10th World Congress of Biomechanics

JULY 11 – 15, 2026 I VANCOUVER, CANADA

WWW.WCB2026.COM

In Conjunction with

CSB SCB

ASB American Society of Biomechanics

European Society of Biomechanics

10th World Congress of Biomechanics

ABSTRACT BOOK

JULY 11–15, 2026

VANCOUVER, BRITISH COLUMBIA, CANADA

In Conjunction with:

Canadian Society for Biomechanics (CSB/SCB)

American Society of Biomechanics (ASB)

European Society of Biomechanics (ESB)

www.wcb2026.com

10th World Congress of Biomechanics

JULY 11 – 15, 2026 I VANCOUVER, CANADA

WWW.WCB2026.COM

In Conjunction with

CSB SCB

ASB American Society of Biomechanics

European Society of Biomechanics

TABLE OF CONTENTS

CSB Competition Abstracts 3

Oral Abstracts 18

Poster Abstracts 2334

Author Index 6070

CSB-01

The Effects of Lumbar Extensor Muscle Fatigue on Trunk Neuromuscular Control during Medio-Lateral Perturbations in Contact-Collision Athletes.

Ms. Juliana Bossom MSc., Dr. Jack Callaghan PhD.

University of Waterloo, Waterloo, Ontario, Canada

Introduction

Muscle fatigue can alter neuromuscular control in sudden-loading, yet prior research mainly examines its effects for the trunk in anterior-posterior directions with minimal between-sex comparisons. Little is known about impact responses to the torso in medio-lateral (M-L) perturbations between sexes. The purpose of this study was to investigate trunk kinematic and muscular responses to M-L sudden-loading in contact-collision athletes, with and without low-back fatigue.

Methods

Twenty-eight contact-collision athletes (14F) experienced bidirectional M-L perturbations before and after low-back fatigue, in a randomized order. Participants were positioned in a semi-seated apparatus restricting lower-extremity motion with cables connecting a chest harness to a pulley-load-supporting system with no external pre-loading. Perturbations were elicited through an unexpected drop force applied to the trunk (30% of side-bending strength) on one side. The fatigue protocol involved sets of trunk flexion-extensions on a Roman chair until the participant could no longer exert 60% of their unfatigued extensor strength. Trunk lateral flexion angles were calculated from passive 3D motion-capture data (128Hz). Peak abdominal and back electromyography (EMG) (2048Hz) response magnitudes and muscle onsets were identified, with onsets detected using a 25ms sliding window at 2 SD above baseline. Responses were evaluated within a 2-second window post perturbation (Figure 1). A two-way linear mixed-effects ANOVA was conducted on dependent variables, with condition and sex as factors.

Results

Condition-sex interactions were found for contralateral lumbar erector spinae (contra-LES) peak ($p<0.05$) and ipsilateral LES (ips-LES) onset ($p<0.05$). Pairwise comparisons with Tukey's HSD revealed males had significantly increased contra-LES peak amplitude when fatigued compared to unfatigued (20vs12.6%MVC, $p<0.05$) and significantly faster ips-LES onsets when fatigued compared to unfatigued (248vs323ms, $p<0.05$).

Discussion

Findings highlight sex-specific neuromuscular strategies in fatigue, with increased contra-LES peaks and faster ips-LES onsets in males. This demonstrates compensatory strategies to maintain stability, since angular displacements were not altered. Females' kinematics were also unaltered, yet muscular compensations were not found. A possible explanation is that female's may have compensated through contributions from muscles not measured in this analysis. Future directions could examine whole-body fatigue to determine if differences in trunk neuromuscular control exist in sport-realistic contexts.

Images (Optional)

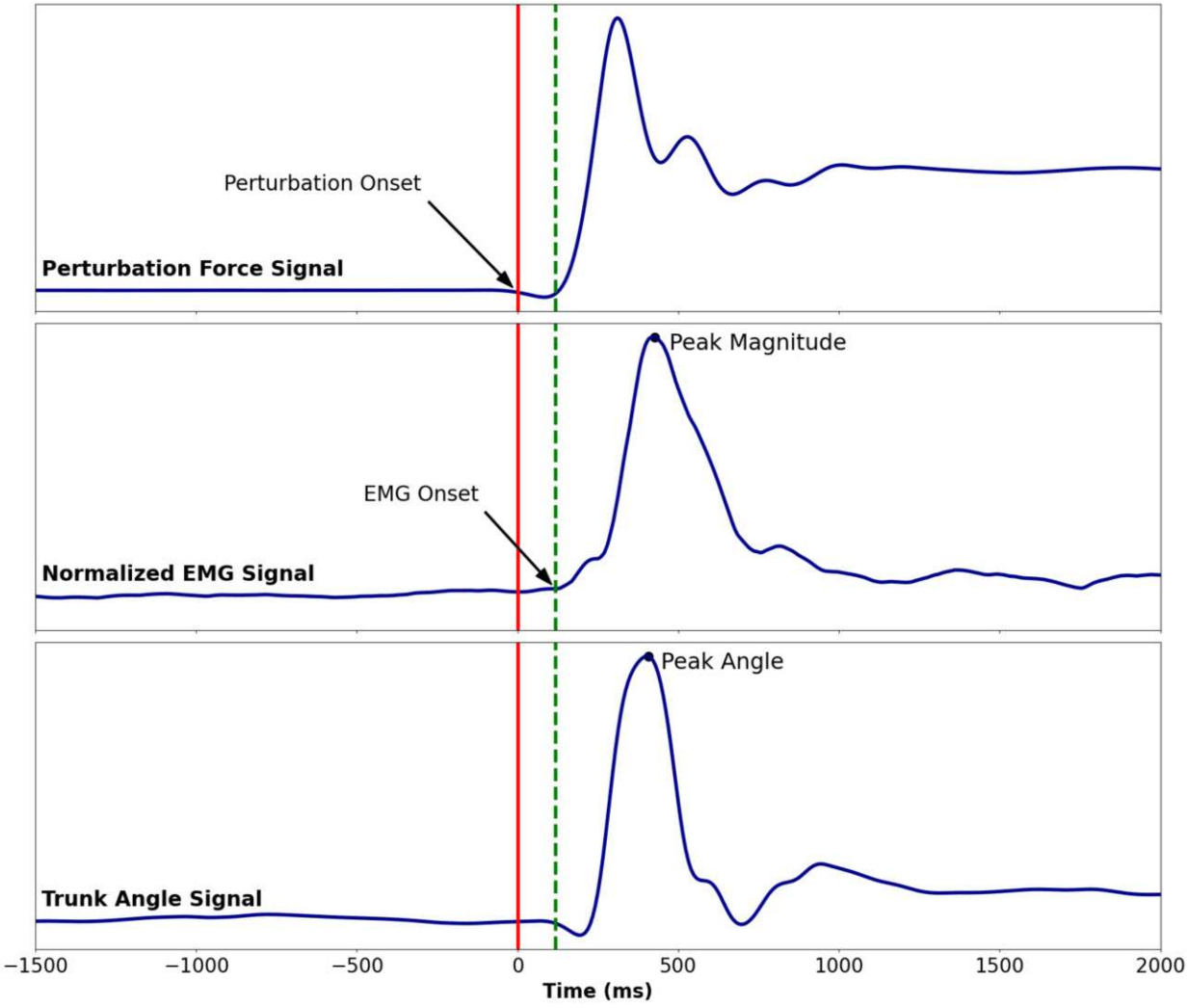


Figure 1: Sample angular (bottom), EMG (middle) and perturbation force (top) signals demonstrating identification of perturbation onset, EMG onset, and peak values.

Session Category

Human Motion and Performance: Balance, Posture and Control

CSB-02

Longitudinal Analysis Reveals the Distribution of Early Peri-Articular Bone Changes Mirrors Traumatic Bone Marrow Lesions Following Acute Knee Injury

Ms. Nina Pavlovic[1,2], Dr. Julio Carballido-Gamio[3], Ms. Callie E. Stirling[1,2], Ms. Sasha M. Hasick[1,2], Dr. Richard E. A. Walker[1,4], Dr. Sarah L. Manske[1,4], Dr. Steven K. Boyd[1,4]

[1]McCaig Institute for Bone and Joint Health, University of Calgary, Calgary, AB, Canada. [2]Department of Biomedical Engineering, University of Calgary, Calgary, AB, Canada. [3]Department of Radiology, School of Medicine, University of Colorado Anschutz Medical Campus, Aurora, CO, United States. [4]Department of Radiology, Cumming School of Medicine, University of Calgary, Calgary, AB, Canada

Introduction

Substantial peri-articular bone loss and structural degradation occur within the first year of anterior cruciate ligament (ACL) injury, with locations of bone marrow lesions (BMLs) experiencing accelerated bone loss relative to adjacent bone. Early peri-articular bone loss may contribute to the development of post-traumatic osteoarthritis (PTOA), yet longitudinal bone remodeling within traumatic BML regions is not well characterized beyond the post-injury period. Understanding longitudinal progression of bone adaptation is needed to inform future interventions. The objective was to quantify and visualize longitudinal peri-articular bone changes for three years following ACL injury and to examine the spatial relationship of these changes to the locations of BMLs.

Methods

Ten participants with an acute ACL injury (50% female; non-surgical management) completed knee dual-energy quantitative computed tomography (DE-QCT) and magnetic resonance imaging (MRI) scans at baseline (~6 weeks post-injury) and 1-, 2-, and 3-year follow-ups. DE-QCT scans were calibrated for bone mineral density (BMD), and bones (femur, tibia, and patella) were segmented, mirrored (if left-sided), and spatially normalized to their corresponding right-sided atlas enabling voxel-wise assessments. Mean BMD maps were created by pooling spatially normalized bones at each timepoint, with difference maps calculated by subtracting the baseline map from the follow-up maps. BMD changes greater than a previously established least-significant change were identified as plausible. Traumatic BMLs were identified on MRIs and spatially normalized to the same atlas for comparison.

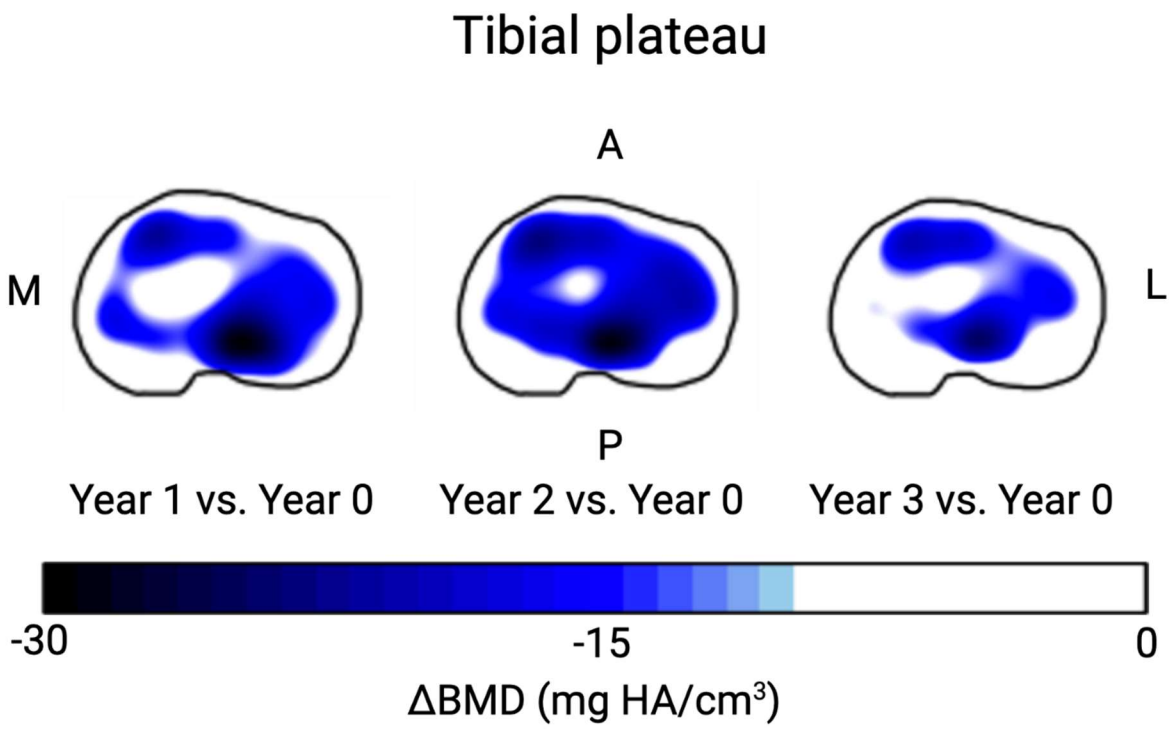
Results

In the ACL-injured limb, voxel-wise BMD loss peaked by at 1 year, extended beyond the initial region at 2 years, and trended toward partial recovery by 3 years. Contralateral limbs remained stable at all timepoints. Spatial analyses revealed an overlap between the regions with the greatest early BMD loss and the locations of BMLs.

Discussion

ACL injury-related peri-articular bone adaptions are region-specific, time-dependent, and tend to align with the distribution of traumatic BMLs. Notably, regions of early BMD loss also exhibited greater BMD recovery between 1- and 2-year follow-ups compared to the surrounding bone. Given that BMLs often reflect the mechanism of injury, peri-articular bone changes following ACL injury may similarly depend on the injury mechanism, which might play a role in the development of PTOA.

Images (Optional)



Session Category

Imaging and Biomedical Devices: Imaging Fundamentals and Applied Research

CSB-03

Applying Load to the Wrist Reveals 3D Carpal Malalignment Following Scapholunate Interosseous Ligament Injury

Mr. Justen Saini[1,2], Dr. Brodie Ritchie[3,4], Dr. Neil White[2,3,4], Dr. Koren Roach[1,2,5,6], Dr. Sarah Manske[2,5]

[1]University of Calgary, Department of Biomedical Engineering, Calgary, Alberta, Canada. [2]University of Calgary, McCaig Institute, Calgary, Alberta, Canada. [3]University of Calgary, Department of Surgery, Calgary, Alberta, Canada. [4]South Campus Research Unit for Bone and Soft Tissue, Calgary, Alberta, Canada. [5]University of Calgary, Department of Radiology, Calgary, Alberta, Canada. [6]University of Calgary, Faculty of Kinesiology, Calgary, Alberta, Canada

Introduction

Current assessments of carpal alignment, including angular and distance relationships between carpal bones, are typically measured on two-dimensional (2D) radiographs. These 2D manual measurements are limited by projection errors, inconsistent wrist positioning, and an inability to capture multiplanar deformities. Manual measurements introduce inter-rater variability, preventing early detection of instability and limiting surgical planning for scapholunate interosseous ligament (SLIL) injuries. Automating these measurements using three-dimensional (3D) imaging techniques, such as weight-bearing computed tomography (WBCT), may help to reduce variability and provide multiplanar assessment of carpal bone position.

Objective: Develop a semi-automated pipeline to measure 3D carpal alignment from WBCT scans and evaluate these measurements in healthy and SLIL-injured wrists.

Methods

WBCT scans were acquired for ten healthy controls and ten SLIL-injured participants in non-weightbearing (NWB), weightbearing pushup bar grip (WBPUB), and weightbearing extension (WBEXT) positions. SLIL injuries were confirmed by fellowship-trained hand surgeons; participants with advanced osteoarthritis were excluded. We developed a semi-automated pipeline in Python to segment 3D carpal bones and define 3D bone axes using principal axes of inertia and curvature patterns. Carpal alignment metrics including the scapholunate interval at five locations, dorsal scaphoid translation (DST), and intercarpal

and radiocarpal angles projected onto simulated lateral and anteroposterior views were assessed (Figure 1). Differences between groups and between positions were evaluated using a mixed-effects ANOVA.

Results

In the NWB position, SLIL-injured wrists showed significantly greater DST (2.18±2.25 mm) compared to controls (0.30±0.98 mm, $p = 0.035$). DST significantly decreased in SLIL-injured wrists in the WBPUB position (1.07±1.49 mm) compared to the NWB position ($p = 0.032$). SLIL-injured wrists exhibited significantly greater scapholunate and radiolunate angles across all positions compared to controls ($p < 0.05$), indicating persistent pathological lunate extension under load.

Discussion

This open-source pipeline enables position-independent, 3D assessments of carpal alignment across multiple wrist postures, reducing reliance on manual radiographic measurements. Through evaluation of multiplanar deformities, this method supports patient-specific surgical planning and corrections. This work may also inform rehabilitation protocols, as evidenced by the reduction in DST in the WBPUB position which may help prevent increased dorsal loading.

Images (Optional)

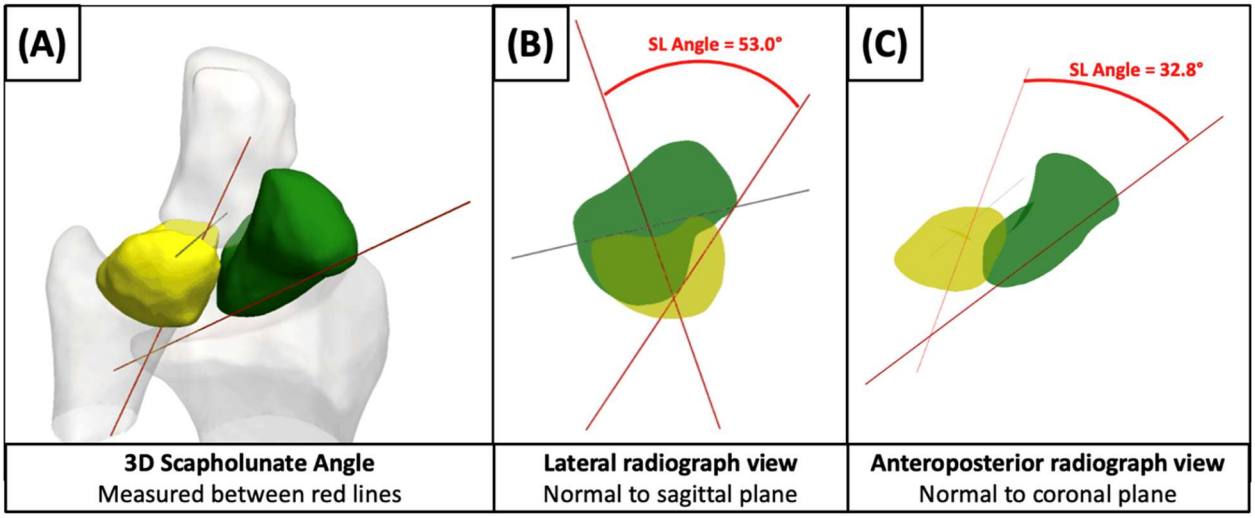


Figure 1: An example of how the three-dimensional (3D) scapholunate angle is calculated for a right-hand weight-bearing computed tomography scan. (A) The 3D representation of the angle measurement, with the axes of the scaphoid and lunate in red. (B) A 2D simulated lateral radiograph projection of the 3D axes, with the angle taken between the red lines, similar to current radiographic techniques. (C) A 2D simulated anteroposterior radiograph projection of the 3D axes, which aims to provide surgeons with additional information on the orientation of carpal bone position.

Session Category

Rehabilitation Biomechanics and Human Factors: Occupational Biomechanics

CSB-04

Using Biplanar Videoradiography to Quantify the Accuracy of Person-Specific Knee Models in Simulating Patellofemoral Kinematics for a Variety of Dynamic Tasks

Ms Annagh Macie[1], Dr. Anthony Gatti[2], Dr. Michael Rainbow[3], Dr. Allison Clouthier[1]

[1]University of Ottawa, Ottawa, Ontario, Canada. [2]Stanford University, Stanford, California, United States. [3]Queen's University, Kingston, Ontario, Canada

Introduction

The ability to measure patellofemoral (PF) joint function in vivo is challenging. PF kinematics can be estimated using person-specific musculoskeletal modelling, but the accuracy of these models is still unclear. Therefore, this study seeks to use biplanar videoradiography (BVR) to quantify the accuracy with which three versions of a person-specific multibody knee model can predict six DOF tibiofemoral (TF) and PF kinematics for a series of dynamic tasks.

Methods

CT scans and MRIs of the right knee of eight participants (4F/4M, 23.8+/-1.4 yrs) and BVR, optical motion capture and force plate data of a lunge ascent and hop task were used. The CT scans were segmented and converted to 3D meshes of the femur, tibia and patella. These meshes were superimposed onto the BVR capture using 3D Slicer AutoScoper which provided relative bone pose at each time frame [1]. The MRIs were segmented to produce three person-specific models of the bone and cartilage of the femur, tibia and patella (Lenhart [2], Smith No Meniscus [3]) as well as the menisci (Smith [3]). These models were then integrated into a generic musculoskeletal model and the participants' trials were simulated by each model via the COMAK routine [4]. The kinematics from the BVR data were compared to the simulated kinematics of the models.

Results

The models simulated kinematics produced relatively low RMSE, which were consistent with previous validation studies [5]; however, maximum errors indicated high between subject variability (Table 1). There was a significant effect of model on total TF rotational RMSE during the hop task
($p = 0.014$), with post-hoc holm corrections indicating the Smith model performed best. No other main effects of model were noted.

Discussion

The high maximum errors and the lack of statistical difference for model performance at the PF joint indicates personalization of other model parameters such as ligament slack length should be investigated to improve person specific performance.

Images (Optional)

Table 1. TF and PF RMSE (per subject average trial error averaged across participants), SEM (standard error of mean RMSE across participants) and maximal errors (largest participant error across trial) for rotation and translation using the Lenhart, Smith and Smith_NM (no meniscus) models during a hop and lunge ascent tasks.

	Hop						Lunge Ascent					
	TF Rotation (deg)			TF Translation (mm)			TF Rotation (deg)			TF Translation (mm)		
Model	RMSE	SEM	Max Error	RMSE	SEM	Max Error	RMSE	SEM	Max Error	RMSE	SEM	Max Error
Lenhart	10.6	1.7	28.5	6.8	0.8	12.9	15.2	2.4	39.5	6.0	0.7	12.3
Smith	8.2	1.3	24.0	6.5	0.4	13.5	13.3	1.7	35.1	7.0	0.9	13.4
Smith_NM	10.8	1.8	30.5	6.9	0.8	13.2	16.0	2.3	39.8	6.2	0.7	13.8
	PF Rotation (deg)			PF Translation (mm)			PF Rotation (deg)			PF Translation (mm)		
Model	RMSE	SEM	Max Error	RMSE	SEM	Max Error	RMSE	SEM	Max Error	RMSE	SEM	Max Error
Lenhart	9.7	1.3	18.1	7.2	1.3	13.0	9.7	1.7	19.3	8.3	1.0	14.8
Smith	9.4	1.1	13.0	6.6	1.1	13.3	8.9	1.4	17.0	7.4	0.7	12.9
Smith_NM	8.7	1.2	17.6	6.3	1.2	12.5	8.3	1.2	17.7	7.4	0.8	16.0

References (Optional)

[1] Akhbari *et al.*, JoVe, 2021.

[2] Lenhart *et al.*, Ann Biomed Eng, 2015.

[3] Smith *et al.*, J Biomech, 2019.

[4] Smith *et al.*, J Knee Surg, 2016.

[5] Dastgerdi et al., Sci Rep, 2023.

Session Category

Musculoskeletal Biomechanics: Methods, Models and Applications

CSB-05

Directional Dependence of Multiscale White Matter and Axonal Injury Metrics from Real-World Head Impacts

Mr. Zaryan Masood[1], Mr. Chaokai Zhang[2], Mr. Daniel Bondi[1], Mr. Alexander Jaffray[1], Mr. David Luke[1], Dr. Rebecca Kenny[1], Dr. Adam Clansey[1], Dr. Paul van Donkelaar[1], Dr. Alexander Rauscher[1], Dr. Songbai Ji[2], Dr. Lyndia Wu[1]

[1]University of British Columbia, Vancouver, British Columbia, Canada. [2]Worcester Polytechnic Institute, Worcester, Massachusetts, United States

Introduction

Traumatic axonal injury (TAI) has shown directional vulnerability in animal studies[1], but this remains less understood in humans, particularly at microstructural scales. Advances in wearable sensors, neuroimaging, and computational modeling now allow large-scale subject-specific simulations of real-world head impacts to estimate deformation from whole-brain to axonal structures. This study examined the directional dependence of white matter fiber strain and axonal substructural damage.

Methods

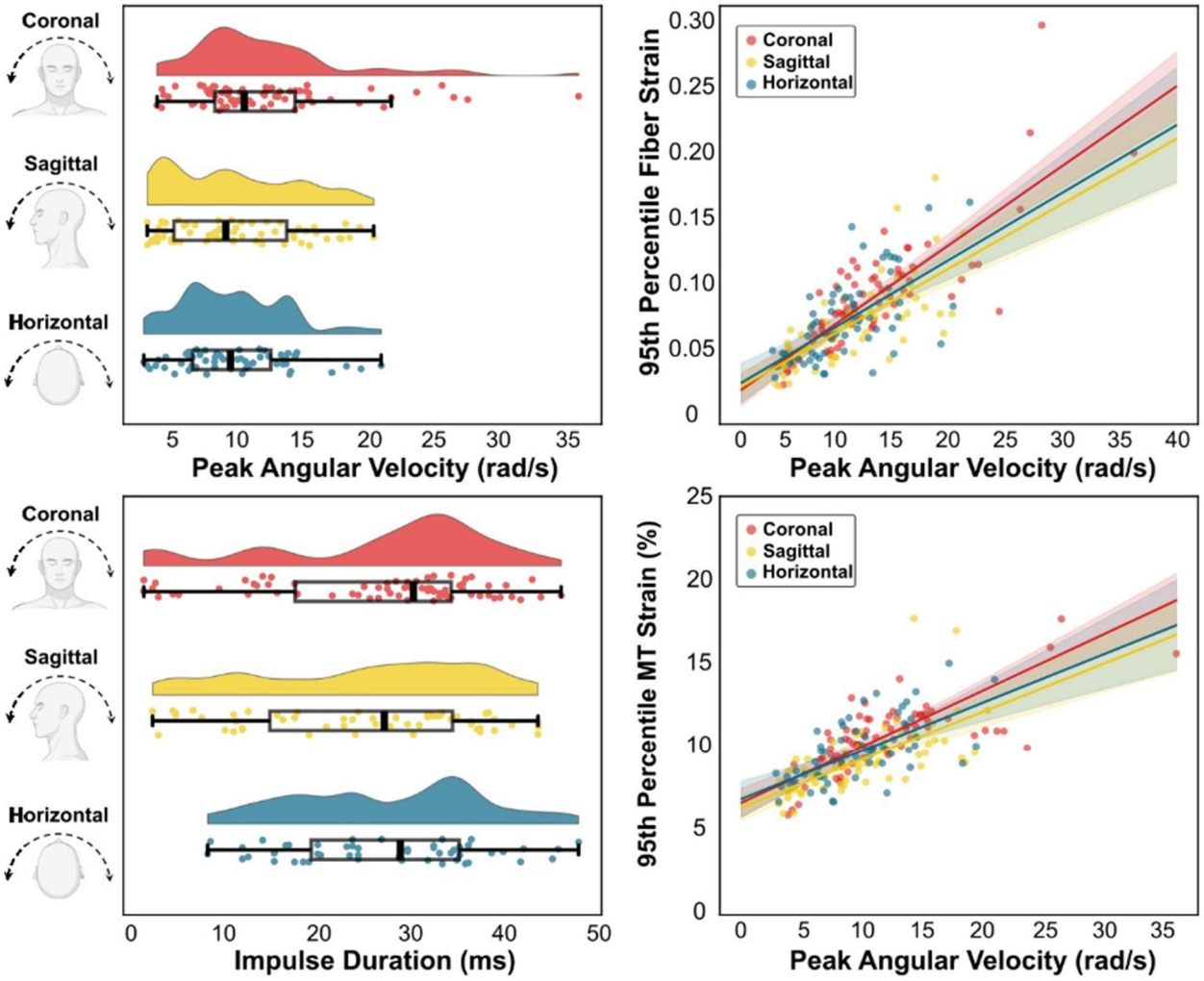
University men's ice hockey athletes (n = 18; UBC ethics: H21-00400) wore custom instrumented mouthguards (iMGs) over one season, and completed a structural brain MRI scan for subject-specific modeling. We simulated voxel-wise white matter fiber strains and axonal substructural deformations using a deep-learning model[2]. An impact was classified coronal-, sagittal-, or horizontal-dominant when the peak angular velocity in that plane exceeded 90% of the resultant magnitude. We used linear mixed-effects models to determine how rotational plane and peak angular velocity influence 95th percentile fiber strains and axonal substructural injury metrics, with subject ID as a random effect.

Results

We analyzed 608 impacts: 88 coronal-dominant, 86 sagittal-dominant, and 61 horizontal-dominant. Coronal-dominant impacts showed the highest median peak angular velocity (10.5 rad/s) and longest impulse durations (30.3 ms) compared with sagittal (8.4 rad/s, 26.1 ms) and horizontal (8.7 rad/s, 29.7 ms). Coronal- and horizontal-dominant impacts produced significantly higher fiber strains (coronal: $\beta = 0.0087$, $p = 0.028$; horizontal: $\beta = 0.0043$, $p = 0.313$) and microtubule strains (coronal: $\beta = 0.801$, $p = 0.004$; horizontal: $\beta = 0.290$, $p = 0.312$) compared with sagittal-dominant impacts. Neurofilament and tau failure did not differ by rotational plane. Between-subject variance was low, indicating consistent directional effects.

Discussion

Our study uniquely examined the directional dependence of microstructural injury risk using real-world head impact data and neuroimaging-enabled subject-specific multiscale modeling. Coronal- and horizontal-dominant impacts may pose a higher risk for axonal damage relative to sagittal-dominant impacts. The directional vulnerability is further compounded by higher severity coronal impacts sustained on-field, warranting protective equipment improvements and potential rule changes to mitigate high-risk impact directions.



References (Optional)

[1] Hill et al., Trends in Neurosciences, 2021

[2] Zhang et al., Biomechanics & Modeling, 2025.

Session Category

Injury Biomechanics: N/A

CSB-06

Normative Modeling of Gait Biomechanics for Personalized and Multisite Clinical Assessment

Mr. Jereme Outerleys[1,2], Mr. Sachitha Wijekoon[1], Dr. Stephen Scott[1], Dr. Kevin Deluzio[1]

[1]Queen's Univeristy, Kingston, Ontario, Canada. [2]Theia, Kingston, Ontario, Canada

Introduction

Clinical gait assessment assumes that the “average” gait is an appropriate benchmark for every patient. This approach ignores variability due to factors such as age, sex, and site, limiting the precision of patient-specific measures. To address this, we apply a normative modeling framework [1] trained on a large, multisite dataset of healthy gait to model expected patterns based on individual characteristics. Applied to knee osteoarthritis (OA), this approach provides a statistical foundation for quantifying biomechanical impairment and supports patient-specific gait evaluation in clinical and multicentre contexts.

Methods

A normative modeling framework using hierarchical Bayesian regression was trained on a markerless gait dataset of healthy adults (N = 607; age 17–92), collected across six sites using Theia3D. Separate models were trained for each time point of hip, knee, and ankle waveforms and spatiotemporal outcomes (408 total). Covariates included age, sex, and site. Trained models were applied to a clinical dataset of 192 individuals with knee OA (55 moderate, 137 severe) to generate patient-specific z-scores quantifying deviations from healthy expectations. Summary deviation scores were calculated using Mahalanobis distance and standardized to a normal distribution [2]. The percentage of participants classified as high deviators ($z > +1.64$) was calculated and compared across the healthy and OA severity groups.

Results

Patient-specific z-scores revealed increasing deviation with OA severity and quantitatively identified joint- and phase-specific abnormalities across the gait cycle. Summary deviation scores classified 5.5% of healthy as high deviators, compared to 67.3% in moderate and 82.7% in severe OA, effectively separating healthy and clinical groups (Figure 1). Z-score distributions in the healthy cohort showed no systematic differences across sites, indicating minimal site effects.

Discussion

Normative modeling enables patient-specific quantification of gait deviations while accommodating demographic and site-related variability. The resulting z-scores offer interpretable, standardized metrics comparable across individuals and sites, distinguish between levels of clinical severity, and identify abnormalities throughout gait. Future work will explore federated modeling, allowing extension to new sites without sharing raw data, an advantage where privacy or resource constraints limit data pooling.

Images (Optional)

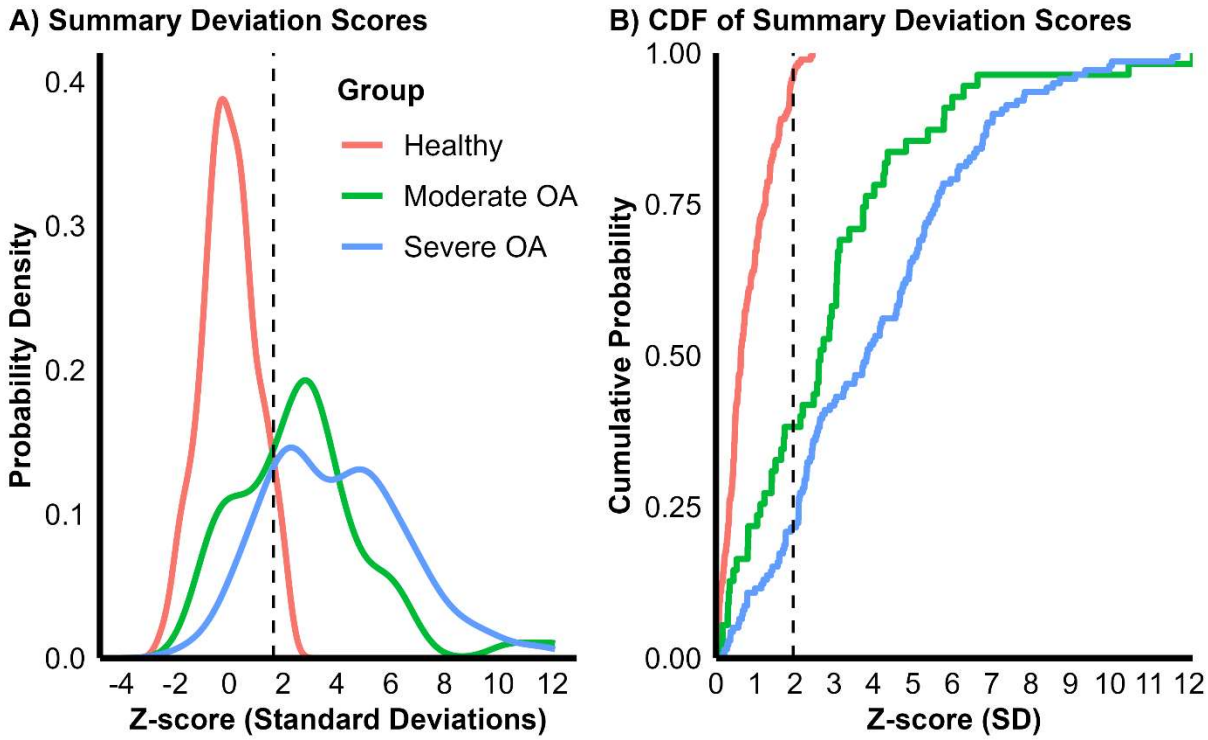


Figure 1. Vertical dashed line at z = +1.64 marks threshold for high deviators.

References (Optional)

[1] Bayer JM et al., NeuroImage, 2022.

[2] Scott et al., NNR , 2023.

Session Category

Human Motion and Performance: Locomotion/Gait

OA1-01

Knee and Ankle Posture Impacts Triceps Surae Muscle Neuromechanics

Mr. Sittinon Nuethong

University of Pennsylvania, Philadelphia, Pennsylvania, United States

Introduction

The three Achilles (AT) subtendons connect medial gastrocnemius (MG), lateral gastrocnemius (LG) and soleus (SOL) muscles to the calcaneus. These muscles differentially strain subtendons that causes non-uniform displacement in AT. The plantar flexor aponeuroses displace and develop internal stresses at different knee angles, foot positions, and ankle angles. This study aims to define the relationships between the joint posture and the subtendon sliding degree with the hypothesis that changing knee-ankle configuration will alter both plantar flexor muscle activation and subtendon sliding extent.

Methods

10 healthy participants (3 men, 7 women, 23 ± 3 years) were provided written informed consent and performed five maximum voluntary isometric contractions (MVICs) on a dynamometer at eight knee-ankle configurations. Surface electromyograms (sEMG) on three plantar flexor muscles and ultrasound images on AT were acquired simultaneously. The differential displacement was calculated from the difference between the deep and superficial displacements of the AT tracked by the Kanade-Lucas-Tomasi point tracking algorithm. The sEMG were normalized to the sum of the maximum sEMG of all three muscles among all configurations. ANOVA with Tukey's post-hoc was used for statistical analysis.

Results

The differential displacement differed only between inversion and dorsiflexion with extended knee (Fig 1A). MG engagement becomes less in the flexed knee position for all ankles (Fig 1B). Moreover, LG was recruited more with flexed knee and plantarflexion compared to the same ankle and both foot orientations (Fig 1C). SOL was activated more in the flexed knee position except in dorsiflexion compared to the knee extended position with the same ankle angles (Fig 1D).

Discussion

Our preliminary study demonstrated the impacts of changing knee-ankle configurations on the plantar flexion muscle activation and subtendon sliding. The higher activations of the SOL and MG muscles in the flexed knee and extended knee positions correspond to the finding of larger displacements in the SOL and MG aponeuroses in these two knee angles. However, few distinct differential displacements were found implying the participant specific quality of this metric. This project is an ongoing study with an expectation to increase statistical power to test the effect of knee-ankle configurations.

Images (Optional)

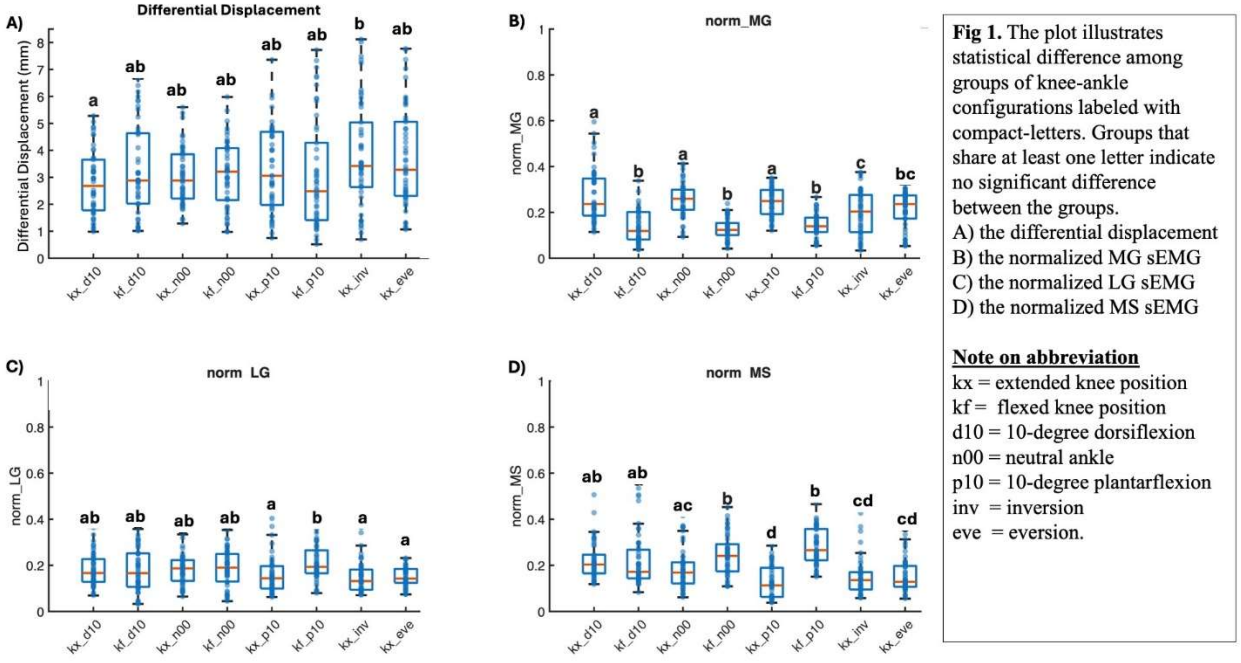


Fig 1. The plot illustrates statistical difference among groups of knee-ankle configurations labeled with compact-letters. Groups that share at least one letter indicate no significant difference between the groups.
A) the differential displacement
B) the normalized MG sEMG
C) the normalized LG sEMG
D) the normalized MS sEMG

Note on abbreviation
kx = extended knee position
kf = flexed knee position
d10 = 10-degree dorsiflexion
n00 = neutral ankle
p10 = 10-degree plantarflexion
inv = inversion
eve = eversion.

References (Optional)

Session Category

Clinical Biomechanics: N/A

OA1-02

Neural Correlates of Knee Flexion-Extension after Unilateral Transtibial Limb Loss

Dr. Courtney Butowicz PhD[1,2,3], Dr. Rujirutana Srikanchana PhD[2], Dr. Brad Hendershot PhD[1,2,3], Dr. Tawnee Sparling MD[2,3], Dr. Sheri Silfies DPT, PhD[4]

[1]Defense Health Agency, Falls Church, VA, United States. [2]Walter Reed National Military Medical Center, Bethesda, MD, United States. [3]Uniformed Services University of Health Sciences, Bethesda, MD, United States. [4]University of Delaware, Newark, DE, United States

Introduction

Nearly 80% of persons with unilateral limb loss (PLL) experience chronic musculoskeletal and/or phantom limb pain, impairing function and quality of life. Amputation induces reorganization in sensorimotor brain regions as representations of the missing limb invade adjacent cortical areas, causing changes in sensory integration, motor control, and pain perception. Yet, evidence has only investigated cortical activity in response to sensory stimulation or during resting state functional magnetic resonance imaging (fMRI), failing to identify how reorganization is linked to movement. The aim of this pilot study was to identify neural correlates of voluntary limb movement among PLL.

Methods

Six participants* (4 with transtibial amputation (2 female) and 2 uninjured (CTR; 1 female)) underwent a T1-W magnetic resonance image (3T Siemens) and then completed 20 repetitions (10/side) of unilateral knee extension/flexion (5s up/5s down/10s rest) in response to visual instructions during fMRI. fMRI measured neural activation via blood oxygen level dependent signal changes. Data were pre-processed in fmriprep; first-level analysis (intact/right>rest, prosthetic/left>rest) processed using SPM in MATLAB. *Larger sample size expected by conference.

Results

Analysis revealed increased cortical activation during intact limb movement vs. rest in sensorimotor regions (primary sensory, primary motor, supplementary motor, premotor cortices) among PLL. Prosthetic vs. rest contrast revealed increased activation in the sensorimotor cortex, precuneus/paracentral lobule, supramarginal gyrus, and anterior cingulate cortex. CTR exhibited a smaller number of active voxels in sensorimotor regions compared to PLL.

Discussion

PLL use brain regions associated with motor control, sensory processing, proprioception, motor sequencing, pain appraisal, and episodic memory to move the lower limbs. Higher activations in pain appraisal and tool use regions during prosthetic side movement suggest pain history associated with prosthesis use may influence motor control. CTR demonstrated highest activations in regions linked to reward evaluation, visual, and language processing for the task.

Our findings support previous work suggesting persons with lower limb injury exhibit increased activation in sensory processing and motor planning brain regions not seen in uninjured controls when performing a voluntary movement task. Characterizing the neuroplastic changes occurring with amputation can guide motor control-based rehabilitation targets to improve sensorimotor function.

Images (Optional)

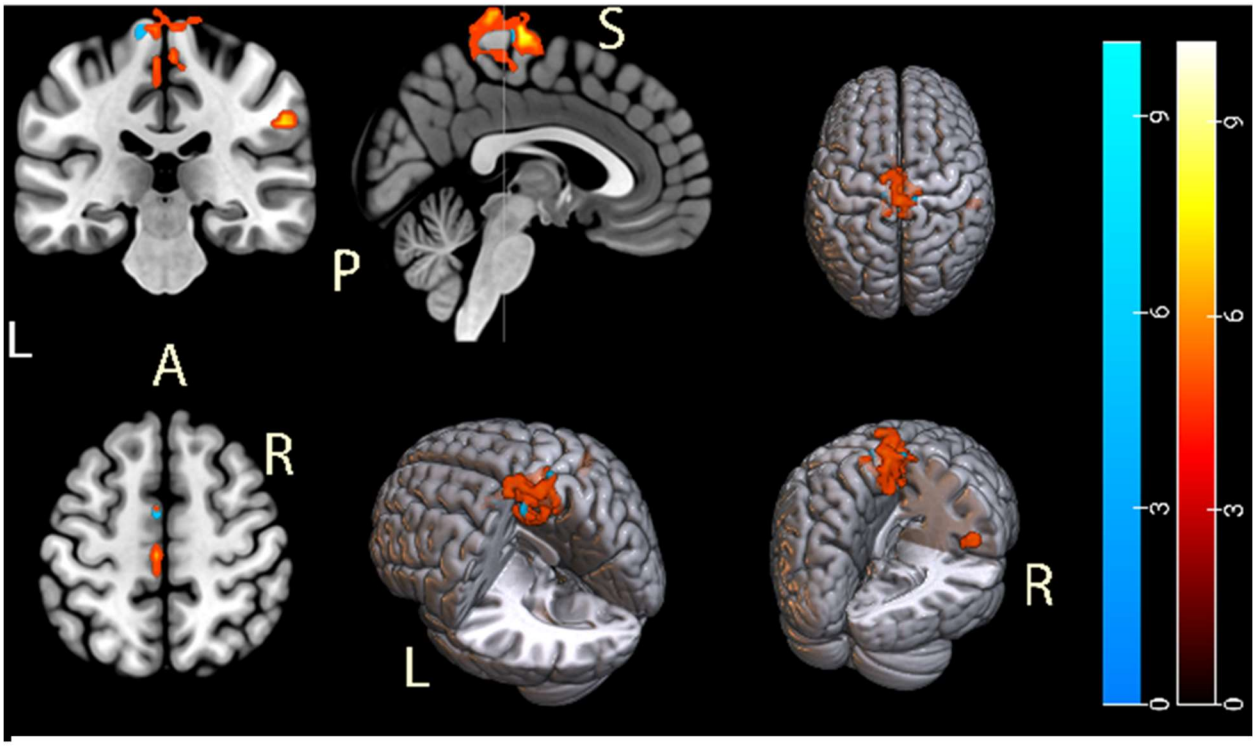


Figure 1: Regions with activation exceeding statistical threshold ($p<0.05$ with family wise error correction, $Z>3.1$, z-score indicated by heat scale) for intact (cool) and prosthetic (hot) movement greater than rest for male subject with left transtibial amputation.

Acknowledgements (Optional)

The views expressed herein are those of the authors and do not necessarily reflect the official policy of the DHA, DoW, USUHS, nor the US Government.

Session Category

Clinical Biomechanics: N/A

OA1-03

Neural Control of Isometric Lower Limb Muscle Contractions in Typically Developing Children and Children with Cerebral Palsy

Mr Andrea Sgarzi[1,2], Dr Agnese Grison[3], Prof Dario Farina[3], Dr Bart Bolsterlee[1,2], Prof Nigel Lovell[1], Dr Luca Modenese[1]

[1]Graduate School of Biomedical Engineering, UNSW, Sydney, NSW, Australia. [2]Neuroscience Research Australia (NeuRA), Sydney, NSW, Australia. [3]Dept of Bioengineering, Imperial College, London, UK, United Kingdom

Introduction

Studying neuromuscular control in children is crucial for understanding typical development and childhood disabilities and, for ethical reasons, requires non-invasive approaches. In cerebral palsy (CP), lower limb impairments may be linked to altered motor unit (MU) activity [1]. While MU behavior has been extensively characterized in adults using high-density surface electromyography (HDsEMG) [2], it remains largely unexplored in children. This study aims to assess MU activity in lower limb muscles of typically developing (TD) children and children with CP.

Methods

To date, fourteen TD children (7 girls, 12 ± 3 years) and fourteen with spastic CP (5 girls, 12 ± 2 years) have been recruited. All procedures were approved by the UNSW Human Research Ethics Committee (iRECS6278). Participants were seated with the knee extended and the foot (dominant side for TD, most affected for CP) strapped to a dynamometer. Each participant performed a maximum isometric voluntary contraction (MVC) and four trapezoidal contractions at 10%, 30%, 50%, and 70%MVC during ankle dorsiflexion and plantarflexion. HDsEMG signals were recorded from the tibialis anterior (TA) and gastrocnemius medialis (GM) using two 64-electrode grids per muscle (4 mm interelectrode distance, OT Bioelettronica, Italy) and decomposed into MU spike trains [3]. MU firing rate (FR) and recruitment threshold (RT) were compared between groups using two-sample t-tests at each intensity.

Results

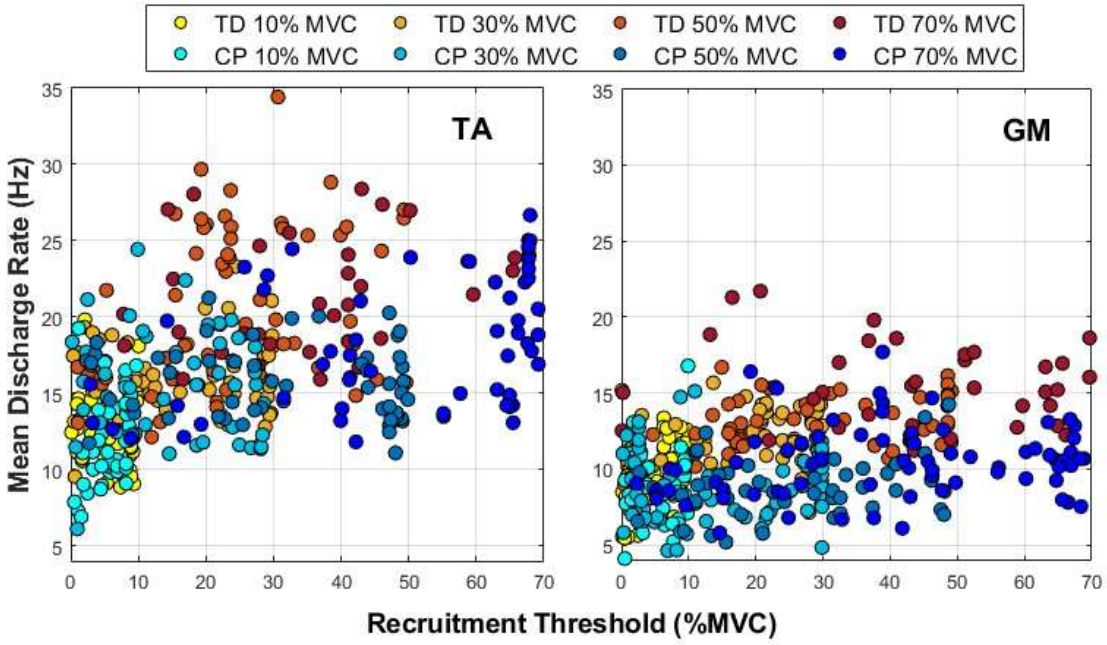
In TD children, up to 46 and 60 MUs per participant were identified in TA and GM respectively, with mean FRs and RTs of 17 ± 5 Hz and 19 ± 15%MVC (TA), and 12 ± 2 Hz and 16 ± 14%MVC (GM). In children with CP, up to 43 MUs per participant were identified in

both muscles, with mean FRs and RTs of 15 ± 4 Hz and 15 ± 15%MVC (TA), and 9 ± 2 Hz and 19 ± 17%MVC (GM). FR was lower in CP for both muscles ($p<10^{-3}$) at intensities >10%MVC. RT never differed significantly.

Discussion

These preliminary findings suggest a limited ability of children with CP to modulate force through FR, consistent with previous intramuscular observations [1].

Images (Optional)



References (Optional)

[1] Rose J *et al.*, Dev Med Child Neurol, 2005.

[2] Avrillon S *et al.*, eLife, 2024.

[3] Avrillon S *et al.*, J Electromyogr Kinesiol, 2024.

Session Category

Clinical Biomechanics: N/A

OA1-04

The Effects of Carpometacarpal Osteoarthritis on Neuromuscular Coordination

Mr Troy Kelly Jr, Mr Benjamin Nowak, Dr Jennifer Nichols

University of Florida, Gainesville, Florida, United States

Introduction

Carpometacarpal osteoarthritis (CMC OA) is a disruptive disease that can impair hand function due to structural joint degeneration. While joint degeneration is well studied, there is a gap in knowledge regarding how muscle coordination adapts to disease progression. This study aims to examine how both co-contraction and intermuscular activation patterns differ between early- and late-stage CMC OA participants.

Methods

Data from 15 participants with CMC OA (73% female; age: 68.5±7.7 years) was analyzed. Using x-rays and the Eaton-Littler grading scale, early-stage CMC OA was classified as grades 1-2, and late-stage CMC OA was classified as grades 3-4. Intramuscular electromyography (EMG) from 8 thumb muscles during a jar grasp task were recorded. Co-contraction was determined using the Co-Contraction Index (CCI) on three thumb muscle pairs: FPL-EPL, FPB-EPB, and APL-ADD. These pairs were selected due to opposing muscle functions. Intermuscular activation patterns were quantified by calculating the Pearson correlation coefficients for all possible thumb muscle pairs (28 total). Higher CCI values indicate greater co-contraction, while higher correlation values indicate stronger synergistic coupling. Group comparisons were conducted using ANOVAs followed by Tukey's post-hoc testing for all analyses.

Results

Individuals with late-stage CMC OA had increased co-contraction relative to those with early-stage CMC OA for all three examined muscle pairs. This difference was statistically significant ($p<0.05$) for FPL-EPL and FPB-EPB (Fig. 1A). Correlation between intermuscular pairs declined in the late-stage CMC OA group across 25 of 28 muscle pairs. Across all assessed intermuscular pairs, significant ($p<0.05$) decline in correlation was found between ADD-FPB, ADD-OPP, FPB-OPP, FPB-FPL, FPL-OPP, and APL-EPL (Fig. 1B).

Discussion

These findings suggest that thumb motor control in individuals with late-stage CMC OA can be characterized as having elevated co-contraction and reduced intermuscular correlation. Increased muscle co-activation may reflect compensatory strategies to improve joint stability in response to joint degradation. In contrast, the reduced intermuscular correlation suggests altered neuromuscular control, similar to changes observed with aging, which can decrease movement efficiency and functional performance. These results suggest that CMC OA is not only associated with joint degeneration but also with altered neuromuscular control.

Images (Optional)

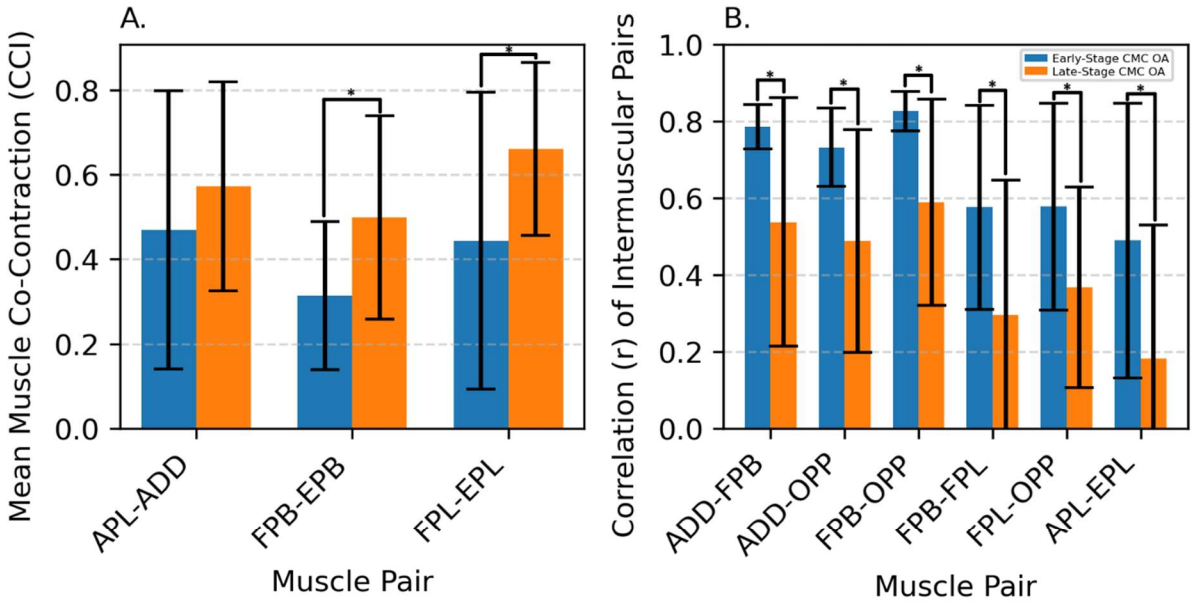


Figure 1. (A) Muscle co-contraction index (CCI) for the three examined muscle pairs and (B) Pearson correlation coefficient (r) for the significant intermuscular pairs. Bars represent mean and standard deviation across participants for early-stage (n = 5, blue) versus late-stage (n = 10, orange) CMC OA. Asterisks indicate significant difference ($p<0.05$).

Acknowledgements (Optional)

Funding from NIH R01AR078817.

Session Category

Clinical Biomechanics: N/A

OA2-02

Sensitivity of Markerless Lower-Limb Kinematics to Camera Height and Capture-Volume Width: Implications for Camera Placement

Mr Alexander Hadwen[1], Mr Jereme Outerleys[1,2], Dr Kevin Deluzio[1]

[1]Queen's University, Kingston, Ontario, Canada. [2]Theia, Kingston, Ontario, Canada

Introduction

Markerless motion capture offers advantages over marker-based systems by eliminating marker placement errors and reducing operator-dependent variability [1]. However, the influence of camera placement on kinematic outcomes remains insufficiently understood. This study quantified the effects of camera layout on lower-limb kinematics estimated using markerless motion capture. We assessed how camera height interacts with capture-volume width to affect joint-angle waveform reliability, aiming to provide practical guidance for camera placement.

Methods

Nine participants performed overground walking trials recorded using 32 synchronized Sony RX0II cameras arranged elliptically. Cameras were organized into four height groups (0.85 m, 1.65 m, 2.45 m, and 3.30 m; eight per group). Participants repeated trials at three camera-horizontal width conditions, changed for each trial: extended (6.9 m), intermediate (5.5 m), and hallway simulation (3.3 m), with capture volume length held constant. Markerless pose estimation was performed using Theia3D (v2025.1.6) and processed in Visual3D and Python. Only strides visible in all 32 cameras were included, and a consistent region of interest ensured identical stride selection, though step count varied by width.

Results

Across all widths, the largest joint-angle difference was 4°, occurring between the 0.85 m and 3.30 m camera groups in the narrowest width condition. This camera pair accounted for the greatest difference in 64% of all joint-plane comparisons (ankle, knee, hip, pelvis; X/Y/Z planes). Peak differences occurred between 60–90% of the gait cycle, corresponding to phases with the greatest self-occlusion, as the hip and knee obscure distal segments. The narrowest width produced the largest variability, followed by the widest, then the intermediate condition.

Discussion

Differences of ≈3–4° between the highest and lowest camera positions indicate that extreme vertical angles increase occlusion and reduce tracking reliability. However, these

effects are small and below the ≈12° inter-laboratory offsets typical of marker-based systems [2], suggesting markerless kinematics remain robust with only minor height-dependent bias. Findings support positioning cameras within a mid-range vertical band, avoiding the highest and lowest placements, to improve reliability. Limitations include no ground-truth comparison and varying walking trials across widths.

Images (Optional)

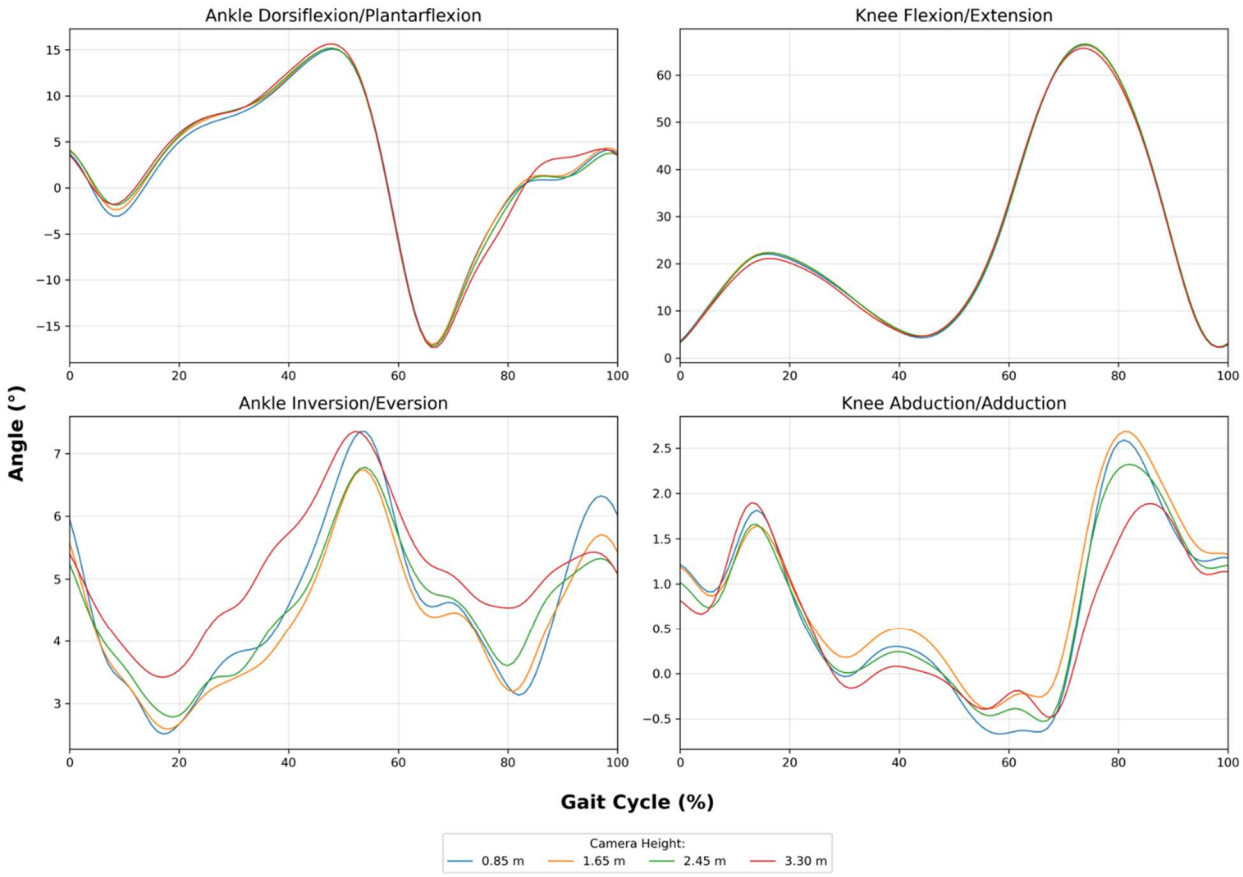


Figure 1: Ankle and knee kinematics in the sagittal and frontal planes across the full gait cycle for the intermediate width condition. Differences between camera-height groups show slight waveform variation in the ankle sagittal plane near mid-swing phase and throughout both joints in the frontal plane.

References (Optional)

[1] C. McFadden et al., J. Biomechanics, 2020

[2] J. C. Schrijvers et al., The Knee, 2021

Session Category

Human Motion and Performance: Locomotion/Gait

OA2-03

Markerless Motion Capture of Wrist Kinematics in Wheelchair Users with Spinal Cord Injury

Mr. Samuel Gillespie MS[1,2], Dr. James Cotton MD, PhD[1,2], Dr. Brooke Slavens PhD[3], Dr. Wendy Murray PhD[1,2]

[1]Northwestern University, Evanston, Illinois, United States. [2]Shirley Ryan AbilityLab, Chicago, Illinois, United States. [3]University of Wisconsin-Milwaukee, Milwaukee, Wisconsin, United States

Introduction

Manual wheelchair users commonly experience upper extremity pain and pathology, particularly carpal tunnel syndrome (CTS), which is especially debilitating given their reliance on their arms for mobility and independence. Wrist kinematics provide insight into joint positions and excursions that influence carpal tunnel pressure and loading. However, quantifying distal upper limb motion is challenging: marker-based systems require complex instrumentation and lengthy setup, while markerless systems struggle with small, fast-moving segments and are typically applied for gross movements . Overcoming this barrier is critical for advancing rehabilitation research and defining best practices for CTS prevention. This work demonstrates a markerless motion capture system capable of tracking wrist kinematics during wheelchair propulsion and differentiating individuals with distinct spinal cord injury levels and functional capacities.

Methods

We implemented a multiview (12 cameras), markerless motion capture workflow using an optimization approach leveraging differentiable physics simulators accelerated on GPUs. Joint trajectories were optimized by minimizing reprojection error between a 3D kinematic model (150 DOF, including wrist and finger articulations) and 2D keypoints detected from multiple cameras. Two adults with SCI completed five 10-meter propulsion trials at self-selected speeds: one with C5 tetraplegia, characterized by limited wrist and finger control, and one with T12 paraplegia, exhibiting full distal upper limb function. Cycle-aligned joint trajectories were extracted for wrist flexion/extension, radial/ulnar deviation, and forearm pronation/supination.

Results

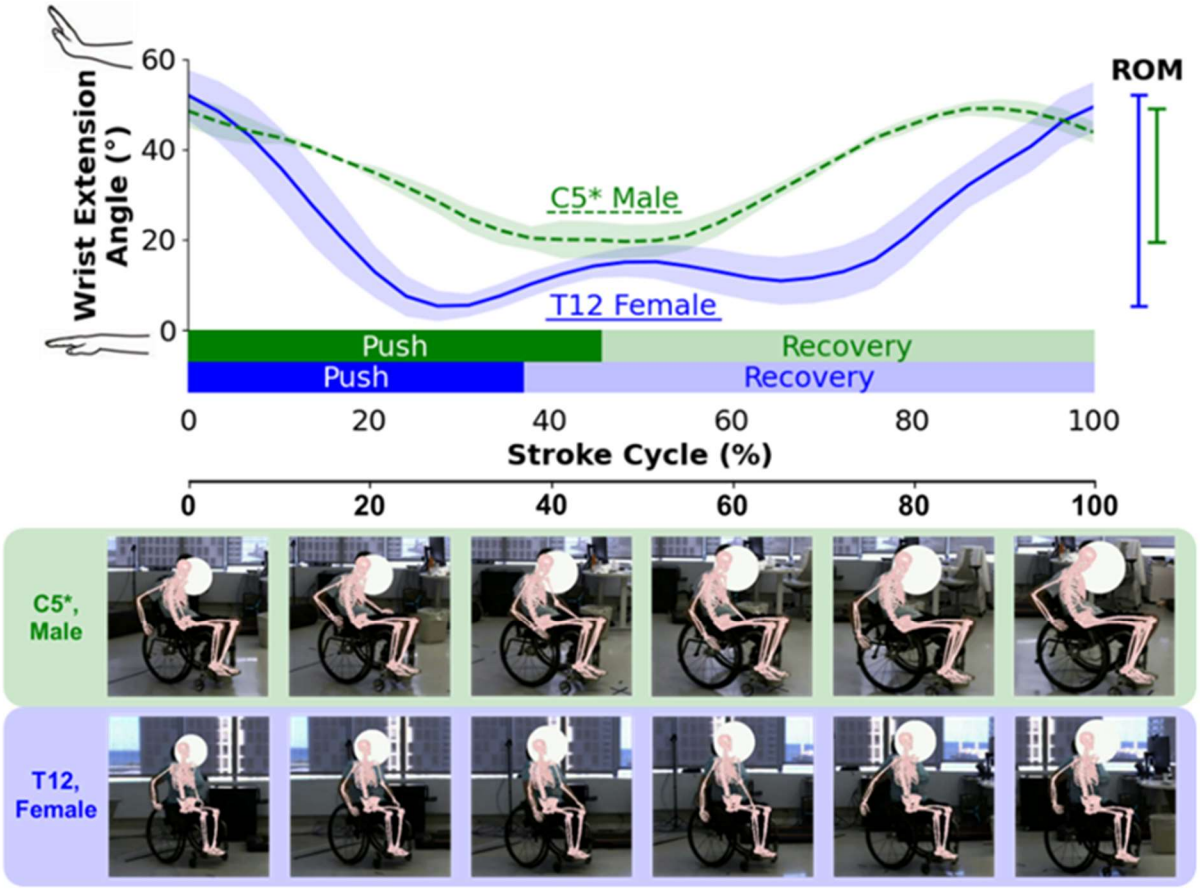
The markerless system successfully captured continuous wrist kinematics during propulsion. Distinct wrist extension trajectories and range of motion (C5: 29.4°; T12: 46.5°)

were observed across the stroke cycle for each participant, reflecting differences in propulsion mechanics.

Discussion

Differences in wrist trajectories observed in this study are consistent with prior marker-based findings [1], suggesting that variations in distal upper limb functional capacity associated with SCI level contribute to distinct propulsion biomechanics, which in turn could influence risk for secondary pathologies such as CTS. This end-to-end markerless approach eliminates marker placement and static calibration trials, enabling efficient, unobtrusive data collection from larger, more representative populations. Future work will leverage these methods in a larger sample to inform best practices for CTS prevention in manual wheelchair users.

Images (Optional)



Cycle-aligned wrist extension trajectories during wheelchair propulsion for two participants with spinal cord injury: one with C5 tetraplegia (green) and one with T12 paraplegia (blue). Solid lines represent mean wrist extension angle across the stroke cycle, with shaded regions indicating standard deviation across stroke cycles. Push and recovery phases are shown below the x-axis, and range of motion (ROM) differences are highlighted on the right. Bottom panels show frames from a single camera overlaid with the reconstructed 3D kinematic model at different points in the stroke cycle for each participant.

References (Optional)

[1] C. J. Newsam et al., Gait Posture, 1999

Session Category

Human Motion and Performance: Locomotion/Gait

OA2-04

Feasibility and Reliability of OpenCap for Assessing Toddler Gait Kinematics

Dr. Ashley Collimore-Doherty PhD, Ms. Kathryn Jemas, Ms. Claire Rohleder, Dr. Jana Iverson PhD

Boston University, Boston, MA, United States

Introduction

Standardized gait assessments are critical for early identification of motor impairments and intervention evaluation for children with neurodevelopmental disabilities. However, gold-standard marker-based motion capture systems are expensive, not portable, and the markers often pose unique sensory challenges for children. Portable, pressure-sensitive walkways are a validated alternative for capturing spatiotemporal metrics but do not provide valuable insight on joint kinematics or kinetics (i.e., force) and require children walk in a straight path. OpenCap (Stanford University) has recently emerged as a portable, cost-effective, markerless motion capture system, but has not been well studied in children. The aim of this study was to determine the feasibility and validity of using OpenCap software to capture toddler walking.

Methods

Four typically developing toddlers (19-41 months) and three toddlers with Down syndrome (31-41 months) completed repeated straight path walking trials of at least 4 consecutive steps. Final data will include 10 participants per group. Spatiotemporal metrics (i.e., step length, step width, stance time) were calculated simultaneously from OpenCap and a portable, pressure-sensitive walkway (Zeno Walkway, ProtoKinetics). ICCs and Bland-Altman plots were used to compare the two systems across each variable on a step-by-step basis.

Results

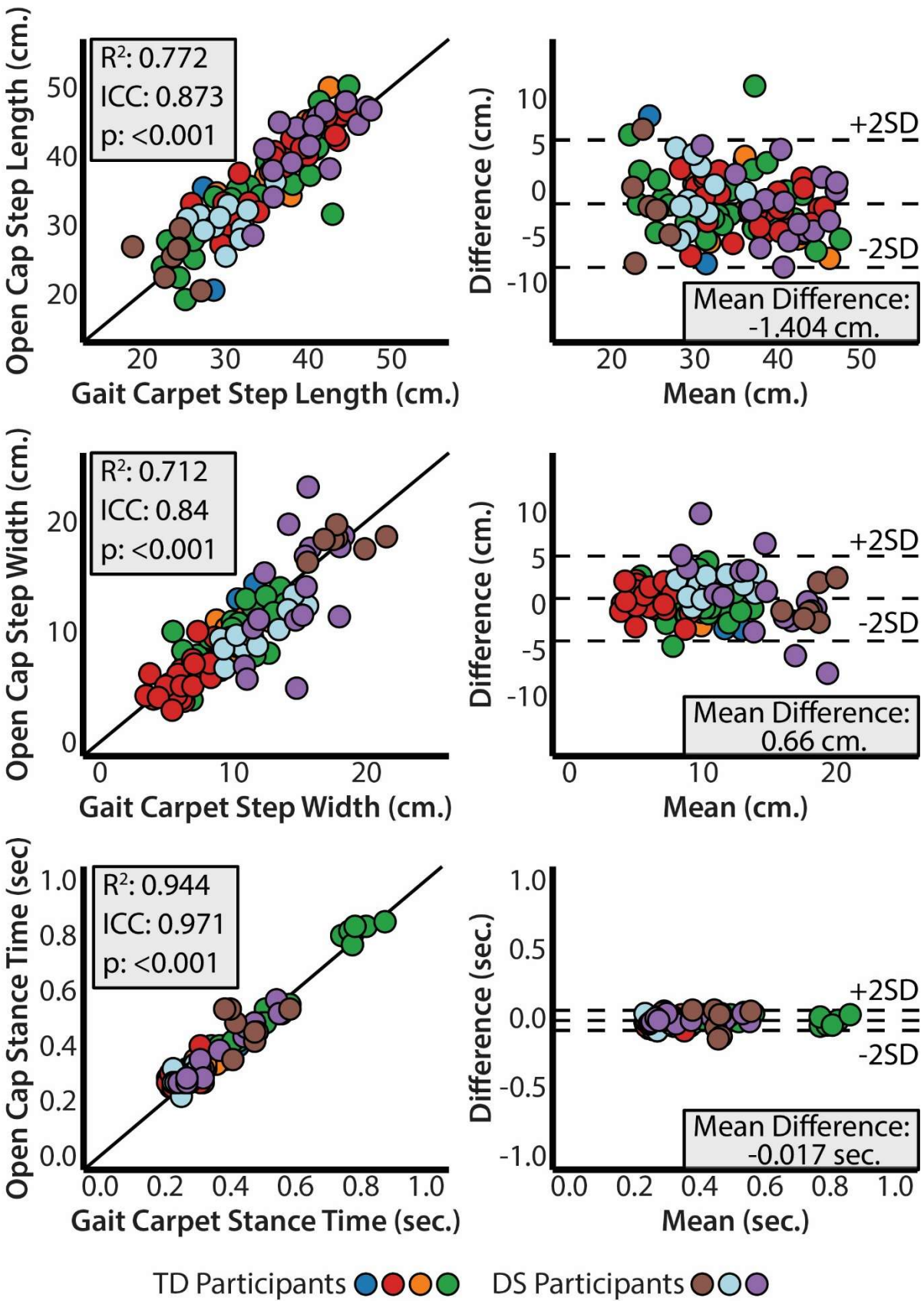
53 trials were captured on the gait carpet, of which 47% were successfully processed using open-source OpenCap code. The most common reasons for unsuccessful OpenCap processing were 1) video synchronization, 2) occlusions, 3) too few matching steps identified, and 4) incorrect order of gait events (i.e., contralateral toe off before ipsilateral heelstrike; issue not found with walkway). In total, 108 steps were used in the comparison (median per participant = 11 [4-31]). Step length, step width, and stance time were all

highly correlated across OpenCap and Zeno Walkway systems (Figure 1; ICCs > 0.84, ps < 0.001).

Discussion

OpenCap may be a feasible and reliable measure of walking kinematics, that offers several advantages over pressure-sensitive walkways. However, the number of usable trials with OpenCap is significantly lower than that with the Zeno Walkway and current algorithms cannot accurately capture heelstrike and contralateral toe-off events when toddlers are close to running. Future work should explore refining OpenCap models for toddler gait and improving consistency in data usability.

Images (Optional)


R²: 0.772
ICC: 0.873
p: <0.001
Open Cap Step Length (cm.)
Gait Carpet Step Length (cm.)
Difference (cm.)
Mean (cm.)
+2SD
-2SD
Mean Difference:
-1.404 cm.
R²: 0.712
ICC: 0.84
p: <0.001
Open Cap Step Width (cm.)
Gait Carpet Step Width (cm.)
Mean Difference:
0.66 cm.
R²: 0.944
ICC: 0.971
p: <0.001
Open Cap Stance Time (sec)
Gait Carpet Stance Time (sec.)
Mean Difference:
-0.017 sec.
TD Participants
DS Participants

References (Optional)

Session Category

Human Motion and Performance: Locomotion/Gait

OA3-01

Velocity-Based Strength Training: The Predictive Use of Mean Concentric Velocity Data

Prof. Silvio Lorenzetti PhD[1,2], Dr. Basil Achermann PhD[1], Mrs Rahel Heynen[3], Mrs Julia Suter[1], Dr. Martin Frey PhD[1], Mrs Naire Regazzi[2]

[1]ZHAW, Winterthur, ZH, Switzerland. [2]DHEST, Zurich, ZH, Switzerland. [3]SFISM, Magglingen, BE, Switzerland

Introduction

We examined the use of a new Velocity based Training (VBT) Framework and linear regression models for predicting the outcomes of a six-week VBT intervention in female floorball players [1].

Methods

A total of 23 female participants were initially enrolled in the study, of which 17 completed the intervention. The participant characteristics at baseline were as follows: body weight = 64.5 ± 9.1 kg, height = 1.69 ± 0.06 m, and age = 22.0 ± 3.7 years.

The intervention was integrated into regular training and consisted of brief 30-min sessions focused on back squats and trap bar deadlifts. Key performance metrics included neuromuscular adaptation, sprint speed, jump performance, stop-and-go performance, and load-velocity profiles. Seventeen participants completed 12 training sessions, a strength block set (Sessions 1–6) and a power block set (Sessions 7–12).

Autoregulative VBT Framework: The intervention was divided into two distinct blocks to target specific neuromuscular adaptations (strength and power development). Velocity was the primary target for load adjustments. If three (Strength) or five (Power) repetitions fell outside the target velocity range, the load for the next set was adjusted by ±5 kg.

For the regression model the change in velocity and load was used as independent variable to predict change in movement velocity and estimated one repetition maximum.

Results

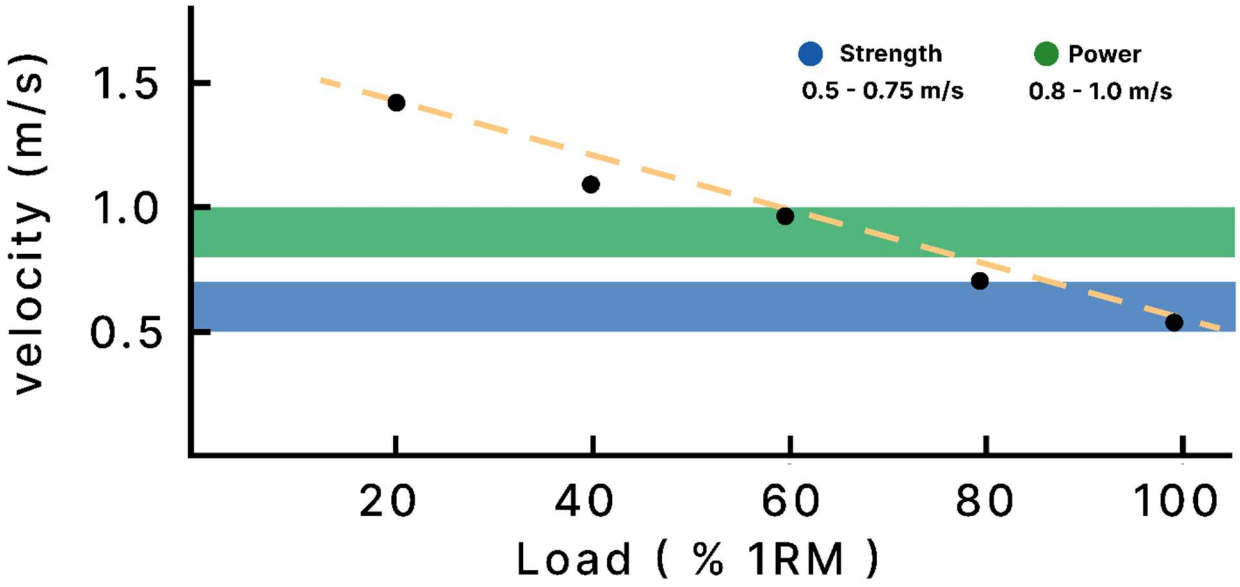
The predictive models explained 54% to 79% (R2 = 0.54–0.79) of the performance improvement in the strength-related tests. Significant gains were observed in neuromuscular metrics, including estimated one-repetition maximum and movement velocity for both exercises.

Discussion

These findings underscore the predictive potential of VBT for enhancing strength and power, while emphasizing the importance of integrating task-specific exercises to optimize sport-specific performance. The proposed VBT framework introduces a novel approach to make capturing metrics meaningful. Load and mean concentric velocity, from VBT measurements, substantially improving model accuracy. Overall, this study provides valuable insights for tailoring VBT strategies to predict performance adaptations in high-demand team sports such as floorball.

Next, we aim to extend the current methodology by applying machine-learning or deep learning models, supported and fine-tuned through the OpenSim framework, to predict anatomical adaptations over time.

Images (Optional)



References (Optional)

[1] Achermann BB *et.al.*, Sports 2025, Doi:10.3390/sports13060175

Acknowledgements (Optional)

Session Category

Human Motion and Performance: Sports

OA3-02

Task-Specific Roles of Upper-Limb Strength in Wheelchair Basketball Performance on Agility, Speed, and Endurance Assessments

Dr. Jennifer Gruenhagen PT, DPT, PhD[1], Dr. Jeffery Rankin MSE, PhD[2], Dr. Kathryn Lucas PT, DPT, PhD[3], Ms. Mia Siong BSE[2], Dr. Hannah Houde PhD[4], Dr. Jill McNitt-Gray PhD[5]

[1]Physical Therapy Program, College of Health Sciences, Midwestern University, Glendale, Arizona, United States. [2]Pathokinesiology Laboratory and Rehabilitation Engineering, Rancho Los Amigos National Rehabilitation Center,, Downey, CA, United States. [3]Physical Therapy Department, Creighton University,, Phoenix, Arizona, United States. [4]School of Health Professions, The University of Texas Medical Branch, Galveston, Texas, United States. [5]Departments of Biological Sciences and Biomedical Engineering, University of Southern California, Los Angeles, California, United States

Introduction

Unlike everyday manual wheelchair propulsion—where individuals contact the handrim—wheelchair basketball (WCBB) athletes contact the tire tread, altering upper-limb loading and increasing the mechanical demands needed for rapid changes in speed, direction, and intensity. Although WCBB propulsion is multifactorial and difficult to predict, upper-limb strength may be a key determinant.[1-2]

This study investigated the ability of three measures of upper-limb function - grip strength, dominant arm girth, and medicine ball throw distance - to predict performance on three common WCBB assessments: the Illinois Agility Test (IAT), a full-court sprint (FCS), and the 6-minute push test (6MPT).

Methods

Data were collected from (n=16) competitive WCBB athletes during early-season fitness screening. Upper limb strength was assessed with three measures: average grip strength (hand force), dominant arm girth (bicep size), and medicine ball put (distance) were measured. Participants then completed FCS (straight-line maximal-speed push with one 180° turn), IAT (agility-focused obstacle course), and 6MPT (endurance assessment of maximal distance covered on an oval track). The contribution of each measure to IAT, FCS, and 6MPT were assessed using backwards regression; semi-partial correlations compared predictive importance.

Results

Dominant arm girth and medicine ball throw distance were moderate predictors of FCS and IAT performance (up to 44% of variance; Table 1). 6MPT performance had weaker relationships, with grip strength and medicine ball throw distance accounting for 24–32% of variance. Due to a small sample size, models did not reach statistical significance (p = 0.09–0.39). However, effect sizes indicate task-specific associations between upper-limb strength measures and WCBB performance: power and arm size relate more to sprint/agility, whereas endurance is less influenced.

Discussion

Measures of upper-limb function had predictive value across performance assessments, although no single measure consistently predicted performance. These findings underscore the multifactorial nature of WCBB performance (including athlete impairments, propulsion techniques, equipment, and task demands) and highlight the need for targeted training strategies: prioritizing explosive strength and power training to improve agility and sprint performance, and further identifying endurance-specific factors to improve sustained mobility.

Images (Optional)

Table 1. Regression Coefficients for Upper Limb Strength predictors across Wheelchair Basketball (WCBB) Performance Assessments.

Wheelchair Basketball Performance Assessments	Dominant Arm Girth (cm)		Medicine Ball Put (cm)		Average Grip Strength (kg)	
	sr	sr^2	sr	sr^2	sr	sr^2
Full Court Sprint (FCS)[a]	0.66	0.44	-0.64	0.41	0.39	0.15
Illinois Agility Test (IAT)[b]	0.44	0.19	-0.48	0.23	0.31	0.10
Six-Minute Push Test (6MPT)[c]			0.57	0.32	-0.49	0.24

a. Measured in seconds, $F(3.8)=3.07$, $R^2=0.54$. $p=0.09$
b. Measured in seconds, $F(3,9)=1.12$, $R^2=0.61$, $p=0.39$
c. Measured in meters, $F(2,10)=2.85$, $R^2=0.36$, $p=0.11$

References (Optional)

[1] Yanci J et al., *Biology of Sport*, 2015.
[2] Neto FR et al., *Journal of Sport Rehabilitation*, 2021.

Acknowledgements (Optional)

This research project was supported by a grant from the Lakeshore Foundation (Alabama, USA; Grant #SSPC003).

Session Category

Human Motion and Performance: Sports

OA3-03

No Relation Between Maximum Hip Abductor Strength and Fatigue-Induced Changes in Hip Adduction Angles During a Near-Maximum 10 Km Run

M.Sc. Laila Sikeler, B. Eng. Mario Kanjuh, M.Sc. Luca Braun, M.Sc. Carlo von Diecken, M.Sc. Bastian Anedda, M.Sc. Sebastian Rehorst, M.Sc. Janina Helwig, Prof. Steffen Willwacher

Institute for Advanced Biomechanics and Motion Studies, Offenburg, Baden-Württemberg, Germany

Introduction

Some running overuse injuries are associated with reduced hip abductor strength and increased peak hip adduction angles ($HipAdd_{peak}$) during running. However, there is no evidence supporting a consistent relationship between hip abductor strength and $HipAdd_{peak}$. Fatigue may modify this relationship, as prolonged running increases $HipAdd_{peak}$, potentially due to the inability to meet the required hip abduction force demands. Whether individuals with lower hip abductor strength exhibit larger fatigue-related increases in hip adduction angles remains unknown. Clarifying this relationship may help explain why runners differ in the magnitude of fatigue-related kinematic changes.

Methods

Marker-based kinematics of 40 healthy runners (18 females) were recorded throughout a near-maximum 10 km treadmill run (5% slower than personal 10 km best time (50:45 ± 08:16 min:s)), with 30-second measurement intervals collected at every kilometer. Perceived exertion (CR10 Borg scale) was reported every 2 kilometers. Blood lactate was sampled before and immediately after the run. Maximum isometric torque of the hip abductors (HipAbd Torque), ankle inverters, plantar flexors, and leg extensors was assessed on a separate day using an isokinetic dynamometer. A linear regression model was used to examine whether HipAbd Torque predicted fatigue-induced changes in $HipAdd_{peak}$ between kilometer 2 and 10 ($\triangle HipAdd_{peak}$) while controlling for post-run lactate, post-run perceived exertion, running speed, body weight, and sex.

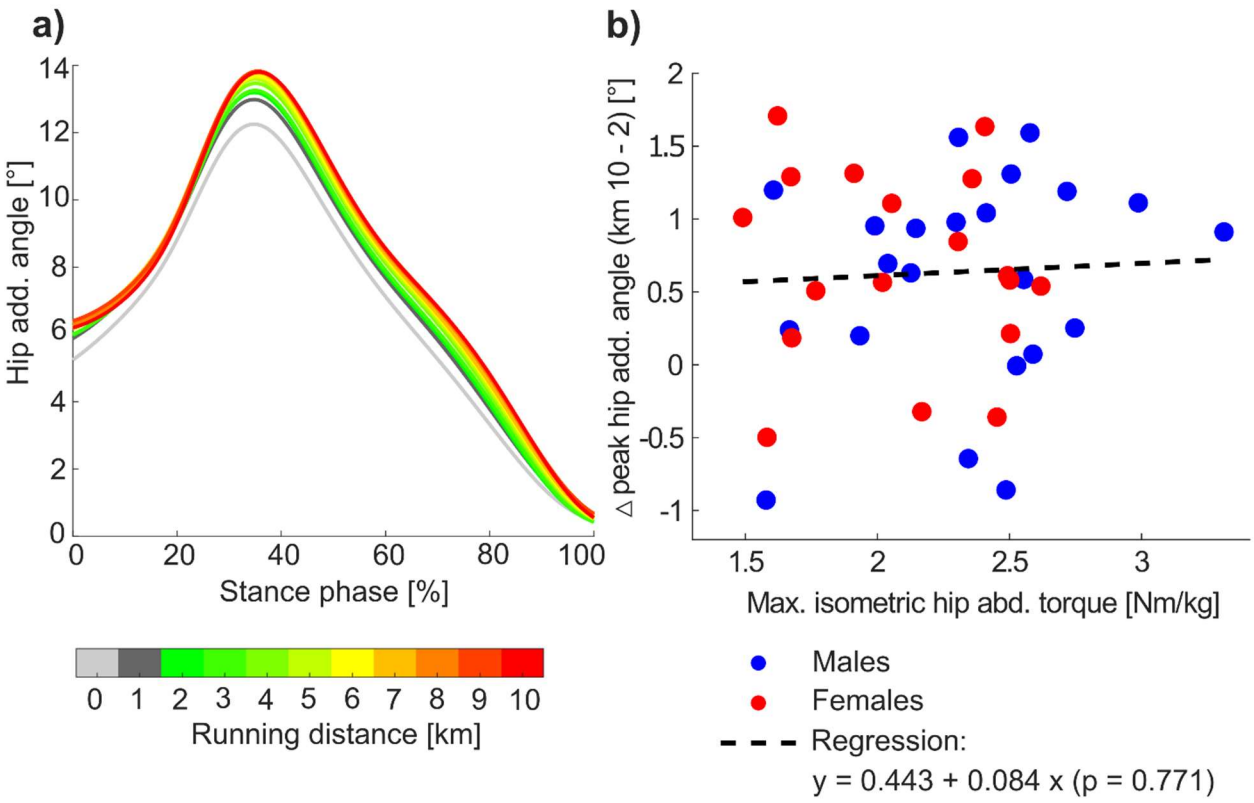
Results

Fatigue was confirmed by increases in perceived exertion (2.45 ± 1.11 to 8.33 ± 1.23) and lactate concentrations (1.64 ± 0.34 to 3.85 ± 1.50 mmol/L). $HipAdd_{peak}$ increased by 0.6 ± 0.7° from kilometer 2 to 10 ($p<0.001$; Figure 1a). In the regression analysis, HipAbd Torque did not predict $\triangle HipAdd_{peak}$ after adjusting for covariates ($\beta=0.052$, $p=0.771$, adjusted $R^2=0.00$), and none of the covariates were significant predictors (all $p>0.05$; Figure 1b).

Discussion

While our results indicate a systematic and significant increase in hip adduction angles during the run, changes are small, likely not clinically relevant, and unrelated to maximum hip abductor strength. In general, investigating how the strength of other muscle groups relates to other fatigue-induced biomechanical changes (e.g., the relationship between plantar flexor strength and joint work redistribution) may clarify the interplay between muscular capacity and fatigue responses in running.

Images (Optional)



Acknowledgements (Optional)

This study was financially supported by the German Federal Institute of Sport Science.

Session Category

Human Motion and Performance: Locomotion/Gait

OA3-04

Improving an Elite-Athlete's Cutting Movement Assessment Score May Improve Their Cutting Performance in Addition to Reducing Their Risk of Injury.

Dr. Evan Dooley PhD[1], Mr. Cody M. O'Cain MS[1], Ms. Anna C. Workman BS[1], Dr. Rachel H. Teater PhD[1], Mr. W. Brody Hicks MS[1], Dr. Kristy B. Arbogast PhD[2], Dr. Laura C. Schmitt PT, PhD, FAPTA[3], Dr. Gwansik Park PhD[1]

[1]Biomechanics Consulting and Research (Biocore), LLC, Charlottesville, Virginia, United States. [2]Children's Hospital of Philadelphia, Philadelphia, Pennsylvania, United States. [3]The Ohio State University, Columbus, Ohio, United States

Introduction

The Cutting Movement Assessment Score (CMAS) is a screening tool that aims to identify movement patterns during cutting that are associated with a high-risk of injury [1]. CMAS may provide practitioners a quick and straightforward way to assess the injury risk of athletes. However, some higher-risk cutting mechanics, like a wider foot plant, may enhance the athlete's performance. Performance is paramount at the elite level, so modifications to an athlete's mechanics must enable them to execute at their highest levels. This work investigates whether performance suffers from using safer mechanics.

Methods

Fourteen elite American football players (age: 28.6 ± 4.5 years; height: 184.5 ± 6.0 cm; weight: 96.3 ± 14.1 kg) performed cutting maneuvers at game speeds [2] and were captured with marker-based motion capture (Vicon, 200 Hz). The postures included in CMAS were quantified from these cuts then scored according to literature-based thresholds, where higher scores indicate higher risk cuts. Cut performance was assessed by the total duration of the cut (time from antepenultimate foot strike to completing the ultimate stride), where faster cuts were considered better performance.

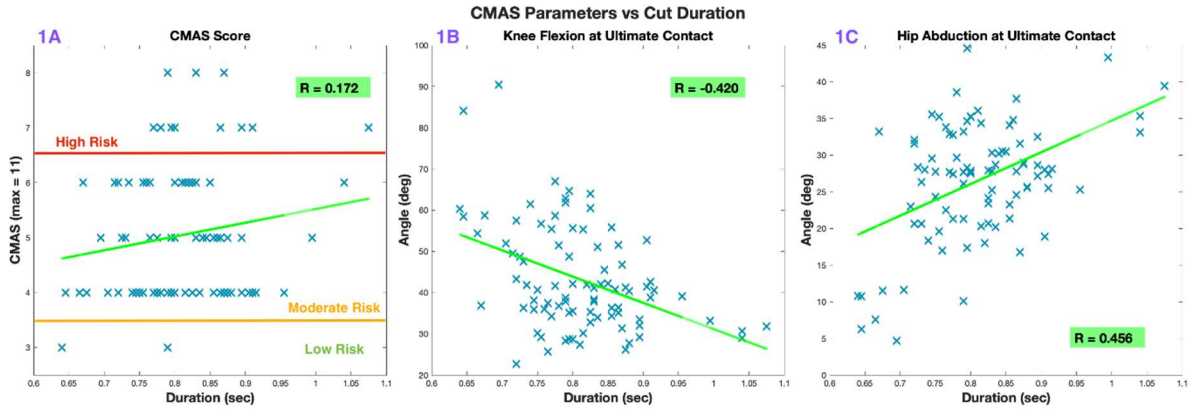
Results

Higher CMAS scores were not correlated with faster cuts (Figure 1A), indicating increased risk does not lead to increased performance. Most of the postures included in CMAS were not related to performance. There was a trend towards faster cuts being executed with a more flexed knee and less abducted hip at the ultimate foot strike (Figure 1BC), suggesting that lower-risk movements may be associated with better performance.

Discussion

These initial results in elite athletes suggest that modifying cutting mechanics may reduce injury risk without decreasing performance. Additionally, specific changes to these mechanics may improve cutting performance. For example, landing with greater knee flexion and less hip abduction on the ultimate step keeps the athlete in a safer posture, while also providing greater access to the posterior chain of muscles they need to fire to send them in their new direction of travel. This shows there are specific components of cutting mechanics that reduce injury risk while improving performance.

Images (Optional)



References (Optional)

[1] *Dos Santos et al.*, Biomechanics, 2021. [2] *O'Cain et al.*, Am J Sports Med, 2025.

Acknowledgements (Optional)

This research was made possible by funding from the National Football League and the National Football League Players Association. The views expressed are solely those of the authors and do not represent the NFL, the NFLPA, or any of its affiliates.

Session Category

Human Motion and Performance: Sports

OA3-05

Preseason Functional Assessments Can Predict Ski Performance in Elite Biathletes

Ms Morgan Koskela, Mr Isaac Burgess MS, Ms Megan Peach DPT, Dr James Becker PhD

Montana State University, Bozeman, MT, United States

Introduction

Functional assessments are commonly used to identify injury risk in high caliber athletes. In paddling sports functional assessments have also been shown to be predictive of performance factors. Whether this predictive ability extends to cross-country skiing is unknown. Therefore, the purpose of this study was to determine if a preseason function assessment provides insight into performance related biomechanical factors while skiing.

Methods

Thirteen biathletes (sex: 7M, 6F, ages: 27.3 ± 3.9 years) from the U.S. National Biathlon team completed the functional assessments. Assessment included measures of dynamic balance (Y-balance test, YBT), active ankle range of motion (goniometry), and isometric hip abductor muscle strength. Following assessment participants roller skied on a treadmill while whole body kinematics were collected using markerless motion capture. Biomechanical variables describing the athlete's ability to balance on the ski and maintain a forward position on the ski were then calculated. Principal component analysis was used to reduce the multiple biomechanical variables to single surrogate variables describing balance and forward lean position and multiple regression was then used to determine whether functional assessment performance predicted the biomechanical variables during skiing.

Results

Mean mediolateral center of mass-ankle inclination angle during the gliding phase (λ = 0.874) and lateral step out distance at ski contact (λ = 0.856) both loaded highly onto the balance surrogate. The regression (R^2 = .405, p = .011) showed that both hip abduction strength (p =.038) and posterior-medial YBT reach distance (p = .008) were predictive of balance on the ski while skiing. Forward lean at pole plant (λ = 0.743) and ankle dorsiflexion at weight acceptance (λ = 0.743) both strongly loaded onto the forward position on ski surrogate. However, regression (R^2 = .055, p = .259) showed that ankle range of motion was not predictive of forward lean on the ski

Discussion

Some aspects from a functional assessment such as hip abductor strength and dynamic balance provide insight into how athletes perform while skiing while others like passive joint range of motion do not. These findings could be used as the basis for developing cross-country specific functional assessments which could be performed in any environment.

Session Category

Human Motion and Performance: Sports

OA3-06

Biomechanical Predictors of Future Success Among High School Baseball Pitchers

Dr. Jonathan Slowik PhD, Dr. Glenn Fleisig PhD

American Sports Medicine Institute, Birmingham, AL, United States

Introduction

Previous studies have linked pitching biomechanics to indirect success metrics (e.g., ball velocity, reduced elbow loading) [1]; however, direct measures of long-term achievement remain largely unexplored. Thus, this study aimed to identify biomechanical factors associated with reaching the highest levels of competitive pitching.

Methods

Motion capture data from 158 high school pitchers [2] were retrospectively analyzed. Biomechanical variables (Fig. 1) commonly used in pitching evaluations were chosen as predictors, along with confounders of handedness, height, weight, and age. Some variables were raw values (e.g., maximum shoulder external rotation), while others were deviations from target values (e.g., shoulder abduction of 90° at foot contact). Follow-up data on each player's highest subsequent competition level were collected from publicly available records (e.g., league, team, and showcase websites), encompassing eight groups from high school through Major League Baseball.

Statistical analyses were conducted in Python. Continuous predictors were standardized, with binary predictors left unstandardized. Univariate associations with highest competition level (controlling for confounders) were evaluated using ordinal logistic regression with bootstrap resampling (n=500) to estimate odds ratios and 95% confidence intervals. A multivariate model was generated using predictors selected via elastic net regression (5-fold cross-validation) followed by AIC-based backward elimination. A final multivariate ordinal logistic model was fit to remaining predictors, with bootstrap resampling to estimate odds ratios and confidence intervals. Odds ratios below 1.0 were inverted for visual comparison, with relationship direction indicated.

Results

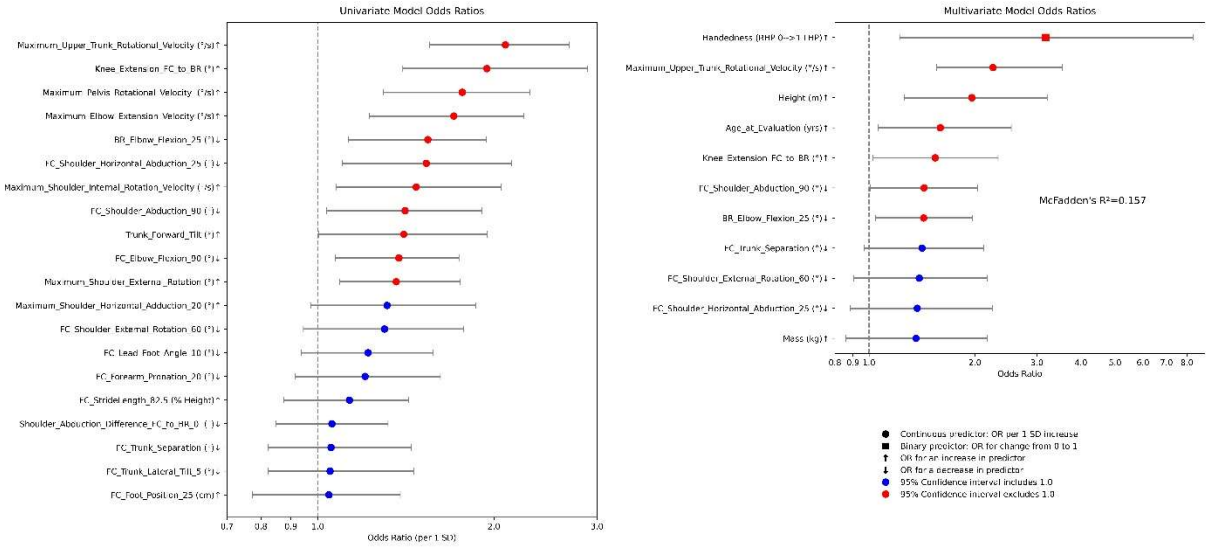
The multivariate model modestly predicted eventual competition level (McFadden's R^2 = 0.157). While the univariate analyses highlighted all four rotational velocities examined, only that of the upper trunk remained in the multivariate model, likely due to correlations across predictors. Across both analyses, maximizing knee extension between foot contact

(FC) and ball release (BR), a shoulder abduction angle 90° at FC, and an elbow flexion of 25° at BR consistently emerged as key biomechanical contributors.

Discussion

These findings highlight specific biomechanical factors that likely contribute to a pitcher reaching advanced levels of competition. Future work may incorporate injury-related follow-up.

Images (Optional)



References (Optional)

[1] Mercier, M.A., et al., BMJ Open SEM, 2020. [2] Slowik, J.S., et al., Orthop J Sports Med, 2025

Session Category

Human Motion and Performance: Sports

OA4-01

Modeling Growth and Remodeling in Tissue-Engineered Heart Valves: Integrating Mechanobiology and Local Density of Macrophages and Tissue-Producing Cells

ir. Justina Ghebryal[1,2], ir. Willem R. Stolk[1,2], prof. dr. ir. Frank P.T. Baaijens[1,2], dr. ir. Sandra Loerakker[1,2]

[1]Department of Biomedical Engineering, Eindhoven University of Technology, Eindhoven, Noord-Brabant, Netherlands. [2]Institute for Complex Molecular Systems, Eindhoven University of Technology, Eindhoven, Noord-Brabant, Netherlands

Introduction

Tissue-engineered heart valves (TEHVs) aim to overcome limitations of prosthetic valves by enabling growth and remodeling (G&R) within the patient. Successful regeneration requires balanced scaffold degradation and neo-tissue formation. Yet, long-term in vivo studies show spatial heterogeneity: hinge regions exhibit high cellularity, rapid scaffold degradation, and increased tissue deposition, whereas the tip regions show lower cellularity and slower degradation [1]. These differences lead to local mechanical variations and influence macrophage behavior, as they shift between proinflammatory M1 and anti-inflammatory M2 phenotypes in response to strain [4]. We developed a computational model to investigate how macrophage-mediated scaffold degradation affects mechano-regulated tissue production as a function of local cell density, explaining spatial heterogeneity in TEHV regeneration.

Methods

To analyze G&R of TEHVs, we developed a homogenized constrained mixture model [3,4]. A linear monocyte distribution from hinge to tip and a time-dependent gamma infiltration profile were prescribed [5,6]. Degradation model 1 assumed full M1 polarization driving scaffold loss, whereas model 2 incorporated strain-dependent M1/M2 ratios [4]. Mechano-mediated glycosaminoglycan and collagen production were scaled by spatially varying the tissue-producing cell (TPC) density [5] (Fig. 1a).

Results

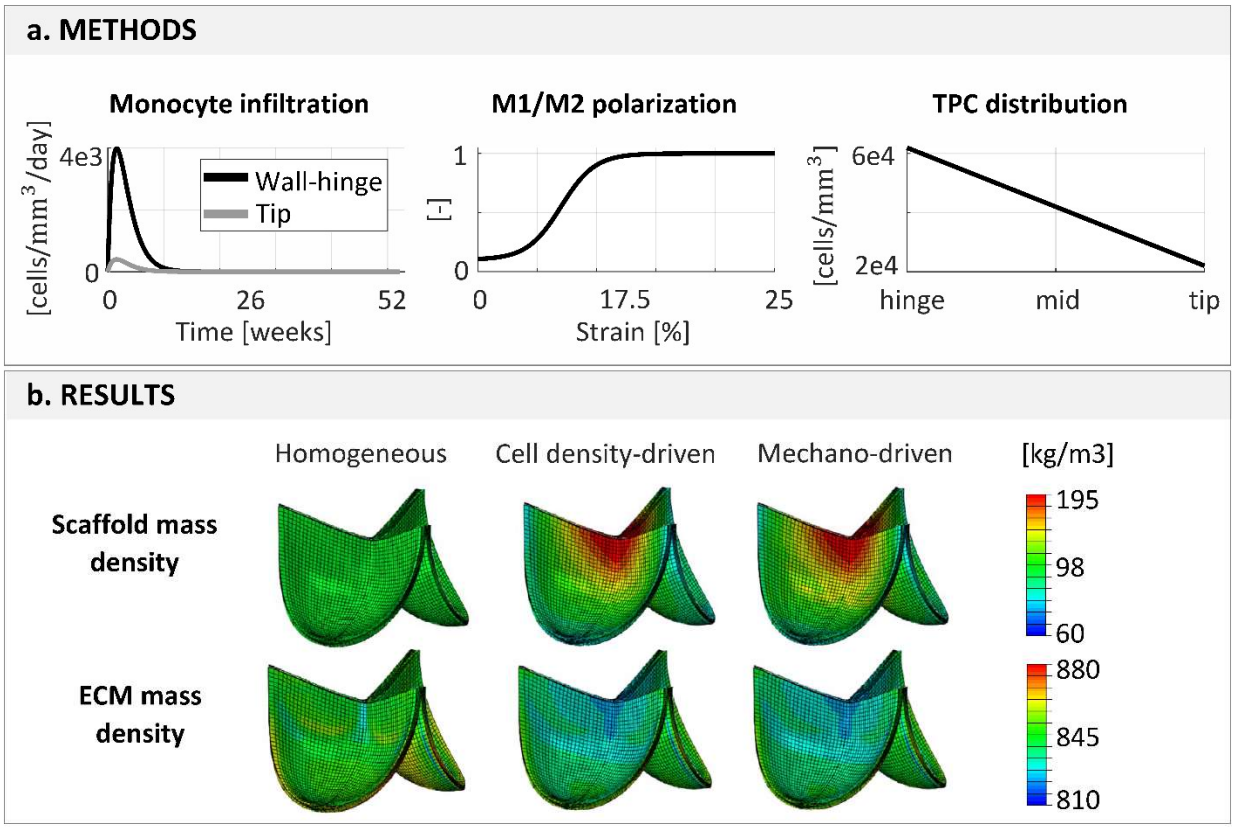
The homogeneous model showed relatively uniform scaffold resorption and matrix (ECM) deposition. The cell density-driven model exhibited more degradation and ECM production in the hinge compared to the tip regions. In the mechano-driven model, strain-dependent

macrophage polarization decreased degradation in the mid-belly regions, while ECM production was similar to the cell density-driven case (Fig. 1b).

Discussion

The cell density-driven model reproduced the experimentally observed heterogeneity [1], with faster scaffold degradation and greater ECM deposition near the hinge. The mechano-driven model produced modest regional differences, yielding ECM deposition similar to the cell-driven case. Future work will examine macrophage-TPC interactions and explore different scaffold properties to understand long-term TEHV remodeling.

Images (Optional)



References (Optional)

[1] Kluin *et al.*, Biomaterials, 2017.

[2] Ballotta *et al.*, Sci. Transl. Med., 2018.

[3] Cyron *et al.*, BMMB, 2016.

[4] Middendorp *et al.*, BMMB, 2024.

[5] Kort *et al.*, Acta Biomaterialia, 2021.

[6] Miller *et al.*, J. Biomech., 2014.

Acknowledgements (Optional)

This project has received funding from the Dutch Research Council (NWO), project no. 19670 of the NWO Talent Program VIDI.

Session Category

Cardiovascular/Cardiorespiratory Biomechanics: Methods, Models and Applications

OA4-02

Incorporating Cell-Mediated Collagen Prestretch to Predict Context-Dependent Growth and Remodeling

Dr. Valery Visser[1,2], Ir. Justina Ghebryal[3], Dr. Sarah Motta[1], Prof. Dr. Simon P. Hoerstrup[1,4], Prof. Dr Frank P. T. Baaijens[3,5], Prof. Dr. Maximilian Y. Emmert[1,6], Prof. Dr. Sandra Loerakker[3,5]

[1]Institute for Regenerative Medicine - UZH, Zurich, Zurich, Switzerland. [2]Institute for Biomedical Engineering - ETH Zurich and UZH, Zurich, Zurich, Switzerland. [3]Biomedical Engineering - TU/e, Eindhoven, Noord-Brabant, Netherlands. [4]WYSS, Zurich, Zurich, Switzerland. [5]Institute for Complex Molecular Systems - TU/e, Eindhoven, Noord-Brabant, Netherlands. [6]Charite Universitatsmedizin, Berlin, Berlin, Germany

Introduction

Homogenized constrained mixture models (HCMMs) are widely used to simulate growth and remodeling (G&R) in soft tissues and tissue-engineered cardiovascular constructs [1,2]. Whereas most studies prescribed collagen prestretch values a priori, experimental evidence suggests that prestretch is context-dependent and driven by cellular traction forces responding to mechanical cues [3].

This limitation reduces the ability of HCMMs to generalize across different mechanical environments. To overcome this, we propose a framework that mechanistically defines cell-driven homeostatic collagen stretch and captures its dynamic adaptation to hemodynamic loading.

Methods

We extend previously developed HCMM frameworks by integrating dynamic target and deposition stress for collagen fibers, linked directly to cellular stress-fiber tension [1,2]. Cellular tension is modeled as a combination of active contractility and passive strain stiffening, giving rise to a non-monotonic stress–strain response (Fig. 1a) [4]. G&R simulations were performed in tubular constructs exposed to low (2.7 kPa) or higher (15 kPa) pressure loads, representing vascular grafts implanted in distinct hemodynamic environments.

Results

The results demonstrate a smooth and rapid convergence of G&R toward homeostatic conditions across both deformation regimes (Fig. 1b). The non-monotonic behavior of the

cellular stress led to a counterintuitive result: constructs exposed to the higher pressure experience lower cellular tension, and therefore converged to a smaller homeostatic elastic collagen stretch (λ_e). Despite this, the higher-pressure environment still led to markedly increased matrix deposition, producing thicker graft walls (Fig. 1c). This is consistent with observations that vessels exposed to higher pressures exhibit thicker walls.

Discussion

We successfully incorporated a dynamic collagen prestretch that is directly linked to cellular tension mediated by the mechanical environment. Consequently, the model predicted context-dependent remodeling, characterized by distinct equilibria in collagen stretch. Results indicate that the definition of cellular stress-strain relationships may strongly influence the G&R response, highlighting the need to further explore these relationships. Overall, the model offers a promising method to develop a more generalizable framework for studying G&R.

Images (Optional)

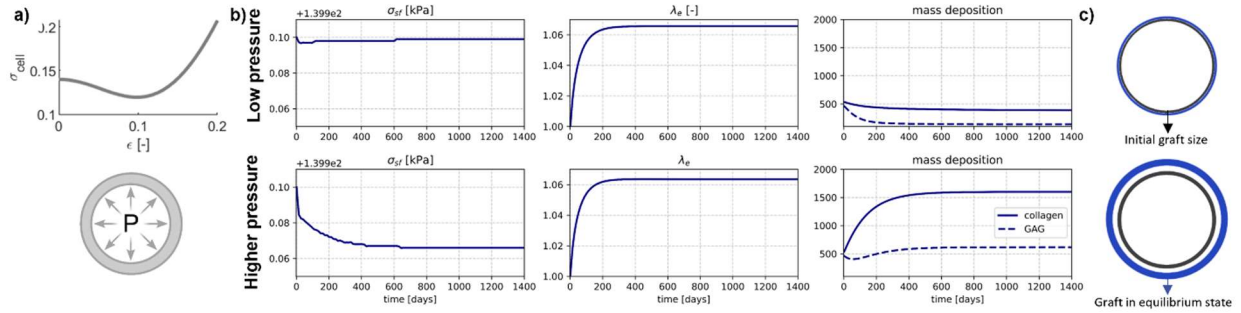


Figure 1 *a) stress-strain relationship of mechano-mediated cellular tension, and a schematic of the simulation configuration. b) cellular stress fiber tension, collagen elastic stretch, and mass deposition in the vascular conduits during G&R. c) Final size of the grafts in their equilibrium state (blue) compared to their initial state (grey).*

References (Optional)

[1] Cyron et al., *BMMB*, 2016

[2] Middendorp et al., *BMMB,* 2024

[3] Latorre et al., *Int. J. Eng. Sci., 2019*

[4] Loerakker et al., *BMMB*, 2014

Acknowledgements (Optional)

This project received funding from the European Research Council (ERC) under the Horizon 2020 program (no. 852814, TAVI4Life)

Session Category

OA4-03

Distinct Remodeling Responses Emerge Across Sex and Castration Groups in Ovine Tricuspid Valve Leaflets

Dr. Colton Kostelnik PhD[1], Ms. Chien-Yu Lin MS[1], Ms. Shreya Sreedhar BS[1], Dr. Magda Piekarska MD[2], Dr. Boguslaw Gaweda MD[2], Mr. Austin Goodyke MS[2], Dr. Tomasz Timek MD[2], Dr. Manuel Rausch PhD[1]

[1]The University of Texas at Austin, Austin, Texas, United States. [2]Corewell Health, Grand Rapids, Michigan, United States

Introduction

Tricuspid regurgitation (TR) severely impacts more than 1.6 million Americans. Most cases are deemed "functional," suggesting that dysfunction arises only from valve-extrinsic factors like right ventricular remodeling [1]. However, our prior work in pulmonary-hypertensive ovine demonstrated that tricuspid leaflets undergo fibrotic remodeling (i.e., maladapt) resulting in increased size, thickness, and stiffness [2]. Although key questions remain, valvular disease is more common in women, and prior studies have focused exclusively on males. Evidence suggests that testosterone may also influence leaflet remodeling [3]. Therefore, we hypothesized that tricuspid leaflet (mal)adaptation differs across sex and castration status.

Methods

We induced pulmonary hypertension via pulmonary artery banding (PAB) in castrated (C-Male) and non-castrated (NC-Male) males and female Dorset ovine (n = 45). After 12 weeks, leaflets were harvested for structural, mechanical, and transcriptomic analyses. Thickness maps were generated using optical profilometry (Figure 1A). Biaxial mechanical testing of the leaflet belly region was performed under equibiaxial tension. Bulk RNA sequencing was used to evaluate differential expression between PAB and control animals.

Results

Echocardiography confirmed that all groups displayed functional TR. Thickness mapping revealed a 37% increase in mean anterior leaflet thickness in C-Males ($p = 0.002$), whereas females showed a 32% increase, and NC-Males exhibited minimal thickening (Figure 1B). Radial tension–stretch curves demonstrated a stiffer response in female PAB anterior leaflets (Figure 1C). RNA-sequencing identified the largest set of differentially expressed

genes (DEGs) in NC-Males, while females and C-Males showed fewer DEG counts, displaying sex-related differences in the transcriptomic response (Figure 1D).

Discussion

All groups exhibited leaflet remodeling, but the magnitude varied across sex and castration status. The similar structural and transcriptomic remodeling observed in females and C-Males suggests a possible role for testosterone in modulating tricuspid leaflet (mal)adaptation. Ongoing integration of structural, mechanical, and transcriptomic data will help clarify mechanobiological pathways contributing to sex-related differences in TR progression. These findings underscore the importance of sex as a critical factor in understanding valve pathophysiology during TR.

Images (Optional)

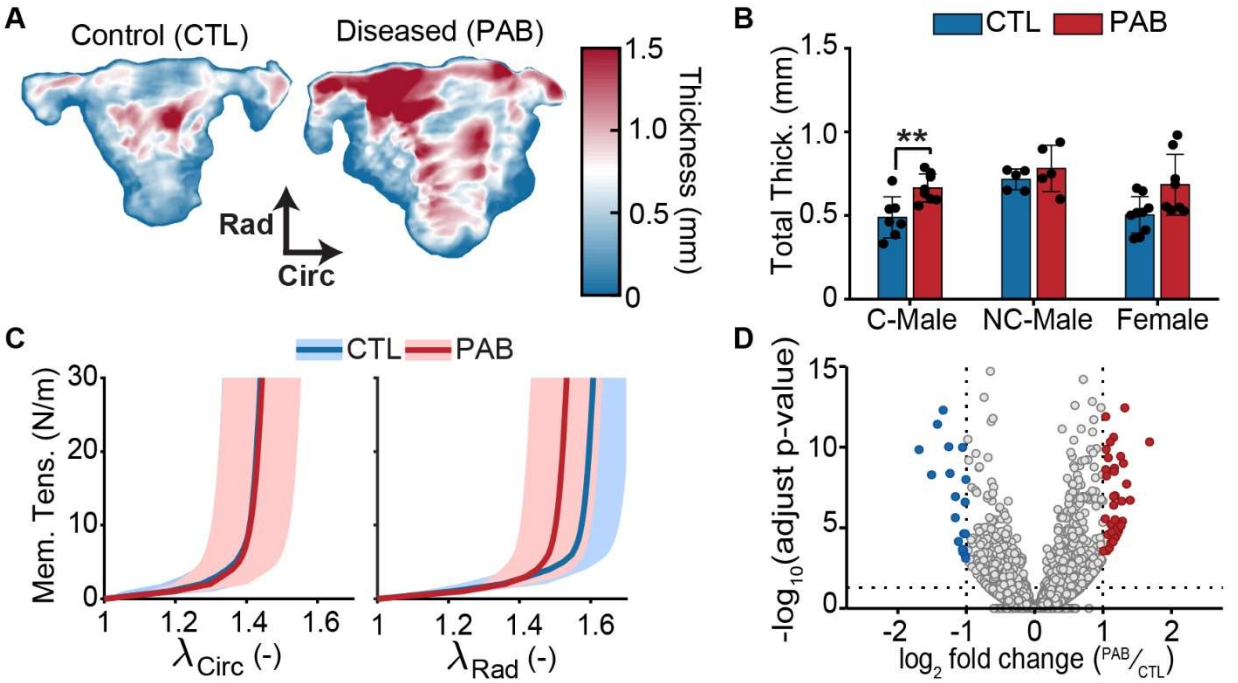


Figure 1. (**A**) Anterior leaflet thickness maps for control (CTL) and diseased (PAB) sheep.(**B**) Total anterior leaflet thickness across all groups. (**C**) Circumferential (Circ) and radial (Rad) membrane tension – stretch responses for CTL and PAB female anterior leaflets. (**D**) Volcano plot of PAB vs. CTL differential gene expression in NC-Male (blue = downregulated genes & red = upregulated genes). ** p<0.01: CTL vs PAB

References (Optional)

[1] Henning, RJ et al., Am J Cardiovasc Dis, 2022.

[2] Iwasieczko, A et al., Eur J Cardiothorac Surg, 2023.

[3] Nitsche, C et al., Wien Klin Wochen, 2020.

Session Category

Cardiovascular/Cardiorespiratory Biomechanics: Methods, Models and Applications

OA4-04

Flow-Mediated Atherosclerotic Growth and Remodeling in Murine Femoral Arteries

Ms. Gloriani Sanchez Marrero[1], Mr. Jake Fernandez[2], Dr. Fujie Zhao[3,4], Dr. Rudy Gleason[1], Dr. Luke Brewster[3,4]

[1]Georgia Institute of Technology, Atlanta, Georgia, United States. [2]Duke University, Durham, North Caroline, United States. [3]Emory University, Atlanta, Georgia, United States. [4]Atlanta VA Medical Center, Decatur, Georgia, United States

Introduction

Peripheral arterial disease (PAD) is the third leading cause of atherosclerotic disease morbidity. PAD often manifests in muscular arteries such as the femoral arteries (FA) in locations of disturbed blood flow (d-flow). Taking into consideration these PAD environmental features (i.e. d-flow, muscular arteries), our research group recently proposed a murine model for PAD [1]. This model uses the partial femoral artery ligation (PFL) surgery to impose pathological blood flows by ligating 4 out of 5 arteries distal to the left FA. Arteries exposed to d-flow undergo arterial growth and remodeling (G&R). The objective of this study is to characterize flow-mediated atherosclerotic G&R in the FA following PFL surgery. Understanding PAD G&R can inform treatment options.

Methods

Five male and five female S129 mice underwent PFL surgery. One week prior, mice were injected with AAV-PCSK9 and introduced to high fat diet to impose hypercholesterolemia [2]. Doppler ultrasound was utilized to measure centerline velocity and vessel diameter at the FAs one day, two weeks, four weeks, and 6 weeks following surgery. During FA dissection, physiological stretch was measured as the ratio of *in vivo* to *ex vivo* length.

Results

Twenty-four hours following PFL surgery, velocity waveforms were dampened in the PFL side when compared to the *in situ* control side (Figure 1A,B). This was confirmed by quantifying average velocity and peak velocity (Figure 1C,D). By the two-week time point, no difference between the FA velocity profiles in the PFL and control sides were found. Atherosclerotic stenosis at the 6-week endpoint was confirmed following dissection. Physiological stretch decreased in the PFL side when compared to the control side (Figure 1E).

Discussion

This novel murine PFL surgery model acutely imposes pathological blood flows in the left FA. Furthermore, under atherogenic conditions the FAs undergo active G&R and normalize velocity profiles. Ongoing work aims to characterize temporal changes to the FA's mechanical properties utilizing biaxial testing.

Images (Optional)

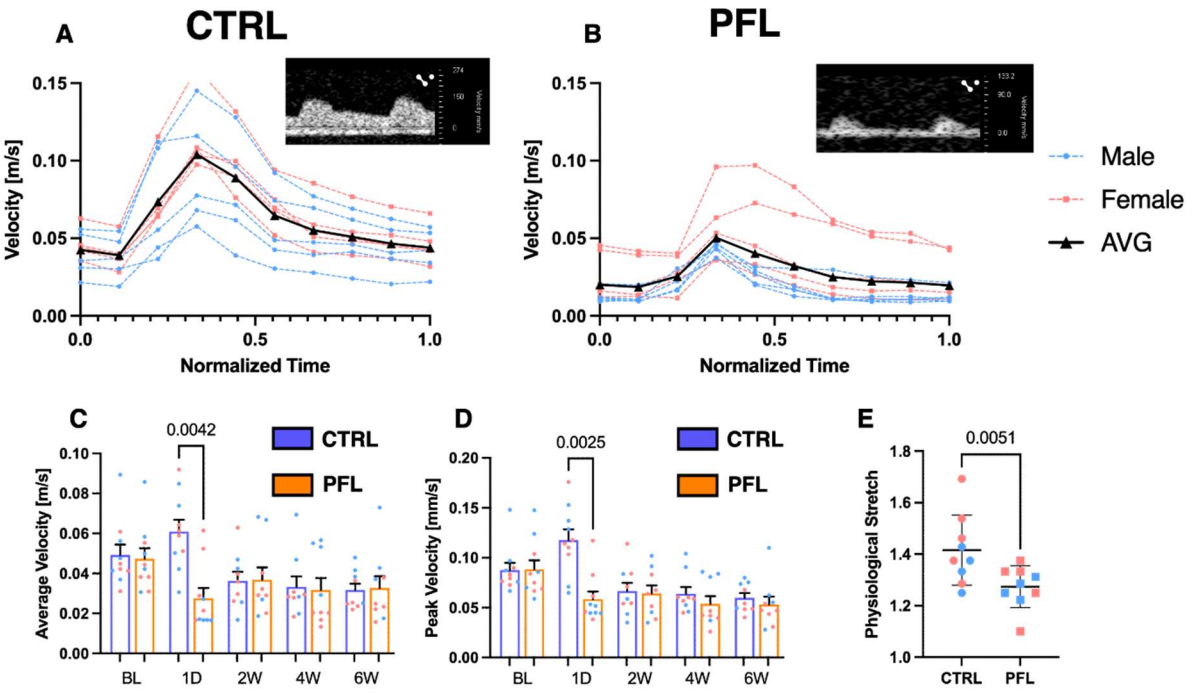


Figure 1. PFL surgery in atherosclerotic mice acutely imposes pathological blood flow and promotes atherosclerotic growth and remodeling. (**A**, **B**) Velocity waveforms over one cardiac cycle one day after partial femoral artery ligation surgery (PFL) for the control (**A**) and PFL (**B**) side. (**C**) Average velocity at the control and PFL femoral arteries across all timepoints studied. (**D**) Peak velocity at the control and PFL femoral arteries across all timepoints studied. (**E**) Physiological stretch of the control and PFL femoral artery 6 weeks after PFL surgery. Statistical significance was assessed with a Student's paired t-test at all timepoints.

References (Optional)

[1] Fujie Zhao et al., JVS-Vascular Science, 2025

[2] Sandeep Kumar et al., Lab Invest, 2017

Acknowledgements (Optional)

AHA 25PRE1354449

NIH T32HL166146

Session Category

OA5-01

Micro Finite Element Models of the Growth Plate Under Physiological Loading

Ms Camille Gardes, Dr Marta Peña Fernández

School of Engineering and Physical Sciences, Heriot-Watt University, Edinburgh, Scotland, United Kingdom

Introduction

The growth plate is a thin cartilaginous layer where longitudinal growth of bone occurs. Growth is regulated by factors, including those arising from mechanical loading, with alterations in the mechanical environment associated to musculoskeletal deformities [1]. Computational models allow to investigate how changes in mechanical stimuli influence growth, however, current models fail to account for the complex microarchitecture and properties of the chondro-osseus junction at the growth plate [2,3]. Here, we develop and validate micro finite element (μFE) models of the bone-growth plate unit to investigate the influence of bone microarchitecture and growth plate cartilage heterogeneity in its mechanical response.

Methods

We performed *in situ* μCT (4μm voxel size) compression testing (2.5%) in ovine bone-growth plate units (5mm). We generated μFE models based on segmented μCT images coarsened to 25μm [4]. Three μFE models were compared: (i) homogeneous bone and cartilage, (ii) heterogenous bone and homogeneous cartilage, and (iii) heterogeneous bone and cartilage (Figure). Bone tissue was modelled as linear elastic (E_0=100MPa, v=0.3) and cartilage as both elastic (E_0= 1MPa, v=0.45) [2] and transversely isotropic poroelastic following [5]. An axial displacement corresponding to 2.5% compression was applied followed by a holding step to allow for stress relaxation.

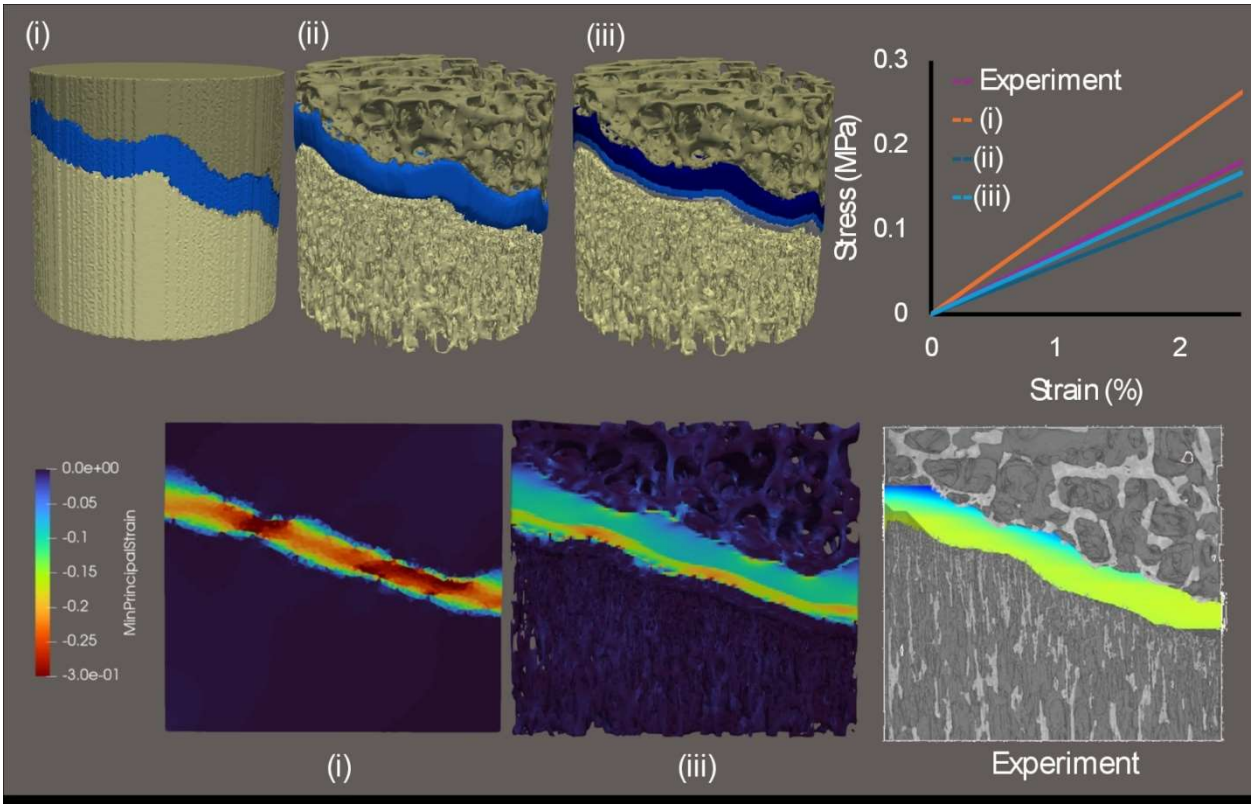
Results

Homogeneous models resulted in high strain concentration in the growth plate cartilage and overestimation of stiffness (Figure), whereas accounting for bone microarchitecture led to better experimental agreement. Transversely isotropic properties for cartilage allow reduction of excessive transverse deformations observed with linear models. Growth plate heterogeneity improved model predictions, with proliferative and hypertrophic zones showing larger deformations than reserve zone.

Discussion

Our results highlight the importance of bone microarchitecture and heterogeneous non-elastic cartilage properties for growth plate strain predictions, which are typically neglected in bone growth simulations [2,3]. These μFE models can be exploited to provide new insight into the mechanical factors that regulate growth plate ossification, enabling predictions of local mechanical environmental under different loading conditions.

Images (Optional)



References (Optional)

[1] Carter & Wong, Philos. Trans. R. Soc. B Biol. Sci., 2003; [2] Gao et al., PLoS One, 2015; [3] Yadav et al., J Biomechanics, 2016; [4] Peña Fernández et al., JMBBM, 2022; [5] Sergerie et al., J Biomech, 2009

Session Category

Musculoskeletal Biomechanics: Methods, Models and Applications

OA5-02

A New Isobaric Mapping Method for the Bone Vascular network.

MD Corentin Serra[1], Prof Natacha kadlub[2,3], Prof Romain Monchaux[1], Associate Professor jean boisson[1]

[1]Laboratory of Mechanics and Interfaces, ENSTA, IP-Paris, Paris, Ile de France, France. [2]Faculté de santé, Université Paris Cité, Paris, Ile de France, France. [3]Maxillofacial and Plastic Surgery, Necker Children Hospital, APHP, Paris, Ile de France, France

Introduction

The vascularization of bone remains largely unknown, yet it is crucial to future developments in reconstructive surgery. For example, in decellularization protocols for bone allografts, precisely tuning perfusion parameters is essential to completely remove all traces of DNA. However, traditional anatomical techniques have difficulty determining the perfusion dynamics of multiple arterial bones, such as the mandible. This study introduces a new method of examining pressure-dependent vascular territories to overcome these limitations.

Methods

We performed contrast agent perfusions on human cadaveric mandibles using an experimental setup that controlled the applied pressure with flow rate adaptation. We used cone beam computed tomography to measure the expansion of the perfused territories for each pressure increment. We identified each newly explored volume at each pressure increment using a custom segmentation pipeline that subtracted the current image from the previous increment. Ten mandibles from six French Caucasian cadaveric donors that were symmetrically dissected were studied. Then, individual pressure maps showing to perfuse different regions of the mandible were generated. An averaged map was finally reconstructed by projecting the ten maps onto a typical mandible mesh.

Results

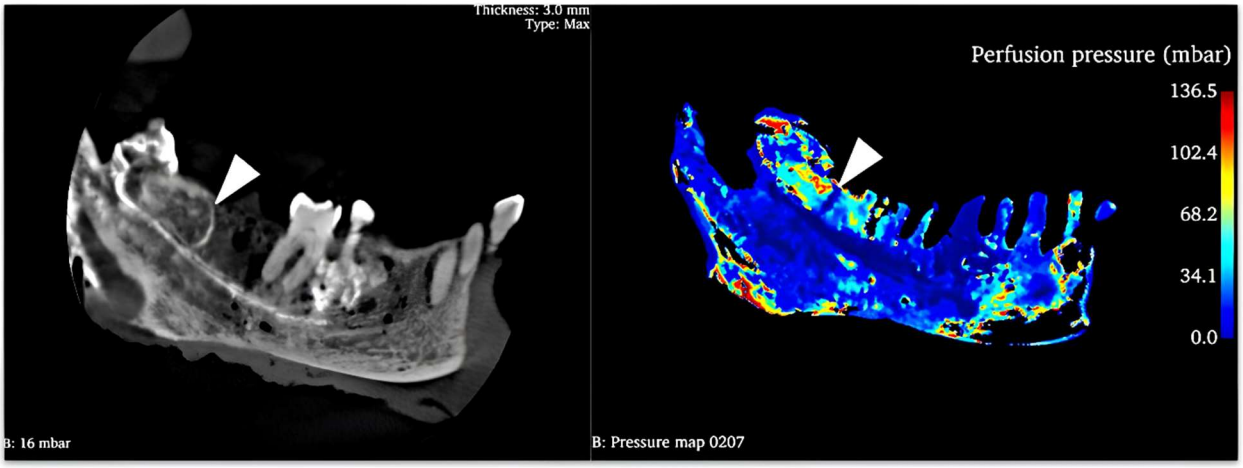
We found that the maxillary artery consistently supplies the entire mandible, with a significant and predictable increase in perfusion volume as pressure rises. Perfusion saturation was achieved at approximately 100–125 mbar, which is consistent with physiological arterial pressures. The study confirms that regions of high bone density, such as cortical areas, require higher perfusion pressure. Additionally, the results suggest different perfusion behaviors in the retromolar area and post-extraction tooth sockets.

Within the studied pressure range, the theoretical perfusion of the mandible from the maxillary and facial arteries appears to be equivalent. However, it is limited by a bottleneck effect at the mental artery anastomosis.

Discussion

These results demonstrate that pressure-driven perfusion analysis provides valuable information about the vascularization of complex bone. Optimizing pressure parameters may enable decellularization by perfusion in massive bone allografts, thereby improving graft integration and viability. This study highlights the importance of pressure-controlled anatomical research because perfusion territories vary significantly with applied pressure, challenging traditional static angiosome models.

Images (Optional)



References (Optional)

[1] Corentin Serra *et al.* , Bone, 2026

Acknowledgements (Optional)

The author thanks the Ecole de Chirurgie, APHP, for the anatomic subject supply. J. Boisson thanks the Agrégation de Science Physique jury for the inspiring experiment. This work is fully supported by funds from the Fondation des Gueules Cassées (NSF: 72-2023).

Session Category

Musculoskeletal Biomechanics: Methods, Models and Applications

OA5-03

Neutral Pose Normalization May Misrepresent Tibiotalar Kinematics in Clinical Populations

Ms Emily Smith-Bregeda[1,2], Mr Robert Chauvet[1,2], Ms Janae Ruzicki[1,2], Dr Elizabeth Condliffe[3], Dr Koren Roach[1,2,4]

[1]Schulich School of Engineering, University of Calgary,, Calgary, Alberta, Canada. [2]McCaig Institute for Bone and Joint Health, Calgary, Alberta, Canada. [3]Alberta Children's Hospital Research Institute, Calgary, Alberta, Canada. [4]Cumming School of Medicine, University of Calgary, Calgary, Alberta, Canada

Introduction

Joint angles are often normalized to a static neutral pose to account for inter-subject anatomical variability, though this method could be detrimental to clinical interpretation. Specifically, when investigating the tibiotalar joint with dual fluoroscopy (DF), individuals who are more dorsiflexed or plantarflexed in their neutral pose may seemingly exhibit resultant joint angles with a baseline offset. This offset may misleadingly represent a joint angle as positive or negative, indicating a motion that is physiologically improbable for that individual. The purpose of this case study was to explore how neutral normalization affects tibiotalar joint angles in healthy controls and individuals with a foot deformity.

Methods

Eight typically-developed control participants (5F/3M; age: 37.9±18.9 yrs; BMI: 23.2±3.6 kg/m^2; REB19-1743), and one participant with plantarflexion contracture foot deformity (F, age: 31.1 yrs; BMI: 29.2 kg/m^2) were recruited (REB23-1432). DF data were collected for neutral (i.e., static) and walking (i.e., dynamic) trials. Computed tomography (CT) scans were acquired and segmented. CT bone models were registered to the DF data to compute tibiotalar kinematics. To assess the effect of neutral normalization, each dynamic relative transformation matrix ("raw") was normalized by post-multiplying with the inverse of the neutral relative matrix ("normalized"). Baseline offset angles were compared between raw and normalized waveforms for control participants using a paired t-test. Positive and negative waveform components for the participant were calculated as positive and negative percent of stance phase.

Results

For the controls, the normalized trials showed a greater baseline offset than raw trials ($p<0.01$). Similarly, the raw baseline offset in the contracture participant was -16°, compared to an offset of -5° when normalized. The contracture participant spent 100% of stance in plantarflexion in the raw condition, compared to only 22% of stance in plantarflexion when normalized (Fig 1).

Discussion

Although the participant had a contracture preventing dorsiflexion, normalized tibiotalar joint angles suggested they were dorsiflexed during 78% of stance. When comparing to a control population, the use of neutral normalization may misrepresent pathology. Similar results were observed in control participants offsets, other joints and planes, suggesting that neutral normalization may not be appropriate for DF analysis, especially for clinical populations.

Images (Optional)

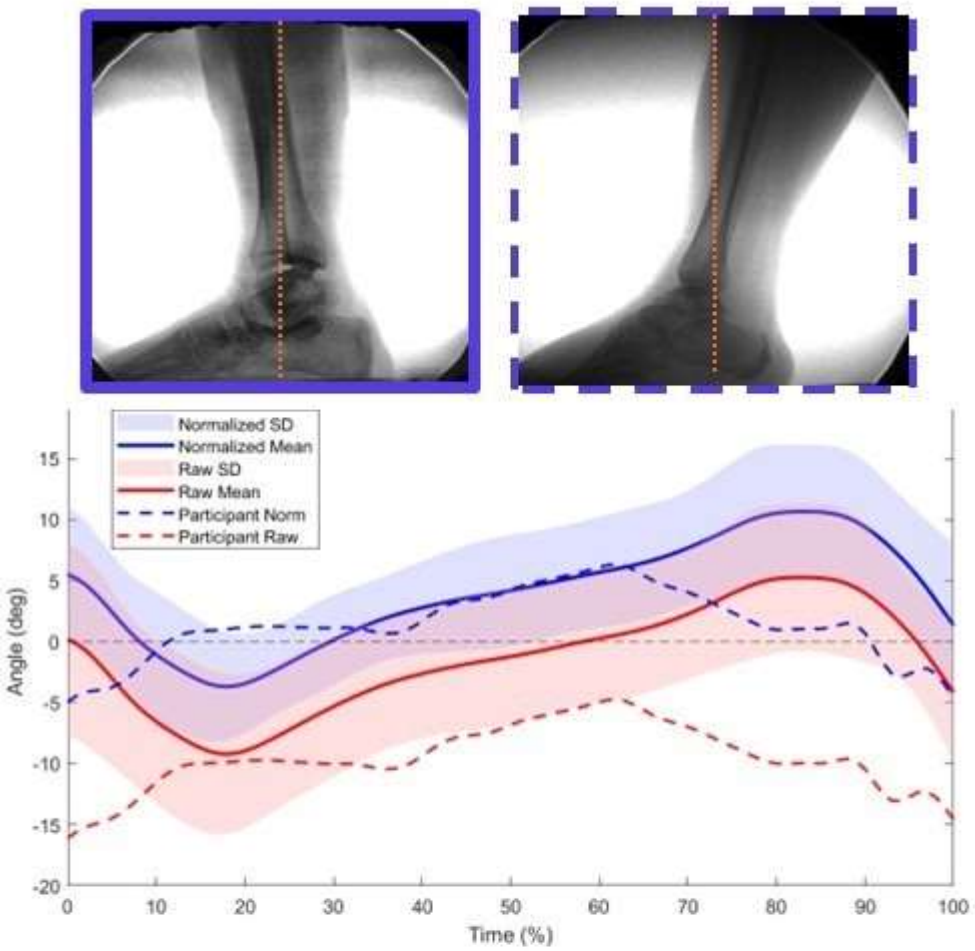


Fig 1. Radiographs of neutral position for a representative control (top left) and equinus foot deformity (top right) with 90° reference displayed as an orange vertical line. Bottom: control mean (solid line), and standard deviation (shaded areas) normalized (blue) and raw (red) tibiotalar dorsi/plantarflexion angles and the equinus participant raw and normalized tibiotalar angles (dashed lines).

References (Optional)

Acknowledgements (Optional)

We gratefully acknowledge funding from the University of Calgary's McCaig Institute for Bone and Joint Health and Department of Biomedical Engineering, Natural Sciences and Engineering Research Council of Canada (NSERC), and Canadian Institute of Health Research (CIHR).

Session Category

Musculoskeletal Biomechanics: Methods, Models and Applications

OA5-04

Feasibility of MRI for Tibial Strain Estimation in Physically Active Adults

Dr Olivia L Bruce, Dr Feliks Kogan

Department of Radiology, Stanford University, Stanford, CA, United States

Introduction

Strain is a key factor associated with bone adaptation and the pathophysiology of bone stress injuries [1]. Finite element modelling using computed tomography (CT) is the current state-of-the-art approach to quantify strain [2]. However, CT is not always available and involves exposure to ionizing radiation. Magnetic resonance (MR) imaging is a potential alternative and would enable opportunistic studies of mechanical risk factors in patients with possible bone stress injuries. The purpose of this study was to evaluate correlations in tibial diaphysis strain measures between finite element models generated from MR and CT images.

Methods

Nine physically active adults (18-56 years) underwent bilateral CT and MR scans of the lower leg. Finite element models of the left and right tibia-fibula with complex boundary conditions and generic muscle and joint contact forces representative of running were generated [2]. The CT-based models were assigned heterogeneous material properties derived from the underlying Hounsfield units and a calibration phantom placed in each scan. The MR-based models used homogeneous material properties for cortical bone, trabecular bone, and marrow regions. Peak pressure-modified von Mises strain and strained volume, defined as the volume of elements experiencing at least 4000 με, normalized to diaphysis volume, were calculated. Correlations were assessed using linear mixed models to account for non-independence of cases.

Results

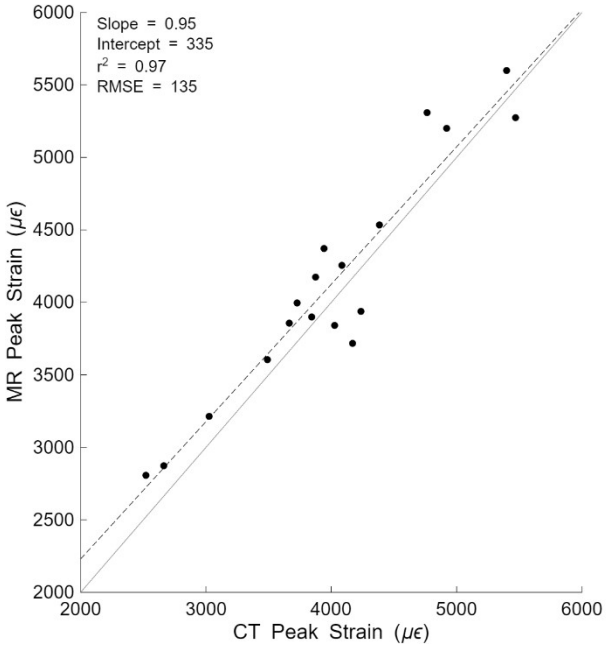
Surface geometry root mean square differences were small (0.85 – 1.11 mm). Mean cortical bone mineral density across participants ranged from 1.83 – 2.00 g/cm^3. Young's modulus differences through the diaphysis were -0.2 to 1.2 GPa. Both peak strain and normalized strained volume measures were very strongly correlated between MR- and CT-based models (slope = 0.95-0.96, r^2 = 0.97-0.98, Figure 1).

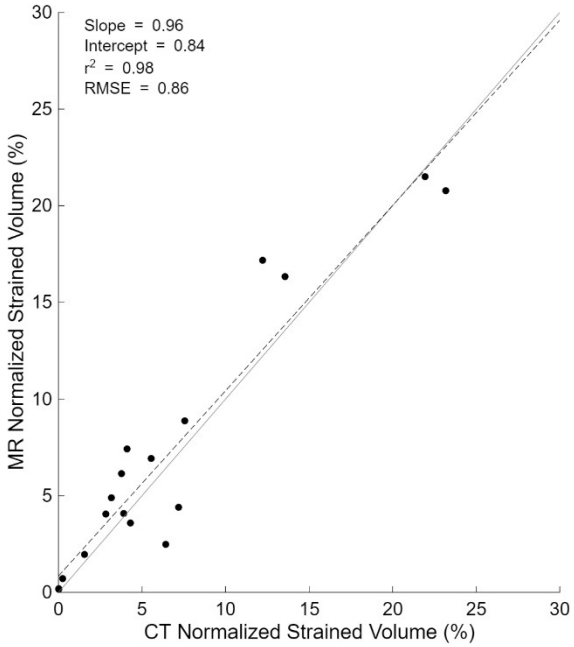
Discussion

Our results suggest that MR is a feasible alternative to CT for finite element modelling of tibial bone strain in physically active adults. This may not be generalizable to studies

involving larger variations in bone density (e.g., comparing runners with and without osteopenia). Future work will investigate adding individualized material property estimates derived from quantitative MR approaches.

Images (Optional)





References (Optional)

[1] Tim Hoenig *et al*. Nat Rev Dis Primers, 2022

[2] Olivia L Bruce & W Brent Edwards. Bone, 2023

Acknowledgements (Optional)

The authors would like to acknowledge funding support for this study: the Wu Tsai Human Performance Alliance, Stanford Medicine Department of Radiology (ISNFR), and GE Healthcare.

Session Category

Musculoskeletal Biomechanics: Methods, Models and Applications

OA5-05

Laplace-Hamming Segmentation Changes Clinical Interpretation of HR-pQCT Microarchitecture and Strength Outcomes in Children With Osteogenesis Imperfecta and Healthy Controls

Dr. Seyedmahdi Hosseinitabatabaei PhD[1,2,3], Dr. Minhao Zhou PhD[4], Dr. Frank Rauch MD[1,5], Dr. Galateia Kazakia PhD[4], Dr. Bettina Willie[1,2,3,6]

[1]Shriners Hospital for Children, Research Center, Montreal, Quebec, Canada. [2]Department of Bioengineering, McGill University, Montreal, Quebec, Canada. [3]Faculty of Dental Medicine and Oral Health Sciences, McGill University, Montreal, Quebec, Canada. [4]Department of Radiology and Biomedical Imaging, University of California, San Francisco, San Francisco, California, United States. [5]Department of Pediatrics, McGill University, Montreal, Quebec, Canada. [6]Department of Biomedical Engineering, McGill University, Montreal, Quebec, Canada

Introduction

High-resolution peripheral-quantitative CT (HR-pQCT) combined with micro-finite element (μFE) models is a powerful tool for assessing bone quality and fracture risk. A Laplace-Hamming (LH) segmentation method has improved microarchitectural accuracy in adults [1]. We investigated its impact in children with osteogenesis-imperfecta (OI) and healthy controls by comparing with data collected using standard segmentation method [2].

Methods

Radius and tibia scans from 20 children with OI and 20 age- and sex-matched controls were obtained using a second-generation HR-pQCT scanner. Microarchitectural and μFE outcomes were derived using both the default (low-pass Gaussian filter) and LH-segmentation. Absolute differences between segmentation methods were assessed using paired t-tests with Benjamini-Hochberg correction. Clinical impact was evaluated by comparing baseline OI vs control differences and 1-year changes using linear mixed-models.

Results

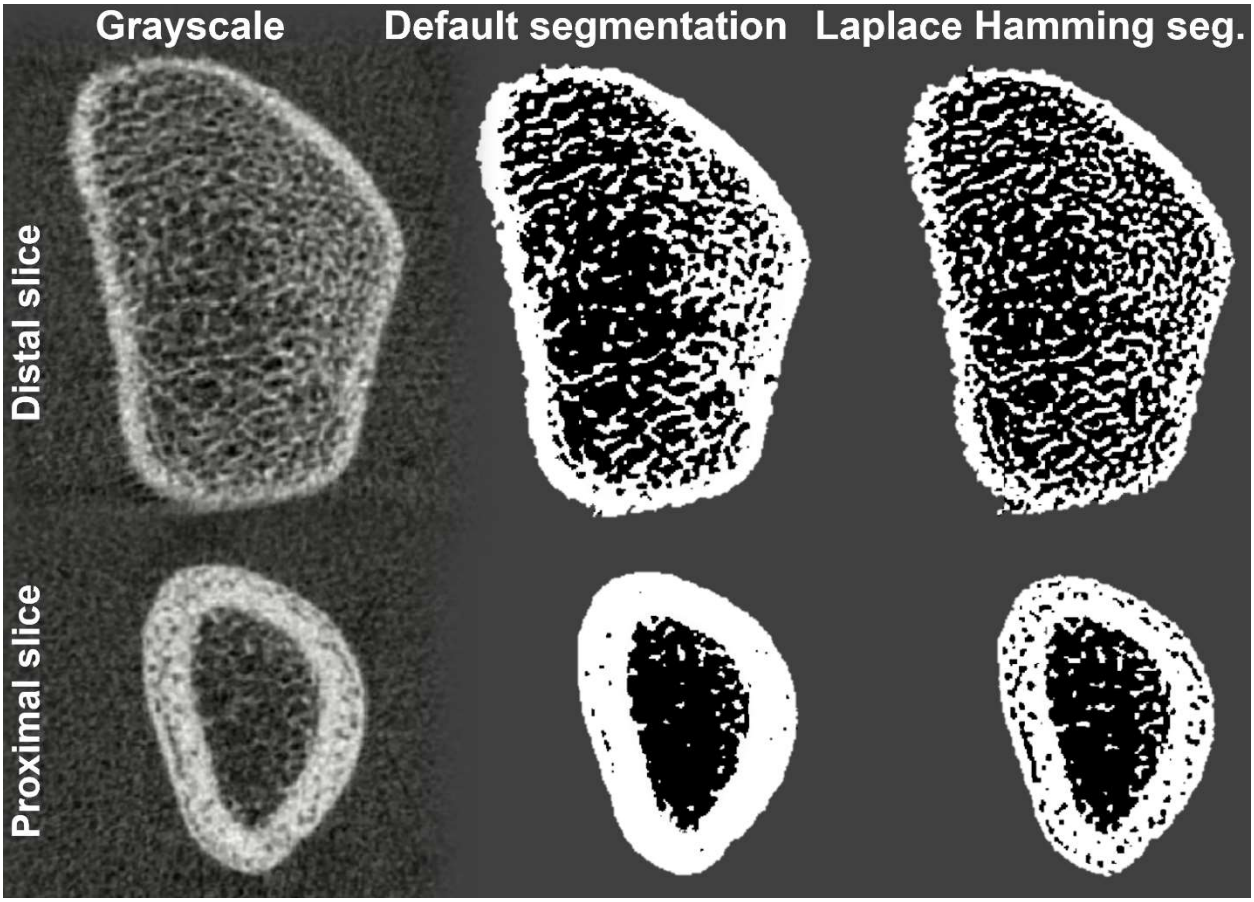
All HR-pQCT and μFE outcomes differed significantly between segmentation methods ($p<0.05$). Cortical porosity (Ct.Po) showed the largest discrepancy, with LH producing 700% and 1250% higher values at tibia and radius, respectively (Figure). Trabecular outcomes differed systematically: LH yielded higher trabecular bone volume fraction (Tb.BV/TV) and number (Tb.Th), and lower thickness (Tb.Th), separation (Tb.Sp), and inhomogeneity (Tb.1/N.SD), with average differences of 9–19% at both sites. Cortical thickness (Ct.Th)

decreased with LH, and estimated bone strength was 6–8% lower. Importantly, LH segmentation altered clinical interpretations. At tibia, only LH detected significant between-group differences in 1-year changes for Tb.BV/TV and Ct.Po, while baseline differences in Tb.N and Tb.Sp were no longer significant with LH. At radius, only LH detected significant group differences in 1-year changes for Tb.BV/TV, Tb.Th, and Ct.Po, and detected baseline differences in Tb.Th and Ct.Th that were not observed using the default method.

Discussion

For these second-generation HR-pQCT images, LH segmentation led to different clinical interpretations for several key outcomes compared to the default method. While strength estimates showed similar directional findings, absolute changes were noticeable. In the absence of microCT gold standards, visual assessment and prior adult data support improved segmentation using LH in children with OI and controls. These results strengthen the evidence that LH offers a more accurate alternative for clinical HR-pQCT evaluation.

Images (Optional)



References (Optional)

[1]Sadoughi et al.,JBMR,2023

[2]Hosseinitabatabaei et al.,JBMR,2025

Acknowledgements (Optional)

We thank all the study participants and staff at the Shriners Hospital for Children-Canada. We also thank Catherine Julien for assisting with data collection. We thank Mereo BioPharma and especially James Clancy for assistance with some data organization. The study was funded by Mereo BioPharma, Shriners Hospitals for Children, and FRQS Programme de bourses de chercheur (BMW, SH). BMW and FR have received institutional research support and materials and have consulted for Mereo BioPharma.

Session Category

Musculoskeletal Biomechanics: Methods, Models and Applications

OA5-06

Reliability of Measuring Meniscal Extrusion in Weightbearing Using Upright Open Magnetic Resonance Imaging

Dr. Jordan Broberg Ph.D., Dr. Honglin Zhang Ph.D., Dr. Parth Lodhia M.D., Dr. David Wilson D.Phil.

University of British Columbia, Vancouver, British Columbia, Canada

Introduction

Meniscal extrusion, defined as abnormal translation of the meniscus beyond the edge of the tibial plateau, is a radiological finding on magnetic resonance imaging (MRI) that suggests altered mechanical function of the meniscus, putting the knee at risk for osteoarthritis. Since menisci distribute loads across a range of knee motion, measuring extrusion in weightbearing and flexed positions would give better insight into mechanical changes caused by injury and treatment. Upright open MRI allows for knee imaging in weightbearing and flexed positions. Our goal was to assess the reliability of measuring meniscal extrusion in weightbearing and flexed positions with an upright open MRI protocol.

Methods

We recruited four healthy participants (3 female/1 male, ages 24-28) and scanned both their knees in four postures with a 0.5T upright open MRI scanner. Each participant had two identical scanning sessions for reliability analysis. Dixon sequences were used to obtain coronal images of the knee. The postures were: a) supine with knees extended; b) unloaded seated at 90° of knee flexion; c) weightbearing standing with knees extended; and d) weightbearing assisted squat with knees flexed to 90°. A MRI-compatible sloped seat supported participants in assisted squatting while still allowing for loading and muscle activation. Medial and lateral meniscal extrusions were calculated on a midcoronal slice as the distance between the edge of the tibial plateau and the external edge of the meniscus. Test-retest reliability was reported using intra-class correlation coefficients (ICC) and standard errors of measurement (SEM).

Results

Mean medial extrusion was 2.50 mm for supine, 1.87 mm for sitting, 2.86 mm for standing, and 2.05 mm for assisted squatting. Mean lateral extrusion was 0.72 mm for supine, 1.21 mm for sitting, 0.39 mm for standing, and 0.67 mm for assisted squatting. ICCs ranged from 0.75-0.96 and SEM ranged from 0.26-0.37 mm (Table 1).

Discussion

Pathological extrusion is around 1 mm greater than normal extrusion for both the medial and lateral meniscus. Our upright open MRI protocol is therefore sufficiently reliable to detect the clinically significant differences in meniscal extrusion in weightbearing and flexed knee positions, making it feasible to study effects of meniscal injury and repair techniques.

Images (Optional)

Table 1. Medial and lateral meniscal extrusion reliability.

	Medial		Lateral	
Posture	ICC	SEM (mm)	ICC	SEM (mm)
Supine	0.88	0.28	0.94	0.32
Sitting	0.78	0.34	0.91	0.37
Standing	0.74	0.37	0.96	0.26
Squatting	0.74	0.36	0.84	0.33

Session Category

Musculoskeletal Biomechanics: Methods, Models and Applications

OA6-02

Prediction of Hip Impact Force From Video-Captured Falls Using Pose-Estimated Kinematics

Mr. Reese Michaels M.S., Dr. Yaejin Moon PhD

Syracuse University, Syracuse, NY, United States

Introduction

Falls are the leading cause of hip fractures among older adults [1,2]. Hip fracture occurs when impact forces exceed the injury threshold of bone [3], yet measuring hip impact force during laboratory falls is challenging due to safety constraints [4]. AI-based pose estimation can extract impact kinematics from video, which machine learning can use to estimate ground reaction forces [5,6]. We evaluated whether pose-estimated kinematics could predict hip impact force in older adult falls, hypothesizing that pose-based models would outperform demographic/observational features and approach IMU performance.

Methods

We analyzed 69 sideways fall trials from 11 older adults (8 male, age=62.6±3.8 years) collected using synchronized video (30 Hz), inertial measurement units (IMU), and force plates [7]. Hip impact velocity, acceleration, and knee flexion angles were extracted using OpenPose and WHAM. Four feature sets were tested: demographic + observational, pose-only, demo + obs + pose, and IMU-only. Models were trained with leave-one-participant-out cross-validation and evaluated using R^2 and mean absolute error (MAE). Prediction errors were compared with repeated-measures ANOVA (Bonferroni-corrected).

Results

The IMU-only model achieved the strongest performance (R^2=0.89; MAE=0.21±0.17 BW). Pose-only features achieved moderate accuracy (R^2=0.68; MAE=0.37±0.27 BW) and improved slightly when demographics and observational features were added (R^2=0.70; MAE=0.35±0.27 BW), outperforming demographics + observational alone (R^2=0.47; MAE=0.48±0.36 BW; p=0.02).

Discussion

This is the first study to predict hip impact forces from video-captured older adult falls. The pose-only model did not match IMU accuracy but added meaningful predictive value, improving performance over demographics and observational features. Notably, model error (MAE=0.35 BW ≈ 270 N) represents only ~4–7% of forces associated with hip fracture

risk (4050 – 6420 N) [3], supporting the potential of video-based approaches. Improving acceleration estimation remains a key target for future work.

Images (Optional)

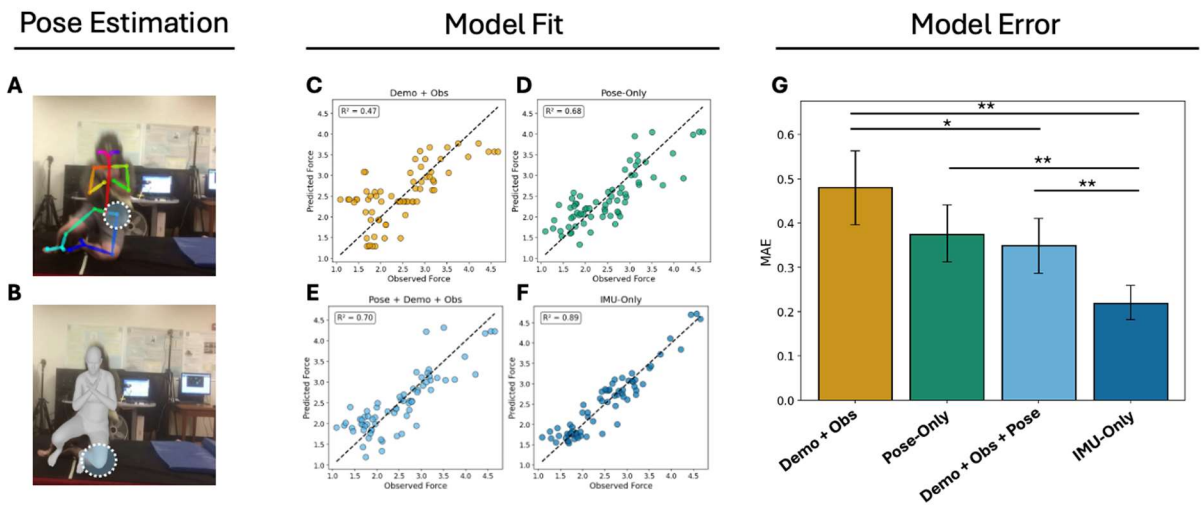


Figure 1. (A) Extraction of vertical hip impact velocity and acceleration from video-captured fall using *OpenPose* algorithm, and **(B)** of knee impact angle using *WHAM* algorithm. **(C-F)** Scatter matrix showing increased model R^2 as impact kinematics are added to the feature set. **(G)** Bar plot showing decreased mean absolute error as models are trained on impact kinematics. All force units are in body weights (BW) to reflect mass-normalization. Results of statistical analyses are denoted as *p<0.05, **p<0.01.

References (Optional)

[1] Centers for Disease Control and Prevention, 2020; [2] Parkkari et al., *Calcif. Tissue Int*, 1999; [3] Nasiri & Luo, *Osteoporos. Int.*, 2017; [4] Moon & Sosnoff, *Arch Phys Med Rehabil., 2017*; [5] Michaels et al., *Sci. Rep.,* 2025; [6] Mundt et al., *Sensors*, 2022; [7] Moon et al, *J of Biomechanics*, 2019

Session Category

Injury Biomechanics: N/A

OA6-03

Using Instrumented Mouthguards to Detect Concussions: Preliminary Findings in Men's Rugby League

Dr James Tooby[1], Dr Cameron Owen[1], Dr Dane Vishnubala[2], Mr Matthew Kitchin[1], Dr Gemma Phillips[3], Professor Kevin Till[1], Professor Ben Jones[1]

[1]Leeds Beckett University, Leeds, West Yorkshire, United Kingdom. [2]University of Leeds, Leeds, West Yorkshire, United Kingdom. [3]Rugby Football League, Manchester, Greater Manchester, United Kingdom

Introduction

The Head Injury Assessment (HIA) protocol is used in rugby league to identify and diagnose concussions. Pitchside doctors initiate the HIA process based on visible signs and symptoms of potential concussion. Instrumented mouthguards (iMGs) record head kinematics during head acceleration events (HAEs), providing objective data that may enhance this process. This study aims to evaluate how well iMG severity measures distinguish HAEs that resulted in HIAs, and further, between HIAs that led to concussion diagnoses.

Methods

A prospective observational study was conducted during the Men's Super League 2025 season, with 73.7% (n=278) of players wearing validated iMGs capturing head kinematics. HAEs linked to each HIA were identified through video analysis by a trained analyst and medical doctor. Among 199 HIAs recorded, iMG data for peak linear acceleration (PLA) and peak angular acceleration (PAA) were available for 47.7% (n=95), with 36 diagnosed concussions. HAEs not resulting in HIAs were selected from the same players and matches (n=2,644). ROC curve analysis assessed PLA and PAA diagnostic performance.

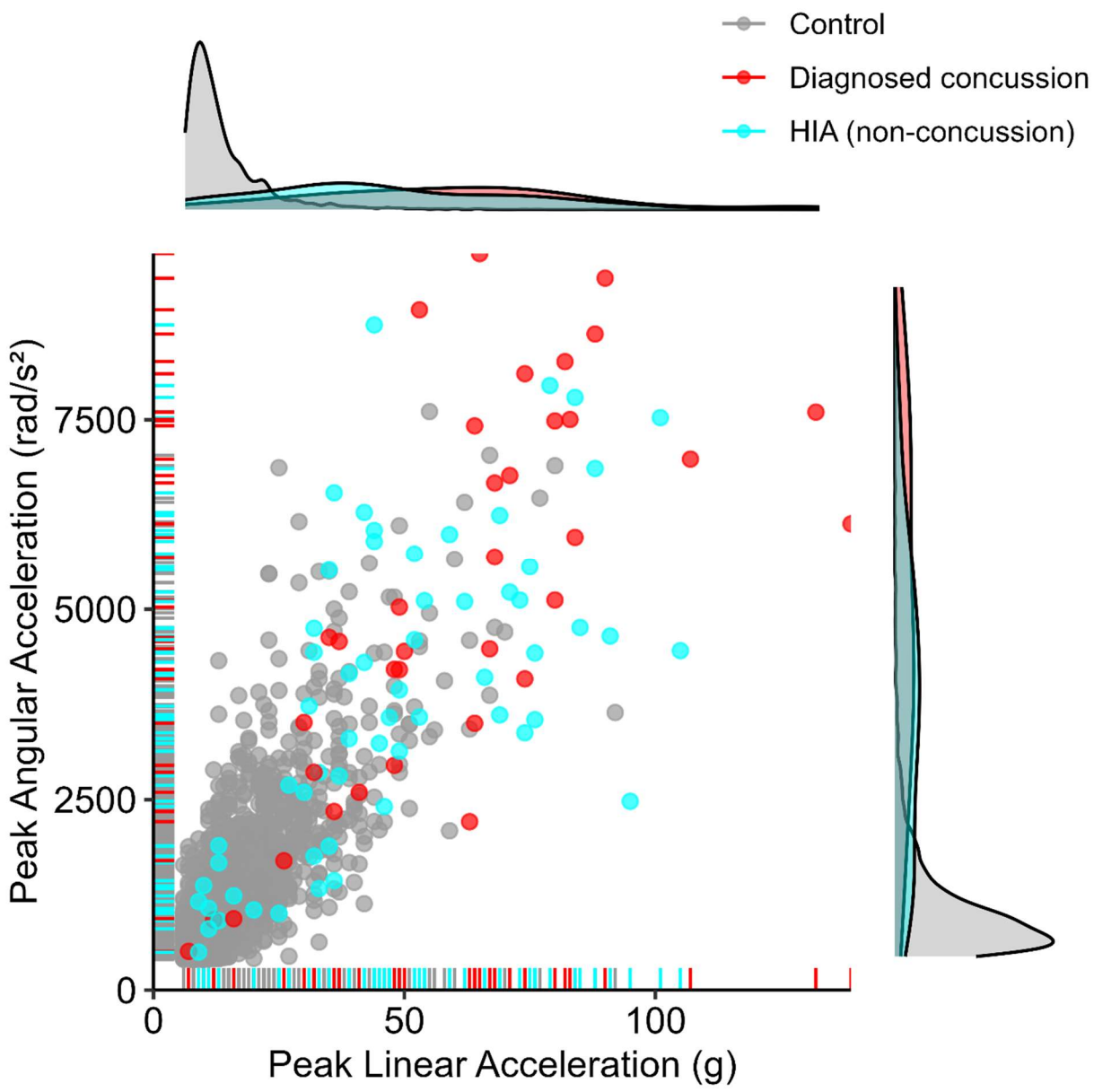
Results

Median (interquartile range [IQR]) PLA and PAA for HAEs resulting in HIA were 49*g* (33-74) and 4,301rad/s^2 (2,596-5,981) compared to 11*g* (9-16) and 885rad/s^2 (630-1,315) for HAEs not associated with HIAs. Among HAEs resulting in HIA, those with diagnosed concussion had PLA and PAA values of 64*g* (39-80) and 4,828rad/s^2 (3,226-7,452), respectively, versus 44*g* (32–69) and 3,728rad/s^2 (2,024-5,199) in non-concussion HIAs. ROC analysis showed excellent accuracy of PLA (AUC: 0.92) and PAA (AUC: 0.92) for distinguishing HAEs leading to HIAs, but poor accuracy (AUC < 0.7) for discriminating concussion diagnosis.

Discussion

Preliminary results suggest iMG-derived PLA and PAA are promising for identifying HAEs warranting medical review; however, concussion diagnosis thresholds based solely on these measures remain elusive. Some HIAs and diagnosed concussions are associated with low-magnitude HAEs (see Figure 1), indicating that detection and diagnosis should not rely exclusively on iMG data. Current analyses focus on 199 HIAs from the Men's Super League 2025 season, with ongoing work incorporating over 300 additional HIAs from other seasons and competitions, including women's leagues. Future analyses will include expanded severity metrics such as brain strain modeling.

Images (Optional)



Session Category

Injury Biomechanics: N/A

OA6-04

Spatial and Positional Patterns of Video-Verified Head Impacts in Men's Collegiate Ice Hockey

Dr. Rebecca Kenny, Mr. Arman Mehrrostami, Dr. Adam Clansey, Mr. Daniel Bondi, Mr. Zaryan Masood, Mr. David Luke, Dr. Lyndia Wu

University of British Columbia, Vancouver, BC, Canada

Introduction

Head impacts in ice hockey contribute to acute concussion risk and cumulative neurological load. Instrumented mouthguards (iMGs) can quantify head kinematics but require video verification to distinguish true impacts from artifacts. This study combined iMG data with synchronized multi-angle video to characterize verified head-impact exposure across two seasons of collegiate men's ice hockey, with emphasis on positional, spatial, and head-location patterns.

Methods

Head impacts were recorded using Prevent Biometrics iMGs. All device-triggered events underwent synchronized multi-angle video review, and only well-coupled impacts—where teeth remained stably seated in the mouthguard—were included to ensure skull-coupled kinematic accuracy. Verified impacts were annotated with player identity, rink zone, and head-impact location. Peak linear acceleration (PLA), angular velocity (PAV), and angular acceleration (PAA) were summarized. Linear mixed-effects models evaluated whether impact severity differed by head-impact location, rink zone, or position.

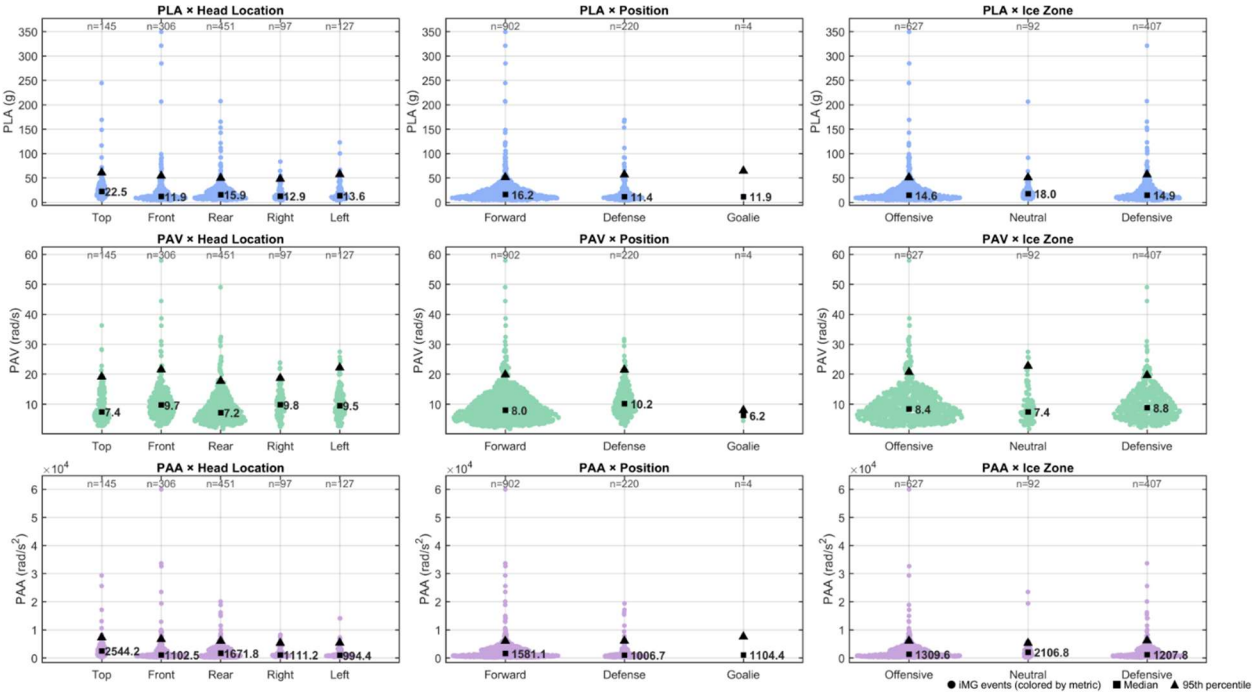
Results

Across 28 athletes and 339 athlete-games, 1,126 well-coupled impacts were analyzed. Median (95th percentile) magnitudes were PLA 15.1 g (52.1 g), PAA 1,311 rad/s^2 (6,070 rad/s^2), and PAV 8.5 rad/s (20.5 rad/s). Impacts occurred primarily in the offensive zone (55.7%), followed by the defensive zone (36.1%) and neutral zone (8.2%). Forwards sustained most impacts (n=902), followed by defence (n=220) and goalies (n=4). Head-location analysis showed clear differences in rotational velocity: right-side (9.8 rad/s), front (9.7 rad/s), and left-side (9.5 rad/s) impacts produced the highest PAV, while top (7.4 rad/s) and rear (7.2 rad/s) impacts were lower. Mixed-effects models found no significant effects of rink zone ($p=0.84$) or position ($p=0.72$), but head-impact location was significantly associated with PAV ($p=0.0018$).

Discussion

This video-verified, well-coupled dataset provides a high-confidence profile of head-impact exposure in collegiate hockey. Lateral and frontal impacts generated the greatest rotational loads, emphasizing the importance of collision direction in impact mitigation. Despite differences in exposure frequency, impact severity remained consistent across rink zones and positions, suggesting that collision mechanics, rather than gameplay role, determine magnitude. Integrating multi-angle video with iMG data strengthens exposure modelling and supports targeted, evidence-based prevention strategies.

Images (Optional)



Session Category

Injury Biomechanics: N/A

OA6-05

Predicting Biomarker-Defined Brain Injury From Instrumented Mouthguard Head Kinematics and Finite Element Brain Strain in Sport-Related Head Impacts

Mr James Hickey[1], Ms Emily Chan[2], Ms Lauren Evans[1], Dr William O'Brien[1], Ms Becca Xie[1], Dr Spencer Roberts[3], Dr Sarah Butler[1], Mr Joel Ernst[4], Mr William Zhou[5], Dr Karl Zimmerman[2], Dr Gershon Spitz[1], Dr Thomas Parker[2], Professor Terence O'Brien[1], Professor Sandy Shultz[1,6], Professor David Sharp[2], A/Prof Mazdak Ghajari[2], A/Prof Stuart McDonald[1]

[1]Monash University, Melbourne, Victoria, Australia. [2]Imperial College, London, South Kensington, United Kingdom. [3]Deakin University, Geelong, Victoria, Australia. [4]University of Melbourne, Melbourne, Victoria, Australia. [5]Old Trinity Grammarians' Football Club, Melbourne, Victoria, Australia. [6]Vancouver Island University, Nanaimo, British Columbia, Canada

Introduction

Identifying head impacts that carry a risk of brain injury in sport remains challenging. Instrumented mouthguards have emerged as a tool to quantify head kinematics and potentially help identify high-risk impacts. Processing this kinematic data using finite element models provides a means of estimating brain tissue strain, potentially offering a more accurate prediction of injury than kinematics alone. However, studies to date have attempted to validate these biomechanical measures against subjective, binary clinical diagnoses rather than objective, biologically grounded markers of brain injury, such as blood-based biomarkers.

Methods

The analysis included 41 video-verified impacts from male amateur Australian football players: 17 resulting in concussion, five assessed but cleared, and 19 not requiring assessment. Instrumented mouthguards recorded peak linear acceleration, peak rotational acceleration, and peak rotational velocity; brain strain was estimated using the Imperial College finite element brain model; and Simoa quantified plasma concentrations of the astroglial injury biomarker glial fibrillary acidic protein (GFAP). Relationships were examined using Spearman correlations and regression.

Results

In the overall sample, plasma GFAP levels were moderately correlated with peak linear acceleration (ρ=0.46, 95% CI:0.20–0.66), peak rotational velocity (ρ=0.53, CI:0.20–0.78),

and brain strain (ρ=0.60, CI:0.32–0.80). These associations were stronger in the concussion subgroup for brain strain (ρ=0.86, CI: 0.58–0.97) and peak rotational velocity (ρ=0.64, CI:0.15–0.93). Comparing the strength of correlations with GFAP, brain strain was stronger than peak linear acceleration (Z=3.10, *P*=0.002), peak rotational acceleration (Z=3.68, *P*=2.35e-04) and peak rotational velocity (Z= 2.30, *P*=0.02) within concussion cases; it was also stronger than peak rotational acceleration for impacts overall (Z=2.60, *P*=0.009). Preliminary piecewise regression analysis identified significant breakpoints for peak rotational velocity and brain strain, above which associations with GFAP strengthened. In concussion cases, exceeding the strain breakpoint was associated with greater symptom severity.

Discussion

Finite element brain strain may better predict brain injury risk following a sport-related impact than peak acceleration metrics. Stronger associations with plasma GFAP, particularly among concussion cases, and evidence of a threshold in the association, support the use of biomarker-informed strain measures in future risk modelling and the development of brain injury screening thresholds.

Session Category

Injury Biomechanics: N/A

OA7-02

Indentation-Based Identifiability of Anisotropic Soft Tissue Material Parameters

Mr. Amit Ashkenazi, Dr. Dana Solav

Technion - Israel Institute of Technology, Haifa, Haifa, Israel

Introduction

Reliable in vivo characterization of anisotropic soft tissues is critical for patient-specific biomechanical modeling. While indentation is a preferred non-invasive testing method, deriving material parameters from force-depth data alone often creates an ill-posed inverse problem, leading to multiple parameter sets fitting the same experimental curve equally well [1]. This study investigates the added contribution of integrating full-field surface deformation measurements with standard force data, and quantifies its ability constrain the solution space and lead to reliable identification of transversely isotropic hyperelastic parameters.

Methods

We utilized a synthetic fiber-reinforced silicone phantom to validate a multimodal indentation framework. Macro-indentation experiments were conducted using spherical indenters, simultaneously recording reaction forces and 3D surface displacement fields via three-dimensional Digital Image Correlation (3D-DIC). Material behavior was described by a transversely isotropic Neo-Hookean model with isotropic (c_1) and anisotropic fiber-direction (c_5) parameters. An inverse finite element analysis (iFEA) pipeline optimized these parameters by minimizing a weighted objective function of force and displacement errors. A comprehensive sensitivity analysis quantified parameter certainty bounds [2], to determine the optimal contribution of each measurement type for maximizing identifiability [3].

Results

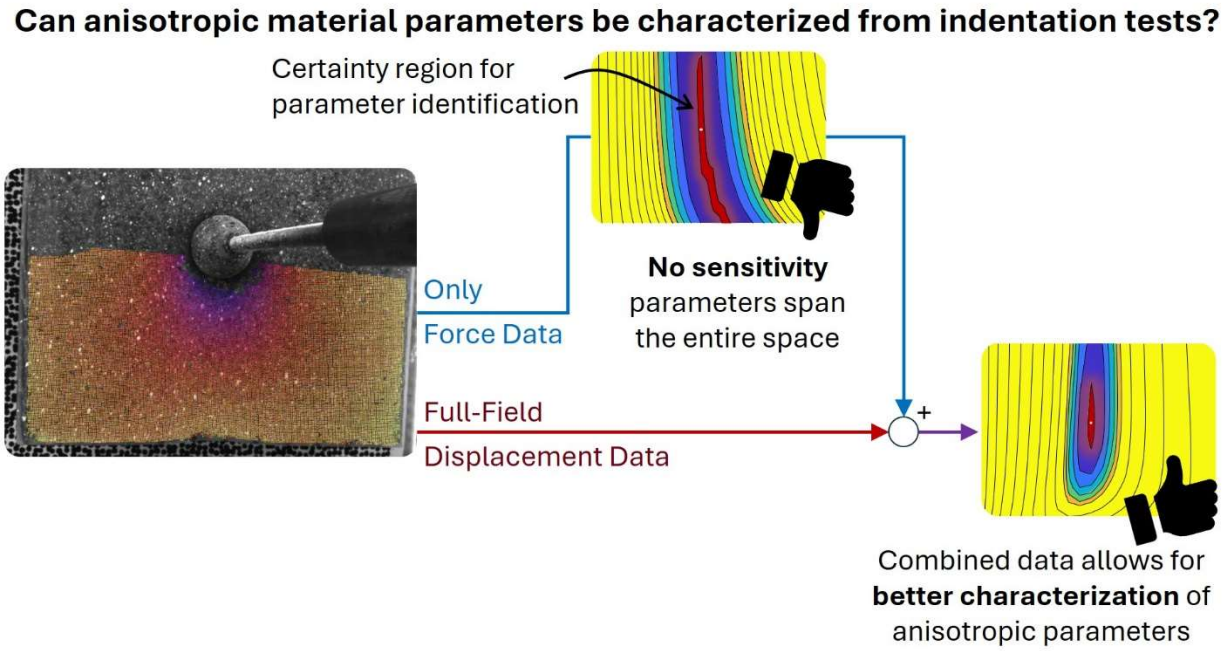
The sensitivity analysis demonstrated that using force data alone yielded poor identifiability, with uncertainty bounds of ±22.5% for c_1 and a massive ±210% for c_5 given a 5% measurement error. However, integrating 3D-DIC data significantly constrained the

solution space, reducing uncertainty to ±5.2% and ±28%, respectively. Experimental application of the optimized multi-modal objective function successfully identified homogenized parameters that matched validation benchmarks [3].

Discussion

The drastic reduction in uncertainty confirms that force-depth curves alone are insufficient for characterizing anisotropy, as they fail to capture directional stiffness contributions. By measuring surface deformations the optimization algorithm can decouple isotropic and fiber responses. These results confirm that surface deformation tracking is essential for reliable indentation-based anisotropic tissue characterization.

Images (Optional)



References (Optional)

1. Zohar Oddes, Dana Solav. *JMBBM,* 2023.
2. Amit Ashkenazi, Dana Solav. *IJES*, 2025.
3. Amit Ashkenazi, et al. *JMPS,* 2026.

Acknowledgements (Optional)

The study was partially funded by the Israel Science Foundation and the Irwin and Joan Jacobs Fellowship.

Session Category

Organ and Tissue Biomechanics: N/A

OA7-03

Full-Field Indentation Microscopy: Inferring Tissue Microstructure From a Single Poke

Mr. Yuvam Kulkarni M.S., Prof. Callan Luetkemeyer Ph.D.

University of Illinois Urbana-Champaign, Urbana, IL, United States

Introduction

Indentation testing is non-destructive, local, and well-suited to layered, spatially heterogeneous soft tissues. Yet traditional approaches rely on unimodal force-displacement curves, which make it challenging to determine nonlinear, anisotropic properties tied to microstructure (e.g., collagen fiber architecture). Thus, we introduce **full-field indentation microscopy (FIM)**: a confocal-imaging-enabled, inverse modeling framework that leverages 3D displacement fields from a *single* spherical indent to estimate microstructure-informed constitutive parameters. Our long-term goal is to employ FIM to develop **mechano-biomarkers**: tissue- and pathology-specific, microstructurally interpretable parameters that can be non-invasively inferred via mechanical imaging.

Methods

FIM uses the weight of a glass microsphere to deform soft tissue samples and acquires 3D confocal images before/after indentation. Full-field displacement maps are computed and fed into a virtual fields method (VFM)-based inverse solver to identify anisotropic and nonlinear elastic parameters (Fig. 1A). We establish the inverse framework for linearly elastic, transversely isotropic materials and then evaluate: (1) virtual-field (VF) selection for accurate anisotropic moduli recovery, (2) extension to hyperelastic constitutive models (Neo-Hookean and Holzapfel-Gasser-Ogden), and sensitivity to (3) reduced experimental field-of-view (FOV) and (4) measurement noise. Synthetic displacement fields, generated via finite element simulations of brain tissue indented with a 1 mm sphere, were used.

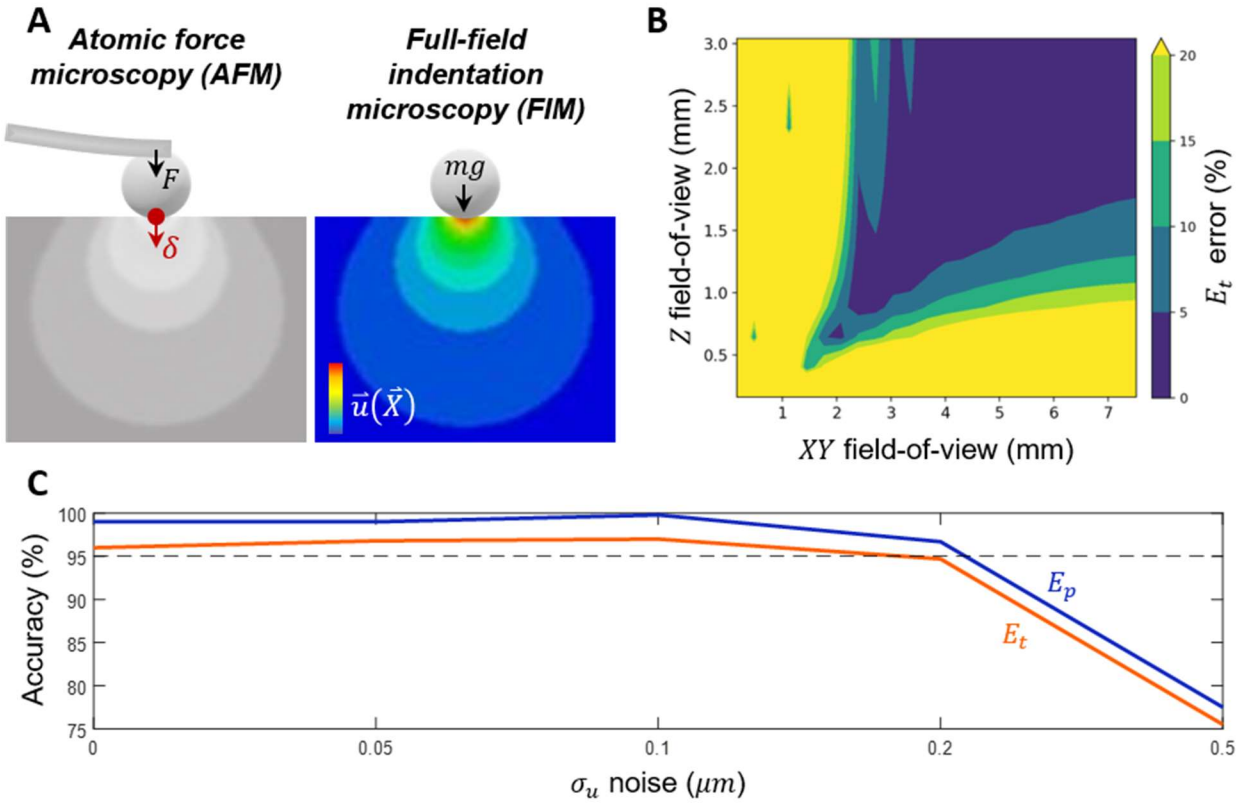
Results

All tested VFs produced cost-function minima near the ground-truth moduli, and VF combinations yielded unique minima with <5% error. The best VF pair was used to assess hyperelastic models, where FIM recovered most nonlinear parameters (including bulk modulus) with ≥98% accuracy for both Neo-Hookean and HGO forms. Reducing the FOV increased error, but even with a 50% FOV reduction in both depth and lateral directions, FIM identified transversely isotropic elastic moduli with <5% error (Fig. 1B). Similarly, FIM was robust to moderate levels of synthetic measurement noise (Fig. 1C).

Discussion

FIM enables microstructure-informed constitutive characterization with a single indentation test, which is especially valuable in layered tissues (e.g., the uterus) where local properties matter. By converting full-field indentation data into parameters with microstructural meaning, FIM offers a pipeline toward in-situ development and validation of mechano-biomarkers. Ongoing work includes experimental validation and open-source software release.

Images (Optional)



Session Category

Organ and Tissue Biomechanics: N/A

OA7-04

Characterization of Human Breast Skin Mechanics for Improved Tissue Expansion in Breast Reconstruction Surgery

Ir. Nicole Ritter, MSc. Gerben Michiels, Prof. Patrick Segers, Prof. Phillip Blondeel

Ghent University, 9000, Ghent, Belgium

Introduction

Tissue expansion remains central to breast reconstruction, yet quantitative data describing the mechanical behavior of human breast skin are limited. Current expansion protocols used in clinics therefore rely on empirical practice rather than biomechanical evidence, restricting the optimization and safety assessment of emerging technologies. This study aims to characterize interpatient variability in breast skin stiffness and evaluate the influence of sample orientation on Young's modulus using combined suction, tensile, histological and patient data.

Methods

In this ongoing six-month study, breast skin is harvested from patients undergoing reduction mammoplasty, mastectomy, or mastopexy at Ghent University Hospital. Immediately following excision, suction testing is performed using a cutometer. After removal of hypodermal and glandular tissue, three punch biopsies per tissue flap are collected for histological analysis. Slides in all planes are stained with Verhoeff–Van Gieson to quantify collagen and elastin content and assess collagen fiber orientation. Remaining skin is sectioned into rectangular (2 × 6 cm) specimens oriented parallel or perpendicular to the longitudinal axis and square (1 × 1 cm) samples aligned with both axes. Rectangular specimens undergo uniaxial tensile testing (four cycles at 15% strain and four at 30%, strain rate 1 s^{-1}). Square specimens are snap-frozen at –80 °C for subsequent biaxial testing under matched strain conditions. Digital image correlation is applied to all tests to generate full-field strain maps. Patient characteristics, including age, weight, and cup size, will be integrated into a regression model to predict stiffness. The study on residual human tissues was approved by the medical ethics committee of the hospital.

Results

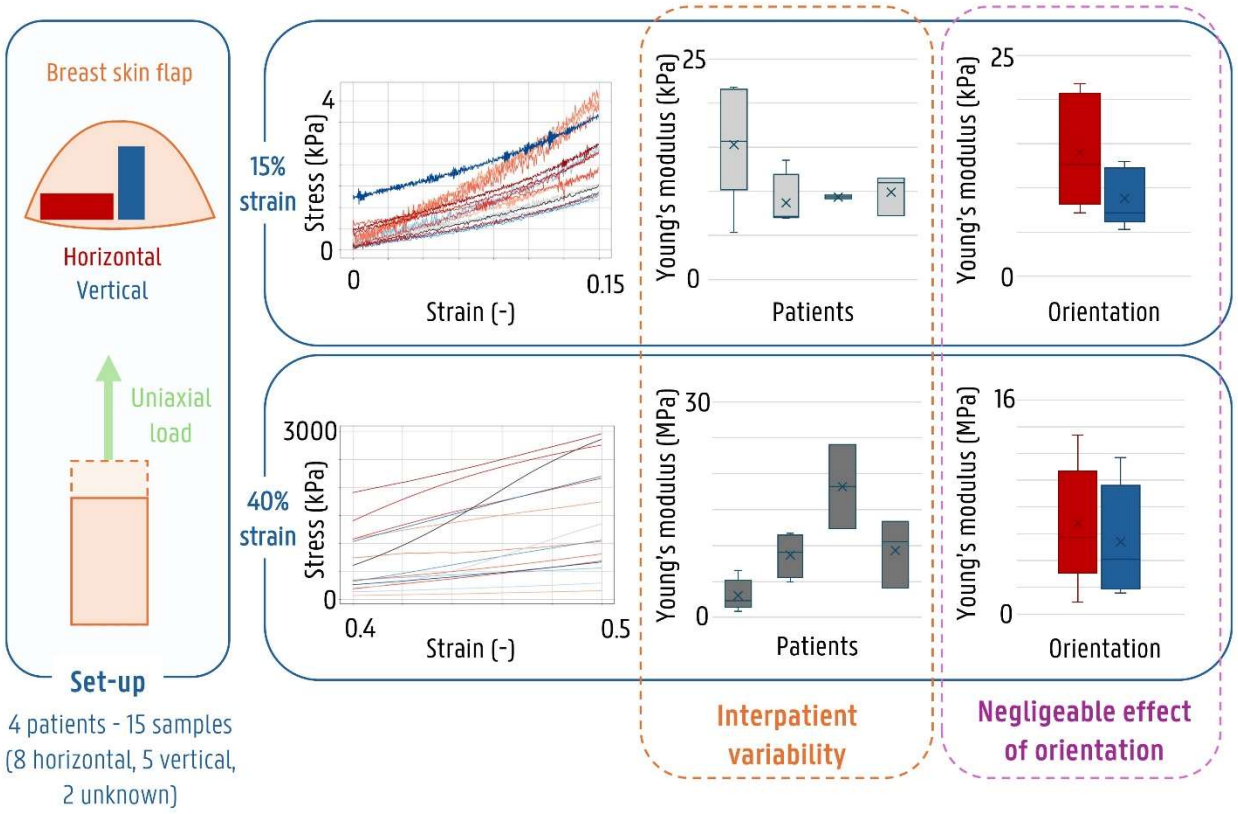
Preliminary data (Fig. 1) from 15 samples across four patients show substantial interpatient variation in Young's modulus at high strain (3–18 MPa; mean 10 ± 6 MPa) and no significant effect of specimen orientation under uniaxial loading. Ongoing collection from up to 30

patients will yield a comprehensive dataset linking ex vivo suction response, ex vivo tensile behavior, and microstructural composition.

Discussion

Improved understanding of patient-specific breast skin mechanics and predictive modeling of stiffness will support safer, individualized tissue-expansion strategies and the development of next-generation expanders that better replicate native tissue behavior.

Images (Optional)



Session Category

Organ and Tissue Biomechanics: N/A

OA8-02

Anterior Cruciate Ligament Elongation During High and Low Impact Movements Using Biplanar Videoradiography

Ms Anastasija Mihic[1], Dr. Allison Clouthier PhD[2], Dr. Michael Rainbow PhD[1]

[1]Queen's University, Kingston, Ontario, Canada. [2]University of Ottawa, Ottawa, Ontario, Canada

Introduction

1 in 3,500 people experience an anterior cruciate ligament (ACL) tear, leading to short-term disability and increasing lifetime risk of knee osteoarthritis eight-fold [1,2]. Nearly 70% of ACL injuries occur during non-contact tasks, highlighting the need to better understand knee mechanics during everyday and sport-specific movements [3]. Direct measurement of ACL strain is rarely feasible; therefore, relative elongation is commonly used as a proxy. Biplanar videoradiography (BVR) provides highly accurate arthrokinematic measurements, enabling in-vivo assessment of ligament loading during motion. This study compared ACL elongation during low-impact (lunge) and high-impact (single-leg hop) tasks. We predicted the high-impact task would produce higher elongation at the same knee flexion angle.

Methods

Five healthy participants performed a forward lunge and single-leg hop. A BVR system recorded motion. CT scans were segmented, generating bone models for tracking the femur and tibia. ACL attachment regions for the anteromedial (AMB) and posterolateral (PLB) were defined [4]. Bundle length was measured as the centroid-to-centroid distance between tibial and femoral attachments, with the maximum length across trials used as the reference for elongation.

Results

All participants exhibited greater elongation during the hop (Figure 1). The AMB showed higher elongation than the PLB. Mean hop elongation was 0.9 (AMB) and 0.9 (PLB), compared with 0.8 (AMB) and 0.7 (PLB) during the lunge. During hop trials, both bundles reached maximum elongation at max extension.

Discussion

Consistent with literature, at similar flexion angles, high-impact movements produced greater ACL elongation [5]. The magnitude of the difference varied across participants, suggesting individual kinematic strategies influence ACL loading. Because flexion alone did not account for these differences, other arthrokinematic factors such as tibial rotation,

ab/adduction, or anterior–posterior translation may contribute. These differences may reflect task-dependent neuromuscular strategies, such as increased co-activation during landing, which could alter ligament loading. These findings underscore that ACL elongation is affected by task intensity and participant-specific movement patterns. Understanding these factors may contribute to improved injury-prevention and personalized training.

Images (Optional)

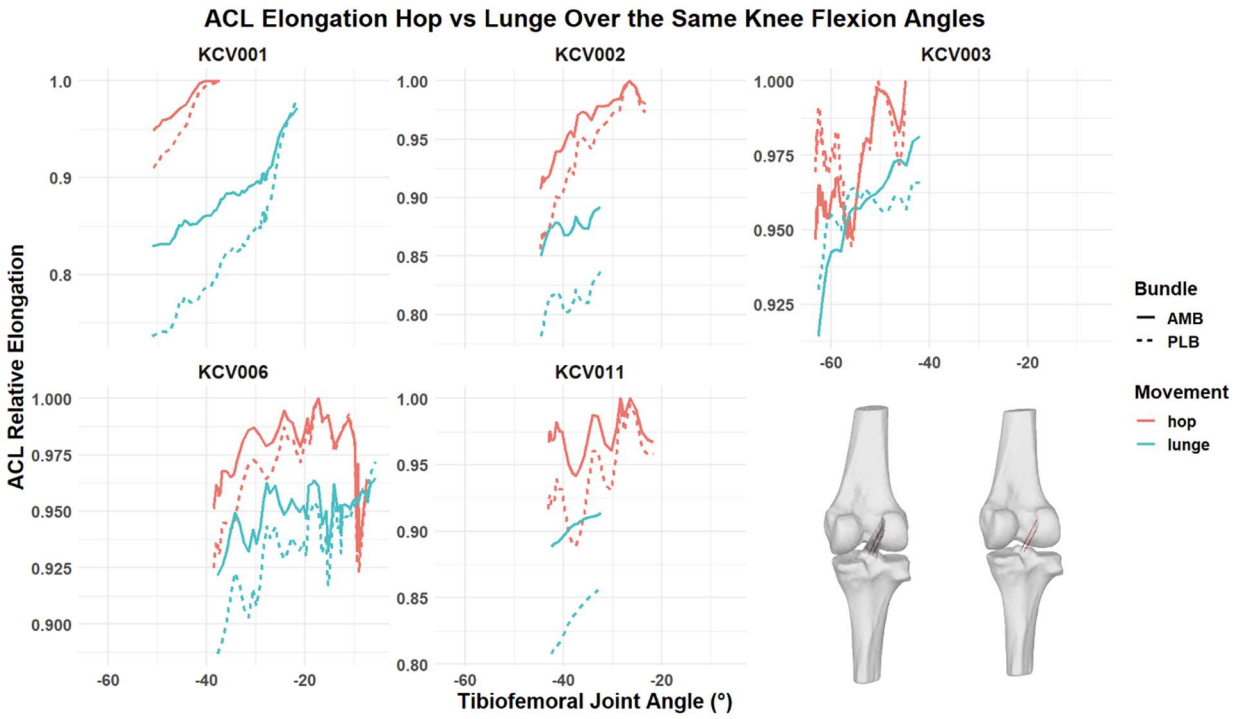


Figure 1 ACL elongation of the anteromedial bundle (AMB; solid lines) and posterolateral bundle (PLB; dashed lines) during the low-impact lunge (blue) and high-impact hop (pink) tasks, plotted over the same knee flexion angles.

References (Optional)

[1] Webster, *Clin J Sport Med* (2022)

[2] Evans, *StatPearls* (2025)

[3] McNair, *N Z Med J* (1990)

[4] Ziegler, *Am J Sports Med* (2011)

[5] Nagai, *J Orthop Res* (2019)

Session Category

Musculoskeletal Biomechanics: Joints and Motion

OA8-03

A Novel Method of Quantifying Changes in Tibiofemoral Joint Stiffness after Ligament Injury via Eigendecomposition Using In Vitro Robotic Testing

Mr. David Shamritsky MEng, Dr. Reza Pourmodheji PhD, Dr. Brian Frondorf MD, Ms. Erin Berube MS, Mr. Philipp Pape, Ms. Lexie Bae, Mr. Bryce Demopoulos, Dr. Carl Imhauser PhD

Hospital for Special Surgery, New York, NY, United States

Introduction

The effect of anterior cruciate ligament (ACL) or medial collateral ligament (MCL) tears on knee stiffness has been primarily assessed via the knee's in vitro uniplanar load-displacement response. We describe a novel, complementary, method that uses eigendecomposition to quantify tibiofemoral stiffness in all three anatomic planes. Using this method, our objective was to measure changes in tibiofemoral stiffness after ACL and MCL sectioning in response to anterior and valgus loads.

Methods

Twelve cadaveric right knees (7 females; mean age: 50, range: 25-65 years) were mounted to a robotic manipulator equipped with a six-axis force-torque sensor. First, equilibrium poses were determined at 15° of flexion under 8 Nm valgus moment and at 30° of flexion under 100 N anterior force. Second, the tibia was translated and rotated by 0.3 mm and 0.3°, respectively, in each anatomic direction other than flexion/extension. Third, during each perturbation, changes in the reaction forces and moments in all directions were recorded to construct the linearized stiffness matrix. Finally, the eigenvalues of each stiffness matrix were calculated. After testing the intact state, the ACL and MCL were sectioned in two cohorts of six knees each, respectively. Steps 2-4 were then repeated at the same equilibrium poses. A system is stable if and only if all eigenvalues of the stiffness matrix are real and positive; thus, the minimum real eigenvalue was used to test our hypothesis. The difference in minimum eigenvalue between the intact and sectioned states was assessed via paired t-tests ($\alpha=0.05$).

Results

After ACL sectioning, the minimum eigenvalue decreased by a median of 11.8 ($p=0.003$) and 7.8 ($p=0.01$) under anterior force and valgus moment, respectively. After MCL sectioning, the minimum eigenvalue decreased by a median of 4.5 ($p<0.001$) and 3.6 ($p=0.02$) under anterior force and valgus moment, respectively.

Discussion

We introduce a novel method to quantify decreases in joint stiffness following ACL and MCL sectioning. Measuring changes in eigenvalues after injury may complement laxity assessments by quantifying stiffness changes simultaneously in all planes. The eigenvectors corresponding to each state's minimum eigenvalue will describe the joint's least stiff direction, which provides novel opportunity to characterize the impact of injury.

Images (Optional)

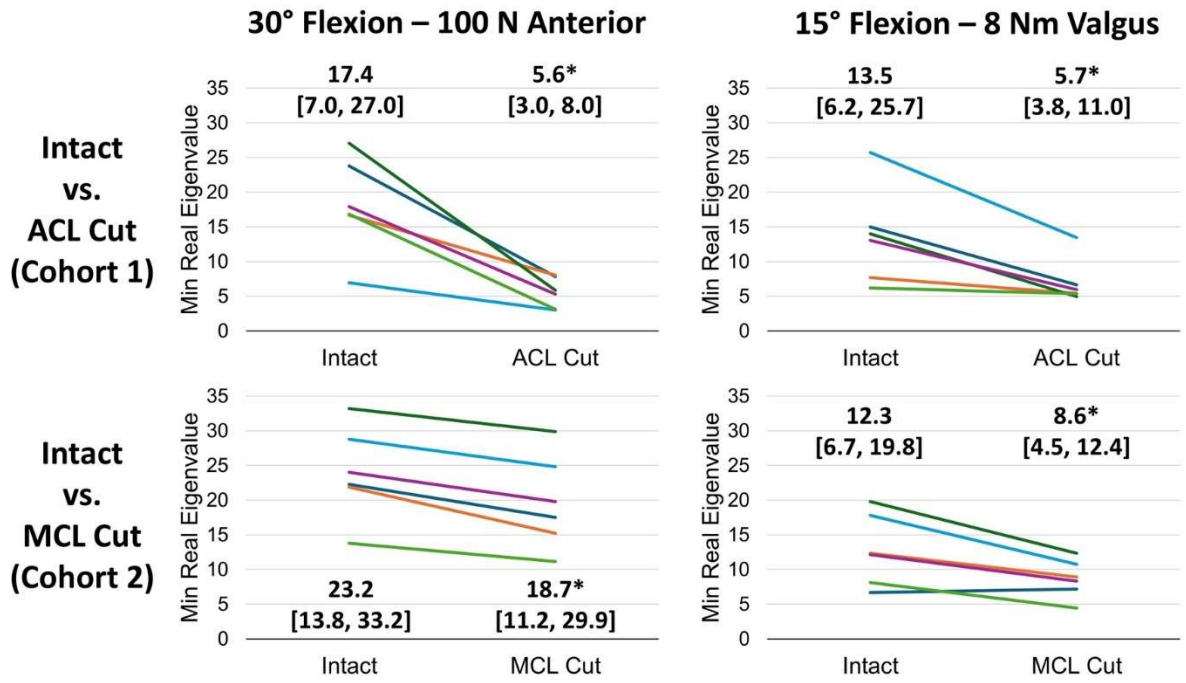


Figure 1. The minimum real eigenvalue of the linearized stiffness matrix for 12 cadaveric knees split into two cohorts. The intact and ACL- (top row) and MCL-cut (bottom row) states were tested under two loading conditions: 100 N anterior force at 30° of flexion (left column), 8 Nm valgus moment at 15° of flexion (right column). Median and range are reported for each condition and state, * indicates $p<0.05$ for the cut state relative to the intact state.

Session Category

Musculoskeletal Biomechanics: Joints and Motion

OA8-04

The Knee You Model is the Knee You Measure: How the Knee Model Degrees of Freedom and Range of Motion Alter the Knee Abduction Moment during Change-of-Direction

M.Sc. Marius Kindermann[1], M.Sc. Lasse Mausehund[2], Dr. Tron Krosshaug[2], Dr. Maurice Mohr[3]

[1]Department of Electrical Engineering, FAU Erlangen-Nürnberg, Erlangen, Bavaria, Germany. [2]Oslo Sports Trauma Research Center, Department of Sports Medicine, Norwegian School of Sport Science, Oslo, Oslo, Norway. [3]Department of Sport Science, University of Innsbruck, Innsbruck, Tyrol, Austria

Introduction

The peak knee abduction moment (pKAM) is a frequently investigated risk factor for non-contact injuries to the anterior cruciate ligament during landing and change-of-direction (COD) maneuvers [1]. The computation of the pKAM, however, relies on a series of analysis and modeling choices including the definition of knee joint rotational degrees of freedom (DOF) and their respective ranges of motion (ROM). The purpose of this study was to analyze the influence of modeled knee DOF and ROM on the pKAM and time to pKAM during a high-intensity 135°COD.

Methods

Twenty-two sports students completed six maximum-speed 135°CODs while their movements were captured by 3D marker-based motion capture and floor-embedded force plates. External knee moments were obtained through model scaling, inverse kinematics and inverse dynamics in OpenSim (v.4.5) and were compared between variations of a full-body biomechanical model [2]. The variations included systematic manipulation of 1) available DOFs related to knee add/abd and knee int/ext rotation and 2) ROM in knee add/abd in a 3DOF model. In a separate model variation (1D-W), secondary knee kinematics were prescribed as a function of knee flexion according to [3]. Repeated measures / Friedman ANOVAs and Spearman's rank correlations were carried out to investigate the model influence on the trial-average pKAM and time to pKAM (alpha = 0.05).

Results

A lower number of DOFs was associated with lower pKAMs ($p<0.001$) and lower time to pKAM ($p<0.001$) (Figure 1). Similarly, a lower ROM in knee add/abd was associated with

lower pKAMs (p<0.001) and lower time to pKAM (p=0.005), however, only below +/-10°. Rank correlations of above 0.8 indicated strong rank consistency among knee models.

Discussion

The magnitude of pKAM and time to pKAM should only be compared across studies if the underlying knee models are equivalent in their available DOFs and ROMs. However, the ranking of athletes according to the pKAM and time to pKAM seems largely unaffected by the modeling choice regarding DOFs and ROMs.

Images (Optional)

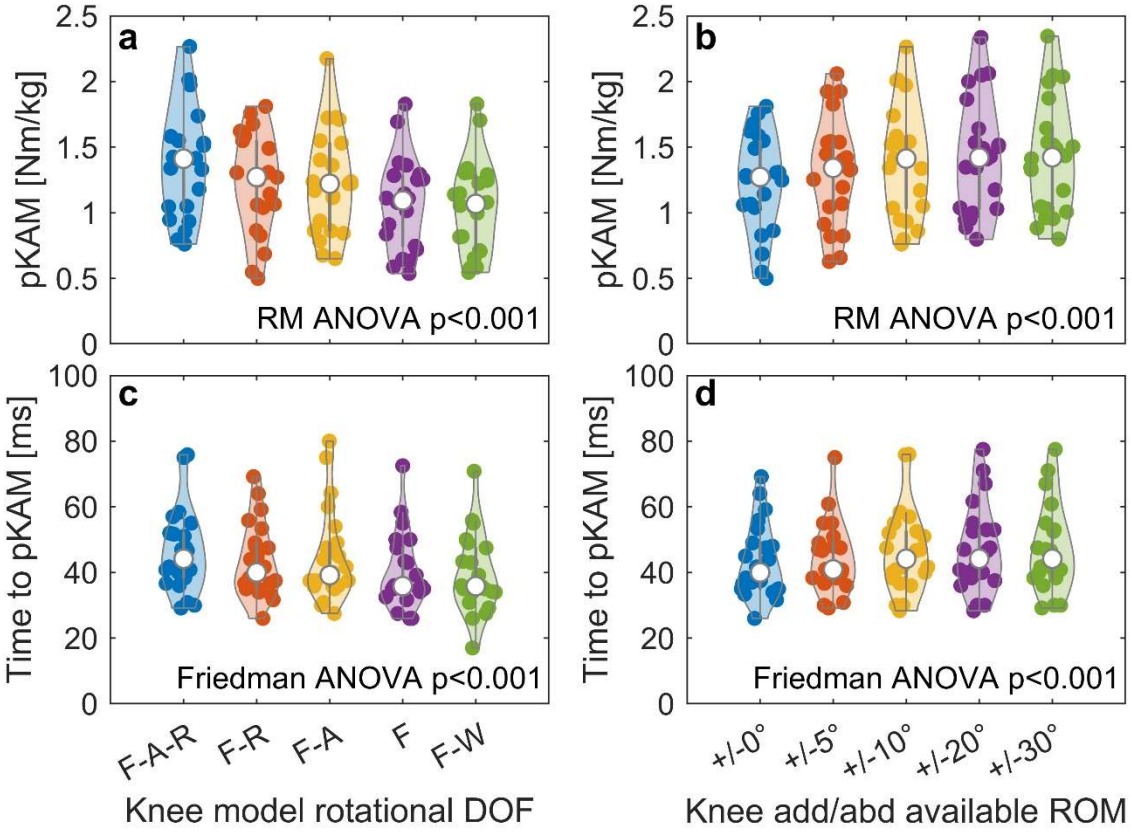


Figure 1. Peak knee abduction moment (pKAM, a&b) and time to pKAM (c&d) during a 135° change-of-direction maneuver for different knee model rotational degrees of freedom (DOFs) and available range of motion (ROM). F-Flexion, A-Add/Abd, R-Rotation, W-Walker

References (Optional)

[1] Besier et al. (2001). *MSSE*. 33(7).

[2] Catelli et al. (2019). *Comput. Methods Biomech. Biomed. Engin.* 22(1).

[3] Walker et al. (1988). *J Biomech*. 21(11).

Acknowledgements (Optional)

This research was funded in whole or in part by the Austrian Science Fund (FWF) [10.55776/I6547].

Session Category

Musculoskeletal Biomechanics: Joints and Motion

OA8-05

Impact of Neurocognitive Reaction Time on the Performance of an Unanticipated Sidestep Cut

Mr Cole Geschwender MS[1,2], Dr Henry Wang PhD[2], Dr Jason Avedesian PhD[3], Dr Clark Dickin PhD[2]

[1]University of Michigan, Ann Arbor, Michigan, United States. [2]Ball State University, Muncie, Indiana, United States. [3]Cleveland Cavaliers, Independence, Ohio, United States

Introduction

An unanticipated sidestep cut is a game-realistic movement commonly performed in cutting sports and is recognized as a key movement associated with non-contact anterior cruciate ligament (ACL) injuries. Neurocognitive reaction time (NCRT) measures the speed an individual responds to an external stimulus and may influence the biomechanics of an unanticipated sidestep cut, but has not been previously investigated. The purpose of this study is to elucidate how NCRT influences unanticipated sidestep cutting in performance and injury prevention.

Methods

Twenty-one right foot dominant healthy subjects (n=11 male) completed a computerized NCRT assessment (Go/No-Go, Simple RT, N-Back, and Stroop) which provided composite RT scores for both dominant and nondominant sides. NCRT was centered across the sample variation. Joint mechanics of the hip, knee, ankle, and trunk were assessed during five unanticipated sidestep cut trials to the left and right. A linear mixed model was used with NCRT, limb dominance, and sex as fixed effects.

Results

Motion capture and force plate technology was used to assess the outcome measures. When adjusting for limb dominance and sex, quicker NCRT response times were associated with less lateral trunk lean (β=0.006, SE=0.002, p =.002), faster approach speed (β=-2.75x10^{-4}, SE=1.05 x10^{-4}, p = .0128), and greater peak hip flexion moment (β=0.001, SE=1.66 x10^{-4}, p < .001). NCRT did not account for any significant differences in knee or ankle mechanics (p>.05).

Discussion

Participants with quicker NCRT scores demonstrated a more upright trunk position during unanticipated sidestep cuts, a position associated with reduced ACL loading. Additionally, NCRT performance was associated with greater hip flexion moments that are indicative of

more explosive and safer unanticipated sidestep cuts. Quicker NCRT scores also had faster approach speeds, suggesting an enhanced ability to quickly position the body during sudden changes of direction. Conversely, individuals with slower NCRT scores had a slower approach speed, potentially indicating that more time was required to perform biomechanically safe cuts, though no joint differences were reported at the knee or ankle. NCRT scores may influence the performance of an unanticipated sidestep cut and should be further considered as a factor for future unanticipated gross motor maneuvers.

Session Category

Musculoskeletal Biomechanics: Joints and Motion

OA9-02

Machine Learning Estimates Ground Reaction Forces with Higher Accuracy than Musculoskeletal Simulation for Anterior Cruciate Ligament Injury-Risk Screening Tasks

Ms. Janelle Kaneda MS, Dr. Julie Kolesar MS, PhD, Dr. Sam Hamner MS, PhD, Dr. Kirsten Seagers MS, PhD, Dr. Krithika Swaminathan MS, PhD, Ms. Julie Muccini MS, OTR/L, Dr. Scott Delp MS, PhD, Dr. Jennifer Hicks MS, PhD

Stanford University, Stanford, CA, United States

Introduction

Millions worldwide sustain anterior cruciate ligament (ACL) injuries, and sometimes these injuries end athletic careers. Kinetic metrics such as peak ground reaction force during drop landings have been identified as risk factors for ACL injury [1]. However, current methods to estimate forces outside of the lab are time-intensive or trained on limited motions. This work aimed to develop and test a generalizable neural network to estimate ground reaction forces during ACL injury-risk screening tasks to enable large-scale injury-risk screening.

Methods

We developed DynamicsNet, a spatiotemporal graph convolutional network that uses physics-based kinematic features to predict ground reaction forces, and trained it with 70+ hours of optical motion capture and force plate data from various activities [2]. We also used the OpenSimAD musculoskeletal simulation framework [3] to estimate ground reaction forces from measured kinematics. We evaluated both methods (DynamicsNet and simulation) on a held-out dataset of OpenCap-based kinematics [4] from adolescent female athletes performing double-leg drop jumps (58 trials, 24 participants) and single-leg squats (90 trials, 23 participants). We computed the mean absolute error of vertical ground reaction force over the region of interest for each movement, as well as at the peaks.

Results

Over the region of interest for both activities, DynamicsNet's error was lower than simulation: 0.21 ± 0.23 versus 0.33 ± 0.33 bodyweights for drop jumps, and 0.08 ± 0.06 versus 0.16 ± 0.17 bodyweights for squats (Figure 1). For peak force, DynamicsNet had about half the error of simulations for drop jumps (0.33 ± 0.24 versus 0.61 ± 0.62 bodyweights) and lower error for squats (0.12 ± 0.06 versus 0.19 ± 0.20 bodyweights).

Discussion

DynamicsNet predicted ground reaction forces with higher accuracy and less variance than physics-based simulation for both drop jumps and squats. Future work will fine-tune DynamicsNet on ACL injury-risk screening activities to ensure sufficient accuracy for detecting clinically meaningful differences in biomechanical risk factors. Our preliminary results suggest that DynamicsNet could enable rapid dynamics estimation for large-scale, effective ACL injury-risk screenings.

Images (Optional)

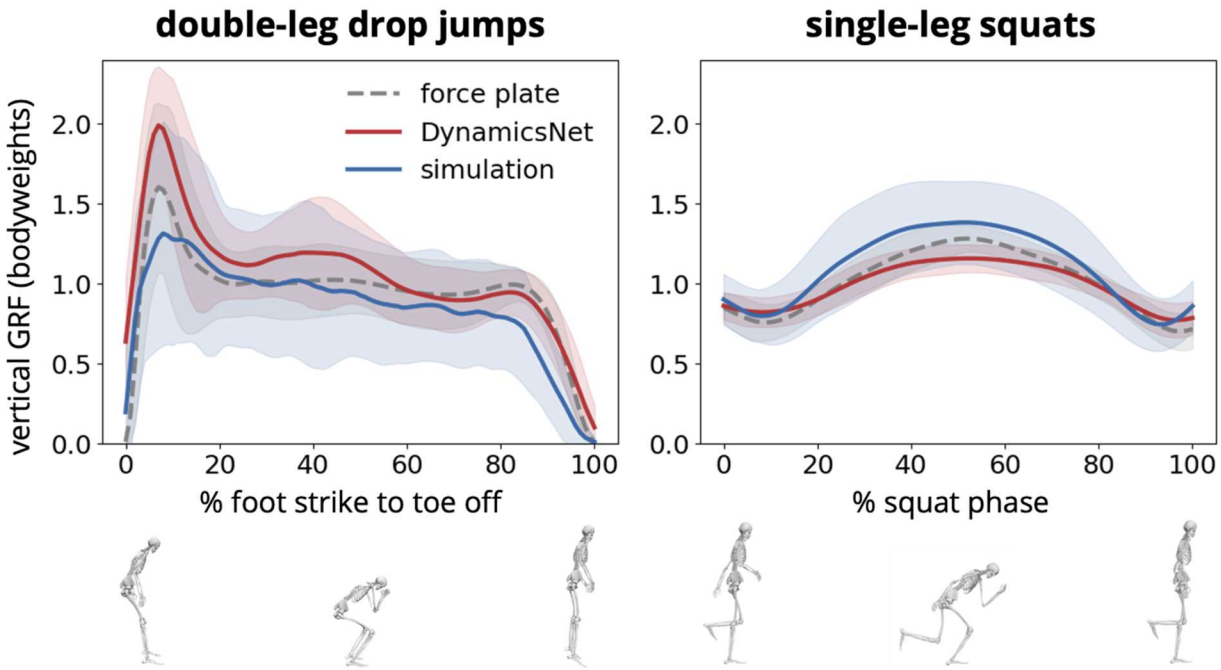


Figure 1. Mean (shaded: ± one standard deviation) vertical ground reaction force (GRF) in bodyweights for DynamicsNet model estimates (red solid line), musculoskeletal simulation estimates (blue solid line), and force plate measurements (gray dotted line) over the region of interest for each ACL injury risk screening task.

References (Optional)

[1] Hewett *et al.*, Am J Sports Med, 2005

[2] Werling *et al.*, Comput Vis ECCV, 2024

[3] Falisse *et al.*, PLoS ONE, 2019

[4] Uhlrich *et al.*, PLoS Comput Biol, 2023

Session Category

Emerging Areas: N/A

OA9-03

Neural Network Surrogates for Musculoskeletal Models: an Application to Implant Alignment in Total Knee Arthroplasty

MSc Linda ten Klooster[1,2], Dr. Ir. Periklis Tzanetis[2], Dr. Ir. Dennis Janssen[1], Dr. Ir. Thom Bitter[1], Prof. Dr. Ir. Nico Verdonschot[1,2], Dr. Jelmer Wolterink[2]

[1]Radboud University Medical Center, Nijmegen, Gelderland, Netherlands. [2]University of Twente, Enschede, Overijssel, Netherlands

Introduction

Musculoskeletal models are widely used to study human movement and simulate joint biomechanics, yet their high computational cost limits their clinical applicability. Artificial neural networks offer a promising solution as fast surrogate models for complex simulations. In this study, a neural network-based surrogate model was used to accelerate estimation of patient-specific optimal implant alignment in total knee arthroplasty (TKA), previously defined as the configuration that best replicates pre-diseased knee function [1]. Our surrogate model rapidly assesses tibiofemoral (TF) kinematics and ligament strains for candidate alignments, enabling accelerated prediction of optimal implant alignment compared to conventional simulations.

Methods

Data from eight TKA patients previously simulated with a patient-specific musculoskeletal TKA model were used [1]. This dataset contains candidate implant alignments evaluated by the root-mean-square deviation (RMSD) in TF kinematics and ligament strains relative to the pre-diseased state. The alignment with the lowest RMSD was defined as optimal. To reduce the configuration space while maintaining clinically viable positions, femoral component rotations were varied while the tibial component was fixed, yielding 125 samples per patient. For each individual patient, a multi-task multilayer perceptron (MLP) with three hidden layers, Adam optimizer, learning rate 0.005, and 80%/10%/10% train/validation/test split was trained to predict kinematics and ligament strains. A gradient-based optimization method was subsequently applied to the frozen MLP outputs to identify optimal alignments. Figure 1 illustrates the workflow.

Results

The multi-task MLP achieved a normalized mean absolute error of ~0.5% between predicted and simulated outputs when trained on the full dataset. On average, ~35

samples per patient were sufficient to keep the error below 1%. Simulation time dropped from 3h to ~50min for musculoskeletal data generation, with subsequent multi-task MLP training taking 2s and optimization less than 1s.

Discussion

Employing a multi-task MLP substantially reduces computational time while maintaining an error below 1% compared to musculoskeletal simulations. Future research will incorporate the implant translations and tibial rotations, as well as data from more patients. This approach represents a critical step toward using biomechanical modeling to determine patient-specific optimal implant alignment during TKA in a clinical setting.

Images (Optional)

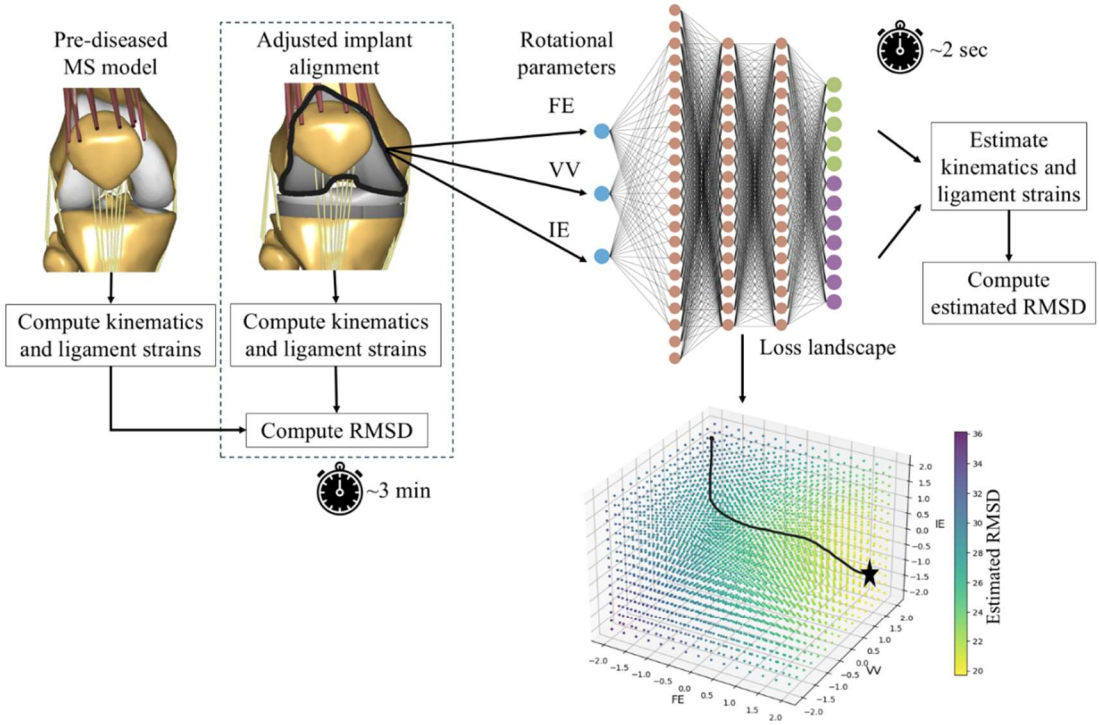


Figure 1 caption: Schematic overview of the methods as applied to one single patient. Training and validation data were obtained using an existing patient-specific musculoskeletal (MS) model that simulates knee kinematics and ligament strains for the pre-diseased state, as well as an implant-aligned femoral and tibial rotation and location. Implant alignment quality is defined by the root-mean-square deviation (RMSD) between these two simulations. We trained a neural network with three hidden layers containing 30, 20, and 20 units, respectively, to predict kinematics, ligament strains, and subsequently RMSD. The frozen trained neural network is then used for gradient-based optimization to identify the optimal implant position for this patient. FE, flexion-extension; VV, varus-valgus; IE, internal-external.

References (Optional)

[1] Tzanetis, P. et al. , The Bone & Joint Journal, 2024.

Session Category

Emerging Areas: N/A

OA9-04

Sit-to-Stand Biomechanical Subgroups Identified from A Large Dataset of Clinically Accessible Smartphone Video Recordings

Ms. Kathryn Blessinger[1], Dr. Manoj Srinivasan[1], Dr. Sarah Roelker[2], Dr. Laura Schmitt[1], Dr. Ajit Chaudhari[1], Dr. Robert Siston[1]

[1]The Ohio State University, Columbus, OH, United States. [2]University of Massachusetts Amherst, Amherst, MA, United States

Introduction

Proposed clinical phenotypes, or subgroups, for common musculoskeletal conditions help tailor physical therapy and exercise recommendations but often overlook task performance factors, such as how individuals leverage available muscle strength to meet task demands, i.e., the potential of muscles to accelerate the center of mass (COM). This study aimed to identify biomechanical subgroups during sit-to-stand (STS), based on patterns in demographics, performance, kinematics, and muscle potentials.

Methods

Seventy participants, a subset of [1], performed five-times STS recorded via smartphone video. Three-dimensional kinematics were predicted from each video, using methods developed by [2]. Sagittal plane kinematics and an induced potential analysis [3] determined muscle potentials to sagittal plane COM accelerations for lower extremity muscles during STS. K-means clustering identified STS subgroups, where participants' age, body mass index (BMI), sex, STS time to completion (TTC), and sagittal plane kinematics and muscle potentials during STS were used as clustering inputs. Kruskal-Wallis or Chi-squared and appropriate post-hoc testing compared demographic, performance and osteoarthritis (OA) prevalence data between resulting subgroups. Descriptive statistics qualitatively compared kinematic and muscle potential data between subgroups.

Results

We identified 3 STS subgroups (Table 1), each of which had similar performance (TTC). Group FEM was older, had a higher proportion of females and higher OA prevalence, the largest BMI, and demonstrated more dorsiflexion, hip flexion, and knee flexion, less lumbar flexion, and smaller plantarflexor and quadriceps muscle potential magnitudes, compared both other groups. The two remaining groups demonstrated similar demographics, performance, and OA prevalence, but Group Q demonstrated less dorsiflexion, compared to both other subgroups. Groups Q and PF showed the largest quadriceps or plantarflexor muscle potential magnitudes, respectively.

Discussion

This pilot analysis suggests that an OA-dominant subgroup characterized by older females with greater BMI (Group FEM), uses a kinematic strategy that yields smaller potentials from muscles that are key for accelerating the COM up (quadriceps and plantarflexors) and forward (plantarflexors) during STS. Our findings may inform future custom kinematic cueing interventions during STS for groups of patients with OA, like many in Group FEM.

Images (Optional)

Table 1. Group medians [interquartile range] or percentages for demographic, performance (sit-to-stand (STS) time to completion (TTC)), and osteoarthritis (OA) prevalence data. Descriptive statistics (average ± standard deviation) for qualitative comparisons of horizontal and vertical muscle potentials from the quadriceps (QUAD) and plantarflexors (PF) at the end of phase 2 during STS and at 100% of STS, respectively. ** Significantly greater than both other subgroups ($p < 0.03$). * Significantly greater than Group PF only ($p < 0.01$).

Group (n)	% Females	BMI (kg/m^2)	Age (years)	TTC (sec)	% OA	QUAD Horizontal @ End of Phase 2 (kg^{-1}) $*10^{-2}$	QUAD Vertical @ End of Phase 2 (kg^{-1}) $*10^{-3}$	PF Horizontal @ 100% of STS (kg^{-1})	PF Vertical @ 100% of STS (kg^{-1}) $*10^{-2}$
PF (n = 45)	51.1%	23.4 [4.7]	29.0 [32.3]	1.43 [0.60]	20.0%	-4.6 ± 5.8	-5.9 ± 7.2	-1.6 ± 0.1	-20.5 ± 1.2
Q (n = 16)	50.0%	23.4 [3.8]	39.5 [42.0]	1.41 [0.43]	31.3%	-7.3 ± 5.9	-12.0 ± 9.2	-1.4 ± 0.1	-14.1 ± 1.0
FEM (n = 9)	88.9%	27.5 [8.3] **	54.0 [33.0]	1.44 [1.13]	66.7% *	-2.7 ± 5.3	-0.9 ± 1.8	-1.0 ± 0.0	6.5 ± 0.3

References (Optional)

[1] Boswell *et al.*, npj Digit. Med, 2023

[2] Cotton, IEEE, 2025

[3] Roelker *et al.*, PLoS One, 2022

Session Category

Emerging Areas: N/A

OA9-05

Bridging OpenCap Outputs to Clinically Useful Gait Reports

Dr. Joseph Mahoney Ph.D.[1], Ms. Keiana Morris[2], Mr. Steve Tello[1], Dr. Allison Altman-Singles Ph.D.[2]

[1]Alvernia University, Reading, PA, United States. [2]Penn State Berks, Reading, PA, United States

Introduction

Quantitative gait measures support clinical decisions, yet traditional motion-analysis labs are costly and require dedicated space and staff. Markerless, open source systems such as OpenCap estimate kinematics and dynamics from smartphone video in small spaces with minimal hardware and training [1]. However, OpenCap typically returns zipped data and raw video or brief web-portal summaries, not a concise report. We developed and tested a low-cost pipeline that lets non-programmers turn OpenCap treadmill sessions into clinician-oriented gait summaries.

Methods

A MATLAB program was developed that ingests the zipped output from an OpenCap treadmill session, unpacks the files, and extracts joint kinematics and marker trajectories from all trials [2]. The code computes stride-averaged kinematics, basic spatiotemporal variables, and symmetry metrics, then compiles subject-level and condition-level tables and plots. To run the analysis, the user downloads the OpenCap zip file from the web portal, selects it in a simple graphical interface, and allows the program to complete all processing automatically. Modular configuration files let developers choose which joints, planes, and metrics appear so that report layouts can be tailored to specific clinical or research needs.

Results

On an initial test dataset of treadmill walking, the pipeline processed OpenCap exports and produced subject-level reports; no additional coding from the user was needed. Each report contained joint-motion plots, stride-averaged spatiotemporal parameters, and symmetry metrics formatted for quick review. From downloading the OpenCap zip file to opening the summarized report, the workflow required only a few simple user actions.

Discussion

These results demonstrate a feasible pathway from smartphone-based markerless motion capture to clinician-ready gait reports that use low-cost hardware and require minimal programming expertise. The pipeline converts high-dimensional OpenCap output into compact, configurable summaries that may support clinical decision-making and remote monitoring. Limitations include reliance on treadmill walking, the quality of video capture, and OpenCap pose estimation. Future work will validate output against gait-lab standards, expand to overground tasks and additional gait metrics, and implement a web-based Python interface that delivers the same customizable reports through a browser.

References (Optional)

[1] Uhlrich et al., PLoS One, 2023

[2] Mahoney, osf.io/v9bhd, 2025

Acknowledgements (Optional)

This work was supported by funding from Alvernia University and Penn State Berks.

Session Category

Emerging Areas: N/A

OA10-02

Exploring Carotid Plaque Rupture Risk Using Non-Invasive MRI-Quantitative Susceptibility Mapping Validated by Comprehensive Multimodal Imaging

Mr Francesco Digeronimo[1,2,3], Ms Jessica Bagnall[1,2], Asst. Prof. Brooke Tornifoglio[1,2], Prof. Karin Shmueli[4], Prof. Caitríona Lally[1,2,3]

[1]Trinity Centre for Biomedical Engineering, Trinity College Dublin, Dublin, Co. Dublin, Ireland. [2]Discipline of Mechanical, Manufacturing and Biomedical Engineering, Trinity College Dublin, Dublin, Co. Dublin, Ireland. [3]Advanced Materials and BioEngineering Research (AMBER) Centre, Royal College of Surgeons in Ireland and Trinity College Dublin, Dublin, Co. Dublin, Ireland. [4]Department of Medical Physics and Biomedical Engineering, University College London, London, England, United Kingdom

Introduction

Carotid Artery Disease (CAD) manifests as atherosclerotic plaque formation, with vulnerable plaque rupture causing ~20% of ischaemic strokes [1]. Identifying plaques vulnerable to rupture is vital for effective patient selection for Carotid Endarterectomy (CEA) surgery, with current approaches, based on arterial narrowing (percentage stenosis), offering limited insights into rupture vulnerability. MRI-Quantitative Susceptibility Mapping (QSM) quantifies tissue magnetic susceptibility (χ), providing deeper compositional insights than conventional MRI [2]. QSM is sensitive to arterial collagen [3], a key determinant of plaque stability [4]. This study investigates QSM's potential to identify rupture-prone plaques in CAD using multi-modal imaging validation and mechanical testing of human plaque tissue.

Methods

Plaques (N=4) from CEAs (Galway Clinic, Ireland) were fixed, mounted in custom-made holders and imaged using multiple modalities: Multi-Echo Gradient Echo MRI (7T-Bruker-BioSpec-70/30) for QSM, and for validation: Micro-CT (μCT), Contrast-Enhanced (CE)-μCT (Nikon-XTH225) and brightfield microscopy. QS-Maps were calculated with a two-pass masking pipeline [5]. QS-Maps were co-registered with CT volumes, and microscopy images aligned for comparison. Fresh plaques (N=7) underwent QSM and uniaxial tensile testing to failure (2-mm-width circumferential strips). Strips were grouped based on QSM features and mechanical differences assessed.

Results

Combined imaging confirmed QSM contrasts and enabled detailed assessment of plaque composition. Heavily diamagnetic ($\chi \ll 0$) and paramagnetic ($\chi \gg 0$) regions corresponded to calcification and intraplaque haemorrhage, aligning with prior work [2]. CE-µCT highlighted highly fibrous regions aligning with QS-Maps diamagnetism, enabling identification of fibrous tissue (Fig.1A, arrows). Based on QSM-groupings (Fig.1B), Group-A showed significantly higher force and strain at failure (Fig.1C), supporting that dense fibrous tissue confers greater plaque stability.

Discussion

By combining imaging and mechanical testing, this study clarifies the compositional basis of QSM contrast and demonstrates its value for assessing plaque mechanical integrity. We have also confirmed QSM feasibility in-vivo, from scanning to post-processing, demonstrating the translational potential of QSM for delivering key insights into plaque composition and vulnerability, supporting improved CEA patient selection.

Images (Optional)

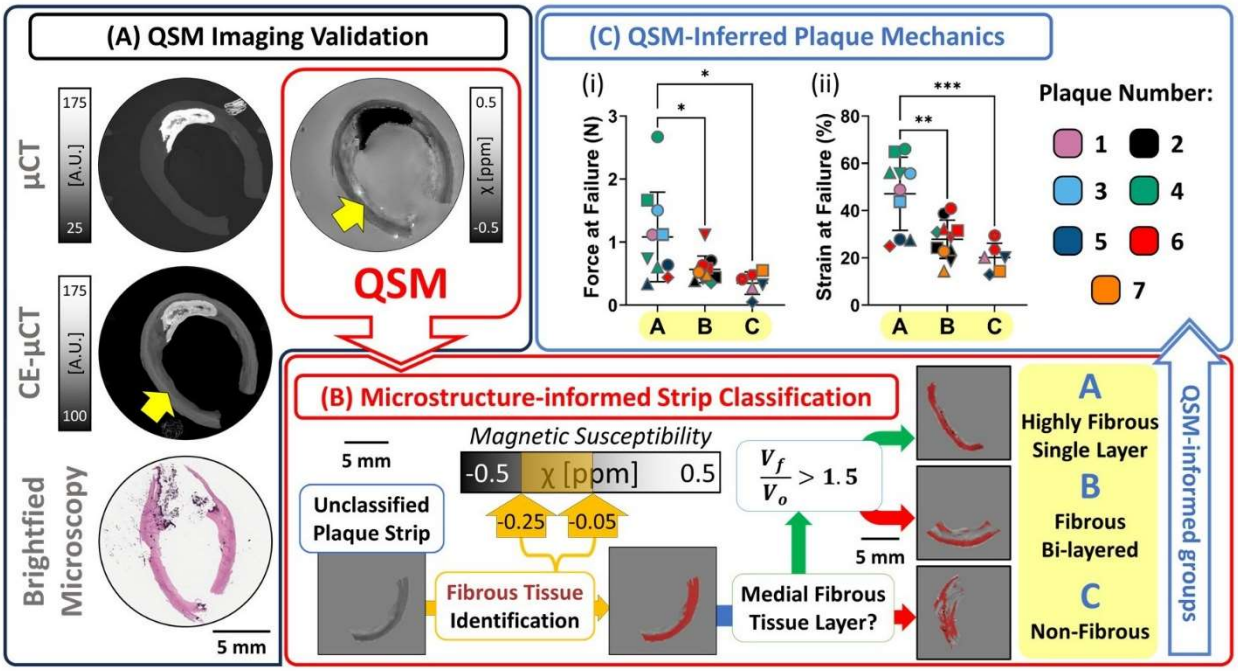


Figure 1. (A) Multi-modal co-registered imaging for validation of QSM: µCT, CE-µCT and 2D brightfield microscopy; (B) Plaque strip classification based on QSM, V_f | fibrous volume, V_o | other volume; (C) Mechanical properties by QSM group: (i) force at failure (N) ($\mu \pm \sigma$), (ii) strain at failure (%) ($\mu \pm \sigma$). Distinct symbols, with matching colour infill, are used to distinguish individual strips originating from the same plaque. One-way ANOVA with Tukey's post-hoc multi-comparison test: p-value ≤ 0.05(*), 0.01(*), 0.001(***). Plaques | N = 7; Strips | n = 27.

References (Optional)

[1] Dossabhoy et al., Seminar Vascular Surgery, 2021.

[2] Wang et al., Journal MRI, 2020.

[3] Stone, Tornifoglio et al., MR Medicine, 2025.

[4] Tornifoglio et al., Biomech. Model. Mechanobiol., 2023.

[5] Karsa et al., ISMRM AGM, 2022.

Acknowledgements (Optional)

This project is funded by the Centre for Doctoral Training in the Advanced Characterisation of Materials and Science Foundation Ireland (SFI) under award reference: 18/EPSRC-CDT/3581.

Session Category

Imaging and Biomedical Devices: Imaging Fundamentals and Applied Research

OA10-03

Steps Toward Understanding Stent Thrombosis

Dr. Hadi Mirgolbabaee[1,2], BSc Karlijn Leussink[1], MSc Yu-Tung Yang[1], MSc Marleen Krommendijk[1], MSc Jan van de Hoek[1], Prof. dr. Bob Geelkerken[1,3], Prof. dr. Michel Reijnen[1,4], Dr. Erik Groot Jebbink[1,4]

[1]Multi-Modality Medical Imaging group, TechMed Centre, University of Twente, Enschede, Overijssel, Netherlands. [2]Physics of Fluids group, TechMed Centre, University of Twente, Enschede, Overijssel, Netherlands. [3]Department of Vascular Surgery, Medisch Spectrum Twente, Enschede, Overijssel, Netherlands. [4]Department of Vascular Surgery, Rijnstate Hospital, Arnhem, Gelderland, Netherlands

Introduction

Stent thrombosis (ST) is a potentially hazardous complication after an endovascular procedure, impacting patients' quality of life. Because ST usually develops abruptly without detectable precursors, its occurrence in clinical practice cannot be predicted, limiting understanding of the thrombus growth mechanism and its relation to local hemodynamics. Existing microfluidic studies provide partial insights but cannot reproduce physiological boundary conditions, realistic stent geometries, or complex vascular anatomy. Hence, current literature is lacking methods for quantifying unfavorable hemodynamics such as blood stasis and recirculation zones, which are known to increase the platelet activation potential and promote ST. To address these gaps, we developed an in-vitro framework to investigate thrombus initiation and progression from hemodynamic and stent-related perspectives.

Methods

3D-printed phantoms were integrated into a closed-loop setup using heparinized (3.5 IU/mL) porcine blood. Ultrasound particle image velocimetry (echoPIV) was used to monitor thrombus formation and obtain time-resolved 2D velocity fields using high frame rate (~2000 fps) ultrasound imaging. In phase one, we evaluated the influence of unfavorable hemodynamic regions on thrombus formation potential by fabricating a step-stenosis phantom to generate regions of stasis and recirculation. In phase two, the repeatability of our experimental setup was evaluated and compared to prior video-microscopy studies. This was done using symmetric 50–75% stenosis phantoms, creating high-shear (>5000 s^{-1}) jets to induce arterial thrombosis. In phase three, stent-grafts were deployed in phantoms to examine graft-dependent effects and dynamics of ST formation.

In all phases, residence time (RT) and vector complexity (VC) were calculated to quantify unfavorable hemodynamics and relate them to thrombus growth.

Results

Step-stenosis experiments showed elevated RT and VC in stasis and recirculation zones, where thrombus formation was observed (Fig 1a–c). Symmetric stenosis phantoms exhibited high-shear jet formation, downstream recirculation, and thrombus formation at their narrowest part (Fig 1d–f). Preliminary stented-phantom results demonstrated thrombus accumulation at the stent's proximal region (Fig 1g,h).

Discussion

These preliminary findings provide valuable insights into the role of unfavorable hemodynamic parameters in predicting thrombus growth potential. Future work will quantify correlations between stent-graft configurations, hemodynamic parameters, and ST to develop a prediction model, which will be validated using in-vivo data.

Images (Optional)

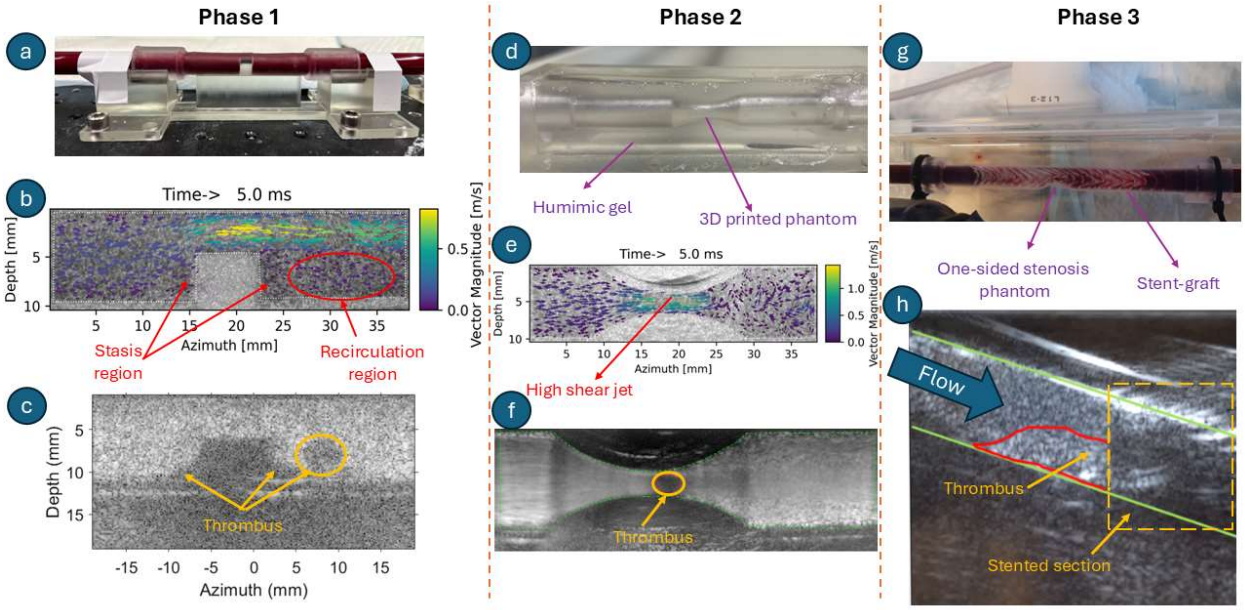


Fig 1. a) *3D-printed (Flexible 80A, Formlabs, Somerville, MA, USA) step-stenosis phantom filled with blood,* ***b)*** *2D velocity field indicating unfavorable hemodynamic regions,* ***c)*** *Thrombosed regions caused by stasis and recirculation patterns,* ***d)*** *symmetrical stenosis phantom encapsulated in tissue mimicking material,* ***e)*** *2D velocity field indicating a jet flow region with high shear,* ***f)*** *Thrombosed region in the stenosis indicating white clot,* ***g)*** *Deployed stent-graft in one-sided stenosis 3D printed phantom,* ***h)*** *Thrombus formation in the proximal section of the stent graft*

Session Category

Imaging and Biomedical Devices: Imaging Fundamentals and Applied Research

OA10-04

TomoSAXS: Full Field 3D X-Ray Scattering Tomography for Biomechanics

Dr Alissa Parmenter PhD, MEng[1], Dr Elis Newham[2], Dr Jishizhan Chen[1], Dr Tim Snow[3], Dr Joseph Brunet[1], Dr Valentin Vinci[4], Dr Jakub Drnec[4], Dr Alexandre Bellier[5], Dr Nick Terrill[3], Professor Peter D Lee[1], Professor Himadri S Gupta[2]

[1]University College London, London, London, United Kingdom. [2]Queen Mary University of London, London, London, United Kingdom. [3]Diamond Light Source, Harwell, Oxfordshire, United Kingdom. [4]European Synchrotron Radiation Facility, Grenoble, Auvergne-Rhône-Alpes, France. [5]Grenoble Alps University, Grenoble, Auvergne-Rhône-Alpes, France

Introduction

Multiscale characterisation of fibre organisation and deformation is essential for understanding the load-bearing behaviour of the intervertebral disc (IVD), yet conventional imaging approaches cannot simultaneously capture nanoscale fibrillar mechanics and tissue-scale architecture in intact specimens. We have recently developed *TomoSAXS* – a combined small angle X-ray scattering (SAXS) and phase contrast computed tomography (CT) approach that enables 3D mapping of micro- to nanoscale collagen structure and mechanics [1]. Here, we reconstruct nano- to microscale properties of collagen fibres across intact human IVD.

Methods

Human IVDs (n=3) were imaged with hierarchical phase contrast tomography (HiP-CT) [2] (4-10µm voxel size, Fig.A) at the European Synchrotron (ESRF) beamline BM18, and correlatively with high energy (75keV) tomographic SAXS (beam size 100µm, Fig.C) at ESRF beamline ID31. Fibre tracing of IVD collagen fibres was performed using Avizo 2024.1, and orientation and curvature calculated. Fibre orientation was fed into the *TomoSAXS* reconstruction pipeline, enabling per-fibre reconstruction of collagen nanoscale properties including D-period and fibril diameter using 3D diffraction modelling and single value decomposition.

Results

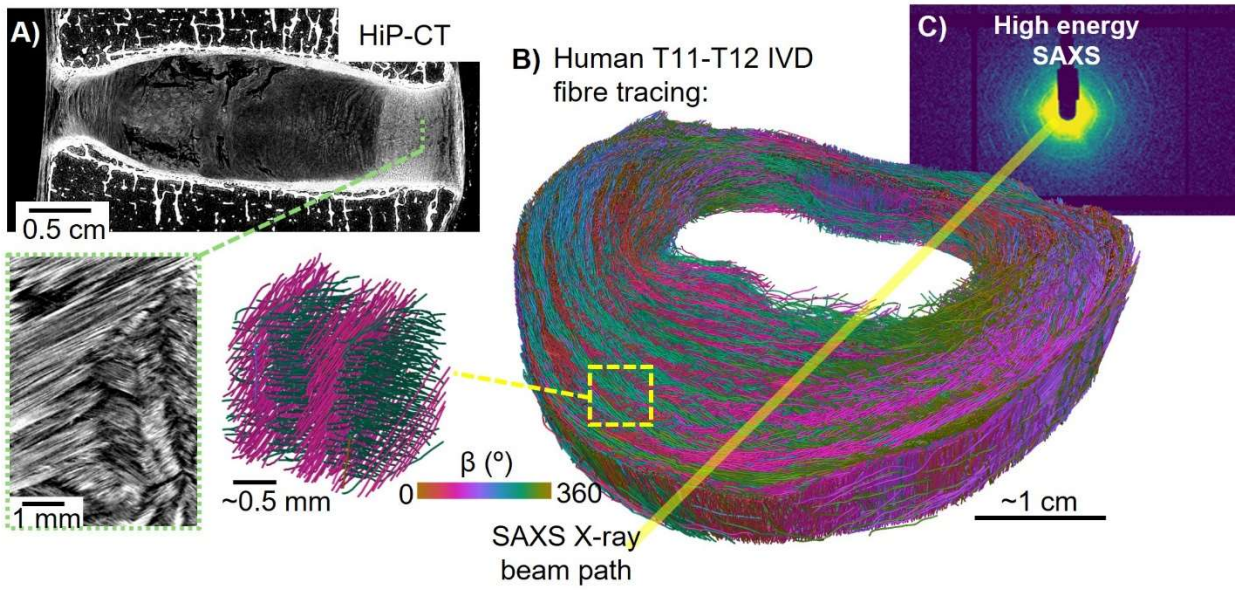
HiP-CT enabled imaging of intact IVD with cellular resolution (Fig.A). Fibre tracing of the annulus fibrosus (Fig.B) provided quantification of orientation and curvature, showing areas of disruption due degenerative changes. *TomoSAXS* enabled per-fibre reconstruction of collagen fibril parameters including fibril diameter and D-period, a measure of fibrillar

pre-strain. The results show gradients in fibril diameter and pre-strain across the IVD, and that these are disrupted around degenerative features such as osteophytes and neovascularisation.

Discussion

This study is the first application of TomoSAXS to human organs, demonstrating the feasibility of the technique to study other systems such as the heart and lungs. We have previously shown that fibre curvature and fibril pre-strain are key determinants of a fibre's response to load [1], so the gradients in nano- to microscale collagen properties observed here likely support the overall mechanical function of the IVD, and could be used to improve computational models. Changes in these properties and their spatial gradients could be a key early indicator of IVD degeneration.

Images (Optional)



References (Optional)

[1] Elis Newham and Alissa Parmenter *et al.*, bioRxiv, 2025

[2] Claire Walsh *et al.*, Nature Methods, 2021

Acknowledgements (Optional)

We acknowledge funding from Back to Back, the UK Engineering and Physical Sciences Research Council (EP/V011235/1, EP/V011006/1, EP/V011383/1, EP/V011065/1), UK Medical Research Council (MR/R025673/1 and MR/V033506/1), Royal Academy of Engineering (CiET 1819/10), Chan Zuckerberg Initiative (CZIF2022-316777), BBSRC

(BB/R003610/1), ESRF HOAHub MD-1389, MD-1290, & ME-1735, Diamond Light Source long-term project (SM29784), & the i4health Centre for Doctoral Training.

Session Category

Imaging and Biomedical Devices: Imaging Fundamentals and Applied Research

OA10-05

Structural Disease Patterns of Early Osteoarthritis in a DMM Mouse Model Relating to Mechanical Changes Revealed Using Time-Lapse *In Vivo* Contrast-Enhanced Micro-Computed Tomography

Dr Jemima E Schadow[1], Ms Emma C Boersma[1], Ms Annunzia M Cagnoni[1], Dr Pholpat Durongbhan[1], Dr Han Liu[1], Prof Rachel E Davey[2], Prof Kathryn S Stok[1]

[1]Department of Biomedical Engineering, The University of Melbourne, Parkville, Victoria, Australia. [2]Department of Medicine, Austin Health, The University of Melbourne, Heidelberg, Victoria, Australia

Introduction

The sequence of early structural tissue changes in the destabilised medial meniscus (DMM) mouse model of osteoarthritis (OA) is undefined. This study aimed to explore structural disease patterns of early OA in the DMM mouse model using time-lapse *in vivo* contrast-enhanced micro-computed tomography (CECT) at high temporal resolution.

Methods

DMM or sham surgery was performed on ten-week-old C57Bl/6 mice (n=22/group). Three mice/group were euthanised weekly until 28-days post-surgery and an additional 3 mice/group were euthanised at 10 weeks-old without surgery for histology. The remaining 10 mice/group underwent weekly microCT scans (10.4 µm, 70 kVp, 114 µA; vivaCT80, Scanco Medical AG) until day 28 and again at day 56 post-surgery. Three mice/group were euthanised for histology. All procedures approved by University of Melbourne, ethics approval #24339. Safranin-O staining and OARSI scoring were used to assess joint pathology. MicroCT images were analysed for cartilage attenuation, joint alignment, joint space and bone morphometry, and osteophyte formation. Effects of OA, time, and laterality were assessed with a mixed-effects model.

Results

OARSI score and mean attenuation were increased on the medial side of DMM mice, which is indicative of glycosaminoglycan depletion (Fig 1A). The number of voxels in the thinnest joint space layer increased on the medial side of DMM mice post-surgery and there was increased variability in dorsal axis and midsagittal axis angles of DMM mice at 14-, 21-, and 28-days post-surgery, indicative of joint space narrowing and increased laxity. Osteophyte formation was visually observed on both sides of the tibia and femur in DMM mice. Cortical porosity and trabecular thickness of medial tibia in DMM mice increased over time before decreasing at 56-days post-surgery (Fig 1B).

Discussion

Non-linear subchondral bone changes were observed in early stages following DMM surgery, likely reflecting altered mechanical loading. Initially, mechanical loading likely increased as joint space narrowed, and joint laxity increased but later decreased as osteophytes matured. These temporal fluctuations in structural disease development, highlight the importance of further research into OA phenotypes and their connection to features such as pain. Furthermore, it could provide indications for disease management, such as targeting joint laxity with physiotherapy.

Images (Optional)

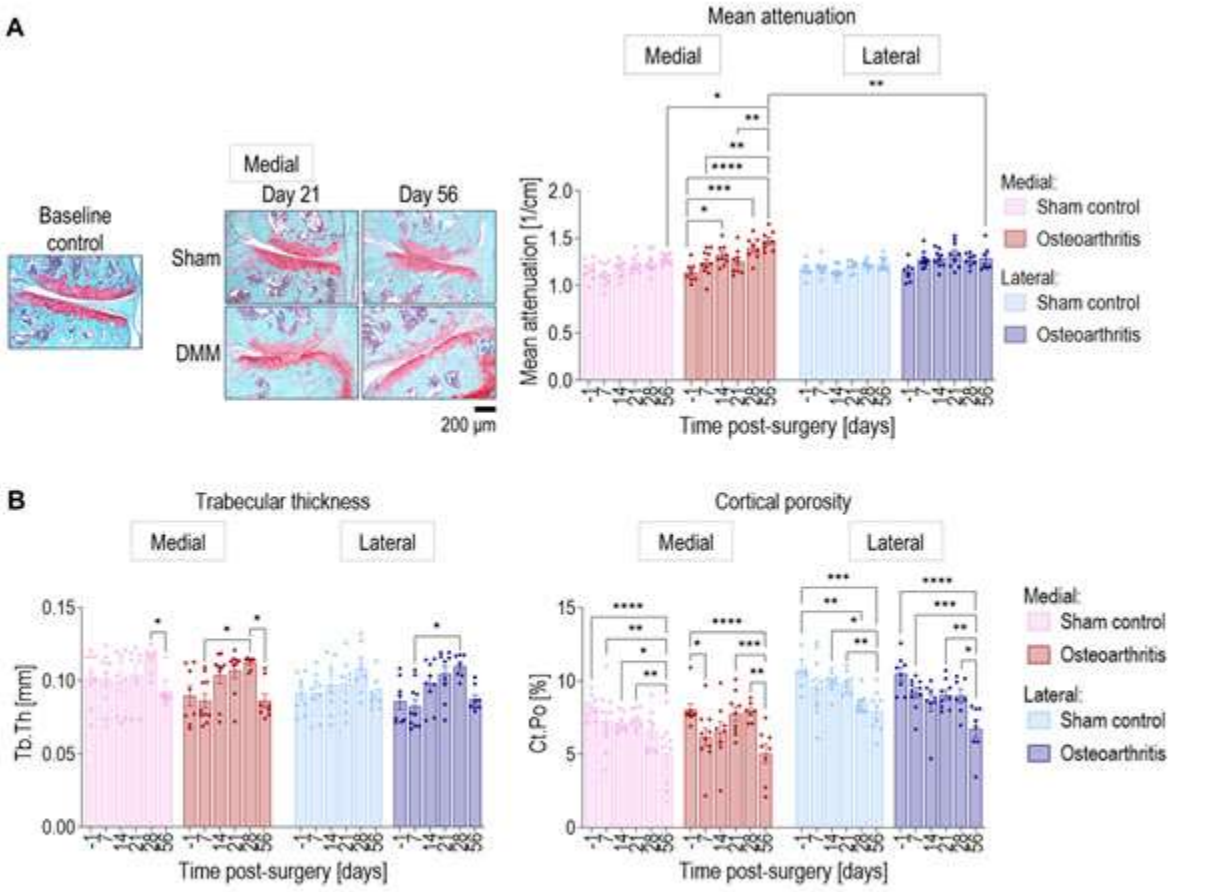


Figure 1 | A) Medial histology images and mean attenuation of tibial cartilage, and B) trabecular thickness (Tb.Th) and cortical porosity (Ct.Po) of tibia DMM and sham control mice. Data shown as mean ± standard error, n=10 per group; * = p<0.05, ** = p<0.01, *** = p<0.001, **** = p<0.0001.

Acknowledgements (Optional)

Funding support from FWO and F.R.S.-FNRS under the Excellence of Science (EOS) programme (EOS No. 40007553) Australian Research Council Discovery programme

(DP180101838), KU Leuven – University of Melbourne International Research Training grant and University of Toronto – University of Melbourne International Research Training grant. We thank Cynthia Louis, PhD from Walter + Eliza Hall Institute of Medical Research, Prof Christopher Little from Kolling Institute, University of Sydney, Melbourne Bioresources Platform, Melbourne Histology Platform and Statistics Consulting Centre from University of Melbourne for their technical assistance with this work.

Session Category

Imaging and Biomedical Devices: Imaging Fundamentals and Applied Research

OA11-01

The Matrix Reintegrated: Engineering Extracellular Matrix Mechanics in Organ-on-Chips

M.Sc. Hazal Kutluk[1,2], Prof. Dr. Iordania Constantinou[1,2]

[1]Institute of Microtechnology (IMT), Technische Universität Braunschweig, Braunschweig, Lower Saxony, Germany. [2]Center of Pharmaceutical Engineering (PVZ), Technische Universität Braunschweig, Braunschweig, Lower Saxony, Germany

Introduction

Mechanical properties of the extracellular matrix (ECM), including stiffness, thickness, and porosity, critically regulate cell proliferation, differentiation, and gene expression; yet current organ-on-chip (OoC) platforms mainly rely on simple protein coatings that poorly recapitulate this complexity. [1] This lack of mechanically tunable ECM analogues constrains the use of OoCs in mechanobiology research. To address this limitation, we present a novel strategy to integrate well-defined polyacrylamide hydrogels, widely used ECM-mimics, onto porous polyethylene terephthalate (PET) membranes commonly employed in OoCs.

Methods

PET membranes were amine-functionalized using different chemistries, concentrations, and treatment times, and functionalization efficacy was assessed via fluorescence labeling. Polyacrylamide gels with tunable stiffness and mesh size were covalently attached to activated PET, with stiffness measured by shear rheology and mesh size inferred from swelling behavior. The functionalized membranes were assembled into multilayer OoC devices, where hydrogel thickness was adjusted via gel precursor volume and quantified by fluorescence microscopy, while porosity was introduced by emulsion templating and visualized by scanning electron microscopy.

Results

Two membrane activation protocols yielded stable attachment of polyacrylamide hydrogels to porous PET membranes for at least 21 days in three different culture media under standard incubator conditions. The method translated to the OoC format, enabling integration of hydrogels with stiffness in the range of 3–30 kPa and tunable internal mesh size at comparable stiffness. Hydrogel thicknesses down to about 40 µm were achieved, with the maximum thickness set by the adjustable microchannel height. Emulsion

templating produced gels with around 50% porosity and mean pore sizes near 0.4 µm, with the potential for further tuning of both parameters. The resulting OoC platform is highly modular, supports thermoplastic or glass sealing, and allows optional electrode integration for non-invasive, real-time readouts.

Discussion

For the first time, our platform introduces tunable, well-defined ECM-mimicking polyacrylamide hydrogels into OoCs. Establishing precise control over hydrogel mechanics overcomes a key limitation of existing OoC systems, expands biological questions addressable on chip, and supports future work connecting ECM mechanics with disease modelling and drug-response profiling.

References (Optional)

[1] Hazal Kutluk *et al.*, Adv Healthc Mater, 2023

Session Category

Tissue Engineering: Methods, Models and Applications

OA11-02

A Microfluidic Platform for Perfused Culture of Organoid Units With Engineered Vascular Networks

Ms. Ayaka Kadotani[1], Dr. Gen Hayase[2], Prof. Daisuke Yoshino[1]

[1]Tokyo University of Agriculture and Technology, Koganei, Tokyo, Japan. [2]National Institute for Materials Science, Tsukuba, Ibaraki, Japan

Introduction

Organoids have attracted considerable interest due to their potential to serve as alternatives to donor organs. These organoids express certain higher-order functions; however, their current size is limited to a few millimeters due to the absence of control over developmental processes and nutrient diffusion. To address these problems, we previously proposed a modular assembly approach, and we have developed the method to fabricate organoid units that replicate the kidney glomerulus rapidly and assemble them in three dimensions [1]. Nevertheless, the absence of vasculature resulted in cell death in organoid units during prolonged culture, thereby limiting the expression of higher-order functions. In this study, we developed a microfluidic device designed to culture units under perfused, physiologically relevant conditions and to analyze their cellular dynamics when combined with hierarchical vascular networks.

Methods

Microfluidic devices were fabricated by casting polydimethylsiloxane (PDMS) onto master molds and bonding PDMS layers to glass coverslips. Organoid units were prepared as previously described [1], and cultured in the designated medium fortwo days. The hydrogel containing human umbilical vein endothelial cells (HUVECs) and pericytes was dispensed into the device's gel channel, and organoid units were embedded within it. Following the incubation period, HUVECs were seeded on media channels. Subsequent to a six-hour static culture, the devices were perfused at a rate of 0.02 milliliters per minute for three days.

Results

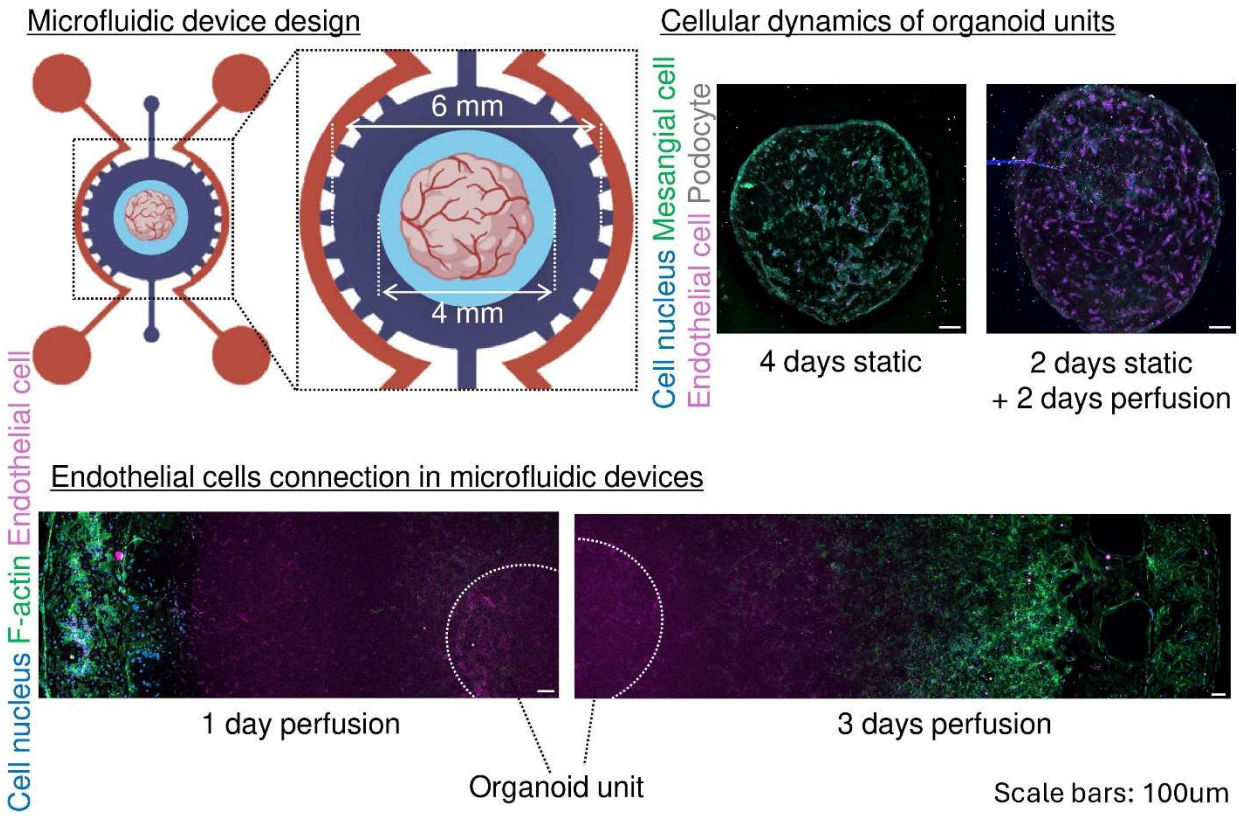
When the organoid units were embedded within the microfluidic device and cultured under perfusion, a confluent endothelial monolayer formed along the media channel within the first day. Furthermore, the endothelial cells lining the channels have been shown to form direct connections with those residing within the organoid units.

A comparison of cellular dynamics between organoid units cultured under static conditions and those embedded in the microfluidic device revealed that the perfused units exhibited markedly improved cell survival, particularly among endothelial populations.

Discussion

The present findings suggest that integrating engineered vascular networks with organoid units supports their long-term culture. Subsequent studies must ascertain whether physiological mechanical stimuli facilitate the development of these higher-order functions, which are essential for fabricating transplantable organoids through the modular approach.

Images (Optional)



References (Optional)

[1] Ayaka Kadotani *et al.*, APL Bioeng., 2024

Session Category

Tissue Engineering: Methods, Models and Applications

OA11-03

Engineered 3D Scaffolds for Modeling Dermal Tissue Regeneration and Macrophage Immune Dynamics

Dr. Chiara Martinelli[1], Dr. Alberto Bocconi[1], Mr. Srijan Chakraborty[1], Mr. Giovanni Buccioli[1], Mr. Matteo Vicini[1], Mr. Leonardo Cherubin[1], Prof. Claudio Conci[1], Dr. Alessandra Nardini[2], Dr. Rebeca Martínez Vázquez[2], Prof. Giuseppe Chirico[3], Prof. Emanuela Jacchetti[1], Prof. Manuela Teresa Raimondi[1]

[1]Department of Chemistry, Materials and Chemical Engineering "Giulio Natta", Politecnico di Milano, Milan, MI, Italy. [2]Institute for Photonics and Nanotechnologies (IFN), CNR, Milan, MI, Italy. [3]Department of Physics, University of Milano-Bicocca, Milan, MI, Italy

Introduction

Subcutaneous implants trigger immune reactions mediated by macrophages, making effective tissue repair essential to re-establish the native dermal environment. Three-dimensional (3D) *in vitro* microstructured scaffolds represent valuable platforms for studying these processes, as they enable the reconstruction of microvascular networks. Upon proper modulation of their physicochemical features, they can play a key role in directing macrophage behavior.

Methods

3D scaffolds were fabricated by two-photon polymerization of the biocompatible photoresist SZ2080 and presented small (15×15×15 μm^3)[1] and large (50×50×20 μm^3)[2] pores. Human dermal fibroblasts (HDF) and HUVEC were cultured in 50×50 scaffolds integrated into a Miniaturized Optically Accessible Bioreactor (MOAB, Figure 1A), perfused at 5µl/min, and administered with VEGF (50ng/mL) and TGF-β1 (5ng/mL). RAW264.7 macrophages were polarized with lipopolysaccharide (M1) or interleukin-4 (M2) in both scaffolds (Figure 1B). Co-cultures were stained for collagen I and CD31 at day 7, inducible nitric oxide synthase (iNOS, M1, Figure 1C), and arginase 1 (Arg1, M2) and acquired by confocal laser scanning microscopy (CLSM). Cytoskeletal changes and metabolic activity of macrophages were analyzed.

Results

The perfused setup provided a robust model of dermal regeneration with the development of early tubular formations (128.1±8.6 µm) and increased deposition of collagen I upon VEGF administration. Both scaffolds markedly influenced macrophage shape,

organization, and metabolic activity in static conditions. In the presence of chemical stimuli, 50×50 pores produced a modest increase in Arg1 expression (+5%), suggesting a shift toward an anti-inflammatory phenotype. Conversely, 15×15 pores strongly enhanced iNOS levels (+121%), promoting a marked pro-inflammatory response.

Discussion

The integration of the 3D scaffolds into the MOAB enabled the generation of a dermal perivascular microenvironment that closely resembles physiological conditions. Thanks to their adjustable architectural features, the scaffolds allowed precise modulation of macrophage functions. Upcoming studies will further explore macrophage dynamics within the perfused bioreactor, in presence of chemical cues.

Images (Optional)

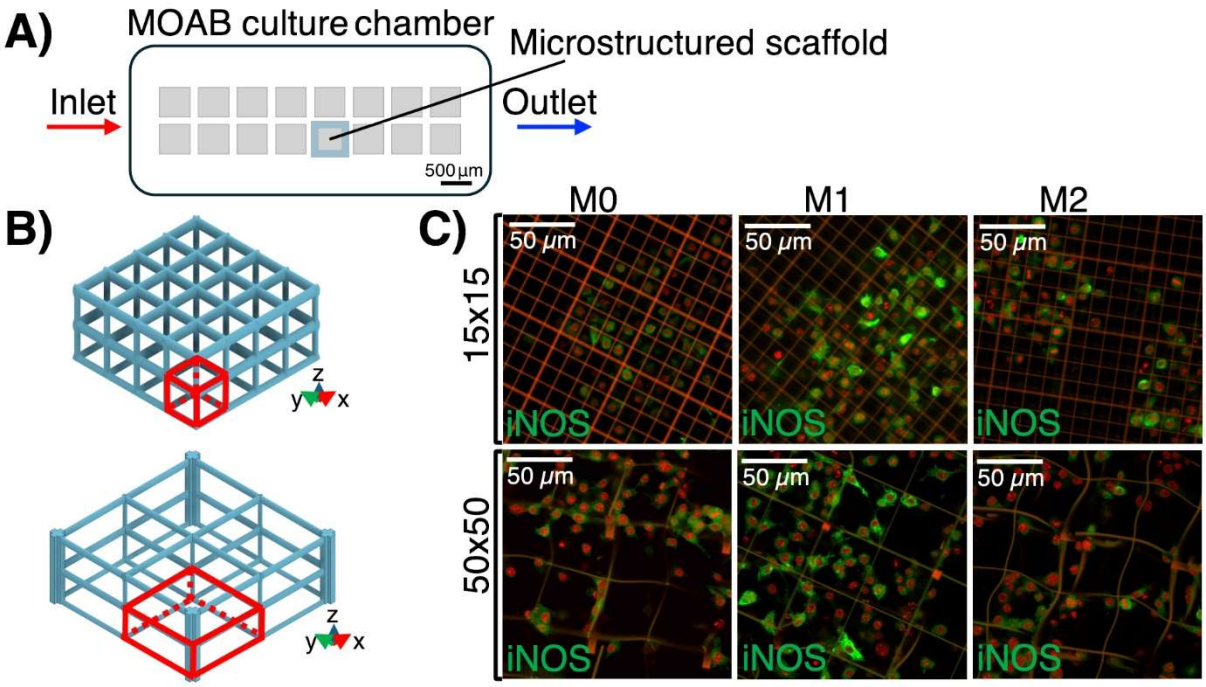


Figure 1: A) Scheme of the MOAB microstructured cell culture chamber. B) CAD of 15×15 (above) and 50×50 (below) scaffolds. C) CLSM images of RAW264.7 (M0, M1, M2) cultured in 15×15 and 50×50 scaffolds (iNOS, green; nucleus, red).

References (Optional)

[1] Chiara Martinelli *et al.*, Mater Today Bio, 2025, 35, 102328

[2] Chiara Martinelli *et al.*, Lab Chip, 2025, 25, 423-439

Acknowledgements (Optional)

ERC, BEACONSANDEGG, G.A.101053122; EU, MSCA-DN, fIIMAGIN3D, G.A.101073507; EU, FET-OPEN, IN2SIGHT, G.A.964481; MUR, VISION, CUP D53D23007890001

Session Category

Tissue Engineering: Methods, Models and Applications

OA11-04

Bending Stiffness Recovery of the Functional Spinal Unit Repaired With Human iPS Cell-Derived Cartilaginous Tissue

Prof. Hiromichi Fujie[1,2,3], Mr. Masaki Nakane[1], Mr. Yuto Noma[1], Mr. Naoto Kuroyama[1], Prof. Takashi Kaito[4], Prof. Noriyuki Tsumaki[5]

[1]Department of Systems Design, Tokyo Metropolitan University, Hachioji, Tokyo, Japan. [2]Medicine-Engineering Collaborative Research Center, Tokyo Metropolitan University, Hachioji, Tokyo, Japan. [3]Graduate School of Medicine, Sapporo Medical University, Sapporo, Hokkaido, Japan. [4]Department of Orthopedic Surgery, Graduate School of Medicine, Osaka University, Suita, Osaka, Japan. [5]Department of Tissue Biochemistry, Graduate School of Medicine, Osaka University, Suita, Osaka, Japan

Introduction

The loss of nucleus pulposus (NP) induces intervertebral disk (IVD) degeneration, which causes back pain. Conservative treatments for IVD may alleviate symptoms but do not restore the degenerated IVD to its healthy state. Yamashita and Tsumaki developed human iPS cell-derived cartilaginous tissue particles (hiPS-Cart). The present authors have performed single-cell RNA sequencing analyses and indicated that hiPS-Cart is a candidate implant for regenerating NP, and preventing IVD degeneration in a rat model. Therefore, the objectives of the present study are to implant hiPS-Cart into NP-removed IVD and assess its bending stiffness recovery in a porcine model.

Methods

hiPS cells, generated from the Center for iPS Cell Research and Application, Kyoto University [1], were chondrogenically differentiated to produce hiPS-Cart following a previously described method [2]. The vertebrae between L2 and L5 from 10-month-old mini pigs were exposed, followed by the removal of the whole NP through the longitudinal, lateral portal of the IVD. Nine hiPS-Cart particles with a diameter of 1.5 mm were inserted into the nuclectomized space. The annulus fibrosus and skin were sutured, and then the operated side was immobilized with surgical tapes. At 3 months after surgery, the vertebral samples were harvested and osteotomized into three vertebra-IVD-vertebra complexes. Histological examination was performed for the complex using safranin-O staining. The remaining complexes were subjected to the bending test using a robotic joint test system [3]. For comparison, the intact complex, sham operation-treated complex, and the non-treated, repaired complex were tested.

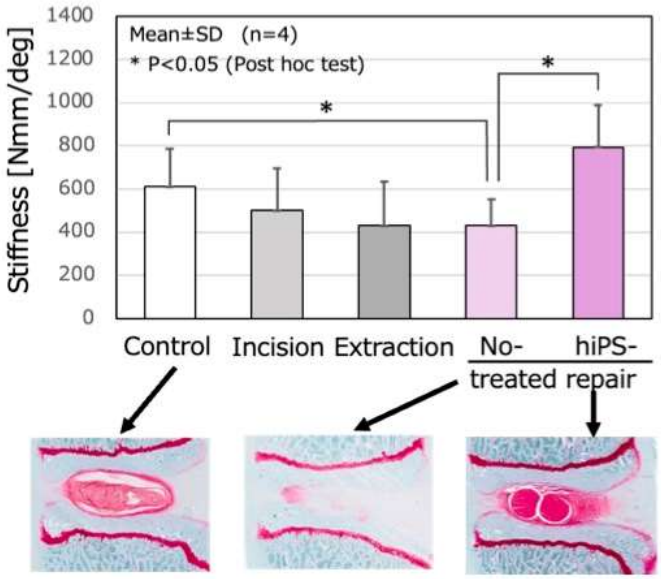
Results

Histological observation indicated that the NP was repaired well with remaining hiPS-Cart particles in the iPS-Cart treated group, although such tissues were not found in the non-treated group. The bending stiffness of the complex was recovered to the control level in the iPS-Cart treated group, with a significant increase compared to the non-treated group.

Discussion

It is suggested that the implantation of hiPS-Cart maintained the potential of cartilaginous tissue formation in the NP and restored the resulting bending stiffness of the vertebra-IVD-vertebra complex.

Images (Optional)



References (Optional)

[1] Okita, et al, Nature Methods, 2011

[2] Yamashita, et al, Stem Cells Translational Medicine, 2020

[3] Kimura and Fujie, Transaction of the JSME (Japanese), 2015

Acknowledgements (Optional)

This research was supported by AMED under Grant Number JP25bm1223014.

Session Category

Tissue Engineering: Methods, Models and Applications

OA12-02

Extracellular Matrix Shape Change Contributes to Skeletal Muscle Passive Force Production

Ms Emily McParland MS, Professor Thomas Roberts PhD

Brown University, Providence, Rhode Island, United States

Introduction

Skeletal muscle is a hierarchically organized composite structure that contains a collagenous extracellular matrix (ECM). Each layer of ECM corresponds and interacts with the scaled layers of the muscle. Epimysium wraps around the whole muscle with large, aligned cables, acting as the most superficial layer of connective tissue. Perimysium encapsulates muscle fascicles and endomysium surrounds and interacts with individual muscle fibers [1] and has obliquely-oriented cables (Figure 1A). Previous work has indicated that ECM undergoes architectural changes during muscle lengthening [2], however, no work has correlated ECM architectural dynamics with passive force production.

Methods

Frog sartorius, trout levator operculi, and mouse soleus muscles were isolated and secured into a custom 3D printed apparatus filled with Ringer's solution. The muscle was fixed to the apparatus and connected to a force transducer secured to an adjustable stage that changed muscle length. Epimysium and endomysium collagen were visualized through second harmonic generation (SHG) using a multiphoton laser scanning microscope (Olympus, Tokyo, Japan). Sarcomere lengths in the same preparation were quantified through visualization of autofluorescent myosin.

Tortuosity was quantified (straight line distance / total collagen fiber length) for both epimysial and endomysial cables [3]. In endomysium, once tortuosity reached a value >0.99, angle relative to the long axis on the muscle was measured. Each of these metrics were compared to force and muscle length.

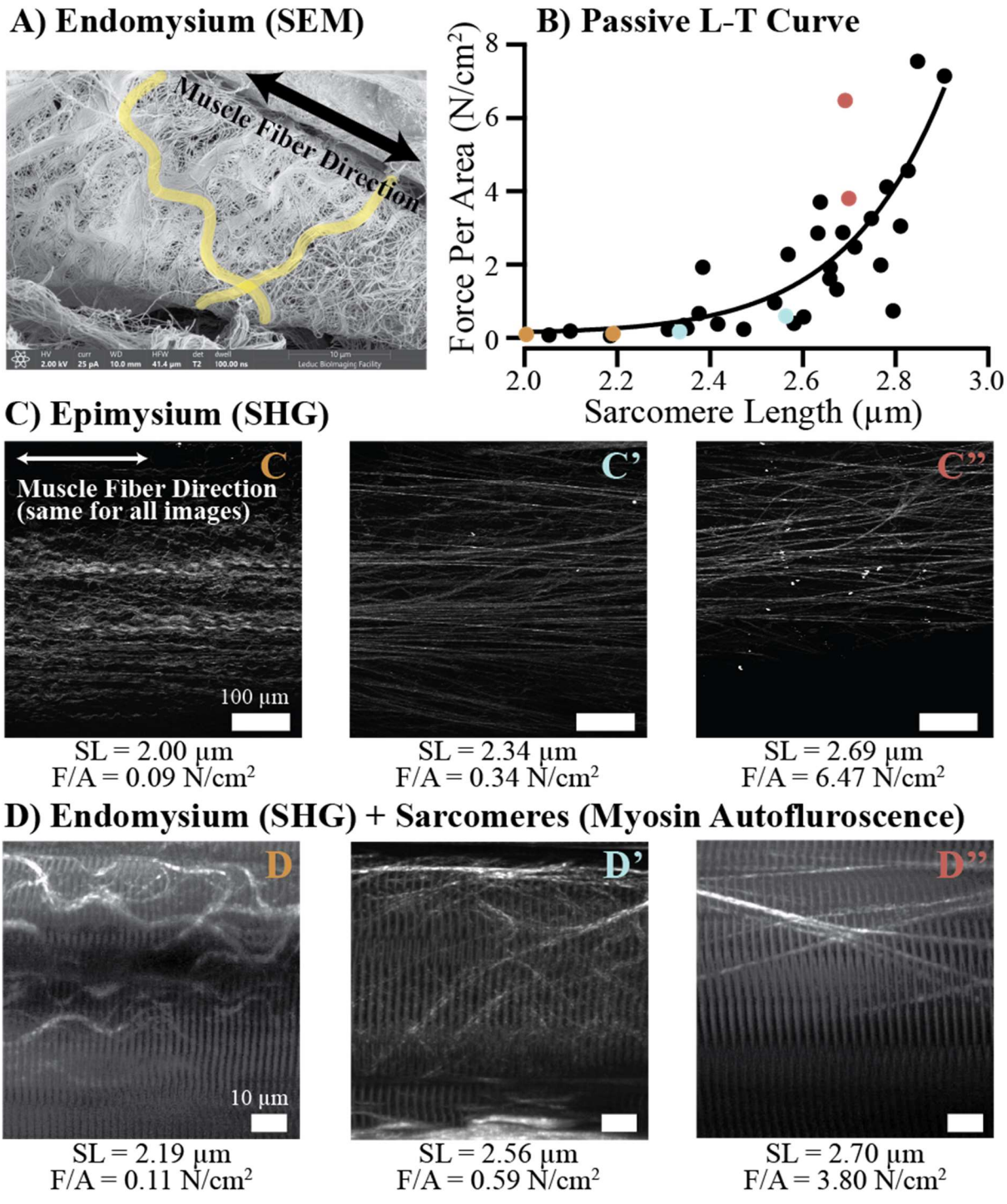
Results

As force rose exponentially during sarcomere lengthening (Figure 1B), epimysial cables uncrimped immediately (Figure 1C-C') and remained uncrimped throughout the muscle stretch (Figure 1C''). As muscles lengthened and force increased, endomysial cables uncrimped (Figure 1D-D'). Once straightened, endomysial cable angle relative to the muscle's long axis decreased (Figure 1D'-D'').

Discussion

Changes in frog, fish, and mouse skeletal muscle collagen architecture correlate with an increase in passive force, indicating that ECM bears some portion of the load during passive force production. Future work will assess how ECM-related pathologies, like fibrosis, impact ECM dynamics.

Images (Optional)



References (Optional)

[1] Sleboda DA *et al.*, J. Morphol, 2019

[2] Purslow, J. Biomech, 1989

[3] Rezakhaniha R, Biomech. Model. Mechanobiol, 2012

Acknowledgements (Optional)

This work was supported by NIH AR55295. We thank Roberts Lab members for their input and support.

Session Category

Comparative Biomechanics: N/A

OA12-03

Scaling Work and Stability: How Two Distal Muscles Partition Propulsion and Landing Control in Guinea Fowl

Dr. Caitlin Bemis, Dr. Monica Daley

University of California, Irvine, Irvine, CA, United States

Introduction

Locomotion on unstable substrates challenges animals to rapidly modulate force and energy, yet how individual muscles contribute to non-steady behaviors remains unclear. Distal muscles, with architecture that favors rapid mechanical responses, are poised to mediate stability at the limb-substrate interface. However, whether different distal muscles perform distinct roles during perturbed movement is unknown.

We investigate *in vivo* dynamics of the lateral gastrocnemius (LG) and digital flexor III (DF) in Guinea fowl (*Numida meleagris*) during jumping and landing on an unstable perch, a task that requires transition from propulsion to reactive stabilization. We hypothesized that LG and DF would exhibit muscle–specific mechanical roles. Specifically, we predicted: (1) LG would produce positive work during take-off; (2) DF would increase activation, force, and positive work during landing; and (3) DF activation would be temporally linked to substrate rotation and amplified at higher jump heights, reflecting increased perturbation magnitude.

Methods

Six adult guinea fowl performed multiple jumps to perches at three heights (20, 30, 40 cm). We recorded muscle force, fascicle length, activation, ground reaction force, and perch motion during landing and stabilization. We quantified muscle work (J/g) from force-length trajectories to compare phase specific mechanical contributions of LG and DF-III. Two-way ANOVAs were performed with muscle and phase as fixed factors on work. Additionally, we used linear mixed-effects models with individual as a random factor to account for repeated measures within birds.

Results

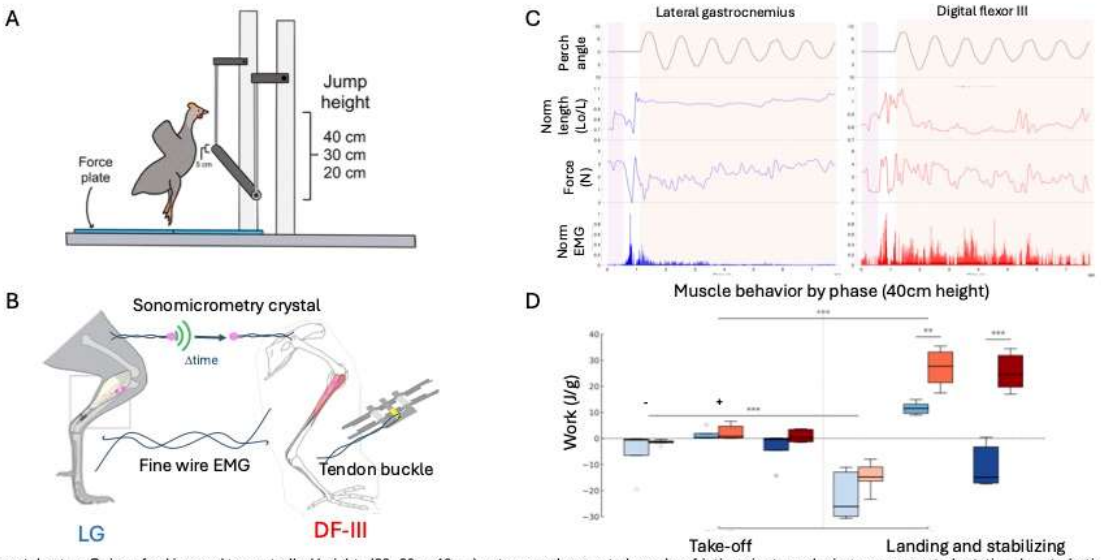
LG produced substantially greater positive work during take-off, confirming a propulsive role. In contrast, DF-III generated significantly greater positive and net work during landing ($p < 0.05$), with activation aligned to perch rotation. DF-III work scaled with jump height, indicating increased energetic contributions under larger perturbations. Both muscles absorbed energy during landing, but only DF-III produced positive work during perch

stabilization, demonstrating a neuromechanical division of labor: LG powers propulsion, whereas DF-III provides stability.

Discussion

Distal muscles do not scale work uniformly under unsteady conditions but adopt complementary strategies shaped by their architecture and mechanical context. This study provides rare *in vivo* evidence that distal muscles partition propulsive and stabilizing functions.

Images (Optional)



A). Experimental setup. Guinea fowl jumped to controlled heights (20, 30 or 40cm) onto a perch mounted on a low friction pivot, producing an unexpected rotational perturbation upon landing. Ground reaction forces were recorded with a force plate. B). *In vivo* muscle recordings. Lateral gastrocnemius (LG; blue) and digital flexor III (DF-III; red) fascicle length (via sonomicrometry), muscle activation (fine-wire EMG), and tendon force (E-buckle transducer) were collected simultaneously during each jump. C) Representative muscle mechanics from a 40cm jump. Perch rotation induces oscillatory perturbation during stabilization. LG and DF-II exhibit distinct mechanical signatures across standing to landing and stabilizing, including fascicle length trajectories (Lo/L), force output and EMG activity. Shaded regions denote the standing and landing responses. D). Muscle work (negative, positive, and net) portioned by movement phase. LG and DF-III perform opposing mechanical roles across take-off and landing/stabilization. Bars show median + interquartile rang; individual trials overlaid. Statistical different across muscles phases indicated (** $p < 0.01$; ****$p < 0.0001$)

Acknowledgements (Optional)

This work was supported by the Integrative Movement Sciences Institute (IMSI) Biological Integration Institute, NSF-DBI-2319710

Session Category

Comparative Biomechanics: N/A

OA12-04

Extreme Heat Production and Thermal Gradients in the Flight Muscles of Bombycoid Moths

Dr Ethan Wold[1], Dr Leo Wood[2], Dr Yash Sondhi[3], Dr Pablo Allen[4], Dr Akito Kawahara[5], Dr Simon Sponberg[6]

[1]University of Chicago, Chicago, IL, United States. [2]Princeton University, Princeton, NJ, United States. [3]Case Western Reserve University, Cleveland, OH, United States. [4]Council on International Educational Exchange, Monteverde, Puntarenas, Costa Rica. [5]University of Florida, Gainesville, FL, United States. [6]Georgia Institute of Technology, Atlanta, GA, United States

Introduction

Skeletal muscle emits heat as a byproduct of force production, but the processes that generate force are temperature dependent. Hawkmoths, for instance, use muscular heat to maintain thoracic temperatures above 40 ºC, enhancing muscle output. Consequently, the thermal gradient between the innermost and outermost fibers causes regional differences in power production. However, across species, it remains unclear whether high temperatures and associated gradients follow from flight power requirements or represent excess heat that boosts muscle function. We performed a field study on Bombycoid moths, extreme animal athletes that produce enough heat to be functional endotherms during flight. We measured depth-resolved intramuscular temperature and tested whether power demands explain variation in temperature and thermal gradient using predictions from a thermodynamic model.

Methods

Light-trapped moths were collected at Monteverde Research Station in Costa Rica. Moths were tethered beneath a high-speed video camera capturing stroke-plane kinematics. During flapping, temperatures were taken progressively deeper into their downstroke muscle. After experiments, photos quantified wing morphology and thoraxes were massed. Wingbeat frequency and amplitude were extracted from videos and flight power costs associated with aerodynamic drag and wing acceleration were estimated using standard formulae.

Results

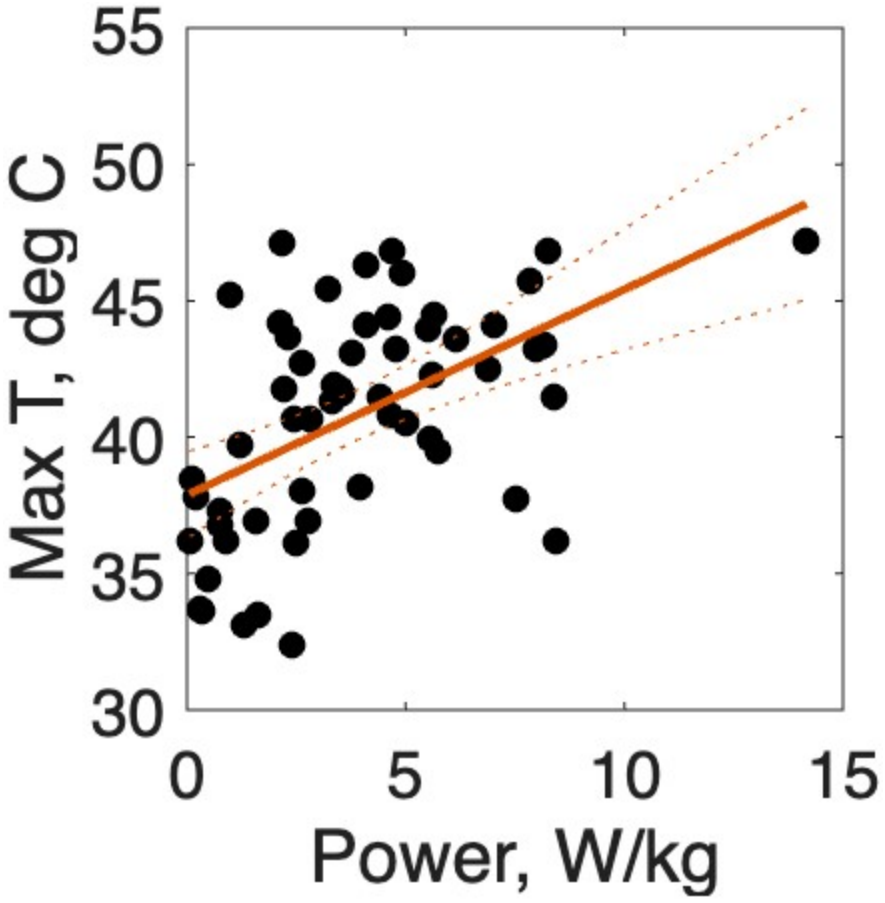
Peak intramuscular flight temperature was 40.7 ± 4.1 ºC, with some moths reaching 47.2 ºC during sustained flapping. Thermal gradients were 0.83 ± 0.26 ºC/mm. Wingbeat frequency and thorax length predicted variation in peak temperature, but not thermal

gradient. Flight power predicted surface and peak muscle temperature, but not gradient. Assuming a spherical thorax and applying the heat equation, we predicted the relationship between power demands and both maximum temperature and thermal gradient. Measured temperatures and gradients were significantly larger than expected scaling.

Discussion

Peak temperatures exceeded model predictions based upon locomotor power costs, suggesting flight muscles produce excess heat that supports muscle function. In contrast, lack of correlation between thermal gradients and power supports that gradients themselves are not important for power production. They may stem from deep elevated temperatures or thermoregulatory responses to overheating. Further comparative tests relating in-vitro optimal muscle temperatures with these data may clarify how high intramuscular temperatures enhance muscle performance.

Images (Optional)



References (Optional)

Session Category

Comparative Biomechanics: N/A

OA12-05

The Effect of Sensory Loss on Jaw Kinematics and Muscle Activation During Mastication

Dr. Jing-Sheng Li, Dr. Fritzie Arce-McShane

University of Washington, Seattle, WA, United States

Introduction

Masticatory behavior involves coordination of sensory and motor systems. Oral sensation can modify and fine-tune jaw movements. In this study, we aimed to investigate the effect of sensory loss on jaw motion and muscle activation. We hypothesized that muscles in the sensory-loss condition have reduced activation and delayed peak timing, and the jaw shows slower opening and a smaller range of motion (ROM) during chewing.

Methods

We collected jaw position and muscle activity while an adult male rhesus macaque (Macaca mulatta, weight: 11.5 kg, age: 8 years) performed a feeding task. In the simulated sensory-loss condition, a temporary anesthetic block was applied to the sensory branches of the trigeminal nerve prior to the experiment. Jaw motions were captured using marker-based biplanar videoradiography at 200Hz. Fine-wire electromyography (EMG) was used to record the activity from temporalis, masseter, and digastricus at 10kHz. Gape cycles identified as chews were included in the analysis. Jaw ROM and duration were evaluated for each chew cycle from maximum gape to the minimum gape. Raw EMG signals were filtered, rectified, and then applied to a moving-average window of 50ms. To quantitatively evaluate the effect of sensory loss, we compared the jaw ROM, gape close phase duration, EMG peak intensity, and time between the EMG peak from the maximum gape and to the minimum gape, with control condition.

Results

In the control condition, the jaw ROM was ~15° with a gape close phase duration of ~191.1ms. EMG peak intensity varies between muscles. Under nerve block, jaw ROM decreased by 11%, gape close phase duration increased by 14%, EMG peak intensity decreased by 7-52%, delayed EMG occurrence by 12-28%, and longer time from EMG peak to minimum gape in most muscles (Table 1).

Discussion

Our study demonstrates that sensory feedback is critical during chewing. Sensory loss changes both kinematics and EMG features. These may further change the loading

mechanics in the oral cavity and TMJ joint. Abnormal loading mechanics have been considered a source of early degenerative changes in the joint. However, the EMG intensity decrease in the nerve block condition may be a potential compensatory mechanism to reduce excessive force generation.

Images (Optional)

Table 1. Jaw kinematics and EMG features

		Nerve block (n= 426 gape cycles) mean (SD)	Control (n = 841 gape cycles) mean (SD)	P-value
ROM (Max gape to Min gape, °)		13.1 (5.6)	14.7 (3.9)	<0.001
Gape close duration (Max to Min gape, ms)		218.0 (48.1)	191.1 (46.0)	<0.001
Peak EMG intensity (au)	Masseter	10532.6 (4074.6)	11274.1 (3952.5)	<0.001
	Temporalis	14800 2 (6322.0)	18688.1 (4148.0)	<0.001
	Digastricus	370.1 (214.2)	764.8 (376.2)	<0.001
Time (Max gape to EMG peak, ms)	Masseter	153.0 (48.8)	119.8 (48.9)	<0.001
	Temporalis	142.0 (48.7)	126.7 (47.0)	<0.001
	Digastricus	299.8 (96.4)	236.9 (80.6)	<0.001
Time (EMG peak to Min gape, ms)	Masseter	65.0 (29.4)	72.5 (33.6)	0.0016
	Temporalis	76.0 (24.3)	65.0 (33.2)	<0.001
	Digastricus	-85.3 (72.4)	-45.3 (65.4)	<0.001

References (Optional)

Acknowledgements (Optional)

We thank the National Institutes of Health for funding support (National Institute of Dental and Craniofacial Research: R01DE027236 and National Institute on Aging: R01AG069227).

Session Category

Comparative Biomechanics: N/A

OA13-03

Can Concomitant Meniscus Injury Modify Jumping Characteristics in Female Adolescents After Acl Reconstruction?

Dr. Karine Velasques Stoelben[1], Dr. Allison Clouthier[2], Dr. Alicia Kerrigan[1], Dr. Daniel Benoit[3], Dr. Sasha Carsen[1]

[1]CHEO Research Institute, Ottawa, Ontario, Canada. [2]University of Ottawa, Ottawa, Ontario, Canada. [3]Lund Univerisity, Lund, Scania, Sweden

Introduction

Meniscal injury often presents as part of initial anterior cruciate ligament (ACL) injury or emerges due to chronic ACL-deficiency. Meniscus injuries can impact joint load absorption, potentially leading to different landing strategies. Ten months after surgery, adult patients with concomitant meniscus and ACL injury and isolated ACL injury presented no differences in jump performance. However, the impact of concomitant injury on jumping strategies and whether it is replicated in adolescent patients is still unclear. Considering that young females are among the highest risk for poor landing mechanics and associated ACL injury, we investigated whether jump outcomes differ between female adolescents who had a concomitant meniscus injury versus an isolated ACL injury after return to activity clearance (RTA).

Methods

We conducted a cross-sectional analysis of 30 female adolescent patients who underwent ACL reconstruction surgery (ACLR) classified into two groups: concomitant (meniscus and ACL injuries) or isolated group (ACL-only injury). All participants were released to RTA and completed five trials of countermovement jump on two force plates. Outcomes measured were: ground reaction force peak (GRFp) and impulse during propulsion phase; GRFp and absorption rate (GRFp/time to peak) during landing phase; and jump height (normalized to participant's body weight or height). Mann-Whitney U, Independent t-tests, or chi-square tests compared demographic characteristics and MANOVA was used to identify group effect.

Results

Seventy-seven percent of patients presented a concomitant meniscus and ACL injury. There was no difference between groups for demographic characteristics, autograft type, or time since surgery. The concomitant injury group presented lower GRFp and higher time

to GRFp in the injured leg than the isolated injury group (Figure 1A-B). The absorption rate was lower in both legs for the concomitant injury group (Figure 1C-D).

Discussion

Female adolescents with concomitant meniscus and ACL injury present a worse strategy in jump landing than those with isolated ACL injury 9 months post-ACLR. Concomitant injury leads to longer landing compensations, which suggests a protective mechanism in favour of the injured leg. Therefore, rehabilitation process and RTA clearance may take longer and require special attention to the landing strategy for patients who have undergone surgery for concomitant injuries.

Images (Optional)

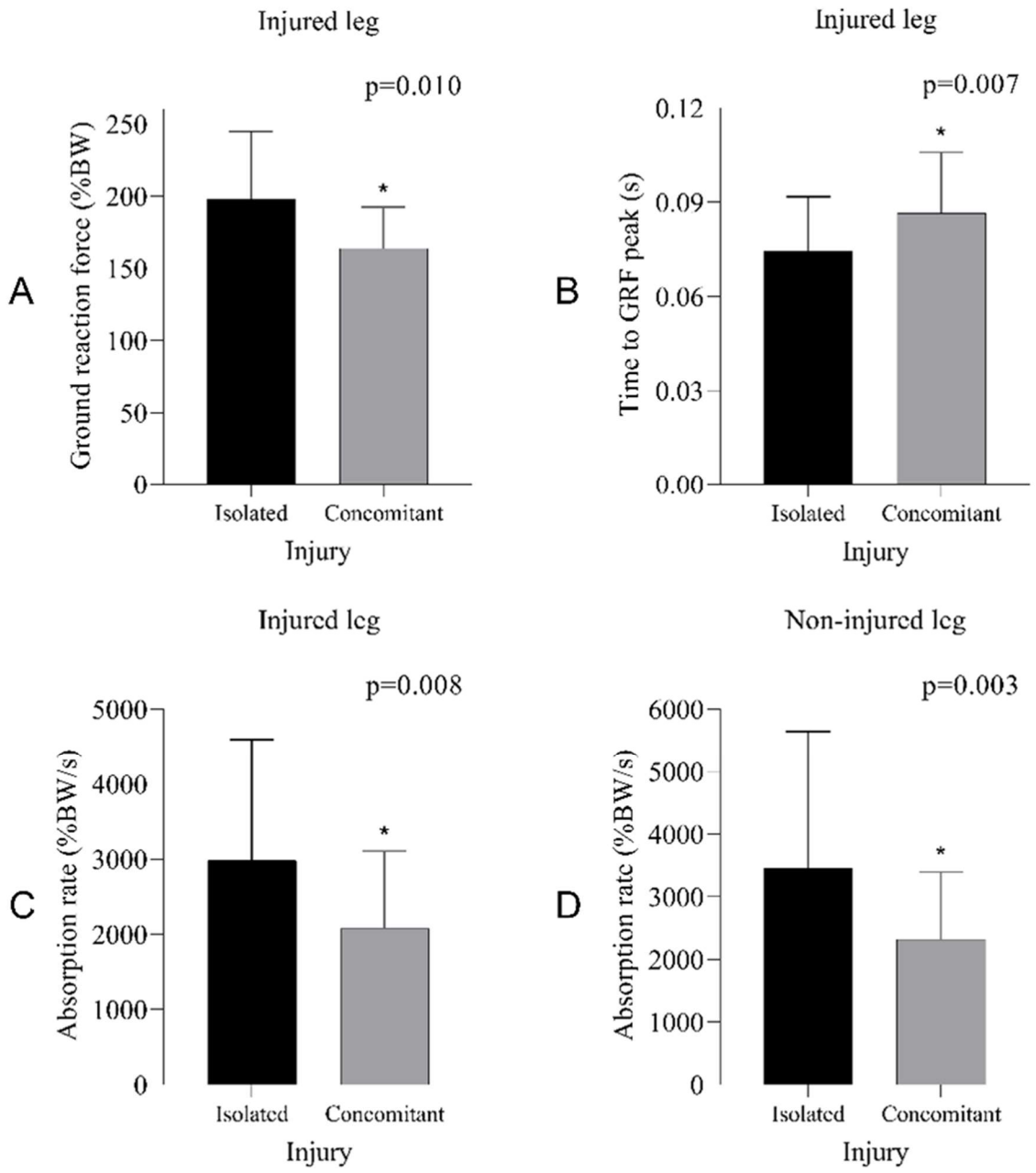


Figure 1. Jump landing differences between female pediatric patients with isolated ACL and concomitant meniscus and ACL injuries.

References (Optional)

Session Category

Orthopaedic Biomechanics: Sports Medicine

OA13-04

Stretch-Shortening Cycle Force-Time and Power-Time SPM Waveform Analysis Indicates Limitations of the Contralateral Limb Benchmark in Athletes After ACLR

Ms. Shadan Al-Saket[1], Mr. Zachary McClean[1], Dr. Nathan Boon-van Mossel[1], Dr. Tanita Botha[2], Dr. Helen Bayne[3,4], Mrs. Cassidy de França[5], Dr. Kati Pasanen[1], Dr. Matthew Jordan[1]

[1]University of Calgary, Calgary, AB, Canada. [2]Deakin University, Geelong, Victoria, Australia. [3]The University of Western Australia, Perth, WA, Australia. [4]Western Australian Institute of Sport, Perth, WA, Australia. [5]University of Pretoria, Pretoria, Gauteng, South Africa

Introduction

Unilateral countermovement jump (CMJ_{SL}) testing is commonly used after anterior cruciate ligament reconstruction (ACLR) to assess stretch-shortening cycle (SSC) function, neuromuscular deficits and return-to-sport (RTS) readiness. However, the impact of ACLR on contralateral limb SSC function is poorly understood and whether the unaffected contralateral limb benchmark overestimates rehabilitation status compared to an objective benchmark from sport- and sex-matched athletes remains unclear. Moving beyond discrete performance, statistical parametric mapping (SPM) may reveal additional regional deficits in CMJ_{SL} biomechanics in athletes after ACLR. This study employed SPM to compare interlimb force- and power-time CMJ_{SL} curves of (i) athletes after ACLR and (ii) healthy athletes with better ($GOOD_{SFI}$) and worse ($POOR_{SFI}$) perceived-limb function, evaluated using the Sport Fitness Index (SFI); and (iii) compare affected & unaffected limbs in ACLR athletes to an enhanced benchmark established from the $GOOD_{SFI}$ group (i.e. the $Control^{+}$ benchmark).

Methods

Canadian university athletes post-ACLR (*n*=20; 11 female; 14±5 months post-op) cleared for RTS and healthy controls (*n*=464; 192 female) performed maximal CMJ_{SL} testing on a force plate. SFI assessed perceived-limb function, and healthy control participants were divided into upper ($GOOD_{SFI}$) and lower ($POOR_{SFI}$) tertiles. The top-ranked jumpers with $GOOD_{SFI}$ were sex- and sport-matched to ACLR athletes to obtain the CMJ_{SL} $Control^{+}$ (enhanced) benchmark. CMJ_{SL} curves were compared within and between-groups using SPM.

Results

No interlimb differences were found in healthy athletes with $GOOD_{SFI}$, whereas healthy control athletes with $POOR_{SFI}$ demonstrated interlimb force and power deficits over 13% and 4% of the CMJ_{SL} movement, respectively ($p<0.001$). Compared to the unaffected limb, the affected limb of ACLR athletes showed reduced force and power over 8% ($p<0.001$) of the CMJ_{SL} propulsive phase. Reflecting greater regions of impairment, the affected limb generated less force over 14% and less power over 25% ($p<0.001$) of propulsion compared to the Control^{+} benchmark.

Discussion

An enhanced biomechanical benchmark provided a better indication of persistent SSC impairments than the contralateral limb benchmark in athletes who had returned to sport post-ACLR. Further, healthy athletes with worse perceived-limb function demonstrated interlimb force and power impairments similar to the ACLR group, highlighting the value of combining biomechanical testing with psychosocial measures in university athletes.

Images (Optional)

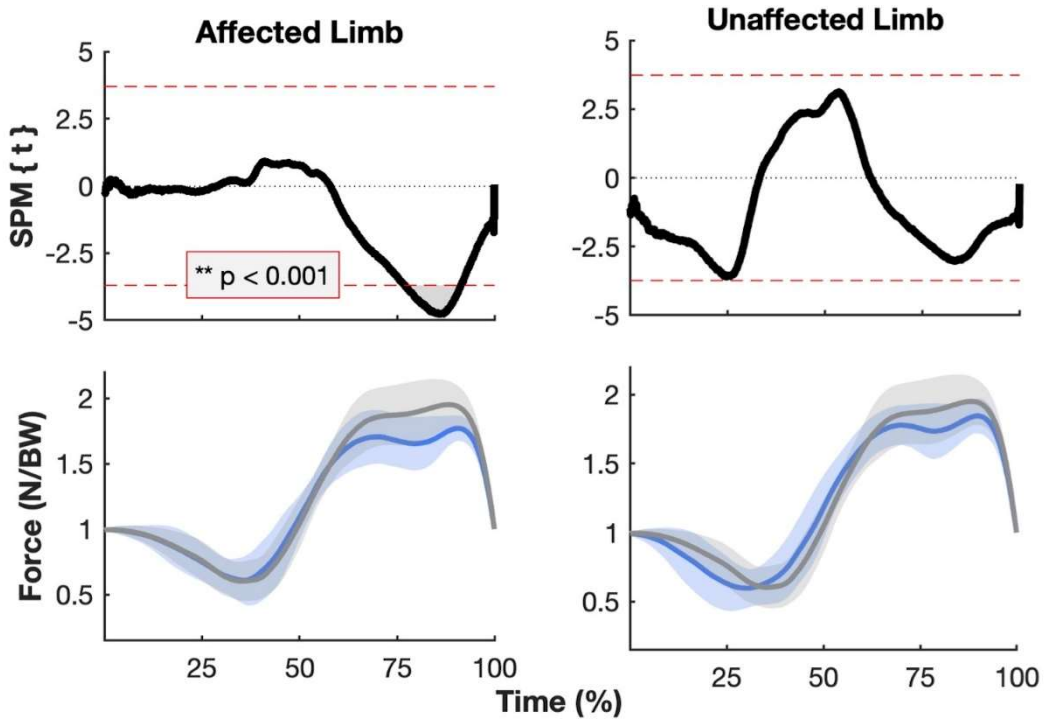


Figure SPM (top) and force-time (bottom) curves of the Control^{+} benchmark (grey) compared to affected limb (left) and unaffected limb (right) of athletes with ACLR (blue).

Session Category

Orthopaedic Biomechanics: Sports Medicine

OA14-01

Comparison of Scapulothoracic and Glenohumeral Kinematics and Muscle Activation in Individuals Undergoing Bankart and Latarjet Repair

Dr. Renato Miyadahira MD[1,2], Dr. Felipe Gonzalez MD, MsC[1,2,3], Dr. João Bonadiman MD[4], Dr. Tiago Zimerman MD[1,2], Mr. Asim Khan MSc[2], Dr. Eliane Guadagnin PhD[1], Dr. Jorge Chahla MD, PhD[2], Dr. Leonardo Metsavaht MD, PhD[1,3], Dr. Gustavo Leporace PhD[1,3], Dr. Grant Garrigues MD[2], Dr. Gregory Nicholson MD[2], Dr. Jonathan Gustafson PhD[2,1]

[1]Instituto Brasil de Tecnologia da Saude, Rio de Janeiro, RJ, Brazil. [2]Rush University, Chicago, IL, United States. [3]Escola Paulista de Medicina, Universidade Federal de São Paulo (UNIFESP), São Paulo, São Paulo, Brazil. [4]Instituto Brasil de Tecnologia da Saude, Rio de Janeiro, RJ, United States

Dr. Renato Miyadahira

Introduction

Bankart repair and the Latarjet procedure are commonly used to treat recurrent anterior shoulder instability. Loss of external rotation (ER) has been seen after the Latarjet procedure, and Bankart repair may also alter muscular control of the shoulder. However, the specific neuromuscular strategies adopted after each procedure remain poorly understood, particularly during positions of high mechanical demand, such as ER with abduction. Our goal was to compare active ER range of motion and neuromuscular activation patterns after Bankart repair and Latarjet procedures, using healthy shoulders as controls.

Methods

Thirty participants (n=30) were enrolled and assigned to three equal groups (n=10 each group): arthroscopic Bankart repair, Bristow–Latarjet–Patte procedure, and healthy controls. Shoulder motion was captured using a 3D optical tracking system, and surface electromyography recorded activity from the deltoid, trapezius, pectoralis major, infraspinatus, teres minor, and serratus anterior. Participants performed ER at 90º of abduction in both weighted and unweighted conditions. Non-normally distributed variables were analyzed using the Kruskal–Wallis test with Dunn post-hoc analysis ($\alpha = 0.05$).

Results

Compared to healthy controls, the Bankart group showed greater humerothoracic flexion–extension during weighted ER (14.6º±6.0º vs 5.5º±8.2º; P=0.04) (Figure). [JG1] Both surgical groups trended (P=0.07) towards increased Scapulothoracic upward rotation during unweighted ER compared with controls (P=0.07). The Bankart repair group demonstrated greater activation of the pectoralis major (sternal head) compared with the Latarjet procedure only in the weighted condition (34.6%±17.1% vs 14.2%±11.3%; P=0.03). The Latarjet group trended towards greater infraspinatus activation in the unweighted condition (43.8%±14.5% vs 33.3%±6.1%; P=0.09).

Discussion

Although total active ER range of motion was similar across groups, Bankart shoulders demonstrated greater humerothoracic flexion–extension and increased activation of the pectoralis major (sternal head) during weighted ER. In contrast, Latarjet shoulders exhibited higher activation of the infraspinatus, indicating more posterior stabilization. The greater anterior recruitment observed in Bankart shoulders under load may be clinically relevant for postoperative rehabilitation planning to prevent potential anterior impingement problems**.**

Images (Optional)

A.

Joint	Bankart	Latarjet	Healthy-Control	P
	Mean ± SD	Mean ± SD	Mean ± SD	
Glenohumeral unweighted (º)	33.3 ± 11.9	24.3 ±12.9	29.7 ± 9.8	0.29
Glenohumeral weighted (º)	32.8 ± 10.3	13.2 ± 5.0	30.5 ± 12.8	0.53
Humerothoracic unweighted (Abduction-Adduction) (º)	3.4 ± 7.4	5.7 ± 6.7	4.6º ± 5.6	0.55
Humerothoracic weighted (Abduction-Adduction) (º)	6.2 ± 8.5	6.2 ± 4.3	5.8 ± 7.2	0.95
Humerothoracic unweighted (Flexion-Extension) (º)	15.6 ± 9.1	10.0 ± 6.0	8.4 ± 7.7	0.16
Humerothoracic weighted (Flexion-Extension) (º)	**14.6 ± 6.0**	**9.5 ± 6.3**	**5.5 ± 8.2**	**0.04**
Scapulothoracic unweighted (Antero-posterior tilt) (º)	-2.5 ± 9.0	3.3 ±10.2	4.4 ± 12.2	0.36
Scapulothoracic weighted (Antero-posterior tilt) (º)	-2.7 ± 11.8	3.7 ± 10.6	5.7 ± 11.9	0.48
Scapulothoracic unweighted (Upwards-Downward rotation) (º)	6.6 ± 5.6	7.9 ± 4.7	3.9 ± 3.5	0.07
Scapulothoracic weighted (Upwards-Downward rotation) (º)	7.9 ± 4.4	8.2 ± 3.9	6.1 ± 3.8	0.28
Scapulothoracic unweighted (Internal-External rotation) (º)	-8.9 ± 4.1	-9.8 ± 3.9	-8.8 ± 5.9	0.60
Scapulothoracic weighted (Internal-External rotation) (º)	-10.3 ± 4.9	-11.1 ± 4.4	-9.7 ± 6.6	0.26

B.

Muscles	Bankart	Latarjet	Healthy-Control	P
	Mean ± SD (%MVC)	Mean ± SD (%MVC)	Mean ± SD (%MVC)	
Pectoralis Major – Clavicular head (Unweighted)	12.8 ± 10.8	8.0 ± 7.5	10.5 ± 13.6	0.47
Pectoralis Major – Clavicular head (Weighted)	17.8 ± 14.5	12.0 ±10.0	14.3 ± 17.2	0.62
Pectoralis Major – Sternal head (Unweighted)	26.6 ± 16.2	10.1 ± 9.1	16.8 ± 13.6	0.08
Pectoralis Major – Sternal head (Weighted)	**34.6 ± 17.1**	**14.2 ± 11.3**	**22.2 ± 16.7**	**0.03**
Anterior Deltoids (Unweighted)	17.4 ± 9.5	18.6 ±6.0	21.8 ± 8.8	0.42
Anterior Deltoids (Weighted)	28.6 ± 12.4	25.4 ± 6.2	28.2 ± 14.8	0.86
Middle Deltoids (Unweighted)	19.5 ± 10.8	17.3 ± 4.6	22.9 ± 9.2	0.31
Middle Deltoids (Weighted)	26.7 ± 16.0	22.4 ± 6.4	29.3 ± 12.1	0.33
Posterior Deltoids (Unweighted)	20.4 ± 11.1	22.1 ± 13.1	18.0 ± 8.6	0.94
Posterior Deltoids (Weighted)	27.6 ± 17.1	27.8 ± 14.6	27.0 ± 10.6	0.96
Upper Trapezius (Unweighted)	24.3 ± 10.1	24.1 ± 10.6	24.1 ± 10.6	0.94
Upper Trapezius (Weighted)	37.6 ± 10.9	40.1 ± 19.4	40.1 ± 19.5	0.82
Middle Trapezius (Unweighted)	36.0 ± 17.3	38.7 ±13.2	27.1 ± 14.0	0.16
Middle Trapezius (Weighted)	40.2 ± 15.2	46.0 ± 14.1	41.0 ± 14.9	0.69
Lower Trapezius (Unweighted)	35.1 ± 17.7	31.4 ± 14.9	25.8 ±15.3	0.55
Lower Trapezius (Weighted)	41.8 ± 21.0	42.2 ± 15.3	38.5 ± 17.2	0.80
Infraspinatus (Unweighted)	34.0 ± 9.0	43.8 ±14.5	33.3 ± 6.1	0.09
Infraspinatus (Weighted)	54.5 ± 13.2	66.5 ± 15.0	61.3 ± 9.7	0.16
Teres Minor (Unweighted)	29.6 ± 12.6	21.6 ± 10.8	21.6 ± 10.7	0.27
Teres Minor (Weighted)	54.3 ± 22.1	51.8 ± 20.0	49.2 ± 21.9	0.80
Serratus Anterior (Unweighted)	23.1 ± 8.9	23.4 ± 10.9	17.5 ± 13.8	0.33
Serratus Anterior (Weighted)	37.4 ± 13.5	40.0 ± 16.5	34.0 ± 23.3	0.67

A: Comparison of joint kinematics and across Bankart, Latarjet, and Healthy-control groups.

B: Superficial electromyographic activations between Bankart, Latarjet, and Healthy-control groups

SD: Standard Deviation; MVC: Maximum Voluntary Contraction.

Session Category

Clinical Biomechanics: N/A

OA14-02

Changes in Shoulder Biomechanics During Forward Flexion After Bankart and Latarjet Procedures

Dr. Renato Miyadahira MD[1], Dr. Tiago Zimerman MD[2,1], Dr. Felipe F. Gonzalez MD, MSc[2,1,3], Ms. Vennela Challagondla BS, MPH[4], Dr. Eliane C. Guadagnin PhD[1], Dr. Jorge Chahla MD, PhD[2,5], Dr. Leonardo Metsavaht MD, PhD[1,3], Dr. Gustavo Leporace PhD[1,3], Dr. Grant E. Garrigues MD[2], Dr. Gregory Nicholson MD[2], Dr. Jonathan A. Gustafson PhD[2,1]

[1]Instituto Brasil de Tecnologias da Saúde (IBTS), Rio de Janeiro, Rio de Janeiro, Brazil. [2]RUSH University Medical Center, Chicago, Illinois, United States. [3]Escola Paulista de Medicina, Universidade Federal de São Paulo (UNIFESP), São Paulo, São Paulo, Brazil. [4]The University of Illinois Chicago College of Medicine, Chicago, Illinois, United States. [5]Midwest Orthopaedics at Rush, Chicago, Illinois, United States

Dr. Renato Miyadahira

Introduction

Both Bankart and Latarjet procedures are well-established techniques for surgically treating anterior shoulder instability. However, their effects on shoulder biomechanics during flexion remain poorly understood. Understanding postoperative adaptations in muscle activation and biomechanical motion can help explain how stability is restored postoperatively. We aimed to compare in vivo glenohumeral and scapulothoracic kinematics, as well as surface electromyographic (EMG) activation during forward flexion, among patients who underwent arthroscopic Bankart repair, open Latarjet procedure, and healthy controls.

Methods

Thirty participants were enrolled and divided into three groups (n=10 each group): Bankart, Latarjet, and healthy controls. Participants conducted active shoulder forward flexion tests without and with weights (1.4 kg in each hand) in our motion analysis lab. Three-dimensional glenohumeral and scapulothoracic kinematics was recorded using an optical motion-capture system synchronized with surface EMG of the deltoid (anterior, middle, posterior portions), pectoralis major (clavicular and sternal heads), trapezius (upper, middle, lower portions), serratus anterior, infraspinatus, and teres minor. Non-normally

distributed variables were compared using the Kruskal–Wallis test with Dunn's post-hoc analysis (α=0.05).

Results

Significant differences (Figure 1) between groups were observed in EMG activation during unweighted, ascending phase of flexion for the middle trapezius (ε^2=0.21, P=0.05), pectoralis major sternal head (ε^2=0.21, P=0.05), infraspinatus (ε^2=0.24, P=0.03), and teres minor (ε^2=0.22, P=0.04). Shoulders with Bankart repair showed greater activation of the middle trapezius and pectoralis major than Latarjet (P=0.04) and higher teres minor activation than healthy controls (P=0.04). Conversely, the Latarjet group presented higher infraspinatus activation than the Bankart group during unweighted ascending (P=0.03) phases and both unweighted (P=0.01) and weighted (P=0.03) descending phases. Kinematic analysis revealed greater scapulothoracic internal/external rotation in the unweighted descending phase in Bankart compared to Latarjet shoulders (ε^2=0.30, P=0.01). No significant differences were found for the glenohumeral joint.

Discussion

Latarjet patients showed increased infraspinatus activity and greater scapular external rotation during the descending phase of flexion, indicating increased stabilization of the shoulder to improve joint compression. These findings suggest that Latarjet patients demonstrate a more mechanically efficient and neuromuscularly balanced shoulder function, which may improve long-term stability compared with isolated soft-tissue repair.

Images (Optional)

A.

Muscles	Comparison	Z	P	Interpretation
Ascending				
Middle_Trapezius (without weights)	Bankart vs. Healthy	1.42	0.46	No significant differences
	Bankart vs. Latarjet	**2.46**	**0.04**	**Significant**
	Healthy vs. Latarjet	1.04	0.89	No significant differences
Pectoralis_Major Sternal Head (without weights)	Bankart vs. Healthy	1.13	0.77	No significant differences
	Bankart vs. Latarjet	**2.45**	**0.04**	**Significant**
	Healthy vs. Latarjet	1.32	0.56	No significant differences
Infraspinatus (without weights)	Bankart vs. Healthy	-1.03	0.91	No significant differences
	Bankart vs. Latarjet	**-2.63**	**0.03**	**Significant**
	Healthy vs. Latarjet	-1.60	0.33	No significant differences
Teres Minor (without weights)	**Bankart vs. Healthy**	**2.51**	**0.04**	**Significant**
	Bankart vs. Latarjet	1.33	0.55	No significant differences
	Healthy vs. Latarjet	-1.18	0.71	No significant differences
Descending				
Infraspinatus (without weights)	Bankart vs. Healthy	-1.02	0.93	No significant differences
	Bankart vs. Latarjet	**-3.02**	**0.01**	**Significant**
	Healthy vs. Latarjet	-2.01	0.13	No significant differences
Infraspinatus (with weights)	Bankart vs. Healthy	-0.79	1.00	No significant differences
	Bankart vs. Latarjet	**-2.64**	**0.02**	**Significant**
	Healthy vs. Latarjet	-1.85	0.19	No significant differences

B.

Muscle	Comparison	Z	P	Interpretation
Descending				
ScapuloThoracic_Z (without weights)	Bankart vs. Healthy	0.91	1.00	No significant differences
	Bankart vs. Latarjet	**2.90**	**0.01**	**Significant**
	Healthy vs. Latarjet	1.98	0.14	No significant differences

Figure 1:
A. Post-hoc pairwise comparisons (Dunn) of **muscle activation** among groups with statistically significant differences during the Flexion ascending and descending phases.
B. Post-hoc pairwise comparisons (Dunn) of **kinematic variables** among groups with statistically significant differences during the Flexion ascending and descending phases.

Session Category

Clinical Biomechanics: N/A

OA14-03

Association Between Glenoid Deformity Correction and Functional Humeral Head Subluxation in Anatomic Total Shoulder Arthroplasty

Dr. Nazanin Daneshvarhashjin[1], Ms. Line Ven[1], Prof. Philippe Debeer[2], Prof. Michael S Andersen[3], Prof. Filip Verhaegen[1,4], Prof. Lennart Scheys[1,4]

[1]KU Leuven University, Leuven, Flanders, Belgium. [2]University Hospital Leuven, Leuven, North Jutland Region, Belgium. [3]Aalborg University, Aalborg, Flanders, Denmark. [4]University Hospital Leuven, Leuven, Flanders, Belgium

Introduction

Recentering the humeral head by correcting glenoid deformity is a key goal of anatomic total shoulder arthroplasty (aTSA) in the treatment of shoulder osteoarthritis. Postoperative humeral head subluxation (HHS) causes eccentric loading and increases the risk of implant loosening. Understanding how intra-operative glenoid correction relates to HHS correction is, therefore, important for reducing implant failure. Previous studies using CT images in supine positions have reported inconsistent findings, and the relationship in upright, functional positions remains largely unexplored. This study aims to address this gap.

Methods

Pre- and postoperative biplanar radiographs in six upright functional arm positions and supine CT images were collected for patients undergoing aTSA (n=28). Radiographs were obtained in relaxed standing (RS), extension (45EX), 45 and 90 degrees of flexion (45F and 90F), and abduction (45AB and 90AB). 3D bone models were reconstructed from CT (Fig1.A-B) and registered to their corresponding 2D biplanar radiographs (Fig1.C). 3D glenoid component models were also registered to CT images. To measure HHS, the (implanted) humeral head center offsets from the native/implanted glenoid center in the anteroposterior (AP) and superior-inferior (SI) directions were measured in each pose and normalized to the (implanted) humeral head diameter (Fig1.D). A stepwise linear regression analysis was conducted to quantify the effects of pre- to post-op glenoid correction—including version, inclination, and center translation — on correction of HHS.

Results

HHS-AP was predicted by glenoid version correction in the supine position ($\beta = 0.46$, $p = 0.03$), but not during functional arm positions. HHS-SI was predicted by inclination correction in supine ($\beta = 0.43$, $p = 0.04$) and several functional positions (45AB, 90AB, 90F, 45F with $\beta > 0.35$ and $p<0.05$). Glenoid center translation in the SI direction was also a

predictor of HHS-SI in functional arm poses (45AB, 90AB, 45F). Additionally, glenoid translation in the ML direction predicted HHS-AP at EX, while glenoid version correction predicted HHS-SI at 90F.

Discussion

Correction of glenoid inclination and superior implant positioning can play a significant role in correcting HHS-SI, whereas glenoid version correction does not predict HHS-AP in functional poses. This lack of surgical control may explain the underlying mechanism behind glenoid component loosening.

Images (Optional)

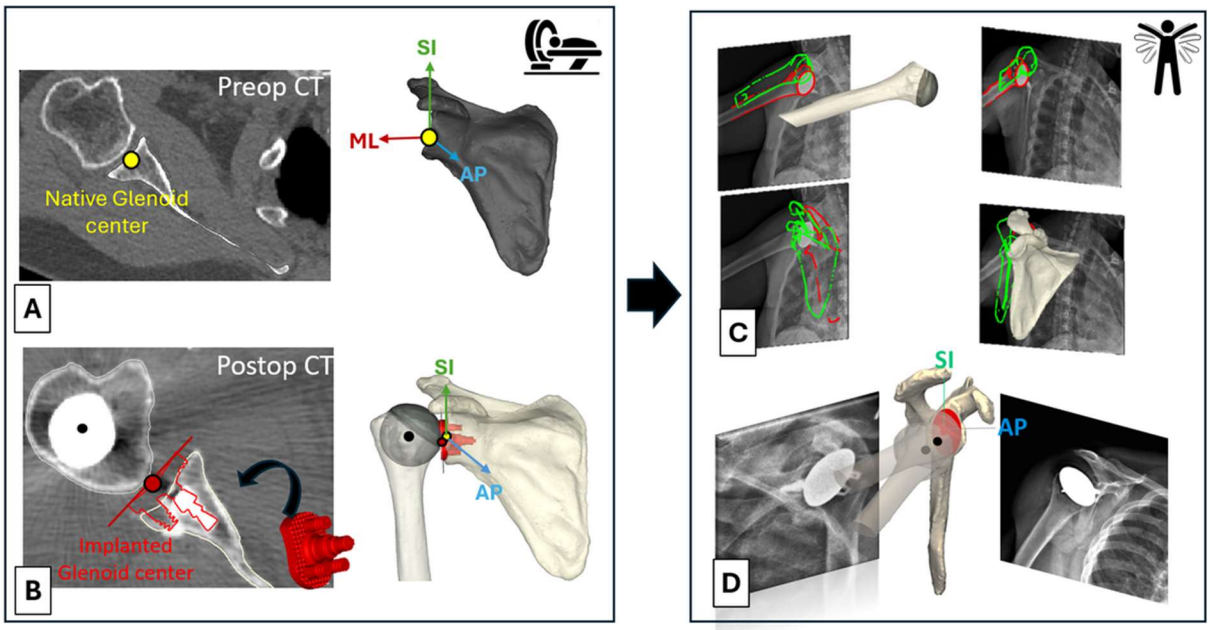


Fig 1. Methodological framework of the study

Acknowledgements (Optional)

The authors thank and PRosPERoS-II Interreg VA Flanders–The Netherlands (2021TC16RFCB041) for financial support.

Session Category

Clinical Biomechanics: N/A

OA14-04

Kinematic and Electromyographic Differences Between Medialized and Lateralized Glenospheres During External Rotation

Dr. João A. Bonadiman MD[1], Dr. Renato Miyadahira MD[2], Dr. Vitor La Banca MD[2], Dr. Felipe F. Gonzalez MD[3,2], Dr. Carolline P. Nunes MD[3,2], Dr. Jorge Chahla MD[3], Dr. Gregory Nicholson MD[3], Dr. Nikhil Verma MD[3], Dr. Brian Forsythe MD[3], Dr. Leonardo Metsavaht PhD[2], Dr. Gustavo Leporace PhD[2], Dr. Grant Garrigues MD[3], Dr. Jonathan Gustafson PhD[4]

[1]Instituto Brasil de Tecnologias da Saúde (IBTS) of Orthopaedics, Rio de Janeiro, Rio de Janeiro, Brazil. [2]Instituto Brasil de Tecnologias da Saúde (IBTS), Rio de Janeiro, Rio de Janeiro, Brazil. [3]Department of Orthopaedics, Rush University Medical Center, Chicago, Illinois, United States. [4]Rush University Medical College, Chicago, Illinois, United States

Introduction

Loss of active external rotation is frequent in rotator cuff arthropathy and a key indication for reverse total shoulder arthroplasty (RTSA). Implant design, especially medialized versus lateralized glenospheres, may alter biomechanics and muscle recruitment, although in vivo comparisons are limited. This study aimed to compare humerothoracic external rotation between RTSA designs and to assess the related electromyographic activity.

Methods

This cross-sectional study included 22 RTSAs with either a medialized (n=12, mean age 71.2 ± 6.1 years, mean follow-up 47 ± 22 weeks) or lateralized design (n=10, mean age 70.8 ± 6.5 years, mean follow-up 68 ± 56 weeks). Three-dimensional optoelectronic motion capture and surface EMG were used to record standardized external rotation tasks with the arm at the side (ER1) and at 90 degrees abduction (ER2). Outcomes included humerothoracic range of motion (ROM), scapulohumeral rhythm, and EMG activity of the deltoid, pectoralis major, infraspinatus, teres minor, trapezius, and serratus anterior. EMG values were normalized to maximal voluntary isometric contraction. Between-group comparisons were performed using Mann-Whitney U-tests, and effect sizes were reported.

Results

In ER2, the medialized group demonstrated greater humerothoracic ROM compared with the lateralized group (16.7°± 10.3° vs. 5.8° ± 7.2°, P = 0.020, r = 0.485) (Table 1-A). No significant difference was observed in ER1 (18.2° ± 10.8° vs. 25.8° ± 8.9° , P = 0.088). Medialized implants demonstrated higher anterior deltoid activation (ER1: 11.0% ± 9.1%

vs. 5.0% ± 4.7%, P = 0.017; ER2: 34.2%± 11.2% vs. 22.0% ± 10.2%, P = 0.038), greater middle deltoid recruitment across tasks, and increased middle trapezius activity (ER1: 33.2% ± 10.8% vs. 20.0% ± 15.0%, P = 0.017) (Table 1-B). Lateralized designs showed lower overall activation of deltoid and trapezius muscles, with more balanced activity across scapular stabilizers.

Discussion

Medialized and lateralized glenospheres influence distinct biomechanical strategies during external rotation. Lateralized implants provided greater ROM in neutral with lower muscular demand, whereas medialized designs enhanced ROM at 90 degrees of abduction but required greater deltoid and trapezius recruitment. These position-specific trade-offs highlight the influence of implant design on motion and neuromuscular load and support individualized implant selection and rehabilitation planning.

Images (Optional)

A. Range of motion

Movement	Position	Axis	RTSA Medialized Glenosphere ROM (Mean ± SD)	RTSA Lateralized Glenosphere ROM (Mean ± SD)	P-value	Effect Size (r)
Humerothoracic Angle (°)	ER1	Axial plane	18.2 ± 10.8	25.8 ± 8.9	0.088	0.356
Humerothoracic Angle (°)	ER2	Coronal plane	16.7 ± 10.3	5.8 ± 7.2	0.020	0.485
Glenohumeral Angle (°)	ER1	Axial plane	6.6 ± 15.4	15.9 ± 6.9	0.13	0.317
Glenohumeral Angle (°)	ER2	Axial plane	16.9 ± 10.3	15.2 ± 8.2	0.49	0.232
Scapulothoracic Angle (°)	ER1	Coronal plane	-1.2 ± 2.5	-0.8 ± 2.8	0.41	0.174
Scapulothoracic Angle (°)	ER2	Coronal plane	10.5 ± 6.3	6.1 ± 5.5	0.28	0.232

B. Electromyographic activation

Muscle	Position	EMG Metric	RTSA Medialized Glenosphere (Mean ± SD)	RTSA Lateralized Glenosphere (Mean ± SD)	P-value	Effect Size (r)
Anterior Deltoid	ER1	Mean	0.110 ± 0.091	0.050 ± 0.047	0.017	0.497
Anterior Deltoid	ER2	Mean	0.342 ± 0.112	0.220 ± 0.102	0.0377	0.433
Anterior Deltoid	ER2	Max	0.508 ± 0.165	0.333 ± 0.152	0.04	0.420
Posterior Deltoid	ER2	Mean	0.168 ± 0.095	0.096 ± 0.065	0.0771	0.369
Middle Trapezius	ER1	Mean	0.332 ± 0.108	0.200 ± 0.150	0.017	0.497
Middle Trapezius	ER1	Max	0.523 ± 0.169	0.323 ± 0.203	0.0236	0.472
Middle Trapezius	ER2	Mean	0.399 ± 0.148	0.264 ± 0.144	0.03	0.433
Middle Trapezius	ER2	Max	0.690 ± 0.281	0.468 ± 0.249	0.02	0.485

Figure 1:
A. Range of motion comparison between medialized and lateralized glenosphere models during external rotation in neutral and 90º of abduction. ROM: Range of Motion; SD: Standard Deviation; ER1: External Rotation in neutral position; ER2: External Rotation in 90º of abduction
B: Electromyographic activation comparison between medialized implant and lateralized implant during external rotations. SD: Standard Deviation; ER1: External Rotation in neutral position; ER2: External Rotation in 90º of abduction

Session Category

Clinical Biomechanics: N/A

OA14-05

Muscle-Tendon Recovery Trajectories Relate to Shoulder Disability in Rotator Cuff Tendinopathy

Dr. Kayla Seymore PhD[1], Dr. Oscar Vila-Dieguez PT, PhD[2], Dr. Matthew Heindel PT, DPT, PhD[1], Dr. Lori Michener PT, ATC, PhD[1]

[1]University of Southern California, Los Angeles, CA, United States. [2]University of California San Diego, San Diego, CA, United States

Introduction

Rotator cuff (RC) tendinopathy is a leading cause of shoulder disability, with up to half of patients experiencing persistent symptoms despite receiving gold-standard exercise treatment. Variability in shoulder disability outcomes following resistance exercise may be driven by distinct responses of common tendon structural and neuromuscular deficits to exercise treatment. However, mechanisms of muscle-tendon recovery for RC tendinopathy are not well understood and remain poorly linked to patient-centered outcomes. This study evaluated the association and contribution of shoulder neuromuscular function and tendon structure to shoulder disability outcomes during an 8-week resistance exercise program in individuals with RC tendinopathy.

Methods

Adults with RC tendinopathy (n=63, 23F/40M) underwent an 8-week standard-of-care resistance exercise program with measures taken at baseline and 8-weeks. Rate of force development from 50-100ms (RFD50-100) and 100-200ms (RFD100-200) during maximal external rotation isometric contraction was recorded with a load cell. Supraspinatus tendon thickness was measured via B-mode ultrasound. The Penn Shoulder Score assessed shoulder disability (0-100,100=no disability). Linear mixed-effect models tested the association of tendon structure and neuromuscular function, as well as contribution of change in neuromuscular function and tendon structure to shoulder disability, over 8 weeks of resistance exercise treatment.

Results

Tendon thickness was positively related to RFD100-200 over 8-weeks of treatment (b(SE)=7.97(3.86), p=0.042;Fig.1A). The main effects of change in tendon thickness and RFD100-200 were not related to shoulder disability, though their interaction with shoulder disability differed over time ($p<0.003$). Greater RFD100-200 at baseline related to less shoulder disability (b(SE)= -0.294(0.91), p=0.002) while reduction in tendon thickness at 8-

weeks related to improved shoulder disability (b(SE)=35.45(6.23), p<0.001;Fig.1B-C). No significant relationship or interactions were observed for RFD50-100.

Discussion

This study took an innovative approach to understand recovery for RC tendinopathy by linking tendon structure and neuromuscular function to shoulder disability outcomes with resistance exercise treatment. Findings provide critical insight into RC muscle-tendon recovery trajectories and identify tendon structural improvement as a key contributor to shoulder disability following resistance exercise treatment. Future work will integrate RC muscle activation and tendon stiffness to define the tendon loading response that drives structural remodeling and improved recovery.

Images (Optional)

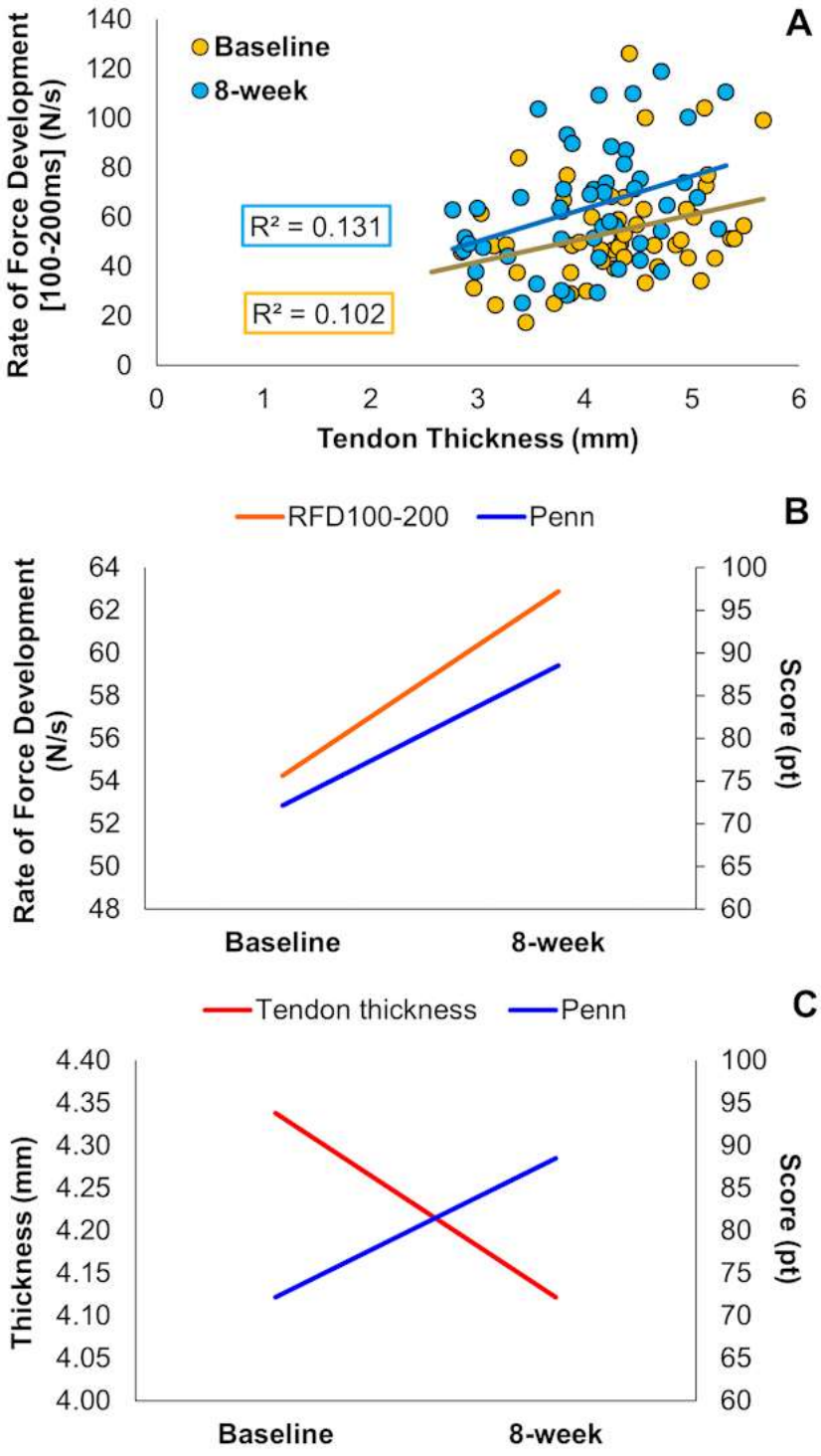


Figure1: [A] Association of neuromuscular function (RFD100-200) and tendon structure (thickness), [B] average shoulder disability (Penn) and neuromuscular function, and [C] average shoulder disability and tendon structure at baseline and 8 weeks of resistance exercise treatment. Higher RFD=improved neuromuscular function. Lower thickness=improved tendon structure. Higher Penn score=improved shoulder disability.

Session Category

Clinical Biomechanics: N/A

OA14-06

Exploratory Kinematic Analysis for Identifying Humeral Elevation Control Strategies in Rotator Cuff Tendinopathy

Mr Chethan Reddy, Mr Daniel McPherson DPT, Dr. Kayla Seymore, Dr. Lori Michener PhD, PT, ATC, FAPTA, FNATA

University of Southern California, Los Angeles, CA, United States

Introduction

Shoulder pain affects up to 25% of the general population, with rotator cuff (RC) tendinopathy accounting for up to 90% of diagnoses. Individuals with RC tendinopathy demonstrate altered kinematics that may modify tissue-loading mechanics and contribute to maladaptive tendon stress. How these altered movement patterns reflect underlying motor control strategies remains unclear. Studies have examined kinematics in discrete and interval differences, which may obscure meaningful temporal features. Continuous-time analysis offers a more complete representation of motor control strategies. In this study, we identify kinematic patterns that may indicate motor control differences in individuals with RC tendinopathy.

Methods

52 participants diagnosed with RC tendinopathy (32M/20F; age 29.0 ± 8.6) and 52 matched controls were examined. Participants performed a standardized bilateral humeral elevation task holding dumbbells, in a constrained scapular-plane motion, following a 75-beats-per-minute verbal cadence. Humeral kinematics for the affected side were collected using a Polhemus Liberty electromagnetic tracking system (240 Hz). Humeral elevation was computed using ISB-recommended Euler angle conventions and filtered with a 6 Hz Butterworth filter. Elevation cycles were extracted using standardized boundaries around each peak corresponding to the duration of movement, and velocity and acceleration profiles were calculated by numerical differentiation. Statistical Parametric Mapping two-sample t-tests were applied to position, velocity, and acceleration waveforms.

Results

Two significant regions of interest emerged for velocity during the eccentric phase: a mid-range (100-75°) interval ($p < 0.001$) and a late-range (30-20°) interval ($p = 0.002$). Patients exhibited higher magnitude velocities during the mid-range interval, but lower magnitude

velocities during the late-range interval. No significant group differences were identified for humeral elevation position or acceleration.

Discussion

Individuals with RC tendinopathy exhibited altered eccentric control strategies characterized by phase-specific modulation of humeral angular velocity. Higher mid-range velocity may reflect reduced active resistance to gravity when the external moment arm is largest, whereas lower late-range velocity may reflect a compensatory slowing strategy near the resting position. This suggests altered regulation of eccentric torque, which may contribute to abnormal tendon loading. These findings indicate that deficits in dynamic eccentric control, rather than positional limitations, may characterize RC tendinopathy.

Images (Optional)

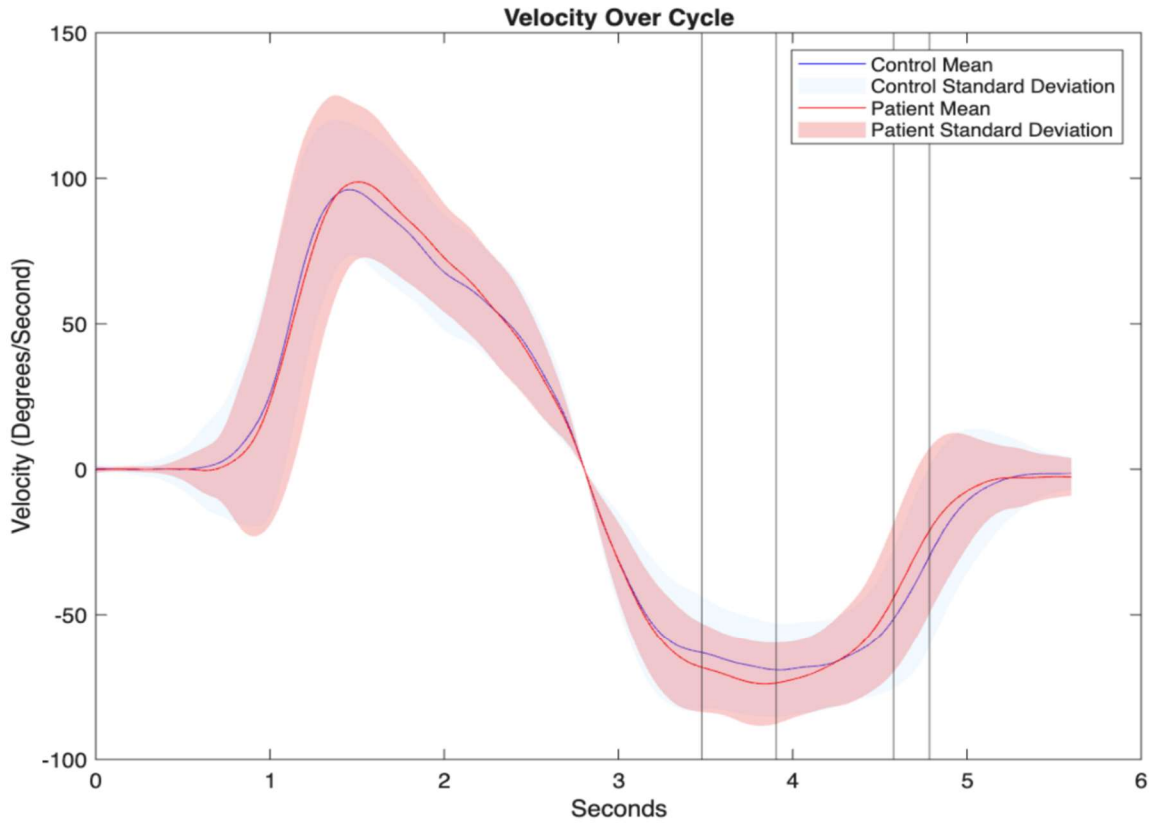


Figure 1. Mean (solid lines) and standard deviation (shaded regions) of humeral elevation angular velocity across the standardized arm-elevation cycle for participants with RC tendinopathy (red) and matched controls (blue). Vertical black lines denote the significant regions of interest identified by the SPM two-sample t-test.

References (Optional)

Acknowledgements (Optional)

Session Category

Clinical Biomechanics: N/A

OA15-02

Full-Body Gait Reconstruction from Arbitrarily Sparse Wearable Sensors via Diffusion Models with Transfer from Healthy to Pathological Populations

PhD Candidate Run Lin[1], Dr. Pavlos E. Evangelidis,[2], Dr. Dong Wang[1], Prof. Helen Dawes[2], Dr. Xijin Hua[1]

[1]Department of Engineering, Faculty of Environment, Science and Economy, University of Exeter, Exeter, Devon, United Kingdom. [2]NIHR Exeter BRC, University of Exeter Medical School, Exeter, Devon, United Kingdom

Introduction

Human motion analysis is essential for monitoring daily activities, tracking disease progression, and guiding rehabilitation. Conventional optical motion capture systems deliver high-fidelity measurements but are expensive, infrastructure-heavy and operationally demanding. Wearable inertial measurement units (IMUs) offer a practical alternative; however, existing approaches remain highly vulnerable to sparse or missing sensor signals and show limited adaptability to pathological gait. This study aimed to develop a unified diffusion-based generative model that reconstructs full-body motion from sparse or arbitrarily positioned IMUs and transfers this capability from healthy to pathological gait.

Methods

We proposed a two-stage diffusion-based framework operating on multichannel IMU data (Fig.1A). In the first stage, the model was trained on data from healthy controls to learn spatiotemporal dependencies across sensors and body segments, enabling reconstruction of complete motion signals under varying degrees of signal sparsity. In the second stage, a transfer-learning procedure fine-tuned the pretrained model using a small dataset of Parkinson's patient to adapt reconstruction to pathological gait patterns. Model performance was evaluated across diverse IMU configurations using R^2. Interpretability analyses were performed to gain a more comprehensive understanding of how different sensors and channels influence both healthy and pathological models.

Results

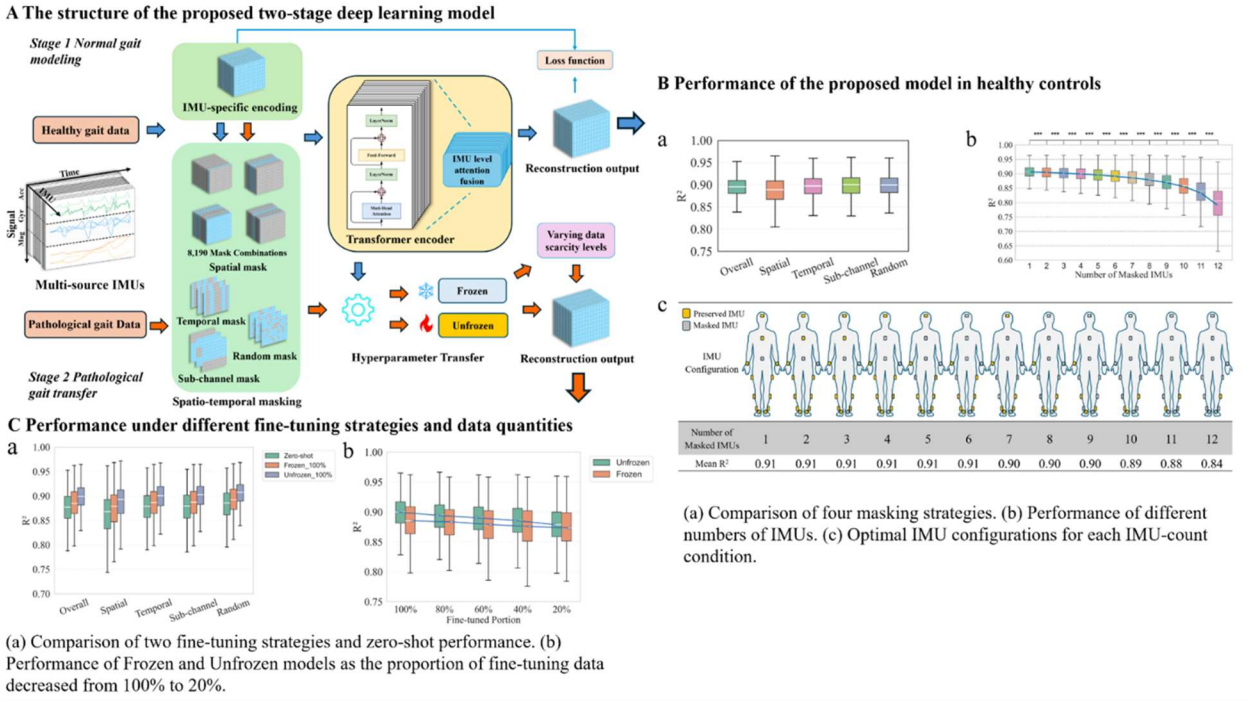
Trained on healthy data, the model accurately reconstructed full-body motion from sparse IMU configurations (mean $R^2 = 0.90$), despite severe signal degradation (Fig. 1B). Zero-shot evaluation on pathological gait showed a reduced R^2 of 0.86. After transfer learning on patient cohorts, the adapted model restored high-fidelity pathological gait reconstruction,

with a best-case R^2 of 0.89 (Fig 1C). Performance remained robust to different IMU placements and missing-sensor configurations.

Discussion

This is the first study to apply diffusion-based modelling to wearable gait analysis, enabling reconstruction of full-body IMU signals from sparse, arbitrarily placed sensors and transfer from healthy to pathological gait. Compared with prior methods relying on fixed configurations, the framework enables consistent biomechanical analyses across heterogeneous sensor configurations, greatly improving flexibility, robustness to missing data, and compatibility with downstream simulations. This has important implications for the design of portable wearables and exoskeletons, and future work will include validation in larger, more diverse populations and development of pathology-informed adaptive training and real-time deployment.

Images (Optional)



(a) Comparison of four masking strategies. (b) Performance of different numbers of IMUs. (c) Optimal IMU configurations for each IMU-count condition.

(a) Comparison of two fine-tuning strategies and zero-shot performance. (b) Performance of Frozen and Unfrozen models as the proportion of fine-tuning data decreased from 100% to 20%.

Session Category

Human Motion and Performance: Locomotion/Gait

OA15-03

IMU-Derived Impact Metrics From an Outdoor Run Are Correlated to Motion Capture-Calculated Joint Kinetics

Ms. Tatiana Djafar[1], Dr. Nicholas Heebner[1], Mr. Tyler Cardinale[1], Dr. Benjamin Cuddy[1], Dr. Jeremy Ross[1], Mr. Andrejs Zalaiskalns[2], Dr. Joshua Winters[1]

[1]University of Kentucky, Lexington, KY, United States. [2]United States Marine Forces Special Operations Command, Camp Lejeune, NC, United States

Introduction

In-depth motion capture assessments of running have been used to identify movement patterns and loading strategies indicative of elevated musculoskeletal (MSK) injury risk. However, in the military, barriers such as available resources and time constraints due to occupational demands can prevent their feasibility within active training environments. Utilizing commercially available inertial measurement units (IMUs) and their outputs may provide a viable option for "invisible monitoring." This study examined the relationship between metrics derived from motion capture and automated outputs from IMUs during overground running.

Methods

15 (4 female) Marine Forces Special Operations Command personnel who were cleared for full, unrestricted duty completed an in-depth running mechanics evaluation using markerless motion capture and integrated force plates as well as a 15-minute outdoor run with tibia-mounted IMUs across separate testing sessions. The middle 10 minutes of the outdoor session were used for analysis. Pearson correlation coefficients (α=0.05) were calculated to examine the relationships between system outputs.

Results

Pearson correlation coefficients can be found in Table 1. Cumulative impact load as calculated by the commercial IMU software was negatively correlated to peak knee extension moments and positively correlated to peak ankle plantarflexion moments, ankle power absorption (dominant limb only), and ankle negative work. Average intensity as calculated by the commercial IMU software was also positively correlated to peak ankle plantarflexion moment, ankle power absorption, and ankle negative work on the dominant limb while the non-dominant limb only exhibited a correlation with peak ankle plantarflexion moment.

Discussion

Outputs determined by commercially available devices worn during the outdoor run demonstrated moderate relationships with joint kinetics calculated from markerless motion capture. These results suggest a potential capability for minimally invasive monitoring during military training that can provide clinically meaningful insights of lower extremity loading, particularly at the ankle. Differences in impact intensity relationships with joint kinetics between the dominant and non-dominant limb may be due to underlying neuromuscular mechanisms and could have training implications. Regular monitoring of impact load metrics may allow for earlier intervention from both a strength and conditioning and clinical perspective to mitigate MSK injury risk while maintaining operational readiness.

Images (Optional)

	Dominant Limb		Non-Dominant Limb	
	Impact Load	Average Intensity	Impact Load	Average Intensity
Peak vGRF	r=0.388, p=0.153	r=0.391, p=0.149	r=-0.096, p=0.735	r=-0.123, p=0.662
vALR	r=-0.339, p=0.216	r=-0.366, p=0.180	r=-0.394, p=0.146	r=-0.356, p=0.193
Peak Knee Extension Moment	**r=-0.522, p=0.046**	r=-0.436, p=0.104	**r=-0.546, p=0.035**	r=-0.459, p=0.085
Peak Ankle PlantarFlexion Moment	**r=0.684, p=0.005**	**r=0.687, p=0.005**	**r=0.602, p=0.017**	**r=0.565, p=0.028**
Peak Knee Power Absorption	r=-0.445, p=0.096	r=-0.378, p=0.164	r=-0.498, p=0.059	r=-0.392, p=0.148
Peak Ankle Power Absorption	**r=0.628, p=0.012**	**r=0.605, p=0.017**	r=0.324, p=0.239	r=0.264, p=0.342
Knee Negative Work	r=-0.366, p=0.180	r=-0.283, p=0.307	r=-0.498, p=0.059	r=-0.395, p=0.145
Ankle Negative Work	**r=0.581, p=0.023**	**r=0.580, p=0.024**	**r=0.567, p=0.028**	r=0.512, p=0.051

Table 1. Pearson correlation coefficients and significance values between IMU (columns) and motion capture (rows) outputs. Bolded values indicate $p<0.05$. Absolute values of variables were used for correlation coefficient calculations. vGRF = vertical ground reaction force; vALR = vertical average loading rate

Acknowledgements (Optional)

Disclaimer: The content is solely the responsibility of the authors and does not necessarily represent the official views of the Office of Naval Research, the US Navy, or the US Special Operations Command. Supported by the Office of Naval Research N0004-21-1-2682.

Session Category

Human Motion and Performance: Locomotion/Gait

OA15-04

Detection of Gait Events during Aquatic Treadmill Walking using Shank Angular Velocity

Mr. Joseph Harrington MS, Dr. David Kingston PhD

University of Nebraska at Omaha, Omaha, NE, United States

Introduction

Time normalization of the gait cycle is essential to quantify walking biomechanics and motor control strategies[1]. Shank angular velocity can identify gait events in various populations on land[2,3]; but it is unknown if this approach translates to aquatic environments. Therefore, this study investigated shank angular velocity characteristics during dry and aquatic treadmill walking in typically developing (TD) and children with cerebral palsy (CP).

Methods

Fifteen TD and 14 children with CP completed three 3-minute walking trials on a dry and aquatic treadmill (9 minutes of walking per environment) at modified self-selected speeds (Slow or 75%, Normal or 100%, and Fast or 125%)[4]. Each participant had seven waterproof intertial measurement untis (WaveTrack IMU, Cometa, Milian, Italy) secured bilaterally to the foot, shank, thigh, and one on the pelvis. A custom algorithm identified gait events using shank angular velocity and was compared to marker-based gait event detection during dry treadmill walking[5]. Dynamic time warping (DTW) assessed morphological similarities of shank angular velocity across environments by matching indices of one signal with one or more indices of the other (Figure 1B), and quantified differences. Statistical parametric mapping (SPM) evaluated magnitude differences pre and post-warping.

Results

Conventional time normalization to 101 data points revealed differences in shank angular velocity between treadmill environments (Figure 1A). However, no normalized differences occurred after DTW (Figure 1C).

Discussion

Conventional time normalization assumes uniform stride structure; however, aquatic walking has altered stride mechanics due to buoyant and hydrodynamic effects[6]. Our results demonstrate that linear time normalization introduces discrepancies between dry and wet treadmill walking, particularly during the swing phase where speed-dependent

hydrodynamic effects would be largest. However, DTW characterizes and demonstrates that while water immersion modifies the temporal structure of the shank angular velocity signal, the signal morphology is unchanged. Overall, these findings suggest that features of shank angular velocity needed to identify gait periods are preserved in water, suggesting the same detection framework developed for dry environments can be used in aquatic environments without additional adjustments.

Images (Optional)

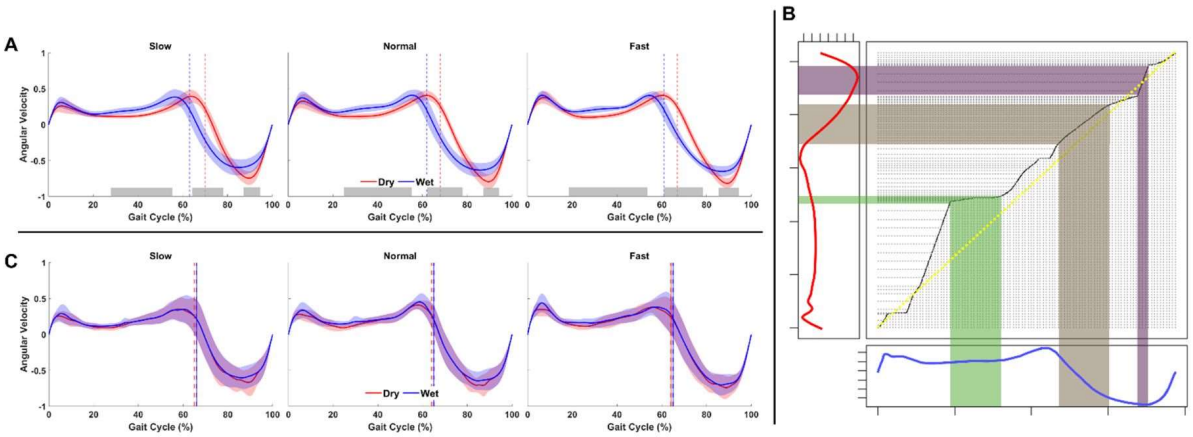


Figure 1: Statistical parametric mapping results of representative shank angular velocity waveforms during Dry (red) and Aquatic (Wet, blue) treadmill walking after normalizing to 101 data points (A) pre- and (C) post- dynamic time warping. Shaded grey areas in A indicate significant differences at α = 0.05. Vertical dashed lines correspond to toe-off. (B) Dynamic time warping of representative shank angular waveforms during Dry (red) and Aquatic (blue) treadmill walking. Dashed yellow line represents perfect similarity, while the warping path is the black line. Dotted black lines and shaded colored regions in B correspond to matching Dry and Aquatic by stretching and compression.

References (Optional)

Session Category

Human Motion and Performance: Locomotion/Gait

OA15-05

Lower Limb Joint Kinematics in Older Adults During Walking in the Home Setting

Mr Mohammad Yavari, Dr Zhou Fang PhD, Dr Yiqun Chen Dr, Dr Davood Shojaei PhD, Prof Abbas Rajabifard PhD, Prof Peter Lee PhD, Prof David Ackland PhD

University of Melbourne, Parkville, VIC, Australia

Introduction

Older adults most commonly experience falls in the home setting [1], yet gait in the home, which is known to differ substantially to that in a controlled laboratory environment [2], is seldom evaluated. The extent to which age-related changes influence gait in the home setting also remains poorly understood. The aim of this study was to evaluate lower limb joint kinematics and spatiotemporal gait parameters during habitual walking throughout a home setting in both younger and older adults.

Methods

Ten healthy young adults (age: 27.7±1.8 years) and ten older adults (age: 74.7±7.0 years) performed nineteen diverse daily activities of daily living over a 2-hour duration throughout a fully furnished single-bedroom apartment that included a kitchen, bathroom, bedroom and living room. Each participant's lower limb joint kinematics and spatiotemporal gait parameters were measured using inertial measurement units (IMUs), and their spatial location throughout the apartment captured using an ultra-wide band system. A mixed-design analysis of variance (ANOVA) was conducted to assess the effects of participant age and living space (room) on peak joint angles and spatiotemporal parameters during walking.

Results

Compared with young adults, older adults exhibited a smaller range of ankle ($p = 0.002$, $\eta^2 = 0.52$) and knee ($p = 0.040$, $\eta^2 = 0.36$) joint flexion angles. Maximum knee flexion in older adults was most significantly smaller to that of younger adults when walking in the bathroom (mean difference: 13.0°, 95% CI = [7.0°, 18.9°], $p < 0.001$). Older age was significantly associated with slower walking speed ($p = 0.006$, $\eta^2_p = 0.74$), and walking speed did not vary significantly between living spaces ($p > 0.05$).

Discussion

Lower limb gait kinematics during walking in the home setting is governed by the internal environment and its associated spatial constraints, which has a substantial impact on the mobility of older adults. The findings have implications for interior design, ergonomics, rehabilitation and fall risk assessment in the home setting.

Images (Optional)

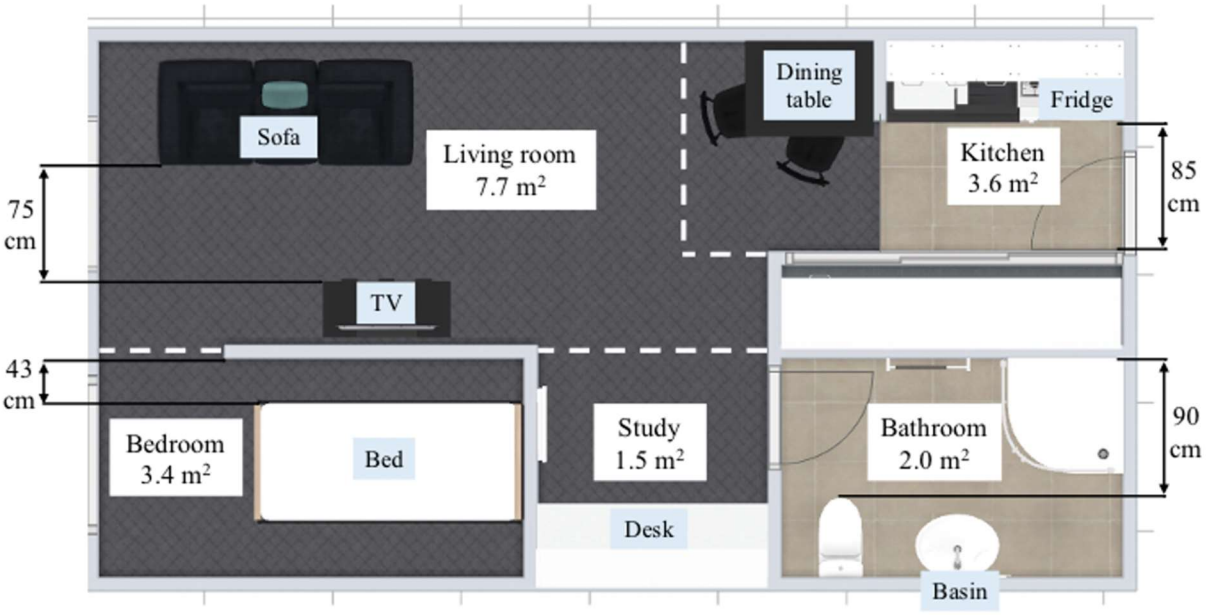


Fig. 1: Floor plan of home setting used in the present study

References (Optional)

[1] Mortazavi *et al.*, Materia Socio-Medica, 2018.

[2] Tamburini *et al.*, Gait & Posture, 2018.

Acknowledgements (Optional)

This project was funded by an Australian Research Council Discovery Project grant (DP230102497)

Session Category

Human Motion and Performance: Locomotion/Gait

OA16-01

Do Shoulder and Elbow Kinetics and Pitching Kinematics Differ Between Pitching On Dirt Surface and Turf Surface Pitching Mounds?

Dr Rafael Escamilla PhD, PT, CSCS, FACSM[1], Dr Jonathan Slowik PhD[2], Dr Rodney Imamura PhD[1], Dr Irwin Thompson EdD, PT[1], Dr Robert Asuncion DPT, PT[1], Dr Arnel Aguinaldo PhD, ATC, CSCS[3], Dr Glenn Fleisig PhD[2]

[1]California State University, Sacramento, Sacramento, CA, United States. [2]American Sports Medicine Institute, Birmingham, AL, United States. [3]Point Loma Nazarene University, San Diego, CA, United States

Introduction

While most baseball fields have dirt pitching mounds, some have turf mounds. Pitching on dirt mounds permits metal cleats, which are discouraged on turf mounds due to turf damage. However, it's unknown if pitching biomechanics differ between dirt and turf mound pitching. Therefore, the purpose was to assess differences in shoulder and elbow kinetics and pitching kinematics in college pitchers between pitching on a dirt mound versus pitching on a turf mound.

Methods

Eighteen college pitchers pitched on both a dirt mound with metal cleats and a turf mound with turf shoes. All pitchers were tested using a 240-Hz, 12-camera motion analysis system, and 28 kinematic and 7 kinetic parameters were calculated. Differences in kinematic and kinetic parameters between dirt and turf mound pitching were assessed with paired t-tests with p-values adjusted (Benjamini-Hochberg method) for multiple comparisons ($p<0.05$).

Results

Significant differences are shown in Table 1. Maximum elbow varus torque, maximum shoulder internal rotation torque, maximum lead knee height, elbow flexion, knee flexion, rotational separation between upper trunk and pelvis, maximum shoulder external rotation, and forward trunk tilt were significantly greater pitching on a dirt mound than a turf mound. Pelvic drift at maximum lead knee height and arm slot angle were significantly greater pitching on a turf mound than a dirt mound.

Discussion

Of the 35 biomechanical comparisons, 10 were significantly different between dirt and turf mound pitching. This implies that pitching mechanics are more similar than different

between dirt and turf mound pitching. However, given several pitching biomechanical differences were found, pitchers who pitch on a dirt mound in-season should only pitch on a turf mound in the off-season and not during pre-season or in-season. Kinematic differences only involved body segment and joint positions and not angular velocity magnitudes or timings. Kinetic differences demonstrated that elbow and shoulder joint torques were overall slightly less pitching on a turf mound than pitching on a dirt mound. Therefore, pitching on a turf mound may decrease throwing elbow and shoulder joint tissue stress and injury risk compared to pitching on a dirt mound, although more research is needed to fully assess injury risk.

Images (Optional)

Table 1. Kinematic and kinetic significant differences (adjusted $p < 0.05$) between pitching on dirt and turf mounds.

	Dirt Mound (n=18)	Turf Mound (n=18)	Unadjusted p-values	Adjusted p-values
Windup				
Max lead knee height (% height)	61±5	56±6	$p < 0.001$	$p = 0.001$
Pelvic drift at maximum lead knee height (cm)	14±4	18±4	$p < 0.001$	$p < 0.001$
Lead foot contact				
Elbow flexion (°)	105±18	102±18	$p = 0.002$	$p = 0.021$
Knee flexion (°)	48±6	45±7	$p = 0.004$	$p = 0.022$
Rotational separation - upper trunk & pelvis (°)	44±10	41±10	$p = 0.005$	$p = 0.022$
Maximum Shoulder External Rotation				
Max elbow varus torque (N•m)	92±11	88±11	$p = 0.004$	$p = 0.022$
Max shoulder internal rotation torque (N•m)	92±11	88±10	$p = 0.002$	$p = 0.021$
Max shoulder external rotation (°)	156±10	153±10	$p = 0.008$	$p = 0.028$
Ball Release				
Forward trunk tilt (°)	34±9	31±9	$p = 0.006$	$p = 0.022$
Arm slot angle (°)	49±11	52±11	$p = 0.005$	$p = 0.022$

Session Category

OA16-02

The Influence of Soft Tissue Glenohumeral Internal Rotation Deficit (ST-GIRD) on Proprioceptive Feedback, Cortical Activity, and Pitching Performance in Baseball Players

Master Student Zong-Han Hsieh, PhD Yi-Hsuan Weng, Professor Jiu-Jenq Lin

School and Graduate Institute of Physical Therapy, College of Medicine, National Taiwan University, Taipei City, Taipei City, Taiwan

Introduction

The traditional Glenohumeral Internal Rotation Deficit (GIRD) overlooks soft tissue changes, whereas Soft Tissue Glenohumeral Internal Rotation Deficit (ST-GIRD) reflects injury mechanisms more comprehensively. GIRD adaptations may lead to proprioceptive deficits at both peripheral and central levels and affect pitching performance. This study aimed to investigate the relationship between ST-GIRD and cortical activity (central level), proprioceptive error (peripheral level), and functional performance, and to compare these measures between groups with and without internal rotation deficit.

Methods

Fifty eight high school baseball players were divided into a deficit (ST-GIRD > 5°, n=32) and no deficit groups (soft tissue glenohumeral internal rotation gain > 5°, n=26). Outcome measurements included proprioceptive error of glenohumeral joint by electromagnetic-based motion analysis system; cortical activity at F3/4 and P3/4 (alpha and beta frequencies) by electroencephalography; and functional performance (muscle strength, pitching velocity and constant error).

Results

In the no deficit group, increased soft tissue glenohumeral internal rotation gain moderately correlated with decreased pitching constant error on the x-axis and y-axis ($r = -0.356$, $p=0.074$ and $r=0.345$, $p=0.084$, respectively) and lower absolute beta frequency power in frontal lobe during the cocking phase ($r = -0.337$, $p=0.093$). There were no significant correlations among measurements in the deficit group ($r= -0113 - 0.201$, $p>0.05$). Compared to no deficit group, the deficit group exhibited significantly weaker strength in middle trapezius (9.4 kg, $p = 0.001$) and lower trapezius (5.9 kg, $p = 0.001$), and slower ball velocity (5.0 km/h, $p = 0.020$). Furthermore, the deficit group demonstrated

significantly lower amplitude of beta frequency in parietal lobe during the ball release phase (8.1%, p = 0.041) relative to no deficit group.

Discussion

ST-GIRD is not solely a problem of soft tissue tightness but is fundamentally linked to broader neuromuscular deficits and central sensorimotor alterations, as evidenced by changes in muscle strength, pitching performance, and cortical activity. This underscores the critical importance of intervention programs that move beyond passive stretching to comprehensively target soft tissue mobility, dynamic scapular control, and significantly sensorimotor retraining.

Images (Optional)

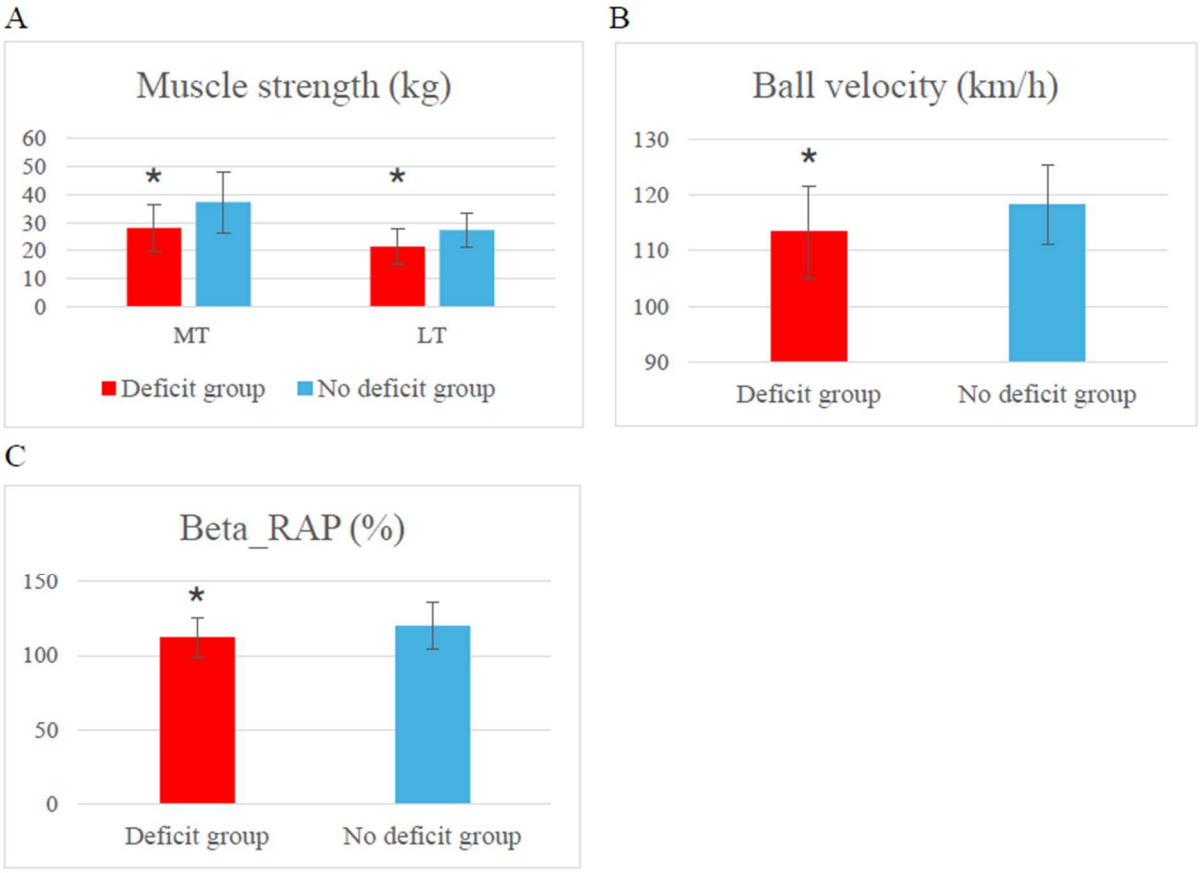


Figure. Comparison of muscle strength (A), ball velocity (B) and beta_RAP (C) between deficit and no deficit groups

Abbreviation: MT, middle trapezius; LT, lower trapezius; RAP, relative amplitude at parietal lobe

*Significant difference between deficit and no deficit group, p value < 0.05

Session Category

Human Motion and Performance: Sports

OA16-03

Intersegmental Coordination in Baseball Pitching: Identifying Skill Level Differences

Mr. Michael Jensen BS, CSCS, Dr. Katherine Boyer PhD

University of Massachusetts Amherst, Amherst, MA, United States

Introduction

In baseball, pitching performance is paramount for success among skill levels. Extensive work on the kinematic sequence has shown that the proximal-to-distal timing of peak joint angular velocities is closely related to pitching performance[1]. However, peak velocities alone do not capture how segments interact throughout the pitching motion. Intersegmental coordination provides a framework for quantifying these interactions. Here, we examined pelvis–torso and torso–arm coordination patterns across skill levels.

Methods

Full-body marker trajectories from 21 baseball pitchers (high-school, collegiate, professional; n=7/group) were obtained from Driveline Baseball's OpenBiomechanics dataset [2]. Three-dimensional pelvis, torso and arm segment angles were calculated in Visual3D. Data were time-normalized from peak leg lift to ball release and separated into three pitch phases: peak leg lift to front-foot contact, front-foot contact to maximum shoulder external rotation (ER), and maximum ER to ball release. Pelvis–torso and torso–arm coordination was quantified using vector coding to obtain coupling angles during each pitch phase [3]. Coupling angles were classified into four coordination patterns; proximal-dominant, distal-dominant, in-phase and anti-phase; across the three pitch phases. Groupwise differences in coordination distributions for each pitch phase were assessed using one-way ANOVAs with post-hoc tests and effect sizes (Cohen's d).

Results

There were no differences in coordination state distributions between groups during early pitching (peak leg lift to front-foot contact; all $p>0.16$), However, professional pitchers exhibited more pelvis-dominant coordination than high school pitchers ($d=0.41$, $p=0.08$).From front-foot contact to maximum external rotation, no coordination pattern differed (all $p>0.38$). From max ER to ball release, moderate effects for trunk and arm dominance was observed between high school and higher skill levels (p=0.08-0.13, d=0.34-0,40).

Discussion

Intersegmental coordination patterns were not significantly different between skill levels. Moderate effect sizes suggest subtle changes in coordination during early and late pitching as skill progresses. These findings suggest coordination strategies are largely conserved, with small refinements at higher levels. Future work should examine whether these refinements can be targeted through coaching and relate to performance.

Images (Optional)

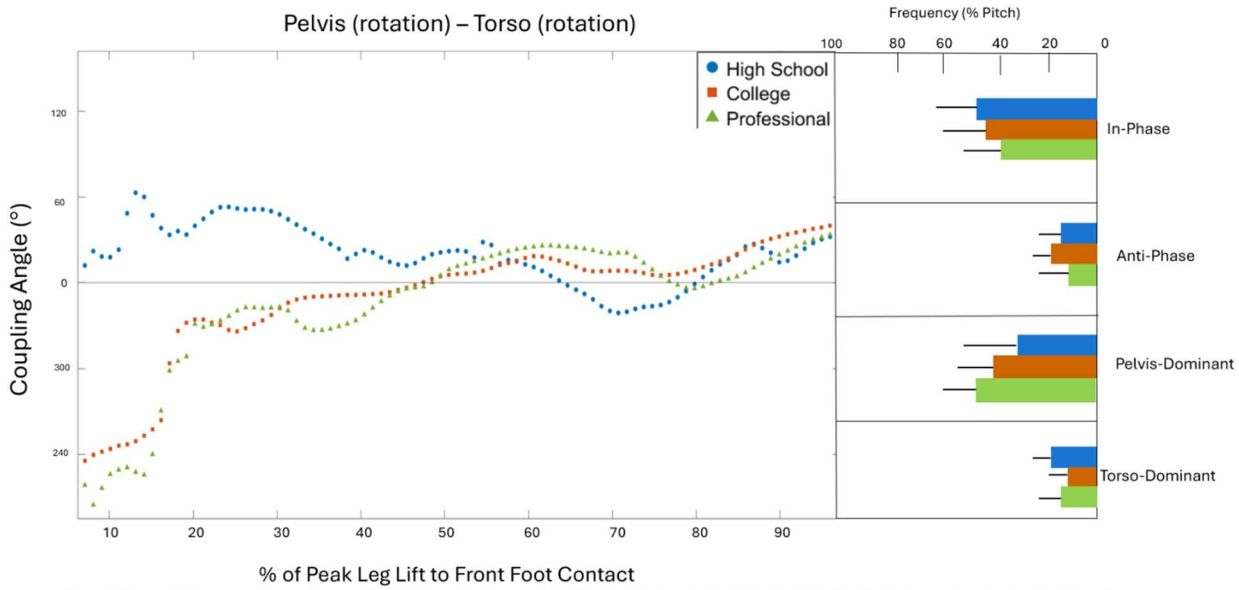


Figure 1. Mean pelvis–torso coupling angle across the pitching motion from peak leg lift to front-foot contact for high school (blue), collegiate (orange), and professional (green) pitchers (left). Horizontal bar charts (right) show the percentage of time spent in each coordination pattern (in-phase, anti-phase, pelvis-dominant, and torso-dominant) over the same phase of the pitch.

References (Optional)

[1] Naito et al., Human Movement Science, 2017

[2] Wasserberger et al., Driveline Baseball Open Biomechanics Project, 2022

[3] Chang et al., Journal of Biomech, 2008

Acknowledgements (Optional)

Data courtesy of Driveline Baseball's OpenBiomechanics Project

Session Category

Human Motion and Performance: Sports

OA16-04

Field Performance of Modern Collegiate Baseball Bats

Prof JJ Trey Crisco[1], Prof Kristen Nicholson[2], Mr Ethan Yoon[1], Prof Richard Greenwald[3]

[1]Brown University, Providence, RI, United States. [2]Wake Forest University, Winston-Salem, NC, United States. [3]Dartmouth College, Hanover, NH, United States

Introduction

The performance of baseball bats has been an intriguing question since the first reports of wood bats being doctored or "corked" by players. Currently, non-wood bats are used almost exclusively in collegiate play, but their field performance has not been previously reported. With the advent of markerless-tracking systems now installed in many baseball stadiums that capture both pitcher and batter kinematic data, we sought to investigate if the data from these systems could be used to determine baseball bat performance.

Methods

Throughout the 2024 collegiate season at one institution, 3,170 hits were analyzed with the markerless KinaTrax motion tracking system. For each hit, pitched ball speed, impact location measured from the tip of the bat, bat speed at the impact location, and batted ball speed were computed. Player performance was intentionally excluded from the calculations. Data analysis was limited to descriptive statistics and graphical evaluation. Units are reported in mph and inches reflecting their historical use in baseball.

Results

Mean bat speed was 64 mph (29 m/s). Mean impact location was 4.3 inches (0.11 m) from the tip of the bat. These bat swings resulted in a mean batted ball speed of 83.5 mph (37.3 m/s). At a bat speed of 63.6±2.5 mph (28.4±1.1 m/s), the top 2% batted ball speeds were 102.1 mph (45.6 m/s), as compared to 92.9 mph (41.5 m/s) with wood baseball bats. The sweet spot for non-wood bats was located 2" to 10.5" (0.05 to 0.27 m) from the bat tip. This sweet spot width for the non-wood bats was substantially greater than the sweet spot for wood bats, located from 3" to 7.5" (0.08 to 0.19 m) from the bat tip (Figure 1).

Discussion

These findings provide a new reference for investigators and governing bodies as to the current field performance of modern collegiate non-wood baseball bats. This field study found that modern non-wood bats used at the collegiate level substantially outperformed wood baseball bats in terms of batted ball speeds at a given bat speed and the width of the sweet spot.

Images (Optional)

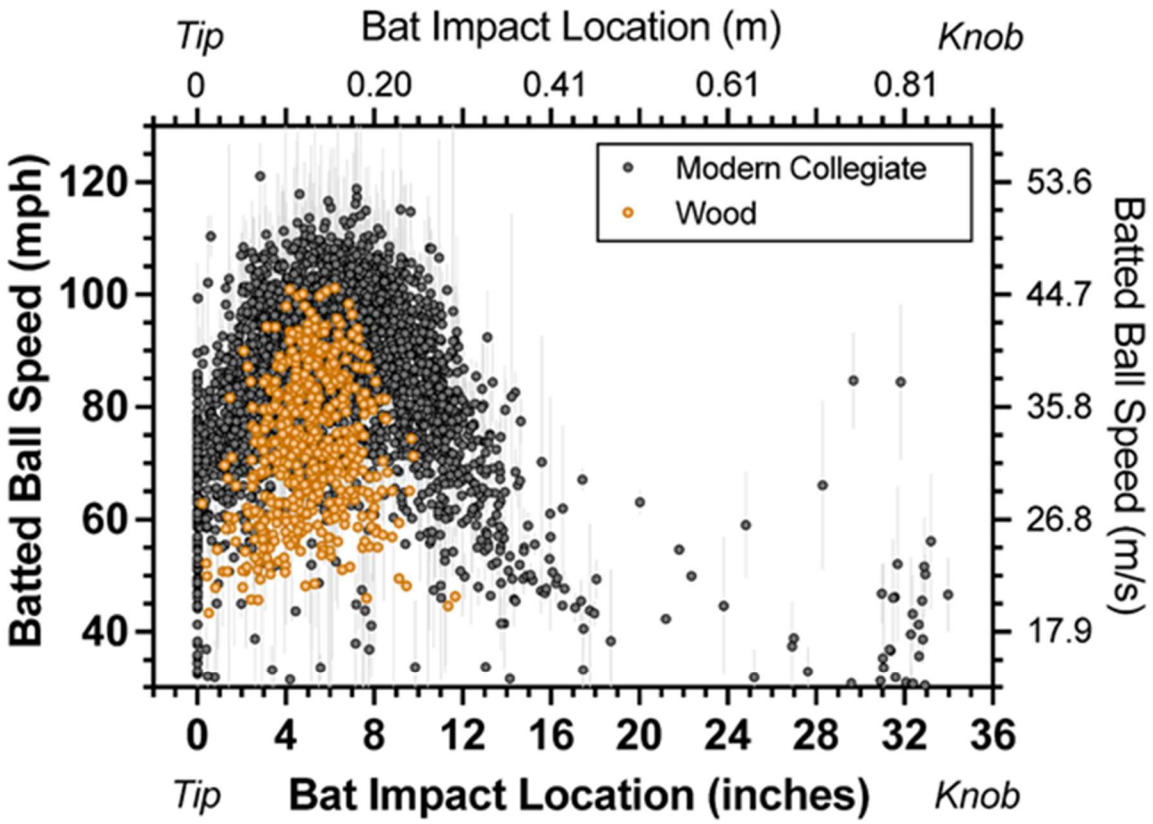


Figure 1. Batted ball speed as a function of impact location on the bat for the modern collegiate non-wood baseball bats and wood bats. The vertical error bars are the SD of the batted ball speeds computed across the six frames of captured ball data for the collegiate non-wood dataset.

Session Category

Human Motion and Performance: Sports

OA16-05

Stride Phase Pelvis Momentum Influences Throwing Arm Load in Collegiate Baseball Pitchers

Mr. Adam Barrack MS, CSCS, TSAC-F

University of Southern California, Los Angeles, CA, United States

Introduction

Introduction: Pitching requires coordinated generation and transfer of energy from the lower extremities to the throwing arm. During the stride phase, the trail leg produces propulsion through home-plate-directed linear momentum and axial angular momentum, reflecting distinct mechanical strategies. Pitchers relying more on angular momentum may generate less linear momentum, equating ball velocity through greater reliance on rotational trunk mechanics. As a result, these strategies may differentially influence throwing arm kinetics. The purpose of this study was to determine how pelvis linear and angular momentum at stride foot contact (SFC) relate to shoulder and elbow joint loading. We hypothesized that pitchers exhibiting greater pelvis angular momentum at SFC would demonstrate higher peak shoulder internal rotator and elbow varus moments and moment impulses, independent of ball velocity and pelvis linear momentum.

Methods

Methods: Thirty-seven healthy collegiate pitchers executed fifteen full-effort fastballs on an instrumented mound while 3-D kinematics (300Hz) and ground reaction forces (1200Hz) were collected. Pelvis momentum was quantified at SFC, with home-plate-directed linear momentum defined in the global +X direction and axial angular momentum defined about the global vertical axis. Peak shoulder internal rotator and elbow varus moments and moment impulses were quantified using inverse dynamics and extracted from SFC to ball release. The ten fastest pitches were analyzed for each pitcher. Linear mixed-effects models with subject-level random intercepts estimated the concurrent effects of pelvis linear and angular momenta on each kinetic outcome, controlling for ball velocity

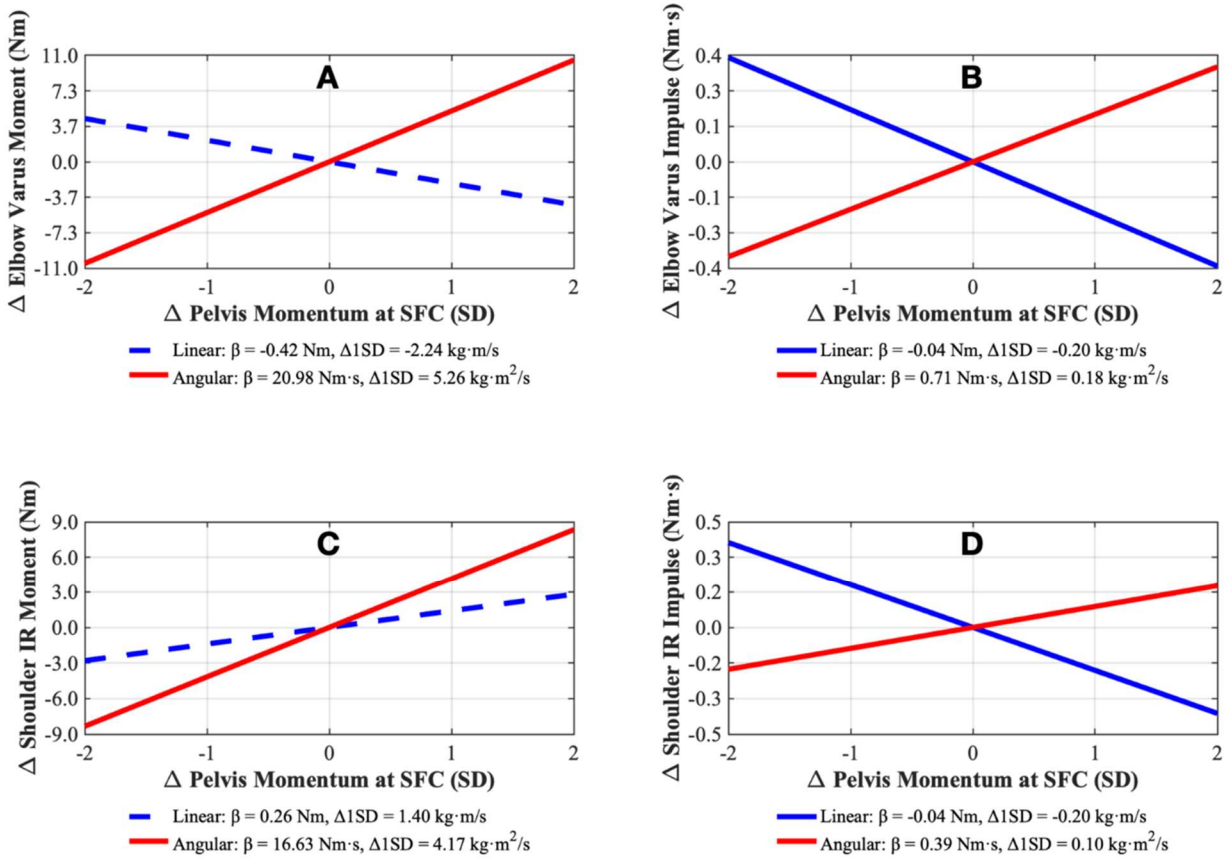
Results

Results: Greater pelvis angular momentum at SFC was significantly associated with increased peak elbow varus (β:21.0Nm,p=0.008) and shoulder internal rotator (β:16.6Nm,p=0.008) moments, and elbow varus (β:0.71Nm·s,p<0.001) and shoulder internal rotator (β:0.39Nm·s,p<0.001) impulses. In contrast, greater pelvis linear momentum was associated with reduced elbow varus (β:–0.04Nm·s,p<0.001) and shoulder internal rotator (β:–0.04Nm·s,p<0.001) impulses. Marginal R^2 values ranged from 15.6%-22.4% across models, while conditional R^2 values ranged from 64.7%-96.1%.

Discussion

Discussion: Pitchers generating greater stride axial pelvis angular momentum experienced greater throwing arm loading, whereas greater linear pelvis momentum attenuated cumulative loading. These findings highlight how trail leg propulsion influences upper-extremity kinetics and may inform performance-enhancing and injury-prevention efforts in baseball pitching.

Images (Optional)



References (Optional)

Session Category

Human Motion and Performance: Sports

OA16-06

The Influence of Shoulder Range-of-Motion on Elbow Valgus Torque Throughout a Baseball Pitch

Dr. Jonathan Slowik PhD, Dr. Glenn Fleisig PhD

American Sports Medicine Insititute, Birmingham, AL, United States

Introduction

Shoulder rotation range-of-motion (ROM) has long been thought to influence pitching biomechanics and elbow loading [1], yet it remains unclear which specific aspects of shoulder ROM are most relevant. The purpose of this study was to determine which ROM-related factors are the most strongly related to elbow valgus loading and how their individual effects may change throughout the phases of a baseball pitch.

Methods

Motion capture data from 267 healthy amateur baseball pitchers (18.7±1.9 yrs) throwing fastball pitches [2] were retrospectively analyzed, along with their shoulder passive ROM measurements. Elbow valgus torque was calculated using inverse dynamics and splined into three 100-point segments spanning foot contact (FC), maximum shoulder external rotation (MER), ball release (BR), and maximum internal rotation (MIR), then expressed as percent pitch (0%=FC, 100%=BR).

We used statistical parametric mapping (SPM) multivariate regression to examine the relationships between time histories of elbow valgus torque and six independent metrics (Variance Inflation Factors<2.5) related to shoulder external/internal ROM (passive non-dominant, ND, passive dominant, Dom, as well as shoulder rotation values reached during pitching). The model included age, height, mass, competition level, and handedness as confounders. Standardized beta curves quantified the independent effect of each metric while holding the others constant, and full-model F-curves identified statistically significant time intervals.

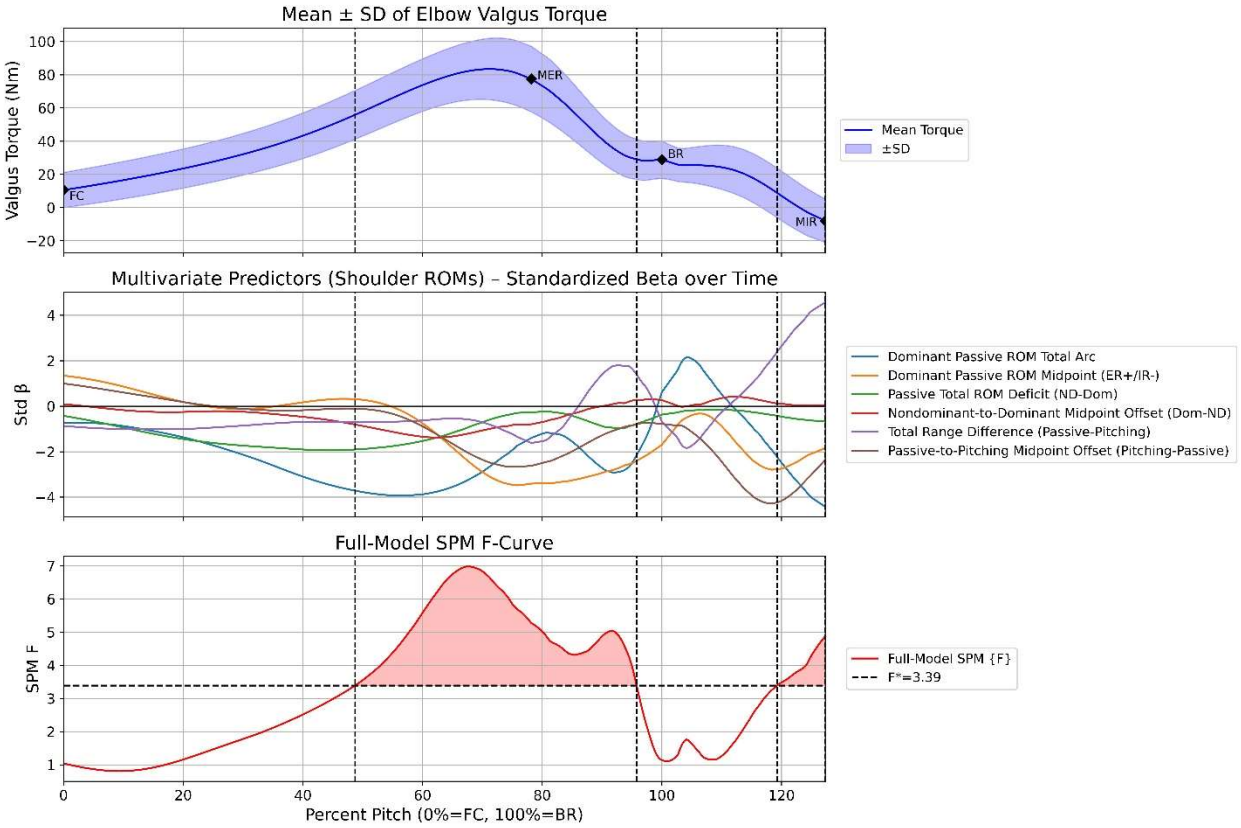
Results

Two significant clusters were identified, with the first occurring during the late arm cocking and arm acceleration phases (48.7-95.8% of the pitch, peak F=6.98), and the second occurring as the shoulder approached maximum internal rotation (119.3-127.3% of the pitch, peak F=4.88). Detailed time histories are provided in Fig. 1.

Discussion

Pitchers with larger total rotation arcs, and shifts towards greater external rotation experienced lower elbow valgus torque, especially around the time of MER, when the torque was near its peak. However, the combined ROM parameters also became significant near the time of MIR, led by the parameter that quantified how much of his full ROM a pitcher may be utilizing. Future work should investigate this often-ignored phase of the baseball pitch.

Images (Optional)



References (Optional)

[1] Bullock, G.S., et al., J Athl Train, 2018. [2] Slowik, J.S., et al., Orthop J Sports Med, 2025

Session Category

Human Motion and Performance: Sports

OA17-02

Disturbed Flow, Cytokine Signaling, and Plaque Growth: Insights from Sensitivity and Flow-Disturbance Analyses Using a Multiscale, Multiphysics Model of Coronary Atherosclerosis

Dr. Jeremy Warren Ph.D.[1,2], Dr. Clark Meyer Ph.D.[1], Dr. Anna Corti Ph.D.[3], Dr. Heather Hayenga Ph.D.[1]

[1]The University of Texas at Dallas, Richardson, Texas, United States. [2]Yale University, New Haven, CT, United States. [3]Politecnico Di Milano, Milan, Italy, Italy

Introduction

Coronary artery disease arises from dysregulated biochemical, biomechanical, and hemodynamic interactions that drive plaque formation. Existing multiscale models couple ABM with either CFD or FEA separately. We developed CAFe, a unified CFD-ABM-FEA framework that simulates hemodynamics, cell–cytokine signaling, and structural mechanics [Figure 1A] [1]. To assess biological robustness, we incorporated results from a sensitivity analysis of ABM rules and mechanistic studies on disturbed flow and pre-existing inflammation.

Methods

Idealized healthy and stenotic arteries were meshed [Figure 1B] and simulated for 6 months. The ABM updated cytokines, leukocytes, ECM, and growth every 6 hours; FEA computed stresses; CFD computed WSS. In the sensitivity analyses, production rates (e.g. TNFα, IL-1, IL-10, TGFβ, and PDGFαβ) were scaled by ×0.1 or ×10. Additional mechanistic studies tested whether disturbed flow alone (10–50% occlusions) or pre-existing plaque cytokines can initiate remodeling [Figure 1C].

Results

Sensitivity analysis: The model was most sensitive to PDGFαβ ×0.1, which reduced multiple cell types and caused 12–15% regional volume loss due to compounded VSMC apoptosis. TNFα ×0.1 and IL-1 ×0.1 markedly reduced leukocytes; IL-1 ×10 increased inflammatory cell numbers. Most ×10 increases produced minimal effects, and IL-10/TGFβ scaling had little impact.

Flow-disturbance study: Disturbed flow alone could initiate plaque formation starting at ≥30% occlusion, enabling leukocyte infiltration and foam-cell formation [Figure 1D]. Severe

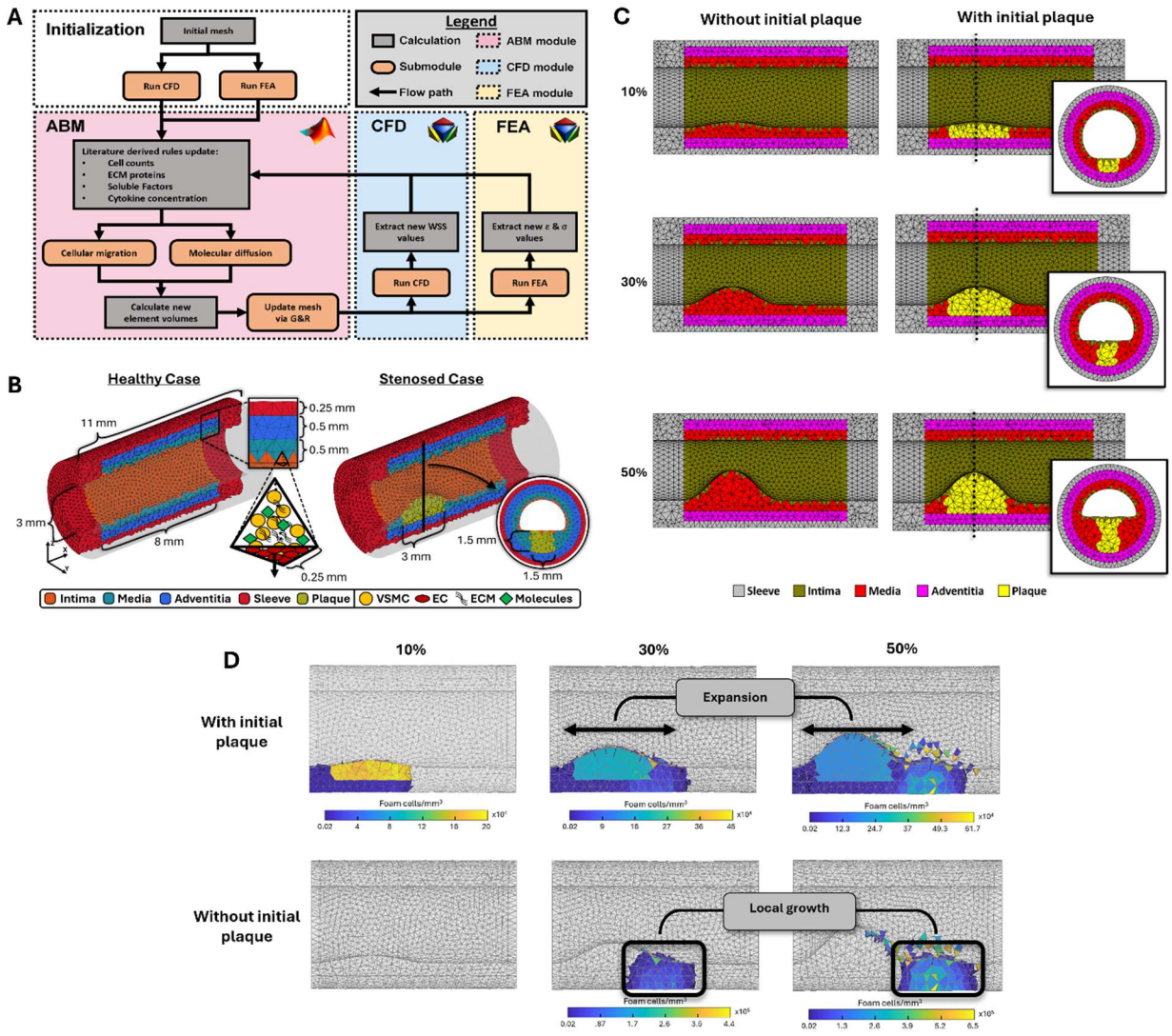
narrowing (50%) generated a secondary downstream stenosis with orders-of-magnitude higher leukocyte counts and foam-cell accumulation.

Pre-existing plaque study: Pre-existing cytokines and foam cells enabled plaque initiation even at 10% occlusion. Unique growth patterns arose; pre-existing plaque expanded whereas plaques initiated from flow disturbance exhibited local growth [Figure 1D]. Remodeling distributions also shifted: simulations with initial plaques showed greater leukocyte buildup in transition regions but reduced downstream accumulation compared to plaque-free cases. Volume patterns reflected these shifts.

Discussion

CAFe captures how growth-factor signaling, inflammation, and hemodynamic disturbances jointly shape plaque progression. PDGFαβ, TNFα, and IL-1 emerged as dominant regulators of model stability. Flow disturbances were sufficient to initiate plaque, while pre-existing cytokines altered spatial remodeling trajectories. Together, these results demonstrate CAFe's ability to resolve nonlinear mechanobiological interactions underlying CAD progression.

Images (Optional)



References (Optional)

[1] Jeremy Warren *et al.* , J Biomechanics, 2025

Session Category

Cardiovascular/Cardiorespiratory Biomechanics: Methods, Models and Applications

OA17-03

A Longitudinal Study on the Association Between Haemodynamics and Early Plaque Formation in Female Coronary Arteries

Dr. Chi Shen[1], Dr. Mingzi Zhang[1,2], A/Prof. Susann Beier[1]

[1]The University of New South Wales, Sydney, NSW, Australia. [2]Torrens University, Sydney, NSW, Australia

Introduction

Haemodynamics play an important role in the development of coronary artery disease (CAD), with evidence indicating different disease presentations in females and males. However, previous work has only focused on haemodynamic effects after disease onset, due to the lack of longitudinal imaging datasets starting from the healthy state. In this study, we investigated the relationship between endothelial shear stress (ESS) and plaque formation in females, using the retrospective GeoCAD dataset featuring 387 patients with at least two longitudinal imaging follow-ups.

Methods

Plaque formation was identified by comparing per-segment CAD-RADS scores of the left coronaries between baseline and follow-up CTCA images. Patients who had no plaque in any segment at baseline and developed plaque in at least one segment at follow-up formed the formation group (21 patients, including 64 diseased segments). Each patient from the formation group was randomly matched with a control (21 patients, including 158 healthy segments), defined as those without plaque across all segments at both baseline and follow-up, after accounting for their age and diabetes status. Eleven haemodynamic factors, including (ESS), were extracted from computational transient simulations on the left coronary trees to evaluate their associations with early plaque formation.

Results

The segments with formation showed lower mean ESS (0.660 [0.505-0.969] vs. 1.055 [0.747-1.547], $p = 0.002$) and ESS gradient (0.251 [0.197-0.506] vs. 0.427 [0.280-0.724], $p = 0.006$). Subsequently, the segments with formation showed a larger percentage area exposed to low ESS <0.5 Pa (33 [14-61] vs. 11 [2-23], $p = 0.002$). In addition, segments with formation exhibited lower helical flow intensity (0.773 [0.298-1.566] vs. 1.883 [0.942-3.976], $p = 0.002$). All other haemodynamic factors showed no statistically significant differences between formation and non-formation segments.

Discussion

This is the first longitudinal study into the blood flow's effects on plaque formation using images taken prior to disease onset. ESS-based haemodynamic factors were associated with early plaque development, while higher helical flow intensity had a protective effect. Overall, haemodynamics were associated with early disease development in females, underscoring their potential for sex-specific risk assessment.

Session Category

Cardiovascular/Cardiorespiratory Biomechanics: Methods, Models and Applications

OA17-04

Plaque Material Stiffness as a Biomechanical Marker Distinguishing ACS from Stable Coronary Lesions

Dr. Jack Wang Ph.D.[1], Mr. Christos Georgiadis B.S.[1], Dr. Caleb Berggren Ph.D.[2], Dr. Steve Maas Ph.D.[2], Dr. Edward Hsu Ph.D.[2], Prof. Jeffrey Weiss Ph.D.[2], Dr. Lucas Timmins Ph.D.[1,2]

[1]Texas A&M University, Houston, TX, United States. [2]University of Utah, Salt Lake City, UT, United States

Introduction

Atherosclerotic plaque rupture remains the leading cause of acute coronary syndromes (ACS), accounting for >1 million heart attacks annually in the US. Stratifying rupture risk remains a diagnostic challenge. Because rupture is a mechanical failure in which tissue stresses exceed material strength, material stiffness may serve as a surrogate marker for rupture risk assessment. This study quantified component-wise material stiffness of diseased human coronary tissue and evaluated its ability to distinguish rupture-prone from stable plaques.

Methods

Coronary arteries (n=3) were dissected from unfixed hearts of individuals who died of non-cardiac causes. Samples were mounted in a custom MR-compatible device enabling acquisition of MR images at 7T under lumen pressures of 10 and 120 mmHg, and subsequently VH-IVUS images at the same loads (Fig. 1A). Material parameters were estimated using our established inverse finite element framework, which incorporates deformable image registration via Hyperelastic Warping. Stiffness values were calculated for VH-IVUS-defined components: fibrous tissue (FT), necrotic core (NC), dense calcium (DC), and healthy media. Stiffness values were used to examine the predictive value of local material stiffness for lesions responsible for an ACS event (n=20) compared with stable controls (n=17) from a prospective clinical dataset.

Results

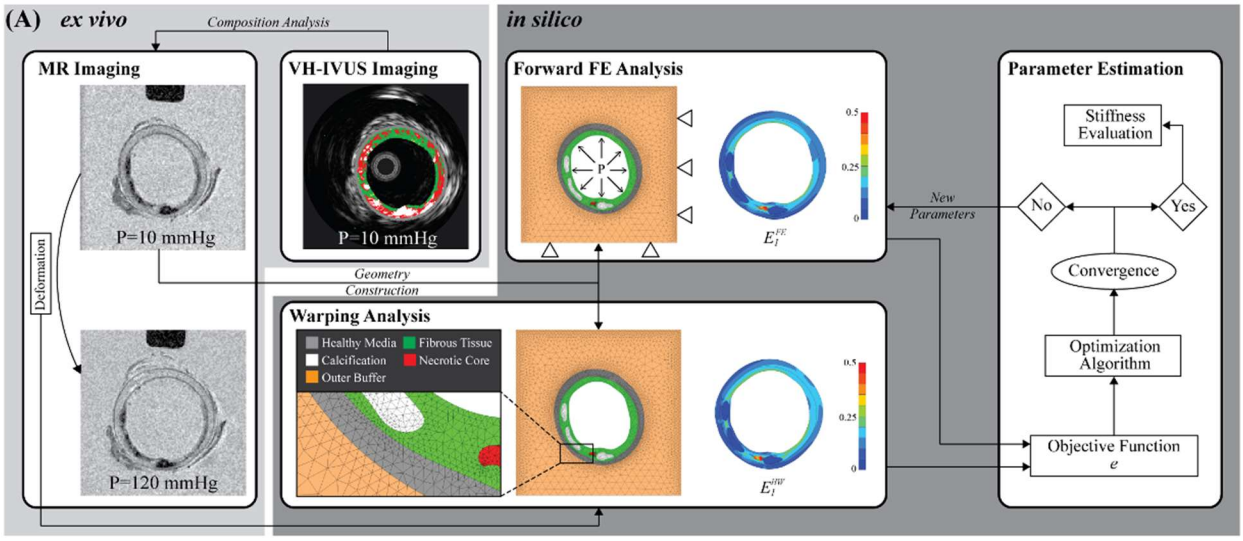
Warping-derived strain magnitudes varied across plaque components, with the highest strains in the NC (0.34±0.24) and the lowest in DC (0.04±0.05). The material optimization scheme achieved strong agreement between Warping-derived and forward FE strains (RMSE=0.03±0.01, mean bias <0.1%), confirming convergence. Stress-stretch curves generated from the estimated parameters demonstrated non-linear behaviors across tissue types. Tangent moduli at 120 mmHg confirmed differences with stiffness values of 0.46±0.28, 0.04±0.04, 4.34±2.65, and 0.21±0.10 MPa for FT, NC (softest), DC (stiffest), and

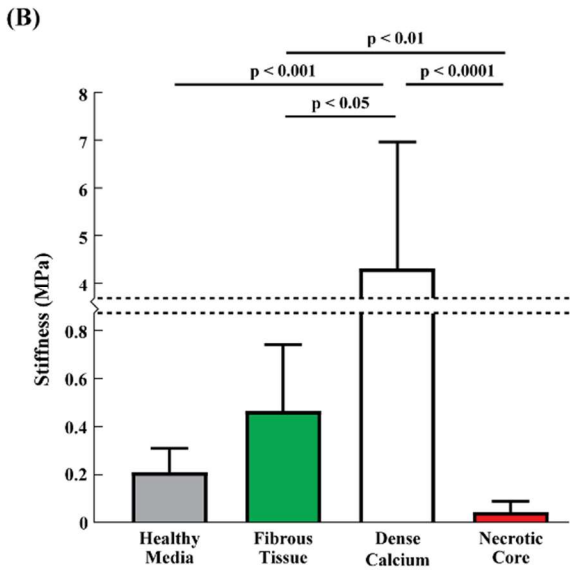
media, respectively (Fig. 1B). Local material stiffness values significantly differed between lesions responsible for an ACS event compared to stable controls with values of 0.63±0.39 and 0.55±0.32 MPa, respectively ($p<0.05$).

Discussion

In conclusion, we implemented an integrated experimental-computational framework to characterize component-wise material stiffness of diseased human coronary arteries and demonstrated its clinical utility. These results support the relevance of plaque material stiffness for advancing ACS risk stratification.

Images (Optional)





References (Optional)

Acknowledgements (Optional)

The Authors thank Prof. Martin Bennett for access to the clinical data. This research was funded, in part, by the National Institutes of Health (R01 HL150608).

Session Category

Cardiovascular/Cardiorespiratory Biomechanics: Methods, Models and Applications

OA17-05

Graph-Derived Mechanochemical Simulations Capture Patient-Specific and Population-Level Variability in Atherosclerosis Progression

Mr Alessandro Mastrofini[1], Dr Aikaterini Tziotziou[2], Prof Daniel Bos[3], Prof Ali C. Akyildiz[3,4], Prof Michele Marino[1]

[1]Multiscale and Multiphysics Mechanics Group (M2M), Department of Civil Engineering and Computer Science Engineering, University of Rome Tor Vergata, Rome, Italy, Italy. [2]Department of Cardiology, Biomedical Engineering, Cardiovascular Institute, Thorax Center, Erasmus MC, Rotterdam, Netherlands, Netherlands. [3]Department of Radiology & Nuclear Medicine, Erasmus Medical Center, Rotterdam, Netherlands, Netherlands. [4]Department of Biomechanical Engineering, Delft University of Technology, Delft, Netherlands, Netherlands

Introduction

Atherosclerosis progression reflects nonlinear interactions among lipid metabolism, inflammatory signaling, cellular phenotype transitions, and arterial biomechanics. Most computational models rely on simplified pathways or large, weakly constrained parameter sets, limiting their ability to reproduce clinically observed heterogeneity [1,2]. We present an application of a graph-derived mechanochemical framework that couples ODE-based phenotype controllers with transport-reaction PDEs and finite-element biomechanics to simulate plaque evolution across both synthetic and patient-specific geometries.

Methods

A curated biological interaction graph, encompassing lipid species, cytokines, macrophage and SMC phenotypes, extracellular matrix turnover, oxidative and osteogenic cues, and mechanical drivers (strain, shear stress), was mapped to a coupled mechanochemical model using standardized operators. A magnitude-based weighting scheme assigned low/medium/high influence levels to pathway edges, ensuring biologically interpretable regulation without excessive parameterization. Phenotype transitions (e.g., M1/M2 macrophages, contractile/synthetic SMCs) were represented using bistable controller ODEs. Biochemical and cellular species were simulated via diffusion-reaction PDEs dynamically coupled to finite-element structural mechanics. Initial and boundary conditions incorporated patient-specific blood biomarkers. Simulations were performed on (i) reduced-order synthetic geometries derived from PARISK population descriptors, and (ii) two patient-specific carotid bifurcations from the PARISK longitudinal study [3].

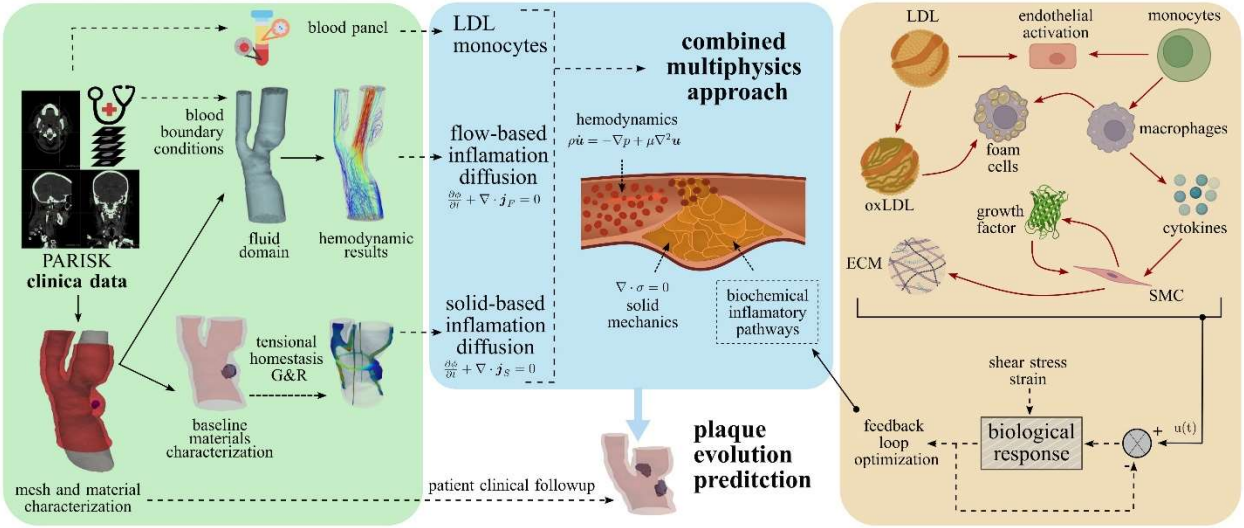
Results

In synthetic geometries, controlled activation or suppression of graph pathways produced a wide spectrum of progression phenotypes, including lipid-dominant plaques, inflammatory amplification loops, and diverging calcification–resorption trajectories. These simulation families qualitatively reproduced patterns of variability observed in PARISK. Patient-specific simulations demonstrated numerical stability and biological interpretability. Differences in LDL levels, monocyte counts, or inflammatory markers translated into distinct spatial distributions of lipid accumulation, macrophage phenotype shifts, and calcification progression. Local predictions of calcification growth or resorption aligned with two-year follow-up imaging, supporting the framework's ability to capture inter-patient variability.

Discussion

The graph-derived mechanochemical framework successfully generated clinically consistent progression scenarios at both population and individual levels. Its ability to integrate blood-derived inputs, reproduce distinct plaque evolution trajectories, and maintain biological interpretability positions it as a promising tool for future risk stratification and personalized simulation of vascular disease.

Images (Optional)



References (Optional)

[1] Ajoolabady A. et al. Cell Death Dis, 2024

[2] Abou-Jaoudé W. et al. Front. Genet, 2016

[3] Truijman MTB et al. International Journal of Stroke. 2013

Session Category

Cardiovascular/Cardiorespiratory Biomechanics: Methods, Models and Applications

OA18-01

Predicting Femoral Fracture in Postmenopausal Women: Multi-Cohort Clinical Validation of the BBCT-Hip Pipeline

Dr. Julia Aleksandra Szyszko[1], Dr. Alessandra Aldieri[1], Dr. Antonino Amedeo La Mattina[2], Mrs. Marilina Amabile[2], M.D. Claudio Ripamonti[3], M.D. Lucia Lisi[3], Dr. Pinaki Bhattacharya[4,5], Mr. Fabio Baruffaldi[3], Prof. Marco Viceconti[1]

[1]Department of Industrial Engineering, Alma Mater Studiorum – University of Bologna, Bologna, Emilia-Romagna, Italy. [2]SC Laboratorio di Tecnologia Medica, IRCCS Istituto Ortopedico Rizzoli, Bologna, Emilia-Romagna, Italy. [3]SSD Medicina e Reumatologia, IRCCS Istituto Ortopedico Rizzoli, Bologna, Emilia-Romagna, Italy. [4]School of Mechanical, Aerospace and Civil Engineering, University of Sheffield, Sheffield, Yorkshire e Humber, United Kingdom. [5]INSIGNEO Institute, University of Sheffield, Sheffield, Yorkshire e Humber, United Kingdom

Introduction

Hip fragility fractures represent one of the most severe manifestations of osteoporosis, associated with increased morbidity, mortality, and significant healthcare burden worldwide [1]. Although aBMD derived from dual-energy X-ray absorptiometry (DXA) is the clinical gold standard for diagnosing osteoporosis, nearly half of patients classified as non-osteoporotic experience fragility fractures [2]. Finite Element (FE) models have emerged as promising tools for improving fracture risk assessment. Within this context, the Bologna Biomechanical Computed Tomography (BBCT)-hip model was developed, which calculates an absolute risk of hip fracture (ARF0) for a subject by coupling a mathematical-stochastic model of the fall used to compute possible subject-specific impact loads with a subject-specific FE model of the femur to estimate its failure load in sideways fall conditions.

Methods

This study assessed the stratification accuracy of BBCT-hip *in vivo* compared to DXA-derived aBMD across multiple clinical cohorts of post-menopausal women, comprising 63 fractured (age: 76.5±8.1; height: 159±6.4; weight: 62.9±13.4) and 293 non-fractured (age: 71.7±7.5; height: 159.6±6.2; weight: 64.5±11.5) subjects. Specifically, three distinct cohorts with CT scans and aBMD available were combined: a retrospective cohort of 94 British women [3]; a retro-prospective cohort of 101 Italian women [4] and a cohort of 161 Italian women collected within an ongoing clinical study at the Rizzoli Orthopaedic Institute. Thanks to the availability of CT scans, weight and height information for each

subject, BBCT-hip pipeline was implemented, and the ARF0 values computed. BBCT-hip stratification accuracy was assessed through a ROC analysis and compared to the stratification accuracy of aBMD.

Results

BBCT-hip showed an AUC of 0.79 (95% CI: 0.73-0.85), which turned out to be statistically significantly higher than the AUC of aBMD, equal to 0.64 (95% CI: 0.55-0.72) (Figure 1).

Discussion

This study demonstrated an improved accuracy of BBCT-hip in separating fractured from non-fractured subjects compared to aBMD. Such a result provides evidence supporting more extensive clinical validation studies to pave the way towards BBCT-hip clinical implementation.

Images (Optional)

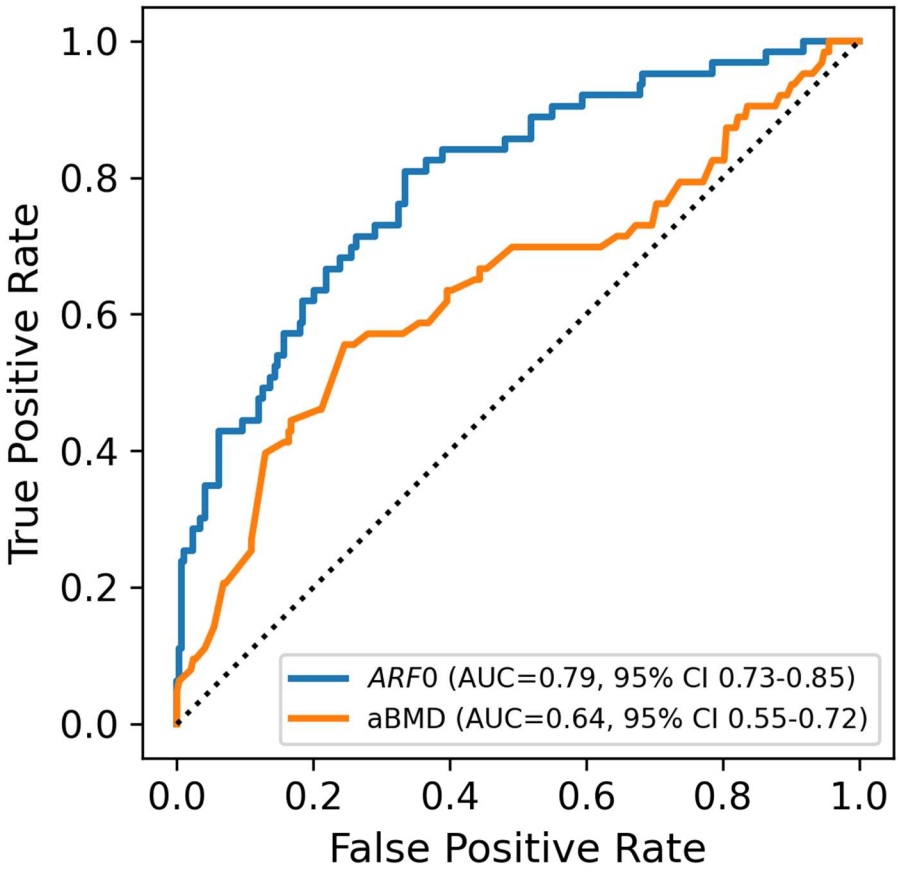


Figure 1. Receiver operating characteristic (ROC) curves for fracture classification in the postmenopausal cohort,showing ROC performance in the combined cohort for aBMD and ARF0.

References (Optional)

[1] A. Odén et al., Calcif Tissue Int, 2013

[2] S.C.E. Schuit et al., Bone, 2004

[3] L. Yang et al., Osteoporos Int., 2014

[4] A. Aldieri et al., AMSActa, 2025

Acknowledgements (Optional)

This research was co-funded by the Italian Complementary National Plan PNC-I.1 'Research initiatives for innovative technologies and pathways in the health and welfare sector' D.D. 931 of 06/06/2022, 'DARE - DigitAl lifelong pRevEntion' initiative, code PNC0000002, CUP: B53C22006230001.

Session Category

Musculoskeletal Biomechanics: Methods, Models and Applications

OA18-02

Associations Between Spinal Parameters and Loads During Gait in Patients With Lumbar Spinal Stenosis: A Combined Clinical and Musculoskeletal Modeling Study

Ms. Alice Caimi[1], Mr. Nicholas Fischlin[1], Mr. David Koch[2,3], Prof. Dr. med. Cordula Netzer[2,3], Dr. Corina Nüesch[2,3], Prof. Dr. Annegret Mündermann[3,4], Prof. Dr. Stephen J. Ferguson[1], Dr. Dominika Ignasiak[1]

[1]ETH Zurich, Zurich, Switzerland, Switzerland. [2]University Hospital Basel, Basel, Switzerland, Switzerland. [3]University of Basel, Basel, Switzerland, Switzerland. [4]Schulthess Clinic, Zurich, Switzerland, Switzerland

Introduction

To alleviate symptoms, patients with lumbar spinal stenosis (LSS) adopt compensatory strategies such as forward trunk inclination and pelvic retroversion [1,2]. While these postural adjustments reduce nerve root compression and provide temporary relief, they may require greater muscular effort and thereby increase spinal loading. Identifying the spinopelvic parameters associated with spinal loads is critical for developing strategies to reduce biomechanical stress and mitigate disease progression. The study aimed to investigate spinal loads in patients with LSS during gait in relation to their spinal parameters, by combining musculoskeletal modeling with motion-capture and radiographic data.

Methods

A full-body musculoskeletal (AnyBody) model was applied to 103 patients with LSS (72.7years±9.6, 52 female, 51 male). Vertebral positions and orientations were extracted from radiographs to reconstruct patient-specific spinal alignment. Inverse-dynamics simulations driven by motion-capture marker trajectories were performed to estimate spinal loads during gait (Figure 1, left). Compressive and shear forces were computed at all lumbar levels, with analyses focused on the predominantly stenotic segment (L4-L5). Associations between sagittal alignment parameters and loads were assessed with Spearman's correlation and corrected for multiple comparisons using the Benjamini-Hochberg method.

Results

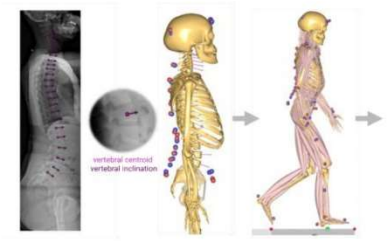
Weak-to-moderate associations were found between maximum L4-L5 spinal loads and spinopelvic alignment parameters during gait (Figure 1, right). Moderate negative associations were observed between compressive loads and T2-T12 kyphosis (ρ=-0.54), and between shear forces and lumbar lordosis (ρ=-0.42) as well as T2-T12 and T5-T12

kyphosis (ρ=-0.41 and -0.40, respectively). Weak but significant positive associations were found between both compressive and shear forces and pelvic tilt, as well as L4-L5 segmental flexion.

Discussion

Spinal loads during gait were estimated for patient-specific full spinal alignment profiles in a large cohort of patients with LSS. Both compressive and shear forces at L4-L5 were associated with spinal alignment parameters, indicating that posture-dependent loading patterns are related to mechanical stress at commonly stenotic levels and may contribute to segmental degeneration over time. Future work should investigate whether spinal loads provide a mechanistic explanation for symptom progression and stenosis recurrence in LSS, supporting targeted clinical decision-making.

Images (Optional)



	Max Compression (/BM)		Max Shear (/BM)	
	Spear. ρ	*p*-value	Spear. ρ	*p*-value
Max SS	-0.15	0.042	**-0.23**	**0.031**
Max PT	**0.32**	**0.017**	0.20	0.036
Max LL	**-0.28**	**0.025**	**-0.42**	**0.006**
Max L4-L5	**0.25**	**0.028**	**0.28**	**0.022**
Max T2-T12	**-0.54**	**0.003**	**-0.41**	**0.008**
Max T2-T5	**-0.23**	**0.033**	-0.01	0.050
Max T5-T12	**-0.33**	**0.014**	**-0.40**	**0.011**
Max T1-T9	-0.12	0.044	-0.07	0.047
Max T1-S1	**-0.31**	**0.019**	-0.15	0.039

Figure 1: (Left) Patient-specific sagittal spinal alignments reconstructed from radiographs for all participants were incorporated into full-body motion-capture-driven musculoskeletal models to simulate gait. (Right) Associations between maximum sagittal spinal alignment parameters and maximum body mass-normalized L4-L5 compression and shear loads. Alignment parameters included sacral slope (SS), pelvic tilt (PT), lumbar lordosis (LL), segmental flexion (L4-L5), thoracic kyphosis angles (T2-T12, T2-T5, T5-T12), sagittal thoracic inclination (T1-T9), and the global spinal angle (T1-S1). Significant correlations, determined after controlling the false discovery rate at 5% using the Benjamini-Hochberg method, are highlighted in bold.

References (Optional)

[1] Tatsuya Igawa *et al.*, PLoS One, 2018

[2] Deed Harrison *et al.*, J Manipulative Physiol Ther, 1999

Acknowledgements (Optional)

This work was funded by SNSF (grant 204461).

Session Category

Musculoskeletal Biomechanics: Methods, Models and Applications

OA18-03

Evaluation of Bicycle Delivery Workers' Load With the 3D-Musculoskeletal Computermodel "Myonardo"

Mag. Norbert Lechner[1], PhD Maarten Van den Heuvel[2], Ing. Harald Bruckner[3], Prof. Heiko Wagner[2], Prof. William H.M. Castro[2], PhD Franziska Mally[1]

[1]AUVA - Austrian Workers Compensation Board, Vienna, Austria, Austria. [2]Predimo GmbH, Münster, Germany, Germany. [3]Chamber of Labour, Vienna, Austria, Austria

Introduction

Recent reports indicate that the physical strain experienced by bicycle delivery workers is excessively high. This study aimed to investigate the load on the riders' joints during cycling in comparison to standing, walking and squat lifting.

Methods

20 healthy male subjects volunteered for the study (184.6 ± 7.1 cm, 79.8 ± 10.9 kg, 27.86 ± 8.18 years). Each subject had to perform cycling in two postures (upright and forward) with and without a loaded delivery backpack (5, 10, 15 kg). Additionally, subjects performed three reference tasks (standing, walking, lifting).

Kinematics were captured using an Xsens Awinda system (Movella, Enschede). External forces were recorded using strain gauges at the handlebar and cranks. Joint loads were calculated with the musculoskeletal model Myonardo (v.7.5.9, Predimo GmbH, Münster, Germany).

Total joint forces were normalized for body weight. 50th and 95th percentile were calculated over 20-30 s of stable cycling, 5-10 s of stable standing/walking and three repetitions of lifting. A generalized linear model analysis was used to determine statistical significance.

Results

The results show that under all weight conditions cycling in an upright position leads to lower joint forces than cycling in forward bent position. In the lower extremities standing, walking and lifting often resulted in higher loads than the cycling tasks. The influence of additional weight during cycling is less in the lower extremities, especially during upright

cycling. The highest loads were found at the L5/S1 segment, which is often an important indicator for occupational risk assessment (Figure 1).

Figure 1: Median (Q50) and peak (Q95) loads at L5/S1 segment (* $p<0.05$, ** $p < 0.01$, *** $p < 0.001$).

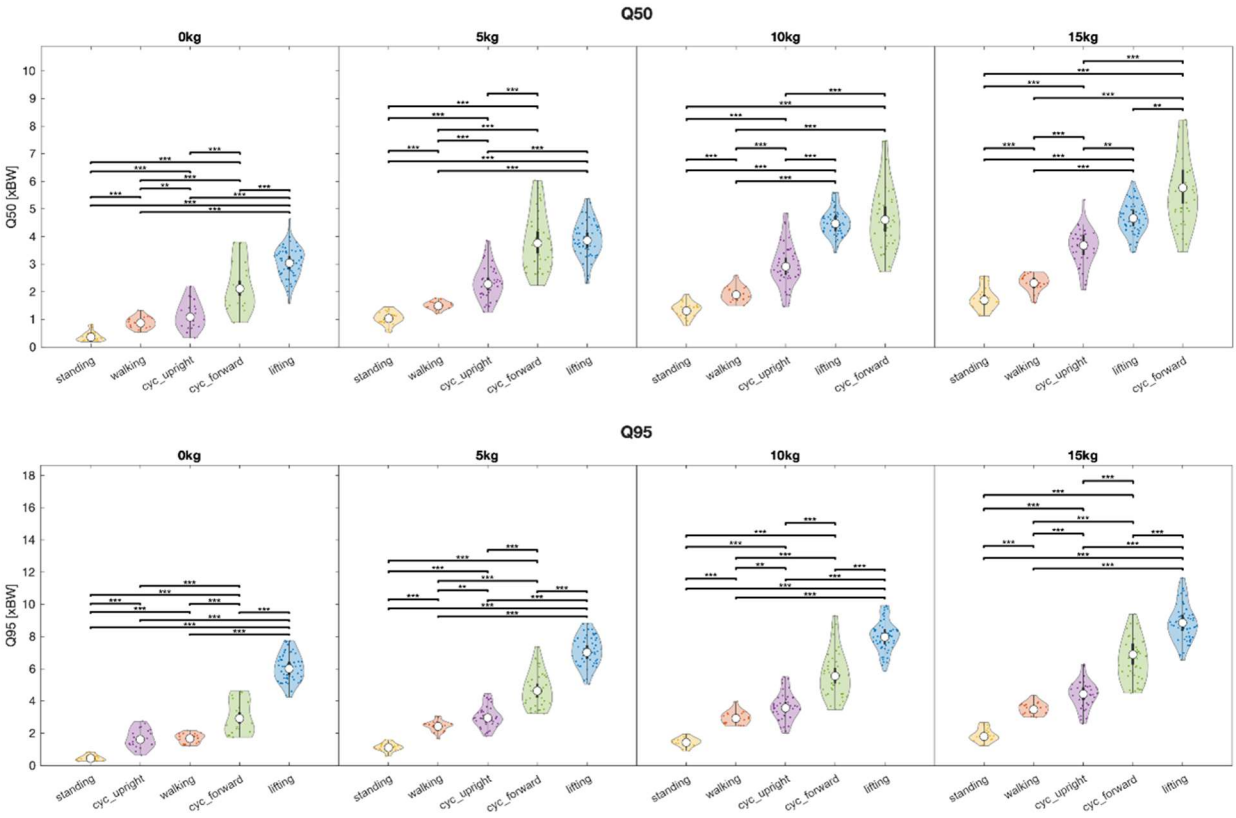
Discussion

To improve the safety and health of delivery riders, future regulations should focus on the reduction the physical stress by technical and personal measures. Additional weight should not be carried on the back and riders should be trained to cycle in good posture.

Next steps could be the analysis and interpretation of

- Remaining joints (i.e. ankle, elbow)
- Shear forces and peak forces
- Forces during sub-tasks (e.g. getting on/off the bike)
- Comparison between computermyography and conventional biomechanical assessment
- Derive measures to improve occupational safety and health of bike delivery riders

Images (Optional)



References (Optional)

Session Category

Musculoskeletal Biomechanics: Methods, Models and Applications

OA18-04

The Influence of Subject-Specific Musculoskeletal Modeling on Contact Stress Predictions in Dysplastic Hips

Dr. Molly Shepherd PhD[1], Dr. Jessica Goetz PhD[2], Dr. Holly Aitken PhD[2], Dr. Michael Harris PhD[1]

[1]Washington University in St. Louis, St. Louis, Missouri, United States. [2]University of Iowa, Iowa City, Iowa, United States

Introduction

Developmental dysplasia of the hip (DDH) is a condition characterized by insufficient acetabular coverage of the femoral head. Discrete element analysis (DEA), a rapidly executing computational technique to quantify joint contact mechanics, has demonstrated higher contact stresses in DDH [1]. However, previous work has focused only on individualized anatomy, despite contact stresses also depending on loading conditions, such as kinematics and joint reaction forces. The objective of this study was to determine the influence of individualized DDH loading conditions from subject-specific musculoskeletal models on DEA-computed contact stresses compared to literature-based loading conditions.

Methods

DEA models were created for 10 individuals with DDH and used to calculate hip contact stresses using two different sets of loading conditions: (1) literature-based average DDH gait kinematics and joint reaction forces [2], and (2) kinematics and forces from individualized gait analysis and musculoskeletal models created by incorporating subject-specific three-dimensional reconstructions of the pelvis and femurs and updating muscle origins and insertions. For both sets of loading conditions, the stance phase of gait was discretized into 13 quasi-static positions for analysis [1].

Results

Subject-specific joint reaction forces and kinematics strongly affected the variability in cartilage contact stresses (Figure 1). While the literature-based model was an average “pusher” loading pattern (larger second peak), subject-specific loading patterns revealed “pusher”, “hard hitters” (larger first peak), “balanced” (similar first and second peaks), and “unimodal” (no distinctive loading peaks) variations. On average, subject-specific mean stresses were significantly higher during early- to mid-stance than literature-based stresses, while there were no significant differences in late stance.

Discussion

These results highlight the importance of incorporating the variability of individualized loading conditions when estimating contact stresses. The individual variations affect not only contact stress magnitudes, but also locations within the hip joint. The larger contact stresses during early stance suggest that this component of gait may contribute more to joint damage than previously assumed. Incorporating individualized loading patterns may improve the accuracy of contact stress predictions and therefore our understanding of patient-specific degenerative risk factors.

Images (Optional)

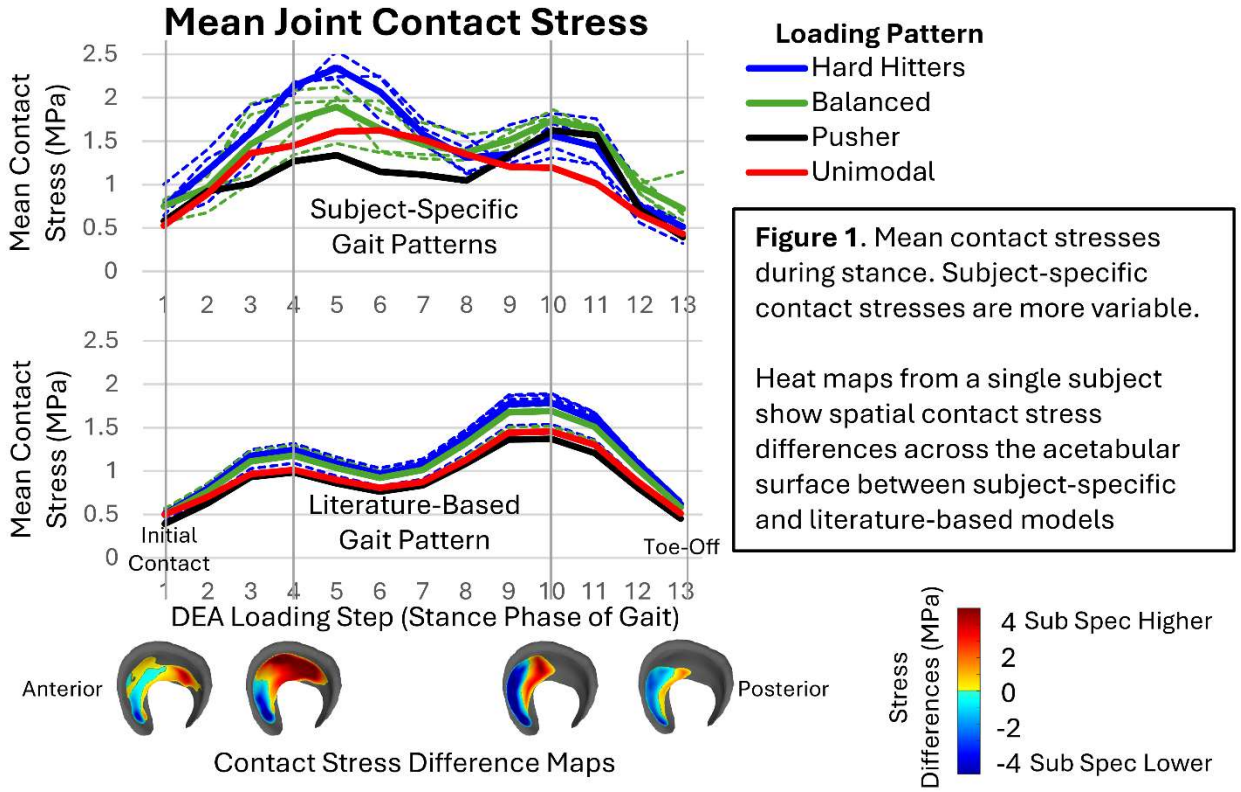


Figure 1. Mean contact stresses during stance. Subject-specific contact stresses are more variable.

Heat maps from a single subject show spatial contact stress differences across the acetabular surface between subject-specific and literature-based models

References (Optional)

[1] Holly Aitken *et al.*, J Orthop Res, 2022. [2] Michael Harris *et al.*, J Biomech, 2017.

Session Category

Musculoskeletal Biomechanics: Methods, Models and Applications

OA18-05

Biomechanical Predictors of Self-Contamination During Medical Gown Doffing: A Motion-Capture Analysis of Hand–Gown Interaction

Dr. Jingeng Li PhD[1], Professor Li-Shan Chou PhD[2]

[1]Iowa State University, Ames, Iowa, United States. [2]Purdue University, West Lafayette, Indiana, United States

Introduction

Proper removal of personal protective equipment (PPE) is essential for preventing self-contamination among healthcare workers. Although previous research has examined gown design and removal techniques, movement behaviors that contribute to contamination during medical gown doffing remain insufficiently understood. This study developed a motion-analysis–based framework to characterize dynamic gown deformation, hand trajectories, and their relationship to contamination during standardized gown removal.

Methods

Eighteen healthy adults performed medical gown doffing following the CDC guidelines. Each participant completed three trials after receiving standardized video and verbal instructions. A consistent amount of fluorescent solution was sprayed onto the gown surface before each trial to simulate contamination. A 12-camera optical motion capture system (240Hz, Qualisys AB, Sweden) recorded three-dimensional trajectories of ten reflective markers placed on the gown and two markers placed on the index finger of each hand. Marker trajectories were used to reconstruct a dynamic 3D contour of the gown and compute two interaction-based variables during the doffing process: hand-to-gown distance and hand-gown contact time. A 12 Hz 4th-order Butterworth low-pass filter was used to remove noise. UV-A inspection identified contaminated body regions post-doffing. Spearman correlations and stepwise regression were used to determine associations and predictors of contamination risk.

Results

Participants averaged 2.04 ± 1.07 contaminated regions per trial, with the dominant hand exhibiting more contamination than the non-dominant hand. Hand-gown distance showed strong negative correlations with contamination across both hands ($r_s = -0.786$ to -0.873, $p < .001$), while hand-gown contact time showed strong positive correlations ($r_s = 0.556$–0.711). Stepwise regression identified dominant hand-to-gown distance and contact time

as significant predictors of dominant-hand contamination (R^2 = .701), while total hand-to-gown distance explained 72.7% of variance in overall contamination risk.

Discussion

This study provides the first quantitative biomechanical evidence that closer hand proximity to the gown and longer contact duration are substantially associated with contamination risk during medical gown doffing. The novel approach enables identification of high-risk movement patterns that may not be detectable through visual observation alone. Future work should validate these findings in clinical populations, examine variations across different gown types, and contamination sources.

Session Category

Musculoskeletal Biomechanics: Methods, Models and Applications

OA18-06

Integrating Models and Muscle-Tendon Function to Understand Sex-Specific Responses to Different Footwear Stiffness during Running

Ms. Vivian Nguyen MSc, BSc[1], Ms. Banin Al-Shimari MSc, BSc[1], Mr. Marco Perizzolo BSc[2], Dr. Jared Fletcher PhD[2], Dr. Brent Edwards PhD[1], Dr. Michael Asmussen PhD[3]

[1]University of Calgary, Calgary, Alberta, Canada. [2]Mount Royal University, Calgary, Alberta, Canada. [3]Vancouver Island University, Nanaimo, British Columbia, Canada

Introduction

Footwear longitudinal bending stiffness (LBS) influences running biomechanics by altering joint energetics [1] and lower-limb muscle-tendon behaviour. However, most studies primarily focus on male participants, despite known sex differences in muscle strength, tendon morphology, and hormonal regulation that may affect muscle-tendon dynamics and how males and females respond to changes in footwear stiffness [2]. Dynamic optimization enables estimation of muscle fiber lengths, velocities, and forces, providing insight into how LBS affects musculotendon dynamics. This study investigated how footwear LBS affects muscle-tendon dynamics between sexes during running using electromyography (EMG)-constrained dynamic optimization.

Methods

Twenty participants (10 male, 10 female) ran at 3.5 m/s on a force-instrumented treadmill in minimalist footwear with three stiffness conditions: no plate (0.05 Nm/deg), 1 mm carbon fiber plate (0.14 Nm/deg), and 1.5 mm carbon fiber plate (0.30 Nm/deg). Motion capture, ground reaction forces, and EMG from the lateral gastrocnemius (LG) and soleus (SOL) were collected. Medial gastrocnemius (MG) fascicle behaviour was recorded using ultrasound. Achilles tendon stiffness and moment arms were measured using ultrasound and dynamometry. A musculoskeletal model [3] was used to perform inverse kinematics and dynamics and an EMG-constrained optimization was used to estimate muscle-tendon dynamics.

Results

A significant interaction effect ($p<0.05$) was found for peak-to-peak normalized MG muscle fiber length, where males exhibited higher values than females in the 1 mm and 1.5 mm footwear conditions. Increased LBS decreased SOL muscle-tendon length and reduced

SOL tendon force. Males showed higher MG and SOL fiber lengths, velocities, and tendon forces, whereas mean normalized fiber velocities were higher in females.

Discussion

These findings indicate that biological sex differences resulted in changes in muscle-tendon behaviour during running. The results reinforce the importance of considering sex when evaluating how LBS influences muscle-tendon dynamics or when designing stiffness-modified footwear. Collected ultrasound fascicle data will validate dynamic optimization outputs and assess how well model estimates reflect *in vivo* behaviour, supporting more accurate, sex-specific predictive modeling.

Images (Optional)

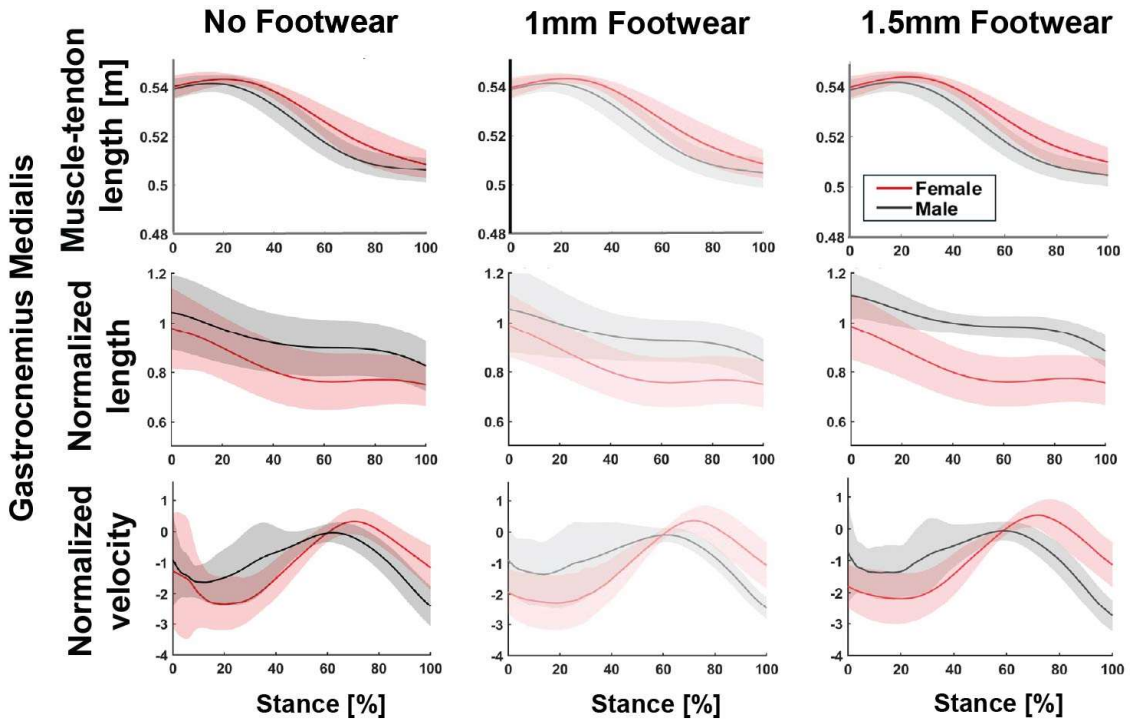


Figure 1: Mean gastrocnemius medialis (MG) muscle-tendon length, normalized muscle fiber length, and normalized muscle fiber velocity during stance across three footwear conditions (n0, 1mm, 1.5mm) and two sexes (male, female). Black line represents males and red line females. Shaded areas indicate variability (± standard deviation).

References (Optional)

[1] Nigg *et al.*, Biomech. Biol. Hum. Mov., 2000

[2] Kubo *et al.*, Eur. J. Appl. Physiol., 2009

[3] Rajagopal *et al.*, IEEE Trans. Biomed. Eng., 2016.

Session Category

Musculoskeletal Biomechanics: Methods, Models and Applications

OA19-02

Neck Muscle Activation during Inverted Freefalls in Human Subjects

Dr. Loay Al-Salehi[1], Dr. Peter A. Cripton[1], Dr. Gunter P. Siegmund[2]

[1]The University of British Columbia, Vancouver, BC, Canada. [2]MEA Forensic Engineers & Scientists, Laguna Hills, CA, United States

Introduction

Understanding the underlying neck injury mechanics of cervical spine fractures and dislocations in headfirst impacts is a prerequisite for potential prevention strategies. Although posture-related injury factors are well studied, the effect of active muscle has received less attention. We therefore quantified the timing and amplitude of neck muscle activation during headfirst freefalls.

Methods

Human subjects (9F/2M) were exposed to 2 initially relaxed and 2 initially braced headfirst freefalls (312.5 ms/0.479 m) on a custom-built freefall device (Fig.1). In relaxed trials, subjects maintained a horizontal head position before freefall without further instructions, while in braced trials, they were instructed to voluntarily brace for an anticipated headfirst impact immediately before freefall. Unilateral neck muscle electromyography (EMG) was recorded using indwelling electrodes which were inserted into seven superficial and deep posterior neck muscles (Fig 1). Surface electrodes were used for the sternohyoid muscle and as reference electrodes on the mid clavicle. Muscle onsets were defined as the time when each muscle's activation reached 10% of its maximum value, and was only quantified in the relaxed condition. Muscle activation levels were calculated as the root-mean square (RMS) and normalized by maximum voluntary isometric contractions. Muscle activation levels were analyzed using linear mixed models to assess the effects of time (before/after freefall start) and condition (relaxed/braced).

Results

Muscle onset times (mean (95% confidence interval)) ranged between 53.7 (49.3; 58.1) ms for STH and 93.6 (80.0; 107.2) ms for SSCAP. Muscle activation levels varied widely between subjects and muscles, and were significantly larger during freefall that before freefall ($p<0.0001$). Bracing increased muscle activation levels in 5 of 8 muscles before freefall ($p\leq0.0298$), but in only 2 muscles (LS and SSCAP) during freefall ($p\leq0.0161$).

Discussion

Muscle activation levels were larger during freefall than before freefall in both conditions, highlighting that an inverted freefall is a strong and robust sensory stimulus, even when braced. The short muscle onset times are consistent with reflex muscle activation, and thus muscle activation would likely precede head contact in many impact scenarios. Therefore, muscles should be included during headfirst impact testing in both cadaveric experiments and computational models.

Images (Optional)

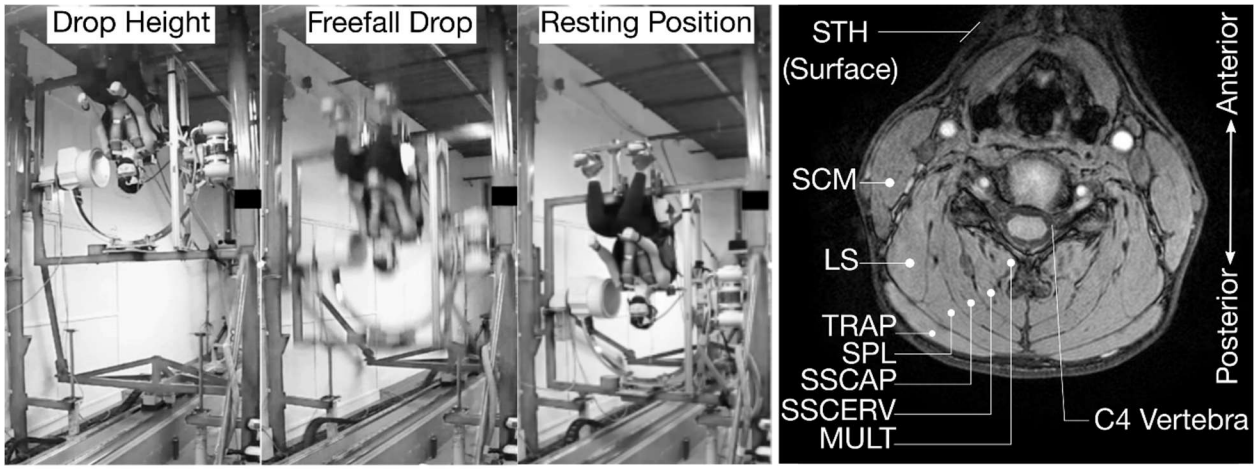


Fig.1 Left: timelapse of the three phases of the experiment. Right: exemplar transverse magnetic resonance image of a neck at C4 level with intended locations of indwelling electrode insertion (circles, levator scapulae (LS), multifidus (MULT), semispinalis capitis (SSCAP), semispinalis cervicis (SSCERV), splenius (SPL), sternocleidomastoid (SCM), and trapezius (TRAP)), and surface electrode (line, sternohyoid (STH)).

Session Category

Injury Biomechanics: N/A

OA19-03

Lesion Angle and Length Correlate in High-Energy Injuries of Articular Cartilage Explants

Dr. Alexander Paz Carvajal PhD.[1,2], Mr. Adnan Tahir MSc.[1], Dr. Atte Eskelinen PhD.[1], Prof. Alan Grodzinsky PhD.[3], Prof. Rami Korhonen PhD.[1], Dr. Mimmi Liukkonen PhD.[2], Assoc. Prof. Petri Tanska PhD.[1,2]

[1]University of Eastern Finland, Kuopio, North Savo, Finland. [2]Kuopio University Hospital, Kuopio, North Savo, Finland. [3]Massachusetts Institute of Technology, Cambridge, Massachusetts, United States

Introduction

Fast loading can injure articular cartilage and trigger a cascade of degenerative changes leading to post-traumatic osteoarthritis. In previous studies, we focused on how degradative changes progress in tissue constituents following high-energy injury and periodic loading with and without exogenous inflammation. Here, the aim was to study whether cartilage structure provides a mechanistic explanation for the initiation and progression of the lesions, which could influence the speed and severity of the subsequent degeneration.

Methods

We harvested 23 cartilage explants (thickness: 1 mm, diameter: 3 mm) from the patellofemoral grooves of 1-to 2-week-old bovines. The explants were subjected to a single high-energy injury (50% strain at 100%/s) in unconfined compression. After the injurious loading, samples were fixed in formalin, dehydrated, and embedded in paraffin. Safranin-O and unstained sections were prepared. Stained sections were imaged with digital densitometry to characterize proteoglycan content and lesion/crack shape and size, while unstained sections underwent polarized light microscopy to evaluate collagen network structure. A custom MATLAB script was used to characterize crack angle with respect to the explant surface (θ, Fig. 1a), the crack length (c), and the crack distance from the explant edge (d).

Results

The protocol fully cracked 4 samples (17%), left 4 visually intact (17%), and induced lesions in 15 samples (66%). From the 30 cracks we observed, the average ([95% confidence interval]) crack length was c = 0.12 [0.09, 0.14] mm occurring at d = 0.62 [0.50, 0.74] mm

from the edge at an angle θ = 56.36 [49.43, 63.28] degrees with respect to the articular surface. In addition, we observed a clear association between a smaller crack angle and longer crack length (Pearson r = – 0.78, r^2 = 0.61; Fig. 1b).

Discussion

Discussion. Longer cracks tended to align more closely with the articular surface. The crack shape and size may be explained by the local collagen arrangement, suggesting that the damage initially develops along the fibers (breaking fiber-to-fiber bonds) rather than transverse to the collagen fibers. This hypothesis needs to be validated by further quantifying the dominant orientation of the collagen fibers in (im)mature cartilage.

Images (Optional)

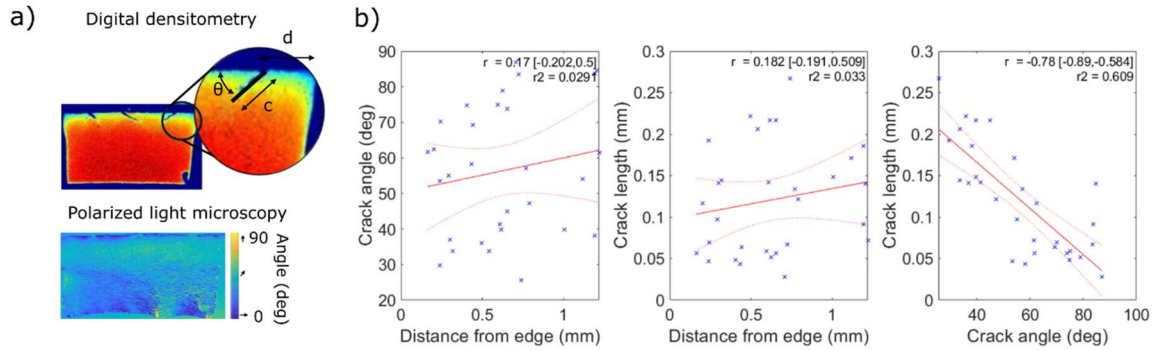


Figure 1. a) Cartilage samples and crack parameters compared: θ, angle with respect to the surface, d, distance from the closest edge, and c, crack length. b) correlation analysis between crack parameters, solid red lines show the linear regressions and corresponding dashed lines, their 95% confidence intervals.

Session Category

Injury Biomechanics: N/A

OA19-04

Fall Detection in Extreme Class Imbalance: A Cascade Architecture for Real-World Deployment

Mr. Ethan Henley[1], Dr. Nicole Stark PhD[1], Ms. Brianna Reilly[1], Dr. Katherine Mayes MD, PhD[2,3], Dr. Damon Kuehl MD[2,3], Dr. Steve Rowson PhD[1]

[1]Virginia Tech, Blacksburg, VA, United States. [2]Virginia Tech Carilion School of Medicine, Roanoke, VA, United States. [3]Carilion Roanoke Memorial Hospital, Roanoke, VA, United States

Introduction

Falls among older adults (≥65 years) result in over 3 million emergency department visits and 32,000 deaths annually in the U.S., generating more than $50 billion in medical costs [1–4]. In long-term care(LTC) settings, many falls are unwitnessed, creating significant challenges for accurately assessing injury Automated fall detection systems offer promise but face a fundamental barrier: extreme class imbalance in continuous monitoring, where falls comprise <2% of recorded footage, leading to high false-positive rates and alarm fatigue [5,6].

Methods

We developed a cascade architecture that decomposes fall detection into two sequential stages optimized for complementary objectives. Stage 1 uses a lightweight 3D convolutional neural network trained via curriculum learning with adaptive focal loss to maximize recall on the minority fall class. Stage 2 implements a feature-based arbiter that evaluates internal CNN representations to validate candidate events, aiming to reduce false positives while preserving sensitivity. The system was validated using 190 videos of simulated falls from the LE2I dataset [7] and 300 spontaneous falls from LTC residents in the Robinovitch dataset [8].

Results

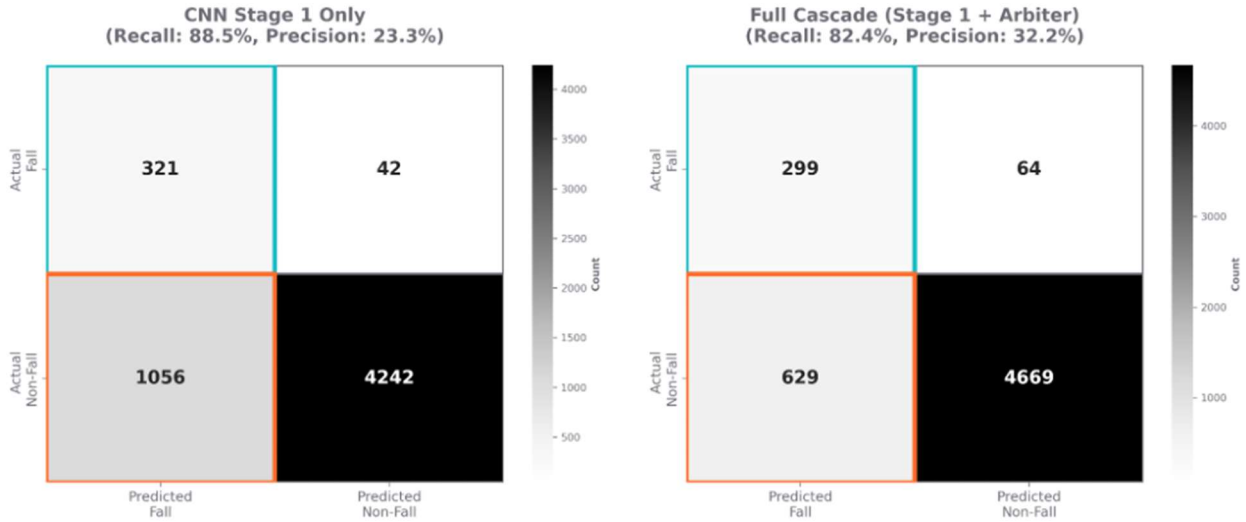
The proposed cascade achieved 82.4% recall and 32.2% precision, yielding a 38% relative improvement in precision over a single-stage CNN baseline (88.5% recall, 23.3% precision). The approach reduced false positives by 40.5% while maintaining sensitivity above 80%.

Discussion

Our findings demonstrate that a two-stage cascade substantially improves the clinical viability of automated fall detection under severe class-imbalance conditions. By

maximizing recall early and applying a discriminative arbiter for refinement, the framework reduces false alarms without compromising sensitivity. This architecture provides a scalable foundation for real-world deployment in LTC environments, where accurate detection is essential yet data constraints remain significant.

Images (Optional)



References (Optional)

[1] Bergen G et al., *MMWR Morb Mortal Wkly Rep*, 2016
[2] Moreland B et al., *MMWR Morb Mortal Wkly Rep*, 2020
[3] Kakara R et al., *MMWR Morb Mortal Wkly Rep*, 2023
[4] Florence CS et al., *J Am Geriatr Soc*, 2018
[5] Sendelbach S et al., *AACN Adv Crit Care*, 2013
[6] Cvach M, *Biomed Instrum Technol*, 2012
[7] Charfi I et al., *J Electron Imaging*, 2013
[8] Robinovitch S et al., *Databrary*, 2018

Session Category

Injury Biomechanics: N/A

OA19-05

Translating Ballet Landing Mechanics to ACL Injury Prevention: A Biomechanical Comparison of Landing Strategies Between Female Dancers and Non-Dancers

Ms. Annabelle Sung Min Kang BS

Yonsei University, Seoul, Seoul, Korea, Republic of

Introduction

Females exhibit a disproportionately high risk of anterior cruciate ligament (ACL) injury, yet female ballet dancers, despite performing frequent jumps, show lower knee injury rates per exposure hour. This study examined whether dancers adopt unique landing strategies that reduce ACL loading and whether these mechanics can inform injury prevention protocols for the general female population.

Methods

10 female ballet dancers (24.88 ± 4.12 yrs; 162.98 ± 3.4 cm; 49.16 ± 5.5 kg) and 10 non-dancers (26.8 ± 3.41 yrs; 161.72 ± 5.4 cm; 57.65 ± 4.93 kg) performed three single-leg hop trials. Kinetic variables (peak vertical ground reaction force [vGRF], time-to-peak vGRF [TTP], loading rate) and sagittal-plane kinematics at initial contact (IC) and peak vGRF were compared using independent t-tests ($\alpha = .05$) and effect sizes.

Results

Dancers showed significantly prolonged TTP vGRF (0.57 ± 0.06 s) compared to non-dancers (0.44 ± 0.16 s; $p = .038$, d = 1.08), indicating slower impact loading. Although loading rate differences were non-significant ($p = .055$), a large effect size (d = -0.98) suggested a notable trend toward reduced impact loading in dancers. Significant kinematic differences emerged only at the ankle. At IC, dancers landed with greater plantar flexion (−17.24 ± 6.70°) than non-dancers (−6.50 ± 9.45°; $p = .009$, d = −1.31), reflecting a forefoot landing strategy. Crucially, no significant differences were observed in kinematics at peak vGRF, revealing a ~1.5-fold greater total ankle excursion (~34° vs. ~22°) in dancers.

Discussion

Lack of kinematic differences at the knee, contrasted with significant ankle excursion, suggests that dancers employ a distal absorption strategy. In this mechanism, the foot and ankle complex acts as the primary shock absorber, filtering impact forces before knee transmission. However, this strategy positions the ankle in a mechanically unstable, open-

packed configuration, consistent with the high incidence of ankle sprains in dancers. Consequently, understanding the muscular control of this mechanism is vital; future research should utilize electromyography (EMG) to quantify the damping role of the triceps surae and the co-activation of the tibialis anterior. For general population application, injury prevention protocols must combine ROM enhancement with neuromuscular training to secure joint stability while leveraging the biomechanical benefits of this soft landing strategy.

Session Category

Injury Biomechanics: N/A

OA20-01

Phase-Specific Neuromechanical Effects of Virtual and Augmented Reality–enhanced Robotic Gait Training After Stroke

Mr. Chaesu Kim M.Sc., Mr. Joshua Sung You Ph.D.

Yonsei university, Wonju, Gangwondo, Korea, Republic of

Introduction

Robotic-assisted gait training (RAGT) is widely used after stroke, but its neuromechanical effects are inconsistent and usually quantified by discrete spatiotemporal measures, so it remains unclear which phases of the gait cycle are modified by RAGT. Virtual reality (VR) and augmented reality (AR) can provide task-oriented visual feedback during RAGT and may differentially modulate impaired phases such as swing foot clearance, initial contact, and paretic propulsion.

Methods

Twenty individuals with chronic hemiparetic stroke trained on a robotic gait system (Walkbot) under four randomized, within-subject conditions: (1) RAGT alone without visual feedback (None), (2) VR-enhanced RAGT with a game-like kicking task emphasizing swing dorsiflexion, (3) AR-enhanced RAGT presenting overground walking scenes aligned with treadmill motion, and (4) VR+AR-enhanced RAGT, in which VR and AR were delivered sequentially (15+15 min) in random order. Robotic parameters (speed, body-weight support, guidance force) were held constant. During the 10–20-min steady-state window of each 30-min session, paretic-side EMG (tibialis anterior, medial gastrocnemius, rectus femoris, biceps femoris), vertical/anterior–posterior ground reaction forces, and COPx/COPy were recorded, time-normalized to 0–100% gait, and analyzed using one-way repeated-measures SPM-ANOVA with Bonferroni-corrected post-hoc SPM t-tests.

Results

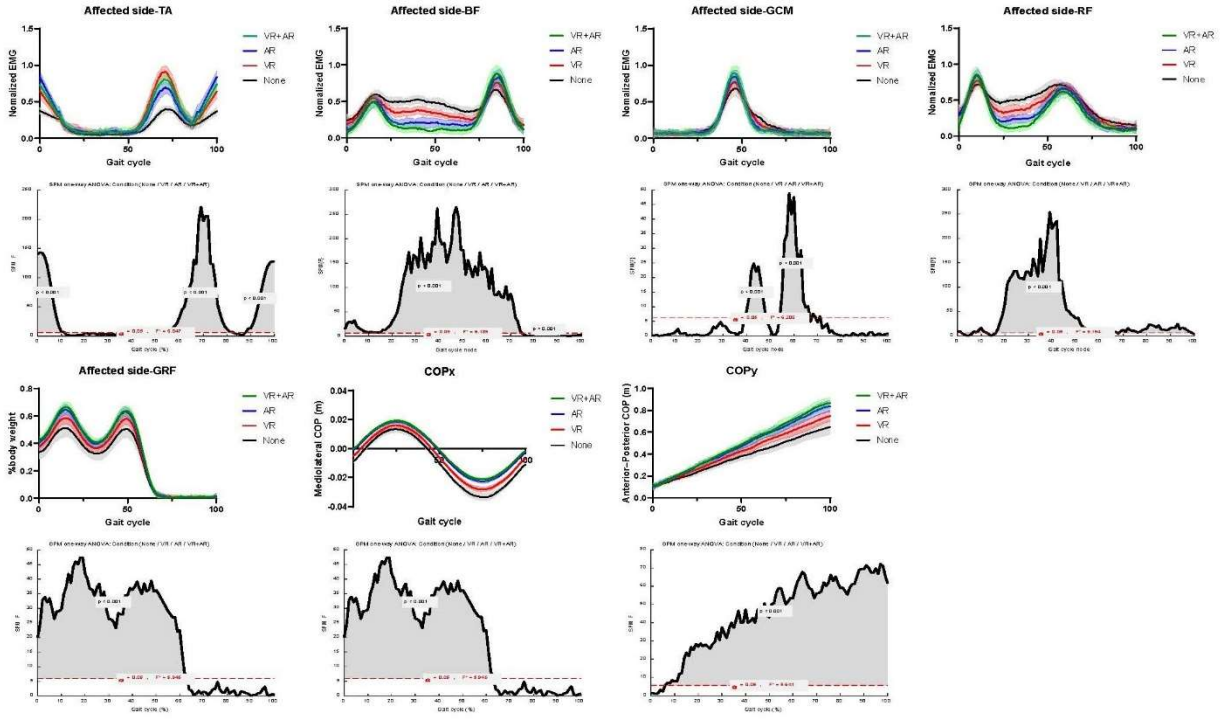
Despite identical robotic assistance, the VR/AR conditions produced phase-specific changes in paretic neuromechanics. VR-enhanced RAGT showed the largest mid-swing tibialis anterior burst (60–80%), consistent with increased dorsiflexor recruitment for toe clearance. AR- and VR+AR-enhanced RAGT increased tibialis anterior activity around initial contact (90–10%), enhanced late-stance gastrocnemius propulsion, and improved heel-to-toe COPy progression with reduced medio-lateral COPx sway. Rectus femoris/biceps

femoris co-contraction during stance was highest with RAGT alone and progressively decreased in VR-, AR-, and VR+AR-enhanced RAGT, indicating more selective knee control.

Discussion

By keeping robotic gait parameters fixed and manipulating only VR/AR visual feedback, this study shows that sensory context can modulate paretic neuromuscular control in a phase-specific manner. VR-enhanced RAGT improves swing-phase dorsiflexor control, whereas AR- and VR+AR-enhanced RAGT better restore loading and propulsion mechanics and reduce maladaptive stiffening. These findings suggest that VR/AR-augmented RAGT can be configured to target specific gait-phase deficits after stroke, rather than simply increasing training intensity.

Images (Optional)



References (Optional)

Acknowledgements (Optional)

This work was supported, in part, by the “Brain Korea 21 FOUR Project” (F21SH8303039), the National Research Foundation of Korea (NRF) for the Department of Physical Therapy in the Graduate School of Yonsei University, and This research was supported by the National Research Foundation of Korea (NRF) grant, funded by the Korean government (MSIT) (RS-

2025-24534569), and This research was supported by the Regional Innovation System & Education (RISE) program through the Gangwon RISE Center, funded by the Ministry of Education (MOE) and the Gangwon State (G.S.), Republic of Korea (2025-RISE-10-006). This research was supported by the National Research Foundation of Korea (NRF) grant, funded by the Korean government (MSIT) (RS-2025-24534569).

Session Category

Rehabilitation Biomechanics and Human Factors: Rehabilitation

OA20-02

Sonified-Biofeedback Training to Improve Postural Control in Older Adults

Ms. Zahava Hirsch, Ms. Erin Kreis, Dr. Antonia Zaferiou

Stevens Institute of Technology, Hoboken, NJ, United States

Introduction

Varied populations have improved their balance and gait using sonified-biofeedback, which conveys biomechanical measures through precise sound cues [1]. Our goal is to understand if sonified-biofeedback training can improve postural control in older adults [2]. We hypothesized that posture angle will improve during training trials versus baseline trials and be retained during a post-evaluation.

Methods

Six older adults (5 f, 74.5 ± 4.55 years) completed an initial assessment visit, four training visits across two weeks, and a one-week post visit. A 13-segment whole-body kinematic model was built using optical motion capture data (OptiTrack USA) [3]. A physical therapist balance guarded as participants completed a walking and turning course (Fig. 1A) at a preferred speed. During the initial assessment visit, participants completed assessments and were familiarized with the turning course. Each training visit consisted of five baseline trials without sonified-biofeedback followed by 10 training trials with sonified-biofeedback, fading by 20% each visit. Posture angle was determined by a vector from the pelvis to the head, using the pelvis anteroposterior axis to determine the sagittal plane. The target posture angle was determined by the participant's baseline trials. When posture approached the target, a low-pitched musical sound played. As the angle increased the pitch increased, informing the participant to self-correct their posture. Participant-level statistics used the Mann Whitney U test. Group-level statistics used the paired t-test.

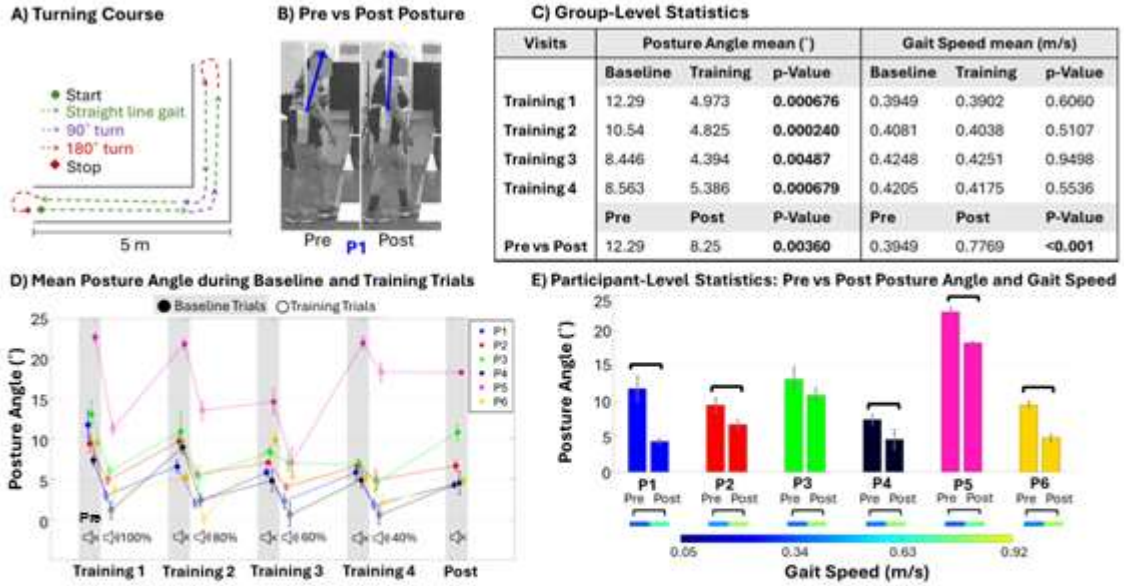
Results

A sample of pre versus post posture is seen in Figure 1B. At the group level, posture angle significantly improved during training versus baseline and pre versus post. There was no significant difference in gait speed during training versus baseline, but gait speed significantly improved pre versus post (Figure 1C). Participants' mean posture angle for each visit's baseline and training can be seen in Figure 1D. Within-participant results revealed five of six participants significantly improved their posture angle and all participants significantly increased gait speed pre versus post (Figure 1E).

Discussion

Results support sonified-biofeedback as a promising approach to help older adults improve dynamic postural control.

Images (Optional)



Visits	Posture Angle mean (°)			Gait Speed mean (m/s)		
	Baseline	Training	p-Value	Baseline	Training	p-Value
Training 1	12.29	4.973	**0.000676**	0.3949	0.3902	0.6060
Training 2	10.54	4.825	**0.000240**	0.4081	0.4038	0.5107
Training 3	8.446	4.394	**0.00487**	0.4248	0.4251	0.9498
Training 4	8.563	5.386	**0.000679**	0.4205	0.4175	0.5536
	Pre	Post	P-Value	Pre	Post	P-Value
Pre vs Post	12.29	8.25	**0.00360**	0.3949	0.7769	**<0.001**

Figure 1: A) Turning course. **B)** Sample image of Participant 1 posture. **C)** Group level statistics for posture angle and gait speed of baseline vs. training trials and pre vs. post. Significant p-values bolded. **D)** Mean posture angle for each participant for each visit's baseline (no sound) and training (with faded sonified biofeedback). **E)** Participant-level results for posture angle and gait speed pre vs post. Brackets indicate significant differences pre vs. post.

References (Optional)

[1] Zaferiou et al. (2025), *J NeuroEng. Rehab*. 22:38 [2] Fernandes et al. (2018), *Fisioter. Mov.* 31 [3] de Leva (1996), *J Biomech.* 29

Acknowledgements (Optional)

National Science Foundation Award #1944207

Session Category

Rehabilitation Biomechanics and Human Factors: Rehabilitation

OA20-03

People With Unilateral Transtibial Amputation Reorganize Muscle Coordination Patterns When Walking With Visual Feedback Targeting Increased Peak Propulsive Horizontal Force

Ms. Ziting Liz Li[1], Prof. Chris Fink[2], Prof. Vincent CK Cheung[3], Dr. Caelyn Hirschman[4], Prof. Alena M. Grabowski[4,5], Prof. Janet Zhang-Lea[1]

[1]Human Biomechanics Lab, University of Oregon, Eugene, Oregon, United States. [2]Department of Physics, Gonzaga University, Spokane, Washington, United States. [3]School of Biomedical Sciences, and The Gerald Choa Neuroscience Centre, The Chinese University of Hong Kong, Hong Kong, Hong Kong, China. [4]Department of Integrative Physiology, University of Colorado Boulder, Boulder, Colorado, United States. [5]Department of Veterans Affairs Eastern Colorado Healthcare System, Denver, Colorado, United States

Introduction

People with unilateral transtibial amputation (UTTA) walk using a passive-elastic prosthesis and apply less peak horizontal propulsive force (PPF) from their affected leg (AL) than their unaffected leg (UL). We previously found that when given visual feedback (VF) to increase AL-PPF by 20%, 3 out of 12 participants with UTTA met the target (≥20% increase), and 6 participants increased AL-PPF <15% compared to baseline. In this study, we used muscle synergy analysis to characterize how groups of muscles were coordinated during walking between high responders (≥20% increase) versus low responders (<15% increase), and hypothesized that high responders would reorganize UL muscle coordination when presented with VF.

Methods

Twelve people with UTTA walked with a passive-elastic prosthesis on a treadmill for 5 minutes at 1.25 m/s in two conditions, without VF as a baseline, and with VF of AL-PPF 20% (20VF) higher than baseline. We recorded surface EMG from lower-limb muscles on both legs, and applied non-negative matrix factorization on the UL EMG signals to extract synergy weightings to describe muscle coordination patterns during the baseline and 20VF trials. We used k-means clustering to identify muscle synergy clusters across participants, which automatically sorts the synergy weightings into a chosen number of clusters so that muscle coordination patterns within the same cluster are as similar as possible.

Results

Participants presented 3 clusters of UL synergies during baseline and 5 clusters during 20VF trials. During baseline, we observed a cluster characterized as a co-activation of the two measured ankle dorsiflexors (Lateral Gastrocnemius and Soleus), and this cluster was regrouped into a co-activation between one of the two measured ankle dorsiflexors and one of the measured hip extensors (Bicep Femoris or Gluteus Maximus) for the 20VF trial . Such reorganization in muscle synergies was observed in all high responders, but not in low responders. Low responders continued to present a synergy cluster with co-activation of both ankle dorsiflexors.

Discussion

People with UTTA using a passive-elastic prosthesis who increased AL-PPF when given VF reorganized their UL muscle synergies to achieve the VF target. A VF-based training program targeting specific synergy profiles may be useful for post-amputation rehabilitation.

Session Category

Rehabilitation Biomechanics and Human Factors: Rehabilitation

OA20-04

Musical Feedback for Medial Knee Load Reduction: Translational Evidence

MS, PT Luisa Cedin, MS Camilla Antognini, PhD Christopher Knowlton, PT, PhD Christopher Ferrigno, PhD Markus Wimmer

Rush University Medical Center, Chicago, IL, United States

Introduction

Medial knee joint overload is a key biomechanical driver of knee osteoarthritis (OA), however existing gait retraining strategies often face barriers in engagement and implementation. We developed a musical feedback system designed to medialize the center of pressure (CoP) and reduce knee adduction moment (KAM) through intuitive, engaging auditory cues [1]. Following initial validation in healthy adults, this study examined feasibility, acceptability, and biomechanical responses in individuals with chronic knee pain as a translational step toward an OA therapeutic tool.

Methods

Healthy (n=12) and chronic knee pain participants (n=10) completed a musical-feedback protocol designed to medialized CoP. Real-time plantar pressure was measured using wireless insoles (Moticon ReGo) and integrated with a low-pass filter that muffled a self-selected playlist whenever lateral CoP exceeded 25% of baseline. Gait analysis was performed using 3D motion capture and force plates. The knee pain cohort also completed the NASA TLX and a custom acceptability questionnaire. Biomechanical analyses focused on responders, those who medialized CoP. Spatiotemporal parameters, CoP, and KAM peaks were compared using paired t-tests.

Results

All healthy participants significantly medialized CoP (average peak -11%) and showed reductions in both KAM peaks without altering speed, cadence, or step width (Table 1). Kinematic adaptations included increased hip and ankle external rotation and reduced inversion/eversion motion. In the knee pain cohort, seven out of ten participants responded and medialized CoP. Those responders reduced their 1st KAM peak without altering spatiotemporal parameters. Interestingly, two non-responders also showed KAM reductions. Participants with knee pain reported high engagement, willingness to use the system, and moderate cognitive workload. Three reported reduced balance confidence and mild arch discomfort from the insole battery position.

Discussion

Across both cohorts, musical feedback successfully cued users to medialize their gait line and reduce knee loading without slowdown. Unloading responses varied with knee pain, likely reflecting heterogeneous gait strategies in symptomatic populations. High acceptability and moderate cognitive load support the system feasibility. Minor comfort or balance concerns indicate improvement opportunities. Together, these findings indicate real-time musical feedback is feasible, acceptable, and effective in COP change, supporting further studies in populations with knee OA.

Images (Optional)

Table 1: Spatiotemporal parameters and knee adduction moment peaks

	Baseline	**Training**	**Baseline**	**Training**
	Healthy cohort (n=12)		Knee Pain cohort (n=7)	
Speed (m/s)	1.25 ± 0.2	1.26 ± 0.1	1.00 ± 0.3	0.91 ± 0.3
Cadence (strides/min)	54.14 ± 3.4	54.80 ± 3.7	49.87 ± 6.7	46.39 ± 10.2
Stride Length (m)	1.40 ± 0.1	1.39 ± 0.1	1.19 ± 0.2	1.14 ± 0.2
KAM 1st Peak (%BW*HT)	-2.47 ± 0.7	-2.29 ± 0.6**	0.63 ± 0.4	0.58± 0.4*
KAM 2nd Peak (%BW*HT)	-2.26 ± 0.4	-1.94 ± 0.4**	0.57 ± 0.4	0.58 ± 0.4

KAM: Knee Adduction Moment, BW: Body Weight, HT: Height. *p = 0.05 **p < 0.01

References (Optional)

[1] L Cedin *et.al*, Healthcare, 2025

Session Category

Rehabilitation Biomechanics and Human Factors: Rehabilitation

OA20-05

Insole-Delivered Forefoot Plantar Force Biofeedback Improves Propulsion in Individuals with Post-Stroke Hemiparesis

Dr. Nicole K. Rendos PhD, LAT, ATC, CSCS, FACSM[1,2], Ms. Jorjie M. Wilson MS[3], Mr. Zahin Alam[4], Dr. Trisha M. Kesar PT, PhD[3]

[1]Florida Institute for Human and Machine Cognition, Pensacola, FL, United States. [2]University of West Florida, Pensacola, FL, United States. [3]Emory University, Atlanta, GA, United States. [4]Hackensack Meridian School of Medicine, Nutley, NJ, United States

Introduction

Individuals with post-stroke hemiparesis exhibit reduced propulsive force from the paretic limb, reflected by decreased anterior ground reaction force (AGRF). This propulsion deficit contributes to slower gait speed, gait asymmetry, and reduced functional mobility. Propulsion biofeedback can improve AGRF but is traditionally limited to laboratory environments. This study examined whether a wearable insole system delivering forefoot plantar force biofeedback could serve as a practical surrogate for propulsion biofeedback.

Methods

Kinematic and kinetic data were recorded as twelve participants with chronic post-stroke hemiparesis (6 male; age=57.0±12.0y; 70.0±57.2 months post-stroke) walked on a split-belt instrumented treadmill wearing 3-sensor loadsol-ACP® insoles. After a baseline walking trial, insoles provided either auditory or haptic biofeedback with a 3-10% target increase in forefoot plantar force in the hemiparetic limb. Gait data were normalized to 100% and root mean square errors (RMSE) were calculated for AGRF, ankle angle, ankle moment, and ankle power to quantify waveform similarity across conditions. Repeated-measures ANOVAs assessed differences in peak values.

Results

AGRF RMSE were 14.006±8.656 N (Baseline-Auditory), 12.819±8.570 N (Baseline-Haptic), and 5.826±3.567 N (Audio-Haptic). Ankle angle RMSE were 3.910±3.224°, 3.631±2.957°, and 1.135±0.531°, respectively. Ankle moment RMSE were .279±3.061 Nm/kg, 1.186±3.097 Nm/kg, and 0.159±0.205 Nm/kg, respectively. Ankle power RMSE were 0.182±0.125 W/kg, 0.188±0.139 W/kg, and 0.064 ± 0.045 W/kg, respectively. Peak AGRF increased significantly across conditions (p=.023), with improvements during auditory (M_{diff}=14.42±5.69 N, p=.032) and haptic (M_{diff}=10.85±6.02 N, p=.096) biofeedback. Peak ankle angle decreased with both auditory (M_{diff}=2.73±0.89°, p=0.014) and haptic

(M_{diff}=3.45±0.96°, p=.006) biofeedback compared to baseline. No differences were observed in peak ankle moment or power.

Discussion

Auditory and haptic forefoot plantar force biofeedback produced similar gait waveform patterns and effectively increased propulsion post-stroke, as reflected by greater peak AGRF without corresponding increases in joint loading. Reductions in peak ankle angle during biofeedback suggest altered limb positioning that may facilitate improved propulsive force generation. The comparable RMSE between auditory and haptic conditions indicates both modalities elicit highly consistent gait responses, supporting their potential utility as propulsion-training strategies in post-stroke rehabilitation.

Acknowledgements (Optional)

K01HD107294, P30DK111024

Session Category

Rehabilitation Biomechanics and Human Factors: Rehabilitation

OA20-06

Effectiveness of Wearable Device-Assisted Gait Retraining in Female Runners with Patellofemoral Pain: A Randomized Controlled Trial

Dr. Hao-Nan Wang PT, PhD, CSCS[1,2], Dr. Pei Luo[3], Prof. Jian Li[1]

[1]Sports Medicine Center, West China Hospital, Sichuan University, Chengdu, Sichuan, China. [2]Department of Orthopedics and Orthopedic Research Institute, West China Hospital, Sichuan University, Chengdu, Sichuan, China. [3]School of Sport Science, Beijing Sport University, Beijing, Beijing, China

Introduction

Patellofemoral pain (PFP) is a common overuse injury among female runners, often impairing running performance and daily activities. Gait retraining has emerged as a potential intervention, and wearable devices with real-time feedback may enhance its efficacy. This study aimed to evaluate the effectiveness of a 6-week wearable watch-assisted gait retraining intervention, which provides real-time cadence feedback to increase step frequency by 10%, in female runners with PFP.

Methods

A randomized controlled trial was conducted between March 2023 and June 2023, recruiting 30 female runners with PFP from running clubs and sports medicine centers in Beijing (15 in each group). Inclusion criteria included age 18-40 years, unilateral or bilateral anterior knee pain for ≥4 weeks (VAS ≥3/10), and insidious symptom onset. Exclusion criteria included traumatic injury history, knee surgery, and other confounding musculoskeletal or systemic diseases. The gait retraining group received 12 sessions of intervention using a wearable watch that provided real-time cadence feedback, with the target of increasing step frequency by 10%. Training duration gradually increased from 15 to 30 minutes per session. The control group received health education. Outcome measures included Visual Analogue Scale (VAS) for pain, AKPS score, and patellofemoral joint (PFJ) stress assessed at baseline and after 6 weeks. Statistical analyses included an independent *T* test, with significance set at $p < 0.05$.

Results

Among a total of 30 participants enrolled and randomized. There were no significant differences in baseline characteristics between the groups. At 6-week follow-up, the intervention group had greater improvements in AKPS compared to the control group (between-group difference, 4.31 [95%CI, 0.53 to 8.10]; P = 0.03). The intervention group showed a larger reduction in VAS pain scores (between-group difference, 5.80 [95%CI, 2.71

to 8.89]; P < 0.01) and more favorable changes in PFJ stress (between-group difference, 1.56 [95%CI, 1.26 to 1.86]; P < 0.01) than the control group. No adverse events were reported during the intervention period.

Discussion

A wearable watch-assisted gait retraining intervention with real-time cadence feedback (targeting a 10% increase in step frequency) significantly reduces pain, improves functional status, and optimizes patellofemoral joint biomechanics in female runners with PFP, demonstrating clinically meaningful effects.

Session Category

Rehabilitation Biomechanics and Human Factors: Rehabilitation

OA21-02

Evaluating Automated Correspondence Approaches for the Scapula using Ground Truth Homologous Landmarks

Dr. Michael Rainbow PhD[1], Dr. Erin Lee PhD[2]

[1]Queen's University, Kingston, ON, Canada. [2]University of Waterloo, Waterloo, ON, Canada

Introduction

3D scapula shape is relevant for injury risk and shoulder biomechanics [1]. An essential step in analyzing shape with statistical shape modelling is to establish point-to-point correspondences that maintain homology (i.e., corresponding points having the same anatomical meaning across bone meshes). Automated methods, such as coherent point drift (CPD), are an attractive alternative to manual landmarking methods because they incorporate the entire 3D surface and capture rich details, like articular curvature, that may be relevant for joint mechanics. Automated correspondence of the scapula is notoriously challenging due to the scapula's branching morphology, but newer CPD algorithms look promising for handling complex geometries. Here, we evaluate two CPD methods for establishing homologous node correspondence in the scapula.

Methods

Eight human scapulae were segmented from CT scans (*Mimics 25*) and landmarked using 29 points that capture scapula morphology (*Stratovan*). To generate meshes with ground-truth correspondences ("warps"), we warped a reference mean mesh to match the landmarks of each participant's scapula using Thin-Plate Spline. This process ensures that the anatomical locations of the warped mesh coordinates are homologous with those of the mean mesh. To evaluate CPD approaches, we generated corresponding meshes for each warped mesh using the mean mesh as the reference. We computed the distance between the ground-truth landmark locations and those produced by the Classic [1] and Bayesian [2] CPD methods.

Results

Both CPD approaches performed well. Within each participant, inter-landmark distances between actual and CPD landmarks were smaller (2 mm) than distances across participants (6 mm). Bayesian CPD had fewer outliers and yielded a smoother mesh. It was also faster, solving in minutes per bone vs. 2 hours without GPU acceleration.

Discussion

CPD approaches can identify homologous landmarks on the scapula, with Bayesian CPD performing better and faster than classic CPD. Our approach of using a thin-plate spline to create homologous landmarks provides a new framework for testing automated correspondence approaches. Future work will investigate how well the CPD approaches reconstruct the geometry of the participant's original bone meshes.

Images (Optional)

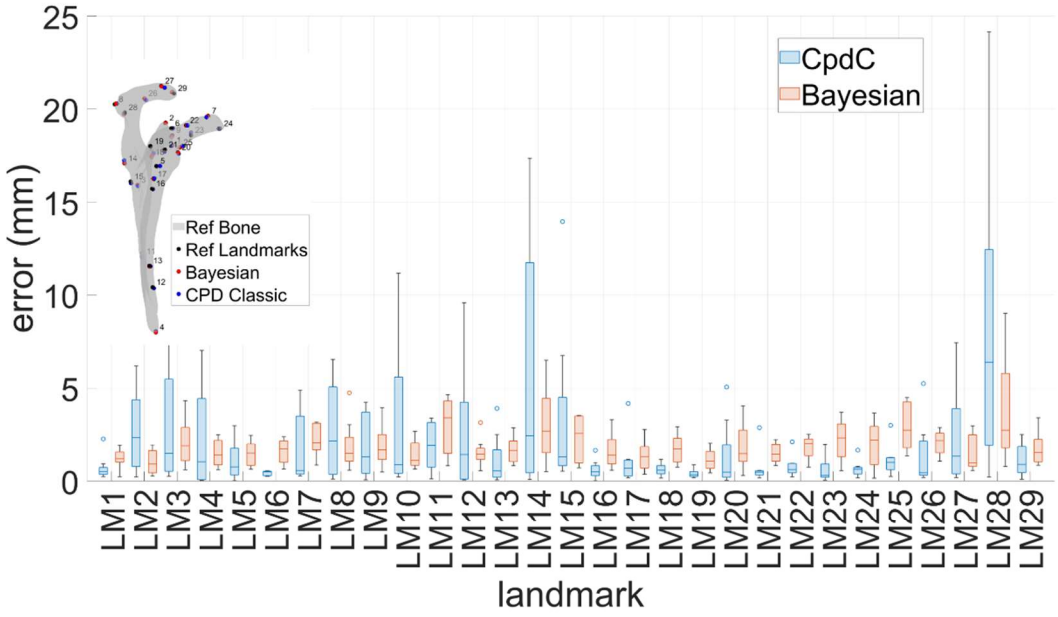


Figure 1. Errors between the gold standard landmarks the two coherent point drift (CPD) approaches – Classic, and Bayesian – for 29 landmarks applied to the scapula.

References (Optional)

[1] Lee *et al.*, *Clin Biomech*, 2020. [2] Myronenko and Song, IEEE TPAMI, 2010. [3] Hirose, IEEE TPAMI, 2020. [3]

Session Category

Musculoskeletal Biomechanics: Joints and Motion

OA21-03

Robot-Assisted Active Shoulder Simulator

Ms. Alina Albert MSc[1], Ms. Julia Sußiek Dr. med.[1], Mr. Willi Engelmann[1], Ms. Jane Gehling BSc[2], Mr. Jens Wermers Prof. Dr.[2], Mr. Michael J. Raschke Univ.-Prof. Dr. med.[1], Mr. J. Christoph Katthagen Prof. Dr. med.[1]

[1]Department of Trauma, Hand and Reconstructive Surgery, University Hospital Münster, Münster, NRW, Germany. [2]Department of Engineering Physics, Münster University of Applied Sciences, Münster, NRW, Germany

Introduction

Accurate evaluation of shoulder biomechanics requires systems that perform muscle driven physiological motion, but also implement clinical test protocols under controlled conditions. Existing simulators provide kinematic and muscle force data but lack integrated kinetic measurements and the capability to apply external loads. A robot-assisted active shoulder simulator is introduced to perform physiological shoulder motion in combination with standardized diagnostic tests, supporting biomechanical research.

Methods

The experimental setup (Fig. 1) integrated a six-degree-of-freedom (DoF) robotic arm equipped with SimVitro-software for measurement of joint kinetics and kinematics, and an active simulator for muscle force application. Actuators applied controlled forces to the rotator cuff and deltoid muscles via steel cables routed along anatomical paths. Tendons were reinforced with FiberWire; infraspinatus and teres minor were combined, and deltoid cables passed over frictionless pulleys. The long head of the biceps was loaded with 22 N, and arm weight simulated as 3.2% of body mass [1]. A LabVIEW-based closed-loop PID controller maintained muscle force accuracy within ±1 N. A load cell mounted on the humerus recorded applied muscle forces, which were transformed into the joint coordinate system for robotic motion. Muscle-induced glenohumeral abduction was performed in 19 cadaveric specimens using EMG and physiological cross-sectional area-based force ratios [2], adjusted every 20°. Internal rotation and horizontal abduction were fixed at 0°, with 25 N compressive force and anterior and superior forces set to 0 N.

Results

Torque compensation enabled abduction from 3° to 60°. Total muscle force increased from 81 ± 36 N/kg arm weight at 20° to 106 ± 28 N/kg. Integrated sensors provided data on joint reaction forces, translations, and muscle forces.

Discussion

Abduction forces were comparable to prior studies [3], validating the approach. The robot-assisted setup offers distinct advantages: application of clinical tests, selective in force- or displacement-controlled DoF, the ability to apply external loads or lock specific motions. Nevertheless, full closed-loop control between the robotic arm and muscle actuators remains challenging. Future work will target adaptive control and machine learning to improve responsiveness and enable more complex motion.

Images (Optional)

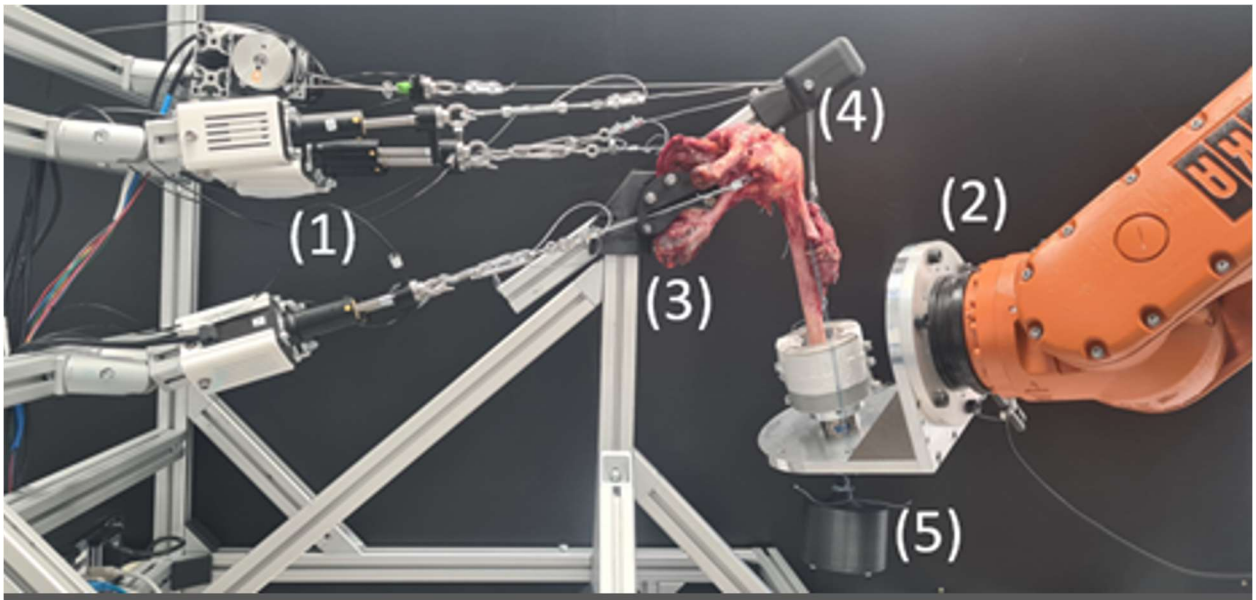


Fig. 1: Active shoulder simulator with six muscle actuators (1), humerus mounted on robotic arm (2), scapula fixed in a 3D-printed shell (3), deltoid pulleys (4), and biceps tension weight (5).

References (Optional)

[1] Wuelker et al., J.Biomech., 1995; [2] Kedgley et al., J.Biomech., 2007; [3] Knighton et al., J.Shoulder-Elbow-Surg, 2022

Session Category

Musculoskeletal Biomechanics: Joints and Motion

OA21-04

Muscle Loading Ratios for Scapular Plane Elevation: Preliminary Results of an In-Vitro Active Shoulder Motion Simulator

Mrs. Inês Santos[1], Ms. Lea-Marie Ocker[1], Mr. Daniel Ritter[1], Mrs. Maxi Tengler MD[1], Mr. Patrick Raiss MD[2]

[1]Arthrex Department of Orthopedic Research, Munich, Bavaria, Germany. [2]OCM, Munich, Bavaria, Germany

Mrs. Inês Santos

Ms. Lea-Marie Ocker

Introduction

Various muscle loading ratio datasets describing glenohumeral motion exist in the literature. Kedgley et al.[1] concluded that combining physiological cross-sectional area with electromyographic signals [2] that vary throughout motion better mimics the in vivo case. These variable muscle loading ratios, however, describe frontal plane abduction, while most shoulder simulators replicate scapular plane abduction. This ongoing study aims to analyze shoulder joint kinematics achieved with this set of muscle loading ratios and experimentally assess adjustments to achieve true scapular plane abduction.

Methods

Two fresh-frozen cadaveric shoulders were assembled in a rotary table using a custom-designed scapula fixation. The anatomic lines of action of the three portions of the deltoid, supraspinatus, subscapularis, and infraspinatus/teres minor, were routed using frictionless pulleys to six electric linear actuators (Fig.1A). Muscle forces were measured with force transducers positioned in line with each actuator. Optical tracking markers were attached to the humerus and scapula, and anatomical landmarks were digitized to create bone-fixed coordinate systems [3], allowing for the acquisition of physiological kinematic data (Fig. 1B). Scapulothoracic rhythm was simulated by rotating the scapula in a 2:1 ratio to the glenohumeral abduction angle. Abduction angles of 7°, 20°, 40°, 60°, and 90° were simulated by applying the literature muscle loading ratios [1], followed by adjusting the ratios to correct the abduction plane.

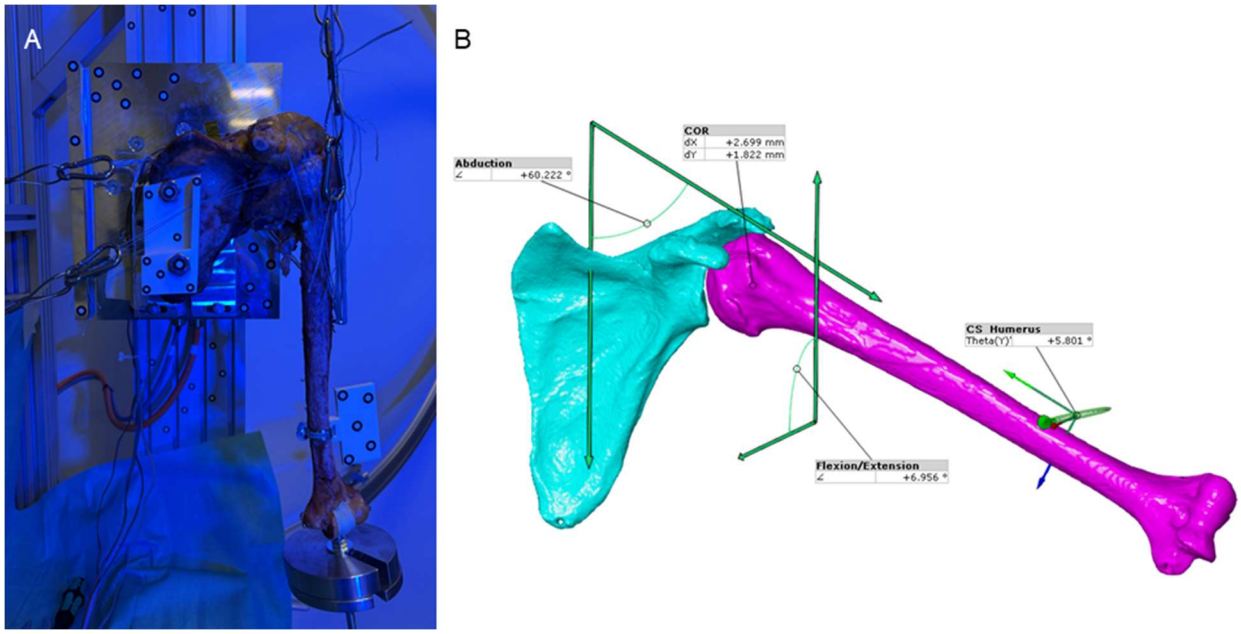
Results

The muscle ratios taken from literature resulted in an abduction plane 12.48±4.99° posterior to the scapular plane. To achieve scapular plane abduction, the middle deltoid force had to be reduced by an average of 12.93±1.03N, while the anterior deltoid had to increase 9.91±2.60N. The main discrepancies between deltoid muscle ratios were observed above 60° of abduction.

Discussion

Scapular plane abduction was not achieved with the muscle loading ratios proposed in literature; instead, they led to an abduction plane closer to the coronal plane. More specimens are being tested to better understand which ratios achieve scapular plane abduction, thereby enabling more accurate motion simulation and accounting for variability in specimen anatomy.

Images (Optional)



References (Optional)

[1] Kedgley et al., J Biomech, 2007

[2] Kronberg et al., Clin Orthop Relat Res, 1990

[3] Wu et al., J Biomech, 2005

Session Category

OA21-05

Dynamic Imaging of the Wrist: Anatomical Shape Variations Do Not Affect Kinematic Parameter Extraction

Drs. Maranda Haenen[1,2], Dr. Stefan Hummelink[1], Prof. Ioannis Sechopoulos[1,3,4], Prof. Brigitte Van der Heijden[1,2]

[1]Radboud University Medical Center, Nijmegen, Gelderland, Netherlands. [2]Jeroen Bosch Ziekenhuis, 's Hertogenbosch, Noord - Brabant, Netherlands. [3]University of Twente, Enschede, Overijssel, Netherlands. [4]Dutch Expert Center for Screening, Nijmegen, Gelderland, Netherlands

Introduction

Four-Dimensional Computed Tomography (4DCT) shows promise in diagnosing wrist pathologies such as scapholunate ligament lesions (SLL). Two parameters indicative of SLL lesions in these scans, the scapholunate angle (SLA) and the capitolunate angle (CLA), might be affected by anatomical shape variations. Therefore, this study characterizes the impact of anatomical shape variations on SLA and CLA estimates from 4DCT scans.

Methods

3D CT images retrieved from 4DCT scans of healthy wrists were used. Scans were segmented using a trained nnU-net and were stored as surface meshes. Meshes were re-meshed and downsampled and then registered to a reference bone using a rigid coherent point drift (CPD) algorithm. The statistical shape model (SSM) was created by performing a principal component (PC) analysis to identify main variation modes, expressing each shape as a linear combination of PCs. The quality of each SSM was evaluated using a leave-one-out approach by calculating the root mean squared error (RMSE) when fitting the SSM to each sample. New bone shapes were generated by adjusting PCs from -2σ to +2σ in 0.2σ increments, yielding 21 variations per PC. A random subset of 3000 new shapes was selected for further analysis. Next, local coordinate systems (LCSs) were assigned to the new shapes. The rotational deviation of the LCSs was calculated by a combined rotation around the three axes. Finally, the SLAs and CLAs were calculated for all new shapes.

Results

The SSM was created using 106 scans with an RMSE of 0.38 mm. The 95th percentile of the rotational deviations of the LCSs was below 5°. The resulting ranges due to anatomical variations in the calculation of the SLA and CLA were 5.7 ° and 6.8°, respectively (Figure 1).

Discussion

Bone shape variations have minimal influence on the determination of LCSs and, consequently, on the resulting SLA and CLA estimates. Based on the naturally occurring variability of carpal angles reported in the literature, the ranges of variation in the SLA and CLA are probably not clinically relevant but should be taken into account when performing inter-subject comparisons.

Images (Optional)

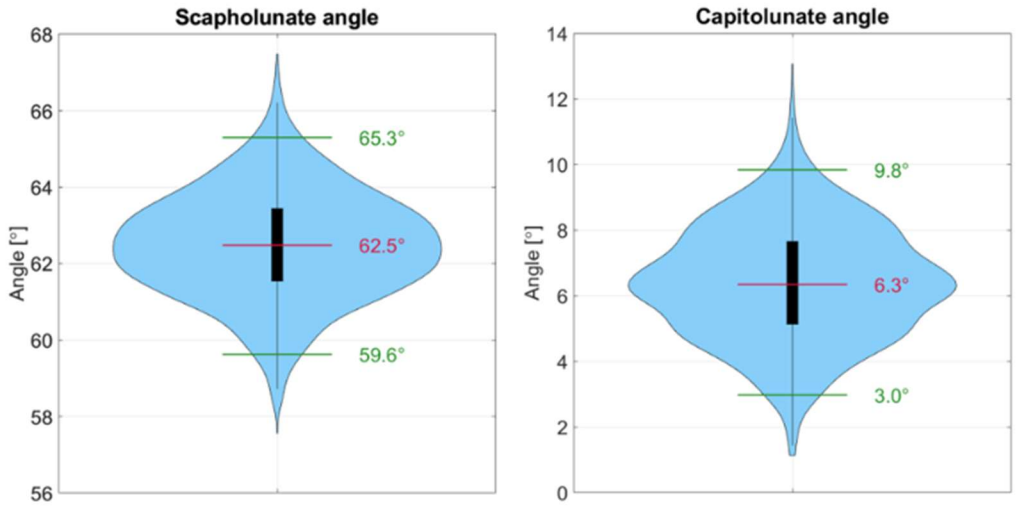


Figure 1: Violin plots illustrating the scapholunate angle range and capitolunate range across 3000 new shapes. In red and green the median and 95th percentiles, respectively, are represented.

Session Category

Musculoskeletal Biomechanics: Joints and Motion

OA22-02

Designing Biomimetic Scaffolds for Bone Tissue Engineering through Machine Learning and Computational Simulation

Miss Yujie Zhang, Prof. Min Wang

The University of Hong Kong, Hong Kong, Hong Kong, Hong Kong

Miss Yujie Zhang

Introduction

In scaffold-based bone tissue engineering (BTE), scaffolds must be porous and mechanically robust. Trabecular bone provides a good template for BTE scaffolds owing to its mechanically resilient structure. Structural parameters such as trabecular thickness (Tb.Th), separation (Tb.Sp) and ellipsoid factor (EF) are key indicators of bone quality. Recent advances in artificial intelligence/machine learning (ML) make it possible to design patient-specific, biomimetic scaffolds. Through designing trabecular bone structure-based scaffolds using a specific region of human femoral head, this study established a framework for designing personalized BTE scaffolds.

Methods

Publicly available medical image datasets of human proximal femur were used for trabecular morphologies across gender and age. Trabecular parameters (Tb.Th, Tb.Sp, EF) were calculated for trabecular characteristics. Image data were processed and augmented using generative adversarial networks (GANs) and variational autoencoders (VAEs) to generate artificial images mimicking trabecular bone. They were converted into 3D BTE scaffold models. Finite element analysis (FEA) using ANSYS Workbench evaluated deformation, stress distribution, and stiffness of these scaffolds. Fluid dynamics simulation (CFD) using ANSYS CFX analyzed mass transport in scaffolds. Biomimetic BTE scaffolds with high structural fidelity were fabricated via fused deposition modeling (FDM) 3D printing using poly(lactic acid) (PLA) and tested under compression.

Results

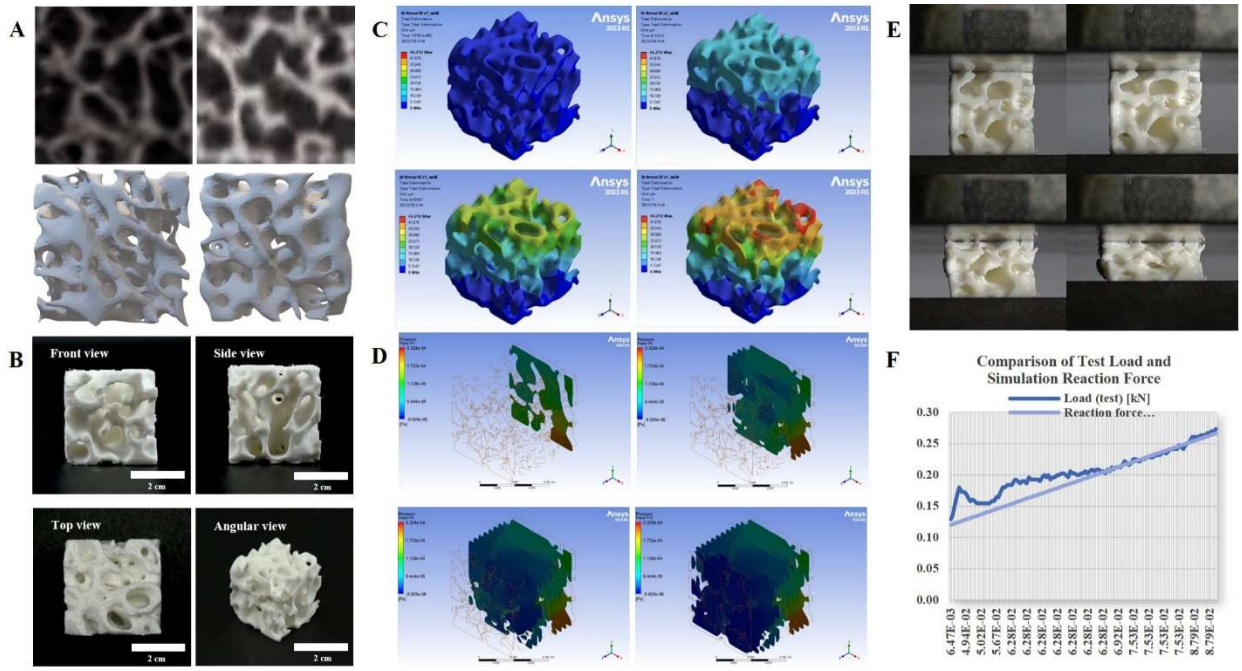
ML-generated synthetic data effectively reproduced trabecular morphologies. FEA simulations revealed heterogeneous but continuous stress distributions in scaffolds similarly found in trabecular bone. Load transfer in scaffolds occurred via interconnected

struts, with stress concentrations in curved and transitional regions. The scaffolds exhibited mechanical responses closely matching experimental results. CFD simulations showed scaffolds supported uniform fluid perfusion. Computed permeability and pressure drop profiles suggested efficient nutrient exchange and metabolite cleaning. In compression tests, biomimetic scaffolds exhibited characteristic porous structure stress-strain behaviour. Reaction force-displacement curves from simulations correlated linearly with experimental data, indicating good predictivity of computational model.

Discussion

The integrated process, which combined medical images, ML-driven data synthesis/augmentation, and computational simulations, enabled creation of biomimetic BTE scaffolds that mimicked both mechanical and mass transport characteristics of trabecular bone. ML for data generation and utilization and FEA and CFD for predictive modeling provide a powerful platform for developing patient-specific, biomimetic BTE scaffolds.

Images (Optional)



(A) Top left: one CT image of the middle region of femur trabecular bone; Bottom left: 3D model of the middle region of femur trabecular bone; Top right: one ML-generated artificial image of the middle region of femur trabecular bone; Bottom right: ML-generated 3D model of the middle region of femur trabecular bone as a scaffold model for bone tissue engineering.
(B) One FDM 3D printed biomimetic bone tissue engineering scaffold using the ML-generated, femur trabecular bone structure-based scaffold model.
(C) FEA result of the total deformation of human trabecular bone structure-based bone tissue engineering scaffold under compression.
(D) CFD result showing pressure (on the XY-plane) of biofluid inside human trabecular bone structure-based bone tissue engineering scaffold.
(E) A series of photos showing the continuous deformation process of a biomimetic bone tissue engineering scaffolds under compression.
(F) Comparison of FEA simulation result and compression test result for the biomimetic scaffold within the elastic deformation region.

Session Category

Emerging Areas: N/A

OA22-03

CEINMS-WEB: A Web-based Application for Ultra Rapid Calibration of Neuromusculoskeletal Models

Mr Matthew Hambly BEng Elec & Biomed (Hons), MMedRes, Dr Alastair Quinn PhD, BE(Mechatronic), Dr Claudio Pizzolato BEng, MEng, PhD

Australian Centre for Precision Health and Technology (PRECISE), Griffith University, Gold Coast, Queensland, Australia

Introduction

Electromyography (EMG)-informed neuromusculoskeletal (NMS) models predict physiologically plausible muscle and joint forces, useful for biomechanical analyses and personalized rehabilitation. However, NMS models require calibration to accurately represent the individual, traditionally taking potentially hours, limiting real-time applicability. Our recent work uses differentiable physics and muscle synergies to calibrate NMS models in minutes while synthesizing unrecorded excitations (CEINMS-NN) [1]. Here, we present a web-based application for ultra rapid NMS model calibration (CEINMS-WEB), providing easy access to users without hardware or software dependencies.

Methods

CEINMS-NN was deployed within a Docker container restricted to 1 CPU core and 1GB of memory with the host having an AMD 5975WX processor. Invited users uploaded datasets consisting of EMG, musculotendon unit kinematics, and inverse dynamics, then calibrated their NMS models. To test CEINMS-WEB, lower limb data from 56 subjects were processed, containing EMG acquired from 8 muscles, driving a model with 40 muscles and 3 degrees of freedom (hip flexion/extension, knee flexion/extension and ankle plantar/dorsiflexion). For comparison, a single-subject calibration was performed using simulated annealing in the CEINMS toolbox [2] and the synergy-hybrid CEINMS-NN calibration, both on a local Windows PC with an Intel Ultra 5 125H processor and 16 GB of memory.

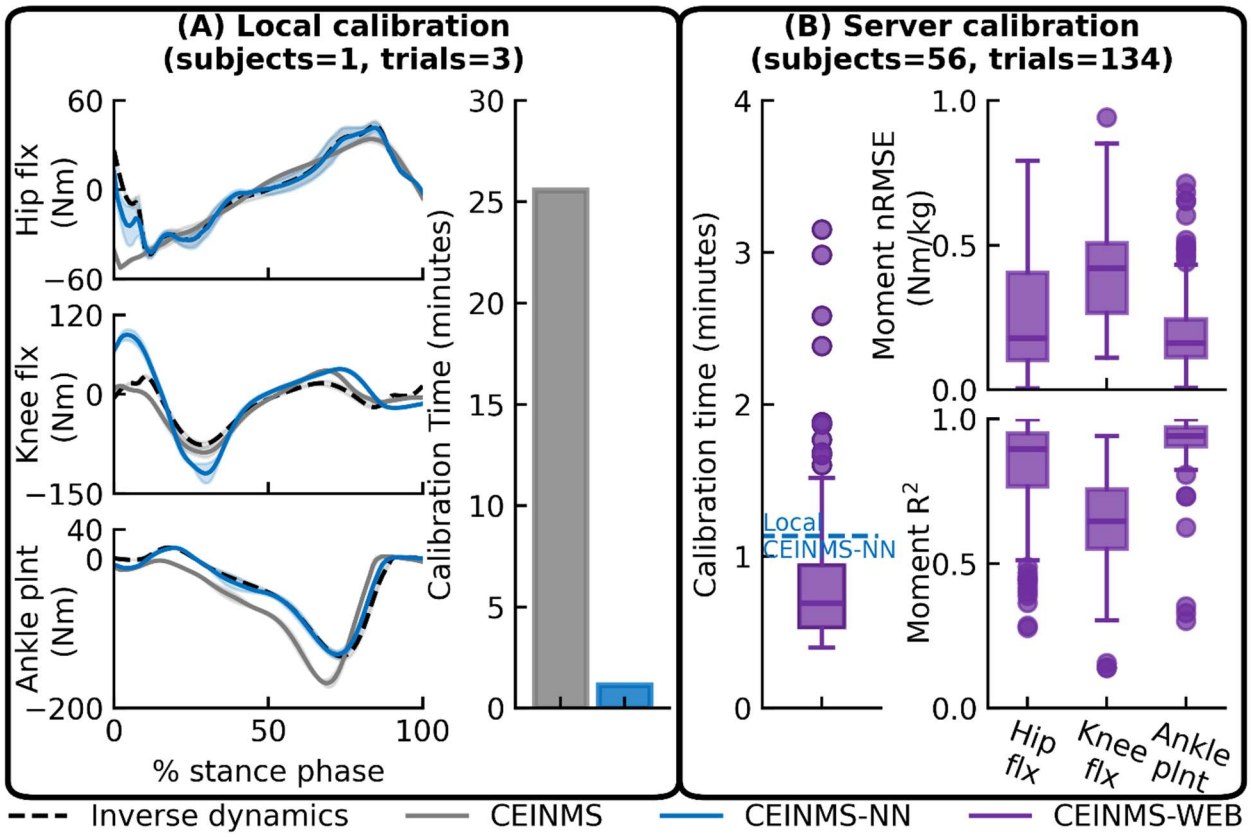
Results

On the local machine, CEINMS-NN showed better overall moment tracking than CEINMS and reduced calibration time from >25 minutes to ~1 minute (figure 1A). Across 56 subjects, CEINMS-WEB reduced calibration time to typically <1 minute, while maintaining good moment prediction accuracy (figure 1B).

Discussion

We developed CEINMS-WEB, allowing users to upload data to a secure server and calibrate NMS models without requiring complex installation or high-performance hardware. By running calibration within minutes, CEINMS-WEB facilitates real-time applications and rapid testing of different modeling configurations, supporting more efficient workflows. Future updates will introduce synergy-based execution, enhanced usability, repeatability, data sharing, automated preprocessing, and results verification, ultimately creating a robust NMS modeling pipeline for the community. This streamlined process makes NMS modeling more accessible, particularly for inexperienced users, while minimizing errors linked to local setups or user error.

Images (Optional)



References (Optional)

[1] Matthew Hambly *et al.* , IEEE TBME, 2025

[2] Claudio Pizzolato *et al.* , J Biomechanics, 2015

Acknowledgements (Optional)

This study was supported by the Motor Accident Insurance Commission, Queensland, Australia (BioSpine project) and by a Griffith University Postgraduate Research Scholarship.

Session Category

Emerging Areas: N/A

OA22-04

A Physics-Informed Federated Learning Approach to Decomposing Bilateral Ground Reaction Forces and Moments from A Single Forceplate for Gait Analysis

Mr. Cheng-Hao Yu[1], Dr. Shiuan-Huei Lu[1,2,3,4], Mr. Yi-Fu Lu[1], Prof. Ting-Ming Wang[1,5], Prof. Tung-Wu Lu[1]

[1]National Taiwan University, Taipei City, Taiwan, Taiwan. [2]Taipei Medical University, Taipei City, Taiwan, Taiwan. [3]Taipei Medical University-Shuang Ho Hospital, New Taipei City, Taiwan, Taiwan. [4]Purdue University, West Lafayette, Indiana, United States. [5]National Taiwan University Hospital, Taipei City, Taiwan, Taiwan

Mr. Cheng-Hao Yu

Dr. Shiuan-Huei Lu

Prof. Ting-Ming Wang

Introduction

Measuring bilateral ground reaction forces and moments (GRF&Ms) is fundamental in gait analysis, requiring subjects to step each foot onto separate forceplates. This requirement often causes multiple trial attempts and alters walking mechanics, particularly in individuals with neuromusculoskeletal disorders. This study introduces a physics-informed federated learning (FL) approach that accurately predicts bilateral GRF&Ms from a single forceplate.

Methods

Retrospective gait analysis data from 4,800 trials across four groups (60 healthy young adults, 60 healthy older adults, 60 healthy children, and 60 individuals with cerebral palsy), each stored at a separate institution, were used. Each participant wore 41 markers and walked without targeted foot placement. Bilateral GRF&Ms were measured using four forceplates (OR6-7-1000, AMTI, USA), and marker trajectories were recorded using a motion capture system (MX-T40, Vicon, UK). These data were used to train and evaluate a physics-informed neural network [1] for predicting bilateral GRF&Ms from a forceplate.

Using FL, each institution trained its model locally using data from 45 participants, periodically sending model-parameter updates to the central server for aggregation into a global model. To accommodate heterogeneity in data and computational resources, a regularisation term was added to local training, and an adaptive normalisation method was applied during aggregation. The global model updated each institution's model at every iteration, enabling large-scale training while maintaining data privacy.

For trials excluded from training, model-predicted GRF&Ms were used to derive the centre of pressure (COP) and to calculate lower-limb intersegmental forces and moments via inverse dynamics. These variables were compared with gold-standard results using root-mean-square errors (RMSE) for COP and relative RMSE (rRMSE) for all other variables.

Results

Model-predicted results showed high consistency with the gold standard, given mean rRMSEs of 0.5%, 0.9%, and 1.2% for GRF, intersegmental forces and moments, respectively, and a mean RMSE of 3.1 mm for COP. No significant differences in prediction errors were observed between groups.

Discussion

The FL-trained model demonstrated strong potential to eliminate the need for step targeting in gait analysis. This approach is promising for developing large-scale AI models across gait laboratories while maintaining privacy.

References (Optional)

[1] Cheng-Hao Yu *et al.*, Gait Posture, 2025

Acknowledgements (Optional)

This study was funded by the National Science and Technology Council, Taiwan (NSTC 113-2221-E-002–043-MY3).

Session Category

Emerging Areas: N/A

OA23-02

Kinematic Constraints Fail to Capture In Vivo Intervertebral Motion Patterns in Adult Spinal Deformity and Healthy Individuals

Mr Tom Leppens MSc[1], Ms Birgitt Peeters MSc[1], Prof Sebastiaan Schelfaut PhD[2], Prof Lieven Moke PhD[2], Prof Lennart Scheys PhD[1]

[1]KU Leuven, Leuven, Vlaams Brabant, Belgium. [2]UZ Leuven, Leuven, Vlaams Brabant, Belgium

Introduction

Musculoskeletal models commonly employ kinematic constraints to reduce computational complexity by limiting intervertebral joint degrees of freedom. These constraints are based on ratios of intervertebral motions derived from limited in vivo datasets [1]. If these ratios misrepresent actual spinal motion, downstream predictions of joint loads and muscle forces may be biased. This study compares coordinate-optimization (CO) ratios against commonly applied kinematic constraint (KC) ratios.

Methods

Three participants performed seated trunk forward flexion and bilateral lateral bending using validated motion capture protocols: one adult spinal deformity patient (64 years), one healthy control (63 years), and one individual with sacralization (28 years). Subject-specific models were created using CT-like MRI for bone geometry, intervertebral joint, and motion-capture marker definition. Recorded motions were simulated using a coordinate-optimization (CO) approach to inversely compute intervertebral kinematics. [2]. CO intervertebral ranges of motion (RoM) were expressed as ratios relative to the total trunk RoM. These CO ratios were compared with KC ratios from the literature [1].

Results

During flexion, CO ratios deviated substantially from KC ratios (Figure 1). KC ratios systematically overestimated lumbar contributions and underestimated thoracic contributions with maximum deviations at L4-L5 (KC: 15.5%, CO: 0-8.4%). Upper thoracic levels showed 2-3 fold higher CO ratios than KC ratios. Lateral bending showed smaller deviations but still failed to capture compensatory patterns. The participant with sacralization exhibited zero L5-S1 contribution in CO ratios, while KC ratios predicted

13.2% in flexion and 3.7% in lateral bending. Consequently, KC ratios failed to capture the adjacent-level compensation at L4-L5, where CO ratios were 60% higher than KC ratios.

Discussion

Widely-adopted KC ratios could misrepresent segmental contributions to overall trunk motion, with error magnitude varying by movement type. Failure to account for anatomical variation highlights the inability of population-derived KC ratios to adapt to individual anatomy. These biases are problematic for applications requiring accurate segmental motion estimates, particularly for predicting joint loads and muscle forces in patients. Future modeling should prioritize patient-specific kinematic characterization over population-derived KC ratios.

Images (Optional)

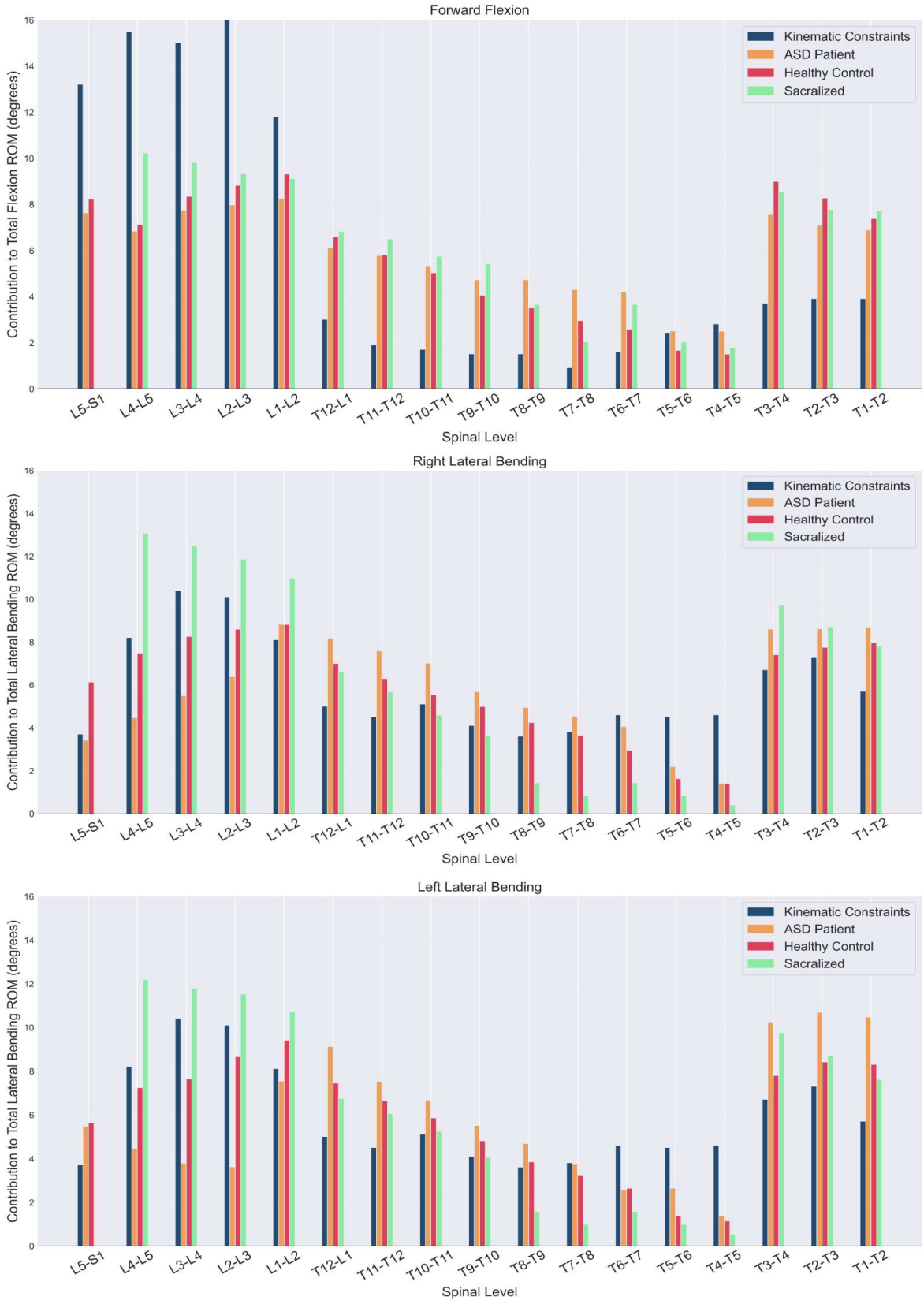


Figure 1. Comparison of intervertebral contribution ratios between coordinate-optimization (CO) and kinematic constraint (KC) approaches across three movement types.

References (Optional)

[1]. Alemi MM *et al.*, Front. Bioeng. Biotechnol., 2021

[2]. Peeters B. *et al.*, JOR Spine, 2025

Session Category

Orthopaedic Biomechanics: Spine

OA23-03

Using Lumbar Spine Intervertebral Motion Sharing as a Kinematics Biomarker for Classifying Individuals with Chronic Low Back Pain

Mrs. Clarissa LeVasseur MS[1,2], Mr. Tom Gale MS[1], Ms. Sabreen Megherhi MPH[1], Dr. Gina McKernan PhD[1], Dr. Nam Vo PhD[1,2], Dr. Gwendolyn Sowa MD, PhD[1,2], Dr. William Anderst PhD[1]

[1]University of Pittsburgh, Pittsburgh, PA, United States. [2]Bethel Musculoskeletal Research Center, Pittsburgh, PA, United States

Introduction

Dynamic assessment of lumbar spine intervertebral kinematics may help identify subgroups of patients with chronic low back pain (cLBP) who may preferentially benefit from specific interventions. One kinematics biomarker to classify individuals with cLBP is motion sharing among intervertebral motion segments. This analysis aimed to classify individuals with cLBP by their dynamic motion sharing, and to evaluate differences in pain, disability, and age between those groupings.

Methods

Individuals fitting the NIH definition of cLBP provided written consent to participate in this IRB-approved study. Participants performed three trials each of maximal lateral bending bilaterally and flexion/extension. Synchronized biplane radiographs of the lumbar spine were captured at 20Hz for each 3s movement trial. Lumbar bone tissues were segmented from CT scans to create subject-specific 3D bone models. Vertebral motion was tracked in the biplane radiographs using a validated tracking process that matched digitally reconstructed radiographs created from the CT-based bones to the biplane radiographs. The percent contribution of each motion segment to the change in L1-S1 angle was computed at each 1° increment of L1-S1 rotation and averaged over corresponding movement trials. Segmental contributions to L1-S1 rotation were concatenated into a single waveform and then clustered using MATLAB's k-means clustering algorithm. Unpaired t-tests compared age, disability (Oswestry Disability Index (ODI)) and pain (10-point VAS in the last 7 days) between clusters.

Results

179 participants were included (86M, 93F; age: 54.7+/-16.5 yrs.; BMI: 26.4+/-3.8kg/m^2). Two clusters of motion sharing were identified for lateral bending and two for flexion/extension (Figure 1). During lateral bending, those with more evenly distributed motion sharing (Group 1) had higher ODI scores (25.5+/-11.9 vs. 21.9+/-10.6, p=0.037) compared to those

with more unequal motion sharing (Group 2). During flexion/extension, age was greater in those with greater contributions from L1-L2 and L2-L3 (Group 3), compared to those with greater contributions from L4-L5 (Group 4) (60.1+/-13.1 vs. 49.6+/-17.0 years, p<0.001).

Discussion

These results suggest individuals with cLBP cluster into two patterns of lumbar spine motion sharing in lateral bending and flexion/extension, with bending motion sharing group associated with disability and flexion/extension motion sharing group associated with age.

Images (Optional)

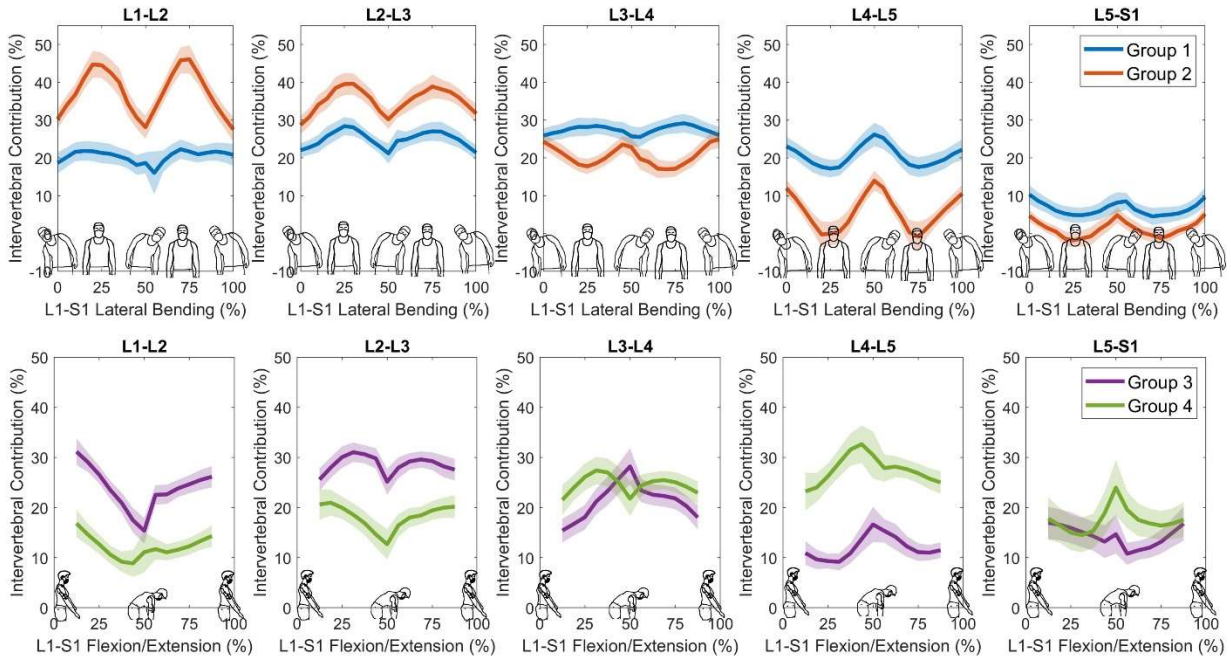


Figure 1: *Kinematics clusters at each motion segment during lateral bending (top) and flexion/extension (bottom). Each color represents a subgroup of participants with similar motion sharing across the entire lumbar spine (a cluster). The mean of each cluster (solid line) and 95% CI within the cluster (shaded region) is shown.*

Acknowledgements (Optional)

This on-going research is supported by the National Institutes of Health through the NIH HEAL Initiative under award number U19AR076725. The content is solely the responsibility of the authors and does not necessarily represent the official views of the National Institutes of Health or its NIH HEAL Initiative.

Session Category

Orthopaedic Biomechanics: Spine

OA23-04

Guiding Spine Flexion and Restricting Pelvic Movement During Flexion and Extension Tasks Has the Potential to Affect Lumbopelvic Kinematics

Dr Mona Frey[1], Dr Alex Breen[2], Dr Diana DeCarvalho[1]

[1]Memorial Univeristy of Newfoundland, St. John's, NL, Canada. [2]Usono B.V., Eindhoven, Noord Brabant, Netherlands

Introduction

Lumbopelvic kinematics are commonly assessed during spine flexion and extension tasks in people with low back pain [1]. However, the movements themselves often vary, reducing comparability. Some methods restrict pelvic movement to isolate lumbar kinematics or pace or guide participants through the movement to reduce variability, but it is unclear if these approaches affect lumbopelvic kinematics. **We compared lumbar and pelvic kinematics through dynamic spine flexion and extension between a free-standing (straight legs) and a guided condition.**

Methods

20 females completed a flexion and extension movement of each condition (free-standing vs guided). Guided motion involved a jig that secured participants' pelvises and used an arm rest to guide them through the motion [2]. Accelerometers (ADXL335, Analog Devices, Norwood, MA, USA) overlaid L2 and S1 spinous processes from which we calculated lumbar (L2-S1) and pelvic (S1) angles. Paired sample t-tests were used to compare lumbar and pelvic angles at standing and peak range of motion (RoM); and statistical parametric mapping (SPM) to compare angles throughout the dynamic movement.

Results

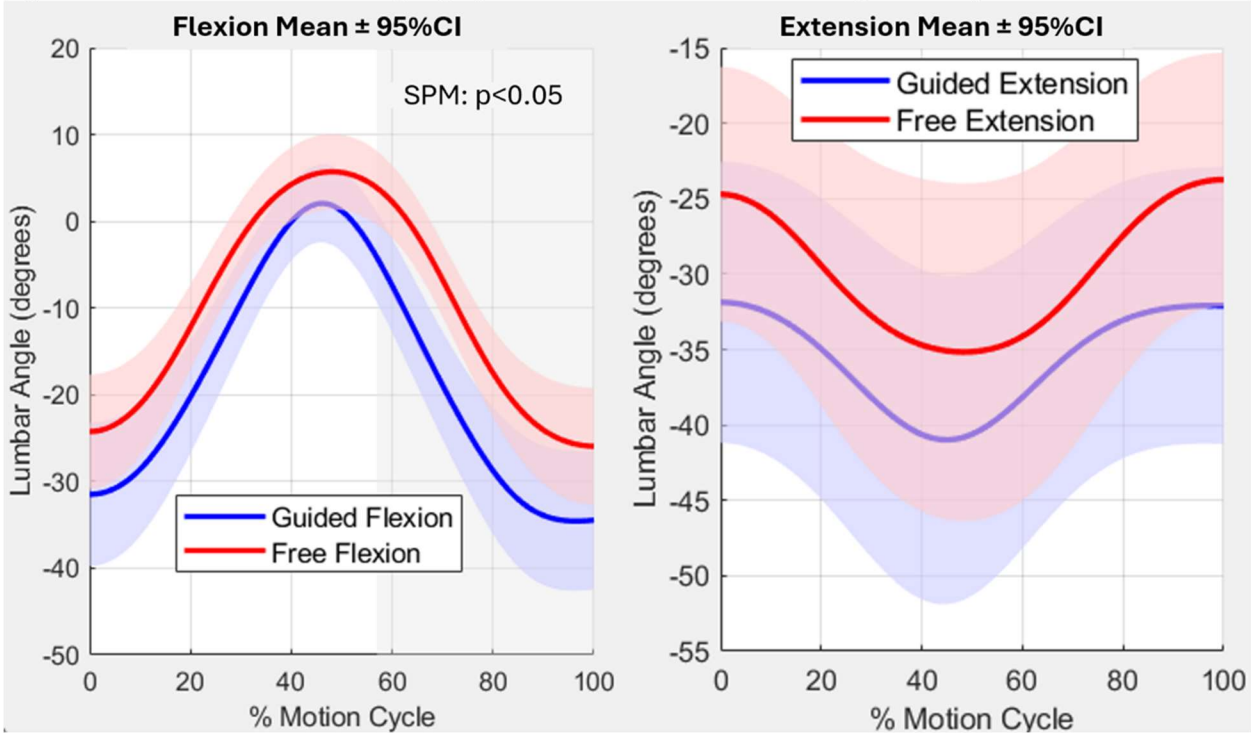
At upright standing, lumbar and pelvic angles were similar between guided (-26.49±24.36° & 17.28±9.11°) and free-standing (-21.05±19.84° & 22.30±15.96°) conditions (p=0.073; p=0.136). Similarly, lumbar and pelvic peak flexion RoM were similar between guided (3.52±9.88°; 29.63±8.23°) and free-standing (6.18±7.75° & 28.87±12.83°) conditions (p=0.807; 0.319). However, while pelvic peak extension RoM was similar between conditions (24.18±14.73° vs 17.64±7.88°; p=0.128), lumbar peak extension RoM was significantly greater in the guided condition (-35.23±27.96° vs -27.72±33.58°; p=0.028). SPM, mean and 95% confidence intervals (Figure 1) show significant differences in lumbar angle during the second half of flexion.

Discussion

Our findings suggest that our guided spine flexion task did not change peak RoM but changed lumbar kinematics during the dynamic range. Conversely, for extension, differences in peak lumbar RoM were observed. Pelvic angle was similar between conditions and its change from standing to full flexion/extension was small (<10°). When comparing studies, methodological differences should be considered as they may impact lumbopelvic kinematics.

Images (Optional)

Figure 1. Mean (line) and 95% confidence intervals (shaded areas) of the lumbar angle during guided and free flexion. The light grey area indicates that data is significantly different.



References (Optional)

[1] Florent Moissenet *et al.*, Scientific reports, 2022.

[2] Alister du Rose *et al.,* BMC Musculoskeletal Disorders, 2016.

Acknowledgements (Optional)

Funding: Chiropractic Research Council, UK. Natural Sciences and Engineering Research Council (NSERC) Discovery Grant. Graduate Student Travel Grant from the Canadian Society for Biomechanics

Session Category

OA23-05

Time-Dependent In Vivo Changes in Spinal Motion After Nucleotomy: Hypermobility or Hypomobility?

Mr. Marcel Simon Reich, Mr. Maxim Bashkuev, Ms. Nicole Bormann, Univ.- Prof. Dr. biol. hum. Hendrik Schmidt, Dr. med. vet. Sandra Reitmaier

Julius-Wolff-Institute, Berlin Institute of Health at Charité – Universitätsmedizin Berlin, Berlin, Berlin, Germany

Introduction

Nucleotomy is among the most common spinal surgeries. While in vitro studies consistently show segmental destabilization and increased range of motion after nucleotomy, in vivo animal studies have reported increased postoperative stiffness [1]. This study investigated the time-dependent in vivo kinematic response to nucleotomy in a controlled large-animal model over 10 weeks to help reconcile these conflicting findings.

Methods

Five female Merino-mix sheep underwent nucleotomy at L3–L4 with removal of approximately 0.2 g nucleus tissue. Flexion-extension kinematics were measured using two cutaneous sensor strips with integrated accelerometers and gyroscopes capturing segmental motion across the lumbar spine. Each animal was assessed twice preoperatively, on postoperative days 1 and 3, and weekly thereafter for 10 weeks. Analyses focused on (1) the index level (L3–L4), (2) the cranial and caudal adjacent segments, and (3) the overall lumbar spine. For all movement parameters, paired two-sided t-tests ($\alpha = 0.05$) were performed comparing preoperative values with week-10 measurements.

Results

At the index level, motion progressively shifted toward smaller excursion ranges over time (Fig. 1). The frequency of 2–4° movements increased above baseline by week 10 (+43.7% flexion, +51% extension), following an early postoperative peak and transient decline. In contrast, large-amplitude excursions (>8°) decreased sharply immediately after surgery and remained markedly reduced through week 10 (e.g., 10-12°: flexion –86.7%, 8-10°: extension –89.1%). Caudal adjacent segments showed a comparable reduction in large-scale motion (extension –59.8%, p=0.0067; flexion –76.7%, p=0.007).

Discussion

Although nucleotomy reduces intrinsic passive stability, the in vivo response was characterized by reduced large-amplitude motion and increased fine-scale adjustments.

This pattern is consistent with a neuromuscular compensation strategy involving increased co-contraction and elevated baseline segmental stiffness. The adaptations at both the index and adjacent segments suggest rapid re-establishment of functional stability rather than hypermobility. These findings help reconcile discrepancies between in vitro destabilization and in vivo reports of increased postoperative stiffness and provide new insight into active stabilization following disc interventions.

Images (Optional)

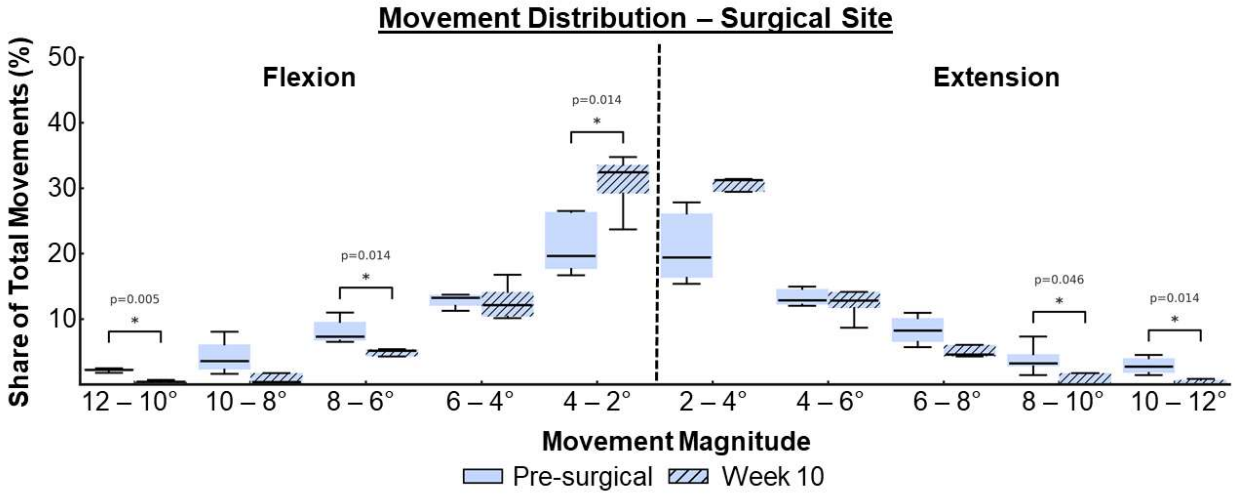


Fig. 1 Flexion and Extension movements prior to and after nucleotomy at the surgical site: After nucleotomy, movement distribution shifted from large-amplitude movements toward smaller movements: larger flexion (12-10° and 8-6°) and extension (8-10° and 10-12°) occurred less frequently, whereas smaller flexion (4-2°) increased significantly at Week 10. Pre-surgical boxes are solid; Week-10 boxes are black-hatched. The y-axis depicts movement distribution (percentage). The x-axis depicts sagittal movement sizes, with flexion to the left of the dotted line and extension to the right. Brackets with a star indicate significant differences (paired, two-sided t-test, $n = 5$, $p < 0.05$).

References (Optional)

[1] Reitmaier et al, J R Soc Interface, 2014

Acknowledgements (Optional)

This study is part of a Research Unit FOR 5177, funded by the German Research Foundation (GZ RE 4292/3-1; SCHM 2572/11-1; SCHM 2572/13-1).

Session Category

Orthopaedic Biomechanics: Spine

OA24-02

Finite Element Analysis of the Biomechanical Interaction Between the Thumb and Carpal Tunnel

Dr. David Jordan PhD, Dr. C. Kent Kwoh MD, Dr. Zong-Ming Li PhD

The University of Arizona, Tucson, Arizona, United States

Introduction

The transverse carpal ligament (TCL) and thumb share an anatomical connection through the thenar muscles which insert along the thumb and originate along the TCL. The biomechanics of these two structures has the potential to become disrupted in the presence of common musculoskeletal disorders, such as trapeziometacarpal (TMC) osteoarthritis. The purpose of this study was to simulate the biomechanical response of the TMC joint and TCL during pinching and the changes to the biomechanical response due to variation of TMC ligamentous stiffness.

Methods

A finite element model of the thumb and distal carpal tunnel was created (Figure 1) from the CT scan of a cadaveric hand. The model included the TCL, articular surface cartilage of the TMC joint, 4 TMC ligaments (dorsal radial ligament, dorsal central ligament, anterior oblique ligament and posterior oblique ligament), five extrinsic muscles represented as nodal forces and three intrinsic muscles represented as a collection of linear springs. A pinching simulation was performed driven by the five extrinsic muscles. First metacarpal rotation and translation, as well as TCL translation during pinching was simulated with percentage variation of TMC ligament stiffness from 100%, 75%, 50% and 25% of the maximum value.

Results

Variation of dorsal radial and anterior oblique ligament stiffness produced the greatest movement changes. A magnitude of 25% dorsal radial ligament stiffness increased metacarpal radial translation, metacarpal internal rotation, and TCL volar translation by 1.3%, 36.9% and 23.8%. A magnitude of 25% anterior oblique ligament stiffness increased metacarpal volar translation, metacarpal internal rotation, and TCL volar translation by 38.7%, 46.3% and 8.1%.

Discussion

TMC ligamentous laxity can alter the biomechanical response of the TCL during common hand activity. Motion changes were the largest for reductions in dorsal radial and anterior oblique ligament stiffness. This observation is supported by previous research which identifies the dorsal radial ligament as the primary ligamentous stabilizer of the TMC joint. Understanding how the biomechanical interaction of the thumb and TCL is altered due to the presence of TMC ligamentous laxity can aid in understanding the potential mechanisms which can alter the interaction and possible implications.

Images (Optional)

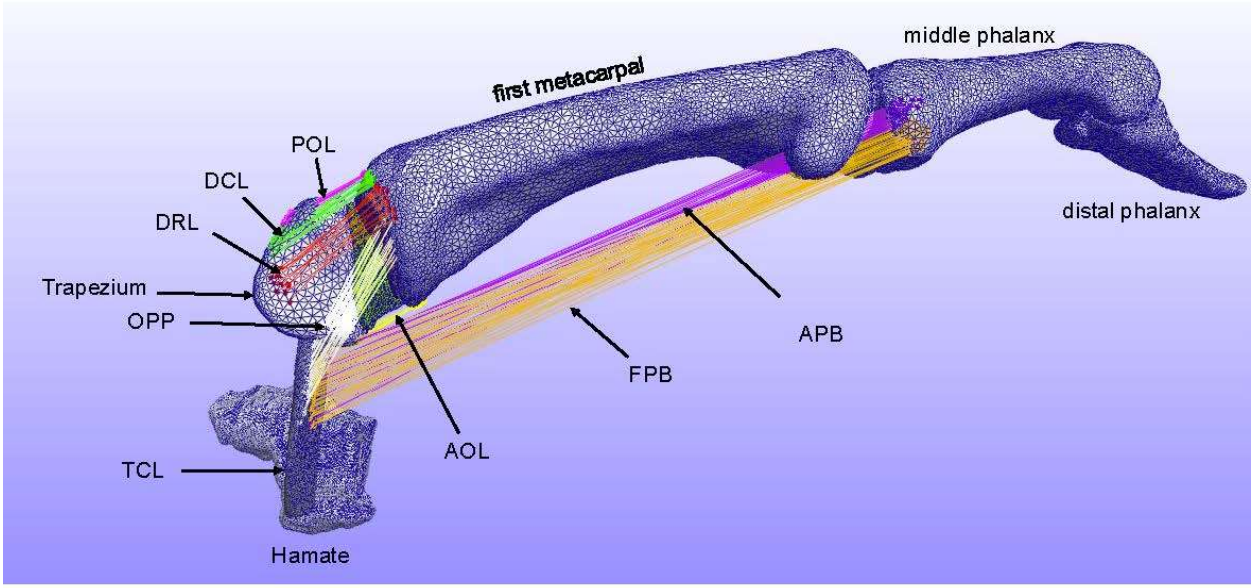


Figure 1: Finite element model of the thumb and distal carpal tunnel.

Session Category

Orthopaedic Biomechanics: Upper Extremities

OA24-03

Personalized Shoulder Musculoskeletal Modeling: A Novel Workflow for Investigations of Glenohumeral Osteoarthritis and Post-Arthroplasty Joint Reaction Loads

Ir. Line Ven[1], Dr. Ir. Nazanin Daneshvarhashjin[1], Prof. Dr. Philippe Debeer[1,2], Prof. Dr. Filip Verhaegen[1,2], Prof. Dr. Ir. Lennart Scheys[1,2]

[1]Institute for Orthopaedic Research and Training, KU Leuven, Leuven, Flanders, Belgium. [2]Division of Orthopaedics, University Hospitals Leuven, Leuven, Flanders, Belgium

Introduction

Glenoid component loosening is a critical complication following anatomic shoulder arthroplasty (aTSA), with the rocking-horse effect considered as primary loosening mechanism. Although musculoskeletal modeling and simulation provide insight into joint loading, personalization of these models for glenohumeral osteoarthritis (OA) and post-aTSA patients remains poorly investigated. This study aimed to develop a workflow for generating personalized shoulder models by uniquely integrating patient-specific geometry and humeral head (HH) translations, as an initial step towards loosening investigations.

Methods

Four OA patients from our prospective clinical study with computed tomography scans and biplanar radiographs (EOS) in multiple flexion and abduction positions were selected for workflow creation. The generic thoracoscapular OpenSim model was enhanced with a detailed scapular mesh, enabling selection of closest nodes to muscle insertions and wrapping surface edges for later personalization. The scapula coordinate frame was updated to align with geometry-defined frames used during EOS-processing, whereafter glenohumeral translations were inserted as additional degrees-of-freedom (DOF).

The automated personalization workflow, built in Python, consisted of: (1) scaling the generic model towards patient-specific HH dimensions, (2) non-rigid morphing of the generic scapula to the segmented patient scapula using MeshMonk, (3) updating muscle insertions based on corresponding nodes on the morphed scapula, and (4) fitting personalized wrapping surfaces to corresponding nodes through Gauss–Newton optimization.

Following personalization, both generic and EOS-derived patient-specific 6DOF-positions were applied to the generic and personalized models, respectively. Muscle forces were

computed using static optimization, joint reaction loads were obtained with OpenSim's JointReactionTool.

Results

Personalized joint reaction forces followed the expected upward trend (Fig.1), but showed considerable variations compared to generic outcomes. Inter-patient HH translation variability seemed associated with differences in out-of-plane glenoid moments, while generic moments remained zero. Translations and moments showed directional shifts between 0-45° and 45-90° elevation.

Discussion

These preliminary findings demonstrate feasibility of the novel workflow for model personalization and joint reaction estimation. By uniquely incorporating HH translations, this workflow achieves more accurate and individualized loading predictions. While preoperative geometry variations appear to affect loading, post-aTSA models remain unexplored. Future work will include additional patients and post-aTSA configurations up to 120° elevation to assess whether loading shifts (rocking-horse effect) persist postoperatively.

Images (Optional)

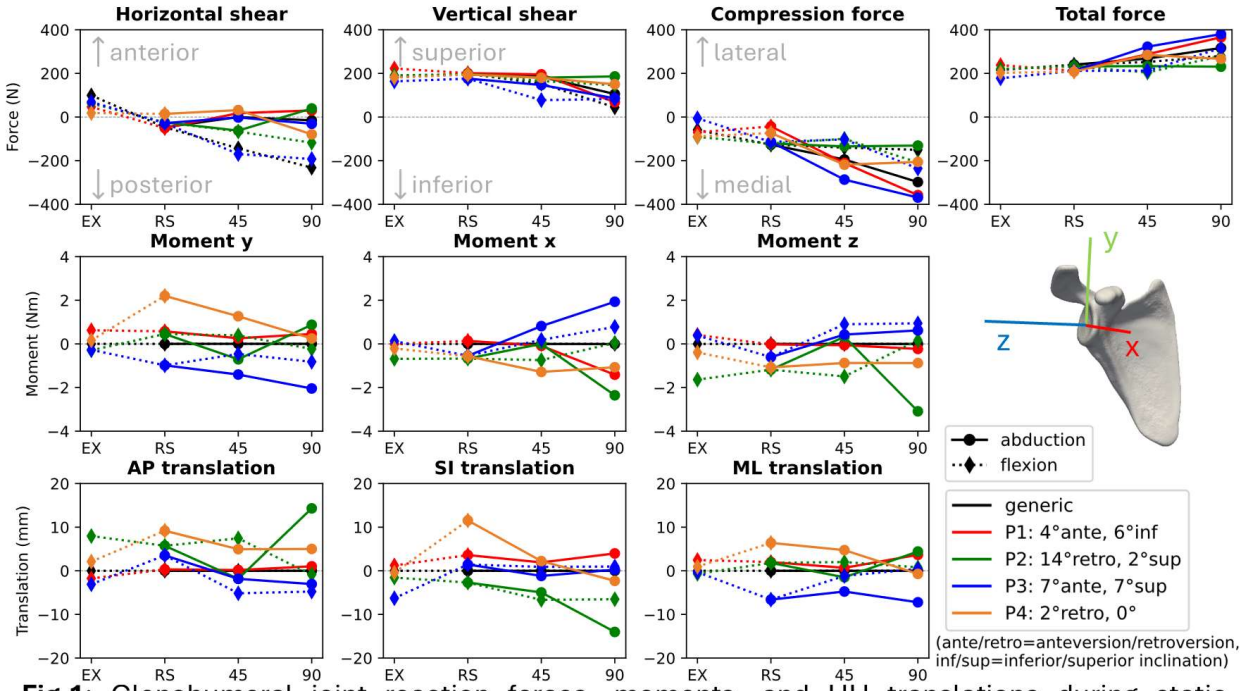


Fig.1: Glenohumeral joint reaction forces, moments, and HH translations during static extension (EX), relaxed standing (RS), 45° (45AB/F) and 90° abduction/flexion (90AB/F). Moments and translations were normalized by the ratio of the generic to the patient HH radius. PAT1+4 didn't perform flexion due to pain. For each scapula, X- and Y-axis were orthogonal to the scapular and transverse plane, respectively. Z-axis was mutually orthogonal.

References (Optional)

Acknowledgements (Optional)

The authors thank Flanders' Fund for Scientific Research (1SA9026N) and PRosPERoS-II Interreg VA Flanders–The Netherlands (2021TC16RFCB041) for financial support.

Session Category

Orthopaedic Biomechanics: Upper Extremities

OA24-04

Relationships between Pain and Glenohumeral Joint Motion and Loading Across Pediatric and Adult Manual Wheelchair Users

Dr. Alyssa Schnorenberg PhD[1], Dr. Amee Seitz PhD, PT[2], Dr. Shubhra Mukherjee MD[3], Dr. Karin Goodfriend MD[4], Dr. Brooke Slavens PhD[1]

[1]University of Wisconsin-Milwaukee, Milwaukee, WI, United States. [2]Northwestern University, Chicago, IL, United States. [3]Shriners Children's Chicago, Chicago, IL, United States. [4]Medical College of Wisconsin, Milwaukee, WI, United States

Introduction

Manual wheelchair propulsion is demanding on the upper extremities (UE), contributing to shoulder pain and pathology that reduce quality of life for individuals with spinal cord injury/dysfunction (SCI/D). Quantitative analyses linking propulsion biomechanics to shoulder pain may help identify injury risk factors and inform prevention strategies. This study examined associations between shoulder pain and glenohumeral (GH) joint dynamics during propulsion in wheelchair users across the lifespan.

Methods

Fifty-nine manual wheelchair users with SCI/D participated: pediatric (n=19, 13.1 ± 3.4 yr), adult pediatric-onset (n=21, 30.0 ± 11.6 yr), and adult adult-onset (n=19, 43.1 ± 13.2 yr). Participants completed the wheelchair users shoulder pain index (WUSPI) and PROMIS Pain Interference (PI) assessments, then propelled their wheelchair while a Vicon system captured their motion. A validated inverse dynamics model quantified GH flexion-extension ROM, peak superior force, and peak extension moment; each metric and its coefficient of variation (CV) were averaged across cycles.

Results

Pediatric users reported significantly less pain interference than adults with adult-onset SCI/D. Biomechanical–pain associations were group-specific. In the adult pediatric-onset group, higher GH extension moment was associated with more pain and pain interference, while children showed the opposite trend with pain interference, suggesting more efficient or protective loading patterns. Additionally, within the adult pediatric-onset group, higher GH superior force and lower superior force variability were associated with less pain interference, indicating possible adaptive propulsion strategies. Across participants, higher pain interference was associated with reduced GH flexion-extension ROM and greater ROM variability, though not significantly different across groups.

Discussion

Overall, disability onset influenced relationships between propulsion biomechanics and pain interference: pediatric users and lifelong adult users demonstrated opposite patterns, while adults with adult-onset SCI/D showed no consistent associations. These findings suggest that propulsion mechanics may have different functional consequences depending on developmental history and years of wheelchair use. Because it remains unclear whether certain loading patterns protect against pain or emerge as compensatory responses, longitudinal studies are needed to clarify their bidirectional links with shoulder pain. Such knowledge will support evidence-based propulsion training and early intervention strategies aimed at reducing overuse-related pain across the lifespan for individuals with SCI/D.

Session Category

Orthopaedic Biomechanics: Upper Extremities

OA24-05

Bi-Fluoroscopy-Informed Machine Learning for Scapula Tracking in Reverse Shoulder Arthroplasty

Dr Maxence Lavaill PhD[1,2], Prof Peter Pivonka PhD[1], Dr Ehsan Sarshari PhD[2]

[1]Queensland University of Technoogy, Brisbane, QLD, Australia. [2]Stryker GmbH, Selzach, Solothurn, Switzerland

Introduction

Accurate assessment of scapular kinematics remains a major challenge in shoulder biomechanics due to substantial soft-tissue artefacts affecting skin-marker–based motion capture (Mocap). Our previous work [1] demonstrated that machine-learning (ML) models trained on concurrent Mocap and bi-fluoroscopy (BF) data from healthy adults can reduce scapular tracking errors by half. However, translating these advances to reverse shoulder arthroplasty (RSA) is essential, as RSA profoundly alters glenohumeral mechanics, increases scapulothoracic compensation, and introduces atypical movement patterns that amplify Mocap errors [2]. This study extends our scapula-tracking BF-informed ML framework to RSA, assessing whether a ML model previously trained on healthy BF and Mocap data [3] could also be applied to RSA patients.

Methods

Newly published concurrent Mocap and BF recordings from nineteen RSA patients performing standard clinical shoulder motions were leveraged [4]. Scapular (AC, AA, AI, TS), thorax and upper-limb Mocap markers served as inputs to the healthy-trained BF-informed ML model, using the same predictor structure and temporal window as originally developed [1]. The model was applied directly to RSA trajectories without retraining. RMS errors were computed against BF ground truth for both raw Mocap and ML-corrected scapular trajectories.

Results

Across all RSA patients and tasks, Mocap scapular landmark errors ranged from 10–30 mm (Figure 1), confirming substantial soft-tissue artefacts. Applying the healthy-trained ML model systematically increased these errors rather than reducing them. The most severe increase occurred for the AI landmark in the Y-direction, with ML-predicted errors reaching ~130 mm, far exceeding the corresponding Mocap error (20 mm). Similar error amplification was observed across all scapular landmarks.

Discussion

The healthy-trained BF-informed ML model did not generalise to RSA shoulders. Instead of correcting soft-tissue artefacts, it produced substantially larger errors and anatomically implausible scapular trajectories. These findings underscore the biomechanical differences between healthy and RSA shoulders, i.e., altered kinematics, compensation patterns and soft-tissue behaviour, and demonstrate that ML models trained solely on healthy data are unsuitable for arthroplasty populations. Future work will focus on developing BF-informed ML models trained on RSA datasets.

Images (Optional)

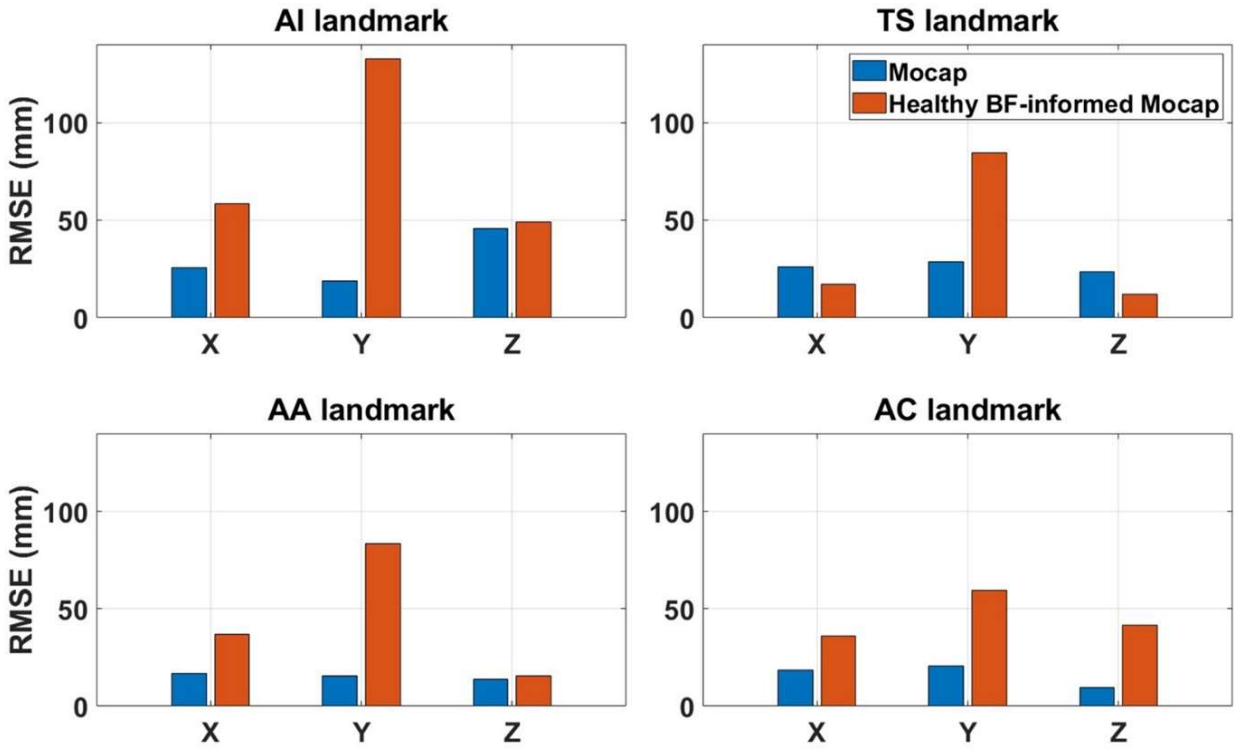


Figure 1: Scapular soft-tissue artefacts of RTSA patients from skin-markers (Mocap) and corrected skin markers from healthy-trained bifluoroscopy-informed machine learning (Healthy BF-informed Mocap, [1])

References (Optional)

[1] Lavaill et al., ESB2025 proceedings, 2025

[2] Terrier et al., JSES, 2013

[3] Henninger, Zenodo, 2024

[4] Henninger, Zenodo, 2025

Acknowledgements (Optional)

This work was supported by an Advance Queensland Industry Research Fellowship. ML and PP also acknowledge support from the Australian Research Council (IC190100020).

Session Category

Orthopaedic Biomechanics: Upper Extremities

OA25-02

Event-Based Image Velocimetry as Alternative to Particle Image Velocimetry for the Experimental Fluid Dynamic Evaluation of Mitral Valve Prostheses

Dr. Elena Torta PhD[1], Mr. Manuel Zannone[1], Mr. Enrico Amico[1], Mr. Girolamo Mastronuzzi[1], Mrs. Emma Giaccone[1], Mr. Daniele Pecchio[2], Dr. Jacopo Serpieri PhD[1], Prof. Gioacchino Cafiero PhD[1], Prof. Diego Gallo PhD[1], Prof. Umberto Morbiducci PhD[1]

[1]Politecnico di Torino, Turin, Piedmont, Italy. [2]Affluent Medical, Colleretto Giacosa, Piedmont, Italy

Introduction

In vitro fluid-mechanics experiments are essential for understanding cardiovascular flows and for design, optimization and characterization of cardiovascular devices, particularly prosthetic heart valves[1,2]. Particle Image Velocimetry (PIV) remains the reference technique but is limited by frame-rate constraints, large data volumes, and complex and expensive setups. Event-Based Imaging Velocimetry[3] (EBIV), a neuromorphic, event-driven imaging technology, offers high temporal resolution and extended dynamic range at reduced costs. Nonetheless, EBIV has never been applied to cardiovascular flows. This study presents the first EBIV investigation of intraventricular dynamics in a left-ventricle (LV) phantom with a transcatheter mitral valve (MV), comparing EBIV to PIV measurements, considered as the reference technique.

Methods

Experiments were performed in a left-heart pulse duplicator (Vivitro System) with a simplified silicone LV phantom and a transcatheter MV prosthesis (Epygon, Affluent Medical), under two flow regimes (3.5 and 5 L/min, 35% systole, 70 BPM). A saline solution seeded with polyamide particles (100 μm diameter) served as working fluid. EBIV and PIV measurements were conducted on the aortomitral plane. The measurement plane was illuminated using a dual-cavity Nd:YAG laser (15 Hz, 200 mJ/pulse). Phase-locked image acquisition was performed simultaneously by two cameras: Prophesee EVK-4 event-based camera (Sony IMX636, 1280×720 pixels^2) and Andor Zyla 5.5 sCMOS camera (2560×2160 px^2). Proper Orthogonal Decomposition (POD) was applied to reduce noise.

Results

Results show that EBIV accurately reproduces PIV-measured valve-related hemodynamic features, including phase-averaged velocity fields (Figure 1), vortex structures (λ_2, Figure 1), circulation, Lagrangian trajectories, and pulsatile kinetic energy, while producing markedly compact datasets and benefiting from an extended dynamic range. A POD-based analysis

further confirms a strong agreement between EBIV and PIV measurements, revealing nearly identical dominant spatial modes.

Discussion

The event-based approach allowed investigating the topology and the temporal evolution of the LV fluid dynamics. These findings establish EBIV as a promising, data-efficient, and real-time capable alternative to PIV. This first biomedical application underscores EBIV's potential for device assessment, intraventricular flow analysis, and broader application in experimental cardiovascular research.

Images (Optional)

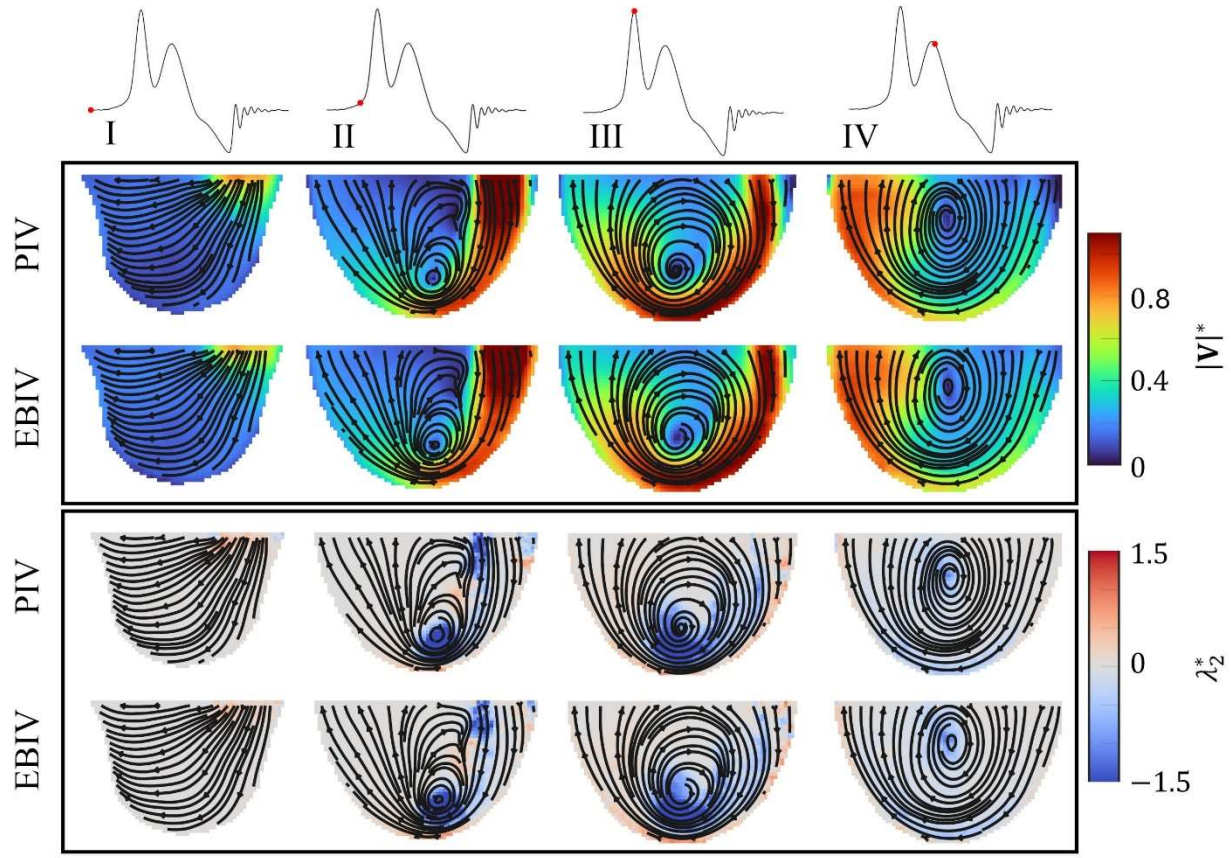


Figure 1: Normalized velocity magnitude $|\boldsymbol{V}|^*$ (top panel) and normalized λ_2^* (bottom panel) maps with streamlines resulting from PIV and EBIV for representative diastolic phases at CO= 5 L/min: early diastole (I), early acceleration (II), E-wave peak (III), A-wave peak (IV). For each phase (ϕ_{ref}), the normalized quantities are obtained by dividing the velocity magnitude and λ_2 fields by a reference quantity, obtained as the 95th percentile of the pooled distribution (respectively $|\boldsymbol{V}_{ref}| = Q_{95}(|\boldsymbol{V}|(\phi_{ref}))$ and $\lambda_{2,ref} = Q_{95}(\lambda_2(\phi_{ref}))$).

References (Optional)

[1] Hicham Saaid et al., J. Biomech., 2019

[2] Yan Qiang et al., Phys. Fluids, 2023

[3] Christian E. Willert, Exp. Fluids, 2023

Acknowledgements (Optional)

The research leading to these results received funding from the NODES project, which has received funding from the Italian Ministry of University and Research (MUR) under PNRR M4C2 1.5, funded by the European Union – NextGenerationEU (Grant Agreement No. ECS00000036). D.P. is employed by Affluent Medical, which provided the transcatheter mitral valve used in the experiments.

Session Category

Imaging and Biomedical Devices: Artificial Organs, Devices

OA25-03

A Validated PIV–CFD Framework for Quantifying Hemodynamic Changes Induced by Left Atrial Appendage Occlusion

PhD Emanuele Gasparotti[1], Eng Ilaria Verdirame[1], PhD Emanuele Vignali[1], PhD Benigno Marco Fanni[1], PhD Francesca Berti[2], Prof Giancarlo Pennati[2], Prof Lorenza Petrini[3], Prof Simona Celi[1]

[1]BioCardioLab, Bioenegineering Unit, Fondazione Monasterio, Massa, Tuscany, Italy. [2]Department of Chemistry, Materials and Chemical Engineering, Politecnico di Milano, Milano, Lombardy, Italy. [3]Department of Civil and Environmental Engineering, Politecnico di Milano, Milano, Lombardy, Italy

Introduction

Left atrial appendage occlusion (LAAO) is used to reduce thromboembolic risk in atrial fibrillation, yet its hemodynamic consequences remain insufficiently quantified and experimentally validated [1]. This study integrates high-resolution Particle Image Velocimetry (PIV) and Computational Fluid-Dynamics (CFD) to characterize pre- and post-LAAO Fluid-Dynamic and evaluate the consistency of numerical predictions against controlled in-vitro measurements.

Methods

Two patient-specific silicone phantoms representing pre- and post-LAAO anatomies were reconstructed from contrast-enhanced CT. The pre-LAAO model was fabricated in PDMS using a Brush–Spin-Coating technique, whereas the post-LAAO chamber incorporated a PDMS model of the device derived from finite-element simulation of LAAO procedure [2]. Phantoms were integrated into a hybrid mock circulatory loop [3] imposing patient-specific boundary conditions. Longitudinal and perpendicular planar velocity fields were acquired with a LED-based PIV system. In parallel, CFD simulations were setup with the same geometries and boundary conditions. PIV velocity fields were computed via double-frame cross-correlation and compared with corresponding CFD slices.

Results

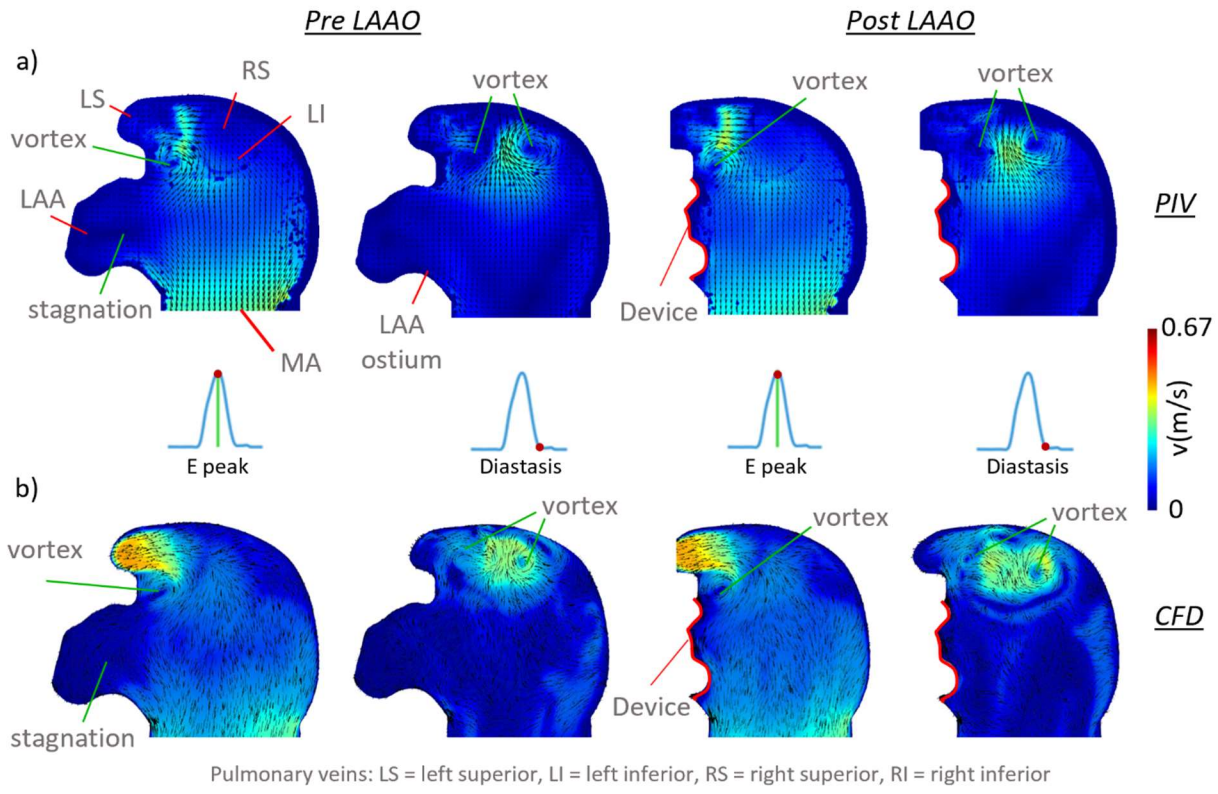
PIV (Fig_a) revealed dominant recirculation within the LAA during peak mitral flow, with velocities decreasing below 0.1 m/s from ostium toward the distal region and coherent vortices forming near LA roof during diastasis. CFD (Fig_b) reproduced these macrostructures, matching vortex location, low-speed distribution, and velocity direction. After occlusion, both PIV and CFD showed a redirected, more coherent mitral jet and a 20% velocity increase in the region formerly occupied by the appendage, eliminating the

dominant intra-LAA recirculation. A confined near-wall recirculation emerged at the device head, consistently captured by both modalities.

Discussion

The combined experimental–numerical investigation demonstrated that LAAO reorganizes atrial hemodynamics, suppressing the large recirculation area in the appendage and reducing low-velocity zones associated with stasis in atrial fibrillation. CFD and PIV reliably reproduced key flow features, supporting its use for patient-specific evaluation of LAAO performance. High inter-cycle repeatability confirmed that observed differences stemmed from anatomical modification rather than measurement variability. The dataset offers robust benchmarks for validating computational LAAO models and strengthens the hemodynamic implications of LAAO.

Images (Optional)



Pulmonary veins: LS = left superior, LI = left inferior, RS = right superior, RI = right inferior

References (Optional)

[1] Marco Viceconti *et al.*, Methods, 2021

[2] Francesca Danielli *et al.*, Int J Numer Method Biomed Eng, 2024

[3] Emanuele Gasparotti *et al.*, Biosystems Biorobotics, 2025

Acknowledgements (Optional)

Session Category

Imaging and Biomedical Devices: Artificial Organs, Devices

OA25-04

Patient-Specific Pediatric Right Heart Simulator for Pulmonary Valve Assessment Using MRI

Dr. Lorenzo Ferrari, Dr. Yellappa Palagani, Ms. Elena S. Martinez, Dr. Alison L. Marsden, Dr. Michael R. Ma, Dr. Doff McElhinney, Dr. Daniel B. Ennis

Stanford University, Stanford, California, United States

Introduction

Early deterioration of pulmonary valve replacements (PVRs) is a critical, yet poorly understood, complication in pediatric patients with repaired congenital heart disease. Existing bench-top flow-driving solutions are unable to replicate the broad range of pulsatile pressure and flow conditions typical of this heterogeneous group. It is also difficult to do so within the MRI environment, which limits the effectiveness of *in vitro* evaluations using this imaging technique. To overcome these challenges and to investigate the underlying valve failure mechanisms, we developed an *in vitro* platform designed to systematically reproduce patient-specific right heart geometries and hemodynamics derived from clinical examinations. Both clinical decision-making and future valve design will benefit from insights gained from our MRI-compatible simulator.

Methods

CT scans from a 10-year-old male subject with pulmonary atresia and an intact ventricular septum were used to create a silicone model of the right heart via 3D-printing and mold casting. Bioprosthetic valves were used in the tricuspid and pulmonary valve anatomical positions. Our computer-controlled pneumatic circuit modulated air inflow and outflow to externally compress and relax the flexible right ventricle, thereby inducing ventricular wall motion and cardiovascular-like flow. Flow sensors and pressure probes monitored the pediatric right heart conditions, which were tuned by adjusting the resistances and compliances downstream of the pulmonary artery. We used a 40% glycerol-based solution, mimicking blood rheological properties, which circulated to a reservoir-like right atrium before returning to the ventricle. The entire circuit is MRI-compatible and amenable to evaluation with advanced flow imaging methods.

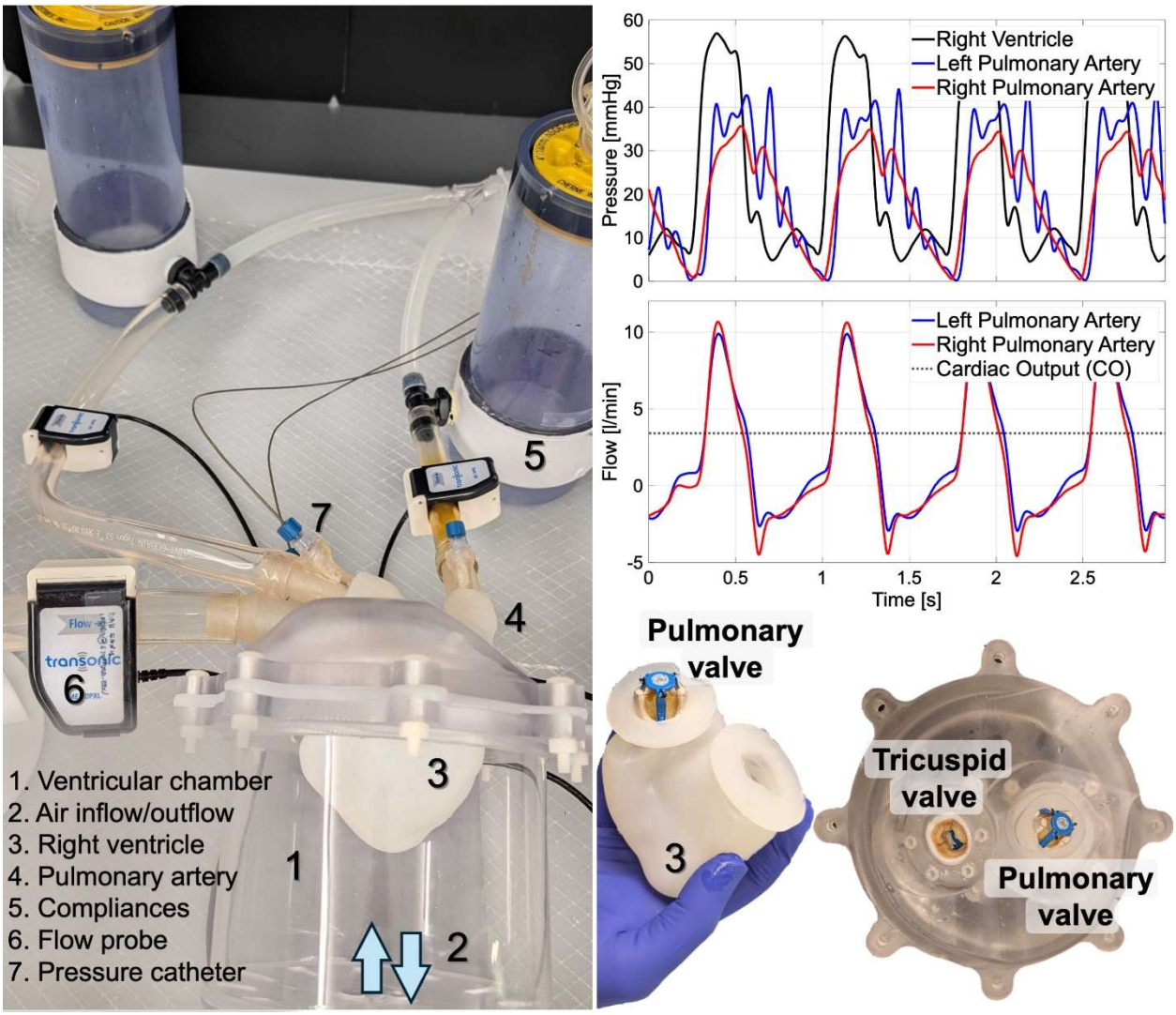
Results

Our right heart simulator reproduced physiological flow and pressure values typically reported for the patient's age group. The computer-controlled pneumatic circuit can control heart rates, right ventricular ejection fraction, diastolic and systolic pressures, and flow profiles.

Discussion

Our *in vitro* setup is the first MRI-compatible right heart simulator for pediatric applications. It reproduces physiological pediatric hemodynamics in patient-specific geometries while incorporating ventricular contraction. Coupled with 4D-Flow MRI, our *in vitro* platform is a powerful and versatile tool for analyzing hemodynamics to assess mechanisms explaining early PVR failure and to identify strategies for enhancing valve durability in pediatric patients.

Images (Optional)



Session Category

Imaging and Biomedical Devices: Artificial Organs, Devices

OA25-05

Set-Up and Interim Results of the PODRACING Trial: A Randomized Controlled Trial to Evaluate Our Renal Perfusion Model During Robot-Assisted Partial Nephrectomy.

Ir Saar Vermijs[1,2,3], Dr Joris Vangeneugden[2,4], Dr Peter De Kuyper[5], Dr Camille Berquin[2,4], Prof Dr Nicolaas Lumen[2,4], Dr Frederic Baekelandt[6], Dr Christophe Ghysel[6], Dr Yannic Raskin[7], Dr Bernard Bynens[7], Dr Kenzo Mestdagh[2,4], Dr Ir Pieter De Backer[2,4,8], Prof Dr Pieter De Visschere[9], Prof Dr Karel Decaestecker[2,4,5], Prof Dr Charles Van Praet[2,4], Prof Dr Ir Charlotte Debbaut[1,3]

[1]IBiTech-Biommeda, Faculty of Engineering and Architecture, Ghent University, Ghent, Flanders, Belgium. [2]Department of Human Structure and Repair, Faculty of Medicine and Health Sciences, Ghent University, Ghent, Flanders, Belgium. [3]Cancer Research Institute Ghent, Ghent, Flanders, Belgium. [4]Department of Urology, Ghent University Hospital, eUROGEN accredited center, Ghent, Flanders, Belgium. [5]Department of Urology, AZ Maria Middelares, Ghent, Flanders, Belgium. [6]Department of Urology, AZ Sint-Jan Brugge, Bruges, Flanders, Belgium. [7]Department of Urology, Ziekenhuis Oost-Limburg (ZOL) Genk, Genk, Flanders, Belgium. [8]ORSI Academy, Melle, Flanders, Belgium. [9]Department of Radiology and Nuclear Medicine, Ghent University Hospital, Ghent, Flanders, Belgium

Introduction

Performing successful selective arterial clamping during partial nephrectomy for kidney tumor removal depends on the surgeon's understanding of the patient-specific vascular anatomy, which is often limited by the quality and interpretability of preoperative imaging. To overcome these limitations, we developed the DIPLANN tool [1], a Class IIa medical device that utilizes 3D modelling and in-house developed algorithms to provide the surgeon with a patient-specific perfusion model (Fig. 1). The device's safety, performance, and clinical efficacy is currently investigated through a randomized controlled trial (RCT): PODRACING [2].

Methods

This ongoing multi-centric, prospective, parallel-group RCT will enroll 235 adult patients with a cT1-2 kidney tumor. Participants are randomized 1:1 to receive either the standard of care (preoperative CT scan) or an additional perfusion model. The primary endpoint includes planned selective clamping success with secondary endpoints addressing clinical outcomes, usability and patients' insight. Data collection occurs at different stages during the one-year follow-up. The study was approved by the Belgian Federal Agency for

Medicines and Health Products and is supported by the Foundation against Cancer and FWO (Flemish Research Foundation) [3-4]. For the interim analysis, the primary endpoint was analyzed in a subgroup of patients where selective clamping was deemed feasible, using a Chi-Squared test.

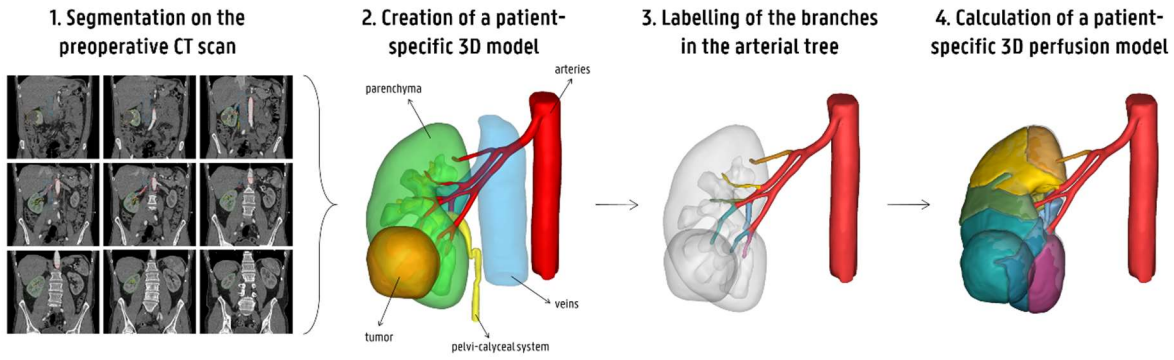
Results

Recruitment and data collection are ongoing (129/235). For the interim analysis, 107 patients who underwent surgery between July 2024 and October 2025 were investigated. In 103 patients, selective clamping was deemed feasible, out of which 50 patients got a perfusion model. In 43 of these 50 patients (86%), selective clamping was performed successfully as preoperatively planned. In the 53 patients in the control group, only 22 patients (41.5%) got successful selective clamping ($p < 0.00001$).

Discussion

The interim analysis of our ongoing PODRACING trial shows that the use of perfusion models is strongly correlated with performing more accurate and more frequent SC during partial nephrectomy. More secondary and exploratory endpoints –including renal function, surgical time and quality of life– are currently being studied.

Images (Optional)



References (Optional)

[1] De Backer P & Vermijs S *et al.*, European Urology, 2023.
[2] ClinicalTrials.gov. Identifier NCT06536439.
[3] Stichting tegen Kanker. Identifier OST-2022-199.
[4] FWO. Identifier 1S64425N

Acknowledgements (Optional)

The authors want to thank the participating patients and surgeons of Ghent University Hospital, AZ Maria Middelares, AZ Sint-Jan Brugge and ZOL Genk.

Session Category

Imaging and Biomedical Devices: Artificial Organs, Devices

OA26-01

Nonlinear Phenomena in Bacterial Turbulence Under Imposed Background Flows

Assoc. Kenji Kikuchi Doctor of Engineering

Tohoku University, Sendai, Miyagi, Japan

Introduction

Dense suspensions of motile bacteria spontaneously generate chaotic mesoscale flows known as bacterial turbulence. While many studies have focused on unconfined or weakly confined systems, how such active turbulence interacts nonlinearly with externally imposed background flows remains poorly quantified. Here we investigate how steady and oscillatory background flows reorganise collective bacterial motion, effective transport and apparent rheology.

Methods

We combine microfluidic experiments in straight and corrugated channels containing concentrated suspensions of rod-shaped bacteria with numerical simulations of an active nematic / active Brownian particle model subjected to imposed Poiseuille and shear flows. Velocity fields are quantified using particle image velocimetry and decomposed into background and active components. By tuning pressure drop and driving frequency, we span regimes from steady weak shear to strong oscillatory forcing, and use cavity depths comparable to the intrinsic vortex size to probe wall trapping and de-trapping of bacteria.

Results

We identify three robust regimes: (i) vortex-dominated bacterial turbulence under weak background flow, (ii) shear-aligned streaming with suppressed vortices under strong background flow, and (iii) an intermediate symmetry-broken state with travelling vortex bands locked to the mean flow. In corrugated channels, bacteria accumulate in wall cavities, where trapped vortices create persistent high-density pockets. Tracer analyses show that axial dispersion and transverse mixing are strongly enhanced in the turbulent and banded states, but are markedly reduced in the shear-aligned regime. The occupancy of individual cavities exhibits intermittent switching between low- and high-density configurations, indicating stochastic transitions between trapped and flushed states driven by the competition of self-propulsion, collective vortices and imposed shear.

Discussion

Our results demonstrate that bacterial turbulence and background flows interact through strongly nonlinear mode competition, leading to bistability and history-dependent transport and mixing properties. These findings provide a physical basis for controlling dispersion in active fluids via externally imposed flows, and suggest design principles for microfluidic devices that harness bacterial turbulence and wall trapping rather than suppress them.

Session Category

Micro/Biofluidics: In Silico Models and Simulation

OA26-02

Measurement of bending stiffness of *Salmonella* flagella

Dr. Hossein Moghimifam[1], Dr. Jamel Ali[2], Mr. Haoxin Huang[1], Dr. Min Jun Kim[3], Dr. Henry Fu[1]

[1]University of Utah, Salt Lake City, UT, United States. [2]FAMU-FSU College of Engineering, Tallahassee, FL, United States. [3]Southern Methodist University, Dallas, TX, United States

Introduction

Bacteria swim by rotating helical flagella like propellers. These flagella are rigid enough to withstand viscous loads during much of swimming, but deform during reorientation events and certain swimming modes. Thus, flagellar stiffness has an important impact on bacterial motility. Earlier efforts to measure the bending stiffness have assumed constant stiffness along the length of the flagellum. We investigate flagella attached at one end to a slide and stretched by an imposed flow in a microfluidic channel, using 3D reconstruction of images and Kirchhoff rod models that enable enough precision to determine strain-dependent bending stiffnesses of flagella.

Methods

Fluorescently labeled flagella from Salmonella typhimurium were bound tightly by one end to a microchannel surface. Imposed flows through the channel were sufficient to deform the filaments, which were observed using fluorescence microscopy. Images of deformed flagella were analyzed by simulating expected images for varying flagellum geometries, using point spread functions that depend on the displacement of flagellum segments from the focal plane. In this way, we could determine the 3D geometry whose image most closely matches experimental observations. We used a numerical method which combines hydrodynamic forces determined using the method of regularized Stokeslets with Kirchhoff rod models of deformation to model the deformations of flagella in the microchannel flow. An input to these models is the bending stiffness of the flagellum. Comparing the results of models with varying bending stiffnesses to experimental observations enables determination of the bending stiffness.

Results

Bending stiffnesses that depend on the deformation or strain in the filament can be incorporated into the Kirchhoff rod model. Model results for bending stiffness that increase as strain increases tend to better reproduce experimental results, suggesting that that these bacterial flagella are strain-stiffening.

Discussion

Strain stiffening behavior of bacterial flagella may have important implications for bacterial swimming and microrobotic propulsion. Our results compare models with and without simple linear models of bending stiffness as a function of flagella deformation. Additional experiments may more precisely quantify the bending stiffness as a function of deformation.

Session Category

Micro/Biofluidics: In Silico Models and Simulation

OA26-03

Ciliary Pumping in the Choanocyte Chambers of Sponges

Dr Takumi Ogawa[1], Mr. Shuji Koyama[1], Prof. Toshihiro Omori[1], Prof. Kenji Kikuchi[1], Dr. Hélène de Maleprade[2], Prof. Raymond E. Goldstein[3], Prof. Takuji Ishikawa[1]

[1]Tohoku University, Sendai, 980-8579, Japan. [2]Sorbonne Université, Paris, F-75005, France. [3]University of Cambridge, Cambridge, CB3 0WA, United Kingdom

Introduction

Sponges, the basalmost members of the animal kingdom, exhibit a range of complex architectures in which microfluidic channels connect multitudes of spherical chambers lined with choanocytes, flagellated filter-feeding cells. Choanocyte chambers can possess scores or even hundreds of such cells, which drive complex flows entering through porous walls and exiting into the sponge channels. One of the mysteries of the choanocyte chamber is its spherical shape, as it seems inappropriate for inducing directional transport since many choanocyte flagella beat in opposition to such a flow.

Methods

We combine direct imaging of choanocyte chambers in living sponges with computational studies of many-flagella models to understand the connection between chamber architecture and directional flow.

Results

We find that those flagella that beat against the flow play a key role in raising the pressure inside the choanocyte chamber, with the result that the flow rate and mechanical pumping efficiency reach a maximum at a small outlet opening angle. Comparison between experimental observations and the results of numerical simulations reveal that the chamber diameter, flagellar wave number, and the outlet opening angle of the freshwater sponge Ephydatia muelleri, as well as several other species, are related in a manner that maximizes the mechanical pumping functions.

Discussion

The obtained results indicate the subtle balances at play during morphogenesis of choanocyte chambers, and give insights into the physiology and body design of sponges.

References (Optional)

Takumi Ogawa, Shuji Koyama, Toshihiro Omori, Kenji Kikuchi, Hélène de Maleprade, Raymond E. Goldstein, Takuji Ishikawa. The Architecture of Sponge Choanocyte Chambers

is Well Adapted to Mechanical Pumping Functions. Proc. Natl. Acad. Sci. USA, 122, e2421296122 (2025).

Session Category

Micro/Biofluidics: In Silico Models and Simulation

OA26-04

Multiphysics In Silico Modeling of Acoustofluidics and Molecular Transport at the Inner Ear–brain Interface: A Multiparametric Analysis of Cochlear fluids–CSF Dynamics in the Cochlear and Vestibular Aqueducts

Dr Andrea Sogno[1], Prof Federica Boschetti[1], Dr Federica Di Berardino[2], Prof Carmen Giordano[1], Dr Diego Albani[3], Dr Simone Perottoni[1]

[1]Department of Chemistry, Materials and Chemical Engineering “Giulio Natta”, Politecnico di Milano, Milan, Lombardy, Italy. [2]Neurodegenerative Diseases Unit, Fondazione IRCCS Ca' Granda Ospedale Maggiore Policlinico, Milan, Lombardy, Italy. [3]Department of Neuroscience, Istituto di Ricerche Farmacologiche Mario Negri IRCCS, Milan, Lombardy, Italy

Introduction

Hearing loss (HL) is a major risk factor for dementia [1]. Impaired cerebrospinal fluid (CSF) clearance of metabolic waste has been associated with both HL and cognitive impairment. Although cochlear fluids communicate with CSF through narrow aqueducts in the temporal subarachnoid space (SAS), their fluid-dynamic properties and their role in solute exchange remain poorly characterized. To address this gap, the EAR2BRAIN project is developing patient-specific in silico and in vitro models of the inner-ear/brain fluidic interface. Here, we present a first multiparametric and multiphysics in silico analysis of the acustofluidics and molecular exchange across the cochlear (CA) and vestibular aqueducts (VA) (Figure 1) towards personalized fully biomimetic model of cochlear–brain communication relevant to HL and neurodegeneration.

Methods

Ranges of width, length and orifice aperture have been collected from human μ-CT scanning and MRI to build 3D geometries of CA and VA to be imported in ANSYS fluent. Physiological and pathological scala tympani pressure (STP) and intracranial pressure (ICP) conditions were imposed at aqueduct inlets and outlets for multiparametric CFD and mass-transport simulations.

Results

Input parameters collection led to an initial idealized CA geometry with a length of 12mm, narrowest diameter of 0.14 mm, and a 3mm opening into the SAS. Three human-observed luminal states will be modeled: patent, connective-tissue filled, and obliterated. STP inputs

from 0–100 dB reproduce acoustic stimuli from 20 Hz to 20 kHz, while ICP ranges from 7 mmHg at rest to 25 mmHg to model hypertension, with oscillatory components mimicking cardiac, respiratory, and sleep–wake contributions.

Discussion

To our knowledge, no biomimetic models comprehensively capture pressure and solute exchange across both aqueducts. This first idealized analysis will reveal how anatomical variability and pressure dynamics influence cochlear–CSF communication relevant for subjects with malformations, HL, or altered intracranial pressures. Ongoing work will extend these models to patient-specific geometries, enabling a broad multiparametric characterization of inner ear–brain fluid dynamics in health and disease.

Images (Optional)

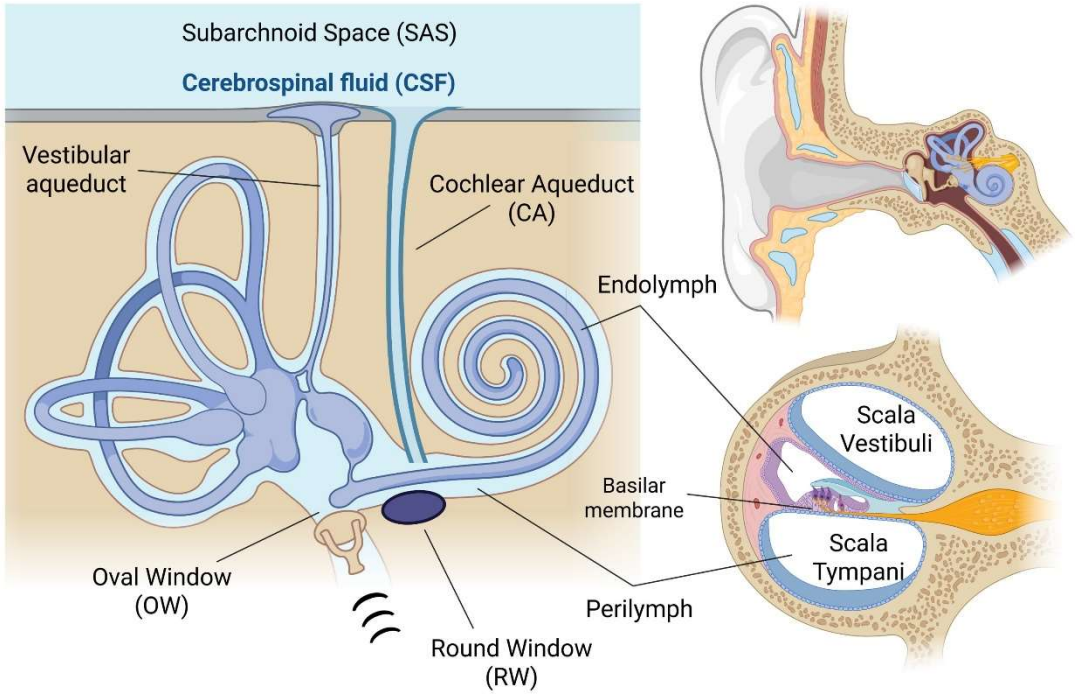


***Figure 1**. Anatomy of the inner ear and its fluidic exchange with the cerebrospinal fluid*

References (Optional)

[1] G. Livingston et al., “Dementia prevention, intervention, and care: 2020 report of the Lancet Commission,” The Lancet, vol. 396, no. 10248, pp. 413–446, Aug. 2020.

Acknowledgements (Optional)

This work has been supported by Fondazione Cariplo, grant n° 2024-1070 "EAR2BRAIN: A biomimetic MRI-compatible artificial cochlea to unravel the role of inner ear-brain fluids exchange on amyloid-beta clearance in dementia".

Session Category

Micro/Biofluidics: In Silico Models and Simulation

OA27-01

Impacts of Transcutaneous Spinal Cord Stimulation on Muscle Activity and Heart Rate Responses During Walker-Based Exoskeleton Use in Children With Cerebral Palsy

Ms. Katie M. Landwehr-Prakel MS[1], Dr. Anna M. Fragomeni PT, DPT, PCS[2], Dr. Kristie F. Bjornson PT, PhD, PCS[3,4], Dr. Chet T. Moritz PhD[5,2], Dr. Heather A. Feldner PT, PhD, PCS[2], Dr. Katherine M. Steele PhD[1]

[1]Department of Mechanical Engineering, University of Washington, Seattle, WA, United States. [2]Department of Rehabilitation Medicine, University of Washington, Seattle, WA, United States. [3]Department of Pediatrics, University of Washington, Seattle, WA, United States. [4]Seattle Children's Research Institute, Seattle, WA, United States. [5]Department of Electrical and Computer Engineering, University of Washington, Seattle, WA, United States

Ms. Katie M. Landwehr-Prakel

Introduction

Children with cerebral palsy (CP) often exhibit muscle weakness and impaired motor control, limiting mobility [1]. The Trexo is a robotic exoskeleton that provides hip and knee actuation to generate walking patterns, which may improve walking function and support rehabilitation [2]. Transcutaneous spinal cord stimulation (tSCS) may further enhance motor output during rehabilitation [3], though its impact during Trexo-assisted walking remains unknown. This case series examined muscle activity and cardiovascular responses during Trexo use with and without tSCS in children with CP.

Methods

Four children with non-ambulatory CP (1M/3F, 32 ± 8.0 months) completed Trexo-assisted walking trials with and without tSCS. Trial duration and device settings were individualized for comfort and engagement. Surface electromyography (EMG) data were recorded bilaterally from the biceps femoris (BF), vastus lateralis (VL), and rectus femoris (RF) and filtered, rectified, and normalized to the 95th percentile maximum of each visit. Heart rate (HR) was collected continuously with an optical HR sensor

Results

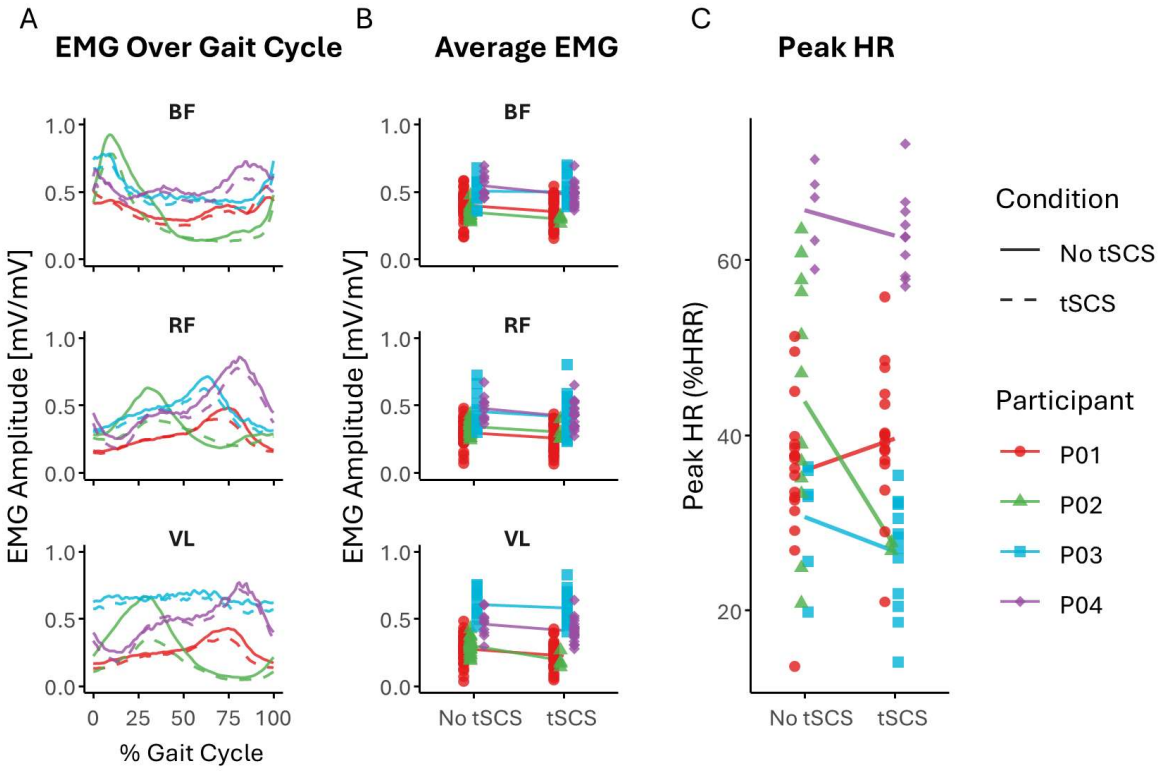
All participants displayed cyclic muscle activity during Trexo use, similar to gait. Heart rate increased with Trexo use by 36.3% (23.1 to 65.3%) compared to resting. Peak heart rate

decreased by 11.2% (-37.9 to +10.2%) for three participants during trials with tSCS. Muscle activity also slightly decreased by 10.1%, 12.1%, and 17.6% for the BF, RF, VL, respectively with tSCS.

Discussion

Muscles were active and heart rate was elevated during Trexo use in young, non-ambulatory children with CP. Adding tSCS may modulate muscle activity and cardiovascular response. Reductions in muscle activation and HR with tSCS may suggest decreased effort or altered control. Prior studies with tSCS and children with CP [3,4] demonstrated decreased co-contraction with tSCS, though we observed minimal changes in our cohort. The Trexo may have provided more constraints on limb movement that altered muscle response. Understanding these physiological responses can guide clinicians in optimizing treatment protocols for children with CP.

Images (Optional)



References (Optional)

[1] Graham et al., *Nat Rev Dis Primers,* 2016; [2] Diot et al., *Disabil Rehabil Assist Technol*, 2021; [3] Solopova et al., *Neurosci Lett*, 2017; [4] Gad et al., *Neurotherapeutics,* 2021

Acknowledgements (Optional)

This work was supported by the Seattle Children's Hospital CP Research Fund and R01NS091056. We would like to thank the participants and their families for their time and participation, as well as Kevin Doherty-Regalia, Avni Sisodiya, and Grace O'Connor for their assistance with data collection.

Session Category

Clinical Biomechanics: N/A

OA27-02

Comparing Split Belt Treadmill Adaptation Rates Between Children with Cerebral Palsy and Typically Developing Peers Using Bayesian Models

Ms. Mackenzie Pitts MS[1], Dr. Alyssa Spomer PhD[2], Dr. Andrew Ries PhD[2,3], Dr. Michael Schwartz PhD[2,3], Dr. Katherine Steele PhD[1]

[1]University of Washington, Seattle, WA, United States. [2]Gillette Children's Hospital, St. Paul, MN, United States. [3]University of Minnesota, Minneapolis, MN, United States

Introduction

Split belt treadmill walking – a paradigm in which individuals adjust step length in response to belts moving at different speeds – has been used to understand coordination and adaptation of gait after stroke [1]. Children with cerebral palsy (CP) also have altered gait due to neurologic injury, and split belt walking may provide insight on adaptation capacity. Particularly, the rate of adaptation is significant as it could be used to identify patient-specific differences in adaptation capacity. The goal of this study was to compare split belt adaptation rates for children with CP and typically developing (TD) peers.

Methods

Twelve children with diplegic CP and seven TD children completed a six-minute split belt protocol following three minutes of treadmill acclimation. TD participants' nondominant limb and CP participants' more-affected limb were subjected to the fast belt, which operated at 1.65-1.8 times self-selected speed (slow belt). Step length asymmetry was computed as the difference between fast and slow limb step lengths divided by stride length. We evaluated step length asymmetry during the first and last 10 gait cycles. We used a Bayesian approach to fit a dual-exponential model to full trial asymmetry, capturing individualized rates for immediate (r_f) and long-term (r_s) responses to adaptation. Coefficient priors were informed by literature [2].

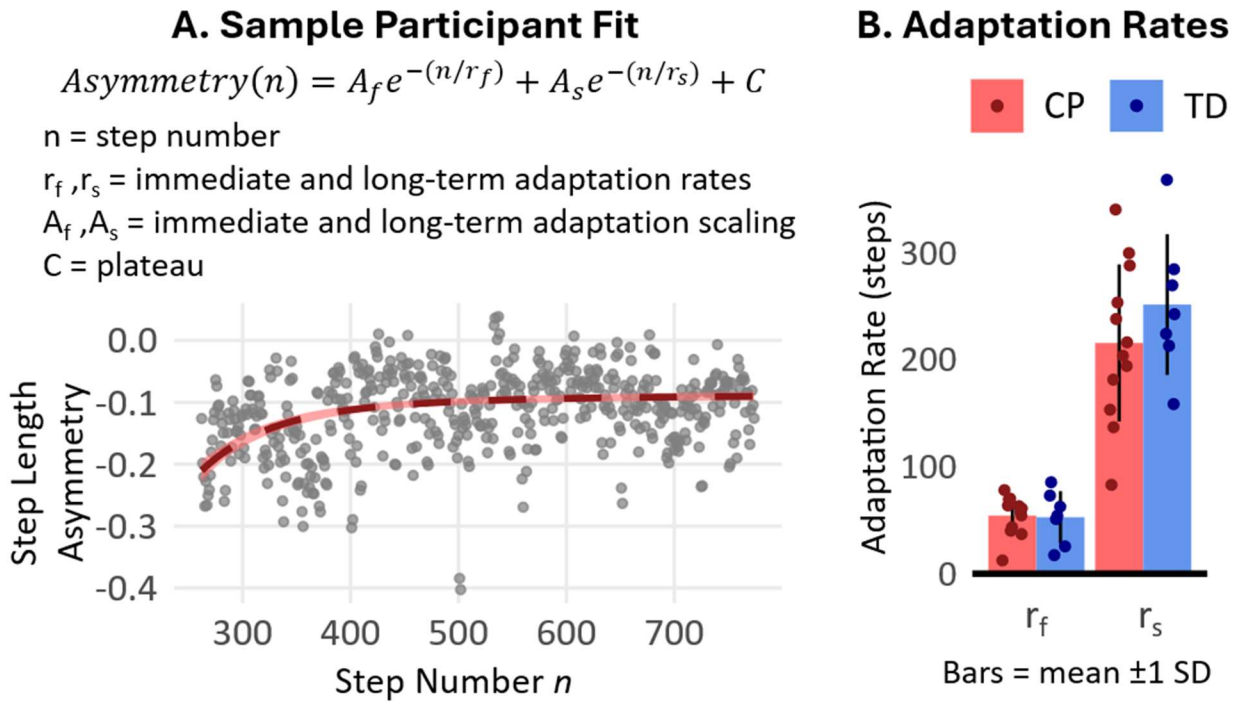
Results

Examining the first and last 10 steps, both cohorts exhibited asymmetry early (average: CP=-0.16; TD=-0.10) and adapted toward symmetry after six minutes (CP=-0.06; TD=-0.04). The immediate adaptation was similar between groups, with a rate of 54±18 (average±SD) steps for CP and 52±24 for TD. The long-term adaptation was smaller (faster) for children with CP at 216±73 steps compared to 252±66 steps for TD.

Discussion

Children with CP adapted similarly to TD peers, with slightly smaller long-term rates. Prior work postulated that having high energetic demands prompts a need to adapt quickly [3], which may explain the smaller rates observed for CP. The Bayesian approach provides a framework to model individualized responses that can inform personalized rehabilitation.

Images (Optional)



References (Optional)

[1] Dorelle Hinton *et al.*, Neuroscience 2020 [2] Sarah Brinkerhoff *et al.*, PLOS One 2023 [3] Sarah Brinkerhoff *et al.*, J Experimental Biology, 2024

Acknowledgements (Optional)

Funding for this research was provided by R01NS091056. We also thank Jennifer Nelson, Rocio Riveros-Charry, Mahamed Abdulahi, and Marissa Esterley for their assistance in collecting data.

Session Category

Clinical Biomechanics: N/A

OA27-03

Examining the Effects of Selective Dorsal Rhizotomy on Kinematics and Synergistic Muscle Activity During Gait in Individuals with Cerebral Palsy

Ms. Amanda L. Vinson MS[1], Mrs. Jessica L. Stockhausen MS[2,1], Dr. James J. Carollo PhD, PE[1,2], Dr. Joyce Oleszek MD[1], Dr. Jason T. Rhodes MD[2,1], Dr. Sayan De MD[2,1], Dr. Kellen T. Krajewski PhD[2,1]

[1]Children's Hospital Colorado, Aurora, CO, United States. [2]University of Colorado School of Medicine, Aurora, CO, United States

Introduction

Spastic cerebral palsy (CP) is characterized by muscle reflex hyperactivity and impaired gait. Selective dorsal rhizotomy (SDR) is a neurosurgical intervention to reduce spasticity that may indirectly improve gait. The purpose was to examine changes in kinematics and muscle activity in individuals with spastic cerebral palsy pre- and post-SDR during overground walking.

Methods

Eight patients with CP who underwent SDR (6M, 2F; 7.6±1.0y/o at SDR) completed overground walking at self-selected speeds. Kinematics (Fs=120Hz) and electromyography (Fs=2160Hz) were collected for six bilateral lower extremity muscles. Dynamic sagittal joint excursions and timing of peak muscle activity were extracted for stance and swing gait periods. Non-negative matrix factorization (NNMF) was used to assess muscle synergies, and total Variance Accounted For (VAF) for one synergy were calculated. Differences pre- and post-SDR were assessed using random effects linear mixed models ($\alpha \leq 0.05$).

Results

See **Figure 1** for kinematics with EMG and NNMF results. Peak hip extension decreased during stance post-SDR ($p=0.043$, 95% CI:-11.06º – -0.50º). Peak knee flexion increased during swing post-SDR ($p=0.002$, 95% CI:3.86 – 14.0). Peak ankle dorsiflexion increased post-SDR during stance ($p<0.001$, 95% CI:9.60º – 27.3º) and swing ($p<0.001$, 95% CI:10.2º – 23.72º). Peak ankle plantarflexion increased post-SDR during stance ($p<0.001$, 95% CI:11.7º – 30.1º) and swing ($p<0.001$, 95% CI:10.6º – 27.8º). Knee and hip excursion increased post-SDR during stance (Knee: $p=0.009$, 95% CI:1.06º – 6.65º; $p<0.001$, 95% CI:4.41º – 9.63º) and swing (Knee: $p<0.001$, 95% CI:7.03º – 13.7º; Hip: $p<0.001$, 95% CI:-3.15º – 7.97º). Peroneal longus and gastrocnemius peak timing during stance occurred

later post-SDR (Peroneal longus: p=0.029, 95% CI:1.52% – 17.4%; Gastrocnemius: p=0.008, 95% CI:2.37% – 12.0%). VAF increased post-SDR (p=0.014, 95% CI:0.007–0.050).

Discussion

Changes in kinematics post-SDR improved gait patterns as patients had larger knee and ankle excursions to better achieve critical events recognized in typically developed gait patterns, such as increased clearance for swing limb advancement. The small changes in muscle activity post-SDR indicate a slight reduction in neuromuscular control complexity potentially due to reduced somatosensory input from the procedure. While a more simplified neuromuscular control system continues to deviate from patterns identified in typically developed individuals, the reduction in muscle tone for this population improved ambulation.

Images (Optional)

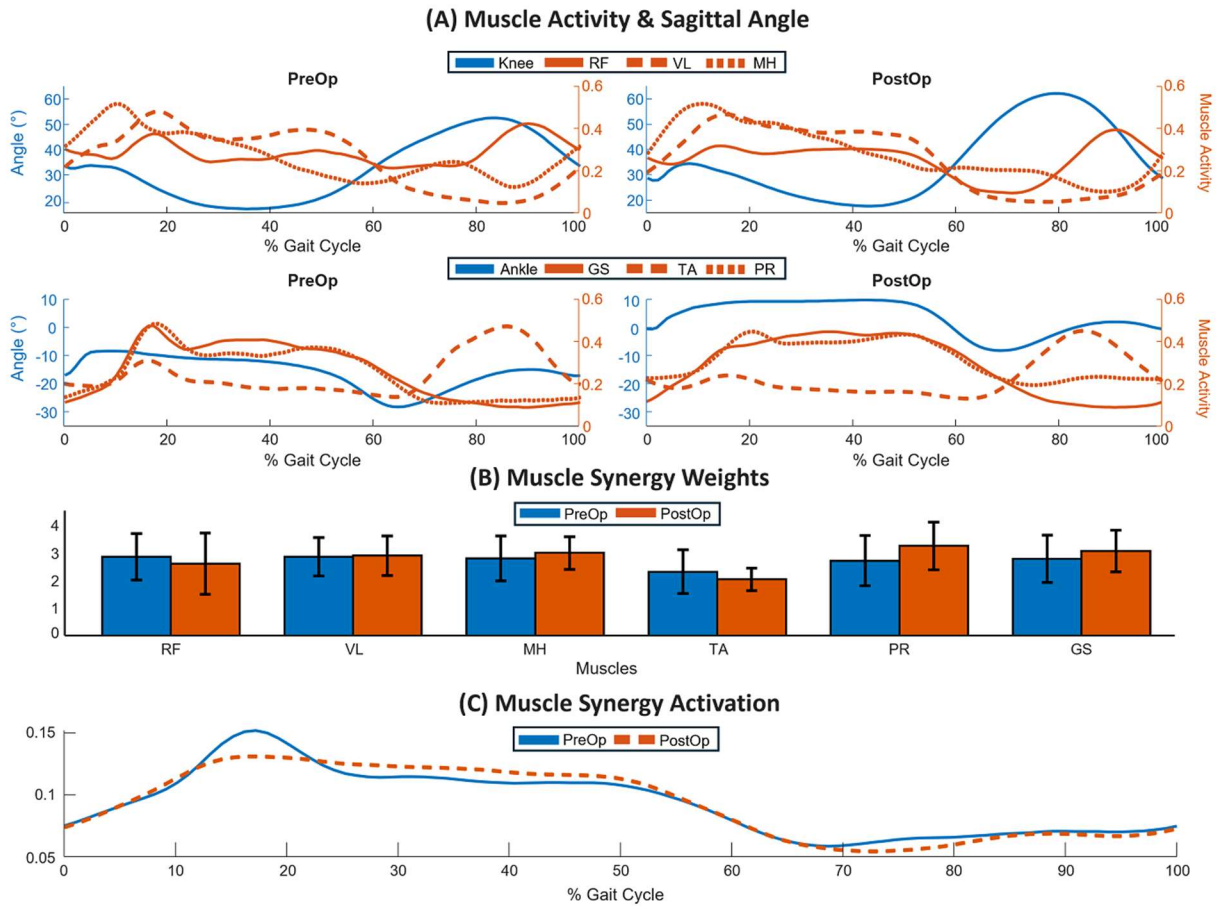


Figure 1. (A) Comparison of muscle activity & sagittal joint angle for the upper and lower leg during a gait cycle (heel-strike to heel-strike). Positive joint angles indicate knee flexion or ankle dorsiflexion, and negative joint angles indicate knee extension or ankle plantarflexion. Muscle activity was normalized to peak magnitude, with 0 indicating 0% and 1 indicating 100% of peak magnitude. Non-negative matrix factorization for one synergy (B) weights and (C) activation of that synergy during a gait cycle. RF=Rectus femoris; VL=Vastus lateralis; MH=Medial hamstring; TA=Tibialis Anterior; PR=Peroneal; GS=Gastrocnemius.

References (Optional)

Session Category

Clinical Biomechanics: N/A

OA27-04

Children with Unilateral Spastic Cerebral Palsy Have Smaller and Weaker Distal Tibias in the Spastic Limb Compared to the Non-Spastic Limb Independent of Physical Activity Habits

Dr Kellen Krajewski PhD[1,2], Mrs Jessica Stockhausen MS[1,2], Dr Julio Carballido-Gamio PhD[1], Dr Jason Rhodes MD[2,1], Dr David Howell PhD[1,2], Dr Sayan De MD[2,1], Dr Patrick Carry PhD[1,2], Dr Christine Swanson MD, MCR[1,3]

[1]University of Colorado School of Medicine, Aurora, CO, United States. [2]Children's Hospital Colorado, Aurora, CO, United States. [3]Veteran Affairs Eastern Colorado Geriatric Research, Education, and Clinical Center (GRECC), Aurora, CO, United States

Introduction

Cerebral palsy (CP) is a neurological condition associated with increased fracture risk even in ambulatory individuals with mild CP (gross motor function classification system (GMFCS) levels I-II). Bone microarchitecture, referred to as bone quality, is believed to reflect mechanical loading history and deficient microarchitecture has been implicated in fracture risk. It is unknown if microarchitecture differs in the area affected by spasticity and whether microarchitecture is associated with physical activity habits in the CP population. The purpose was to examine the difference in tibial microarchitecture between the spastic and non-spastic limbs in children with CP and to examine the association between physical activity habits with spastic limb tibial microarchitecture.

Methods

Ambulatory children with unilateral spastic CP (GMFCS I-II) affecting muscles crossing the ankle completed bilateral high-resolution peripheral quantitative computed tomography (HR-pQCT) scans of the distal tibia metaphysis (4% site) to assess microarchitecture metrics. Metrics were then used to conduct a finite element analysis, modeling a uniaxial compression stress test yielding stiffness and failure load estimates. To assess physical activity habits, participants completed the bone specific physical activity questionnaire (BPAQ) which estimates osteogenic potential based on cumulative mechanical loading exposure. Paired t-test were used to assess tibial microarchitecture metrics between limbs. Linear regressions were conducted to assess the association between BPAQ and tibial microarchitecture. Alpha set $p \leq 0.05$.

Results

18 participants (6 males, 12 females; 7.6±1.5years; 124.8±14.2cm; 26.7±7.7kg) had usable scans for both limbs and were included. See **Table 1** for tibial microarchitecture metrics

stratified by limb and results of between-limb comparisons. Total area, trabecular area, cortical area, cortical perimeter, cortical thickness, stiffness, and failure load were less in the spastic limb than the non-spastic limb. There were no significant associations between BPAQ scores and tibial microarchitecture.

Discussion

The distal tibia metaphysis of the spastic limb had similar bone density but was smaller and weaker compared to the non-spastic limb. Differences in bone quality likely accounted for between-limb differences in estimated bone strength. Altered mechanical loading patterns specific to the spastic limb may explain lack of association between microarchitecture and BPAQ, but prospective research is needed to confirm this mechanism.

Images (Optional)

	Parameter	Non-Spastic Limb	Spastic Limb	p value	Effect Size (Cohen's d)
Total	**LL (mm)**	**281.86±34.86**	**279.50±31.13**	**0.023**	**0.591**
	TtAr (mm^2)	**368.68±57.61**	**348.68±51.46**	**0.013**	**0.657**
	TtvBMD (mg HA/cm^3)	228.09±30.73	218.53±43.66	0.133	0.372
Trabecular	**TrAr (mm^2)**	**316.96±54.14**	**301.37±49.19**	**0.035**	**0.539**
	TrMetaAr (mm^2)	**128.16±21.75**	**121.91±19.78**	**0.035**	**0.540**
	TrInnAr (mm^2)	188.80±32.36	219.91±169.49	0.450	0.182
	TrvBMD (mg HA/cm^3)	141.02±24.19	135.03±33.19	0.266	0.271
	TrMetavBMD	215.54±26.41	211.37±36.79	0.488	0.167
	TrInnvBMD	90.42±23.47	83.18±32.51	0.180	0.329
	TrBV/TV (%)	0.19±0.05	0.19±0.05	0.268	0.270
	TrN (#)	1.31±0.12	1.28±0.25	0.509	0.159
	TrTh (mm)	0.23±0.23	0.23±0.23	0.112	0.395
	TrSp (mm)	0.74±0.09	0.80±0.23	0.211	0.306
	Tr1/NSD	0.31±0.07	0.40±0.25	0.104	0.405
Cortical	**CtAr (mm^2)**	**55.51±12.00**	**51.02±12.98**	**0.008**	**0.712**
	CtvBMD (mg HA/cm^3)	737.41±39.67	728.46±38.94	0.066	0.464
	CtPm (mm)	**73.34±5.82**	**71.28±5.41**	**0.012**	**0.664**
	CtPo (mm)	0.01±0.01	0.01±0.01	0.585	0.131
	CtTh (mm)	**0.87±0.17**	**0.81±0.21**	**0.046**	**0.509**
	CtPoDm (mm)	0.17±0.02	0.16±0.02	0.189	0.322
FEA	**Stiffness (N/mm)**	**73952±23391**	**66205±22310**	**0.010**	**0.678**
	Failure Load (kN)	**4145±1281**	**3707±1251**	**0.008**	**0.703**

Table 1. Distal tibia metaphysis bone microarchitecture parameters.
FEA=Finite element analysis based outcomes; LL=Limb length; TtAr=Total area; TtvBMD=Total volumetric bone mineral density; TrAr=Trabecular area; TrMetaAr=Trabecular and metaphyseal area; TrvBMD=Trabecular volumetric bone mineral density; TrBV/TV=Trabecular bone volume tissue volume fraction; TrN=Trabecular number; TrTh=Trabecular thickness; TrSpa=Trabecular spacing; CtAr=Cortical area; CtvBMD=Cortical volumetric bone density; CtPm=Cortical perimeter; CtPo=Cortical porosity; CtTh=Cortical thickness; CtPoDm=Cortical pore diameter;

Session Category

Clinical Biomechanics: N/A

OA27-05

Mediolateral Forces and Walking Stability in Children with Cerebral Palsy

Ms. Allyson Clarke[1], Dr. Andrew Ries[2], Dr. Michael Schwartz[2], Dr. Katherine Steele[1]

[1]University of Washington, Seattle, WA, United States. [2]Gillette Children's, St. Paul, MN, United States

Introduction

Children with cerebral palsy (CP) experience greater gait instability compared to typically developing (TD) peers when walking, increasing energetic costs and fall risk [1]. Children with CP often walk with increased step width (SW), minimum margin of stability (MMOS), and gait variability- indicating challenges with stability [2]. Applying mediolateral forces can improve gait stability for aging and poststroke individuals, and may promote stability for children with CP [3, 4]. The aim of this study was to evaluate how gait stability changes with mediolateral forces for children with CP and TD peers.

Methods

Twelve individuals with CP and 10 age-matched TD peers were recruited. Participants walked on a treadmill with mediolateral forces applied by a mechatronic system (Humotech) to mimic a hysteretic spring. Four spring stiffnesses between 50-1500 N/m were evaluated during 5-minute trials in randomized order. SW, MMOS, step length (SL), step width variability (SWV), and step length variability (SLV) were computed from motion capture, normalized to leg length (L), and assessed with Bayesian multilevel linear models.

Results

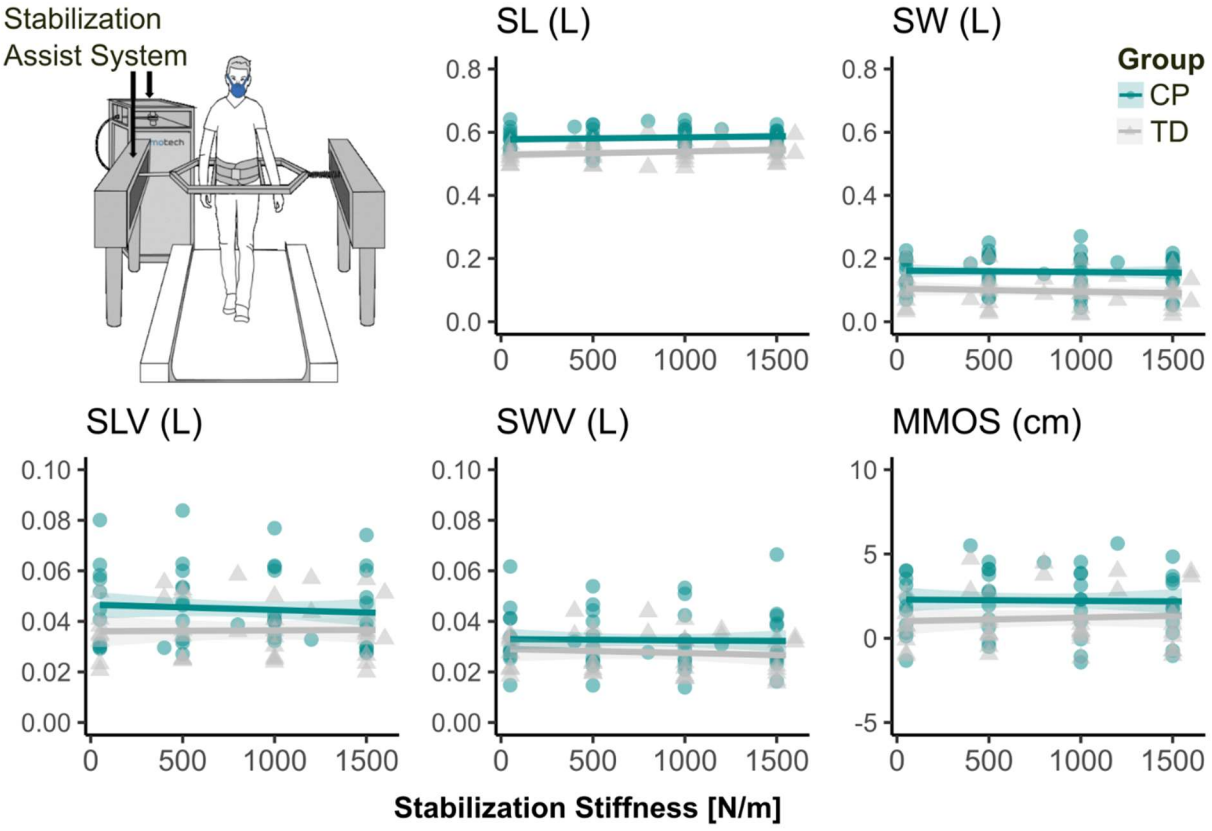
Across all conditions, the CP group had higher SW (average = 0.16L) and MMOS (average= 2.2cm) compared to TD peers (SW= 0.10L, MMOS= 1.0 cm). However, there were negligible changes in SW, SWV, SL, SLV, or MMOS with increasing stabilization stiffness for either group.

Discussion

Mediolateral forces mimicking a hysteretic spring applied via a mechatronic system did not impact biomechanical measures of stability for either group. These findings contrast prior literature, where SW, SWV, and MMOS decrease with mediolateral forces for nondisabled adults, aging adults, and individuals after stroke. Prior work has used linear springs in experimental design, but our use of a hysteretic spring may have affected responses. As we did not observe changes for the TD group, children may also be less responsive to mediolateral forces. Our use of Bayesian statistical methods, rather than typical

frequentist methods, allows for robust analysis of small datasets and a framework for analyses of null results.

Images (Optional)



References (Optional)

[1] Donelan et al., *JBiomech*, 2004 [2] Hof et al., *JBiomech*, 2005 [3] Dean et al., *TBME*, 2007 [4] Frame et al., *Clin Biomech,* 2020

Acknowledgements (Optional)

Supported by R21HD104112 and R01NS091056.

Session Category

Clinical Biomechanics: N/A

OA27-06

Active and Passive Force Variability Between Gracilis and Adductor Longus Muscle Fibres From Children With Cerebral Palsy

Mr. Faizan Syed[1], Mr. Latif Omerkhil[1], Ms. Sunnie Vuong[1], Ms. Ruth-Anne Seerattan[1], Dr. Jason Howard[2], Dr. Tim Leonard[1], Dr. Venus Joumaa[1], Dr. Walter Herzog[1]

[1]University of Calgary, Calgary, AB, Canada. [2]IWK Health Centre, Halifax, NS, Canada

Introduction

Cerebral palsy (CP) is associated with impaired muscle growth, contractures, and spasticity. Whole muscle and single fibre studies have shown variable passive stiffness, altered sarcomere lengths, fat infiltration and fibrosis in spastic muscles, but these investigations typically examined a single muscle. However, it remains unknown whether different spastic muscles within the same child demonstrate similar fibre mechanical properties or exhibit heterogeneous adaptations.

Methods

Biopsies of the GR and AL were obtained from 11 children with CP (Gross Motor Function Classification System levels IV–V). Skinned fibres (3–5 per biopsy) were mounted between a length controller and force transducer. Maximal active stress and instantaneous stiffness (rapid, short stretch) were measured at an average sarcomere length (SL) of 2.4μm, and passive steady-state stress was measured during stepwise stretches from SL 2.6–3.4μm.

Actin, myosin, titin, and nebulin content were quantified using SDS-PAGE. Collagen, fat, and fibre size were quantified using Picrosirius Red, Oil-Red-O, laminin staining, respectively.

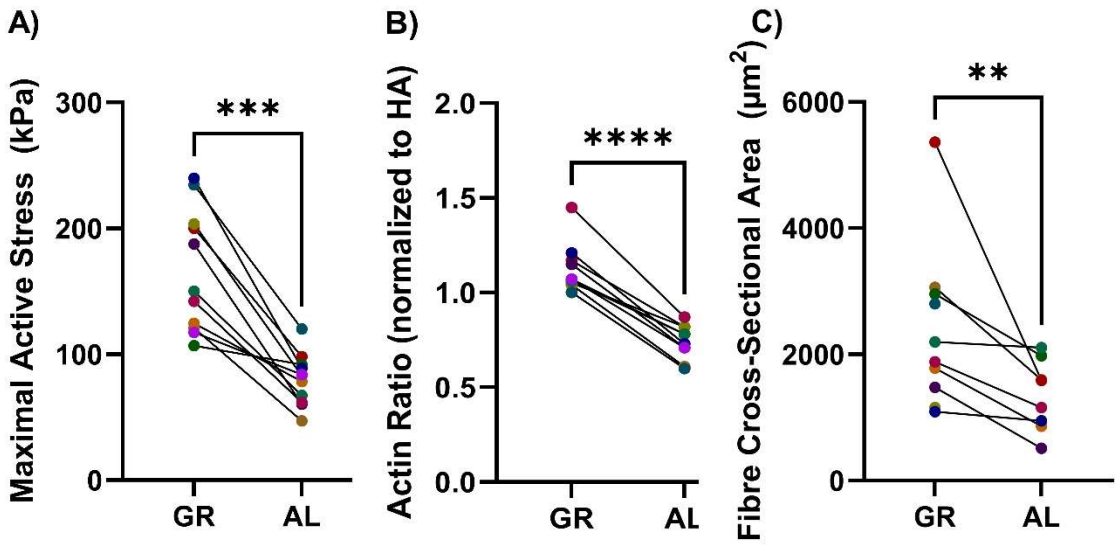
Results

Compared to GR, AL fibres produced significantly less maximal active stress (80 ± 20 vs. 166 ± 49 kPa, p=0.001), had lower instantaneous stiffness (5.5 ± 1.8 vs. 9.9 ± 3.0 MPa, p=0.003) and smaller fibres (1344 ± 564 vs. 2477 ± 1349 μm^2, p=0.008). Passive stress was significantly lower in AL at SLs of 3.0–3.4μm (p<0.05). Actin and nebulin content were approximately 35% (p<0.001) and 47% (p<0.01) lower, respectively, in AL than in GR. Myosin, titin, collagen, and fat content did not differ between muscles.

Discussion

Our results demonstrate muscle-specific heterogeneity in fibre properties in children with CP. Compared with GR, AL fibres are significantly smaller and weaker, possibly due to reduced actin content. Future work should explore the molecular mechanisms underlying these deficits and determine whether similar patterns occur in other spastic muscles of children with CP, so that particularly vulnerable muscles can be identified and considered when planning surgical and rehabilitative interventions.

Images (Optional)



References (Optional)

Session Category

Clinical Biomechanics: N/A

OA28-02

Sex-specific Effects of Load Carriage and Locomotion Speed on Achilles Tendon Loading

Mr. Charles Minerd[1], Mr. Fisher Adkisson[1], Dr. Patrick Corrigan PT, DPT, Ph.D.[2], Dr. Alex Reiter Ph.D.[1]

[1]Saint Louis University, St. Louis, MO, United States. [2]Cleveland Clinic, Cleveland, OH, United States

Introduction

Musculoskeletal injuries account for over two million medical visits annually among military personnel, with Achilles tendinopathies representing a leading cause.[1] The physical demands of military service, including marching, running, and load carriage, contribute substantially to these injuries.[2] Previous studies have examined load carriage effects on Achilles tendon loading during walking.[3,4] This study investigated load carriage during running and assessed sex-based adaptations.

Methods

Physically active adults completed treadmill trials under four conditions: walking (1.34 m/s) and running (3.13 m/s) with and without an additional 30 percent body-weight load. Achilles tendon loading was measured using a shear-wave tensiometer.[5] Tendon wave speed measurements captured with tensiometry were used to derive force via a previously established calibration technique.[5] Data were processed in MATLAB to time normalize each gait cycle and extract peak tendon force and impulse normalized to participant body weight. Differences in loading variables were analyzed with repeated measures linear mixed effects models ($p<0.05$); locomotion condition and sex were included as fixed effects.

Results

Fourteen adults participated in this study (7/7 males/females, age: 23.5±1.3 years, height: 1.78±0.09 m, mass: 74.0±11.8 kg). Peak force increased from walking without load carriage to walking with load carriage, as expected, but not between running without and with load carriage (Fig. 1A-B). However, impulse increased when load carriage was added within both walking and running (Fig 1A,C). Significant interactions ($p<0.001$) between sex and condition were observed across both variables, indicating that the response to load carriage and speed differed between sexes (Fig. 1B-C). This sex-based

difference was observed in tendon force during running without and with load carriage, and in impulse across all conditions (Fig. 1B-C).

Discussion

These findings suggest females employ different ankle strategies than men when running with and without load carriage, as indicated by reduced force. Differences in force and impulse will be compared with kinematics to better understand these adaptations. This insight may help guide training programs that reduce injury risk in military populations.

Images (Optional)

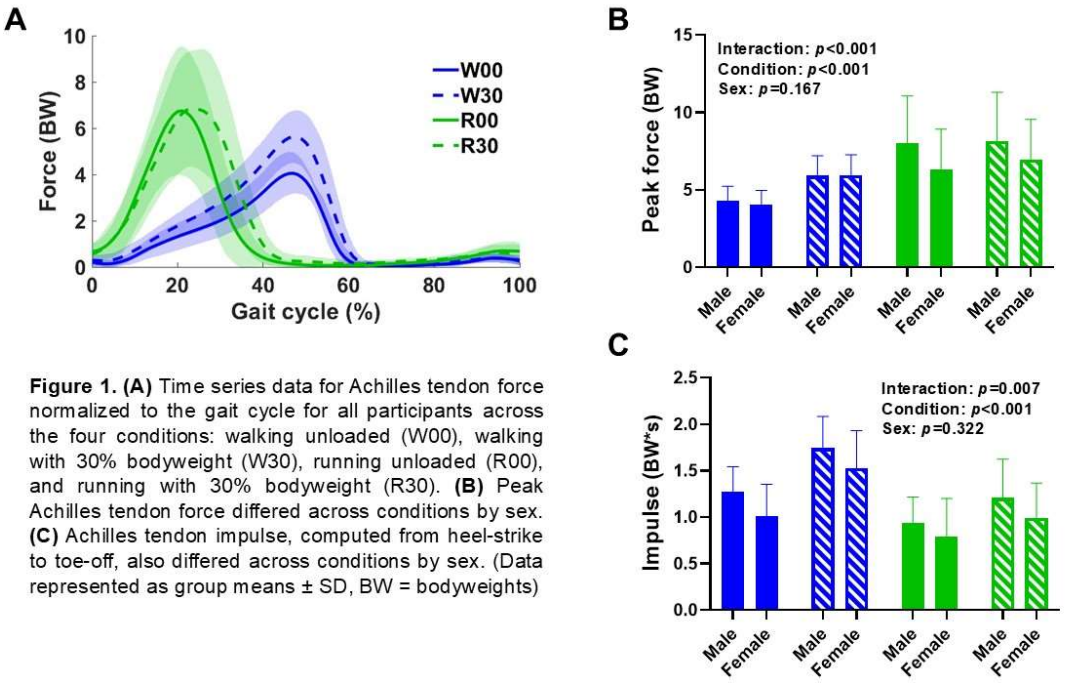


Figure 1. (A) Time series data for Achilles tendon force normalized to the gait cycle for all participants across the four conditions: walking unloaded (W00), walking with 30% bodyweight (W30), running unloaded (R00), and running with 30% bodyweight (R30). **(B)** Peak Achilles tendon force differed across conditions by sex. **(C)** Achilles tendon impulse, computed from heel-strike to toe-off, also differed across conditions by sex. (Data represented as group means ± SD, BW = bodyweights)

References (Optional)

[1] Fox, *JOOS*, 2020. [2] Knapik, *MilMed*, 2013. [3] Willy, *MilMed*, 2019. [4] Schmitz, *SciRob*, 2022. [5] Reiter, *MSSE*, 2024.

Acknowledgements (Optional)

Funding from the Saint Louis University Research Institute.

Session Category

Human Motion and Performance: Locomotion/Gait

OA28-03

Effect of an Ankle Assistive Device With Printed Textile-Based Motion Sensing Suit on Muscle Activation During Walking: A Pilot Study

Ms. Minyoung D. Cho, Dr. Pankwon Kim, Mr. Yundong Kim, Mr. Hyun Seong Shin, Mr. Eun Seong Jeon, Mr. Min Soo Park, Prof. Namkeun Kim, Prof. Sang Yup Kim, Prof. Seokhwan Jeong, Prof. Choongsoo S. Shin

Department of Mechanical Engineering, Sogang University, Seoul, Mapo-gu, Korea, Republic of

Introduction

Active ankle assistive devices can improve human walking performance with supporting plantarflexion[1]. The gastrocnemius and soleus play important roles as ankle plantarflexors[2], which generate propulsive power during late stance of walking[3]. Many conventional ankle assistive devices have relied on inertial measurement units or pressure type sensors[4] for gait event detection. However, kinematics can be inferred by strain of skin[5]. We developed an ankle assistive device with strain sensors printed directly onto the suit to control the device, eliminating the need for extra sensors. The purpose of this pilot study was to evaluate the effects of the developed ankle assistive device on selected muscle activation during walking.

Methods

Strain sensors were printed on the following locations: the middle of the anterior thigh, the medial side of the ankle, the Achilles tendon, and the patella. To control the device, a learning-based control algorithm was developed using synchronized sensor signals, joint kinematics of lower extremity, and ankle moment obtained from experimental trials. To assess the effect of the developed device, the electromyography (EMG) data of soleus and medial gastrocnemius (MG) were obtained from three healthy male participants during walked on treadmill at a speed of 3.5 km/h. The participants completed the tasks wearing the device under power-on and power-off conditions. The integrated EMG (iEMG) and the mean EMG during stance phase were compared between two conditions.

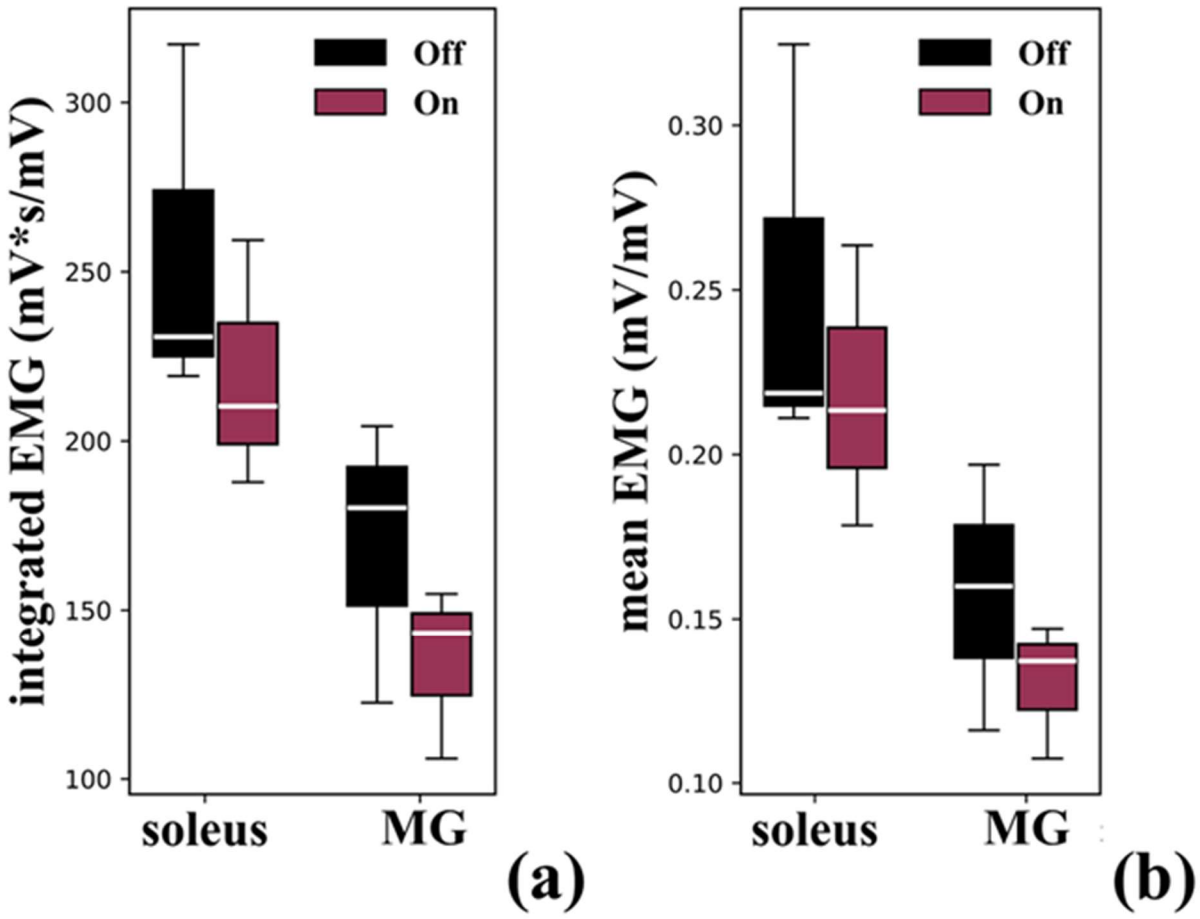
Results

During the stance phase, both mean EMG and iEMG of soleus and MG showed reduction under the power-on condition compared to power-off condition (mean EMG: soleus -13%, MG -18%; iEMG: soleus -14%, MG -20%).

Discussion

The observed reductions in ankle plantarflexor EMG activation suggest that the assistive torque generated by the ankle assistive device successfully supported the biological torque of ankle. In conclusion, our new developed ankle assistive device effectively reduced the muscular demand required for ankle plantarflexion during walking while maintaining the walking speed.

Images (Optional)



References (Optional)

[1] Weiqi Lin et al., *Technologies*, 2025

[2] Lenhart et al., *J Biomechanics*, 2014

[3] Meinders et al., *Scand J.Rehabil Med*, 1998

[4] Netukova et al., *Sensors*, 2022

[5] Mengüç et al., *Int.J.Robotics Research*, 2014

Acknowledgements (Optional)

This work is supported by the National Research Foundation (NRF) of Korea grant funded by the Korean Government through the Ministry of Science and Information Communication Technology (MSIT) (RS-2023-00218379).

Session Category

Human Motion and Performance: Locomotion/Gait

OA28-04

Determinants of Enhanced Propulsive Capacity When Walking With Powered Ankle Exoskeleton Assistance

Mr. Ethan Simaitis[1,2], Mr. Oluranti Olatosi[1,2], Dr. Michael Lewek PT, PhD[1,2], Dr. Jason Franz PhD[1,2]

[1]University of North Carolina at Chapel Hill, Chapel Hill, NC, United States. [2]North Carolina State University, Raleigh, NC, United States

Introduction

Human plantarflexor muscles are vulnerable to age- and disease-related decline, and conventional interventions fail to restore sufficient ankle push-off power in walking. Adaptive torque assistance via ankle exoskeletons (EXOs) offers a promising strategy to replace, or even supplement plantarflexor function during habitual walking to enhance *propulsive capacity* and community accessibility. Despite previously confirming this premise [1], the mechanistic determinants of EXO-enhanced propulsive capacity remain unclear. We hypothesized EXO assistance would increase propulsive capacity proportional to: (i) trailing limb angle (TLA) and (ii) total (Biological + EXO) ankle moment (AMOM) – mirroring known determinants of walking propulsion [2]. We also used invariant soleus excitation to confirm that participants maximized plantarflexor engagement, independent of EXO assistance.

Methods

Fifteen younger adults (age: 22.4 ± 3.0 yrs) walked at preferred speed on a treadmill wearing a powered ankle EXO (Biomotum) under four randomized assistance levels (0, 5, 15, 25% body weight [BW], peaks scaled to biological AMOM). At each assistance level, participants performed a 'biomechanical stress test' where an impeding force at the waist increased linearly at +1 %BW/s. The test terminated following an inexorable 0.5-m posterior displacement of the sacrum. We analyzed the stride immediately preceding termination.

Results

12 of 15 participants increased propulsive capacity (i.e., test duration and propulsive impulse, $p \leq 0.013$) without changes in soleus excitation when walking with assistance. Among those 12, the top-performing EXO condition had no effect on peak anterior ground reaction force (AGRF), peak TLA (**Fig 1A**), or peak AMOM (**Fig 1B**). Performance improvements correlated with changes in AGRF ($r^2=0.50$, $p=0.010$) but not in TLA nor AMOM. However, between-condition differences in AGRF correlated significantly with AMOM and TLA (multivariate $r^2=0.78$, $p<0.001$).

Discussion

EXO assistance preserved soleus muscle excitation while enhancing propulsive capacity during walking, but without concomitant changes in peak ankle joint moment or trailing limb posture. Significant between-condition correlations between propulsive capacity and biomechanical determinants suggest a common but unaccounted factor. The next step is to extend this approach to individuals with insufficient push-off (i.e., older adults).

Images (Optional)

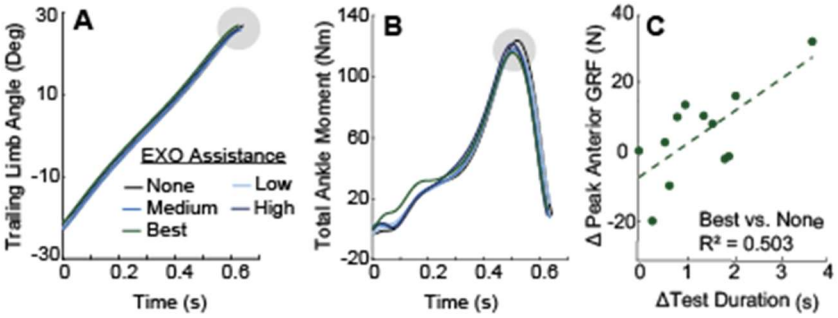


Figure 1. Determinants of walking propulsion - (A) trailing limb angle and (B) total peak ankle moment - across all exoskeleton assistance conditions (None, Low, Medium, High, and each participant's Best-performing condition, defined as the assistance level at which they achieved maximum propulsive capacity). EXO-related changes in trailing limb angle (A) and total peak ankle moment (B) together correlate with those in peak anterior GRF, which itself is positively correlated with those in propulsive capacity (C).

References (Optional)

[1] Simaitis et al. (2025) *ASB*. [2] Hsiao et al. (2015) *Hum Mov Sci*.

Session Category

Human Motion and Performance: Locomotion/Gait

OA28-05

Running With an Exotendon: Biomechanical Insights Into Metabolic Savings Across Running Speeds

Ms. Olivia Felton, Mr. Chadwick Healy, Mrs. Alaa Ahmed, Ms. Cara Gonzalez Welker

University of Colorado Boulder, Boulder, CO, United States

Introduction

Passive assistive devices can influence metabolic rate and alter running mechanics. Previously, the exotendon, a spring connecting a runner's legs, was shown to reduce metabolic rate by an average of 6.4% when running at 2.67 m/s [1]. Here, we examine individual biomechanical adaptations that influence these reductions and test whether the metabolic benefits of the exotendon persist across additional speeds.

Methods

Sixteen recreational runners completed treadmill running trials with and without the exotendon at 2.67 m/s. Participants that reduced metabolic rate with the exotendon subsequently completed trials at ±10% of their self-selected speeds. Metabolic rate was measured using indirect calorimetry, and joint kinematics were estimated using OpenCap [2]. Spatiotemporal parameters, joint angles, and ground reaction forces were analyzed to identify gait adaptations associated with metabolic changes when running with the exotendon at all speeds.

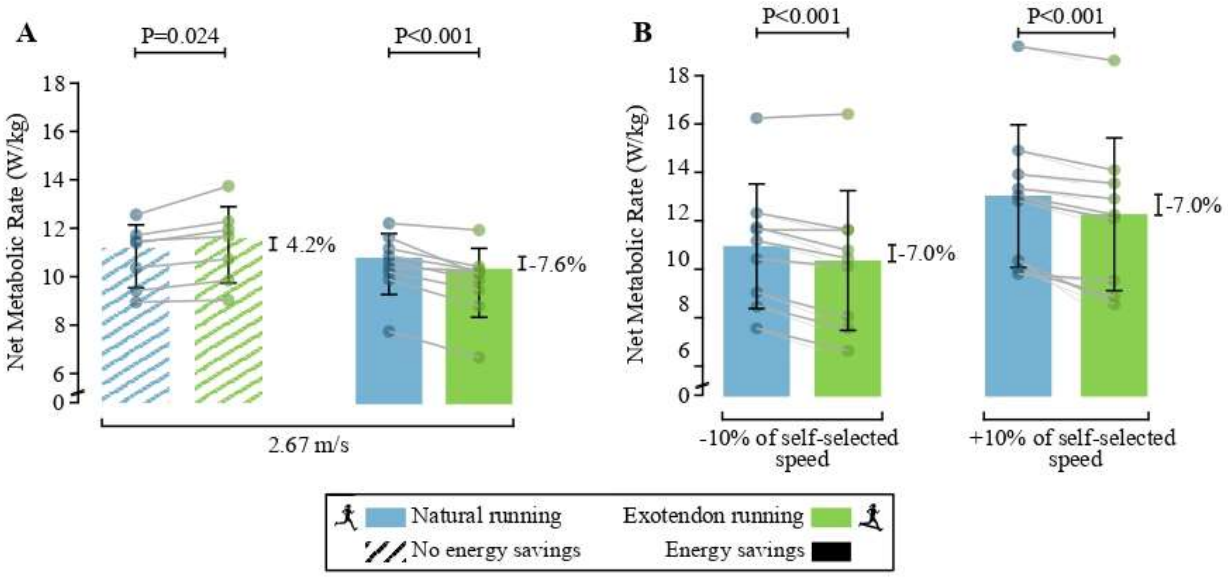
Results

Nine of sixteen participants reduced metabolic rate when running with the exotendon. Reductions in responders were associated with specific biomechanical adaptations, including increased stride frequency ($P<0.001$); decreased peak knee flexion angles ($P=0.04$); decreased peak hip flexion and extension angles ($P=0.01$, $P=0.004$, respectively); and lower peak vertical and horizontal ground reaction forces ($P<0.001$, $P<0.001$, respectively). For the participants who benefited at 2.67 m/s, metabolic reductions were consistent across speeds (see figure). The biomechanical patterns associated with metabolic savings at 2.67 m/s were consistent across speeds, suggesting that these gait adaptations influence metabolic benefits.

Discussion

This study demonstrates that the metabolic benefits of running with an exotendon generalize across speeds, but are selective for runners who adopt specific gait strategies. By promoting gait patterns associated with reduced peak joint angles and lower peak ground reaction forces, the exotendon may also offer additional benefits, such as reduced injury risk. A key limitation is the use of markerless motion capture, which may introduce small kinematic errors. These findings emphasize the importance of designing assistive devices that account for both metabolic efficiency and individual human adaptability. Future work should investigate long-term adaptation and real-world conditions to maximize the effectiveness of passive assistive technologies.

Images (Optional)



References (Optional)

[1] Simpson *et al*. J Exp Biol, 2019

[2] Uhlrich *et al.* PLoS Comput Biol, 2023

Session Category

Human Motion and Performance: Locomotion/Gait

OA29-02

Wrist Biomechanics During Handstands: Effect of Wrist Position on the Soft Tissues

Ms Mercedes Aramayo Gomes Rezende, Dr Angela Kedgley

Department of Bioengineering, Imperial College London, London, Greater London, United Kingdom

Ms Mercedes Aramayo Gomes Rezende

Introduction

Up to 88% of gymnasts experience wrist pain [1]. It is believed that this is related to the use of the upper extremities for weight bearing, where the wrist can reach extreme extension angles [1], subjecting the joint's soft tissues to high passive moments. It was hypothesised that doing handstands on parallettes, rather than on the floor, would decrease wrist extension, thereby decreasing the passive moments at the joint and protecting the soft tissues.

Methods

Ten participants (four females and six males, 29.3 ± 9.6 years) volunteered. Wrist extension [2] was measured with an optical motion capture system (Qualisys AB, Gothenburg, Sweden) during four 10 seconds assisted handstand tasks (two on the floor and two on parallettes). Passive moments were calculated from the wrist angles [3].

Based on Shapiro-Wilk tests for normality, paired t-tests or Wilcoxon Signed-Rank tests were used to compare maximum wrist extension angles and corresponding passive moments as a function of wrist position. Significance was defined as $p < 0.05$.

Results

No differences were found due to hand dominance; therefore, averages of right and left hands across the four trials were taken. Handstands on the floor had greater wrist extension angles (by 12.7°) and passive moments (by 280 N.mm) compared to those on the parallettes ($p \leq 0.005$, Figure 1).

Discussion

Handstands on the floor had a wider range of passive moments than those on the parallettes (Figure 1C). This was because passive moments exponentially increased when

approaching the maximum range of motion [3] (Figure 1A). At extreme extension angles the palmar ligaments' lengths can increase by up to 25% [4]. By performing handstands on parallettes, wrist extension angles decrease, potentially decreasing wrist pain prevalence as the ligaments are be subjected to less elongation.

Images (Optional)

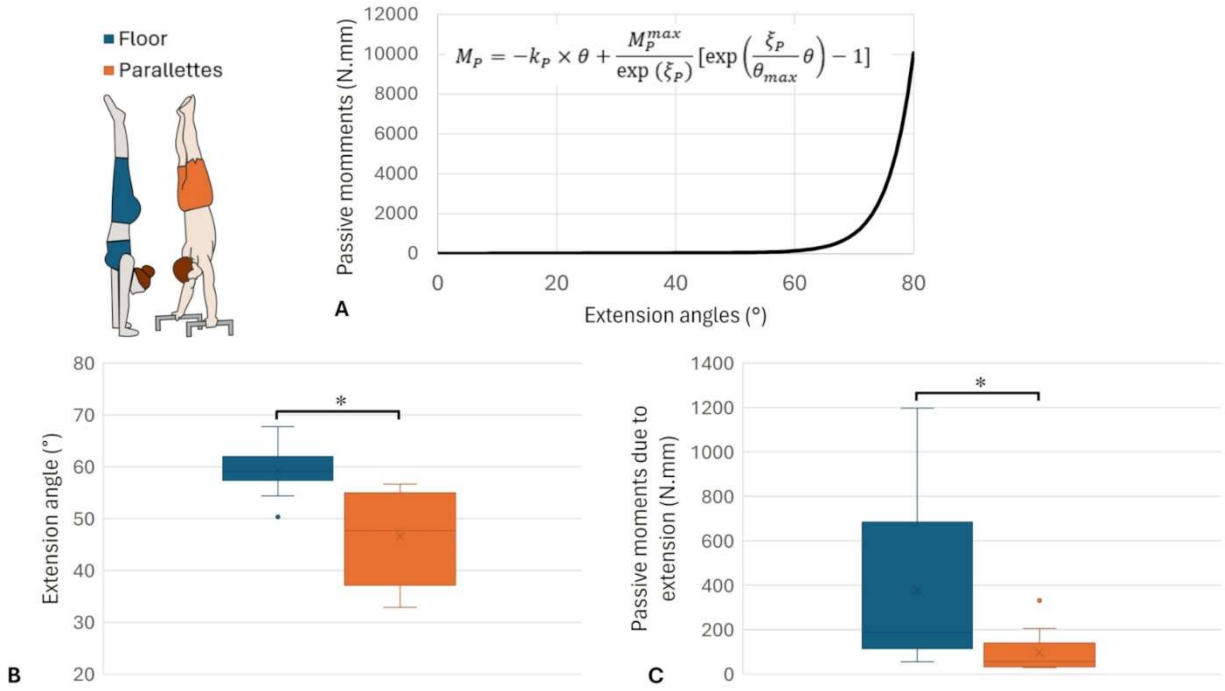


Figure 1: (A) Passive moments (M_P) as a function of wrist extension angle (θ), where M_P^{max} is the maximal passive moment, θ_{max} is the joint angle at which the maximal passive moment occurs, k_P is the linear stiffness and ξ_P is the shape parameter for the non-linear elastic component [3]. (B) Wrist extension angle and (C) passive moments compared between handstand on the floor and parallettes. * indicates p ≤ 0.005.

References (Optional)

[1] Benjamin Mauck *et al.* , Orthop Clin North Am, 2020

[2] Oluwalogbon Akinnola *et al.* , J Biomech, 2021

[3] Benjamin Goislard De Monsabert *et al.* , Ann Biomed Eng, 2018

[4] Jun Tan *et al.* , J Hand Surg Eur Vol, 2014

Acknowledgements (Optional)

MAGR work was supported by FCT – Fundação para a Ciência e Tecnologia (https://doi.org/10.54499/2023.00375.BD)

Session Category

OA29-03

Scapulo- and Humerothoracic Kinematics of a Simulated Volleyball Spike Using Biplane Videoradiography

Dr. Aaron Hellem DPT, PhD, Dr. Arin Ellingson PhD, Dr. Paula Ludewig PT, PhD

University of Minnesota, Minneapolis, MN, United States

Introduction

Kinematics literature for the shoulder in overhead sports is dominated by optical surface motion capture despite significant limitations associated with skin motion artifact [1,2]. The purpose of this analysis was to describe scapulothoracic (ST) and humerothoracic (HT) kinematics of a simulated volleyball spike minimizing the limitation of skin motion artifact associated with surface motion capture.

Methods

17 volleyball players (8M, 14R, mean age 24.1) without play-limiting shoulder pain were included in this cross-sectional, descriptive analysis. Biplanar videoradiography (BVR) captured subject-specific kinematics of a simulated volleyball spike. CT scans of the scapula and humerus were obtained and semi-automated 2D/3D shape matching performed to align digitally reconstructed radiographs to BVR images. Kinematics Toolbox [3] was employed to extract and describe (mean ± 1SD) ST and HT kinematics relative to the trunk using YX'Z'' and XZ'Y'' rotation sequences. Rotations are expressed using the R-hand rule.

Results

Mean ST initial position was 36.1° ± 12.85 internal rotation; -2.1° ± 6.93 upward rotation; and -8.8° ± 7.55 of anterior tilt. Mean HT initial position was -6.3° ± 7.3 elevation; 2.3° ± 8.1 anterior to the scapular plane; and -51.1° ± 19.6 of external rotation (ER). The scapula achieved mean maximum external rotation of -25.7° ± 20.3, upward rotation of -49.5° ± 5.9, and a peak of posterior tilt (~22°) just prior to arm cocking (i.e. maximum ER). This was followed by rapid IR, downward rotation, and anterior tilt of the scapula during arm acceleration. The humerus reached mean maximum elevation of -149.6° ± 19.0 posterior to the plane of the scapula (-44.3° ± 17.6) and a mean maximum ER of -118.4° ± 21.5.

Discussion

This is the first study to describe ST and HT kinematics of a dynamic sporting task minimizing skin motion artifact. Qualitative comparison of these results with previous surface motion capture of the volleyball spike demonstrates similar HT elevation magnitudes and substantially smaller HT ER magnitudes suggesting that surface motion capture may overestimate HT ER [4]. This may be attributed to known skin motion artifact that is amplified in HT elevation angles greater than 120° and may grow with increasing movement velocity [1,5].

Images (Optional)

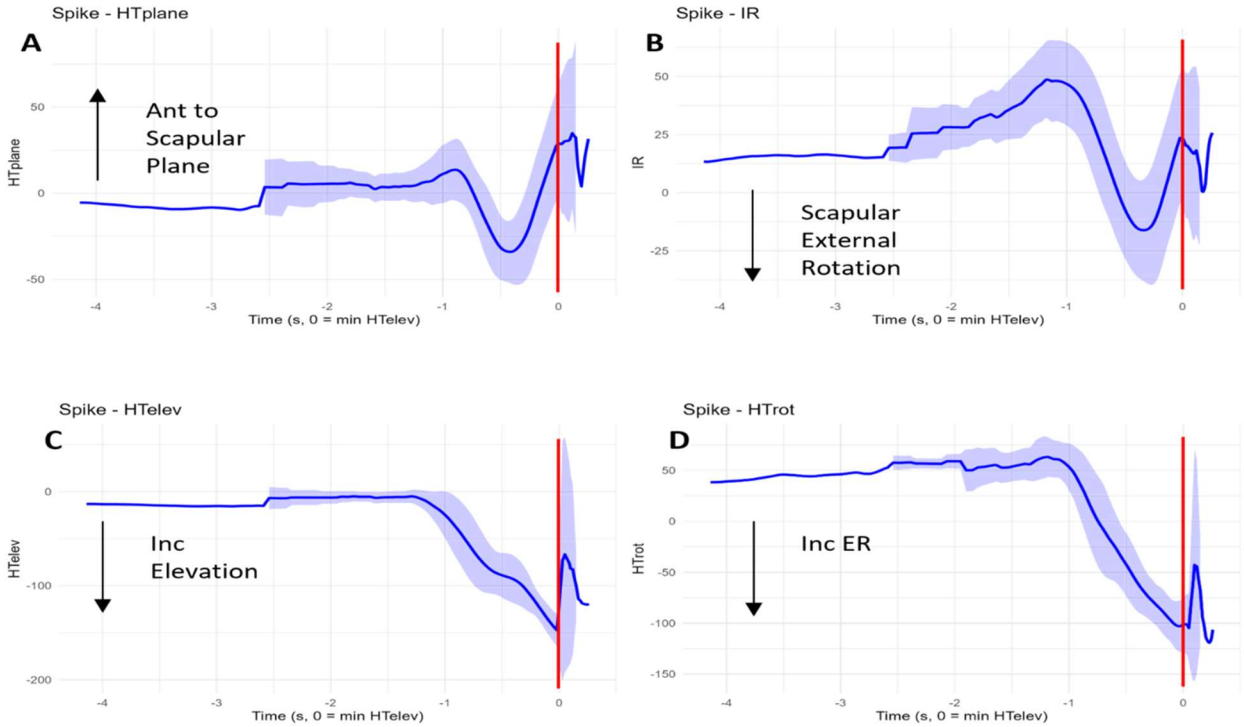


Figure 1. Scapulothoracic (left) and Humerothoracic (right) kinematics (mean ± 1 SD) of the Simulated Volleyball Spike centered at maximum elevation (t = 0, red line). Temporally, HT horizontal abduction peaked (A) just prior to ST ER (B), followed by maximum HT elevation (C) and ER (D) which occur almost simultaneously.

References (Optional)

[1]Karduna,JBiomechEng,2001[2]Benoit,Gait&Posture,2006[3]Lawrence,KinematicsToolbox,2023[4]Reeser,SportsHealth,2010[5]Hamming,JBiomechanics,2012

Session Category

Human Motion and Performance: Sports

OA29-04

Modulation of Rein Tension and Rider's Elbow Joint Angle in Show Jumping

PhD student Nolwenn Regnault[1], PhD Nicolas Bideau[1], PhD Agnès Olivier[2]

[1]M2S Laboratory, Bruz, Bretagne, France. [2]Institut Français du cheval et de l'équitation, Saumur, Pays de la Loire, France

Introduction

In show jumping, horse–rider pairs continually adapt to clear obstacles and manage varying constraints. Rider–horse dynamics have been examined through rein tension, which is naturally asymmetrical at the canter due to the gait itself [1]. Postural adjustments enable riders to modulate forces and compensate for these inherent imbalances [2]. This study therefore investigates how the presence of an obstacle influences dynamic variables of the rider–horse interaction.

Methods

Twelve amateur riders performed a canter jumping task on the same horse, equipped with IMUs (XSens MVN). Rein tension was recorded using instrumented strain-gauge reins (Shimmer Sensing). Riders completed six straight-line (SL) canters and four straight lines including an obstacle. Elbow flexion–extension and rein tension were analysed on straight lines and during the approach phase (AP). Right–left asymmetries were tested separately for right- and left-lead canter, and for inside vs. outside rein, using paired t-tests ($\alpha = 0.05$). Pearson correlations between rein tension and elbow angle were computed for each rider and condition.

Results

No significant right–left rein tension differences were found for SL right-lead, AP right-lead or AP left-lead canter. In SL left-lead canter, however, right-rein tension was higher (RR: 21.9 ± 5.4 N vs. LR: 18.3 ± 5.3 N, $p = 0.034$). Inside–outside comparisons showed no significant effects (table 1).

In SL, most riders showed significant negative correlations between rein tension and elbow angle ($r = –0.20$ to $–0.53$, $p < 0.05$). In AP, these correlations became more heterogeneous, with both positive and negative relationships observed among riders.

Discussion

These findings result partly support previously reported natural canter asymmetries [3]. The significant asymmetry found only in left-lead canter (RR > LR), together with the tendency for higher right-rein tension when cantering right, may reflect horses' lateral preferences. This asymmetry disappears in the approach phase, suggesting that riders standardise their rein aids before the jump. The increased variability in rein–elbow coordination during AP highlights individual adaptation strategies, potentially reflecting different technical approaches.

Images (Optional)

Type	Mesure	Right (mean±sd)	Left (mean±sd)	t_stat	p
SL Right-lead Canter	Rein tension (N)	24,9±9.4	21,8±4.8	1,627944	0,131814
SL Right-lead Canter	Elbow Flexion/Extension (°)	35,1±7.7	36,7±10.5	-0,64293	0,501762
SL Left-lead Canter	Rein tension (N)	21,9±5.4	18,3±5.3	2,427858	0,53344
SL Left-lead Canter	Elbow Flexion/Extension (°)	35,3±8.7	35,9±11.4	-0,26761	0,251639
AP Right-lead Canter	Rein tension (N)	31,5±11.6	30,6±9.2	0,405501	0,691704
AP Right-lead Canter	Elbow Flexion/Extension (°)	43,2±10.9	43,6±11.0	-0,15244	0,88118
AP Left-lead Canter	Rein tension (N)	34,1±15.2	30,4±12.6	1,312605	0,212018
AP Left-lead Canter	Elbow Flexion/Extension (°)	44,0±7.7	41,9±9.6	0,944825	0,361979
Type	**Mesure**	**Inside (mean±sd)**	**Outside (mean±sd)**	**t_stat**	**p**
SL Inside–outside	Rein tension (N)	21,6±5,5	21,9±4,7	-0,573845	0,577616
SL Inside–outside	Elbow Flexion/Extension (°)	35,5±8,9	35,9±8,6	-0,796753	0,442451
AP Inside–outside	Rein tension (N)	31,1±10,5	33,4±11,6	-1.6505	0.119618
AP Inside–outside	Elbow Flexion/Extension (°)	43,1±9,3	24,58072736	-0.89722	0.383774

References (Optional)

[1] Symes, D., & Ellis, R., *The Veterinary Journal*, *2009*

[2] Trabelsi, I. et al, *Computers in Biology and Medicine*, 2022

[3] Egenvall, A. et al, *Comparative Exercise Physiology*, *(2015)*

Session Category

Human Motion and Performance: Sports

OA29-05

Trunk and Arm Coordination in the Wheelchair Tennis Serve Across Athletes With Varied Abilities

Post Doctoral Research Fellow 1 Hannah Houde PhD.[1], Co-Director, Pathokinesiology Laboratory & Director, Rehabilitation Engineering Program Jeffrey Rankin PhD[2], Research Assistant Mia Siong BS[2], Assistant Professor Kathryn Lucas PhD, DPT[3], Assistant Professor Jennifer Gruenhagen PhD, DPT[4], Professor, Director of the Sealy Center on Aging, Co-Director NIA P30 UTMB Pepper Center Melissa Morrow PhD[1], Professor in the Departments Biological Sciences and Biomedical Engineering and Director of the Integrative and Evolutionary Biology Graduate Program Jill McNitt-Gray PhD[5]

[1]The University of Texas Medical Branch, Galveston, Texas, United States. [2]Rancho Los Amigos National Rehabilitation Center, Downey, CA, United States. [3]Creighton University, Pheonix, Arizona, United States. [4]Midwestern University, Glendale, Arizona, United States. [5]University of Southern California, Los Angeles, California, United States

Post Doctoral Research Fellow 1 Hannah Houde

Co-Director, Pathokinesiology Laboratory & Director, Rehabilitation Engineering Program Jeffrey Rankin

Research Assistant Mia Siong

Assistant Professor Kathryn Lucas

Assistant Professor Jennifer Gruenhagen

Professor, Director of the Sealy Center on Aging, Co-Director NIA P30 UTMB Pepper Center Melissa Morrow

Introduction

In adaptive sport, how an athlete's control strategy affects performance and injury risk remains poorly understood. For wheelchair tennis athletes, effective overhead serve mechanics are essential for improving performance and distributing upper-extremity loading [1-3]. This study examined trunk and arm contribution during the wheelchair tennis serve, hypothesizing that athletes with limited trunk control would display different control patterns than those with greater trunk control.

Methods

A convenience sample of wheelchair tennis athletes at different career stages performed serves during a practice session on an outdoor court. As part of a larger protocol assessing upper body strength (dominant arm girth, grip strength), power (medicine ball throw), and ROM (multidirectional reach), calibrated inertial measurement units (Equilibrium, Vayu Tech, 100 Hz) were secured to the wheelchair back and the lumbar, trunk, head, and bilateral upper arm and forearm segments to capture kinematics during the serve. Data from the Ball Toss, Execution, and Follow-Through phases were analyzed.

Results

Muscle strength and playing experience influenced serve kinematics (Table 1, exemplar athletes). Athlete 1, with reduced upper body power, showed limited trunk motion (13–25° max) across phases and used an arm-driven Ball Toss strategy (mean shoulder external rotation [ER]: 11°; max: −48°) with minimal ER during Execution (mean: 24°, max: 28°). Athlete 2, with impaired passive ROM and power, used a trunk–arm strategy, rotating the trunk away from the racket arm during Ball Toss (max: 24°), maintaining this trunk position during Execution (max: 22°) while externally rotating to −61°. Athlete 3, with full function, showed extensive trunk rotation during Toss and Execution (max: −73° and −43°, respectively), with reduced ER at Follow-Through. Peak shoulder ER occurred during Execution (max: −176°), indicating strong trunk–shoulder coupling to enhance serve performance.

Discussion

This exploratory series of case studies illustrates distinct serving strategies among wheelchair tennis athletes with varied impairment profiles. These results emphasize the need to consider an individual's trunk-shoulder coordination when designing training interventions to improve serve effectiveness and manage shoulder loading.

Images (Optional)

Athlete (Age, Sex, yrs playing tennis)	Arm Dominance	Functional Deficit	Serve outcome	Ball Toss: ER mean / max (°)	Ball Toss: trunk rot. mean / max (°)	Execution : ER mean / max (°)	Execution : trunk rot. mean / max (°)	Follow-Through : ER mean / max (°)	Follow-Through : trunk rot. mean / max (°)
1 (51, M, 16)	Right	MP	0	11.29 / −48.33	−5.18 / 13.00	24.26 / 27.68	18.94 / 24.69	−49.58 / −49.80	69.34 / 69.55
2 (55, M, 3)	Right	MP & ROM	1	−24.97 / 45.06	11.92 / 23.61	−61.16 / −59.31	21.02 / 21.57	−47.54 / −45.71	15.36 / 16.06
3 (63, M, 7)	Right	None	1	25.40 / 127.19	−60.75 / −72.54	−190.98 / −175.74	−36.49 / −43.01	−119.51 / −85.43	−15.50 / −29.08

References (Optional)

[1] Courel-Ibáñez, J., et al. (2022)

[2] Martin, C., et al. (2022)

[3] Reid, M., Elliott, B., & Alderson, J. (2007)

Acknowledgements (Optional)

Acknowledgements: Funding: Lakeshore Foundation (Grant #SSPC003); NSF DBI 2319710; ASB Up & Comer Award.

Session Category

Human Motion and Performance: Sports

OA30-02

Personalized Cardiac Mechanics: Evaluating Diffusion Tensor Imaging and Rule-Based Methods for Cardiomyocyte Orientation

Mr. Devin Seyler[1], Dr. Aaron Brown PhD[1], Dr. Tyler Cork PhD[1], Dr. Javiera Jilberto PhD[1], Dr. Luigi Perotti PhD[2], Dr. Daniel Ennis PhD[1], Dr. Alison Marsden PhD[1]

[1]Stanford University, Stanford, California, United States. [2]University of Central Florida, Orlando, Florida, United States

Introduction

Achieving clinically relevant accuracy for personalized cardiac biomechanics models requires assimilating extensive patient-specific data, including the complex, highly organized architecture of the myocardium. Cardiac diffusion tensor imaging (cDTI) can estimate aggregate cardiomyocyte orientation but is limited by physiological motion and low resolution *in vivo*. Consequently, Laplace-Dirichlet rule-based methods (LDRBMs) are widely used to algorithmically assign cardiomyocyte orientations but lack patient specificity [1]. Here, we present a method for tuning personalized cardiac models incorporating either ex vivo cDTI or LDRBM-derived cardiomyocyte orientations and investigate how this choice influences simulated ventricular function.

Methods

A biventricular model was generated from cine MRI of a healthy adult pig with corresponding LV pressure measurements and *ex vivo* cDTI [2]. Cardiac mechanics were simulated for both cDTI and LDRBM cardiomyocyte orientations using the open-source svMultiPhysics solver from SimVascular. The 3D model was coupled to a 0D lumped-parameter network tuned to match LV pressure and chamber volumes. Material parameters and an unloaded configuration were obtained via an inverse finite element method fitting the observed passive inflation [3]. A periodic active stress was prescribed using a double Hill model. Kinematics, pressures, and volumes were compared between simulations using cDTI-derived or LDRBM-derived cardiomyocytes.

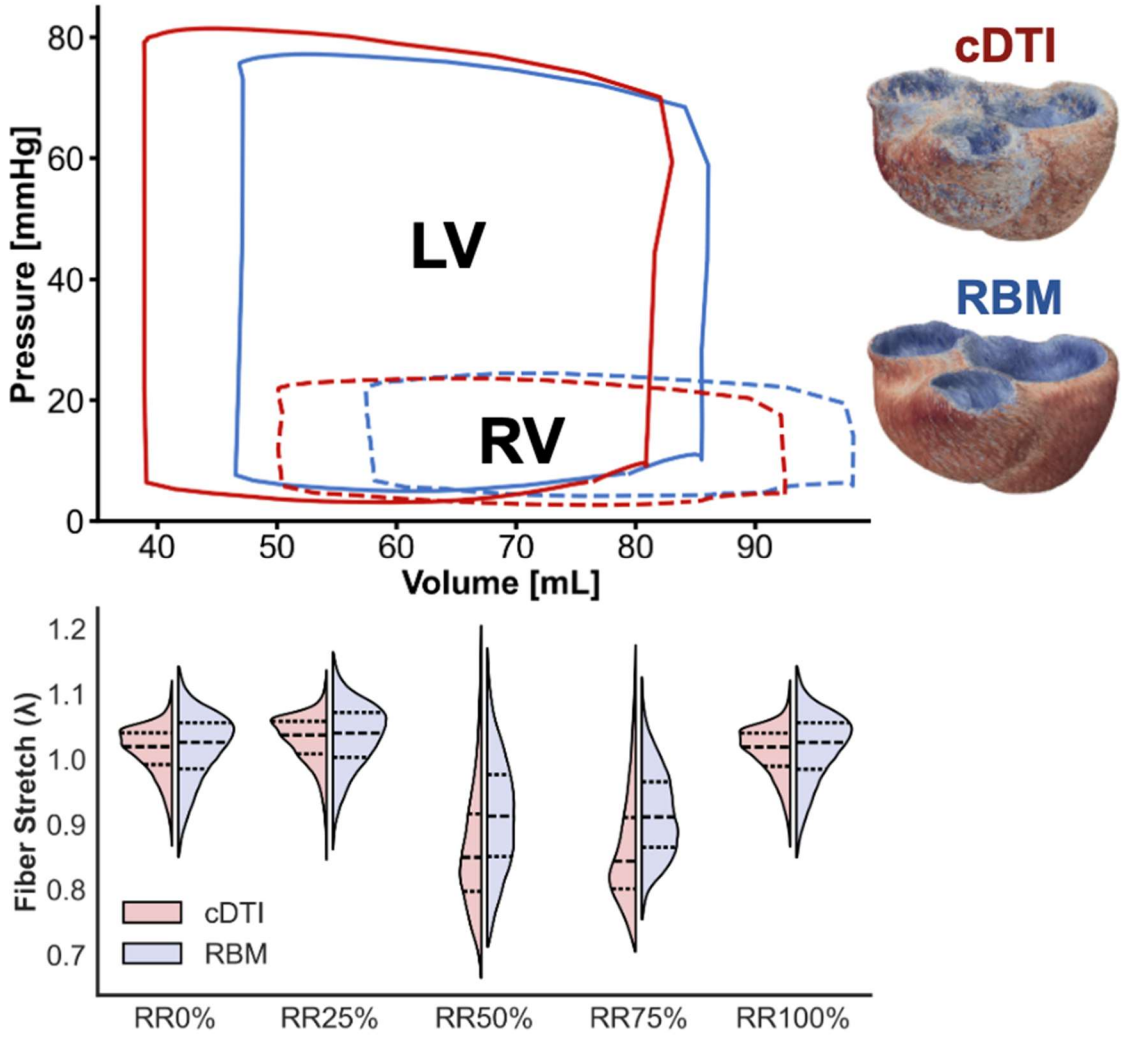
Results

Significant discrepancies exist between cDTI and LDRBM aggregate cardiomyocyte orientations, particularly near the apex (~45°) and within the RV (~40°). After tuning the LPN, all pressures and chamber volumes were within 10% of their *in vivo* targets. Preliminary simulation results demonstrate a greater LV ejection fraction using cDTI (53.2% vs 45.9%) and more homogenous fiber-stretch distribution.

Discussion

This work demonstrates a method for constructing subject-specific cardiac mechanics models and evaluating the impact of cardiomyocyte orientation. Observed kinematic differences between cDTI and LDRBM models indicate the need for RBMs with greater spatial variation. Future work will extend to congenital heart disease patients for whom deviations between LDRBMs and anatomy are likely more pronounced.

Images (Optional)



Top: Pressure-volume loops for cDTI and RBM models. cDTI exhibits a higher LV ejection fraction.
Bottom: Fiber stretch over the cardiac cycle. cDTI shows more uniform stretch during systole (RR50%).

References (Optional)

[1] Bayer, J.D. *et al.*, Ann Biomed Eng, 2012

[2] Cork, T.E. *et al*., Funct Imaging Model Heart, 2019

[3] Shi, L. et al., Comp Meth Appl Mech Eng, 2024

Acknowledgements (Optional)

NIH (R01HL173845), NSF GRFP

Session Category

Cardiovascular/Cardiorespiratory Biomechanics: Methods, Models and Applications

OA30-03

4D-Flow MRI Measurements and Computational Analyses of Pulsatile Cerebrospinal Fluid Flow in the Human Third Ventricle

Mr. Fuga USHIO[1], Assoc. Prof. Tomohiro OTANI PhD[1], Mr. Atsuhito TAISHAKU[2], Assoc. Prof. Shigeki YAMADA MD[2], Prof. Yoshiyuki WATANABE PhD[3], Prof. Shigeo WADA PhD[1]

[1]The University of Osaka, Toyonaka, Osaka, Japan. [2]Nagoya City University, Nagoya, Aichi, Japan. [3]Shiga University of Medical Science, Otsu, Shiga, Japan

Introduction

Cerebrospinal fluid (CSF) in the ventricular system exhibits bidirectional motion synchronized with cardiac pulsation and contributes to the transport of hormones and waste products, particularly within the third ventricle (3V) [1]. However, detailed flow patterns and their driving mechanisms remain unclear due to anatomical and physiological complexities. This study aimed to characterize 3V CSF flow and identify underlying mechanical factors by computational fluid dynamics (CFD) simulation based on four-dimensional flow magnetic resonance imaging (4D flow MRI).

Methods

CFD simulations of 3V CSF flow were performed following our previous study [2] using subject-specific MRI data (Fig. 1(a)). MRI-derived flow rate was imposed at cerebral aqueduct (CA), traction free was applied at foramen of Monro, and no-slip wall conditions were assigned on the ventricle surface (Fig. 1(b)). First, rigid walls were assumed and the total CSF flow rate through the 3V cross-section was compared between MRI and CFD. Next, prescribed wall motion was applied to the 3V superior-posterior region, which is anatomically formed by a thin membrane (velum interpositum) [3], to match the MRI-derived 3V total flow rate balance.

Results

Figure 1(c) shows time courses of the CSF flow rate through the 3V cross-section in MRI and CFD, and representative snapshots of CSF flow velocity on the midsagittal plane at cardiac systole. CFD results with rigid-wall assumptions markedly underestimated the 3V flow rate compared with MRI (Fig. 1(c)). Although the moving-wall assumption produced flow rates closer to MRI, local CSF flow velocity was still underestimated, particularly on the 3V inferior side.

Discussion

These results suggest that the 3V does not behave as a rigid conduit driven solely by the CA flow rate, and that pulsatile wall motion plays an essential role in forming actual CSF flow pattern. Further investigation of the wall motion to better reproduce local CSF flow distributions may provide new insights into 3V physiological functions.

Images (Optional)

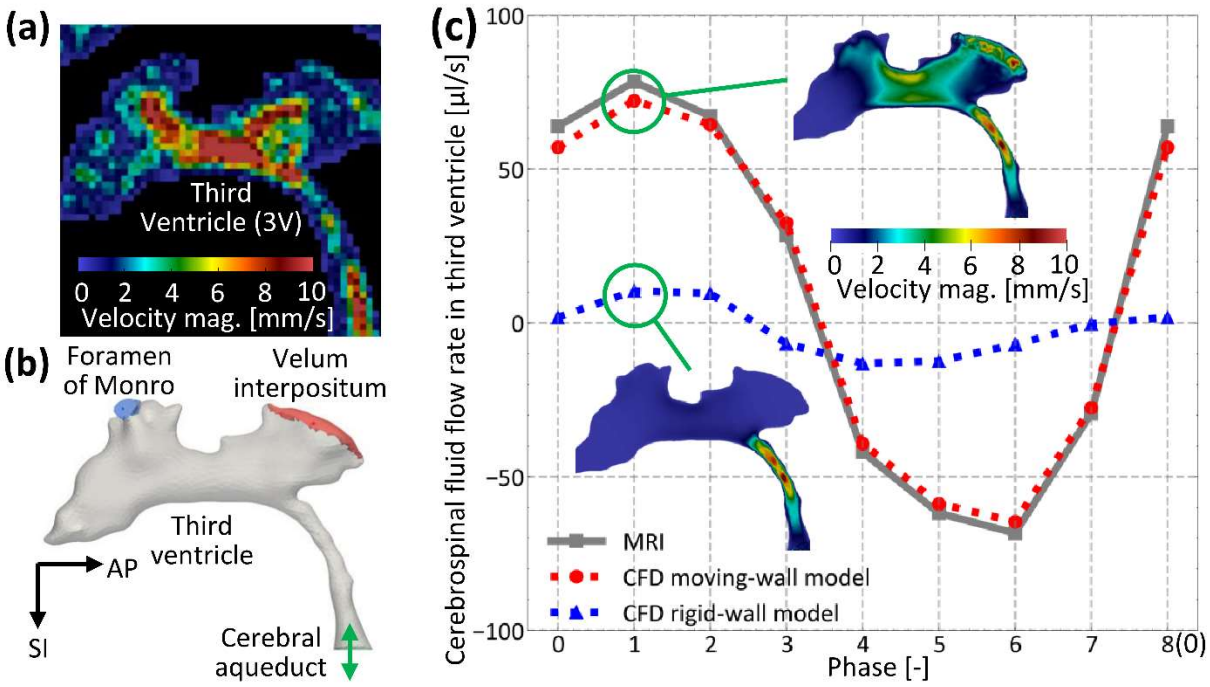


Fig. (a) Cerebrospinal fluid (CSF) flow velocity fields on the midsagittal plane in the third ventricle (3V) acquired from 4D flow MRI. Fig. (b) 3V geometry and boundary conditions. Fig. (c) Time courses of CSF flow rate in the 3V and representative snapshots of CSF flow computational simulations with rigid and moving-wall boundary conditions.

References (Optional)

[1] Wu et al., Neurobiol Aging, 2007

[2] Maeda et al., J Biomech, 2023

[3] Park et al., J Neurosurg: Pediatrics. 2011

Acknowledgements (Optional)

This study is partly supported by JSPS Scientific Research (23K11830, 24K02557, 25K03452) and MEXT program for promoting research on the Supercomputer Fugaku (JPMXP1020230118).

Session Category

Cardiovascular/Cardiorespiratory Biomechanics: Methods, Models and Applications

OA30-04

A Computational Fluid Dynamics Study of Human and Porcine Hearts: Implications for Cardiac Xenotransplantation

Dr. Chanikya Valeti, Dr. Sairam Pamulaparthi Venkata, Prof. Philip Cardiff

School of Mechanical and Materials Engineering, University College Dublin, Belfield, Dublin, Ireland

Dr. Chanikya Valeti

Dr. Sairam Pamulaparthi Venkata

Introduction

Cardiac transplants are widely used to treat patients with critical heart conditions. However, donor availability is a major limitation for the life-saving treatment. The University of Maryland School of Medicine recently demonstrated the potential of cardiac xenotransplantation: nonetheless, long-term success requires a deeper understanding of the physiological and biomechanical challenges introduced by anatomically dissimilar xenotransplants [1]. The present computational fluid dynamics study establishes numerical simulations for the analysis and comparison of the blood flow structures in human and porcine heart models.

Methods

Computational fluid dynamics is a powerful tool for analysing complex haemodynamics in the human circulatory system. Significant progress has been made in both computational and experimental analysis of the haemodynamics of the human heart: nonetheless, detailed cross-species examination of cardiac haemodynamics remains unexplored. Human and pig hearts are reconstructed from the CT data. The left atria and aortas are assumed rigid, whereas the left ventricles expands and contracts according to prescribed mesh movements over the cardiac cycle. A moving ventricle solver is developed in OpenFOAM to facilitate the dynamic mesh movements. Pressure conditions are specified at the pulmonary veins (inlets) and mass flowrates are prescribed at the aortas (outlet).

Results

Transient flow analyses are performed on both human and porcine left heart models. A custom left ventricle mesh motion procedure has been developed to approximate physiological chamber expansion and contraction. A stroke volume of 78 ml, and an ejection fraction of 56% are assumed for the human left ventricle. Blood is taken as the Newtonian, and wall-compliance effects are ignored. Various hemodynamic and biomechanical features, such as vortical structures, Q-criteria, Wall Shear Stresses (WSS), Oscillatory Shear Indices (OSI), Relative Residence Time (RRT), are compared between the porcine and human heart models.

Discussion

The genetically modified porcine model is a promising donor for xenotransplantation. Nonetheless the hemodynamic and biomechanical compatibility needs to be investigated considering significant anatomical dissimilarities between two heart models. The key anatomical difference is pigs have only two pulmonary veins, while human heart has four, which results in different flow partitioning into left atrium.

Images (Optional)

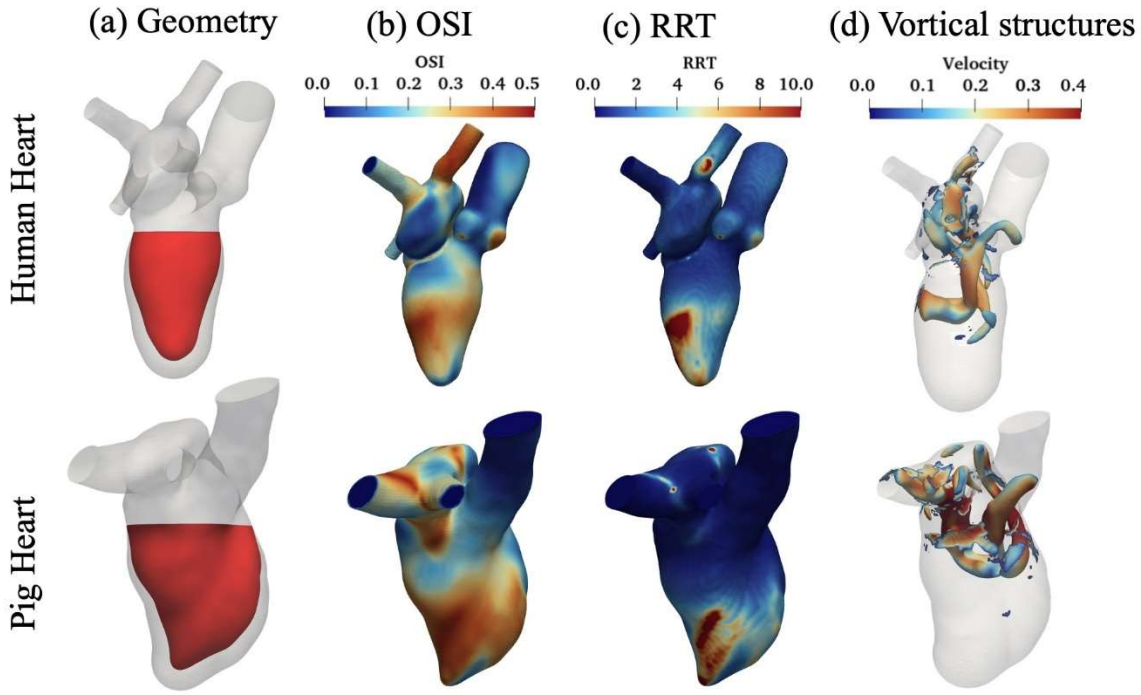


Fig: Top row represents the human heart model, and bottom row represents the pig heart model. (a) Left heart geometry at two instants of cardiac cycle: the moving ventricle patch is colored with red. (b) Oscillatory shear index. (c) Relative residence time and (d) Q-criteria: vortical structures at filling phase using threshold $300s^{-2}$ colored with velocity magnitude.

References (Optional)

[1] Griffith BP et al., 10.1056/NEJMoa2201422, New England Journal of Medicine.

Acknowledgements (Optional)

Funded by the European Union (ERC, XenoSim, 101088740). Views and opinions expressed are however those of the author(s) only and do not necessarily reflect those of the European Union or the European Research Council Executive Agency. Neither the European Union nor the granting authority can be held responsible for them.

Session Category

Cardiovascular/Cardiorespiratory Biomechanics: Methods, Models and Applications

OA30-05

Simulation of Purkinje-Mediated Left Bundle Branch Block and Cardiac Resynchronization Therapy

Dr Sandra Hager[1], Dr Vahid Ziaei-Rad[1], Dr Jenny Choy[2], Dr Mengjun Wang[2], Dr Ghassan Kassab[2], Dr Lik Chuan Lee[1]

[1]Michigan State University, East Lansing, Michigan, United States. [2]California Medical Innovations Institute, San Diego, California, United States

Introduction

Synchronized ventricular contraction is maintained by rapid electrical conduction through the Purkinje fiber network. Disruption of this conduction pathway, such as in left bundle branch block (LBBB), often associated with cardiomyopathy or valvular disease, leads to delayed ventricular excitation, mechanical dyssynchrony, and reduced cardiac performance. Understanding these conduction abnormalities and predicting the response of therapeutic interventions such as cardiac resynchronization therapy (CRT), requires a unified electromechanical modeling framework. In this work, we present a multiphysics model that couples cardiac electrophysiology, ventricular mechanics, and closed-loop hemodynamics in a biventricular (BiV) finite element modeling framework.

Methods

An idealized BiV geometry with rule-based fiber architecture was utilized [1]. A fractal-tree–based Purkinje network was generated using a modification of an existing algorithm and mapped onto the endocardial surfaces of both ventricles. Electrical activation was initiated at the His bundle and propagated within the Purkinje system and myocardium employing a modified FitzHugh–Nagumo (FHN) formulation with an anisotropic diffusion tensor, adapted to match physiological conduction properties in both tissues [2-4]. A transversely isotropic constitutive law was used to model time-varying active and passive myocardial stress [5]. Systemic and pulmonary hemodynamics were represented using a closed-loop circulatory model [6]. Left bundle branch block (LBBB) was introduced by setting diffusion in the left bundle branch to zero immediately after bifurcation from the His bundle. Cardiac resynchronization therapy (CRT) was simulated with a lateral left-ventricular epicardial pacing site.

Results

Baseline simulations reproduced physiological activation patterns, strain profiles, and pressure–volume dynamics (Figure 1). In the LBBB case, the myocardial wall was activated after 165ms, accompanied by reduced peak circumferential (Ecc) and

longitudinal (Ell) strains of -0.17 and –0.15, respectively. Standard CRT pacing improved ventricular synchrony, where the myocardium was activated after 100.5ms and peak strains were restored with Ecc = -0.18 and Ell = -0.16.

Discussion

This computational model provides a focused framework for examining the effects of LBBB and CRT pacing on ventricular electromechanics. Based on the modular model design, the framework can be extended to incorporate ischemic regions and alternative pacing strategies, such as His-bundle or left bundle branch pacing, and can be adapted for patient-specific simulations.

Images (Optional)

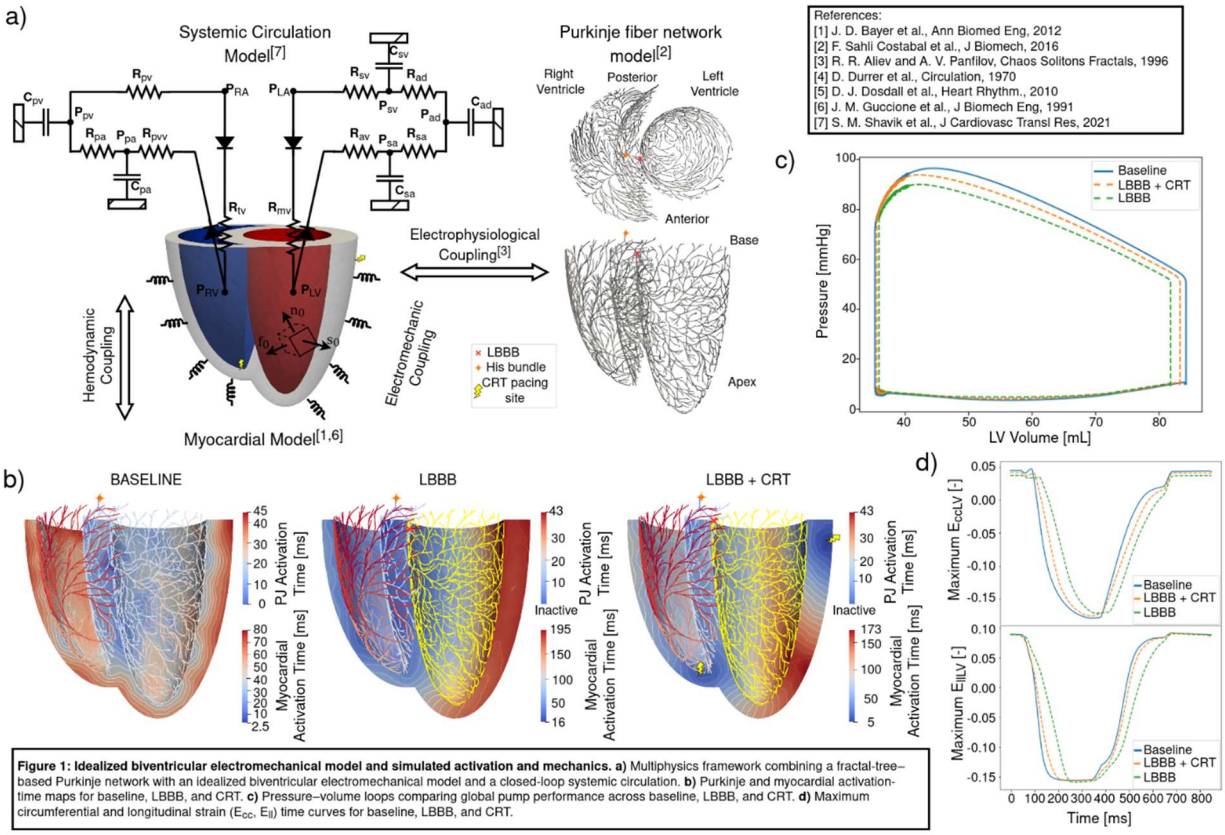


Figure 1: Idealized biventricular electromechanical model and simulated activation and mechanics. a) Multiphysics framework combining a fractal-tree–based Purkinje network with an idealized biventricular electromechanical model and a closed-loop systemic circulation. **b)** Purkinje and myocardial activation-time maps for baseline, LBBB, and CRT. **c)** Pressure–volume loops comparing global pump performance across baseline, LBBB, and CRT. **d)** Maximum circumferential and longitudinal strain (E_{cc}, E_{ll}) time curves for baseline, LBBB, and CRT.

References (Optional)

Session Category

Cardiovascular/Cardiorespiratory Biomechanics: Methods, Models and Applications

OA31-01

Integrating Paediatric Statistical Shape and Density Model Prediction to *in Silico* Finite Element Modelling of the Femur and Tibia

Miss Yidan Xu, Dr. Laura Carman, Professor Thor Besier, Dr. Julie Choisne

The University of Auckland, Auckland, Auckland, New Zealand

Introduction

Subject-specific Finite Element (FE) models have demonstrated high accuracy in biomechanical computations; however, they are limited by cost and time. Generic models are inaccurate for paediatric populations. To overcome these limitations, statistical shape-density models (SSDM) have shown promising results in predicting bone geometry and bone mineral densities (BMD) for FE analysis. The aim was to evaluate the accuracy of stress and strain distribution in personalised femoral and tibial FE models derived from paediatric SSDMs using different predictive inputs and algorithms.

Methods

SSDMs of the paediatric femur and tibia were built from 330 paediatric calibrated CT scans (136F, 12 ±5 y.o., N=657 femora and 652 tibiae)[1]. These SSDMs were used to predict femoral and tibial geometry and BMD in a leave-one-out analysis from the following inputs: 1) full medical imaging, 2) partial medical imaging (15% proximal and distal bone) and 3) no medical imaging. Three predicting algorithms were compared: 1) shape only fitting (bone geometry as input), 2) shape and density fitting (bone shape and BMD as input) and 3) Partial Least Squares Regression (from demographics). SSDM-based FE models were built based on each SSDM geometry and BMD prediction. Subject-specific FE models were built based on CT information. For each FE model, boundary conditions were applied to represent single-leg standing. Von Mises stress and 1st and 3rd principal strain from each SSDM-based model were compared to the subject-specific FE Model using element-wise normalised root-mean-square error (NRMSE).

Results

Femoral average NRMSEs for stress, 1st and 3rd principal strain were below 6%, 1% and 2% respectively, for all SSDM-based FE models. Tibial NRMSEs were higher (8%, 2%, and 5%, respectively). Adding medical imaging as input, compared to PLSR, reduced the average NRMSE for stress. Shape and density fitting further reduced stress errors and decreased

NRMSEs in the 1st and 3rd principal strains compared to shape-only fitting. Shape-only fitting with partial imaging produced similar errors to full shape-only fitting (Figure 1).

Discussion

Our SSDM-based FE models can accurately reproduce stress and strain distributions, approaching the gold standard. This is valuable in paediatric clinical settings where imaging is limited.

Images (Optional)

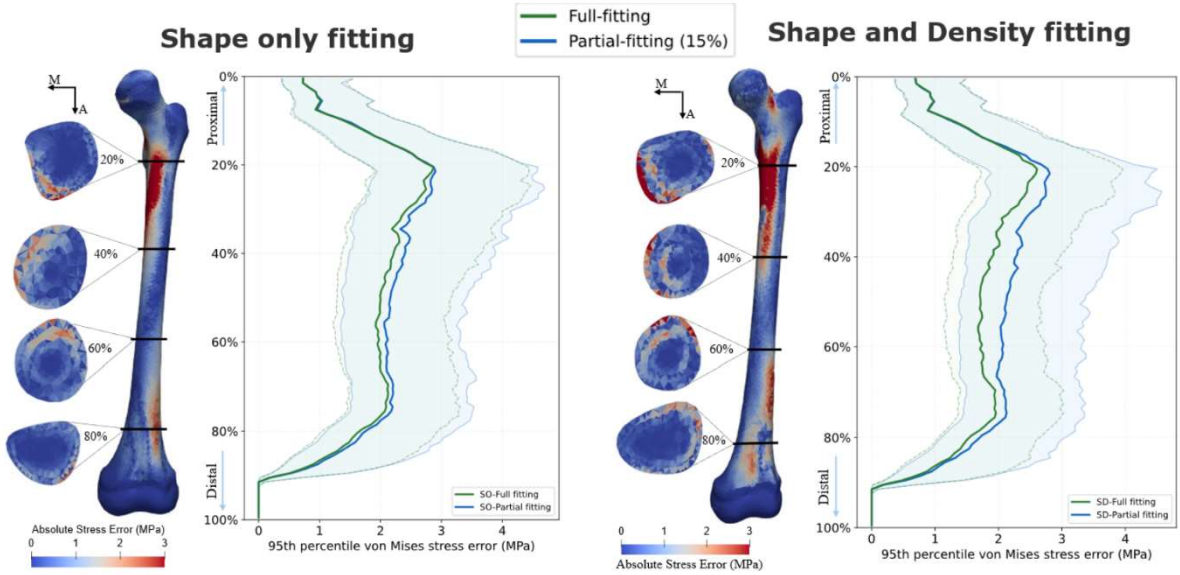


Figure 1: Slice-wise 95th percentile von Mises stress error (MPa) along the femoral axis. For each a) shape only fitting and b) shape and density fitting algorithm: left image is a representative median femur in frontal view with cross-sectional slices at 20%, 40%, 60%, and 80% of total length. Slice maps display element-wise absolute stress error relative to the subject-specific reference; A (anterior) and M (medial). The right image represent the population profiles of the 95th percentile stress error versus normalised femoral length. Curves represent the group median (solid line) and 5th - 95th percentile range (shaded area) for the Full fitting in green and Partial fitting in blue.

References (Optional)

[1] Xu Y et al., Bone; 117419 (2025)

Session Category

Musculoskeletal Biomechanics: Methods, Models and Applications

OA31-02

An Automated Pipeline for Paediatric Musculoskeletal Model Development Utilising Articulated Statistical Shape Modelling and OpenSim

Dr Laura Carman, Dr Julie Choisne, Dr Thor Besier

Auckland Bioengineering Institute, Auckland, Auckland, New Zealand

Introduction

Children are not small adults, bone morphology changes significantly throughout growth. Traditional linear scaling of adult musculoskeletal models to represent children yields large inaccuracies. Accurate paediatric musculoskeletal modelling is crucial for clinical applications such as surgical planning, and orthotic design. Statistical shape modelling has emerged as an effective tool for predicting paediatric lower limb bone geometries [1]. The aim of this study was to develop and implement an automated pipeline to generate personalised paediatric musculoskeletal models directly from motion capture data.

Methods

A dataset of 327 paediatric CT scans (4-18years (12±5years), 137F) were used to develop an articulated shape model (ASM) of the pelvis, femora, and tibiae/fibulae. Bone geometries were predicted using twelve common skin surface landmarks (ASIS, PSIS, femoral epicondyles, and tibial malleoli). These skin markers were obtained by projection from bony landmarks to the skin surface on the CT scans. The articulated shape model predicts individualized bone geometry by optimizing principal component analysis (PCA) weights and joint articulations. Model accuracy was evaluated using leave-one-out cross-validation, quantifying bone surface reconstruction error, clinical measurement error, and anatomical landmark error. The performance of the new 2-sided-ASM was compared to our previously developed shape models (1-sided-ASM, and single bone shape models (SSM)) and linear scaling of adult bone (LSA). The generated bone geometries and landmarks were used to create subject-specific musculoskeletal models via the OpenSim Python API, enabling inverse kinematic and kinetic analyses.

Results

The average RMSE for bone surface reconstructions were 2.64±0.99mm, 1.91±0.59mm, and 1.69±0.55mm in the pelvis, femur, and tibia/fibula respectively. The 2-sided-ASM performed similarly to the 1-sided-ASM and produced on average significantly lower bone surface errors compared to the SSM models and LSA, indicating the importance of personalised bone geometry in paediatric populations. Additionally, clinical bone

measurements showed low errors. The automated pipeline successfully generated OpenSim models and performed kinematic and kinetic analyses.

Discussion

This study presents a novel, fully automated workflow for paediatric musculoskeletal model generation using sparse skin surface landmarks, eliminating the need for medical imaging and enabling accurate, personalised gait analysis in clinical and research settings.

Images (Optional)

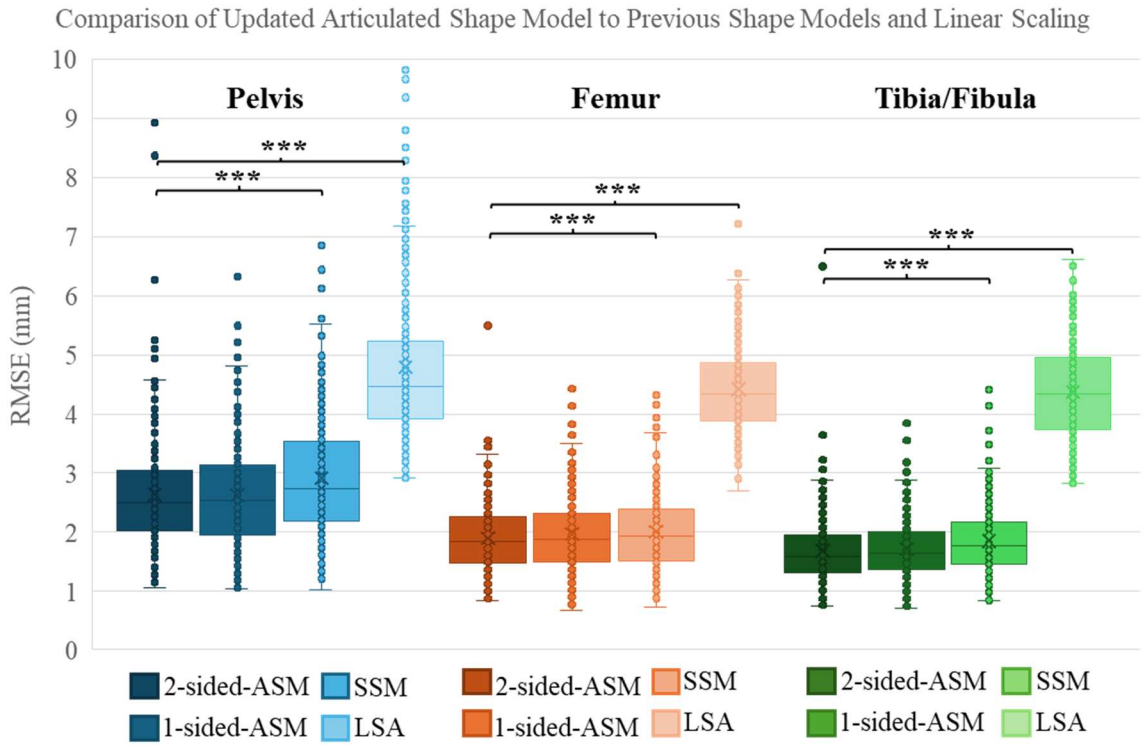


Figure 1: Box plot of bone surface geometry errors for the pelvis, femur, and tibia/fibula predicted from skin surface landmarks using the new articulated shape model (2-sided-ASM), compared to errors when predicted from bone surface landmarks using an articulated shape model (1-sided-ASM), errors when predicted using PLSR in single bone shape models (SSM), and errors when performing linear scaling of adult bone geometry from the opensim gait2392 model (LSA).

References (Optional)

[1]*L. Carman et al.*,J Biomechanics,2024

Session Category

Musculoskeletal Biomechanics: Methods, Models and Applications

OA31-03

Automated Statistical Shape Modelling of the L4-L5 Functional Spinal Unit for Population-based Computational Studies

Dr Sherif Zantiba PhD, Dr Gavin Day PhD

University of Leeds, Leeds, West Yorkshire, United Kingdom

Introduction

Vertebral geometry is a critical determinant of load transfer and fusion outcomes at the L4-L5 functional spinal unit (FSU). However, current computational studies largely rely on generic models, neglecting population-level variability. In this study a Statistical Shape Model (SSM) of the L4-L5 FSU is used to quantify how specific anatomic variations drive spinal mechanics.

Methods

L4 and L5 surface meshes were derived from 25 segmented lumbar CT scans [1]. A fully-automated Python-based automated workflow utilised Coherent Point Drift [2] to non-rigidly register all specimens to a common template, ensuring nodal correspondence. Principal Component Analysis identified dominant modes of shape variation. FE models were automatically reconstructed for the mean shape and ±1/±2σ of the first three modes (13 models), crucially, this included procedural generation of the nucleus and annulus, and ligament attachment mapping via nodal correspondence. A Young's modulus distribution, derived from the population mean intensity, was mapped onto all shape variants. Range of Motion (ROM) was assessed under a 400 N follower load and 10 Nm moments.

Results

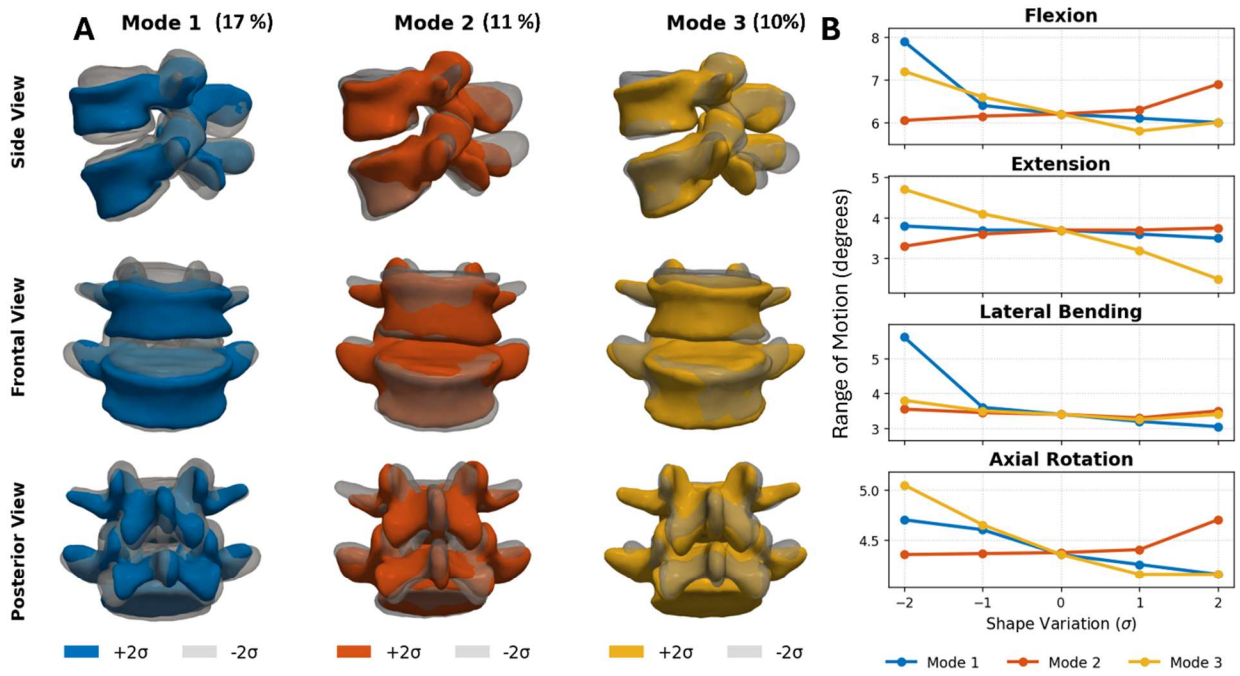
The pipeline achieved a symmetric mean surface error of 0.83±0.07 mm, with leave-one-out generalisation errors of 2.0±0.4 mm. The first three modes captured 38.7% of geometric variance. Broadly, Mode 1 captured vertical scaling (17% variation in body height), Mode 2 characterised posterior element morphology, and Mode 3 represented sagittal wedging. The models reproduced experimental ROM ranges from the literature. Finite element sensitivity analysis revealed distinct kinematic drivers: Mode 1 (-2σ; increased body) caused a twofold increase in lateral bending ROM. Conversely, Mode 3 (wedging) was the dominant sensitivity factor for extension and axial rotation stiffness.

Discussion

This study demonstrates an automated, scalable workflow for generating FE-ready spinal models with high geometric fidelity. The mechanical sensitivity analysis highlights that

specific morphological features, specifically vertical aspect ratio and sagittal wedging, drive distinct kinematic responses. These differences underscore the limitations of single-geometry models for device evaluation. While the current dataset validated the pipeline, the framework is designed for application to large-scale medical imaging databases to robustly evaluate implant–geometry interactions.

Images (Optional)



Geometric characterisation and mechanical sensitivity of the L4-L5 statistical shape model. (A) Visualisation of the first three principal component modes (capturing 38% of total variance). Solid coloured meshes represent the +2 σ geometry overlaid on the -2 σ geometry (transparent grey). Mode 1 (blue) captures vertical scaling, Mode 2 (orange) posterior element morphology, and Mode 3 (yellow) sagittal wedging. **(B)** Finite element predicted Range of Motion (ROM) sensitivity to geometric variation under 10 Nm pure moments. Key results are the non-linear, twofold increase in Lateral Bending ROM associated with Mode 1 geometry at -2 σ (increased vertebral height), and the influence of Mode 3 (wedging) on Extension and Axial Rotation stiffness.

References (Optional)

[1] Ibragimov, *IEEE TMI*, 2014. **[2]** Khallaghi, *pycpd* (GitHub), 2025.

Session Category

Musculoskeletal Biomechanics: Methods, Models and Applications

OA31-04

Effect of Shoulder Bone Shape on Glenohumeral Joint Forces: A Population-Based Analysis

Mr Francois Bruyer-Monteleone, Dr Maxence Lavaill

Queensland University of Technology, Brisbane, Queensland, Australia

Mr Francois Bruyer-Monteleone

Introduction

Shoulder anatomy varies between individuals, affecting the glenohumeral joint (GHJ) mechanics. Musculoskeletal (MSK) models can study these internal loadings across anatomies. Medical image-based models require resources and detailed anatomy, limiting result generalizability. Population-based modelling can use statistical shape models (SSMs) derived from principal component analysis (PCA) to capture anatomical variability across a population. These models can automatically generate large cohorts, for instance, to clarify how anatomy relates to joint loading at a population level. Despite this potential, population-based MSK models remain underexplored - an important gap this study seeks to address.

Methods

Shoulder girdle bones - humerus, scapula, clavicle – were 3D modelled from 61 healthy subjects. Bones and patient height were used to build a multi-segmented SSM via PCA. The SSM was then leveraged to develop 500 instances to non-uniformly scale a generic MSK model's segments [1], with randomized body mass following a normal distribution from underweight (> 18) to overweight (< 30). Overhead scaption and flexion motions were analyzed with an optimization solver which constrains the GHJ force within the glenoid's border [2]. Simulations were run with and without a 3-kg weight in hand. GHJ forces were normalized over body weight (BW) and distribution across models were reported.

Results

During flexion, GHJ force rose from 30% to 100%BW, and tripled with the weight (100% to 300%BW; Fig.A). During scaption, the unweighted pattern was similar to flexion, but with the weight the force doubled at the start and tripled by the end (Fig.B). Overall, patterns were comparable with and without the weight.

Discussion

The population-based MSK model integrates shape variability and reproduces forces comparable to the published weighted and unweighted data -from in vivo [3], in vitro [4] and in silico [5] studies- though sometimes lower in our models. Population-based models can help elucidate loading patterns in patients whose anatomies deviate from the population average, potentially explaining the limited success of certain surgical procedures and supporting more personalized treatment strategies.

Images (Optional)

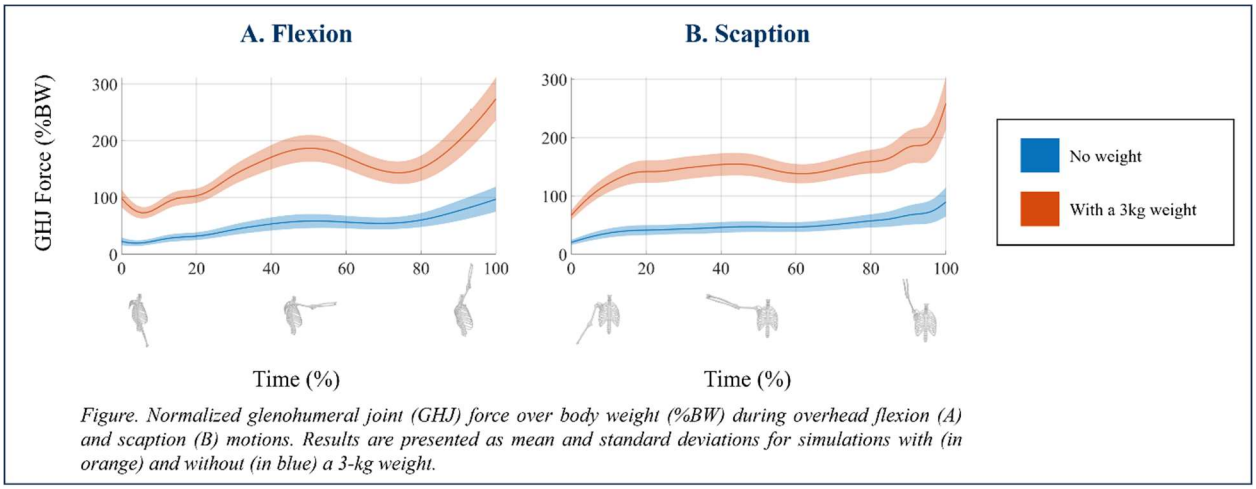


Figure. Normalized glenohumeral joint (GHJ) force over body weight (%BW) during overhead flexion (A) and scaption (B) motions. Results are presented as mean and standard deviations for simulations with (in orange) and without (in blue) a 3-kg weight.

References (Optional)

[1] Seth et al., *PLoS One*., 2016

[2] Belli et al., *PLoS One.*, 2023

[3] Bergmann et al., *JB.*, 2011

[4] Genter et al., *JB.*, 2024

[5] Lavaill et al., *JB.*, 2023

Session Category

Musculoskeletal Biomechanics: Methods, Models and Applications

OA31-05

Sensitivity of Knee Contact Mechanics to Statistical Cartilage Thickness Models Derived From a Single and Multiple Imaging Modalities

Dr Roberto Leonardo Diaz, Prof Sophie Williams, Prof Ruth Wilcox

University of Leeds, Leeds, West Yorkshire, United Kingdom

Introduction

Accurate cartilage thickness distribution is essential for realistic contact mechanics simulations [1]; however, obtaining bone and cartilage surfaces from the same imaging source is not always possible. Statistical shape models (SSMs) offer the potential to apply cartilage layers to bone models derived from radiographic imaging that does not capture the soft tissue, however SSMs often combine data from different imaging modalities. The aim of this study was to compare contact mechanics predictions from models with different SSM-derived cartilage layers.

Methods

A SSM, based on a single imaging source, was developed in which the subject-specific cartilage thickness was derived from the bone geometry. Bone and cartilage masks of tibiofemoral joints (n=8) were first segmented from high-resolution CT scans (voxel size 82μm). Articular cartilage surfaces were extracted (bone shape), resampled for node correspondence and assigned with a cartilage thickness value per node. Training samples were aligned and scaled to a template for a subsequent Principal Component Analysis (PCA), applied independently to bone shape and cartilage thickness distribution. The predictive model was verified with a control sample. Contact mechanics were compared using FE models with the (original) segmented cartilage and with cartilage derived using the above SSM (‘SSM-CT’), a 1 SD shift of this model (‘SSM-CT-1SD'), and a SSM derived from MRI data (‘SSM-MRI’)[2].

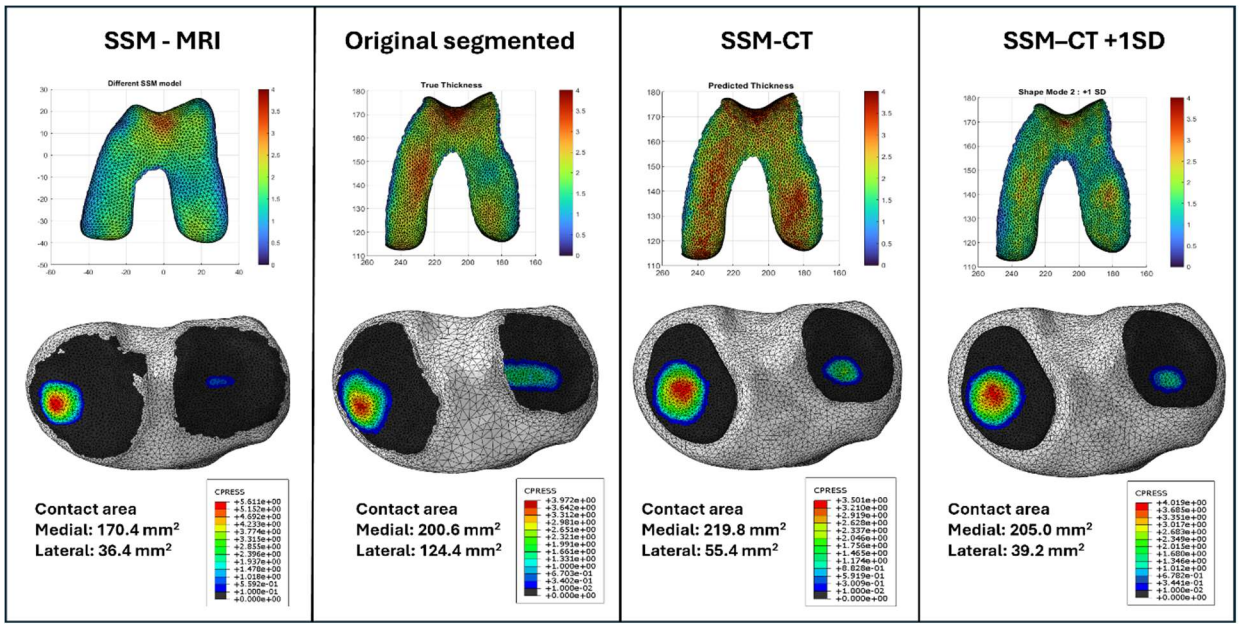
Results

The predicted mean cartilage thickness distribution of SSM-CT was consistent with the segmented case but 20% larger in volume, while the SSM-CT-1SD shifted case reduced the volume error to 11%. The contact mechanics simulation showed that, compared to the segmented case, the SSM-CT case had lower peak stress (−11.9%) and contact area (−15.3%), the SSM-CT+1SD case had similar peak stress (+1.2%) but reduced contact area (−24.8%), and the MRI-derived SSM had larger errors.

Discussion

The SSM-CT model produced cartilage thickness with a systematic overestimation but maintained a similar distribution. Crucially, better results were achieved when both cartilage and bone models were derived from a single, consistent imaging modality like µCT. Despite the limited sample size to train the model, this method demonstrates strong potential for adding cartilage to image-derived bone models for contact biomechanics research.

Images (Optional)



References (Optional)

[1]Cooper,doi:10.1177/09544119241307793

[2]Ovevelen,doi:10.3389/fbioe.2023.1055860

Acknowledgements (Optional)

This project is funded by the EPSRC, grant:EP/W003139/1

Session Category

Musculoskeletal Biomechanics: Methods, Models and Applications

OA31-06

Sex Differences in Ankle Muscle Morphology Revealed Through MRI-Derived Statistical Shape Models

Mr. Mario E. Garcia, Dr. Silvia S. Blemker

University of Virginia, Charlottesville, Virginia, United States

Introduction

Despite established sex-related and architectural variability, muscle morphology remains under explored. As such, this study leverages our large dataset of MRI-derived lower-limb muscle volumes and paired functional assessments to develop statistical shape models for the ankle's plantar and dorsiflexor muscles. These models reduce geometries into principal components (PC) that capture morphology features, enabling comparison across landmarks, functional capacity, and sex.

Methods

Participants (n=103, female:55, male:48) of representative heights (average:1.70±0.08m, female:1.64±0.05m, male:1.76±0.06m) and masses (average:71.52±13.92kg, female:64.32±10.72kg, male:79.78±12.59kg) were recruited. The study was approved by the University of Virginia Institutional Review Board and conducted in accordance with the Declaration of Helsinki. Participants underwent MRI scans and the ankle's functional capacity was evaluated isometrically, using a Biodex System 4. Muscle volumes were identified using automated segmentation with manual vetting (Springbok Analytics, Charlottesville, VA). Shape models for plantar and dorsiflexors (n=206, female:110, male:96) were generated using Generalized Procrustes Analysis and screened using leave-one-out cross-validation with Mahalanobis distances. Selected morphology landmarks included CSA, curvature length, maximum Feret diameter, perpendicular thickness (PTH), curvature deviation (CDV), and axial-CSA proxy. Principal component analysis was performed and related to landmarks and torque capacity using linear regressions. PC sex differences were analyzed using Welch's t-test. Reported results focused on PC1-5 for the soleus (SOL) and tibialis anterior (TA) for brevity.

Results

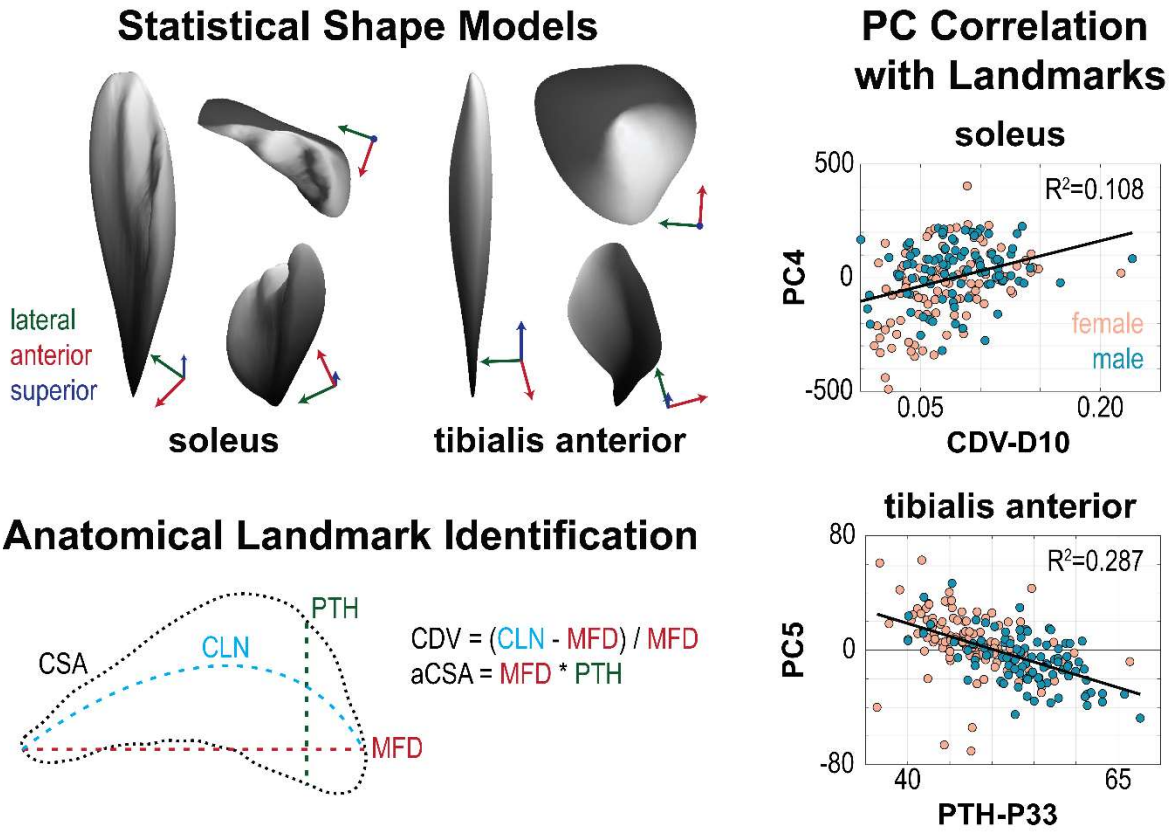
For SOL, PC4 was significantly greater in males and positively correlated with CDV in the distal-tenth (R^2=0.11, $p<0.05$). This PC indicated greater distal curvature in female participants. For TA, PC5 was significantly greater in females and negatively correlated with

PTH in the distal-third (R^2=0.29, $p<0.05$). This PC indicated that females' higher values correspond to reduced distal thickness.

Discussion

Utilizing our dataset, we found sex differences across multiple PCs in our shape models. These results suggest that sex differences in muscle morphology are most apparent in the distal regions of the SOL and TA, near the muscle-tendon junction, where tapering, curvature, and transitions are most pronounced. These models enable targeted investigation of morphological differences driving these differences and their links to functional capacity, and future work will compare pooled, female, and male models to further delineate variation.

Images (Optional)



References (Optional)

Session Category

Musculoskeletal Biomechanics: Methods, Models and Applications

OA32-01

Fall Experiments from Stepladders Using a Hybrid III Pedestrian Dummy

Dr. HIROKI TAKAHASHI Researcher, Dr. HAEYOUNG KIM Researcher, Mr. YASUMICHI HINO Researcher, Dr. KATSUTOSHI OHDO Researcher

National Institute of Occupational Safety and Health, Japan, Kiyose, Tokyo, Japan

Introduction

Falls from low heights, particularly from stepladders, remain a major cause of fatal and severe occupational injuries in the construction industry. In Japan, falls account for approximately 40% of all fatal construction accidents, and incidents involving stepladders have shown an increasing trend. Understanding head impact mechanisms during short-distance falls is essential for developing effective prevention strategies. This study experimentally investigates head acceleration responses during stepladder falls using the Hybrid III Pedestrian dummy.

Methods

Experiments were conducted in the fall-testing facility at the National Institute of Occupational Safety and Health, Japan. A stepladder was placed on a 50-cm-high platform, and female and male Hybrid III Pedestrian dummies were positioned on the ladder. A release mechanism initiated controlled falls at three inclination angles relative to the ground surface: 10°, 20°, and 30°. Dummy posture was varied between a straight-torso configuration and a flexed-waist configuration. A tri-axial accelerometer mounted at the dummy's head measured impact accelerations. Helmet and non-helmet conditions were also tested to evaluate protective effects.

Results

Greater inclination angles consistently produced higher peak head accelerations. For the female dummy at a 10° inclination, the straight-torso posture generated approximately 550 G, while the flexed-waist posture generated about 400 G. The flexed posture allowed the hip, back, and shoulders to contact the ground before the head, enabling partial energy absorption. Helmet use substantially decreased measured head acceleration compared with non-helmet conditions, reinforcing the importance of protective equipment.

Discussion

The findings indicate that even low-height falls can produce severe head impacts when the head directly contacts the ground. Fall posture strongly influences injury severity, and preventing direct head impact—together with consistent helmet use—is essential for

reducing risk. These results provide fundamental data for improving fall-prevention strategies and will be extended using biomechanical injury indices such as **HIC（Head Injury Criterion）** and **BRIC（Brain Injury Criterion）** to enable more quantitative injury assessment.

Images (Optional)



Session Category

Injury Biomechanics: N/A

OA32-02

Novel Direct Assessment of Bulk Fracture Propagation Speed in Bone

Mr Souren Moradi Undergraduate Student[1], Mr Samuil Miah Undergraduate student[1], Mr Heytham Mohilldeen BS[1], Mr Charles Bass BS[2], Dr. Cameron Bass PhD[1]

[1]Wayne State University, Detroit, MI, United States. [2]Virginia Commonwealth University, Richmond, VA, United States

Introduction

Rib fractures remain common traumatic injuries, yet the mechanics of fracture propagation in bulk is poorly understood, particularly the speed of crack propagation under dynamic loading. Most existing studies investigate slow fatigue cracking at microscale. Modern Lagrangean finite element model (FEM) injury biomechanics models are is fundamentally compromised by sub-element level bony failure, often partially addressed using nonbiofidelic heuristic element deletion procedures. However, the stress-strain behavior in bulk relies sensitively on crack propagation speed. To rectify this deficiency, this study introduces and validates a novel three-point bone breaking apparatus to directly track high-speed dynamic fractures in bulk bone.

Methods

A three-point bending apparatus was constructed using a large-stroke, 10-ton hydraulic cylinder mounted in a rigid frame. The cylinder was attached to a transparent, acrylic indentor that provided access for overhead illumination of the rib specimen (30,000 lumen backlighting across ~625 mm^2). The outer margin of dry bovine rib specimens (n=11) were placed on cylindrical supports. Fracture propagation was recorded using a high-speed camera (Phantom V711) at 210,000-390,000 frames/sec. Crack tip positions from video were tracked using Tracker (v.6.2.0). Fracture velocity was calculated by differentiation of the displacement data.

Results

Crack propagation illuminated through bulk bone was successfully tracked for 3-6 frames (~400 um/pixel at 390,000 f/s). Typical fracture profiles were linear during the time tracked with an average R^2 of 99±0.8%. Mean fracture velocity was assessed as 1370±200 m/s, with no statistically significant difference in assessed velocities between the datasets with the smaller number of frames (3) and larger number of frames (4-6) ($p=0.05$).

Discussion

Fracture propagation speed is an essential input into biofidelic human FEMs that include fracture. This study demonstrated a novel and effective methodology to accurately track bulk fracture propagation in whole bone for use in improved bone injury models. Crack propagation speed in dried bovine bone is comparable to Rayleigh wave speed in dry cortical bone. Novel aspects of this study include high intensity backlighting through the indentor. With this approach, bone cracks at > 3000 m/s can be seen propagating on both sides of the rib specimens used in this study.

Images (Optional)

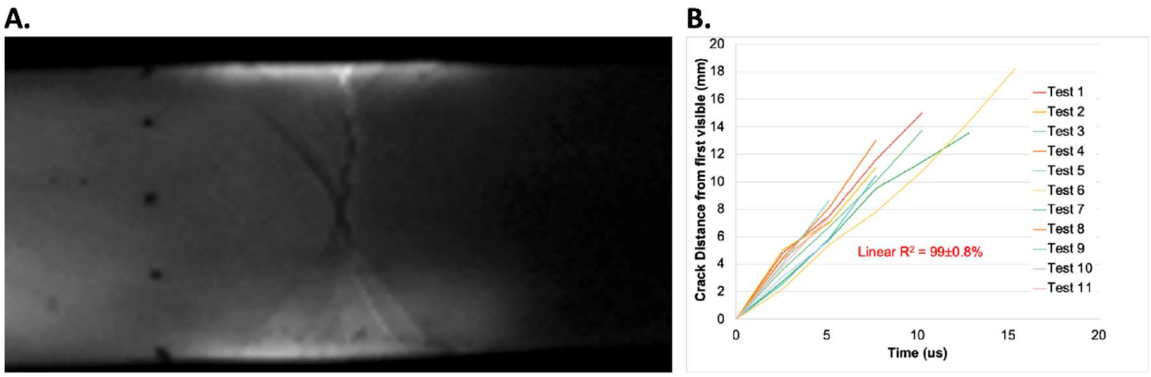


Figure: High speed tracking of bulk bone fracture propagation. A. Video frame with fracture propagated across the bone backlit through the three-point bend indentor. B Video position tracking of crack position.

Session Category

Injury Biomechanics: N/A

OA32-03

In-Vivo Imaging of Harmonic Brain Motion Correlates Head Rotation With Increased Mechanical Vulnerability of the Adolescent and Adult Human Brain

Dr. Ruth Okamoto[1], Dr. Jordan Escarcega[1], Dr. Curtis Johnson[2], Dr. Ahmed Alshareef[3], Dr. Philip Bayly[1]

[1]Washington University, St. Louis, MO, United States. [2]University of Delaware, Newark, Delaware, United States. [3]University of South Carolina, Columbia, South Carolina, United States

Introduction

Cadaver studies and in-silico models have linked the location and direction of head impacts to the relative risk of brain injury [1, 2]. Non-injurious experimental studies are needed to confirm these findings in living humans [3]. We used magnetic resonance elastography (MRE) to measure the response of the brain to occipital and lateral excitations and characterize contributions of rotational and translational motion to the non-dimensional strain energy - kinetic energy ratio, SE/KE [4].

Methods

96 participants in 4 age cohorts underwent an MRI exam including standard anatomical imaging and MRE with harmonic skull excitation in the lateral or occipital direction at [20, 30,50] Hz (Fig. 1). Image volume were aligned to an MNI-152 template, then processed to obtain bulk motion, dynamic deformation fields, strain fields, brain mass, m, and moment of inertia tensor, $\boldsymbol{I}$. The ratio of rotational kinetic energy to translational kinetic energy, RKE/TKE was computed at each frequency f using bulk angular displacement ($\boldsymbol{\theta}$) and centroid translation ($\boldsymbol{u_0}$) vectors. Strain energy was computed using frequency-dependent shear storage moduli for each age cohort. We used a linear, mixed-effects model (LMEM) to fit power-law relationships between SE/KE and RKE/TKE as functions of frequency for each cohort.

Results

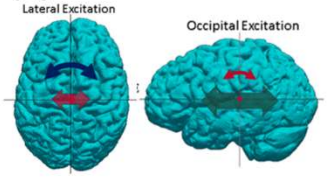
RKE/TKE and SE/KE were highly correlated for all cohorts using the LMEM: $\log_{10}(SE/KE) = -1.4 + 0.74 \log_{10}(RKE/TKE) + 0.74*\log10(f)$. Including age cohorts and excitation direction improved the fits modestly (Fig 1E).

Discussion

RKE/TKE was larger for lateral excitation than for occipital excitation and decreased with frequency. Variations in RKE/TKE within cohorts may occur due to differences in head positioning and head shape during imaging, and explain the variability of SE/KE within cohorts. Higher SE/KE ratios for low frequency motions with large RKE/TKE suggest that longer-duration impacts lead to proportionally higher values of shear strain and possibly higher likelihood of injury across all age cohorts studied.

Images (Optional)

(A)



(B)

$$\frac{\text{RKE}}{\text{TKE}} = \frac{\frac{1}{2}\left[\frac{1}{2}(2\pi f)^2 \boldsymbol{\theta}\, \mathbf{I}\, \boldsymbol{\theta}^*\right]}{\frac{1}{2}\left[\frac{1}{2}(2\pi f)^2 m \boldsymbol{u_o}\, \boldsymbol{u_o^*}\right]}$$

(C)

$$\frac{\text{SE}}{\text{KE}} = \frac{\sum_{i=1}^{n} V_{vox} \frac{1}{2}[G'(f)\boldsymbol{\varepsilon}_{dev} : \boldsymbol{\varepsilon}^*_{dev}]}{\sum_{i=1}^{n} V_{vox} \frac{1}{2}\left[\frac{1}{2}\rho(2\pi f)^2 \boldsymbol{u}\, \boldsymbol{u}^*\right]}$$

(D)

	G' (kPa)		
Age Cohort	***20 Hz***	***30 Hz***	***50 Hz***
14Y-17Y	1.31	1.69	2.46
18Y-21Y	1.34	1.72	2.46
22Y-49 Y	1.29	1.66	2.41
50Y-80Y	1.13	1.47	2.15

(E)

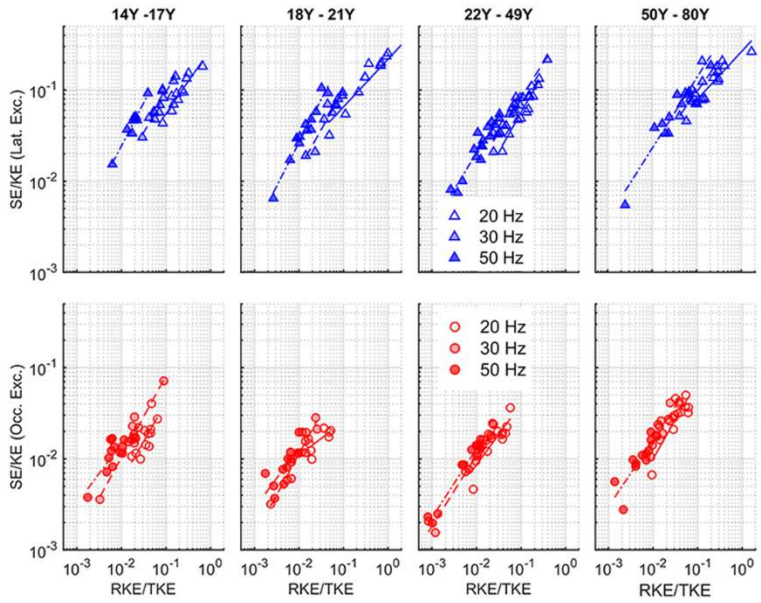


Figure 1. (A)Typical rigid-body motion for lateral and occipital excitation
(B) Rotational/translational kinetic energy ratio (see text for variable def'ns)
(C) Strain energy/ kinetic energy ratio. (D) Age-stratified shear storage moduli.
(E) Fit of SE/KE using linear mixed-effects model fit for four age cohorts and two excitation directions. Symbols in (E) denote data, lines denote model fits. N=12 for each cohort, but participant data for an individual frequency may be missing.

References (Optional)

[1] Ahmed Alshareef et al. , J Neurotrauma, 2020

[2] Fidel Hernandez et al. , Biomech Model Mechanobiol, 2019

[3] Philip Bayly et al. , Ann Biomed Eng, 2021

[4] Ruth Okamoto et al. J Biomech Eng, 2023

Acknowledgements (Optional)

NIH U01 NS112120

Session Category

Injury Biomechanics: N/A

OA32-04

Apparent Shear Softening Present in *Ex Vivo* Bovine Brain Tissue Captured with MR Elastography

Ms Olivia Bailey[1], Ms Alexa Diano[1], Dr. L. Tyler Williams[1,2], Mr Ali Lateef[1], Dr. Kshitiz Upadhyay[3], Dr. Elise Corbin[1,4], Dr. Curtis Johnson[1,4]

[1]University of Delaware, Newark, DE, United States. [2]Children's Hospital of Philadelphia, Philadelphia, PA, United States. [3]University of Minnesota, Minneapolis, MN, United States. [4]Nemours Children's Hospital, Wilmington, DE, United States

Introduction

Traumatic brain injury (TBI) models require advanced experimental data on brain mechanical properties, potentially acquired using magnetic resonance elastography (MRE). Traditional *in vivo* MRE is limited to capturing linear mechanical properties within the small-strain regime. However, modeling high-strain and strain-rate injuries should consider nonlinear mechanical tissue behavior. Here, we modify our MRE experiment to induce large strain in *ex vivo* tissue to capture mechanical nonlinearity.

Methods

Bovine brains were encapsulated in agarose (0.75wt.%) to create phantoms and were scanned with a custom EPI-MRE sequence on either Siemens 3T (2.5 mm isotropic resolution, 30-100 Hz) or Bruker 9.4T (0.5 mm isotropic resolution, 200-500 Hz) MRI scanners. Octahedral shear strain and maps of shear modulus, estimated with a nonlinear inversion [1], were calculated. Typically, micron-level displacements induce minor shear strain; however, here we maximize applied displacement to increase the strain induced into tissue-agar phantoms.

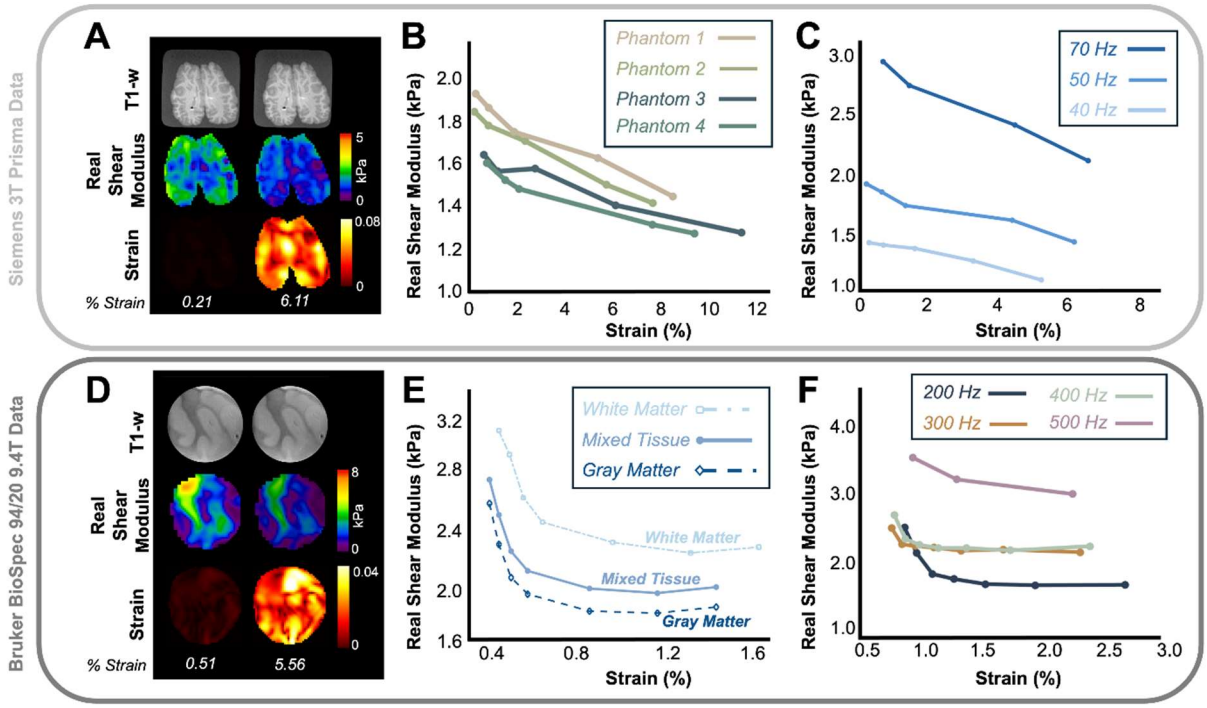
Results

In larger samples tested on the 3T clinical scanner, we induced 6.11% strain into the tissue, causing a 25.1% decrease (1.93 to 1.45 kPa) in shear modulus. This trend remained consistent across multiple phantoms and frequencies (Figure 1A-C). In smaller samples on the 9.4T high-resolution scanner, we induced 5.56% strain, causing a 38.16% decrease (3.15 to 1.95 kPa) in shear modulus. Comparison between tissues showed a 28.7% decrease in gray matter (2.58 to 1.84 kPa) and a 26.9% decrease (3.10 to 2.27 kPa) in white matter (Figure 1D-E). Figure 1C,F demonstrates that data collected at lower frequencies typically achieves higher strain and results in higher percent modulus change.

Discussion

Results indicate success in achieving large strain using MRE and match similar nonlinear strain softening behavior previously identified in bovine brain under shear stress [2]. We achieved peak strains of approximately 6-12%, whereas typical *in vivo* brain MRE experiments induce strains less than 0.05% [3]. Future work will assess strain-softening in fresh tissue and further investigate the influence of frequency and tissue-type. Experimental data will be incorporated into computational models to capture the large-strain nonlinear tissue response relevant to TBI.

Images (Optional)



References (Optional)

[1] McGarry *et al.*, Med. Phys., 2012

[2] Bilston *et al.*, Biorheology, 2001

[3] Okamoto *et al.*, J. Exp. Neurosci., 2019

Acknowledgements (Optional)

This work was supported by the NIH grant U01-NS112120, an NIH Bench-to-Bedside grant and the NSF grant CMMI-2331296.

Session Category

Injury Biomechanics: N/A

OA32-05

Video Analysis of Human Lateral Head Impacts Reveals Muscle Co-Contraction Reduces Head Excursion Relative to Torso

Dr Pawel Kudzia PhD[1], Ms Gabrielle R. Booth[2], Dr. Kristen Reynier PhD[1], Dr. Matthew Panzer PhD[3], Dr. Peter A. Cripton PhD[1]

[1]University of British Columbia, Vancouver, BC, Canada. [2]MEA Forensic Engineers & Scientists, Laguna Hills, CA, United States. [3]University of Virginia, Charlottesville, VA, United States

Dr Pawel Kudzia

Ms Gabrielle R. Booth

Dr. Kristen Reynier

Dr. Matthew Panzer

Introduction

Anthropomorphic test devices (ATDs) and human body models require empirical head and torso kinematic data to better predict injury risk. Reynier et al. (2020) characterized head kinematics during non-injurious lateral impacts under different muscle activation conditions, but their analysis focused exclusively on head motion [1]. We performed secondary analysis of their high-speed video data to quantify simultaneous head and torso kinematics for ATD biofidelity assessment.

Methods

We digitized high-speed video recordings from 19 male participants who received standardized lateral head impacts under passive and co-contracted muscle conditions. A 3.7 kg padded impactor struck participants at 2 m/s while cameras captured motion at 500 Hz. We tracked head and torso positions from video and computed velocity and

acceleration metrics. We detected impact onset using a velocity threshold and compared conditions using paired t-tests with effect sizes.

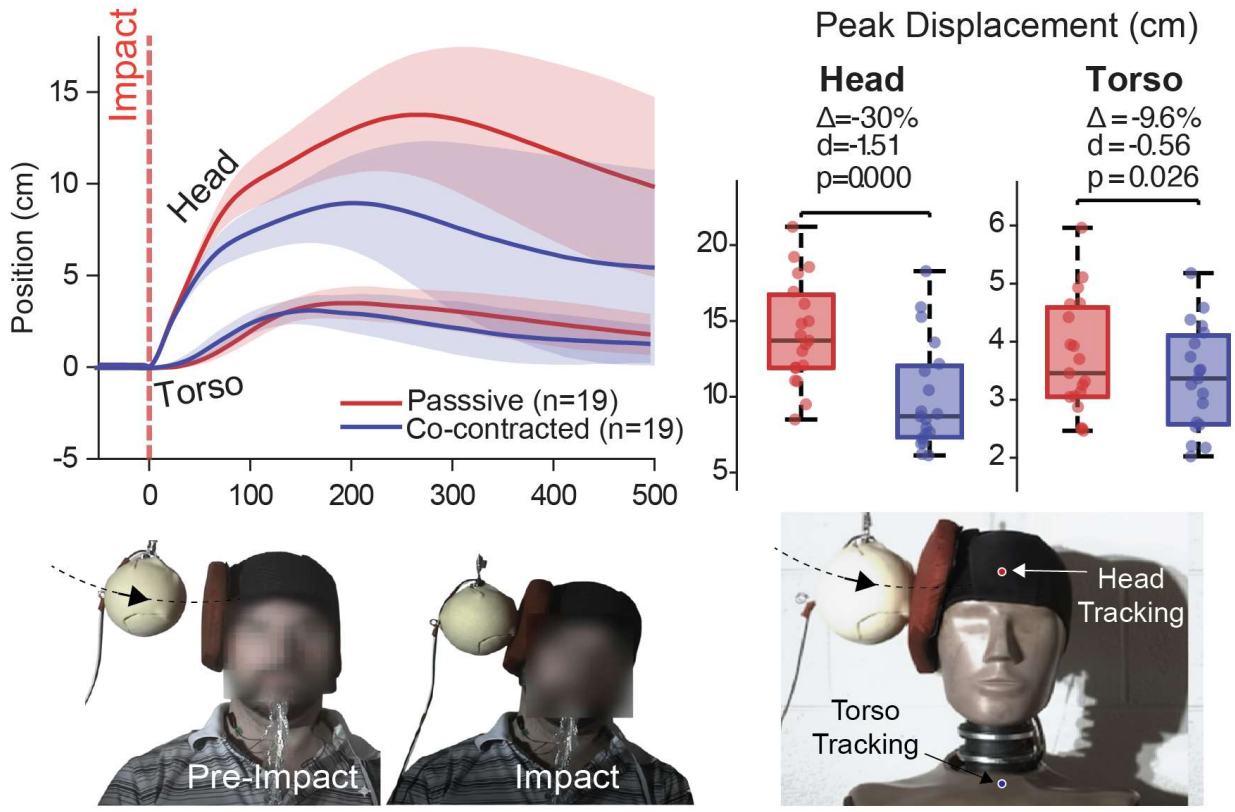
Results

Muscle co-contraction reduced peak head displacement by 30% (passive: 14.2 ± 3.4 cm; co-contracted: 10.0 ± 3.6 cm; $p < 0.001$, $d = 1.51$). Peak head velocity decreased by 6.4% ($p = 0.003$, $d = 0.78$). Torso velocity and acceleration showed no significant differences between conditions ($p > 0.05$). Head excursion relative to torso decreased 36% with co-contraction (passive: 11.3 ± 3.3 cm; co-contracted: 7.2 ± 3.2 cm; $p < 0.001$, $d = 1.35$). Individual displacement responses demonstrated consistent proportional reductions across conditions (slope = 0.70, $R^2 = 0.46$).

Discussion

While peak acceleration remained unchanged, muscle co-contraction reduced head displacement and excursion relative to the torso following lateral impact. Our video-based approach captured displacement trajectories that can be tricky to capture using accelerometer-only methods. The time-series data and head excursion metrics address a need for developing more biofidelic ATDs used in automotive safety and sports injury research. The consistent proportional reduction in head displacement across participants supports development of scalable muscle activation factors.

Images (Optional)



References (Optional)

[1] K.A. Reynier et al., Ann Biomed Eng, 2020

Session Category

Injury Biomechanics: N/A

OA32-06

Poroelastic Inversion of the Human Brain at 3T Using Amplified MRI

Mr. Tyson Lam M. S.[1], Dr. Patrick Fillingham Ph. D.[1], Dr. Matthew McGarry Ph. D.[2], Ms. Caitlin Neher M. S.[1], Dr. Em Triolo Ph. D.[3], Dr. Fargol Rezayaraghi Ph. D.[1], Dr. Mehmet Kurt Ph. D.[1]

[1]University of Washington, Seattle, Washington, United States. [2]Dartmouth College, Hanover, New Hampshire, United States. [3]Children's Hospital of Philadelphia, Philadelphia, Pennsylvania, United States

Introduction

Cardiac pulsations drive subtle, measurable brain deformations on the order of ~100 μm [1], observable with cine-MRI and amplified-MRI (aMRI) [2, 3], which amplifies subtle motion for quantification. Harnessing natural actuation offers a unique opportunity to probe low-frequency mechanics and enable elastography without external drivers. These motions serve as inputs to poroelastic nonlinear inversion (peNLI), a fluid-solid coupled iterative mesh framework [4]. The objective is to demonstrate the feasibility of aMRI-peNLI at 3T by estimating stiffness maps of the human brain at cardiac frequencies.

Methods

Healthy adults (n=18) were scanned at 3T using a 16-channel head coil and a cardiac-gated balanced steady-state free precession sequence ($1.0\times1.0\times1.0 mm^3$). 3D-aMRI was applied to the cine-MRI data, followed by Demons-based registration to obtain voxel-wise displacements across the cardiac cycle [2, 3], later served as inputs to the peNLI solver modeling poroelastic behavior with Darcy-type fluid transport by estimating the real component of the shear modulus. Soft-prior regularization [5] was applied to CSF, and ventricular regions were masked out to mitigate numerical instability and non-uniqueness.

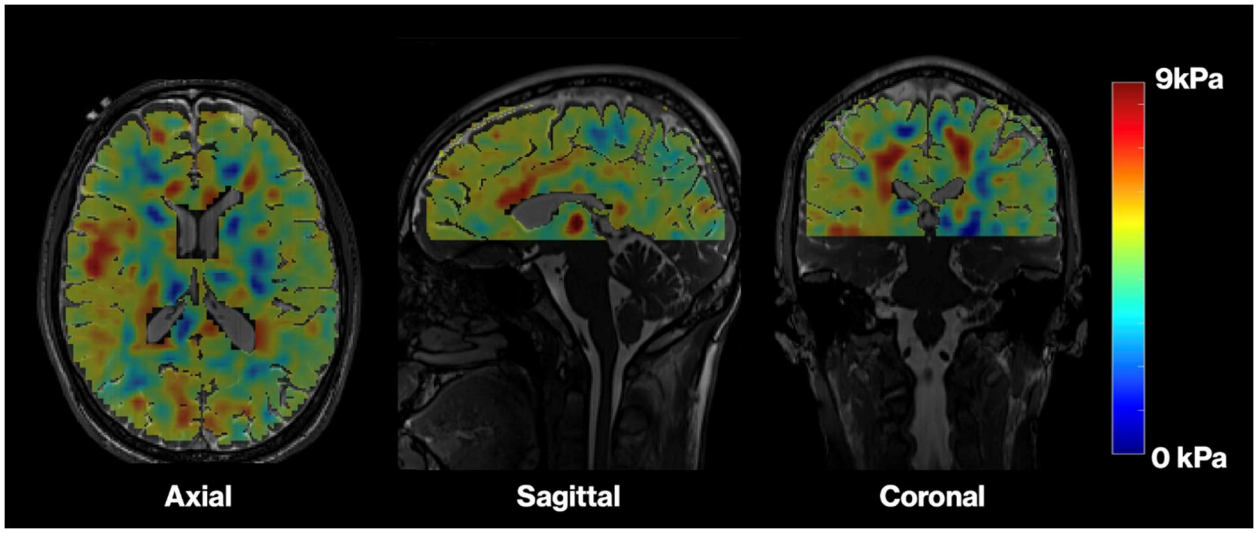
Results

Preliminary stiffness maps/elastograms from peNLI were able to differentiate gray matter (GM) from white matter (WM) regions and yielded ratios similar to typical 50Hz magnetic resonance elastography (MRE) ranges. Since absolute stiffness values are not physically meaningful for ~1 Hz MRE, regional ratios (e.g., GM/WM) were reported for performance comparison. Residual "hotspot" clusters appeared near tissue boundaries and regions limited by registration confidence.

Discussion

Results showcase feasibility of 3D-aMRI driven peNLI at 3T, with stiffness maps broadly consistent with prior MRE studies. Deviations (e.g. thalamus softer relative to WM, -0.79±0.17 vs +0.06±0.16 literature) may reflect CSF shielding around deep GM nuclei or anisotropic fiber organization in WM. Residual hotspots likely reflect interstitial fluid forces not yet captured. Future work will incorporate poroviscoelastic models to better capture clinically relevant changes in compliance and pulsatility.

Images (Optional)



References (Optional)

[1] Adams AL *et al.* , NeuroImage, 2020

[2] Abderezaei J *et al.* , Brain Multiphysics, 2021

[3] Terem I *et al.* , Magn Reson Med, 2021

[4] McGarry MD *et al.* , Med Phys, 2015

[5] McGarry M *et al.* , IEEE Trans Med Imaging, 2013

Acknowledgements (Optional)

This work was supported by NSF CMMI 2227232 and NIH 1R21NS111415-01. The authors thank Ms. Aislinn Diaz for volunteer coordination, and Javid Abderezaei and Itamar Terem for contributions to 3D-aMRI. Data collection for this work was partially funded by the UW Center for Human Neuroscience and the UW Student Technology Fee.

Session Category

Injury Biomechanics: N/A

OA33-01

Multi-day Co-adaptation of Ankle Exoskeleton Assistance for Poststroke Gait

Ms Tara Kimiavi, Dr. Santiago Canete PhD, Dr. Conor Walsh PhD, Dr. Patrick Slade PhD

Harvard University, Cambridge, MA, United States

Introduction

Ankle exoskeletons can enhance poststroke mobility [1], but effectiveness depends on user adaptation [2] and assistance personalization [3]. Poststroke users often show reduced adaptability and endurance [4], limiting co-adaptation. Hemiparetic compensation shifts power to the hip or non-paretic limb [5], so leveraging ankle assistance may require gait readaptation. We personalized ankle assistance across multiple days to characterize poststroke human-robot co-adaptation and test how training time and continuous exoskeleton personalization influence device efficacy. We hypothesized that with increasing training, the human-exoskeleton system converges: device parameters approach an optimum while the user converges to an internal gait pattern that better exploits ankle push-off.

Methods

Two chronic poststroke adults completed four overground walking visits with an ankle exoskeleton at a comfortable speed. We measured kinematics, kinetics, cost of transport, and spatiotemporal metrics during validation trials comparing no exoskeleton, generic assistance, and optimized assistance. After each day's validations, assistance was personalized online using CMA-ES [3] to maximize overground walking speed. On the final visit, we performed a double-reversal validation of the three conditions. The generic condition was periodically retested during optimization to track adaptation.

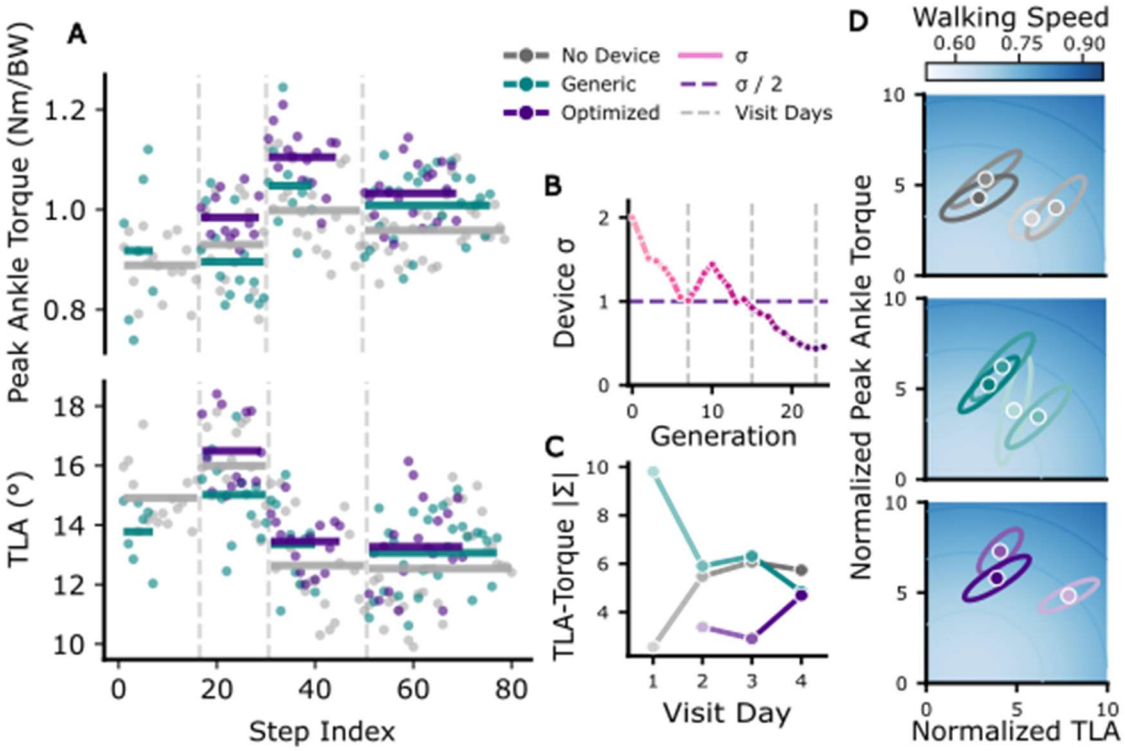
Results

For one participant, the exoskeleton converged to an optimal assistance profile after 160 minutes of training (1B). Walking speed improved with exoskeleton assistance compared to no device on all days, with greater differences observed between the optimized controller (0.78 ± 0.1, 0.75 ± 0.1 m/s) and the generic (0.67 ± 0.1,0.73 ± 0.1 m/s) after visits 1 and 2. Covariance between paretic TLA and peak ankle torque across all validation steps (1A, 1D) indicates convergence towards a gait pattern that increases walking speed relative to the no device condition. Covariance decreased in the generic condition but remained stable in the optimized condition, indicating the participant did not adopt a strategy that better leveraged optimized assistance.

Discussion

This study will provide insights into better training protocols for people post-stroke to move towards community device use.

Images (Optional)



References (Optional)

"[1] Awad et al., IEEE Open J. Eng. Med. Biol., 2020"

"[2] Poggensee et al., Sci. Robot., 2021"

"[3] Slade et al., Nature, 2022"

"[4] Otter et al., Exp. Brain Res., 2005"

"[5] Farris et al., J. NeuroEng. Rehabil., 2015"

Session Category

Rehabilitation Biomechanics and Human Factors: Rehabilitation

OA33-02

Effects of Backpack Loads on Bone Mechanical Stimulus in Persons with Spinal Cord Injury during Exoskeletal-assisted Walking: A Simulation Study

Ms. Gabriela B. De Carvalho[1], Dr. Ann M. Spungen[2], Dr. William A. Bauman[3], Dr. Saikat Pal[1,2]

[1]New Jersey Institute of Technology, Newark, NJ, United States. [2]James J. Peters Veterans Affairs Medical Center, Bronx, NY, United States. [3]Icahn School of Medicine at Mount Sinai, New York, NY, United States

Introduction

Severe osteoporosis is a secondary consequence of spinal cord injury (SCI). Exoskeletal-assisted walking (EAW) offers a promising approach to mitigate bone loss by providing sustained loading of bones in an upright position. However, knowledge of EAW dosing to improve bone health is non-existent. The **goals** of this study were (1) to quantify exercise dose using Bone Density Index (BDI), an established metric to quantify mechanical stimulus [1], and (2) evaluate the effects of backpack loads during EAW from persons with SCI.

Methods

We recorded the 3-D motion of three persons with SCI during EAW in the ReWalk P6.0. A generic OpenSim musculoskeletal model was scaled to match each participant's anthropometry. Human-robot interaction forces were applied to regions of exoskeletal support cuffs/bands. Knee joint forces were computed during EAW using muscle-driven simulations with muscle control signals constrained to a maximum value of zero to simulate muscle inactivity in SCI. We calculated BDI (Equation 1) for EAW steps ranging from 10 to 2000, where $\beta=1$ and $m=6$. Next, we simulated backpack loads ranging from 10 to 40lbs and calculated BDI for the range of EAW steps.

$$BDI = [\sum n * (\beta * F)^m]^{1/2m} \quad \text{(Equation 1)}$$

Results

Average peak knee joint forces during EAW with no added backpack loads were 0.88 BW, which is substantially lower than a previously defined osteogenic threshold [2]. Adding backpack loads increased average peak knee forces to up to 1.09 BW, resulting in linear increases in BDI (Fig.1A-C). More interestingly, adding a backpack load of just 10lbs reduced the number of EAW steps per day by 64%, from ~1,400 to ~500 steps to maintain a

BDI of 1.75 (Fig.1C-D). These results are exciting because many persons with SCI cannot take several thousands of EAW steps per day.

Discussion

The results from this simulation study suggest that addition of modest backpack loads during EAW may greatly improve bone mechanical stimulus in persons with SCI.

Images (Optional)

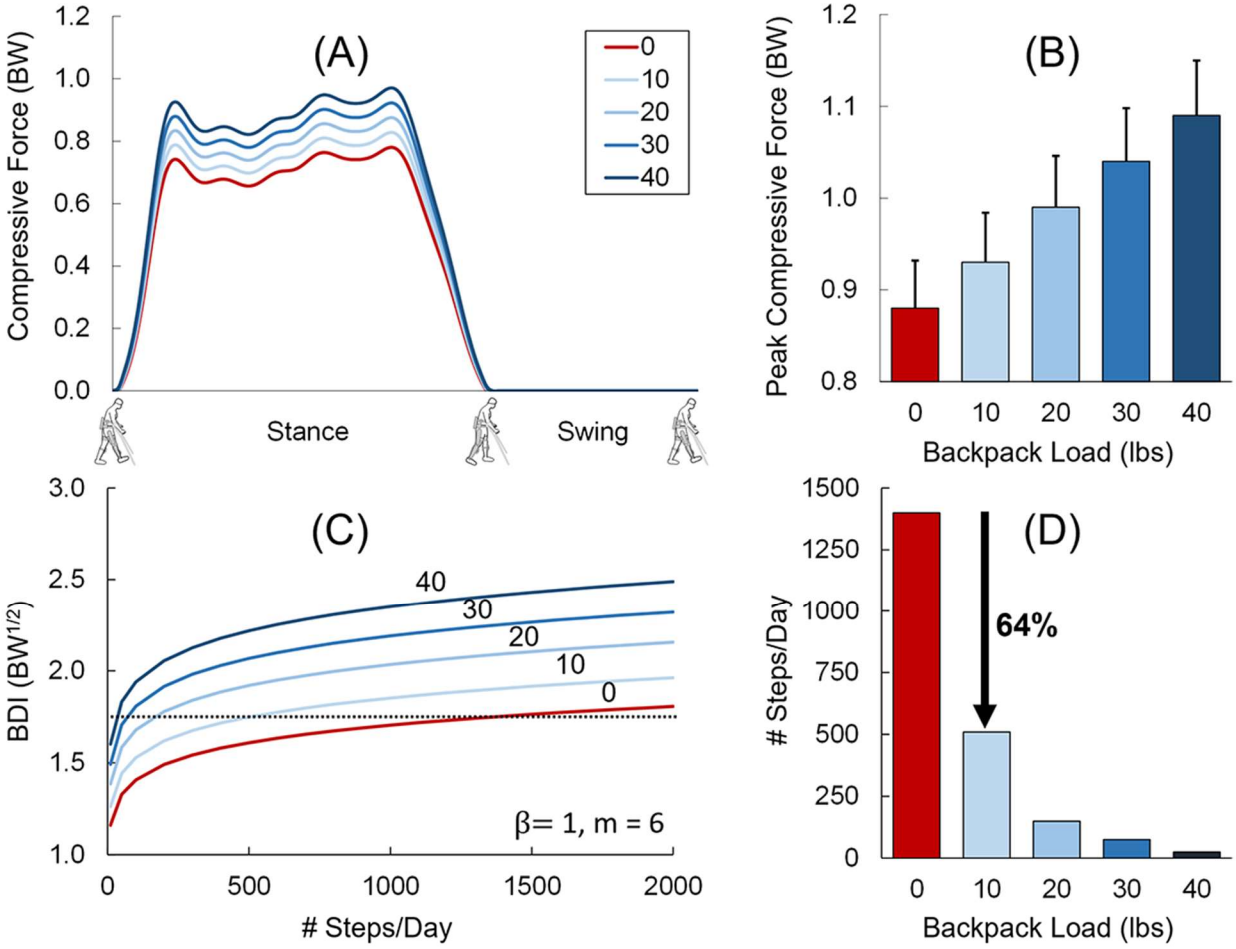


Figure 1. (A-B) Average knee compressive forces from 3 participants with SCI were computed during EAW with 0 to 40lbs backpack loads. The error bars represent +1 SD. (C) BDI was calculated from the peak knee compressive forces and number of steps of EAW per day for each backpack load condition. The horizontal dotted line denotes a representative BDI of 1.75. (D) Number of steps per day to maintain a BDI of 1.75 for each backpack load condition was highly non-linear. Our results show a 64% decrease in the number of steps required per day with a 10lb backpack load.

References (Optional)

[1] Bowley et al., *Orthop Res Soc*, 2001;

[2] Dudley-Javoroski et al., *Osteoporos Int*, 2012.

Acknowledgements (Optional)

VA RR&D #1 I01 RX003561; NSF GRFP 1000346414 (Fellow ID: 2022346414).

Session Category

Rehabilitation Biomechanics and Human Factors: Rehabilitation

OA33-03

Biological Ankle Mechanics During Walking with an Ankle Exoskeleton and Limb Angle Feedback in Individuals with Chronic Stroke

Mr. Steven Thompson BS[1,2], Dr. Jason Franz PhD[1,2], Dr. Gregory Sawicki PhD[3], Dr. John Baratta MD, MBA[1], Dr. Michael Lewek PT, PhD[1]

[1]University of North Carolina at Chapel Hill, Chapel Hill, NC, United States. [2]North Carolina State University, Raleigh, NC, United States. [3]Georgia Institute of Technology, Atlanta, GA, United States

Introduction

Following stroke, reduced paretic ankle plantarflexor moment and trailing limb angle (TLA) contribute to decreased paretic propulsion. Ankle exoskeletons (EXOs) address reduced ankle moment by supplying torque in parallel with weakened plantarflexor muscles. EXO assistance, however, does not reliably increase paretic propulsion due to concurrent reductions in TLA [1]. We addressed reduced TLA with visual feedback, but found that only TLA feedback, not EXO assistance, improved propulsion in those with and without stroke [2,3]. Here, to ascertain why EXO assistance did not improve propulsion, we investigated the role of human "motor slacking," in which users reduce their biological output, as a potential explanation. We predicted that as EXO assistance increased, biological ankle moment would decrease, resulting in no change in total mechanical output from the ankle during walking.

Methods

To date, seven individuals post-stroke walked at their comfortable speed while wearing an ankle EXO (Biomotum) providing paretic plantarflexor assistance (0%-,15%-,25%-body weight [BW]). Participants walked with each combination of EXO assistance and either no TLA feedback, feedback of typical TLA, or feedback of typical+5° TLA. We used inverse dynamics to obtain total ankle moment (peak and impulse). We subtracted EXO torque from the total to obtain the underlying biological contribution for comparison between conditions.

Results

Data from five participants are reported. Total peak ankle moment remained unchanged as EXO assistance increased (1.29±0.16, 1.30±0.15, 1.29±0.14 $Nmkg^{-1}$ for the 0%-,15%-,25%-BW EXO conditions), while peak biological moment appeared to decrease (1.29±0.16,

1.20±0.15, 1.17±0.13 $Nmkg^{-1}$, respectively) (**Fig. 1A**). Similarly, total ankle angular impulse remained largely unchanged while biological impulse appeared to decrease with EXO assistance (**Fig. 1B**).

Discussion

Here, EXO assistance did not enhance total ankle moment because of a reduction in biological ankle moment comparable to the prescribed EXO assistance. For some goals (e.g., reducing metabolic cost) motor slacking is a positive outcome. Conversely, to assist stroke survivors in augmenting gait capacity, preventing motor slacking is desired. Future work will instruct users to maintain biological ankle function while walking with an EXO to improve paretic propulsion and walking speed.

Images (Optional)

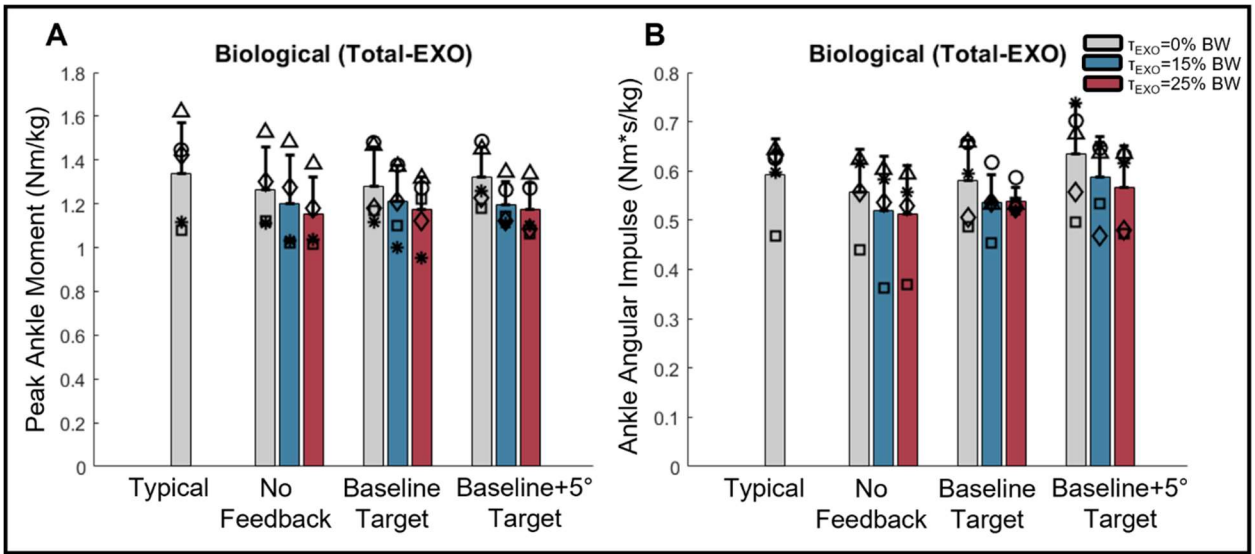


Fig. 1. A) Peak biological ankle moment and **B)** biological ankle moment impulse. Bars are grouped by feedback condition while color denotes EXO condition.

References (Optional)

[1] McCain, JNER, 2019. [2] Thompson, PLoSOne, 2025. [3] Thompson, ASB, 2025.

Acknowledgements (Optional)

NIDILRR – RERC: 90REGE0017: Assisting Stroke Survivors with Engineering Technology (ASSET). NSF 2306660: Improving Older Adults' Mobility and Gait Ability in Real-World Ambulation with a Smart Robotic Ankle-Foot Orthosis. We thank Sonia Wrobel, PT, DPT and Benjamin Killen, PT, DPT, NCS for their assistance with testing sessions.

Session Category

OA33-04

Back Exosuits Enhance Physical Therapy Outcomes Improving Recovery From LBP

Dr. D. Adam Quirk PhD[1], Dr. Diane Dalton DPT[2], Dr. Conor Walsh PhD[1], Dr. Lou Awad PhD[2]

[1]Harvard University, Cambridge, MA, United States. [2]Boston University, Boston, MA, United States

Introduction

Low back pain (LBP) is a costly condition. With physical therapy (PT), one in three individuals with LBP will fail to recover, in part, due to pain and fear during exercise [1]. Wearable exosuits offload back muscles, making lifting tasks easier [2]. This study sought to determine whether a back exosuit could augment PT, hypothesizing that the device would enable individuals to complete functional activities with less effort, thereby improving recovery rates.

Methods

This single-arm clinical trial (CT) evaluated participants completing up to 12 PT visits, including the use of an exosuit [2]. On visits 1, 3, 6, 9, and 12, patient function was appraised using a 2.5-minute asymmetric lifting task performed with assistance ON and OFF (A). At each visit, modified disability questionnaires tracked recovery rates, defined as a 30% reduction in disability [1]. Recovery was compared with a historical control dataset of individuals who received PT at the same clinic without an exosuit, matched for LBP type, and selected to span a comparable age range, baseline disability, and pain-visit frequency to our CT. To assess effectiveness, generalized estimating equations were used to examine whether device assistance could change the number of lifts performed and perceived effort, and whether those in the CT would have a higher % recovery.

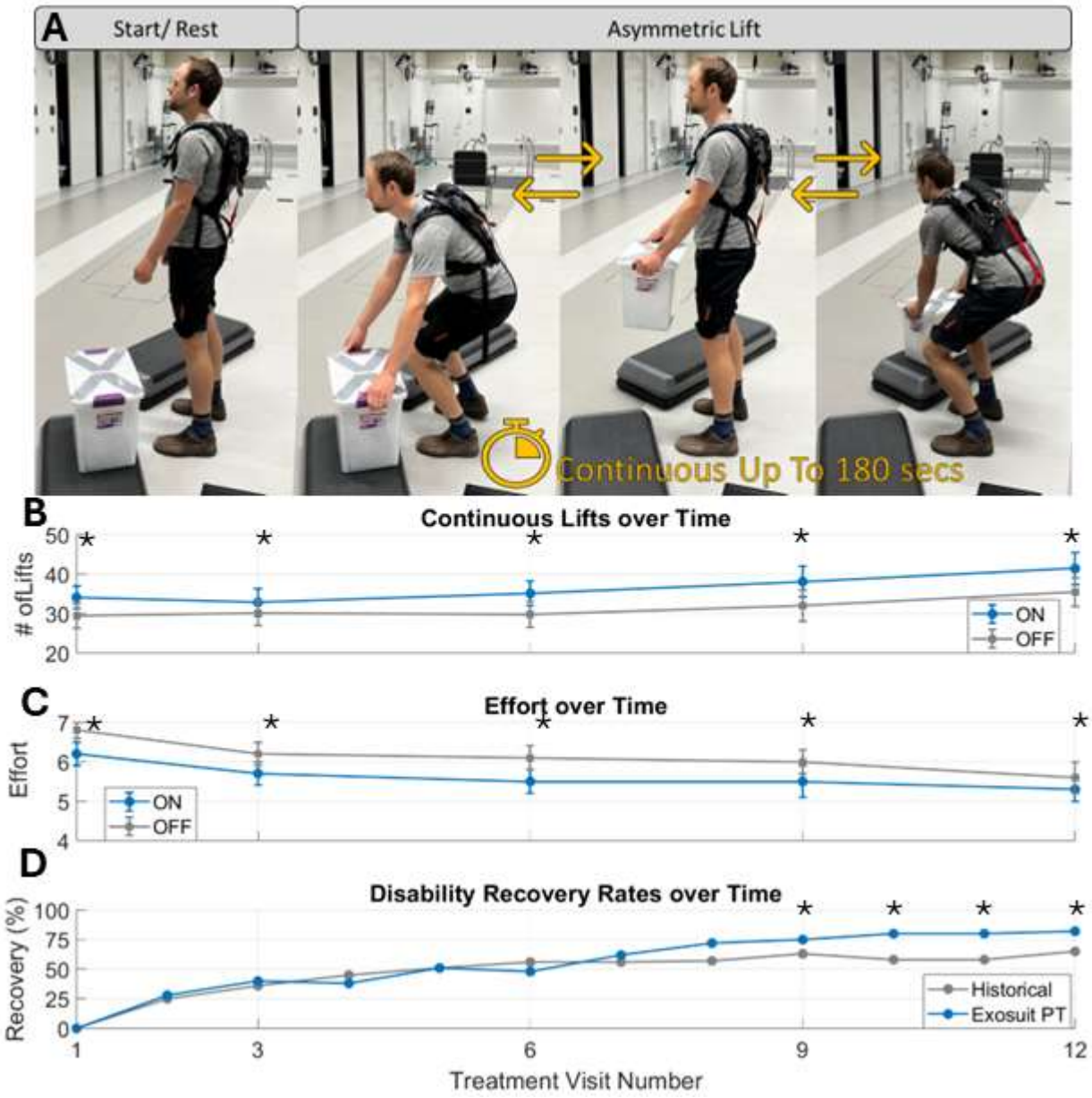
Results

44 participants completed 431 visits with the exosuit. Across all time points, compared to lifting with assistance OFF, individuals can complete 16% more repetitions (B) with a 9-10% reduction in perceived effort (C) with assistance ON ($p<0.001$). Compared with 300 matched control patients, group-by-visit interactions ($p=0.047$) showed higher recovery rates (13-22%) when PT is performed with an exosuit (D).

Discussion

We show that an exosuit can enable patients to complete more repetitions of functional activities with less effort over multiple PT visits. While recovery rates in our historical control group were consistent with the literature [1], we found that our clinical trial participants were more likely to recover from LBP, suggesting that exosuits may augment PT. However, these results will need to be confirmed in parallel randomized clinical trials.

Images (Optional)



References (Optional)

[1] Hill et al., Lancet, 2011

[2] Quirk et al., Pain Medicine, 2023

Session Category

Rehabilitation Biomechanics and Human Factors: Rehabilitation

OA33-05

3D-Printed Tunable Stiffness Chain-Mail Fabric With a Data-Driven Model Enabling Inverse Design for Rehabilitation and Assistive Devices

Mr Jiawen Xu PhD, Prof Ghita Oana Professor, Prof Evans Ken Professor, Mr Xijin Hua Dr

University of exeter, Exeter, Devon, United Kingdom

Introduction

Rehabilitation and occupational tasks require devices that stay compliant during natural motion yet rapidly stiffen to stabilize joints or support loads when needed[1]. Existing stiffness-modulation methods lack the mechanical robustness and adaptive performance required for applications such as tremor suppression in Parkinson's disease. We develop an interlocked chain-mail-inspired fabric that provides tunable, reversible, pressure-controlled stiffness for wearable rehabilitation devices via 3D printing, together with a data-driven inverse-design framework that enables application-specific customization of its mechanical response[2].

Methods

We 3D-printed hollow interlocking chain-mail particles and encapsulated them in a thin elastomeric membrane to form pressure-tunable fabrics (Fig. 1A). Compression, three-point bending, and low-velocity impact tests were performed to characterise stiffness modulation and energy absorption (Fig. 1B). A validated finite-element model was used to generate a stiffness–pressure database, on which a Random Forest classifier enabled inverse design of geometries within prescribed stiffness bands; the workflow and a conceptual wrist-support integration are shown in Fig. 1C–D.

Results

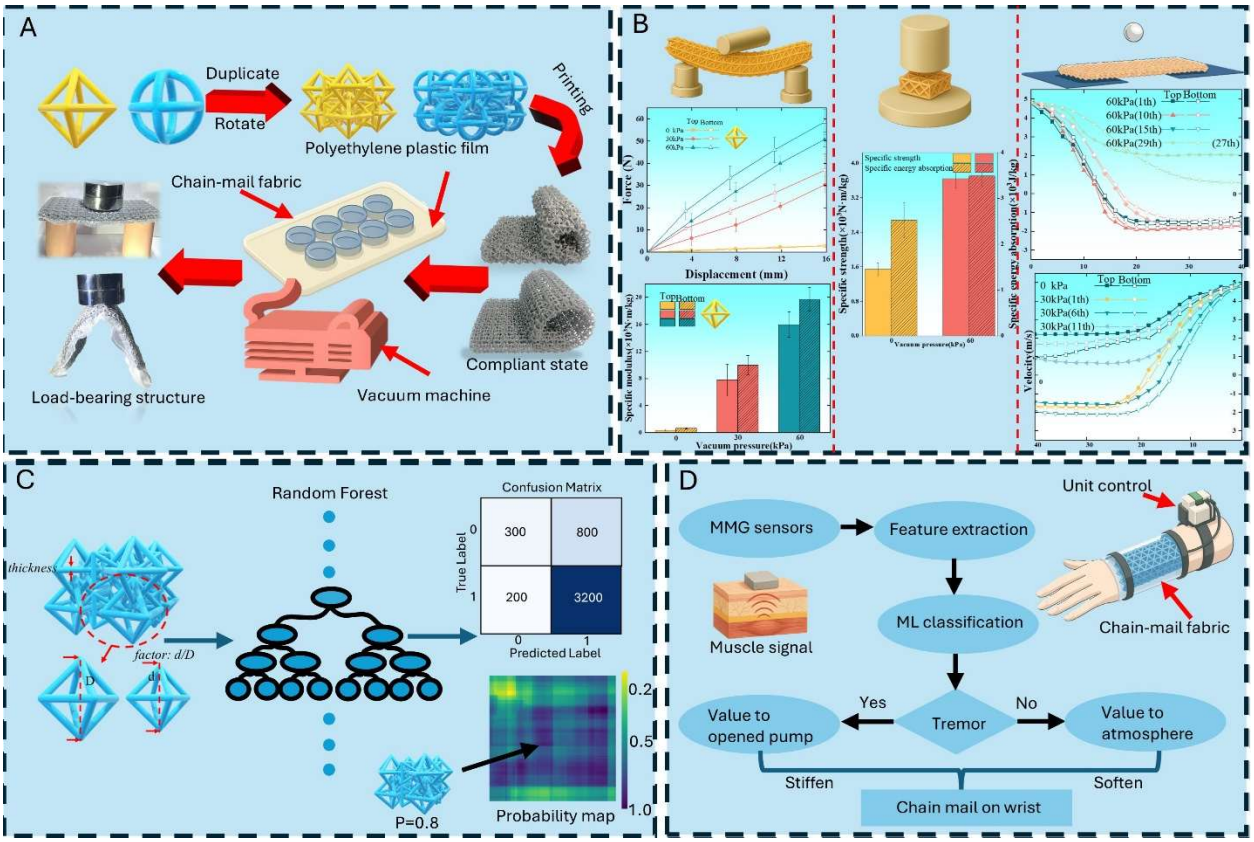
The chain-mail fabric exhibits more than an eight-fold increase in bending modulus upon vacuum-induced jamming. Pressure-dependent compression and impact tests further confirm that increasing confinement enhances load-bearing capacity and specific energy absorption, while maintaining reversible, repeatable stiffness over multiple cycles (Fig. 1B).Using the FE-generated stiffness–pressure dataset, the Random Forest surrogate achieved strong classification performance (F1 ≈ 0.84) and separated designs that do and do not meet the target stiffness band (Fig. 1C). Compared with surrogate GA and CMA-ES,

the RF-based inverse design reached >85% success after two FE evaluations and 100% after three, with improved robustness and design diversity.

Discussion

The experimental and computational results indicate that the inverse-designed tunable-stiffness chain-mail structures combine rapid stiffness activation with high flexibility in the unjammed state under loading and confinement levels relevant to wearable devices. These characteristics suggest that such fabrics are promising building blocks for future wrist and upper limb supports in rehabilitation and occupational settings, where the level of mechanical assistance can be tailored to individual needs, for example in tremor management and repetitive manual tasks.

Images (Optional)



References (Optional)

1.Y. Wang *Nature* **2021**

2.J. Xu *Composites Part B* **2025**

Acknowledgements (Optional)

Session Category

Rehabilitation Biomechanics and Human Factors: Rehabilitation

OA33-06

Hip Exoskeleton Contributions to Leg Swing Initiation During Walking for Individuals Post-Stroke

Ms. Kristen Stewart[1], Dr. Gregory Sawicki[2], Dr. Aaron Young[2], Dr. Richard Neptune[1]

[1]The University of Texas at Austin, Austin, Texas, United States. [2]Georgia Institute of Technology, Atlanta, Georgia, United States

Introduction

Individuals post-stroke with hemiparesis often have asymmetric gait patterns, impaired paretic leg swing initiation [1] and reduced walking speed [2]. Bilateral hip exoskeleton assistance has been shown to improve walking speed [3], but such net measures may not fully reflect the exoskeleton's role in improving gait. Modeling and simulation can be used to determine the direct impact of exoskeleton assistance on gait mechanics. Further, it is unclear which limb assistance strategy most effectively improves walking performance given post-stroke inter-limb differences. The purpose of this study was to determine how a powered hip exoskeleton with different assistance strategies (unilateral versus bilateral) contributes to leg swing initiation during walking for individuals post-stroke. We expect that unilateral assistance will be more effective in directly providing swing initiation due to limb asymmetry.

Methods

Five individuals with chronic post-stroke hemiparesis walked on an instrumented treadmill with a powered Samsung hip exoskeleton with flexion-extension assistance in four conditions: unassisted (UN), unilateral paretic limb (P), unilateral nonparetic limb (NP) and bilateral (BI) assistance [3]. A 23 degrees-of-freedom model with 92 musculotendon actuators was scaled for each subject and simulations were performed in OpenSim [4]. A torque actuator with the exoskeleton controller was applied to the hip. Contributions to leg swing initiation were quantified by calculating the exoskeleton work delivered to the leg during pre-swing.

Results

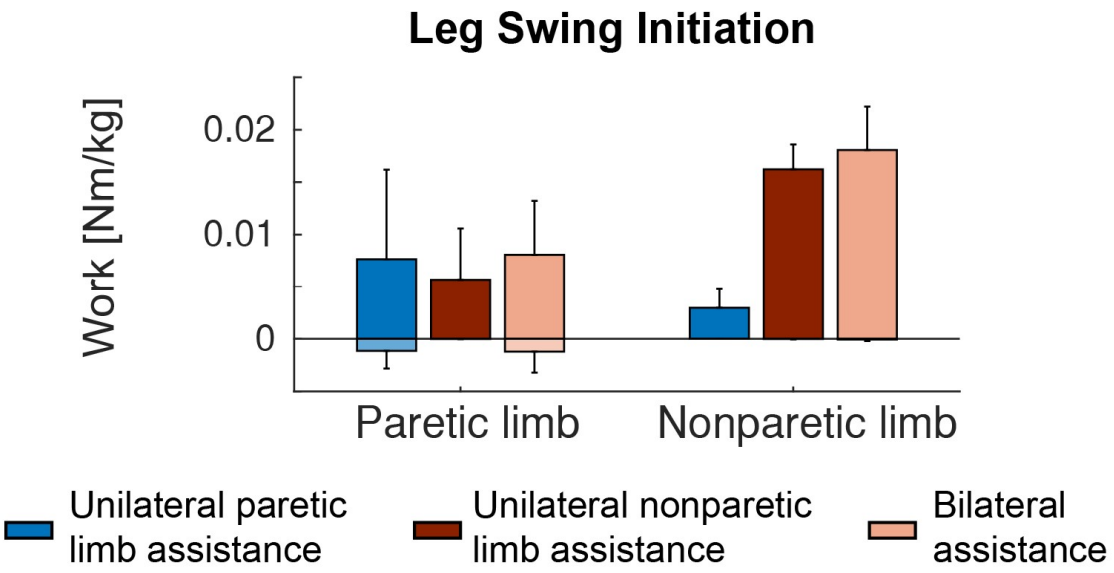
P and BI assistance provided the greatest paretic leg swing initiation (0.0078 Nm/kg), while NP and BI assistance provided greater nonparetic leg swing initiation (0.017 Nm/kg) (Fig. 1).

Discussion

Individuals post-stroke have reduced pre-swing contributions from the paretic limb iliopsoas [1]. Thus, hip exoskeleton assistance acting with the hip flexors can increase

power for swing initiation. For the same assistance magnitude, more power was delivered to the nonparetic limb, which may help explain why only BI assistance improved walking speed [3]. These results begin to elucidate how exoskeleton assistance directly impacts walking performance, which cannot be measured experimentally. Next steps include investigating other biomechanical functions of walking.

Images (Optional)



References (Optional)

[1] Peterson et al., *Gait Posture*, 2010

[2] Olney & Richards, *Gait Posture,* 1996

[3] Pan et al., *Ann. Biomed. Eng*, 2023

[4] Delp et al., *TBME*, 2007

Session Category

Rehabilitation Biomechanics and Human Factors: Rehabilitation

OA34-02

CT-Based Workflow to Generate Subject-Specific Articular Cartilage Models

Ms Nancy Kim[1], Mr Marco Schneider[2], Ms Vickie Shim[1], Mr Thor Besier[1]

[1]Auckland Bioengineering Institute, Auckland, Auckland, New Zealand. [2]FormusLabs, Auckland, Auckland, New Zealand

Introduction

Computational models of the knee have promising clinical applications, but their uptake is limited by challenges in accurately segmenting and reconstructing patient-specific articular cartilage. Failure to capture cartilage surfaces, thickness, and edge boundaries can result in non-physiological stress concentrations and simulation convergence issues [1]. We present an approach to predict articular cartilage geometry using information from bone morphology. The advantage of this approach is that it is applicable to CT scans, which are less costly and more amenable to automated segmentation approaches than MR imaging.

Methods

Our workflow integrates bone point clouds (from segmented CT scans), cartilage thickness measurements (from population models), and subchondral bone surface normal of the femur, tibia, and patella (from fitted statistical shape models). Using these data, we performed a principal component analysis to predict cartilage geometry solely from bone morphology and validated the approach with leave one out analysis using manually segmented MR images from 51 participants.

Results

Fitting bone shape models to segmented geometries resulted in discrepancies below 0.3 mm across the femur, tibia, and patella (Figure 1). For cartilage, the median differences between predicted and segmented point clouds were 0.4 mm for the patella, 0.37 mm for the femur, 0.36 mm for the lateral tibial cartilage, and 0.34 mm for the medial tibial cartilage.

Discussion

Considering MRI voxel sizes of 0.3 × 0.3 × 1.0 mm and manual segmentation errors ranging from 0.1 to 0.5 mm, these results indicate prediction within expected error margins [2]. Our new approach accurately predicted femoral and tibial cartilage, particularly in the central region of the joint. Patellar cartilage predictions were not as good, but further refinement with larger datasets might improve these predictions. Extending cartilage boundaries could

help to reduce stress concentrations by providing smoother transitions at cartilage margins. The comparison between cartilage predicted from articulated bones and from individual bones is currently in progress, along with mesh generation from the predicted cartilage point clouds.

Images (Optional)

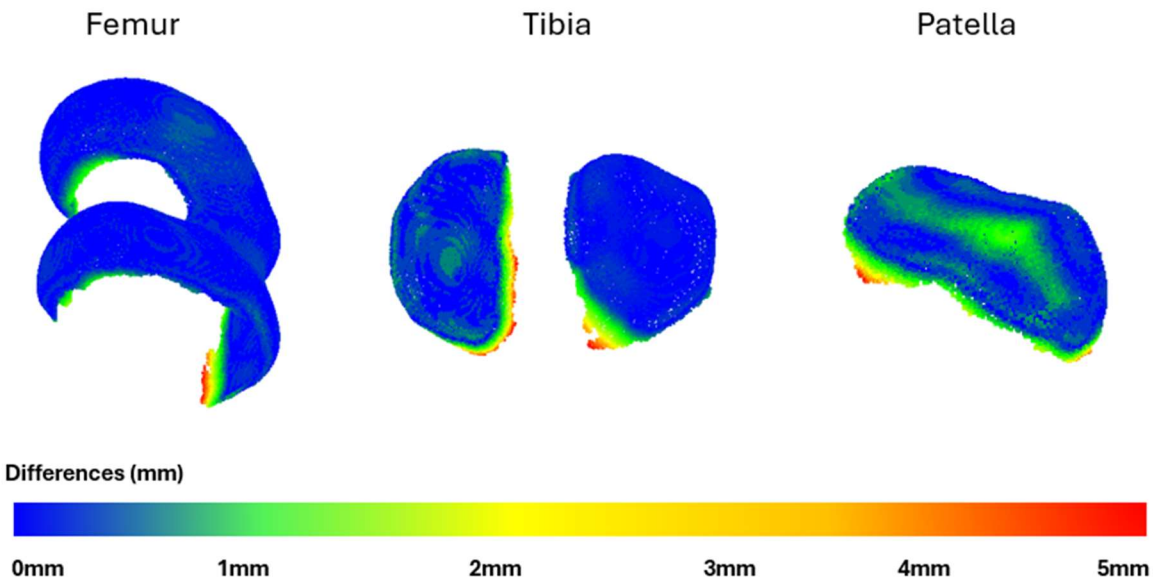


Figure 1. Differences between predicted and segmented femoral, tibial, and patellar cartilages. Colour scale (in mm) indicates the magnitude of differences, with the corresponding bar displayed at the bottom.

References (Optional)

1. H. Donahue et al., J. Biomech. Eng., vol. 124, pp. 273–280, 2002.

2. J. Alibert et al., J. Magn. Reson. Imaging, vol. 45, no. 3, pp. 769–777, 2 017.

Session Category

Musculoskeletal Biomechanics: Joints and Motion

OA34-03

A Biomechanical Assessment of a Two-Foot Vertical Jump at Baseline, 6-month and 12-month following Return to Play from ACL Reconstruction

Mr. Pratham Singh, Dr. Timothy Burkhart

University of Toronto, Toronto, ON, Canada

Introduction

Approximately 3% - 30% of ACL reconstruction patients experience re-injury following return-to-play (RTP) [1]. Current RTP tests do not assess the neuromuscular strategies that a patient may adopt. Therefore, the purpose was to quantify knee biomechanics in ACLR patients in response to a two-foot vertical jump.

Methods

Data was collected on 27 ACLR patients who had been cleared to return to sport (M:14; F:13; Age: 24.92 [5.14]) and 27 recreationally active healthy participants (M:17; F:10; Age: 24.44 [3.27]). Motion data, ground reaction forces (GRFs) and muscle activations were collected while a two-foot vertical jump was performed. Data were analyzed from landing to 200ms after landing. Each patient also performed resisted knee extension/flexion on a dynamometer. Limb symmetry index (LSI = involved limb/uninvolved limb) was quantified for all variables.

Results

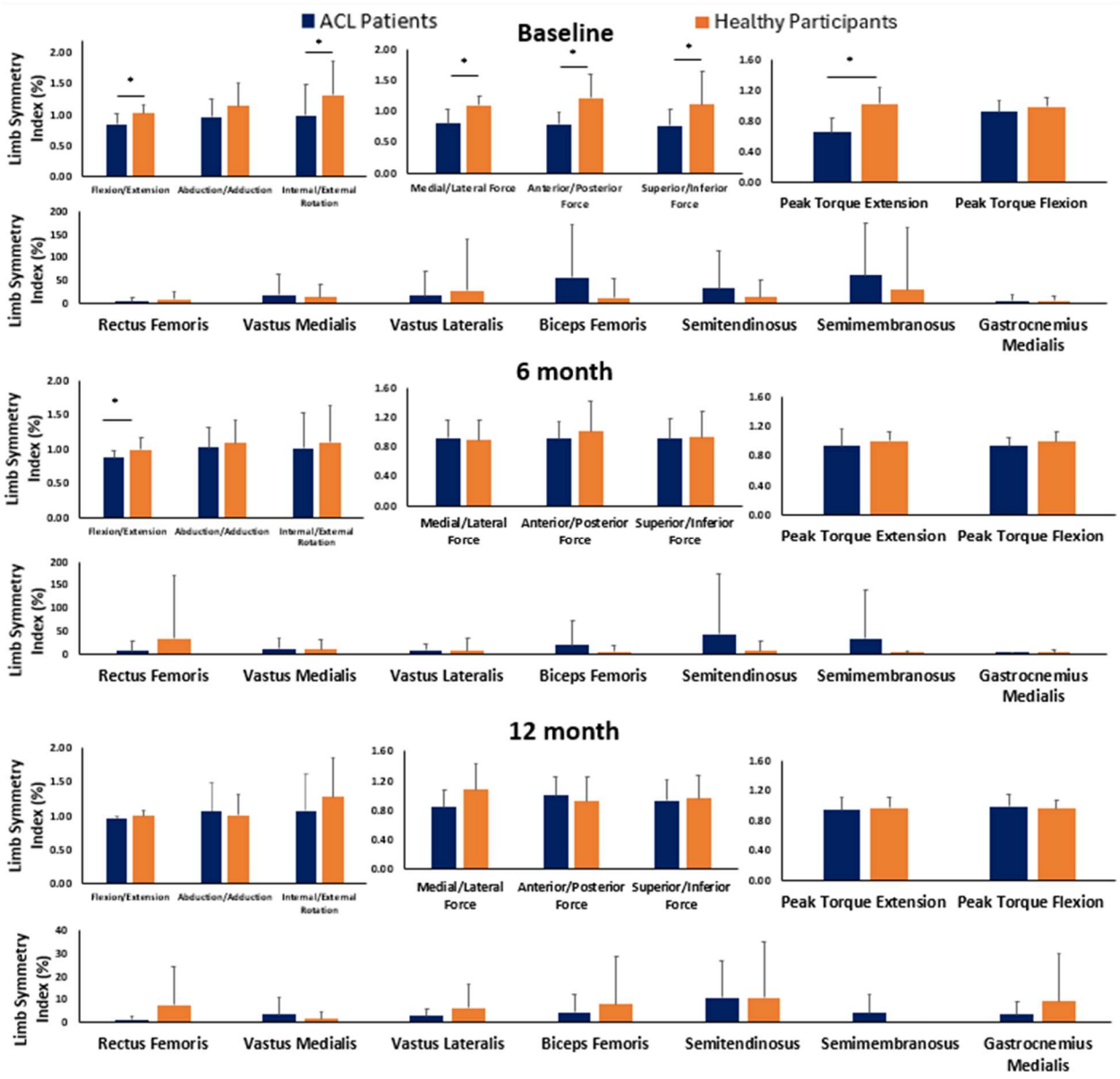
At baseline, the ACL patients had a significantly lower LSI than the healthy participants for knee flexion/extension (0.85 vs 1.02) as well as knee internal/external rotation (0.98 vs 1.32) angles. The ACL patients also had significantly smaller LSI values for GRFs in the AP (0.80 vs 1.10), ML (0.78 vs 1.21) and SI (0.76 vs 1.10) direction. The ACL patients also had significantly smaller LSI values for peak torque extension (0.66 vs 1.03) on the dynamometer. There was no significant difference in LSI values of muscle activation patterns. After 6 months, ACL patients had significantly lower LSI for knee flexion/extension (0.87 vs 0.99) angles. After 12 months, there was no significant difference in LSI values for knee joint kinematics, GRFs, muscle activation patterns or peak torque values.

Discussion

Despite greater peak muscle activation being observed, strength deficits in the involved limb persisted up to 12 months post RTP (baseline). This may indicate that neuromuscular contributions are adapting to injury where increased neural drive is required to achieve similar or less output. This may indicate that these patients were not yet ready to RTP

despite passing a commonly used vertical jump test. Understanding neuromuscular contributions during dynamic movements may provide a better indication of when patients are ready to RTP following ACLR.

Images (Optional)



References (Optional)

[1] Morris et al., Clin Sports Med, 2016

Session Category

Musculoskeletal Biomechanics: Joints and Motion

OA34-04

Walking With Enhanced Ankle Plantarflexor Muscle Leverage Modulates Muscle Neuromechanics in Older Adults

Dr. Daniel Davis[1], Mr. Andrew Peterson[1], Dr. Jason Franz[2], Dr. Kota Takahashi[1]

[1]University of Utah, Salt Lake City, UT, United States. [2]UNC Chapel Hill and NC State, Chapel Hill, NC, United States

Introduction

Musculoskeletal impairment reduces quality of life and longevity. Deficits in the ankle plantarflexor musculature with age are particularly impactful [1], given these muscles' importance to walking function. Changes in plantarflexor muscle operating condition in younger adults - slower fascicle shortening and increased force - have been demonstrated when walking with greater ankle muscle leverage via increased footwear longitudinal bending stiffness [2]. Improvements to muscle force-velocity behaviour position footwear stiffening as a potentially useful intervention for improving plantarflexor muscle function and overall walking performance in older adults. Thus, the purpose of the present study was to examine plantarflexor muscle operating conditions in older adults when walking with greater footwear bending stiffness.

Methods

Twenty older adults (9F; 70±6 yrs) walked at 1.2 m/s in three different footwear stiffness conditions (termed Low, Medium, and High stiffness). We employed cine B-mode ultrasonography and motion capture to characterize stance-phase medial gastrocnemius (MG) and soleus fascicle dynamics and surface electromyography to quantify stance-phase muscle excitation. We compared variables across conditions using one-way repeated measures ANOVA and post-hoc pairwise comparisons.

Results

Ultrasound data for three participants were excluded due to image quality issues. Enhancing plantarflexor muscle leverage via increased footwear stiffness slowed the average stance-phase fascicle velocity for the MG ($p=0.02$) and soleus ($p<0.01$) (Figure 1A&D). Stance-phase integrated excitation increased with greater stiffness for the MG ($p=0.02$; Figure 1B) but not the soleus ($p=0.79$; Figure 1E). Lastly, greater footwear stiffness increased average estimated MG and soleus muscle forces (both $p<0.001$; Figure 1C&F).

Discussion

Older adult ankle plantarflexor muscle operating conditions, specifically shortening velocity and estimated force, were improved when walking with greater plantarflexor muscle leverage via footwear stiffening. Acutely, improving plantarflexor muscle function may enhance older adult's capacity for meeting the propulsive demands of everyday walking. Used as a longer-term intervention, the increase in muscle force and medial gastrocnemius excitation could serve as useful stimuli to address age-related ankle muscle atrophy and subsequent walking performance deficits.

Images (Optional)

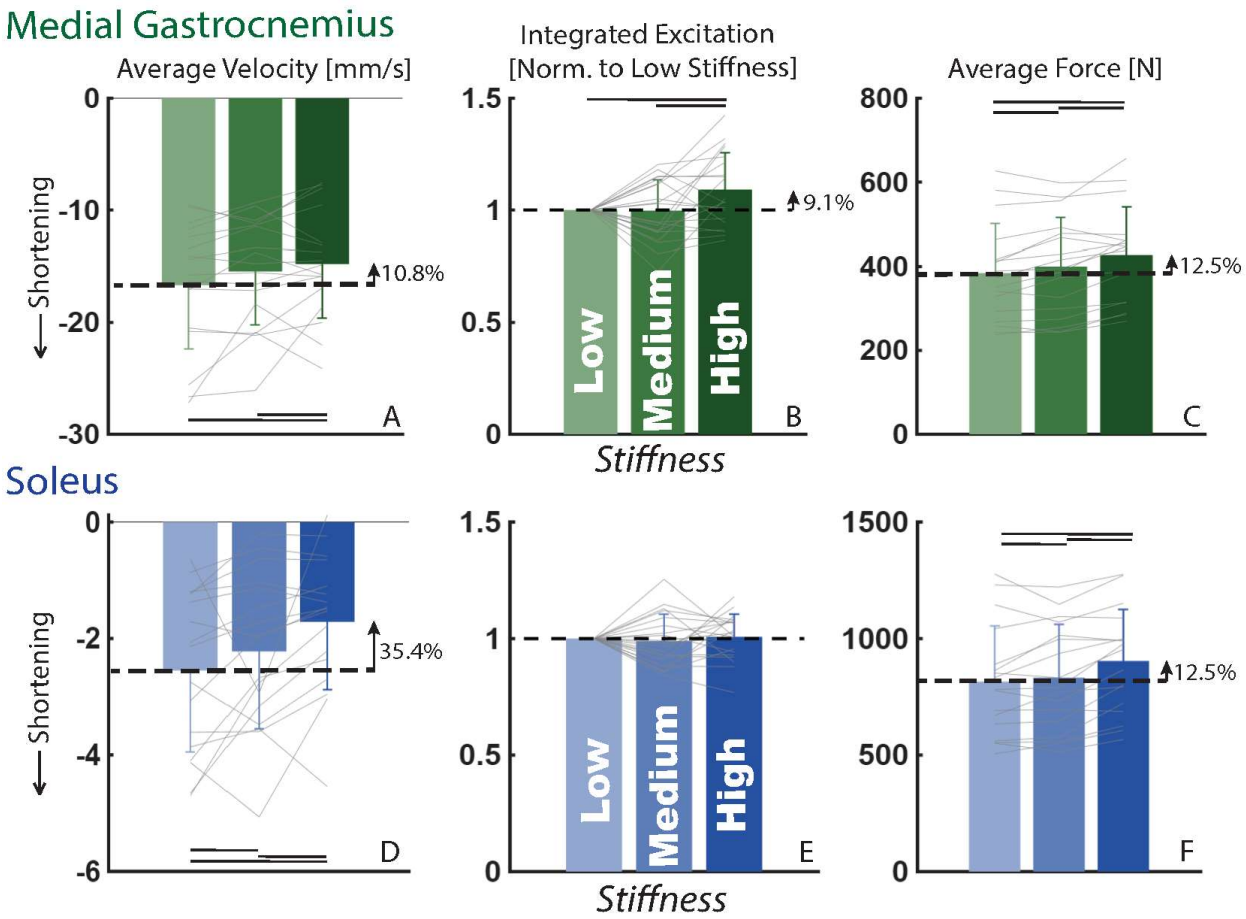


Figure 1: Medial gastrocnemius (top row) and soleus (bottom row) stance-phase average velocity (panels A & D), integrated excitation normalized to the Low stiffness condition (B & E), and stance-phase average force along the fascicle (C & F). Increasing footwear stiffness is represented by darkening color from left to right. Horizontal bars indicate statistically significant pairwise differences ($p < 0.05$).

References (Optional)

[1] Graf *et al.*, Arch Phys Med Rehabil, 2005.

[2] Takahashi *et al.*, Sci Reports, 2016.

Acknowledgements (Optional)

This work was supported by NIH T32TR004394 (DJD) and NIH R01AR081287 (KZT, JRF).

Session Category

Musculoskeletal Biomechanics: Joints and Motion

OA34-05

Longitudinal Analysis of Hip Joint Contact Pressure in Growing Children using Subject-Specific Multi-Scale In-Silico Simulations

Dipl.-Ing. Kevin Kitir[1], Dr. Alexander Synek[2], Univ.-Prof. Dieter Pahr[2], Assoc.-Prof. Hans Kainz[1]

[1]University of Vienna, Vienna, Vienna, Austria. [2]Technical University of Vienna, Vienna, Vienna, Austria

Introduction

Mechanical loading plays a central role in skeletal development during childhood. While bone adaptation has been widely studied [1,2], considerably less is known about how articular cartilage responds to loading during growth. Finite Element (FE) studies in pediatric hip dysplasia have shown abnormally high peak contact pressures [3], but investigations in typically developing children are scarce and mostly cross-sectional. Understanding longitudinal changes in physiological hip joint loading is essential for establishing normative reference data and identifying early deviations preceding orthopedic disorders. **We hypothesized that growth-related increase in body weight is compensated by increased contact area due to bone growth, maintaining relatively stable cartilage contact pressures over time** [4].

Methods

Typically developing children underwent MRI-based anatomical imaging and gait analysis at two time points approximately two years apart. Subject-specific 3D models of pelvis, femur, and hip cartilage were reconstructed from MRI using manual segmentation for bone and parametric extrusion for cartilage. Musculoskeletal simulations based on MRI-informed models were used to calculate joint kinematics and joint contact forces, which served as boundary and loading conditions for FE simulations. For both time points, peak contact pressures (95th percentile) were computed throughout the stance phase of a representative gait trial.

Results

Data of three from nine available participants was analysed so far. Contrary to our hypothesis, preliminary results indicate an increase in cartilage contact pressure between time points in both qualitative and quantitative comparisons (Figure 1). However, given the

small preliminary sample and marked inter-subject variability, paired t-tests did not reach conventional statistical significance ($\alpha = 0.05$).

Discussion

Although preliminary and limited by sample size, these results suggest that hip cartilage loading may increase during growth despite structural adaptation. The proposed longitudinal pipeline demonstrates the feasibility of combining MRI, motion analysis, musculoskeletal modeling, and FE simulation in pediatric cohorts. The emerging normative data will support future comparisons with orthopedic pathologies and may help identify early indicators of abnormal joint loading.

Images (Optional)

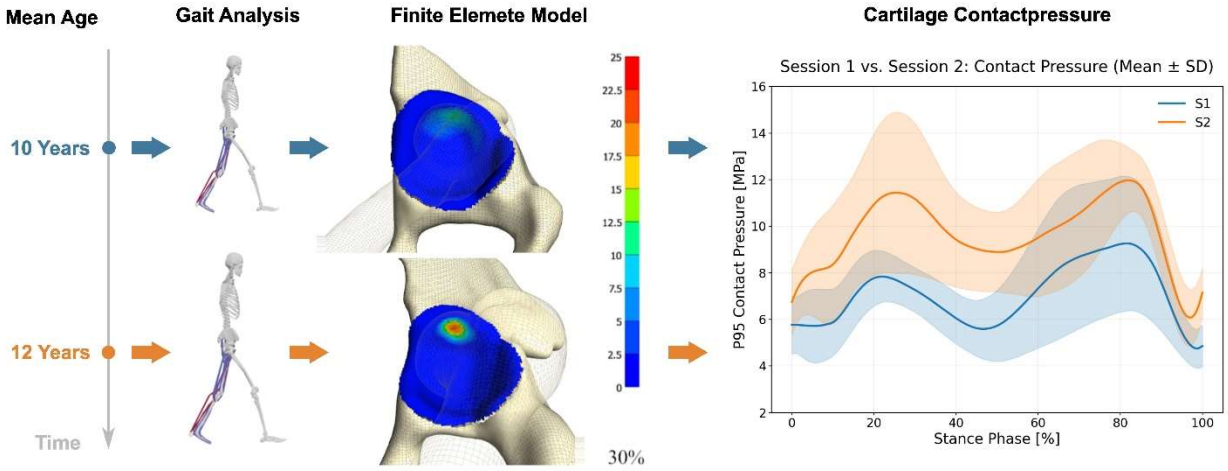


Figure 1: Method workflow and hip cartilage contact-pressure results. Left: timeline showing mean participant age at Session 1 and Session 2. Next: schematic OpenSim models used to compute loads and kinematics. Center: qualitative contact-pressure maps for one subject; acetabular cartilage and hip bone shown, femur position semi-transparent, pressure distribution shown at 30% of the stance phase; color scale in MPa. Right: group-averaged contact pressure (mean ± SD across subjects) over the duration of the stance phase, comparing Session 1 and Session 2 (MPa).

References (Optional)

[1] Frost, The Anatomical Record, 2001

[2] Pivonka et al., CISM International Centre for Mechanical Sciences, 2018

[3] Incze-Bartha et al., Journal of Personalized Medicine, 2023

[4] Kainz et al., Gait & Posture, 2024

Acknowledgements (Optional)

This research was partly funded by the European Research Council (ERC-2024-COG, 101170218, INSIDE-BONE).

Session Category

Musculoskeletal Biomechanics: Joints and Motion

OA35-02

Graph Neural Network Surrogates for Finite Element Modeling of Femur Mechanics: A Comparative Study

Ms Sikha O K[1], Mr Morteza Rasouligandomani[1], Ms Elham Alizadeh[1], Mr Jakka Prasad[1], Mr Sai Natarajan[1], Mr Miguel A González Ballester[1,2], Mr Ludovic Humbert[3], Mr Jérôme Noailly[1], [4]

[1]Universitat Pompeu Fabra, Barcelona, Barcelona, Spain. [2]Icrea, Barcelona, Barcelona, Spain. [3]3D-Shaper Medical, Barcelona, Barcelona, Spain. [4]

Introduction

Finite Element analysis is the standard for femur biomechanics but is computationally expensive.Machine-learning surrogates—especially Graph Neural Networks (GNNs)—provide a faster alternative by modeling FE meshes as graphs (nodes ↔ mesh-nodes, edges ↔ connectivity) and predicting node-level stress/strain [1,2]. This study compares hybrid deep-GNNs to find models that best balance accuracy, speed, and generalizability for femur biomechanics.

Methods

Figure.1 illustrates the surrogate-modelling workflow. We analyzed 128 FE femur models (64 controls, 64 fractures) with lateral-fall simulations, generating mechanical fields at 132,120 nodes and 126,800 hexahedral elements. FE meshes were converted to graphs, with nodes representing FE nodes and edges encoding connectivity. Each node included geometric labels, femoral parameters, density-derived stiffness, and spatial coordinates, and the model predicted six node level stress values. Graphs were normalized and trained using a DeepHybridGNN combining GIN(MLP-aggregation), GraphSAGE(stabilizes neighbor propagation), and GAT(weights neighbors via attention) within residual blocks (prevent overfitting). Training used neighborhood sampling, Adam optimizer with Smooth L1 loss,LR 0.0005, gradient accumulation, mixed precision, and a plateau-based LR scheduler, with all graph splits and normalization statistics verified beforehand.

Results

The results in Table.1 show that incorporating richer anatomical and mechanical features substantially improves surrogate performance. Models using only density and spatial coordinates (GIN–SAGE–GAT) achieve moderate accuracy, with $R^2 \approx 0.36$-0.44 and MAE ≈ 3.6–4.5. Increasing hidden dimensions does not improve performance, suggesting limited

benefit from scaling depth alone. In contrast, the SAGE–GAT model using geometric labels, femoral parameters, and nodal stiffness achieves a much higher R^2 (0.85–0.87) and markedly lower MAE, indicating that feature quality—rather than architecture size—is the dominant factor in accurately predicting node-level stress fields.

Discussion

GNNs can effectively surrogate finite-element femur models, predicting node-level stress with much lower computation time. Models using detailed biomechanical features outperform those with only density and coordinates, highlighting the importance of informative inputs. The DeepHybridGNN, combining GIN, GraphSAGE, and GAT, captures both local and global structure, offering a fast and accurate framework for clinically scalable fracture risk assessment.

Images (Optional)

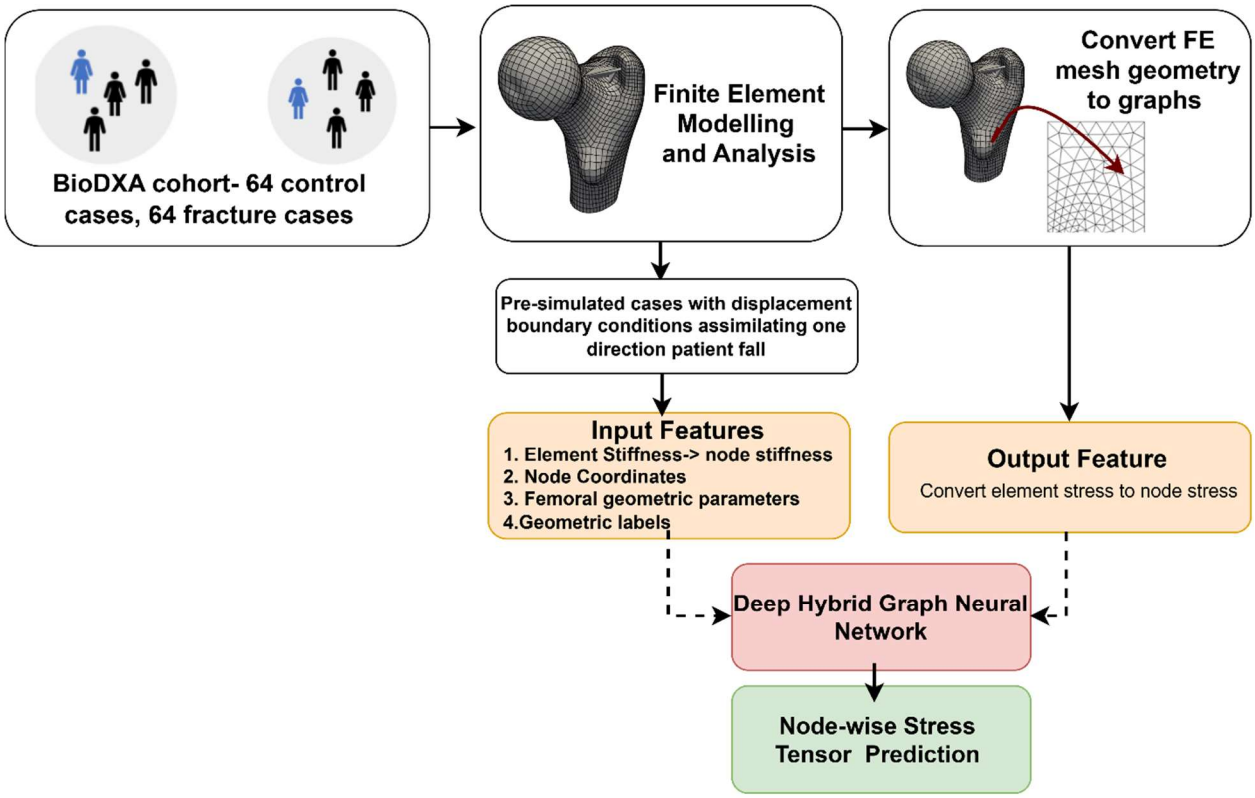


Figure.1 Graph neural network based surrogate modelling overview

GNN Architecture	Input Features	R2 Score		Mean Absolute Error	
		Train	Test	Train	Test
GIN->SAGEConv-> GAT with residual connections Hidden layers: 64	Node level density, (X,Y,Z) coordinates	0.3689	0.3606	4.33	4.54
GIN->SAGE->GAT with residual connections Hidden layers: 128 6 layers	Node level density, (X,Y,Z) coordinates	0.4432	0.4356	3.66	4.10
SageConv->GAT Hidden layers: 64	Geometric labels, Femoral geometric parameters, Nodal Stiffness	0.8671	0.8482	0.0182	0.0554

Table.1 Quantitative comparison of Graph neural network based surrogate models in predicting nodal stress

References (Optional)

1. Awal, R., Naznin, M., & Faisal, T. R., Expert Syst. Appl., 264:125916 (2025)
2. Franco, N. R., et al., Chaos, 33:123456 (2023)

Acknowledgements (Optional)

Funding by the Spanish Government (SpineFX-CPP2023-010970), AGAUR (BoneFX-2023 BP 00224), and by the European Research Council (ERC-2021-CoG-O-Health-101044828)

Session Category

Emerging Areas: N/A

OA35-03

Sensor-less Prediction of Posture-Specific Peak Interface Pressures from Anthropometry Using Machine Learning

Ms. Seohyun Lee M.S. Candidate, Ms. Seoyoung Kim Undergraduate Student, Prof. Taeyong Lee Ph.D.

Ewha Womans University, Seoul, Seoul, Korea, Republic of

Introduction

Pressure ulcers are a major complication in immobilized patients, yet most predictive systems either stratify patient-level risk from electronic health records or reconstruct pressure maps using dedicated sensors, with few models directly estimating posture-specific interface pressures from anthropometry alone. This study proposes a sensor-less, machine learning–based framework that predicts peak interface pressures at ulcer-prone regions using a minimal set of anthropometric variables.

Methods

Interface pressure and overhead RGB data were collected from 81 adults in standardized supine, left-lateral, and right-lateral postures. Peak pressures were extracted by reconstructing 32 × 64 pressure maps, detecting local maxima, and mapping these to ulcer-prone regions via MediaPipe-based skeletal landmarks. Using BMI, body weight, waist circumference, and hip circumference as inputs, region-wise deep neural network (DNN) and Gaussian process regression (GPR) models were trained with 5-fold GroupKFold cross-validation, Elastic-Net–based stable feature selection, and permutation importance analysis. To evaluate usability, test samples were categorized as intra-range or extra-range depending on whether all anthropometric values lay within or outside the training bounds.

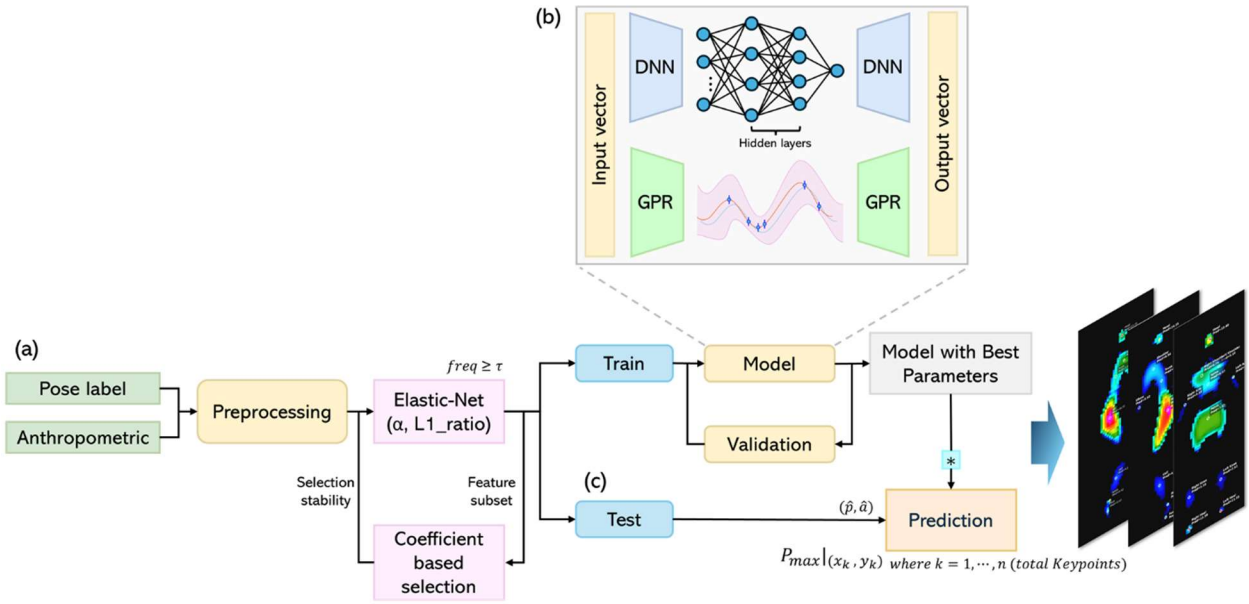
Results

Cross-validated performance across 27 posture–region combinations was high, with R^2 values of approximately 0.82–0.98 (grand mean ≈ 0.93) and MAE values of 0.06–0.59 kPa (mean ≈ 0.22). The DNN slightly outperformed the GPR overall (R^2 ≈ 0.94 vs. 0.93; MAE ≈ 0.21 vs. 0.24). In intra-range tests using inputs within the training anthropometric bounds, the DNN achieved R^2 ≈ 0.93 with MAE ≈ 0.29 kPa, whereas the GPR achieved R^2 ≈ 0.89 with MAE ≈ 0.36 kPa. Under extra-range conditions, the DNN and GPR attained R^2 ≈ 0.85/0.77 and MAE ≈ 0.44/0.65 kPa, respectively.

Discussion

These findings show that posture-specific peak interface pressures can be estimated from a compact anthropometric feature set without pressure sensing at prediction time, enabling low-cost, sensor-less, individualized pressure-risk estimation that is agnostic to bed hardware or camera availability. However, the current framework is limited to static posture snapshots and does not model temporal changes in pressure during repositioning. As a next step, the model will be extended to predict how interface pressures decrease as the bed or trunk angle is gradually adjusted, enabling angle-specific guidance for pressure-relief maneuvers.

Images (Optional)



Acknowledgements (Optional)

This work was funded by grants from Korea Health Industry Development Institute (RS-2023-KH141374).

Session Category

Emerging Areas: N/A

OA35-04

Generating Physically Realistic Footwear Contact Pressure Distributions with Diffusion Models

Mr. Gerard Aristizábal Pla, Prof. Kurt Beschorner

University of Pittsburgh, Pittsburgh, Pennsylvania, United States

Introduction

Diffusion models excel at image generation with flexible input prompts. Their use in biomechanics, where outputs must be realistic, remains underexplored. Shoe-ground contact mechanics are a biomechanical metric relevant to user performance and safety that may be predicted by diffusion models. We evaluated diffusion models for predicting shoe-tread contact pressure distributions trained from frustrated total internal reflection (FTIR) data.

Methods

A method that calibrates and converts pixel intensities from FTIR to vertical force was used to capture pressure maps for 10 shoes at varying shoe angles and force levels (using ~1500 frames of data). For generative modeling, we fine-tuned two large Stable Diffusion–based models (≈860M parameters each), ControlNet and IP-Adapter (Figure 1). IP-Adapter [1] predicted contact masks from smartphone outsole images, foot angles, and vertical forces (evaluated using Dice score). ControlNet [2] generated pressure distributions from contact masks and force inputs (evaluated using mean absolute error, MAE). During fine-tuning, only LoRA adapters attached to the U-Net attention layers were trained (≈5–8M trainable parameters), while the base diffusion weights and the VAE remained frozen. All models were trained and evaluated using leave-one-shoe-out cross-validation to assess generalization to unseen footwear and variability in loading conditions, with each fold trained for 30 epochs (~20,000 optimization steps). To incorporate biomechanical inputs, the U-Net was conditioned on force and foot-angle scalars via positional encodings.

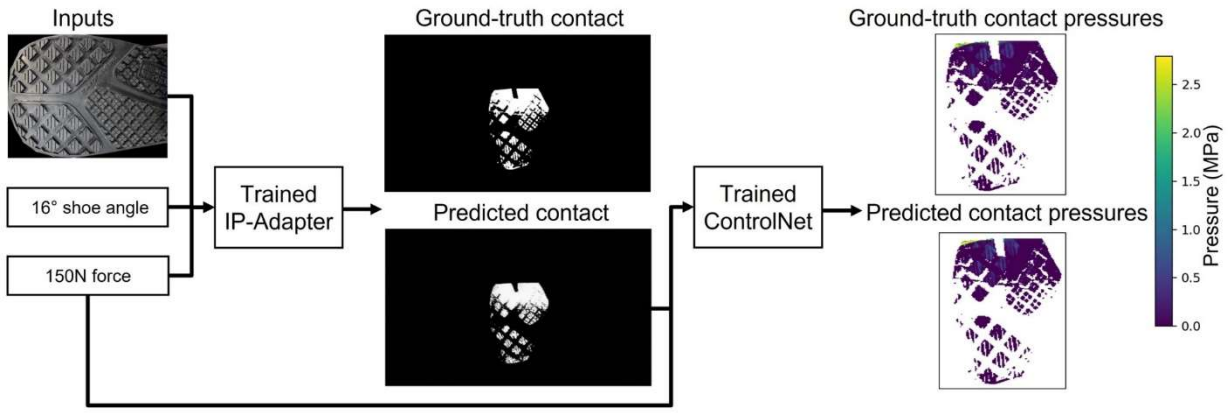
Results

The FTIR intensity-to-force calibration achieved an average R^2 of 0.97. Across ten folds, ControlNet produced pressure maps with a mean MAE of 2 kPa, and IP-Adapter generated contact masks with a mean Dice score of 0.61.

Discussion

A sequence of diffusion models was developed and was able to accurately predict contact regions and pressures within these regions. ControlNet produced pressure distributions that learned physics, whereas the IP-Adapter generated contact regions from readily available visual and biomechanical inputs. Together, these findings show that diffusion models can generate physically realistic pressure distributions across diverse footwear conditions. Future work can extend generalizability of this model and integrate it within footwear digital twins.

Images (Optional)



References (Optional)

[1] Ye *et al.* , arXiv, 2023; [2] Zhang *et al.* , arXiv, 2023.

Acknowledgements (Optional)

We thank Jun-Yan Zhu for sharing his insights.

Session Category

Emerging Areas: N/A

OA35-05

Development of a Novel Neural Network-Based Approach for Estimating Ground Reaction Forces From Kinematic Data in Gait Analysis

Mr. Giulio Rigoni[1], Ms. Maria Dalle Vacche[1], Mr. Oier Zazpe[1,2], Ms. Federica Beghetti[1], Ms. Fabiola Spolaor[1], Prof. Damiano Varagnolo[1], Prof. Zimi Sawacha[1]

[1]University of Padova, Padova, Veneto, Italy. [2]Mondragon Unibertsitatea, Mondragòn, Basque country, Spain

Introduction

Kinematic and kinetic data (i.e., ground reaction forces, GRFs) are pivotal to human movement analysis. The growing need for real-world applications requires gathering these data out of laboratories. Even though this has been partially covered by markerless motion analysis, the provision of GRFs in absence of force plates is still an open challenge.

The present study aims to present a novel Spatio-Temporal Graph Convolutional Network (ST-GCN) based approach to predict GRF from solely kinematics input and seeks to assess its accuracy in regards to different state of the art GRF estimation methods.

Methods

A ST-GCN to predict the 3 GRF components during gait was developed based on 19 marker trajectories (IORgait protocol) maximizing informativeness through Partial Least Squares regression. Graph neural network approach was applied to implement awareness of markers spatial connections. 401 complete gait cylces were collected (8 Vicon cameras, 2 Bertec force plates) from 39 healthy (45.40 ± 20.47 years; 24.58 ± 3.57 kg/m^2) and 26 Parkinson's Disease individuals (70.74 ± 7.56 years; 25.78 ± 3.39 kg/m^2) and used as training dataset. The resultant GRFs were compared with 3 state of the art GRF estimators: OpenGRF [1]; GaitDynamics [2]; an image-based NN [3] re-trained on the same proprietary dataset. The validation of all four solutions was performed by comparing the predicted GRFs with the experimental one of 10 healthy individuals (22.70 ± 2.60 years; 21.16 ± 2.59 kg/m^2) not included in the training; RMS, coefficient of multiple correlation (CMC), and SPM [4] were used as comparison metrics.

Results

The ST-GCN training phase achieved an overall root mean square error (RMS) of 0.633 N/m.

Both GaitDynamics and the image-based NN reported the highest correlation (CMC > 0.81) and the lowest RMS (**Figure 1**). Among the three GRF components, the mediolateral direction revealed the lowest agreement.

Discussion

In this study, NN demonstrated a potential for on the field GRFs estimation. Future developments will focus on expanding the training dataset, including additional tasks as well as pathologies.

Images (Optional)

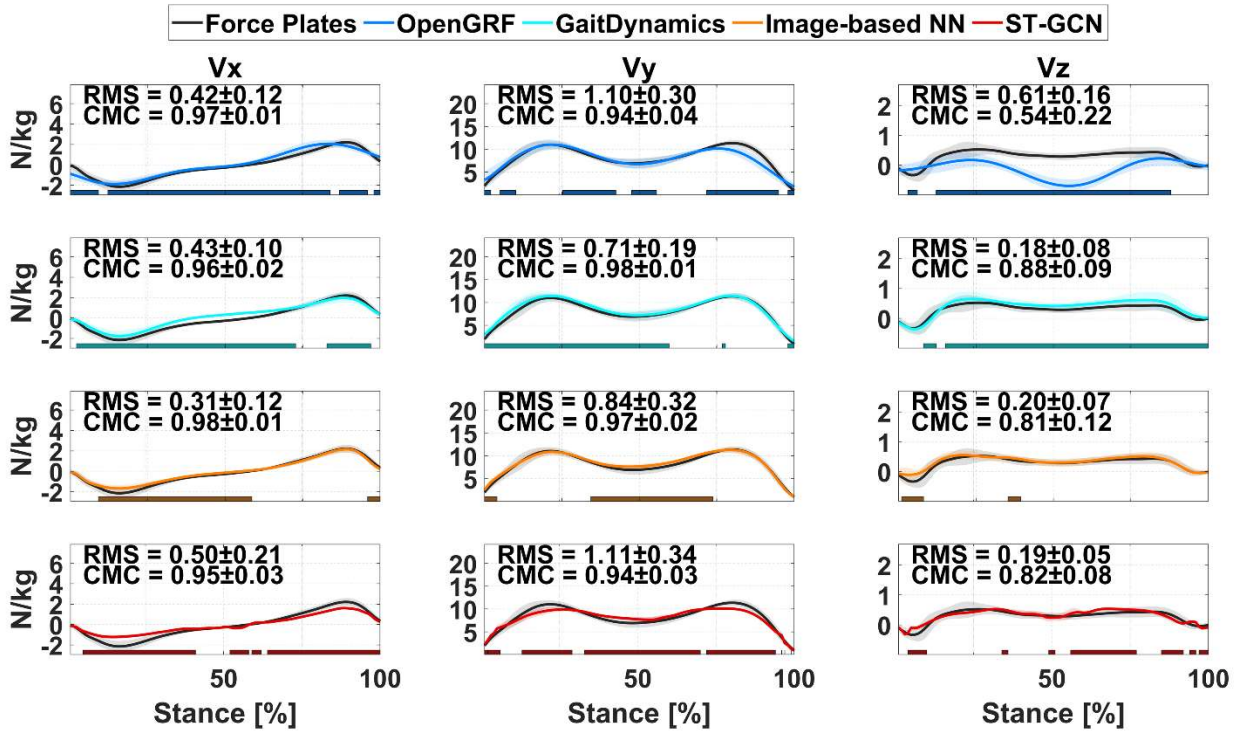


Figure 1. Estimated GRFs compared with force plate data (grey): OpenGRF (blue), GaitDynamics (light blue), Image-based NN (orange), ST-GCN (red). Mean ± std. *statistical significance (p<0.05)

References (Optional)

[1] Di Pietro A, *et al.* bioRxiv. 2025.

[2] Tan T, *et al.* Research Square. 2025.

[3] Johnson WR, et al. TBME. 2019.

[4] Pataky TC, et al. CMBBE. 2012.

Session Category

Emerging Areas: N/A

OA36-01

An Experimental Framework for Measuring Trabecular Bone Strains Surrounding Pedicle Screws

Ms Léa Slive, Ms Ye Young Shin, Prof Martine McGregor PhD, Prof Stewart McLachlin PhD, Prof Jonathan Kusins PhD

University of Waterloo, Waterloo, Ontario, Canada

Introduction

Pedicle screws are essential for postoperative construct stability in spinal fusion surgeries. However, screw loosening remains a common clinical complication, with a reported prevalence of ~13% at 6 months postoperatively [1], often linked to excessive loading that induces damaging trabecular bone strains at the screw–bone interface. This study aims to enhance pre-clinical assessment of pedicle screw fixation by establishing the feasibility of combining microCT imaging with digital volume correlation (DVC) techniques to directly characterize internal trabecular bone strains at the screw–bone interface.

Methods

Pedicle screws were surgically implanted into human lumbar vertebrae specimens (n=6). Each specimen underwent microCT imaging (225 kV, 150 µA, 37.5 µm voxel size) (Figure 1). For three specimens, paired unloaded scans were analyzed using a standard DVC uncertainty workflow. To mitigate local bone–metal artifacts, bone segmentation was performed using a deep learning convolutional neural network with a U-net architecture, trained on 90 independently annotated slices from the six vertebrae (training: 48 slices, validation: 12 slices, testing: 30 slices). Segmentation accuracy was quantified using the Sørensen-Dice similarity coefficient. DVC trabecular bone strain measurement accuracy and precision was evaluated within peri-screw volumes of interest (VOIs) defined as proximal, middle, and distal along the screw trajectory. VOI differences were analyzed using the Friedman test (α=0.05).

Results

The deep learning model reproduced manual segmentations with high fidelity (Dice=0.90). DVC accuracy and precision depended on the spatial resolution of strain measurement; at a spatial resolution of 2.4 mm, strain estimates were reliable with low error across all peri-screw bone VOIs (accuracy: 316±82 µε; precision: 195±78 µε). No significant differences in strain errors were observed between VOIs along the screw trajectory (p=0.052).

Discussion

This study established a DVC workflow for quantifying experimental strains surrounding pedicle screws. Coupling deep learning segmentation with DVC enabled spatially resolved strain measurements along the bone–screw interface which can complement traditional pullout tests by revealing how load is transferred into surrounding bone. This workflow provides a foundation for future studies involving loaded tests, further optimization of imaging/segmentation to suppress artifacts, and validation across larger cohorts and implant designs.

Images (Optional)

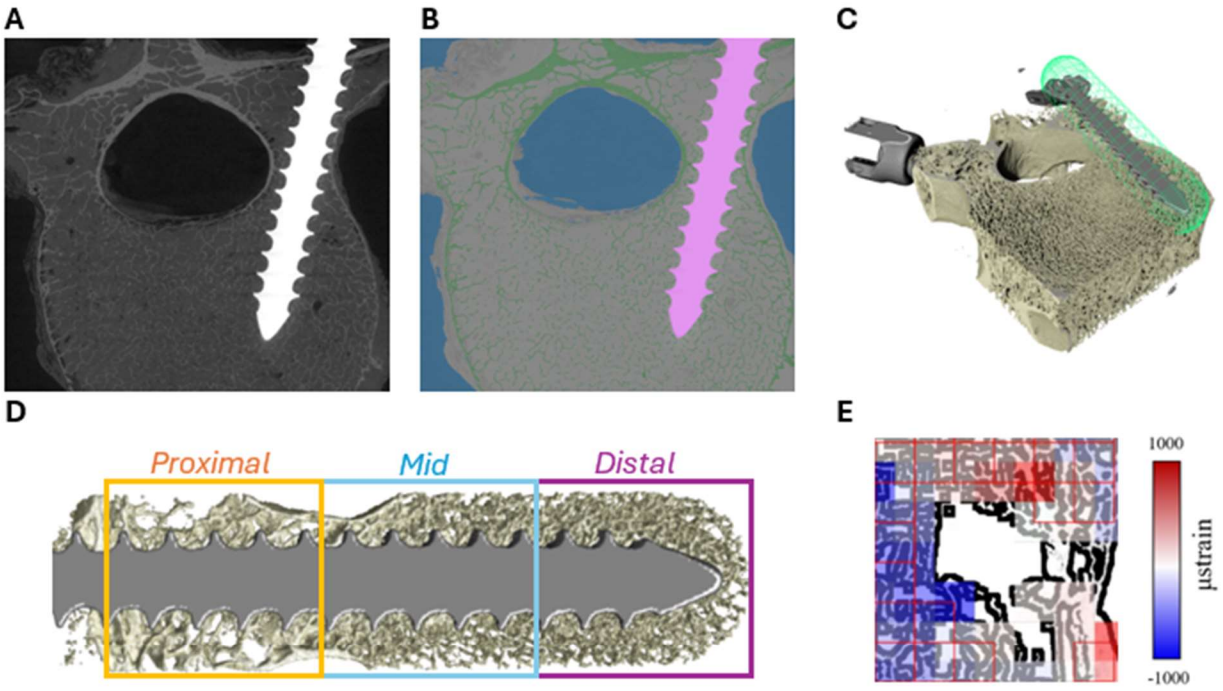


Figure 1 : *MicroCT images (A) were acquired of vertebrae samples implanted with pedicle screws. Annotation (B) was performed to generate training data for deep learning–based segmentation of the bone–implant region. An isometric three-dimensional rendering of the bone–implant interface (C) is shown, with varying volumes of interest (VOIs) defined and analyzed (D). These VOIs were subsequently used for volumetric trabecular bone strain analysis (E).*

References (Optional)

[1] Kim *et al., TSJ,* 2020

Session Category

Orthopaedic Biomechanics: Spine

OA36-02

Pre-Clinical Mechanical Evaluation of Anatomically and Mechanically Conforming Patient-Specific Spinal Fusion Cages Designed by Full-Scale Topology Optimization

Dr. Xiaoyu Du, Dr. Thijs Smit, Mr. Charles Cheruparambil, Prof. Stephen Ferguson

ETH Zurich, Zurich, Zurich, Switzerland

Introduction

Lumbar disc herniation often necessitates fusion surgery when conservative care fails. However, subsidence remains a concern due to the stiffness mismatch between the cages and the vertebral bone. Although porous and lattice architectures aim to reduce stress, they overlook patient-specific variation. Topology optimization offers individualized implant design to improve load distribution and minimize local stress peaks within the underlying bone [1]. This pre-clinical mechanical evaluation study aims to clarify the potential of anatomically and mechanically conforming patient-specific implants to reduce stress in the endplates and vertebral bodies, thereby mitigating subsidence.

Methods

Six human lumbar spines yielded sixteen functional spinal units (FSUs), which were allocated by bone density to topology-optimized (TOD) or off-the-shelf (OTS) groups. Each FSU underwent micro-CT imaging, potting, and implantation according to standard surgical methods. TOD and OTS cages were 3D-printed using titanium alloy and evaluated using pressure film to visualize endplate contact. Compression testing to failure (1 mm/min) was performed on a dynamic testing machine (Instron E10000) with optical displacement tracking (Epsilon). After testing, a force-displacement curve was generated, and the force at subsidence/failure was determined by the first local maximum of the force measurement for each FSU.

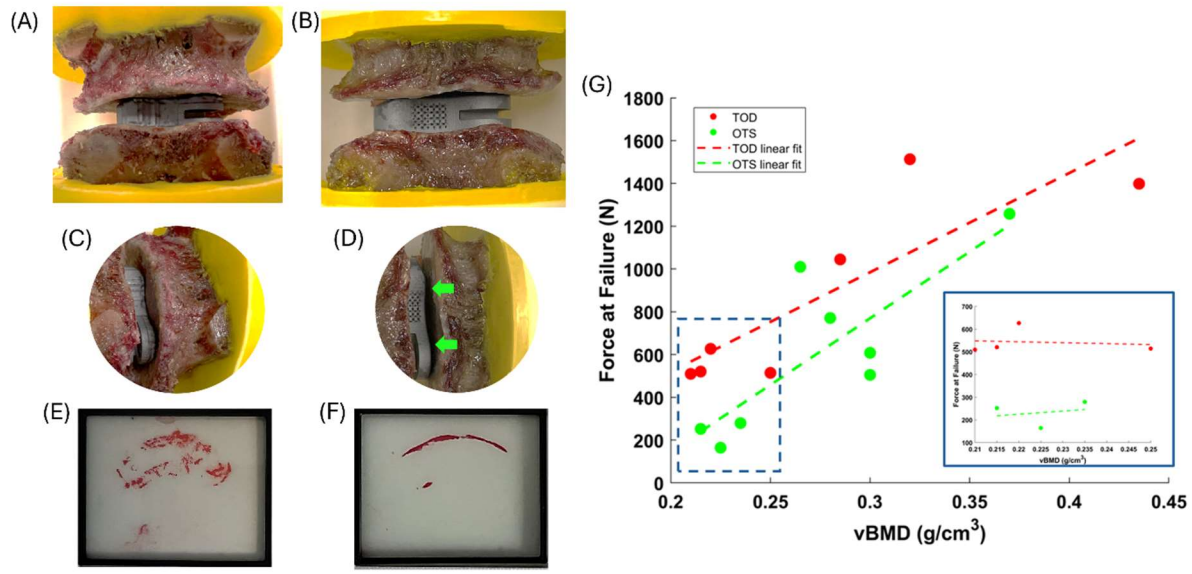
Results

The pressure film measurements illustrate that the TOD implants produced broader, more uniform endplate contact, whereas OTS implants showed concentrated edge loading. Mean subsidence force was higher with TOD (875 N; range 510–1513 N) than OTS (606 N; range 164–1258 N). Both groups showed increasing subsidence force with higher vBMD (integral volumetric bone mineral density), though correlations were weak. In low-vBMD FSUs, TOD implants performed significantly better (552 ± 65 N vs. 232 ± 60 N).

Discussion

These findings suggest that subsidence risk can be meaningfully reduced through implant topology optimization rather than material changes. The personalized TOD design improved endplate conformity and contact distribution, which has been shown to reduce local stress peaks while mimicking bone-like mechanical behavior with minimal material use. TOD implants showed higher forces at subsidence than OTS, especially in low-vBMD spines, highlighting their advantage for fragile bone. Limitations include small sample size and cadaveric specimens.

Images (Optional)



References (Optional)

[1] Thijs Smit et al., Front Bioeng Biotech, 2024

Session Category

Orthopaedic Biomechanics: Spine

OA36-03

Hyperhydration and Endplate-Annulus Disintegrity Provoke Cervical Disc Herniation - An In Vitro Study

M.Eng. Ann-Kathrin Greiner-Perth, PhD Morten Vogt, PhD Christian Liebsch, Prof. Dr. Hans-Joachim Wilke

Ulm University Medical Center, Ulm, Baden-Wuerttemberg, Germany

Introduction

Mechanisms underlying cervical disc herniation remain poorly understood. Particularly, astronauts show a 21-fold higher risk compared to the standard population, potentially due to excessive disc swelling [1]. This study explored swelling-induced alterations in intradiscal pressure (IDP), range of motion (ROM), and neutral zone (NZ), and examined whether hyperhydration combined with compromised endplate-annulus integrity under complex loading contributes to disc herniation.

Methods

Six fresh frozen human cervical spinal motion segments (1x C3-C4, 3x C5-C6, 2x C6-C7; 17–42 years; 2 female / 4 male) were hydrated in distilled water for 14 h, with IDP being measured via fiberoptic pressure transducers. A standardized posterior defect between cranial endplate and annulus fibrosus was created paramedially under x-ray control. Specimens underwent complex loading for 3,000 cycles at 1 Hz in a dynamic disc-loading simulator [2], combining 100 N compression with flexion/extension (FE), lateral bending (LB), and axial rotation (AR) according to physiological ROM values [3]. Flexibility was assessed before and after hydration and loading using pure moments of 2.5 Nm. Data was analyzed using the Friedman test with Bonferroni correction in SPSS29.

Results

Hyperhydration increased intrinsic IDP by 243% ($p<0.05$) and reduced NZ (FE: -46%, LB: -56%; $p<0.05$). Complex loading immediately provoked herniation in one disc, showing posterior extrusion of nucleus pulposus material into the spinal canal paramedially from the cranial endplate defect site (Fig. 1). Following complex loading, ROM and NZ increased compared to the hyperhydrated condition ($p<0.05$; ROM: FE: +36%, LB: +56%, AR: +31%; NZ: FE: +148%, LB: +216%, AR: +138%).

Discussion

Hyperhydration increases IDP, thus reflecting amplified mechanical stress on annulus structures. Combined with complex loading, excessive hydration was shown to contribute to cervical disc herniation. However, induction of a paramedian defect at the upper endplate–annulus transition did not consistently provoke herniations, indicating that defects do not further augment their risk of occurrence.

Images (Optional)

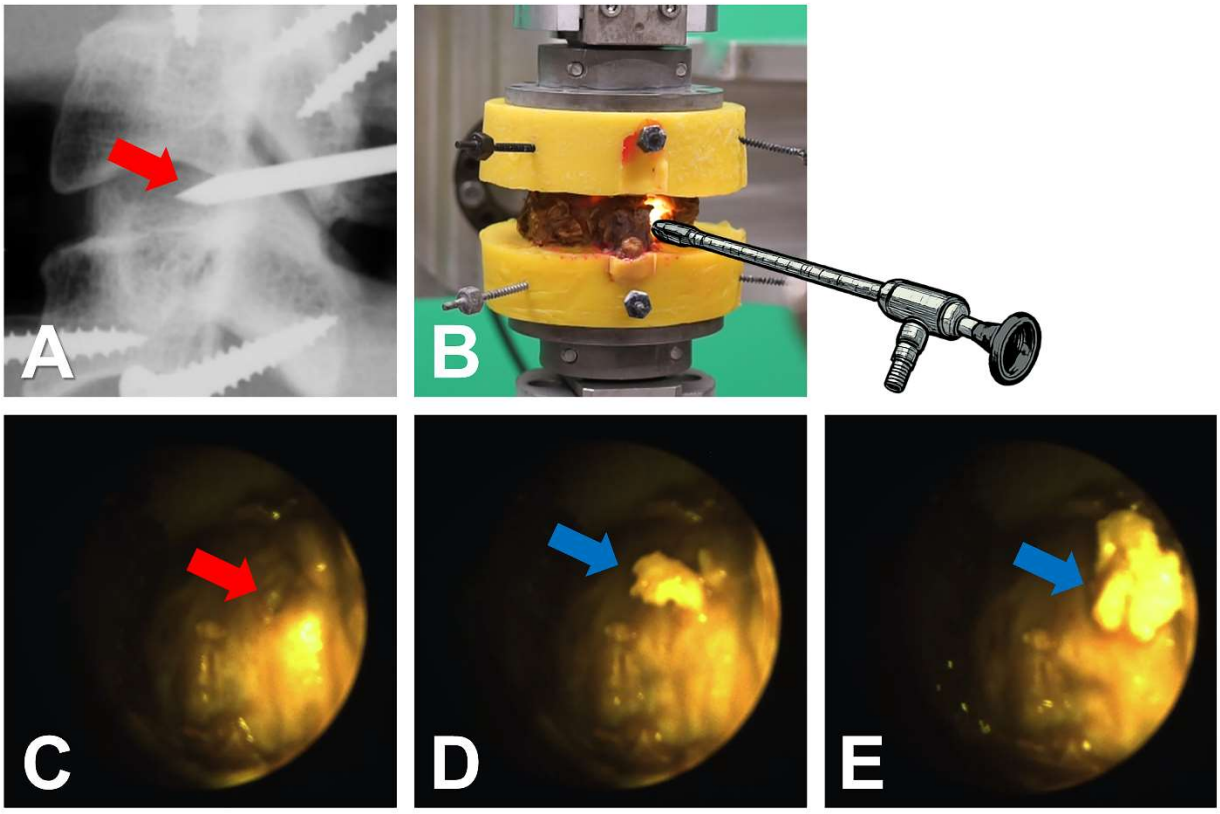


Fig. 1. *In vitro* model for cervical disc herniation.

(A) **Defect** generation at the cranial endplate-annulus transition via pin (red arrow).
(B) Endoscopic monitoring of the posterior disc wall through laminotomy under complex loading conditions.
(C–E) Sequential endoscopic imaging from posterior oblique view illustrating the development of cervical disc **herniation**: Artificial **defect** (red arrow) and provoked disc **herniation** at C3–C4 level (blue arrow) with extrusion of nucleus pulposus material into the spinal canal.

References (Optional)

[1] Belavy *et al.*, Eur Spine J, 2016.

[2] Wilke *et al.*, Eur Spine J, 2016.

[3] Anderst *et al.*, J Biomech, 2015.

Acknowledgements (Optional)

Funded by the German Research Foundation (DFG, 72128423) and the German Aerospace Center (DLR, 50WB2424D).

Session Category

Orthopaedic Biomechanics: Spine

OA36-04

Mechanical Loading Affects the Swelling Behavior of the Intervertebral Disc - An In Vitro Study

M.Eng. Ann-Kathrin Greiner-Perth, Ms. Hanna Unseld, Prof. Dr. Hans-Joachim Wilke, PhD Christian Liebsch

Ulm University Medical Center, Ulm, Baden-Wuerttemberg, Germany

Introduction

Intervertebral discs are known to undergo daily fluctuations in water content, dehydrating under daily loading and rehydrating overnight via osmotic processes [1]. While being of major importance for model validation and data interpretation, effects of constant hydration and mechanical loading on disc swelling and consequent motion segment flexibility remain insufficiently explored. This study therefore investigated the effects of disc loading on intradiscal pressure (IDP), range of motion (ROM), neutral zone (NZ) and disc height (DH).

Methods

18 fresh ovine lumbar motion segments (6x L1-L2, 6x L3-L4, 6x L5-L6) were hydrated for 24 h in 0.9% saline solution and randomized regarding segmental level into three groups (each n=6) using different axial compressive loading: 0 N (unloading), 58 N (loading during recovery phase), 130 N (loading during active phase) [2]. ROM and NZ were determined using pure moments of 7.5 Nm [3] at baseline, after 2 h, 4 h, 8 h, and 24 h. IDP was measured using fiberoptic pressure sensors. Statistical analysis was performed using Friedman's test with Dunn-Bonferroni post-hoc correction in SPSS29.

Results

Unloaded discs showed increased IDP after 8 h and 24 h of hydration ($p<0.05$) and elevated DH after all hydration intervals ($p<0.05$). Flexibility testing revealed increased IDP in all motion directions after 8 h (except flexion) and 24 h ($p<0.05$, Fig. 1). ROM decreased in lateral bending after 8 h and 24 h, and NZ in flexion/extension after 24 h ($p<0.05$). At 58 N, IDP increased during extension after 8 h and 24 h ($p<0.05$). At 130 N, no significant changes were observed ($p>0.05$).

Discussion

Lumbar ovine discs exhibit limited hydration capacity under low or recovery loads, while no fluid uptake was measurable under active load, suggesting that sustained loading reduces rehydration. In contrast, unloaded discs undergo osmotic swelling, leading to increased IDP and reduced flexibility. These effects might affect the transferability of experimental data to in vivo conditions. Future studies will verify these findings in human discs.

Images (Optional)

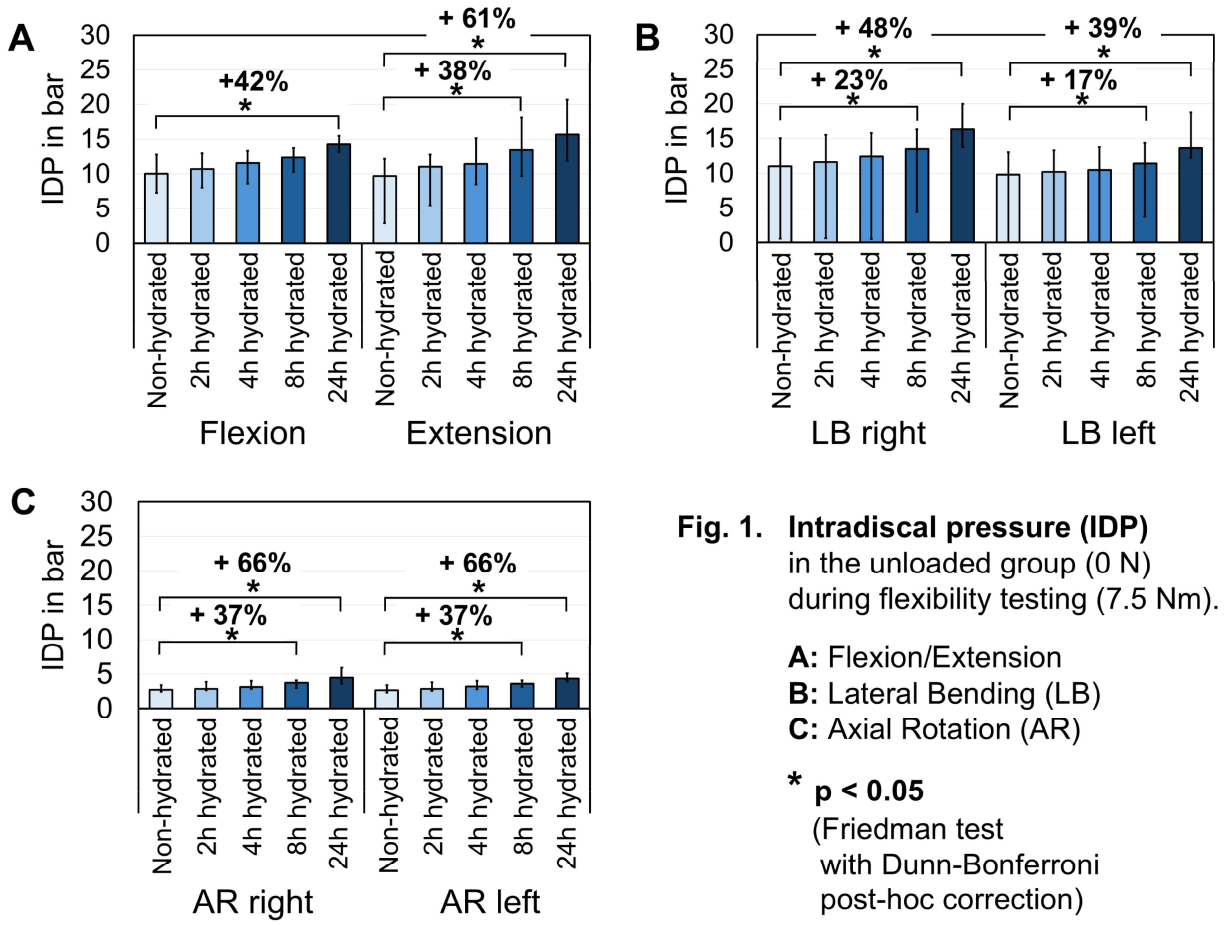


Fig. 1. Intradiscal pressure (IDP) in the unloaded group (0 N) during flexibility testing (7.5 Nm).

A: Flexion/Extension
B: Lateral Bending (LB)
C: Axial Rotation (AR)

* **p < 0.05** (Friedman test with Dunn-Bonferroni post-hoc correction)

References (Optional)

[1] Wilke *et al.*, Spine, 1999.

[2] Reitmaier *et al.*, PloS One, 2013.

[3] Wilke *et al.*, Spine, 1997.

Acknowledgements (Optional)

Funded by the German Aerospace Center (DLR, 50WB2424D).

Session Category

OA36-05

Post-fusion Facet Biomechanics are Influenced by Disc Degeneration and Facet Anatomy: Insights from Experimental and Computational Modelling of Cadaveric Human Lumbar Segments

Dr Shambo Bhattacharya, Dr Sophie Hutchinson, Ms. Sophie Clark, Dr Sherif Zantiba, Dr V. Nagitha Wijayathunga, Dr James Warren, Dr Marlene Mengoni

Institute of Medical and Biological Engineering, School of Mechanical Engineering, University of Leeds, Leeds, West Yorkshire, United Kingdom

Introduction

Despite Facet Joints' (FJ) critical role in governing spine biomechanical function, their biomechanics is understudied, with limited facet-specific data to evaluate their mechanical contribution or effects of interventions. Further, this hinders validation of FJ forces, often used as key outputs in computational models. The present study aimed to experimentally assess the effect of spinal fusion on FJ biomechanics, to calibrate and validate a FJ contact model, and comparing outcomes to imaging features.

Methods

Following ethical review (Yorkshire and the Humber REC15/YH/0096), human lumbar functional spinal units (FSUs) (N=7, three donors) were prepared after 3T MR imaging (Siemens-Vida), followed by a mock fusion procedure. Posteriorly off-axis compression experiments were carried out, with FJ local displacements and normal loads measured through respective motion capture and pressure-sensitive wafer-sensors. Micro-CT image-based finite element (FE) models of fused FSUs (N=4, substantial modic changes excluded) were developed. FJs were modelled as a pressure-overclosure contact defined with parameters calibrated against force-displacement curves. Validation was performed by comparing local FJ displacements. Outcomes were correlated with imaging features.

Results

Mock fusion significantly reduced FJ relative motion ($p=0.032$) with some FSUs shifting from extension to flexion. Changes in FJ normal force and motion following mock fusion negatively correlated with IVD Griffith grades ($R^2=0.42$ and $R^2=0.87$). Post fusion, relative FJ motion correlated negatively with facet space ($R^2=0.36$). Calibration yielded a good agreement between experimental and FE FJ displacements (CCC=0.92). Computational parameters for maximum contact pressure correlated positively with FJ Weishaupt grades ($R^2=0.71$), and parameter for contact initial clearance correlated positively with facet space ($R^2=0.78$), with the latter showing high variability (CoV=42%).

Discussion

This study provides the first experimental evaluation of post-fusion FJ biomechanics and development of an experimentally validated FJ contact model. Findings demonstrate IVD degeneration is a key determinant for changes in FJ kinematics and load transfer, while facet anatomy governs post-fusion kinematics. With mock fusion eliminating confounding factors of IVD modelling, findings showed FJ contact models were highly specimen-specific with dependence of facet space and facet grades. Albeit, small sample size, outcomes demonstrate high variability in FJ kinematics and role in load transfer overlooked in other spine FE models.

Session Category

Orthopaedic Biomechanics: Spine

OA36-06

Process-Driven Mechanical Tuning of 3D Printed Foaming Thermoplastic Polyurethane for Age-Specific Cervical Intervertebral Disc Modelling

Mr Rajan S. Vraitch[1], Dr Xianghong Ma[1], Dr Francesco Giorgio-Serchi[2], Dr Eirini Theodosiou[1], Prof Adrian Gardner[1,3], Dr Jean-Baptiste R.G. Souppez[4]

[1]Aston University, Birmingham, West Midlands, United Kingdom. [2]University of Edinburgh, Edinburgh, Scotland, United Kingdom. [3]Royal Orthopaedic Hospital, Birmingham, West Midlands, United Kingdom. [4]Birmingham City University, Birmingham, West Midlands, United Kingdom

Introduction

Additive Manufacturing (AM) enables patient-specific cervical spinal models, however, while anatomical accuracy is derived from medical imaging, achieving physiologically relevant intervertebral discs (IVDs) mechanics that account for age and disease variations in mechanical behaviour remains challenging. Previous work demonstrated feasibility of modulating compressive properties using material selection and AM parameters [1], however limited understanding remains regarding how extrusion conditions govern microstructural foaming, and mechanical performance of foaming thermoplastic polyurethane (TPU). Consequently, this study investigates the process-structure-property relationship of 3D printed foaming TPU, enabling age-specific IVDs within anatomically accurate geometries.

Methods

Foaming TPU samples were manufactured with variations of extrusion temperature T (200-240°C), flow ratio f (0.60-0.90), layer height L_H (0.12-0.28 mm), and print speed S_P (40-60 mm s^{-1}). Compression tests were conducted following ISO 604:2003, with compressive modulus E_C determined using least-squares regression. For density and microstructural analysis, cubic samples were produced, with density used to characterise foaming behaviour and scanning electron microscopy (SEM) to analyse pore morphology.

Results

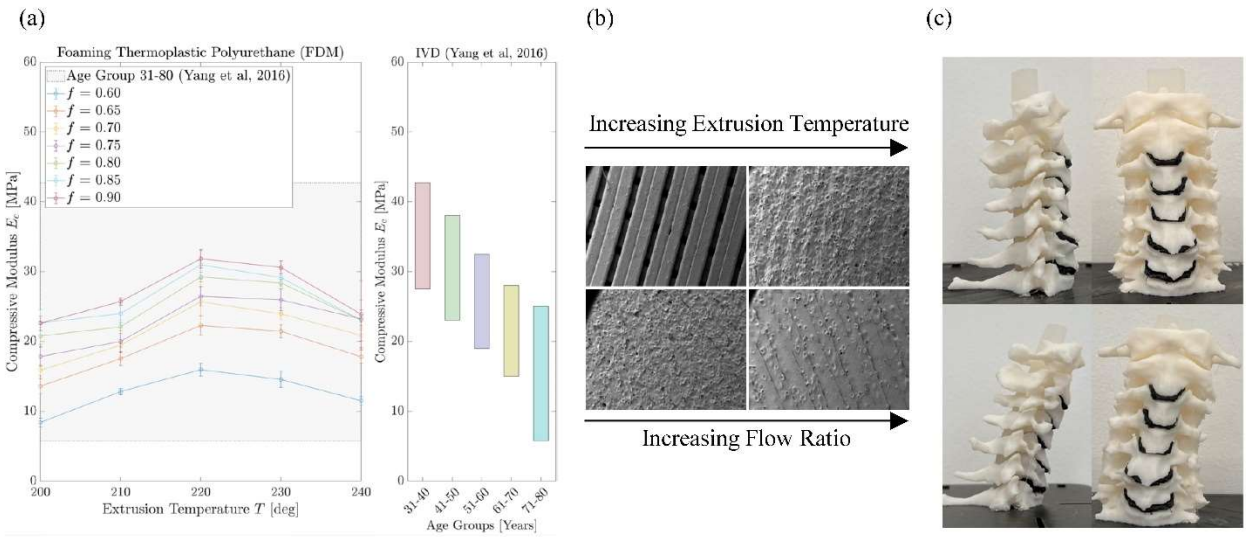
T and f were identified as the dominant variables governing foaming behaviour and compressive mechanical response. Increased T and lower f resulted in lower density and E_C. Conversely, conditions that restricted foaming yielded stiffer samples, representative of younger IVDs [2] (Figure 1a). In contrast, changes in L_H and S_P produced

no statistically significant changes in E_C. SEM revealed microstructural changes, with increasing T and decreasing f producing greater expansion of the foaming agent, while higher E_C was attributed to denser filament packing with few pores and overlapping of filament tracks (Figure 1b).

Discussion

These findings demonstrate that foaming TPU enables controllable replication of age-specific IVDs through extrusion-driven changes of foaming behaviour. The relationship between processing parameters, pore morphology, density, and E_C enables predictive control of mechanical behaviour. Importantly, stiffness tuning was achieved without changing geometry or material, enabling models to exhibit physiologically relevant behaviour (Figure 1c). This approach enhances the biomechanical accuracy of spinal models used for surgical simulation, thereby improving their value in clinical training and decision-making for personalised treatment.

Images (Optional)



References (Optional)

[1] Vraitch et al., Proc. 29th Congress of the European Society of Biomechanics, 2024.

[2] Yang et al., Journal of Biomechanics, 2016.

Acknowledgements (Optional)

This work was funded by the inaugural Spine Research Fellowship from ORUK, BASS and BSS, as well as Aston University's College of Engineering and Physical Sciences.

Session Category

Orthopaedic Biomechanics: Spine

OA37-02

Defining New Carpal Bone Anatomical Reference Systems Optimized for Kinematic Description

Mr. Daniel McDermott Sc.B.[1], Dr. Nicola Sancisi Ph.D.[2], Dr. Michael Rainbow Ph.D.[3], Dr. Michele Conconi Ph.D.[2]

[1]Harvard Medical School, Boston, MA, United States. [2]University of Bologna, Bologna, BO, Italy. [3]Queen's University, Kingston, ON, Canada

Introduction

Previous carpal bone reference systems definitions follow two main approaches: one defines all reference systems as parallel to the radius's in a neutral wrist [1]; another relies on carpal bones' principal axes of inertia [2]. Parallel axes do not distinguish healthy from pathological individuals, and joint angles derived from inertial axes are difficult to interpret. Based on the method developed for the foot [3], we propose a new definition of anatomical reference systems (ARS) from the articular surface shape and bone morphology, optimized for kinematic description while remaining clinically interpretable.

Methods

The proposed approach fits geometrical primitives on the articular surfaces, approximating them with elementary kinematic pairs. It was hypothesized that these features allow the definition of ARS that incorporate elements of articular coupling, such as the relative center of spherical motion. To test the effectiveness of the approach, we reconstructed wrist kinematics from CT scans of 9 wrists in 11 postures [4]; the instantaneous helical axes of all the articular pairs were computed between adjacent wrist poses, together with mean helical axis (MHA), mean pivot point (MPP), mean dispersion angle and mean axis-to-MPP distance of the IHA's. These data were used to identify the principal joint motions and their correspondence with the ARS axes.

Results

Motion occurs primarily between the scaphoid-radius, lunate-radius, and capitate-scaphoid joints, resembling spherical motion, as demonstrated by the small axis-to-MPP distance (2.7±1.1, 2.6±0.92, and 3.4±1.4mm) and large mean dispersion angles (18.9±4.1, 29.1±1.2, and 21.8±2.2°). The small distances between the MPP and the ARS's centers (4.1±1.8, 3.7±0.78, and 2.8±1.3mm) demonstrate the alignment of our ARS with the

kinematic pairs (Fig. 1, top row). Qualitatively, the distribution of the ARS is clinically sound, for instance following the natural curvature of the carpal tunnel.

Discussion

Our ARS method effectively captures joint kinematics, is clinically relevant, and will allow for more accurate principal component analysis.

Images (Optional)

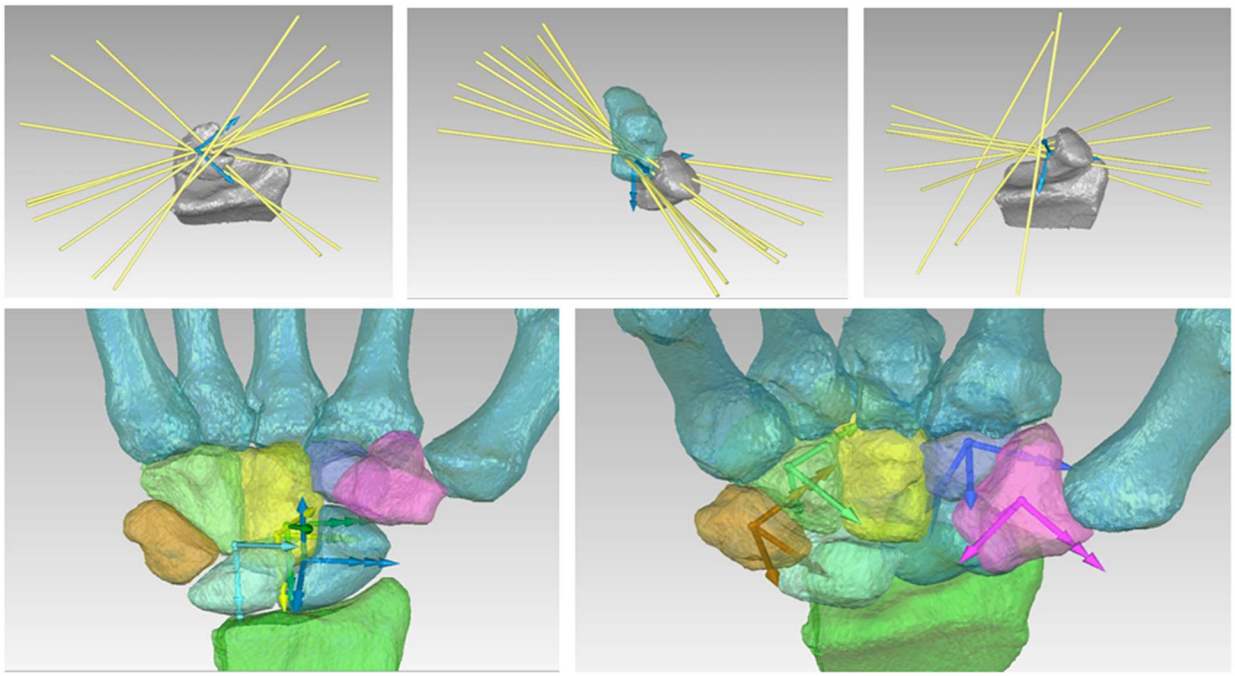


Figure 1: Distribution of the IHA for: the radius-lunate motion in the lunate ARS (top row, left); the scaphoid-capitate motion in the capitate ARS (top row, middle); the radius-scaphoid motion in the scaphoid ARS (top row, right). Visualization of the ARS distribution in a neutral wrist (bottom row)

References (Optional)

[1] Wu *et al.* , J Biomechanics, 2005

[3] Coburn *et al.* , J Biomechanics, 2007

[4] Conconi *et al.* , J Foot Ankle Res, 2021

[5] Rainbow *et al.* , J Hand Surg Eur Vol, 2016

Session Category

Orthopaedic Biomechanics: Upper Extremities

OA37-03

Dual Dysfunction: Central and Peripheral Factors of Recovery in Rotator Cuff Tendinopathy

Dr. Matthew Heindel PT, DPT[1], Dr. Oscar Vila-Dieguez PT, PhD[2], Dr. Jason Kutch PhD[1], Dr. Lori Michener PT, ATC, PhD[1]

[1]University of Southern California, Los Angeles, CA, United States. [2]University of California - San Diego, San Diego, CA, United States

Introduction

Rotator cuff (RC) tendinopathy is the most common cause of shoulder pain. Resistance exercise is effective, but outcomes are highly variable, with 40-50% developing recurrent or chronic pain. Deficits in tendon structure incompletely explain the variability in outcomes. Understanding the contribution of central factors – specifically, brain network activity – has not been explored. Other chronic pain conditions have shown decreased within-network connectivity of the default mode network (DMN), which is responsible for self-referential thought, mind wandering, and assists in descending pain modulation. No study has assessed the role of DMN connectivity in the presence or recovery with resistance exercise in RC tendinopathy. Defining the role of central and peripheral factors contributing to RC tendinopathy will aid in identifying intervention targets for personalized treatment approaches.

Methods

Adults with RC tendinopathy (n=58) completed an 8-week progressive resistance exercise program. Supraspinatus tendon structure of thickness and collagen disorganization (via peak spatial frequency radius–PSFR) were measured on ultrasound tendon images at baseline, 2, 4, and 8 weeks. DMN connectivity was measured with resting-state fMRI at baseline and 8 weeks. Shoulder disability was assessed with the Penn Shoulder Score. A linear mixed effects model was used to determine if change in tendon structure from baseline to 2, 2 to 4, and 4 to 8 weeks predicted change in shoulder disability. A general linear model was used to determine if a change in DMN connectivity, controlled for tendon structure, predicted shoulder disability change.

Results

Decreased supraspinatus tendon thickness over baseline to 2 weeks were associated with improved shoulder disability at 8 weeks, but later changes in thickness and PSFR were not. Increased medial prefrontal cortex connectivity to the DMN from baseline to 8 weeks was related to improved disability.

Discussion

Both tendon structure and central factors contribute to recovery, but brain connectivity better explains outcomes following resistance exercise. Early tendon adaptation marks the initial peripheral response to loading, but increased DMN connectivity is related to better shoulder disability, independent of tendon structure. This may indicate improved descending pain modulation. This central biomarker could be a therapeutic target for future interventions for those who do not respond to resistance exercise.

Session Category

Orthopaedic Biomechanics: Upper Extremities

OA37-04

Co-Contraction Patterns of Forearm Muscles During Cylindrical Grasp Differ Between People With Hand Osteoarthritis and Healthy Individuals

Mr. Mahdi Mohseni[1], Dr. Verónica Gracia-Ibáñez[2], Dr. Angela Kedgley[1]

[1]Department of Bioengineering, Imperial College London, London, Greater London, United Kingdom. [2]Department of Mechanical Engineering and Construction, Universitat Jaume I, Castelló de la Plana, Valencian Community, Spain

Introduction

Muscle coordination analysis provides valuable information about the neuromuscular system function and may lead to improved rehabilitation strategies [1]. This study aimed to quantify forearm muscle synergy patterns for healthy individuals and participants with hand osteoarthritis (HOA) during cylindrical grasp, one of the most frequently used grasps in activities of daily living. Grasp activates most forearm muscles to generate strength and stability. We hypothesised that HOA would change forearm muscle coordination.

Methods

Seven electromyography (EMG) sensors were placed on the forearm to acquire muscle activation signals during grasp (Figure 1) [2]. EMG signals were collected while performing maximum painless cylindrical grasp from 21 healthy women and 20 women with HOA [3]. Signals were filtered and normalised to maximum voluntary contraction values. Non-negative matrix factorisation was recruited to extract synergy modules for each trial. The consistency of these synergy patterns across both groups was examined using the k-means method.

Results

Three synergy patterns (S1-S3) were extracted from EMG signals of each participant group (variance accounted for: 99.62 ± 0.07 % and 99.63 ± 0.11 % for healthy and HOA groups, respectively). In both groups, the S1 module was associated with the generation of grip force, S2 with wrist posture in extension and radial-deviation, and S3 with wrist flexion and ulnar-deviation (Figure 1).

Discussion

Participants with HOA primarily used their finger flexor muscles to apply grip force, while healthy participants used their thumb muscles as well. Both groups used almost the same

pattern for controlling wrist posture in flexion and ulnar-deviation; however, to control wrist posture in extension and radial-deviation, participants with HOA used finger extensor muscles instead of wrist extensor/radial-deviator muscles. These differences could be due to pain around the thumb and radial side of the wrist in participants with HOA. These results can be used to develop rehabilitation protocols based on the changes in forearm muscle coordination patterns and to distinguish HOA patients from healthy people using non-invasive EMG signals.

Images (Optional)

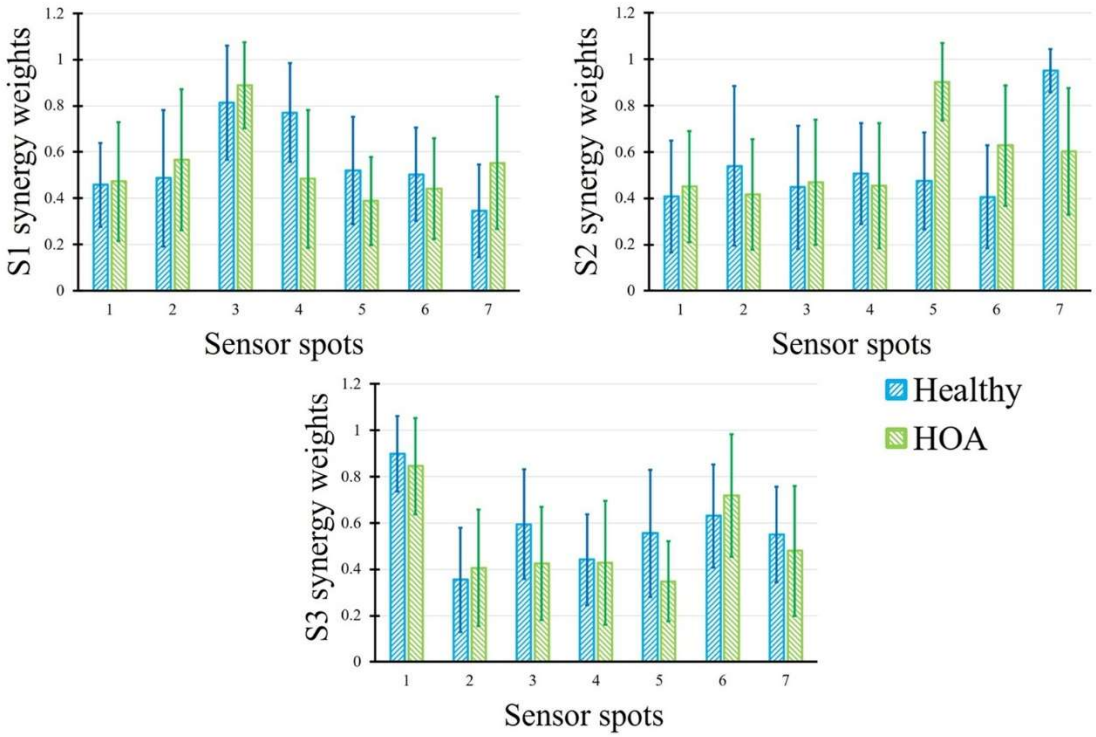


Figure 1: Synergy patterns for seven electromyography sensors collecting signals that represented muscle activity during: 1: wrist flexion/ulnar-deviation, 2: wrist flexion/radial-deviation, 3: thumb and finger flexion, 4: thumb extension/abduction/adduction, 5: finger extension, 6: wrist extension/ulnar-deviation, and 7: wrist extension/radial-deviation [2] for both healthy and hand osteoarthritis (HOA) groups.

References (Optional)

[1] Natalie Cole and A Bolu Ajiboye, J Neural Eng, 2019.

[2] Néstor J Jarque-Bou *et al.*, J Neuroeng Rehabil, 2018.

[3] Verónica Gracia-Ibáñez *et al.*, Sensors, 2024.

Acknowledgements (Optional)

This study was funded by the Regional Government (CIBEST/2023/202) and by U. Jaume I (UJI-A2021-03).

Session Category

Orthopaedic Biomechanics: Upper Extremities

OA37-05

Assessing Shoulder Pain-Related Range of Motion Limitations with Markerless Motion Capture

Ms. Vienna Liu, Ms. Belzora Lovett, Dr. David Lipps Ph.D.

University of Michigan, Ann Arbor, MI, United States

Introduction

Shoulder pain affects one in five adults, diminishing quality of life and independence by limiting shoulder mobility and hindering the ability to perform daily tasks [1]. Quantifying shoulder kinematics is vital for informing rehabilitation treatment plans to improve functional shoulder movements. Markerless motion capture is both highly valid [2] and more clinically accessible than marker-based systems; however, its application in upper-extremity assessments remains limited. We hypothesized that individuals with chronic shoulder pain would exhibit reduced shoulder range of motion as measured by markerless motion capture.

Methods

15 individuals with chronic shoulder pain (≥3 months, SPADI ≥20, pain on ≥ 3/8 clinical tests) were compared to 15 age- and sex-matched controls (14 M, 16 F, mean age 60 yr, 172 cm, 80 kg). Participants completed four shoulder range-of-motion tasks with kinematics derived using Theia markerless motion capture (16 Qualisys Miqus cameras): flexion/extension, abduction/adduction, internal/external rotation at 90° flexion, and internal/external rotation at 90° abduction. Visual3D was used to compute joint angles (YXZ rotation). Cohen's d effect sizes and independent t-tests examined the effect of shoulder pain on shoulder kinematics.

Results

Individuals with shoulder pain exhibited reduced range of motion in abduction ($d = 0.89$, $p = 0.02$), external rotation with 90° elbow flexion ($d = 1.07$, $p = 0.007$), and internal rotation in 90° shoulder abduction ($d = 0.95$, $p = 0.01$) (Figure 1). No other shoulder kinematics reached significance.

Discussion

This study highlights that individuals with shoulder pain exhibit reduced internal/external rotation and abduction range-of-motion tasks measured by markerless motion capture. Markerless motion capture has shown shoulder kinematic patterns similar to those of marker-based systems [3]. This study further suggests that markerless motion capture is

useful for distinguishing shoulder kinematics between individuals with and without pain. Future research should examine a wider range of activities of daily living and develop standardized protocols for markerless motion capture to improve reproducibility and expand clinical applications.

Images (Optional)

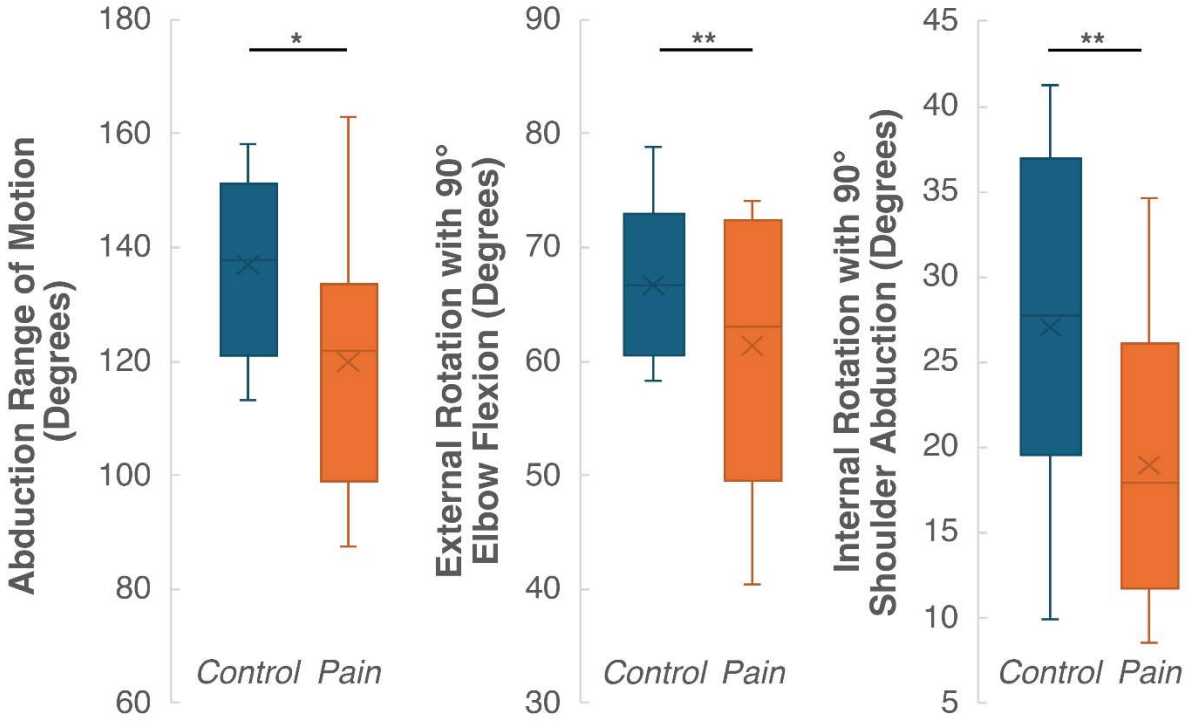


Figure 1: Abduction range of motion, external rotation with 90° elbow flexion, and internal rotation with 90° shoulder abduction in individuals with and without shoulder pain. Asterisks indicate significant between-group differences ($p < 0.05$ = *, $p < 0.01$ = **).

References (Optional)

[1] Patel et al. *Pain*. 2013;154(12)

[2] Hansen et al. *Adv Biomed Eng*. 2024;4

[3] Croci et al.. J Biomech. 2025;191

Session Category

Orthopaedic Biomechanics: Upper Extremities

OA38-01

An Actuated Encapsulation Implant for Cell Therapy

Dr. Eimear Dolan[1], Ms Parand Shokrani[1], Dr. Lesley Trask[1], Dr. Niamh Ward[1], Dr. Hannah Prendeville[1], Dr. Aoibhin Sheedy[1], Dr. Ellen T. Roche[2], Dr. Garry P. Duffy[1]

[1]University of Glaway, Galway, Galway, Ireland. [2]Massachusetts Institute of Technology, Cambridge, Massachusetts, United States

Introduction

Medical implants encapsulating therapeutic cells are being developed for chronic diseases[1]. However, many have limited long-term performance due to the foreign body response (FBR) impeding vital transport[2]. Our group previously demonstrated that cyclically actuating (inflating and deflating) an implant can reduce the FBR in rodents and improve drug delivery[3]. However, previous designs were not suitable for cell encapsulation. The actuatable cell encapsulation (ACE) implant, was designed (Fig 1A) and validated *in vivo* as described herein.

Methods

Implants were manufactured using variations of previously published techniques[3] and delivered subcutaneously to C57BL6 mice. Actuation (13.8kPa, triangular, 1Hz) occurred 10 minutes daily using an Elveflow OB1 controller. Mouse mesenchymal stem cells transfected with firefly luciferase (F-cells, $0.5x10^6$) and a fluorescent therapy analog (Genhance, 30µL), were delivered via transcutaneous port at key times. Cell viability and therapy spread were quantified via Spectrum In Vivo Imaging System (IVIS®).

Results

Preliminary *in vivo* results are shown in Fig 1. Progressive cell death, indicated by loss of bioluminescent signal (>90%), was observed in all implants (**Fig 1B**). However, the actuated implant demonstrated a plateau in bioluminescent signal beginning at Day 7, in contrast to the non-actuated controls.

The ability of the ACE implant to deliver a therapy analog was evaluated. Significant drops in the therapy's raw fluorescent signal and the area under the curve (AUC) were observed over time in all groups (**Fig 1C,D**). However, early data indicates that actuated implants show improving trends compared to non-actuated controls at Day 13.

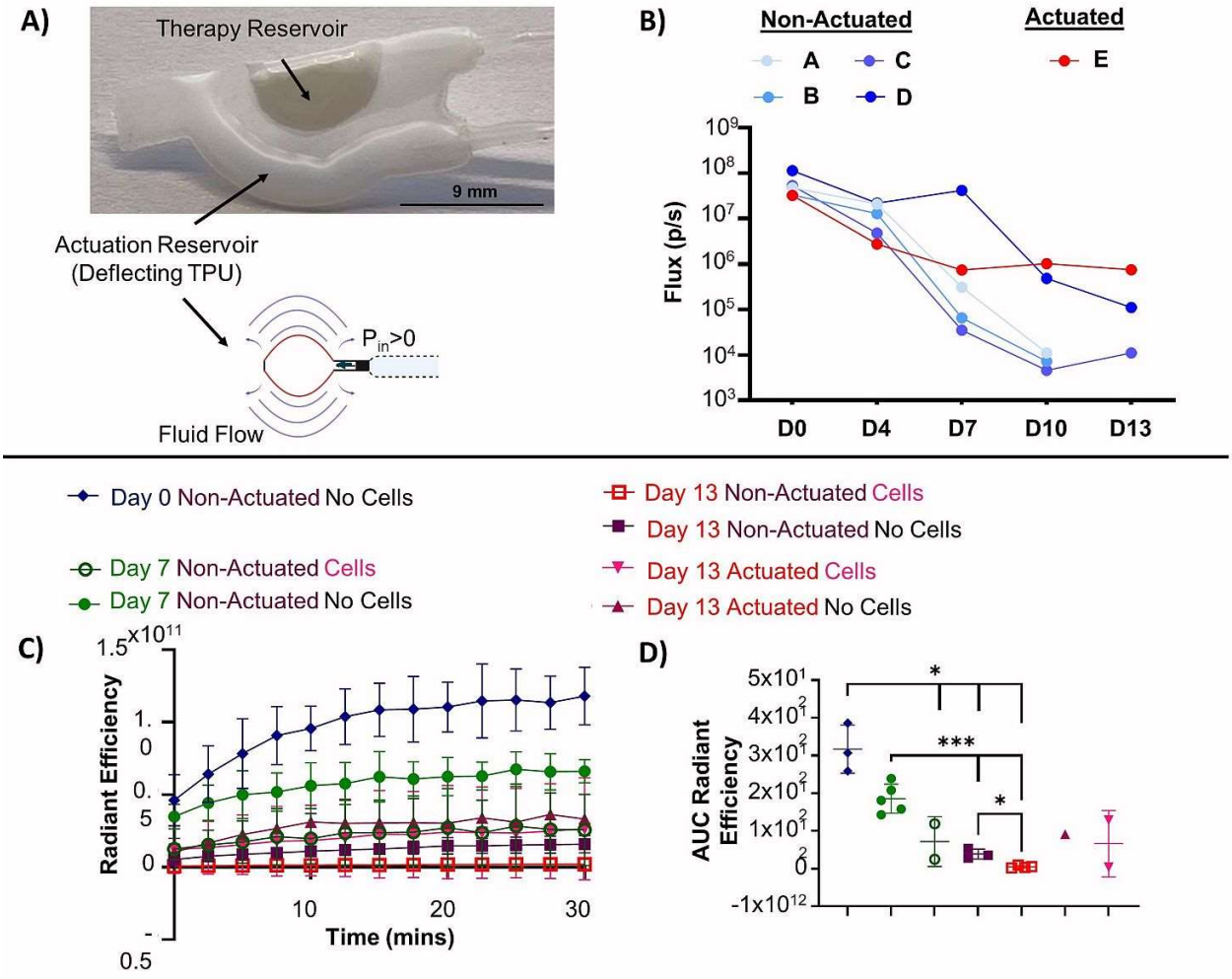
(Figure 1 here)

Figure 1 **A**) ACE implant in the inflated state. **B**) F-cell viability Day 0 (D0) to Day 13 (D13). **C**) Fluorescent intensity of therapy analog 30 minutes following delivery. **D**) AUC fluorescent intensity of therapy analog.

Discussion

This study is ongoing. These preliminary trends show promise for actuated implants to support cell viability up to 13 days in the challenging subcutaneous space, and improve therapy delivery compared to non-actuated controls.

Images (Optional)



References (Optional)

[1] Keymeulen B et al., *Nat Biotech*, 47:1507-1514, 2024. [2] Veiseh O et al., *Adv Drug Deliv Rev*. 144:148–161, 2019. [3] Whyte W et al., *Nat Comm*. 13:4496, 2022

Session Category

Imaging and Biomedical Devices: Artificial Organs, Devices

OA38-02

Experimental Validation of a Mechanically Intelligent Bone Anchor

Dr Sean Thomas, Ms Sachi Bansal, Dr Ophelie M. Herve, Dr David R. McAllister, Dr Tyler R. Clites

University of California, Los Angeles, Los Angeles, CA, United States

Dr Sean Thomas

Ms Sachi Bansal

Dr Ophelie M. Herve

Dr David R. McAllister

Introduction

Secure fixation is central to the success of orthopaedic implants, particularly in applications where implants remain in the body for extended periods. Conventional bone anchors typically rely on uniform thread engagement [1], which may not adequately adapt to bone morphology and can permit micro-motion that impedes osseointegration leading to aseptic loosening [2]. In this study, we present a mechanically intelligent bone anchor that adapts passively to the surrounding bone architecture without the use of sensors, electronics, or active control. The design leverages compliant mechanisms and force-gated mechanical fuses to achieve sequential engagement of cortical and cancellous bone while maintaining stability for osseointegration and long term implantation.

Methods

The anchor, centred around a mechanical fuse, was parametrised according to key geometric features (blade thickness, width, length, etc.). A design of experiments was conducted to sweep through the parameter space and >2000 finite element analysis (FEA) simulations were conducted to predict the buckling load and Poisson ratio of the fuse.

Using a random forest regressor [3], the partial dependence of each parameter on the two output parameters is estimated. Prototypes were fabricated using wax casting (Fig1A) and assessed through experimental validation. Motion capture was used to confirm the intended sequence of mechanical engagement.

Results

Predictions from the FEA were used to design a fuse that buckles allowing the two stages of the bone anchor to be activated sequentially (Fig1B). While blade thickness and length had opposing effects on the buckling load, the number of blades in the fuse showed a pathway to increase the required buckling loads without any effect on the Poisson ratio, critical to prevent radial expansion against the surrounding bone. Upon contact with a simulated cortical layer, the compliant fins achieved immediate fixation, followed by controlled deployment of the mechanical fuse (Fig1C).

Discussion

This study provides the first experimental validation of a mechanically intelligent bone anchor capable of passive, morphology-responsive fixation. By integrating compliant mechanisms tailored to bone anatomy, the anchor minimises micro-motion and offers a promising architecture for long-term orthopaedic implantation and future translational testing.

Images (Optional)

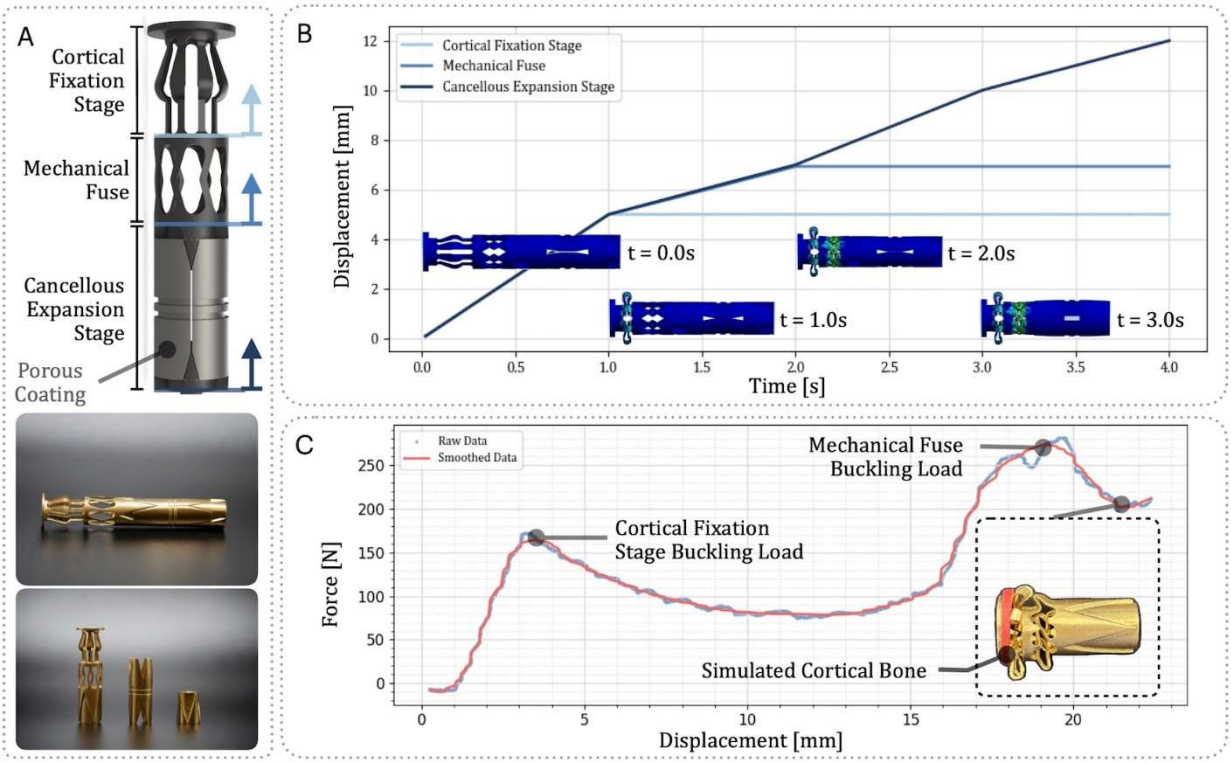


Figure 1: (A) Mechanically intelligent bone anchor prototype. (B) Finite element validation of the behaviour. (C) Experimental results

References (Optional)

[1] Nouri et al. (2023) [2] Apostu et al. (2018) [3] Breiman, L (2001)

Session Category

Imaging and Biomedical Devices: Artificial Organs, Devices

OA38-03

A Versatile Bioreactor Enabling Perfusion and Mechanical Stimulation of 3D Scaffolds: Design, CFD Assessment, and In Vitro Validation

Mr. José I. Contreras Raggio[1,2], Prof. Dr. Carola Millán[3], Mr. Usama Qayyum[2], Mr. Bernhard Weisse[2], Prof. Dr. Ameet K. Aiyangar[2,4,5], Prof. Dr. Juan F. Vivanco Morales[1]

[1]Facultad de Ingeniería y Ciencias, Universidad Adolfo Ibáñez, Viña del Mar, Valparaíso, Chile. [2]Laboratories for Mechanical Systems Engineering, Swiss Federal Laboratories for Materials Science and Technology (EMPA), Dübendorf, Zürich, Switzerland. [3]Facultad de Artes Liberales, Universidad Adolfo Ibáñez, Viña del Mar, Valparaíso, Chile. [4]Faculty of Medicine, University of Bern, Bern, Bern, Switzerland. [5]Department of Diagnostic, Interventional and Paediatric Radiology (DIPR), Inselspital, University Hospital, Bern, Bern, Switzerland

Introduction

Dynamic 3D in vitro culture systems are essential for evaluating engineered scaffolds under physiologically relevant conditions, providing mechanical and biochemical cues that 2D cultures cannot replicate [1]. They enable realistic modeling of nutrient transport, shear stress, and mechanotransduction, all critical in bone tissue engineering [2]. We present a dynamic bioreactor capable of delivering controlled perfusion and axial compression to scaffolds from 2.3 to 14 mm in height, supporting both small-scale and clinically relevant testing. The system replicates key mechanical and metabolic features of the bone microenvironment while enabling long-term culture.

Methods

The polycarbonate bioreactor chamber was designed to enable simultaneous perfusion and compression. CFD simulations using a 50% porous, 400 µm scaffold assessed flow uniformity, shear stress, and stagnant regions. Mechanical behavior was evaluated through in situ microCT compression tests, and material stability through chemical and mechanical degradation studies on polycaprolactone scaffolds. Biological validation included 14-day cell cultures, sterility checks, and viability assays to confirm compatibility and lack of cytotoxicity.

Results

CFD simulations demonstrated uniform perfusion flow across scaffold heights from 3–10 mm, with <0.1% stagnant regions, confirming efficient internal circulation. The chamber

maintained mechanical stability under repeated compression cycles, with microCT analyses showing no structural deformation of the chamber or scaffold mounts. Biological assays indicated no contamination or cytotoxic effects during 14 days of continuous dynamic culture, validating biocompatibility of the system.

Discussion

The system was validated for fluid dynamics, mechanical performance, and biocompatibility. A perfusion rate of 0.1 mL/min provided homogeneous flow without excessive shear in 10 mm scaffolds. The bioreactor offers a versatile, scalable platform that bridges static assays and in vivo models. Its capacity to support various scaffold sizes with controlled mechanical stimulation makes it a strong tool for mechanobiology, biomaterial testing, and preclinical evaluation. Future work will extend culture duration, vary loading and flow conditions, and integrate sensors for real-time monitoring. Overall, the system enables more reproducible, physiologically relevant in vitro models and may reduce reliance on animal studies in bone tissue engineering.

Images (Optional)

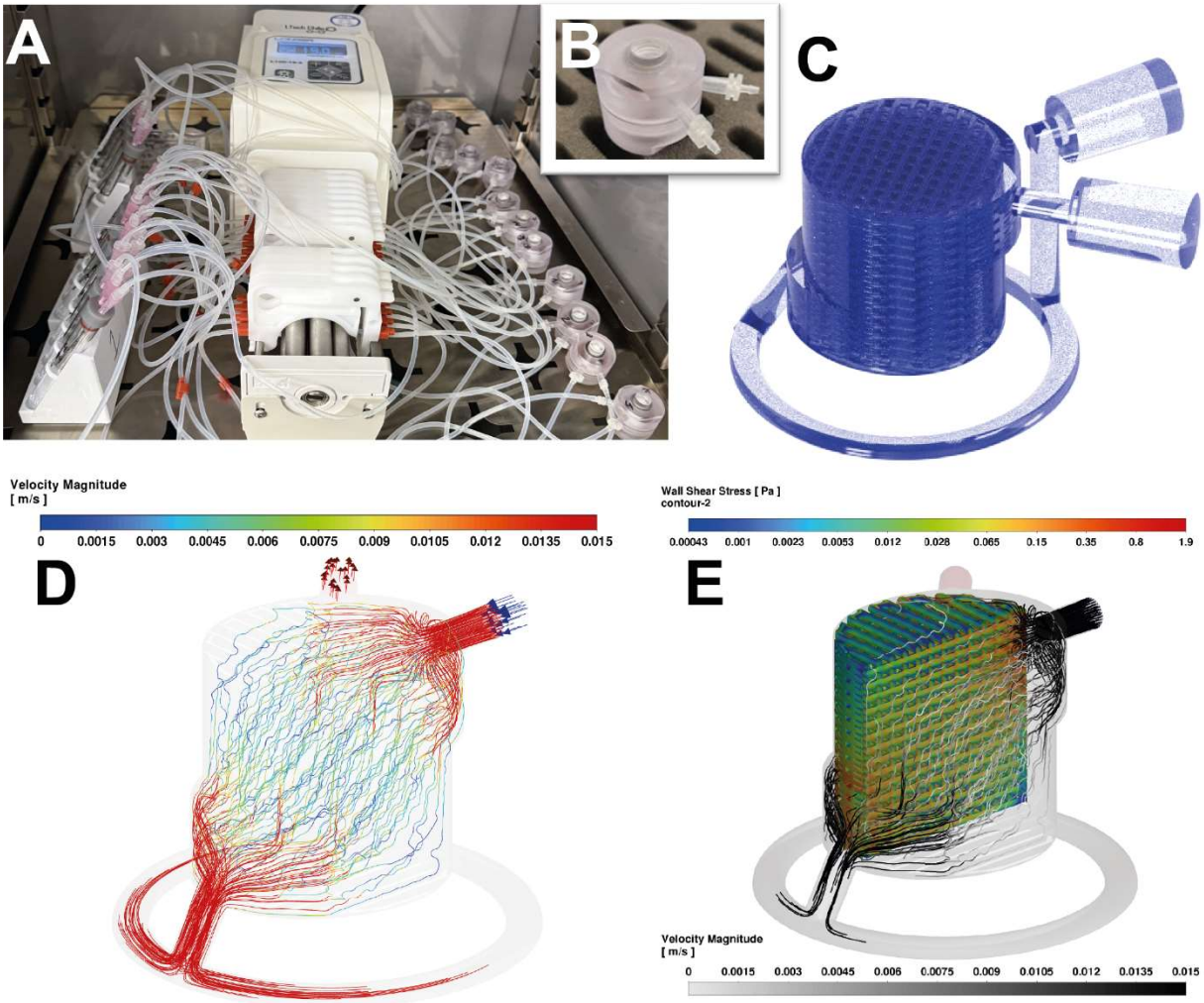


Figure 1. (A) Full bioreactor setup inside the incubator. (B) Fabricated bioreactor chamber. (C) Schematic representation of the perfusion flow path. (D–E) Representative CFD simulations illustrating fluid movement from the top-right inlet across the scaffold toward the bottom-left outlet, demonstrating a homogeneous and well-distributed flow profile throughout the chamber.

References (Optional)

[1] Zhang J. et al., Int. J. Mol. Sci., 2021.

[2] Yeatts A.B., Fisher J.P., Bone, 2011.

Session Category

Imaging and Biomedical Devices: Artificial Organs, Devices

OA38-04

Impact on Thrombus Morphology by Local Flow Structures in Extracorporeal Membrane Oxygenation Circuits Evaluated Using X-Ray Scattering, Electron Microscopy and Computational Fluid Dynamics

PhD Frida Nilsson[1], PhD Sheran Nanayakkara[1], MD Marcus Brynolf[2,3], PhD Monica Emendi[1], PhD Nils Hauff[4], PhD Sara Henriksson[4], PhD Kim Nygårds[5], PhD Sarathlal Koyiloth Vayalil[6], Professor Stephan Roth[7,8], Assoc. Prof, MD Lars Mikael Broman[2,3], Professor Lisa Prahl Wittberg[1]

[1]KTH Dept. Engineering Mechanics, Stockholm, N/A, Sweden. [2]ECMO Centre Karolinska, Astrid Lindgren Children's Hospital, Karolinska University Hospital, Stockholm, N/A, Sweden. [3]Dept. of Physiology and Pharmacology, Karolinska Institutet, Stockholm, N/A, Sweden. [4]Umeå Centre for Electron Microscopy, Umeå, N/A, Sweden. [5]MaxIV, Lund University, Lund, N/A, Sweden. [6]P03 Deutsches Elektronen-Synchrotron(DESY), Hamburg, N/A, Germany. [7]Deutsches Elektronen-Synchrotron(DESY), Hamburg, N/A, Germany. [8]KTH Dept. Fiber and polymer technology, Stockholm, N/A, Sweden

Introduction

Extracorporeal membrane oxygenation (ECMO) is a lifesaving support where the patient's blood is oxygenated outside the body via a membrane lung. Besides the membrane lung, the ECMO circuit consists of a blood pump, cannulae, tubing and several connectors. It is well-known that the flow in these medical devices exposes the blood to supraphysiological stress conditions generated by the highly unsteady flow. Today, common indicators used to assess risk of thrombogenicity are time-averaged where the stress tensor is represented in a scalar form. To improve these indicators, increased knowledge of the detailed flow structures and their effect on thrombus formation is needed.

Methods

In this work, a combined analysis of human thrombi was applied. Small angle x-ray scattering (SAXS) and scanning electron microscopy (SEM) was used to characterize structure and morphology of thrombi collected from used ECMO circuit components (pump, cannula and membrane lung). Large eddy simulation (LES) was applied to obtain detailed understanding of the flow structures developing in the different components of the ECMO circuit.

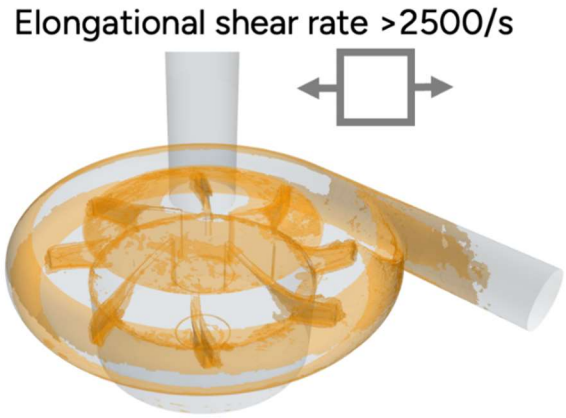
Results

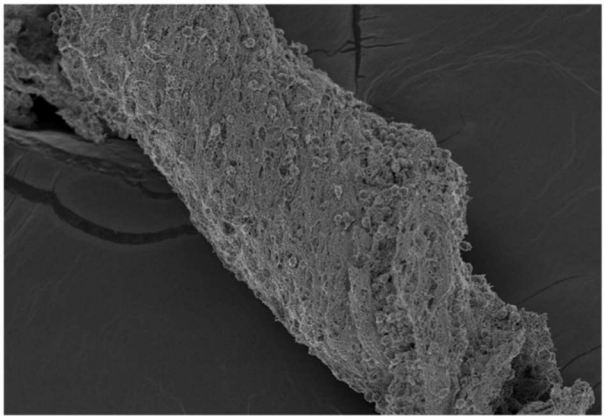
The flow in both pump and the membrane lung showed shear rates and elongational shear exceeding levels know to initiate von Willebrand factor unfolding, platelet activation, and hemolysis. All thrombi displayed a fibrin matrix with an outer fibrin alignment resembling the large-scale flow structures. Moreover, the fibrin matrix density varied between the different locations and samples. Besides fibrin, red blood cells (normal, echinocytes, and hemolyzed), activated platelets, and leukocytes were observed.

Discussion

Taylor-Couette-like systems used to provide data to form platelet activation and hemolysis models offer repeatability. However, they significantly differ from the fluid dynamical conditions in life supporting devices as in ECMO. An ECMO circuit exposes the blood to multidirectional and elongational flow characterized by strong shear layers, highly fluctuating, and stagnant flow regions. Our results highlight the importance of coupling knowledge of complex flow fields with the morphological characteristics of thrombi, pinpointing details in the flow promoting thrombus formation. This in turn may enable improved models for risk assessment and provide knowledge regarding parts of the different components that may benefit from re-design.

Images (Optional)





Acknowledgements (Optional)

The research was founded by Swedish Research Council through grant agreement no. 2019-04800 and the European Union (ERC CoG 2021: Project 101045453 - fitsCAN). Views and opinions expressed are however those of the author(s) only and do not necessarily reflect those of the European Union or the European Research Council Executive Agency. Neither the European Union nor the granting authority can be held responsible for them.

The computations were enabled by resources provided by the National Academic Infrastructure for Supercomputing in Sweden (NAISS), partially funded by the Swedish Research Council through grant agreement no. 2022-06725. For sample preparation of the blood clot and the scanning electron microscopy measurements, the authors acknowledge the facilities and technical assistance of the Umeå Centre for Electron Microscopy (UCEM) at the Chemical Biological Centre (KBC), Umeå University, a part of the National Microscopy Infrastructure NMI (VR-RFI 2019-00217). For the SAXS experiments we acknowledge Petra III, DESY (Hamburg, Germany), a member of the Helmholtz Association HGF and ForMAX at MaxIV, Lund, Sweden.

Session Category

Imaging and Biomedical Devices: Artificial Organs, Devices

OA39-01

Numerical-Experimental Estimation Spanning Single Red Blood Cell Dynamics to Bulk Suspension Rheology

Dr Naoki Takeishi Associate Professor[1], Prof Naoto Yokoyama Professor[2], Prof Masako Sugihara-Seki Professor[3]

[1]Kyushu University, Fukuoka, Fukuoka, Japan. [2]Tokyo Denki University, Adachi-ku, Tokyo, Japan. [3]Kansai University, Suita, Osaka, Japan

Introduction

The deformability of human red blood cells (RBCs), which comprise almost 99% of the cells in whole blood, is largely related not only to pathophysiological blood flow but also to the levels of intracellular compounds. Therefore, statistical estimates of the deformability of individual RBCs are of paramount importance in the clinical diagnosis of blood diseases. However, there is no established method to estimate individual RBC deformability from the rheological data of RBC suspensions, and the possibility of this estimation has not been proven.

Methods

To address this issue, we conducted an integrated analysis of a model of the rheology of RBC suspensions, coupled with macrorheological data of human RBCs suspended in plasma. The contribution of the individual deformed RBC to the bulk suspension rheology is quantified by the stresslet tensor [1].

Results

Assuming a nonlinear curve of the relative viscosity of the suspensions as a function of the cell volume fraction, the statistical average of the membrane shear elasticity was estimated for individual intact RBCs or hardened RBCs. Both estimated values reproduced well the experimentally observed shear-thinning non-Newtonian behavior in these suspensions.

Discussion

We hereby conclude that our complementary approach makes it possible to estimate the statistical average of individual RBC deformability from macrorheological data obtained with usual rheometric tests [2].

References (Optional)

[1] Naoki Takeishi et al., J Fluid Mech., 2019.

[2] Naoki Takeishi et al., J Rheol., 2024

Acknowledgements (Optional)

N.T. acknowledges funding from the Japan Society for the Promotion of Science (JSPS) KAKENHI JP25K07570 and JKA promotion funds from AUTORACE (2025M-480).

Session Category

Micro/Biofluidics: In Silico Models and Simulation

OA39-02

The Effect of Vessel Curvature on Flow Patterns of Red Blood Cells

Mr. Yu Terada[1], Dr. Tomoaki Watamura[1], Dr. Satoshi Ii[2], Dr. Shu Takagi[1]

[1]The University of Tokyo, Tokyo, Kanto, Japan. [2]Institute of science tokyo, Tokyo, Kanto, Japan

Introduction

Distinct flow patterns of red blood cells (RBCs) emerge in micrometer-scale capillary vessels depending on the vessel radius [1]. A single-file flow, in which RBCs align in a line, develops in narrow vessels whereas a double-file flow, characterized by alternating RBC alignment, appears within slightly wider vessels. These previous findings are based on straight vessels, even though curved vessels are frequently observed. In this study, we aim to clarify the transition conditions between single-file and double-file flow in curved vessels.

Methods

We performed direct numerical simulations to examine flow including RBCs in toroidal vessels with constant vessel curvature. Navier-stokes equations were solved. Red blood cells were modeled as Newtonian fluid covered by an elastic membrane with infinite small thickness. Immersed boundary method [2] was employed to exert RBCs' membrane force to fluid. No-slip boundary conditions were imposed on the surface of the toroidal vessel. The Reynolds number was on the order of 10^{-2}.

Results

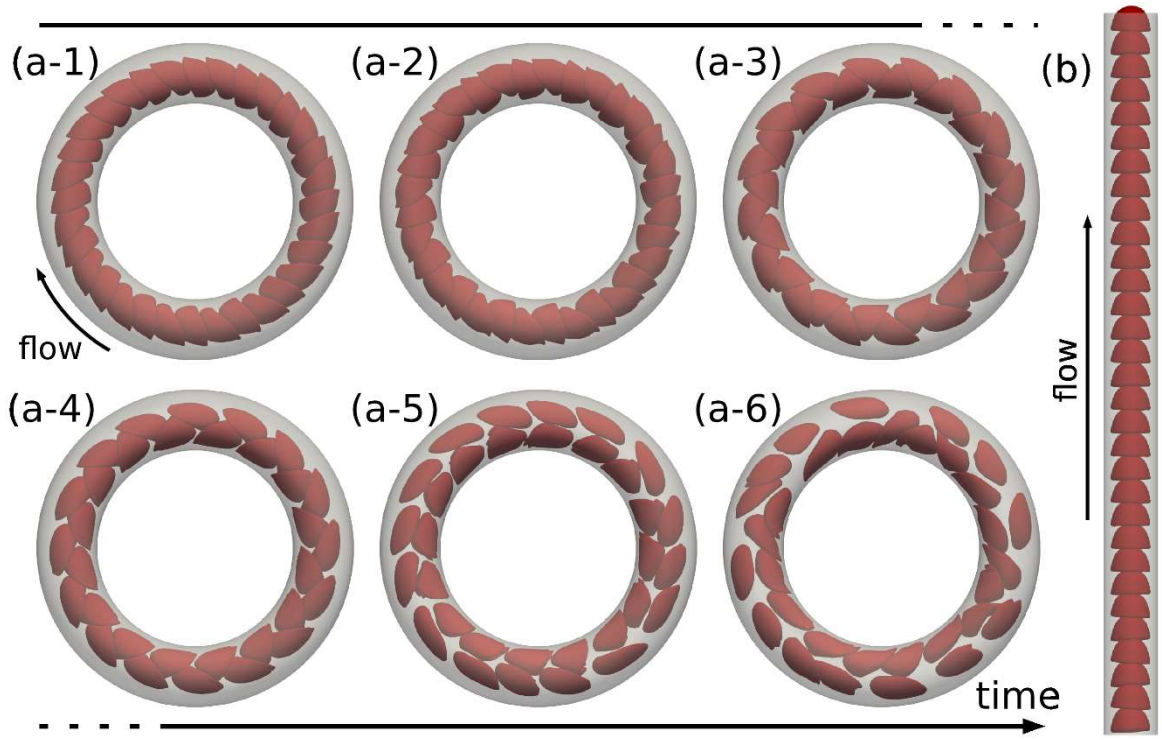
We investigated the effect of vessel curvature on the flow patterns at the quasi-steady state. Although single-file flow was observed in a straight vessel with a vessel radius of $R_d=4.75 \mu m$, in a toroidal vessel with an identical radius and with a curvature radius of $R_c=20 \mu m$, double-file flow emerged as indicated in the Figure. We mapped a transition diagram in radius and curvature radius space. Double-file flow was observed for larger vessel radii and smaller vessel curvature radii.

Discussion

The effect of vessel radius on these flow patterns is primarily attributed to whether sufficient space exists. To understand the influence of vessel curvature radius, we first consider the velocity field of single-phase flow in toroidal vessels. Although the maximum mainstream velocity is located at the vessel center in straight vessels, it shifts toward the inner wall of toroidal vessels [3]. Consequently, the shear rate profile in toroidal vessels

becomes asymmetric. Since a capsule migrates towards zero shear rate position, the asymmetric profile promotes the formation of double-file flow.

Images (Optional)



References (Optional)

"[1]C. Pozrikidis, Phys Fluids, 2005"

"[2]C. Peskin, Acta Numerica, 2002"

"[3]W. R. Dean, Lond Phil J. 1927"

Session Category

Micro/Biofluidics: In Silico Models and Simulation

OA39-03

Beyond Blood Flow: Combined Use of CFD and DOE to Predict Microsphere Distribution

Ms. Marta Gutiérrez de San Miguel, Dr. Jorge Aramburu, Professor Raúl Antón

Tecnun, Universidad de Navarra, San Sebastián, Guipúzcoa, Spain

Introduction

Hepatic radioembolization (RE) delivers Yttrium-90-labeled microspheres through the hepatic artery to irradiate liver tumors. Treatment efficacy depends on intrahepatic microsphere distribution, which is influenced by potentially physician-controlled parameters such as catheter axial and radial positioning. Although low Stokes number suggests microspheres follow blood streamlines and distribute proportionally to branch flow [1], clinical and computational evidence shows that small variations in catheter placement or flow conditions can significantly alter delivery, highlighting the need for personalized modeling [1,2]. Computational fluid dynamics (CFD) can simulate hepatic hemodynamics and microsphere transport, while Design of Experiments (DOE) identifies influential parameters and reduces computational cost. This work quantifies how catheter position affects microsphere distribution at the first bifurcation in three scenarios by combining CFD with DOE.

Methods

Three idealized hepatic artery bifurcations were created, with a catheter located at the parent vessel. Catheter-tip position was defined by axial (x_c) and radial (y_c, z_c) coordinates relative to the inlet plane. DOE was conducted to evaluate the influence of these three parameters under fixed geometry and flow conditions. Each parameter was set at three levels (low, medium, high), and a central composite design with 15 CFD simulations was executed per scenario. Microsphere trajectories were computed, and the response variable was the percentage of microspheres exiting a target daughter branch. Response surface models (RSM) were fitted and statistically evaluated.

Results

RSMs exhibited excellent fit and significance (R^2>0.96; ANOVA, p<0.05). Pareto charts identified dominant effects and interactions. Contour plots revealed how microsphere distribution varies with lateral (y_c) and vertical (z_c) catheter offsets for each axial position, highlighting regions highly sensitive to positional changes and others with stable, low-variability responses.

Discussion

Case-specific contour maps provide an intuitive and rapid tool to identify optimal catheter positions to achieve a desired microsphere distribution, while minimizing sensitivity to operator variability. Findings confirm that microsphere transport at the first bifurcation is a multifactorial process strongly influenced by both patient-specific and operator-controlled parameters. These DOE-CFD framework supports personalized RE planning and may contribute to more predictable dose delivery.

References (Optional)

[1] Wondergem, *et al*. Jour Nuc Med 2013;54(8):1294-1301.

[2] Roncali *et al.* Ann Biomed Eng 2020;48(5):1499-1510.

Session Category

Micro/Biofluidics: In Silico Models and Simulation

OA39-04

In Vitro and *In Silico* Study of Red Blood Cell Deformation in a Microfluidic Sudden Expansion

Ms Hannah Palahnuk, Dr. Nicolas Tobin, Dr. Keefe Manning

Pennsylvania State University, University Park, PA, United States

Introduction

Hemolysis occurs in mechanical circulatory support devices (MCSDs) at a rate of 5-18%[1]. Strain-based hemolysis models, those governed by red blood cell (RBC) deformation, may aid in the design of MCSDs to decrease the hemolytic rate. In this study, we modify a droplet deformation-based numerical approach to capture RBC behavior in a microfluidic channel and validate *in silico* results using *in vitro* data.

Methods

In silico droplet and *in vitro* RBC deformation were quantified in a 575x580 μm area in a microfluidic sudden expansion (**Figure 1A**). The region of interest produces spatially varying strain rates with shear, rotational, and extensional components at supraphysiological magnitudes (>2,000 s^{-1}) to emulate MCSD flows. The deformation model, an evolution equation for a morphology tensor (***S***), was coupled to steady flow in the microchannel using OpenFOAM (**Figure 1B**). The symmetric (***E***) and antisymmetric (***W***) components of the velocity gradient tensor govern deformation along with constitutive parameters τ, f_1, and f_2, which were tuned to represent RBCs. The eigenvalues of ***S*** (λ_i) represent the droplet's principal axes' lengths and were used to quantify deformation (**Figure 1C**). For the *in vitro* experiments, human RBCs were suspended at 0.5% hematocrit in Hanks balanced salt solution with 13.5 or 6.5 wt.% Dextran-40,000 (viscosity of 4.17 or 2.05 cP, respectively). The channel was mounted to an inverted microscope stage and perfused with either suspension at 100 μL/min; images were captured in the region of interest (**Figure 1A**). RBC and droplet deformation indices (DIs) were compared for model validation (**Figure 1C**).

Results

The model reproduces spatially varying RBC deformation: high magnitude DI in the channel throat and the shear-dominant regions along the channel walls (DI ~0.5 or ~0.25 for 4.17 cP and 2.05 cP, respectively), and DI<0 for x>150 μm as RBCs compress when flow

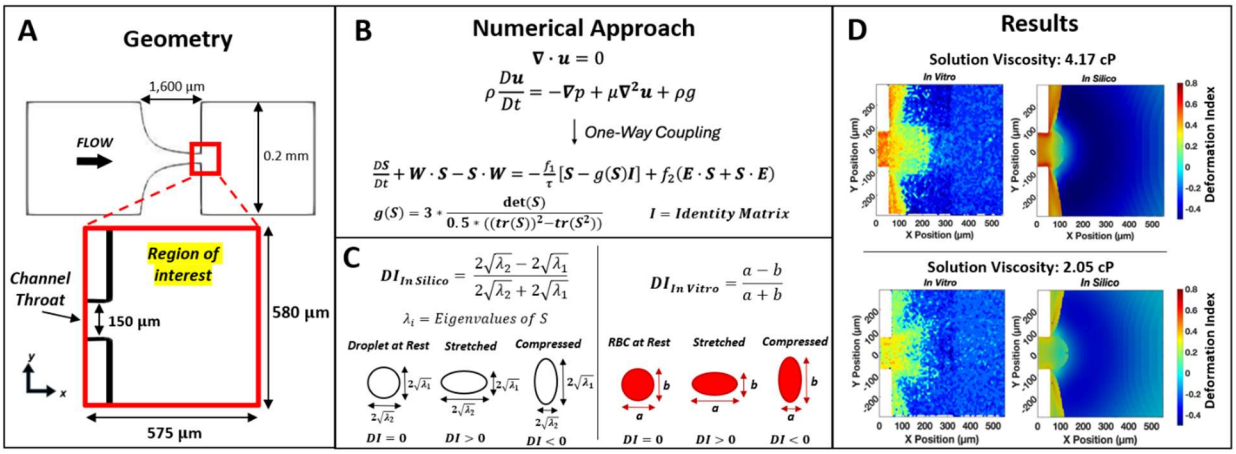
decelerates (**Figure 1D**). Further, the magnitude of *in vitro* deformation increases with higher viscosity, as reflected in the *in silico* data (**Figure 1D**).

Discussion

The model reproduces RBC deformation in a heterogeneous environment akin to MCSDs. The model will be extended to capture RBC lysis in future studies.

Images (Optional)

Figure 1.



References (Optional)

[1] Christos Papanastasiou *et al.,* World J. Cardiol., 2020

Acknowledgements (Optional)

Session Category

Micro/Biofluidics: In Silico Models and Simulation

OA40-01

Effect of Aging and Beta-Amyloid Deposition on Movement Variability during Single- and Dual-Task Walking

Dr. Lisa Zukowski PhD[1], Dr. Katherine Hsieh PhD[2], Dr. Samuel Lockhart PhD[3,4], Dr. Christina Hugenschmidt PhD[3], Dr. Jamie Kronenberg PT, DPT, PhD, SCS[1]

[1]High Point University, High Point, NC, United States. [2]Georgia State University, Atlanta, GA, United States. [3]Wake Forest University School of Medicine, Winston-Salem, NC, United States. [4]Perceptive Inc., Burlington, MA, United States

Introduction

Alzheimer's disease (AD), a progressive neurodegenerative disease characterized by beta-amyloid deposition (Aβ), negatively impacts cognition, mobility and quality of life. Aβ deposition may therefore alter healthy movement variability, which is characterized by having variable, yet stable movement solutions to accommodate multifactorial environmental demands. We sought to determine if movement variability as characterized by recurrence quantification analysis (RQA) variables of interest, differed between older adults at elevated risk of developing AD (OAer), older adults at low risk of developing AD (OAlr), and young adults (YA) during single- and dual-task walking.

Methods

Twenty-one OAer (78.6±5.0 years, 9 females, 55.0±33.2 Aβ-PET Centiloid), 31 OAlr (78.0±4.6 years, 14 females, -2.1±5.9 Aβ-PET Centiloid), and 28 YA (30.6±3.5 years, 17 females, no Aβ-PET) completed two 2-minute trials: single-task fast walking (ST) and dual-task fast walking while completing an auditory working memory task (DT). Linear acceleration in the anterior/posterior direction was recorded with an APDM opal sensor worn on the lower back. Predictability (percent determinism; %DET) and stability (max line; MaxL) were calculated using RQA of anterior/posterior linear acceleration to characterize movement variability during each task. A 2x2 mixed ANOVA assessed group (OAer/OAlr/YA) and task (ST/DT) effects on %DET and MaxL.

Results

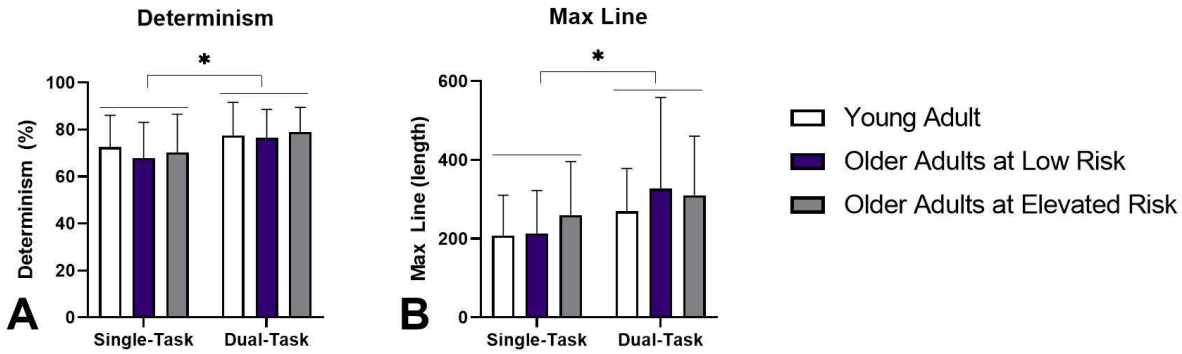
There were no significant interactions of group and task on %DET ($p=0.349$; $h^2=0.027$) or MaxL ($p=0.170$; $h^2=0.045$). There was no main effect of group on %DET ($p=0.638$) or MaxL ($p=0.455$), but there was a main effect of task on %DET ($p<0.001$) and MaxL ($p<0.001$), with participants demonstrating greater predictability and stability during DT compared to ST (Figure 1).

Discussion

While there was no interaction of group and task on %DET or MaxL, main effects of task suggest that movement variability changes when responding to DT walking conditions independent of group. The increase in predictability and stability from ST to DT may indicate altered movement variability, suggesting increased automaticity of the gait task during DT performance to attend to the cognitive task. Future directions should include more complex gait tasks and different types of cognitive tasks to further assess the impact of aging and Aβ deposition on movement variability.

Images (Optional)

Figure 1. Percent determinism and max line results of YA, OAlr, and OAer during ST and DT trials.



Session Category

Clinical Biomechanics: N/A

OA40-02

Longitudinal Changes in Walking Speed Reserve May Be an Indicator of pTau and Amyloid Beta Changes: A Pilot Study

Mr. John Tebbetts MS, Ms. Breanna Morales MS, Dr. Jack Manning PhD, Dr Jennifer Yentes PhD

Texas A&M University, College Station, Texas, United States

Introduction

Functional reserve is related to resilience. Resilience is defined as the ability to recover from a stressor while reserve is the capacity. An individual's functional reserve is the difference between baseline and maximal function, representative of their capacity to respond to perturbations. Reserve narrows with age through decrease in maximal capacity and/or increase in baseline requirements to maintain function. If reserve decreases over time, this may be an indicator of accelerated cognitive decline (measured by Plasma phosphorylated Tau (pTau) and Amyloid-Beta (AB)) and increased vulnerability to disease and injury. It is currently unknown if walking speed reserve may be indicative of a change in these markers of dementia risk.

Methods

Five middle aged (60.4±3.2yrs) and 4 older (67.8±2.6yrs) individuals underwent gait assessments and a blood draw twice, one year apart. Walking speed reserve (WSR) was quantified by subtracting preferred walking speed from their maximum walking speed. Levels of pTau181, pTau217, total pTau, AB 40, and AB 42 were quantified. pTau ratios to total Tau and AB42/40 were calculated for both years. Longitudinal changes were calculated by subtracting year one from year two. Spearman correlations between WSR and markers of dementia were run.

Results

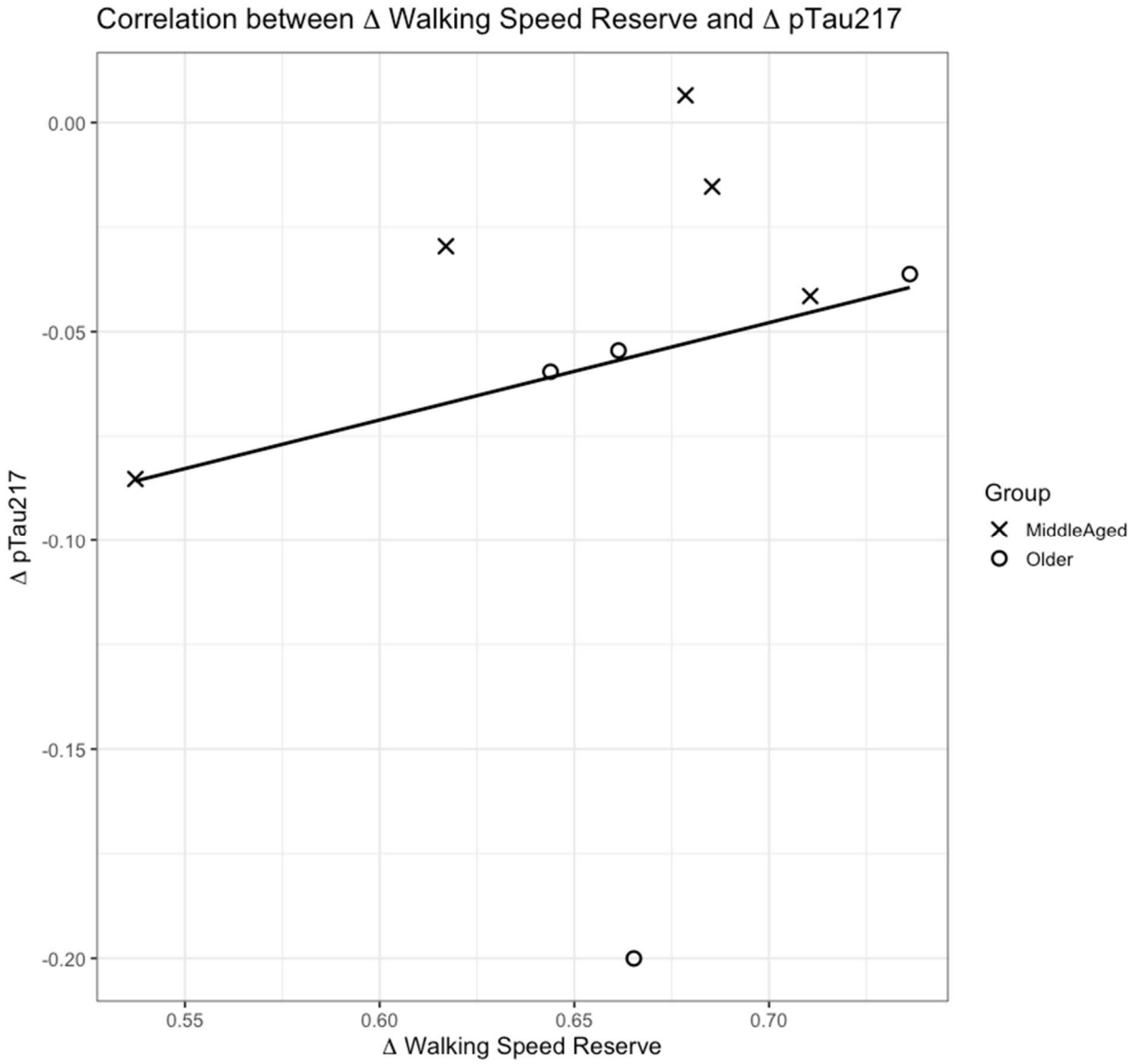
Longitudinal change in WSR was moderately correlated with pTau217 ($r=0.42$, $p=0.27$), although not significant. WSR had non-significant weak relationships with pTau181 ($r=-0.13$, $p=0.74$) and AB ($r=0.28$, $p=0.46$).

Discussion

At this sample size, longitudinal change in WSR was associated with pTau217, and weakly with AB. Indicating that greater changes in WSR were associated with greater changes in blood biomarkers of dementia. Changes in walking speed are indicative of mobility and

mortality. These results provide some evidence that WSR may be an early indicator of cognitive decline and should be investigated in studies with larger samples.

Images (Optional)



Session Category

Clinical Biomechanics: N/A

OA40-03

Dementia with Lewy Bodies Worsens Reactive Responses to Walking Balance Perturbations Compared to Older Adult Controls

Dr. Emily Eichenlaub[1], Dr. Andrea Bozoki MD[2], Dr. Jason Franz PhD[1]

[1]University of North Carolina at Chapel Hill and North Carolina State University, Chapel Hill, NC, United States. [2]University of North Carolina at Chapel Hill, Chapel Hill, NC, United States

Introduction

As our aging population continues to grow, the prevalence of dementia is expected rise. Specifically, Dementia with Lewy Bodies (DLB) affects memory, executive function, and motor planning, making individuals nearly two-times more likely to fall than age-matched controls. When faced with an oncoming threat to balance, cognitive impairments may reduce DLB patients' ability to make proactive adjustments; when responding to a threat to balance, motor impairments may reduce their ability to effectively deploy reactive responses. To our knowledge, no studies have deployed ecologically relevant lab-based perturbations to understand changes in proactive and reactive balance control caused by DLB. We hypothesized that DLB patients would exhibit smaller proactive adjustments (via whole-body angular momentum, WBAM) for anticipated perturbations and larger reactive responses (via WBAM), particularly for unanticipated perturbations, compared to controls.

Methods

11 older adult controls (Controls; 6F; age: 71.4±4.8 years; walking speed: 1.38±0.16 m/s) and 11 older adults diagnosed with DLB (DLB; 2F; age: 71.6±4.4 years; walking speed: 1.04±0.24 m/s) were age- (±2 years) and BMI- (±2.5 pts) matched. Participants responded to treadmill-induced perturbations delivered at the instant of heel-strike in which the belt accelerated or decelerated over 200ms at 6m/s^2 delivered either unexpectedly (unanticipated) or after a 3-s verbal countdown (anticipated). We calculated WBAM and WBAM ranges ($WBAM_{range}$) in all three planes of motion during the preceding, perturbed, and recovery strides to determine the effects of cognition, anticipation, and their interaction effect on proactive adjustments and reactive responses.

Results

Preceding a perturbation, DLB did not exhibit any differences in proactive adjustments compared to controls. When responding to accelerations, DLB exhibited greater $WBAM_{range}$ in the transverse and frontal planes (perturbed stride) compared to Controls (**Fig.** 1A). When responding to decelerations, DLB exhibited greater $WBAM_{range}$ in

the sagittal (perturbed stride) and frontal planes (perturbed and recovery strides) compared to Controls (**Fig.** 1B).

Discussion

These results suggest that DLB negatively affects reactive responses to balance perturbations, independent of anticipation. Our findings have significant implications for understanding the effects of cognitive decline on balance control to inform the design of rehabilitation programs and assistive devices to mitigate patients' risk of falling.

Images (Optional)

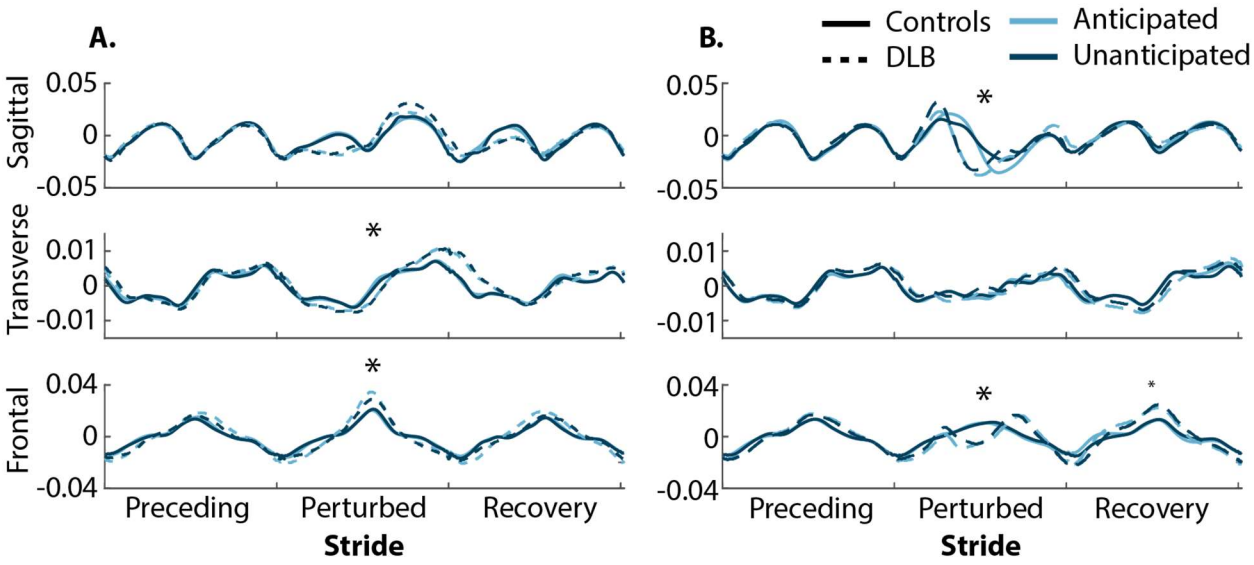


Figure 1. WBAM profiles in the frontal, transverse, and sagittal planes of motion in response to treadmill-belt (A) accelerations and (B) decelerations. Statistical significance on WBAMrange is denoted as: cognition (*), anticipation (#), and a cognition x anticipation interaction effect (&).

Acknowledgements (Optional)

Supported by the National Institutes of Health (F31AG084241).

Session Category

Human Motion and Performance: Balance, Posture and Control

OA40-04

The Effects of Mild Cognitive Impairment on Kinematic and Neuromuscular Responses to Novel Slip-Like and Trip-Like Perturbations During Walking

Ms. Jessica Pitts, Dr. Tanvi Bhatt

University of Illinois at Chicago, Chicago, IL, United States

Introduction

Older adults with mild cognitive impairment (OAwMCI) fall 2x more than cognitively intact older adults (CIOA) and show impaired reactive balance responses to unexpected perturbations. However, most studies in OAwMCI have delivered unidirectional stance-perturbations, whereas most real-life falls are caused by multi-directional gait-perturbations (e.g., slips and trips). This study compared kinematic and neuromuscular responses to both slip-like (backward balance loss) and trip-like (forward balance loss) gait-perturbations in OAwMCI vs. CIOA.

Methods

25 OAwMCI (Montreal Cognitive Assessment (MoCA): 18-25) and 25 CIOA (MoCA: 26-30) experienced a novel slip and trip during treadmill walking, caused by sudden belt deceleration (-6 m/s^2) or acceleration (5 m/s^2). An overhead load cell detected falls (>30% body weight), and Chi-Square tests assessed group differences in fall rate. 2x3 ANOVAs examined the effect of group and time (pre-perturbation touchdown (TD), recovery TD1, recovery TD2) on margin of stability (MOS). Muscle synergies were extracted from bilateral EMG (biceps femoris (BF), vastus lateralis (VL), medial gastrocnemius (MG), tibialis anterior (TA)) from perturbation onset to recovery TD2. Synergy structures (M) were compared between groups using Pearson's correlations.

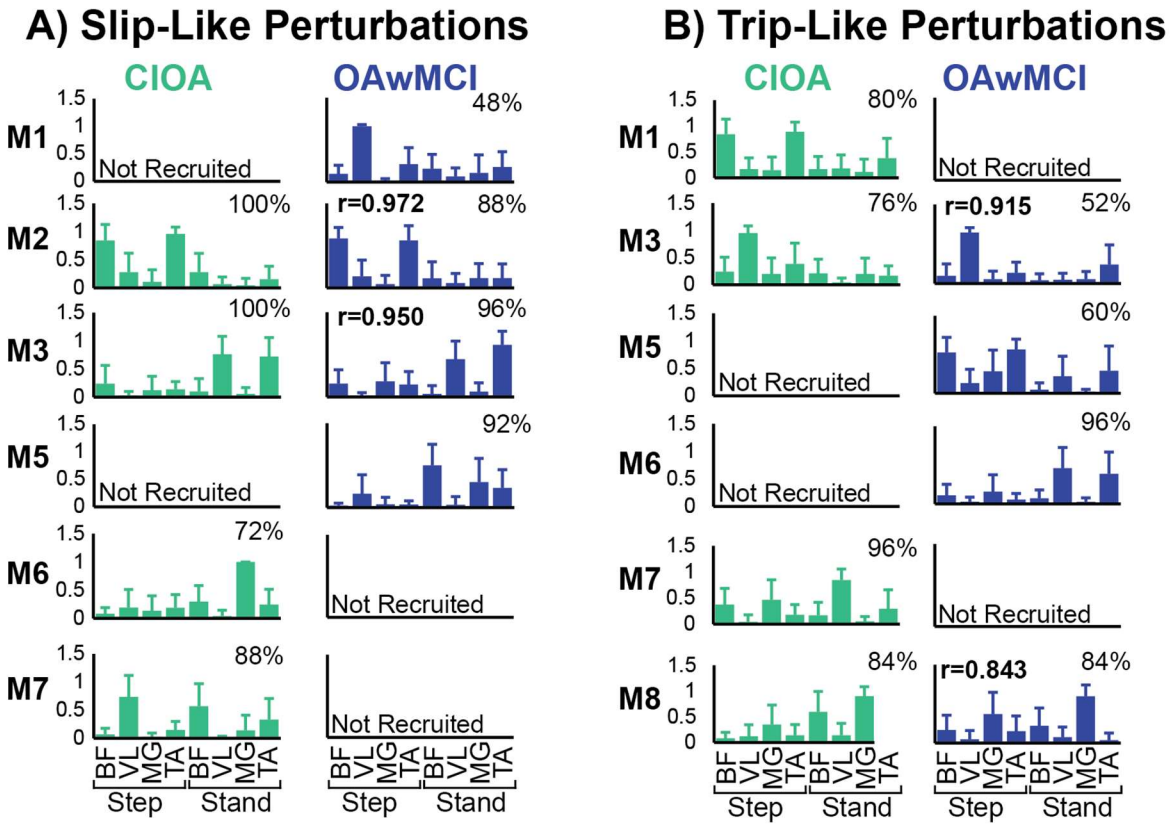
Results

Fall rates were not significantly different between groups ($p \geq 0.123$), although OAwMCI showed 16-20% higher fall rate for both slips (64% vs. 44%) and trips (92% vs. 76%). OAwMCI showed significantly lower MOS during slip recovery (recovery TD1, $p=0.004$), although no group differences in MOS were found for trips ($p>0.05$). For both perturbations, 2-3 muscle synergies were highly similar between groups ($r>0.843$), although each group also recruited 2-3 unique synergies. For example, M7 (slips) was only recruited by CIOA (*mostly VL step, BF stand*), which could reflect greater interlimb coordination, whereas M5 (trips) was only recruited by OAwMCI (*mostly BF & MG step, bilateral TAs*) and could indicate defensive co-contraction/stiffening.

Discussion

OAwMCI showed lower reactive COM stability than CIOA during slip recovery, although not trip recovery. Trips may have posed a higher biomechanical challenge than slips (given ~30% higher fall rate) and been difficult for all older adults, regardless of cognition. However, OAwMCI still recruited distinct muscle synergies during both slips and trips, suggesting the use of different neuromuscular strategies to implement reactive stepping.

Images (Optional)



Session Category

Clinical Biomechanics: N/A

OA41-02

Predictive Neuromechanical Simulation Explains Gait Biomechanics in Obesity

Dr. Chi-Whan Choi PT, PhD, MPH[1], Mr. Vincent Ton MS[2], Dr. Simone V. Gill PhD, OTR, FAOTA[1], Dr. Seungmoon Song PhD[2]

[1]Boston University, Boston, MA, United States. [2]Northeastern University, Boston, MA, United States

Introduction

Individuals with obesity exhibit characteristic gait adaptations, including reduced early-stance knee flexion, altered muscle activation, and slower walking speeds. Although these patterns are well documented experimentally, the mechanisms driving them remain unclear because inverse-dynamics and tracking-based approaches cannot determine why specific gait strategies emerge. This study used predictive neuromechanical simulation to identify how obesity-related changes and gait-related objectives shape walking biomechanics.

Methods

We investigated baseline and obese models using predictive neuromechanical simulations. The baseline model represented a 1.8 m, 80 kg adult. We adapted segmental inertia properties and muscle strength according to the literature to represent a nominal obese model (1.8 m, 140 kg), as well as more apple-like and more pear-like variants with identical height and mass. Control parameters were optimized using CMA-ES to generate stable, steady walking. The cost function combined muscle effort and knee loading, and we identified optimal weightings by matching early-stance knee kinematics, one of the key gait changes observed in individuals with obesity. Using these weights, we simulated gait across walking speeds for baseline and obese models and evaluated resulting kinematics, kinetics, and muscle activations.

Results

The baseline model achieved its best match to experimental knee kinematics using the muscle effort cost alone, while the obese model required a combination of muscle effort and knee loading costs (w_{effort}=0.6 & w_{load}=0.4). With this weighting, the obese model reproduced experimentally observed gait features, including reduced early-stance knee flexion and increased muscle demand, as well as a shift toward slower preferred walking speeds. Differences in body-mass distribution produced modest but consistent variations:

the more apple-like model showed slightly greater knee flexion and vastii activation, whereas the more pear-like model exhibited slightly higher gastrocnemius activation.

Discussion

Predictive neuromechanical simulation provided mechanistic explanations for gait adaptations associated with obesity. The combination of altered physiology and an objective that penalizes knee loading reproduced stiff-knee gait features, and elevated muscle effort at faster speeds explained the emergence of slower speeds. Although the effects of mass distribution were modest, they demonstrated how morphological variation can influence knee mechanics and muscle demand. These findings highlight the value of predictive simulation for probing gait mechanisms relevant to obesity.

Images (Optional)

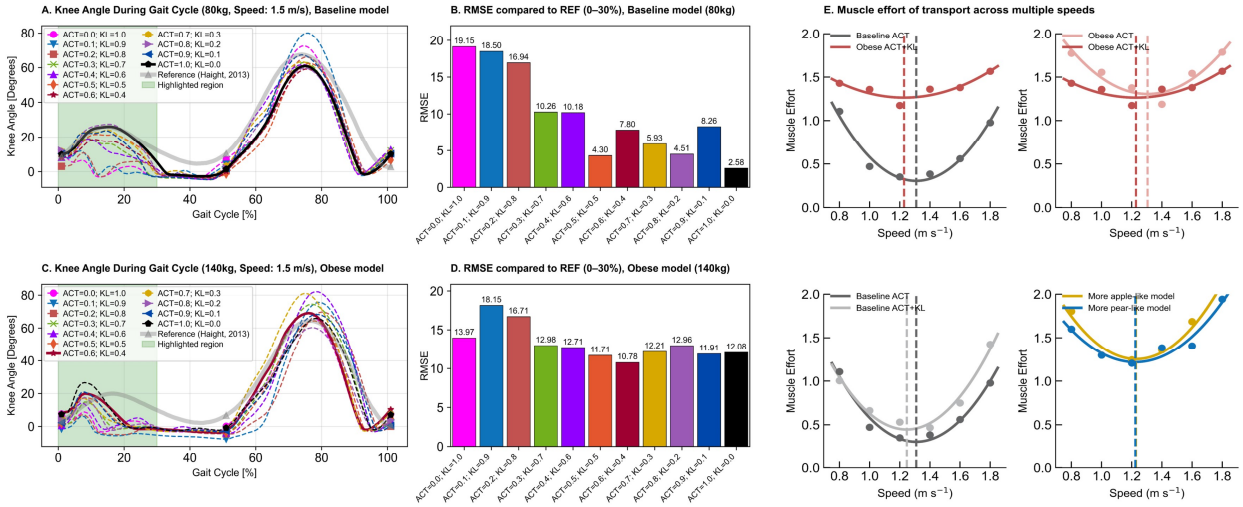


Figure 1 (A) Baseline (80kg) model: The black solid line represents the knee angle from the best weight combination based on Root Mean Square Error (RMSE) compared to knee angle (bold gray line) in individuals without obesity from the reference (REF, Haight 2014) when optimized for different costs with each weight combination of weight for muscle activation (w_{effort}: ACT) and weight for knee loading (w_{load}: KL). (B) RMSE compared to REF (0–30% during gait cycle) in Baseline model. (C) Nominal obese (Obese, 140kg) model: The dark red solid line represents the knee angle from the best weight combination based on RMSE. Bold gray line represents knee angle in individuals with obesity from REF. (D) RMSE compared to REF (0–30% during gait cycle) in Obese model. (E) Muscle effort of transport during walking simulations at each speed using the Baseline model (80kg, gray line: Baseline ACT) with the best weight combination (ACT=1.0, KL=0.0) and Nominal obese model (140kg, red line: Obese ACT+KL) with the best weight combination (ACT=0.6, KL=0.4), Nominal obese model (140kg, light red line: Obese ACT) with the weight combination (ACT=1.0, KL=0.0), Baseline model (80kg, light gray line: Baseline ACT+KL) with weight combination (ACT=0.6, KL=0.4), more apple like model (140kg, yellow line), and more pear like model (140kg, blue line) with the weight combination (ACT=0.6, KL=0.4). Each vertical line indicates the point of minimum muscle effort cost for each model.

References (Optional)

Session Category

Human Motion and Performance: Locomotion/Gait

OA41-03

A Neuromusculoskeletal Digital Twin for Personalized Stroke Gait Rehabilitation

Dr. Liangliang Xiang[1], A/Prof. Ruoli Wang[1,2], Prof. Elena Gutierrez-Farewik[1,2]

[1]KTH Royal Institute of Technology, Stockholm, Stockholm, Sweden. [2]Karolinska Institute, Stockholm, Stockholm, Sweden

Introduction

Stroke commonly leads to muscle weakness, spasticity, and abnormal gait, substantially limiting mobility and increasing fall risk. Conventional biomechanical approaches, such as optimization-based estimators, cannot adapt to individual neuromuscular deficits. Deep reinforcement learning (DRL) offers a promising alternative, having demonstrated the ability to learn physiologically plausible control strategies, model neuromechanical interactions, and assist in locomotion and exoskeleton control [1]. Its capacity to discover individualized motor policies makes it suitable for modeling heterogeneous stroke gait impairments. We propose a neuromusculoskeletal digital-twin framework that combines personalized musculoskeletal modeling with DRL to simulate and analyze muscle coordination in stroke gait.

Methods

A public dataset of 48 stroke participants (age 64 ± 14 yr; body mass 72 ± 14 kg; height 1.70 ± 0.08 m) was used for training and evaluation. Forty-five subjects were used for training and three for testing [2]. Subject-specific kinematics were used to generate individualized anatomical constraints, and a DRL controller was trained to reproduce gait patterns through muscle excitations. The RL state included joint angles and velocities (37 dimensions), body positions and orientations (49 dimensions), and segment velocities (21 dimensions). Stroke severity (mild, moderate, and severe) was modeled by adjusting activation/deactivation delays, muscle force capacity, and passive stiffness [3]. A Mixture-of-Experts (MoE) architecture trained three severity-specific expert policies, and Proximal Policy Optimization (PPO) optimized muscle-driven control. The reward combined joint tracking, pelvis stabilization, and metabolic cost minimization.

Results

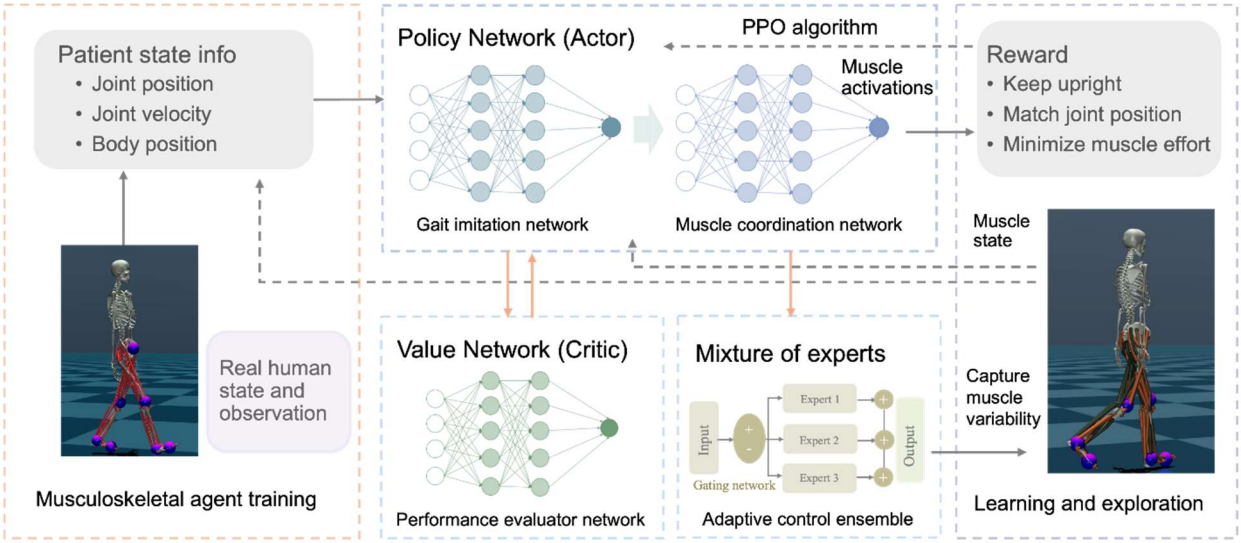
The framework reproduced subject-specific joint trajectories with low error (<10°) and generated muscle activation patterns resembling EMG references. The severe-stroke expert captured reduced plantarflexor activity and delayed quadriceps activation, while the

mild expert produced more physiological profiles. The MoE gating network appropriately selected policies across intermediate impairment levels according to Functional Ambulation Categories scores of 2.67 ± 1.07 (severe), 3.05 ± 1.08 (moderate), and 3.79 ± 0.88 (mild).

Discussion

This digital-twin approach provides adaptive, physiologically grounded insights into impaired muscle coordination and supports "what-if" analyses for weakness, spasticity, or exoskeleton assistance. It offers a scalable foundation for personalized rehabilitation and assistive-device design in stroke gait.

Images (Optional)



References (Optional)

[1] Luo *et al.*, Nature, 2024

[2] Van Criekinge *et al.*, Sci Data, 2023

[3] Dorsch *et al.*, Arch Phys Med Rehabil, 2016

Session Category

Human Motion and Performance: Locomotion/Gait

OA41-04

Revisiting How We Model Psoas Geometry in Musculoskeletal Models - Implications for Simulating Walking in Duchenne Muscular Dystrophy

Dr. Ines Vandekerckhove[1], Mr. Lars D'Hondt[2], Prof. Kaat Desloovere[1,3], Prof. Friedl De Groote[2]

[1]Department of Rehabilitation Sciences, KU Leuven, Leuven, Vlaams-Brabant, Belgium. [2]Department of Movement Sciences, KU Leuven, Leuven, Vlaams-Brabant, Belgium. [3]Clinical Motion Analysis Laboratory, University Hospital Leuven, Pellenberg, Vlaams-Brabant, Belgium

Introduction

Predictive simulations in Duchenne muscular dystrophy (DMD) fail to capture increased hip flexion, anterior pelvic tilt and posterior trunk lean. The psoas muscle is often contracted in DMD and is thought to contribute to these gait features. However, in most lower-limb musculoskeletal models, the psoas incorrectly attaches to the pelvis rather than the lumbar spine. This study corrects psoas geometry and tests its impact on predictive DMD gait simulations.

Methods

We previously generated predictive gait simulations of three DMD gait patterns (DMD1: mild, DMD2: tiptoeing, DMD3: flexion pattern), identified from a longitudinal dataset of 137 measurements in 30 boys with DMD. Simulations were based on an extended version of OpenSim's 2392 model scaled to the average dimensions of boys with the corresponding gait pattern. DMD impairments were incorporated by estimating average muscle weakness from fixed dynamometry and contractures from goniometry and clinical scales.

Here, we replaced the simplified psoas geometry with a detailed, anatomically accurate psoas derived from the Anderson lumbar-spine model and repeated all simulations with the updated model. The differences between the DMD models and the TD model with simplified psoas (original simulations) were compared to the differences between DMD models and TD model with complex psoas, and to the differences between DMD and TD experimental data.

Results

The effect of the adapted psoas geometry was minimal for lumbar and pelvic joints but slightly larger for the hip joint. The updated psoas improved agreement between

experimental and simulated differences in hip flexion during terminal stance in DMD1 and during swing in DMD3 although it reduced agreement during terminal swing and early stance (Figure 1).

Discussion

Overall, improving anatomical realism of the psoas had modest effects on the predicted gait pattern. A possible reason is that we underestimated psoas contracture. Indeed, increasing psoas contracture improved the agreement between experimental and simulated differences between DMD3 and TD gait patterns. In addition, alterations in the gait pattern might be the consequence of interactions between lower limb muscle contractures and increased spine mobility. We believe that refining trunk-hip mechanics is critical for using simulations to guide targeted interventions aimed at prolonging ambulation in DMD.

Images (Optional)

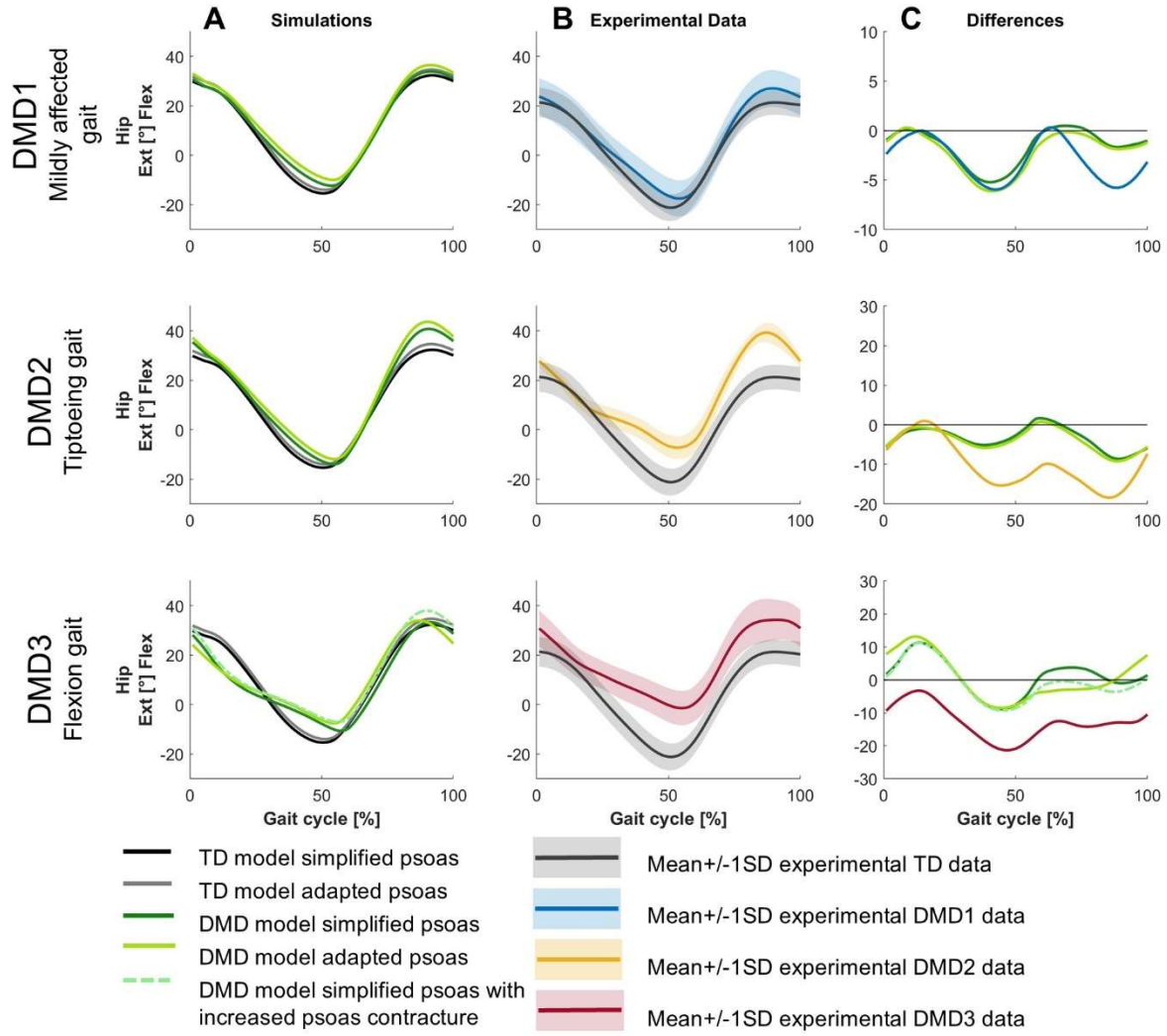


Figure 1: Comparison of simulated and experimental hip flexion angle for DMD1, DMD2 and DMD3. (A) Simulated gait of TD and DMD models with simplified and adapted psoas. (B) Experimental gait. (C) Differences in hip flexion angle between TD and DMD models with simplified psoas (dark green), TD and DMD models with adapted psoas (light green), TD and DMD model with adapted psoas and increased psoas contracture. DMD, Duchenne muscular dystrophy; Ext, extension; Flex, flexion; SD, standard deviation; TD, typically developing.

References (Optional)

Session Category

Human Motion and Performance: Locomotion/Gait

OA41-05

Practical Inter-Laboratory Variations in Motion Capture Measurements and Implications for Personalized Musculoskeletal Modeling

MSc. Parham Sadeghinia[1], BSc. Leendert Schaake[2], Dr. Vera Kooiman[3], BSc. Lise Wilders[4], Prof. dr. Nico Verdonschot[1,3], Dr. Periklis Tzanetis[1]

[1]Department of Biomechanical Engineering, University of Twente, Enschede, Overijssel, Netherlands. [2]Roessingh Research and Development, Enschede, Overijssel, Netherlands. [3]Orthopaedic Research Laboratory, Radboud University Medical Center, Nijmegen, Gelderland, Netherlands. [4]Department of Rehabilitation, Sint Maartenskliniek, Nijmegen, Gelderland, Netherlands

Introduction

Gait analysis is essential for understanding human movement, yet reproducibility across laboratories remains challenging due to examiner- and lab-specific factors, especially marker placement [1]. This study aimed first to determine how inter-laboratory variations in protocol-execution, including marker placement or execution of an activity, affect knee joint angles and net moments; and second, to assess whether a personalized musculoskeletal model mitigates these effects through its marker optimization process.

Methods

A healthy subject performed walking and step-down activities at three independent gait laboratories following a standardized protocol. All laboratories used the Vicon motion-capture system (Nexus v2.12) and the Conventional-Gait-Model 2.4 (CGM2.4) marker set. Knee joint angles and net moments were computed based on marker-trajectories and ground reaction forces. A subject-specific musculoskeletal model was subsequently developed in the Anybody Modeling System (AnyBody Technology A/S, Denmark) driven by the motion capture data. Marker positioning optimization and then kinematic analysis was performed to calculate joint angles, and inverse dynamics analysis to evaluate the resulting net joint moments. Inter-laboratory differences were quantified using absolute differences (Δ) in peak knee flexion angle and net moment.

Results

Table 1 summarizes absolute differences in knee joint angles and net moments across the three laboratories using the CGM2.4 and the musculoskeletal model. By utilizing the personalized musculoskeletal model, the differences in knee joint angles decreased by

maximally 38.4% and 77.9% for walking and step-down trials, respectively; the corresponding decrease in net joint moments was 74.9% and 77.6%.

Discussion

This study showed that inter-laboratory differences in kinematics and kinetics are affected by examiner-dependent marker placement and task execution, which is more variable if the task is more complex. Greater variability during step-down further reflected factors such as foot placement and balance. Multi-site studies therefore require consistent marker placement and step-by-step instructed task execution. Using a personalized musculoskeletal model can reduce both kinematic and kinetic differences through marker positioning optimization, thereby supporting a more reliable interpretation of gait analysis outcomes.

Images (Optional)

Table 1. Inter-laboratory differences in peak knee joint flexion angle and net moment computed using the CGM2.4 and personalized musculoskeletal model.

Analysis Method	Parameter	Activity	Δ Lab1 VS. Lab2	Δ Lab1 VS. Lab3	Δ Lab2 VS. Lab3
CGM2.4	Knee joint Flexion angles (°)	Walk	2.6	6	3.7
		Step-Down	5.8	8.6	3.7
	Knee joint Flexion net moments (Nm)	Walk	16.9	24.1	41
		Step-Down	32.3	25	7.3
Musculoskeletal Model	Knee joint Flexion angles (°)	Walk	1.6	5.4	3.7
		Step-Down	1.6	1.9	3.6
	Knee joint Flexion net moments (Nm)	Walk	4.2	23.6	27.9
		Step-Down	7.2	13.5	6.3

References (Optional)

[1] Bendetti *et al*, Gait Posture, 2013

Session Category

Human Motion and Performance: Locomotion/Gait

OA42-01

Cutting Technique of ACL-Reconstructed Professional Handball Players: On-Field Kinematic Assessment using IMUs

Dr. Margherita Mendicino[1], Dr. Stefano Di Paolo[1], Dr. Raffaele Zinno[2], Dr. Carlo Simonelli[3], Prof. Laura Bragonzoni[2], Prof. Stefano Zaffagnini[1,4]

[1]2nd Orthopaedic and Traumatologic Clinic, IRCCS Rizzoli Orthopaedic Institute, Bologna, Emilia Romagna, Italy. [2]Department for Life Quality Studies, University of Bologna, Rimini, Emilia Romagna, Italy. [3]Department of Biotechnology and Life Sciences, University of Insubria, Varese, Lombardia, Italy. [4]Department of Biomedical and Neuromotor Sciences, University of Bologna, Bologna, Emilia Romagna, Italy

Introduction

Anterior cruciate ligament (ACL) injuries are common in handball, mostly occurring during non-contact cutting maneuvers [1]. While lab-based studies have identified biomechanical risk factors, on-court duels remain unexplored [1]. Wearable technologies (IMUs) allow on-field assessments during dynamic tasks. This study compared ACL-reconstructed (ACLR) and healthy handball players using IMUs during on-field sport-specific injury-related tasks.

Methods

Twenty-five professional handball players (23.7±3.9 years; 14 males), including 7 ACLR players (RTS>24 months), performed two high-dynamic cutting tasks: a change of direction with a passive opponent and a response to an active, real-game opponent (n=300 trials collected, Figure1). Based on dominant hand and movement direction, trials were classified as sidestep cuts (SSC) or crossover cuts (XOVER). Lower-limb and trunk kinematics were recorded using eight IMUs (100Hz, MTw Awinda, Movella), validated for high-dynamic movements. Joint kinematics was assessed in the three anatomical planes at initial contact (IC), peak knee flexion (pKF), and range of motion (ROM). Speed and acceleration/deceleration during approach/exit phases were evaluated. A linear mixed-effects model tested effects of injury (ACLR vs. healthy), opponent (passive vs. active), and their interaction effect (injury×opponent) on kinematics.

Results

Significant injury×opponent interactions indicated altered kinematics in ACLR players. Active-opponent conditions amplified kinematic differences between ACLR and healthy players (SSC: 9 vs. 2 significant variables). In SSC ($p<0.001$-0.042), ACLR showed greater

trunk sagittal ROM and ipsilateral rotation at pKF, increased contralateral pelvic rotation at IC, higher hip flexion, larger frontal-plane knee ROM, and greater ankle eversion, more pronounced with active opponent. In XOVER ($p<0.006$-0.048), ACLR demonstrated increased trunk rotation and flexion, greater pelvic flexion, higher hip flexion, reduced knee internal rotation with more varus, and increased ankle ROM with greater external rotation. ACLR players showed significant differences in performance, including higher lateral exit velocity in SSC ($p=0.023$), and lower approach velocities and higher peak accelerations in XOVER ($p\leq0.048$).

Discussion

ACLR handball players adopted altered cutting techniques compared to healthy controls, especially against active opponents. These findings highlight the need for sport-specific ecological assessment of players' motion to detect residual impairments and promote data-driven return-to-play decisions.

Images (Optional)



SSC, PASSIVE



SSC, ACTIVE



XOVER, PASSIVE



XOVER, ACTIVE

References (Optional)

[1] Lasse Mausehund, *et al.*, Am J Sports Med, 2024.

Session Category

Human Motion and Performance: Sports

OA42-02

Concurrent Validation of Markerless Motion Capture Systems for Measuring Player Kinematics During Ice Hockey Skating Starts

Mr. Minori Iizuka[1], Ms. Kelsey Klug[1], Mr. Philippe Renaud[1], Dr. Glenn Fleisig[2], Dr. Philippe Dixon[1], Dr Shawn Robbins[1]

[1]McGill University, Montreal, Quebec, Canada. [2]American Sports Medicine Institute, Birmingham, Alabama, United States

Introduction

Ice hockey biomechanics has focused on marker-based motion capture systems to measure player kinematics, but these technologies are subject to skin motion artifact, and marker-placement biases. Thus, markerless motion capture systems offer a potential alternative to measuring biomechanics. However, this technology has not been validated for ice hockey tasks. This study aims to validate the kinematic measurements of a commercial markerless against a marker-based motion capture system during ice hockey skating starts.

Methods

Ten participants (six males, four females) were fitted with an adapted cluster-based marker set and performed five "V-Starts" for this cross-sectional study. A 10-camera Vicon marker-based system (240 Hz) and an eight-camera Qualisys video system (120 Hz, 720p resolution) with Theia Markerless software measured kinematics. Marker and video data were filtered using a 10Hz low-pass Butterworth filter and a 10Hz Generalized Cross-Validation Spline Filter, respectively. Lower extremity joint angles were compared using root mean squared error (RMSE) and coefficient of multiple correlations (CMC). Joints sides were categorized as lead (side that steps forward first) or push (back leg that pushes off at the start).

Results

The mean and standard deviation players' ages were 24 ± 4 years old. Table 1 highlights each joint's RMSE and CMC. The sagittal plane (flexion/extension, plantar/dorsi-flexion) joints measures had very good to excellent agreement; frontal (ab-/ad-duction, pronation/supination) and transverse plane (internal/external rotation) measures had poor to moderate agreement. The mean RMSE values for the sagittal, frontal, and transverse plane were 7.95°, 9.34°, and 11.75 °.

Discussion

The sagittal plane measures had highest agreement and lowest differences. Each biomechanical model's segment coordinate system definition likely impacted observed differences as these definitions alter joint angles calculations in secondary/tertiary segment axes [1]. Additionally, the skating start's explosive, dynamic movement may explain the results as previous markerless validation studies found larger errors with increased running speeds [2]. Angle measurements were different between systems, thus, researchers should use caution when comparing markerless and marker-based studies. Future validation studies should investigate other hockey shooting and skating tasks.

Images (Optional)

Table 1. Summary of the RMSE and CMC values for each joint in each plane

Joint	Side	Sagittal		Frontal		Transverse	
		RMSE	CMC	RMSE	CMC	RMSE	CMC
Hip	Lead	8.54°	0.97	7.36°	0.64	10.48°	0.41
	Push	9.29°	0.96	10.16°	0.23	11.89°	0.505
Knee	Lead	8.41°	0.96	10.72°	0.24	14.64°	*
	Push	9.64°	0.97	10.97°	0.18	13.28°	*
Ankle	Lead	5.49°	0.92	9.70°	0.19	9.77°	0.48
	Push	6.33°	0.94	7.16°	0.41	10.42°	0.47

References (Optional)

[1] Antognini C, et al, J Biomech, 2025

[2] Tang H, et al., J Sport Health Sci, 2024

Acknowledgements (Optional)

Session Category

Human Motion and Performance: Sports

OA42-03

Development of a Wearable Feedback System for Wheelchair Racing Athletes: A Participatory Design Approach

Prof Jason Bouffard OT., Ph.D.[1,2], Mr Ismael Breton B.Sc.[1,2], Mr Mohammed El Bahry M.Sc.[1,2], Mr Raphaël Ouellet M.Sc.[1,2], Prof Katia Turcot Ph.D.[1,2], Prof Félix Chénier Ph.D.[3,4], Miss Nathalie Séguin B.Sc.[5], Mr Anthony Bouchard PLY[5]

[1]Université Laval, Quebec, Qc, Canada. [2]Centre interdisciplinaire de recherche en réadaptation et en intégration sociale (Cirris), Quebec, Qc, Canada. [3]Université du Québec à Montréal, Montreal, Qc, Canada. [4]Centre de recherche interdisciplinaire en réadaptation du Montréal métropolitain (CRIR), Montreal, Qc, Canada. [5]Club d'athlétisme de l'Université Laval, Quebec, Qc, Canada

Introduction

Wearable sensors are widely used in both recreational and elite sports to monitor performance and prevent injuries. Recent studies have demonstrated that wearable sensors, when paired with appropriate analytical algorithms, can yield reliable data in wheelchair sports [1,2]. Yet, tailored feedback systems for para-athletes and their coaches remain limited [1]. This study aims to develop a real-time feedback system specifically designed for wheelchair racing athletes and their coaches.

Methods

An iterative design thinking methodology was employed, beginning with focus group interviews involving five wheelchair racing para-athletes and three coaches to identify key needs and preferences. Based on these insights, a wheelchair velocity measurement system was developed using inertial motion units (IMUs). The system underwent multiple field-testing iterations, involving up to three para-athletes, one coach, and twelve able-bodied individuals. Usability was assessed through participatory observations and semi-structured interviews, while validity was evaluated by comparing the system's output with a Lidar-based reference system and by following the evolution in performance of an elite athlete over a six-month period.

Results

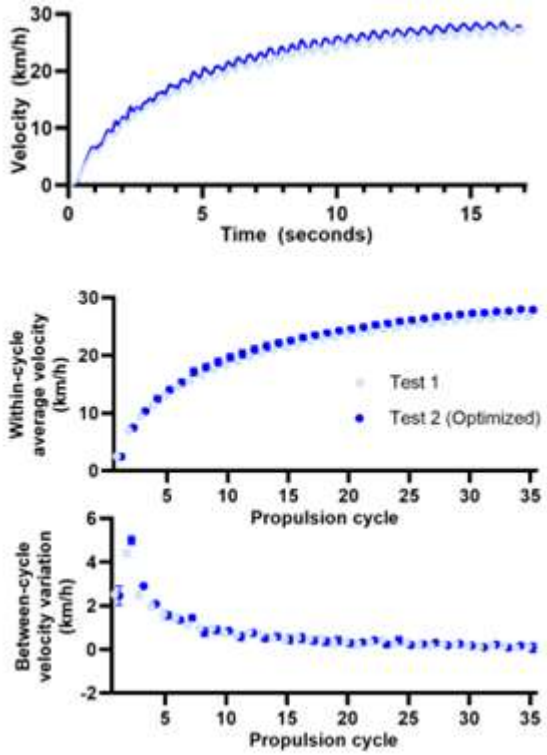
The current prototype (4th iteration) calculates wheelchair velocity at 20 Hz using a gyroscope mounted on the wheel. It also communicates with a smartphone via Bluetooth for data collection control and includes onboard data storage. The system provides

sufficient spatiotemporal resolution to capture intracycle velocity variations, a key requirement identified by athletes and coaches. Longitudinal data collected during 100 m races over six months with an elite athlete demonstrated the system's sensitivity to detect a 3.9% gain in maximal velocity ($p<0.001$) following a wheelchair optimization intervention. Notably, velocity gains during the initial propulsion cycles (Figure 1) aligned with the athlete's perceived improvements in start performance.

Discussion

This project highlights the value of a participatory approach involving engineers, motor performance researchers, athletes, and coaches. The resulting system is both robust and valid for short-distance wheelchair racing. Future iterations will focus on enhancing the software interface to promote greater autonomy for users and facilitate integration into training routines.

Images (Optional)



References (Optional)

[1] Van Der Slikke et al. , Eur J Sport Sci. 2023.

[2].Ouellet et al. , Sensors. 2025.

Acknowledgements (Optional)

The research was funded by grants and scholarships from Mitacs, Société Inclusive, FRQNT (Interactive Technologies of Engineering in Rehabilitation strategic network), Université Laval, FRQS (Réseau provincial de recherche en adaptation et readaptation), and the Cirris.

Session Category

Human Motion and Performance: Sports

OA42-04

Concurrent Validity of Portable Inertial Sensors versus Force Plates for Assessing Countermovement and Drop Jump Kinetics in Basketball

Prof. Carlos Quintana Matoses[1,2], Dr. Francisco García-Muro San José[2], Dr. Néstor Pérez Mallada[3,4,5], Prof. Daniel Iordanov López[2], Prof. Carlos Santo Domingo Berzosa[1,2]

[1]Researcher in training in the Translational Medicine Program at CEU International Doctoral School (CEINDO), Urbanización Montepríncipe, 28660, Boadilla del Monte, Madrid, Spain. [2]Neuromusculoskeletal and biomechanics research group, Department of Physiotherapy, Faculty of medicine, Universidad San Pablo-CEU, CEU Universities, Urbanización Montepríncipe, 28660, Boadilla del Monte, Madrid, Spain. [3]San Juan de Dios Foundation, 28016, Madrid, Madrid, Spain. [4]Health Sciences Department, San Juan de Dios School of Nursing and Physical Therapy, Comillas Pontifical University, 28350, Ciempozuelos, Madrid, Spain. [5]Institute for Research in Technology (IIT), ICAI School of Engineering, Comillas Pontifical University, 28008, Madrid, Madrid, Spain

Prof. Carlos Quintana Matoses

Dr. Francisco García-Muro San José

Dr. Néstor Pérez Mallada

Prof. Daniel Iordanov López

Introduction

Monitoring jump kinetics is vital for assessing performance, neuromuscular fatigue, and injury risk factors in basketball, as landing dynamics and asymmetries are critical predictors [1, 2]. While force plates represent the gold standard, their high-cost limits daily application. Low-cost inertial measurement units (IMUs) could offer a feasible, reliable field-based alternative [3]. This study wants to validate DOTS IMUs against Hawkin Dynamics force plates during countermovement and drop jumps, assessing their accuracy in measuring key biomechanical variables for practical player monitoring.

Methods

In this study 47 healthy athletes of both sexes participated (age: 26.42 ± 5.01 years; mass: 77.55 ± 24.47 kg; height: 1.77 ± 0.11 m). The technologies used were inertial movement units (IMUs) DOTS (120Hz, Movella Technologies B.V.) and force plates (Hawkin Dynamics, 1000Hz) were used to evaluate 2 repetitions of each of the following jump tests: counter-movement jump (CMJ) and drop jump (DJ). Data processing was performed in Python (v 3.7). SPSS (v 31) was used for statistical analysis (p-value < 0.05).

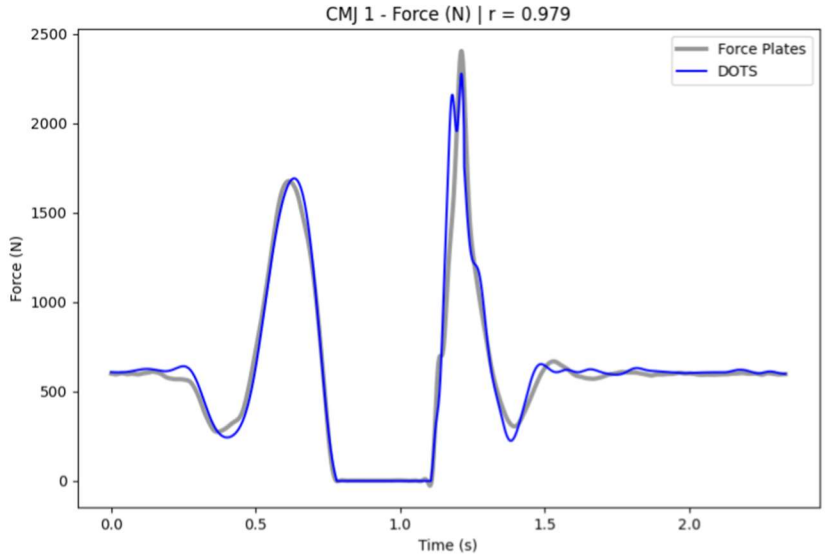
Results

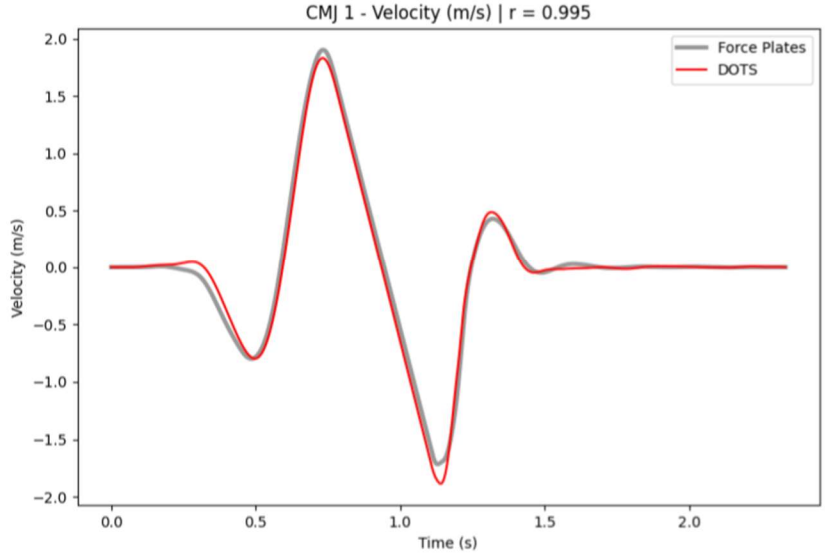
Signal correlation between DOTS and force plates was strong (r>0.9) for both CMJ and DJ (View Figure 1). Bland-Altman analysis indicated good agreement, with the majority of data points falling within the limits of agreement across variables. SPM revealed significant differences only during the initial (0–13%) and final (75–100%) phases, attributed to IMU sensitivity to non-essential movement noise. Despite mean differences in some of the variables IMU system tracked performance metrics consistently.

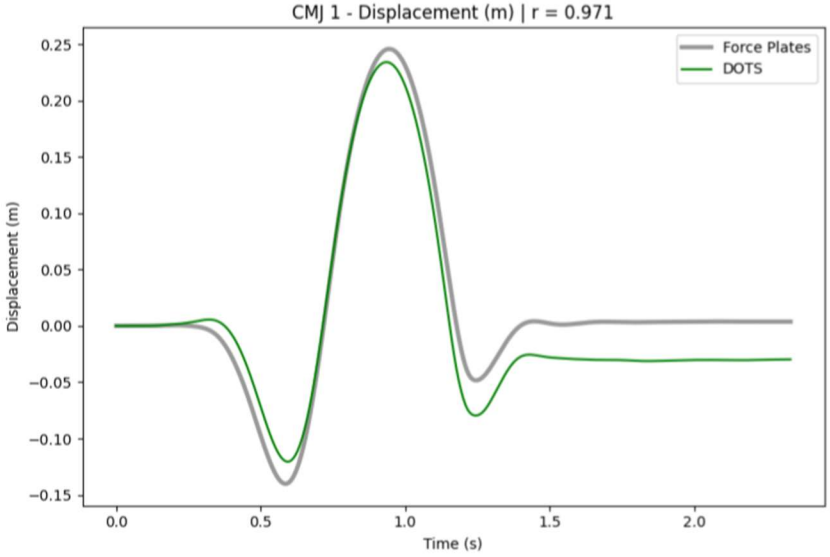
Discussion

The findings validate DOTS as a practical alternative to force plates for monitoring basketball players. High correlations in key metrics support their use for performance profiling, neuromuscular fatigue, and return-to-play assessments. While IMUs showed sensitivity to noise during stabilization phases (start/end of the signal), the critical force-production phases remained accurate. Consequently, DOTS provides a valid, portable and low-cost solution for daily field monitoring of variables like peak propulsive force and RSImod, overcoming the logistical limitations of stationary force plates in team sports settings.

Images (Optional)


CMJ 1 - Force (N) | r = 0.979
Force Plates
DOTS
Force (N)
Time (s)


CMJ 1 - Velocity (m/s) | r = 0.995
Force Plates
DOTS
Velocity (m/s)
Time (s)


CMJ 1 - Displacement (m) | r = 0.971
Force Plates
DOTS
Displacement (m)
Time (s)

References (Optional)

[1] Pedley *et al.*, J Of Science In Sport And Exercise, 2020

[2] Acar *et al.*, BMC Sports Science, Medicine and Rehabilitation, 2025

[3] Villa *et al.*, Sensors, 2024

Session Category

Human Motion and Performance: Sports

OA42-05

Revisiting the Illinois Agility Test as a Wheelchair Sport Coaching Assessment: Segmenting Biomechanical Approaches to Generate Actionable Insights into Athlete Performance

Ms. Mia Siong[1], Dr. Kathryn Lucas PT, DPT, PhD[2], Dr. Jennifer Gruenhagen PT, PhD[3], Dr. Hannah Houde PhD[4], Dr. Jill McNitt-Gray PhD[5], Dr. Jeffery Rankin MSE, PhD[1,6]

[1]Pathokinesiology Laboratory, Rancho Los Amigos National Rehabilitation Center, Downey, CA, United States. [2]Physical Therapy Department, Creighton University, Phoenix, AZ, United States. [3]Physical Therapy Program, College of Health Sciences, Midwestern University, Glendale, AZ, United States. [4]School of Health Professions, The University of Texas Medical Branch, Galveston, TX, United States. [5]Departments of Biological Sciences and Biomedical Engineering, University of Southern California, Los Angeles, CA, United States. [6]Rehabilitation Engineering, Rancho Los Amigos National Rehabilitation Center, Downy, CA, United States

Introduction

Recent work demonstrated that an adaptation of the Illinois Agility Test (IAT) for wheelchair athletes is a reliable measure [1]. The IAT measures how quickly athletes navigate an obstacle course using straight-line and weaving movements (Figure 1A). Beyond execution time, biomechanical tools (e.g., video recordings, wearable sensors) can reveal additional movement insights. This study aimed to understand how an athlete's capacity for trunk control (CTC) influences IAT execution and performance.

Methods

Five competitive wheelchair athletes (3 basketball, 2 tennis) with varying impairments performed the IAT using their own sport chair. Spatiotemporal parameters and upper extremity joint kinematics were collected using high speed video and inertial measurement units (Equilibrium, Vayu Technology, USA). CTC was estimated through sport classification or self-report. IAT phases (e.g., straight-line, turning) were defined, and relationships between performance (i.e., phase completion times), movement technique (e.g. trunk angle), and CTC were investigated.

Results

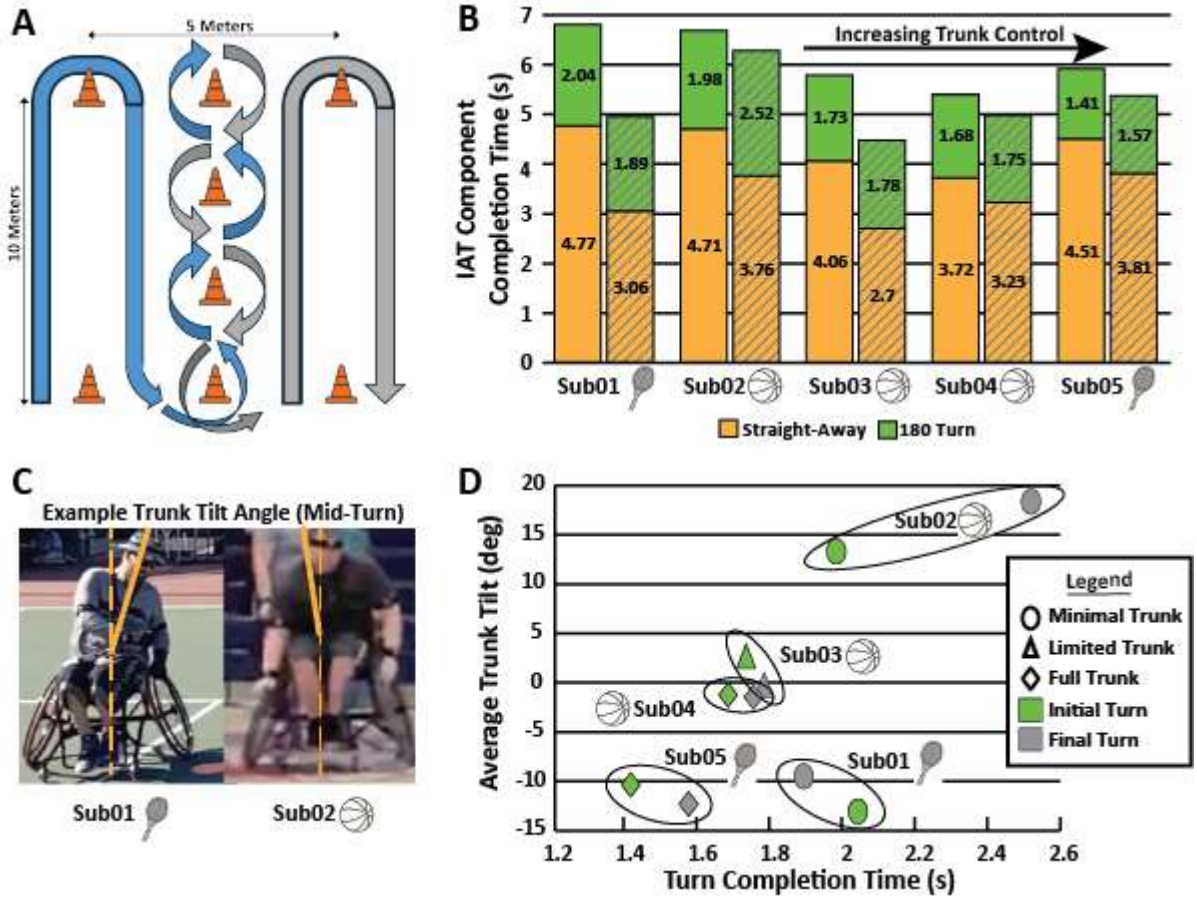
IAT completion times were between 29.8-35.6 seconds. Analysis of the first and third straight-aways and subsequent turns (Fig 1A, bold outline) revealed strategy differences: athletes with less CTC took longer times to prepare and execute turns (Fig 1B). Surprisingly, the participants with similar CTC used different turn techniques as evidenced

by differences in average trunk side-to-side tilt: those with minimal CTC used opposite tilts (Fig 1C-D). These findings highlight that athletes with similar CTC can use varying strategies to achieve the same objective; emphasizing the need for training protocols tailored for individual capacities.

Discussion

This pilot study demonstrates that biomechanics tools are easily integrated into sport activities, providing wheelchair athletes and coaches with additional, sport-relevant insights into IAT performance. Evaluating straight line (speed) and turning (agility) IAT components, alongside trunk kinematics such as trunk tilt, revealed multiple viable performance approaches, suggesting optimal technique is influenced by CTC. Although IAT is widely used by parasport coaches and athletes, additional work is needed to contextualize the rich biomechanical data available during execution of the IAT [2,3].

Images (Optional)



References (Optional)

[1] Salimi & Ferguson-Pell, PloS One, 2020

[2] Usma-Alvarez et al., Sports Technology, 2010.

[3] Shepherd et al., Sports, 2018.

Acknowledgements (Optional)

Project funded by Lakeshore Foundation (Grant #SSPC0003) and NSF-DBI-2319710.

Session Category

Human Motion and Performance: Sports

OA42-06

Field-Based Biomechanical Analysis of Ski Mountaineering Using Smartphone Video and Open-Source Pose Estimation Methods

Dr. Pawel Kudzia PhD, Ms Naomi Clements, Dr. Peter A. Cripton PhD

University of British Columbia, Vancouver, BC, Canada

Dr. Pawel Kudzia

Ms Naomi Clements

Introduction

Ski mountaineering debuts at the 2026 Milano-Cortina Winter Olympics, yet we know remarkably little about how athletes actually move in mountain environments. Unlike downhill skiing, ski mountaineers spend most of their time ski touring: walking uphill with skis attached, using specialized bindings that release the heel and skins that grip the snow to prevent backward sliding [1]. During ski touring, athletes also loosen their boots to allow greater ankle mobility. This ascending phase is physically demanding and technically complex, yet nearly all biomechanical research relies on laboratory treadmills and roller skis that cannot replicate snow properties or glide characteristics. We used smartphone video and open-source pose estimation to demonstrate that meaningful kinematic analysis of ski touring is feasible in natural mountain environments.

Methods

We recruited 11 participants (ages 22-54, intermediate to expert) and recorded video using an iPhone 13 (1080p, 60 Hz) in the mountains of Sḵwx̱wú7mesh (Squamish), British Columbia, Canada. Participants ski toured under six conditions varying speed (slow, natural, fast) and boot configuration (loose touring mode vs. tight skiing mode). We extracted body landmarks using a general pose estimation algorithm (BlazePose) and then estimated hip, knee, and ankle joint angles, trunk inclination, and ski stride rate across segmented ski strides.

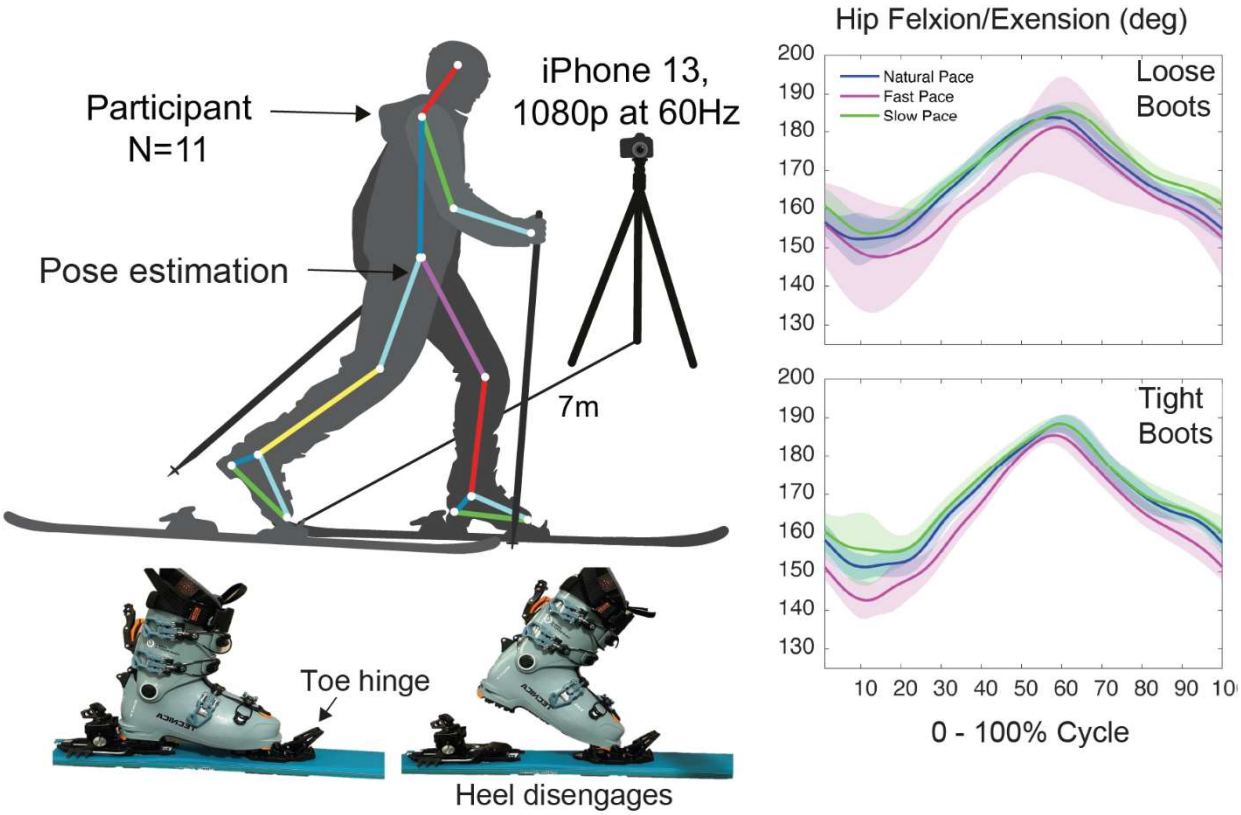
Results

Using this free, and easily implemented method, we found consistent hip and knee joint angle patterns across the ski stride cycle. Boot configuration altered how participants moved: tight boots reduced hip range of motion (both $p < 0.001$) but increased knee range of motion ($p \leq 0.025$), suggesting participants compensated for restricted ankle mobility through greater knee flexion. Participants also leaned further forward as stride rate increased. However, our pose estimation algorithm struggled to well track ski boot landmarks, producing inconsistent ankle angles.

Discussion

To our knowledge, this represents the largest in-field ski touring biomechanics dataset collected to date. We demonstrate that smartphone-based pose estimation can detect meaningful kinematic patterns and condition differences in natural environments. Future work will focus on improving landmark tracking on ski equipment and validate results against wearable systems such as inertial measurement units.

Images (Optional)



References (Optional)

[1] L. Bortolan et al., Front Physiol, 2021

Session Category

Human Motion and Performance: Sports

OA43-02

Patient-Specific Multiphysics Modeling for Accurate Recapitulation of Patent Ductus Arteriosus Stenting Interventions

Mr. Luis Rene Mata Quinonez ME, MS[1,2], Dr. Thangam Natarajan PhD[1], Mr. Leon Cheng B.S.[1], Ms. Emma Chang B.S.[1], Mr. Burke Thompson B.S.[3], Dr. Lakshmi Prasad Dasi PhD[1,2], Dr. Holly Bauser MD, PhD[4]

[1]Georgia Institute of Technology, Atlanta, Georgia, United States. [2]Emory University, Atlanta, Georgia, United States. [3]Georgia Institute of Technology, Atlanta, Georgia, Norway. [4]University of Texas Health Science Center at Houston, Houston, Texas, United States

Introduction

In patients with cyanotic congenital heart diseases, a common treatment is Patent Ductus Arteriosus (PDA) stenting, a minimally invasive palliative procedure that keeps the ductus open, improves oxygen saturation, and provides a more stable source of pulmonary blood flow (PBF). Even though the mortality of this procedure is low, some of the complications associated to proper stent length selection are: partial PDA coverage and risk of pulmonary artery jailing. In the former case, an implanted stent that is too short may leave segments of the PDA uncovered, accelerating ductal stenosis resulting in cyanosis, and the second issue occurs when a long stent obstructs the blood flow of the side branch pulmonary artery (PA), which often results in PBF imbalance and asymmetric PA growth.

Methods

Physical samples of the stent, angioplasty balloon, and guidewires, were micro-CT scanned to enable computational reconstruction, CAD modeling, meshing, and crimping to generate their undeployed configurations. Patient-specific PDA anatomy was reconstructed from pre-procedural CT scans. We simulated the guidewire tracking by first segmenting and 3D reconstructing the guidewire from procedural fluoroscopy videos and then deforming a PDA centerline to this configuration. The pre-deployment stent and balloon geometries, pre-bent to the guidewire path, were then positioned within the PDA model, and stent deployment was simulated through balloon inflation and deflation. For the fluid dynamics analysis, echocardiography-derived velocity waveforms were applied as boundary conditions to the post-deployment geometry, and CFD simulations were conducted to evaluate local hemodynamics. (Fig. 1A-B)

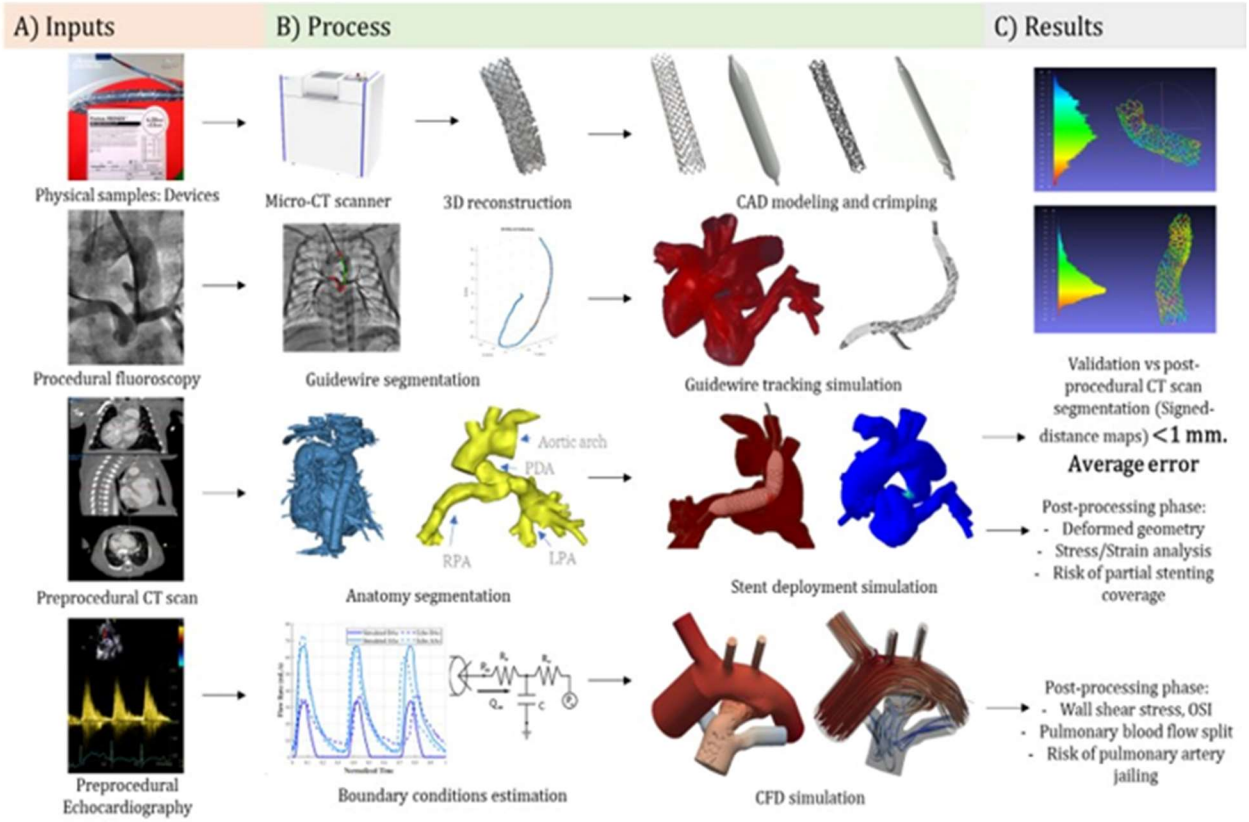
Results

We applied the pipeline to ten patients with varying PDA tortuosity. The deformed PDA and stent geometries from our FEA simulations were validated against post-procedural segmentations, yielding a mean signed-distance error below 1 mm. We developed semi-automatic tools to identify regions of elevated stress/strain and to estimate areas at risk of partial coverage. For CFD post-processing, we quantified wall shear stress, OSI, pulmonary blood-flow split, and introduced metrics to assess the risk of pulmonary artery jailing. (Fig. 1C)

Discussion

In this retrospective work, we showed a multi-physics FEA-CFD simulation pipeline to recapitulate the outcomes of PDA stenting procedures and predicted the risks of partial stenting coverage and pulmonary artery jailing.

Images (Optional)



Session Category

Cardiovascular/Cardiorespiratory Biomechanics: Methods, Models and Applications

OA43-03

Influence of Inherent and Exercise-Induced Aerobic Capacity on Cardiac Structure and Function in a Rat Obesity Model

Mr. Dhairya Desai, Mrs. Jeannine Turnbull, Mr. Griffin Wong, Mr. Abel Mebrahtu, Mr. Darsh Tripathi, Mr. Mauricio Delgado, Dr. Walter Herzog PhD

University of Calgary, Calgary, Alberta, Canada

Introduction

Obesity is now the leading global risk factor for early cardiovascular (CV) death and contributes to heart dysfunction through metabolic and endothelial damage [1]. Aerobic capacity is a measure of metabolic processes using maximal oxygen uptake rate and serves as a protective factor against CV degeneration. Differences between inherent (genetic) and acquired (exercise-based) aerobic capacity in the context of obesity remain unclear. Therefore, studying animal models selectively bred for high aerobic capacity (HAC) and low aerobic capacity (LAC) can help further our understanding of protective mechanisms and pathways that aerobic capacity has against the effects of obesity on the heart. We hypothesize that high inherent aerobic capacity and increased acquired aerobic capacity will lessen the negative cardiac effects of diet-induced obesity.

Methods

Forty-seven male N:NIH rats , comprised of 24 HAC and 23 LAC underwent a 12-week exercise intervention, and then were split into four groups; HAC/LAC rats undergoing a12-week diet intervention (high-fat, high-sucrose - HFS - or control chow). The primary outcome of this study is the measurement of cardiac function obtained using echocardiography taken longitudinally throughout the intervention periods every 4 weeks.

Results

Cardiac output (CO) increased during the exercise phase in both HAC and LAC rats. During the diet intervention, CO generally declined in HAC and LAC rats. LAC rats on the HFS diet showed an earlier drop in CO, though the chow-fed LAC rats converged to a similar CO level by Week 24.

Discussion

Our results suggest that inherent aerobic capacity influences cardiac resilience during metabolic stress, as reflected in literature. While both HAC and LAC rats maintained or improved CO during the exercise phase, strain differences emerged once the diet intervention began. LAC rats, especially those on the HFS diet, showed an earlier and more

pronounced decline in CO, indicating greater vulnerability to diet-induced cardiac dysfunction. In contrast, HAC rats generally preserved CO regardless of diet, suggesting intrinsic protective mechanisms linked to higher aerobic capacity.

However, interpretation is limited by the small sample size and incomplete dataset, and additional HAC and LAC rats will be incorporated as analyses continue.

References (Optional)

[1] Sari DCR *et al*., Medical j. Malaysia, 2022

Session Category

Cardiovascular/Cardiorespiratory Biomechanics: Methods, Models and Applications

OA43-04

Computational Framework for Studying myocardial Bridging

Dr. Giuseppe De Nisco[1], Dr. Sara Zambon[1], Mr. Stefano Elia , MD[2], Prof. Fabrizio D'Ascenzo , MD[3], Prof. Giuseppe Patti , MD[2], Prof. Diego Gallo[1], Prof. Domenico D'Amario , MD[2], Prof. Umberto Morbiducci[1]

[1]PolitoBIOMed Lab, DIMEAS, Politecnico di Torino, Turin, Piedmont, Italy. [2]Department of Translational Medicine, University of Eastern Piedmont, Novara, Piedmont, Italy. [3]Hemodynamic Laboratory, Department of Medical Sciences, University of Turin, Turin, Piedmont, Italy

Introduction

Myocardial bridging (MB) is a congenital anomaly in which a segment of a coronary artery tunnels within the myocardium. Traditionally regarded as benign, MB has been recently associated with ischemia, arrhythmias, and sudden cardiac death [1], possible consequences of systolic compression and alterations in wall shear stress (WSS). This study proposes a personalized computational framework to characterize MB morphology and hemodynamics and demonstrates its feasibility in three patients.

Methods

The workflow (Figure 1) used segmentation of dynamic cardiac Computed Tomography images acquired over multiple cardiac phases to reconstruct patient-specific MB geometries on patients P1, P2 and P3—in P1 covering the diastolic phase; in P2 and P3 the entire cardiac cycle. Each phase-specific geometry was meshed and registered using the Coherent Point Drift algorithm to reproduce vessel motion [2]. Computational fluid dynamics simulations were performed by prescribing personalized velocity and pressure data at the inflow and outflow boundaries, respectively [3]. A *Moving Boundary* condition was imposed to the wall. Anatomical features were assessed in terms of local luminal surface area, shape index, curvature, and torsion [4]. Hemodynamics was evaluated in terms of WSS-based quantities: TAWSS, OSI, RRT and TSVI.

Results

In all patients, MB segment showed marked lumen reduction (up to 70%, Figure 1C) across systole and diastole (e.g., in P2 mean MB luminal area was 5.02 mm^2 in systole and 5.64 mm^2 in diastole). MB modestly affected lumen eccentricity, with negligible changes in

curvature and torsion. MB consistently altered WSS, with higher shear disturbances in the proximal segment than bridged tract (Figure 1D).

Discussion

This pilot study proposes a patient-specific framework for morphological and hemodynamic assessment of MB. Ongoing extension to ten cases will confirm the observation,first reported here, that MB lumen reduction persists across the entire cardiac cycle (not only in systole). The proposed framework candidates as a tool to identify higher-risk MB patients who may benefit from closer surveillance or targeted management.

Images (Optional)

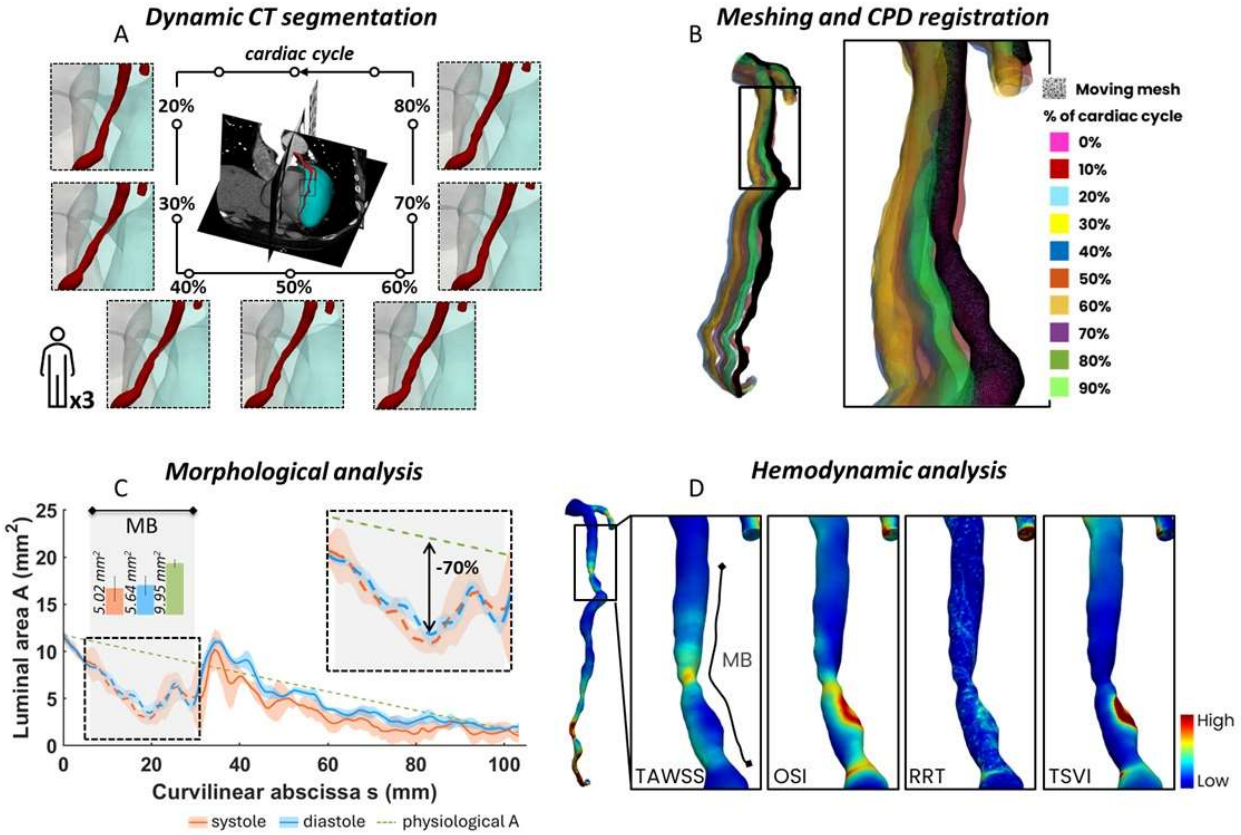


Figure 1. *Main steps of the computational approach for patient P2, as explanatory case: A - Segmentation of dynamic cardiac Computed Tomography (CT) acquisitions across ten cardiac phases; B - Generation of the computational mesh and Coherent Point Drift (CPD) registration; C - Morphological analysis, exemplified by the variation of luminal area along the lumen centerline throughout the cardiac cycle phases; D - Hemodynamic analysis, exemplified by the luminal distribution of WSS-based quantities.*

References (Optional)

[1] Sternheim *et al.*, J Am Coll Cardiol, 2021

[2] Myronenko and Song, IEEE Trans Pattern Anal Mach Intell, 2010

[3] Khan *et al.*, Cardiovasc Eng Technol, 2022

[4] Gallo *et al.*, Ann Biomed Eng, 2015

Session Category

Cardiovascular/Cardiorespiratory Biomechanics: Methods, Models and Applications

OA43-05

Computational Fluid Dynamics Validation of Left Atrial Hemodynamics Incorporating Physiological Wall Motion and Occluder Device Conditions

MSc Manal Barrouhou[1], Ph.D. Manisha Singh[2], Ph.D. Andy L. Olivares[1], Ph.D. Carlos Albors[1], Ph.D. Jordi Mill[3], Ph.D. Keegan Mendez[2,4], Prof. Ellen T. Roche[2,5], Prof. Oscar Camara[1]

[1]Department of Engineering, Universitat Pompeu Fabra, Barcelona, Catalonia, Spain. [2]Institute for Medical Engineering and Science, Massachusetts Institute of Technology, Cambridge, Massachusetts, United States. [3]Virtest Technologies, Barcelona, Catalonia, Spain. [4]Harvard-MIT Program in Health Sciences and Technology, Massachusetts Institute of Technology, Cambridge, Massachusetts, United States. [5]Department of Mechanical Engineering, Massachusetts Institute of Technology, Cambridge, Massachusetts, United States

Introduction

Computational fluid dynamics (CFD) is increasingly used to study left atrial (LA) hemodynamics in atrial fibrillation (AF) and to support evaluation of left atrial appendage occlusion (LAAO) devices. However, validation of patient-specific CFD models, particularly those incorporating physiological wall motion and implanted devices, remains limited. To address this gap, this work introduces a validation framework integrating CFD with a soft-robotic dynamic atrial phantom capable of reproducing patient-specific atrial contractility in AF and post-LAAO conditions.

Methods

A patient-specific LA was reconstructed from pre-LAAO computed tomography (CT) images. This geometry was used to create a soft-robotic phantom whose actuation reproduced atrial wall motion via CT-derived displacement fields. Integrated within a closed-loop mock circulatory system, the phantom enabled pressure and flow measurements at the pulmonary veins (PVs) and mitral valve (MV) [1]. To extend validation to device-implanted conditions, the same LA was adapted to a post-LAAO configuration by virtually implanting a 25 mm Amplatzer Amulet device and reproducing the occlusion with a mechanical clip at the LAA ostium (Figure 1a: LA with virtual implanted device and phantom with mechanical LAA occlusion.). Corresponding CFD simulations were performed in ANSYS Fluent 2021R2 using the virtually cut LA geometry. Atrial wall motion was prescribed through CT-derived displacement fields, while PVs pressure and MV flow

waveforms measured in the phantom were applied as boundary conditions. Ten cardiac cycles were simulated and compared with the in-vitro recordings.

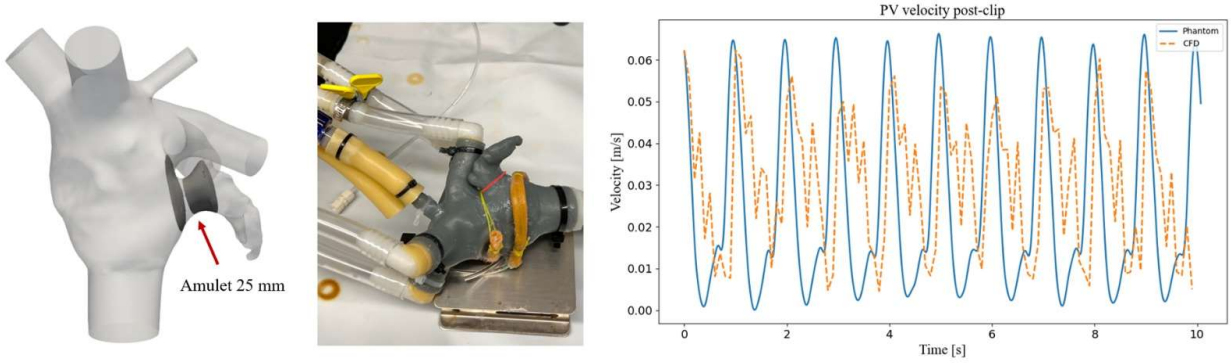
Results

CFD analysis reproduced the global features of the PV velocity waveforms measured in the phantom, capturing peak timing and waveform morphology in both pre- and post-LAAO configurations. Simulated velocities were generally lower near peak inflow and showed higher-frequency fluctuations, attributed to geometric fidelity near the PV inlets and differences between soft-robotic actuation and numerical motion mapping (Figure 1b: Phantom and CFD PV velocity waveforms in the post-LAAO scenario).

Discussion

This study provides the first validation of LA CFD under dynamic wall motion and device-implanted conditions. The agreement in global hemodynamics supports the use of CFD for benchmarking studies covering wall mechanics and LAAO devices, while remaining discrepancies motivate improvements in geometric fidelity and motion transfer methods.

Images (Optional)



(a) (b)

References (Optional)

[1] E. Roche et al., [Preprint], 2025.

Acknowledgements (Optional)

This project has received funding from the European Union's Horizon 2020 research and innovation programme under grant agreement, No. 101016496 (SimCardioTest) and No.101136438 (GEMINI). We also acknowledge the support by the Spanish Ministry of Science, Innovation and Universities under the Proyectos the Generación del Conocimiento Programme (GENERALITAAT project, PIT2022-143239OB-I00).

Session Category

Cardiovascular/Cardiorespiratory Biomechanics: Methods, Models and Applications

OA44-01

Comparing Ex Vivo MRI and Dissection Methodology to Derive Muscle Parameters for Musculoskeletal Models: The Impact of Fixation and Dehydration

ir. Iris van Kan[1], dr. ir. Bart Bolsterlee[2,3], dr. Hilco Theeuwes[4,5], Bsc. Lucas Visscher[4,5], Bsc. Sjoerd van de Weerd[4,5], Bsc. Esmee Eikelenboom[4,5], dr. ir. Eline van der Kruk[1]

[1]Department of Biomechanical Engineering, Faculty of Mechanical Engineering, Delft University of Technology, Delft, Zuid-Holland, Netherlands. [2]Neuroscience Research Australia (NeuRA), Sydney, New South Wales, Australia. [3]Graduate School of Biomedical Engineering, University of New South Wales, Sydney, New South Wales, Australia. [4]Skills & InnovationLab Healthcare, Erasmus University Medical Center, Rotterdam, Zuid-Holland, Netherlands. [5]Department of Neuroscience-Anatomy, Erasmus University Medical Center, Rotterdam, Zuid-Holland, Netherlands

Introduction

Muscle parameters in generic musculoskeletal models are typically derived from combined datasets that include in-vivo, ex-vivo, and in-vitro measurements from limited studies [1]. Magnetic resonance imaging (MRI) could provide larger in-vivo datasets for a subset of these muscle parameters. However, validating MRI against anatomical-dissection is methodologically challenging. Fixation prevents decay during dissection but possibly introduces artifacts, while dissection causes dehydration that alters muscle volume. This study aimed to quantify ex-vivo volumetric differences across three stages within the same donor: MRI of fresh tissue, MRI of fixated tissue, and physical dissection.

Methods

MRI scans of the lower extremities in a fresh-frozen human were acquired before, and one week after AnubiFIX fixation [2]. Three-dimensional models were generated from manual segmentations of 20 muscles bilaterally (n=2) to calculate fresh ($V_{MRI,f}$) and fixated ($V_{MRI,fix}$) muscle volumes. Subsequently, these same muscles were dissected, and their physical volumes ($V_{Dis,fix}$) measured via water displacement. We compared: (1) the volumetric effect of fixation ($V_{MRI,f}$ vs. $V_{MRI,fix}$), (2) the methodological consistency between imaging ($V_{MRI,fix}$) and dissection ($V_{Dis,fix}$) and (3) total volumetric change ($V_{MRI,f}$ vs. $V_{Dis,fix}$).

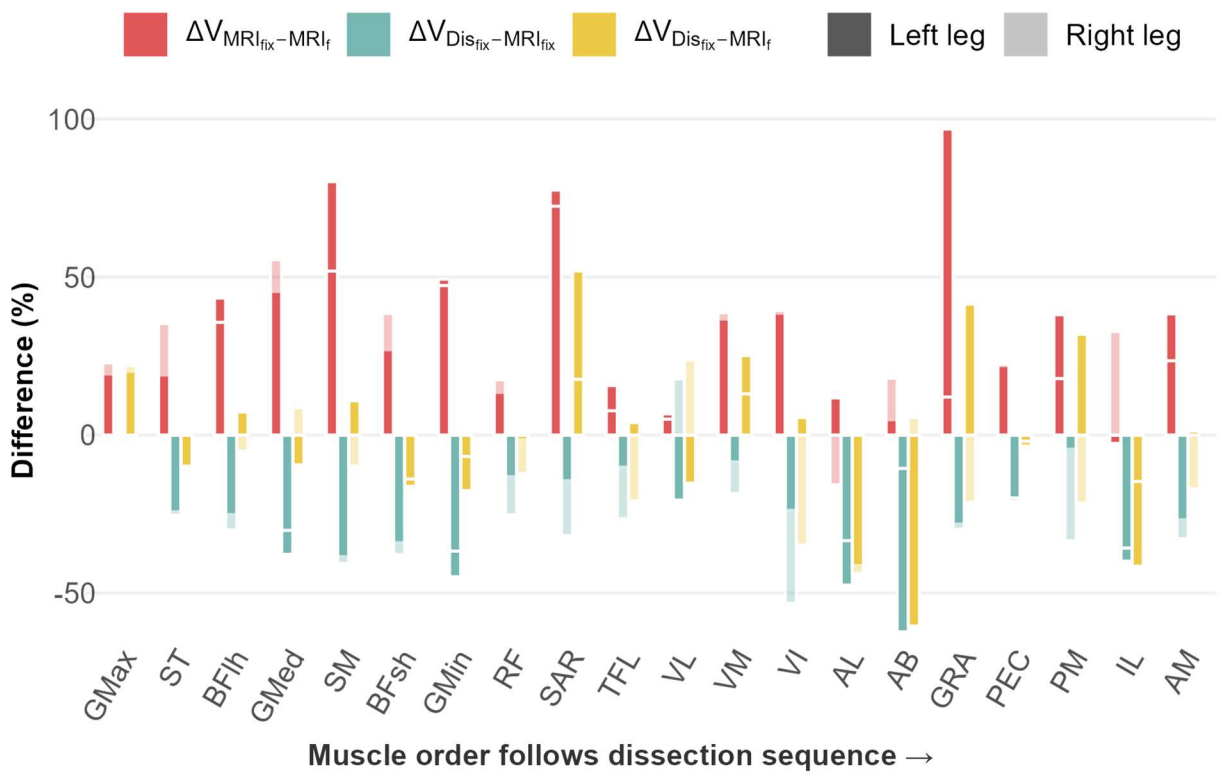
Results

The mean percentage change between $V_{MRI,f}$ and $V_{MRI,fix}$ was +31.5% (SD 23.3%). The high SD indicates variable swelling between muscles. Transitioning from fixated MRI to physical dissection revealed a mean volume change of −26.5% (SD 15.4%).

Discussion

Results demonstrate substantial volumetric alterations between fresh, fixed, and dissected muscle tissue, varying inconsistently across muscles. While the volume increase aligns with post-fixation swelling, the high variability implies fixation effects are nonuniform, likely influenced by muscle hydration, fat content, and anatomy. This is an important finding for the accuracy of musculoskeletal simulations [1]. Furthermore, the average volume loss between fixated MRI and dissection indicates significant tissue dehydration occurred. This was time-dependent: muscles dissected later in the sequence - and thus exposed longer - exhibited greater volume deviations. Quantifying these effects on a larger scale is important to ensure that the combined data from dissection and MRI are reliable for musculoskeletal modeling.

Images (Optional)



References (Optional)

[1] Maarleveld et al. , J Biomechanics, 2025

[2] Theeuwes et al. , Anatomy Physiol Biochem Int J, 2017

Session Category

Musculoskeletal Biomechanics: Methods, Models and Applications

OA44-02

An “Uplifting” Exploration: What Global or Local Anthropometry Best Predicts Pelvic Floor Muscle Volume?

Ms. Amanda Knizley[1], Mr. Brendan S. Shea[1], Dr. Lara Riem[2], Mr. Mario E. Garcia[1], Dr. Neha Yadu[3], Dr. Silvia Blemker[1]

[1]University of Virginia, Charlottesville, Virginia, United States. [2]Springbok Analytics, Charlottesville, Virginia, United States. [3]University of Texas at Southwestern, Dallas, Texas, United States

Introduction

Pelvic floor dysfunction (PFD), experienced by up to 46.50% of females worldwide, results in one or more of the following symptoms: urinary incontinence, fecal incontinence, and prolapse [1]. Even with state-of-the-art current treatments, up to 50% of females still experience dysfunction with risk increasing with age [2], greatly limiting quality of life. Little is known about what geometrical pelvic floor muscle (PFM) features may predispose individuals to PFD, limiting early intervention and preventing more tailored treatment. A quantitative framework describing anatomical predictors relative to normal PFM variability is needed to contextualize PFD. The goal of this work is to measure the variability in PFM volume and examine how this variability relates to mass, height, bone geometry, and other muscle volumes.

Methods

Static high-resolution MRI scans of the pelvic floor were collected from (n=20) female subjects between the ages of 20 and 49 with no history of musculoskeletal injury. The PFM, lower limb muscles, and lower limb bones were segmented through a combination of a trained AI system and manual editing. PFM volume was measured in 3D Slicer and related as a linear regression with measurements of pelvic cavity (including the lesser pelvis space only) depth, width, and height; pelvis volume; hip and lower limb muscle volumes; and body mass and height measurements.

Results

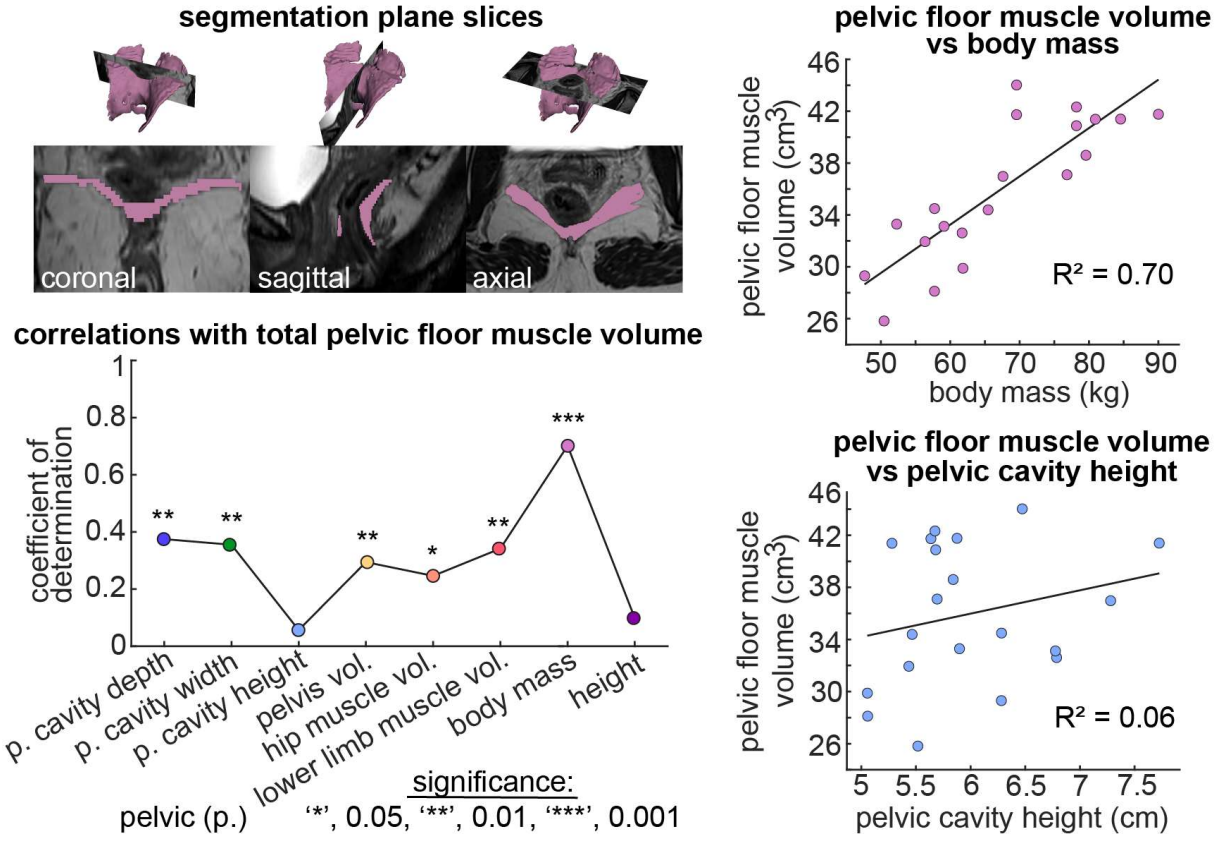
Across all predictors, PFM volume varied most strongly with body mass ($R^2 = 0.70$, model p-value < 0.001). The weakest predictors were pelvic cavity height ($R^2 = 0.06$, model p-value > 0.05) and body height ($R^2 = 0.10$, model p-value > 0.05). The remaining predictors (pelvic

cavity depth and width, pelvis volume, and hip and lower limb muscle volumes), all showed similar low-to-moderate correlations (R^2 = 0.37, 0.36, 0.29, 0.24, 0.34 respectively).

Discussion

PFM volume scaled most strongly with body mass, suggesting functional adaptation to support demands associated with whole-body loading and intra-abdominal pressure, rather than being primarily constrained by pelvic bony dimensions. Future studies will investigate PFMs in dysfunctional cases and see if deviation occurs in relation to healthy relationship trends.

Images (Optional)



References (Optional)

[1] Rocío Adriana Peinado-Molina *et al.*, BMC Public Health, 2023.

[2] Gabriela Kołodyńska *et al.*, Prz. Menopauzalny, 2019.

Acknowledgements (Optional)

UVA, M3 Lab, Springbok Analytics, BHH Training Program

Session Category

OA44-03

Influence of Pelvis and Femur Morphology on Hip and Knee Joint Loading

Dr. Ekaterina Stansfield[1], Ing. Dr. Andreas Kranzl[2], OA Priv.-Doz. Dr. Jochen Hofsädter[2], Dr. Basilio Gonçalves[1], Dr. Hans Kainz[1]

[1]University of Vienna, Vienna, Vienna, Austria. [2]Speising Orthopaedic Hospital, Vienna, Vienna, Austria

Introduction

Hip and knee joint contact forces (JCF) during daily activities are central to orthopedics and sports science. Although implanted force gauges in joint-replacement patients provide gold-standard measurements (1), most estimates rely on musculoskeletal models. Here, we investigate how individual morphology of the lower girdle (pelvis, femora, tibiae) influences hip and knee JCF.

Methods

MRI images and 3D gait data of 25 women and 22 men was collected and used to create highly personalized musculoskeletal models (2). Morphology of the pelvis, femora, patellae, tibiae and fibulae was quantified using homologous anatomical landmarks. Muscle paths were wrapped onto skeletal structures using non-linear functions and refined with MRI views. Muscle forces were obtained through static optimization, and hip and knee joint contact forces were consequently calculated.

Principal components summarized skeletal shape variation. These components, combined with foot-position measures and pelvis, hip and knee kinematics, were used to predict JCF. Peak JCF during early- and late-stance phase were analyzed, yielding four dependent variables (HipPeak1, HipPeak2, KneePeak1, KneePeak2). In total, 36 independent variables were included in the regression model.

LASSO regressions were run for each dependent variable using three predictor sets: (a) speed+shape+foot position+kinematics; (b) speed+shape+kinematics; (c) speed+shape. LASSO selected up to five predictors, and Ridge regression with cross-validation assessed over-fitting and coefficient significance.

Results

HipPeak1 depended strongly on pelvic and femoral morphology and hip flexion (Fig. 1). HipPeak2 was driven mainly by speed. Knee JCF was primarily determined by knee and hip flexion, with KneePeak2 additionally influenced by foot position.

Discussion

Previous work based on generic-scaled models showed that JCF can be predicted from kinematics and anthropometry (3). This study presents the first statistical analysis using highly personalized MRI-based models with morphology-specific lower-girdle bones and muscle paths. The results underscore the importance of pelvis and femur morphology for early-stance hip JCF and confirm the overarching influence of joint kinematics and speed on hip and knee loading.

Images (Optional)

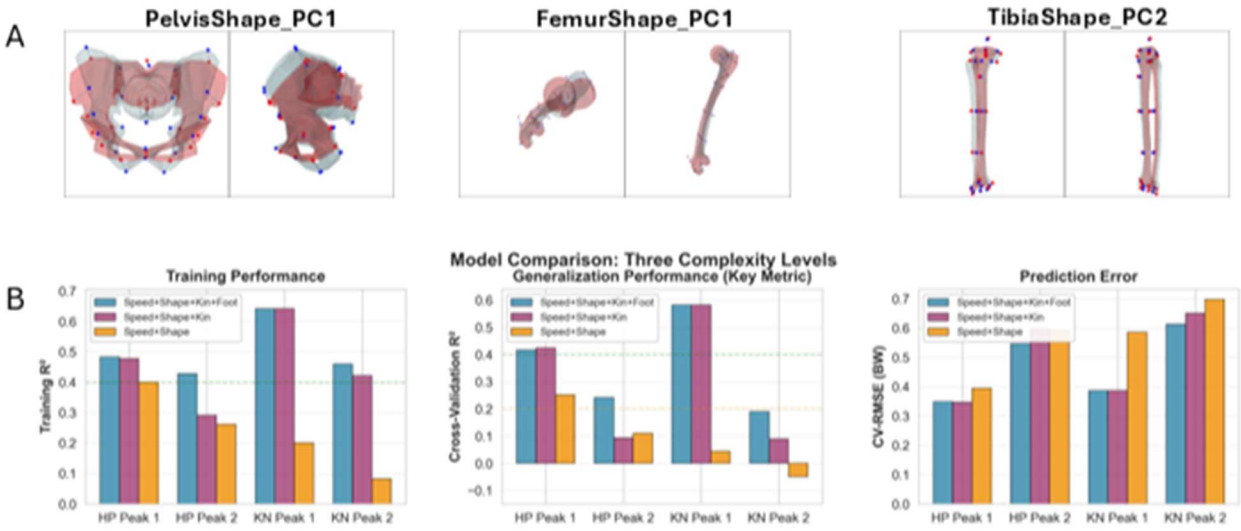


Figure 1. (A) Examples of shape independent variables; (B) Prediction performance.

References (Optional)

1. Bergmann et al., 2016. *PloSone*,11(5), p.e0155612.
2. Stansfield et al., 2025. BioRxiv, 2025, 10.1101/2025.07.23.666289
3. Krondorfer et al.,2025. *Gait&Posture,*121, S126-128.

Session Category

Musculoskeletal Biomechanics: Methods, Models and Applications

OA44-04

An Anatomy Based Technique For Predicting Knee Natural Motion

Dr. Lorenzo Capetta, Professor Nicola Sancisi, Professor Michele Conconi

University of Bologna, Bologna, Emilia Romagna, Italy

Introduction

Quantifying subject-specific kinematics is essential for identifying articular pathologies, planning treatments, and developing musculoskeletal models [1]. Accurate in-vivo measurements remain challenging, necessitating the development of predictive joint motion models. We propose a method that directly predicts subject-specific knee kinematics from joint anatomy, using only a description of articular surfaces and ligament insertions from medical images. This approach fulfils the experimentally observed reciprocity between natural motion and articular constraints: ligament fibres remain nearly isometric, while ligaments and articular contact lines of action intersect the instantaneous helical axis (IHA) throughout the entire range of motion [2]. Results were validated against experimental measurements [3], and the RMSE values were compared with those reported in the literature [4].

Methods

Six fresh-frozen leg specimens were analysed. Joint anatomy was manually segmented in MITK from CT and MRI scans. Insertions of 7 ligaments (ACL, PCL, LCL, ALL, deep MCL, proximal anterior MCL, proximal posterior MCL) were identified, and 5 fibres per ligament were extracted (35 total). Two contact lines of action were derived at each predicted pose as the weighted average of the normals of the condylar contact surfaces applied to their geometrical centroid, yielding 37 total constraints. Joint kinematics was obtained by minimising, for each flexion step, ligament length variation and the line-to-line distance between each constraint line of action and the IHA [2].

Results

Rotational and translational RMSE across subjects were 3.57 ± 3.93° and 2.70 ± 3.18 *mm*, with the highest errors observed in IE rotation and AP translation [Figure 1].

Discussion

The proposed model, based on standard CT and MRI, showed good results without requiring any calibration to experimental kinematics. Its RMSE values were lower than

those reported for calibrated predictive models of the literature (4.60° and 3.54 mm) [6], making it a promising tool for subject-specific knee motion prediction.

Images (Optional)

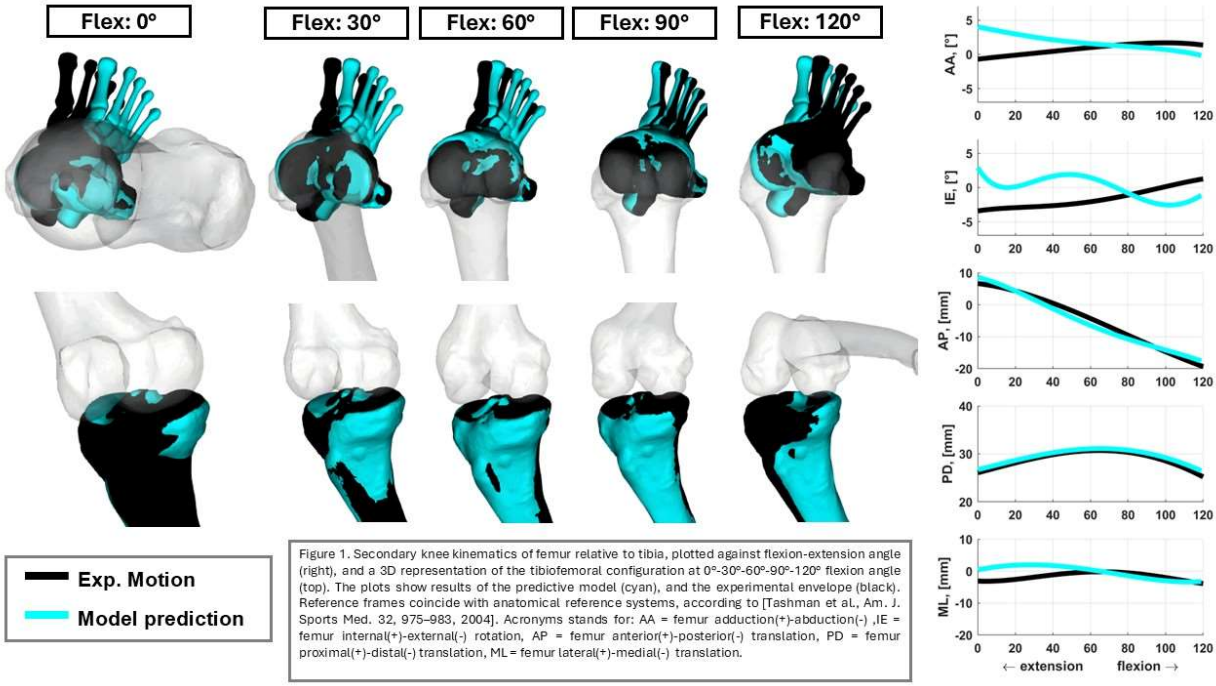


Figure 1. Secondary knee kinematics of femur relative to tibia, plotted against flexion-extension angle (right), and a 3D representation of the tibiofemoral configuration at 0°-30°-60°-90°-120° flexion angle (top). The plots show results of the predictive model (cyan), and the experimental envelope (black). Reference frames coincide with anatomical reference systems, according to [Tashman et al., Am. J. Sports Med. 32, 975–983, 2004]. Acronyms stands for: AA = femur adduction(+)-abduction(-) ,IE = femur internal(+)-external(-) rotation, AP = femur anterior(+)-posterior(-) translation, PD = femur proximal(+)-distal(-) translation, ML = femur lateral(+)-medial(-) translation.

References (Optional)

1. Coats-Thomas et al., J. Orthop. Res., 2013
2. Conconi et al., J. Biomech. Eng., 2019
3. Conconi et al., ESB2023, 2023
4. Andreassen et al., J. Biomech. Eng., 2023

Session Category

Musculoskeletal Biomechanics: Methods, Models and Applications

OA44-05

Estimating the Patient-Specific Gravitational Loads Acting on the Spine

Dr. Benedikt Schlager[1], Dr. Peter Stauffert[1], Mr. Robert Graf[2], Mr. Hendrik Möller[2], Prof. Jan Kirschke[2], Prof. Hans-Joachim Wilke[1]

[1]Institute of Orthopaedic Research and Biomechanics, Centre for Trauma Research Ulm, Ulm, BW, Germany. [2]Department of Diagnostic and Interventional Neuroradiology, School of Medicine, TUM University Hospital, Technical University of Munich, Munich, Bayern, Germany

Introduction

A key challenge for the biomechanical analysis of patient-specific orthopedic treatment is identifying the loads which act within the individual patient.

Goal of this study was to quantify the gravitational loads and load distribution which act on the individual spine, as well as correlate these loads with the individual spinal shape.

Methods

Full body MRI images from a random retrospective subset of 270 patients (121 female, 149 male, age 21-72 years, BMI 17.4-50.6) of the German National Cohort (NAKO) were analyzed. 112 anatomical structures within the torso including the abdominal organs, lung, heart, spine and muscles were segmented using the DL-tools VibeSegmentator [1], SPINEPS [2] and MuscleMap [3]. The extracted parameters included the volume and center position of each anatomical structure, as well as the morphological parameters of the spinal shape (Fig). Density values for each anatomical structure was obtained from literature. The coordinates were transformed to a subject-specific coordinate system and the moments were calculated by the lever arm relative to the spinal vertebra L5. The data was evaluated statistically, and compared with literature and metric data of the patients.

Results

The estimated weight of the torso correlated significantly with the measured weight of the subjects (R2=0.9). The overall induced mean moment within the sagittal plane was 0.17 +/- 0.27 Nm, while the structures positioned anterior of the spine induced a mean moment of 0.3 +/-0.2 Nm and the posterior structures -0.16 +/-0.05 Nm. The subcutaneous fat induced a mean moment of 0.06 +/-0.09 Nm. No significant correlations between the shape of the spine and the weight or moments were obtained.

Discussion

Using segmented organs within the torso appears to be a promising approach for quantifying the distribution of gravitational loads acting on the individual spine. Limitations include the lying posture during MRI acquisition and the general methodological challenges of measuring and validating in-vivo loads. Nevertheless, the findings represent an important step toward individualized biomechanical analysis and orthopedic treatment.

Images (Optional)

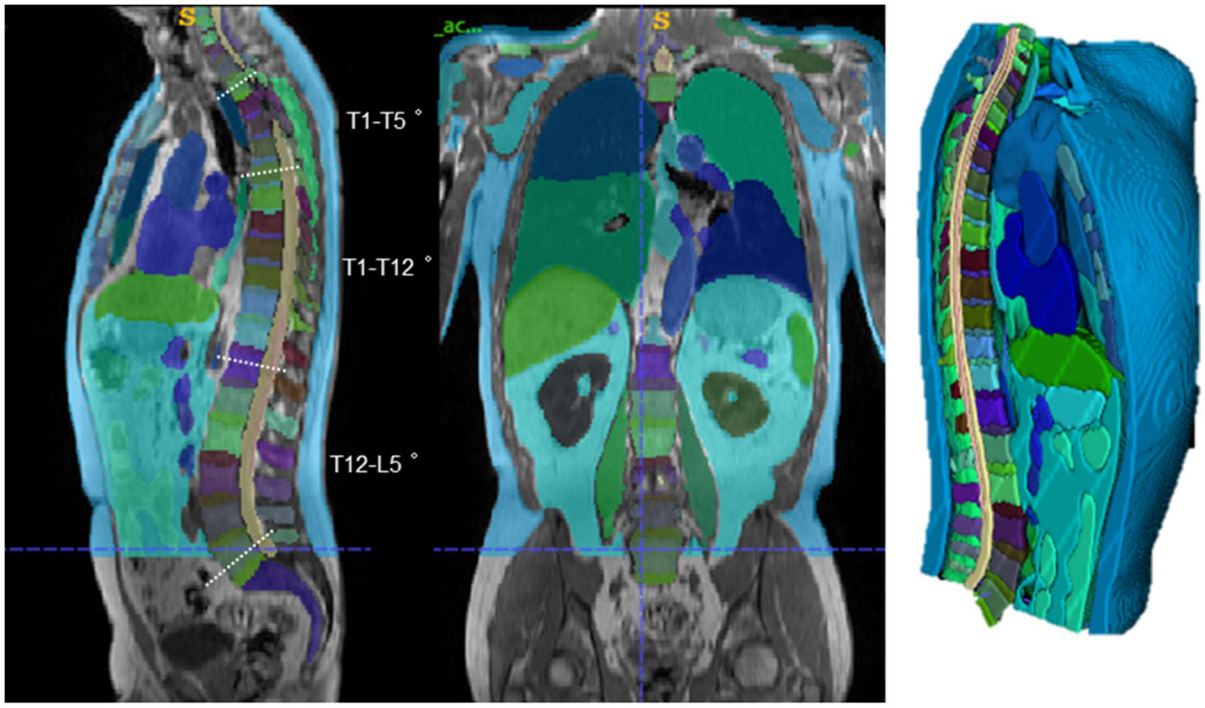


Fig: Extracted anatomical structures from MRI images to estimate spinal loading

References (Optional)

[1] Graf et al. Eur Radiol (2025), [2] Möller et al. Eur Radiol (2025), [3] McKay et al. J Imaging (2024)

Acknowledgements (Optional)

Funded by the German Research Foundation grand 422439870 (WI 1352/23-2). We thank all participants who took part in the NAKO study and the staff in this research program, as well as their funding agencies.

Session Category

Musculoskeletal Biomechanics: Methods, Models and Applications

OA44-06

Prediction of Adult Foot Bones Through Statistical Shape Modelling

Mr. Michael Oborn[1], Prof. Thor Besier[1,2]

[1]Auckland Bioengineering Institute, University of Auckland, Auckland, New Zealand. [2]Department of Engineering Science and Biomedical Engineering, Faculty of Engineering, University of Auckland, Auckland, New Zealand

Introduction

Statistical shape modelling provides a means to predict personalised geometry with a greater accuracy than generic model scaling, with application to musculoskeletal modelling. Statistical shape models have effectively described the coupled relationship between the pelvis, femur, tibia and fibula geometries. However, prior models have not included the foot geometry. A coupled shape model of the foot bones would enable accurate prediction of personalised foot geometry using physiological constraints. This study describes the coupled relationship of bone shape and size variation in an adult foot population, and evaluates the performance of a combined shape model of the foot to predict bone morphology.

Methods

The tibia, fibula, and all 28 bones of the foot were automatically segmented from 418, and 368 CT scans of adults for the left and right foot, respectively. Variation in combined bone geometries was determined through principal component analysis. Separate shape models were created to predict the combined geometry of the left and right feet, through partial least squares regression, from demographic and linear bone measurements. Predictions were validated through k-fold validation, comparing RMSE and dice scores between predicted and ground truth segmentations.

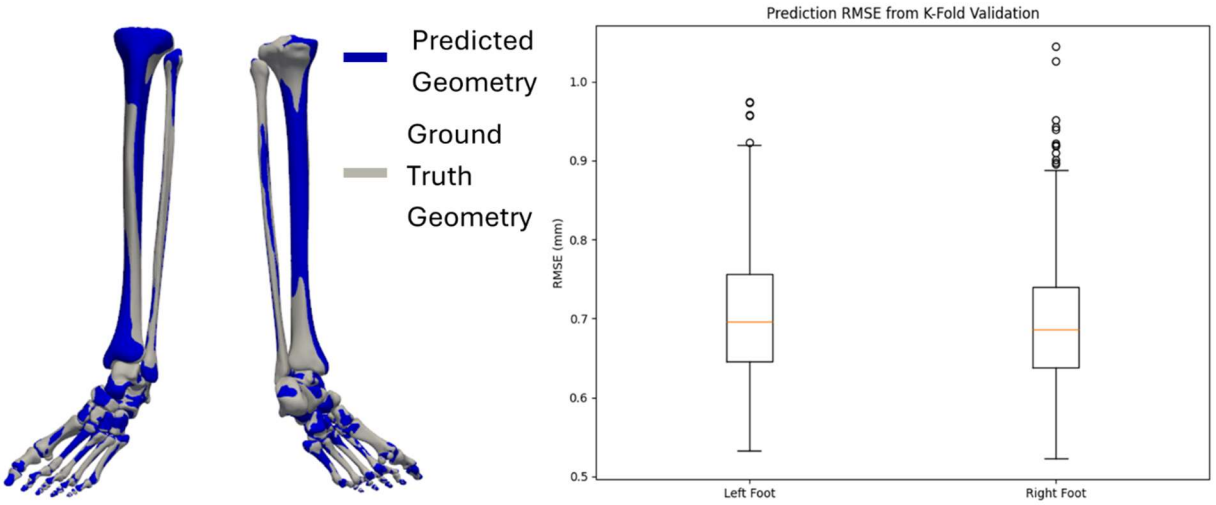
Results

The first 5 principal components of the dataset described 81 % of variation in the left foot, and 85 % of variation in the right foot. These principal components described variation in overall bone size and shape, along with bone variations such as tibial torsion. K-fold validation of combined geometry prediction produced average prediction RMSE of 0.7 ± 0.4 mm for both the left and right foot. Dice scores of the predicted geometries were 0.9 ± 0.1 for the left and right foot.

Discussion

Our combined shape model of the foot provides a novel method to accurately scale all the foot bones, consistent with the lower limb anatomy, from anthropometric measurements. These patient specific models can be used in future musculoskeletal modelling workflows or clinical analysis of morphological variation.

Images (Optional)



Session Category

Musculoskeletal Biomechanics: Methods, Models and Applications

OA45-02

A Support Vector Machine Regression Model for Rapid Predictions of ACL Forces Based on Finite-Element Knee Simulations.

PhD-student Maximilian Ebenbichler, Dr. Robert Eberle, Dr. Dieter Heinrich, PhD Maurice Mohr

University of Innsbruck, Innsbruck, Tirol, Austria

Introduction

Anterior cruciate ligament (ACL) force (F_{ACL}) is commonly estimated using FE knee models and regression models. FE models allow a wide range of loading conditions but are computationally expensive, whereas regression models offer rapid predictions. However, most existing regression models are derived from in-vitro testing [1], which is typically restricted to low-loading conditions and thus limits their application to high-loading scenarios.

The objectives of this work were to 1) train and test a support vector machine regression (SVMR) model to predict FE model-based F_{ACL} under high-loading conditions with reduced computation time, and 2) compare the SVMR model-based F_{ACL} to an existing regression model [1].

Methods

A modified version [2] of the OpenKnee(s) OKS008 FE knee model [3] was used. The FE simulations were performed by fixing the femur and applying 600 random combinations of forces and rotations to the tibia: three forces (100N < compression force < 5000N, -500N < posterior force < 500N, -500N < medial force < 500N) and three path-controlled angles (0° < flexion angle < 60°, -15° < adduction angle < 15°, -25° < internal rotation angle < 25°). From these simulations, 6000 data points were extracted to train and test the SVMR model using a second order polynomial kernel function. SVMR model-based F_{ACL} were compared to 1) the FE model and 2) the regression model by Weinhandl et al. [1] using Bland-Altman plots.

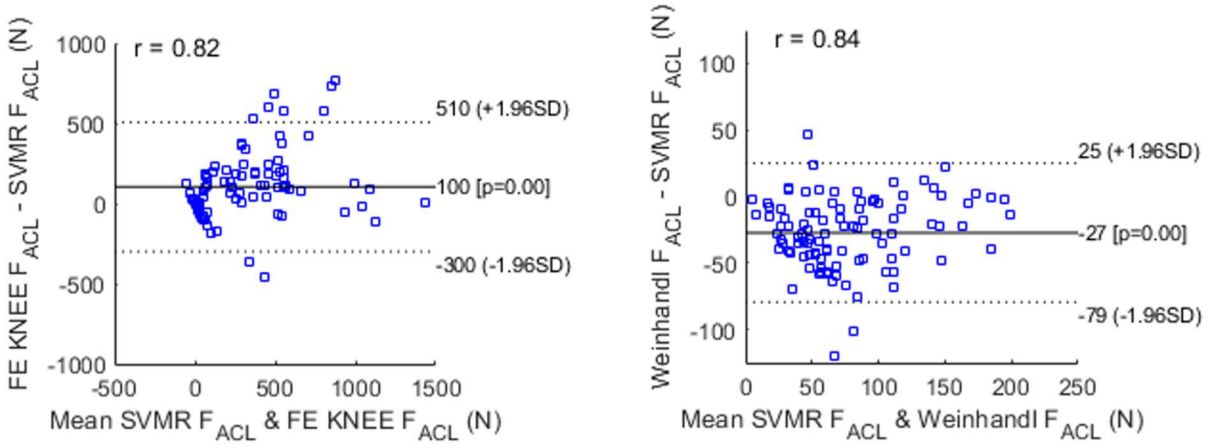
Results

The SVMR model reduced the computation time to predict F_{ACL} under high-loading conditions from 3h to 0.3s. However, the SVMR model poorly predicted FE model-based F_{ACL} in some loading conditions (Figure 1(a)), while overestimating the regression model-based F_{ACL} (Figure 1(b)). Nevertheless, there was a strong correlation between the models.

Discussion

In its current form, the SVMR model was not accurate enough for some loading conditions. However, rapid machine learning algorithms based on FE simulation generated data could be a promising method. Future work will test a reinforcement learning approach to improve the SVMR model's accuracy in predicting F_{ACL} for different loading scenarios.

Images (Optional)



(a) (b)

Figure 1 Two Bland-Altman plots are shown to compare the ACL force predicting models (a) FE knee testing data to SVMR model in high loading conditions and (b) Weinhandl model to SVMR model in low loading conditions, as the cadaver testing data in Weinhandl et al. [1]. Additionally the Pearson r-value (r) is shown for each comparison.

References (Optional)

[1] Joshua Weinhandl *et al.* , Clinical Biomechanics, 2013

[2] Maximilian Ebenbichler *et al.* , Current Issues in Sport Science, 2024

[3] Snehal Chokhandre *et al.* , Annals of Biomedical Engineering, 2023

Session Category

Injury Biomechanics: N/A

OA45-03

Computational Model Distinguishes Mechanical Injury- and Inflammation-Driven Temporal Protease Activity Underlying Collagen and Aggrecan Loss in Cartilage

Mr. Moustafa Hamada MSc[1], Dr. Atte S.A. Eskelinen PhD[1], Dr. Joonas P. Kosonen PhD[1], Dr. Cristina Florea PhD[1], Prof. Alan J. Grodzinsky PhD[2], Dr. Petri Tanska PhD[1,3], Prof. Rami K. Korhonen PhD[1]

[1]University of Eastern Finland, Kuopio, North Savo, Finland. [2]Massachusetts Institute of Technology, Cambridge, Massachusetts, United States. [3]Kuopio University Hospital, Kuopio, North Savo, Finland

Introduction

Cartilage collagen and aggrecan loss are key hallmarks of post-traumatic osteoarthritis (PTOA) [1]. However, the underlying mechanobiological pathways governing their temporal dynamics following mechanical injurious overloading of cartilage versus exogeneous inflammation remain unclear. We present a finite element model simulating post-injury cartilage degeneration that disentangles the respective temporal contributions of injury (INJ)- and interleukin-1 (IL-1)-induced catabolic cell activity to protease-mediated collagen and aggrecan loss.

Methods

Experiment: Cartilage explants from calf knee joints were cultured for 3 and 12 days in free-swelling conditions and under combination of single injurious loading and continuous IL-1α treatment [2] (fig. 1A). Aggrecan and collagen contents were quantified depth-dependently using digital densitometry and infrared microspectroscopy.

Computational model: A 2-D finite element model simulated cartilage response to injurious loading at day 0, followed by 12-day IL-1 diffusion. Excessive shear strain triggered cell catabolism, followed by release of collagen-degrading matrix metalloproteinases (MMPs) and aggrecan degrading aggrecanases. Similarly, IL-1 induced release of MMPs and aggrecanases via IL-receptor binding [3]. Model results were compared to experiments on days 3 and 12. Relative contributions of injurious loading and IL-1 to total protease activity over time in the model were analyzed.

Results

On day 3, INJ+IL model and experiment showed negligible bulk aggrecan loss versus control. Collagen loss remained negligible in the model but reached 9% in the experiment within 20%–60% tissue depth. On day 12, model predicted 14% collagen and 25% aggrecan loss, matching experimental losses (12% and 20%, respectively; Fig.1C–D). Injurious loading accounted for 70% of collagen- and 57% of aggrecan-targeting protease activity by day 2 (Fig.1E). By day 12, the IL-1-diffusion dominated, contributing 90% and 97% of protease activity against collagen and aggrecan, respectively.

Discussion

Our model reproduced the experimentally observed depth-dependent collagen and aggrecan losses following injury and inflammation. It quantified the distinct temporal contributions of injury- and IL-1-mediated protease activity, revealing an early burst of injury-mediated enzymatic degradation followed by sustained IL-1-mediated degradation. This framework provides a novel basis for examining therapeutic time windows for protease-inhibitor drugs at PTOA onset.

Images (Optional)

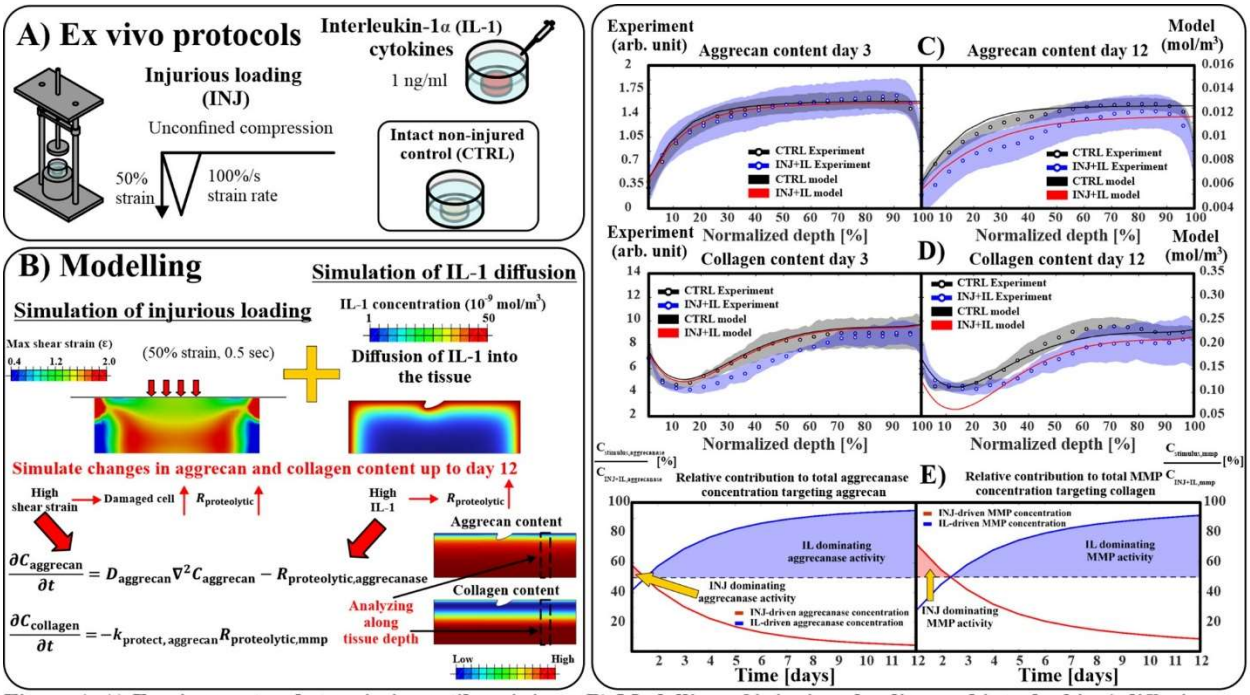


Figure 1. A) Ex vivo protocols to mimic cartilage injury, B) Modelling of injurious loading and interleukin-1 diffusion to simulate aggrecan and collagen loss, C)&D) Model results compared to experiments for aggrecan and collagen content respectively, E) Relative contributions of INJ and IL to total aggrecanase and MMP activity in INJ+IL model. INJ = injurious loading, IL= Interleukin-1, CTRL = control non-injured

References (Optional)

1.Krishnan, Matrix Biology, 2018, 2.Hamada, J Orthop Res, 2025, 3.Kar, Arch. Bichem. Biophys, 2016.

Session Category

Injury Biomechanics: N/A

OA45-04

Combined Experimental-Computational Framework for Assessing Traction Forces and Fetal Brain Deformation in Vacuum-Assisted Delivery

PhD candidate Estelle Pitti[1,2], Assistant Professor, MD Lotta Herling[2,3], Associate professor, MD Gunilla Ajne[2,3], Professor Matilda Larsson[1], Associate professor Xiaogai Li[1]

[1]KTH Royal Institute of Technology, Stockholm, Stockholm, Sweden. [2]Karolinska Institutet, Stockholm, Stockholm, Sweden. [3]Karolinska University Hospital, Stockholm, Stockholm, Sweden

Introduction

Vacuum-assisted delivery (VAD) facilitates complicated vaginal deliveries by applying traction to the fetal head. Excessive traction may increase neonatal morbidity risk, but the underlying injury mechanisms remain poorly understood, partly due to the lack of robust experimental and computational models of fetal head biomechanics during VAD [1]. This study aims to develop a combined experimental-computational framework to allow for investigation of the impact of traction on fetal brain deformation during VAD.

Methods

The fetal head geometry for both experimental and computational models was derived from CT segmentation of a newborn [2]. The experimental setup [3] included a 3D-printed skull phantom (Fig. 1a) and a brain phantom of composite hydrogel (6% PVA, 0.85% Gellan Gum) (Fig. 1b). Six sonomicrometry crystals were embedded in the phantom to estimate brain strain and traction of 30–110 N was applied in the VAD experimental setup (Fig.1c). The computational fetal head model was obtained by morphing the baseline 2-month Infant PIPER head model [4] to the target geometry (segmented CT images) using Demons registration. The dice coefficient was computed to quantify the accuracy of the morphed model with respect to the target fetal head geometry used for the phantom.

Results

Crystal motion followed traction direction, confirming the feasibility of the experimental VAD setup with traction up to 112 N and brain strains up to 4% which correlated significantly with traction ($p < 0.05$) (Fig. 1d). The computational model presented a morphed fetal head model (Fig. 1e, 1f) with a dice coefficient of 0.75 (skull and sutures) and 0.92 (intracranial structures).

Discussion

The high dice coefficients confirm the computational model's fidelity to the patient-specific phantom, while its complexity supports ongoing work for deeper investigation of traction effects on fetal brain deformation. Framework validation is provided by the experimental framework, offering direct biomechanical measurements despite practical limitations. This integrated experimental–computational framework could help identify injury risk factors and promote safer clinical use of VAD.

Images (Optional)

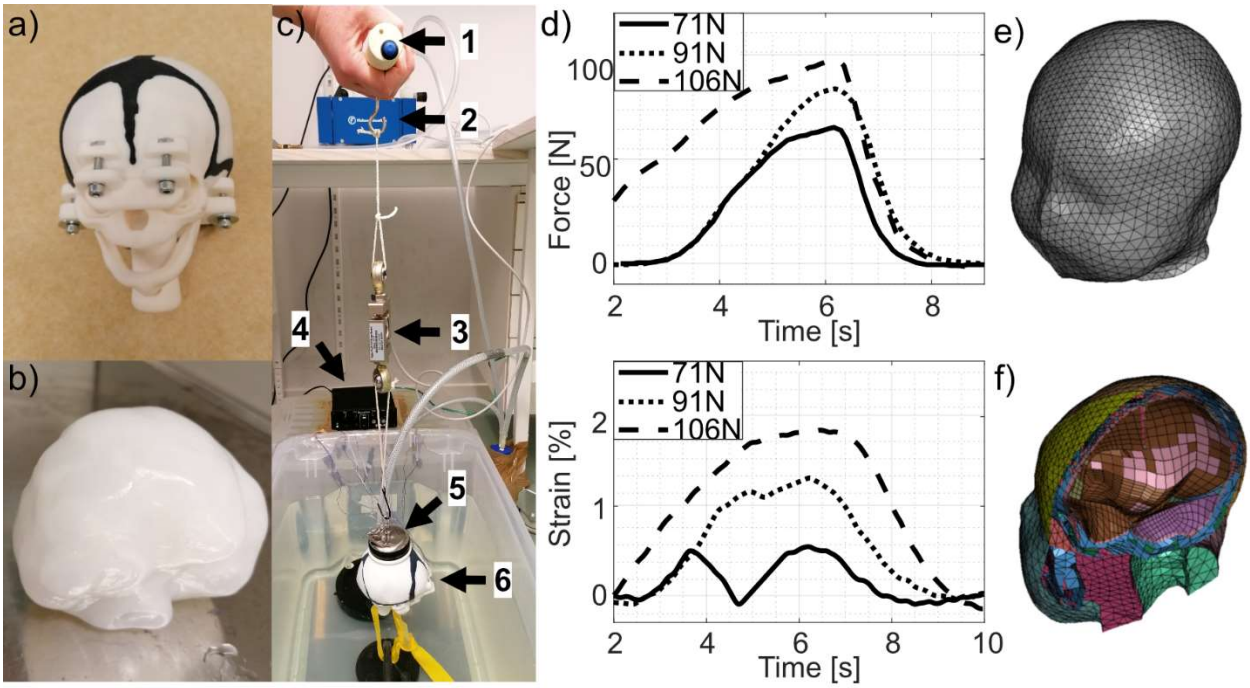


Figure 1 a) Fetal head phantom b) Fetal brain phantom c) Experimental VAD setup, 1; VAD handle, 2; vacuum pump, 3; force gauge, 4; sonomirometry, 5; VAD cup, 6; fetal head phantom d) Sample traction force and strain curves e) Morphed fetal head model f) Element view of the morphed fetal head model (each color represents one element)

References (Optional)

[1] Goordyal D et al., J Med Eng, 2020

[2] Edgar H.D.B et al., U.N.M, 2020

[3] Pitti E et al., Ann Biomed Eng, 2025

[4] Chen S et al., IRCOBI, 2024

Session Category

Injury Biomechanics: N/A

OA46-01

Effects of Agonist-Antagonist Myoneural Interface on Whole-Body Angular Momentum During Perturbed Walking Among Individuals With Transtibial Limb Loss

Mr. Kiichi Ash MS[1,2], Dr. Courtney Butowicz PhD[2,3,4], Dr. Brad Hendershot PhD[2,3,4], Dr. Paolo Bonato PhD[5], Dr. Pawel Golyski PhD[2,3]

[1]Henry M. Jackson Foundation, Bethesda, MD, United States. [2]Walter Reed National Military Medical Center, Bethesda, MD, United States. [3]Extremity Trauma & Amputation Center of Excellence, Falls Church, VA, United States. [4]Uniformed Services University of the Health Sciences, Bethesda, MD, United States. [5]Harvard Medical School, Boston, MA, United States

Introduction

Traditional lower limb amputation anchors transected muscles to bone, removing some proprioceptive feedback which may have detrimental effects on walking stability. The agonist-antagonist myoneural interface (AMI) procedure reestablishes agonist-antagonist muscle pairs, restoring proprioceptive feedback and muscle dynamics which are in turn leveraged by a neuroprosthesis. However, the effect of AMI on stability during walking in patients who use conventional prostheses is unknown. Thus, we evaluated stability during perturbed walking using sagittal whole-body angular momentum (WBAM) among individuals with unilateral transtibial limb loss (UTTLL) with and without AMI using a conventional prosthesis. We hypothesized patients with AMI vs. a traditional amputation would have improved stability, as evidenced by 1) a smaller WBAM range during unperturbed walking and 2) a smaller WBAM range during the perturbed (S0) and recovery steps (S+1).

Methods

7 service members with UTTLL, 2 with AMI (37.0 ± 2.8 y) and 5 without (38 ± 11.1 y), completed a full-body gait evaluation on a split-belt treadmill at a controlled velocity (1.0 m/s) with unexpected perturbations occurring every 20-35 steps. Perturbations were created with brief (200 ms duration), rapid (10 m/s^2 acceleration/deceleration) increases (“slip”) or decreases (“trip”) in unilateral treadmill velocity targeted to begin at 40% of the stance. Ten trials were collected for each condition. WBAM was calculated using OpenSim (v4.4) and custom MATLAB (2024b) scripts. Group differences were assessed with independent-samples t-tests (α=0.05).

Results

Sagittal WBAM ranges were similar between patients with AMI and those with traditional amputations during unperturbed walking ($p>0.159$), during the perturbed step ($p>0.327$), and during the first recovery step after a perturbation ($p>0.085$), across both slips and trips.

Discussion

In this work, we investigated sagittal WBAM ranges during unperturbed and perturbed walking in patients with UTTLL with and without AMI when donning a conventional prosthesis. Our findings suggest that sagittal walking mechanics before, during, and after sagittal plane perturbations are not influenced by AMI, indicating a neuroprosthesis may be necessary to obtain walking stability benefits from AMI. However, given the small sample size and modest magnitude of WBAM differences observed, definitive conclusions are premature. The study remains ongoing, with continued enrollment to strengthen future analyses.

Images (Optional)

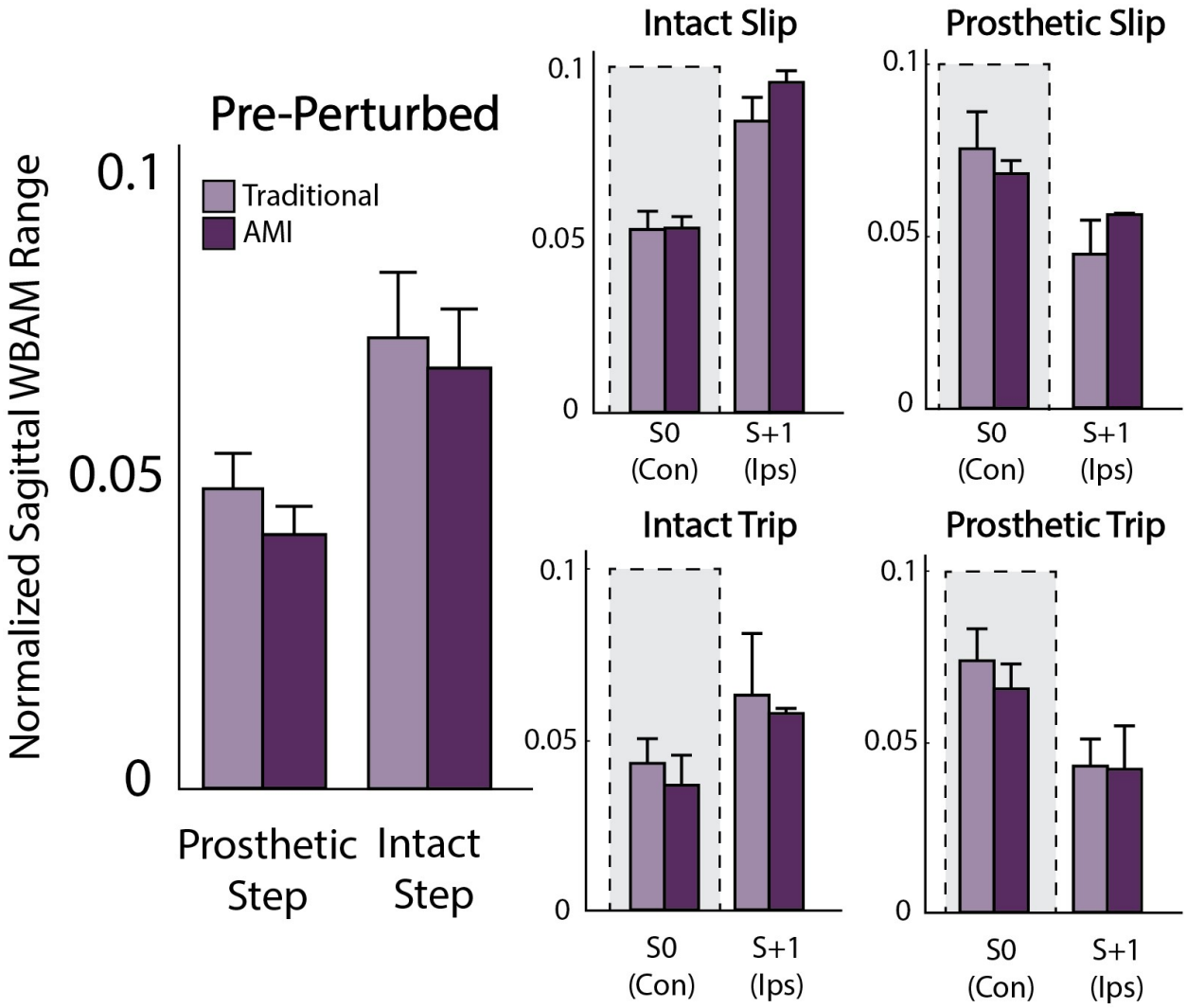


Figure 1: Sagittal whole-body angular momentum (WBAM) ranges before (Pre-Perturbed), during (S0), and after (S+1) treadmill perturbations in patients with UTTLL with and without AMI. WBAM was normalized to body mass. "Con/Ips" indicates step side relative to the perturbed side (i.e., the effect of the perturbation is first apparent at the contralateral heelstrike). S0 (gray-shaded box): Perturbed step. S+1: Recovery step

Acknowledgements (Optional)

This work was supported by NIH award 1R03HD114176-01. The views expressed herein are those of the authors and do not reflect the views of Henry M. Jackson Foundation for the Advancement of Military Medicine, Inc.. The views expressed in this abstract are those of the authors and do not necessarily reflect the official policy of USUHS, DHA, DoW, VA, nor the U.S. Government.

Session Category

Rehabilitation Biomechanics and Human Factors: Rehabilitation

OA46-02

Minimally Invasive Muscle Implant Captures Greater Muscle Activation Complexity Than Surface EMG

Ms. Paige Dzenutis, Dr. Jennifer Leestma Ph.D., Ms. Kristín Helga Jónsdóttir, Mr. Alexander Madinger M.S., Dr. Shriya Srinivasan Ph.D.

Harvard University, Cambridge, MA, United States

Introduction

Electromyography (EMG) is commonly used to decode human intent. Minimally invasive, high-density EMG can improve myoelectric control, compared to low-density and surface EMG (sEMG), while avoiding invasive surgery, a benefit over traditional intramuscular EMG [1]. We have designed a minimally invasive neural implant (MINI) to provide precise and high-density EMG via ~1cm incision. We hypothesized that MINI provides greater muscle activation complexity in dynamic tasks compared to sEMG.

Methods

Under a protocol approved by the Harvard Institutional Animal Care and Use Committee, we placed 36 electrodes into a rat's hind limb, targeting superficial and deep compartments in anterior and posterior regions. For comparison, we covered the surface of the hind limb with 8 sEMG sensors. We recorded all sEMG and either anterior or posterior MINI channels (due to a 32-channel acquisition limit) while the rat locomoted through a custom 'jungle-gym' (Figure 1). We used principal component analysis (PCA) during movement periods, sectioned by laps around the 'jungle gym', to evaluate data complexity captured by the MINI and sEMG.

Results

To match channel count, we randomly subsampled 30 combinations of 8 MINI channels. For each subsample, we computed the number of principal components (PCs) required to explain 95 percent of the variance. In the anterior compartment, MINI exhibited higher dimensionality than sEMG (6.5 ± 0.7 PCs vs. 5.0 ± 0.0 PCs; $p = 0.0955$). In the posterior compartment, MINI also showed greater dimensionality than sEMG (5.5 ± 0.7 PCs vs. 4.0 ± 1.4 PCs; $p = 0.3118$).

Discussion

The MINI captured greater complexity than sEMG in both the posterior and anterior regions, given its improved access to non-superficial muscles and detection of varying activation levels throughout a single muscle due to higher spatial density [2]. Such improved motor intent signal capture will enable enhanced control of prostheses and other assistive robots, especially for dextrous movements or those elicited by smaller or deeper muscles that are classically inaccessible by sEMG.

Images (Optional)

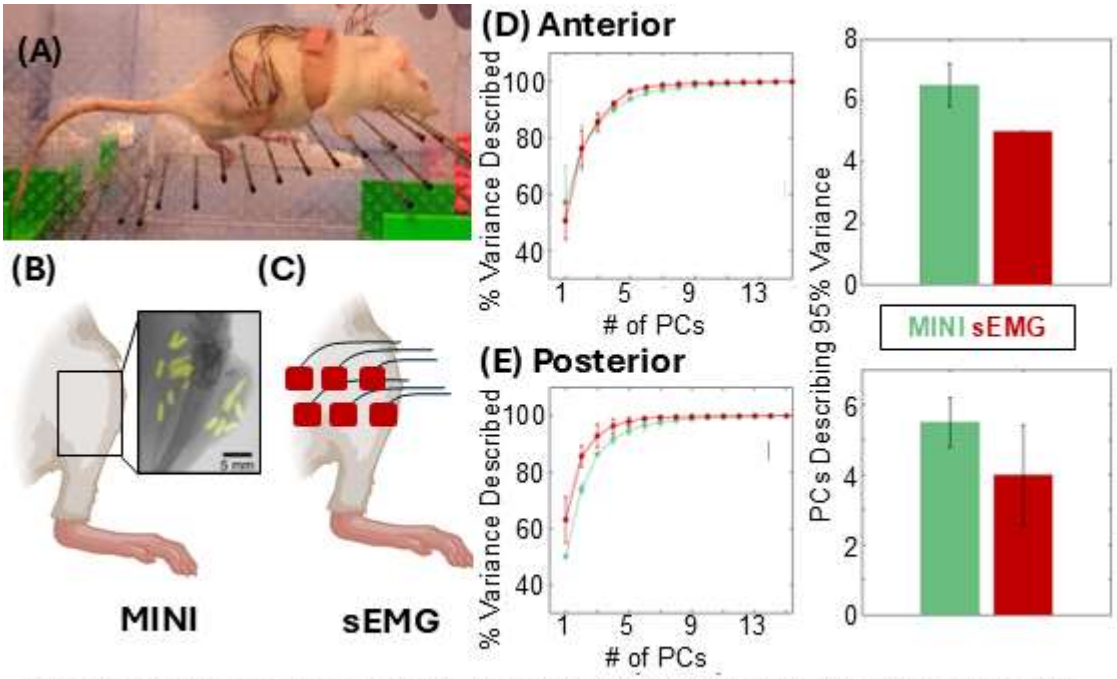


Figure 1: (A) Rat locomoting on jungle gym, (B) MINI in rat's hind limb, (C) sEMG on rat's hind limb, (D) Principal Component Analysis for Anterior region, (E) PCA for Posterior Region

References (Optional)

[1] D. Sussillo, et al., Nature, 2025

[2] B. R. Schlink et al., Physiol Rep, 2020

Acknowledgements (Optional)

This work was funded by the K. Lisa Yang Center for Bionics and the Harvard Mind Brain Behavior Postdoctoral Fellowship.

Session Category

Rehabilitation Biomechanics and Human Factors: Rehabilitation

OA46-03

Bone-Anchored vs. Socket-Suspended Transfemoral Prosthesis Users Do Not Differ in Intact Limb Knee Mechanics

Mr. John Pope CPO[1], Mr Ross Miller PhD[1], Garui Desai[2]

[1]University of Maryland, College Park, MD, United States. [2]Standford University, Stanford, CA, United States

Introduction

Transfemoral prosthetic users (TFPU) have high rates of knee osteoarthritis partly attributed to mechanical loading on the intact limb[1]. Peak knee flexion moments (pKFM), adductor moments (pKAM) and impulses (KAM*i*) are indicators of medial knee loading and associated with knee osteoarthritis[2]. Fit issues with traditional socket-suspended prostheses can impair gait and affect loading of the intact-limb[3]. Bone-anchored prostheses lack the fit-related issues of socket-suspension, but their effect on mechanical loads in the intact-limb is unclear. The purpose of this study is to examine differences in knee joint biomechanics during walking between physically fit TFPU with bone-anchoring versus socket-suspension. Because bone-anchoring minimizes uncontrolled movement between the prosthetic socket and the residual-limb, it may promote more symmetric weight bearing and lower intact limb knee joint loads. Therefore, we hypothesized that TFPU with bone-anchoring vs. socket-suspension would exhibit lower pKFM, pKAM and KAM*i* during walking.

Methods

Twelve bone-anchored (49±9years, 75.6±19.9kg) and twelve socketed (40±14years, 80.01±15.2kg) TFPU walked across a 15-meter walkway at a target speed (~1m/s). Participants all had K3/K4 mobility and participated in a variety of sports and exercise more demanding than walking. Knee moments were determined by inverse dynamics and scaled by total body weight and height. Comparisons between groups of pKAM, KAMi, and pKFM were made using independent Student's t-tests with a Bonferroni-adjustment (threshold $p<0.017$).

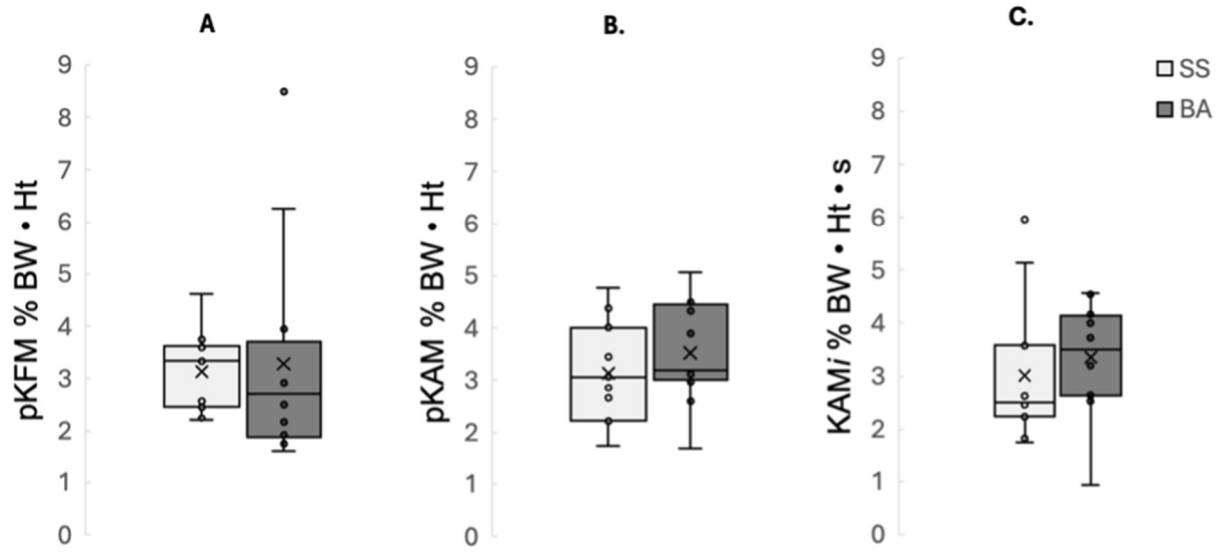
Results

There was no significant difference in knee moments found in either the sagittal or frontal plane for bone-anchored vs. socketed TFPU (Fig.1): pKFM p=0.50; pKAM p=0.34; KAMi p=0.50.

Discussion

Compared to physically fit socketed TFPU, bone-anchored revision appears to allow TFPU who previously had low function with sockets to achieve knee mechanics that do not differ from high-functioning socketed users. The cross-sectional study design can help isolate the mechanical effects of bone-anchored prostheses on intact limb loads, complementing longitudinal data where baseline mobility is low. Future studies should examine how prosthesis mechanics interact with bone-anchored suspension to affect gait and intact-limb loading.

Images (Optional)



Peak external knee flexion moment (pKFM, A.), adduction moment (pKAM, B.) and knee adduction moment impulse (KAM*i*, C.) during stance on the intact limb side of socket-suspended (SS) and bone-anchored (BA) TFPU. Joint moments are normalized to BW *Ht (m) and presented as %.

References (Optional)

[1] Morgenroth DC, et al. *PMR* **4**, S20-S27,2012. [2] Manal K, et al. *OA and Cart* ***23.7****, 1107-1111,2015*. [3] Gale T, et al. J Biomech **112**, 110050,2020.

Acknowledgements (Optional)

Funded: CDMRP HT9425-23-1-0103

Session Category

Rehabilitation Biomechanics and Human Factors: Rehabilitation

OA46-04

Increasing Prosthetic Limb Torque Decreases User Effort at the Cost of Symmetry in Individuals with Above-Knee Amputation during Stair Ascent

Ms. Clare Severe[1], Dr. Lukas Gabert[1], Dr. Tommaso Lenzi[1,2]

[1]University of Utah, Salt Lake City, UT, United States. [2]Rocky Mountain Center for Occupational and Environmental Health, Salt Lake City, UT, United States

Introduction

Stair ascent is biomechanically demanding, requiring substantial positive power that conventional passive prostheses cannot provide. Consequently, amputees must rely entirely on their sound side and residual limb to generate the energy needed for stair ascent. Previous research shows that active prostheses can reduce users' effort by generating positive power through their electrical motors. However, their energy contribution has yet to match the physiological energy contribution [1-3]. Therefore, reliance on biological joints remains an ongoing challenge. This study aims to assess the user's effort, measured by positive biological work, as an active knee prosthesis delivers increasing levels of extension torque. We hypothesize that increasing prosthesis extension torque will increase positive mechanical work, thereby reducing energy demands on biological joints.

Methods

Eight individuals with above-knee amputation ascended a seven-step instrumented staircase using an active knee-ankle prosthesis controlled to provide six randomized levels of knee extension torque (0.20-1.20 Nm/kg, Figure 1a). Full-body motion capture was recorded. We calculated total positive biological joint work by integrating positive joint power over stance, then summing the positive work at the residual hip and the sound hip, knee, and ankle. We also assessed symmetry by calculating the peak knee torque and power symmetry indexes.

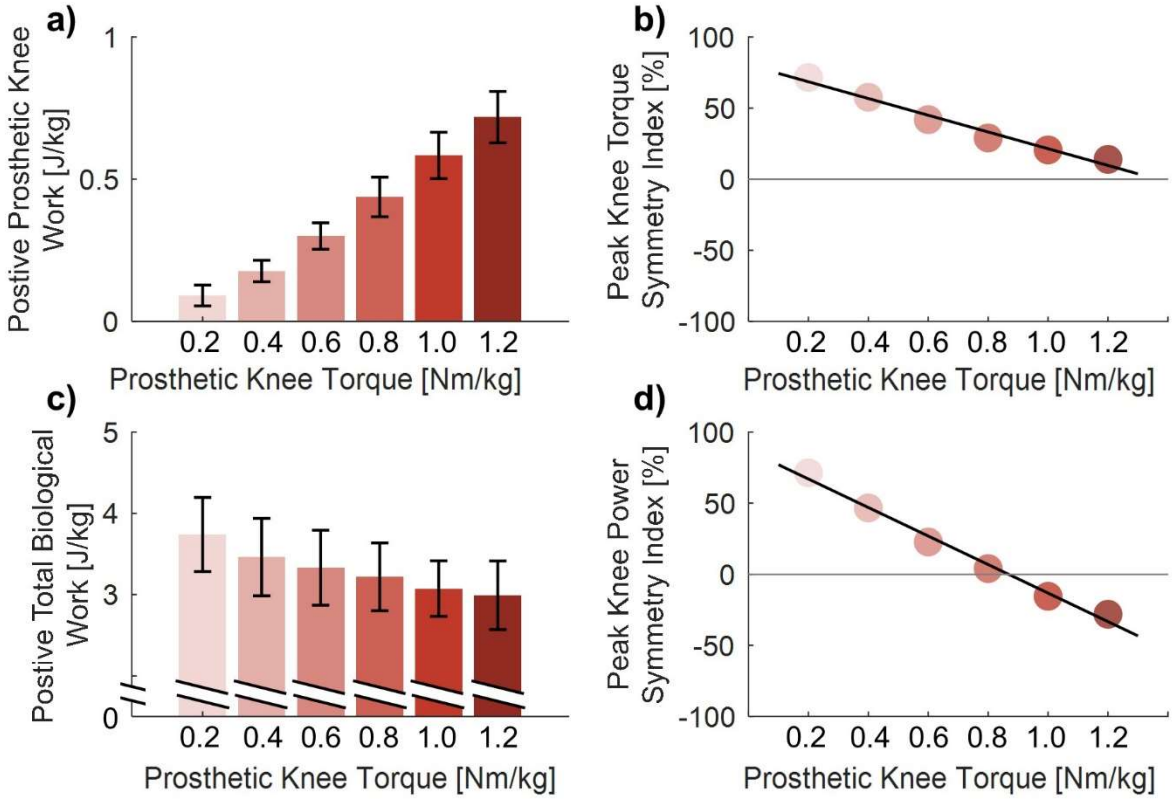
Results

Positive biological joint work varied inversely with prosthetic knee torque, achieving its lowest level (3.0+/-0.4 J/kg) at the highest torque level (Figure 1a,c). This highest torque level resulted in the best peak torque symmetry (13.9+/-1.0%, Figure 1b). However, peak power symmetry did not follow this trend, with best results at intermediate levels of knee torque (0.80 Nm/kg) and worsening at maximum torque (Figure 1d).

Discussion

Increasing extension knee torque successfully offloads the biological joints, decreasing the user's effort. However, results indicate a trade-off: higher torque improves torque symmetry, but it degrades power symmetry, suggesting that high torque levels result in excessive, uncontrolled knee velocity. Therefore, increasing prosthesis torque is not always biomechanically advantageous. Proper device tuning requires balancing effort reduction with movement control to ensure users can comfortably climb stairs.

Images (Optional)



References (Optional)

[1] Camargo *et al.*, J Biomech Eng, 2023. [2] Kestur *et al.*, J Biomech, 2024. [3] Zhou *et al.*, J Biomech, 2025.

Acknowledgements (Optional)

We thank Jim Liston, CPO, Kyle Rasmussen, CPO and Brian Kaluf, CP for helping with prosthesis fitting and alignment. This work was funded in part by the National Institutes of Health under grant #R01HD098154 and by the Department of Defense under grant #W81XWH2110037 and #HT94252410811.

Session Category

Rehabilitation Biomechanics and Human Factors: Rehabilitation

OA46-05

Bioinspired peptide therapy to augment skin mechanics in lower limb amputees

Dr Jack Hayes PhD[1], Miss Ella Beattie-Edwards[1], Miss Min Waye Chew[1], Miss Ireen James[1], Dr Summik Limbu PhD[1], Mr Jia Jun Lee[1], Miss Anna Rhodes[1], Mr Charles Sawyer[2], Dr David Gaboriau PhD[1], Dr Marc Masen PhD[1], Dr Claire Higgins PhD[1]

[1]Imperial College London, London, UK, United Kingdom. [2]University of Florida, Gainesville, Florida, United States

Introduction

Following lower limb amputation, an individual's life changes forever. However, despite significant advances in artificial limb function, 1 in 5 individuals with limb difference abandon their device before 1 year citing skin injury from device use (a problem that affects 75% of amputees). We hypothesise that the biomechanics of amputee skin make it unable to sustain the shear present during ambulation. This is in contrast to skin on the soles of our feet, which is designed to be load bearing. Our previous research has shown that despite 27 years of prosthesis use amputee skin is softer, has higher friction, shows minimal increase in skin thickness and has higher inflammation compared to the intact limb. Overall, prosthetic use does not transition skin to a load bearing identity, like that seen on the foot (figure 1a). Here we demonstrate how a bioinspired peptide can augment skin mechanics to that of plantar skin.

Methods

To investigate the role reprogramming plays at a cell scale, nanoindentation was utilised to characterise changes primary human keratinocyte monolayers.

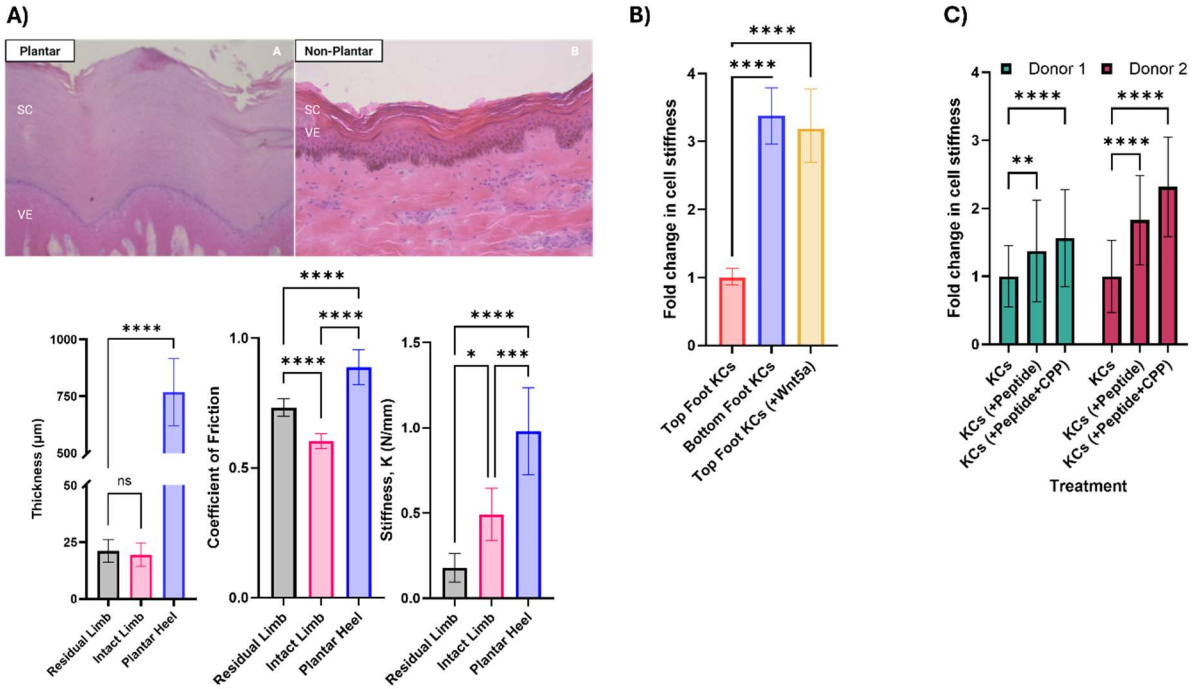
Results

Our results highlight differences in mechanical properties between plantar and non-plantar skin observed in vivo (figure 1a) are retained by keratinocytes in culture (figure 1b). Nanoindentation of patient matched plantar and non-plantar keratinocytes reveals that plantar keratinocytes are 3.4-fold stiffer that non-plantar keratinocytes (figure 1b). Addition of a plantar fibroblast derived protein, Wnt5a, to non-plantar keratinocytes increases indentation stiffness by 3.2-fold (figure 1b). Use of a novel peptide inspired by plantar skin led to 1.4-fold and 1.8-fold increase in cell stiffness, for donors 1 and 2 respectively and was further increased to 1.6-fold and 2.3-fold when conjugated with a cell-penetrating-peptide (CPP) (figure 1c).

Discussion

The results presented show how a peptide treatment can augment skin mechanics, increasing the stiffness of non-plantar keratinocytes in vitro. We envisage use of a such a therapy to improve skin resilience at medical device interfaces, a currently clinically unmet need, by reengineering skin on the residuum to a load bearing identity. We are currently evaluating the effect peptide treatment has on the resistance to frictional shear of human keratinocytes both in vitro and ex vivo.

Images (Optional)



Session Category

Rehabilitation Biomechanics and Human Factors: Rehabilitation

OA46-06

Evaluating Vibrotactile Sensory Feedback During a Foraging Task: A Case Series of Three Individuals With Partial Hand Amputations

Ms. Fatima Gafoor MASc[1], Mr. John Milkovich MEng[1], Mr. Arman Arezoomand MSc, PhD(c)[2], Dr. Chloe R. Wong MD, PhD(c)[3], Ms. Bettina Oghinan BEng[2], Ms. Zixin Gao[4], Ms. Sophie Wong Shi Kam[5], Ms. Paige Hughes BEng[2], Mr. Daniel Antflek BSc[6], Dr. Faezeh Azhari MASc, PhD[2], Dr. Heather L. Baltzer MD, MSc, FRCSC, FACS[3,6]

[1]Temerty Faculty of Medicine, University of Toronto, Toronto, ON, Canada. [2]Department of Mechanical and Industrial Engineering, University of Toronto, Toronto, ON, Canada. [3]Division of Plastic, Reconstructive & Aesthetic Surgery, Department of Surgery, University of Toronto, Toronto, ON, Canada. [4]Division of Engineering Science, University of Toronto, Toronto, ON, Canada. [5]Department of Civil Engineering, University of Western Ontario, London, ON, Canada. [6]Schroeder Arthritis Institute, Division of Plastic, Reconstructive and Hand Surgery, University Health Network, Toronto, ON, Canada

Introduction

Current partial hand (PH) prostheses provide adequate grip and cosmesis but are often abandoned due to lack of sensory feedback [1], which can limit rehabilitation and return-to-work. Previous work has identified tactile sensation as a design priority for thumb prostheses [2]. Vibrotactile feedback has been shown to improve grip strength and reduce cognitive workload in trans-radial prostheses but has not been incorporated in PH prostheses [3,4]. This study aimed to assess the effect of vibrotactile feedback on task performance across different levels of PH amputation.

Methods

A vibrotactile feedback system was developed, comprising a 3D-printed wristband connected to a force-sensing resistor on the volar pad of the thumb and a linear resonating actuator within the prosthetic socket for haptic feedback. Three participants with varying levels of PH amputation completed a Foraging Task Test, sorting blocks of three stiffnesses with and without vibrotactile feedback. Visual and auditory cues were blocked with frosted goggles and noise-cancelling headphones, ensuring participants relied solely on tactile cues. Task performance was evaluated using accuracy (percent correct) and efficiency (search time and accuracy per second). Results were compared between conditions (vibrotactile feedback on/off for stiffness levels 1-3) for each participant, and semi-structured interviews assessed user experience and impact.

Results

Participants with more extensive amputation saw the most significant improvement with vibrotactile feedback. Accuracy rose from 31.4% to 50.0% in the participant with D1-5 amputations and from 61.4% to 81.4% in the participant with a proximal D2 amputation. Accuracy remained stable in the participant with a distal D1 amputation, however they demonstrated improved efficiency with faster average search times when the feedback was on (4.78s) compared to when it was off (5.12s). Overall, participants reported greater object awareness, confidence, and control with vibrotactile feedback, and all requested to continue using the vibrotactile feedback system at home.

Discussion

Integration of vibrotactile sensory feedback improved task performance in individuals with more extensive PH amputation. These findings highlight the potential of vibrotactile feedback to improve rehabilitation outcomes, task efficiency, and prosthesis embodiment.

References (Optional)

[1] Cordella, Frontiers Neuroscience, 2016

[2] Moltaji, Disability Rehabilitation, 2023

[3] Saunders, J NeuroEngineering Rehabilitation, 2011

[4] Raveh, Clinical Rehabilitation, 2018

Session Category

Rehabilitation Biomechanics and Human Factors: Rehabilitation

OA47-02

The Effect of Alignment Variability on the Primary Fixation of Cementless Femoral TKA

MSc. Verena Helgers[1], Dr. Periklis Tzanetis[2], Dr. Thom Bitter[1], Dr. Adam Briscoe[3], Prof.Dr. Nico Verdonschot[1,2], Dr. Dennis Janssen[1]

[1]Radboud University Medical Center, Nijmegen, Gelderland, Netherlands. [2]University of Twente, Enschede, Overijssel, Netherlands. [3]Invibio Ltd, Thornton Cleveleys, Lancashire, United Kingdom

Introduction

Ensuring a proper primary fixation is essential for long-term fixation and total knee arthroplasty (TKA) survival. It is, however, poorly understood how differences in surgical alignment techniques impact implant fixation and TKA survival. The aim of mechanical alignment is to obtain a neutral knee joint alignment, while in kinematic alignment the native joint alignment defines the post-operative alignment, which may have implications for fixation. The aim of this computational study was therefore to investigate the effect of variations in coronal knee alignment on the primary fixation of femoral cementless polyetheretherketone (PEEK-OPTIMA™) and cobalt-chrome (CoCr) TKA in a patient population.

Methods

Patient-specific finite element (FE) models were created using 295 pre-operative CT images of TKA patients. The natural knee alignment of these patients was determined automatically using CPAK classification. 276 FE models of kinematically aligned femoral reconstructions of 69 varus patients were created, varying the implant material (CoCr and PEEK) and applying patient-specific gait and squat loading determined from musculoskeletal models. The primary fixation of the implant was quantified by the peak and median (99th and 50th percentile) values of the resulting micromotions on the bone-implant surface.

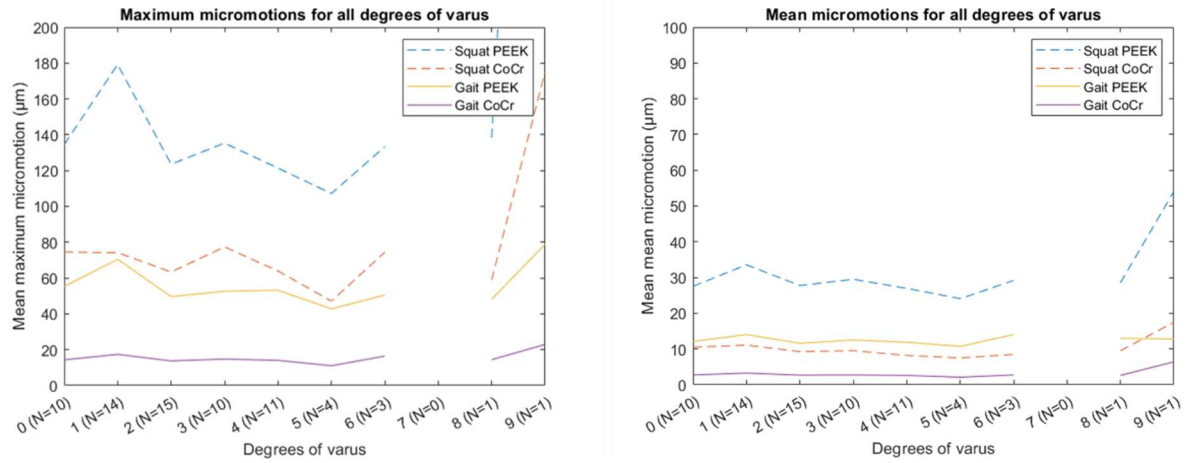
Results

Micromotions remained stable across different degrees of varus for both PEEK and CoCr models. Overall, PEEK models generated larger micromotions than CoCr models for the various degrees of varus. However, both CoCr (6 μm) and PEEK (21 μm) displayed mean micromotions that remained below the threshold of 112 μm for osseointegration (Figure 1).

Discussion

This study presents the results of a novel workflow investigating the effect of implant material and kinematic alignment on primary fixation of TKA reconstructions in varus patients. The current results do not suggest an effect of varus alignment on primary fixation, although the number of cases with larger varus angles was relatively low. We intend to further expand the number of cases and to compare these outcomes with mechanical alignment applied to the same cohort. Differences in fixation between different alignment strategies (i.e. kinematic vs. mechanical) may become more pronounced at larger native varus angles.

Images (Optional)



Acknowledgements (Optional)

This study was financially supported by Invibio Ltd. PEEK-OPTIMA™ is a trademark of Invibio Ltd.

Session Category

Orthopaedic Biomechanics: Lower Extremities

OA47-03

How Closely Mechanical Alignment in Total Knee Arthroplasty Reproduces Normal Biomechanics: A Cohort-Based in Silico Study

BSc. Andrés Álvarez Gual de Torrella[1], Prof.dr. Nico Verdonschot[1,2], Prof.dr. Sara Checa[3], Dr. Periklis Tzanetis[1]

[1]Department of Biomechanical Engineering, University of Twente, Enschede, Overijssel, Netherlands. [2]Orthopaedic Research Laboratory, Radboud University Medical Center, Nijmegen, Gelderland, Netherlands. [3]Institute of Biomechanics, Hamburg University of Technology, Hamburg, Hamburg, Germany

Introduction

Surgeons continue to widely use the traditional mechanical alignment (MA) technique in total knee arthroplasty (TKA) to achieve a neutral lower-limb mechanical axis. It remains unclear, however, how closely MA can reproduce osteophyte-free knee biomechanics on a population level. This study compared osteophyte-free musculoskeletal knee models with MA-TKA models to quantify the extent to which MA alters tibiofemoral kinematics and ligament strains.

Methods

We used a database of 53 TKA patients, including osteophyte-free reconstructed knee bones, cartilage, and anatomical landmarks required to virtually plan MA. Utilizing this information, we generated patient-specific musculoskeletal models for both osteophyte-free and MA-TKA configurations using a previously established modeling workflow [1]. All models simulated a flexion-extension movement from 0° to 90°. Differences between osteophyte-free and MA-TKA models were quantified by calculating the root-mean-square-deviation (RMSD) in kinematics, in terms of tibial rotations and translations relative to the femur, as well as ligament strains. We defined thresholds for “close to osteophyte-free” biomechanics as ±1° and ±1 mm, consistent with the reported accuracy of validated models in predicting tibiofemoral kinematics [2]. Ligament strains were evaluated using a 3% RMSD threshold, selected as a conservative boundary below the onset of fiber micro-damage, occurring approximately at 5% strain [3].

Results

Across all 53 patients, MA-TKA models consistently exhibited deviations larger than the specified thresholds of ±1° and ±1 mm for at least one kinematic parameter, and 3% for at least one of the ligaments relative to the osteophyte-free state. The average differences

between osteophyte-free and MA-TKA models across the patients peaked at 4.4° and 5.3 mm, with ligament strain differences peaking at 8.7% (Table 1).

Discussion

In this cohort, MA resulted in substantial changes in both kinematics and ligament strains relative to the osteophyte-free state, supporting the need for more personalized alignment strategies such as kinematic or restricted kinematic alignment. The selected thresholds for "close to osteophyte-free" restoration are necessarily estimates that may be relatively restrictive; further investigation is therefore necessary to determine their appropriate values and clinical relevance.

Images (Optional)

Table 1. Average root mean-square-deviation (RMSD) in tibiofemoral kinematics and ligament strains between osteophyte-free and MA-TKA musculoskeletal models across all patients

Tibiofemoral Kinematics (°/mm)	
Varus-Valgus (°)	4.4
External-Internal Rotation (°)	3.8
Proximal-Distal Translation (mm)	1.7
Anterior-Posterior Translation (mm)	5.3
Lateral-Medial Translation (mm)	3.1
Ligament Strains (%)	
Posterior Cruciate Ligament	1.0
deep Medial Collateral Ligament	8.7
superficial Medial Collateral Ligament	5.3
Lateral Collateral Ligament	2.7
Oblique Popliteal Ligament	2.2
Anterolateral Ligament	6.4
Posterior Capsule	2.1

References (Optional)

[1] Tzanetis *et al*, Bone Joint J, 2024

[2] Marra *et al*, J Biomech Eng, 2015

[3] Provenzano *et al*, J Appl Physiol, 2002

Session Category

Orthopaedic Biomechanics: Lower Extremities

OA47-04

Quantifying the Influence of Patellar Morphology on Patellofemoral Kinematics During Active Knee Extension in Healthy Knees

Ms. Erin Teule[1], Dr.ing. Sebastiaan van de Groes[1], Prof.dr.ir. Nico Verdonschot[1,2], Dr.ir. Dennis Janssen[1]

[1]Radboudumc, Nijmegen, Gelderland, Netherlands. [2]University of Twente, Enschede, Overijssel, Netherlands

Introduction

Understanding how knee morphology influences patellofemoral (PF) kinematics is essential for advancing patient-specific assessment of PF disorders. While femoral morphology has been studied, the role of patellar morphology remains underexplored. This study investigated how patellar morphology contributes to variation in PF kinematics during knee extension in healthy participants.

Methods

Six degrees-of-freedom (DOF) PF kinematics were derived from dynamic CT data from 100 healthy participants during active knee extension. Four patellar morphology features (height , width, Wiberg index, and Wiberg angle) were automatically extracted from a static CT scan. Mixed-effects models were fitted for each DOF, with patella features and knee angle as fixed effects and random intercepts and slopes per participant. Univariable analyses identified significant predictors ($p < 0.05$), which were entered into multivariable models. Due to collinearity ($r = 0.80$), patella width was retained over height when both were significant.

Results

After excluding 20 dynamic scans, unilateral data from 80 participants (78% female, mean age 24.3 ± 3.4 years, 60% right knees) were analysed. Knee angle explained most variance across all DOFs (R2=0.938-0.997). After controlling for knee angle, patellar morphology features contributed significantly to PF flexion, AP and PD position. Univariable models showed that patella height, width and Wiberg angle significantly predicted PF flexion and AP position, and that patella height and width predicted PD position. No morphology features contributed to PF rotation, tilt, or ML position. Multivariable models for PF flexion and AP position indicated that patella width (β=-0.23, 95%CI [-0.41,-0.05]; β=-0.50, 95%CI [-0.65,-0.35], respectively) and Wiberg angle (β=-0.21, 95%CI [-0.34,-0.08]; β=-0.12, 95%CI

[-0.23,-0.01], respectively) were independent significant predictors. For PD position, patella width was the only significant predictor (β=0.34, 95%CI [0.17,0.50]).

Discussion

Patellar morphology modestly but significantly influenced PF flexion, AP, and PD position, whereas other PF DOFs were unaffected. Larger patellae and greater Wiberg angles (i.e., a flatter patella) were associated with slightly reduced flexion and a more anterior and, for larger patellae, more distal position. Flatter patellae may exhibit reduced trochlear-patellar congruence, potentially leading to a more anterior patellar position and reduced PF flexion. Overall, knee angle remained the dominant determinant of PF kinematics.

Session Category

Orthopaedic Biomechanics: Lower Extremities

OA47-05

Total Knee Arthroplasty Implications on the Patellofemoral Joint Contact Forces

Dr. Mounir Boudali[1,2], Mr. Jobe Shatrov[1,3], Dr. Koki Abe[4], Dr. David Parker[1,3], Prof. William Walter[1,5], A/Prof. Elizabeth Clarke[1,2,6]

[1]The University of Sydney, Sydney, NSW, Australia. [2]The Kolling Institute Sydney MSK Health, St. Leonards, NSW, Australia. [3]Landmarks Orthopaedics, St. Leonards, NSW, Australia. [4]Yokohama City University, Yokohama, Yokohama, Japan. [5]The Royal North shore Hospital, St. Leonards, NSW, Australia. [6]The Murray Maxwell Biomechanics Laboratory, St. Leonards, NSW, Australia

Introduction

Total knee arthroplasty (TKA) is an effective intervention for end-stage knee osteoarthritis, yet some patients remain dissatisfied. Persistent pain is a leading cause of revision (7.2%), including patellofemoral-related pain (6%) according to the Australian Orthopaedic Association Annual Report 24/25 [1].

Contemporary surgical philosophy emphasises restoration of native anatomy, including articular geometry, joint line, and patellar thickness. However, standard implants often fail to replicate the individual patient morphology, potentially altering joint mechanics and soft tissue tension.

This study quantifies differences in patellofemoral biomechanics between the native and the reconstructed knee following robotically assisted TKA in a cadaveric model.

Methods

Eleven fresh-frozen pelvis-to-toes specimens were prepared and mounted on the simVITRO® Universal Musculoskeletal Simulator (Jupiter 3000, Cleveland Clinic, Cleveland, OH) following the protocol described in [2].

Each specimen was tested under three conditions: **Native** (intact knee – only skin and subcutaneous fat removed), **Neutral** (patella resurfaced after a medial parapatellar incision), and **TKA** (after completion of TKA). Passive knee flexion from 0° to 100° was simulated for all conditions replicating what a surgeon would perform intraoperatively to assess the knee joint. Patellofemoral joint forces were measured with a custom patella force sensor.

All surgical procedures were performed by a single senior surgeon using the CORI robotic system (Smith & Nephew, Memphis, TN) to ensure consistency and precision across specimens.

Results

Results show a significant increase in forces between **Neutral** and **TKA** conditions. On average, we saw a 43% increase in the resultant load in the patellofemoral joint.

The lateral side of the patella saw a larger increase in the load compared to the medial side.

Discussion

The forces increased after TKA across all specimens in a non-uniform fashion. The lateral loading increase could imply the trochlear is not ideally placed and therefor the use of femoral components with lateralised trochlear groove should be prioritised over the centrally aligned designs, which could help reduce the loading of the patella and hence help mitigate abnormal soft tissue strain.

In the absence of navigation systems, surgeons could still compensate for the potential increase of the articular forces by lateralising the placement of the patellar implant.

Images (Optional)

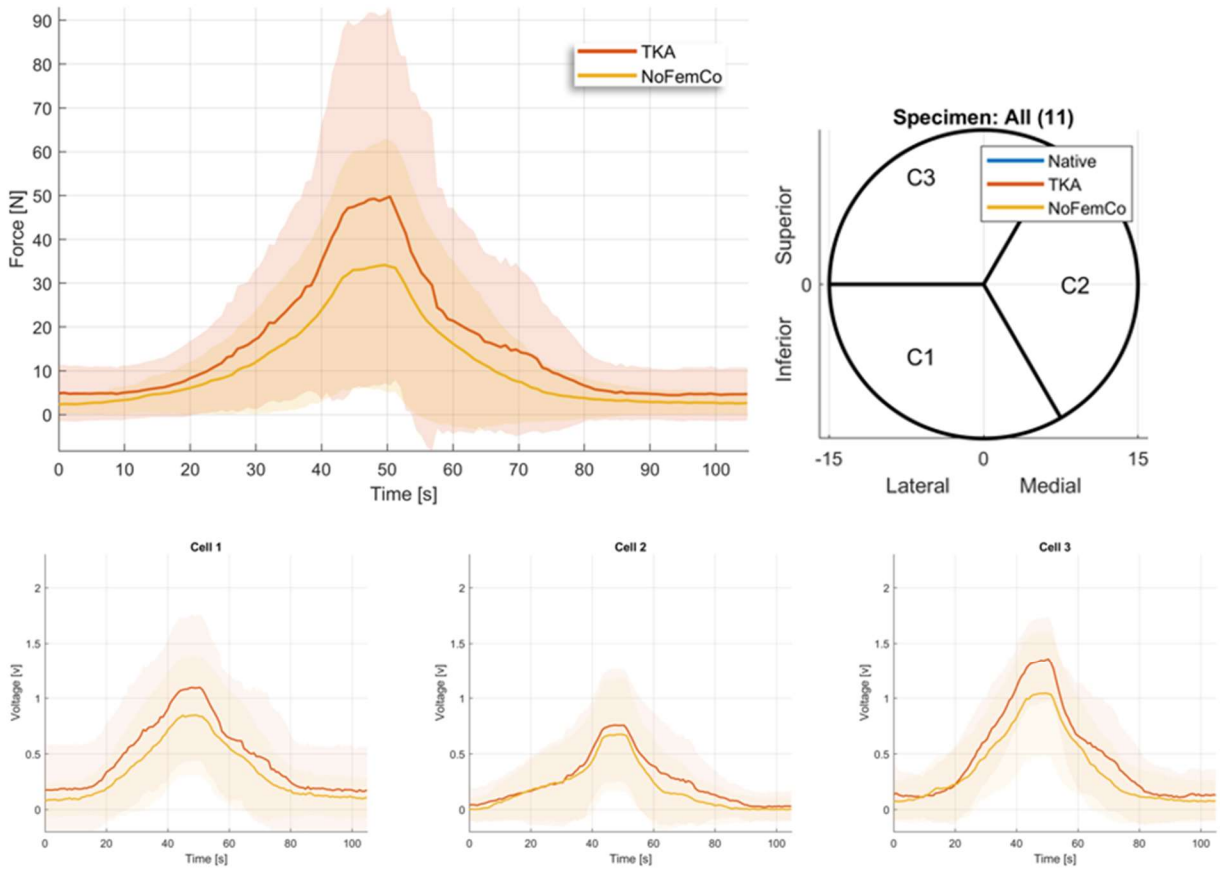


Figure1: Top left shows the resultant force in the PFJ. Top right shows an illustration of the patellar sensor. Bottom panels show each force sensing cell.

References (Optional)

AOANJRR Annual Report 25.

doi:10.1051/sicotj/2025043

Session Category

Orthopaedic Biomechanics: Lower Extremities

OA48-02

Can a Behavioral Foundation Model Predict Human Locomotion?

Dr. Jeonghwan Lee, Dr. Nidhi Seethapathi

Massachusetts Institute of Technology, Cambridge, MA, United States

Introduction

Building predictive models of human biomechanics remains challenging. Traditional optimal control models provide key insights but are limited to restricted behaviors such as steady-state locomotion. Behavioral Foundation Models (BFMs) now generate complex whole-body motions from large-scale data [1], yet it is unclear whether they learn fundamental biomechanical principles such as speed-dependent gait and energy minimization. This study evaluates the biomechanical fidelity of BFMs against optimal control, imitation learning, and experimental data.

Methods

We trained two BFMs with Forward-Backward representations with Conditional Policy Regularization [1]: a “Task-Agnostic” model (BFM-TA; 8,902 motions including non-locomotor tasks) and a “Task-specific” model (BFM-TS; 1,107 locomotion-only motions). We generated 200 straight-line motions (0.5–5 m/s) in MuJoCo and compared them with an imitation learning model, Adversarial Motion Prior (AMP) [2], an optimal control model (OPT-CTL) [3], and experimental data (EXP) [4–6]. Speed-dependent manifolds for stride length, frequency, and cost of transport were fitted using generalized additive models, and transition speeds were identified from duty factor. Agreement with experimental manifolds was quantified using Spearman’s rank correlation.

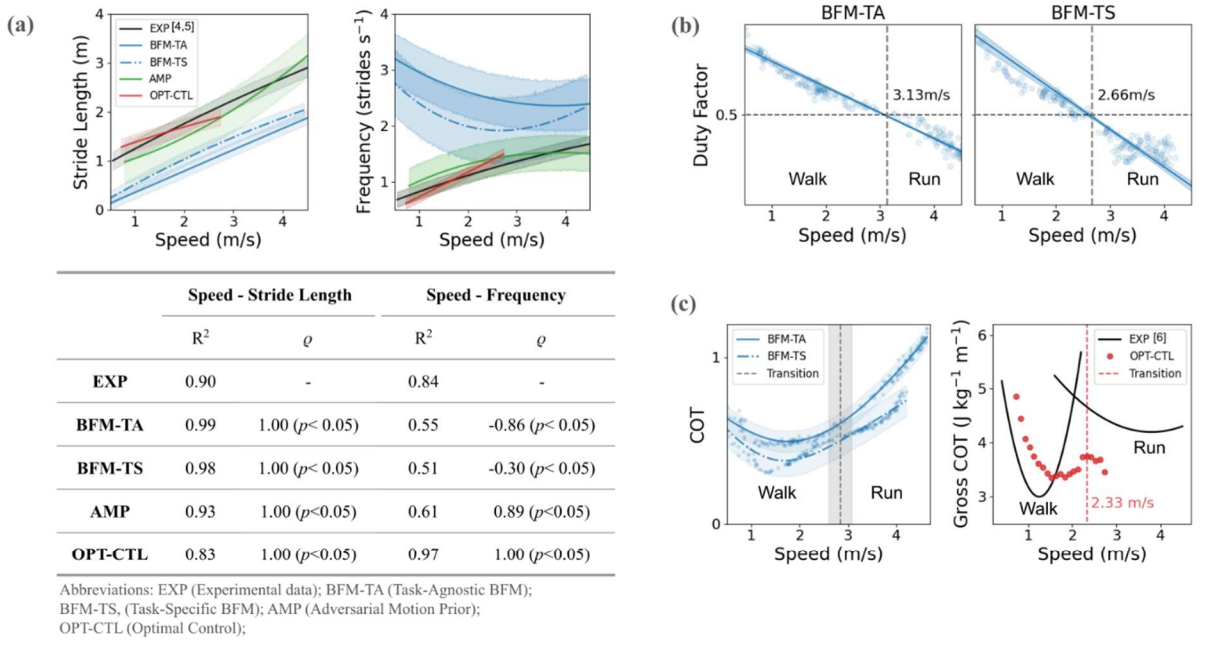
Results

Both BFM variants reproduced the speed–stride length manifold (ρ=1.00, p<0.05) found in human data. However, they failed to capture the speed–stride frequency manifold (BFM-TA: ρ=-0.86; BFM-TS: ρ=-0.30, p<0.05 for both). In contrast, AMP and the optimal control model matched human trends for both manifolds (ρ=~0.90, p<0.05). BFMs overestimated the walk-to-run speed (BFM-TA: 2.66 and BFM-TS: 3.13) compared to the optimal control model (2.33) and failed to replicate the energetic landscape of human locomotion.

Discussion

Our findings reveal a distinction between the ability of BFMs to generate visually plausible locomotion and their ability to capture the underlying biomechanical principles; although BFMs captured the speed–dependent manifold, they failed to reproduce the temporal manifold and energetic landscape. These findings underscore the need to integrate the generative capacity of BFMs with fundamental biomechanical principles to advance next-generation predictive models for biomechanics.

Images (Optional)



	Speed - Stride Length		Speed - Frequency	
	R^2	ϱ	R^2	ϱ
EXP	0.90	-	0.84	-
BFM-TA	0.99	1.00 (p< 0.05)	0.55	-0.86 (p< 0.05)
BFM-TS	0.98	1.00 (p< 0.05)	0.51	-0.30 (p< 0.05)
AMP	0.93	1.00 (p<0.05)	0.61	0.89 (p<0.05)
OPT-CTL	0.83	1.00 (p<0.05)	0.97	1.00 (p<0.05)

Abbreviations: EXP (Experimental data); BFM-TA (Task-Agnostic BFM); BFM-TS, (Task-Specific BFM); AMP (Adversarial Motion Prior); OPT-CTL (Optimal Control);

Figure 1. Benchmarking the locomotor features predicted by BFMs. (a) Speed-dependent manifolds fitted by generalized additive modeling with 2000 bootstrapping (bold lines). Shaded area indicates 95% prediction intervals. The inset table lists the R^2 goodness-of-fit values and Spearman's rank correlation coefficient (ϱ and p-value) with respect to experimental human data. (b) Walk-to-run transition speeds derived from BFMs based on duty factor. The transition speed is identified where a linear fit of speed-duty factor intersected a duty factor of 0.5 (c) Comparison of speed-dependent energetic landscapes across BFMs, the optimal control model, and human experimental data. Unlike human data and the optimal control model, BFMs do not exhibit distinct landscapes for walking and running.

References (Optional)

[1] A. Tirinzoni et al., arXiv, 2025; [2] XB. Peng et al., ToG, 2025; [3] A. Falisse et al., J R Soc Interface, 2019; [4] J. Camargo et al., CMBBE, 2020; [5] C. Clemente et al., Nat Commun, 2024; [6] M. McAllister et al., J Exp Biol, 2025;

Session Category

Emerging Areas: N/A

OA48-03

Smartphone Video–based Estimates of the Knee Extension Moment During Chair Rise Relate to MRI Measures of Muscle Function

Mr. R. Daniel Magruder[1], Dr. Mary Hall[2], Ms. Yael Vainberg[2], Ms. Jessica L. Asay[2], Dr. Jennifer L. Hicks[2], Dr. Scott L. Delp[2], Dr. Garry E. Gold[2], Dr. Valentina Mazzoli[3], Dr. Scott D. Uhlrich[1]

[1]University of Utah, Salt Lake City, Utah, United States. [2]Stanford University, Stanford, California, United States. [3]New York University Langone Health, New York City, New York, United States

Introduction

Preserving muscle function is critical for maintaining mobility, balance, and independence as we age [1]. However, muscle function is not routinely assessed clinically due to a lack of accessible, sensitive tools. Muscle volume and quality both contribute to its force-generating capacity [2]. MRI provides high-fidelity measures of muscle volume and quality, while dynamometry quantifies maximum voluntary joint torque production. Both modalities are costly, so low-fidelity tests, like the five times sit-to-stand [5xSTS], are used in clinical studies instead [3]. Here we evaluate whether OpenCap, a scalable smartphone video–based tool for estimating musculoskeletal dynamics [4], during 5xSTS is sensitive to muscle volume and microstructure from MRI.

Methods

We collected MRI of the quadriceps, isometric and isokinetic dynamometry, and 5xSTS time with concurrent OpenCap from healthy adults across the lifespan (n=19, 30–78 y). We computed quadriceps volume and radial diffusivity (relates to fiber size) from MRI. We computed the peak knee extension moment from OpenCap during chair rise, and from isometric and isokinetic (120°/s, concentric) dynamometry. We compared OpenCap, 5xSTS time, and dynamometry to MRI measures of muscle function using linear regression.

Results

The OpenCap-derived knee extension moment correlated with quadriceps volume (r=.63, p=.004), radial diffusivity (r=.61, p=.005), and a combined metric ($volume_{standardized} \cdot$ radial $diffusivity_{standardized}$; r=.77, p<.001). Isokinetic torque correlated with volume (r=.66, p=.002), radial diffusivity (r=.52, p=.023), and the combined metric (r=.73, p<.001); isometric torque correlated with volume (r=.75, p<.001), but not radial diffusivity (r=.04, p=.862). 5xSTS time and a kinematic compensation for quadriceps weakness (torso orientation) were not correlated with MRI features (r=-.16–.35, p=.14–.97).

Discussion

Joint moments—measured with OpenCap or isokinetic dynamometry—predict aspects of muscle size and microstructure, unlike time or kinematic features. OpenCap smartphone video–based kinetics are a scalable assessment of muscle force-generating capacity that can be conducted rapidly without specialized equipment. This enables assessment of muscle function in the clinic and large-scale studies where imaging and dynamometry are impractical.

Images (Optional)

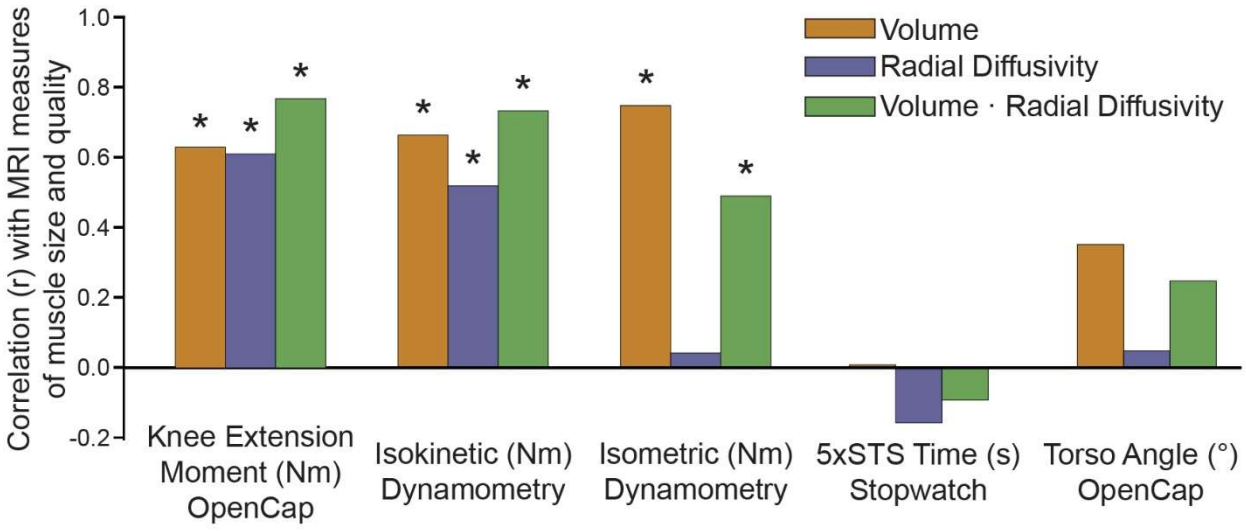


Figure 1: Pearson correlation coefficients relating biomechanical measures of quadriceps function to MRI measures of muscle force-generating capacity. The sit-to-stand knee extension moment (KEM) estimated by OpenCap correlates with quadriceps volume, radial diffusivity, and a combined metric ($volume_{standardized}$ · $radial\ diffusivity_{standardized}$). Isokinetic dynamometry has similar relationships to MRI, while the clinical standard five times sit-to-stand time did not correlate with any MRI measures. * denotes $p<.05$

References (Optional)

[1] dos Santos *et al.*, *J Cachexia, Sarcopenia & Muscle*, 2016. [2] Goodpaster *et al.*, *J Applied Physiology*, 2001. [3] Cruz-Jentoft *et al.*, *Age & Aging*, 2019. [4] Uhlrich *et al.*, *PloS Comp Bio*, 2023.

Session Category

Emerging Areas: N/A

OA48-04

Mind the Gaps: Robustness of DNN Ankle Joint Angle Prediction Models to Unexpected Sensor Flatlines

Mr. Ryan Pollard, Ms. Jacquelyn Brokamp, Mr. Matheus Ferreira-Shornack, Dr. Roberto Molinari, Dr. Ivan Nail-Ulloa, Dr. Michael Zabala

Auburn University, Auburn, AL, United States

Introduction

Despite promising results for deep neural network (DNN)-based lower-limb kinematic prediction, these models' robustness to sensor loss during deployment is unclear, raising uncertainty about the effectiveness and safety of their use in real-world exoskeleton control. In real-time settings, wearable sensor disconnection or detachment often manifests as data flatlined at the last known value. Thus, this study investigates the effect of flatlined wearable sensor data on DNN model performance and proposes a simple, sensor-agnostic training modification to mitigate the effect of erroneous sensor input on ankle joint angle prediction.

Methods

Data from eleven lower-limb biomechanical sensors (three accelerometers, three gyroscopes, three electromyography sensors, and two goniometers) from 21 participants performing five unique actions (walking, ramp ascent/descent, and stair ascent/descent) were extracted from a *Journal of Biomechanics* open-source dataset [1]. Nine Long Short-Term Memory (LSTM) models were trained to predict sagittal-plane ankle angles at a t_{hzn} = 200 ms prediction horizon, each model being informed by a unique subset of the eleven wearable sensors. Each LSTM model was trained while intermittently simulating that $0 \leq N_{dropped,train} \leq 3$ random sensors were flatlined for each input window (i.e., sensor data replaced by a random constant value within the sensor's recorded range). Model performance was then evaluated on a held-out dataset where $0 \leq N_{dropped,test} \leq 3$ sensors were randomly simulated as flatlined.

Results

No matter the number of sensors flatlined during training (i.e. $N_{dropped,train}$), LSTM model performance degraded as the number of flatlined sensors during testing (i.e. $N_{dropped,test}$) increased ($p < 0.001$). However, performance robustness to flatlined sensor data during testing improved as the number of flatlined sensors increased during training ($p < 0.001$).

Discussion

The results indicate that, during model testing, flatlined sensor data is significantly detrimental to model performance, posing a limitation to LSTM-based model implementation in practice. However, purposeful intermittently flatlined sensor data during LSTM model training ($N_{dropped,train} > 0$) was shown to improve model performance robustness during flatlined sensor test. Thus, LSTM joint angle prediction models may benefit from intermittently flatlining sensor data during training to ensure robustness to sensor failure during deployment.

Images (Optional)

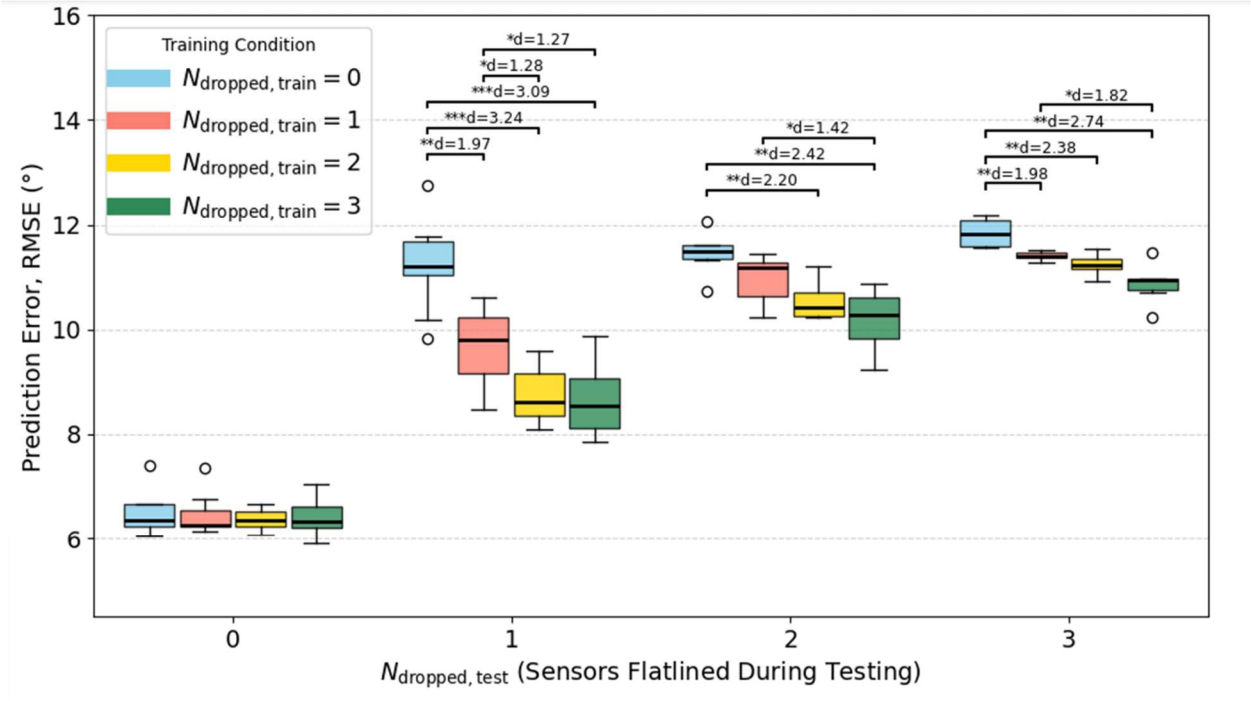


Figure 1: *Ankle joint angle prediction error of LSTM models as a function of flatlined sensor data during both training (legend, unique box-plot colors) and testing (horizontal axis).*

References (Optional)

[1] Jonathan Camargo *et al.,* J Biomechanics, 2021.

Session Category

Emerging Areas: N/A

OA48-05

Large Movement Models: Transformer-Based Models of Individual Movement in the Real World Using Data From Consumer Headphones

Dr. Alexandra Hammerberg[1,2], Dr. Samuel Grunblatt[3,1], Dr. Patricia Kramer[4]

[1]hominin labs, Seattle, WA, United States. [2]European Society of Biomechanics, London, London, United Kingdom. [3]University of Alabama, Tuscaloosa, AL, United States. [4]University of Washington, Seattle, WA, United States

Dr. Alexandra Hammerberg

Dr. Samuel Grunblatt

Introduction

Developing AI solutions that leverage existing wearable technology such as Apple AirPods or other body-worn devices to understand unconstrained walking mechanics in individuals has been a goal since this data became available, but few models address the hierarchical nature of real-world motion data and even fewer incorporate data that contextualize real-world gait mechanics such as environmental conditions. In this work we propose a novel foundation model for human movement - a Large Movement Model (LMM): a nested hierarchical and flexibly multimodal transformer-based model of individual human movement in the real world.

Methods

We utilize data from existing inertial measurement unit (IMU) sensors embedded in spatial audio-enabled headphones. Like genetic sequencing, the individual's gait pattern can be discerned by decomposing the movement signal into its fundamental features in each coordinate direction, forming the backbone of the LMM. At each layer, multimodal features (e.g., environmental conditions) are fused prior to passing through the transformer. Each layer of the model builds upon the outputs from the prior layer as initial embeddings, following a characters -> words -> sentences convention. We evaluate the LMM using a previously collected dataset consisting of AirPod Pro IMU data from 17 adults (age: 18 - 67 years, 11F) without known pathology walking outside normally and while wearing orthopaedic braces to simulate gait pathology.

Results

We found that our model outperformed a basic multilayer perceptron (MLP) neural net in identifying normal vs non-normal walking at the level of the individual (MLP: 62.4%, LMM: 76.7%). The individual-level model also outperformed the population-level model (Population: 73.6%).

Discussion

By 2050, 22% of the global population will be over the age of 60 with greater than 40% risk of developing life-altering neuromusculoskeletal pathologies. The potential of wearables to provide personalized preventative and predictive health monitoring outside of the clinic is nascent, but large quantities of open-ended data that capture movement in the physical world now exist. We demonstrate that by designing an AI model with architecture informed by the structure of the system, LMMs have the potential to expand on-body monitoring at scale.

Session Category

Emerging Areas: N/A

OA49-02

Age-Related Changes in Spinal Load Distribution: Predictive Simulation of Active Spine Movements

Dr. Maria Hammer[1], apl. Prof. Dr. Patrick Strube[2], Prof. Dr. Matthias Woiczinski[1]

[1]Experimental Orthopedics, University Hospital Jena, Campus Eisenberg, Jena/ Eisenberg, Thüringen, Germany. [2]Spine Department, University Hospital Jena, Campus Eisenberg, Jena/ Eisenberg, Thüringen, Germany

Introduction

Age-related changes in the spine often lead to instability, altered movement patterns, and degenerative conditions, whose mechanical origins remain partly unclear. At the same time, surgical interventions in older adults show limited success, with revision rates reaching up to 30%. Biomechanical simulations could support preoperative planning but currently poorly capture the complex, age-dependent load distributions - particularly during dynamic active movements. Therefore, we developed an aged spine model to quantify changes in spinal load distribution in elderly people using predictive, muscle-driven simulations.

Methods

A population-based multibody spine model of a healthy young male, which is fully articulated and includes detailed musculature and ligament structures, was further enhanced based on [1,2]. Age-related biomechanical alterations in the intervertebral discs, ligaments, muscles, and facet joints were implemented using reported data by adjusting soft tissue stiffnesses, muscle cross-sectional areas, prestrains, and other geometric and mechanical parameters to correspond to a biological age of 60 years. By varying spinopelvic parameters, four anatomical variations were derived. For each model, muscle, ligament, disc, and facet joint forces were quantified in predictive simulations [1] of flexion–extension, lateral bending, and axial rotation, and subsequently compared with corresponding values obtained from young spine models.

Results

The results indicate a reduced stiffness of the lumbar segments and increased global instability in the upright posture when considering aging effects in all soft tissue compartments including muscle atrophy. We observe increased disc forces during active forward bending, as well as elevated facet joint forces, particularly during lateral bending.

Considering degeneration of isolated tissue elements shows the counteracting mechanism of ligament stiffening (see Fig. 1) leading to a reduced flexibility and range of motion. In general, the magnitude and location of these effects vary substantially with individual spinal curvature.

Discussion

The simulation results are consistent with experimental and clinical findings and provide deeper insight into the biomechanical load distribution in aged spines during daily-life movements. The large impact of spinopelvic parameters highlights the importance of a patient-specific assessment. Predictive simulations could therefore assist in identifying individual mechanical risk factors.

Images (Optional)

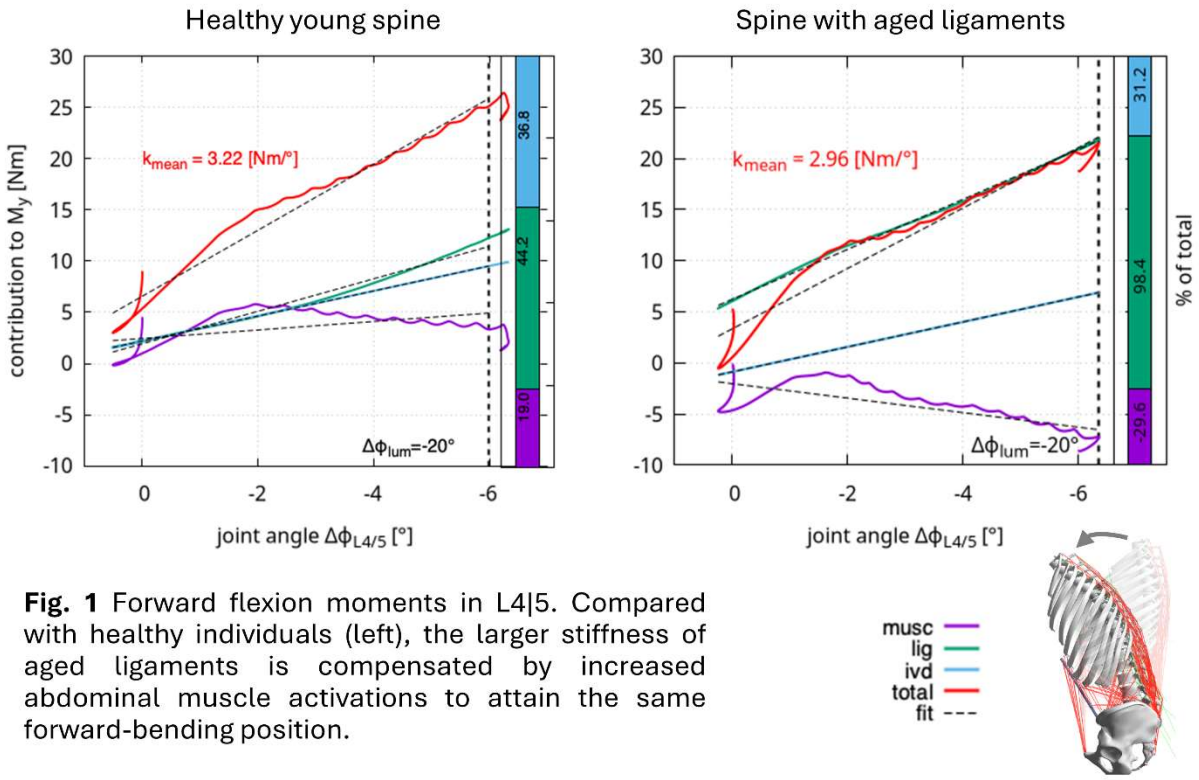


Fig. 1 Forward flexion moments in L4|5. Compared with healthy individuals (left), the larger stiffness of aged ligaments is compensated by increased abdominal muscle activations to attain the same forward-bending position.

References (Optional)

[1] Meszaros-Beller et al., BMMB, 22(2):669-694, 2023.

[2] Hammer et al., DaRUS, 2022. https://doi.org/10.18419/DARUS-2814

Session Category

OA49-03

Automated Workflow of Vertebral Finite Element Models: Impact of Coordinate Systems and Boundary Conditions on Fracture Load

Mr Daniel Strack[1], Ms Sara Amenini[1,2], Prof Nico Sollmann[3,4,5,6], Prof Jan S. Kirschke[3], Prof Dario Gastaldi[2], Prof Karupppasamy Subburaj[1]

[1]Aarhus University, Aarhus, Central Denmark Region, Denmark. [2]LaBS - Department of Chemistry, Materials and Chemical Engineering "Giulio Natta", Politecnico di Milano, Milan, Lombardy, Italy. [3]Department of Diagnostic and Interventional Neuroradiology, School of Medicine and Health, TUM Klinikum Rechts der Isar, Technical University of Munich, Munich, Bavaria, Germany. [4]TUM-Neuroimaging Center, TUM Klinikum Rechts der Isar, Technical University of Munich, Munich, Bavaria, Germany. [5]Department of Diagnostic and Interventional Radiology, University Hospital Ulm, Ulm, Baden-Württemberg, Germany. [6]Department of Nuclear Medicine, University Hospital Ulm, Ulm, Baden-Württemberg, Germany

Introduction

Patient-specific finite element (FE) models derived from clinical CT can support vertebral fracture risk assessment, but their translation into routine care remains limited by the time-consuming manual tasks, including the definition of vertebral coordinate systems (CYS) and boundary conditions (BC). Because, loading direction and BC specification can substantially influence output [1], robust automation is needed. This study evaluated whether an automatic, standardized CYS and BC setup yields vertebral fracture load predictions comparable to those defined by experts.

Methods

Twenty vertebrae (10 thoracic, 10 lumbar) from an ongoing clinical study were used to generate CT-based FE models and applied density–elasticity material mapping. In the reference condition, an experienced operator manually defined the vertebral CYS and applied compression BC. The automatic pipeline [2] determined vertebral axes from geometric extreme points and extracted superior and inferior endplates using normal vectors of the elements, applying Gaussian and median filtering. From these, standardized compression BC was applied.

Three configurations were compared with the manual reference: (1) automated BC only (BC), (2) automated CYS only (CYS), and (3) fully automated CYS+BC (Auto). Agreement in FL was evaluated using linear regression (R^2) and Bland–Altman bias.

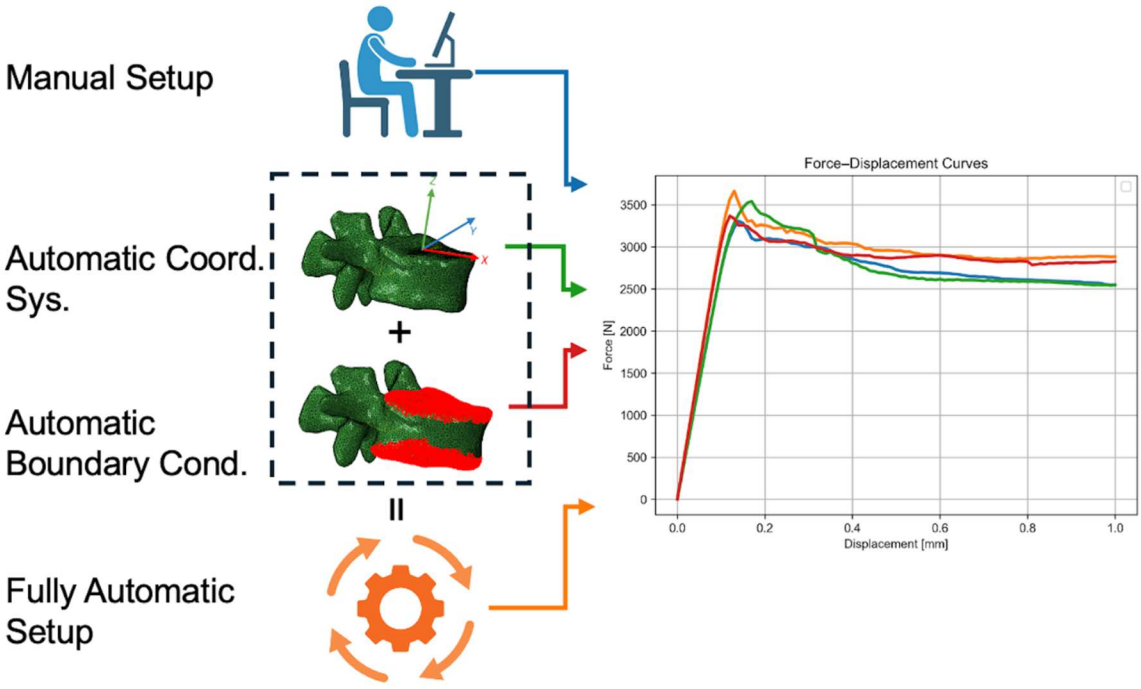
Results

All automated configurations showed excellent correlation with the manual reference ($R^2 >$ 0.97; BC: 0.98; CYS: 0.978; Auto: 0.971). Bland-Altman analysis revealed the smallest mean bias for CYS (31 N), followed by BC (230 N) and Auto (308 N).

Discussion

Both partially and fully automated setups preserved vertebral FL predictions with high agreement with manual expert models. However the automated setup was approximately 20 times faster than the manual process. The smallest bias observed for CYS suggests that modest variations in loading direction exerted a limited influence on FL in this cohort, whereas BC definition contributed more substantially to deviations. Ongoing work will expand the dataset and quantify how specific CYS and BC discrepancies propagate to FL, with the goal of establishing clinically robust and scalable automation strategies.

Images (Optional)



References (Optional)

[1] Jonah Dimnik et al., Bone, 2025

[2] Sara Amenini, Masterthesis Polimi, 2025

Acknowledgements (Optional)

This research was supported by the Aarhus University Research Foundation under the grant AUFF-E-2022-7-12 (Karupppasamy Subburaj).

Session Category

Orthopaedic Biomechanics: Spine

OA49-04

How Treatment Therapies Shape Mechanics in Osteoporotic Vertebral Fracture Repair: A Computational Study

Dr Robert Johnston[1], Dr Ciara Murphy[1,2,3]

[1]Tissue Engineering Research Group, Department of Anatomy & Regenerative Medicine, Royal College of Surgeons (RCSI), Dublin, Ireland, Ireland. [2]Trinity Centre for Biomedical Engineering, Trinity College Dublin, Dublin, Ireland, Ireland. [3]Advanced Materials and Bioengineering Research Centre (AMBER), RCSI and TCD, Dublin, Ireland, Ireland

Introduction

Osteoporotic vertebral fractures are the most common complication of osteoporosis and are often treated with PMMA-based vertebroplasty or kyphoplasty, but PMMA's stiffness mismatch can alter spinal biomechanics, causing stress shielding and adjacent fractures. Tunable hydrogels may offer a stabilization and regenerative alternative. This study uses finite element analysis to evaluate how PMMA and hydrogels influence lumbar stress distribution under biomechanically realistic loading conditions, aiming to guide improved treatment strategies.

Methods

T2-weighted spine MRI scans were segmented in 3D Slicer to isolate the L2–L4 vertebrae and discs using intensity-based thresholding, followed by smoothing, see Fig. 1A. The segmented geometry was exported to Abaqus as an IGES file, partitioned, and meshed in Abaqus CAE with C3D8H hexahedral elements. Material sections were assigned for healthy, osteoporotic, PMMA-treated, and hydrogel-treated models, see Fig.1B. Six biomechanical movements were simulated (flexion, lateral flexion, compression, lateral bending, extension, rotation) by constraining L4 and applying displacement or rotation to L2. Loads were 500N, 1000N, 500N, 10Nm, 20Nm, and 10Nm, with penalty contact (μ=0.1), see Fig.1C.

Results

Across all simulated loading conditions, osteoporotic vertebrae showed higher peak von Mises stresses (57.37, 33.06, 35.97, 30.06, 79.12, 58.45 MPa) and a greater bone volume exposed to elevated stress than healthy vertebrae (47.65, 15.06, 21.24, 16.28, 73.18, 47.42 MPa) , see Fig.1D-E. PMMA treatment reduced stress at the implant site but increased high-

stress volumes in adjacent vertebrae. In contrast, the stiffest hydrogel increased stress locally at the implant site while reducing stress transmission to adjacent levels, lowering the proportion of bone in higher stress bands, see Fig.1E. Although this suggests improved stress mitigation, the hydrogel may lack sufficient structural strength for fracture stabilization. Notably, the stiffest hydrogel did carry measurable internal stresses, indicating active participation in load transfer.

Discussion

Osteoporotic bone exhibits elevated stress levels, PMMA further increases loading in adjacent vertebrae, while the stiff, high-volume hydrogel formulation effectively participates in load transfer under biomechanically relevant loading. The findings demonstrate that treatment choice significantly alters lumbar stress distributions and offer a strong foundation for developing improved, patient-specific devices and biologically informed therapies that preserve spinal biomechanics, reduce secondary fracture risk, and enhance long-term clinical outcomes.

Images (Optional)

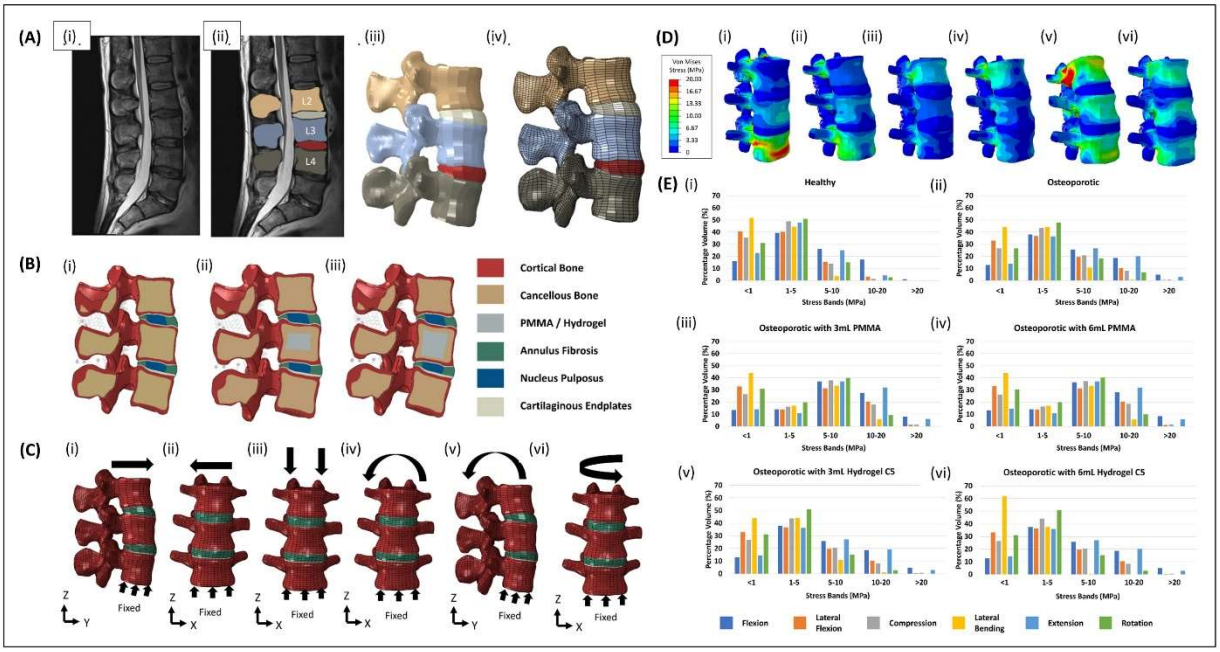


Fig 1: (A) L2-L4 lumbar segment created from in-vivo MRI images and subsequently meshed for finite element analysis (B) Material property assignment for the lumbar segment for (i) healthy, osteoporotic and (ii-iii) treatment therapies of two volumes respectively (C) Implemented boundary conditions for (i) flexion (ii) lateral flexion (iii) compression (iv) lateral bending (v) extension and (vi) rotation (D) Finite element simulations of a healthy lumbar segment undergoing (i) flexion (ii) lateral flexion (iii) compression (iv) lateral bending (v) extension and (vi) rotation (E) Percentage volume of stress plots of the L2-L4 lumbar vertebrae under 6 biomechanical loading conditions (i) Healthy (ii) Osteoporotic (iii) Osteoporotic with 3mL PMMA (iv) Osteoporotic with 6mL PMMA (v) Osteoporotic with 3mL Hydrogel C5 (vi) Osteoporotic with 6mL Hydrogel C5

References (Optional)

Acknowledgements (Optional)

This study is funded by the European Research Council (ERC) under the consolidator grant agreement GAP-101125820 (RESTORE). Views and opinions expressed are however those of the author(s) only and do not necessarily reflect those of the European Union or the European Research Council. Neither the European Union nor the granting authority can be held responsible for them. It has been stated by the ERC that this should be included in acknowledgement of ERC funding.

Session Category

Orthopaedic Biomechanics: Spine

OA49-05

Multiscale Investigation of Spinal Fixation Failure Risk: The Interplay Between Global Alignment and Local Bone Properties

PhD Student Sara Panero[1,2], Dr. Simone Borrelli[1,2], Dr. Giovanni Putame[1,2], Prof. Alberto Audenino[1,2], Prof. Mara Terzini[1,2], Dr. Alessandra Aldieri[1,2,3]

[1]PolitoBIOMed, Politecnico di Torino, Turin, Piedmont, Italy. [2]Department of Mechanical and Aerospace Engineering, Politecnico di Torino, Turin, Piedmont, Italy. [3]Department of Industrial Engineering, Alma Mater Studiorum - University of Bologna, Bologna, Emilia Romania, Italy

Introduction

At present, the interplay between biomechanical factors across spatial scales remains poorly investigated when assessing implant failure risk [1]. This study proposes an integrated multibody-finite element pipeline connecting global spinal alignment and local bone quality to improve implant loosening prediction.

Methods

Subject-specific multiscale models of the T12-S1 segment were generated from CT scans of six female subjects,with different lumbar lordosis (LL: [38.7°,67.6°]) and bone quality (T-score: [-3.6,1.1]). Assuming an L3 fracture, three titanium implant fixations were modelled for each subject (long-segment, Lf: L1-L2-L4-L5 and short-segment, Sf4: L2-L4, Sf6: L2-L3-L4).

For MB simulations, rigid vertebrae were connected via nonlinear bushings [2]. Rods deformability was described through modal analysis and screw stiffness derived from cantilever beam theory (Figure 1a). Follower loads accounted for muscle contribution. The sacrum was fully constrained, and pure moments were applied on T12 within Cone of Economy range of motions.

FE analyses were performed on L4 applying MB outputs as boundary conditions. Material properties were mapped element-wise from CT-derived HU [3]. A bonded contact at the screw-bone interface was implemented, and principal stress values at the bone were considered to investigate the regions at greater risk.

Results

At this stage, simulations were performed on the three spine models. Long and short fixations were compared, showing the outer instrumented vertebrae experiencing higher pull-out and shear forces, whereas the central vertebrae were comparatively shielded (~24% less). No clear dependence between spinal alignment and maximum shear forces at the pedicle screws emerged (Figura1b). Small deviations were observed on the L4 screws during axial rotation (~4%), whereas a linear trend was observed under lateral bending, the resulting worst-case scenario. Stress distribution (Figure 1c) appeared to be influenced by T-score, with the highest peaks occurring at the screw-bone interface and along the pedicles of osteoporotic vertebrae.

Discussion

Further analyses will be conducted on the entire cohort to refine preliminary results and achieve a multiscale understanding of how microscale and joint-level parameters contribute to implant stability and failure risk.

Images (Optional)

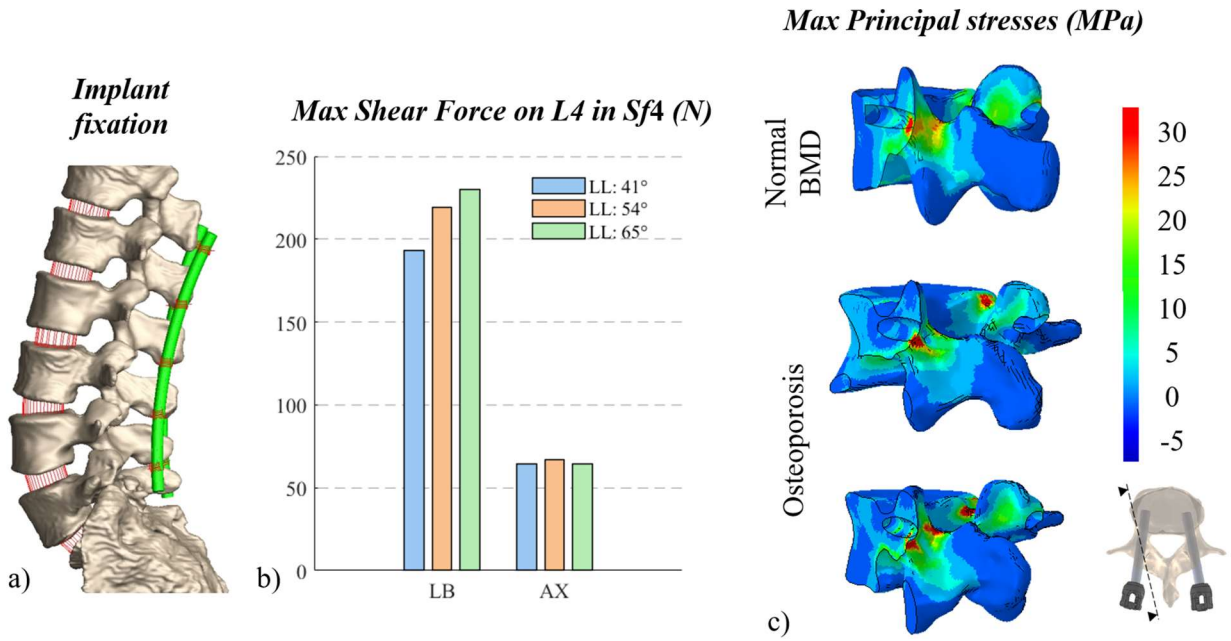


Figure 1: a) Example of implant-fixation; b) Comparison of maximum shear forces at L4 in subjects with increasing lordosis and c) maximum principal stress distribution for different T-scores

References (Optional)

[1] Fasser M.R. et al, Eur Spine J, 2022

[2] Zhang C. et al., J. Biomech., 2020

[3] Szyszko J.A. et al., PLoS ONE, 2024

Session Category

Orthopaedic Biomechanics: Spine

OA50-01

Two-Photon Subtractive Manufacturing of Mesoscale Porosity for Structure-Function Optimization of Electrospun Vascular Grafts

Ms. Tiffany Moreno[1], Ms. Colleen OMalley[1], Mr. Brock Pemberton[1], Mr. Markus Boettcher[2], Dr. William Wagner PhD[1,3,4], Dr. Jonathan Vande Geest PhD[1,5]

[1]Department of Bioengineering, University of Pittsburgh, Pittsburgh, PA, United States. [2]Miltenyi Biotec B.V. and Co. KG, Bielefeld, NRW, Germany. [3]Department of Surgery, University of Pittsburgh, Pittsburgh, PA, United States. [4]Department of Chemical Engineering, University of Pittsburgh, Pittsburgh, PA, United States. [5]Vascular Medicine Institute, University of Pittsburgh, Pittsburgh, PA, United States

Introduction

Small diameter tissue engineered vascular grafts (TEVGs) often fail from early thrombosis and late intimal hyperplasia, due to limited vascular smooth muscle cell (VSMC) infiltration and inadequate tissue remodeling. Introducing mesoscale porosity (50–250 μm) has been proposed to facilitate cell migration, however, existing fabrication approaches, including salt-leaching and thermally induced phase separation, often lack geometric precision, limited control over pore size, spacing, and distribution. The objective of this study was to develop and characterize a two-photon (2P) laser subtractive manufacturing approach to introduce tunable pore architectures into electrospun scaffolds for TEVG applications.

Methods

Electrospun PCL/PLCL sheets were fabricated from a 10% (w/v) solution in HFP using a high-voltage system (15 kV, 10 μL/min) on a 9 cm rotating mandrel (300 rpm), producing 90 μm sheets. Four binary templates (Gradient I, Gradient II, Stent Mesh, Dodecagon Mesh) were generated in MATLAB to test cutting precision across varying complexities and applied via two-photon subtractive manufacturing (Miltenyi Biotec) with an Olympus XL Fluor 4× objective, creating 10–260 μm pores. Images were analyzed using thresholding, artifact filtering, and DICE coefficient calculation.

Results

Two-photon manufacturing generated pores 10–260 μm with high geometric fidelity (DICE 0.74–0.95). As shown in Figure 1, overlays of design masks (magenta) and 2P cuts (green) illustrated alignment quality, with higher DICE indicating stronger overlap. Welch's ANOVA ($n = 4$/group) revealed significant differences in DICE values ($p < 0.05$), with Gradient I

showing highest accuracy and Gradient II lowest. Coefficient of variation indicated repeatability, with Gradient II most variable and Gradient I least variable. These results demonstrate reliable patterning performance for evaluating structure function relationships.

Discussion

Two-photon subtractive manufacturing reliably produces mesoscale pore architectures with high fidelity and reproducibility across varying pattern complexities, enabling controlled investigation of how geometry influences cell infiltration. Variability between templates highlights the importance of pattern selection in TEVG design. This method supports engineering pore architectures tailored to biological and mechanical needs. Current work with these two-photon cut sheets focuses on forming tubular graft-like constructs and matching their compliance to native arteries, as compliance mismatch influences hemodynamic stress and contributes to small-diameter graft failure.

Images (Optional)

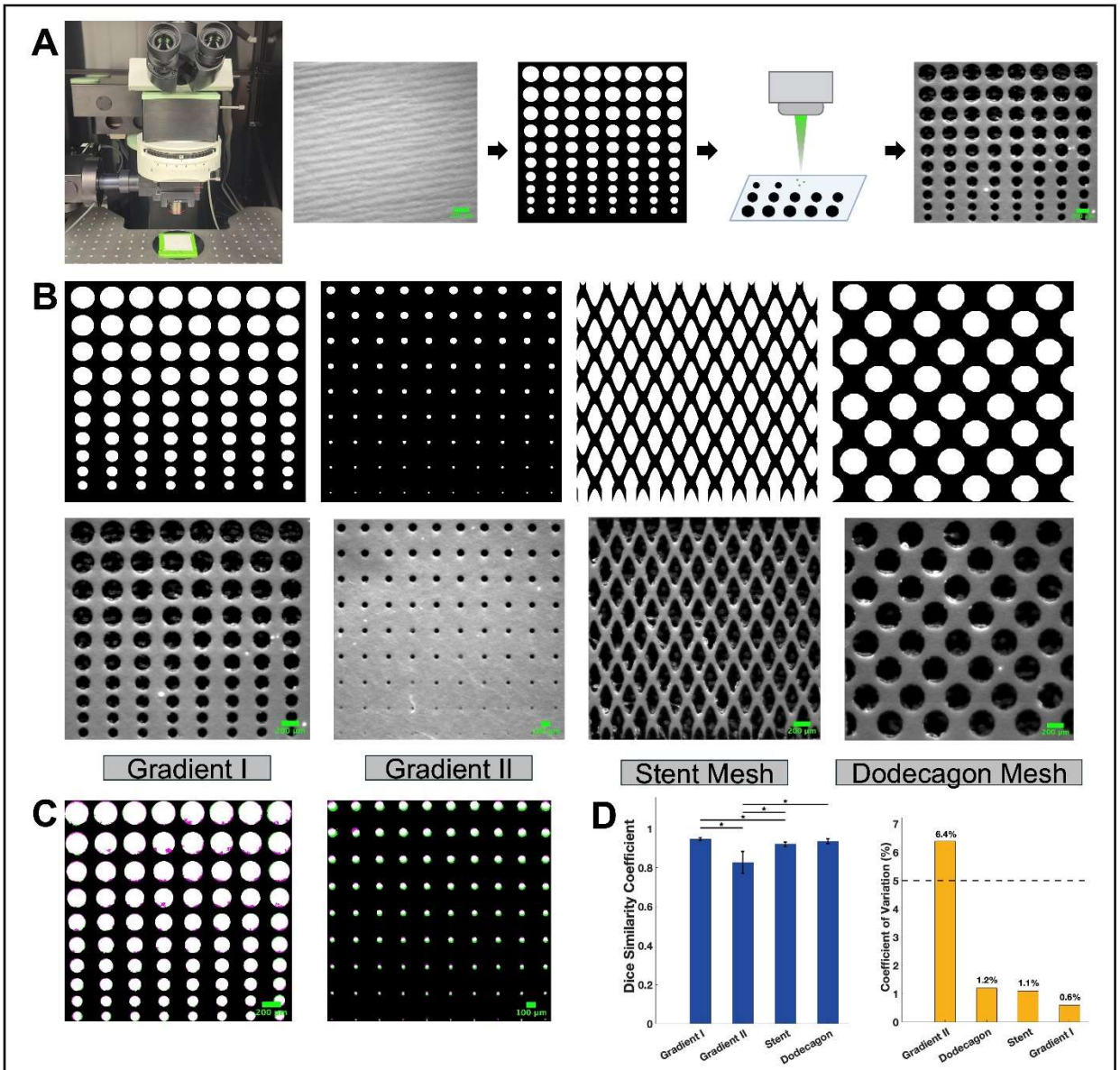


Figure 1: **(A)** Two-photon workflow (scale bar = 200um). **(B)** ***(top)*** Binary masks; ***(Bottom)*** respective two-photon cut images (Gradient I, Stent Mesh, and Dodecagon Mesh scale bar = 200um, Gradient II scale bar = 100um). **(C) DICE visualization:** Overlay of design mask (magenta) and 2P cut (green). ***(Left)*** High DICE (0.95) shows strong alignment; ***(Right)*** Low DICE (0.74) shows mismatch. DICE = spatial overlap (1 = perfect). **(D)** ***(Left)*** Welch's ANOVA (n = 4 per group) revealed significant differences in Dice similarity coefficients ($p < 0.05$); ***(Right)*** CV highlights repeatability; Gradient II is most variable.

References (Optional)

Acknowledgements (Optional)

This research was funded by NIH R01 (HL157017), NIH Diversity Supplement (3R01HL157017-03S2), and NIH T32 (T32HL076124) Cardiovascular Bioengineering Training Program.

Session Category

Tissue Engineering: Methods, Models and Applications

OA50-02

Digital Light Processing (DLP) 3D Printing of β-TCP/PDLLA-co-TMC Nanocomposite Scaffolds for Bone Tissue Engineering

Miss Yujie Zhang, Dr. Xiaodie Chen, Prof. Min Wang

The University of Hong Kong, Hong Kong, Hong Kong, Hong Kong

Miss Yujie Zhang

Dr. Xiaodie Chen

Introduction

Bone tissue engineering (BTE) scaffolds, which combine mechanical integrity, bioactivity and controlled biodegradation, promote new bone formation in human bodies. Digital light processing (DLP) 3D printing can produce complex BTE scaffolds. β-tricalcium phosphate (β-TCP) is a biodegradable bioceramic with good osteoconductivity and hence often used in BTE. Combining β-TCP with biodegradable poly(D,L-lactide-co-trimethylene carbonate) (PDLLA-co-TMC) polymer can balance biological and mechanical properties and produce shape-morphing scaffolds for BTE. In this study, a β-TCP/PDLLA-co-TMC composite printing ink system was established and inks were optimized for DLP 3D printing. DLP 3D printed composite scaffolds were subsequently assessed.

Methods

Printing inks were made by dissolving PDLLA-co-TMC in acetone, followed by adding PEGDA-600 as crosslinker. β-TCP nanoparticles were dispersed in PDLLA-co-TMC solutions at 5, 10, 15, 20 vol% loading. LAP and curcumin were photoinitiator and photoabsorber, respectively. Curcumin-Na served as a free radical inhibitor. BTE scaffolds were 3D printed on a DLP printer. Printed composite scaffolds were characterized using various techniques. Cytocompatibility was assessed using MC3T3-E1 cells through live/dead staining and CCK-8 assay.

Results

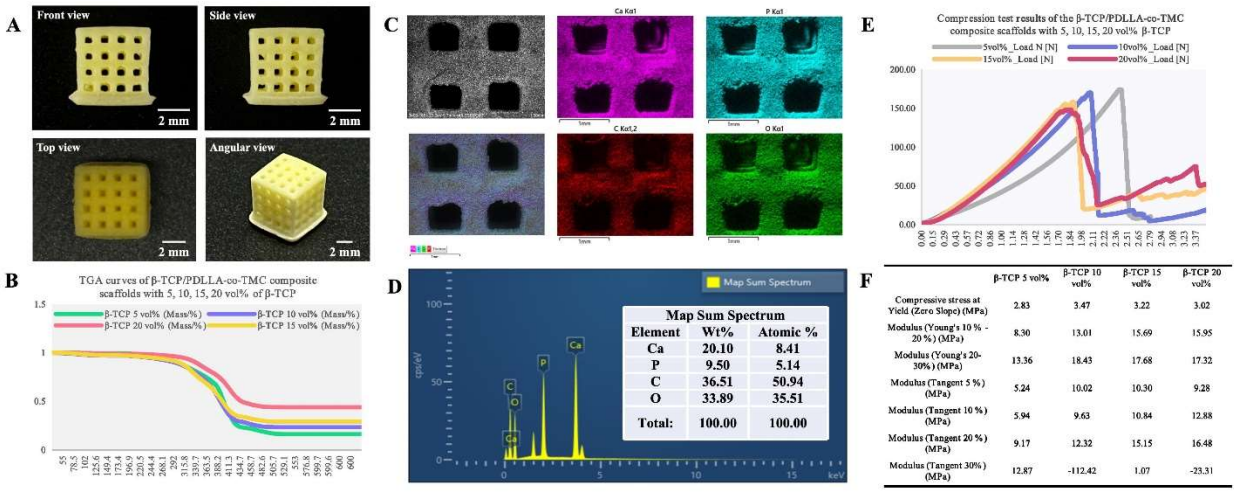
Optimized printing inks containing 5, 10, 15, and 20 vol% β-TCP exhibited viscosities, which increased with increasing β-TCP loading, suitable for layer-by-layer printing in DLP

processes. Take the 10 vol% β-TCP formulation for example. DLP successfully produced scaffolds with high dimensional fidelity and uniform pore morphology (pore sizes of 800, 600 and 400 μm, with porosities of 55.4%, 41.7% and 27.9%, respectively). The compressive strength of β-TCP/PDLLA-co-TMC scaffolds with 5, 10, 15 and 20 vol% β-TCP reached 2.83, 3.47, 3.22 and 3.02 MPa, which are within the range for human cancellous bone (2–12 MPa), indicating their suitability for BTE. MC3T3-E1 cells cultured on composite scaffolds exhibited well-spread morphology and good biocompatibility. They showed increased proliferation over the 7-day culture period.

Discussion

This study showed feasibility of formulating suitable inks for DLP 3D printing of β-TCP/PDLLA-co-TMC scaffolds and also their high-fidelity printing via DLP. Like other composite scaffolds for BTE, the bioceramic content affected mechanical and biological properties of β-TCP/PDLLA-co-TMC scaffolds.

Images (Optional)



(A) A β-TCP/PDLLA-co-TMC composite scaffold (10 vol% of β-TCP) with 600 μm pore size made by DLP 3D printing.
(B) TGA curves of β-TCP/PDLLA-co-TMC scaffolds with 5, 10, 15, 20 vol% of β-TCP, confirming β-TCP contents in the composite scaffolds.
(C) An SEM image showing the porous structure of a β-TCP/PDLLA-co-TMC scaffold (10 vol% of β-TCP, with 600 μm pore size) and element distribution maps for Ca, P, C and O in the scaffold as determined by energy-dispersive X-ray spectroscopy (EDS).
(D) Summary of the EDS element analysis results for the β-TCP/PDLLA-co-TMC scaffold (10 vol% of β-TCP, with 600 μm pore size).
(E) Selected compression test stress-strain curves for β-TCP/PDLLA-co-TMC composite scaffolds with 5, 10, 15, 20 vol% of β-TCP.
(F) Mechanical properties of β-TCP/PDLLA-co-TMC composite scaffolds with 5, 10, 15, 20 vol% of β-TCP.

Session Category

Tissue Engineering: Methods, Models and Applications

OA50-03

Biosourced Molecules as Photoinitiators for Light-Based 3D Printing of Tunable Biomaterials

Ms. Hailey McCoy-Munger, Dr. Kristan Worthington

University of Iowa, Iowa City, Iowa, United States

Introduction

Two-photon polymerization (TPP) is a high-resolution additive manufacturing technique uniquely suited for biomaterial fabrication due to its inherent spatial and temporal control. Unfortunately, many common TPP resins are cytotoxic and key material properties such as stiffness are difficult to predict and control. However, using bio-sourced molecules and exploiting TPP printing parameters may address these challenges. Here, we present a cytocompatible TPP resin that employs curcumin as a photoinitiator for polyethylene glycol dimethacrylate (PEGDMA) to fabricate biomaterials with tunable stiffnesses.

Methods

Prepolymer solutions comprising curcumin (18 mM) in 550 Mn PEGDMA were used for TPP using a Nanoscribe Photonic Professional GT. Cuboid (25 x 25 x 5 μm) arrays were created using three laser powers (LP; 80, 90, 100%) and scanning speeds (SS; 70, 85, 100 mm/sec). A complex structure with void features <20 μm was also printed to demonstrate scale-up feasibility. Cuboid arrays were sterilized in 70% ethanol, laminin coated, and seeded with primary human dermal fibroblasts (HDFs). Cell viability was assessed after 24 hours using a live/dead assay (n=3). Stiffnesses (DMT modulus) of cuboids printed at select parameters were measured using atomic force microscopy. Differences in moduli (n=3) were determined using a one-way ANOVA with subsequent Tukey's test.

Results

Cuboids printed effectively at all combinations of LP and SS (Fig. 1A). HDFs seeded on the TPP structures maintained high viability (> 80%) across all printing conditions (Fig. 1B-C). The PEGDMA-curcumin resin could also form more complex, high-resolution TPP structures (Fig. 1D). At 80% LP, DMT modulus varied significantly with SS (Fig. 1E). However, changing SS did not significantly change the stiffness of structures printed at 70 mm/sec (Fig. 1F).

Discussion

Our results demonstrate the feasibility of using PEGDMA-curcumin as a biocompatible, readily tunable TPP resin. Printed structures support high cell viability and the resin can be

used to create intricate microstructures. Furthermore, the stiffness of cuboids was modulated by simply changing scanning speed, which may enable creating stiffness gradients within a single structure. In our ongoing work, we are expanding to other monomer and cellular systems, with long-term goals of creating cytocompatible, stiffness-tunable tissue-mimicking structures with encapsulated cells.

Images (Optional)

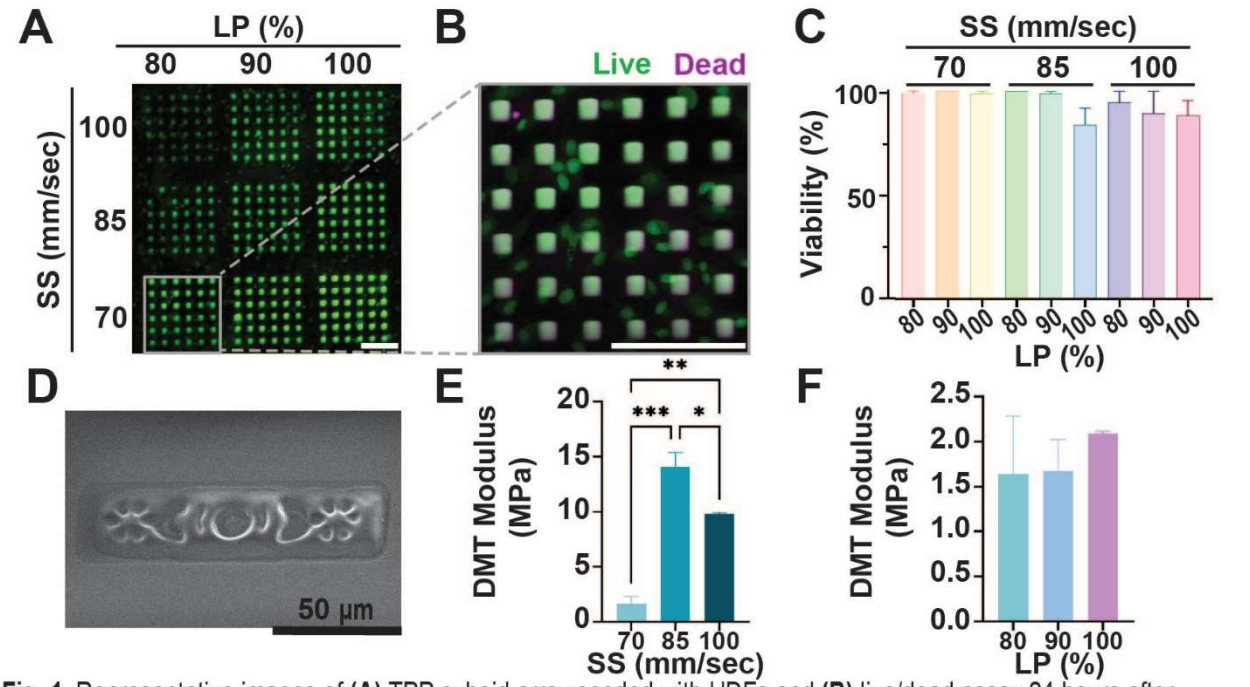


Fig. 1. Representative images of **(A)** TPP cuboid array seeded with HDFs and **(B)** live/dead assay 24 hours after seeding on structures; live (green) and dead (magenta) cells are stained by HCS NuclearMask and NucGreen Dead, respectively (scale bars = 150 µm). **(C)** Percent viability of HDFs 24 hours after seeding onto structures at all printing conditions, shown as mean ± SE (n=3). **(D)** Example TPP structure produced using PEGDMA-curcumin (scale bar = 50 µm). DMT moduli measurements of structures printed at **(E)** 80% LP or **(F)** 70 mm/sec SS; plots are mean ± SE, with n=3 for each, and *p<0.05, **p<0.01, and ***p<0.001.

Acknowledgements (Optional)

This work was funded by the NSF (2142246). The authors would also like to acknowledge use of the University of Iowa Central Microscopy Research Facility, a core resource supported by the University of Iowa Vice President for Research, and the Carver College of Medicine.

Session Category

Tissue Engineering: Methods, Models and Applications

OA50-04

Multi-Metamaterial and Region-Specific Biomimetic Auxetic Scaffolds Guide the Regeneration of the Whole Bone-Enthesis-Tendon Chain: A Multiscale In-Vitro and In-Vivo Study

Dr. Alberto Sensini[1], Dr. Olga Stamati[2], Dr. Francesca Giacomini[1], Dr. Pierpaolo Fucile[1], Dr. Sandra Ruiz Alonso[3], Dr. Tim Ten Brink[1], Dr. Carlos Peniche Silva[1], Prof. Alberto Maria Crovace[4], Dr. Riccardo Giorgino[5], Prof. Antonio Crovace[5], Prof. Laura Saenz del Burgo[3], Prof. Jose Luiz Pedraz Munoz[3], Dr. Bratislav Lukic[6], Dr. Julie Villanova[6], Dr. Henry Proudhon[7], Dr. Maryse Gille[7], Dr. Gregorio Marchiori[8], Dr. Gianluca Giavaresi[8], Prof. Gianluca Tozzi[9], Prof. Zeinab Tahmasebi Birgani[1], Prof. Roman Truckenmüller[1], Prof. Martijn van Griensven[1], Prof. Lorenzo Moroni[1]

[1]MERLN Institute, Maastricht University, Maastricht, 6229 ER, Netherlands. [2]University Grenoble Alpes, Grenoble, F-38000, France. [3]University of the Basque Country, Vitoria-Gasteiz, 01006, Spain. [4]University of Sassari, Sassari, 07100, Italy. [5]University of Bari, Bari, 70010, Italy. [6]ESRF Synchrotron, Grenoble, 38043, France. [7]MINES Paris, PSL University, Evry Cedex, 91003, France. [8]IRCCS Istituto Ortopedico Rizzoli, Bologna, 40136, Italy. [9]University of Greenwich, Chatham Maritime, ME4 4TB, United Kingdom

Introduction

Enthesis injuries are critical for extracellular-matrix organization-composition and auxetic mechanics [1]. Merge hierarchical electrospinning (HE) with 3D-printing (3DP) is suitable for replicate bone–enthesis–tendon chain. Enthesis fascicle-inspired auxetic electrospun bundles (EB) and hierarchical multi-material scaffolds (HMS) were fabricated mimicking structure-mechanics of sheep calcaneal tendon–enthesis–bone complex. Scaffolds' in-vitro-in-vivo performances were investigated, while in-situ Synchrotron X-ray tomography (SXCT) stepwise-tensile tests with digital volume correlation (DVC) elucidated their auxetic strain behaviour.

Methods

PLLA-Collagen-I blend EB were electrospun on a drum collector obtaining regions with controlled nanofiber orientations: mineralized fibrocartilage (random+aligned), non-mineralized fibrocartilage (conical junction, aligned), and tendon (aligned). EB morphology was examined via SEM-SXCT. EBs were seeded with human mesenchymal stromal cell (hMSC) spheroids (28days) and evaluated by qPCR, ELISA, and confocal microscopy. EB mechanics were assessed with tensile tests (strain-rate:0.4, 10, 100%/s), and full-field

strain distribution was analysed through in-situ SXCT stepwise-tensile tests with DVC. HMSs were produced grouping EBs with HE epitenon-inspired electrospun membranes resembling native tendon–enthesis tissue. STL models were generated segmenting a sheep calcaneal bone SXCT scan and used to 3DP PLA scaffolds on HMS mineralized fibrocartilage region, reproducing the whole bone–enthesis–tendon chain. HMSs with different numbers of internal EB were prepared (sHier, wHier). HMS morphology was examined via SEM/microCT, and mechanics was assessed with tensile tests at 100%/s. wHier auxetic expansion was evaluated through stepwise-tensile tests with DVC adapting the EB protocol. Custom sHier scaffolds were implanted in-vivo in sheep calcaneal bone–tendon defects, with follow-up x-rays, echography for six months.

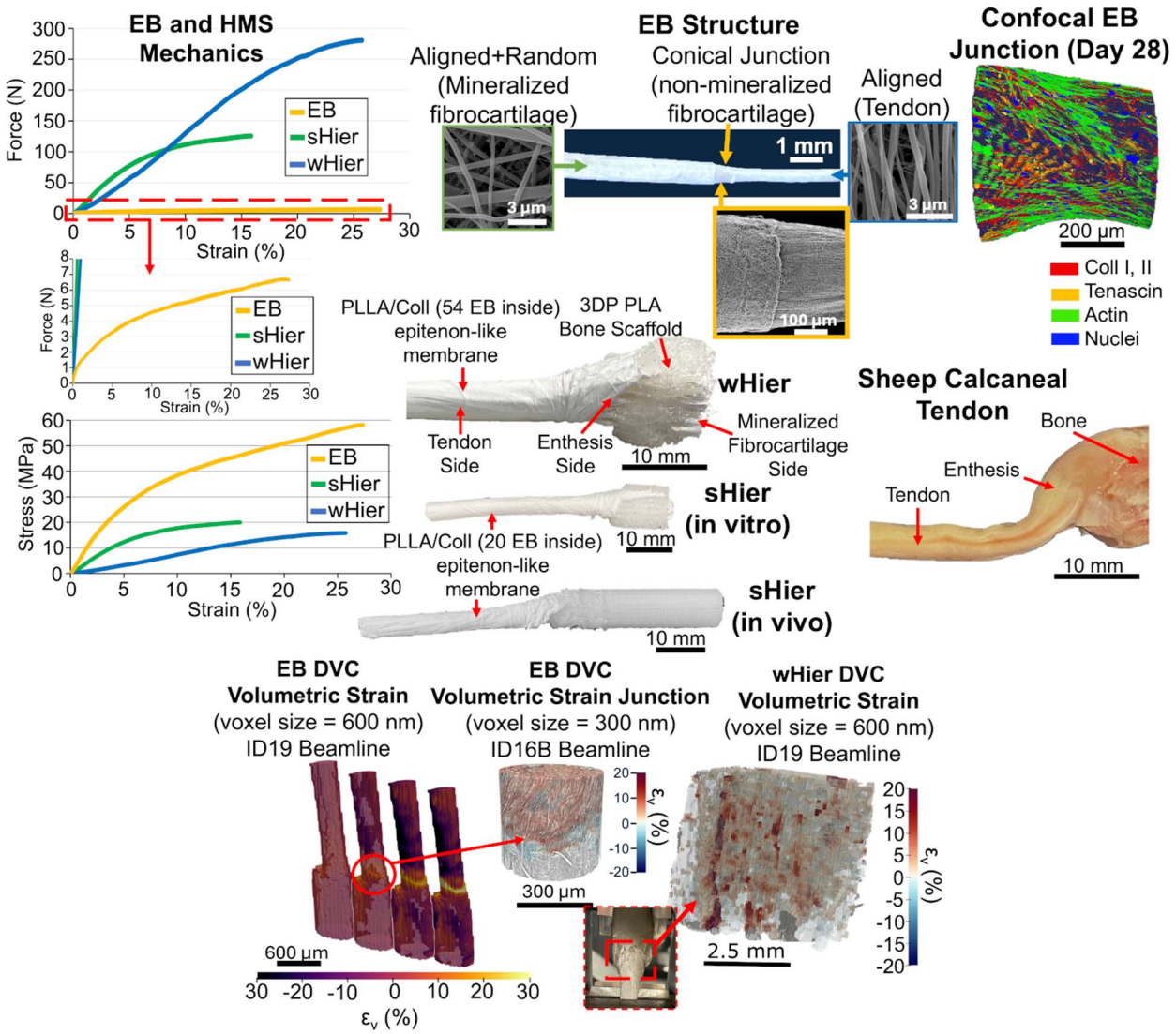
Results

SEM-SXCT confirmed biomimetic EB-nanofibers morphology [1]. EB mechanical tests revealed tendon fascicles-like mechanics. Confocal imaging verified EB colonization by hMSCs with enthesis-specific extracellular-matrix production. EB qPCR highlighted bone/enthesis/tendon markers expression. ELISA showed Collagen-II-Tenomodulin production. DVC revealed EB junction volumetric expansion verifying auxetic behavior. Volumetric auxetic strains were confirmed with HMSs' DVC. SEM-microCT HMS investigations revealed natural tissue biomimicry while mechanical tests showed HMSs mechanical reductions complexity-dependent like natural tissues. X-rays and echography showed in-vivo bone-enthesis-tendon regeneration.

Discussion

Multi-metamaterial scaffolds for bone-enthesis-tendon regeneration were realized. SXCT-DVC confirmed electrospun scaffolds' metamaterial nature.

Images (Optional)



References (Optional)

[1] Sensini et al.,Front.Bioeng.Biotech.,2021

Acknowledgements (Optional)

Horizon Europe MSCA 3NTHESES (n.101061826)

Session Category

Tissue Engineering: Methods, Models and Applications

OA51-03

Dynamic Air–liquid Interface Culture in a Milli-Fluidic Biomimetic Bioreactor for Advanced Skin Tissue Engineering

Dr. Beatrice Masante[1,2], Dr. Simona Villata[3,2], Dr. Stefano Gabetti[1,2], Eng. Pompeo Gaudiosi[3], Dr. Elena Torta[1,2], Prof. Diego Gallo[1,2], Prof. Francesca Frascella[3,2], Prof. Diana Massai[1,2]

[1]Dept of Mechanical and Aerospace Engineering and PolitoBIOMed Lab, Politecnico di Torino, Torino, Piemonte, Italy. [2]Interuniversity Center for the Promotion of the 3Rs Principles in Teaching and Research, Torino, Piemonte, Italy. [3]Dept of Applied Science and Technology, Politecnico di Torino, Torino, Piemonte, Italy

Introduction

Epithelial tissues (ET) are naturally exposed to external environment [1], a condition reproduced *in vitro* through the air–liquid interface (ALI) approach [2]. Conventional ALI systems employ transwell inserts to separate air and liquid compartments [3]; however, their static configuration does not adequately replicate the dynamic exchange of nutrients and gases occurring *in vivo*, often resulting in uneven tissue development. In this context, we present a biomimetic bioreactor, designed to support ALI culture with continuous medium recirculation (CMR) to enhance physiological relevance for skin tissue engineering.

Methods

The bioreactor culture chamber is composed of two screwable parts, 3D-printed with biocompatible autoclavable resins, housing transwells for ensuring effective separation between air and liquid phases. The chamber is integrated in a hydraulic circuit for guaranteeing CMR under the construct (working volume = 5mL). Air bubble accumulation is prevented by specific design. Preliminary biological validation was performed culturing 3D skin-like constructs. Human fibroblasts were embedded in a GelMa hydrogel, then poured on the transwell and coated with keratinocytes. The constructs were cultured in bioreactor for 14 days (flow rate = 0.5mL/min, n=4) (Fig.1A).

Results

Performances tests confirmed the bioreactor operational suitability and proper flow circulation under continuous operation. Biological tests demonstrated that constructs subjected to dynamic culture conditions displayed markedly improved epidermal

stratification, achieving epidermal layers exceeding 100 µm in thickness (Fig.1B), together with a significant upregulation of dermis-associated genes (Fig.1C). These findings indicate a more advanced level of tissue maturation relative to static controls.

Discussion

Overall, the bioreactor provides a controlled culture environment enabling both air exposure and CMR, improving nutrient and oxygen transport, while maintaining sterility and operational ease of use. Moreover, its modularity allows parallel culture of multiple samples, supporting reproducibility and scalability. By reproducing the ET microenvironment, the bioreactor overcomes the inherent limitations of static approaches, representing a versatile tool for advanced ET engineering studies.

Images (Optional)

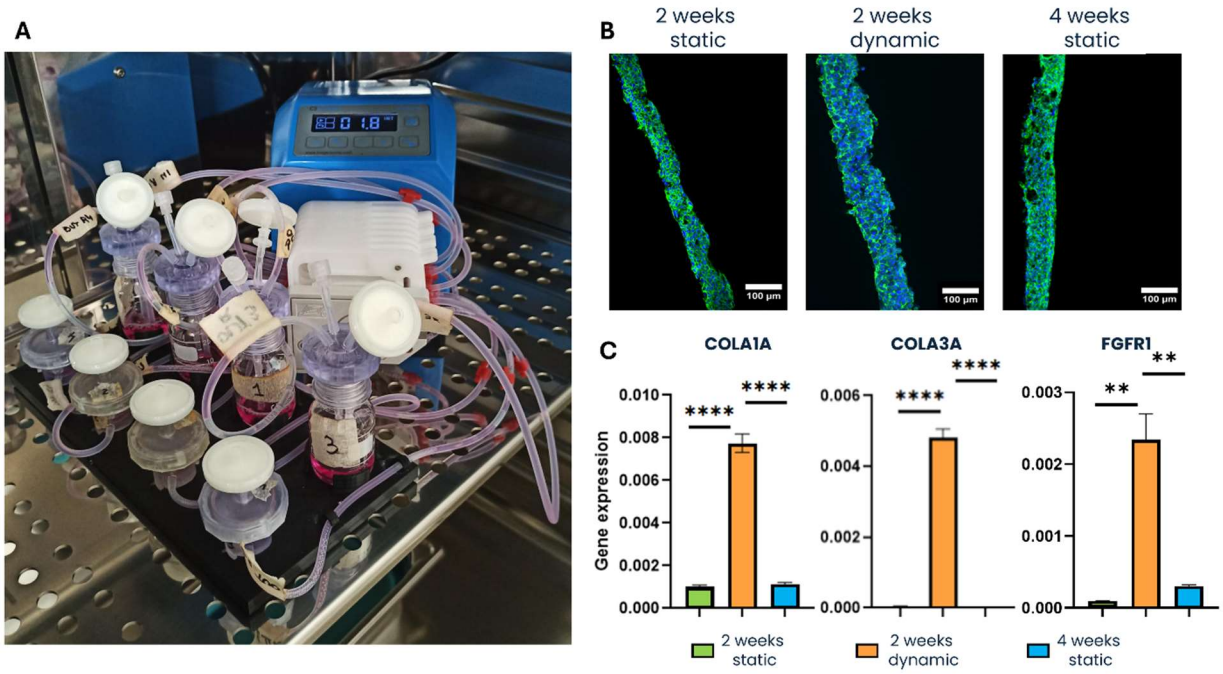


Figure 1. A) Parallelized milli-fluidic bioreactor with 4 culture chambers. B) DAPI/Phalloidin staining of the epidermis layer, scale bar = 100 µm. C) Gene expression analysis of collagen type 1 (COLA1A), type 3 (COL3A1) and receptor 1 fibroblast growth factor (FGFR1) (n = 2).

References (Optional)

[1] Rimal, et al, Appl. Mater. Today, 2021.

[2] Chen, et al, Reprod. Domest. Anim, 2019.

[3] Bluhmki, et al, Sci.Rep, 2020.

Acknowledgements (Optional)

Study partially supported by ALIce-MIRROR funded by Politecnico di Torino.

Session Category

Micro/Biofluidics: Experiments

OA51-04

Cyclic Hypoxia Modulates Endothelial Permeability in a Microvascular Network Formed in an Oxygen-Controllable Microfluidic Device

Mr. Shohei Yanagita, Dr. Kenichi Funamoto

Tohoku University, Sendai, Miyagi, Japan

Introduction

Ischemia–reperfusion injury arises when hypoxic tissues are reoxygenated, triggering abrupt increases in reactive oxygen species (ROS), endothelial barrier dysfunction, and inflammation. Conversely, controlled cycles of hypoxia and reoxygenation can induce ischemic conditioning, a protective phenomenon that enhances vascular resilience. Despite extensive research, the cellular mechanisms that distinguish injury-inducing from protective oxygen fluctuations remain incompletely understood, partly due to limitations of conventional in vitro models that cannot impose dynamic oxygen changes within a 3D microvascular network. Here, we used an oxygen-controllable microfluidic device containing a self-assembled microvascular network to investigate how cyclic hypoxia regulates redox dynamics and endothelial integrity.

Methods

A 3D microvascular network was formed by co-culturing human umbilical vein endothelial cells and fibroblasts in fibrin for 7–10 days. The formed microvascular networks were then subjected to one of three oxygen conditions for 180 min: normoxia (N, 21% O_2), steady hypoxia (H0, 0.3% O_2), or cyclic hypoxia (CyH0, alternating between 0.3% and 21% O_2 every 30 min). ROS generation was quantified using a CellROX fluorescence reagent. Endothelial permeability was assessed by quantifying diffusion of FITC-labeled dextran through the vascular network. Intracellular proteins Nrf2 and VE-cadherin were observed by immunofluorescence microscopy to assess antioxidant response and cell–cell junction integrity.

Results

ROS levels decreased and reached a low steady state under the H0 condition, whereas the CyH0 condition produced oscillatory ROS fluctuations synchronized with oxygen cycling. Endothelial permeability slightly increased under the H0 condition compared with the N condition, but was reduced under the CyH0 condition, indicating endothelial barrier reinforcement. Nuclear localization of Nrf2 increased under both hypoxic conditions (H0

and CyH0), suggesting activation of antioxidant defenses. In addition, VE-cadherin junctional area increased under the CyH0 condition, indicating enhanced endothelial adhesion.

Discussion

Cyclic hypoxia elicits coordinated redox and structural adaptations in a microvascular network. The combination of oscillatory ROS dynamics, Nrf2 activation, and VE-cadherin–mediated junctional reinforcement suggests that the CyH0 condition promotes a protective endothelial state resembling ischemic conditioning, whereas steady hypoxia lacks these adaptive features. Our microfluidic platform provides a powerful tool for dissecting oxygen-pattern–dependent vascular responses and for informing strategies to mitigate ischemia-reperfusion injury or harness conditioning-based protection.

Session Category

Micro/Biofluidics: Experiments

OA51-05

Cancer Associated Fibroblasts and Leader Cells Drive Collective Migration of Breast Cancer Metastasis Through Chemo-Mechanical Signaling

Mrs. Jessica Williamson B.S., Mr. Jesee Rolston B.S., Mr. Musaddiq Lodi, Dr. Jessanne Lichtenberg PhD, Dr. Preetam Ghosh PhD, Dr. Priscilla Hwang PhD

Virginia Commonwealth University, Richmond, Virginia, United States

Introduction

Heterogeneous tumor clusters can detach from primary tumors and travel to distant organs via collective cell migration (CCM), where cells move as a coordinated unit. *In vivo*, tumor clusters include various tumor phenotypes, immune, and stromal cancer associated fibroblasts (CAFs) [1]. Using 3D microfluidic models we designed, we demonstrated that leader cells at the front drive directional migration and CAFs physically associate with leaders [2-4]. This project investigates how CAFs and leaders communicate to coordinate migration using our microfluidic models and single-cell RNA sequencing (scRNA-seq) assays. We hypothesize that chemo-mechanical feedback between CAFs, leaders, and mechanical matrix cues directs CCM.

Methods

Primary mouse tumor (MMTV-PyMT) organoids were cultured in 3D microfluidic devices under biomechanical gradient (interstitial flow, 12 μm/s) to induce CCM [3,4]. A non-migratory control was included. After 16 hours, organoids were isolated for scRNA-seq. Data was analyzed after principal component analysis (PCA), using Seurat's default parameters, and CAF to leader ligand-receptor interactions were assessed using CellChat. Ingenuity Pathway Analysis was used to reveal signaling pathways and to validate scRNA-seq results against *in vivo* datasets.

Results

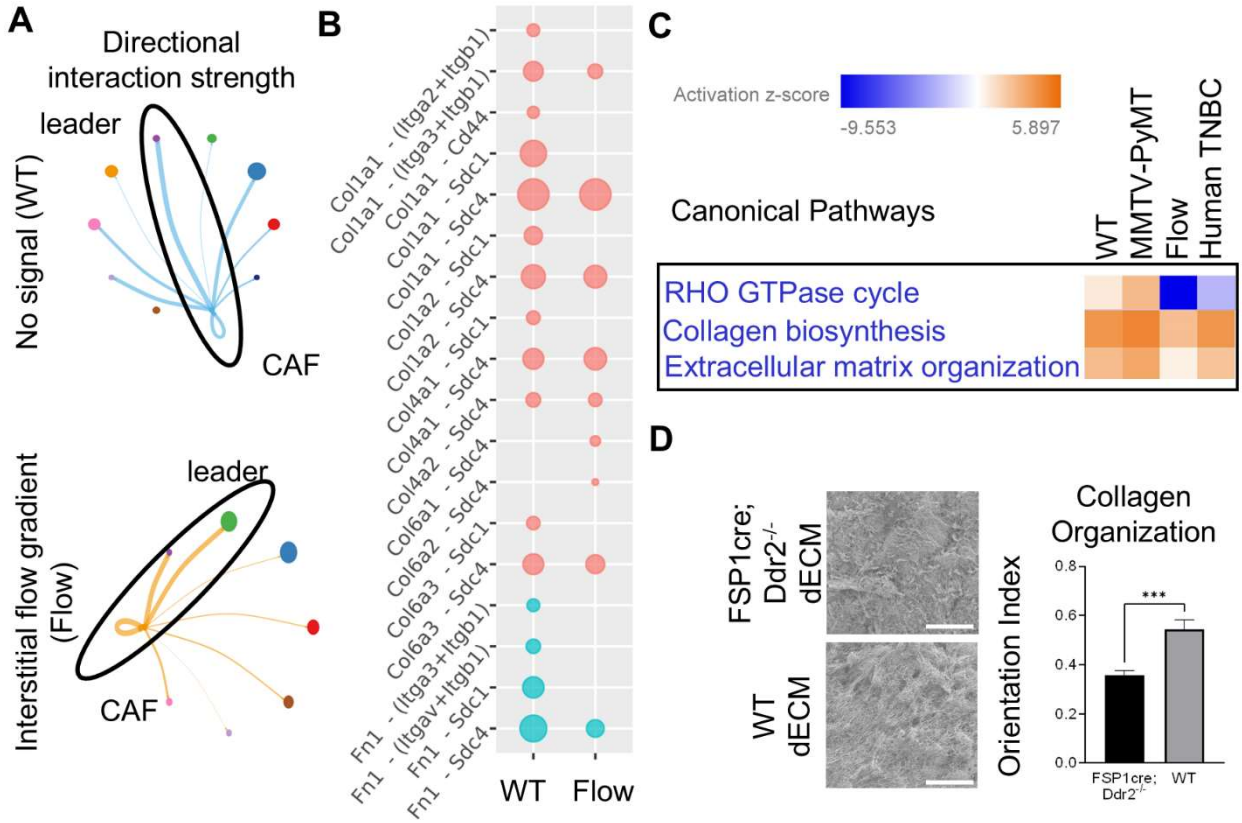
scRNA-seq revealed 10 cell clusters without flow and 8 under flow. CAFs and leaders had the greatest number and strength of interactions (Fig1A). CAFs send signals to leaders through matrix ligands such as collagen and fibronectin interacting with syndecan (Sdc) receptors (Fig1B). Pathway analysis identified "RHO GTPase", "Collagen Biosynthesis," and "Matrix organization" as significant pathways (Fig1C). We validated our analysis with metastatic human and primary MMTV-PyMT data, finding similar pathway activation (Fig1C). Scanning electron microscopy (SEM) imaging of tumors with and without CAFs

ablated revealed differences in matrix organization, validating our scRNA-seq analysis (Fig1D).

Discussion

We demonstrate CAF ligands communicate with leader cell receptors within organoids, and our model correlates with *in vivo* conditions. This work contributes to the mechanistic understanding of how biomechanics regulate CCM in breast cancer metastasis. In the future we will perform loss/gain-of-function experiments to validate genes identified as potential therapeutic targets.

Images (Optional)



References (Optional)

[1] Keller & Pantel, Nat. Rev. Cancer, 2019

[2] Morikis et al., Cell Rep., 2025

[3] Hwang et al., Dev. Cell, 2023

[4] Hwang et al., Cancer Res., 2019

Session Category

Micro/Biofluidics: Experiments

OA52-02

Using Biomechanical Simulation for Generalizing and Personalizing Assistance From a Supernumerary Robotic Limb for Diverse Single-Shot Activities

Mr. Haedo Cho, Ms. Zoe Kutulakos, Dr. Patrick Slade

Harvard University, Cambridge, MA, United States

Introduction

Assistive robotic devices aim to improve mobility, but providing assistance that improves biomechanical outcomes across many different activities is challenging. State-of-the-art devices use either generalizable controllers that provide modest mobility improvements for all activities, or task-specific controllers that achieve field-leading mobility improvements for a single activity by personalizing assistance to the user. This personalization requires researchers to carefully define many settings, like assistance parameterization, informed by prior experiments. We present a framework that uses biomechanical simulation to generalize assistance to diverse single-shot activities and automatically set up assistance personalization.

Methods

Our framework (Fig 1A-B): 1) records the user's unassisted motion with OpenCap smartphone motion capture, 2) determines an idealized assistive force profile in simulation using OpenSim Moco [1], 3) personalizes the simulation-informed assistance using human-in-the-loop optimization [2]. We evaluated this approach on three single-shot activities of daily living (Fig 1C) using a wearable supernumerary robotic limb with two revolute joints, a passive end effector interfacing with the user's body or environment, and an adjustable base attached to a chest brace. Nine healthy participants (5 male and 4 female; age, 27 ± 4 yr) completed the study. During human-in-the-loop optimization, a Bayesian optimizer minimized muscle excitation for a target muscle (vastus medialis or biceps brachii), measured using surface electromyography, as participants performed 100 repetitions of each activity. Sim-informed and personalized assistance were compared to an unassisted condition for each participant and activity in a validation experiment (Fig 1D).

Results

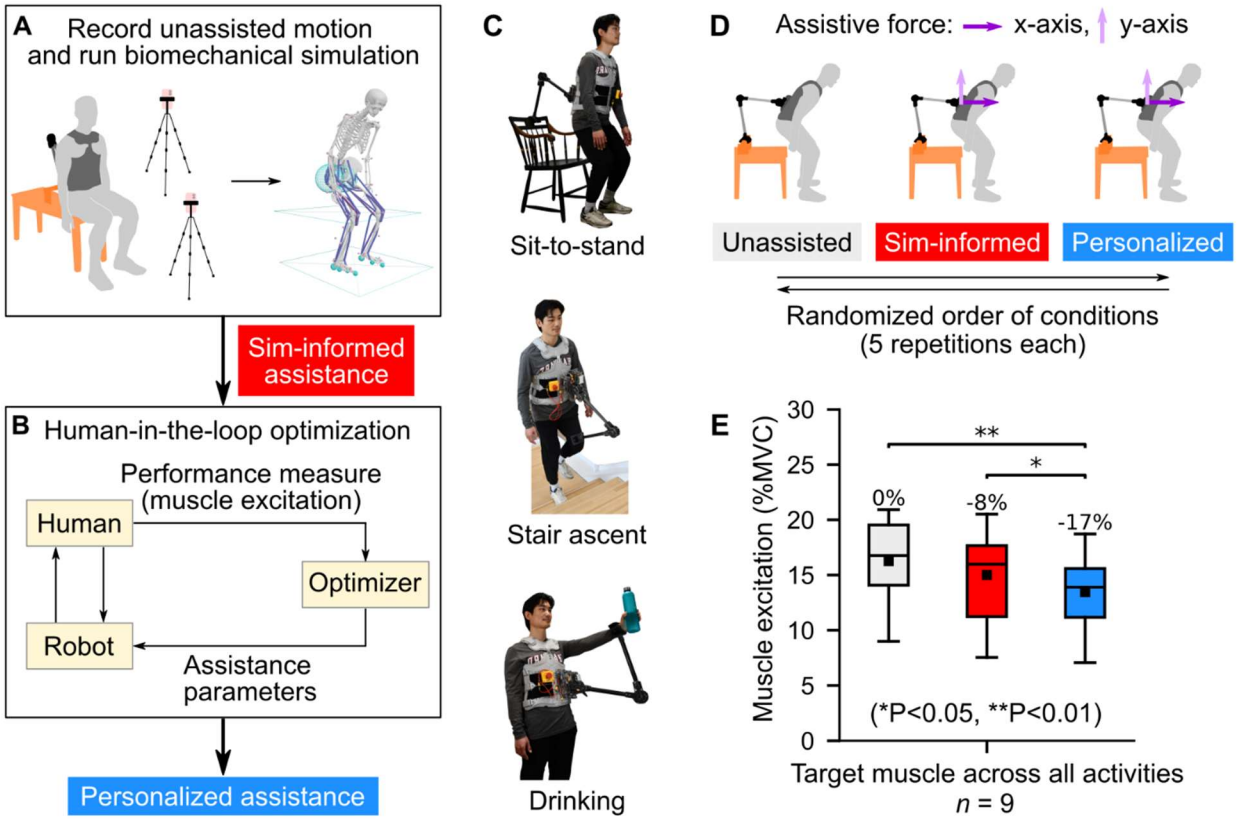
Personalized and sim-informed assistance reduced participants' target muscle excitation by 17% and 8% compared to unassisted, respectively (Fig 1E). The simulations met best

practice benchmarks [3]. Human-in-the-loop optimization converged and identified unique assistance parameters for each participant, providing significant benefits beyond sim-informed assistance.

Discussion

These results support the feasibility of using biomechanical simulation to systematically generalize and personalize assistance. Populations like older adults or workers with physically demanding jobs could benefit from personalized assistance across many diverse upper- and lower-limb tasks.

Images (Optional)



References (Optional)

[1] Christopher L Dembia *et al.*, PLoS Comput Biol, 2020

[2] Patrick Slade *et al.*, Nature, 2024

[3] Jennifer L Hicks *et al.*, J Biomech Eng, 2015

Session Category

Imaging and Biomedical Devices: Assistive Technologies

OA52-03

Stair Walking-Mode Classification Using Minimal Biomechanically Relevant Features Optimized for Powered Prosthetic Knees

Mr. Ryan Busch A.S., A.A., Dr. Stephen Cain PhD

West Virginia University, Morgantown, West Virginia, United States

Mr. Ryan Busch

Introduction

Current powered prosthetic knees lack the ability to seamlessly switch modes when a user begins to ascend or descend stairs, making ambulation more difficult. The aim of our work was to develop a stair classification model using only data from sensors commonly integrated into powered knees that could inform the controller when to change the mode of the prosthetic knee.

Methods

Our model was developed based on a powered prosthetic knee with a motor encoder and shank IMU, which provides the angular position of the knee as well as the acceleration and angular velocity of the shank. The vertical position can be calculated using inertial navigation principles, knee angle is the direct output of the encoder, and thigh angle is the difference between knee angle and the integral of shank angular velocity. Using visual inspection, vertical position range, knee angle maximum, mean thigh angle, and thigh angle variance, calculated using a one-second reverse sliding window, were the features selected for classification. Classification was performed by a KNN model using 15 neighbors. Motion capture and goniometer data from an open dataset created by the EPIC lab at Georgia Tech was used to test our model; we used walking and stair-climbing data from the legs of 20 subjects [1]. The training group consisted of 15 randomly selected subjects, and the testing group consisted of the remaining five subjects. The best model was selected using leave-one-subject-out cross-validation and evaluated on the testing dataset. A 0.5-second debounce filter was applied to the classification output before statistics were calculated.

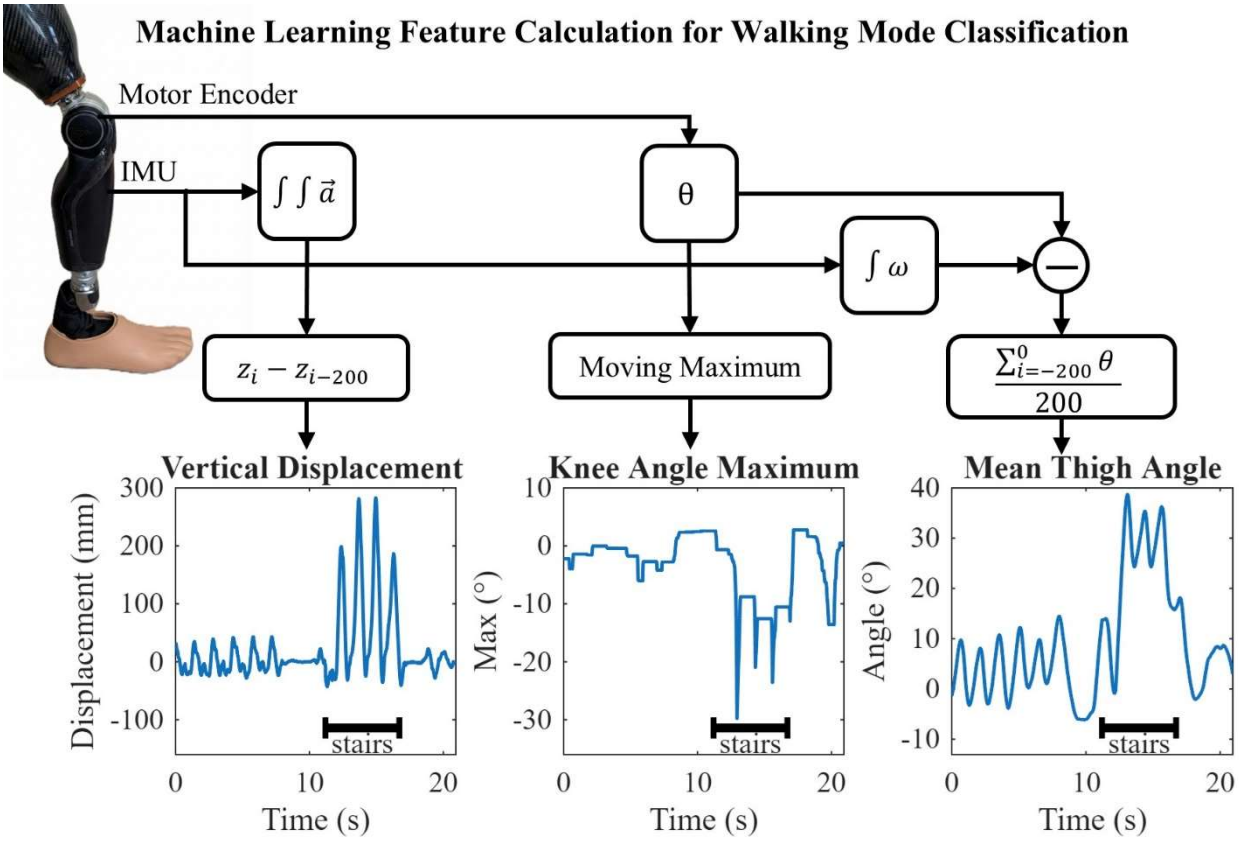
Results

The final model had an accuracy of 92.8%, an F1 score of 88.8%, and an AUROC of 88.6% when tested on the five held-out subjects.

Discussion

This model utilized only four features and a simple KNN model, achieving high accuracy and never confusing stair ascent with stair descent. Given these promising initial results from testing on a dataset with a wide range of subjects, we believe this system could be further refined and developed to build a robust mode detector for powered prostheses.

Images (Optional)



References (Optional)

[1] J. Camargo *et al.* , J Biomechanics, 2021

Acknowledgements (Optional)

We thank Dr. Michael Davidson of Loma Linda University for his insights into the needs of amputees who use powered prostheses.

Session Category

Imaging and Biomedical Devices: Assistive Technologies

OA52-04

Efficacy of a Frugal Inertial Sensor-based Motion Capture System to Quantify Upper Limb Kinematics for Remote Monitoring Rehabilitation

Mr. Apoorv Shrivastava PhD Student[1], Ms. Aliki Statiri[2], Dr. Samrat Sagar[1], Dr. Angela E. Kedgley[2], Dr. Darshan S. Shah[1]

[1]BiOME Lab, Department of Mechanical Engineering, Indian Institute of Technology Bombay, Mumbai, Maharashtra, India. [2]Department of Bioengineering, Faculty of Engineering, Imperial College London, London, London, United Kingdom

Introduction

The need for portable home-based training systems for monitoring rehabilitation for neuromuscular disorders, such as stroke, is growing. Although inertial measurement unit (IMU) based sensors are a viable tool for remotely assessing joint kinematics, their application for monitoring upper limb kinematics is minimal, perhaps due to varying accuracies for different joints, motions and IMU-related protocols [1]. Hence, a frugal IMU-based motion capture system, developed for more accessible and customizable biomechanical analyses, was used to quantify upper limb motions, and compared to values from a commercial IMU system and a benchmark 10-camera optical motion capture system (OMC; Qualisys, Sweden).

Methods

IMUs from the frugal system – MPU9250 (InvenSense, USA) with custom signal processing, drift compensation and Madgwick filter-based sensor fusion algorithm – and the commercial system (Blue Trident, Vicon, UK) were rigidly affixed to each other, and manually aligned to the upper arm, forearm and hand segments of 9 participants (6F, 27±7yrs), following institutional ethics approval. Elbow and wrist kinematics were captured for three trials of elbow flexion-extension (E_{FE}), pronation-supination (E_{PS}), wrist flexion-extension (W_{FE}) and radioulnar deviation (W_{RUD}) following ISB recommendations [2, 3]. Root mean square error (RMSE) was used to compare the accuracy of the two sets of IMU-derived elbow and wrist kinematics to those from OMC.

Results

RMSE in joint kinematics between IMUs and OMC was lower than clinically acceptable threshold (5°) for E_{FE}, but higher for E_{PS}, W_{FE} and W_{RUD} (Fig. 1). RMSE for the custom and commercial IMU systems were within 2.65˚ of each other for all motions.

Discussion

Both IMU systems displayed lower accuracy for smaller ranges of motion and secondary degrees of freedom. Larger errors during E_{PS} could be attributed to the more proximal placement of the two IMUs, leading to an inherent difference from OMC. Higher errors observed for W_{FE} could be improved with more robust sensor-to-segment alignment protocols. Following kinematic quantification during activities of daily living, the use of custom IMUs for remote monitoring and tele-rehabilitation applications will be explored by embedding them in orthotic devices.

Images (Optional)

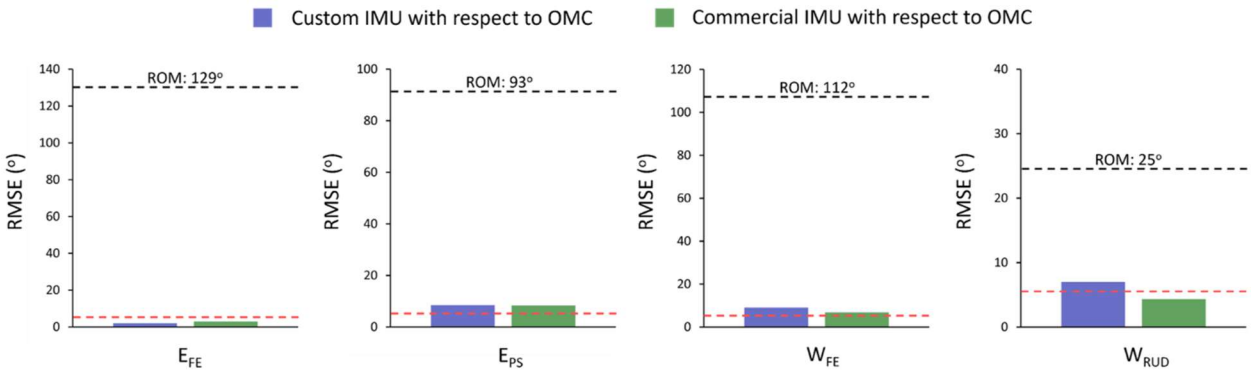


Figure 1: Root mean square error (RMSE) of elbow and wrist kinematics from custom and commercial inertial measurement units (IMUs) with respect to optical motion capture (OMC) for upper limb motions with their range of motion (ROM; dotted, black) and clinically acceptable RMSE (5°; dotted, red)

References (Optional)

[1] Fang *et al.*, Sensors, 2023

[2] Cereatti *et al.*, J Biomechanics, 2024

[3] Wu *et al.*, J Biomechanics, 2005

Acknowledgements (Optional)

The study was supported by Imperial-India Connect Fund, Imperial College London. Apoorv Shrivastava was supported by Prime Minister Research Fellowship, Government of India.

Session Category

Imaging and Biomedical Devices: Assistive Technologies

OA52-05

Designing a Lower-Limb Exoskeleton Controller to Alter the Energetics of Gait Symmetry

Dr. Anthony Chen, Ms. Tiana A. Wertelecky, Dr. Jessica C. Selinger

Queen's University, Kingston, Ontario, Canada

Dr. Anthony Chen

Ms. Tiana A. Wertelecky

Introduction

Persistent gait asymmetries affect over half of persons post-stroke, and often the level of asymmetry exceeds what can be explained by muscle weakness or spasticity alone [1]. Many persons post-stroke can transiently reduce asymmetries through conscious effort, but more implicit and permanent changes often remain elusive [2]. Exoskeletons that alter gait energetics have been used to change preferred step length, rate, and width in healthy individuals, but never symmetry, which may be less modifiable [3]. Here, our aim was to develop an exoskeleton controller that manipulates the relationship between step-time asymmetry and metabolic cost—incentivizing asymmetry in healthy individuals. We view this as an important proof of concept that supports our longer-term goal of incentivizing symmetric gait post-stroke.

Methods

We developed a custom controller for ankle exoskeletons (Humotech, USA) that scaled assistive plantarflexion torque in real-time based on step-time symmetry measured from an instrumented treadmill (Bertec, USA). To do so, we first modeled the interactions between step asymmetries, natural costs, assistive torque profiles, and cost reductions using literature data. We arrived at a controller that we predicted would reduce cost by approximately 9% at a +3.5% asymmetry (**Fig. 1**). To test our controller, we then had one participant walk in the exoskeleton at various step-time asymmetries, commanded with visual feedback, on four separate days while instrumented with indirect calorimetry (COSMED, Italy).

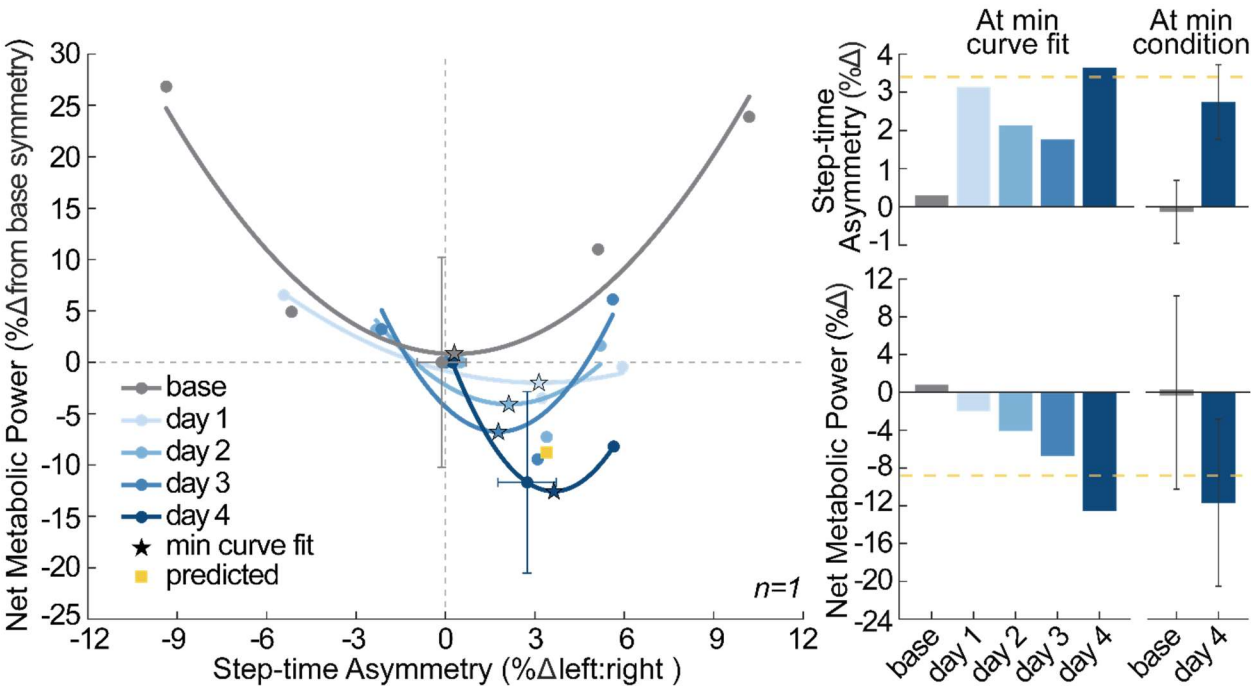
Results

Our controller accurately scaled peak assistive plantarflexion torque in real-time based on step-time symmetry and altered the energy-optimal step-time (**Fig. 1**). By day four, the participant reduced metabolic cost by 12.6% at +2.7% asymmetry, well matching model predictions.

Discussion

Our controller reliably altered the energy-optimal step-time to an asymmetric gait. We will next test if healthy naïve participants adopt energy-optimal asymmetries and adapt our controller to incentivize symmetry in persons post-stroke. Our approach—of leveraging energy optimization to incentivize clinically desirable gait adaptations—could have broad applications in assistive robotics and rehabilitation.

Images (Optional)



References (Optional)

[1] Little *et al.* , Gait Posture, 2020

[2] Roemmich *et al.* , Neurorehabil Neural Repair, 2019

[3] Ellis *et al.* , Proc R Soc B, 2013

Session Category

Imaging and Biomedical Devices: Assistive Technologies

OA53-01

Effects of Mirror Therapy Combined with Transcranial Direct Current Stimulation on Bimanual Coordination in Chronic Stroke: A Double-Blind Randomized Controlled Trial

Dr. Tsai-Yu Shih[1], Prof. Ching-Yi Wu[1,2,3], Prof. Chia-Lun Liu[1], Dr. Ken-Hsien Su[1]

[1]Department of Occupational Therapy and Graduate Institute of Behavioral Sciences, College of Medicine, Chang Gung University, Taoyuan, Taiwan, Taiwan. [2]Department of Physical Medicine and Rehabilitation, Linkou Chang Gung Memorial Hospital, Taoyuan, Taiwan, Taiwan. [3]Department of Occupational Therapy and the Healthy Aging Research Center, Chang Gung University, Taoyuan, Taiwan, Taiwan

Dr. Tsai-Yu Shih

Introduction

Mirror therapy (MT) is a prominent intervention to enhance upper extremity (UE) motor function [1]. Performing MT tasks may enhance bimanual coordination through bilateral movement practice, and mirror visual feedback may further enhance attention to the covered UE [1]. Applying anodal tDCS may further restore interhemispheric balance, potentially strengthening these effects. Therefore, this study compared MT combined with tDCS applied over the premotor cortex (PMC) or primary motor cortex (M1) to evaluate their efficacy on bimanual coordination.

Methods

Thirty-six patients with stroke were recruited and randomly allocated to the PMC, M1 or Sham group to receive MT combined with tDCS on different regions. UE kinematics were recorded using a 7-camera motion analysis system. Participants were instructed to perform bilateral reaching as rapidly as possible, and bimanual coordination was assessed before and after the intervention. Temporal synchronization was assessed using differences in movement onset ($Diff_{onset}$), movement offset ($Diff_{offset}$) and peak velocity onset ($Diff_{PV}$) between the two UEs. Total movement time (TMT) and movement overlap time (MOT) were calculated to indicate bimanual efficiency. Generalized estimating equations were applied with group (PMC, M1, and Sham) and time (baseline and post-intervention) as factors. The level of significance was set at 0.05.

Results

$Diff_{offset}$ and MOT showed significant Group×Time interactions (Waldχ2 = 9.625, p = .008; Waldχ2 = 4.063, p = .046). Post hoc analysis indicated participants in the M1 group exhibit significantly smaller $Diff_{offset}$ and greater MOT at post-intervention compared to baseline (p < .001). TMT exhibited a significant main effect of time (Waldχ2 = 4.220, p = .040), with participants across all groups showed shorter TMT at post-intervention compared to baseline. No significant interaction or main effect was found for $Diff_{onset}$ or $Diff_{PV.}$

Discussion

Applying ipsilesional M1 stimulation in combination with MT improved bimanual coordination. Participants demonstrated more synchronous bimanual reaching movements after the intervention, suggesting that their UEs operated in a more coordinated manner similar to healthy adults [2]. combining MT with M1 stimulation appears to produce beneficial effects on bimanual motor performance in patients with stroke.

Images (Optional)

Table 1. Mean values and standard deviations of the bimanual coordination by group and time.

Variables	PMC	M1	Sham	Group	Time	Group *time
$Diff_{onset}$				.952	.131	.341
Baseline	0.10 (0.07)	0.09 (0.09)	0.10 (0.06)			
Post-intervention	0.10 (0.09)	0.14 (0.12)	0.11 (0.05)			
$Diff_{offset}$				.698	.017*	.008*
Baseline	0.38 (0.20)	0.39 (0.21)	0.27 (0.17)			
Post-intervention	0.32 (0.24)	0.21 (0.14)	0.29 (0.17)			
$Diff_{PV}$				.269	.519	.557
Baseline	0.29 (0.14)	0.29 (0.17)	0.23 (0.13)			
Post-intervention	0.36 (0.22)	0.26 (0.16)	0.25 (0.09)			
MOT				.776	.087	.046*
Baseline	0.53 (0.25)	0.52 (0.26)	0.63 (0.18)			
Post-intervention	0.57 (0.26)	0.66 (0.23)	0.60 (0.20)			
TMT (millisecond)				.248	.040*	.796
Baseline	197.10 (72.11)	180.72 (47.43)	232.11 (109.15)			
Post-intervention	177.99 (47.81)	144.36 (37.60)	216.05 (135.25)			

Abbreviations: $Diff_{onset}$, time differences between movement onset of the 2 hands; $Diff_{offset}$, time differences between movement offset of the 2 hands; $Diff_{PV}$, time differences between time of peak velocity of the 2 hands; MOT, Movement overlap time; TMT, Total movement time.

References (Optional)

[1] Rossiter, H.E., et al., Neurorehabil Neural Repair, 2015

[2] Wu, C.-Y., et al., Disability and Rehabilitation, 2009.

Acknowledgements (Optional)

This study was supported in part by Chang Gung Memorial Hospital , under Grant BMRP553; and in part by National Science and Technology Council , under Grant NSTC-113-2314-B-182-049-MY3; and in part by National Health Research Institutes , under Grant NHRI-EX114-11105PI; and in part by Healthy Aging Research Center in Taiwan , under Grant URRPD1Q0181.

Session Category

Clinical Biomechanics: N/A

OA53-02

Individual Baseline Factors May Predict Increased Paretic Propulsion On an Adaptive Split-belt Treadmill in People with Chronic Stroke

Ms. Rucha Kulkarni, Dr. Jill S. Higginson

University of Delaware, Newark, DE, United States

Introduction

Stroke affects over 100 million people worldwide. However, motor impairments in stroke survivors present heterogeneously. There are often differences in baseline walking function and ability, and training paradigms often lead to mixed responses and improvements. Prior work has shown that individual baseline factors can predict changes in step length asymmetry and cost of transport. The purpose of this study was to determine the baseline factors that might predict the capacity to volitionally increase paretic propulsion (push-off) on an adaptive (user-driven) treadmill.

Methods

We developed an adaptive split-belt treadmill (sATM) that changes the speed of each belt independently based on the user's gait mechanics and can be modified to increase propulsion demand (higher propulsion to maintain belt speed) unilaterally. Fourteen stroke survivors walked on a tied-belt adaptive treadmill (Baseline) and the sATM with increased propulsion demand on the paretic side. We calculated Spearman correlations to determine the baseline factors correlated with change in paretic propulsion (peak AGRF). To determine their contribution, we modelled the baseline factors (overground walking speed, baseline peak AGRF asymmetry, and Borg's Rating of Perceived Exertion (RPE)) to the change in paretic propulsion using multiple linear regression.

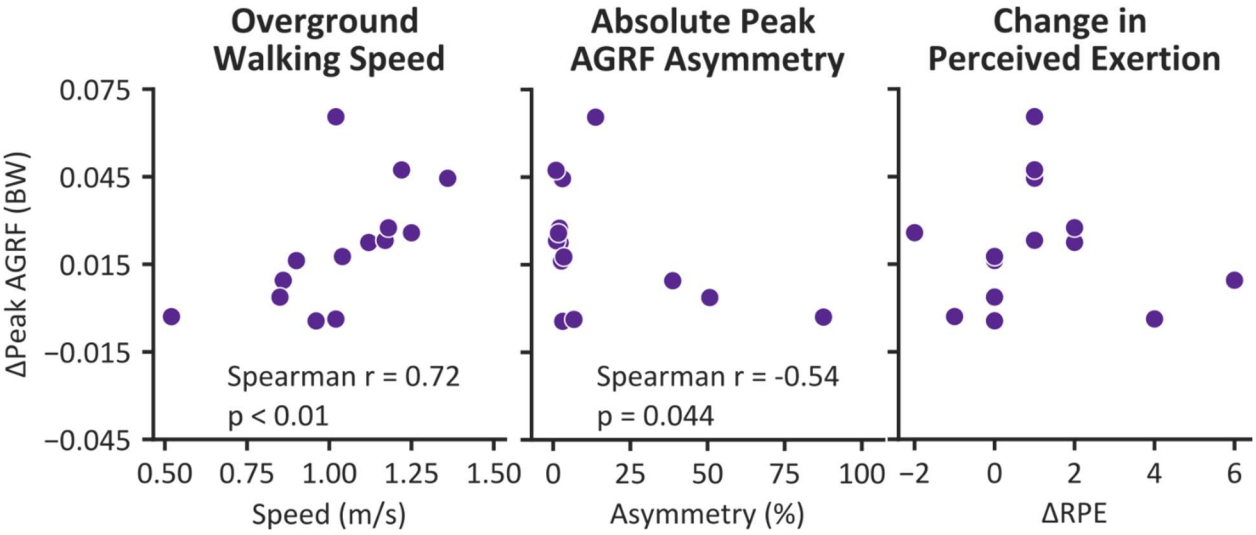
Results

We observed significant correlations between baseline factors (overground walking speed and baseline propulsion asymmetry) and change in paretic propulsion compared to Baseline (Δ). We also observed a binomial distribution of ΔRPE. The best linear regression contained only a factor of overground walking speed and was determined using the lowest AIC score, highest observed R^2 (0.60) and predictive R^2 (0.26).

Discussion

Our results suggest that overground walking speed may be the best predictor of the change in peak paretic AGRF on an sATM. While the best model did not contain baseline propulsion asymmetry, it is possible that this asymmetry is minimized due to the equal speeds on both belts on the tied-belt treadmill, and we may see an association with overground asymmetry. The binomial distribution of ΔRPE suggests that increased propulsion demand may be most effective when the perceived exertion is roughly increased by 1 in comparison to baseline. This study represents a step towards developing personalized treatments to individual impairments for maximal improvement.

Images (Optional)



Session Category

Clinical Biomechanics: N/A

OA53-03

Stroke Survivors Retain the Ability to Harness Mediolateral Assistance to Improve Weight Transfer During Walking

Mr. Jason Tsai, Dr. Hao-Yuan Hsiao Ph.D.

University of Texas at Austin, Austin, Texas, United States

Introduction

Post-stroke gait is characterized by impaired frontal-plane control and inefficient weight transfer [1]. Walking on a lateral oscillating treadmill provides a unique means to deliver mediolateral forces that may help restore more efficient body transfer mechanics. Understanding whether stroke survivors can harness external energy to enhance weight transfer performance has implications for gait rehabilitation and designing assistive devices.

Methods

Five stroke survivors and five elderly controls walked on a mediolateral sinusoidally oscillating treadmill (1-cm amplitude; oscillation frequency = stride frequency). Participants completed non-oscillation and oscillation trials at self-selected comfortable speeds after familiarization. Kinematics and kinetics were collected using motion capture and an instrumented treadmill. We quantified synchronization between weight transfer and treadmill motion, treadmill mediolateral mechanical energy input, vertical ground reaction force (vGRF), and weight-transfer time (WTT) toward the leading limb (paretic in stroke; nondominant in controls).

Results

Both groups synchronized to similar oscillation phases during mid–weight transfer (stroke: 0.74–0.85π; controls: 0.71–0.86π), indicating comparable weight transfer timing strategies. All participants received similar amounts of net positive treadmill energy during weight transfer (stroke: 0.004–0.009 J/kg; controls: 0.005–0.013 J/kg). Stroke survivors showed larger increases in paretic vGRF (≈ +0.02–0.04 N/kg) and greater reductions in WTT (≈ –0.02s to –0.05 s) than controls (vGRF ≈ –0.02–0.03 N/kg; WTT ≈ 0.00 to –0.02 s), indicating a more pronounced effect of oscillation on weight-transfer mechanics.

Discussion

Across groups, participants synchronized weight transfer with the oscillation that delivered net positive mechanical energy, demonstrating a shared strategy that accepts external

assistance. This conserved behavior indicates that stroke survivors retain the capacity to exploit predictable mediolateral assistance.

However, healthy controls showed only minor changes in vGRF and WTT, reflecting their minimal need to alter baseline efficient weight-transfer and limb-loading strategies. In contrast, stroke survivors displayed larger increases in vGRF and greater reductions in WTT, indicating that the mechanical energy was redirected toward supporting limb loading and weight-transfer demands. These findings suggest that oscillatory assistance may preferentially benefit individuals with impaired frontal-plane control, highlighting its potential to enhance weight transfer after stroke.

Images (Optional)

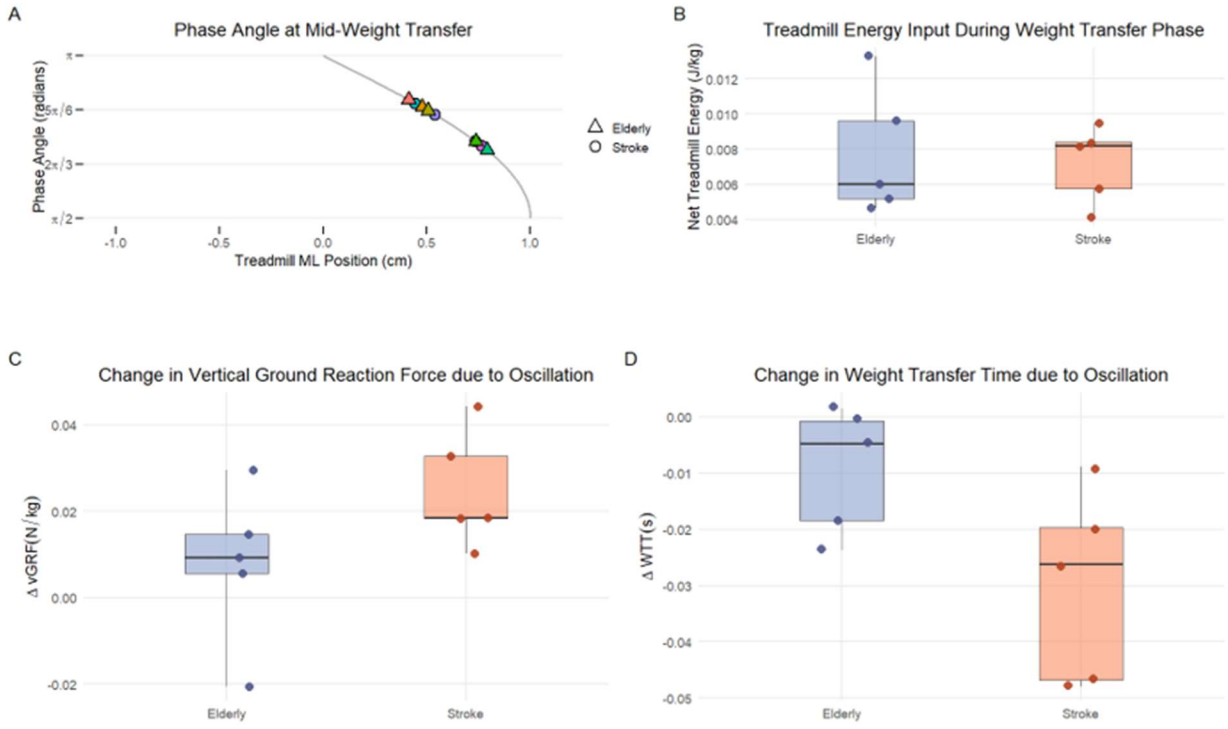


Figure 1: *(A) Symbols (Triangles for elderly, Circles for stroke) indicate average phase angle along the treadmill oscillation path at mid-weight transfer during treadmill oscillation walking. Weight transfer phase was defined as the period in which Center of Mass velocity is positive toward the paretic/nondominant side. (B) Net energy input from the treadmill during the weight transfer phase in elderly and stroke. (C) Changes in Vertical Ground Reaction Force for the nondominant/paretic limb in elderly and stroke between Treadmill Oscillation Walking compared to normal treadmill walking. (D) Changes in Weight Transfer Time towards the nondominant/paretic limb between Treadmill Oscillation Walking compared to normal treadmill walking.*

References (Optional)

[1] Hsiao et al. , J. Neuroengineering Rehabil., 2020

Session Category

Clinical Biomechanics: N/A

OA53-04

Effect of Stroke on Limb Contributions to the Lateral Center of Mass Trajectory During Walking

Ms. Grace Kellaher[1], Ms. Sarah Overby[1], Dr. Elisa Arch[1], Dr. Jason Franz[2,3], Dr. Darcy Reisman[1], Dr. Jeremy Crenshaw[1]

[1]University of Delaware, Newark, Delaware, United States. [2]University of North Carolina at Chapel Hill, Chapel Hill, North Carolina, United States. [3]North Carolina State University, Raleigh, North Carolina, United States

Introduction

Individuals with chronic stroke have known balance impairments that contribute to their higher risk of falling. A large percentage of falls occur during walking, and the frontal-plane is the primary direction where instability while walking occurs, but the biomechanical contributors to frontal-plane balance during walking are unclear. Therefore, the purpose of this study was to characterize the contributions of the leading (a_{Lead}) and trailing (a_{Trail}) limbs to the lateral center of mass acceleration (a_{COM})– an aspect directly influencing frontal-plane balance during walking– in those with and without chronic stroke.

Methods

Nine adults with chronic stroke (4M/5F;65.4±4.0yrs;30.4±4.6kg/m^2;76.1±47.8 months post-stroke) and nine adults without chronic stroke (5M/4F;63.3±6.2yrs;25.1±3.9kg/m^2) have thus far participated. Kinematic and force data were recorded while participants walked on an instrumented, split-belt treadmill for 60 seconds at a self-selected speed (Stroke:0.85±0.26m/s;Non-Stroke:1.35±0.18m/s). We calculated a_{Lead} and a_{Trail} according to methods described in Figure 1 (Panel A). Two-way ANOVAs assessed the effects of Group (Stroke, Non-Stroke) and Limb (Paretic/Non-Dominant, Non-Paretic/Dominant) on contributions to a_{COM}.

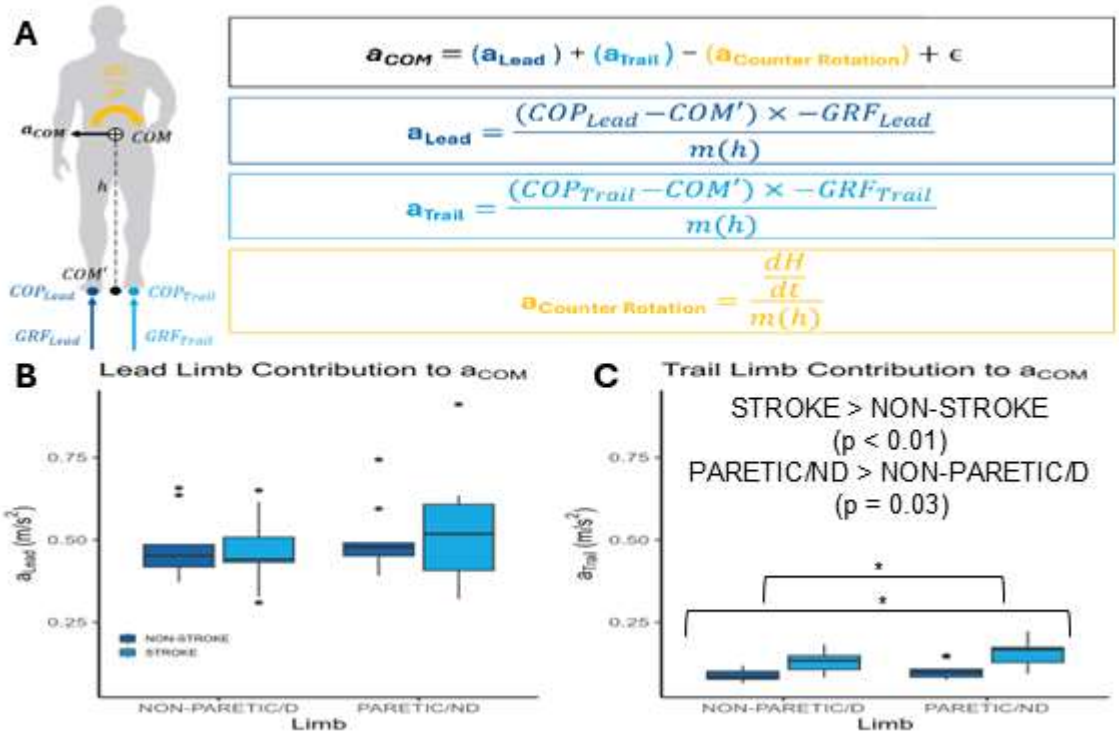
Results

We found no significant main effects or interactions containing Group or Limb ($p>0.05$, $\eta_p^2<0.04$) for a_{Lead} (Figure 1, Panel B). For a_{Trail}, we found significant main effects of Group ($p<0.01$, $\eta_p^2=0.39$) and Limb ($p=0.03$, $\eta_p^2=0.13$) (Figure 1, Panel C). Individuals with chronic stroke demonstrated significantly larger a_{Trail} compared to non-stroke individuals, regardless of limb ($p<0.01$, Cohen's $d=1.15$). Across all participants, the paretic/non-dominant limb demonstrated significantly larger a_{Trail} contributions compared to the non-paretic/dominant limb ($p=0.03$, Cohen's $d=0.74$).

Discussion

These findings suggest that chronic stroke is associated with an increase in a_{Trail} contributions affecting both limbs. Since individuals with chronic stroke exhibit wider step widths and a more laterally placed paretic limb, this result may be driven by larger COM-COP separation. It remains to be seen how a_{Trail} of those with chronic stroke changes when step widths are constrained. Despite demonstrating increases in a_{Trail}, individuals with chronic stroke did not appear to compensate with smaller a_{Lead} contributions compared to non-stroke individuals. Overall, these findings help identify a new, specific aspect of frontal-plane balance while walking that is altered after a stroke.

Images (Optional)



Acknowledgements (Optional)

This research was supported by the Eunice Kennedy Shriver National Institute Of Child Health & Human Development of the National Institutes of Health under Award Number F31HD115311. This work was also supported by the 2024 American Society of Biomechanics Graduate Student Grant-in-Aid Award and the University of Delaware Department of Kinesiology & Applied Physiology Doctoral Dissertation Award.

Session Category

Clinical Biomechanics: N/A

OA54-02

Toward Standardized Gait Event Detection: A Multicenter Evaluation of the Deep Learning-Based *IntellEvent A*lgorithm

MSc. Bernhard Dumphart[1,2,3], Dr. Djordje Slijepčević[4], Dr. Andreas Kranzl[5], MSc. Fabian Unglaube[5], Dr. Nathalie Alexander[6], MSc. Florian Dobler[6], Prof. Stéphane Armand[7], MSc. Marys Revaz[7], Dr. Britta Krautwurst[8,9], MSc. Gianna Klucker[9], Prof. Arnold Baca[10], Prof. Brian Horsak[1]

[1]Center for Digital Health & Social Innovation, University of Applied Sciences St. Pölten, St. Pölten, Lower Austria, Austria. [2]Institute for Health Sciences, University of Applied Sciences St. Pölten, St. Pölten, Lower Austria, Austria. [3]Vienna Doctoral School of Pharmaceutical, Nutritional, and Sport Sciences, University of Vienna, Vienna, Vienna, Austria. [4]Institute for Creative\Media/Technologies, University of Applied Sciences St. Pölten, St. Pölten, Lower Austria, Austria. [5]Laboratory of Gait and Movement Analysis, Orthopaedic Hospital Vienna-Speising,, Vienna, Vienna, Austria. [6]Laboratory for Motion Analysis, Department of Paediatric Orthopaedics, Children's Hospital of Eastern Switzerland, St. Gallen, St. Gallen, Switzerland. [7]Laboratory of Kinesiology, Geneva University Hospitals and University of Geneva, Geneva, Geneva, Switzerland. [8]Pediatric Orthopedics and Traumatology, University Children´s Hospital Zurich, Zurich, Zurich, Switzerland. [9]Pediatric Orthopedics and Traumatology, University Hospital Balgrist, Zurich, Zurich, Switzerland. [10]Centre for Sport Science and University Sports, University of Vienna, Vienna, Vienna, Austria

Introduction

Accurate gait event detection is essential for clinical gait analysis (CGA) [1]. However, commonly used heuristic approaches are sensitive to pathology and laboratory-specific differences [2]. Deep learning-based models demonstrate improved performance but are typically trained on single-center datasets [3]. Consequently, their generalizability remains uncertain due to variability in acquisition protocols, including capture frequency, walkway lengths, and marker placement. This study investigates the performance of *IntellEvent* [3] on three large-scale CGA datasets from different laboratories and examines whether multicenter training can mitigate laboratory-specific differences.

Methods

CGA data from gait laboratories in Vienna (OSS, 150Hz), St. Gallen (GL1, 200Hz), Geneva (GL2, 100Hz), and Zurich (GL3, 200Hz) were included, comprising 4,300 patients, totaling

over 26,000 trials. 70% of each laboratory's data was used for training, while the remaining 30% was used for evaluation. Data comprised pathologies like orthopaedic disorders (OD), neurological disorders (ND) and cerebral palsy (CP). Two approaches were compared: (1) *IntellEvent*, the original single-center model trained only on OSS data [3], and (2) *IntellEvent-Multicenter,* evaluated using a leave-one-lab-out cross-validation (Figure 1A). Performance was evaluated using mean absolute error (MAE) and detection rate (DR) within ±20ms [1] for initial contact (IC) and foot off (FO), based on force plate ground truth events.

Results

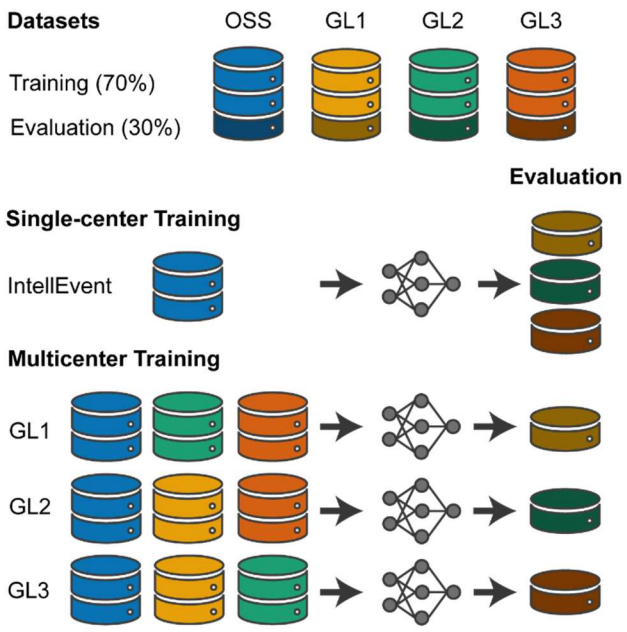
IntellEvent performed accurately across diverse laboratory-specific settings. IC was detected with MAEs of 2.3-7.0ms and DRs of 96.4-99.9%. FO showed higher variability with MAEs of 7.9-21.0ms and DRs of 77.4-96.0%. *IntellEvent-Multicenter* demonstrated small improvements for IC in GL2 and GL3, and consistently improved FO detection, reducing MAE to 6.4-17.4ms and increasing DRs to 80.7–98.8% (Figure 1B).

Discussion

These results underline that *IntellEvent* generalizes strongly across laboratories despite single-center training, yet multicenter training offers additional improvements, particularly for FO. This highlights that laboratory-specific differences can influence ML methods. Multicenter training is one approach to mitigate these effects by exposing the model to diverse data distributions, strengthening its suitability as a standardized tool for CGA. Future work could investigate fine-tuning as another alternative strategy.

Images (Optional)

A)



B)

Center	Patho.	Events	Initial Contact				Foot Off			
			IntellEvent		Multicenter		IntellEvent		Multicenter	
			ms (±SD)	*DR [%]*	*ms (±SD)*	*DR [%]*	*ms (±SD)*	*DR [%]*	*ms (±SD)*	*DR [%]*
GL1	OD	3013	**2.3 (3.2)**	99.9	3.3 (3.0)	**100.0**	9.1 (7.7)	94.6	**6.4 (5.7)**	**98.8**
	ND	696	4.2 (5.3)	98.3	**4.2 (4.5)**	**99.3**	10.6 (9.1)	91.2	**7.8 (7.9)**	**94.3**
	CP	597	**3.4 (4.6)**	**99.5**	4.2 (4.9)	98.8	10.6 (9.6)	89.9	**8.9 (9.8)**	**94.0**
	All	4306	**2.8 (3.9)**	99.6	3.5 (3.6)	**99.7**	9.6 (8.3)	93.4	**7.0 (6.9)**	**97.4**
GL2	OD	810	6.1 (6.3)	99.1	**5.2 (6.1)**	**99.5**	11.1 (12.7)	91.7	**9.4 (11.7)**	**95.8**
	ND	332	6.8 (7.9)	96.4	6.8 (9.2)	**97.0**	21.0 (27.7)	77.4	**17.4 (23.4)**	**80.7**
	CP	841	7.0 (7.6)	98.2	**6.0 (6.9)**	**98.9**	13.7 (13.4)	87.6	**11.6 (14.5)**	**91.0**
	All	1983	6.6 (7.1)	98.3	**5.8 (7.1)**	**98.8**	13.9 (16.8)	87.6	**11.7 (15.6)**	**92.6**
GL3	OD	1675	3.9 (4.5)	99.5	**3.5 (3.2)**	**99.9**	9.4 (7.7)	94.0	**7.2 (6.3)**	**97.6**
	ND	348	4.9 (5.9)	98.6	**4.1 (4.2)**	**99.7**	8.7 (7.1)	96.0	**7.5 (6.5)**	**98.6**
	CP	67	5.8 (10.2)	97.0	**5.2 (5.9)**	97.0	13.9 (14.5)	80.6	**10.4 (15.0)**	**92.5**
	All	2090	4.1 (5.1)	99.3	**3.7 (3.6)**	**99.8**	9.4 (8.0)	93.9	**7.5 (3.6)**	**97.4**

Figure 1. *A) Methodological workflow B) Performance of IntellEvent vs. IntellEvent-Multicenter across three large-scale gait laboratories. Mean absolute error (MAE) is reported in ms (±SD). Detection rate (DR) within ± 20 ms is reported in percent. Bold values highlight the best performance.*

References (Optional)

[1] B. Dumphart et al., Gait Posture, 2026

[2] R. Visscher et al., Gait Posture, 2021

[3] B. Dumphart et al., PLOS ONE, 2023

Session Category

Human Motion and Performance: Locomotion/Gait

OA54-03

Evaluation of Fall Risk of Elderly by Convolutional-Transformer Neural Network Using Time-Series Gait Data

PHD Student Jie Mao, Prof. Toshiaki Oda, Prof. Shigeho Noda, Prof. Zhe Sun, Prof. Ryutaro Himeno

Juntendo University, Graduate School of Health Data Science, Urayasu, Chiba, Japan

Introduction

Early identification and prevention of falls are pivotal for maintaining the health span of an aging global population. Traditional fall risk assessment relies on manual evaluation. Wearable IMU sensors offer a scalable solution for community screening, but most existing analysis methods rely on calculated biomechanical features, such as average stride length. This approach discards critical time-series information inherent in the signals. To address this limitation, we propose a Transformer-based model that learns directly from raw IMU sequences. This method achieves accurate assessment of fall risk, balance, and muscle strength, demonstrating superior performance and robustness compared to traditional feature engineering.

Methods

We collected data from 145 elderly individuals to assess Fall Risk and Physical Performance. Standardized scores from the CDC 4-Stage Balance Test and CS-30 test were used to categorize balance and strength into 5 levels. Combined with fall history, Fall Risk was categorized as high, medium, or low. Subsequently, subjects performed a 10m walk test while wearing IMUs on the lower back and toe tips.

To establish a baseline, we first evaluated traditional classifiers (SVM and Random Forest) using extracted gait features. Subsequently, we proposed our Convolutional-Transformer neural network. By leveraging attention mechanisms, this model captures complex long-range dependencies directly from raw IMU signals, thereby enhancing representation capability.

Results

The results demonstrated that traditional biomechanical features failed to generalize effectively when applied to a large-scale population. K-means clustering based on gait features failed to correspond effectively with risk categories (accuracy: 58.62%). The accuracy of SVM for binary classification was 65.38%, and the Random Forest model reached only 69.23%.

In contrast, the Transformer model, learning directly from raw IMU data, exhibited superior robustness and accuracy. For the 5-level balance ability classification, the model achieved an average accuracy of 75.25%; for the 5-level strength classification, accuracy reached 73.30%; and for the 3-level fall risk classification, the model achieved an accuracy of 70.4%, effectively identifying high-risk individuals.

Discussion

Deep learning on raw IMU data overcomes the generalization limitations of traditional averaged features. By leveraging attention mechanisms to identify complex non-linear gait dependencies, the Transformer offers a superior and more robust representation of physical performance.

Session Category

Human Motion and Performance: Locomotion/Gait

OA54-04

Biomechanics-Informed Energy Expenditure Estimation Durning Walking and Running Using a Single IMU

Dr. Jinsung Jung Ph.D[1], Prof. Hyerim Lim Ph.D[2], Prof. Sukyung Park Ph.D[1]

[1]KAIST, Yuseong-gu, Daejeon, Korea, Republic of. [2]Kumoh National Institute of Technology, Gumi-si, Gyeongsangbuk-do, Korea, Republic of

Dr. Jinsung Jung

Prof. Hyerim Lim

Introduction

Energy expenditure (EE) is a key indicator of metabolic cost and is widely used in fields such as sports science, daily activity monitoring, and wearable robotics. However, indirect calorimetry, the gold standard for EE measurement, suffers from limited wearability and practicality. Recent approaches using wearable sensors often require multiple sensors or rely on purely data-driven models with high data demands and low interpretability. Since prior studies have shown that mechanical joint power explains most EE [1], reducing the required biomechanical information is essential for practical single-sensor use. In this study, we propose a single-IMU EE estimation framework grounded in biomechanical domain knowledge for both walking and running. By analyzing joint-level mechanical contributions, we identify dominant segments and use them to construct an accurate yet lightweight EE estimation method.

Methods

We collected walking data from 13 participants and running data from 8 participants at five treadmill speeds each. Whole-body motion capture, GRF, and indirect calorimetry were recorded. Joint powers were computed using inverse dynamics, and dominant segments were selected based on their contributions. A sacrum-mounted IMU was used to estimate lower-limb dynamics, given its proximity to the COM [2]. Weighted joint power—using efficiency-based weights for positive and negative work—was computed for the dominant segment, and a scale factor mapping this to EE was derived and tested using leave-one-subject-out evaluation.

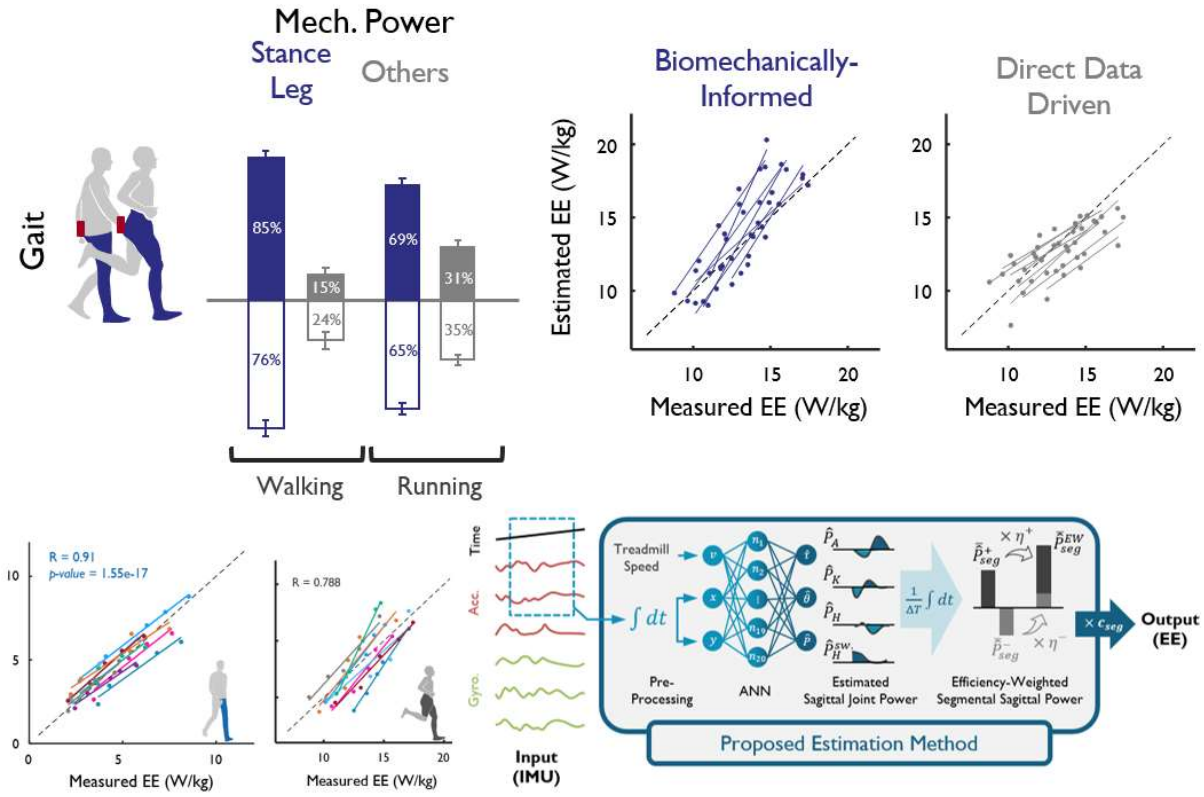
Results

Stance-leg joint power accounted for ~80% of whole-body power during walking and ~70% during running, confirming its dominant biomechanical role. IMU-estimated stance-leg dynamics enabled accurate EE prediction: walking RMSE was 0.69 W/kg, outperforming a prior deep-learning model (0.95 W/kg). In running, our method showed comparable RMSE (1.40 vs. 1.32 W/kg) but higher linearity (R=0.838 vs. 0.717) and no EE-dependent residual trends.

Discussion

Overall, incorporating biomechanical structure enabled a practical, interpretable, and high-performance single-sensor EE estimation framework suitable for daily monitoring applications.

Images (Optional)



References (Optional)

[1] R. Riddick and A. Kuo, Sci. Reports, 2022

[2] H. Lim et al., Sensors, 2019

Acknowledgements (Optional)

This work was supported by the National Research Foundation of Korea (NRF) grant funded by the Korea government (MSIT) (RS-2024-00356657)

Session Category

Human Motion and Performance: Locomotion/Gait

OA54-05

Detecting Slips on Ice Using Wearable Inertial Sensors: *Identifying Kinematic Features for Classifying Slip Events*

Mr. Davood Dadkhah[1,2], Dr. Hamed Ghomashchi[2], Dr. Hosna Movahhedinia[1], Dr. Tilak Dutta[1,2]

[1]University of Toronto, Toronto, Ontario, Canada. [2]University Health Network, Toronto, Ontario, Canada

Introduction

Falls due to slips on icy surfaces remain a persistent public health challenge, causing injuries and placing significant burdens on healthcare systems in cold-weather regions. The ability to identify slip events from data collected using wearable sensors would allow for comparing the potential for reducing the risk of slipping across different interventions, including different types of winter footwear or slip-prevention training. The objective of this project was to identify the best feature set from our wearable sensor data that could be used to identify slip events during gait.

Methods

Data was collected from 27 healthy adults walking on a 5m by 5m ice surface in WinterLab at the KITE Research Institute using inertial measurement units (IMU) that were attached to each foot, as well as a Vicon motion capture system that provided ground-truth labels. Each participant wore three different commercially available winter boots and walked on a range of slopes from level to 13 degrees. Over 400 features were engineered from the IMU measurements using a combination of time, frequency, and nonlinear domains. A leave-one-participant-out cross-validation was performed to evaluate the created features using XGBoost classifiers, and feature importance was ranked for discriminating slip events.

Results

Results revealed three biomechanical signatures that robustly distinguished slips from non-slips on the anterior-posterior (AP) axis: (1) dominant spectral amplitude of acceleration, (2) positive Hilbert envelope area, and (3) number of rotational peaks in AP-axis angular velocity. Slip steps consistently demonstrated stronger, more energetic AP acceleration frequency components and greater cumulative movement intensity, alongside markedly increased oscillations. For the most important feature, dominant spectral

amplitude on the AP axis, the median value was approximately 50% higher for slip steps compared to non-slip steps.

Discussion

These findings establish, for the first time, the specific kinematic features that best discriminate naturally occurring slips on ice during controlled ice walking. By identifying the signal characteristics of slips, this work enables more targeted design and development of wearable systems for real-time slip detection, as well as objective methods for measuring the slip resistance performance of winter footwear, advancing both fundamental understanding and practical solutions for injury prevention in icy environments.

Session Category

Human Motion and Performance: Locomotion/Gait

OA55-01

Lower Extremity Kinematics During Ice Hockey Goaltender Stances

Ms. Margaret Harrington BKin, Dr. Timothy Burkhart PhD

University of Toronto, Toronto, Ontario, Canada

Introduction

Goaltending techniques have evolved to include goaltenders dropping to their knees to cover the lower part of the net, utilizing stances such as the butterfly and reverse vertical horizontal (RVH). These stances are suggested to place considerable stress on the hip, knee, and ankle joints compared to traditional stances (e.g., standing, vertical horizontal (VH)) [1,2]. However, the kinematic differences between these techniques and potential injury risk implications have not been fully explored. Therefore, this study aimed to quantify three-dimensional lower extremity joint kinematics during key goaltending stances.

Methods

Twenty-six goaltenders (mean (SD) age = 19.5 (2.3) years, six females) performed four key goaltending stances: butterfly, standing ready, RVH post-play, and VH post-play. For the post-plays, the post-side and net-side limbs were analyzed separately. Eight synchronized Sony 2D video cameras and Theia3D were used to quantify 3D hip, knee, and ankle angles. One-way repeated-measures ANOVAs or Friedman tests assessed differences in joint angles across tasks, along with effect sizes and Bonferroni-corrected post hoc comparisons.

Results

There were statistically significant differences ($p < 0.001$) between the tasks for all joint angles. Large effect sizes were shown for all hip angles, knee flexion and internal rotation, and ankle dorsiflexion. Medium effect sizes were shown for knee adduction, ankle external rotation and inversion. The butterfly and RVH, compared with the standing ready and VH, demonstrated higher mean hip internal rotation (16.6-22.2° vs. 5.2-11.4°) and ankle external rotation (11.7-15.9° vs. -1.6-10.8°) (Figure 1). Compared to the standing ready, the kneeling stances involved higher knee abduction (12.4-15.1° vs. 5.6°) and external rotation (13.0-21.3° vs. 0.7°) (Figure 1).

Discussion

The butterfly and RVH showed riskier kinematics for common hip, knee, and ankle injuries in goaltenders. Such injuries may result from the high hip internal rotation (e.g., femoroacetabular impingement syndrome and labral tears), knee abduction and external rotation (e.g., medial collateral ligament injuries and meniscal tears), and ankle external rotation (e.g., high ankle sprains). These findings provide new insights into the biomechanical demands of goaltending and how they may correspond to injury risk.

Images (Optional)

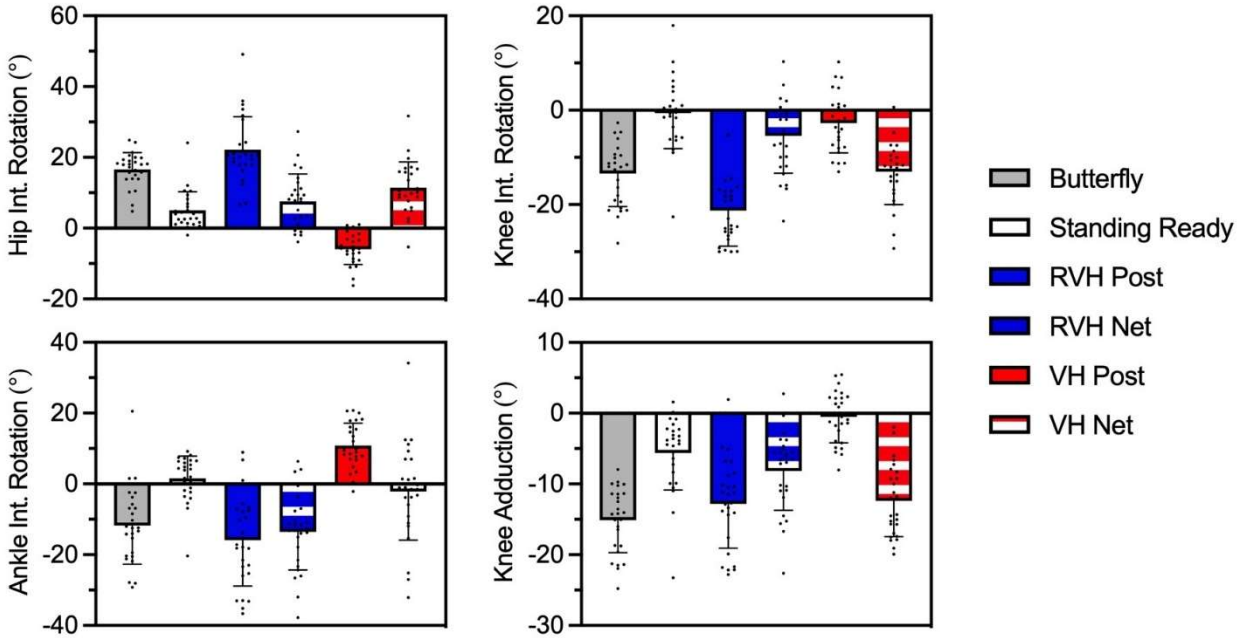


Figure 1. Group mean (SD) 3D hip, knee and ankle internal rotation and knee adduction angles. Y-axis labels indicate positive motion directions. Dots represent individual participant averages across three trials.

References (Optional)

[1] Wörner *et al.,* Orthop J Sports Med, 2021; [2] Keshen *et al.,* Am J Sports Med, 2025

Session Category

Human Motion and Performance: Sports

OA55-02

Ground Reaction Force Characteristics During Salcow and Loop Jumps in a Novice and a Junior Figure Skater: A Case Study

Ms Ami Koga, Dr Jingmin Liu

Tsinghua University, Beijing, Beijing, China

Introduction

Youth figure skaters are often exposed to substantial overuse injury risks due to repetitive and high-impact jump practices. Previous figure skating biomechanical studies have mostly focused on jump kinematics, and there are limited studies on examining on-ice force generation patterns and impact on the lower limbs across different skill-level skaters. Therefore, this study aims to compare the ground reaction force characteristics between jumps of two different skill-level skaters.

Methods

One novice level skater and one junior level skater performed single salcow, double salcow, single loop and double loop jumps. Two high speed cameras (Sony FDR-AX700, 100Hz) were used to record skaters' kinematics. W-INSHOE system from Medicapteur (8 sensors per foot, 100 Hz) was used for plantar pressure measurements at jump's take-off and landing. Ground reaction force (GRF) data obtained using plantar pressure insole were normalized using body weight (BW). Peak GRF and loading rate between skaters were compared. Due to limited data, only descriptive analysis was conducted.

Results

Detailed results of GRF variables of two skaters can be seen in Table 1. Junior skater's GRF variables including peak GRF and loading rate at jump take-off and landing are generally greater than novice skater. While junior skater's take-off force-time curves during salcow jumps followed monomodal patterns, novice skater's curves followed bimodal patterns. Landing force-time curves of all jumps showed similar patterns, which the landing leg's GRF spikes upon initial contact at the landing, then slightly decreases as lower limbs flex to stabilize the body and to absorb impact force.

Discussion

The differences in salcow jump take-off force-time curve patterns between two skaters potentially indicate technical differences between them. Moreover, junior skater

demonstrated higher peak GRF and loading rate at take-off, which indicate that junior skater applies more explosive and faster force generation to achieve greater take-off vertical velocity and jump height. However, higher impact forces especially at the landing also indicate higher risks of lower limb injuries. Novice skaters are in earlier stage of their technical development and focused more on controlled force distribution rather than explosiveness. Therefore, novice skater may benefit from more strength training.

Images (Optional)

Table 1. Ground reaction force variables during figure skating salcow jump and loop jump

	Novice	Junior	Differences (%)
Single Salcow			
Take-off 1st peak GRF (BW)	1.25	-	-
Take-off 2nd peak GRF (BW)	0.73	2.01	93.4
Landing peak GRF (BW)	2.86	2.52	12.6
Take-off 1st loading rate (BW/s)	3.95	-	-
Take-off 2nd loading rate (BW/s)	0.85	5.58	147.9
Landing loading rate (BW/s)	10.5	23.3	76.1
Double Salcow			
Take-off 1st peak GRF (BW)	0.99	-	-
Take-off 2nd peak GRF (BW)	0.78	2.07	90.6
Landing peak GRF (BW)	3.36	3.85	13.6
Take-off 1st loading rate (BW/s)	4.17	-	-
Take-off 2nd loading rate (BW/s)	1.11	5.58	66.3
Landing loading rate (BW/s)	11.5	23.6	69.0
Single Loop			
Take-off peak GRF (BW)	3.07	3.68	18.1
Landing peak GRF (BW)	2.74	4.19	41.8
Take-off loading rate (BW/s)	2.21	8.99	121.4
Landing loading rate (BW/s)	13.2	21.8	48.9
Double Loop			
Take-off peak GRF (BW)	2.94	3.81	25.8
Landing peak GRF (BW)	2.74	4.31	44.5
Take-off loading rate (BW/s)	1.99	8.49	124
Landing loading rate (BW/s)	9.75	20.8	72.3

Session Category

Human Motion and Performance: Sports

OA55-03

Kinematic Differences Across Development Levels in Elite Biathletes

Mr Ethan Livingood, Mr Isaac Burgess MS, Dr. James Becker PhD

Montana State University, Bozeman, MT, United States

Introduction

Numerous studies have described differences in physiological parameters between junior (JN), national (NC), and world class (WC) biathletes. However, how global movement patterns while skiing differ between these groups is unknown and addressing this gap might highlight important technique points which coaches can target when working with athletes progressing from junior to world class ranks. Thus, the purpose of this study was to compare full-body kinematics during V2 skate skiing between JN, NC, and WC biathletes.

Methods

Thirteen WC (sex: 8M/5F, age: 27 ± 3.8 years) eight NT (sex: 6M/3F, age: 25 ± 3.9 years), and nine JN (sex: 4M/5F, age: 18 ± 1.1 years) biathletes skied on a ski treadmill at race intensity while whole body 3D kinematics were recorded using markerless motion capture. Joint angles at the shoulder, elbow, trunk, hip, knee, and ankle were calculated using a 12-segment biomechanical model. Cycles were normalized to 100% of cycle and Statistical Parametric Mapping (SPM1D) was used to assess temporal differences in joint kinematics between the groups.

Results

SPM revealed JN demonstrated greater sagittal and lateral trunk flexion than both NC and WC athletes before pole plant ($p < 0.05$), more elbow flexion during the poling phase ($p < 0.05$), less hip flexion during the transition from one ski to the other ($p < 0.05$), and, reduced hip abduction during the return phase of the cycle ($p < 0.05$).

Discussion

The differences between JN and NC and WC athletes reveal deficits in ski technique in younger athletes. Increased elbow flexion during the poling phase suggests JN athletes are allowing greater collapse of the arms while poling which reduces the force transmitted through the poles. Reduced hip abduction during the leg recovery might indicate decreased lateral balance, requiring JN athletes to bring the leg closer to their center of

mass after the push. Overall, the differences observed here highlight specific phases of a V2 skate skiing cycle where JN level athletes show different movement patterns than NC or WC athletes which could be targeted for technique interventions to help these athletes progress to NC or WC levels.

Images (Optional)

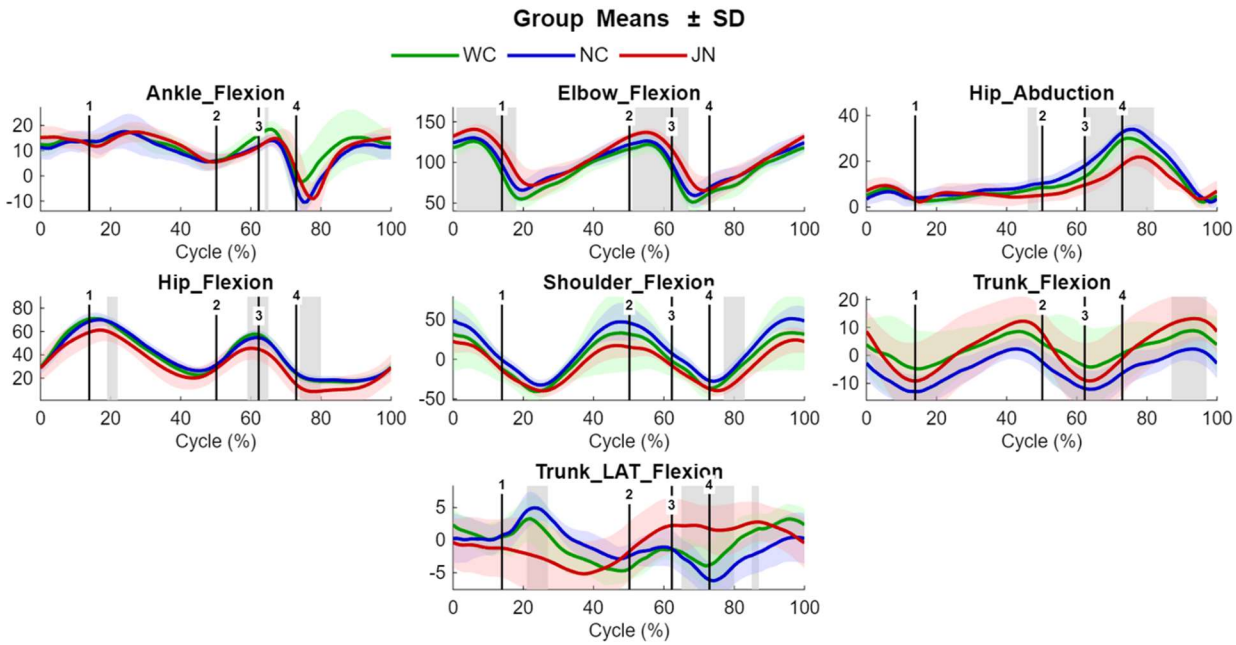


Figure 1. Group mean right leg joint angles (± SD) normalized to 100% V2 skate skiing cycle, defined from pole plant on the right ski to the subsequent plant. Vertical markers indicated events in the ski cycle: 1) right pole off; 2) right leg peak force; 3) left ski contact; 4) left ski peak force. Gray shaded bands show regions in the cycle with significant differences between groups as identified by SPM with an $\propto$ of 0.05.

Session Category

Human Motion and Performance: Sports

OA55-04

Comparison of Fully-Rotated and Under-Rotated Figure Skating Jumps by Key Performance Metrics

Dr. Mia Caminita PhD[1], Dr. Dustin Bruening PhD[2], Ms. Elizabeth Klemm MS[3], Dr. Michael Jones PhD[2], Dr. Sarah Trager Ridge PhD[4]

[1]Children's National Hospital, Silver Spring, MD, United States. [2]Brigham Young University, Provo, UT, United States. [3]East Carolina University, Greenville, NC, United States. [4]University of Hartford, West Hartford, CT, United States

Introduction

In competition, figure skating jumps are evaluated by technical specialists who determine if the jump was fully-rotated. According to the International Judging System (IJS), up to 90° rotation after landing is permitted for a jump to still be considered fully-rotated. Jumps under-rotated by >90° are assigned a downgraded score. However, no studies have identified key performance metrics (KPMs) that quantitatively distinguish fully-rotated ("good") from under-rotated jumps. Therefore, the purpose of this study was to compare KPMs between fully rotated and under-rotated jumps using a waist mounted IMU to support technique optimization and training decisions.

Methods

Fifty-nine competitive skaters performed double (DJ) and triple (TJ) jumps (n=157) wearing a waist-mounted IMU synchronized with video to identify take-off and landing events and full rotation status according to IJS standards. TJ were performed by high and elite skaters (U.S. Figure Skating (USFS) levels Novice and above), while DJ were performed by lower-level skaters (USFS Preliminary-Intermediate). KPMs calculated were: air time (t_{air}), peak angular velocity (ω_p), % of expected rotations completed ($R_{\%}$), and angular velocity at landing as a percent of peak angular velocity ($\omega_{Land\%\omega p}$). One-way ANOVAs were performed with Tukey pairwise post-hoc tests (a=0.05).

Results

All KPMs showed significant main effects ($p<0.001$). Under-rotated triple jumps (URTJ) demonstrated significantly decreased t_{air} ($p=0.019$) and $R_{\%}$ ($p=0.003$) compared with good triple jumps (GTJ) (Figure 1). Similarly, under-rotated double jumps (URDJ) demonstrated significantly decreased $R_{\%}$ ($p<0.001$) compared with good double jumps (GDJ). ω_p was not significantly different between GTJ and URTJ ($p=0.182$), however, ω_p decreased significantly

in URDJ compared to GDJ (p=0.04). $\omega_{Land\%\omega p}$ of URTJ was significantly increased as compared to GTJ (p=0.039), while no difference was observed between URDJ and GDJ (p=0.343).

Discussion

Both URDJ and URTJ had significantly decreased t_{air} demonstrating this as a KPM. Further, our findings demonstrate that even fully-rotated figure skating jumps judged under IJS standards achieve only 73% of the nominal three rotations for triples and 64% of the two rotations for doubles. This is likely due to on-ice pre-rotation during take-off. Awareness of this discrepancy is important for interpreting wearable-sensor data. Monitoring these KPMs may guide technique adjustments, training-load, and competition-readiness decisions.

Images (Optional)

Jump Type	t_{air} (s)	$R_{\%}$	ω_p (deg/s)	$\omega_{Land\%\omega p}$
Good Triples (High/Elite)	0.54 ± 0.05	72.9 ± 5.5	1747 ± 122.2	90.8 ± 10.9
Under-rotated Triples (High/Elite)	0.50 ± 0.04	65.6 ± 4.3	1681 ± 116.9	95.9 ± 5.3
Good Doubles (Low)	0.38 ± 0.06	64.3 ± 3.4	1410 ± 127.1	79.3 ± 13.2
Under-rotated Doubles (Low)	0.31 ± 0.06	49.8 ± 9.3	1318 ± 129.1	88.1 ± 12.9
Statistics				
Main Effects	p<0.001	p<0.001	p<0.001	p<0.001
Triple Jumps GTJ vs. URTJ	p=0.019	p=0.003	p=0.182	p=0.039
Double Jumps GDJ vs. URDJ	p<0.001	p<0.001	p=0.004	p=0.343

Session Category

Human Motion and Performance: Sports

OA56-02

Biventricular Heart Model with Novel Pseudo-Fluid Domains and Thermodynamically-Motivated Growth & Remodeling

Mr. Darshan Senthil, Dr. Jamie Concannon, Dr. Ryan Coleman, Prof. Patrick McGarry

University of Galway, Galway, Galway, Ireland

Introduction

A common flaw in finite element (FE) heart models is the unphysical specification of predetermined ventricle pressure or volume. We propose a novel "pseudo-fluid" framework in which active myocardium contractility drives changes in ventricular volume and pressure, both of which are computed model outputs. We also develop a novel thermodynamically-based model for cardiomyocyte and myocardium growth and remodelling.

Methods

We process MRI images of healthy human hearts to create 3D patient-specific biventricular meshes with distinct myocardium and "pseudo-fluid" domains representing blood in each ventricular cavity (Fig.1A). Our constitutive law for myocardial tissue includes active contractility of cardiac myocytes [1] and passive anisotropic collagen in the ECM [2]. The "pseudo-fluid" material model incorporates bespoke windkessel-type constitutive laws based on aortic and pulmonary compliance and peripheral resistance.

Our novel thermodynamic model entails the computation of the myocardium free energy, which consists of active free energy due to cardiomyocyte contractility, and passive strain energy due to deformation of inter-cellular collagen. Deviation of the total free energy from a healthy homeostatic free energy acts a driver for evolution of cell morphology and sarcomere/myofibril remodelling.

Results

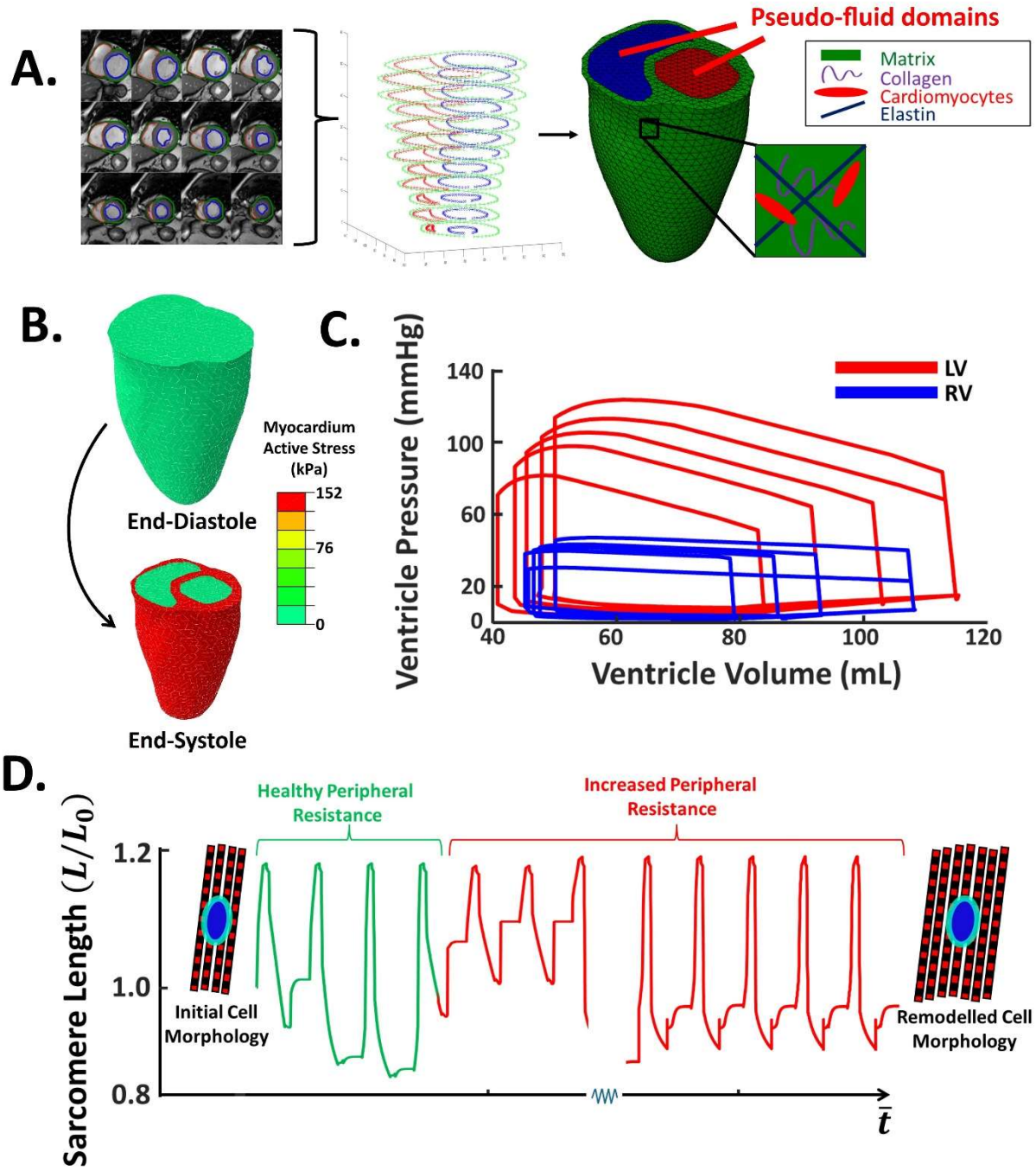
The deformation and active stress distribution in a patient-specific heart is shown in Fig.1B. Physiologically accurate levels of deformation and twist are computed during systole. Fig.1C shows predicted changes in PV loops following inferior vena cava occlusion (IVCO). Physiological accurate reductions in pressure, stroke volume and end-diastole volume are computed. Predictions of sarcomere remodelling in response to increased peripheral resistance are shown in Fig.1D. Initially, sarcomeres are unable to shorten sufficiently during systole, increasing the myocardium free energy over the course of a

cardiac-cycle. This results in the addition of sarcomeres in parallel, leading to enhanced contractility and a restoration of homeostatic free energy. The increase in cell thickness results in concentric hypertrophy.

Discussion

At a run time of approximately 20 minutes per cardiac cycle, our framework can potentially be used as a real-time clinical diagnostic tool. We accurately predict the short-term response to IVCO[3]. Furthermore, we uncover a thermodynamic cell-level mechanism for concentric hypertrophy[4].

Images (Optional)



References (Optional)

[1]Concannon et.al.,Acta.Biomater.2021.

[2]McEvoy et.al.,J.Mech.Behav.Biomed.Mater.2021.

[3]Seemann et.al.,J.Cardiovasc.Mag.Reson.2023

[4]Sharifi et.al.,Ann.Biomed.Eng.2024

Session Category

Cardiovascular/Cardiorespiratory Biomechanics: Methods, Models and Applications

OA56-03

Patient-Specific Investigation of Septal Repositioning Effects on Intraventricular Hemodynamics in Pediatric Dilated Cardiomyopathy

Ms. Weiru Luo PhD Candidate

Waseda University, Shinjuku, Tokyo, Japan

Introduction

Pulmonary artery banding (PAB) has emerged as a promising therapy for pediatric dilated cardiomyopathy (DCM), yet the mechanism by which PAB-induced interventricular septal (IVS) repositioning improves left ventricular (LV) function remains unclear. Clinical observations consistently report an acute leftward septal shift after PAB. However, its impact on intraventricular flow organization, vortex dynamics, and energetic efficiency has not been quantitatively characterized. This study aimed to elucidate the fluid-mechanical consequences of PAB-induced septal repositioning using a patient-specific computational hemodynamics framework.

Methods

Pre- and post-PAB LV geometries were reconstructed from cine MRI, with septal repositioning characterized by echocardiography and incorporated into the patient-specific post-PAB model. Transient blood flow was simulated in ANSYS Fluent using an Arbitrary Lagrangian–Eulerian (ALE) formulation with dynamic-mesh ventricular wall motion. Hemodynamic indices including flow patterns, vortex structures (Q-criterion), kinetic energy (KE), and volume-normalized viscous dissipation were quantified across the cardia cycle and compared.

Results

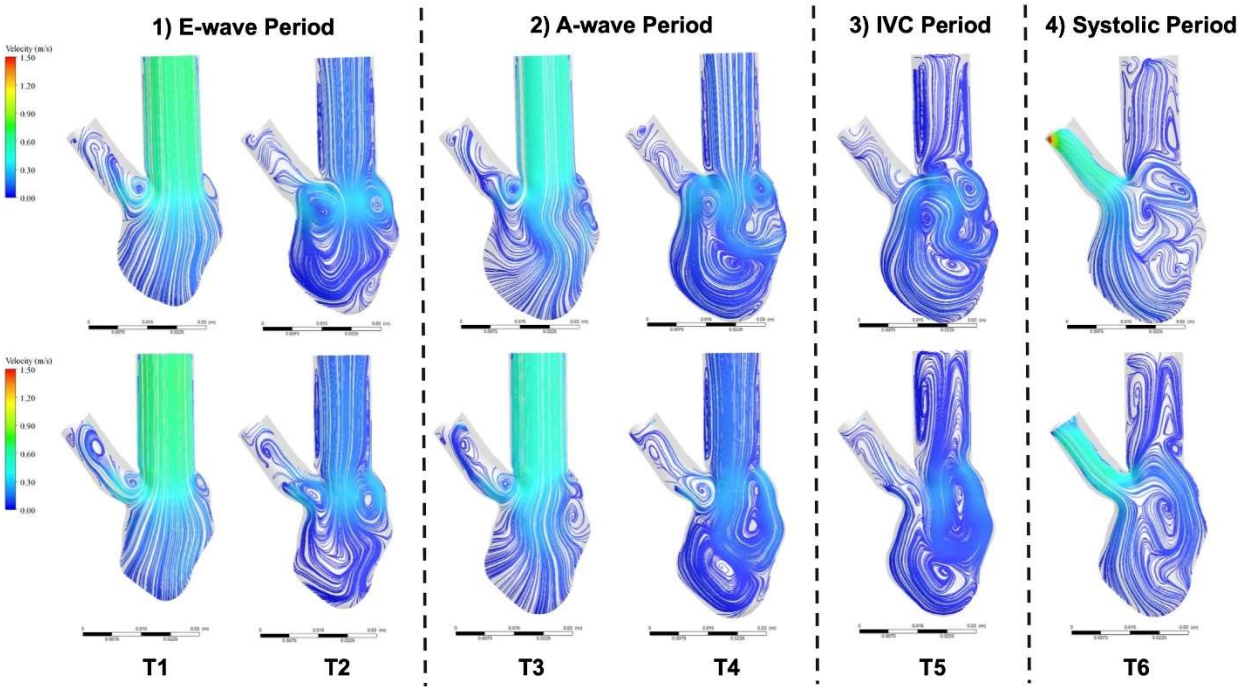
Echocardiography revealed a spatially heterogeneous leftward septal shift, most pronounced in the basal region, resulting in substantial LV geometric reconfiguration. As illustrated in Fig.1, this displacement compressed diastolic vortex rings (E-wave and A-wave) and redirected their propagation toward the aortic outflow tract. The apical vortex was repositioned closer to the apex, suggesting enhanced apical washout. During systole, the pre-PAB ventricle exhibited multiple dissipative vortices, whereas the post-PAB model was dominated by a single coherent jet-oriented vortex. Energetically, the post-PAB model demonstrated lower mean systolic KE, indicating a reduction in inefficient fluid recirculation. Conversely, viscous dissipation increased following PAB, reflecting the

shear cost associated with accelerating blood through the narrowed septal-outflow channel.

Discussion

PAB-induced septal repositioning reorganizes intraventricular flow, suppressing disordered vortices and promoting a more coherent ejection jet. The associated energetic trade-off, lower recirculatory KE but higher viscous dissipation, suggests a physiologically meaningful redistribution of mechanical energy that enhances systolic efficiency. However, this sustained elevation in viscous dissipation may impose a long-term energetic burden on the myocardium. Furthermore, the altered flow near the mitral annulus suggests a potential risk for valvular dysfunction, highlighting the importance of longitudinal patient monitoring. These findings provide fluid mechanistic insight into the therapeutic effects of PAB on pediatric DCM.

Images (Optional)



Session Category

Cardiovascular/Cardiorespiratory Biomechanics: Methods, Models and Applications

OA56-04

Modeling Cardiac Growth and Fiber Remodeling in a Finite Element model of Left Ventricular Mechanics

Ir. Britt van Kerkhof, Ir. Kelly Keulen, Dr. Ir. Peter Bovendeerd

Eindhoven University of Technology, Eindhoven, North Brabant, Netherlands

Introduction

The heart adapts via changes in mass (growth) and tissue properties (remodeling). Computational models of cardiac growth and remodeling (G&R) can be used to describe G&R in response to disease or treatment. However, published computational G&R models focus on growth alone [1]. In reality, G&R occur concurrently, with fiber orientation likely to be subject to remodeling. We combined the growth model of [1] with fiber remodeling of [2] in a Finite Element (FE) model of cardiac mechanics to simulate cardiac G&R under physiological loading conditions, where a stable end configuration is to be expected.

Methods

This study builds on the FE model in [3]. Remodeling of fiber orientation is assumed to minimize mechanics-induced reorientation during the cardiac cycle [2]. Local tissue growth is driven by the deviation of tissue work density from a homeostatic set point [1]. After each G&R step the grown state is adopted as the new stress-free state for the subsequent mechanics step. Three simulations were performed: no G&R (INIT), growth only (G), and both processes (GFR), each covering 6 cycles.

Results

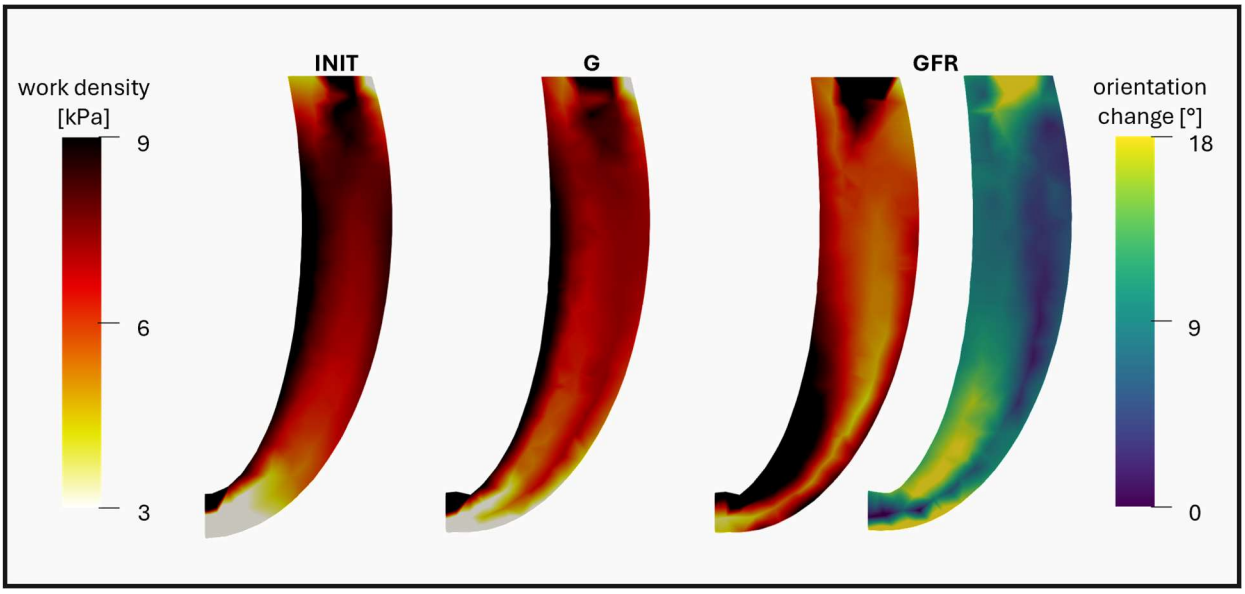
In both G and GFR, the left ventricular (LV) geometry shows apical thinning and midwall thickening. Spatially averaged work density evolves towards the homeostatic value of 6.7 kPa, from 7.4±1.8 kPa in INIT, to 6.9±1.9 kPa in G, and in 6.9±2.2 kPa in GFR (Fig. 1). Wall and cavity volume rise from 136 ml and 44 ml in INIT to 145 ml and 52 ml in both G and GFR. Fiber orientation changes by 8.3° on average in GFR (Fig. 1).

Discussion

We investigated whether a combined G&R model could reproduce a stable healthy LV configuration, based on a local stimulus-effect relation. Preliminary results show that the LV geometry grows from ellipsoidal to more spherical. FR affects work density, and slightly

affects growth. Additional cycles are needed to evaluate whether the combined G&R model evolves to a steady state.

Images (Optional)



References (Optional)

[1] Van Osta *et al.*, FIMH, LNCS, 2019.

[2] Kroon *et al.*, Med.Imag.Anal., 2009.

[3] Bovendeerd *et al.*, Am.J.Physiol.Heart.Circ.Physiol, 2009.

Acknowledgements (Optional)

This research was supported by the European Union's Horizon 2020 research and innovation program under grant agreement 874827 (BRAVƎ).

Session Category

Cardiovascular/Cardiorespiratory Biomechanics: Methods, Models and Applications

OA56-05

An Integrated Experimental-Computational Approach to Modeling the Mechano-Energetic Cost of Cardiac Contractility

Mr. Tanmay Mukherjee MS, Mr. Emilio Mendiola BS, Dr. Sunil Venkategowda PhD, Dr. Carl Tong MD, PhD, Dr. Mahua Choudhury PhD, Dr. Reza Avazmohammadi PhD

Texas A&M University, College Station, TX, United States

Introduction

Cardiac remodeling in cardiometabolic disease is increasingly linked to reduced ATP availability needed to support normal myofiber contraction. When energy supply becomes insufficient, the mechanical processes that enable force generation are affected. While separate endeavors have been devoted to studying the mechanical and metabolic mechanisms of cardiac structure-function, the mechanistic link across mechano-metabolic cues governing contractility remains understudied. In this study, we present an experimental-computational model devoted to delineating the mechano-energetic cost of cardiac contractility.

Methods

The left ventricular free wall (LVFW) was harvested from 8-10-week-old wild-type mice and immediately placed in PBS at 1°C. Mechanical testing was performed to measure passive stiffness at 30% equibiaxial stretch (M and F; n = 4 each). Energetics were quantified by homogenizing 10 mg of LVFW tissue using buffer A and analyzing the supernatant ATP concentration (M and F; n = 4 each, Fig. 1A). A constitutive model of mechano-energetics was implemented to recapitulate myofiber shortening using experimentally obtained ATP concentration (Fig. 1B).

Results

Bias in passive stresses towards the circumferential axis, in comparison to the longitudinal direction was evidenced, indicating the inherent anisotropy in the cardiac tissue (Fig. 1C). Sex-specific changes were also confirmed via LVFW stiffness (Fig. 1D). Baseline ATP concentration was measured in the supernatant LVFW tissue with significant sex-specific changes (Fig. 1E). The model represented metabolite production (*ATP, NADH,* and *ADP*) using simple ordinary differential equations of respective mass fractions ( ), and incorporated a hyperelastic formulation of the passive LV tissue to compute total stresses consistent with experimentally measured values.

Discussion

The alterations in stiffness and ATP levels suggest that sex-specific disruptions in mechano-metabolic coupling may be vital in examining early disease progression. Importantly, the mechano-metabolic measures presented herein may provide insight into fiber-level remodeling even before measurable cardiac dysfunction appears. For example, impaired relaxation in diastolic dysfunction has been linked to metabolic or “active” deficits at the protein level, as well as increased “passive” stiffness of the myocardial tissue, while preserving the heart’s ejection fraction. Our results indicate the ability to model the complex mechano-metabolism within the heart by establishing the mechano-energetic cost of cardiac contractility.

Images (Optional)

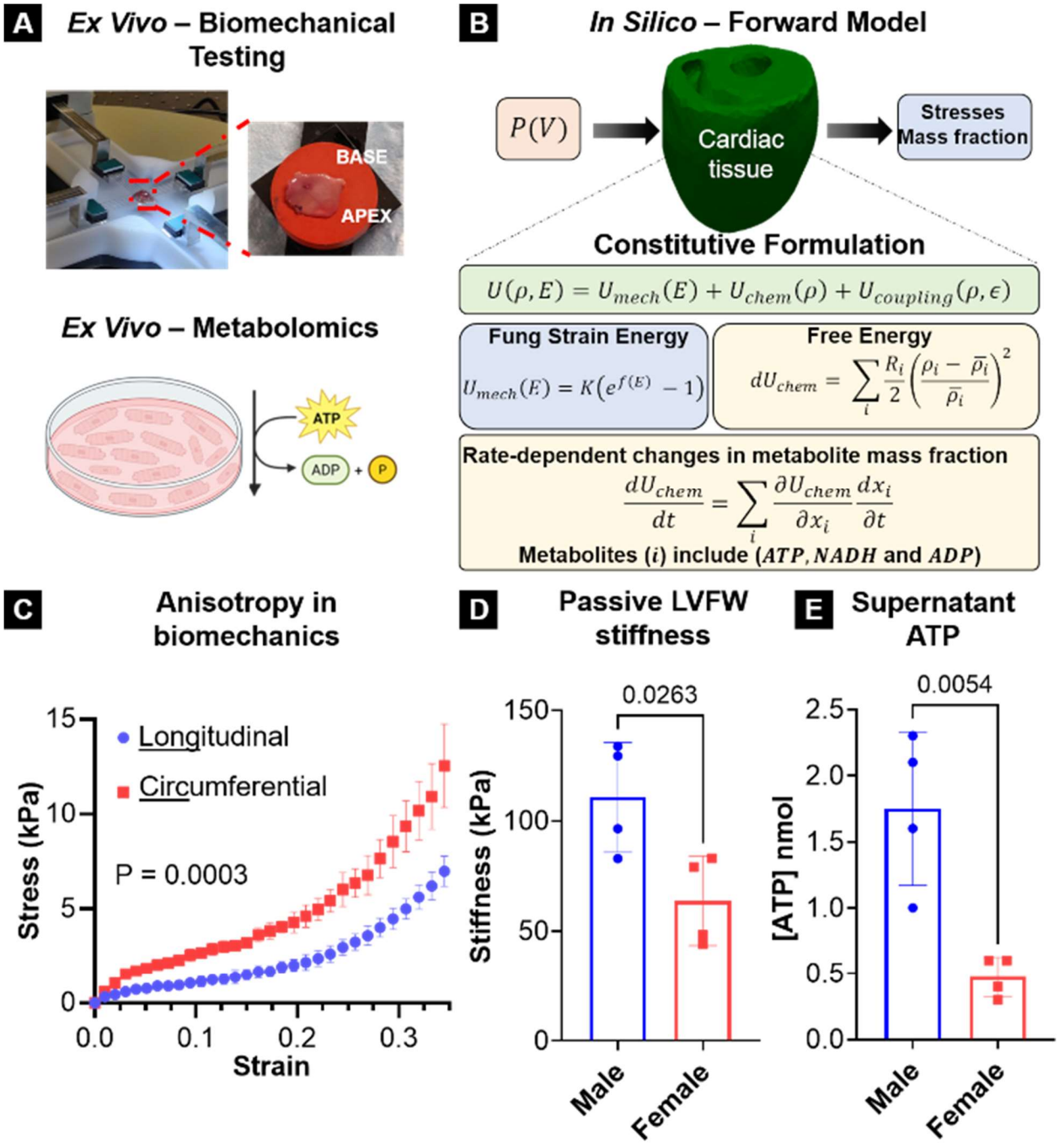


Figure 1. (A) Ex-vivo benchtop testing of the left ventricular free wall (LVFW) tissue. **(B)** Schematic of the constitutive model to formulate cardiac mechano-energetics through Hyperelastic stress formulation (E) and Free energy-based model of metabolite mass fraction (ρ). **(C)** Representative passive stress of the LVFW at an equibiaxial stretch of 30%. **(D)** Passive LVFW stiffness, measured as the tangent modulus of the stress-strain curve at 30% stretch. **(E)** Supernatant ATP concentration measured through a luciferase-based assay. Statistical analysis was performed using two-way ANOVA for the growth-curves and Student's t-test for the mechano-metabolic measures of cardiac contractility.

Acknowledgements (Optional)

This research was supported by the National Institutes of Health R01HL168368 to R.A and American Heart Association (AHA) predoctoral fellowship 24PRE1240097 to T.M.

Session Category

Cardiovascular/Cardiorespiratory Biomechanics: Methods, Models and Applications

OA57-01

Frame Alignment Improves Agreement between Marker-Based and Markerless Knee Kinematics in Children with Cerebral Palsy

Dr. Eric Dugan PhD[1,2], Dr. Ariana Ortigas-Vásquez PhD[3], Dr. Adrian Sauer PhD[4], Ms Katelyn Campbell MS[1]

[1]Texas Children's Hospital, The Woodlands, TX, United States. [2]Baylor College of Medicine, Houston, TX, United States. [3]ETH Zürich, Zürich, Zürich, Switzerland. [4]Aesculap AG, Tuttlingen, Baden-Württemberg, Germany

Introduction

Markerless motion capture offers a promising alternative for clinical gait analysis, but notable differences from marker-based data have been reported in children with cerebral palsy (CP) [1]. These discrepancies may arise from differences in segment coordinate frame definitions. Ortigas-Vásquez et al. introduced the REFRAME method, which reconciles coordinate frames across modalities using a constrained optimization [2], and Antognini et al. showed that this alignment substantially reduced apparent knee kinematic differences [3]. In children with CP, we hypothesized that 1) REFRAME would markedly reduce systematic differences between marker-based and markerless knee kinematics and 2) markerless data would capture both the magnitude of stride-to-stride variability and, after alignment, the same trial-specific deviation patterns observed in marker-based measurements.

Methods

Fifty-one children with CP (GMFCS I–III) participated in simultaneous marker-based and markerless three-dimensional gait analysis during barefoot walking. Markerless segment orientations were optimized to marker-based orientations using REFRAME. Knee joint angles from both systems were compared before and after alignment. The primary outcome was root-mean-square error (RMSE) across the gait cycle. Secondary outcomes evaluated stride-to-stride variability using within-subject standard deviation (wSD) and directional agreement based on correlations of trial-specific deviation vectors.

Results

Before alignment, sizable between-system differences were present, particularly in frontal and transverse motions. REFRAME reduced RMSE by approximately 50 to 75 percent across planes, yielding post-alignment values below a conservative 3-degree clinical threshold (Figure 1). Within-subject variability was similar between marker-based and markerless measurements even before alignment, and equivalence testing confirmed that

wSD differences were biomechanically trivial. Directional agreement increased significantly after frame harmonization, indicating that both systems detected trial-to-trial deviations more consistently once coordinate-frame differences were removed.

Discussion

REFRAME improved agreement between marker-based and markerless knee kinematics in children with CP while preserving natural stride-to-stride variability. These findings indicate that most pre-alignment discrepancies likely reflected coordinate-frame inconsistencies rather than differences in how each system tracked the underlying movement. Incorporating frame harmonization may enable markerless motion capture to serve as a reliable and scalable tool for pediatric gait assessment.

Images (Optional)

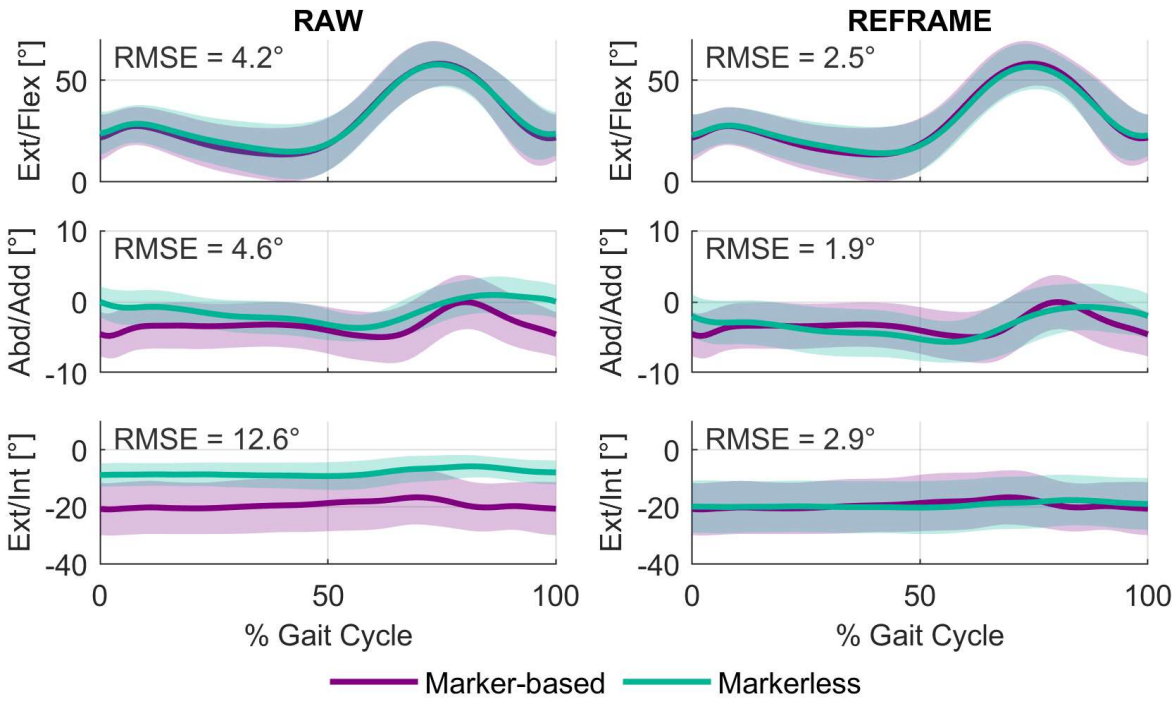


Figure 1. Knee angles: marker-based (purple) vs. markerless (green), before (left) and after REFRAME (right). Mean ± SD over gait cycle. RMSE shown in subplots.

References (Optional)

[1] Wren et al., *Gait & Posture*, 2023

[2] Ortigas Vásquez et al., *Scientific Reports*, 2023

[3] Antognini et al., *Journal of Biomechanics*, 2025

Session Category

Musculoskeletal Biomechanics: Methods, Models and Applications

OA57-02

Development and Validation of a Multi-Camera Dynamic 3D Foot Scanning System for Kinematic Analysis in Flexible Flatfoot

Mr. LEI LI, Dr. Hok Sum MAN, Dr. Ming ZHANG

the Hong Kong Polytechnic University, Hong Kong, Hong Kong, Hong Kong

Introduction

Flatfoot is a common deformity characterized by medial longitudinal arch collapse, often leading to pain and impaired gait. Current orthotic design relies heavily on static assessments, which fail to capture dynamic foot morphology during walking. This study aims to develop and validate a novel dynamic 3D foot scanning system to capture high-frame-rate foot shapes during gait, enabling markerless multi-segment foot tracking and kinematic analysis in individuals with flexible flatfoot.

Methods

A dynamic 3D foot scanning system was constructed using eight synchronized Intel RealSense D455 cameras, capturing both geometric and texture data at 60 Hz. System repeatability and accuracy were validated using a rigid foot model compared against a commercial laser scanner (XPOD-S). Four foot segments (shank, rearfoot, forefoot, hallux) were defined using anatomical landmarks, and a two-step point-to-plane iterative closest point (PL-ICP) algorithm was implemented for segment tracking. Kinematic parameters were derived from segment transformations and compared between flatfoot (FPI ≥ 6, n=8) and normal foot (n=18) groups during walking.

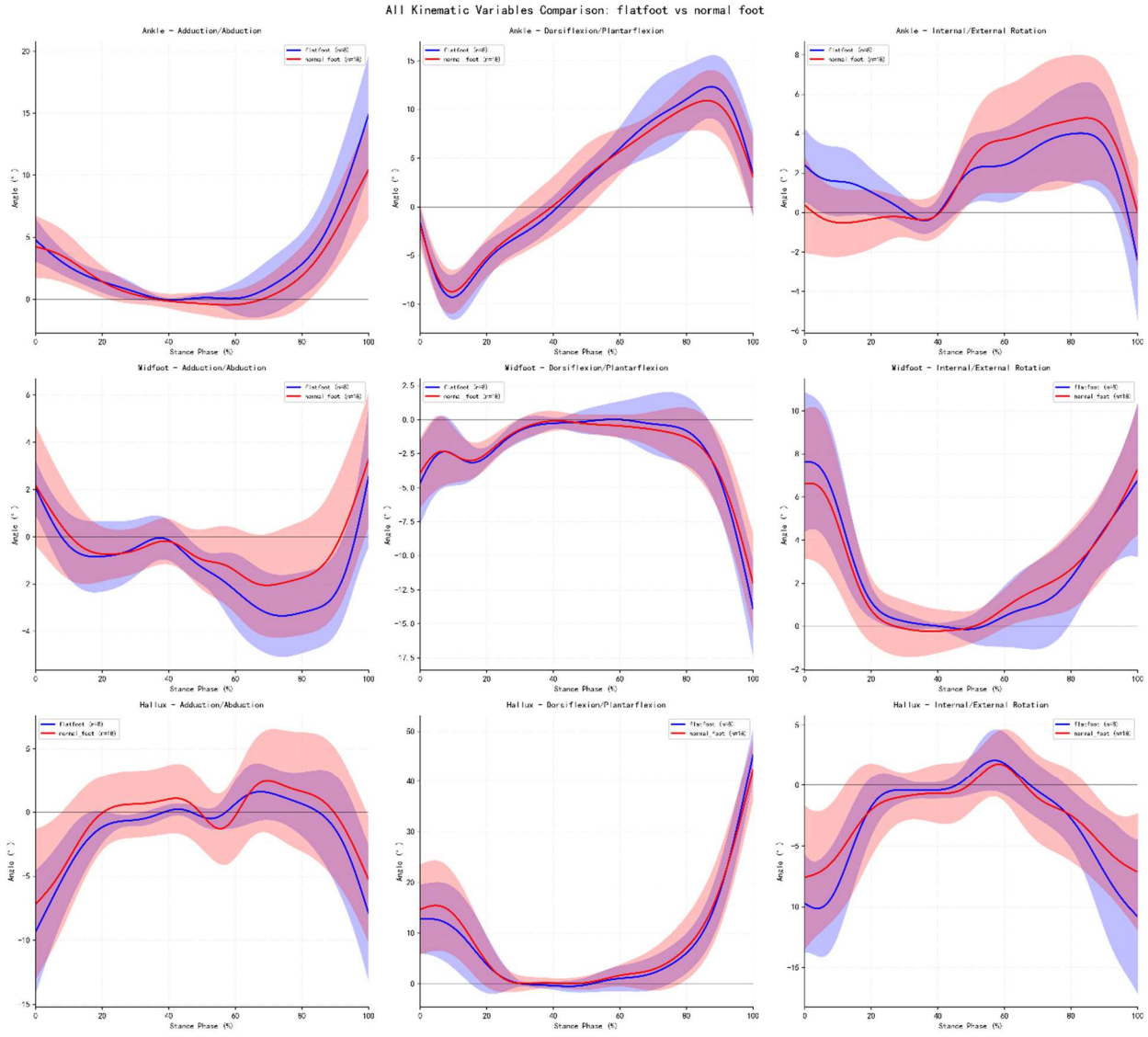
Results

The system demonstrated good repeatability, with 94.3% of static scan overlap area within ±0.5 mm deviation, and 90% of dynamic scans within 1.34 mm of the reference model. Segment tracking achieved high fitness scores (≥0.90) and sub-millimeter RMSE across all segments. Kinematic analysis revealed that individuals with flatfoot exhibited significantly greater rearfoot abduction ($p=0.0256$) and coronal-plane range of motion ($p=0.0289$) compared to normal feet, while other spatiotemporal and kinematic parameters were comparable.

Discussion

The developed system provides a cost-effective, accurate, and repeatable method for dynamic 3D foot assessment. The proposed tracking algorithm outperforms existing methods in stability and accuracy, particularly during high-velocity gait phases. The observed kinematic differences highlight specific compensatory patterns in flatfoot gait, supporting the potential for dynamic morphology to inform orthotic design. Future work will include validation against gold-standard motion capture and application of principal component analysis to quantify foot deformation modes for personalized orthotic development.

Images (Optional)



Session Category

Musculoskeletal Biomechanics: Methods, Models and Applications

OA57-03

Estimating Lower Limb Joint Moments, Muscle Forces, and Joint Contact Forces from Video

Dr Amir Esrafilian[1,2], Dr Tian Tan[1], Dr Nicholas Bianco[1], Dr Anthony Gatti[1], Asst Professor Akshay Chaudhari[1], Dr Jennifer Hicks[1], Professor Scott Delp[1]

[1]Stanford University, Stanford, California, United States. [2]University of Eastern Finland, Kuopio, North Savo, Finland

Introduction

Quantifying joint moments, muscle forces, and joint contact forces (JCFs) is valuable for understanding musculoskeletal conditions. While video-based motion analysis can estimate body kinematics accurately, estimating internal forces remains limited to resource-demanding marker-based motion capture (Mocap) and computational modeling. Here, we adapted a machine learning (ML) model to estimate lower-limb joint moments, muscle forces, and JCFs from video-based kinematics.

Methods

We used an OpenSim musculoskeletal model [1] and Mocap and ground reaction force data from the AddBiomechanics Dataset [2] (273 individuals, 6-84 years) to obtain gold-standard kinematics, joint moments, muscle forces (static optimization), and JCFs. Ten individuals had videos synced with Mocap data. We adopted GaitDynamics ML model [3], and trained it using 70% of Mocap and 30% of video-based data. ML model inputs were lower-limb joint coordinates, velocities, and accelerations. We used pelvis-ground and bilateral hip, knee, and ankle joints, totaling 15 degrees of freedom (Fig. 1-A). The ML model outputs were joint moments (3 components per joint), muscle forces (40 muscles per leg), and JCFs (3 components per joint) time series. Here, we reported results for seven unseen individuals, with kinematics obtained from (i) single and (ii) dual video camera [4,5].

Results

Compared to musculoskeletal model, the ML model had an overall normalized root mean square error (NRMSE) of 9.2±3.1% for dual and 10.3±3.8% for single camera systems in estimating joint moments, muscle forces, and JCFs. Demonstrated for a selected subject (Fig. 1-B, dashed lines), ML model estimated magnitudes and temporal patterns of kinetics consistent with musculoskeletal modeling.

Discussion

The ML model estimated subject-specific and task-specific lower-limb kinetics from kinematics, surpassing the accuracy of previous studies and predicting a larger set of outputs (e.g., our JCF-NRMSE: 4.8-12.7% vs. literature: 4.5-32.5%). Our ML model enables fast (few minutes from camera setup to results) and low-cost movement analysis, offering the potential to assist in personalized musculoskeletal disorder management and performance optimization.

Images (Optional)

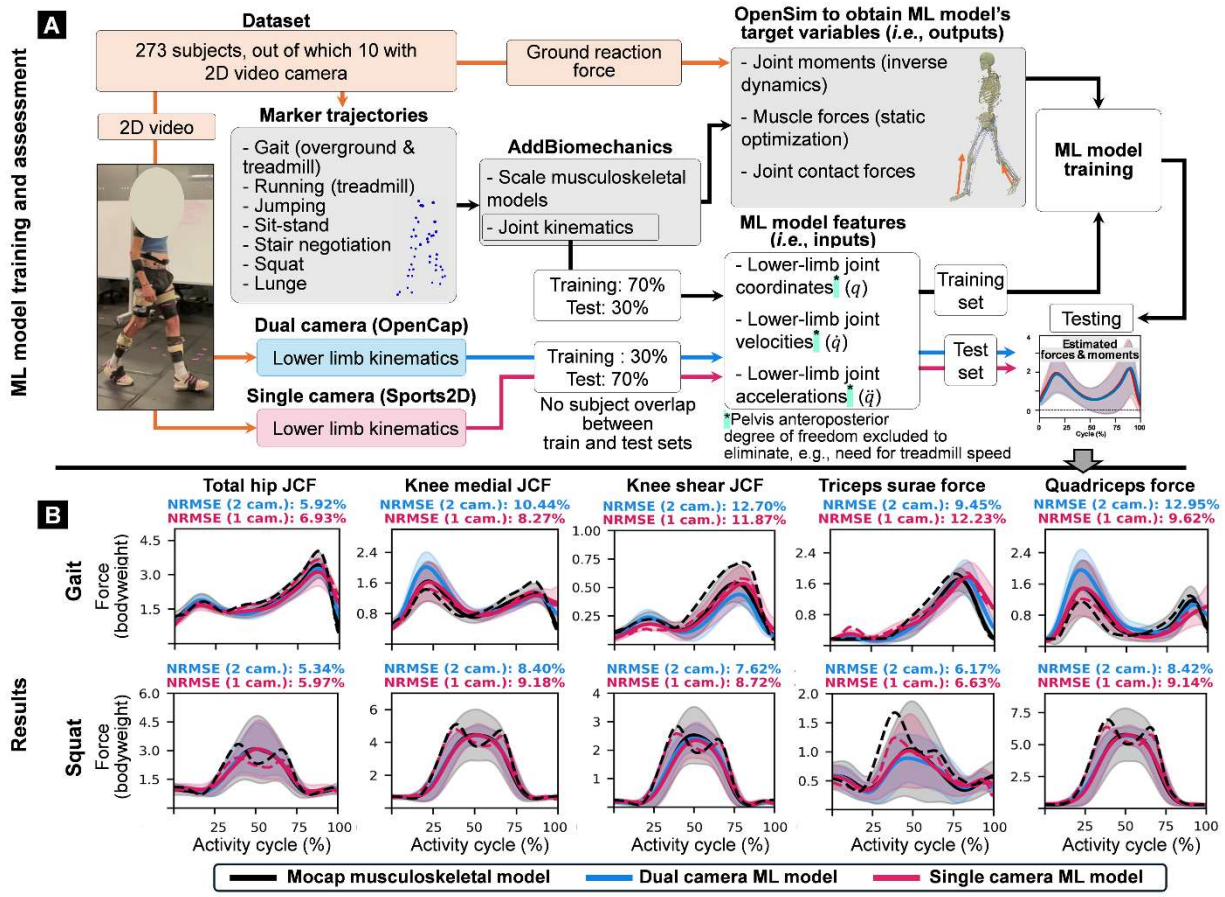


Fig. 1: A) Study workflow; ML model training using the AddBiomechanics dataset. **B)** A subset of ML outputs based on kinematics from dual (in blue) and single (in red) video camera, along with musculoskeletal analysis of Mocap data (in black). The mean NRMSE of all trials is reported, comparing the corresponding ML model with musculoskeletal analysis. Solid lines in plots illustrate mean ± one standard deviation, and dashed lines illustrate results from one representative subject.

References (Optional)

[1] Apoorva Rajagopal *et al.*, IEEE-TBME, 2016; [2] Keenon Werling *et al.*, PLoS ONE, 2023; [3] Tian Tan *et al.*, Nat Biomed Eng, 2025; [4] David Pagnon *et al.*, JOSS, 2024; [5] Scott Uhlrich *et al.*, PLoS Comput Biol, 2023.

Acknowledgements (Optional)

European Union’s Horizon 2020 MSCA-IF #101108335, Finnish Cultural Foundation #00230091.

Session Category

Musculoskeletal Biomechanics: Methods, Models and Applications

OA57-04

Quantifying Marker-Wise Kinematic Sensitivity in the Shriner Children's Gait Model Using Individual Marker Error Analysis

Grant Schwiebert[1,2], Matthew Parrett M.Ed.[1], Mallory Rowan M.S.[1], Jessica Lewis PT, DPT[1], Dr. Sean Tabaie MD[1], Dr. Kirsten Tulchin-Francis PhD[1]

[1]Nationwide Children's Hospital, Columbus, Ohio, United States. [2]The Ohio State University, Columbus, Ohio, United States

Introduction

Marker placement error (MPE) and soft tissue artifact (STA) produce well-documented deviations in gait kinematics. Most clinical models, including the Shriner Children's Gait Model (SCGM), provide qualitative guidance on which markers most strongly influence joint angles. However, no
quantitative placement sensitivity or tolerances accompany these qualitative statements. This study used an Individual Marker Error Analysis (IMEA) pipeline to map marker-specific perturbations to resulting kinematic deviations for the SCGM.

Methods

A walking trial from a healthy adult was processed using a vectorized Python re-implementation of SCGM. Each marker was perturbed individually representing 3-D MPE. Perturbations were applied in segmental anatomical coordinate systems and mapped into global space to emulate bone-fixed offsets. For each perturbation, the SCGM static calibration and dynamic kinematics were recomputed. A finite-difference gradient-descent search identified the perturbation directions that maximized angle error for each axis, while linear interpolation estimated mean sensitivities (deg/mm). For each marker–axis pair, an allowable placement tolerance was computed based on preserved angle errors of ≤2% of gait cycle range of motion.

Results

IMEA quantitatively confirmed most SCGM-designated critical alignment axes. Markers identified by SCGM as essential for segment-axis definition, particularly the ASIS and medial/lateral knees and malleoli, showed the highest sensitivity to marker placement upwards of 3.0 to 6.6°/mm (Table 1) and represented errors seen across all planes.

Similarly, most markers which SCGM classified as having minimal critical alignment (e.g. PSIS) displayed correspondingly low sensitivities, often <0.01°/mm confirming negligible influence on lower-limb joint angles.

Discussion

IMEA provides the first numerical placement tolerances for SCGM, quantitatively validating the model's most influential alignment axes while identifying several markers whose true kinematic impact is far lower than implied by their qualitative labels. While IMEA characterizes marker-wise kinematic sensitivity, it does not model soft-tissue artifacts. Incorporating probabilistic STA distributions and marker-placement variability would allow for fully probabilistic IMEA weighting. Integrating these distributions with fuzzy-logic or Bayesian frameworks could enable real-time, uncertainty-aware estimation of true joint kinematics across gait cycles, enhancing clinical interpretation, surgical planning, and treatment evaluation. Future work will expand to multi-participant, multi-session datasets to establish population-level sensitivity ranges and subject-specific placement tolerances.

Images (Optional)

Marker Sensitivities

Angle	Marker	X sens (°/mm)	Y sens (°/mm)	Z sens (°/mm)
Ankle Dorsiflexion	ASIS	0.010	0.020	0.009
Foot Progression	ASIS	0.001	0.002	0.004
Hip Ab/Adduction	ASIS	0.707	2.575	0.309
Hip Flexion	ASIS	0.389	2.392	0.244
Hip Rotation	ASIS	0.287	2.696	0.582
Knee Flexion	ASIS	0.089	0.805	0.191
Knee Rotation	ASIS	0.048	0.127	0.180
Knee Var/Valgus	ASIS	0.110	0.337	0.104
Pelvic Obliquity	ASIS	0.869	1.785	0.253
Pelvic Rotation	ASIS	0.254	1.762	0.877
Pelvic Tilt	ASIS	0.338	1.811	0.178
Trunk Lateral Bend	ASIS	0.124	0.381	0.156
Trunk Rotation	ASIS	0.012	0.034	0.013
Trunk Tilt	ASIS	0.035	0.305	0.067
Ankle Dorsiflexion	Lateral Malleolus	0.379	0.357	0.259
Foot Progression	Lateral Malleolus	2.103	0.569	2.282
Knee Flexion	Lateral Malleolus	0.110	0.171	0.154
Knee Rotation	Lateral Malleolus	1.174	0.881	1.540
Knee Var/Valgus	Lateral Malleolus	0.522	0.141	0.549
Ankle Dorsiflexion	Lateral Malleolus	0.774	0.433	0.526
Foot Progression	Medial Malleolus	0.107	0.047	0.066
Knee Flexion	Medial Malleolus	0.130	0.088	0.236
Knee Rotation	Medial Malleolus	1.225	0.795	2.284
Knee Var/Valgus	Medial Malleolus	0.046	0.029	0.017
Ankle Dorsiflexion	Lateral Knee	0.477	0.159	0.334
Foot Progression	Lateral Knee	0.510	0.098	0.541
Hip Ab/Adduction	Lateral Knee	0.791	0.111	0.280
Hip Flexion	Lateral Knee	0.655	0.154	0.686
Hip Rotation	Lateral Knee	5.119	0.996	5.179
Knee Flexion	Lateral Knee	1.610	0.365	1.772
Knee Rotation	Lateral Knee	4.517	0.875	4.550
Knee Var/Valgus	Lateral Knee	3.374	0.562	2.818
Ankle Dorsiflexion	Medial Knee	0.136	0.129	0.077
Foot Progression	Medial Knee	0.005	0.005	0.004
Hip Ab/Adduction	Medial Knee	0.008	0.007	0.008
Hip Flexion	Medial Knee	0.073	0.112	0.063
Hip Rotation	Medial Knee	0.616	0.936	0.530
Knee Flexion	Medial Knee	0.252	0.321	0.189
Knee Rotation	Medial Knee	0.578	0.873	0.493
Knee Var/Valgus	Medial Knee	0.211	0.317	0.270

Session Category

Musculoskeletal Biomechanics: Methods, Models and Applications

OA57-05

Accuracy of Markerless Motion Capture Tibiofemoral Rotations Benchmarked Against Biplane Videoradiography

Miss Lauren Swain, Miss Janine Flohr, Prof Cathy Holt, Dr David Williams

Cardiff University, Cardiff, Wales, United Kingdom

Introduction

Markerless motion capture is an emerging technology for human motion analysis, with the potential to replace marker-based motion capture as it removes the need for marker placement, a time-consuming process requiring skilled personnel. Markerless motion capture has been shown to produce average joint angle differences of 2.6-13.2° compared to marker-based equivalents [1]. However, the true accuracy of markerless motion capture can only be determined by comparison to a gold standard, such as biplane videoradiography (BVR) [2].

Methods

Video footage from 10 Miqus cameras was captured simultaneously with BVR whilst 3 healthy volunteers (2M/1F) carried out a sit-down activity. Theia3D (Theia) was used to calculate whole-body kinematics from the video footage, including 3 degrees-of-freedom at the knee. Bone models segmented from MRI (Simpleware, ScanIP) were registered to pairs of X-rays (SlicerAutoscoperM [3]) for each frame of the activity. Anatomical coordinate systems were applied to the bone models [4] and 3 DOF BVR knee rotations were calculated from the bone poses (MATLAB, Mathworks) using the joint coordinate system approach [5]. An adaptive lowpass Butterworth filter was applied to all rotations.

Results

Figure 1 shows the 3 rotations for both methods, normalised to percentage activity. Flexion was generally well predicted (RMSE±SD: 6.21±1.22°); however, the total range of motion was underestimated by Theia3D. Adduction had the smallest RMSE of the three rotations (4.79±3.37°), whereas external rotation had the largest differences between the two methods (13.86±9.98°). Theia3D struggled to track the knee for HV02 due to occlusion by the X-ray equipment, leading to drop out and worse agreement when filtering was applied.

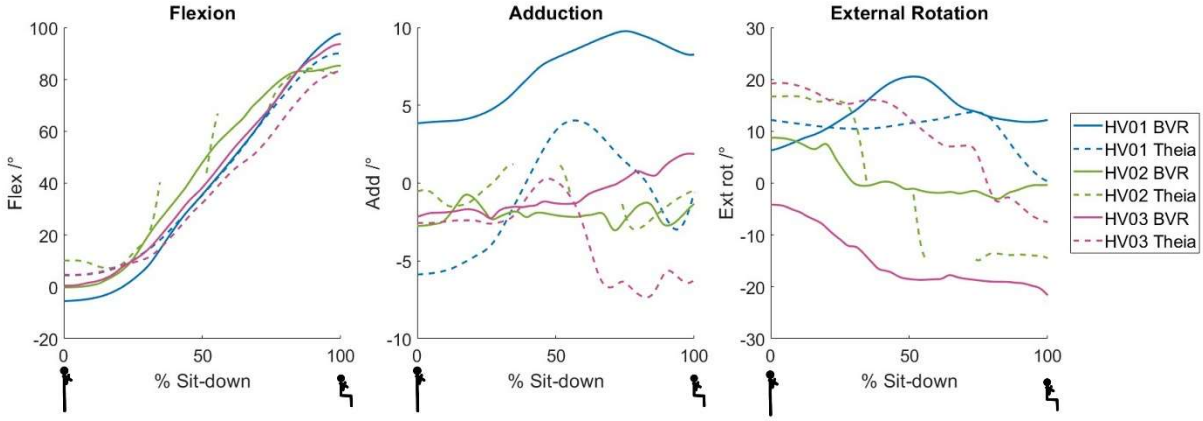
Discussion

These pilot results show the importance of comparing markerless motion capture kinematics to gold-standard BVR to understand its true accuracy. Future work will expand the comparison to more activities and participants, including pathological cohorts, as well

as comparison with marker-based motion capture to gauge markerless performance against the current clinical gold-standard.

Images (Optional)

Figure 1 – The three knee rotations for a sit-down calculated by Theia3D and BVR for the three healthy participants.



References (Optional)

[1] Robert Kanko *et al.*, J Biomechanics, 2021
[2] Logan Wade *et al.*, J Biomechanics, 2022
[3] Amy Morton *et al.*, J Biomechanics, 2025
[4] Daniel Miranda *et al.*, J Biomechanics, 2010
[5] Grood and Suntay, J Biomechanical Engineering, 1983

Acknowledgements (Optional)

Funding from the Engineering and Physical Sciences Research Council (EPSRC): EP/X039870 (Holt & Williams) and EPSRC UKRI3014 POST DOCTORAL PATHWAYS FUNDING (Swain)

Session Category

Musculoskeletal Biomechanics: Methods, Models and Applications

OA57-06

Pelvic Tracking During Gait in Overweight and Obese Individuals

Mr. Niels Dur MSc, MD[1], Ms. Lianne Damink MSc[2], Ms. Erin Macri PhD[1], Ms. Mariska Wesseling PhD[1,3], Mr. Jaap Harlaar Professor, PhD[1,3], Mr. Wouter Schallig PhD[1]

[1]Erasmus MC University Medical Center, Rotterdam, Zuid-Holland, Netherlands. [2]Haaglanden Medical Center, The Hague, Zuid-Holland, Netherlands. [3]TU Delft Technical University, Delft, Zuid-Holland, Netherlands

Introduction

Given the global rise of obesity, accurate 3D motion analysis methods tailored to this population is needed. Pelvic kinematics measured with conventional marker models using skin-mounted anterior superior iliac spine (ASIS) markers, such as CGM 2.4, may be inaccurate due to substantial soft tissue artifacts [1]. An alternative approach uses a sacral marker cluster combined with pointer-based calibration of virtual ASIS markers. This method showed promise in individuals with a normal body mass index (BMI) [2], but has not yet been evaluated in an overweight population. This study aimed to compare pelvic kinematics and hip joint center (HJC) locations derived from these two models in a healthy-weight group and an overweight group.

Methods

Ten healthy-weight (mean BMI 23.0±1.7) kg/m^2) and ten overweight/obese (mean BMI 33.7±5.2 kg/m^2) adults were included. Gait analysis was conducted on a treadmill using CGM 2.4 and an additional sacral marker cluster to track the pelvis. A probe was used to calibrate the virtual ASIS in the sacral cluster. Pelvic kinematics and HJC locations were calculated for three consecutive steps with and without the cluster. Statistical parametrical mapping paired t-tests were performed to test for significant differences over the gait cycle in pelvic kinematics and HJC.

Results

No differences were observed in pelvic kinematics between methods for the healthy-weight group. In the overweight group, significant mean differences up to 10° were observed for pelvic obliquity throughout most of the gait cycle (see Figure 1). For HJC trajectories, statistically significant differences were observed in the anteroposterior direction in healthy-weight (mean 15mm) and overweight groups (mean 28mm) and in the superoinferior direction in the overweight group (mean 22mm).

Discussion

The use of a sacral cluster with pointed virtual ASIS markers provided different, and potentially more accurate, estimates of pelvic orientation and HJC in overweight individuals compared to a conventional model. It does, however, affect HJC estimates in healthy-weight individuals. While confirmation in a larger sample is required, this method may be more accurate than conventional models when performing gait analysis in overweight or obese individuals.

Images (Optional)

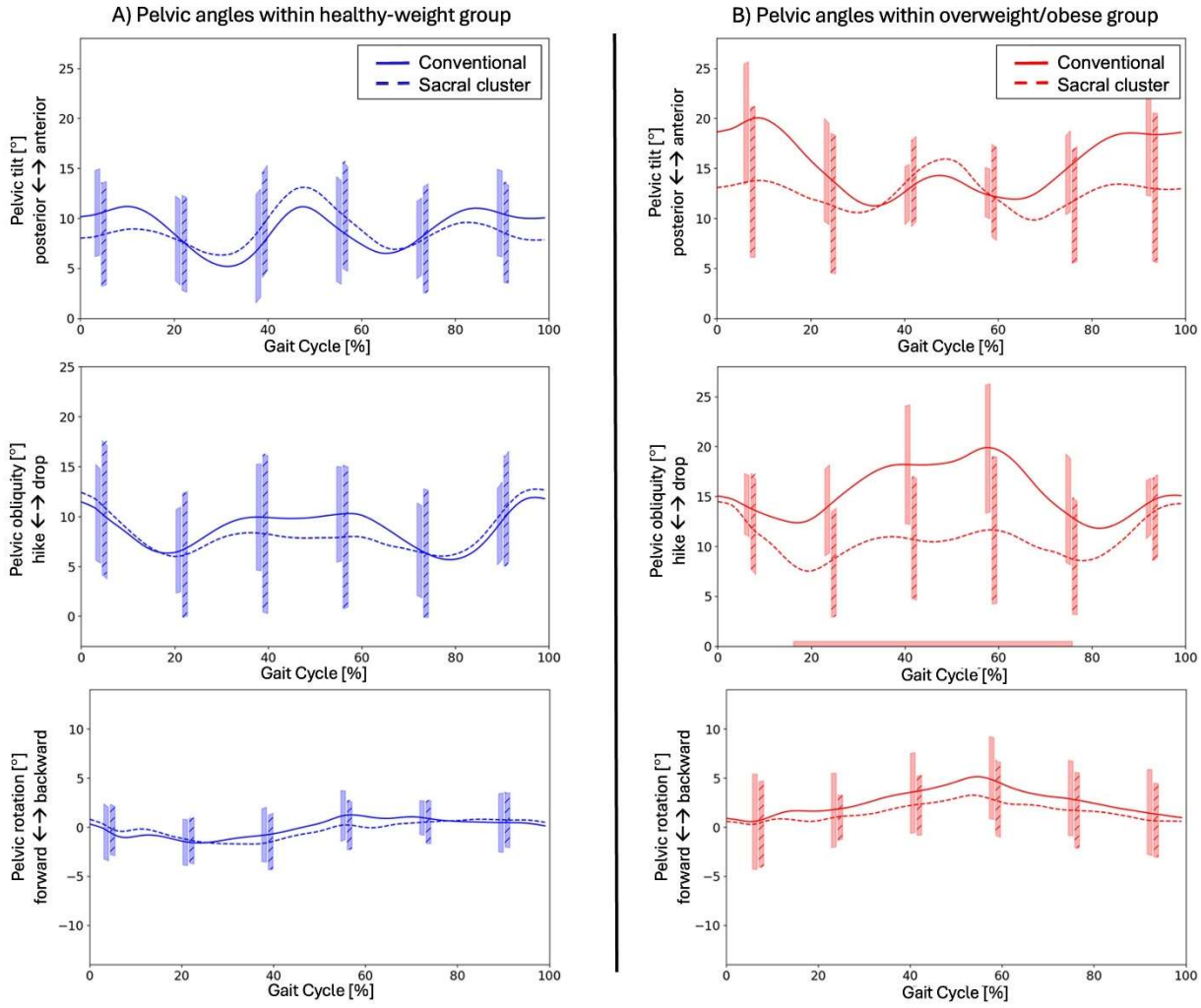


Figure 1: Pelvic angles (mean [degrees] ± SD) within (A) the healthy-weight and (B) overweight/obese group. Angles are shown in: sagittal plane (pelvic tilt), frontal plane (pelvic obliquity), the transverse plane (pelvic rotation) for conventional (continuous line) and sacral cluster (dashed line) models. Trajectories with statistically significant differences between methods are indicated with horizontal boxes.

References (Optional)

[1] Peters *et al.*, Gait Posture, 2010.

[2] Langley *et al.*, Gait Posture, 2019.

Session Category

Musculoskeletal Biomechanics: Methods, Models and Applications

OA58-01

Representative Sampling Using Realisation-Dependent Stopping Algorithm to Quantify the Relationship Between Brain Volume, Impact Severity, and Brain Strain

Ms Emily Yik Kwan Chan[1], Mr Vahid Darvishi[1], Dr Thomas Parker[2], Dr Anthony Quinn[1,3], Dr Mazdak Ghajari[1]

[1]Dyson School of Design Engineering, Imperial College London, London, London, United Kingdom. [2]Department of Brain Sciences, Imperial College London, London, London, United Kingdom. [3]School of Engineering, Trinity College Dublin, Dublin, Dublin, Ireland

Introduction

Subject-specific neuroanatomy influences finite-element(FE)-predicted brain strain. Larger brain volume yields higher strain under identical impact kinematics, and the volume–strain relationship varies with impact severity (Figure-1A) [1]. Exhaustive simulation across subjects and impacts to determine this relationship is computationally infeasible. Meanwhile, naïve down-sampling risks bias. This study uses a realisation-dependent, statistical stopping algorithm to select representative subjects and impacts to enable unbiased characterisation of volume–severity–strain relationship [2]. The aim is to determine whether using this algorithm will lead to representative samples, which are small enough to make FE runs feasible.

Methods

We used 211 MRI-scans of a large range of subjects, and 3,687 head impacts from boxing, mixed-martial-arts and rugby, captured by instrumented mouthguards (Figure-1C) [3]. Impact severity was defined as 90th-percentile maximum principal strain at corpus callosum estimated by Imperial College FE model developed from a 50th-percentile anatomy (Figure-1B) [4].

The stopping algorithm was applied separately to the two variables, volume and severity. The algorithm iteratively draws random samples of size n from the full N-sample distribution and evaluates the change in the sub-sampled distribution caused by the latest sample via the n-dependent Kullback–Leibler divergence (KLD). Sampling stops when KLD falls below a predefined tolerance, returning a stopping size n (typically $n<<N$). The tolerance was validated using 500 Monte-Carlo repeats. Representativeness was assessed by comparing the summary statistics of the n-sample to the N-sample, reporting error in standardised error (σ) unit of N. The KLD at stopping also quantifies the closeness between the n- and N-sample distributions.

Results

The algorithm independently selected 25 subjects and 75 impacts.Errors relative to full distributions were 0.33σ (volume) and 0.18σ (severity), indicating that selected samples accurately represent the full distributions (Figure1-D).

Discussion

Exhaustive simulations require 211×3,687=777,957 FE runs.The algorithm reduced this to 25×75=1,875, reducing the number of simulations by ~415times.This ensures computational feasibility while providing a KLD-based guarantee of distributional accuracy at stopping.The resulting dataset supports robust estimation of volume–severity–strain relationship and facilitates subject-specific strain prediction.

Images (Optional)

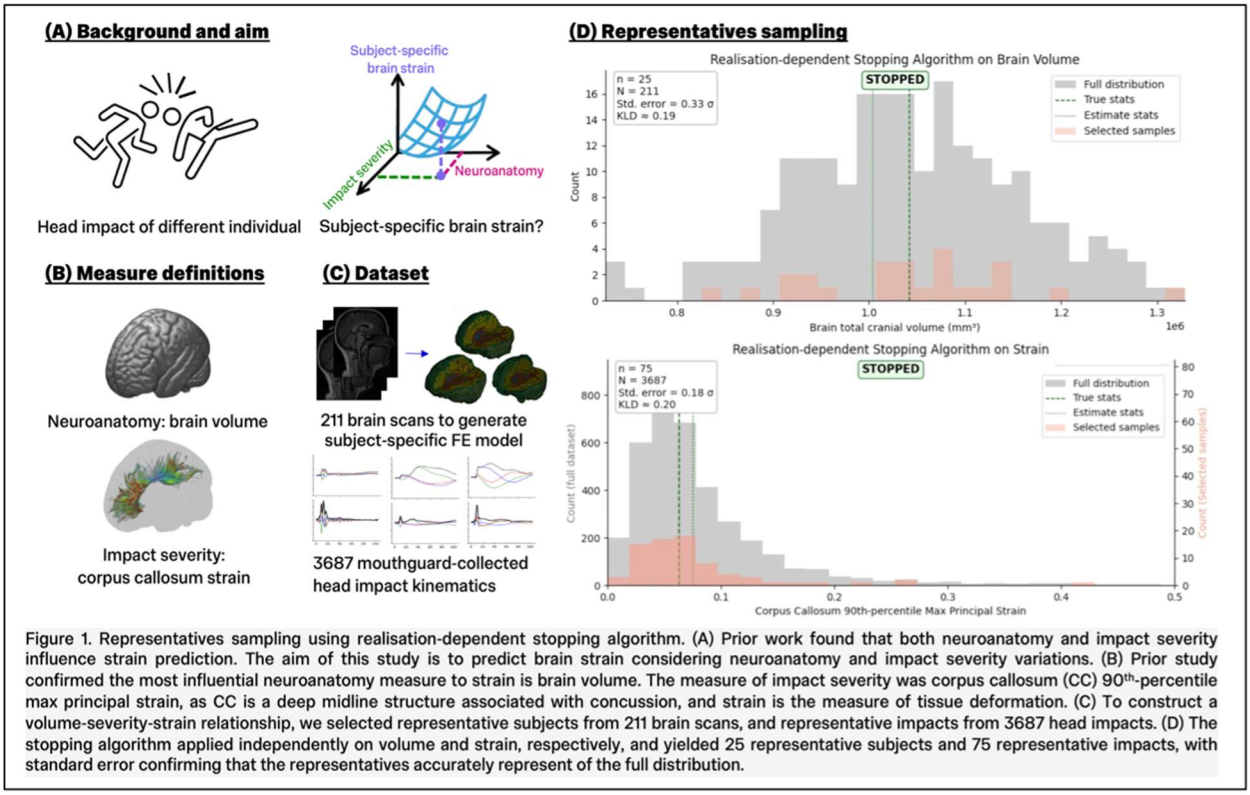


Figure 1. Representatives sampling using realisation-dependent stopping algorithm. (A) Prior work found that both neuroanatomy and impact severity influence strain prediction. The aim of this study is to predict brain strain considering neuroanatomy and impact severity variations. (B) Prior study confirmed the most influential neuroanatomy measure to strain is brain volume. The measure of impact severity was corpus callosum (CC) 90th-percentile max principal strain, as CC is a deep midline structure associated with concussion, and strain is the measure of tissue deformation. (C) To construct a volume-severity-strain relationship, we selected representative subjects from 211 brain scans, and representative impacts from 3687 head impacts. (D) The stopping algorithm applied independently on volume and strain, respectively, and yielded 25 representative subjects and 75 representative impacts, with standard error confirming that the representatives accurately represent of the full distribution.

References (Optional)

[1] Giudice JS et al.,J.Neurotrauma,2023

[2] Quinn A, Kárný M,Int.J.Adapt.Control,2007

[3] Jones CM et al.,Sensors,2023

[4] Ghajari M et al.,Brain,2017

Session Category

Injury Biomechanics: N/A

OA58-02

Subject-Specific In Silico Modeling of Brain Interstitial Fluid Transport Under Traumatic Loading

Dr. Ge He[1], Mr. Chenghan Cai[2], Dr. Lei Fan[2]

[1]Lawrence Technological University, Southfield, Michigan, United States. [2]Michigan State University, East Lansing, Michigan, United States

Introduction

Interstitial fluid (ISF) transport within brain tissue is essential for nutrient delivery, waste clearance, and intracranial pressure regulation. Traumatic brain injury (TBI) disrupts ISF flow through rapid mechanical loading, tissue swelling, and microstructural damage, contributing to edema, impaired clearance, and long-term neurodegeneration. However, capturing real-time dynamic ISF flow during and after TBI is highly challenging because brain's intricate porous architecture and millisecond-scale loading response prevent direct in vivo measurement. Computational modeling provides a controlled framework to quantify ISF dynamics and investigate mechanisms of impact-induced and post-traumatic fluid transport impairment.

Methods

In this work, we extend our previously developed hyper-poroelastic constitutive model of brain tissue to characterize ISF transport at the tissue scale by implementing the constitutive model into subject-specific whole-brain geometries to computationally investigate how head impact forces affect ISF flow across anatomically realistic structures and, ultimately, to enable simulations over large cohorts of human subjects. Brain parenchyma was modeled as a deformable porous medium saturated with ISF, governed by mass continuity, Darcy flow, and a hyperelastic constitutive relation, and implemented using a finite element formulation in FEniCSx.

(1) Tissue-Level Model: A one-dimensional consolidation test was reproduced to calibrate permeability, porosity, solid stiffness, fluid viscosity, and bulk modulus. A parametric study evaluated how these parameters influence the consolidation ratio.

(2) Whole-Brain Model: A patient-specific 3D brain geometry was used to simulate transient ISF pressure and flow rate following rapid loading. Spatial distributions of ISF pressure, flow rate, parenchymal strain, and stress were quantified, and simulations across different subjects will evaluate inter-subject variability.

Results

The parametric study showed that higher permeability and fluid bulk modulus increased the consolidation ratio, whereas higher fluid viscosity delayed fluid transport. Increased porosity produced a weaker effect. Whole-brain simulations revealed a transient, spatially heterogeneous ISF response, with peak flow rates near the impact site ($\approx 10^{-5}$–10^{-4} mm/s) at 5 ms, followed by rapid dissipation. Wave-like propagation and poroelastic lag behavior were observed, reflecting tight fluid–solid coupling.

Discussion

This modeling framework reveals how TBI-like loading perturbs ISF pressure and flow rate during and after impact, providing insight into post-traumatic fluid redistribution and potential mechanisms underlying edema and neurodegeneration.

Session Category

Injury Biomechanics: N/A

OA58-03

AI-based Positioning of Finite Element Human Body Models *Co-corresponding authors: Henrik Abrahamsson and Xiaogai Li

Mr. Giorgio Diena[1], Ms. Yuju Son[2], Mr. Siyuan Chen[1], Dr. Henrik Abrahamsson[2], Dr. Xiaogai Li[1]

[1]KTH - Royal Institute of Technology (KTH), Stockholm, Stockholm, Sweden. [2]RISE - Research Institutes of Sweden, Stockholm, Stockholm, Sweden

Introduction

Finite element human body models (HBMs) are essential for biomechanical injury analysis. Since most HBMs are developed in specific postures (e.g., seated or standing), they need to be repositioned for real-world applications. While existing simulation-based, lightweight physics or interpolation-based methods exist (e.g., [1-4]), they remain computationally intensive and sometimes time-consuming. This study evaluates the potential of several machine-learning approaches for HBM positioning, aiming at near-real-time generation of quality HBM meshes.

Methods

A dataset of 149 manually positioned six-year-old PIPER HBM was generated using the PIPER framework [5] and expanded to more than 1300 postures using controlled augmentation. Three AI models were trained to predict FE nodal coordinates from joint-angle inputs: (1) a Multi-Layer Perceptron (MLP) with noise injection and relative nodal coordinates; (2) a Generative Adversarial Network (GAN); and (3) a Random Forest (100 trees) included for comparison. Training used five-fold random splits (80%/20%). Performance was evaluated using mean squared error (MSE), coefficient of determination (R^2), and mesh quality via Jacobian metrics. Statistical analysis was used to compare and evaluate model performance.

Results

All models showed substantial improvements when increasing the training dataset from 149 to 1300+ poses. The MLP with noise injection and relative node achieved best-case MSE≈ 0.3 mm^2, significantly outperforming its non-noise counterparts. GAN models exhibited preliminary behavior consistent with trends observed for the MLP. Random Forest demonstrated stable performance with $R^2 = 0.86 \pm 0.02$ and MSE = 107.28 ± 13.56 across five independent splits.

Discussion

Noise injection and relative node representation markedly enhanced MLP performance, making it a promising option for HBM positioning. Some positioned HBMs exhibited localized mesh distortion, highlighting the need for future architectural refinement or post-processing to improve local element quality. Overall, this work demonstrates the potential of AI-based methods for near-real-time HBM positioning.

References (Optional)

[1] Lindgren et al. Traffic Injury Prevention. 2025.

[2] Chen S, Li X. Front Bioeng Biotech, 2025.

[3] Beillas et al. (2015) IRCOBI

[4] Hwang et al. SAE Technical Paper, 2016.

[5] PIPER Project http://piper-project.org

Acknowledgements (Optional)

Digital Futures Research Pair and Consolidator grant.

Session Category

Injury Biomechanics: N/A

OA58-04

Investigating the Effects of Cerebral Atrophy and Tissue Softening on Brain Deformation Response in Older Adults

Mr. Bashar L. Elkhatib[1], Dr. Aaron Carass[2], Dr. Jerry L. Prince[2], Dr. Ahmed Alshareef[1]

[1]University of South Carolina, Columbia, SC, United States. [2]Johns Hopkins University, Baltimore, MD, United States

Introduction

Traumatic brain injury (TBI) disproportionately affects older adults, who account for most TBI-related hospitalizations and deaths in the United States, mainly due to falls. With healthy aging, the brain undergoes pronounced structural and mechanical changes, including cerebral atrophy, ventricular enlargement, and reduced tissue stiffness (Figure 1A). These alterations can potentially change the vulnerability of the brain to tissue deformations from head impact, yet their influence on biomechanical response remains unclear. This study examines how age-related cerebral atrophy and tissue softening affect brain deformation under rotational loading using subject-specific models.

Methods

Longitudinal T1-weighted magnetic resonance imaging (MRI) data from 40 older adults (68–96 years, 3-5 scans per subject) were used to create subject-specific finite element (FE) models (Figure 1C). Age-dependent material properties were derived from MR elastography (MRE) data of 89 participants from the Brain Biomechanics Imaging Resource (BBIR) (Figure 1D). For each subject, two FE models were generated: a stable model incorporating structural changes alone with middle-age material properties and an age-adjusted model that also incorporated softening of the brain tissue. All models were simulated with a half-sine rotational pulse (peak velocity 40 rad/s, acceleration 5000 rad/s^2) similar to high severity falls onto hard surfaces from a standing height, applied across axial, sagittal, and coronal directions, totaling 960 simulations.

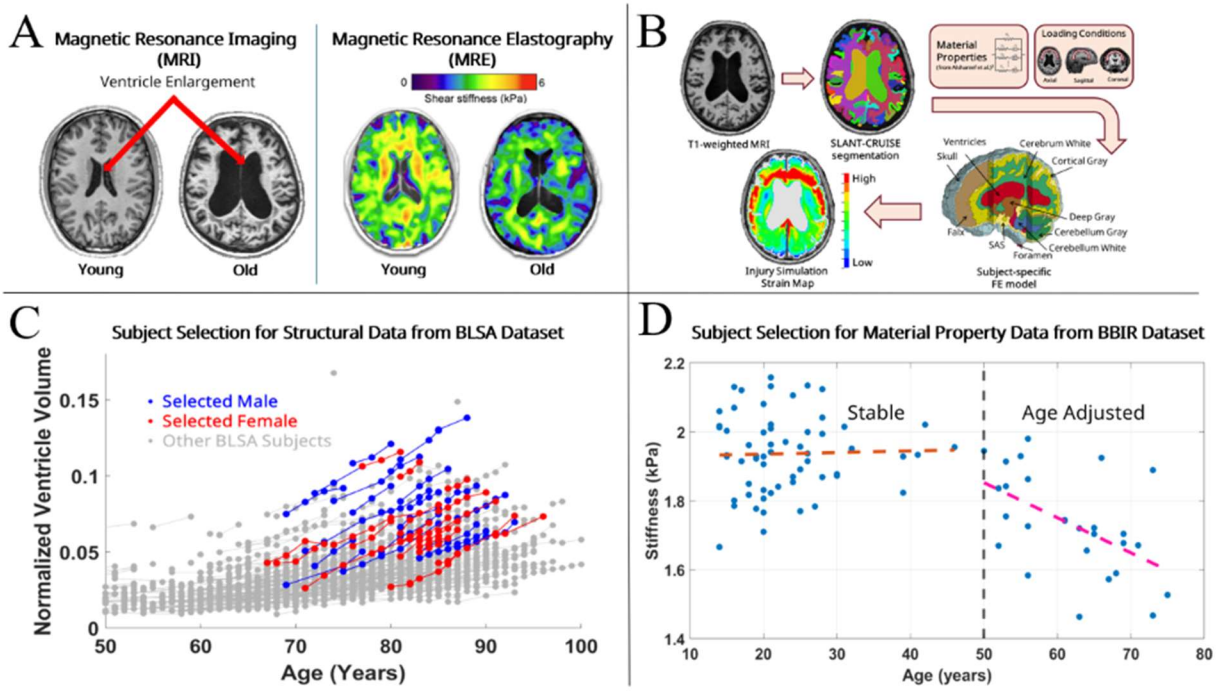
Results

Maximum principal strain (MPS) decreased with increasing normalized ventricle volume, indicating lower global brain deformation with greater atrophy. When material softening was incorporated, MPS values increased significantly relative to the stable models ($p < 0.05$), with softening increasing the deformation and vulnerability of the older adult brain. Models with higher degrees of atrophy showed greater sensitivity to softening, suggesting that geometric and material aging processes interact to shape overall deformation behavior and brain vulnerability.

Discussion

The results demonstrate that structural and mechanical aging exert competing influences on brain deformation during impact. While atrophy appears to reduce strain magnitude, concurrent softening amplifies deformation, leading to greater variability in biomechanical response among older adults. Integrating MRI- and MRE-derived datasets enables a data-driven modeling framework that captures these coupled effects and provides a more accurate representation of the aging brain.

Images (Optional)



References (Optional)

Acknowledgements (Optional)

NIH NINDS R01NS112120 (Alshareef)

NIH NINDS U01NS112120 (Bayly)

Baltimore Longitudinal Study of Aging

Session Category

Injury Biomechanics: N/A

OA58-05

Tract Morphing: A Novel Integration of Finite Element Modelling With Diffusion MRI for White Matter Tract Analysis in Mild Traumatic Brain Injury With Multimodal Fusion

Mr. Christian John Saludar[1,2], Dr. Maryam Tayebi PhD[1,3], Dr. Eryn Kwon PhD[1,3], Dr. Joshua McGeown PhD[3,4,5], Mr. Tuterangi Nepe-Apatu[3], Dr. William Schierding PhD[3,6], Mātai mTBI Group[3], Ms. Leigh Potter[3], A/Prof. Alan Wang PhD[1,3,4], Prof. Justin Fernandez PhD[1,3], A/Prof. Samantha Holdsworth PhD[3,4], Dr. Vickie Shim PhD[1,3]

[1]Auckland Bioengineering Institute, University of Auckland, Auckland, Auckland, New Zealand. [2]University of the Immaculate Conception, Davao City, Davao del Sur, Philippines. [3]Mātai Medical Research Institute, Gisborne, Gisborne, New Zealand. [4]Faculty of Medical and Health Sciences & Centre for Brain Research, University of Auckland, Auckland, Auckland, New Zealand. [5]Brain Health Research Institute, Auckland University of Technology, Auckland, Auckland, New Zealand. [6]Vision Research Foundation, University of Auckland, Auckland, Auckland, New Zealand

Introduction

Diffusion MRI (dMRI) enables in-vivo investigation of brain's microstructural organisation, but conventional analysis aggregates complex microstructural information, discarding significant spatial variation. To overcome this, a novel framework is introduced that projects the full voxel-wise dMRI metrics onto a subject-morphed finite element (FE) model, conforming to the subject-specific tract geometry and fibre orientation to preserve microstructural detail and enable fine-grained analysis. We applied this method to investigate effects of head acceleration events (HAE) and mild traumatic brain injury (mTBI) in rugby players on the corticospinal tract (CST) which is mostly implicated in sports-related head injuries.

Methods

Thirty-three male high school rugby players (HAE group) underwent multi-shell dMRI brain scan (3.0T GE Scanner) at early, mid-, and post-season. Ten rugby players with in-season mTBI were scanned at 1, 3, and 8 weeks post-injury. Twenty age and sex-matched non-contact-sport athlete controls were scanned once. dMRI were preprocessed, and diffusion tensor (DTI) and kurtosis (DKI) metrics were extracted. Fibre orientation distributions were estimated, and bilateral CST was segmented using TractSeg. A tetrahedral FE CST template (TetGen) was free-form deformed to each CST's mask, and nearest-neighbour mapping assigned all DTI and DKI metrics to each FE node. Permutation t-tests identified elements

showing significant group differences, and principal component analysis (PCA) was used to visualise clustering across groups and timepoints.

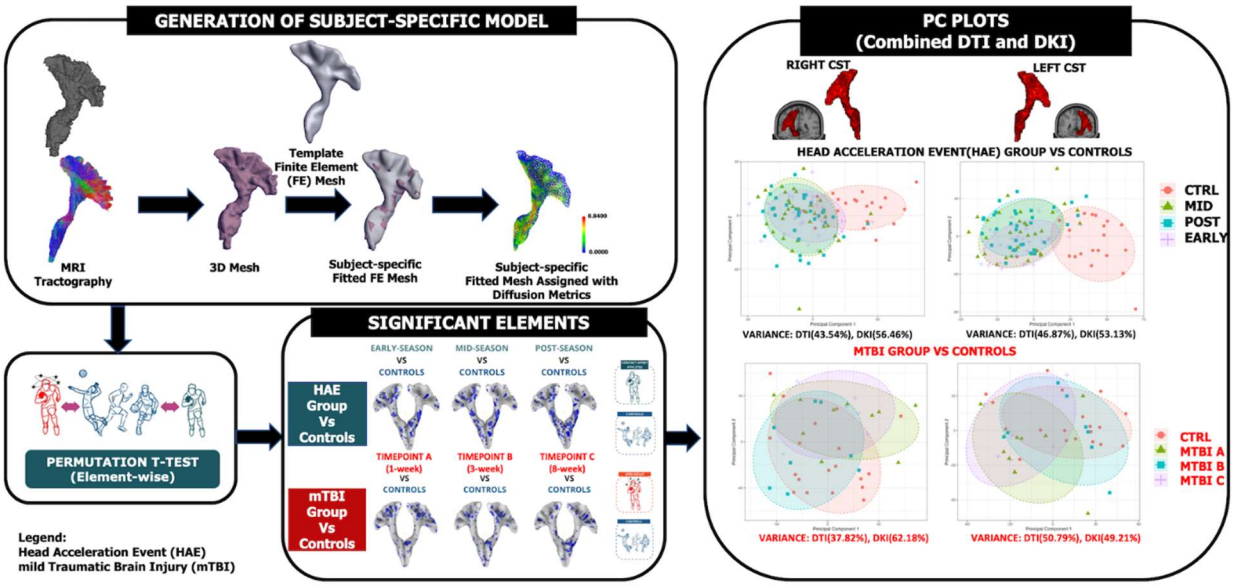
Results

Permutation testing revealed bilateral CST regions with significant and temporally increasing differences between controls and the HAE group across the season. In controls vs. mTBI, significant regions increased along the spine but decreased in the crown from Timepoints A to C. PCA (PC1–PC2) demonstrated separable clusters for both comparisons, with DTI and DKI contributing similarly to variance. HAE clusters overlapped across timepoints, whereas mTBI clusters showed partial separation from 1 week to 8 weeks, indicating evolving post-injury microstructural changes.

Discussion

This framework preserves maximum dMRI data within subject-specific FE models, enabling sensitive, localized detection of HAE/mTBI alterations. Morphing a common FE model increases inter-subject comparability priming outputs for machine-learning integration. In addition, this model can be extended to multimodal data fusion (e.g., strain) for inclusion in analysis, making it a powerful tool for comprehensive analysis.

Images (Optional)



References (Optional)

Acknowledgements (Optional)

We sincerely thank all participants, Gisborne Boys High School, and Mātai Ngā Māngai Māori for their engagement. Support for research: Kānoa – Regional Economic Development & Investment Unit; Trust Tairāwhiti; NZ MBIE Catalyst Strategic Fund; Neurological Foundation; Fred Lewis Enterprise Foundation; Hugh Green Foundation; JN & HB Williams Foundation; Health Research Council of New Zealand; Anonymous Donation; NZ Rugby Foundation; and Te Tītioki Mataora. We also thank GE Healthcare for MRI protocol assistance and acknowledge use of the eResearch Infrastructure Platform hosted by REANNZ Ltd. Support to researchers: C.J. Saludar – DOST-SEI Foreign Graduate Scholarship; W. Schierding – Vision Research Foundation Fellowship; J. McGeown – Neurological Foundation Philip Wrightson Fellowship; M. Tayebi and E. Kwon – Hugh Green Foundation Senior Fellowships.

Session Category

Injury Biomechanics: N/A

OA59-01

Multi-Site Wearable Ultrasound for Tracking Neuromuscular Adaptation in ACL Rehabilitation: A Pilot Study

Dr. Erica L. King Ph.D., Ms. Morgan Lamarre M.S., Mr. Connor Delaney M.S., Dr. Qi Wei Ph.D., Dr. Siddhartha Sikdar Ph.D., Dr. Margaret T. Jones Ph.D., Dr. Parag V. Chitnis Ph.D.

George Mason University, Fairfax, VA, United States

Introduction

Anterior cruciate ligament (ACL) injuries often lead to significant quadriceps weakness and asymmetry, which can impair knee stability and delay functional recovery. Musculoskeletal ultrasound (MSK-US) can provide real-time assessment of muscle activity during rehabilitation. However, conventional MSK-US relies on handheld, single-site probes that are bulky, operator-dependent, and unsuitable for dynamic tasks. To address these limitations, this study introduces a wearable ultrasound (WUS) system designed for hands-free monitoring of muscle function during movement. The system employs multiple transducers positioned over key muscles, enabling simultaneous acquisition of quantitative biofeedback signals for bilateral assessment.

Methods

A custom four-channel Time Delay Spectrometry Ultrasound (TDS-WUS) system was developed to capture M-mode data during rehabilitation exercises. The system transmitted 20-ms frequency sweeps (3–5 MHz) and recorded echo signals at 50 lines/s from transducers placed bilaterally over the vastus lateralis (VL) and vastus medialis oblique (VMO). Automated processing using Composite Factorization Principal Component Analysis (CF-PCA) extracted contraction dynamics and computed a muscle-specific bilateral symmetry index (BSI). One subject with a left ACL-III tear was monitored weekly for four weeks during three trials of bilateral bodyweight squats. Instrumented insoles measured plantar force, and a modified SMFA survey assessed functional status. Data were analyzed using repeated-measures ANOVA ($p = 0.05$).

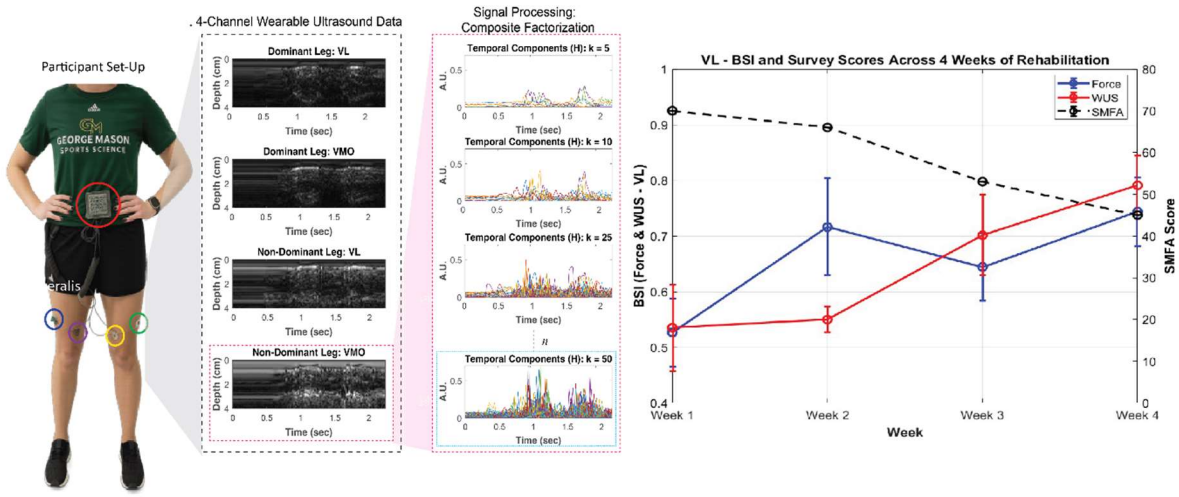
Results

Results showed a significant main effect of day on plantar force ($F(3,15) = 24.35$, $p < 0.001$), with Week 1 values significantly lower than Week 2 and 4. VL-BSI also improved significantly across sessions ($F(3,6) = 16.22$, $p = 0.003$) with Week 1 lower than Week 3 and Week 3 lower than Week 4, while VMO-BSI changes were not significant. SMFA scores improved from 70 to 45, paralleling objective measures of force and symmetry.

Discussion

This pilot study demonstrates the feasibility of WUS for tracking muscle function symmetry during ACL rehabilitation. Unlike traditional MSK-US, WUS enables simultaneous, hands-free monitoring of multiple muscles during dynamic tasks, providing richer insights into neuromuscular adaptation. While limited by a single-subject design and short duration, these findings support further validation in larger cohorts and expansion to additional muscle groups. WUS offers a scalable, real-time solution for personalized rehabilitation and remote monitoring.

Images (Optional)



Acknowledgements (Optional)

Effort sponsored by the Government under Other Transactions Number W81XWH-15-9-0001

Session Category

Rehabilitation Biomechanics and Human Factors: Rehabilitation

OA59-02

Objective Free-Living Metrics Challenge Traditional Prosthetic Classification Standards

Mrs Sydney Lundell M.S., Dr. Kenton Kaufman PhD, P.E.

Mayo Clinic, Rochester, MN, United States

Introduction

In the United States, the Medicare Functional Classification Level (K-Level) scale, (K0-K4) reflects a patient's functional mobility potential and ability to safely ambulate using a prosthesis. K-levels guide insurance coverage for prosthetic components, but no gold standard exists, making classification subjective and reliant on clinician judgment. K1/2 individuals typically receive mechanical components with fixed resistance, while K3/4 individuals are provided advanced devices that adapt joint resistance in response to changes in walking speed. The primary distinction between K2 and K3 is the ability to ambulate with variable cadence. Falls in K2 users decrease significantly with microprocessor-controlled knees, yet clinical walking tests fail to capture real-world function. The goal of this study was to determine whether objective free-living data can classify functional mobility in this population.

Methods

The cohort included 51 amputees rated K2–K4 (male 27; 54±15.6 years). They wore tri-axial accelerometers on the ankles and waist for three days. Metrics for activity [1] and cadence [2] were calculated and averages for each metric was calculated for a total of 60 unique metrics. These metrics were then fed into an unsupervised Self-Organizing Map over a 5×5 neuronal grid for 500 epochs. Subjects were grouped according to resulting topological clusters.

Results

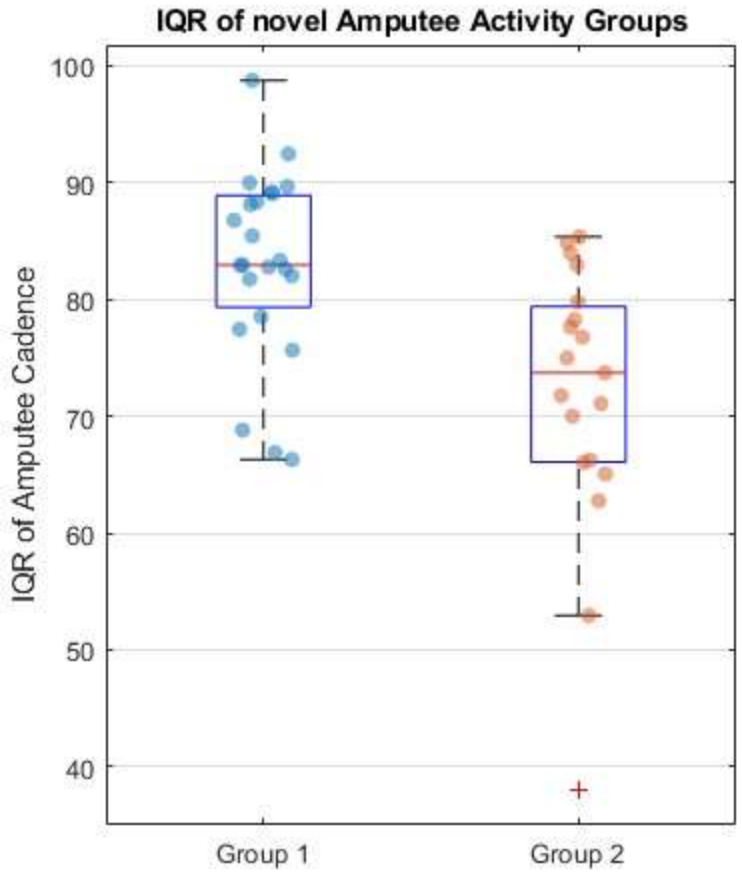
Two distinct clusters were identified across the 51 amputees. The strongest differentiator was the average interquartile range of cadence ($p = 0.001$; Figure 1), followed by percentage of the day spent static ($p = 0.027$). Cluster grouping did not correspond to K-levels.

Discussion

Our results indicate that real-world activity patterns among amputees differ from traditional K-level classifications and instead consist of two groups. Both groups ambulate

with a variable cadence; with the range of variability across three days having no direct relationship to K-level. K-levels had no significance in amputee cadence variability. These findings raise important questions about the adequacy of K-levels as the sole determinant for prosthetic prescription coverage, suggesting a new clinical direction that leverages wearable sensors to improve prescription and subsequently reduce fall-related healthcare costs.

Images (Optional)



References (Optional)

1. Lugade, V et al., *Med Eng & Phys*, 2014
2. Fortune, E. et al.,*Med Eng Phys, 2014*

Session Category

Rehabilitation Biomechanics and Human Factors: Rehabilitation

OA59-03

Wearable Sensor Calibration for Sports Knee Injury Rehabilitation

Ms. Rosalind Bendell B.S., Mr. Joey Scilla, Dr. Sagar Doshi Ph.D., Dr. Erik Thostenson Ph.D., Dr. Jill Higginson Ph.D.

University of Delaware, Newark, Delaware, United States

Introduction

Wearable sensors have the potential to help prevent injury and monitor rehabilitation progress beyond laboratory settings. Our collaborators have developed carbon nanocomposite sensors that change electrical resistance when elongated[1]. These sensors are integrated into a compressive knee sleeve - the Smart Sleeve - to measure knee flexion angle (KFA). Our objectives are to calibrate the Smart Sleeve to measure knee angles during movement and validate the Smart Sleeve accuracy.

Methods

In this IRB approved study, participants (n=4, 1F, 3M) were outfitted with the Smart Sleeve (centered over the right knee) and retroreflective motion capture markers. Participants performed a sensor calibration trial of five seated leg extensions with KFA from 0° at full extension to approximately 90° and holds at 0° and 90°. Next, participants performed four validation trials, three consisting of 20 seated leg extensions and one 30 second walking trial at 1.0 m/s between the second and third validation trials. Motion capture data (Qualisys, 100 Hz) and sensor resistances (ohms, 20 Hz) were collected.

The percent change in resistance was normalized to recorded resistance values at 0° (baseline). For seated leg extension validation trials, a 4^{th} order polynomial equation was used to fit knee angles to sensor resistance measurements from the calibration trial. The calculated knee angles were compared to the experimental knee angles from the validation trial. A linear regression between experimental and calculated angles was applied to evaluate Smart Sleeve accuracy.

Results

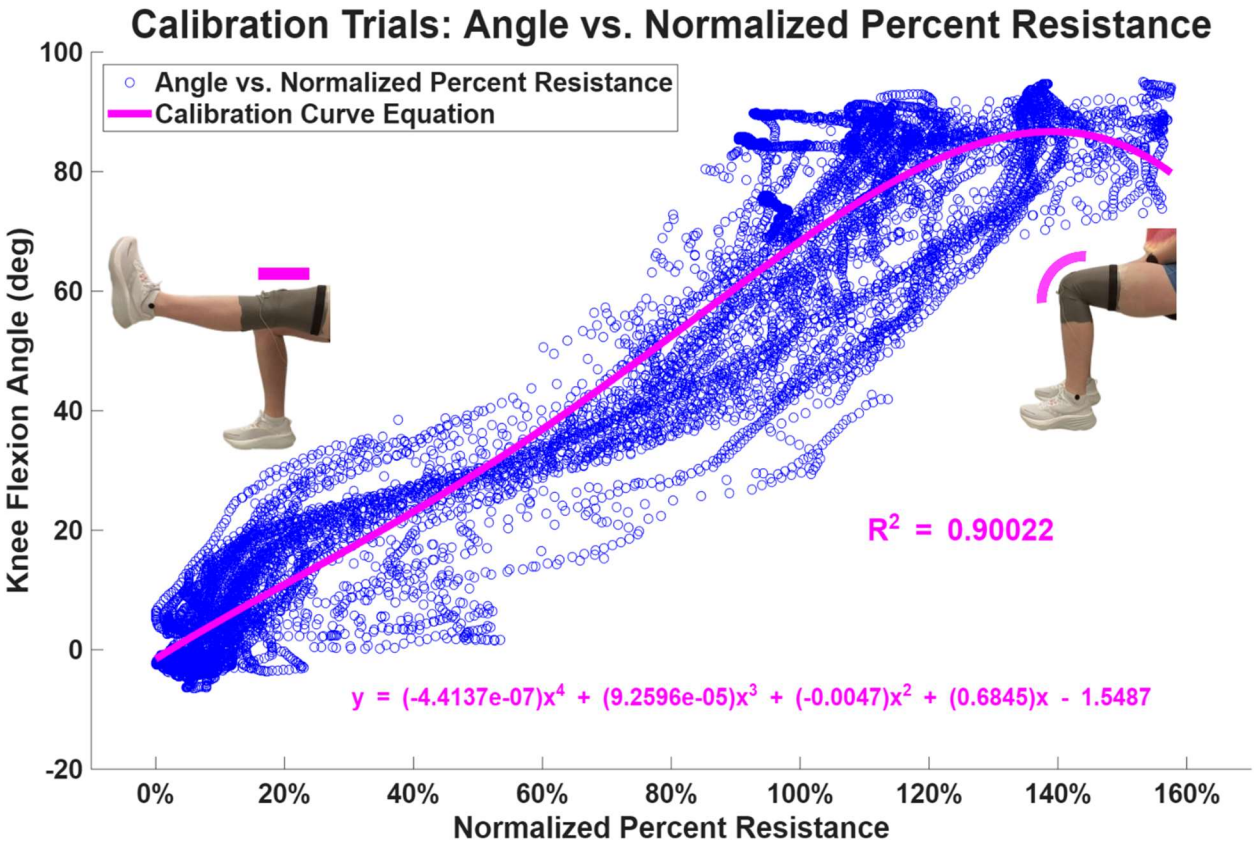
The calibration equation (normalized percent resistance in ohms to degrees) for each participant had an R^2= 0.932±0.067 and RMSE=7.396±3.247°. When the calibration equation was applied to a seated leg extension validation for each participant, the linear

regression had R^2 = 0.942±0.029 and RMSE=7.865±1.901°. The calibration equation for all participants (Fig.1) had R^2=0.90022 and RMSE=10.885°.

Discussion

Linear regression R^2 values indicate a high angle detection accuracy. This work shows calibration of the Smart Sleeve to measure KFA during seated leg extensions. Future work will continue collecting data for this protocol. Then, we will calibrate and validate the Smart Sleeve for walking, running, and jumping for sports motion tracking during knee injury rehabilitation.

Images (Optional)



References (Optional)

[1] Doshi, J.Mater.Chem.C, 2022

Session Category

Rehabilitation Biomechanics and Human Factors: Rehabilitation

OA59-04

Capturing Individual Recovery Trajectories After ACL Injury Using Principal Component-Derived Countermovement Jump Data

Ms. Tamar D. Kritzer, Dr. Dylan Kobsar

McMaster University, Hamilton, Ontario, Canada

Introduction

Anterior cruciate ligament (ACL) tears are among the most common and severe knee injuries in sports, leading to more than 400,000 reconstructions and costing approximately $3 billion annually across North America [2,4]. Despite surgical intervention, only 50–65% of athletes return to their previous level of competition, often at reduced performance and elevated risk of re-injury [1,3]. Current return-to-play (RTP) protocols remain largely generalized and emphasize subjective performance benchmarks, while overlooking continuous biomechanical and neuromuscular factors [1,3]. This study presents an approach that captures individualized, sex-specific recovery patterns to inform more evidence-based RTP decision-making.

Methods

Varsity women's basketball athletes (n = 14) completed weekly countermovement jumps (CMJs) throughout a full season. Two athletes sustained ACL injuries and were tracked through recovery. CMJs were recorded using a dual force plate system (Hawkin Dynamics, ME, USA) following a 5-minute warm-up. Weekly averages were computed for jump height and biomechanical force-time metrics. Recovery trajectories were quantified using principal component analyses of nine primary CMJ metrics (e.g., Jump Height, Time-To-Takeoff, mRSI, Left/Right Peak Braking and Propulsive Force, and Left/Right Average Braking RFD) applied at both the individual and team levels. Euclidean distances from each athlete's postoperative observations to their pre-injury or team-based centroids served as change metrics and were modeled over time to characterize recovery patterns.

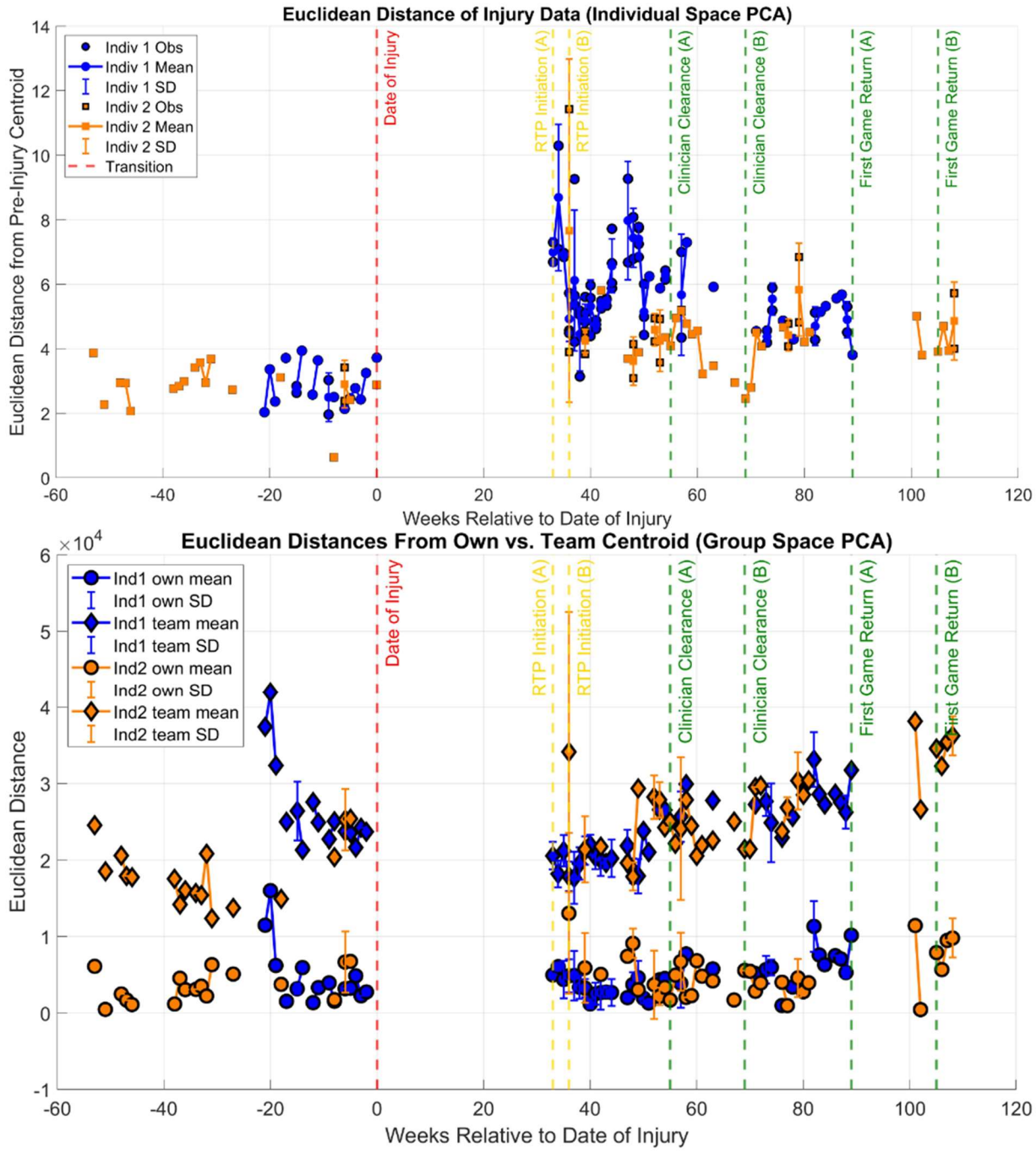
Results

Distances between postoperative observations and each athlete's individual centroid showed deviation from pre-injury patterns and heightened day-to-day variability during return-to-play, with a progressive trajectory toward pre-injury values. In contrast, trajectories referenced to team-based centroids masked these deviations and recovery patterns, illustrating how generalized benchmarks can overlook meaningful individual differences, thereby emphasizing the need for personalized assessment (Figure 1).

Discussion

Individualized monitoring of ACL recovery using holistic PCA-derived CMJ patterns reveals athlete-specific deficits that may serve as an overarching indicator of return to pre-injury form. This approach has the potential to improve evidence-based decision-making, reduce re-injury risk, and optimize performance outcomes.

Images (Optional)



References (Optional)

[1] Davies et al. (2020). Sports Medicine, 50: 485-495.

[2] Devana et al. (2022). Rev. Musculoskel. Medicine, 1-9.

[3] Jordan et al. (2024). J. Strength & Conditioning, 46: 406-414.

[4] Larose et al. (2022). J. Surgery, 65(2): E269.

Session Category

Rehabilitation Biomechanics and Human Factors: Rehabilitation

OA59-05

Task-Independent Continuous Prediction of Whole-Body and Segmental Balance during Multi-Terrain Ambulation Circuits

Ms. Marissa Pirritano, Ms. Juliana Iverson, Dr. Nicholas Fey

University of Texas at Austin, Austin, TX, United States

Introduction

Accurately quantifying whole-body angular momentum (H) and its segmental contributions offer biomechanical insight into balance control during ambulation. Current methods to evaluate H typically rely on expensive motion capture systems that are restricted to a confined tracking space. Previously, linear acceleration and angular velocity data derived from motion capture have been used to represent *signals* from a sparse set of inertial measurement units (IMUs) and when combined with machine learning, segmental contributions to H were accurately predicted [1]. This suggests that a sparse set of IMUs could enable accessible and quantitative assessment of balance in real-world settings. To validate this approach, we apply temporal convolutional networks (TCNs) to predict segment-level contributions to H using data collected from wearable IMU *sensors*.

Methods

Six able-bodied participants were instrumented with five 9-axis IMUs: one placed on the dorsal aspect of each wrist, one superior to each lateral malleolus, and one over the sternum. Each participant traversed a multi-terrain circuit comprised of a five-step staircase, raised level platforms, and a 2.5 m ramp. Each participant completed the circuit a total of 140 times over 7 trials. Kinematics were obtained using a markerless motion capture system. Ground truth segmental contributions to H were computed about the body center of mass and expressed in the pelvis reference frame. A TCN was trained on the IMU data to predict the 3D contributions to H from five body segments (each leg, each arm, and the trunk) for each participant. Performance was evaluated using RMSE between the sum of the segmental predictions and ground truth H per axis (X-sagittal, Y-frontal, and Z-transverse) on held out circuit laps.

Results

Across participants, the mean RMSE (m/s) was 0.0273 ± 0.0030 for the X-axis, 0.0275 ± 0.0058 for the Y-axis, and 0.0121 ± 0.0018 for the Z-axis.

Discussion

These results further demonstrate that a small set of wearable IMUs can reliably predict H across tasks. This approach provides a practical method for “real-world” assessment of dynamic balance which could additionally be leveraged to provide real-time feedback for human-in-the-loop control of exoskeletons and prostheses.

Images (Optional)

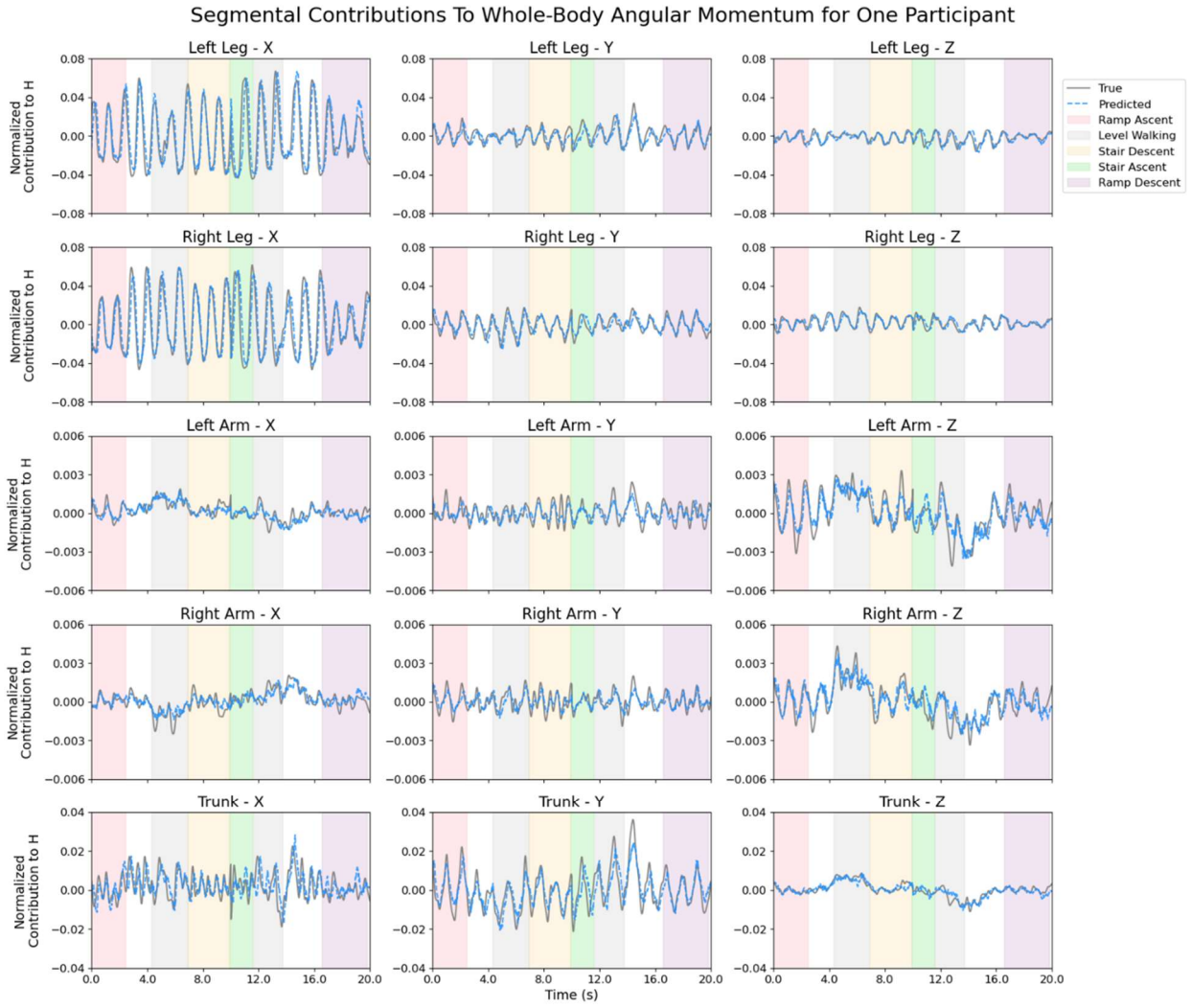


Figure 1: Comparison of ground-truth (gray) and predicted (blue) segmental contributions to whole-body angular momentum (H) during various locomotor tasks (shaded regions). The segmental contributions to H have been normalized by subject mass and height. Please note different scales across segments.

References (Optional)

[1] Pickle, Nathan. et al, J Neuroengineering and Rehab, 2019.

Session Category

Rehabilitation Biomechanics and Human Factors: Rehabilitation

OA60-02

An AO Classification-Based Virtual Testing Framework for Mechanobiological Evaluation of Tibial Shaft Fracture Healing and Fixation Strategies

M.Sc Felix Scherf, M.Sc Robin Reinardt, B.Sc. Yana Böhr, Dr. rer. nat. Michael Roland, Prof. Dr.-Ing. Stefan Diebels

Applied Mechanics, Saarland University, Saarbrücken, Saarland, Germany

Introduction

Fracture healing is driven by coupled mechanical and biological processes and is sensitive to the local mechanical environment [1,2]. To systematically study how implants and fixation strategies influence this process, standardized tibial fracture configurations based on AO/OTA patterns are required [3]. We present a virtual testing framework that uses artificially created, AO-classified tibial shaft fractures to analyse the mechanobiological impact of different implants and fixation constructs.

Methods

A finite element–based mechanobiological model was implemented in COMSOL® Multiphysics with LiveLink™ for MATLAB®, building on our own developed established mechanoregulation concepts for tissue differentiation [1,2]. As shown in figure 1, based on a statistical shape model of the tibia, three-dimensional bone geometries were generated and assigned AO/OTA tibial fracture patterns and callus geometries according to the current classification system [3]. For each virtual fracture, multiple fixation concepts (e.g. plate configurations, screw layouts, working lengths) were created, yielding a library of implant–fracture combinations. Quasi-static structural analyses provided the local mechanical environment for each construct under physiological loading [1–3]. These mechanical stimuli were coupled to partial differential equations describing tissue differentiation and key biological regulators. Temporal changes in tissue properties updated the structural analyses, capturing the evolving fracture stiffness. MATLAB® scripts automated model generation, parameter variation, and post-processing, enabling systematic comparison of implants across tibial fracture types.

Results

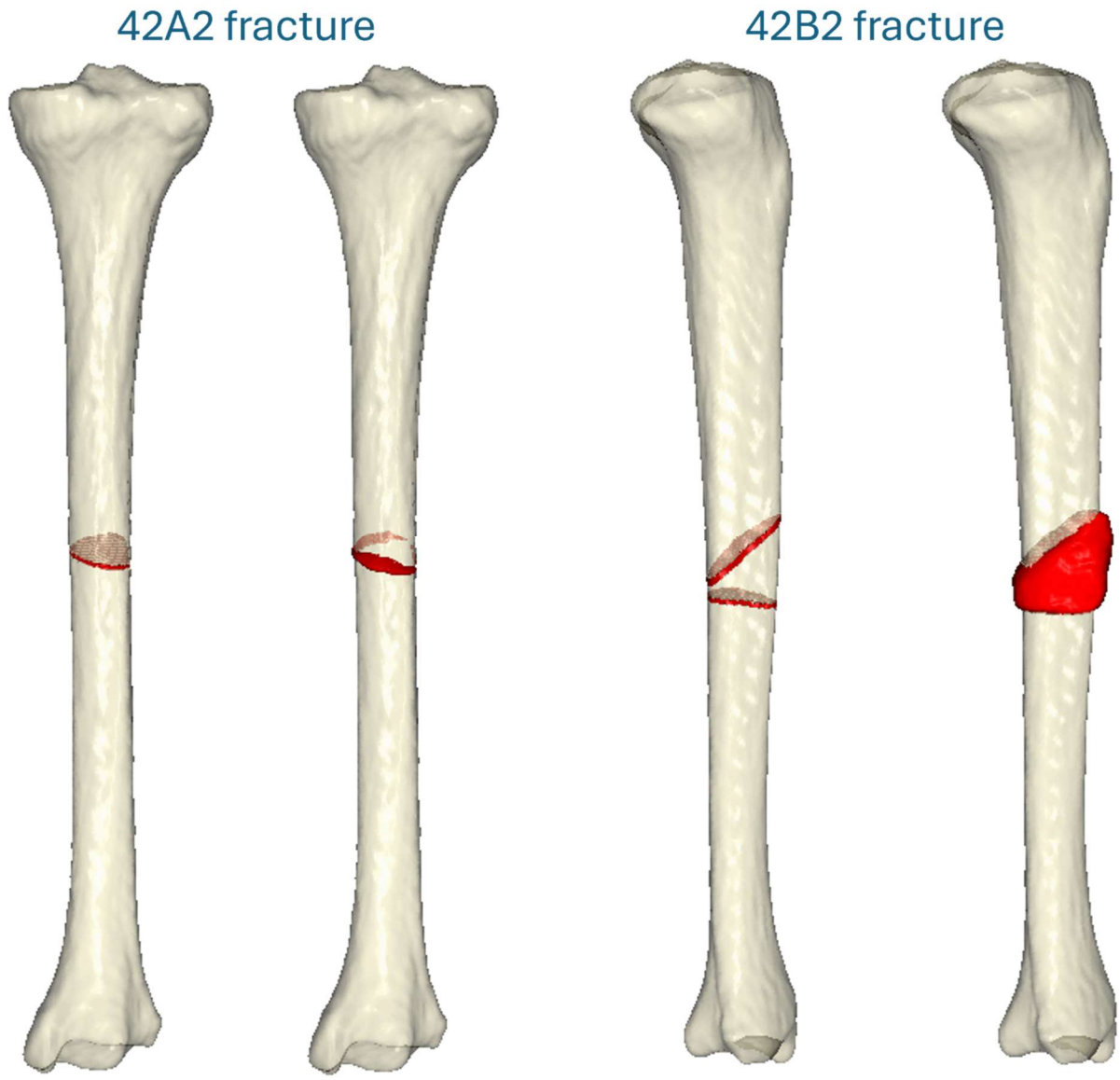
The framework produced consistent, anatomically plausible tibial AO-fracture geometries and fixation constructs. Mechanical indicators relevant for healing, such as interfragmentary motion and strain, varied systematically between implant designs,

fracture classes, and loading conditions. Simulated tissue differentiation patterns reflected these differences, revealing construct-specific trends in predicted tissue matrix formation, cortical bridging, and risk of delayed or asymmetric healing.

Discussion

The proposed virtual fracture workflow enables standardized, AO-based in silico testing of implants and fixation strategies for tibial fractures without relying on patient-specific imaging. Future work will expand the catalogue of tibial fracture types and implants, refine biological submodels, and investigate how virtual trial results can support preclinical implant assessment, design optimization, and clinical fixation planning.

Images (Optional)



References (Optional)

[1] Claes et al., J Biomech, 1999

[2] Ghiasi et al., Bone Rep., 2017

[3] J. Orthop. Trauma, 2018

Session Category

Orthopaedic Biomechanics: Lower Extremities

OA60-03

A Computational–experimental Framework for Reproducible Biomechanical Testing Through Standardised Acetabular Defect Models in Hip Revision Arthroplasty

M.Sc. Carina Micheler[1,2], Dr.-Ing. Jan Lang[1,3], PD Dr. med. Igor Lazic[1], Dr. med. Benjamin Schloßmacher[1], Dr.-Ing. Maximilian Fischer[4], M.Sc. Christian Fritz[2], Univ.-Prof. Dr. med. Rüdiger von Eisenhart-Rothe[1], Prof. Dr. med. Rainer Burgkart[1]

[1]Department of Orthopaedics and Sports Orthopaedics, TUM University Hospital, Munich, Bavarian, Germany. [2]Institute for Machine Tools and Industrial Management, TUM School of Engineering and Design, Munich, Bavarian, Germany. [3]Chair of Artificial Intelligence in Healthcare and Medicine, TUM School of Computation, Munich, Bavarian, Germany. [4]AQ Solutions GmbH, Cologne, North Rhine–Westphalia, Germany

Introduction

Acetabular defects that arise during hip revision surgery are highly patient-specific, which makes it challenging to establish reproducible experimental conditions for evaluating revision implants and treatment strategies. This study addresses this limitation by presenting a computational–experimental framework that generates geometrically standardised acetabular defect models and transfers them to pelvic specimens. This enables controlled and comparable biomechanical testing.

Methods

From a dataset of 18 female revision cases, a geometrically defined multi-sphere model representative of Paprosky IIIA defects was generated (Fig.(a)) using a previously developed computational workflow for 3D reconstruction after revision arthroplasty [1]. A milling setup was designed to implement this digital defect model into pelvis specimens (Fig.(b)), supported by positioning aids and stop geometries to ensure accurate execution. The setup comprises a tilting xyz-milling attachment for linear toolpaths and a gimbal suspension for producing the multi-sphere contours. To validate the accuracy of the manufacturing process (Fig.(c)), three 3D-optical scans (Miraco, Revopoint) were performed after milling and evaluated using a custom MATLAB-based ICP deviation analysis tool [2]. Additionally, a biomechanical test setup was developed on a hydraulic tensile–compression testing machine (Zwick) to enable standardised evaluation of revision implants (Fig.(d)).

Results

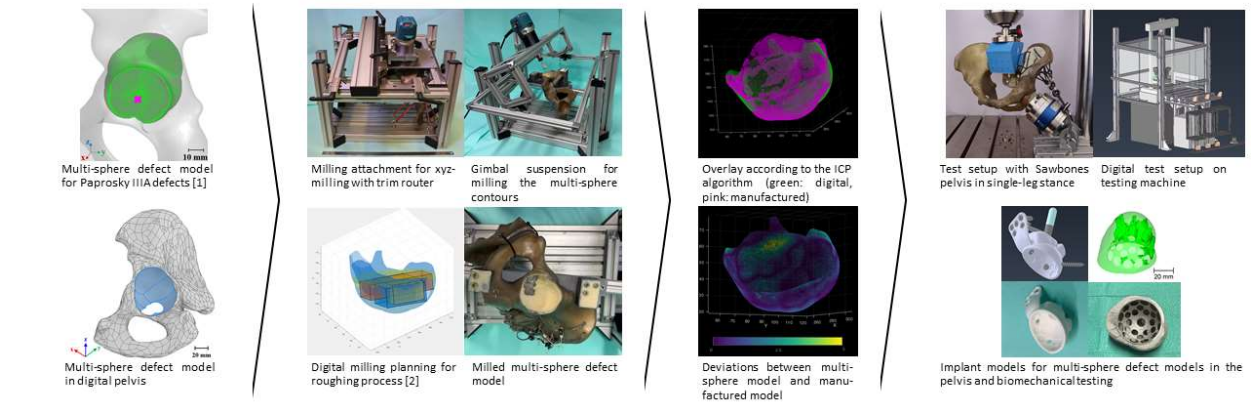
Analysis of the patient dataset yielded a geometrically standardised, multi-sphere defect model that is representative of Paprosky IIIA morphology (Fig.(a)). The defect model

consists of six spheres with an equal diameter of 23.64 mm, and provides a reproducible and scalable representation of bone loss patterns. The deviation analysis between the digitally defined multi-sphere model and the manufactured defect model demonstrated a mean geometric deviation of 0.88 ± 0.21 mm. This confirms that the geometry of a multi-sphere acetabular defect can be reproduced with high accuracy.

Discussion

The results show that the proposed multi-sphere defect model is robust, scalable and experimentally manufacturable, providing a standardised geometric basis for biomechanical investigation of acetabular revision cases. This approach establishes reproducible conditions for systematic implant testing and paves the way for future comparative studies involving artificial pelvises and human specimens in hip revision arthroplasty.

Images (Optional)



References (Optional)

[1] Micheler et al., IEEE Access, 2025.
[2] Micheler, Matlab Central File Exchange, 2025.

Acknowledgements (Optional)

Ethical approval: TUM Ethics Committee, 2025-413-S-KK.

Session Category

Orthopaedic Biomechanics: Lower Extremities

OA60-04

Implant Design Affects Knee Kinematics During Chair Rise After Total Knee Arthroplasty

Mr. Tom Gale[1], Ms. Lauren Gross[1], Dr. Kenneth Urish[2], Dr. William Anderst[1]

[1]University of Pittsbugh, Pittsburgh, PA, United States. [2]UPMC, Pittsburgh, PA, United States

Introduction

Total knee arthroplasty (TKA) surgery has a reported dissatisfaction rate of up to 20%. One unexplored possible cause of dissatisfaction is knee kinematics asymmetry post-TKA. TKA implant designs, such as posterior stabilized (PS), medially congruent (MC), and cruciate retaining (CR), are believed to affect post-TKA kinematics. However, the association between outcomes and bilateral symmetry in kinematics after receiving these prostheses remains unknown. This study compared the kinematics asymmetry post-TKA for CR, PS, and MC designs and explored relationships between patient-reported outcomes and asymmetry. We hypothesized that CR-TKA, which retains the native cruciate ligaments, would lead to better symmetry than PS- or MC-TKA.

Methods

Participants undergoing TKA using the same robotic system were recruited for this IRB approved study. Both knees were imaged using dynamic biplane radiography at 100Hz during a chair rise activity 12 months post-surgery. A validated tracking method was used to track bone and implant motion with accuracy better than one millimeter in translation and one degree in rotation. Six degree-of-freedom kinematics were calculated and expressed relative to tibiofemoral flexion. The side-to-side difference (SSD) in kinematics waveforms post-TKA were compared among implant designs using SPM 1-way ANOVA with a post-hoc t-test, and the association between average SSD and patient-reported KOOS scores were tested using Spearman's correlation.

Results

7 CR, 13 PS, and 9 MC participants were included. The anterior-posterior (AP) translation SSD after CR was significantly greater than after MC during deep flexion ($p<0.001$)(Figure 1). No other differences in SSD were detected. No correlation between average SSD and KOOS scores were detected (mean scores 74.5+/-8.0 vs 63.3+/-11.7, CR and MC respectively).

Discussion

The differences found in AP translation SSDs between the MC and CR designs suggest that the MC design replicates native knee kinematics most closely while the CR design was the least similar. This may indicate that geometrically constrained implant designs are more capable of restoring native knee-like kinematics rather than relying on partial and possibly degenerated soft tissues surrounding the joint. Although no correlation between post-TKA KOOS scores and AP SSD were detected, other activities of daily living with differing loads and flexion angles need to be investigated.

Images (Optional)

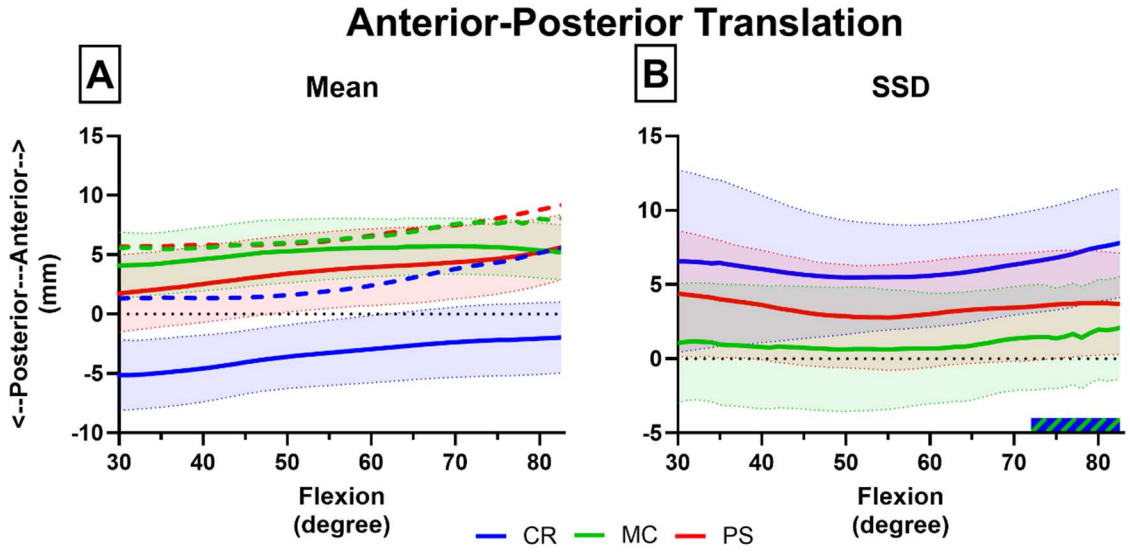


Figure 1: A) Mean tibial anterior-posterior translation relative to femur is shown, with solid lines indicating post-TKA kinematics with the shaded regions for standard deviation and dashed lines indicating native contralateral kinematics. B) The SSD for each group, with the two-toned dashed lines indicating angles of significant differences between CR and MC.

Session Category

Orthopaedic Biomechanics: Lower Extremities

OA60-05

Wear Behaviour of Total Hip Replacements During Subject-Specific Walking and Running: A Finite Element Study

Dr Zainab Altai[1,2], Dr Alican Tuncay Alpkaya[3], Dr Leiming Gao[4], Associate Professor Stephen McDonnell[5], Dr Wenxing Guo[6], Dr Ahmed Soliman[7], Dr Stefan Maas[8], Professor Nelson Cortes[8], Dr Bernard X.W. Liew[8]

[1]School of Sport, Rehabilitation and Exercise Sciences, Colchester, Essex, United Kingdom. [2]Institute of Public Health and Wellbeing, Colchester, Essex, United Kingdom. [3]Mechanical Engineering Department, Izmir Institute of Technology, Izmir, Izmir, Turkey. [4]Department of Engineering, School of Science and Technology, Nottingham Trent University, Nottingham, Nottingham, United Kingdom. [5]Division of Trauma and Orthopaedic Surgery, University of Cambridge, Cambridge, Cambridge, United Kingdom. [6]School of Mathematics, Statistics and Actuarial Science, University of Essex, Colchester, Essex, United Kingdom. [7]Department of Engineering, Faculty of Science, Technology and Medicine, University of Luxembourg, Luxembourg, Luxembourg, Luxembourg. [8]School of Sport, Rehabilitation and Exercise Sciences, University of Essex, Colchester, Essex, United Kingdom

Introduction

The accurate assessment of wear rates in total hip arthroplasty is essential for estimating implant longevity [1]. Current implants are predominantly tested under pure walking conditions, although other high-impact activities may impose additional wear [2]. Incorporating activities such as running into preclinical evaluation could yield predictions that align more closely with clinical outcomes. This study aimed to characterise the effect of running compared to walking on wear in total hip replacements (THRs).

Methods

Wear rates for CoCr-on-XLPE THRs under walking and running were analysed for 11 participants (55.9[9.8] years) with a THR using explicit finite element analysis in LS-DYNA. Each simulation ran for 5 million cycles (Mc) [3]. Archard wear law was employed to predict sliding wear, with worn geometry updated after each simulation using a 250,000-cycle scaling factor. Joint loadings were estimated from motion data using musculoskeletal simulations in AnyBody for each participant.

Results

Across subjects, cumulative linear wear over 5 Mc ranged from 0.236–0.421 mm during walking and 0.382–1.036 mm during running. Mean linear wear rates were 0.064 ± 0.012 mm/Mc (walking) and 0.115 ± 0.037 mm/Mc (running), an ~1.8-fold increase during running. Cumulative volumetric wear was 143.90–276.80 mm^3 for walking and 258.86-777.82 mm^3 for running, with the mean rising from 207.76 ± 41.37 to 412.15 ± 146.95 mm^3 (1.98× higher). Mean contact area increased from 645 ± 39 mm^2 (walking) to 714 ± 51 mm^2 (running), indicating greater loading and variability during running.

Discussion

Relative to the commonly cited critical wear threshold of 0.1 mm/Mc for polyethylene cups [3], mean linear wear during walking was 35–40% below the limit, whereas running exceeded it by ~15%. This shows that high-impact activities substantially elevate wear risk and may contribute to aseptic loosening through periprosthetic osteolysis. Wear predictions based solely on walking therefore underestimate true loading exposure. Comprehensive assessments should incorporate multiple daily activities, including running. Ongoing work in our group is examining how realistic activity combinations influence long-term implant wear.

Images (Optional)

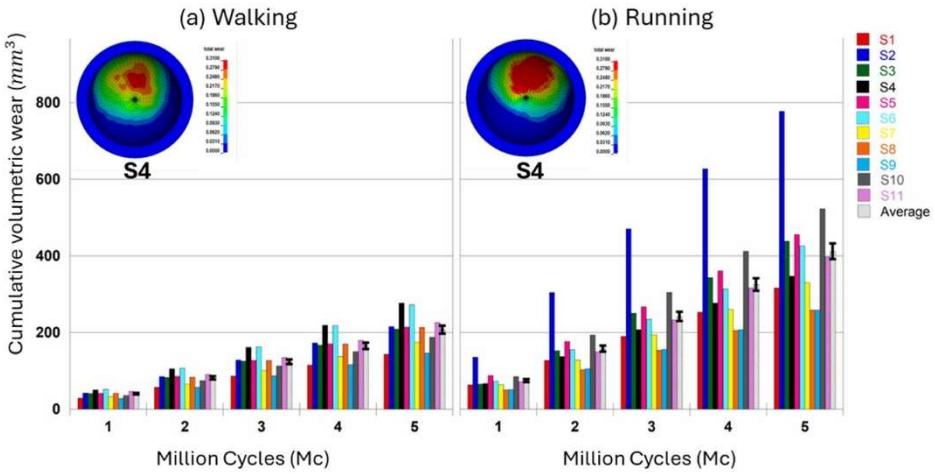


Figure1. Cumulative volumetric wear under five million cycles of walking (a) and running (b) for all subjects. The distribution of the volumetric wear is also illustrated for a representative case (S4)

References (Optional)

[1] Pourzal et al, Clin Orthop Relat Res, 2016.

[2] Bergmann et al, Biomed Mater Eng, 2010

[3] Alpkaya et al, Med Eng Phys, 2024

Acknowledgements (Optional)

This work was funded by the Medical Research Council (MR/Y013557/1)

Session Category

Orthopaedic Biomechanics: Lower Extremities

OA61-02

Video-Based Hip Kinematic Analysis and Machine Learning for Screening of Sarcopenia During the Five Times Sit-to-Stand Test

Ms Hejin Cai[1], Mr Jialiang Xu[1], Dr Guoxin Zhang[2], Dr Tony Lin-Wei Chen[1], Ms Linjuan Wei[1], Dr Qitao Tan[1], Prof Ming Zhang[1]

[1]The Hong Kong Polytechnic University, Hong Kong, Kowloon, Hong Kong. [2]Beihang University, Hangzhou, Zhejiang, China

Introduction

Sarcopenia leads to marked impairments in lower-limb strength and movement control in the aging population. The five-times sit-to-stand (5STS) test is widely used in clinical assessment of sarcopenia, but stopwatch-based timing of the test often lacks the sensitivity to detect subtle, joint-level functional deficits indicative of early-stage disease. This study aimed to examine whether smartphone video-derived kinematics combined with interpretable machine learning can accurately distinguish sarcopenia from healthy older adults and identify key movement predictors of the condition.

Methods

Forty-four adults aged ≥65 years (22 sarcopenic, 22 healthy) each performed three standardized 5STS trials recorded by a smartphone. Object detection and pose estimation algorithms (YOLOv8 and SMPLer-X) provided 3D hip and knee kinematics. Each sit-stand-sit cycle was segmented into forward, upward, downward, and backward phases, from which 40 biomechanically interpretable angular and temporal features were extracted. Training and validation sets were split at the participant level (7:3). A physiologically constrained augmentation strategy with Gaussian noise and KNN-based label filtering expanded the training dataset to 255 samples. Six classifiers (GBDT, KNN, LR, MLP, RF, and SVM) were trained using 10-fold cross-validation. Performance metrics included accuracy, recall, specificity, F1-score, and AUC. Feature importance was quantified using permutation analysis. The top 10 features were further statistically compared between groups.

Results

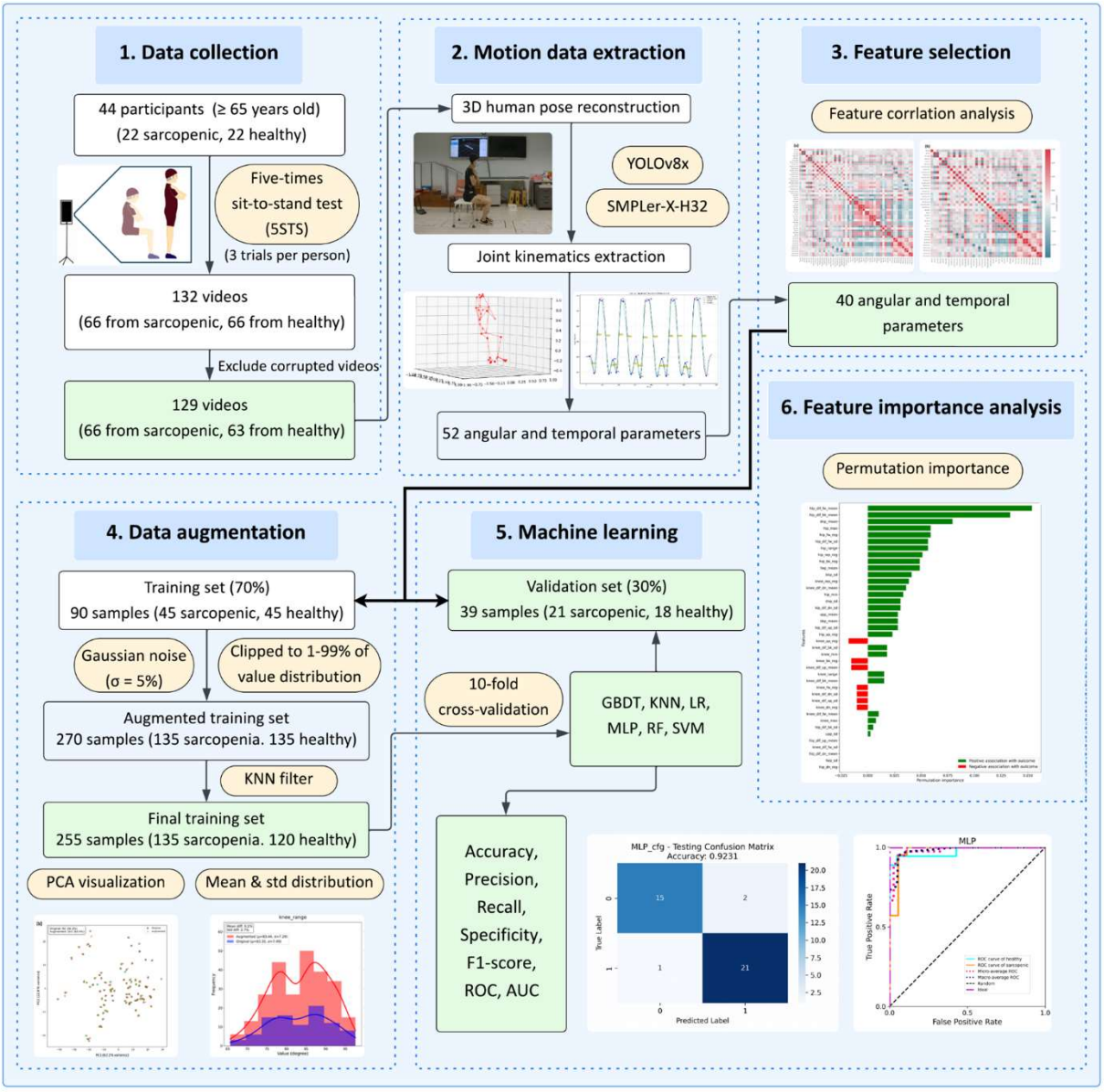
Augmented samples preserved the distribution of original features without forming artificial clusters. The multilayer perceptron (MLP) achieved the strongest performance (validation accuracy: 0.95; recall: 1.00; specificity: 0.89; AUC: 0.98). Hip-related variables

were the most discriminative biomarkers. Greater hip range of motion in the forward (12.48° vs. 8.05°, p=0.010) and backward phases (11.48° vs. 6.78°, p=0.019) showed the strongest predictive value.

Discussion

Smartphone video-based 3D motion analysis offers a feasible, low-cost method for capturing joint-level biomechanics relevant to sarcopenia. The proposed augmentation strategy preserved physiological plausibility and improved classifier performance. The findings emphasize the central role of altered hip motion, particularly enlarged forward- and backward-phase hip range of motion, as a compensatory strategy in sarcopenia. This pipeline demonstrates the potential of accessible motion analysis and machine learning to offer a scalable, precise, and objective tool for early sarcopenia screening in both clinical and community settings.

Images (Optional)



Session Category

Emerging Areas: N/A

OA61-03

World-Grounded 3D Pose Estimation for Marker-Less Motion Analysis in Children

Ms. Josephine Wang, Mr. Daniel Seong, Dr. Nidhi Seethapathi

Massachusetts Institute of Technology, Cambridge, MA, United States

Introduction

Motor development research is limited by the cost and practical challenges of using motion capture with young children. Recent work shows that marker-less video-based approaches recover clinically acceptable lower limb kinematics, but assume stationary cameras [1], while at-home videos of children tend to have a moving frame. Here, we develop and validate a computer vision (CV) pipeline that extracts world-grounded 3D pose estimation from videos of children, including ones with moving cameras.

Methods

Videos of 6 children were processed with WHAM to extract 3D keypoints in a world frame [2]. For comparison, we ran AlphaPose and MotionBERT to characterize movements in the camera frame [3, 4]. The child was identified in each clip via manual bounding boxes labeled in CVAT, and adult individuals were masked with opaque overlays. From the tracked heel trajectories, we applied Savitzky-Golay filtering and peak detection to identify heel strikes, then computed stride length, stride frequency, and walking speed to compare their relationships with those obtained from ground truth motion capture (MoCap). To validate the CV-inferred heel strikes, we manually labeled left and right step events.

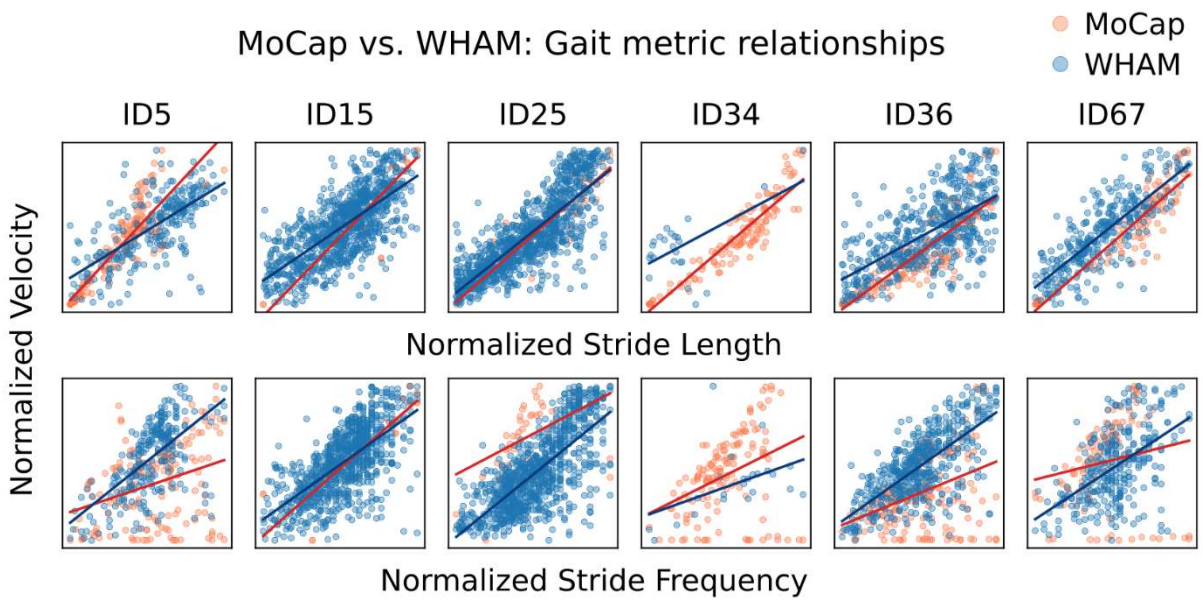
Results

Across all CV methods (WHAM, AlphaPose, and MotionBERT), we found that stride length was more strongly correlated with walking speed than stride frequency, consistent with MoCap (MoCap: $r = 0.896$ vs $r = 0.434$; AlphaPose: $r = 0.457$ vs 0.015; MotionBERT: $r = 0.689$ vs -0.098; WHAM: $r = 0.708$ vs 0.616). For step-detection precision, defined as the fraction of CV-identified heelstrikes that aligned with manually labeled steps, WHAM achieved the highest precision (89.7%), compared to MotionBERT (48.9%) and AlphaPose (45.0%). Across CV methods, WHAM showed the strongest agreement with MoCap.

Discussion

Comparing different CV methods, we demonstrate that world-grounded CV is more accurate than camera-fixed CV tools with the same constraints. Easy-to-use and accurate CV from video has the potential to transform the scope and scale of biomechanics through improved gait analysis from naturalistic, at-home recordings.

Images (Optional)



References (Optional)

[1] Greaves *et al.*, Sensors, 2025

[2] Shin *et al.*, arXiv:2312.07531 (preprint), 2024

[3] Fang *et al.*, arXiv:2211.03375 (preprint), 2022

[4] Zhu *et al.*, arXiv:2210.06551 (preprint), 2023

[5] Anderson *et al.*, Front. Digit. Health, 2025

Session Category

Emerging Areas: N/A

OA61-04

Markerless Motion Tracking Powered by Synthetic Data Outperforms Alternatives in Estimation of Lower-Extremity Joint Moments

Mr. Soyong Shin[1], Ms. Chaeeun Lee[1], Ms. Sijia Li[1], Mr. Zhixiong Li[1], Mr. Kunwoo Lee[1], Dr. Hanz Cuevas Velasquez[2], Mr. Anastasios Yiannakidis[2], Dr. Michael J. Black[2], Eni Halilaj[3]

[1]Carnegie Mellon University, Pittsburgh, PA, United States. [2]Max Planck Institute for Intelligent System, Tübingen, Germany, Germany. [3]Carnegie Mellon University (Department of Mechanical Engineering), Pittsburgh, Pennsylvania, United States

Introduction

Markerless motion tracking is expanding opportunities for scalable biomechanics by reducing reliance on expensive and cumbersome marker-based systems. While recent studies have assessed kinematics accuracy, it remains unclear how reliably existing markerless tools estimate joint moment and how performance depends on the number of cameras. We compared the performance of OpenCap [1], Theia3D [2], and DeepGaitLab [3] in lower-extremity joint-moment estimation. OpenCap is a two-camera open-source solution, Theia3D is a commercial tool requiring at least six cameras, and DeepGaitLab is a flexible open-source tool that operates with any number of cameras and has shown superior kinematics tracking capabilities [3].

Methods

Twelve healthy participants performed overground walking, single-leg squat, and lateral step-down while recorded with 20 infrared cameras, 10 RGB cameras, and force plates. Marker-based inverse dynamics served as the reference. We evaluated the agreement (relative root mean square difference) between Theia3D (10 cameras), OpenCap (2 cameras), and DeepGaitLab (both 10-camera and 2-camera configurations) with marker-based analysis. Head-to-head comparisons assessed DeepGaitLab against OpenCap (both using 2 cameras), DeepGaitLab against Theia3D (both using 10 cameras), and DeepGaitLab (2 cameras) against Theia3D (10 cameras). A linear mixed-effects model assessed the effect of tracking method, activity, and joint degrees of freedom, with Wilcoxon signed-rank tests and Bonferroni correction for pairwise comparisons.

Results

DeepGaitLab yielded the highest accuracy across configurations. With two cameras, DeepGaitLab outperformed OpenCap (0.27±0.07 vs. 0.42±0.17, $p<0.0001$), with the largest difference observed during single-leg squat (0.30±0.12 vs. 0.54±0.26, $p<0.0001$), hip abduction/adduction (0.41±0.14 vs. 0.69±0.27, $p<0.0001$) and internal/external rotation

(0.17±0.05 vs. 0.33±0.15, p<0.0001) moments. With ten cameras, DeepGaitLab and Theia3D performed comparably (0.26±0.08 vs. 0.29±0.09, p=0.6797). However, DeepGaitLab reached comparable accuracies even with two cameras (0.27±0.07 vs. 0.29±0.09, p=0.0991).

Discussion

These findings demonstrate that DeepGaitLab, built using synthetic data and designed for flexible hardware, is more powerful than other existing tools in estimation of lower-extremity joint moments. These results help contextualize accuracy–accessibility trade-offs among emerging markerless tracking solutions and underscore the potential of scalable biomechanics tools.

Images (Optional)

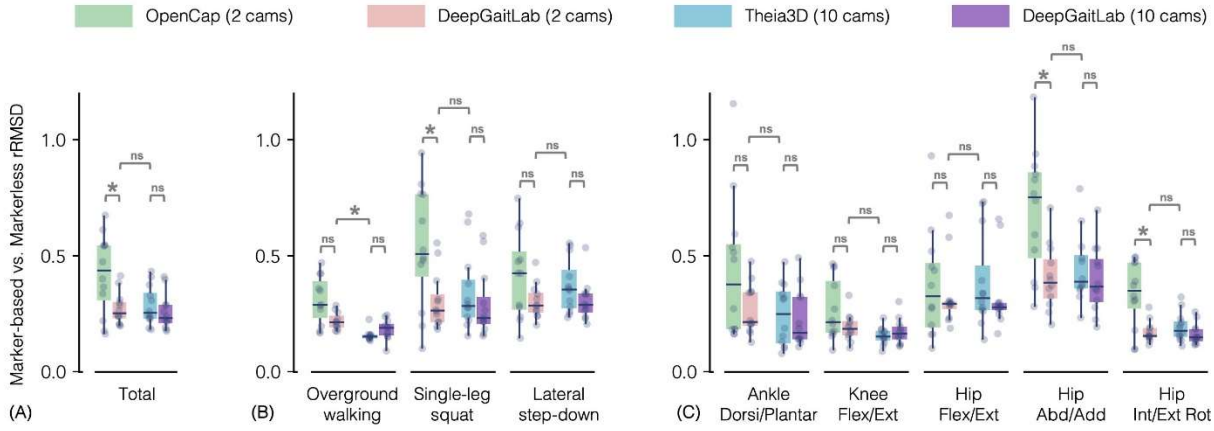


Figure 1. Performance Evaluation. (A) Overall, DeepGaitLab (2 cams) surpassed the performance of OpenCap (2 cams) and matched that of Theai3D (10 cams). (B) DeepGaitLab (2 cams) particularly outperformed OpenCap on single-leg squat and it matched Theia3D (10 cams) during single-leg squat and lateral step down. In overground walking, DeepGaitLab and Theia3D performed comparably only when using the same camera density, given the spatial coverage requirements of this type of activity. (C) DeepGaitLab (2 cams) shows greater accuracy than OpenCap (2 cams) particularly in non-sagittal degrees of freedom.

References (Optional)

This project was funded by the NSF (CBET 2145473) and Chan Zuckerberg Initiative.

Acknowledgements (Optional)

[1] Uhlrich et al., 2023, [2] Kanko et al., 202, [3] Shin et al., 2025.

Session Category

Emerging Areas: N/A

OA61-05

Influence of Camera Orientation on Joint-Angle Estimation Using Single-Camera 2D and 3D Markerless Motion Capture

Ms. Ishi Arora, Ms. Sarah Dumont, Dr. Calvin Kuo PhD

University of British Columbia, Vancouver, BC, Canada

Introduction

Markerless motion capture has strong potential for large-scale movement analysis in real-world settings, but accuracy and applicability in out-of-laboratory conditions remain limited. In single-camera systems, changes in camera angle can reduce joint visibility, increase occlusion, and lead to issues with observing multi-axial movements, which can affect the accuracy of joint-angle estimates in 2D (OpenPose) and 3D (GVMHR) reconstructions [1,2]. This study examines how camera angle influences joint-angle estimation in single-camera markerless systems to guide optimal camera placement for higher-quality data collection.

Methods

29 participants (24±4.1yo; 15F) performed dynamic movements while wearing 50 active LED markers. Marker trajectories were captured using an 8-camera PhaseSpace system (960 Hz), then interpolated, filtered, and downsampled to match video data. 3D knee joint angles were computed using inverse kinematics.

Simultaneously, eight Sony RX0II cameras (60Hz) were placed 2m from participants at 45° intervals. Movements were performed facing the front camera (180°) and at 15° and 30° deviations. Videos were processed with OpenPose and GVMHR to extract 2D and 3D joint centers of the knee, hip, and ankle. Data was interpolated and filtered to compute knee joint-angles (cosine law).

We then computed knee joint-angle normalized root mean square error (RMSE) and peak error relative to the marker-based system.

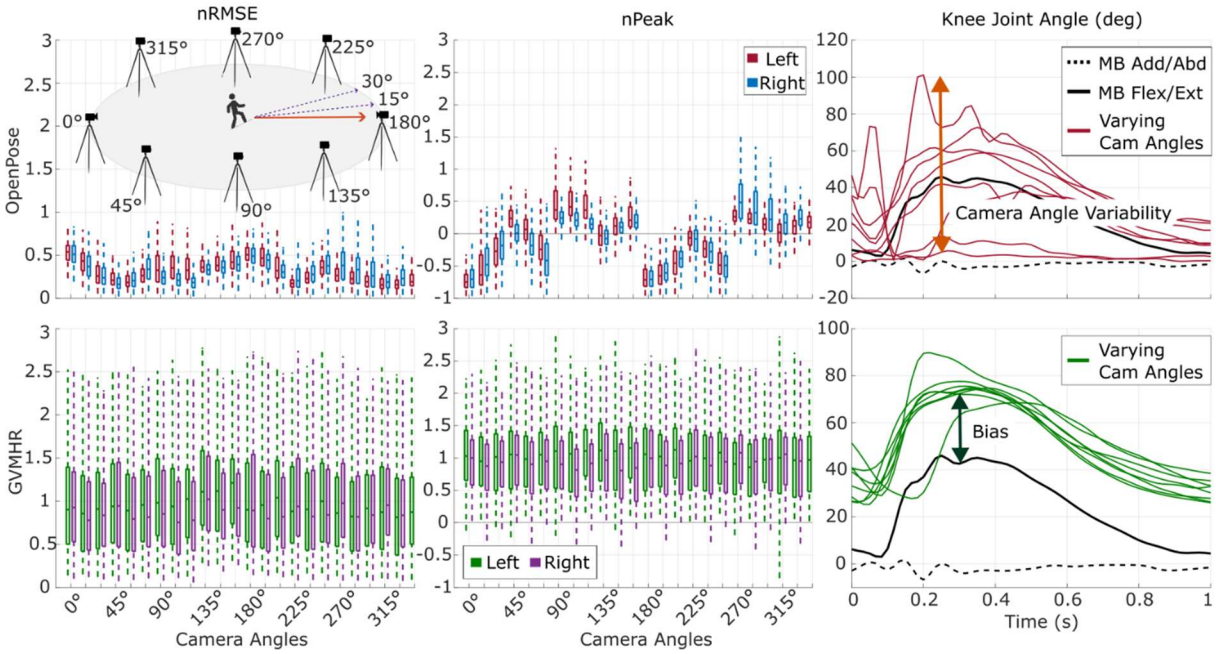
Results

OpenPose provides 2D pose estimation, which shows high variability in joint-angle calculations between camera angles. Oblique views, particularly rear oblique views (45°, 315°), yielded the most accurate knee joint-angle estimates. GVMHR reconstructs a 3D pose, which produced similar results across varying camera angles. However, there is a bias in knee joint-angle leading to high error bars within the plots.

Discussion

Using 2D pose estimation (OpenPose) for joint-angle measurement requires careful camera placement, while adding a 3D mesh model (GVMHR) helps generalize estimates across orientations. However, joint centers in these mesh models are not anatomically defined, introducing bias in the results that must be calibrated. By quantifying how joint-angle outputs vary with camera angle across systems, this study offers practical guidance for system setup and clarifies the limitations and capabilities of single-view markerless motion capture for kinematic assessment.

Images (Optional)



References (Optional)

[1] Cao Z. (2019). IEEE.

[2] Shen Z. (2024). SIGGRAPH.

Acknowledgements (Optional)

Funded by the Canadian Foundation for Innovation John R Evans Leadership Fund and Mitacs Accelerate.

Session Category

Emerging Areas: N/A

OA62-01

Establishing the 3D Asymmetry of the Intervertebral Disc in Adolescent Idiopathic Scoliosis

Miss Anna Iacocca[1], Mr. Jacob Jordan[2], Mr. Thomas Coleman[2], Dr. Patrick Cahill MD[2], Dr. Axel Moore PhD[1]

[1]Carnegie Mellon University, Pittsburgh, PA, United States. [2]Children's Hospital of Philadelphia, Philadelphia, PA, United States

Introduction

Adolescent idiopathic scoliosis (AIS) is an abnormal lateral curvature of the spine that develops prior to skeletal maturity. Though primarily defined by the coronal deformity, AIS is realistically a 3-dimensional disease that afflicts the spine in all three planes. While differential growth of the vertebrae is well-established, the effect of AIS on the 3-dimensional structure of the intervertebral disc (disc) has yet to be established. Given the tenet that structure follows function, and the function (kinematics and kinetics) of the AIS spine is inherently asymmetric, we hypothesized that AIS discs would be structurally asymmetric.

Methods

Following IRB approval, we retrospectively analyzed magnetic resonance (MR) images from 10 pre-surgical AIS patients (7 F) with Cobb angles ranging from 45 to 71 deg (**Fig 1A**). The disc and nucleus pulposus (NP) were manually segmented from the MR image stacks (**Fig 1B)**. Following segmentation, we quantified disc wedging in the coronal plane as well as anterior-posterior and left-right symmetry in the transverse plane. Disc wedge was quantified from planar fits to the superior and inferior surfaces of the disc (**Fig 1C**). Symmetry was quantified using the dice similarity coefficient, defined as the normalized area of overlap of a mirrored disc (**Fig 1D**).

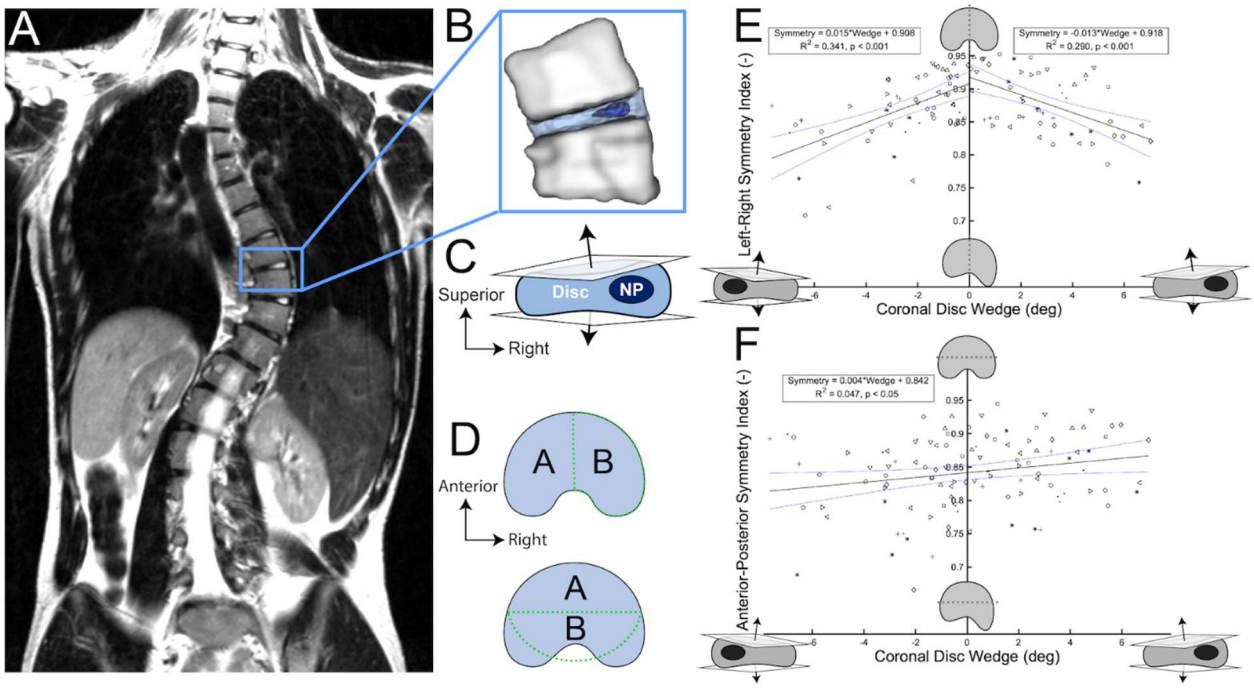
Results

Our results demonstrate that the AIS disc is coronally wedged, and this wedging opens toward the convexity of the curve and follows vertebral wedging. In the transverse plane, the AIS disc is asymmetric about the anterior-posterior and left-right axes (**Fig 1E&F**). The symmetry about the anterior-posterior axis was correlated with disc wedging—more wedge = less symmetry. The symmetry about the left-right axis was not correlated with disc wedging; however, even non-scoliotic discs lack symmetry about this axis.

Discussion

In this work we demonstrate that the AIS disc is structurally asymmetric in all 3 dimensions. Currently, it is unknown whether these results stem from structural remodeling, damage, or poro-visco-elastic deformations of the disc. The observed structural asymmetry suggests that AIS discs will also display asymmetric mechanics. This work takes a critical first step towards establishing the structural, compositional, and functional state of the AIS disc.

Images (Optional)



Acknowledgements (Optional)

The authors acknowledge support from the Wyss/Campbell Center for Thoracic Insufficiency Syndrome, Achievement Rewards for College Scientists Foundation, and Biomechanics in Regenerative Medicine Training Program (NIH T32-EB034216).

Session Category

Orthopaedic Biomechanics: Spine

OA62-02

Quantification of Vertebral Bone Morphology in Young Adults Using Ultrashort Echo Time MRI Sequence

MSc Salvatore Conticello[1,2], Dr. Bernd Jung[3], Dipl. Radiologiefachfrau HF Scilla Dozio[3], Dipl. Radiologiefachfrau HF Verena Beutler-Minth[3], MSc Philippe Bähler[1,2], Dr. Stefan Schmid[2,4], Prof. Dr. Philippe Büchler[1]

[1]ARTORG Center for Biomedical Engineering Research, University of Bern, Bern, Bern, Switzerland. [2]Spinal Movement Biomechanics Group, School of Health Professions, Bern University of Applied Sciences, Bern, Bern, Switzerland. [3]Department of Diagnostic, Interventional and Pediatric Radiology, University Hospital Bernof Diagnostic, Interventional and Pediatric Radiology, Bern, Bern, Switzerland. [4]Faculty of Medicine, University of Basel, Basel, Basel, Switzerland

Introduction

MRI is the preferred modality for soft tissue imaging, yet its capacity to visualize bone remains limited. In contrast, CT provides superior bone imaging but the associated ionizing radiation makes it unsuitable for repeated imaging in pediatric populations. High-resolution imaging is crucial for detecting subtle morphological changes and for assessing growth at the level of individual vertebral bodies. This study evaluates the feasibility of using Ultrashort Echo Time (UTE) MRI sequences to visualize vertebral bone anatomy and to enable reliable morphometric assessments over time.

Methods

Ten volunteers adolescent (16 ± 1 years) underwent two MRI examinations using UTE sequences of the thoracic and lumbar spine, acquired within a 30 minutes time interval. The vertebrae were automatically segmented using a deep learning algorithm. Vertebral morphology between the two acquisitions was then compared using surface distance metrics such as the Hausdorff distance. In addition, several anatomical measurements were evaluated, including, whole vertebra height (WVh) and width (WVw), endplate width (EPW) and depth (EPD), vertebral body height (VBH), and processus spinosus length (SPl).

Results

The segmentation achieved high repeatability with the mean difference between time points of 0.46 ± 0.05 mm. Region-specific results showed slightly better agreement in the lumbar region with a mean difference of 0.44 ± 0.04 compared to the thoracic spine where the difference between repeated acquistions was 0.47 ± 0.06. All anatomical

measurements were within 0 and 0.5 mm between the two acquisitions, except for WVw and SPl, which showed a difference between 1.5 to 2 mm (Figure 1).

Discussion

UTE MRI provides enhanced bone contrast and allows accurate, repeatable vertebral segmentation. Vertebral surface can be reconstructed with an accuracy below 0.5mm, which is smaller than the expected yearly vertebral growth in healthy children (0.8–1.2 mm/year). This level of precision supports longitudinal monitoring without radiation exposure, particularly in multi-year follow-up studies. Segmentation quality appears adequate for modeling and quantifying bone growth over one to two years, with the potential to reveal spatial patterns of bone growth, that may improve our understanding of scoliosis progression and the evaluation of conservative treatments such as bracing and physiotherapy. Future work will include comparisons vertebral morphology with CT.

Images (Optional)

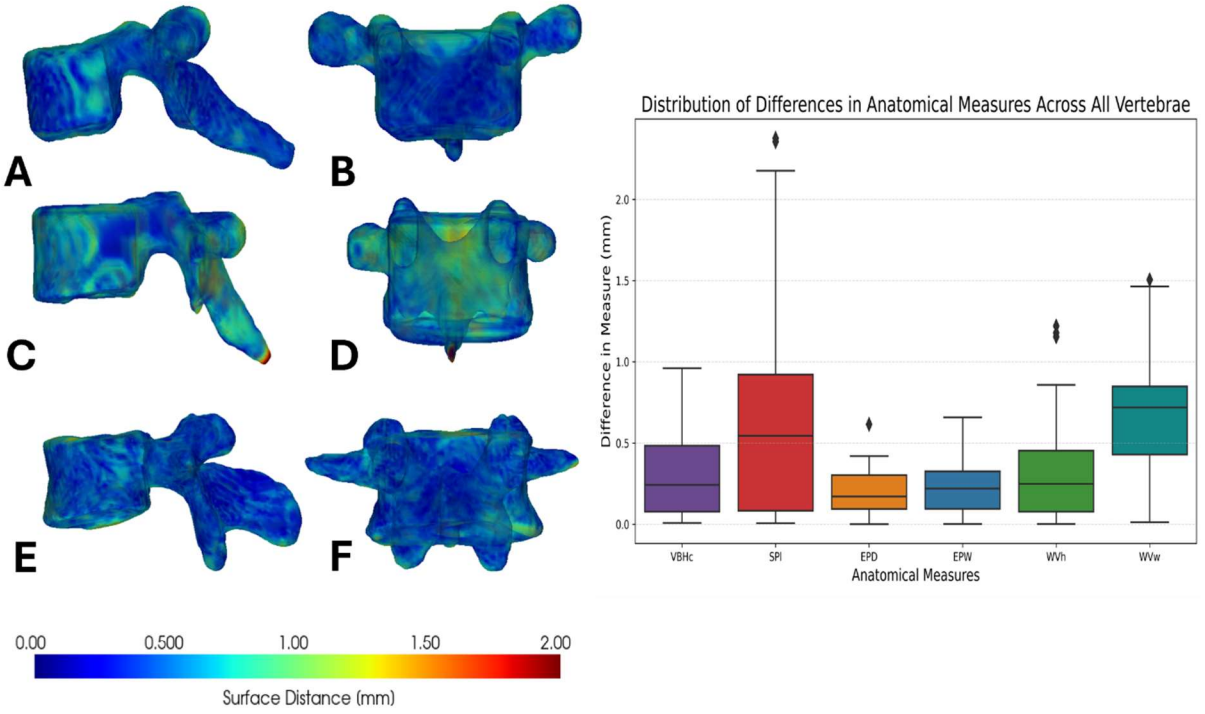


Figure 1 3D vertebrae reconstructed from UTE MRI with a heat map illustrating the Hausdorff distance. A–B) Sagittal and coronal view of the T1 vertebra, C–D) sagittal and coronal view of the T8 vertebra, and E–F) sagittal and coronal view of the L2 vertebra.
The accompanying plot shows the distribution of differences in anatomical measurements across all vertebrae, including whole vertebra height (WVh) and width (WVw), endplate width (EPW) and depth (EPD), vertebral body height (VBH), and spinous process length (SPl).

Acknowledgements (Optional)

This work was supported by the Swiss National Science Foundation (SNSF; Grant-no.: 214986).

Session Category

Orthopaedic Biomechanics: Spine

OA62-03

Generating Standing Posture Finite Element Models of the Spine Based on Radiation-Free Imaging

MsC Federica Incatasciato[1], Mr. Peter P.G. Lafranca[2], Prof Dr. Tom P.C Schlosser[2], Dr. Bert van Rietbergen[1], Prof Dr. Keita Ito[1,2], Dr. Joeri Kok[1]

[1]Eindhoven University of Technology, Eindhoven, N/A, Netherlands. [2]University Medical Center Utrecht, the Netherlands, Utrecht, N/A, Netherlands

Introduction

Patient-specific Finite Element (FE) spine models are typically created from CT scans acquired in supine position. To obtain the clinically relevant standing posture, these models can be morphed to standing radiographs. However, the radiation exposure limits this approach in children. Synthetic CT (sCT) generated from MRI, combined with emerging ultrasound (US) techniques that estimate 3D spinal curvature in standing position, offers a radiation-free alternative [1]. This study aims to integrate sCT and US imaging to develop a radiation-free method for generating patient-specific FE spine models in standing posture.

Methods

A cohort of 8 subjects (8-13 years old) at risk for scoliosis development undergoing upright US and supine MRI as part of a study, were included (informed consent by patients and parents/legal guardians; IRB approval MedNed 22-999). Subject-specific T3–L5 FE models were created from MRI and sCT, including vertebrae, intervertebral discs, and ligaments [2]. US scans acquired in standing position visualized posterior vertebral elements. Supine FE models were converted to standing posture by aligning T12 laminae and applying a rigid rotation that minimized the distance between the model and a curve fitted through US-measured laminae. Remaining distances were used as displacements in FE analysis to enforce the standing curvature. For validation, spinal curvature was prescribed using radiograph-derived laminae measurements, and common clinical curvature measures were calculated and compared to direct radiographic measurements (Fig.1).

Results

The procedure successfully transformed each supine model to standing position, with deviations from prescribed curvature <1 mm. Validation against radiographs showed mean within-subject differences of 7.1 ± 6.1° for thoracic kyphosis, 5.6 ± 2.5° for lumbar lordosis,

1.5 ± 0.8° for thoracic tilt, and 1.8 ± 1.3° for lumbar tilt. Non-parametric Wilcoxon signed-rank test showed no significant differences between the two modalities ($p>0.05$).

Discussion

The proposed radiation-free method accurately represented the prescribed spinal curvature at the laminae, while keeping vertebrae undeformed. Validation revealed differences in vertebral inclination between model and radiographs. These differences were small, suggesting that the morphed model will be an accurate representation of the standing spinal alignment and morphology.

Images (Optional)

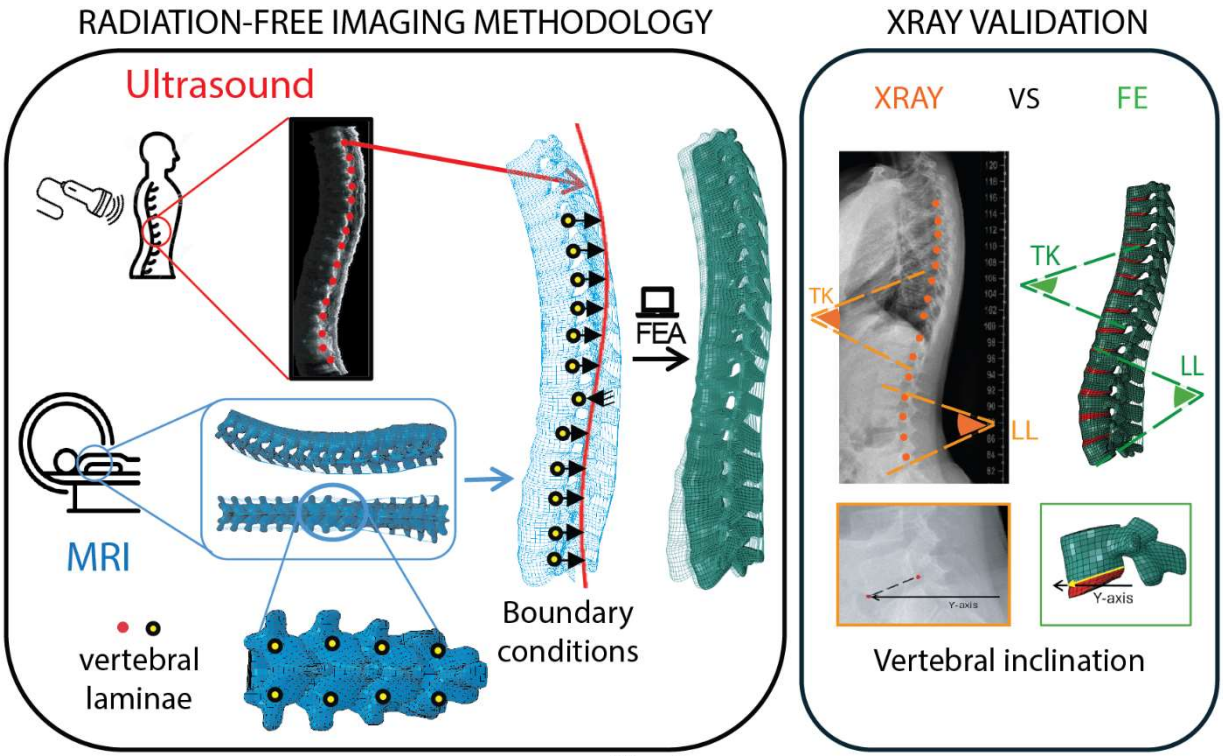


Fig. 1

References (Optional)

[1] Timothee Lee *et al.*, J. Orthopaedic Translation, 2021

[2] Joeri Kok *et al.*, Frontiers Bioengineering Biotechnology, 2023

Acknowledgements (Optional)

Financial support was provided by the European Research Council (Grant no: 101020004)

Session Category

Orthopaedic Biomechanics: Spine

OA62-04

Mechanics-Informed Stability and Morphological Descriptors for Predicting Adolescent Idiopathic Scoliosis Progression

Mr David Landinez Leon[1], Mr Javier Bayod[2], Mr Christian Cifuentes-De La Portilla[1]

[1]Universidad de los Andes, Bogotá, Cundinamarca, Colombia. [2]Universidad de Zaragoza, Zaragoza, Aragon, Spain

Introduction

Adolescent idiopathic scoliosis (AIS) burdens young recruits in Latin-American militaries, where access to 3D imaging is scarce and fitness-for-duty decisions rely almost exclusively on Cobb angle from plain radiographs [1]. Angle cut-offs do not capture three-dimensional mechanical stability, cumulative disc compression or morphological balance, despite their relevance for curve progression and duty limitations. There is a need for objective, interpretable biomechanical indices computable from routine standing X-rays and compatible with existing accession and follow-up workflowS.

Methods

We retrospectively analysed 209 standing posteroanterior radiographs of AIS in young members of the Colombian military health system. A convolutional neural network segmented the spine and extracted a smooth midline. A parametric finite-element digital twin was fitted by matching the radiographic curve to a precomputed simulation library under axial load. From the fitted model we derived an energy-based stability index (Rayleigh quotient), disc-height loss as a magnitude proxy, and a symmetry index describing morphological balance. After standardisation, a Gaussian mixture model identified unsupervised risk clusters in this three-dimensional energetic–morphological space.

Results

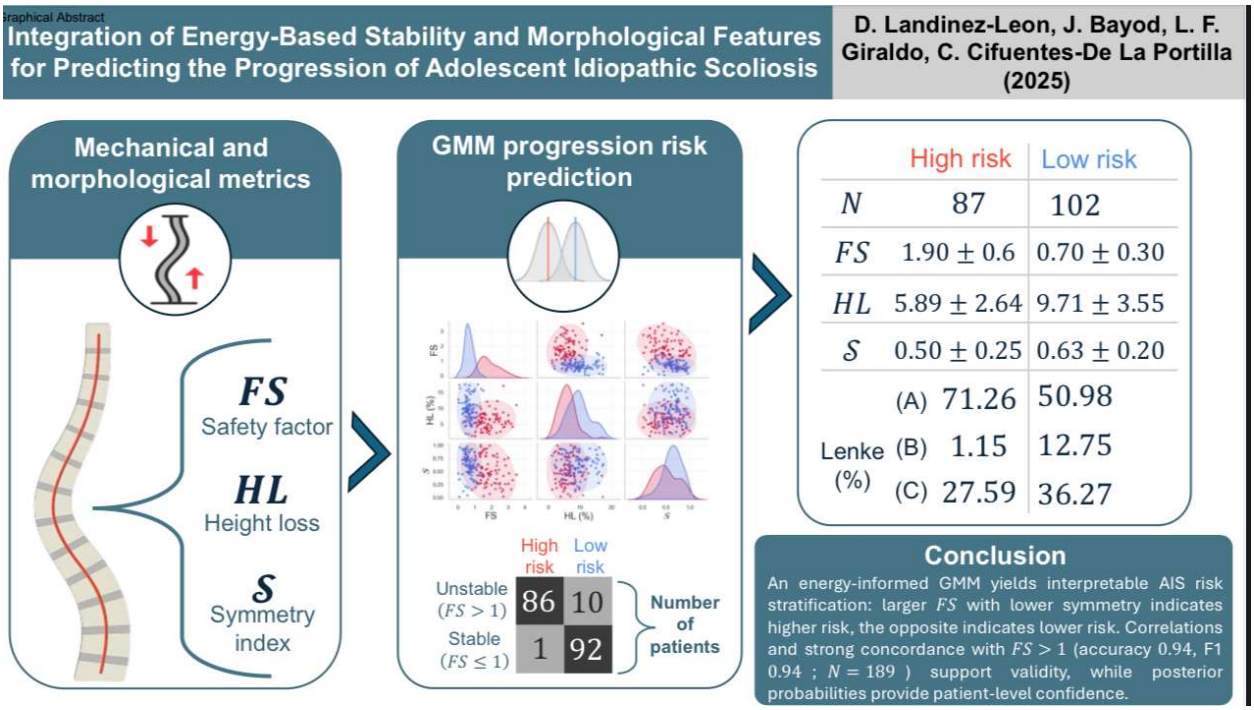
Two well-separated phenotypes emerged. The low-risk cluster showed higher mechanical stability, lower disc-height loss and higher symmetry index, indicating mechanically safer, more balanced curves. The high-risk cluster concentrated cases with reduced stability, greater cumulative compression and more asymmetric morphology. Cluster membership

probabilities were sharply peaked, suggesting limited ambiguity and good internal separability of phenotypes.

Discussion

This mechanics-informed, radiography-first pipeline enriches conventional AIS assessment without changing imaging infrastructure. Combining patient-specific digital twins with energetic and morphological descriptors yields interpretable risk phenotypes aligned with curve-type labels and intuitive notions of mechanical vulnerability. Because it operates on plain radiographs and commodity computing, the approach can support Latin-American military screening and follow-up, standardising documentation, guiding referral and potentially reducing attrition related to spinal deformity.

Images (Optional)



References (Optional)

[1] Li M, Wang X, Li S, et al. Prevalence of scoliosis in children and adolescents: a systematic review and meta-analysis. Front Pediatr. 2024;12:1399049

Session Category

OA62-05

In-Vivo Identification of Adolescent Idiopathic Spine Properties through Intraoperative Measurement and FE Modelling

Mr. Till van der Reijden Msc.[1], Prof. Dr. Philippe Büchler[1], Prof. Dr. med. Carol Hasler[2], PD Dr. med. Daniel Studer[2], Associate Prof. Dr. sc. Georg Rauter[3]

[1]ARTORG Center for Biomedical Engineering Research, Bern, Bern, Switzerland. [2]Universitäts-Kinderspital beider Basel, Basel, Basel, Switzerland. [3]Bio-Inspired RObots for MEDicine-Lab (BIROMED-Lab), Basel, Basel, Switzerland

Introduction

Adolescent Idiopathic Scoliosis (AIS) is a complex three-dimensional spinal deformity that often requires surgical intervention to prevent progression. Although spinal fusion provides reliable correction, it limits spinal mobility and can cause serious adverse effects. Developing new treatment strategies is challenging due to limited access to *in-vivo* spinal mechanics. Cadaveric specimens are rare and cannot mimic physiological conditions. To address these limitations, this study combines intraoperative measurements collected during AIS correction surgery with patient-specific finite-element (FE) simulations to identify the biomechanical properties of the scoliotic spine.

Methods

Patient-specific FE models of three functional spinal units of a single patient were automatically generated from MRI images, capturing bone and soft-tissue anatomy (e.g., intervertebral disc, annulus, and ligaments). The annulus was modelled using the Holzapfel–Gasser–Ogden formulation, and the nucleus as a fluid-filled cavity. The vertebrae were represented as rigid bodies, and ligaments were modelled as truss elements with a user-defined stretch-dependent, tension-only response. The lateral bending moment was derived from *in-vivo* measurements [1] and applied to the cranial vertebra, while caudal vertebra displacements were constrained. Material parameters were identified using a Bayesian optimisation, which minimised the difference between model-predicted and measured *in-vivo* rotation.

Results

Simulated moment–angle curves closely matched experimental measurements, indicating reliable model performance. Material parameters converged within each analysed segment, suggesting a robust optimisation process, and the overall combined RMSE

ranged from 0.08 to 0.2 degrees. The calibrated models successfully reproduced the characteristic asymmetry observed in *in-vivo* measurements (Figure 1), showing that the calibrated models can capture the biomechanical behaviour of the scoliotic spine.

Discussion

These initial results showed that integrating intraoperative measurements with patient-specific FE modelling enables reliable estimation of *in-vivo* spinal mechanics in AIS patients. This is a major step forward, given the scarcity of representative cadaveric material and the challenges of directly measuring spinal behaviour. This integrated approach can predict subject-specific mechanical properties, supporting improved surgical decision-making and the development of personalised, mobility-preserving interventions.

Images (Optional)

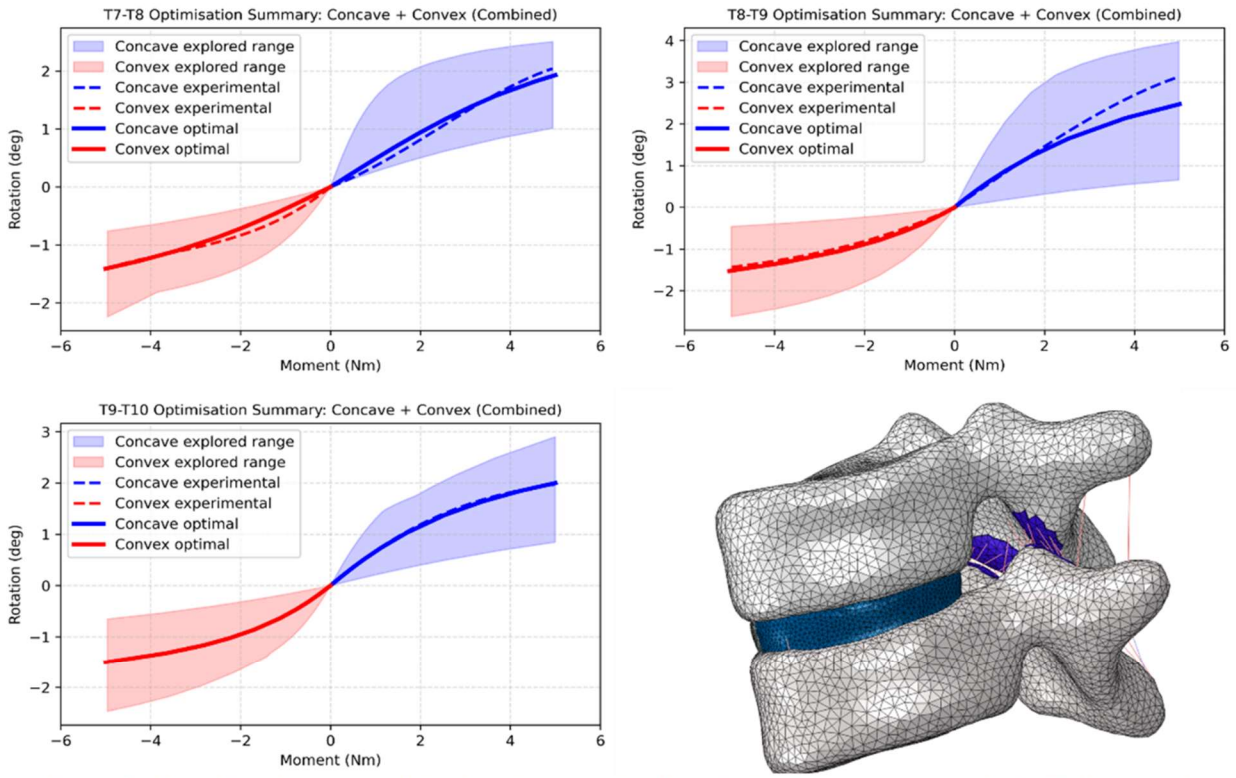


Figure 1: Combined concave (blue) and convex (red) optimisation summaries for initially tested segments (top left: T7-T8, top right middle: T-8-T9, lower right: T9-T10) of the same patient. The shaded regions show the range of moment-angle responses explored during the Bayesian optimisation process. Experimental curves are represented as dashed lines, while solid lines represent the simulations using the respective set of optimal parameters. An example of the reconstructed Abaqus model including all soft tissue structures is shown in the lower left.

References (Optional)

[1] C. Reutlinger et al., 'Intraoperative determination of the load–displacement behavior of scoliotic spinal motion segments: preliminary clinical results', *Eur Spine J*, vol. 21, no. S6, pp. 860–867, Aug. 2012, doi: 10.1007/s00586-012-2164-8.

Acknowledgements (Optional)

This work was supported by the Swiss National Science Foundation (#205320_219970).

Session Category

Orthopaedic Biomechanics: Spine

OA63-01

A Novel Biomechanical Bioreactor Platform Reveals that Tensional Homeostasis in Soft Tissues Arises from a Balance Between Cell Contractility and Extracellular Matrix Densification

Mr. Andrew Glick[1,2], Mr. Victor Ngyuen[1,2], Mr. Bishan Karki[1], Dr. Daniel Paukner[3], Dr. Margherita De Marzio[4], Dr. Huocong Huang[5,6], Dr. Christian J. Cyron[3], Dr. Jacopo Ferruzzi[1,2]

[1]Department of Bioengineering, University of Texas at Dallas, Richardson, Dallas, TX, United States. [2]Department of Biomedical Engineering, University of Texas Southwestern Medical Center, Dallas, TX, United States. [3]Hamburg University of Technology, Hamburg, Germany, Germany. [4]Channing Division of Network Medicine, Brigham and Women's Hospital and Harvard Medical School, Boston, MA, United States. [5]Department of Surgery, University of Texas Southwestern Medical Center, Dallas, TX, United States. [6]Department of Immunology, University of Texas Southwestern Medical Center, Dallas, TX, United States

Introduction

To ensure optimal physiological function, cells maintain tensional homeostasis around a tissue-specific set-point. With fibrosis, the biomechanical function of tissues is lost due to a breakdown of this set-point, as well as excessive production of a collagen-rich extracellular matrix (ECM) by resident fibroblasts. However, it remains unclear how interactions between fibroblasts and the ECM give rise to a mechanically homeostatic state compatible with normal tissue function. Common models to study tensional homeostasis are fibroblast-populated collagen gels. Such tissue equivalents develop tensile forces in presence of a physical constraint, suggesting the existence of a homeostatic setpoint. However, the steady-state force varies in different collagen concentrations, suggesting the existence of a complex homeostatic target.

Methods

We developed the first biomechanical bioreactor fully integrated with a confocal microscope. Our platform was designed to be capable of dynamic measurements of force, structural remodeling of collagen, and tissue cross-sectional area, thereby allowing for the estimation of the Cauchy stress generated by tissue equivalents.

Results

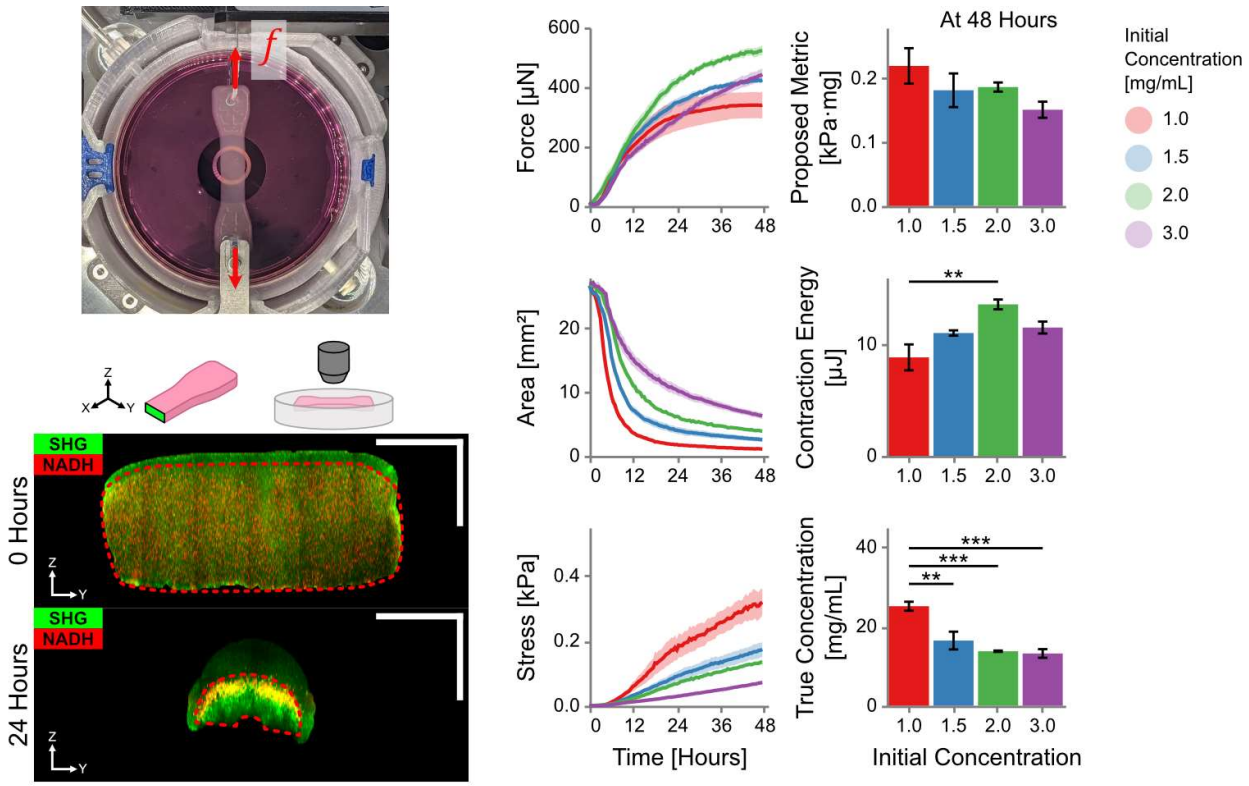
By culturing NIH/3T3 fibroblasts in increasing concentrations of collagen, we observe that cell-generated forces reach a plateau after 24 hours[JF1] . At steady-state, force (f) increases with higher initial collagen concentrations while the cross-sectional area (a) decreases. Surprisingly, we found that stress (σ=f/a) is not conserved. Rather, tissues with

the lowest initial collagen density develop the highest stresses due to higher densification and earlier alignment of collagen fibers. We found that the product between the contraction energy W and the true collagen density ρ is maintained. We validated the trend in W by quantifying the intensity of α-smooth muscle actin via immunofluorescence and the trend in ρ by measuring the densification of collagen via confocal reflection microscopy. Bulk RNA sequencing indicates that the homeostatic state is maintained at the protein level and is disrupted by culturing fibroblasts in high collagen concentrations.

Discussion

In this work we developed a new biomechanical bioreactor and used it as a tissue engineering platform to show that the homeostatic state in tissues may not be driven by a single factor (such as the stress) but rather arises from a balance between fibroblast contractility and ECM compaction.

Images (Optional)



Acknowledgements (Optional)

We acknowledge Professor Jay D. Humphrey (Yale University) and Professor Patrick W. Alford (University of Minnesota) for fruitful conversations on bioreactor design. This project was funded, in part, by The University of Texas at Dallas Jonsson School Research Initiative.

Session Category

Tissue Engineering: Methods, Models and Applications

OA63-02

Tissue Maturation In Engineered Ligaments is Synergistically Improved Via Combined Slow Elongation and Rapid Intermittent Cyclic Stretch

Mx. Leia Troop, Dr. Jenny Puetzer

Virginia Commonwealth University, Richmond, VA, United States

Introduction

Hierarchical collagen fibers are the primary source of strength in ligaments; however, these fibers don't regenerate after injury.[1] Engineered replacements are promising, but it remains challenging to regenerate hierarchical fibers. Mechanical cues, including slow-growth elongation and rapid-cyclic muscle activity are critical for fiber formation *in vivo,*[1] but occur at strain rates orders-of-magnitude apart, likely effecting cells differently.[1,2] Previously, we developed a system which guides anterior cruciate ligament (ACL) fibroblasts in high-density collagen gels to form hierarchical fibers over 6 weeks,[1] and have shown slow-growth elongation and intermittent cyclic stretch individually and differentially improve fiber maturation. However, further maturation is needed to be clinically relevant. Here we evaluated whether combined slow-elongation and rapid-intermittent cyclic stretch results in synergistic fiber maturation. We hypothesize this combined loading regime will drive cells to produce significantly stronger replacements than either load alone.

Methods

Neonatal bovine ACL fibroblasts were mixed with collagen to form constructs (20mg/mL collagen, $5x10^6$cells/mL), and cultured up to 6 weeks.[1] Controls were statically clamped or stimulated with slow stretch(0.1 mm/day)[2] or intermittent cyclic stretch(1 Hz, 5% strain, 1 mm/sec)[1] every other day (Fig.1**A-B**). Combined-stretch constructs were loaded with alternating days slow and cyclic stretch. Post-culture, collagen organization, composition, and tensile properties were evaluated.

Results

Mechanical stimulation drove increased maturation, with combined load producing larger fibers with larger, more regularly spaced crimps by 6 weeks (Fig.1**C-D**). Loading drove increased fibril level alignment with combined load appearing to have increased, native-like fibril bundling (Fig.1C-SEM). Loading accelerated DNA and GAG accumulation (not shown), and combined load increased collagen accumulation over other groups by 6 weeks (Fig.1**D**). Individual loads improved LOX activity at different timepoints, while

combined had increases at both. All constructs significantly improved tensile properties, with combined load having the strongest elastic and toe moduli by 6 weeks.

Discussion

Here the combination of slow and rapid-cyclic stretch synergistically improved fiber organization, composition, and tissue strength. This study demonstrates differential strain rates drive variable cellular responses, which when combined results in synergistic improvements. Understanding how mechanical cues regulate fiber formation will help engineer replacements and develop better rehabilitation protocols.

Images (Optional)

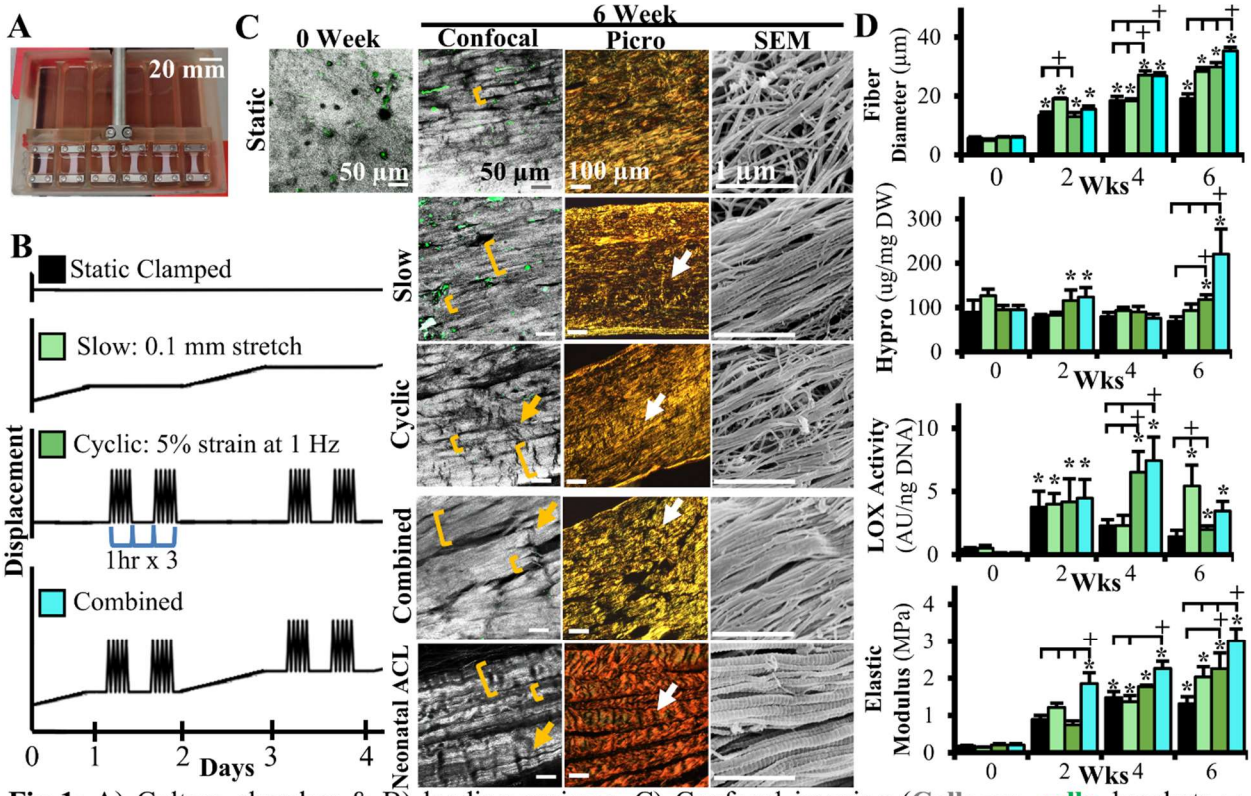


Fig 1: A) Culture chamber & B) loading regimes. C) Confocal imaging (Collagen, cells, brackets = fibers or early fascicles, arrows = crimp), Picrosirius Red Staining, & SEM imaging. D) Image analysis of average fiber diameter (N=3-6, n=6-8 images). E) Collagen content (hypro) normalized to dry weight (DW), LOX activity, & Tensile properties. N=5-8. Data are mean±S.E.M. Significance determined via 2-way ANOVA with Tukey's post-hoc ($p<0.05$). Significance to *0wk or +bracket.

References (Optional)

1.Troop+Acta Biomat2024;2.Cone+PloS ONE2019

Session Category

OA63-03

Cyclic Mechanical Stimulation of TDPCs Improves Tendon Tissue Maturation in Vitro by Enhanced Collagen Fibril Formation

MSc Ekaterina Oleinik[1,2], MSc Felix Gross[1], MSc Magdalena Fuchs[1], MSc Lune Teplitchi-Menou[1], MSc George Gourgi[2], PhD Andreas H. Teuschl-Woller[2], PhD Philipp J. Thurner[1]

[1]TU Wien, Vienna, Vienna, Austria. [2]UAS Technikum Wien, Vienna, Vienna, Austria

Introduction

Mechanical loading is key regulator of tendon development, maintenance, and repair, and thus an essential parameter in tendon tissue engineering (TTE). Despite progress in in vitro TTE, standardized tendon model is lacking. Existing approaches either use static or cyclic mechanical loading, and it is debated in the TTE community, which approach is advantageous. This study compared the effects of static (SL) and cyclic loading (CL) on tendon-derived progenitor cells (TDPCs) to identify optimal conditions for maintaining tenocyte function in TTE.

Methods

Rat TDPCs ($4x10^6$ cells/mL) were embedded in fibrin scaffolds (10 mg/mL fibrinogen, 0.625 KIU thrombin) and subjected to mechanical stimulation in a custom-made bioreactor (MagneTissue). We applied 10% uniaxial tensile strain for 6 hours daily, followed by an 18-hour resting period at 3 % strain, over 7 consecutive days. CL was applied with 0.5Hz frequency to replicate physiological conditions. Cell proliferation (EdU), survival (TUNEL), and morphology (Actin/DAPI) were evaluated. Gene expression was analysed by RNAseq and RT-qPCR for extracellular matrix (ECM) and tendon-specific markers. Construct functionality was assessed by uniaxial tensile testing (Zwickiline, Zwick), collagen deposition by MSB staining, and fibril formation by atomic force microscopy (AFM) (Nanowizard Ultraspeed A, Bruker-JPK).

Results

CL induced pronounced cell alignment, along with higher cell proliferation and survival compared to SL. RNAseq identified two distinct transcriptomic clusters: CL upregulated tendon-specific and ECM-related genes (Scx, Tnc, Tnmd, Sparc, Col1a1, MMP3), indicating enhanced ECM remodelling and mature tendon phenotype, while SL upregulated inflammatory markers (Il6, Ccl2, Cxcl1/3). Histological and AFM analyses confirmed enhanced collagen deposition and fibril formation upon CL (Fig. 1A,B). Mechanical testing

revealed a threefold higher tensile modulus in CL constructs, indicating superior remodeling upon CL (Fig. 1C).

Discussion

This study demonstrates that CL provides markedly superior microenvironment for TTE compared to SL conditions. Enhanced cell viability, proliferation, alignment, and upregulated tendon-specific markers reflect improved tenocyte functionality. CL enhanced ECM remodeling and mechanical performance without eliciting inflammatory responses, thereby more closely mimicking physiological conditions of tissue growth and adaptation. These findings highlight the necessity of incorporating controlled cyclic mechanical stimulation in in vitro tendon modelling to achieve more functional and biomimetic tissue constructs

Images (Optional)

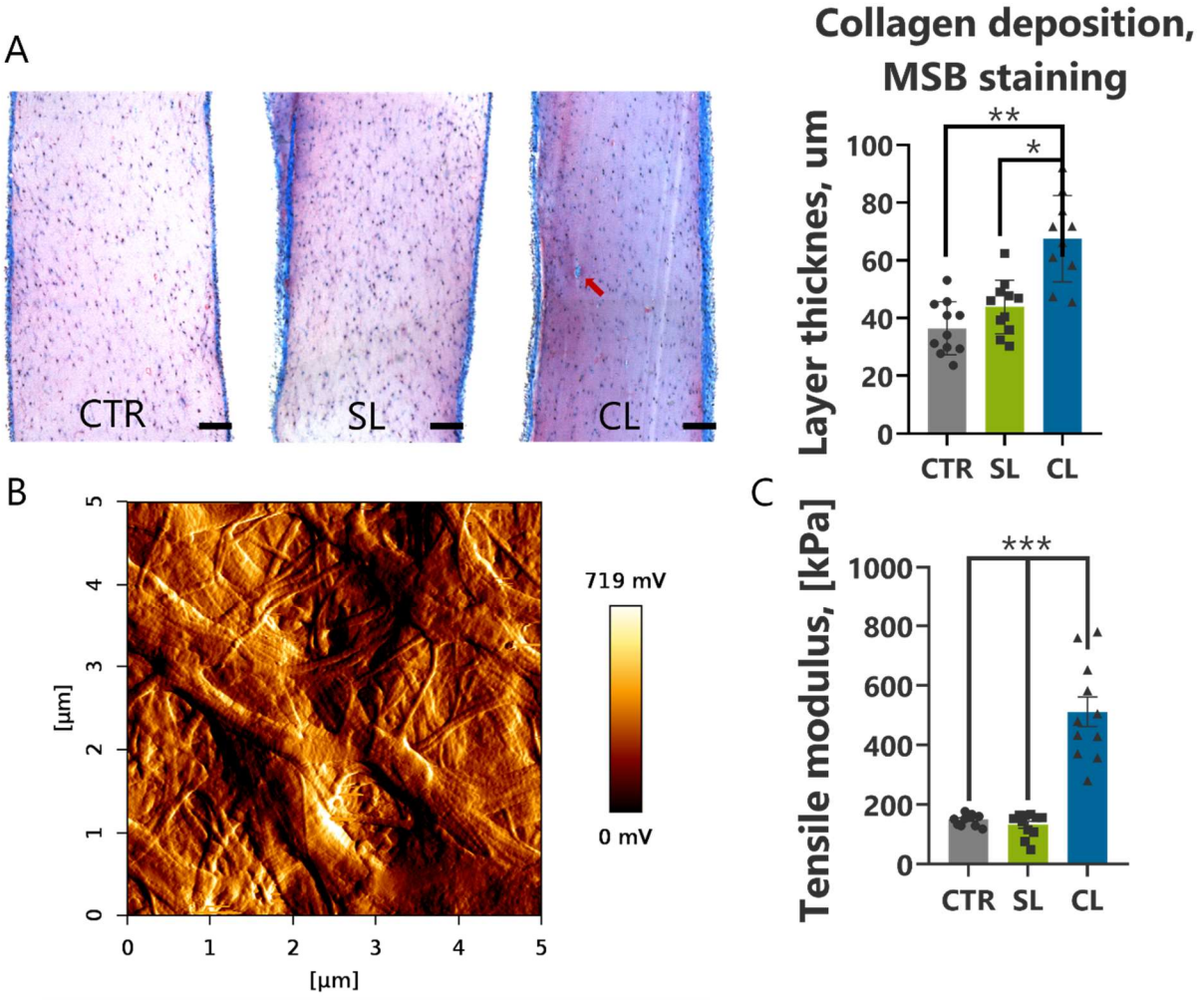


Fig 1. ECM remodeling upon different loading protocols.
A. Images of MSB staining and statistical analysis of collagen layer thickness, showing fibrin replacement (shown in purple) with collagen (blue). Scale bar = 200 µm.
B. AFM-based imaging of longitudinal section. Collagen fibrils are identified via characteristic D-banding.
C. Tensile moduli of the different groups, derived from first linear region of each test via linear fit. Data are shown as mean ± SEM, n=11.

Session Category

Tissue Engineering: Methods, Models and Applications

OA64-02

Cell Size Orchestrates Osteogenic Commitment of Adipose-Derived Stem Cells via H3K9me3 Demethylation

Dr. Han Wang PhD Candidate[1], Dr. Tianmian Liu PhD Candidate[2], Dr. Xuran Li PhD Candidate[1], Prof. Mengning Yan Professor[1], Prof. Xiaobo Gong Professor[2], Prof. Zhifeng Yu Professor[1]

[1]Shanghai Ninth People's Hospital,Shanghai Jiao Tong University School of Medicine, Shanghai, Shanghai, China. [2]Key Laboratory of Hydrodynamics (Ministry of Education), Department of Engineering Mechanics, School of Ocean and Civil Engineering, Shanghai Jiao Tong University, Shanghai, Shanghai, China

Dr. Han Wang

Dr. Tianmian Liu

Dr. Xuran Li

Prof. Mengning Yan

Prof. Xiaobo Gong

Introduction

Adipose-derived stem cells (ADSCs) exhibit size heterogeneity, yet whether cell size functions as an endogenous regulatory cue has not been mechanistically defined. Using a spiral microfluidic chip to isolate size-specific subpopulations, we identified large-size ADSCs in the upper ~30th percentile as displaying markedly enhanced osteogenic potential. This suggests that size acts not merely as a morphological descriptor but as a deterministic biophysical signal encoding lineage predisposition. Building on this observation, we investigated how cell size integrates cytoskeletal architecture, nuclear mechanics, and epigenetic regulation to direct osteogenic fate.

Methods

Human ADSCs were isolated from subcutaneous adipose tissue and size-fractionated using a microfluidic device to obtain large-, medium-, and small-size subpopulations. Osteogenic differentiation was assessed through alkaline phosphatase and Alizarin Red staining, qPCR, and Western blot. Cell and nuclear morphology were quantified via immunofluorescence. Mechanical properties were analyzed using atomic force microscopy. RNA-seq and CUT&Tag profiling for H3K9me3 were performed to identify transcriptional and epigenetic differences. Functional assays were conducted following PALM knockdown or inhibition of RhoA/ROCK signaling.

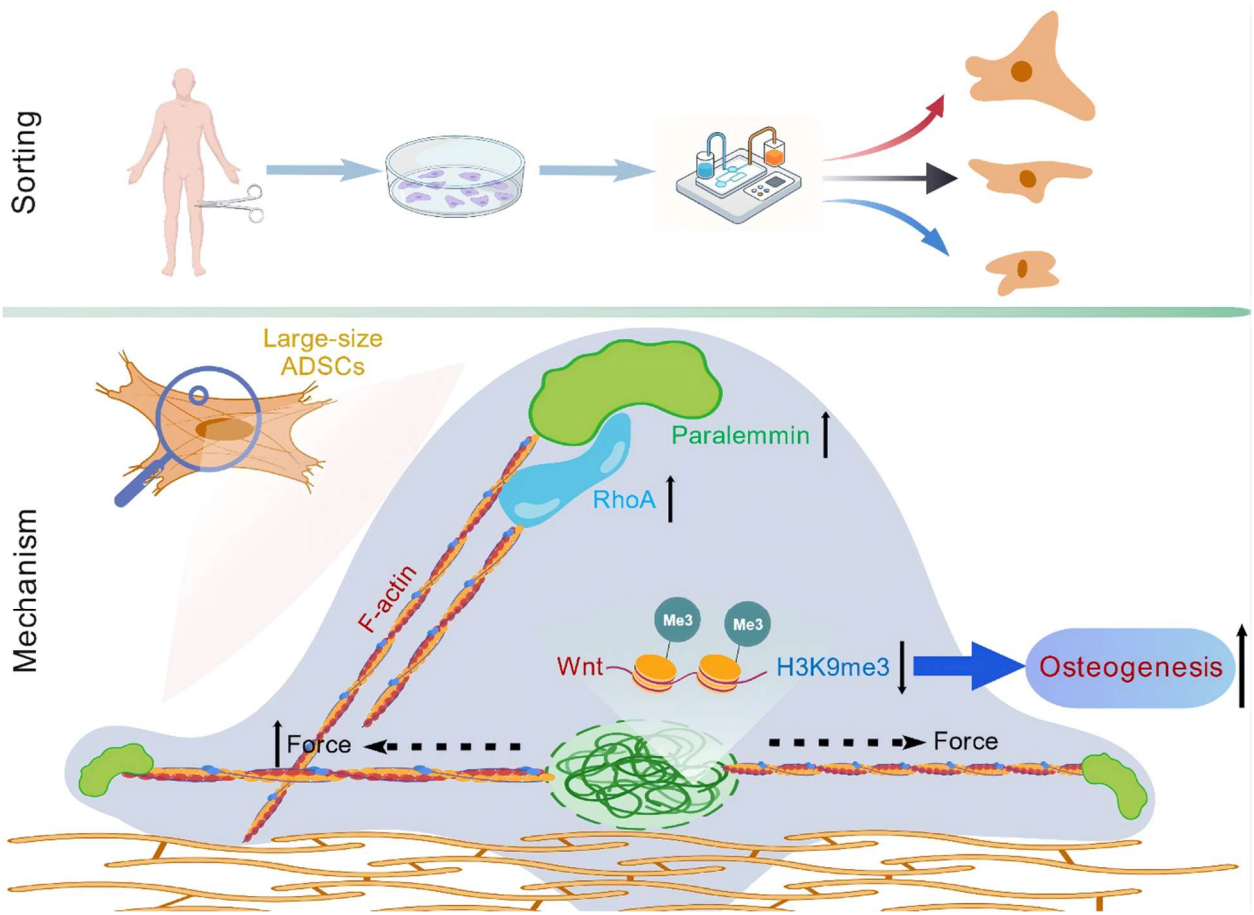
Results

We used microfluidic sorting to isolate ADSCs of distinct diameters. Large-size cells exhibited stronger osteogenic differentiation, greater spreading, and increased fiber formation. RNA-seq revealed enrichment of osteogenic Wnt signaling, with PALM (Paralemmin) prominently upregulated. PALM knockdown disrupted cytoskeletal organization, reduced cell and nuclear spreading, and impaired osteogenesis. Paralemmin interacted with RhoA, and large-size cells showed elevated RhoA/ROCK levels; inhibiting this pathway similarly suppressed osteogenesis. CUT&Tag profiling showed reduced H3K9me3 at WNT1 and WNT5A promoters in large cells, consistent with their higher expression. Cytoskeleton disruption increased nuclear H3K9me3 and diminished osteogenesis.

Discussion

Through precise sorting of ADSC subpopulations, we quantitatively elucidated how intrinsic cell size regulates stem cell state and lineage selection. Large ADSCs exhibit superior osteogenic potential through a Paralemmin–RhoA/ROCK cytoskeletal axis that shapes nuclear architecture, redistributes heterochromatin, and reduces H3K9me3 repression of WNT genes. The biophysical–epigenetic coupling reveals how intrinsic physical states instruct cell fate, offering a practical strategy to isolate high-potential MSC subsets and enhance bone regeneration for skeletal tissue engineering.

Images (Optional)



Session Category

Tissue Engineering: Mechanobiology

OA64-03

Mechanobiological Effects of Dynamic Loading Modalities in Engineered Cartilage: A Meta-Analysis

Mr. Jiaqi K. Shen[1], Mr. Tony B. Huang[1], Dr. Catherine E. Davey PhD[1], Dr. Elias Salzer PhD[2], Prof. Gerjo J. V. M. Van Osch PhD[2,3,4], Prof. Sandra J. Shefelbine PhD[5,6], Prof. Marcus G. Pandy PhD[7], Prof. Kathryn S. Stok PhD[1]

[1]Department of Biomedical Engineering, The University of Melbourne, Parkville, Victoria, Australia. [2]Department of Orthopaedics and Sports Medicine, Erasmus MC, University Medical Center Rotterdam, Rotterdam, South Holland, Netherlands. [3]Department of Otorhinolaryngology, Head and Neck Surgery, Erasmus MC, University Medical Center Rotterdam, Rotterdam, South Holland, Netherlands. [4]Department of Biomedical Engineering, University of Technology, Delft, South Holland, Netherlands. [5]Department of Mechanical and Industrial Engineering, Northeastern University, Boston, Massachusetts, United States. [6]Department of Bioengineering, Northeastern University, Boston, Massachusetts, United States. [7]Department of Mechanical Engineering, The University of Melbourne, Parkville, Victoria, Australia

Introduction

Cartilage mechanoadaptation can be driven by dynamic microenvironmental cues induced by various mechanical loading modalities in bioreactor systems. This influences both extracellular matrix composition and functional properties. While dynamic mechanical cues have been shown to possess chondrogenic potential in diverse cartilage tissue engineering studies [1], the lack of standardisation has long hindered quantitative comparison and consensus on a gold-standard stimulation protocol [2]. This study systematically evaluates how different loading modalities influence matrix development in tissue-engineered cartilage constructs.

Methods

Following a PRISMA-guided systematic approach, published *in vitro* studies were included if dynamic mechanical stimulation was implemented to culture engineered hyaline articular cartilage tissue constructs. Studies using cartilage explants and qualitative assessment methods were excluded. A total of 95 studies were analysed under six conventional loading modalities: compression, tension, shear, hydrostatic pressure, fluid-induced shear, and combined stimuli. Meta-analysis using standardised effect measures (Hedges' *g*) was conducted for conventionally assessed chondrogenic outcomes, including

aggrecan and collagen-II gene expression, glycosaminoglycan and collagen deposition, and compressive equilibrium modulus.

Results

The overall chondrogenic response to dynamic mechanical stimulation across all six loading modalities showed that combined stimulation of compression and shear was particularly effective in promoting matrix production (Figure 1). This suggests that heterogeneous mechanical cues more effectively promote cartilage mechanoadaptation compared to single-modality stimulation. Meta-regression revealed a parameter-dependent relationship between fluid-induced shear showing decreasing benefits at higher intensities, suggesting that mechanical stimulation must be tuned for optimal matrix development.

Discussion

This systematic approach highlights the value of using standardised effect measures to enable cross-study comparison in cartilage tissue engineering, despite methodological heterogeneity. To identify optimal mechanobiological environments for cartilage matrix development, loading parameters must be optimised at the microstructural scale under standardised culture conditions. Addressing gaps identified in this work, such as inconsistent reporting, variation in outcome assessment, and the lack of sub-tissue mechanical histories, will be critical for improving reproducibility, guiding the development of future bioreactor systems, and advancing mechanically stimulated chondrogenesis for cartilage regeneration.

Images (Optional)

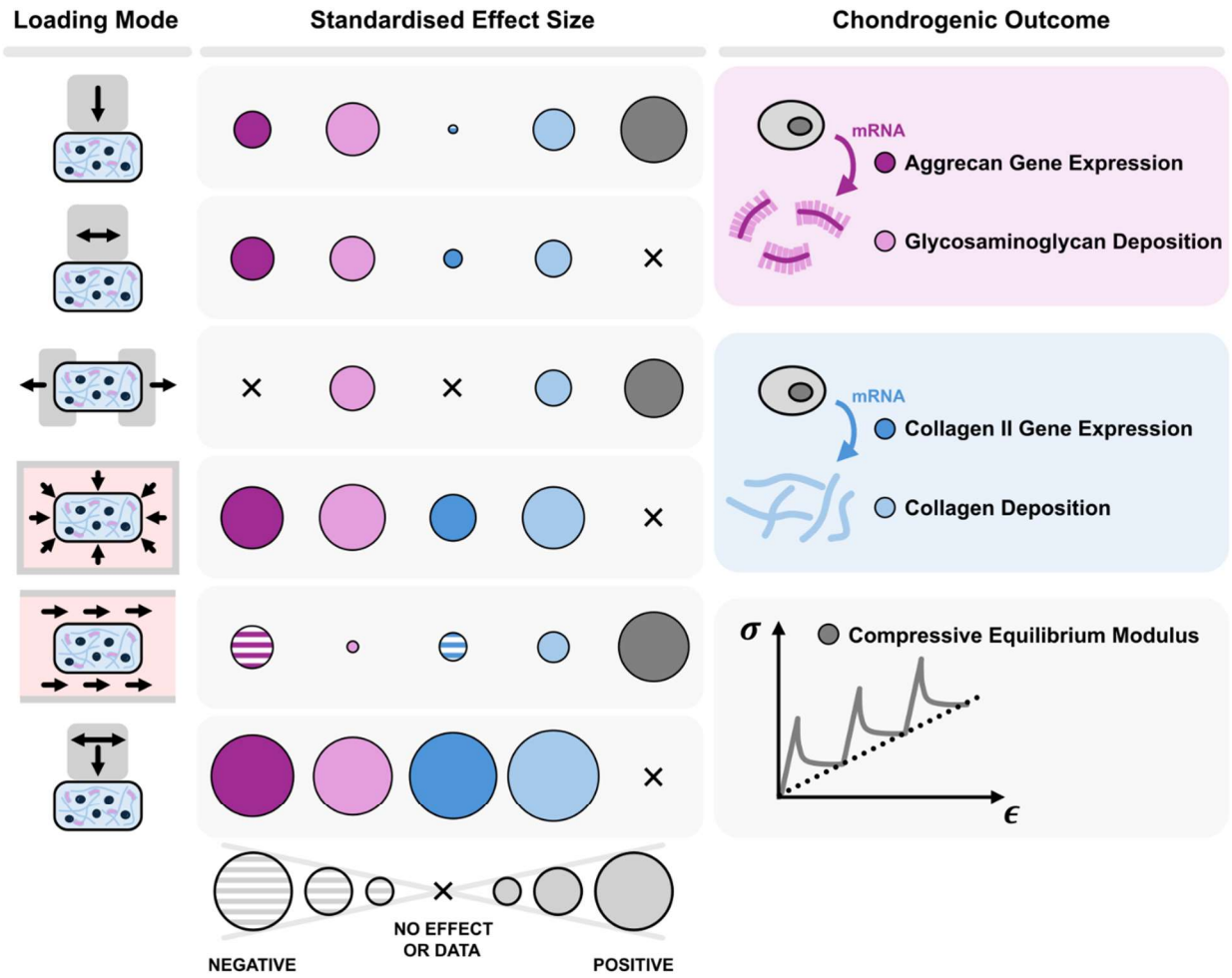


Figure 1: An overview of chondrogenic effects across six conventional mechanical loading modalities. Colours represent different outcome measures. Bubble size scales with the standardised effect size.

References (Optional)

[1] Byumsu Kim & Lawrence J. Bonassar, *Electromechanobiology of Cartilage and Osteoarthritis*, Springer, 2023.

[2] Devon E. Anderson & Brian Johnstone, *Front. Bioeng. Biotechnol.*, 2017.

Acknowledgements (Optional)

We thank Dr Jeremy Silver (Statistical Consulting Centre, The University of Melbourne, Australia) for his valuable statistical advice and guidance in data analysis. This project is supported by the Australian Research Council Discovery Project funding scheme (DP240102160), and Jiaqi K. Shen and Tony B. Huang are recipients of Melbourne Research Scholarship from the University of Melbourne. Elias Salzer and Gerjo van Osch are partly

financed by the Dutch Research Council (NWO) through the LoaD NWA-ORC research programme (NWA1389.20.009).

Session Category

Tissue Engineering: Mechanobiology

OA64-04

Mechanobiological Regulation of Transport and Shear in Hierarchical Bio-Inspired Scaffolds for Bone Repair

Dr. Federica Buccino[1], Dr. Sara Sebastiani[1], Prof. Giuseppe Banfi[2], Prof. Laura Vergani[1]

[1]Politecnico di Milano, Milano, Lombardy, Italy. [2]IRCCS Galeazzi Orthopaedic Institute, Milano, Lombardy, Italy

Introduction

Mechanical cues such as fluid-induced WSS regulate osteogenic differentiation [1–2], yet achieving uniform stimulation in complex 3D scaffolds remains challenging [3]. Native bone accomplishes this through its hierarchical trabecular and lacuno–canalicular architecture, which shapes flow and local mechanical signals [4]. However, how such features interact with perfusion to generate meaningful WSS is poorly understood [4]. This study compares two hierarchical scaffold designs—one regular, the other canalicular-like—to assess how topology influences early cellular responses.

Methods

Hierarchical scaffolds were generated from a high-resolution STL of human trabecular bone and enriched with a biomimetic lacuno–canalicular layer of ellipsoidal lacunae and microchannels. Two variants were produced: a regular scaffold with ordered features and a canalicular-like scaffold with randomly distributed lacunae and Delaunay-derived interconnections. Both were fabricated with submicron fidelity via two-photon polymerization (Nanoscribe Quantum X). Representative subvolumes underwent CFD analysis in COMSOL Multiphysics under free-flow conditions using Newtonian DMEM at 10^{-5}–10^{-4} m/s, with mesh convergence and mass-balance error <0.1%. Human hBMSCs were statically cultured for 28 days, and endpoint evaluation by SEM and synchrotron micro-CT (SYRMEP beamline) provided high-resolution, non-destructive assessment of cellular organization and mineral-like matrix deposition across the architecture.

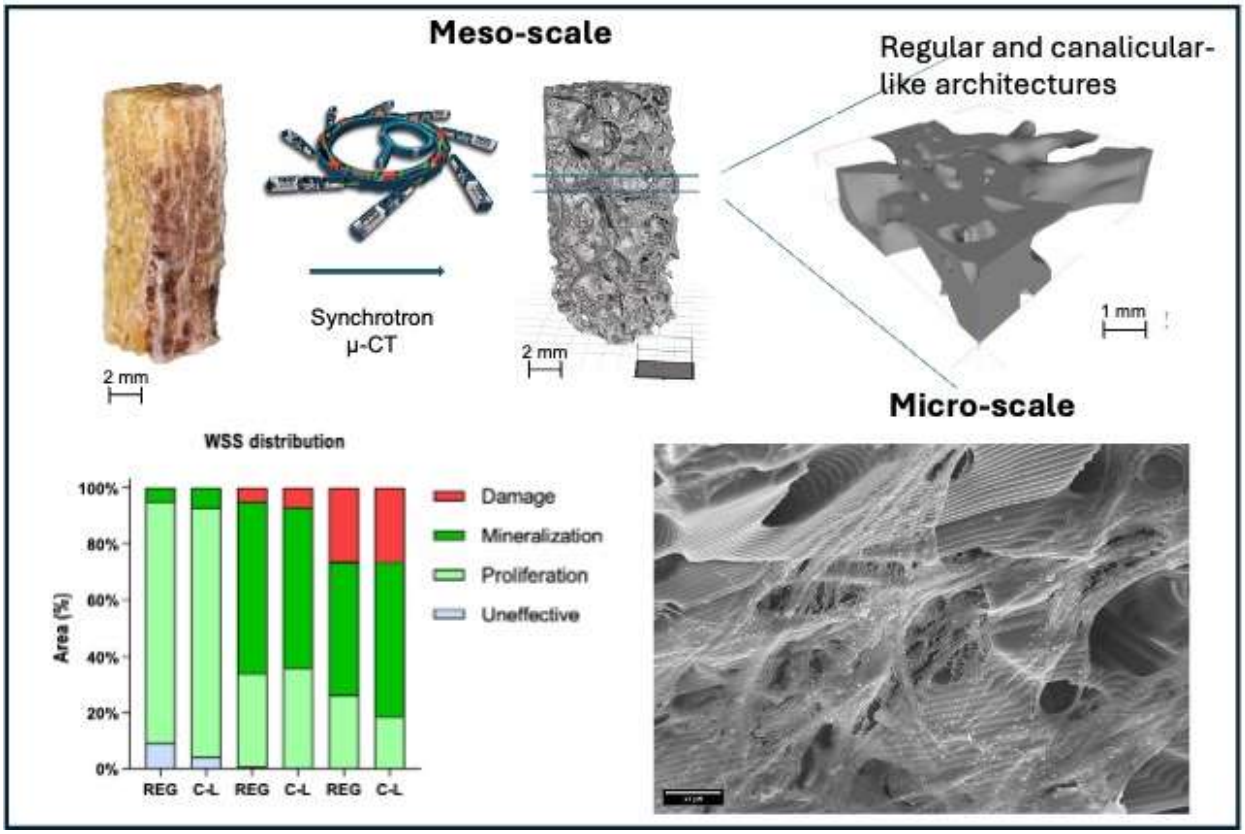
Results

Under free-flow, bypass reduced Δp (<1 Pa) and intrapore shear, with >85% of surfaces below 5 mPa and minimal osteogenic-range stimulation, leading to rim-localized matrix deposition. The regular scaffold showed long high-WSS corridors, whereas the canalicular-like design produced shorter, more diffuse hotspots. Forced-flow shifted WSS into the osteogenic window. Cell studies reflected these trends: hBMSCs penetrated more deeply and formed more internal ECM in the canalicular-like network, confirming its enhanced support for early osteogenic activity.

Discussion

The canalicular-like scaffold distributed shear more uniformly and exposed more internal surfaces to osteogenic WSS, while the regular design created high-shear corridors and under-stimulated regions. Forced-flow, especially at low velocity, improved interior perfusion and maintained WSS within the osteogenic window.

Images (Optional)



References (Optional)

[1] Seunghun S. Lee et al., *Matter*, 2022.
[2] E. Maevskaia et al., *J. Mech. Behav. Biomed. Mater.*, 2023.
[3] L. Roseti et al., *Mater. Sci. Eng. C*, 2017.
[4] Ieva Bružauskaitė et al., *Cytotechnology*, 2016.

Acknowledgements (Optional)

The authors acknowledge that the presented work was realized using the infrastructure provided by the Euro-BioImaging initiative https://www.eurobioimaging.eu/

F.B and L.M.V. acknowledge the financial support from the European Union Horizon Europe research and innovation programme under the Marie Skłodowska-Curie (MSCA) grant agreement No 101120290 (GAP).

F.B. and L.M.V. acknowledge financial support under the National Recovery and Resilience Plan (NRRP), Mission 4, Component 2, Investment 1.1, Call for tender No. 104 published on 2.2.2022 by the Italian Ministry of University and Research (MUR), funded by the European Union – NextGenerationEU– Project ARCHIMEDES – CUP D53D23003940006 - Grant Assignment Decree No. 2022R4KA9X adopted on 02/02/2022 by the Italian Ministry of Ministry of University and Research (MUR)

Session Category

Tissue Engineering: Mechanobiology

OA64-05

Activation of Mechanotransduction in Redifferentiating Human Articular Chondrocytes in response to Short-Term Mechanical Stimulation

Ms. Sriranjani Seshadri[1], Ms. Ruxin Yang[1], Dr. Weiping Li[2], Ms. Kiera Downey[1], Dr. Cheri Deng[2], Dr. Rhima Coleman[1]

[1]University of Michigan, Ann Arbor, Michigan, United States. [2]Michigan State University, East Lansing, Michigan, United States

Introduction

Autologous chondrocyte implantation (ACI) is less effective in patients over 45 because expanded cells dedifferentiate and lose redifferentiation capacity. Mechanical loading may help restore chondrocyte function, but the response of early OA cells remains to be elucidated. The objective of this study was to compare the early response of early OA human articular chondrocytes (HACs) to young HACs.

Methods

HACs from young or OA donors were encapsulated (20 million cells/mL) in hydrogels composed of 5% polyethylene glycol (PEG), type I collagen, and hyaluronic acid. Cyclic mechanical loading was applied using tensile acoustic rheometry (TAR) at 10% strain and 1 Hz for 30 minutes per session, repeated over five days with a two-day rest period. Free-swelling hydrogels served as controls. Mechanotransduction and chondrocyte-specific gene expression was evaluated using RT-qPCR, protein levels were assessed by immunofluorescence (not shown).

Results

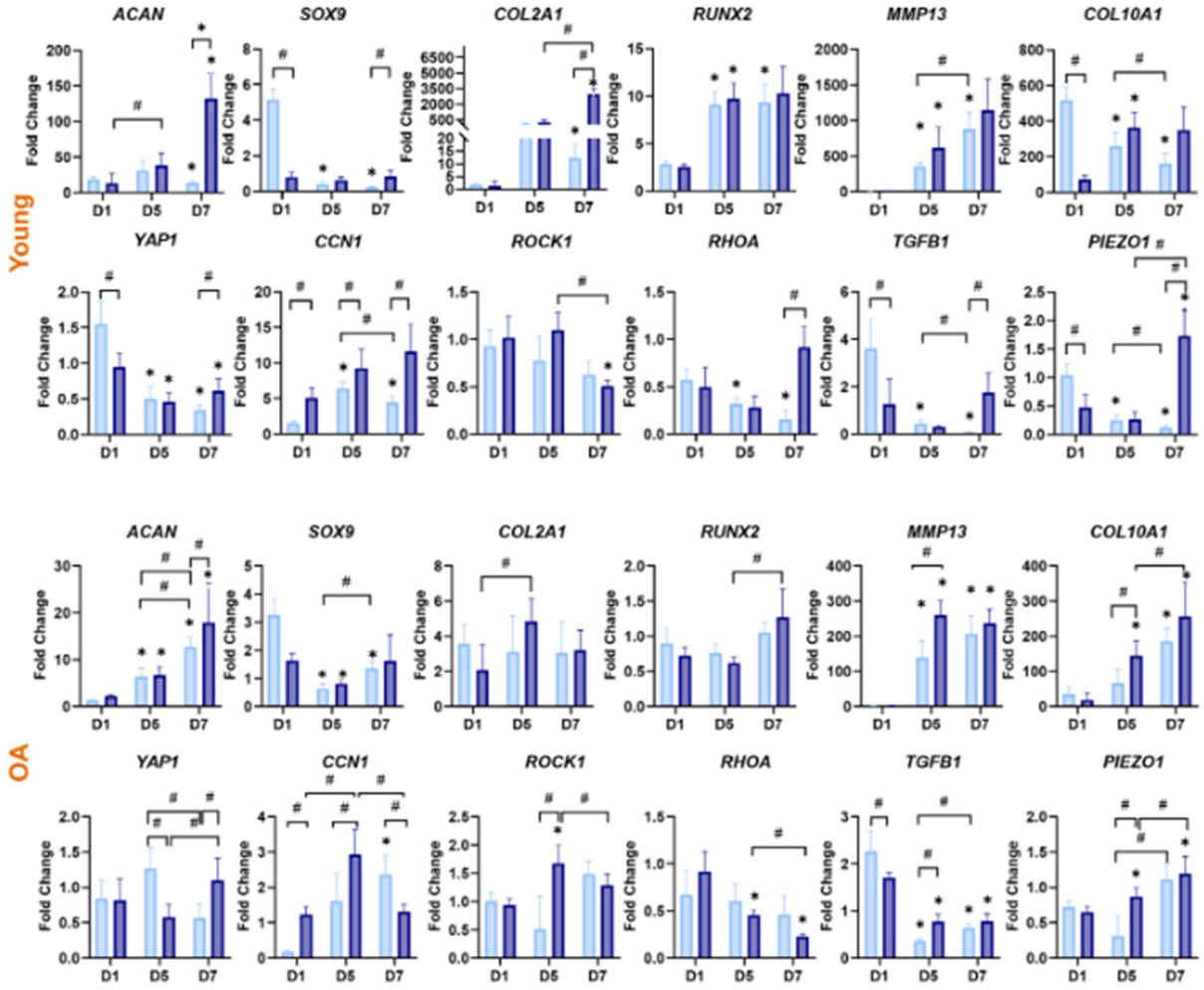
Mechanical loading enhanced ACAN, COL2A1, and hypertrophic gene expression in young HACs, (Figure 1), consistent with increased matrix synthesis and chondrocyte maturation. In OA HACs, loading did not increase chondrogenic gene expression; however, aggrecan and collagen protein levels were higher than young HACs as confirmed by immunofluorescence, suggesting that post-transcriptional mechanisms contribute to matrix deposition; protein expression in young HACs remained largely unchanged. TGF-β signaling was generally similar between cell types, though OA HACs exhibited slightly reduced SMAD1/5/9 activation and increased SMAD2/3 activation compared to young HACs, consistent with a phenotype favoring tissue remodeling processes. Hypertrophic protein markers decreased in OA HACs after loading but remained unchanged in young HACs, indicating that loading may selectively suppress pathological hypertrophy in OA HACs. Loading induced variable YAP1 and increased CCN1 expression in OA HACs, similar

to young HACs but to a lesser extent, suggesting that mechanotransduction pathways remain partially responsive in disease-altered cells.

Discussion

Short-term mechanical stimulation modulated behavior in both young and early OA HACs, but with different magnitudes. Overall, brief loading benefited OA HACs by enhancing matrix deposition and reducing hypertrophy.

Images (Optional)



Session Category

Tissue Engineering: Mechanobiology

OA65-02

Exoskeleton Reduces Knee Contact Force Through Consistent Decreases in Intersegmental Forces and Varied Changes in Muscle Forces Across People

Ms. Ashley Brown, Mr. Dominic Locurto, Dr. Patrick Slade

Harvard University, Cambridge, MA, United States

Introduction

Knee osteoarthritis (OA) is the most common cause of adult musculoskeletal pain, affecting over 14 million people in the US. High peak mechanical loading in the knee during walking is strongly correlated with knee OA progression. Knee contact force (KCF) is the measure of total loading at the knee joint and is comprised of intersegmental and muscle forces. There is a need for new interventions that target a key mechanism of knee OA progression by reducing loading and subsequent pain. We developed a bilateral exoskeleton capable of offloading muscle forces and intersegmental loads by providing whole-leg assistance proportional to the individual's ground reaction force (GRF).

Methods

Healthy young adults (N=9) were recruited for a two day protocol. On day 1, participants walked in the exoskeleton for 40 minutes at progressively higher assistance levels proportional to their GRF. On day 2, participants walked in the exoskeleton at four proportional GRF magnitudes linearly spaced between 10% and the comfortable maximum value that the participant identified on day 1. GRF, motion capture, and electromyography (EMG) from 7 knee spanning muscles were collected. EMG-informed musculoskeletal simulation in OpenSim Moco was used to estimate KCF as described in [1].

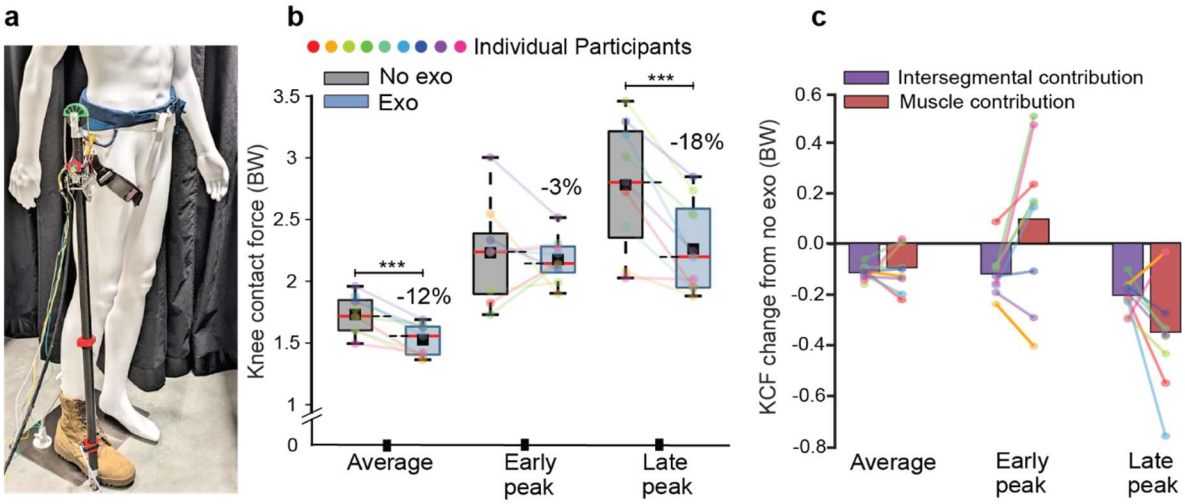
Results

For each participant, we identified the assistance condition that minimized the RMS of the early and late stance KCF peaks. This selected condition was then compared to normal shoes walking to evaluate device efficacy. Across 9 participants, average KCF over stance decreased by 12%, early peak KCF decreased by 3%, and late peak KCF decreased by 18%. Five subjects showed meaningful increases in muscle contribution to KCF during early stance, while four subjects decreased their early peak KCF.

Discussion

The results suggest the device is capable of providing assistance to reduce early peak KCF, but individuals' natural coordination patterns may affect its benefits. Some participants naturally adopted an effective coordination strategy indicating that such patterns are feasible, and targeted retraining may promote more consistent and larger benefits. Combining this novel exoskeleton assistance and additional user training could represent a breakthrough in knee OA treatment.

Images (Optional)



References (Optional)

[1] Delaney Miller et al. , *PLoS Comput. Biol.*, 2025

Session Category

Imaging and Biomedical Devices: Assistive Technologies

OA65-03

Tuning Twisted and Coiled Artificial Muscles (TCAMs) for a Combined Passive-Active Ankle-Foot Orthosis

Mr George Elias[1], Ms. Katherine Vaiciulis[1], Mr. Braeden Harrell[1], Dr. Kirsten M. Anderson PhD[1], Ms. Xandra McGlasson[2], Prof. Jason Wilken PT, PhD[1], Prof. Caterina Lamuta PhD[1], Prof. Deema Totah PhD[1]

[1]University of iowa, Iowa City, IA, United States. [2]University of Iowa, Iowa City, IA, United States

Introduction

Passive ankle-foot orthoses (AFOs) typically use mechanical components like leaf springs and/or dampers to store and release user energy, providing limited gait support. Active AFOs can supplement ankle power through actuators but are often bulky leading to metabolically inefficient systems. Twisted and coiled artificial muscles (TCAMs), a new smart material actuator, can provide both *passive and active support in a single component* with high force output and low mass on the distal limb [1]. This work presents an experimental characterization of a TCAMs-actuation module, within a powered AFO, undergoing flexion through a gait cycle's range of motion. The unique contribution lies in the TCAM's significantly higher torque-to-mass ratio compared to existing active exoskeletons.

Methods

Manufacturing TCAMs involves twisting a carbon fiber/silicone rubber yarn and forming a helical coil after a curing process. The coiled structure has *passive* elastic properties. Further, applying voltage across the TCAMs produces thermal expansion, resulting in uncoiling and shortening of the artificial muscle, producing *active* contractile force. This passive-active TCAM actuation module was incorporated into a custom carbon-fiber AFO with a metal ankle joint. Four passive and three active support levels were tested by pre-tensioning the TCAMs and varying voltage, respectively. An encoder and in-line loadcell measured ankle angle and torque while the AFO was flexed through a normative gait cycle in a custom apparatus.

Results

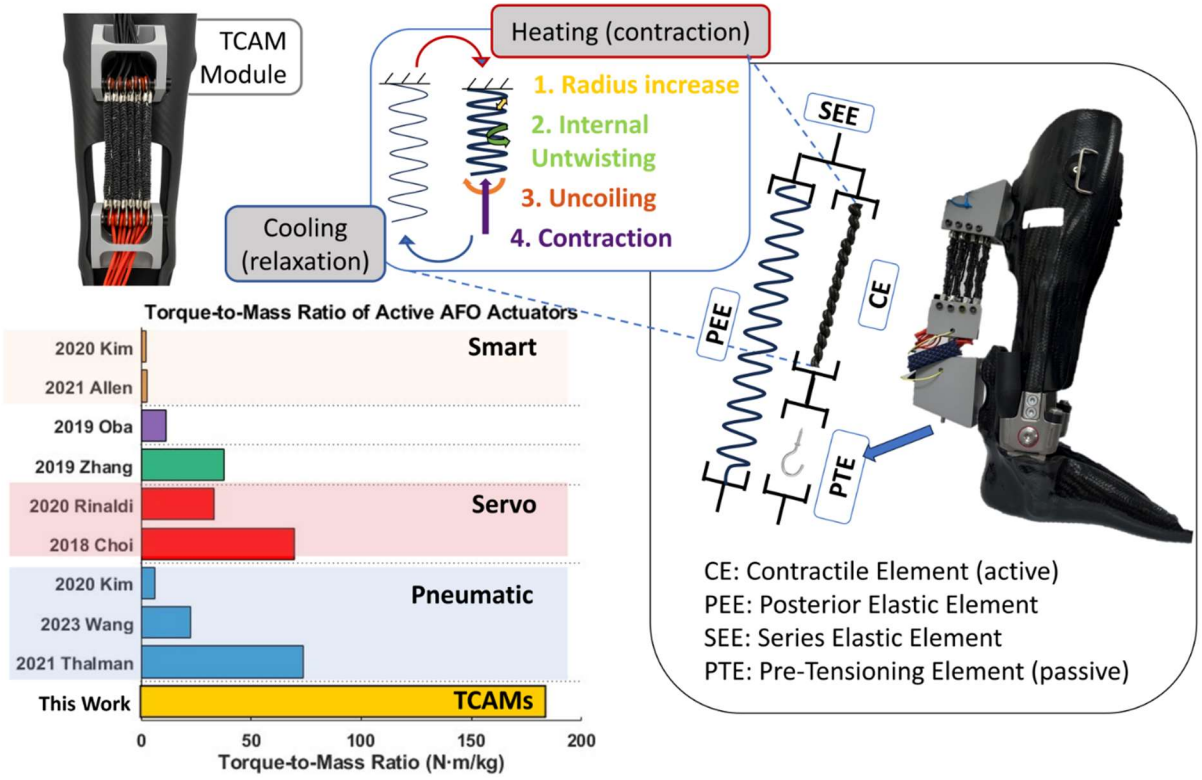
The TCAMs produced peak torque ranging from 10 to 50 Nm over the gait cycle demonstrating the ability to provide meaningful assistance during the stance phase. By strategically configuring both passive and active components of the actuator system, the

device was able to reproduce up to 40% of peak healthy ankle moment, augmenting the plantarflexor muscles.

Discussion

These results suggest that TCAM-based actuators can supplement lost ankle function in individuals with neuromuscular impairments and represent a clinically significant step toward adaptable, low-profile orthotic devices with broad applicability. Future work will test this technology with a clinical population and validate its use for creating adaptable, user-optimal, low-weight, and flexible robotics customized to increase mobility and improve gait performance for its specific user.

Images (Optional)



References (Optional)

[1] Kotak *et al.*, ASME *J Biomech Eng*, 2022

Session Category

Imaging and Biomedical Devices: Assistive Technologies

OA65-04

Mechano-Luminescence-Optoelectronic Health Monitoring Wearables for Physical Health Digital Twin

Dr. Donghyeon Ryu[1,2], Mr. Alexander Watts[1], Mr. Joseph Gallegos[1,2], Mr. Aaron Madrid[1], Dr. Peter Anselmo[2]

[1]New Mexico Tech, Socorro, NM, United States. [2]RD Health Sensing Inc., Socorro, NM, United States

Introduction

This study aims to propose a novel physical sensing technology-based health monitoring wearable platform to help improve our knowledge base about a human neuromuscular system. A model mimicking physical phenomena (namely, physical health digital twin) is created in a digital environment using long-term in-plane strain sensor data from the wearable platform. The physical health digital twin (PHDT) keeps improving the similarity in physical behaviors of the actual human body as it keeps being updated with continuous inflow of strain data. This PHDT serves as a baseline to detect anomalies through data processing of the strain data during daily activities. It is hypothesized that the data anomalies are attributed to neuromuscular health disorders because physical behaviors are outputs of the neuromuscular system with numerous known/unknown inputs. Throughout this study, we plan to verify the hypothesis using the novel strain sensor technology.

Methods

A highly stretchable and self-powering strain sensing fiber (HSF) is designed using the patented design platform of multifunctional mechano-luminescence-optoelectronic (MLO) composites and manufactured using two functional mechano-luminescent (ML) and mechano-optoelectronic (MO) constituents. The MLO-based HSF produces direct current (DC) when subjected to mechanical strain and the DC varies with the strain and strain rate. The HSF at major joints can produce DC and sense in-plane strain by tracking change in DC on a human body. As a validation test, we perform a fitness bike riding with a single HSF instrumented at a knee cap on a human body subject.

Results

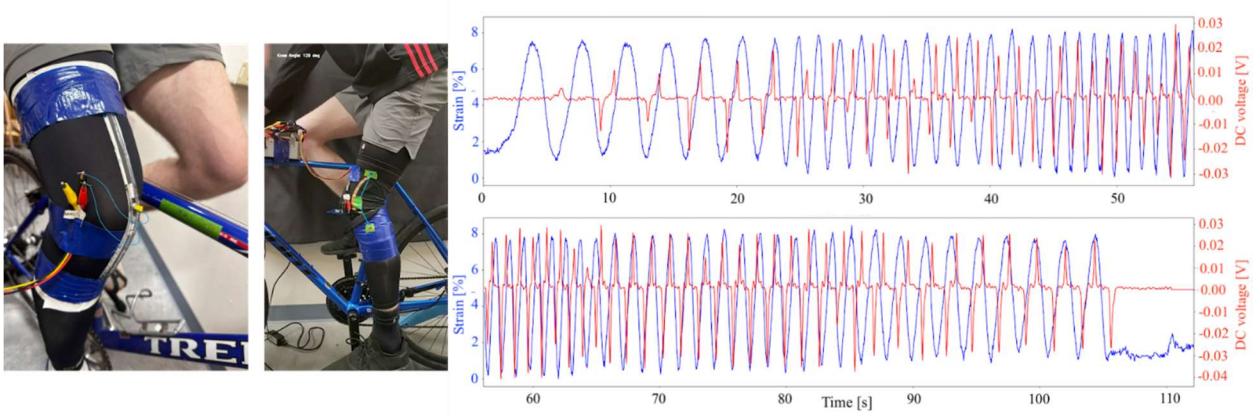
DC from HSF was shown to vary with a leg movement during a bike riding. We train long short-term method (LSTM) model using the DC sensor data as well as reference in-plane strain data that were produced after processing video footages recording leg movement.

The trained LSTM model is used for quantifying the in-plane strain and strain rate with the DC sensor data.

Discussion

The DC responds well to the in-plane strain and strain rate on the knee cap under a large strain up to 15% strain. We are in process of building one-leg PHDT using strain and strain rate from the trained LSTM model with the DC sensor data.

Images (Optional)



References (Optional)

Session Category

Imaging and Biomedical Devices: Assistive Technologies

OA65-05

Second Harmonic Generation-Derived Collagen Fraction as a Biomarker for Early Osteoarthritis Detection in Human Tibial Cartilage

Ms Benafsha Tughra[1,2], Dr. Ziad Abusara PhD[1,2], Mr. Azim Jinha MSc[1,2], Mrs. Sue Miller MSc[2,3,4], Dr. Scott Timmermann MD[2,3], Dr. Walter Herzog PhD[1,2]

[1]Human Performance Laboratory, Faculty of Kinesiology, University of Calgary, Calgary, AB, Canada. [2]McCaig Institute for Bone and Joint Health, Cumming School of Medicine, University of Calgary, Calgary, AB, Canada. [3]Section of Orthopedic Surgery, Department of Surgery, University of Calgary, Calgary, AB, Canada. [4]Taylor Institute for Teaching and Learning, University of Calgary, Calgary, AB, Canada

Introduction

Early osteoarthritis (OA) involves subtle disruptions in the collagen network that appear before clinical detection. Because collagen architecture governs cartilage mechanical behavior, methods to detect early microstructural change are needed to improve OA diagnosis and monitoring. Second Harmonic Generation (SHG) imaging provides a label-free measure of collagen volumetric fraction (Φ_{col}), while indentation stiffness (E_{inst}) reflects mechanical function. Our previous work across the OA range (regions 0–2, where 0 is healthy and 2 represents severe degeneration) showed a strong linear relationship between Φ_{col} and E_{inst} ($\Phi_{col} = 0.081\ E_{inst} + 0.007$, $R^2 = 0.92$) [1]. This study evaluated whether this association persists in healthy or minimally degenerated knees (regions 0–1) and SHG can detect early tissue deviations indicative of incipient OA.

Methods

Following institutional approval, tibial plateaus were obtained from the Alberta Tissue Bank (three donors, 68 regions). Each region was tested for the instantaneous indentation modulus (E_{inst}) and then imaged to compute Φ_{col}, and regions were graded as 0 or 1 using streaming-potential–based criteria [1, 2]. Linear regressions relating Φ_{col} to E_{inst} were compared with our previously published region 0–2 OA dataset.

Results

In the current cohort of healthy knees (regions 0–1), $\Phi_{col} = 0.026\ E_{inst} + 0.15$, $R^2 = 0.54$ (Fig. 1). The OA slope was approximately 3.05× steeper, and the two regression models for healthy and replaced knee joints intersected at $E_{inst} \approx 2.6$ MPa, $\Phi_{col} \approx 22\%$, marking the point at which their structure–function profiles began to diverge.

Discussion

SHG imaging detected measurable reductions in Φ_{col} from region 0 to 1 despite minimal gross degeneration, demonstrating sensitivity to early matrix disruption. The steep and high correlation between Φ_{col} and E_{inst} in the otherwise healthy knees reflects a tight coupling between collagen loss and mechanics, whereas the lower R^2 relative to replaced knees indicates greater baseline heterogeneity in the replaced joints. The intersection highlights stimulus-dependent inversion of contrast that may refine diagnostic protocols. SHG-derived Φ_{col} shows strong promise as a non-destructive biomarker for early OA detection, progression monitoring, and future clinical translation.

Images (Optional)

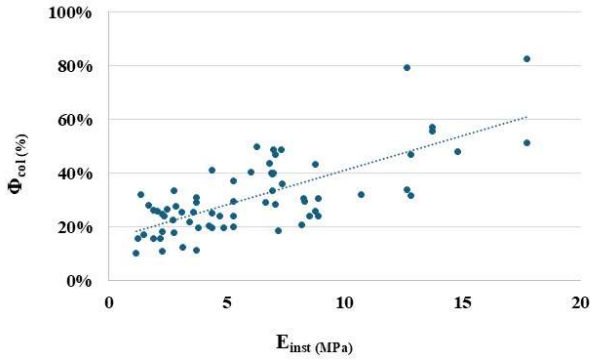


Figure 1. Correlation between SHG-derived collagen volumetric fraction (Φ_{col}) and instantaneous elastic modulus (E_{inst}) in human tibial cartilage of healthy/asymptomatic knees (regions 0–1)

References (Optional)

[1] Abusara Z. et al. ,Ann Biomed Eng, 2024

[2] Sim S. et al. ,Osteoarthritis Cartilage, 2014

Session Category

Imaging and Biomedical Devices: Assistive Technologies

OA66-01

Replicating Physiological Stance Knee Flexion Reduces Residual Hip Torque in Above-Knee Amputees

Ms. Karen Walker, Dr. Grace Hunt PhD, Dr. Lukas Gabbert PhD, Dr. Tommaso Lenzi PhD

University of Utah, Salt Lake City, Utah, United States

Introduction

The biological knee functions as a shock absorber during stance, absorbing energy to soften impacts with the ground and returning energy to assist forward momentum, a process known as "Stance Knee Flexion" (SKF) [1]. Unfortunately, above-knee amputees typically lack SKF, as conventional passive prostheses cannot generate the positive power required for physiological energy return [2]. Active prostheses can theoretically address this limitation, as their motors can produce both positive and negative power needed for physiological SKF. However, previous studies have not fully replicated physiological SKF kinetics [3]. This study aimed to evaluate gait biomechanics with an active knee prosthesis controlled to deliver physiological SKF. We hypothesized that replicating physiological knee energy absorption/return would reduce compensatory strategies by decreasing residual hip extension torque. The rationale is the energy stored and returned during SKF will supplement forward propulsion, reducing the need for the user to pivot over a fully extended leg.

Methods

Eight unilateral above-knee amputees walked on an instrumented treadmill at a self-selected speed using an active knee prosthesis (Fig.1A) first controlled in a high-impedance mode to prevent SKF, and then with the same device controlled to enable physiological SKF. Lower-limb joint kinetics and kinematics were calculated using ViconNexus and Visual3D.

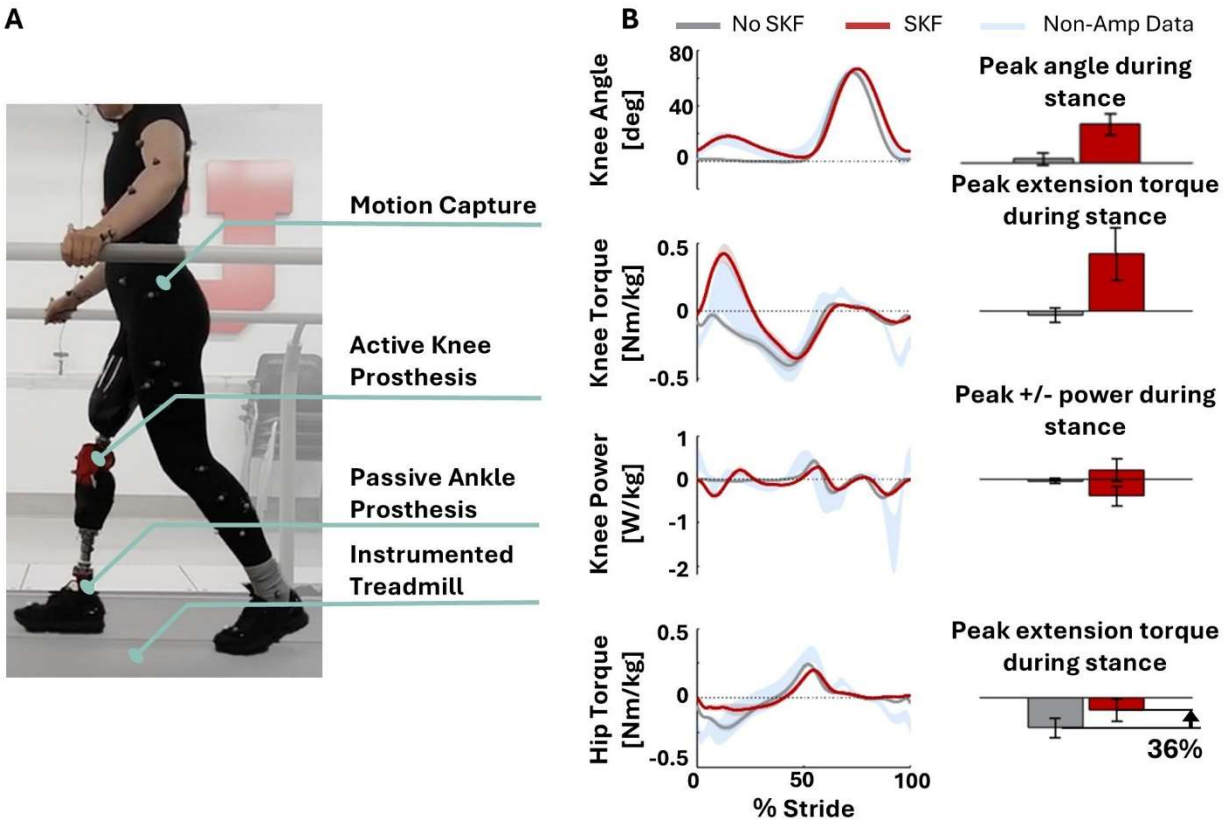
Results

Without SKF, the prosthetic knee remained fully extended in early stance. In contrast, with SKF, the knee prosthesis successfully matched biological knee behavior, flexing to 18.9+/-5.0°and generating up to 0.46+/-0.19 Nm/kg of extension torque, while absorbing/returning up to -0.25+/-0.26/0.44+/-0.22 W/kg of power (Fig.1B). Crucially, residual hip extension torque decreased by 36% when walking with SKF (0.14+/-0.06 Nm/kg) compared to walking without SKF (0.22+/-0.07 Nm/kg).

Discussion

To our knowledge, this is the first demonstration of an active prosthesis fully replicating the kinematics and kinetics of physiological SKF. Our results suggest that properly replicating SKF facilitates forward movement and reduces the effort required from the residual joint. This reduction in compensatory hip loading could improve mobility and reduce fatigue in above-knee amputees.

Images (Optional)



References (Optional)

[1] Zhang *et al*. Appl Bionics Biomech, 2020; [2] Goldfarb *et al*. J of Prost and Ortho, 2013; [3] Zhou *et al*. IEEE TMRB, 2025.

Acknowledgements (Optional)

We thank Brian Kaluf, CP; Kyle Rasmussen, CPO; Jim Liston, CPO; and Mike Reynolds, CPO, for their assistance with prosthesis fitting and alignment. This work was funded in part by the National Institutes of Health under grant # R01HD098154 and by the U.S. Department of War under grant # W81XWH2110037.

Session Category

Clinical Biomechanics: N/A

OA66-02

Isometric Hip Extensor Torque-Angle Relationships Differ Between the Residual and Intact Limb of Transfemoral Prosthesis Users.

Mrs. Ashlyn Wormsley BS, Dr. Hannah D. Carey PhD, Mrs. Julie Ferrell-Olson MSc, Dr. Andrew Sawers CPO PhD

University of Illinois Chicago, Chicago, Illinois, United States

Introduction

Hip muscle strength is critical to walking speed, balance, and endurance in transfemoral prosthesis users (TFPU) [1]. How amputation and/or subsequent inactivity and disuse alters muscle physiology – particularly the force-length relationship - remains unclear, this limits mechanistic insight and intervention development. The objective of this study was to compare hip extensor torque-angle (force-length) relationships between the residual and intact limbs of TFPUs. We hypothesized that the residual limb would have a flatter torque-angle slope and a more extended peak torque angle due to amputation and/or inactivity.

Methods

Sixteen TFPUs (8 females; 50.3±17.3 years) performed bilateral maximum voluntary isometric hip extension contractions on a motor-driven dynamometer. Each participant completed three trials at nine randomized hip flexion angles between 85° and 165° in 10° increments. Torque-angle relationships were plotted as trial-averaged torque against hip angle (Figure 1). Peak torque angle, linear-fit slope, and R^2 values from torque-angle curves were compared between residual and intact limbs using paired t-tests.

Results

Isometric hip extension torque decreased as hip flexion decreased (Figure 1). Linear models fit the data similarly in both limbs (residual R^2=0.45±0.35; intact R^2=0.54±0.26; p=0.18). Peak torque angle did not differ significantly between limbs (residual=101±17°; intact=106±21°; p=0.48). Residual limb torque-angle slopes were significantly flatter (-0.16±0.17) than intact limb slopes (-0.29±0.22), p=0.03.

Discussion

Consistent with unimpaired adults [2], residual and intact limbs exhibited descending hip extension torque-angle relationships with moderate linear fits. Because peak torque angle was similar between limbs, isometric hip extension strength testing could be standardized at a single, evidence-based hip angle (e.g., 100°-105°). These findings also suggest TFPUs' hip extension strength is underestimated, since many studies use more extended hip

angles during testing [1,3]. Flatter residual limb torque-angle slopes suggest reduced hip extensor torque-generating capacity across muscle lengths, especially at more flexed angles where hip extensors are longest. Between-leg asymmetry in slope suggests that amputation -rather than inactivity or disuse - disrupts the torque-angle (force-length) relationship, since inactivity would likely affect both hips similarly. Direct comparisons to unimpaired adults are ongoing.

Images (Optional)

References (Optional)

[1] Sawers et al., 2025; [2] Kulig et al., 1984; [3] Bevacqua et al., 2023

Session Category

Clinical Biomechanics: N/A

OA66-03

Preferred Gait Symmetry and Energetic Cost in Unilateral Below-Knee Prosthesis Users

Mr John Kerr BEng, MSc[1,2], Dr Luca Modenese PhD[1], Dr Lucy Armitage BAppSci, BEng, MBiomedE, PhD[1], Associate Professor Lauren Kark BE (Hons), MBiomedE, PhD[1], Dr Key Nahan BPodMed, MSc, PhD[3,1,2], Dr Kirsty McDonald BSc (Hons), PhD[4,1,2]

[1]University of New South Wales, Sydney, NSW, Australia. [2]Neuroscience Research Australia, Sydney, NSW, Australia. [3]University of Massachusetts Amherst, Amherst, MA, United States. [4]Edith Cowan University, Perth, WA, Australia

Introduction

Anatomical and functional asymmetries from unilateral transtibial limb loss may make asymmetric walking more energy-efficient than symmetric patterns. While preferred stance time asymmetries minimise metabolic cost [1], it remains unclear whether other biomechanical variables demonstrate symmetry or asymmetry during the user's preferred, and likely energetically optimal, gait condition. We aimed to determine whether the preferred walking speed (PWS) of unilateral below-knee prosthesis users reflects the speed that minimises metabolic cost of transport (COT) and/or yields the greatest symmetry in spatiotemporal, vertical ground reaction force (vGRF) and limb work metrics.

Methods

Nine unilateral below-knee prosthesis users (age: 46.3±13.2 years; body mass: 83.0±14.2kg; mean±SD) provided informed consent. The protocol was approved by the University of New South Wales Human Research Ethics Committee. Despite an inclusive, extended recruitment period, a male-only convenience sample was sourced. Markers on the malleoli/prosthesis were tracked (200Hz; Bonita, Vicon) as participants walked on an instrumented split-belt treadmill (1000Hz; M-Gait, Motek Medical) at their PWS and 0.8, 1.0, 1.2, 1.4 and 1.6m/s. Each five-minute trial included metabolic gas collection. Generalised linear mixed models identified speed effects for all variables; optimal values were predicted from fitted functions and compared to PWS.

Results

PWS (1.26 m/s) COT (3.98 J/kg/m [3.50, 4.46]; mean [95%CI]) did not differ from the optimal predicted value (4.04 J/kg/m [3.87, 4.22]; $p=0.21$). The Robinson Symmetry Index [2] was not different between measured values at the PWS and predicted optima for step time ($p=0.889$), step length ($p=0.35$), negative limb work ($p=0.329$) and first peak vGRF ($p=0.692$). Positive limb work ($p<0.001$) and second peak vGRF ($p=0.007$) differed.

Discussion

This study contextualises metabolic cost and key symmetry variables across walking speeds, showing prosthesis users favour speeds that optimise energy cost and, at least in some measures, symmetry. Greater overall symmetry was achievable at slower-than-preferred speeds (5/6 variables could have been simultaneously optimised), but these speeds were likely avoided due to higher metabolic cost. Despite the clinical emphasis on symmetry, asymmetry may serve a functional role, possibly minimising energy expenditure.

References (Optional)

[1] Wedge *et al.*, Clin. Biomechanics, 2022

[2] Robinson, J. Manipulative Physiol. Ther., 1987

Session Category

Clinical Biomechanics: N/A

OA66-04

The Effect of Prosthetic Foot Stiffness on Gait Stability

Mr. Tyler Ho BS[1], Dr. Elizabeth Halsne PhD, CPO[1,2], Dr. Sara Koehler-McNicholas PhD[3,4], Dr. Andrew Hansen PhD[3,4], Mrs. Alexandria Lloyd MS[3], Mr. Juan Cave CPO[3], Mrs. Nicole Schaumann MS[3], Dr. Andrew Sawers PhD[5], Mrs. Christina Carranza CPO[1], Dr. David Morgenroth MD[1,2]

[1]Center for Limb Loss and Mobility (CLiMB), VA Puget Sound Health Care System, Seattle, WA, United States. [2]Department of Rehabilitation Medicine, University of Washington, Seattle, WA, United States. [3]Rehabilitation & Engineering Center for Optimizing Veteran Engagement & Reintegration (RECOVER), Minneapolis VA Health Care System, Minneapolis, MN, United States. [4]Department of Rehabilitation Science, University of Minnesota, Minneapolis, MN, United States. [5]Department of Kinesiology, University of Illinois Chicago, Chicago, IL, United States

Introduction

Falls are common among lower limb prosthesis (LLP) users. Prosthetic foot stiffness is believed to affect LLP users' stability. Previous research on foot stiffness used experimental feet or provided limited accommodation time, limiting the clinical relevance of these findings. This study aimed to determine whether the stiffness of commercially-available prosthetic feet influenced unilateral transtibial LLP users' stability after a week-long accommodation period.

Methods

Using mechanical testing (ISO 10328), we characterized the sagittal-plane stiffness of commonly-prescribed prosthetic feet. Subsequently, unilateral transtibial LLP users wore three different feet of varying stiffnesses for one week, in a randomized order and while masked to foot type. Following each foot accommodation period, participants walked at self-selected walking speeds (controlled within-participant across feet) on level (LVL) and uneven terrain treadmills (UNV) for at least 30 seconds. Using kinematics recorded with optical motion capture during walking, we calculated minimum mediolateral margin of stability (MoS) during each step. [1] Participants rated their balance confidence with each foot on a 0-10 scale. We used linear mixed-effects regression to test for within-participant associations between foot stiffness (N/mm) and gait outcomes (MoS, step width, and balance confidence), controlling for foot type.

Results

Nine male LLP users [mean(SD) age=61.7(9.9)years] have completed the study. Participants selected slower walking speeds for UNV [0.58(0.12)m/s] compared to LVL [0.93(0.22)m/s]. For every 10N/mm increase in prosthetic foot stiffness: 1) prosthesis-side MoS decreased by -0.64±0.10cm on LVL ($p<0.001$) and -0.56±0.12cm on UNV ($p<0.001$); 2) step width decreased on LVL (-0.48±0.17cm, $p<0.05$), but did not change on UNV; and 3) participants' balance confidence decreased (-0.3±0.1, $p<0.001$).

Discussion

Reduced prosthesis-side MoS suggests poorer lateral gait stability with stiffer commercially-available prosthetic feet, especially on UNV where step width was unchanged. Reduced participant-reported balance confidence with stiffer feet corroborates the MoS findings. These results agree with those of previous studies which showed that increased stiffness in experimental prosthetic feet was associated with reduced participant-reported balance confidence. These findings could be useful to clinicians when selecting feet for transtibial LLP users to reduce fall risk.

Images (Optional)

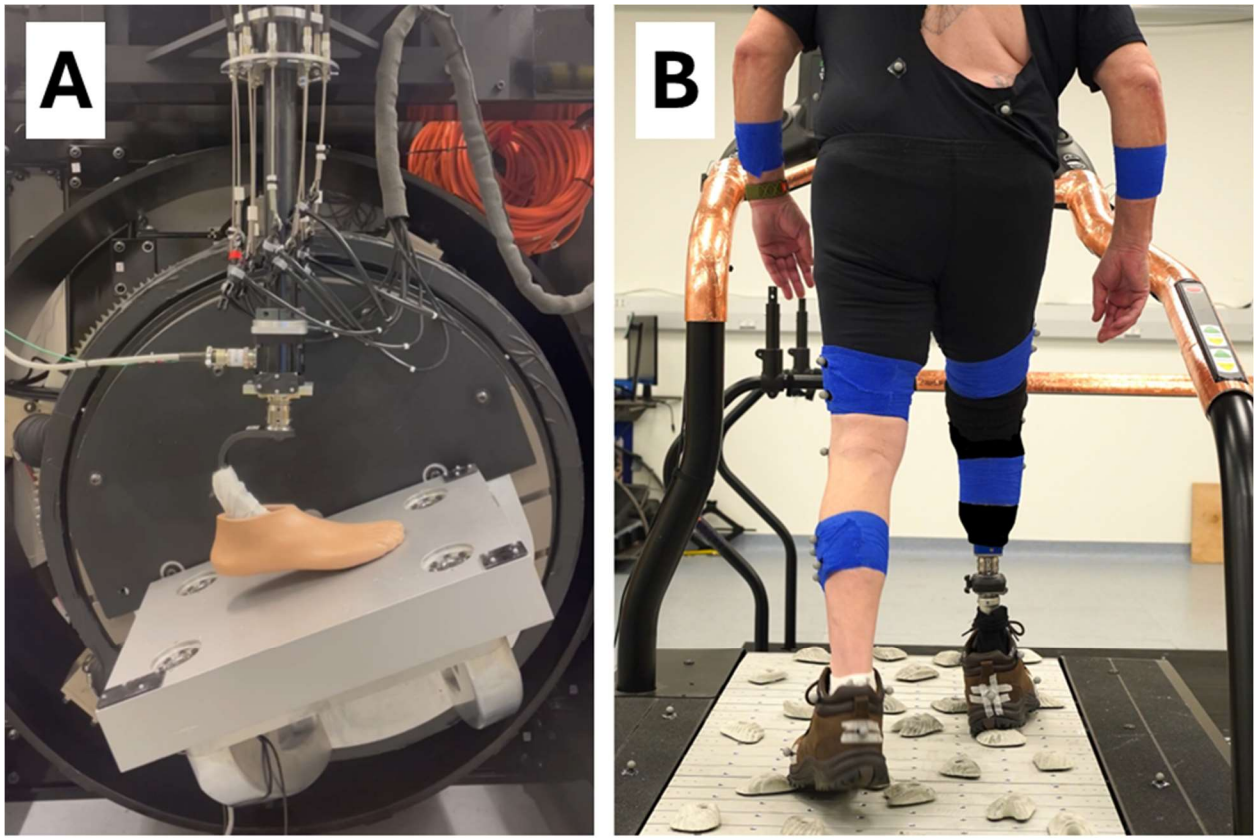


Figure 1. A) Example study prosthetic foot undergoing mechanical testing to characterize stiffness in a robotic gait simulator B) A participant walking on the uneven ground treadmill.

References (Optional)

[1] Gates, et al., Gait Posture, 2013

Acknowledgements (Optional)

Session Category

Clinical Biomechanics: N/A

OA66-05

Hip Muscle Co-Contraction in Transfemoral Prosthesis Users May Not Be an Inherent Consequence of Amputation

Dr Hannah Carey, Mrs. Ashlyn Wormsley, Mrs. Julie Ferrell-Olson, Dr. Andrew Sawers

University of Illinois Chicago, Chicago, IL, United States

Introduction

Walking with a transfemoral prosthesis is believed to involve pronounced co-contraction, potentially due to compensations for missing knee/ankle function, muscle weakness, user experience, or task context (e.g. effort). However, these assumptions have rarely been tested [1]. As a first step towards understanding how amputation affects co-contraction in transfemoral prosthesis users (TFPU), we compared hip co-contraction between residual and intact limbs across effort levels. We used a seated isometric task to remove walking-specific mechanical demands that could mask amputation-related differences in co-contraction. We hypothesized greater co-contraction in the residual than intact limb.

Methods

Thirteen TFPUs (6 females; 50±16 years old) performed isometric hip extension and abduction contractions with their residual and intact limbs on a motor-driven dynamometer at three effort levels: 30%, 60% and 100% MVC. Submaximal efforts were obtained using a visual torque-matching task. Surface EMG was collected from rectus femoris, biceps femoris, gluteus medius, and adductor magnus. Co-contraction values were calculated as the ratio of the less active to more active muscle multiplied by the sum of both muscles [2]. Values were compared using separate two-way repeated measures ANOVAs for extension and abduction.

Results

There was a main effect of effort ($p=0.009$) but not leg ($p=0.454$) for co-contraction during hip extension. However, post-hoc tests revealed no significant pairwise differences between effort levels. For hip abduction there was a main effect of effort ($p<0.001$) but not leg ($p=0.247$). Post-hoc tests revealed higher co-contraction at 100% versus 30% ($p=0.01$) and 60% effort ($p=0.016$).

Discussion

Because hip co-contraction did not differ between limbs during the isometric task, elevated co-contraction during walking in TFPUs likely reflects compensations for lost knee and ankle function or muscle weakness, not amputation per se. Consistent with

unimpaired adults [3], hip abduction co-contraction increased with effort. This trend may reflect greater demands for joint stability and torque accuracy as effort increases, or a common descending command to agonist-antagonist muscle pairs [4] that scales with effort. Direct comparisons to age- and sex-matched controls are ongoing.

Images (Optional)

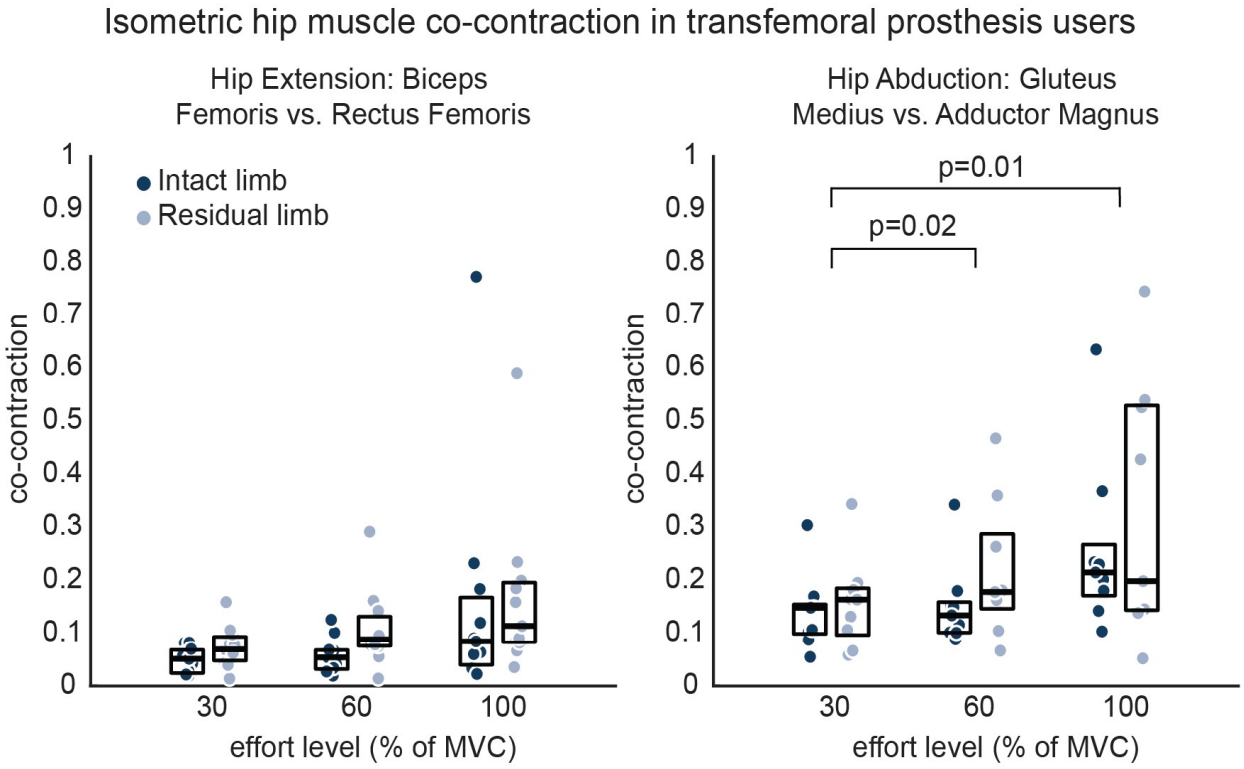


Figure 1. Agonist-antagonist co-contraction during isometric maximum voluntary contractions (MVC, i.e., 100%) and submaximal contractions (30% and 60% of MVC) for hip extension (left panel) and hip abduction (right panel). Dark blue indicates the intact limb and light blue indicates the residual limb.

References (Optional)

[1] Bae *et al.*, JMedEngTechnol. 1999; [2] Rudolph *et al*. KSSTA, 2000; [3] Wu *et al.*, AmJSportsMed, 2017; [4] DeLuca *et al.*, JNeurophysiol, 1987

Session Category

Clinical Biomechanics: N/A

OA66-06

A Comparison of Gait Adaptations During Two Types of Dual-Task Walking in Individuals With Unilateral Lower Limb Amputation: Part 1- Gait Spatiotemporal Outcomes

Ms. Emily Parsowith M.S., CSCS[1], Dr. Lisa Zukowski Ph.D[2], Dr. Paul Kline PT, DPT, Ph.D[1]

[1]Virginia Commonwealth University, Richmond, VA, United States. [2]High Point University, High Point, NC, United States

Introduction

Following lower limb amputation (LLA), spatiotemporal gait asymmetries are common with prosthesis use and adversely affect gait efficiency and functional performance [1]. Cognitive-motor dual-task assessments have been utilized in people with LLA to assess readiness for real-world walking, but there is large variation in the type of cognitive task used [2]. The purpose of this study is to compare gait spatiotemporal parameters between single-task walking, vision-based cognitive-motor dual-task walking, and non-vision-based cognitive-motor dual-task walking in people with unilateral LLA.

Methods

16 participants were enrolled; 14 (11 males, 3 females; age=55.3±13.4 yrs, BMI=29.7±4.0 kg/m2, 10 transtibial, 4 transfemoral) had complete data for analysis. Three walking tasks were performed, each two minutes in duration: single-task (ST), serial subtraction dual-task (SS; non-vision-based), and visual puzzles dual task (VP; vision-based). The two cognitive tasks were evaluated to compare between types of cognitive-motor dual-tasking. APDM Opal 3-sensor wireless inertial sensors, attached to the dorsal aspect of the left and right feet and the posterior of the lower back at the L4/L5 lumbar spine, were used to measure gait speed, cadence, stance time, step duration, and stride length. Normalized symmetry index (NSI) was calculated to compare the effect of task on stance, step duration, and stride length. A NSI value of 0% is considered perfect symmetry.

Results

A repeated measures ANOVA revealed a significant main effect of task condition on gait speed ($F=17.313$, $p<0.001$), cadence ($F=17.332$, $p<0.001$), stride length in the amputated limb ($F=16.633$, $p<0.001$) and stride length in the non-amputated limb ($F=15.869$, $p<0.001$). Post-hoc paired-samples t-tests indicated that gait speed, cadence, and stride length in the amputated and non-amputated limb were greater for ST compared to SS and VP.

Notably, VP had a higher cadence than SS (p=0.007, d=-0.845). Complete results from the statistical analysis can be found in Table 1.

Discussion

These findings suggest type of cognitive task during cognitive-motor dual-tasking influences cadence in people with LLA. Additional research on dual-task performance based on types of cognitive task and real-world walking are needed.

Images (Optional)

Outcome Variable	Task	Mean±SD	F	*p*-value	Paired Samples t-test	Mean difference±SD	*p*-value	Cohen's *d*
Gait Speed (m/s)	ST	1.07±0.14	17.31	<0.001*	SS-VP	-0.03±0.07	0.08	-0.51
	SS	0.96±0.09			ST-SS	0.12±0.09	<0.001*	1.32
	VP	0.99±0.12			ST-VP	0.08±0.07	<0.001*	1.16
Cadence (steps/min)	ST	109.3±8.5	17.3	<0.001*	SS-VP	-2.4±2.8	0.01*	-0.8
	SS	104.1±6.5			ST-SS	5.2±3.6	<0.001*	1.4
	VP	106.5±6.4			ST-VP	2.8±3.4	<0.001*	0.8
Stance NSI (%)	ST	-3.36±4.11	0.07	0.93				
	SS	-3.30±4.18						
	VP	-3.26±4.18						
Step Duration NSI (%)	ST	1.75±7.45	0.02	0.98				
	SS	1.77±7.94						
	VP	1.67±7.65						
Stride Length NSI (%)	ST	-0.21±3.38	0.42	0.66				
	SS	-0.41±3.69						
	VP	-0.36±3.57						
Stride Length-Amputated Limb (m)	ST	1.18±0.12	16.63	<0.001*	SS-VP	-0.01±0.05	0.40	-0.24
	SS	1.10±0.10			ST-SS	0.07±0.06	<0.001*	1.25
	VP	1.12±0.12			ST-VP	0.06±0.04	<0.001*	1.47
Stride Length-Non-Amputated Limb (m)	ST	1.18±0.12	15.87	<0.001*	SS-VP	-0.01±0.05	0.38	-0.77
	SS	1.11±0.09			ST-SS	0.07±0.06	<0.001*	0.50
	VP	1.12±0.12			ST-VP	0.06±0.04	<0.001*	-0.66

Table 1. Within-subjects analysis of task condition effect on kinematic variables. Statistical significance is designated by an *. Negative mean NSI indicates a greater non-amputated limb peak loading, impulse, and loading rate, respectively. Negative mean difference values indicate improved symmetry or greater values in the second task compared to the first.

References (Optional)

[1] Pantera et al., Gait Posture, 2025

[2] Hunter et al., Gait Posture, 2018

Session Category

Clinical Biomechanics: N/A

OA67-02

Wearable Ankle Resistance Training to Enhance Gait Function in Older Adults: A Proof-of-Concept Feasibility Study Using a Smart Passive Device

Mr. Ethan Simaitis[1,2], Mr. Benit Namahoro[1,2], Mr. Max Trnonja[1,2], Mr. Roshan Ragu[1], Dr. John Batsis MD, PhD[1], Dr. Michael Lewek PT, PhD[1,2], Dr. Zachary Lerner PhD[3], Dr. Jason Franz PhD[1,2]

[1]University of North Carolina at Chapel Hill, Chapel Hill, NC, United States. [2]North Carolina State University, Raleigh, NC, United States. [3]Northern Arizona University, Flagstaff, AZ, United States

Introduction

Preventing walking disability in our rapidly aging population is a significant public health challenge. Reduced strength and functional output from muscle-tendon units spanning the ankle (i.e., plantarflexors) during push-off represent known determinants of walking disability due to the aging process and a potential target for intervention [1]. To overcome the poor compliance of conventional interventions, we theorized that targeted and context-specific ankle resistance holds potential to revolutionize therapeutics to restore plantarflexor function and gait biomechanics for older adults. We conducted a proof-of-concept test to determine the feasibility and early efficacy of wearable ankle resistance training to enhance plantarflexor and gait function older adults.

Methods

A pilot cohort of n=3 slow-walking (1.01±0.14 m/s) and physically inactive older adults (aged 65-74) completed a 6-week training study. In each of 12, 20-min sessions, participants walked while using a novel wearable ankle resistance system designed with a carbon fiber leaf spring and embedded sensors on the foot and ankle. The device provided real-time audio-visual ankle power biofeedback to promote plantarflexor muscle engagement during push-off. Walking speed and ankle resistance increased progressively based on 70% success in exceeding a target ankle power of 110% of habitual walking. Primary outcome measures included feasibility (compliance and retention), gait performance (comfortable/fast walking speeds), and plantarflexor function (maximum voluntary isometric contraction [MVIC] strength via dynamometry and medial gastrocnemius thickness via *in vivo* ultrasound).

Results

Participants reported no safety or comfort concerns, completed 100% of their 12 training sessions, and averaged 70% success in plantarflexor engagement. Compared to pre-

training, 6 weeks of wearable ankle resistance training elicited on average a 27% increase in calf muscle strength and a 13% increase in calf muscle thickness. Functionally, local muscle improvements were accompanied by up to 20% (0.18 m/s) and 6% (0.10 m/s) increases in preferred and fastest possible walking speeds, respectively.

Discussion

Preliminary safety and feasibility data, as well as early gait and muscle-level efficacy data, support moving to more rigorous evaluations of wearable ankle resistance training with on-board ankle power biofeedback as an effective therapeutic strategy to enhance gait function for older adults.

Images (Optional)

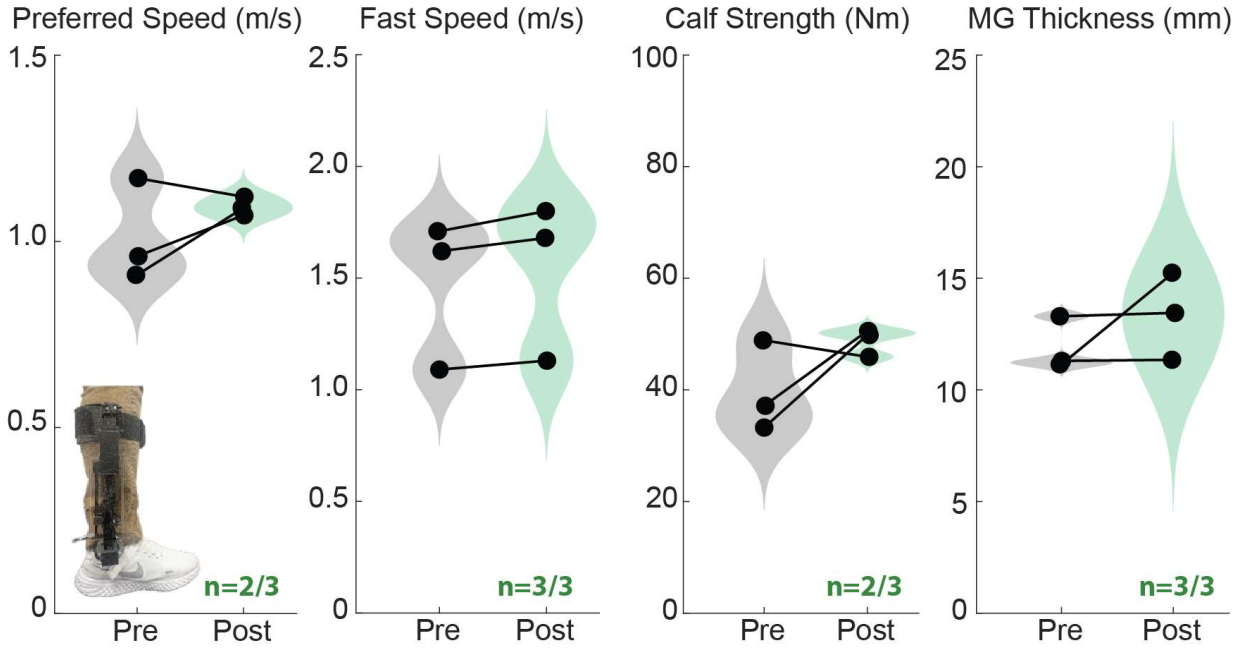


Figure 1. Pre-post comparisons for a pilot cohort of n=3 older adults who participated in a 6-week wearable ankle resistance training program. The passive device (shown) was worn bilaterally and provided plantarflexor resistance via carbon fiber leaf springs and ankle power biofeedback via embedded sensors to encourage plantarflexor engagement in walking.

References (Optional)

[1] Franz JR. ESSR, 2016.

Acknowledgements (Optional)

Acknowledgements. This project was support by a generous gift from the Winston Family Foundation.

Session Category

Human Motion and Performance: Locomotion/Gait

OA67-03

Bottom-Up and Top-Down: Learning Physiologically Plausible Exoskeleton Control via Physics-Informed Musculoskeletal Simulation

Dr. Inseung Kang, Mr. Itak Choi, Mr. Ilseung Park

Carnegie Mellon University, Pittsburgh, PA, United States

Dr. Inseung Kang

Mr. Itak Choi

Introduction

Wearable exoskeletons have advanced rapidly, yet real-world deployment remains limited by the difficulty of creating control policies that generalize across users, tasks, and environments. Current controllers often require hardware-in-the-loop tuning under narrow conditions, restricting scalability. Advances in musculoskeletal simulation and AI now enable digital twins capable of physiologically plausible motion, providing a scalable platform for exploring user variability without exhaustive physical experiments. Here, we compare two complementary strategies, bottom-up reinforcement learning (RL) and top-down imitation learning (IL), to assess their potential for exoskeleton control.

Methods

We evaluated RL and IL using a 21-DOF, 90-muscle musculoskeletal model. The RL agent learned locomotion through reward shaping (reduced muscle activation) combined with domain randomization to promote robustness across walking conditions. The top-down agent tracked reference kinematics, receiving future target states and generating muscle excitation commands. The IL reward emphasized kinematic tracking while penalizing excessive kinetics. Biomechanical fidelity was assessed by comparing simulated joint moments to physiological profiles. As a proof of concept, the learned digital twin was integrated with a hip-exoskeleton model to train an assistance controller.

Results

The RL agent produced biomechanics profiles bounded within human-like motion while maintaining stable locomotion across settings (Moment R^2=0.79, RMSE=0.25~Nm/kg;

Angle R^2=0.919, RMSE=4.30°). Deploying the RL-trained controller on a physical hip exoskeleton yielded torque profiles with R2=0.60 and RMSE=0.048 Nm/kg, indicating a manageable sim-to-real gap. The IL agent reproduced highly human-like gait patterns, with hip and knee angle errors of 4.82° and 2.46°, and moment estimation errors of 0.13 and 0.09 Nm/kg.

Discussion

The two strategies provide complementary strengths rooted in how they learn. RL acquires locomotion directly from physics, producing behaviors that remain stable across settings. Its independence from motion references enables broad exploration and strong robustness to out-of-distribution conditions. In contrast, IL generates physiologically realistic biomechanics for personalization. However, this reliance on reference data also makes it sensitive to conditions not represented in the demonstrations, limiting its generalizability. These trade-offs motivate a hybrid framework that anchors motion within physiological norms through IL while leveraging RL for stability, enabling exoskeleton controllers that are personalized for real-world use.

Images (Optional)

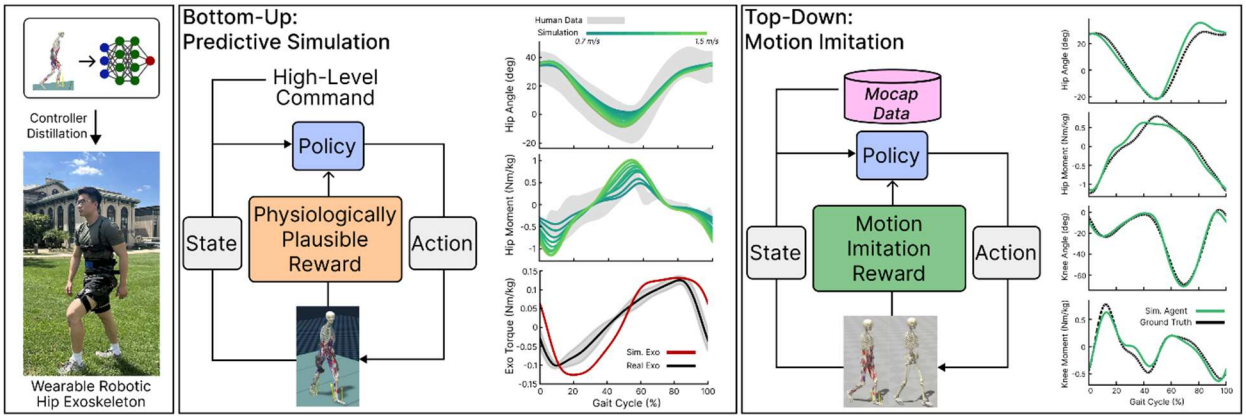


Figure 1: Bottom-up and top-down motion generation strategies used for developing exoskeleton control policies through simulation-to-real distillation. The bottom-up agent optimizes biomechanical objectives, yielding broad generalization across tasks and enabling the training of a viable hip exoskeleton assistance controller directly from the learned policy. The top-down agent imitates human motion trajectories, producing physiologically plausible biomechanics. Together, these complementary approaches highlight the need for a hybrid framework that integrates human-likeness with robustness for reliable real-world exoskeleton control.

Session Category

Human Motion and Performance: Locomotion/Gait

OA67-04

Powered Footwear System Designs Must Account for Athlete Kinematic Changes in Response to Ankle Assistance and System Compliance

Dr. Julia Butterfield, Ms. Kristin Quah, Ms. Kristin DeHart, Ms. Hannah Frame, Dr. Alison Sheets-Singer

Nike, Inc., Beaverton, Oregon, United States

Introduction

Nike is designing powered footwear systems (PFS) to provide metabolic benefits during walking and running. The systems aim to provide large torques in late stance as literature [1,2] suggests are important for large metabolic reductions. They include compliance at the device-body interfaces for comfort and wearability, even though torque-induced deformations of compliant interfaces may negatively impact device function. Nike's first PFS prototype (Fig.1) did not produce the expected metabolic benefits, and participants felt assistance stopped too early; therefore, this study aims to investigate potential causes including: ankle plantarflexion changes with assistance, electro-mechanical limitations impacting the system's on-body performance, and interactions between these factors.

Methods

Six athletes gave informed consent and completed two 90-second, 6-mph running trials on a Bertec treadmill: shoes-only, and wearing the PFS. Motion capture (Vicon) of the athlete and PFS were collected during the final 20-seconds, and stance-phase metrics were calculated: difference in peak biological ankle plantarflexion angle with and without the PFS; and difference between biological ankle and mechanical PFS ankle range of motion (ROM), peak plantarflexion angle, and peak and average angular velocity.

Results

Wearing the PFS increased all athletes' peak stance-phase biological plantarflexion angle (mean difference from shoes: 6.0±3.1°). The biological and mechanical PFS ankle angle in the powered trials also differed due to system compliance: the PFS moved through a larger ROM than the athlete's biological ankle (difference: 12.0±2.5°), reached larger peak plantarflexion angles (difference: 8.4±3.2°), larger maximum angular velocities (difference: 125.5±73.1°/sec), and had larger average angular velocity between maximum dorsiflexion and toe-off (difference: 34.9±16.8°/sec).

Discussion

The PFS torque increased biological plantarflexion, and system compliance allowed increased mechanical ROM, meaning the PFS had larger-than-expected mechanical plantarflexion which shifted it into a region with limited torque-production capability. Additionally, the larger-than-biological PFS angular velocity suggests the system must be able to generate higher electro-mechanical power since power is a function of torque and angular velocity. Recent Nike PFS iterations that include these updated specifications are more capable of delivering metabolic and perception benefits when optimally controlled.

Images (Optional)

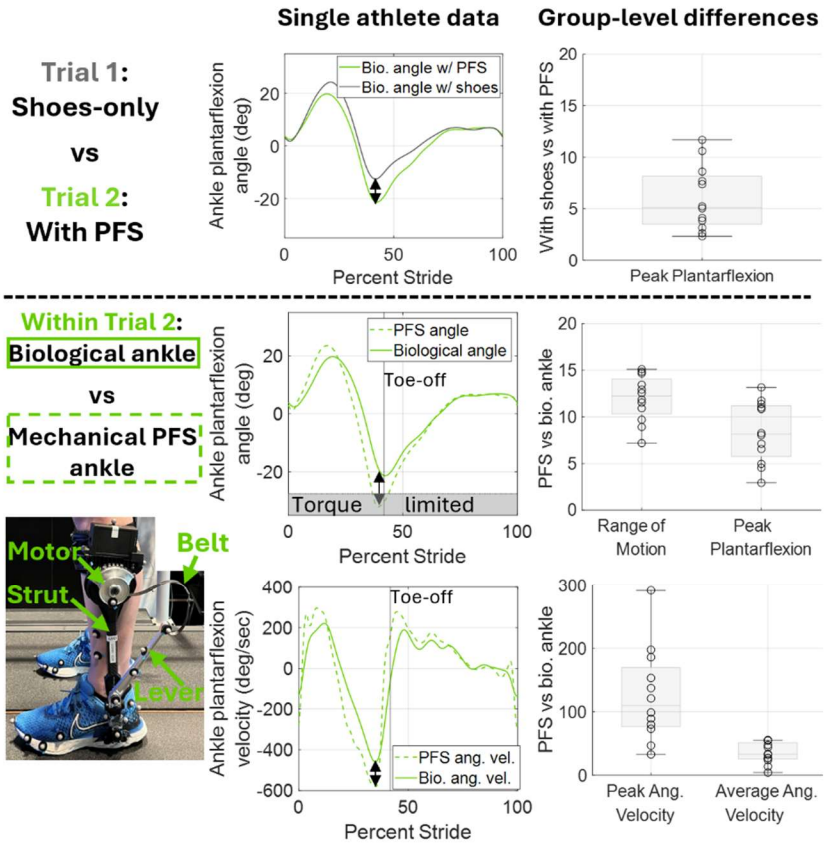


Figure 1. Athletes completed motion capture trials with shoes-only and with a powered footwear system (PFS). The PFS produces torque about the ankle by spinning the motor to shorten the belt, causing the lever to rotate relative to the strut. As the lever nears alignment with the strut, the PFS's ability to apply torque decreases as the moment arm approaches zero. The biological ankle angle is defined using markers on the shoe and the shank. The mechanical PFS ankle angle is defined using markers on the PFS lever and strut. **(Top)** Athletes reached larger biological plantarflexion angles during stance when running in the PFS compared to running in shoes. **(Middle)** The mechanical PFS ankle joint moved through a larger sagittal range of motion than the biological ankle and reached a higher peak plantarflexion angle in stance. For some athletes, the PFS plantarflexed enough that the system's ability to produce torque was severely limited due to strut-lever alignment. **(Bottom)** The mechanical PFS ankle also had larger peak plantarflexion angular velocity during stance and larger average plantarflexion angular velocity between maximum dorsiflexion angle and toe-off than the biological ankle. Data are shown for the right leg of a representative athlete (left column, lines represent the average across all strides within a trial) and for the group (right column, circles represent individual athlete data with separate circles for the left and right sides). Positive values in the group-level data indicate that the mechanical PFS ankle had a larger range of motion and more plantarflexed peak position than the biological ankle, and that athletes have a larger peak stance-phase biological plantarflexion angle when wearing the PFS compared to running in shoes.

References (Optional)

[1] Juanjuan Zhang *et al.*, Science, 2017

[2] Kirby Witte *et al.*, Science Robotics, 2020

Session Category

Human Motion and Performance: Locomotion/Gait

OA67-05

Control of a Modular Hip-Knee Exoskeleton via Reinforcement Learning for Sit-to-Stand and Squatting Assistance

Dr Neethan Ratnakumar, Ms. Mariya Tohfafarosh, Dr. Xianlian Zhou

New Jersey Institute of Technology, Newark, New Jersey, United States

Introduction

As the global population ages, the demand for wearable assistive technologies that can enhance mobility, independence, and quality of life continues to rise. Sit-to-stand(STS) transitions and squatting are two of the most biomechanically demanding daily movements, requiring substantial lower-limb strength, joint coordination, and balance control. Developing adaptive and intuitive control strategies for lower-limb exoskeletons is therefore essential to provide safe, timely, and personalized assistance for these tasks.

Methods

We developed a new hip–knee exoskeleton by augmenting an existing hip exoskeleton[1] with powered knee joints. The 8.5-kg system was engineered for high backdrivability, easy adjustability across users, and compatibility with multiple sensing and control frameworks. The device incorporates an IMU-based kinematic measurement system that streams data wirelessly to an onboard Raspberry Pi for real-time processing and control. To design task-specific assistance profiles, we employed a reinforcement learning (RL) framework that generated muscle-driven human motion simulations and jointly optimized hip and knee torque assistance for STS and squatting. A human-subject evaluation involving five healthy adults assessed the feasibility, safety, and physiological impact of the RL-driven controller using indirect calorimetry, heart rate, electromyography (EMG), and full-body kinematics.

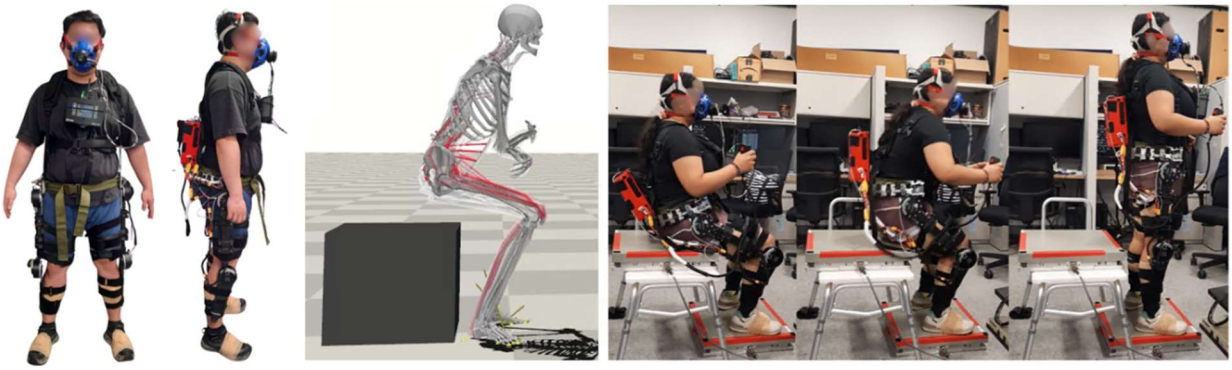
Results

In simulation, the RL-trained controller produced torque assistance patterns that closely matched the timing and shape of muscle-generated joint moments, substantially reducing predicted muscle activation and joint loading. When implemented on hardware, the controller demonstrated robust user adaptation, generating personalized torque profiles (kept below 10 Nm for safety) that aligned with each participant’s natural motion. During repetitive squatting, active assistance reduced net metabolic rate by approximately 10%. STS assistance yielded smaller metabolic reductions, likely due to suboptimal control near the seat-contact phase. Ongoing EMG analysis will further quantify changes in muscle recruitment and fatigue across assistance conditions.

Discussion

These preliminary findings demonstrate that RL-based control is a promising strategy for adaptive, task-specific exoskeleton assistance and can reduce physiological effort during high-demand movements. Observed performance sensitivities, such as fit, user acclimation, comfort, and latency, highlight opportunities for hardware refinement and improved sensing integration. This work establishes a streamlined framework for rapid development, simulation-based optimization, and real-world deployment of advanced exoskeleton controllers.

Images (Optional)



Hip-Knee Exoskeleton Simulation and Learning Experimental Evaluation

References (Optional)

Tohfafarosh et al., 2025 ICORR.

Session Category

Human Motion and Performance: Locomotion/Gait

OA68-01

Same Jump Height, Different Movement Strategy: Five Force Production Phenotypes in Elite Athletes

Dr. Bahman Adlou M.Sc., Ph.D.[1,2], Mr. John Grace MS[1], Dr. Christopher Wilburn Ph.D.[1], Dr. Wendi Weimar Ph.D.[1]

[1]Auburn University, Auburn, Alabama, United States. [2]US Soccer Federation, Fayetteville, Georgia, United States

Introduction

Jump height remains the predominant metric for countermovement jump (CMJ) assessment in high-performance athletes, yet this single value cannot distinguish how athletes achieve their performance. If multiple coordination strategies produce equivalent outcomes, practitioners may fail to detect meaningful neuromuscular changes even with consistent monitoring. This study applied functional data analysis [1] to determine whether distinct force production strategies exist in elite athletes and whether different strategies can yield similar jump heights.

Methods

Force-time data from 17,767 verified CMJ trials across 448 NCAA Division I athletes (323 male, 125 female; 9 varsity sports; 6,200 testing sessions; 2022-2025) were sampled at 500 Hz and underwent phase-linked temporal normalization and functional principal component analysis (fPCA). K-means clustering identified movement strategies, validated through gap statistic, silhouette coefficient (0.31), and bootstrap resampling (1,000 iterations; Jaccard similarity=0.82). Statistical parametric mapping (SPM) quantified temporal force differences. Within-athlete consistency was evaluated using intraclass correlation coefficients.

Results

Four principal components captured 95.50% of force-time variance. Five stable strategies emerged (Figure 1) with jump heights ranging from 31.6±6.9 cm (Strategy 4) to 48.4±5.6 cm (Strategy 3). Within-athlete consistency was high (ICC=0.66) while sport-specific clustering was weak (Cramér's V=0.066), indicating stable individual phenotypes. Critically, two high-performing strategies achieved comparable jump heights (Strategy 2: 45.7±7.7 cm; Strategy 3: 48.4±5.6 cm) through different coordination: Strategy 3 produced 4.7% greater peak force (2.92 vs. 2.79 BW; $p<0.001$, $d=0.47$) with distinct temporal force application during

braking and propulsive phases (18-92% vs. 14-92% of movement cycle). These two strategies represented 41% of all testing sessions.

Discussion

Elite athletes employ multiple distinct strategies to accomplish the CMJ task, though individuals remain consistent, and equivalent jump heights do not guarantee equivalent neuromuscular function. An athlete transitioning between strategies while maintaining jump height would appear stable under conventional assessment, potentially masking fatigue, compensation, or early-stage injury. Force-time waveform analysis detects coordination changes invisible to discrete metrics and should be integrated into performance monitoring and return-to-play decision-making. Limitations include absence of prospective injury data. Future work should examine whether strategy-matched training interventions produce superior individualized adaptations.

Images (Optional)

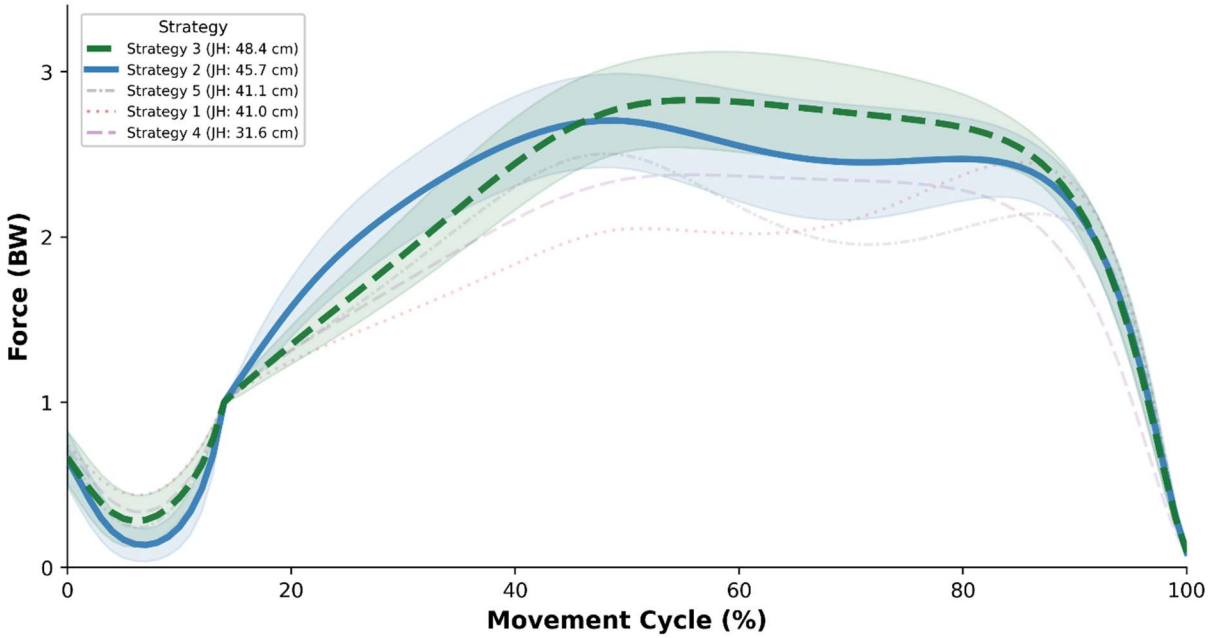


Figure 1. Mean body weight-normalized force-time curves (shaded regions: ±1 SD) for five movement strategies identified via functional principal component analysis and k-means clustering in 17,767 countermovement jumps from 448 NCAA Division I athletes. Strategies 2 and 3 (emphasized) achieve similar jump heights (45.7 and 48.4 cm) through distinct temporal force production patterns, illustrating coordination differences undetectable by discrete performance metrics.

References (Optional)

[1] Warmenhoven J *et al.*, J Biomechanics, 2021.

Acknowledgements (Optional)

The authors gratefully acknowledge Dr. Michael Goodlett, Chief Medical Officer, and participating sport performance coaches, including Bryan Karkoska and Dom Studzinski, for facilitating athlete testing.

Session Category

Human Motion and Performance: Sports

OA68-02

Joint Loading and Performance Implications of an Isolated Reduction in Footwear Rotational Traction

Lead Biomechanics Researcher Marlon Rainville, Senior Biomechanics Researcher Amanda Cann, Lead Biomechanics Researcher Nick Frank, Director of Footwear Biomechanics Elysia Davis

Nike Sport Research Lab, Beaverton, Oregon, United States

Introduction

Mechanically available traction between footwear and playing surface describes the resistance to relative motion and can be measured in translational and rotational components [1]. Footwear traction is critical for athletic performance [2], but high rotational traction is linked to lower extremity non-contact injuries [1] and high joint loading [3] in field sports. NIKE Inc. designed a novel forefoot cleated traction pattern that reduces rotational but maintains translation traction compared to traditional patterns. The purpose of this study was to measure the effects of reduced rotational traction footwear on agility performance and knee joint loading during cutting.

Methods

Twenty athletes (6F, 14M) completed seven maximal effort 180° shuttle cuts in two footwear conditions on artificial turf with embedded force platforms. Mechanical testing measured the NIKE Phantom Luna (“LowRT”) cleat reduced rotational traction by 47% and maintained translational traction compared to the NIKE Phantom GT2 (“Control”) cleat (**Table 1a**).

Kinematic and kinetic data were collected to quantify agility performance, ground reaction forces, and stance leg kinematics and kinetics. A two-way mixed ANOVA was used to test for interaction effects between footwear and gender. For variables without an interaction effect, gender was collapsed to identify significant main effects ($\alpha < 0.05$) of footwear using paired t-tests.

Results

A significant interaction exists between gender and footwear for agility performance time, with female athletes performing faster in the LowRT cleat (-2.6% Female x LowRT, $p = 0.04$) and male athletes showing no performance difference (0% Male x LowRT, $p > 0.05$).

Footwear did not affect utilized translational traction. The LowRT cleat significantly reduced peak free moment in early stance. The LowRT cleat significantly reduced peak knee abduction moment and peak knee transverse external rotation moment in late stance. Athletes exhibited greater transverse-plane internal foot rotation during stance, starting from a more externally oriented foot position at ground contact in the LowRT cleat (**Table 1b**).

Discussion

Footwear that maintains sufficient available translational traction but reduced rotational traction reduces knee joint loading without compromising agility performance.

Images (Optional)

	Dependent Variable	Footwear Condition		
a.	**Mechanical Testing (US M7)**	**LowRT**	**Control**	
	Rotational Traction [Nm]	19.7	37.3	
	A/P Translational Traction Coefficient	1.3	1.1	
	M/L Translational Traction Coefficient	1.1	1.2	
b.	**Footwear Effects**	**LowRT**	**Control**	***p***
	Agility Performance [sec]	**(Gender x FW Interaction)**		**0.02**
	Female	**1.47 ± 0.16**	**1.51 ± 0.14**	**0.04**
	Male	1.42 ± 0.13	1.42 ± 0.12	0.88
	Utilized Traction @ Peak Shear GRF	0.94 ± 0.10	0.94 ± 0.09	0.86
	Peak Knee Abduction Moment [Nm BWL^{-1}]	**0.45 ± 0.18**	**0.50 ± 0.19**	**<0.01**
	Peak Knee Ext. Rot. Moment [Nm BWL^{-1}] (Early Stance)	0.073 ± 0.020	0.071 ± 0.021	0.26
	Peak Knee Ext. Rot. Moment [Nm BWL^{-1}] (Late Stance)	**0.056 ± 0.015**	**0.060 ± 0.014**	**0.02**
	Peak (+) Free Moment [Nm BW^{-1}] - Early Stance	**0.017 ± 0.007**	**0.021 ± 0.007**	**<0.01**
	Peak (-) Free Moment [Nm BW^{-1}] - Late Stance	-0.017 ± 0.007	-0.016 ± 0.008	0.27
	Foot Angle Transverse Plane [deg] - Foot Contact	**21.9 ± 9.0**	**20.4 ± 8.6**	**0.04**
	Foot Internal Rotation Excursion [deg]	**14.1 ± 8.5**	**11.5 ± 6.3**	**<0.01**

References (Optional)

[1] Wannop et al., American College of Sports Medicine, 2013.

[2] Luo & Stefanyshyn, Footwear Science, 2011.

[3] Wannop et al., American Journal of Sports Medicine, 2010.

Session Category

Human Motion and Performance: Sports

OA68-03

Height or Hops: Why Do Female Hoopsters Rarely Dunk?

Dr. Emily Haag PhD, CSCS, Dr. Peter Weyand PhD

Texas Christian University, Fort Worth, Texas, United States

Introduction

Since dunking data has been available for both men's and women's professional basketball (2002), there have been over 200,000 regular-season dunks recorded for men and 34 total for women. Indicating that the men's hoopsters dunk 6,000 times more often than the women.

The 10-foot rim is the same for both sexes; therefore, the deficit could be attributable to either (1) women being shorter than men, and therefore having to jump higher to attain the same jump and reach height, or (2) women being less able to elevate the body to attain the height needed, or both.

We hypothesize that the basis for the sex difference in dunking frequency is equally attributable to stature and jumping ability.

Methods

To determine the relative contributions of stature and jumping ability to maximal projected jump and reach height of professional men and women basketball players, mean reported heights of NBA and WNBA players were acquired (2.00 ± 0.08 m, 1.85 ± 0.07 m, respectively). Standing reach heights of professional players were determined using reported arm length/ height ratios. The sex difference in jumping ability was assessed by measuring kinetics and maximal vertical countermovement jump and reach height for 20 athletic men and 20 athletic women subjects, jumping off laboratory force platforms.

Results

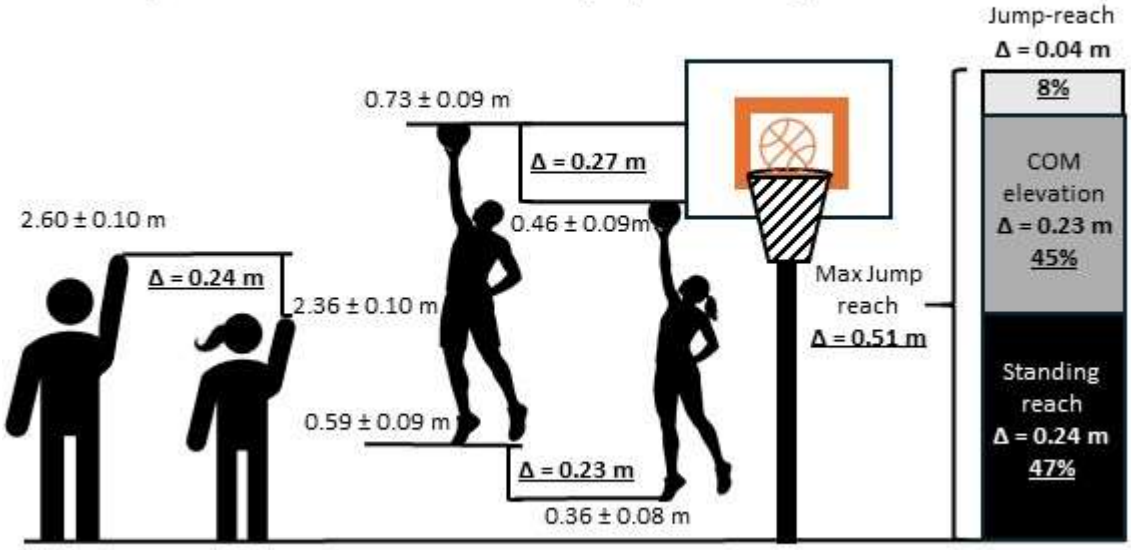
As seen in Figure 1, the mean sex difference in the maximal projected jump and reach height was Δ=0.51 m. The relative contributions of stature and jumping ability to this overall differential were broken down into standing reach (Δ=0.24 m; 47%), center of mass (COM) jumping elevation (Δ=0.23 m, 45%), and jump and reach height difference from COM elevation (Δ=0.04 m, 8%).

Discussion

In contrast to our initial hypothesis of equally attributable factors, stature and reaching ability account for relatively more (55%) of the differential than jumping ability (45%). In conclusion, the sex difference in dunking frequency is primarily attributable to sex differences in stature and secondarily to vertical jumping ability/heights. We also identified a small additional contribution from differences in jump and reach height that were greater than standing reach height differences.

Images (Optional)

Figure 1. Left: Standing reach height for average male and female NBA & WNBA players (n=710 & n=206, respectively). Middle: Measured COM elevation and jump-reach heights for male and female athletes (n=20 males, n=20 females). Right: Relative contributions of jump-reach, COM elevation, and standing reach of the sex difference in maximal jump and reach height.



References (Optional)

Acknowledgements (Optional)

Session Category

Human Motion and Performance: Sports

OA68-04

Quantifying Execution Variability in the CMJ: Phase-Specific Responses to Practice-Induced Fatigue

Mr. Anil Palanisamy, Mr. Aniakh Randhawa, Dr. Dylan Kobsar

McMaster, Hamilton, ON, Canada

Introduction

Fatigue can disrupt motor control, leading to changes in movement variability, defined as the trial-to-trial fluctuations in repeated skill execution. Execution variability captures the subtle adjustments performers use to maintain a stable coordination strategy in well-learned, multi degrees-of-freedom (DOF) movements(2). Because execution variability is sensitive to coordination shifts, complex goal-directed tasks offer an effective model for studying how fatigue influences movement control (6). The countermovement jump (CMJ), a coordination-intensive task used in athlete monitoring, is well suited for this purpose. When paired with force-plate analysis, the CMJ allows phase-specific analysis of jump execution, making it a practical tool for detecting fatigue-related changes in execution (3). However, how fatigue affects the magnitude of execution variability remains unclear (4).This study tested whether basketball practice alters the magnitude of execution variability, quantified using the coefficient of variation (CV) (5). We hypothesized increased post-practice variability, particularly in eccentric-phase metrics sensitive to fatigue(7).

Methods

This repeated-measures study assessed pre- to post-practice changes in CMJ execution variability in thirty basketball athletes (14 males, 16 females). CMJs were performed on dual uniaxial force plates (ForceDecks FDLite, VALD Performance), which recorded vertical ground reaction forces at 1,000 Hz (1). Force–time data were processed using ForceDecks software to derive phase-specific CMJ metrics with established accuracy and reliability relative to laboratory force plates (1). Within-subject CV was calculated to quantify the magnitude of changes in execution variability(4).

Results

Eccentric-phase variability increased in Braking RFD ($\beta = 20.6\%$, $p = 0.050$) and Deceleration RFD ($\beta = 23.3\%$, $p = 0.014$). Concentric variability increased: Concentric Impulse Phase 1 (first 50% of concentric; $\beta = 36.1\%$, $p = 0.001$) and Concentric Impulse–100 ms ($\beta = 33.6\%$, $p = 0.001$) both increased. Jump-height variability also increased ($\beta = 24.5\%$, $p = 0.014$).

Discussion

Despite reductions in mean force and jump performance, most CMJ variability metrics remained stable, indicating preserved coordination under typical training loads. Larger changes emerged in the concentric phase, where variability in early (Phase 1) and rapid (100-ms) impulse production increased. In contrast, increases in Braking and Deceleration RFD variability suggest diminished tolerance to eccentric loading under fatigue (2).

Images (Optional)

Metric	Phase	β % Change (95% CI)	p-value	Female Pre	Female Post	Male Pre	Male Post
Braking RFD (N/s)	Eccentric	19.0% (2.8%, 37.6%)	0.050	4615.8 ± 1059.0	4370.1 ± 880.6	5053.2 ± 1240.3	4481.1 ± 1356.5
Deceleration RFD (N/s)	Eccentric	23.3% (6.7%, 42.5%)	0.014	5341.4 ± 1347.8	5056.1 ± 1350.8	5773.4 ± 1778.9	5009.1 ± 1880.4
Concentric Impulse Phase 1 (N·s)	Concentric (first 50%)	36.1% (15.8%, 59.8%)	0.001	109.8 ± 12.1	107.0 ± 11.8	129.3 ± 17.0	120.3 ± 17.9
Concentric Impulse–100 ms (N·s)	Concentric	33.6% (14.1%, 56.5%)	0.001	86.2 ± 13.8	84.8 ± 15.0	100.0 ± 18.1	91.0 ± 19.3
Jump Height (cm)	Performance	24.5% (7.1%, 44.7%)	0.014	27.6 ± 4.6	26.3 ± 4.6	40.9 ± 4.7	38.9 ± 6.1

Significant pre–post changes in CMJ execution variability. Values represent overall percent changes in within-subject variability (β) with corresponding 95% confidence intervals, along with pre- and post-practice mean ± SD for females and males. All metrics shown demonstrated significant pre–post effects following FDR correction.

Session Category

Human Motion and Performance: Sports

OA68-05

ACL Injury Resilience Score Distinguishes Risky and Protective Biomechanics with In-Lab and Out-of-Lab Measurement Tools

Dr. Kirsten Seagers MS, PhD[1], Dr. Krithika Swaminathan MS, PhD[1], Dr. Julie Kolesar MS, PhD[1], Dr. Sam Hamner MS, PhD[1], Ms. Julie Muccini MS, OTR/L[1], Dr. Gregory Myer PhD, FACSM, CSCS*D[2], Dr. Jennifer Hicks MS, PhD[1], Dr. Scott Delp MS, PhD[1]

[1]Stanford University, Stanford, CA, United States. [2]Emory University School of Medicine, Atlanta, GA, United States

Introduction

ACL injuries are among the most debilitating in sports, but many occur during non-contact incidents and are preventable through targeted training [1]. A metric is needed to assess injury risk across multiple sport-related movements and target neuromuscular training to individualized risk factors. In this study, we aimed to develop a score that reflects an athlete's overall biomechanical performance during movements that differentiate injury risk. We compared this score between in-lab (motion-capture) and out-of-lab (OpenCap) measurement tools.

Methods

We collected concurrent 3D motion-capture and OpenCap video data for 26 uninjured female athletes (15.7±1.2 yrs) during five common injury-risk screening activities (Figure 1A)[2, 3]. We calculated activity-specific biomechanical risk factors and compared these factors to existing literature on injured groups to establish an injury resilience distribution (high resilience = low injury-risk). By defining a sample-adjusted injury threshold, we calculated resilience factor-specific z-scores (Figure 1B). The ACL Injury Resilience (AIR) Score was derived by averaging z-scores, with higher scores indicating greater resilience. We compared musculoskeletal model visualizations from athletes with low and high AIR scores to literature-derived profiles of injury-prone versus injury-resilient movements. AIR scores computed with kinematics from motion-capture and OpenCap were compared with a Pearson correlation.

Results

Musculoskeletal visualizations showed the athlete with the lowest AIR Score (red) exhibited riskier mechanics, while the athlete with a high AIR Score (green) displayed protective movements (Figure 1C). AIR Scores calculated from motion-capture and OpenCap kinematics were strongly correlated ($r=0.73$, $p<0.005$; Figure 1D)[4].

Discussion

The AIR Score assesses injury resilience during multiple movements using literature-derived thresholds linking biomechanical factors to ACL injuries. Musculoskeletal visualizations highlight vulnerable and injury-resilient movements, suggesting the AIR Score can guide targeted neuromuscular training programs to reduce injury risk. Moreover, the AIR Score can be reliably captured with smartphone-video data. Larger datasets collected out-of-lab with injury incidence outcomes are required to validate and refine the AIR Score framework.

Images (Optional)

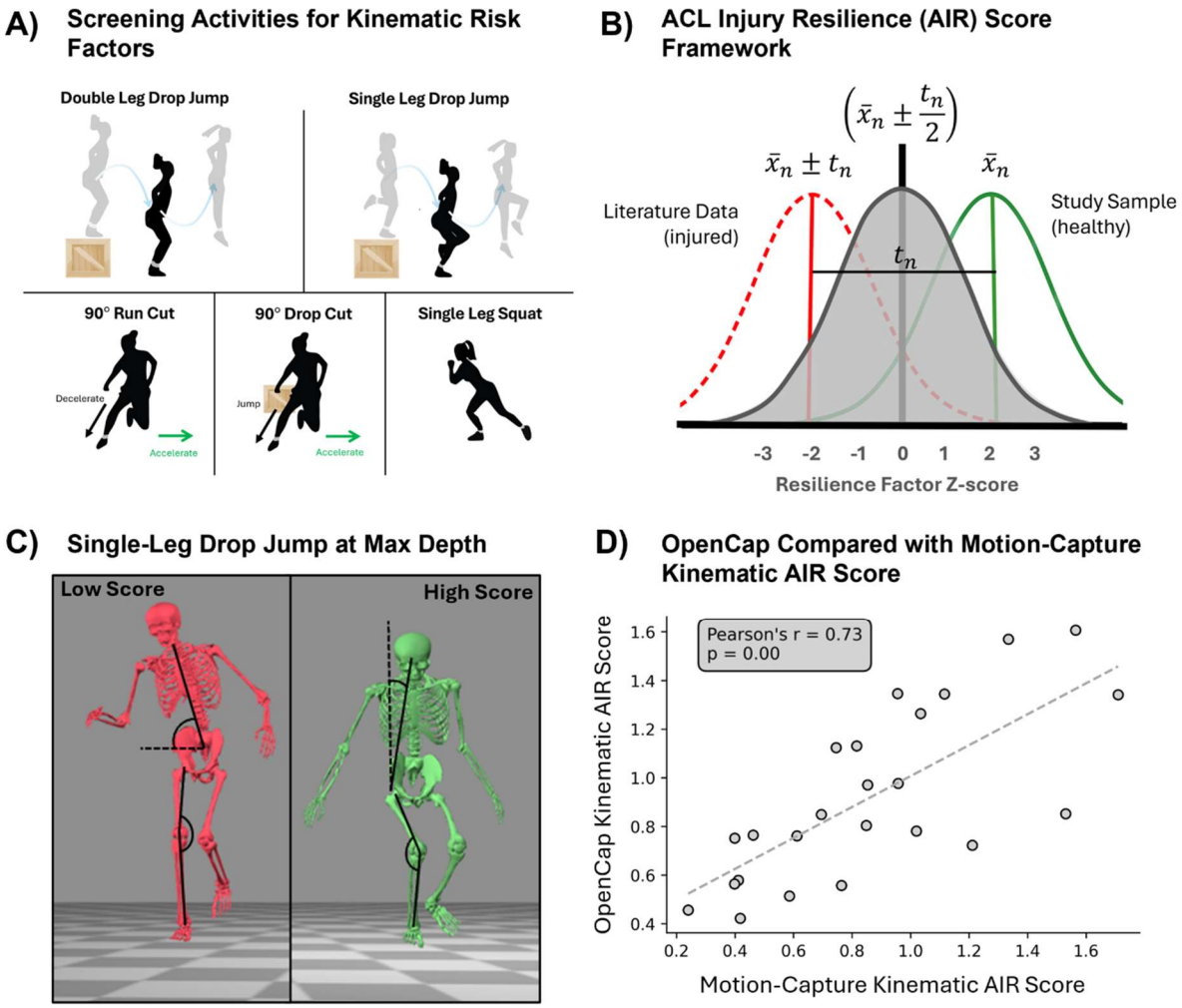


Figure 1: A) Kinematic risk factors from five screening activities are used in the B) ACL Injury Resilience (AIR) Score framework. The AIR Score identifies athletes with risky (red) and protective (green) biomechanics. C) Musculoskeletal models of representative participants with low (red) and high (green) AIR Scores at the maximum depth of a single-leg drop jump's landing phase. D) There is strong agreement between AIR Scores calculated from 3D motion-capture (in-lab gold standard measurement) and OpenCap, a video-based out-of-lab measurement.

References (Optional)

[1] Myer et al., (2007). BMC Musculoskelet Disord

[2] Schweizer (2022). Int J Environ Res Public Health

[3] Uhlrich et al., (2023). PLoS Comput Biol

[4] Schober et al., (2018). Anesth Analg

Acknowledgements (Optional)

Session Category

Human Motion and Performance: Sports

OA68-06

Upward Movement Velocity and Acceleration Strategies That Enable the Minimum-Velocity Advantage in Basketball Free Throws

Ms Kaitlin Jackson[1], Dr. Kirk Goldsberry[2], Dr. Owen Beck[1]

[1]University of Texas, Austin, TX, United States. [2]University of Texas, Austin, Texas, United States

Introduction

Free-throw success depends on ball-release parameters. Prior research indicates that skilled shooters release the ball near the minimum velocity required for a made shot, reducing the sensitivity of ball in-ring position to small execution errors in release parameters (e.g. release angle) (1). We examined the kinematics of how free-throw shooters produce their individualized minimum release speed.

Methods

Basketball shooters (12 NCAA D1 females, 16 NBA males, 12 novice females, and 12 novice males; novices highest level = high school) completed 50 free throws. Three-dimensional ball-trajectory and full body kinematic data were collected using 3D motion capture. Each player's probability of a made free throw based on ball release speed and angle was calculated using projectile motion equations, including release height and distance from the hoop. We used Pearson correlations and multivariate regressions.

Results

Actual and minimum-required ball release speeds were strongly related ($r=0.96$, $p<0.001$), and release speed was less variability than release angle ($p<0.001$) indicating that shooters may prioritize their consistency in release speed versus angle. Shooters who shot nearest to their model-predicted minimum speed were more consistently (std of release speed, $r=0.66$, $p<0.001$) and had better shooting accuracy ($r=0.74$. $p<0.001$). Higher release height was associated with slower release speed ($r=0.87$, $p<0.001$), suggesting taller shooters require a lower minimum release speed. Lower elbow upward velocity at release predicted better accuracy ($p<0.001$). Peak acceleration timing: earlier pelvis and elbow peak upward accelerations were associated with slower release speed ($p<0.001$and $p=0.0024$, respectively) and better accuracy ($p<0.001$and $p = 0.045$, respectively), whereas earlier wrist peak acceleration was associated with higher release speed ($p<0.001$) and reduced accuracy ($p=0.029$).

Discussion

Shooters with superior shot accuracy better prioritized and demonstrated more consistent minimum release speed. While NBA data require further analyses, our current findings imply that free throw shooters should release the ball with a relatively slow release speed while focusing on earlier acceleration of the pelvis and elbow and delaying wrist acceleration closer to release.

Images (Optional)

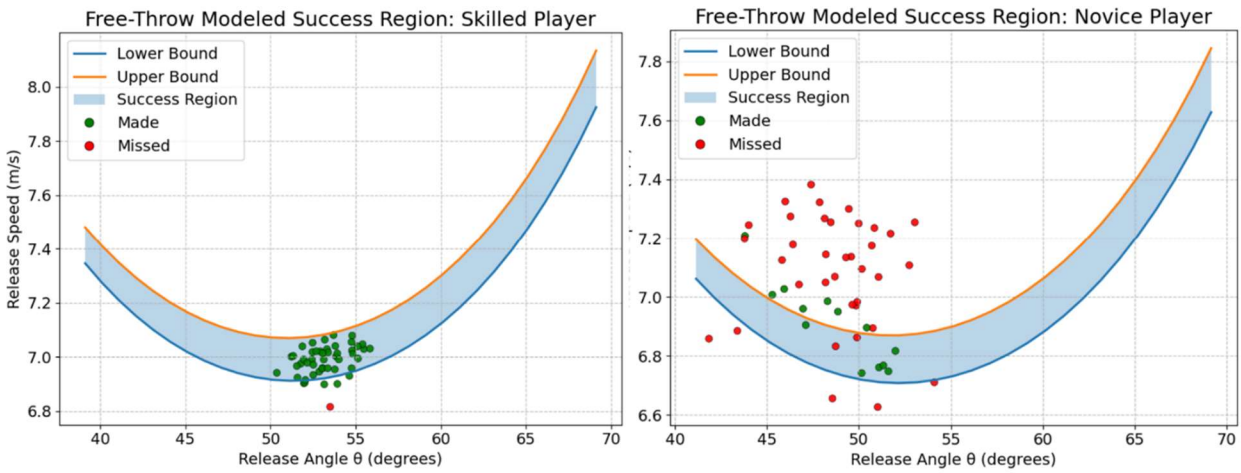


Figure 1. **Skilled shooters release the ball near their minimum possible speed.** Model-based estimation of each player's optimal success region represented by upper and lower bounds of the angle–speed combinations of a successful free throw with actual shot data of made (green) and missed (red) shots. Skilled shooters (left) exhibit the minimum-velocity strategy, demonstrating high accuracy, low variability, and repeated selection of their individualized minimal release speed. Novice shooters (right) exhibit poor minimum-velocity strategy (reduced accuracy, greater variability, and higher-than-necessary release speeds).

References (Optional)

[1] Nakano et al. , *Hum Mov Sci,* 2020

Session Category

Human Motion and Performance: Sports

OA69-01

Integrating In-Silico and In-Vitro Approaches to Elucidate the Role of Flow-Induced Vascular Wall Vibrations in Arteriovenous Fistula Failure

Dr. Luca Soliveri[1], Ms. Elena Carrara[2], Ms. Sofia Poloni[1], Dr. Kristian Valen-Sendstad[3], Dr. Anna Caroli[2], Prof. Andrea Remuzzi[1], Dr. Chiara Emma Campiglio[1], Dr. Michela Bozzetto[2]

[1]University of Bergamo, Dalmine, Bergamo, Italy. [2]Mario Negri Institute for Pharmacological Research IRCCS, Bergamo, Bergamo, Italy. [3]Simula Research Laboratory, Oslo, Oslo, Norway

Introduction

The arteriovenous fistula (AVF) is the preferred vascular access for hemodialysis, but 40% fail within 1 year due to stenosis. We have recently shown that turbulent-like flow induces AVF wall vibrations, and we observed in a case study that elevated vibration amplitude localized in the venous segment where stenosis subsequently manifested [1]. The aim of this investigation was to computationally identify relevant vibration frequencies and amplitudes associated with vascular remodeling and then experimentally investigate how such mechanical stimuli affect human umbilical vein endothelial cells (HUVECs) and aortic smooth muscle cells (HASMCs) behavior.

Methods

We monitored with magnetic resonance images and Doppler ultrasound 6 patients within 1 year after AVF creation. We performed high-fidelity fluid-structure interaction (FSI) simulations [2] in patient-specific AVF models and analyzed the frequency content of the vascular wall vibrations to identify relevant frequency bands related to AVF failure. Then, we exposed HUVECs and HASMCs to vertical vibrations at frequencies computationally determined from patients who developed stenosis, for 1 and 24 hours, with static cultures serving as controls. Cell viability was assessed by LDH assay. Proliferation, adhesion, mechanotransduction, and endothelial activation were evaluated by immunofluorescence, quantifying Ki67-positive cells, VE-cadherin and paxillin distribution, YAP localization and ICAM-1 expression. The effect of conditioned medium from vibration-exposed HUVECs on HASMC proliferation was examined through Ki67 quantification.

Results

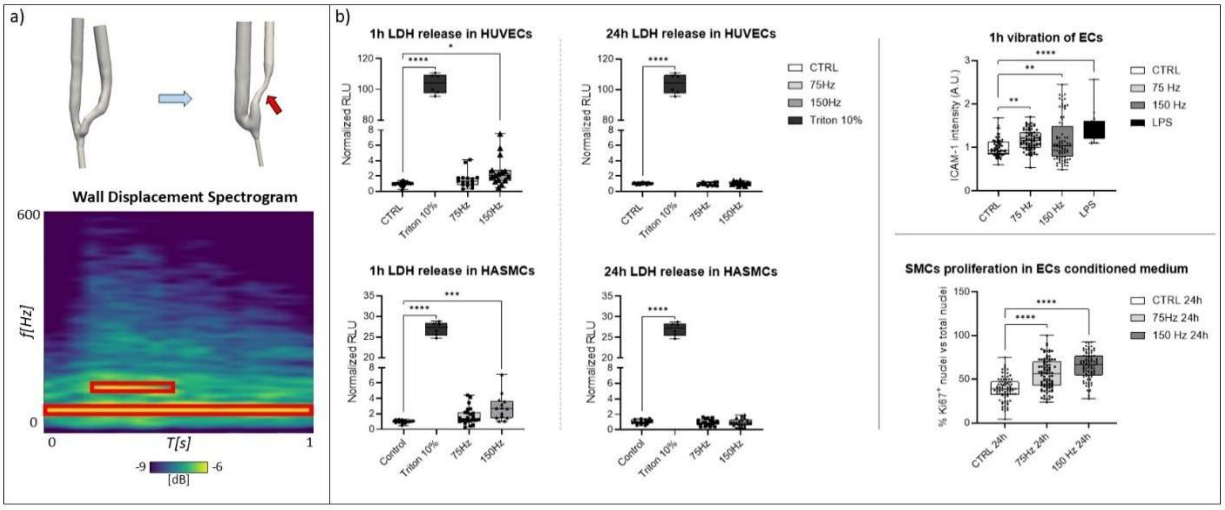
FSI results revealed the presence of relevant frequency bands around 75-150 Hz in the patients who later developed stenosis (Figure 1a). Mechanical vibrations at these

frequencies induced transient membrane perturbations without long-term cytotoxicity and promoted HASMC proliferation. VE-cadherin (HUVECs) and paxillin (HASMCs) distribution shifted toward patterns associated with greater cell motility. HUVECs showed mild YAP activation and increased ICAM-1, indicating mechanotransduction pathways and endothelial activation. Conditioned medium from vibration-exposed HUVECs enhanced HASMC proliferation, revealing a paracrine endothelial contribution to smooth muscle cell responses (Figure 1b).

Discussion

These findings suggest that flow-induced vibrations modulate vascular cell behavior through multiple mechanobiological mechanisms that may contribute to vascular remodeling. Integrating in-silico and in-vitro approaches can elucidate these mechanisms and allow the identification of new therapeutic targets.

Images (Optional)



References (Optional)

[1] Soliveri et al., Kidney Medicine, 2025

[2] Yamamoto et al., Softwarex, 2025

Session Category

Cardiovascular/Cardiorespiratory Biomechanics: Methods, Models and Applications

OA69-02

Relationship Between Wall Shear Stress and Coronary Computed Tomography Angiography-Derived Features in Diseased Coronary Arteries

Dr. Maurizio Lodi Rizzini PhD[1], Dr. Marco Stefanati PhD[2], Prof. Diego Gallo PhD[1], Prof. Claudio Chiastra PhD[1], Mr. Marco Stimolo MSc[1], Prof. Fabrizio D'Ascenzo MD, PhD[3], Prof. Stefano Salizzoni MD, Phd[3], Prof. José Félix Rodríguez Matas PhD[2], Prof. Umberto Morbiducci PhD[1]

[1]Politecnico di Torino, Torino, Piemonte, Italy. [2]Politecnico di Milano, Milano, Lombardia, Italy. [3]Città della Salute e della Scienza di Torino, Torino, Piemonte, Italy

Introduction

Coronary computed tomography angiography (CCTA) allows non-invasive evaluation of both anatomical stenosis severity and plaque morphology, including features of plaque vulnerability [1]. Additionally, CCTA enables accurate 3D reconstruction of the coronary lumen, facilitating quantification of wall shear stress (WSS) via computational fluid dynamics (CFD). WSS is a key mediator of hemodynamic stimuli on endothelial biopathways and has been associated with adverse clinical events [2].

This study investigated the relationship between CCTA-derived morphological features and WSS in coronary atherosclerotic plaques, with the aim of refining plaque vulnerability assessment.

Methods

The study included 14 patients (16 coronary arteries) who underwent CCTA. Lumen reconstruction and plaque characterization were performed using the QAngioCT Research Edition software (Medis Medical Imaging). Morphological metrics were extracted at (i) lesion volumetric level, and (ii) cross-sectional site of maximal obstruction. Transient CFD simulations were performed using the finite volume method [2]. Hemodynamics were characterized by Time-Averaged WSS (TAWSS) and the Topological Shear Variation Index (TSVI) [2]. Hemodynamic quantities were spatially averaged over each lesion surface, and associations with morphological features were evaluated.

Results

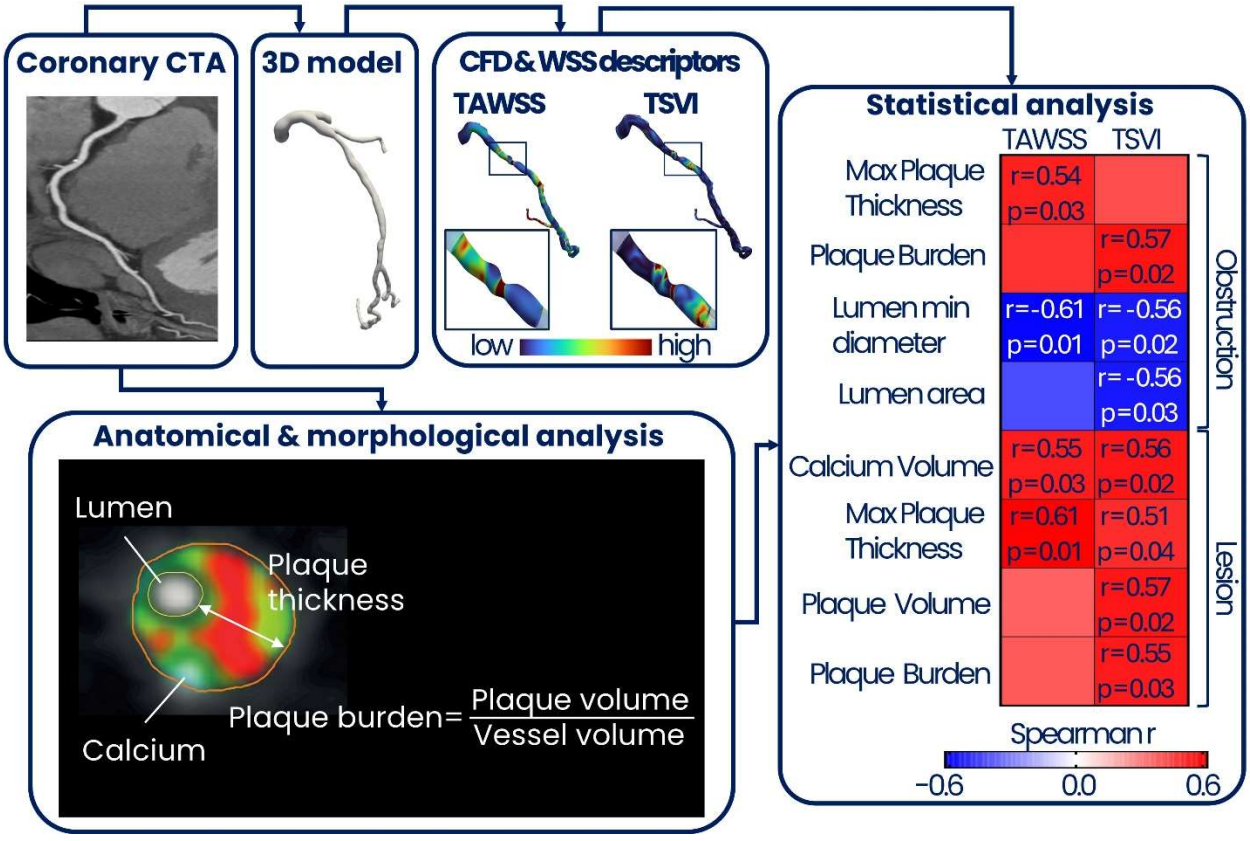
At the lesion level, both TAWSS and TSVI were positively correlated with calcium volume (TAWSS: $r=0.55$, $p=0.03$; TSVI: $r=0.56$, $p=0.02$) and maximum plaque thickness (TAWSS: $r=0.61$, $p=0.01$; TSVI: $r=0.51$, $p=0.04$). Only TSVI showed significant correlations with

plaque volume (r=0.57, p=0.02) and plaque burden (r=0.55, p=0.03). At the site of maximal obstruction, both TAWSS and TSVI were inversely correlated with lumen minimum diameter (TAWSS: r=-0.61, p=0.01; TSVI: r=-0.56, p=0.02). TAWSS alone was correlated with maximum plaque thickness (r=0.54, p=0.03), whereas TSVI alone was correlated with lumen area (r=-0.56, p=0.03) and plaque burden (r=0.57, p=0.02).

Discussion

These findings suggest a mechanistic link between plaque morphology and local hemodynamics. While TAWSS predominantly reflects stenosis severity, TSVI demonstrates additional sensitivity to overall plaque burden, suggesting that WSS topological dynamics reflect global plaque characteristics more comprehensively than WSS magnitude alone. The integration of CCTA-derived morphological features with advanced hemodynamic descriptors may provide a more comprehensive plaque vulnerability profile and ultimately enhance risk stratification.

Images (Optional)



References (Optional)

[1] Pál Maurovich-Horvat *et al.*, Nat. Rev. Cardiol., 2014.

[2] Alessandro Candreva *et al.*, Atherosclerosis, 2022.

Acknowledgements (Optional)

Marco Stefanati, Fabrizio D'Ascenzo, Stefano Salizzoni, José Félix Rodríguez Matas, and Umberto Morbiducci, acknowledge financial support provided by the Italian Ministry of University and Research (PRIN 2022, grant 2022ZKEP8S).

Session Category

Cardiovascular/Cardiorespiratory Biomechanics: Methods, Models and Applications

OA69-03

Large-Scale Studies to Investigate the Prognostic Utility of Computational Hemodynamics in Coronary Artery Disease

Dr Diego Gallo[1], Dr Alessandro Candreva[2], Dr Maurizio Lodi Rizzini[3], Dr Claudio Chiastra[1], Dr Gianluca Campo[4], Dr Simone Biscaglia[4], Dr Bernard De Bruyne[5], Dr Carlos Collet[6], Prof Umberto Morbiducci[1]

[1]Politecnico di Torino, Torino, TO, Italy. [2]Zurich University Hospital, Zurich, CH, Switzerland. [3]Politecnico di Torino, Torino, T, Italy. [4]University of Ferrara, Ferrara, FE, Italy. [5]Cardiovascular Center Aalst, Aalst, BE, Belgium. [6]Cardiovascular Research Foundation, New York, NY, United States

Introduction

Recent trials have demonstrated the prognostic value of hemodynamics-based assessment of coronary atherosclerosis to determine the risk of future adverse events. However, such assessment is mostly limited to the evaluation of the pressure drop across luminal narrowing [1]. Here, we tested whether wall shear stress (WSS)-based quantities obtained from personalized in silico hemodynamic models provide additional prognostic information in the largest patient cohorts to date.

Methods

Two patient populations from recent randomized clinical trials were analyzed. From the FIRE trial [2], 335 patients who experienced myocardial infarction (MI) and had one lesion non-culprit for MI were included. A second cohort of 331 patients from the FAME2 trial [1] consisted of patients with stable coronary artery disease treated with medical therapy. FIRE patients had 1-year follow-up, whereas FAME2 patients had follow-up at 3, 5, and 10-years.

Personalized computational fluid dynamics (CFD) simulations were performed in angiography-reconstructed geometries. Lesion-level descriptors included the time-average WSS magnitude (TAWSS) and the topological shear variation index (TSVI), which quantifies the variability of the contraction/expansion action exerted by WSS on the endothelium along the cardiac cycle [2].

Outcome events included MI, death, or revascularization. For each cohort, Cox proportional-hazard models were fitted to estimate hazard ratios (HRs).

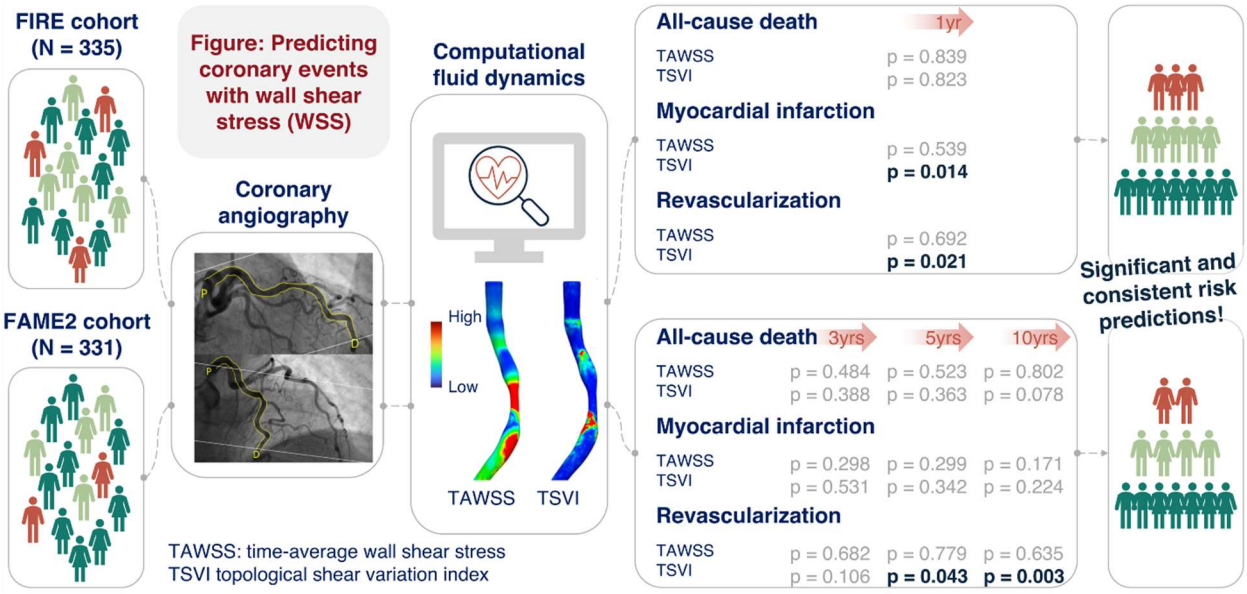
Results

In the FIRE cohort, higher lesion TSVI was associated with a higher risk of future MI (HR 1.01, p=0.014), and revascularization (HR 1.06, p=0.021). In the FAME2 cohort, TSVI predicted revascularization at 5 and 10 years (HR 1.03, p=0.043; HR 1.02, p=0.003, respectively), but not at 3 years (HR 1.02, p=0.106). TAWSS did not predict events in either cohort (Figure).

Discussion

The results confirm and expand the utility of WSS characteristics captured by TSVI for assessing the propensity of coronary lesions to cause acute events. The observed associations in acute (FIRE) versus stable (FAME2) patients suggest distinct mechanisms of action of hostile WSS conditions, with short-term effects in acute MI settings and longer-term effects in stable coronary artery disease.

Images (Optional)



References (Optional)

[1] Panagiotis Xaplanteris *et al.*, N Engl J Med, 2018

[2] Alessandro Candreva *et al.*, Atherosclerosis, 2025

Session Category

Cardiovascular/Cardiorespiratory Biomechanics: Methods, Models and Applications

OA69-04

Computational Analysis of Posture-Dependent Cerebrovascular Hemodynamics Using a Multiscale Model with Vascular Autoregulation

Mr. Youngjae Choi[1], Prof. Hyun Jin Kim[1], Mr. Chang Min Lee[1], Prof. Hyeyeon Chang[2], Prof. Keun-Hwa Jung[3]

[1]Korea Advanced Institute of Science and Technology, Daejeon, Daejeon, Korea, Republic of. [2]Konyang University Hospital, Daejeon, Daejeon, Korea, Republic of. [3]Seoul National University Hospital, Seoul, Seoul, Korea, Republic of

Introduction

Cerebral blood flow (CBF) is tightly regulated through autoregulatory mechanisms that counteract changes in arterial pressure and gravitational loading. Although several modeling studies have examined cerebrovascular responses to pressure or posture changes, most have focused on localized vascular regions rather than the integrated system. This study quantifies the effects of aortic pressure and posture on cerebrovascular hemodynamics using a multiscale blood flow model comprising arterial, venous, and microvascular domains with embedded autoregulation.

Methods

Arterial, venous, and tissue domains were segmented from brain imaging, and the microvasculature was extended to precapillary and postcapillary levels via a synthetic vascular tree generation algorithm. One-dimensional blood flow equations were solved in the extended vasculature, while capillary flow was modeled as Darcy flow by treating brain tissue as a porous medium. Explicit coupling ensured mass conservation across domains. Vessel wall mechanics was represented using a hyperelastic tube law, and active autoregulation was implemented by modulating arteriolar radius in response to local metabolic demand. Simulations were conducted for aortic pressures ranging from 30 to 150 mmHg and under supine, upright, and inverted postures, with wall stiffness varied to assess the impact of vascular compliance.

Results

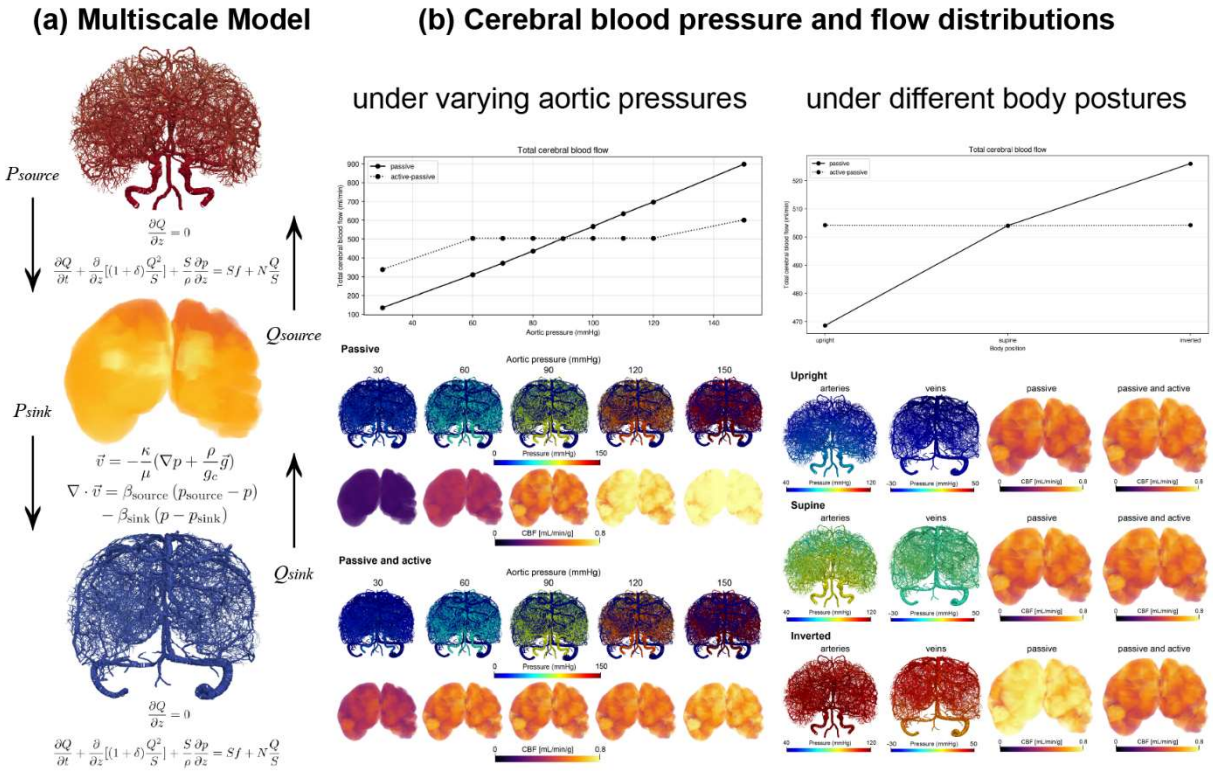
Without active regulation, total CBF increased nearly linearly with aortic pressure, while the inclusion of autoregulation maintained CBF within a physiological pressure range. Posture changes produced CBF differences in the passive model due to hydrostatic effects; however, the full autoregulatory model preserved near-constant perfusion across

postures. Arterial volume increased with aortic pressure, whereas venous volume was relatively insensitive to pressure but varied with posture. Increased vessel compliance amplified posture-induced variations in venous volume and arteriolar radius, while stiffer vessels dampened these responses.

Discussion

The proposed multiscale cerebrovascular model, integrating passive mechanics and arteriolar autoregulation, demonstrates how cerebral perfusion is maintained across a wide range of arterial pressures and postures. Arteries deform passively in response to pressure, while arterioles serve as the primary regulators of CBF. The venous system functions as a reservoir containing a substantial fraction of intracranial vascular volume. This framework provides a physiologically grounded tool for studying how altered vessel compliance or impaired autoregulation may impact cerebrovascular hemodynamics in health and disease.

Images (Optional)



References (Optional)

Acknowledgements (Optional)

This work was supported by the National Research Foundation of Korea (NRF) grant funded by the Korea government (RS-2022-NR070832), Ministry of Food and Drug Safety (RS-2023-00215667), Ministry of Health and Welfare (RS-2024-00512384), and Samsung Research Funding and Incubation Center for Future Technology (SRFC-IT2401-04).

Session Category

Cardiovascular/Cardiorespiratory Biomechanics: Methods, Models and Applications

OA70-01

Muscle Contributions to the Hip and Knee Articular Contact Forces in Highly Functional Unilateral Transtibial Amputees During Gait

Mr Bryan Rivera Calagua[1], Dr. Anthony M. J. Bull[2], Dr. Pouya Amiri[1]

[1]Queen's University, Kingston, Ontario, Canada. [2]Imperial College London, London, London, United Kingdom

Introduction

Unilateral transtibial amputees (UTAs) adopt compensatory strategies in the intact limb, increasing joint loading and the risk of knee and hip osteoarthritis [1]. Since muscles are the primary contributors to joint loading [2], understanding how muscle forces influence joint contact forces may support improved prosthetic designs. This study investigated muscle contributions to hip and knee joint contact forces in highly functional UTAs compared to non-amputees using musculoskeletal modeling.

Methods

Gait data were collected from 12 UTAs (32.9 ± 3.2 years; BMI 26.6 ± 2.6 kg/m^2) and 10 controls (32.1 ± 4.6 years; BMI 25.3 ± 3.8 kg/m^2) using 10 optical cameras and force plates. Musculoskeletal simulations were performed in OpenSim 4.4 using the Rajagopal model for controls and a modified version for UTAs [3]. Static optimization estimated muscle forces and hip and knee joint contact forces. Statistical parametric mapping (SPM1D) compared the control, intact, and amputated limbs using parametric or non-parametric ANOVA with post-hoc tests.

Results

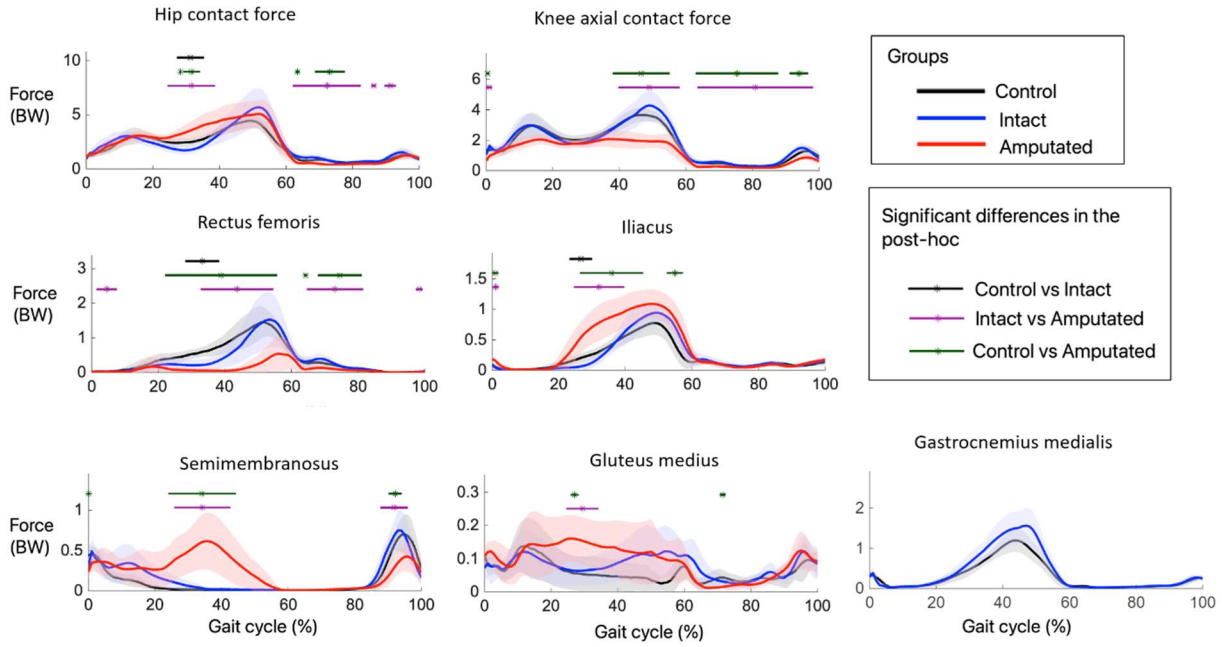
The figure shows the joint contact forces, muscle forces, and significant differences. Hip contact forces differed during mid-stance: the intact limb showed the lowest forces, the control limb intermediate forces, and the amputated limb the highest. Increased iliopsoas, gluteus medius, and hamstring forces in the amputated limb may contribute to this higher loading. For knee contact forces, the amputated limb exhibited the lowest forces during late stance, likely due to the absence of gastrocnemius force generation.

Discussion

Amputees walked with higher mid-stance hip contact forces on the amputated side, associated with increased hip flexor and abductor forces. However, unlike previous work [4], we did not observe elevated intact-limb knee contact forces, potentially because gastrocnemius forces did not differ from controls. Hip contact forces appeared elevated

overall, consistent with known overestimation of muscle forces in the Rajagopal model [5]. Future work will focus on modifying the model to bring hip contact forces within physiological bounds.

Images (Optional)



References (Optional)

[1] Struyf et al., Arch Phys Med Rehabil, 2009.

[2] Erdemir et al., Clin Biomech, 2007.

[3] Willson et al., Comput Methods Biomech Biomed Engin, 2023.

[4] Ding et al., J Orthop Res, 2021.

[5] Uhlrich et al., Sci Rep, 2022.

Session Category

Musculoskeletal Biomechanics: Methods, Models and Applications

OA70-02

Modeling the Infant Head-Neck Complex to Investigate Positional Asphyxia Risk in Inclined Environments

Graduate Assistant Andrew Bossert BS, Mechanical Engineering[1], Associate Professor of Orthopedic Surgery Dennis Anderson PhD, Engineering Mechanics[2], Associate Professor Clare Fitzpatrick PhD, Mechanical Engineering[1], Associate Professor Erin Manned PhD, Mechanical Engineering[1]

[1]Boise State University, Boise, ID, United States. [2]Beth Israel Deaconess Medical Center, Boston, MA, United States

Introduction

Of the 3600 sudden infant death cases in the United States each year, nearly 1/3 are from asphyxia [1]. Chin-to-chest positioning increases risk of asphyxia, and an infant's ability to achieve and self-correct from this posture in common inclined environments is poorly understood. It's unethical to expose living infants to dangerous experiments; thus, robust computational models are critical to elucidate mechanics of positional asphyxia. This study created a novel infant model to understand risks of chin-to-chest postures.

Methods

Experimental data (neck kinematics, head ground reaction force) were generated using a physical surrogate of an infant allowing neck flexion-extension. At body incline angles of 0°, 15°, 30°, and 45°-representing incline angles of common infant products- starting from a chin-to-chest position, the neck was extended to contact the force plate, and then flexed to return to the chin-to-chest position. An OpenSim cervical-musculoskeletal model [2] was adapted into a novel infant model to simulate the experimental setup. Muscle forces to flex and extend the neck at each inclination angle were predicted from static optimization. Grouped neck flexor and extensor muscle forces were analyzed.

Results

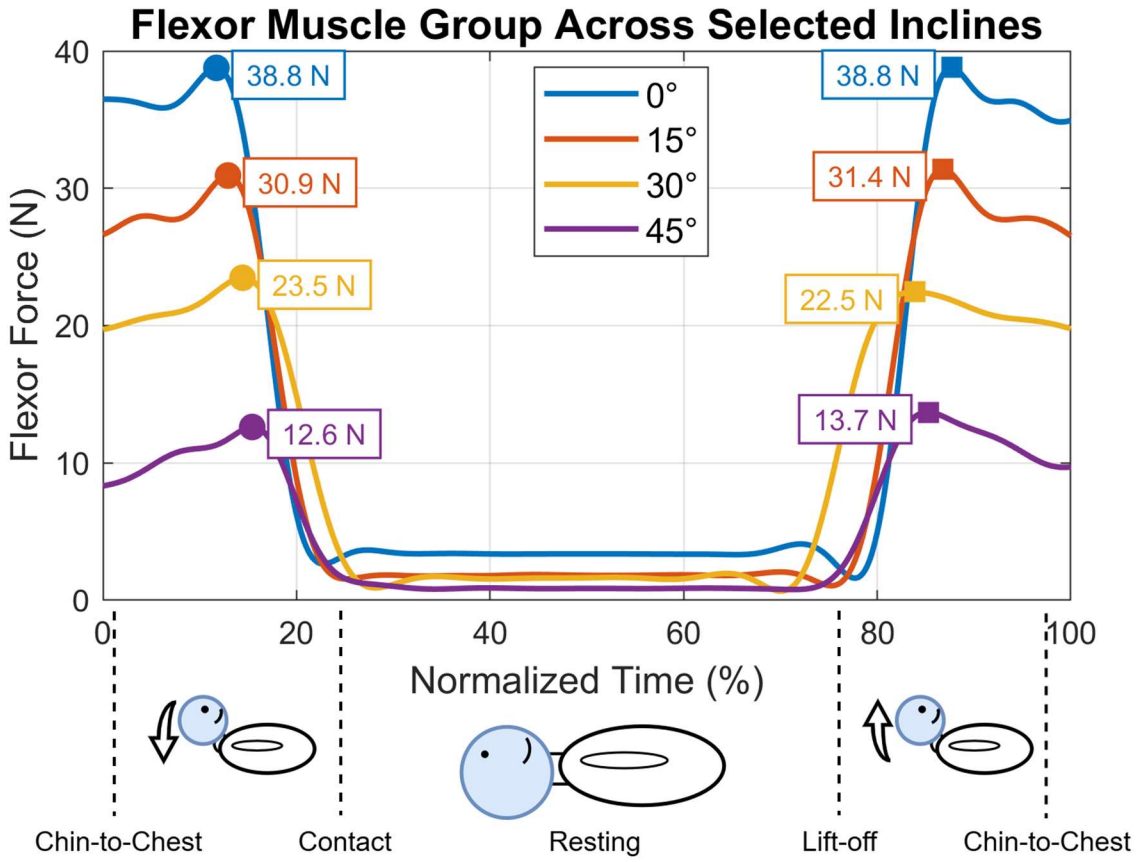
As incline angle increased, peak force necessary to lift the head decreased in sinusoidal proportion. Figure 1 shows peak forces prior to the head contacting the platform, coming to rest, and peak forces to lift the head from the platform. At 45° body incline, 65.7% less force was required to lift the head off the platform compared to 0°.

Discussion

The lower force required to achieve chin-to-chest posture at greater body inclines demonstrates an inherent vulnerability for infants to assume positions associated with

elevated asphyxia risk. Notably, many infant products currently on the market feature back-rest incline angles between 15-45°, placing infants in situations where chin-to-chest postures are more easily achieved. Our computational model provides a framework for comparing how positional changes contribute to asphyxia risk across product designs. Future work incorporating EMG measurements to validate muscle activation patterns may further clarify the relative muscle forces involved in chin-to-chest motion, ultimately informing design features that prioritize infant safety.

Images (Optional)



References (Optional)

[1] Shapiro-Mendoza et al., *Pediatrics,* 2023
[2] Mortensen et al., *PloS-One*, 2018

Acknowledgements (Optional)

This research is supported by the National Institutes of Health, Eunice Kennedy Shriver National Institute of Child Health and Human Development, NIH Grant No. 1R01HD113921.

Session Category

Musculoskeletal Biomechanics: Methods, Models and Applications

OA70-03

The Development and Implementation of a Computational Framework to Simulate Patellofemoral Joint Mechanics: Direct Comparisons Between Musculoskeletal Modeling and Finite Element Analysis

Mr. Mahmood Rashedi[1], Dr. Mark Seeley[2], Dr. Brecca Gaffney[3], Dr. Benjamin Wheatley[1]

[1]Bucknell University, Lewisburg, Pennsylvania, United States. [2]Geisinger, Danville, Pennsylvania, United States. [3]University of Colorado Denver, Denver, Colorado, United States

Introduction

Anterior knee pain occurs in nearly 25% of adults and is linked to altered patellofemoral joint (PFJ) mechanics. PFJ modeling varies widely, with no clear gold standard. Simplified muscle-driven musculoskeletal models estimate joint kinetics but lack relevant tissue-level mechanics. Finite Element (FE) models overcome this limitation by solving for cartilage contact mechanics, but at a higher computational cost. This project establishes a workflow to test the correlation between musculoskeletal-predicted joint loads and FE-predicted cartilage contact pressure in a healthy individual.

Methods

Marker-based motion capture was performed during squatting on one adult male using a 12-camera VICON system and AMTI force plates (Figure 1A). Optimal control and a Rajagopal Opensim model with polynomial-based patellar kinematics were used to generate kinetics and patellofemoral joint reaction force (PFJRF) (Figure 1B). A left PFJ FE model was built in Abaqus using OpenKnee (OKS009), with rigid bones, neo-Hookean cartilage, and ligament/tendon springs. Tibiofemoral kinematics were applied via cylindrical joints in addition to muscle forces computed from musculoskeletal simulations (Figure 1C).

Results

Musculoskeletal-predicted PFJRF reached 6.47×BW at 100° flexion (Figure 1E). FE model results, reported as the mean of the top 5% patellar cartilage contact hydrostatic pressure, reached 12.90 MPa at 100° flexion. PFJRF and FE-predicted patellar cartilage pressure increased with knee flexion (R^2=0.92, Figure 1F), and deeper squats produced larger contact areas, with greater loading on the lateral facet (Figure 1D).

Discussion

This study developed a workflow integrating musculoskeletal and FE modeling to compare PFJ mechanics. Results supported our hypothesis: higher musculoskeletal-predicted PFJRF corresponded to greater FE cartilage contact pressure. Muscle activation profiles, PFJRF values, and patellofemoral contact area distributions matched prior reports, providing key model validation. Ongoing work will increase sample size from n=1. This framework can be applied to pathological conditions such as muscle weakness, morphological abnormalities, and soft tissue laxity to better understand how different modeling approaches simulate patellofemoral mechanics.

Images (Optional)

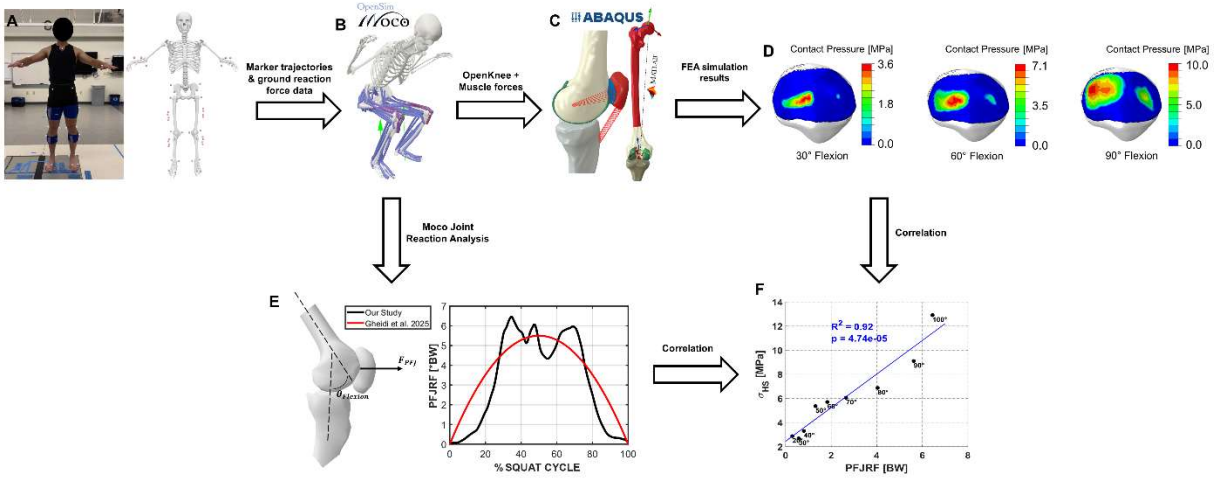


Figure 1. A) Motion analysis participant and marker set in a static pose. B) OpenSim Moco musculoskeletal simulation, with activated quadricep muscles shown in red. C) Finite element model of the patellofemoral joint developed in Abaqus using OpenKnee (OKS009) geometries, with aligned OpenSim and OpenKnee frames to ensure consistent quadriceps force vector definitions. D) Patellar cartilage contact pressure heat maps at 30°, 60°, and 90° of knee flexion during squatting (MPa) showing deeper squats produced larger contact areas, with greater loading on the lateral facet. E) Patellofemoral joint reaction force computed using Moco joint reaction analysis across the squat cycle, compared with Gheidi et al. (2025). F) Correlation between patellofemoral joint reaction force from the musculoskeletal model and the mean of the top 5% patellar cartilage contact pressure from the finite element model across knee flexion during squatting.

Session Category

Musculoskeletal Biomechanics: Methods, Models and Applications

OA70-04

Impact of Personalized Model Using the Opensim-Torsion Tool on Muscle Contribution for CG Acceleration Estimation in CP Children

Prof. António Veloso[1], Dr. Basílio Gonçalves[2], Dr. Filipa João[1], MSc Rodrigo Mateus[1], MSc Carolina Silva[1]

[1]Faculdade de Motricidade Humana, Cruz-Quebrada, Lisboa, Portugal. [2]University of Viena, Viena, Viena, Austria

Introduction

Children with cerebral palsy CP frequently present pathological gait patterns, with crouch gait CG being one of the most prevalent and severe. Musculoskeletal MSK modelling is commonly used to study CG, but generic models based on healthy adults overlook subject specific anatomy [1]. This limits their applicability to pathological gait. To address this, personalized MSK models have been developed, the OpenSims torsion tool offers a way to incorporate femoral and tibial torsions and improve personalization [1]. This study examined the impact of this tool on CG biomechanics and on induced acceleration (IAA) estimations of body center of mass (CM) in a child with spastic diplegic CP.

Methods

The participant was a 13 year old height 169.7 cm 60.6 kg GMFCS III who underwent clinical gait analysis one month before SEMLS. Kinematic and kinetic data were collected. Four OpenSim scaled MSK models were created a generic Gait2392 model, a personalized model based on clinical and radiographic torsion values, and two additional models incorporating upper and lower limits of agreement for femoral anteversion tibial torsion and femoral neck shaft angle. Muscle forces were estimated during single support and normalized to each muscles maximum isometric force. IAA analysis quantified muscle contributions to CM dynamics.

Results

Pre surgery antero-posterior center of mass contributions showed pronounced differences in the right leg. The generic model predicted higher soleus propulsion while models including torsional deformities showed reduced contribution. This shows that excessive tibial torsion diminishes the soleus ability to support and propel the body. After surgery differences between models decreased and by one and ten years post surgery model

outputs became similar indicating reduced influence of torsional deformities after correction.

Discussion

Torsion personalization strongly influenced muscle force predictions and center of mass accelerations particularly before surgery. Only the personalized model captured the expected improvement in soleus function after SEMLS. These findings support the need for subject specific MSK modelling for accurate assessment of crouch gait and surgical outcomes.

Images (Optional)

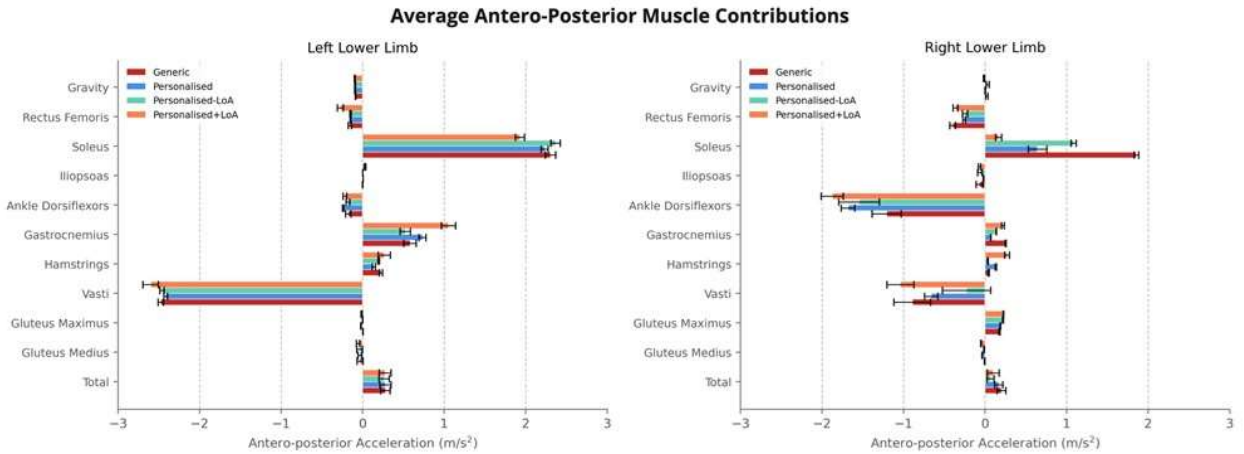


Figure 1 Pre-surgery avg muscle contributions to A-P CM acceleration for all four models. The total acceleration and contributions from gravity are also shown. Positive values indicate anterior acceleration, while negative values posterior acceleration.

References (Optional)

[1] K. Veerkamp, et all, J Biomech, vol. 125, 2021

Acknowledgements (Optional)

This study is supported by the project: https://doi.org/10.54499/PTDC/EMD-EMD/5804/2020, and project CIPER Doi 10.54499/UIDB/00447/2020 and 10.54499/UIDP/00447/2020.

Session Category

Musculoskeletal Biomechanics: Methods, Models and Applications

OA70-05

Automated Subject-Specific Modeling of 6 DoF Glenohumeral Kinematics

Dr. Eva C. Herbst[1,2], Dr. John E. Lloyd[3], Dr. Heath B. Henninger[4], Prof. Dr. med. Philipp Moroder[2], Professor Stephen J. Ferguson[1]

[1]ETH Zurich, Zurich, ZH, Switzerland. [2]Schulthess Klinik, Zurich, ZH, Switzerland. [3]University of British Columbia, Vancouver, Vancouver, Canada. [4]University of Utah, Salt Lake City, UT, United States

Introduction

Semi-constrained joints are typically used to reduce kinematic tracking error in inverse dynamic musculoskeletal simulations. However, the sub-mm accuracy of biplanar fluoroscopy data, coupled with subject-specific bone models from CT, can be used to kinematically validate subject-specific models that achieve joint constraint solely through realistic contact conditions and muscle activation. Our goal was to develop an automated method to generate subject-specific musculoskeletal models of the glenohumeral joint capable of replicating subject-specific kinematics.

Methods

Our pipeline automatically generates 6 DoF glenohumeral joint models in Artisynth, using a 3 DoF OpenSim template model [1]. Subject-specific bones directly replace template bones. The glenohumeral joint is modeled as contact between elastic bodies, with cartilage geometry automatically generated from glenoid and humeral anatomic neck boundaries, incorporating cartilage thickness variation (Fig. 1A). Large passive glenohumeral bounds were defined to test whether glenohumeral translations can be stabilized with muscular activity. Muscle parameters were based on per-muscle scaling without optimization algorithms and wrap objects and landmarks were deformed and transferred using affine and deformable transforms representing anatomical changes between template and target bones. Nineteen models were tested, with inverse simulation input tracking biplanar fluoroscopy kinematics during coronal abduction (Fig. 1B).

Results

Our method enables incorporation of subject-specific anatomy and kinematics, is entirely automated except for the selection of the glenoid and humeral anatomic neck boundaries, and solves common wrap object issues (e.g., muscle via points ending up inside wrap object, muscle wrapping around wrong side of wrap object). Thirteen of nineteen subjects achieved glenohumeral translations within a few mm of target values, i.e., not approaching the bounds of the glenoid (Fig. 1C).

Discussion

The majority of models were able to stabilize glenohumeral joint translations through muscular activity alone, mimicking the *in vivo* condition. The main advantage of our model is that the capacity for dislocation requires active recruitment of the rotator cuff for realistic muscle stabilization; dislocations (6/19 cases) indicate insufficiency of the template model or subject modeling pipeline. Future work will aim to resolve dislocations by testing the effect of the template model and muscle parameters and wrapping on kinematic tracking accuracy.

Images (Optional)

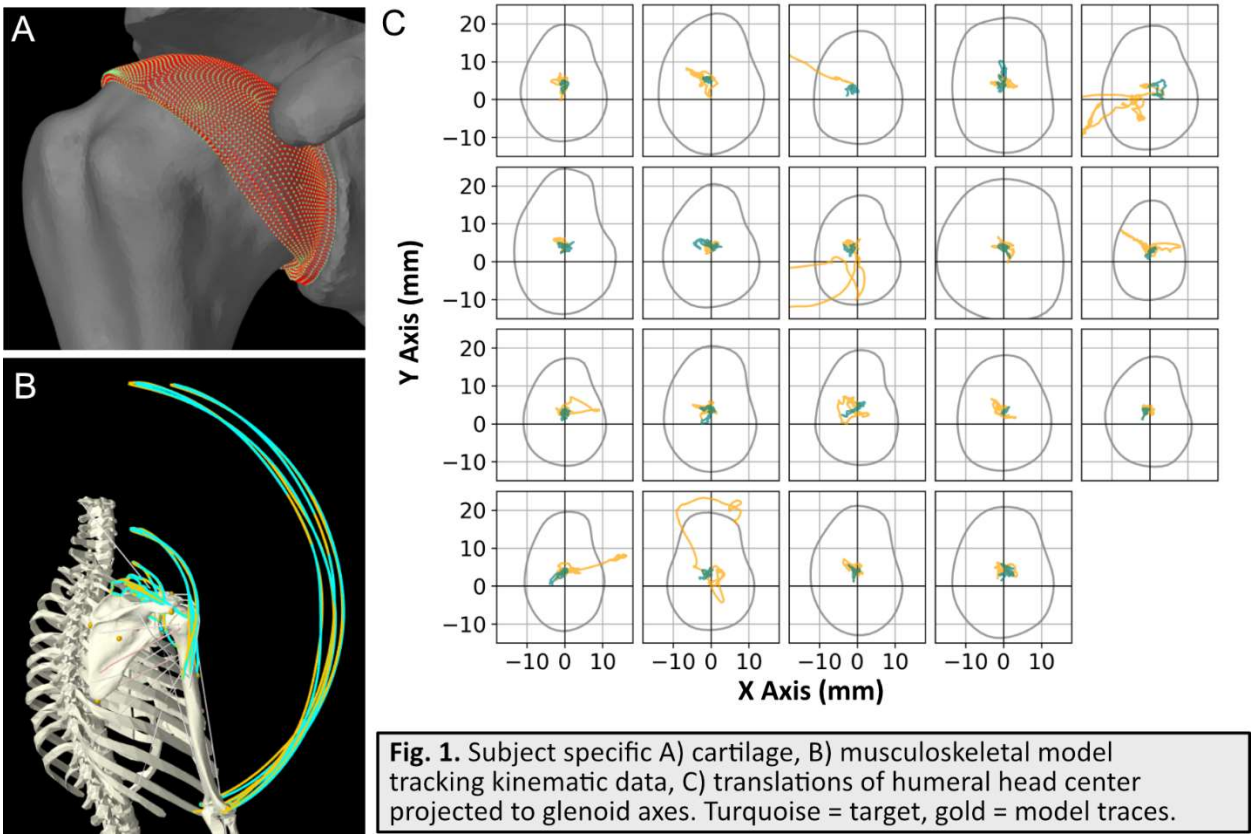


Fig. 1. Subject specific A) cartilage, B) musculoskeletal model tracking kinematic data, C) translations of humeral head center projected to glenoid axes. Turquoise = target, gold = model traces.

References (Optional)

[1] Seth *et al.*, Frontiers Neurorobotics, 2019

Acknowledgements (Optional)

We thank the Schwyzer Foundation for funding this research. We thank Liam Roth and Anna Luong for development of subject specific cartilage modeling algorithms, and Max Modelhart for selecting glenoid and humeral neck boundaries as inputs for the model.

Session Category

Musculoskeletal Biomechanics: Methods, Models and Applications

OA70-06

Design of Patient-specific High Tibial Osteotomy Surgery using Predictive Simulations of Walking

Prof. Benjamin Fregly Ph.D., Mr. Spencer Williams B.S.

Rice University, Houston, TX, United States

Introduction

High tibial osteotomy (HTO) is a useful yet oftentimes unreliable surgery for medial knee osteoarthritis. By cutting the tibia and angling it outward, surgeons make a bow-legged (varus) individual knock-kneed (valgus), thereby shifting some tibiofemoral contact force from the diseased medial to the healthy lateral side of the knee. Reducing the peak knee adduction moment to approximately 2.5% BWxHt during post-surgery walking produces the best long-term clinical outcome. However, for any patient, surgeons currently have no way of predicting the amount of tibial valgus correction needed to achieve this post-surgery functional target. The objective of this study was to investigate whether patient-specific predictive simulations of post-surgery walking can be used to perform such predictions.

Methods

Experimental walking data collected from a subject with bilateral medial knee osteoarthritis were used in the Neuromusculoskeletal Modeling Pipeline [1] with OpenSim [2] to 1) create a personalized full-body skeletal model of the subject, 2) generate a dynamically consistent walking simulation that closely tracked experimental data, 3) perform virtual HTO surgeries on both tibias of the model using valgus corrections of 3, 6, and 9°, 4) perform predictive walking simulations to determine corresponding values of post-surgery peak knee adduction moments, 5) estimate optimal amount of valgus correction for each tibia via quadratic fit, and 6) perform a final predictive walking simulation using optimal valgus correction values to verify final post-surgery peak knee adduction moments of 2.5% BWxHt.

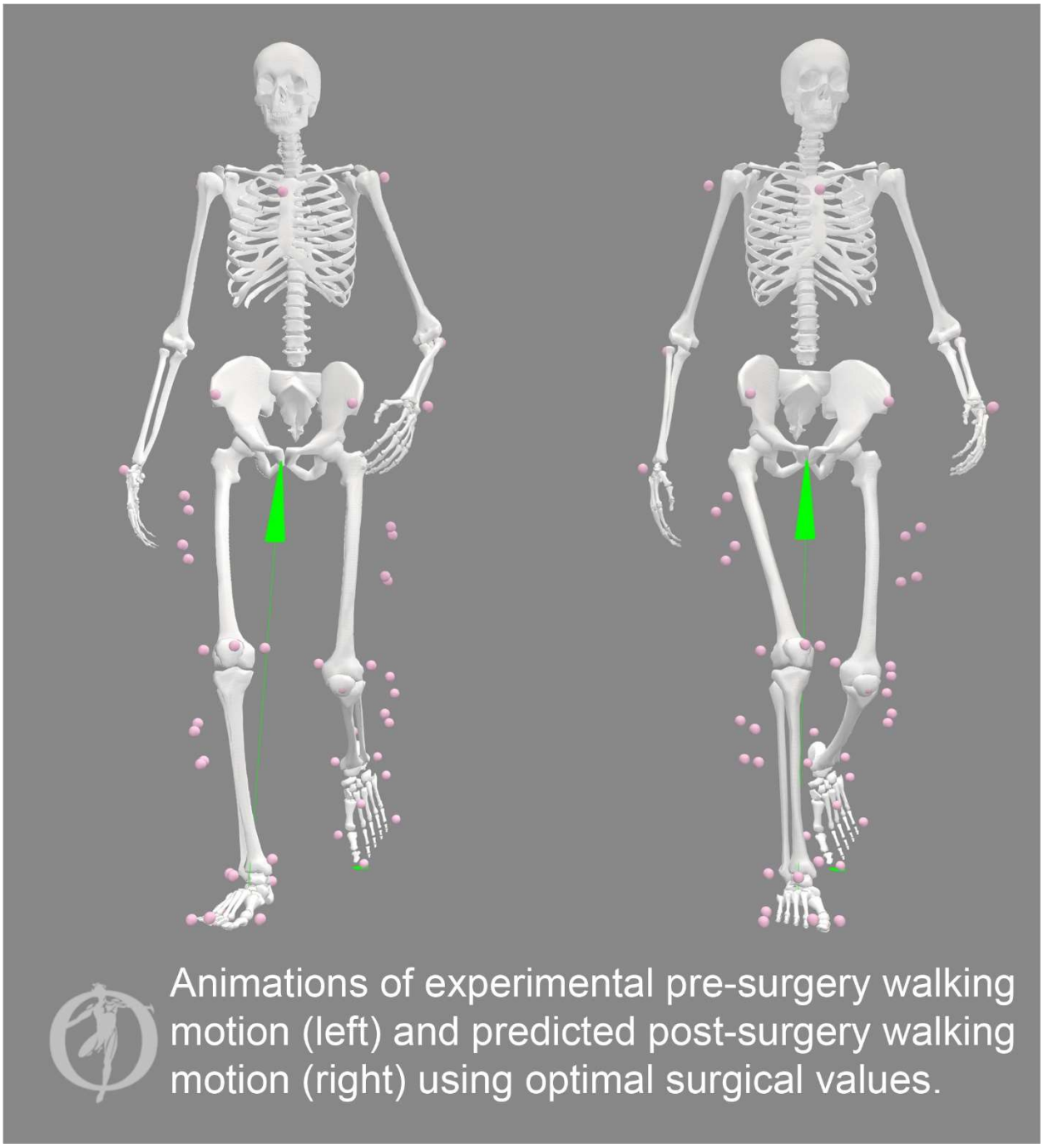
Results

Patient-specific predictive simulations of post-surgery walking yielded a near-linear relationship between amount of tibial valgus correction and value of post-surgery peak knee adduction moment. Using the optimal amounts of correction (5.5 and 6.5° for the right and left tibia, respectively), a final predictive simulation produced a peak adduction moment of 2.5% BWxHt for each knee as desired.

Discussion

HTO surgeries are currently planned using a target value of post-surgery *static knee alignment*. In contrast, this study demonstrates that patient-specific predictive simulations of post-surgery walking could potentially be used to plan HTO surgeries using a target value of post-surgery *dynamic knee loading*.

Images (Optional)



References (Optional)

[1] C. Hammond *et al*., J. NeuroEng. Rehab., 2025.

[2] A. Seth *et al*., PLoS Comput. Biol., 2018.

Acknowledgements (Optional)

NIH R01EB030520

Session Category

Musculoskeletal Biomechanics: Methods, Models and Applications

OA71-02

Spatially-Resolved Multiscale Mechanics of the Mouse Achilles Tendon Enthesis Unveiled by *in Situ* X-Ray Scattering

Dr. Isabella Silva Barreto[1], Dr. Claire Camy[2], Mr. Moritz L. Stammer[1], Dr. Moritz P.K. Frewein[1], Dr. Juraj Todt[3], Dr. Michael Meindlhumer[3], Dr. Jozef Keckes[3], Dr. Stefano Checchia[4], Dr. Sandrine Roffino[2], Dr. Martine Pithioux[2,5], Dr. Tilman A. Grünewald[1]

[1]Aix-Marseille Univ, CNRS, Centrale Med, Institut Fresnel, Marseille, Provence-Alpes-Côte d'Azur, France. [2]Aix-Marseille Univ, ISM, Marseille, Provence-Alpes-Côte d'Azur, France. [3]Montanuniversität Leoben, Leoben, Styria, Austria. [4]European Synchrotron Radiation Facility, Grenoble, Auvergne-Rhône-Alpes, France. [5]Aix-Marseille Univ, AP-HM, Marseille, Provence-Alpes-Côte d'Azur, France

Introduction

The enthesis is the insertion site of tendon into bone. Its high durability stems from gradients in its collagen and mineral content, organization and structure on multiple hierarchical length scales [1]. However, its regeneration after injury is poor and surgical repair often fails. Despite extensive research into its structure and mechanics, the local deformation mechanisms are poorly understood. This study aims to characterize the spatially resolved multiscale mechanical response of the enthesis by combining *in situ* mechanical testing with scanning small- and wide-angle X-ray scattering.

Methods

Hindlimbs were dissected from 12 mice. Scattering measurements were performed at the European Synchrotron Radiation Facility. Samples were loaded *in situ* in steps of 200µm using a custom-built tensile loading device (Fig.1A). 2D maps including the calcaneal bone and Achilles tendon were collected at preload and displacement steps after relaxation (Fig1.B). Collagen fibril and molecule as well as mineral particle and crystal strains were extracted [2,3].

Results

At the tissue scale, displacement steps resulted in ~10% strain each. Nanoscale and molecular differences were observed between regions (Fig.1B-D). While mineral particles remained unchanged, collagen fibrils strained ~2%, with the region close to the enthesis exhibiting a stronger axial response than the Achilles tendon (Fig1.B-C). The tendon exhibited ~0.5% molecular strain but the region close to the enthesis remained unstrained

(Fig1.D). Minerals exhibited ~0.05% strain along their c-axis, with a stronger response close to the enthesis compared to the calcaneal bone.

Discussion

Decreasing strain was observed across the hierarchical structure with 10%, 2%, 0.5% and 0.05% strain in the tissue, nanoscale fibrils, collagen molecules and mineral crystals respectively, indicating a strong strain partitioning across length scales. Differences in both structure at preload as well as their mechanical response were observed depending on the proximity to the enthesis, indicating a regional heterogeneity in the activation of deformation mechanisms of different components. These findings support the notion of a tissue adopted to a complex and changing mechanical environment with an outstanding ability to dissipate energy through its hierarchical structure and tissue organization.

Images (Optional)

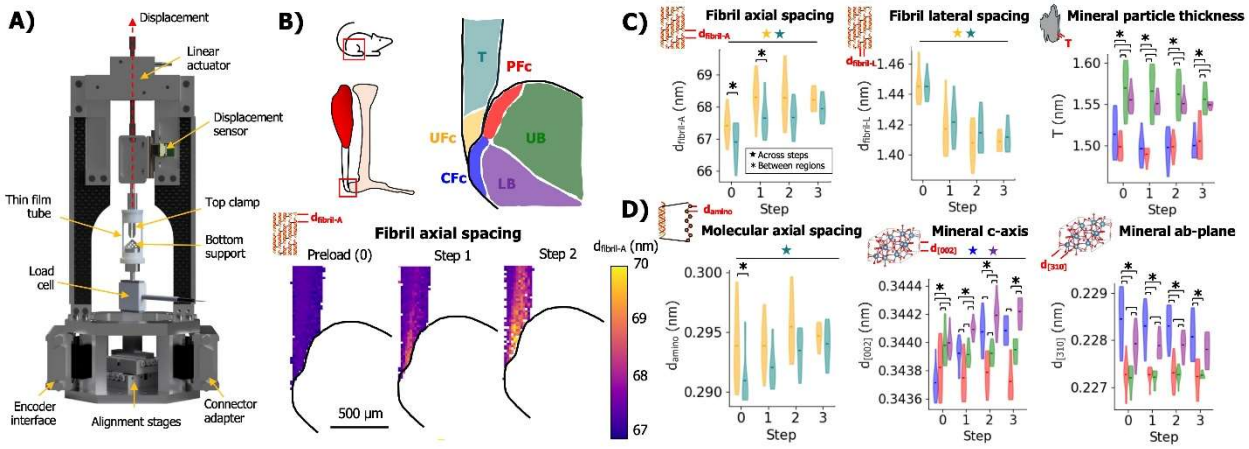


Figure 1. A) Design of *in situ* loading device. B) Illustration of investigated regions (T – tendon, UFc – uncalcified fibrocartilage, CFc – calcified fibrocartilage, PFc – periosteal fibrocartilage, LB – lower bone, UB – upper bone) and representative 2D map of collagen fibril axial d-spacing. C) Nanoscale and D) molecular scale response of collagen and mineral structures in different regions to strain steps.

References (Optional)

[1] Rossetti et al., *NatMater,* 2017 [2] Sharma et al., *ActaBiomat,* 2025, [3] Silva Barreto et al. *AdvSci,* 2020

Acknowledgements (Optional)

This project has received funding from the European Research Council (ERC) under the European Union's Horizon Europe research and innovation program (grant agreement No 101041871). We acknowledge the European Synchrotron Radiation Facility, Grenoble, France, for providing beamtime at the ID15A beamline under proposal LS3372, as well as their beamline staff.

Session Category

Organ and Tissue Biomechanics: N/A

OA71-03

Image-to-Mechanics Mapping of Bone via DECT-Quantified Composition: A Numerical Study

Professor Yunhua Luo Y.

University of Manitoba, Winnipeg, Manitoba, Canada

Introduction

Accurate characterization of bone mechanical behavior using imaging is critical for assessing bone quality, screening osteoporosis, and evaluating fracture risk. Clinical methods relying solely on bone mineral density are limited because bone is a composite of inorganic minerals (primarily hydroxyapatite), organic proteins (mainly type I collagen), and water, each influencing stiffness, strength, and toughness. We are developing a dual-energy CT (DECT)–based framework to quantify these three components and predict mechanical properties from their spatial distribution. This study presents preliminary numerical results demonstrating the feasibility of linking DECT images with mechanical performance.

Methods

A representative bone volume (RBV) with prescribed fractions of mineral, protein, and water was generated. Virtual DECT scanning was performed using MATLAB implementations of the Radon transform and filtered back-projection to simulate low- and high-energy CT acquisitions. Image noise, beam-hardening artefacts, and partial-volume effects were included to approximate realistic DECT conditions. Constitutive behavior for hydroxyapatite, collagen, and water was assigned using stress–strain data extracted from the literature. A finite element model of the RBV was then constructed, and uniaxial compression was simulated to obtain its apparent elastic modulus, strength, and toughness as functions of the underlying composition.

Results

The simulated DECT images captured distinct attenuation differences corresponding to variations in mineral, protein, and water fractions. Preliminary finite element results showed a monotonic increase in elasticity modulus with increasing mineral fraction and a pronounced reduction in strength when protein or water fractions were elevated, accompanied by a substantial improvement in toughness—a key parameter for mitigating fall-induced hip fractures. The mapping between DECT-derived voxel intensities and

mechanical outputs exhibited strong monotonic trends, demonstrating that variations in composition captured by DECT can be used to predict key mechanical properties within the generated dataset.

Discussion

These initial findings support the feasibility of predicting bone mechanical behavior directly from DECT-quantified composition. Ongoing work includes characterizing stress–strain data, particularly for collagen in human bone, validating the computational framework using experimental measurements, and developing regression and machine-learning models to generalize the image–mechanics relationship. The long-term goal is to establish a clinically viable DECT-based tool for voxel-wise assessment of bone strength.

References (Optional)

Session Category

Organ and Tissue Biomechanics: N/A

OA71-04

Unique Deformation Mechanisms in Teleost Intermuscular Bones

Dr Imke A. K. Fiedler[1,2], Dr Eric Schaible[3], Dr Boliang Yu[4], dr Murielle Salome[5], Dr Max Langer[4], Ms Svetlana Zeveleva[1], Dr James Rosenberg[6], Dr Cecile Olivier[4], Dr Robert Richie[7], Dr Tamara Alliston[8], Dr Francoise Peyrin[4], Dr Claire Acevedo[9], Dr Jean-Philippe Berteau[1]

[1]Department of Physical Therapy, Division of Science and Technology, College of Staten Island, City University of New York,, Staten Island, NY, United States. [2]Department of Osteology and Biomechanics, University Medical Center Hamburg-Eppendorf, Hamburg, Hamburg, Germany. [3]Lawrence Berkeley National Laboratory, Advanced Light Source, Berkeley, CA, United States. [4]INSA Lyon, Univ Claude Bernard Lyon 1, CNRS, Inserm, Creatis UMR 5220, Lyon, AURA, France. [5]ESRF, The European Synchrotron, Grenoble, AURA, France. [6]UNiversity of Utah, Salt Lake City, UT, United States. [7]Department of Materials Science and Engineering, University of California, Berkeley, CA, United States. [8]Department of Orthopaedic Surgery, University of California San Francisco, San Francisco, CA, United States. [9]Department of Mechanical and Aerospace Engineering, University of California, San Diego,, San Diego, CA, United States

Introduction

Intermuscular bones (IB) are exclusively found in the skeleton of bony fish. This specialized mineralized tissue, derived from ossified tendon, exhibits a unique combination of mechanical properties: strength comparable to mammalian bone and the capacity for large deformation typically associated with mammalian tendons. This unusual pairing of stiffness and extensibility challenges conventional assumptions about mineralized tissue behavior. To identify the factors underpinning the unique whole-bone mechanical behavior of IB, we extended our investigation to smaller length scales than previously examined. We hypothesized that their ability for large deformation is reflected at the level of mineralized collagen fibrils and associated with structural features at microscopic and sub-microscopic length scales.

Methods

To test our hypothesis, we analyzed mineral composition using thermogravimetric analysis (TGA), assessed tissue- and fibril-level mechanics using synchrotron small-angle X-ray scattering (SAXS) combined with in situ uniaxial tensile testing, and characterized micro- and sub-microstructural organization using synchrotron phase-contrast nano-computed

tomography (nanoCT). In total, 293 IB were collected from twenty freshly obtained Atlantic herring.

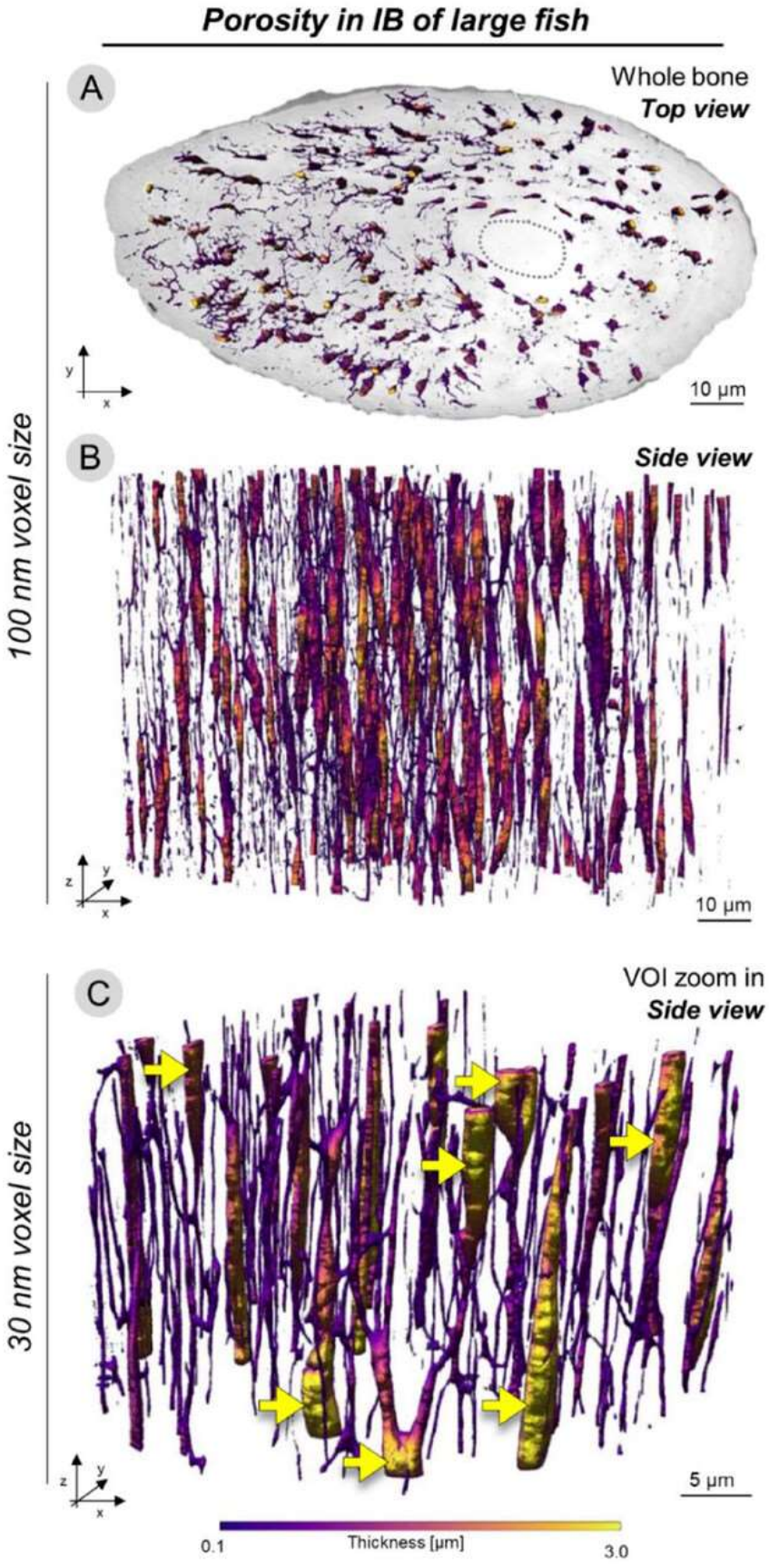
Results

IB from large fish exhibited a 50% higher strain-to-failure—reaching up to 4.5%—compared with IB from small fish ($p = 0.015$). The applied macroscopic strain was almost entirely transmitted to the collagen fibrils, indicating highly efficient fibrillar load transfer. Although IB from larger fish showed greater mineral maturity, their overall mass density did not differ substantially from that of smaller fish. NanoCT imaging revealed concentric patterns of hypo- and hyper-mineralized regions in both groups, with these features being more pronounced in larger IB. Furthermore, larger IB displayed an extensive porous network, with tissue porosity increased by 180% relative to smaller IB ($p = 0.036$).

Discussion

Extending previous findings, our results indicate that the pronounced deformation capacity of IB arises from a combination of factors: marked tissue heterogeneity with concentric layers of differing mineral density, high strain transmission and stretching at the collagen fibril level, and potential cellular (re-)modeling processes that shape local microstructure. This unusual integration of stiffness, extensibility, microstructural heterogeneity, and distinct mineralization patterns positions intermuscular bones as a compelling biological template for the design of composite biomaterials with tailored structure–function relationships.

Images (Optional)


Porosity in IB of large fish
A
Whole bone
Top view
y
x
10 µm
100 nm voxel size
B
Side view
z
y
x
10 µm
C
VOI zoom in
Side view
30 nm voxel size
z
y
x
5 µm
0.1
Thickness [µm]
3.0

Session Category

Organ and Tissue Biomechanics: N/A

OA71-05

Modeling Immuno-Mechanics in Vascular Adaptation

Professor Jay Humphrey PhD[1], Professor Ana Estrada PhD[2]

[1]Yale University, New Haven, CT, United States. [2]Fairfield University, Fairfield, CT, United States

Introduction

Accumulating data for arteries reveal that mechanobiological responses tend to contribute to homeostasis whereas immunobiolological responses tend to compromise homeostasis. There is, therefore, a pressing need for a theoretical framework that can account simultaneously for these often-competing drivers of vascular (mal)adaptation.

Methods

In response to this critical need, we developed two complementary modeling frameworks: a constrained mixture-based growth and remodeling model that can be coupled easily to fluid-solid-interaction models to achieve tissue-to-circulation level understanding and a logic-based cell signaling model that can be coupled easily to the constrained mixture model to achieve transcript-to-tissue level understanding. Fundamental to both models is constitutive relations for constituent-specific rates of mass production, mass removal, and material behavior.

To parameterize and test these computational models, we collected data from 20 adult mice (with IACUC approval) that were rendered hypertensive for 4 weeks via chronic infusion of the potent vasoconstrictor angiotensin II. Data were collected at 2 or 4 weeks and included bulk RNA-sequencing, histological, immunohistochemical, and biomechanical.

Results

We found that we could capture time-course changes in key geometric and mechanical metrics by augmenting our traditional constrained mixture model with a stress-threshold based immunobiological function that alters rates of cell and matrix turnover. We also found that we could parameterize a three-cell (smooth muscle, fibroblast, and macrophage) logic-based cell signaling model that was capable of capturing phenotypic modulation of the cells (e.g., M1-type to M2-type macrophage expression). In particular,

both models were capable of capturing differential thickening of the medial and adventitial layers and both models successfully captured the loss of homeostatic control of wall stress in the presence of strong inflammation, with homeostatic responses recovered when neglecting inflammation.

Discussion

Notwithstanding accumulating multiscale data on vascular (mal)adaptations under many different conditions, the complexity of in vivo behaviors demand multiscale computational models to increase understanding. We submit that the present modeling approaches can contribute in this regard. Indeed, given that both models include a tissue-level constrained mixture module, we submit that transcript-to-tissue-to-circulation models should soon be possible, hence enabling basic biological data to predict (patho)physiological outcomes, with further promise for identifying new pharmacotherapies.

Session Category

Organ and Tissue Biomechanics: N/A

OA72-01

Community-Based RoboGym Circuit Training Improves Gross Motor Function, Independence, and Quality of Life in Children With Cerebral Palsy

Mr. Chaesu Kim M.Sc., Mr. Joshua Sung You Ph.D.

Yonsei university, Wonju, Gangwondo, Korea, Republic of

Introduction

Children with cerebral palsy (CP) frequently experience lifelong deficits in gross motor function, balance, and independence, and many are unable to maintain regular self-directed exercise without external support. Conventional hospital- or community-based rehabilitation (CBR) often provides insufficient intensity, task specificity, and long-term continuity, leading to regression of gains after discharge. To address these limitations, we developed a community-based RoboGym (CRG) program that integrates multiple task-specific robotic modalities into a circuit-style intervention for long-term CP management.

Methods

Thirty-one children with CP (mean age 12.8 ± 4.1 years, GMFCS II–III) were randomly allocated to CRG or conventional CBR. Both groups received 90-minute sessions, twice weekly, for 6 months (48 sessions). CBR emphasized activity-based, neurodevelopmental treatment approaches. CRG delivered a structured robotic circuit including therapeutic robotic horse-riding (TRH), automated motorized cycling (AMC), robotic-assisted reciprocal upper- and lower-limb gait trainer (RGT), robot-assisted gait training (RAGT), and overground suspension gait (OSG). Outcomes were assessed pre- and post-intervention using the Gross Motor Function Measure-66 (GMFM-66), Pediatric Balance Scale (PBS), Functional Independence Measure (FIM), and Pediatric Quality of Life Inventory (PedsQL). Group differences over time were analyzed using ANOVA/ANCOVA with Bonferroni correction.

Results

CRG produced significantly greater improvements than CBR in multiple domains. GMFM-66 total and key subdomains (lying/rolling, crawling/kneeling, standing) improved more in CRG, with medium-to-large effect sizes, indicating meaningful gains in gross motor capacity. PBS scores increased by ~38% in CRG versus ~7% in CBR, reflecting superior enhancements in static and dynamic balance. FIM scores improved by ~50% in CRG compared with modest gains in CBR, demonstrating clinically relevant increases in self-

care, transfer, and locomotion independence. PedsQL physical, emotional, social, and school functioning improved by approximately 20–30% in CRG versus 8–10% in CBR, indicating better translation of motor gains into participation and quality of life.

Discussion

A multi-modal, community-based RoboGym circuit produced larger and more comprehensive improvements in gross motor function, balance, functional independence, and quality of life than conventional CBR in children with CP. These findings support CRG as a feasible, intensive, and sustainable community model that leverages complementary robotic modalities to deliver long-term, task-specific rehabilitation across ICF domains.

Images (Optional)

Device / Training Type	Purpose / Functional Domain	Volumetric Intensity (Frequency × Duration × Program Length)	Parametric Intensity(Device-Specific Adjustable Parameters)	Clinical Decision-Making Rationale
TRH – Therapeutic Robotic Horse 	Stability: Improve dynamic postural control, head–trunk alignment, and proximal stability.	30 min/session, 1 session/week, for 6 months.	Frequency: 10–80 HzSpeed: 0.1–2.0 km/hAmplitude: adjustable oscillation up to 5–10 cm vertical displacement.Mode: forward/reverse astride, side-sit, kneel, quadruped.	Clinicians increase frequency and amplitude progressively to stimulate vestibular and proprioceptive inputs without inducing spastic responses. For GMFCS III–IV, lower frequency and greater postural support are maintained early. For GMFCS II, dynamic transitions and higher oscillation enhance trunk control and adaptive equilibrium responses.
AMC – Automatic Motorized Cycling 	Mobility: Enhance reciprocal lower-limb coordination and endurance within functional range.	30 min/session, 1–2 sessions/week, for 6 months.	Speed: 10–15 km/hResistance: 5–25 N·m torque, auto-adjusted to cadence and muscle tone.Mode: passive → active-assist → resistive.Pedal symmetry feedback integrated.	Clinicians titrate cycling speed and resistance based on lower-limb selective motor control and endurance. Passive or active-assist modes are used initially for GMFCS IV, progressing to resistive loads as coordination improves. Higher torque promotes muscle activation symmetry and cardiopulmonary endurance.
RGT – Robotic Gait Trainer (Upper–Lower Coupled Trainer) 	Transitional Mobility: Re-educate interlimb coordination for walking and postural transfer.	30 min/session, 1–2 sessions/week, for 6 months.	Speed: 0.4–1.0 km/hResistance: graded 0–30 N·mSupport mode: 30–60% body weight assist.Arm–leg reciprocal control module synchronized with trunk sensor feedback.	Parametric control of resistance and speed allows individualized motor learning. Clinicians reduce body-weight support as trunk control stabilizes, and increase step frequency for rhythm entrainment via central pattern generators (CPG). Target progression: slow repetitive walking → dynamic reciprocal stepping → dual-task control.
RAGT – Walkbot Robotic-Assisted Gait Training 	Skilled Mobility: Optimize functional gait symmetry, endurance, and selective control.	40 min/session, 1–2 sessions/week, for 6 months.	Speed: 1.0–2.0 km/hSuspension: 50% → 30% body weight unloadingResistance: 10–50 N·m torque modulationMode: passive → active → interactive assist-as-needed (AAN).	Clinicians adjust speed and unloading according to gait stability, spasticity, and energy efficiency. Lower speeds and higher support promote postural safety; progressive load and speed enhance task-specific neuroplasticity. Resistance promotes eccentric control and interlimb coordination via spinal CPG activation. Target: symmetrical gait with improved hip–knee–ankle phasing.
OSG – Overground Suspension Gait Trainer 	Transitional / Dynamic Mobility: Promote balance and independent stepping in a partial weight-bearing environment.	20 min/session, 1 session/week, for 6 months.	Suspension: adjustable 10–40% body weightSpeed: clinician-determined overground cadence (0.4–1.2 km/h)Tasks: forward, backward, lateral, and obstacle walking.Support harness with multi-directional pelvic control.	Used after sufficient trunk and hip control from TRH/AMC/RGT. Clinicians reduce suspension gradually to challenge balance and anticipatory control. Progressive reduction of support encourages autonomous dynamic balance, weight-shifting, and gait adaptability under task-specific contexts.

References (Optional)

Acknowledgements (Optional)

This work was supported, in part, by the “Brain Korea 21 FOUR Project” (F21SH8303039), the National Research Foundation of Korea (NRF) for the Department of Physical Therapy in the Graduate School of Yonsei University, and This research was supported by the National Research Foundation of Korea (NRF) grant, funded by the Korean government (MSIT) (RS-2025-24534569), and This research was supported by the Regional Innovation System & Education (RISE) program through the Gangwon RISE Center, funded by the Ministry of Education (MOE) and the Gangwon State (G.S.), Republic of Korea (2025-RISE-10-006). This research was supported by the National Research Foundation of Korea (NRF) grant, funded by the Korean government (MSIT) (RS-2025-24534569).

Session Category

Rehabilitation Biomechanics and Human Factors: Rehabilitation

OA72-02

Relative Demand on the Knee Extensors During Running Following an Anterior Cruciate Ligament Reconstruction

Dr. Meredith Owen PhD, Dr. Darren Johnson MD, Dr. Brian Noehren PT, PhD

University of Kentucky, Lexington, KY, United States

Introduction

Return-to-running following anterior cruciate ligament reconstruction (ACLR) is an essential milestone of recovery. Adequate quadriceps strength is critical to successful return-to-running to control knee loading. When task demands exceed the maximal force-producing capacity of the quadriceps, compensatory movement strategies may emerge to ensure task completion, potentially increasing the risk of future injury. However, the relative demand on the quadriceps during running across the first year of recovery is unknown. The purpose of this work was to determine relative demand on the knee extensors during running across late-stage ACLR rehabilitation.

Methods

20 individuals (13 F/7 M, 20.1 years, 1.7 m, 70.1 kg) were assessed at 6, 9, and 12 months post-ACLR. Participants completed an instrumented running assessment with marker (200 Hz) and ground reaction force (2000 Hz) data sampled synchronously. Peak knee extension moment (KEM) was determined and averaged across 5 steps. Peak knee extensor strength was taken as the peak of four maximum voluntary quadriceps contractions. Relative demand on the extensors was estimated as the ratio of peak KEM of the uninjured limb (e.g. the goal needed for symmetrical running) to peak isometric torque of the injured and noninjured limbs. Differences between limbs and timepoints were assessed using a two-way repeated-measures ANOVA with Tukey's post-hoc tests.

Results

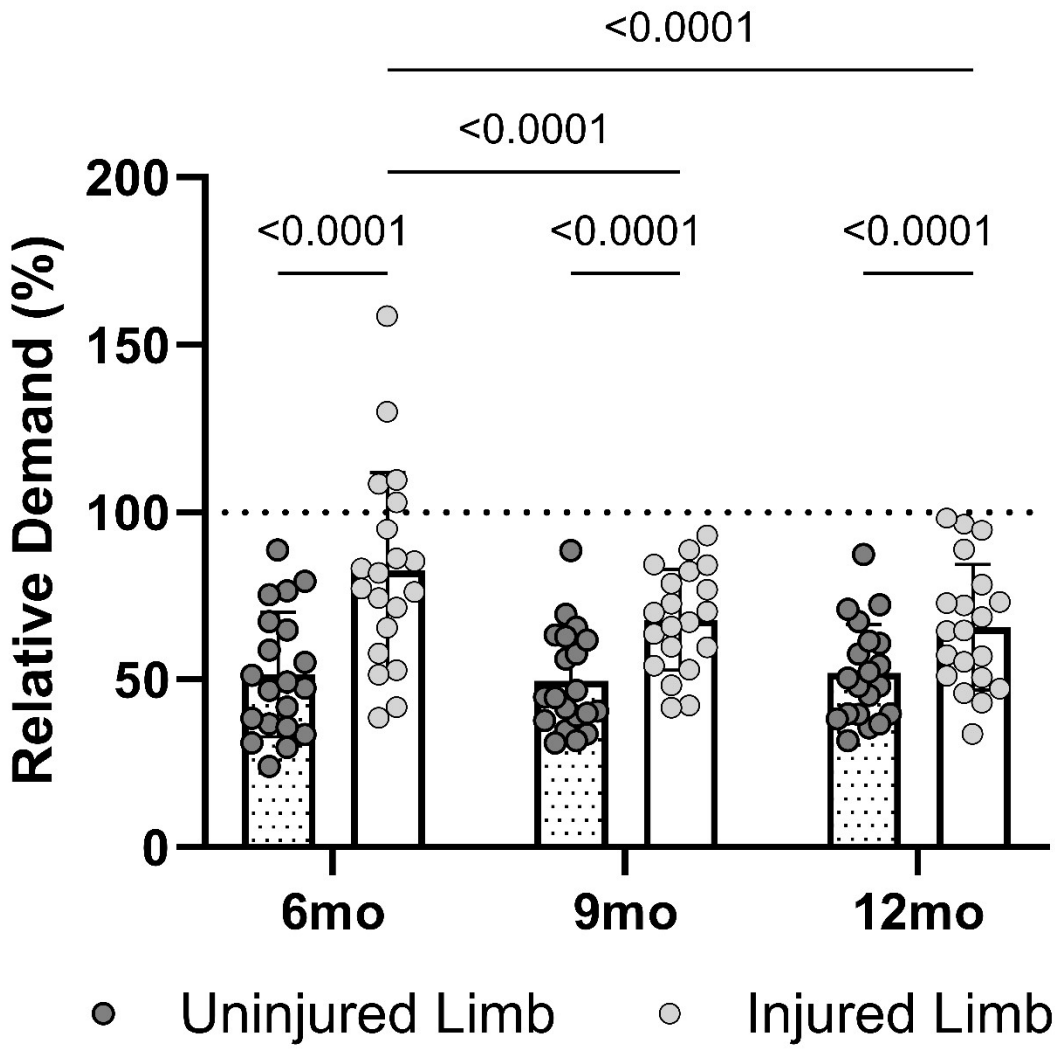
Peak PKEM was significantly lower in the ACLR limb than the healthy limb across all timepoints (6mo: -58.9 Nm; 9mo: -53.9 Nm, 12mo: -45.9 Nm difference between limbs; all $p<.01$). Relative demand on the ACLR limb was significantly higher than for the uninjured limb for all time points and decreased significantly over time (Figure 1).

Discussion

We show that the relative demand on the quadriceps required to achieve symmetric joint moments is significantly higher for the injured limb across all timepoints. Further, even though individuals possess the strength to run symmetrically at 12 months, with relative

demand reduced below suggested normative values (~60% relative demand during running), asymmetries in the peak KEM still exist. Persistent asymmetries could be due to learned disuse or fear of reloading, suggesting the potential need for gait retraining throughout the return-to-run phase of rehabilitation after ACLR.

Images (Optional)



Session Category

Rehabilitation Biomechanics and Human Factors: Rehabilitation

OA72-03

Assessing the Posteriorly Directed Forces Applied to Pediatric Knees by ACL Orthoses

Dr Alexandria Mallinos PhD, Dr Kerwyn Jones MD, Ms Kristen Smith RN

Akron Children's Hospital, Akron, Ohio, United States

Introduction

Functional anterior cruciate ligament (ACL) orthoses are used to limit anterior tibial translation and valgus loading, providing external stabilization during healing and return-to-sport. These devices apply posteriorly directed forces (PDF) through anterior tibial pads, yet the magnitude of these forces across brace designs in pediatric populations is not well defined. This study quantified PDF generated by custom-fit (CF) and off-the-shelf (OTS) ACL orthoses in pediatric patients.

Methods

Thirty patients within one year of ACL reconstruction (17 females, 13 males; mean age 16.3 years; mean weight 71.6 kg) were enrolled. Inclusion criteria required unilateral ACL reconstruction. Patients with additional ligament injury or neuromuscular impairments were excluded. Participants brought their prescribed CF DonJoy Defiance orthosis and were fitted with an OTS DonJoy Playmaker II. LoadPad sensors (Novel Electronics) were placed under the proximal and distal anterior tibial pads to measure PDF.

Static testing was performed at 0°, 30°, 60°, and 90° of knee flexion, with each angle held for 5 seconds and repeated three times. Dynamic testing consisted of three pivot shift tests (PST) following standard clinical protocols. LoadPad data were processed in MATLAB to compute average PDF for each condition. Descriptive statistics and independent t-tests compared forces between orthosis types.

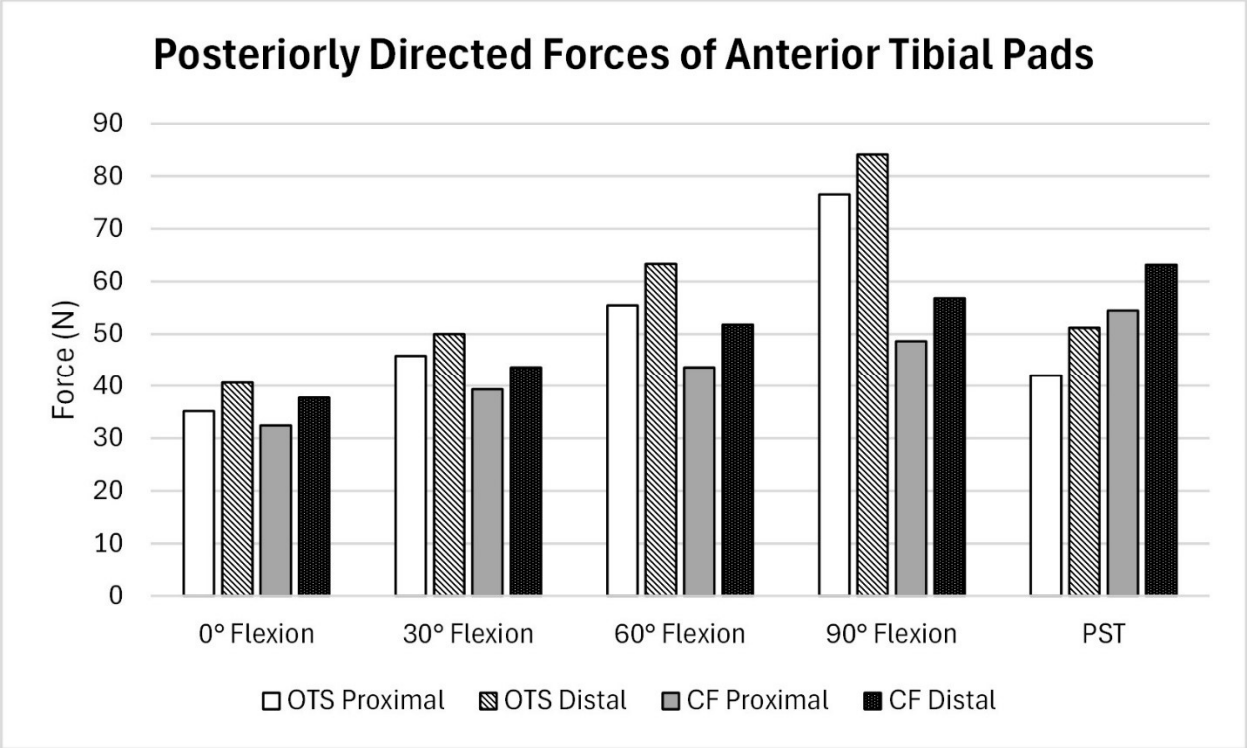
Results

PDF measurements showed that both orthosis types produce increasing loads with greater knee flexion (Figure 1). The OTS orthosis consistently generated higher forces during static flexion, whereas the CF orthosis experienced greater PDF during the PST. Although the OTS orthosis demonstrated significantly higher proximal pad forces at 90° of flexion ($p = 0.043$), no other differences between orthosis types reached statistical significance.

Discussion

Both orthoses demonstrated increasing PDF with flexion, consistent with prior studies. The higher static forces observed in the OTS brace may reflect its total-contact design, whereas the CF brace's superior performance during dynamic loading suggests improved conformity and contact maintenance. Although most differences were not significant, these trends indicate that brace design may influence load transfer and dynamic knee stabilization. Limitations include a single postoperative cohort and two brace models. Future work should incorporate broader brace designs, full-surface pressure mapping, and links between PDF, knee stability, and patient outcomes.

Images (Optional)



Session Category

Rehabilitation Biomechanics and Human Factors: Rehabilitation

OA72-04

Mechanisms of Plantar Load Transfer in Custom Accommodative Insoles for People With Diabetes

Research Engineer Dylan Heino MS[1,2], Principal Investigator Scott Telfer EngD[1,2,3], Research Engineer Kimberly Nickerson BS[1,2], Research Prosthetist Christina Carranza L/CPO[2], Postdoctoral Scholar Mathew Sunil Varre PhD[1,2], Research Engineer Avocet Nagle-Christensen BS[1], Principal Investigator William Ledoux PhD[1,2,3], Principal Investigator Brittney Muir PhD[1,2]

[1]VA RR&D Center for Limb Loss and MoBility (CLiMB), Seattle, WA, United States. [2]Department of Mechanical Engineering, University of Washington, Seattle, WA, United States. [3]Department of Orthopaedic Surgery and Sports Medicine, University of Washington, Seattle, WA, United States

Introduction

Custom accommodative insoles are commonly prescribed to reduce plantar pressures in people with diabetes who are at elevated risk for foot ulceration. We have developed 3D-printed custom accommodative insoles that incorporate patient-specific geometry and tunable material properties, resulting in improved offloading performance compared with standard-of-care designs. Although these insoles effectively reduce forefoot pressures, the mechanisms by which they redistribute load throughout the entire plantar surface are not fully understood. The objective of this study was to characterize and compare load redistribution pathways across nine anatomical plantar regions for standard of care and 3D-printed insoles using a quantitative load-transfer algorithm.

Methods

Twenty-six feet from 17 adults with diabetes and elevated forefoot plantar pressures in the first-to-third metatarsals were analyzed. Each participant was provided with three types of custom accommodative insoles: a standard of care clinical insole, a finite-element–optimized 3D-printed insole, and a pressure-based 3D-printed insole. Plantar pressures were collected during walking using an in-shoe pressure measurement system (pedar-X), and peak plantar pressure and force-time integral were computed for each anatomical region. A load transfer algorithm was then applied to quantify how reductions in loading in one region corresponded to increases in another, enabling identification of redistribution pathways unique to each insole design.

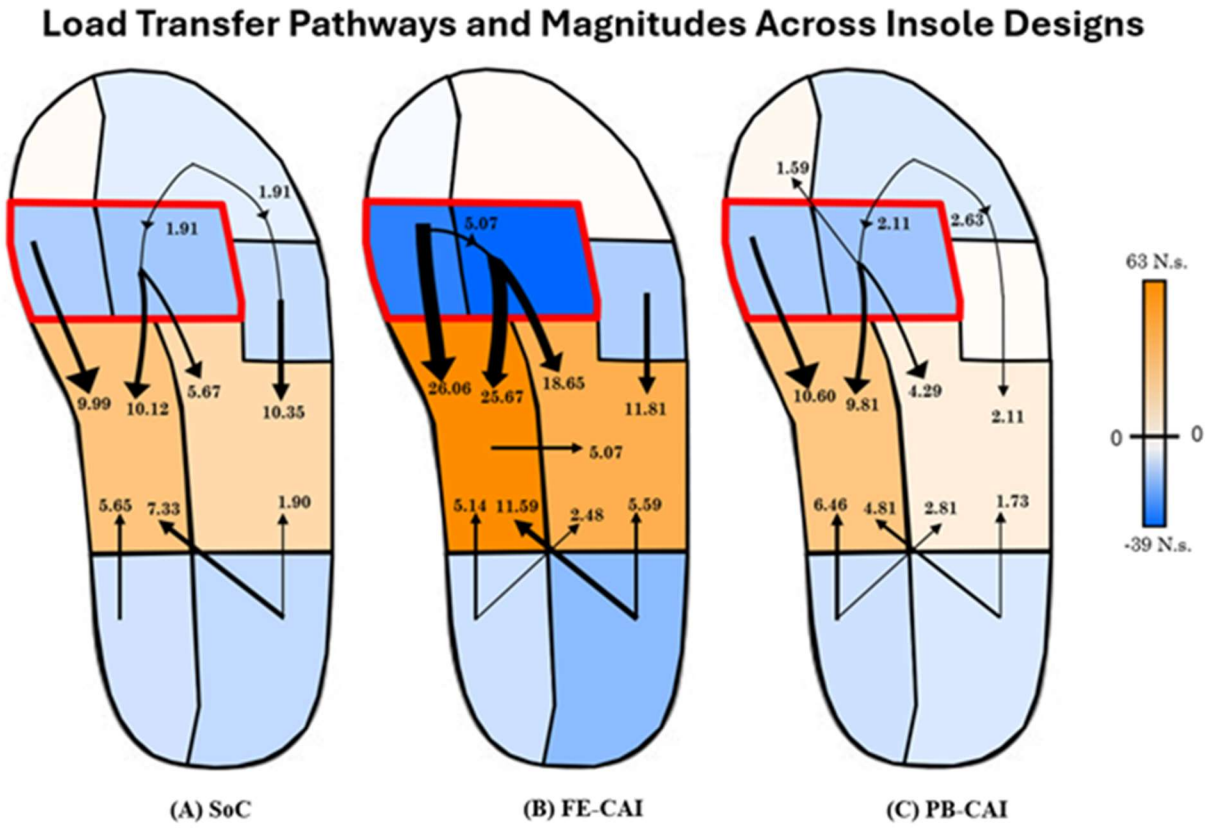
Results

Across all insole conditions, the dominant load-transfer pathway occurred from the metatarsal heads to the midfoot, with the strongest redistribution observed from the first metatarsal head to the medial midfoot. The finite-element–optimized 3D-printed insoles produced the largest reductions in metatarsal loading and the largest corresponding increases in midfoot loading, indicating more effective and targeted redistribution compared with the standard-of-care and pressure-based designs.

Discussion

Design features such as arch height, metatarsal bar geometry, and targeted offloading zones strongly influenced the redistribution pathways identified. These results highlight the capacity of advanced custom insole designs to offload high-risk plantar regions while more effectively engaging the midfoot as a load-bearing structure. The load-transfer framework provides an additional metric for evaluating insole performance and may help guide future patient-specific design strategies, although individual variability in loading patterns remains a critical consideration.

Images (Optional)



Acknowledgements (Optional)

We acknowledge Ellen Y. Li, Ellen Clarissimeaux, and Leo Gagnon from the Department of Veterans Affairs for their contributions to data collection.

Session Category

Rehabilitation Biomechanics and Human Factors: Rehabilitation

OA72-05

A Biomechanical-Social Analysis of Multijoint Leg Extensor Eccentric-Concentric Force Output in Healthy and Post-ACL Reconstructed Female University Athletes

Ms Dana J Hunter MSc[1,2,3], Mr Zachary J McClean MKin, MSc, PhD Candidate[1,3], Dr Kati Pasanen PT, MSc, PhD[1,3,4,5], Dr. Matthew J Jordan PhD, CSCS[1,2,3,4,5]

[1]Faculty of Kinesiology, University of Calgary, Calgary, Alberta, Canada. [2]Sport Medicine Centre, University of Calgary, Calgary, Alberta, Canada. [3]Integrative Neuromuscular Sport Performance Lab, University of Calgary, Calgary, Alberta, Canada. [4]McCaig Institute of Bone and Joint Health, University of Calgary, Calgary, Alberta, Canada. [5]Alberta Children's Hospital Research Institute, University of Calgary, Calgary, Alberta, Canada

Introduction

Lower-limb eccentric and concentric strength are important for performance and injury prevention in **youth female athletes**, who **experience disproportionately high ACL injury rates**. However, most assessments rely on single-joint dynamometers that do not reflect the multijoint, high-velocity actions of real-world ACL injury mechanisms (i.e., rapid braking/deceleration) [1]. Eccentric strength deficits after ACL reconstruction (ACLR) may impair movement and increase reinjury risk [2]. Social factors, including strength-training attitudes, may influence force production, supporting a biomechanical–social view of ACL injury risk [3]. This abstract **(i)** quantifies multijoint maximal eccentric (MEF) and concentric (MCF) leg extensor force in female athletes with ACLR and healthy controls, and **(ii)** examines associations between strength-training attitudes and force production.

Methods

Healthy female athletes (n=177) and female athletes with **ACLR** who returned to sport (n=13) performed **MEF and MCF leg extensions on a robotic servomotor leg press**. Body mass–normalized force outputs were obtained for the ACLR limbs, contralateral limbs, and healthy control limbs. Participants rated their agreement with the statement, "**I prefer strength training with light/bodyweight versus heavy weights**," on a 7-point Likert scale. Linear mixed-effects models accounted for repeated limb measurements, and Holm-adjusted estimated marginal means assessed group differences.

Results

ACLR limbs demonstrated significantly lower MCF than contralateral (β:–2.17 N/kg, p=0.006) and **healthy limbs** (β:–2.27 N/kg, p=0.008). Contralateral and healthy limbs did not differ (β:–0.10 N/kg, p=0.90). MEF did not differ by limb condition (ACLR vs healthy: β:–0.89 N/kg, p=0.51), though contralateral limbs showed a non-significant trend toward

higher MEF than healthy limbs (β:2.17 N/kg, p=0.108) (**Figure1**). **Athletes preferring light/bodyweight training produced lower maximal force** (β:–1.12 N/kg, p=0.05), with no differences between healthy and contralateral limb conditions (β:0.43 N/kg, p=0.72) or contraction type (MEF versus MCF) (p=0.46).

Discussion

ACLR limbs showed significant MCF deficits relative to contralateral and healthy limbs, while MEF was preserved. Preference for light/bodyweight training was linked to lower strength, **supporting a biomechanical–social approach to evaluating ACLR and healthy female athletes.**

Images (Optional)

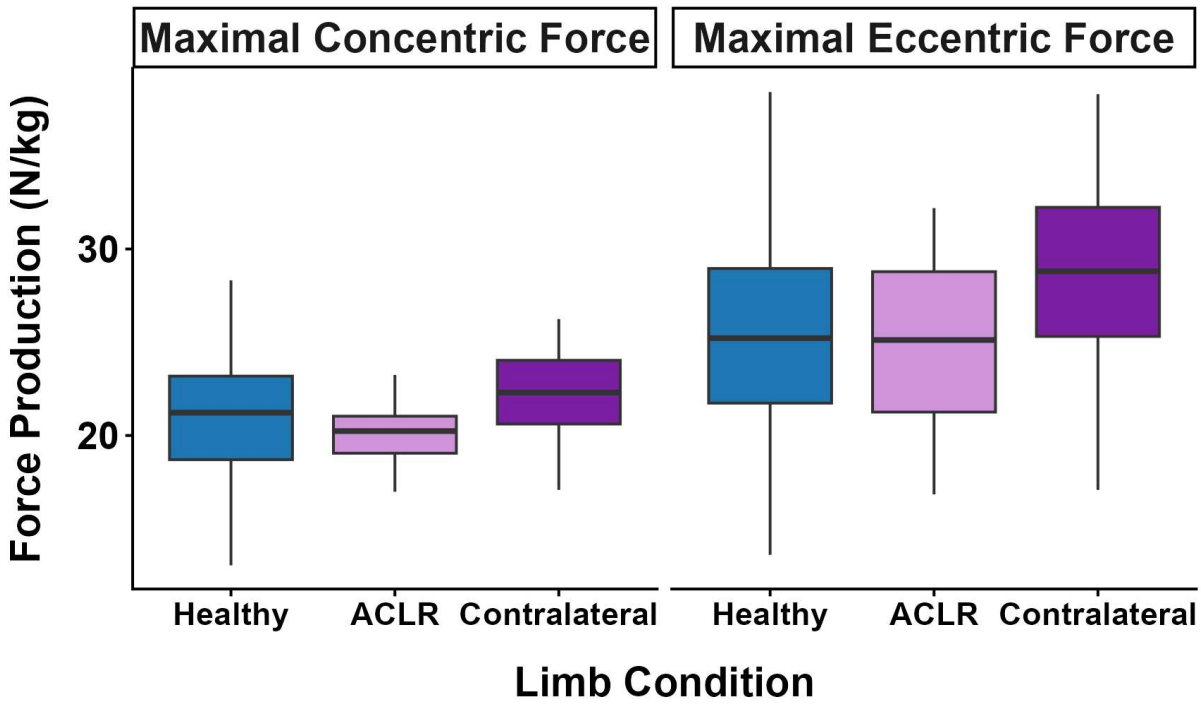


Figure 1. Maximal Concentric Force (MCF) and Maximal Eccentric Force (MEF) by Healthy, ACLR, and Contralateral Limbs of Female University Athletes.

References (Optional)

[1] Boden et al.,2023,*J Orthop Res*.; [2] Drake et al.,2017,Sport Med O.; [3] Vasudevan et al.,2021,*Prev Sci*.

Session Category

Rehabilitation Biomechanics and Human Factors: Rehabilitation

OA72-06

Biomechanical Correlates of Positive Hip Joint Work and Symmetry in Post-Stroke Gait

Mr. Dongwon Jeong[1,2], Mr. Dongho Park[3,4], Dr. Aaron Young[3,4]

[1]School of Computing, Georgia Institute of Technology, Atlanta, Georgia, United States. [2]Bio-Convergence, Integrated Science and Engineering Division, Yonsei University, Seoul, Seoul, Korea, Republic of. [3]George W. Woodruff School of Mechanical Engineering, Georgia Institute of Technology, Atlanta, Georgia, United States. [4]Institute for Robotics and Intelligent Machines, Georgia Institute of Technology, Atlanta, Georgia, United States

Mr. Dongwon Jeong

Mr. Dongho Park

Introduction

A vast majority of stroke survivors exhibit asymmetric gait, leading to metabolic inefficiency and long-term musculoskeletal consequences. Driven by hemiparetic deficits, individuals commonly compensate by shifting joint work from the paretic to the non-paretic limb. This reliance on the non-paretic side reinforces inefficient gait strategies. Although real-time gait biofeedback is widely used, target selection has often relied on theoretical assumptions rather than on quantitative analyses on metrics directly tied to hip joint mechanics. Given the hip joint's substantial capacity to generate positive work, understanding the specific biomechanical correlates of positive hip joint work (PHJW) is essential. This study aimed to quantify the correlations between commonly used biomechanical variables and PHJW magnitude and symmetry in post-stroke gait.

Methods

Treadmill walking data were analyzed from 20 post-stroke subjects across multiple speeds. We computed PHJW and 15 biomechanical variables for both limbs, including: peak hip/knee/angle moments and angles, trailing limb angle (TLA), stride length, step length, step width, cadence, stance time, swing time, single limb stance time, and peak anterior-posterior ground reaction force (AP-GRF). Pearson correlation coefficients (R^2) were calculated to determine linear relationships between: (1) each variable and paretic limb PHJW, and (2) the symmetry index of each variable and the PHJW symmetry index.

Results

A subset of variables showed meaningful correlations with paretic PHJW: paretic hip flexion moment (R^2=0.35±0.29), non-paretic hip extension moment (R^2=0.42±0.53), paretic knee extension moment (R^2=0.25±0.27), paretic hip extension angle (R^2=0.25±0.23), TLA (R^2=0.26±0.30), and stride length (R^2=0.28±0.28). Across nearly all metrics, non-paretic limb variables were more strongly correlated with PHJW than paretic limb variables. However, the symmetry index showed that only hip flexion angle (R^2=0.23), knee flexion angle (R^2=0.33), ankle dorsiflexion moment (R^2=0.26), and step width (R^2=0.21) were associated with PHJW symmetry (all p<0.05).

Discussion

These findings demonstrate that despite high inter-subject variability, several clinically actionable feedback variables do recur across subjects and that even if a variable is correlated with PHJW, it may not be a suitable biofeedback target to meet PHJW symmetry. Furthermore, this study provides data-driven insights for designing future biofeedback strategies aimed at post-stroke gait rehabilitation.

Images (Optional)

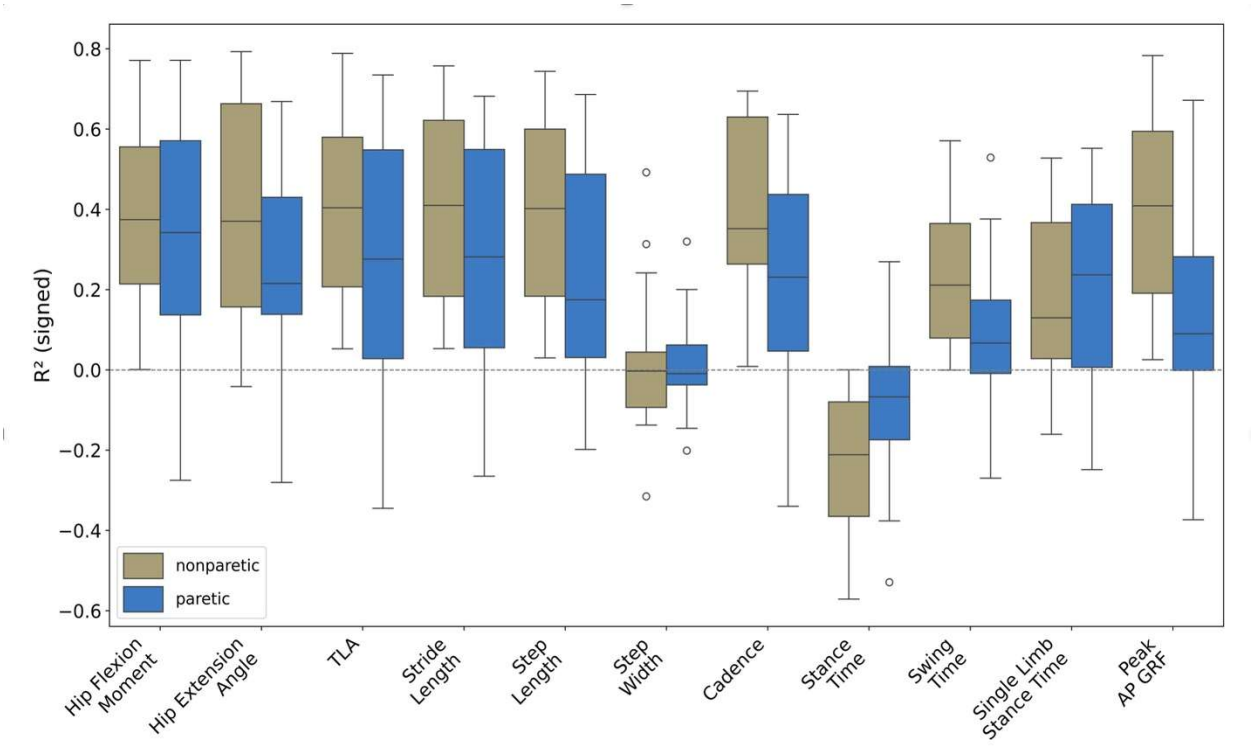


Figure 1: Boxplot of signed R^2 distributions showing correlations of each biofeedback target against positive hip joint work (PHJW) across 20 post-stroke subjects for both paretic and non-paretic limbs.

Session Category

Rehabilitation Biomechanics and Human Factors: Rehabilitation

OA73-01

Simulated Medial Knee Contact Force is More Predictive of Cartilage Thinning Than Static Alignment: An Analysis of 3,301 OAI Subjects

Dr. Anthony Gatti, Dr. McKenzie S. White, Dr. Nicos Haralabidis, Ms. Anoosha Pai, Dr. Constance Chu, Dr. Seth Sherman, Dr. Gatti E. Gold, Dr. Scott Delp, Dr. Feliks Kogan, Dr. Akshay Chaudhari

Stanford University, Stanford, CA, United States

Introduction

Systematic reviews confirm knee adduction moment predicts osteoarthritis (OA) progression. While High Tibial Osteotomy (HTO) slows progression by surgically redistributing knee load, surgical planning relies solely on static alignment, ignoring mechanical load. Predictive simulations could bridge this gap by estimating joint loads under varying surgical plans. Purpose: To demonstrate feasibility of using predictive simulations for surgical planning, we tested whether predictive simulations personalized to Osteoarthritis Initiative (OAI) subjects predicted longitudinal cartilage thinning.

Methods

We generated personalized predictive gait simulations for 3,301 Osteoarthritis Initiative participants (6,602 knees). Subject-specific musculoskeletal models were created by scaling a generic model[1] using femoral/tibial lengths, Hip-Knee-Ankle (HKA) alignment extracted from full lower limb radiographs, and body mass. We simulated a full gait cycle, normalizing the walking speed to a Froude number of 0.25 to account for subject size. We used the OpenSim AD pipeline minimizing the cost function as previously described[2] with an additional cost term tracking generic reference kinematics. Medial knee contact force (MCF) was estimated using a frontal plane static equilibrium model.

To test predictive power, we auto-segmented medial femoral cartilage of each subject from all available OAI MRI timepoints and computed the annual rate of thinning per knee. We compared the correlation of static clinical metrics (Body Mass, BMI, HKA) and simulation-derived MCF metrics (Peak 1, Peak 2, Impulse) against the rate of cartilage thinning.

Results

Simulation-derived MCF was moderately correlated with HKA alignment (**corr**: peak 1=-0.61, peak 2=-0.57, impulse=-0.58). HKA alignment was the strongest clinical predictor of cartilage thinning (corr: HKA=0.20, body mass=-0.13, BMI=-0.14). MCF peak 1 and impulse had a significantly stronger correlation (**corr**: peak 1=-0.22, peak 2=-0.19, impulse=-0.21) with cartilage thinning ($p<0.001$ vs HKA).

Discussion

The data show that predictive simulations can be deployed at epidemiological scale to estimate joint loads. Predictive simulation-based MCF better predicted disease progression than clinical metrics. Integrating pre-operative kinematics into the physics-based simulations could further improve simulations for surgical planning.

Images (Optional)

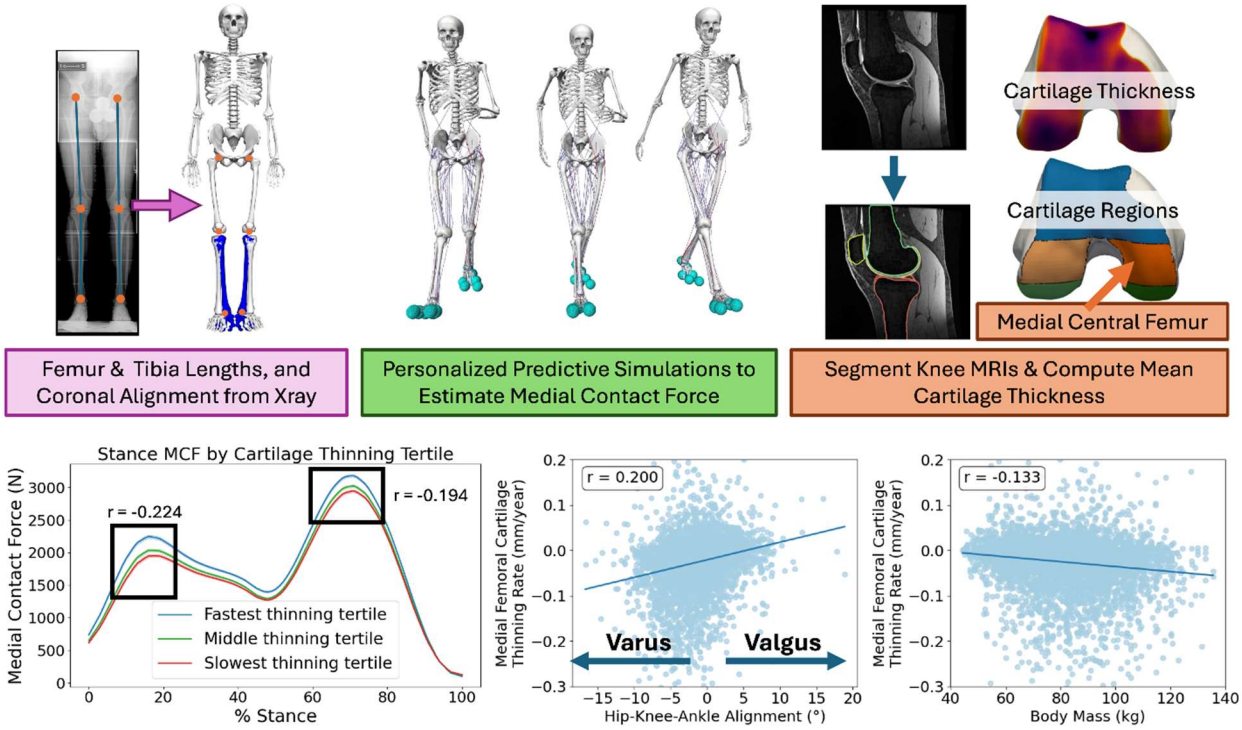


Figure 1. Personalized musculoskeletal models were scaled using radiographic HKA and limb lengths to drive predictive simulations for estimating MCF. Longitudinally, medial femoral cartilage thinning rates were quantified via automated MRI segmentation. The left lower plot shows mean +/- 95% confidence intervals for MCF over stance for the lowest, middle, and highest tertiles of cartilage thinning; black boxes annotate correlations per peak with thinning rate. Scatter plots show association of thinning rate with Body Mass, and HKA.

References (Optional)

[1] Hamner S. et al., JOB, 2010

[2] Falisse A. et al., J. R. Soc. Interface, 2019

Session Category

Orthopaedic Biomechanics: Lower Extremities

OA73-02

Cartilage Biomechanical Responses Are Reduced by Valgus Bracing in Varus Malaligned Knees With Medial Osteoarthritis

Mr. Joose Peitola MSc[1], Dr. Amir Esrafilian PhD[1], Dr. Atte Eskelinen PhD[1], Dr. Scott Starkey PhD[2], Assoc. Prof. David Saxby PhD[3], Assoc. Prof. Laura Diamond PhD[3], Assoc. Prof. Michelle Hall PhD[4], Prof. Rami Korhonen PhD[1,3]

[1]University of Eastern Finland, Kuopio, Northern Savo, Finland. [2]The University of Melbourne, Melbourne, Victoria, Australia. [3]Griffith University, Gold Coast, Queensland, Australia. [4]The University of Sydney, Sydney, New South Wales, Australia

Introduction

Valgus bracing is a common intervention method to reduce medial knee compartment loading. However, its effects on cartilage tissue-level biomechanics have not been examined using advanced fibril-reinforced material models. Such models consider how the collagen fibril network provides tensile stiffness and structural integrity, and how its interaction with fluid pressure governs tissue deformation and stress [1]. We investigated how valgus bracing affects cartilage biomechanics in individuals with knee varus malalignment and medial knee osteoarthritis (KOA) using fibril-reinforced poroviscoelastic (FRPVE) and -poroelastic (FRPE) materials for cartilage and menisci, respectively.

Methods

Twenty-five participants (aged ≥50 years) with varus-malaligned medial KOA (Kellgren–Lawrence grade ≥ 2) completed unbraced and braced (Unloader One©, Össur) walking trials. Personalized knee geometries from magnetic resonance imaging were implemented into a validated 12-degree-of-freedom knee model and combined with electromyography-informed neuromusculoskeletal simulations [2] (Figure 1A) to estimate tibiofemoral kinematics and kinetics as inputs for the finite element (FE) analysis (Figure 1B). Next, the cartilage and meniscus geometries were imported into an FE model [3] with FRPVE and FRPE material models and meshed using hexahedral elements. A soils consolidation analysis (Abaqus 2023) was performed. We report maximum principal stress (MPa), maximum shear strain (%), and collagen fibril strain (%) (Figure 1C) as indicators of cartilage damage.

Results

Bracing reduced medial tibial cartilage stress and strain at the second peak in contact loading during stance (i.e., 70–90% of stance). The maximum principal stress, maxium shear shear strain, and collagen fibril strain within medial tibial cartilage decreased from

9.5±3.9 MPa to 8.5±3.6 MPa (p=0.01), 31.0±5.1% to 29.5±5.2% (p=0.025), and 4.4±0.7% to 4.2±0.7% (p=0.014), respectively.

Discussion

Valgus bracing applies an external abduction moment to the knee, and our analysis indicates this reduces biomechanical stresses and strains in the medial tibial knee cartilage. This may help limit collagen fibril network damage in individuals with varus malalignment, potentially slowing medial KOA progression.

Images (Optional)

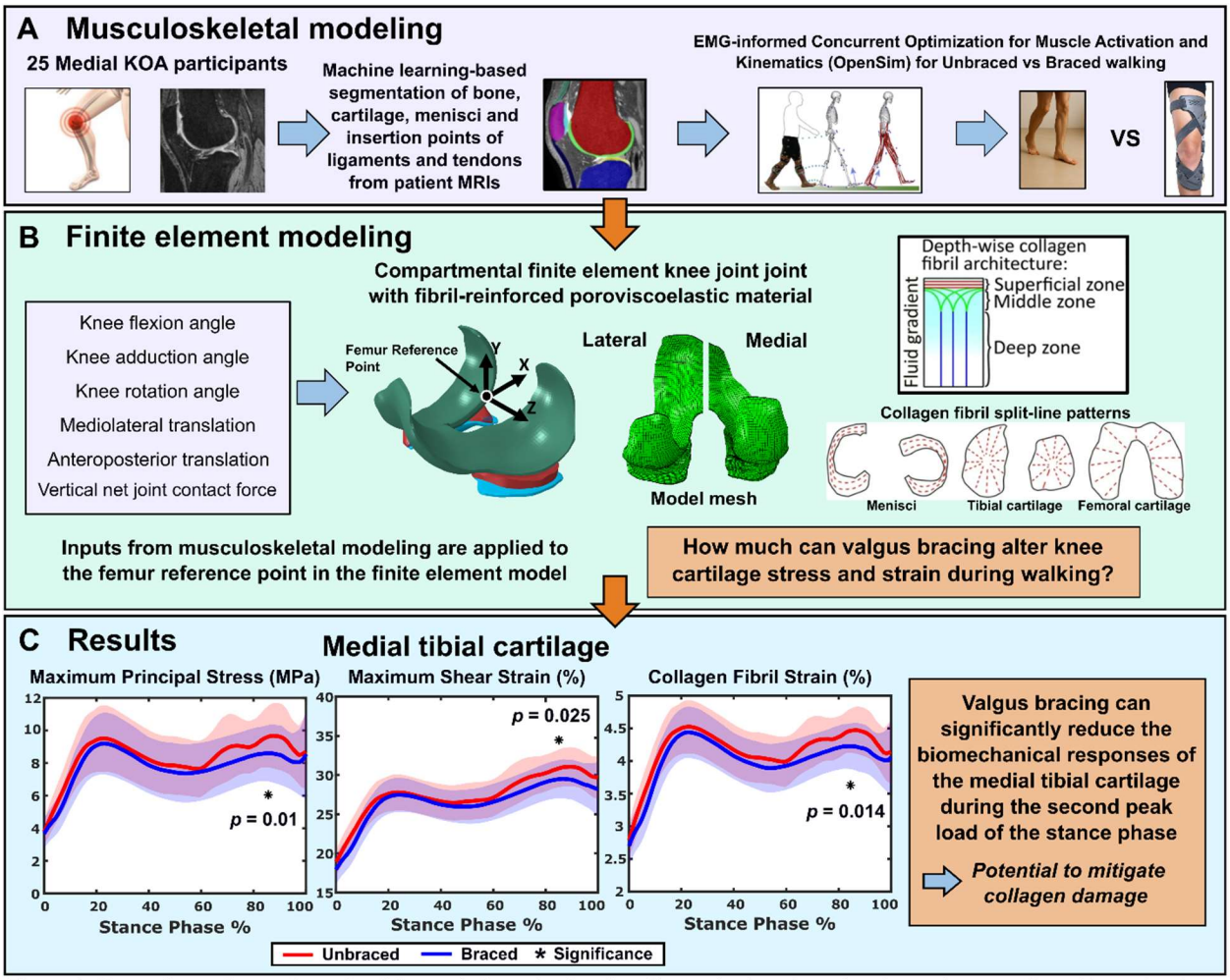


Figure 1: General overview and results of the study investigating the effects of valgus knee bracing on knee cartilage biomechanics.

References (Optional)

[1] Mika Mononen *et al.* J. Biomech, 2012. [2] Scott Starkey *et al.* Clin. Orthop. Relat. Res., 2025. [3] Amir Esrafilian *et al.* IEEE Trans. Biomed. Eng., 2024.

Acknowledgements (Optional)

NNF, RCF, Väisälä Foundation, NHMRC, MSCA, SKR, DREAM pilot.

Session Category

Orthopaedic Biomechanics: Lower Extremities

OA73-03

The Impact of Estrogen on Stress Relaxation Properties and Collagen Content in Chondrocyte-Seeded Alginate Gels

Ms. Emma Stevens, Mr. Marcus Torres-Negron, Dr. Jill Middendorf Ph.D.

Johns Hopkins University, Baltimore, MD, United States

Introduction

Women make up a disproportionate share of osteoarthritis cases [1], yet mechanisms linking sex hormones to cartilage biomechanics remain poorly defined. Estrogen, a key sex specific hormone, has been shown to upregulate collagen II and downregulate matrix metalloproteinases gene expressions [2]. However, changes in mechanical properties and measures of matrix production due to estrogen is unknown. Therefore, the goal of this study was to identify how estrogen alters matrix production and the mechanical properties of chondrocyte seeded alginate gels.

Methods

Chondrocytes were isolated from porcine femoral condyles and embedded in alginate at 10^7 cells/ml. Hydrogel samples were placed in control (complete) or estrogen media (+1pM 17*b* estradiol) and incubated for 1, 2, or 3 weeks. After culture, stress relaxation tests, comprised of 6 steps of 5% strain, was performed ($N \geq 6$). Stress-time plots were fit to a biphasic model to find instantaneous and equilibrium moduli and tissue permeability [3,4]. Hydroxyproline assay assessed collagen content (N=3).

Results

No significant changes in instantaneous modulus, equilibrium modulus, or permeability based on media condition were observed (Fig 1A). Trends suggest that estrogen produces a slightly weaker, more permeable construct than control media. Time dependent decreases in construct mechanics may be due to alginate degeneration [5]. A significant decrease in collagen content between estrogen and control conditions occurred at week 2 ($p = 0.014$, Fig 1B).

Discussion

Since compressive properties often correlate strongest with aggrecan content, insignificant mechanical changes due to estrogen likely indicates no significant changes in proteoglycan concentrations. However, contrary to prior data on chondrocyte gene

expression [2], this study showed decreased collagen production and trends towards decreasing compressive mechanics due to estrogen. Since estrogen's impact changes with chondrocyte age and sex [6,7], these contradictions may stem from these factors. Nevertheless, our results demonstrate that estrogen may predispose the joint to degeneration in women as estrogen concentrations fluctuate.

Images (Optional)

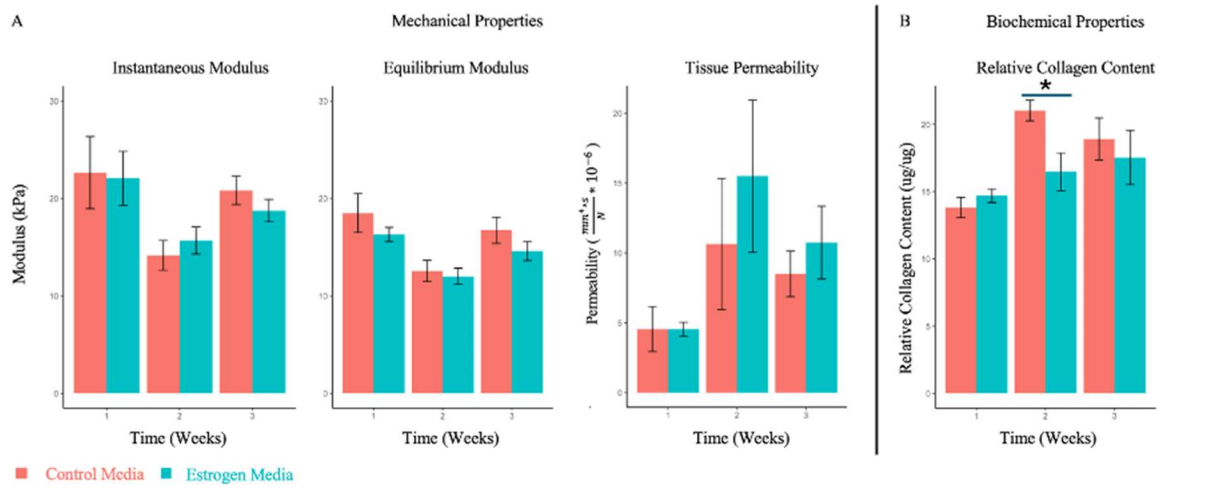


Figure 1: A) Stress relaxation properties demonstrate changes over time supersede changes by media condition. Trends show samples treated with estrogen generally have lower equilibrium and instantaneous moduli and higher permeability compared to samples treated with control media (n≥6/condition). B) Hydroxyproline assay demonstrates lower moduli correspond with lower relative collagen content when normalized by wet weight (n=3/condition). (* p<.05)

References (Optional)

[1] Roman-Blas *et al*, Arthritis Research & Therapy, 2009 [2] Wang *et al*, Bone Research, 2023[3] Armstrong *et al.*, J Biomech Eng, 1984 [4] Cloyd, Eur Spine J., 2007[5] Bouhadir Biotechnol Prog, 2001 [6] Zhong *et al.*, Endocrinology, 2010; [7] Kinney *et al*, Osteoarthritis & Cartilage, 2005

Session Category

Orthopaedic Biomechanics: Lower Extremities

OA73-04

Cartilage Thickness not Pain Variability is Associated with Higher Stride Length Variability in Knee Osteoarthritis

Dr. Skylar Holmes[1], Dr. Garry Gold[1], Dr. Anthony Gatti[1], Dr. Katherine Boyer[2]

[1]Stanford University, Stanford, CA, United States. [2]University of Massachusetts Amherst, Amherst, MA, United States

Introduction

Knee osteoarthritis (KOA) has been linked to movement adaptations, specifically greater spatiotemporal gait variability than age-matched controls[1]. However, it is unclear whether increases in variability are driven by pain, a primary symptom of OA, or structural differences. Therefore, the purpose of this work was to determine whether pain variability or structural severity would predict spatiotemporal gait variability in KOA. It was hypothesized that greater pain variability and structural severity would predict greater spatiotemporal gait variability in KOA.

Methods

Seventeen adults with KOA (9F, age: 70±4y, BMI: 25.9±3, KOOS Pain: 69.3±12) participated in this study. Participants completed a 30-minute treadmill walk (30MTW) at preferred speed. The standard deviation of stride length and step width (spatiotemporal variability) were calculated with 7 – 30 strides of data collected at min 2 of the 30MTW. Knee pain was reported on an 11-point verbal numeric rating scale (NRS) every 6 minutes during the 30MTW. Change in pain (Δpain) was the difference between NRS at minutes 30 and 0 of the 30MTW. The standard deviation of the 1st derivative of pain scores (Δpain/Δtime) and Δpain were used to quantify pain variability. Affected knee MR images were obtained using a 3-dimensional Double Echo Steady State sequence. The medial-to-lateral (M/L) cartilage thickness ratio was defined as mean medial femoral weight-bearing thickness divided by mean lateral femoral weight-bearing thickness. Separate linear regression models were used to assess the relationships between change in pain, pain variability, M/L cartilage thickness ratio with measures of gait variability ($\alpha = 0.05$).

Results

Pain variability was not associated with stride length nor step width variability. There was a positive association between M/L thickness ratio and stride length ($p=0.03$, Table 1). KOA

individuals who have a larger M/L thickness ratio or thicker medial relative to lateral cartilage (less severe medial OA) have greater stride length variability.

Discussion

M/L ratio not pain predicted gait variability suggesting structural severity may independently impact movement adaptations in KOA. These findings suggest that while pain is an important clinical symptom it may not underly movement variability in KOA.

Images (Optional)

Table 1. Regression Models

Outcome Variable	ΔPain Beta (95% CI)	Pain Derivative	M/L Ratio
Stride Length Variability	0.01(-0.01 0.03)	-0.02(-0.09,0.06)	0.06(0.07,0.04)*
Step Width Variability	0.01(-0.02,0.02)	-0.01(-0.08,0.05)	0.05(-0.01,0.11)

* indicates p<.05

References (Optional)

[1] Tanpure et al., J Orthop,2023

Session Category

Orthopaedic Biomechanics: Lower Extremities

OA73-05

Longitudinal Bone and Joint Changes After High Tibial Osteotomy for Medial Knee Osteoarthritis

Mr. Tadiwa Waungana MSc.[1], Miss Elisa Moretta[2], Dr. Giacomo Dal Fabbro MD[2], Prof. Stefano Zaffagnini MD[2], Mr. Enrico Schileo PhD[2], Mr. W. Brent Edwards PhD[1], Mrs. Sarah Manske PhD[1], Mrs. Fulvia Taddei PhD[2]

[1]University of Calgary, Calgary, Alberta, Canada. [2]Istituto Ortopedico Rizzoli, Bologna, Emilia-Romagna, Italy

Introduction

Varus joint alignment is common and contributes to knee osteoarthritis (OA) progression through cartilage degeneration, typically observed as joint space narrowing, and bone sclerosis in the medial compartment[1]. Medial opening wedge high tibial osteotomy (MOWHTO) is a surgical procedure that corrects varus malalignment and redistributes compartmental loads, whilst preserving the native joint surfaces, to alleviate pain and restore joint function[2]. However, we have limited understanding of its effects on articular structures and whether it slows load-mediated joint degeneration. This clinical trial investigated the efficacy of MOWHTO on restoring bone and joint structure.

Methods

51 patients (9 female, mean age 53 ± 8.6 yrs) with medial knee OA (KLG ≤ 3, varus knee alignment > 4°) were assigned to non-surgical or surgical MOWHTO groups. All patients underwent baseline and one-year knee imaging using weight bearing computed tomography (Onsight 3D, Carestream). We quantified changes in three-dimensional tibiofemoral joint space width (ΔJSW) and subchondral bone plate thickness (ΔSbp.Th) to determine the effects of MOWHTO.

Results

We observed consistent trends of decreasing femoral Sbp.Th, with moderate ($0.53 < d < 0.96$) and small to moderate ($0.27 < d < 0.75$) effect sizes in lateral and medial ΔSbp.Th, respectively. Compared to non-surgical patients, we observed a significant decrease in Sbp.Th in the lateral trochlea ($p = 0.015$) of surgical patients. Overall, Sbp.Th increased in the lateral tibia of surgical patients ($-0.64 < d < -0.53$), whilst changes in the medial tibia varied by region. Trends towards increased medial JSW were accompanied by decreased lateral JSW in surgical patients ($d_{Medial} = -0.60$, $d_{Lateral} = 0.54$), but these changes were not significant compared to non-surgical patients.

Discussion

Whilst the decrease in Sbp.Th and increase in JSW in the medial compartment was consistent with unloading due to MOWHTO, we were surprised to find decreased Sbp.Th in the lateral femur, suggesting that load redistribution may affect the femur and tibia differently. Our results suggest that load redistribution may lead to bone adaptations that may underpin extended joint survivorship in MOWHTO patients[2] and have important implications for OA treatment strategies.

References (Optional)

[1] L. Sharma *et al.*, 2010. *Ann Rheum Dis*

[2] L. Murray *et al.*, 2021. *J Am Academy Orth Surg*

Session Category

Orthopaedic Biomechanics: Lower Extremities

OA74-01

Craniofacial CBCT: Addressing Volume-Resolution Dilemma using Generative Artificial Intelligence

Dr. Seyedmahdi Hosseinitabatabaei[1], Dr. Andrew Nelson[2], Dr. Nicolas Piché[3], Dr. Didem Dagdeviren[4], Dr. Natalie Reznikov[1,4,5]

[1]Department of Bioengineering, McGill University, Montreal, Quebec, Canada. [2]Department of Anthropology, University of Western Ontario, London, Ontario, Canada. [3]Comet Technologies Canada Inc., Montreal, Quebec, Canada. [4]Faculty of Dental Medicine and Oral Health Sciences, McGill University, Montreal, Quebec, Canada. [5]Department of Anatomy and Cell Biology, McGill University, Montreal, Quebec, Canada

Introduction

A dilemma in cone-beam computed-tomography (CBCT) is resolution vs field-of-view: one can get either a large volume or high resolution. In low resolution CBCT, fuzzy and diffuse edges result in poor segmentation that affect biomechanical analysis of bone. Super-resolution can recover sharp details, but most such AI-based algorithms rely on artificially downgraded images, phantoms, or excised specimens, limiting real-world applicability. Using real low- and high-resolution image pairs, we developed a Generative-Adversarial-Networks (GAN)-based super-resolution method for clinical CBCT that recovers sharp edges while avoiding hallucinations.

Methods

CBCT scans of 1 human skull, 4 cadaveric human heads, and 6 sheep heads were acquired at 270µm and 135µm voxel, and a GAN (Unet-Structure-Preserving Super-Resolution [UNetSPSR]) was designed to recover fine image details in low-resolution images. The low- and high-resolution pairs were registered and used for training and testing using pixel-, edge-, and perceptual-accuracy loss terms. Performance was benchmarked against state-of-the-art methods using peak signal-to-noise ratio (PSNR) and learned perceptual image patch similarity (LPIPS), and further evaluated through downstream segmentation of trabecular bone using paired t-tests. Independent clinical CBCT scans from five patients with osteogenesis imperfecta and an external public dataset (n=50) were used for generalization testing.

Results

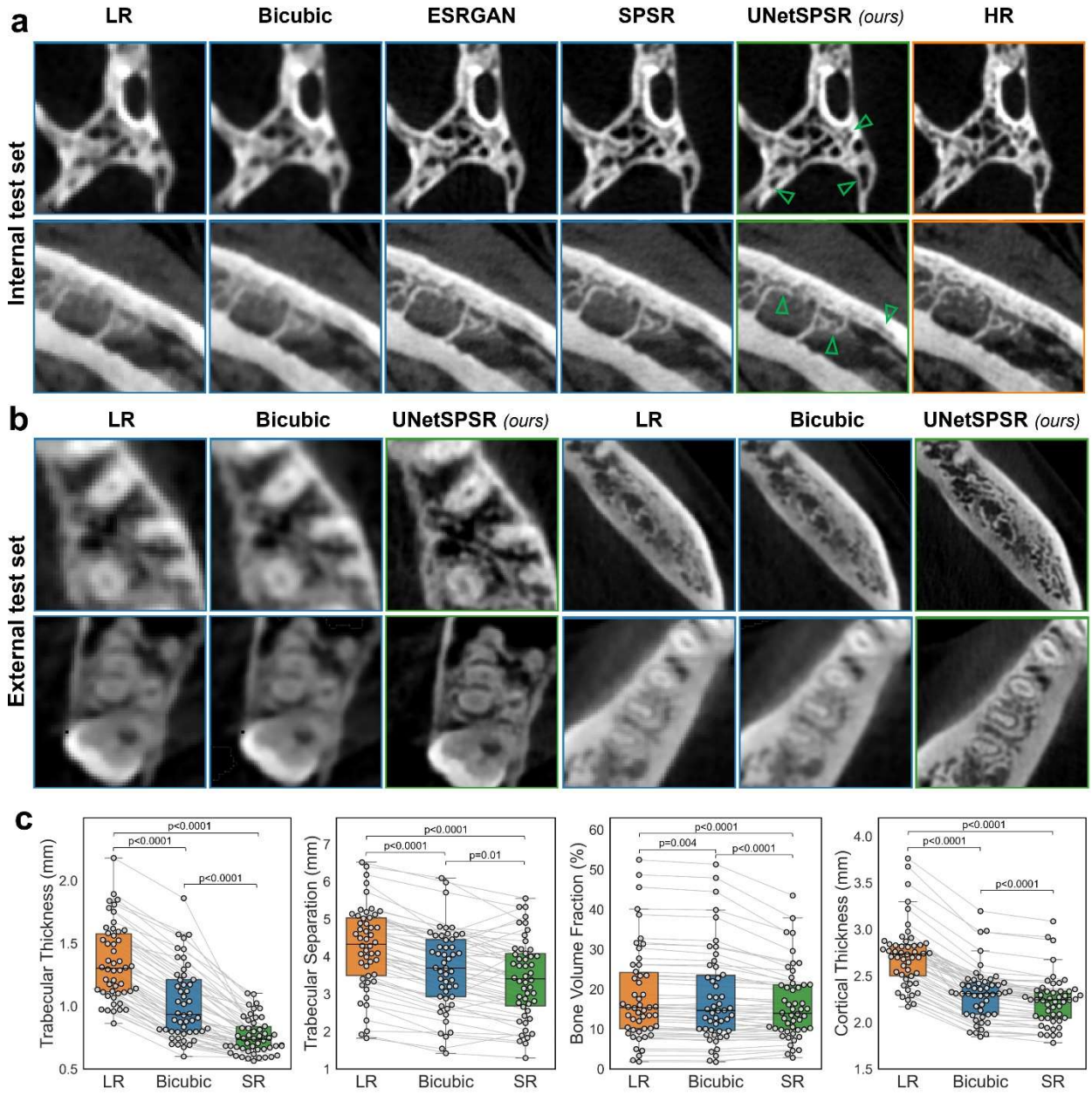
UNetSPSR achieved the highest PSNR (+0.66 seen, +0.11 unseen compared to the runner-up method) and lowest LPIPS (−0.01), indicating improved detail recovery (Figure 1a). Its similar performance on seen and unseen sets demonstrates generalization, effectively

recovering sharp gradients from diffuse patterns instead of ‘memorization’. It further recovered fine details without introducing artifacts in independent clinical low-resolution scans of individuals with osteogenesis imperfecta, despite varying imaging parameters, as well as external data, supporting its generalizability (Figure 1b). UNetSPSR reduced overestimation of trabecular bone morphology, notably lowering trabecular thickness overestimation from 61% to 11%. The network generalized well to external data, significantly improving microarchitectural measures ($p < 0.05$) with patterns similar to the internal dataset (Figure 1c).

Discussion

Our proposed network, UNetSPSR, accurately recovered sharp features in CBCT without introducing artifacts and generalized across cadaveric, clinical, and external datasets. With further validation, UNetSPSR holds promise as a practical tool for both retrospective data enhancement and prospective clinical imaging.

Images (Optional)



Acknowledgements (Optional)

We thank the donors of McGill University Body Donation Program, and the staff of the Division of Anatomical Sciences, especially Dr. Gabriel Venne, Jamie Brisebois, and Robert L'Heureux. We also thank the members of the Brittle Bone Disease Consortium (BBDC) including Drs. Brendan Lee, V. Reid Sutton, Sandesh CS Nagamani, Frank Rauch, Jean-Marc Retrouvey, Janice Lee, Jeanne Franzone, Danielle Gomez, Karen Kruger, Tracy Hart, Mahim Jain, Deborah Krakow, Eric Orwoll, Lindsey Nicol, Cathleen Raggio, Pamela Smith, Peter Smith, Laura Tosi, Danita Valesco, Maegen Wallace. Former PIs of the BBDC include

Francis Glorieux, Michael Bober, Gerald Harris, Eric Rush, and Paul Esposito. This research was enabled in part by support provided by the Digital Research Alliance of Canada.

Session Category

Emerging Areas: N/A

OA74-02

4D Reconstruction of Fetal Left Ventricles from Echocardiography via Geometric-Aware Radial Segmentation and Graph-Fourier Reconstruction

Mr. Haziq Shahard[1], Mr. Kamrul Hasan[1], Mr. Qifeng Wang[2], Mr. Lucas Iljima[1], Ms. Nida Ruseckaite[1], Mr. Yihao Luo[1], Dr. Iris Scharnreitner[3], Dr. Andreas Tulzer[3], Prof. Bin Liu[2], Dr. Guang Yang[1], Dr. Choon Hwai Yap[1]

[1]Imperial College London, London, England, United Kingdom. [2]Dalian University of Technology, Dalian, Liaoning, China. [3]Medical Faculty, Johannes Kepler Uni- versity Linz, Linz, Upper Austria, Austria

Introduction

Deep learning (DL) 3D fetal left ventricle (LV) reconstruction from echocardiogaphy images is useful for congenital malformation detection and biomechanics modelling. Here, we developed the first public 3D+time fetal echo dataset to enable training such a network. Further, we developed a novel 2.5D reconstruction approach, utilizing 2D segmentation via SCOPE-Net (Symmetry-COnsistent, Prompt-Enhanced Network), followed by 3D mesh reconstruction. Rather than planar Cartesian slicing, radial slices revolving around the LV longitudinal axis are extracted to enhance performance.

Methods

Image dataset: 3D+time fetal echocardiograms of 52 patients from the Kepler University Hospital (ethics approval 1009/2017), complete with 2D segmentations and 3D mesh reconstructions over the cardiac cycle, are publicly shared at https://feecho4d.github.io/Website/. DL 3D Reconstruction: SCOPE-Net performs 2D segmentation on all radial image slices, followed by 3D mesh reconstruction via the Graph Harmonic Deformation (GHD) approach [1] (shape modelling with Fourier surfaces). SCOPE-Net's 2D segmentation employs a self-supervised novel geometric inductive bias, which aligns the latent features of symmetrically opposed radial slices with attention and contrastive learning.

Results

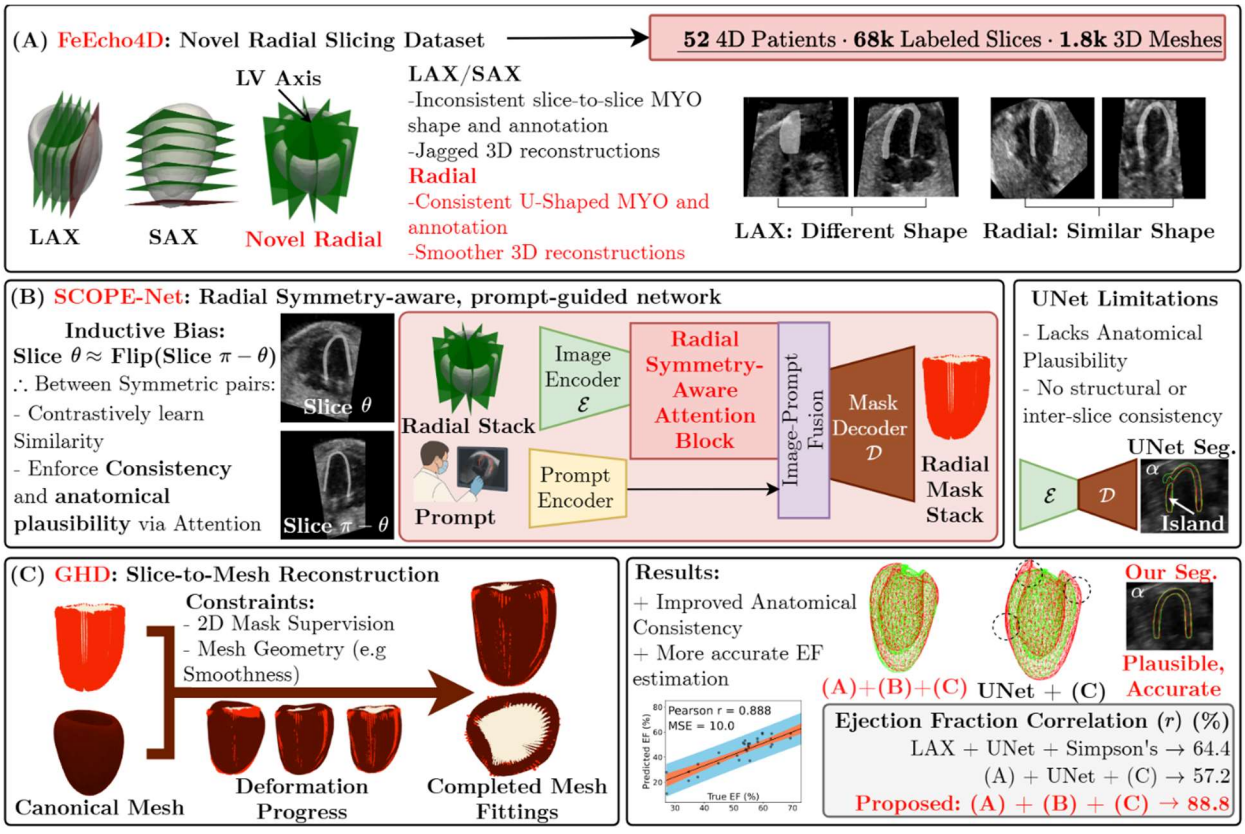
Experiments with UNet and SAM showed that radial slicing of the 3D image enabled more accurate 2D DL segmentation and 3D mesh reconstruction compared to planar Cartesian slicing. SCOPE-Net achieves superior Dice (0.893 ± 0.044) compared to the UNet (0.838±0.140) and SAM (0.881±0.040), and lowers the percentage of erroneous

segmentation islands: 0.0036% vs SAM's 0.025% and UNet's 1.39%. The reconstructed 3D mesh was used to quantify ejection fraction. SCOPE-NET achieved Pearson's r=0.888 compared to ground truths, exceeding performance of 2DUNet+GHD (r=0.572), and 3DUNet(r=0.731). Similar enhanced accuracy is observed for global longitudinal strain quantifications.

Discussion

Results show that our LV radial sampling outperformed standard slicing in segmentation due to the more consistent myocardium "U" shape, allowing for more natural 3D shape reconstructions. Our 2.5D approach outperformed other methods, with less computational expense. Further testing may be performed with other modalities, and finite element modelling with our meshes. Anatomically asymmetric cases, such as severe congenital deformations, may cause our inductive bias to fail; future work is necessary with broader sample sizes and asymmetry-aware network modifications.

Images (Optional)



References (Optional)

[1] Yihao Luo *et al.*, arXiv preprint, 2024

Acknowledgements (Optional)

Session Category

Emerging Areas: N/A

OA74-03

oNLI: Operator Nonlinear Inversion of Magnetic Resonance Elastography Data for Real-Time Viscoelasticity Reconstruction

Mr. Juampablo Heras Rivera MS, Ms. Caitlin Neher MS, Dr. Mehmet Kurt PhD

University of Washington, Seattle, WA, United States

Introduction

Magnetic resonance elastography (MRE) is a quantitative method for noninvasively obtaining the mechanical properties of tissues, such as the liver, brain, and kidneys. MRE involves three steps: 1) mechanical actuation of the tissue, 2) a specialized phase-contrast MRI sequence to capture spatiotemporal displacement fields, and 3) an inversion algorithm to reconstruct material properties. Time-efficient inversion methods typically approximate tissue as a linear, incompressible and locally homogeneous material. Alternatively, nonlinear inversion (NLI) relaxes these assumptions at a high computational cost. Here, we frame inversion as done in NLI as a neural operator learning problem (oNLI), where the goal is to learn a mapping between displacement fields and complex shear stiffness in the infinite-dimensional function space, effectively learning a general operator that maps any subject's MRE displacement data to their respective shear moduli in one sub-second forward pass.

Methods

This retrospective study used publicly available data from 61 subjects (34F/27M, 14-75 years old), including anatomical T1 and multifrequency MRE at 30, 50, and 70 Hz with pneumatic anterior-posterior actuation. Elastograms were calculated using NLI and served as training targets. Three models were trained on the multifrequency displacement inputs: a baseline U-Net, a Fourier neural operator (oNLI), and a SPADE-oNLI variant incorporating a spatially-adaptive normalization block at each layer. Ten-fold cross-validation with held-out data was used for evaluation. Whole-brain and regional analyses quantified reconstruction accuracy relative to NLI.

Results

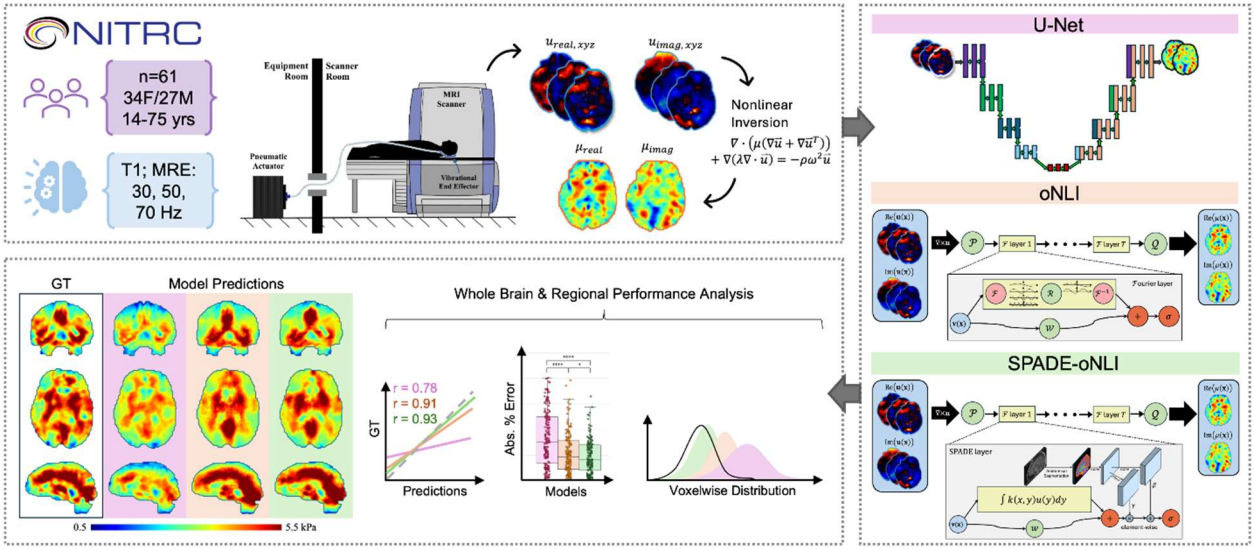
The oNLI framework enabled real-time inversion (30,000x speedup) while preserving the fine-grained spatial accuracy of NLI. Across evaluation metrics, the operator-learning approach consistently outperformed the U-Net, yielding improved correlation (r = 0.934 vs.

0.782), reduced absolute percent error (8.4% vs. 15.8%), and lower Wasserstein distance (0.035 vs. 0.063).

Discussion

This study introduces a data-driven operator-learning framework for real-time MRE inversion and demonstrates its extension with anatomical priors (SPADE-oNLI). The approach rapidly predicts heterogeneous tissue mechanical properties, representing progress towards real-time high-fidelity MRE for complex organs such as the brain.

Images (Optional)



Acknowledgements (Optional)

Data were provided by the Brain Biomechanics Imaging Repository (http://www.nitrc.org/projects/bbir). Principal Investigators: P. Bayly, D. Pham, C. Johnson, J. Prince, K. Ramesh, through grants U01 NS11212 and R56 NS055951.

Session Category

Emerging Areas: N/A

OA74-04

Sex-Specific Morphological Determinants of Cardiac Ageing in a Healthy Population

ir. Beatrice Moscoloni[1,2,3], Mr. Cameron A. Beeche[3], Prof. Dr. Julio A. Chirinos[3], Prof. Ir. Patrick Segers[1], Dr. ir. Mathias Peirlinck[2]

[1]Institute of Biomedical Technology - BioMMedA, Ghent University, Ghent, East Flanders, Belgium. [2]Department of BioMechanical Engineering, TU Delft, Delft, South Holland, Netherlands. [3]Division of Cardiovascular Medicine, UPenn, Philadelphia, PA, United States

Introduction

Despite growing awareness of sex differences in cardiovascular disease, the mechanisms underlying sex dimorphism in cardiac remodelling remain poorly understood. Recent analyses leveraging statistical shape modelling have revealed intrinsic sex differences in cardiac anatomy, even after accounting for body size, blood pressure and age [1]. Ageing is one of the most important unmodifiable risk factors for heart disease, and understanding its sex-specific effects on cardiac morphology is fundamental to uncover sex-specific pathways of structural remodelling.

Methods

In this study, we developed sex-specific models to investigate the morphological determinants of cardiac ageing in 2064 healthy participants from the UK Biobank, aged 46 to 83. Specifically, we employ an open-source image-to-mesh pipeline to reconstruct biventricular meshes from cardiac magnetic resonance images [2]. Then, we apply a previously developed shape modelling pipeline to derive a set of 3D morphological descriptors (principal modes) characterizing cardiac anatomy [1]. Then, we use automatic relevance determination regression to predict chronological age from the first 28 normalized modes as model inputs. Finally, we perform SHapley Additive exPlanations (SHAP)-based feature importance analysis stratified by sex, by combining the five most predictive features for each sex and quantifying each feature's percentage contribution to age prediction [3].

Results

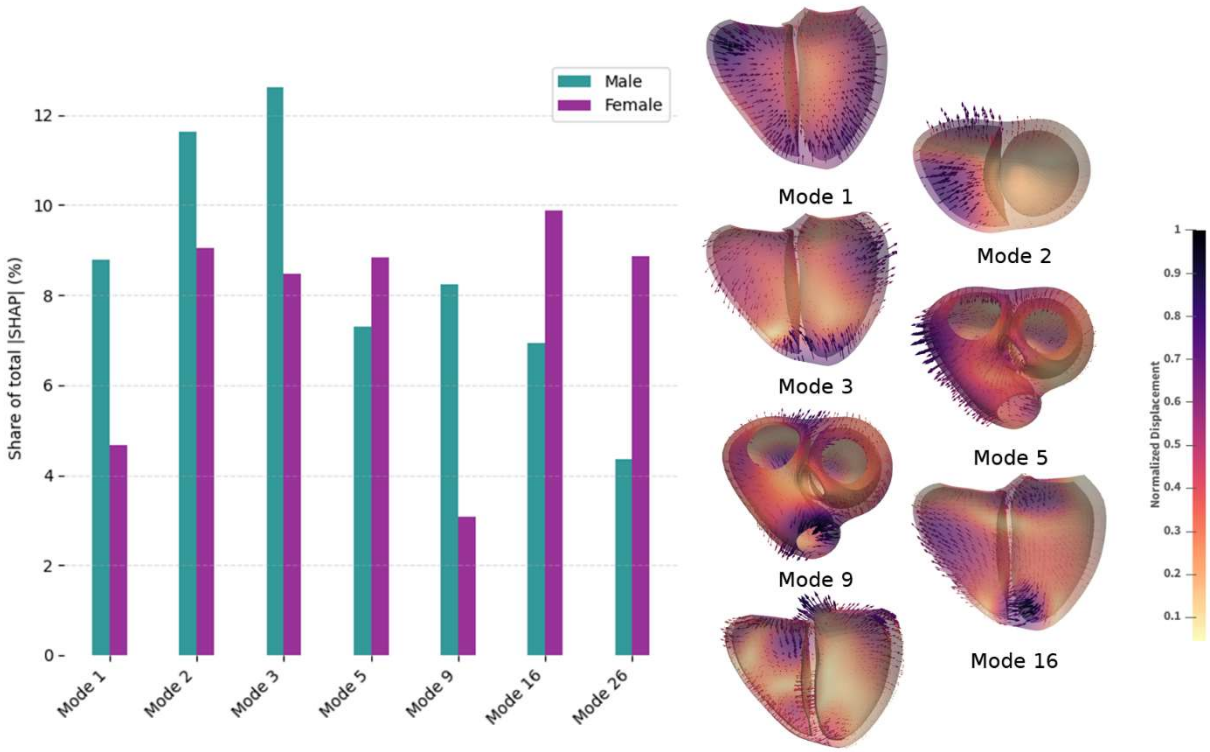
Modes 2 (increased anterior–posterior chamber width), 3 (eccentric structural remodelling), 5 (right ventricle -RV - lateral-septal width) and 16 (apical septal bulging) emerged as shared predictors of cardiac age, with mode 3 being 1.5× more important in males and mode 16 being 1.4× more important in females. Male-dominant features

included mode 1 (overall chamber size reduction) and mode 9 (tilting of the RV outflow tract), whereas mode 26 (basal septal bulging) was a female-specific determinant, contributing approximately four times more to cardiac age estimation in females than in males (Figure).

Discussion

Our findings reveal sex-specific patterns in the morphological determinants of cardiac ageing and identify shape features that differentially associate with heart ageing in males and females. These results provide important new insights into sex-specific patterns in structural cardiac remodelling.

Images (Optional)



References (Optional)

[1] Moscoloni, B., et al. J. Physiol., 2025

[2] Dillon, J. R, et al., LNCS, 2025

[3] Lundberg S., arXiv, 2017

Acknowledgements (Optional)

We thank Research Foundation Flanders (Grant No: 1PS524N) and the European Union's Horizon Europe research and innovation program (VITAL – Grant No.101136728) for funding of the project.

Session Category

Emerging Areas: N/A

OA74-05

Surface Topography-Based Analysis for Automated Classification of Adolescent Idiopathic Scoliosis (AIS)

Grad Research Assistant Mahmoud Hashim, Grad Research Assistant Mariam Ezzat, Postdoctoral Scholars Bruna da Rosa, Assistant Lecturer Behzad Vafaeian, Assistant Professor Qipei Mei, Professor Samer Adeeb, Associate Professor Lindsey Westover

University of Alberta, Edmonton, Alberta, Canada

Introduction

Adolescent Idiopathic Scoliosis (AIS) is the most common spinal deformity in youth, affecting 1–3% of children aged 10–16 years [1]. Diagnosis is based on a Cobb angle ≥10° on X-ray [1, 2], and while AIS occurs in both sexes, it is more progressive in females [3]. Posterior-anterior radiographs are the gold standard for monitoring [2]. Key limitations include the Cobb angle's poor representation of 3D deformity [3] and the radiation burden from repeated imaging and subjective screening referrals. This study aims to leverage machine learning methods for scoliosis screening, with the goal of reducing unnecessary radiographic referrals.

Methods

Torso scans from healthy volunteers (n = 482) and AIS participants (n = 602), aged 10–18, were collected using an infrared 3D structure sensor. AIS cases were confirmed through radiographic exams with Cobb angles of 10°–60°. Deviation maps were obtained using surface topography analysis. Each scan was mirrored, aligned to the sagittal symmetry plane, and mapped to a 102×102 grid. A corresponding 102×102 depth map was generated for the model's second pathway. A two-pathway CNN was trained for 100 epochs with early stopping. The dataset was split 70% training, 20% validation, and 10% testing, with severity levels balanced. Performance was evaluated using sensitivity and specificity.

Results

The model showed excellent training performance and strong validation generalization, with a sensitivity of 0.87 and a specificity of 0.98. On the independent test set, it achieved a sensitivity of 0.96 and a specificity of 0.94, indicating reliable performance with only minor specificity reduction.

Discussion

This model maintained high sensitivity and specificity across training, validation, and testing, indicating strong generalization and effective feature learning from depth and deviation features. Minor sensitivity reduction on the validation set did not affect overall stability, and test results confirmed reliable detection of AIS while limiting unnecessary referrals. These outcomes highlight the potential of 3D surface-based AI screening as a radiation-free complement to standard radiographic assessment.

References (Optional)

[1] Konieczny M.R. et al., J Children's Orthopaedics, 2013.

[2] Weinstein S.L. et al., The Lancet, 2008.

[3] Lechner R. et al., International Orthopaedics, 2017.

Session Category

Emerging Areas: N/A

OA74-06

Super-Resolution and Denoising of Left Ventricle 4D Flow Images

Mr. Yusuf Ozturk[1], Dr. Jie Zheng[2], Dr. Fanwei Kong[1]

[1]Washington University in Saint Louis, St. Louis, Missouri, United States. [2]Washington University in Saint Louis Medicine, St. Louis, Missouri, United States

Introduction

4D Flow Magnetic Resonance Imaging (MRI) is a non-invasive imaging technique that quantifies 3D blood velocity fields throughout the cardiac cycle. However, its clinical applications have been limited by substantial image noise, low temporal(40ms<) and spatial resolutions(2.5mm<), and prolonged acquisition time. Although recent work has applied deep learning (DL) methods to super-resolve and denoise 4D Flow MRI, prior approaches [1, 2, 3] focused primarily on vascular applications and assumed rigid blood vessels. We propose a strategy that integrates physics-informed DL with CFD simulations of the cardiac flow to denoise and super-resolve cardiac 4D flow MRI.

Methods

Our model leverages a Convolutional Neural Net to extract latent representations of the low-resolution velocity fields. We then sample this latent volume at arbitrary coordinates for an Multilayered Perceptron to predict velocity-pressure values. The network generates highly resolved velocity-pressure fields through physics-informed loss function. The physics loss is formulated using the Arbitrary Lagrangian–Eulerian form of the incompressible Navier–Stokes equations due to deforming left-ventricle. The datasets are generated using CFD simulations of six left-ventricle geometries with prescribed motions. The simulations for synthetic data are performed in svFSI[4]. Error measurements are used to assess model accuracy on validation dataset.

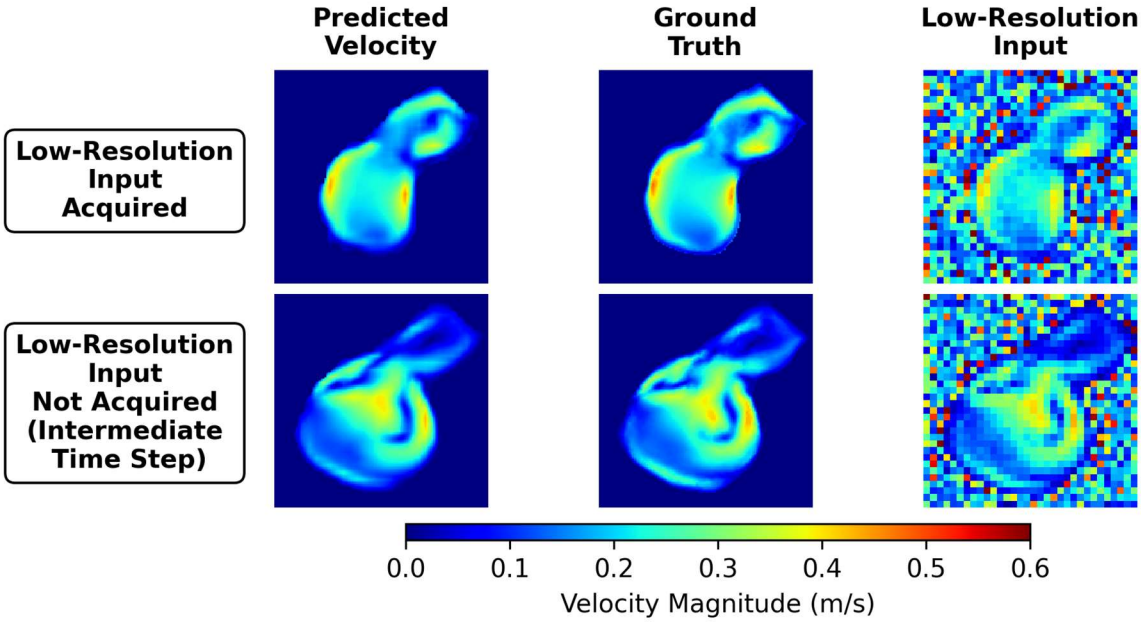
Results

Our model successfully predicts high-resolution velocity fields (up to a four-times increase in both spatial-temporal resolution) from low-resolution noisy images. Figure 1 shows the predicted fields from a low-resolution time step, along with predictions at an intermediate step that demonstrates the model's temporal super-resolution capability. However, the predictions at time steps where low-resolution input was acquired were more accurate. The difficulties in generalizing to real 4D Flow MRI after training solely on synthetic datasets are noted.

Discussion

Our study demonstrates a framework that successfully predicts high-resolution, denoised flow fields from low-resolution ventricular flow with moving boundaries. Future work includes validation on real 4D flow MRI and improving the temporal super-resolution capability.

Images (Optional)



References (Optional)

[1] Edward Ferdian et al. Frontiers in Physics, 2020.

[2] Mojtaba F Fathi et al. Computer Methods and Programs in Biomedicine, 2020.

[3] Suprosanna Shit et al. Frontiers in Artificial Intelligence, 2022.

[4] Chi Zhu et al. Journal of Open Source Software, 2022.

Session Category

Emerging Areas: N/A

OA75-02

Hydrostatic Pressure Reconfigures Nuclear Mechanics to Activate Proliferative Signaling in Cancer Cells

Ms. Norino Uenaka M.E., Prof. Daisuke Yoshino Ph.D.

Tokyo University of Agriculture and Technology, Koganei, Tokyo, Japan

Introduction

Cancer cells proliferate rapidly within confined tissue environments, where they experience elevated hydrostatic pressure generated by surrounding tumor masses. While mechanical forces are increasingly recognized as regulators of tumor progression, the mechanism by which hydrostatic pressure influences nuclear mechanics and cell behavior remains unclear. This study aims to elucidate how sustained hydrostatic pressure affects nuclear structure, chromatin organization, and cell-cycle regulation in pancreatic cancer cells.

Methods

MIA Paca-2 pancreatic cancer cells were exposed to controlled hydrostatic pressure (0, 50, or 100 mmHg for 24 hours) by subjecting the culture medium to compression. The nuclear stiffness was evaluated using atomic force microscopy (AFM). Immunofluorescence imaging was performed to visualize Lamin A/C, F-actin, and heterochromatin marker H3K9me3. The role of histone H3 methylation in Lamin A/C localization was assessed through pharmacological inhibition. The expression levels of the methyltransferase SUV39H1 and various cell-cycle regulators (Cyclin D1/E2, CDK4, phosphorylated Rb) were analyzed through the use of immunoblotting and immunostaining techniques.

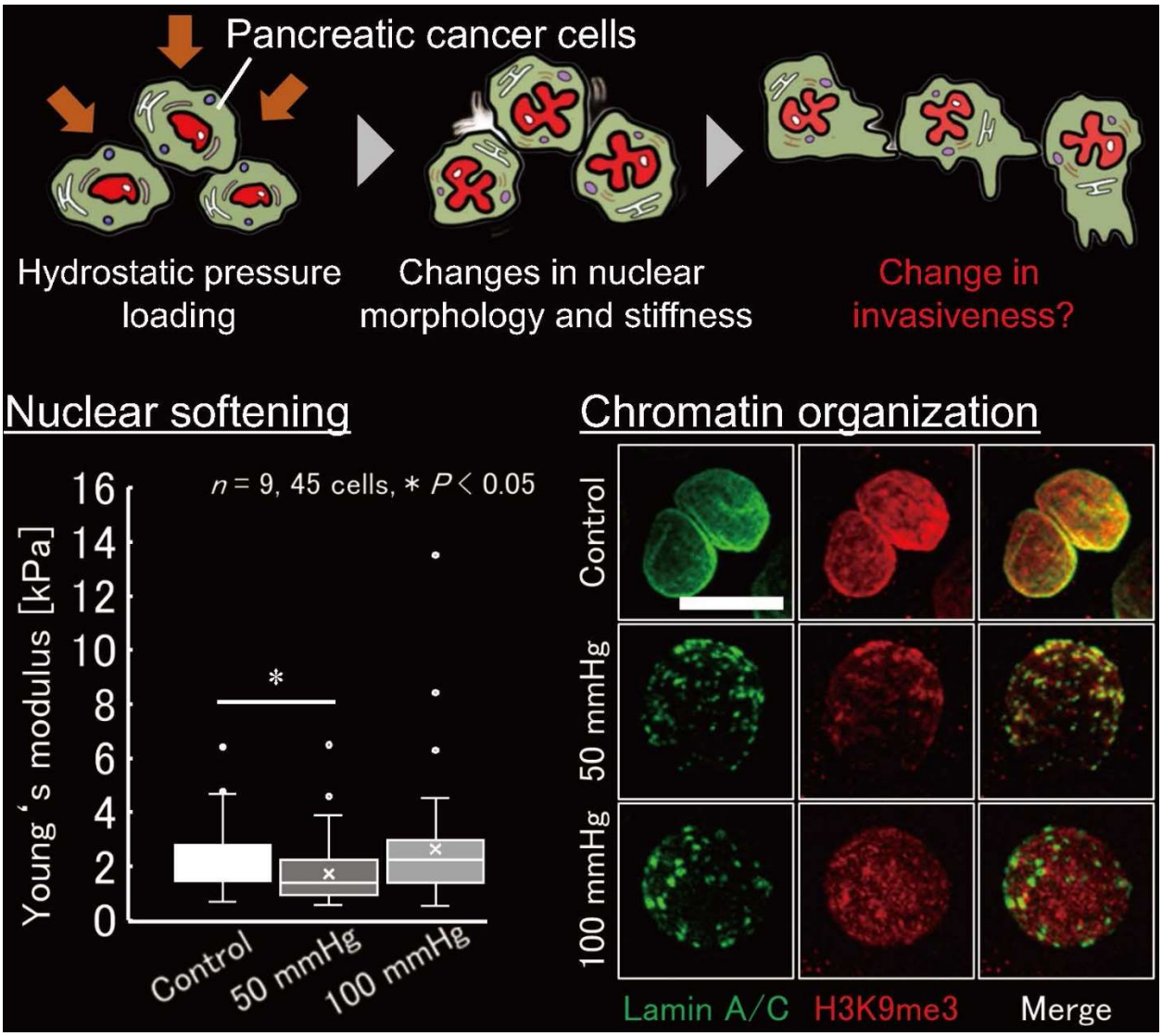
Results

Hydrostatic pressure induced a significant decrease in nuclear stiffness, indicating nuclear softening. Lamin A/C displayed pressure-dependent reorganization, characterized by a dotted distribution at the nuclear periphery. H3K9me3 exhibited altered nuclear localization under pressure, and inhibition of histone H3 methylation suppressed Lamin A/C redistribution, suggesting that chromatin modification is required for nuclear mechanoadaptation. SUV39H1 expression increased under elevated pressure, supporting an epigenetic regulatory mechanism. Pressure also enhanced cell proliferation, as evidenced by increased Ki-67 positivity and upregulation of G1–S transition proteins, including Cyclin D1/E2, CDK4, and phosphorylated Rb.

Discussion

These findings indicate that hydrostatic pressure acts as a potent mechanical cue that remodels chromatin, repositions Lamin A/C, and softens the nucleus through epigenetically regulated pathways. The concurrent activation of cell-cycle signaling suggests that nuclear mechanical adaptation facilitates tumor cell proliferation in confined environments. This mechanobiological mechanism potentially contributes to enhanced invasiveness and metastatic competence. Targeting nuclear stiffness regulation or histone modification pathways may represent a promising strategy to suppress pressure-driven malignant progression.

Images (Optional)



Session Category

OA75-03

Bioenergetic Pathways Regulate Distinct Patterns of Invasion and Matrix Remodeling in Breast Cancer Cells Upon YAP/TAZ Activation

Mr. Adil Khan[1,2], Mr. Haider Ali[1], Mr. Bishant Karki[1], Dr. Xaralabos Varelas[3], Dr. Jacopo Ferruzzi[1,2]

[1]University of Texas at Dallas, Richardson, TX, United States. [2]University of Texas Southwestern Medical Center, Dallas, TX, United States. [3]Boston University, Boston, MA, United States

Introduction

Breast cancer invasion depends on intracellular signaling and microenvironmental factors. Central to this process are the transcriptional coactivators YAP and TAZ, two regulators of the Hippo pathway [1]. YAP/TAZ are known to respond to biomechanical and metabolic cues by translocating to the nucleus, where they regulate genetic programs that promote tumor progression. In the tumor microenvironment, extracellular matrix (ECM) remodeling and altered cell metabolism modulate invasion. However, how YAP/TAZ coordinate ECM mechanics and cancer cell metabolism during invasion remains unclear.

Methods

MCF-10A cells and doxycycline-inducible MCF-10A YAP(5SA) and TAZ(4SA) mutants [2] were used to generate spheroids and conduct invasion assays in collagen. Micro-mechanical changes in collagen during invasion were monitored using 3D Magnetic Twisting Rheometry (3D-MTR), a technique developed in our lab to assess heterogeneous mechanical properties [3]. Metabolic changes in invading cells were monitored using Fluorescence Lifetime Imaging Microscopy (FLIM) of NAD(P)H [4]. To probe the role of metabolic pathways in YAP/TAZ-driven invasion, we inhibited oxidative phosphorylation (OxPhos) using rotenone/antimycin A (50nM each), and glycolysis using 2-deoxyglucose (5 mM).

Results

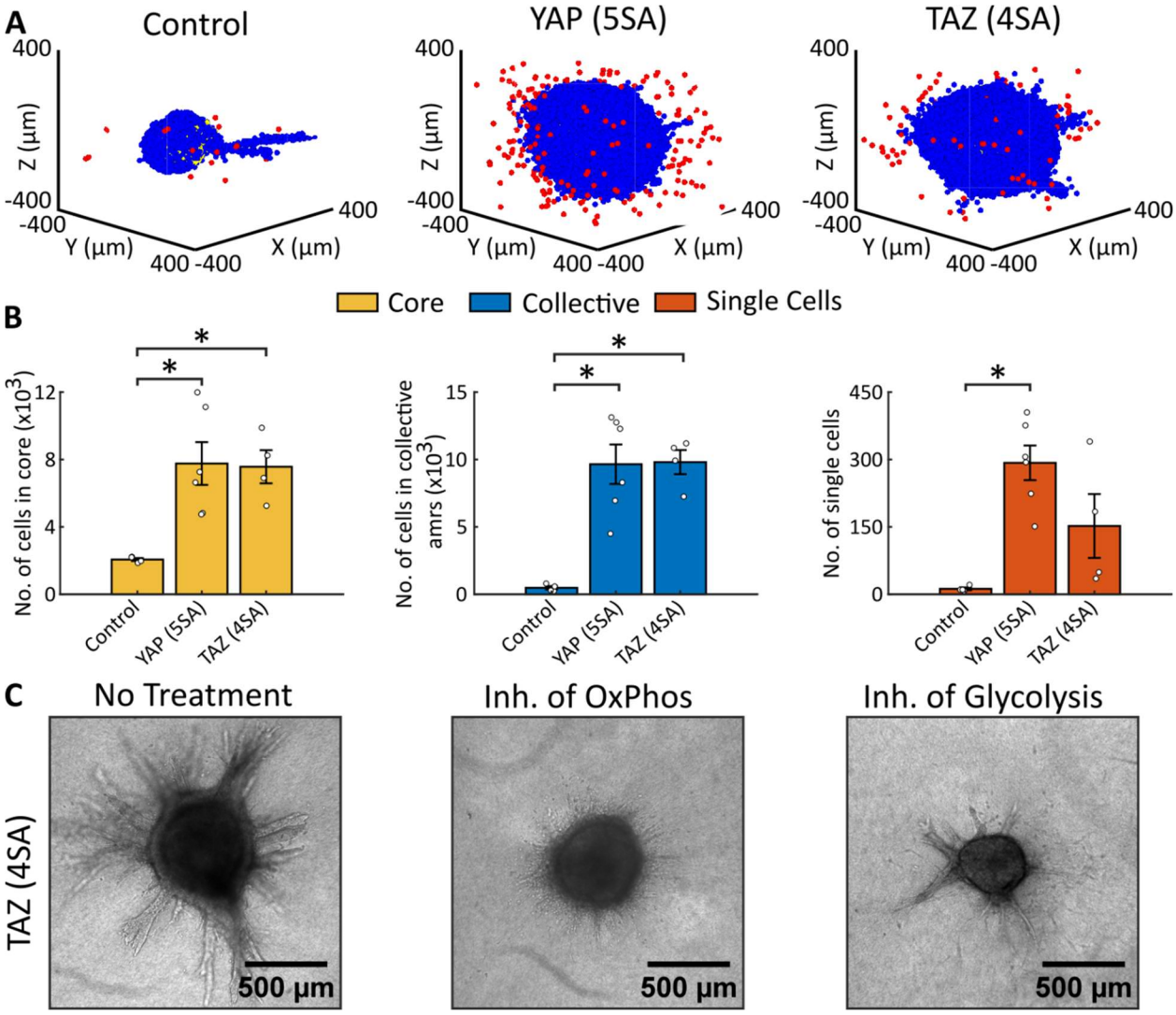
Control MCF-10A spheroids exhibited limited ECM remodeling and invaded collectively while YAP/TAZ-activated spheroids displayed increased proliferation and invaded aggressively through both collective protrusions and single-cell migration (Fig. 1A-B). 3D-MTR showed that YAP/TAZ-activated spheroids stiffened peritumoral collagen by increasing collagen alignment. FLIM showed that, upon YAP/TAZ activation, the spheroid core

exhibited an optical signature consistent with glycolysis, while the periphery adopted a mix of glycolysis and OxPhos. In YAP/TAZ-activated spheroids, inhibition of OxPhos shifted invasion from collective to single-cell modality (Fig. 1C). Conversely, inhibition of glycolysis reduced single-cell migration, shifting invasion towards collective migration (Fig. 1C).

Discussion

We found that YAP/TAZ activation couples ECM stiffening with metabolic plasticity to regulate invasion modality. Inhibiting oxidative metabolism shifted invasion from collective to single-cell migration, while inhibiting glycolysis had the opposite effect, suggesting that the metabolic state controls both cancer cell contractility and invasion modality.

Images (Optional)



References (Optional)

[1] Piccolo *et al.*, Nat Cancer, 2023.

[2] Hiemer *et al.*, J Biol Chem, 2014.

[3] Khan *et al.*, in preparation.

[4] DeCamp *et al.*, Sci Rep, 2020.

Acknowledgements (Optional)

This project was funded, in part, by The UT Dallas Office of Research and Innovation through the SPIRe program and by NIH grant R01 EB034360.

Session Category

Cell Biomechanics: Mechanobiology

OA76-02

Hyper-Selective Neurectomy Shifts Sarcomere Length in Spastic Human Biceps Toward Normal Values

Dr. Zheng Wang[1], Dr. Rajeswari Pichika2[2,3], Dr. Peter Rhee[1], Dr. Kenton Kaufman[1], Dr. Richard Lieber[2,3]

[1]Mayo Clinic, Rochester, MN, United States. [2]Northwestern University, Chicago, IL, United States. [3]Hines V.A. Hospital, Mayowood, IL, United States

Introduction

Spasticity after upper motor neuron injury causes muscle overactivity and structural remodeling. Neurectomy is known to reduce spasticity, and hyper-selective neurectomy (HSN) is emerging as a targeted technique with advances in anatomy and intraoperative mapping. Although HSN's clinical benefits are established, its structural impact on human muscle remains unclear. To address this knowledge gap, this study quantified sarcomere length (SL) before and after HSN.

Methods

Individuals with elbow flexor spasticity undergoing planned two-stage HSN were prospectively enrolled (n = 10). Stage 1 released the elbow flexors and provided a pre-HSN biceps brachii biopsy. Stage 2 performed three months later to treat forearm flexors, provided a post-HSN bicep brachii biopsy. All biopsies were obtained with customized clamps at predefined elbow angles (50°, 90°, 135°), fixed, and analyzed for SL. Clinical spasticity was assessed before Stage 1 and again before Stage 2 using the Modified Ashworth Scale (MAS). Control samples were obtained from biceps brachii in individuals undergoing cubital tunnel release at 50° and 90° due to limited exposure. A mixed-effects model tested within-subject pre-to-post differences and comparisons with controls.

Results

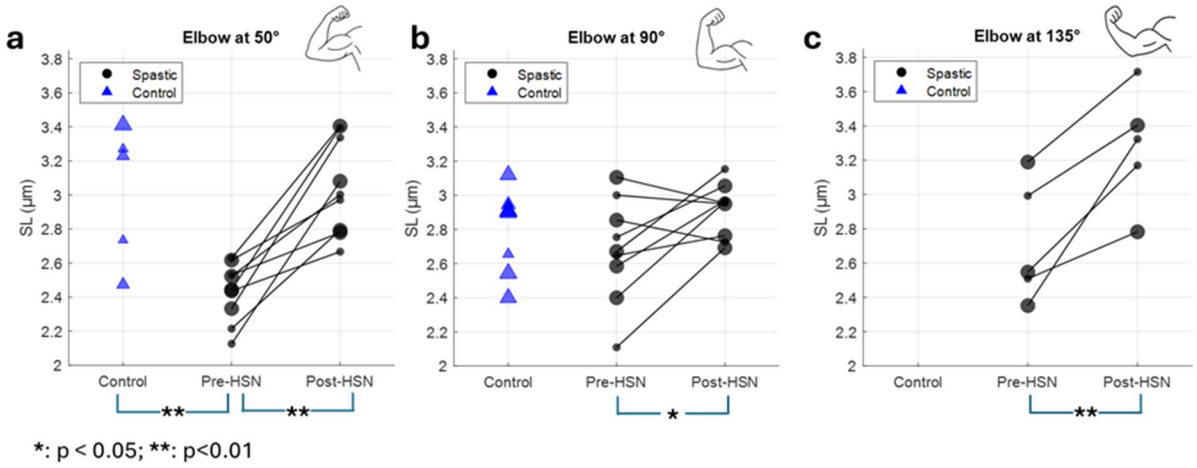
MAS scores decreased significantly, from 1.89 ± 0.93 to 0.35 ± 0.53 ($p < 0.05$) after HSN. At 50° of elbow flexion, spastic biceps exhibited significant shorter sarcomeres preoperatively (2.45 ± 0.18 μm), compared to control values (3.02 ± 0.40 μm, $p < 0.01$). After HSN, SL (3.05 ± 0.28 μm) increased significantly ($p<0.01$), no longer different from controls (Fig. 1a.). At 90°, neither pre-HSN (2.70 ± 0.29 μm) nor post-HSN SL (2.91 ± 0.16 μm) differed significantly from controls (2.81 ± 0.23 μm) ($p >0.05$). However, paired analysis showed a

significant increase in SL from pre- to post-HSN ($p<0.05$, Fig. 1b). At 135°, SL significantly increased ($p<0.05$, Fig. 1c) from pre-HSN (2.72 ± 0.36 μm) to post-HSN (3.24 ± 0.32 μm).

Discussion

Spastic muscles showed measurable increases in sarcomere length (SL) toward normal values when excessive neural input was reduced with a HSN. These changes highlight the muscle fiber capacity to undergo rapid structural remodeling, with sarcomere organization in response to altered activation patterns.

Images (Optional)



References (Optional)

Acknowledgements (Optional)

This work was supported by Mayo Clinic internal grant, Veterans Affairs (VA) Grant 1 I01RX002462, Research Career Scientist Award Number IK6 RX003351 from the US Department of Veterans Affairs Rehabilitation R&D Service and the W. Hall Wendel Jr. Musculoskeletal Research Professorship.

Session Category

Orthopaedic Biomechanics: Upper Extremities

OA76-03

Accelerated Rotator Cuff Degeneration in Manual Wheelchair Users with Spinal Cord Injury: Longitudinal MRI and 5-Year Transition Modeling

Dr. Omid Jahanian[1], Ms. Meegan Van Straaten[1], Dr. Jiefei Wang[2], Dr. Hannah Houde[2], Ms. Kathylee Pinnock Branford[3], Dr. Stephen Cain[3], Dr. Naveen Murthy[1], Dr. Melissa Morrow[2]

[1]Mayo Clinic, Rochester, Minnesota, United States. [2]The University of Texas Medical Branch, Galveston, Texas, United States. [3]West Virginia University, Morgantown, West Virginia, United States

Introduction

Manual wheelchair (MWC) use places high biomechanical demand on the shoulder, potentially accelerating rotator cuff tendon degeneration. This study compares 2-year progression of rotator cuff tendon tears between MWC users with spinal cord injury (SCI) and age- and sex-matched able-bodied (AB) individuals, and estimates 5-year probabilities of tendon pathology progression.

Methods

In this longitudinal cohort study, 37 MWC users with SCI and 44 AB individuals completed baseline and 2-year follow-up shoulder MRI. Rotator cuff tendon health was graded using a novel scoring system from normal tendon to full-thickness tear, and progression was defined as an increase in tear score from baseline to follow-up [1]. Presence of shoulder pain was recorded at both visits. Logistic regression examined factors associated with tear progression. 5-year transition probabilities among tendon states (normal, tendinopathy, tear) were estimated using multi-state Markov transition models using all available longitudinal data.

Results

Over two years, MWC users showed significant increases in tendon tear scores in both dominant ($p=0.001$) and non-dominant shoulders ($p=0.016$), whereas AB individuals showed no significant progression. After adjusting for age, sex, and baseline tendon scores, MWC users had 2.26 times higher odds of tear progression (95% CI:1.05–5.00; $p=0.04$). Older age was associated with progression in both cohorts. Shoulder pain remained more common in MWC users but did not consistently correspond with rotator cuff tendon pathology progression.

Five-year transition estimates showed markedly faster progression in MWC users (Figure 1). The probability of progressing from normal to tear in the dominant supraspinatus was

37.3% in MWC users versus 3.1% in AB individuals, and the probability of progressing from tendinopathy to tear was 70.8% versus 10.0%, respectively.

Discussion

MWC users with SCI showed greater 2-year progression of rotator cuff pathology than AB individuals and higher 5-year probabilities of transitioning from normal or tendinopathy to tear states. Age contributed to progression, while shoulder pain did not reliably reflect changes in tendon health. These findings highlight the need for early detection and targeted strategies to preserve shoulder integrity in individuals with SCI.

Images (Optional)

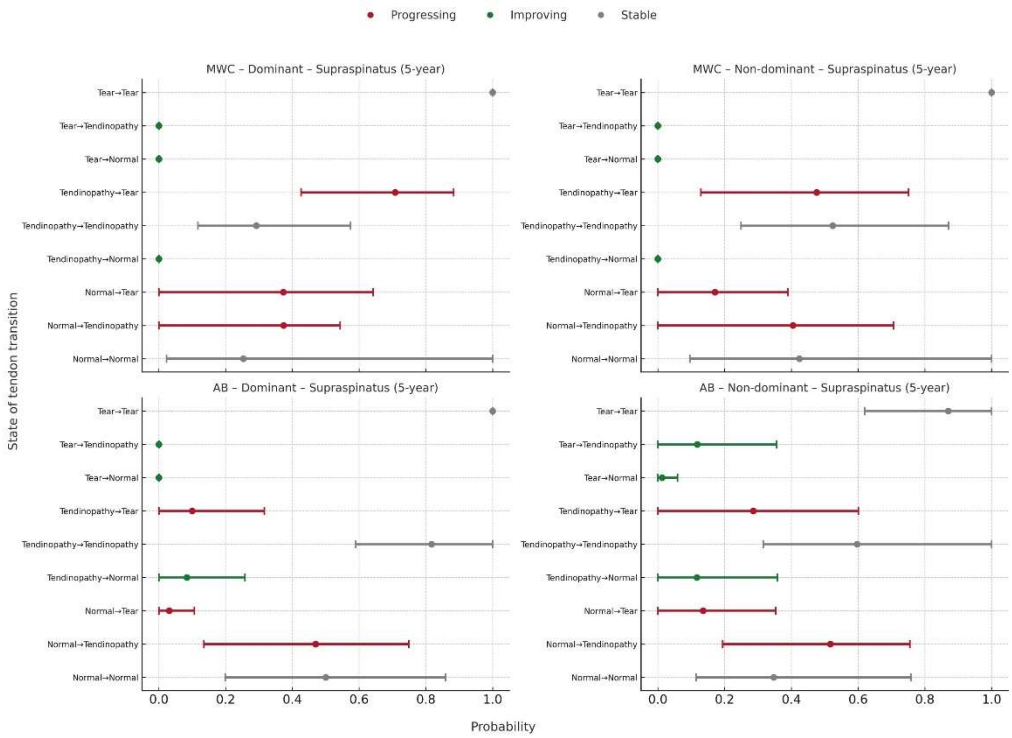


Figure 1. Five-year transition probabilities for supraspinatus tendon health in manual wheelchair (MWC) users and able-bodied (AB) individuals with 95% confidence intervals. Forest plots display the probability of transitioning between tendon states (normal, tendinopathy, tear) for dominant and non-dominant shoulders.

References (Optional)

[1]: Jahanian O et al. (2023). *J Spinal Cord Med*, 46(3):466–476.

Acknowledgements (Optional)

NIH Eunice Kennedy Shriver National Institute of Child Health and Human Development (R01HD084423)

Session Category

Orthopaedic Biomechanics: Upper Extremities

OA76-04

Compensatory Scapulothoracic Mechanisms and Glenohumeral Deficits in Rotator Cuff Pathology: A Multi-Site 3D Motion Capture Biokinetic Analysis of 76 Shoulders

Dr. Renato Miyadahira MD[1], Dr. Felipe F. Gonzalez MD[2,1], Ms. Vennela Challagondla BS, MPH[3], Mr. Cauã Neves[1], Dr. Eliane Guadagnin PhD[1], Dr. Marcos Amstalden Barros MD[2,1], Dr. Tiago Zimerman MD[2,1], Dr. Caroline Popovicz Nunes MD[2,1], Mr. Joshua M. Samaniego BS[2], Dr. Gustavo Leporace MSc, PhD[1], Dr. Jonathan A. Gustafson PhD[2,1], Dr. Leonardo Metsavaht PhD[1], Dr. Jorge Chahla MD, PhD[2,4]

[1]Instituto Brasil de Tecnologias da Saúde (IBTS), Rio de Janeiro, RJ, Brazil. [2]Rush University, Chicago, IL, United States. [3]The University of Illinois Chicago, Chicago, IL, United States. [4]Midwest Orthopaedics at Rush, Chicago, IL, Brazil

Dr. Renato Miyadahira

Introduction

Rotator cuff pathology often presents along a spectrum of functional limitations. These disorders affect shoulder strength, range of motion (ROM), and scapulohumeral rhythm, yet few studies have evaluated these biokinetic factors simultaneously. This study aimed to compare shoulder kinematics during arm elevation, as well as measures of strength and passive ROM, between affected shoulders and their contralateral healthy shoulders in individuals with rotator cuff pathology.

Methods

This cross-sectional observational study evaluated 38 adults who presented with unilateral rotator cuff pathology and a healthy contralateral shoulder (mean age 47 ± 12.8 years; 31.6% female) across five motion analysis laboratories. Bilateral 3D scapulothoracic and glenohumeral kinematics during scapular-plane elevation, passive ROM testing, and isometric strength testing (normalized to body weight) were obtained. Kinematic data were collected using a four-camera high-speed motion capture system using International Society of Biomechanics standards. Variables included glenohumeral elevation, scapular upward rotation, tilt, internal/external rotation, vertical displacement, maximum humeral elevation, and scapulohumeral rhythm. Passive shoulder ROM was measured using a digital inclinometer, and isometric strength was assessed using a hand-held dynamometer.

Paired t-tests ($p < 0.05$) compared affected and contralateral shoulders and effect sizes were reported using Cohen's d.

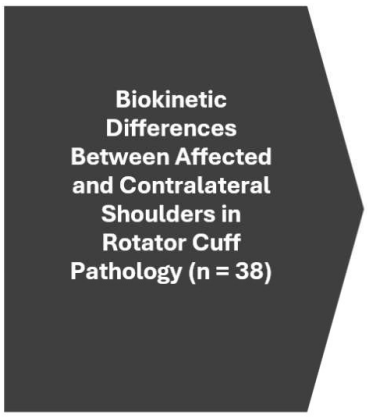
Results

Kinematic differences emerged only above 90° of elevation (Table 1). Compared with the contralateral shoulder, the affected side showed reduced glenohumeral elevation (61.5° ± 8.8° vs. 64.3° ± 6.8°; $p = 0.011$), reduced maximum humeral elevation (153.6° ± 15.2° vs. 158.7° ± 14.9°; $p = 0.003$), greater scapular upward rotation (29.9° ± 6.7° vs. 27.3° ± 5.4°; $p = 0.011$), and increased scapulohumeral rhythm (0.50 vs. 0.43; $p = 0.002$). No significant differences were observed below 90°. Passive ROM did not differ between sides. Strength deficits were limited to external rotation in the neutral position ($p < 0.05$). Effect sizes ranged from 0.23–0.35.

Discussion

Individuals with rotator cuff pathology demonstrated increased scapular upward rotation and decreased glenohumeral elevation during higher-range arm elevation, consistent with compensatory mechanisms reported in prior studies. These adaptations may increase joint reaction forces, potentially contributing to long-term dysfunction. Integrating strength, ROM, and kinematic assessments can identify impairments and compensatory strategies to address clinically.

Images (Optional)



Domain	Variable	Affected Shoulder	Contralateral Shoulder	P Value	Effect Size (d)
Kinematics > 90°	Glenohumeral elevation (°)	61.5 ± 8.8	64.3 ± 6.8	0.011	0.23
	Maximum humeral elevation (°)	153.6 ± 15.2	158.7 ± 14.9	0.003	0.35
	Scapular upward rotation (°)	29.9 ± 6.7	27.3 ± 5.4	0.011	0.31
	Scapulohumeral rhythm	0.50	0.43	0.002	0.35
Kinematics < 90°	All variables	No significant differences	—	> 0.05	—
Passive ROM	All measures	No significant differences	—	> 0.05	—
Strength	External rotation (neutral)	Decreased	—	< 0.05	—

Table 1: Comparison of scapulothoracic and glenohumeral kinematics, passive range of motion, and isometric strength between affected and contralateral shoulders in individuals with unilateral rotator cuff pathology (n=38). Significant differences were observed only above 90° of humeral elevation, including reduced glenohumeral elevation and maximum humeral elevation, and increased scapular upward rotation and scapulohumeral rhythm on the affected side. No significant differences were identified below 90° or in passive range of motion. Values are reported as mean ± standard deviation where applicable. Effect sizes are reported as Cohen's d.

Session Category

Orthopaedic Biomechanics: Upper Extremities

OA76-05

It is Worth the RASL: Scapholunate Ligament Reconstructive Surgery Aids Restoration of Healthy Kinematic Patterns

Mr. Justen Saini[1,2], Dr. Brodie Ritchie[3,4], Dr. Neil White[2,3,4], Dr. Koren Roach[1,2,5,6], Dr. Sarah Manske[2,5]

[1]University of Calgary, Department of Biomedical Engineering, Calgary, Alberta, Canada. [2]University of Calgary, McCaig Institute, Calgary, Alberta, Canada. [3]University of Calgary, Department of Surgery, Calgary, Alberta, Canada. [4]South Campus Research Unit for Bone and Soft Tissue, Calgary, Alberta, Canada. [5]University of Calgary, Department of Radiology, Calgary, Alberta, Canada. [6]University of Calgary, Faculty of Kinesiology, Calgary, Alberta, Canada

Introduction

Scapholunate interosseous ligament (SLIL) injuries are the most common wrist ligament injury, often resulting from a fall on an outstretched hand. These injuries disrupt normal carpal biomechanics, including altered load transmission and carpal kinematics. A hallmark symptom of these injuries is pain in load-bearing positions. SLIL surgical reconstructions, such as the Reduction and Association of the Scaphoid and Lunate (RASL) procedure, can be employed in an attempt to restore normal biomechanics. However, the efficacy of these procedures in restoring wrist function and stability in functionally load-bearing positions remains unclear, due to limitations with current unloaded imaging modalities.

Objective: Evaluate the efficacy of the RASL procedure to restore healthy carpal kinematics and arthrokinematics in functionally load-bearing positions using weight-bearing computed tomography (WBCT).

Methods

Healthy controls, SLIL-injury participants, and minimum 1-year post-RASL participants (n = 10/group) underwent WBCT scans in a non-weightbearing position (NWB), a weight-bearing pushup bar grip position (WBPUB), and a weight-bearing extension position (WBEXT). Participants with advanced osteoarthritis were excluded. Helical axis orientations, bone rotations, contact area between neighbouring bones, and contact centroid shifts were compared between groups using a repeated measures ANOVA.

Results

SLIL-injured wrists demonstrated altered carpal bone rotations compared to controls when loaded, including significantly greater scaphoid rotation (WBPUB: p=0.027, WBEXT: p=0.012) and significantly decreased lunate rotation (WBPUB: p=0.037, WBEXT: p=0.012). Radioscaphoid contact area increases from the NWB position to WBEXT were significantly greater for injured wrists compared to controls (p=0.002) and RASL-reconstructed wrists (p=0.001). Contact centroid shifts were similar in the controls and RASL-reconstructed wrists, indicating healthy load distribution is restored following surgery (Figure 1).

Discussion

SLIL-injured wrists had altered kinematics and contact behaviour under load, particularly in the extended position, which may contribute to accelerated degenerative changes. In contrast, RASL-reconstructed wrists demonstrated rotational coupling and load distribution comparable to healthy wrists under load, indicated by centroid shifts consistent with healthy wrists and significantly reduced radioscaphoid contact area compared to injured wrists. These findings support RASL reconstruction as an option to restore functional biomechanics under physiologic loading. WBCT provides a clinically relevant tool to assess post-surgery biomechanics under load, supporting future improvements in surgical planning and outcome assessments.

Images (Optional)

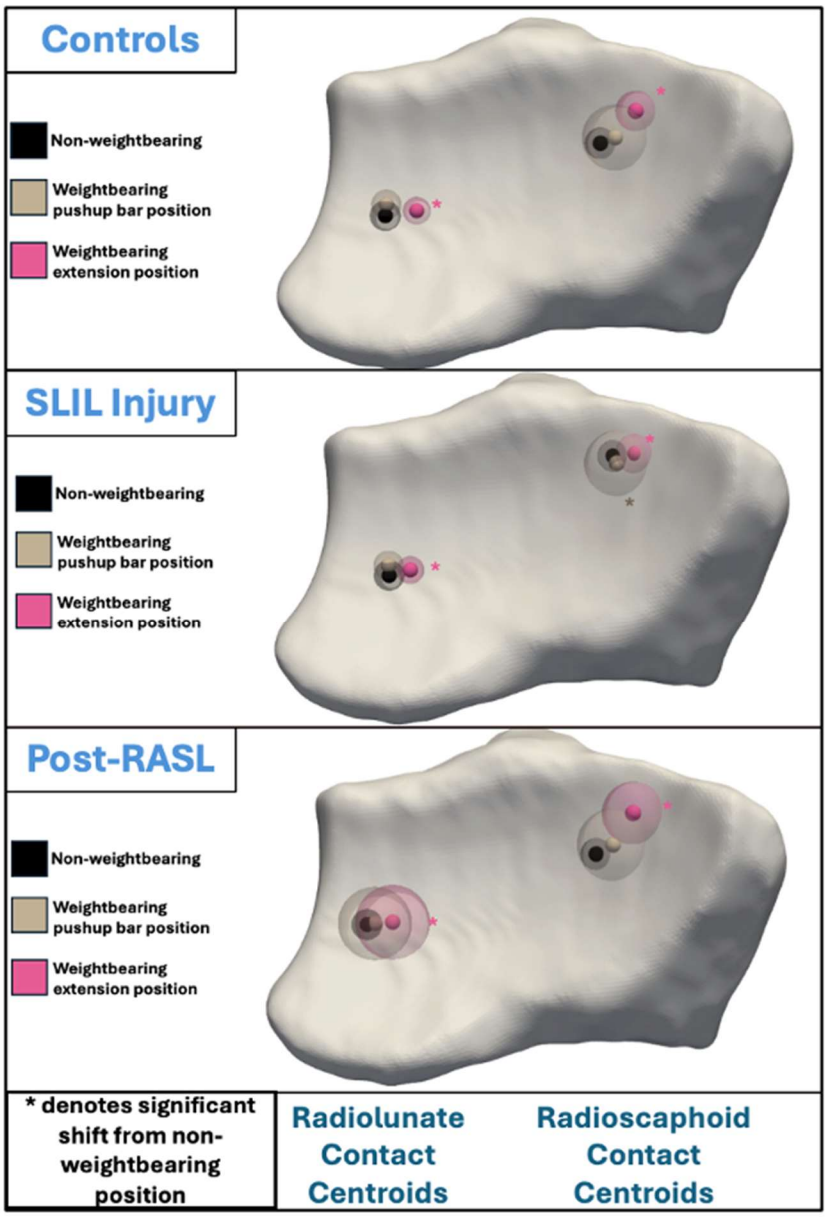


Figure 1: Locations of the contact centroids in the radiolunate and radioscaphoid articulations projected onto a distal view of the radius for non-weightbearing (black), weightbearing push-up (tan), and weightbearing extension (pink) positions. The smaller opaque sphere represents the mean location of the centroid, with the larger transparent sphere representing the standard deviation in the centroid location.

Session Category

Orthopaedic Biomechanics: Upper Extremities

OA77-02

Developing a Collagen Fiber-Mimetic Strain Model of the Meniscus Cell Mechanoresponse After Injury

Ms. Janie Johnson, Dr. Katherine Meinhold Ph.D., Dr. Jennifer Robinson Ph.D.

University of Washington, Seattle, Washington, United States

Ms. Janie Johnson

Dr. Katherine Meinhold

Introduction

Meniscal injuries are the most common intraarticular knee injury, with radial meniscus tears exhibiting the poorest healing potential partly due to collagen fiber structure and anisotropy. We hypothesize that the loss of residual strain occurring when collagen fibers are torn leads to increased apoptosis and fibrosis, similar to prior results in intervertebral disc fibrocartilage [1]. Our poly(caprolactone) (PCL) electrospun fibrous meshes recapitulate the structure and material properties of native meniscus collagen fibers, but there remains a need to develop an *in vitro* injury model using these meshes to incorporate fiber mechanical properties. Thus, the objective herein is to establish an *in vitro* injury model and examine the human meniscal cell (hMC) response to physiological strain after a partial tear.

Methods

Material Properties: Two approaches were tested to develop a model that captures residual strain loss and resultant hMC behavior. First, plastic deformation of aligned and non-aligned samples was characterized at 100% strain in a CellScale Mechanoculture J. Second, a 1.5mm cut (37.5% total width) was created in aligned fibrous meshes, mimicking a tissue-level radial tear (***Figure 1A***). Physiological 10% strain was applied to aligned meshes (2-3 technical replicates, per condition) for 3 hours and resultant stress determined. Cell Response: Morphology, apoptosis, collagen production and fibrotic marker αSMA were assessed from MCs subjected to 500mN pre-load, 10% strain, and 100% strain for 48 hours.

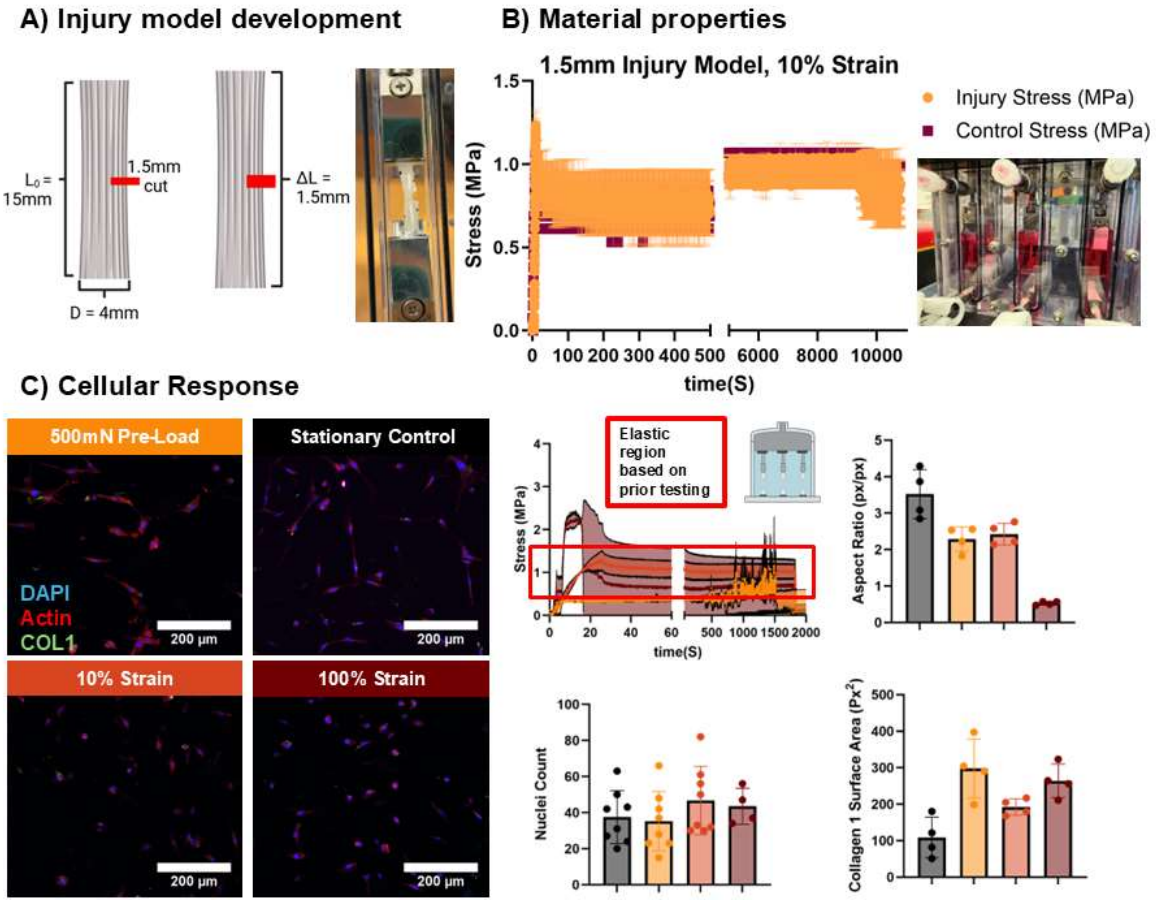
Results

Both tear models achieve mechanical properties in the range of native menisci without substantial stress relaxation (***Figure 1B:*** *1.5mm cut,* ***1C:*** *100% strain*). The evaluated stress of 1.5mm-tear (0.91±0.1MPa) and control (1.3±0.3MPa) samples at 10% strain matches the elastic region of 100% strain samples. Quantification of MC alignment on non-aligned fibers showed a modest decrease in aspect ratio after 10% strain (***Figure 1C***, 2.4 vs. 3.5 control) whereas 100%, injurious strained cells displayed dramatic rounded morphology (aspect ratio 0.5), indicating aberrant behavior. Current studies are focused on 10% strain in the1.5mm-tear injury model to characterize YAP/TAZ response in hMCs.

Discussion

By establishing an *in vitro* mechanobiology system we can investigate regenerative strategies to combat aberrant mechanosignaling.

Images (Optional)



References (Optional)

[1] Bonnevie, ED *et al. Nat. Biomed. Eng.* (2019)

Session Category

Tissue Engineering: Mechanobiology

OA77-03

Architected 3D Micro-Scaffold as a Mechanotransduction Platform for Stemness Preservation in Mesenchymal Cells

Mr Giovanni Buccioli[1], Ms Cristina Cortesi[1], Dr Chiara Martinelli[1], Mr Morteza Behrouzitabar[2], Ms Benedetta Gavazzoni[3,4], Dr Claudio Conci[1], Dr Alessandra Nardini[4], Dr Rebeca Martínez Vázquez[4], Dr Stephana Carelli[5], Dr Renzo Vanna[4], Prof Dario Polli[3], Dr Giuseppe Antonacci[6], Prof Manuela Teresa Raimondi[1], Prof Emanuela Jacchetti[1]

[1]Department of Chemistry, Materials and Chemical Engineering "Giulio Natta", Milan, Italia, Italy. [2]Department of Physics, Università di Milano-Bicocca, Milan, MI, Italy. [3]Department of Physics, Politecnico di Milano, Milan, MI, Italy. [4]Institute for Photonics and Nanotechnologies, CNR, Milan, MI, Italy. [5]Center of Functional Genomics and Rare Diseases, Buzzi Children's Hospital, Milan, MI, Italy. [6]Specto Photonics, Milan, MI, Italy

Introduction

Mesenchymal stromal/stem cell (MSC) therapies offer potent immunomodulatory and anti-inflammatory benefits, making them attractive for regenerative medicine [1]. However, translation is limited by low expandability ex vivo and a risk of differentiation with loss of stemness during standard 2D cell expansion. Preserving MSC phenotype requires recapitulating mechanotransduction pathways in vivo-like. Therefore, we present an architected 3D microscaffold to evaluate stemness maintenance without biochemical inducers, which are often undesirable prior to clinical re-implantation.

Methods

The 3D microscaffold, the Niche, consists of a lattice of cubic pores (15×15×15 μm^3) fabricated by two-photon polymerisation of the biocompatible resin SZ2080 directly onto glass coverslips [2]. Rat bone-marrow–derived MSCs were cultured either on flat glass (2D) or within the Niche. F-actin organisation and nuclear morphology were quantified from confocal immunofluorescence images. Fluorescence-lifetime imaging microscopy (FLIM) inferred cell metabolism, while Brillouin microscopy quantified cell stiffness. Bulk RNA sequencing was performed to assess differential gene expression and pathway enrichment between 2D and 3D conditions.

Results

Cells cultured in the Niche showed fewer actin stress fibres than in 2D, with F-actin redistributed into a cortical rim (Fig. 1a,b). Nuclear shape modelling showed rounder nuclei

in 3D compared with 2D (Fig. 1c,d). Brillouin microscopy revealed a difference in cell stiffness between 2D and 3D conditions (Fig. 1e,f). FLIM indicated a shift towards a more glycolytic metabolic state in 3D culture. Pathway enrichment analysis identified significantly overexpressed mechanotransduction and stemness-related programmes in 3D versus 2D.

Discussion

These results indicate that the architected 3D scaffold provides defined structural cues that reorganise actin towards a cortical pattern, reshape nuclear geometry and shift cell mechanical properties, with a coherent move towards a glycolytic state. The enrichment analysis supports the view that this environment helps preserve a mesenchymal, non differentiated phenotype compared with 2D. This makes the scaffold a robust, reagent free platform for standardised MSC expansion and biomechanics informed screening.

Images (Optional)

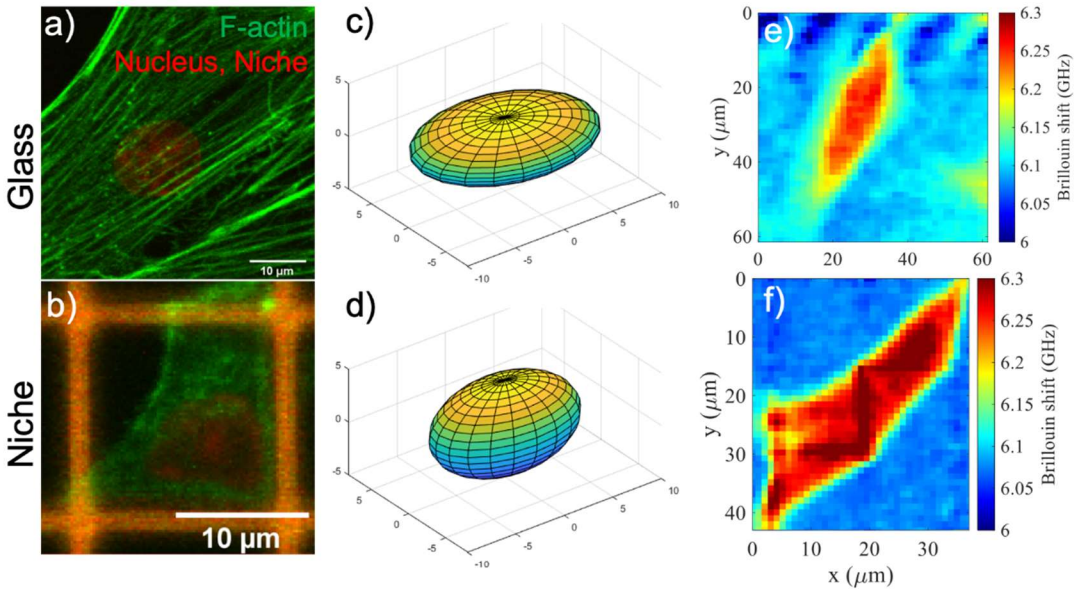


Fig. 1 Representative characterisation of MSCs on 2D glass and in the 3D Niche. (a,b) Immunofluorescence of F-actin (green), nuclei and Niche scaffold (red), showing stress fibres in 2D and predominantly cortical actin in the Niche. (c,d) Nuclear shapes modelled from morphometric parameters, flatter in 2D and rounder in 3D. (e,f) Brillouin shift maps highlighting differences in intracellular mechanical properties between 2D and 3D culture.

References (Optional)

[1] Donnaloja et al., APL Bioeng 7, 036112, 2023.

[2] Martinelli et al., Mater Today Bio 35, 102328, 2025.

Acknowledgements (Optional)

MIUR (PRIN2022-VISION, cod. 2022FLXS8T); ERC (BEACONSANDEGG, G.A. 101053122); EU H2020 (flIMAGING3D, G.A. 101073507). We thank Letizia Messa and Bianca Barzaghini for preparing the samples for transcriptomic analyses.

Session Category

Tissue Engineering: Mechanobiology

OA77-04

Wavy Topography Enhances Contractile Phenotype and YAP Nuclear Localization in Primary Vascular Smooth Muscle Cell

Mr. Wei-Chen Leo Lin, Dr. Pen-hsiu Grace Chao

National Taiwan University, Taipei, Taiwan, Taiwan

Introduction

Vascular smooth muscle cells (VSMCs), located in the medial layer of blood vessels, regulate vascular tone and maintain vessel function. Pathological stimuli and aging can drive VSMCs from a contractile to a synthetic phenotype [1]. We previously demonstrated that wavy fibrous scaffolds, which mimic the native arterial structure, enhance contractile marker expression and suppress proliferation [2]. Yes-associated protein (YAP), a mechanosensitive regulator has been implicated in VSMC phenotype regulation [3-5]. In this study, we hypothesize that wavy structures modulate VSMC phenotype through YAP-dependent mechanotransduction.

Methods

Polylactic fibrous scaffolds were manufactured based on previously reported protocols [6]. Primary VSMCs isolated from murine thoracic aortas via explant culture were cultured on straight or wavy electrospun scaffolds for 3 weeks. VSMC phenotype was assessed via fluorescent staining and gene expression analysis for contractile markers.

Results

VSMCs on wavy fibers followed the fiber structure with curved actin cytoskeletal organization, reduced alignment, and significantly increased expression of contractile markers SM22 and calponin (Fig A-C). The immunocytochemistry findings were consistent with increased transgelin expression, which encodes SM22 (Fig. D). At the same time, VSMCs on wavy fibers exhibited higher YAP nuclear localization (Fig. E), supporting the involvement of morphology-dependent mechanotransduction.

Discussion

Mechanical cues such as substrate stiffness, dimensionality, and fiber alignment are known to control VSMC phenotype [7]. Our results indicate that wavy and straight fibers create distinct structural cues that regulate VSMC phenotype and YAP signaling. Part of the Hippo pathway, YAP plays complex roles in VSMC regulation, associating with both contractile maintenance and synthetic transition [4,5]. Our findings suggest that YAP may contribute to preserving the contractile phenotype in native structure. Future studies will

investigate the role of YAP in topography-mediated phenotypic regulation and evaluate VSMC responses under physiologic and pathologic mechanical stimulation.

Images (Optional)

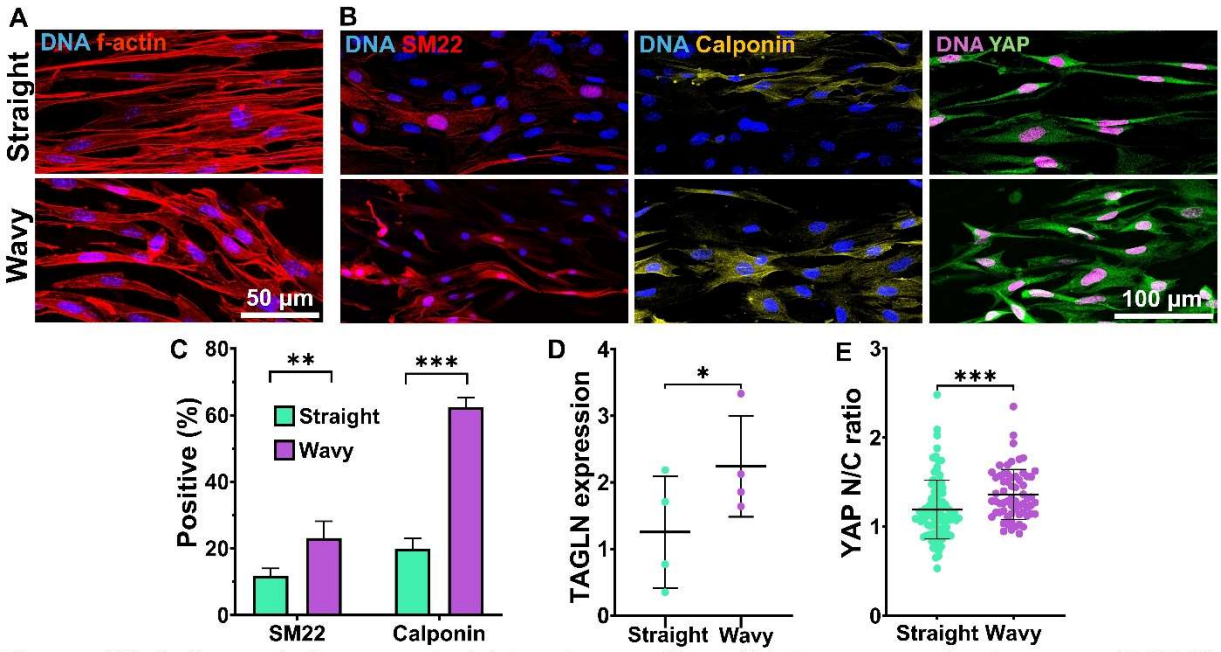


Figure (A) Cell morphology on straight and wavy fiber. (B) Representative images of VSMCs stained for contractile markers and YAP. (C) Percentage of cells staining positive for the contractile markers. (D) Contractile gene transgelin expression in straight and wavy fibers. (E) Quantitative results for YAP nuclear/cytoplasmic ratio.
*: p<0.05 **: p<0.01 ***: p<0.001

References (Optional)

[1] Chen+, JAHA, 2023.

[2] Lin+, SB3C, 2021.

[3] Piccolo+, Physiological Reviews, 2014

[4] Xie+, J Biol Chem, 2012.

[5] Sladitschek-Martens+, Nature, 2022.

[6] Chao+, Biofabrication, 2014.

[7] Nagayama+, J Mech Behav Biomed Mater, 2019.

Acknowledgements (Optional)

This study was supported by the Taiwanese National Science and Technology Council (NSTC 114-2221-E-002-091-MY3, 114-2923-E-002-017-MY3, and 114-2122-M-001-002).

Session Category

Tissue Engineering: Mechanobiology

OA77-05

TGF-β2 and Matrix Stiffening Elicit Mesenchymal Transition of Choroidal Endothelial Cells In Vitro

Mr. Richard Cliver, Dr. Kristan Worthington

The University of Iowa, Iowa City, Iowa, United States

Introduction

Age-related macular degeneration (AMD) is a prevalent cause or irreversible blindness. Although its underlying pathophysiology is complex, endo- and epithelial-to-mesenchymal transition (EMT) is implicated in AMD. EMT involves aberrant de-differentiation, proliferation, and matrix production. In other tissue systems, EMT can be caused by biochemical signaling factors and by increases in tissue stiffness. Given that retinal and vascular tissues stiffen with age, our goal is to characterize the extent to which these biomechanical changes contribute to retinal cell EMT compared to classical biochemical instigators.

Methods

Due to their involvement in early AMD pathology, we focused our initial efforts on choroidal endothelial cells using an immortalized ChEC line (imChECs) for our preliminary studies. We characterized the extent to which three canonical drivers of EMT (TGF-b1, TGF-b2, and TNF-a) impact cell proliferation, morphology, endothelial phenotype (e.g., expression of VE-Cadherin and PECAM-1), and EMT (a-SMA, N-Cadherin, SNAI1, and Vimentin) for one week. Age-related biomechanical tissue changes were simulated using an accelerated *in situ* matrix stiffening model: imChECs were seeded and allowed to attach to a GelMA hydrogel, followed by a secondary photocrosslinking to increase the matrix compressive modulus. We validated imChEC viability before and after secondary photocrosslinking and characterized cell response as described above.

Results

Exposure to TGF-b1 caused moderate upregulation of EMT markers in imChECs within 7 days while TGF-b2 elicited a substantial EMT response (**Fig.1A**). Secondary photocrosslinking of GelMA hydrogels produced a change in compressive modulus from

approximately 5 kPa to more than 10 kPa (**Fig.1B**), which mimics age-related biomechanical changes. ChECs readily attached to GelMA substrates and remained viable (>95%) after being subjected to secondary photocrosslinking (**Fig.1C**). Within two days of matrix stiffening, imChECs demonstrated transcriptomic downregulation of VE-cadherin and upregulation of α-SMA (**Fig.1D**).

Discussion

Our results demonstrate the feasibility of using secondary photocrosslinking to increase matrix stiffness without disrupting existing cell attachments or causing cell death. We also show that imChECs are susceptible to EMT, as instigated by either canonical biochemical signal or biomechanical cues. Our ongoing studies that utilize human iPSC-derived ChEC and RPE cells and additional timepoints and assays will further elucidate the mechanisms driving EMT in AMD pathophysiology.

Images (Optional)

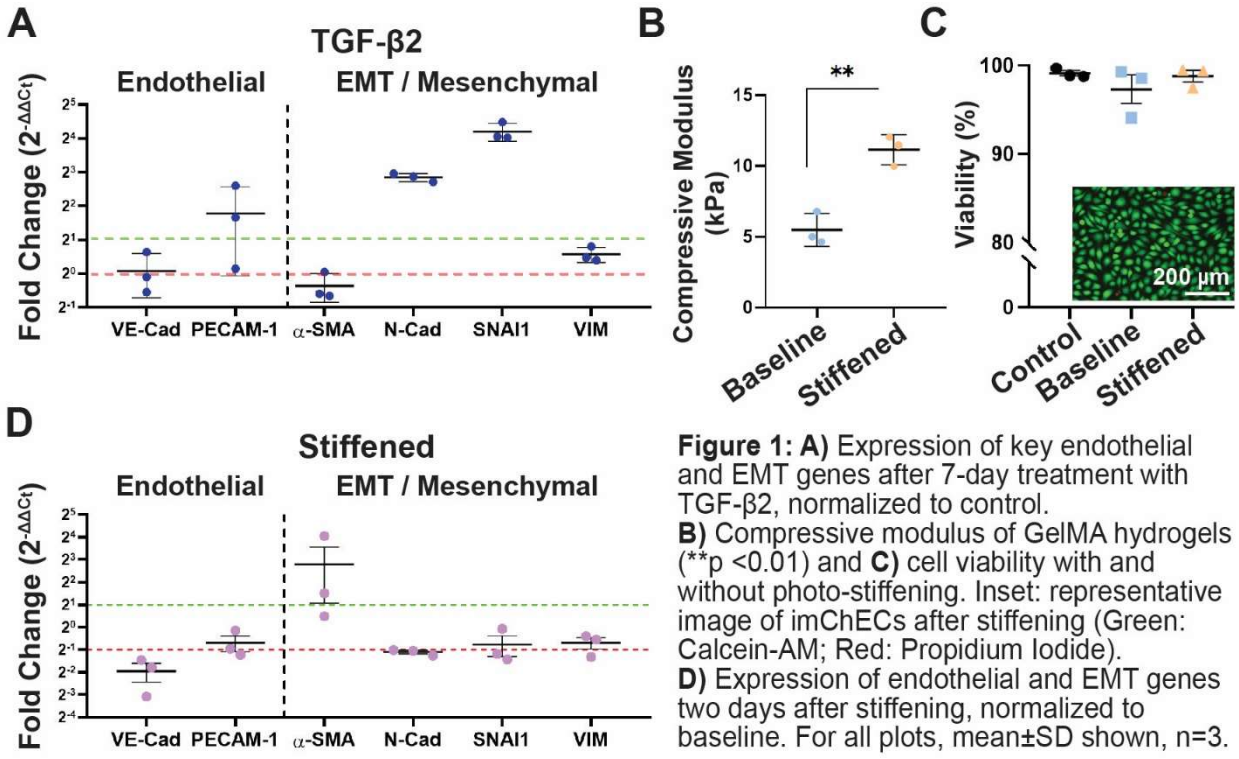


Figure 1: A) Expression of key endothelial and EMT genes after 7-day treatment with TGF-β2, normalized to control. **B)** Compressive modulus of GelMA hydrogels (**p <0.01) and **C)** cell viability with and without photo-stiffening. Inset: representative image of imChECs after stiffening (Green: Calcein-AM; Red: Propidium Iodide). **D)** Expression of endothelial and EMT genes two days after stiffening, normalized to baseline. For all plots, mean±SD shown, n=3.

Acknowledgements (Optional)

This work was funded by the National Eye Institute (1R01EY036467-01) and University of Iowa Office of the Vice President for Research (KSW Early Career Scholar Award). The authors would also like to acknowledge the labs of Budd Tucker and Robert Mullins (University of Iowa Institute for Vision Research) for generating and donating the ChEC cell line.

Session Category

Tissue Engineering: Mechanobiology

OA78-01

Automating the Simulation of Cough Induced Csf Flow in Subject-Specific Models of Chiari Malformation Using Machine Learning

Dr Rob Lloyd[1,2], Dr Adam Martinac[2,1], Prof. Marcus Stoodley[3], Prof. David Fletcher[4], Prof. Lynne Bilston[1,2]

[1]UNSW, Sydney, NSW, Australia. [2]NeuRA, Sydney, NSW, Australia. [3]Macquarie University, Sydney, NSW, Australia. [4]University of Sydney, Sydney, NSW, Australia

Dr Rob Lloyd

Dr Adam Martinac

Prof. Marcus Stoodley

Prof. David Fletcher

Introduction

Chiari malformation is a disorder where the cerebellar tonsils herniate into the spinal canal. This is assumed to obstruct normal cerebrospinal fluid (CSF) flow and cause cough-associated headache. Recent real-time phase contrast (PC) MRI [1] showed that the CSF velocities were two times greater in patients with Chiari than healthy controls. Additionally, the CSF space around the vertebrobasilar arteries anterior to the pons were more restricted. These findings suggested that high velocity CSF flow during coughs may stress the vertebrobasilar and contribute to headaches.
In this study, machine learning was used to construct subject-specific computational models from anatomical and PC-MRI data. These models were used to evaluate whether cough induced CSF flow increased the stresses acting on the vertebrobasilar arteries in patients with cough associated headache.

Methods

Previously trained U-Net segmentation models [1] were used to extract the CSF regions from the T1-weigthed anatomical images, and real-time PC-MRI taken at mid-C3 and the foramen magnum. Models were generated for 27 Chiari patients (7 without cough headache), and 12 matched controls. The fluid domain was meshed using Simpleware. The outlet at the suprasellar cistern was given a 7mmHg [2] static pressure. A CSF flow waveform measured at mid-C3 that included both cardiac and cough pulses was applied to the inlet. Simulated flow was validated against PC-MRI measurements taken at the foramen magnum, and peak shear stress on the vertebrobasilar artery was collected.

Results

Simulated CSF velocities were similar to those measured at the foramen magnum during the cardiac cycle (-0.6±1.7cm.s^{-1}) and the cough (-0.11±3.5cm.s^{-1}), in pilot models of a control and patients with and without cough headache (N=3). The peak shear stresses on the vertebrobasilar arteries were greater in Chiari patients than controls at all time points (Fig.1). During the coughs shear stress was twice as great in patients with coughing headache than those without.

Discussion

These results suggest that differences in cranial anatomy and greater arterial stresses could contribute to cough headaches. Additional models are required to determine if this is consistent within the larger cohort.

Images (Optional)

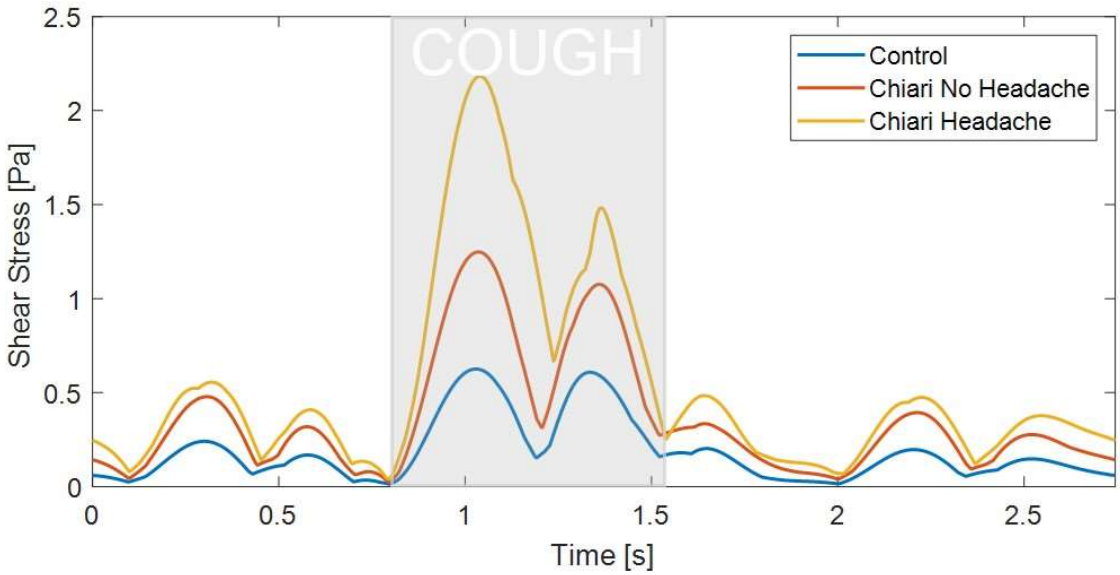


Fig. 1: Shear stress acting on the vertebrobasilar arteries before, during and after a cough.

References (Optional)

[1] Lloyd et al., Comput. Biol. Med., 2025

[2] Frič & Eide, J. Nurosurg., 2017

Acknowledgements (Optional)

The Column of Hope, the NHMRC, and NeuRA Imaging.

Session Category

Micro/Biofluidics: In Silico Models and Simulation

OA78-02

Process-Specific Numerical Simulations as an Optimization Tool of Microfluidic Nanoparticles Synthesis

Doctor Marco Bellotti[1], Doctor Enrica Chiesa[1], Doctor Elia Bari[2], Professor Michele Conti[1,3], Professor Ferdinando Auricchio[1], Doctor Alessandro Caimi[1]

[1]Università degli studi di Pavia, Pavia, Pavia, Italy. [2]Università del Piemonte Orientale, Novara, Novara, Italy. [3]IRCCS Policlinico San Donato, San Donato Milanese, Milano, Italy

Introduction

Conventional nanoparticles (NPs) synthesis methods offer limited control over size, polydispersity, and reproducibility. Microfluidic technologies overcome these limitations by enabling precise control of flow, mixing, and residence times [1]. However, optimization still relies largely on Design of Experiment (DoE) strategies, which are time-consuming, expensive, and focus on outcomes rather than underlying physicochemical mechanisms. Integrating numerical simulations with knowledge of NPs formation mechanisms can streamline formulation optimization, improve reproducibility, and facilitate translation across different microfluidic devices. This approach could reduce experimental workload and supports the rational design of new microfluidic geometries tailored to specific NPs synthesis requirements [2].

Methods

CFD simulations were employed to examine mixing patterns of various binary mixtures and NPs (i.e. liposomes, Eudragit L100, PLGA, fibroin) precursors in microfluidic chips with different geometries. Both transient and steady-state species transport simulations were performed depending on domain complexity. Formation-specific mechanisms were integrated during post-processing to derive new variables linked to NPs properties. Complementary experimental data were obtained by synthesizing model-drug-loaded NPs and characterizing their morphology using Dynamic Light Scattering , Nanoparticle Tracking Analysis , and Transmission Electron Microscopy, enabling correlation between simulations and experimental outcomes.

Results

Numerical results highlighted that fluid physical properties, such as viscosity, strongly influence mixing patterns within microfluidic chips. Incorporating NPs-specific precipitation curves for polymeric NPs and self-assembly curves for liposomes revealed that formation zones are highly dependent on the binary mixtures used. Key fluid dynamics parameters, including total flow rate and flow rate ratio , impact internal velocities,

residence times, and the speed at which optimal dilution occurs, directly influencing NPs morphology. Microfluidic chip geometry further modulates these effects by shaping internal flow and mixing (Figure 1A,C,E). Experimental data validated these findings, linking specific numerical and experimental boundary conditions to observed NP morphological features (Figure 1B,D,F).

Discussion

CFD simulations combined with mechanistic insight into NPs formation can reveal new morphology-linked variables, simplifying DoE approaches and reducing time and cost. These insights also ease the transfer of optimized formulations across microfluidic chips and guide the design of chips tailored to specific processes for more efficient synthesis.

Images (Optional)

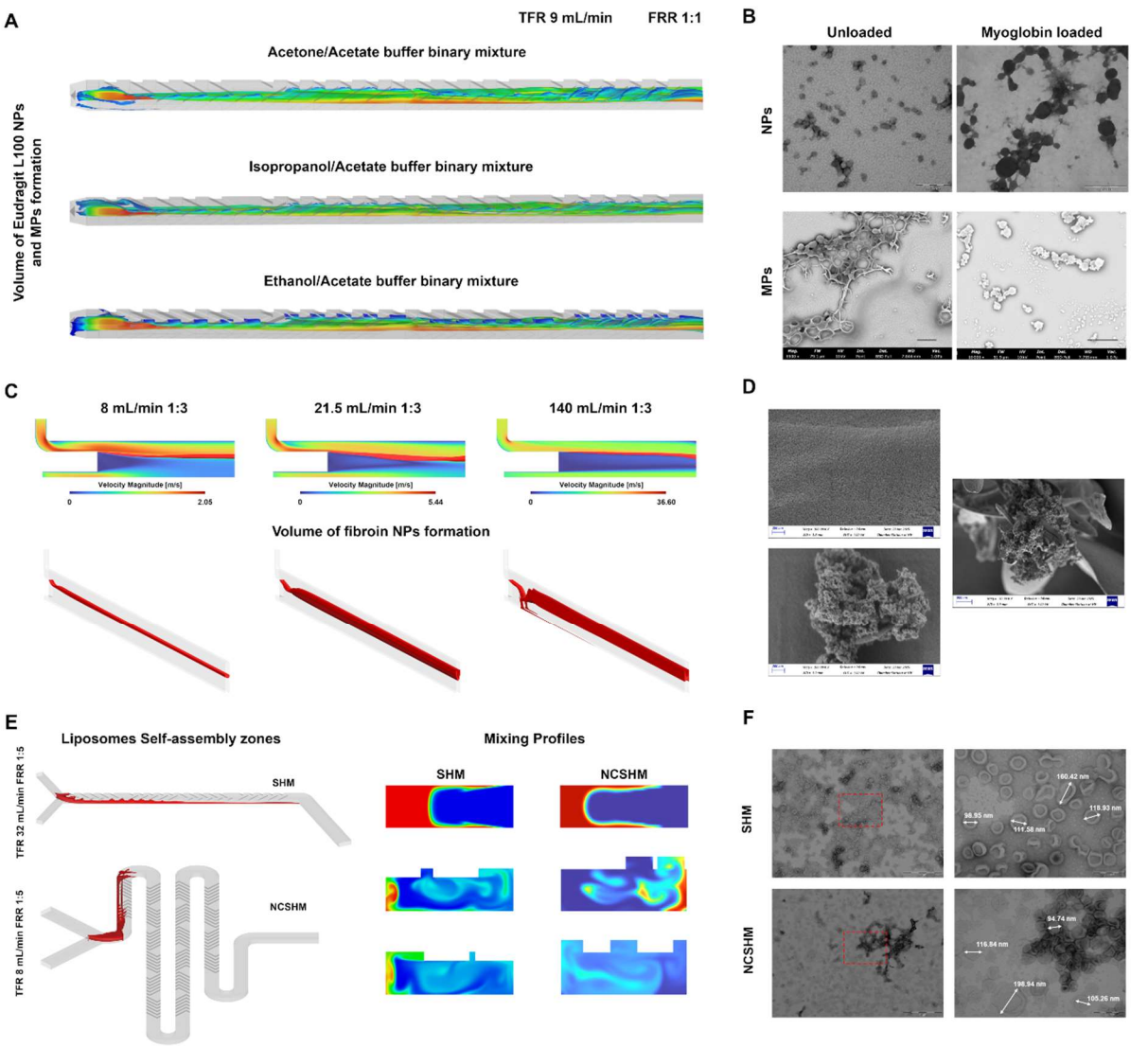


Figure 1 A) Volume of precipitation for Eudragit L100 pH-sensitive polymer identified by numerical simulation at fixed Total Flow Rate (TFR) and Flow Rate Ratio (FRR) and different binary mixture; **B)** TEM images of Eudragit L100 NPs (top row) and SEM images of MPs (bottom row), unloaded (left column) and loaded with myoglobin (right column); **C)** Numerical study about the impact of TFR on the velocity profiles (top row) and Volumes involved in the formation of silk fibroin NPs (bottom row); **D)** TEM images of silk fibroin NPs populations obtained in the study; **E)** Numerical results regarding the volumes involved in liposome self-assembly and respective mixing profile along the staggered herringbone mixer (SHM) and narrow curved staggered herringbone mixer (NCSHM); **F)** TEM images of the obtained liposomes populations (left column). A magnification with size measurement is reported for each case (right column).

References (Optional)

[1] Chiesa et al., J Pharmaceutics 2022

[2] Bellotti et al., A Biomedical Engineering, 2024

Session Category

Micro/Biofluidics: In Silico Models and Simulation

OA78-03

Artificial Microswimmer Propulsion in Blood: Surface-Active Designs Reduce Resistance and Improve Trajectory Stability

Dr. Chenjun Wu[1], Associate Prof. Toshihiro Omori[2], Prof. Takuji Ishikawa[2,3]

[1]School of Advanced Studies Sant'Anna, Pontedera, Pisa, Italy. [2]Graduate School of Engineering, Sendai, Miyagi, Japan. [3]Graduate School of Biomedical Engineering, Sendai, Miyagi, Japan

Dr. Chenjun Wu

Associate Prof. Toshihiro Omori

Introduction

Blood is a dense suspension of deformable red blood cells (RBCs) that generates strong hydrodynamic resistance and destabilizing interactions for artificial microswimmers (1). Although such microswimmers have shown promise for biomedical applications, the influence of RBC mechanics on their propulsion efficiency and trajectory stability remains poorly quantified (2). In particular, how surface-active propulsion fundamentally differs from inert designs remains unclear, especially when swimmers are controlled by external magnetic actuation in crowded RBC environments (3). This study addresses these gaps using an RBC-resolved computational framework to evaluate locomotion performance across propulsion modes.

Methods

We simulated microswimmer–RBC interactions using a fluid–structure interaction framework that couples boundary-element hydrodynamics with finite-element modeling of deformable RBC membranes, while treating the microswimmer as a rigid body (Fig. A and B). Surface-active swimmers were implemented using a squirmer formulation with prescribed slip velocities representing puller, pusher, and neutral modes. Inert designs were modeled as non-slip swimmers actuated solely by externally applied magnetic forces. Simulations were performed under varying magnetic actuation strengths to assess propulsion behavior in crowded RBC environments.

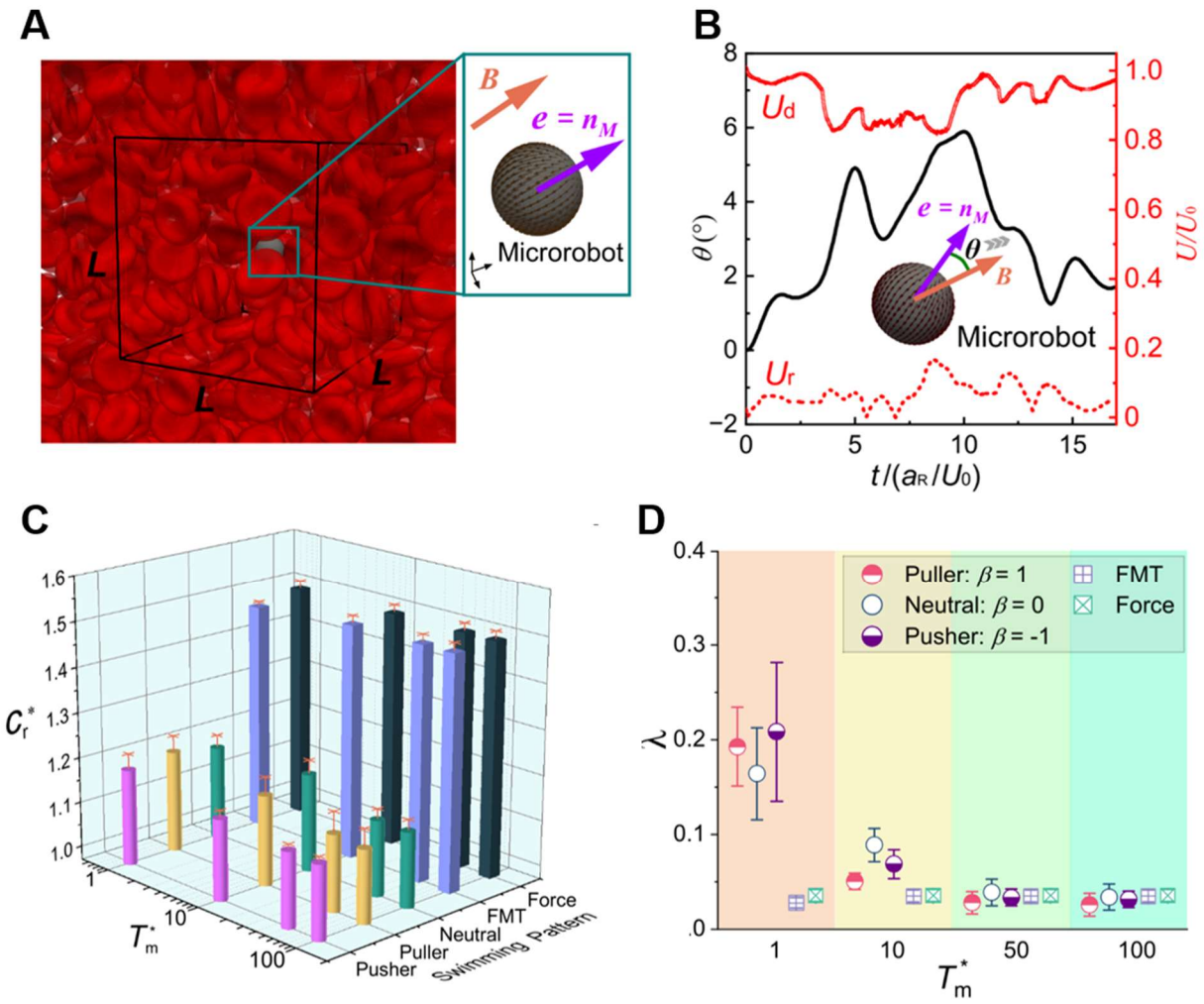
Results

Surface-active microswimmers exhibited consistently lower hydrodynamic resistance than inert designs across all magnetic actuation levels (Fig. C). For inert microswimmers, the force-magnetic-torque-driven (FMT) microswimmer differs from purely force-driven motion and it only induces slight orientational perturbations, leading to minor variations in the relative resistance coefficient (C^*_r). In contrast, C^*_r or squirmer microswimmers decreased more notably with increasing magnetic torque, with an slightly drop when dimentionless magnetic torque (T^*_m) is greater than 10. Besides, surface-active microswimmers showed markedly reduced lateral drift (λ) and suppressed angular fluctuations (Fig. D).

Discussion

Our findings show that surface-active propulsion fundamentally alters microrobot–RBC interactions, generating slip flows that redirect nearby RBCs and reduce both hydrodynamic resistance and destabilizing collisions. These results suggest that integrating slip-based actuation with magnetic control is a promising strategy for reliable navigation in dense blood environments and motivate future validation in microvascular-scale experiments.

Images (Optional)



(A) Schematic of an artificial microswimmer navigating through an RBC suspension under magnetic actuation. (B) Representative trajectory, orientation angle, and velocity components of a neutral microswimmer. (C) The relative resistance coefficient (C_r^*) of different propulsion modes under varying magnetic torques. (D) Lateral drift of microswimmers as a function of dimensionless magnetic torque T_m^*

References (Optional)

1. Toshiro Yamanaka and Fumihito Arai, IEEE RA-L, 2018.

2. Chenjun Wu et al. , Communications Physics, 2024.

3. Chenjun Wu et al. , PNAS Nexus, 2024.

Session Category

Micro/Biofluidics: In Silico Models and Simulation

OA79-01

Early Biomechanical Insights into the Association between Offloading Adherence and Gait Mechanics in Diabetic Foot Ulcer Patients Offloaded with Removable Cast Walkers

Mr. Nahir Negron-Fernandez MS, Dr. Ryan Crews PhD, Mr. Sanam Jhaveri BS, Dr. Noah Rosenblatt PhD

Rosalind Franklin University, North Chicago, IL, United States

Introduction

While removable cast walkers (RCWs) are commonly prescribed to offload diabetic foot ulcers (DFUs), adherence with RCWs is low. To optimize offloading adherence (OA), this ongoing, multi-site trial aims to evaluate the impact of existing RCW designs on OA and to collect preliminary data to quantify the effect of RCW design biomechanical correlates of usability and their ability to predict OA.

Methods

Data was analyzed from an initial set of eight participants in an ongoing clinical trial focused on offloading DFU. Participants in the trial were randomized to receive one of two RCW offloading interventions. OA with the RCW was monitored via dual accelerometers over four weeks, after which participants visited the motion capture lab for a single session to assess 10 biomechanical correlates of usability related to energetics, joint loading, and stability. Principal component analysis (PCA) was performed on the set of biomechanical variables, and Spearman correlations were used to evaluate the strength of association between PCA component scores and OA.

Results

PCA resulted in three components explaining 81.7% of the variance in the data. Component 1 loaded heavily on vertical ground reaction forces, non-boot external knee adduction moments (EKAM), overground walking velocity, and posterior perturbation thresholds; component 2 on pelvic tilt measures, cost of transport, and anterior perturbation thresholds; and component 3 on boot-condition EKAM and pelvic tilt range of motion. OA was indexed separately by walking (steps) and standing time (minutes). Correlations between OA and the principal component scores were of weak to moderate strength ($0.2< \rho<0.5$; all $p \geq 0.29$).

Discussion

These preliminary findings demonstrate the feasibility of capturing OA and rich gait mechanics data in DFU patients following a one-month acclimation period to an assigned RCW. While underpowered to vet the PCA approach, small-to-moderate effects are encouraging for a behavioral outcome like OA, which is influenced by biomechanics and psychological factors captured in the larger trial. Biomechanical data clustered into three components (loading, pelvic mechanics, stability), and additional measures such as trunk dynamic stability, which have been collected but not yet analyzed, may further clarify OA, highlighting the value of biomechanical methods for addressing clinically important questions.

Images (Optional)

Table 1. Principal component loadings for biomechanical correlates and correlation coefficients for OA

			Component		
			1	2	3
Biomechanical Correlate (ρ)	Loading/Joint Pain	Peak EKAM RCW	0.155	0.595	0.711
		Peak vGRF RCW	0.801	0.286	0.216
		Peak EKAM nonRCW	0.825	0.479	-0.074
		Peak vGRF nonRCW	0.898	0.264	-0.094
		Mean Pelvic Tilt	-0.283	0.688	-0.244
		ROM Pelvic Tilt	0.602	0.246	-0.648
	Stability	Walking speed	0.863	-0.019	-0.013
		Anterior Step Threshold	0.524	-0.698	0.438
		Posterior Step Threshold	0.804	-0.171	0.259
	NRG	Cost of Transport	-0.425	0.707	0.335
		Correlation - Walking OA	**-0.429**	**-0.333**	**0.238**
		Correlation - Standing OA	**-0.381**	**-0.048**	**0.310**

Notes: ρ = Spearman correlation coefficient; EKAM = external knee adduction moment; vGRF = vertical ground reaction force, RoM = Difference between local peaks; darker colors represent larger loading with orange and blue for positive and negative values, respectively.

Session Category

Clinical Biomechanics: N/A

OA79-02

Postural Instability in Diabetes Mellitus: Insights from Rambling-Trembling and Non-linear Approach

Dr. Kai Cheng PhD[1], Dr. Carl Luchies PhD[2], Dr. John Miles MD[1], Dr. Jianghua He PhD[1], Dr. Hannes Devos PhD, PT[1], Dr. Chun-Kai Huang[1]

[1]University of Kansas Medical Center, Kansas City, KS, United States. [2]University of Kansas, Lawrence, KS, United States

Introduction

Diabetes mellitus (DM) is a chronic condition that causes microvascular damage and impairments in sensory processing, leading to postural instability and an increased risk of falls. Both peripheral and central sensory processing are crucial for balance maintenance, but the relative contributions of each to postural instability in DM are not well understood. Previous research suggests that DM-related neuropathy, retinopathy, and vestibular dysfunction all contribute to poor balance, but how these systems interact in postural control remains unclear. The objective of this study is to investigate sensory system contribution to postural control using center-of-pressure decomposition and nonlinear approaches.

Methods

A VR-based Sensory Organization Test that simulated sensory conflicts among somatosensory, visual, and vestibular inputs were adopted. The center-of-pressure data were decomposed into Rambling (RM) and Trembling (TR) components, representing central and peripheral postural control, respectively. Variables such as root mean square, velocity, acceleration, and jerk were calculated for both RM and TR in anteroposterior (AP) and mediolateral (ML) directions. Sample Entropy was used to assess the predictability and regularity of postural control dynamics.

Results

DM showed significantly greater sensory ratios in RM jerk (ML), particularly when relying on visual input, indicating reduced central processing. Additionally, DM exhibited increased velocity and acceleration in TR (AP), especially under visual and vestibular reliance conditions, suggesting inefficient peripheral reflex adjustments. SampEn analysis revealed decreased predictability and regularity in central processing (RM) and peripheral responses (TR), particularly when relying on the vestibular system.

Discussion

The findings suggest that DM leads to altered postural control, characterized by impaired central processing and inefficient peripheral compensation when relying on visual or vestibular systems. These results align with the hypothesis that DM affects both the central and peripheral processing contributing to balance impairment. The increased jerk in RM components and excessive velocity and acceleration in TR components indicate that DM participants engage in maladaptive strategies, possibly due to impaired sensory integration. Future interventions targeting both central and peripheral mechanisms, such as multisensory integration exercises and gaze stabilization, may improve postural control in individuals with DM.

Session Category

Clinical Biomechanics: N/A

OA79-03

Comparing Upper Limb Muscle Activation Following Unilateral and Prophylactic Contralateral Mastectomy for Unilateral Breast Cancer

Ms. Sarah Fitzgerald MHSc, Dr. Kenzie Friesen PhD, Dr. Angelica Lang PhD

University of Saskatchewan, Saskatoon, Saskatchewan, Canada

Introduction

Breast cancer (BC) is the most commonly diagnosed cancer among women in Canada[1]. Unfortunately, treatment often results in upper limb morbidities[2]. Commonly performed surgical treatments for unilateral breast cancer include unilateral mastectomies (UM) with or without prophylactic contralateral mastectomy (PCM). However, the merits of both these options are debated. To the best of our knowledge, no previous literature has examined the relative impact of UM alone or with PCM on upper limb biomechanics and function. As such, the objective of this study is to examine the impact of PCM and UM alone on shoulder biomechanics.

Methods

Sixteen participants (N = 10 PCM | N = 3 right-sided UM | N = 3 left-sided UM) are included in this abstract, with data collection ongoing. Activity of the bilateral upper trapezius, lower trapezius, serratus anterior, infraspinatus, pectoralis clavicular, and middle deltoid was measured during a range of functional and range of motion tasks. EMG activity was normalized to maximum voluntary contractions and smoothed with a second order Butterworth bandpass filter. Data was then compared between PCM shoulders (n=20), UM affected shoulders (n=6), and UM unaffected shoulders (n=6) using one-way SPM ANOVAs ($p < .05$).

Results

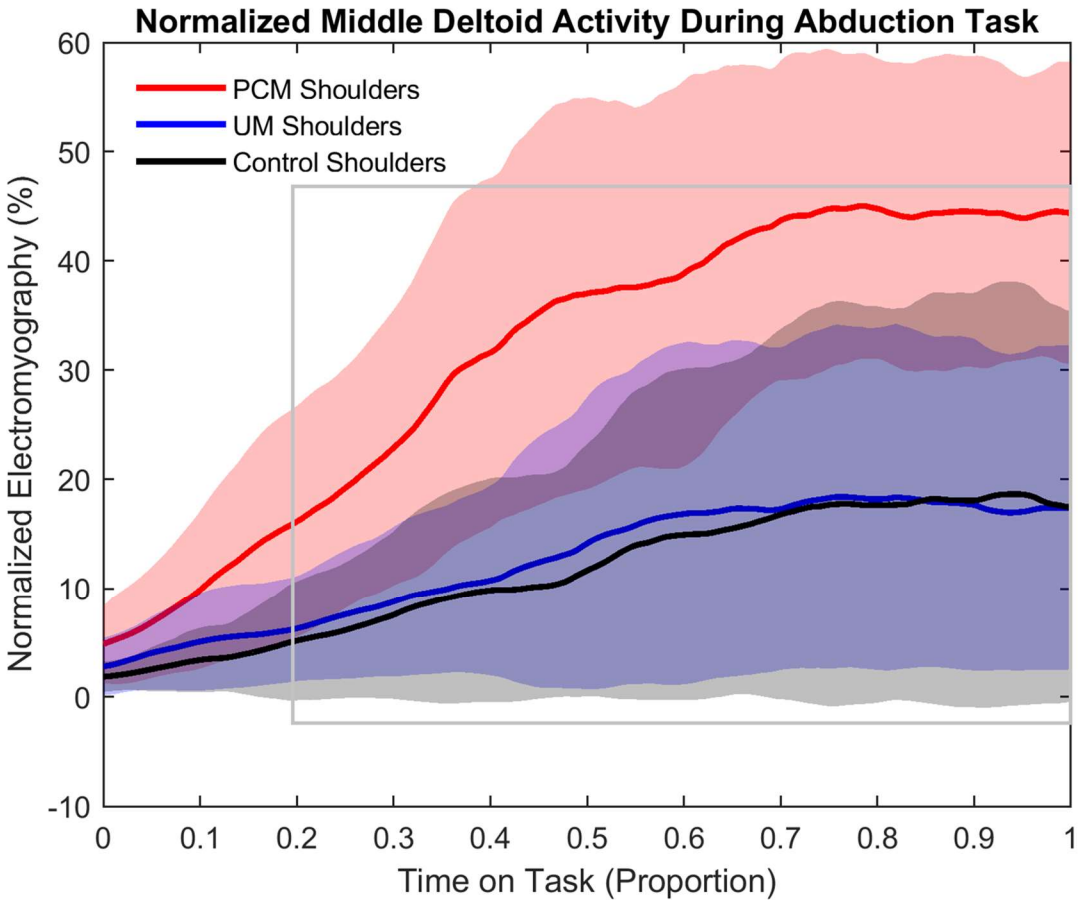
Preliminary analyses demonstrated elevated middle deltoid activity among PCM shoulders as compared to both groups of UM shoulders during arm elevation tasks (Figure 1; $p < 0.001$).

Discussion

Preliminary results demonstrate interesting trends of elevated middle deltoid activity among PCM shoulders as compared to UM and control shoulders. This may reflect reduced middle deltoid strength among these participants. Data from this work are expected to contribute to improving resources available to support BC survivorship. Improved

understanding of these biomechanical effects of PCM and UM will supplement shared decision-making with patients and surgeons.

Images (Optional)



References (Optional)

[1] Brenner, D. R. *et al.,* CMAJ, 2024

[2] Lang, A. E. *et al.,* Ann. Med., 2022

[3] Findlay-Shirras, L. *et al.,* Breast Cancer Res. Treat, 2021

Session Category

Clinical Biomechanics: N/A

OA79-04

Gait Variability and Velocity Improve With Partnered Dance Intervention Among Individuals With Breast Cancer and Chemotherapy-Induced Neuropathy: A Pilot Study

Dr. Aya Alwan[1], Ms. Kristen Lantis[2], Dr. Ashley Hawke[3], Dr. Madeleine Hackney[4,5], Dr. Maryam Lustberg[3], Dr. Lise Worthen-Chaudhari[6]

[1]The Ohio State University College of Medicine, Columbus, Ohio, United States. [2]Sarepta Therapeutics, Columbus, Ohio, United States. [3]Yale School of Medicine, New Haven, Connecticut, United States. [4]Emory University School of Medicine, Atlanta, Georgia, United States. [5]Atlanta VA Health Care System, Birmingham/Atlanta, Virginia, United States. [6]The Ohio State University College of Medicine, Columbus, OH, United States

Introduction

Breast cancer (BC) survivors with chemotherapy-induced neuropathy (CIN) experience sensorimotor deficits, altered gait patterns, and increased fall risk. We evaluated partnered, adapted, Argentine Tango dance training (Tango) as nonpharmacologic treatment for these deficits. Here, we report intervention effects on gait function, specifically. The intervention was designed to decrease gait variability through step and support motor learning techniques unique to Tango. Because gait variability is believed to represent a trainable mechanism underlying fall risk, improvements in this metric are clinically relevant. We hypothesized that Tango intervention would reduce gait variability as measured by coefficient of variation in stride-to-stride speed (CV_{speed}).

Methods

Eleven female BC survivors with CIN and demonstrated balance deficits were randomized to receive the Tango intervention (TEX, 2x/week for 8-weeks, ~30-minute dose/session). Effects were measured during an instrumented 6-minute walk test (6mwt) performed pre- and post-intervention. From inertial measurement units (IMUs) placed on the sacrum and feet, we computed spatiotemporal gait metrics during straightaway bouts of walking using *gaitmap* library. Across all strides per participant and timepoint, we calculated CV_{speed} as the primary outcome and additional measures as exploratory outcomes (e.g., mean, standard deviation (SD), and coefficient of variation (CV) of stride time and length). We used paired t-tests to assess change with intervention (significance level $p < 0.05$).

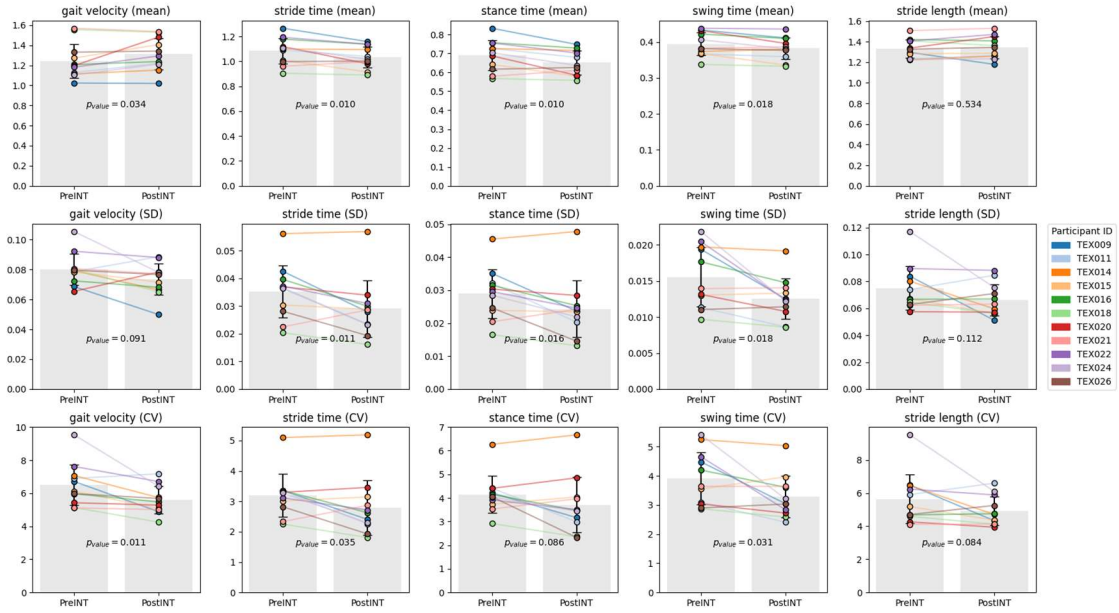
Results

The primary outcome (CV_{speed}) decreased with intervention (p = 0.011). Exploratory analysis identified additional functional gains associated with the intervention such as increased gait speed (p = 0.034; mean(SD) improvement = ~5.6(8.1)%) and decreased CV stride time (p = 0.035) and swing time (p = 0.031). Stride length did not change with intervention.

Discussion

Tango training improved stride-to-stride variability and other aspects of gait variability among BC survivors with CIN. The intervention improved gait speed, although we did not target this outcome. While the small sample limits clinical generalizability, the dataset is sufficient for biomechanical inferences. Future work will examine turning-specific gait metrics, foot placement control (step-to-step error correction), dynamic stability (resilience to small perturbations), and post-intervention falls incidence to explore the potential for nonpharmacologic treatment through Tango among BC survivors with CIN.

Images (Optional)



References (Optional)

Acknowledgements (Optional)

This project was funded by R21-AG068831 and R01-AG084676. We thank Jackie Wilder, Courtney Bland, Nelson Glover, and Shawanee Patrick for assistance with data collection.

Session Category

Clinical Biomechanics: N/A

OA79-05

A Personalised Intervention Integrating Pressure-Optimized Footwear, Self-Management and Education Reduces the Incidence of Foot Ulcer Recurrence in Diabetes: The DIASSIST Multicenter Randomised Controlled Trial

Prof. dr. Sicco Bus[1], MSc Lisa Vossen[1], Dr. Chantal Hulshof[1], MD Heleen Berendsen[2], Dr. Chantal Bakker MD[3], Dr. Louise Sabelis MD[1], Prof. dr. Marcel Dijkgraaf[1], Dr. Jaap van Netten[1]

[1]Amsterdam UMC, University of Amsterdam, Amsterdam, NH, Netherlands. [2]Reinier de Graaf Gasthuis, Delft, ZH, Netherlands. [3]Maxima Medisch Centrum, Veldhoven, Brabant, Netherlands

Introduction

The prevention of foot ulcers in diabetes helps reduce the large patient and healthcare burden of diabetic foot disease. To prevent foot ulcers, guidelines recommend patient education, self-management, appropriate foot care and pressure-optimized footwear [1]. For the latter, protocol-based footwear design and modifications guided by in-shoe plantar pressure analysis is used [2]. We assessed the effect of an integrated multimodal and personalized intervention on the incidence of diabetes-related foot ulcer recurrence.

Methods

In a parallel-group multicentre superiority randomized controlled trial in 5 hospitals in the Netherlands, 126 participants with diabetes, peripheral neuropathy, ulcer history, and custom-made footwear, were randomly assigned to usual care or enhanced treatment. Enhanced treatment consisted of pressure-optimized custom-made footwear, pressure-optimized indoor footwear; at-home foot temperature monitoring; and structured education, including motivational interviewing. Participants were followed for 12 months, with incident foot ulcer recurrence as primary outcome, which was assessed masked to group allocation and with all participants included. Trial registration: clinicaltrials.gov, ID: NCT05236660.

Results

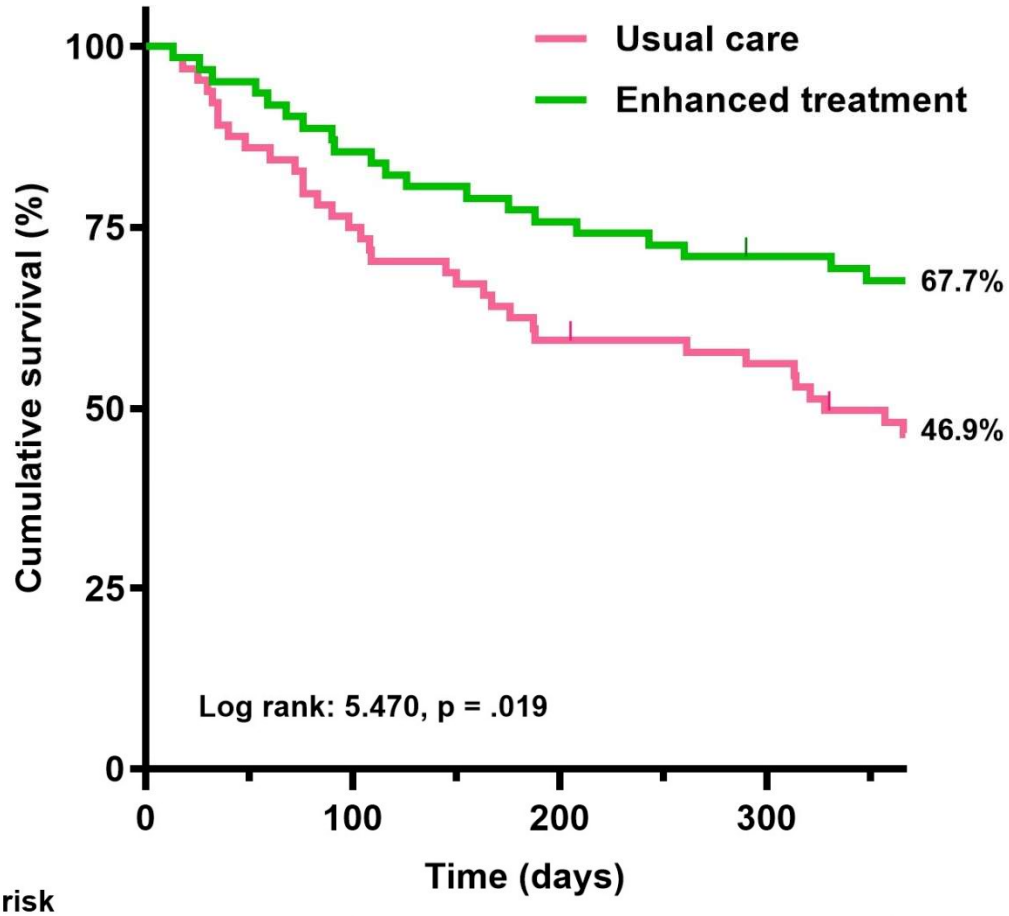
Participants were assigned between 2/3/2022 and 25/9/2024: 64 to usual care (54 male; 10 female), 62 to enhanced treatment (52 male; 10 female). On the basis of intention-to-treat, 20 (32.1%) participants in enhanced treatment and 34 (53.1%) in usual care had a recurrent foot ulcer (RR 0.607 [95%CI 0.396-0.931], p=0.018). There were significantly more ulcer-free days for enhanced treatment (mean ± SD 320±87) than for usual care (298 ± 94, p=0.039). Of the 10 participants in enhanced treatment who wore their pressure-optimized

footwear >10h/day and adhered to foot temperature-monitoring recommendations, 1 (10%) had an ulcer, significantly fewer than the 53.1% in usual care (RR 0.188 [95%CI 0.029-1.226], p=0.015).

Discussion

Integrated multimodal and personalized treatment including pressure-optimized custom-made footwear and pressure-optimized indoor footwear, significantly reduces incidence of foot ulcer recurrence in people with diabetes, and this effect can be further improved when patients adhere to self-management recommendations and prescribed footwear use. These outcomes help reduce the burden of diabetic foot disease in high-risk persons.

Images (Optional)



Numbers at risk

Usual care	64	48	38	35	28
Enhanced treatment	62	53	47	43	41

References (Optional)

[1] Bus SA, et al. *Diabetes Metab Res Rev* 2023

[2] Bus SA, et al. *Diabetes Metab Res Rev* 2020

Session Category

Clinical Biomechanics: N/A

OA79-06

Myofascial Massage Reduces Pain in Breast Cancer Survivors but Does Not Induce Acute Changes in Tissue Stiffness- a Pilot Study.

Ms. Layla Lynch MS, CSCS[1], Ms. Margit Fried[1], Mrs. Diane Mastnardo BS, LMT[2], Dr. Suzi Wolfram PhD[3], Dr. David Lipps PhD[1]

[1]University of Michigan, Ann Arbor, Michigan, United States. [2]Mastnardo Massage Therapies, Westlake, Ohio, United States. [3]Northumbria University, Newcastle, Northeast England, United Kingdom

Introduction

Up to 50% of breast cancer survivors (BCS) experience persistent upper quadrant myofascial pain[1], which impairs their quality of life. Myofascial massage reduces pain and increases shoulder mobility in BCS[2], but its underlying mechanisms are poorly understood. Surgery and radiation therapy can cause fibrosis and stiffness, leading to thickening and tightening of connective tissue. Myofascial massage may counter these changes and break down fibrotic tissue. This study examined how myofascial massage affects pectoralis major stiffness and pain in BCS. We hypothesized that a single session of myofascial massage would reduce tissue stiffness and pain.

Methods

Twenty breast cancer survivors with upper quadrant myofascial pain (mean ± SD, age: 53.5 ± 11.3) participated after providing written consent. Each participant received a 30-minute individualized myofascial massage to the chest wall and axilla. Ultrasound shear wave elastography (SWE) assessed tissue stiffness before, immediately after, and 60 minutes after the intervention at six distinct sites on the pectoralis major. A linear mixed-effects model tested the effect of myofascial massage on shear wave velocity (SWV) with site, time, radiation exposure, and their interaction (time x radiation) as fixed effects. Patient-reported outcomes at enrollment assessed average pain in the past week (PEG), and one week post-intervention, PEG and change in condition (PGIC) were evaluated.

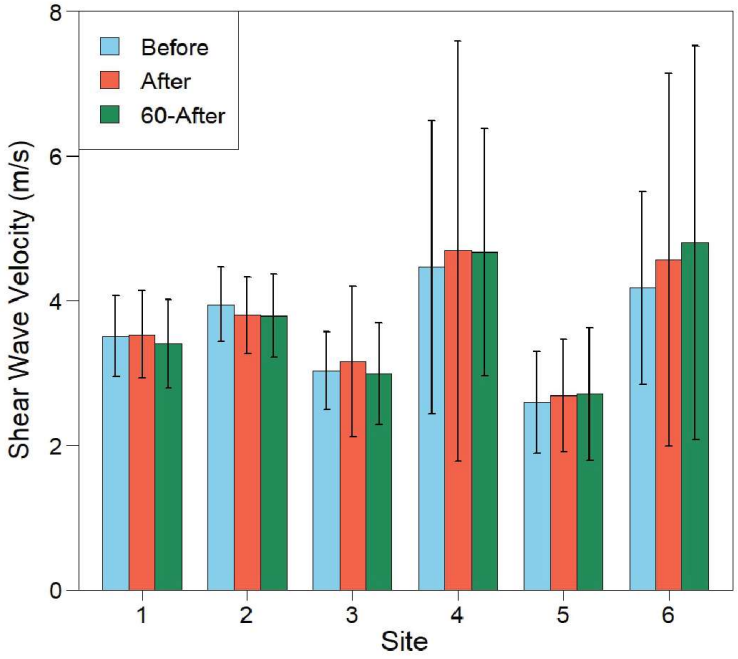
Results

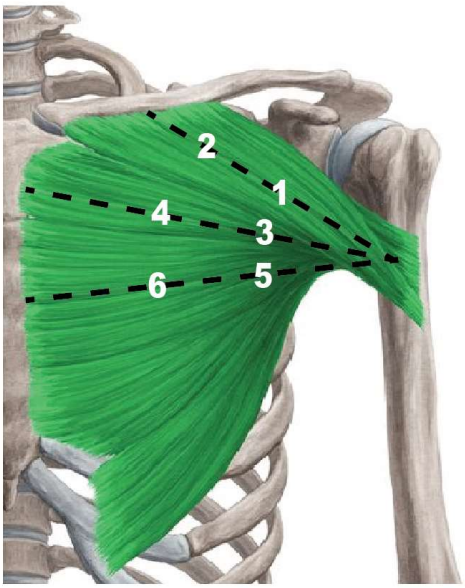
Following treatment, most participants (17/20) reported improvement and reduced pain (PEG: $p = 0.001$). SWV significantly differed between site locations ($p = 0.039$) (Fig. 1), with greater stiffness in the medial portion of the sternocostal region. Time, radiation, and their interaction did not exhibit statistically significant relationships with SWV (all $p > 0.51$).

Discussion

Myofascial massage improved patient condition and reduced pain, but did not change SWV within 60 minutes of the intervention. SWV varied significantly across sites, suggesting regional differences in general tissue properties. Limitations included a small sample size, variable massage histories, and the possibility of multiple sessions needed to alter tissue biomechanics. Following this pilot study, future research should consider extended intervention periods and larger, more controlled samples to better assess the effects of myofascial massage.

Images (Optional)





References (Optional)

1. Lacomba et al., *Clin J Pain*, 2010

2. Serra-Añó et al., *Support Care Cancer*, 2019

Acknowledgements (Optional)

Financial support for this work was provided by a ForceNet pilot grant through the National Institutes of Health (NCCIH/NINDS) U24-AT011969

Session Category

Clinical Biomechanics: N/A

OA80-02

Optimizing Prosthesis Knee Damping Minimizes Intact-Knee Contact Forces During Ramp Descent in Transfemoral Amputees

Ms. Elise Nielsen, Ms. Marissa Cowan, Dr. Lukas Gabert, Dr. Scott Uhlrich, Dr. Tommaso Lenzi

Univeristy of Utah, Salt Lake City, UT, United States

Introduction

Individuals with transfemoral amputations are 40% more likely to develop knee osteoarthritis than non-amputees [1], a risk linked to elevated knee contact forces on the intact limb [2]. These forces are particularly high during activities that require lowering the center of mass, like ramp descent [3]. Knee prostheses use damping to resist knee flexion and control the descent. However, the influence of this damping on intact-knee contact forces remains unknown. Our objective was to assess the effect of damping on transfemoral amputees' intact-knee contact forces during ramp descent. We hypothesize that intermediate levels of damping will minimize intact-knee contact forces. The rationale is that high damping prevents the necessary knee flexion for a smooth center-of-mass descent, while low damping results in excessive knee velocity. Both extremes force users to abruptly transfer weight to the intact limb for stabilization, increasing knee loading.

Methods

Eight transfemoral amputees walked on a declined (7.5º) instrumented treadmill with an active knee prosthesis. After training, we recorded kinematics and ground contact forces at three speeds (0.4, 0.6, and 0.8 $m \cdot s^{-1}$) across five randomized damping levels (0.004-0.016 $Nm \cdot s \cdot deg^{-1} \cdot kg^{-1}$). We estimated intact-knee contact forces using static optimization in OpenSim and fitted quadratic curves to identify the optimal damping level.

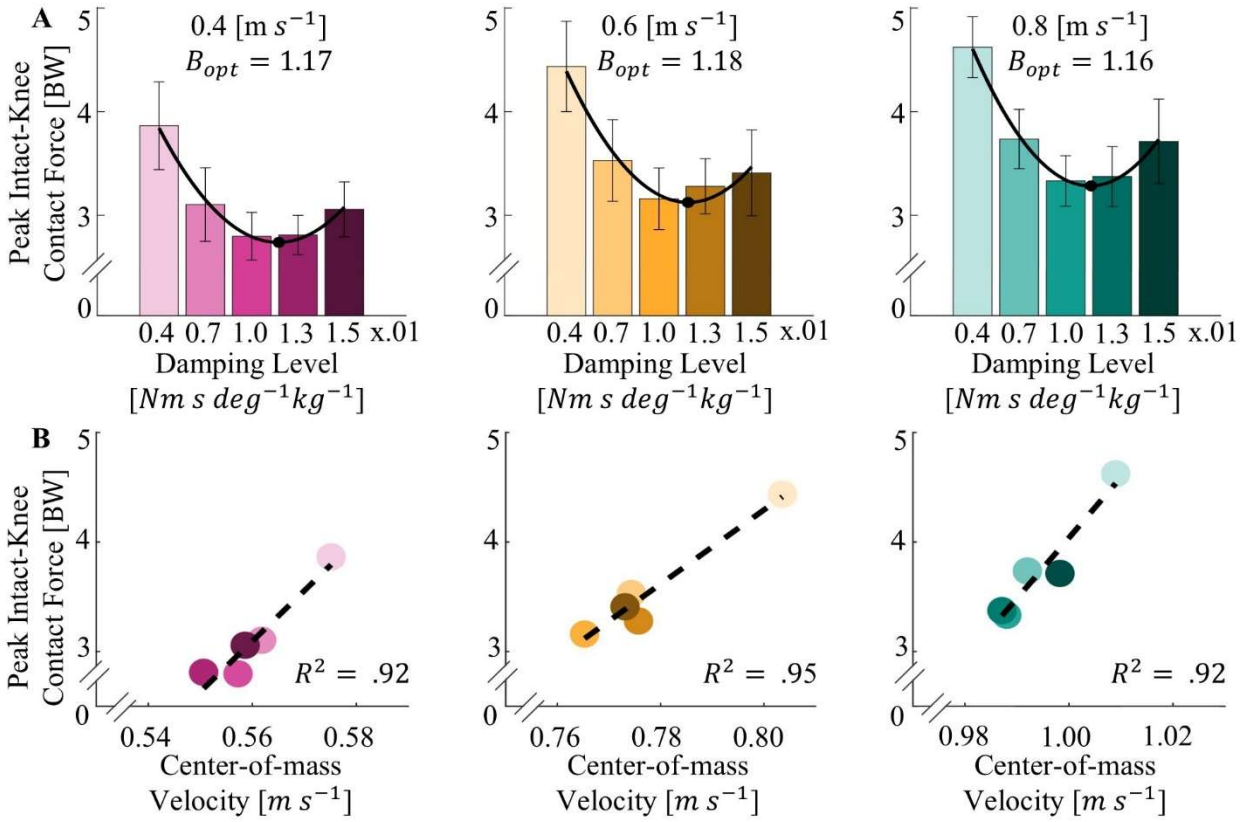
Results

We found a quadratic relationship between damping and intact-knee contact force, with a theoretical minimum (B_{opt}) occurring at an intermediate damping level (0.012 $Nm \cdot s \cdot deg^{-1} \cdot kg^{-1}$) across all speeds (*Figure 1A*). At B_{opt}, peak contact forces were reduced by 30% and 10% compared to the lowest and highest damping, respectively. Additionally, peak contact forces correlated strongly with center-of-mass velocity (R^2 0.92-0.95, *Figure 1B*), indicating that B_{opt} facilitates controlled lowering of the body.

Discussion

Our findings indicate that prosthesis damping directly influences intact-knee contact forces. Notably, B_{opt} remained constant across walking speeds, simplifying future controller implementation. Tuning prosthesis damping to B_{opt} limits the center-of-mass velocity, reducing the mechanical stress on the intact joint and potentially lowering the risk of osteoarthritis.

Images (Optional)



References (Optional)

[1] Daniel Norvell *et al.*, Arch Phys Med Rehabil., 2005; [2] Nicholas Brisson *et al.*, Arthritis Rheumatol, 2021; [3] Shawn Farrokhi *et al.*, Knee, 2016;

Acknowledgements (Optional)

We thank Brian Kaluf, CP, Kyle Rasmussen, CPO, Jim Liston, CPO, and Mike Reynolds, CPO for helping with prosthesis fitting and alignment. This work was funded in part by the National Institutes of Health under grant # R01HD098154 and by the Department of War under grant # W81XWH2110037.

Session Category

Clinical Biomechanics: N/A

OA80-03

Current Clinical Practice for Prosthesis Alignment Does Not Yield Lowest Interlimb Asymmetry in People With Unilateral Transtibial Amputation during Walking

Ms. Kelsie Heffernan[1], Dr. Alena Grabowski[2,3], Dr. Janet Zhang-Lea[1]

[1]University of Oregon, Eugene, Oregon, United States. [2]University of Colorado Boulder, Boulder, Colorado, United States. [3]Department of Veterans Affairs Eastern Colorado Healthcare System, Denver, Colorado, United States

Introduction

Proper alignment of prostheses is critical for reducing interlimb asymmetry and secondary injury risk for people with unilateral transtibial amputation (UTTA). Currently, aligning a prosthesis is done by a prosthetist based on their subjective evaluation. In this study, we modified prosthesis alignment by systematically changing 3D angular rotations from a neutral alignment. We aimed to investigate whether prosthetic alignment based on current clinical practice (baseline) yields the lowest interlimb asymmetry during walking compared to the modified alignment. We hypothesized that the baseline alignment will yield the smallest symmetry index (SI) for both step length and peak horizontal ground reaction force (hGRF) compared to 3° and 6° alignment changes.

Methods

Five participants with UTTA walked on an instrumented treadmill at 1.25 m/s for 3 minutes with 13 alignment conditions for the same low-profile passive-elastic prosthesis. We started with a baseline trial, with the prosthesis set to a neutral alignment by a prosthetist. The prosthetic alignment between the socket and pylon was then changed by ±3° and ±6° in the three planes (sagittal, coronal, and transverse), 6 directions total (plantarflexion/dorsiflexion, abduction/adduction, internal/external rotation; Figure 1). We assessed the SI of step length and hGRF at baseline, and all alignment conditions. SI=0 means perfect symmetry.

Results

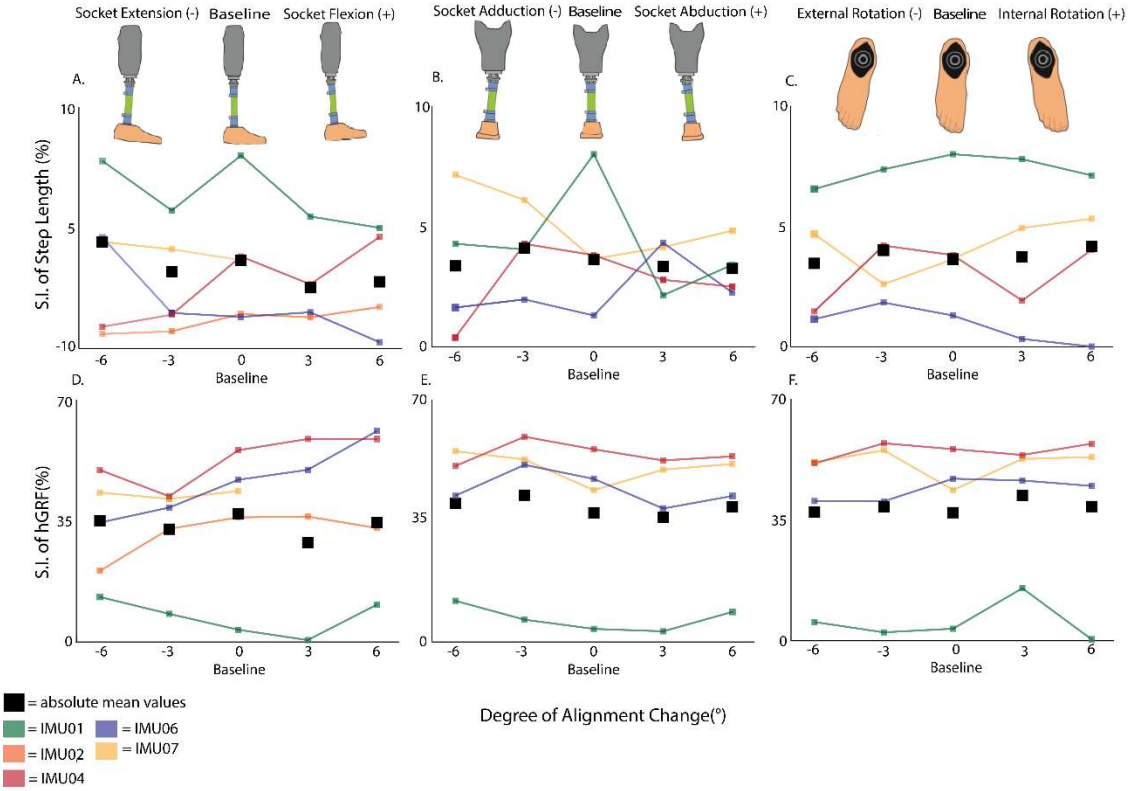
None of the 5 participants presented the lowest SI for step length or hGRF at baseline (Figure 1). SI at baseline was averaged at 3.64±4.89% (step length) and 37.06±20.09% (hGRF). Modifying alignment with +3° change in sagittal plane yielded the lowest SI for step length (2.53±3.46%) and hGRF (28.37±30.04%) SI of step length was the highest (4.43±5.46%) with -6° change on the sagittal

plane alignment. SI of hGRF was the highest (42.16±30.33%) with -3° change on the coronal plane.

Discussion

The baseline alignment did not yield the lowest interlimb asymmetry compared to the 3° and 6° alignment changes in 3 directions. Our results suggest that subjective evaluation may not be the most effective tool to reduce interlimb asymmetry during walking in people with UTTA. We suggest the need for a more objective tool to quantify prosthesis alignment in the future.

Images (Optional)



Session Category

Clinical Biomechanics: N/A

OA80-04

A Comparison of Gait Adaptations During Two Types of Dual-Task Walking in Individuals With Unilateral Lower Limb Amputation: Part 2- Limb Loading Symmetry

Ms. Emily Parsowith M.S., CSCS[1], Dr. Lisa Zukowski Ph.D[2], Dr. Paul Kline PT, DPT, Ph.D[1]

[1]Virginia Commonwealth University, Richmond, VA, United States. [2]High Point University, High Point, NC, United States

Introduction

Individuals with unilateral lower limb amputation (LLA) exhibit limb-loading asymmetry that impairs function and may increase risk of knee osteoarthritis [1]. Cognitive-motor dual-task assessments reveal altered joint loading in response to additional cognitive demands, but this response may vary by the type of cognitive task utilized. The purpose of this study was to compare kinetic parameters between single-task walking, vision-based cognitive-motor dual-task walking, and non-vision-based cognitive-motor dual-task walking in people with unilateral LLA.

Methods

16 participants were enrolled, 14 with complete data for analysis (9 males, 5 females; age = 56.9±11.1 yrs, BMI = 29.1±4.5 kg/m^2, 10 transtibial, 4 transfemoral). Three walking tasks were performed, each two minutes in duration: single-task (ST), serial subtraction dual-task (SS; non-vision-based), and visual puzzles dual task (VP; vision-based). The two cognitive tasks were evaluated to compare between types of cognitive-motor dual-tasking. Loadsol® wireless force-sensing insoles were placed in the shoes of the amputated and non-amputated limb to measure peak loading, impulse, and loading rate. Normalized symmetry index (NSI) was calculated to compare the effect of task condition (ST, SS, and VP) on peak loading, impulse, and loading rate normalized to body weight. An NSI value of 0% is considered perfect symmetry between amputated and non-amputated limbs.

Results

A repeated measures ANOVA revealed a significant main effect of task condition on peak loading NSI ($F=3.547$, $p=0.043$). Post-hoc paired-samples t-tests indicated that peak loading NSI was significantly improved during VP compared to ST ($p=0.022$, $d= -0.697$). Differences between ST and SS ($p=0.344$, $d= -0.263$) and SS and VP ($p=0.06$, $d= -0.55$) were not significant. There were no significant main effects of task condition on impulse

(F=0.361, *p*=0.700) or loading rate (F=0.827, *p*=0.449) Additional results from the statistical analysis can be found in Table 1.

Discussion

These findings suggest that the VP task resulted in greater between-limb peak loading symmetry, primarily through increased loading of the amputated limb. These findings suggest unique adaptations based on cognitive task during cognitive-motor dual-task walking, including potential deviations from the individuals' preferred loading strategy, warranting further investigation.

Images (Optional)

Outcome Variable (NSI)	Task	Mean±SD	F	*p*-value	Paired Samples t-test	Mean difference±SD	*p*-value	Cohen's *d*
Peak Loading (%)	ST	-3.09±9.00	3.55	0.04*	ST-SS	-0.85±3.25	0.34	-0.26
	SS	-2.24±8.36			ST-VP	-1.92±2.75	0.02*	-0.70
	VP	-1.17±9.39			SS-VP	-1.07±1.94	0.06*	-0.55
Impulse (%)	ST	-6.50±8.03	0.36	0.70				
	SS	-6.74±8.77						
	VP	-6.34±8.82						
Loading Rate (%)	ST	-12.35±13.40	0.83	0.45				
	SS	-14.02±16.13						
	VP	-11.58±16.00						

Table 1. Within-subjects analysis of task condition effect on kinetic variables. Statistical significance is designated by an *. Negative mean NSI % indicates a greater non-amputated limb peak loading, impulse, and loading rate, respectively. Negative mean difference values indicate improved symmetry in the second task compared to the first.

References (Optional)

[1] Ding et al., J Orthop Res, 2021

Session Category

Clinical Biomechanics: N/A

OA80-05

Amputee Motor Control During Steady-State Overground Walking with Non-Prescribed Feet

Mr. Satria Ardianuari M.S.[1,2], Dr. Richard Neptune Ph.D.[3], Dr. Glenn Klute Ph.D.[1,2]

[1]Center for Limb Loss and MoBility (CLiMB), VA Puget Sound Health Care System, Seattle, WA, United States. [2]Department of Mechanical Engineering, University of Washington, Seattle, WA, United States. [3]Walker Department of Mechanical Engineering, The University of Texas at Austin, Austin, TX, United States

Introduction

Transtibial amputees (TTA) demonstrate altered muscle activations with increased co-contraction but preserved motor modules (co-excited muscles) during level and non-level ground walking [1-3]. How changing foot prescription (i.e., stiffer foot (SF) or powered foot (PW)) affects their overall motor control is unknown. Thus, this study investigated how foot prescription influences muscle activations and motor complexity (i.e., the number of independent modules).

Methods

Twelve unilateral TTA (46 ± 15 y; 10 M) completed motion analysis at preferred speed using their prescribed foot (PR) and SF. Seven subjects also walked with a PW. EMG data from eight intact-limb muscles: tibialis anterior (TA), medial gastrocnemius (MGAS), peroneus longus (PL), vastus medialis (VASM), rectus femoris (RF), biceps femoris (BFLH), gluteus medius (GMED), and gluteus maximus (GMAX) were filtered, rectified, and normalized to peak activation. Integrated EMG (iEMG) was calculated to quantify muscle excitations, and an index $(CCI) = iEMG_{min} / \Sigma iEMG_{ago_antago}$ was used to compute co-contraction [4]. Non-negative matrix factorization (NNMF) extracted modules (W) and their activations (C) such that $muscle\ activations = W \times C + error$ [5]. Total variance accounted for by n modules ($tVAF_n$) assessed motor complexity. Linear-mixed effects regression tested for differences between feet.

Results

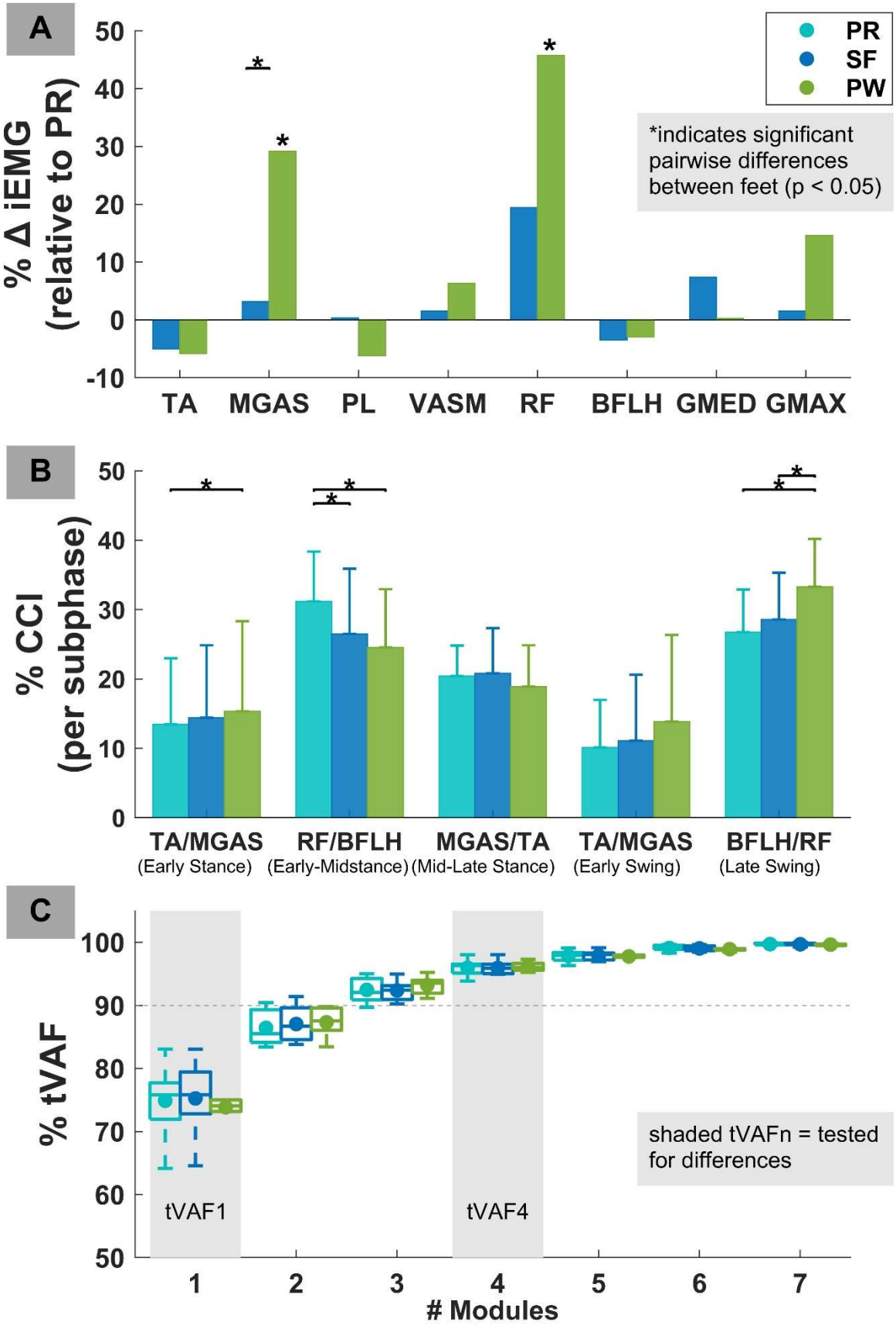
MGAS and RF activations increased with the PW foot (Fig. A). Ankle co-contraction increased with the PW foot (early stance) while knee co-contraction decreased (early-

midstance) but then increased (late swing) with SF and PW feet (Fig. B). No differences were observed in complexity (n=4) across feet for the selected $tVAF_n$ (Fig. C).

Discussion

In early swing, the heavier, higher-inertia PW foot may require increased MGAS activation for forward propulsion [6] and increased ankle and knee co-contractions for limb stability [4]. Despite changes in key support muscles like MGAS, similar modules across feet suggest preserved overall motor complexity. Thus, the influence of prosthetic feet on motor control may be insignificant.

Images (Optional)


A
% Δ iEMG (relative to PR)
50
40
30
20
10
0
-10
PR
SF
PW
*indicates significant pairwise differences between feet (p < 0.05)
TA
MGAS
PL
VASM
RF
BFLH
GMED
GMAX
B
% CCI (per subphase)
50
40
30
20
10
0
TA/MGAS
(Early Stance)
RF/BFLH
(Early-Midstance)
MGAS/TA
(Mid-Late Stance)
TA/MGAS
(Early Swing)
BFLH/RF
(Late Swing)
C
% tVAF
100
90
80
70
60
50
tVAF1
tVAF4
shaded tVAFn = tested for differences
1
2
3
4
5
6
7
Modules

References (Optional)

[1] Seyedali et al., J Neuroeng Rehabil, 2012; [2] Mehryar et al., IEEE-EMBS, 2017; [3] Mehryar et al., Gait Posture, 2020; [4] Kim et al., J Biomech, 2021; [5] Shuman et al., J Neuroeng Rehabil, 2019. [6] Lefranc et al., J Biomech, 2024

Acknowledgements (Optional)

Funded by the VA awards RX003138 and RX002974.

Session Category

Clinical Biomechanics: N/A

OA81-01

Using Stereoradiography to Investigate Ankle Motion with a Powered Footwear System

Mr. Destan Norman[1], Dr. Peter Laz[1], Dr. Alison Sheets-Singer[2], Dr. Kris Quah[2], Dr. Casey Myers[1]

[1]University of Denver, Denver, CO, United States. [2]Nike, Beaverton, OR, United States

Introduction

Powered footwear and exoskeletons can enhance human performance. Despite load-reduction benefits [1,2], ankle motion under exoskeleton use is not well understood. Marker-based motion capture (MOCAP) may lack accuracy in describing ankle joint movement. Stereoradiography offers an accurate description of bone motion [3], but has limited field of view and metal components may obscure bones. The objective of this study was to investigate the feasibility of using stereoradiography to measure ankle motion during walking and running with a powered footwear system (PFS).

Methods

Following IRB approval, MOCAP and stereoradiography data were collected on four adult subjects (3 female, 1 male) wearing a PFS during walking and running. A scaled OpenSim model was used to compute dorsiflexion from marker data. Models of the tibia/fibula, talus, and calcaneus were segmented from CT and assigned coordinate systems per [4,5]. Components of the FPS were also assigned anatomical coordinate systems. Models of the bone and device were registered to each stereoradiographic frame to generate a 3D pose throughout the activity. Ankle dorsiflexion from stereoradiography was represented as relative bone rotation (tibia-talus and tibia-calcaneus) and device rotation (shin strut-heel strut) where each was calculated about the mediolateral axis.

Results

Stereoradiography visualization of bony anatomy and device components was clearly defined for model registration using calibrated imaging settings (Figure 1). The bones and mechanical structures were tracked during stance phase of walking and running (Figure 1).

While kinematics from MOCAP and stereoradiography were strongly correlated (R= 0.961-0.984) throughout stance, notably less tibia-talus and tibia-calcaneus dorsiflexion was observed between mid-stance and toe-off compared to MOCAP.

Discussion

Stereoradiography was effective at dynamically visualizing ankle bone kinematics during exoskeleton use. This study identified distinct movement patterns of the ankle compared to those derived from motion capture, including the relative contributions at multiple bony joints. Understanding the true bone motion patterns can support the design (e.g. sizing, alignment, control) of powered footwear systems.

Images (Optional)

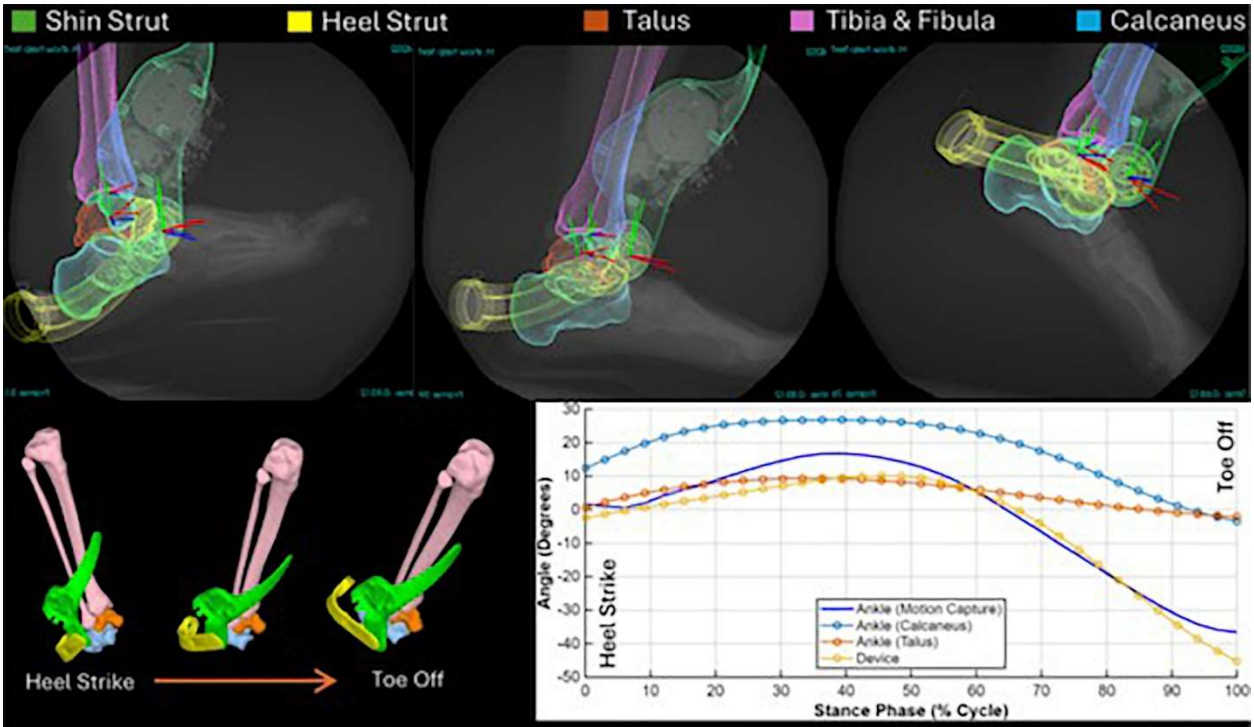


Figure 1: Stereographic tracking of subject-specific bone anatomy and powered footwear during running. Inset: Ankle dorsiflexion for a representative subject (male, age 27) comparing MOCAP, stereoradiography (talus-tibia and calcaneus-tibia), and device components.

References (Optional)

1. Sawicki et al., J Neuroeng Rehabil, 2020, 2. Mooney and Herr, J Neuroeng Rehabil, 2016. 3. Hogg-Cornejo et al., Foot Ankle Orthopaedics, 2020. 4. Peterson et al., Front Bioeng Biotech, 2023. Wu et al., J Biomech, 2002.

Session Category

Human Motion and Performance: Sports

OA81-02

Experience Led Biomechanics: Multivariate Links Between Foot and Ankle Kinematics and Transition Perception with a New Footwear FlexZone Technology

Ms. Megan Saftich MEng, Dr. Evan Day PhD, MS, Mr. Eddie Martinez MSc, Dr. Jennifer Sumner PhD, MS

Brooks Sports, Seattle, Washington, United States

Introduction

Foot torsion, defined as frontal-plane motion of the forefoot relative to the rearfoot [1], is often overlooked in running footwear design, where flexibility typically targets sagittal-plane metatarsophalangeal (MTP) motion. This study investigated how a shoe built for enabling more foot torsion influences biomechanical and perception metrics.

Methods

Biomechanical and perception data (n=10; 3.35 m/s treadmill running) were collected in the Brooks Glycerin Flex ("Flex", with "FlexZone" technology, Figure1) and Brooks Glycerin 23 (neutral counterpart). Kinematics (sagittal and frontal-plane MTP and ankle joint) and center of pressure (COP) trajectories were analyzed alongside Likert-scale ratings for transition (fluidity, speed, flexibility, energy return, and overall satisfaction). Paired t-tests compared biomechanics between shoes. Relative differences (Glycerin – Flex) were calculated to control for inter-subject variability. Principal component analysis (PCA) was used to reduce dimensionality and identify meaningful biomechanical change patterns between shoes. Pearson's correlations were used to relate biomechanical PCs to perception data.

Results

Frontal-plane MTP range of motion (ROM), ankle ROM, and medial-lateral COP excursion (late stance) were significantly higher in the Flex ($p<0.05, <0.001, <0.04$). PC2 (22.6% variance) showed a strong-negative correlation with fluidity ($r= –0.72, p= 0.02$). PC2 was characterized by high positive loading for the average medial-lateral COP velocity in the midfoot (+0.56) and moderate negative loadings for frontal and sagittal-plane landing angles (-0.48, -0.34), as well as frontal-plane MTP ROM and ankle ROM in the late stance (-0.31, -0.36).

Discussion

This study demonstrated that footwear with FlexZone technology influences kinematics and perception. FlexZone, designed to enable foot torsion in push-off, led to an expected higher medial-lateral COP excursion and frontal-plane ROM (MTP, ankle) in late-stance. In a shoe, if runners demonstrated greater late-stance frontal-plane ROM, combined with slower medial-lateral COP velocity in the midfoot; and landed more dorsiflexed and everted (PC2) they tended to perceive that shoe as more fluid. The landing angle influence suggests that in a shoe with midfoot-focused technology, such as the FlexZone, heel strikers may feel a more fluid transition.

Images (Optional)

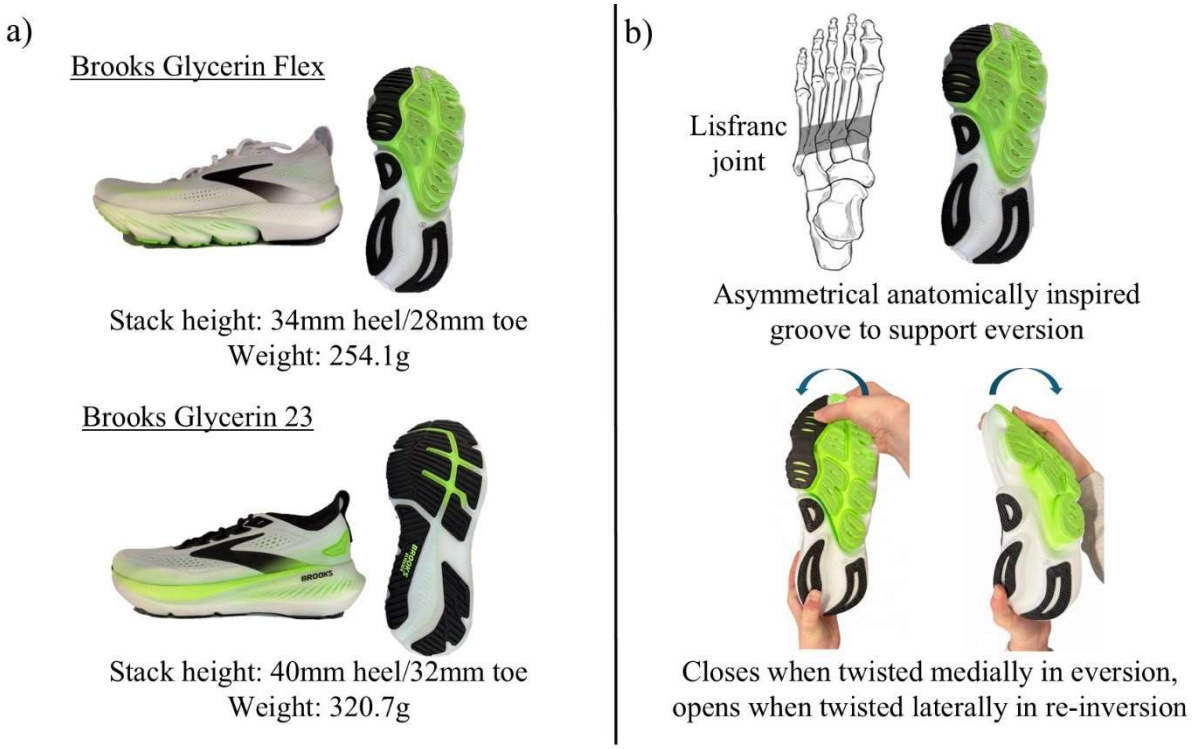


Figure1. a) Shoes tested (Brooks Glycerin Flex and Brooks Glycerin 23) and their geometries. b) Specific geometry of the Flex and it's S-shaped "FlexZone."

References (Optional)

[1] Stacoff et al., MSSE, 23(4), 482-490, 1991

Acknowledgements (Optional)

Thank you to all Brooks' Run Research Team members who assisted with data collection and processing.

Session Category

OA81-03

Analysis of Backpedal Mechanics and Achilles Tendon Loading in Elite American Football Athletes

Dr. Rachel H. Teater PhD[1], Ms. Anna C. Workman BS[1], Mr. W. Brody Hicks MS[1], Mr. Cody M. O'Cain MS[1], Dr. Evan A. Dooley PhD[1], Dr. Kristy B. Arbogast PhD[2], Dr. Laura C. Schmitt PT, PhD, FAPTA[3], Dr. E. Meade Spratley PhD[1]

[1]Biomechanics Consulting and Research (Biocore), LLC, Charlottesville, Virginia, United States. [2]Children's Hospital of Philadelphia, Philadelphia, Pennsylvania, United States. [3]The Ohio State University, Columbus, Ohio, United States

Introduction

In the National Football League, Achilles tendon (AT) ruptures often occur when players attempt to accelerate forward by pushing off their back limb extended behind their center-of-mass. "Breaking out of a backpedal" is a common defensive maneuver in which the final back step requires a powerful eccentric-concentric plantarflexor action. Understanding AT loading during this movement and whether trainable movement patterns might reduce load without compromising performance could inform injury prevention strategies. This study examined how backpedal technique, specifically foot orientation during the final back step, influences AT load and performance in American football athletes.

Methods

Fifteen elite American football athletes (male, 27 ± 5 yrs; 1.93 ± 0.26 m; 100.9 ± 14.2 kg) performed a standardized backpedal-to-sprint task on an outdoor synthetic turf field. Athletes were retrospectively classified as using a "Bicycle step" (in-line foot), "T-step" (out-turned foot), or "Other strategy" based on visual inspection of their final back step. Data were collected using marker-based motion capture and embedded force plates. AT force was estimated by dividing the ankle plantarflexion moment by a 5 cm moment arm and normalized to body weight (BW). Transverse plane foot angle relative to the direction of travel was computed at 50% stance, and task completion time quantified performance. A two-sample t-test compared peak AT force between Bicycle step and T-step groups, and linear correlations were computed between key variables (α=0.05).

Results

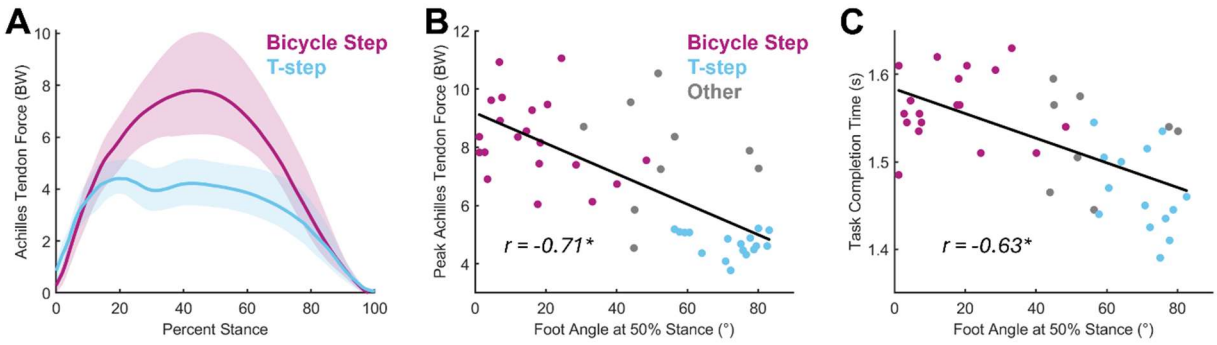
Seven athletes used a Bicycle step, five used a T-step, and three used other strategies. Average peak AT force across all trials was 6.8 ± 2.1 BW, with 8.3 ± 1.4 BW for Bicycle step

and 4.7± 0.4 BW for T-step ($p<0.001$). A more out-turned foot angle correlated with lower peak AT forces (Fig. 1B) and slightly improved performance (Fig. 1C) ($p<0.001$).

Discussion

Elite American football athletes who used a more out-turned foot during the final back step experienced lower peak AT forces without compromising performance. These findings suggest that adopting a T-step may be one strategy to mitigate AT loading when initiating forward acceleration. Understanding how these athlete movement variations distribute load across lower-limb joints could inform coaching and training strategies to reduce AT rupture risk while optimizing on-field performance.

Images (Optional)



Acknowledgements (Optional)

This research was made possible by funding from the National Football League (NFL) and the National Football League Players Association (NFLPA). The views expressed are solely those of the authors and do not represent the NFL, the NFLPA, or any of its affiliates.

Session Category

Human Motion and Performance: Sports

OA81-04

Fifth Metatarsal Cumulative Loading Across Rugby-Specific Movements in Elite Athletes Assessed via Plantar Pressure Measurement

Dr. Zixiang Gao Postdoctoral Researcher, Dr. Robin Trama Postdoctoral Researcher, Mr. David McNish Master's Student, Prof. Darren Stefanyshyn Professor, Dr. John Wannop Assistant Professor

Human Performance Laboratory, Faculty of Kinesiology, University of Calgary, Calgary, Alberta, Canada

Introduction

Fifth metatarsal (MT5) fractures (Jones fracture) are common in turf-based sports involving rapid acceleration and direction changes such as rugby, with 4.1% of foot injuries consisting of metatarsal fractures [1]. These injuries are associated with prolonged recovery and high recurrence rates despite surgical intervention [2]. However, it remains unclear which specific movements impose the greatest cumulative loads on the MT5, limiting the development of targeted injury-prevention strategies. Plantar pressure analysis provides a practical means to estimate MT5 loading and infer potential pathways relevant to MT5 injury risk.

Methods

Thirty elite North American rugby players (8 males, 22 females) performed five rugby-specific movements: sprinting, running pass, 90° V-cut, 180° turn, and ruck. All tasks were executed on an infilled artificial turf (FieldTurf) laid over the laboratory floor (3 trials per movement). Plantar pressure data were recorded using an Xsensor system (235 sensors) during stance. The MT5 region was manually defined using the sensor-coordinate grid by selecting sensors corresponding to the anatomical location of the MT5, and its force–time integral (FTI) and relative load ratio (MT5 FTI \total-foot FTI) were computed to assess cumulative 5th-metatarsal loading. Repeated-measures ANOVA with Bonferroni-adjusted pairwise comparisons were used for statistical analysis (a=0.05) to compare the different movements.

Results

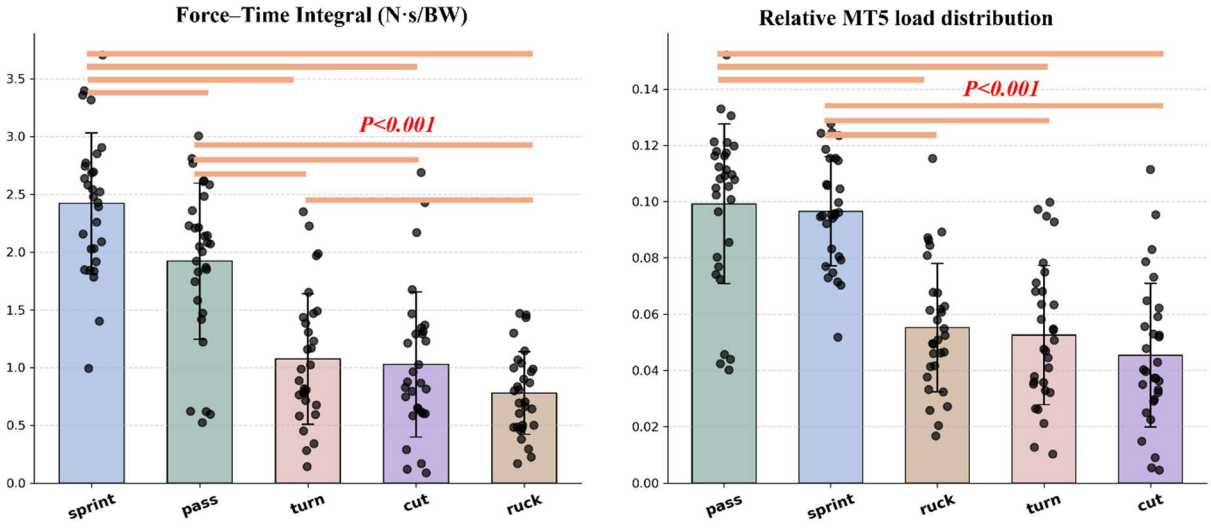
Significant effects of movement were present for both the MT5 FTI ($F(4,112)=113.94$, $p<0.001$) and relative load ratio ($F(4,112)=70.35$, $p<0.001$). Post-hoc comparisons indicated that sprinting produced the highest MT5 FTI and running pass had the highest load ratio,

which were both significantly greater than the cutting, turning, and ruck movements ($p<0.001$).

Discussion

This pattern indicates that MT5 loading is strongly influenced by lateral–medial pressure distribution. Sprinting showed the greatest MT5 cumulative load, reflecting the higher overall mechanical demand of straight-line sprinting, while the running pass produced the highest MT5 load ratio due to its more lateral pressure during trunk rotation. Cutting, turning and ruck actions demonstrated more medial pressure tendencies, reducing MT5 loading. Future work should incorporate finite element modeling to determine the MT5 internal loading.

Images (Optional)



References (Optional)

[1] Wright RW et al. Am J Sports Med. 2000.

[2] Miyamori T et al. BMJ Open. 2019

Session Category

Human Motion and Performance: Sports

OA81-05

Acute Effect of Incremental Exhaustive Treadmill Running on Running Biomechanics in Well-Trained Runners

Prof. Dr. Steffen Mueller[1], B.Eng. Leah Reiter[2], M.Sc. Marco Rahner[1], Prof. Dr. Jörg Lohscheller[3], Dr. Juliane Mueller[1]

[1]Trier University of Applied Sciences; Department of Computer Science – Therapeutic Sciences, Trier, RLP, Germany. [2]Trier University of Applied Sciences; Department of Engineering, Trier, RLP, Germany. [3]Trier University of Applied Sciences; Department of Computer Science, Trier, RLP, Germany

Introduction

Understanding the biomechanical responses of runners to increasing metabolic load and exhaustion is essential for optimizing running performance and minimizing fatigue-related injury risk. This study aimed to quantify acute changes in running biomechanics including vertical peak force, contact time, and vertical stiffness during progressive incremental treadmill running.

Methods

Eight well-trained male runners (31±6y; 178±2cm; 70±4kg; 65±24.5km in 6.5±1.8h training/week) performed an incremental treadmill test to exhaustion. The test started with 8km·h^{-1} (MIN) up to termination (3minutes steps, 2km/h per step increase). Capillary blood samples were taken to determine lactate thresholds (LT1: aerobic 2mmol·L^{-1}; LT2: anaerobic 4mmol·L^{-1}). Ground reaction force (GRF) data were recorded on each increment after 30s(A) and 150s(B) for 20s using an instrumented treadmill (h/p/cosmos 3D/Gaitway). The parameters peak vertical GRF (Fz: normalized/bodyweight [%BW]), contact time (CT: percent/stride time [%ST]) and vertical stiffness (k_v [a.u.]) were analysed at initial START (8km), LT1 (14.7±1.2 km/h), LT2 (17.0±1.4 km/h) and FINAL (20.3±1.6 km/h) running increment. Differences for acute fatigue (B-A [%]) were calculated. Descriptive analysis was followed by repeated-measures ANOVA using post hoc Tukey-Kramer ($\alpha = 0.05$).

Results

Fundamentally, with increasing running speed, Fz [%BW] increased from START 228.4±25.8 to FINAL 296.6±32.3 ($p<0.001$). CT [%ST] decreased from START 40.2±3.0 to FINAL 27.2±2.7 ($p<0.001$). Stiffness increased from START 4754±437 to FINAL 6766±999 ($p<0.001$). Acute fatigue during an increment (difference B-A [%]) showed for Fz [%] no differences at START 1.1±4.3, LT1 -0.3±2.6 and LT2 -1.0±1.2 ($p>0.05$), but a significant reduction

at FINAL -3.1±3.4 ($p<0.05$). For CT [%ST] no difference at any increment (START -0.5±1.2, LT1 0.1±3.0, LT2 -0.6±1.8 to FINAL 1.9±4.2 ($p>0.05$)) appeared and for stiffness no differences at START 0.1±1.2, LT1 0.0±2.0, LT2 0.1±2.8 ($p>0.05$) and a small reduction at FINAL -3.5±4.5 ($p=0.07$) was present (Fig. 1).

Discussion

Acute fatigue affects biomechanics only near exhaustion, suggesting relatively stable running patterns until maximal load. These findings highlight important implications for performance optimization and fatigue-related injury prevention.

Images (Optional)

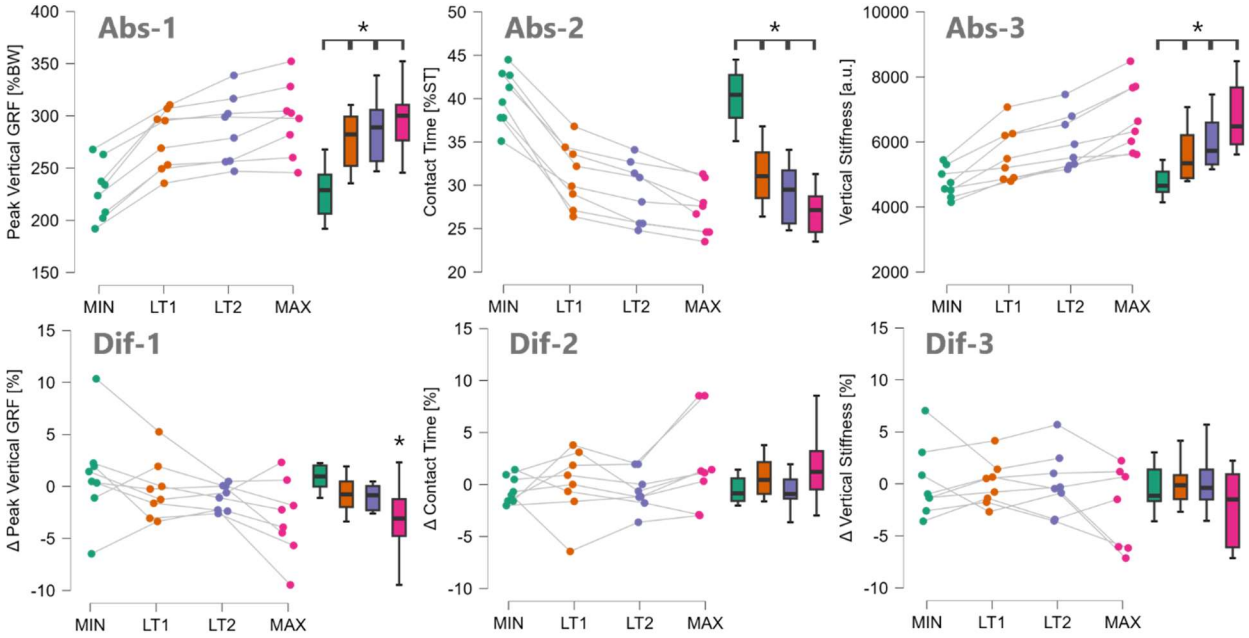


Fig. 1: Absolute between-increment changes in peak vertical GRF (Abs-1), contact time (Abs-2), and vertical stiffness (Abs-3) for the measurement A, and relative within-increment changes (Dif-1, Dif-2, Dif-3) for the increments (MIN, LT1, LT2, MAX) in well-trained runners. Significant differences are indicated: $p<.05$*

Session Category

Human Motion and Performance: Sports

OA81-06

Assessment of Achilles Tendon Loading During Outdoor Running Using a Novel Wearable System

Mr. Fisher Adkisson[1], Ms. Lindsay Rehme[1], Ms. Megan Thompson[1], Mr. Brady Huggins[1], Dr. Patrick Corrigan[2], Dr. Alex Reiter[1], Mr Charlie Minard[3], Mr Charlie Minard[4]

[1]Saint Louis University, St. Louis, MO, United States. [2]Cleveland Clinic, Cleveland, Ohio, United States. [3]Saint Louis University, St. Louis, Missouri, United States. [4]St Louis University, St. Louis, missouri, United States

Introduction

Achilles tendon injuries are highly prevalent in athletes. Because clinicians lack the ability to measure tendon loading, they often rely on symptomatology to guide rehabilitation decisions, including running volume and intensity. Shear wave tensiometry has emerged as a noninvasive tool that directly assesses *in vivo* muscle-tendon loading [1]. Recent work has deployed the technology for assessing Achilles tendon loads during real-world walking with favorable results. However, it remains unknown if this technology can characterize loading during running in real-world settings [2]. This preliminary study investigated the capacity of an updated wearable tensiometer system to track changes in Achilles tendon loading during outdoor running.

Methods

Healthy, physically active adults completed 100-meter outdoor walking (1.34 m/s) and running (2.68, 3.35, and 4.47 m/s) trials. Participants donned a custom wearable data acquisition system that measured Achilles tendon loading via tensiometers (Fig 1A) [2]. Using a previously established calibration technique, tendon force was derived from wave speed [2-3]. Data were processed in MATLAB to normalize time for each gait cycle. Preliminary wave speed results were compared with descriptive statistics.

Results

To date, four adults have participated in this study (3/1 males/females, age: 21.8±2.3 years, height: 1.82 ± 0.12 m, mass: 75.6±14.0 kg). Preliminary results for outdoor locomotion show peak wave speed increased with increasing locomotion speed from 36.9±3.6 m/s during walking to 46.8±12.6 m/s during the fastest running speed (Fig 1B). Furthermore, stance phase decreased from ~60% of the gait cycle during walking to ~40% during running (Fig 1B). Recruitment of additional participants and calibration of wave speed to force are ongoing.

Discussion

The wearable system successfully captured expected time series trends and changes in wave speed magnitude, which were also similar to previous work using tensiometry during indoor running [3]. Advances in wearable sensors such as these present an exciting opportunity to track tendon loading during high-dynamic, unobstructed movement in real-world environments, with the goal of improving patient outcomes by providing clinicians with objective ways of progressing rehabilitation.

Images (Optional)

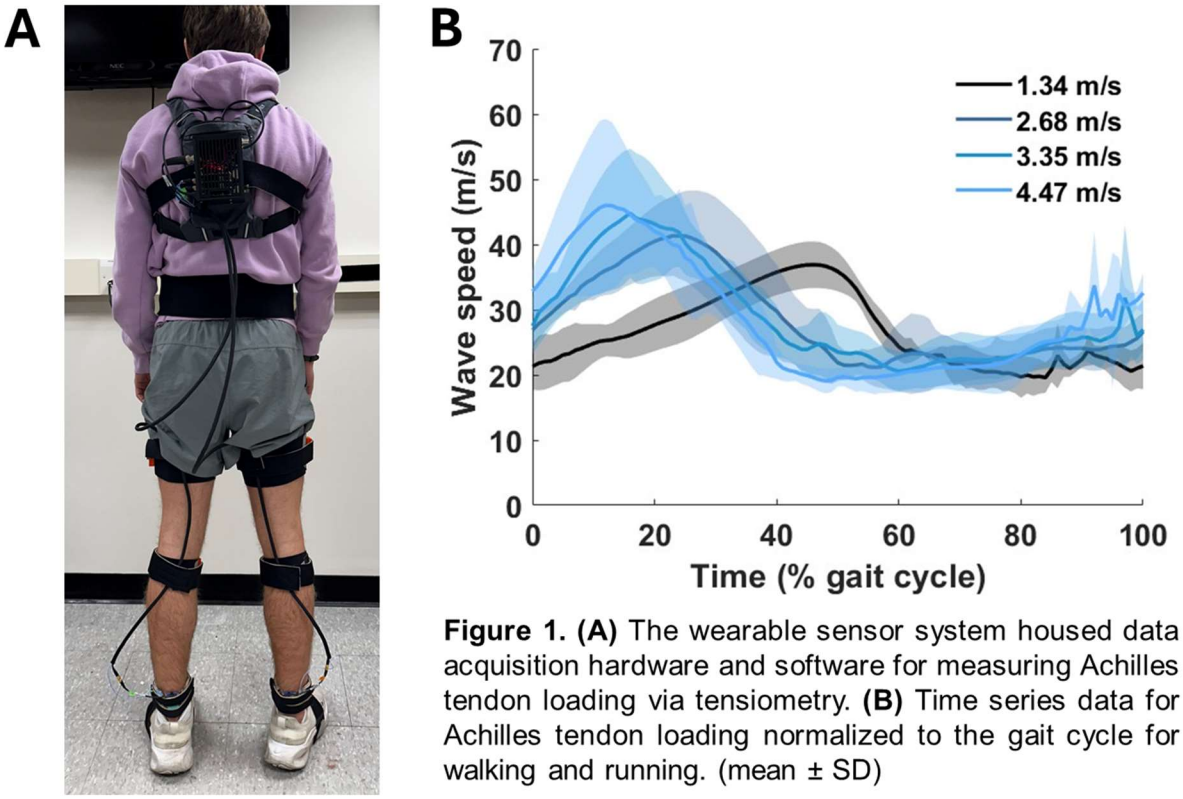


Figure 1. (A) The wearable sensor system housed data acquisition hardware and software for measuring Achilles tendon loading via tensiometry. **(B)** Time series data for Achilles tendon loading normalized to the gait cycle for walking and running. (mean ± SD)

References (Optional)

[1] Martin, *Nat Comm*, 2018. [2] Reiter, *JBME*, 2025. [3] Reiter, *MSSE*, 2024.

Acknowledgements (Optional)

Funding from the Saint Louis University Research Institute.

Session Category

Human Motion and Performance: Sports

OA82-02

Predicting Post-TEVAR Endoleaks: A Novel Pre-Operative Hemodynamic Risk Factor From Fluid-Structure Interaction simulations

MSc Francesca Duca[1], MSc Silvia Tavarone[1], MD Maurizio Domanin[2,3], MD Daniele Bissacco[2,3], PhD Santi Trimarchi[2,3], PhD Francesco Migliavacca[1], PhD Christian Vergara[1]

[1]LaBS, Department of Chemistry, Materials and Chemical Engineering ”Giulio Natta”, Politecnico di Milano, Milan, Lombardia, Italy. [2]Department of Clinical Sciences and Community Health, Università degli Studi di Milano, Milan, Lombardia, Italy. [3]Section of Vascular Surgery, Cardio Thoracic Vascular Department, Fondazione I.R.C.C.S. Ca’ Granda Ospedale Maggiore Policlinico, Milan, Lombardia, Italy

Introduction

To avoid endoleak formation after Thoracic Endovascular Aortic Repair (TEVAR), adequate stent-graft stability must be ensured at the device fixation sites (i.e., landing zones, LZs). In this work, we apply a Fluid-Structure Interaction (FSI) computational framework to ten pre-operative patient-specific Thoracic Aortic Aneurysms (TAA) cases, for which post-TEVAR outcomes are known, to propose a hemodynamic risk factor useful to predict the formation of type I and III endoleaks.

Methods

A cohort of ten patients, who underwent TEVAR for a diagnosis of TAA, was selected for this study and, at the time of the last follow-up, five patients showed an endoleak. Following the pipeline already presented in [1] and using the finite element library life^X [2], we performed an FSI simulation in each pre-operative scenario to compute the Drag Forces (DFs). These were then used to calculate the risk factor R in each LZ: $R = (DF_{\perp}^2 * DF_{||} * p_{tortuosity})/10^6$, where $DF_{\perp}$ and $DF_{||}$ are the DFs’ perpendicular and parallel components to the vessel centerline, and $p_{tortuosity}$ is the endoleak formation probability based on the LZ tortuosity. R was then scaled between 0 and 1 in each LZ. The patients’ cohort was divided into two groups: an eight-patient calibration set, used to associate specific R values with different risk levels, and a two-patient test set, employed to validate the predictive capability of R.

Results

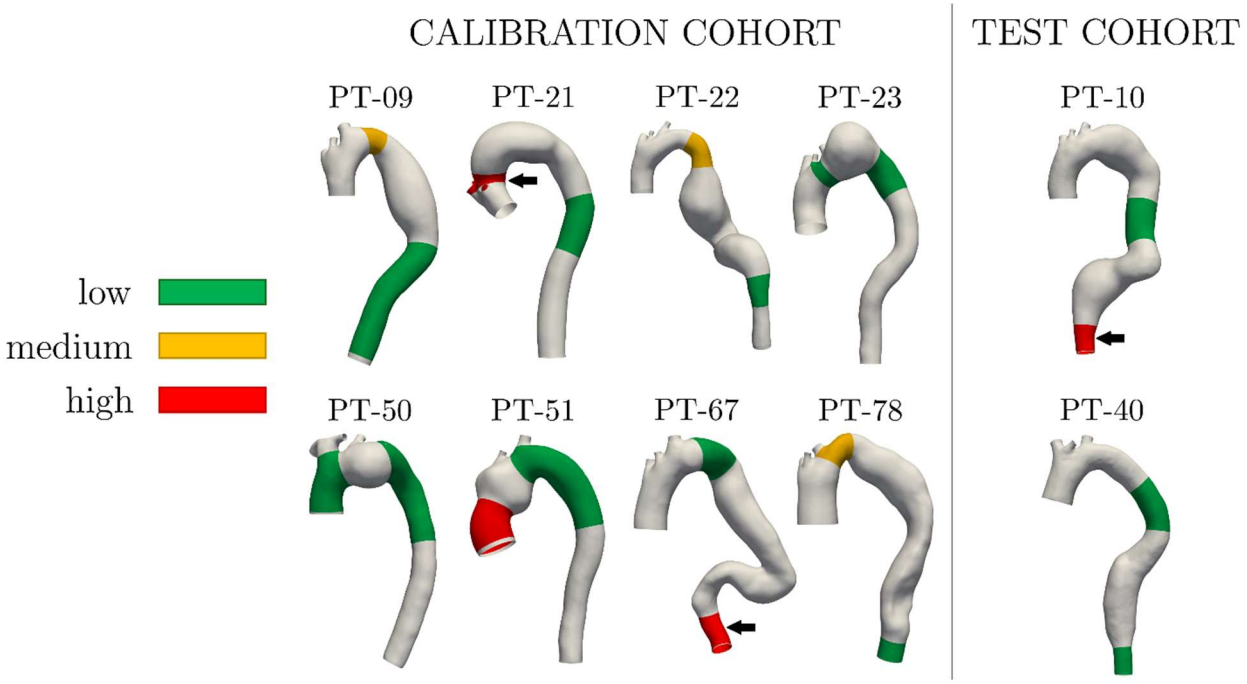
In the calibration set, all the type I endoleak cases occurred in landing zones with $R \geq 0.95$. Black arrows in Figure highlight the LZs where the type I endoleak occurred. For type

III endoleak, LZs with R ≤ 0.30 had no endoleak, those with 0.31 ≤ R ≤ 0.75 showed endoleaks in some cases, and all the LZs with R ≥ 0.76 presented an endoleak.

Discussion

Based on the results obtained (Figure), LZs with R ≤ 0.30 could be considered at low risk, those with 0.31 ≤ R ≤ 0.75 at medium risk, and those with R ≥ 0.76 at high risk. When we applied this classification to the test cohort, the patients follow-up outcomes were correctly predicted.

Images (Optional)



References (Optional)

[1] Francesca Duca et al., The Journal of Physiology, 2025. [2] Pasquale C. Africa et al., SoftwareX, 2022.

Session Category

Cardiovascular/Cardiorespiratory Biomechanics: Methods, Models and Applications

OA82-03

Onset and Nature of Flow Instabilities in Cerebral Venous Diseases

Ms. Rojin Anbarafshan[1], Dr. David A. Steinman[1,2]

[1]Department of Mechanical Engineering, University of Toronto, Toronto, Ontario, Canada. [2]Institute of Biomedical Engineering, University of Toronto, Toronto, Ontario, Canada

Introduction

Morphological abnormalities in cerebral venous sinuses are strongly implicated in disorders like pulsatile tinnitus (PT). Recent CFD studies have demonstrated presence of high-frequency, turbulent-like flow instabilities plausibly linked to PT sounds; however, their onset mechanisms and fluid mechanical nature remain poorly characterized, and hampered by a lack of patient-specific flowrates. Here we aimed to systematically investigate the emergence and evolution of these flow instabilities and associated sounds as a function of inlet flowrate.

Methods

Three patient-specific PT anatomies with transverse sinus (TS) stenosis, previously studied under pulsatile conditions, were simulated under linearly increasing inlet flowrate (Qin) ramped up through a physiologically plausible range of 2-10 ml/s. Fluid mechanics were inspected using velocity isosurfaces, streamlines, and Q-criterion to identify vortical structures and instabilities. Time-resolved spectral power index (SPI) and spectrograms of wall pressure fluctuations were used as first-order proxies of flow-induced sound.

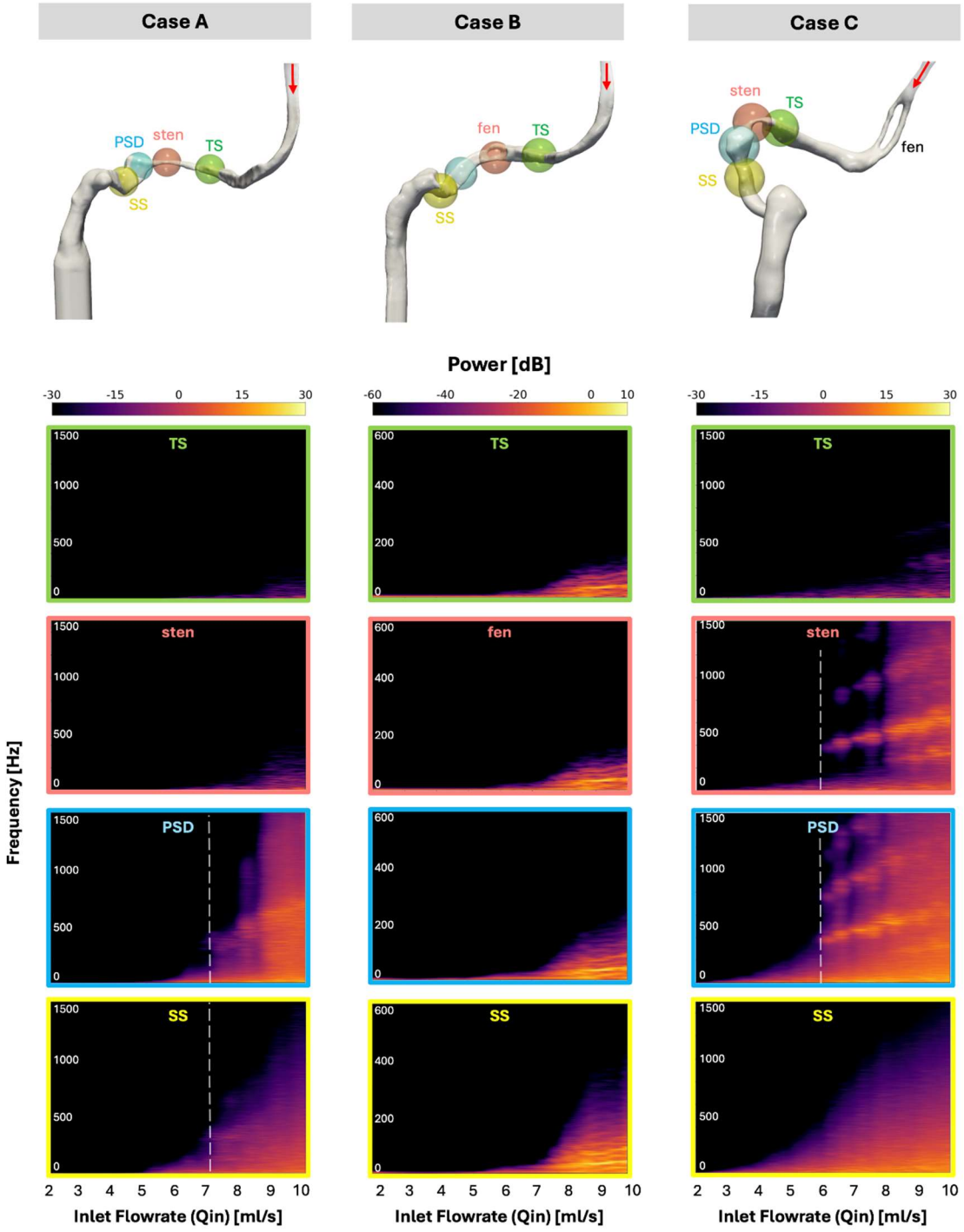
Results

In cases A and C, high-frequency vortical flow instabilities emerged at or distal to the stenosis at roughly 5 and 3 ml/s respectively. Spectrograms revealed onset of pseudo-acoustic activity at roughly 7 and 6 ml/s (dashed lines in figure), with discrete harmonic bands at the post-stenotic dilatation (PSD) indicative of periodic vortex–wall interactions, and more broadband, turbulent-like flow downstream in the sigmoid sinus (SS). Case B, which has a fenestration (fen) instead of a true stenosis, generated only weak, low-frequency spectral content even at highest Qin (note different frequency range and dB scales in figure).

Discussion

Strong flow instabilities near auditory structures can manifest as either or both narrowband and broadband characteristics, consistent with the disparate nature of PT sounds that have been recorded. The relationship between Qin and both flow instability and sound generation is strongly nonlinear, where modest changes (~10%) in inflow in the physiological range can shift the system to different flow and acoustic signatures. This is consistent with postural and diurnal variations in PT sounds reported by patients, and highlights the need for patient-specific vs. generic inflow information—potentially via reduced-order modeling of the cerebral venous network—to pinpoint the fluid dynamic sources of sound production, especially when multiple anomalies might be present.

Images (Optional)



References (Optional)

Acknowledgements (Optional)

This research was supported by a Discovery grant (RGPIN-2018-04649) to DAS from the Natural Sciences & Engineering Research Council of Canada (NSERC). RA was additionally supported by an NSERC Canada Graduate Scholarship–Doctoral (CGS-D) and by a Mr. John H. Weber and Dr. Eleanor Connie Mariano Graduate Scholarship in Biomedical Engineering.

Session Category

Cardiovascular/Cardiorespiratory Biomechanics: Methods, Models and Applications

OA82-04

Ultrasound-Based Fluid Structure Interaction Modelling of Diseased Carotid Arteries

Ir. Lotte Piek[1,2], Ir. Joerik de Ruijter[1], Prof. Dr. Marc van Sambeek[2], Prof. Dr. Ir. Richard Lopata[1]

[1]Eindhoven University of Technology, Eindhoven, Noord-Brabant, Netherlands. [2]Catharina Hospital, Eindhoven, Noord-Brabant, Netherlands

Introduction

Carotid artery disease poses significant risks such as stroke and transient ischemic attacks. Current interventions are primarily based on diameter measurements. There is a need for patient-specific computational models to support clinical decision-making. Ultrasound (US) offers a cost-effective, rapid, and safe solution for geometry assessment as basis for such biomechanical models. This study presents a framework to aid personalized treatment strategies through the use of US-informed fluid structure interaction models for patient-specific geometries, making it suitable for diagnostic and monitoring in subsequent patient studies.

Methods

To obtain the geometries with sufficient resolution, ultrasound scans were acquired using manual sweeps (N=5). Data were segmented automatically using our in-house method. The resulting contours were smoothed (Fig A).Inlet conditions were set using a clinically measured velocity profile, while distal vasculature was represented by Windkessel models.The wall was modeled as a Neo-Hookean material (shear modulus: 250 kPa), chosen for its suitability for the pressure range given. Plaques were also modeled as Neo-Hookean solids, with shear moduli of 50 kPa for lipid-rich regions and 1.3 MPa for calcified regions.

Results

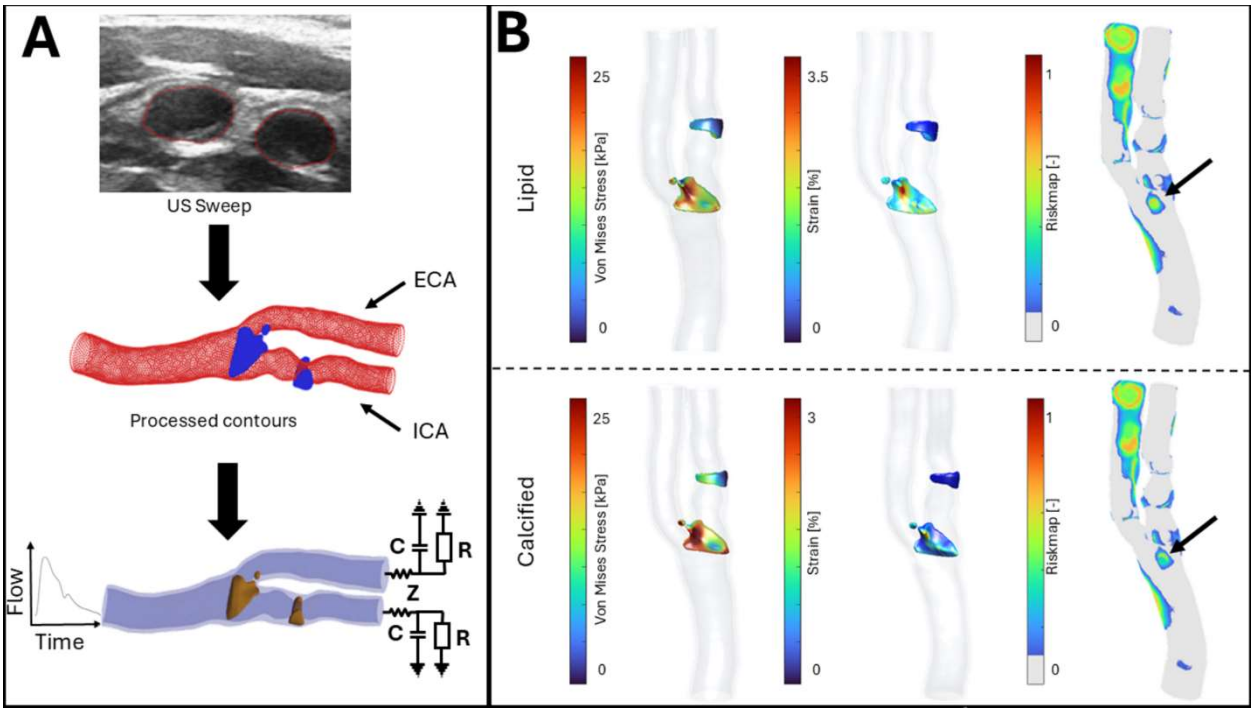
Fluid-structure interaction (FSI) simulations revealed distinct structural and hemodynamic behaviors for lipid- and calcified plaques (Fig B). Lipid plaques exhibited lower von Mises stress but higher strain, indicating greater compliance and deformation under pulsatile loading. Calcified plaques showed markedly higher stress and minimal strain, confirming their rigidity. The fluid-derived risk map highlighted disturbed flow near plaque shoulders

for both cases, with the largest local differences occurring at the most prominent plaque (arrows in Figure B). Overall risk map differences between plaque types were minor.

Discussion

The minor differences in risk maps suggest that flow-based metrics alone, even when derived from FSI, may not fully capture plaque vulnerability. Structural metrics such as stress and strain provide critical complementary information, underscoring the value of combining fluid and structural analysis.By integrating patient-specific ultrasound-based geometries with FSI, this approach enables simultaneous evaluation of wall mechanics and flow-derived risk factors in a clinically feasible workflow. Such combined insights could improve stratification beyond diameter or flow-based criteria, supporting personalized treatment planning

Images (Optional)



References (Optional)

Session Category

OA82-05

A Proper Orthogonal Decomposition-Based Approach to Expedite Transient Clinical-Use CFD in Coronary Arteries

Mr. Girolamo Mastronuzzi MSc[1], Dr. Maurizio Lodi Rizzini PhD[1], Prof. Diego Gallo PhD[1], Dr. Valentina Mazzi PhD[1], Mrs. Bianca Griffo MSc[1], Prof. Claudio Chiastra PhD[1], MD. Alessandro Candreva PhD[2], MD. Carlos Collet PhD[3,4,5], Prof. Umberto Morbiducci PhD[1]

[1]Politecnico di Torino, Torino, TO, Italy. [2]Department of Cardiology, Zurich University Hospital, Zurich, Zurich, Switzerland. [3]Cardiovascular Center Aalst, OLV-Clinic, Aalst, East Flanders, Belgium. [4]Division of Cardiology, New York Presbyterian Hospital Columbia University, New York, NY, United States. [5]Clinical Trial Center, Cardiovascular Research Foundation, New York, NY, United States

Introduction

Emerging evidence shows that wall shear stress (WSS)–derived quantities can help identify/predict coronary disease [1] and outcome [2]. As WSS cannot be measured directly, personalized in silico models are required, but transient Computational Fluid Dynamics (CFD) simulations remain computationally expensive within a clinical framework. This study introduces an approach based on Proper Orthogonal Decomposition (POD) that reconstructs full transient hemodynamics from partial CFD data, markedly reducing computational cost and supporting clinical translation.

Methods

Three-dimensional geometries of mildly stenosed coronary arteries were reconstructed from coronary angiography. The dataset originated from a clinically adjudicated cohort of 80 patients and comprised 80 lesions culprit of future myocardial infarction (MI) and 107 non-culprit lesions [2]. Transient CFD simulations were carried out on the reconstructed geometries. For each case, instantaneous WSS data over a hemodynamically representative window (22%) of the cardiac cycle were extracted and decomposed using POD. The three main POD modes (capturing >99% of variability) were linearly combined using the inlet flow rate waveform and its first and second derivatives, enabling WSS reconstruction over the entire cardiac cycle. Accuracy was assessed through lesion-averaged, clinically relevant WSS quantities, including time-averaged WSS (TAWSS) and the Topological Shear Variation Index (TSVI), the latter capturing topology-aware WSS features [1]. The prediction capability for future MI of TSVI from CFD and CFD-POD was then evaluated in terms of area under the curve (AUC) and compared.

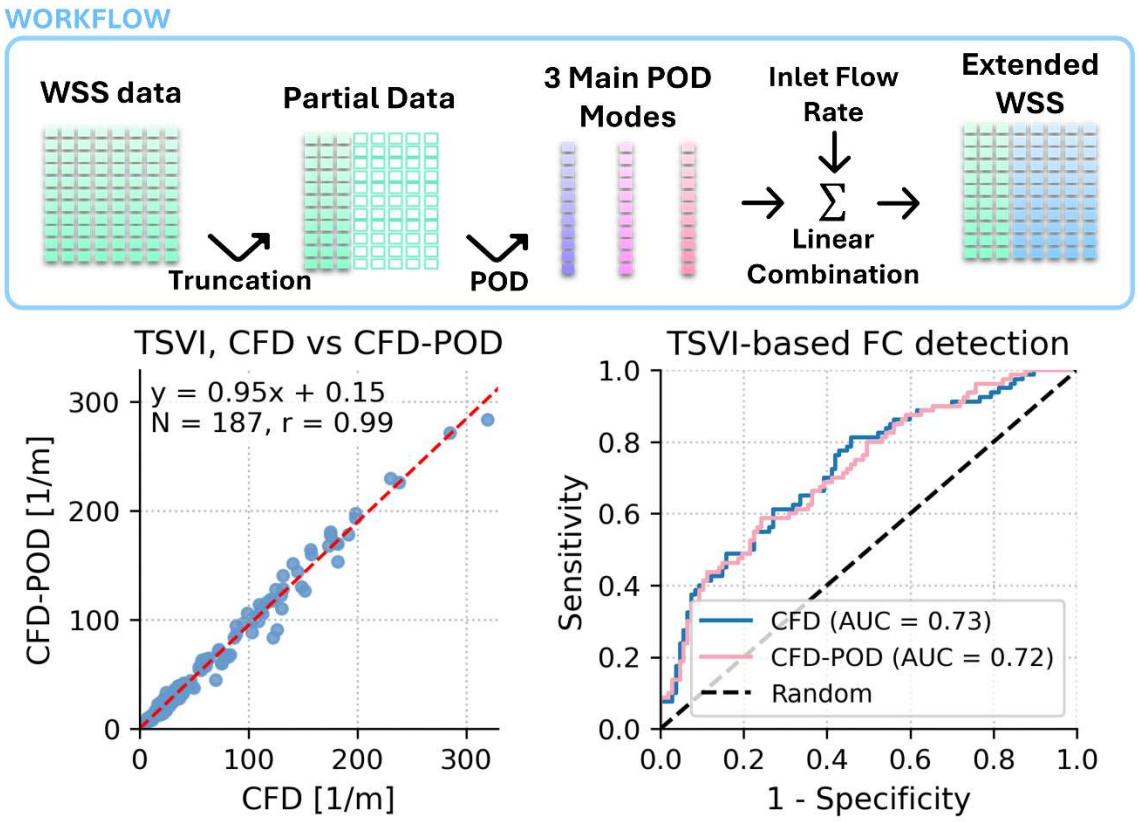
Results

CFD-POD reconstruction of cycle-averaged WSS-based quantities required ~1s, yielding a computational cost reduction of ~78% with respect to traditional CFD. The reconstructed TAWSS and TSVI showed a remarkable proportional relationship with quantities calculated from CFD ($r > 0.99$). When predicting future MI, TSVI from CFD-POD achieved identical performance as traditional CFD (AUC=0.72, $p<0.0001$ vs. 0.73, $p<0.0001$), confirming preservation of prediction power.

Discussion

The proposed POD-based framework accurately reconstructs WSS fields while markedly reducing computational cost. Its agreement with CFD demonstrates robustness and suitability for efficient characterization of coronary hemodynamics. These findings support integration of accelerated WSS-based risk assessment into routine practice, enabling broader adoption of personalized, simulation-driven diagnostics.

Images (Optional)



References (Optional)

[1] Valentina Mazzi *et al.*, Ann Biomed Eng, 2021

[2] Alessandro Candreva *et al.*, Atherosclerosis, 2022

Acknowledgements (Optional)

Session Category

Cardiovascular/Cardiorespiratory Biomechanics: Methods, Models and Applications

OA83-01

Biofidelic Foot Models for *In Vitro* Gait Simulation Must Include a Compliant Plantar Surface

Dr Antony Crossman, Dr Angela Kedgley

Imperial College London, London, Greater London, United Kingdom

Introduction

In vitro gait simulation is used in the development of surgical methods and implant designs. Although the research field is almost thirty years old [1], control methods have remained broadly the same. Previous systems have applied pre-calculated average muscle forces to specimens, leaving kinematics unconstrained. One reason for the lack of progression may be the cost and ethical considerations of testing new methods on cadaveric specimens. Therefore, a multi-segment foot and ankle model that replicates joint kinematics and enables the application of muscle forces, with anatomically accurate moment arms, would benefit the gait simulation community. The hypothesis was that such a model must include compliance on the plantar surface for accurate vertical ground reaction force (vGRF) control.

Methods

A five-segment, nine-tendon, multi-articulated foot and ankle model was designed and manufactured (Figure 1a). Segments were 3D printed with PLA plastic (80% infill), totalling a weight approximately that of an average 75kg male's foot [2]. Tendons were represented by steel wires running through nylon-coated brake cable sheaths. A second model incorporated a 10mm TPU compressible heel (30% infill).

Both models were tested by simulating 10 repetitions of the stance phase of gait (vGRF scaled to one eighth of in vivo). Accuracy and repeatability were defined as mean kinetic and kinematic errors, and mean standard deviations between trials, respectively.

Results

The rigid heel model achieved vGRF accuracy of 37.5N ± 20.7N, with a repeatability of 14.0N ± 7.1N (Figure 1b). The soft heel improved the kinetic accuracy to 7.7N ± 4.8N, with a repeatability of 3.7N ± 1.5N. The soft heel also improved kinematic accuracy by 36% across all controlled joints.

Discussion

Introducing compliance into a foot and ankle model, to test in vitro simulation methods, improved load acceptance at the beginning of stance. Without this, contact of the foot with the ground resulted in a sharp increase in vGRF, which caused instability within the control system. The instability propagated throughout the remainder of the simulation as the controller was never able to recover the accuracy.

Images (Optional)

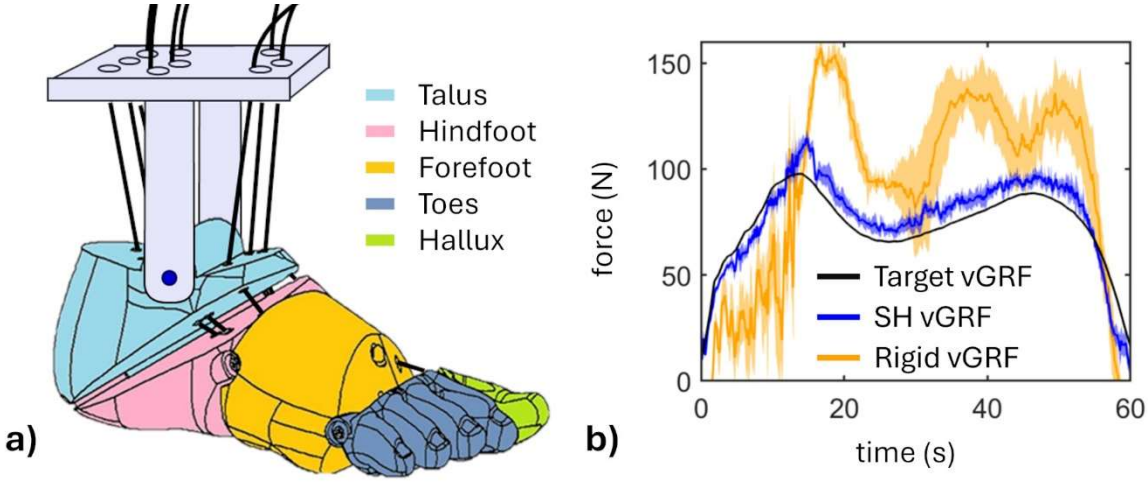


Figure1: a) Rigid foot model, b) Desired and average (± one standard deviation) achieved stance phase vertical ground reaction force (vGRF) using the rigid foot model (orange) and soft heel (SH) model (blue)

References (Optional)

[1] Sharkey N.A. et al. Clinical Biomechanics, 1998

[2] Winter D.A. Biomechanics and Motor Control of Human Movement, 2009

Acknowledgements (Optional)

AJC was supported by the UK Engineering and Physical Sciences Research Council (EPSRC) grant EP/S02249X/1 for the Centre for Doctoral Training in Prosthetics and Orthotics.

Session Category

Musculoskeletal Biomechanics: Methods, Models and Applications

OA83-02

Construct Validity of a Novel Arthrometer-Based First Ray Relative Mobility Index: A Cadaveric Biomechanical Study

PD Dr Florent Moissenet[1,2], Dr Mickaël Chollet[2], Mr Quentin Praz[2], Mr Spyridon Schoinas[2], Dr Alberto Bailez[3], Dr Antoine Acker[4], PD Dr Mathieu Assal[4], Pr Stéphane Armand[2,1]

[1]Geneva University Hospitals, Geneva, Geneva, Switzerland. [2]University of Geneva, Geneva, Geneva, Switzerland. [3]Clínica Corachan, Barcelona, Catalonia, Spain. [4]Foot and Ankle Surgery Centre, Centre Assal, Geneva, Geneva, Switzerland

Introduction

First ray hypermobility contributes to several forefoot disorders and is a key mechanical factor in hallux valgus development. Clinical assessment remains largely subjective, relying on manual tests of absolute first ray mobility that poorly capture the functional loading behaviour. A new automated arthrometer quantifies an alternative metric, the first ray relative mobility (FRRM), by comparing the first ray displacement to that of the lesser metatarsals under equal loads [1]. This study evaluated its construct validity against the superior translation of the first tarsometatarsal joint, the principal biomechanical marker of the first ray instability [2].

Methods

Ten fresh-frozen lower limbs without major degeneration or prior surgery were instrumented for controlled loading. The Achilles, tibialis anterior, tibialis posterior, and peroneus longus tendons were attached to a loading system applying physiologic forces, with additional tibial loading to maintain heel contact. The arthrometer applied equal loads (10-50 N, 5 N increments) to the first and lesser metatarsal columns. The FRRM was defined as the change in vertical displacement difference between these columns from 10 to 50 N. The superior translation of the first tarsometatarsal joint was measured using 3D motion capture with intracortical pins. After preconditioning, averaged data from six trials were analysed using Spearman correlations with bootstrap intervals (10,000 resamples) and leave-one-out robustness testing.

Results

Construct validity was very strong, with a significant correlation between the FRRM and the superior translation of the first tarsometatarsal joint (Spearman r = 0.87, 95% CI [0.40-

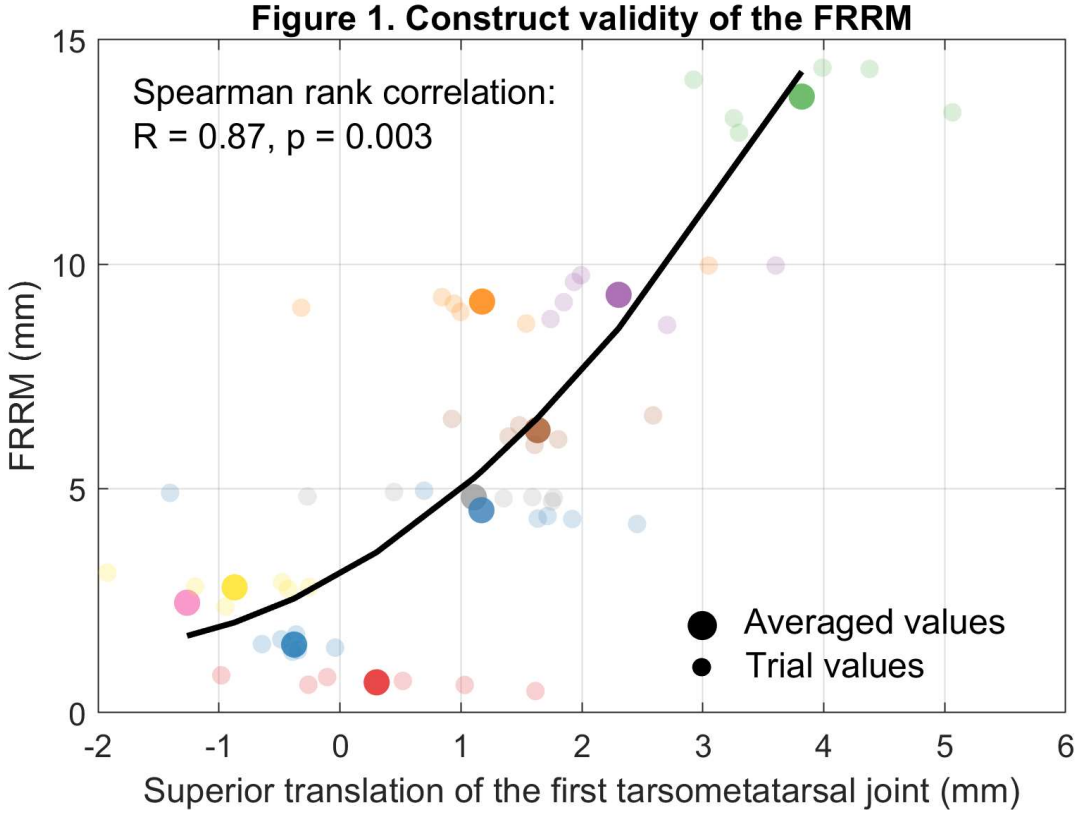
1.00], p = 0.003; Fig. 1). The association was non-linear and remained highly stable across specimens in leave-one-out testing, with variations in r below 0.10 (range 0.82-0.92).

Discussion

The FRRM showed a very strong construct validity, indicating that the relative first ray excursion closely reflects the superior translation of the first tarsometatarsal joint under physiological loading. These results support FRRM as a meaningful biomechanical measure of forefoot instability and a potential alternative to absolute displacement metrics. Confirmation in larger in vivo cohorts is warranted.

Images (Optional)

Figure 1. Construct validity of the FRRM



References (Optional)

[1] Pierobon F. et al., Foot Ankle Surg, 2025
[2] Glasoe W.M. et al., Foot Ankle Int, 2005

Acknowledgements (Optional)

This work was supported by Innosuisse, the Swiss innovation agency (Grant No. 123.305 IP-LS).

Session Category

Musculoskeletal Biomechanics: Methods, Models and Applications

OA83-03

A Combined MRI and Inverse Finite Element Analysis (iFEA) Workflow for Subject-Specific Characterisation of Meniscus Material Properties *In Situ*

Dr Sherif Zantiba, Dr Nagitha V.N.Wijayathunga@leeds.ac.uk, Dr Marlène Mengoni, Prof. Ruth Wilcox

University of Leeds, Leeds, England, United Kingdom

Introduction

Over 375 million people worldwide are afflicted by knee OA. The meniscus is a critical load-bearing structure, and its damage can cause or accelerate knee OA. Understanding its mechanical behaviour is essential for developing effective treatments. Traditional mechanical testing is destructive and fails to capture the tissue's functional behaviour while computational models are limited by a lack of subject-specific, *in-situ* material properties. This study aimed to develop and validate a novel workflow combining MR-imaging of *in-vitro* loaded joints with iFEA to characterise the *in-situ* meniscus material properties.

Methods

A novel, calibrated MRI-compatible loading rig was developed (*Figure-1*) to apply physiological compressive loads to in-vitro knee joints, uniquely permitting tibial axial rotation to accommodate the screw-home mechanism.

Three porcine knee joints were imaged (Siemens 3T Vida) under stepped compressive loads (to 1500N) in the neutral position. A new kinematic measurement technique was developed to quantify meniscus radial distance from the MR images, using the tibial eminence as a stable reference point to account for tibial rotation.

Subject-specific FE models were generated from specimen MR and CT images. A preliminary sensitivity study was performed to identify which transverse isotropic material parameters most influenced meniscus radial movement. An iFEA workflow, driven by a particle swarm optimiser, then calibrated these candidate parameters by minimising the error between FE-predicted and MRI-measured radial distances in the neutral configuration.

Results

The sensitivity study confirmed fibre, in-plane, and shear stiffness values as the dominant parameters influencing radial movement. The subsequent iFEA calibration successfully identified these properties for all samples. The in-plane stiffness was consistently found to be 20 MPa, while fibre stiffness ranged from 161–250 MPa and shear from 13–30 MPa. The optimised models achieved a good fit, with a normalised root mean squared error between 7% and 11%.

Discussion

A novel, *in-vitro* methodology for characterising subject-specific, *in-situ* meniscus material properties was successfully developed and applied to derive meniscus properties from axially-loaded experiments. This workflow provides a robust foundation for future patient-specific stratification and the pre-clinical assessment of meniscal replacement devices.

Images (Optional)

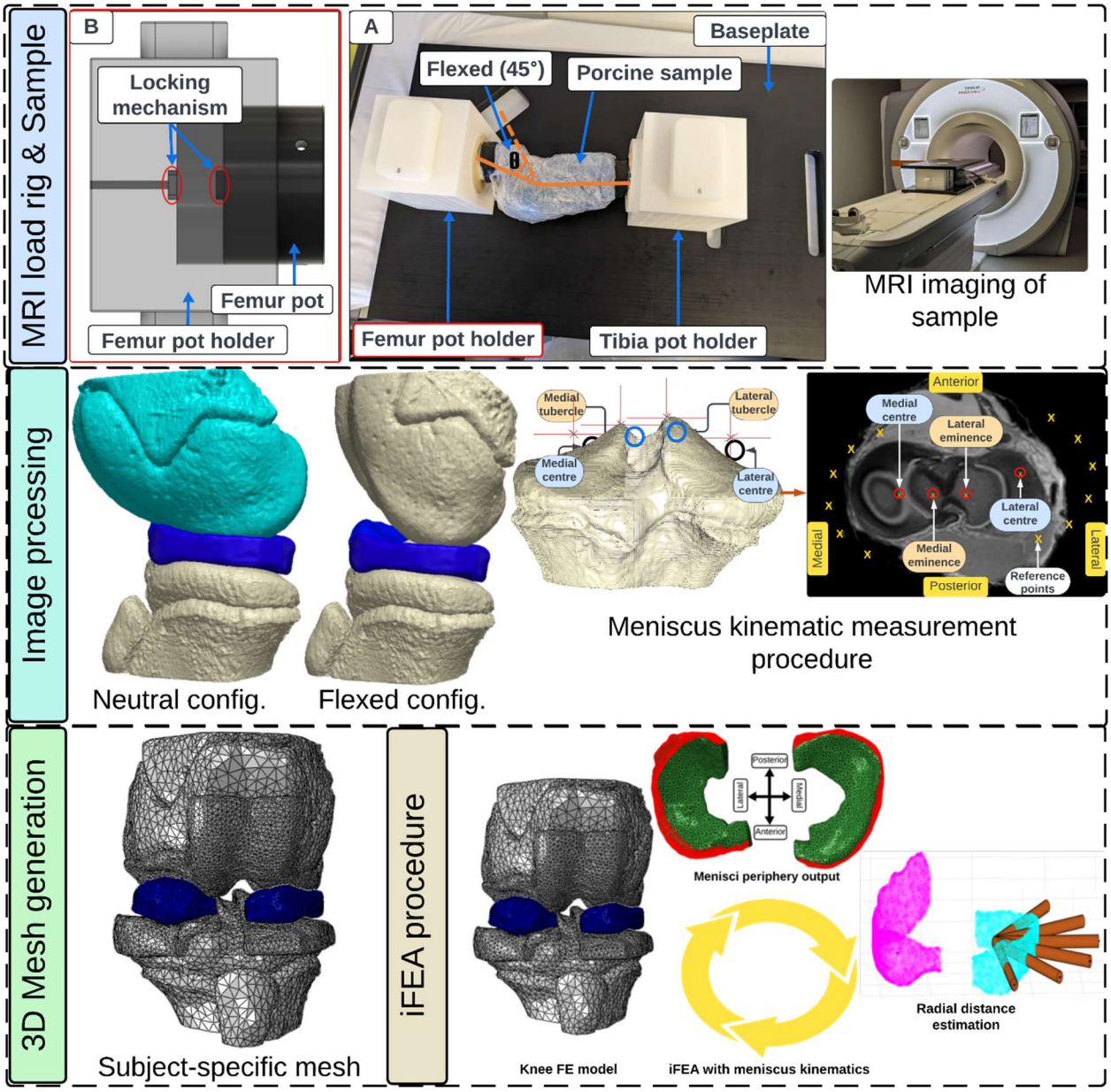


Figure 1: Workflow for meniscus tissue characterisation.

Session Category

Musculoskeletal Biomechanics: Methods, Models and Applications

OA83-04

In Vitro Biomechanical Assessment of Nucleus Augmentation for the Treatment of Degenerated Intervertebral Discs

Dr Andrew Dixon PhD, Dr James Warren PhD, Dr Nagitha Wijayathunga PhD, Dr Marlene Mengoni PhD, Prof Ruth Wilcox PhD

University of Leeds, Leeds, West Yorkshire, United Kingdom

Introduction

Nucleus augmentation is an emerging intervention for intervertebral disc (IVD) degeneration. Previous nucleus replacement procedures have shown poor outcomes clinically due to device expulsion or fragmentation. One challenge in the development of successful interventions is the lack of effective *in-vitro* biomechanical models. The aim of this study was to develop and apply cyclic loading testing methods to evaluate a nucleus augmentation biomaterial.

Methods

A peptide-glycosaminoglycan hybrid hydrogel was developed previously [1]; it self-assembles *in*-situ, allowing delivery down a fine needle to prevent annulus damage. The hydrogel was tested in bovine and human IVDs. The IVDs were imaged and cyclically loaded (loading range dependent on specimen size) in their native state, following artificial degeneration (bovine specimens) and following augmentation with the hydrogel. Specimens were held under load in a fluid bath for 24 hours between each stage to allow hydration equilibrium. Bovine IVDs were first tested to 1000 cycles to optimise the procedure [2]. Tests were then extended to 20000 cycles at either the native, degenerated or treated stage to examine the longer-term performance, using a mathematical model based on the first 1000 cycles to compare between states. Human IVDs were tested in both the native (naturally degenerated) and augmented state to 5000 cycles.

Results

In the bovine specimens tested to 1000 cycles, nucleus augmentation restored bovine IVD height and stiffness to the native levels, which were significantly different to the degenerated levels (Figure-1A inset). After 20,000 cycles, there was no observed hydrogel expulsion in treated IVDs and the stiffness restoration was generally maintained (Figure-1B). In human IVDs, the augmentation increased height and reduced stiffness although the change was more variable, with limited effect on specimens exhibiting calcification (Figure-1C).

Discussion

This in-vitro biomechanical assessment allows early optimisation of nucleus augmentation procedures prior to costly animal or clinical studies. The hydrogel provided sustained stiffness restoration in the bovine model and promising results in the human model, which will help guide patient selection for future clinical studies.

Images (Optional)

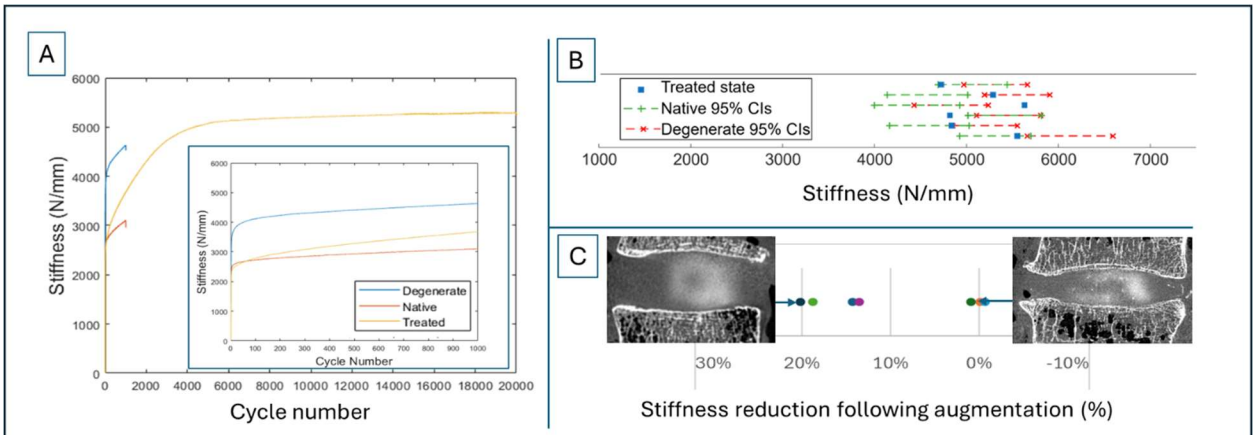


Figure 1: A: typical bovine specimen stiffness over each cycle showing 0-1000 cycles (inset) and to 20,000 cycles for the treated stage (following nucleus augmentation). B: comparison of stiffness at 20000 cycles for treated bovine specimens (n = 6) with predictions for native and degenerated. C: change in stiffness of human tissue specimens (n = 7) showing uCT images of two examples.

References (Optional)

[1]:Danielle Miles *et al.* J.Mat.Chem.B, 2016

[2]:James Warren *et al*. JOR Spine, 2025.

Acknowledgements (Optional)

Work funded by EPSRC and NIHR

Session Category

Musculoskeletal Biomechanics: Methods, Models and Applications

OA83-05

Tendon Injury Mechanism and Severity Alter Musculotendon Mechanics in an *ex-Vivo* Rabbit Model

Ms. Kathryn Rex[1], Dr. Joshua Pataky PhD[1], Dr. Meghan Vidt PhD[1,2]

[1]Pennsylvania State University, University Park, Pennsylvania, United States. [2]Penn State College of Medicine, Hershey, Pennsylvania, United States

Introduction

Achilles tendon injuries vary in severity, from partial- to full-thickness tears, and in mechanism, either traumatic or chronic [1]. Musculoskeletal models help quantify how injury variation affects biomechanics, which is unclear *in vivo*. Previous work assumed musculotendon force decreased linearly as injury severity increased [2]. The validity of this assumption is unconfirmed, therefore, this study experimentally defined how injury severity and mechanism influence musculotendon mechanics.

Methods

New Zealand White rabbit Achilles tendons (N=46) were grouped by injury mechanism: uninjured (0%), traumatic, or chronic. Partial tendon transection simulated traumatic injury and mechanical overload simulated chronic injury at 3 severity levels (25%, 50%, 75%). Mechanical testing (MTS 858 Bionix, MTS Systems, MN, USA) occurred immediately post-injury and musculotendon mechanics were calculated [3]. The impact of severity and mechanism were assessed using 1-way ANCOVAs with sex as a covariate and Pearson correlation tests (Kruskal Wallis and Spearman tests for non-parametric data) with $p<0.05$ ($\chi^2<0.05$) considered significant (SAS Institute, NC, USA).

Results

Traumatic yield stress ($\chi^2=0.0014$), maximum force (Fig. 1A), maximum stress ($\chi^2=0.0007$), and cross-sectional area (CSA) ($p=<0.0001$) decreased with increased severity. Stiffness increased ($p=0.0395$), percent relaxation ($p<0.0001$) and yield stress ($p=0.0013$) decreased, and CSA did not change with increased chronic severity. Chronic injuries had greater stiffnesses (25%: $\chi^2=0.025$, 50%: $\chi^2=0.0104$, 75%: $p=0.0237$), lower yield stress (25%: $p=0.0009$, 50%: $\chi^2=0.0039$, 75%: $p=0.0237$), and lower maximum stress (25%: $p=0.0023$, 50%: $p=0.002$, 75%: $\chi^2=0.0062$) than traumatic injuries at those same severities. Maximum force was positively correlated with traumatic CSA but had no correlation to chronic CSA (Fig. 1B).

Discussion

Results revealed that maximum force decreases linearly with increased traumatic injury severity. Chronic injuries impact musculotendon elasticity but not force transmission. Traumatic CSA decreases while chronic CSA is not altered with increased severity. This suggests that structural damage from chronic injury does not impede force transmission like traumatic injury. Findings suggest that tendon compliance and maximum force should be considered when modeling chronic injury. Continued work will evaluate ways to implement injury severity and mechanism into computational models.

Images (Optional)

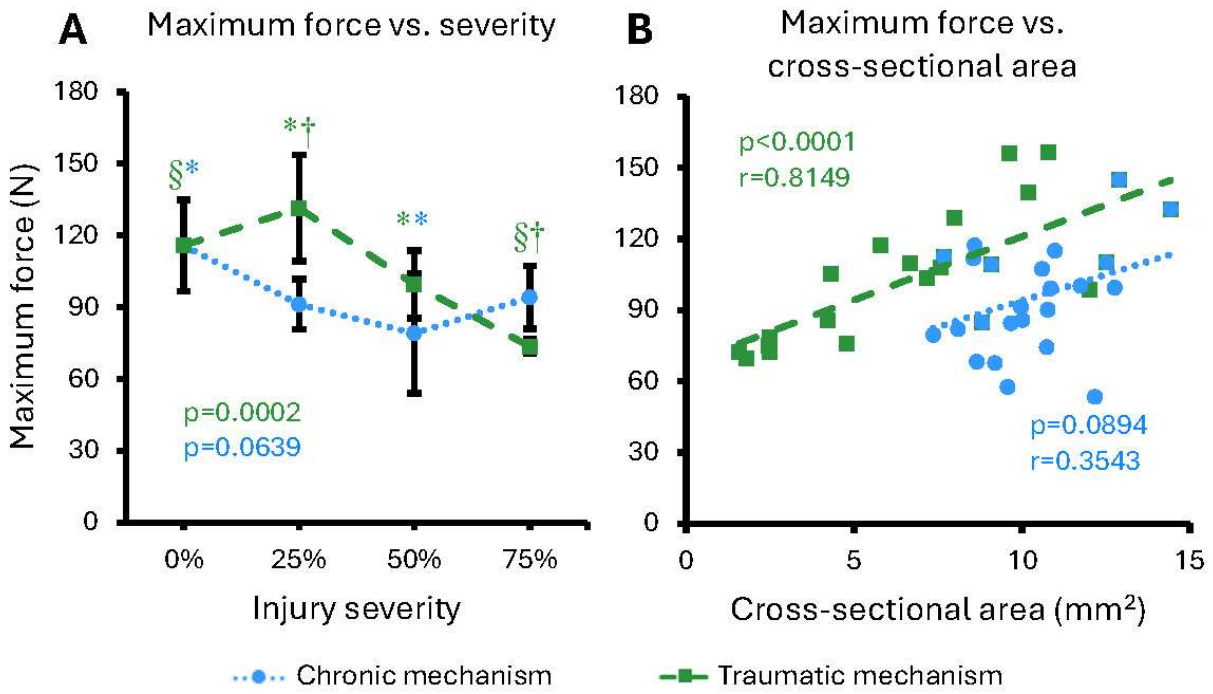


Figure 1: A) Mean maximum force for each severity group. B) Maximum force of each sample by the cross-sectional area measured after injury. Samples that underwent traumatic injury are shown by green squares and samples that underwent chronic injury are shown in blue circles.

References (Optional)

[1] Wu *et al.*, EFORT Open Rev, 2017

[2] Pataky *et al.*, Clin Biomech, 2021

[3] Khandare *et al.*, J. Biomech, 2021

Acknowledgements (Optional)

NIH-R01AR079999; Start-up funds (Vidt); Penn State IACUC #: PROTO201800257

Session Category

Musculoskeletal Biomechanics: Methods, Models and Applications

OA83-06

Digital Image Correlation for Measuring Strain in the Achilles Tendon During Cyclic Loading

Mr Nisal Jayaneththi, Dr Hans Gray, Prof Peter Lee

The University of Melbourne, Melbourne, Victoria, Australia

Introduction

We aimed to develop a novel method for measuring strains using digital image correlation (DIC) in cadaveric Achilles tendon specimens during a prolonged physiologically representative cyclic loading experiment.

Methods

A specimen comprising the distal half of the calf muscles, the Achilles tendon, and the calcaneus was obtained (Age 85, female). The calcaneus was potted and mounted to the base of a tensile testing machine, and the proximal end of the specimen was held in a custom cryogenic clamp (Fig. 1A).

The specimen was subjected to published loads occurring in daily activities scaled to account for age - jogging (490N at 1.35Hz for 2656 cycles), running (690N at 1.43Hz for 3040 cycles), sprinting (1300N at 2.33Hz for 3536 cycles) and unilateral jumping and landing (640N and 600N at 0.658Hz for 208 cycles).

Two synchronised cameras imaged the tendon, on which a speckle pattern had been applied. A purpose-built programmable module synchronised the cameras with the testing machine and enabled recording predetermined cycles. Every 15th cycle for jogging, 9th cycle for running, 5th cycle for sprinting, and 5th cycle for jumping were recorded (50Hz).

Surface displacements, strains and projection errors were calculated using a DIC software (VIC-3D, correlated solutions, SC, USA). The correlation coefficient was calculated between the displacement of the proximal end of the specimen calculated using DIC, and the displacement of the actuator.

Results

The projection error (0.0291 ± 0.004px) was below the recommended threshold (0.100px) for accurate measurement (Fig. 1B). A total of 424.8GB of data was generated during the experiment. Correlation coefficients between the DIC displacement and the testing

machine displacement for jogging, running, sprinting and jumping were 0.978, 0.986, 0.982 and 0.963, respectively.

Discussion

The developed method could measure tendon displacements using DIC during all loading conditions. The low projection errors and the high correlation for displacements are indicative of acceptable measurement accuracy. The capability to capture data for a sample set of cycles reduced the required storage capacity by 87% compared to capturing every loading cycle. This is of significant importance as it greatly increases the capacity for continuous experimentation.

Images (Optional)

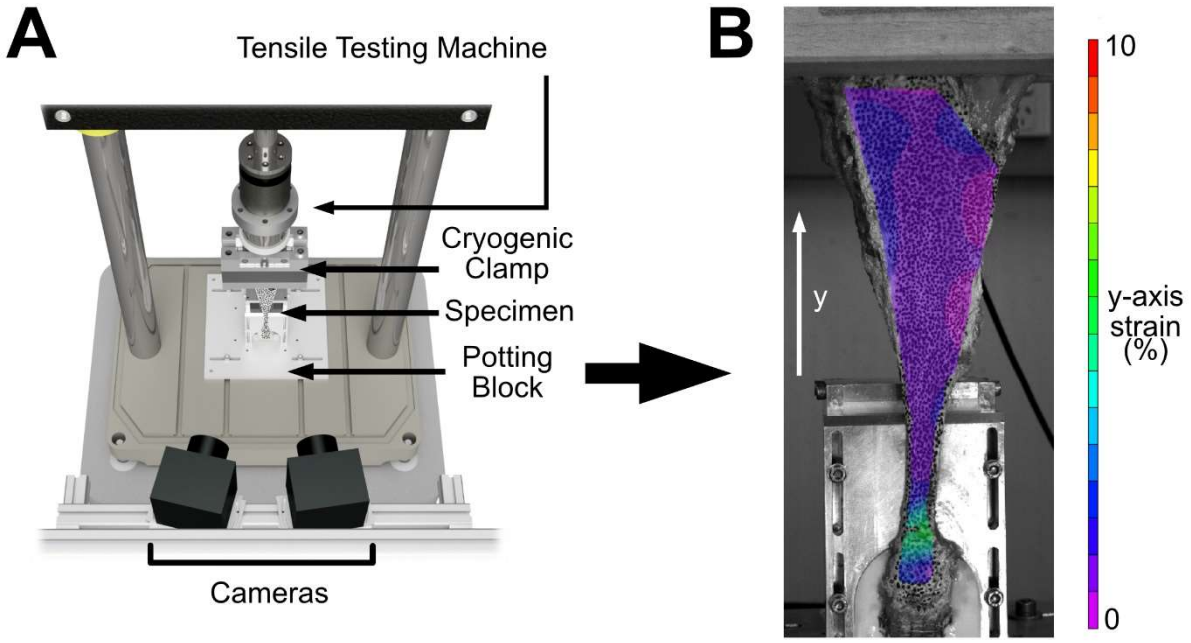


Figure 1 - A) Mechanical testing setup with two cameras mounted on a frame, recording the specimen. The distal end of the specimen is potted and mounted to the base of the testing machine and the proximal end is clamped cryogenically. A black speckle pattern has been applied to the surface of the tendon. B) A strain map along the y axis for the 422nd sprinting cycle generated by the DIC software.

Session Category

Musculoskeletal Biomechanics: Methods, Models and Applications

OA84-02

JAX-based High-Speed Simulations of Mitral Valve Transcatheter Edge to Edge Repair

Mr. Kenneth Meyer[1,2], Dr. Michael Sacks[1,2]

[1]The University of Texas at Austin, Austin, Texas, United States. [2]The Oden Institute for Computational Engineering and Sciences, Austin, Texas, United States

Introduction

Mitral Valve (MV) regurgitation (MR) is a deadly disease affecting 2% of the world. Various MV repair techniques such as transcatheter edge-to-edge repair (TEER) provide minimally-invasive treatments. However, long-term clinical outcomes remain poorly understood. To better understand the post-treatment state and to guide clinicians for optimal methods for MR repair, we have developed a Google JAX-based Finite Element package, CARDIAX-MV, to simulate patient specific TEER procedures. This new platform greatly accelerates simulations through GPU-based parallelization and provides a differentiable framework for determining patient-specific MV mechanical states. Coupled with time-dependent modeling of MV leaflets, we aim to predict patient-specific long-term outcomes to TEER.

Methods

Patient-specific reconstructions of the MV are required for TEER procedure predictions; 3D spline-based discretizations are used to represent MVs. Isogeometric Analysis (IGA) is integrated into CARDIAX-MV via an extraction-based approach. Another major feature of CARDIAX-MV is contact; Incremental Potential Contact provides a robust and high-speed approach for MV closure simulations. To determine patient-specific mechanical states, we compute MV leaflet and chordae tendinae (CT) pre-strains. The adjoint method is used to determine these pre-strains. Lastly, to characterize MV leaflet remodeling caused by medical devices used in TEER procedures, structural and Neural-Network based material models will be tested to elucidate MV leaflet remodeling mechanisms.

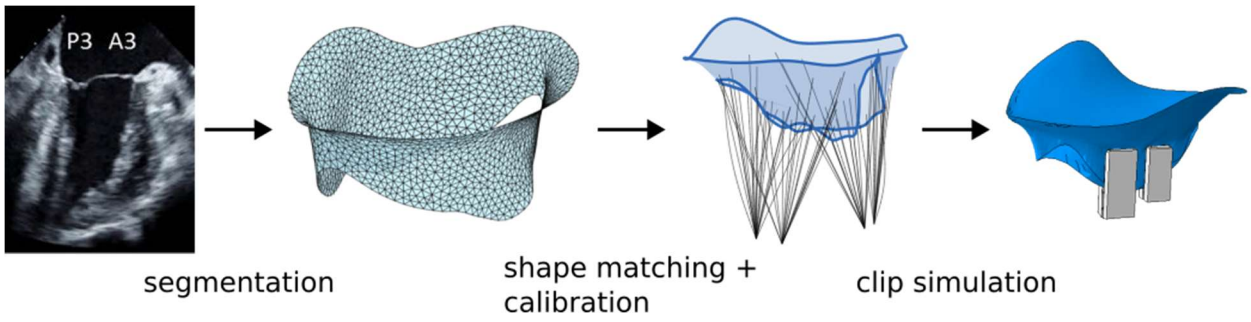
Results

Current results have shown that CARDIAX-MV can dramatically accelerate inverse modeling of organ-level function when compared to pipelines that use commercial FE codes (ABAQUS). Speedups of 24x, using 5x more data, were observed [1]. Similar speedups are also being evaluated when applying the same CARDIAX inverse modeling pipelines to MV pre-strain calculations.

Discussion

In this work, we developed a high-speed pipeline that determines patient-specific 3D MV mechanical states with higher fidelity than existing MV modeling pipelines. This will be useful to cardiologists to understand the mechanisms behind in-silico predictions of surgical repair outcomes, and time-dependent MV remodeling will be used to help explain this.

Images (Optional)



References (Optional)

[1] Thomas, Ben *et al.*, CARIDAX: A JAX-based platform for Rapid Cardiac Functional Simulations, *preprint, engrxiv,* 2025

Session Category

Organ and Tissue Biomechanics: N/A

OA84-03

Mechanical Vulnerability of the Hypertensive Marfan Aorta

Mr Gavin Mays BS, MS, Professor Jay Humphrey PhD

Yale University, New Haven, CT, United States

Introduction

Marfan syndrome (MFS) is a hereditary connective tissue disorder that affects multiple tissue systems, notably the proximal thoracic aorta which becomes susceptible to dilatation (aneurysm) and dissection (intramural failure). Mouse models having different induced genetic mutations yield a spectrum of aortic phenotypes from mild to severe. Uncontrolled hypertension is a strong risk factor in patients but has not been studied in detail in the mouse. We report detailed biomechanical and histological evidence of a hypertension-induced increase in disease severity in an otherwise mild MFS phenotype in mice.

Methods

To mimic human risk factors, with IACUC approval we combined a high salt diet (8% NaCl in the chow) with endothelial dysfunction (blocking nitric oxide synthase with L-NAME) to render adult wild-type (WT) and *Fbn1*(*C1041G/+*) MFS mice hypertensive, with systolic blood pressures ~160 mmHg. To assess potential aortic vulnerability, we further exposed sub-sets of mice to BAPN, an inhibitor of the extracellular matrix cross-linker lysyl oxidase. After four weeks, the ascending aorta was excised and subjected to biaxial mechanical testing and histological examination.

Results

The aorta of both the WT and MFS mice evidenced what appeared to be mild hypertensive remodeling, including increases in wall thickness and homeostatic control of wall stress. When further exposed to BAPN, the WT aortas showed modest differences from hypertensive alone whereas ~60% of the MFS mice exhibited aortic dissection with ~50% mortality. Biaxial data revealed a marked decrease in in vivo axial stretch and storage of elastic energy in the dual-treated MFS, but not WT, mice which suggests marked vulnerability of the elastic laminae in the medial layer of the Marfan aorta, which was confirmed histologically. Data similarly revealed a marked structural stiffening in the dual-

treated MFS, but not WT, mice which histology revealed was due in large part to an increased accumulation of adventitial collagen that was likely not functional.

Discussion

The healthy aorta exhibits a remarkable resilience to a hypertensive-challenge whereas the Marfan aorta contains an underlying vulnerability within the medial layer that is exacerbated in hypertension. Compensatory collagen deposition and cross-linking can offset this vulnerability in part and should be a target for adjuvant therapies.

Session Category

Organ and Tissue Biomechanics: N/A

OA84-04

Evaluation of the Role of Macrostructure in the Anisotropy of the Atrial Appendage Tissue

PhD student Kundry Reibel[1], PhD Baptiste Pierrat[1], Prof Stéphane Avril[1], Mrs Claudia Cino[2], M Nicolas Curt[1], PhD Fanette Chassagne[1]

[1]Mines Saint-Etienne, INSERM, U1059 Sainbiose, Saint-Etienne, Auvergne-Rhône-Alpes, France. [2]Università degli Studi di Palermo, Palermo, Sicilia, Italy

Introduction

Atrial appendage mechanics remains poorly understood, and its highly trabeculated macro-structure produces strong and spatially variable thickness. To clarify the role of macro-structure in the mechanical response, this study combines full-field 3D thickness mapping, uniaxial testing, and modeling to evaluate how structural variability influences apparent anisotropy in atrial appendage tissue.

Methods

Porcine atrial appendages (n=40) were dissected to obtain paired longitudinal and transverse rectangular specimens, tested under uniaxial loading. Dimensions were first measured with a caliper, and samples were then scanned using high-resolution 3D imaging. The scans were processed in MATLAB to generate full-field thickness maps. Mechanical behavior was modeled using an isotropic Veronda–Westmann law through two approaches: (1) a direct analytical model using the scan-derived mean thickness, and (2) an inverse finite element (FE) model incorporating each specimen's full 3D geometry. First, material parameters were identified individually. Secondly, longitudinal parameters were transferred without re-fitting to predict the transverse response. Finally, effective thicknesses were determined by fixing these parameters and optimizing thickness to best match the experimental data.

Results

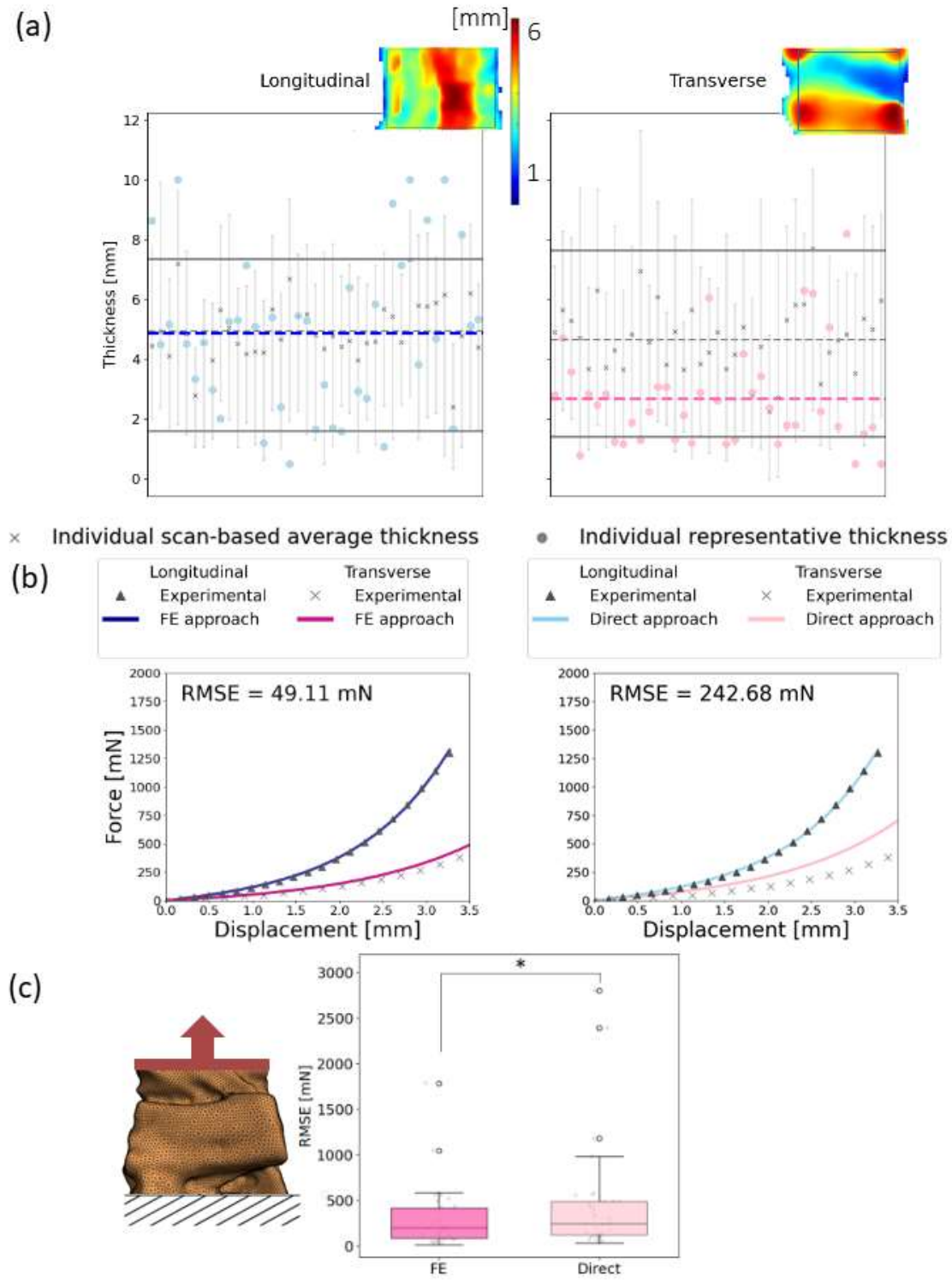
Thickness maps revealed pronounced intra- and inter-sample heterogeneity, with calipers underestimating scan-based average thickness by ~25%. All specimens showed nonlinear behavior with substantial variability. Identified C1 values were consistently higher in the longitudinal direction. When longitudinal parameters were used to predict the transverse response, FE models yielded lower error than the direct analytical approach ($p<0.03$), demonstrating that geometry improves predictive accuracy. However, errors in prediction

were non-null, indicating that geometry alone cannot fully account for the mechanical response. Effective thicknesses in transverse specimens often approached the minimal local thickness, whereas effective thicknesses for longitudinal samples were larger and more variable, reflecting different engagement of trabecular structures under loading.

Discussion

These results show that geometric heterogeneity strongly influences atrial appendage mechanics and contributes to apparent anisotropy. Nonetheless, residual discrepancies between FE predictions and experiments indicate additional contributions from meso- and microstructural organization, such as fiber orientation and layered composition. Preliminary micro-CT imaging supports this interpretation by revealing abrupt structural transitions. Overall, the study highlights the need for geometry-informed constitutive modeling to accurately describe the mechanics of these highly heterogeneous cardiac tissues.

Images (Optional)



(a) Example thickness maps for longitudinal (left) and transverse (right). For each direction, scan-based average thickness values (gray crosses) are compared with the representative thicknesses (blue and pink markers). Gray lines show mean minimum and maximum scan-based thicknesses. Blue and pink dashed lines denote the representative longitudinal and transverse model thicknesses. **(b)** Representative transverse prediction curves for scan-based (left) and direct (right) approaches corresponding to the lowest FE RMSE. **(c)** RMSE distributions for both approaches.

Session Category

Organ and Tissue Biomechanics: N/A

OA84-05

A Microstructure-Driven Arterial Representative Volume Element Framework Using Contrast-Enhanced Microfocus Computed Tomography for Constitutive Model Discovery

Dr. Maïté Pétré[1,2,3], Mr. Hannes Wolfs[1,2,3], Dr. Thibault Vervenne[2], Ms. Isabelle Gennart[1,3,4], Prof. Greet Kerckhofs[1,3,4,5], Prof. Nele Famaey[2,6]

[1]Institute of Mechanics, Materials and Civil Engineering (iMMC), UCLouvain, Louvain-la-Neuve, Belgium. [2]Department of Mechanical Engineering, KU Leuven, Leuven, Belgium. [3]Institut de recherche expérimentale et Clinique (IREC), UCLouvain, Louvain-la-Neuve, Belgium. [4]Department of Materials Engineering, KU Leuven, Leuven, Belgium. [5]Prometheus, Division of Skeletal Tissue Engineering, KU Leuven, Leuven, Belgium. [6]FIBEr, KU Leuven Core Facility for Biomechanical Experimentation, Leuven, Belgium

Introduction

Accurate modeling of arterial mechanics is critical for understanding cardiovascular pathologies. Traditional phenomenological constitutive models, such as the Gasser-Ogden-Holzapfel model, rely on fitting parameters to macroscopic mechanical data. While effective for fitting, these models often impose a fixed functional form that may not capture the complex behavior of heterogeneous tissues. We propose a workflow that derives governing constitutive behavior from microstructural data obtained via contrast-enhanced microfocus computed tomography (CECT), using Constitutive Artificial Neural Networks (CANNs) [1] to learn the specific mechanical response generated by microstructural simulations.

Methods

We present a framework integrating CECT-informed Representative Volume Elements (RVEs) [2] and CANNs. Microstructural features of the medial porcine descending thoracic aorta, such as collagen and elastic lamellae volume fractions, are quantified using CECT. These metrics guide the generation of 3D finite element RVEs that incorporate elastic lamellae, elastin fibers, collagen fibers, and smooth muscle cells. The RVEs undergo virtual biaxial tensile testing to generate stress-stretch datasets. These datasets are subsequently used to train a CANN. In this framework, the CANN acts as a surrogate, learning the complex stress-stretch behavior outputted by the RVE without relying on phenomenological formulas.

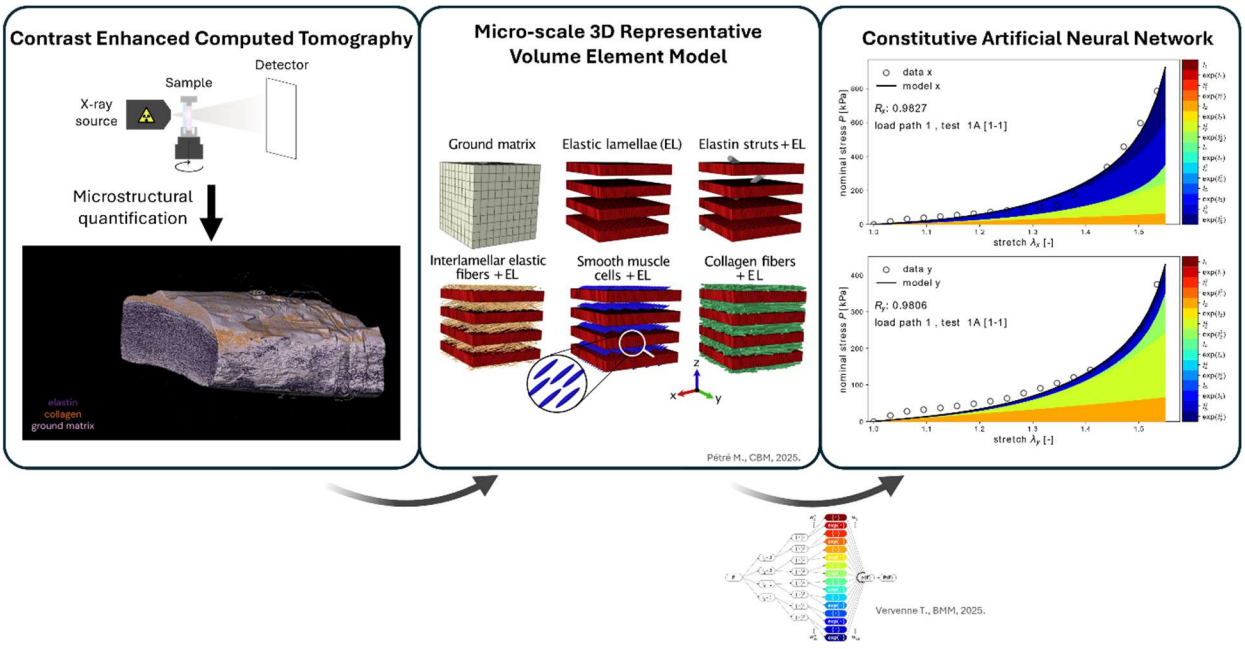
Results

RVE simulations revealed that microstructural variations significantly modulated the macroscopic mechanical response. The trained CANNs successfully captured these complex anisotropic behaviors, reproducing the RVE-derived stress-stretch curves with high fidelity where traditional fixed-form models struggle. Furthermore, the application to RVEs adapted to infrarenal arteries highlighted distinct mechanical phenotypes. Therefore, the framework can be generalized for RVEs that are adapted to varying microstructural environments, such as with different species or arteries.

Discussion

This study establishes a direct link between microstructure and computational mechanics. By training CANNs on RVE-derived data, we create constitutive models that are inherently faithful to the underlying microstructure. This approach allows us to easily vary the microstructural composition of the arterial wall in the RVE stage and observe changes on the tissue-scale via the trained CANN, offering a scalable method to generate high-fidelity material models for finite element simulations of diverse arterial diseases.

Images (Optional)



References (Optional)

[1] Thibault Vervenne *et al.*, Biomechanics and Modeling in Mechanobiology, 2025

[2] Maïté Pétré *et al.*, Computers in Biology and Medicine, 2025

Session Category

Organ and Tissue Biomechanics: N/A

OA85-01

Effects of Proactive and Reactive Perturbations on Foot Placement Modulation in People With Chronic Stroke

Dr. Jesse Dean PhD

Medical University of South Carolina, Charleston, SC, United States

Introduction

Mediolateral foot placement modulation is an important strategy for ensuring walking balance [1], but is disrupted in many people with chronic stroke (PwCS). Such foot placement modulation deficits are associated with poorer clinical balance performance and increased falls [2]. Foot placement modulation can be strengthened using appropriately applied swing leg perturbations, with sustained effects following repeated exposure [3]. By pushing the swing leg medially when lateral foot placement is warranted (and vice-versa), individuals appear able to relearn this proactive balance strategy. The objective of this randomized controlled trial was to compare the effects of Proactive perturbations with simpler Reactive perturbations, in terms of post-stroke foot placement modulation.

Methods

PwCS were randomly assigned to a Proactive perturbation group (n=43) or a Reactive perturbation group (n=43). Both interventions lasted 8-weeks, with 2 training sessions per week, and up to 30-minutes per session of perturbed walking. As before, the Proactive group experienced mechanics-dependent weak mediolateral pushes to their legs. The Reactive perturbation group experienced mediolateral trunk forces every ~15 seconds, with timing and direction randomized. These forces progressively increased from 3% to 15% of body weight. Our primary analyses focused on the partial correlation between mediolateral pelvis displacement and foot placement, a measure of foot placement modulation [2]. We used a linear mixed model to assess the effects on foot placement modulation of Time (pre- vs. post- intervention), Group (Proactive vs. Reactive) and Stepping Leg (Paretic vs. Non-paretic), as well as their interactions.

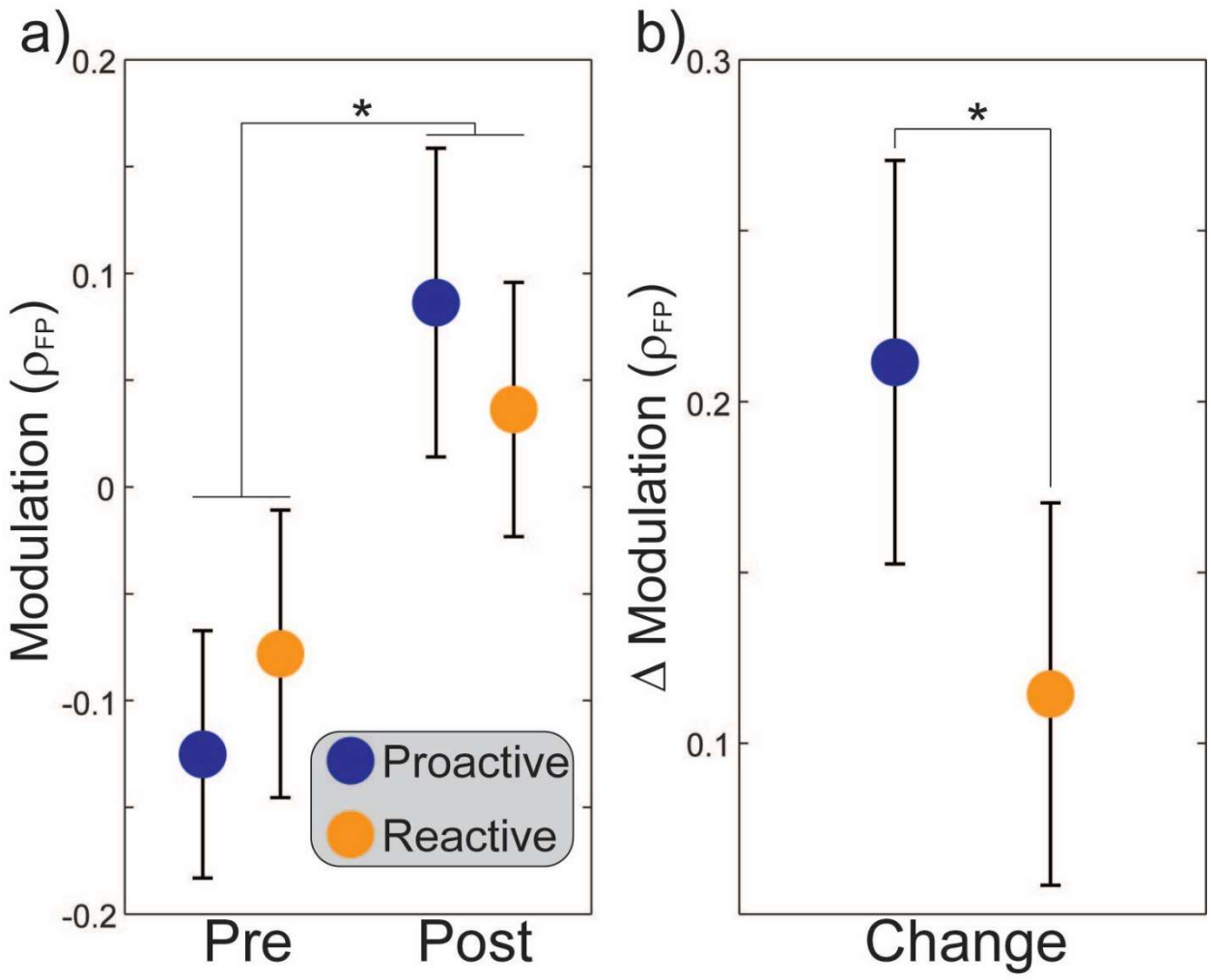
Results

From before to after the intervention, foot placement modulation increased significantly (Fig. 1a; Time, $p<0.001$). However, this increase was significantly larger in the Proactive than the Reactive group (Fig. 1b; Time X group, $p=0.01$).

Discussion

The present results demonstrate that traditional Reactive perturbation methods – while useful – are not as effective as a more specifically targeted Proactive approach in terms of strengthening foot placement modulation. Future analyses will investigate whether similar unique benefits of Proactive perturbations are present in other balance strategies, as well as real-world falls.

Images (Optional)



References (Optional)

[1] Sjoerd Bruijn *et al.*, J Roy Soc Interface, 2018

[2] Keith Howard *et al.*, Gait Posture, 2024

[3] Alexa Krause *et al.*, PLOS One, 2024

Session Category

Rehabilitation Biomechanics and Human Factors: Rehabilitation

OA85-02

Neuromuscular Fatigue-Integrated Balance Training Does Not Improve Fatigue Resilience of Dynamic Postural Control in Individuals With Chronic Ankle Instability: Double-Blinded Randomized Controlled Trials

PhD Student Suji Yoon[1], Professor Hyunsoo Kim[2], PhD Student Kyungeon Kim[1], PhD Student Eun Ji Hong[1], PhD Student Kyoung Uk Oh[1], Postdoctoral Researcher Hyung Gyu Jeon[3], Professor Sae Yong Lee[1,4]

[1]Department of Physical Education, Yonsei University, Seoul, N/A, Korea, Republic of. [2]Department of Kinesiology, West Chester University, West Chester, Pennsylvania (PA), United States. [3]Department of Sports Culture, Dongguk university, Seoul, N/A, Korea, Republic of. [4]International Olympic Committee Research Centre Korea, Seoul, N/A, Korea, Republic of

Introduction

Chronic ankle instability (CAI) is characterized by recurrent giving way, proprioceptive deficits, and neuromuscular control impairments that compromise postural stability and elevate re-injury risk. Although balance training (BT) is central to CAI rehabilitation, it is rarely performed under fatigued conditions despite evidence that most ankle sprains occur during neuromuscular fatigue. Fatigue disrupts sensory reweighting, force production, and cortical–spinal motor control, potentially exacerbating postural deficits. Training under fatigue may promote performance-relevant neuromuscular adaptation. However, previous studies relied on localized or isokinetic fatigue that do not reflect functional, multi-joint fatigue. Therefore, this study investigated whether four weeks of fatigue-integrated BT improves dynamic balance and fatigue resilience in individuals with chronic ankle instability.

Methods

Sixteen CAI meeting International Ankle Consortium criteria were randomized to traditional BT (BAL; n = 8) or fatigue-based BT (F-BAL; n = 8). Both completed a four-week hop-to-stabilization program. In the F-BAL group, BT were performed immediately after a fatigue protocol combining sprinting, directional changes, hopping, and jumps. Fatigue was confirmed by: <80% MVJH, ≥90% HRmax, and RPE ≥17. Dynamic balance (SEBT reach; normalized to leg length) was assessed pre-/post-intervention under non-fatigued/fatigued conditions. Fatigue resilience was calculated as Δ(NF–F). A 2×2 mixed ANOVA tested Time (PreΔ, PostΔ) × Group (BAL vs. F-BAL). Secondary analysis compared absolute performance under fatigue (Pre-F vs. Post-F).

Results

No significant Time or Time × Group interaction effects were found for Δ(NF–F) in any SEBT direction (all $p > .69$). No significant improvements occurred in absolute balance performance under fatigue across groups.

Discussion

Four weeks of BT performed under neuromuscular fatigue did not improve fatigue resilience of dynamic balance in individuals with CAI. This suggests that fatigue sensitivity may represent a stable neuromechanical characteristic not readily altered through short-term balance interventions. Fatigue-integrated BT may also stimulate a different adaptation pathway, reflecting the demands of dynamic sport tasks rather than postural stabilization. Moreover, unchanged SEBT performance does not rule out adaptation; dynamic balance represents task success, but underlying kinematic and kinetic strategies may still differ. Future research should incorporate biomechanical analyses and longer, higher-demand interventions to determine whether fatigue-specific neuromuscular adaptation occurs.

Session Category

Rehabilitation Biomechanics and Human Factors: Rehabilitation

OA85-03

A Minimally Invasive Implant Acts as a Digital Nervous System for Manipulating Limb Mechanics

Dr. Jennifer Leestma Ph.D.[1], Mr. Alexander Madinger M.S.[2], Dr. Shriya Srinivasan Ph.D.[1]

[1]Harvard University, Cambridge, MA, United States. [2]Massachusetts Institute of Technology, Cambridge, MA, United States

Introduction

Various conditions and diseases influence the function of the peripheral nervous system and inhibit everyday movement, despite biological actuators remaining intact. Our goal was to design a minimally-invasive muscle implant to act as a 'digital nervous system', capable of both reading muscle activity and inducing muscle activation via stimulation, to restore and manipulate biomechanics [1,2]. We hypothesized that we could continuously modulate ankle and toe joint motion, avoiding discrete 'bang-bang' behavior that is common in non-invasive stimulation.

Methods

We surgically implanted the shank segment of seven rats with a custom 36-lead muscle implant via a 1cm incision in this study approved by the Harvard University Institutional Animal Care and Use Committee. We targeted the anterior and posterior superficial and deep compartments of the shank musculature (see Figure). We stimulated all possible pairs of leads at 1000, 3000, and 5000 microamperes. We collected video data from the sagittal, frontal, and transverse planes at 240 Hz. We attained kinematics using custom-trained DeepLabCut models [3,4].

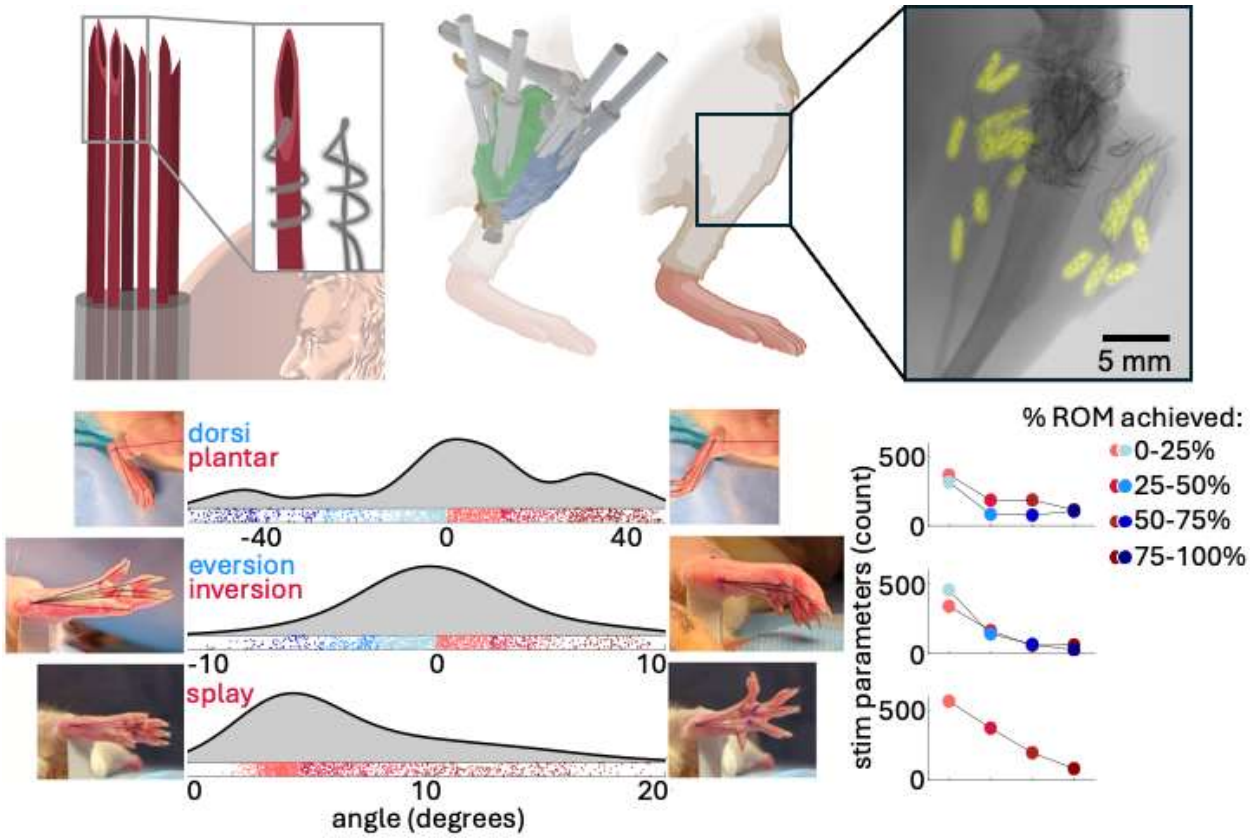
Results

We implanted all rats without any perforation or adverse consequences. With stimulation, we induced a maximum of 48° plantarflexion, 57° dorsiflexion, 9° inversion, and 10° eversion at the ankle. We induced a maximum of 20° of mean finger splay. Stimulation conditions were able to reliably access and hold small position changes relative to the overall achievable range of motion (ROM), while also achieving large overall joint position changes (see Figure).

Discussion

The implant produced a wide range of joint motions while demonstrating smoothly graded responses at lower stimulation levels, supporting its potential to restore naturalistic muscle-driven motion characterized by varying magnitudes of desired joint excursions. A current limitation is the pending direct comparison to standard surface stimulation, which we are in the process of evaluating. Our related ongoing work includes how muscle stimulation can be used to induce proprioceptive sensation and maintain accurate forces in the presence of stimulation-induced fatigue.

Images (Optional)



References (Optional)

[1] Ethier et al. (2012), *Nature* [2] Ferrante et al. (2025), *Nat Biomed Eng*, [3] Mathis et al. (2018), *Nat Neurosci,* [4] Nath et al. (2019) *Nat Protoc*

Acknowledgements (Optional)

This work was funded by the K. Lisa Yang Center for Bionics and the Harvard Mind Brain Behavior Postdoctoral Fellowship.

Session Category

Rehabilitation Biomechanics and Human Factors: Rehabilitation

OA85-04

Relating Mechanical Stiffness to Quasi-Stiffness at the Knee During Walking Using an Adjustable Stiffness Leg Brace

Ms. Sierra Foley, Mr. Jack Wallace, Dr. Edward Washabaugh

Wayne State University, Detroit, MI, United States

Introduction

Neuromusculoskeletal injuries can alter joint stiffness and lead to gait impairments. Having a metric to measure stiffness during functional tasks (e.g., walking) would improve clinicians' ability to treat altered joint stiffness (e.g., using nerve blocks or braces); however, measuring mechanical stiffness requires equipment that is not currently clinically feasible. Quasi-stiffness is a more clinically feasible metric that estimates stiffness behavior, but it is unclear how quasi-stiffness relates to mechanical stiffness; hence, the purpose of this study was to determine how alterations in mechanical stiffness during walking relate to changes in quasi-stiffness.

Methods

We developed a leg brace with interchangeable leaf springs to introduce mechanical stiffness to the knee during walking. We conducted a human subjects experiment on uninjured individuals (n = 9) to measure quasi-stiffness as participants walked with varying levels of mechanical stiffness (k = 0.12, 0.20, 0.31, 0.41, and 0.53 Nm/deg). Participants first performed a 1-minute baseline where they walked without stiffness, then the stiffness levels were introduced in a randomized order. Quasi-stiffness during stance was estimated using linear regression on the moment-angle curve. A linear mixed-effects regression (random slope) was performed to compare the change in mechanical stiffness to the measured change in quasi-stiffness from baseline while the knee was flexing and extending.

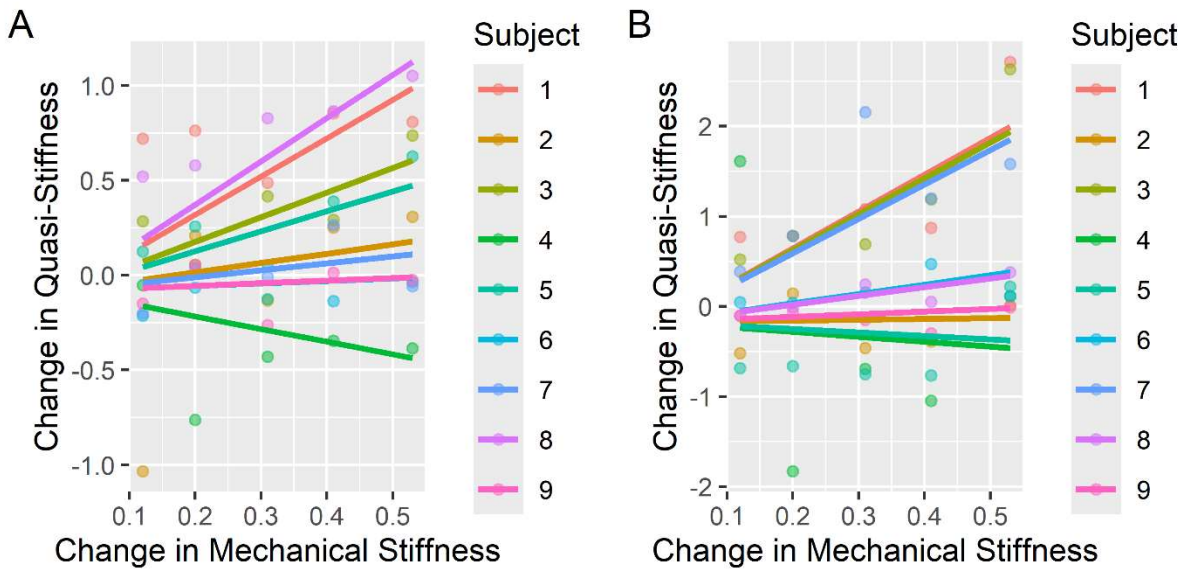
Results

Mixed effects regression showed that quasi-stiffness and mechanical stiffness were moderately correlated when accounting for random subject effects during knee flexion (Slope = 0.79, R^2 = 0.64; Figure 1A) and extension (Slope = 1.48, R^2 = 0.63; Figure 1B). When removing random subject effects, mechanical stiffness had a poor correlation with quasi-stiffness (R^2 < 0.06).

Discussion

These results suggest that quasi-stiffness is correlated with mechanical stiffness on an individual subject level. Increasing mechanical stiffness tended to increase quasi-stiffness; however, individuals showed large variance in the extent to which these increases occurred. One reason for this variation could be differences in how subjects adapted to walking with increased stiffness. Notably, quasi-stiffness alone is a poor predictor of mechanical stiffness on a population level. However, this study supports the idea that quasi-stiffness could be used as a surrogate to track changes in stiffness for individual patients.

Images (Optional)



Session Category

Rehabilitation Biomechanics and Human Factors: Rehabilitation

OA85-05

Influence Of Delayed Onset Muscle Soreness On Joint Stiffness In Different Jumps Landing Tasks

PhD Andressa Lemos[1], PhD Karine Stoelben[2], MSc Inaê de Oliveira[1], PhD Felipe Carpes[1]

[1]Federal University of Pampa, Uruguaiana, RS, Brazil. [2]Children Hospital of Eastern, Ottawa, ON, Canada

Introduction

Delayed onset muscle soreness (DOMS) may reduce joint range of motion and transiently impair strength, potentially altering joint moments, stiffness, and support torque in landing biomechanics. However, DOMS symptoms do not always translate into biomechanical changes. Understanding its effects on landing tasks is essential for managing injury risk and ensuring proper movement technique. Here we aimed to determine whether exercise-induced DOMS changes joint stiffness during landings from different jumps.

Methods

Twenty-six physically active adults (15 women and 11 men) underwent a lower-limb DOMS induction protocol using squatting exercises. Before and 48 hours after this protocol, DOMS was assessed using a numerical pain scale, and a 3D motion analysis system was used to collect kinetic and kinematic data of forward jump, vertical jump, and drop jump. Joint stiffness was determined during the landing phase of each jump.

Results

The protocol effectively induced DOMS, with pain ratings increasing from baseline to 48 hours. Across vertical, forward, and drop jumps, DOMS did not alter hip, knee, or ankle joint stiffness. In all tasks, joint stiffness differed consistently between joints: hip stiffness was highest, knee was intermediate, and ankle was lowest. No joint-by-day interactions were observed. A small overall time effect appeared only for ankle stiffness, which was slightly higher under DOMS, independent of jump type.

Discussion

Our findings do not support the hypothesis that DOMS alters joint stiffness or landing technique in drop jumps. Hip and knee control during landing remained stable, which is favorable given the importance of hip strength in these tasks. Knee stiffness exceeded ankle stiffness during vertical jump landings, suggesting a more dominant role of the knee

in lower-limb stiffness organization. Although joint stiffness patterns were similar across tasks, forward jumps were less affected by DOMS, likely because this movement relies more on hamstrings, whereas soreness was induced mainly in the quadriceps. Despite moderate pain, participants maintained stiffness and impact control, adopting protective strategies.

Session Category

Rehabilitation Biomechanics and Human Factors: Rehabilitation

OA86-01

Interim Report on Foot Structure and Function after Minimally Invasive Distal Chevron Osteotomy vs Lapidus Bunion Corrections

Ms Minah Waraich BS[1], Ms Silvia Zanini MS[1], Dr Howard Hillstrom PhD[1], Dr Holly Johnson MD[1], Dr Matthew Conti MD[1], Dr Rajshree Hillstrom PhD[2], Dr Constantine Demetracopoulos MD[1], Dr Mark Drakos MD[1], Ms Isabella Voellmicke BS[1], Mr Lance Ward BS[1], Dr Scott Ellis MD[1]

[1]Hospital for Special Surgery, New York, New York, United States. [2]Biomed Consulting, New York, New York, United States

Introduction

Hallux valgus (HV) is a common forefoot deformity associated with first ray hypermobility and pes planus foot type which can have substantial impact on physical function. Surgical intervention is common and includes the selection of a wide variety of treatments. The modified Lapidus procedure addressed the bunion through fusion of the 1st metatarsal-cuneiform joint, however it requires a longer postoperative healing time. The minimally invasive (MIS) distal chevron osteotomy is performed with a smaller incision yielding a faster recovery yet its ability to correct foot structure and function is unknown. The objective of this study is to evaluate changes in foot structure and function pre- and post-operatively between Lapidus and MIS chevron procedures.

Methods

In this prospective IRB approved study, 27 participants with HV (2M, 25F; 47.69 ± 17.49 years; 163.22 ± 8.09 cm; 63.59 ± 15.22 kg) who underwent surgical treatment were recruited: 15 received Lapidus and 12 received MIS chevron bunionectomies. Structural foot measurements while sitting (Arch Height Index (AHI), First ray mobility (FRM)) and functional foot parameters (peak plantar pressures (PP) at the hallux, 1st metatarsophalangeal (MTP) joint, and 2nd MTP joint) at self-selected walking speed while barefoot were collected from each subject preop and at 6 months post-op. Radiographically, hallux valgus angle (HVA) and intermetatarsal angle (IMA) was acquired at preop and 6 months post-op. Repeated-measures ANCOVA across visits and surgical procedure was examined with significance at $p<0.05$.

Results

The Lapidus procedure significantly increased AHI, improved IMA and HVA, decreased PP under MH2 and hallux, while the MIS procedure only significantly improved IMA and HVA. As a pooled cohort of 27 patients, CPEI was significantly different pre vs post-op (p =

0.031). When comparing the two surgeries, Lapidus significantly decreased PP under MH2 compared to MIS, but there was no difference in IMA, HVA, and CPEI improvement.

Discussion

Both surgeries are successful at realigning the 1st ray. However, the more involved Lapidus procedure also improves arch height and pressures under the foot during ambulation. Other trends in the data may become significant as our full cohort (40 people) returns for follow-up in the next few months.

Images (Optional)

		Lapidus	MIS
CPEI	Pre	14.712 (±4.51)	15.8702 (±6.14)
	Post	16.77 (±6.53)	17.6101 (±5.89)
	P value*	0.211	0.294
AHI	Pre	0.3413 (±0.021)	0.3583 (±0.023)
	Post	0.3536 (±0.021)	0.358(±0.026)
	P value	**0.015**	0.938
HVA	Pre	32.780 (±8.19)	28.477 (±5.82)
	Post	7.533 (±3.96)	6.2875 (±4.56)
	P value	**< 0.001**	**< 0.001**
IMA	Pre	17.040 (±3.45)	14.750 (±3.96)
	Post	6.3667 (1.615)	4.4358(±2.33)
	P value	**< 0.001**	**< 0.001**
PP_MH2^	Pre	66.2714 (±26.22)	48.7083 (±20.0)
	Post	48.7912 (±27.12)	44.4936 (±16.36)
	P value	**0.031**	0.252

Table 1: Pre-operative and post-operative values (mean ± SD) for Lapidus and MIS procedures across key metrics. *P-values represent within-group comparisons (Pre vs Post). Significance was set at $p<0.05$. ^When comparing both surgeries, PP_MH2 decreased significantly in Lapidus compared to MIS ($p = 0.041$).

Acknowledgements (Optional)

This study was funded by the HSS Surgeon-in-chief fund.

Session Category

Orthopaedic Biomechanics: Lower Extremities

OA86-02

Joint Space Distance Measurements of Controls and Individuals With Asymptomatic Flatfoot Across the Stance Phase of Walking

Ms. Elizabeth Bowman BS[1], Mr. Andrew Peterson MS[1], Mr. Tradd Rector[1], Dr. Kassidy Knutson PhD[1], Dr. Karen Kruger PhD[2], Dr. Amy Lenz PhD[1]

[1]University of Utah, Salt Lake City, UT, United States. [2]University of Wisconsin-Milwaukee, Milwaukee, WI, United States

Introduction

Individuals with asymptomatic flatfoot (AFF) exhibit altered hindfoot alignment, specifically increased subtalar eversion and external rotation, as well as increased tibiotalar inversion. By analyzing changes in joint space distance from heel strike to toe-off, we aim to characterize how altered kinematics affect the motion of the subtalar, tibiotalar, tibiofibular, and talofibular joints between individuals with AFF and healthy controls (CNO).

Methods

Weight-bearing CT and biplane fluoroscopy gait data from twenty-three participants (10 AFF, 13 CNO) were used to generate group-specific statistical shape models to drive the joint measurement analysis (JMA). Joint space distances for the subtalar, tibiotalar, tibiofibular, and talofibular joints were computed using the JMA toolbox during both static and dynamic movements. This toolbox utilizes a correspondence-based approach to register shape models with dynamic biplane fluoroscopy data, computing point-to-surface distances between articulating surfaces at each frame. A two-sample Student's T-test (α=0.05) compared AFF and CNO joint space distances for both static and dynamic trials.

Results

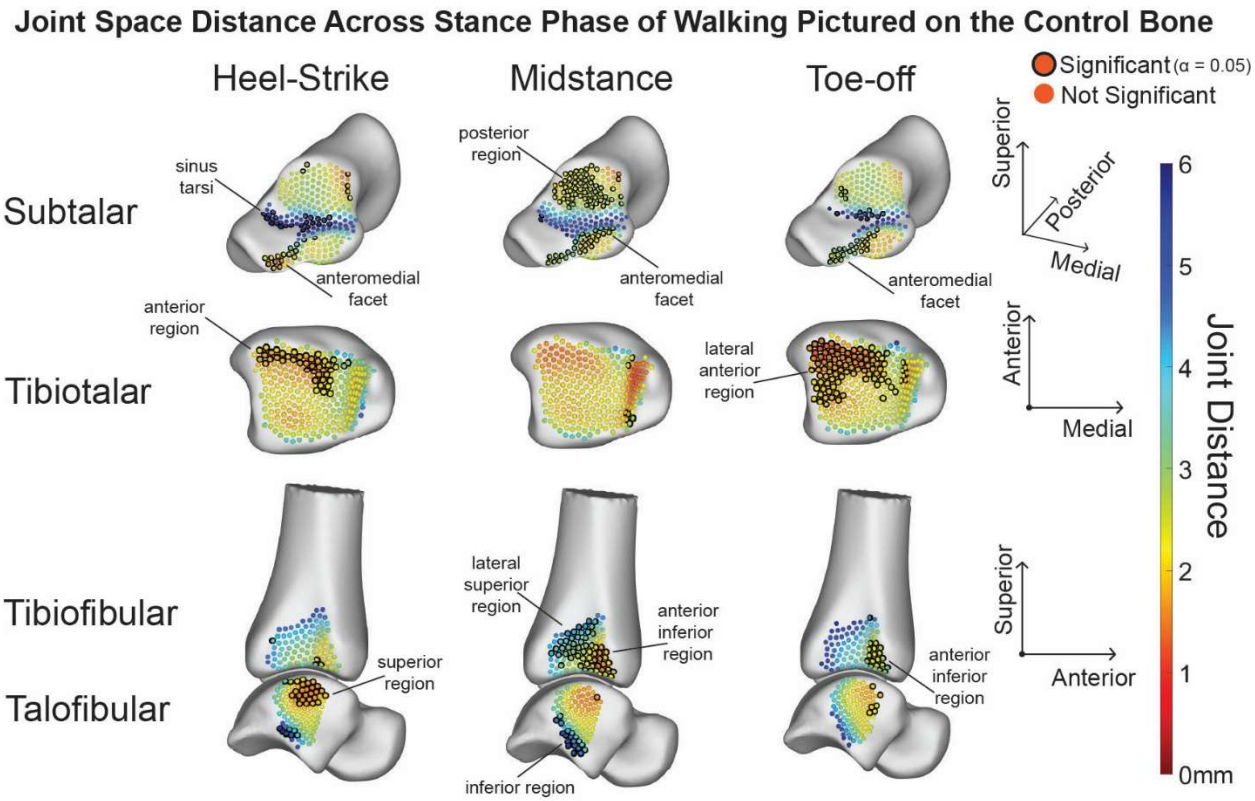
Differences in static joint space distance between AFF and CNO were observed in the subtalar, tibiotalar, and tibiofibular with minor differences in the talofibular joint. Dynamic analyses revealed significant differences in each joint across the stance phase of gait, as seen in Figure 1.

Discussion

In the subtalar joint, individuals with AFF demonstrated significantly increased sinus tarsi spacing and reduced anteromedial facet spacing, indicating greater eversion and talar

medial rotation throughout stance. In the tibiotalar joint, the AFF group showed significantly reduced anterior-lateral joint space at heel strike and toe-off, implying altered ankle alignment during high-loading phases when stability demands are greater. This also suggests that the AFF talus sits more plantarflexed and drives increased forefoot abduction. In the tibiofibular and talofibular joints, the fibula rotates and translates, likely compensating for medial collapse at the subtalar and tibiotalar complex. These joint redistributions may elevate localized stress and alter how the joints articulate, supporting AFF as a dynamic, multi-joint alteration in hindfoot function. Even without symptoms, these deviations may predispose individuals to pain or progressive conditions, highlighting the value of joint-level quantification for early risk identification and intervention.

Images (Optional)



Session Category

Orthopaedic Biomechanics: Lower Extremities

OA86-03

SSM-Guided Segmentation of the Bones of the Foot in CT Data with Extremely Narrow Inter-Bone Joint Spaces

Mr. Kuan-Hsien Wu[1], Ms. Han-Chieh Hsieh[1], Dr. Tung-Wu Lu[2,3,4]

[1]Department of Biomedical Engineering, National Taiwan University, Taipei, Daan, Taiwan. [2]Department of Biomedical Engineering, National Taiwan University, Taipei, Daan District, Taiwan. [3]Department of Orthopedic Surgery, School of Medicine, National Taiwan University, Taipei, Zhongzheng District, Taiwan. [4]Health Science and Wellness Research Centre, National Taiwan University, Taipei, Daan District, Taiwan

Introduction

Segmentation of individual foot bones from CT is challenging because the joint spaces are extremely narrow, causing conventional automatic or semi-automatic methods to merge adjacent bones into a single structure. This limitation prevents accurate biomechanical modeling and subject-specific analysis. To address this unmet need, we developed an SSM-guided multi-bone segmentation framework that can separate all 28 foot bones even when only a single fused CT segmentation is available. The objective was to create a robust, anatomically constrained method capable of restoring physiologically valid bone boundaries from imperfect surface data.

Methods

Ten manually segmented feet were decomposed into 28 bones to construct a multi-part SSM, with ICP/CPD establishing point correspondence and each vertex labeled by bone identity and articular surface. For new CT data where segmentation produced a single fused foot surface, decomposition was performed in two stages. First, the SSM mean model was aligned to the target and its shape parameters optimized using a cost function combining weighted surface fitting and a constraint separation across joint surfaces. Second, each bone underwent localized refinement, and non-articular vertices were snapped back to the CT surface to restore geometric detail while preserving bone separation.

Results

The proposed SSM-guided decomposition framework was tested on 29 CT-derived foot models that initially failed to yield separate bones using standard segmentation approaches. The method successfully decomposed 28 of the 29 datasets into clean, anatomically plausible 28-bone models. Bones were fully separated without topological overlap, and joint surfaces were preserved with physiologically consistent spacing. The

final refinement step restored detailed cortical geometry from the original CT data while maintaining separation enforced by the SSM constraints.

Discussion

Conventional CT segmentation methods struggle to distinguish individual foot bones due to extremely narrow joint spaces. By incorporating anatomical priors and joint-surface constraints within a multi-stage SSM-guided optimization, the proposed approach reliably segments a fused CT-derived foot surface into 28 anatomically separate bones. The high success rate (28/29 cases) highlights its robustness and utility for downstream biomechanical analyses. The primary limitation is the dependence on reasonable initial CT surface quality. Future work will expand the SSM training set and improve pre-processing to enhance generalizability.

Session Category

Orthopaedic Biomechanics: Lower Extremities

OA86-04

Foot and Ankle Statistical Shape Modeling Reveals Morphological Similarities Between Inherent Foot Types and Osteoarthritis Presentations

E. Renae Lapins[1,2], Dr. Megan Mills[3], Dr. Charles Saltzman[4], Dr. Amy Lenz[5]

[1]Dept. of Biomedical Engineering, University of Utah, Salt Lake City, UT, United States. [2]Dept. of Mechanical Engineering, University of Utah, Salt Lake City, UT, United States. [3]Dept. of Radiology and Imaging Sciences, University of Utah, Salt Lake City, UT, United States. [4]Dept. of Orthopaedics, University of Utah, Salt Lake City, UT, United States. [5]University of Utah, Dept. of Mechanical Engineering, Salt Lake City, UT, United States

Introduction

Foot and ankle osteoarthritis (OA) can affect the subtalar, tibiotalar, or both joints, and it remains unclear whether inherent foot types (high/low arch) predispose individuals to specific OA presentations. Identifying morphological risks could improve early detection and surgical planning. Radiographs lack the dimensionality necessary to capture complex anatomy or subtle variations associated with OA. Statistical shape modeling (SSM) offers a 3D framework for comparing joint anatomy across populations, potentially revealing patterns underlying different OA manifestations. This study aimed to identify morphological and alignment similarities between foot types and OA presentations using SSM, joint measurement analysis (JMA), and radiographic measurements.

Methods

204 weightbearing computed tomography scans from 138 OA patients (50 subtalar OA (STOA), 44 tibiotalar OA (TTOA), 44 combined subtalar/tibiotalar OA (TTSTOA)) and 66 asymptomatic individuals (19 cavus, 26 planus, 21 rectus/neutral) were used to make a 14-bone SSM. Principal component analysis (PCA) evaluated shape and alignment variations between groups, and Hotelling's T^2 test identified localized discrepancies. Radiographic measurements, describing arch height and hindfoot alignment, were automatically calculated using anatomic coordinate systems. JMA assessed joint space distance and variations along articulating surfaces.

Results

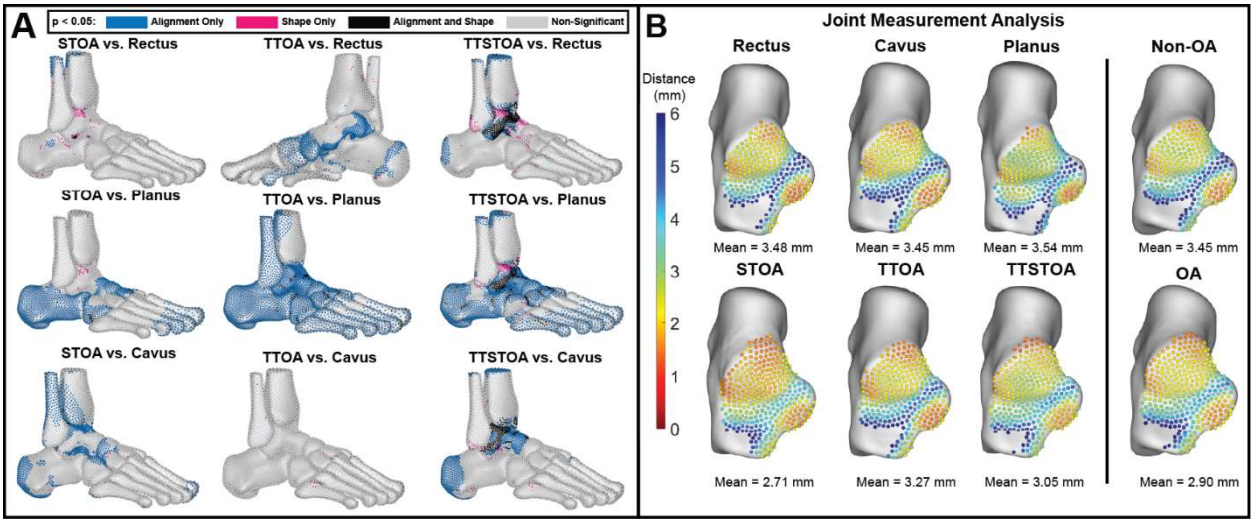
PCA mode 1 revealed statistical differences between foot types and between the STOA and TTOA groups. No statistical differences were observed between STOA and rectus

alignment, nor between TTOA and cavus alignment. PCA mode 3 distinguished OA from non-OA, highlighting joint space narrowing. Hotelling's T^2 results confirmed these variation patterns, and JMA demonstrated joint space narrowing in all OA groups relative to non-OA data. Radiographic measurements reinforced similarities between STOA and rectus groups, and between TTOA and cavus alignment.

Discussion

This study identified morphological similarities between rectus and STOA groups, and cavus and TTOA groups. Rectus alignment may predispose individuals to subtalar joint degeneration, whereas cavus alignment may increase the risk of TTOA. Load distribution and joint kinematics likely drive these patterns, but further investigation is needed to confirm these mechanisms. Recognizing alignment-specific patterns enhances our understanding of the biomechanical OA risk factors and may support earlier identification of at-risk individuals. These findings emphasize the importance of considering inherent foot type during OA assessment and surgical planning.

Images (Optional)



Session Category

Orthopaedic Biomechanics: Lower Extremities

OA86-05

Pediatric Flatfoot Tarsal Morphology Variation via Statistical Shape Modeling

Mr. Nick Slavik[1,2], Ms. Renae Lapins[3], Dr. Amanda Whitaker MD[4], Dr. Amy Lenz PhD[3], Dr. Karen Kruger PhD[1,2,5]

[1]Medical College of Wisconsin, Milwaukee, WI, United States. [2]Marquette University, Milwaukee, WI, United States. [3]University of Utah, Salt Lake City, UT, United States. [4]Shriners Children's - Northern California, Sacramento, CA, United States. [5]Shriners Children's - Chicago, Chicago, IL, United States

Introduction

Pediatric flatfoot is among the most prevalent disorders affecting children and adolescents. The growing availability of weightbearing computed tomography (WBCT) has the potential to identify early abnormal bone development. This exploratory pilot study aimed to compare bone morphology in children with flatfoot to asymptomatic controls using statistical shape modeling (SSM).

Methods

This IRB approved study included a control group of typically developing children (n=20 feet, age=11±2.4 yrs) and a flatfoot group of children who underwent clinical WBCT for assessment of flatfoot deformity (n=16 feet, age=13±2.5 yrs). Segments were aligned and Procrustes analysis was used to remove orientation and size as variation modes. Single-domain SSMs were generated to assess bone geometry and alignment [1]. Principal component analysis (PCA) with Holm-Sidak corrected parallel analysis was conducted to identify significant modes of shape variation statistically separating our sample cohorts.

Results

PCA identified significant shape variation modes for all assessed bones; cumulative explained variance 63.9%, 74.4%, 62.1%, 68.9% for calcaneus, talus, navicular, and cuboid SSMs, respectively.

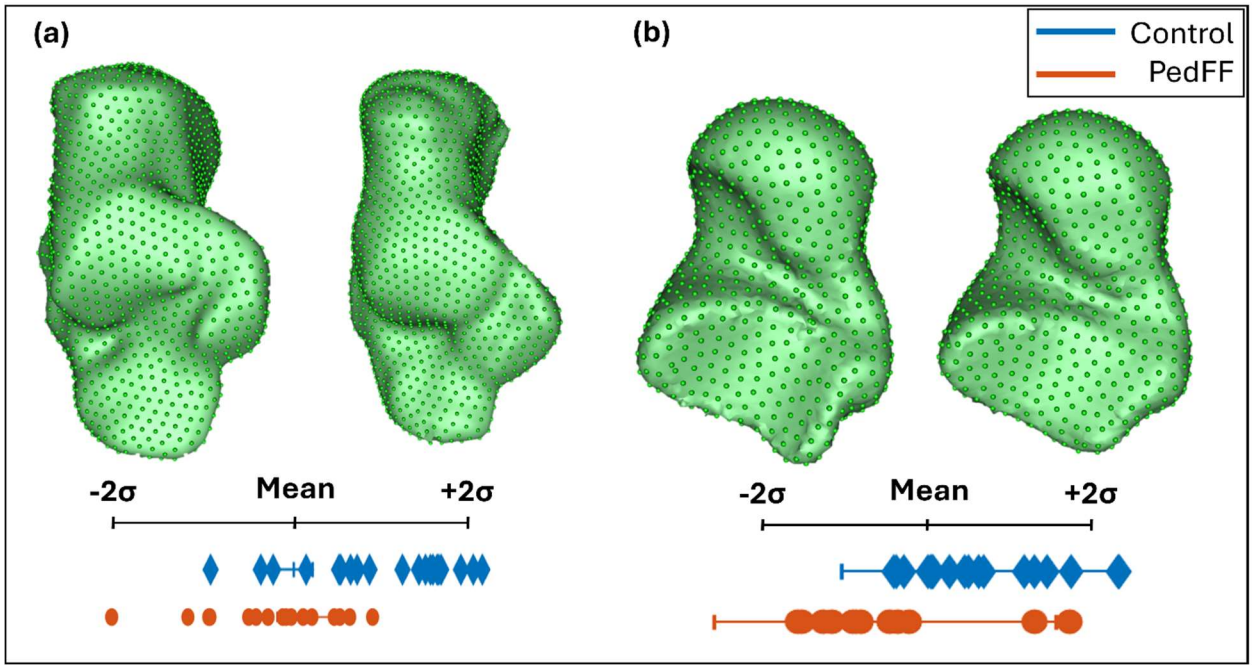
Discussion

Significant group differentiating PCA modes revealed morphology variation in pediatric flatfeet, relative to control cohort. **Calcaneus SSM:** Reduction in medial and posterior facet bone volume, and a larger, more pronounced anterior facet (Figure 1a). **Talus SSM:** Complimentary to calcaneus SSM, talus bone volume increased for the posterior and

medial facet articulations and anterior facet volume reduction (Figure 1b). **Navicular SSM:** Increased bone thickness of superior-medial aspect and reduced volume of the inferior-medial aspect. **Cuboid SSM:** Reduced bone volume between calcaneal-cuboid and navicular-cuboid articulations that results in less defined and smaller articular surfaces.

These findings support our hypothesis that children with flatfoot deformity will have different morphologic development than a typically developing child. For each of the hindfoot bones analyzed, we identified at least one significant shape variation mode statistically separating the flatfoot cohort from the typically developing. Our future work will focus on greatly increasing our sample sizes for all cohorts, with the aim of better understanding the clinical significance and relevance of these morphological differences.

Images (Optional)



References (Optional)

[1] Lenz et al. , Sci Rep 11, 2021.

Acknowledgements (Optional)

This work is supported by Shriners Grant #79135 and NIH-R01HD118205

Session Category

OA86-06

Fracture and Non-Fracture Tibiotalar Osteoarthritis Present Distinct Morphologies in the Midfoot and Ankle Joint

Mr. Jordan Langford[1], Ms. Elana Lapins[1], Mr. Andrew Peterson[1], Mr Jacob Benna[1], Dr. Curran Reddy[1], Dr. Maryam Soltanolkotabi[1], Dr. Donald Anderson[2], Ms. Julie Agel[3], Dr. Conor Kleweno[3], Dr. Justin Haller[1], Dr. Amy Lenz[1]

[1]University of Utah, Salt Lake City, UT, United States. [2]University of Iowa, Iowa City, IA, United States. [3]Harborview Medical Center, Seattle, WA, United States

Introduction

Ankle osteoarthritis (OA) is an understudied OA type affecting an estimated 1% of the global population. Unlike in other joints, ankle OA is predominantly trauma-induced. Trauma-induced OA includes both OA subsequent to fracture and OA subsequent to non-fracture trauma, such as sprains or strains. However, fracture and non-fracture ankle OA are often considered *en banc*, with little distinction being made between the fracture and non-fracture OA. Here, we hypothesize that fracture and non-fracture ankle OA present with distinct morphological typologies.

Methods

Weight-bearing computed tomography scans of 31 pilon fracture patients with post-fracture tibiotalar osteoarthritis (PF-TTOA) and 44 non-fracture tibiotalar osteoarthritis (TTOA) patients were collected at the University of Utah, Harborview Medical Center, and the University of Iowa. The scans were processed into 3D models for analysis, and fourteen-bone statistical shape models were generated for each patient cohort. The shape models were analyzed for shape and alignment differences using a Hotelling's T^2 test, and the joint distances were analyzed using the joint measurement analysis toolbox.

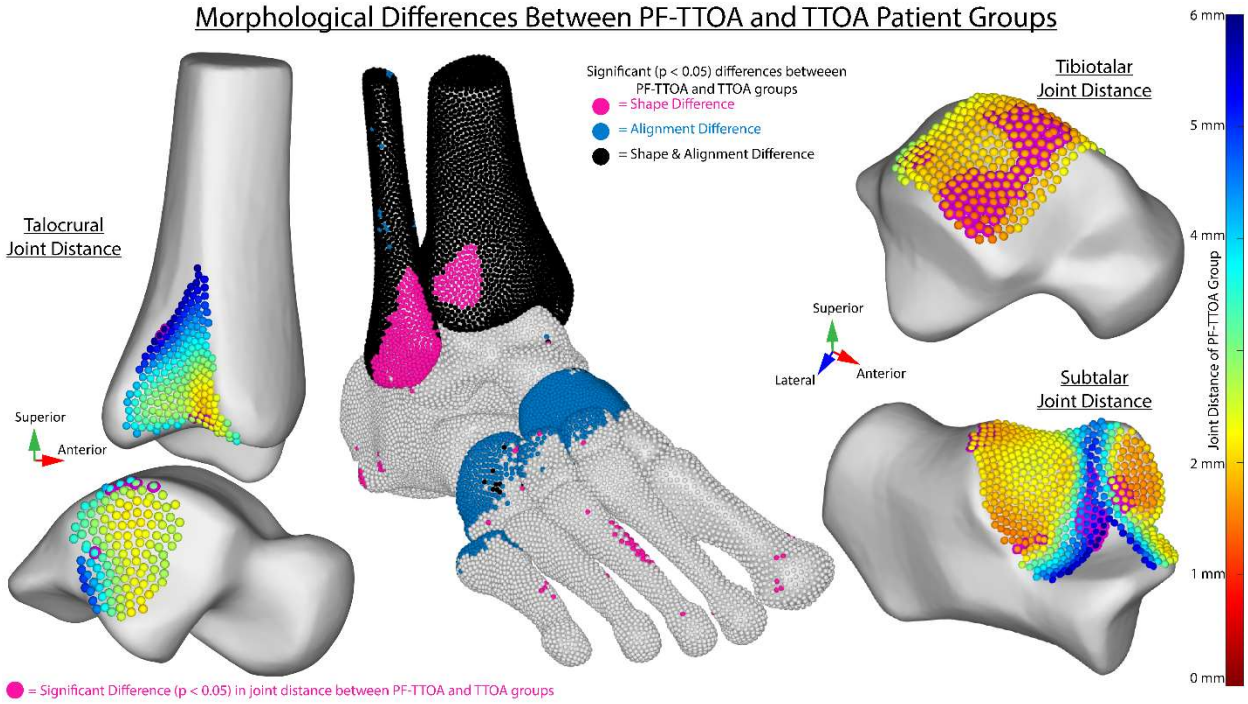
Results

Statistically significant differences in alignment were observed in the navicular and cuboid (Fig 1). Differences in both alignment and shape are visible throughout the tibia and fibula (Fig 1). Joint distances significantly differed between PF-TTOA and TTOA groups in several regions, including the talar dome (PF-TTOA narrower than TTOA), facies articularis talaris posterior (TTOA narrower), sulcus calcanei (TTOA narrower), and talocrural joint (TTOA narrower) (Fig 1).

Discussion

Significant differences in midfoot and ankle joint alignment indicate that PF-TTOA and TTOA present differently morphologically. These differences can be summarized as PF-TTOA patients having a more collapsed tibiotalar joint space, while TTOA patients tend to have reduced joint distances in other joints. Additionally, PF-TTOA midfeet are generally more everted. Differences in alignment, shape, and joint distance may indicate distinct mechanisms of compensation and different regions of joint space narrowing that contribute to OA. These differences in morphology necessitate further investigation and may suggest that PF-TTOA and TTOA are distinct phenotypes that may follow divergent mechanobiologic pathways, which could justify separate consideration in clinical decision-making and future OA classification systems.

Images (Optional)



Session Category

Orthopaedic Biomechanics: Lower Extremities

OA87-01

Full-Field Strains of the Anterior Cruciate Ligament under Physiologic Loading Configurations

Ms. Charlotte Andreasen, Ms. Chloe Stacey, Dr. Ulrich Scheven, Dr. Ellen Arruda

University of Michigan, Ann Arbor, MI, United States

Introduction

Anterior cruciate ligament (ACL) tears are a common, traumatic injury among athletes that are often non-contact, so understanding the failure mechanics is vital to prevention. Mechanically characterizing biological materials like ligaments can be challenging because of the geometric irregularity, non-linearity, heterogeneity, and visco-elasticity. To simplify mechanical characterization of the ACL, it is generally untwisted, straightened, and the anteriomedial (AM) and posterolateral (PL) bundles are separated during uniaxial loading. However, macroscale geometry, including factors like splay, is known to impact the mechanical behavior. Therefore, we believe that the bone insertion angle, twist, and offset between the axis of loading and main axis of fiber direction in the ACL will impact the mechanical response of the ACL under tension.

Methods

In this study, we designed a fixture that accommodates the entire ACL with femoral and tibial attachments for loading in the MRI to collect full-field strain data throughout the entire volume of the ACL. Our new design allows for controlled twist angles at 45° increments of the tibial insertion relative to the femoral insertion. It also gives us control of the medial-lateral and proximal-distal offsets between the two bones of up to 4mm in both directions. This allows us to replicate the twist and insertion offsets that the ACL experiences during anterior tibial translation (ATT), a motion of the knee that primarily loads the ACL.

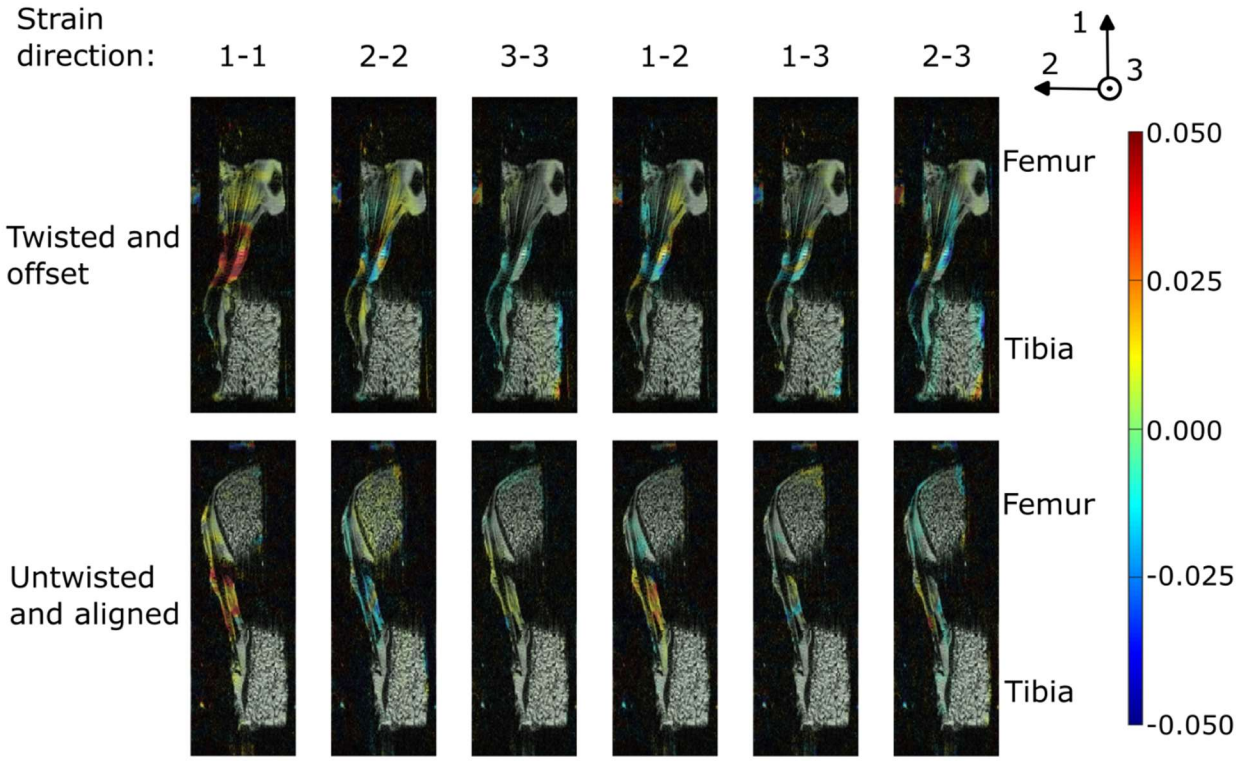
Results

Preliminary data indicate that we can identify differences in the full-field strain with different offsets and twist angles. As shown in figure 1, when the ACL is twisted and insertions offset, we see shifts in strain magnitudes and locations. Specifically, we see strains closer to zero in the 3-3 direction in the untwisted configuration; as well as higher 1-1 strains through the entire mid-tendon in the twisted, offset configuration.

Discussion

This novel testing method allows us to determine the strains the ACL AM and PL bundles undergo from being in their twisted configuration *in vivo*. We are beginning to characterize the response of the ACL to more complex loading conditions, which will eventually be used to identify individuals at a higher injury risk and lead to injury prevention.

Images (Optional)



Session Category

Musculoskeletal Biomechanics: Tissues

OA87-02

Effects of Wrist Posture and Pinch Force on Median Nerve Flattening in the Carpal Tunnel

Mr. Trevour Greene MS, Dr. David Jordan PhD, Dr. Zong-Ming Li PhD

The University of Arizona, Tucson, Arizona, United States

Introduction

The median nerve (MN) and flexor tendons pass through the carpal tunnel. Wrist flexion-extension (FE), radioulnar deviation (RUD), and pinch force may increase MN compression by changing contact with surrounding tissues and carpal tunnel pressure. This study investigated the independent and combined effects of wrist posture and pinch force on MN flattening.

Methods

Eleven healthy young adults were immobilized in a hand splint set to one of nine wrist postures combining FE at 30° flexion, 0°, and 30° extension with RUD at 15° radial, 0°, and 30° ulnar. Ultrasound at the distal carpal tunnel captured cross-sectional videos. Participants performed a thumb-index pinch that increased from 0 to 20 N. MN perimeter was manually traced and MN flattening ratio was calculated. A three-way repeated-measures ANOVA examined effects of FE, RUD, Force, and interactions. Tukey post-hoc tests were used for pairwise comparisons ($\alpha=0.05$).

Results

MN flattening ratio was affected by the main factors FE and RUD ($p<0.05$) but not Force ($p=0.20$). All the two- and three-way interactions were significant ($p<0.05$). At 0 N, flattening ratio was most influenced across RUD postures and increased from ulnar to radial deviation. For example, flattening ratio increased 57% from 30° ulnar to 15° radial deviation when FE was fixed at 30° flexion ($p<0.05$, Figure 1a). At 20 N, flattening ratio was most influenced across FE postures and increased from extension to flexion. For example, flattening ratio increased 184% from 30° extension to 30° flexion when RUD was fixed at neutral ($p<0.01$, Figure 1b). Flattening ratio was influenced by factor interactions and increased with radial deviation, flexion, and 20 N force. For example, flattening ratio increased 84% from 0° FE with 30° ulnar deviation at 0 N to 30° flexion with 0° RUD at 20 N ($p<0.001$, Figure 1a and 1b).

Discussion

In this study, we found MN deformation is driven primarily by wrist posture and interactive effects of pinch force. RUD had the strongest influence on MN shape without pinch force, and FE became the most influential when pinch force was applied. Our study suggests everyday tasks involving flexion and radial deviation under load may increase MN compression risk.

Images (Optional)

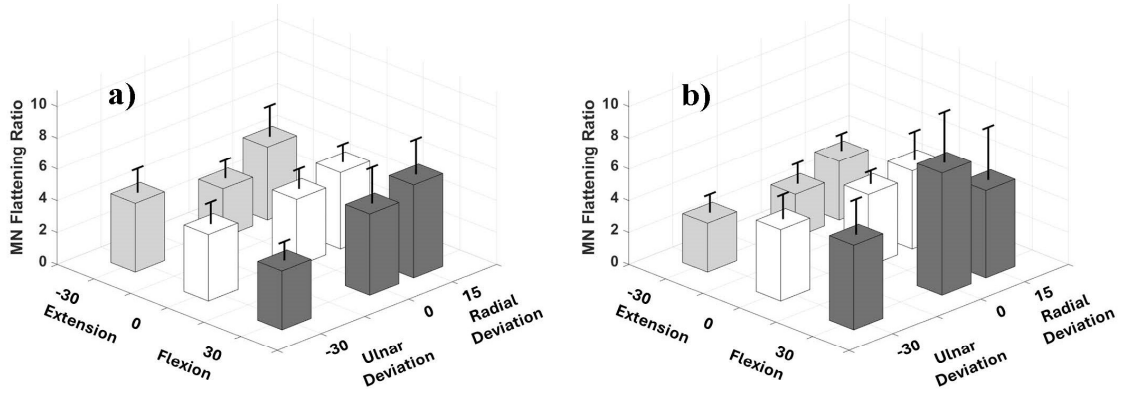


Figure 1. MN flattening ratio (mean ± SD) at each FE and RUD postures under pinch forces of 0 N (a) and 20 N (b).

Session Category

Musculoskeletal Biomechanics: Tissues

OA87-03

Abrocitinib Induces Hypertrophy in an Engineered Human Ligament Model

Dr. Adam Kositsky PhD[1], Dr. Alec Avey PhD[2], Mr. Jared Ong[2], Assoc. Prof. Lauri Stenroth PhD[1], Prof. Rami Korhonen PhD[1], Prof. Keith Baar PhD[2]

[1]University of Eastern Finland, Kuopio, North Savo, Finland. [2]University of California, Davis, CA, United States

Introduction

Abrocitinib is an FDA-approved prescription medicine used to treat patients with atopic dermatitis through systemic inhibition of janus kinase 1 (JAK1), reducing inflammation. A different JAK1 inhibitor, itacitinib, has been shown to alter engineered human ligament (EHL) function [1]. Therefore, use of this class of drug may have secondary effects on connective tissues. Accordingly, we used an EHL model to investigate the potential effects of abrocitinib on ligament development.

Methods

Twenty-eight EHLs were constructed using standardized protocols [1,2] from human fibroblasts of anterior cruciate ligament remnants obtained during reconstructive surgery (IRB #779755). Every second day, EHLs were fed a standardized growth media supplemented with ascorbic acid, proline, and transforming growth factor beta-1. From day 8, EHLs were fed this growth media supplemented with either 0 (control), 0.1 (low), 1.0 (medium), or 10 (high) μM doses of abrocitinib (n = 7 per group). On Day 14, cross-sectional area was determined by measuring width and thickness using optical coherence tomography (OQ LabScope, Lumedica) and assuming an elliptical shape. For mechanical tensile testing (68SC-1, Instron), EHLs were housed in a saline solution maintained at 37°C. After applying a tare load (0.05 MPa), EHLs underwent 10 preconditioning cycles (0.10 MPa at 1%/s) followed by a ramp to failure (0.5%/s). Data were low-pass filtered at 10 Hz and analyzed as true stresses and strains using MATLAB (R2023b). One-way ANOVAs ($p < 0.05$) were performed using GraphPad Prism (v10.6.1).

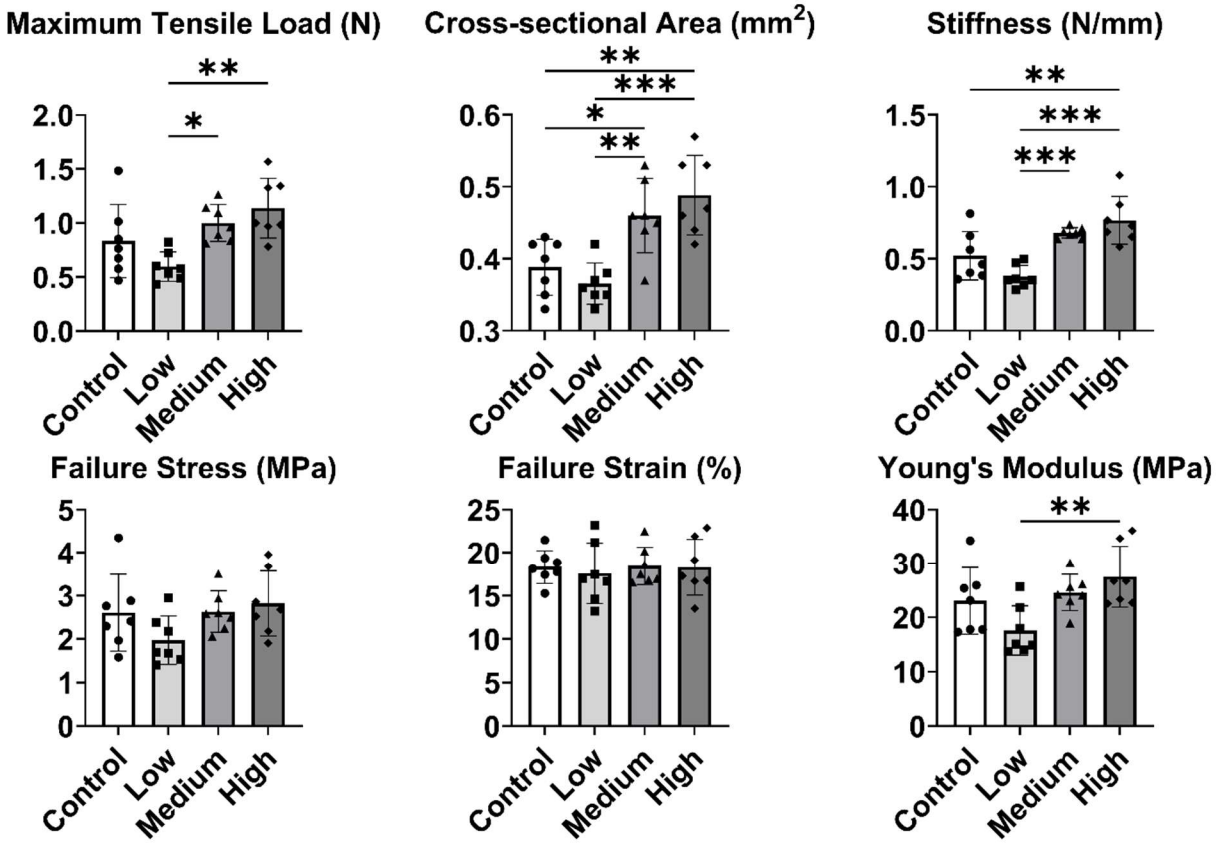
Results

At medium and high abrocitinib doses, EHLs were generally stronger, stiffer, and bigger than those of control and/or low dose groups (Figure 1). There were no significant differences between the control and low dose groups or between medium and high doses.

Discussion

Here, we show that an FDA-approved drug (abrocitinib) alters the morphology and mechanical properties of EHLs. Clinical examination of ligament and tendon properties in patients taking this medicine may thus be warranted. Investigation of the mechanistic pathway of JAK1 on ligament and tendon mechanics is ongoing.

Images (Optional)



References (Optional)

[1] A Avey *et al.*, Matrix Biol, 2024. [2] A Avey *et al.*, Matrix Biol Plus, 2024.

Acknowledgements (Optional)

Fulbright Finland Foundation, Orion Research Foundation, Novo Nordisk Foundation, Peretz Family Foundation for Connective Tissue Research.

Session Category

Musculoskeletal Biomechanics: Tissues

OA87-04

A New Mechanical Clamping System for Bone-Ligament-Bone Tensile Testing

MSc. Minoo Tehrani[1,2], Dr Adam Kositsky Ph.D.[1], Dr. Aapo Ristaniemi[1,2], Dr. Rami Korhonen[1]

[1]University of Eastern Finland, Kuopio, North Savo, Finland. [2]Kuopio University Hospital, Kuopio, North Savo, Finland

Introduction

Accurate mechanical testing of bone-ligament-bone specimens requires stable boundary conditions, yet reliable gripping in knee ligament tensile tests is difficult due to limited bone contact and variable geometry. Existing solutions, such as roughened flat grips, cryogenic clamps, PMMA potting [1], and mechanical bone-locking, often suffer from slippage, uneven load transfer [2], thermal effects, or long sample preparation time. Therefore, we aimed to design a new mechanism that overcomes these limitations.

Methods

We developed a novel mechanical clamping system with several integrated features (Fig. 1A-B). The gripping mechanism relies on downward-oriented grooves that create a self-locking effect as load increases. To enhance the fixation, sharp screws are used to tighten the specimen to the jaws. The clamp is easy to assemble onto the machine, and the jaw components can be detached and replaced when needed.
To experimentally test the new design, one bovine lateral collateral ligament (LCL) was mounted (Fig. 1C) and subjected to an incremental stress-relaxation and ultimate tensile testing protocol (Instron 8874). For comparison, a second bovine LCL was tested in the same manner using a conventional clamping system with flat pyramid-serrated jaws. (4-mm serration depth).

Results

No slipping at the grips was evident throughout stress relaxation or ultimate tensile tests. The ultimate force reached 1289 N compared to 216 N with conventional clamping.

Discussion

The designed clamping system eliminated slippage, which helps to achieve repeatability and accuracy in estimating mechanical parameters of bone-ligament-bone samples. The ultimate force of 1289 N is higher than reported for human LCLs (up to 629 N [1]), demonstrating good applicability of the new clamps to bone-ligament-bone testing. Repeatability tests are being performed.

Images (Optional)

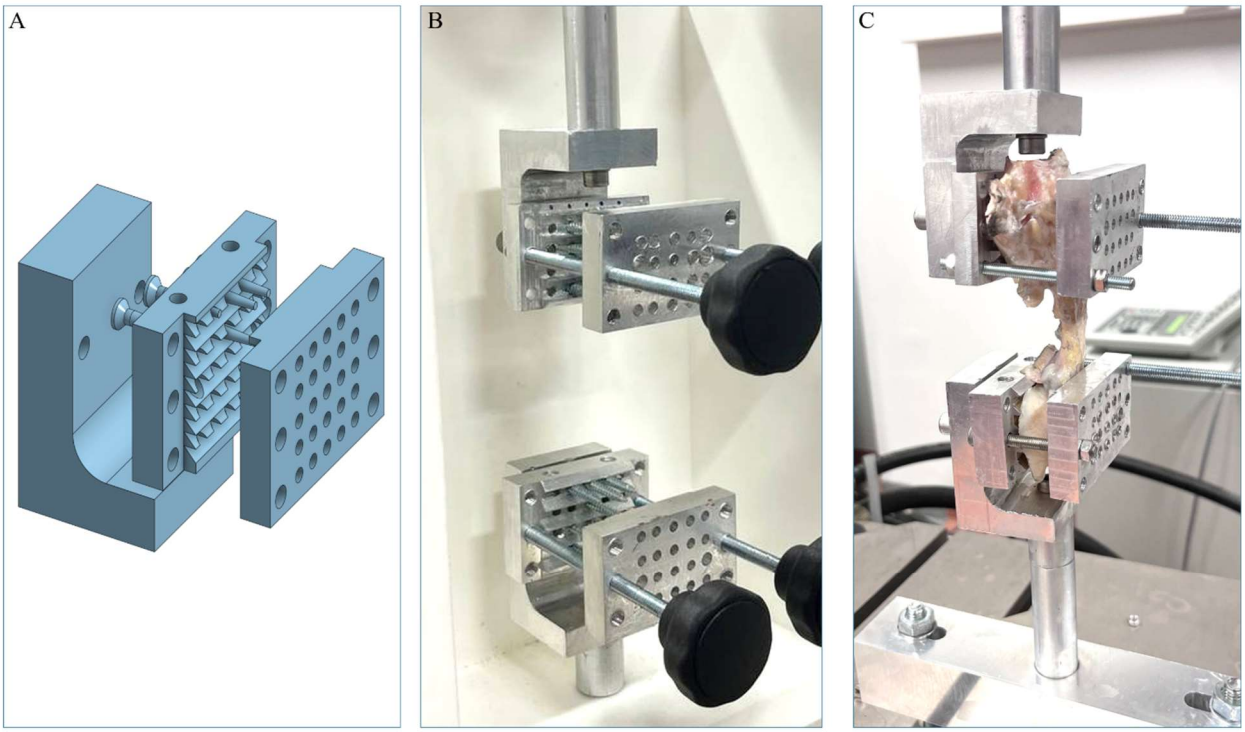


Fig.1. Overview of the clamp development and testing workflow: (A) CAD model of the new clamp design, (B) physical assembly corresponding to the CAD model, and (C) clamp setup with the tissue sample mounted for mechanical testing.

References (Optional)

1. Peters AE et al., Front Bioeng Biotechnol, 10:954837, 2022.
2. Jiang et al., J Mech Behav Biomed Mater, 103:103503, 2020.

Acknowledgements (Optional)

Orion Research foundation, Instrumentarium Science foundation, and Kuopio University Hospital, Wellbeing services county of North Savo

Session Category

Musculoskeletal Biomechanics: Tissues

OA87-05

Sarcomere Length and Force Behavior in Skeletal Muscle Myofibrils

Mr. Taiki Ino

University of Calgary, Calgary, Alberta, Canada

Introduction

Muscles can produce two types of force: active and passive. Active and passive forces are dependent on the length of the sarcomere [1]. Active force is generated through cross-bridge cycling, while passive force in myofibrils depends virtually exclusively on the protein titin [2]. Within a myofibril, sarcomeres are arranged in-series, thus they transmit identical forces at any instant in time. When active force production in sarcomeres differs, passive forces should compensate for the lack of active force by elongating until passive force reaches the required magnitude. This adjustment of sarcomere length has been thought to lead to so-called sarcomere "popping", which has been proposed as a mechanism of muscle injury, residual force enhancement, and force depression [3]. We developed a novel technique to locally deactivate one sarcomere in an otherwise fully activated myofibril with the purpose to test if deactivated sarcomeres will "pop" when active force is eliminated.

Methods

We used single myofibrils from rabbit psoas muscle. A single myofibril is suspended between a needle (for length control) and a cantilever pair (for force measurement). A large and a small-bore pipette are used for activation and deactivation of the myofibril and single sarcomeres, respectively.

Results

We found that locally deactivated sarcomeres did not overstretch in an otherwise fully activated myofibril as predicted by the popping sarcomere theory. Deactivated sarcomeres lengthened by about 0.6μm from about 2.6 to 3.2μm (Fig. 1). At 3.2μm, rabbit psoas sarcomeres have a small passive force (about 127nN/μm^2), thereby questioning how these deactivated sarcomeres can sustain the active stresses exceeding 370nN/μm^2.

Discussion

We propose that activated sarcomeres form a linked framework between actin and titin, which enhances passive force and thereby protects against "popping" and sarcomere damage under these experimental conditions. Activation induces a titin–actin linkage that stabilizes sarcomeres, and this linkage is not immediately broken upon deactivation. Our

findings reveal a novel built-in safety mechanism in previously activated sarcomeres that prevents them from being overstretched and damaged when deactivated.

Images (Optional)

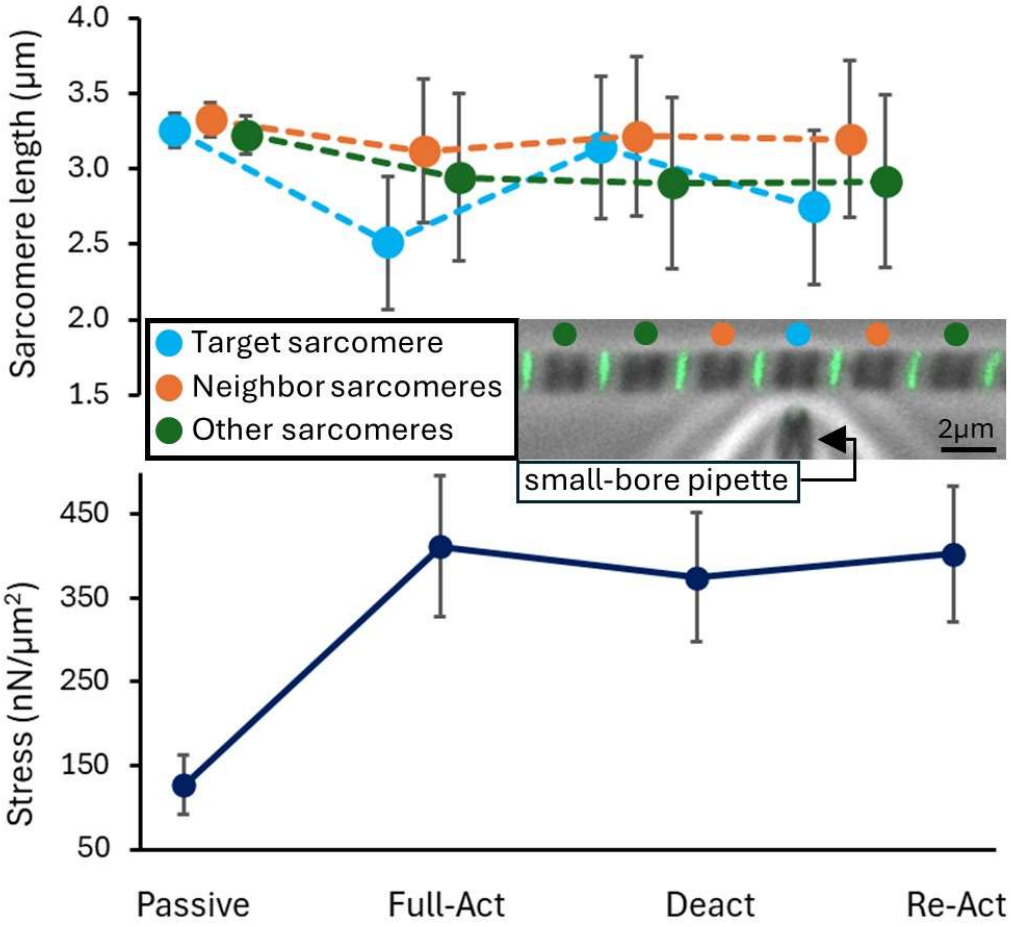


Figure 1: Sarcomere length and stress changes as a function of experimental conditions. The target sarcomere is the one being deactivated. The neighbor sarcomeres are the sarcomeres on either side of the target sarcomere. The other sarcomeres are sarcomeres not immediately neighboring the target sarcomere.

References (Optional)

[1] Gordon *et al.*,J. Physiol, 1966

[2] Trombitas *et al.*, J. Cell Biol,1998

[3] Morgan, Biophys. J, 1990

Acknowledgements (Optional)

CIHR, KMGS and KDDS-University of Calgary scholarship to T.I.

Session Category

Musculoskeletal Biomechanics: Tissues

OA88-02

Resilient Biomechanical Phenotype of Memory CD4⁺ T Cells in Long-Lived Mice

PhD Aldo Abarca-Ortega[1], PhD Blanca González-Bermúdez[2,3,4], PhD Gustavo R. Plaza[2,3,4]

[1]Universidad de Santiago de Chile, Santiago de Chile, Región Metropolitana, Chile. [2]Center for Biomedical Technology, Universidad Politécnica de Madrid, Madrid, Madrid, Spain. [3]Departamento de Ciencia de Materiales, ETSI Caminos, Canales y Puertos, Madrid, Madrid, Spain. [4]Instituto de Investigación Sanitaria Hospital Clínico San Carlos, Madrid, Madrid, Spain

Introduction

Immunosenescence drives functional alterations in T cells, often correlated with increased cellular stiffness as previously reported in longitudinal studies [1]. However, the biophysical evolution of these cells in individuals achieving exceptional longevity remains unexplored. While aging typically correlates with progressive mechanical deterioration [1], we hypothesized that survivors reaching extreme age might exhibit a distinct phenotype. This study investigates the mechanical and structural properties of memory CD4⁺ T cells in a murine model of extreme longevity to identify signatures of mechanical resilience.

Methods

We performed a cross-sectional analysis on memory CD4⁺ T cells isolated from female ICR-CD1 mice across three distinct age groups: Old (72 weeks), Very Old (96 weeks), and Long-lived (>120 weeks), following established longevity criteria [2]. Cellular stiffness (apparent Young's modulus) was quantified via micropipette aspiration (Fig. 1) utilizing a linearized elastic model [3]. Functional motility was assessed through spontaneous migration assays in Boyden chambers. To correlate mechanics with intracellular architecture, we employed 3D confocal microscopy to analyze the relative nuclear size (R_n/R_c) and cytoskeletal anisotropy, alongside flow cytometry for protein expression.

Results

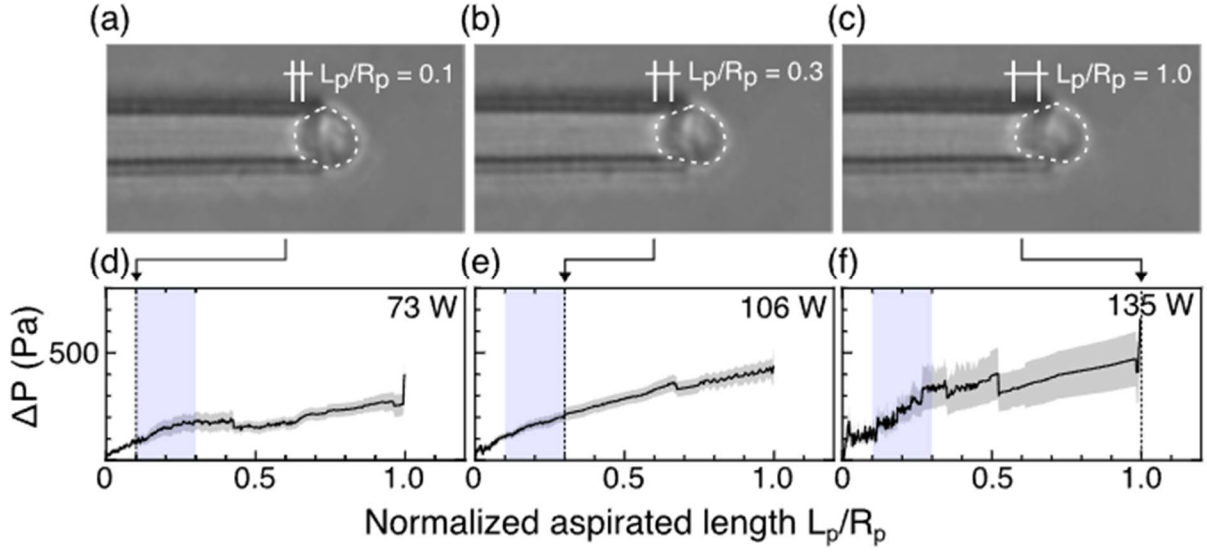
As expected, T cells from the Very Old group exhibited significant stiffening and reduced migration compared to the Old group, consistent with standard aging trajectories. However, this trend did not persist in the Long-lived group. Remarkably, cells from long-lived individuals displayed a mechanical phenotype comparable to the younger Old cohort, with stabilized stiffness values and significantly recovered migratory capacity compared to the "Very Old" group. Conversely, flow cytometry showed no significant differences in

cytoskeletal protein abundance (actin, myosin, vimentin) or senescence markers (p16) across groups.

Discussion

These findings demonstrate a decoupling between chronological age and cellular biomechanical decline in extreme longevity. The preservation of deformability and motility challenges the assumption of continuous stiffening in the immune system. We propose that this distinct biophysical phenotype in long-lived survivors allows for sustained immune surveillance, identifying cell mechanics as a potential biomarker for successful aging distinct from traditional biochemical markers.

Images (Optional)



References (Optional)

[1] González-Bermúdez B, et al. 2022. doi: 10.1111/imm.13559

[2] Martínez de Toda I, et al. 2019. doi: 10.1155/2019/4574276

[3] Plaza GR, et al. 2015. doi: 10.1039/c5sm00125k

Acknowledgements (Optional)

The authors received support from the Comunidad de Madrid, Spain, project TecNanoBio-CM. Ref. TEC-2024/TEC-158, and from the Spanish Ministry of Science, Innovation and Universities, project PID2024-158773OB-I00. A.A-O. gratefully acknowledges the support provided by the Chilean National Agency for Research and Development (ANID) through FONDECYT project N° 11251174.

Session Category

Cell Biomechanics: Mechanobiology

OA88-03

Integrated mRNA–miRNA Profiling Reveals Dysregulation of Mechanotransduction Pathways in Osteoporotic Bone

Dr. Syeda Masooma Naqvi BSc, MSc, PhD[1], Mr. Munam Bukhari[1], Mr. Colin Murphy[2], Prof. Laoise McNamara[1]

[1]University of Galway, Galway, Connacht, Ireland. [2]University Hospitals Galway, Galway, Connacht, Ireland

Introduction

Osteoporosis is not solely a disease of bone loss; it involves disruption of cell–matrix signalling, mechanotransduction, and ECM homeostasis, diminishing bone quality. The mechanobiological basis of impaired osteocyte mechanosensing in osteoporotic bone remains unclear. Although circulating microRNAs (miRNAs) implicated in osteoporotic remodelling have been identified, transcriptional and post-transcriptional regulation within human bone tissue remains insufficiently characterised. To address this, we present the first integrated mRNA–miRNA mechanobiological profile of human osteoporotic femoral head bone to identify regulatory signatures linked to disrupted osteocyte mechanosensation.

Methods

Femoral head samples were collected from female patients undergoing total hip replacement and categorised as Non-OP (n = 8; age 55.6 ± 11.6 years) or OP (n = 4; age 80.7 ± 9.0 years). Total RNA was analysed using custom RT^2 Profiler arrays targeting anabolic, catabolic, and mechanosensitive genes. For miRNA profiling, cDNA was synthesised using the miRCURY LNA RT Kit and amplified via customised miRCURY PCR panels. Relative expression was determined using the comparative Cq ($2^{-}\Delta\Delta$Cq) method. Data dimensionality reduction and differential expression analysis identified clusters.

Results

mRNA profiling revealed transcriptional separation between groups, with PCA distinguishing OP from Non-OP samples (Fig. 1A). OP bone exhibited significant upregulation of anabolic and ECM-related genes (FN1 ↑22.7-fold, DMP1 ↑10.92-fold, BMP2 ↑8.8-fold, OPN ↑8.1-fold), osteocyte- regulation of osteoclasts (SOST) (Fig. 1B-D) and mechanosensitive genes encoding Axin-1, β-catenin, connexin-43, and integrin-β1 (Fig. 1C). miRNA profiling also distinguished OP from Non-OP bone (Fig. 1A). OP samples had

higher expression of osteogenic miRNAs (miR-29 family, miR-148a ↑57.9-fold) and the resorptive regulator (miR-27a) (Fig. 1B-D), while mechanotransduction-associated miRNAs (miR-141, miR-182, miR-183) remained unchanged (Fig. 1C), suggesting a selective disruption of mechanosensitive miRNA pathways.

Discussion

Integrated mRNA–miRNA analysis reveals a mechanobiologically imbalanced, high-turnover yet dysfunctional phenotype in osteoporotic bone, where elevated anabolic transcripts coexist with miRNA-mediated repression that may constrain effective matrix production. Increased expression of mechanosensitive genes highlights dysregulated osteocyte mechanotransduction, particularly within Wnt signaling, integrin–ECM interactions, and connexin-43–mediated communication. We propose that osteoporosis represents a maladaptive, mechanosensory-impaired state driven by discordant transcriptional and post-transcriptional regulation. This research identifies potential targets for therapies aimed at restoring load-responsive bone remodeling.

Images (Optional)

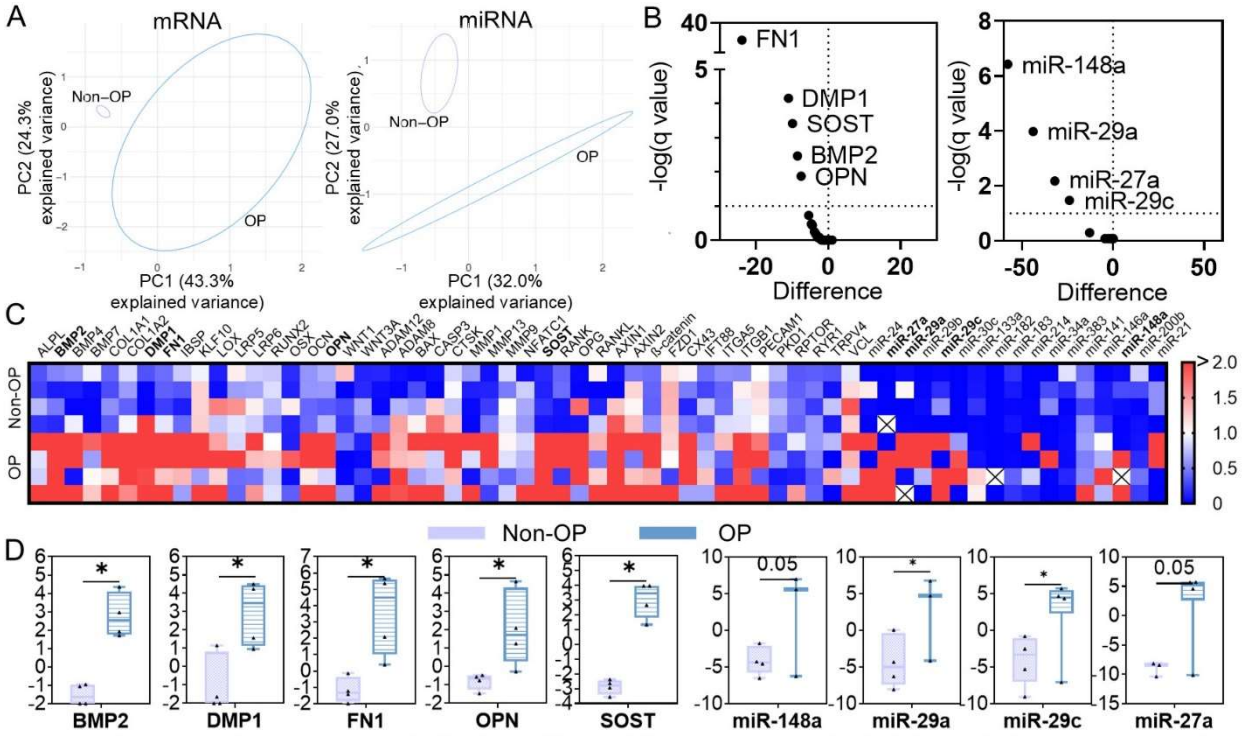


Figure 1: (A) PCA showing distinct profiles. (B) Volcano plot of differential expression. (C) Heatmap of anabolic, catabolic, and ECM-related mRNAs and miRNAs. (D) Selected box plots. Bars = mean ± SD. *p < 0.05; numeric values indicate p < 0.1.

Session Category

OA88-04

Mechanotransducers Downstream of LFA-1 Control Leukocyte Upstream Migration in the KG-1a Cell Line

Dr. Ai Mochida[1], Miss Emily Valerio[1], Dr. Janis Burkhardt[1,2], Dr. Daniel Hammer[1]

[1]University of Pennsylvania, Philadelphia, PA, United States. [2]Children's Hospital of Philadelphia, Philadelphia, PA, United States

Introduction

Leukocyte migration is critical for an effective immune response. During homing, leukocytes experience high shear stresses as they crawl on the endothelium before transmigrating into tissues. On surfaces with intercellular adhesion molecule-1 (ICAM-1), which engages the integrin lymphocyte functional antigen-1 (LFA-1), lymphocytes preferentially migrate upstream, or against the direction of shear flow. Previous studies showed that signaling through LFA-1, including Crk and c-Cbl adaptor proteins but not PI3K, Arp2/3, or Cdc42 were critical for upstream migration. However, it is unclear if there are other intermediate molecules that link LFA-1 to actuating networks that modulate migration in response to shear flow. We studied the role of actin nucleation promoting factors (NPFs) WASP and Hem1; Ena/VASP-like (EVL) protein; CasL, which binds to Crk; and molecules linking the actin cytoskeleton to integrins including vinculin, L-plastin, and RIAM.

Methods

We used the human HSPC-like KG-1a cell line to generate CRISPR/Cas9-mediated knockouts. Migration on ICAM-1 under shear flow (n=3, at least 30 cells/experiment) was analyzed to calculate the mean migration index (MI), where negative MIs represent upstream migration and positive MIs represent downstream migration. Lifeact-GFP videos (at least 5 cells/KO) were analyzed for leading edge dynamics. For statistical analysis, we used one-way ANOVAs with Dunnett’s multiple comparisons.

Results

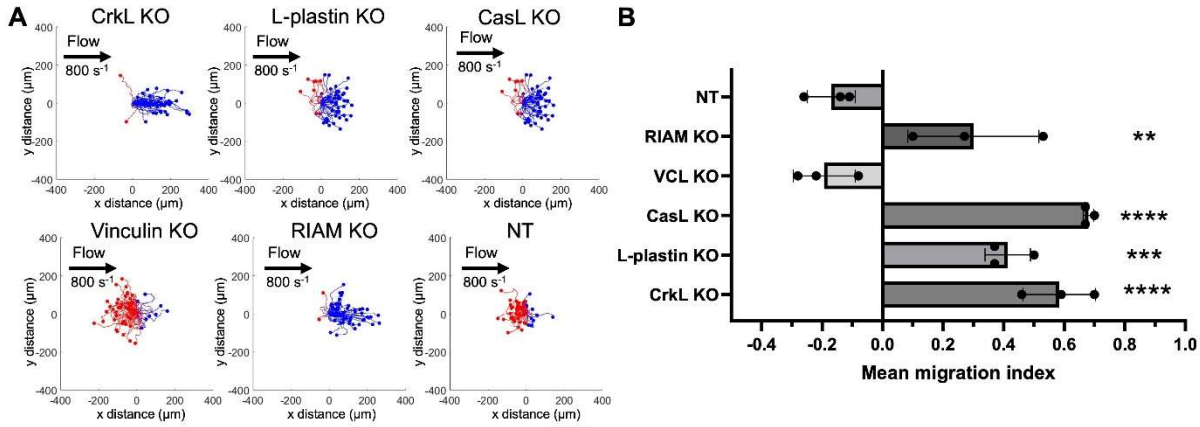
We found that L-plastin, CasL, CrkL, and RIAM-deficient cells were unable to migrate upstream. Meanwhile, Hem1, WASP, EVL, and vinculin were dispensable for upstream migration. Compared to upstream-migrating cells, knockouts that reversed direction of migration appeared to have F-actin localized to the uropod instead of the lamellipod. In

addition, the knockouts protruded continuously along the direction of shear flow and did not retract compared to upstream-migrating cells.

Discussion

We have identified 3 novel molecules that controlled the direction of cell migration under shear flow in KG-1a cells. Leukocyte upstream migration has been observed *in vivo*, with studies indicating upstream migration may enable more effective transmigration, leading to increased homing to target organs. Future work includes assessing transendothelial migration on a HUVEC monolayer to investigate the physiological relevance of upstream migration. This study provides insights into mechanotransduction and integrin signaling that regulate leukocyte migration under shear flow.

Images (Optional)



References (Optional)

Acknowledgements (Optional)

This work was supported by the NIH (GM123019, GM133060, and GM143357) and the NSF (DGE-1650441).

Session Category

Cell Biomechanics: Mechanobiology

OA88-05

HIV-1-Tat-Induced Stiffening of Burkitt Lymphoma Cells Is Reversed by Chemical Disruption of the Cytoskeleton

Mr. Arthur Ndeh MSc Biomedical Engineering[1], Mr. Majahonkhe Shabangu Postdoctoral fellow Biomedical Engineering[1], Ms. Ghodeejah Higgins Lecturer Biomedical Engineering[1], Ms. Elizabeth Kruse Postdoctoral fellow Biomedical Engineering[1], Mr. Thomas Franz Professor in Division of Biomedical Engineering[1], Mrs. Shaheen Mowla Associate Professor in Division of Haematology[2], Mr. Ben Fabry Professor Head of Department of Physics[3]

[1]Biomedical Engineering Research Centre, Division of Biomedical Engineering, Department of Human Biology, Faculty of Health Sciences, University of Cape Town, Cape Town, Western Cape, South Africa. [2]Pathology : Division of Hematology, Department of Human Biology, Faculty of Health Sciences, University of Cape Town, Cape Town, Western Cape, South Africa. [3]Department of Physics, Friedrich-Alexander University Erlangen-Nuremberg, Erlangen, Bavaria, Germany

Mr. Arthur Ndeh

Mr. Majahonkhe Shabangu

Ms. Ghodeejah Higgins

Ms. Elizabeth Kruse

Mr. Thomas Franz

Mrs. Shaheen Mowla

Introduction

Burkitt lymphoma (BL), an aggressive type of B-cell lymphoma, is highly overrepresented among people living with HIV. Intriguingly, the risk of developing HIV-related BL remains high even when viral load is well-controlled. In BL patients with HIV, the HIV-1 Trans-activator of Transcription (Tat) protein is internalised within tumour cells. Emerging evidence suggests that the HIV viral proteins can promote oncogenic events in bystander cells. It is unclear whether this impacts BL cell mechanics, which may have implications for BL pathogenesis and treatment. This research aimed to determine if and how Tat expression modifies the mechanical properties of BL cells, and whether such changes can be chemically adjusted by targeted treatment.

Methods

Shear-flow deformation cytometry was used to compare the mechanical properties of Tat-expressing Burkitt lymphoma cells (BL-41-Tat) with their parental line under two conditions: 2 μM cytochalasin D for actin disruption or 1% DMSO vehicle control. Cells were cultured under standard conditions, treated for 30 minutes, and suspended in 2% (w/v) sodium alginate. Cell suspensions were driven through a straight 200 μm × 200 μm square microchannel and imaged using a CMOS camera at 50 frames per second. Cell deformations were analysed with a UNet-based neural network to extract single-cell mechanical parameters, including stiffness, storage and loss moduli, and fluidity. Two independent biological repeats were performed, each comprising 10 runs with an average of 500 cells per run for each group.

Results

BL 41-Tat cells were stiffer and less fluid than BL 41 cells. With cytochalasin D treatment, the elastic (G') and viscous (G'') response of BL-41-Tat indicated a reversal to BL-41 values. Stiffness and fluidity shifted towards the parental BL-41 mechano-phenotype (Figure 1).

Discussion

Tat expression shifted BL-41 cells toward a more solid-like, less deformable mechanical state, consistent with reinforcement of the actin cytoskeleton and a potentially more aggressive lymphoma phenotype. Cytoskeletal disruption with cytochalasin D largely reversed this Tat-induced mechanical behaviour, indicating that the altered cell mechanics are predominantly actin driven, with residual differences likely reflecting additional cytoskeletal reorganisation. Further research will elucidate whether these mechano-phenotypic changes can inform strategies targeting invasiveness and chemoresistance of HIV-associated BL.

Images (Optional)

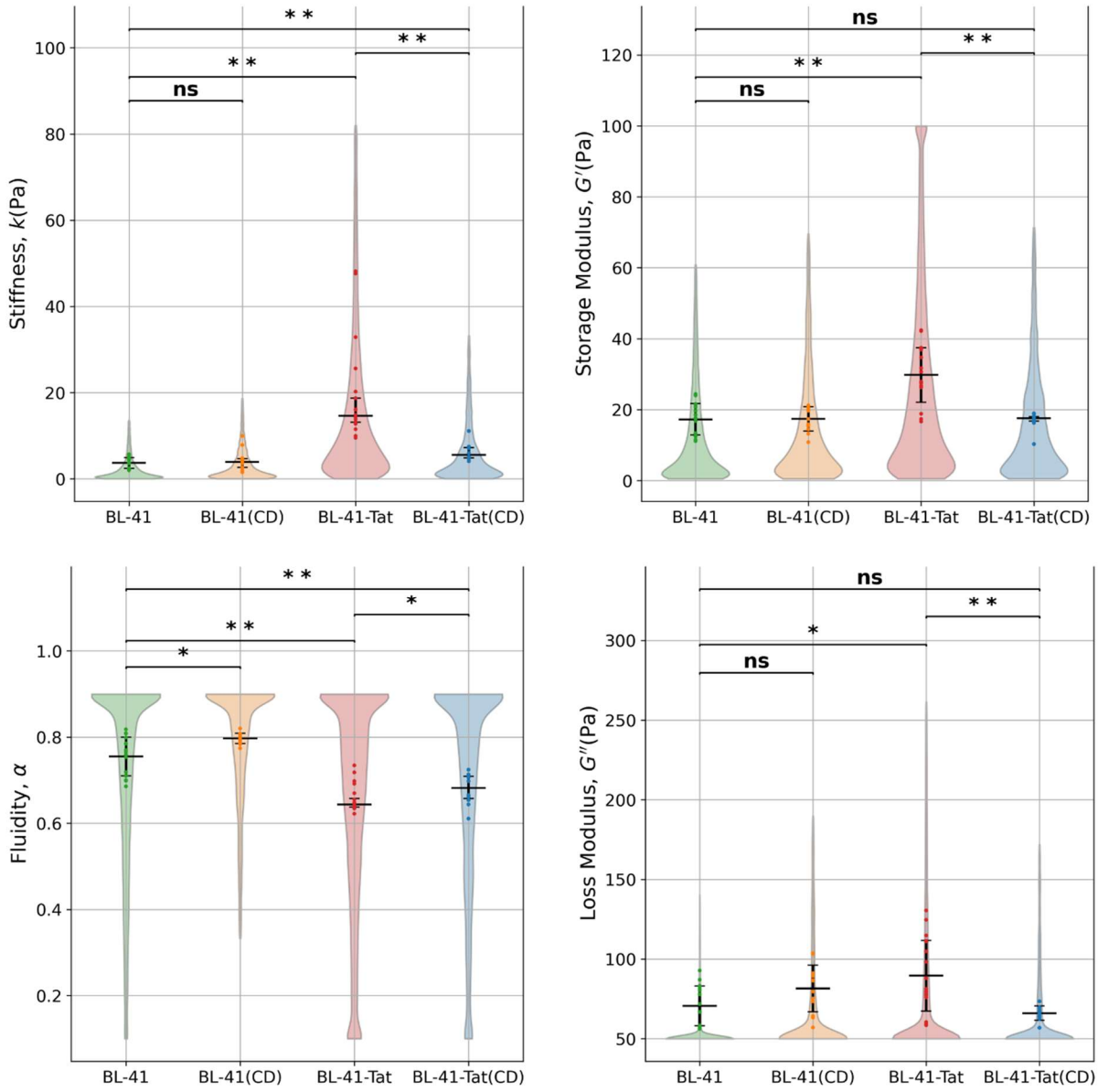


Figure 1: Cell mechanical properties for experimental groups. Plots show median (95% CI). CD: Cytochalasin D, * $p < 0.05$, ** $p < 0.01$, ns: non-significant. Fluidity ranges from 0 (solid-like) to 1 (fluid-like).

Acknowledgements (Optional)

Prof Georgia Schaefer (ICGEB Cape Town) kindly provided laboratory space to perform the shear-flow deformation cytometry experiments.

Session Category

Cell Biomechanics: Mechanobiology

OA89-02

Fibre Architecture Governs Calcification-Driven Failure in Porcine Pericardium

Mr. Luke Guerin[1,2], Dr. Celia Hughes[2,3], Mr. Benjamin J. Thomas[4,5], Mr. Kenneth Meyer[4,5], Dr. Evelyn Campbell[3], Dr. Emily Growney[3], Dr. Michael S. Sacks[4,5,6,7], Dr. Caitríona Lally[1,2,8]

[1]Trinity Centre of Biomedical Engineering, Trinity College Dublin, Dublin, Leinster, Ireland. [2]Department of Mechanical, Manufacturing and Biomedical Engineering, Trinity College Dublin, Dublin, Leinster, Ireland. [3]Structural Heart Division, Boston Scientific Corporation, Galway, Connaught, Ireland. [4]James T. Willerson Center for Cardiovascular Modeling and Simulation, Austin, Texas, United States. [5]The Oden Institute for Computational Engineering and Sciences, Austin, Texas, United States. [6]Department of Biomedical Engineering, Austin, Texas, United States. [7]Department of Mechanical Engineering, Austin, Texas, United States. [8]Advanced Materials and Bioengineering Research Centre (AMBER), Trinity College Dublin, Dublin, Leinster, Ireland

Introduction

Severe aortic stenosis (AS) is a life-threatening condition that narrows and stiffens the aortic valve, with a four-year mortality rate of 44.9% [1]. Minimally invasive bioprosthetic heart valve (BHV) implantation has transformed AS treatment. However, device durability remains limited by regurgitation or stenosis [2]. Calcification and structural damage are key contributors to device failure, yet their interaction is debated [3]. This study investigates interactions between calcification and structural damage and the influence of fibre architecture, and uses these insights to inform CARDIAX, a rapid cardiac mechanics simulation platform [4], with a view to extending pericardial tissue durability.

Methods

Porcine pericardium (PP) was screened non-destructively using a small angle light scattering (SALS) system to separate highly aligned (HA) and highly dispersed (HD) fibre groups [5]. Samples underwent in-vitro calcification in a cyclic bi-directional bulge inflation rig for 30 million cycles. Structural damage and calcification were quantified throughout using digital image correlation (DIC) and μCT imaging respectively [3]. Calcified samples were compared to uncalcified PP loaded in the same conditions. A finite element (FE) model was developed in CARDIAX using a modified fibre-ensemble constitutive equation based on Sacks et al. [6], calibrated with inverse modelling across three pressurisation levels.

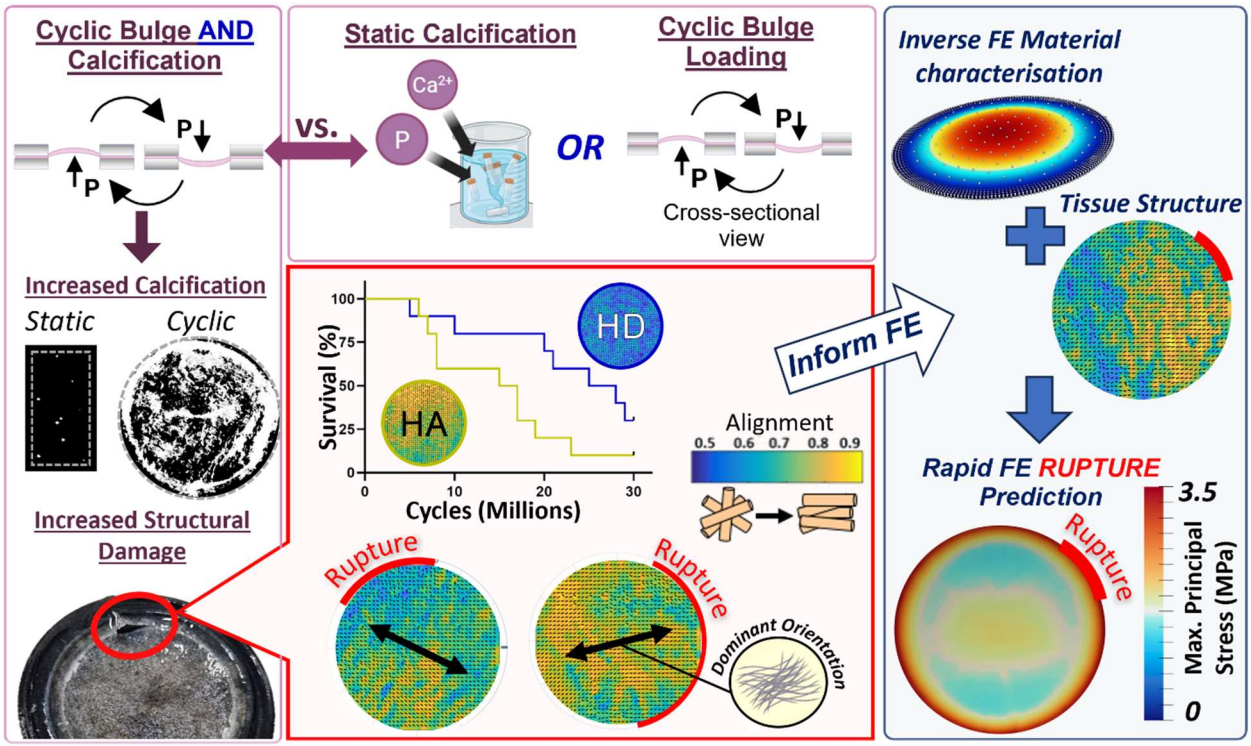
Results

16 of 20 samples loaded in calcification solution ruptured; a behaviour absent in saline-loaded samples. HA tissue ruptured at approximately twice the rate of HD, with rupture sites dictated by dominant fibre direction, see Figure 1. FE simulations of HA PP reveal stress concentrations along the dominant fibre alignment, indicating a predictive link between fibre architecture and rupture.

Discussion

Calcification and structural damage act together to induce pericardium failure. The 2x increase in rupture rate observed in HA calcified tissue substantiates that fibre-mediated tissue mechanics affect leaflet durability in prosthetic valves. GPU-accelerated simulations combined with non-destructive fibre screening provide a pathway for optimising leaflet selection, improving long-term outcomes for patients treated with BHVs.

Images (Optional)



References (Optional)

[1] Généreux et al. , JACC., 2023.

[2] Blackman et al. , JACC., 2019.

[3] Guerin et al. , Acta Biomater., 2025.

[4] Thomas et al. , engrxiv, 2025.

[5] Guerin et al., JMBBM., 2025.

[6] Sacks et al. , Interface Focus., 2016.

Session Category

Cardiovascular/Cardiorespiratory Biomechanics: Materials and Devices

OA89-03

Validation and Verification of Patient-Specific TAVI Simulations for Paravalvular Leakage Prediction

Eng Benedetta Grossi[1,2,3], Miss Letizia Maria Perri[2,3], Miss Valeria Raona[3,2], Dr Ottavia Cozzi[1,3], Prof Gianluigi Condorelli[1,3], Prof Giulio Stefanini[1,3], Prof Francesco Migliavacca[2,4], Prof Giulia Luraghi[2]

[1]IRCCS Humanitas Research Hospital, Milan, Lombardy, Italy. [2]Department of Chemistry, Materials and Chemical Engineering, Politecnico di Milano, Milan, Lombardy, Italy. [3]Department of Biomedical Sciences, Humanitas University, Milan, Lombardy, Italy. [4]Fondazione IRCCS Cà Granda Ospedale Maggiore Policlinico, Milan, Lombardy, Italy

Introduction

Transcatheter aortic valve implantation (TAVI) is an established treatment for aortic stenosis, yet paravalvular leakage (PVL) remains a clinically relevant complication. Patient-specific numerical simulations offer powerful tools for predicting procedural outcomes. However, current models are limited by methodological heterogeneity and incomplete validation against clinical data[1]. Specifically, most studies rely on qualitative echocardiographic comparisons, and none incorporate cardiac MRI, limiting translational reliability.

To fill this gap, this study aims to validate different numerical strategies for PVL prediction by quantitively comparing in-silico outputs with post-TAVI MRI measurements, to identify the modelling approach with the highest clinical accuracy.

Methods

Ten patients undergoing TAVI were prospectively enrolled, and dedicated post-procedural MRI images were acquired. Patient-specific anatomies were reconstructed from pre-operative CTs, and device models were calibrated using ad-hoc crimping tests[2]. FEA simulations reproduced device deployment within each native anatomy. Subsequently, diastolic CFD simulations were performed using patient-specific transvalvular pressure gradients as boundary conditions (BCs). A novel FSI framework was also implemented, setting intraoperatively acquired pressure waveforms as BCs, with calibrated Windkessel models at coronary outlets.

FSI-based systolic flow directionality was visually compared against cine MRI to confirm correct prosthesis orientation. For each strategy (FEA, CFD, FSI), the regurgitant fraction (RF) was quantified, and its absolute deviation from MRI-derived RF was computed. Figure1a depicts the workflow.

Results

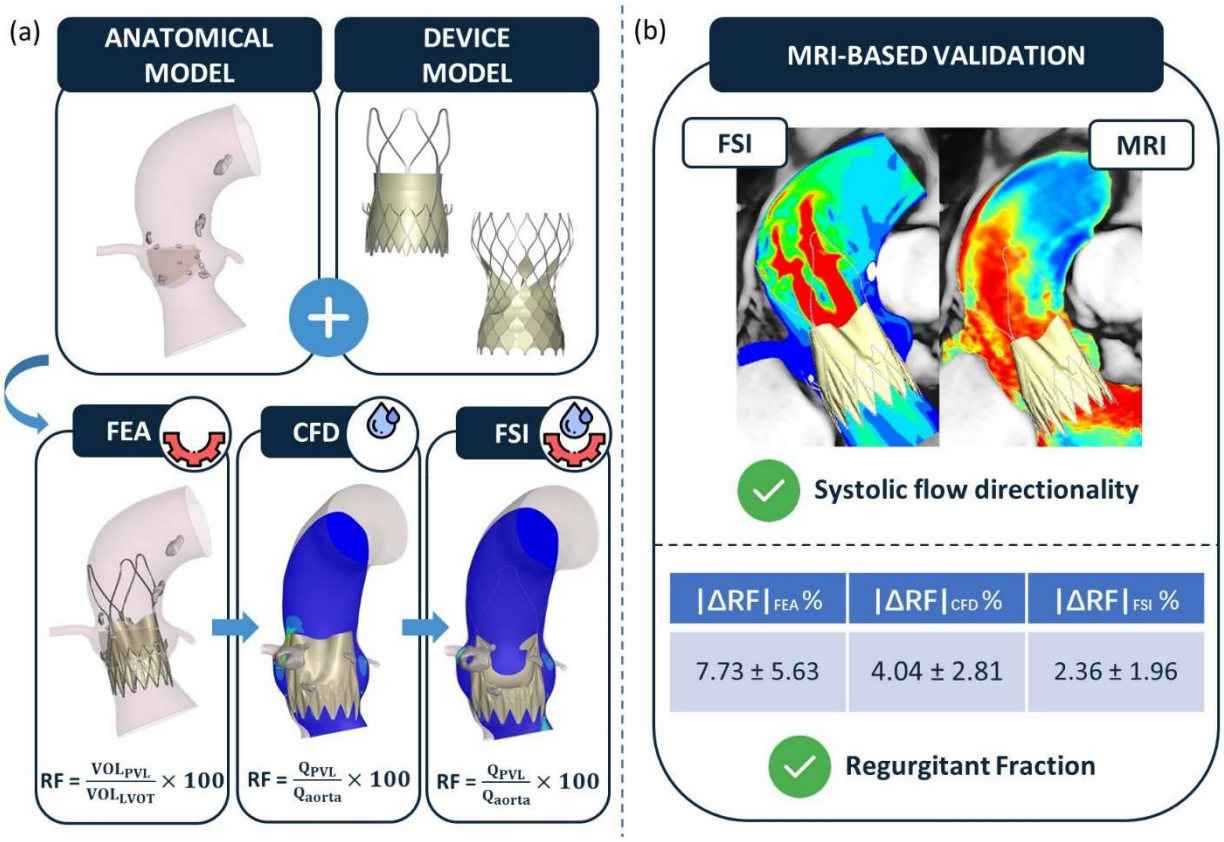
Simulations were successfully completed for all patients. The directionality of systolic flow within the aortic root exhibited good qualitative agreement with MRI acquisitions(Figure1b). The average absolute RF deviation with respect to MRI-based measurements was 7.73±5.63% for FEA-based geometric assessment, 4.04±2.81% for CFD and 2.36±1.96% for FSI analysis.

Discussion

Among the investigated numerical strategies, FSI demonstrated the highest accuracy in predicting post-TAVI PVL. By integrating patient-specific, time-dependent boundary conditions within a deformable anatomical domain, FSI captures the dynamic interaction between the prosthesis and the cardiovascular system, yielding the most physiological haemodynamic representation.

These findings represent a methodological advancement over current state-of-the-art, identifying the validated FSI simulations developed in this study as an accurate in-silico strategy for assessing TAVI outcomes and guiding patient-tailored procedural planning.

Images (Optional)



References (Optional)

[1] Benedetta Grossi et al.,Progress-in-Biomedical-Engineering,2026

[2] Benedetta Grossi et al.,Comput-Biol-Med,2024

Acknowledgements (Optional)

The study is supported by a research grant of the Italian Ministry of University and Research (PRIN 2022 PNRR, grant P20227KTBZ under the Program Next Generation EU, Mission 4, Component 1). B.G.,L.M.P.,F.M. and G.L. are supported by the European Research Council(ERC, project PROTEGO, G.A. 101162753).

Session Category

Cardiovascular/Cardiorespiratory Biomechanics: Materials and Devices

OA89-04

In-Silico Modelling and Validation of Post-Dilation in TAVI Patients

Miss Letizia Maria Perri[1,2], Eng. Benedetta Grossi[3,2,1], Prof. Francesco Migliavacca[1,4], Prof. Gianluigi Condorelli[3,2], Prof. Giulio Stefanini[3,2], Prof. Giulia Luraghi[1]

[1]Department of Chemistry, Materials and Chemical Engineering, Politecnico di Milano, Milan, Lombardy, Italy. [2]Department of Biomedical Sciences, Humanitas University, Milan, Lombardy, Italy. [3]IRCCS Humanitas Research Hospital, Milan, Lombardy, Italy. [4]Fondazione IRCCS Cà Granda Ospedale Maggiore Policlinico, Milano, Lombardy, Italy

Introduction

Transcatheter Aortic Valve Implantation (TAVI) is a minimally invasive treatment for aortic stenosis. Balloon post-dilation, commonly performed to optimize device expansion and reduce paravalvular leakage (PVL), critically influences final device–tissue interaction and clinical outcomes. Despite its clinical importance, post-dilation is often omitted in computational models, limiting their ability to replicate real-world behaviour and predict procedural risks. This study develops and validates patient-specific numerical simulations of TAVI post-dilation to improve the mechanical realism and predictive power of existing models. Simulation results are validated based on post-operative CT images, and their impact is assessed by comparing them with models without post-dilation.

Methods

Four patients were included. The Edwards Lifesciences post-dilation balloon was reconstructed, discretized, and its material properties calibrated through uniaxial tensile tests. Experimental and computational compliance tests were then performed to validate the material model. Finally, the calibrated balloon was integrated into patient-specific anatomies, after simulating TAVI deployment, to carry out finite-element post-dilation simulations. The orifice area (OA), averaged across three cross-sectional stent planes, and the eccentricity were extracted from both the segmented and simulated stent configurations to quantify the predictive accuracy of the simulations as outlined in our previous work [1]. Prediction errors from simulations with and without post-dilation were then compared to evaluate its impact. Figure 1 illustrates the workflow and previous results.

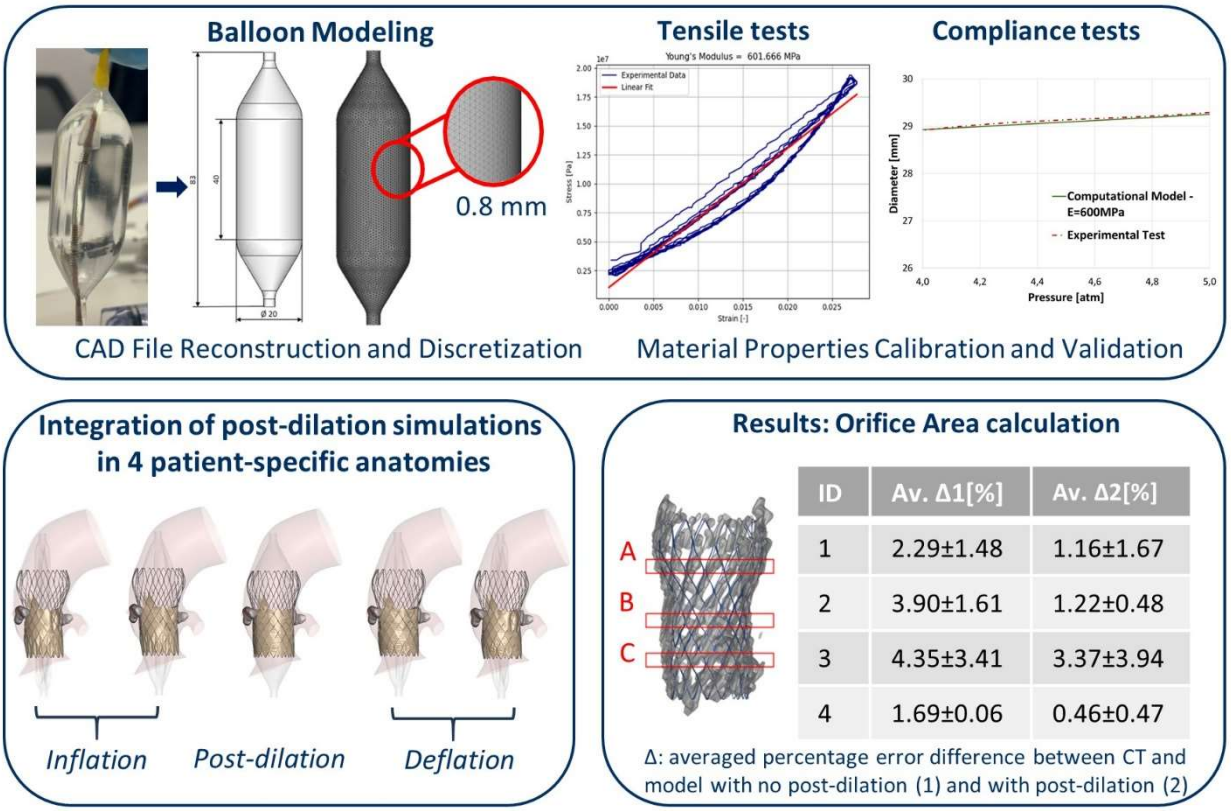
Results

Post-dilation simulations were successfully performed on the previously implanted TAVI devices. The average absolute deviation of OA percentage difference error between the simulated and CT-derived stent configurations decreased from 3.06±1.27% in simulations without post-dilation to 1.55±1.26% when post-dilation was included. A similar improvement was observed for eccentricity percentage error, decreasing from 5.70±5.80% to 1.62±1.08% when post-dilation was simulated.

Discussion

A dedicated computational workflow was established to model balloon post-dilation, with material properties calibrated and validated experimentally. The effect of post-dilation on stent deformation was systematically assessed. This work is novel, as previous studies have not modelled this clinically critical step, despite its role in optimizing valve expansion and improving outcomes, especially in complex anatomies.

Images (Optional)



References (Optional)

"[1] Benedetta Grossi *et al.* , Computers in Biology and Medicine, 2024"

Acknowledgements (Optional)

L.M.P., B.G., F.M. and G.L. are supported by the European Research Council (ERC, project PROTEGO, G.A. 101162753).

The study is supported by a research grant of the Italian Ministry of University and Research (PRIN 2022 PNRR, grant P20227KTBZ under the Program Next Generation EU, Mission 4, Component 1).

Session Category

Cardiovascular/Cardiorespiratory Biomechanics: Materials and Devices

OA89-05

A Mechano-Mimetic Mitral Valve for Evaluation of Repair in Grades of Mitral Regurgitation – In Vitro and In Silico Findings

Dr Sina Javadpour[1], Prof Fergal O'Brien[1,2], Dr Claire Conway[1,2]

[1]RCSI, Dublin, Leinster, Ireland. [2]Trinity College Dublin, Dublin, Leinster, Ireland

Dr Sina Javadpour

Prof Fergal O'Brien

Introduction

Mitral valve mechanics play a significant role in its function and alterations in mechanics are classical indicators of valvular disease. As minimally invasive treatments emerge the modes of study of the mitral valve need to advance. In-vitro flow rigs with ex-vivo mitral valves lack pathology, have low anatomical consistency, and varied material properties. Therefore, synthetic mitral valves are being developed for flow examinations, but to-date lack anisotropy and capacity for physiological pressures.

Methods

A novel mechano-mimetic synthetic mitral valve with anisotropic leaflet mechanical properties is presented. A left heart simulator for a mechano-mimetic mitral valve loading under physiological flow conditions (70 beats per minute, cardiac output 4-6 L/min, transmitral pressure ~120 mmHg) and related computational models (FEA - finite element analysis) are presented. The mechano-mimetic valve (MM) is compared to two other polymeric valves with varying types of reinforcement (R1, R2 – Fig1A). Grades of mitral regurgitation (MR) are introduced via annular dilation, via extension in the posterior leaflet direction, and edge-to-edge repair (EER) is investigated for centrally placed single and double clips (Fig1B).

Results

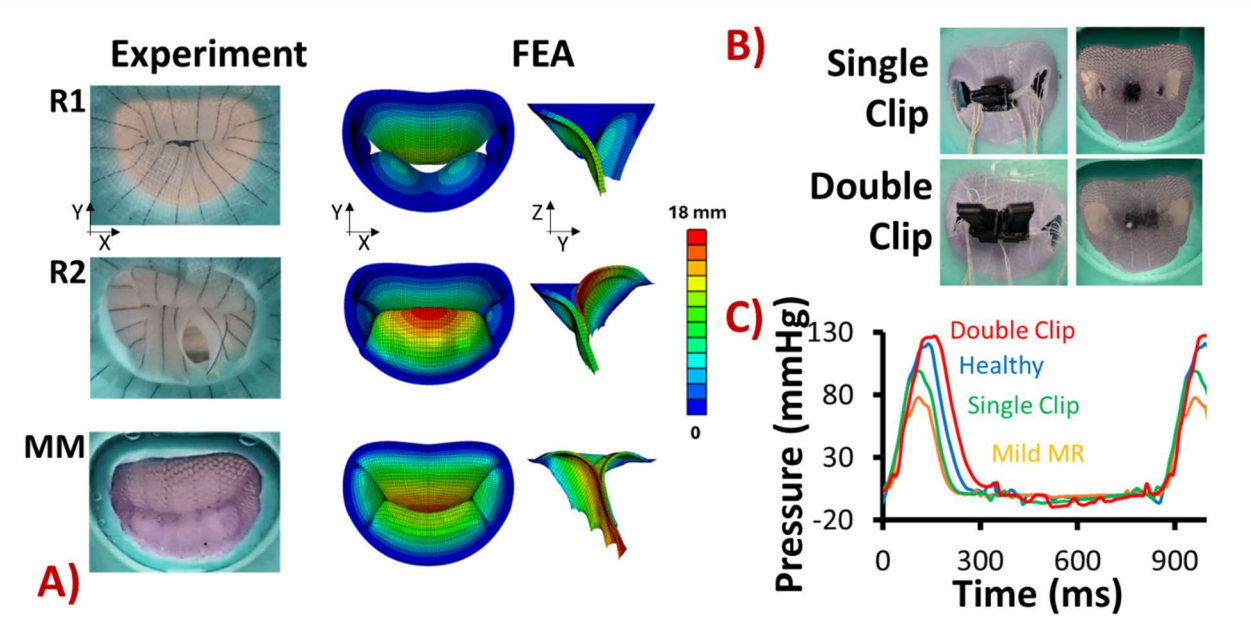
The left heart simulator successfully tested the mechano-mimetic mitral valve under physiological conditions. Left atrial viewing of coaptation profiles, during systolic ventricular ejection, mimicked clinical features, in particular, with anterior mitral leaflet

dominance noted in MM. FEA predicted a similar coaptation profile, healthy range of leaflet bulge, and quantification of coaptation length in mm (Fig1A). EER for grades of MR revealed clipping repair most suited to mild levels of MR (Fig1C). There were minimal improvements with single or double clipping for moderate and severe grades of MR.

Discussion

This novel, low-cost physical model addresses the compelling need for anatomically representative, repeatable, and durable synthetic mitral valves with precise control over leaflet thickness and incorporating anisotropic material properties to advance our understanding mitral mechanics. With the capability to simulate controlled grades of MR, it represents a vital advancement for device testing, as demonstrated here for EER clipping scenarios.

Images (Optional)



Acknowledgements (Optional)

This study was supported by the RCSI Strategic Academic Recruitment (StAR) Lectureship (C Conway) and Research Ireland Frontiers for the Future Programme Project grant (20/FFP-P/8588 – C Conway).

Session Category

Cardiovascular/Cardiorespiratory Biomechanics: Materials and Devices

OA90-03

Label-Free Particle Accumulation in Helical Microtubes with Secondary Flows

Mr Tianmian Liu[1], Mr Deyun Liu[1], Mr Shenghong Zhang[1], Prof Kazuyasu Sugiyama[2], Prof Xiaobo Gong[1]

[1]Shanghai Jiao Tong University, Shanghai, Shanghai, China. [2]The University of Osaka, Toyonaka, Osaka, Japan

Introduction

Curved microfluidic channels utilizing secondary flows offer a label-free strategy for sorting rare and heterogeneous targets such as exosomes, T cells, and mesenchymal stem cells. However, limited understanding of particle dynamics constrains sorting efficiency and precision. This study aims to elucidate the hydrodynamic mechanisms driving the formation and transition of distribution patterns of rigid particles and deformable cells in three-dimensional helical microtubes.

Methods

We develop a three-dimensional microfluidic platform with helical microtubular channels that generates steady, tunable secondary flows across a broad range of Reynolds (Re=1–224) and Dean numbers (De=0.056–25.04) to visualize cross-sectional particle distributions using fluorescence microscopy. The force balance between inertial lift and Dean drag, together with particle trajectories, is further analyzed using semi-analytical approaches and the immersed boundary method.

Results

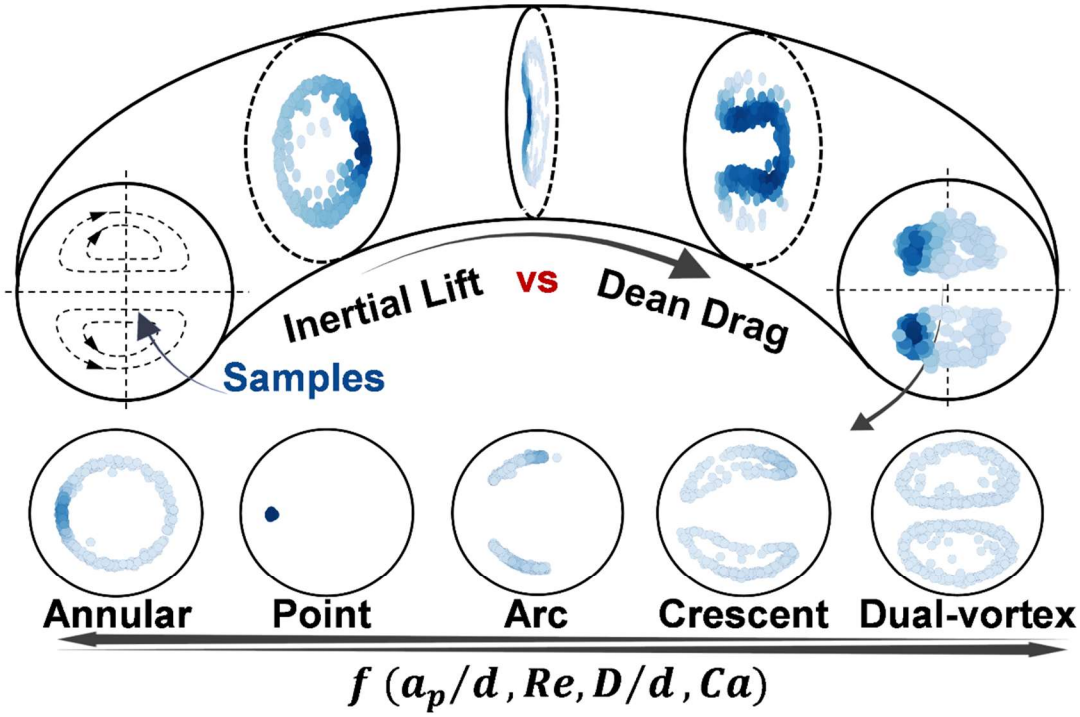
Within the parameter ranges of Reynolds number $1 \leq Re \leq 224$, normalized helical diameter $80 \leq D/d \leq 320$, and particle-to-channel diameter ratio $0.06 \leq ap/d \leq 0.27$, five distinct cross-sectional distribution patterns are observed. A dimensionless parameter, the characteristic inertial force ratio (γ), defined as the ratio of the maximum inertial lift to the maximum Dean drag, is introduced to elucidate the transition of distribution regimes from lift-dominated to drag-dominated states, providing a quantitative basis for predicting pattern evolution.A trade-off between focusing efficiency and size resolution is revealed, and an off-axis collection strategy is proposed to exploit non-horizontal equilibrium positions for improved sorting accuracy. Furthermore, a comparison between rigid particles and Jurkat cells show that cell deformability alters equilibrium positions and focusing patterns in the helical flow. The deformation-induced lift force, characterized by

the Capillary number (Ca), emerges as a key parameter governing the lateral migration behavior of cells.

Discussion

This work establishes a unified physical framework for understanding particle and cell migration in secondary-flow microfluidics. The combined parameters γ and Ca govern distribution transitions, offering design guidance for optimizing focusing efficiency and sorting precision in label-free microfluidic platforms.

Images (Optional)



References (Optional)

[1] Tianmian Liu et al., Anal Chem, 2025.

Acknowledgements (Optional)

We acknowledge support from Key Project of the National Natural Science Foundation of China (No. 12432014) and the National Key Research and Development Program of China (No. 2025YFE0107500).

Session Category

Micro/Biofluidics: Experiments

OA90-04

Analysing the Effect of RBC Aggregation and Deformability in the Microhaemodynamics

Miss Gladys Diaz Armas, Dr. Joseph van Batenburg-Sherwood

Imperial College London, London, London, United Kingdom

Introduction

In diabetes, red blood cell (RBC) aggregation increases and deformability decreases, likely contributing to microvascular symptoms by raising blood viscosity, altering the flow dynamics, and impairing oxygen transport. Although aggregation and deformability have been studied individually, their combined effects remain unclear. Our work aims to determine how these two mechanical properties jointly shape blood flow in health and disease. We began with a simple model, a straight channel, to examine how RBC velocity and concentration change with altered aggregation and deformability.

Methods

We built an optical system that alternates blue and red illumination to capture image pairs at high-speed. Red-light images yield velocity profiles via Particle Image Velocimetry (PIV), with underestimation corrected using a flow sensor. Blue-light images provide local haematocrit based on the principles of optical densitometry and the Beer–Lambert law. Healthy RBCs were washed and suspended at 25% haematocrit in solutions of 0.5% or 1% Dextran 500 kDa to induce normal or increased aggregation. Deformability was reduced by incubating cells with 0.04% or 0.08% glutaraldehyde before resuspension in low-aggregation media. A 43x40 μm channel was used, and flow was controlled by pressure differences between the inlet and outlet.

Results

At low flow rates, RBC migration increases with aggregation (Fig. 1a). At higher flow rates, the difference is subtler but present (Fig. 1c). Velocity profiles appear blunter with increased migration, indicating a negative correlation between velocity and haematocrit bluntness (Fig. 1b,d).

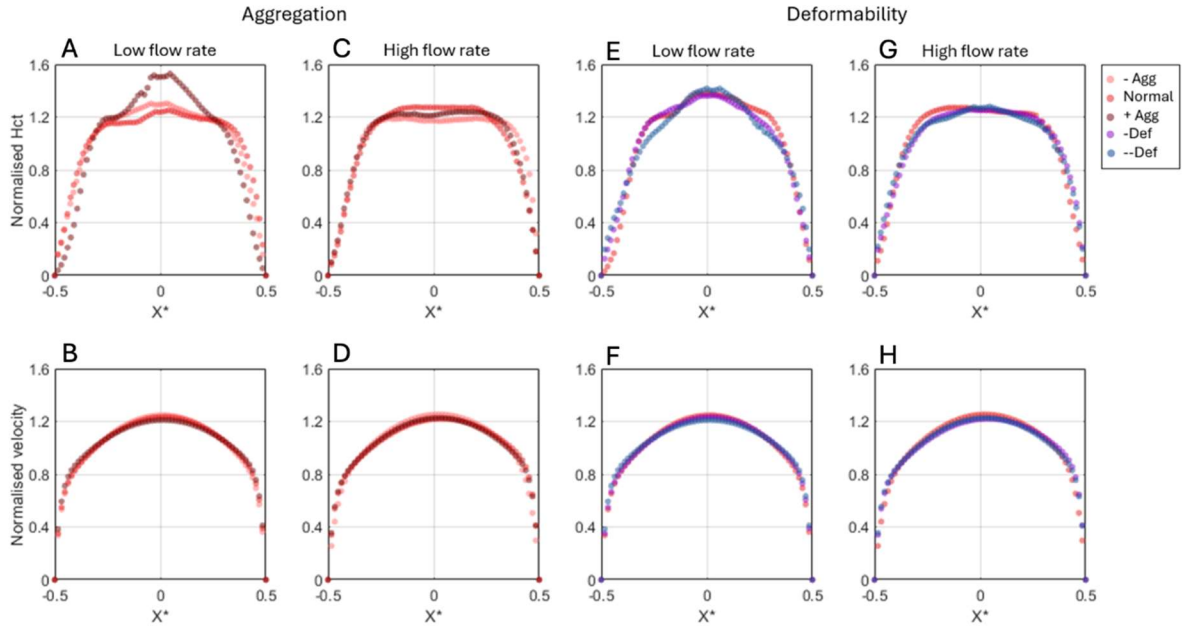
A similar trend is observed with varied deformability. Consistent with [1], stiffer cells showed increased migration, contrasting with what is generally expected for rigid discs (Fig.

1e,g). Velocity profile bluntness also shows a negative correlation with haematocrit bluntness (Fig. 1f,h).

Discussion

Both increased aggregation and decreased deformability increase migration, affecting the local viscosity at the walls and therefore changing the shear stress. The different profiles will impact how RBCs are distributed at bifurcations, which could lead to some branches having low Hct, causing hypoxia in specific locations. Next steps include analysing these samples in networks that better represent the microvasculature to better understand the role of RBC mechanical properties in blood flow.

Images (Optional)



References (Optional)

[1] Andreas Passos et al., Phys. Fluids, 2019

Session Category

Micro/Biofluidics: Experiments

OA90-05

Multimodal Intravital Observation of Drugs Induced Reaction in Bioengineered Avian Embryos Using Nonlinear Microscopy and Magnetic Resonance Imaging

Prof. Claudio Conci[1], Mr. Leonardo Cherubin[1], Dr. Alberto Bocconi[1], Eng. Matteo Laganà[2], Dr. Chiara Martinelli[1], Ms. Giulia Lodola[1], Mr. Marco Vigneri[1], Dr. Domenico Aquino[3], Dr. Federica Mazzi[3], Dr. Cristina Chirizzi[3], Prof. Emanuela Jacchetti[1], Prof. Manuela Raimondi[1]

[1]Department of Chemistry, Materials and Chemical Engineering "Giulio Natta", Politecnico di Milano, Milan, Lombardia, Italy. [2]Gemma Prototipi, Erba, Lombardia, Italy. [3]Neuroradiology, Fondazione IRCCS Istituto Neurologico "Carlo Besta", Milan, Lombardia, Italy

Introduction

The chick embryo is a valuable model for studying the effects of new drugs on the vascular system, a knowledge crucial to understand vascular related diseases. Intravital imaging of animal vasculature is limited by upright microscopes, invasive windows or reduced signal-to-noise ratio. We developed the "Eggs&Beacon" platform for performing longitudinal intravital imaging on avian embryos on inverted microscopes and MRI-systems. We used this platform to quantify immune reaction to implanted human breast cancer tumors and we developed a predictive model of druggability.

Methods

We created an artificial eggshell assuring a sufficient oxygen influx and transparency. Eggshell's supported by a plastic case (Form3B+, Formlabs) made of a body, a cap and an imaging window (Fig.1a). This platform fit embryos on inverted microscopes (EclipseTi-2, Nikon). We observed the same embryo at different time-points (EID 8,11,14). The imaging window is a millifluidic device imaged with a water-immersion objective (40X, NA=1.1, WD=0.8mm) where fluids were used to correct optical distortions. We performed MRI imaging (Bruker, Ettlingen) on a 7T scanner (BioSpec70/20), with a 72mm 1H-linear radiofrequency coil (T2-RARE echo-time=100ms;rep-times=8400ms;slice=1mm).

Results

The platform enabled embryo survival >33% and longitudinal imaging up-to 14days. Nonlinear microscopy showed inflammatory reaction at the tumor-implanted region with a drug controllable modulation. SHG revealed referentially oriented collagen-I in

microenvironments. The realized membranes (thickness<130µm) enabled the embryos to survive until EID14 (Fig.1a). Eggs&Beacon allowed to expose the vasculature to the microscope objective, without compromising the embryo's viability (Fig.1b-e). We quantified angiogenesis with TPEF (Z=600µm, λexc=800nm, λem<450nm, Fig.1c,e). SHG (Z=600µm, λexc=910 nm, λem=450/55nm, Fig.1e,f) showed collagen-I matrix and enabled us to measure amount and direction of fibers. By MRI, we quantified the vascular network growth and the embryo's body dimension (Fig.1d-f).

Discussion

We developed a multimodal imaging platform compatible with inverted microscopy and MRI to monitor living avian embryos up to EID14. By enabling the longitudinal quantification of fibrosis, as blood vessel density, and collagen production allows for the assessment of anti-angiogenic drugs and systemic responses. Crucially, this versatile approach offers a method to evaluate pharmaceutical efficacy and safety in-vivo while significantly reducing the reliance on mammals' models.

Images (Optional)

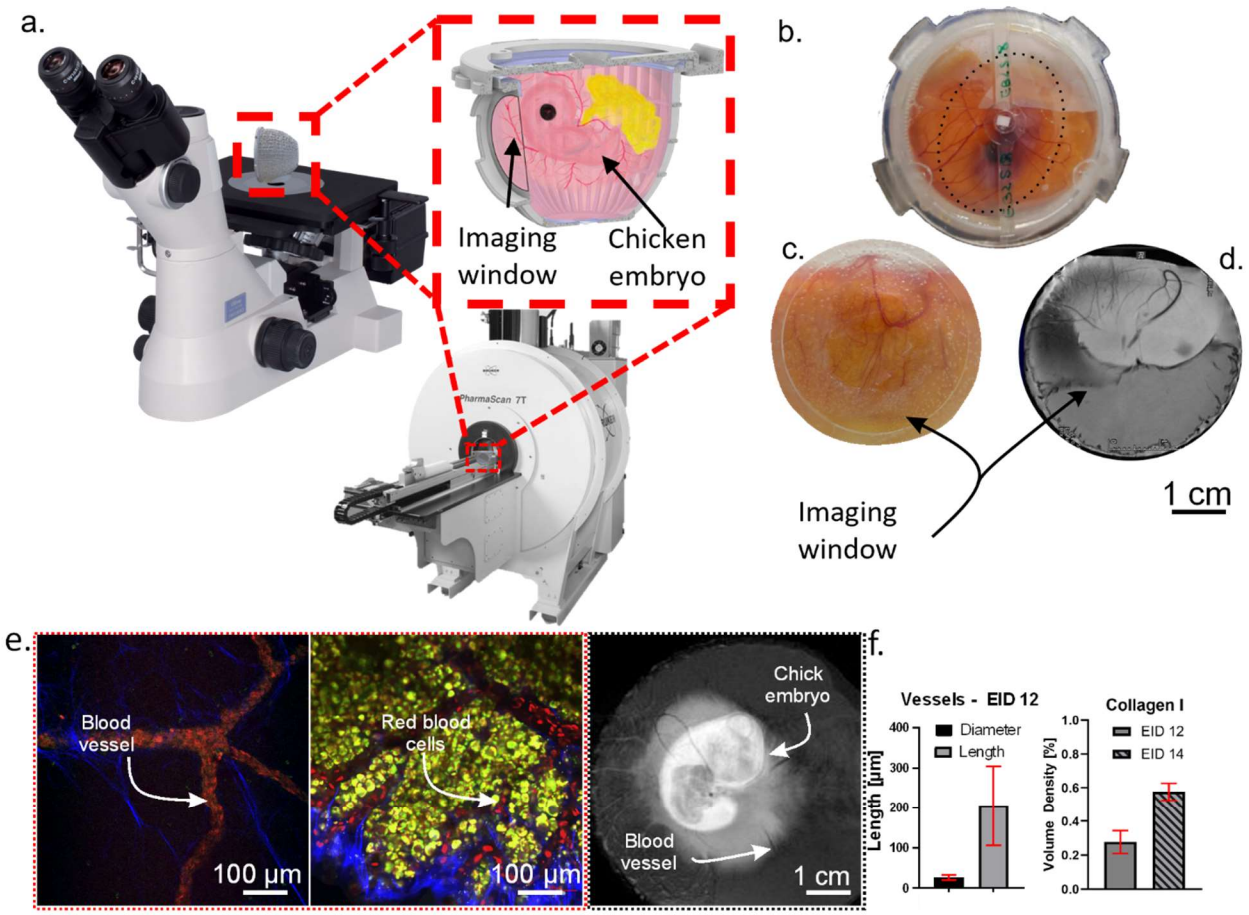


Fig.1: *(a)Eggs&Beacon, made of a plastic eggshell, a permeable membrane, a plastic casing, a cap and an imaging window. (b) Top, Chick embryo at EID14. (c-d) Lateral view and MRI through the imaging window. (e-f) Microscopy/MRI images of the capillaries (TPEF, red – MRI, BW) and of collagen matrix (SHG, blue) Z=600µm, EID12. (f) Data from live images.*

References (Optional)

[1] Conci et al. AplBioeng, 2023

Acknowledgements (Optional)

ERC-BEACONSANDEGG, G.A.101053122, ERC-ALFRED 101221323.

Session Category

Micro/Biofluidics: Experiments

OA90-06

The Influence of Red Blood Cell Deformability on Endothelial Cell Nitric Oxide Signalling: A Biomicrofluidic Approach

Miss Ioana Esanu, Dr Joseph van Batenburg-Sherwood

Imperial College, London, London, United Kingdom

Introduction

The endothelial cells (ECs) lining the vessels experience shear stress imposed by blood flow, which is detected by ECs and modulates behaviour like vasoregulation, permeability and inflammation. Microvascular flow and the resulting shear stress are determined by the physical properties of red blood cells (RBCs), particularly deformability, which decreases in diabetes and even more in diabetic retinopathy. We therefore hypothesise that reduced RBC deformability modifies local shear stress, contributing to microvascular dysregulation in diabetes.

Methods

Microfluidic channels (50x900µm) were fabricated from laser-cut adhesive tape, acrylic layers and a glass coverslip bottom, on which HUVECs were grown under continuous media turnover via hydrostatic pressure. A pressure controller then supplied 24mbar, generating an arteriolar-level shear stress of 30dyn/cm^2, irrespective of fluid. Channels were perfused for 1h with culture media or with 25% haematocrit RBC suspensions from human donors (healthy or glutaraldehyde-stiffened to mimic diabetes). Immunofluorescence intensity of cytosolic phosphorylated eNOS was quantified relative to a static control within each blood donor and HUVEC batch, averaged across 4 images per channel.

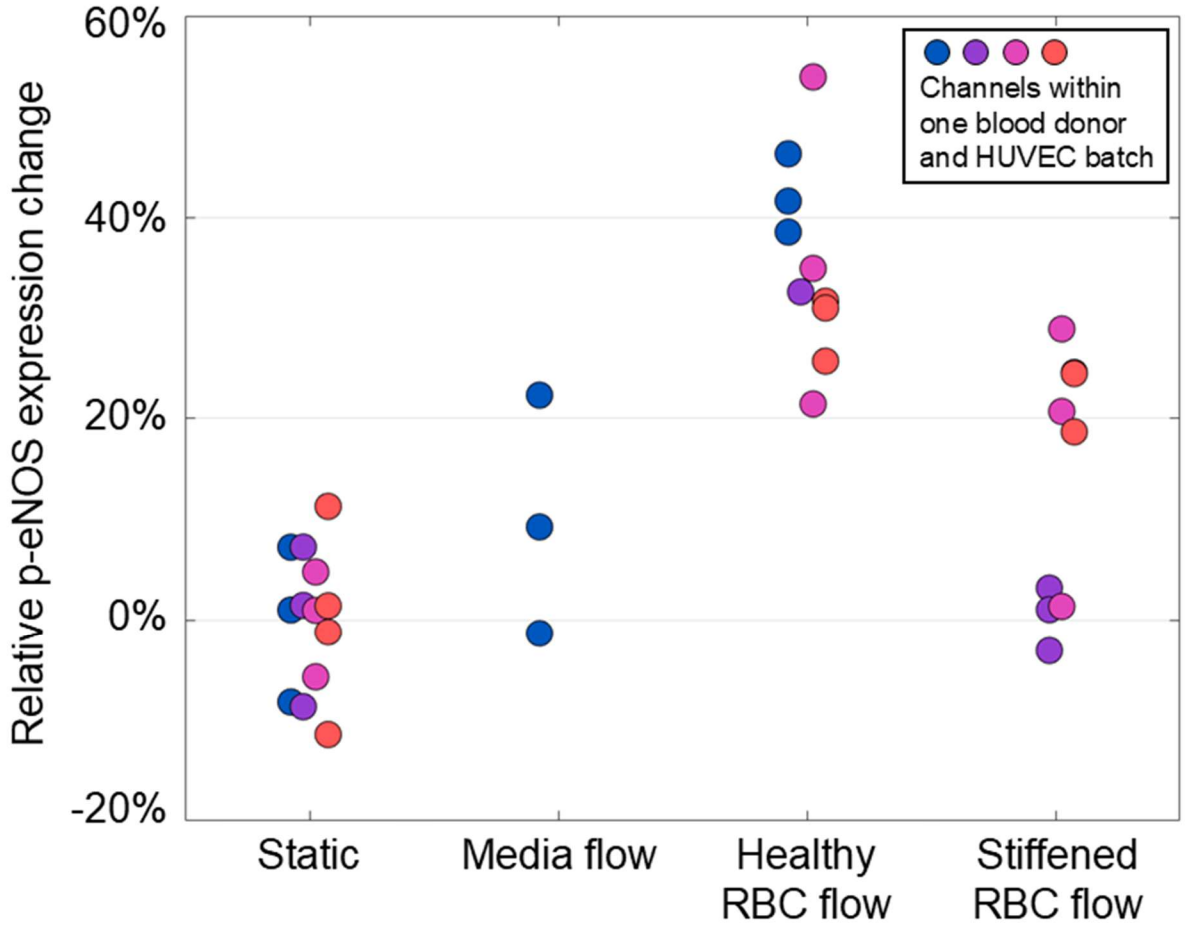
Results

Perfusion with healthy RBCs increased p-eNOS intensity by 23 [17, 29]% compared to media flow (mean [95% CI], p<0.002, one-way ANOVA, Tukey post-hoc). Stiffened RBC flow resulted in a change of 3 [-6,12]% compared to media (p>0.05), which was statistically different from healthy RBCs (p<0.001). As the same average shear stress was applied with all perfusates, we attribute these differences to local, transient, RBC-driven changes in blood flow. Linear mixed-model ANOVA showed no dependence on blood donor or HUVEC batch.

Discussion

RBCs enhance EC mechanical activation via the nitric oxide signalling pathway, but the response is supressed when RBCs are stiffened, despite the same average shear stress. We posit this is due to enhanced migration of stiff RBCs towards the vessel centre [1], reducing discrete EC-RBC interactions. We believe this points to a key role of RBCs in endothelial mechanotransduction, which upon disruption may contribute to microvascular dysfunction, emphasising the need to include RBCs more widely in EC flow studies. Future work will examine long-term and spatial effects of RBC flow in branching microfluidic networks.

Images (Optional)



References (Optional)

[1] Andreas Passos *et al.*, Physics of Fluids, 2019

Session Category

Micro/Biofluidics: Experiments

OA91-02

Composition-Dependent Mechanics and Stability of Collagen Proteins

Dr. Alaa Al-Shaer, Ms. Janine Srocka, Ms. Kassandra Richard, Mr. Daniel Sloseris, Prof. Nancy Forde

Simon Fraser University, Burnaby, BC, Canada

Introduction

As the predominant proteins in our bodies, collagens are the building blocks of connective tissues and the extracellular matrix, where they perform critical structural and mechanical roles. Surprisingly, individual collagen proteins are structurally unstable at body temperature [1]. We apply atomic force microscopy (AFM) imaging to characterize the bending stiffness and structural stability of different types of collagen, thereby learning about the interplay among stability, mechanics and chemical composition in these essential proteins.

Methods

We imaged different types of collagen proteins (collagens I, III and IV) using AFM, and deposited collagen samples at different temperatures to investigate their thermal stability. Collagen I was treated with ribose as a chemical model of aging. We used our SmarTrace software [2] to analyse the conformations of hundreds of collagen proteins, determining contour lengths and bending stiffnesses. For collagen samples with a globular end, we mapped the chain flexibility as a function of position, providing a mapping between protein sequence and bending stiffness [3].

Results

We observed collagens to be unstable at 37°C [4], consistent with previous bulk measurements [1]. Our analysis of large ensembles of denaturing and renaturing collagens allowed us to map the thermally induced unfolding and refolding pathways of collagen IV, and we determined that disulfide bonds are critical for renaturation [4]. We also found that interruptions in the (Gly-X-Y)n sequence within collagen IV enhance flexibility [3], and that aging causes collagen proteins to destabilize and stiffen [5].

Discussion

Our results demonstrate the power of AFM imaging to provide insight into the mechanics and structural stability of collagen proteins. Because these proteins are not amenable to high-resolution structural study with conventional approaches, AFM can fill a valuable niche in mapping sequence and compositional changes, e.g. arising in disease, to their

effects on local mechanics and structural stability. Increasing spatial resolution will further deepen our mechanistic understanding of this key structural building block of our tissues.

References (Optional)

[1] Leikina *et al.*, PNAS 2002

[2] Rezaei *et al.*, Biophys J 2018

[3] Al-Shaer *et al.*, Biophys J 2021

[4] Al-Shaer and Forde, PNAS 2025

[5] Sloseris and Forde, Matrix Biol 2025

Acknowledgements (Optional)

This research was funded by the Natural Sciences and Engineering Research Council of Canada (NSERC)

Session Category

Molecular Biomechanics: N/A

OA91-03

Structural Determinants of Microtubule Mechanics: A Computational Analysis of Protofilament Architectures

Dr. Eric Adriano Zizzi[1], Dr. Maco Cannariato[1], Dr. Marcello Miceli[2,1], prof. Umberto Morbiducci[1,3], prof. Marco Agostino Deriu[1]

[1]PolitoBIOMed Lab, Department of Mechanical and Aerospace Engineering, Politecnico di Torino, Turin, TO, Italy. [2]Dalle Molle Institute for Artificial Intelligence IDSIA. USI/SUPSI, Lugano-Viganello, CH, Switzerland. [3]Department of Life Sciences, Università Degli Studi di Modena e Reggio Emilia, Modena, MO, Italy

Introduction

Microtubules (MTs) are αβ-tubulin polymers that govern key cellular processes and exhibit a considerable architectural heterogeneity, with protofilament (PF) numbers varying depending on assembly conditions, cellular context and tubulin isotypes [1,2]. This heterogeneity has been shown to determine functional consequences. However, how architectural differences determine emergent mechanical properties of the MT has not been fully elucidated. Herein, we conducted an *in-silico* investigation of the structure–mechanics relationships in MTs.

Methods

We constructed human αIb-βIII tubulin patches from the 3J6F PDB template, subsequently fitted to architecture-specific cryo-EM maps [3] to generate 11, 13, 16 PF systems (Figure 1A). We performed 500-ns molecular dynamics (MD) simulations using GROMACS 2021.4 and the AMBER ff99SB-ILDN force field, and evaluated the root mean square deviation (RMSD) and fluctuation (RMSF), inter-tubulin contact probabilities, electrostatics, and performed dynamic network (DN) analysis. Conformations were extracted to reconstruct 400-nm MTs for the elastic network modelling – normal mode analysis (ENM–NMA).

Results

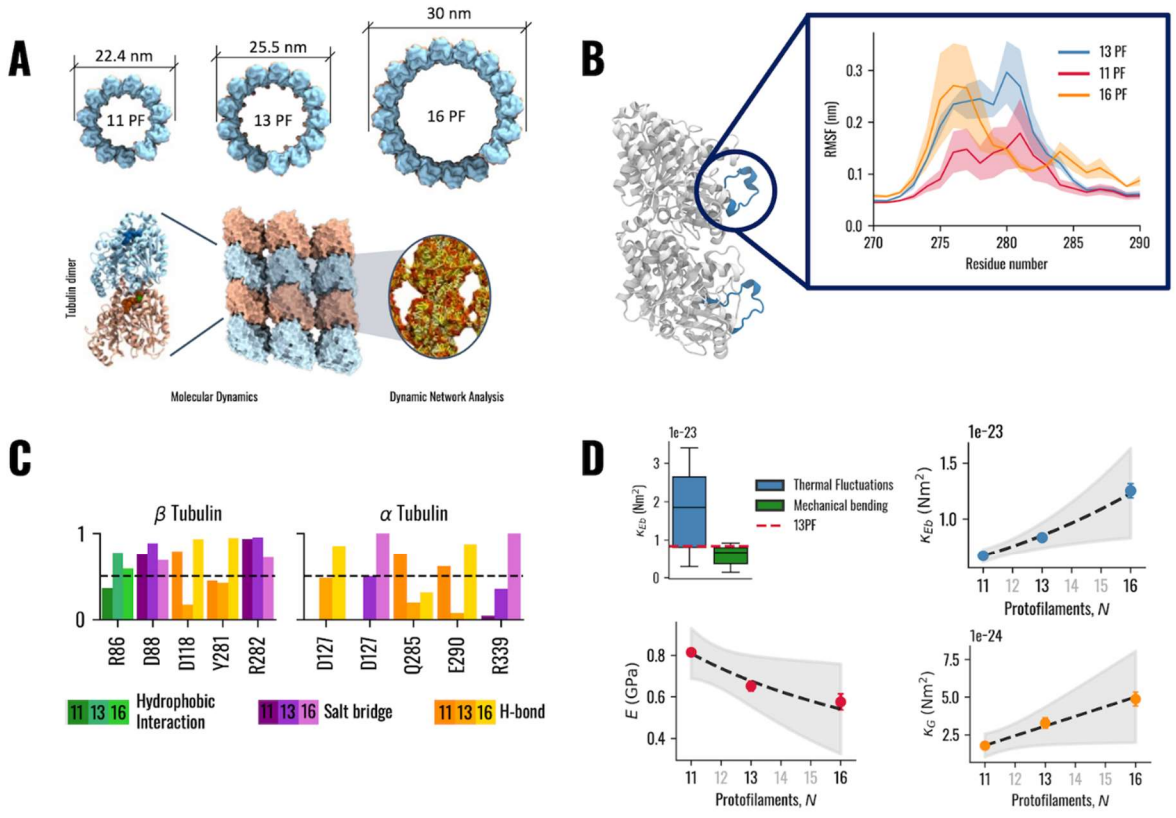
Architecture-dependent differences in βM-loop dynamics emerged from simulations (Figure 1B), with 16PF architecture also exhibiting C-terminal stabilization. The 16PF architecture also featured larger buried interface, the 11PF higher hydrophobic character, and each lattice showed residue-specific interactions (Figure 1C). The DN analysis revealed how mechanical communication path lengths increased with PF number, while the ENM yielded persistence lengths consistent with experimental measurements [4], and demonstrated that bending (k_{Eb}) and torsional (k_G) stiffnesses increased with PF count (Figure 1D). The Young's modulus *E*decreased from ~ 0.8 GPa to about 0.6 GPa with

increasing numbers of PFs (Figure 1D), revealing a competing effect between MT material properties and geometrical characteristics.

Discussion

PF number is a tunable architectural parameter determining MT mechanics: lower PF lattices exhibit more efficient vibrational communication, whereas higher PF architectures provide enhanced stiffness, supporting the view that MT architecture encodes function and revealing the design principles underlying cytoskeleton mechanics. Ongoing work extending this framework to different tubulin isotypes will further elucidate how molecular-level variations modulate emergent MT mechanical behavior.

Images (Optional)



References (Optional)

[1] Ti SC et al., *Dev Cell.* , 2018

[2] Chaaban S et al., *Mol Biol Cell.* , 2017

[3] Sui, H et al., *Structure,* **2010**,

[4] Hawkins, T. L et al. , *Biophys. J.,* **2013**

Acknowledgements (Optional)

We acknowledge ISCRA for awarding this project access to the LEONARDO supercomputer, owned by the EuroHPC Joint Undertaking, hosted by CINECA (Italy). The research leading to these results has received funding from the European Union—NextGenerationEU through the Italian Ministry of University and Research under PNRR—M4C2-I1.3 Project PE_00000019 “HEAL ITALIA” to M.M. and U.M., CUP E93C22001860006. This work was supported by the project FISA-2023-00313 “LangMol” funded by the "Fondo Italiano per le Scienze Applicate (FISA)" programme of the Italian Ministry of University and Research (MUR).

Session Category

Molecular Biomechanics: N/A

OA91-04

High-Resolution Imaging of Untwisted and Melted DNA in a Cell Nucleus

Assoc. Prof. Koichiro Maki PhD[1], Dr Jumpei Fukute PhD[2,3], Mr Shu Kanikawa BS[1], Ms Miwa Rokudo BS[1], Mr Akira Kumano BS[1], Prof Taiji Adachi PhD[1]

[1]Kyoto University, Kyoto, Kyoto, Japan. [2]The University of Tokyo, Bunkyo, Tokyo, Japan. [3]Karolinska Institute, Stockholm, Stockholm, Sweden

Introduction

Cellular mechanotransduction is mediated by various kinds of mechano-sensors. Recently, nuclear chromatin is reported to contribute to mechanotransduction under hydrostatic pressure, by altering the architecture for transcriptional regulation [1]. Although one of the possible mechanisms is deformation of DNA duplex (e.g. untwisting and melting) under mechanical environment, which would be critical in the regulation of chromatin architecture and transcription, there are few available techniques for detecting deformed DNA duplex. In addition, DNA deformation would be highly depending on local mechanical environment in a cell nucleus. Therefore, the development of *in situ* imaging technique is required to explore how DNA is deformed under local mechanical environment in a nucleus.

Methods

In order to fluorescently label untwisted DNA, we utilized a psoralen, which is an intercalator that preferentially binds to untwisted DNA [2]. Cells were gently permeabilized with digitonin and treated with biotinylated psoralen followed by UV irradiation for crosslinking untwisted DNA and psoralen. After fixation by paraformaldehyde and further permeabilization, incorporated biotinylated psoralen was fluorescently detected by NeutrAvidin Protein, DyLight 488. SYBR Green II was utilized to label single-stranded DNA after RNase A treatment.

Results

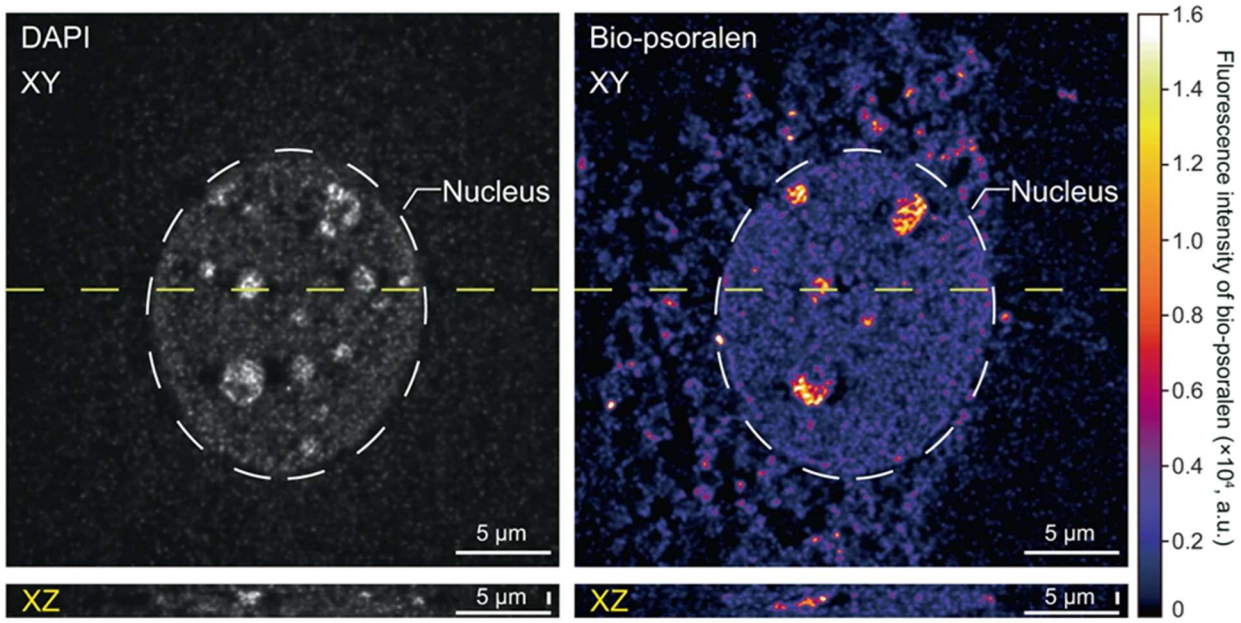
As a result, we observed that untwisted DNA is abundant inside nucleolus (Figure). The abundance of untwisted DNA was reduced by inhibition of RNA polymerase I (RNAPI) as well as by blocking G-quadruplex (G4) structure, implying the importance of RNAPI-based torque-generation coupled with its G4-based constraints of axial rotation by NPM1, which forms phase separated condensates. More interestingly, single-stranded DNA was found to be accumulated surrounding the nucleolar shell [3]. This suggests a positive feedback

mechanism in which untwisted DNA produced in the nucleolar core transits to single-stranded DNA toward the shell, to supply G4 structures for further DNA untwisting.

Discussion

We revealed that DNA deformation (untwisting and melting) occurs under endogenous mechanical environment. In future, we explore how endogenous mechanical forces such as hydrostatic pressure affects the deformation state of DNA for transcriptional regulation.

Images (Optional)



References (Optional)

[1] Koichiro Maki et al., *Journal of Cell Science,* 2021

[2] Jumpei Fukute, Koichiro Maki and Taiji Adachi, *Commun. Biol.* 2024

[3] Koichiro Maki, Jumpei Fukute and Taiji Adachi, *Journal of Cell Science,* 2024

Session Category

Molecular Biomechanics: N/A

OA91-05

Mechanomic Profiling of Cytoskeletal Architecture and Intracellular Forces in Senescent Fibroblasts

Prof. Shinji Deguchi Ph.D., Ms. Yuika Ueda, Ms. Intan Chairun Nisa, Dr. Pirawan Chantachotikul, Dr. Takumi Saito Assistant Professor

The University of Osaka, Toyonaka, Osaka, Japan

Introduction

Cellular senescence involves extensive remodeling of intracellular architecture, but the molecular and physical distinctions between senescent and young cells remain incompletely understood. Our previous work revealed systematic remodeling of stress-fiber-associated proteins and partial rejuvenation by molecular modulation [1,2]. Here, we investigate how cytoskeletal architecture and intracellular mechanics are reorganized in senescent human fibroblasts.

Methods

Primary human fibroblasts were driven into replicative senescence and verified by molecular markers. Intracellular forces were quantified using fluorescence correlation spectroscopy with tandem GFP probes (Figure). Force landscapes were reconstructed using spatial statistical modeling [3,4]. Pharmacological perturbations targeting actin and myosin were applied, and active-force magnitude and spatial heterogeneity were analyzed quantitatively.

Results

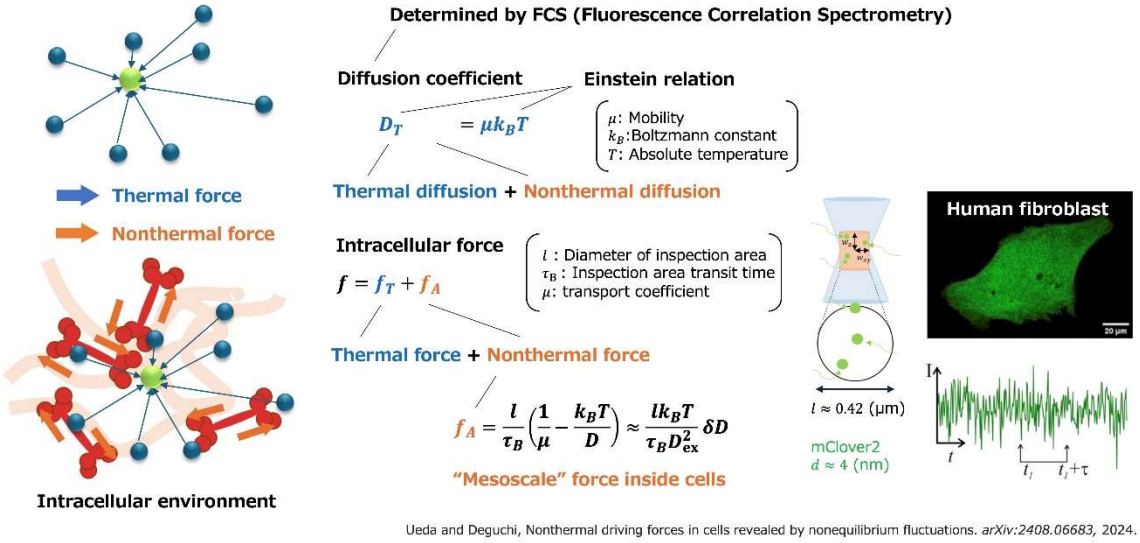
Fibroblasts exhibited nonequilibrium intracellular fluctuations driven by active forces on the order of ~100 pN. Inhibition of actin polymerization or myosin II significantly reduced force levels, while microtubule motor inhibition had minimal effect, indicating actomyosin dominance. Senescent cells generated higher forces than young cells but displayed fewer fluctuation modes, revealing simultaneous amplification and simplification of intracellular dynamics.

Discussion

Our results identify actomyosin activity as the primary intracellular force source and demonstrate that senescence is characterized by reduced dynamic complexity, suggesting that senescent cells rely on restricted mechanical pathways. Together with our previously

developed methods [5-7], this study provides a physical framework for understanding senescence as a mechanical state transition. Thus, our approach establishes a new approach for mechanistic analysis and potential intervention in cellular senescence.

Images (Optional)



Ueda and Deguchi, Nonthermal driving forces in cells revealed by nonequilibrium fluctuations. *arXiv:2408.06683,* 2024.

References (Optional)

1. Pirawan Chantachotikul et al., Cell. Signal., 2025

2. Shiyou Liu et al., Mol. Biol. Cell, 2022

3. Yohei Okabe et al., Biophys. J., 2025

4. Takumi Saito et al., Biophys. J., 2022

5. Shihang Ding et al., eLife, 2024

6. Honghan Li et al., Commun. Biol., 2022

7. Honghan Li et al, PLOS Comput. Biol., 2024

Acknowledgements (Optional)

This study was supported in part by JSPS KAKENHI grants (23H04929 and 24KJ1649) and JST ACT-X (JPMJAX25L2).

Session Category

Molecular Biomechanics: N/A

OA92-01

Using Self-Generated Rhythmic Cues to Enhance Gait in Parkinson: Preliminary Analysis of a 12-Week Intervention

Dr. Sidney T. Baudendistel PhD, MS[1], Dr. Ryan P. Duncan PT, DPT, MSCI[1], Ms. Alison J. Cole MBA, MT-BC[2], Dr. Kerri S. Rawson PhD, MS[1], Dr. Gammon M. Earhart PT, PhD, FAPTA[1]

[1]Washington University in St. Louis School of Medicine, St. Louis, MO, United States. [2]Alison Cole, LLC, St. Louis, MO, United States

Introduction

People living with Parkinson disease (PD) walk with shorter, slower, and more variable steps compared to controls resulting in mobility impairment and reduced quality of life. Rhythmic auditory cueing, such as matching steps to the rhythm of an externally played song, is an accepted method to enhance gait performance. Our previous work showed that, in a single session, mentally singing a song in one's head without playing it externally may produce similar, or even greater, benefits than listening to the song. It is not known whether repeated practice of internal or external cues produce greater gains in walking ability among people with PD. This study aimed to address this gap.

Methods

Participants were included in one of two interventions led by a music therapist and physical therapist. Both interventions included 24 one-hour group classes (twice weekly). Classes focused on standard elements of training in beat perception, production, and synchronization. Individuals focused on either rhythmic movement training using external musical cues (MUSIC) or rhythmic movement training using self-generated, internal singing cues (MENTAL). Participants were asked to practice what they learned on their own for an additional 90 minutes per week. Six sensors (APDM) measured velocity and stride time variability during uncued, preferred walking before and after the intervention while participants were on anti-PD medication. We modeled the data with a RM-ANOVA (2x2, group x time).

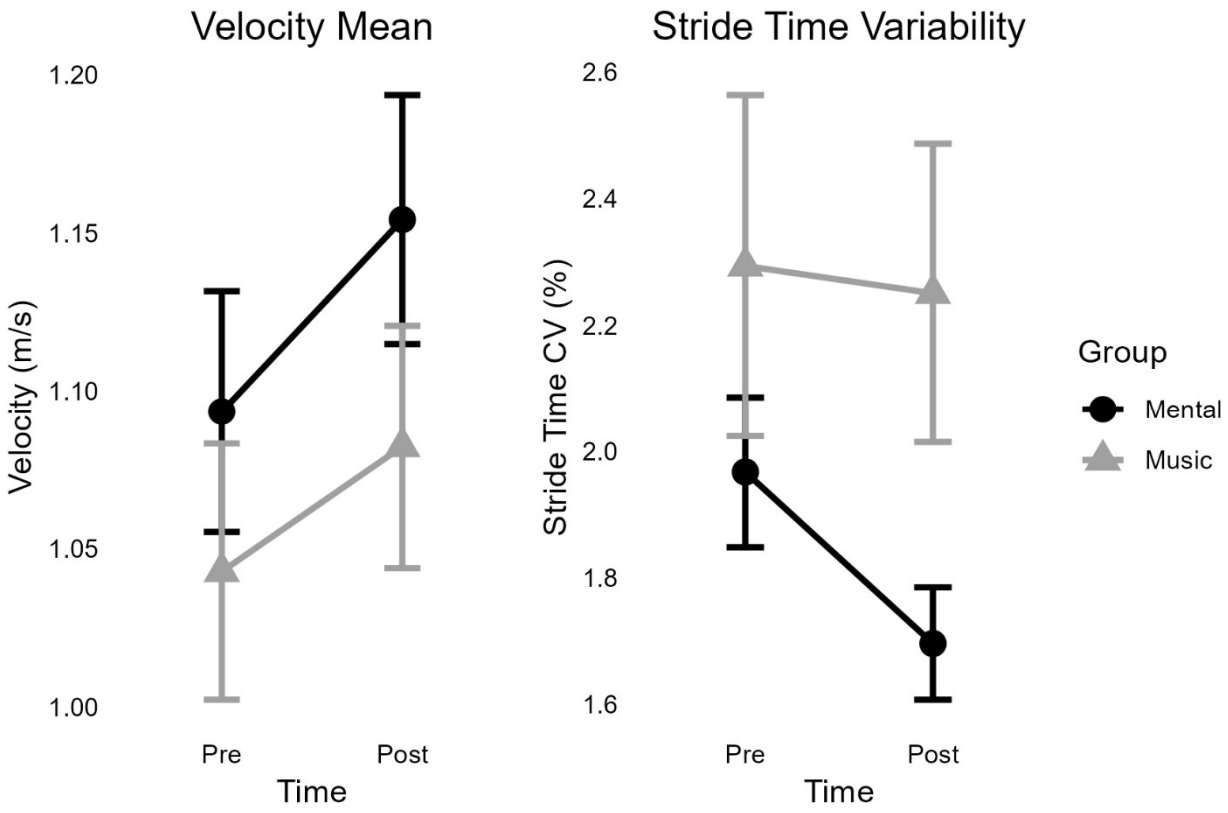
Results

Sixty-one participants with mild-moderate PD completed the intervention (MENTAL=28, MUSIC=33). There were no significant differences in velocity or stride time variability between groups at baseline ($p \geq .301$). For both variables, there was no interaction effect ($p \geq .132$), nor an effect of group ($p \geq .124$). The effect of time was significant for velocity ($F(1,59)=17.840$, $p<.001$) and stride time variability ($F(1,59)=4.426$, $p=.040$), indicating the interventions improved these measures for both groups (Figure 1).

Discussion

This preliminary analysis suggests both internal and external- based rhythmic auditory cueing training provides significant improvement in key measures of gait in PD. As MENTAL cueing does not require a device and can be deployed covertly, this may be an alternative treatment strategy to enhance gait parameters in PD.

Images (Optional)



Session Category

Clinical Biomechanics: N/A

OA92-02

Quantifying Contributions From Individual Wrist Muscles to Hand Tremor in Persons With Essential Tremor

Mr. Nolan Howes BS[1], Prof. Dario Farina PhD[2], Prof. Steven Charles PhD[1]

[1]Brigham Young University, Provo, UT, United States. [2]Imperial College London, London, Greater London, United Kingdom

Introduction

Tremor is the most common movement disorder, and many individuals remain unsatisfied with outcomes from standard treatments, which intervene at the level of the central nervous system. Peripheral suppression methods, including injections of botulinum toxin A, low-level electrical stimulation, or filtering orthoses/exoskeletons, show promise but could be optimized by identifying the muscles most responsible for tremor. This study aimed to quantify the contribution of individual wrist muscles to hand tremor.

Methods

Surface electromyography from the four prime wrist muscles and motion capture of hand translation were recorded in 14 individuals with Essential Tremor. Subjects attempted to maintain a neutral wrist posture while the upper limb was constrained to isolate the wrist joint. Contributions of individual muscles to hand tremor were determined using excluded coherence between muscle activity and hand motion. Excluded coherence is a novel measure capable of estimating input contributions in multi-input systems with correlated inputs [1]. It describes the portion of output power (in this case, tremulous motion of the hand) that would be removed if a given input (tremorogenic muscle activity) were excluded.

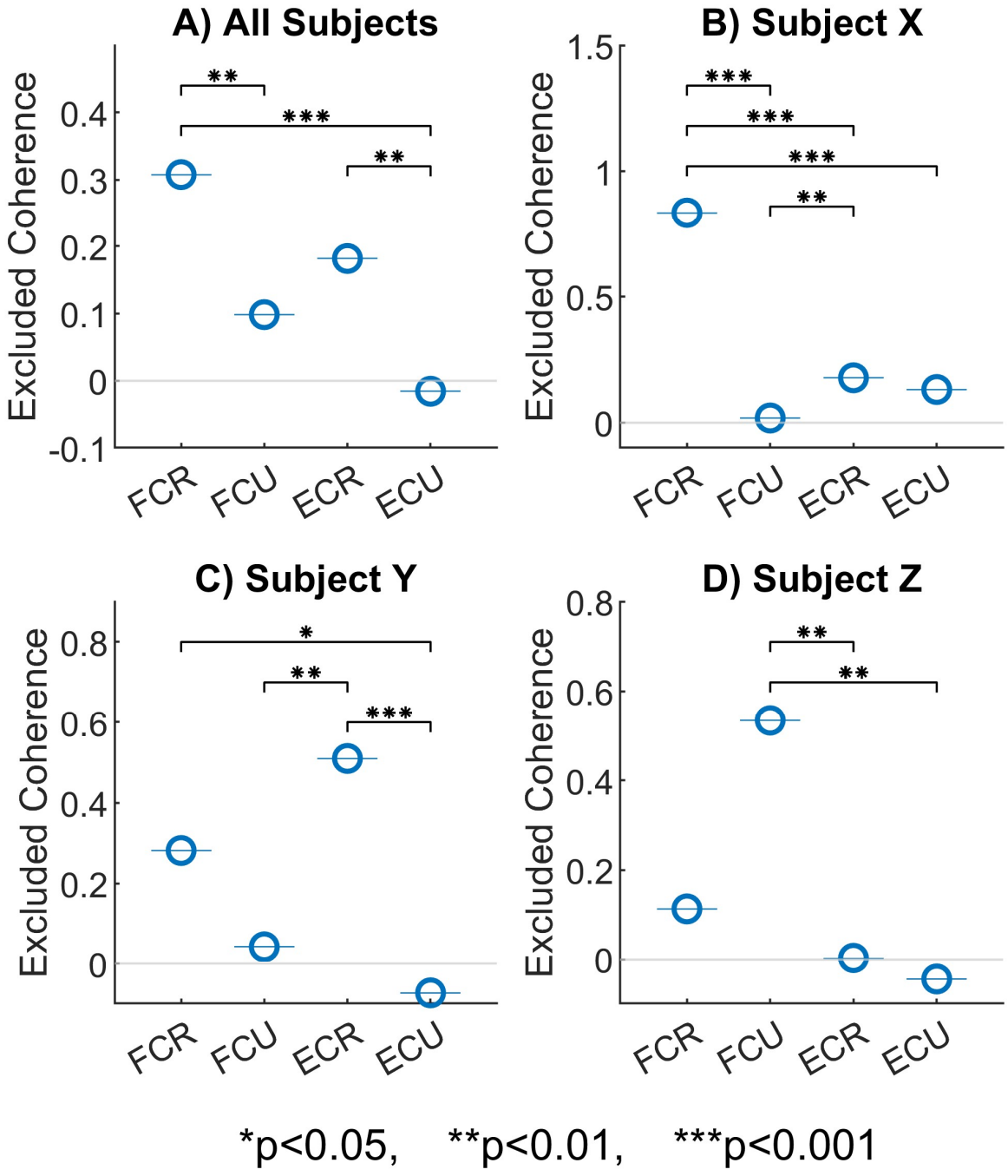
Results

We found many statistically significant differences in tremor contributions between muscles. Averaged across all subjects, the flexor carpi radialis (FCR) contributed the most to tremor, followed by the extensor carpi radialis (ECR) and flexor carpi ulnaris (FCU), with the extensor carpi ulnaris (ECU) consistently contributing very little (Figure 1A). However, the dominant contributing muscles varied between individuals (Figure 1B-D). The majority of tremor power was caused by direct contributions from individual muscles rather than constructive interference between muscles. Also, we found that although suppressing certain muscles could theoretically increase tremor (because they interfere destructively with other muscles), this is unlikely to occur.

Discussion

This is the first quantification of muscle-specific contributions to tremor in multiple subjects. The presence of significant trends across subjects suggests that a general peripheral tremor suppression plan targeting the same muscles for all subjects could be effective, but personalized treatment based on subject-specific contribution patterns would be optimal. Excluded coherence analysis provides an effective tool for calculating these contributions.

Images (Optional)



References (Optional)

1. NH Howes *et al.*, Biomed Signal Process Control, 2025.

Acknowledgements (Optional)

This study was funded by NIH grant R15NS087447.

Session Category

Clinical Biomechanics: N/A

OA92-03

A Single Thigh-worn Accelerometer and Context-Specific Features to Predict Fall Risk in Persons with Multiple Sclerosis

Dr. Guido Mascia[1], Dr. Josh Cherian[1], Mr. Dheeraj Kairamkonda[1], Dr. Brett Meyer[2], Dr. Andrew Solomon[3], Dr. Ryan McGinnis[1]

[1]Center for Remote Health Monitoring, Wake Forest School of Medicine, Winston-Salem, NC, United States. [2]Medidata Solutions, New York, NY, United States. [3]Department of Neurological Sciences, University of Vermont College of Medicine, Burlington, VT, United States

Introduction

People with Multiple Sclerosis (PwMS) experience motor function decay that negatively impact their ability to generate lower-limb strength, increasing the probability of falling [1]. Recent advancements in wearable technology may allow for a more granular assessment of fall risk than infrequent clinical visits. The 30-second chair test (30CST) used to quantify functional capacity and lower limb strength is perfectly suited this hybrid approach. The aim of the study is to predict fall risk in PwMS performing multiple 30CST by leveraging signals extracted from a single accelerometer.

Methods

Sixty recording sessions from 36 PwMS were analyzed. For each, participants reported whether they fell at least once in the past 6 months (32/60 fallers). Participants completed the Activity-specific Balance Confidence Scale (ABC), the Modified Fatigue Index Scale (MFIS) and the Multiple Sclerosis Walking Scale (MSWS). Participants went home wearing an accelerometer on their right thigh, where they performed a series of unsupervised 30CSTs. Sit-to-stands were automatically segmented and leveraged for extracting signals used as inputs for convolutional neural networks, long-short-term memory networks, and gated-recurrent neural networks, along with the corresponding ABC, MFIS, and MSWS scores, leading to a total of 13 features. An attention layer was added to track feature importance. Models were evaluated using Leave-One-Subject-Out Cross-Validation.

Results

A total of 8870 transitions (4502/8870 fallers) were used for training, validating, and testing 45 models. Mean feature attention from the 5 best performing models (AUC = 0.80—0.83) was computed, and features for each model were sorted based on their average rank. The analysis revealed Rotational Power [2] as the most important one, whereas negligible contribution was exerted by the clinical scores (Fig. 1).

Discussion

The current study demonstrated the possibility to predict fall risk in PwMS leveraging a single, thigh-worn accelerometer outside of the clinic. This is encouraging, given the recent trends in remote monitoring and large clinical studies employing similar experimental setups. Future studies may benefit from the inclusion of a chest sensor, accounting for trunk-flexion strategies, naturally implemented by PwMS.

Images (Optional)

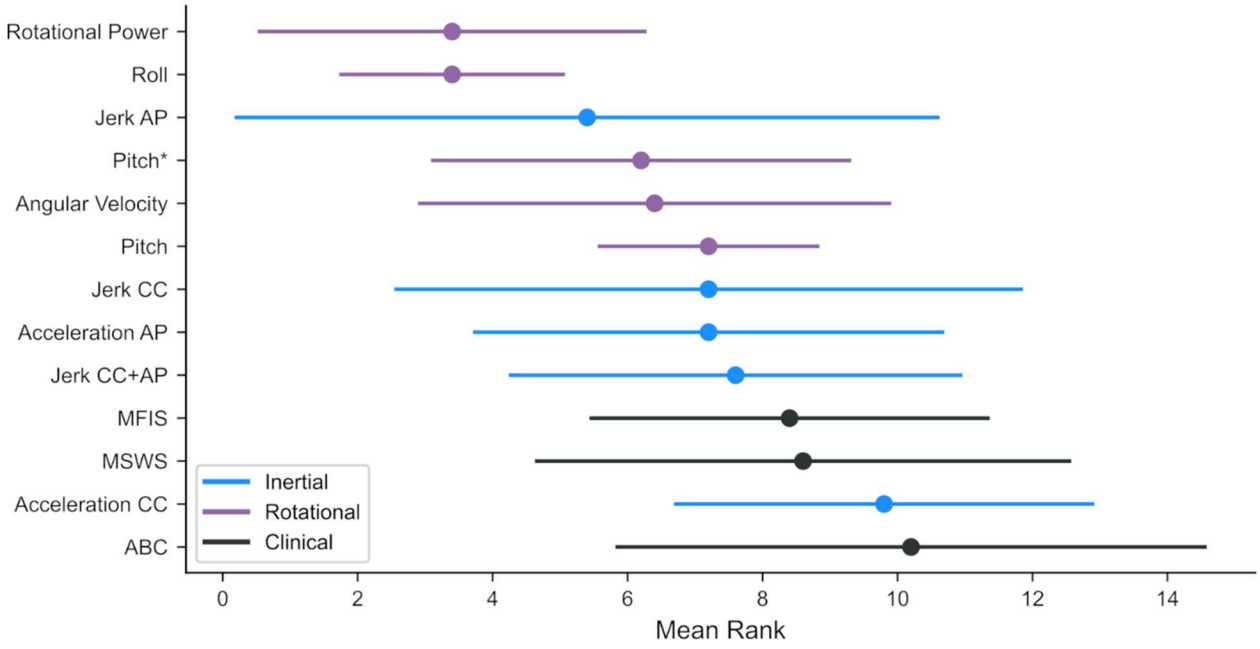


Fig. 1: Mean consensus feature attention ranking for the 5 best performing deep learning models in terms of AUC. The marker indicates the mean ranking, while the continuous line represents the standard deviation. AP = Anterior-Posterior; CC = Cranial-Caudal; MFIS = Modified-Fatigue Index Scale; MSWS = Multiple Sclerosis Walking Scale; ABC = Activity-Specific Balance Confidence Scale.

References (Optional)

[1] Michelle H. Cameron *et. al.*, Handb Clin Neurol, 2018

[2] Guido Mascia *et. al.*, IEEE TNSRE, 2025

Session Category

Clinical Biomechanics: N/A

OA92-04

Biomechanical and Sensory-Cortical Interactions During Postural Control in Parkinson's Disease

Dr. Ashwini Sansare[1], Mr. Hossein Soroushi[1], Ms. Taylor Gauss[2], Dr. Jan Hondzinski[2], Dr. Deanna Kennedy[1], Dr. Yuming Lei[1]

[1]Texas A&M University, College Station, TX, United States. [2]Louisiana State University, Baton Rouge, LA, United States

Introduction

Postural stability requires coordinated integration of sensory input with biomechanical control strategies. Individuals with Parkinson's Disease (PD) often exhibit peripheral sensory deficits and atypical cortical processing of somatosensory information, yet how these neural alterations influence standing balance remains unclear. During functional tasks, afferent nerve stimulation typically produces sensory gating, i.e. reduction of somatosensory-evoked potential (SEP) amplitude, to suppress irrelevant input and optimize neural resources for movement control. Altered SEP responses have been linked to poor upper limb function in PD, but their implications for balance are unknown. We investigated how PD affects the interplay between sensory-cortical activity and postural sway across increasingly challenging conditions. We hypothesized reduced sensory gating in PD, particularly as task difficulty increased.

Methods

Forty-eight adults participated: 16 high-functioning individuals with PD, 16 neurologically healthy older adults (OA), and 16 neurologically healthy young adults (YA). Participants completed three 60-second standing trials under four randomly ordered conditions: eyes open (EO), eyes closed (EC), eyes open on foam (EOF), and eyes closed on foam (ECF). We quantified center-of-pressure (COP) on an AMTI force plate. The primary biomechanical outcome was COP 95% confidence ellipse area; secondary metrics included mean COP velocity, RMS COP displacement, and frequency dispersion. SEPs (P38 component) were recorded via EEG during tibial nerve stimulation. Mixed-Model repeated-measures ANOVAs revealed effects of group as the between-subject factor and the condition (EO, EC, EOF, ECF) as the within-subject factor.

Results

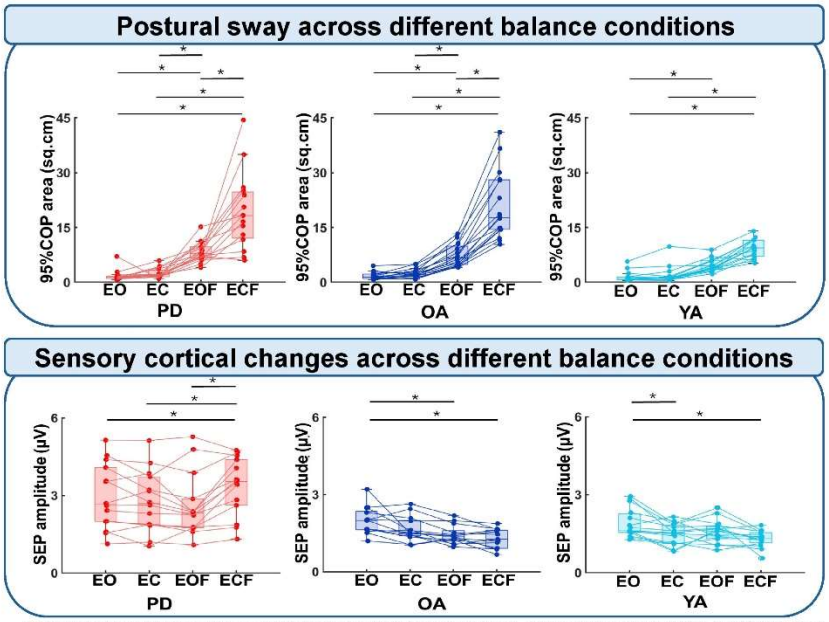
PD and OA exhibited greater 95% COP ellipse area, COP velocity, RMS displacement, and frequency dispersion than YA, consistent with age-related changes in balance. No significant differences between PD and OA suggests similar sway characteristics in aging

and PD. In contrast, cortical responses diverged. YA and OA showed the expected decline in SEP amplitude as task difficulty increased, reflecting intact sensory gating. PD showed minimal SEP modulation across conditions, indicating reduced adaptability of sensory-cortical processing.

Discussion

Despite exhibiting sway characteristics comparable to age-matched controls, individuals with PD demonstrated markedly impaired sensory gating. These findings suggest that sensory-cortical dysfunction may precede observable declines in balance and highlight a dissociation between neural and mechanical aspects of balance control.

Images (Optional)



Box and whisker plots, with scattered dots indicating each subject, showing the trend in the 95%COP area (top panel) and SEP amplitude (bottom) as the balance conditions become increasingly challenging from eyes open (EO), eyes closed (EC), eyes open on foam (EOF) to eyes closed on foam (ECF) for the three group, PD (red), OA (dark blue) and YA (light blue).

References (Optional)

Acknowledgements (Optional)

Funding: Parkinson's Foundation grant (PF-VSA-1300-235) to AS.

Session Category

Clinical Biomechanics: N/A

OA93-01

Real-Time Amplitude-Based Haptic Feedback Enhances Arm Swing and Spatiotemporal Gait Parameters in Older Adults

Ms. Ines Khiyara M.S., Dr. Babak Hejrati PhD

University of Maine, Orono, Maine, United States

Introduction

Arm swing supports gait stability, yet older adults show reduced motion linked to slower gait, shorter strides, and increased fall risk. While voluntary modulation and timing-based cueing can alter gait, amplitude-based feedback remains underexplored. Therefore, the study evaluated how real-time haptic feedback influences arm range of motion (ROM), arm-swing symmetry, gait speed, and stride length (SL) in older adults.

Methods

Eleven older adults (72.8±4.2 years) completed nine 200-m trials: Baseline (B), Exaggerated (E), Fast (F) and six error-feedback (FB) conditions in a 3×2 design (vibration location: flexion/extension/combined × intensity: 100%/200% of baseline amplitude). Participants were ≥65 years, walked independently, and reported no neurological or gait-affecting musculoskeletal disorders. Arm/foot kinematics were captured with Movella DOT IMUs, and a custom Android app delivered cues when amplitude fell below targets. Outcomes included gait speed, SL, and arm ROM/symmetry (Right/Left ratio). Repeated-measures one-way ANOVA compared Baseline, Exaggerated, Fast, and Feedback; symmetry was tested using one-sample t-tests; and a two-way ANOVA assessed Location×Intensity effects.

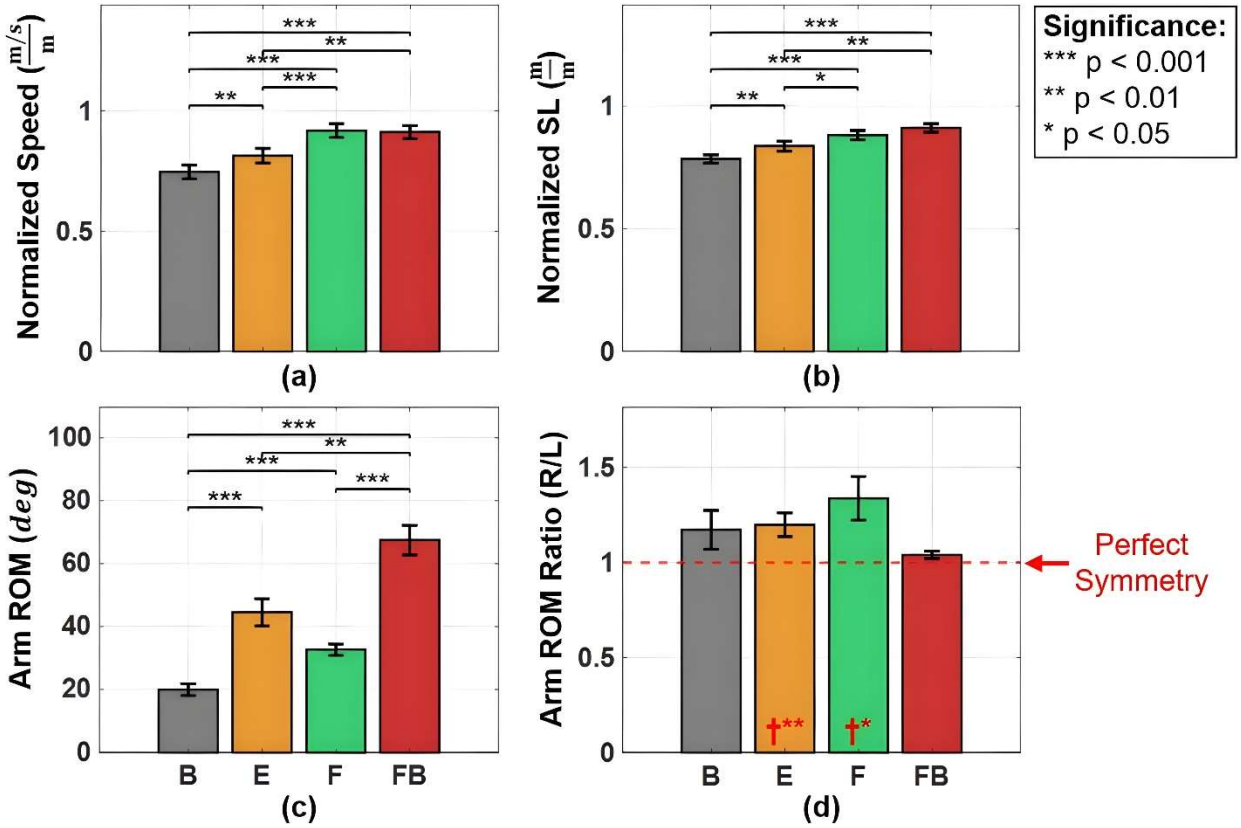
Results

Significant condition effects were found (Figure 1) for speed ($F(3,30)=35.20$, $p<0.001$, $\eta^2=0.78$), SL ($F(3,30)=35.29$, $p<0.001$, $\eta^2=0.78$), and arm ROM ($F(3,30)=55.32$, $p<0.001$, $\eta^2=0.85$). Feedback significantly increased ROM beyond Baseline ($p<0.001$), Exaggerated ($p=0.006$), and Fast ($p<0.001$). Symmetry improved under Feedback (ratio=1.041, $p=0.061$), whereas Exaggerated ($p=0.009$) and Fast ($p=0.015$) deviated significantly from 1.0. Feedback speed and SL matched Fast but exceeded Baseline ($p<0.001$) and Exaggerated ($p=0.005$). In the 3×2 ANOVA analysis, 200% intensity increased ROM, combined-location showed the highest ROM, and no Location×Intensity interaction was found ($p=0.19$).

Discussion

Amplitude-based haptic feedback substantially enhanced arm swing—238% over Baseline, 52% over Exaggerated, and 107% over Fast—while restoring symmetry. Compared to our prior timing-based cueing (18% speed, 30% ROM increases), amplitude-based feedback produced larger improvements in both speed (22% over Baseline) and ROM. The stronger 200% intensity and absence of interaction suggest independently optimizable feedback parameters. These results support wearable IMU-driven feedback as a promising rehabilitation tool, where quantitative amplitude cues outperform instructional strategies for improving gait biomechanics in older adults.

Images (Optional)



References (Optional)

Session Category

Human Motion and Performance: Locomotion/Gait

OA93-02

Rhythmic Cues with Different Modalities and Structures Distinctly Affect Spatial and Temporal Structure of Gait Kinematics

Mr Seung Kyeom Kim[1], Mr Vasileios Mylonas[1], Ms Marilena Kalaitzi Manifrenti[1], Dr Nick Stergiou[1,2], Dr Aaron Likens[1]

[1]University of Nebraska at Omaha, Omaha, NE, United States. [2]Aristotle University of Thessaloniki, Thessaloniki, Thessaloniki, Greece

Introduction

Humans readily synchronize movements to rhythmic cues (RC) across modalities (e.g., vision, auditory). RCs also modify gait variability (GV; subtle timing and spacing changes across gait cycles) by entraining to external rhythms. Healthy GV is fractal, meaning spatiotemporal features are related over time, but becomes random with age and disease. RCs are a promising tool for restoring GV; however, most studies deliver constant auditory inter-beat intervals that may differ from natural GV. Previous work focused on basic gait measures like stride intervals or length, leaving joint or segment angles–the variables of interest–less explored. Modality and rhythm structure (e.g., fractal(FRAC), random(RAND)) influence GV, but their impact on gait kinematics (GK) is unclear. This study investigated the effect of modality and rhythm structure on gait kinematics.

Methods

Eighteen participants were assigned to one of three groups (non-musical-auditory, AUD(Age=26.286±4.096); Female=3); visual, VIS(Age=27.667±3.249); Female =1); music, MUS(Age=25.429±2.718); Female =3) and walked for 12-min, self-paced, then two 12-min walks synchronized to each of two rhythmic structures (FRAC, RAND). Spatial characteristics of thigh GK were quantified using box counting dimension (BCD); higher values reflect less constrained movement in space. Temporal characteristics of thigh GK were quantified using sample entropy (SampEn); higher values reflect less predictable movement over time. Metrics were computed on sagittal plane. Multilevel models were analyzed to examine the modality×rhythm structure interaction on BCD and SampEn.

Results

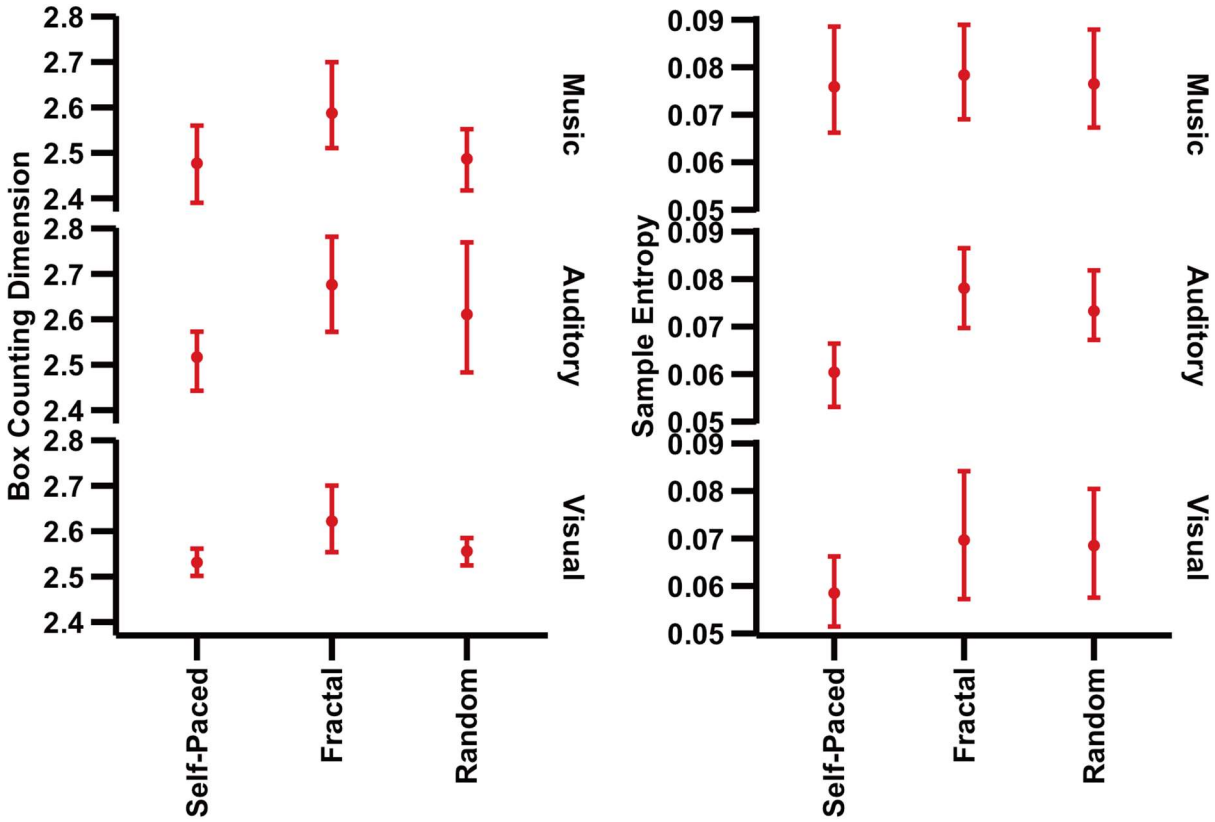
Models revealed a modality×rhythm structure interaction for both metrics. Rhythm structure induced large effects within each modality (Figure 1). In AUD, FRAC increased BCD (D=1.2845) and SampEn (D=1.2231), indicating less constrained and more irregular

coordination. In VIS, FRAC increased only SampEn (D=0.7759). In MUS, FRAC increased only BCD (D=0.8854).

Discussion

These findings demonstrate RCs affect the spatial and temporal characteristics of GK in a modality-specific manner. FRAC consistently affected both characteristics of GK in AUD, whereas only temporal and spatial characteristics were affected in VIS and MUS, respectively. This implies a distinct entrainment mechanism across cue modalities and rhythm structures. Therefore, modality and rhythm structure should be chosen based on the purpose of RC-based rehabilitation.

Images (Optional)



Acknowledgements (Optional)

National Institutes of Health [grant number: P20GM109090]

National Institutes of Health [grant number: 1P20GM152301-01]

National Institues of Health [grant number: P20GM152301]

National Institutes of Health [grant number: P30GM159554]

Session Category

Human Motion and Performance: Locomotion/Gait

OA93-03

A Variability-Embedded Music System (VEMS) Modulates Gait Variability as Effectively as Auditory or Visual Cueing

Mr Vasileios Mylonas MSc[1], Ms Marilena Kalaitzi Manifrenti MSc[1], Dr Nick Stergiou PhD[1,2], Dr Aaron Likens PhD[1]

[1]Department of Biomechanics and Center for Research in Human Movement Variability, University of Nebraska at Omaha, Omaha, Nebraska, United States. [2]Department of Physical Education and Sport Science, Aristotle University of Thessaloniki, Thessaloniki, Thessaloniki, Greece

Introduction

Human gait of healthy individuals varies from one step to the next. These variations over many gait cycles create a structured (fractal-based) pattern where gait patterns are related over time. With pathology, this structure degrades, making gait overly periodic or overly random. This degradation reflects reduced adaptability of the locomotor system and has been associated with gait instability and increased fall risk. Restoring the gait variability structure requires external variable cueing. We developed Variability Embedded Music System (VEMS), a novel auditory cueing approach that embeds fractal patterns into the inter-beat intervals of commercial music, providing an alternative to traditional cueing methods. Here, we compare VEMS to auditory and visual cueing on the temporal structure of gait variability.

Methods

18 healthy adults (6 per group) were assigned to one of three cueing conditions (non-musical auditory (NMA): 3F, 27.6±3.25 years, visual (VIS): 1F, 26.3±4.1 years, VEMS: 3F, 25.3±2.72 years) and completed a 12-min baseline walk, followed by two randomly ordered 12-min cued (fractal and random). Cues were delivered via headphones or a lightweight head-mounted display. The standard deviation of the step-to-beat relative phase was computed. Detrended Fluctuation Analysis (α-exponent) was used to assess the temporal structure of gait variability in the form of the α-exponent. Cueing preference was also obtained. Statistical analysis involved a 3×3 multilevel model. Type-1 error= 0.05.

Results

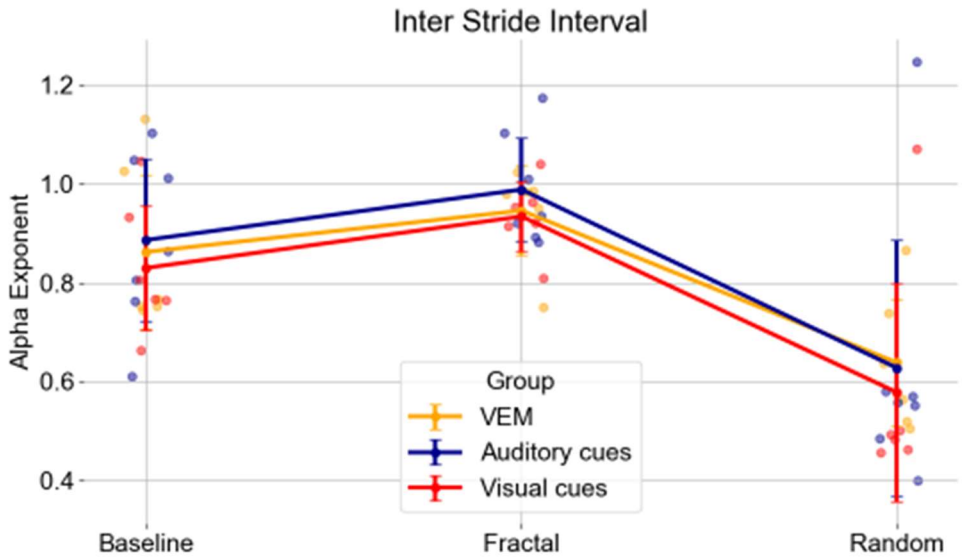
A significant main effect of cue type was found ($F_{(2,36)}$=24.86, p<0.001, η^2_p=0.58; Figure 1). Random trials were associated with significantly lower α-exponents than both baseline (p<0.001, d=1.57) and fractal (p<0.001, d=2.22) trials. Step-to-beat synchronization was

similar across groups and cue types. Preference differed across groups ($F_{(2,16)}$=4.24, p=0.033, η^2_p=0.27); VEMS was preferred over NMA (p=0.032, d=0.35).

Discussion

Our results indicate that VEMS is as effective as VIS and NMA in modulating gait variability, with similar synchronization accuracy across modalities. Fractal cues preserved the temporal structure of healthy gait, whereas random cues significantly reduced the α-exponent, showing that all three modalities can alter gait dynamics. VEMS, therefore, offers an effective and more enjoyable alternative for restoring heathy, fractal patterns in gait variability.

Images (Optional)



Acknowledgements (Optional)

NIH: P30GM159554, P20GM152301

Session Category

Human Motion and Performance: Locomotion/Gait

OA93-04

Effects of Delay and Amplification of Auditory Feedback for Gait: Variability and Cadence Adaptation

MS. Jingxian Gu, Dr. Dobromir Dotov

University of Nebraska Omaha, Omaha, NE, United States

MS. Jingxian Gu

Introduction

Rhythmic auditory cueing of gait with exogenous stimuli is a widely studied technique for improving symptoms of gait disorders. Less is known about the effects of self-cueing, such as endogenously generated sounds of one's own footsteps. We adopted the delayed auditory feedback (DAF) paradigm which is known to improve symptoms of speech disorders in various populations such as Parkinson's disease but has not been studied in gait.

Methods

Young healthy adults (N=30, 19 to 35 years old) participated. They were instructed to walk overground at a comfortable self-selected pace on a circular track. Feedback consisted of the lateralized continuous sound of their footsteps, captured with shoe-worn microphones and relayed to closed-cup headphones (15 ms delay) via a belt-worn mini-computer. The feedback manipulations consisted of delay (zero, eighth, and quarter step), amplification (half or full self-selected amplitude), and masking pink noise (half or full self-selected amplitude). Baseline cadence was recorded in a pre-test trial without auditory manipulation. Participants wore an IMU system to record gait parameters. Additionally, we used mobile brain imaging (fNIRS) to measure the activation in prefrontal cortical areas involved in purposeful attention, reported separately.

Results

Statistical analysis with linear mixed-effects models revealed that gait variability and cadence were influenced by delay and amplification. We found that amplification without delay had the effect of reducing variability ($p<.05$), see Figure 1. Interestingly, delay had the effect of increasing cadence ($p<.05$) which is opposite to the prediction derived from DAF for speech.

Discussion

These findings confirm the hypothesis that auditory information from self-produced action is used for sensorimotor integration and gait regulation. The increase of cadence with delay contradicts traditional internal model theories of motor control but can be explained either by a Bayesian account of sensory uncertainty or by a dynamic model for anticipatory synchronization with delayed feedback that we adopted. The combination of delay and amplification, particularly the reduction in variability with amplified feedback, suggests that this simple technique may be used for daily in-community rehabilitation and re-training of gait.

Images (Optional)

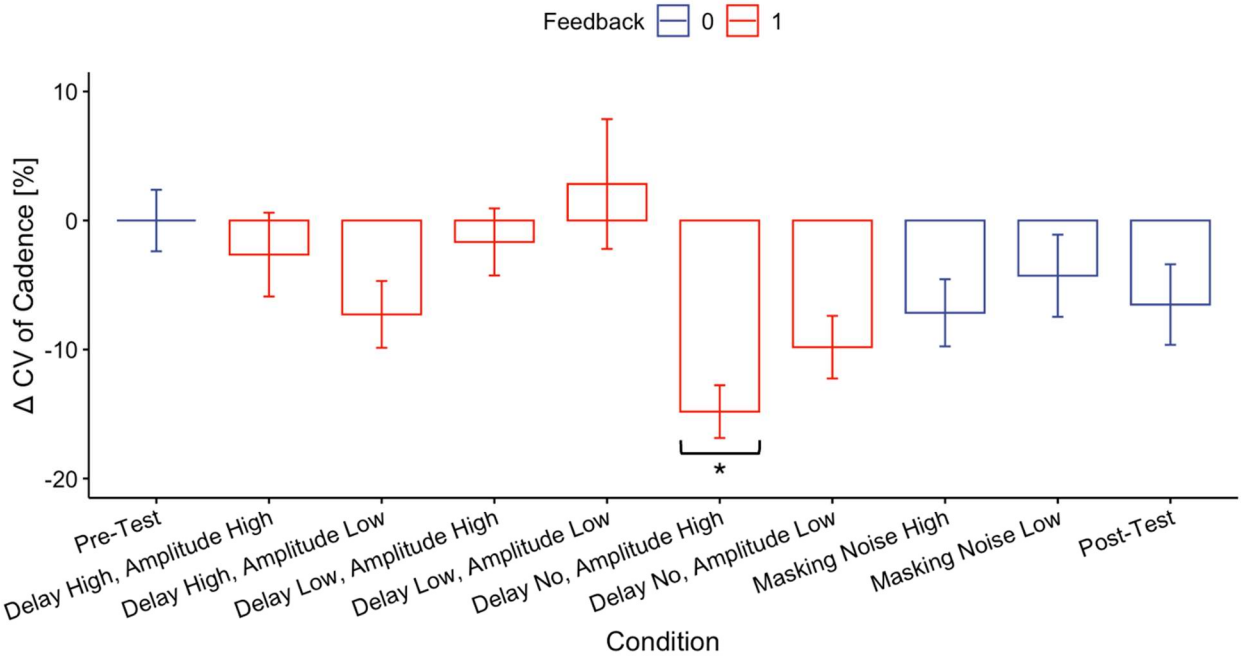


Figure 1. Change in gait variability relative to pretest (Mean±95% CI).

Acknowledgements (Optional)

J.G. was supported by NIHP20GM109090 and NIH5P20GM152301-02.

Session Category

Human Motion and Performance: Locomotion/Gait

OA93-05

Does Nordic Walking Affect Ground Reaction Forces, Joint Angles, and Joint Moments?

Ms. Hyemin Han[1], Mr. Taewoong Kong[1], Mr. Dongho Ha[1], Dr. Hoon Kim[1,2]

[1]Department of Software Convergence, Soonchunhyang University, Asan-si, Chungcheongnamdo, Korea, Republic of. [2]Department of Sports Medicine, Soonchunhyang University, Asan-si, Chungcheongnamdo, Korea, Republic of

Introduction

Nordic walking, that uses poles, is considered to reduce push-off ground reaction forces (GRF) and lower-limb loading compared with normal walking, which may be beneficial for older adults. However, differences in study methods (e.g., Nordic walking techniques) and limitations in previous studies have left other biomechanical characteristics unclear and led to inconsistent findings for GRF and joint biomechanics. Notably, research on the "defensive" Nordic walking style, with poles placed nearly perpendicular to the ground, remains limited despite its frequent use in rehabilitation. Therefore, the purpose of this study was to comprehensively examine GRF and lower-limb biomechanics of defensive-technique Nordic walking.

Methods

Twelve healthy adults performed normal and Nordic walking. GRF and 3-dimensional motion data were recorded using three force plates (lead-foot (right), trail-foot (left), and left-pole) and nine motion-capture cameras (Fig.A and B), respectively. Joint angles and moments were calculated through inverse kinematics and dynamics tools in OpenSim, respectively. GRF and joint moment were normalized by body weight. Statistical parametric mapping paired t-tests were compared for GRF, joint angles, and moments between normal and Nordic walking.

Results

Nordic walking exhibited smaller vertical (13–38% of stance) and braking (13–23%) GRF of lead-foot (p<0.001) (Fig.C and D). Nordic walking also showed a more flexed hip joint angle (2–57%, p<0.001) than normal walking, whereas knee and ankle angles showed no significant differences (Fig.E). In addition, Nordic walking showed a smaller knee extension moment (14–22%, p=0.009) than normal walking. Although hip extension moment was smaller in Nordic walking (1–7%, p=0.010) (Fig.F), this difference occurred before the pole-loading phase.

Discussion

Defensive-technique Nordic walking selectively reduced knee moments without altering ankle or hip moments during the pole-loading phase. This occurred together with smaller vertical and braking GRF at the lead foot and a more flexed hip posture throughout stance. Thus, the pattern reflects targeted unloading at the knee rather than a global reduction in lower-limb mechanical demand, as propulsion-related mechanics were largely preserved. Such selective unloading may be clinically meaningful for older adults or individuals with knee pain and supports defensive Nordic walking as a knee-targeted gait modification.

Images (Optional)

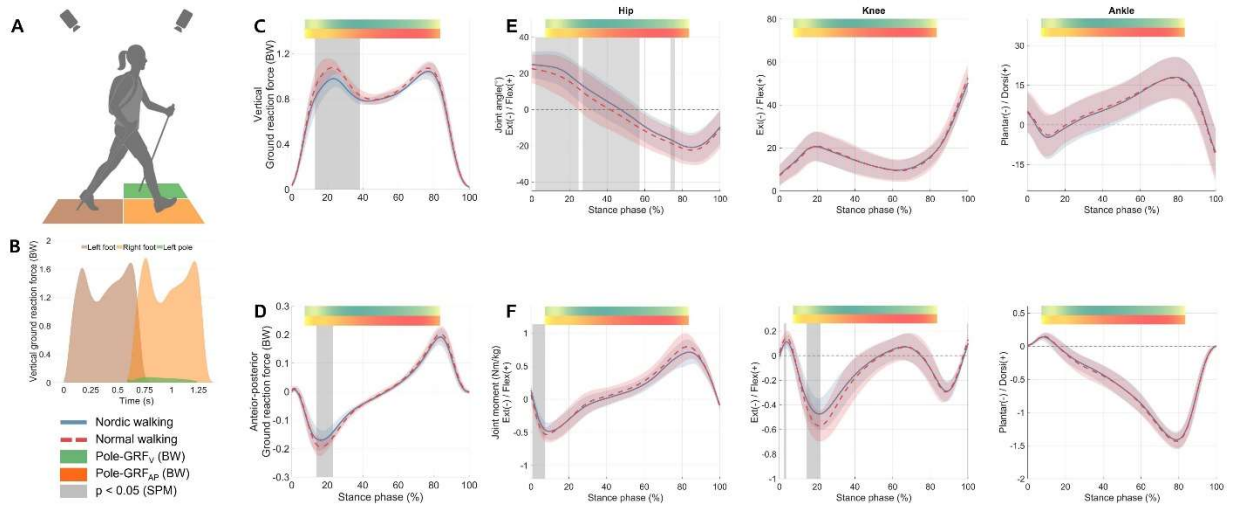


Figure 1. Experimental protocol and biomechanical outcomes comparing normal and Nordic walking. A. Experimental protocol using force plates and motion capture. B. Vertical ground reaction forces (GRF) during Nordic walking. C–D. Vertical and anteroposterior GRF during the stance phase for normal (red) and Nordic walking (blue). Shaded regions show the phase where significant differences exist based on statistical parametric mapping. The green–yellow and orange–yellow color-coded bar represents the pole's vertical and anteroposterior GRF, respectively. E–F. Hip, knee, and ankle joint angles and moments.

References (Optional)

Acknowledgements (Optional)

We thank Jaehun Lee for providing the shoes and poles used in this study and for offering valuable input. This work was supported by the Soonchunhyang University Research Fund and BK21 FOUR (Fostering Outstanding Universities for Research) (No. 5199990914048).

Session Category

Human Motion and Performance: Locomotion/Gait

OA93-06

Effects of Body Weight Support on Temporal Features of Walking and Crawling Gait in Near-Walking Infants

Mr. Tristan McCarty[1], Ms. Melanie Barahona[1], Dr. Cole Galloway[2], Dr. Elena Kokkoni[1]

[1]University of California, Riverside, CA, United States. [2]Baylor University, Waco, TX, United States

Introduction

The development of independent locomotion in infancy, like crawling and walking, is critical for overall development [1]. Temporal gait abnormalities, such as those often seen in infants diagnosed with Down Syndrome (DS), can affect gait stability, resulting in delays to the onset of independent locomotion [2]. While exposure to dynamic body-weight support (BWS) has been shown to immediately alter the temporal features of walking gait in adults, its influence on infant gait parameters is less understood. Here, we report how immediate exposure to BWS alters temporal walking and crawling gait in near-walking infants.

Methods

Eleven typically developing (TD) infants (M=9.9±1.2 months) and five infants diagnosed with DS (M=17±3 months) participated in two experimental sessions. In each session, infants performed crawling and walking trials before BWS exposure (Pre), with BWS (IN), and after BWS exposure (Post). Multi-view video recordings were collected for digitization of limb contact and lift-off events in each gait segment. For each segment, temporal variables of interest (cycle duration, duty factor, cadence, and continuous relative phase) were calculated and assessed using non-parametric Friedman tests to examine differences between the three conditions.

Results

In a preliminary analysis of a subset of participants, we saw significant decreases in crawling gait cadence ($p=.041$) and more synchronized crawling gait as measured by the continuous relative phase ($p=.015$) when TD infants were exposed to BWS (Pre vs. IN). While not significant, a trend was observed of more asynchronous continuous relative phase for walking gait in infants with DS ($p=.097$, Pre vs. IN). However, none of these changes were retained once the infants were removed from BWS (Pre vs. Post).

Discussion

This work demonstrates infants' ability to immediately alter their temporal gait features during both crawling and walking in response to BWS exposure. While these changes were significant during immediate exposure, they were not retained after removal from BWS, suggesting that longitudinal exposure may be needed for long-term retention of these effects.

References (Optional)

[1] Adolph & Franchak, *Wiley Interdiscip Rev Cogn Sci*., 2016.

[2] Ulrich et al., *Pediatrics*, 2001.

Session Category

Human Motion and Performance: Locomotion/Gait

OA94-02

Machine Learning Estimation of Peak Elbow Varus Torque in Baseball Pitching Using a Sensor-Embedded Ball

Mr. Atsuki Kageyama[1], Mr. Takeru Ojima[2], Mr. Haruki Takaoka[1], Dr. Takahiko Sato[3,4], Dr. Gen Horiuchi[2], Dr. Shohei Shibata[5], Mr. Yuki Yamada[5], Dr. Akinori Nagano[2]

[1]Ritsumeikan University, Graduate School of Sport and Health Science, Kusatsu, Shiga, Japan. [2]Ritsumeikan University, Faculty of Sport and Health Science, Kusatsu, Shiga, Japan. [3]Biwako Professional University of Rehabilitation, Faculty of Rehabilitation, Higashi-Omi, Shiga, Japan. [4]Ritsumeikan University, Institute of Advanced Research for Sport and Health Science, Kusatsu, Shiga, Japan. [5]Mizuno Corporation, Global Equipment Product Department, Osaka, Osaka, Japan

Introduction

Ulnar collateral ligament (UCL) injury in baseball pitchers requires prolonged rehabilitation before returning to play. Peak elbow varus torque during pitching has been identified as a primary risk factor for UCL injury. Although sensor-based estimation methods have been proposed, their accuracy remains insufficient. The purpose of this study was to develop a new method for estimating the peak elbow varus torque using a sensor-embedded ball.

Methods

Twenty collegiate baseball pitchers each threw twenty-four pitches (eight each of four-seam fastballs, sliders, and curveballs). Measurements were conducted using a sensor-embedded ball (500 Hz) equipped with an accelerometer (±32 G), a high-range accelerometer (±400 G), a gyroscope, and a magnetic sensor, each with three axes. The pitching motion was recorded using a three-dimensional motion capture system (500 Hz), and inverse dynamics analysis was performed with a three-link model. An elastic net machine-learning model ($\alpha = 0.01$, L1 ratio = 0.5, maximum iterations = 10,000) was used to estimate the peak elbow varus torque. Model performance was evaluated using the coefficient of determination (R^2) and root mean square error (RMSE) derived from a 10-fold cross-validation procedure that independently partitioned the training and testing datasets. Time-series data from a high-range accelerometer and a gyroscope in the sensor-embedded ball were segmented into two phases: within 0.06 s before ball release and an earlier phase. For each phase, variables showing consistent time-series trends across trials were represented by their mean, while variables with large intertrial variability were represented by their range, resulting in ten derived features. The height and body mass of

each pitcher were added to these, giving a total of twelve features used in the machine learning model. The high-range acceleration data were transformed into a fixed coordinate system aligned with the velocity vector of the ball immediately after release.

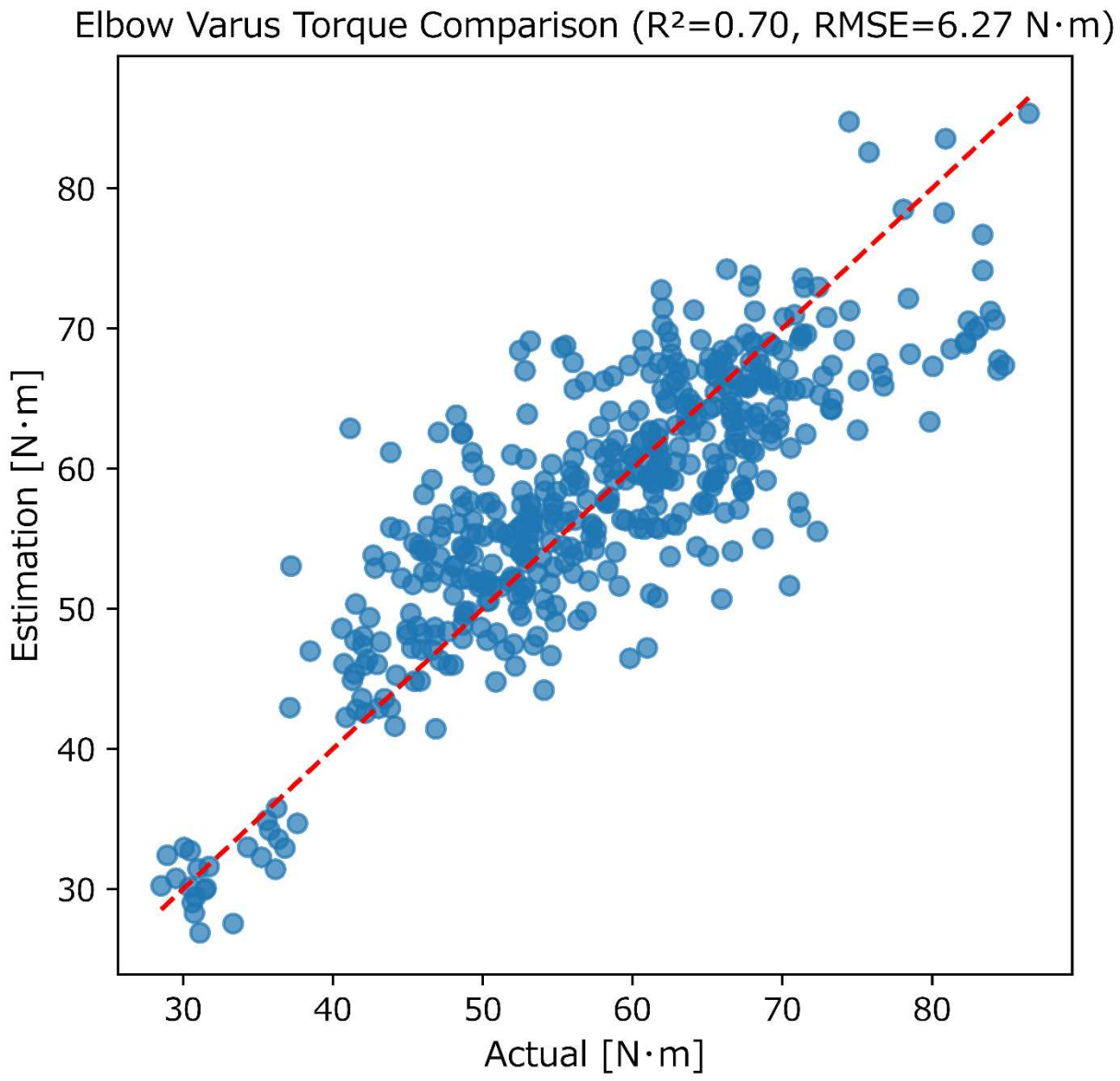
Results

The estimation model achieved an R^2 of 0.70 and an RMSE of 6.27 N·m.

Discussion

These results indicate that the new method can sufficiently estimate peak elbow varus torque using data obtained from the sensor-embedded ball. These findings suggest that this novel measurement is useful for evaluating a risk factor for UCL injury in field settings.

Images (Optional)



Session Category

Human Motion and Performance: Sports

OA94-03

Biokinetic Profiles of Single-Leg Hop Landing in Healthy and Orthopedic Patients: A Machine Learning-Based Functional Classification Of1878 Lower Limbs

Dr. Gustavo Leporace PhD[1,2], Dr. Felipe F. Gonzalez MD, MSc[1,2,3], Dr. Eliane C. Guadagnin PhD[1], Dr. Felipe Carpes PhD[4], Dr. Tiago Zimerman MD[1,3], Dr. Marcos Amstalden Barros MD[1,3], Dr. Carolline P. Nunes MD[1,3], Dr. Alexandre Maioli MD Candidate[1], Dr. Jonathan A. Gustafson PhD[5,1], Dr. Jorge Chahla MD, PhD[6,3], Dr. Moisés Cohen MD, PhD[7], Dr. Leonardo Metsavaht MD, PhD[1,2]

[1]Instituto Brasil de Tecnologia da Saúde (IBTS), Rio de Janeiro, Rio de Janeiro, Brazil. [2]Universidade Federal de São Paulo (UNIFESP), Escola Paulista de Medicina, Departamento de Diagnóstico por Imagem, São Paulo, São Paulo, Brazil. [3]Rush University Medical Center, Illinois, Chicago, United States. [4]Laboratory of Neuromechanics, Federal University of Pampa (Universidade Federal de Pampa), Uruguaiana, Rio Grande do Sul, United States. [5]Rush University Medical Center, Illinois, Chicago, Brazil. [6]Midwest Orthopaedics at Rush (MOR), Illinois, Chicago, United States. [7]Departamento de Ortopedia e Traumatologia, Escola Paulista de Medicina, Universidade Federal de São Paulo (UNIFESP), São Paulo, São Paulo, Brazil

Dr. Felipe F. Gonzalez

Introduction

Single-leg hop landing tests are widely used in orthopedic rehabilitation and return-to-play decisions, but traditional assessments often rely on performance metrics or inter-limb symmetry, which may not capture compensatory movement strategies or neuromechanical deficits. Our objective was to establish a generalizable functional classification by identifying unique biokinetic profiles of a single-leg hop landing test across both healthy individuals and orthopedic populations, using unsupervised machine learning on a large-scale clinical dataset, and to classify these profiles based on clinical parameters.

Methods

Kinematic data from 1878 lower limbs (n=939 adults) were captured via three-dimensional motion analysis during single-leg hop landings. Twenty-four variables were processed through a previously validated five-step unsupervised machine learning pipeline (including

kernel-based normalization, self-organizing maps, and k-means clustering). Subgroups were characterized according to performance (hop distance), isometric strength, flexibility, pain, self-reported functional capacity, and diagnosis distribution. Statistical comparisons were made using ANOVA, post hoc Tukey tests, and chi-square analyses ($p<0.05$). Effect sizes were interpreted using Cohen's d.

Results

Six profiles (P1–P6) emerged (Figure 1). P1 was marked by proximal compensation and stiff landing, associated with higher pain ($p=0.0006$) and ankle/foot disorders ($p=0.005$). In contrast, P6 showed a distal compensation strategy in response to proximal mobility deficits, evidenced by reduced hip flexion and higher ankle eversion, possibly linked to its lower soleus strength ($p=0.02$). P3 showed a higher prevalence of post-anterior cruciate ligament reconstruction cases and reduced dorsiflexion, stiff landing, and knee varus thrust ($p<0.0001$). P5 demonstrated dynamic valgus and a higher prevalence of knee disorders ($p=0.005$). P4 showed globally stiff mechanics, and P2 combined optimal biomechanics with the highest asymptomatic proportion ($p<0.001$). P2 and P5 exhibited higher hop performance ($p<0.0001$), while P1, P3, and P4 performed worse. Despite some group-pathology associations, diagnoses were distributed across profiles.

Discussion

This study demonstrates that single-leg hop landing profiles, identified through unsupervised machine learning, provide a clinically meaningful functional classification that is not captured by traditional diagnostic categories. Incorporating biokinetic profiling into clinical assessment enables more precise identification of neuromechanical deficits and supports the development of patient-specific rehabilitation strategies, optimizing return-to-play decisions.

Images (Optional)

A.

	P1	P2	P3	P4	P5	P6	p value
Peak Trunk Flexion (°)	9.1 ± 8.0	26.7 ± 12.4	12.7 ± 9.8	12.5 ± 10.3	16.3 ± 10.9	12.0 ± 8.8	<0.0001
Peak Trunk Ipsilateral Lean (°)	-7.9 ± 4.5	-11.0 ± 7.0	-9.6 ± 5.0	-9.3 ± 6.5	-8.9 ± 5.1	-9.3 ± 5.4	<0.0001
Peak Anterior Pelvic Tilt (°)	7.3 ± 6.8	21.6 ± 10.0	21.5 ± 6.7	14.3 ± 8.7	9.6 ± 8.5	6.4 ± 7.1	<0.0001
Peak Contralateral Pelvic Drop (°)	-2.4 ± 3.7	-3.9 ± 5.2	-3.5 ± 4.6	-5.0 ± 5.3	-1.4 ± 3.7	-4.0 ± 3.5	<0.0001
Peak Hip Flexion (°)	36.1 ± 7.6	61.8 ± 12.1	50.3 ± 8.3	38.4 ± 12.0	43.7 ± 10.1	38.7 ± 8.4	<0.0001
Peak Hip Adduction (°)	2.5 ± 4.2	0.7 ± 5.7	-1.1 ± 5.0	0.4 ± 5.1	3.4 ± 4.5	-3.0 ± 4.2	<0.0001
Peak Hip Internal Rotation (°)	-1.2 ± 6.1	-2.5 ± 5.8	0.9 ± 5.7	-3.1 ± 6.1	-1.6 ± 6.1	-5.3 ± 5.0	<0.0001
Peak Knee Flexion (°)	38.0 ± 6.0	55.4 ± 10.2	35.2 ± 7.0	35.6 ± 12.0	46.5 ± 8.9	44.9 ± 7.8	<0.0001
Peak Knee Varus (°)	2.6 ± 4.4	2.0 ± 4.3	4.7 ± 3.5	-0.1 ± 3.8	1.6 ± 4.2	4.0 ± 3.9	<0.0001
Peak Knee Internal Rotation (°)	-14.3 ± 9.6	-7.9 ± 9.1	-12.8 ± 9.0	-14.6 ± 8.0	-13.0 ± 8.8	-3.8 ± 7.9	<0.0001
Peak Ankle Dorsiflexion (°)	5.2 ± 4.6	11.1 ± 6.4	2.7 ± 4.8	8.4 ± 5.0	7.5 ± 6.2	7.5 ± 5.5	<0.0001
Peak Ankle Eversion (°)	8.1 ± 3.7	6.3 ± 4.9	8.5 ± 4.3	3.6 ± 4.2	6.6 ± 4.6	10.1 ± 3.8	<0.0001
ROM Trunk Flexion (°)	-2.2 ± 3.0	7.3 ± 7.3	-0.2 ± 3.3	-0.8 ± 2.6	1.2 ± 5.3	-2.0 ± 4.4	<0.0001
ROM Trunk Lateral Lean (°)	-0.9 ± 2.4	-1.9 ± 4.0	-1.6 ± 2.4	-0.7 ± 2.2	-0.9 ± 3.2	-2.2 ± 2.8	<0.0001
ROM Anterior Pelvic Tilt (°)	-5.3 ± 2.9	2.9 ± 5.4	-2.4 ± 3.4	-1.8 ± 3.0	-3.4 ± 4.0	-5.2 ± 3.3	<0.0001
ROM Contralateral Pelvic Drop (°)	7.2 ± 2.3	6.1 ± 3.1	5.8 ± 2.0	3.2 ± 3.1	9.0 ± 2.6	6.9 ± 2.5	<0.0001
ROM Hip Flexion (°)	4.0 ± 3.6	18.0 ± 7.5	8.7 ± 4.4	3.4 ± 4.9	8.1 ± 6.8	5.1 ± 5.3	<0.0001
ROM Hip Adduction (°)	9.0 ± 3.2	11.0 ± 4.6	7.6 ± 2.8	4.0 ± 3.7	12.6 ± 3.8	8.1 ± 3.3	<0.0001
ROM Hip Internal Rotation (°)	1.2 ± 3.4	1.0 ± 4.7	1.6 ± 3.4	-0.4 ± 2.5	1.8 ± 4.1	0.8 ± 3.7	<0.0001
ROM Knee Flexion (°)	29.9 ± 5.7	44.4 ± 8.7	31.0 ± 5.4	17.8 ± 14.9	37.9 ± 7.3	35.0 ± 6.1	<0.0001
ROM Knee Varus (°)	2.9 ± 3.0	1.1 ± 3.7	3.6 ± 3.0	0.1 ± 1.8	1.8 ± 3.5	1.9 ± 2.9	<0.0001
ROM Knee Internal Rotation (°)	1.4 ± 2.7	3.1 ± 3.9	2.4 ± 2.9	-0.1 ± 1.9	0.9 ± 3.3	4.1 ± 2.8	<0.0001
ROM Ankle Dorsiflexion (°)	12.6 ± 12.0	14.4 ± 13.6	9.7 ± 10.2	8.5 ± 10.0	12.9 ± 13.6	11.9 ± 11.8	<0.0001
ROM Ankle Eversion (°)	9.3 ± 5.2	8.7 ± 5.6	8.7 ± 4.6	2.8 ± 3.9	9.6 ± 5.0	12.1 ± 4.2	<0.0001

B.

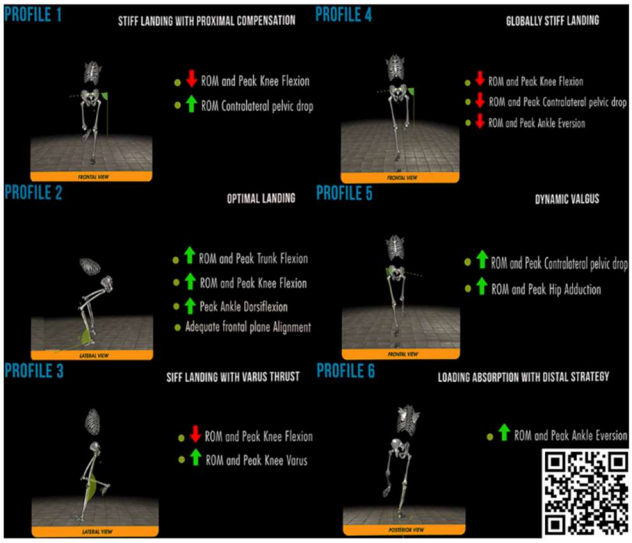


Figure 1: A. Kinematic characteristics of each biokinetic profile (mean ± standard deviation). P: Profile; ROM: range of motion. Positive values: Trunk Flexion/Contralateral Lean; Pelvis: Anterior tilt, Contralateral Pelvic Drop; Hip: Flexion/Addiction/Internal Rotation; Knee: Flexion/Varus/Internal Rotation; Ankle: Dorsiflexion/Eversion. **B.** The video illustrates the six functional landing profiles identified through machine learning analysis during the single-leg hop landing task. ROM = range of motion. The QR code links to the video demonstration of all hop landing profiles.

Session Category

Human Motion and Performance: Sports

OA94-04

Predicting Peak Elbow Varus Torque from Ball Tracking Release Metrics with Machine Learning in Professional Baseball Pitchers

Dr. Connor Moore PhD[1,2], Ms. Brittany Dowling MS[3], Dr. Jason Avedesian PhD[4], Dr. Edward Mitchell PhD[5], Dr. Melissa Boswell PhD[6], Dr. Reed Gurchiek PhD[1]

[1]Clemson University Department of Bioengineering, Clemson, SC, United States. [2]Maven Baseball Lab, Atlanta, GA, United States. [3]Midwest Orthopaedics at Rush, Chicago, IL, United States. [4]Cleveland Cavaliers Basketball Operations, Cleveland, OH, United States. [5]Joe Gibbs Human Performance Institute, Huntersville, NC, United States. [6]Rethink Health LLC, Charlotte, NC, United States

Introduction

Ball tracking and biomechanics technologies are increasingly used in baseball to optimize performance and monitor pitcher health. Current applications lack the ability to estimate injury-related joint loads on a pitch-by-pitch basis without using motion capture, restricting the potential of biomechanics-informed workload monitoring in baseball pitching. However, no attempt has been made at leveraging popular ball tracking technology for predicting clinically relevant elbow load metrics (e.g., peak elbow varus torque), which are needed as rates of major elbow injury rise across levels of play. The study at hand thus sought to address this gap by predicting peak elbow varus torque directly from ball tracking release metrics.

Methods

Two separate machine learning models were trained and compared: random forest (RF) and linear regression (LR). Both models used a historical data source consisting of marker-based motion capture and ball tracking data from 150 professional pitchers (2,901 pitches). Peak elbow varus torque was calculated with an OpenSim pipeline, and models were developed and trained in Python. The models were trained with leave-one-subject-out-cross-validation to maximize out-of-sample data available for evaluation, and both modeling approaches were compared using root mean square error (RMSE) computed across all held out pitches. The best performing model was further evaluated with a Bland-Altman analysis and permutation-based feature importances.

Results

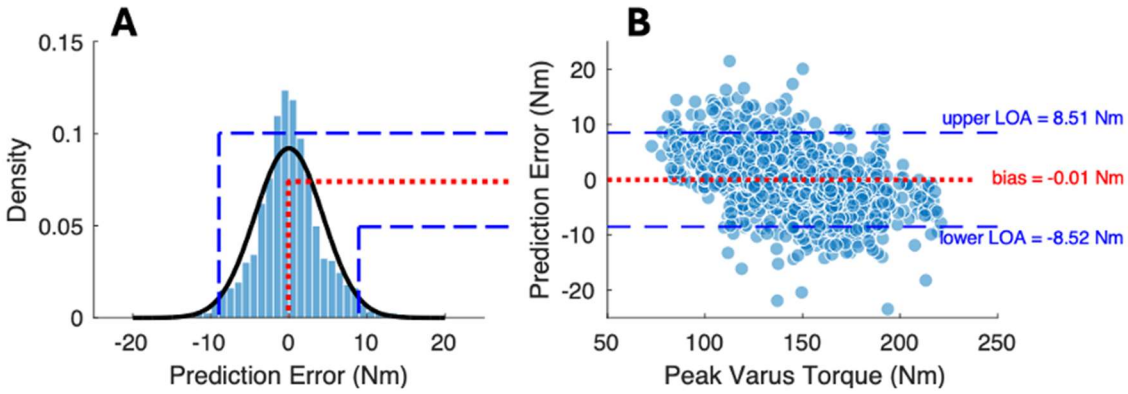
The RF model predicted peak elbow varus torque with an RMSE of 4.61 Nm, substantially outperforming LR (21.41 Nm RMSE). Limits of agreement (−8.52 Nm to 8.51 Nm) from the Bland-Altman analysis fell within previously established ranges distinguishing injured from

non-injured pitchers. Permutation-based feature importance analysis identified release speed, release position (vertical and horizontal), and spin rate as the most important predictors of peak torque.

Discussion

Despite limitations related to sample size and the range of torque values (142 ± 24.8 Nm) compared to previous research, this study demonstrated that peak elbow varus torque can be predicted directly from ball flight metrics using machine learning. Such results demonstrate the feasibility of leveraging ball tracking technology as a scalable, non-invasive tool to monitor biomechanical workload, and in the future can support more informed decisions around performance enhancement and injury prevention in baseball.

Images (Optional)



References (Optional)

Acknowledgements (Optional)

The Robert H. Brooks Sports Science Institute at Clemson University provided funding support for this research with a seed grant. The presenters would like to thank them for support of the project.

Session Category

Human Motion and Performance: Sports

OA94-05

A Machine Learning Approach for Predicting the Grade of Execution of Triple Axel Jumps in Male Figure Skaters Using Real-World Kinematic Data from the World Championships

Dr. Seiji HIROSAWA

Toin University of Yokohama, Yokohama, Kanagawa, Japan

Introduction

In figure skating competition, the Grade of Execution (GOE) of jumps as well as their difficulty is important. However, current criteria—such as “very good height and length” and “good take-off and landing”—leave interpretive flexibility even for kinematic characteristics. Previous studies on women’s double Axel jumps have shown that greater horizontal distance and landing distance are associated with higher GOE[1]. However it remains unclear whether these findings apply to the more difficult triple Axel by male skaters. To provide objective and practically applicable indicators for technical instruction, this study examined the relationship between GOE and kinematic characteristics in men’s triple Axel jumps.

Methods

The dataset comprised 49 triple Axel jumps performed at the 2019 and 2023 World Championships, limited to jumps that received non-negative GOE from all nine judges. The object variable was the trimmed-mean GOE (maximum = 5). Kinematic variables were obtained using a media-oriented tracking system based on two-dimensional DLT reconstruction and included vertical height (VH), horizontal distance (HD), landing distance (LD), and ratio-derived features: (HD+LD)/VH, LD/HD, and HD/VH. Because of strong multicollinearity, Elastic Net regression was used to select influential variables and compared with standard multiple regression.

Results

The Elastic Net model showed superior performance (adjusted R^2 = 0.266, Mean Absolute Error = 0.581, Root Mean Squared Error = 0.726) and identified VH, LD, and LD/HD as positive predictors of GOE.

Discussion

These results indicate that greater jump height as well as smoother flow after landing contributes to higher GOE. Interestingly, HD—identified as important in women's double Axel—was not selected, suggesting that the kinematic features emphasized in GOE evaluation differ by rotation level and athlete category. The model's MAE was smaller than errors previously reported for novice judges and skaters estimating GOE from video [2], indicating its usefulness as an objective reference in training. This study provides the first quantitative evidence that the kinematic features valued in subjective evaluation differ across categories and technical levels, offering data-driven insights for technique optimization and coaching strategies.

Images (Optional)

Regression Coefficients of Each Feature for GOE in the Elastic Net Model

Features	Standardized Coefficient	Unstandardized Coefficient
Intercept	2.349	-2.202
Vertical Height (VH)	0.259	5.164
Horizontal Distance (HD)	0.000	0.000
Landing Distance (LD)	0.271	1.486
(HD + LD) / VH	0.000	0.000
LD / HD	0.210	3.375
HD / VH	0.000	0.000

References (Optional)

[1] Seiji Hirosawa et al. J Sports Sciences, 2022

[2] Seiji Hirosawa et al. Sensors, 2023

Session Category

Human Motion and Performance: Sports

OA95-01

A Framework for Simulating the Geometric Evolution of Abdominal Aortic Aneurysms with Hemodynamic Validation

Prof. Tingting Fan, Dr. Jinhang Wang, Prof. Haixia Zhang

School of Bioengineering, Capital Medical University, Beijing, Beijing, China

Introduction

Abdominal aortic aneurysm (AAA) rupture is associated with high mortality. Current clinical surveillance, which relies primarily on maximum diameter measurements, fails to adequately characterize long-term three-dimensional morphological progression. We propose a region-specific spatiotemporal (RSS-AAA) modeling framework for the longitudinally fitting and prediction of AAA centerline .

Methods

Centerlines were extracted from AAA geometries at multiple follow-up time points. A modified Coherent Point Drift algorithm was employed for non-rigid registration, incorporating lesion-segment weighting, arc-length and path consistency, and segment-wise anisotropic stiffness to achieve "lesion-prioritized" alignment across time. Subsequently, a temporal global least-action model was formulated, integrating velocity/acceleration priors and bending-energy regularization. This model was used to infer unobserved morphological states and to predict future AAA geometry. Geometric accuracy was assessed using length-weighted point-wise distance, curvature error, and bending-energy error. Computational Fluid Dynamics (CFD) simulations were performed on both real and predicted geometries, and flow fields were compared.

Results

(1) In the AAA segment, the length-weighted centerline distance error was ~4.15 mm and the relative bending-energy error was 3.26%–14.62%, indicating that the algorithm can reliably infer the overall pattern of morphological change in the diseased region.

(2) For interpolated and predicted AAA shapes, maximal diameter errors were ~5.22% and 4.27%, respectively, with volume errors <0.5% and ~0.02%, demonstrating good morphologic prediction performance.

(3) CFD showed close agreement between real and predicted models in main jet path, recirculation/vortex structures, and high-/low-shear regions, supporting the hemodynamic validity of RSS-AAA reconstructions.

Discussion

The RSS-AAA framework synthesizes anatomical priors, temporal constraints, and AAA-specific bending energy to achieve temporally consistent reconstruction and short-term prediction of AAA morphology, while preserving essential hemodynamic characteristics. This work offers substantial and potential technical support for aneurysm research, serving as a tool for studying the morphological evolution of aneurysms, and also can provide quantitative support for early AAA rupture risk assessment.

Acknowledgements (Optional)

This research is supported in part by National Natural Science Foundation of China (12202292) and the R&D Program of Beijing Municipal Education Commission (KM202310025021).

Session Category

Cardiovascular/Cardiorespiratory Biomechanics: Methods, Models and Applications

OA95-02

Predicting Patient-Specific TEVAR Outcomes With Finite Element Models: A Proof-of-Concept Study

MEng Giulia De Campo[1], Dr. Anna Ramella[1,2], Dr. Sara Barati[1,2], Dr. Giulia Luraghi[1], Dr. Maurizio Domanin[3], Dr. Irene Fulgheri[3], Prof. Robin Heijmen[4], Prof. Santi Trimarchi[3], Prof Francesco Migliavacca[1,3]

[1]Politecnico di Milano, Milan, Italy, Italy. [2]AllStent srl, Milan, Italy, Italy. [3]Fondazione IRCCS Ca' Granda Ospedale Maggiore Policlinico, Milan, Italy, Italy. [4]Radboud University Medical Centre, Nijmegen, Netherlands, Netherlands

Introduction

The thoracic endovascular aortic repair (TEVAR) has become the preferred treatment option for thoracic aortic pathologies. The current procedural planning relies on manual and geometric assessment, overlooking the complex device–aorta interaction [1]. This study presents the application of a validated high-fidelity finite element methodology [2,3] to replicate the TEVAR procedure in a cohort of twelve patient-specific anatomies presenting aneurysms and acute aortic syndromes with variable curvature and tortuosity. Pre-operative and post-operative computed tomography angiography (CTA) images of patients who underwent TEVAR using a specific stent-graft were analysed. To ensure the accuracy and reliability of the TEVAR digital twin, the simulation results were validated against post-operative image-based reconstructions.

Methods

Patient-specific geometries were segmented from CTA using the level set technique (VMTK). Digital twins of the pre-operative anatomy and stent-graft models were generated. Explicit finite element numerical simulations were conducted to replicate the stent-graft deployment (Fig.1-A). Simulation validation consisted of comparing the simulated stent configuration to the stent reconstructed from post-operative CTA, using the stent ring opening area percentage errors (eOA%) as quantitative metric (Fig.1-B)[2].

Results

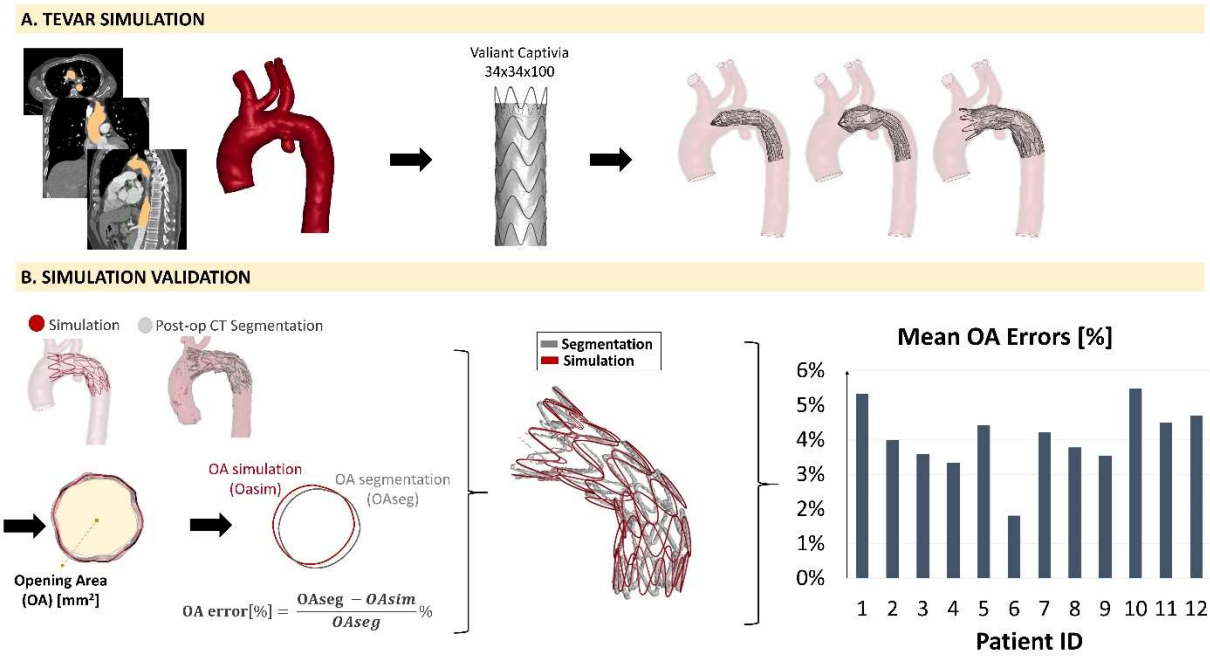
The simulations successfully replicated stent-graft implantation across all anatomies, with eOA% consistently remaining below 10% per stent each ring and below 6% on average (Fig.1-B). Particularly, low errors were observed in the proximal and distal stent rings, critical for ensuring sealing (<3.7% average). These findings demonstrated improved

accuracy compared to values previously reported in the literature (error range 5% - 30%) [4].

Discussion

This study establish the credibility of the TEVAR digital twin for clinical use, providing a reliable tool for pre-procedural planning. Although the patient cohort is limited, the preliminary results support the capability of numerical simulations to predict short-term post-operative outcome in anatomies with diverse pathologies, curvatures and tortuosity.

Images (Optional)



References (Optional)

[1]-Kaladji, Eur-Vasc-Endovasc-Surg-2013;46(1):82-6.
[2]-Ramella, Ann-Biomed-Eng-2022;50(12):1941-53.
[3]-DeCampo, J-Biomech-2025;190:112875.
[4]-Kan, Comp-Meth-Prog-Biomed-2024;244:107994.

Acknowledgements (Optional)

PRIN-2022-Mission 4-Component-1:2022L3JC5T- project, funded by the EU–NextGenerationEU, under the National Recovery and Resilience Plan (CUP:D53D23014380006).
MUSA–"Multilayered-Urban-Sustainability-Action"–project, funded by the EU–

NextGenerationEU, under the National Recovery and Resilience Plan Mission-4-Component-2-Investment-Line-1.5: Strengthening of research structures and creation of R&D “innovation ecosystems”, set up of “territorial leaders in R&D”.

Session Category

Cardiovascular/Cardiorespiratory Biomechanics: Methods, Models and Applications

OA95-03

Simplified LV Hemodynamic Forces via Automated Short-Axis Cine MRI Integration: Preliminary Comparison With 4D Flow MRI

Dr. Sofia Di Filippo[1], Dr. Giandomenico Disabato[2,3], Dr. Riccardo Gorla[4], Dr. Alessandra Riva[1], Dr. Davide Astori[5], Dr. Karima Tissir[6], Dr. Pietro Spagnolo[6], Prof. Emiliano Votta[5], Prof. Francesco Bedogni[4], Dr. Massimo Lombardi[2], Dr. Francesco Sturla[1,5]

[1]3D and Computer Simulation Laboratory, IRCCS Policlinico San Donato, San Donato Milanese, Lombardia, Italy. [2]Multimodality Cardiac Imaging Section, IRCCS Policlinico San Donato, San Donato Milanese, Lombardia, Italy. [3]Universitary Cardiology Department, IRCCS Policlinico San Donato, San Donato Milanese, Lombardia, Italy. [4]Department of Clinical and Interventional Cardiology, IRCCS Policlinico San Donato, San Donato Milanese, Lombardia, Italy. [5]Department of Electronics, Information and Bioengineering, Politecnico di Milano, Milano, Lombardia, Italy. [6]Unit of Radiology, IRCCS Policlinico San Donato, San Donato Milanese, Lombardia, Italy

Introduction

Hemodynamic forces (HDFs) exchanged between blood and left ventricle (LV) wall are emerging as markers of LV dysfunction and adverse remodeling [1]. 4D Flow MRI is the gold standard for HDF assessment; a simplified approach using only long-axis bSSFP images has been proposed but it does not exploit the short-axis stack nor account for valvular regurgitation [2]. We aimed to automate short-axis data integration into simplified HDF calculation and compare the resulting HDFs with those from 4D Flow MRI.

Methods

A training set (n=150) was created by annotating LV endocardial wall on short-axis bSSFP images in Segment (Medviso). A ResNet34 was trained to predict endocardial control points, starting from upper-layer training and progressively unfreezing deeper layers. The tool, integrated into an in-house pipeline, reconstructed LV endocardial 3D surface frame-by-frame, tracking wall motion via diffeomorphic shape matching in Deformetrica. Simplified HDFs were computed according to [2] with enforced mass conservation. HDFs were also computed from 4D Flow MRI and analyzed using Medis suite. Preliminary tests were conducted in a healthy male (71y) and in a female patient (89y) with LV hypertrophy due to severe aortic stenosis (AS) and aortic regurgitation (AR), using 2D phase-contrast (PC-MRI) to correct HDFs.

Results

Network performance improved by retraining head and layers, yielding a Dice score of 0.941±0.073 and Hausdorff distance of 2.05±1.72mm., simplified HDFs captured the temporal pattern seen with 4D Flow in the healthy subject: systolic apex-base and septal-lateral components were higher with 4D Flow, while simplified HDFs showed a higher apex-base peak for diastolic E-wave. Flow rates from mass conservation well resembled PC-MRI measurements. In the patient, systolic apex-base and septal-lateral HDF magnitudes were comparable when using 4D Flow while the simplified method showed a HDF pattern with septal-lateral predominance and greater diastolic values. AR estimates agreed with 2D PC-MRI, despite 24% (aortic) and 29% (mitral) lower mean flow rates.

Discussion

The proposed approach captured the overall pattern of 4D Flow HDFs in healthy conditions. Under pathological LV conditions, extensive analysis and further testing are required to improve agreement.

Images (Optional)

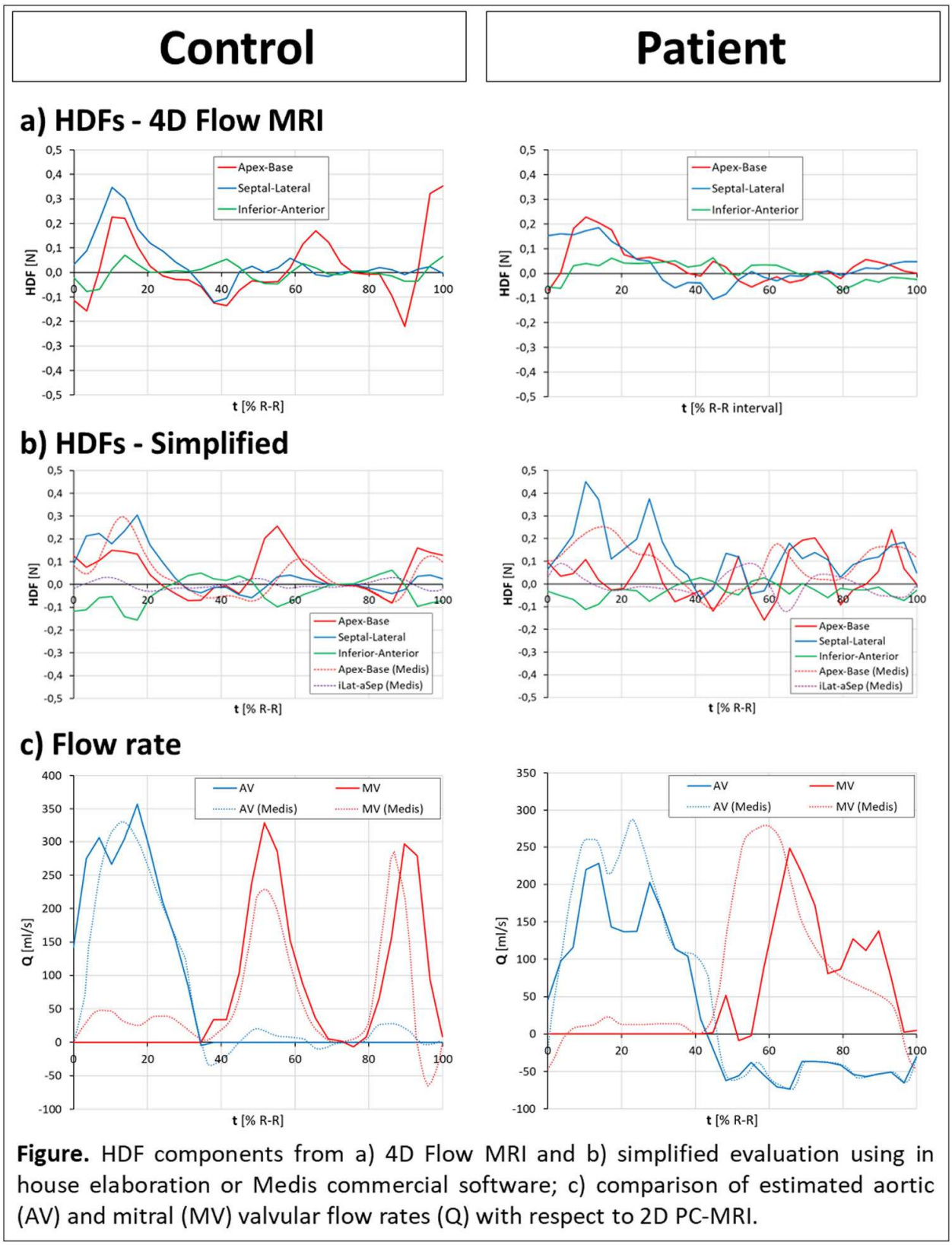


Figure. HDF components from a) 4D Flow MRI and b) simplified evaluation using in house elaboration or Medis commercial software; c) comparison of estimated aortic (AV) and mitral (MV) valvular flow rates (Q) with respect to 2D PC-MRI.

References (Optional)

[1] Aimo *et al.*, EHJIMP, 2024

[2] Pedrizzetti *et al.*, J Biomech, 2017

Acknowledgements (Optional)

TRANSLATE project (Phenotyping lefT ventRicle fAilure with hemodyNamic biomarkerS from 4D FLow mAgneTic rEsonance imaging) was funded by the National Plan for NRRP Complementary Investments, project n. PNC0000003 - AdvaNced Technologies for Human-centrEd Medicine (ANTHEM) - Cascade Call launched by SPOKE 3 POLIMI.

Session Category

Cardiovascular/Cardiorespiratory Biomechanics: Methods, Models and Applications

OA95-04

A 0D Simulation-Based Framework for Fast and Accurate Boundary Condition Optimization in Coronary Arteries Steady-State and Transient CFD Simulations

Mr Luca Mariani MSc[1,2], Ms Marta Pillitteri MSc[1], Ms Giulia Frigerio MSc[1], Mr Gianluca Pontone MD[3,4], Mr Alberto Redaelli PhD[1]

[1]Department of Electronics Information and Bioengineering, Politecnico di Milano, Milano, Lombardy, Italy. [2]European Society of Biomechanics (ESB), Milano, Italy, Italy. [3]Department of Perioperative Cardiology and Cardiovascular Imaging, Centro Cardiologico Monzino IRCCS, Milano, Lombardy, Italy. [4]Department of Biomedical, Surgical and Dental Sciences, Università degli Studi di Milano, Milano, Lombardy, Italy

Introduction

Coronary artery disease represents one of the leading causes of death worldwide. Predicting plaque progression using CFD-derived indices, which have been shown to correlate strongly with plaque growth and remodelling [1], is therefore crucial in the early identification of culprit lesions. However, a spread limitation lies in the reliable estimation of patient-specific boundary conditions (BCs) from limited clinical data, and in the high computational cost of 3D transient CFD simulations. We propose a framework that leverages 0D models to optimize BCs for both steady-state (R) and transient (RCRCR) simulations, enabling patient-specific flow-rate waveforms and outlet impedances in minutes.

Methods

Coronary geometries from 20 patients were segmented from CT images using an in-house automatic segmentation tool. Initial inlet flowrates and outlet BCs were estimated from literature formulas and assigned to a baseline 3D simulation and to its equivalent 0D model. Results from the 3D simulation were used to calibrate the internal parameters of the 0D circuit through a optimization algorithm. The calibrated 0D model was then used to optimize steady and transient output BCs to match the patient's measured mean arterial pressure (MAP) at the coronary ostium (Figure 1). Wall shear stress (WSS), WSS topological skeleton, oscillatory shear index (OSI), and wall pressure gradient (WPG) were computed through 3D simulations using the optimized BCs.

Results

Following internal calibration, 0D models showed strong agreement with 3D simulations when using identical BCs, yielding a relative MAP error of 0.15%. Compared to conventional iterative frameworks, our method reduced computational time for transient

and steady BC estimation respectively by 59% and 54% using a 120-core CPU, with further gains with lower-end CPUs. The approach achieved a mean ostial pressure error, compared to MAP, of 0.13% for steady simulations and 2.31% for transient. Moreover, simulations accuracy was proved by comparing vFFR with invasive iFFR values [2], resulting in a mean error of 4.10%.

Discussion

The proposed 0D-based framework enables fast, reliable patient-specific BCs estimation while substantially reducing computational cost, facilitating more efficient CFD-based assessment of coronary hemodynamic and plaque-progression predictors.

Images (Optional)

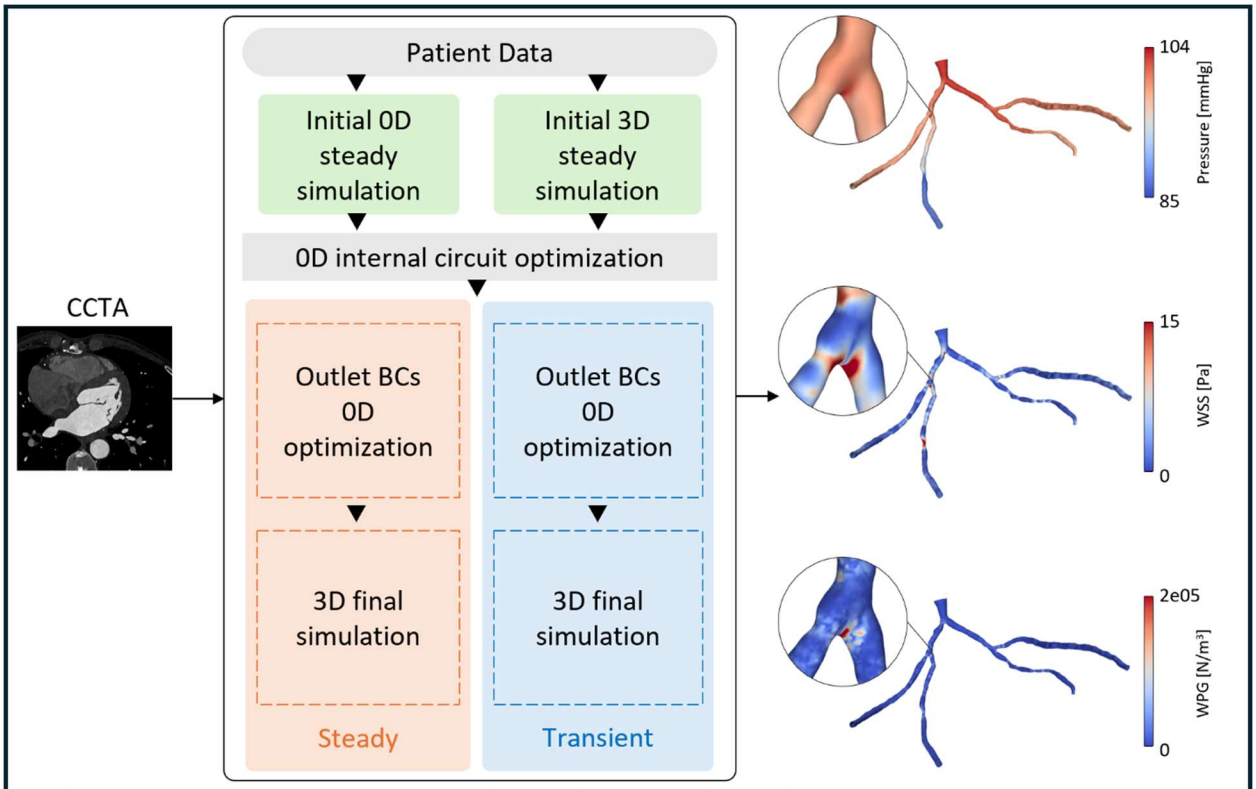


Figure 1: Representation of the workflow followed for the 0D-based optimization of coronary BCs

References (Optional)

[1] Habib Samady et al., Circulation, 2011

[2] Guido Nannini et al., Comput Methods Programs Biomed, 2024

Acknowledgements (Optional)

This work has been supported by Fondazione Regionale per la Ricerca Biomedica (Regione Lombardia). Project 3432721 - AI-CORPS.

Session Category

Cardiovascular/Cardiorespiratory Biomechanics: Methods, Models and Applications

OA96-01

Coupled Eulerian-Lagrangian Modelling of Orthopaedic Trauma Bone Screw Pullout

Dr. Lin Wang[1], Dr. Dana Coombs[2]

[1]DePuy Synthes, Leeds, West Yorkshire, United Kingdom. [2]DePuy Synthes, West Chester, Pennsylvania, United States

Introduction

To ensure patients' safety, evaluating mechanical fixation of bone screws is critical. However, the typically used cadaveric or standard benchtop tests (ASTM F543) are limited by the large variations of donor bone quality and costly design-prototyping-testing iterations. To address those limitations, an innovative computational method is developed to simulate pullout of six trauma screws and validated against benchtop testing.

Methods

An advanced ABAQUS/Explicit R2024 solver using Coupled Eulerian-Lagrangian (CEL) is employed to model the ultra large material deformation and highly nonlinear process. Pullout models of DePuy Synthes locking and cortex self-tapping screws, each with three sizes (1.5x20, 3.5x20 and 4.0x20mm), were built as per benchtop testing (Figure 1a). For computing efficiency, the insertion step was simplified with geometrical Boolean between screws at the full insertion depth (Figure 1b) and 20PCF polyurethane foam (Sawbone™) which was modelled as elastic-plastic material, while the much stiffer screws were assumed to be rigid bodies. Their interactions were simulated with a frictional "penalty" algorithm.

Results

Under the current assumptions, it is predicted that for both locking and cortex screws studied, a larger diameter results in a higher peak pullout force, broadly following the rank order of benchtop testing (Figure 1c). However, the computational models underpredict the experimental peak forces by 10% to 20%, which could result from a few factors such as material variations of Sawbone foam and simplification of the insertion step. When comparing the pullout force history, predicted peak force occurs slightly earlier than measured force (Figure 1d), where the experimental fixtures may take longer to "settle", while neglected numerically.

Discussion

CEL modelling has been successfully developed to simulate bone screw pullout, which would otherwise be extremely challenge for other solvers e.g. Finite Element Analysis, due to severe element distortion. In general, the CEL approach is able to capture the rank order of screws as per benchtop testing. Notably, the models solve in a few hours, which is considerably less time than prototyping and benchtop testing. Moreover, this approach offers a valuable "controlled" platform which only evaluates screw designs while keeping all other variables consistent in contrast to cadaveric tests.

Images (Optional)

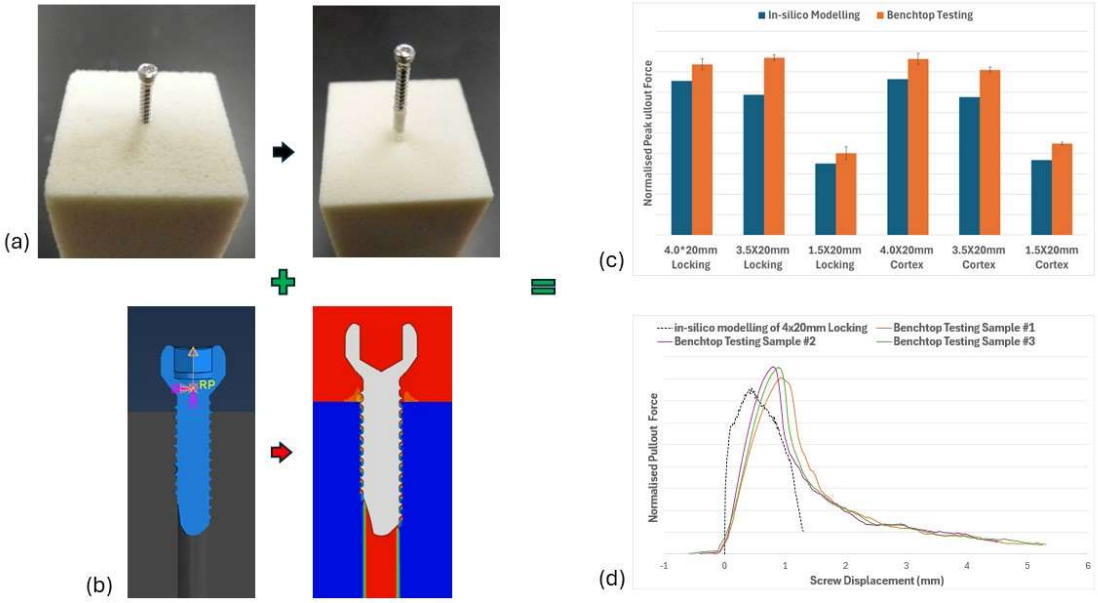


Figure 1 (a) Benchtop testing of screw insertion-pullout ; (b) in-silico modelling of screw pullout; (c) Peak pullout force results of six screws studied; (d) Illustration of pullout force history (Synthes 4x20mm locking screw)

Session Category

Musculoskeletal Biomechanics: Methods, Models and Applications

OA96-02

Finite Element Investigation of Load-Driven Bone Density Distribution in Dysplastic and Normal Hips

Mr. Mohammad Mahmoodi[1,2], Prof. dr. Sita Bierma-Zeinstra[2], Dr. Rintje Agricola[2], Dr. ir. Nazli Tumer[1,2], Prof. dr. ir. Amir Zadpoor[1]

[1]Delft University of Technology, Delft, Zuid Holland, Netherlands. [2]Erasmus University Medical Center, Rotterdam, Zuid Holland, Netherlands

Introduction

Bone tissue adapts to its mechanical environment [1], making bone density distribution (BDD) an essential indicator of physiological and pathological loading. This study investigates how dysplastic hips (DH), a strong risk factor for hip osteoarthritis [2], differ from normal hips (NH) in BDD under representative loading conditions.

Methods

Ten dysplastic and ten normal hips were semi-automatically segmented from publicly available CT scans [2, 3] using TotalSegmentator. Acetabular regions and their corresponding coverage areas on each femur were automatically identified, and muscle attachment sites were mapped using a 3D statistical shape model of the proximal femur to ensure consistent muscle force application across all the specimens. First, joint contact forces and muscle forces, including magnitudes and directions, were obtained from individuals without any known hip pathologies [4]. These forces, referred to here as normal loading, were then applied in our simulations. A multi-phasic tissue adaptation model implemented in FEBio [5] was used to simulate BDD. All modelling steps (e.g., discretization, material assignment) were automated using a custom GUI-based pipeline that generated FEBio input files and managed the complete workflow. The adaptation model was first validated against CT-derived densities. Adaptation simulations were then conducted for all hip geometries under normal loading conditions, and statistical comparisons were performed to assess the normal loading effects on DH and NH geometries. In the next phase, dysplastic loading conditions obtained from dysplastic patients will be incorporated into the analysis.

Results

BDD revealed clear differences between NH and DH under normal loading conditions (Fig. 1). The BDD was higher in the head and neck region for NH. Overall, dysplastic cases

demonstrated a 25% lower average total density, with the femoral head density reduced by 21% compared with normal hips.

Discussion

Normal loading revealed consistent differences in adaptation between NH and DH, demonstrating the model's ability to detect geometry-dependent remodelling patterns and supporting its use for evaluating pathological loading effects.

Images (Optional)

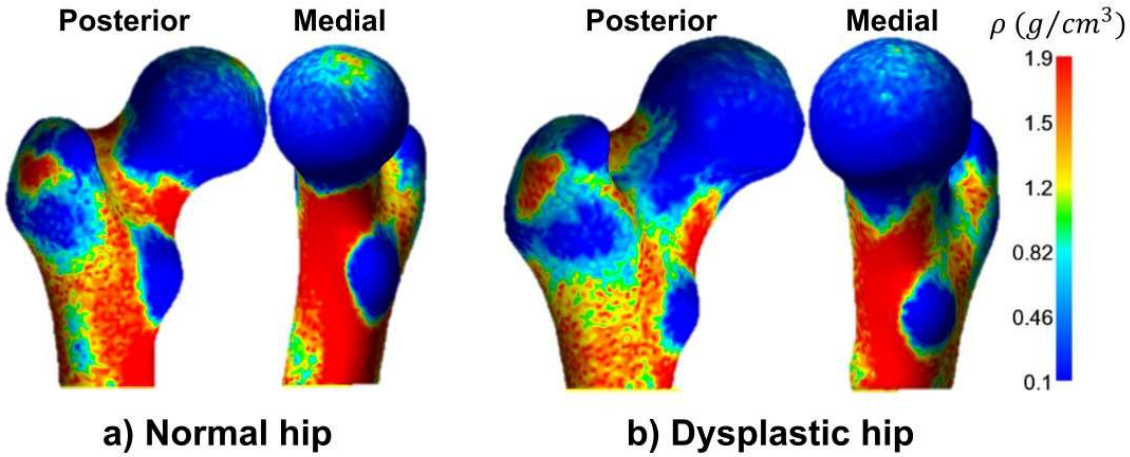


Fig.1 BDD [g/cm^3] for exemplar a) NH and b) DH cases under normal loading

References (Optional)

[1] Wolff J, Springer, 2012.

[2] Henak CR et al., Osteoarthr. Cartil., 2014.

[3] Harris MD et al., J. Orthop. Res., 2012.

[4] Campoli G et al, J. Mech. Behav. Biomed. Mater., 2012.

[5] Maas S and Weiss J, "Theory Manual"

Session Category

Musculoskeletal Biomechanics: Methods, Models and Applications

OA96-03

A High-Fidelity Finite Element Model of the Lumbar Spine to Quantify Load Sharing Across Functional Tasks

Ms Linda Carpenedo, Prof. Luigi La Barbera

LaBS, Dept. of Chemistry, Materials and Chemical Engineering, Politecnico di Milano, Milan, Italy, Italy

Introduction

Spinal stability relies on the coordinated action of passive (vertebrae, ligaments), active (muscles), and neural subsystems, and any deficits in one of them require compensation by others. Because direct measurements of spinal loads are invasive or unfeasible, computational models are used. This study proposes a fully deformable musculoskeletal finite element model to examine how soft tissues contribute to load sharing across different tasks.

Methods

The geometry from a validated parametric CAD model of the lumbar spine is used, and all structures are represented as continuous deformable bodies in Abaqus [1]. Body weight is applied eccentrically at each vertebral level. Eight muscle groups are included and discretized into 28 uniaxial fascicle connectors per side, whose stiffness k=qF/l adapts to task demands (Fig.1a). Muscle activations are estimated through an energy-based-optimization informed by a Plackett–Burman screening and a surrogate-optimization based on a generalized linear model predicting the activation patterns needed to satisfy the desired kinematics at each spinal level during standing and 10°/20° flexion. Optimized muscle forces and assessed intradiscal pressures are compared to *in vivo* data [2]. Compressive and shear forces (CFs, SFs) are extracted to assess the soft tissues' load sharing.

Results

The energy-based-optimization estimates physiologically plausible muscle forces (Fig.1b) [2]. Intradiscal pressures increase from standing to 10° and 20° flexion (e.g., at L5–S1: 0.50, 0.57, 0.90 MPa). The anterior column bears the highest CFs and SFs, exceeding 140% of total CFs in flexion (Fig.1a), mainly supported by the anulus. Among posterior ligaments, facet capsules (FCLs) contribute most to load sharing (±40% CFs, ±35% SFs).

Discussion

Estimated muscle forces and spinal loads align with *in vivo* references [2]. The anterior column and FCLs are crucial in standing and flexion, matching the results of other computational strategies and supporting model credibility [3]. The FE model offers detailed insight into soft tissue contributions during daily activities. Future work includes sensitivity analyses on muscle architecture and examining additional tasks under more severe loading conditions.

Images (Optional)

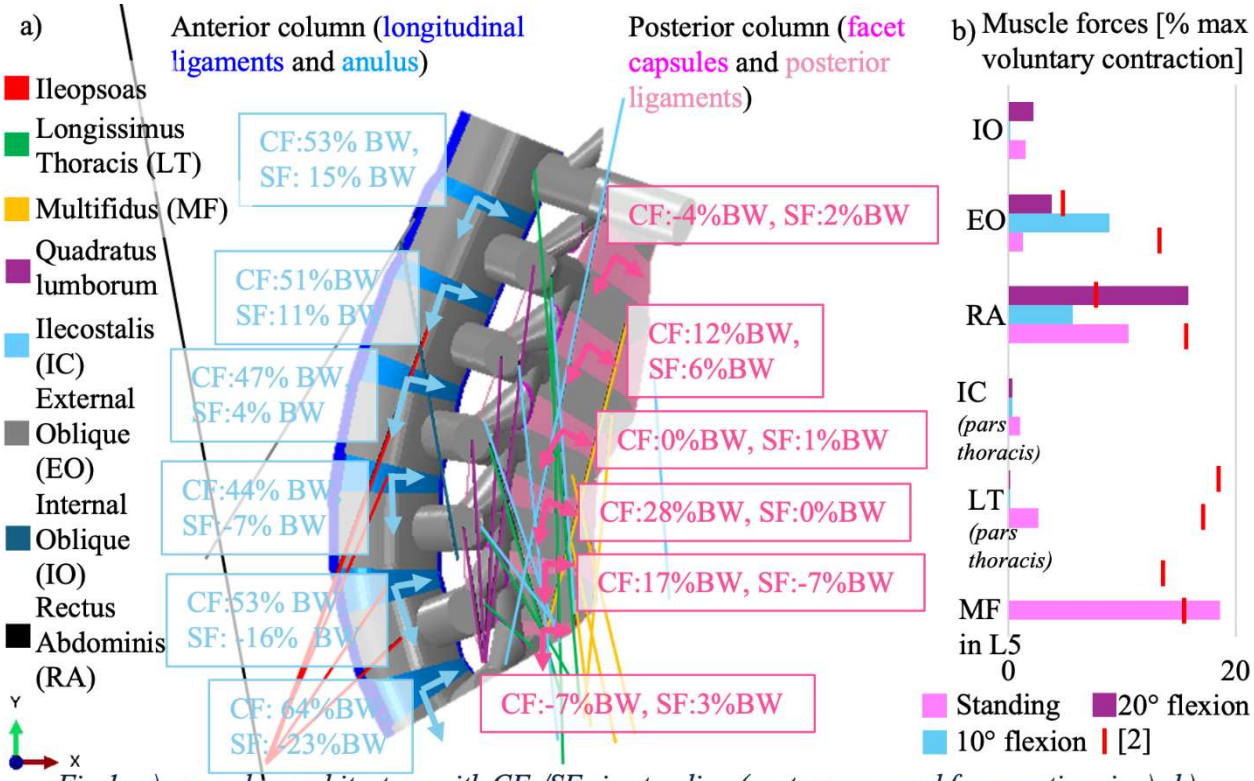


Fig.1: a) muscular architecture with CFs/SFs in standing (vectors reversed for negative sign); b) estimated muscle forces for some fascicles for different tasks.

References (Optional)

[1] Bellina E et al., J Biomech, 2024

[2] Arjmand N et al., J Biomech, 2006

[3] Liu T et al., Front Bioeng Biotechnol, 2019

Session Category

Musculoskeletal Biomechanics: Methods, Models and Applications

OA96-04

Fabric and Density Based Determination of Habitual Bone Loading with Homogenised Finite Element Models

MSc Gabriela Gerber, Prof. Dr. Philippe Zysset

ARTORG Center for Biomedical Engineering Research, University of Bern, Bern, Bern, Switzerland

Introduction

A bone's morphology is closely tied to its mechanical function. Computational inverse remodelling allows to estimate personalised habitual load cases based on local bone density and microstructural orientation obtained from high-resolution CT images. Homogenised finite element (FE) models substantially improve computational performance compared to the traditionally used micro-FE approach but have so far only been considered for density-based remodelling [1]. This study aims to include both density and microstructural (fabric) orientation in homogenized inverse bone remodelling algorithms for the estimation of bone's habitual loading history.

Methods

Homogenised FE models of n=24 left human distal tibia sections were created following established procedures [2]. The habitual load case for each bone was defined as a linear combination of scaled unit forces and moments. Appropriate scale factors were determined by minimising the cumulative local difference between the element stress resulting from the combined habitual loading and the ideal local stress based on the element's density and fabric [3]. This optimisation was once performed with the sample's local fabric distribution, and once with an isotropic fabric. The statistical difference between the two methods was evaluated with a paired sign test.

Results

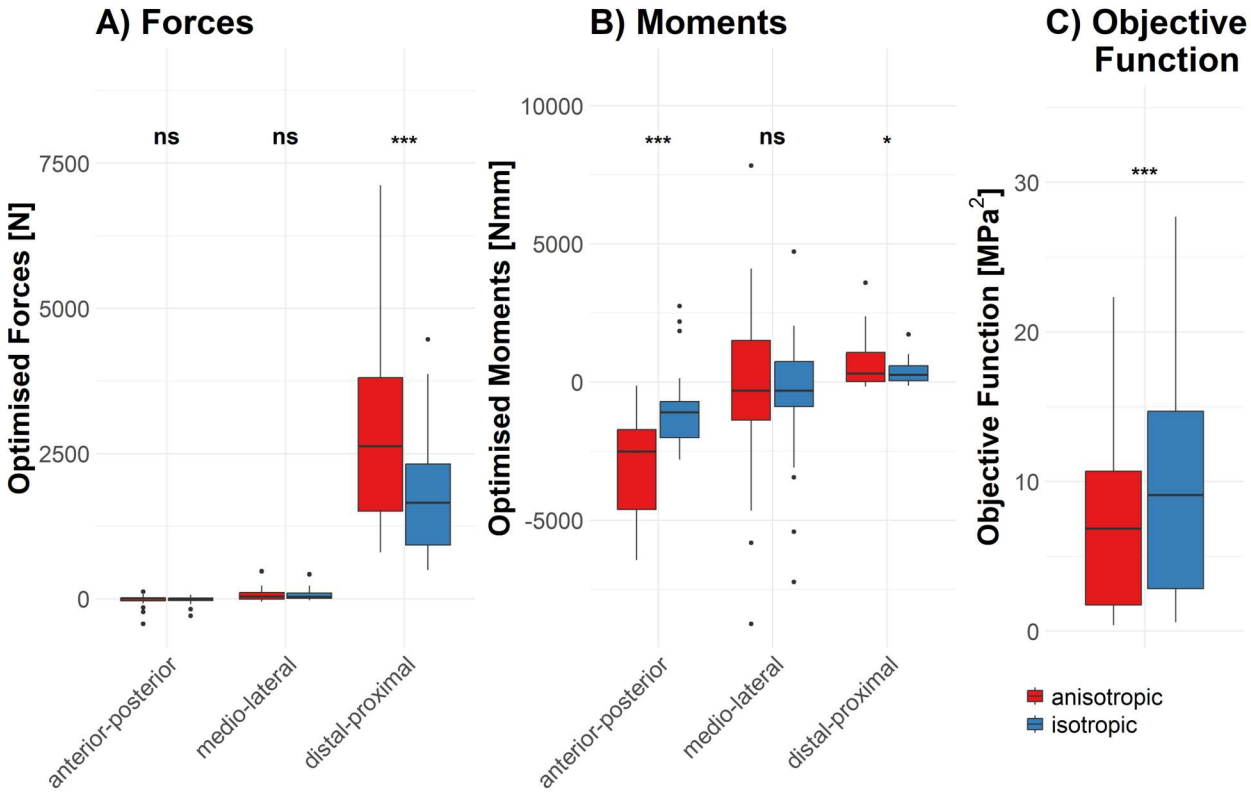
The figure presents (A) optimised forces, (B) optimised moments, and (C) the objective function for isotropic and anisotropic optimisation approaches.

Discussion

During walking, compressive axial forces acting on the distal tibia are slightly shifted laterally [4], inducing a negative moment around the anterior-posterior axis, which corresponds to the largest moment emerging from our inverse analysis. Considering the

fabric orientation in homogenized inverse remodelling leads to an increase in the dominant force and moment and reduces the objective function by 27%, indicating that the osseous structure is better adjusted to this load case than the purely density based remodelling solution. Future analysis will include quantification of St.-Venant's effect on the optimisation results and the estimation of a safety factor relating the habitual load case to the bone's compressive yield force.

Images (Optional)



References (Optional)

1. Bachmann et al., Ann Biomed Eng, 2023
2. Schenk et al., J Mech Behav Biomed Mater, 2022
3. Zysset, Biomech Model Mechanobiol, 2025 (accepted)
4. Rajaeirad et al., J Orthop, 2024

Acknowledgements (Optional)

This work was financially supported by grant no 200365 of the Swiss National Science Foundation.

Session Category

Musculoskeletal Biomechanics: Methods, Models and Applications

OA96-05

Rapidly Converging, Patient-Specific Finite Element Modeling of Foot-Ground Interactions on Variable Terrains and Surface Compliances

Mr Samuel Allen, Dr Nelly Andarawis-Puri

Cornell University, Ithaca, NY, United States

Mr Samuel Allen

Introduction

From rigid hardwood to compliant sneakers, daily locomotion spans a wide range of terrains and surface compliances. However, existing biomechanical tools struggle to accurately capture interactions of the body with diverse surfaces. Multi-body dynamics platforms, such as OpenSim [1], are patient tailored but oversimplify the foot-ground interface. In contrast, finite element models (FEM) can offer greater fidelity [2] but are too computationally expensive to pair with inverse dynamics and patient individualization. This project bridges this gap by developing an automated, patient-specific global foot FEM in Ansys. By simplifying soft-tissue representation and joint contacts, the model predicts tendon loads and plantar pressures within 10 minutes.

Methods

Bone and skin geometries were reconstructed from T1-weighted MRI scans (5 mm slice spacing). Bones were represented as rigid bodies and skin as shell elements. Inter-bone kinematics were simplified to revolute or spherical joints based on the shape of articular surfaces. Joint passive stiffness was calibrated using clinical tests of ankle and longitudinal/lateral arch flexibility. To improve computational efficiency and stability, volumetric soft tissue was approximated with a non-linear spring network. The simulation was driven by ankle inverse-dynamics loads, with loading of tendons within the foot solved via minimization of Hill-type tendon actuators throughout the walking gait cycle.

Results

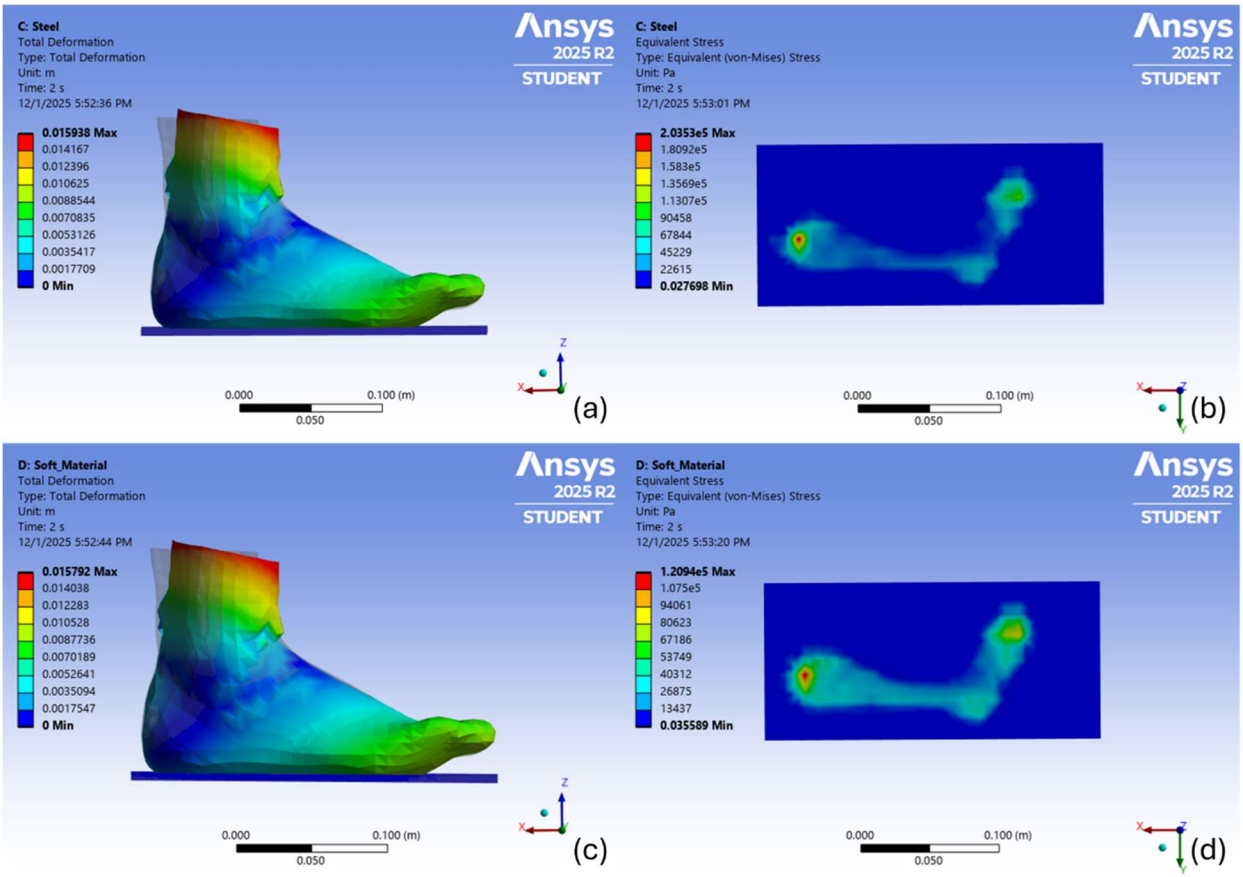
For a standing load case on rigid steel versus compliant foam (~4000x more compliant), the model converged in 8 and 7 minutes. Peak pressures were localized under the heel and metatarsophalangeal joint (Fig 1b, d). On the compliant surface, peak pressure decreased

while contact area increased. Total deformation (Fig 1a, c) shows the model's large deformation capability.

Discussion

This framework combines the patient-specificity of multibody dynamics with the high-fidelity contact mechanics of FEM. By achieving rapid convergence across a four-orders-of-magnitude compliance range, this model is a robust platform for simulating real-world locomotion. Critically, the automated generation of a patient-specific model using standard clinical MRI scans and mobility tests establishes a practical tool. This efficient process will allow isolation and prediction of the effects of specific footwear materials and insole designs on individual patients.

Images (Optional)



References (Optional)

[1] Seth *et al.*, PLoS Comput Biol, 2018

[2] Cheung *et al.*, J Biomechanics, 2005

Session Category

Musculoskeletal Biomechanics: Methods, Models and Applications

OA96-06

Changes in Biomechanical Properties of Paediatric Femora With Age Estimated by Finite Element Methods

Mr George Allison[1,2], Mr Salman Almutairi[3], Professor Amaka C Offiah[3,2], Dr Xinshan Li[1,2]

[1]School of Mechanical, Aerospace & Civil Engineering, University of Sheffield, Sheffield, England, United Kingdom. [2]Insigneo Institute, University of Sheffield, Sheffield, England, United Kingdom. [3]School of Medicine and Population Health, University of Sheffield, Sheffield, England, United Kingdom

Introduction

There is currently a lack of understanding of bone strength (failure load) in children, which is important to understand normal skeletal growth and development. One of the main challenges is the difficulty in obtaining paediatric bone samples. Therefore, finite element (FE) modelling utilizing post-mortem computed tomography (CT) images is a useful method to non-invasively investigate femoral bone strength in children through a range of loading conditions.

Methods

Seventy anonymized and retrospective post-mortem CT scans of children (0-15 years old) were obtained from the Sheffield Children's Hospital and processed through the PyPeCT2S pipeline to create 3D FE models. Personalised heterogeneous material properties were derived through CT attenuation. Three loading conditions were applied (Figure 1): (1) 4-point bending with two equidistant forces applied to the femoral shaft and partially fixed ends. (2) external rotation and (3) internal rotation torsion, where the proximal end was fixed with multi-point constraints and a moment was applied to the distal end. The region of interest for all boundary conditions was the femoral diaphysis. Values of interest were defined as critical moments where the predicted peak strain exceeded a yield strain of 0.73% for tension and 1.04% for compression (1).

Results

FE predicted critical moment increased with age and a quadratic fit was a better predictor than linear. Bending tests produced the highest values and the highest critical moment. Torsion predicted maximum critical moments of 86 Nm and 146 Nm for internal and external rotations, respectively, while 4-point bending predicted values up to 168 Nm. Both

bending and torsional results exhibited the same trend with increasing age, which were also in line with previous results from (2).

Discussion

This study presents a sizeable cohort of data with a well-spaced age range, and the largest dataset of CT-based paediatric biomechanical femoral models in infants. The results of this study reinforce age as a key predictive factor for bone strength and show good correlation with previous experimental studies. Additionally, the results offer insight regarding the rate of change of bone strength during normal growth and development in children.

Images (Optional)

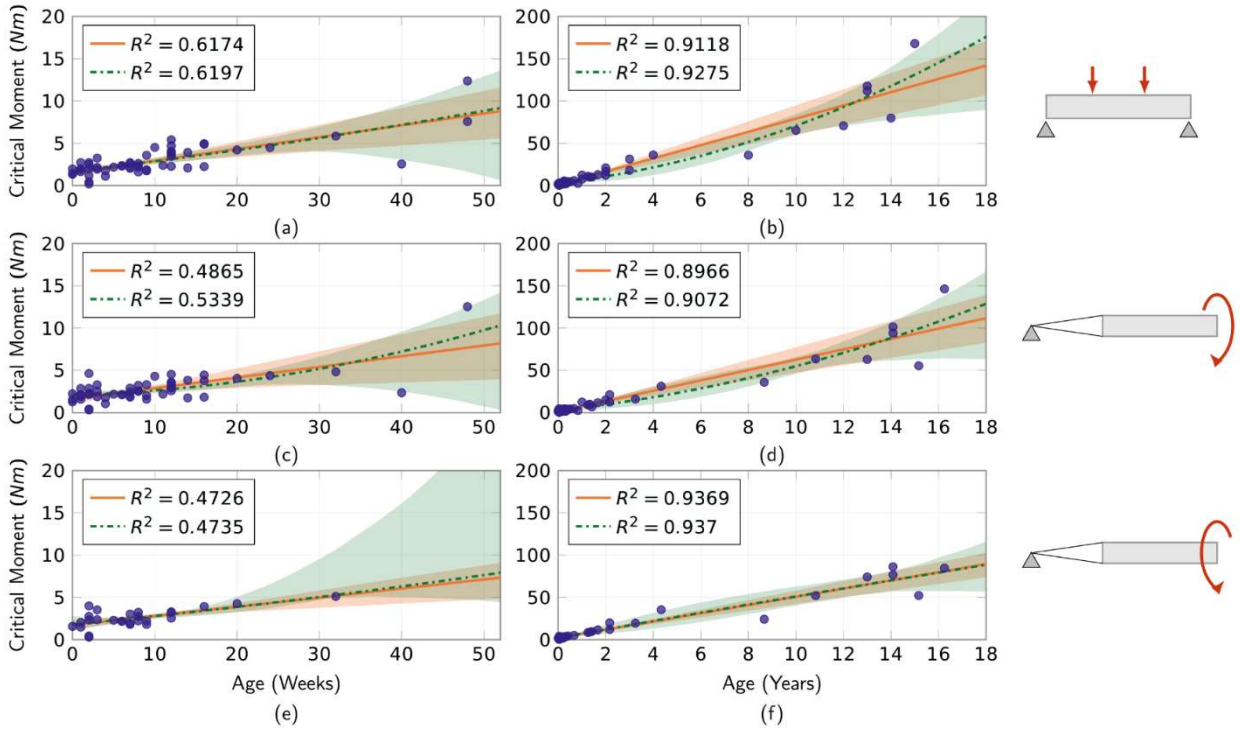


Figure 1: Figures in the left column are representative of children up to 1-year-old, while figures on the right are the entire age range of the cohort (n=70). Linear and quadratic regressions were performed on all data sets, where linear regression is shown in orange, and quadratic regression in green. (a) and (b): the 4-point bending. (c) and (d): torsion with external rotation. (e) and (f): torsion with internal rotation.

References (Optional)

[1] Bayraktar et al., J Biomechanics, 2004

[2] Ouyang et al., CJCA 2003

Session Category

Musculoskeletal Biomechanics: Methods, Models and Applications

OA97-01

Biophysical Modeling of Human Colonic Motor Patterns in Health and Disease

Dr. Ahilan Anantha Krishnan PhD[1], Prof. Phil Dinning PhD[2], Prof. Maria Holland PhD[1]

[1]University of Notre Dame, Notre Dame, IN, United States. [2]Flinders University, Bedford Park, South Australia, Australia

Introduction

Colonic motility disorders such as diarrhea predominant irritable bowel syndrome (IBSD) and slow transit constipation (STC) are common and can significantly impact quality of life. These conditions involve disrupted bowel function, often linked to abnormalities in colonic motility. For example, two key motor patterns observed in healthy individuals, high amplitude propagating contractions and cyclic motor patterns, are frequently reduced or absent in affected patients as shown by high resolution colonic manometry. Understanding how these patterns interact, along with the pacemaker, neural, and mechanical mechanisms that generate them, is essential for developing more effective treatments.

Methods

In this study, we developed a biophysical whole colon model that represents the colon as a chain of coupled oscillators driving smooth muscle activation. The model incorporates enteric nervous system reflexes, a pressure gated cyclic motor pattern (the rectosigmoid brake), and a nonlinear tube law describing colon wall mechanics. By adjusting a small set of physiologically grounded parameters, specifically pacemaker drive, coupling strength, directional spread, and distal gating, we reproduced three distinct motility phenotypes: healthy function, IBSD, and STC. Simulated pressure maps were compared with representative high resolution colonic manometry recordings, and local sensitivity analysis identified the parameters most strongly influencing peak pressure and motility index.

Results

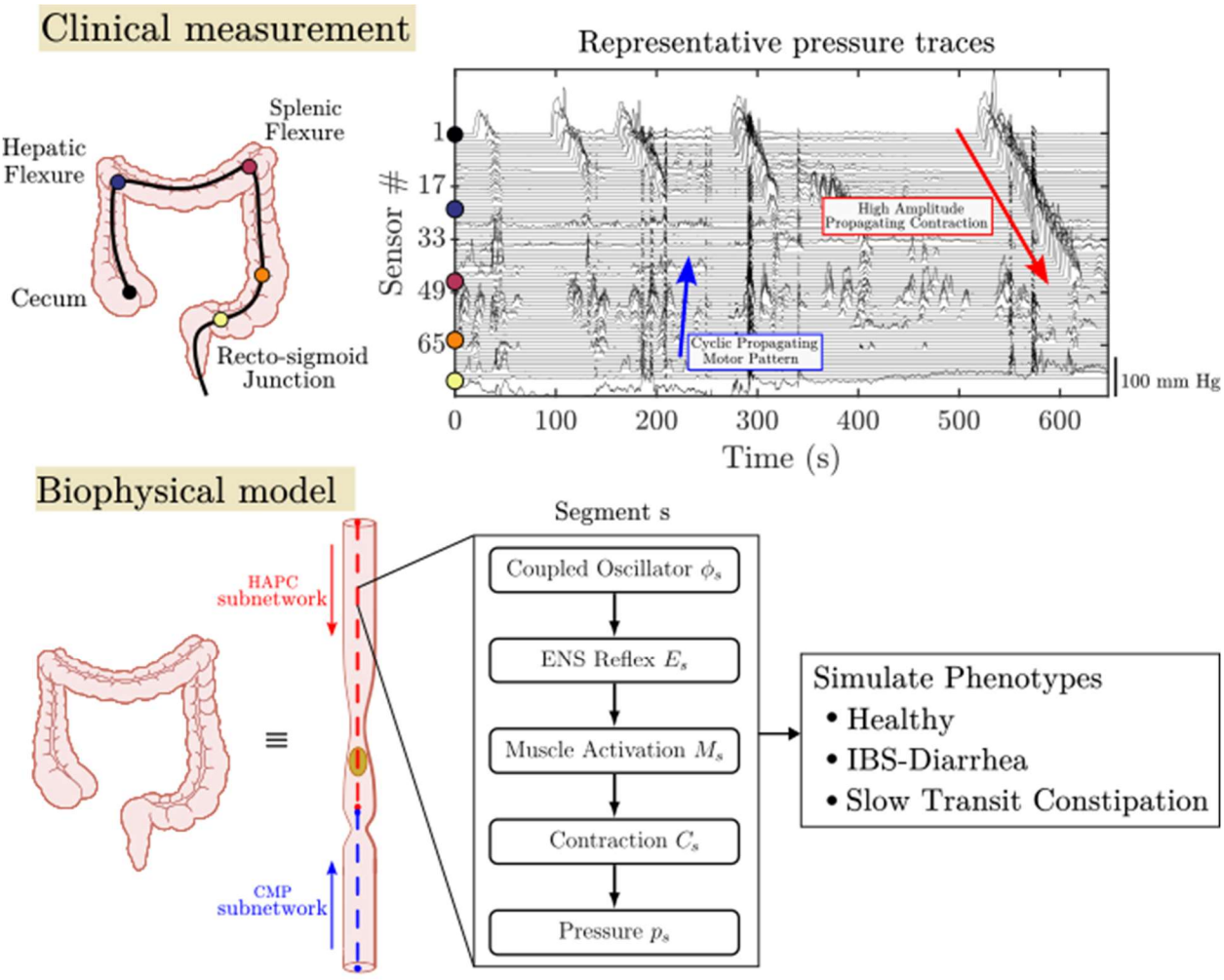
The model reproduced key features observed in clinical manometry, including high amplitude propagating contractions, a retrograde cyclic motor pattern, and phenotype-specific differences in amplitude and coordination. Increased pacemaker activity and reduced distal gating generated a hypermotile pattern consistent with manometric findings in IBSD [1], while reduced coupling and added stochasticity produced fragmented, low amplitude activity characteristic of STC [2]. Sensitivity analysis identified proximal

pacemaker amplitude, coupling strength, and directional spread as dominant regulators of the global pressure response.

Discussion

This biophysical framework links measurable manometry metrics to specific physiological mechanisms controlling colonic motility. It provides a first step towards a mechanistic basis for interpreting high-resolution colonic motility, supports hypothesis-driven in silico exploration of motility disorders, and offers a platform for future patient-specific calibration to guide individualized therapeutic strategies.

Images (Optional)



References (Optional)

[1] Wiklendt L et al. Am J Physiol Gastrointest Liver Physiol, 2023

[2] Dinning PG et al. Neurogastroenterol Motil, 2015

Session Category

Organ and Tissue Biomechanics: N/A

OA97-02

The Generalized-Kelvin-Voigt-Based Visco-Hypoelastic Model Describes the Rate-Dependent Thixotropic Behavior of Individual Collagen Fibrils Under Uniaxial Tension

Msc You-Rong Chiang[1,2], Dr Orestis G. Andriotis[1], Prof Claire Morin[3], Prof Christian Hellmich[2], Prof Philipp J. Thurner[1]

[1]Institute of Lightweight Design and Structural Biomechanics, TU Wien, Vienna, Vienna, Austria. [2]Institute for Mechanics of Materials and Structures, TU Wien, Vienna, Vienna, Austria. [3]Mines Saint-Étienne, Université Jean Monnet, Saint-Étienne, Auvergne-Rhône-Alpes, France

Introduction

Collagen fibrils provide mechanical support for most biological tissues and exhibit rate-dependent and thixotropic behavior under uniaxial tension by atomic force microscopy (AFM) [1,2]. Using the Mooney-Rivlin (MR) model in rate form within a visco-hypoelastic framework, we have previously decoupled the elastic part from the fibril total response [3]. In this process we have identified two dissipation regimes associated with molecular straightening and twisting, respectively. Here, we present an extension of our model including the dissipative behavior by implementing the generalized Kelvin-Voigt (GKV) rheological model into the visco-hypoelastic formulation.

Methods

We re-formulate the visco-hypoelastic model analogously to the GKV model. The elastic portion is governed by the MR model, while the viscous portion is represented by the Kelvin-Voigt (KV) element in series to the elastic portion. The spring in the KV element is also specified as MR type. Material parameters are determined through a two-step least-squares procedure: the first step is to identify the elastic MR properties and the latter to identify the viscous KV properties.

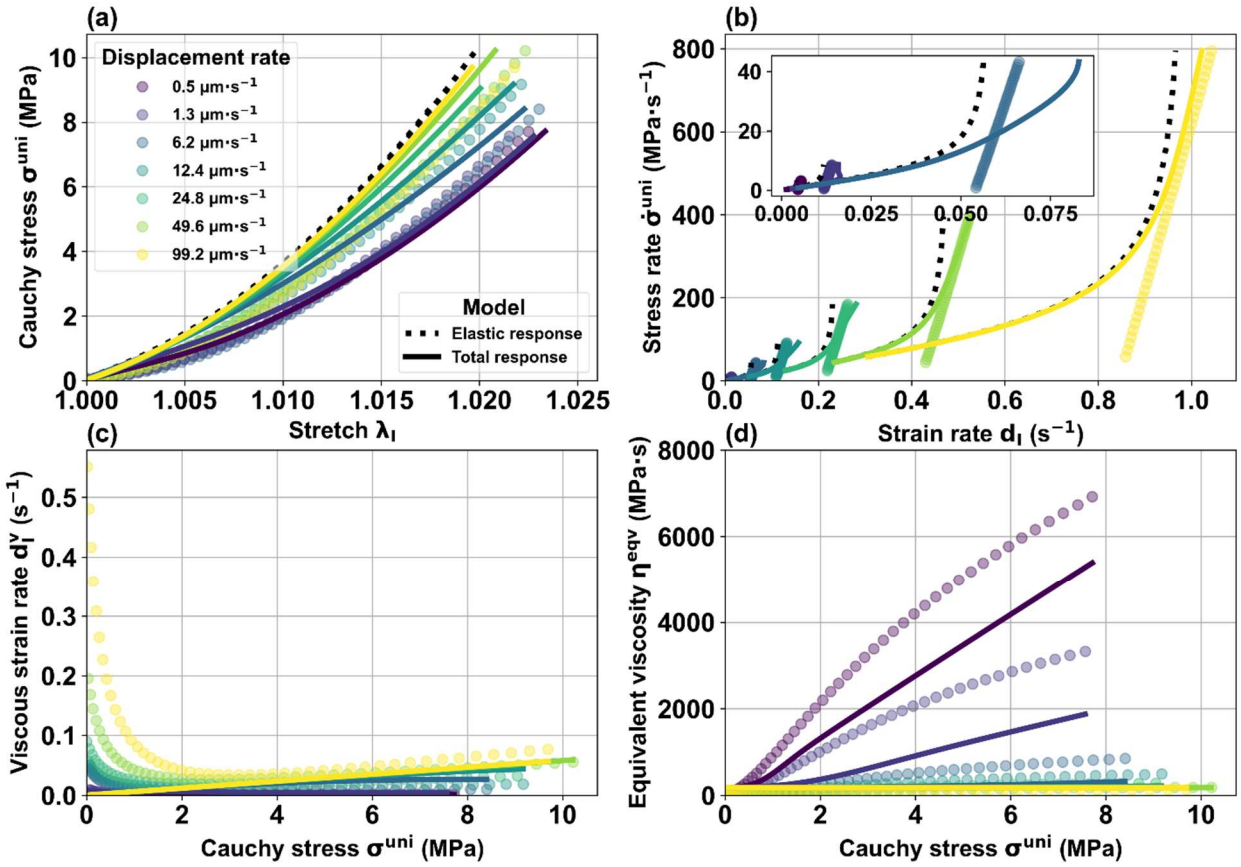
Results

The rate-type MR model yields an initial hypoelastic modulus of about 188 MPa, corresponding to the stiffest fibril response at the infinite strain rate (black dotted line in Figure a and b). Two dissipation regimes are found and separated at around 2 MPa , whereupon the second regime is well-described by the GKV model (Figure c). The model also captures the thixotropic behavior of collagen fibrils, as the equivalent viscosity increases with the decreasing displacement rates (Figure d).

Discussion

The GKV-based visco-hypoelastic model presented describes the rate-dependent and thixotropic behavior of individual collagen fibrils. Nevertheless, the current model is restricted to describing the second dissipation regime only (Figure c). The dissipative portion represented by the KV element alone leads to the underestimation of the equivalent viscosity at low displacement rates (figure d). The current study represents a first step toward a comprehensive visco-hypoelastic description of collagen fibrils, with further refinements needed.

Images (Optional)



References (Optional)

[1] Orestis G. Andriotis et al. , ACS NANO, 2018.

[2] Martin Handelshauser et al. , J. Biomech. Behav. Biomed. Mater., 2023.

[3] You-Rong Chiang et al. , Mech. Adv. Mater. Struct. [Manuscript Submitted for publication].

Acknowledgements (Optional)

This project was financially supported by EU Horizon 2020 Marie Skłodowska-Curie programme (grant number 101034277) and ERASMUS+ 2023 EULiST project (grant number 101124310).

Session Category

Organ and Tissue Biomechanics: N/A

OA97-03

Microscale Structure-Mechanics Coupling in Hypertrophic Cardiomyopathy

Mr Dimosthenis Giannopoulos[1], Dr Maja Schlittler[2], Dr Marzia De Bortoli[2], Prof Raffaele Coppini[3], Dr Mina Petrovic[4], Mrs Ekaterina Oleinik[1], Mr Kariem El Saedi[1], Prof Elisabetta Cerbai[3], Prof Philipp J. Thurner[1], Dr Alessandra Rossini[2], Dr Orestis G. Andriotis[1]

[1]Institute of Lightweight Design and Structural Biomechanics, TU Wien, Vienna, Vienna, Austria. [2]Institute for Biomedicine, Eurac Research, Bolzano, South Tyrol, Italy. [3]Department of Neurosciences, Psychology, Drug Research & Child Health, University of Florence, Florence, Tuscany, Italy. [4]Institute of Materials Science and Technology, TU Wien, Vienna, Vienna, Austria

Introduction

Hypertrophic cardiomyopathy (HCM) is strongly associated with interstitial fibrosis, a key regulator of ventricular stiffening. Cardiac fibroblasts (CFs), mediators of extracellular matrix (ECM) remodeling, are highly mechanosensitive and respond to matrix stiffening, which may drive disease progression. Three-dimensional cell spheroids (CSs) mimic the native cellular microenvironment and enable micromechanical testing via parallel-plate compression. Yet the micromechanics of HCM CFs-derived CSs remain insufficiently characterized. Here, we employed compression, stress-relaxation analysis, and confocal imaging to characterize the viscoelastic-structural properties in healthy and HCM CF-derived CSs.

Methods

Four CS groups were studied: control untreated (CU) and treated with TGF-β (CT), HCM untreated (HCMU) and treated with TGF-β (HCMT). TGF- activation in fibrosis is linked to collagen synthesis - a key response to inflammation. Parallel-plate compression (CellScale MicroSquisher) tests were performed in a quasi-static ramp at 50% strain and 0.5μm/s displacement rate. Force-displacement data analyzed using a Mooney–Rivlin hyperelastic model with nonlinear contact effects. Stress-relaxation tests (30% strain, 90s hold) were fitted with a generalized Maxwell model. Confocal imaging detected collagen (picrosirius red) and α-smooth muscle actin (α-SMA). Statistical analysis used Kruskal-Wallis or ANOVA with post hoc tests ($\alpha < 0.05$).

Results

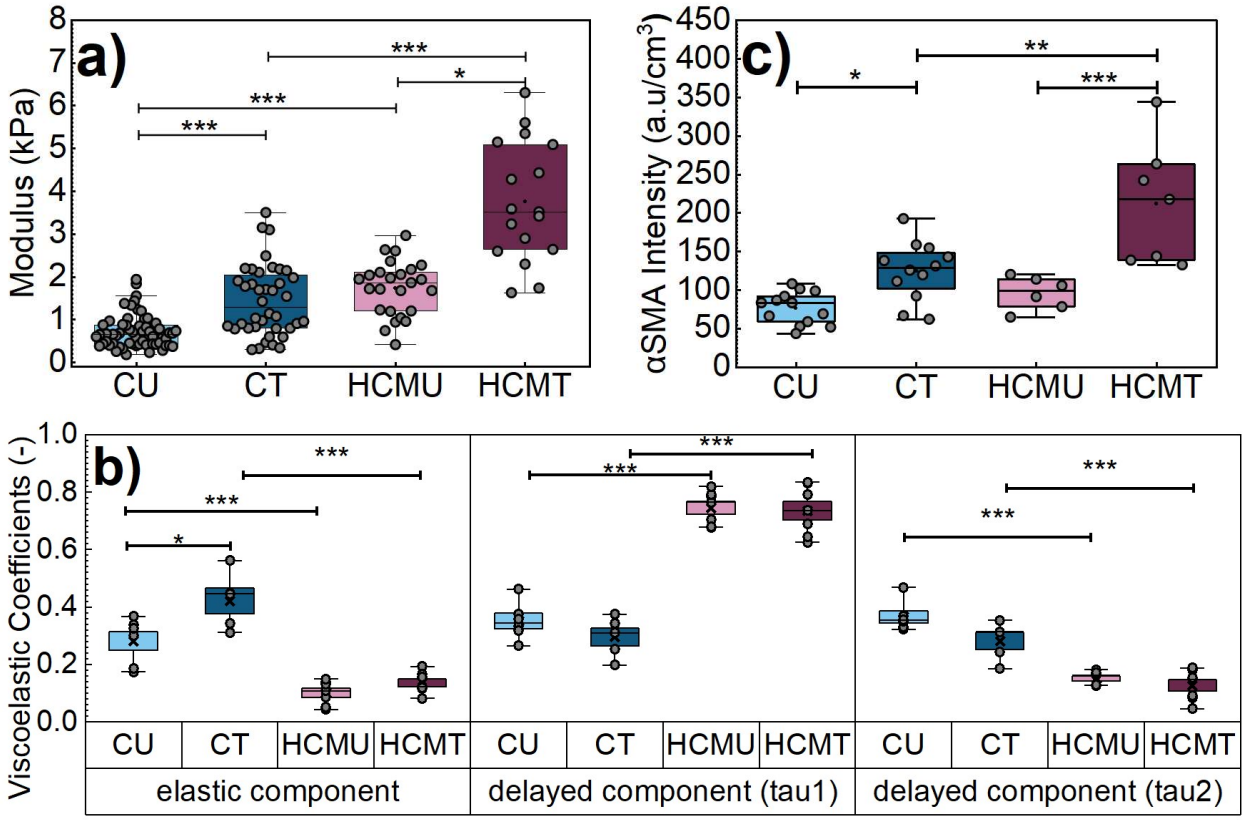
Figure1 shows results obtained from mechanical testing and confocal imaging on CSs derived from primary human CFs. Each scatter represents a measurement from one CS. HCM spheroids exhibited a nearly three-fold higher modulus than controls, with TGF-β

inducing an additional two-fold increase (Figure1a). Stress-relaxation revealed two-phase decay, successfully captured by the Wiechert model. HCM CSs showed higher viscous components. TGF-β increased elastic components, especially in controls, with slight viscous reduction (Figure1b). Confocal imaging revealed a marked induction of α-SMA by TGF-β, particularly in HCMT (Figure1c).

Discussion

In summary, the mechanical and structural analysis demonstrates that HCM CFs–derived CSs possess a distinct viscoelastic and structural phenotype consistent with fibrotic remodeling. However, further research is required to elucidate all aspects of this model, with particular emphasis on pathways such as TGF-β and HIF, which are known to contribute to other types of fibrosis, i.e. lung interstitial fibrosis.

Images (Optional)



Session Category

Organ and Tissue Biomechanics: N/A

OA97-04

Frequency-Dependent Changes in the Viscoelastic Properties of Porcine Brain Tissue

Ms. Laura Ruhland, Prof. Dr.-Ing. habil. Kai Willner

Institute of Applied Mechanics, Friedrich-Alexander University of Erlangen–Nuremberg, Erlangen, Bavaria, Germany

Introduction

A persistent problem in the mechanical characterization of brain tissue is the inconsistency in responses that result from different testing techniques. Particularly challenging are experiments with different time scales [1]. The aim of this study is to combine mechanical responses obtained in varying time scales and consequently characterize brain tissue over an extended time range.

Methods

To obtain the frequency-dependent material response Magnetic Resonance Elastography (MRE) was performed in three different brain areas, as well as in liver tissue. The liver tissue serves as a comparative material due to its widespread clinical and experimental use in MRE applications [2]. A tabletop MRE system, which is described in detail in [3], was used to acquire the responses for frequencies from 300 to 2100Hz. The material behavior of the brain tissue in the quasi-static time domain was examined through multi-modality rheometer experiments under cyclical loading and relaxation. From both experimental responses the frequency-dependent storage and loss moduli were calculated, with the modulus obtained from the time-domain measurements corresponding to 0Hz. A viscoelastic model was calibrated using the combined material response over the whole frequency range.

Results

Fig. 1 shows the measured storage and loss moduli as well as the calibrated model for the brain areas and the liver. The storage modulus indicates the elasticity of the material, whereas the loss modulus quantifies the viscous dissipation. All tissues exhibit a higher storage than loss modulus at low frequencies, while at high frequencies the loss modulus surpasses the storage modulus. However, the frequency point at which the loss modulus exceeds the storage modulus varies for every tissue.

Discussion

The findings indicate that the viscoelastic behavior of brain and liver undergoes a transition from an elasticity-dominated to a viscous-dominated response with increasing frequency. Furthermore, every tissue type has a unique frequency at which the material behavior transits. Therefore, we propose the crossover frequency as a model-independent material parameter to describe the viscoelastic properties of brain and liver tissue.

Images (Optional)

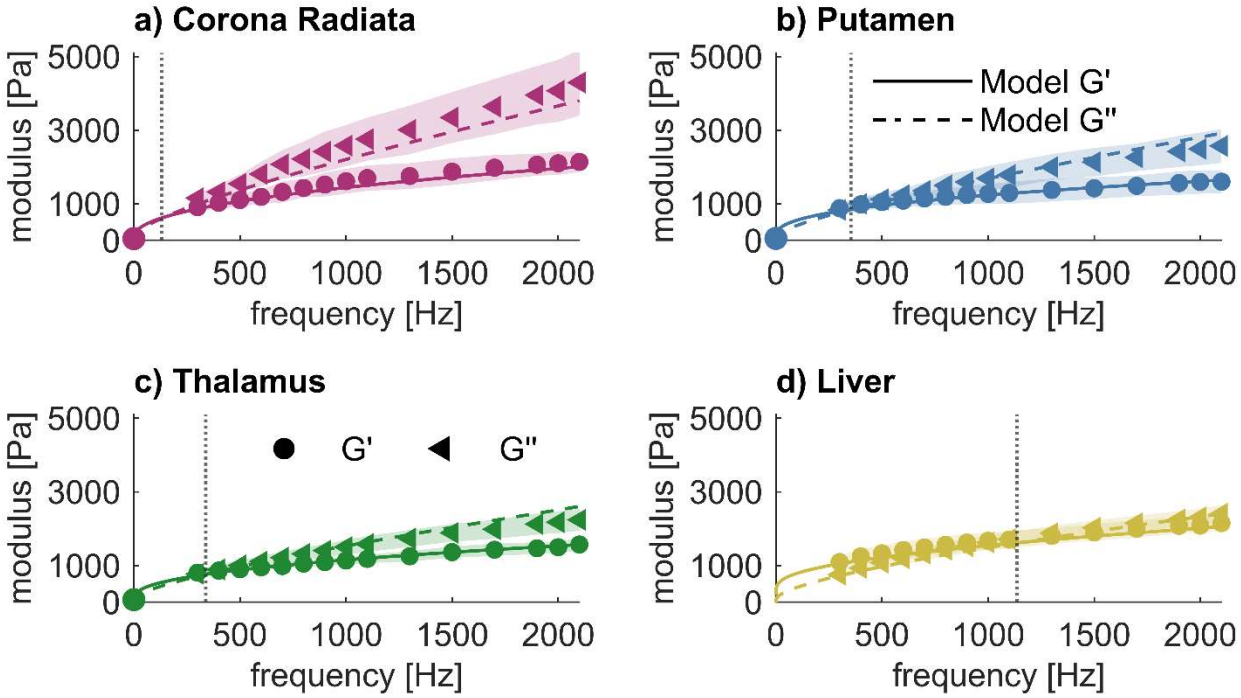


Figure 1: Measured (Mean ± Std) and modeled storage (G') and loss modulus (G"). The dotted line indicates the crossover frequency at which the loss modulus exceeds the storage modulus.

References (Optional)

[1] Faber, Jessica et al. , Current protocols, 2022

[2] Venkatesh, Sudhakar K. et al. , Journal of Magnetic Resonance Imaging, 2013

[3] Braun, Jürgen et al. , Magnetic resonance in medicine, 2018

Session Category

Organ and Tissue Biomechanics: N/A

OA97-05

Decidualization during pregnancy alters collagen microarchitecture and mechanical response of the endometrium

Ms. Catalina Bastias, Dr. Matthew Dean, Dr. Callan Luetkemeyer

University of Illinois Urbana-Champaign, Urbana, IL, United States

Introduction

Infertility affects 8-12% of reproductive-age couples [1], and endometrial dysfunction—specifically, impaired decidualization—is believed to account for ~20% of cases. The endometrium, the uterus's innermost layer, undergoes cyclical proliferation, differentiation, and shedding with each menstrual cycle [2]. Decidualization is the process marked by dramatic cellular changes, thickening, and extensive extracellular matrix (ECM) remodeling to create a receptive environment for embryo implantation [2]. Because the ECM is heavily implicated, mechanical imaging techniques such as elastography may enable diagnosis and guide the development of treatments, which remain elusive. Thus, this study examines how decidualization influences endometrial stiffness and collagen microstructure.

Methods

8-week-old C57BL/6 female mice (n=6) were mated, then euthanized on day 8 of pregnancy. One uterine horn was cut along the antimesometrial (AM) pole (implantation pole) and the other along the mesometrial (M) pole. Samples were stained, then indented using a glass ~1 mm microsphere. 3D confocal microscopy images were captured during and after indentation at the decidualized implantation site (IS) and undecidualized inter-implantation sites (IIS). Indentation depth was estimated, from which an indentation modulus was calculated using the Hertz model (Fig.1A). Collagen microstructure was assessed via second harmonic generation imaging. Custom Python code quantified fiber orientation (azimuth and elevation); the alignment index was calculated as the inverse of the standard deviation in azimuth angle. Two-way ANOVA evaluated effects of pole (AM vs. M) and decidualization (IS vs. ISS), with significance defined as $p<0.05$.

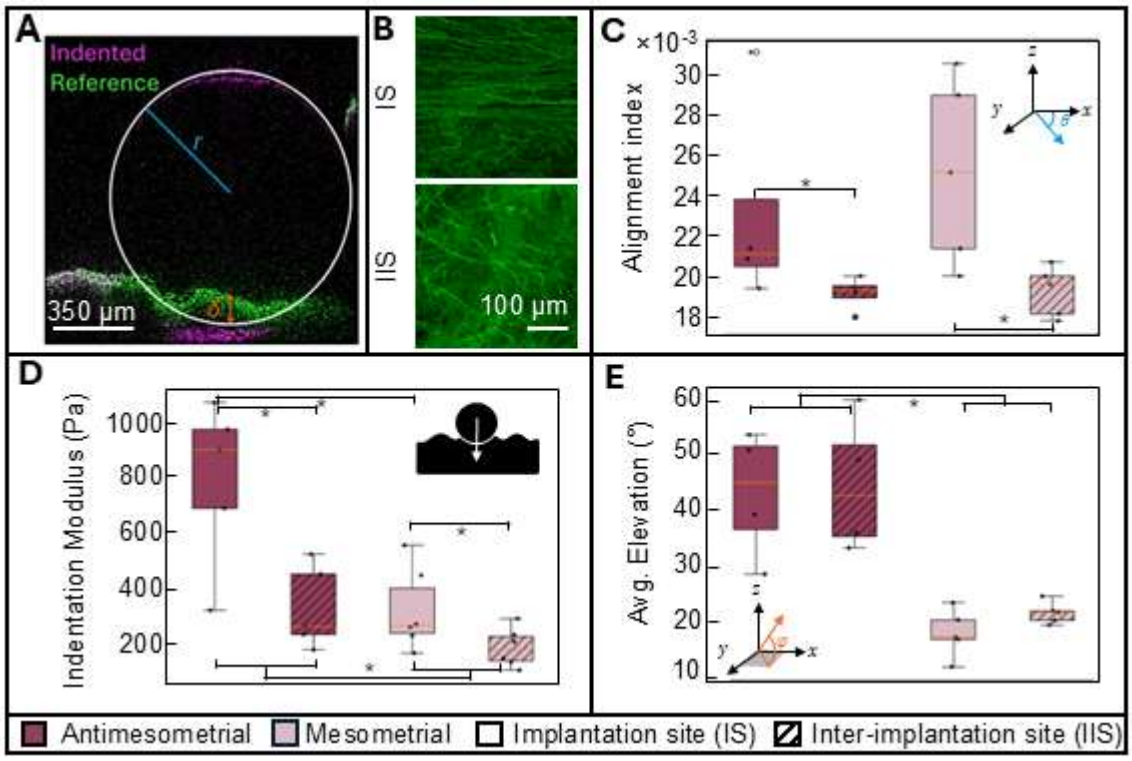
Results

Both decidualization and pole significantly affected indentation modulus. Stiffness was higher at the AM pole and increased with decidualization, with post-hoc differences in AM-IS vs. AM-IIS and AM-IS vs. M-IS (Fig.1D). Collagen fibers were more aligned at the IS (Fig.1B-C), and elevation angle was larger at the AM pole regardless of decidualization status (Fig.1E).

Discussion

This is the first study to jointly characterize mechanical and microstructural changes during decidualization; results demonstrate that decidualization causes circumferential collagen alignment and an increase in indentation stiffness. Future work will examine mechanical anisotropy and models of impaired decidualization to inform mechanics-based diagnostics of uterine infertility.

Images (Optional)



References (Optional)

[1] Hanson et al., *J Assist Reprod. Genet,* 2017

[2] Strowitzki et al., *Hum. Reprod Update,* 2006

Session Category

Organ and Tissue Biomechanics: N/A

OA98-01

COP Jump Metrics Reveal Bilateral Compensation and Increased Movement Variability Following ACL-Reconstruction

Dr Suzanne M Konz PhD, ATC, CSCS

Marshall University, Huntington, West Virginia, United States

Introduction

Countermovement jumps (CMVJ) are viewed as symmetrical tasks that mask neuromuscular deficits after anterior cruciate ligament reconstruction. However, the center of pressure (COP) behavior and force-time metrics may reveal compensation strategies that are not visible in traditional bilateral outputs. This study examined whether participants with ACL reconstruction (ACL-R) demonstrate altered control, loading patterns, and movement consistency during double-leg jumping compared with healthy teammates.

Methods

420 participants (323 controls particpants, 97 ACL-R (54 males, 43 females) completed force plate (Sparta Science, Sparta Plate) CMVJ testing protocol. Variables extracted included COP sway velocity, unweighting and eccentric COP displacement, landing rate of deceleration, unweighting and concentric timing, time to takeoff, time to peak acceleration, modified reactive strength index, and force expression metrics. Group differences were evaluated using Mann-Whitney U tests or independent t tests. Variance differences were assessed using Levene tests.

Results

ACL-R participants demonstrated lower COP sway velocity in the frontal plane ($p \approx 0.000002$) and greater eccentric displacement in the frontal plane ($p \approx 0.000048$). Landing rate of deceleration was lower in the ACL-R group ($p \approx 1.5 \times 10^{\wedge} -15$). Timing differences were seen in concentric duration ($p \approx 0.025$), time to takeoff ($p \approx 0.0038$), and time to peak acceleration ($p \approx 0.005$). Force expression metrics were significantly lower in the ACL reconstructed group, including modified reactive strength index ($p = 3.04 \times 10^{-14}$), relative force at zero velocity ($p = 1.72 \times 10^{-9}$), average maximum force ($p = 3.04 \times 10^{-8}$), eccentric impulse ($p = 0.00003$), and concentric impulse ($p = 7.89 \times 10^{-16}$). Variance analyses indicated greater variability in COP sway, eccentric displacement, unweighting

displacement, landing deceleration, eccentric time, and modified reactive strength index (all $p < 0.05$).

Discussion

ACL-R participants displayed differences in COP control, loading strategy, timing, and force expression during a CMVJ. They demonstrated greater variability across several control and performance measures. These findings show that ACL-R patients do not exhibit unilateral deficits but instead demonstrate bilateral compensation strategies characterized by altered COP control, prolonged timing, reduced force expression, and increased movement variability. COP-based metrics and timing variables may provide sensitive indicators for monitoring recovery and informing return-to-sport decisions.

Images (Optional)

Table 1. Means and Standard Deviation of CMVJ Outcomes.

	Healthy	fACL-R
COPx Sway Velocity Mean (m/s)	0.03 ± 0.13	0.009 ± 0.134
COPy Sway Velocity Mean (m/s)	0.29 ± 0.18	0.201 ± 0.163
COPx Eccentric Displacement)0 (m)	0.002 ± 0.016	0.001 ± 0.032
COPy Eccentric Displacement (m)	0.04 ±0.035	0.024 ± 0.029
COPx Unweighting Displacement (m)	-0.004 ± 0.024	-0.001 ± 0.029
COPy Unweighting Displacement (m)	-0.019 ± 0.037	-0.017 ± 0.029
Avg Landing Rate of Deceleration (m/s^3)	522.562 ± 187.455	366.62 ± 151.083
Unweighting Time (s)	0.385 ± 0.1625	0.400 ± 0.181
Eccentric time (s)	0.368 ± 0.10425	0.395 ± 0.129
Concentric time (s)	0.298 ± 0.052	0.312 ± 0.057
Time to Take Off (s)	1.051 ± 0.166	1.107 ± 0.203
Time to Max Acceleration (s)	0.916 ± 0.17	0.969 ± 0.217
mRSI - Modified Reactive Strength Index (m/s)	0.384 ± 0.126	0.275 ± 0.09
Relative Force at Zero Velocity (N/kg)	9.892 ± 3.007	7.823 ± 2.599
Average Max Force (N)	2139.475 ± 773.378	1666.481 ± 787.414
Eccentric Impulse (N/kg)	0.59 ± 0.192	0.496 ±0.157
Concentric Impulse (N/kg)	2.518 ± 0.41	2.113 ± 0.358

Session Category

Rehabilitation Biomechanics and Human Factors: Rehabilitation

OA98-02

Knee Contact Forces of TKA Patients with Asymmetrically Shortened Crankarm Lengths during Ergometer Cycling

Professor Songning Zhang PhD, FNAK, FACSM[1], Dr. Walter Menke PhD[1], Mr. Alejandro Ovispo-Martinez[1], Mr. Tsung-Lin Lu[1], Dr. Katie Stevens DPT[2], Dr. Harold Cates MD[2]

[1]University of Tennessee, Knoxville, TN, United States. [2]Tennessee Orthopaedic Alliance, Knoxville, TN, United States

Introduction

Stationary cycling is a common method used for rehabilitation of patients post total knee arthroplasty (TKA) and crankarm shorting on the replaced showed reduced knee range of motion (ROM) and unaltered knee extension moment (1). However, it is still unknown what effects of these adjustments may have on knee joint loading. The purpose of this study was to quantify the knee contact forces during cycling with asymmetrical crank arm shortening in individuals 1-2 months after TKA.

Methods

Seven participants who received a cruciate retaining implant cycled at 70 W and 70 RPM in three cycling conditions: 170mm standard crank arms on both side, and shortened 155mm and 140mm crank arms on the replaced limb and 170mm on the non-replaced limb. Kinematic (240 Hz) and pedal reaction force (PRF, 1200 Hz) data were collected simultaneously using a 12-camera motion analysis system (Vicon, Oxford, UK). The cycling tasks were conducted with a cycle ergometer (Lode). Static optimization and joint reaction analysis were conducted using a knee model in OpenSim to estimate the total knee contact force (TCF), and medial (MCF) and lateral (LCF) compartment contact forces. A one-way repeated measures ANOVA was used to assess the potential effects on MCF, LCF, and TCF as well as peak muscle forces ($p<0.05$).

Results

Decreases in crank length led to significantly reduced TCF and LCF within the replaced limb at 140mm and 155mm compared to 1700mm with $p=0.002$ and $p=0.011$, respectively (Table 1).

Discussion

Findings from this work along with the reduced knee ROM and unchanged knee extension moment previously reported, suggest that asymmetric crankarm shortening can accommodate the reduced knee ROM without overloading the knee joint. The current simulation results actually showed added benefits of reduction in knee compressive contact forces with reduced crankarms. These results suggest that stationary cycling with shorter crankarms can be implemented early in the rehabilitation process of patients with TKA to accommodate their knee stiffness while not adversely affecting estimated internal knee loading and altering knee muscle forces.

Images (Optional)

Table 1: Peak knee contact forces, vertical pedal reaction force, and knee muscle forces (N, mean ± std).

Variable	C1 (140/170)	C2 (155/170)	C3 (170/170)	p-value (η_p^2)
Total Contact Force	830.99 ± 301.94 [a]	857.75 ± 282.16 [a]	1036.28 ± 264.34	**0.002** (0.660)
Medial Contact Force	432.71 ± 203.15	447.01 ± 153.66	502.53 ± 168.63	0.082 (0.341)
Lateral Contact Force	434.20 ± 148.92 [a]	446.81 ± 180.72 [a]	551.79 ± 129.60	**0.011** (0.660)
PRF	227.51 ± 47.82	225.22 ± 47.49	230.29 ± 42.00	0.876 (0.022)
Quadriceps Force (N)	932.17 ± 321.10	942.80 ± 395.74	1101.88 ± 487.82	0.151 (0.270)
Hamstrings Force (N)	288.57 ± 65.91	321.00 ± 72.58	353.50 ± 197.52	0.428 (0.113)

a: significant difference from C3, η_p^2: partial eta squared.

References (Optional)

1. Menke et al. 2025 *2025 Congress of ISB*.

Acknowledgements (Optional)

Funded by 2024 ISB Matching Dissertation Grant.

Session Category

Rehabilitation Biomechanics and Human Factors: Rehabilitation

OA98-03

Biomechanical Performance Profiling Demonstrates a Lack of Performance Readiness Compared to Isolated Benchmarks in Athletes 14 Months Post ACL Reconstruction

Mr. Zachary McClean PhD Candidate[1], Dr. Ricardo da Silva Torres PhD[2], Dr. Walter Herzog PhD[1], Dr. Kati Pasanen PhD[1], Dr. Matthew Jordan PhD[1]

[1]University of Calgary, Calgary, AB, Canada. [2]Wageningen University & Research, Wageningen, Wageningen, Netherlands

Introduction

In addition to a high risk for subsequent anterior cruciate ligament (ACL) injury, athletes who have returned-to-sport (RTS) after ACL reconstruction (ACLR) demonstrate long-term disruptions in neuromuscular performance related to a loss of power, explosive strength and impaired biomechanics. However, the best approach to measure neuromuscular performance-readiness in this population is unclear. RTS readiness is typically determined using isolated metrics and tests (e.g., quadriceps strength, jump biomechanics) and the interlimb asymmetry index (AI). This yields numerous neuromuscular and biomechanical outcome measures. Beyond additive models based on isolated tests and outcomes, supervised machine learning (ML) has been used successfully in healthy athletes to generate performance profiles based on a weighted combination of characteristics. Additionally, ML model explainability has been used in health care settings to gain insights into the output of ML models to identify functional limitations at the individual level. Whether biomechanical performance profiling using ML and model explainability provides enhanced information on athlete performance-readiness after their RTS from ACLR compared to isolated AI measures using the contralateral limb benchmark has yet to be tested. The purpose of this study was to compare the proportion of athletes who meet an AI benchmark < 10% based off isolated metrics to the proportion of athletes classified into a target profile using BPP_{ML}.

Methods

A supervised BPP_{ML} was developed to classify healthy control athletes to sport-specific and sex-specific biomechanical profiles based on their maximal leg extensor strength, vertical jump and repeat hop testing mechanics. Competitive athletes with ACLR beyond RTS (n=19; post-op: ~14 months) performed the same biomechanical assessment. The proportion of athletes meeting a <10% AI criteria were compared to the BPP_{ML} classification.

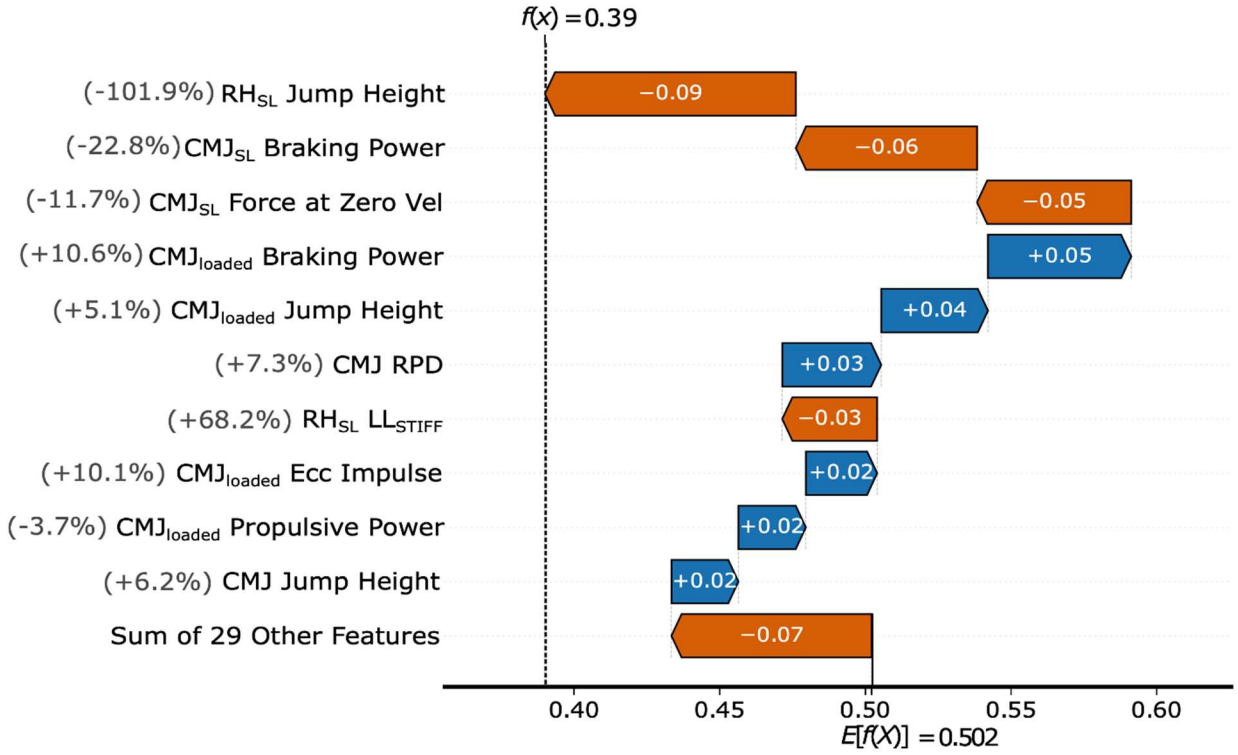
Results

After training, the BPP_{ML} showed >93% classification accuracy in healthy controls. ACLR athletes were less likely to belong to the target profile using a BPP_{ML} (16% ACLR athletes) compared to the AI criteria (43-63%, mean=54%) (p=0.01). ML explainability identified individualized biomechanical features influencing the classification outcome (Fig 1).

Discussion

This BPP_{ML} approach should be tested in clinical and performance settings to better understand its applicability for highlighting the long-term impact of ACLR on biomechanical and neuromuscular performance after RTS.

Images (Optional)



Session Category

Rehabilitation Biomechanics and Human Factors: Rehabilitation

OA98-04

Rotator Cuff Activation in Post-operative Rehabilitation Exercises

Ms Minah Waraich BS, Ms Silvia Zanini MS, Dr Andreas Kontaxis PhD, Dr Julia Retzky MD, Dr Michael Fu MD, Ms Bridget Assip PT, DPT, PCS, C/NDT, Dr Jennifer Jezequel PT, DPT, PCS, EdD, Ms Sophia Wang BS

Hospital For Special Surgery, New York, New York, United States

Introduction

Rotator cuff (RC) tears are a common shoulder injury, with supraspinatus repairs being the most frequent, and a high prevalence of complications and re-tears. Excessive muscle load is considered a factor contributing to repair failure. Standard rehabilitation involves 6 weeks of immobilization, with gradual progression to passive ROM and active ROM. Immobilization, however, increases risk of stiffness and muscle atrophy. The objective is to characterize RC muscle activations, with a focus on supraspinatus, during common post-operative rehabilitation exercises. This will inform clinicians to progressively increase load during rehabilitation to minimize complications.

Methods

Nine healthy volunteers (9M, 28.3±5.14years; 180.7±6.23cm; 87.28±13.38kg) performed 9 commonly prescribed post-operative RC exercises (Figure 1). Participants performed maximal voluntary isometric contractions (MVICs). Muscle activity of the infraspinatus, supraspinatus, and subscapularis was recorded using fine-wire EMG.

The raw EMG data were processed using MATLAB. Raw signals were scaled, rectified, and DC offsets were removed. The linear envelope was normalized to 1000 points for time alignment. The peak linear envelopes (PLE) were defined with repetition's averaged. Average PLE was normalized by MVICs. The mean %MVIC across subjects for each muscle and exercise was categorized based on the following literature thresholds: Low (0–20%), Moderate (21–40%), High (41–60%), and Very High (>60%).

Results

The supraspinatus exhibited low activation in: pendulum (9%), shoulder stabilization with ball on wall (18%), shoulder IR Isometric (9%), shoulder IR with Band (9%), and shoulder ER (15%), and moderate activation in: walking hand up wall (31%), Row (34%), shoulder IR ROM Towel Pass (24%) and scaption (39%). High activation was shown in the infraspinatus

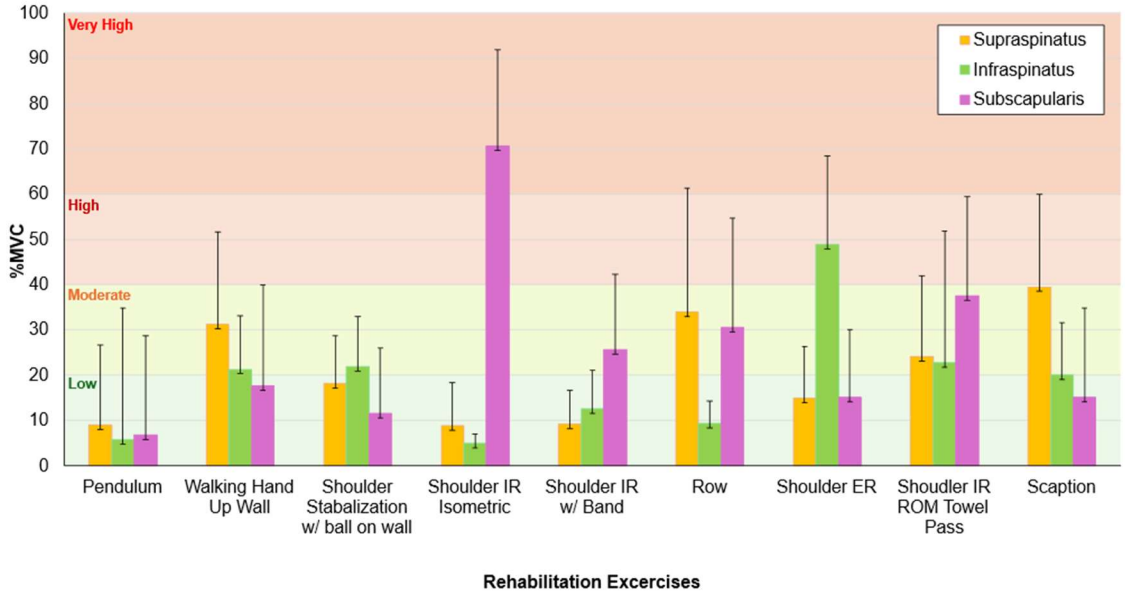
during shoulder ER (49%), and very high activation in the subscapularis during shoulder IR isometric (71%).

Discussion

During early-phase rehabilitation low activation exercises are appropriate for rehabilitation, while moderate activation exercises should be implemented during later phases. For supraspinatus, pendulum, shoulder stabilization, and IR/ER rotation with bands are recommended for early phase. Scaption, row, and walking hand up the wall exercises should follow later. Future work will incorporate a computational model to define muscle loading, for optimized rehabilitation.

Images (Optional)

Figure 1: Average %MVIC of supraspinatus, infraspinatus, and subscapularis during 9 shoulder rehabilitation exercises.



Acknowledgements (Optional)

This study was funded by the Hospital for Special Surgery Surgeon-in-Chief Grant (SIC).

Session Category

Rehabilitation Biomechanics and Human Factors: Rehabilitation

OA98-05

The Relationship Between Changes in Cartilage Thickness and Knee Joint Contact Stress: A Comparison of Walking and Running

Mr Shinya Ogaya PhD, Ms Riona Kaizu BS, Ms Moko Kitahara BS, Mr Satoshi Horiguchi BS, Mr Kenta Horiuchi MS, Mr Masahiko Shimamura PhD

Saitama Preferctural University, Koshigaya, Saitama, Japan

Introduction

Repetitive weight-bearing loads on the knee joint compress cartilage, reducing its water content and thickness. However, it remains unclear whether changes in cartilage thickness are correlated with the magnitude of joint contact force. In this study, we used walking and running to vary the magnitude of cartilage loading and examined the resulting changes in cartilage thickness.

Methods

We recruited 11 recreational runners aged over 45 years who reported knee pain and had no history of knee surgery. The study included measurements of cartilage thickness, motion analysis, and imaging (X-ray and MRI). Cartilage thickness was assessed using ultrasound at four sites: medial and lateral tibiofemoral (mTF, lTF) and medial and lateral patellofemoral (mPF, lPF) joints. Measurements were performed before and after 10 minutes of treadmill walking or running. Motion analysis was performed using a three-dimensional motion capture system while participants walked or ran on a treadmill. The tibio-femoral and patella-femoral joint alignment of musculoskeletal model were individually adjusted using X-ray-derived femoro-tibial angle and MRI-based patellofemoral facet orientation, respectively. Vertical contact forces normalized to squared height at mTF, lTF, mPF, and lPF were estimated during the stance phase using OpenSim. Paired t-tests compared walking and running; Pearson correlation was used to examine the force-thickness relationships.

Results

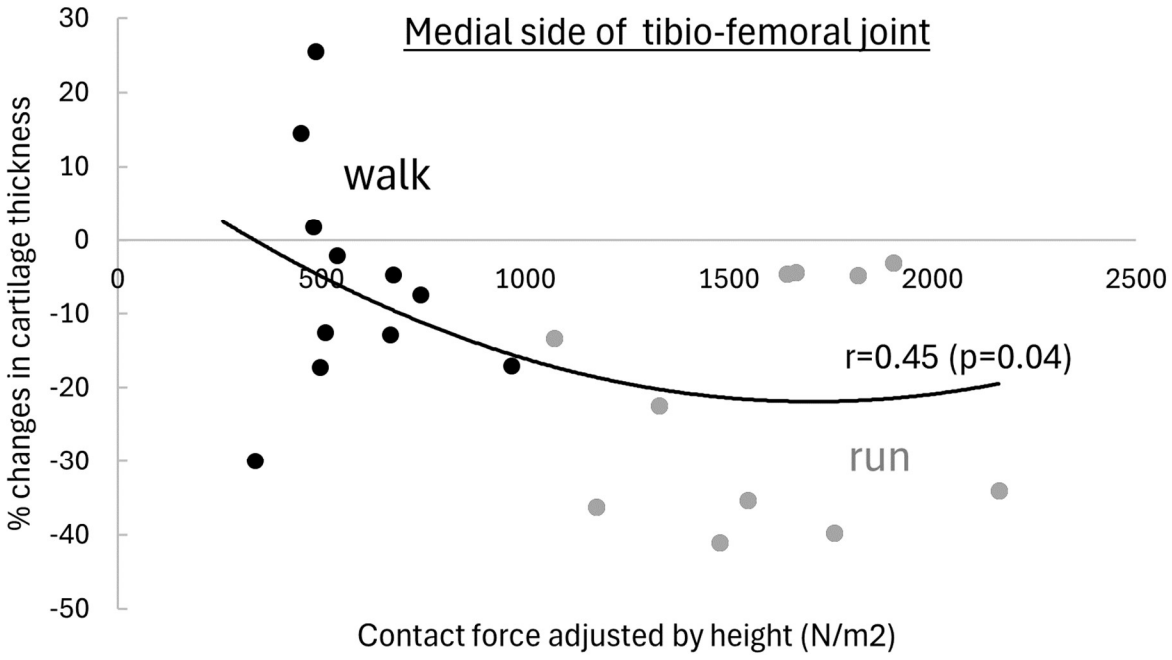
Contact forces at all joint sites were significantly higher during running compared to walking. Percentage change in cartilage thickness at the mTF joint decreased significantly more after running (-21.1%) than after walking (-5.6%). When the walking and running data were combined, the percentage change in cartilage thickness was significantly associated

with the contact force at the mTF in a quadratic manner (r=0.45, p=0.04) with higher contact forces corresponding to larger decreases in cartilage thickness shown in Figure.

Discussion

Cartilage thickness decreased more after running than after walking, suggesting that cartilage is more susceptible to deformation under higher mechanical stress. This finding indicates that the cartilage thickness response may be associated with the magnitude of joint loading.

Images (Optional)



Session Category

Rehabilitation Biomechanics and Human Factors: Rehabilitation

OA98-06

Understanding Hip–Spine Compensations in Low Back Pain through Biokinetic Analysis

Dr. Felipe Gonzalez MD, MSc[1,2,3], Dr. Gustavo Leporace PhD[1,2], Dr. Jonathan Gustafson PhD[3], Dr. Dino Samartzis PhD[3], Dr. Eliane Guadagnin PhD[2], Mr. Joshua Samaniego MD Candidate[4], Dr. Jose Dutra MD[2], Dr. Carolline Popovicz MD[2,3], Dr. Matheus Vilela MD[2,3], Dr. Jorge Chahla MD, PhD[3], Dr. Leonardo Metsavaht MD, PhD[1,2], Dr. Marcus Luzo MD, PhD[1,5]

[1]Universidade Federal de São Paulo, Department of Diagnostic Imaging, São Paulo, SP, Brazil. [2]Instituto Brasil de Tecnologias da Saúde (IBTS), Department of Research in Biomechanics, Rio de Janeiro, RJ, Brazil. [3]Rush University, Department of Orthopedic Surgery, Chicago, Illinois, United States. [4]Rush Medical College, Chicago, Illinois, United States. [5]5. Universidade Federal de São Paulo, Department of Orthopedics and Trauma, São Paulo, SP, Brazil

Dr. Felipe Gonzalez

Introduction

The spine and hips are biomechanically interconnected, and disorders affecting both are often categorized under hip-spine syndrome. This study explores the link between pelvic motion impairments and hip physical characteristics in low back pain patients with increased contralateral pelvic drop and anterior tilt during gait. The hypothesis was that hip strength and flexibility would correlate with pelvic gait kinematics.

Methods

This cross-sectional retrospective study included participants with a mean age of 44.6 (Range: 21–60) years, presenting acute or chronic low back pain and independent gait. Participants had been previously categorized into distinct gait profiles (P1: Flexed trunk, P2: Lumbar rectification; P3: Pelvic impairment; P4: Trunk extension and rotation; P5: Tight axial control) based on three-dimensional gait kinematics using machine learning algorithms. The current analysis examined intra-profile correlations between pelvic motion during gait (pelvic drop and anteversion) and clinical measures of hip function (hip abductor strength and hip flexor/extensor flexibility). Spearman's rho was used to assess linear correlations and normalized mutual information was computed to explore non-linear associations. Statistical significance was set at 5%.

Results

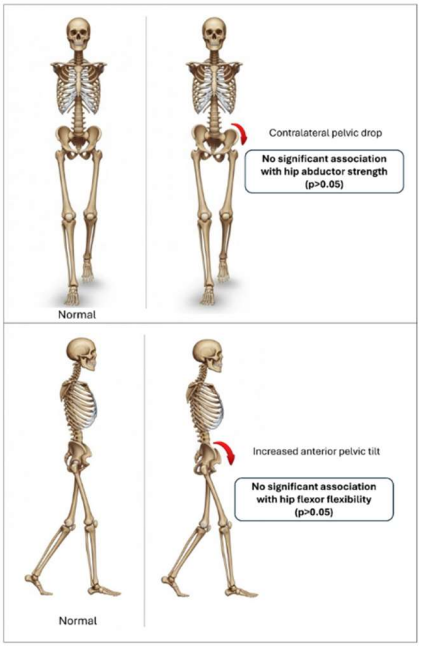
No statistically significant correlations were found for profiles 3, 4, and 5 ($p > 0.05$) (Figure 1). Although significant correlations between hip strength/flexibility and pelvic kinematics emerged within profiles 1 and 2, as well as when considering profiles 1–5 as a single group ($p < 0.05$), these lacked clinical relevance due to low biomechanical plausibility.

Discussion

This study builds on previous literature on gait profiles in low back pain and provides new insights into the mechanisms underlying hip-spine syndrome. There was no association between hip strength or flexibility and altered pelvic kinematics during gait in individuals with low back pain. These findings suggest that the observed pelvic motion impairments are likely compensatory responses rather than primary deficits in the hip musculature. As such, interventions aiming to increase strength or flexibility are likely insufficient, and interventions that may further restrict spinal mobility could exacerbate compensatory pelvic mechanics and potentially contribute to the progression of underlying hip pathology. These findings support adding motion analysis to clinical assessment to identify compensatory patterns and refine treatment selection.

Images (Optional)

A



B Spearman's rho

Comparison	Profile 1	Profile 2	Profile 3	Profile 4	Profile 5	Profiles 1-5 combined
Hip Flexor Flexibility vs Mean Pelvic Anteversion	0.49**(0.020)***	-0.19(0.441)	0.04(0.830)	-0.22(0.271)	0.34(0.252)	0.01(0.884)
Hip Flexor Flexibility vs Pelvic Anteversion ROM	0.05(0.837)	-0.33(0.187)	0.01(0.953)	0.17(0.408)	0.04(0.892)	-0.04(0.696)
Hamstrings Flexibility vs Mean Pelvic Anteversion	-0.37(0.093)	-0.28(0.265)	0.21(0.297)	-0.01(0.959)	-0.10(0.735)	-0.06(0.567)
Hamstrings Flexibility vs Pelvic Anteversion ROM	0.03(0.911)	-0.09(0.727)	-0.24(0.234)	-0.21(0.308)	0.24(0.418)	**-0.24(0.014)***
Hip Abductor Strength vs Mean Contralateral Pelvic Drop	0.18(0.426)	**0.57(0.016)***	0.13(0.521)	-0.06(0.757)	-0.50(0.060)	0.00(0.974)
Hip Abductor Strength vs Pelvic Anteversion ROM	0.10(0.649)	-0.19(0.456)	0.17(0.394)	0.28(0.168)	-0.25(0.360)	0.10(0.300)

ROM: Range of Motion. *p<0.05.

C Normalized Mutual Information

Comparison	Profile 1	Profile 2	Profile 3	Profile 4	Profile 5
Hip Flexor Flexibility vs Mean Pelvic Anteversion	0.27	**0.43***	0.11	0.34	**0.43***
Hip Flexor Flexibility vs Pelvic Anteversion ROM	**0.41***	0.32	0.18	0.29	0.39
Hamstrings Flexibility vs Mean Pelvic Anteversion	0.22	0.33	0.27	0.26	**0.51***
Hamstrings Flexibility vs Pelvic Anteversion ROM	0.34	0.19	0.32	0.33	0.21
Hip Abductor Strength vs Mean Contralateral Pelvic Drop Coronal	0.21	**0.40***	0.18	0.26	0.38
Hip Abductor Strength vs Pelvic Anteversion ROM Coronal	0.17	0.22	0.19	0.20	0.13

Higher NMI values indicate stronger correlation between physical measures and pelvic motion patterns. ROM: Range of motion; * indicates moderate or stronger associations (NMI ≥ 0.40)

Figure 1: A. Illustration of pelvic compensations observed during gait in a subgroup of patients with low back pain (Pelvic Impairment profile or Profile 3) and the correlation with hip strength and flexibility. Top: Contralateral pelvic drop compared to normal gait, showing no significant association with hip abductor strength. Bottom: Increased anterior pelvic tilt compared to normal pelvic alignment, showing no significant association with hip flexor flexibility.
B and C: Top Panel: Correlation between hip flexor/extensor flexibility and pelvic sagittal kinematics during gait, and between hip abductor strength and contralateral pelvic drop. Values are reported as Spearman's rho (R) and corresponding p-values. **Bottom Panel:** Normalized Mutual Information (NMI) between hip flexor/extensor flexibility and pelvic sagittal kinematics during gait, and between hip abductor strength and contralateral pelvic drop.

References (Optional)

Session Category

Rehabilitation Biomechanics and Human Factors: Rehabilitation

OA99-01

Joint Implant Contact Force During High-Impact Exercises in People With Hip and Knee Replacements

Dr Bernard Liew PhD[1], Dr Leiming Gao PhD[2], Dr Stephen McDonnell PhD[3], Dr Ahmed Soliman PhD[4], Prof Stefan Maas PhD[4], Dr Wenxing Guo PhD[1], Dr Zainab Altai PhD[1], Prof Nelson Cortest PhD[1]

[1]University of Essex, Colchester, Essex, United Kingdom. [2]Nottingham Trent University, y, Nottingham, y, Nottingham, United Kingdom. [3]University of Cambridge, Cambridge, Cambridge, United Kingdom. [4]University of Luxembourg, Luxembourg City, Luxembourg, Luxembourg

Introduction

Subjects with hip or knee joint replacement are commonly advised to avoid high-impact physical activities (PA) because of concerns about implant integrity. Yet high-impact PA can be important for mitigating age-related bone loss. However, the safety of such PA on the joint implants remains uncertain. This study quantified implant loads across a spectrum of high-impact PA in people with hip or knee joint replacement.

Methods

Eleven participants with total hip (55.9 [9.8] years), four with a total knee (63.7 [4.8] years), and three with a unicompartmental knee (65.3 [2.5] years) replacement who had successfully returned to high-impact PA participated. Optical motion capture (Vicon) with in-ground force plates (Kister) and an instrumented treadmill (Bertec) were used. Participants performed both overground and treadmill walking and running (various slopes and cadences), countermovement jumps, unilateral and bilateral hopping, drop landing, and change of direction (COD) at various intensity levels.

Results

For participants with a total hip replacement, COD, unilateral hopping, and running produced >1.5x greater hip implant loads than walking (~ >8BW; all $P < 0.001$) as shown in Figure 1a. Treadmill walking (with/slopes) and jumping produced similar loads on the hip implant compared to level walking. For participants with a total knee replacement, unilateral hopping, running, and COD produced >1.5x greater knee implant loads than walking (7-9BW, all $P < 0.001$) (Figure 1b).

Discussion

Determining optimal loads that stimulate bone adaptations without compromising implant integrity is needed. These rankings provide initial comparative data to inform training programs aimed at preventing bone loss in persons with a hip or knee joint replacement, and to guide future hip or knee implant load-testing protocols.

Images (Optional)

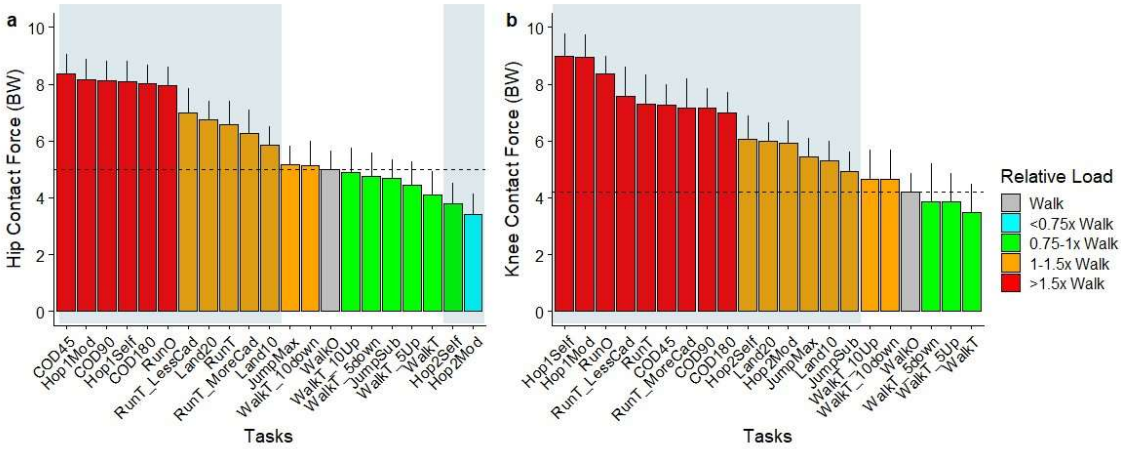


Figure 1. Predicted (with 95%CI) resultant implant contact forces at a) the hip for total hip replacement, and b) the knee for total knee replacement. The shaded regions indicate a statistically significant ($p < 0.05$) difference from overground walking (WalkO). **Abbreviations.** COD: change of direction (45°, 90°. 180°); Hop1Mod/Hop2Mod (unilateral/bilateral hopping 2.6Hz); Hop1Self/Hop2Self (unilateral/bilateral hopping self-paced); RunT/RunT_LessCad/RunT_MoreCad (running treadmill self-paced, with lesser or greater cadence); Land10/Land20 (drop land bilateral 10cm or 20cm); WalkT (walking treadmill self-paced, level surfaced); 5up/5down/10up/10down (5° or 10° upslope or downslope); JumpMax/JumpMod (maximal or moderate effort countermovement jumps).

References (Optional)

[1] Mooiweer Y, et al. Eur Rev Aging Phys Act 2022;19:7.

[2] Clynes MA, et al. Br Med Bull 2020;133:105-17.

Session Category

Orthopaedic Biomechanics: Lower Extremities

OA99-02

Individuals With Symptomatic Hip Osteoarthritis Ambulate With Different Hip Stress Contact Locations

Mrs. Holly Elliott M.S.[1], Dr. Kate Jochimsen Ph.D.[2,3], Dr. Anthony Mangino Ph.D.[1], Dr. Aaron Fain M.D.[4], Dr. Brecca Gaffney Ph.D.[5,6], Dr. Sebastian Bawab Ph.D.[7], Dr. Stephen Duncan M.D.[4], Dr. Michael Samaan Ph.D.[1]

[1]University of Kentucky, Lexington, KY, United States. [2]Harvard Medical School, Boston, Massachusetts, United States. [3]Massachusetts General Hospital, Boston, Massachusetts, United States. [4]University of Kentucky Healthcare, Lexington, KY, United States. [5]University of Colorado Denver, Denver, CO, United States. [6]University of Colorado Anschutz, Denver, CO, United States. [7]Old Dominion University, Norfolk, VA, United States

Introduction

Peak hip stress occurs within the anterior hip joint during loading response in normal gait. Individuals with hip osteoarthritis exhibit higher peak hip flexion angle during loading response. It is not well understood how these altered kinematics during loading response relate to hip cartilage mechanics resulting in severe structural abnormalities. The goal of this study was to compare hip cartilage mechanics in individuals with symptomatic hip osteoarthritis (sHOA) and asymptomatic controls without radiographic hip OA by utilizing subject-specific, magnetic resonance (MR) imaging-based finite element models (FEMs).

Methods

FEMs were developed for three individuals with sHOA (Kellgren Lawrence [KL]=2–3 and HOOS pain score of < 80) and three asymptomatic controls (KL=0-1 and HOOS pain score > 90). MR-images of the bony and cartilage morphologies were segmented for each individual to develop subject-specific mesh. Subject-specific hip kinematics and moments at the peak vertical ground reaction force during loading response were applied to each model to estimate maximum shear stresses (MSS) on the acetabular and femoral cartilage layers. Due to the small sample size, Cohen's d effect sizes were used to assess between group differences in MSS magnitudes, kinematics and hip moments.

Results

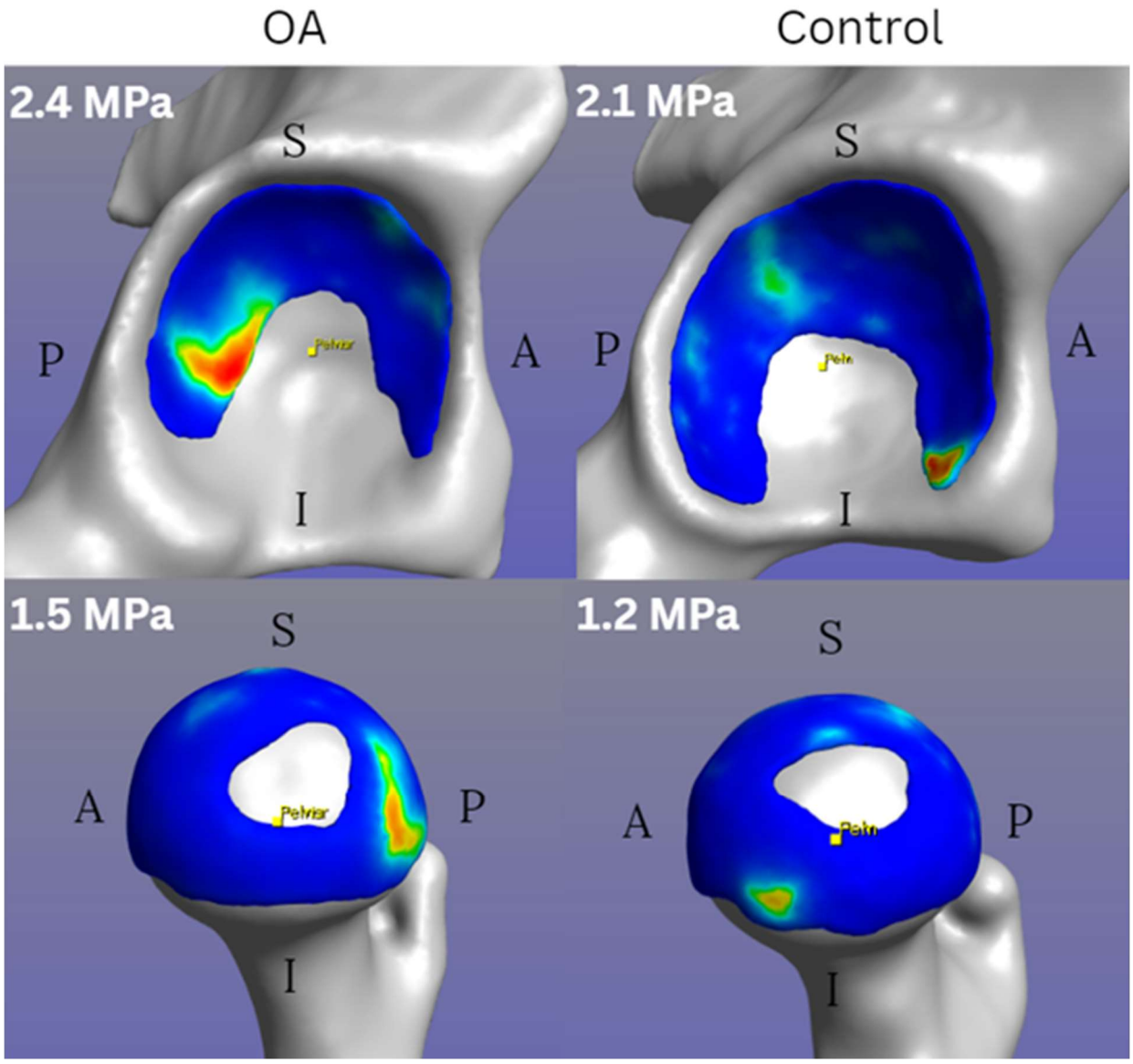
The sHOA self-reported worse hip-related pain (lower HOOS pain scores) compared to the control group (sHOA: 98.3±2.36, Control: 57.5±2.04, d=2.70). Peak MSS for the sHOA group

were located more posterior on both the acetabular (sHOA: 1.14±0.92MPa, Controls: 1.87±0.56MPa, d=0.787) and femoral (sHOA: 0.82±0.49MPa, Control: 1.10±0.37MPa, d=0.525) cartilage layers, whereas the peak MSS for the control group were located within the anterior acetabular and femoral cartilage layers. The sHOA group exhibited a smaller femur internal rotation angle (sHOA: 2.43±0.81degrees; Control: 7.25±4.78degrees, d=1.148) and larger hip extension moment (sHOA: -0.37±0.20Nm, 0.06±0.18Nm, d=1.318) compared to the control group.

Discussion

The sHOA group exhibited more posteriorly oriented peak acetabular and femoral cartilage MSS compared to the control group. Future work should assess the association between hip muscle dysfunction and proximal hip morphology with these altered cartilage contact mechanics to inform future exercise and gait retraining interventions to optimize hip contact mechanics and mitigate hip joint disease.

Images (Optional)



Acknowledgements (Optional)

Funding support via NIH (K01-AG073698, K23-AT011922, K01-AR080776) and the College of Education Office of Research at the University of Kentucky.

Session Category

Orthopaedic Biomechanics: Lower Extremities

OA99-03

Retrospective Analysis of Hip Joint Morphology: Affected versus Unaffected Joints of Hip Resurfacing Arthroplasty Patients

Ms. Emily Cameron PhD Candidate, MASc, BASc[1], Mr. Utomobong Essien BASc Candidate[1], Mr. Bishoy Awad BSc Candidate[2], Ms. Ella Connop BASc Candidate[1], Dr. John Rudan MD, FRSC(C), FCAHS,[3], Dr. Heidi Ploeg Ph.D., P.Eng., FASME, FORS[1]

[1]Mechanical Engineering, Queen's University, Kingston, Ontario, Canada. [2]Health Sciences, Queen's University, Kingston, Ontario, Canada. [3]School of Medicine, Queen's University, Kingston, Ontario, Canada

Introduction

Aging and degenerative joint diseases alter pelvic and acetabular morphology, affecting joint orientation, load distribution and mechanical function. Pelvic tilt, acetabular orientation, centre-of-rotation (CoR) alignment, and depth-width geometry are clinically relevant structural markers and may be associated with joint replacement success. This retrospective study aimed to assess hip morphology in pre-operative hip resurfacing (HRA) patients from computed tomography (CT) data.

Methods

Clinical CT scans of the pelvis from HRA patients (n=158; age≈51.9 years, male = 143, female = 19) were reconstructed (Mimics v.26) (ethics # 6006471). A data pipeline (MATLAB 2025) applied ISB-standardized pelvic coordinate systems, quantified pelvic tilt, acetabular orientation, femoral/acetabular CoR, acetabular CoR-to-CoR distance, radii, femoral-acetabular radius mismatch and acetabular width, depth and depth-to-width ratios (Fig 1.A).

Morphology differences were analyzed using linear mixed-effects models (SPSS Statistics v.29.0.2), with patient identification for paired left-right hips. Fixed effects were Affected Status (affected vs. unaffected), with models adjusted for age, pelvic tilt, and acetabular CoR-to-CoR distance (α=0.05; Bonferroni-corrected).

Algorithm accuracy was validated against physical (vernier caliper) and virtual (Artec Studio 19 Professional) measurements of surface models (Artec Eva) of male and female Sawbones pelves (model # 1301, 1302). Bland-Altman analysis and ICCs (95% CI) were used for comparison.

Results

Affected Status significantly influenced morphology. Affected hips had larger femoral head radii ($p<0.001$), differences between affected and unaffected acetabular radius ($p=0.04$) and femoral-acetabular radius mismatch ($p<0.001$). Pelvic tilt was strongly associated with radius- and depth-based measures (all $p<0.001$). Age was not significant.

When normalized to acetabular CoR-to-CoR distance, femoral head radius remained significantly larger ($p<0.001$), indicating disproportionate radial enlargement independent of pelvic size (Fig 1.B). Acetabular depth also showed pelvic size-independent increase ($p<0.001$), indicating disproportionate acetabular deepening (Fig 1.C).

Validation confirmed excellent agreement across measurement modalities with minimal bias and ICC(3,1) of 0.80-0.98.

Discussion

Normalization to acetabular CoR-to-CoR distance confirmed that femoral head enlargement and acetabular deepening represent true morphological changes rather than pelvic size variation. Increased radii, femoral-acetabular radius mismatch, and pelvic-tilt effects indicate reduced joint congruency and altered load transfer, with implications for moment-arm geometry, implant sizing accuracy, and restoring hip biomechanics.

Images (Optional)

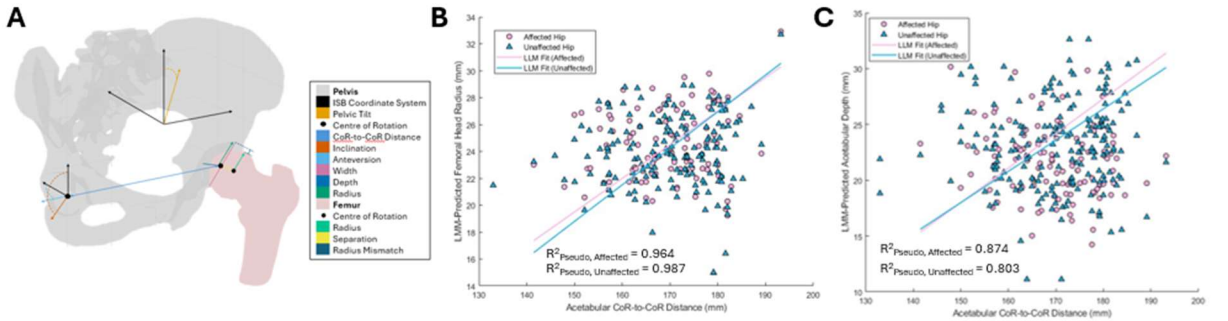


Figure 1. A) 3D visualization of the pelvic morphology pipeline; B) Linear mixed-effects model predictions of femoral head radius as a function of acetabular CoR–to–CoR distance; C) Linear mixed-effects model predictions of acetabular depth as a function of acetabular CoR-to-CoR distance.

Session Category

Orthopaedic Biomechanics: Lower Extremities

OA99-04

Altered Hip and Knee Between-Limb Symmetry During Sit-to-Stand in Cam-Type Femoroacetabular Impingement

Mr. Patrick Ippersiel PhD[1], Ms. Ariane Parisien MSc[2], Mr. Andrew Tucker B.Sc. (Hons)[2], Mr. Andrew Spiers PhD, P.Eng[3], Mr. Mario Lamontagne PhD[1], Dr. Paul Beaulé MD, FRCSC FAAOS CHE[2]

[1]University of Ottawa, Ottawa, Ontario, Canada. [2]The Ottawa Hospital, Ottawa, Ontario, Canada. [3]Carleton University, Ottawa, Ontario, Canada

Introduction

Cam-type femoroacetabular impingement (FAI) is associated with altered hip mechanics, joint loading, and early osteoarthritis, yet the extent of between-limb asymmetry during demanding functional tasks remains unclear.[1] Asymmetry provides insight into compensatory strategies and uneven loading patterns. This work compared lower-limb kinematic and kinetic symmetry between individuals with and without FAI during a sit-to-stand (STS) task. We hypothesized greater between-limb asymmetry in FAI patients, compared to controls.

Methods

FAI patients (n=12; 11 males; iHOT-33=44.3) and healthy controls (n=9; 9 males; iHOT-33=98.45) completed 5 standardized STS trials. Forty-five reflective markers tracked 3-d joint kinematics at 200Hz with a 10-camera system (Vicon MX, UK), and kinetic data were collected from a bench-mounted and two floor-embedded force plates (Kistler, 1000 Hz). Data were processed in Nexus (modified Plug-in-Gait) and MATLAB (R2023b). STS was partitioned into early (movement initiation to seat-off) and late (seat-off to upright) phases using bench-mounted force plate data. Between limb symmetry (affected vs. un-affected) was quantified using the Zifchock method for peak hip/knee flexion, sagittal hip/knee ROM, and vertical ground reaction force (vGRF).[2] Mixed ANOVAs tested the effects of group (FAI/healthy), phase (early/late) and their interaction (group*phase) on kinematic outcomes. Mann-Whitney U tests compared kinetic outcomes.

Results

A group*phase interaction was observed for hip ROM symmetry ($p=0.02$, $\eta^2_p=0.233$), with post-hoc Tukey's tests showing less between-limb symmetry in the FAI group during the early phase (mean difference=1.79, $p=0.049$, Fig.1). A group effect showed greater peak knee flexion symmetry ($p=0.043$, $\eta^2_p=0.198$), in the FAI group, independent of phase. Mann-

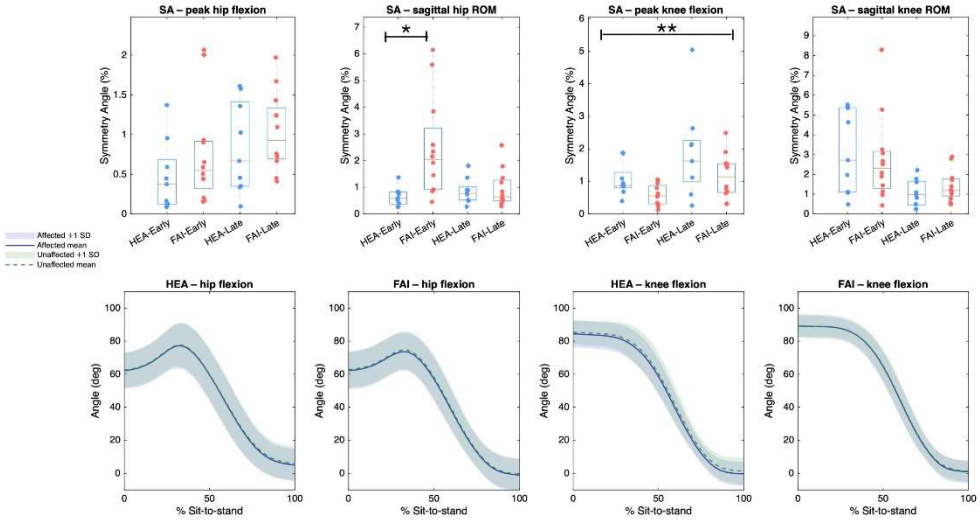
Whitney U tests revealed more vGRF symmetry in the FAI group during early phase (p=0.009, mean difference=13.89; cohen's d=1.043).

Discussion

Group differences in early-phase between-hip ROM symmetry may be related to reduced hip flexion in the affected limb in FAI patients. Greater symmetry in vGRF and peak knee flexion across limbs reflects more even weight bearing in FAI patients. This suggests movement adaptations that preserve external weight bearing while modifying joint mechanics in ways that might lessen mechanical demand on the symptomatic hip.

Images (Optional)

Figure 1. Sit-to-Stand Symmetry Angles and Sagittal Hip and Knee Joint Angles in Individuals With and Without FAI



Top row indicates symmetry angles in FAI (red) and Healthy (blue) group across early and late STS phases for kinematic metrics. Larger symmetry angles (SA) values indicate greater asymmetry. Bottom row indicates group means +/- 1 SD for affected (solid blue) and unaffected (dashed green) limb joint angles for the hip and knee. (*) denotes statistical significance (p<0.05) based on post-hoc Tukey's tests. (**) denotes significant group effect (p<0.05). HEA: Healthy; FAI: Femoroacetabular impingement; ROM: Range of Motion.

References (Optional)

[1] Kennedy et al., Gait Posture. 2009.

[2] Zifchock et al., Gait Posture. 2008.

Session Category

Orthopaedic Biomechanics: Lower Extremities

OA99-05

Head Center Restoration With the Cutting Guide Q-Ring During Total Hip Arthroplasty

Mrs. Katja Brand[1], Dr.-Ing. Gerd Huber[1], Ms. Celina Ibrahim[1], Prof. Michael Morlock[1], Prof. David Beverland[2]

[1]Institute of biomechanics, TUHH, Hamburg, Hamburg, Germany. [2]Primary Joint Unit, Musgrave Park Hospital, Belfast, North, Ireland

Introduction

Restoration of the femoral head center is a crucial aspect to achieve native biomechanics and reduce the risk of instability after total hip replacement surgery (THA) [1]. This is usually determined based on the surgeon's experience and anatomical landmarks as references. The present study evaluated the accuracy of a standardized workflow using a cutting guide for the head resection during posterior-approach for cementless stem insertion.

Methods

Eight cadaveric femoral pairs (5f/3m, Ø 77.1 years) were CT-scanned before head resection by an experienced surgeon using a cutting guide (Q-Ring, enztech, NZ, Fig. 1a). After compaction broaching (Corail, Johnson&Johnson MedTech, US), trial neck and head components were selected to reconstruct the head center. The laser scan models of assembled THAs (scan resolution 0.012 mm; HandySCAN Black+™|Elite, Creaform, CA) were aligned with the femur models derived from CT-scans (root mean square error: 0.1 mm, PolyWorks|Inspector, InnovMetric Software, CA). Differences between native and THA head center position were determined relative to the anatomical axis (Fig. 1b; MATLAB 2023b, MathWorks, US). Stem orientation in varus/valgus and the anterior-posterior offset were assessed.

Results

The reconstructed head center was on median 2.7 mm (inter quartile range [-0.2, 4.6]) higher and 3.7 mm [2.6, 4.8] more medial compared to the native head center. Stem orientation showed a varus tilt of 2.2° [3.4, 0.4], with an anterior-posterior offset of 3.8 mm [1.4, 5.6] compared to native.

Discussion

The largest reconstruction mismatch occurred in the anterior-posterior offset, likely due to the cutting guide controlling height and lateral offset but not 3D-stem orientation. Deviations are slightly larger than those reported for 3D-digital planning [1] which, however, is not widely used in clinical settings. With a similar range to typical stem migration (<2.7 mm [2]) the observed mismatch should clinically be acceptable. The Q-ring cutting guide standardizes head resection and helps to reconstruct the native head center better than a purely manual approach [3]. Results are limited by the precision of determining the native head center, particularly in patients with arthritis.

Images (Optional)

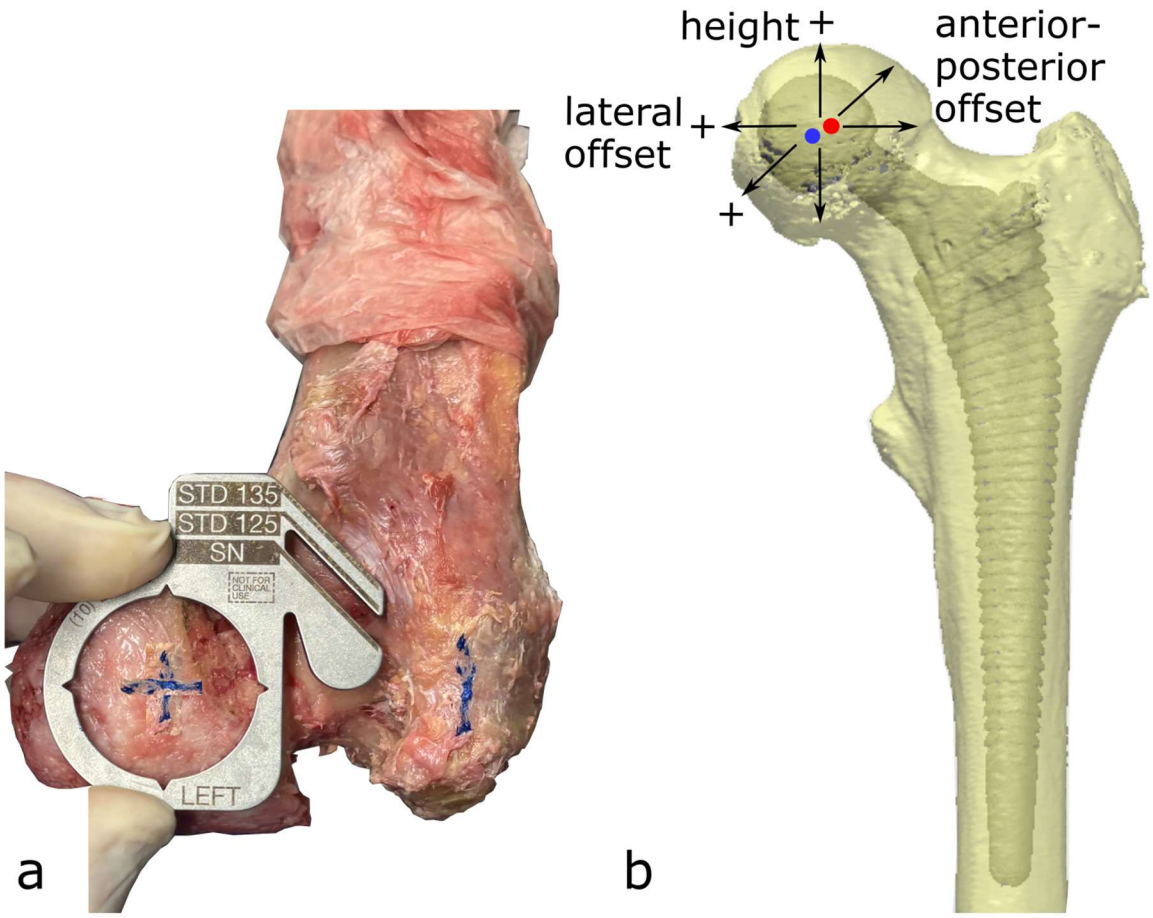


Figure 1: a) Use of the Q-Ring cutting guide for femur head resection;
b) Position of the native (red) and the reconstructed head center (blue) based on [1].

References (Optional)

[1] LaCour *et al.*, JOR, 2024

[2] Kastner *et al.*, JOR, 2023

[3] Bjarnason, Reikeras, Ann Transl Med, 2015

Acknowledgements (Optional)

The authors thank Johnson&Johnson MedTech for providing implants, instruments and institutional financial support.

Session Category

Orthopaedic Biomechanics: Lower Extremities

OA99-06

Comparative Biomechanics of Gluteus Medius Repair: A Finite Element Analysis

Mr. Matthew Allen[1], Mr. Yuan Liu[2], Mr. Brendan Rockwell[3], Dr. Stefano Bini[1]

[1]University of California, San Francisco, San Francisco, California, United States. [2]Touro University, Vallejo, California, United States. [3]University of California, Berkeley, Berkeley, California, United States

Introduction

Surgical repair of Gluteus Medius tendon (GMed) tears is complicated by constant post-operative mechanical load during ambulation. Suture Anchor (SA) repairs are standard, but suffer from a 6-7% structural failure rate, characterized by suture pull-through due to focal stress concentrations. We hypothesized that augmenting the repair with a scaffold would reduce these stress concentrations. We used Finite Element Analysis (FEA) to systematically evaluate the benefit of two simulated repair configurations on the mechanical properties of tendon-to-bone repair in a 3D volumetric mesh derived from a normal hip MRI.

Methods

High-fidelity 3D volumetric meshes were generated from patient-specific hip MRI using nnU-Net segmentation. Using SolidWorks, we simulated two repairs: SA as control and a Collagen/PLLA mesh augmentation (AR). The AR scaffold was modeled to span from the distal footprint to the proximal musculotendinous junction, permitting direct load transfer. This offers a potential solution to the 'cheese-wiring' phenomenon by converting focal suture points into a distributed area of compression.

A nonlinear FEA solver was utilized to model soft tissue hyperelasticity. The tendon was assigned hyperelastic Neo-Hookean material properties. A distributed tensile load of 200N was applied to the proximal face of the tendon-scaffold composite to simulate the clinical failure threshold of degenerative tendon during early rehabilitation.

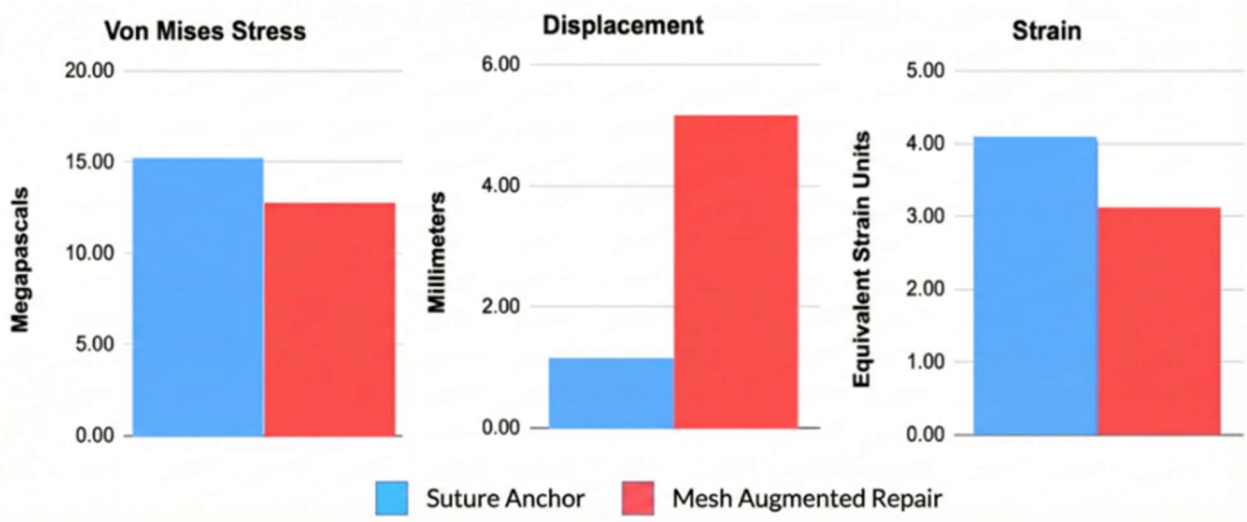
Results

Compared to SA, AR demonstrated peak Von Mises stress decrease of 15.7% (12.80 MPa vs 15.18 MPa), and equivalent strain reduction of 24.6% (3.06 vs 4.06). Conversely, the AR exhibited a 355% increase in displacement (5.15 mm vs 1.13 mm).

Discussion

GMed repair biomechanics are poorly studied. We show that augmenting repair constructs with a mesh decouples tissue strain from construct displacement at time-zero. By acting as a compliant load-sharing element, the augmented repair reduces peak Von Mises stress, potentially mitigating the "cheese-wiring" failure mode observed in rigid standard suture anchor repairs. Limitations of this study include the use of static loading which does not replicate cyclic gait mechanics, and the assumption of idealized friction interfaces. Despite these constraints, the data supports that shifting load-bearing to a distributed surface area protects the distal tendon. Next steps will validate these analyses in vitro using cadaveric models.

Images (Optional)



References (Optional)

Session Category

Orthopaedic Biomechanics: Lower Extremities

OA100-02

Collagen Fiber Orientation in Human Achilles Tendons Affects the Mechanical Response

Dr Chiara Garavelli PhD[1], Dr Hector Dejea PhD[2], Dr Joseph Brunet PhD[2,3], Miss Renate Janssen MSc[1], Dr Maria Pierantoni PhD[1], Prof Hanna Isaksson PhD[1]

[1]Department of Biomedical Engineering, Lund University, Lund, Skåne, Sweden. [2]European Synchrotron Radiation Facility, Grenoble, Auvergne-Rhône-Alpes, France. [3]Department of Mechanical Engineering, University College London, London, Greater London, United Kingdom

Introduction

The Achilles tendon (AT) is frequently subjected to overuse, contributing to the rise of tendinopathy. Collagen fiber distribution is important for mechanical response; however, clinical imaging modalities are unable to resolve it. This limits the possibility to mimic real tissue behavior. Therefore, this work aimed at assessing the effect of simplification in fiber modeling on the strain distributions, through the integration of synchrotron experimental data and finite element modelling.

Methods

Five entire human ATs (age: 59-73 y) were imaged at BM18 of ESRF (The European Synchrotron) within the Human Organ Atlas Hub, using Hierarchical Phase-Contrast Tomography (HiP-CT) [1] (voxel size 10.1µmx10.1µmx10.1µm). 3D orientation distribution of collagen fibers was determined through structure tensor analysis [2]. Parallelly, the ATs contours were segmented, meshed and assigned a poro-visco-hyperelastic material model. The collagen fibers were assigned as: I) following the tendon axis (idealized); II) approximated as the global average orientation from HiP-CT (global); and III) extracting the local distribution from HiP-CT within each element (local) [3]. The finite element (FE) models were subjected to stress-relaxation (10% strain at 1%/s), and the strain distributions were compared between specimens and fiber modeling approaches.

Results

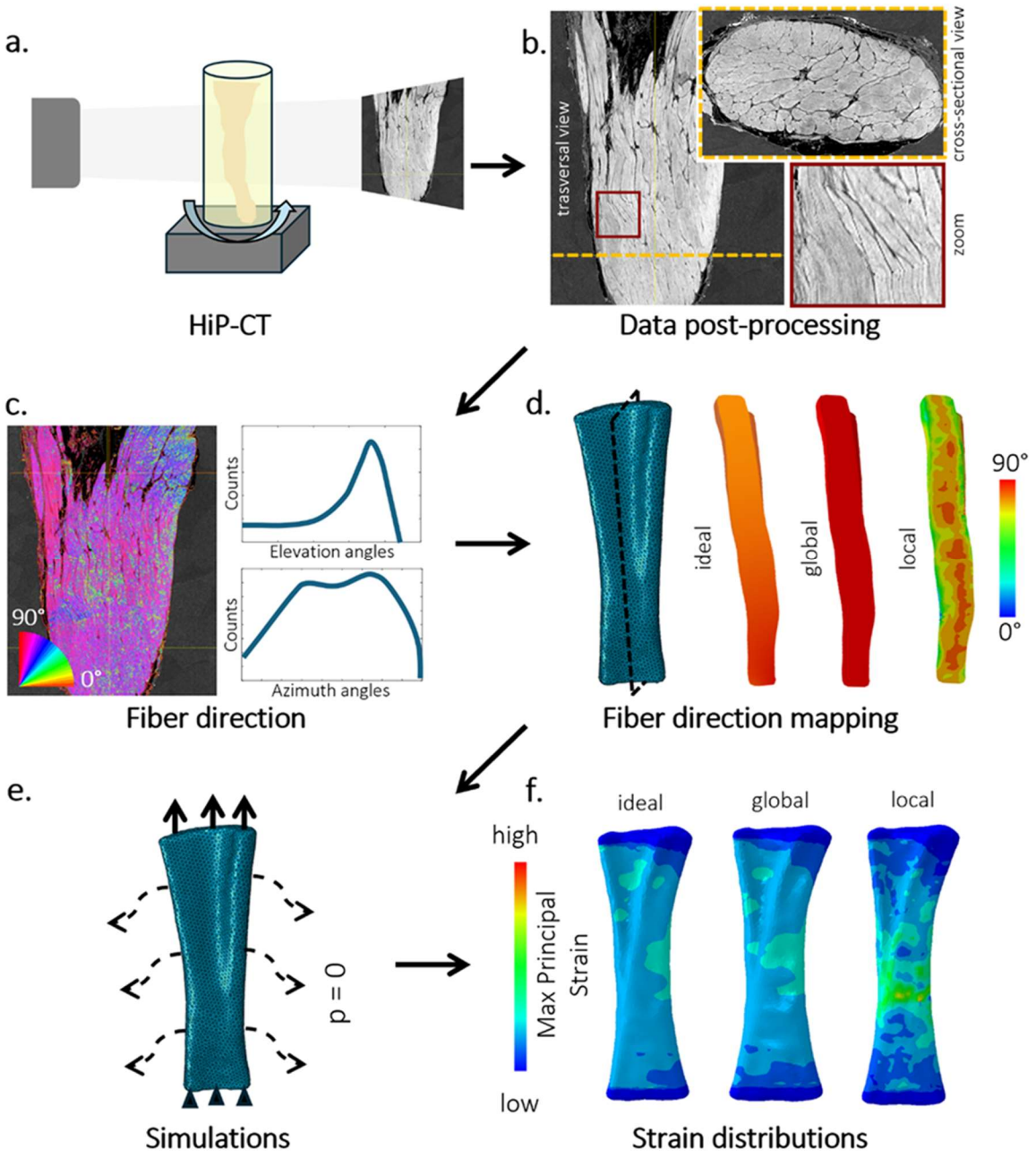
HiP-CT allowed to resolve the fiber orientation, assessing variation in fiber distributions between (20% difference between donors) and within AT (wider azimuth angles in the free tendon region). The different fiber orientations (ideal, global, local) resulted in significantly different ($p<0.001$, Wilcoxon signed rank test) strain distributions. The full-width at half-

maximum of the strain distribution increased with increasing model complexity (ideal to local: +6.8%; global to local: +6.6%). Peak reaction forces differed between 19-66% between the different model approaches.

Discussion

Fiber orientations derived from HiP-CT enabled us to assess the variations in FE-based strain predictions depending on the level of donor-specific fiber information. These results highlighted the strength of the synergy between high-resolution imaging and FE modelling in understanding tendon biomechanics.

Images (Optional)



Project workflow. Tendon data acquired with HiP-CT (a, b) were used to obtain collagen fiber direction information at each point, (colormap shows elevation angles (c)), and to segment the tendon outer contour. Inside each element the collagen fibers were oriented with an ideal, global or local distribution (d), while the other components of the poro-visco-hyperelastic material model were kept constant. The models were loaded under the same boundary condition in stress-relaxation (e). The resulting strain distributions were compared (f).

References (Optional)

[1] Walsh et al. 2021, Nature Methods

[2] Pierantoni et al., 2023, *Acta Biomaterialia*

[3] Janssen et al., 2025, BMMB

Acknowledgements (Optional)

Funding from ERC (ID:101002516), Mats Paulsson Foundation, and Chan Zuckerberg Initiative Foundation (CZIF2022-316777). We thank the HOAHub and ESRF (proposal MD1389) for beamtime allocation.

Session Category

Musculoskeletal Biomechanics: Tissues

OA100-03

Influence of Collagen Network Dispersion on Torsional Shear Loading of Articular Cartilage With Synchrotron-Based Fibril-Reinforced Finite Element Models

Mr Viktor Jönsson MSc, Assistant Professor Lorenzo Grassi PhD, Assistant Professor Anna Gustafsson PhD, Dr Maria Pierantoni PhD, Professor Hanna Isaksson PhD

Lund University, Lund, Scania, Sweden

Introduction

The collagen network plays a critical role during shear loading of articular cartilage [1], and its dispersion affects the response during axial loading [2]. The objective of this study was to determine the influence of collagen dispersion during torsional shear. To achieve this, we employed fibril-reinforced poro-visco-hyperelastic (FRPVE) FE models based on in situ torsional shear loading with synchrotron phase-contrast micro-tomography (PhC-µCT) of cartilage (Fig.1A), using three collagen orientation models with increasing complexity.

Methods

In situ PhC-µCT (TOMCAT, SLS) imaging (2.75µm isotropic voxel size, 5.54x3.85mm^2 field of view) with concurrent stress relaxation was performed on cylindrical (4mm ⌀) knee femoral cartilage samples (bovine N=1, human N=4). Mechanically, compression (10% strain, 1%s) was followed by torsional shear (10% applied strain, 1%/s), FRPVE [3] FE models were generated with both idealized and segmented geometry (Fig.1B,C). The Benninghoff arcade pattern was used as basis for the three collagen orientation models: #1 no dispersion(arcade), #2 isotropic dispersion [3] (isotropic) and #3 x-ray scattering based dispersion (SAXS) [4] (Fig.1D,E). The three orientations were implemented in the FE models and the simulated stress relaxation results were compared, using one set of material properties.

Results

The idealized geometry (Fig.1B) shows that the isotropic and SAXS collagen models are both comparable with the experimental data for compression and torsion loading (Fig.1F,G). In contrast, the arcade model shows less time dependency and does not match experimental data well for torsion (Fig.1G).

Discussion

We show that the classical Benninghoff arcade collagen pattern does not contribute to the time-dependent torsional behavior, likely due to fibrils buckling during compressive loading. The time dependency is instead attributed to fiber dispersion, seen with the isotropic and SAXS-based collagen models. Next step is to simulate the different collagen models with sample specific models (Fig.1C) to determine the influence of realistic sample geometries with collagen orientation.

Images (Optional)

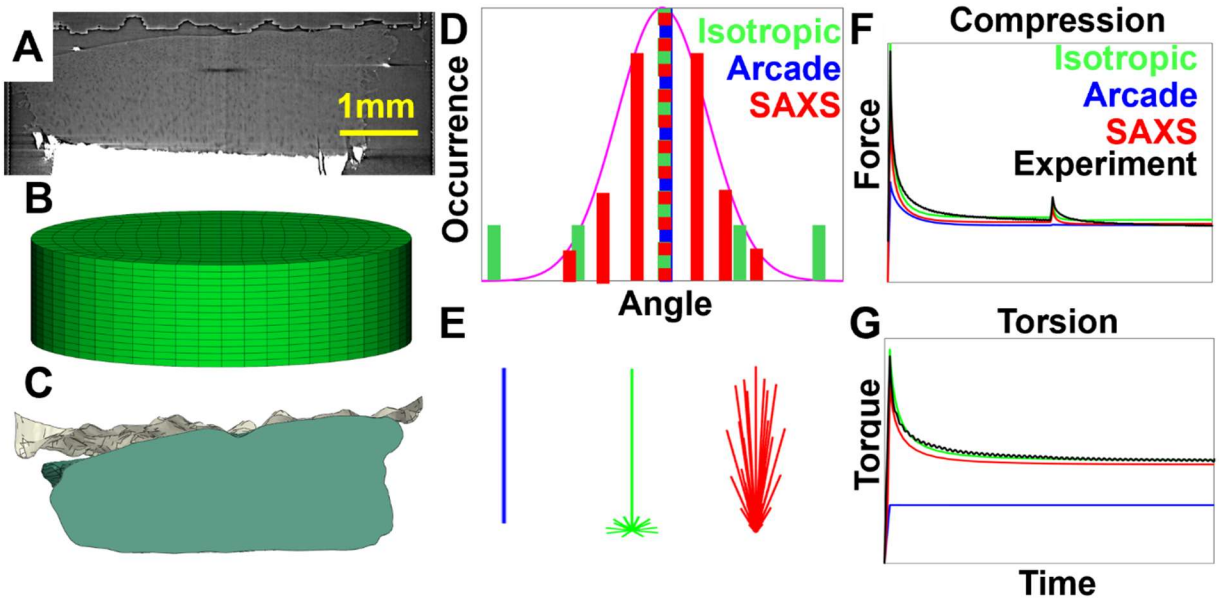


Figure 1. A) PhC-μCT longitudinal slice of sample at beginning of loading, B) Idealized cylindrical FE model, C) Cut through segmented FE model during loading. D-E) Example fibril distribution(pink) and visualization for the collagen orientation models. F-G) Comparison between experiment and simulated compression and torsion stress relaxation, note torque is only shown after torsion is applied.

References (Optional)

[1] Maier et al. Osteoarthritis and Cartilage, 2019
[2] Ateshian et al. Journal of Biomechanical Engineering, 2009
[3] Wilson et al. Journal of Biomechanics, 2004
[4] Aspden et al. Proceedings of the Royal Society of London, 1981

Acknowledgements (Optional)

Funding from Swedish Research Council (2023-04099) and Novo Nordisk Foundation through MathKOA (NNF21OC0065373). We thank the Paul Scherrer Institute, Villigen, Switzerland for the beamtime at TOMCAT(20220313).

Session Category

Musculoskeletal Biomechanics: Tissues

OA100-04

Heterogeneous Strain Distribution in Rat Achilles Tendon From Physiological Loading: A Finite Element Study

Dr. Yeswanth Pydi PhD, Dr. Maria Pierantoni PhD, Assiatant Professor Anna Gustafsson PhD, Professor Hanna Isaksson PhD

Lund Universitry, Lund, Skåne, Sweden

Introduction

The rat Achilles tendon comprises three subtendons originating from the medial gastrocnemius (MG), lateral gastrocnemius (LG), and soleus (SOL) muscles. Knowledge of region-specific strain variations in rat tendons during physiological activities is lacking in the literature; however, it is critical for understanding their load-sharing and injury mechanisms. The goal of the current study was to evaluate the strain distribution resulting from rat subtendons under physiological loads.

Methods

FE models, including the three subtendons, were developed from three rat Achilles tendons that earlier underwent phase-contrast synchrotron-based X-ray tomography [1]. Images were segmented using 3D Slicer, and FE models were generated using ANSA (Fig. 1a). This study uses experimentally measured subtendon MG forces from literature during walking, trotting, and galloping (Fig. 1b) [2]. These experimentally derived MG loads were scaled to estimate forces in the LG and SOL based on physiological cross-sectional areas [3]. The simulations were performed in Abaqus using a fibril-reinforced poro-visco-hyperelastic material model [4]. The fiber orientations were determined from the synchrotron images, assuming the average fiber orientation in the whole tendon [1].

Results

The forces applied on the subtendon were heterogeneous (4.1 N on MG, 5.2 N on LG, and 0.6 N on the SOL) (Fig. 1c). The subtendons deformed non-uniformly, which can significantly influence the strain distribution and the energy storage (Fig. 1d) [2]. Throughout the loading phase, the maximum principal strain varied from 0.01 to 0.19 (Fig. 1e). Higher strains were observed on the medial (MG) side and minimal strain on the posterior (SOL) side, indicating uneven load transfer between subtendons.

Discussion

These findings provide insight into the mechanical interaction between subtendons under physiological loading conditions. The work will be extended by incorporating local fiber orientations per element [4], which will further elucidate the role of subtendon structure on strain heterogeneity and load transfer.

Images (Optional)

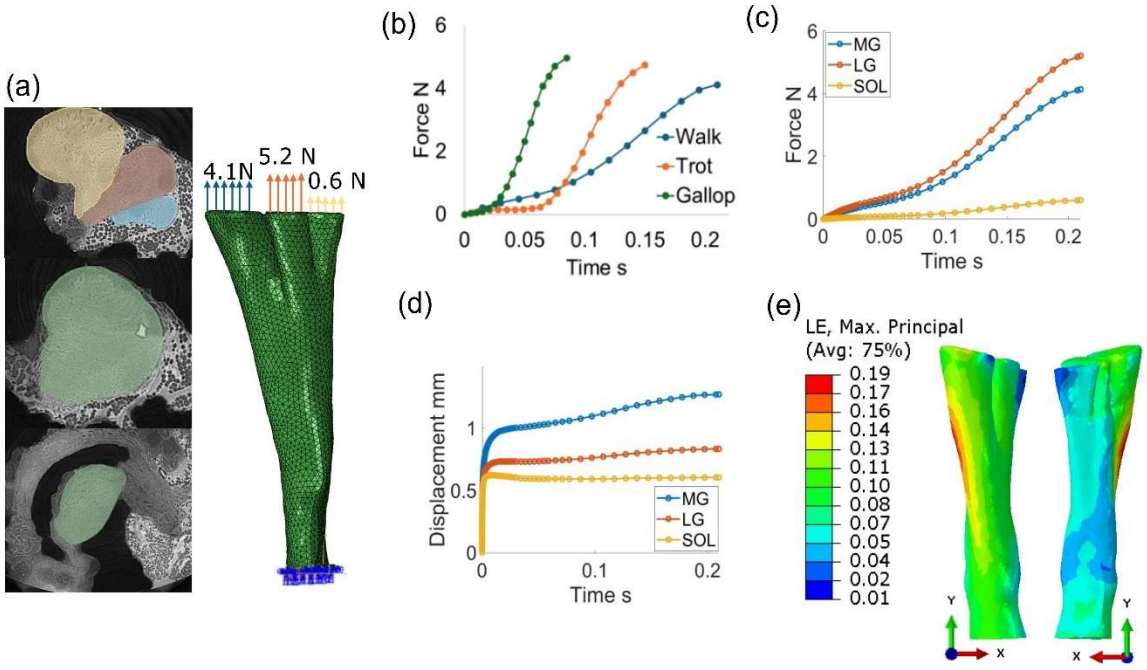


Figure 1. (a) Segmented micro-tomographic images showing the rat subtendon structure. (b) Experimentally derived MG loads for Walking, Trotting, and Galloping [2]. (c) Subtendon loads applied as boundary conditions. (d) Resulting individual subtendon displacements from the top surface. (e) Spatial distribution of maximum principal strain in the X–Y and Y–X orientations.

References (Optional)

[1] Pierantoni M, Acta Biomaterialia 2025; 246-257; [2] Eng C. M, JExpBiol, 2019; jeb205559; [3] Maarleveld R, JBiomech.2025; 112976; [4] Janssen R, BMMB 2025; 1959–1972.

Acknowledgements (Optional)

Funding from the European Research Council (ERC) under the European Union's Horizon 2020 research and innovation program (101002516) is greatly acknowledged.

Session Category

Musculoskeletal Biomechanics: Tissues

OA100-05

Modelling of Diffusion in a Hydrated Tissue Using Gyration Tensor Analysis

Ms. Leila Shahsavari, Mr. Mohsen Hassani, Dr. Kotaybah Hashlamoun, Dr. Amir Sanati-Nezhad, Dr. Salvatore Federico

University of Calgary, Calgary, Alberta, Canada

Ms. Leila Shahsavari

Mr. Mohsen Hassani

Dr. Kotaybah Hashlamoun

Dr. Amir Sanati-Nezhad

Introduction

Diffusion of macromolecules through tissues is critical for nutrient/drug transport, especially for avascular tissues, e.g., articular cartilage. Conventional diffusion models assume that the molecules are spheres or revolution ellipsoids, and miss the effect of more complex molecular conformations. The purpose of this work is a diffusion model that accounts for more general molecular conformations via the gyration tensor, a measure of how far a geometrical shape is from a sphere.

Methods

We assume that the preferred direction of diffusion for a molecule is that associated with the smallest eigenvalue of its gyration tensor: roughly speaking, the direction associated with the smallest cross-section. Since the molecules of the same species are randomly oriented in the solvent, the effective diffusion tensor is isotropic and given by a certain average of the directional diffusivities for the molecule. We choose the harmonic average, i.e., the reciprocal of the sum of the reciprocals of the diffusivities (hindrances). The model

was validated against Perrin's classical model [1] for revolution-ellipsoidal molecules, across a wide range of shape ratios.

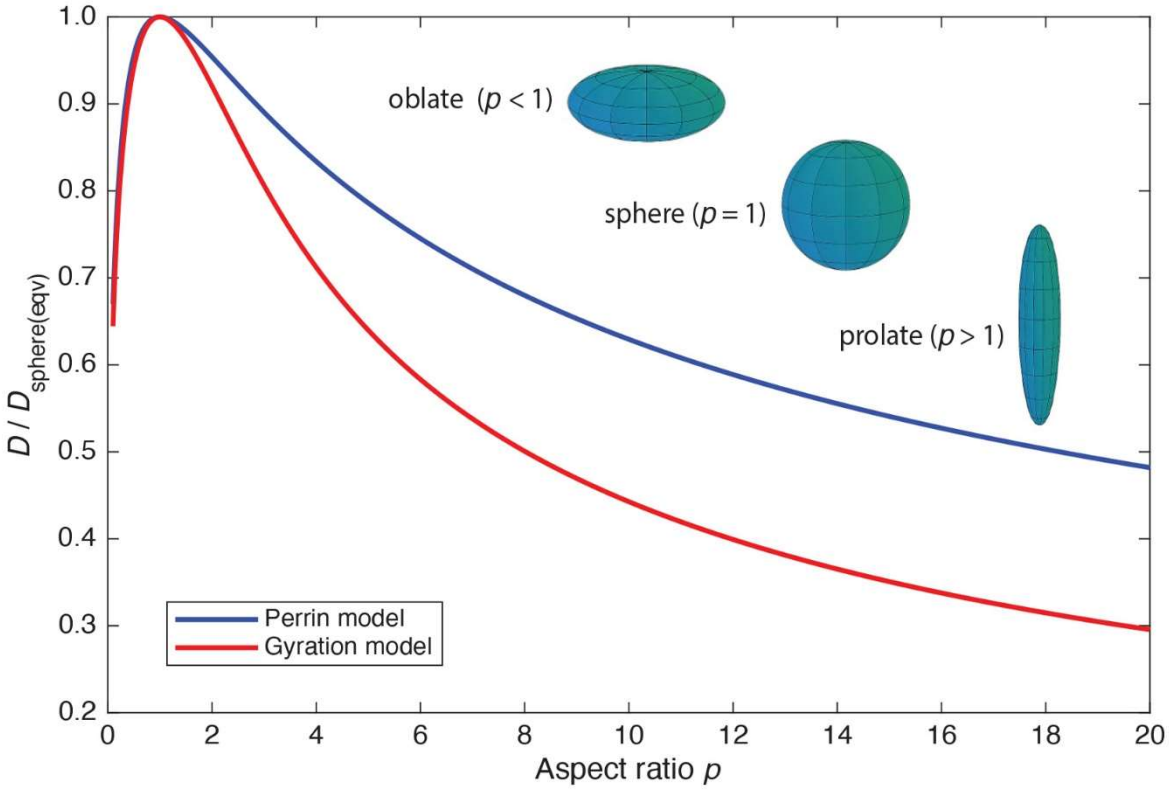
Results

For spherical molecules, the model reproduced the classical Stokes–Einstein prediction. For elongated molecules, anisotropy significantly reduced the effective diffusion. Compared to Perrin's model, our approach predicted lower diffusion for highly anisotropic shapes. This is because of the use of the harmonic average: the smallest directional diffusion causes the highest hindrance effect. This result is especially significant for highly anisotropic molecules, for which diffusion tends to zero. Overall, for rod-like (prolate) molecules, our results showed lower diffusion compared to Perrin's model, while for disk-like (oblate) molecules, our model is close to Perrin's model.

Discussion

This work introduces a versatile analytical framework that moves beyond idealised revolution-ellipsoidal molecules, enabling the prediction of anisotropic diffusion for complex macromolecules. The model provides a mechanistic basis for quantifying nutrient transport and designing drug delivery systems [2]. Future work will incorporate the model into a framework for diffusivity in anisotropic porous media [3], such as articular cartilage.

Images (Optional)



References (Optional)

[1] Martin Hoffmann *et al.*, J ACS Nano, 2009

[2] Liujing Wang *et al.*, J Polymer Science, 2025

[3] Kotaybah Hashlamoun and Salvatore Federico, J Biomech Eng, 2020

Session Category

Musculoskeletal Biomechanics: Tissues

OA101-02

Investigating Leader Cell Mechanics of Breast Cancer Collective Invasion Using Tumor Decellularized Matrices and Microphysiological Systems

Mrs Jessica Williamson, Dr Jessanne Lichtenberg, Dr Priscilla Hwang Associate Professor

Virginia Commonwealth University, Richmond, VA, United States

Introduction

Collective invasion, where cells move together and are connected via cell-cell adhesions, is an essential component of breast tumor invasion. During collective invasion, a few cells at the front (i.e. leaders) define the front, integrate signals from the extracellular matrix (ECM) and send signals to neighboring (follower) cells. Our work demonstrated leader cells must arrive (or polarize) at the front to begin invasion. The tumor microenvironment contains many mechanical cues including matrix architecture and fluid flow gradients, yet their impact on invasion or leader cell response is not fully understood. Here we investigated how matrix architecture and fluid flow gradients work together to drive invasion. We hypothesize leader cells biophysics are primary sensors of mechanical matrix cues, and a sub-group of followers directly reorganize the matrix to prime the environment for invasion.

Methods

We used our previously designed *ex vivo* 3D microfluidic model and primary mouse breast tumor organoids (MMTV-PyMT) to incorporate native cell heterogeneity. We generated decellularized matrix (dECM) integrated in our model to maintain inherent properties of native ECM. We identified a sub group of followers (cancer associated fibroblasts (CAFs)) that remodel the surrounding matrix via collagen receptor, discoidin domain receptor 2 (DDR2). Thus, we generated a PyMT mouse model to knockout DDR2 in CAFs only (FSPcre;DDR2$^{f/f}$), and synthesized dECM. We performed live-cell imaging, tracked invasion, and measured changes in focal adhesions.

Results

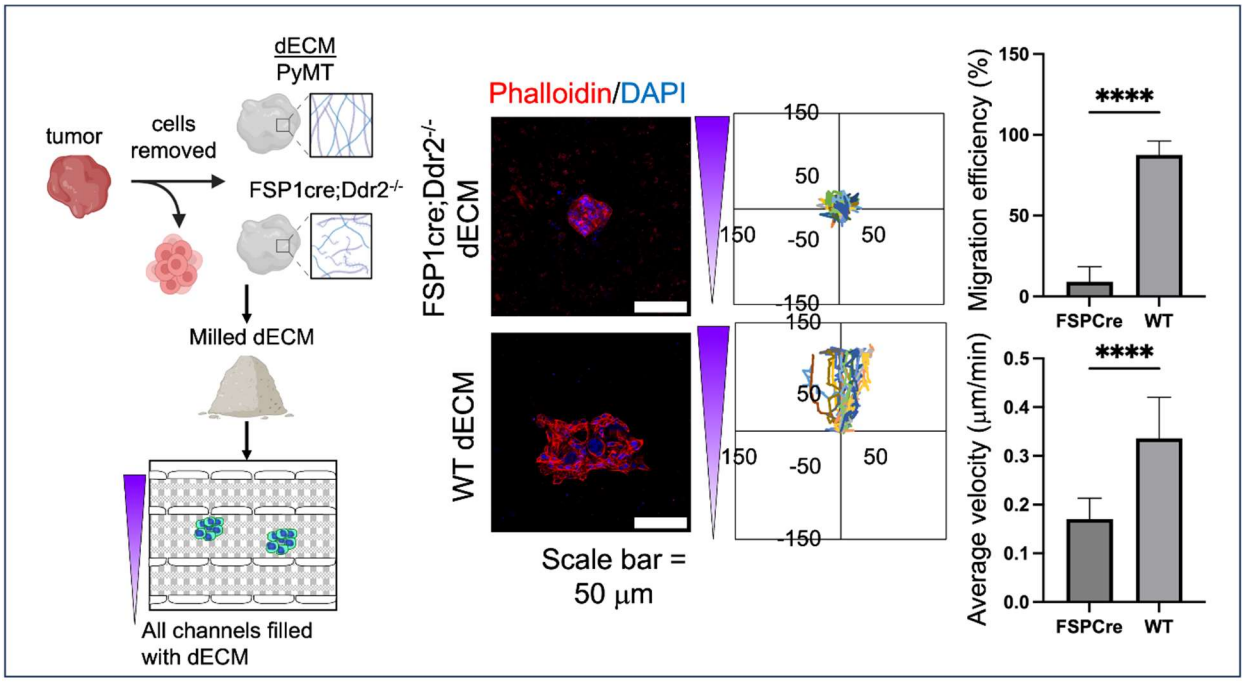
Tumor organoids migrated significantly slower and without direction when cultured in decellularized matrix where DDR2 is knocked out in CAFs (FSPcre;DDR2$^{f/f}$) (Fig 1). Further, tumor organoids had smaller and less number of vinculin focal adhesions when cultured on FSPcre;DDR2$^{f/f}$ dECM. From our single cell sequencing analysis, we also identified

ligand-receptor pairs responsible for leader-CAF communication. These ligand-receptor pairs were all associated with matrix remodeling pathways.

Discussion

We demonstrate mechanical environment cues can dictate tumor invasion, specifically via interactions between the mechanical environment, CAFs, and leader cells. Our work contributes new perspectives which can bring new approaches for therapy design. Further, our work can provide new mechanical signatures of collectively invading tumor clusters, which can add more universal biomarkers that can diagnose or predict cluster-based metastasis in patients.

Images (Optional)



Session Category

Cell Biomechanics: Mechanobiology

OA101-03

Beta-Amyloid42 Oligomers Soften Neuronal Cells by Reorganization of Cytoskeleton

Prof. Yuan Feng[1], Ms. Huijing Jin[1], Ms. Qian Suo[1], Dr. Shengyuan Ma[1], Mr. Xingqun Gao[1], Mr. Peijun Zhao[1], Prof. Aili Zhang[1], Prof. Yaohui Tang[1], Prof. Yue Zhou[1], Prof. Assaf Zemel[2], Prof. Shengce Tao[1], Prof. Daniel Czajkowsky[1], Prof. Linyong Zhu[1], Prof. Zhifeng Shao[1], Prof. Guang-Zhong Yang[1]

[1]Shanghai Jiao Tong University, Shanghai, Shanghai, China. [2]Hebrew University of Jerusalem, Jerusalem, Jerusalem, Israel

Introduction

Alzheimer's disease (AD) is the leading cause of dementia and is characterized by progressive neuronal loss and cognitive decline. Central pathological features include extracellular deposition of β-amyloid (Aβ) peptides and intraneuronal accumulation of tau neurofibrillary tangles. Although amyloid plaques are mechanically rigid, multiple studies have shown that AD brains are globally softer than those of healthy individuals, raising an unresolved conflict at the interface of pathology and biomechanics.

Methods

SH-SY5Y human neuroblastoma cells were cultured and treated with Aβ42 oligomers. Live-cell mechanics were measured with AFM in fluid. Global stiffness was probed using bead-functionalized cantilevers. Elastic modulus was extracted from force–displacement curves using the Hertzian contact model (v=0.5). RNA sequencing was performed on cells treated with Aβ42. Differentially expressed genes were identified with DESeq2, and pathway enrichment was assessed using GO and KEGG databases.

Results

Quantitative analysis revealed that global Young's modulus declined significantly in a concentration-dependent manner. Both actin filaments and microtubules underwent extensive disintegration, accompanied by further increases in microtubule porosity and pronounced shortening of axons. KEGG pathway analysis revealed significant downregulation of focal adhesion and ECM–receptor interaction pathways, indicating impaired cell–cell and cell–matrix contacts as well as reduced responsiveness to extracellular stimuli. Such adhesion deficits disrupt the intracellular tension network, thereby weakening actin retrograde flow mediated by adaptor proteins and impairing actin

polymerization. This reduction in cytoskeletal tension is expected to lower cellular stiffness, reflected in decreased Young's modulus values.

Discussion

The precise molecular mechanisms underlying Aβ42-mediated neurotoxicity remain incompletely defined, and the full scope of its cellular effects is still under active investigation. Here, we show that oligomeric Aβ42 alters neuronal mechanics, highlighting a previously underappreciated mechanobiological dimension of Alzheimer's pathology. The biomechanical properties of cells offer rich diagnostic and therapeutic potential, and our findings place cytoskeletal remodeling at the center of Aβ42-driven dysfunction.

Acknowledgements (Optional)

This work was supported by the National Natural Science Foundation of China (grant 32322042, 32271359), 2024 Shanghai Jiao Tong University - Hebrew University of Jerusalem Joint Seed Funding, Science and Technology Commission of Shanghai Municipality (grant 21TS1400600, 20DZ2220400), Shanghai Municipal Science and Technology Major Project (grant 2021SHZDZX).

Session Category

Cell Biomechanics: Mechanobiology

OA101-04

Mechanobiology of Schlemm's Canal Inner Wall Endothelial Cells in Glaucoma

Prof. C. Ross Ethier[1,2], Dr. Hiayan Li[1], Dr. Seyed Mohammad Siadat[2], Ms. Kristin Perkumas[3], Prof. W. Daniel Stamer[3], Prof. Darryl Overby[4]

[1]Emory University, Atlanta, GA, United States. [2]Georgia Tech, Atlanta, GA, United States. [3]Duke University, Durham, NC, United States. [4]Imperial College, London, England, United Kingdom

Introduction

Glaucoma, the leading cause of irreversible blindness, is treated by lowering intraocular pressure (IOP). Schlemm's canal (SC), a fluid collecting duct in the eye, is lined by specialized endothelial cells that experience significant stretch *in vivo* and whose permeability influences IOP. Here we use an *in vitro* assay to study the mechanobiology of SC cells.

Methods

Human SC cells from normal and glaucomatous donors were cultured on microspheres to induce cellular stretch, and transcellular pore formation was quantified [1]. SC cells were also cultured on substrates of different stiffness and subcortical cell stiffness was measured by AFM (10 um spherical tip). To gain insight into mechanosensing pathways in SC cells, we modulated the activity of the mechanosensitive ion channel TRPV4 [2] using the antagonist HC067047 (10 μM) or the agonist GSK1016790A (100 nM). To investigate the role of microtubule stability, known to affect IOP [3], we treated SC cells with paclitaxel (10 μM, microtubule stabilizer) or nocodazole (10 μM, microtubule destabilizer), and additionally used siRNA targeting GEF-H1, a microtubule-associated Rho guanidine exchange factor.

Results

Stiffer substrates increased SC cell stiffness and F-actin levels, and decreased microtubule stability (acetylated tubulin levels). These responses were strongly modulated by TRPV4 activity. Specifically, transcellular pore formation was potentiated by short-term (<2 mins) TRPV4 activation (1.5-fold increase, $p < 0.05$), and by long-term (2 days) TRPV4 inhibition (1.6-fold increase, $p<0.0001$). However, these effects were dampened/absent in glaucomatous SC cells. Microtubule stabilization potentiated pore formation and reduced cell stiffness. In contrast, microtubule destabilization increased cell stiffness by 1.5-fold

($p<0.001$), and enhanced F-actin levels (1.9-fold, $p<0.0001$). Knockdown of GEF-H1 attenuated the effects of microtubule destabilization. Taken together, pore forming ability showed a strong inverse correlation with cell stiffness (Figure 1).

Discussion

SC cells are mechanoresponsive to substrate stiffness (altered in glaucoma) and to stretch. This mechanosensitivity is dependent in part on TRPV4 and is altered by microtubule stability, both of which affect SC cell transcellular pore formation. These processes offer novel targets for IOP-lowering therapies in glaucoma.

Images (Optional)

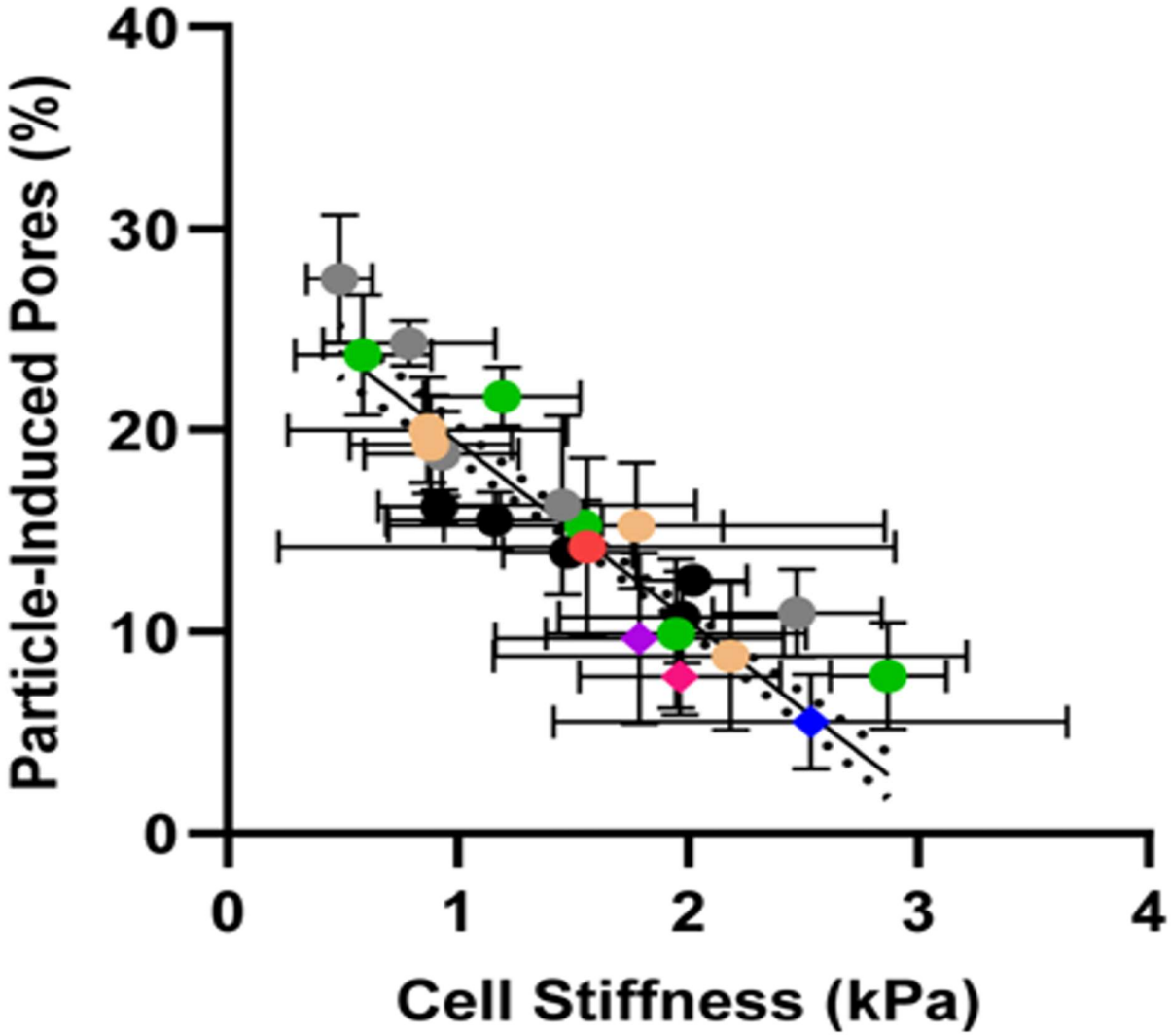


Figure 1: SC cell pore forming ability vs. cell stiffness. Each color represents one cell strain, some of which were treated to alter cell stiffness (rho-kinase inhibitor or S1P).

References (Optional)

[1] Siadat et al., 2025. PMID: 39554025

[2] Li et al., 2025. PMID: 41022289.

[3] Su et al., 2025. PMID: 39820277

Acknowledgements (Optional)

BrightFocus Foundation G2024003F, NIH R21 EY033142, Georgia Research Alliance (CRE), Emory Ophthalmology Departmental funds (CRE).

Session Category

Cell Biomechanics: Mechanobiology

OA101-05

P-Cadherin Regulates Collective Migration Phenotypes During Epithelial Morphogenesis via Rho Signaling

Ms. Corinne Leonard B.S.[1], Dr. Jessanne Lichtenberg Ph.D.[1], Ms. Hazel Sterling[1], Mr. Jesse Rolston B.S.[1], Dr. Priscilla Hwang Ph.D.[1,2]

[1]Virginia Commonwealth University, Richmond, Virginia, United States. [2]Massey Comprehensive Cancer Center, Richmond, Virginia, United States

Introduction

Epithelial cells undergo different modes of collective cell migration (CCM) during morphogenesis. For example, cells spinning (rotational collective migration (RCM)) in a coordinated manner can develop acinar structures, and cells collectively invading (invasive collective migration (ICM)) can develop duct-like tissues. Cadherins are cell-cell junctions that support CCM and act as force transmitters driving tissue remodeling. Our lab demonstrated P-cadherin (CDH3) regulates CCM in breast cancer invasion and morphogenesis, but it's unclear what drives adoption of different phenotypes. In this study, we investigate how CDH3 impacts RCM or ICM phenotypes during epithelial morphogenesis, by quantifying cell-matrix interactions. We hypothesize CDH3 controls establishment of mature cell protrusions, a first step for ICM phenotype, that is regulated by extracellular matrix (ECM) deformation rates and Rho signaling.

Methods

Using our previously published epithelial morphogenesis microfluidic model [1], we integrated the ability to measure ECM deformation rates in real-time. We used epithelial clusters (wild-type (WT) or CDH3-depleted (CDH3-/-). We performed live-cell imaging before and after inducing cell protrusions (hepatocyte growth factor (HGF) treatment), and quantified changes in migration phenotypes (ICM vs RCM), morphology, and ECM deformation rates. We also treated samples with RhoA activator.

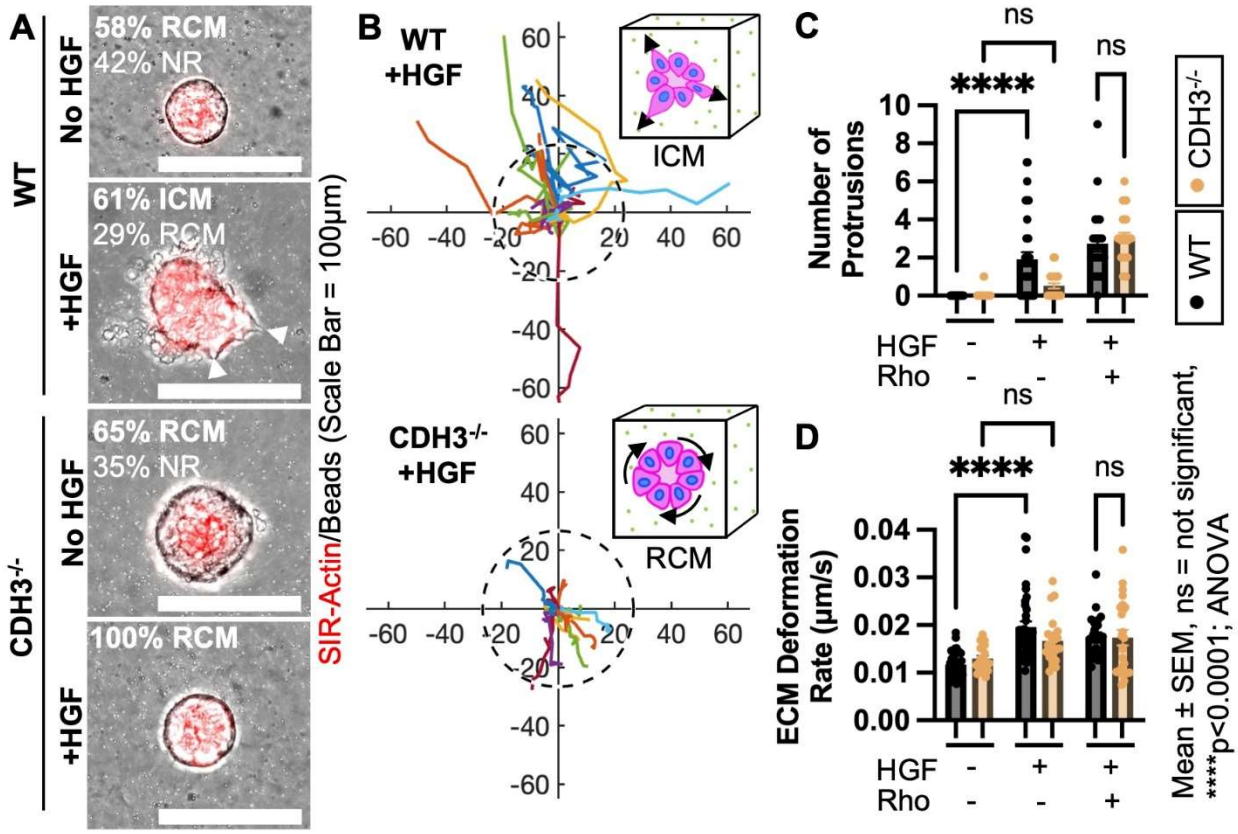
Results

Most WT epithelial cysts adopt RCM phenotype and transition to ICM phenotype upon HGF stimulation (Figure 1A,B). CDH3-/- cysts lose their ability to transition from RCM to ICM after HGF stimulation (Figure 1A,B), revealing CDH3-/- cysts are unable to generate mature cell protrusions (Figure 1C). ICM cysts have higher ECM deformation rates compared to RCM cysts (Figure 1D). Treatment of CDH3-/- cysts with RhoA activator rescues their ability to adopt an ICM mode with matrix deformation rates and protrusion formation like WT cysts (Figure 1C,D).

Discussion

Our findings demonstrate CDH3 is a mechanosensor regulating CCM modes through dictating the generation of mature cell protrusions and changing matrix deformation rates, modulated by RhoA signaling. This knowledge is essential in understanding developmental processes and can be applied to broader applications such as cancer progression. Future directions include investigation of cell-matrix adhesions regulated by CDH3 and Rho signaling, to understand their direct impact in regulating ECM deformations.

Images (Optional)



References (Optional)

[1] Lichtenberg *et al.*, ACS Biomater Sci Eng, 2024

Session Category

Cell Biomechanics: Mechanobiology

OA102-02

Engineering Reliable Bioabsorbable Magnesium Stents: A Pipeline From Computational Design Optimization to *In Vitro* Testing

M.Sc. Diego Blunda[1,2], M.Sc. João Cruz[2,3], M.Sc. Simon Pöstges[2], PhD Alexander Kopp[2], Prof. Claudio Chiastra[4], PhD Dario Carbonaro[4], Prof. Ted J. Vaughan[1]

[1]University of Galway, Galway, Galway, Ireland. [2]Meotec GmbH, Aachen, Nordrhein-Westfalen, Germany. [3]Chair for Laser Technology (LLT), Aachen, Nordrhein-Westfalen, Germany. [4]PoliToBIOMed Lab, Dept. Mechanical and Aerospace Engineering, Torino, Piemonte, Italy

Introduction

Drug-eluting stents are effective for treating coronary artery disease, but remain associated with long-term complications due to their permanent structure. Bioabsorbable magnesium stents (BMgS) can potentially avoid these issues, providing temporary support and then degrading [1]. However, BMgS are prone to acute mechanical failure, requiring rigorous design and manufacturing control. This study presents a comprehensive workflow for BMgS design, optimization, and fabrication.

Methods

The workflow comprises design and manufacturing phases. In the design phase, a parametric stent geometry was evaluated using a finite element (FE) framework incorporating crimping on a balloon catheter, expansion, and radial compression (ASTM F3067-14). Simulations of multiple geometric variants trained surrogate models for key metrics, enabling an NSGA-III multi-objective optimization. From the resulting Pareto front, an optimal design was selected and compared with a baseline configuration. In the manufacturing phase, WE43 magnesium billets were extruded into microtubes and laser-cut using a femtosecond ultra-short-pulse system to reproduce the optimized geometry. Three stents based on the optimized geometry were fabricated and experimentally tested through crimping, deployment, and radial compression to validate the FE predictions.

Results

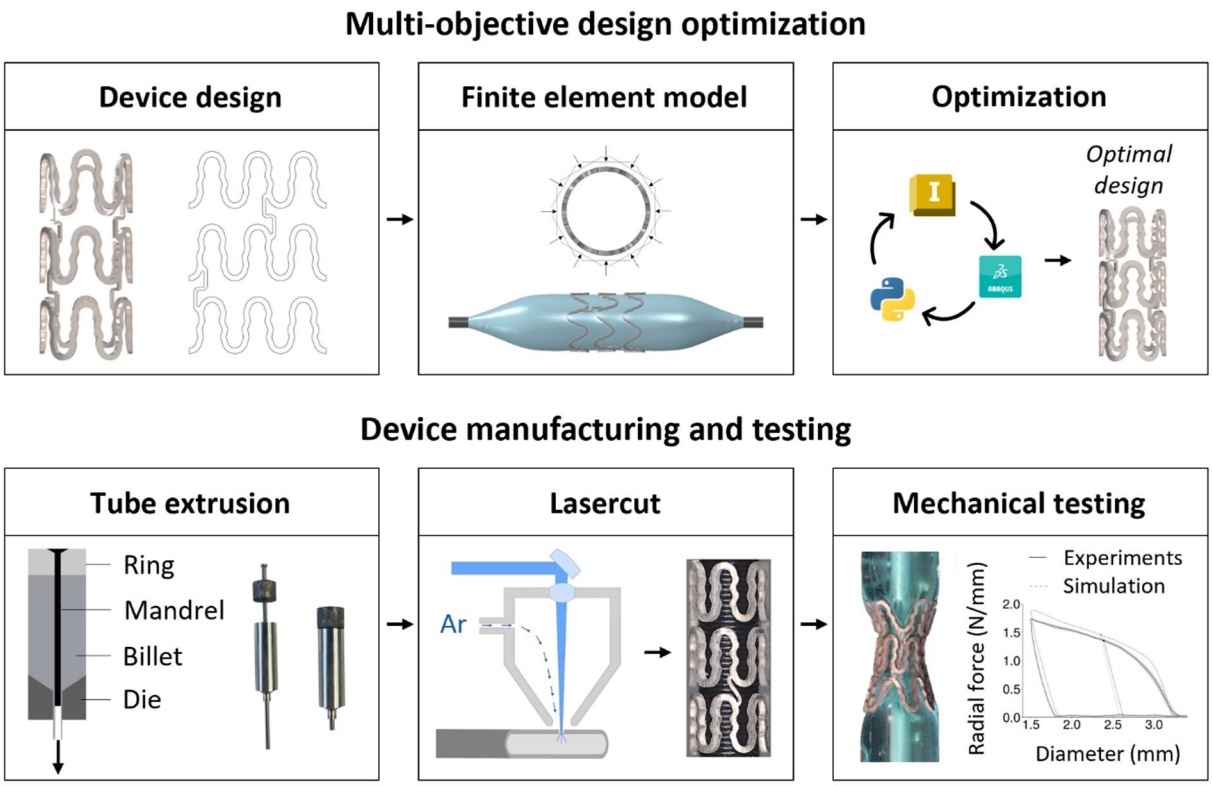
The surrogate models showed high predictive accuracy ($R^2_{pred} > 0.93$), and NSGA-III optimization yielded a clear Pareto front. Relative to the baseline, the identified optimized stent reduced material damage by 4.5 %, increased radial strength by 57.7 %, and lowered the surface-to-volume ratio by 17.9 %. Fabricated stents were successfully crimped,

deployed, and radially compressed. Experimental radial recoil was 8.45 ± 0.31 %, closely matching simulation (8.4 %; 0.6 % relative error). Radial strength at 20 % diameter reduction was 1.363 ± 0.020 N/mm versus 1.456 N/mm in simulation (6.8 % relative error), confirming strong agreement between FE model and experiments.

Discussion

This study demonstrates the feasibility of an integrated computational-experimental workflow for developing BMgS. The optimization framework identified a design that outperformed the baseline, and the strong agreement between simulations and *in vitro* tests confirmed the reliability of the FE model in capturing acute stent mechanics. Successful extrusion and femtosecond laser cutting further validated manufacturability. Overall, the workflow provides a solid foundation for accelerating the design and translation of next-generation BMgS.

Images (Optional)



References (Optional)

[1] Raymond Haddad *et al.*, Catheterization and Cardiovascular Interventions, 2021.

Acknowledgements (Optional)

This project has received funding from the European Union's Horizon Europe research and innovation programme under Marie-Sklodowska-Curie grant agreement ID No 101120006.

Session Category

Cardiovascular/Cardiorespiratory Biomechanics: Materials and Devices

OA102-03

Biomechanically Optimized Peripheral Artery Stent Remonstrates Reduced Intimal Hyperplasia and Stenosis In a Swine Model

Professor and Chair Alexey Kamenskiy Ph.D.[1], Postdoctoral Fellow Barbara Batista de Oliveira M.D.[2], Associate Professor Anastasia Desyatova Ph.D.[1], Research Scientist Frazer Heinis Ph.D.[1], Research Scientist Jordan Rosenbohm Ph.D.[1], Research Scientist Paul Deegan MSc[1], Professor Jason MacTaggart M.D.[2]

[1]University of Nebraska Omaha, Omaha, Nebraska, United States. [2]University of Nebraska Medical Center, Omaha, Nebraska, United States

Introduction

Endovascular treatment of peripheral artery disease (PAD) remains limited by high restenosis rates, particularly when stents are placed in biomechanically active regions such as the adductor hiatus or behind the knee. Commercial stents often fail to accommodate large limb-flexion-induced deformations, producing adverse stent-artery interactions that impair healing.

Methods

A computational Design-of-Experiments framework with response-surface methodology was used to optimize the geometry of a NiTi PAD stent for improved apposition, reduced wall stress, and minimized pinching under physiologic axial compression, bending, and torsion. The optimized design was manufactured, crimped into a custom delivery system, and implanted in 8-month-old Yucatan swine (n=6). Each animal received the optimized stent on one side and a commercial Zilver stent - representing average biomechanical behavior - contralaterally. Stents were deployed behind the inguinal ligament to replicate the severe deformation environment near the human adductor hiatus. Animals survived 12 weeks on a high-fat, high-sugar diet with interim CTA in straight and flexed postures. After sacrifice, μCT and histology quantified intimal hyperplasia and stenosis.

Results

All treated arteries remained patent with preserved side branches. CTA showed that the optimized stent accommodated limb-flexion deformations more effectively (Figure), exhibiting greater physiologic axial compression (13 ± 3% vs. 7 ± 2%) and smoother transitions at stent ends. In contrast, Zilver stents frequently produced distal-end kinking during flexion. μCT analysis demonstrated substantially reduced neointimal hyperplasia

with the optimized design (251 ± 86 mm^3) compared with Zilver (407 ± 90 mm^3). Correspondingly, maximum stenosis (47 ± 9% vs. 63 ± 7%) and mean stenosis (32 ± 10% vs. 47 ± 7%) were significantly lower in the optimized stents (all $p<0.001$, Figure).

Discussion

A stent engineered explicitly for lower-limb biomechanics demonstrated superior ability to accommodate limb-flexion-induced deformations and produced markedly improved vascular healing in vivo. These findings underscore that biomechanical compatibility - particularly in regions of high dynamic strain - should be a core design requirement for next-generation PAD stents.

Images (Optional)

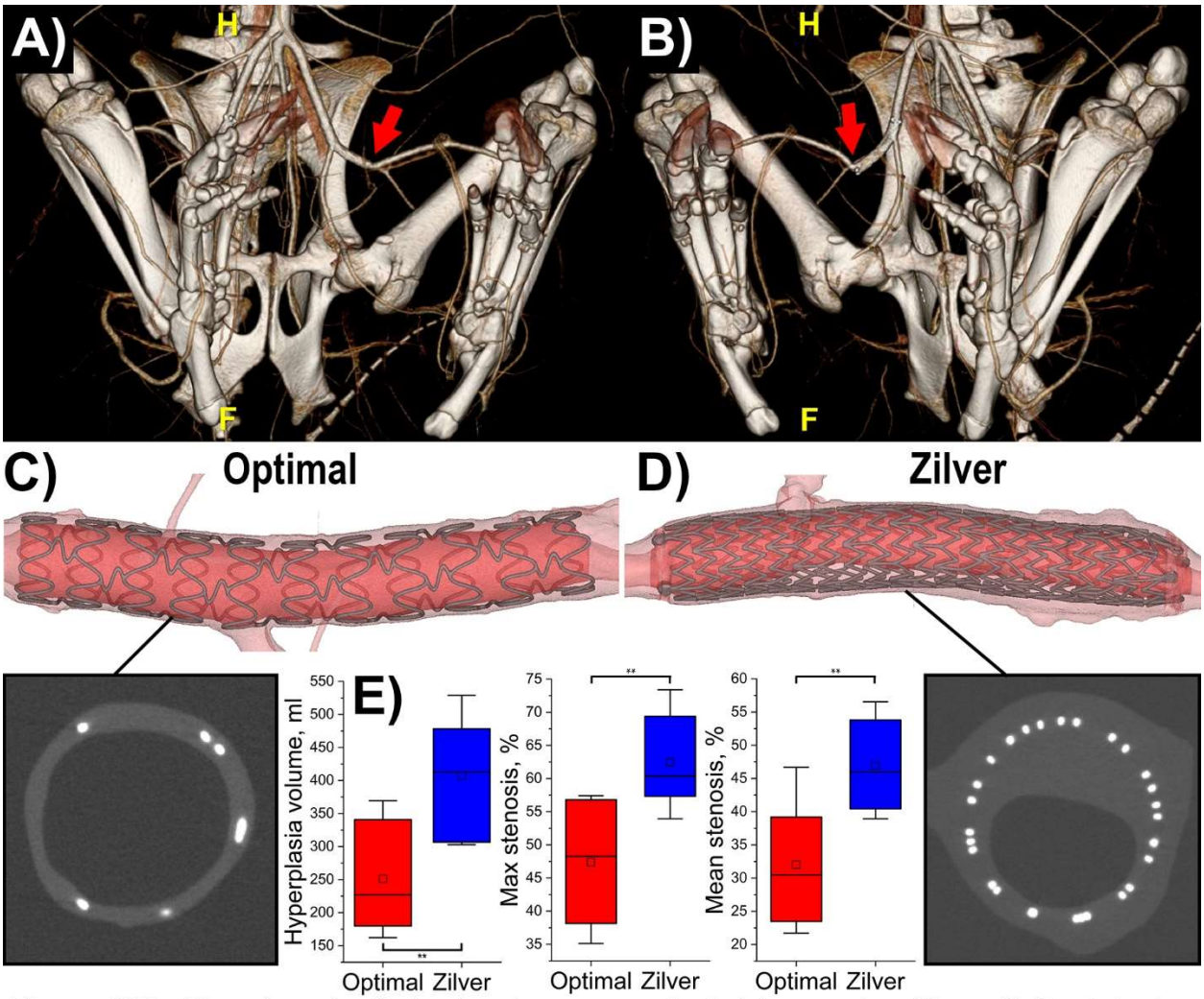


Figure. CTA of flexed porcine limbs showing preserved arterial geometry with our Optimal stent **(A)** versus acute kinking with the Zilver stent **(B)**. µCT reconstructions after 12 weeks illustrate significantly reduced neointimal hyperplasia with Optimal **(C)** compared to Zilver **(D)**.
E) Quantification of hyperplasia volume, maximum stenosis, and mean stenosis (n = 6; $p < 0.001$).

Acknowledgements (Optional)

This work was supported in part by the NIH awards HL125736, HL180371, and P20GM152301.

Session Category

Cardiovascular/Cardiorespiratory Biomechanics: Materials and Devices

OA102-04

Numerical Analysis of Knee Bending Effects on Blood Flow in a Femoral Arterial Stent Using a Centerline-Based Deformable Model

Professor Marie Oshima Ph.D, Mr. Kotaro Onoue, Dr. Katsuyuki Hoshina M.D.

The University of TOkyo, Tokyo, Tokyo, Japan

Introduction

Revascularization procedures are routinely performed for patients with severe femoral artery stenosis caused by progressive atherosclerosis to prevent critical limb ischemia. However, some patients experience poor postoperative outcomes due to stent migration or collapse associated with knee bending motion. Regular follow-up imaging is therefore essential to detect morphological changes over time. Because medical images obtained at different time points produce different geometric models, a new mesh must be generated for each model. Therefore, it becomes difficult to conduct quantitative comparison of simulation results between analysis models in an efficient manner. To solve this issue, we developed a centerline-based deformable modeling method to investigate the effects of knee bending motion on hemodynamics in the femoral artery.

Methods

The proposed method transforms a standard analysis model into a target model using vascular centerlines. First, three-dimensional vascular geometries at multiple time points are segmented from medical images to construct both the standard and target models. After centerline extraction for each model [1], the analysis mesh of the standard model is generated using Gmsh [2]. A transformation matrix is then derived from the correspondence between the two centerlines. This matrix is used to deform the standard analysis model so that its centerline matches that of the target geometry. The surface mesh of the target model is generated using the same correspondence, and a smoothing procedure is implemented to reduce distortions in the transformed surface.

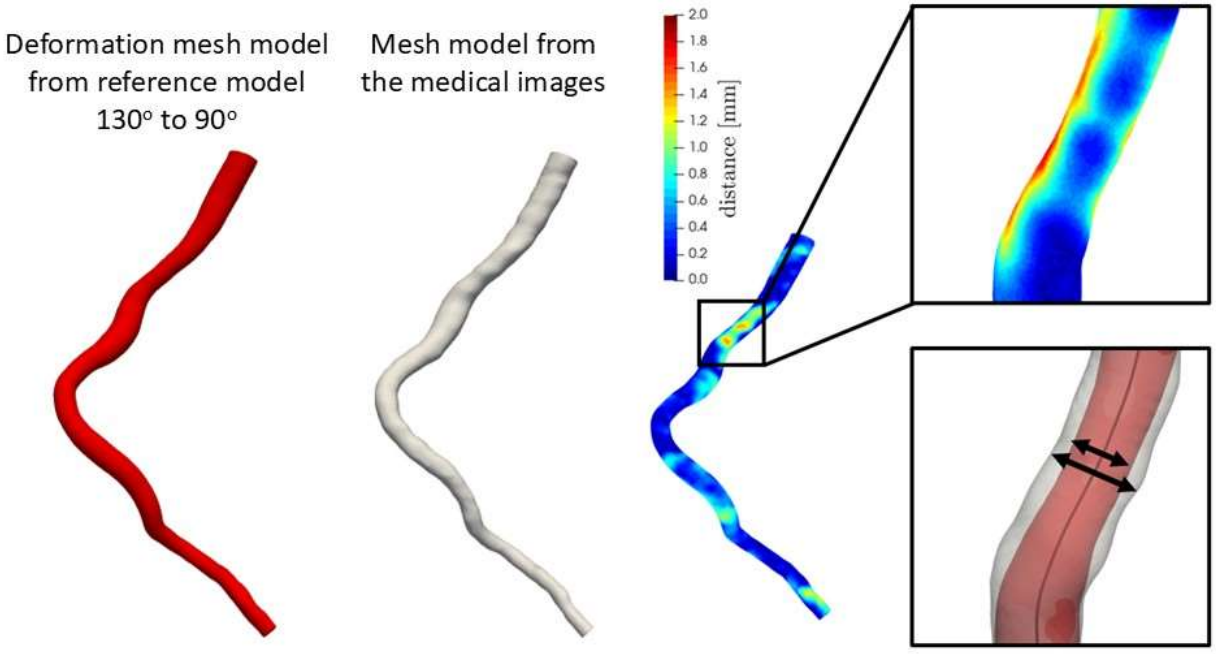
Results

The target analysis model was successfully created by transforming the centerline and surface mesh of the standard model according to the derived transformation matrix. The smoothing algorithm effectively improved mesh quality by reducing distortions in highly deformed regions.

Discussion

Verification and validation of the proposed method were performed using simplified geometries. The method was further applied to patient-specific femoral artery simulations using CT images acquired at three different knee bending angles. Geometric differences and hemodynamic outcomes were compared across the three configurations. The results demonstrated the capability of the method to enable consistent quantitative analysis across time-varying vascular geometries.

Images (Optional)



References (Optional)

[1] Kobayashi, M., et al., Comput. Med. Imaging Graph. , 2020
[2] Geuzaine, C. et al., Int. J. Numer. Methods Eng., 2009

Session Category

Cardiovascular/Cardiorespiratory Biomechanics: Materials and Devices

OA102-05

Hemodynamic Testing of a Composite Leaflet Material for Transcatheter Aortic Valve Replacement (TAVR)

Ms. Vivienne Zacher BS[1,2], Ms. Shweta Karnik MS[1,2], Dr. Sanchita Bhat Ph.D.[1,2], Ms. Mabel Prejean BS[3], Ms. Abbey Nkansah BS[3], Dr. Elizabeth Cosgriff-Hernandez Ph.D.[3], Dr. Lakshmi Prasad Dasi Ph.D.[1,2]

[1]Georgia Institute of Technology, Atlanta, GA, United States. [2]Emory University, Atlanta, GA, United States. [3]The University of Texas at Austin, Austin, Texas, United States

Introduction

Aortic Stenosis (AS) obstructs blood flow from the left ventricle to the aorta, often leading to the need for an aortic valve replacement. Transcatheter Aortic Valve Replacement (TAVR) is a minimally invasive option to treat severe AS where a stent with bioprosthetic leaflets is most commonly deployed via access from the femoral artery [1]. Bioprosthetic leaflets have limited long-term durability due to calcification and degeneration [2]. Therefore, there is a need for an alternative leaflet material to prolong TAVR durability. Here, we hypothesize that the use of hydrogel-coated electrospun (HES) composite leaflets will improve the hemodynamic performance and durability of TAVRs.

Methods

The leaflets were fabricated as illustrated in previous studies [3]. The polyurethane will provide enhanced mechanical properties, and the hydrogel coating provides thromboresistance.

HES leaflets were sutured on a cobalt-chromium stent (MP35N). A left heart simulator was used to test the hemodynamic performance at physiological aortic conditions. The downstream fluid velocity through the valve was analyzed using phase-locked particle image velocimetry (PIV). The left heart simulator fluid was seeded with fluorescent particles to track the fluid motion and the data was recorded using a high-speed camera. The peak velocity for an average of 100 cardiac cycles was obtained using DaVis 8.4, a software used to analyze raw PIV images.

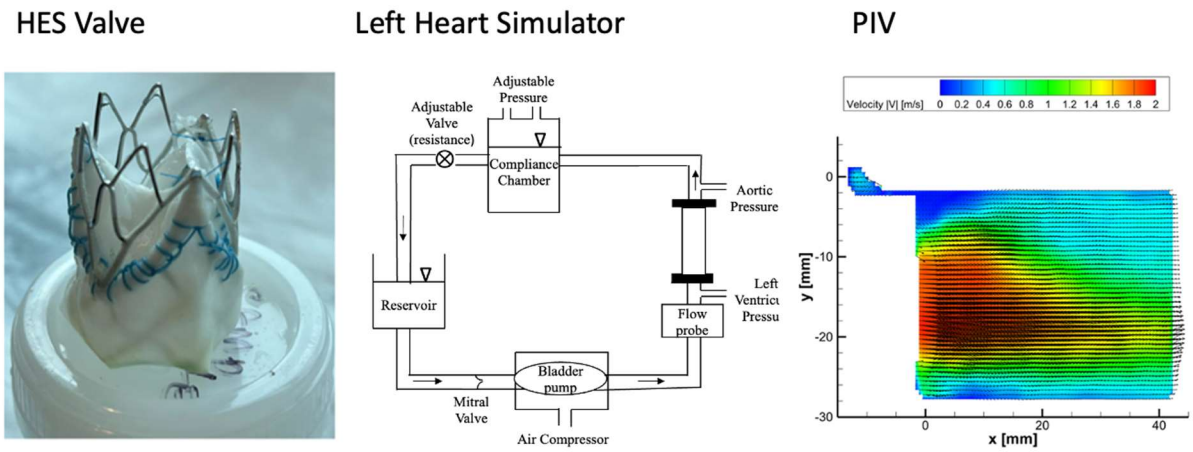
Results

The effective orifice area and regurgitation fraction were 1.52 ± 0.34 cm^2 and 9.6 ± 1.8%, respectively. The velocity magnitude at peak systole was 1.93 m/s.

Discussion

The effective orifice area and regurgitation fraction met ISO 5840 standards. The mean transvalvular pressure gradient was also comparable to current clinical devices [3]. Future studies will include finite-element simulations of stents to improve stent design and minimize stress concentrations, therefore preventing fracture of stent frames. These simulations will illustrate the stresses on the stent while loading it into the catheter and expanding it using a balloon during the TAVR procedure. Additionally, accelerated wear testing will be completed to access mechanical durability.

Images (Optional)



References (Optional)

[1] C. Banceu, et al., *Journal of Clinical Medicine*, 2025.

[2] E. Wium, et al., *Asian Cardiovascular and Thoracic Annals*, 2019.

[3] A. Robinson, et al., *Journal of Biomedical Materials Research*, 2024.

Session Category

Cardiovascular/Cardiorespiratory Biomechanics: Materials and Devices

OA103-03

Not All Hoppers Are Built for the Desert: Effects of Substrate on Hopping Kinematics of Kangaroo rats.

Ms. Sage Murthy[1], Ms. Kaylee Nguyen[2], Ms. Mary Pena[1], Dr. Craig McGowan PhD[1]

[1]University of Southern California, Los Angeles, California, United States. [2]University of California, Irvine, Irvine, California, United States

Introduction

Bipedal hopping is often associated with arid environments and it has been suggested that this mode of locomotion offers selective advantages under these conditions. In a recent study we showed that desert kangaroo rats are capable of hopping on soft sand with almost no changes in kinematics, relative to hard surfaces [1]. However, not all kangaroo rats live in sandy dunes and it remains unclear if bipedal hopping alone provides a unique ability to hop on soft substrates. In this study, we examined the kinematics of hopping on solid vs sand surfaces by California kangaroo rats, a species whose native habitat is grasslands. We hypothesized that, similar to desert kangaroo rats, there would be little difference in kinematics for California kangaroo rats hopping on sand vs solid surfaces.

Methods

To test our hypothesis, we collected high-speed sagittal plane video (300 Hz) from 9 California kangaroo rats (*D. californicus*) while hopping on a custom built rotary treadmill at 1.8 m/s on solid and sand (25 mm) surfaces. The animals' fur was shaved and the hindlimb joint centers were marked and digitized in order calculate limb and joint angles. A repeated measures ANOVA was used to test for differences between the conditions.

Results

Ours results showed several significant differences between hopping on solid and sand surfaces. Hopping frequency decreased on the sand while duty factor increased. The animals hopped with a more couched posture on sand, characterized by a shorter effective leg length, and there were significant changes in joint angles leading to increased limb extension at foot off. Joint angle changes were most pronounced at the knee and ankle.

Discussion

Our hypothesis was not supported. Unlike desert kangaroo rats, California kangaroo rats change their hopping kinematics significantly when hopping on the sandy substrate. The changes in kinematics are consistent with the animals having to do more mechanical work, presumably to replace energy lost to the movement of the sand under the foot. These

outcomes indicate that, while some bipedal hoppers are able to locomote on sand with little apparent energetic penalty, it is not a function of the hopping gait alone.

References (Optional)

Acknowledgements (Optional)

This work was supported by the Integrative Movement Sciences Institute (IMSI) Biological Integration Institute, NSF-DBI-2319710.

Session Category

Comparative Biomechanics: N/A

OA103-04

Influence of EMA and Musculoskeletal Stress Reduction on Postural Changes in Walking vs Climbing in Rats

Mrs. Cassandra Shriver, Dr. David Hu, Dr. Young-Hui Chang

Georgia Institute of Technology, Atlanta, GA, United States

Introduction

Climbing is a challenging type of locomotion requiring constant ascent against gravity, yet there are many scansorial animals capable of both walking and climbing. How do limb positions and body posture change between horizontal and vertical locomotion? We hypothesize different locomotor constraints impacting musculoskeletal stress in walking versus climbing induce postural changes that reduce pitchback torque and improve the effective mechanical advantage (EMA) of limb muscles.

Methods

We conducted preliminary experiments with six rats (*Rattus norvegicus)* in a GT IACUC-approved protocol (#A100530). Individuals completed ten horizontal walking trials on a treadmill and ten vertical climbing trials on a ladder. Kinematics were collected using a biplanar x-ray system. We used DeepLabCut [1] to train point-tracking models for labeling limb joints. Markers were fed into XMALab [2] to obtain 3D-coordinate positions. We calculated forelimb and hindlimb effective limb lengths and joint angles to assess postural changes between the locomotor modes. Differences in musculoskeletal stress were estimated with the Effective Mechanical Advantage (EMA) of the limb using a quasi-static inverse model [3].

Results

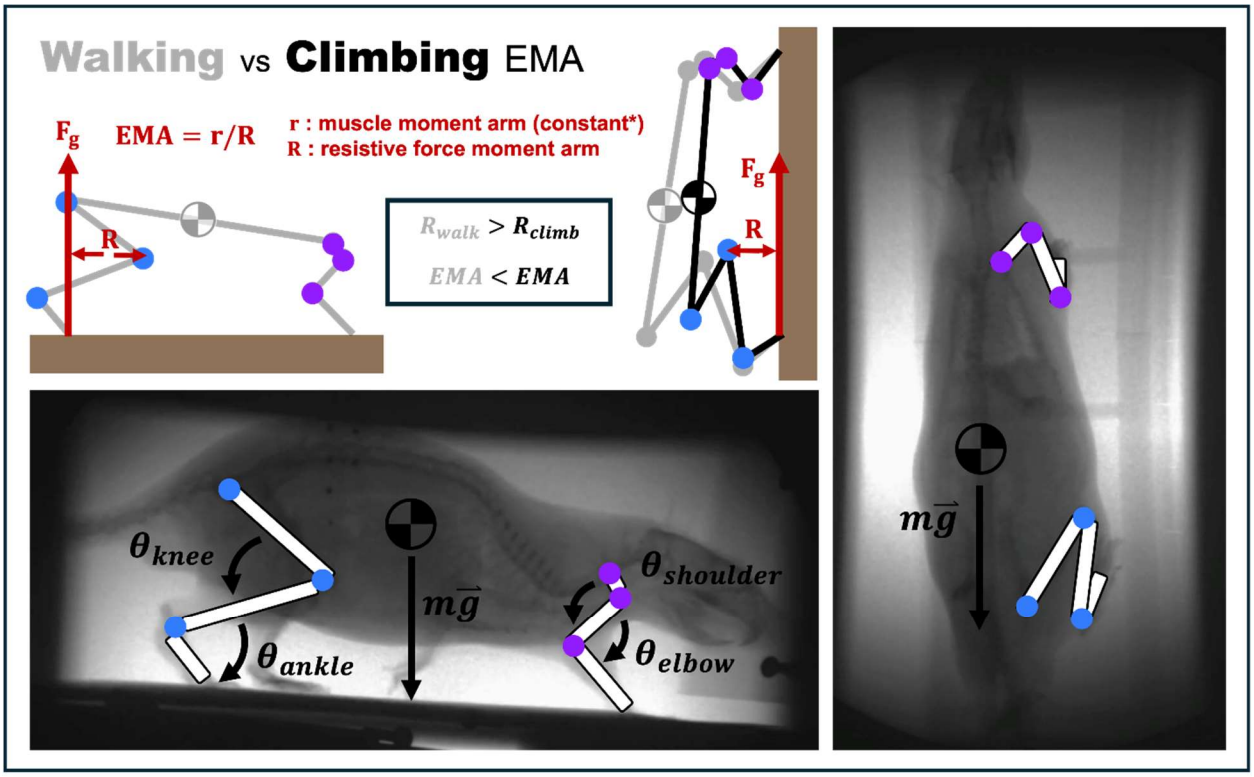
Preliminary analyses on two rats support our hypothesis that limb posture becomes more crouched during climbing. Effective hindlimb length decreased by 1.5±0.5 cm. This was achieved by decreasing joint angles, but maintaining similar contact patterns, as opposed to a sprawled limb posture. Similar changes were observed in elbow angles, reducing effective forelimb lengths (0.5±0.3 cm).

Discussion

Bringing the hips and shoulders closer to the locomotor surface during climbing reduces musculoskeletal stresses via an increased EMA. An increased EMA reduces torques

associated with a smaller moment arm of the substrate reaction force. In contrast to larger walking animals that display a more upright posture to increase their EMA, we propose that larger climbers likely adopt more crouched postures to increase EMA, due to biomechanical differences from body orientation relative to gravity. Future work will examine how these changes are exacerbated by mass scaling in larger climbers subject to proportionally greater gravitational constraints.

Images (Optional)



Effective mechanical advantage (EMA) differences in walking vs climbing. *The muscle moment arm (r) is assumed to be constant in comparison to the magnitude of change in the resistive force moment arm (R). In horizontal locomotion, more crouched postures increase the moment arm of the gravitational resistive force about distal joints, resulting in reduced EMA compared to more upright postures. In vertical locomotion, the opposite is true. Rats crouch more during climbing than walking, improving EMA in comparison to applying the same walking posture to climbing.

References (Optional)

[1] Nath, T. et al. (2019). Nat Protoc 14, 2152–2176.

[2] Knörlein, B.J. et al. (2016). J Exp Biol 219, 3701–11.

[3] Biewener. (1989). Science 245, 45-48.

Session Category

Comparative Biomechanics: N/A

OA103-05

Multimaterial Models Reveal Functional Principles of Armored Fish and Bioinspired Devices

Dr. Cassandra Donatelli[1], Ms. Megan Vandenberg[2], Dr. Karly Cohen[3], Mr. Lorenzo Martinez[4], Mr. Brody Anderson[5], Mr. John Racy[2], Dr. Adam Summers[2,3]

[1]University of Washington Tacoma, Tacoma, WA, United States. [2]University of Washington, Seattle, WA, United States. [3]Friday Harbor Laboratories, Friday Harbor, WA, United States. [4]Rhodes College, Memphis, TN, United States. [5]Washington State University, Pullman, WA, United States

Introduction

Armored fishes are extraordinary, exhibiting morphological diversity ranging from interlocking bony plates, to fused strut systems, to flexible embedded scales. They are ideal models for understanding how rigid elements and flexible joints can be arranged to balance protection, mobility, and efficiency. These natural structures face the same constraints seen in engineered protective systems such as the need to dissipate forces, restrict harmful deformation, and maintain flexibility, which makes them useful sources of bioinspiration. Understanding how those demands are balanced requires computational and physical models that let us probe mechanics directly. Advances in multi-material 3D printing and computational fluid dynamics allow us to model biological complexity using accessible, low-cost tools, enabling rapid prototyping and testing. These models inform our biological understanding and engineered design.

Methods

We quantified the diversity of shapes and plate arrangements in one family of armored fishes, the poachers (Agonidae, Figure 1.A). Using micro-CT scanning. microscopy, and geometric morphometrics, we explored plate shape (Figure 1.B), body shape (Figure 1.D), and plate arrangement. We examined the tissues with dissection and histology to understand how plates are connected. With these data, we designed and mechanically tested multimaterial 3D-printed models that incorporated embedded fabrics (Figure 1.C, E) and flexible materials (Figure 1.E,G) to mimic the geometry and the material differences of natural armor.

Results

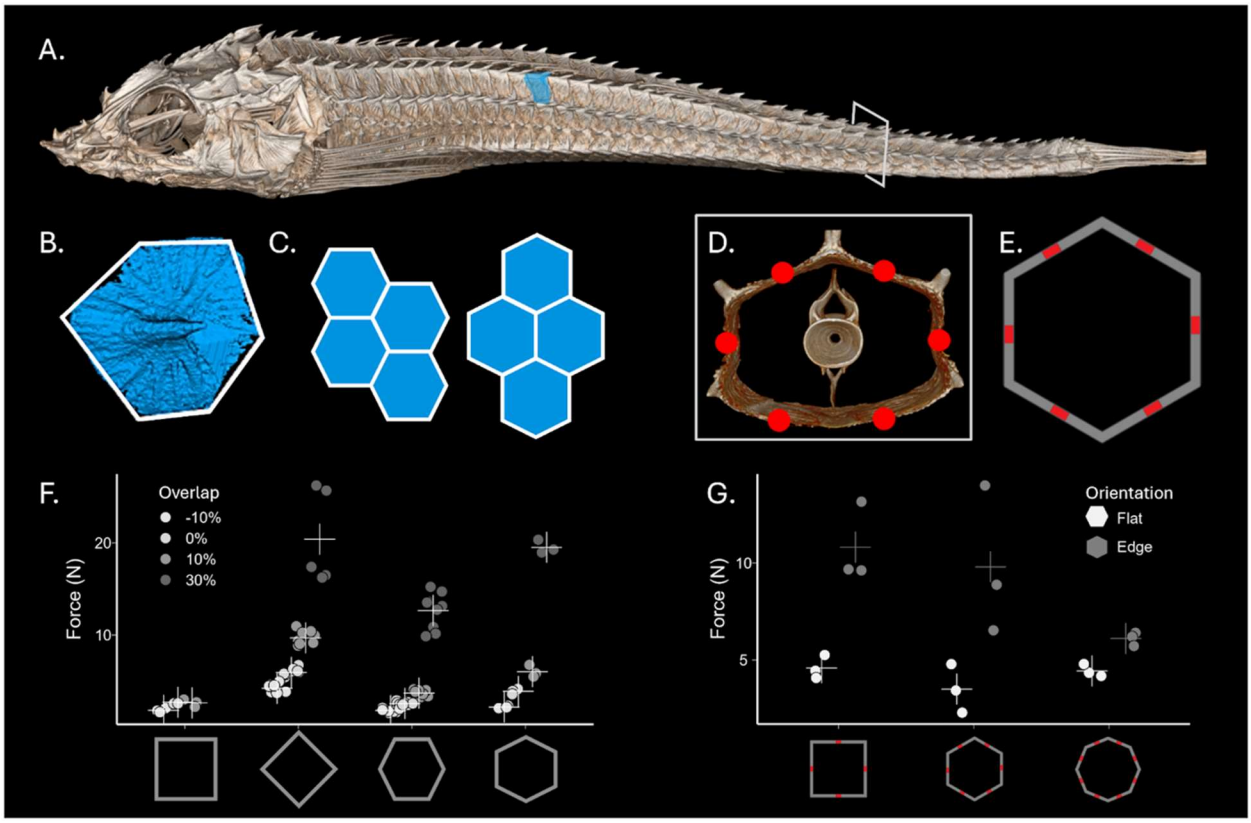
Our models show that the shape and arrangement of rigid components, and the integration of soft materials, influence the mechanical performance of armored systems (Figure 1. F, G). Bioinspired models that closely mimic natural morphology and tissue organization tend

to resist compression and bending more effectively than other designs. Variation in joint placement, material flexibility, and fiber reinforcement all affect system mechanics, demonstrating the importance of testing the combination of segment shape and overlap, soft–hard interfaces, and composite-material anisotropy.

Discussion

These models show how natural armor balances protection and flexibility. Our multimaterial composite additive manufacturing framework provides a systematic approach for continued evaluation of the geometric, interfacing, and material drivers of armor performance. In addition to helping us understand biological armor, we also use these approaches to inform human-focused design challenges such as bioinspired prosthetics and medical braces.

Images (Optional)



Session Category

Comparative Biomechanics: N/A

OA104-01

Numerical Study of Drag Influence on Magnetic Micro-Particle Aggregates in Magnetic Resonance Navigation for Tumor Embolization

Mr Mahdi Rezaei Adariani[1,2], Dr Jiří Pešek[2], Dr Cyril Tous[1], Dr Ning Li[1], Prof Gilles Soulez[1], Prof Irene Vignon-Clementel[2]

[1]CRCHUM, Montreal, QC, Canada. [2]Inria, Saclay Ile-de-France, Palaiseau, France

Introduction

Magnetic resonance navigation (MRN) of medicinal particles is an emerging technique for liver cancer treatment. MRN relies on particle clusters formed via interactions induced by the MRI scanner's magnetic field. These aggregates are injected into the blood flow and steered toward target vessels by blood drag, magnetic gradient forces, and gravity. A critical challenge is understanding aggregate motion near vessel walls, which remains inadequately addressed by existing models. This study investigates these factors using numerical simulations to provide insights into aggregate behavior and improve computational models for targeted embolization.

Methods

Magnetic micro-bead aggregates were simulated in hepatic artery geometry under physiologically relevant flow conditions and validated against in-vitro phantom experiments. Inlet conditions were derived from phase-contrast MRI, with outlet flow rates measured manually. Particle motion was modeled using a Lagrangian point-particle approach based on the Maxey-Riley equation. Drag was estimated by the bead drag model for chain-like aggregates, with near-wall corrections available in the literature. While these simplifications neglect shape effects and flow complexity, they provide a framework for analyzing aggregate behavior near vessel walls, which is key for the application. Hydrodynamic forces on individual particles were further analyzed using direct numerical simulation (DNS) to better capture aggregate dynamics close to walls.

Results

The study began with chains of spherical particles oriented parallel or perpendicular to flow. Total drag predictions were validated against experimental data and the bead-chain drag model. Near-wall corrections were further validated using DNS for a particle moving in stationary flows and a particle fixed in shear flow. Strong agreement between analytical

solutions and numerical results confirms the model's accuracy for these configurations. Moving particles in flow were also analyzed.

Discussion

The simplified model was verified and validated against phantom experiments. Preliminary results suggest that the method provides reasonable estimates of drag. However, the bead drag model is limited to rigid chains of spherical particles, and further research is needed to generalize hydrodynamic effects on aggregates of varying shapes in arterial flow. Ongoing work aims to develop a semi-empirical model to better bridge the gap between one-way coupling simulations and experiments, providing a foundation for optimizing MRN-based tumor embolization in-vivo.

Session Category

Micro/Biofluidics: In Silico Models and Simulation

OA104-02

A Physics-Informed Computational Model Based on Diffusion MRI for Predicting Ischaemic Stroke Evolution

PhD student Hsuan-Ju Chen[1], Dr. Stephen Payne[2,1]

[1]Institute of Applied Mechanics, National Taiwan University, Taipei city, Da'an District, Taiwan. [2]School of Engineering Mathematics and Technology, University of Bristol, Bristol, South West England, United Kingdom

PhD student Hsuan-Ju Chen

Introduction

Current clinical imaging techniques, particularly DWI and PWI, are central to stroke diagnosis but capture only a single time point in stroke evolution. Dynamic prognosis requires predicting how perfusion deficits evolve into permanent tissue damage by integrating these data into a physics-based model.

We propose a physics-informed FEM brain model, based on our previous cerebral perfusion work [1], integrating DWI-derived parameters to simulate restricted water motion, which is highly sensitive to early ischaemic changes.

Methods

The study utilized a longitudinal dataset from 3 large animals, with each scanned at three checkpoints post-intervention: immediate (post-cooling), 24-48 hours, and 30 days. A voxel-wise diffusion coefficient map, D(x,y,z), was generated from raw DWI data.

The spatio-temporal evolution of the stroke was modeled using the partial differential equation (PDE): $\partial u/\partial t = \nabla \cdot (D(x)\nabla u)$, where, u represents the evolving diffusion measurement, governed by a diffusion field. The lesion ROI was manually delineated on the DWI maps and a corresponding contralateral normal ROI was also generated by mirroring the lesion geometry across the midline.

Results

In the immediate group, the lesion ROI was found to exhibit a marked reduction in mean diffusivity (0.758 vs. 0.887 x 10^{-3} mm^2/s) compared to the contralateral normal tissue, which is consistent with restricted water motion. The 24-48 hours group demonstrated

pseudonormalization (0.862 vs. 0.838 x 10^{-3} mm^2/s), while the 30-day group showed elevated diffusivity (0.981 vs. 0.855 x 10^{-3} mm^2/s), which may reflect structural changes associated with subacute to chronic stroke evolution.

Discussion

Results from the Immediate group highlight energy failure, helping to explain the high-intensity signals in clinical DWI. The transition from acute restriction to chronic tissue liquefaction mirrors temporal dynamics previously seen in stroke models [2]. The acute slower decay serves as a robust biomarker for the severity of the ischaemic core. Persistent restricted diffusion indicates areas where metabolic suppression may not have fully prevented cellular injury. Ultimately, this helps to validate our physics-informed computational model as a framework for characterizing and predicting ischaemic stroke evolution.

Images (Optional)

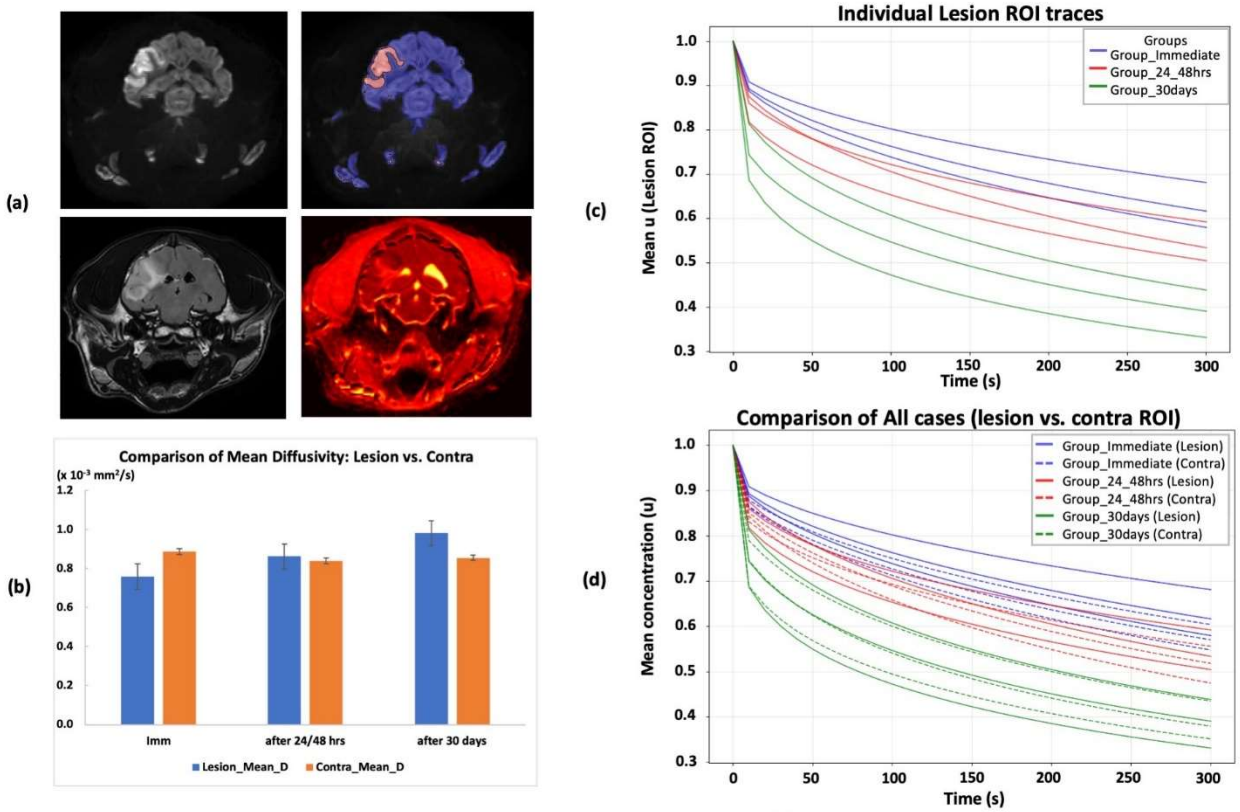


Figure 1. Simulation of spatiotemporal diffusion dynamics in a canine stroke model. (a) Representative DWI, anatomical MRI, and diffusivity maps with lesion segmentation. **(b)** Bar chart comparison showing the transition from acute restricted diffusion to chronic elevated diffusivity. Note the pseudonormalization at 24/48 hours. **(c)** Simulated concentration decay curves for lesion ROIs. **(d)** Comparison of lesion (solid) vs. contralateral (dashed) transport. A clear crossover is observed in the 30-day group (green).

References (Optional)

[1] Józsa, T. I. et al., Interface Focus, 2021

[2] Boudreau, E. et al., Frontiers in Veterinary Science, 2022

Acknowledgements (Optional)

We acknowledge NSTC funding for the GEMINI project, thank UMass Chan and Prof. Robert King for the canine data, and also thank Prof. Alfons Hoekstra and Prof. Tamás Józsa for their guidance.

Session Category

Micro/Biofluidics: In Silico Models and Simulation

OA104-03

Sensitivity Analysis of Ventricular Shunt Obstructions on Cerebrospinal Fluid Drainage

Dr. Bryan Good PhD, Dr. Stephanie TerMaath PhD

University of Tennessee, Knoxville, TN, United States

Introduction

Hydrocephalus is a condition where an excessive amount of cerebrospinal fluid (CSF) accumulates within the ventricles of the brain resulting in elevated intracranial pressure (ICP) that can cause permanent brain damage and impairment. The primary treatment is the implantation of a ventricular shunt to drain excess CSF. While effective in controlling ICP, ventricular shunts have extremely high failure rates, with most patients requiring a shunt replacement within two years. Approximately 85% of pediatric patients will require a shunt revision, with 5% requiring 10 or more revision procedures over their lives. Therefore, our objective is to determine the sensitivity of ventricular shunt CSF drainage to different obstruction scenarios within the proximal catheter.

Methods

OpenFOAM and its 'porousSimpleFoam' solver was used to simulate CSF flow within a simplified lateral ventricle and proximal catheter model (**Fig. 1A**). The catheter featured 2 rows of 8 drainage holes, with each designated a "porous" zone in the model. An inlet flow rate of 21 ml/hr was prescribed, representing choroid plexus CSF production, with a fixed outlet pressure. Since no data of shunt obstruction properties exists, we varied the Darcy coefficient (inverse of material permeability) from $1e^{0}$-$1e^{10}$ m^{-2} in each catheter hole to determine the sensitivity of catheter performance to obstructions.

Results

When normalized by baseline "unobstructed" flow (**Fig. 1B**), obstructions with Darcy coefficients $<1e^{7}$ had no significant effect on CSF drainage. On the other extreme, Darcy coefficients of $1e^{10}$ were sufficient to completely obstruct CSF drainage. We also found that obstruction of Hole 8 (closest to outlet) had the greatest effect on other holes' CSF flows, increasing between 42-51% over baseline. Hole 1 obstruction (closest to inlet) had the least impact, only increasing Hole 2-4 flows by 2-10%.

Discussion

These results provide baseline data for our ongoing machine-learning study to determine the combined effects of catheter hole obstructions on shunt performance. We have narrowed our range of obstruction permeabilities and also determined the effect of single hole obstructions on overall catheter drainage. Our ultimate goal is to optimize shunt performance, while minimizing the effects of catheter obstructions, to decrease the number of shunt revisions for hydrocephalus patients.

Images (Optional)

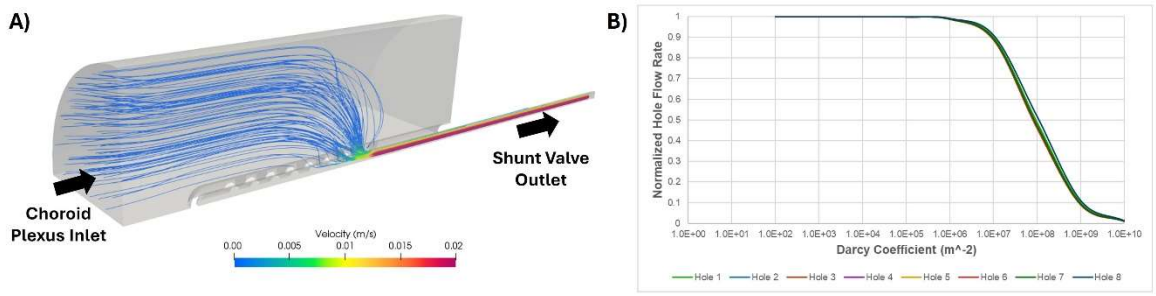


Fig. 1: A) Example of CSF flow through our simplified ventricle and catheter model, showing the influence of a Hole 1 obstruction on overall drainage flow patterns. **B)** Effect of obstruction permeability (Darcy Coefficient) on flow rate through each catheter drainage hole.

Session Category

Micro/Biofluidics: In Silico Models and Simulation

OA104-04

Mechanical Responses and Key Parameter Identification in a Finite Element Model of the Mouse Cervical Spinal Cord under CSF Pulsatile Loading

Doctoral student Duzhi CHEN

Laboratoire de Biomécanique Appliquée, Marseille, Provence-Alpes-Côte d'Azur, France

Introduction

Numerous numerical spinal cord models exist, yet analyses of the mechanical loading environment due to cerebrospinal fluid (CSF) pulsation remain sparse. Reported mechanical properties vary widely across species, sample preparations, experimental protocols, and constitutive assumptions, while the dynamics of CSF pulsation are not well defined. This study aimed to clarify the spinal cord's mechanical response under pulsatile CSF loading by reviewing previous work to establish realistic parameter ranges and identify dominant factors, and then running simulations and a sensitivity analysis to evaluate the influence of those parameters.

Methods

A finite element model of the mouse cervical spinal cord was developed, modelling grey matter (GM) and white matter (WM) separately and employing a generalized Maxwell model to capture viscoelastic behavior (elastic moduli $E_{WM} \approx 0.2$ MPa for and $E_{GM} \approx 0.025$ MPa). CSF pulsation was represented as a sinusoidal pressure load acting on the lateral surface (mean pressure at 0.00267 MPa, 1Hz). The first principal strain, von Mises stress and Lode angle were extracted from a 15-cycles simulation as an output for a sensitivity analysis using the Morris method, screened the effects of material parameters and loading conditions.

Results

Stress and strain evolved over time; although steady state was not reached within 15 s, analysis focused on this point. The Lode angle indicated predominantly compressive states in GM and tensile states in WM. Stress ranged from 0.003 to 0.5 kPa, and the first principal strain from roughly 0.0005 % to 0.1 %, with higher values in WM. Maximum strains occurred in the lateral funiculus; stress concentrations appeared at the grey–white interface near the dorsal and ventral horns. The sensitivity analysis found Poisson's ratio to be the most influential parameter, followed by loading-related variables and overall stiffness.

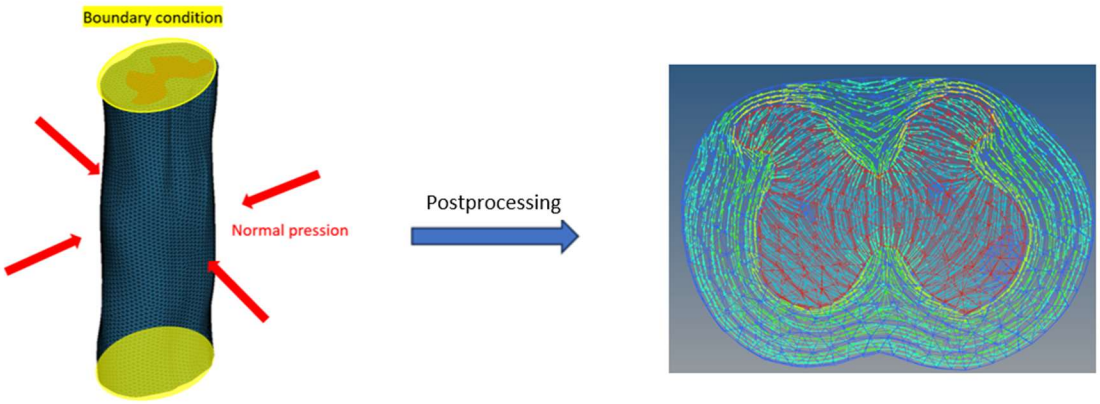
Viscoelasticity had limited effect; the stiffness ratio between grey and WM was negligible. Base pressure amplitude and Poisson's ratio showed pronounced nonlinear interactions.

Discussion

These simulations provide quantitative ranges for stress and strain, showing deformations are sufficiently small and that linear elasticity is adequate under CSF pulsation. Strong influence of Poisson's ratio underscores the importance of incompressibility assumptions. Accurate characterisation of CSF pulsation parameters is essential for predicting spinal cord response.

Images (Optional)

Snapshot of the model and its corresponding simulation results



Preprocessing(definition of boundary conditions)

First principal strain vector field (transverse view)

Session Category

Micro/Biofluidics: In Silico Models and Simulation

OA105-01

Longitudinal Assessment of Sensor-Derived Gait Quality and Clinical Functional Outcomes Following Total Hip Arthroplasty.

Ms. Jiahui Wang[1], Dr. Abner Sergooris[2], Prof. Annick Timmermans[2], Prof. Benedicte Vanwanseele[1]

[1]KU Leuven, Leuven, Leuven, Belgium. [2]Hasselt University, Hasselt, Hasselt, Belgium

Introduction

Total hip arthroplasty (THA) is highly effective for end-stage hip osteoarthritis, yet gait biomechanics don't always fully normalize despite substantial improvements in pain and self-reported function [1]. These gait abnormalities are clinically relevant because they may influence mobility, loading, and fall risk. While functional tests often miss subtle gait abnormalities, wearable inertial measurement unit (IMU) offers a biomechanics-driven approach to quantify sensor-derived gait quality in clinics [2]. In addition, most individuals undergoing THA are middle-aged and older adults, distinguishing surgery-related recovery from age-related changes is essential. This study evaluated longitudinal changes in IMU-derived gait quality after THA and examined whether these changes were independent of aging.

Methods

Seventy-seven THA participants were assessed preoperatively and at 6 weeks, 3 months, and 1 year, while forty-five age-matched healthy individuals were assessed at baseline, 3 months, and 1 year to characterize aging effects. A trunk-mounted IMU (200 Hz) recorded habitual 25-m straight-line walking, providing step symmetry and stability in the vertical (VT), mediolateral (ML), and anteroposterior (AP) directions. Clinical assessments included the 30-s Chair Stand Test (30sCST), 40-m Fast Walk (40MFW), and hip muscle strength. Linear mixed-effects models analyzed all outcomes.

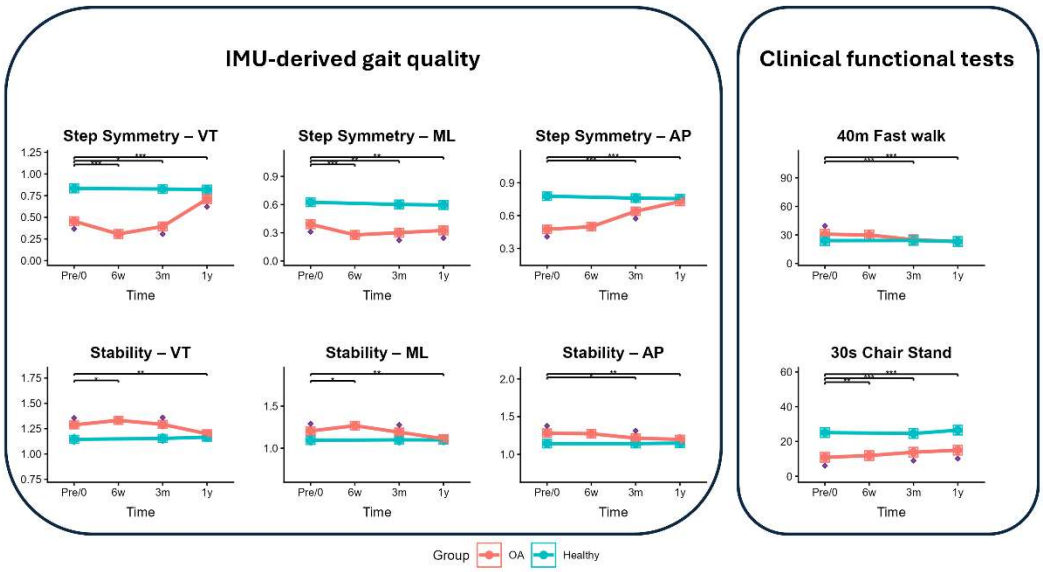
Results

IMU gait measures showed postoperative changes not explained by aging. VT and ML symmetry worsened at 6 weeks; VT improved by 1 year, while ML did not return to preoperative values. VT and ML stability decreased at 6 weeks and improved by 1 year. AP symmetry and stability improved by 3 months. Hip strength on the operated side declined until 3 months and improved by 1 year, except for external rotation. The 40MFW matched healthy performance by 3 months, whereas the 30sCST improved but remained below healthy levels at 1 year.

Discussion

ML symmetry remained impaired at 1 year, which may relate to prosthesis-altered hip rotator mechanics or residual strength asymmetry. AP measures recovered more rapidly, possibly due to preserved AP structures and earlier restoration of flexor–extensor strength. As these patterns were not explained by aging, ML gait quality represents an important target for postoperative rehabilitation.

Images (Optional)



References (Optional)

[1] J. S. Bahl et al., *Osteoarthritis Cartilage*, 2018

[2] Jill Emmerzaal et al., *Sensors (Basel)*, 2022

Session Category

Clinical Biomechanics: N/A

OA105-02

Longitudinal Changes in Strength, Physical Activity, Mobility, and Pain Following Periacetabular Osteotomy for Hip Dysplasia

Ms. Christina Bourantas BA, Dr. Molly Shepherd PhD, Ms. Madison Wissman BS, Dr. John Clohisy MD, Dr. Michael Harris PhD

Washington University in St. Louis, St. Louis, Missouri, United States

Introduction

Developmental dysplasia of the hip (DDH) is characterized by abnormal bony geometry that reduces hip joint stability [1,2]. Many individuals with DDH are active but limit activity and seek surgery because of insidious pain. Periacetabular osteotomy (PAO) surgically reorients the acetabulum [3], yet outcomes remain variable [4]. Assessing short-term changes in activity, strength, and self-reported outcomes during the period when rehabilitation can be optimized is critical. The objective of this study was to evaluate longitudinal changes in pain, function, strength, and activity during one-year post-PAO.

Methods

Fifteen individuals with DDH completed assessments preoperatively and every 2 months post-PAO for 12 months. Participants wore a Fitbit for 7 days to measure steps and heart rate; moderate activity was defined as minutes above 50% of estimated max heart rate. Self-reported outcomes included iHOT-12 and PROMIS Pain Interference, Physical Function, and Anxiety. Isometric hip strength was assessed using a handheld dynamometer pre-PAO, 4-, and 12-months post-PAO. Paired t-tests compared outcomes across timepoints.

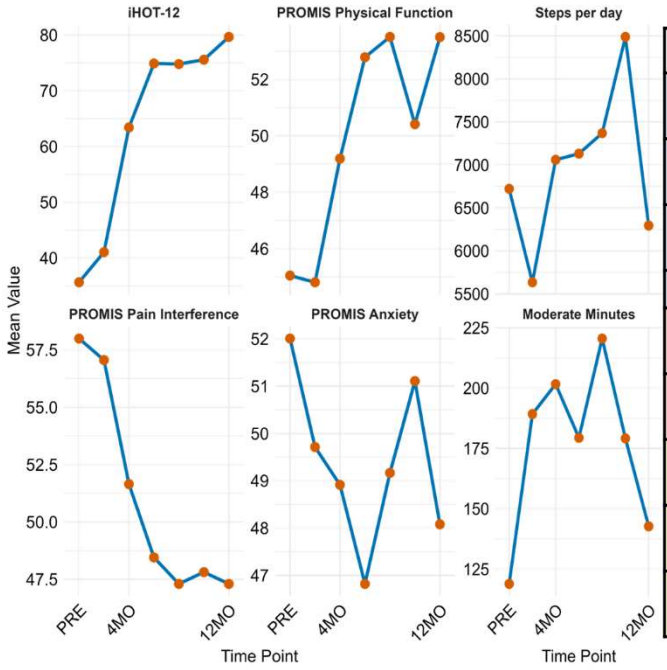
Results

iHOT-12, PROMIS Pain Interference, and Physical Function significantly improved at 4- and 12-months post-PAO (Figure 1). For activity, steps per day were not different pre to 12-months post-PAO, but moderate minutes changed significantly from pre to 4-months post-PAO and 4- to 12-months post-PAO. Strength significantly decreased at 4-months post-PAO but increased at 12-months post-PAO. Despite these group-level changes, variability remained high across participants, with large standard deviations in self-reports, activity, and strength measures.

Discussion

These findings demonstrate variable changes in pain, function, strength, and activity during early recovery after PAO. While self-reported outcomes improved, activity measures were inconsistent, and strength recovery decreased initially before returning to preoperative values. The variability in outcomes suggests that self-reported improvements may mask persistent functional deficits for some individuals, while others recover more rapidly. Comprehensive monitoring revealed diverse recovery patterns, reinforcing the need for individualized rehabilitation strategies. Addressing variability during this critical recovery window may help reduce long-term dissatisfaction and optimize functional outcomes.

Images (Optional)



Outcome	PRE	4MO	12MO
iHOT-12	35.6 ± 11.0	63.4 ± 13.9*	79.7 ± 15.7#^
Pain Interference	58.0 ± 5.2	51.6 ± 5.4*	47.3 ± 7.6#^
Physical Function	45.0 ± 5.4	49.2 ± 8.1	53.5 ± 6.8#^
Anxiety	52.0 ± 6.7	48.9 ± 9.7	48.1 ± 12.3
Steps per day	6722 ± 3799	7060 ± 3591	6295 ± 3140
Moderate Minutes	118.8 ± 66.5	201.7 ± 109.8*	142.7 ± 110.9^
Hip Flexion (lbs)	42.9 ± 14.9	34.0 ± 12.4*	43.6 ± 8.6^
Hip Extension (lbs)	61.5 ± 27.6	45.2 ± 26.3*	59.0 ± 22.4^
Hip Abduction (lbs)	48.6 ± 22.0	34.5 ± 14.8*	43.2 ± 12.5^

Figure 1. Averages across 1-year following PAO. Table: average ± standard deviation at PRE, 4- and 12-months post-PAO.
Significant differences ($p<0.05$): *PRE vs 4MO, #PRE vs 12MO, ^4MO vs 12MO

References (Optional)

[1] Cody Wyles *et al.,* Clin Orthop, 2017; [2] Reinhold Ganz *et al*., Clin Orthop, 2008; [3] John Clohisy *et al*., JBJS, 2005; [4] Julie Boje *et al*., Hip Preserv Surg, 2019

Acknowledgements (Optional)

Funding from NIH-R01AR081881.

Session Category

Clinical Biomechanics: N/A

OA105-03

A DXA-Based Hip 3D Finite Element Model Predicts Hip Fractures Better Than Hip aBMD Independently of FRAX Scores in a MrOS Sub-Cohort

Dr Lorenzo Grassi[1], Mr Lars Jehpsson[2,3], Dr Helena Johansson[4], Dr Magnus K Karlsson[2,3], Dr Björn E Rosengren[2,3], Dr Hanna Isaksson[1]

[1]Department of Biomedical Engineering, Lund University, Lund, Skåne, Sweden. [2]Department of Clinical Sciences, Lund University, Lund, Skåne, Sweden. [3]Department of Orthopedics, Skane University Hospital, Malmö, Skåne, Sweden. [4]Sahlgrenska Osteoporosis Centre, Institute of Medicine, Sahlgrenska Academy, University of Gothenburg, Gothenburg, Gothenburg, Sweden

Introduction

Areal bone mineral density (aBMD) measured by dual-energy x-ray absorptiometry (DXA) is a moderate predictor of bone strength, while more resource-demanding computed tomography derived 3D finite element (FE) models provide superior accuracy. We have previously presented a method to reconstruct 3D shape and BMD distribution of the femur from a single DXA image and created subject-specific FE models [1]. The aim of this pilot study was to evaluate the feasibility of using the method to predict hip fractures.

Methods

We used a sub-cohort of men from the population based MrOS Sweden study (Malmö, Uppsala). The sub-cohort (n=609) included men without previous hip fracture who had undergone evaluation by DXA and FRAX (Fracture Risk Assessment Tool) at age 75±2 years. We reconstructed 3D FE models from 2D DXA scans and predicted femoral strength for 10 different side-fall configurations using a validated technique [2,3]. We ran time-to-event analysis (hip fracture) with competing risk (death) with Fine-Gray sub-distribution hazard models 5 years after the DXA scans were performed. We predicted fractures using aBMD and FE-predicted femoral strength, with and without adding FRAX scores as covariate. Fracture risk prediction accuracy was evaluated with area under the receiver operating characteristics (AUROC) curve.

Results

Twentynine men sustained a hip fracture during the 5-year study period. FE-predicted femoral strength was useful to identify hip fracture cases (AUROC=0.72, 95% confidence interval [0.60–0.87]) and in the examined sub-cohort was superior to aBMD (AUROC=0.66

[0.46–0.86], ΔAUROC=0.06, figure 1). The differences, however, did not reach statistical significance. Similar results were seen when adjusted for FRAX (ΔAUROC=0.06, figure 1).

Discussion

FE-predicted femoral strength was useful to identify fracture cases and in the examined sub-cohort also had better discriminatory ability than aBMD (with or without FRAX). The superiority to aBMD was not statistically significant, but the observed effect size suggests potential clinical relevance. Our future work will focus on including larger sub-cohorts to the analysis to increase statistical power and verify or oppose our current inferences.

Images (Optional)

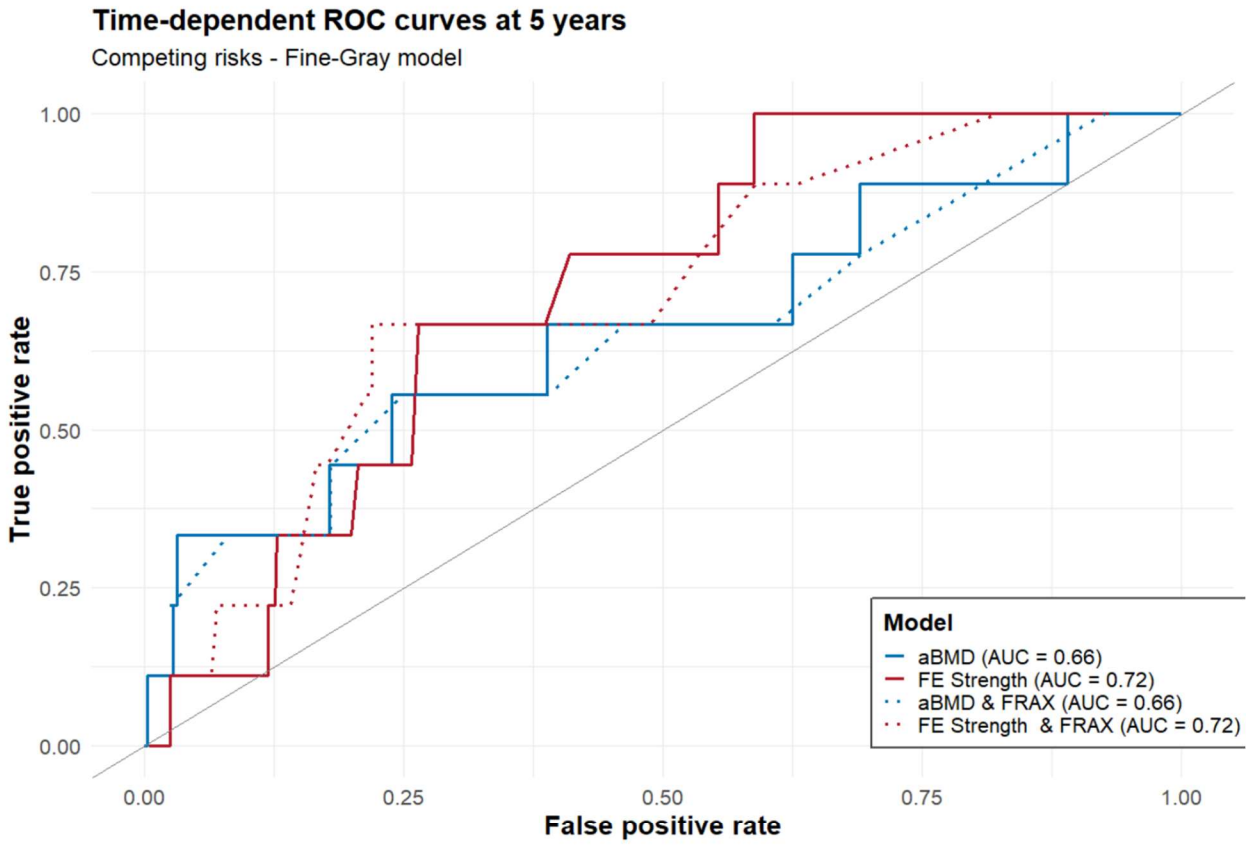


Figure 1: Receiver operating characteristics (ROC) curves for the predictions of the Fine-Gray models obtained using finite element (FE)-predicted proximal femoral strength (red) and areal bone mineral density (blue) as predictors. The dotted lines show the same predictions when FRAX scores were added as covariate to both predictons.

References (Optional)

[1] Väänänen et al., MedImagAnal 2015

[2] Grassi et al., JBMR 2023

[3] Schileo et al., jBiomech 2014

Acknowledgements (Optional)

The study received funding from Swedish Research Council [no. 2015-04795; 2019-04517; 2022-03474] and the Mats Paulsson's foundation. The computation of the 2D-to-3D reconstructions was enabled by resources provided by LUNARC (the center for scientific and technical computing at Lund University).

Session Category

Clinical Biomechanics: N/A

OA105-04

Phenotypic Variability in Developmental Dysplasia of the Hip: Linking Acetabular Geometry to Pain, Function, Activity, and Strength

Ms. Christina Bourantas BA, Ms. Emma Behrman, Dr. Keith Lohse PhD, PStat, Dr. John Clohisy MD, Dr. Michael Harris PhD

Washington University in St. Louis, St. Louis, Missouri, United States

Introduction

Developmental dysplasia of the hip (DDH) presents with a range of morphologic abnormalities, yet most studies consider affected individuals as a homogeneous group. This approach risks masking anatomical differences that may influence pain, function, and treatment response. Prior work showed geometric subgroups, like anterior or lateral coverage deficiencies, may be linked to patterns of intra-articular damage [1,2]. It remains unclear whether these subgroups also differ in activity or self-reported mobility and function. By classifying DDH using multiple measures of geometry rather than single radiographic thresholds, we aimed to capture phenotypic variability and examine how acetabular geometry may impact pain, function, activity, and strength.

Methods

18 individuals with DDH underwent radiographic assessment of lateral center edge angle (LCEA) and acetabular inclination (AI), along with 3D measures of anterolateral and posterolateral femoral head coverage [3]. Unsupervised K-means clustering using the elbow method [4] identified two geometric subgroups reflecting more versus less severe DDH. Participants wore a Fitbit for 7 days to record steps and heart rate; moderate activity was defined as minutes above 50% of estimated maximum heart rate. Self-reported outcomes included iHOT-12 and PROMIS Mental Health, Mobility, Pain Interference, Physical Health, and Anxiety. Isometric hip strength was assessed using a handheld dynamometer.

Results

Cluster 1 (more severe DDH), defined by decreased LCEA, lateral femoral coverage, and increased AI, demonstrated lower iHOT-12 scores and fewer daily steps than Cluster 2 (less severe DDH) (Table 1). Other self-reported outcomes were similar between clusters. Flexion strength was greater in Cluster 1, but abduction and extension were comparable.

Discussion

Geometric subgrouping captures some variability in pain, function, and activity. More severe acetabular deficiency was associated with reduced mobility and activity. However, small sample size limits generalizability and statistical power. Larger cohorts are needed to validate these preliminary cluster differences and determine whether geometric profiles consistently predict pain, mobility, and activity variation. Stratifying DDH by geometry may improve pre-operative assessment and inform personalized treatment strategies.

Images (Optional)

Outcome	Cluster 1: More severe DDH	Cluster 2: Less severe DDH
iHOT-12	33.0 ± 13.4	38.1 ± 11.9
PROMIS Mental Health	52.7 ± 9.5	50.2 ± 7.7
PROMIS Physical Health	44.1 ± 7.2	45.3 ± 3.5
PROMIS Mobility	41.4 ± 5.4	43.8 ± 3.1
PROMIS Anxiety	50.6 ± 9.3	53.7 ± 7.2
PROMIS Pain Interference	58.8 ± 4.8	57.9 ± 5.2
Average Steps	6748 ± 3225	8703 ± 5063
Moderate Minutes	111 ± 70	109 ± 57
Hip Flexion (lbs)	48.0 ± 16.4	38.8 ± 5.9
Hip Abduction (lbs)	49.0 ± 24.9	51.2 ± 11.2
Hip Extension (lbs)	64.7 ± 30.1	59.7 ± 16.2

Table 1. Average ± standard deviation of each outcome for both clusters.

References (Optional)

[1] Jeffery Nepple *et al.*, CORR, 2017; [2] Charlotte Hartig-Andreasen *et al.*, Acta Orthop, 2013; [3] Christina Bourantas *et* al., Clin Biomech, 2025; [4] Seth Higgins *et al.*, CMBBE, 2024

Acknowledgements (Optional)

Funding from NIH-R01AR081881.

Session Category

Clinical Biomechanics: N/A

OA105-05

The Effect of Simulated Movement Training on Joint Forces in Patients with Hip Dysplasia

Ms. Madison Wissman, Dr. Molly Shepherd, Ms. Christina Bourantas, Dr. Michael Harris

Washington University in St. Louis, St. Louis, Missouri, United States

Introduction

Developmental dysplasia of the hip (DDH) is characterized by inadequate femoral head coverage, abnormal joint reaction forces (JRFs), high risk for early osteoarthritis, and functional limitations [1,2]. Patients with DDH may exhibit altered movement patterns [3]. Movement training rehabilitation aims to normalize kinematics during pain-evoking movements and has been shown to reduce pain and improve function [4]. However, its effect on joint loading is unknown, especially in DDH. Our objective was to quantify gait compensations in DDH and simulate movement training to assess its impact. We hypothesized that DDH kinematics differ from healthy gait, and that enforcing healthy kinematics would reduce hip JRFs.

Methods

We collected motion, electromyography, and ground reaction forces from 12 individuals with DDH and 15 controls without hip pathology. Patient-specific musculoskeletal models were created from magnetic resonance imaging using OpenSim. One representative gait cycle on the symptomatic limb was analyzed with OpenSim Moco to determine muscle forces and hip JRFs. Average “healthy” kinematics and ground reaction forces were computed from controls. Movement training was simulated by applying healthy kinematics to patients’ models. Joint angles and JRFs from patients’ natural motion and trained motion were compared using statistical parametric mapping.

Results

Natural kinematics revealed up to ±15° differences in flexion, adduction, and rotation from trained kinematics. Peak hip extension and abduction were larger during trained motion than natural motion. Trained JRFs were elevated in all directions during early stance; superior hip JRF was 50% greater at heel strike.

Discussion

Our hypothesis was partially supported; we observed differences between natural and trained joint angles, but JRFs increased with simulated training. Kinematic variation among patients may represent beneficial adaptations that prevent pain and reduce JRFs. Therefore, training toward one "healthy" gait pattern may not be beneficial in DDH. Movement training may be more effective for other activities (i.e. squat), with individualized target kinematics, or in conjunction with surgical intervention.

Images (Optional)

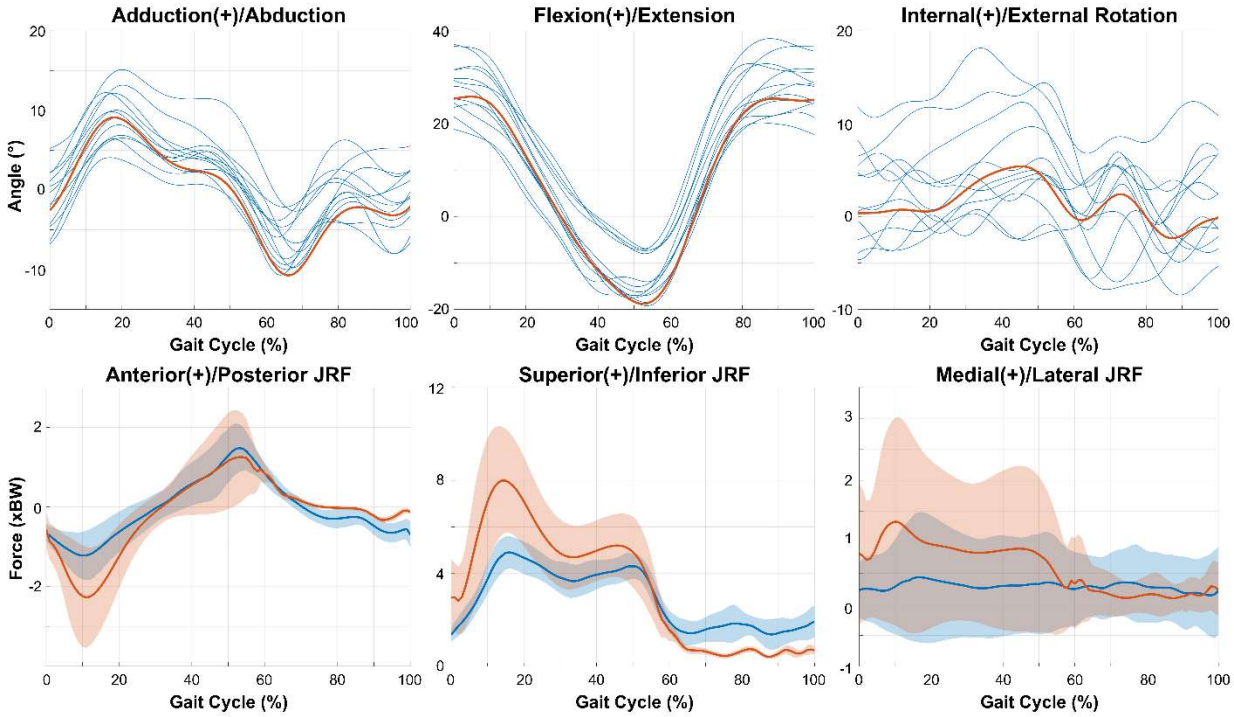


Figure 1: Hip joint angles (adduction, flexion, and rotation) and JRFs (anterior/posterior, superior/inferior, and medial/lateral) for patients' natural (blue) and trained (red) motion.

References (Optional)

[1] Cody Wyles *et al.*, CORR, 2017; [2] Michael Harris *et al.*, JBiomech, 2017; [3] Ole Skalshøi *et al.*, Gait&Posture, 2015; [4] Marcie Harris-Hayes *et al.*, JOrthop Sports Phys Ther, 2018.

Acknowledgements (Optional)

Supported by NIAMS-R01AR081881/K01AR072072.

Session Category

Clinical Biomechanics: N/A

OA105-06

Hip Range of Motion Is a Weak Predictor of Femoral Neck Version in Patients With Patellofemoral Pain Syndrome

Dr. Lucas Pallone MD[1,2], Dr. Felipe F. Gonzalez MD, MSc[1,3,4], Dr. Tiago Zimerman MD[1,3], Ms. Aleksandra Kozicka BS[3], Dr. Talissa Generoso MD[1], Dr. Eliane C. Guadagnin PhD[1], Dr. Carolline Popovicz Nunes MD[1,3], Dr. Marcos Amstalden Barros MD[3,1], Dr. Matheus Vilela MD, MSc[1,3], Dr. Patricia Martins e Souza MD, PhD[5], Dr. Jorge Chahla MD, PhD[3,6], Dr. Jonathan A. Gustafson PhD[3,1], Dr. Gustavo Leporace PhD[1,4], Dr. Leonardo Metsavaht MD, PhD[1,4]

[1]Instituto Brasil de Tecnologias da Saúde, Rio de Janeiro, RJ, Brazil. [2]Universidade de São Paulo, Ribeirão Preto, SP, Brazil. [3]Rush University Medical Center, Chicago, IL, United States. [4]Universidade Federal de São Paulo, São Paulo, SP, Brazil. [5]Clinica Felippe Mattoso, Radiology, Grupo Fleury, Rio de Janeiro, RJ, Brazil. [6]Midwest Orthopeadics at Rush, Chicago, IL, United States

Dr. Felipe F. Gonzalez

Introduction

Rotational lower-limb deformities are associated with many conditions, including patellofemoral pain syndrome (PFP). The femoral neck version (FNV), an important rotational parameter of the lower limb, is essential in managing PFP. Traditionally, physical examinations using passive hip range of motion (ROM) have been used to estimate FNV. However, the accuracy of this method in patients with patellofemoral pain remains uncertain. This study aimed to investigate the relationship between passive hip ROM and FNV in patients with PFP.

Methods

In this retrospective cross-sectional study, 49 patients with PFP (73 symptomatic lower limbs) were evaluated. Passive hip ROM measurements, including internal and external rotation, abduction, flexion, and Ober and Thomas tests, were recorded using a digital inclinometer following validated protocols. FNV was measured on computerized tomography scans by using the posterior femoral condyle and the femoral neck as parameters. The associations between hip ROM and FNV were analyzed using Pearson

(normally distributed) and Spearman (non-normal) correlation coefficients, linear regression models, and ANOVA. Statistical significance was set at $p < 0.05$.

Results

The mean FNV was 13.2º (SD: 8.0º), ranging from 2º to 36º of anteversion. Weak but statistically significant correlations were found between FNV and hip internal ($r = 0.28$, $P = 0.015$) and external rotation ($r = -0.24$, $P = 0.036$). In the linear regression analysis, these variables remained significant predictors of FNV, with the model explaining a small portion of the variance (10.6%; $R^2 = 0.106$, adjusted $R^2 = 0.080$, $P = 0.02$). ANOVA across retroverted, normal, and anteverted groups showed a significant difference only for internal rotation ($P = 0.019$), with post-hoc analysis revealing a 7.6° greater internal rotation in the normal version group compared to the retroversion group. No other significant associations were found between FNV and the other passive ROM tests (Figure 1).

Discussion

Passive hip ROM was significantly associated with FNV in PFP patients but only explained a small part of its variance. Given the limited predictive value and multifactorial nature of PFP, these findings indicate that physical examination alone is insufficient to accurately assess femoral torsion in this population, reinforcing the need for imaging in clinical decision-making.

Images (Optional)

A.

ROM parameters	Spearman's rho	n	p-value
Hip Internal Rotation	0.284	73	0.015*
Hip External Rotation	-0.245	73	0.036*
Total Hip Rotation ROM	0.067	73	0.574
Hip Abduction	0.018	26	0.931
Thomas test	0.029	71	0.809
Hip Flexion	-0.140	58	0.293
Ober Test	0.043	66	0.730

FNV=femoral neck version; ROM= range of motion; *p<0.05; n = sample

B.

Variable	α	SE	p-value	R^2	Adjusted R^2
Intercept	13.899	4.8581	0.006	0.106	0.080
	β				
Hip Internal Rotation	0.180	0.0845	0.037		
Hip External Rotation	-0.185	0.0888	0.040		

SE=Standard Error

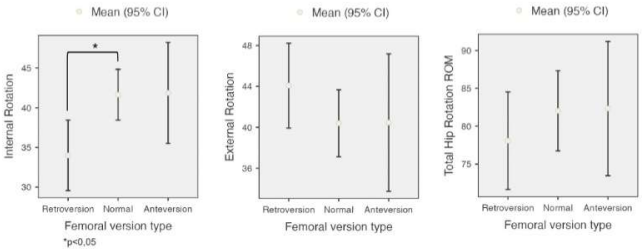
C.

Table 4: Comparison of Hip Internal and External Rotation among FNV groups

Group	Femoral version type	n	Mean	SD
Internal Rotation	Retroversion (<10º)	25	34	10.75
	Normal (10-20º)	33	41.6	9.02
	Anteversion (>20º)	15	41.9	11.5
External Rotation	Retroversion (<10º)	25	44.1	10.06
	Normal (10-20º)	33	40.4	9.21
	Anteversion (>20º)	15	40.5	12.14
Total Hip Rotation ROM	Retroversion (<10º)	25	78.1	15.57
	Normal (10-20º)	33	82.0	14.88
	Anteversion (>20º)	15	82.3	16.01

n=sample; SD=Standard Deviation

D.



A: Correlation between femoral neck version vs range of motion parameters; **B**: Linear regression analysis of femoral neck version vs hip internal and external rotations; **C**: Comparison of hip internal and external rotation among femoral neck version groups (ANOVA); **D**: Internal rotation, external rotation, and total rotation range of motion distribution among the femoral neck version groups (Post-hoc analysis).

Session Category

Clinical Biomechanics: N/A

OA106-01

Understanding How People Prioritize Movement Goals During Overground Walking

Prof Patrick Slade, Ms. Jordan Feldman

Harvard University, Boston, MA, United States

Introduction

Walking requires managing competing movement goals shaped by the demands of everyday activity. Several important goals during overground walking include maintaining a desired walking speed, achieving an intended foot placement, preserving postural and locomotor balance, and reducing energy expenditure. Biomechanical simulation and motor control-based methods use goal-related cost functions or structured models to identify people's movement priorities but are often restricted to simple movement scenarios and are currently impractical for broad deployment. Here, we systematically vary four movement goals during an overground walking experiment, characterize the resulting trade-offs in spatiotemporal gait metrics, and show that these trade-offs are sufficient to estimate participants' perceived ranking of movement goals.

Methods

Twelve healthy young adults (6 men and 6 women; age = 25.8 ± 3.7 years; body mass = 70.9 ± 10.2 kg; height = 1.75 ± 0.08 m) completed a series of walking conditions on an indoor track while wearing biomechanical measurement equipment and a visual perturbation headset (Fig. 1a). Participants performed a series of overground walking conditions guided by one of three walking speed prompts, foot placement prompts, and visual perturbation intensities, forming a three-by-three cube of 27 conditions (Fig. 1b). Baseline conditions were collected before and after the 27 conditions to determine if the unpowered visual perturbation headset altered participants' gait and evaluate if participants adapted to the headset over the course of the protocol (Fig. 1c).

Results

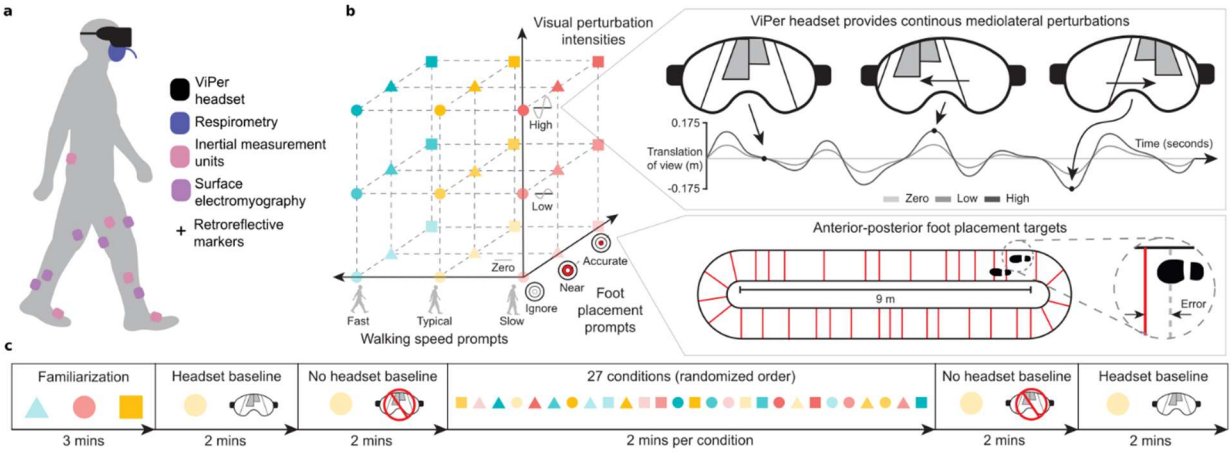
Gait metrics across participants became more heterogenous as combinations of movement goal prompts became more complex, suggesting person-specific movement strategies. Participants' perceived prioritization of movement goals showed systematic associations with corresponding gait metrics, with the strongest relationships observed for visually guided goals such as balance and foot placement. Subject-agnostic regression

models estimated the perceived order of importance of movement goals with 21% error, and subject-specific models reduced this error to 11%.

Discussion

Future studies could extend this framework toward more ecological and naturalistic contexts, incorporating additional goals and environmental factors to better approximate the complex prioritization processes that underlie mobility. This work establishes an approach for low-burden estimation of movement priorities and could support adaptive rehabilitation, personalized assistive devices, and an improved understanding of gait in real-world environments.

Images (Optional)



Session Category

Human Motion and Performance: Locomotion/Gait

OA106-02

Biomechanical Factors Influencing Effort and Risk Trade-Offs in Walking

Ms Jackeline Tafur-Oviedo MS, PT, Prof James Finley PhD

University of Southern California, Los Angeles, California, United States

Ms Jackeline Tafur-Oviedo

Introduction

In challenging walking conditions, we may trade off physical effort to minimize the risk of falling. However, the extent to which these trade-offs guide walking remains limited. We propose that such trade-offs depend not only on walking conditions but also on the subjective value assigned to effort and risk. Here, we used a utility-based computational model to estimate how individual differences in biomechanical measures of effort and risk influence participants' walking decisions.

Methods

We asked participants to choose between pairs of experienced walking bouts that differed in physical effort and risk. In the Effort-Only Bout, the treadmill was set to one of six participant-specific walking speeds, while in the Risky Bout, participants walked while experiencing two unexpected increases in speed of 20%, 30%, 40%, 50%, or 60% of their self-selected speed. We quantified effort and risk using the total positive leg work during each bout and changes in antero-posterior margins of stability (AP MoS) in response to perturbations. We used these variables as predictors in a mixed-effect, logistic regression to estimate the probability of choosing the Risky Bout on each trial.

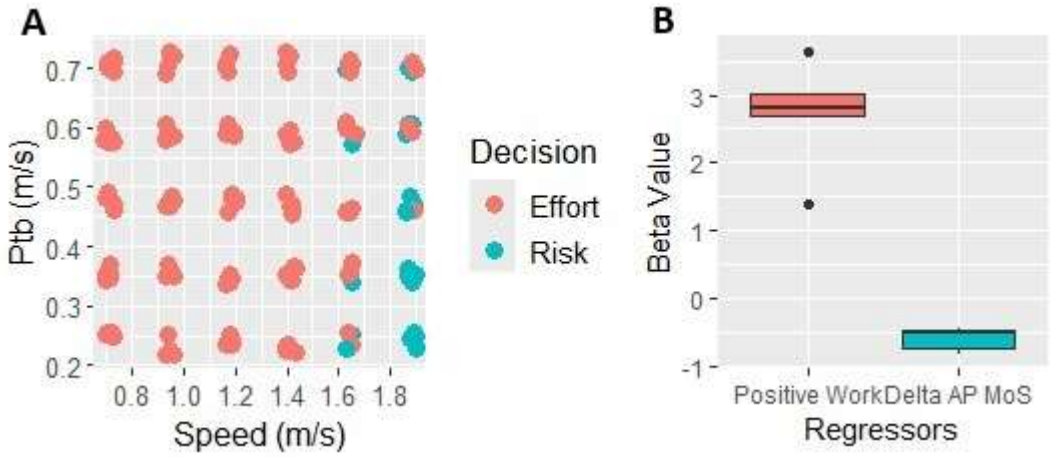
Results

Both effort, as measured by positive leg work, and risk, as measured by deviations in the AP MoS, were significant predictors in the logistic regression model. In general, participants were most sensitive to effort and preferred the Risky Bout when the speed associated with the Effort-Only Bout was high (Fig. 1A). In contrast, choices were less influenced by risk as the regression coefficients for effort were, on average, three times larger than those for risk (Fig. 1B). Overall, the regression model fit the decision data well with an area under the curve (AUC) of 0.83 and an accuracy of 0.76.

Discussion

When balancing trade-offs between risk and effort, young adults appear to make decisions that are largely explained by minimizing effort. Since our participants were willing to accept a greater level of risk to avoid exerting more effort, this may be attributed to their intact ability to recover successfully from balance disturbances. Ongoing studies will determine if age-related changes in balance capacity influence the trade-off between risk and effort.

Images (Optional)



Session Category

Human Motion and Performance: Locomotion/Gait

OA106-03

Poincaré-Based Metrics Detect Cognitive–Motor Impairment During Dual-Task Gait

Ms Adeline Smith, Ms Juliana Bostock, Mr Colin Slavin, Mr Jacob Packer, Ms Cassidy Considine, Dr Kristin Morgan

University of Connecticut, Storrs, CT, United States

Introduction

When cognitive and motor tasks are performed concurrently, the increased load it places on the central nervous system can impair both cognitive performance and motor control [1]. The interference of cognitive and motor processes during dual-task conditions often manifests as changes in gait variability [1]. Quantifying changes in gait variability can be valuable for evaluating cognitive induced motor impairment. Here, we hypothesized that novel gait variability metrics would possess the sensitivity to detect cognitive-motor impairment induced disruptions in motor control.

Methods

Seventeen individuals (age: 22.0±3.1 years; height: 1.6±0.2m; mass: 65.5±13.8kg; gender: 12 females:5 males) performed a dual-ask cognitive-gait protocol. Participants walked on an instrumented treadmill for 3 minutes at a self-selected speed under single- and dual-task conditions: Auditory Stroop (AST), Visual Stroop (VST), and combined AST + VST task administered via a custom headset (Fig. 1).

Stride-time series for each limb were derived from consecutive strides collected from the treadmill. Poincaré analysis served to quantify stride time variability (Fig. 1) [2].

Differences in gait features (stride time, SD1, SD2, SD2/SD1, dual-task cost) across the single- and dual-task conditions, were assessed using Kruskal-Wallis tests with Dunnn-Šidák post hoc comparisons ($\alpha=0.05$).

Results

Poincaré-derived metrics revealed significant differences in gait variability across single- and dual-task conditions (Table 1). The combined AST+VST task produced a significant change in variability, reflected by a decreased SD2/SD1 ratio ($p<0.01$), despite note differences in mean stride time or dual-task cost. Additionally, SD2 was significantly reduced during the AST condition ($p=0.048$).

Discussion

The study demonstrated that Poincaré analysis is sensitive to cognitive-motor impairment-related alterations in motor control, by detecting changes not captured by traditional gait measures. These findings are significant and suggest that Poincaré-derived metrics could aid in the early identification of cognitive-motor dysfunction in pathological populations. Future work will investigate these metrics sensitivity to varying cognitive loads and whether it can serve as reliable biomarkers of impairment.

Images (Optional)

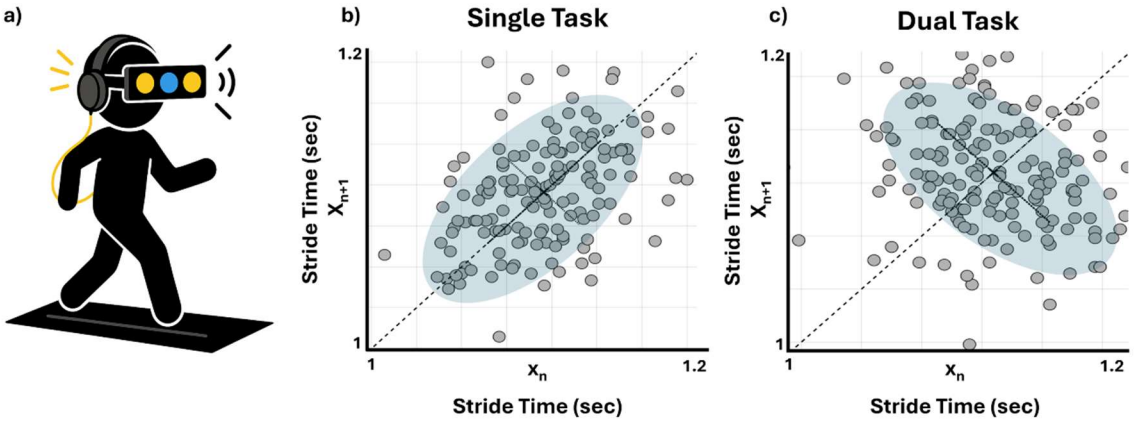


Figure 1. (a) Illustration of dual-task cognitive-gait protocol in which participants walked while responding to a visual and auditory stimuli. (b - c) Representative Poincare plots for an individual perform the single-task and combined Auditory Stroop + Visual Stroop tasks, respectively.

Table 1. Comparison of gait variability measures across single-task and dual-task cognitive conditions.

Variable of Interest	Self-Selected	Dual-Task: Auditory (AST)	Dual-Task: Visual (VST)	Dual-Task: AST+VST	P-value
Stride Time (sec)	1.1 ± 0.1	1.1 ± 0.1	1.1 ± 0.1	1.1 ± 0.1	0.56
SD1	16.1 ± 4.2	13.9 ± 3.4	15.4 ± 4.5	15.9 ± 4.4	0.18
SD2	20.1 ± 5.5[a]	16.2 ± 3.7[b]	17.5 ± 4.8[a]	18.1 ± 7.4[a]	0.048*
SD2/SD1	1.3 ± 0.2[a]	1.2 ± 0.2[a]	1.2 ± 0.2[a]	1.1 ± 0.3[b]	<0.01*
Dual-Task Cost (%)	---	-1.1± 1.5	-1.3 ± 1.3	-1.3 ± 1.7	0.33

*a, b denotes groups with significantly different mean ($p<0.05$)

References (Optional)

[1] Plummer *et al.*, Ach of Phys Med and Rehab, 2013.

[2] Brennan *et al.*, IEEE Trans Biomed Eng, 2001.

Session Category

Human Motion and Performance: Locomotion/Gait

OA106-04

Effects of One Night of Sleep Deprivation on Gait: Evidence From Single- and Dual-Task Walking

Ms. Maura Seynaeve[1], Dr. Anna C. Render[2], Prof. Peter C. Fino[2], Prof. Toon de Beukelaar[1]

[1]KU Leuven, Leuven, Vlaams-Brabant, Belgium. [2]University of Utah, Salt Lake City, Utah, United States

Introduction

Sleep deprivation reduces higher-order cognitive control, potentially impacting movements that depend on these processes, like walking. To test whether gait changes after one night of sleep deprivation reflect reduced cognitive capacity, we compared its effects to those of dual-task walking, which similarly taxes cognitive resources. We hypothesize that sleep deprivation will produce gait changes similar to those under dual-task conditions.

Methods

We employed a randomized cross-over design to test eighteen healthy adults (9 female, 9 male; M=22.2 (s.d. 2.3) yrs) in two conditions: after a night of regular sleep (CON) and after a night of sleep deprivation (SDEP). The morning after each condition, participants completed two 2-min treadmill trials: single-task walking (ST) and walking with a concurrent 2-back working memory task (DT, dual-task). Using 3D marker trajectories of the lateral foot and pelvis, we calculated spatiotemporal gait variables, foot placement error (FPE) and mediolateral margin of stability (MoS_{ML}), along with variability of these measures. FPE was calculated as the difference in foot placement predicted by the center of mass (CoM) state and actual foot placement in antero-posterior (AP) and mediolateral (ML) directions [1]. Data were analyzed using linear mixed models with sleep condition and task as fixed effects and subjects as random effects.

Results

While SDEP increased average step time (CON: M=0.542 (s.d. 0.044) s; SDEP: M=0.549 (s.d. 0.046) s, $p<0.001$) and step length (CON: M=0.620 (s.d. 0.046) m; SDEP: M=0.627 (s.d. 0.048) m, $p=0.001$), DT reduced spatiotemporal variability. FPE_{AP} decreased in both SDEP (CON: M=0.010 (s.d. 0.002) m; SDEP: M=0.009 (s.d. 0.002) m, $p = 0.001$) and DT (ST: M=0.010 (s.d. 0.002) m; DT: M=0.008 (s.d. 0.001) m, $p<0.001$), while FPE_{ML} decreased in DT only (ST: M=0.010 (s.d. 0.002) m; DT: M=0.008 (s.d. 0.001) m, $p<0.001$). Additionally, mean

MoS_{ML} decreased only in SDEP (CON: M=0.093 (s.d. 0.010) m; SDEP: M=0.089 (s.d. 0.009) m, p=0.011).

Discussion

DT and SDEP influence gait through distinct mechanisms, affecting different spatiotemporal and stability metrics. Therefore, these findings suggest that the effects of sleep deprivation on gait cannot be fully explained by reduced cognitive resources alone.

References (Optional)

[1] Wang, Y. & Srinivasan, M., Biol Lett (2014)

Session Category

Human Motion and Performance: Locomotion/Gait

OA106-05

Dual-Task Effects on Gait Balance Control Stability in Older Adults Using A Single IMU with AI Techniques

Mr. Cheng-Hao Yu[1], Ms. Yi-Yun Cheng[1], Mr. Chia-Han Hu[1], Dr. Shiuan-Huei Lu[1,2,3,4], Mr. Hsiang-Yu Tsai[1], Mr. Jeng-Heng Lin[1], Prof. Yi-Chun Kuan[1,2,3], Prof. Tung-Wu Lu[1]

[1]National Taiwan University, Taipei City, Taiwan, Taiwan. [2]Taipei Medical University, Taipei City, Taiwan, Taiwan. [3]Taipei Medical University-Shuang Ho Hospital, New Taipei City, Taiwan, Taiwan. [4]Purdue University, West Lafayette, Indiana, United States

Mr. Cheng-Hao Yu

Ms. Yi-Yun Cheng

Mr. Chia-Han Hu

Dr. Shiuan-Huei Lu

Mr. Hsiang-Yu Tsai

Mr. Jeng-Heng Lin

Prof. Yi-Chun Kuan

Introduction

Divided attention, often induced by dual-task (DT) demands, is known to disrupt balance and increase fall risk during walking, particularly among older adults. However, its effects on the control variability of dynamic gait balance outside laboratory environments remain unclear. This study aims to identify the DT effects on gait balance control variability in older

adults using a single waist-worn inertial measurement unit (IMU) with artificial intelligence (AI) techniques in real-world community environments.

Methods

At the community centres, 102 older adults wore an IMU on the waist and completed two 10-m walking trials: a single-task (ST) walk, and a DT walk with an arithmetic task. For each trial, the IMU signals were filtered and segmented into individual gait cycles. These data were used as inputs to a validated physics-informed recurrent neural network model [1] to extract the inclination angles (IAs) between the body's centre of mass (COM) and the centre of pressure (COP) in the sagittal and frontal planes, as well as their rates of change.

For each participant, phase angles (PA) at each condition were obtained from the phase plots of the model-predicted IA. The root-mean-squared differences (RMSD) in the PA curves between conditions were calculated. The deviation phase (DP) of the PA was also calculated to quantify gait balance variability; a lower DP indicates smaller variability. A paired t-test was used to identify the DT effects on DP values during double-limb and single-limb support phases (α=0.05).

Results

The older adults exhibited similar coordination patterns of gait balance control during ST and DT walking, with RMSD values below 1°. During the double-limb support phase, they showed significantly higher DP values in the frontal plane during DT walking than during ST walking. No significant DT effects were found in any other variables.

Discussion

This study is the first to investigate the DT effects on gait balance control variability in older adults using an IMU with AI techniques in community settings. The findings revealed DT-induced alterations in gait balance control in ageing populations, potentially increasing fall risk. This approach demonstrates strong potential for real-life monitoring of gait balance.

References (Optional)

[1] Cheng-Hao Yu et al., Sensors, 2023

Acknowledgements (Optional)

This study was funded by the Ministry of Science and Technology, Taiwan (MOST 110-2221-E-002-027-MY3).

Session Category

OA106-06

Influence of Cognitive Dual-Task on Stride Frequency in Older Adults

Miss Haley Hentnik, Dr. Reed Gurchiek

Clemson University, Clemson, SC, United States

Introduction

Cognitive processes are thought to influence gait control to some extent based on observed within-person gait changes in cognitive dual-task gait. Reduced gait speed is commonly observed, a finding which contributes to initiatives that seek to leverage slow gait speed as a digital biomarker for cognitive impairment. However, a better understanding of the control principles that underlie speed changes may improve the specificity of gait-based biomarkers (since slow gait speed manifests in many clinical conditions). In our prior (unpublished) work, we observed changes in the speed-frequency relationship under dual-task conditions in healthy young adults. In this study, we conducted a similar experiment in older adults with variable cognitive abilities.

Methods

Nineteen older adults (mean age: 73 years, range: 65-92 years), ranging from high to low cognitive functioning, walked on a treadmill (0.8, 1.0, and 1.2 m/s) for 15 seconds both with a cognitive dual-task (sequential subtracting of serial 7's) and without (single-task gait). We calculated stride frequency using foot contact events identified from shank-worn gyroscope data. To determine the effect of the cognitive dual-task on the speed-frequency relationship, we performed a one-sample t-test on the person-specific differences in stride frequency observed during dual-task compared to single-task gait at each speed.

Results

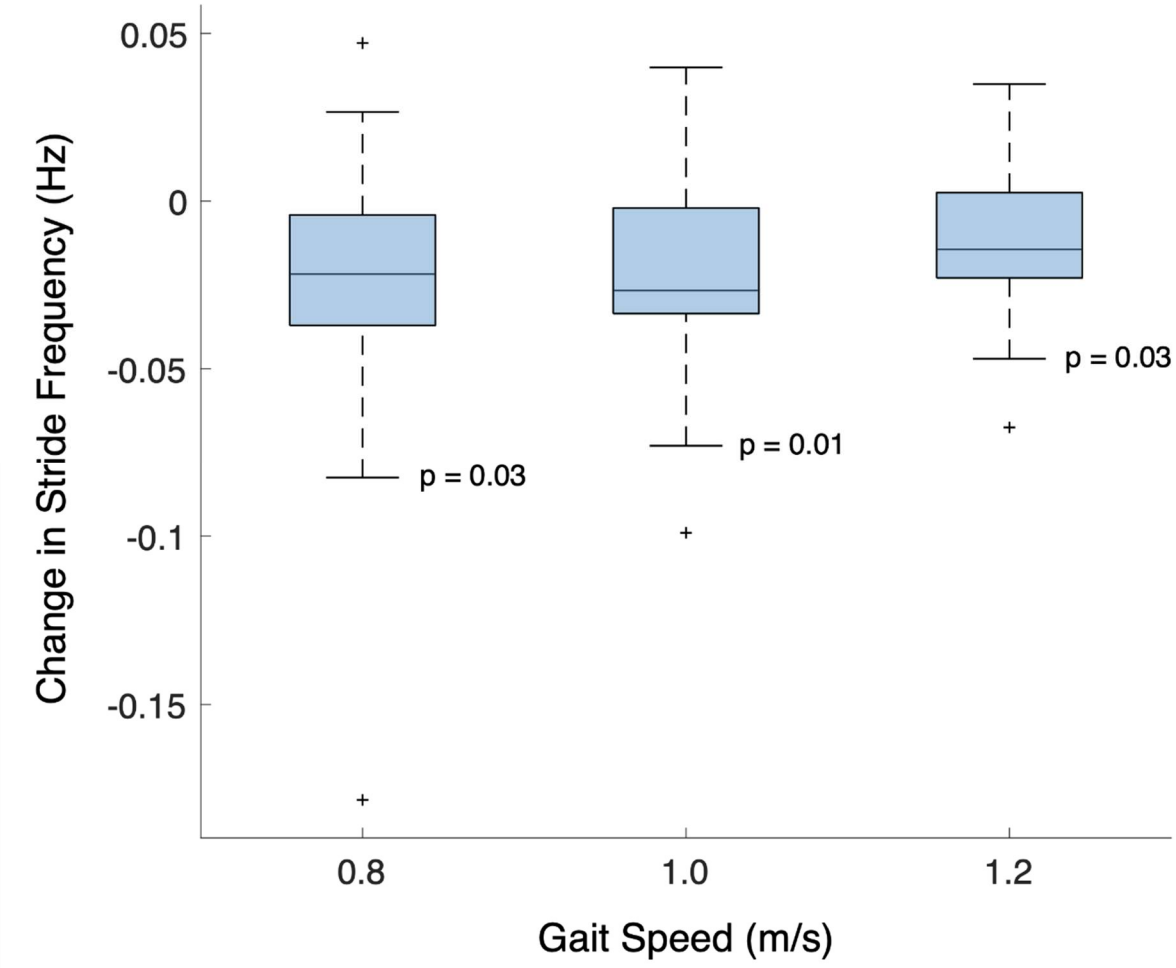
Participants decreased stride frequency at each speed during the dual-task condition compared to single-task gait at all speeds (average change in stride frequency: -0.026 Hz for 0.8 m/s (p=0.03), -0.021 Hz for 1.0 m/s (p=0.01), and -0.012 Hz for 1.2 m/s (p=0.03)).

Discussion

Our findings suggest older adults adopt a lower stride frequency under cognitive dual-task conditions when compared with single-task walking at the same speed. However, while statistically significant, these changes were relatively small (the greatest average

difference, -0.026 Hz for 0.8 m/s, is only 3.12 steps per minute). In our prior (unpublished) work, we observed the opposite effect which was more pronounced during overground gait; a phenomenon we plan to explore in future work with older adults. Moreover, future work should explore potential explanations of the observed effect (e.g., based on control complexity or dynamic stability).

Images (Optional)



Acknowledgements (Optional)

This work was supported by the Clemson University Office of Research Development and NIH-NIGMS (SC-INBRE: P20GM103499).

Session Category

Human Motion and Performance: Locomotion/Gait

OA107-02

Why Foot Model Choice Matters: Rethinking Ankle Kinematics in Running Shoe Research

Dr. Jamie Ferris, Mr. Ben Hazelwood, Dr. Jinger Gottschall

New Balance, Boston, MA, United States

Introduction

Ankle kinematics during running are frequently estimated using a rigid mid- and rearfoot distal segment, despite midfoot deformation (Zelik & Honert, 2018). This study evaluated how this assumption influences ankle kinematic estimates and conclusions in footwear investigations.

Methods

Two cohorts of 10 experienced runners tested advanced footwear technology prototypes varying in (1) longitudinal bending stiffness (LBS) or (2) rocker geometry. LBS prototypes included: no plate, plate with medial-lateral cuts, lower-stiffness plate, and higher-stiffness plate. Rocker prototypes featured forefoot rockers with early, mid, or late onset. Ankle kinematics were computed using two different foot models: mid/rearfoot (calcaneal and metatarsophalangeal foot-mounted markers) and rearfoot (calcaneal markers only). Dorsi/plantarflexion (D/P) trajectories were compared using statistical parametric mapping RMANOVA of the angle after offset removal (angle – mean). Footwear effects under each model were analyzed with RMANOVA and Tukey's HSD ($\alpha = 0.05$).

Results

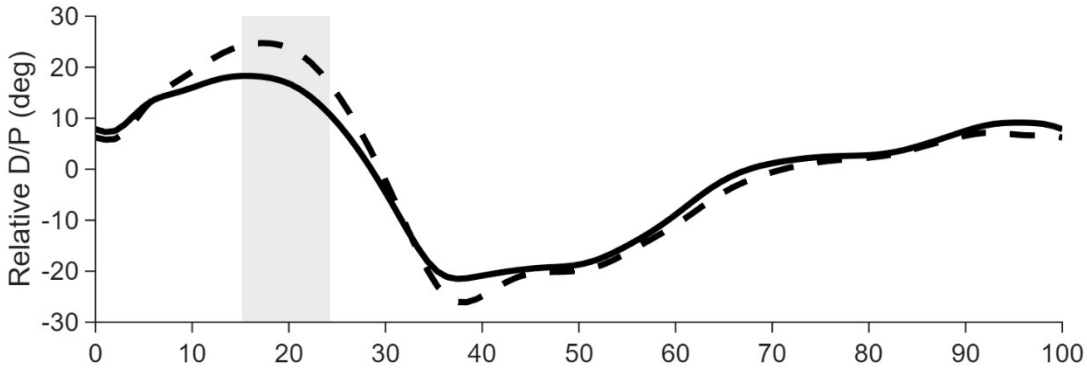
Foot model significantly altered ankle D/P trajectory, even after offset removal (Figure 1). With the rearfoot model, LBS had no effect on ankle kinematics. With the mid/rearfoot model, LBS influenced ankle kinematics including D/P ROM ($p < 0.001$; significant differences between no plate/lower stiffness and no plate/higher stiffness) and peak plantarflexion velocity ($p = 0.006$; cut/higher). Rocker geometry effects also differed between foot models. For example, stance-phase D/P ROM differed with the rearfoot model ($p < 0.001$; mid/late), while stride D/P ROM differed with the mid/rearfoot model ($p = 0.020$; early/late).

Figure 1. Average D/P angle after offset removal (angle – mean) throughout the stride cycle using mid/rearfoot (solid) and rearfoot (dashed) foot models. Shaded regions indicate significant differences.

Discussion

Assuming mid/rearfoot rigidity produced D/P trajectory differences and changed conclusions about footwear effects in both cohorts. These findings underscore the importance of anatomically valid foot models in footwear and running research.

Images (Optional)



References (Optional)

Zelik, K. & Honert, E.C. (2018). Ankle and foot power in gait analysis: Implications for science, technology and clinical assessment. *Journal of Biomechanics, 75*, 1-12.

Session Category

Human Motion and Performance: Sports

OA107-03

Evaluating the Shifty Agility Drill: Repeatability and Footwear Sensitivity of a Novel Court Sport Agility Test

Lead Researcher Bryan Picco M.S., Senior Researcher Jason Hashimoto M.S., Senior Researcher Amanda Cann M.S., Director of Footwear Research Elysia Davis Ph.D.

Nike Sport Research Lab, Beaverton, OR, United States

Introduction

Athletic footwear should support sport-specific demands, yet agility drills can lack relevance, repeatability [1], and sensitivity to footwear effects. This study introduces the Shifty Agility Drill for court sports like basketball, evaluates its repeatability, and tests if drill performance varies with footwear. These insights can guide designers in creating shoes that measurably enhance agility.

Methods

The Shifty Agility Drill consists of two forward steps (left foot first), a lateral cut around a mannequin off the right foot into a left foot euro-step, and two steps toward the hoop simulating a lay-up (Figure 1). Ten athletes (93±13.1 kg; 31.6±2 yrs) performed the drill in two footwear conditions. A counterbalanced crossover design (Shoe 1–Shoe 2–Shoe 2–Shoe 1; order randomized) was used, with seven trials per condition block. Ten step-back jump shots were performed between blocks as active recovery. Motion capture (250hz), force plates (2500hz), and timing gates recorded performance.

Each shoe's mechanical properties differed. Shoe 1 was lighter (333.6 g), flexible (bending: 6.4 Nm; torsional: 348 Nmm/deg), with lower traction (DCOF: 1.06), higher impact peak (33.1 G), and lower energy efficiency (61%). Shoe 2 was heavier (355.8 g), stiffer (bending: 12.1 Nm; torsional: 472 Nmm/deg), with greater traction (DCOF: 1.14), reduced impact peak (13.2 G), and higher energy efficiency (79%).

Statistical analyses included coefficients of variation (CV1, CV2) to assess repeatability and paired t-tests to evaluate footwear sensitivity. Bland–Altman analyses assessed agreement. Two-tailed paired t-tests compared total drill and cut step times between shoes for sensitivity to footwear.

Results

The drill demonstrated strong repeatability, with mean CV1 and CV2 values ≤0.0608 and ≤0.0660. For the cut step, Shoe 1 showed lower variability (CV1: 0.0536 vs 0.0608; CV2: 0.0494 vs 0.0660). Bland–Altman analyses revealed trivial biases and symmetric variability across blocks. Shoe 2 was significantly slower than Shoe 1 ($p < 0.05$) in total drill (≈0.031 s) and cut step times (≈0.01 s)

Discussion

The Shifty Agility Drill demonstrated strong repeatability and was sensitive to footwear differences, supporting its use as a reliable, sport-relevant tool for evaluating footwear performance.

Images (Optional)

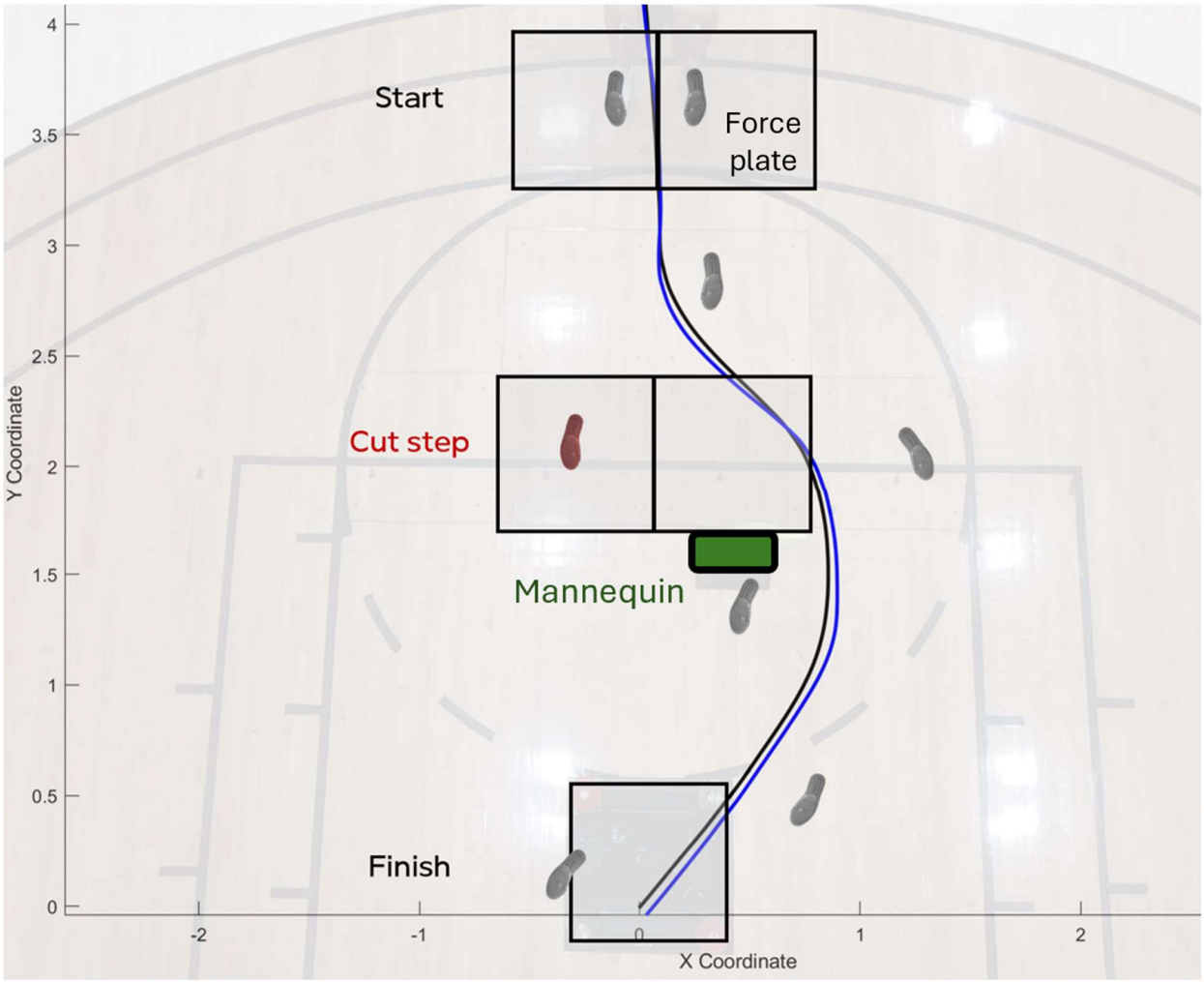


Figure 1: Top-down view of Shifty Agility Drill. Lines are representative pelvis tracing through the drill for Shoe 1 (**black**) and Shoe 2 (**blue**)

References (Optional)

[1] Paul, D. J. et al., Sports Medicine, 2016.

Session Category

Human Motion and Performance: Sports

OA107-04

On-Field Validation of Second-Generation Female-Specific Soccer Cleats Using Wearable Sensors and Predictive Computational Modeling

Dr. Alex Denton PhD[1], Ms Danielle Page MS[2], Mr Rory Tatterton BEng[2], Ms. Laura Healey MS[2], Mr. Maximilian Grüttner MS[2], Dr. Michael Hahn PhD[1]

[1]University of Oregon, Eugene, Oregon, United States. [2]PUMA SE, Herzogenaurach, Bavaria, Germany

Introduction

Soccer cleats are historically designed based on male biomechanics, which may contribute to greater anterior cruciate ligament (ACL) injury risk in female athletes [1]. However, soccer cleat traction and lower limb mechanics of female athletes can be modified through stud parameters [2]. We identified optimal stud length, shape, and position in our initial female-specific soccer cleat prototypes 1.1 & 1.2 [3 & 4] and further optimized prototype 2.0 for evaluation in the present study. It was hypothesized that prototype 2.0 would reduce the overall mechanical demand of the knee during lateral cutting maneuvers pre- and post-fatigue.

Methods

Fifteen competitive female soccer athletes (20.3±2.1 yrs, 163.6±5.8 cm, 64.2±6.2 kg) performed unanticipated lateral cutting maneuvers targeting 120° from a running approach at 80% of perceived maximum velocity on an artificial turf field in the PUMA Future 8 and prototype 2.0 cleats on separate days. Athletes were tested pre- and post-Shuttle Fatigue Protocol, consisting of a 180 m sprint and 1440 m run with cutting steps every 30 m. Knee mechanics indicative of ACL injury risk were estimated using predictive model ensembles driven by insole pressure data (XSensor, 100 Hz). A two-way repeated measures ANOVA (cleat x fatigue) with Tukey HSD was used to evaluate knee mechanics.

Results

Peak knee flexion angle was 13.5% greater, and anterior shear force was 9.7% lower in prototype 2.0 ($p<0.001$ and $p=0.02$, respectively) (Figure 1). No significant differences were observed for valgus angle, internal knee extensor moment, or external knee valgus moment ($p>0.05$). Fatigue did not significantly affect knee mechanics ($p>0.05$).

Discussion

Prototype 2.0 demonstrated promising potential to reduce the risk of ACL injury among female soccer athletes by lowering the overall mechanical demand at the knee. However,

the absence of significant changes in frontal plane mechanics suggests future iterations may further benefit from design innovations targeting valgus loading. A refined version of prototype 2.0 will be released in anticipation of the 2027 Women's World Cup.

Images (Optional)

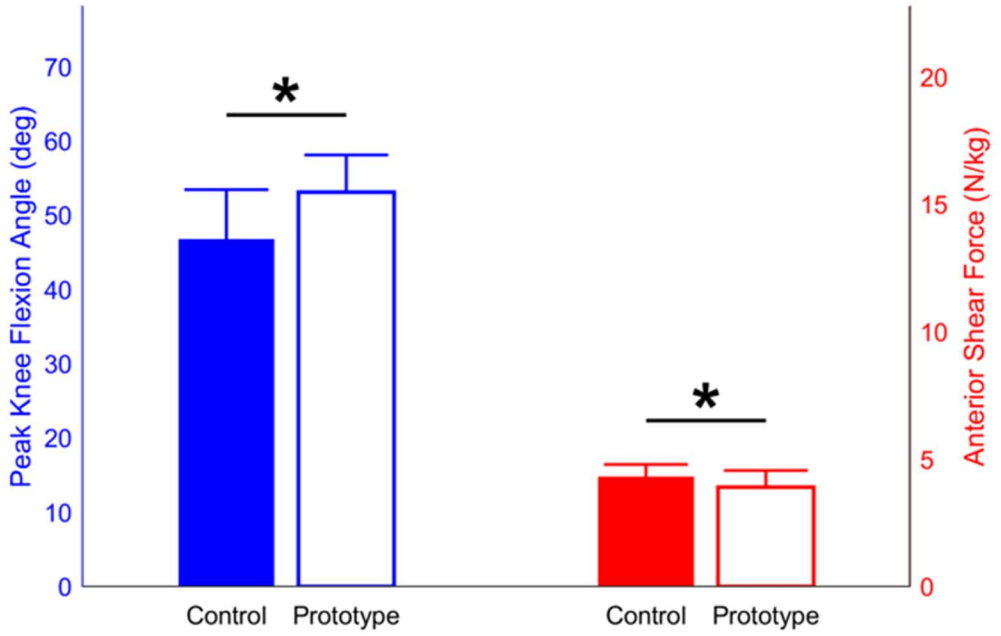


Figure 1. Peak knee flexion angle and anterior shear force during lateral cutting maneuvers in female soccer athletes wearing control and prototype cleats. * $p<0.05$

References (Optional)

[1] Waldén *et al.*, KSSTA, 2010 [2] Butler *et al.*, 2012 [3] Denton *et al.*, Footwear Sci, 2025 [4] Karolidis *et al.*, Footwear Sci, 2025

Session Category

Human Motion and Performance: Sports

OA107-05

Wrapping Cycling Shoes Improves Cycling Performance Over Laces

Dr. Eric Honert, Ms. Milena Singletary, Ms. Bethany Kilpatrick, Mr. Adam Luftglass, Dr. Daniel Feeney, Dr. Kathryn Harrison

BOA Technology Inc., Denver, CO, United States

Introduction

Cycling shoe fit systems vary between BOA, Velcro, Lace, amongst others. BOA wrapping fit systems can improve performance over shorter durations compared to Velcro by increasing steady-state power output at a similar energy expenditure and increasing sprint power [1]. Physical exhaustion impacts cycling energy expenditure [2], and fit systems may impact energy expenditure after exhaustion. This study evaluated the differences between BOA and Lace fit systems prior to and after exhaustion.

Methods

This two-part study compared lace (Lace) and wrapping BOA (Wrap) shoes. First, nine participants completed two trials in each footwear condition. Each trial included 4 minutes at 80% of functional threshold power and a 10-second maximal sprint. Heel contact area (HCA) and peak power were extracted from the steady-state and sprint portions, respectively. Separately, participants underwent two testing sessions, using a different shoe for each session. Gas exchange was collected for five minutes before and after an exhaustion protocol (similar to [2]). Net energetic expenditure (netEE) was evaluated during the last two minutes. Bayesian linear mixed models were used to estimate differences between outcomes. The percentage of the posterior above zero (% Post.) and average difference is presented for each metric.

Results

In the first portion, the HCA was 6.6% higher in the Wrap shoe compared to the Lace (%Post: 95%). The peak sprinting power was 2.5% greater in the Wrap shoe (%Post: 96%). In the second portion, the Wrap shoe reduced netEE by 1.7% (%Post: 86%) prior to the exhaustion protocol. The difference increased to 2.2% (%Post: 88%) after the exhaustion protocol.

Discussion

This study examined how fit systems impact energy expenditure after physical exhaustion. The 2% improvement in energy expenditure in the Wrap shoe is similar in magnitude to changes observed in running shoes with supercritical foams, which are the standard in

marathon racing. The improvement in energy expenditure, as well as sprint performance, in the Wrap shoe is likely due to improved fit quantified by increased heel contact area.

References (Optional)

[1] Kilpatrick *et al.*, NACOB, 2022.

[2] Spragg *et al.*, Med Sci Sports Exerc, 2023.

Acknowledgements (Optional)

Session Category

Human Motion and Performance: Sports

OA107-06

Effects of Advanced Footwear Technology (AFT) on Running Biomechanics

Hyeong-Sik Kim M.S.[1], Jae-Won Kang M.S.[1], Yun-Bae Jeong M.S.[1], Jungmin Yoon M.S.[1], Dr. Sejin Kong Ph.D.[2], Prof. Sang-Kyoon Park Ph.D.[1]

[1]Korea National Sport University, Seoul, Seoul, Korea, Republic of. [2]LS Networks, Seoul, Seoul, Korea, Republic of

Introduction

Running mechanics are influenced by external factors such as surface conditions and footwear [1]. Carbon-plated shoes have recently been developed to improve mechanical efficiency by enhancing energy transfer and lowering metabolic cost. However, previous research has mainly examined the presence or stiffness of carbon plates, leaving the influence of carbon-plate curvature on joint mechanics and running efficiency unclear. This study investigated whether curvature variations improve mechanical efficiency and performance.

Methods

Participants were ten male recreational runners who ran over 20 km per week, including three trained middle and long distance athletes. They tested three shoe conditions: (1) a carbon-plated running shoe, (2) a lightweight carbon-plated shoe with enhanced cushioning, and (3) a customized shoe with modified carbon plate curvature. All runners completed trials on an instrumented treadmill at 3.3 m/s and 4.0 m/s in randomized order. For each condition, they performed a 5-minute familiarization, and the final minute was analyzed. Kinematic data were recorded at 100 Hz, and ground reaction forces at 1,000 Hz. A one-way repeated-measures ANOVA assessed biomechanical differences.

Results

Shoe 3 demonstrated greater stride and step length with a corresponding reduction in step frequency compared with Shoe 1. Furthermore, Shoe 3 exhibited increased ankle range of motion and higher ankle joint power than Shoes 1 and 2. In addition, Shoe 3 generated a larger propulsive ground reaction force during running compared with Shoe 1.

Discussion

Carbon plates enhance energy transfer and alter lower extremities mechanics during running [2]. In this study, the increased stride parameters, greater ankle motion, and higher

ankle power and propulsion in Shoe 3 indicate that modified carbon-plate curvature improves ankle mechanical efficiency, suggesting its importance as a design factor for enhancing running performance.

Images (Optional)

Table 1. Spatiotemporal and ankle joint kinetic variables over time

Variables	Shoe 1	Shoe 2	Shoe 3	F(*p*)	Post-hoc
Strid Time (sec)	0.70(0.02)	0.70(0.02)	0.72(0.02)	**10.759(.01) ***	3>1
Cadence(step/min)	170.28(6.06)	168.49(6.45)	166.48(5.78)	**7.664(.01) ***	3>1
Maximum Ankle Negative Power (Watt/BW)	-5.61(1.34)	-5.62(1.46)	-6.29(1.95)	**5.119(.02) ***	3>1, 2
Maximum Ankle Positive Power (Watt/BW)	8.54(1.21)	8.52(1.23)	9.23(1.56)	**5.681(.01) ***	3>1, 2

* Indicates significant differences between Shoes

Shoe 1: a carbon-plated running shoe, Shoe 2: a lightweight carbon-plated shoe with enhanced cushioning, and Shoe 3: a customized running shoe manufactured with modified carbon-plate curvature.

References (Optional)

[1] Devita, P., & Skelly, W. A. (1992). Effect of landing stiffness on joint kinetics and energetics in the lower extremity. Medicine & Science in Sports & Exercise, 24(1), 108-115.Wright, R. L.,

[2] Song, Y., Cen, X., Chen, H., Sun, D., Munivrana, G., Bálint, K., ... & Gu, Y. (2023). The influence of running shoe with different carbon-fiber plate designs on internal foot mechanics: A pilot computational analysis. Journal of biomechanics, 153, 111597.

Acknowledgements (Optional)

This study was supported by LS Networks.

Session Category

Human Motion and Performance: Sports

OA108-02

Tornadic Phenomena in Cerebral Aneurysms: Towards New Definitions of Hostile Hemodynamics

Dr. Valentina Mazzi PhD[1], Prof. Diego Gallo PhD[1], Dr. Thangam Natarajan PhD[2], Dr. Jonas Schollenberger PhD[3], Dr. Karol Calò PhD[1], Prof. David Saloner PhD[3], Prof. David A. Steinman PhD[4], Prof. Umberto Morbiducci PhD[1]

[1]Politecnico di Torino, Torino, Piemonte, Italy. [2]Georgia Institute of Technology, Atlanta, Georgia, United States. [3]University of California, San Francisco, San Francisco, California, United States. [4]University of Toronto, Toronto, Ontario, Canada

Introduction

Extreme atmospheric events arise when intense airflows, such as tornadoes, produce damaging effects upon interacting with the ground (Figure 1A). Cerebral aneurysms (CAs, Figure 1B) can also develop complex hemodynamic environments shaped by their anatomy and pulsatile inflow. Recent work linking wall shear stress (WSS) topology to near-wall vorticity has shown that specific vortical structures imprint characteristic “ground effects” on the vessel wall [1]. Despite differences in underlying physics, we demonstrate that CAs can exhibit a spectrum of previously unrecognized tornadic-like flow phenomena that can be identified through a topology-based taxonomy, providing a mechanistic alternative to elusive notions of “hostile hemodynamics”.

Methods

CA hemodynamics were analyzed using high-fidelity computational fluid dynamics (CFD) simulations [2]. WSS fixed points (Figure 1C) were extracted [3], and their dynamics were analyzed. The topology-based taxonomy, grounded in the theoretical relationship between WSS and near-wall vorticity [1], enabled unambiguous identification of tornadic phenomena in the near-wall domain. 4D flow MRI datasets were analyzed to validate *in vivo* the presence of these tornadic fluid structures.

Results

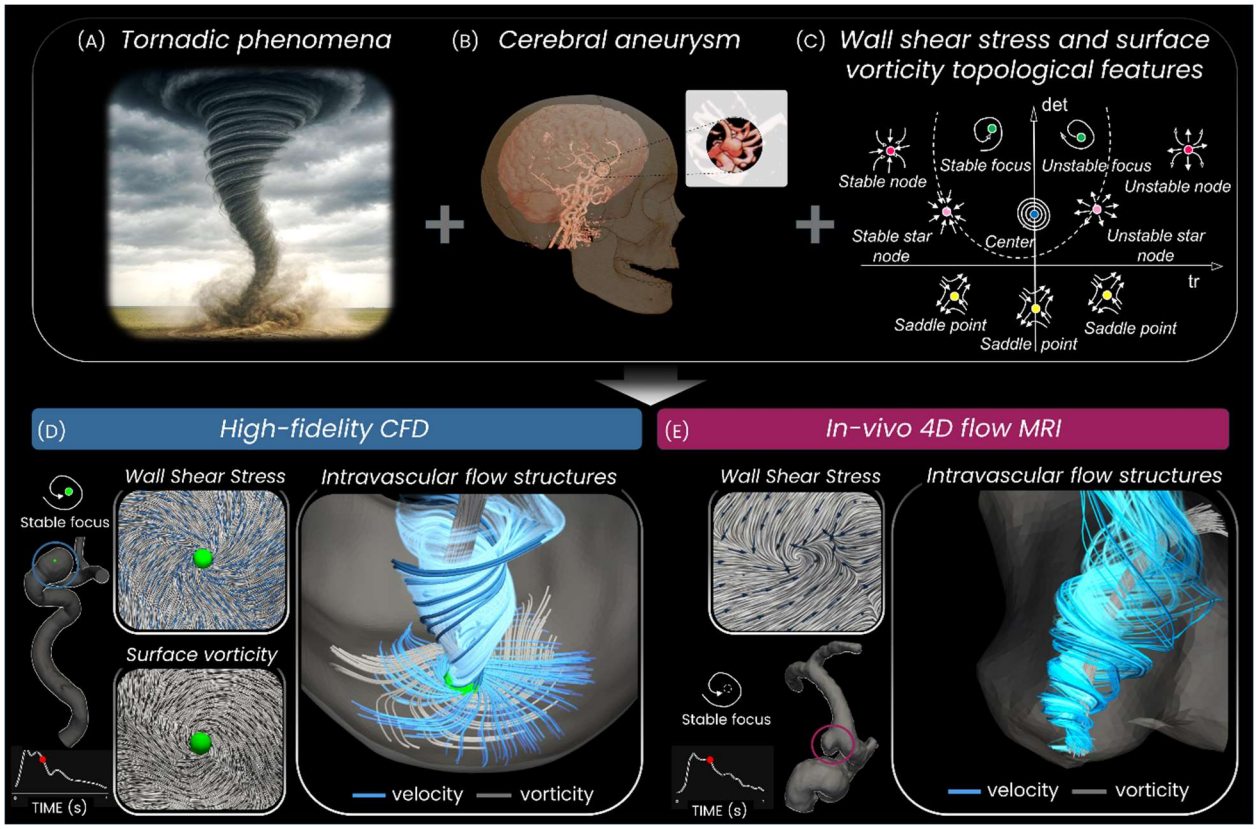
According to the adopted topology-based taxonomy, a tornado-like fluid structure in the near wall emanates from a WSS (and surface vorticity) stable focus, whose presence is revealed by the configuration of instantaneous velocity streamlines wrapping around vorticity lines (Figure 1D, CFD data). The existence of tornado-like structures and their imprints on the wall was further confirmed *in vivo* using 4D MRI (Figure 1E). Additional

atmospheric analogues, including downbursts, multiple-tornado systems, tornado-downburst combinations, and roll clouds, were likewise identified in CAs when the proposed taxonomy was applied.

Discussion

By translating concepts from atmospheric physics to vascular biomechanics, and specifically considering ground-effects analogues, this study elucidates how rotational and non-rotational fluid structures analogous to tornadic phenomena may impose distinct mechanical stimuli on the aneurysm wall. These stimuli may contribute to inflammation, remodeling, and eventual rupture. The agreement among theory, CFD simulations, and *in vivo* measurements highlights the translational potential of the topology-based framework for standardized hemodynamic phenotyping and improved risk stratification.

Images (Optional)



References (Optional)

[1] Mazzi *et al.*, Physics of Fluids, 2025.

[2] Natarajan *et al.*, Journal of Biomechanical Engineering, 2025

[3] Mazzi *et al.*, Biomech. Model Mechanobiol. ,2020

Acknowledgements (Optional)

The author V.M. is supported by the project NODES, which has received funding from the MUR-M4C2 1.5 of PNRR funded by the European Union-NextGenerationEU (Grant agreement no. ECS00000036). The author D.A.S. acknowledges the support of a Discovery grant (RGPIN-2018-04649) from the Natural Sciences & Engineering Research Council of Canada. Priority core-hours for high-fidelity CFD were provided by SciNet, which is funded by the Canada Foundation for Innovation, the Government of Ontario, the Ontario Research Fund - Research Excellence, and the University of Toronto.

Session Category

Cardiovascular/Cardiorespiratory Biomechanics: Methods, Models and Applications

OA108-03

Effect of Estrogen on Thoracic Aortic Aneurysm Development and Progression in a Mouse Model of Marfan Syndrome

Professor Jessica Wagenseil Jessica, Dr. Krashn Dwivedi krashn, Ms. Yufan Wu Viola

Washington University in Saint Louis, Saint Louis, Missouri, United States

Introduction

Thoracic aortic aneurysm (TAA) is a life-threatening disorder involving progressive aortic dilation and rupture risk [1]. TAA is associated with Marfan syndrome (MFS) [1]. Despite similar prevalence of MFS in males and females, TAA progression and outcomes differ significantly by sex [1, 2]. This study investigates how sex hormones, specifically estrogen, contribute to sex-specific TAA growth and adverse events using a mouse model of MFS.

Methods

A severe mouse model of MFS (*Fbn1*$^{mgR/mgR}$ = MU) was used in this study. Mice exhibiting marked dilation at 30 days of age (defined as a diastolic diameter in MU mice at least ~1.2× that of their WT littermates) were included. 30 day old male MU mice had either a 17-β estradiol (bioactive estrogen) or a placebo pellet (release rate 0.25 mg/day for 60 days) subcutaneously implanted. In 30 day old female MU mice, either bilateral oophorectomy (BO) or sham surgery was performed (Fig. 1A). The ascending aortic (ASC) diameter of each mouse was then measured using ultrasound every 7 days for the entire lifespan. An autopsy was performed on each mouse after death, and the ASC was dissected. Multiphoton microscopy was performed to assess extracellular matrix (ECM) remodeling in the aortic wall.

Results

Figs. 1B–F show changes in ASC diastolic diameter with age and Figs. 1G-J show multiphoton images of the ECM after ASC dissection. Estrogen-treated male MU mice exhibited slower TAA progression and longer survival than placebo-treated male MU mice. BO-operated female MU mice displayed a marked acceleration in TAA growth and substantial ASC enlargement compared to sham-operated female MU mice. Both placebo-treated males and BO-operated females demonstrated severe elastic fiber fragmentation and increased collagen deposition in the ASC wall.

Discussion

Our preliminary results suggest that estrogen contributes to the sex-specific differences in TAA progression and outcomes in MU mice. This study is ongoing, and we are continuing to collect data to further clarify how estrogen influences vascular mechanics, ECM remodeling, and gene-regulatory pathways during TAA development and progression.

Images (Optional)

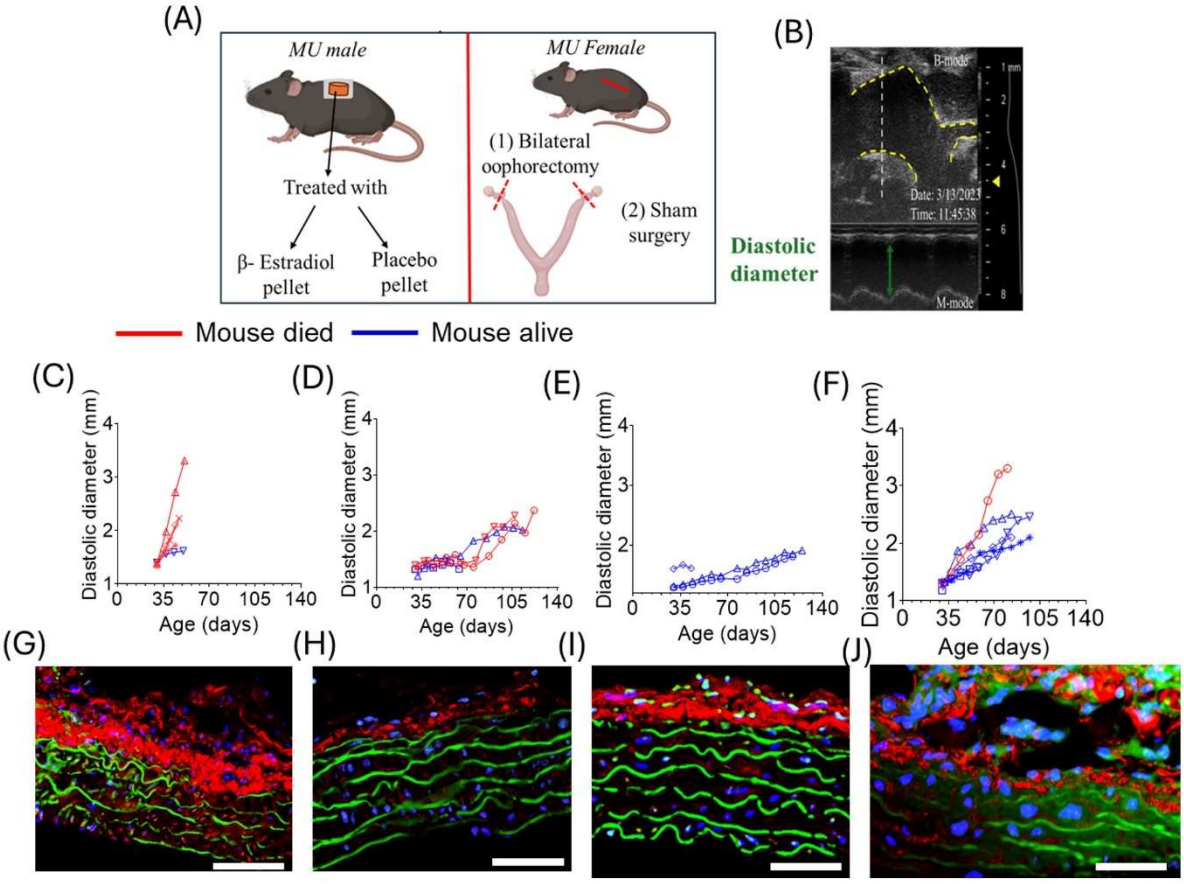


Figure 1. (A) Schemic of experimental procedures. (B) Representative ultrasound image of ASC and diastolic diameter measurement. Diastolic diameter vs. age in (C) male mice with placebo pellet, (D) male mice with β-estradiol pellet, (E) female mice with sham surgery, and (F) female mice with bilateral oophorectomy (BO) surgery. Mice traced with red lines died at the latest timepoint on the graphs, while mice traced with blue lines were still alive at the latest timepoint on the graphs. Multiphoton images of ASC wall ECM for (G) male mouse with placebo pellet, (H) male mouse with β-estradiol pellet, (I) female mouse with sham surgery, and (J) female mouse with BO surgery. Collagen fibers = red, elastic fibers = green, cell nuclei = blue. Lumen is at the bottom of the images. Scale bar = 50 μm.

References (Optional)

[1] Jain D, et al., *Cardiovasc. Pathol*, 20:15-25, 2009.

{2] Detaint., et al., *Eur Heart J*, 31:2223-2229, 2010.

Acknowledgements (Optional)

AHA 25POST1379021 and NIH R01164800

Session Category

Cardiovascular/Cardiorespiratory Biomechanics: Methods, Models and Applications

OA108-04

Geometry-Aware Abdominal Aortic Aneurysm Digital Twins for Patient-Specific Wall Stress Mapping

PhD Candidate Julian Carvajal Rico[1], M.D Satish C. Muluk[2], M.D Mark K. Eskandari[3], PhD Ender A. Finol[1]

[1]Department of Mechanical, Aerosp., and Ind. Engineering, UT San Antonio, San Antonio, TX, United States. [2]Department of Cardiothoracic Surgery, Allegheny Health Network, Pittsburgh, PA, United States. [3]Division of Vascular Surgery, Northwestern University School of Medicine, Chicago, IL, United States

Introduction

Abdominal aortic aneurysm (AAA) rupture risk is assessed largely by geometric surrogates (maximum diameter and growth rate), despite evidence that rupture depends on the balance between wall stress and wall strength. In the present work, we frame each image-derived reconstruction as a geometry-aware digital twin and study fast graph-based surrogates that map individual anatomy to clinically relevant wall stress endpoints.

Methods

Computed tomography angiography (CTA) scans from a multi-institution cohort were processed as geometry-aware digital twins. CTA images were segmented using a U-Net pipeline with expert refinement **(Fig.1b)**. Outer wall surfaces were standardized to nodes and enriched with node-wise descriptors, wall thickness, thrombus thickness, principal/mean/Gaussian curvature, and centered coordinates **(Fig.1c)**. Finite element analysis (FEA) simulations provided the ground truth wall stress fields, which were projected onto the outer wall surface **(Fig.1d)**. We compared two Graph Neural Network (GNN) families; GraphSAGE as a scalable inductive baseline for graph-level endpoints and a Graph Transformer (GT) with edge-aware, relative positional encodings for long-range interactions. Both yielded wall stress predictions as in **Fig.1e**. During the training process we used standardized features, AdamW, early stopping, and tail-aware readouts/losses; evaluation included graph-level RMSE-R^2, node-level errors, and spatial correlations versus FEA.

Results

For an exemplary AAA shown in **Fig.1f**, the best-performing GT model reproduced the FEA wall stress distribution with close agreement in both central tendency and tail behavior. The FEA-derived stress field had a mean of 2.54 N/cm^2 and 99th percentile of 12.19N/cm^2, whereas the GT predictions yielded a mean of 3.81 N/cm^2 and 99th percentile of 12.00

N/cm^2. Spatially, high stress regions along the sac and neck were preserved, and the corresponding histograms, PDFs, and ECDFs show near overlap across most of the distribution with mild deviations in the extreme tail.

Discussion

Treating CTA reconstructions as AAA digital twins enables patient-specific, near real-time wall stress mapping once models are trained. GraphSAGE suits rapid prediction of scalar endpoints, while GT improves full-field fidelity and tail calibration, better representing biomechanically coupled regions such as sac–neck interactions. This geometry-aware, graph-based pipeline reduces reliance on time-intensive simulations and is extensible to other vascular surfaces naturally represented as meshes.

Images (Optional)

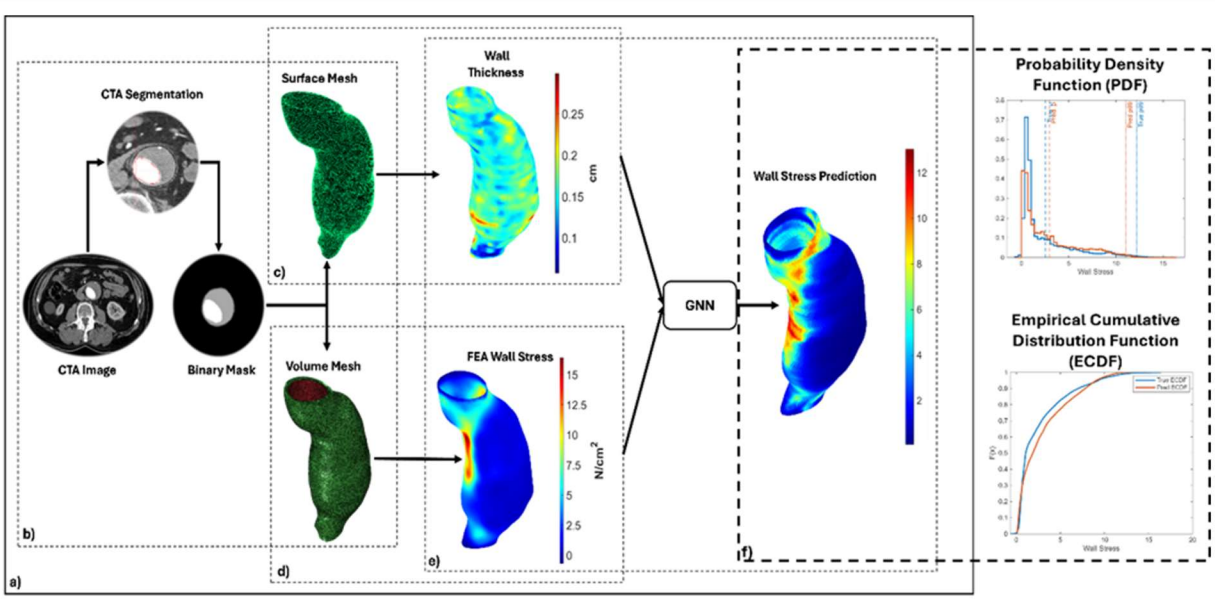


Figure 1. a) End-to-end, geometry-aware digital-twin pipeline for patient-specific AAA wall stress mapping. (b) Segmentation to binary masks followed by 3D reconstruction of surface/volume meshes. (c) Feature engineering on the standardized outer wall surface (e Graph-based prediction of wall stress (GraphSAGE/Graph Transformer) from geometric features. f) Probability Density Function (PDF) and Empirical Cumulative Distribution Function (ECDF) predicted wall stress vs. ground truth wall stress for a representative test case using Graph Transformer (GT).

Session Category

Cardiovascular/Cardiorespiratory Biomechanics: Methods, Models and Applications

OA109-01

Reversal of Dominant Loading Direction Along the Cervical Spine During Multidirectional Head Resistance: Insights From a Nonlinear 3D FE Model

Dr. Wissal Mesfar[1], Dr. Kodjo Moglo[2]

[1]King Saud University, Riyadh, Riyadh, Saudi Arabia. [2]Royal Military College of Canada, Kingston, Ontario, Canada

Introduction

Quantifying stabilizing muscle moments along the head–neck (HN) complex is essential for understanding cervical loading and predicting muscle forces. Global neck-strength measures, however, provide only overall head force and cannot detect how mechanical demands vary or shift across cervical levels. This study addresses this limitation by determining the isometric muscle moments required at each HN bony structure to resist multidirectional axial-plane loads under physiological head weight, providing the level-specific data needed for accurate cervical muscle modeling.

Methods

A validated 3D nonlinear finite element (FE) model of the HN complex was used to simulate resistance to external static loads. Forces ranging from 25–150N were applied at the head in five directions—Anterior, Posterior, Right, Anterior-Right, and Posterior-Right—while a constant 40N head weight acted at the center of mass. The T1 vertebra was fixed, while the head and cervical vertebrae were allowed translations but not rotations, reproducing the constraint normally imposed by coordinated muscle action. Reaction moments at the head and at vertebral levels C1–C7 were extracted as the net muscle moments required to maintain neutral posture. All simulations were performed using Abaqus 6.14.

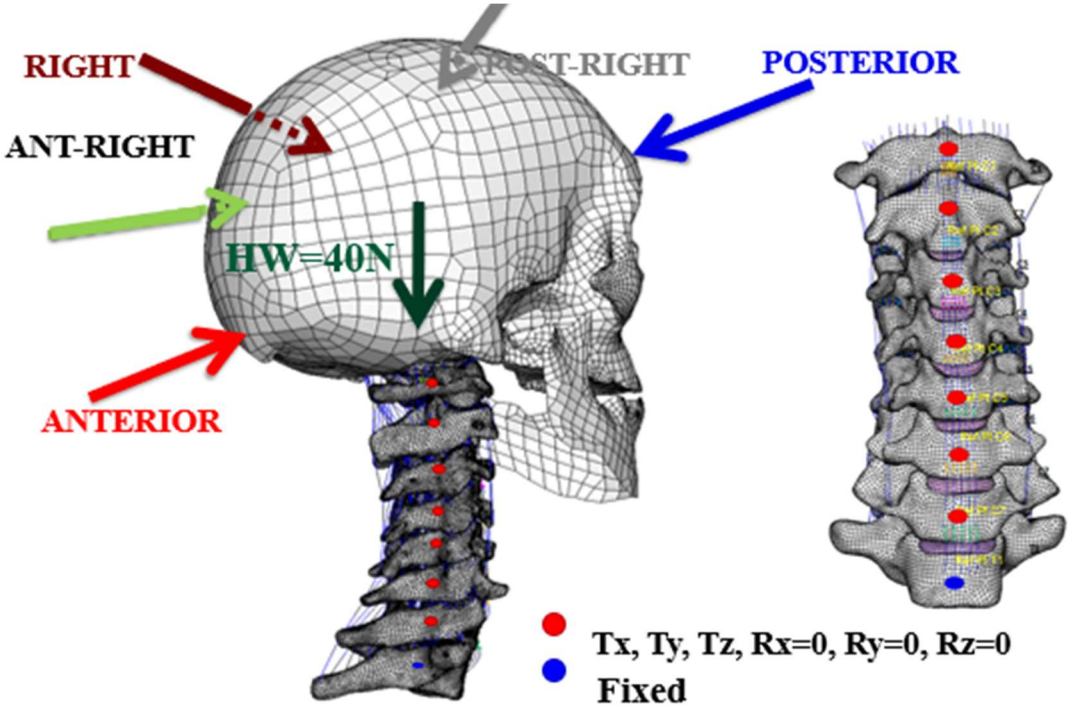
Results

Stabilizing moments increased nearly linearly with load at all cervical levels. At the head, moments ranged from ≈1.7N·m (25N) to 10.1N·m (150N) under posterior loading, the highest across all directions. Right-directed loading produced the lowest head moment (≈1.1–6.4N·m). Mid-cervical levels (C3–C6) showed a directional reversal: right-directed loads generated the largest moments (≈3.5–4.2N·m at 150N) versus posterior loading (≈2.6–3.0N·m). Upper levels (C1–C2) showed minimal directional variation, while lower levels (C7) had low demands (<2N·m), highlighting strong level- and direction-specific differences.

Discussion

The head experiences the highest stabilizing moments—up to 10.1N·m—reflecting its long lever arm. Mid-cervical levels exhibit a reversal of dominant loading: right-directed moments exceed posterior by ≈30–40%, showing that moment transmission is segment-specific and shaped by vertebral geometry and soft tissues. Low C7 moments (<2N·m) indicate its supportive role. These patterns demonstrate that global neck-strength measures cannot capture the pronounced segmental and directional variations revealed by detailed FE modeling.

Images (Optional)



Session Category

Musculoskeletal Biomechanics: Methods, Models and Applications

OA109-02

Late-Stage Knee Osteoarthritis Patients with Joint Pain Experience Small Variability in Knee Joint Contact Forces During Walking

Doctoral Researcher Fatemeh Jalali[1], Postdoctoral Researcher Amir Esrafilian[1], Postdoctoral Researcher Atte Eskelinen[1], Associate Professor Lauri Stenroth[1], Project Researcher Paavo Vartiainen[1], University Researcher Laura Säisänen[1,2], Professor Petro Julkunen[1,2], Professor Petteri Nieminen[3], Professor Rami K. Korhonen[1]

[1]Department of Technical Physics, University of Eastern Finland, Kuopio, North Savo, Finland. [2]Department of Clinical Neurophysiology, Kuopio University Hospital, Kuopio, North Savo, Finland. [3]Institute of Biomedicine, University of Eastern Finland, Kuopio, North Savo, Finland

Introduction

Gait biomechanics in late-stage knee osteoarthritis (KOA) patients is poorly understood, partly because standard musculoskeletal models assume normal joint structure, which can lead to inaccurate force estimates in osteoarthritic knees. As patients often experience prolonged pain before surgery, understanding altered joint loading could support non-surgical pain relief. Using the Concurrent Optimization of Muscle Activations and Secondary Knee Kinematics (COMAK) framework, we estimated subject-specific joint contact forces (JCFs) in patients with self-reported joint pain and severe KOA.

Methods

16 participants were recruited, including 8 patients with late-stage KOA and 8 healthy controls. The patients met criteria for moderate to severe radiographic changes and joint pain [1]. Motion data, including marker trajectories and ground reaction forces, were collected during five gait trials at habitual walking speed for both groups. Additionally, Visual Analogue Scale (VAS) pain scores were obtained from patients before surgery. We utilized a musculoskeletal model with a personalized 12-degree-of-freedom knee model, based on MRI scans [2] (Fig. 1), and simulated the movements using the COMAK algorithm.

Results

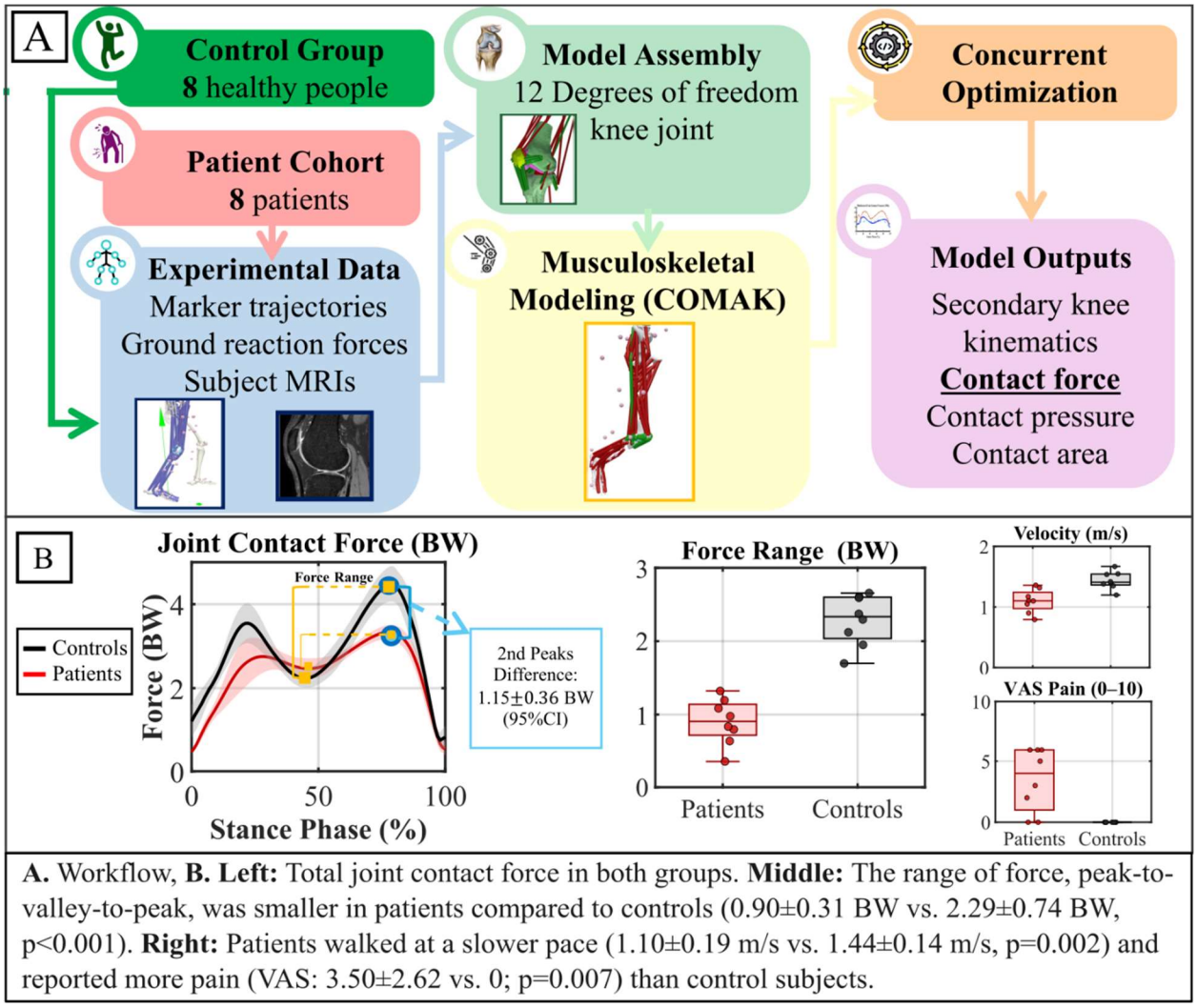
Controls had higher total and compartmental JCF peaks than patients, with the second peak greater by 1.15±0.36BW ($p<0.001$) (Fig. 1). Beyond peak magnitudes, the within-stride force range between peaks (peak-to-valley-to-peak) was smaller in patients than controls, indicating a flatter mid-stance profile in late-stage KOA (0.90±0.31 vs. 2.29±0.74BW,

p<0.001). Patients walked slower (1.10±0.19 vs. 1.44±0.14m/s, p=0.002) and reported more intense pain (VAS: 3.50±2.62 vs. 0; p = 0.007) compared to controls. Within the patient cohort, pain showed no significant correlation with any biomechanical parameter (p>0.05).

Discussion

The reduced peak force and force variability in late-stage KOA patients during walking likely resulted from pain that can trigger compensatory strategies, such as reduced walking speed and altered gait. Yet, pain alone did not have a direct correlation with the JCF. It may be that more patients with larger variability in pain scores are needed, or pain is influenced by multiple factors, including biochemical and biological elements [1].

Images (Optional)



A. Workflow, **B. Left:** Total joint contact force in both groups. **Middle:** The range of force, peak-to-valley-to-peak, was smaller in patients compared to controls (0.90±0.31 BW vs. 2.29±0.74 BW, p<0.001). **Right:** Patients walked at a slower pace (1.10±0.19 m/s vs. 1.44±0.14 m/s, p=0.002) and reported more pain (VAS: 3.50±2.62 vs. 0; p=0.007) than control subjects.

References (Optional)

[1] Mustonen AM et al., Biochim Biophys Acta Mol Cell Biol Lipids,2025

[2] Esrafilian A et al., IEEE TBME,2025

Acknowledgements (Optional)

Finnish Ministry of Education and Culture (pilot project DREAM), the European Union's H2020 (#101108335), the Research Council of Finland (#322429), Novo Nordisk Foundation.

Session Category

Musculoskeletal Biomechanics: Methods, Models and Applications

OA109-03

Neuromusculoskeletal Control of Foot Stabilization During Ground Contact

Dr. Michael Asmussen[1], Dr. Simon Danner PhD[2]

[1]Vancouver Island University, Nanaimo, BC, Canada. [2]Drexel University, Philadelphia, Pennsylvania, United States

Introduction

Neuromuscular control of stabilization of the foot during locomotion can involve both anticipatory muscles (co-)activation in expectation of a perturbation and feedback-driven neural responses once a perturbation occurs during the early stance phase. Relying solely on human experimentation limits our ability to sytematically probe these mechanisms (i.e., participant safety reasons). Here, we present a neuromechanical model that helps overcome these limitations and allows us to examine how the human foot adapts to ground perturbations during early stance.

Methods

The model included twelve muscles that control an ankle joint with three degrees of freedom [1]. Ligaments crossing the ankle joint were modelled as bushing torques derived from cadaveric data. We added a simulated neural network such that each muscle was controlled by a population of motoneurons activated by descending drive. Ia spindle and Ib Golgi tendon feedback of all muscles was connected to the network to simulate stretch reflex pathways, Ib disynaptic excitation and inhibition, recurrent inhibition, and phasic presynaptic inhibition of Ia afferents [2].

The neuromusculoskeletal model received simulated perturbations similar to locomotion forces. Multi-objective optimization that minimized ankle torques, ligament torque, and metabolic power was used to find weights of the synaptic connections in the neural model. The model was trained with and without neural feedback. To assess the contribution of afferent feedback to ankle stabilization, simulations with feedback connections silenced were performed.

Results

When the model was trained with feedback, but tested without it (Fig. 1A, B), the foot exhibited excessive dorsiflexion and stabilizing it required substantially increased ligament force. Models trained with and without feedback exhibited similar kinematic responses to

perturbations (Fig. 1C), but afferent feedback reduced metabolic cost by limiting muscle pre-activation (Fig. 1D).

Discussion

During locomotion, afferent feedback is important for economical and safe foot control; without it, the model either over-loads ligaments or uses excess energy to maintain stability.

Images (Optional)

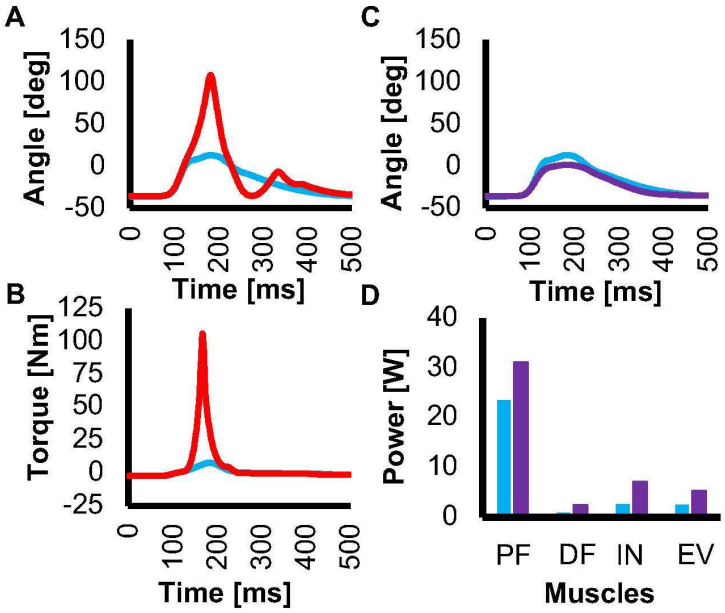


Figure 1: **A:** The angular deviation both with (blue) and without (red) reflexes. **B:** The required ligament torque to stabilize the foot with (blue) and without (red) reflexes. **C:** The angular deviation of a model trained with (blue) and trained without (purple) feedback. **D:** The metabolic cost of plantarflexor (PF), dorsiflexor (DF), invertor (IN), or evertor (EV) muscles to stabilize the foot with (blue) and without (purple) feedback.

References (Optional)

[1] Rajagopal et al., IEEE Bio Med, 2016

[2] Ausborn et al., Int J. Mol. Sci., 2022

[3] Chen et al,. J Biomech. Eng., 1988

Acknowledgements (Optional)

NSERC and MSHR-BC to MJA, and NIH grant nos. R01NS115900 and R01NS112304 to SMD.

Session Category

Musculoskeletal Biomechanics: Methods, Models and Applications

OA109-04

Neuromuscular Modeling of the Human Eyelid

Mr Jinyoung Kim, MD Daniel Rootman, Dr Tyler Clites

University of California, Los Angeles, Los Angeles, CA, United States

Introduction

Crucial eyelid functions are driven by the *orbicularis oculi* muscle (OOM). We showed in a recent study that precise spatiotemporal control of the OOM drives different eyelid motions to perform specific functions [1]. Current eyelid models are based on statistics, and cannot recapitulate this complex relationship between OOM activation and eyelid motion [2]. Neuromuscular models (NMM) based on mechanistic dynamics offer a more complete understanding of this relationship. We present a new NMM architecture for the eyelid, built around segmental control of the OOM.

Methods

The model was built using OpenSim Creator (Fig. 1A). The OOM is designed as a series attachment of four Hill-Type muscle actuators across the eyelid. Ligaments, tendons, and levator palpebrae superioris (LPS) were modelled as passive springs to support eyelid weight and stabilize the initial condition of the eyelid-open position. The model is simulated using OpenSim Computed Muscle Control (CMC). Eyelid kinematics were derived from motion capture tracking of five markers spread across the upper eyelid margin during different blink types. Muscle excitations (U1-U4) calculated by CMC were compared to EMG data collected from bipolar fine wire electrodes (Fig. 1B) during the same behaviors.

Results

CMC results showed that input kinematics can be well tracked by the model with reserve and residual force less than 0.1 N (Fig 1C). Simulation results showed similar spatiotemporal activation patterns in the OOM to experimental data. To be specific, the medial electrodes (U1 and U2) showed a faster onset time and higher amplitude than the lateral electrodes (U3 and U4) during spontaneous blink, but not during reflex blink. This medially biased activation pattern causes eyelid movement in the medial direction during closure, which is critical to spontaneous blink function.

Discussion

A predictive mechanistic NMM would have critical implications for diagnosis and treatment of eyelid paralysis. With an accurate mechanistic model, eyelid behaviors can be simulated by changing parameters of the NMM such as reduced muscle strength and lack of OOM activation. We anticipate that this work will also serve as a starting point for model-based control of stimulation for eyelid paralysis.

Images (Optional)

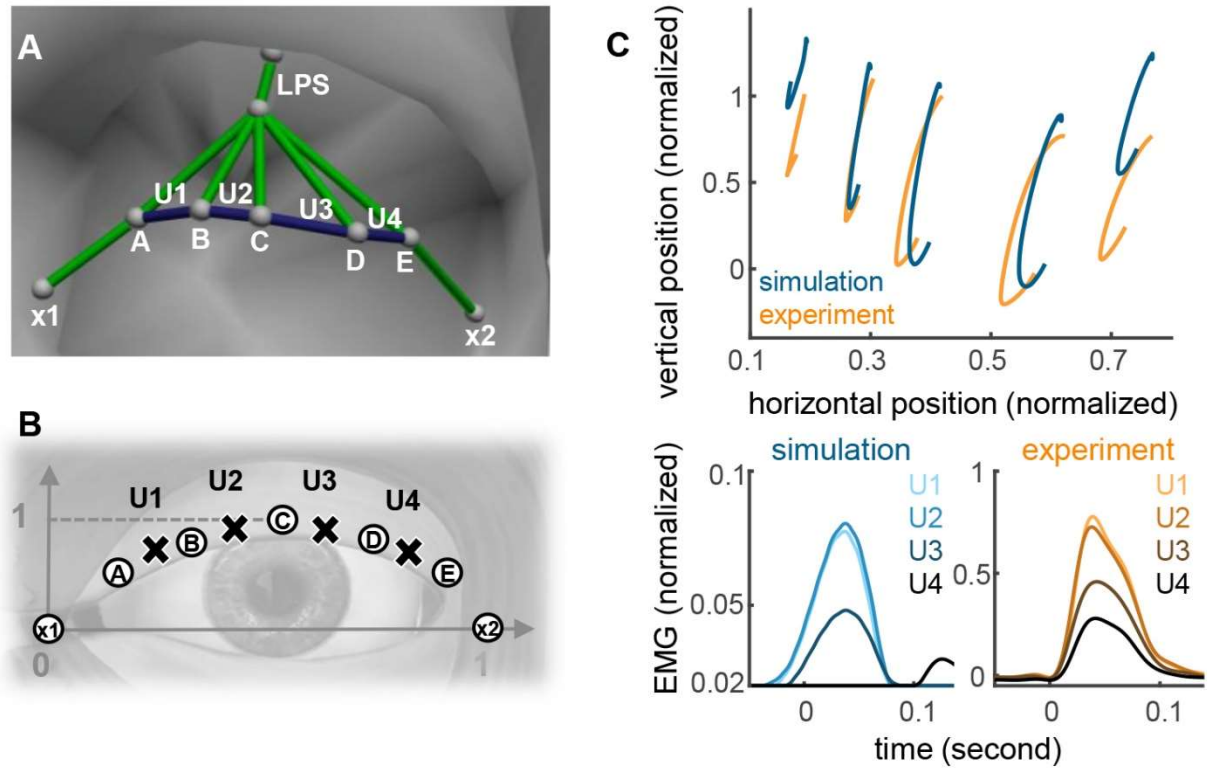


Figure 1: (A) Modeling of OOM (blue), tendon and ligament (green). (B) Electrode (x) and marker (circle) placement in the OOM. (C) Trajectory of markers (A-E) and normalized EMG activation of pretarsal region (U1-U4) for simulation and experiment during spontaneous blink.

References (Optional)

[1] Kim et al.,PNAS122(32), 2025; [2] Jowett et al.,PlasticAndReconstructiveSurgery143(1)

Acknowledgements (Optional)

This work was supported in part by the NIH National Eye Institute (award #1R21EY036680-01)

Session Category

OA109-05

The Muscle Spindle Behaves as a Tunable Feedback Controller During Perturbed Locomotion

Dr. Surabhi N. Simha[1,2], Dr. Gregory S. Sawicki[2], Dr. Timothy C. Cope[2,1], Dr. Lena H. Ting[1,2]

[1]Emory University, Atlanta, Georgia, United States. [2]Georgia Institue of Technology, Atlanta, Georgia, United States

Introduction

Muscle spindles, tunable sensors in skeletal muscles, may facilitate sensing and correcting perturbations to gait. Muscle spindles receive two gamma motor drives that are modulated independent of the alpha motor drive to the parent skeletal muscle, decoupling spindle firing from joint motion. Current technology limits direct probing of how tuning of spindle firing through gamma motor drive affects voluntary behavior. Thus, we developed a biophysical computational model of muscle spindle Ia firing. We hypothesized that gamma drive serves as an efference copy, encoding intended movement, so Ia firing reflects the feedback signal that corrects for deviations from the intended movement.

Methods

We simulated modulation of Ia firing by gamma drive during sinusoidal length changes mimicking locomotion. We modelled two types of intrafusal spindle-specific muscle fibers (bag1 and chain) as half sarcomeres, whose force is determined by rate equations governing cross-bridge attachment and detachment [1,2]. Gamma dynamic drives Bag1 fiber activation, while gamma static drives chain fiber activation. Force and yank of the intrafusal fibers are linearly combined to generate a receptor potential that drives Ia firing. The parent extrafusal skeletal fiber is modelled in parallel to the intrafusal fibers, is governed by different rate equations, and receives alpha activation.

Results

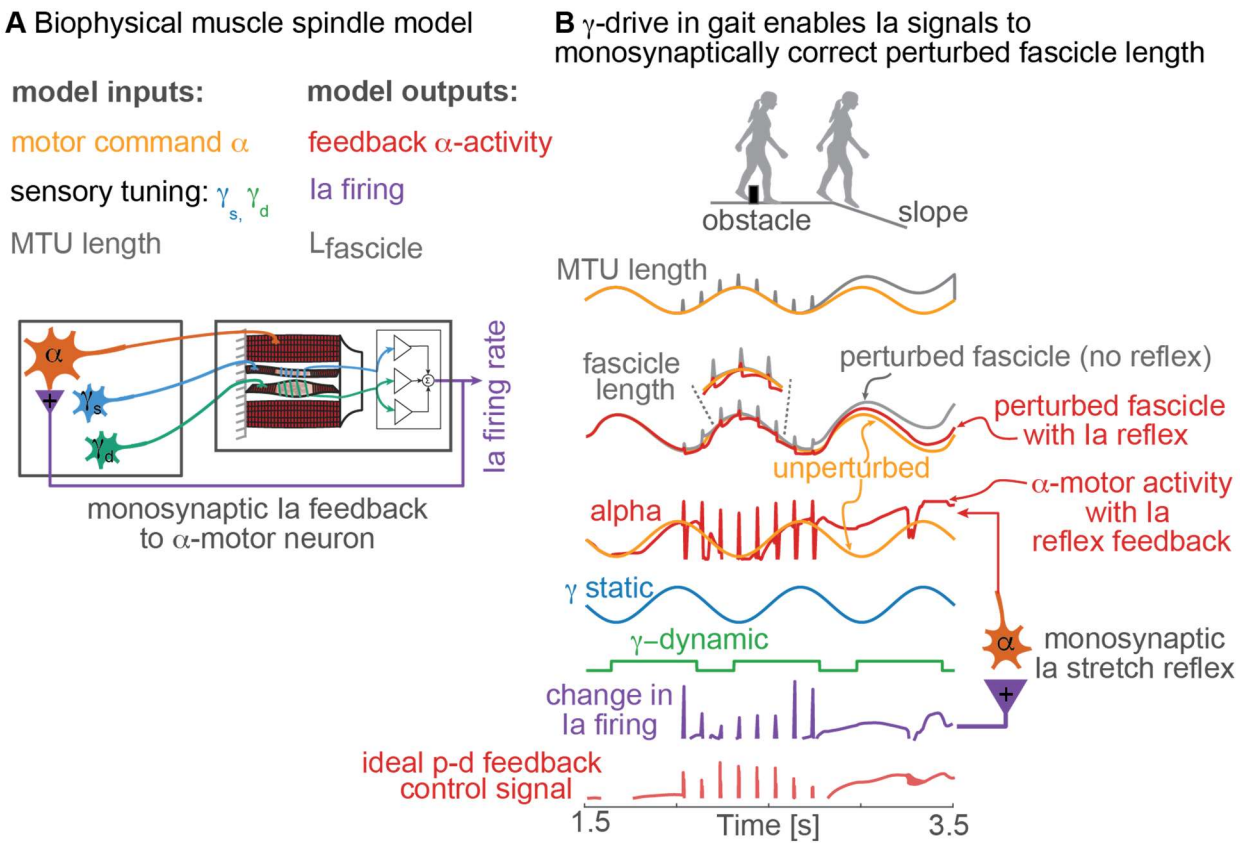
Our model, tuned to relaxed stretch conditions, reproduced profound changes in muscle spindle firing seen in locomotion due to changes only in gamma motor drive. When the model received sinusoidal muscle length changes and Ia firing measured from cat locomotion, it predicted measured patterns of each gamma drive [3]. We leveraged the generalizable nature of our model to identify that the phasic gamma drive during locomotion modulates Ia firing such that when muscle length was perturbed away from

nominal movement, Ia firing encoded a position-and-velocity-error feedback control signal, correcting muscle fascicle length through the monosynaptic stretch reflex (figure).

Discussion

Our model, grounded in biophysical properties of muscle fibers, demonstrates that spindle signals, dissociated from joint motion, can be tuned to generate error signals to correct perturbations to gait.

Images (Optional)



References (Optional)

[1] Blum et al., eLife, 2020 [2] Simha & Ting, Exp. Physiol., 2024 [3] Taylor et al., J. Physiol., 2006

Acknowledgements (Optional)

NIH-R01-HD90642, NIH-R21-HD117352, NSF-DBI-2319710

Session Category

Musculoskeletal Biomechanics: Methods, Models and Applications

OA109-06

An EMG-Informed 6DOF Knee Musculoskeletal Model for Deep Squat Tasks: Application in ACL Injury Prevention

Ms. Maria Dalle Vacche, Mr. Giulio Rigoni, Ms. Fabiola Spolaor, Prof. Zimi Sawacha

University of Padova, Padova, Veneto, Italy

Introduction

Anterior Cruciate Ligament (ACL) injuries affect 30–78/100,000 individuals annually [1], highlighting the need for prevention and deeper understanding of knee biomechanics. State of the art musculoskeletal models (MSMs) consider the knee as a 1-degree-of-freedom (DOF) joint and even when 6DOF are available either they are not suitable for deep squat movements [2] or they don't include ligaments [3].

This study introduces a 6DOF knee MSM with customizable ligament parameters [4], enabling estimation of: muscle activity (MA) and forces, ligament forces and strain, joint reaction forces. Two different EMG-informed methods (Computed Muscle Control (CMC), Moco [5]) were applied to represent individualized motor control patterns in the analysis.

Methods

Ten healthy (age 26.1 ± 1.5 yrs, BMI 22.6 ± 2.0 kg/m^2) and five ACL-injured subjects (19 ± 2.82 yrs; 26.65 ± 2.04 kg/m^2) performed three bipodalic leg drop landings and squats. Kinematics and kinetics were acquired with a stereophotogrammetric system and two force plates. An 8-channel surface-EMG (sEMG) system (1000 Hz) acquired the MA as listed in **Fig.1**.

Data were processed in OpenSim (**Fig.1**) using a 6DOF knee MSM purposely developed for deep squat movement, EMG informed through Moco or CMC. sEMG envelopes were calculated via bandpass filtering (10–450 Hz) with a fifth-order Butterworth filter. Results were compared between EMG-informed methods and Static optimization; simulated MA and experimental sEMG were also compared: root mean square error (RMSE), coefficient of multiple correlation α were computed. SPM analysis [5] was performed across all methods.

Results

The best agreement between simulated and experimental MA profiles was obtained for Moco EMG-informed approach (see **Fig.1**: $\alpha > 0.97$; RMSE < 0.05, Tibialis Anterior, controls' data))

Discussion

Results support the introduction of a 6DOF knee MSM informed by sEMG signals to investigate the knee joint biomechanics for application in ACL injury screening.

Images (Optional)

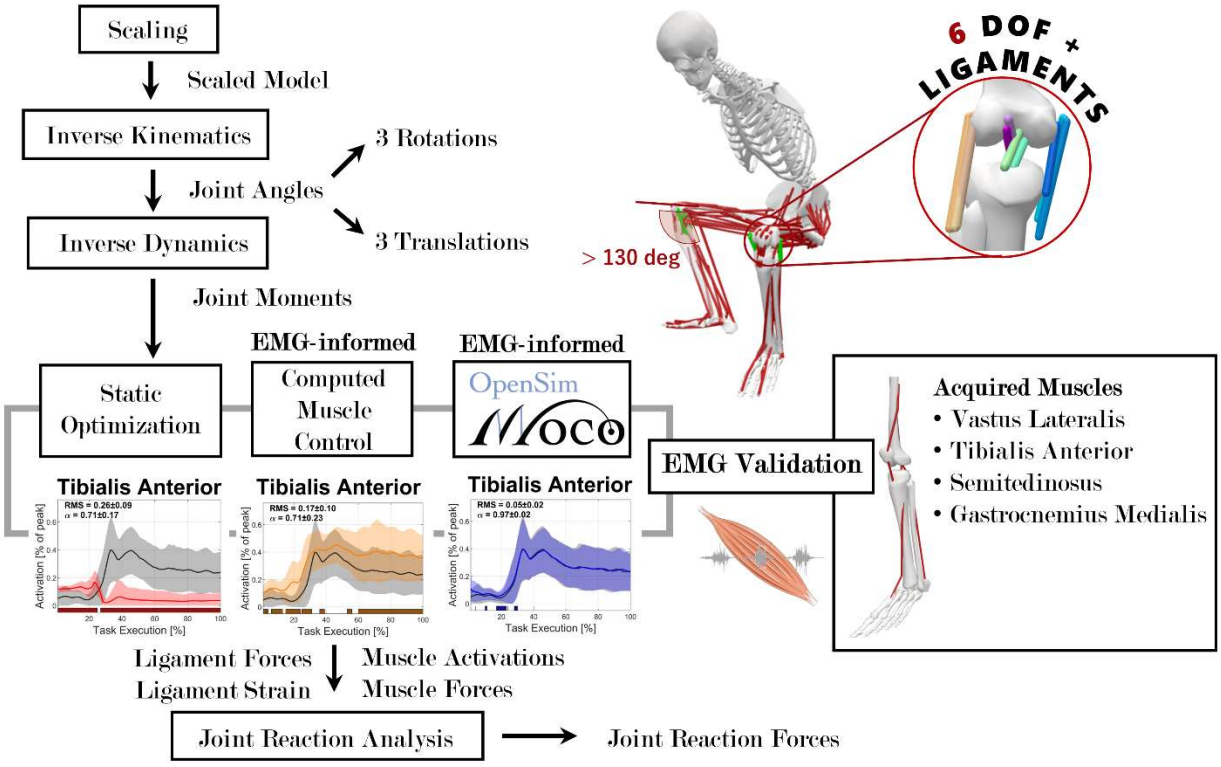


Figure 1: Proposed Musculoskeletal Modeling Framework.

References (Optional)

[1] Singh N, et al. Orthop Res Online J. 2018.

[2] Xu H, et al. CMBBE. 2015.

[3] Catelli DS, et al. CMBBE. 2019.

[4] Blankevoort L, Huiskes R. J Biomech Eng. 1991.

[5] Dembia CL, et al. PLoS Comput Biol. 2020.

[6] Pataky TC. CMBBE. 2012.

Session Category

Musculoskeletal Biomechanics: Methods, Models and Applications

OA110-02

Experimental and Computational Modelling Framework for Detecting Bladder Microcontractions

Mr. James Fox[1], PD Dr. Francesco Clavica[1,2], Prof. Dr. Dominik Obrist[1], Dr. Silje Ekroll Jahren[1]

[1]ARTORG Center for Biomedical Engineering Research, University of Bern, Bern, Bern, Switzerland. [2]Department of Urology, Inselspital, Bern University Hospital, University of Bern, Bern, Bern, Switzerland

Introduction

Overactive bladder is a common urological disorder. It is characterised by urgency, frequency, and nocturia. Diagnosis relies on filling and voiding cystometry; about half of symptomatic patients exhibit detrusor overactivity, detected as involuntary pressure rises during filling. However, many bladder microcontractions generate pressure changes below standard detection limits ($5 cmH_2O$) yet may contribute to symptoms. Treatment often involves intradetrusor botulinum toxin injections that suppress global bladder contractility and frequently lead to intermittent catheterisation. We hypothesised that adapting Pressure Volume (PV) catheters to the bladder would enable detection and localisation of microcontractions and support more targeted therapy. Ex-vivo and computational models of microcontractions were used to assess PV catheter performance.

Methods

A multielectrode PV catheter (Millar, Inc.) applying a constant current along the lumen was adapted for bladder use. Voltage measurements at evenly spaced electrodes were used to infer segmental impedance and compute local volume. Viable ex-vivo porcine bladders were collected after euthanasia; removal of central neural inhibition resulted in spontaneous microcontractions. Bladder surface motion was recorded using particle tracking by applying fiducial markers to the bladder surface.

These marker trajectories were used as inputs to a computational bladder model. Bladder geometry was reconstructed by laser scanning four lateral facets, stitching surfaces into a closed topology. Fluid–structure interaction (FSI) simulations coupled an FE-model of the bladder wall with a CFD model of the contained fluid, exchanging boundary conditions until convergence.

Results

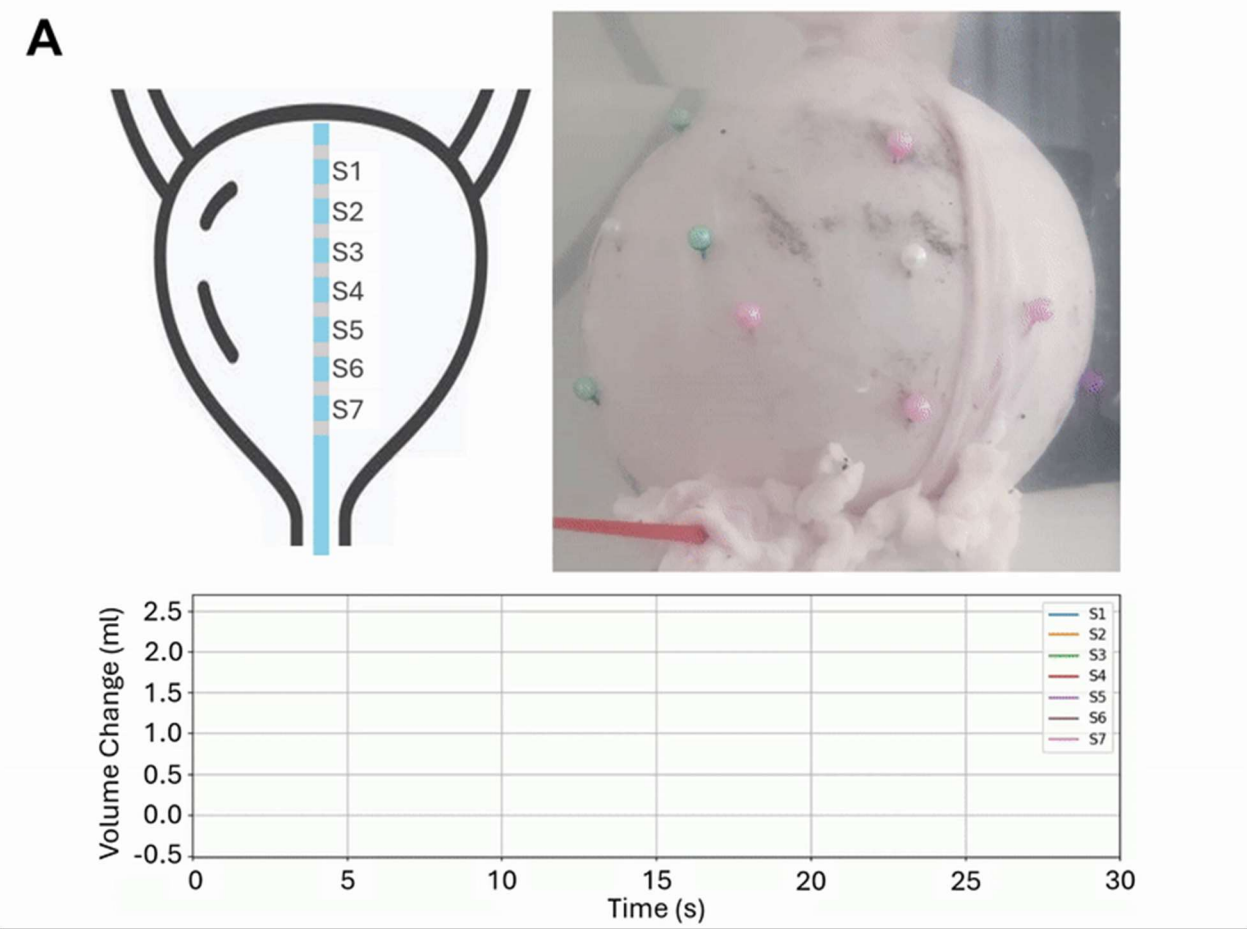
In the ex-vivo study, the PV catheter measurements reliably detected segmental volume changes associated with microcontractions. These contractions produced pressure excursions below $1 cmH_2O$ (undetectable by standard urodynamics) yet generated distinct local volume changes (Figure A).

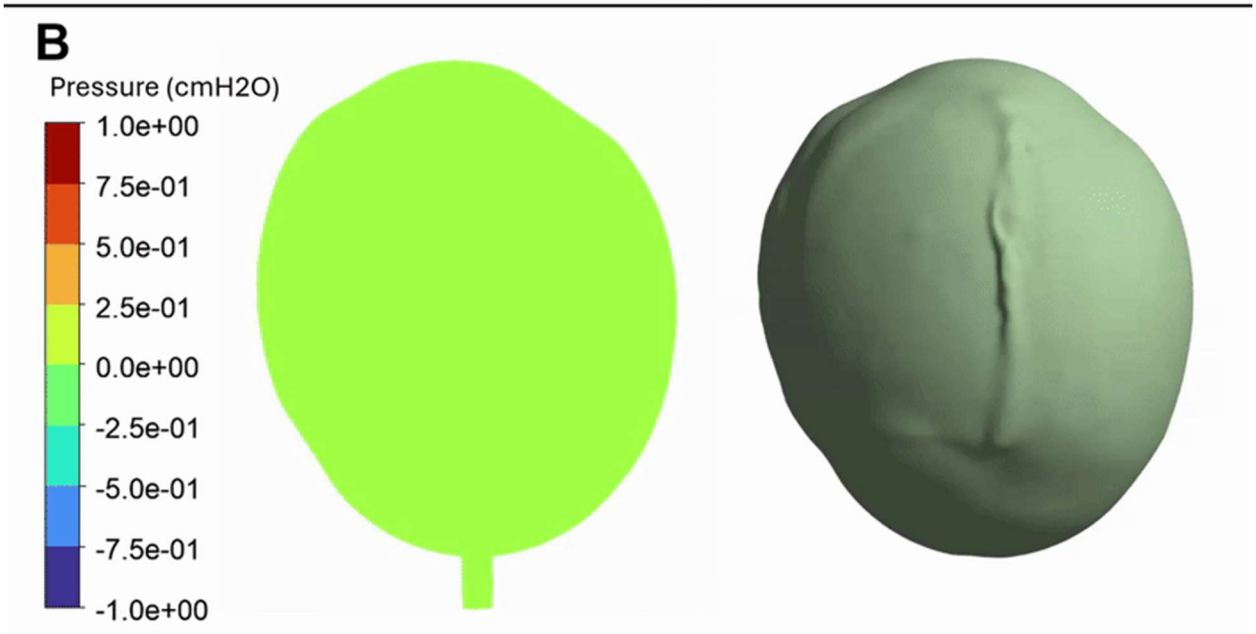
The computational model reproduced the experimental surface kinematics, and simulations replicated the maximal-change segment and the minimal pressure response (Figure B). Both experiment and simulation localised the largest relative volume change in S1.

Discussion

Segmental volume mapping can detect microcontractions, not measurable using pressure-only urodynamics. Identifying a dominant contracting segment (S1) suggests potential for targeted intradetrusor injections, by reducing toxin use by over 85% and preserving bladder function. This represents the first combined experimental and FSI-based characterisation of bladder microcontractions. Further in-vivo validation is required.

Images (Optional)





Session Category

Organ and Tissue Biomechanics: N/A

OA110-03

Temporal Differential Growth Drives Sequential Midgut Protrusion, Rotation, and Retraction: A Computational Simulation Study.

Ms. Michina Saiki Ph.D student[1], Mr. Hironori Takeda[2], Mr. Yuto Kawabata Ph.D student[1], Mr. Shunichi Ishida Assistant Professor[1], Mr. Yohsuke Imai Professor[1]

[1]Kobe University, 1-1,Rokkodai,Nada,Kobe, Hyogo, Japan. [2]Kyoto University, 53 Shogoin-Kawahara-cho, Sakyo, Kyoto, Japan

Introduction

Midgut morphogenesis proceeds through a characteristic sequence of protrusion, rotation, looping, and retraction during embryonic development. However, the mechanical basis underlying these transitions remains unclear. Differential growth between the midgut and the mesentery has been proposed as a mechanism for loop formation[1], which motivates us to investigate whether this growth-based mechanism could also contribute to other stages of midgut morphogenesis, including protrusion, rotation, and retraction. In this study, we aim to determine whether temporal changes in differential growth can reproduce the sequential transitions of protrusion, rotation, and retraction observed in embryos[2].

Methods

We constructed a continuum-mechanics model representing the midgut as a compressible hyperelastic tube whose reference configuration mimics embryonic geometry. To model differential growth, we defined a mesentery region attached to the tube wall with a slower growth rate and higher stiffness than the midgut. Tissue growth was represented using multiplicative decomposition of the deformation gradient, allowing us to simulate axial elongation driven by growth. The hyperelastic response was described by a compressible Neo-Hookean model, and the governing equations were solved using isogeometric analysis with Newton–Raphson iterations. We conducted parameter studies by varying the growth stretch and stiffness to identify mechanical regimes that yield protrusion, rotation, or retraction.

Results

Uniform growth without differential properties caused the tube to deform into a U-shaped protrusion when elongated under fixed-end constraints, indicating that herniation can arise from geometric confinement alone. When differential growth was introduced, the model generated a 90° rotation. As the growth differential was further increased, the tube subsequently retracted.

Discussion

Our findings suggest that temporal differential growth is sufficient to generate major phases of midgut morphogenesis. Protrusion emerges from compression-induced buckling, rotation arises from tension redistribution caused by a stiffer, slower-growing mesentery, and retraction occurs when the growth imbalance becomes large. Although the model simplifies mesentery geometry and omits interactions with surrounding tissues, it provides a unified mechanical explanation for midgut development and offers a basis for future, more detailed simulations.

References (Optional)

[1]Thierry Savin et al., Nature, 2011

[2]Michina Saiki et al., Biomech Model Mechanobiol, 2025

Session Category

Organ and Tissue Biomechanics: N/A

OA110-04

A Computational Framework for Evaluating AMS 800 Artificial Urinary Sphincter Behaviour Across Patient-Specific Urethral Anatomies

Dr Conall Quinn PhD

Trinity College, Dublin City, Dublin, Ireland

Introduction

Urinary incontinence affects up to 32% of men worldwide, severely impacting quality of life [1]. The AMS 800 artificial urinary sphincter is the gold-standard treatment for male stress urinary incontinence, yet complications remain frequent, with mechanical failure and urethral erosion common long-term issues [2]. Erosion is linked to excessive circumferential compression, but urethral stress cannot be measured clinically, limiting optimisation of pressure settings and device performance [3]. Computational modelling enables evaluation of internal stresses under realistic deployment [4]. This work presents a patient-specific framework to assess AMS 800 performance across varying urethral geometries.

Methods

AMS 800 cuff and balloon geometries (Boston Scientific) were reconstructed in Abaqus (2020). Patient-specific urethral geometries and nonlinear tissue behaviour were derived from mechanical characterisation of nine male urethras (Cunnane et al. [5]). A full preprocessing pipeline was developed to automatically generate device–tissue models, assign material behaviour, and simulate AMS 800 deployment (Fig. 1).

Device components used hyperelastic/elastic formulations based on manufacturer data whilst urethral tissues were fitted to patient-specific constitutive laws (Fig. 1C). Balloon inflation pressure, intraluminal pressure, and cuff sizing were controlled as input variables. Outputs included luminal reduction, contact pressure, and stress distribution.

Results

The pipeline successfully generated models for all urethral anatomies. Preliminary simulations demonstrated stable closure and realistic mechanical outputs, demonstrating sensitivity to cuff pressure. Increased balloon pressure raised urethral reopening thresholds and sustained continence over a wider pressure range. A complete parameter sweep assessing stress concentration and closure mechanics is ongoing.

Discussion

This framework enables quantitative evaluation of AMS 800 behaviour across varied urethral anatomies. Integrating device geometry, tissue data and automated simulation provides a scalable platform for analysing forces not measurable *in vivo*. Future work will map stress–pressure relationships, informing optimum cuff sizing and balloon inflation to reduce erosion risk.

Images (Optional)

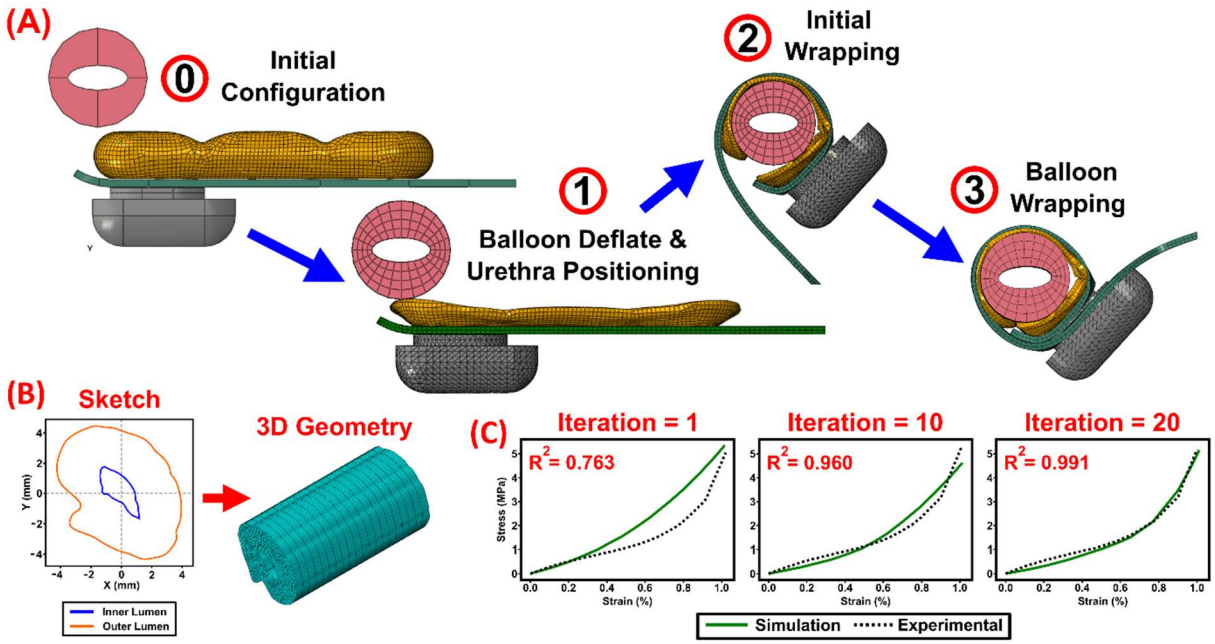


Figure 1 Workflow: (A) Cuff placement, (B) Patient-specific model generation, (C) Material calibration.

References (Optional)

[1] Shamliyan (et al.), Rev Urol. 11(3):145-65, 2009. [2] Kim (et al.), *Journal of Urology* 179:1912–1916, 2008. [3] Carson (et al.), *Asian Journal of Andrology* 22:154–157, 2020. [4] Mascolini (et al.), Artificial Organs 48:1112–1125, 2024. [5] Cunnane (et al.), *Biomaterials* 269:120651, 2021.

Acknowledgements (Optional)

Boston Scientific Clonmel

Session Category

Organ and Tissue Biomechanics: N/A

OA111-01

NeuroRecoVR: Split-Belt Virtual Reality Treadmill Training for Subacute Stroke

Ms. Alexa Boyer PhD Student[1], Dr. Zaid Alsaaran MD[2], Dr. Isabelle Poitras PhD[3], Dr. John Bertram PhD[1,4], Dr. Sean Dukelow MD, PhD[2,3,4]

[1]Department of Biomedical Engineering, Schulich School of Engineering, Calgary, AB, Canada. [2]Division of Physical Medicine and Rehabilitation, Calgary, AB, Canada. [3]Department of Clinical Neurosciences, Calgary, AB, Canada. [4]Cumming School of Medicine, Calgary, AB, Canada

Introduction

Up to 80% of stroke survivors experience mobility challenges, including hemiparesis, which can cause difficulties with walking and balance. This hemiparesis can lead to asymmetric and functionally limited propulsive forces generated by the paretic and non-paretic limbs, potentially resulting in injury and decreased quality of life. The split-belt treadmill (SBT) assists individuals with hemiplegia and asymmetric gait to relearn symmetrical walking and may reduce propulsive asymmetry. Although the SBT has proven effective for improving walking quality in chronic stroke, its effects on those in the subacute phase remain uncertain. Traditional walking therapies often lack engagement, but incorporating virtual reality (VR) with standard care could enhance outcomes. This study aimed to evaluate the safety, feasibility and preliminary efficacy of the VR-SBT system for rehabilitation in subacute stroke patients.

Methods

Fifteen participants, 40 days post-stroke (range 18-86), completed 10 sessions of walking using the NeuroRecoVR system. The sessions involved 27 minutes of total walking, including 15 minutes of SBT walking along a virtual reality mountain pathway reminiscent of the Rocky Mountains. Baseline clinical assessments included walking speed (10-metre walk test) and endurance (6-minute walk test), which were repeated on days 5 and 10. Ground reaction forces and centre of pressure were recorded using force plates embedded in the treadmill to calculate the power of each limb, both paretic and non-paretic, over the 10-day intervention. The asymmetry in power generated by each limb was measured, with lower asymmetry values indicating greater symmetry.

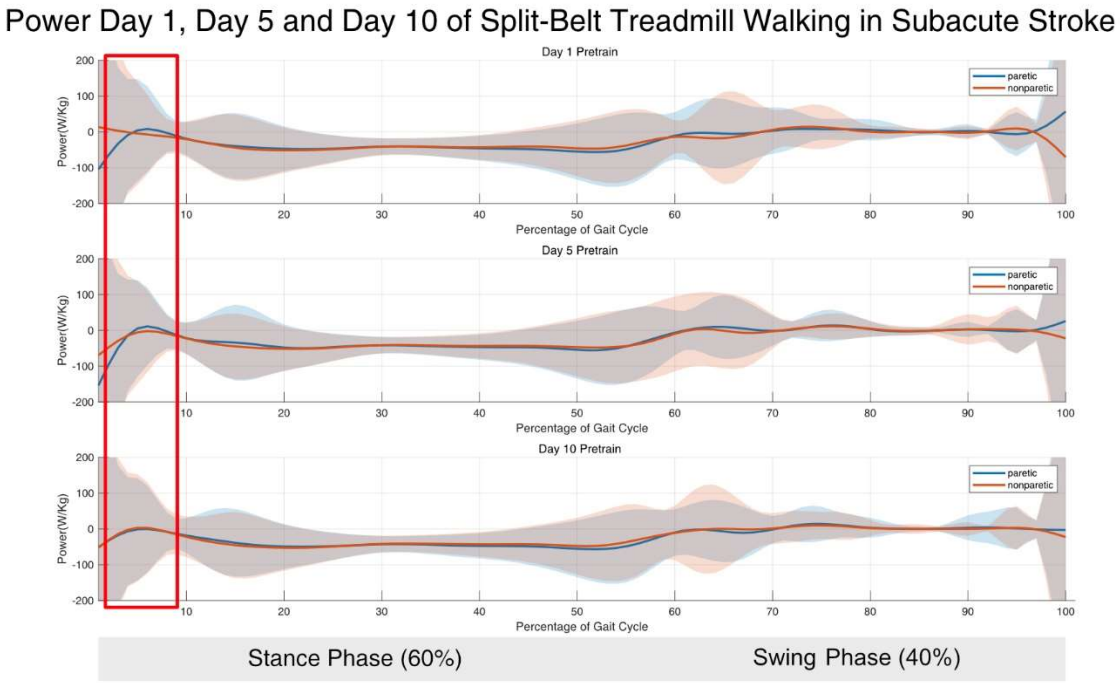
Results

All participants completed the 10-day SBT training without any falls. Participants reduced their average peak heel-strike power asymmetry by 0.66 W/Kg ($p<0.93$, t-test) over 10 days (Figure 1), indicating that they were learning and maintaining a more symmetrical walking pattern. On average, participants increased their walking speed by 0.24 m/s (±0.24 SD, $p=0.002$) and their endurance by 71.1 meters (±55.7 SD, $p< 0.001$).

Discussion

The NeuroRecoVR initiative was safe and feasible, and improved post-stroke patients' walking speed and endurance, meeting the minimal clinically important difference for these clinical scores. Symmetry of heel strike power between the paretic and non-paretic limbs also improved over the 10-day intervention, with no significant adverse events.

Images (Optional)



Session Category

Rehabilitation Biomechanics and Human Factors: Rehabilitation

OA111-02

Sit, Stand, Activate! Quantifying Muscle Activity During Mobility Aid Use in Young Children With Developmental Disabilities

Mia Hoffman PhD, Mr. Spencer Hensley, Ms. Katie Leija, Ms. Shariphine Agoalikum BS, MPhil, MPH, Ms. Allyson Clarke BS, Dr. Heather Feldner PT, PhD, PCS Emeritus, Dr. Katherine Steele PhD

University of Washington, Seattle, WA, United States

Introduction

Mobility aids can support independent movement for young children with developmental disabilities [1]. While device type and positioning may affect muscle activity [2] changes in muscle activity with and without mobility aids remains largely unknown. We compared muscle activity without mobility aids (NO-AID) and with a partial bodyweight support (PBWS) system or powered mobility device (PMD) in seated (PMD-sit) or standing (PMD-stand) postures. We hypothesized that muscle activity would be greatest in PBWS and PMD-stand.

Methods

Nine children with developmental delays and atypical muscle tone (AGE: 22 ± 11 months, 3M/6F) completed four, 30-minute play sessions randomized to NO-AID, PBWS, PMD-sit, or PMD-stand. Electromyography data from the tibialis anterior (TA), medial gastrocnemius (GAS), biceps femoris (BF), and quadriceps (QUAD) were filtered, rectified, and normalized to the 95^{th}-percentile across visits. Session-level muscle activity was calculated as the mean of 15-second window averages. Differences across conditions were assessed using Friedman tests with post-hoc Wilcoxon tests and Holm-Šidák corrections. One participant's PMD-stand data was missing.

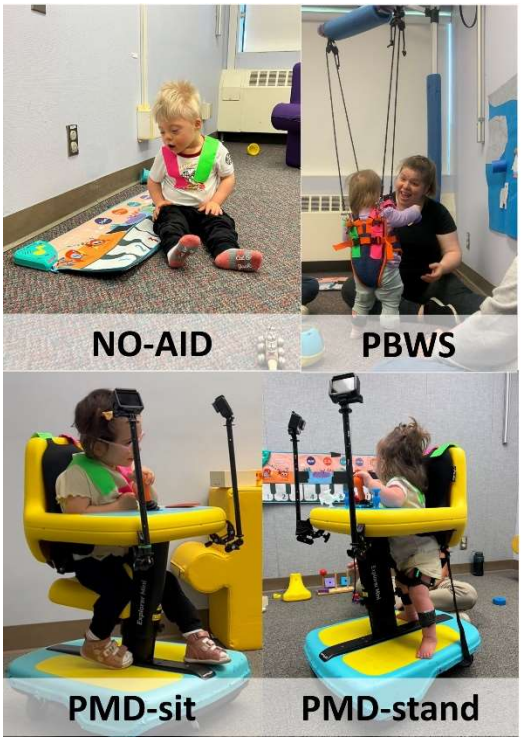
Results

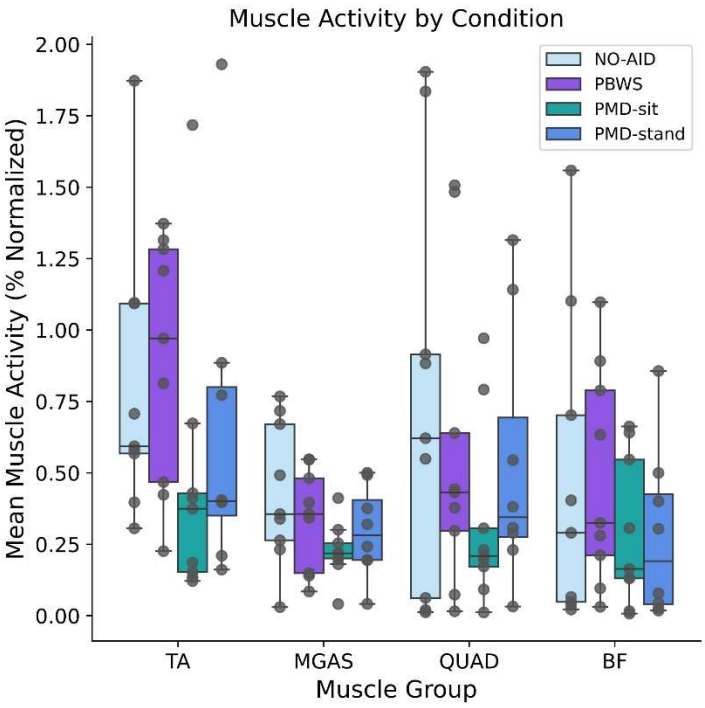
BF activity differed significantly across conditions ($p = 0.047$), with higher activity in PBWS than PMD-stand ($p = 0.008$) and a trend toward higher activity in NO-AID than PMD-stand ($p = 0.04$). TA activity trended towards significance ($p = 0.0503$), with PBWS higher than PMD-sit ($p = 0.039$). MGAS and QUAD activity were similar across conditions. Rank analyses showed TA and BF were most active during PBWS, while MGAS and QUAD were most active in NO-AID. The majority of participants showed higher QUAD (6/8 participants) and TA activity (7/8 participants) in PMD-stand than PMD-sit.

Discussion

Children with developmental delay used their lower-limb muscle during all play sessions and activity was influenced by mobility aid use. Consistent with a prior case series, PMD-stand elicited higher QUAD activation than PMD-sit [2]. Increased TA and BF activation in PBWS may reflect postural stabilization in a novel environment. Muscle activity may not fully capture functional changes, as participants ranged from early sitting to cruising. These findings challenge assumptions that PMD use requires minimal effort and highlight dynamic positioning's potential to increase physical engagement.

Images (Optional)





References (Optional)

[1] Feldner *et al.,* DRAT, 2016

[2] Zaino *et al.*, AT, 2024

Acknowledgements (Optional)

This work was supported by the NIH under grant TL1TR002318.

Session Category

Rehabilitation Biomechanics and Human Factors: Rehabilitation

OA111-03

Memory-Anchored Gestures and Visual Feedback Improve Motor Learning Efficiency and Consistency in VR

Mr. Zachary Marvin[1], Ms. Sophie Dewil[1], Mr. Yu Shi[1], Dr. Noam Harel[2,3], Dr. Raviraj Nataraj[1]

[1]Stevens Institute of Technology, Hoboken, NJ, United States. [2]James J. Peters Veterans Affairs Medical Center, Bronx, NY, United States. [3]Icahn School of Medicine at Mount Sinai, New York, NY, United States

Introduction

Neurological disorders such as spinal cord injury (SCI) and Parkinson's disease (PD) significantly impair hand dexterity and function, compromising the ability to perform important manual activities of daily living (ADLs). While practice of gestural biomechanics in physical therapy can improve dexterity, traditional methods often lack the neural engagement required to facilitate robust neuroplasticity [1]. We propose a VR-based rehabilitation approach designed to bridge this gap. In this study, we integrate augmented sensory feedback (ASF) to enhance motor awareness [2] with memory-anchored gestures inspired by American Sign Language (ASL) to leverage intuitive cognitive-motor coupling [3].

Methods

We recruited and tested 10 neurotypical adults for this pilot study. The neurotypical adults were seated in front of a webcam and were tasked to replicate target hand gestures displayed within an immersive VR environment. Participants performed gesture-matching across four conditions: 1) control, 2) visual ASF, 3) memory, and 4) memory + visual ASF. We assessed motor performance according to measures for accuracy (spatial matching to the target gesture), learning efficiency (time to reach the 80% accuracy threshold), and consistency (minimizing standard deviation past the 80% threshold).

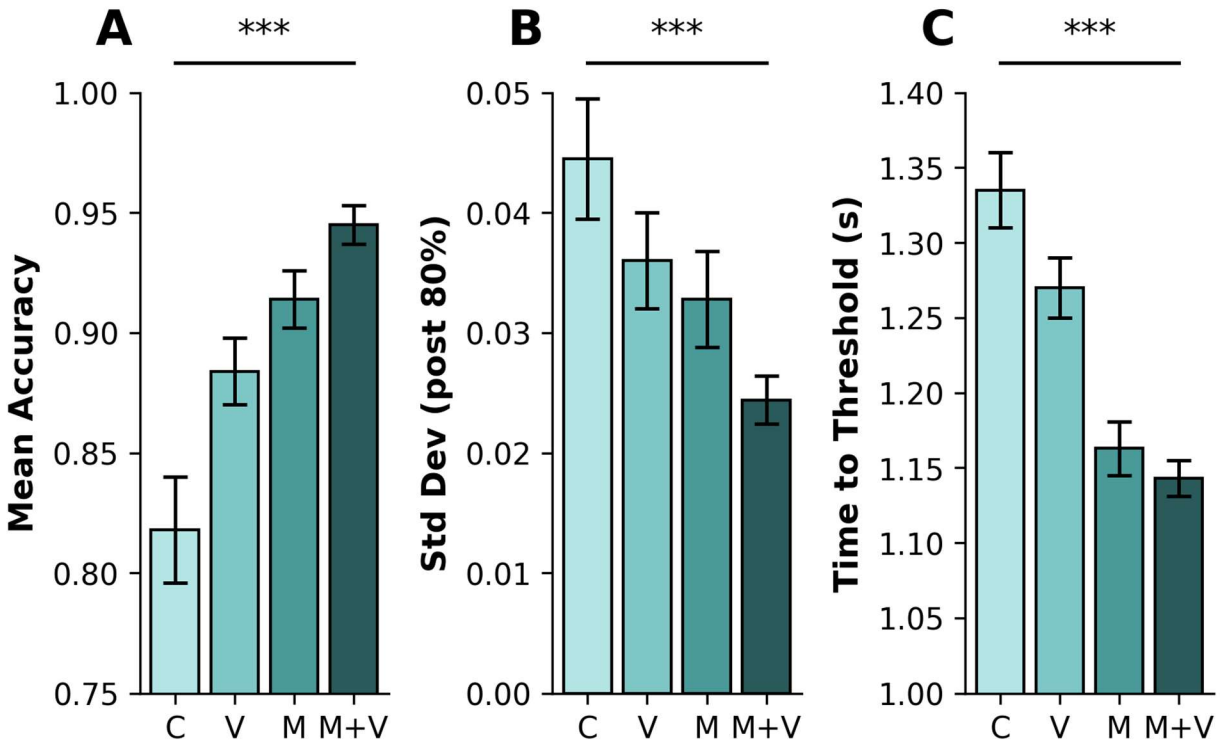
Results

Significant main effects were observed across all conditions. The combined memory + visual ASF condition achieved the highest accuracy (94.3%), a 12.6% improvement over control. Also in this combined condition, learning efficiency improved by 15% (1.13s vs. 1.33s; $p<0.001$), and consistency increased by 51%, indicating significantly more consistent motor execution.

Discussion

The findings from this pilot study establish proof-of-concept of a framework for cognitively-enhanced sensorimotor integration for rehabilitative training. This approach could be extended by integrating multisensory activation with augmented feedback that further reinforces cognitive scaffolding during motor training. Our memory-anchored approach improved performance by converting otherwise repetitive tasks into cognitively-enriched, memory-supported training activities. Future work will translate this approach to clinical populations to assess its therapeutic efficacy in restoring manual ADL function.

Images (Optional)



C=Control, V=Visual ASF, M=Memory, M+V=Memory+Visual ASF
*Error bars: ±SEM. ***p < 0.001 (one-way ANOVA)*

References (Optional)

[1] Kleim et al., Journal of Speech, Language, and Hearing Research. 2008

[2] Nataraj R et al., *Bioengineering*. 2025

[3] Corina DP et al., *Current Biology.* 2020

Acknowledgements (Optional)

Supported by the Provost Fellowship from the Stevens Institute of Technology Provost's Office.

Session Category

Rehabilitation Biomechanics and Human Factors: Rehabilitation

OA111-04

Real-Time Modulation of Split-Belt Treadmill Speed Enhances Gait Propulsion and Neuromuscular Engagement in Post-Stroke Hemiparesis

Ms. Adriele Rivera[1], Mr. Hyunje Park[1], Dr. Seoung Hoon Park[1], Dr. Jooeun Ahn[2], Dr. Beom Chan Lee[1,2]

[1]University of Houston, Houston, Texas, United States. [2]Seoul National University, Seoul, N/A, Korea, Republic of

Introduction

In individuals with post-stroke hemiparesis, limited forward propulsion arising from paretic plantarflexor and knee extensor deficits impedes functional walking recovery [1, 2]. Although split-belt treadmill training ameliorates step asymmetry through error-based learning, it does not explicitly target the deficit in push-off generation. To address this limitation, this study evaluated the Adaptive Propulsion Enhancement eXperience (APEX) system [3], specifically its propulsion-facilitating mode designed to reinforce paretic-limb propulsion via real-time, phase-dependent belt speed modulation.

Methods

Ten adults ndividuals with chronic post-stroke hemiparesis completed a single-session treadmill protocol comprising baseline, training, and post-training periods. In the training period, the propulsion-facilitating mode applied a transient deceleration to the belt ipsilateral to the paretic leg during late stance, effectively extending ground contact time to augment propulsive effort (Fig. 1). Ground reaction forces were sampled at 1000 Hz using instrumented treadmill force plates, and EMG signals were acquired at 1926 Hz from the medial gastrocnemius (MG), soleus (SOL), vastus medialis (VM), and rectus femoris (RF). Outcomes included normalized peak paretic propulsive force and mean EMG amplitudes for the targeted muscles during the propulsive phase. Statistical differences across the three periods were evaluated using a one-way repeated measures ANOVA.

Results

One-way repeated measures ANOVA revealed significant period effects for all outcomes ($p < 0.0001$). Normalized peak paretic propulsive force increased from 0.78 ± 0.09 at baseline to 1.33 ± 0.14 during training and remained increased post-training (1.32 ± 0.12). MG and SOL exhibited increases from 0.97 ± 0.05 to 1.20 ± 0.10 and 1.16 ± 0.08, respectively, during and after training, demonstrating greater engagement of the plantarflexors during

push-off. Similarly, VM increased from 0.98 ± 0.07 to 1.22 ± 0.09, and RF from 0.98 ± 0.06 to 1.27 ± 0.11.

Discussion

The propulsion-facilitating mode of the APEX system significantly increased forward propulsion and neuromuscular activation of the paretic limb, demonstrating immediate and sustained improvements in push-off mechanics. These results indicate that phase-specific belt-speed modulation during late stance effectively re-engages underactive plantarflexors and knee extensors, promoting active contribution to forward propulsion.

Images (Optional)

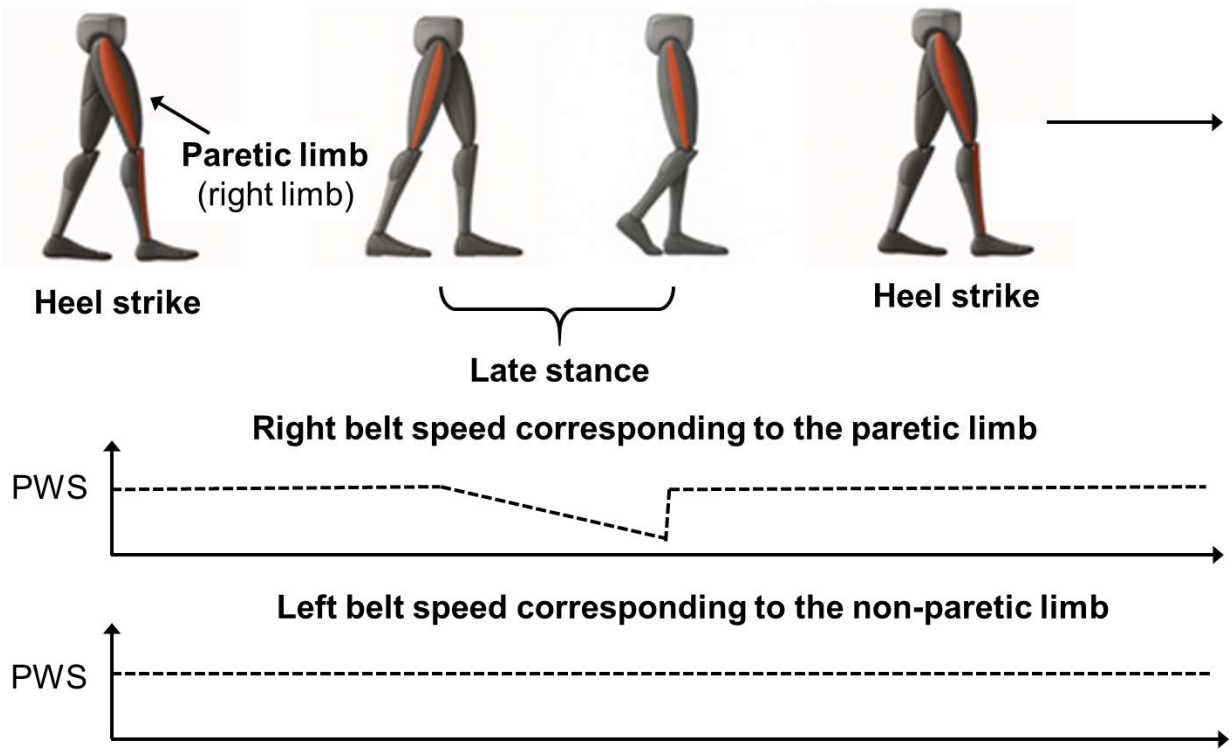


Fig. 1: Phase-specific belt-speed modulation implemented in the propulsion-facilitating mode of the APEX system. The treadmill belt under the paretic limb undergoes transient deceleration during late stance to prolong ground contact and facilitate greater propulsive engagement, followed by restoration to the preferred walking speed (PWS) after toe-off.

References (Optional)

[1] Mark G. Bowden et al., Stroke, 2006

[2] Sarah A. Roelker et al., Gait Posture, 2019

[3] Seoung Hoon Park et al., IEEE Trans Neural Syst Rehabil Eng, 2025

Acknowledgements (Optional)

This work was supported by the Brain Pool Program funded by the Ministry of Science and ICT (MSIT) through the National Research Foundation of Korea under Grant RS-2024-00446461. It was also supported in part by Korea Health Technology Research and Development Project through Korea Health Industry Development Institute (KHIDI) funded by the Ministry of Health and Welfare under Grant HK23C0071, and in part by the National Research Foundation of Korea Grant funded by Korean Government (MSIT) under Grant RS-2023-00208052.

Session Category

Rehabilitation Biomechanics and Human Factors: Rehabilitation

OA111-05

Functional Mobility and User-Defined Goals in Active Individuals with Transfemoral Amputation: A randomized cross-over trial assessing objective and subjective parameters

Dr Victoria Spartacus[1], Dr Marta Da Costa[2], Dr Lisa Gaffino[3], Dr Sandrine Rey[4], Dr Isabelle Loiret[5,6], Ms Laurine Calistri[7]

[1]PROTEOR, 6 rue de la redoute, CS 37833, CEDEX, Dijon, Bourgogne-Franche Comté, France. [2]Physical and Rehabilitation Department, Maubreuil & La Tourmaline, Saint-Herblain, Loire-Atlantique, France. [3]Cliniques du Docteur Ster, Lamalou les Bains, Occitanie, France. [4]Hôpital Léon Bérard, Hyères, Provence-Alpes-Côte d'Azur, France. [5]Centre Louis Pierquin, Institut Régional de Réadaptation de Nancy – UGECAM Nord-Est, Nancy, Grand-Est, France. [6]Université de Lorraine, Nancy, Grand-Est, France. [7]PROTEOR, 6 rue de la redoute, CS 37833, CEDEX, Dijon, Bourgogne - Franche Comté, France

Dr Victoria Spartacus

Dr Marta Da Costa

Dr Lisa Gaffino

Dr Sandrine Rey

Dr Isabelle Loiret

Introduction

Microprocessor-controlled prosthetic knees (MPKs) are prescribed to active individuals with above-knee amputations (AKA), offering advantages such as stumble recovery and adaptability to variable walking speeds. Compared with mechanical knees, MPK users often report improved mobility and quality of life, suggesting benefits that extend to both

physical and psychological well-being [1]. Yet, differences in functional mobility and satisfaction across MPK models remain unclear. Given the variability in environmental demands and individual lifestyles, evaluating multiple MPKs is essential to identify the device that best meets each patient's functional needs and expectations. This study aimed to compare functional mobility, patient-defined outcomes, and quality of life across different MPKs to inform more personalized prosthetic prescription and targeted rehabilitation.

Methods

A randomized crossover trial was conducted in five rehabilitation centers with K3–K4 participants. Each participant used two devices: their usual MPK and the QUATTRO, for at least four weeks before assessment. Objective outcomes were assessed during the 6-Minute Walk Test with Loadsol© insoles and goniometers measuring ground reaction forces (GRF) and knee angles, respectively. GRF data were used to compute impulse and step symmetry. Subjective outcomes included the Patient-Specific Functional Scale (PSFS), where participants rated 2–3 daily tasks (0–10 scale), and the SF-36 questionnaire to assess quality of life. Wilcoxon tests compared device outcomes.

Results

Seventeen AKA (15 men, 2 women) completed the trial. Usual MPKs included the C-Leg (n=11), Rheo Knee (n=5), and Orion (n=1). No significant differences were observed in step or impulse symmetry, nor in knee angles, between devices. In contrast, PSFS scores were significantly higher with QUATTRO ($p < 0.05$), as were SF-36 physical health component scores ($p < 0.05$).

Discussion

Objective gait metrics did not distinguish between MPK systems, whereas subjective outcomes revealed meaningful differences. Patient-defined goals and perceived quality of life appear more sensitive to inter-device differences than standardized gait analyses. However, it remains essential to monitor biomechanical parameters to ensure that emphasizing subjective outcomes does not compromise gait performance or safety. A patient-centered approach combining gait assessment with user-reported outcomes is recommended to guide prosthetic prescription, ensuring optimal functional performance and long-term satisfaction.

Images (Optional)

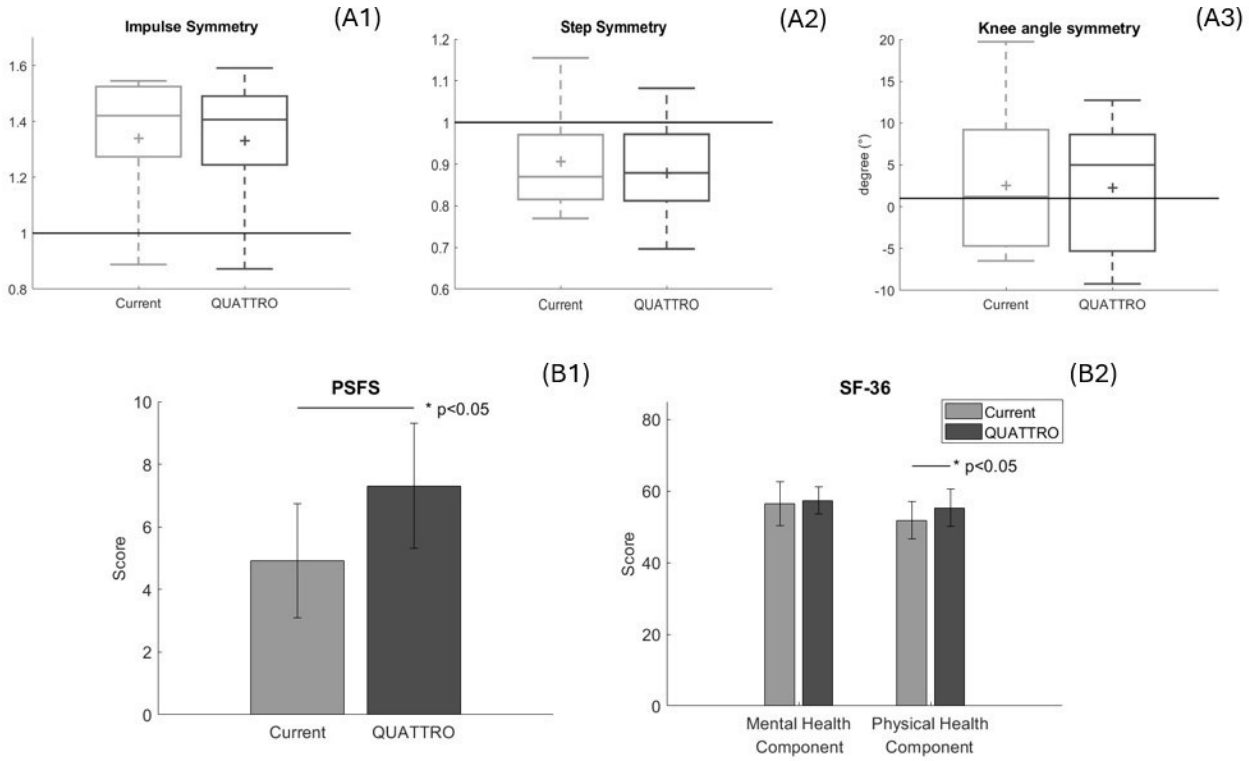


Figure 1: (A1-3): Objective outcomes: impulse, step and knee angle symmetry.
A value of 1 (line) represents perfect symmetry
(B1-2): Subjective outcomes: score on daily life activities (PSFS) and on perceived quality of life (SF-36)

References (Optional)

[1] Kaufman et al., Gait & Posture, 2007

Session Category

Rehabilitation Biomechanics and Human Factors: Rehabilitation

OA113-02

High Dietary Phosphate and Simulated Microgravity Affect Bone Mechanical Integrity in a Spaceflight Animal Model

Ms. Alejandra Correa-Belloso Ph.D. (c)[1], Ms. McKinley Van Klei M.A.Sc. (c)[1], Ms. Emily G. Cameron Ph.D. (c)[1], Mr. Phoenix Hsuen[2], Mr. Eric B. P. Fernandes[3], Ms. Trisha Singh[3], Mr. Daniel Wang[3], Mr. A. Eduard Popescu[3], Mr. Heshanth Rasalingam[3], Ms. Emilie C. Ward[3], Dr. Elahe Alizadeh[4], Dr. Mandy E. Turner[5,6], Dr. Michael A. Adams[3], Dr. Rachel M. Holden[7,3], Dr. Heidi Ploeg[1]

[1]Dept. of Mechanical and Materials Engineering, Queen's University, Kingston, Ontario, Canada. [2]Faculty of Health Sciences, Queen's University, Kingston, Ontario, Canada. [3]Dept. of Biomedical and Molecular Sciences, Queen's University, Kingston, Ontario, Canada. [4]Translational Institute of Medicine, Department of Medicine, Queen's University, Kingston, Ontario, Canada. [5]Brigham and Women's Hospital, Center for Interdisciplinary Cardiovascular Sciences, Boston, Massachusetts, United States. [6]Harvard Medical School, Boston, Massachusetts, United States. [7]Dept. of Medicine, Queen's University, Kingston, Ontario, Canada

Introduction

During spaceflight, astronauts experience 1-2% bone mass loss per month, resulting in increased risks of fractures and osteoporosis. High amounts of inorganic phosphate additives are very common in processed foods (40-70% of top-selling grocery items) and may be linked to bone demineralization. As a result, astronauts consume 3-4x higher amounts of phosphate than recommended [1] and yet, the impact of this excess on microgravity-induced bone loss is unknown. The purpose of this study was to explore the impact of dietary phosphate in accelerating bone weakening using a rat model for simulating microgravity.

Methods

Twenty-five female Sprague-Dawley rats were subjected to a 3-week (n=5-6/group, n=3 baseline controls), 2×2 design combining dietary normal (NP) or high-phosphate (HP), with ambulatory (AMB) or hindlimb unloading (HLU) conditions (Figure-A). Bone volume, material, and structural properties of rat tibias were obtained *ex vivo* via 4-point-bending mechanical tests (Figure-B). Left tibias were scanned using micro-computed tomography (μCT; 50kV, 75ms with 1440 projections) prior to mechanical testing. The tibias were preconditioned and loaded 3 times within the elastic region before inducing structural failure. Bone volume and second moment of area of each specimen were measured from

reconstructed µCT images (10µm voxel-size). A 2×2 factorial Aligned-Rank-Transform, followed by post-hoc tests, were used to assess statistical significance (α=0.05).

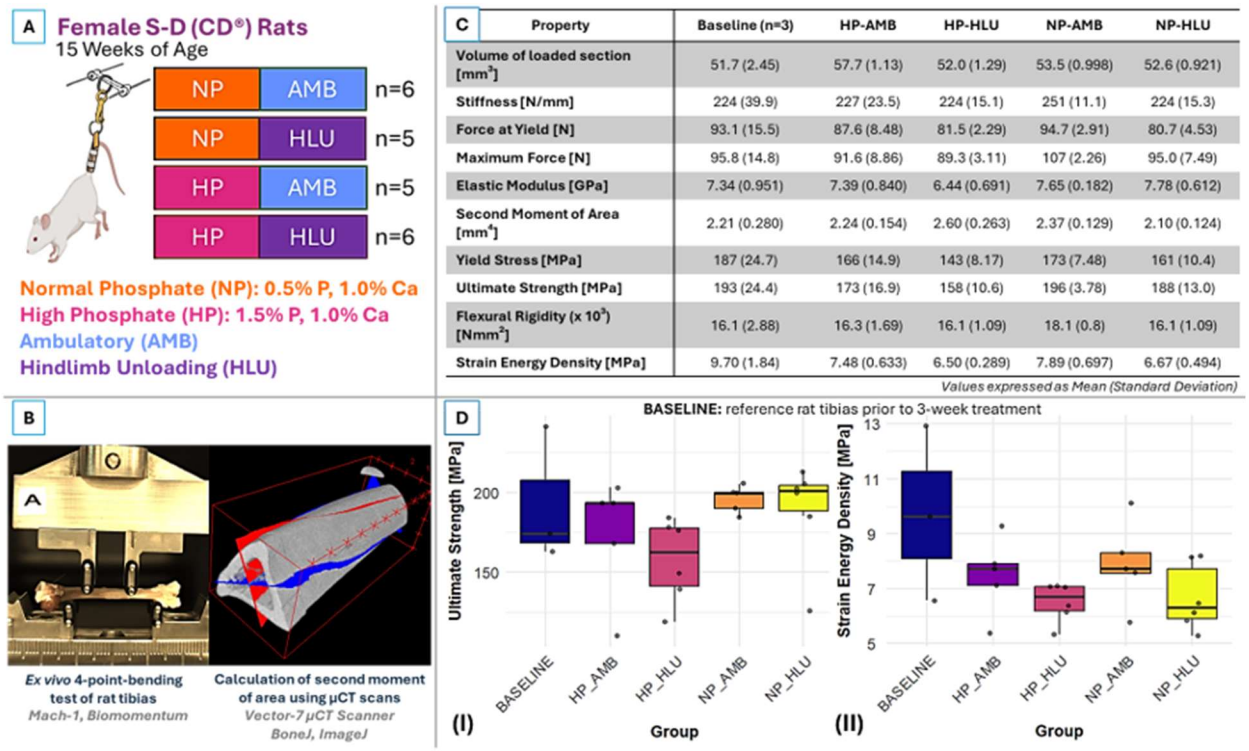
Results

Bone volume, material, and structural properties were summarized (Figure-C). The HP diet groups showed 14.8% lower ultimate strength when compared to NP (p=0.006, Figure-D-I). HLU groups had both 11.7% and 15.4% lower force-at-yield and strain energy density (p=0.028 and 0.041), respectively, than AMB (Figure-D-II). No statistically significant interactions between diet and HLU effects were found.

Discussion

Our main findings suggest that **(1)** diet significantly impacts bone mechanical properties, confirming high dietary phosphate negatively affects bone strength and functional integrity, and **(2)** HLU negatively impacts energy-to-yield, indicating that under non-loading conditions, bone stores less energy before permanent deformation. Combined, these results highlight significant risks when considering the recommencement of normal bone loading of female astronauts returning to Earth following exposure to microgravity. Future work will include morphological analyses of bone and sex-specific responses.

Images (Optional)



References (Optional)

[1] S.M. Smith *et al.*, Space Science, 2009

Session Category

Musculoskeletal Biomechanics: Tissues

OA113-03

A 3D Perspective on Morphological Changes in Cortical Bone of the Femur from Growth to Ageing

Dr Julie Kim, Dr Conrad Werkhoven, Dr Julie Choisne, Professor Thor Besier

University of Auckland, Auckland Central, Auckland, New Zealand

Introduction

Bone adapts throughout life, but understanding of this lifelong dynamism is limited by sparse 2D measurements, small cohorts, and demographic under-representation, especially of paediatric groups [1].

This study addresses this knowledge gap by developing 3D statistical shape models of the femur based on a large, demographically stratified population, offering a comprehensive view of morphology integrated with cortical thickness.

Methods

Right femurs were segmented from CT scans of 996 individuals (460 females, aged 4 – 89 years). To achieve intersubject nodal correspondence, a template mesh was fitted to each segmented femur, and all meshes were aligned to their anatomical axes to remove positional variations. Diaphyseal endosteal surfaces were constructed using an automated cortical thickness calculation method [2].

Principal component analysis was performed on periosteal and endosteal meshes to generate a mean model for each age group (Figure 1). Moment of inertia - a metric of bending resistance, and the ratio of its minimum to maximum values - a biomechanical shape index, were computed along the diaphysis.

Results

During growth (4 – 18 years), the diaphysis showed increases in cross-sectional size and cortical thickening, with the greatest changes along the linea aspera. These growth-related changes produced a more asymmetrical shape around the mid-diaphysis and greater anterior–posterior bending rigidity.

With ageing (20 – 89 years), cross-sectional enlargement continued but mainly on the medial and lateral sides. Cortical thinning appeared, prominently along the linea aspera and anterior regions. These parallel changes led to a more symmetrical shape and shifted the direction of maximum moment of inertia towards the medial–lateral axis.

Discussion

Cortical thickness variation was more dominant near muscle attachment sites. Cross-sectional enlargement remained active into ageing on the medial and lateral sides, where higher stresses concentrate during walking or standing. Transitions between symmetrical and asymmetrical cross-sections - also seen in modern compared to pre-industrial populations [3] - was noted. Together, these findings suggest that alterations in mechanical loading could underlie lifespan-related morphological adaptations, and the model can support further numerical studies of form–function relationships.

Images (Optional)

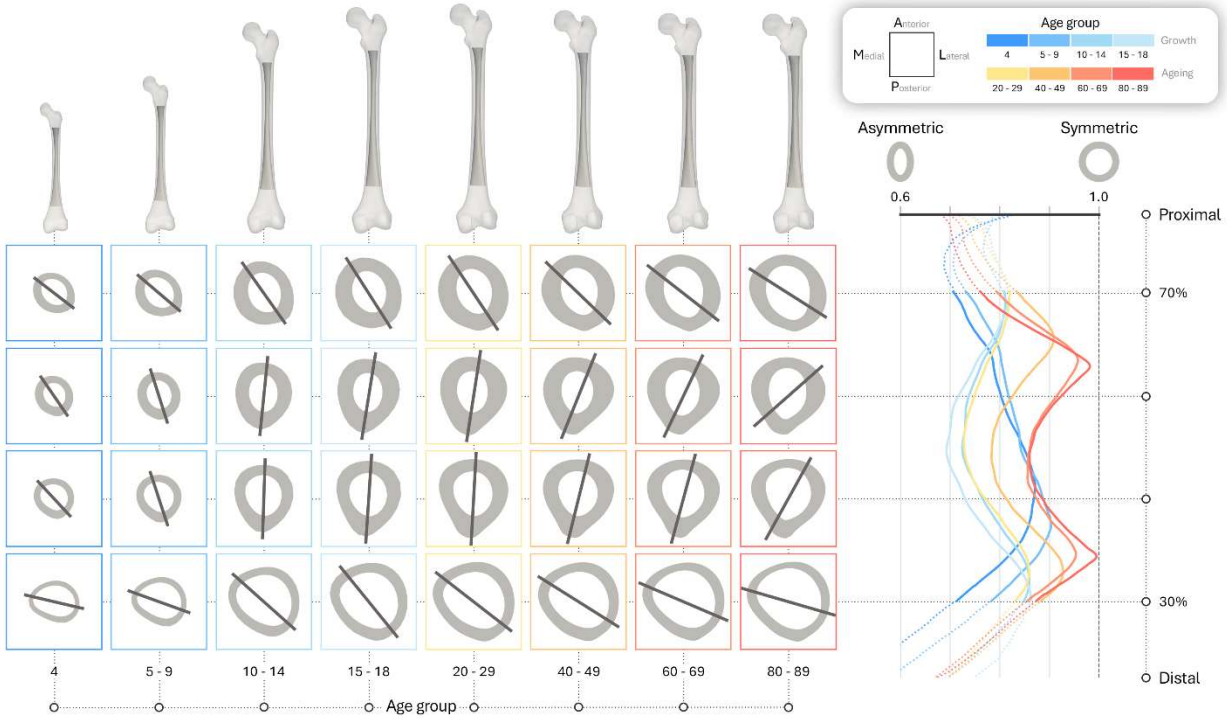


Figure 1. Top row shows 3D mean femoral models for each age group, and below are their cortical bone cross-sections (grey) with the direction of maximum moment of inertia (black line) at 30–70% of total length. Right is the shape index based on moment of inertia computed along the diaphysis (20–80% of total length), with colored curves representing age groups as shown in the legend.

References (Optional)

1. Szabo *et al.*, J Mech Behav Biomed Mater, 2022
2. Kim *et al.*, J Biomechanics, 2025
3. Ruff *et al.*, Am J Phys Anthropol, 1983

Acknowledgements (Optional)

Funding has been awarded to the project through the Ministry of Business, Innovation and Employment's Catalyst Strategic Fund.

Session Category

Musculoskeletal Biomechanics: Tissues

OA113-04

A New Perspective on Cartilage Biology: 3D Characterisation of Chondrocyte Morphology and Organisation Across Postnatal Development.

Ms. Karin Vancíková[1], Ms. Sarah Moore[1], Dr. Nidal S Khatib[2], Dr. Maria Pierantoni[3], Ms. Margot C Labberté[1], Dr. Shashidhara Marathe[4], Prof Hanna Isaksson[3], Prof Pieter AJ Brama[1], Prof Niamh C Nowlan[1]

[1]University College Dublin, Dublin 4, Dublin, Ireland. [2]Queen Mary University of London, London, England, United Kingdom. [3]Lund University, Lund, Skåne, Sweden. [4]Diamond Light Source, Oxfordshire, England, United Kingdom

Introduction

Articular cartilage is a specialised tissue maintained by chondrocytes. While early postnatal cartilage contains densely packed, disorganised cells, mature cartilage exhibits a highly ordered zonal architecture [1]. However, how this zonal structure emerges during postnatal maturation remains poorly understood, largely due to limitations in 2D histology. To address this gap, we used synchrotron-based phase-contrast tomography to visualise and quantify chondrocyte organisation and properties across multiple postnatal stages, enabling depth-resolved characterisation of cartilage maturation and providing a developmental reference to inform regenerative strategies.

Methods

Goat osteochondral cores (4 mm) were collected post-mortem from the second phalanx of Saanen goats, under approval from UCD's Animal Research Ethics Committee (AREC-21-22). Samples from seven developmental stages (neonate to adult, n = 5–6 per group) were imaged at the Diamond Light Source, beamline I139 (UK; pixel resolution = 1.625 µm). Data were reconstructed (with SAVU), followed by machine-learning-based cell segmentation and analyses (Fiji, Matlab).

Results

Neonatal and 6-week cartilage contained high cell numbers and larger chondrocytes in comparison to the more mature stage, with a layered distribution marked with two peaks in chondrocyte volumes through the depth (Fig.1a, b) and cells oriented predominantly perpendicularly to obliquely to the articular surface (Fig.1c). By 6 months, cell volume and number variation was reduced compared with the earlier organisation. A stratification emerged by 12 months, with increased mid-zone cell volume, higher cell numbers near the

surface, decreased deep-zone volume and a shift in cell orientation toward a zonal pattern, with surface-perpendicular and deep-parallel alignment to the surface (Fig. 1c, d). In the adult stage, this organisation was fully established.

Discussion

This work demonstrates the postnatal transformation of cartilage from a hypercellular, layered immature tissue into a zonally organised, mechanically specialised structure. In early development, cartilage displayed a three-layer organisation with distinct depth-dependent changes in volume and count, which diminished in 6 months. Zonal architecture became established by 12 months and fully matured in adulthood. These 3D analyses reveal organisational features not observable in 2D histology and provide a depth-resolved developmental reference essential for understanding cartilage maturation and guiding regenerative medicine approaches.

Images (Optional)

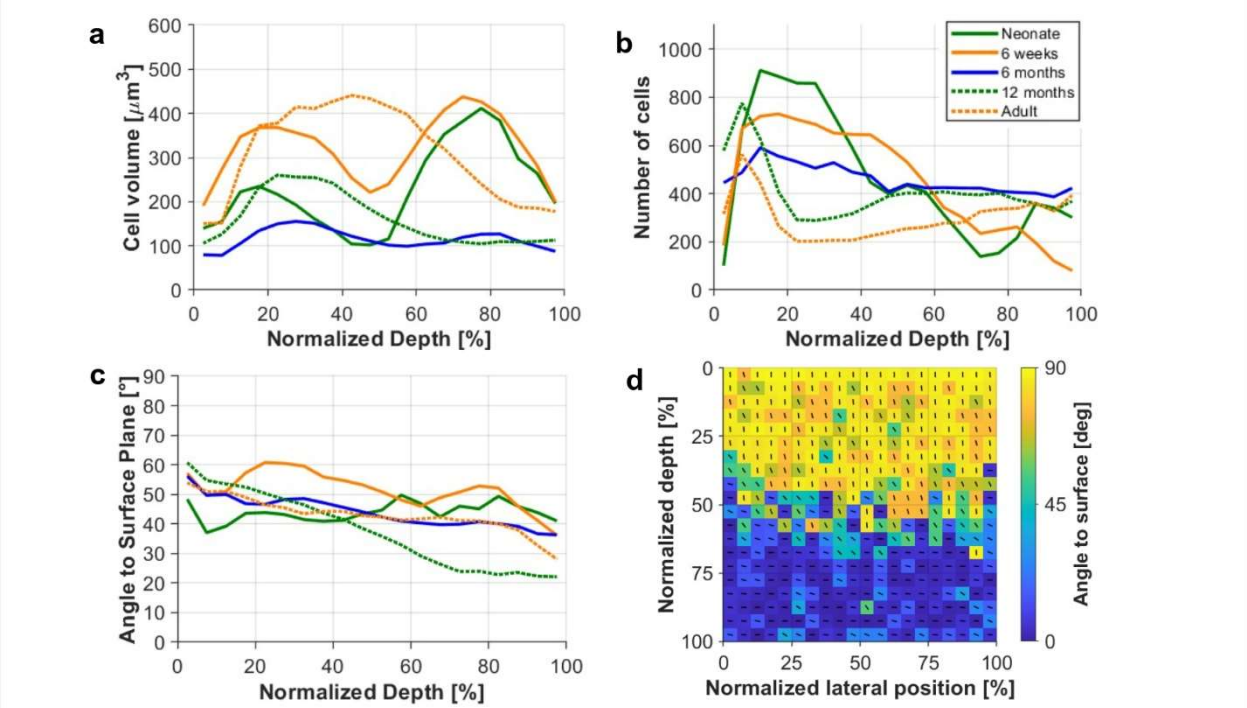


Figure 1 Chondrocyte organization transitioned from a layered, highly cellular structure in early stages to a zonally organized, orientation-aligned architecture in maturity. Shown are depth-wise profiles of cell volume (a), number (b), and orientation (c) with (d) heatmap illustrating orientation at 12 months, along normalized depth (0–100%) from the cartilage surface to the calcified front.

References (Optional)

[1] Rebekah S Decker et al. ,Dev. Biol, 2017

Acknowledgements (Optional)

Funding: Research Ireland (21/FFP-A/9090); Diamond Light Source (I13-2, MG31326).

Session Category

Musculoskeletal Biomechanics: Tissues

OA113-05

In Vivo Mechanical Loading Induces Site-Specific, Partially Reversible Tissue Adaptation in Vertebrae

Licensed Pharmacist Cosima Erhard PhD Student[1,2], Dipl.-Ing. Tobias Thiele[1,2], Dr. med. Lukas Schönnagel Resident Physician[1,3], PD Dr. rer. nat. Katharina Schmidt-Bleek PI[1,2], Dr. Melih Özgür Celik[4], Univ.-Prof. Dr.-Ing. Georg Duda PI[1,2,3]

[1]Julius Wolff Institute, Berlin Institute of Health at Charité, Berlin, Berlin, Germany. [2]BIH Center for Regenerative Therapies, Charité, Berlin, Berlin, Germany. [3]Center for Muskuloskeletal Surgery, Charité, Berlin, Berlin, Germany. [4]Department of Anesthesiology and Intensive Care Medicine Campus Benjamin Franklin, Charité, Berlin, Berlin, Germany

Introduction

The role of mechanical loading in spinal adaptation eventually resulting in spinal degeneration is not fully understood. Clinically, many patients associate back pain with mechanical overloading while therapeutic strategies often focus on correcting for structural changes in the spine [1]. While load-induced bone remodeling via osteoblasts and osteoclasts is well characterized in long bones, this study investigates whether mouse caudal vertebrae also respond to defined mechanical loading with structural changes, and whether these changes are reversible following load cessation [2].

Methods

Female C57BL/6 (n= 49, 11 weeks old) mice underwent mechanical loading applied via clinical grade titanium pins inserted into caudal vertebrae 5 and 7, allowing for axial cyclic compression (10 Hz, 5 min/session, 3×/week over four weeks). The sham control only underwent pinning without loading. This was followed by four weeks of non-loading. For quantification, longitudinal in vivo micro-CT (µCT; MILabs U-CT xuhr) scans were performed. Image registration and post-processing were conducted using a semi-automated workflow (Xploraytion GmbH). µCT data were compared with histological stainings, including a quantification of collagen organization and vascular structures.

Results

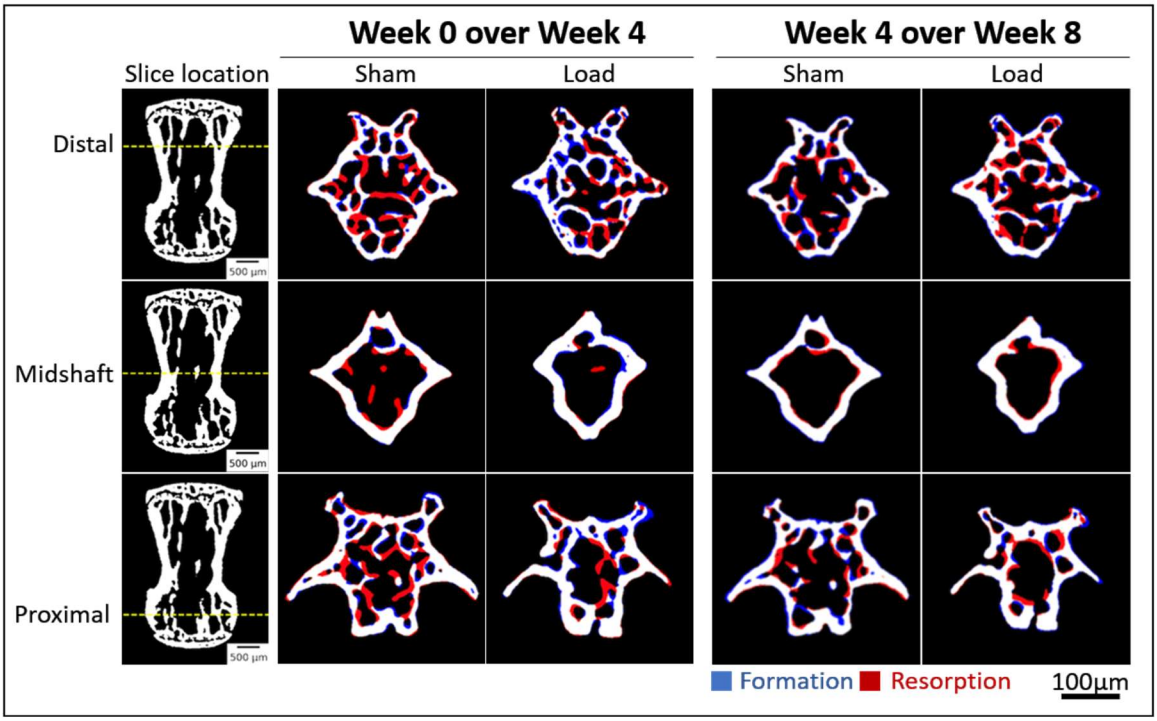
µCT imaging revealed distinct, region-specific bone adaptations in response to loading. Bone formation (blue) increased especially in the endplate regions, while bone resorption (red) was reduced in the loaded compared to the sham group (Fig. 1). In the midshaft area, characterized by less trabecular bone, fewer structural changes were observed. Some of

the adaptations persisted even during non-loading, suggesting only a partial reversibility of bony adaptations. Histology showed a pronounced vascular ingrowth in the endplates and the presence of osteoprogenitor cells in regions with pronounced bone formation.

Discussion

These results show that caudal vertebrae adapt to mechanical loading in a site-specific manner, with endplates being particularly responsive. These structural changes were only partially reversible after load cessation, pointing to time- and location-dependent remodeling behavior. Our future work will focus on the detailed effects at the endplates and the associated angiogenesis. Finally, our findings have to be benchmarked against patient data from clinical scenarios of vertebral overloading.

Images (Optional)



References (Optional)

[1] Vlaeyen et al, Nat Rev Dis Primers, 2018.

[2] Birkhold et al, Bone, 2014.

Session Category

Musculoskeletal Biomechanics: Tissues

OA114-02

Engineering Aortic Valves via Transdifferentiating Fibroblasts Into Valvular Endothelial Cells Without Using Viruses or IPS Cells

Professor Junwei Chen, Professor Fuxiang Wei, Dr. Peng Tang, PhD Candidate Xinyu Zhang, PhD Candidate Chenyang Ji, PhD Candidate Xinman Chen, PhD Candidate Anqi Wang, PhD Candidate Wuhuang Liu

Huazhong University of Science and Technology, Wuhan, Hubei, China

Introduction

Valve replacement is the primary treatment for end-stage valvular heart disease (VHD), with hundreds of thousands of surgeries annually worldwide[1,2]. Existing bioprosthetic/mechanical valves lack growth/regeneration, challenging pediatric patients, making tissue-engineered valves an urgent need[3]. Induced pluripotent stem cells (iPSCs) offer cell replacement potential but carry tumorigenic risks and require pluripotent intermediates. The key challenge is generating valvular endothelial cells (VECs) efficiently without pluripotent states or viruses.

Methods

Mouse embryonic fibroblasts (NIH/3T3) and human primary dermal fibroblasts (HDF) were used. Transdifferentiation combined soluble factors (5-azacytidine, BMP4, VEGF, etc.) and PDMS10 (2.1 MPa, mimicking native aortic valve stiffness). Cells were seeded on PGG-crosslinked decellularized porcine valves. Assays included flow cytometry (CD31/CD144), immunofluorescence, Western blotting, DiI-Ac-LDL uptake, tube formation, teratoma formation, and ChIP-qPCR (H3K9me3, RNA polymerase Ⅱ at Flk1/CD31/CD144 promoters). In vivo validation in nude rats used Doppler ultrasonography, histology, and coagulation tests. Statistics: Student's t-test, ANOVA, Bonferroni correction.

Results

PDMS10 optimized transdifferentiation: ~70% mouse iAECs and 10% human hiVECs were $CD31^{+}CD144^{+}$ pre-sorting, reaching 95%-97% purity post-seeding. ChIP-qPCR showed lowest H3K9me3 and highest RNA polymerase Ⅱ binding at endothelial gene promoters in PDMS10 groups. iAECs/hiVECs expressed VEC markers (NFATC1, Flk1) without pluripotency markers, functionally matching native VECs. Engineered valves functioned

intact for 60 days in rats (no thrombosis/teratomas), while iPSC-derived cells had 40%-80% teratoma risk.

Discussion

This study achieved virus/iPSC-free transdifferentiation of fibroblasts into functional VECs via soluble factors and PDMS10. Core mechanism: PDMS10 reduces H3K9me3, relieving endothelial gene suppression to enhance efficiency and purity. It overcomes iPSC tumorigenic risks and viral safety concerns, offering autologous valves for pediatric patients. Limitations: non-xeno-free media, lower human cell efficiency, unclear H3K9me3 downstream mechanisms. Future work: develop xeno-free systems, optimize human transdifferentiation, and validate in large animals.differentiation, and validate clinical translational value in large animal models.

References (Optional)

[1] M. H. Yacoub *et al.*, Nat. Clin. Pract. Cardiovasc. Med, 2005

[2] J. L. d'Arcy *et al.*, Heart, 2011

[3] E. S. Fioretta *et al.*, Nat. Rev. Cardiol, 2021

Acknowledgements (Optional)

This work was supported by National Natural Science Foundation of China grants (12422212,32071306,11902121) (JC)

Session Category

Cell Biomechanics: Mechanobiology

OA114-03

Substrate Convexity Induces Nuclear Flattening That Triggers Phenotype Marker Expression Change in Vascular Smooth Muscle Cells

Mr. Yuga Isobe PhD student[1], Mr. Takuya Nishina[1], Mr. Yudai Ishida[2], Ms. Tomoe Kamiya[2], Prof. Ryo Sudo Pfrofessor[1,2], Prof. Tadahiro Yamashita Associate Professor[1,2]

[1]School of Integrated Design Engineering, Keio University, Yokohama, Kanagawa, Japan. [2]Department of Systems Design Engineering, Keio University, Yokohama, Kanagawa, Japan

Introduction

Numerous studies in mechanobiology have revealed that the geometrical constraints in two-dimensions are transduced to biochemical signalling . Recently, the biological significance of curved surfaces at a scale equivalent to or larger than that of cells (microcurvatures) has been revealed [1]; such microcurvatures indeed change cellular protein expression and even differentiation. However, the mechanism by which the substrate curvature influences protein expression remains to be elucidated. We here hypothesise that nuclear deformation, known to mediate cellular response to geometrical inputs in two-dimentsions [2], also facilitates curvature-dependent protein expressions.

Methods

To test hypothesis, we cultured vascular smooth muscle cells (VSMCs) on substrates containing hemispherical convexes with radii spanning from 50 to 500 μm for 72h. The dependency of the expression levels of αSMA, a marker of VSMCs in the contractile phenotype, on the substrate curvature was examined by immunofluorescence and confocal microscopy. Next, we inhibited expression of nesprin1, which transmits cytoskeletal forces to the nucleus, using siRNA. Additionally, the cells were externally compressed by placing an agarose pad onto the top of the cells to test the contribution of nuclear deformation to curvature-dependent protein expression. Based on the stack of confocal images, nuclear sphericity index (NSI) representing the roundness of nuclear morphology was calculated (FigureA). The correlation between NSI and αSMA expression levels at a single cell level was examined.

Results

Elevated αSMA was observed on the convex surfaces rather than on the flat surface. αSMA expression increased as the curvature radius increased from 50 to 500 μm (FigureB).

Nesprin1 inhibition rounded the nucleus and decreased the αSMA expression, whereas the external compression flattened the nucleus and increased the αSMA expression. Overall, a moderate negative correlation between NSI and αSMA expression was observed regardless of the curvature of substrate (*R*=0.42, FigureC).

Discussion

Our results suggest that nuclear deformation is the key mediator that transduces substrate curvature to the phenotype marker expression, possibly via well-known nuclear mechanotransduction pathways [2] Our study provides fundamental knowledge on cellular geometry sensing; it may contribute to the cutting-edge biomaterials design with growing structural complexity .

Images (Optional)

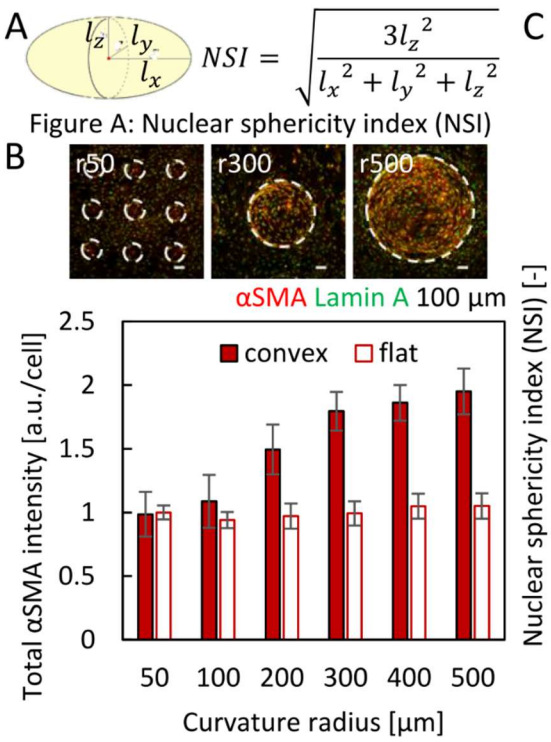


Figure A: Nuclear sphericity index (NSI)

Figure B: αSMA expression of VSMCs on convex surface, *N*=3, *n*=30, Mean ± 95%CI

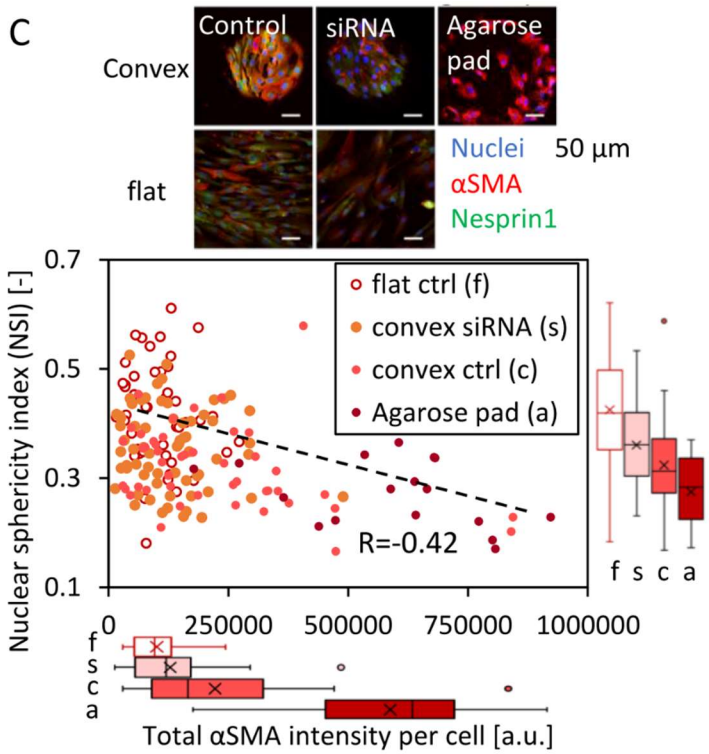


Figure C: Correlation of αSMA expression and NSI, *N*=3, 17≦*n*≦65

References (Optional)

[1] Callens *et al.*, Biomaterials, 2020

[2] Kalukula *et al.*, Nat. Rev. Mol. Cell. Bio., 2022

Acknowledgements (Optional)

This work was funded by KAKENHI grants (21K18041, 23H04089 and 24K03252) from Japan Society for the Promotion of Science.

Session Category

Cell Biomechanics: Mechanobiology

OA114-04

In Vitro Validation of an Implantable 3D Microengineered Tumor Model for Investigating Fibrosis Remodelling-Associated Drug Response

Ms. Giada Mainieri[1], Dr. Chiara Martinelli[1], Dr. Claudio Conci[1], Dr. Alberto Bocconi[1], Mr. Leonardo Cherubin[1], Mr. Marco Vigneri[1], Dr. Rebeca Martinez Vázquez[2], Prof. Giulio Cerullo[2], Prof. Roberto Osellame[3], Prof. Manuela T. Raimondi[1]

[1]Department of Chemistry, Material and Chemical Engineering "Giulio Natta" Politecnico di Milano, Milan, Lombardy, Italy. [2]Department of Physics, Politecnico di Milano, Milan, Lombardy, Italy. [3]Institute of Photonics and Nanotechnologies (IFN)-CNR, Milan, Lombardy, Italy

Introduction

Fibrotic remodelling alters the biomechanical properties in the tumor microenvironment, mainly due to increased collagen deposition, representing one of the main barriers to anticancer drug penetration into solid tumors [1]. To better understand and modulate these mechanisms, we developed an innovative approach combining a mechanically controlled 3D breast cancer microenvironment capable of reproducing a gradient in fibrosis, upon implantation in chick embryo chorioallantoic membrane (CAM), to provide a predictive model of chemotherapeutic drug efficacy.

Methods

Microscaffolds were fabricated by Two-Photon Polymerization (SZ2080) with different pore sizes, in which tumor cell lines MDA-MB-231, HCC1937 and BT-474 were locally seeded thanks to a 3D-printed stencil preventing surrounding substrate adhesion. In 2D, protein expression was analyzed by Western-blotting while toxicity to Doxorubicin was evaluated by metabolic assays. Fitting the acquired fluorescence data of Doxorubicin with one-phase exponential model ($F(t)=F_{max}(1 - e^{-kt})$) provided the drug release kinetic constant (k), subsequently used to estimate the Diffusion coefficient (D) in MDA-MB-231 in 2D and 3D.

Results

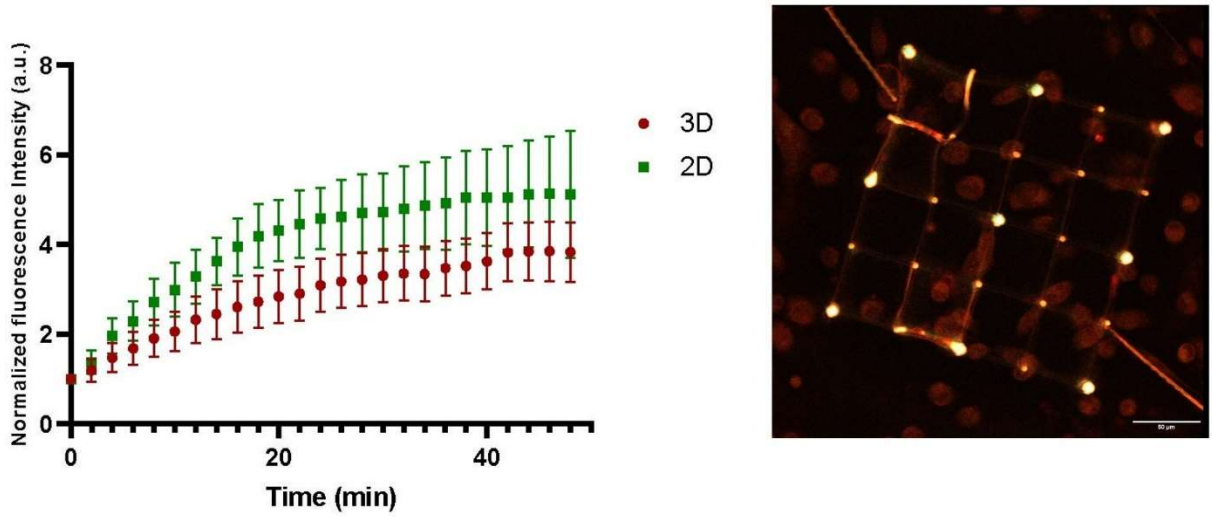
Tumor cell lines showed increased proliferation over time in both 2D and 3D. Preliminary protein expression results confirmed the mesenchymal phenotype of MDA-MB-231 (N-cadherin) and the epithelial phenotype in HCC1937 and BT-474 (E-cadherin). The in vitro half-maximal inhibitory concentration (IC_{50}) of Doxorubicin on controls was ~ 0.28 µM (MDA-MB-231), 0,72 µM (HCC1937), 4,95 µM (BT-474). Prior to in vivo administration,

Doxorubicin diffusion was assessed in vitro. In 2D, diffusion rate $k \approx 0.094\ min^{-1}$ yielded a diffusion coefficient of $D \approx 8 \times 10^{-14}\ m^2/s$. In 3D, the k value decreased from 0.122 to 0.062 min^{-1} inversely to scaffold height from $D \approx 1.9 \times 10^{-13}$ to $6.7 \times 10^{-13}\ m^2/s$.

Discussion

Our 3D microenvironments with optimized pore dimensions enabled cell adhesion and sustained proliferation over time, confirming their suitability for in vitro tumor cell culturing. Following implantation in the CAM chicken embryo, upon administration of antitumor drugs in combination with the antifibrotic compounds, non-linear optical microscopy combined with Raman spectroscopy will allow evaluation of collagen remodelling and correlation between drug penetration and fibrotic capsule modulation. [2]

Images (Optional)



Panel: (a) Normalized fluorescence intensity of Doxorubicin in MDA-MB-231 cells, in 2D and 3D, as a readout of drug diffusion. (b) Lifetime imaging by Confocal microscopy to monitor autofluorescence signal of Doxorubicin (λ_{em} =575 nm) in MDA-MB-231 cells embedded in the microscaffold.

References (Optional)

[1] Moradi F. et al., "WIREs Mech Dis, 2025"

[2] Lee M. et al., "Intravital , 2015"

Acknowledgements (Optional)

ERC-BEACONSANDEGG,G.A.101053122

Session Category

Cell Biomechanics: Mechanobiology

OA114-05

The Role of Focal Adhesion Kinase in ACL Fibroblast Response to Slow Stretch Elongation Depends on Degree of Hierarchical Fiber Formation

Ms. Kelly Ott, Dr. Jennifer Puetzer

Virginia Commonwealth University, Richmond, VA, United States

Introduction

Hierarchically-organized collagen fibers strengthen tendons and ligaments but don't regenerate after injury. Previously, we developed a static system that guides cells to form hierarchical collagen fibers over 6 weeks[1] and found that addition of slow stretch at neonatal and postnatal ACL growth-rates drives further maturation.[2] However, effects of stretch changed with collagen organization, suggesting shifts in mechanotransduction.[2] Slow stretch is key in fiber maturation but difficult to replicate in adult tissue, so understanding relevant mechanotransduction pathways could help improve fiber regeneration after injury. Cells on aligned fibrils primarily sense tensile-loads via focal adhesions and focal adhesion kinase (FAK), but how they sense once larger fibers and fascicles form is unknown. This study evaluates the role of FAK in cellular sensing of slow stretch at different degrees of collagen organization.

Methods

Neonatal bovine ACL fibroblasts were mixed with collagen to form constructs at 20mg/ml collagen and $5x10^6$cells/ml[1] and cultured statically for 0, 2, or 4 weeks to obtain unorganized collagen, aligned collagen fibrils, or fibers, respectively. After, they were transferred to a tensile bioreactor and stretched at neonatal (1mm/day) or postnatal (0.1mm/day) ACL growth-rates for 1 week (Fig.1A).[2] FAK was inhibited with 10μM PF-228[3] (FAK-I) during stretch (Fig.1A). Controls were statically clamped throughout culture or dosed with DMSO during stretch. Post-culture, collagen organization, composition, and tensile strength were analyzed.[1] Data are mean±SEM.

Results

Loading increased collagen organization and mechanical properties at all timepoints (Fig.1). FAK-I reduced organization, DNA, GAG, collagen turnover, and tissue strength in unorganized collagen (Fig.1, 1wk data) but had little effect once aligned fibrils formed (Fig.1, 3wk data). FAK-I once fibers formed increased collagen organization and concentration for both stretch-rates and tensile strength with neonatal (Fig.1, 5wk data).

Discussion

FAK-I blocked stretch-driven improvements in unorganized collagen, but had little effect once fibrils had formed. Further, FAK-I improved organization and mechanics with stretch applied once fibers formed. This suggests FAK is an important mechanosensor during fibril formation, but other mechanosensors dominate cellular response to slow stretch at higher levels of collagen organization. Understanding these mechanosensors could help stimulate collagen repair after injury.

Images (Optional)

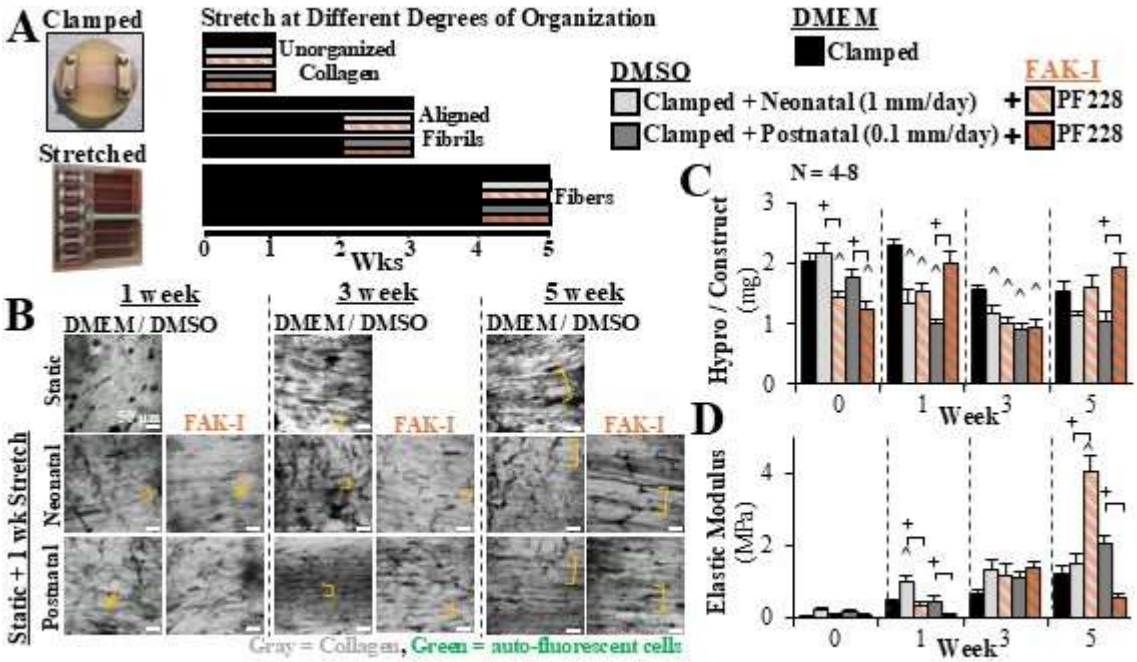


Fig 1: A) Experimental setup, B) Collagen organization with FAK-I, scale bar = 50 μm, C) collagen (hypro) content per construct, and D) tensile elastic modulus. Statistics performed by 2-way ANOVA with Tukey's post-hoc ($p<0.05$). Significance to ^clamped constructs at same timepoint or + bracket

References (Optional)

1.Puetzer+*Biomat* 2021; 2.Ott+*TERMIS* 2024; 3.Rajshankar+*J Cell Physiol* 2020

Session Category

Cell Biomechanics: Mechanobiology

OA115-02

Sensitivity of Frictional Interactions During Mechanical Thrombectomy: In Silico and In Vitro Investigations

Dr. Mahesh S. Nagargoje[1], Ms. Demitria Poulos[2], Ms. Virginia Fregona[3], Dr. Giulia Luraghi[3], Prof. Francesco Migliavacca[3], Dr. Bryan Good[2], Prof. Jose Felix Rodriguez Matas[3]

[1]Politecnico di Milano, Milan, Lombardy, Italy. [2]University of Tennessee Knoxville, Knoxville, Tennessee, United States. [3]Politecnico di Milano, Milan, Lombardia, Italy

Introduction

Mechanical thrombectomy (MT) has revolutionised the treatment of Acute Ischemic Stroke; however, procedural failures persist due to device–vessel friction, catheter navigation difficulties, and uncertainties in clot–device interaction mechanics [1]. Stent compression, catheter kinking, and navigation resistance are strongly influenced by vessel tortuosity and frictional forces, yet current in silico models lack validated friction coefficients and realistic catheter-tracking mechanics. This work investigates the sensitivity of frictional interactions during SR retrieval and catheter navigation, combining benchtop experiments with virtual mechanical thrombectomy (VMT) simulations in flexible vessels.

Methods

A benchtop circulatory loop was developed using a silicone ICA/MCA phantom to study SR retrieval and Aspiration thrombectomy. A Solitaire X 6×40 mm SR was deployed via a Phenom 21 microcatheter and retrieved at 2 mm/s using a programmable syringe pump. Catheter navigation tests were performed by advancing microcatheters (Plato 27B) and aspiration catheters (Sofia Plus) through tortuous pathways. Navigation resistance and catheter bending/kinking behavior were recorded.

VMT simulations were developed for the same model used for in vitro experiments. SRs were modeled with shape-memory alloy beam elements; catheters were modeled as linear orthotropic structures calibrated using experimental bending tests. Simulations reproduced crimping, deployment, retrieval, and catheter pushing in flexible vessels using finite element modeling [2]. Quantitative comparisons of stent compression, catheter path, and retrieval forces were made between experiments and simulations.

Results

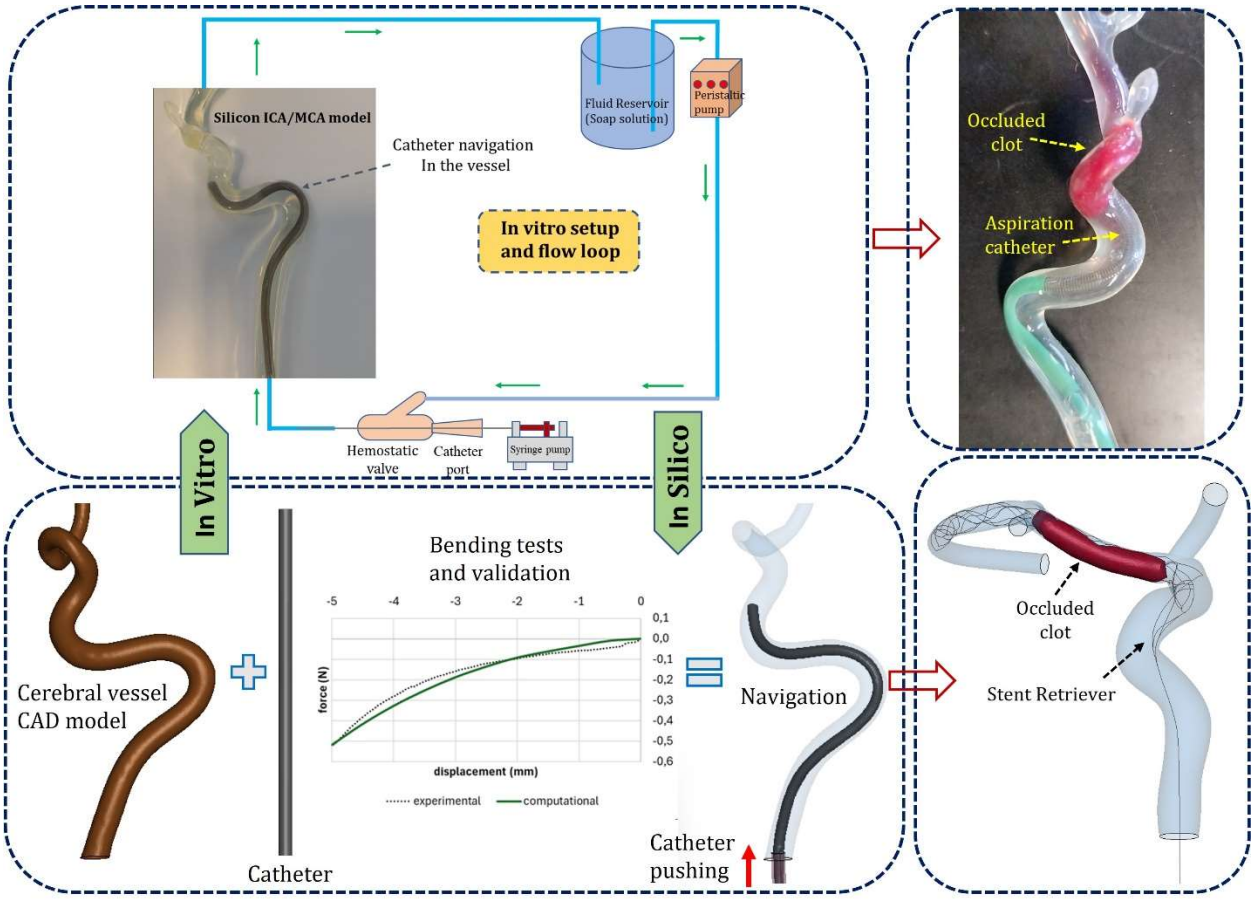
High-friction conditions increased SR compression, clot fragmentation, and retrieval resistance, particularly in curved MCA regions. Lubrication reduced SR deformation and

improved clot entrapment. Catheter navigation experiments and simulations showed significantly increased resistance, kinking, and vessel traction in acutely curved vessels. Flexible-vessel MT accurately reproduced experimental catheter paths and failure modes.

Discussion

The combined analysis demonstrates that friction critically affects both SR mechanics and catheter navigability. Accurate friction modeling and flexible-vessel simulations are essential for predicting MT success, understanding failure pathways, and guiding next-generation device design. This work provides a validated framework for realistic in silico thrombectomy and catheter navigation modeling to support surgical planning and future in silico clinical trials.

Images (Optional)



References (Optional)

[1] Nagargoje, M. S., Journal of Biomechanics, 2025.

[2] Nagargoje, M. S., Computer Methods and Programs in Biomedicine, 2025.

Acknowledgements (Optional)

This project has received funding from the European Union's Horizon 2020 research and innovation program under the Marie Sklodowska-Curie grant agreement No. 101104493.

Session Category

Cardiovascular/Cardiorespiratory Biomechanics: Materials and Devices

OA115-03

Modelling Mechanical Thrombectomy in Silico: A Validation Study

MSc Virginia Fregona[1], PhD Giulia Luraghi[1], MSc Ciaran Gillespie[2], PhD Shahd Horie[2], PhD Ray McCarthy[2], PhD Jose Felix Rodriguez Matas[1], PhD Francesco Migliavacca[1,3]

[1]Dept. of Chemistry, Materials and Chemical Engineering, Politecnico di Milano, Milan, Lombardy, Italy. [2]J&J MedTech Neurovascular, Galway, County Galway, Ireland. [3]Fondazione IRCCS Cà Granda Ospedale Maggiore Policlinico, Milan, Lombardy, Italy

Introduction

Mechanical Thrombectomy (MT), a minimally invasive treatment for acute ischemic stroke, aims to remove a clot from a large cerebral vessel using stent-retrievers and/or aspiration catheters. To investigate key aspects of this procedure (e.g. effect of devices, clot mechanical properties [1] or vessel morphology [2]), Finite Element Analysis (FEA) can be employed. This work aims to validate the MT FE analyses by comparing them with in vitro MTs performed using the three techniques: stent-retriever, aspiration, and combined approach.

Methods

A silicone anatomical model of the cerebral vasculature, with physiological pressures and flow rates, was used to perform the experiments with twelve different combinations of techniques (three), devices (two stent-retrievers and two aspiration catheters) and clot compositions (two: 5% and 30% RBCs, ovine clot analogues [3]). The four devices used in the tests were mechanically characterised and then modelled in silico. Finally, FE analyses were generated to reproduce each of the twelve experiments, mimicking the in vitro procedure as closely as possible. Each in vitro – in silico pair was compared in terms of success or failure of clot removal and qualitatively in terms of clot fragmentation and device-clot kinematics.

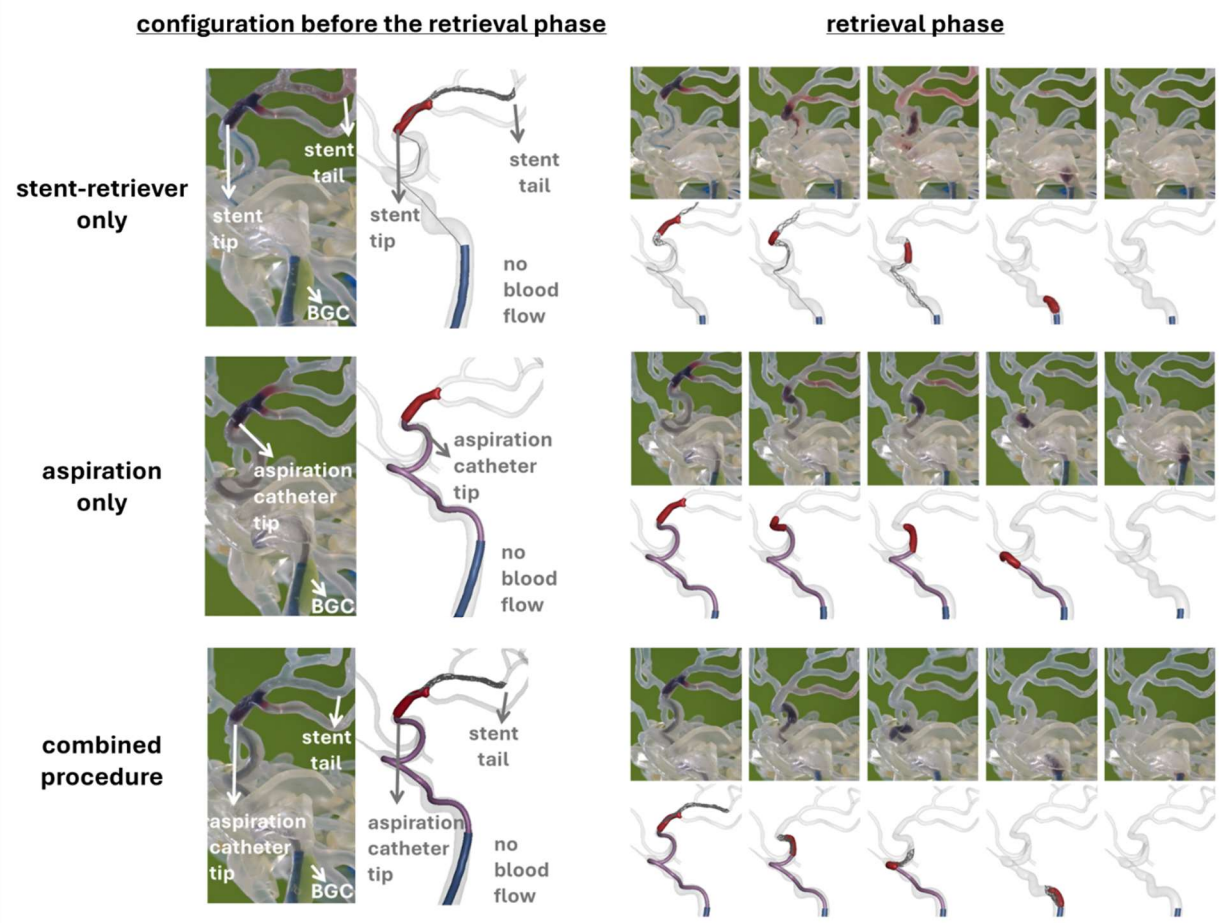
Results

Eight MTs could be reproduced with structural simulations, whereas four would require fluid-structure interaction to model aspiration and combined procedure in the presence of highly fragmentable clots (30% RBCs). All eight structural simulations reproduced the in vitro outcome, and half of them also showed a matching kinematic. One representative example per MT technique is shown in the attached figure.

Discussion

This study demonstrates that FE analyses can, in general, replicate the identified quantities of interest (namely, thrombus removal and fragmentation). However, further work is needed to model MTs in condition where purely structural simulations fail. Overall, this validation provides a foundation for an applicability analysis of MT FE analyses in clinical contexts.

Images (Optional)



References (Optional)

[1] Fregona *et al.*, J. Mech. Behav. Biomed. Mater., 2025

[2] Bridio *et al.*, Front. Med. Technol., 2021

[3] Johnson *et al.*, Ann. Biomed. Eng., 2021

Acknowledgements (Optional)

This project has received funding from the European Union's Horizon Europe research and innovation programme under the grant agreement No 101136438.

Session Category

Cardiovascular/Cardiorespiratory Biomechanics: Materials and Devices

OA115-04

Effect of Stent Retriever Behavior on Clot Removal Success During Mechanical Thrombectomy

Ms. Demitria Poulos[1], Dr. Michael Froehler[2], Dr. Bryan Good[1]

[1]University of Tennessee, Knoxville, TN, United States. [2]Vanderbilt University Medical Center, Nashville, TN, United States

Introduction

Stent retriever mechanical thrombectomy (SR MT) is an endovascular therapy to remove a thrombus from an occluded vessel causing a stroke. The first pass effect (FPE), a measure of complete revascularization with a single SR pass, is only achieved in 27% of patients. MT proves to be more complex when the occlusion occurs in tortuous anatomies, strongly influencing the rate of FPE.

Methods

A circulatory flow loop with a tortuous ICA/MCA arterial model was developed. Each curve of the model was separated into distal, center, and proximal regions to track SR deformation. Control MTs, tests without clots, were first performed to investigate SR collapse in the arterial model. Next, 50% hematocrit clots were injected into the flow loop and lodged downstream in the arterial model. Benchtop MTs were then performed (**Fig. 1A**) with both Solitaire (4x15, 4x40, 6x40 mm) and EmboTrap (5x22, 5x37 mm) commercial SRs.

Results

Control tests proved that the center and proximal regions of all SRs experienced the most collapse around a curve, while the distal segment remained generally expanded during retrieval. Overall, 30 MTs were performed with 50% hematocrit clots and SR stretching was found to negatively impact MT outcomes (i.e. failed FPE) in 13 cases. FPE was achieved in 60% of cases with the 4x40 SR and only 20% of cases with the 6x40 SR. Shorter SRs (4x15, 5x22 mm) resulted in similar FPE rates (**Fig. 1B**).

Discussion

Sufficient SR-clot integration is a key factor for successful thrombus removal with MT. Without EAs present, SR collapse was observed and varied across devices sizes, limiting the possibility for SR-clot integration. However, we suspect the expansion of the distal portion of longer SRs assists in the clot removal process despite the collapse. We hypothesize that lower rates of FPE are observed with the 6 mm SR due to SR overlap, caused by deployment of a 6 mm device within a 3 mm diameter tubing. Future studies will

continue to investigate FPE in more realistic arterial models and with clots of varying composition and mechanical properties.

Images (Optional)

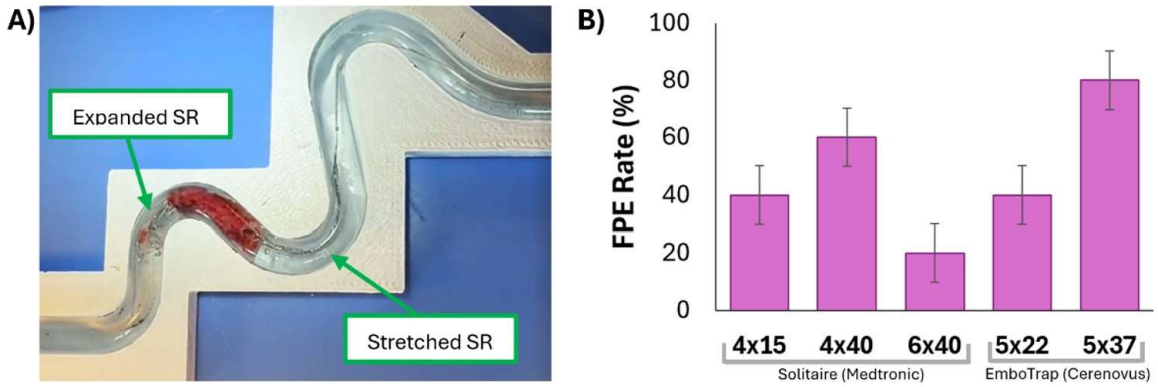


Figure 1: A) Image highlighting blood clot retrieval with a Solitaire 4x40mm SR. **B)** Comparison of FPE rates (%) across SRs.

Session Category

Cardiovascular/Cardiorespiratory Biomechanics: Materials and Devices

OA115-05

How Histopathological Determinants Shape Viscoelastic Mechanical Properties of Thrombi in Acute Ischemic Stroke

Mr. Luca Bontempi[1,2], Ms. Janneke Cruts[1], Dr. Rachel Cahalane[1,3], Dr. Nikki Boodt[1], Dr. Daniel Bos[1], Dr. Behrooz Fereidoonnezhad[2], Mr. Pieter Jan van Doormaal[1], Prof. Aad van der Lugt[1], Prof. Diederik Dippel[1], Prof. Frank Gijsen[1,2]

[1]Erasmus MC, University Medical Center, Rotterdam, South Holland, Netherlands. [2]Delft University of Technology, Delft, South Holland, Netherlands. [3]University of Limerick, Limerick, Limerick, Ireland

Introduction

Cerebral thrombus mechanical properties influence endovascular thrombectomy (EVT) success in acute ischemic stroke (AIS). Understanding the relationship between thrombus mechanics and composition is essential to predict thrombus–device interactions. [1] While in vitro thrombus analogues are well characterized, ex vivo cerebral thrombi remain poorly described. [2] This study provides the first characterization of AIS thrombus viscoelastic mechanical properties and identifies the histopathological determinants of stiffness, softening, and energy dissipation in thrombi retrieved during EVT.

Methods

Thrombi retrieved from 73 EVT-treated patients were sectioned for mechanical testing and processed for histology within six hours (Fig.1A). Unconfined quasi-static compression tests using a custom-built device measured bulk low- and high-strain stiffness (10% and 75%-strain secant moduli), softening (stiffness variation between first and last cycle), and dissipation (strain-normalized hysteresis area). [3] A total of 346 sections (median per patient=6.5) were compressed to 80% strain for 20 cycles, at a strain rate of 10%. Histology quantified RBCs, fibrin and platelets. Linear mixed-effects regression first examined associations among mechanical properties, then assessed histological determinants.

Results

Median patient-averaged thrombus stiffness was 0.779 kPa (IQR 0.289–1.663), softening 0.897 (0.821–0.970), and dissipation 0.333 kPa (0.072–1.086). Stiffness correlated positively with dissipation (β=0.162, 95% CI 0.084; 0.240), while softening correlated negatively with dissipation (β=–0.008, 95%CI –0.013; –0.003).

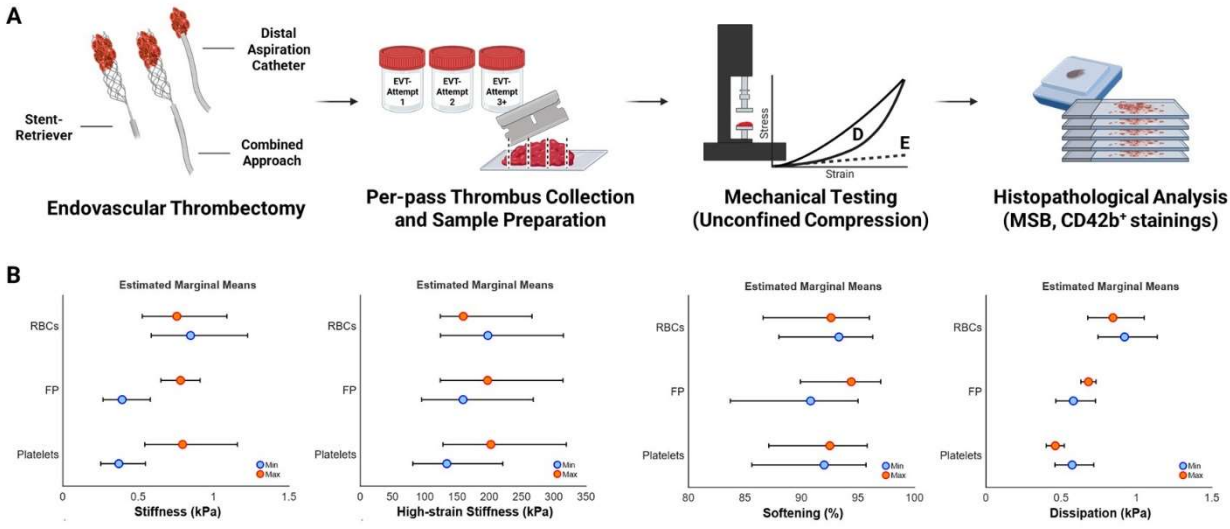
Thrombus stiffness was positively associated with platelets (β=0.008, 95%CI 0.004;0.012) and negatively with RBC content (β=–0.008, 95%CI –0.012;–0.005). Fibrin showed a positive

trend with softening (β=0.021, 95%CI −0.001;0.044). Dissipation was negatively associated with RBCs content (β=–0.007, 95%CI –0.011;–0.003). Fig.1B shows the marginal effects from the regressions.

Discussion

Stiffer thrombi, enriched in platelets and fibrin and depleted in RBCs, dissipate more energy per cycle, while softer thrombi, RBC-rich, progressively lose stiffness during cyclic loading and thus might be more prone to fragment. These findings underscore the relevance of thrombus mechanical properties and composition for EVT, as mechanical variability may create distinct procedural challenges requiring tailored retrieval strategies and may inform device design and intervention planning.

Images (Optional)



References (Optional)

[1] R.Cahalane *et al.*, J Biomech, 2021

[2] N.Boodt *et al.*, Stroke, 2021.

[3] R.Cahalane *et al.*, Ann Biomed Eng, 2023.

Acknowledgements (Optional)

LB, BF, and FG are supported by GEMINI, funded by the European Union's Horizon Europe research and innovation programme under grant agreement No. 101136438.

Session Category

Cardiovascular/Cardiorespiratory Biomechanics: Materials and Devices

OA116-02

Impact of a Humanoid Robot-Assisted, Space-Themed, Physical Activity Program

Ms Georgia Roula Kouvoutsakis[1], Ms. Martha Spanou[2], Mr. Konstantinos Soutos[3], Dr. Sofoklis Sotiriou[3], Dr. Foteini Venetsanou[2], Dr. Konstantinos Karydis[1], Dr. Elena Kokkoni[1]

[1]University of California, Riverside, Riverside, California, United States. [2]National & Kapodistrian University of Athens, Athens, Attica, Greece. [3]Ellinogermaniki Agogi, Athens, Attica, Greece

Introduction

Sedentary behavior in children, caused by factors like prolonged screen time, critically reduces opportunities and motivation for physical activity (PA) with negative effects (e.g., risk for obesity) persisting into adulthood [1]. Incorporating thematic elements in children's PA, such as NASA's "Train Like an Astronaut" (TLA) challenge, leverages children's curiosity to strengthen health knowledge and stimulate PA interest [2]. Further, socially assistive robots may capture children's attention, motivating participation in movement-based educational activities [3]. This work assesses the feasibility of a robot-assisted program that integrates motivational space-themed activities and the social appeal of a humanoid with the aim of increasing PA engagement and enjoyment, and attenuating perceived exertion compared to traditional instruction.

Methods

The cohort comprised 136 children (10–11 years old) recruited from physical education classes for a 6-week program involving two 20-minute sessions weekly. The program was integrated into an ongoing long-term STEM intervention, "Stories of Tomorrow" (focused on organizing a Mars mission and colony [4]). Participants were randomly assigned to the Human-Robot (HR) experimental group, where the robot NAO provided primary instructions supported by the instructor, or the Human-Only (HO) control group, where sessions were solely instructor-led. Both groups were engaged in high-intensity interval training exercises (e.g., plank, quadruped crawl), adapted from NASA's TLA challenge and modified to maintain participant interest. Activity was recorded via Fitbit trackers. The Physical Activity Enjoyment Scale quantified PA enjoyment every other session, while the Dalhousie Dyspnea and Perceived Exertion Scales measured perceived exertion immediately post-session. Participants' knowledge of human space exploration and health behaviors was surveyed pre- and post-study.

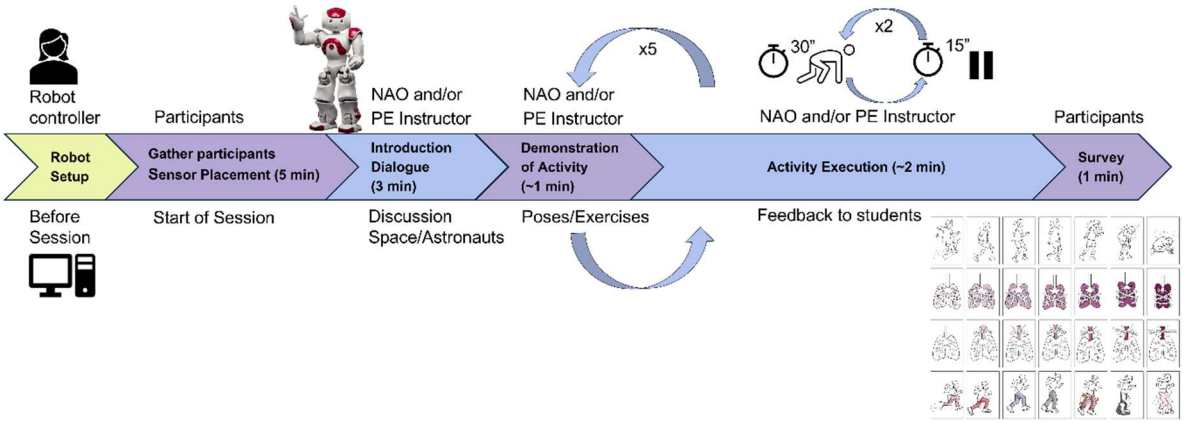
Results

All participants completed the sessions, attempting each exercise. Preliminary analysis supports high enjoyment scores (HO:4.4±0.90, HR:4.0±1.16), declining perceived exertion over time (HO:-38.4%, HR:-20.5%), and low baseline knowledge score (2.98±1.60).

Discussion

This study confirms the program's feasibility, with ongoing analysis assessing post-study knowledge acquisition and between-group differences.

Images (Optional)



References (Optional)

[1] Hills et al., Br. J. Sports Med., 2011

[2] Min et al., Am. J. Health Promot., 2018

[3] Papadopoulos et al., Computers & Education, 2020

[4] Bogner and Sotiriou, CSCI Conference, 2018

Acknowledgements (Optional)

This work was supported by the NASA California Space Grant Consortium (CaSGC) Fellowship, 2024.

Session Category

Biomechanics Education, Knowledge Translation and Outreach: N/A

OA116-03

Cardiovascular Biomechanics Workshop for High School Students

Dr. Fanette Chassagne[1], Dr. Raphaëlle Jarrige[2], Ms. Lina Abssi[2], Mr. Simon Fontaine[2], Dr. Baptiste Pierrat[1]

[1]Mines Saint-Etienne, Sainbiose INSERM U1059, Saint-Etienne, Loire, France. [2]Mines Saint-Etienne, Saint-Etienne, Loire, France

Introduction

Explora (https://explora.saint-etienne.fr/discover-explora/) is a dedicated center for scientific outreach located in Saint-Étienne, France. It is managed by La Rotonde, the Center for Scientific, Technical and Industrial Culture of Mines Saint-Étienne. A few years ago, Explora launched the "Research Workshop" program, specifically designed to give high school students direct exposure to the processes and realities of scientific research. Each two-hour workshop ensures maximum student engagement through active participation and includes a dedicated discussion with a professional researcher.

Methods

The workshop, defined in collaboration with scientific outreach specialists, focused on the biomechanics of abdominal aortic aneurysms and was designed to maximize student autonomy. Following a pilot test with one student group (approx. 25 students), feedback was used to refine the format. The final version was successfully implemented for nine student cohorts, engaging approximately 250 students in total.

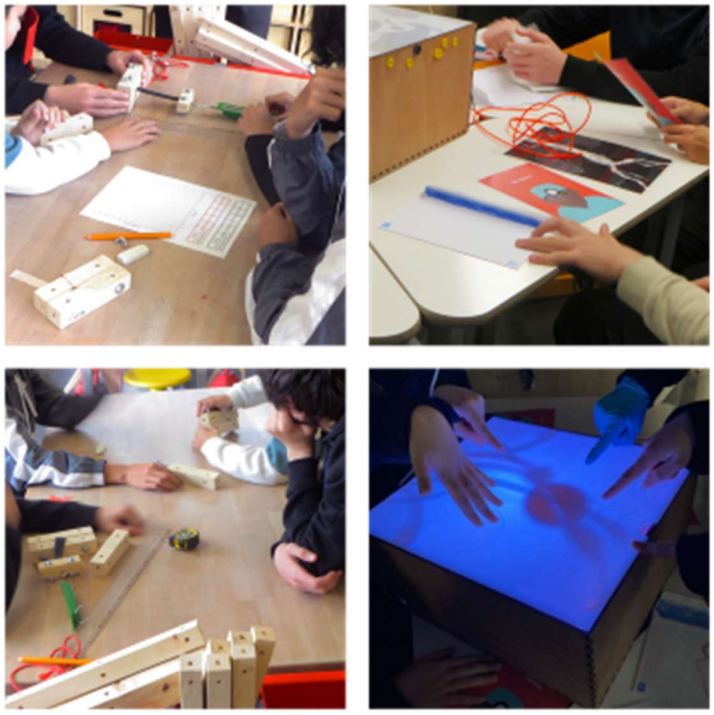
Results

The final two-hour workshop was structured into four interactive parts. It began with an introduction using a phone-based quiz on the cardiovascular system and aneurysms. Next, during hands-on mechanical characterization, students designed improvised tensile testing devices with common tools (ruler, luggage scale, ...) to obtain force-displacement curves for materials like rubber gloves and inner tubes, comparing their results to data for human aortic tissue. The third phase focused on clinical application, where a researcher demonstrated endovascular aneurysm repair using a surgical simulator. Students then participated in a role-play, manipulating their own simulators with fake catheters and X-ray tools to experience the surgical challenges. The workshop concluded with an open Q&A with the researcher and the opportunity for students to manipulate preserved porcine aorta.

Discussion

The workshop achieved a high level of student engagement, evidenced by their demonstrated curiosity and enthusiasm for the interactive components. The design effectively integrated hands-on mechanics, clinical simulation, and direct researcher interaction. Future projects will concentrate on adapting this effective model for delivery directly within classrooms.

Images (Optional)



Session Category

Biomechanics Education, Knowledge Translation and Outreach: N/A

OA117-01

Stance-Phase Kinematic Biomarkers Differentiate Total Knee Replacement From Conservative Management in Women With Moderate Knee Osteoarthritis

Ms Mayra Alejandra Loayza-Saldaña[1], Dr. Simone Tassani[1], Dr. Laura Tío[2], Dr. Jordi Monfort[2,3], Dr. Gil Serrancolí[4,5], Dr. Gemma Piella[1], Dr. Jérôme Noailly[1]

[1]Universitat Pompeu Fabra, Barcelona, Barcelona, Spain. [2]Hospital del Mar, Research Institute, Inflammation and Cartilage Research Group, Barcelona, Barcelona, Spain. [3]Hospital del Mar, Rheumatology Service, Barcelona, Barcelona, Spain. [4]Simulation and Movement Analysis Lab, Universitat Politècnica de Catalunya, Barcelona, Barcelona, Spain. [5]Institut de Robòtica i Informàtica Industrial (CSIC-UPC), Barcelona, Barcelona, Spain

Introduction

Total knee replacement (TKR) is the primary treatment for knee osteoarthritis (KOA) with severe symptoms, yet decision-making is influenced by subjective judgment. Long-term outcomes for 10-34% of patients are unclear, prompting the need for objective patient stratification. This study aimed to identify biomechanical descriptors differentiating TKR-scheduled from conservatively managed KOA patients and to examine their association with patient-reported outcomes.

Methods

Sixty-six women (27 TKR, 39 conservative) with moderate KOA (Kellgren–Lawrence grades 2-3) underwent gait analysis. Participants were classified by age, body mass index and treatment at baseline. The effect of these factors on joint kinematics was assessed across three stance sub-phases (loading response (t1), mid-stance (t2), and terminal stance (t3)) using repeated-measures multifactorial MANOVA. Stance-phase kinematic changes (D = t3 -t1) were analyzed using Random Forest models with nested cross-validation and exhaustive feature selection, and their associations with clinical variables were examined through logistic regression. Clinical construct consistency was assessed against the Osteoarthritis Initiative dataset.

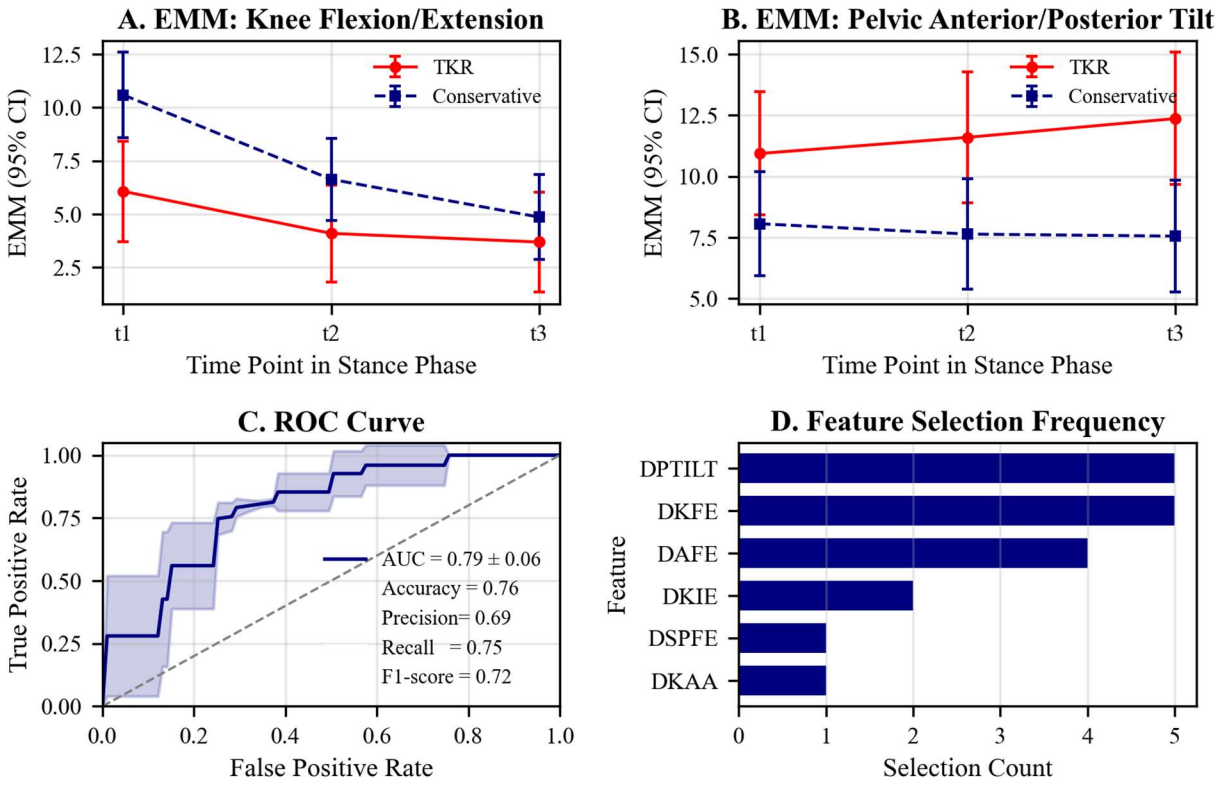
Results

MANOVA revealed significant Time × Treatment interactions (p-value = 0.001). The univariate test showed knee flexion-extension (KFE) and pelvis tilt (PTILT) associated with treatment. At initial loading (t1), patients in the conservative group exhibited greater knee flexion angles, whereas the TKR group showed stiffer joints across all three time points (Fig. A). Moreover, the TKR group demonstrated greater pelvic tilt during the stance phase compared to the conservative group (Fig. B). Machine learning achieved mean ROC-AUC of 0.79 and F1-score 0.72 (Fig. C), with DKFE, DPTILT, and DAFE as the most stable predictors (Fig. D). DPTILT predicted functional limitation (AUC 0.71), pain (0.80), and depression (0.73). Clinical construct structure was preserved between datasets, though WOMAC subscales alone yielded poor classification accuracy (<0.70).

Discussion

Stance-phase kinematics differentiate treatment pathways demonstrating that biomechanical features outperform patient-reported outcomes for treatment stratification. Strengths include comprehensive 3D gait analysis with repeated-measures multifactorial MANOVA and rigorous feature selection and hyper-parameter tuning. Limitations comprise the cross-sectional design, and the use of delta features that condense continuous trajectories. Machine learning classifiers using biomechanical sets show promise for supporting decision making, but validation in larger, sex-balanced cohorts and multimodal integration are essential.

Images (Optional)



References (Optional)

Acknowledgements (Optional)

Spanish Government (STRATO-PID2021-126469OB-C21) and European Union and European Research Council (ERC-591 2021-COG-O-Health-101044828).

Session Category

Clinical Biomechanics: N/A

OA117-02

Knee Adduction Moment Is Associated With Acute Cartilage Deformation Following Walking in Adults With Clinical Knee Osteoarthritis

Dr. Erin C.S. Lee PhD[1], Dr. Kendal A. Marriott PhD[1], Dr. Anthony A. Gatti PhD[2], Ms. Natasha K. Ivanochko MSc[1], Dr. Jacquelyn M. Maciukiewicz PhD[1,3], Dr. Lauren Straatman PhD[1], Ms. Emily Wiebenga[1], Dr. Jonathan D. Adachi[4], Dr. Michael D. Noseworthy PhD[4], Mr. Paul W. Stratford MSc[4], Dr. Monica R. Maly PhD[1]

[1]University of Waterloo, Waterloo, ON, Canada. [2]Stanford University, Palo Alto, CA, United States. [3]Waterloo Regional Health Network, Waterloo, ON, Canada. [4]McMaster University, Hamilton, ON, Canada

Introduction

The knee adduction moment (KAM) during walking predicts future cartilage loss in knee osteoarthritis (OA) [1]. However, the validity of the KAM as a proxy for medial knee load has been questioned [2] and there is a lack of data showing how KAM relates to cartilage response *in vivo*. The purpose of this study was to investigate the association between peak KAM and acute cartilage deformation following a standardized walking exposure in adults with clinical knee OA.

Methods

89 adults with clinical knee OA (females/males=59/30, age=65±7 years, BMI=28.9±5.2 kg/m^2) participated. In the first visit, 3D overground walking data were collected with optical motion capture and a synchronized force plate. Peak KAM was averaged over five trials. Approximately one week later, participants underwent magnetic resonance imaging (MRI) before and immediately after a 25-minute walk at a speed standardized to leg length [3]. We computed acute deformation as the mean difference in thickness between the pre- and post-walk scans in the medial and lateral tibia and medial and lateral weight-bearing femur. For each region, regression models determined the association between peak KAM and acute deformation after adjusting for age, sex, BMI, and pre-walk cartilage thickness.

Results

Higher peak KAM, indicating a higher medial-to-lateral load ratio, was associated with greater cartilage deformation (or thickness reduction) in the medial femur (β=-0.21 [-0.39, -0.04], p=0.02). We also observed nonsignificant trends where higher peak KAM tended to

associate with greater deformation in the medial tibia (β=-0.12 [-0.26, 0.02] p=0.08) and less deformation in the lateral tibia (β=0.11 [-0.01, 0.23], p=0.07).

Discussion

Here, we directly link KAM to *in vivo* cartilage deformation in clinical knee OA for the first time. Our findings indicate that tibiofemoral cartilage regions that experience higher loads exhibit greater deformation in adults with clinical knee OA. This deformation likely reflects increased fluid flow to dissipate loading [4]. Future work will investigate whether there is a threshold of excessive deformation that could be a mechanism contributing to cartilage degradation over time.

Images (Optional)

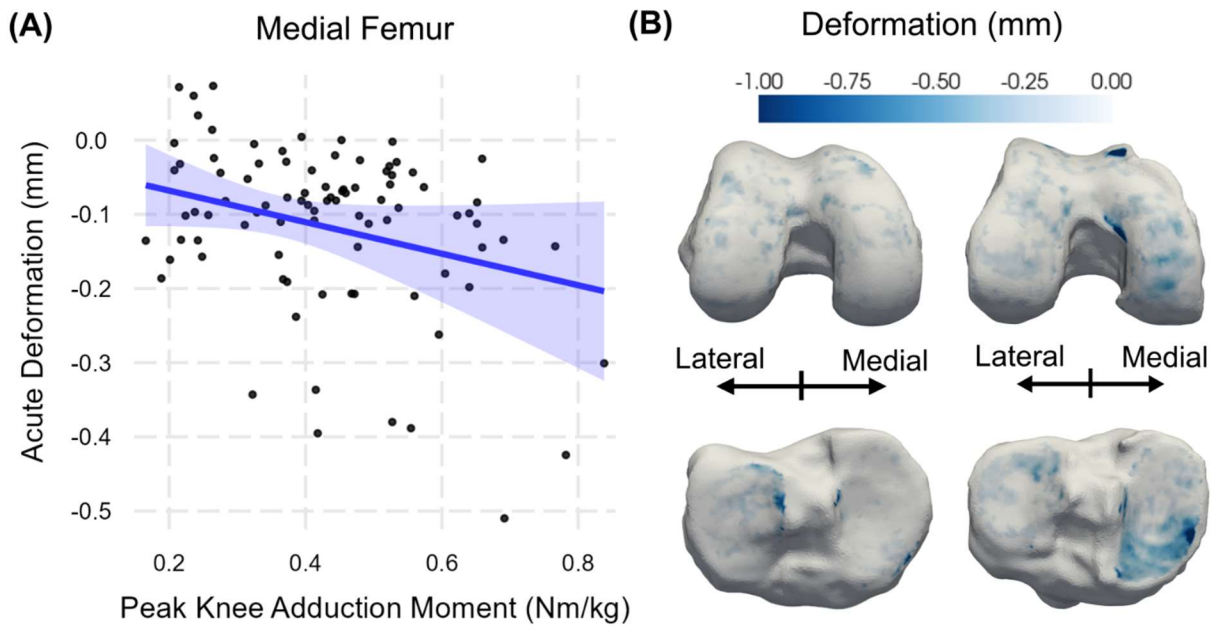


Figure 1: (A) Acute deformation associated with peak KAM in the medial femur. Negative deformation indicates a reduction in cartilage thickness after walking. **(B)** Deformation maps for a participant with low KAM and low deformation (left) and a participant with high KAM and high deformation (right) in the medial femur and tibia.

References (Optional)

[1] Chang, OAC, 2015. [2] Walter, JOR, 2010. [3] Paranjape, Sci Reports, 2018. [4] Eckstein, Anat Embryol, 1999.

Acknowledgements (Optional)

Arthritis Society Canada Training Postdoctoral Fellowships (TPF 24-117, TPF 21-39), Canadian Institutes of Health Research (CIHR) Fellowship, CIHR Project #175169.

Session Category

Clinical Biomechanics: N/A

OA117-03

Cartilage Volume and Composition in Masters Runners With and Without Knee Osteoarthritis: Changes Immediately Following a Run and After a 12-Week Progressive Distance Running Program

Dr. Michael A. Hunt PhD, PT[1], Ms. Michaela C.M. Khan MSc[1], Ms. Natasha M. Krowchuk BSc[1], Dr. Anthony A. Gatti PhD[2], Dr. Alexander Rauscher PhD[1], Dr. Eric C. Sayre PhD[3], Dr. Jean-Francois Esculier PhD, PT[4]

[1]University of British Columbia, Vancouver, BC, Canada. [2]Stanford University, Stanford, CA, United States. [3]BC Centre on Substance Use, Vancouver, BC, Canada. [4]The Running Clinic, Lac Beauport, QC, Canada

Introduction

Recreational running provides significant physical and mental health benefits throughout the lifespan, with the number of masters runners (those aged >35 years) at an all-time high. With the increasing age of the running community comes questions about the appropriateness of running for knee joint health, especially for those with knee osteoarthritis. While there is growing evidence that running is generally not harmful to younger, healthy knees, there are still many questions regarding running with knee osteoarthritis. We aimed to address these gaps by comparing how knee cartilage in masters runners with and without knee osteoarthritis recover from a single run and react to a 12-week progressive distance running program.

Methods

47 runners with (KOA), and 27 control runners without (CON), knee osteoarthritis underwent magnetic resonance imaging of knee cartilage before (Baseline) and after (Follow-up) a 12-week progressive volume running program. We measured changes in cartilage volume and composition (T2 and T1ρ relaxation times) across 8 regions of interest in the tibia, femur, and patella immediately before and after a 30-minute treadmill run at each testing session. Within- and between-group contrasts were examined both within and between testing sessions to assess the immediate and longer-term effects of running on cartilage.

Results

Statistically significant decreases in relaxation times and volumes were observed in most regions of interest immediately following the treadmill run in both groups at both testing

sessions. Relative differences immediately following the runs were modest (T2 < 5%; T1ρ < 11%; volume < 5%). Between-group differences were observed in patellar and lateral tibial volumes at Follow-up, as well as the change in immediate responses when comparing Follow-up and Baseline (greater loss in CON in all comparisons showing a difference).

Discussion

These data indicate that osteoarthritic and non-osteoarthritic cartilage generally respond similarly to a single bout of running and to a running program focused on increasing distance. Our findings suggest that running with knee osteoarthritis does not have deleterious effects on cartilage health, thus providing important and unique information that will inform clinicians and runners in the management of knee symptoms and overall joint health.

Session Category

Clinical Biomechanics: N/A

OA117-04

A Markerless, Autoencoder-Derived Gait Quality Index for Knee Osteoarthritis

Ms. Julia Irvine[1], Mr. Jereme Outerleys[1], Dr. Elise Laende[1,2], Dr. Kevin Deluzio[1]

[1]Queen's University, Kingston, Ontario, Canada. [2]University of Waterloo, Waterloo, Ontario, Canada

Introduction

Radiographic severity and symptom scores in knee osteoarthritis (OA) often fail to reflect the biomechanical contributors to functional decline, despite gait impairment being a central to disability. Traditional gait summary metrics rely on linear dimensionality reduction techniques, which may overlook the nonlinear, multi-joint compensations characteristic of OA. Recent work demonstrated that autoencoders can condense high-dimensional gait data into low-dimensional representations while retaining substantially more information than linear approaches [1]. However, this methodology has not been translated to OA populations or applied with markerless motion capture, which offers a scalable pathway for routine, clinic-ready gait assessment. This study aimed to derive an autoencoder-based markerless gait index for knee OA and evaluate its discriminative ability and association with patient-reported outcomes.

Methods

The study included 294 subjects: 230 with OA (67.3 ± 8.47 years) and 64 asymptomatic controls (58.3 ± 18.6 years). Overground gait kinematics were processed using Theia3D v2023. Seventy gait variables (63 kinematic, 7 spatiotemporal) per subject were extracted and min-max normalized. A two-layer autoencoder was optimized via five-fold cross validation. Principal component analysis (PCA) was applied to the same inputs for comparison, with both methods reducing the data to a single dimension [1]. Feature importance was assessed using a tuned random forest model. The relationship between the resulting gait index and EQ-5D mobility scores were quantified using Spearman correlation.

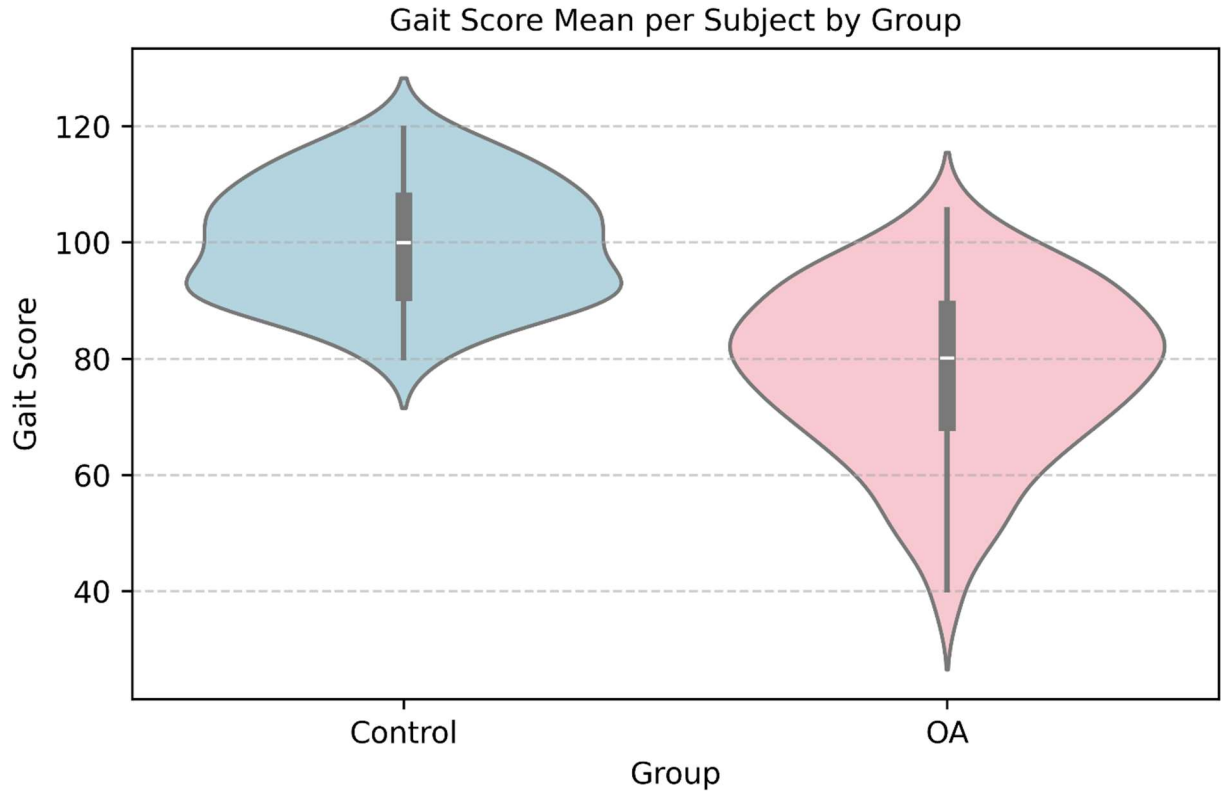
Results

The optimized autoencoder retained 56.0±2.67% of input variance (maximum 58.4%), substantially exceeding PCA's first principal component (22.3%). OA participants exhibited significantly lower gait scores than controls with a very large effect size (Cohen's d=-1.60, $p<0.0001$). Scores correlated strongly with EQ-5D mobility (Spearman's $\rho=-0.614$; $p<0.0001$). Top contributing features included mean foot-progression angle during stance, maximum knee flexion, and hip-adduction range.

Discussion

A markerless, autoencoder-derived single-score gait index effectively distinguishes OA gait patterns and reflects mobility related quality of life. The autoencoder's superior variance retention versus PCA suggest that OA gait adaptations involve nonlinear biomechanical relationships. Limitations include cross-sectional design and single-dimension compression, which may oversimplify OA gait complexity. Future directions should validate sensitivity to change following treatment and explore whether higher-dimensional representations improve groups discrimination.

Images (Optional)



References (Optional)

"[1] Shou-Jen Wang *et al.,* J Biomechanics, 2024"

Acknowledgements (Optional)

The authors thank all participants who volunteered for this study. Data were collected at the Human Mobility Research Laboratory, Queen's University.

Session Category

Clinical Biomechanics: N/A

OA117-05

Infrapatellar Fat Pad Volume and Knee Joint Running Biomechanics in Runners With a History of Knee Surgery: Data From the TRAIL Cohort

Dr Danilo De Oliveira Silva Associate Professor[1], Dr Benjamin Mentiplay Senior Lecturer[1], Dr Kay Crossley Professor[1], Dr Prasanna Sritharan Research Fellow[1], Ms Melissa Haberfield PhD student[1], Dr Michael Girdwood Research Fellow[1], Ms Elizabeth Sylvestre[2], Mr Peter Hartley[2], Ms Yimo Wang[2], Mr Zaid Faiz[2], Ms Bhavana Billapaty[2], Mr Brody McCarthy PhD student[1], Ms Fernanda Serighelli[1], Dr Harvi Hart[3]

[1]La Trobe University, Melbourne, VIC, Australia. [2]Western University, London, Ontario, Canada. [3]Michigan State University, East Lansing, Michigan, United States

Introduction

Individuals at increased risk of post-traumatic knee osteoarthritis often show altered sagittal-plane biomechanics. The infrapatellar fat pad (IPFP) has also been linked to post-traumatic knee osteoarthritis, but the relationship between these biomechanical changes and IPFP involvement remains poorly understood. Therefore, we explored whether peak knee flexion angle and internal knee flexion moment during running are associated with IPFP volume in runners with a history of knee surgery.

Methods

Runners with a history of knee surgery who ran at least 3 times and >10km a week underwent quantitative gait analysis using a 10-camera motion capture system synchronised with force plates. Running trials were collected at 3–3.5 m/s and 5–6 m/s in participants' habitual footwear. Peak knee flexion angle and peak internal knee flexion moment for the surgical limb were calculated over the stance phase using OpenSim. IPFP volume (cm^3) was quantified from sagittal T2-mapped MRI by manually digitising the IPFP boundaries slice-by-slice. Separate linear regression models examined associations between each biomechanical variable at each speed and IPFP volume, whilst adjusting moments for body mass and sex, and angles for sex.

Results

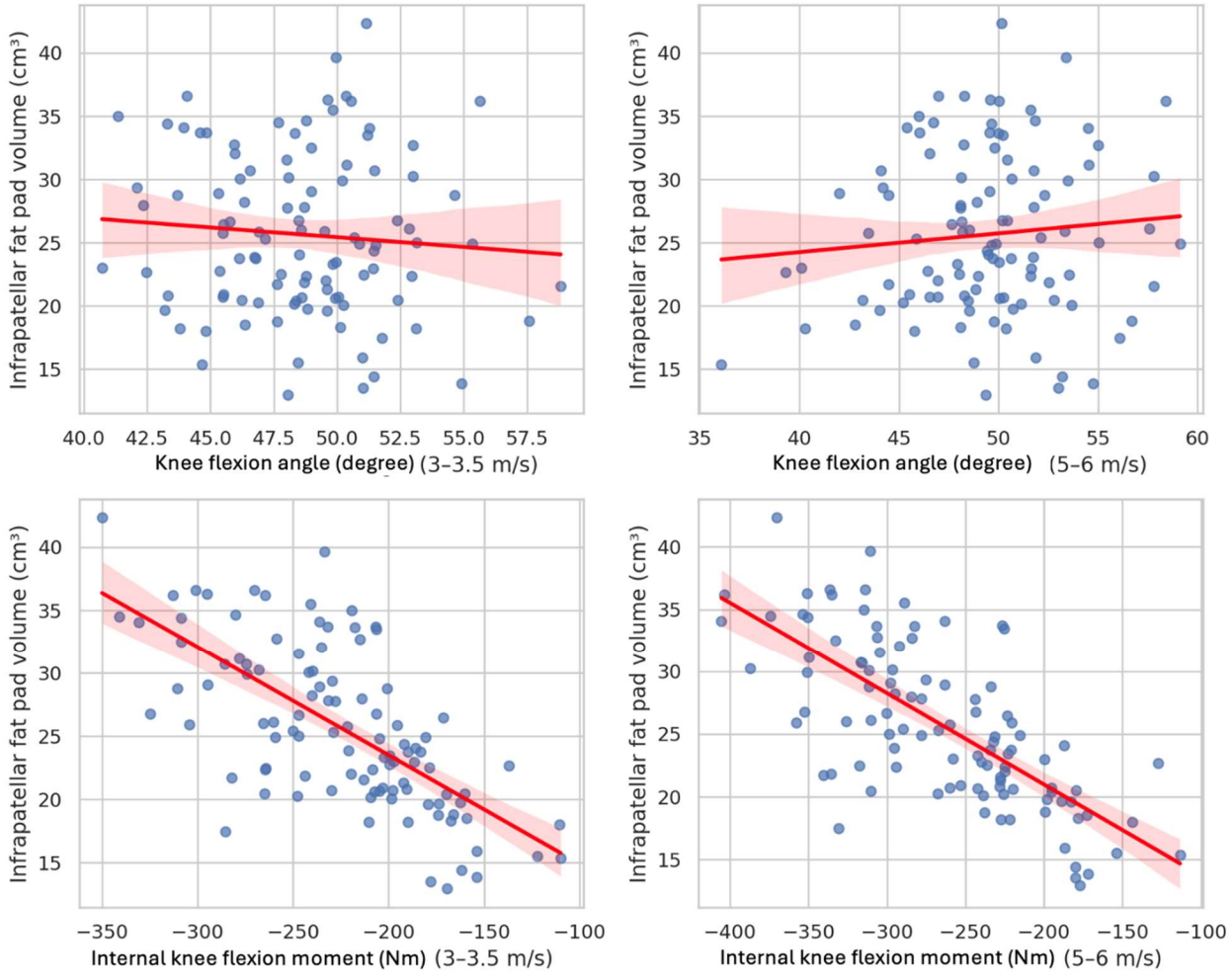
106 runners (52 females; mean age 34±7 years, mass 77±13 kg) were included. The IPFP volume ranged from 12.9-42.3cm^3. The peak knee flexion angle was not associated with IPFP volume at 3–3.5m/s (B [95% CI]: 0.01 [−0.23 to 0.26]) or at 5–6m/s (0.08 [−0.12 to 0.28]). Lower peak internal knee flexion moment was associated with smaller IPFP volume

at both 3-3.5m/s −0.04 [−0.07 to −0.01]; R^2=0.59) and 5-6m/s (−0.04 [−0.07 to −0.02]; R^2=0.60). This indicates that a 10Nm lower peak internal knee flexion moment is associated with approximately a 0.4 cm^3 smaller IPFP volume.

Discussion

Among runners with a history of knee surgery, lower peak internal knee flexion moments, but not knee flexion angles, were associated with smaller IPFP volume. As lower moments reflect reduced quadriceps demand, these findings align with underloading frameworks in post-traumatic knee osteoarthritis, where insufficient mechanical stimulation may influence IPFP morphology. Clinically, interventions that restore knee extensor loading, if confirmed longitudinally, may help maintain IPFP health.

Images (Optional)



Session Category

Clinical Biomechanics: N/A

OA117-06

Time-Frequency Analysis of Muscle Activation Patterns in People With Knee Osteoarthritis During Walking

Mr. Taewoong Kong[1], Dr. Hoon Kim[1,2]

[1]Department of Software Convergence, Soonchunhyang University, Asan-si, Chungcheongnamdo, Korea, Republic of. [2]Department of Sports Medicine, Soonchunhyang University, Asan-si, Chungcheongnamdo, Korea, Republic of

Introduction

Knee osteoarthritis (KOA) is a degenerative disease that impairs neuromuscular function, including quadriceps and hamstring weakness and prolonged activation, which are reflected in altered electromyography (EMG) amplitudes. However, EMG amplitudes cannot fully explain neuromuscular alterations in KOA, given that the underlying motor unit recruitment and firing behavior can usually be captured in the frequency domain of EMG. Therefore, the purpose of this study was to investigate lower-limb muscle activation patterns in time-frequency domain in people with KOAs.

Methods

Muscle activation data of 8 lower-limb muscles from a public dataset, including ten KOA patients and ten healthy older adults, were used. Four walking trials per subject were analyzed. Wavelet transformation and principal component analysis (PCA) were applied to decompose EMG data in time-frequency domain. Two-way mixed ANOVAs and post-hoc pairwise comparisons were used to test group and muscle effects on PC scores.

Results

PCA captured contrasts between low-mid frequencies in the early/late phase and the full band in the middle phase (PC1), and low frequencies early vs. the full band in the middle-late phase (PC2). Significant group x muscle interaction was observed for PC1 ($p<0.001$) and PC2 ($p=0.001$). In addition, patients with KOA exhibited lower PC1 scores in vasti and medial hamstring, greater PC1 scores in gastrocnemius and soleus, and greater PC2 scores in hamstrings compared with healthy controls.

Discussion

People with KOA exhibited distinct deficits in muscle activations in the time-frequency domain. PC1 indicated a partial “pattern swap,” whereby vasti and hamstring activation

became more plantar-flexor-like and plantar-flexor activation more proximal knee-like, so that these muscles were not predominantly active during the phases in which they are normally most needed, consistent with a less efficient neuromuscular strategy during walking. Higher PC2 scores in hamstrings showed relatively greater low-frequency activation early in the gait cycle and reduced broadband activation during a functionally critical phase, particularly terminal swing for the hamstrings. Together, these PC1 and PC2 alterations indicate a temporally mistimed and spectrally altered knee-ankle activation strategy, reflecting a protective and inefficient strategy during early stance and compromised deceleration capability during terminal swing, which might affect gait function.

Images (Optional)

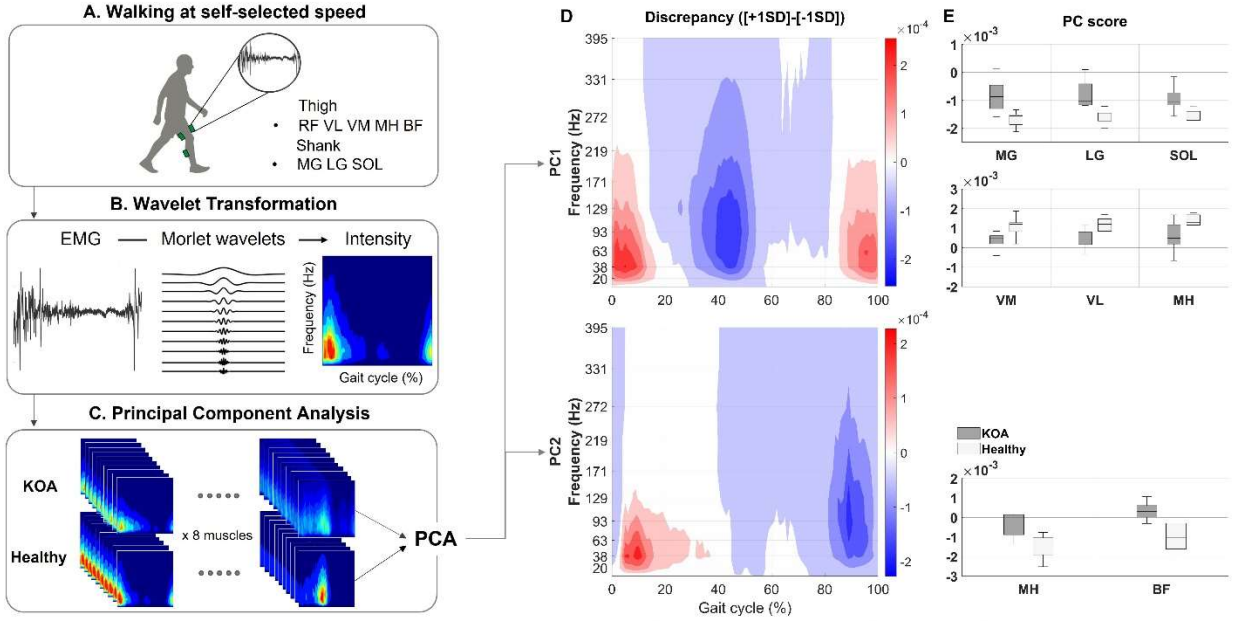


Figure 1. **A**. Experimental protocol showing walking at self-selected speed with EMG data from eight lower-limb muscles (RF: rectus femoris, VL: vastus lateralis, VM: vastus medialis, MH: medial hamstrings, BF: biceps femoris, MG: medial gastrocnemius, LG: lateral gastrocnemius, and SOL: soleus). **B**. Wavelet transformation of EMG data using Morlet wavelets to obtain time-frequency intensity across the gait cycle. **C**. Principal component analysis (PCA) applied to time-frequency intensity matrices from people with knee osteoarthritis (KOA) and healthy groups across eight muscles. **D**. Discrepancy of effect of +1SD and -SD of PC scores. E. PC scores of muscles showing significant differences based on pairwise comparisons.

Acknowledgements (Optional)

This work was supported by the Soonchunhyang University Research Fund and BK21 FOUR (Fostering Outstanding Universities for Research) (No. 5199990914048).

Session Category

Clinical Biomechanics: N/A

OA118-01

Anterior Trunk Leaning Does Not Alter Recovery Time and Sagittal Whole-Body Angular Momentum After Perturbations in Human Running

M.Sc. Luca Braun[1,2], PhD Brian R. Umberger[2], M.Sc. Carlo von Diecken[1], PhD Varun Joshi[2], M.Sc. Laila Sikeler[1], M.Sc. Sebastian Rehorst[1], M.Sc. Janina Helwig[1], M.Sc. Bastian Anedda[1], PhD Steffen Willwacher[1]

[1]Institute for Advanced Biomechanics and Motion Studies, Offenburg University of Applied Sciences, Offenburg, Baden-Württemberg, Germany. [2]School of Kinesiology, University of Michigan, Ann Arbor, Michigan, United States

Introduction

Given the substantial mass and inertia of the trunk, anterior trunk leaning (ATL) is an effective strategy to redistribute lower extremity joint moments in running, specifically reducing knee extension moments at the cost of increased hip extension and external rotation moments. By shifting the centre of mass forward relative to the base of support, ATL may influence perturbation recovery, an essential determinant for preventing falls and related injuries. However, whether ATL affects perturbation recovery - defined here as perturbation recovery time (PRT) and sagittal whole-body angular momentum (WBAM) range after slip-like anterior–posterior perturbations (SLAPPs) - remains unclear.

Methods

Sixteen recreational runners completed six treadmill runs (2.5 m/s) at one self-selected and five predefined ATL conditions spanning −4° to 28°. Each condition included five standardised SLAPPs at pseudorandomized time intervals. Kinematics and kinetics during baseline and perturbed steps were captured. Subject-specific 95% prediction bands around time-normalised baseline sagittal WBAM curves were generated. PRT was defined as the time from perturbation onset to the final time point at which WBAM re-entered this band (Fig. 1A). Linear mixed-effects models were applied to PRT (condition) and sagittal WBAM range, defined as peak-to-peak WBAM (condition, step, interaction), with subject as a random intercept.

Results

PRT did not differ across ATL conditions ($p=0.63$; Fig. 1B). WBAM range showed significant main effects of step ($p<0.001$; Fig. 1C) and condition ($p<0.001$; Fig. 1D) with no interaction

(p=0.59). WBAM range decreased with increasing ATL. Relative to baseline, WBAM range increased after the perturbation, peaked at step 3, and returned to baseline by step 5.

Discussion

ATL did not affect recovery time following SLAPPs in running. Although sagittal WBAM range was sensitive to SLAPPs and differed across ATL conditions, the sagittal plane perturbation recovery strategy on a whole-body level is unaffected by ATL, given the absence of an interaction between factors. Thus, using ATL, which reduces knee extension moments and may reduce the risk of running-related overuse injuries, does not appear to affect perturbation recovery, suggesting that fall risk after SLAPPs might be unaffected. Future work should investigate joint-level changes to determine whether recovery mechanics differ across ATL conditions.

Images (Optional)

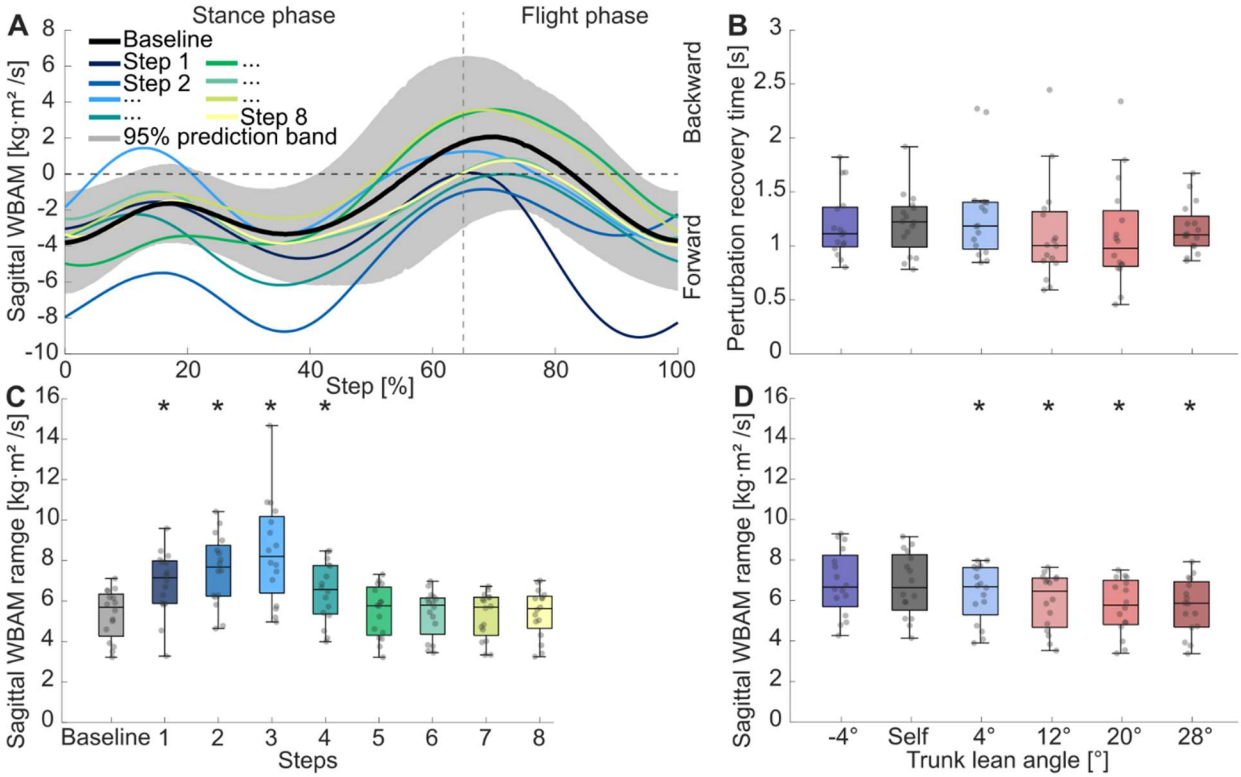


Fig.1: Prediction band of sagittal WBAM and post-perturbation steps (A), PRT (B), sagittal WBAM range across steps (C) and ATL conditions (D). Asterisks mark significant pairwise differences relative to baseline (C) or self (D).

Session Category

Human Motion and Performance: Locomotion/Gait

OA118-02

Watch Your Step: Stepping Error Increases With Age in Response to Perturbing Visual Cues

Mr Adam Grimmitt, Mr Jonaz Moreno, Mr Paul McDonnell, Dr Douglas Martini, Dr Wouter Hoogkamer

University of Massachusetts Amherst, Amherst, MA, United States

Introduction

Globally, 35% of adults over the age of 65 experience a fall annually [1]. Missteps directly increase their fall risk, and reactive step training improves their fall outcomes [2,3]. However, relationships between visual processing and missteps are largely unknown. This study compared stepping error among young adults, older adults, and older adult fallers during visually cued walking and visually cued walking with perturbations. We hypothesized that (1) stepping error would be larger in older adults, and that (2) during visually cued walking with perturbations, stepping error would be the largest in older adult fallers.

Methods

31 young adults, 30 older adults, and 22 older adult fallers walked on a treadmill for two three-minute trials at their habitual speed with visual cues (stepping targets) projected onto the surface of the treadmill at matched speeds. During visually cued walking with perturbations, random stepping targets were shifted in a forward, backward, or lateral direction. Stepping error was quantified as the average distance between the foot center at midstance and the nearest stepping target. We used a linear mixed effects model and Bonferroni corrected t-tests to compare the effects of age group across stepping target conditions: steady, perturbed lateral, perturbed backward, and perturbed forward.

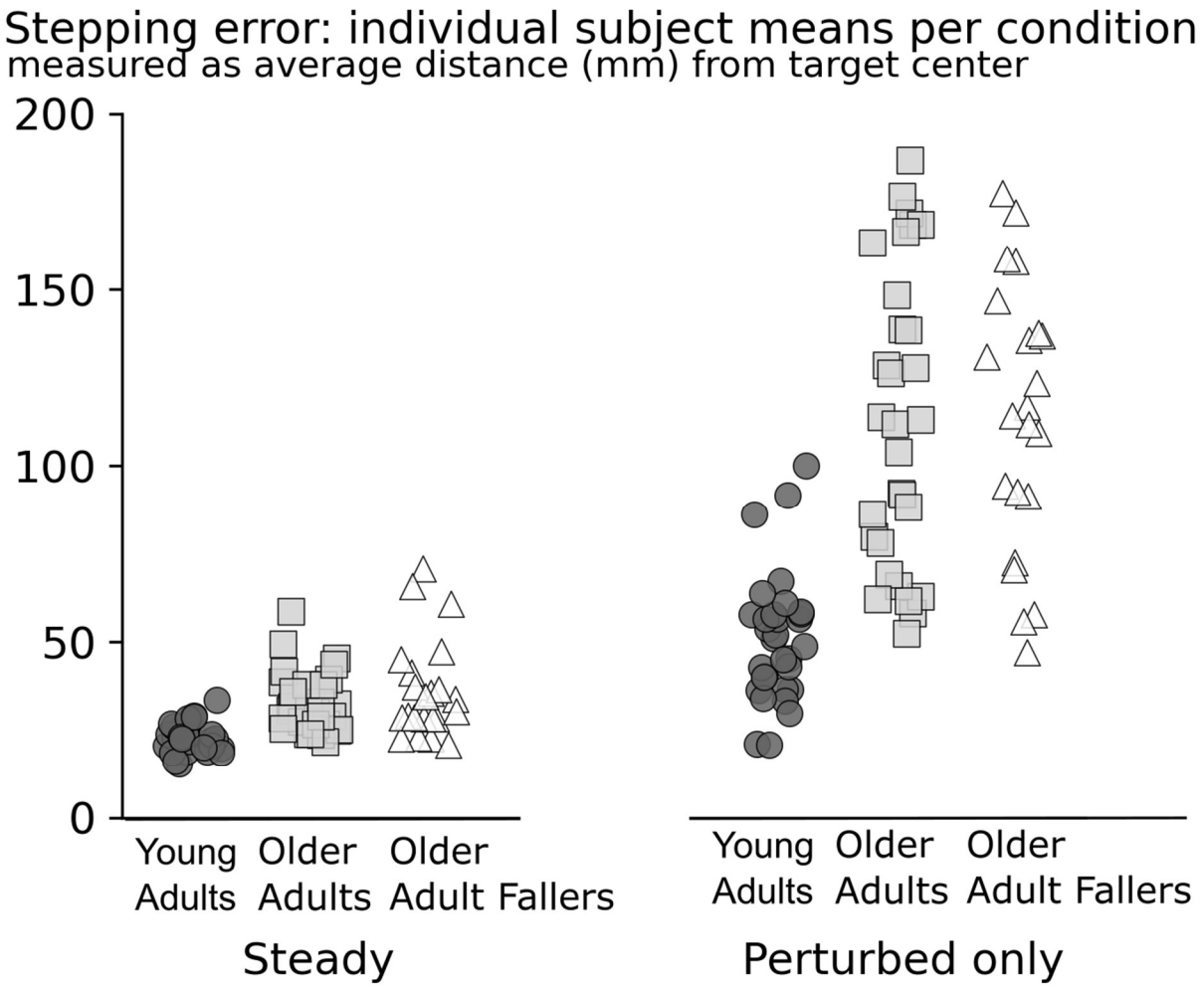
Results

Our model revealed main effects of age $F_{(1,83)} = 39.17$, $p<0.001$, target condition $F_{(1,249)} = 209.24$, $p<0.001$, and an age × target condition $F_{(1,249)} = 19.29$, $p<0.001$. Specifically, stepping error was larger in older adults compared to young, $t_{(86.1)} = 8.67$, $p<0.001$. Furthermore, compared to young adults, older adult and older adult fallers were less accurate when responding to perturbed targets, $t_{(97.8)} = 10.54$, $p<0.001$, although they were not different from each other $t_{(97.8)} = 0.27$, $p=0.830$.

Discussion

Older adults exhibited larger stepping error, indicating an age-related response to virtual cues.There was no difference in perturbed target stepping error between older adults and older adult fallers. Stepping error before and after a perturbed step could elucidate differences between fallers and non-fallers, however our current findings suggest that aging, but not fall history, is associated with stepping error.

Images (Optional)



References (Optional)

1. WHO.2008
2. S.Robinovitch et al.,Lanclet,2013
3. Y.Okubo et al.,BJSM,2017

Acknowledgements (Optional)

We thank Adam Knight for his role in developing methodology. The work was supported by: R21AG075489.

Session Category

Human Motion and Performance: Locomotion/Gait

OA118-03

Preferred Locomotor Patterns Minimize Head Motion Variability

Mr Liam Foulger, Dr Jesse Charlton, Dr Jean-Sébastien Blouin

University of British Columbia, Vancouver, BC, Canada

Introduction

The ability to sense the world around us is crucial for movement and navigation. Given visual and vestibular sensors in the head contribute to self-motion estimates, it is important to reduce variability (i.e., noise) in head motion. Head movement variability is lowest near preferred walking speeds, similar to how our preferred locomotor patterns minimize energetic cost. This suggests that sensory demands – in addition to energetic cost – shape our movement. To determine if minimizing sensory variability is associated with other well-defined locomotor behaviours, we tested if preferred walk-run transition speeds (~2m/s) also minimize head motion variability. Secondarily, we quantified if head movement variability is lowest near our preferred running speeds.

Methods

Five participants (2F) walked and ran outdoors across a range of speeds (<0.5m/s to >5m/s). We quantified head kinematic variability by calculating the mean ratio (V_{res}) of residual variability (deviation from average stride cycle) to total magnitude of head linear accelerations and angular velocities. We fitted second-order polynomial functions to each participant's walking and running data.

Results

Participants preferred to walk at 1.39±0.20m/s and run at 3.15±0.82m/s. For the mean V_{res} calculated from net head linear acceleration, the polynomials fit well for walking (R^2=0.97±0.04, minima=1.53±0.11m/s) and running (R^2=0.95±0.05, minima=2.94±0.59m/s). The ideal walk-run transition point (intersection of the polynomials) was 1.92±0.29m/s. The mean V_{res} polynomial fits for net head angular velocity had worse fits for walking (R^2=0.74±0.31, minima=1.56±0.58m/s) and running (R^2=0.75±0.16, minima=5.85±0.57m/s). The transition point was 2.36±0.38m/s.

Discussion

We found that head kinematic variability during walking exceeded that during running around the speed (~2m/s) where humans transition from walking to running (hypothesized

to be energetically optimal). Head kinematic variability was lowest near preferred walking speeds. This relationship was less clear for running given head variability changed minimally across speeds, similar to previously reported energetic cost landscapes. Although our work presents evidence that head motion variability influences how we move, it is not clear how sensory and energetic constraints interact to shape motion. Future work should address if these are competing demands or if sensory noise is a proxy for optimizing energy expenditure.

Images (Optional)

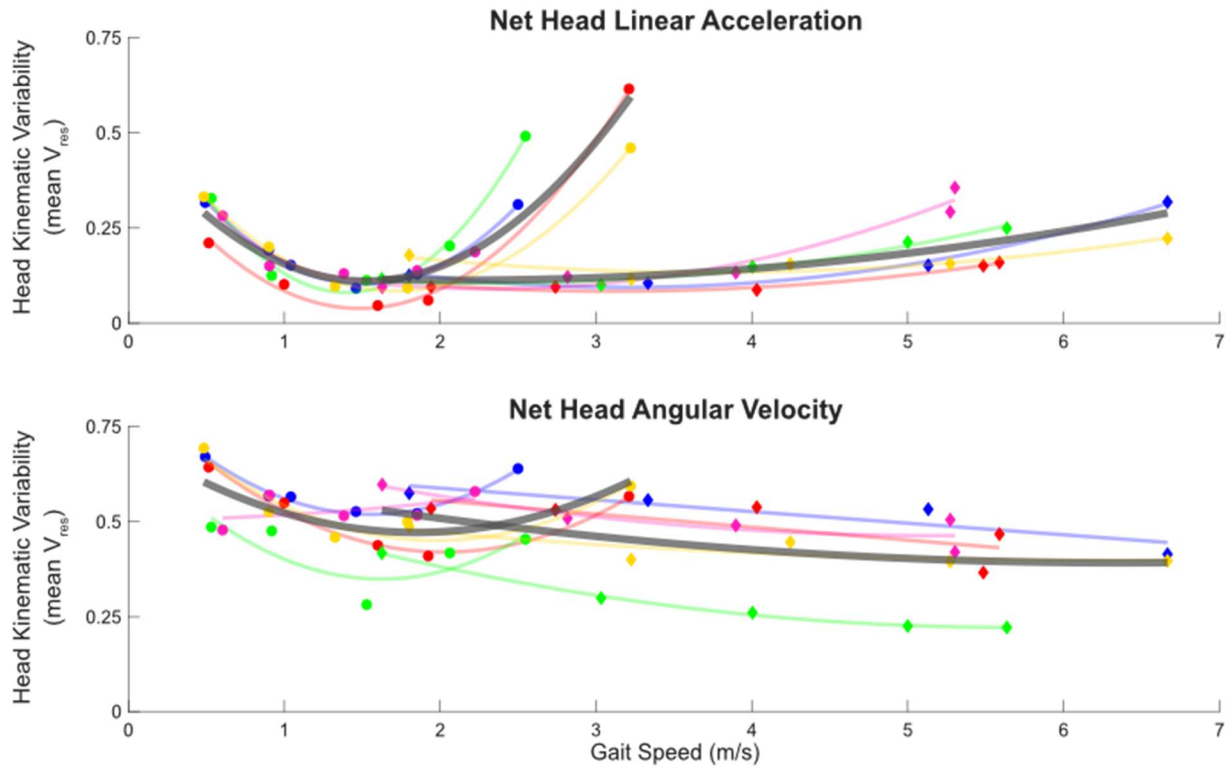


Figure 1. Head kinematic variability as quantified by the mean proportion of residual variability (V_{res}) from net head linear acceleration (top) and net head angular velocity (bottom). Participants walked (circles) and ran (diamonds) at various speeds on an outdoor track. Thin coloured lines represent fitted second-order polynomial functions for each participant's walking and running. Thick grey lines represent second-order polynomial functions fitted to the entire group data.

Session Category

Human Motion and Performance: Locomotion/Gait

OA118-04

Does Peripheral Vision Restriction Alter Walking Function?

Ms Jasmaine Bubier-Hunter BS, Dr Frankie Wade Ph.D.

San Diego State University, San Diego, CA, United States

Introduction

As adults age, they rely more on visual feedback to maintain balance and locomotor stability; however, declines in peripheral vision can impair gait [1]. When visual information is altered, individuals adjust their gait to stay stable [2]. We isolated the effect of peripheral vision on walking function in healthy adults and hypothesized that restricted vision would lead to wider, shorter steps, reduced arm swing, stooped posture, and increased variability.

Methods

Fourteen healthy adults (28+-11 years; 70.7+-17.0 kg; preferred speed: 1.19+-0.15 m/s) walked for 2 minutes in full (VIS) and restricted-vision (LOW_VIS, 30-70°, SwivelVision Goggles) conditions on an instrumented treadmill (AMTI Tandem) at their preferred speed. 43 markers (Plug-in Gait plus greater trochanter and 5^{th} metatarsophalangeal) were sampled at 100 Hz (Vero 2.2, Vicon). Spatiotemporal gait parameters, postural measures, and sagittal plane joint kinematics were extracted. Paired t-tests compared VIS and LOW_VIS (α=.05).

Results

Restricted peripheral vision did not significantly alter spatiotemporal averages or arm swing. Trunk angle, the angle between the vector from C7 to the pelvis and the vector from the pelvis to the stance heel, did not differ between conditions. Heading, the angle between the anteroposterior axis and the vector connecting anterior and posterior superior iliac crest midpoints, showed no change. Variability in heading reduced and lower limb range of motion increased with LOW_VIS (Table 1).

Discussion

Despite reduced visual input, participants did not adopt the expected cautious gait strategy, contrary to our hypothesis and prior evidence [3]. Instead, variability reduced in heading and the only significant differences occurred at the joint level, where range of motion increased in the lower limb. This suggests healthy adults compensate for reduced peripheral vision through greater sagittal-plane joint excursions rather than altering whole-body posture. These findings align with evidence that individuals adapt to decreased sensory environments through joint-level adjustments rather than gross postural changes [4]. We continue to expand this work to incorporate aging adults in our collections.

Images (Optional)

Table 1. Mean ± SEM for each variable of interest across full vision (VIS) and restricted vision (LOW_VIS) trials

		VIS	LOW_VIS	p-value	Effect Size
Step Width (m)	Mean	.61 ± .02	.61 ± .02		
	SD	.02 ± .001	.02 ± .002		Small (d=.42)
Step Length (m)	Mean	.09 ± .01	.10 ± .01		Small (d=.24)
	SD	.02 ± .002	.03 ± .01		Small (d=.26)
Toe Clearance (m)	Mean	.13 ± .005	.13 ± .01		
	SD	.01 ± .001	.01 ± .001		Small (d=.44)
Trunk Angle (°)	Mean	11.01 ± .91	11.05 ± 1.08		
	SD	1.22 ± .08	1.56 ± .31		Small (d=.30)
Arm Swing RoM (°)	Mean	23.48 ± 2.46	22.31 ± 2.49		Small (d=.35)
	SD	6.49 ± 1.20	6.87 ± 1.01		Small (d=.27)
Ankle RoM (°)	Mean	33.09 ± 1.99	34.03 ± 2.13	.01	Large (d=.80)
	SD	5.94 ± 2.33	7.41 ± 3.06		Small (d=.49)
Knee RoM (°)	Mean	57.00 ± 1.34	57.70 ± 2.13	.022	Medium (d=.69)
	SD	5.02 ± .80	4.94 ± .78		
Hip RoM (°)	Mean	44.94 ± 1.26	45.39 ± 1.28	.042	Medium (d=.60)
	SD	2.07 ± .21	2.38 ± .28		Small (d=.39)
Heading (°)	Mean	−1.05 ± .88	−1.06 ± .93		
	SD	1.60 ± .13	1.51 ± .13	0.007	Large (d=.85)

RoM = range of motion in sagittal plane. SEM = standard error of the mean

References (Optional)

[1] O'Connor, S. M., & Kuo, A. D. , *J Neurophys,* 2009.

[2] Lord, S. R. *Age Ageing,* 1997.

[3] Chamberlin, M. E., *et al.*, *J Gerontol A,* 2005.

[4] McCrum, C., *et al.*, *J Biomechanics,* 2016.

Acknowledgements (Optional)

We thank Averi Noel, Taryn Lawas Morales, and Jacob Liu for their help with data collection and processing.

Session Category

Human Motion and Performance: Locomotion/Gait

OA118-05

Brachial Plexus Injury Impairs Upper Limb and Trunk Kinematics during Self-Selected Walking and Tandem Gait

MSc. Aline Dalfito Gava[1,2], PhD. Ana de David[1], MSc. Carlos Passos Goncalves[1,2], MSc. Marcio Mendonca Cardoso[2]

[1]Universidade de Brasilia, Brasilia, DF, Brazil. [2]Sarah Network of Rehabilitation Hospitals, Brasilia, DF, Brazil

Introduction

Traumatic brachial plexus injury (BPI) reduces upper limb function and motion, which pays a crucial role in postural control and gait stability, particularly in challenging conditions. No previous studies were found investigating upper limb and trunk kinematics during gait in individuals with BPI. These comprehensions could guide future rehabilitation interventions. This study aimed to compare upper limb, trunk, and pelvis kinematics between individuals with BPI and healthy controls during self-selected walking speed (SSWS) and tandem gait (TG).

Methods

Forty adults (20 unilateral BPI; 20 controls matched for sex, age, and body mass index) performed SSWS and TG (3 meters distance). Inclusion criteria: confirmed BPI and age ≤20 years; exclusion criteria: previous surgical treatment, any musculoskeletal or neurological disorders. A motion-capture system (Vicon System, USA) with 11 cameras at 120 Hz rate was used to measure kinematics in sagittal, frontal and transverse planes using a full-body plug-in-gait marker set. Group differences were assessed by statistical parametric mapping (SPM) and t-tests ($p \leq 0.05$).

Results

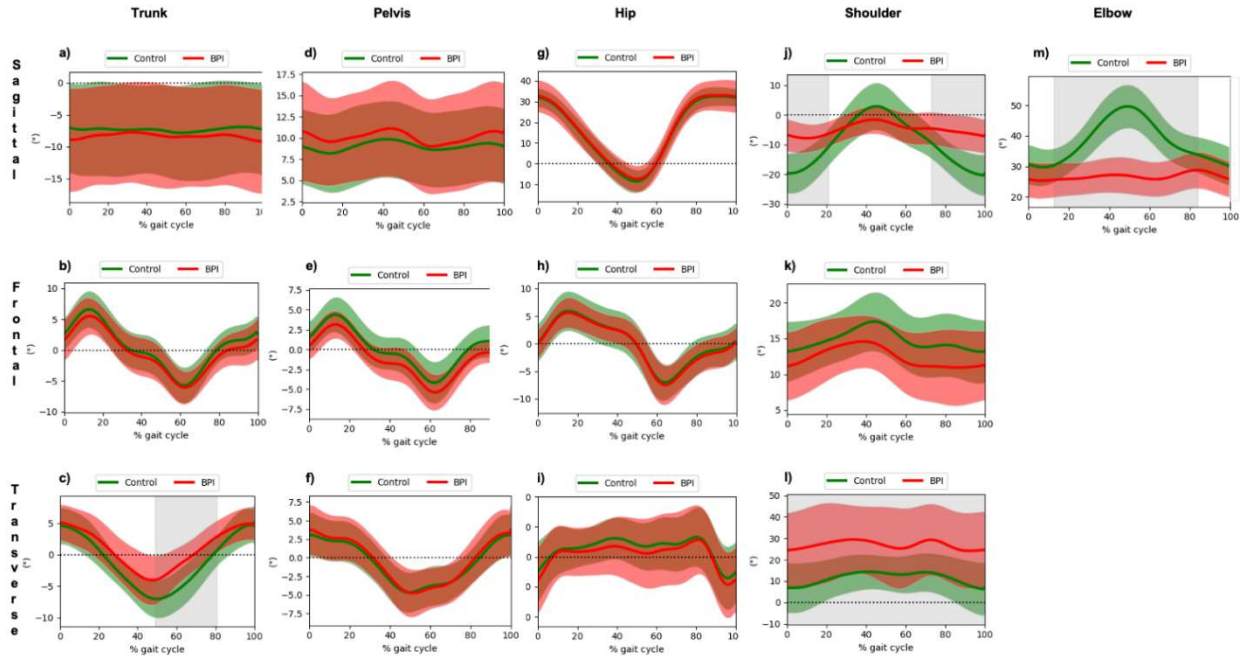
Compared to controls, BPI participants walked more slowly and with shorter step lengths across both tasks ($d = -0.87$ to -1.05). The affected limb exhibited no shoulder or elbow angular motion during either task. During SSWS, the BPI group showed trunk rotation toward the affected side during terminal stance and early swing (Figure 1). Across TG, pelvic drop toward the affected side was observed during medial swing. Furthermore, the non-affected shoulder showed an add compensatory increases in internal rotation during

early and medial stance, and during medial to late swing. Participants with BPI required 36.4% more time to complete the 3-meter TG task.

Discussion

Upper limb–trunk–pelvis coupling is increased during SSWS and TG in individuals with BPI. It may reflect compensatory mechanisms linked to impaired arm swing. In TG, more challenger task than SSWS, there was a add compensatory strategy in the unaffected shoulder. These findings emphasize the importance of rehabilitation strategies that integrate upper-limb recovery in gait and postural control training. Future studies should explore whether targeted interventions can restore more symmetrical arm–trunk–pelvis coordination and improve dynamic stability.

Images (Optional)



Session Category

Human Motion and Performance: Locomotion/Gait

OA118-06

Different Visual Scanning Strategies Are Associated With Improved Mobility in Adults With and Without Glaucoma

Dr. Michelle Harter, Dr. J. Patrick Mayo, Ms. Galen Holland, Dr. Rakié Cham

University of Pittsburgh, Pittsburgh, Pennsylvania, United States

Introduction

Glaucoma causes peripheral visual field loss and significant mobility limitations [1]. However, even those with severe glaucoma still have residual central vision, which, if leveraged appropriately, can be useful for mobility. Systematic movement of the eyes / head, called visual scanning, can help salient objects fall within an individual's preserved visual field as they walk through complex real-world environments. People with vision loss adopt different visual scanning strategies than those without vision loss [2], but it remains unclear which strategies are beneficial. This work examined how head and eye scanning patterns relate to mobility performance in individuals with glaucoma.

Methods

Seven adults with normal vision (63±8 years; 4F) and five adults with glaucoma (68±4 years; 4F; glaucoma severity ranging from mild to advanced) walked an outdoor garden path representative of real-world mobility demands while head kinematics and eye movements were tracked (Opal V2R IMUs; Tobii Pro Glasses 3). Magnitude of head scanning was quantified by peak-to-peak head pitch and yaw. Magnitude of eye scanning was quantified by the percentage of spatial area over which the participant fixated during the task. Mobility was quantified by completion time. Pearson correlation coefficients (ρ) were identified to find associations between head / eye scanning and mobility (moderate or strong correlations reported).

Results

Head and eye scanning showed different relationships with mobility in adults with glaucoma compared with those without glaucoma. In adults without glaucoma, greater head yaw and larger spatial area of fixations were associated with slower completion time (head yaw: ρ=0.85; spatial fixation area: ρ=0.60). In contrast, adults with glaucoma who showed greater head yaw and greater spatial area of fixations tended to have faster completion time (head yaw: ρ=–0.57; spatial fixation area: ρ=–0.39).

Discussion

These results highlight that head and eye scanning may be beneficial for improving mobility efficiency in people with glaucoma. These findings will be expanded in future work with the goal of developing a visual scanning training program to teach people with glaucoma effective visual scanning strategies for maintaining real-world mobility.

References (Optional)

[1] Mihailovic *et al.*, TVST, 2017. [2] Kübler *et al.*, Optometry & Vision Science, 2015.

Session Category

Human Motion and Performance: Locomotion/Gait

OA119-01

Cleat Engagement Patterns used by Elite American Football Athletes during Peak Utilized Translational Traction

Mr. Cody M. O'Cain[1], Mr. W. Brody Hicks[1], Dr. Evan A. Dooley[1], Dr. Kristy B. Arbogast[2], Dr. Laura C. Schmitt[3], Mr. Antonius Prader[1], Dr. Jason R. Kerrigan[1], Dr. E. Meade Spratley[1]

[1]Biomechanics Consulting and Research (Biocore), LLC, Charlottesville, Virginia, United States. [2]Children's Hospital of Philadelphia, Philadelphia, Pennsylvania, United States. [3]The Ohio State University, Columbus, Ohio, United States

Introduction

For decades, researchers have used mechanical devices to evaluate footwear traction characteristics for investigating athlete safety and performance [1, 2]. These mechanical tests typically employ a few standardized footwear engagement patterns that often do not reflect the wide variety of footwear engagement patterns utilized by athletes during play. The goal of this study was to quantify the cleat engagement patterns utilized by elite American football athletes during peak utilized translational traction to inform more representative cleat testing.

Methods

Twenty-seven male athletes (mean ± SD: age, 27 ± 5 y; height, 1.88 ± 0.2 m; body mass, 95.6 ± 13.8 kg; shoe size, US Men’s 12 ± 1) with college or professional American football experience performed four sport-relevant motions using two commonly worn cleat models while 3D motion and ground reaction forces were captured. 3D scans were taken of the cleats, and the 3D surface mesh of each cleat was dynamically deformed based on the athlete cleat kinematics to derive the contact patch between the cleat and surface. Peak utilized traction, contact patch, center-of-force, and ground reaction force were aggregated for each motion, cleat, and loading and unloading phases. SPM1D was used to test significant differences.

Results

Contact area increased as athletes applied more vertical force during all motions and reached a maximum area between 2.5 and 3.25 bodyweight of vertical force during the loading phase. Contact area remained at this maximum until 2.5 to 1.25 bodyweight during the unloading phase. Contact area rapidly decreased below 0.25 bodyweight during the unloading phase, which corresponded with a rapid increase in utilized traction for all

motions. Significant differences were observed for utilized traction between the two cleats and the loading and unloading phases below 0.25 bodyweight.

Discussion

Prior studies have designed tests with cleat engagement patterns that mimic athletes to better evaluate the traction characteristics of cleats and surfaces [3]. This research presents a method for deriving cleat-surface engagement patterns. The applied method identified associations between peak utilized traction, applied vertical force, and cleat contact area.

Images (Optional)

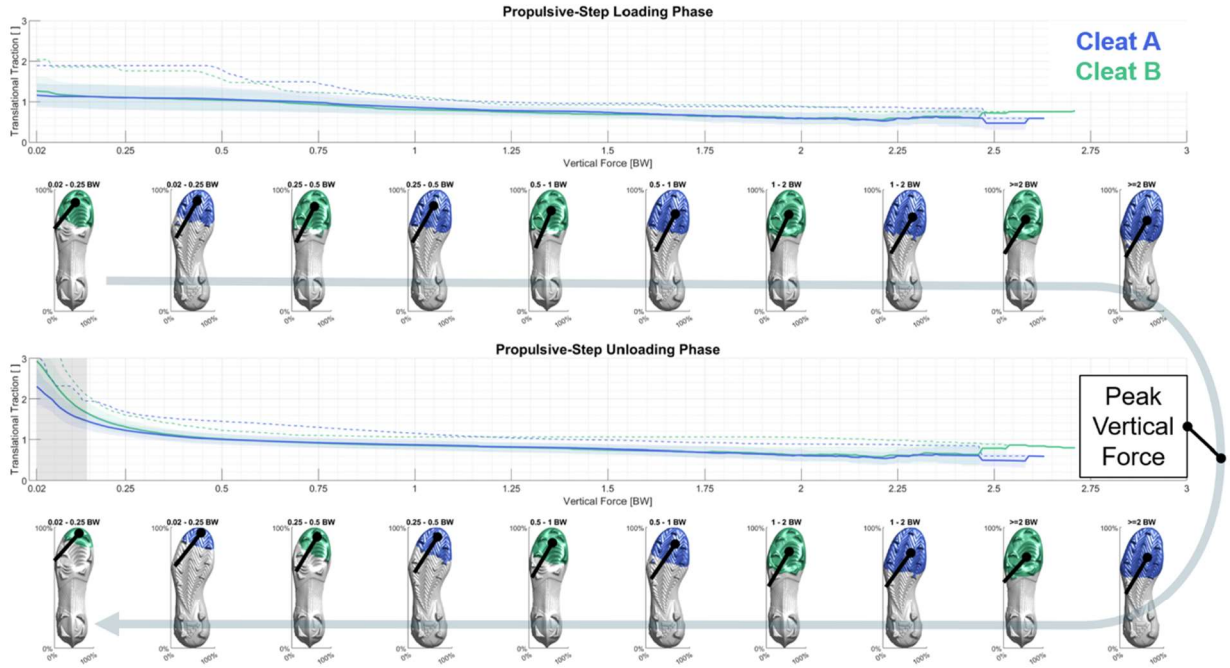


Figure 1: The cleat engagement and peak translational traction utilized for the propulsive step the population of athletes. The solid lines on the two graphs represent the average peak utilized translational traction as a function of vertical force, shade region represents +/- 1 standard deviation, and the dashed line represents the population max. The grey shaded region represents a significant difference in utilized traction between cleat A and cleat B. The blue and green shaded region on each cleat represents the average contact patch for the population during peak utilized traction, and the black dot and vector represents the center-of-pressure and cleat reaction force vector. The transparent arrow depicts time starting with touch-down in the top left, peak vertical force on the right, and ending with toe-off on the bottom left.

References (Optional)

[1] Torg et al. , J Sports Medicine, 1974

[2] Wannop et al. , J Sports Sciences, 2015

[3] Loud et al. , Orthopaedic J Sports Medicine, 2024

Acknowledgements (Optional)

This research presented was made possible by funding from the National Football League and the National Football League Players Association. The views expressed are solely those of the authors and do not represent the NFL, the NFLPA, or any of its affiliates.

Session Category

Human Motion and Performance: Sports

OA119-02

Absolute Energy Returned from the Forefoot of Advanced Footwear is Strongly Related to Reduced Metabolic Cost

Mr. Eddie Martinez, Mr. Jesse Frank, Mr. Daniel Shull, Dr. Bryan Conrad, Dr. Jennifer Sumner

Brooks Sports, Seattle, Washington, United States

Introduction

While greater percentage of energy return in running shoes has been associated with reduced metabolic cost (MC), recent literature suggests that energy returned from the forefoot region may be the most metabolically relevant due to the energy stored and returned from this region being later in stance [1]. Forefoot energy return can be expressed as absolute forefoot energy out (FFEO) and as the percentage of stored-to-returned energy (FFER%). The purpose of this study was to understand how FFEO and FFER% in advanced footwear technology (AFT) are associated with MC, and which may be the most relevant.

Methods

Respiratory gas exchange (Cosmed K5) was collected from 23 runners (11 male, 12 female) while running in two AFT conditions (Hyperion Elite 4, HE4; Hyperion Elite 5, HE5) at their individually estimated marathon pace. Shoe order was randomized, mirrored, and counterbalanced with five-minute bouts of running separated by five-minute rests. MC (W/kg) was averaged over the last two minutes of the two trials run in each shoe. Mechanical testing was conducted on each AFT using a biofidelic forefoot force-compression protocol with a peak force of 730N (ElectroPuls E3000, Instron). Linear mixed-effects regression models assessed the relationship between both FFEO and FFER% and MC.

Results

HE5 exhibited 38% greater FFEO (HE4: 2.1J, HE5: 2.9J) and 23% greater FFER% (HE4: 68.2%, HE5: 83.8%). Runners demonstrated 1.5% lower MC in HE5. Both FFEO and FFER% significantly predicted MC ($p < 0.001$), but FFEO demonstrated a substantially stronger negative relationship ($\beta = –0.318$) than FFER% ($\beta = –0.016$). Greater FFEO corresponded to lower MC (Fig. 1).

Discussion

A strong relationship exists between mechanically measured FFEO and runners' MC at their estimated marathon pace, exceeding that of FFER%. Given that the 25g mass difference between shoes should reduce MC by only ~0.25%, the observed 1.5% decrease indicates that HE5's greater FFEO drives metabolic savings beyond what mass alone can explain. These findings emphasize FFEO as a potentially key determinant of MC in AFT. Future work will explore this relationship and the possible application to understanding physiological performance across speeds and runner populations.

Images (Optional)

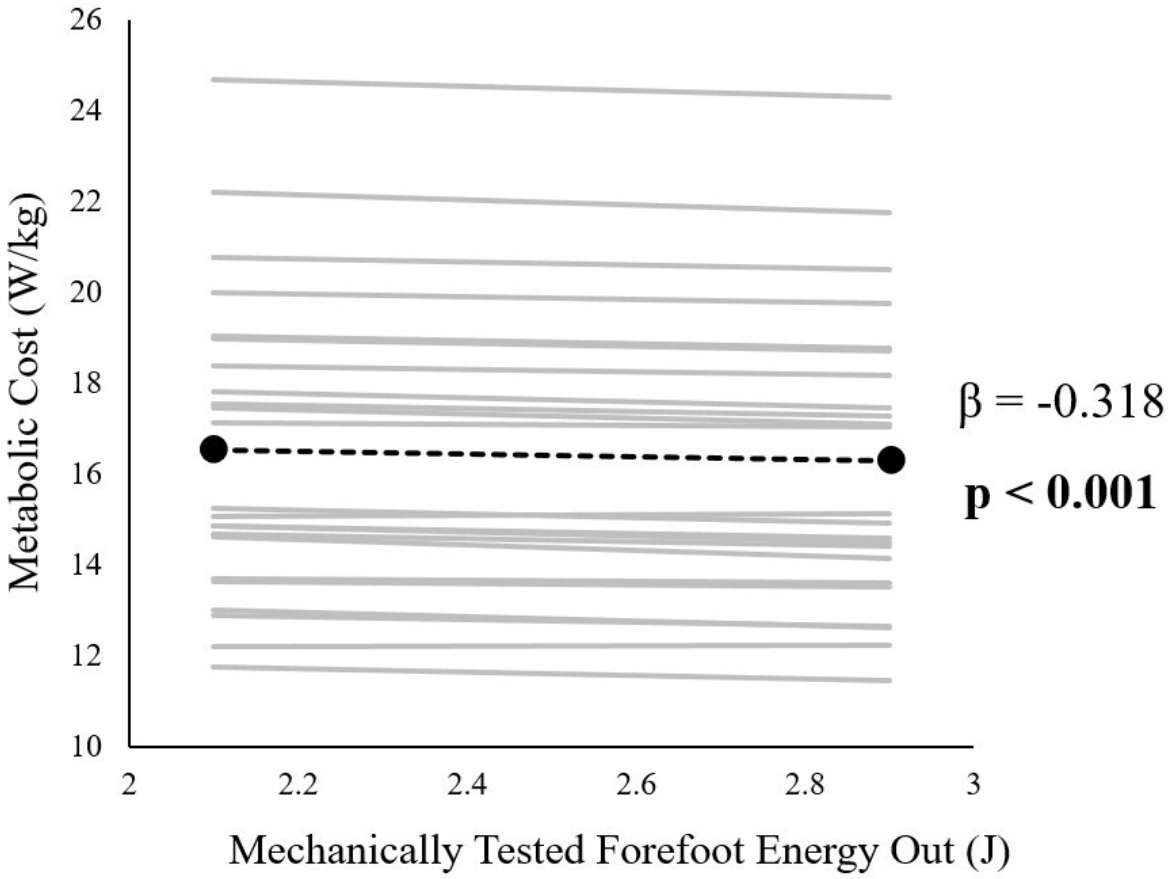


Figure 1. Metabolic cost (MC) of 23 individual runners (grey lines) plotted across the forefoot energy out (FFEO) of each shoe condition. The average MC for each condition (larger black dots connected by a dashed line) is shown to represent the overall relationship.

References (Optional)

[1] E. S. Matijevich *et al.*, Footwear Science, 2023

Acknowledgements (Optional)

Thank you to all Brooks Run Research Team members who contributed to this project.

Session Category

Human Motion and Performance: Sports

OA119-03

The Effects of Advanced Footwear Technology Shoes on Hip Joint Loading in Female Runners

Ms Maria J. Rodriguez, Dr. Colin R. Firminger PhD, Ms Chinaza Enyinnaya-Okidi, Dr. W. Brent Edwards PhD

University of Calgary, Calgary, Alberta, Canada

Introduction

Advanced footwear technology (AFT) shoes have been shown to improve running economy by 4%, resulting in performance increases of 2% [1]. However, recent evidence suggests that AFT shoes may increase injury incidence at the hip [2], which could be related to the shoes, performance increases, or both. The increased injury risk is particularly disconcerting for females, who experience higher rates of hip running-related injuries than males [3]. The primary objective of this study was to examine the effects of AFT shoes and running speed on hip joint moments in trained female runners.

Methods

To date, eight trained female runners (18-45 years; 165.46±6.1 cm; 61.63±7.2 kg) completed treadmill running trials while motion capture and force plate data were collected concurrently in three shoe conditions: the Nike Structure and Nike Infinity (both non-AFT), as well as Nike Alphafly (AFT). Each shoe condition was tested at two speeds: a 10-km race pace and a speed reflecting a hypothetical 4% improvement in running economy. Peak, mass-normalized three-dimensional hip joint moments were computed during the stance phase of running using inverse dynamics and compared using repeated-measures ANOVA.

Results

A significant effect of speed, but not shoe ($p^3$0.156), was observed for peak sagittal (p=0.029) and frontal plane (p=0.005) moments (Figure 1); however, this was driven heavily by the non-AFT shoes. A significant interaction was observed between shoe and speed for peak transverse plane moment (p=0.037), whereby hip joint moments increased with speed in the AFT shoe only.

Discussion

The significant interaction for peak transverse plane moment between shoe and speed conditions suggests that the increased speeds achieved when running in AFT shoes, but not the shoes themselves, may contribute to elevated rotational loading at the hip in female runners. Increasing sample size may help clarify and strengthen these observed statistical trends.

Images (Optional)

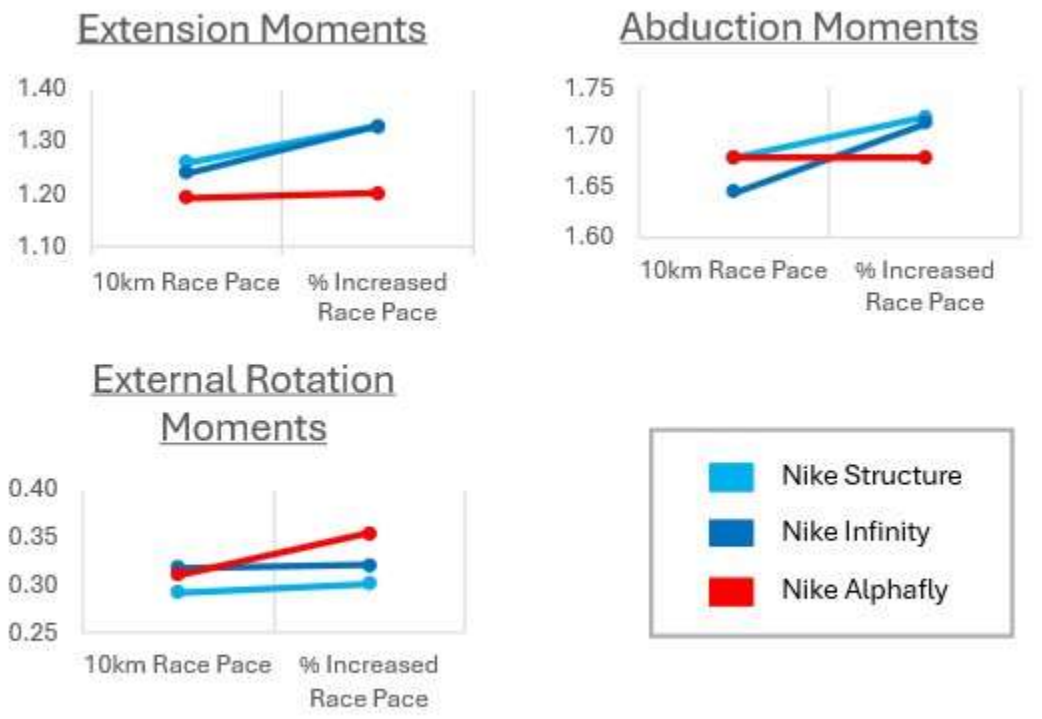


Figure 1 : Subject-averaged peak joint moments normalized to body mass.(Nm/kg)

References (Optional)

[1] Hoogkamer et al., Sports Medicine, 2018

[2] Aoyagi et al., J. Sci. Med. Sport, 2025

[3] Francis et al., J. Sports Sci. Med., 2019

Session Category

Human Motion and Performance: Sports

OA119-04

The Effect of Advanced Footwear Technology Spikes' Midsole Stiffness on the Biomechanics and Metabolic Cost of Running of Elite and Sub-Elite Distance Runners

Mr. Luis Morata-Moreno, Mr. Bradley Needles, Dr. Alena Grabowski

University of Colorado Boulder, Boulder, Colorado, United States

Introduction

Distance runners have experienced improved race performance and running economy when wearing compliant (low stiffness) advanced footwear technology (AFT) spikes compared to stiffer traditional spikes [1], [2], [3], which may be due to increased leg stiffness and ground contact time [1]. Thus, we evaluated the effects of elite and sub-elite distance runners wearing AFT spikes with different midsole foam stiffness on the biomechanics and metabolic cost of running. We hypothesized that when distance runners wore AFT spikes with decreased midsole foam stiffness, leg stiffness and contact time would increase and the metabolic cost of running would decrease.

Methods

10 (7 male, 3 female) elite and sub-elite distance runners (10 km race ≤37 min or equivalent within the past 6 months) completed six 5-min running trials (three shoe conditions *x* two replicates) at 4.17 m/s on a force-measuring treadmill. Participants wore three custom AFT spikes (AFT A, B, and C) that were otherwise identical but had midsole stiffness values of 170, 159 and 140 kN/m, respectively. We measured ground reaction forces (1000 Hz) and metabolic rates, and calculated and compared leg stiffness, ground contact time, and metabolic power (W/kg) across AFT spikes using linear mixed models.

Results

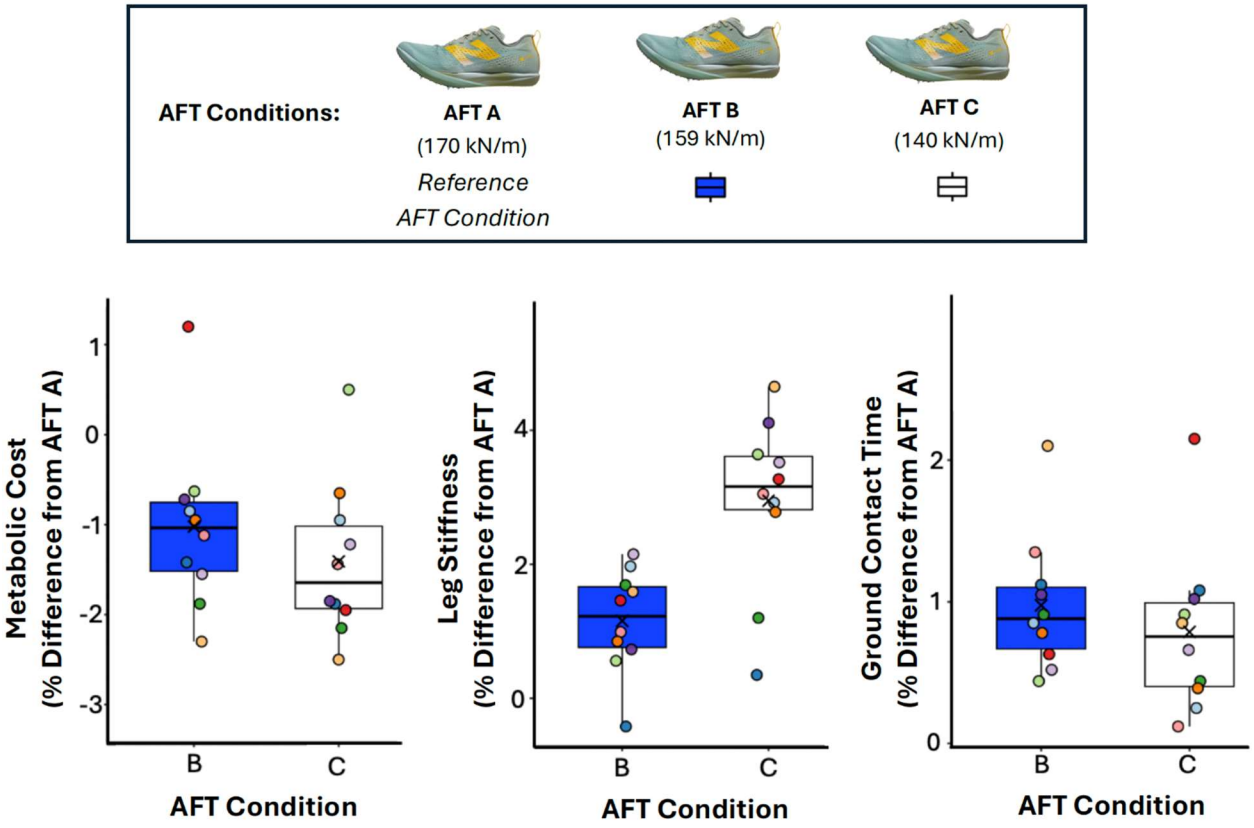
For elite and sub-elite distance runners wearing AFT spikes, the linear mixed models revealed that for every 1 kN/m decrease in AFT midsole stiffness, leg stiffness increased by 0.31% ($p = 0.018$) and metabolic cost decreased by 0.20% ($p = 0.041$). However, AFT midsole stiffness did not significantly influence ground contact time ($p = 0.49$) within the range of footwear tested.

Discussion

Reducing midsole stiffness in AFT spikes may decrease the metabolic cost of running, likely through increased leg stiffness. As a result, runners may experience race

performance improvements with lower midsole stiffness of AFT spikes. Consequently, further reductions in midsole stiffness within AFT spikes, relative to current commercial models, may offer a viable strategy for further enhancing distance-running performance.

Images (Optional)



References (Optional)

[1] Needles et al., JAP, 2024

[2] Joubert et al. IJSPP, 2024

[3] Rodrigo-Carranza et al. IJSPP, 2025

Acknowledgements (Optional)

New Balance Athletics, Inc.

Wu Tsai Human Performance Alliance

Session Category

OA119-05

The Effect of Footwear Stack Height and Outsole Traction on Ankle and Knee Kinematics during Downhill Trail Running

Ms. Kathy Reyes[1], Dr. J.J. Hannigan[2]

[1]Oregon State University, Corvallis, OR, United States. [2]Oregon State University - Cascades, Bend, OR, United States

Ms. Kathy Reyes

Introduction

Trail running is the most popular form of off-road running, often including downhill segments and uneven terrain [1]. These factors have influenced trail running footwear design, particularly midsole stack height and outsole traction. Despite these developments, trail runners continue to face high rates of running-related injuries at the ankle and knee [2]. Therefore, the purpose of this study was to examine the effect of midsole stack height and outsole traction on ankle and knee kinematics during downhill trail running.

Methods

Twenty-one trail runners averaging ≥15 miles/week participated in the study. After a 10-minute warm-up, participants ran five successful downhill trials at their comfortable pace (±10%) in three zero-drop footwear conditions in random order: maximal shoe with traction lugs (MAX; 35mm stack height), traditional shoe with traction lugs (TRAD; 25mm stack height), and traditional shoe without traction lugs (TRAD-NL; 20mm stack height).

Ten Sony RX0 II cameras captured running trials at 120 Hz along the downhill slope. Videos were processed in Theia3D, and frontal and sagittal knee and ankle kinematics (initial contact, peak, excursion, toe-off angles) were calculated in Visual3D. Differences between shoes were identified using repeated-measures ANOVAs (α=0.05) with Bonferroni-corrected pairwise comparisons, with effect sizes also calculated (η_p^2).

Results

A significant main effect of shoe was found for ankle inversion at initial contact (p=.019, η_p^2=.181) and toe-off (p=.025, η_p^2=.169), with the MAX shoe exhibiting greater inversion than the TRAD shoe (Table 1). No other significant differences were identified,

although a trending ~2-degree difference was observed in peak knee flexion with a moderate effect size (p=.073, η_p^2=.123) between the MAX shoe and the TRAD-NL shoe (Table 1).

Discussion

Inversion at initial contact and toe-off were significantly higher in the MAX shoe compared to the TRAD shoe during downhill trail running. Greater inversion at initial contact, observed in the MAX shoe, may increase the risk of sustaining a lateral ankle sprain [3]. Further research is needed to clarify how trail footwear features affect joint kinematics and injury risk.

Images (Optional)

Table 1. Selected variables of interest

Variable	MAX	TRAD	TRAD-NL	p-value	η_p^2
Inversion at Initial Contact (°)	4.2 ± 4.0	3.0 ± 3.4	3.0 ± 3.5	.019*	.181
Inversion at Toe-Off (°)	4.9 ± 3.5	3.6 ± 2.6	3.8 ± 3.1	.025*	.169
Peak Knee Flexion (°)	62.9 ± 6.8	61.6 ± 7.5	60.9 ± 6.9	.073	.123

*denotes a significant main effect of footwear

References (Optional)

[1] Scheer et al., *Int J Sport Med*, 2020.

[2] Hamill et al., *Foot Sci*, 2022.

[3] Chinn et al., *Phys Ther Sport*, 2013.

Acknowledgements (Optional)

The authors would like to acknowledge Loren Trottman, Anna Bennes, Kelsey Goertzen, Amy Farley, Austinn Rossetti, Dylan Schmidt, Katherine Swanson, and Gayatheri Iyer for their assistance with data collection.

Session Category

Human Motion and Performance: Sports

OA119-06

Foot-Stiffening Socks May Improve Running Economy

Ms. Kamen Wong, Ms. Hui Tang, Dr. Owen Beck Ph.D.

University of Texas at Austin, Austin, Texas, United States

Introduction

The foot splays with each ground contact. Due to cross-axis coupling, tightly wrapping the transverse arch mitigates foot splay and stiffens the entire foot, including the medial longitudinal arch [1]. Running with wrapped transverse foot arches improves ankle gear ratio during stance and reduces the metabolic cost of barefoot running [2], similar to the function of adding carbon fiber plates to shoe soles [3]. Here, we developed socks that are stiff along the distal metatarsal region (foot-stiffening socks) and assessed whether they decrease the metabolic cost of shod running, similar to that of carbon fiber plates.

Methods

Fifteen athletes performed 9 x 5-min treadmill running trials at 3.5 m/s with 5-min rest preceding each trial. After a familiarization, participants performed two running trials in each footwear condition using a counterbalanced trial order (ABCDDCBA). The footwear conditions included each sock and shoe combination: traditional athletic socks (control), foot-stiffening socks (stiff), flexible running shoes (control), running shoes with carbon fiber plates (carbon) embedded in the midsoles.

Results

The foot-stiffening socks applied 40 ± 4 N (Avg ± SD) more compressive force to the distal transverse foot than athletic socks ($p < 0.001$). The three-point bending stiffness of shoes with carbon fiber plates was 174.5% stiffer than athletic shoes. Foot-stiffening socks reduced the net metabolic power of running across shoes by 0.82% ($p = 0.030$), whereas carbon fiber plates did not reduce the metabolic power across sock conditions ($p = 0.341$). Moreover, the change in distal foot pressure applied by foot-stiffening socks versus traditional athletic socks was associated with a greater decrease in net metabolic power during running in control shoes ($r = -0.77$, $p = 0.007$).

Discussion

Foot-stiffening socks reduced the metabolic cost of shod running. The mechanisms underlying the greater metabolic reduction using foot-stiffening socks versus carbon fiber plates requires further analysis but may relate to the difference in metatarsophalangeal

joint mobility. Here, we present the first sock design that may be able to improve running performance.

Images (Optional)

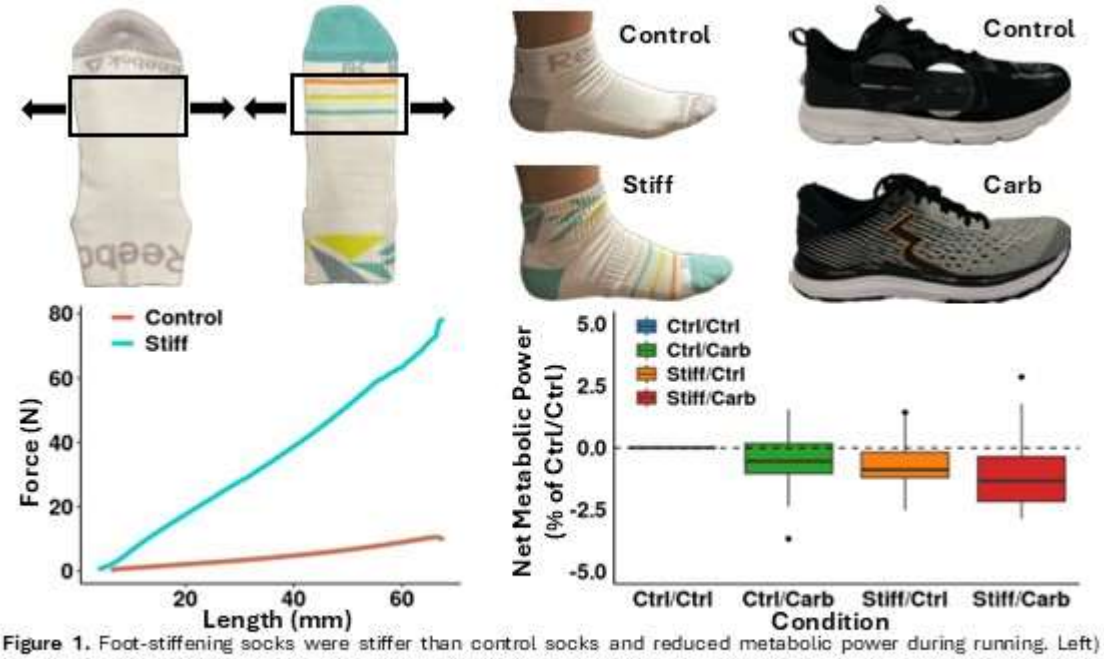


Figure 1. Foot-stiffening socks were stiffer than control socks and reduced metabolic power during running. Left) Control and foot-stiffening socks with boxed region that underwent mechanical testing as well as the corresponding force versus length results. Right) The tested socks and mass-matched shoes with and without carbon fiber midsoles. Net metabolic power during running in each footwear condition (sock/shoe) : control + control (Ctrl/Ctrl), control + carbon-fiber (Ctrl/Carb), stiff + control (Stiff/Ctrl), and stiff + carbon-fiber (Stiff/Carb).

References (Optional)

[1] Venkadesan et al., *Nature*, 2020

[2] Tang & Beck, *J Exp Biol,* 2025

[3] Roy & Stefanyshyn, *Med Sci Sports Exerc,* 2006

Session Category

Human Motion and Performance: Sports

OA120-02

Comparative Analysis of Resistive Immersed Surface and Immersed Boundary Methods for Aortic Valve Hemodynamics

Dr. Han Zhao[1], Dr. Alexander Kaiser[1], Dr. Fanwei Kong[2], Dr. Alison Marsden[1]

[1]Stanford University, Stanford, California, United States. [2]Washington University in St. Louis, St. Louis, Missouri, United States

Introduction

The modeling of aortic valve fluid-structure interaction (FSI) is essential for accurately predicting hemodynamics in normal and diseased valves. However, heart valve simulation remains a challenging task due to the significant motion and contact of valve leaflets. The resistive immersed surface (RIS) [1] method and the immersed boundary (IB) [2] method are two contrasting approaches for simulating heart valves. These two methods differ in coupling strategies and whether valve motion is prescribed or emergent. This study presents a comparative analysis of the RIS and IB methods for aortic valve hemodynamics and practical trade-offs.

Methods

We employ open-source implementations of the RIS and IB methods for aortic valve simulation. The RIS method is developed within the svMultiPhysics finite element solver. Valve leaflets are modeled with prescribed motion, and represented as thin resistive surfaces with a penalty force using an unfitted mesh. The framework thus uses one-way coupling, so valve motion influences hemodynamics, but hemodynamic changes do not alter valve motion. In contrast, the IB method is implemented using the IBAMR software, where valve leaflets are modeled as deformable elastic structures immersed in the fluid domain. The two-way coupled Navier–Stokes equations and structural dynamics are solved simultaneously. Both simulations use the same aorta geometry and boundary conditions, while the prescribed opening and closing leaflet motions in the RIS simulation are extracted from the IB simulation to ensure a consistent comparison.

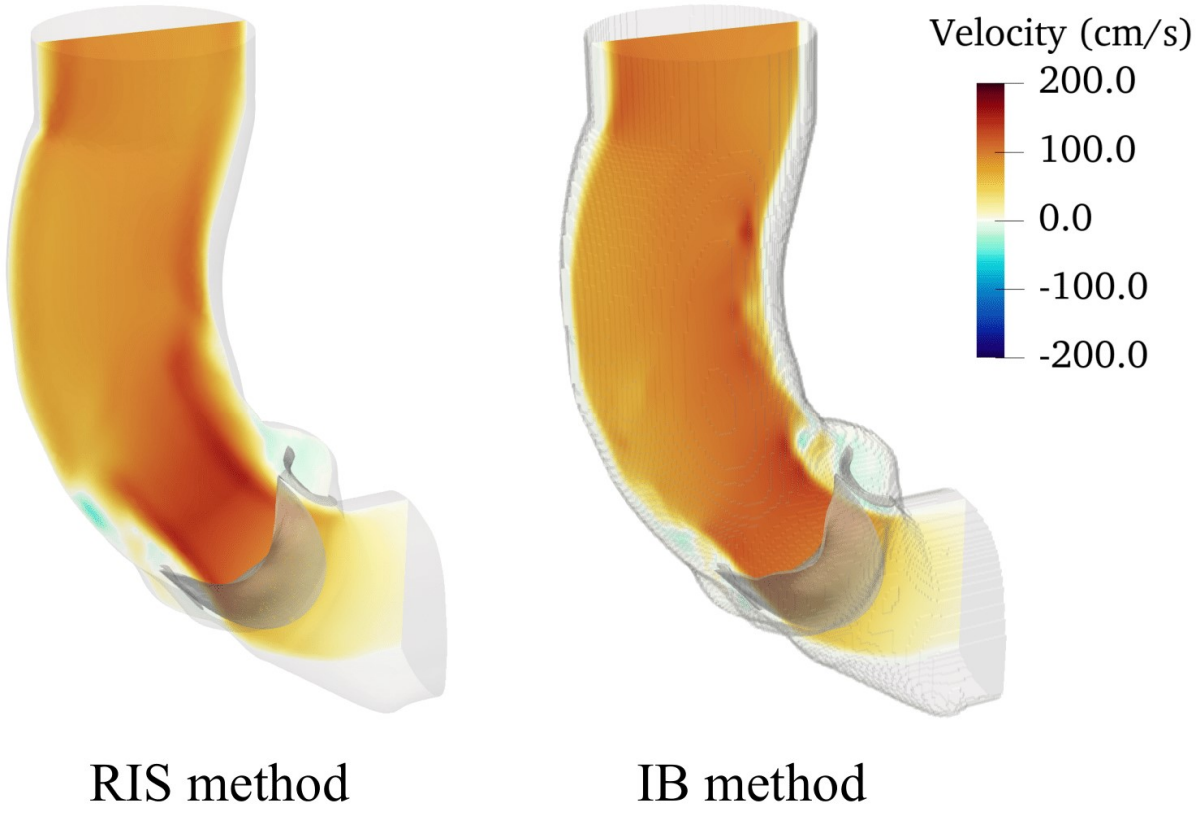
Results

Numerical results demonstrate that both methods produce pressure gradients within 5% relative difference across the valve and comparable bulk flow motion. However, the RIS simulation does not capture the fine-scale leaflet motion or allow for potential physiologic regurgitation due to prescribed valve kinematics. Conversely, the IB method resolves the emergent leaflet kinematics and deformation and more detailed flow patterns.

Discussion

The comparison shows that the RIS method can produce comparable bulk hemodynamics in situations where valve kinematics are known prior to running simulations and prescribed. This work offers guidance for method selection depending on the objectives and known data of the application.

Images (Optional)



References (Optional)

[1] Alberto Zingaro et al., Int J Numer. Methods Eng., 2023

[2] Boyce E. Griffith et al., J. Comput. Phys., 2007

Acknowledgements (Optional)

This work was supported by the National Science Foundation #2310909. ADK was funded in part by a grant from the National Institutes of Health #K25HL175208 and by the American Heart Association Grant #24CDA1272816.

Session Category

OA120-03

A Novel Computational Pipeline to Predict Hypoattenuating Leaflet Thickening Following Transcatheter Aortic Valve Replacement Using Pre-Procedural Computed Tomography Scans

Mr. Aniket Venkatesh MS[1], Mr. Noah Tregobov BS[2], Dr. Wenyuan Song PhD[1], Dr. Shantanu Bailoor PhD[3], Dr. Breandan Yeats PhD[1], Mr. Colin Jamieson BS[2], Mr. Joshua Yoon BS[2], Dr. Hoda Hatoum PhD[4], Dr. Huang Chen PhD[5], Mr. Beom Jun Lee MS[3], Dr. Milad Samaee PhD[1], Ms. Malvika Sawant[1], Ms. Megan De Jesus[1], Ms. Shreya Vavilala[1], Mr. John Khoo BMed[2], Dr. Philipp Blanke MD[2], Dr. Jonathon Leipsic MD[2], Mr. Gaurav Gulsin BMed[6], Dr. Vinod Thourani PhD[7], Dr. David Meier MD[2], Dr. Stephanie Sellers PhD[2], Dr. Lakshmi Dasi PhD[1]

[1]Georgia Institute of Technology, Atlanta, Georgia, United States. [2]St. Paul's Hospital and University of British Columbia, Vancouver, British Columbia, Canada. [3]DASI Simulations, Dublin, Ohio, United States. [4]Michigan Technological University, Houghton, Michigan, United States. [5]University of Nevada, Las Vegas, Las Vegas, Nevada, United States. [6]University of Leicester and the NIHR Leicester Biomedical Research Centre, Glenfield Hospital, Leicester, East Midlands, United Kingdom. [7]Marcus Heart Valve Center, Piedmont Heart Institute, Atlanta, Georgia, United States

Introduction

Leaflet thrombosis is often detected after transcatheter aortic valve replacement (TAVR) as hypoattenuating leaflet thickening (HALT) on computed tomography (CT). In our prior work, we predicted HALT risk in a retrospective cohort of patients with tricuspid aortic valves undergoing TAVR with a balloon-expandable valve using geometric and hemodynamic features. Among the metrics included in the model (e.g., normalized circulation (NC) in the neo-sinuses), no single parameter demonstrated strong predictive power for HALT. The model also relied on actual post-deployment TAV dimensions and positioning, thus limiting its clinical translatability. In this study, we developed a computational pipeline to predict HALT risk in a retrospective cohort of patients with either tricuspid or bicuspid aortic valve anatomy, using only pre-TAVR CT.

Methods

Aortic anatomies of 151 patients who underwent balloon-expandable TAVR with a SAPIEN 3 platform were reconstructed from pre-TAVR CTs to simulate post-CT TAVR deployment at peak systole using reduced order modeling (ROM) and finite element analysis (FEA) (Figure

1A). Aortic annulus area was measured to determine TAV size based on SAPIEN 3 guidelines. For each patient, the TAV was expanded nominally and deployed at conventional and high depths depending on TAV size and rotated about its vertical axis at each depth (Figure 1B). Algorithms were developed to predict post-TAVR geometric and hemodynamic features from simulation outputs (Figure 1C), which were used to compute NCs across all deployments. NC threshold vs density plots were produced by varying NC and determining number of values that either fall below that NC (high HALT risk region) or above (low HALT risk region).

Results

Following training with a subset of 27 patients with known HALT outcomes (n=12 HALT-, n=15 HALT+), NC and density thresholds of 106-107 and 20%, respectively, resulted in highest area under ROC curve (AUC=0.78) (Figure 1D).

Discussion

This novel computational pipeline performed adequately in the initial training cohort and is now suitable for testing on the remaining 124 patients with unknown HALT outcomes. With further refinement and training and validation in a larger, distinct patient population, this tool may eventually support procedural planning. Future development may also involve adapting the pipeline for other transcatheter valve platforms.

Images (Optional)

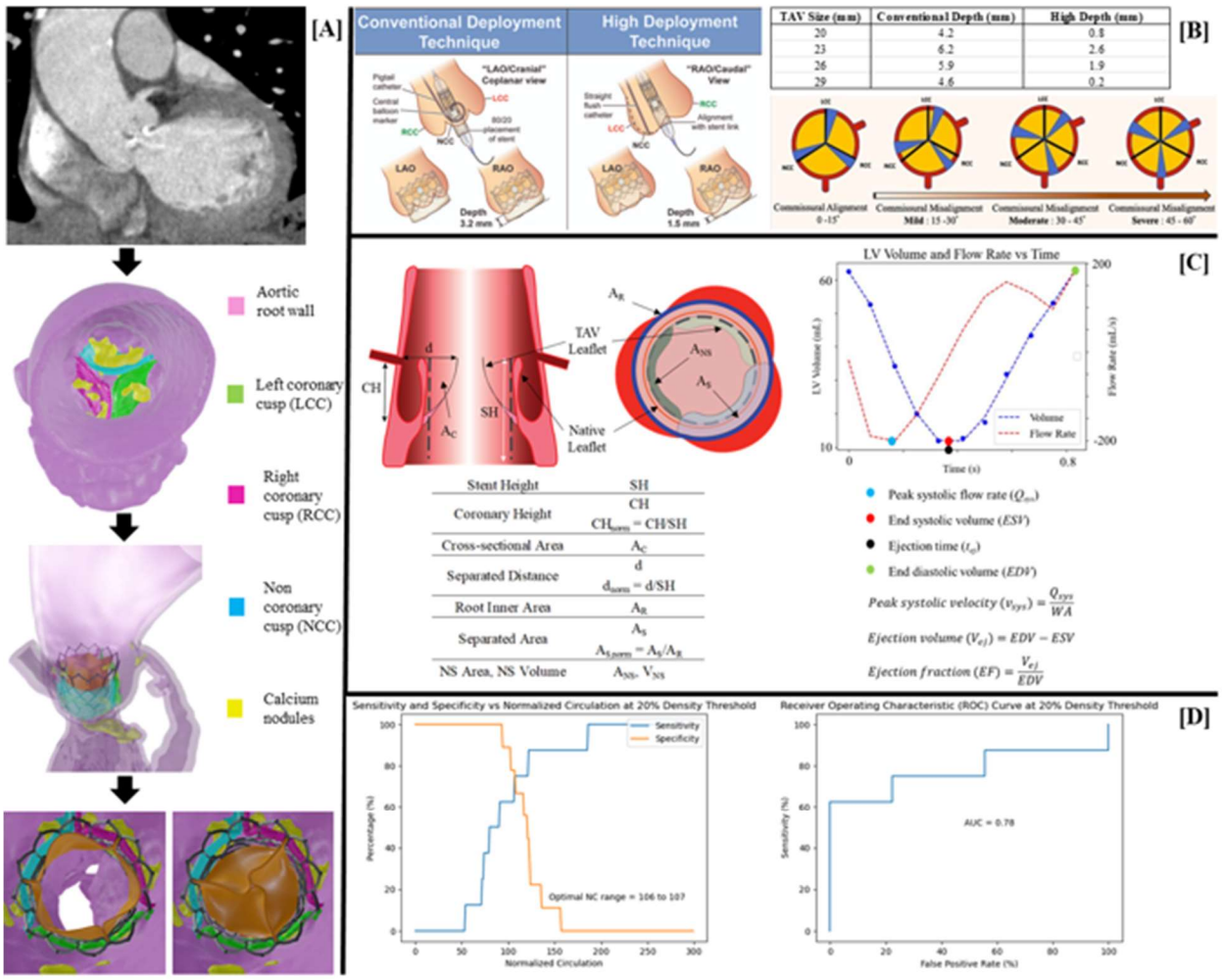


Figure 1: TAVR ROM and FEA simulations using pre-TAVR CT aortic segmentation (A), different TAV depths and commissural alignments simulated for each patient (B), post-TAVR geometric and hemodynamic features predicted using ROM and FEA outputs (C), and optimal NC and density thresholds determined through sensitivity vs specificity analysis on the training cohort (D).

References (Optional)

Session Category

Cardiovascular/Cardiorespiratory Biomechanics: Methods, Models and Applications

OA120-04

Fluid-Structure Interaction Model of a Neonatal Quadricuspid Valve

Dr Karoline-Marie Bornemann, Dr Perry S. Choi, Mr Jay Huber, Dr Alexander K. Reed, Mr Amit Sharir, Dr Shiraz A. Maskatia, Dr Michael R. Ma, Dr Alison L. Marsden, Dr Alexander D. Kaiser

Stanford University, Stanford, CA, United States

Introduction

Quadricuspid valve morphology is a rare congenital valve anomaly in which the valve has four instead of three cusps of various size distributions. It commonly occurs in truncus arteriosus (TA), accounting for around 25% of patients. TA is a rare, severe congenital heart disease (CHD) in which blood from both ventricles enters a truncal valve through a ventricular septal defect (VSD) and exits the heart through only one great artery instead of two. In this study, we simulate the interaction between a quadricuspid valve of a neonate after TA repair in a patient-specific geometry with the surrounding blood flow.

Methods

The quadricuspid valve is constructed using an elasticity-based design approach. Based on the patient valve's gross morphology extracted from ECHO and the assumption that the valve supports a prescribed pressure, we derive its mechanical equilibrium equations. Their solution predicts a loaded configuration from which we derive a constitutive law with scaled membrane stiffnesses to achieve the predicted tensions. By solving the equilibrium equations with the derived constitutive law under zero pressure, we obtain an open valve configuration serving as initial condition. The aortic wall geometry is segmented from CT imaging using SimVascular. Fluid-structure interaction simulations are performed with the Immersed Boundary Method. Boundary conditions are derived from patient data and optimized using a 0D-model to reflect neonatal hemodynamics.

Results

During valve opening, an accelerating jet emerges which deflects toward the outer aortic curvature. An initial four-lobed starting vortex is formed which transitions into multiple elongated streamwise vortices. During systole, free edge displacement and fluttering dynamics of the thickened leaflets are highly influenced by the proximity to the surrounding vessel. During systolic deceleration, the adverse pressure gradient across the valve leads

to transient backward flow in the ascending aorta. Although the valve model is symmetric, we observe asymmetric closure kinematics and central coaptation.

Discussion

Our study provides the first fluid-structure interaction simulation of a patient-specific aortic geometry with quadricuspid valve in neonatal hemodynamic conditions. Analysis of both blood flow patterns and leaflet kinematics reveal insights into quadricuspid valve performance and can aid in predicting individual outcomes in affected patients.

Images (Optional)

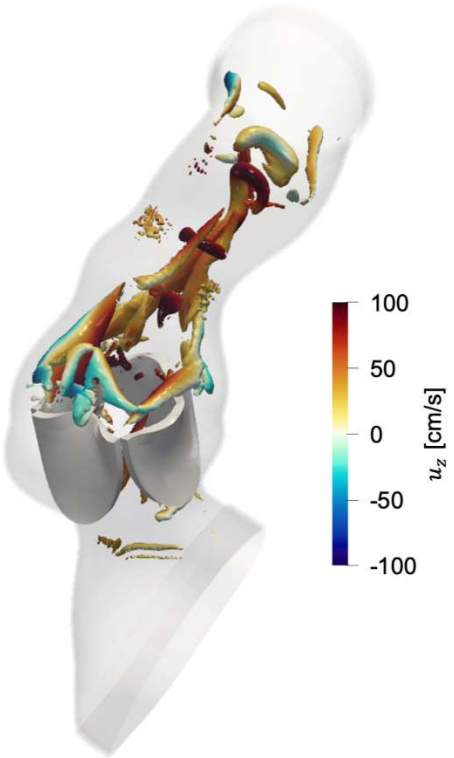


Figure: Neonatal quadricuspid valve in a patient-specific geometry: Iso-surfaces of λ_2-criterion colored in streamwise velocity.

Acknowledgements (Optional)

NIH grant K25HL175208, AHA Career Development Award 24CDA1272816, MCHRI Instructor K Award Support to ADK

Session Category

Cardiovascular/Cardiorespiratory Biomechanics: Methods, Models and Applications

OA120-05

3D Simulations of Electrospun Biomaterials for Replacement Heart Valves

PhD Student Ulas Akyuz[1,2], Dr. Michael Sacks[1,2,3]

[1]The University of Texas at Austin James T. Willerson Center for Cardiovascular Modeling and Simulation, Austin, Texas, United States. [2]The University of Texas at Austin Department of Mechanical Engineering, Austin, Texas, United States. [3]The University of Texas at Austin Department of Biomedical Engineering, Austin, Texas, United States

Introduction

Current replacement heart valves (RHVs) remain limited by inadequate long-term durability, thrombogenic risks, and the intrinsic variability of pericardial biomaterials. For example, despite the current success of transcatheter aortic valve replacement (TAVR), long-term durability remains unknown. Existing leaflet materials, derived from chemically treated pericardium, continue to fail from calcification and mechanical fatigue. To address these limitations, we investigate hydrogel-coated electrospun (HES) biomaterials as a new platform for RHV, leveraging their tunable mechanical behaviours and decoupled structural (mesh) and blood-contacting (gel) feature. We hypothesize that systematic, simulation-guided development of HES-based RHVs can yield designs with superior durability.

Methods

We use our novel HES constitutive model, which incorporates fiber alignment, fiber properties, and fiber–fiber interactions, along with separate gel and mesh components, to capture a broad fabrication space and support high-fidelity hyperelastic simulations.This constitutive model formed the foundation of an in-silico parametric design pipeline that utilized NURBS-based geometric representations with a neural-network finite element (NNFE) solver trained directly from the governing PDE across physiological loading states. To evaluate tri-leaflet mechanics under quasi-static peak tensile conditions, we performed all computations using CARDIAX, a JAX-based FE and isogeometric analysis (IGA) platform that leverages GPUs, providing at least a 20-fold speedup over traditional solvers and, when combined with the NNFE surrogate framework, enabling rapid predictions without experimental training data.

Results

Our results demonstrate that subtle modifications in leaflet fiber architecture can homogenize strain fields, a key determinant of durability. Eleven major design variables derived from current TAVR geometries were systematically explored to maximize strain homogenization and leaflet longevity. The HES simulations spanned the full known

fabrication space, enabling systematic optimization of fiber distributions, thickness variations, and leaflet geometry. To date, our simulations have identified leaflet shapes that substantially reduce peak tensile concentrations and promote more uniform load sharing. Several candidate designs exhibit markedly improved predicted durability compared with current pericardial-based TAVR leaflets.

Discussion

This work establishes a customizable, rationally engineered biomaterial platform coupled with a high-speed modeling pipeline for next-generation RHVs. The resulting framework supports rapid iteration, compatibility with evolving HES formulations, and direct translation toward clinical applications, including patient-specific TAVR designs.

Session Category

Cardiovascular/Cardiorespiratory Biomechanics: Methods, Models and Applications

OA121-01

Anti-Rotation Load-Leg in Infant Car Seats Under Misuse Conditions

Mr. Hossein Bahreinizad Ph.D. Student[1], Dr. Antonio Fernandes Human Factors Engineer[2], Dr. Suman Chowdhury Associate Professor[1]

[1]University of Florida, Gainesville, Florida, United States. [2]Uppababy, Boston, massachusetts, United States

Introduction

Motor vehicle crashes (MVCs) remain a leading cause of fatal or near-fatal injuries for infants and young children. Rear-facing child restraint systems (CRS) can help reduce these injuries by limiting the head, neck, and chest movements during a crash. However, misuse of these restraints is common, despite various safety awareness programs. Issues such as loose harnesses or improper installation can significantly diminish their protective effectiveness. This study aimed to evaluate whether an anti-rotational load leg can help counteract the negative effects of CRS misuse by conducting the CR 35/35 test.

Methods

We conducted CR-35/35 sled tests using a rear-facing CRS with a CRABI 12-month infant dummy, as per standard procedures. Four installation conditions reflected proper use and common misuses: 1) proper seat with proper harness (Baseline), 2) proper seat with loose harness (Misuse 1), 3) loose seat with proper harness (Misuse 2), and 4) loose seat with loose harness (Misuse 3). We tested each condition with and without the load leg. To assess load leg performance, we estimated several commonly used injury metrics, including HIC_{36} and HIC_{15} for head injuries, Nij for neck injuries, and 3-ms chest acceleration for chest or trunk injuries.

Results

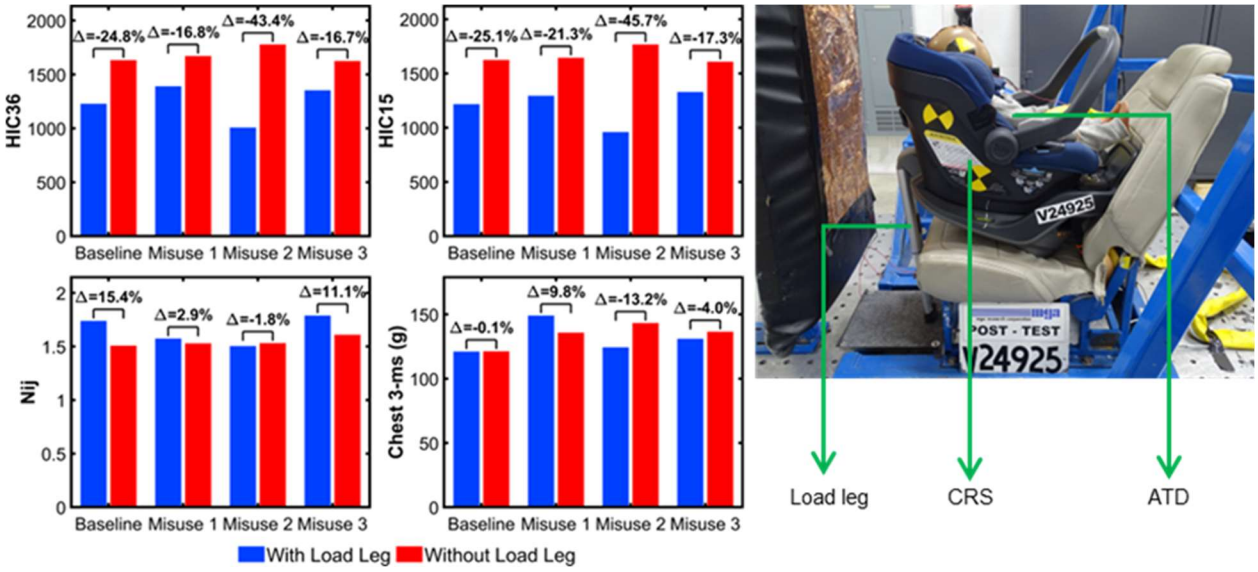
The load leg reduced head injury metrics across all conditions: HIC_{36} decreased by 24.8% in Baseline, 16.8% in Misuse 1, 43.4% in Misuse 2, and 16.7% in Misuse 3. HIC_{15} showed similar reductions of 25.1%, 21.3%, 45.7%, and 17.3%, with the highest reduction occurring in Misuse 2.

However, the load leg increased Nij in most conditions, increasing by 15.4% in Baseline, 2.9% in Misuse 1, and 11.1% in Misuse 3, and decreased by 1.8% only in Misuse 2. Chest 3-ms acceleration also showed mixed responses, slightly reduced in Baseline and Misuse 3 but increased in Misuse 1 and Misuse 2.

Discussion

Overall, the use of load legs provides improved head protection under both proper and misuse conditions, with consistent reductions in HIC_{36} and HIC_{15}. Interestingly, it showed increased Nij across most conditions and mixed chest responses, indicating the need to replicate its performance evaluation across other CRS and dummy types to understand the full spectrum of its benefits.

Images (Optional)



Session Category

Injury Biomechanics: N/A

OA121-02

Identifying Predictors of Lap-Belt Submarining Through ROC-Based Metric Selection in Finite Element Simulations of 50th Percentile Male HBMs and ATDs

Mr. Alex Kalmar-Gonzalo B.S.[1], Mr. Bharath Koya M.S., B.E.[1], Dr. Karan Devane Ph.D, M.Tech, B.E.[1], Dr. Fang-Chi Hsu Ph.D, B.S.[1], Mr. Don Sherman M.S., B.S.[2], Dr. Cynthia Bir Ph.D, M.S., B.S.[2], Dr. Dale Bass[2], Dr. F. Scott Gayzik Ph.D, M.S., B.S.[1]

[1]Wake Forest University School of Medicine, Winston-Salem, NC, United States. [2]Wayne State University, Detroit, MI, United States

Introduction

Lap-belt submarining is associated with severe injury and has become an increased concern in the automotive safety field [1]. We present a computational study using two finite element models, intended to identify and evaluate candidate submarining metrics (CSMs) for classifying submarining outcomes in frontal impacts.

Methods

400 simulations were conducted using the Global Human Body Models Consortium (GHBMC) M50 THAN-OS v.2.3, and the THOR 50M v.1.9.2 (Farmington Hills, Michigan). Prior to simulation the M50-THAN-OS, a variant of the M50-OS model sized to match the THOR ATD, was validated against 4 studies of reclined occupant loading. Each model was run in an identical set of frontal impact simulations that varied seatback recline angle, seat pan angle, seatbelt anchor position, knee bolster presence, load limiting and pretensioning values, and delta-v. Submarining outcomes for each simulation were determined based on belt kinematics relative to the ASIS, providing a binary classification of submarining. A set of approximately 70 candidate submarining metrics including displacements, accelerations, rotational velocities, pressures, forces, moments, and strains were extracted. Receiver Operating Characteristic (ROC) analysis was completed for each CSM and the area under the ROC curve (AUC) was calculated to quantify the performance of each.

Results

ROC analysis revealed that several CSMs performed well in identifying submarining outcomes. The CSM with the greatest AUC value was pelvic rotation with an average AUC value of 0.82 across both models. A range of AUC values were observed with some candidate metrics being deemed non-predictive.

Discussion

This ROC analysis provides a systematic and quantitative method for evaluating submarining outcomes based on intrinsic model outputs and extrinsic environmental-based outputs. These findings offer insight into how HBMs and ATDs respond physically in both submarining and non-submarining scenarios and importantly show that certain outputs can be quite predictive in both types of surrogates. We provide suggested CMSs for use in large scale design of experiments studies or high throughput studies where individual analysis of simulation outcomes is impractical. This research contributes to the broader goal of mitigating abdominal and spinal injury in vehicle crash.

References (Optional)

[1] Leung, Y.C. et al. , SAE Transactions, 1982

Acknowledgements (Optional)

This study was funded by the National Highway Traffic Safety Administration (693JJ921D000024) and supported by the Global Human Body Models Consortium.

Session Category

Injury Biomechanics: N/A

OA121-03

Computational Reconstruction of 30 Real-World Motorcycle Collisions With Facial Impact to Guide Future Helmet Standards

Dr Lucas Low[1], Dr Claire Baker[1], Dr Will Dawber[1], Dr Shiyang Meng[2], Dr Mazdak Ghajari[1]

[1]Imperial College London, London, Greater London, United Kingdom. [2]Autoliv Research, Vårgårda, Vårgårda Municipality, Sweden

Introduction

Motorcycle helmets are a major focus for improving motorcyclists' safety, as they substantially reduce the rate of head injuries [1]. However, facial impacts are minimally tested in helmet safety standards internationally [2], despite accounting for over 50% of head impacts [3]. Facial impact often presents with injury remote to the location of impact, such as base of skull fracture (BSF), which is over-represented in fatal cases [3]. The aim of this study is to reconstruct real-world motorcycle collisions leading to facial impacts, to better understand the loading conditions and associated injuries, and inform future helmet standards.

Methods

The cost-free UK Road Accident In-Depth Studies (RAIDS) database was parsed for motorcycle collisions with confirmed facial impact. Reconstructions were developed in Madymo using an ellipsoid pedestrian model and helmet, as well as case-specific motorcycle and car models. Photographic evidence was used to verify the kinematics of the reconstructions, and an uncertainty analysis of motorcycle speed, orientation, rider posture, and rider stature (50th and 95th percentile male) was conducted to capture a range of possible impact configurations. Accelerations and loads significantly larger in BSF cases were used to calculate injury risk curves.

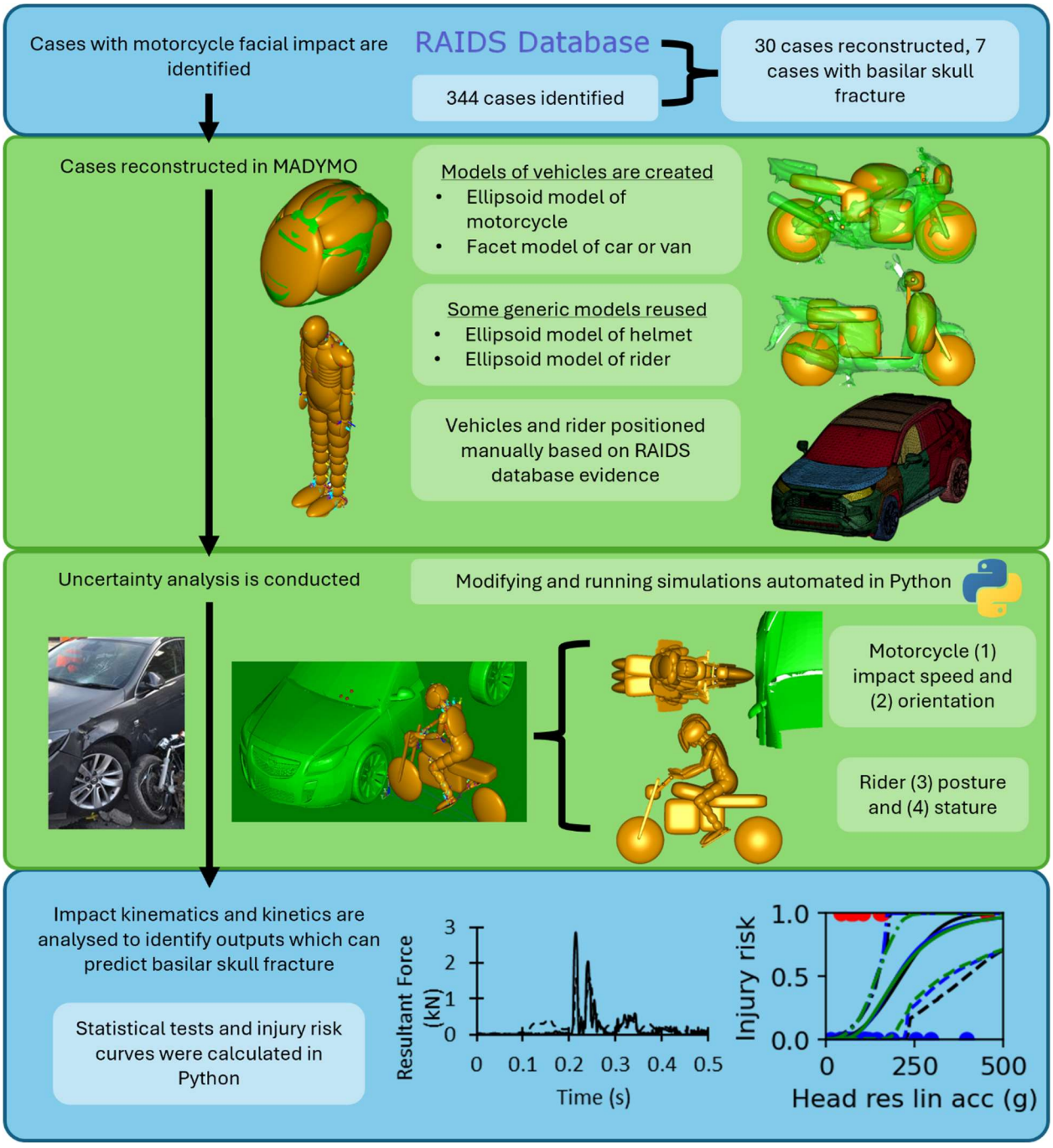
Results

30 real-world cases were reconstructed, producing 1,476 simulations from the uncertainty analysis. The head impact speeds and angles had medians of 8.7m/s and 47.5° (interquartile ranges 5.1-15.0m/s and 32.7°-60.7°). In the head and neck, cases with BSF had larger linear and rotational acceleration, and higher loads in extension, towards the posterior, and in tension. Injury risk curves were developed for the resultant accelerations and loads.

Discussion

The reconstructions provide insight into typical facial impact configurations of motorcycle collisions. The dataset may inform the head orientation, impact velocity, and angle of a future helmet facial impact test. Additionally, injury risk curves developed to predict BSF provides a biomechanical basis for the injury criterion for helmet design. Overall, this study establishes the evidence base for defining typical motorcycle facial impact conditions and helmet assessment criterion, to inform future helmet standards.

Images (Optional)



References (Optional)

[1] Rice, T., *et al.*, Accid. Anal. Prev., 2016
[2] Smith, T., *et al.*, GRSP, 2025
[3] Baker, C. *et al.*, IRCOBI, 2025

Acknowledgements (Optional)

The funding of Autoliv Research, and the support of the RAIDS database and TBI-REPORTER, is all gratefully acknowledged.

Session Category

Injury Biomechanics: N/A

OA121-04

Advancing Biofidelity: Subject-Specific Validation of Whole-Body Human Models for Frontal Impacts

Dr. Sujata Khandare, Mr. Yang-Shen Lin, Mr. Kyle Boyle, Ms. Anne Bonifas, Mr. Carl Miller, Dr. Matthew Reed, Dr. Jingwen Hu

University of Michigan Transportation Research Institute, Ann Arbor, MI, United States

Introduction

Finite element HBMs are typically validated using population-averaged PMHS response corridors [1], but these methods rely on geometric and mass scaling and do not capture specimen-specific variation in body shape, bone morphology, or posture, factors that strongly affect belt interaction, especially in reclined seating. As virtual testing expands to diverse occupants, these limitations have become clearer. Subject-specific validation, achieved by morphing HBMs to individual PMHS geometry and posture [2], was developed and evaluated in this study.

Methods

Eight male PMHS (mean age 68.6±9.0 years, stature 172.4±4.0cm, BMI 23.8±3.1kg/m^2) were tested at 32/50 km/h and 25°/45° recline. Subject-specific HBMs were created by morphing the simplified GHBMC model using statistical posture and external shape [3,4], and ribcage/pelvis/lower-extremity geometry models [5,6], with RBF morphing [7] and joint-based positioning. Simulations matched belt, seat, and pulse conditions, and CORA with Signal Magnitude Factor weighting [8] was applied.

Results

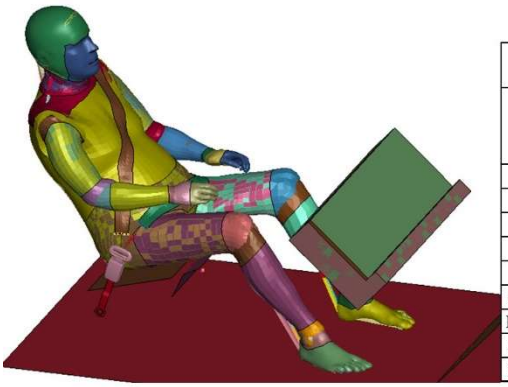
At 32 km/h, 25°, improvements were observed at the head (0.73→0.76), T1 (0.67→0.80), T8 (0.66→0.72), T12 (0.65→0.72), and L4 (0.58→0.67). At 32 km/h, 45°, head, T1, and T8 correlations increased (0.68→0.75, 0.77→0.85, 0.69→0.75). At 50 km/h, 25°, head, T1, and T8 again improved, with T12 unchanged. At 50 km/h, 45°, head correlations increased (0.69→0.82), while thoracic and lumbar responses showed variability. Pelvic and lower-extremity changes were modest and condition-dependent.

Discussion

Subject-specific HBMs better reproduced PMHS head and upper thoracic motion, reflecting the influence of specimen-specific spinal curvature and belt interaction. Lumbar, pelvic, and leg responses were more variable due to differences in pelvis orientation and

belt fit. Results emphasize the value of individualized validation, with future work extending to small female PMHS.

Images (Optional)



Signal	Velocity 32 km/h, Recline 25°		Velocity 32 km/h, Recline 45°		Velocity 50 km/h, Recline 25°		Velocity 50 km/h, Recline 45°	
	GHBMC Midsize Male	Subject-specific HBM	GHBMC Midsize Male	Subject-specific HBM	GHBMC Midsize Male	Subject-specific HBM	GHBMC Midsize Male	Subject-specific HBM
Head CG	0.73	0.76	0.68	0.75	0.71	0.76	0.69	0.82
T1	0.67	0.80	0.77	0.85	0.59	0.67	0.78	0.76
T8	0.66	0.72	0.69	0.75	0.55	0.70	0.68	0.62
T12	0.65	0.72	0.67	0.66	0.59	0.59	0.68	0.53
L4	0.58	0.67	0.65	0.58	0.45	0.40	0.62	0.56
Left Hip Joint Center	0.60	0.61	0.57	0.75	0.46	0.47	0.53	0.53
Right Hip Joint Center	0.71	0.70	0.60	0.57	0.46	0.45	0.73	0.56
Left Femur Midshaft	0.72	0.77	0.83	0.85	0.53	0.54	0.72	0.62
Right Femur Midshaft	0.74	0.75	0.71	0.72	0.60	0.61	0.77	0.63

Figure 1: Subject-specific finite element human body model (HBM) configured to match the anthropometry and posture of an 80-year-old male post-mortem human subject (PMHS) with a stature of 169.1 cm and a BMI of 27.75. The model is shown positioned in the experimental seating environment used for sled testing. Table shows the weighted CORA scores comparison between the baseline GHBMC midsize male model and subject-specific HBMs across four frontal-impact conditions (32 and 50 km/h; 25° and 45° recline). Values represent the average CORA score of the two PMHS specimens tested in each condition.

References (Optional)

[1] Nicholas Vavalle *et al.* Ann Biomed Eng, 2015

[2] Kai Zhang *et al.* J Biomech, 2017

[3] Matthew Reed *et al.* Hum Factors, 2002

[4] Byoung-Keon Park *et al.* Ergonomics, 2022

[5] Erik Brynskog *et al.* J Biomech, 2021

[6] Katelyn Klein *et al.* Ann Biomed Eng, 2015

[7] Jingwen Hu *et al.* 25th ESV, 2017

[8] Jeremy Schap *et al.* Ann Biomed Eng, 2019

Acknowledgements (Optional)

National Highway Traffic Safety Administration - Contract no. 693JJ921D000021/693JJ923F000218

Session Category

Injury Biomechanics: N/A

OA122-01

Tendon Fibrils and Fascicles of the *oim* Mouse Model of Osteogenesis Imperfecta Exhibit Signs of Increased Advanced Glycation End Product (AGE) Crosslinking

Ms. Magdalena Fuchs[1], Dr. Mathis Uelner[1], Ms. Lauren Battle[2], Ms. Anxhela Docaj[2], Mr. Felix Groß[1], Dr. Orestis G. Andriotis[1], Dr. Alessandra Carriero[2], Univ.Prof. Dr. Philipp J. Thurner[1]

[1]TU Wien, Vienna, Vienna, Austria. [2]The City College of New York, New York City, NY, United States

Introduction

The *oim/oim* mouse model of Osteogenesis Imperfecta (OI) produces solely homotrimeric collagen I. In *oim/oim* bone, Advanced Glycation End Products (AGEs) are increased [1]. We hypothesize that the presence of homotrimeric collagen I and AGEs alter *oim/oim* collagen fibrils' properties and consequently collagenous tissue mechanical properties. Therefore, we quantified the mutations' effect on tail tendon (TT) fibrils' and fascicles' mechanical properties.

Methods

TT fibrils and TT fascicles from 14-week-old, *oim/oim* (OIM) and wild-type (WT) mice were tested in tension at $5\%s^{-1}$ and $0.1\%s^{-1}$, respectively. For fibrils, a custom-built tensile testing device [2] was used. Fibril diameters and hydration-induced swelling were assessed using Atomic Force Microscopy (AFM).

TT fascicles' cross-sectional areas were determined via Micro-CT imaging, and tensile tests were conducted using a tensile testing machine (zwickiLine z2.5, Zwick-Roell). AGEs were quantified via the fluorescence of tissue hydrolysates.

Results

While tensile moduli and ultimate stresses of WT fibrils are lower than *oim/oim* fibrils (n=21 WT, n=18 *oim/oim*), *oim/oim* fascicles (n=20 WT, n=28 *oim/oim*) did not differ in tensile modulus and ultimate stress, but showed lower ultimate strains. Despite being similar in material parameters, since *oim/oim* fascicles were thinner than WT fascicles, at the whole-organ level their mechanical competence is compromised as described in [3].

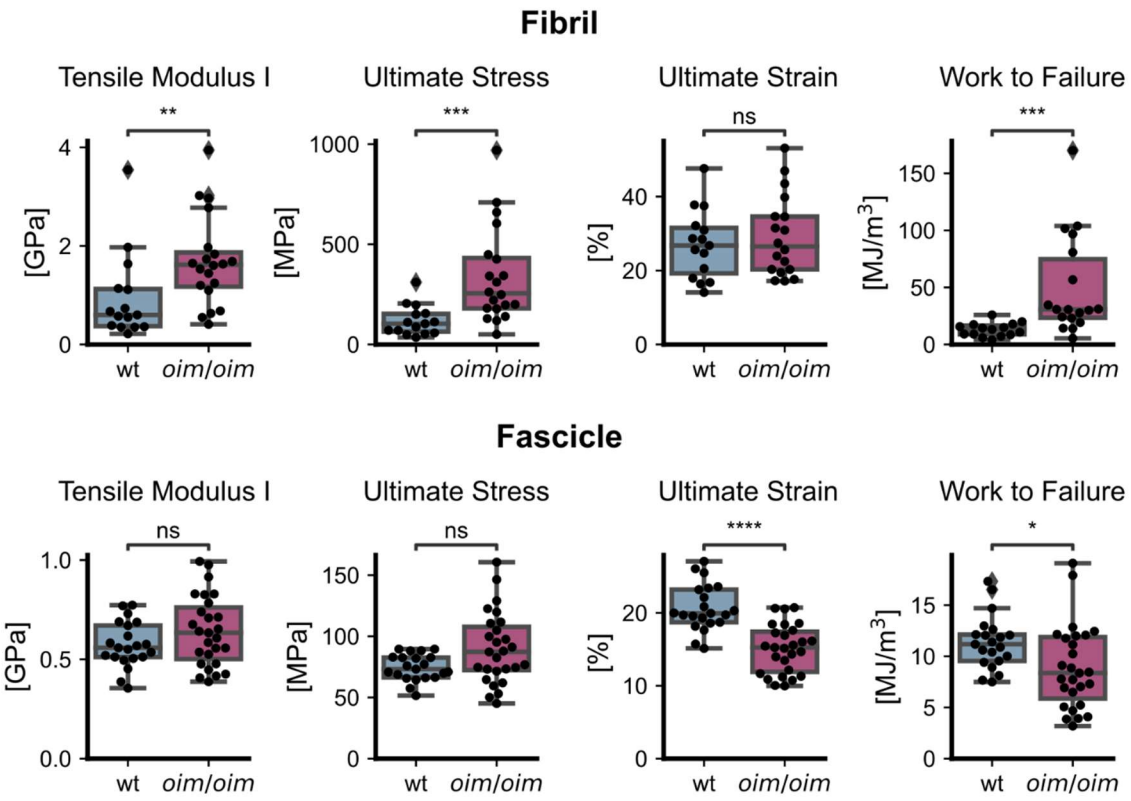
Eight of the 21 *oim/oim* fibrils tested displayed increased tensile modulus pre-rupture, not present in WT-CFs. WT fascicles exhibited decreased tensile modulus before failure, not present *oim/oim* fascicles.

Fluorescent AGEs are increased twofold in *oim/oim* TT vs. WT ones (n=5/group).

Discussion

Effects observed in *oim/oim* fibrils, and fascicle-level decreased ultimate strain, and more "brittle" failure, resemble changes due to in-vitro induced AGEs [4,5]. This highlights the importance of considering altered crosslinking for the understanding of collagen mutations. Whether AGEs potentiate or partially rescue impaired tissue mechanical properties caused by homotrimeric collagen I, remains to be elucidated.

Images (Optional)



References (Optional)

[1] A. Carriero *et al.*, *J. Bone Miner. Res.*,2014

[2] M. Nalbach *et al.*, *Rev. Sci. Instrum.*,2022

[3] K. Misof *et al.*, *J. Clin. Invest.*,1997,

[4] R. B. Svensson *et al.*, *Acta Biomater,*2018,

[5] A. Gautieri *et al.*, Matrix Biol.,2017

Acknowledgements (Optional)

This work was sponsored by National Science Foundation (Grant NSF 1829310) for AC, LB, AD.

Session Category

Organ and Tissue Biomechanics: N/A

OA122-02

The Hidden Influence of Osteoporosis on Bone Regeneration During Distraction Osteogenesis

Mr Juan José Toscano-Angulo[1], Dr Juan Mora-Macías[2], Dr Pablo Blázquez-Carmona[3], Dr Antonia Pajares[4], Dr Juan Morgaz[5], Dr Esther Reina-Romo[1]

[1]University of Seville, Seville, Andalucía, Spain. [2]University of Huelva, Huelva, Andalucía, Spain. [3]University of Cadiz, Cadiz, Andalucía, Spain. [4]University of Extremadura, Badajoz, Extremadura, Spain. [5]University of Cordoba, Cordoba, Andalucía, Spain

Introduction

Osteoporosis is characterized by trabecular microarchitecture deterioration, raising fracture risk. Osteoporotic post-fracture regeneration remains a clinical challenge due to the low prevalence of successful consolidation. Although the bone transport procedure is recognized for promoting bone healing, the effect of osteoporosis on its clinical efficacy has not been proven.

In this study, we conducted an *ex vivo* characterization of the regenerated woven bone and the adjacent cortical tissue to investigate the impact of osteoporosis on distraction osteogenesis.

Methods

Fifteen sheep underwent osteoporosis induction. Subsequently, distraction osteogenesis treated a 15 mm bone defect surgically created in the right hind metatarsus, stabilized by an external fixation. The subjects were randomly sacrificed at days 40 or 100 after surgery. The dorsal half of the woven tissue formed (W) and the adjacent cortical tissue (C_P, proximal, and C_D, distal) were used for μCT and nanoindentation. The plantar half of W was used for analysis of volumetric composition and elemental mineral mass. Cortical samples from the contralateral metatarsus (C_C) served as control measurements. Osteoporotic results were compared with non-osteoporotic similar studies.

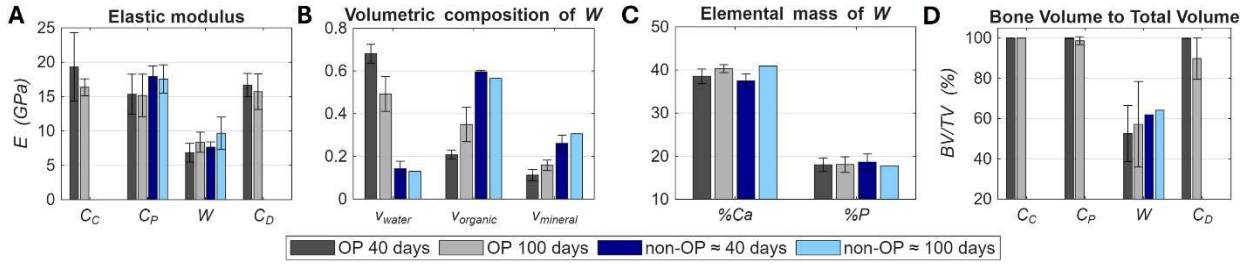
Results

Figure 1A revealed similar elastic modulus of woven and adjacent cortical tissue between groups, without differences among osteoporotic cortical samples. Figure 1B reported a significantly higher specific water volume in the osteoporotic group. Consequently, specific organic and mineral volumes were significantly lower in this group. Figure 1C did not show differences in woven mass percentage of calcium and phosphorus. Figure 1D also revealed no significant differences in woven *BV/TV*. Meanwhile, *BV/TV* decreased in the adjacent cortical tissues over time compared to control data.

Discussion

These findings indicate that osteoporosis does not compromise the intrinsic bone quality of the newly formed woven tissue. However, it markedly reduces the amount of woven bone matrix produced within the distraction callus, suggesting a disease-related delay. Moreover, the mineral of adjacent cortical bone appears to be resorbed and mobilized to support woven bone ossification.

Images (Optional)



Acknowledgements (Optional)

Grant PID 2023-148828OB-I00 funded by MICIU/AEI/10.13039/501100011033 and by ERDF/EU.

Session Category

Organ and Tissue Biomechanics: N/A

OA122-03

3D-DXA–Based Finite Element Models Improve Hip Fracture Prediction versus aBMD in the Japanese Population-Based Osteoporosis (JPOS) Cohort Study

Dr Elham Alizadeh[1], Dr Junko Tamaki[2], Dr Takahiro Tachiki[3], Dr Yuho Sato[4], Dr Masami Hamada[5], Dr Kouji Tsuda[2], Dr Asako Kudo[2], Dr Kuniyasu Kamiya[6], Dr Nami Imai[7], Dr Akemi Nitta[8], Dr Kumiko Ohara[9], Dr Naoyuki Takashima[9], Dr Jun Kitagawa[10], Dr Katsuyasu Kouda[8], Dr Akemi Morita[11], Dr Kazuhiro Uenishi[12], Dr Etsuko Kajita[13], Dr Sadanobu Kagamimori[14], Dr Ludovic Humbert[15], Prof Jérôme Noailly[1], Dr Masayuki Iki[8]

[1]Pompeu Fabra University, Barcelona, Catalonia, Spain. [2]Osaka Medical and Pharmaceutical University, Osaka, Osaka Prefecture, Japan. [3]University of Kochi, Kochi, Kochi Prefecture, Japan. [4]Jin-ai University, Echizen, Fukui, Fukui Prefecture, Japan. [5]Josai International University, Chiba, Chiba Prefecture,, Japan. [6]Kobe City College of Nursing, Kobe, Hyogo Prefecture, Japan. [7]Nihon Pharmaceutical University, Kita-ku, Tokyo, Tokyo Metropolis, Japan. [8]Kansai Medical University, Osaka, Osaka Prefecture, Japan. [9]Kyoto Prefectural University of Medicine, Kyoto, Kyoto Prefecture, Japan. [10]Kitasato University, Sagamihara / Tokyo region, Kanagawa Prefecture, Japan. [11]Tottori University, Yonago, Tottori, Tottori Prefecture, Japan. [12]Kagawa Nutrition University, Saitama, Saitama Prefecture, Japan. [13]Nagoya University, Nagoya, Aichi Prefecture, Japan. [14]University of Toyama, Toyama, Toyama Prefecture, Japan. [15]3D-Shaper Medical, Barcelona, Catalonia, Spain

Introduction

Areal bone mineral density (aBMD) derived from dual-energy X-ray absorptiometry (DXA) is the clinical gold standard for diagnosing osteoporosis. Quantitative computed tomography (QCT)-based finite element (FE) simulations can improve hip fracture prediction compared with aBMD, but need for QCT scans limits clinical adoption. Advances in 2D–3D modelling enable the generation of patient-specific 3D-DXA models from standard DXA images, offering potential for fracture risk prediction when combined with 3D FE analyses of osteoporosis patient cohorts [1]. This study aimed to evaluate whether the exploitation of 3D-DXA-FE simulations for fracture prediction can be extended to population cohorts.

Methods

We conducted a case–control study including 1,636 women of the JPOS Study, 85 of whom suffered a hip fracture over 20-year follow-up. 3D-DXA-FE models were generated from hip DXA scans out of 3D-Shaper® (v2.14) appearance and shape modelling [2]. Side-

fall was simulated by applying displacement to the femoral head under rigid-body constraints, with the greater trochanter and shaft fixed. A perfect elastoplastic material model used bone density-dependent material properties and tension- and compression-specific yield parameters, distributed over the mesh. Failure was defined from the nonlinear force–displacement curve at the onset of force decline. Global mechanical descriptors, including strength, nonlinear deformation, and energy absorption, were quantified from FE analyses and used for fracture discrimination [1]. Figure 1 illustrates the overall methodology.

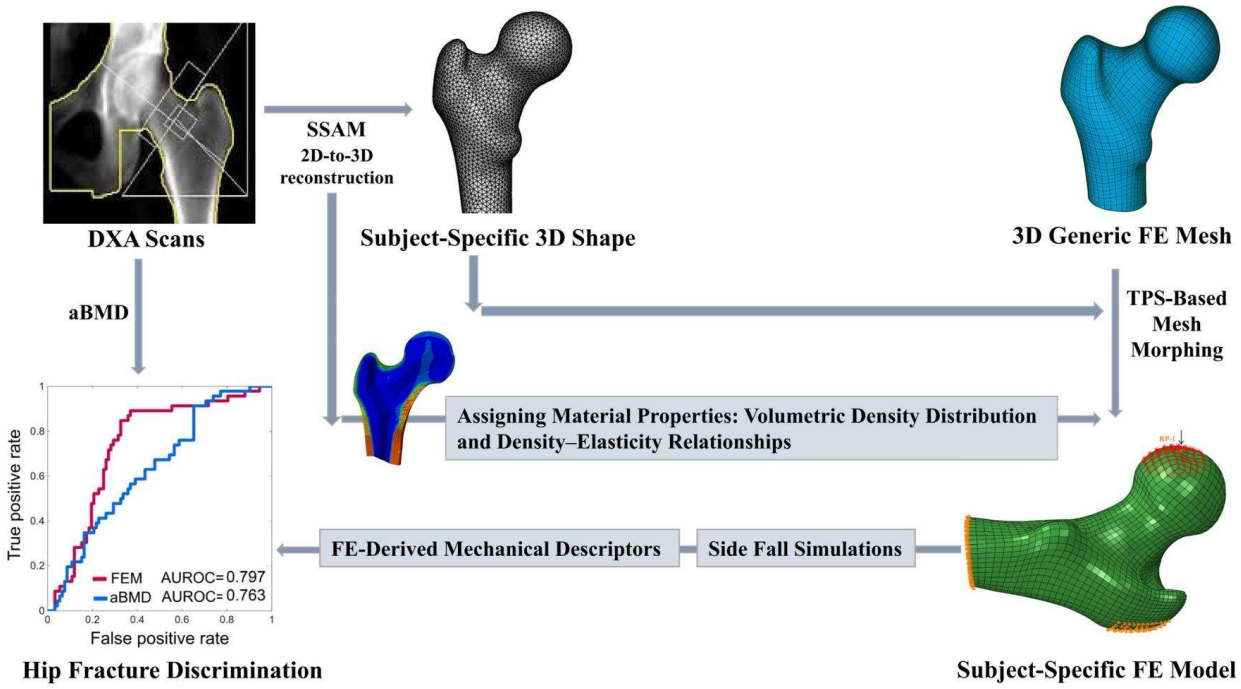
Results

The area under the receiver operating characteristic curve (AUROC) with leave-one-out cross-validation showed that combining strength and residual energy (AUROC: 0.797) improved fracture prediction compared with total hip aBMD (AUROC: 0.763). The difference between the two AUROCs was statistically significant according to the DeLong test ($p = 0.0267$).

Discussion

This is the first study demonstrating that global mechanical descriptors obtained from standard hip DXA scans outperform aBMD in predicting incident hip fractures in a population-based, prospectively followed cohort of women. These findings highlight the potential of integrating 3D-DXA and FE modelling into existing DXA-based clinical workflows to enhance fracture risk assessment.

Images (Optional)



References (Optional)

[1]Alizadeh et al., Front. Bioeng. Biotechnol., 13: 1673339, (2025)

[2] Ruiz Wills et al., Bone, 121: 89–99, (2019)

Acknowledgements (Optional)

Spanish Government (CPP2021-008574, CPP2023-010970); AGAUR (2023 BP 00224)

Session Category

Organ and Tissue Biomechanics: N/A

OA122-04

Mechanical Loading Supports Targeted Modeling More Than Remodeling When Combined With Anabolic Pharmacological Treatment

Dr. Friederike A Schulte[1], Dr. Francisco C Marques[1], Dr. Julia K Griesbach[1], Dr. Claudia Weigt[1], Dr. Marcella von Salis-Soglio[1], Dr. Floor M Lambers[1], Dr. Clemens Kreutz[2], Dr. Michaela Kneissel[2], Dr. Peter J Richards[2,3], Dr. Gisela A Kuhn[1], Prof. Dr. Ralph Müller[1]

[1]Institute for Biomechanics, ETH Zurich, Zurich, Zurich, Switzerland. [2]Musculoskeletal Disease Area, Novartis Institutes for Biomedical Research, Basel, Basel, Switzerland. [3]Bone and Stem Cell Research Group, CABMM, University of Zurich, Zurich, Zurich, Switzerland

Introduction

Mechanical loading increases bone strength, whereas postmenopausal osteoporosis compromises it. This suggests that the systemic character of pharmacological treatments could be improved by mechanical loading to focus treatment effects where mechanical competence is most needed. Because mechanical loading can stimulate both remodeling and targeted modeling-based bone formation, it remains unclear which process primarily contributes to strength gains under combined interventions. Here, we investigated how mechanical loading with three pharmacological treatments influences modeling, remodeling, and their relationship to trabecular bone strength.

Methods

Time-lapsed *in vivo* micro-computed tomography images of the 6th caudal vertebra were obtained from C57BL/6 mice ovariectomized at 15 weeks-of-age and treated from week 20 to 24 without (VEH; n=25) or with mechanical loading (ML; n=26), bisphosphonates (BIS; n=9; BIS+ML: n=9), parathyroid hormone (PTH: n=10; PTH+ML: n=9), or sclerostin antibodies (SclAB: n=9; SclAB+ML: n=8). Strain energy density (SED) was computed by micro-finite element analysis, and trabecular bone strength predicted using the Pistoia criterion [1]. Modeling and remodeling amounts per bone surface were quantified from biweekly registered images [2] and correlated with changes in bone strength.

Results

SED decreased and predicted bone strength increased in all treatment groups (Fig. 1a, $p<0.05$). Remodeling amounts were lowest in the SclAB+ML and PTH+ML group, modeling amounts were highest in these same groups (Fig. 1b). Neither modeling nor remodeling

amounts in BIS differed from BIS+ML. Modeling amounts correlated highly with predicted strength gains (R=0.928, p<0.0001; Fig. 1c). Remodeling amounts correlated moderately inversely with predicted strength gains using a power-law fit (rho=0.476, p<0.0001, Fig. 1c).

Discussion

Mechanical loading, when combined with anabolic treatments such as PTH and SclAB, enhances bone strength primarily through increased modeling rather than remodeling. The strong correlation between modeling amount and predicted strength gains identifies modeling as a key driver of mechanical adaptation, whereas only substantial suppression of remodeling yields any strength benefit. The lack of significant response in BIS-groups indicates that antiresorptives alone are insufficient to support mechanically guided adaptation. These findings suggest that incorporating controlled mechanical loading into osteoporosis therapies could selectively stimulate modeling-based bone formation thus enhancing mechanical competence.

Images (Optional)

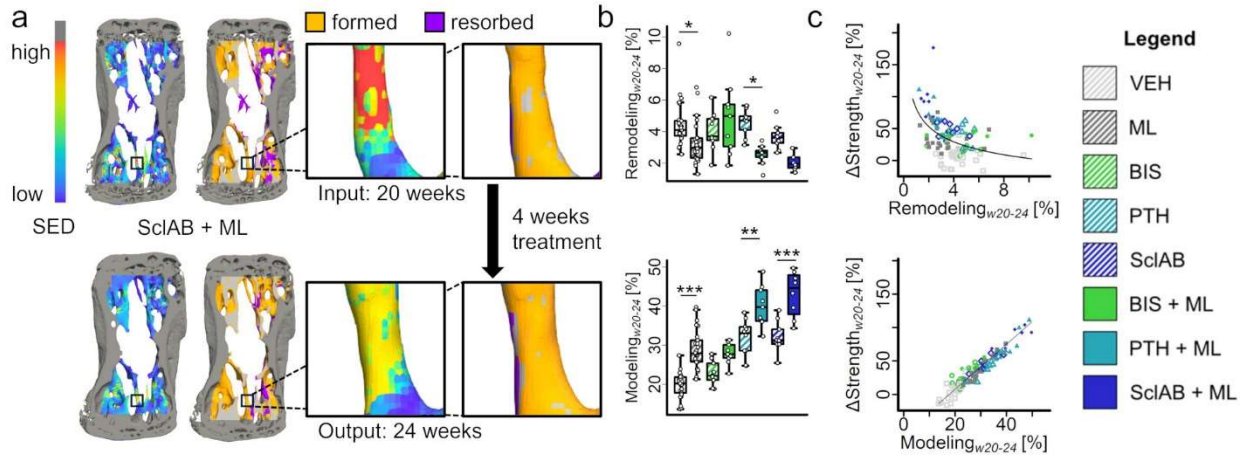


Figure 1: (a) Finite-element and registered time-lapsed *in vivo* micro-CT image of the sixth caudal vertebra from a sclerostin-antibody-treated mouse subjected to mechanical loading (SclAB + ML). A magnified view highlights a highly loaded modeling site, which results in a more homogeneous strain energy density (SED) distribution after 4 weeks of treatment. **(b)** Remodeling expressed as a percentage of bone surface in VEH, ML, BIS, BIS+ML, PTH, PTH+ML, SclAB, and SclAB+ML groups. Significance is shown only between each treatment and its corresponding combination group; *p<0.05, **p<0.01, ***p<0.001 **(c)** Regression analyses showing the relationship between remodeling (power-law fit) and modeling (linear fit) activity and the predicted changes in trabecular bone strength over 4 weeks.

References (Optional)

[1] Pistoia *et al.,* Bone, 2002

Session Category

Organ and Tissue Biomechanics: N/A

OA122-05

The Effect of Short-Term Continuous Administration of Alendronate on Bone Quality and Strength of Rabbit Tibia

Dr. Tsolmonbaatar Khurelbaatar, Mr. Andrew Sawatsky, Ms. Ariunzaya Dorj, Dr. W. Brent Edwards

University of Calgary, Calgary, Alberta, Canada

Introduction

Alendronate (ALN) is a potent bisphosphonate used to treat osteoporosis and other bone diseases [1]. In preclinical studies, ALN is typically delivered several times per week via subcutaneous injection, but the efficacy of continuous drug delivery remains unknown. This study quantified the effects of four weeks of continuous ALN administration on cortical bone quality and strength in the rabbit tibia.

Methods

Thirteen female rabbits received ALN (85.7 μg/kg/day, ALN, n = 7) or injectable water (VEH, n=6) for four weeks via subcutaneous osmotic pumps (ALZET 2ML4). Fluorochrome bone labels were injected throughout drug treatment, and changes in areal bone mineral density (aBMD) were measured using dual-energy X-ray absorptiometry. The rabbit tibiae were harvested after treatment and rectangular beams (0.9 mm×1 mm×16 mm) were prepared from anterior, posterior, medial, and lateral quadrants of the cortical shaft at the distal, middle, and proximal regions of the left tibiae (Figure 1). The contralateral tibial shafts of the right tibiae were used for dynamic histomorphometry. Micro-computed tomography images (voxel size=5 μm) from the middle 3 mm of each beam were used to quantify cortical porosity (Ct.Po), vascular canal thickness (Ca.Th), and canal number per volume (Ca.N). Beams were then monotonically tested in four-point bending to compute the ultimate bending stress (σ_{bend}) and elastic modulus (E).

Results

A statistically significant increase in aBMD at the leg was observed in the ALN ($p<0.01$), but not the VEH ($p=0.46$) group. This corresponded with a significantly lower number of labeled osteons in the ALN compared to the VEH group ($p=0.03$). Linear mixed-effects models revealed that σ_{bend} and E varied by region and quadrant, but treatment did not affect σ_{bend} or E. There were also no effects of ALN on Ct.Po, Ca.Th, or Ca.N.

Discussion

Short-term, continuous administration of ALN increased aBMD and decreased remodeling activity in the rabbit tibia; however, significant effects of ALN on cortical bone microstructure and strength were not observed. Thus, improvements in aBMD with this model were likely localized to trabecular regions, and more prolonged duration therapy may be required to influence cortical microarchitecture and strength.

Images (Optional)

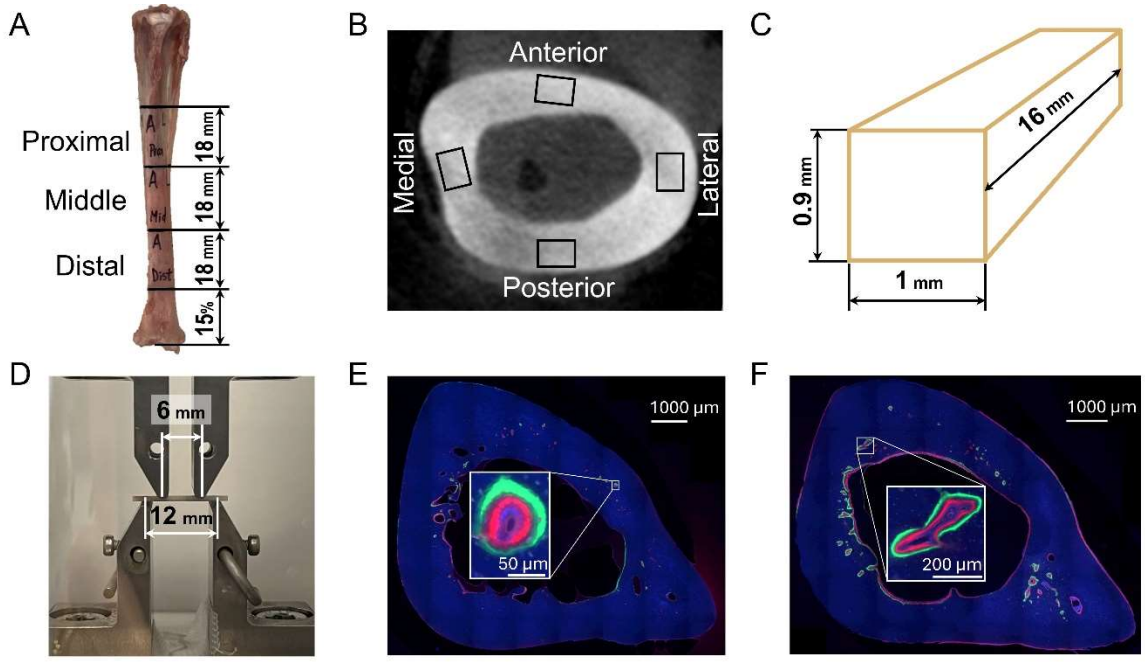


Figure 1. (A) Proximal, middle, and distal regions. **(B)** Rectangular beam samples were prepared from each quadrant. **(C)** Beam sample dimensions. **(D)** Test setup for four-point bending test. Representative fluorescence microphotograph of tibial cross-section at the midshaft in ALN **(E)** and VEH **(F)** groups. Here, green, red, and blue colors correspond to the Calcein, Alizarin Complexone, and Calcein Blue fluorochromes, respectively.

References (Optional)

[1] Steven Cummings *et al.*, Bone, 2020

Session Category

Organ and Tissue Biomechanics: N/A

OA122-06

Evaluating Hip Fracture Risk Through 3D-DXA FE Mechanical Descriptors: A Comparison of Abaqus and MoFEM

PhD Abdollah MoslemiVaraki[1], Dr Elham Alizadeh[1], Dr Veera Venkata Satya Varaprasad Jakka[1], PhD Callum J. Runcie[2], PhD Andrei G Shvarts[2], Professor Łukasz Kaczmarczyk[2], PhD Carlos Ruiz Wills[1], Dr Luis Del Rio[3], Dr Silvana Di Gregorio[3], PhD Ludovic Humbert[4], Professor Jérôme Noailly[1]

[1]Pompeu Fabra University, Barcelona, Barcelona, Spain. [2]Glasgow Computational Engineering Centre (GCEC), James Watt School of Engineering, Glasgow, Glasgow, United Kingdom. [3]CETIR Ascires, Barcelona, Barcelona, Spain. [4]3D-Shaper Medical, Barcelona, Barcelona, Spain

Introduction

3D modeling from femoral DXA scans can enhance aBMD-based fracture-risk assessment through subject-specific FE analyses [1]. This study evaluates global descriptors from 3D-DXA-based FE models to distinguish patients with incident hip fractures, comparing the open-source MoFEM with Abaqus to facilitate 3D-DXA-FE simulations in software-as-a-medical-device.

Methods

Hip DXA scans from 64 fracture and 64 control patients were retrospectively processed with 3D-Shaper® (v2.14) to obtain femur geometries [2]. Side-fall was simulated, imposing displacement on the femoral head and constraining the greater trochanter [2]. FE simulations were performed with both Abaqus and MoFEM. Each solver used a perfect elastoplastic formulation with bone density-dependent material properties with Asymmetric Compression–Tension Yield Criterion.

The initial decline of the global force-displacement response indicated the failure point. Extracted descriptors were bone strength (Fu), maximum displacement (Du), and nonlinear energy (Wu). A piecewise linear model further provided elastic quantities (FLE, DLE, WLE), nonlinear deformation (D1), and post-yield residual displacement (DR) and dissipated energy (WD) [2]. Fracture discrimination by FE-derived metrics, aBMD, and 3D-DXA trabecular vBMD was assessed using AUROC from logistic regression with leave-one-out validation.

Results

Bone strength (Fu) achieved an AUROC similar to vBMD (72%) for both solvers (Table 1). When Fu was combined with Du, Wu, or D1, discrimination with Abaqus, reached 79%. MoFEM reproduced elastic-domain results well but underperformed Abaqus with post-yield quantities. Combining FLE and WD provided MoFEM's highest AUROC (75%), compared to 77% with Abaqus.

Discussion

3D-DXA-FE-based descriptors surpassed aBMD and vBMD in fracture discrimination, particularly when post-yield behavior was captured. MoFEM matched Abaqus in the elastic range but diverged for post-yielding. This difference is mainly linked to differences in yield surface: 'Von Mises' in Abaqus, while not being the most elegant model, imposed a sudden tension-compression transition, which seemed to favor discrimination. The 'Paraboloidal' in MoFEM, with a smooth surface, probably led to more subtle differences among models, as elements entered plasticity. **Current developments target plasticity models common to MoFEM and ABAQUS with smooth yield surfaces.**

Images (Optional)

Table 1. AUROC values for fracture discrimination

Descriptors	AUROC		Difference (%)
aBMD	0.69		-
vBMD	0.72		-
	Abaqus	MoFEM	
$\boldsymbol{F_u}$	**0.72**	**0.72**	**0**
D_u	**0.78**	0.72	7.72
W_u	0.52	0.51	**1.16**
$\boldsymbol{F_u + D_u}$	**0.79**	0.74	6.67
$\boldsymbol{F_u + W_u}$	**0.79**	0.74	7.08
$\boldsymbol{F_u + D_1}$	**0.79**	0.74	6.67
$F_u + W_R$	0.73	0.73	**0.69**
$F_{LE} + D_{LE}$	0.74	0.73	**0.95**
$F_{LE} + W_{LE}$	0.74	0.73	**1.09**
$F_{LE} + D_1$	**0.78**	0.74	**4.72**
$F_{LE} + W_D$	**0.77**	0.75	**2.90**

References (Optional)

[1] Ruiz Wills et al, Bone, 2019

[2] Alizadeh et al, Frontiers, 2025

Acknowledgements (Optional)

Spanish Government (CPP2021-008574, CPP2023-010970); AGAUR (2023 BP 00224)

Session Category

Organ and Tissue Biomechanics: N/A

OA123-01

A Shoe-Integrated Soft Actuator System for Augmenting Plantarflexion During Walking

Dr. Sahel Mohammadi Ghalehney, Dr. Ahad Behboodi

University of Nebraska-Omaha, Omaha, NE, United States

Dr. Sahel Mohammadi Ghalehney

Introduction

Weak ankle plantarflexion in children with neuromuscular disorders and adults with mobility impairments reduces push-off power and leads to inefficient gait. Passive ankle–foot orthoses improve stability but cannot actively restore propulsion, and existing robotic orthoses are often bulky, noisy, and visually obtrusive—especially for pediatric users. Stacked dielectric elastomer actuators (SDEAs) offer a lightweight, compliant, and silent alternative capable of rapid longitudinal contraction, enabling compact and muscle-like actuation. The goal of this work is to embed SDEAs within a shoe midsole to provide unobtrusive push-off assistance. We call this device the Flash-Sole. **Objective**: To quantify the capability of SDEAs to power Flash-Sole.

Methods

An instrumented pediatric foot–ankle model was developed to quantify the plantarflexion moment generated by the Flash-Sole. Ankle torque was measured using a FUTEK TDD400 reaction torque sensor mounted coaxially with the joint (Fig. 1a, b). SDEAs were integrated beneath the heel region to serve as the active push-off elements (Fig. 1c). The actuators were pre-compressed to 95% of their original 40 mm length and activated using a Trek HA51U-3B high-voltage amplifier driven by a National Instruments NI-9263 module. Torque data were collected through an NI-9237 bridge module at 1 kHz. To reflect gait biomechanics, the measured ankle torque was scaled to an equivalent metatarsal-joint moment using a 137 mm heel-to-metatarsal lever arm.

Results

The Flash-Sole generated 16.87 Nm of plantarflexion moment, compensating for approximately 60–85% of the typical biological push-off demand for a 25 kg child (≈20–28 Nm).

Discussion

These findings demonstrate that embedding SDEAs into footwear can provide meaningful plantarflexion assistance while remaining lightweight, silent, and unobtrusive. The device can partially restore push-off power in children with ankle control deficits and represents a promising step toward shoe-integrated soft robotic assistance. Current limitations include the modest strain capacity of SDEAs (~11%) and the need for a low-power (~1 W) but high-voltage (~1200 V) driver, which constrains the availability of portable electronics suitable for wearable use. Future work will focus on redesigning the midsole to improve SDEA integration, optimizing actuator placement beneath the heel to maximize push-off moment, and incorporating gait-synchronized control to enable real-world walking assistance.

Images (Optional)

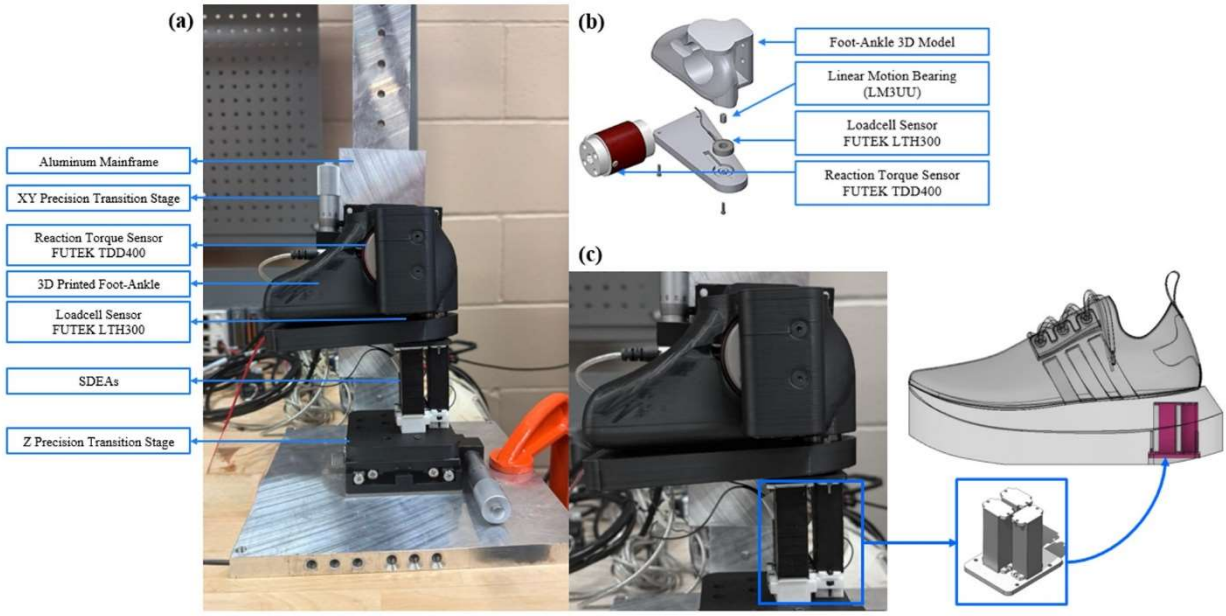


Figure 1. Experimental hardware used to benchmark the push-off force and ankle torque of the pediatric foot–ankle model. (a, b) A rigid aluminum frame supports a 3D-printed foot–ankle model instrumented with a FUTEK TDD400 reaction torque sensor and a FUTEK LTH300 heel load cell. (c) Artificial muscles are integrated beneath the heel as active push-off elements. X–Y–Z translation stages enable precise alignment and preload adjustment during testing.

References (Optional)

Acknowledgements (Optional)

This study received support from the National Institutes of Health (NIH) through Grants P20GM109090 and P20GM152301.

Session Category

Rehabilitation Biomechanics and Human Factors: Rehabilitation

OA123-02

Virtual Reality Design Influences Biomechanical Adaptation and Motor Strategies to a Novel Prosthesis Sorting Task

Mr. Kenneth M Mazariegos B.A.[1], Mr. Gerbert Funes Alfaro B.S.[2], Mr. Marek Kwasek B.S.[1], Dr. Peter Bishay Ph.D.[1], Dr. Stefanie Drew Ph.D.[1], Dr. Thomas Chan Ph.D.[1], Dr. Jacob Hinkel-Lipsker Ph.D.[2]

[1]California State University, Northridge, Northridge, CA, United States. [2]California State University, Northridge, Northridge, CA, United Kingdom

Mr. Kenneth M Mazariegos

Mr. Gerbert Funes Alfaro

Mr. Marek Kwasek

Dr. Peter Bishay

Dr. Stefanie Drew

Dr. Thomas Chan

Introduction

Evidence suggests that the visual fidelity (i.e., visual realism) and cognitive demand (i.e., psychological realism) of a virtual reality (VR) rehabilitation paradigm may influence motor learning [1]. However, the combined effects of these features on learning and real-world transfer remain untested; a crucial gap given that variability in VR fidelity may underlie mixed reports of VR training efficacy. Thus, the purpose of this study is to determine how these VR design features impact reaching biomechanics during learning and real-world transfer of a novel arm prosthesis control task.

Methods

Participants with and without a transradial amputation (anticipated *n* = 40 without and *n* = 10 with amputation) are being recruited for this ongoing study. Each participant learns to perform a block sorting task using a custom foot-controlled below-elbow prosthesis. After a real-world baseline assessment, participants practice this task twice per week for five weeks in a virtual environment that differs in terms of visual fidelity (high (HV) or low (LV)) and cognitive demand (high (HC) or low (HC)). All participants then perform a real-world transfer test. Inertial measurement units (IMUs) placed on the trunk and arm are used to calculate sagittal-plane reaching kinematics as well as forearm linear jerk.

Results

Preliminary results (*n* = 4, all without amputation) indicate that training in HV/HC VR resulted in large changes in reaching kinematics between baseline and transfer, including a large decrease in shoulder flexion and a large increase in elbow extension compared to the other groups. Moreover, this group demonstrated a drastic increase in forearm linear jerk during transfer, indicating a less smooth reaching strategy.

Discussion

These results indicate that high-fidelity (instead of highly realistic) VR conditions (both visual and cognitive) alter (or modify) participants' reaching strategies. Across groups, VR training also promoted a more distal, elbow-dominant control strategy. Preliminary results indicate that VR design features modify motor learning and biomechanical behavior, reinforcing the need for rehabilitation protocols to consider how fidelity levels influence movement quality and real-world transfer.

Images (Optional)

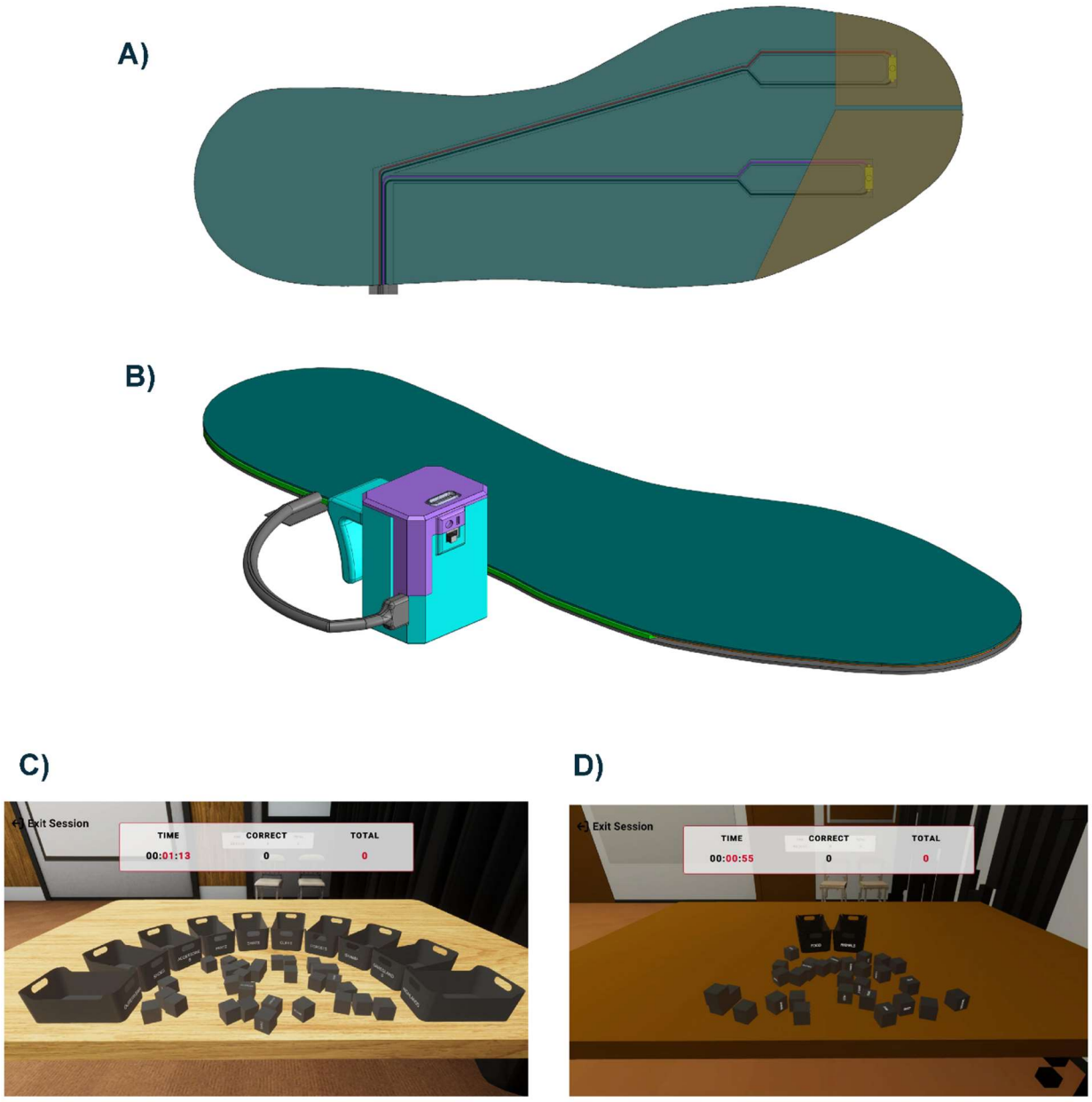


Figure 1. Overview of prosthesis control and VR experience. A) Toe button diagram to control grip configurations; B) IMU to control hand orientation; C) User view of block sorting task in high visual fidelity, high cognitive demand VR; D) User view of block sorting task in low visual fidelity, low cognitive demand VR

References (Optional)

[1] Howard, M. C. , Comp Hum Behav , (2017)

Acknowledgements (Optional)

This project is funded by the National Science Foundation's Mind, Machine, and Motor Nexus (M3X) program (NSF Award Number 2225135).

Thank you to all other members of the Gait, Oculomotor, and Lower-extremity Dynamics (GOLD) Lab, Design of Smart Mechanical And Reconfigurable Technologies (SMART) Lab, Visual Information Science and Neuroscience (VISN) Lab, Positive Aging Research and Development (PAR-D) Lab for data collection and analysis.

Session Category

Rehabilitation Biomechanics and Human Factors: Rehabilitation

OA123-03

Hands-On vs. Teleoperated Assistance: Exploratory Findings from a Single Therapist Training Artificially Impaired Treadmill Walkers

Dr. Julia Manczurowsky PT, DPT, PhD[1], Ms. Samantha Steer[2], Mr. Om Prajapati[2], Dr. Sheng-Che Yen PT, PhD[2], Dr. Lester Leung MD, MSc[3,4], Dr. Peter Whitney PhD[2], Dr. Charles Hillman PhD[2,5], Dr. Christopher Hasson PhD[2]

[1]University of British Columbia, Vancouver, BC, Canada. [2]Northeastern University, Boston, MA, United States. [3]Tufts Medical Center, Boston, MA, United States. [4]Tufts University School of Medicine, Boston, MA, United States. [5]Institute for Cognitive and Brain Health, Boston, MA, United States

Introduction

During rehabilitation, physical therapists vary assistive forces to facilitate motor adaptation, yet assistance is subjectively described as minimal, moderate, or maximal, making skilled strategies hard to interpret. Quantifying assistance is essential for improving clinical practice and robotic systems, which currently rely on algorithms agnostic to therapist behavior. To address this gap, we analyzed one therapist's assistance forces across two similar gait-training studies: hands-on through an instrumented leg brace and teleoperated through a robotic arm attached to the leg. We examined whether assistance modality or visual feedback modulated these forces.

Methods

Interaction forces were extracted from two assisted gait-training datasets involving healthy adults treadmill-walking with an artificial impairment of elastic resistance and hamstring stimulation to disrupt right leg swing (N= 35 hands-on; N = 23 telerobotic). Across four 2.5-minute trials and 1 trial the next day, the same therapist assisted participants to increase stride length and reach a mechanical work target. Visual feedback, assigned randomly, showed either participant and therapist summed work (control), or their work relative to the therapist (comparative). Feedback of stride-length accuracy helped the therapist adjust assistance. Anterior-posterior forces were averaged per trial and group. A linear mixed model tested effects of assistance modality, time, and feedback on mean force, with participant identity as a random effect and AR1 for repeated time.

Results

Assistance forces were less frequent and more discrete with telerobotics, reflected by a main modality effect on average force ($p < .001$). Target stride length was equally achieved in both studies. Although programmed to closely follow participants' leg motion, a small baseline resistance from the robotic arm produced negative mean forces during swing. Feedback also interacted with modality ($p = .005$): hands-on assistance was greater for control participants, whereas feedback type did not affect assistance during teleoperation.

Discussion

Therapeutic assistance is shaped by how participants and therapists adapt, how they are physically connected, and the feedback provided. Physical proximity may change engagement, while robotic constraints may temper therapist forces but increase participant effort. The observed assistance differences with a single therapist are hypothesis-generating for testing factors that could enhance or impede motor adaptation in gait retraining.

Session Category

Rehabilitation Biomechanics and Human Factors: Rehabilitation

OA123-04

Quantifying Play Interactions: Implementation of a Digital Switch-Accessible Play Kit for Young Children Receiving Early Intervention Services

Mia Hoffman PhD[1], Ms. Alisha Bose[1], Ms. Riley Bernas[2], Ms. Kate Bokowy BS[1], Dr. Heather Feldner PhD, PT, PCS Emeritus[1], Dr. Katherine Steele PhD[1]

[1]University of Washington, Seattle, WA, United States. [2]University of Connecticut, Mansfield, CT, United States

Introduction

Play-based therapeutic activities are essential for young children with disabilities, yet accessible play options remain limited due to market constraints and financial barriers [1]. We collaborated with clinical and family stakeholders to develop the Switch Kit, an open-source switch interface compatible with homemade, low-cost switches and interactive Scratch-based games. This study aimed to understand and measure how early interventions providers integrated the Switch Kit into their practice.

Methods

Ten early intervention service providers (3 – 22 years' experience) received a Switch Kit to use for 4-6 weeks with clients. A data logger embedded in Scratch games tracked device usage and interaction metrics for each switch press. These data were combined with provider-completed logs detailing client characteristics and activities. At study completion, each provider completed clinical-implementation surveys and a semi-structured interview.

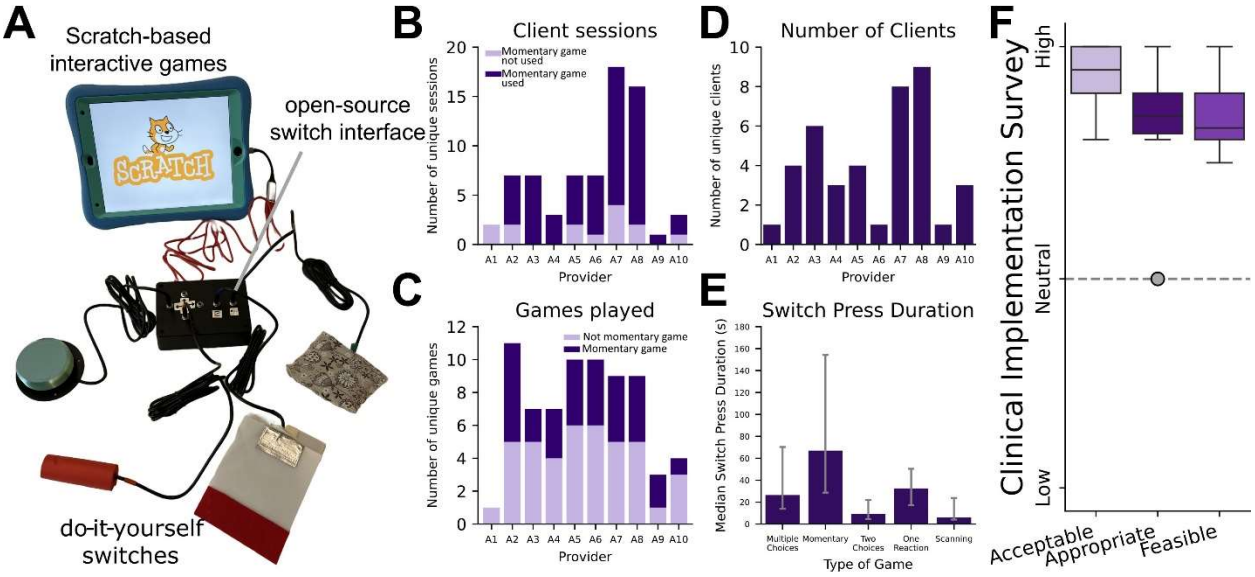
Results

Providers used the Switch Kit with one to nine clients (ages: 9 months – 4 years) with diagnoses including cerebral palsy and autism spectrum disorder. Momentary games, which played music during switch activation, were the most frequently selected. This game type also yielded the longest median press duration (67.5 seconds) and highest median presses (80.1) compared to other game types. All providers rated the Switch Kit as acceptable and feasible for classroom, outpatient, and in-home settings. All but one provider deemed it appropriate for their clients. Providers reported that the Switch Kit offered insights into each child's preferences, cognitive abilities, and readiness for other assistive technologies, such as augmentative and alternative communication.

Discussion

Providers used the Switch Kit to promote play participation for children with sensory challenges or significant motor involvement. Providers reported using the Switch Kit more frequently and with more clients than other switch-adapted toys, echoing prior findings that children engaged more with socially-assistive robots than switch-adapted toys [2]. The Switch Kit provides a practical, low-cost, and open-source solution (https://miahoffmannd.github.io/switchkit/) for integrating assistive technology into early intervention. By expanding access to play and offering insights into developmental readiness, it addresses a critical gap in technology use for young children with disabilities and supports clinicians in tailoring future interventions.

Images (Optional)



References (Optional)

[1] Rasmussen *et al.,* CCHD, 2023

[2] Clark *et al.*, AHCI, 2019

Acknowledgements (Optional)

This work was supported by the NIH under grants TL1TR002318 and R01NS091056, and the University of Washington Center for Research and Education on Accessible Technology and Experiences.

Session Category

Rehabilitation Biomechanics and Human Factors: Rehabilitation

OA123-05

The Effects of Spasticity on Gait: A Comparison Between Predictive Simulations and Expert Consensus

Ms. Stefanie de Jager MSc[1,2], Dr. Niels Waterval PhD[1,3], Dr. Ajay Seth PhD[2], Dr. Kirsten Veerkamp PhD[4,3,1], Dr. Marjolein van der Krogt PhD[1,3]

[1]Amsterdam UMC, Department of Rehabilitation Medicine, Amsterdam, NH, Netherlands. [2]Delft University of Technology, Department of Biomechanical Engineering, Delft, SH, Netherlands. [3]Amsterdam Movement Sciences, Rehabilitation & Development, Amsterdam, NH, Netherlands. [4]Vrije Universiteit Amsterdam, Department of Behavioural and Movement Sciences, Amsterdam, NH, Netherlands

Introduction

Spasticity can have a detrimental impact on gait [1], but the specific effects of individual muscle spasticity on gait kinematics are poorly understood. Here we compare two approaches that attempt to elucidate this effect, i.e. predictive simulations of gait and expert consensus. By comparing these approaches, we intend to gain further insight in the effect of spasticity on gait and obtain confidence in each of these methods.

Methods

We employed a predictive simulation framework [2], using a planar neuromusculoskeletal model, featuring nine musculotendon units per leg [3]. Muscles were activated by reflex-based controllers, while minimizing cost of transport, head movements, and foot-ground impacts [4]. Spasticity was modelled for the soleus, gastrocnemius, hamstrings, and rectus femoris muscles separately, by increasing velocity-dependent or force-dependent reflexes [3], or a combination of both, with five increasing gain values. Kinematic deviations from the unperturbed simulation were compared against spasticity-related gait features based on expert consensus, as previously obtained using a Delphi study [5].

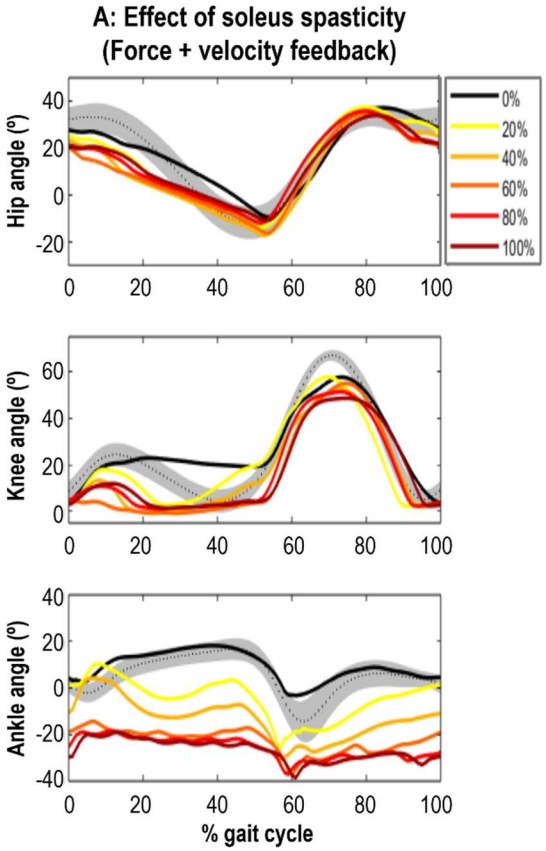
Results

The combined force+velocity-dependent simulations showed the best match with expert consensus, followed by velocity-dependent reflexes alone. The simulations of soleus and gastrocnemius muscles matched well with expert consensus for most gait features (7/8 and 8/8, respectively, Fig.1). Simulations with hamstrings and rectus femoris spasticity did not match as well (1/3 and 1/2 features, respectively) and showed additional gait features that were not expected by experts.

Discussion

Our findings indicate that spasticity may be best represented by multi-factorial reflex pathways, rather than by purely velocity- or force-dependent reflexes. The mismatches found may be due to compensations by the model to prevent the muscles from stretching or producing force not typically seen in patients. In addition, length-dependent reflex activity was absent in our model but may play a significant role particularly in more proximal muscles [6]. Ultimately, predictive simulations may help to further refine clinical understanding by yielding deeper insight in the mechanisms underlying spasticity and its impact on gait.

Images (Optional)



B: Match with expected gait features based on expert consensus

Gait Features: Soleus

Joint	Feature	Phase	
Knee	Extension movement	LR	✗
Knee	Extension increased	EST–LST	✓
Ankle	PF increased	LSW	✓
Ankle	PF increased	LR–LST	✓
Ankle	PF peak too early	EST–LST	✓
Foot	Early heel rise (v)	EST	✓
Foot	Toe walking (v)	Stance	✓
Foot	FF/MF contact (v)	IC	✓

Abbreviations: LR: loading response; EST: early stance; LST: late stance; LSW: late swing; PF: plantarflexion; (v): based on video; FF/MF: forefoot/midfoot; IC: initial contact

References (Optional)

[1] Cans. Dev.Med.Child.Neurol.2000-1;42(12):816–24.

[2] Geijtenbeek. J.OpenSourceSoftw.2019-4-1421.10.21105/joss.01421.

[3] Veerkamp *et al*.J.Appl.Biomech.2023-2;39(5):334–46.

[4] Veerkamp *et al*. J.Biomech.2021-18;123:110530.

[5] Van der Krogt *et al*. Front.Hum.Neurosci.2022-20:16:907565.

[6] Bar-On *et al*. PLoSOne.2014-20;9(3):e91759.

Session Category

Rehabilitation Biomechanics and Human Factors: Rehabilitation

OA124-02

Mechanical Demand Shapes Anticipatory Kinematic Adjustments in Landing From a Countermovement Jump: Evidence From a Microgravity Paradigm

Dr Romain Bechet[1], Prof Benedicte Schepens[2], Dr Clement Gambelli[3,2]

[1]Institut de Biomécanique Humaine Georges Charpak, Paris, Ile de France, France. [2]Laboratoire de Physiologie et biomécanique de la Locomotion, Institute of NeuroScience, Université catholique de Louvain, Louvain-la- Neuve, Brabant Wallon, Belgium. [3]Physical Activity, Sport and Recreation Research Focus Area (PhASRec), North-West University (NWU), Potchefstroom, North-West, South Africa

Introduction

Landing from a jump presents distinct challenges that require the integration of sensory information to accurately predict both the timing of ground contact and the characteristics of the forthcoming impact forces, to generate the appropriate motor command. Gravity is central to these predictions, as the central nervous system (CNS) relies on internal models assuming constancy to overcome sensory feedback delays. When gravity changes, touchdown (TD) joint angles and muscle activity adjust, suggesting sensory reweighting [1]. Yet, the mechanisms guiding pre-landing kinematic adjustments remain unclear.

Methods

Six participants performed countermovement jumps (CMJ) under simulated microgravity (0.2g, 0.4g, 0.6g, 1g) during parabolic flights, using a subject loading system to apply downward force in weightlessness (0g). Ground reaction forces and sagittal plane kinematics were recorded and used to compute hip, knee, and ankle joint angles and angular velocities, computed from a left derivative. The onset of joint flexion was defined as the first moment angular velocity became positive and remained so until TD. A linear mixed model examined the effect of gravity.

Results

The *p*-values, mean and standard deviation (SD) of flight time (FT), flexion onsets, relative flexion onsets (expressed as a percentage of FT) and joint velocities at TD are presented in Table 1. Gravity significantly altered FT, with longer FT in lower gravity. It also significantly altered hip and knee flexion onsets, with earlier onsets in lower gravity. In contrast, gravity had the inverse effect for relative joint onset, with later relative onsets in lower gravity.

Gravity also significantly affected hip, knee and ankle velocities at TD, with lower angular velocities in lower gravity.

Discussion

Earlier absolute but later relative onsets in lower gravity indicate that the CNS does not rely on a fixed timing reference to adjust joint angular velocity at touchdown. Instead, pre-landing control appears to be flexibly scaled to the mechanical constraints imposed by reduced gravity.

Images (Optional)

Table 1

Variable	Gravity	1g (mean ± SD)	0.6g (mean ± SD)	0.4g (mean ± SD)	0.2g (mean ± SD)
Flight time (ms)	$p < 0.001$	307 ± 26	516 ± 54	683 ± 52	905 ± 92
Hip onset (ms)	$p = 0.002$	100 ± 21	142 ± 27	146 ± 25	211 ± 61
Knee onset (ms)	$p = 0.009$	116 ± 26	163 ± 38	152 ± 21	203 ± 53
Ankle onset (ms)	$p = 0.101$	78 ± 7	110 ± 23	100 ± 31	130 ± 62
Hip onset (%FT)	$p = 0.006$	32 ± 5	28 ± 5	21 ± 4	24 ± 6
Knee onset (%FT)	$p = 0.008$	37 ± 7	33 ± 10	22 ± 4	23 ± 7
Ankle onset (%FT)	$p = 0.007$	26 ± 3	22 ± 6	15 ± 5	15 ± 8
Hip velocity ($°.s^{-1}$)	$p = 0.013$	137 ± 41	143 ± 47	129 ± 38	95 ± 33
Knee velocity ($°.s^{-1}$)	$p = 0.010$	290 ± 66	297 ± 49	277 ± 35	196 ± 38
Ankle velocity ($°.s^{-1}$)	$p < 0.001$	428 ± 42	416 ± 59	404 ± 34	296 ± 26

References (Optional)

[1] Clement N Gambelli *et al.* , J Appl Physiol, 2015

Session Category

Human Motion and Performance: Balance, Posture and Control

OA124-03

Elevated Mediolateral Slip Risk through Comprehensive Friction Demands during Walking in Unilateral Transfemoral Amputees

Mr. Shunta Kobayashi B.Sc.[1], Mr. Kai Kobayashi B.Sc.[1], Prof. Chien-Chi Chang Ph.D.[2], Prof. Takeshi Yamaguchi Ph.D.[3], Assoc. Prof. Hiroaki Hobara Ph.D.[1]

[1]Tokyo University of Scinence, Tokyo, Tokyo, Japan. [2]National Tsing Hua University, Hsinchu, Hsinchu, Taiwan. [3]Tohoku, Sendai, Miyagi, Japan

Introduction

Individuals with unilateral transfemoral amputation (uTFA) exhibit an elevated fall risk than non-amputees, and slipping is a major factor in both populations [1, 2]. The required coefficient of friction (RCOF)—the minimum shoe–floor friction needed to prevent slipping—has been characterized in non-amputees' gait. In contrast, research on RCOF in individuals with uTFA remains limited, particularly regarding its dependence on walking speed. To address this gap, the present study compares RCOF between individuals with uTFA and non-amputees across multiple controlled walking speeds.

Methods

Thirty individuals with uTFA and thirty sex-, age-, and body mass-matched non-amputees were recruited. All participants walked at eight prescribed speeds (2.0–5.5 km/h) on an instrumented split-belt treadmill, and ground reaction forces (GRFs) were collected at 1 kHz. RCOFh was defined as the ratio of the resultants GRF to the vertical GRF (Fh/Fz), where

$$Fh = \sqrt{(Fx^2 + Fy^2)}$$

Higher RCOF reflects greater frictional demand and increased slip risk, whereas lower RCOF indicates reduced slipping potential. For each trial, the peak RCOF (RCOFh) and its mediolateral and anteroposterior components (RCOF_ML and RCOF_AP) were calculated as Fx/Fz and Fy/Fz at the instant of peak RCOF during the braking phase [3]. Normality was assessed using the Shapiro–Wilk test; when assumptions were violated, the Friedman test and Kruskal–Wallis test were applied ($p < 0.05$).

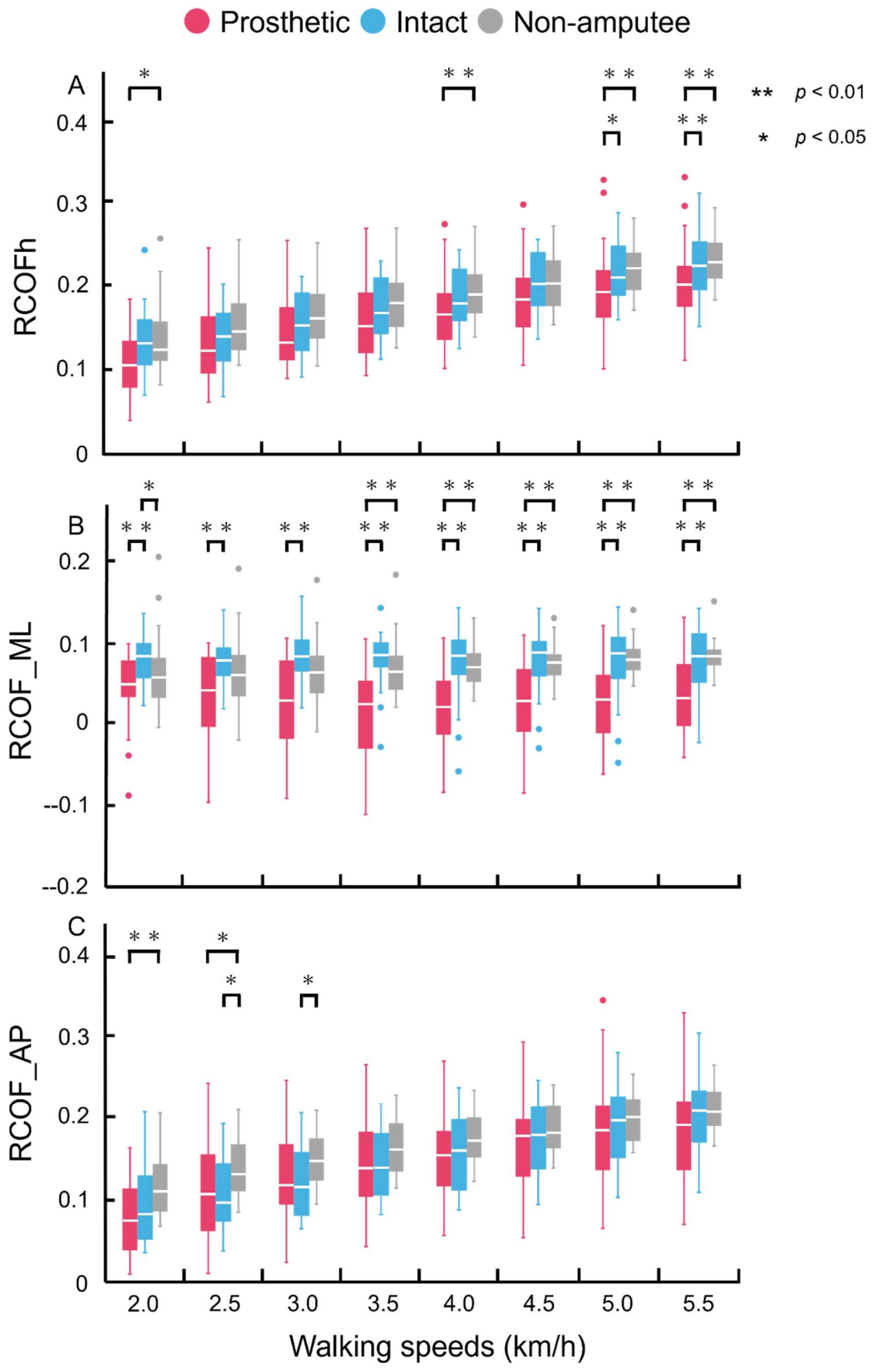
Results

RCOFh was higher in the non-amputee limb than in the prosthetic limb at 2.0, 4.0, 5.0, and 5.5 km/h, and higher in the intact limb than in the prosthetic limb at 5.0–5.5 km/h. RCOF_ML was higher in the intact limb than in the prosthetic limb across all speeds, and higher in the non-amputee limb at 2.0 and 3.5–5.5 km/h. RCOF_AP was higher in the non-amputee limb at 2.0–2.5 km/h and higher in the intact limb at 2.5–3.0 km/h.

Discussion

These results suggest that individuals with uTFA may benefit from asymmetric outsoles designed to enhance slip-resistance in the lateral direction.

Images (Optional)


Prosthetic
Intact
Non-amputee
A
B
C
RCOFh
RCOF_ML
RCOF_AP
** p < 0.01
* p < 0.05
0.4
0.3
0.2
0.1
0
--0.1
--0.2
2.0
2.5
3.0
3.5
4.0
4.5
5.0
5.5
Walking speeds (km/h)

References (Optional)

[1] Kim J et al., *PM R*, 2019

[2] Talbot LA et al., *BMC Public Health*, 2005

[3] Chang WR et al., Ergonomics, 2012

Acknowledgements (Optional)

This work was partly supported by JSPS KAKENHI (19K11338) and JST-Mirai Program (JPMJMI21H5).

Session Category

Human Motion and Performance: Balance, Posture and Control

OA124-04

Visuospatial Attention and Trip Avoidance Throughout Pregnancy

Dr. Robert Catena PhD[1], Dr. Jason Moore DPhil[2], MS. Xueying Wu BEng[1], Dr. Pegah Jamali PhD[1], Dr. Alan Godfrey PhD[2], Dr. Lisa Fournier PhD[1]

[1]Washington State University, Pullman, WA, United States. [2]Northumbria University, Newcastle, Tyne and Wear, United Kingdom

Introduction

The fall rate at seven months gestation is 25x greater than the first month [1]. An introspective shift of attention [2] may sacrifice needed extrospective attention to trip hazards. Our aim was to determine if visuospatial attention allocation to obstacle avoidance changes during pregnancy to explain some of the increase in fall risk.

Methods

Seventeen healthy pregnant participants were tested at ~13, ~19, ~25, ~31, and ~37 weeks of gestation. They walked continuous laps for 2 minutes through a 24m obstacle course consisting of six obstacles between 5% and 12.5% of body height (figure 1 left). Pupil kinematics and scene video were tracked with a mobile eye tracker. A YoloV8 algorithm classified scene objects and gaze overlap with objects to measure gaze distances relative to obstacle- and distractor-related scene information (figure 1 right) [3]. An 11-camera motion capture system tracked Euclidian distances between feet and obstacles [4]. Linear mixed models statistically analyzed changes over gestational time.

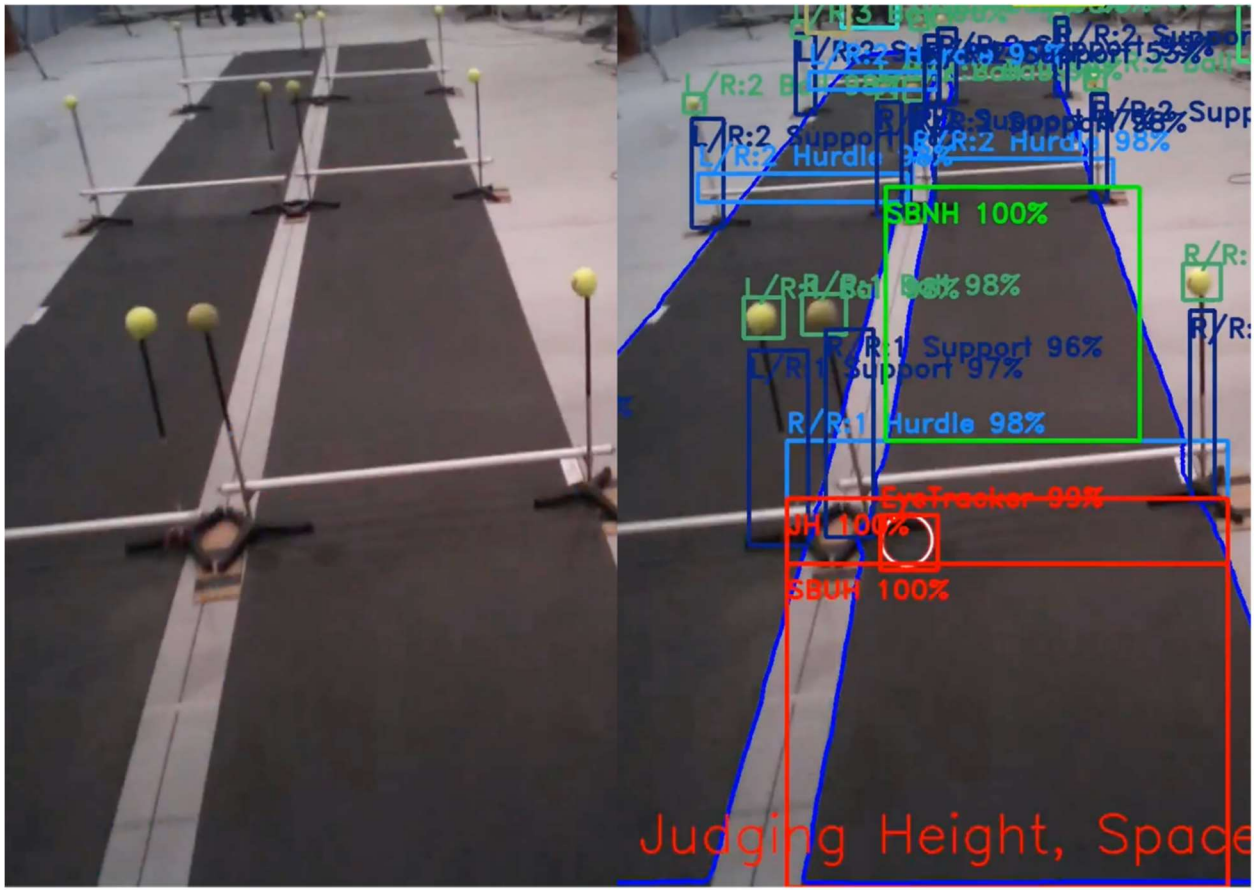
Results

Attention magnitude (blink rate, pupil size) did not change throughout pregnancy. Through the 2nd trimester, attention location (gaze distance) moves 10% closer to the current obstacle being crossed ($p=0.05$) and time spent attending to future obstacles decreased by 75% ($p=0.05$), allowing for 15% reduction in foot crossing heights ($p=0.03$). These changes suggest a safer and more energy efficient crossing strategy in the 2nd trimester. However, by week 31, visuospatial attention shifts away from the current trip hazard, while at the same time, crossing height further decreased by 20%, suggesting a riskier crossing strategy in the early 3rd trimester.

Discussion

With reduced attention allocated to the current trip hazard and low crossing heights, trip risk is greatest in week 31 (~7 months) of pregnancy. This timepoint also corresponds with degraded balance control [5] and degraded perception of obstacle heights [4], suggesting a combination of cognitive and mechanical reasons for the increased trip rates at 7 months gestation [1].

Images (Optional)



References (Optional)

[1] Dunning et al., Maternal Child Health J, 2010; [2] Crawley et al., Psychology Psychotherapy, 2003; [3] Moore et al., J Neuroengineering Rehabilitation, 2024; [4] Jamali et al., Experimental Brain Research, 2024; [5] Flores et al., Gait Posture, 2018.

Acknowledgements (Optional)

This research was funded by the American Society of Biomechanics - 2019 Junior Faculty Research Award.

Session Category

OA124-05

Whole-Body Balance Control Strategies During Obstacle Negotiation in Older Adults with Mild Cognitive Impairment

Dr. Shiuan-Huei Lu[1,2,3], Prof. Yi-Chun Kuan[1,2], Prof. Kuan-Wen Wu[1], Prof. Ting-Ming Wang[1], Prof. Tung-Wu Lu[1]

[1]National Taiwan University, Taipei, Taiwan, Taiwan. [2]Taipei Medical University, Taipei, Taiwan, Taiwan. [3]Purdue University, West Lafayette, Indiana, United States

Introduction

Mild cognitive impairment (MCI) represents a transitional stage between normal aging and dementia and is associated with deficits in executive function, attention, and motor coordination. These impairments challenge dynamic balance regulation during complex locomotor tasks such as obstacle negotiation. Whole-body balance control, quantified through center of mass-center of pressure (COM-COP) inclination angle (IA) and its rate of change (RCIA), provides a mechanistic framework for understanding fall-prone gait patterns. This study examined whole-body balance control strategies in older adults with MCI across obstacles of varying heights.

Methods

Eighteen adults with MCI (8 males, 10 females; 67.5 ± 4.2 years) and 18 healthy controls (10 males, 8 females; 67.8 ± 4.5 years) walked at preferred speed and crossed obstacles set at 10, 20, and 30% of leg length. Whole-body kinematics were recorded using a Vicon motion system, and ground reaction forces were measured using forceplates. COM position was estimated as the weighted sum of body-segment centres of mass, and COP position was derived from forceplate measurements. IA and RCIA were calculated in sagittal and frontal planes. Crossing speed and endpoint parameters, IA, and RCIA were analyzed using two-way mixed-design ANOVA with group as the between-subject factor and obstacle height as the within-subject factor.

Results

Crossing speed and endpoint parameters, including toe-obstacle clearance, did not differ between groups. However, the MCI group demonstrated increased sagittal-plane posterior IA and RCIA during double-limb support (DLS) and increased anterior RCIA during leading-limb swing ($p<0.05$). In the frontal plane, the MCI group exhibited increased medial IA and RCIA during swing and the first half of DLS ($p<0.05$).

Discussion

The phase-specific increases in IA and RCIA suggest impaired neuromechanical regulation of the inverted-pendulum-like COM-COP system in MCI, reflecting deficits in both anticipatory and reactive balance mechanisms. Although toe clearance was preserved, compensatory adjustments were required to maintain stability, potentially narrowing the margin of stability and elevating fall susceptibility. These results establish a biomechanical signature of instability in MCI and highlight COM–COP dynamics as sensitive indicators for early detection of impaired obstacle negotiation. Future work incorporating control-theoretic modeling and neuromusculoskeletal simulations may further elucidate the mechanistic pathways linking cognitive decline to gait instability.

Acknowledgements (Optional)

Financial support: NSTC 113-2628-E-038 -001 -MY3.

Session Category

Human Motion and Performance: Balance, Posture and Control

OA125-02

Organic Bone Matrix Predictors of Fracture Toughness in Type 2 and Non-diabetic Cortical bone from Cadaveric, Femoral Midshafts

Ms. Emily Berestesky BS[1], Mr. Sasidhar Uppuganti MS[2], Dr. Paul Voziyan PhD[2], Dr. Thomas Willett PhD[3], Dr. Jeffry Nyman PhD[2]

[1]Vanderbilt University, Nashville, Tennessee, United States. [2]Vanderbilt University Medical Center, Nashville, Tennessee, United States. [3]University of Waterloo, Waterloo, Ontario, Canada

Ms. Emily Berestesky

Introduction

The risk for fragility fracture is assessed by Dual-energy x-ray absorptiometry (DXA) scans, which measure bone mineral density (BMD). T2D patients are at a greater risk of sustaining a fracture than non-diabetic age, sex & BMD-matched adults suggesting T2D weakens bone matrix quality. However, we recently reported that fracture toughness (FT) of human cortical bone is not different between donors with T2D (≥ 10 years) and without diabetes despite thermal stability of the organic matrix being higher with T2D [1]. Since matrix properties and porosity influence FT of cortical bone, we hypothesized that T2D affects the relationship between FT and matrix- and structural-related properties of the mechanical specimen while accounting for sex and age of the donor.

Methods

Single-edge notched beams (SENBs) from 120 cadaveric femoral midshafts (60 with T2D, 60 non-diabetic; sex-equivalence) were scanned by μCT (cortical porosity, Ct.Po; volumetric BMD, Ct.vBMD) and ^{1}H nuclear magnetic resonance relaxometry (bound water volume fraction, BW) [2] before micro-notch fracture toughness testing (crack initiation toughness, K_{init}; total crack energy dissipation, J_f) [3]. SENB sections underwent high performance liquid chromatography (pentosidine, PE; pyridinoline, PYD) and differential scanning calorimetry (temperature at maximum recorded heat flow, T_{peak}). To test the hypothesis, the ability of either Ct.Po, Ct.vBMD, PE, PYD, BW, or T_{peak} to predict FT properties was assessed with linear regression models, which included covariates: donor group (Non-diabetic/T2D), age, and sex. Group and each predictor interaction was not significant ($p > 0.3$), therefore excluded.

Results

Disproving our hypothesis, diabetic status was not a significant covariate of any FT property (Table). Only BW and Ct.Po were significant predictors of K_{init} and J_f. Female donors had higher FT for a given bone property than males. J_f but not K_{init} significantly depended on age.

Discussion

Present results suggests that fracture risk would benefit from measurements of Ct.Po and BW in long bones of patients since these properties could predict bone's ability to resist crack growth. The high-than-expected fracture risk in T2D cannot be attributed to alterations in how porosity and the matrix confer fracture toughness.

Images (Optional)

Table. Estimates (β) and p-values from linear regression models of Fracture Toughness properties and matrix- and structural-related properties.

Equation	Value Type	Parameters				
		Covariate	Group (No Dia)	Age (years)	Sex (F)	Intercept
K_{init} = **Ct.Po** + Group + Age + Sex + Intercept	β	-0.07002	0.1932	-0.008405	0.5956	7.741
	p	**0.0213**	0.4976	0.4647	**0.0362**	<0.0001
K_{init} = **Ct.vBMD** + Group + Age + Sex + Intercept	β	0.005716	0.1706	-0.01004	0.6402	2.051
	p	*0.0594*	0.5527	0.3841	**0.027**	0.5081
K_{init} = **PE** + Group + Age + Sex + Intercept	β	0.1575	0.09228	-0.01335	0.5824	7.627
	p	0.6631	0.7609	0.2901	**0.0475**	<0.0001
K_{init} = **PYD** + Group + Age + Sex + Intercept	β	0.0005501	0.04293	-0.0108	0.569	7.566
	p	0.8779	0.8853	0.3768	0.0556	<0.0001
K_{init} = **BW** + Group + Age + Sex + Intercept	β	0.2832	0.1078	-0.005097	0.5639	1.51
	p	**0.0347**	0.7003	0.6664	**0.0477**	0.6183
K_{init} = $\mathbf{T_{peak}}$ + Group + Age + Sex + Intercept	β	-0.01914	0.02719	-0.01164	0.5724	8.847
	p	0.8558	0.9281	0.3262	0.0529	0.1734
Jf = **Ct.Po** + Group + Age + Sex + Intercept	β	-0.1313	0.6988	-0.05968	1.237	12.77
	p	**0.0246**	0.2032	**0.0078**	**0.0238**	<0.0001
Jf = **Ct.vBMD** + Group + Age + Sex + Intercept	β	0.005942	0.552	-0.0638	1.256	6.803
	p	0.3103	0.3234	**0.0051**	**0.0255**	0.2592
J_f = **PE** + Group + Age + Sex + Intercept	β	-0.6673	0.224	-0.05641	1.089	12.89
	p	0.3357	0.6997	**0.0207**	0.0527	<0.0001
J_f = **PYD** + Group + Age + Sex + Intercept	β	-0.005242	0.326	-0.07005	1.23	13.85
	p	0.4454	0.5679	**0.0033**	**0.0313**	<0.0001
J_f = **BW** + Group + Age + Sex + Intercept	β	0.9244	0.6251	-0.04487	1.18	-7.487
	p	**0.0003**	0.2283	**0.0417**	**0.0252**	0.1825
J_f = $\mathbf{T_{peak}}$ + Group + Age + Sex + Intercept	β	-0.1414	0.2861	-0.06765	1.25	21.27
	p	0.4839	0.6206	**0.0034**	**0.0278**	0.0885

References (Optional)

[1] Berestesky et al. JBMR, 2025, [2] Creecy et al. Bone, 2020, [3] Ritchie et al. Bone, 2010

Acknowledgements (Optional)

This study was supported by the National Institute of Arthritis and Musculoskeletal and Skin Diseases (AR063157), the VA Office of Research and Development (BX005866), and the National Center for Research Resources (S10RR027631).

Session Category

Musculoskeletal Biomechanics: Tissues

OA125-03

Adaptation of the Mouse Tibia to Fatigue Under Weekly Pathological *in Vivo* Axial Loading

Dr Vincent Stadelmann[1], Dr Claudia Siverino[2], Dr Stephan Zeiter[2], Prof Claire Acevedo[3]

[1]Schulthess Klinik, Zürich, ZH, Switzerland. [2]AO Research Institute, Davos, GR, Switzerland. [3]UC San Diego, San Diego, CA, United States

Dr Vincent Stadelmann

Dr Claudia Siverino

Dr Stephan Zeiter

Introduction

The causes of stress fractures are not yet fully understood. Stress fractures likely develop from the accumulation of microdamage caused by repetitive loading. Under normal circumstances, bone cells continuously renew damaged bone; however, changes in physical activity, estrogen deficiency, and the use of corticosteroids (CS) or antiresorptive medications like bisphosphonates (BP) can disrupt this process. The study aimed to develop a murine model to investigate the response of bone to pathological fatigue loading, assess microcrack accumulation, and evaluate the role of CS/BP on resistance to fatigue.

Methods

Eighty-four 10 weeks old female C57BL6 mice were divided into 6 groups (Table 1). Animals in groups 1 to 3 underwent ovariectomy at week 12. From w20 on, groups 2 and 3 received BP (zoledronic acid weekly). Group 3 received CS (Prednisolone pellets - PRED). From w25 on, the left tibia in groups 1-4 were axially loaded (3-18N, 0.5Hz until 140% deformation). Group 4-5 were not loaded. Group 5 received analgesics only. The tibias were scanned bi-weekly with microCT. After sacrifice 6 tibias per group were tested in axial fatigue, the others were reserved for histology.

Results

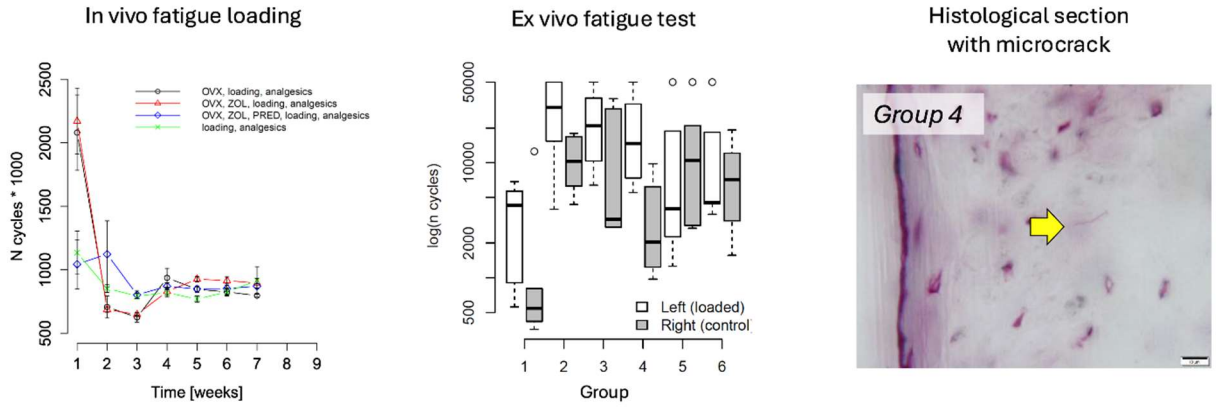
The number of loading cycles until 140% deformation was very variable at w1 (1500±1000 cycles) but by W4 all groups had converged to 860±100. Groups 3 and 4 exhibited the most notable increases in cortical thickness (ct.th) and bone volume (BV) at proximal ROIs, reaching or surpassing the control levels. However, no significant changes were observed at the distal ROIs.

Imaging revealed that bone formation was greater in loaded tibias compared to non-loaded ones, while bone resorption showed only minor changes. Significant formation of woven bone was observed in the proximal region of the loaded tibias, and mechanical tests demonstrated that these tibias were significantly more resistant to fatigue than the non-loaded controls. Only 3 microcracks were observed in all histological slides (Fig. 1).

Discussion

The increased strength and absence of microdamage in the bones under fatigue loading indicates that mouse tibias adapt to mechanical loading even under intense weekly fatigue stress regardless of estrogen levels or CS/BP exposure.

Images (Optional)



Session Category

Musculoskeletal Biomechanics: Tissues

OA125-04

Micromechanical Properties of Human Femoral Neck Compact Bone - Influence of Age, Sex and Anatomical Site

BSc Alex Bieri[1], BSc Simon Walker[2], MSc Jorge de Oliveira[3], Dr Christian Minnert[3], Dr Kevin Both[3], MSc Valeria Zanrè[3], Prof Beat Neuenschwander[2], Dr Jakob Schwiedrzik[3], Prof Philippe Zysset[1], Dr Tatiana Kochetkova[1]

[1]ARTORG Center for Biomedical Engineering Research, University of Bern, Bern, BE, Switzerland. [2]Institute for Applied Laser, Photonics and Surface Technologies ALPS, Bern University of Applied Sciences, Burgdorf, BE, Switzerland. [3]Empa, Swiss Federal Laboratories for Materials Science and Technology, Dübendorf, ZH, Switzerland

Introduction

The femoral neck site is the most burdensome location of fragility fractures. Anatomically, this site has a thicker inferior cortex compared to the thinner superior counterpart, the latter being the nucleation point for the majority of femoral neck fractures. While numerous studies focused on macro- and microarchitectural differences within the neck quadrants, there is limited data addressing their mechanical properties at the tissue level. We are interested in comparing the elastic, yield and post-yield mechanical properties of the inferior versus superior quadrants in ageing. This knowledge is relevant for understanding the fracture mechanism that leads to whole-organ failure.

Methods

Inferior and superior quadrants were cut from the femoral neck sections of 40 donors (24 female and 16 male, 57-96y.o.). In each quadrant, 12-20 bone micropillars were fabricated using the refined laser ablation protocol, providing, for the first time, sufficiently straight micropillars (~3° taper) in a high-throughput manner without exposing the sample to vacuum (fig-a). Micropillars were compressed under ambient conditions using an *ex-situ* indenter setup in a displacement-controlled quasi-static loading protocol with an intermittent unloading segment, to assess elastic, yield and post-yield properties (fig-b). A total of 1053 micropillars were compressed, with 1028 included in the final analysis.

Results

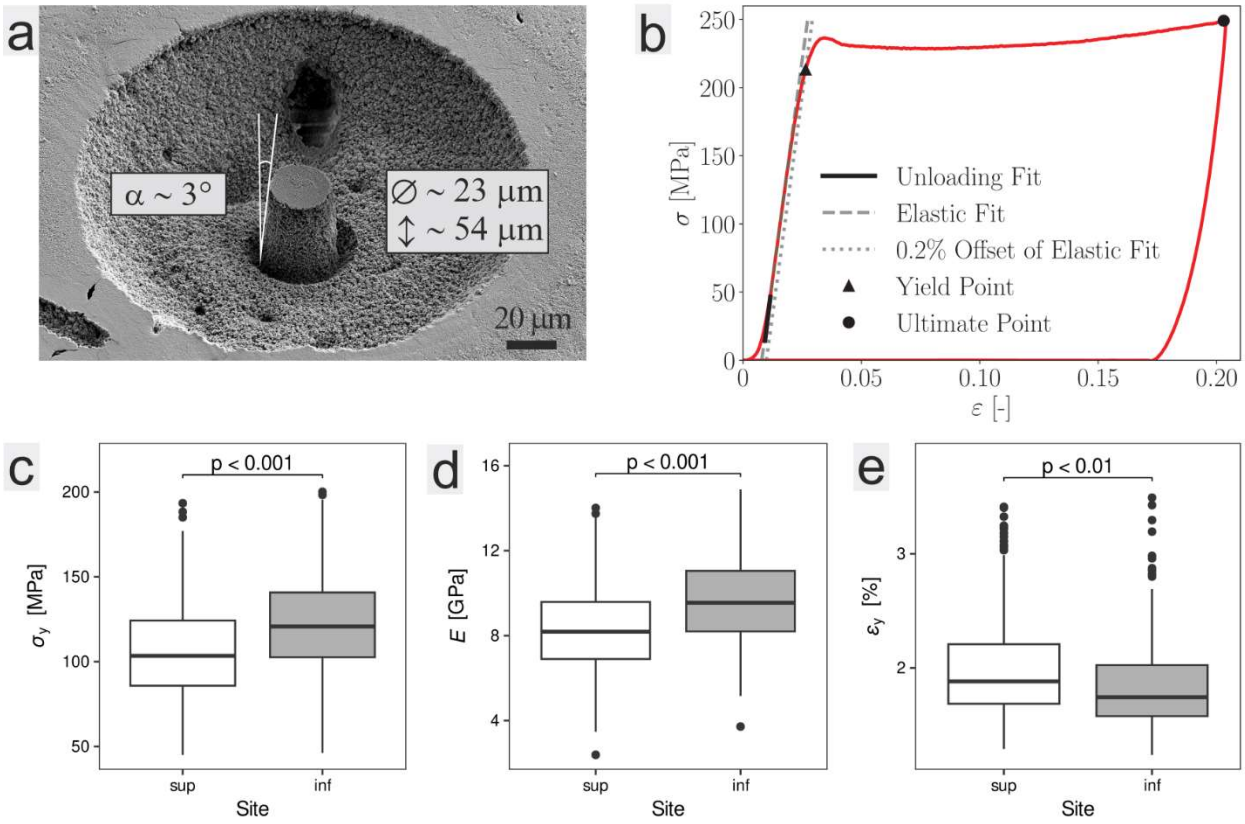
Inferior cortex exhibited 16-18% higher tissue-level E, σ_y, and 8% lower ε_y, in comparison to the superior quadrant (fig-c-e-d). All mechanical properties were largely constant across the examined donors' ages and sex, as anticipated [1]. Four types of failure modes were identified for both quadrants: homogeneous deformation (39%), mushrooming (21%), and

a combination of the first two with shear localization (34% and 6%), consistent with existing observations from ion-milled micropillar compressions [2].

Discussion

Observed variations in the femoral neck quadrants' tissue-level mechanical properties are attributed to the different mineralization levels [3] and/or internal lamellar organization, both of which are to be investigated with polarized Raman spectroscopy and second harmonic generation microscopy. Combined data will shed light on the microscale structure-property relationship within the inferior and superior femoral neck quadrants.

Images (Optional)



References (Optional)

[1] Kochetkova et al., Bone, 177:116920, 2023

[2] Schwiedrzik et al., Nature Mat, 13:740-747, 2014

[3] Fratzl-Zelman et al., Calcif Tissue Int, 85:335-343, 2009

Acknowledgements (Optional)

Grant no 200365 of the Swiss National Science Foundation (SNSF) is gratefully acknowledged.

Session Category

Musculoskeletal Biomechanics: Tissues

OA125-05

Evaluating Regional Bone Loss in Patients With Brachial Plexus Injury

Dr. Karyne Rabey PhD, Ms. Nikala Bochinski, Ms. Takeisha Wang, Dr. Mithun Rajshekar PhD, Ms. Stephanie Ramage, Dr. Matthew Curran MD, Dr. Ming Chan MD

University of Alberta, Edmonton, Alberta, Canada

Introduction

Peripheral nerve injuries can render an affected limb flaccid and insensate. Our rodent models have shown that there is a significant loss of bone mineral density (BMD), bone innervation, and bone strength post injury. Whether these peripheral nerve injuries also lead to BMD loss in humans, has not yet been tested. This represents a major knowledge gap as untreated bone loss in an arm already lacking motor and sensory protection could increase the risk of fractures and further exacerbate functional decline.

Methods

Twenty-eight adult participants (22 males and 6 females) with a brachial plexus injury resulting in shoulder and/or elbow deficits were recruited. Time since their injury ranged from 6 months to 17 years. Each patient underwent a full body DEXA scan using General Electric iDXA encore-based X-ray Bone Densitometer (Fig 1A). Results from the region of interest (ROI) in the injured humerus were compared to those from the uninjured arm.

Results

Results revealed a significant decrease in both BMD (82 ± 13%) and lean tissue mass (83 ± 9%) with an increase in fat tissue mass (157 ± 45%) in the injured arm. All changes began 1 year since injury and persisted over time. There were no differences in BMD between patients with motor recovery and patients with little to no motor recovery. Data indicated that male and female patients were classified to have either regional osteopenia (T-score between -1.0 and -2.5) or regional osteoporosis (T-score -2.5 and below) (Fig 1B-C).

Discussion

Patients with peripheral nerve injuries have significant loss of BMD and lean tissue mass, accompanied by infiltration of fat tissue, in the region of their injury. These findings are persistent even in those with motor recovery and those who are 10+ years post injury. This suggests that loss of BMD is not due to weakness or lack of arm use. Rather, recent data from our animal studies show an intimate relationship between sensory and sympathetic

nerves and bone turnover. This highlights the importance of early detection and early integration of osteoporosis management into the treatment of nerve injuries to prevent irreversible bone loss and to minimize the risk of fractures.

Images (Optional)

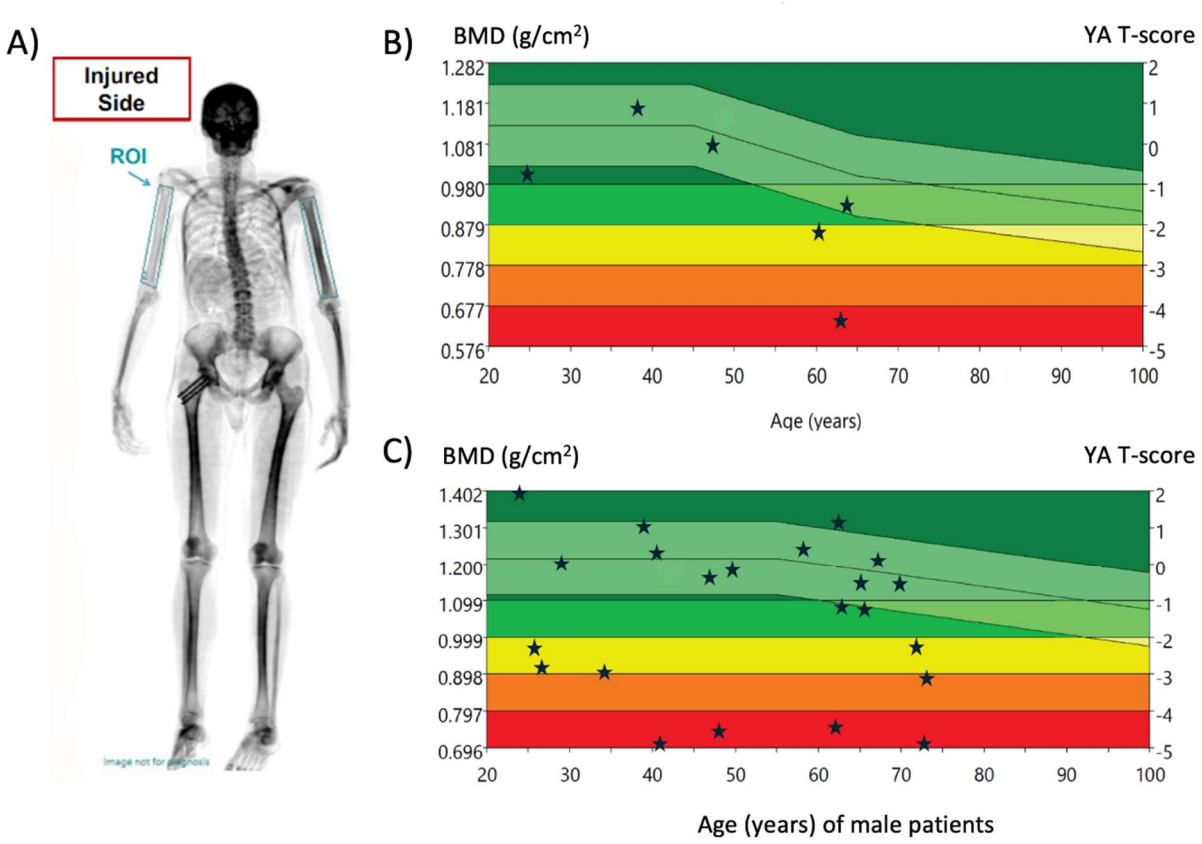


Figure 1: **A**) DEXA scan image showing the humeral regions of interest (ROI – blue boxes) used for comparison. **B-C**) Bone mineral density (BMD) of injured arm in female (**B**) and male (**C**) participants as related to their sex-matched T-scores to predict future fracture risk. Reference database classified 2 female patients and 4 male patients with regional osteopenia (T-score -1.0 to -2.5); 1 female patient and 7 male patients classified with regional osteoporosis (T-score -2.5 and below).

Session Category

Musculoskeletal Biomechanics: Tissues

OA126-02

Chemomechanical Modeling of Time-Delayed Feedback in Cell–ECM Adhesion Regulation

Mr Eiji Matsumoto PhD student, Mr Shinji Deguchi Professor

Graduate School of Engineering Science, The University of osaka, Toyonaka, Osaka, Japan

Introduction

Cell–ECM adhesion plays a central role in how cells integrate mechanical forces and biochemical signals to regulate their behavior. This interaction is mediated by focal adhesions (FAs), which physically link the extracellular matrix (ECM) to actomyosin fibers (AMs), the contractile structures that generate intracellular tension, thereby enabling chemomechanical coupling. Dysregulation of this adhesion process contributes to pathological conditions such as fibrosis and atherosclerosis, highlighting the need to understand its regulatory principles. Although the relevant biochemical cascades have been well characterized, a fundamental question remains unresolved: how diverse adhesion dynamics can coexist within a single cell. This study aims to elucidate the minimal chemomechanical principle that accounts for the coexistence of distinct adhesion dynamics.

Methods

Live imaging of FA-associated proteins combined with traction force microscopy revealed two distinct dynamical modes coexisting within single cells: a stable mode and an oscillatory mode. To clarify the chemomechanical origin of these dual modes, we developed a minimal chemomechanical model that captures the key feedback loops coupling FA size and AM tension. The model incorporates tension-dependent FA maturation and the antagonistic RhoA–Rac1 signaling pathway, formulated as a bidirectional feedback system with an effective time delay. This delay acts as a coarse-grained representation of the reaction-time delays accumulated within biochemical signaling cascades.

Results

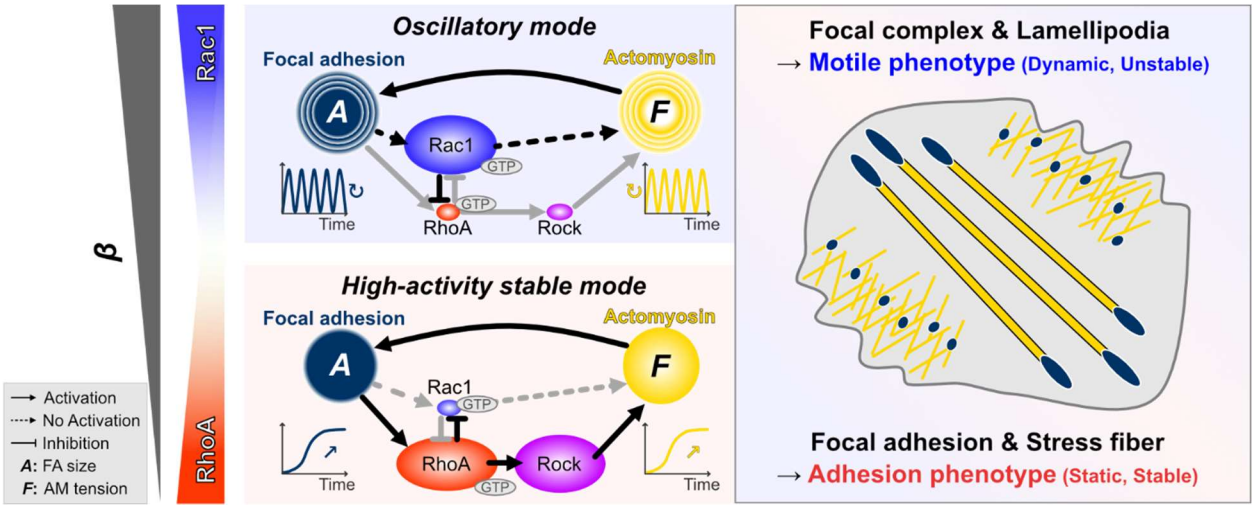
The model yields a dynamical phase diagram that predicts the coexistence of stable and oscillatory regimes, reproducing time-course behaviors consistent with experimental observations. The oscillatory period follows a scaling relationship determined by the chemomechanical feedback strength, and the phase lag between FA size and AM tension

remains robustly locked at 90 degrees. Oscillation amplitudes are regulated hierarchically by model parameters, revealing how biochemical and mechanical factors together shape adhesion dynamics.

Discussion

The model provides a physical mechanism suggesting that time-delayed chemomechanical feedback acts as the essential driver of both stable and oscillatory adhesion behaviors. This framework generalizes beyond adhesion dynamics to broader chemomechanical regulation and provides a mechanistic basis for interpreting pharmacological perturbations as modifications of underlying bifurcation structures. By connecting chemomechanical control of adhesion to pathological phenotypes, the model offers a conceptual foundation for therapeutic strategies targeting cell–ECM mechanics.

Images (Optional)



Session Category

Cell Biomechanics: Mechanobiology

OA126-03

Type V Collagen Regulates Nascent Matrix Templating and Cell-Mediated Reorganization in Embryonic Meniscus

Mr. Neil Patel[1], Dr. Meghan Kupratis PhD[2], Dr. Karen Xu PhD[2], Mr. Thomas Li[1], Dr. Eiki Koyama PhD[3], Dr. Nathaniel Dyment PhD[2], Dr. Robert Mauck PhD[2], Dr. Lin Han PhD[1]

[1]Drexel University, Philadelphia, PA, United States. [2]University of Pennsylvania, Philadelphia, PA, United States. [3]The Children's Hospital of Philadelphia, Philadelphia, PA, United States

Introduction

Meniscus injury often leads to the onset of post-traumatic osteoarthritis, but there is limited success in meniscus repair due to poor understanding of its fibrocartilaginous matrix and cell-matrix cross-talk. Our prior work showed collagen V plays key roles in the initial establishment of meniscus matrix and mechanosensitive signaling of meniscal cells in vivo. This study investigates how collagen V directs embryonic meniscal cell–matrix interactions under well-controlled in vitro scenarios.

Methods

Meniscal cells were harvested from E84 pigs and were transfected with *Col5a1*-siRNA to reduce Col5a1 expression. Cell-derived matrices (CDMs) were generated at 7-10 days to assess mechanical properties via AFM-nanoindentation and architecture (fibril alignment and density). Additionally, cell-mediated matrix contraction was evaluated in collagen I gels with and without the addition of exogenous collagen V. Cell level fibril reorganization was assessed via second harmonic generation (SHG).

Results

The reduction of Col5a1 expression by siRNA was validated up to 3-5 days by qPCR and immunofluorescence imaging (**Fig. 1a,b**). As a result, the production CDM was significantly impacted. At day 7, siRNA-CDMs exhibited reduced fibril alignment and density (**Fig. 1c**), which was recovered by day 10. However, AFM-nanoindentation found significantly lower micromodulus for siRNA-CDMs compared to the controls, indicating impaired matrix assembly (**Fig. 1d**). Meanwhile, Col5a1 knockdown led to significant delay in cell-mediated gel contraction (**Fig. 1e**) and reduced collagen I fibril organization at the cell-gel interface via SHG (**Fig. 1f**). Conversely, treatment of exogenous collagen V was able to partially restore gel contraction (**Fig. 1e**) and cell-mediated reorganization (**Fig. 1f**).

Discussion

This study highlights a pivotal role of collagen V in regulating meniscus matrix functional elaboration and cell-mediated matrix organization. This is supported by the impairment of CDMs, delayed gel contraction and diminished collagen fibril reorganization by siRNA-treated embryonic meniscal cells. Meanwhile, such effects caused by a loss of endogenous collagen V can be partially rescued by exogenous collagen V. Therefore, our results also indicate the therapeutic potential of applying collagen V for improving meniscus repair by augmenting matrix assembly and cell-matrix interactions.

Images (Optional)

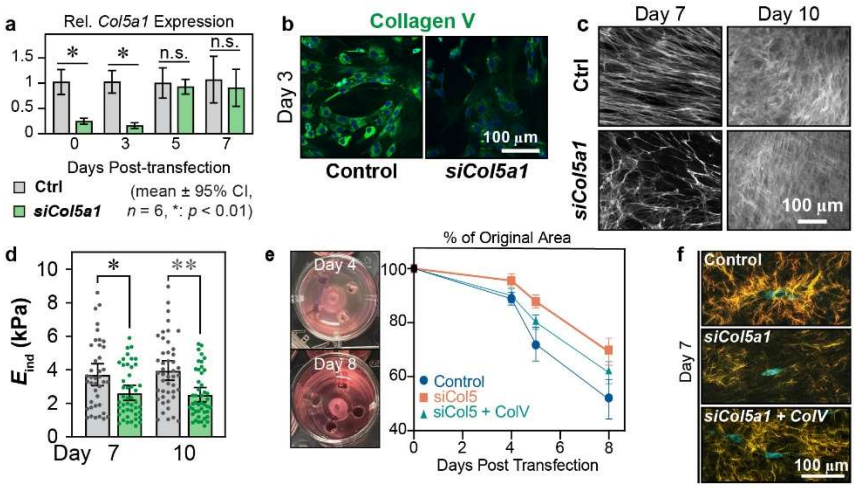


Fig. 1 a) qPCR shows temporal reduction of *Col5a1* expression by siRNA (mean ± 95% CI, *: $p < 0.01$). **b)** IF of collagen V (green, blue: DAPI) at day 3. **c)** NHS-Primary amine staining shows the alignment of cell derived matrices (CDMs, gray). **d)** Indentation Modulus, E_{ind} of CDMs at days 7 and 10 (mean ± 95% CI, *: $p < 0.05$, **: $p < 0.01$). **e)** Representative images of collagen gel contraction at days 4, 8. **f)** Gel contraction over time ($n = 5$, mean ± SEM). **c)** Representative SHG images showing fibril organization (yellow/red) surrounding meniscal cells (blue) at day 7.

Session Category

Cell Biomechanics: Mechanobiology

OA126-04

Critical Cell Spacing Governs Mechanical Communication via Strain-Stiffened Tension Bands in Fibrous ECM

Prof Guy Genin[1], Dr Xiangjun Peng[2], Mr Yuxuan Huang[1], Dr Wenyu Kong[2], Prof Yanan Du[2], Prof Elliot Elson[1], Prof Xi-Qiao Feng[2]

[1]Washington University, St. Louis, MO, United States. [2]Tsinghua University, Beijing, Beijing, China

Introduction

Cells communicate mechanically through the extracellular matrix (ECM), influencing neighbors' contractility, polarization, and migration during wound healing, fibrosis, and cancer progression. However, the physical principles governing the range of this mechanical communication remain unclear. Understanding what determines whether cells can "sense" each other through the matrix is essential for predicting collective cell behavior and developing mechanical interventions for fibrotic disorders.

Methods

We developed a bio-chemo-mechanical model integrating three components: (1) a motor-clutch framework for cell contractility, incorporating actin polymerization, myosin motor activity, and integrin-mediated adhesion; (2) nonlinear fibrous ECM mechanics capturing strain-stiffening behavior through a fiber recruitment model; and (3) mechanosensitive signaling via YAP/TAZ nuclear translocation. We simulated cell pairs at varying separations and ECM properties, then extended the model to multicellular systems to examine collective behavior.

Results

Mechanical communication between cells exhibited a nonmonotonic dependence on ECM stiffness: communication was optimized at intermediate stiffness values where cells could both generate sufficient contractile forces and create strain-stiffened tension bands in the ECM. This balance established a critical cell spacing threshold of approximately 100-200 μm, which was remarkably conserved across different cell types and collagen densities, consistent with experimental observations. The critical stretch ratio at which fibrous networks transition from compliant to strain-stiffening governed this threshold through tension band formation between neighboring cells. In multicellular simulations, these mechanical communication networks drove a collective phase transition from disordered

to ordered polarization states when cell density exceeded an effective percolation threshold.

Discussion

Our model provides a mechanistic explanation for the experimentally observed phenomena of "optimal ECM rigidity" and "paratensile signaling," revealing how microscale cell-ECM interactions control emergent tissue-level mechanical properties. The conserved critical spacing offers a quantitative design parameter for tissue engineering and suggests that manipulating ECM mechanics or cell density near this threshold may enable more effective treatments for chronic wounds, fibrosis, and cancer invasion.

Acknowledgements (Optional)

Natural ScienceFoundation of China (Grant 12402364,T2488101,12032014), and the Human Frontier Science Program (https://doi.org/10.52044/HFSP.RGP0162024.pc.gr.194164)

Session Category

Cell Biomechanics: Mechanobiology

OA126-05

Mechanotransduction Modeling of Stiffness-Sensitive Gene Regulation in Human Mesenchymal Stem Cells

Dr Jean-Philippe Berteau[1], Dr Abdennasser Chekroun[2], Dr Laurent Pujo-Menjouet[3], Dr Kevin Yueh-Hsun Yang[4]

[1]Department of Physical Therapy, Division of Science and Technology, College of Staten Island, City University of New York,, New York, NY, United States. [2]Laboratoire d'Analyse Nonlinéaire et Mathématiques Appliquées, University of Tlemcen, Tlemcen, Tlemcen, Algeria. [3]Universite Claude Bernard Lyon 1, CNRS, Centrale Lyon INSA Lyon, Université Jean Monnet, I CJ UMR5208, Inria, Lyon, AURA, France. [4]Translational Tissue Engineering Center, Johns Hopkins University School of Medicine, Baltimore, MD, United States

Introduction

Bone is a dynamic, load-responsive tissue whose structure and function are shaped by mechanical forces. Through mechanotransduction, osteogenic cells convert mechanical cues such as stiffness, strain, and fluid shear into biochemical signals that regulate proliferation, differentiation, and matrix mineralization. In mesenchymal stem cells, these signals modulate the bone Gene Regulatory Network (GRN), directing lineage commitment and the expression of key osteogenic proteins. Understanding how mechanical inputs interface with gene regulatory mechanisms is essential for explaining bone adaptation, pathological remodeling, and the design of biomaterials that exploit mechanically guided osteogenesis. The aim of our study was to determine how a defined segment of the bone GRN governs mineralization in response to stiffness. We hypothesized that a system of differential equations could model stiffness-sensitive gene regulation in human mesenchymal stem cells by capturing the epistatic interactions between stiffness-activated pathways (e.g., WNT–β-catenin) and five major transcription factors and bone proteins (RUNX2, BSP, OSX, OC, and OPN)

Methods

To test this hypothesis, we (i) performed in-vitro experiments culturing bone cells on different stiffness, (i) adapted our previously published model from being continuously time-dependent to continuously stiffness-sensitive, and (iii) simulated protein production in function of stiffness and other protein production from the best estimate of parameters coming from the experimental work.

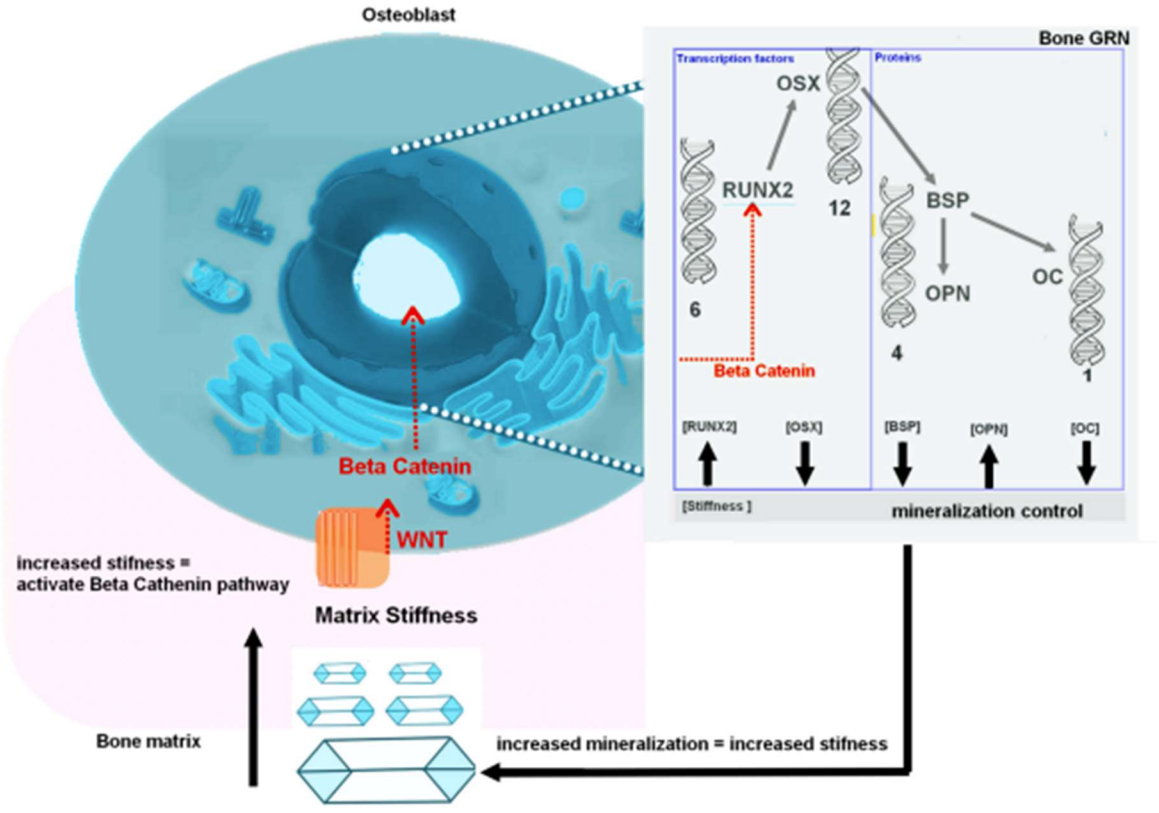
Results

Our experiments show a non-parametric relationship between stiffness and RUNX2 expression, with no clear linear trends for the other proteins. The modeling results indicate that continuous changes in stiffness allow accurate simulation of bone-GRN gene expression and fit our new experimental dataset. In particular, the model predicts maximal OPN production at low stiffness (8 kPa), whereas RUNX2, OSX, and OC reach their highest expression at higher stiffness (64 kPa). This agreement highlights the model's ability to reproduce the experimental observations

Discussion

Our model predicts that WNT–β-catenin activation enhances OPN and BSP production. It also identifies a negative feedback–like interaction between OC and BSP. Variations in stiffness exert a strong influence on OC and BSP expression and a moderate effect on OPN. By incorporating stiffness-dependent gene regulation, the approach provides mechanistic insight into mineralization patterns through the predicted dynamics of bone protein expression.

Images (Optional)



Session Category

OA127-02

Impact of Stent-Graft Compliance on Regional Aortic Remodeling

Dr. Ramin Shahbad[1], Ms. Sivapriya Kuniyil[1], Dr. Jason MacTaggart[2], Dr. Anastasia Desyatova[1]

[1]University of Nebraska Omaha, Omaha, NE, United States. [2]University of Nebraska Medical Center, Omaha, NE, United States

Introduction

Endovascular aortic repair is the first-line therapy for treating aortic pathologies such as aneurysm, dissection, and blunt thoracic injury. However, implantation of currently available stent-grafts introduces a substantial compliance mismatch with the native aorta, which can disrupt wall biomechanics, promote pathological remodeling, and contribute to long-term cardiovascular complications. To investigate the impact of this compliance mismatch, we compared aortic remodeling four months after implantation of a conventional stiff stent-graft (CS-SG) with a newly developed compliant nanofibrillar stent-graft (NF-SG) designed to mimic native vessel properties.

Methods

Aortas were harvested from 20 porcine animals that underwent endovascular surgery 18 weeks earlier to receive either a stiff polyethylene terephthalate stent-graft (CS-SG, N=8), a compliant nanofibrillar stent-graft (NF-SG, N=5), or sham-operated (control, N=7). Tissue samples were collected from proximal, stented, and distal aortic regions. Post-sacrifice analyses included planar biaxial mechanical testing to quantify intrinsic wall stiffness and nonlinearity, and histological assessment of elastin, collagen, and smooth muscle cell densities across the medial depth using Movat's Pentachrome and Masson's Trichrome (MTC) stains. These metrics were compared between treatment groups and across anatomical locations (proximal, stented, and distal segments) to characterize regional remodeling patterns.

Results

Remodeling in the CS-SG group was mainly localized to regions in direct contact with the stent-graft and was characterized by marked collagen accumulation (~25–30% vs. ~15% in the inner media), elastin fiber compaction, substantial SMC loss (~10–15% vs. ~20–25% in the inner media), and formation of a thick neointima. These structural changes corresponded to increased aortic stiffness (0.47 MPa vs. 0.37 MPa) and reduced non-linearity, most notably in the distal stented segments, while non-stented remote regions showed minimal alterations. In contrast, NF-SG implantation resulted in significantly

milder remodeling, with preserved SMC density, less collagen compaction, minimal neointima, and greater compliance in both stented and neighboring regions.

Discussion

A compliant stent-graft reduced wall loading at stent–tissue contact, limiting excessive remodeling and preventing early stiffening. In contrast, the stiff graft restricted expansion and generated higher localized stresses that promoted maladaptive structural changes. These findings highlight the importance of compliance-matching of stent-grafts in maintaining healthy aortic biomechanics.

Acknowledgements (Optional)

This work was supported in part by the NIH awards HL147128 and P20GM152301.

Session Category

Cardiovascular/Cardiorespiratory Biomechanics: Materials and Devices

OA127-03

Large-Scale Virtual Population Modeling of the Internal Carotid Artery Derived from the Nagahama Cohort

Mr. Vedhino Bima Aryaputra Ahnaf[1], Mr. Kazuyoshi Jin[1], Dr. Jing Liao[1], Dr. Masaharu Kobayashi[2], Dr. Yan Chen[3], Prof. Yoichiro Kamatani[4], Prof. Marie Oshima[3], Prof. Fumihiko Matsuda[5], Prof. Takahisa Kawaguchi[5], Prof. Makoto Ohta[1], Dr. Hitomi Anzai[1]

[1]Tohoku University, Sendai, Miyagi, Japan. [2]CHI CO., LTD, Kokubunji, Tokyo, Japan. [3]University of Tokyo, Meguro, Tokyo, Japan. [4]University of Tokyo, Shirokanedai, Tokyo, Japan. [5]Kyoto University, Sakyo, Kyoto, Japan

Introduction

The geometry of the internal carotid artery (ICA) strongly influences flow patterns and the initiation of vascular diseases. Large ICA datasets support data-driven analysis, yet are challenging to obtain because of ethical and cost constraints. Previous studies have proposed Multivariate Normal Distribution (MVND) based artery virtual population generation [1], but these efforts relied on limited datasets (<20 ICAs), restricting their ability to represent natural anatomical variability. In this study, we extend the virtual population approach to a substantially larger and more diverse community dataset. ICA data from the Nagahama cohort (1,883 left and 1,927 right) were analyzed to construct a large-scale, statistically grounded virtual ICA population that better captures population-level shape diversity for downstream vascular research.

Methods

ICA centerlines and diameter profiles were extracted, resampled, and smoothed from the Nagahama MR images. The 3D coordinates and corresponding diameter values of each landmark points were used as the input for MVND modeling, from which 10,000 virtual ICA samples were generated. Geometric descriptors, including vessel length, distance metrics, local maximum curvature, and minimum diameter, were then computed for both real and virtual populations. Distributional similarity between real and virtual populations was quantified using Kullback–Leibler (KL) divergence for each geometric descriptor. All procedures were performed separately for left and right ICAs to preserve laterality-specific anatomical characteristics.

Results

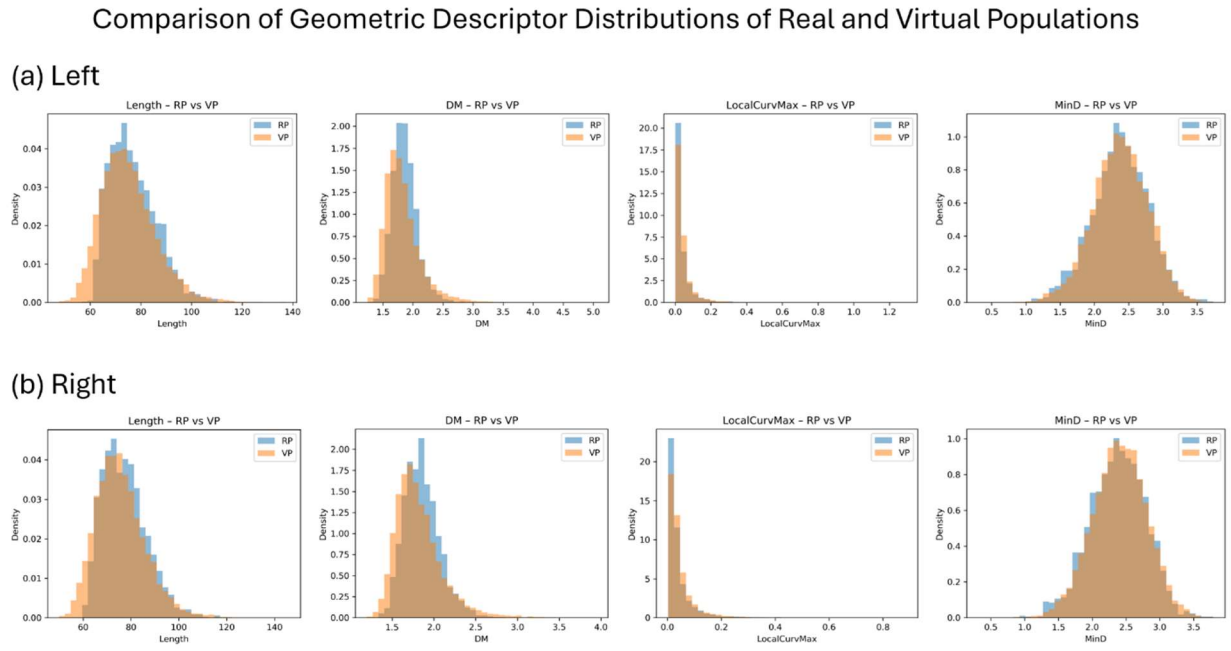
The distributions of key geometric descriptors in the virtual population closely matched those of the real Nagahama dataset. Similar trends were observed for both left and right ICAs. KL divergence values were consistently low to moderate, with <0.10 for minimum

diameter and local curvature maxima, ~0.29–0.39 for distance metrics, and ~0.58–0.90 for vessel length, indicating good agreement between real and virtual populations. The model faithfully reproduced major ICA morphological trends and variability patterns observed in the cohort.

Discussion

This work demonstrates that a large community-based cohort enables construction of a statistically representative virtual ICA population with significantly greater anatomical diversity than prior small-sample models. The resulting virtual population provides a robust foundation for uncertainty quantification, large-scale flow simulations, and future studies on ICA-related cerebrovascular risk.

Images (Optional)



References (Optional)

[1] Jin et al., Int J Numer Meth Biomed Eng, 2025

Session Category

Cardiovascular/Cardiorespiratory Biomechanics: Materials and Devices

OA127-04

Abluminal Watertight Lining in Porcine Carotid Arteries: Biomechanical Role and Impact on Decellularization Efficiency

Prof. Jin-Jia Hu, Mr. Yi-Jing Chen

Department of Mechanical Engineering, National Yang Ming Chiao Tung University, Hsinchu, Taiwan, Taiwan

Introduction

Tissue-engineered vascular grafts (TEVGs) have gained increasing attention as alternatives to autologous conduits for vascular reconstruction. Decellularized blood vessels provide native extracellular matrix scaffolds with favorable mechanical properties and biocompatibility, yet efficient decellularization without compromising structural integrity remains challenging. Our previous work identified an abluminal watertight lining in human umbilical arteries; its removal altered vessel mechanics and markedly improved perfusion decellularization efficiency. Determining whether similar structures exist in other vascular beds is essential for optimizing decellularization strategies and producing high-quality scaffolds for TEVG development.

Methods

Porcine carotid arteries (PCAs) were used to investigate the presence and functional role of an abluminal lining. A highly viscous collagenase solution was applied to the external surface to selectively degrade this lining. Histological staining with three complementary methods assessed extracellular matrix preservation. Vessel-wall permeability was measured to quantify transmural flow. Mechanical behavior was evaluated using circumferential ring testing. A custom perfusion system was then used to assess decellularization efficiency using a 1% SDS solution for 48 hours followed by a 10% calf serum wash for 18 hours. Residual DNA content and histology were used to confirm decellularization effectiveness.

Results

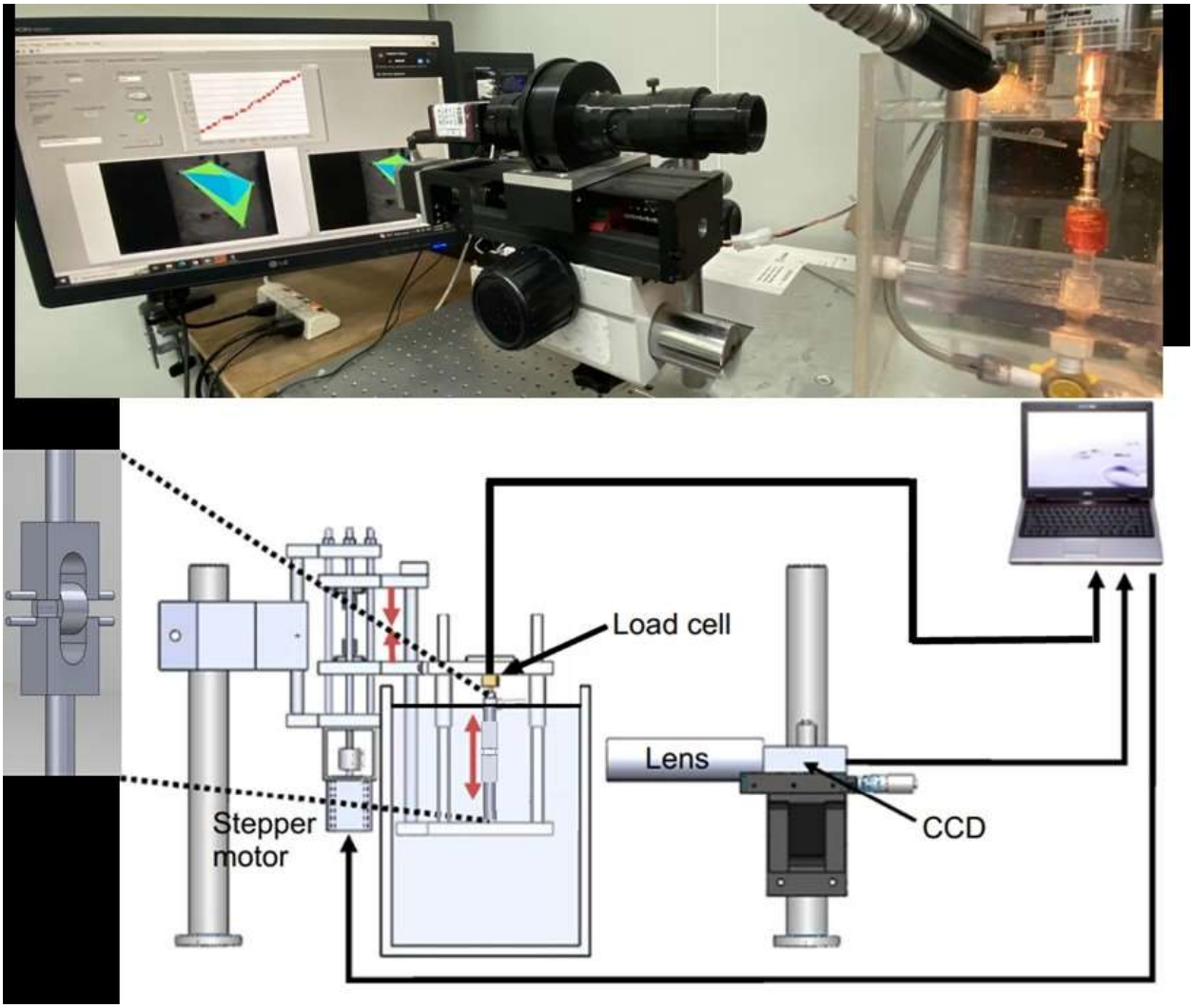
Histology confirmed that medial extracellular matrix components were preserved after collagenase treatment. Permeability testing showed a substantial increase in transmural flow, supporting the existence and successful removal of an abluminal watertight lining. Ring testing demonstrated increased compliance after treatment, indicating that the lining contributes to the artery's passive mechanical response. Following perfusion decellularization, histological analyses showed extensive cell removal, and residual DNA decreased to approximately 100 ng/mg. Ring testing of decellularized arteries exhibited a

leftward shift in the stress–strain curve, suggesting the loss of compliant constituents during SDS treatment.

Discussion

Selective removal of the abluminal watertight lining significantly enhanced perfusion decellularization efficiency in PCAs without damaging medial extracellular matrix. This approach enabled preparation of fully decellularized vessels within three days. These findings highlight the biomechanical relevance of abluminal linings and support the potential of decellularized PCAs as scaffolds for tissue-engineered vascular grafts.

Images (Optional)



Session Category

Cardiovascular/Cardiorespiratory Biomechanics: Materials and Devices

OA127-05

Prediction of Stent-Graft Placement After the EVAR Procedure: A High-Fidelity Computational Model

Eng Giulia De Campo[1], Dr Sara Barati[1,2], Dr. Anna Ramella[1,2], Dr. Francesco Migliavacca[1,3], Dr. Irene Fulgheri[3], Dr. Santi Trimarchi[3,4], Dr. Giulia Luraghi[1]

[1]Politecnico di Milano, Milan, Lombardy, Italy. [2]AllStent, Milan, Lombardy, Italy. [3]Foundation IRCCS Ca' Granda Ospedale Maggiore Policlinico,, Milan, Lombardy, Italy. [4]Department of Clinical Sciences and Community Health, University of Milan, Milan, Lombardy, Italy

Introduction

Endovascular aortic repair (EVAR) is a minimally invasive techniques commonly used to treat abdominal aortic aneurysm (AAA). The procedure consists in the deployment of a stent-graft in the pathological region of the aorta to exclude the aneurysm from the blood circulation. Variability in the pre-operative planning measurement, may results in inconsistent device positioning and sizing, leading to post operative complications [1]. In this context, computational models can provide information about stent-graft placement, varying device location and size. The aim of this work is to validate a finite element (FE) model of the EVAR procedure and to provide support to clinicians in the pre-operative planning phase.

Methods

Stent-graft models are carefully designed with material properties tuned accordingly to the results of crimping tests. The device comprises either the main body and the limb component.

The FE model replicates the entire EVAR process, including device crimping, delivery, and gradual release in the aorta [2]. Those steps are replicated for the limb component which is introduced from the contralateral femoral artery.

A 3D-printed rigid anatomy is used to reproduce the EVAR procedure in-vitro. CT images of different stages of the stent-graft release are acquired to validate the simulation results, by comparing the opening area (OA) and the distance between the centers (c-c distance) of the simulated and segmented stent rings (Figure1). The same evaluation is performed on 3 patient-specific anatomies.

Results

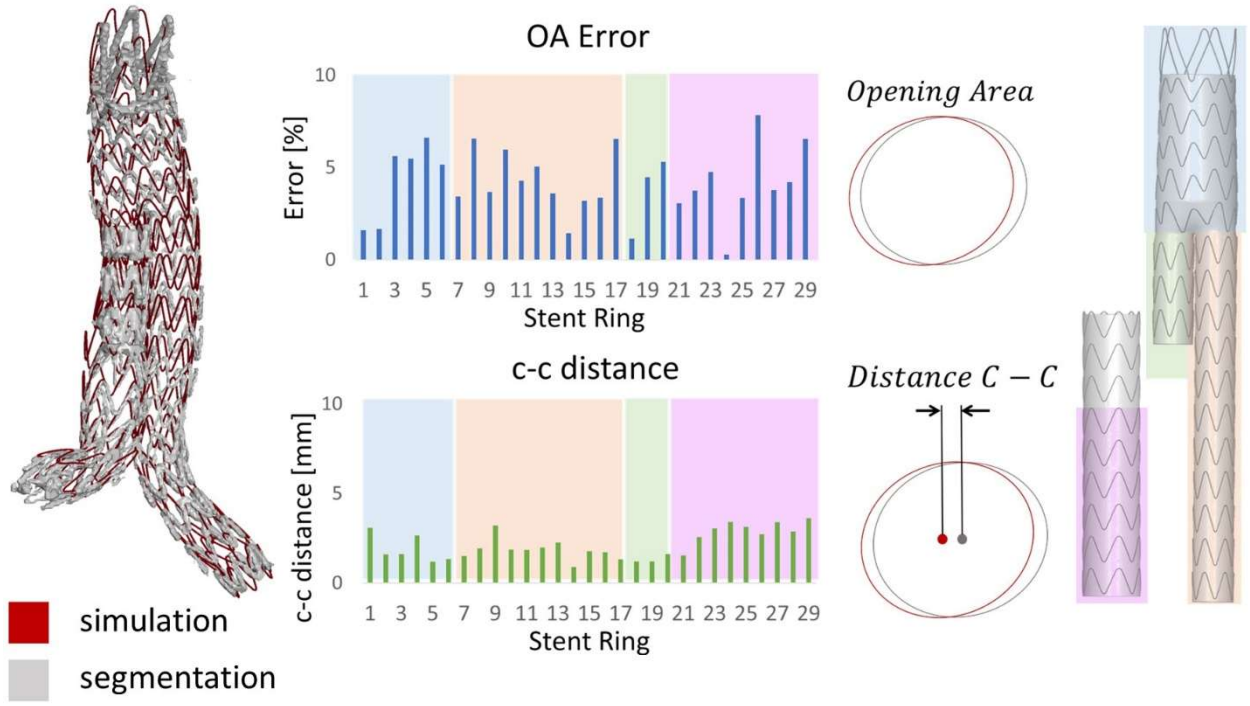
The validation with the 3D-printed rigid model, resulted in a mean error in the OA between the simulated and segmented stent-graft of 4.2% and a mean c-c distance of 2.15mm (Figure1).

Preliminary results on a first patient specific anatomy are in agreement with the ones achieved on the rigid model, with a mean OA error of 4.47% and a mean c-c distance of 2.18mm.

Discussion

This work shows the importance and the usefulness of numerical simulation in predicting the outcome of EVAR implantation. The possibility of virtually testing different device sizes and landing zones can provide clinicians with valuable support during the pre-operative planning phase.

Images (Optional)



References (Optional)

[1] Stéphane Avril et al., Int-J-Numer-Method-Biomed-Eng.2021.

[2] Anna Ramella et al., Ann-Biomed-Eng.2022.

Session Category

Cardiovascular/Cardiorespiratory Biomechanics: Materials and Devices

OA128-01

Clinician Requirements of a Home-Based Gait-Retraining System With Real-Time Feedback and Remote Monitoring

Ms Christy Oi-ying Chan Master's student[1,2], Dr. Jos Runhaar PhD[1], Dr. Selma Papegaaij PhD[3], Dr. Lennard Voogt PhD[4], Dr. Mariska Wesseling PhD[1], Dr. Martin Schepers PhD[3], Dr. Ignazio Aleo PhD[3], Ms Antoinette Torsij Master's student[5], Dr. ir. Eline van der Kruk PhD[5], Prof.dr.ir. Jaap Harlaar PhD[1,5], Dr. Erin Macri PT PhD[1]

[1]Erasmus MC University Medical Center, Rotterdam, South Holland, Netherlands. [2]Erasmus University Rotterdam, Rotterdam, South Holland, Netherlands. [3]Moveshelf Labs BV, Utrecht, Utrecht, Netherlands. [4]Rotterdam University of Applied Sciences, Rotterdam, South Holland, Netherlands. [5]Delft University of Technology, Delft, South Holland, Netherlands

Introduction

Altering foot progression angle (FPA) will affect the Knee Adduction Moment, and thereby knee-load. Consequently it may reduce pain, and slow down knee osteoarthritis progression. We recently developed a gait-retraining system with real-time feedback and remote monitoring to facilitate home-based gait-retraining programs. We interviewed physiotherapists to guide further development of our gait-retraining system.

Methods

This preliminary analysis is part of a larger feasibility study. Our system includes a single foot-mounted inertial measurement unit (IMU), a mobile app with a previously-validated algorithm to estimate FPA and provide real-time feedback, and a mock-up for a remote-monitoring dashboard (Figure). We recruited 10 physiotherapists who: have ≥2 years' experience, treat ≥2 knee-related cases per week, and have affinity for technology. We performed and recorded semi-structured interviews, during which we demonstrated the system, and inquired about opinions regarding usability and usefulness of the system, and what information clinicians desired to feel competent prescribing gait-retraining programs. So far, we have transcribed and thematically coded 5 interviews (Nvivo software).

Results

The first five participants were male physiotherapists located in North and South Holland. Regarding usability, clinicians preferred to see all summary statistics on a single screen/page to enhance interpretation. They confirmed the importance of showing FPA,

adherence to training, and patient-reported outcomes on the dashboard. Concerning usefulness, clinicians reported the system would help them to verify and monitor their patients' home programs, for example *"Is [my patient] on the right track?"*. They felt the system overall may motivate patients to adhere to treatment. Clinicians expressed a desire for the system to track additional parameters (e.g. spatiotemporal gait patterns) and different activities (e.g. stair climbing). Physiotherapists expressed that a system that could be operated fully outside of a lab would support patient care. Regarding decision support, clinicians expressed a lack of clinical practice guidelines or known literature to guide the design and monitoring of gait-retraining interventions.

Discussion

In this preliminary assessment, clinicians found our system to be supportive for monitoring home-based gait-retraining programs, though they sought broader functionality of the device and they lacked decision-making support. More sample diversity may enrich our dataset. Analyses are ongoing.

Images (Optional)

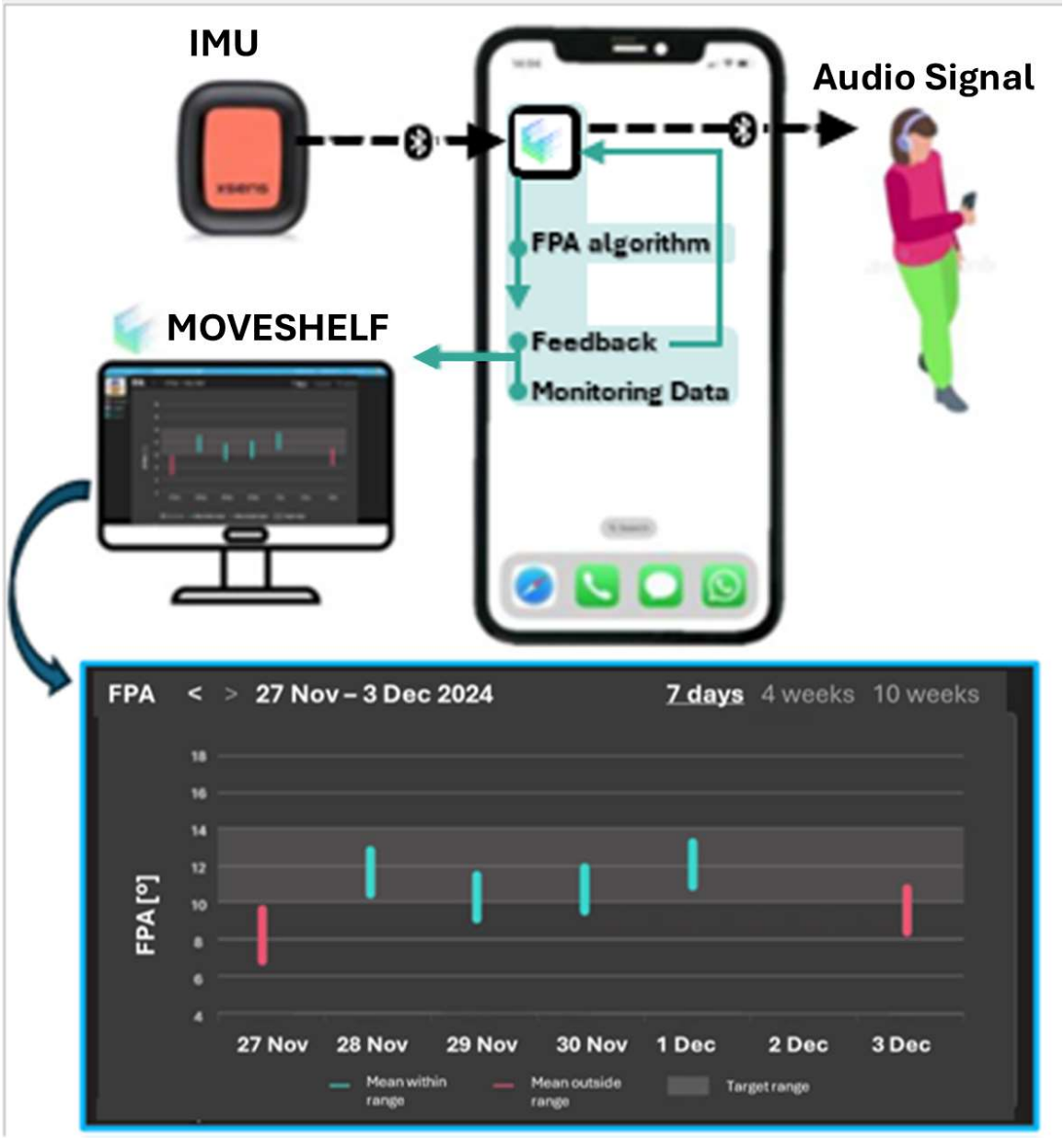


Figure. Top: Gait-retraining system. Bottom: Clinical dashboard with foot progression angle summary report

References (Optional)

Acknowledgements (Optional)

This project was supported by a Health Holland Public Private Partnership grant (#EMCLSH23038).

Session Category

Biomechanics Education, Knowledge Translation and Outreach: N/A

OA128-02

Traumatic Risk Assessment for Cerebral Exposure (TRACE): A Digital Platform for Real-Time Brain Health Monitoring in Sport

Ms Eleni Koumantou, Ms Emily Yik Kwan Chan, Mr Vahid Darvishi, Assoc. Prof. Mazdak Ghajari

Imperial College London, London, Greater London, United Kingdom

Introduction

Head impacts pose brain health risks. The impact kinematics can be collected by instrumented mouthguards (iMGs) and translated to brain strain. This translation typically relies on finite element (FE) models that are time- and resource-consuming. Machine learning (ML) models on the contrary, provide real-time estimation of brain strain, yet they are inaccessible to non-experts. Therefore, we introduce TRACE, a user-ready digital platform that provides real-time estimates of brain deformation, enabling accessible, interpretable brain health monitoring.

Methods

Technical design. TRACE integrates a validated ML surrogate model that approximates FE brain strain predictions to quantify post-impact biomechanical response (Fig. 1a). The model is designed to be pitch-side available as it uses kinematic features that can be reliably streamed to pitch-side receivers from iMGs [1].

Usability test designs. Current version of TRACE has been developed to handle iMG-recorded impact kinematics and generate immediate brain strain visuals (Fig. 1c), after an iterative process to decide feature selection and UI design tailored to user groups. To test TRACE's usability, pilot testing has been designed in collaboration with our industry partner, an iMG manufacturer and head-impact surveillance provider. Evaluation criteria include technical validity, user interface and interaction (UI/UX) design.

Results

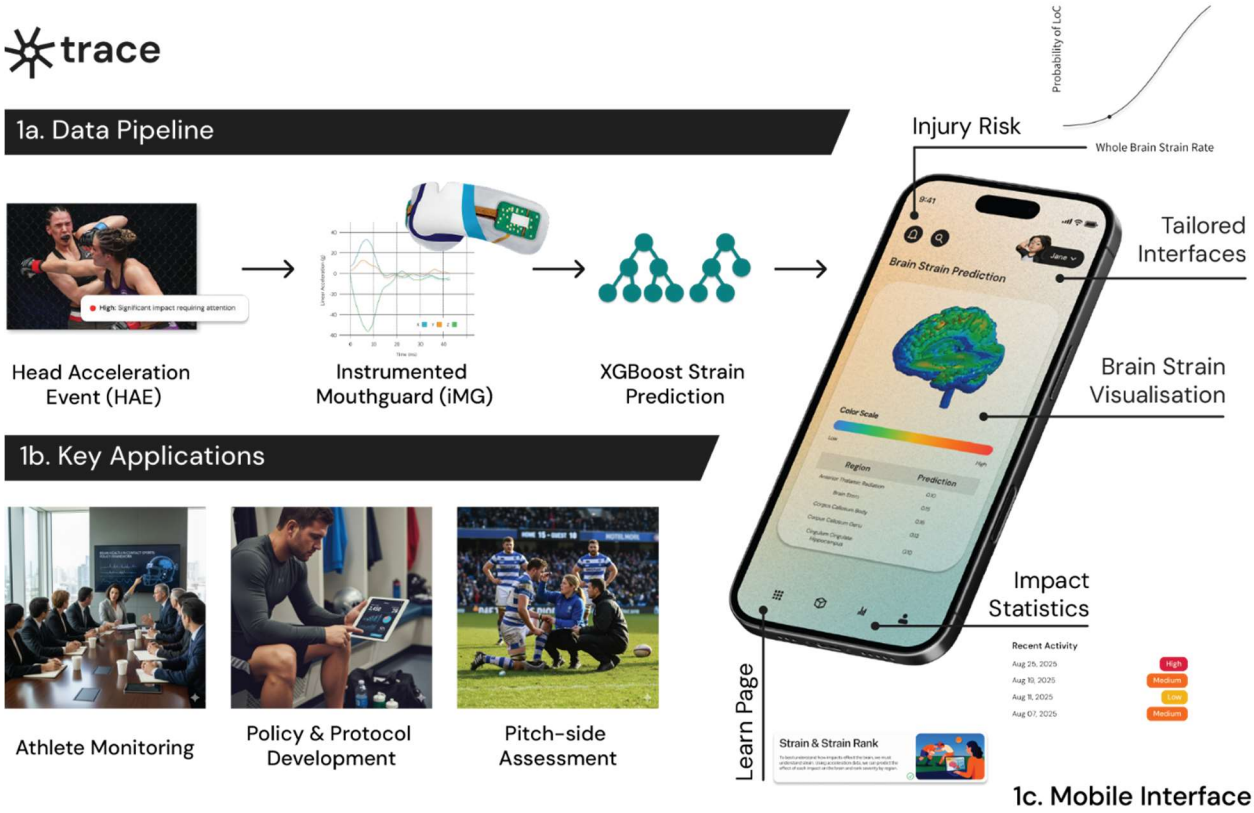
Technical validation. The ML model provides strain estimation under 0.1 seconds and has pitch-side availability enabled by its minimal requirement from iMG-collected kinematics.

UI/UX designs. TRACE provides brain strain estimation in interactive visuals and implements role- and sport-specific interfaces and features tailored for coaches, clinicians, and parents/guardians.

Discussion

This project is a translational initiative that aims to bridge the gap between on-field impact kinematics with biomechanical measures. TRACE will enable non-experts to make biomechanics-informed brain health decisions (Fig. 1b). This will ultimately benefit underrepresented groups like amateur and youth athletes who do not have excessive access to brain health experts, but also policy makers as they will gain insights from a wider range of populations often overlooked in studies. Future steps include: 1) conducting usability testing and interviews with athletes and coaches, 2) refining platform design based on user feedback, and 3) quantifying measurement uncertainty.

Images (Optional)



References (Optional)

Chan E. Y. K. et al., Eng. Appl. Artif. Intell, 2025

Session Category

Biomechanics Education, Knowledge Translation and Outreach: N/A

OA128-03

Presenting Gait Analysis Results to Older Adults Undergoing Joint Arthroplasty: A Qualitative Study and Patient-Centred Report Development

Mr. Gabriel Lonuzzo B. Eng, Mr. Imad Kashir, Alexandra Pop, Ms. Madeline Rao Shishis, Ms. Kassidy Appiah-Kubi, Ms. Maya Drozdov, Dr. Vincenzo Di Bacco, Dr. Matthew Ruder, Dr. Anthony Adili P.Eng, MD, FRCSC, Dr. Kim Madden, Dr. Dylan Kobsar

McMaster University, Hamilton, Ontario, Canada

Introduction

Motion capture provides objective biomechanical data that can inform clinical decisions surrounding joint arthroplasty. However, results are often communicated through technical figures and terminology that patients find difficult to interpret. Clear, accessible reporting is essential to support shared decision-making and engagement in perioperative treatment and rehabilitation. This study examined older adults' preferences for how gait analysis results should be communicated. Based on these findings, we developed a patient-centred gait report and software pipeline that translates complex biomechanical data into accessible formats.

Methods

Ten adults undergoing elective knee or hip arthroplasty participated in semi-structured interviews. Purposive sampling captured diverse demographics and surgical experiences. Interviews (~30 minutes) were recorded, transcribed, de-identified, and analyzed using thematic analysis. These insights informed the development of a prototype clinical gait report.

To automate report generation, custom Python software was developed to integrate clinical and biomechanical data, compute mobility metrics, and generate personalized reports featuring simplified diagrams, plain-language explanations, and colour-coded indicators. A clinician dashboard enables the selection of specific metrics and timepoints. The system was deployed in a longitudinal knee and hip arthroplasty cohort (n>200), and sample reports were shown to patients to collect feedback on clarity and perceived usefulness.

Results

Participants preferred results directly tied to daily activities, including walking speed, step length, joint angles, and stair performance. Comparative metrics (pre-/post-operative changes, bilateral symmetry, and age-matched benchmarks) were viewed as highly valuable for contextualizing progress. Tables were preferred for clarity, while graphs were

acceptable only when clearly labelled and had consistent colour-coding to improve interpretability. These findings informed a multimodal gait-reporting system that retrieves data from secure servers, computes personalized metrics, and presents results through simplified visuals. The software has generated 121 reports to date (Figure 1), with initial feedback indicating strong usability.

Discussion

This study demonstrates the importance of incorporating patient perspectives when communicating gait analysis results. Older adults prefer personalized, visually intuitive reports grounded in meaningful comparisons. By integrating automated data processing with user-centred design, the reporting tool improves the accessibility of biomechanical outputs and may enhance comprehension, engagement, and shared decision-making. Future work will continue to evaluate long-term usability, clinical integration, and effects on perioperative care.

Images (Optional)

St. Joseph's Healthcare Hamilton

Gait Report

McMaster University

Joint Angle Metrics (Details)

Peak Angle during Stance: Typical range: >10.0 | L: 20.1° | R: 17.8°

This angle represents how much your knee bends when your foot is on the ground. More bending = better shock absorption. Less = possible stiffness.



Peak Angle during Swing: Typical range: >50.0 | L: 54.2° | R: 61.3°

This angle represent how much your knee bends as your leg moves forward when you take a step. A larger angle means more flexibility.



Range of Motion (ROM): Typical range: >5.00 | L: 12.7° | R: 10.5°

Your knee's range of motion (or excursion) represent how much your knee moves while supporting weight. More range of motion often means better joint function.



Outward (Varus) Thrust: Typical range: < 2.50 | L: 2.23° | R: 2.47°

When you place weight on your knee, it can move outward (like a bowed-leg). Less thrust can indicate better alignment and recovery.

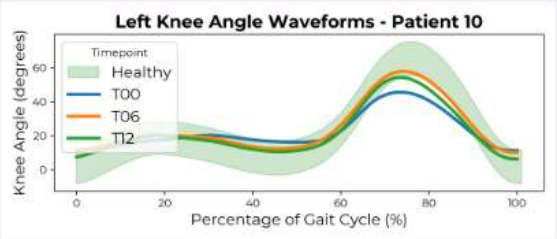


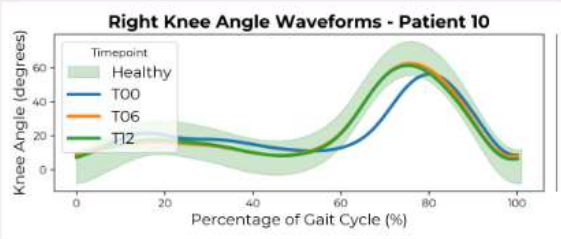
Knee Alignment: Typical range: -5.00 - 5.00 | L: -4.17° | R: -6.08°

This indicates how aligned your leg is while walking. Ideally, your thigh and shin line up. Angling out or in can suggest alignment issues.



Knee Angle Waveforms:





Acknowledgements (Optional)

We gratefully acknowledge St. Joseph's Healthcare Hamilton and the Smart Mobility for the Aging Population (sMAP) program at McMaster University for their ongoing support of this study.

Session Category

Biomechanics Education, Knowledge Translation and Outreach: N/A

OA128-04

Who Really Knows Strength Training Biomechanics? An Experience and Occupation-Based Comparison

Dr Tron Krosshaug[1,2], Dr Erich Petushek[3,4], Dr Sarah Breen[5], Dr Gregory D. Myer[6,7,8], Dr Beau P. Dupuis[9], Dr Sandor Dorgo[10], Dr William Ebben[11]

[1]Department of Sports Medicine, Norwegian School of Sport Sciences, Oslo, Oslo, Norway. [2]Oslo Sports Trauma Research Center, Oslo, Oslo, Norway. [3]Department of Psychology and Human Factors, Michigan Technological University, Houghton,, Michigan, United States. [4]Health Research Institute, Michigan Technological University, Houghton, Michigan, United States. [5]Stephenson School of Biomedical Engineering, The University of Oklahoma, Norman, Oklahoma, United States. [6]Emory Sports Performance and Research Center (SPARC), Flowery Branch, Georgia, United States. [7]Emory Sports Medicine Center, Atlanta, Georgia, United States. [8]Department of Orthopaedics, Emory University School of Medicine, Atlanta, Georgia, United States. [9]Aspirus Health, Calumet, Michigan, United States. [10]Department of Kinesiology, University of Texas at San Antonio, San Antonio, Texas, United States. [11]Northland Analytics, Mountain, Wisconsin, United States

Introduction

Undergraduate and professional education in strength-training biomechanics requires integration of anatomical knowledge, force vectors, and movement principles into applied exercise contexts. Despite widespread training and credentialing, it remains unclear how well these principles are retained across career pathways and experience levels. This study evaluated overall strength training biomechanics knowledge among individuals engaged in strength training and examined whether professional role, years of experience, age, or gender predicted performance. We further compared observed performance to expected guessing accuracy to assess baseline knowledge levels.

Methods

Participants (N = 435) from diverse exercise-related backgrounds (academics, physical therapists, fitness professionals, sport coaches, students, and others) completed an online strength training biomechanics assessment focused on exercise technique, moments and moment arms, and joint loading concepts. Percent correct was calculated for each participant. Linear regression modeled performance as a function of occupation, years of experience evaluating exercise technique (0–1, 2–5, 6–10, 11–20, 20+ years), age, and gender. Estimated marginal means were used to characterize experience trends.

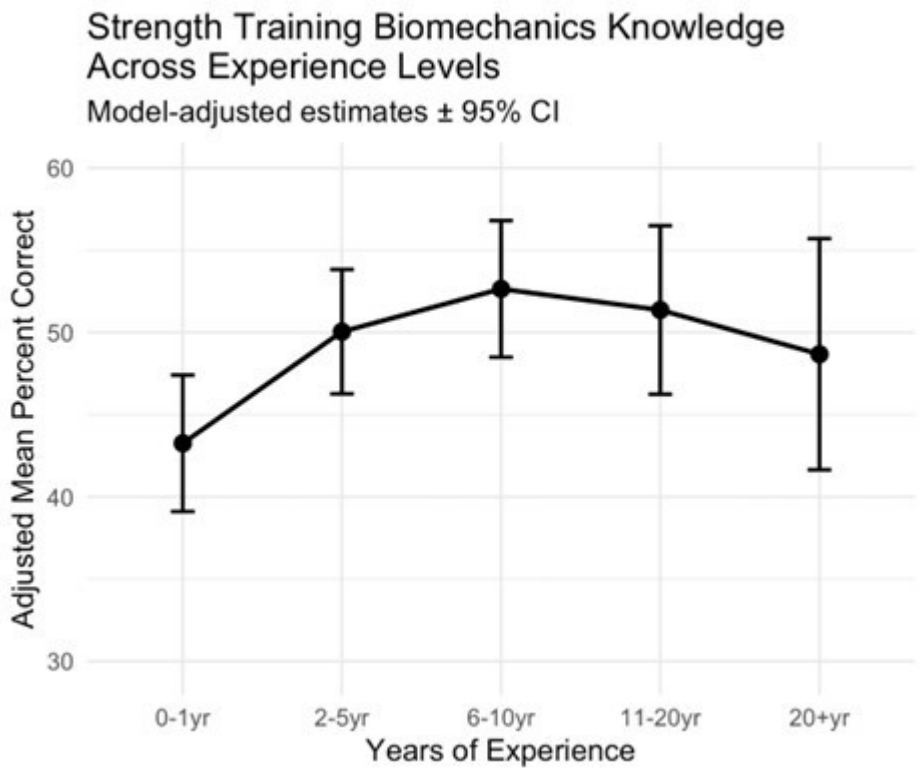
Results

Overall performance was low (M = 50.1% correct, 95% CI [48.8, 51.3]), only modestly exceeding expected guessing performance (29.47%), indicating limited mastery across the cohort. The regression model was significant ($F(11,416)=4.20$, $p<.001$) but explained limited variance (Adj. $R^2 = .08$), suggesting substantial unexplained heterogeneity. Years of experience emerged as the strongest predictor, with higher scores observed for 2–5 years (+6.8%), 6–10 years (+9.4%), and 11–20 years (+8.1%) of experience relative to 0–1 year, demonstrating a performance curve peaking at mid-career (see Figure 1). Professional occupation showed modest effects; fitness professionals scored lower than academics (−5.6%), while physical therapists, coaches, students, and others did not differ reliably. Age was not predictive. Female participants scored lower on average (−5.0%).

Discussion

Biomechanics knowledge in applied strength training was low overall and highly variable, with experience—rather than professional role—serving as the primary differentiator. The modest explanatory power of demographic predictors highlights the need for structured, accessible, and engaging instructional tools to bridge persistent learning gaps and promote equitable acquisition of biomechanics competence across training pathways.

Images (Optional)



References (Optional)

Session Category

Biomechanics Education, Knowledge Translation and Outreach: N/A

OA128-05

Evaluating COACH: Time in Live Tackling Drills and Associated Head Acceleration Events in Youth Football

Mr. Giovanny A. Romero A. MS[1,2], Mr. William S. Carter[1,2], Dr. N. Stewart Pritchard PhD[1,2], Dr. Garret D. Bullock DPhil[1], Dr. Justin B. Moore PhD[1], Dr. Ty D. Holcomb PhD[1,2], Dr. Madison E. Marks PhD[1,2], Dr. Christopher M. Miles MD[1], Dr. Johna Register-Mihalik PhD[3], Dr. Joel D. Stitzel PhD[1,2], Dr. Kristie L. Foley PhD[1], Dr. Jillian E. Urban MPH, PhD[1,2]

[1]Wake Forest University School of Medicine, Winston-Salem, NC, United States. [2]Virginia Tech – Wake Forest University, Winston-Salem, NC, United States. [3]University of North Carolina at Chapel Hill, Chapel Hill, NC, United States

Introduction

Communities Aligned to Reduce Concussion and Head Impact Exposure (COACH) is an intervention to improve coaches' knowledge, skills, and attitudes for safer youth football practices. COACH aligns with National Federation of State High Schools (NFHS) guidelines, which recommend no more than 30 minutes of live tackling (full speed, to the ground) per practice. This study examines the relationship between minutes of live tackling and head acceleration events (HAEs) outcomes in youth tackle football players.

Methods

Athletes from seven youth football teams participated: three control (C) teams (12U_1C, n=18; 13U_1C, n=17; 13U_2C, n=14) and four intervention (I) teams (11U_1I, n=15; 12U_1I, n=14; 12U_2I, n=16; 13U_1I, n=21). Intervention teams coaches were trained in COACH guidelines before the season began. All athletes wore instrumented mouthguards to record HAEs. Trained staff collected biomechanical and video data in all practices and games to quantify live tackling time and verify HAEs. A linear mixed-effects model examined associations between HAEs, minutes of live tackling, intervention status (intervention vs control), and their interaction, with random effects for player and team.

Results

A total of 3,416 verified HAEs were recorded during live tackling across 146 practices. Control teams spent more time in live tackling (44.6±27.6 min) than intervention teams (18.6±26.1 min) and had more HAEs per minute (1.75±2.71 vs. 1.08±4.17). Across all practices, HAE rates increased by 0.04 events/min in control teams (SE = 0.004, 95% CI: 0.03–0.05) and 0.07 events/min in intervention teams (SE = 0.004, 95% CI: 0.06–0.08), with a slope difference of −0.03 events/min ($p < 0.0001$).

Discussion

Results show differences in HAEs between intervention and control teams during live tackling, with control teams sustaining more HAEs per practice and spending more time in live tackling. Control teams had higher mean HAEs and greater live-tackling minutes, whereas intervention teams showed a steeper increase in HAEs per minute, indicating greater head-impact burden per unit of live exposure. This pilot highlights how coaches implemented the COACH program in real-world settings and the need to balance live tackling time.

Session Category

Biomechanics Education, Knowledge Translation and Outreach: N/A

OA128-06

The Misuse of Biomechanical Evidence in Shaken Baby Cases

Professor Barbaram Pfeffer Billauer J.D. ,M.A., PhD

Elon University School of Law, Greensboro, NC, United States. University of Port, Porto, Portugal, Portugal. Institute of World Politics, Washington, DC, United States

Introduction

The diagnosis of *Shaken Baby Syndrome (SBS)* has recently come under legal attack. A small group of physcians and biomechanics professionals claim that biochemical evidence does support the diagnosis - which is caused by repeated shaking resulting in the brain banging against the skull (a *contre coup* lesion). using non-representative studies. In one recent case, the medical diagnosis was rejected by NJ's highest court based on these non-representative studies regarded as the consensus in the biomechanics community.

Methods

This research evaluates the biomechanical/medical evidence adduced in *State of New Jersey v. Darryl Neives and Michael Cafelli [4],* leading to the courts rejecting the SBS diagnosis entirely. The evidence submitted by the defendants' biomechanics expert relies on six articles, plus amici briefs by legal organizations supporting the defendants' rights. The studies relied on were evaluated for scientific reliability and validity and legal relevance. The studies are assessed for their relevance to human subjects (babies) typically diagnosed with the condition to determine whether the results and testimony based thereon are reliable, relevant, and valid to assess the issue.

Results

The studies relied on via expert testimony require a double extrapolation (from dolls or animals to adult humans and then to babies) which ethically cannot) be done). The tests do not assess the biological/physiological effects of *repeated* shaking in humans. They merely calculate the *external* force generated by a single shake in a dummy or an animal (where 33% of the test subjects actually sustained injuries consistent with SBS). Further the test conditions do not represent real life conditions and hence are invalid to determine

the effects of repeated shaking in a premature or vulnerable child. SBS involves internal injuries caused by forces generated by a cascade of physiological responses and hence are outside the purview of conclusions generated by testing external forces.

Discussion

This work demonstrates the misuse of biomechanics when the science is taken beyond its limits in a legal setting. Lawyers representing defendants are advocating these limited studies, while the child who has been severely damaged (or has died) is without redress.

References (Optional)

References: . *State of New Jersey v. Nieves, (2025)*

Session Category

Biomechanics Education, Knowledge Translation and Outreach: N/A

OA129-01

Athletes With ACL Reconstruction Demonstrate Altered Movement Variability When Preparing to Respond to Perturbations: A Preliminary Analysis

Dr. Jamie Kronenberg PT, DPT, PhD, SCS[1], Dr. Michael Riley PhD[2], Dr. Laura Schmitt PT, MPT, PhD[3]

[1]High Point University, High Point, North Carolina, United States. [2]University of Cincinnati, Cincinnati, Ohio, United States. [3]Ohio State University, Columbus, Ohio, United States

Introduction

Athletes returning to sport following anterior cruciate ligament reconstruction (ACLR) must be prepared to respond to the dynamic nature of their sport. Complex, variable movement solutions are required to match specific situational contexts, such as responding to a perturbation in sport. The purpose of this study was to test the hypothesis that when preparing to respond to perturbations, athletes with ACLR would demonstrate altered movement variability, as characterized by recurrence quantification analysis (RQA), compared to uninjured athletes.

Methods

Twelve athletes with primary ACLR (6 female, age 21.1 ± 2.7 years) at the time of medical clearance for sports participation and 12 age-, sex- and activity-matched controls (CTRL) completed 3-dimensional motion analysis of walking on a self-paced treadmill. Each athlete completed baseline walking (BASE), walking before an anticipated gait perturbation (ANT; informed of perturbation prior to trial) and walking before an unanticipated gait perturbation (UNT; not informed prior to trial). Participants in the ACLR group received the perturbations in a random order and their matched-CTRL received the perturbation in the same order. Time periods of interest (POI) included the 10 seconds preceding the ANT and UNT perturbations. Movement variability was assessed using percent determinism (%DET) as calculated by RQA of involved limb (ACLR; non-dominant CTRL) sagittal plane knee kinematics during POI. A 2x2 mixed ANOVA tested group and anticipation effects.

Results

There was no significant difference in %DET between groups at BASE ($p=0.836$) and no significant group by anticipation interaction ($p=0.536$; $h^2=0.018$). There was no main effect of anticipation ($p=0.752$; $h^2=0.005$), but there was a main effect of group

($p=0.016$; $h^2=0.235$). Athletes with ACLR demonstrated significantly higher %DET compared to CTRL independent of anticipation (Table1).

Discussion

No significant interaction was found between group and anticipation, but athletes with ACLR showed higher %DET than CTRL when preparing for both perturbations. Higher %DET indicated greater gait predictability, indicating alterations in movement variability that may reflect differences in strategies used to prepare for a perturbation between groups. Future studies are warranted to further understand the impact of ACLR on movement variability and its potential impact on how athletes with ACLR prepare for and respond to perturbations.

Images (Optional)

Baseline			Anticipated	Unanticipated
ACLR	86.8 ± 3.2%	ACLR	89 ± 3.3%	89.9 ± 2.2%
CTRL	86.5 ± 4.7%	CTRL	87 ± 2.3%	87.7 ± 4.2%
Difference	p= 0.836	Group x Anticipation	p=0.536	
		Group	p=0.016	
		Anticipation	p=0.752	

Table 1. Average %DET ± standard deviation for each group. Larger values of %DET indicate increased predictability or repetitiveness.

References (Optional)

Session Category

Clinical Biomechanics: N/A

OA129-02

Stretch-Shortening Cycle Mechanics and Leg Strength in Adolescent Male and Female Athletes Following ACL Injury

Mr. Landon Foley BSc., Dr. Nathan Boon-van Mossel DC, MSc., Dr. Kati Pasanen PhD, Dr. Karen Ballinger MD, Dr. Matthew Jordan PhD

University of Calgary, Calgary, Alberta, Canada

Introduction

Biomechanical testing is recommended to support athlete clearance for return to sport (RTS) following anterior cruciate ligament reconstruction (ACLR). Previous work has suggested that biomechanical outputs during stretch-shorten cycle tasks such as jumping may be useful at detecting lower limb deficits in adolescent athletes compared to traditional performance metrics (jump height) [1]. Additionally, there is a significant lack of literature examining stretch-shortening cycle mechanics and eccentric lower limb strength in adolescent athletes with ACLR. This study therefore aimed to investigate the lower limb stretch-shortening cycle and maximal strength characteristics in adolescent athletes following ACLR.

Methods

Adolescent athletes with ACLR (age: 14-17 years; n=21; females: n=11: mean post-op = 13 months +/- 7 months) performed maximal isokinetic concentric and eccentric contractions on a robotic leg press and maximal effort single leg vertical jumps on a force plate system. Paired t-tests were used to compare athlete performance between the ACLR and the contralateral limb. One-sample t-tests were used to compare athlete performance to established sex-based youth athlete benchmarks. Cohen's *d* was used to determine effect sizes. This study is currently ongoing.

Results

All athletes demonstrated significant deficits in stretch-shorten cycle performance between the ACLR limb and the contralateral limb ($p<0.001$, $d = 1.76$), and in stretch-shorten cycle braking phase strategy such as peak braking power ($p<0.001$, $d = 1.51$) and contact time ($p=0.02$, $d = 0.54$). Both male and female athletes presented significant deficits in stretch-shorten cycle performance and braking phase strategy relative to established youth athlete benchmarks. All athletes demonstrated significant deficits in both maximal concentric ($p<0.001$, $d = 0.87$) and maximal eccentric strength ($p<0.001$, $d = 1.00$) between the ACLR and the contralateral limb. Female athletes displayed greater deficits

in maximal concentric strength between limbs ($p<0.001$, $d = 1.79$) relative to male athletes ($p=0.159$, $d =0.49$).

Discussion

Adolescent athletes with ACLR demonstrate significant biomechanical deficits in both stretch-shorten cycle and maximal strength tasks, despite being at the time course of clinical RTS. Both biomechanical outputs and performance metrics may provide insight into deficits related to recovery from ACLR in this population.

Images (Optional)

Table 1

Differences Between ACLR and Contralateral Limb in Maximal Strength and Stretch-Shortening Cycle Measures in Adolescent Athletes by Sex

	Limb			
Female Adolescent Athletes	ACLR	Contralateral	Effect Size (*d*)	p-value
Maximal Concentric Strength (N/Kg)	13.23 (3.41)	17.11 (3.33)	1.79	<0.001
Maximal Eccentric Strength (N/Kg)	18.22 (3.89)	21.38 (3.96)	0.90	0.014
Jump Height (cm)	5.04 (2.84)	8.76 (3.10)	-2.54	<0.001
Peak Braking Power (W/Kg)	9.36 (2.64)	12.27 (2.26)	-1.84	<0.001
Whole Body Eccentric Stiffness ([N/m]/Kg)	100.87 (56.24)	100.38 (49.71)	0.05	0.874
Contact Time (s)	0.859 (0.100)	0.881 (0.173)	-0.19	0.542

	Limb			
Male Adolescent Athletes	ACLR	Contralateral	Effect Size (*d*)	p-value
Maximal Concentric Strength (N/Kg)	17.78 (5.18)	20.02 (5.03)	0.49	0.159
Maximal Eccentric Strength (N/Kg)	19.77 (5.97)	23.90 (6.01)	1.07	0.008
Jump Height (cm)	9.34 (4.59)	13.24 (4.64)	-1.36	0.002
Peak Braking Power (W/Kg)	12.30 (2.65)	14.52 (2.89)	-1.21	0.004
Whole Body Eccentric Stiffness ([N/m]/Kg)	100.52 (65.34)	97.62 (55.15)	0.22	0.503
Contact Time (s)	0.849 (0.156)	0.937 (0.206)	-1.14	0.006

Note . All limb measures presented as mean (SD).

References (Optional)

[1] Matthew J. Jordan *et al.* J Sport and Health Science, 2018

Acknowledgements (Optional)

The authors would like to thank Dr. Lisa Phillips in her assistance with the recruitment of participants for this work.

Session Category

Clinical Biomechanics: N/A

OA129-03

Disentangling Movement Variability with Principal Component Analysis of Full-Waveform Motion Capture in Adolescent Athletes Post-ACL Reconstruction

Ms Mona Behrouzian BASc[1], Dr Tim Bhatnagar PhD, BEng, BSc, MASc[2,3], Dr Lise Leveille MD, PhD, MHSc, BSc[2,4,5], Dr Calvin Kuo PhD, PEng[1]

[1]School of Biomedical Engineering, University of British Columbia, Vancouver, BC, Canada. [2]The Motion Lab, Sunny Hill Centre at BC Children's Hospital, Vancouver, BC, Canada. [3]Department of Pediatrics, Faculty of Medicine, University of British Columbia, Vancouver, BC, Canada. [4]BC Children's Hospital Research Institute, Vancouver, BC, Canada. [5]Department of Orthopedics, University of British Columbia, Vancouver, BC, Canada

Introduction

Anterior Cruciate Ligament (ACL) tears are severe knee injuries, with re-injury rates up to 32% in adolescents. Return-to-sport (RTS) assessments for post-ACL reconstruction (ACLR) have been adopted by hospitals worldwide to screen for re-injury risk. However, no functional-testing RTS assessments have shown a significant association with reduced ACL re-injury rates in adolescents. Threshold-based pass-fail criteria with motion capture are common, but fail to consider the substantial movement variability exhibited by adolescents, caused by heterogeneity in size, sex, and age. To address this gap, the full waveforms of motion capture can be analyzed with Principal Component Analysis (PCA), which reduces multivariate datasets into a minimized set of key biomechanical parameters.

Methods

32 adolescent athletes (16.5±1.6 years, 23F) 9-12 months post-ACLR performed three 45-degree run-to-cut trials on each leg, while instrumented with motion capture (12-camera Qualisys system, 50-marker PRiSM set) to analyze full-body 3D joint kinematics (Visual3D) [1]. PCA was applied across the aggregated knee flexion angle of both legs during foot-strike. Extracted principal components (PCs) captured knee flexion movements that explained the greatest variability across the injured and uninjured legs and across athletes. PC coefficients (relative weight per knee flexion angle trace) of the injured and uninjured legs were compared with a t-test. This demonstrates whether a PC is differentially represented in the injured and uninjured legs.

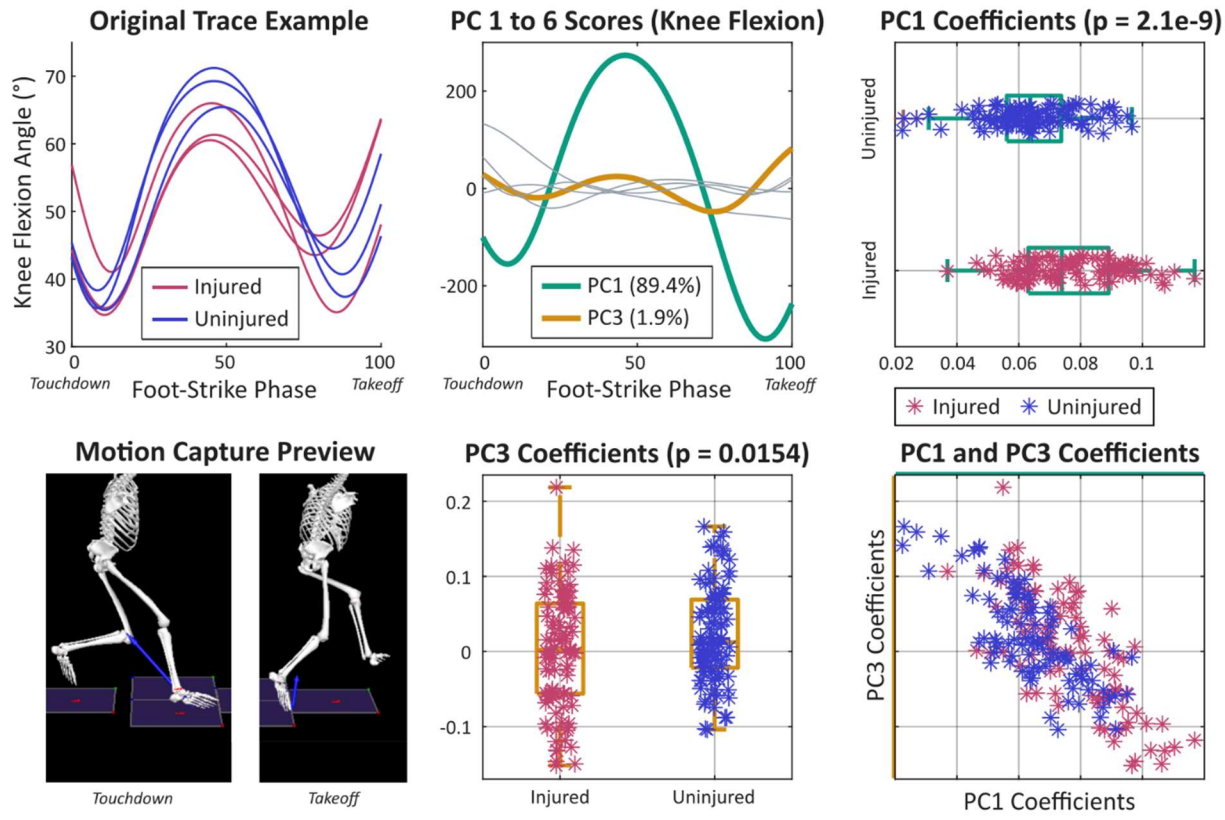
Results

Two PCs (89.4%, 1.9% explained variance) showed significant differences (p=2.1e-9, 1.5e-2 respectively) between injured and uninjured legs. The former PC captures the variability in magnitude of knee flexion motion throughout foot-strike, while the second corresponds to stiffness in landing strategy, indicated by increased flexion during touchdown and takeoff.

Discussion

Using PCA in RTS screening can help to both disentangle movement variability and uncover the small adaptations (such as landing strategies) that are associated with injury. PCs from full-waveform analysis may be a stronger indicator of injury compared to traditional threshold-based criteria. This method can be expanded with additional joints to provide insights into inter-joint coordination and movement compensation. This enables future work exploring adolescents who exhibit abnormal movement patterns related to injury or other health conditions that affect movement.

Images (Optional)



References (Optional)

[1] PRiSM, Motion Analysis RIG, 2022

Session Category

Clinical Biomechanics: N/A

OA129-04

In Vivo MR Elastography Reveals Cartilage Stiffness Changes Linked to Altered Gait Patterns Post-ACL Surgery

Dr. Emily Miller[1], Dr. Timothy Lowe[1], Dr. Hongtian Zhu[1], Dr. Stéphane Avril[2], Dr. Corey Neu[1]

[1]University of Colorado Boulder, Boulder, CO, United States. [2]Ecole des Mines de Saint-Etienne, Saint-Etienne, Auvergne-Rhône-Alpes, France

Introduction

Following ACL reconstruction, altered gait mechanics often persist despite surgical repair and may drive divergent cartilage remodeling patterns that initiate osteoarthritis [1]. However, the relationship between joint loading and early cartilage mechanical changes remains poorly characterized because conventional imaging cannot detect cartilage stiffness alterations before structural damage occurs. This study developed an MRI-based elastography method to quantify *in vivo* cartilage stiffness heterogeneity and examined how regional stiffness patterns relate to gait mechanics and patient outcomes in ACL reconstructed patients.

Methods

Twenty participants (mean age 24.9 years, BMI 23.5) underwent bilateral MRI scans and KOOS questionnaires approximately 12 months post-ACL reconstruction. Participants also completed gait analysis using markerless, smartphone-based motion capture, with musculoskeletal modeling estimating peak knee adduction moments and medial contact forces. DENSE MRI captured cartilage displacement during cyclic loading. An inverse elastography pipeline combining the virtual fields method [2] and adjoint optimization [3] generated stiffness maps with less than 6% reconstruction error in validation studies. Three stiffness heterogeneity metrics quantified mechanical organization: zonal stiffness contrast (depth-dependent gradient), zonal pattern irregularity (spatial consistency), and surface stiffness variability (regional differences).

Results

Significant gait-stiffness relationships emerged exclusively in the reconstructed limb, indicating local mechanoadaptation. In tibial cartilage, higher knee adduction moments strongly correlated with increased stiffness gradient and variance, suggesting overloading-driven stiffening. Conversely, femoral cartilage showed opposite patterns, where greater mechanical heterogeneity correlated with reduced knee adduction moments, consistent with underloading-induced softening. Lower KOOS physical function scores correlated

with increased tibial stiffness variance, while femoral patterns showed distinct regional associations. No gait-stiffness relationships appeared in the contralateral limb.

Discussion

This study presents the first *in vivo* cartilage elastography in humans, revealing that altered gait mechanics after ACL reconstruction correlate with spatially divergent cartilage remodeling. The contrasting pattern of femoral softening under reduced loading and tibial stiffening under elevated loading reflects loss of mechanical homeostasis that may drive early osteoarthritis progression. These findings support rehabilitation strategies targeting harmful loading patterns to restore mechanical balance and potentially slow cartilage degeneration.

Images (Optional)

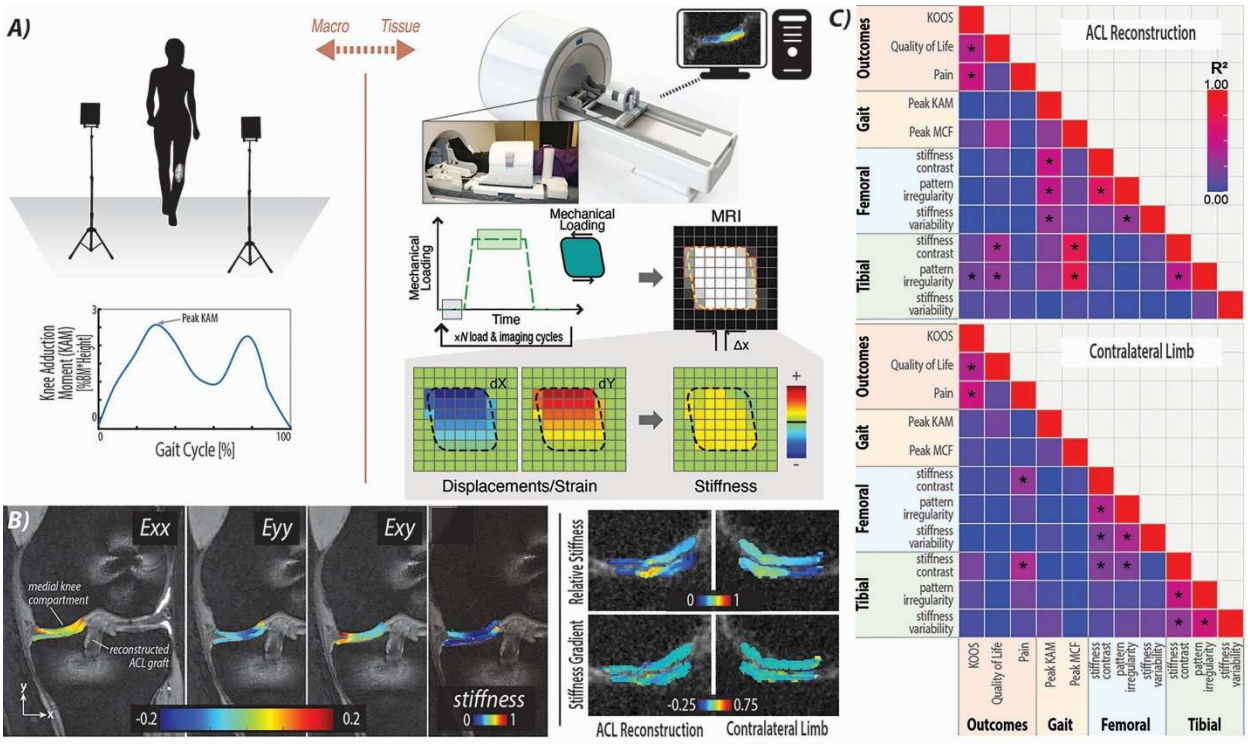


Figure 1. *In vivo* stiffness in articular cartilage was measured and related to human gait in the same patients post-ACL reconstruction. Markerless motion capture was compared to MRI-based measures of stiffness. *(A-B)* Noninvasive measurement of displacements/strain, and in combination with inverse modeling, enabled calculation of stiffness in tibiofemoral cartilage of ACL reconstructed and contralateral knees. *(C)* Correlations were found between stiffness and gait in both femoral and tibial cartilage.

References (Optional)

[1] Wang *et al.*, *Arthritis Res Ther*, 2020.

[2] Mei *et al.*, *Comput Mech,* 2021.

Acknowledgements (Optional)

NIH 2 R01 AR063712

Session Category

Clinical Biomechanics: N/A

OA129-05

Three-Year Bone Changes Following Acute ACL Injury: Bone Density and Microarchitecture Analysis Using HR-pQCT

Ms. Callie Stirling, Ms. Nina Pavlovic, Dr. Nathan Neeteson, Dr. Sarah Manske, Dr. Richard Walker, Dr. Steven Boyd

University of Calgary, Calgary, Alberta, Canada

Introduction

Anterior cruciate ligament (ACL) injuries frequently lead to post-traumatic osteoarthritis (PTOA). High-resolution peripheral quantitative computed tomography (HR-pQCT) allows precise assessment of bone density and microarchitecture, enabling tracking of periarticular bone changes over time. This study used HR-pQCT to quantify three-year bone changes, providing insight into processes contributing to PTOA.

Methods

This longitudinal prospective cohort study was approved by the Conjoint Health Research Ethics Board at the University of Calgary (REB19–1184). Baseline imaging was performed ~6 weeks post-injury with annual follow-ups. Participants either did not undergo ACL reconstruction (ACLR) or completed at least two visits before surgery; visits after ACLR were excluded. Bilateral HR-pQCT (XtremeCT II) imaging was performed at each visit and processed using automated methods developed in our lab. Weight-bearing compartments of the femur and tibia were analyzed at the subchondral plate and periarticular trabecular bone. Subchondral plate measures included bone mineral density (Sc.BMD; mg HA/cm^3) and thickness (Sc.Th; mm). Trabecular bone within 7.5 mm of the articular surface was assessed for BMD (Tb.BMD; mg HA/cm^3), thickness (Tb.Th; mm), and separation (Tb.Sp; mm). Longitudinal changes in HR-pQCT outcomes in injured and contralateral knees were modeled using mixed-effects models (R 4.2.2).

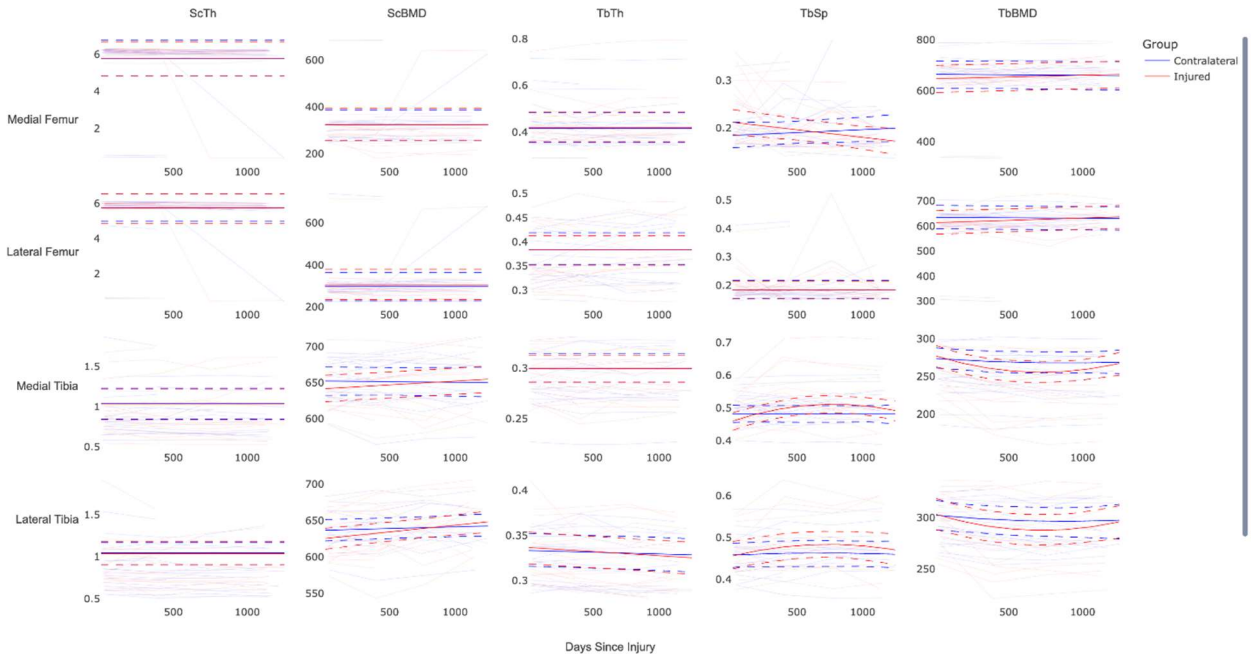
Results

Twenty participants (mean age 33.5 years, SD 10.2; 11 female) were included. Injured knees showed Tb.BMD losses in the medial and lateral tibia (−2.9% and −2.6%) and increases in the femur (+3.1% and +3.5%). Tb.Sp increased in the medial and lateral tibia (+6.2% and +4.1%) but decreased in the femur (−10.3% and −6.9%). Sc.BMD increased in the tibia (~+3%) and decreased slightly in the femur (~−1%). Contralateral knees showed minimal median changes (<1%). Injured knees exhibited larger, time-varying remodeling patterns (Figure 1).

Discussion

Early changes in subchondral and periarticular trabecular bone were observed following ACL injury. In the tibia, subchondral bone shifts toward a thinner trabecular network beneath a slightly denser plate, whereas femoral trabecular bone becomes denser and more compact under a less dense plate. This asymmetric, time-dependent remodeling aligns with early PTOA mechanisms, where alterations in local stiffness gradients and trabecular architecture of the joint can modify contact mechanics and may contribute to subsequent joint degeneration.

Images (Optional)



Session Category

Clinical Biomechanics: N/A

OA129-06

Analysis of Muscle Synergy Strategies During High-Risk Tasks in Patients Following ACL Reconstruction

Mr Ze Gong[1,2], Dr Di Ao[2], Dr Le Li[2], Dr Ming Zhang[1]

[1]The Hong Kong Polytechnic University, Hong Kong, Hong Kong, Hong Kong. [2]Northwestern Polytechnical University, Xi'an, Shaanxi, China

Introduction

Over 2 million annual anterior cruciate ligament (ACL) injuries lead to knee instability and osteoarthritis. ACL reconstruction (ACLR) restores structure, but only 50-60% return to pre-injury sports, with 6-time higher re-injury risk (driven by biomechanics)[1]. Muscle synergy—central nervous system's modular activation for stable movement—is critical for knee control in high-risk tasks, yet its role in ACL re-injury (e.g., if altered patterns raise risk) is understudied. This study explored ACLR patients' synergy strategies in single-leg tasks and biomechanical links, to define synergy's significance for re-injury prevention.

Methods

Thirty-three healthy subjects (17 males, 16 females) and 24 ACLR patients (14 males, 10 females) were enrolled, divided into Control (healthy dominant sides), Affected (ACLR patients' injured sides), and Nonaffected (ACLR patients' uninjured sides) groups. Data collection included electromyography, marker trajectory for kinematics, and ground reaction forces data during a single-leg landing and lateral jumping task. Non-negative Matrix Factorization decomposed EMG data to spatial and temporal components, with Variance Accounted For (VAF ≥95%) determining synergy number[2]. Temporal (CoA, FWHM, RMS) and spatial (vector weights) synergy characteristics were analyzed, alongside joint kinematics (angles) and kinetics (moments). Mixed-effects models compared parameters across groups, and Pearson correlation explored synergy-biomechanics relationships.

Results

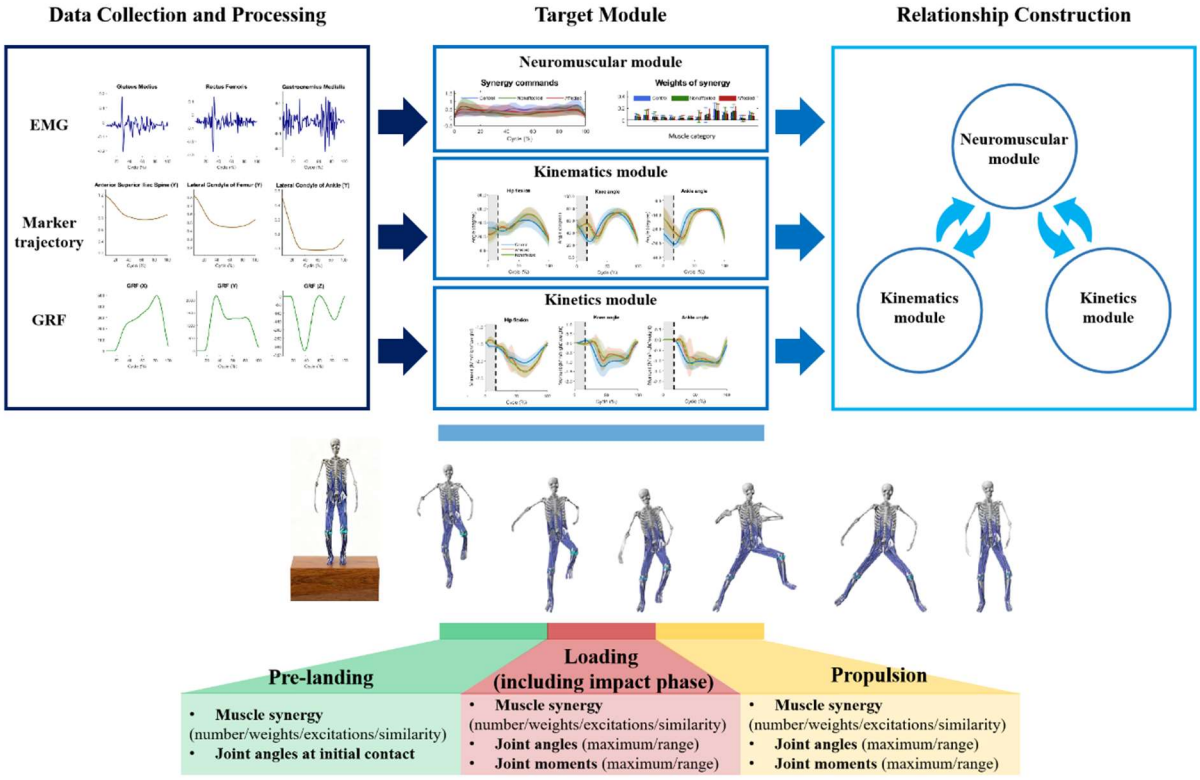
During the impact phase (50ms post-initial contact), the Control group used more muscle synergies than ACLR groups, including an additional peroneus longus/gluteus medius-dominated synergy. Controls also had delayed knee extensor/flexor synergy activation, higher synergy activation RMS ($p<0.05$), and distinct biomechanics (greater hip flexion angles/moments) vs. ACLR subgroups; no FWHM differences existed. In the Affected limb,

synergy number correlated negatively with max hip/knee flexion angles and positively with max ankle plantar flexion.

Discussion

ACLR patients' altered synergy (fewer synergies, reduced activation, unspecialized patterns) links to adverse biomechanics: fewer synergies in the Affected limb associate with lower hip/knee flexion (poor shock absorption) and higher ankle plantarflexion (increased knee load)—key re-injury drivers. Controls' extra synergy boosts hip-ankle coordination for stability, confirming muscle synergy as a critical re-injury mediator and recovery biomarker.

Images (Optional)



References (Optional)

1. Dunn et al., *Am J Sports Med* 38(10):2040-2050.

2. Shin et al., *J Neuroeng Rehabil* 18(1):58.

Acknowledgements (Optional)

This work was supported in part by the National Natural Science Foundation of China under Grant 32071316, Grant 32211530049, and Grant 32301090. The authors thanked all the participants in this study.

Session Category

Orthopaedic Biomechanics: Sports Medicine

OA130-01

Energetic Consequences of a Distal-to-Proximal Shift in Positive Joint Work During Gait are Opposite for Mobility Impaired vs Non-Mobility Impaired Older Adults

Dr. Jacob Thomas PhD[1], Ms. Zoe Smith MS[1], Dr. Brian Umberger PhD[2], Dr. Jane Kent PhD[1], Dr. Katherine Boyer PhD[1]

[1]University of Massachusetts-Amherst, Amherst, MA, United States. [2]University of Michigan, Ann Arbor, MI, United States

Introduction

Redistribution of positive joint work from ankle to hip during gait is a candidate mechanism for increased energetic cost of walking (CoW) in older age. Muscle weakness, which can differ by mobility status, may necessitate such redistribution [1]. We quantified groupwise differences in maximal isokinetic ankle extensor power (AEP_{Max}) and relationships between positive mechanical work distribution and both CoW and AEP_{Max}, to understand the energetic consequences of age-related positive mechanical work redistribution and the role of ankle extensor weakness in such redistribution.

Methods

Sixty-one participants; fourteen younger (6Female, 35.3±3.7yr, preferred walking speed (PWS):1.38±0.19m$\cdot s^{-1}$), nineteen older highly active (OHA) (8F, 73.3±2.8yr, PWS:1.49±0.21), fourteen non-mobility impaired older control (OC) (10F, 72.9±3.0yr, PWS:1.34±0.14), and fourteen older impaired (OI) (9F, 73.1±3.2yr, PWS:1.42±0.24); underwent overground gait analysis, isokinetic plantar flexion power testing (60 deg$\cdot s^{-1}$; dynamometry), and Short Physical Performance Battery (SPPB) measures before a seven-minute PWS treadmill walk with indirect calorimetry to quantify net CoW ($J \cdot kg^{-1} \cdot m^{-1}$). Stance-phase joint work was used to calculate redistribution ratio (RR; [$Work^{+}_{Ankle}$-$Work^{+}_{Hip}$]/[$Work^{+}_{Ankle}$+$Work^{+}_{Hip}$]). Physical activity was tracked for one week via accelerometry. Grouping was based on SPPB and physical activity. Statistical analyses included Pearson correlation coefficients and one-way ANOVA with Tukey's tests.

Results

AEP_{Max} was lowest for OI (0.71±0.17W/kg) and different (p<0.01) from younger (1.06±0.22W/kg), with no other groupwise differences. For OC, greater RR (greater hip relative to total work) was associated with greater CoW (r=0.50), while the opposite was observed for OI (r=-0.47, Figure 1). There were no associations between AEP_{Max} and RR for younger, older groups, or all older adults combined (p≥0.28).

Discussion

Opposite relationships between RR and CoW for OC and OI suggest group-specific energetic consequences of redistribution from ankle to hip during walking. AEP_{Max} was not related to RR in older adults, but may still have implications for age-related mobility loss, as AEP_{Max} was lowest for OI and different from younger. These results challenge popular hypotheses about mechanisms for, and energetic consequences of, age-related distal-to-proximal redistribution of mechanical work during walking.

Images (Optional)

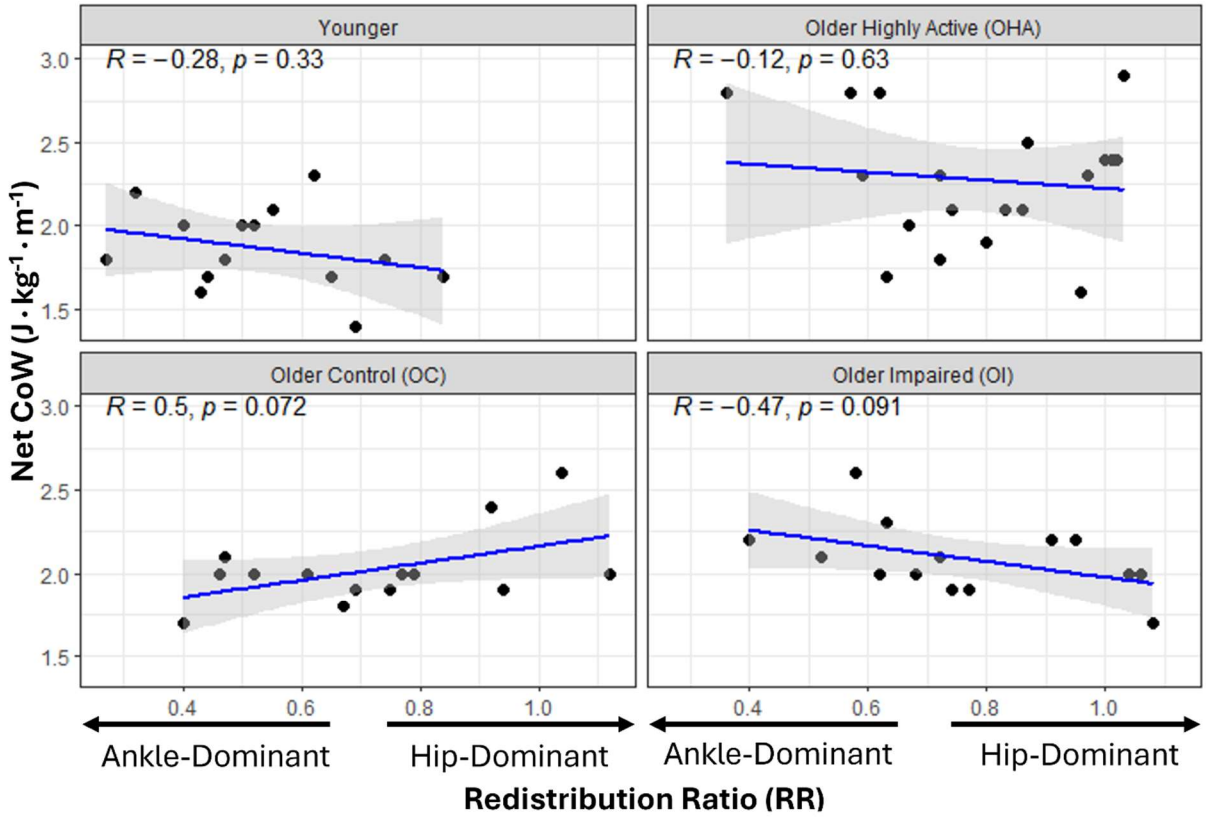


Figure 1. Scatter plots with correlation trendlines showing opposite relationships between RR and Net CoW for OC and OI groups, with weak relationships for Younger and OHA groups.

References (Optional)

[1] Katherine Boyer *et al.*, Exp Gerontol, 2023

Acknowledgements (Optional)

NIA grant R01AG068102

Session Category

Human Motion and Performance: Locomotion/Gait

OA130-02

Investigating the Potential to Reduce the Risk of Slips on Icy Surfaces With Gait training:*Preliminary Evidence of Gait Adaptation During Repeated Sessions of Walking on Ice*

Mr. Mohammadali Shahiri[1,2], Mr Pedram Karimi[1,2], Dr. Tilak Dutta[1,2]

[1]University of Toronto, Toronto, Ontorio, Canada. [2]KITE - Toronto Rehabilitation Institute – University Health Network, Toronto, Ontorio, Canada

Introduction

Falls are a major cause of injury-related hospitalizations in Canada, and winter conditions add to this risk due to reduced traction on icy surfaces. Existing prevention strategies, environmental control, slip-resistant footwear, and public awareness initiatives offer partial benefit but remain limited by cost, low adoption, and the lack of structured practice. Gait training has emerged as a promising complementary approach showing that individuals with winter-walking experience develop adaptive gait strategies that reduce slip likelihood. The objective of this study was to investigate whether repeated short-term ice-walking training can reduce slip risk.

Methods

The study took place in the WinterLab at KITE, University Health Network, using a custom ice walkway with embedded force plates. WinterLab is a self-contained laboratory mounted on a tilting platform (up to 15°). The ice surface was kept in a melting state (0°), and participants wore a safety harness. Three-dimensional kinematics were captured with an eight-camera Vicon system, along with video. Slip resistance was measured using the Maximum Achievable Angle test, which quantifies the steepest slope angle participants can safely walk up and down without slipping. Eight healthy young adults completed seven consecutive daily sessions (60 minutes each), consisting of level-walking trials, the Maximum Achievable Angle test, and force-plate walking. Participants wore curling sliders on both feet to increase task difficulty and matched their gait cadence to a metronome set to 40 bpm.

Results

Our preliminary results showed improvement in Maximum Achievable Angle across all participants. Most individuals began the study able to complete walking trials at slopes of

only 4°, but the majority achieved 8° after their fourth session. The ground reaction forces demonstrated declining anteroposterior shear forces at both level (0°) and at the maximum achieved slopes across participants.

Discussion

These findings suggest that repeated exposure to icy surfaces can facilitate gait adaptations that improve dynamic stability and reduce forces contributing to slip initiation. While preliminary and limited by sample size, findings indicate that experience-based gait training may serve as a useful slip-prevention strategy. Future work will include larger cohorts and detailed analysis of the biomechanical mechanisms underlying these adaptations.

References (Optional)

Session Category

Human Motion and Performance: Locomotion/Gait

OA130-03

What Is The *recovery Time* after a Perturbation?

PhD Student Ariane Lallès[1,2], Postdoc Romain Bechet[1], Professor Hélène Pillet[1], Professor Bruno Watier[2]

[1]Institut de Biomecanique Humaine Georges Charpak, Arts et Metiers Institute of Technology, EPF Engineering School, Universite Sorbonne Paris Nord, Paris, 75013, France. [2]LAAS-CNRS, Université de Toulouse, CNRS, UPS, Toulouse, 31400, France

Introduction

Balance control mechanisms can be assessed in the laboratory using several parameters, one of them, the distance between the body center of mass and minimal moment axis (**d**BCoM-MMA) has been shown to be sensitive to external perturbations [1]. Reaction to perturbation can be quantified by the perturbation recovery time (PRT). A recent method based on nonlinear dynamic system theory proposed a time-based analysis [2]. The goal of the study is to introduce the **d**BCoM-MMA as a balance feature in this method and to assess the time required to consistently return to steady-state gait.

Methods

38 healthy adults walked on a dual belt instrumented treadmill (1000 Hz, Treadmetrix®) with 50 markers tracked by 9 optoelectronic cameras (100 Hz, Vicon®). Participants walked at 1.2 m/s and experienced 8 slips and 8 trips at heel strike (target speeds: 2.04 and 0.36 m/s), with two intensities (±3 and ±10 m/s^2). 608 randomized perturbations were recorded. Following [2], we computed each participants' limit cycle and steady-state neighborhood from pre-perturbation data using anteroposterior (AP) and mediolateral components of **d**BCoM-MMA and AP and vertical BCoM acceleration. For each perturbation, we computed the current state's deviation from the limit cycle. A 1-second sliding window identified the earliest time at which 79.8% [2] of values remained below a threshold (80th percentile of pre-perturbation deviation). All other parameters followed [2].

Results

Participants returned faster to their steady-state gait after a slipping perturbation (Fig. 1). A significant number of trials resulted in PRT greater than 6 seconds. The contribution of the selected features, especially for BCoM acceleration components depends on the perturbation type.

Discussion

The results show average PRT consistent with the values reported in [2] for some waist-pull perturbations. The contribution of the acceleration of the BCoM appears as a predominant balance feature. For real-world instability assessment, BCoM acceleration is especially relevant and measurable by wearable sensors. Unlike discrete instability outcomes, PRT enables a continuous monitoring of multifactorial balance changes over time.

Images (Optional)

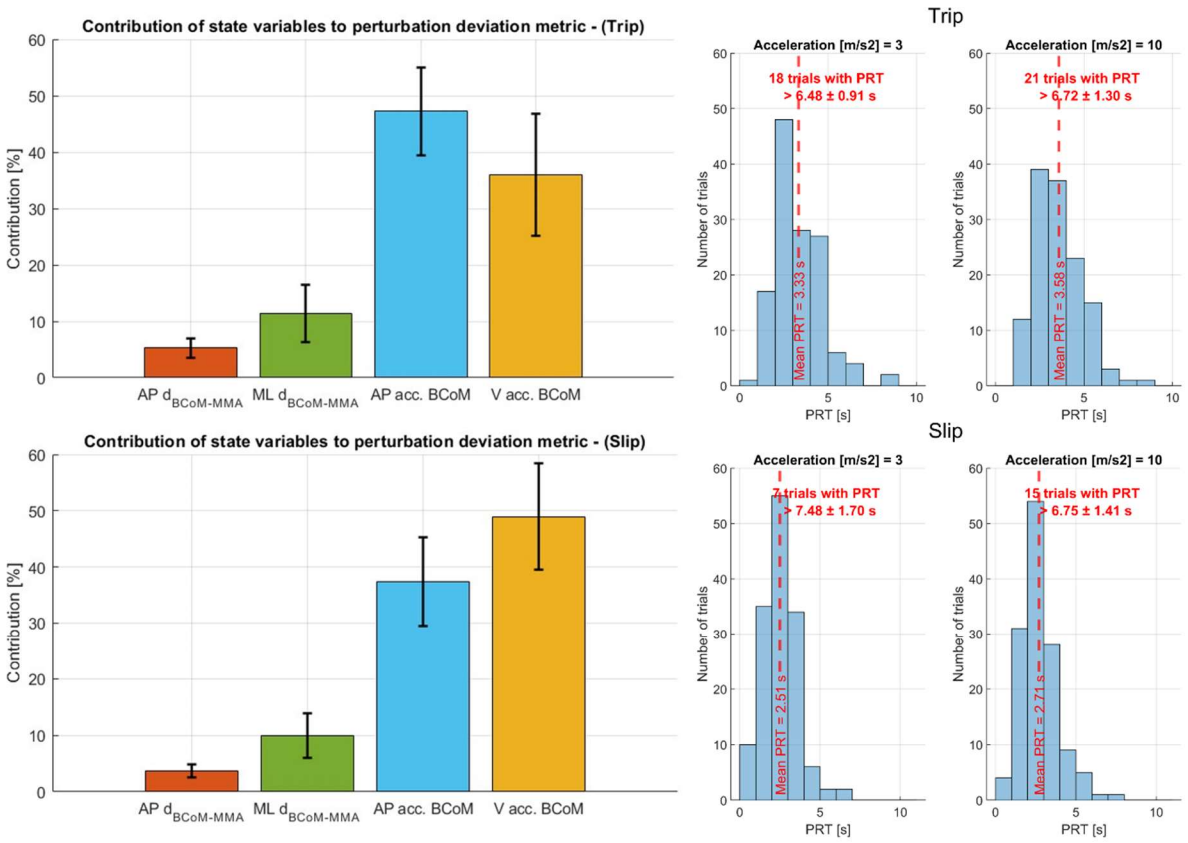


Figure 1: Contribution of selected features on the deviation metric for Trip and Slip perturbations. PRT is presented as a histogram for all recorded trials.

References (Optional)

[1] Lallès, et al., *2024 International Symposium on 3D Analysis of Human Movement (3DAHM)*, 2024.

[2] Wu, et al., bioRxiv, 2025.

Acknowledgements (Optional)

This research was funded in whole or in part by the National Research Agency (ANR) under project ANR-22-CE19-0003- 01.

Session Category

Human Motion and Performance: Locomotion/Gait

OA130-04

Timing of Trunk and Leg Reorientation During Turns Performed by Older Adults

Ms. Athena Efthymiou, Ms. Erin Kreis, Ms. Zahava Hirsch, Dr. Jun Liu PhD, Dr. Mitchell Tillman PhD, Dr. Antonia Zaferiou PhD

Stevens Institute of Technology, Hoboken, NJ, United States

Introduction

Falls are the leading cause of non-fatal and fatal injuries for older adults [1]. Turning maneuvers are closely associated with falls [2]. Many studies characterize gait patterns during turns [3] however, there are limited sources on balance states during a turn. This study compares the timing of maxima trunk and leg mediolateral lean angles during a walking turn, to better understand older adults' balance states during turns. From timing, we can learn if stepping or trunk lean initiates gait modifications during turns.

Methods

Ten healthy older adults (72.2 ± 6.03 years) completed 10-12 trials of straight-line gait, 90-degree leftward turns. The pelvis mediolateral axis and a vertical vector defined the frontal plane that allowed calculation of mediolateral trunk and leg lean angles. The leg angle used a vector from the right foot's center of mass to the hip joint center. Turn phase was defined based on [4]. Time of maxima in terms of percent time of the turn phase was also calculated. The time and percent time of maxima were compared using two-sided paired sample t-tests ($\alpha = 0.05$).

Results

During turns, the leg preceded the trunk in reaching its lean maximum (Fig.1A, $p=0.023$, Fig.1B, $p=0.009$).

Discussion

This study contributes further details regarding the cascade of gait modifications during turn initiation. Specifically, we found that older adults step outward such that the leg lean angle maximum precedes that of the trunk for most of the older adults in our cohort. Understanding the sequencing in turning provides more insight into balance control during turns. These findings help inform future fall-risk diagnoses and physical rehabilitation practices to reduce fall risk.

Images (Optional)

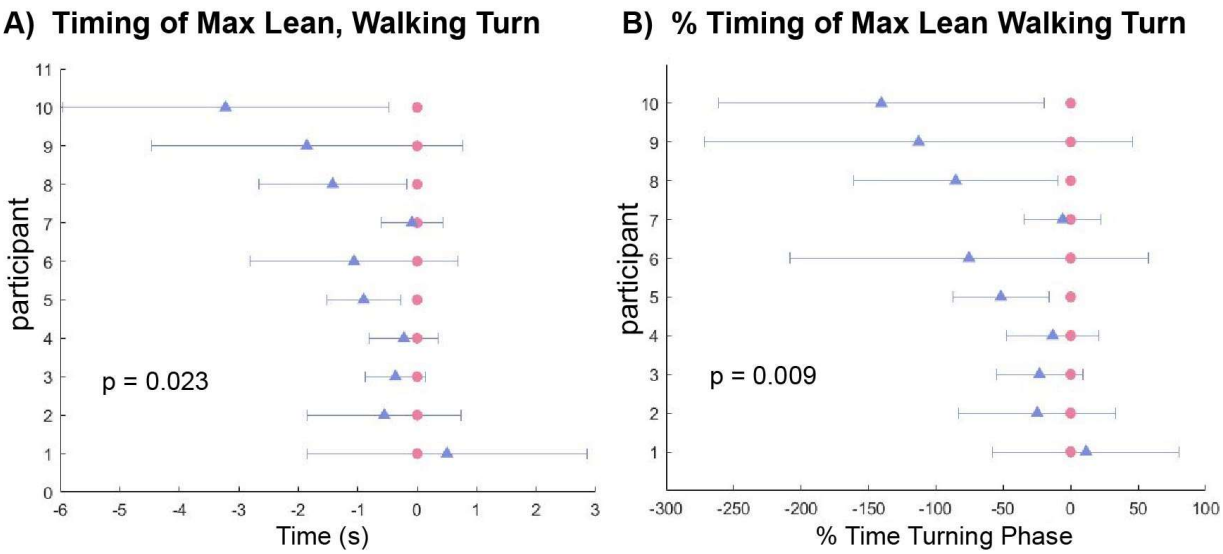


Figure 1. Leg lean represented by purple triangles while trunk lean represented by pink circles **A)** maximum trunk and leg lean angles timing **B)** maximum trunk and leg lean angles percent timing of turning phase

References (Optional)

[1] Kakara, Ramakrishna *et al.* , CDC Morb Mortal Wkly Rep, 2023

[2] Martina Mancini *et al.* , J Gerontol A Biol Sci Med Sci, 2016

[3] Ting-Ting Yeh, *et al.* , Int J Rehabil Res, 2022

[4] Mitchell Tillman et al., J. Biomech, 2022

Acknowledgements (Optional)

This study was supported by NSF Award #1944207

Session Category

Human Motion and Performance: Locomotion/Gait

OA130-05

Gait Dynamics in Space and Time Reveal Distinct Impacts of Aging Across the Lifespan

Mr Seung Kyeom Kim[1], Dr Tyler Wiles[2], Dr Nick Stergiou[1,3], Dr Aaron Likens[1]

[1]University of Nebraska at Omaha, Omaha, NE, United States. [2]University of Florida, Gainesville, Florida, United States. [3]Aristotle University of Thessaloniki, Thessaloniki, Thessaloniki, Greece

Introduction

Human movement emerges from continuous interactions among multiple body components and the environment. Those interactions can be observed in a *state space*, a coordinate system that defines all possible states of a motor behavior. Within this space, stable movement trajectories form *attractors*, whose structures reflect how the system organizes and adapts. Movement variability analyses have focused on the attractor's temporal structure (how motion evolves over time) as well as spatial structure (how motion is distributed in space). We demonstrate a novel approach to the latter (i.e., spatial structure) by applying a multidimensional box counting dimension (BCD) on human gait kinematics and distinguish gait dynamics of adults across the lifespan.

Methods

126 adults (35 young(YA); 50 middle-aged(MA); 41 older(OA)) performed 4-minute overground walking trials. The spatial structure of gait was quantified using BCD of sagittal thigh kinematic; higher values indicate less constrained movement trajectories in space. Temporal structure of sagittal thigh kinematics was quantified using sample entropy (SampEn); higher values indicate more unpredictable movements over time. Metrics were computed for both thighs and *z*-scored. Multilevel modeling, a modern alternative to ANOVA, was used to examine age-related differences and limb effects.

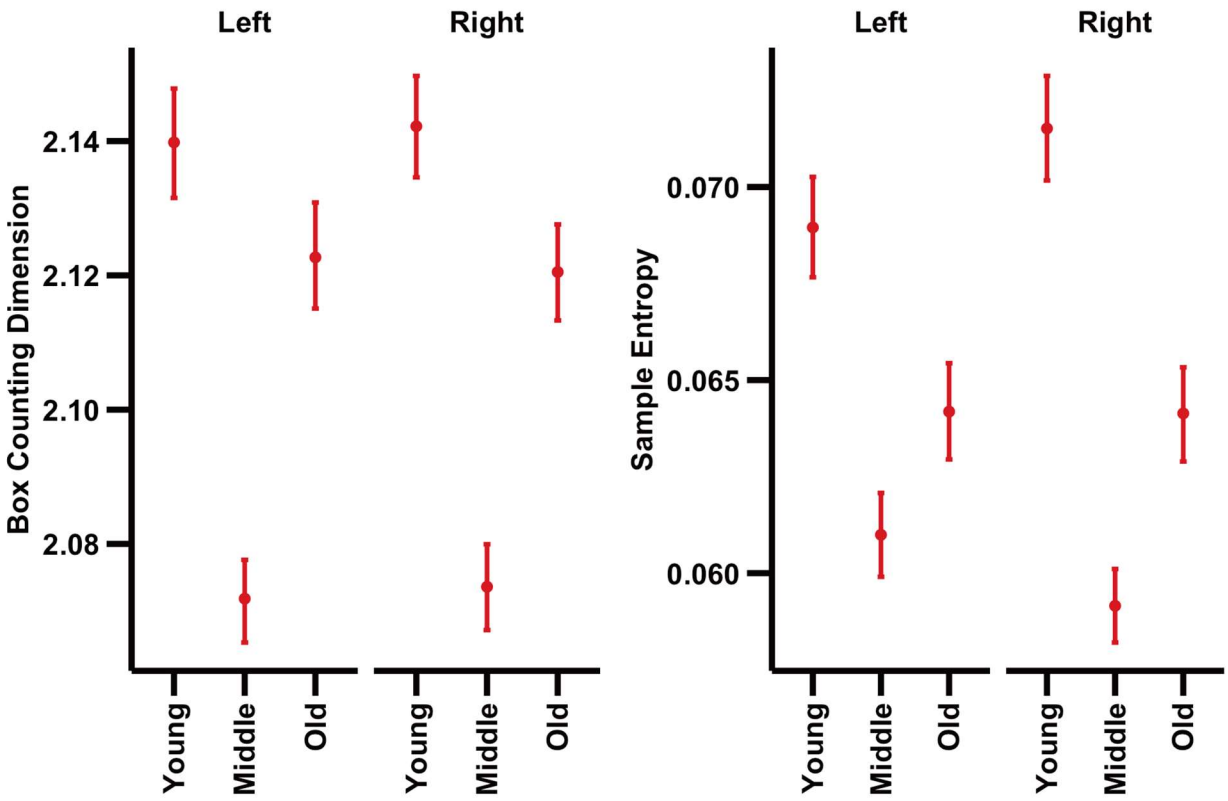
Results

The multilevel model revealed moderate to large age effect on BCD (Figure 1). MAs exhibited lower BCD than young and OAs (D=0.418-0.585), indicating more spatially constrained coordination. Age and limb interactively modified SampEn. Post-hoc analysis within each thigh revealed moderate to large age differences for SampEn. YAs showed higher SampEn than MAs and OAs (D=0.386-0.653), indicating more temporally irregular, yet potentially more exploratory, movement patterns.

Discussion

MAs experienced more spatially constrained and more temporally predictable gait patterns than YAs. In contrast, OAs showed only increased predictability. Both results may be a byproduct of our sample; our OA were quite active and healthy, whereas MAs had the highest body mass index, on average, perhaps reflecting more sedentary lifestyles. Were the results to survive replication, one might speculate that spatial and temporal dimensions of gait have distinct mechanisms. Perhaps spatial changes in MAs compensate for changes in body mass, whereas temporal changes in timing dynamics reflect a more general pattern of aging.

Images (Optional)



References (Optional)

Acknowledgements (Optional)

National Institutes of Health [grant number: P20GM109090]

National Institutes of Health [grant number: 1P20GM152301-01]

National Institues of Health [grant number: P20GM152301]

National Institutes of Health [grant number: P30GM159554]

Session Category

Human Motion and Performance: Locomotion/Gait

OA130-06

When Age Isn't Enough: Testing Recruitment Validity and Functional Decline in Biomechanical Gait Data

Dr. Jason Franz, Dr. Eran Dayan, Dr. Michael Lewek

UNC Chapel Hill, Chapel Hill, NC, United States

Introduction

The field of biomechanics has long been central to enhancing understanding of age-related gait changes and to the development and evaluation of modifiable factors and therapeutic interventions. Much of our experimental work is based on a single fundamental premise – that our enrollment practices, to include our inclusion and exclusion criteria, are capable of capturing demographics that will lead to generalizable discoveries. One way to determine the efficacy of those practices is by testing measured in-lab data against the basic principle that physical function declines with advancing age. We use this retrospective analysis of previously-collected data across several domains of physical function to do just that. As an altogether alternative goal - one difficult to disentangle from our primary goal - we use the same analysis to inform the broader discussion of biological age versus chronological age in our biomechanical study of gait and instability.

Methods

Data from three studies with routine sample sizes (*i.e.*, n=16-29) were included that enrolled individuals ≥ 65 yrs who could walk without an assistive device, with normal or corrected to normal vision, who self-reported no neurological, musculoskeletal, cardiopulmonary diseases, self-reported no recent musculoskeletal injury, and with BMI ≤ 30 kg/m^2. Outcome measures spanned: (i) *functional performance* (i.e., timed up-and-go, dynamic gait index [DGI], 5x sit-to-stand, and comfortable walking speed), (ii) *balance* (i.e., anterior-posterior and mediolateral margins of stability and fear of falling), and (iii) *foot-ankle function* (i.e., plantar sensation and, during walking, foot-ankle leverage and ankle moment). Cross-sectional comparisons demonstrated that nearly every outcome was significantly worse for older vs. younger participants.

Results

Enrollment ages spanned 65-87 years. Only DGI score (r^2=0.19, p=0.017) correlated with chronological age; a weak trend approaching significance was observed for speed (r^2=0.13, p=0.055). No other outcome exceeded 10% variance explained by chronological age.

Discussion

Chronological age is a poor predictor of physical function among older adults enrolled in biomechanics studies using routine inclusion/exclusion criteria. Although differences between biological versus chronological age may be relevant, we are more convinced that our results reflect restrictive enrollment criteria that should be reconsidered to enhance the generalization and impact of our discoveries.

Images (Optional)

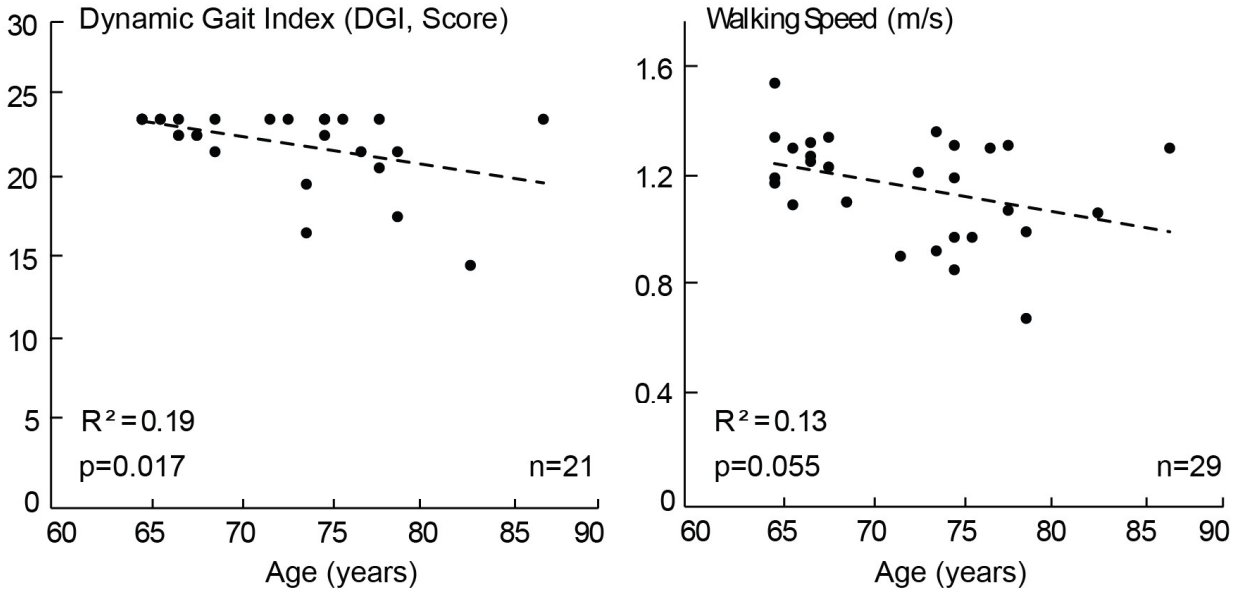


Figure 1. Scatter plots showing the distribution of DGI scores and walking speeds as a function of age. Only DGI score correlated with chronological age; a weak trend approaching significance was observed for speed. No other outcome exceeded 10% variance explained by chronological age.

Acknowledgements (Optional)

We thank the members of the UNC Applied Biomechanics Laboratory for their unwavering commitment to collecting meaningful data to support the independent mobility of those in our aging population.

Session Category

Human Motion and Performance: Locomotion/Gait

OA131-01

Shoe Fit and Downhill Cycling Performance

Dr. Kathryn Harrison PhD, Dr. Daniel Feeney PhD, Ms. Bethany Kilpatrick, Ms. Milena Singletary, Mr. Adam Luftglass, Dr. Eric Honert PhD

BOA Technology, Denver, CO, United States

Introduction

Skill in navigating technical terrain is critical to performance in Downhill Mountain biking. This requires dynamically responding to obstacles to maintain balance while not losing speed. A rider's footwear may influence their proprioception and ability to respond to the terrain, as seen in trail running. Sample entropy has been used to evaluate aspects of footwear on athletes' adaptability to technical terrain; shoes with a wrapping upper designed to conform to the foot improved ability to navigate technical terrain[1]. This study explored whether a similar benefit exists in mountain biking.

Methods

Twenty-one expert downhill mountain bikers (10F/11M) completed three laps of a 5km black diamond downhill trail. The first lap was for familiarization. During the next two laps, riders completed the course in two different pairs of shoes: a clipless downhill shoe with standard lace and hook and loop closure, and the same base shoe with a wrapping closure activated by two dials. Data were collected from inertial measurement units mounted on the heel, the top tube of the bike frame, and the rider's sacrum. Sample entropy was calculated for each axis of the IMU acceleration signals throughout the trail. Sample entropy values were converted to subject specific z-scores and were compared between shoe conditions using Bayesian linear mixed effects models.

Results

In the wrap shoe, sample entropy of the foot was 4% greater in the vertical direction (97% posterior>0). On the bike, it was 2% greater in the mediolateral direction (88% posterior>0) and 1% greater in the anteroposterior direction (81% posterior>0). Sample entropy of the sacrum in the vertical direction tended to be 1% lower in the wrap shoe (74% posterior<0).

Discussion

The greater entropy of the foot and bike suggest that in the wrap shoe, riders were better able to adapt to changing terrain. This allowed them to maintain more consistent motion of

their torso, an indication of balance and skill. The improvements in the wrap shoe may be driven by more consistent contact of the riders foot with the shoe, similar to trail running[1].

References (Optional)

1. Harrison et. al. ISBS. 2024.

Acknowledgements (Optional)

The authors are employed by BOA Technology.

Session Category

Human Motion and Performance: Sports

OA131-02

SplitCranks: A New Technological Device for Leg-Independent Control of Bilateral Power Output in Cycling

PhD Marcos Kunzler, PhD Felipe Carpes

Applied Neuromechanics Research Group, Federal University of Pampa, Uruguaiana, RS, Brazil

PhD Marcos Kunzler

Introduction

Power output during cycling results from bilateral motion of both legs in a synchronous way using coupled cranks. Previous studies show that the use of decoupled cranks alters lower limb muscle activation and coordination, promoting balanced recruitment and reducing asymmetry [1, 2]. However, each leg may present different motion patters, and training and rehabilitation strategies may benefit of leg-independent movement control. Such insights come from split-belt treadmills in locomotion research and use of decoupled cranks by cycling athletes. To the date, to reproduce leg-independent movement control in cycling ergometers is not possible with commercial devices. In this study we describe the concept, construction, and pilot testing of SplitCranks, a new device now under patent registration.

Methods

SplitCranks adapts the concept of split-belt treadmills to cycling by using two fully independent cranks, each connected to its own electromagnetic resistance unit and controlled by custom electronics and software (Figure 1). A prototype was built from a standard cycle ergometer, enabling leg-independent resistance, power, and cadence monitoring (Figure 1). A pilot test with a 42-year-old man recreational cyclist evaluated the system's feasibility. He completed two 5-minute sessions at 100 W - one with coupled cranks and one with decoupled cranks. Bilateral power and cadence were recorded with a Favero Assioma Duo powermeter. Left-right balance, energy distribution, and peak power phase were recorded.

Results

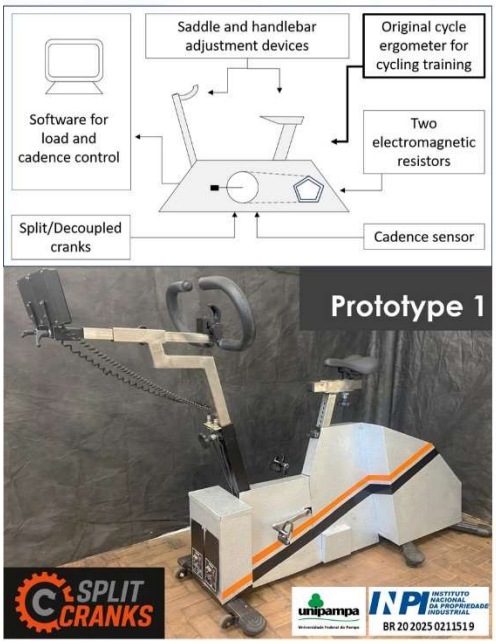
SplitCranks allowed individualization of mechanical load on each crank during pedaling. Using our prototype (Figure 2) we properly adjusted body positioning on the bike and

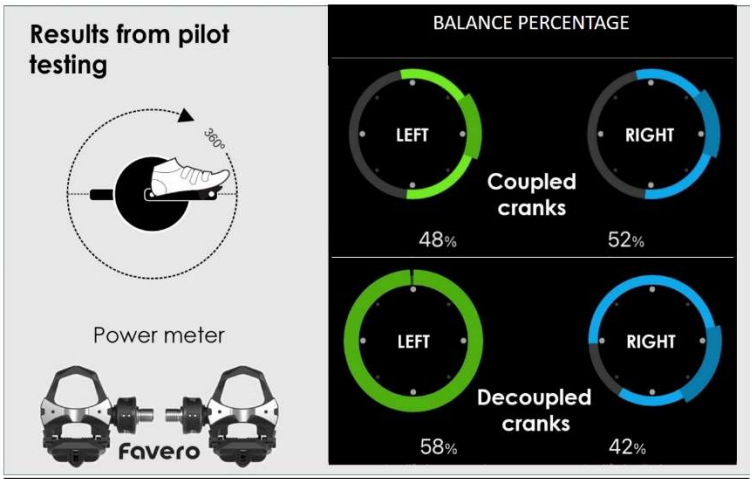
recorded unilateral power output and cadence during bilateral cycling. The pilot tests confirmed that participants comfortably adapted to the system while data are recorded. Results are in Figure 1.

Discussion

SplitCranks allows unilateral workload manipulation. Compared with traditional coupled cranks, the decoupled condition using SplitCranks seems to elicit more homogeneous power distribution along pedaling cycle and increased contribution from the non-preferred limb to power ouput, indicating strong potential for improving pedaling symmetry. Overall, SplitCranks provides a promising platform for performance optimization, technique refinement, rehabilitation, and research on motor control and biomechanics.

Images (Optional)





	Coupled cranks		Decoupled cranks	
	Left leg	Right leg	Left leg	Right leg
Energy distribution	349° - 186°	346° - 186°	0° - 357°	267° - 212°
Peak power phase	55° - 111°	51° - 110°	0° - 357°	77° - 150°

References (Optional)

[1] Hug F, *et al.,* Front Physiol, 2013

[2] Bourdon E, *et al.,* J Sports Sci Med, 2017

Acknowledgements (Optional)

National Council for Scientific and Technological Development (CNPq) and Rio Grande do Sul State Research Support Foundation (FAPERGS).

Session Category

OA131-03

A Comparison of Cycling Positional Differences Between Tandem Stokers and Pilots Before and After Wind-Tunnel Optimisation

Mr Sean Husband PhD candidate[1], Prof Ciaran Simms Professor In, Mechanical, Manuf & Biomedical Eng[1,2,3], Mr Paul Carragher Physiotherapist[2], Mr Robert Coulthard-Wragg BSc, MSc[1]

[1]Trinity College Dublin, Dublin, Dublin, Ireland. [2]Sport Ireland Institute, Dublin, Dublin, Ireland. [3]Cycling Ireland, Dublin, Dublin, Ireland

Introduction

Tandem cycling is a specialized category of cycling regulated by the UCI. Visually impaired athletes, referred to as stokers, compete alongside their guides, commonly known as pilots. The inclusion of an additional cyclist introduces complexity to cyclist positioning for aerodynamic optimisation, necessitating the simultaneous optimisation of both cyclist. Research on tandem cycling is limited, with Mannion et al. (2018) and Kopacz et al., (2014) being the only studies in this domain, examining various overall positions and aerodynamic properties, such as upright, crouched, time-trial, and frame-clench (where the stoker holds the frame instead of the handlebars). The present study sought to elucidate the whole-body kinematic differences between the stoker and pilot both before and after wind-tunnel optimisation, and at different cycling intensity levels

Methods

Twelve elite tandem cyclists participated in a study conducted in a wind-tunnel in the UK (comprising six tandems: three male pilots with three female pilots, and three male stokers with three female stokers). Each participant pairing had reflective markers placed on the anatomical sites of interest. A single side-view camera was positioned to record the sagittal plane of the cyclist and bicycle. A calibration image was captured with participants straddling the bicycle, arms in front of their shoulders to prevent occlusion of markers.

Trials were conducted successively across two cycling intensities for 3 minutes, with participants instructed to maintain their race positions throughout the trials. Cycling intensities were derived from physiological laboratory testing.

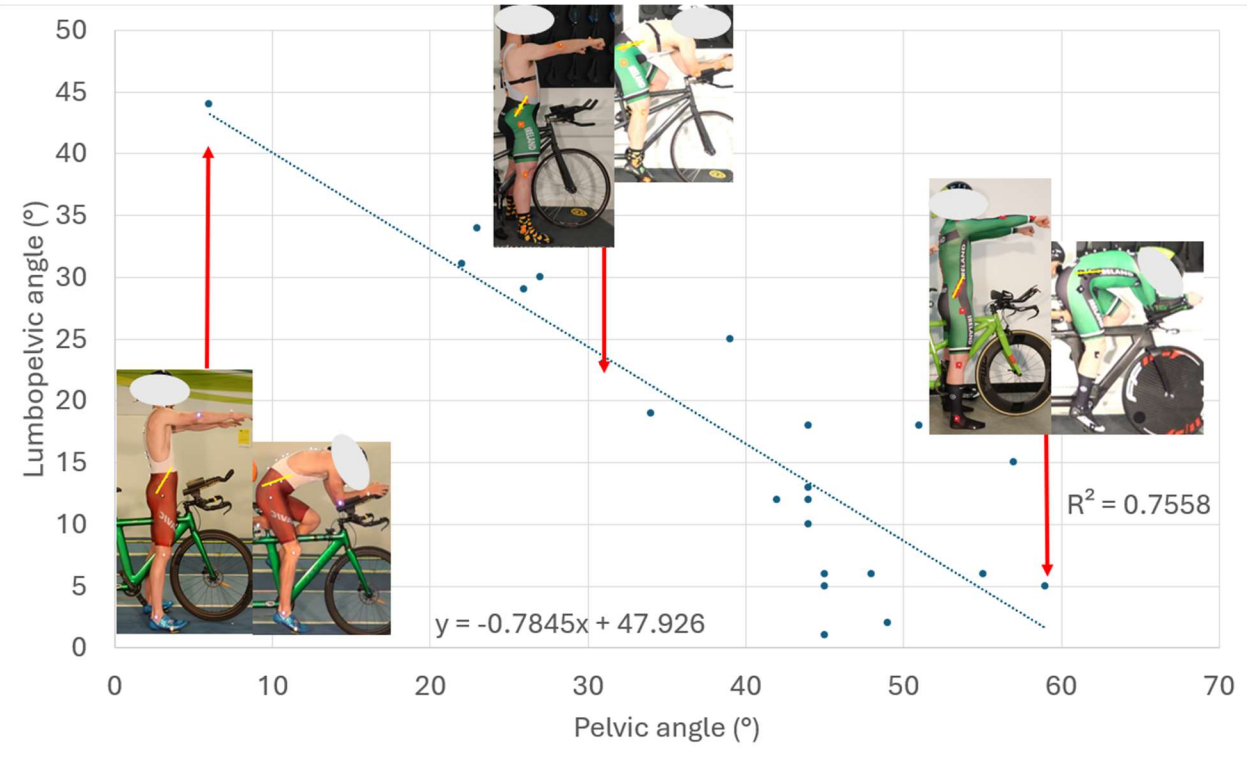
Results

Pilots (M = 77°, SD = 12.9) demonstrated significantly lower elbow flexion angles compared to stokers p= 0.023 (M = 117°, SD = 34.8). Higher lumbopelvic tilt angles were associated with lower pelvic tilt angles. -.89, p=<.001,95% CI [-.96,-.53]

Discussion

The most significant differences were identified in the elbow and ankle angles, with pilots demonstrating greater elbow flexion and stokers consistently exhibiting greater ankle plantar flexion. A strong inverse correlation was observed for lumbopelvic tilt and pelvic tilt in pilots, but not stokers.

Images (Optional)



References (Optional)

Sean Husband *et al.*, Journal of Sport Sciences, 2024

Paul Mannion *et al.*, Journal of Wind Engineering and Industrial Aerodynamics, 2018

Karolina Kopacz *et al.*, Journal of Kinesiology and Exercise Sciences, 2016

Acknowledgements (Optional)

Trinity College Dublin

Cycling Ireland

Sport Ireland Institute

Research Ireland

Session Category

Human Motion and Performance: Sports

OA131-04

Head Acceleration Event Burden in Competition Downhill Mountain Biking: Insights from the Whistler Crankworx Competition

Mr. Matthew G. Neill MSc[1,2], Dr. James Tooby PhD[3], Mr. Nicholas Devert BSc[1,2], Dr. Cameron Owen PhD[4,5], Ms. Ember Larson BSc.[1,2], Dr. Jonathan D. Smirl PhD[1,2], Dr. Carolyn A. Emery PT, PhD[1,2]

[1]Sport Injury Prevention Research Center, University of Calgary, Calgary, Alberta, Canada. [2]Faculty of kinesiology, University of Calgary, Calgary, Alberta, Canada. [3]Carnegie Applied Rugby Research (CARR) Centre, Leeds Beckett University, Leeds, West Yorkshire,, United Kingdom. [4]Carnegie Applied Rugby Research (CARR) Centre, Leeds Beckett University, Leeds, West Yorkshire, United Kingdom. [5]England Performance Unit, Rugby Football League, Machester, North West England, United Kingdom

Introduction

There is growing interest in quantifying the cumulative head acceleration event (HAE) burden in downhill mountain biking (MTB). Recent studies have detected neural differences post-ride compared to pre-ride in MTB riders, though the contribution of repetitive HAE exposure to this difference is not well quantified. Thus, the purpose of this study was to evaluate the number of HAEs sustained per day of competition in elite competitive MTB athletes.

Methods

Participants, recruited pre- or mid-competition, were fit with an instrumented mouthguard (iMGs; Prevent Biometrics) with a 5g linear acceleration trigger threshold and instructed to wear the iMG while riding. iMGs were synced pre-ride, provided to each rider before competition or training, and recovered post-ride for syncing and charging. False positives were removed using Prevent Biometrics integrated filtering. Teeth proximity sensor data confirmed mouthguard use. Poisson regression was used to calculate the incidence rate of HAEs greater than 5g's, per-athlete per-day.

Results

Twenty-one athletes (18 male,3 female) wore the iMGs for a cumulative total of 51 days of MTB riding, recording 101 true positive impacts. Thus, an incidence rate of 1.98 HAEs per person day (95% CI: 1.61,2.41) was observed.

Discussion

A previous study using accelerometers adhered to the skin reported 1031 HAEs >10g in 16 MTB riders over two sessions [1]. Our data suggests that the rate of HAE accumulation is much lower, likely due to the improved coupling between the iMG and the skull. Accumulation of HAEs may not be a major target for injury prevention in MTB and acute traumatic injuries such as concussion may be more burdensome. Human kinematics are likely impacted by the suspension geometry of the mountain bikes. Thus, future work should evaluate if iMG filtering developed in team sport is suitable for delineating true positive from false positive impacts sustained during MTB.

References (Optional)

[1] Hurst, *et al*. , JSAMS, 2018

Acknowledgements (Optional)

Thank you to all the athletes for their participation. Funding for iMGs was provided by Canada Foundation for Innovation. CAE holds a Canada Research Chair (Tier 1) in Concussion. This project received support from a MITACS Accelerate Grant (MGN), and NSERC Discovery Grant (JDS).

Session Category

Human Motion and Performance: Sports

OA131-05

Examining Muscular Fatigue Across Repeated Golf Swings and Its Relationship With Performance

Mr Stephen Boulanger Ph.D.(c)[1], Mr John Li[1], Mr Nishad Rajmalwar Ph.D.(c)[2], Mr John McPhee Ph.D.[2], Mr Clark Dickerson Ph.D.[2], Mrs Jaclyn Chopp-Hurley Ph.D.[1]

[1]York University, Toronto, Ontario, Canada. [2]University of Waterloo, Waterloo, Ontario, Canada

Introduction

The golf swing is a highly coordinated movement that requires high muscular demands which dictate performance. Over repeated swings, the risk of muscle fatigue increases thereby potentially compromising overall swing performance. The aims of this study were to assess muscle fatigue through repeated golf swings and determine whether these patterns are related to psychophysical measures (rate of perceived exertion; RPE), and performance measures (ball speed, club speed, carry distance).

Methods

Thirteen male golfers have been recruited for this study (Age: 25.7 ± 2.6 years, BMI: 26.7 ± 2.1 kg/cm^2, Registered Golf Handicap: 8.6 ± 5.6) with additional participants forthcoming. Delsys Avanti and Snap Lead surface electromyography (EMG) sensors were affixed to thirteen upper limb and trunk muscles, bilaterally (Figure 1). Muscle specific maximal (MVIC) and submaximal isometric voluntary contractions (SVIC) at 50% MVIC were performed prior to swing trials. Swing trials were performed in sets of twenty repetitions with EMG data collected during the first five swings of each set. After each set, RPE was recorded. Once participants reached an RPE of $\geq$ 9 or 200 swing repetitions, the protocol was completed. SVICs were then performed to assess post-trial muscular fatigue.

Results

One-way ANOVAs revealed no significant differences in EMG amplitude in trailing or leading arms between pre- and post-swing SVICs. Trailing latissimus dorsi (LD; $p = 0.23$), external oblique ($p = 0.14$), leading anterior deltoid (AD; $p = 0.26$), and LD ($p = 0.07$) were nearing significance for effects of fatigue. Mean power frequency as well performance-related and skill level-related results will be forthcoming for further analyses.

Discussion

It was anticipated that the muscles, which are responsible for powerful exertions of the golf swing, would fatigue over the course of our swing protocol. Specifically, the LD and AD were expected to fatigue as they are responsible for forceful exertions of the shoulders. We suspect that the non-significant results indicate potential load sharing and muscular compensation as the swing protocol progressed which enabled muscles to recover. Further analyses are being performed to potentially identify these trends, in addition to assessing muscular demands during the swing protocol.

Images (Optional)



Session Category

Human Motion and Performance: Sports

OA131-06

Predictive Accuracy of Golf Clubhead Speed from Body-Derived Kinematic Variables

Dr. Bryndan Lindsey[1], Mr. Yuanshuo Tan[1], Mr. Xiujie Sun[1], Ms. Chunping Liang[1], Mr. Kezhe Zhu[1], Mr. Huiming Pan[1], Mr. Bo Xiao[2], Dr. Shenglong Le[2], Dr. Peter Shull[1]

[1]State Key Laboratory of Mechanical System and Vibration, School of Mechanical Engineering, Shanghai Jiao Tong University, Shanghai, Shanghai, China. [2]Department of Physical Education, Shanghai Jiao Tong University, Shanghai, Shanghai, China

Introduction

Wearable sensors have the potential to provide golfers with objective feedback on swing performance in real-time. Clubhead speed, in particular, is a critical determinant of driving performance resulting in increased carry distance and fewer strokes per round. Prior research has shown that body-derived kinematic variables, including pelvis–trunk separation (X-factor) and segmental rotational velocities, can discriminate skill level and predict ball speed. However, the ability to predict clubhead speed directly from these variables has not been established. Therefore, our purpose was to determine whether body-derived kinematics can accurately predict clubhead speed across golfers of varying proficiency.

Methods

Data were collected from 24 participants (male=17, age=25±0.7yrs, height=1.75±0.8m, mass=69±13kg) using a whole-body motion-capture system. A Random Forest regression model was developed to predict clubhead speed using kinematic and temporal variables previously associated with swing performance. Validation was performed using leave-one-subject-out (LOSO) cross-validation and performance was quantified using mean absolute error (MAE), root mean squared error (RMSE), and overall R^2. Variable importance was assessed using permutation-based increases in prediction error, and recursive feature elimination (RFE) identified a minimal predictor set on which model results are based.

Results

Model validation results demonstrated strong predictive performance (R^2 = 0.84) with an RMSE of 3.21 m/s and MAE of 2.5 m/s. Variable importance analysis showed that predictive performance was driven primarily by time from top of backswing to peak lead arm angular velocity as well as peak trunk rotational velocity prior to impact (Figure 1). Pre-impact peak X-factor and lead arm velocity also contributed to the prediction.

Discussion

These results demonstrate that body-derived kinematic and temporal metrics can meaningfully predict golf clubhead speed with a small set of motion-based variables. The four-variable model explained 84% of the variance in clubhead speed, with mean absolute error of 2.5 m/s indicating low prediction error relative to typical speed differences across golfers. Variable importance revealed that rotational power generated by the trunk prior to impact, together with timing of downswing lead-arm acceleration, were the strongest predictors of speed. Addition of acceleration-based and sequencing metrics may enhance biomechanical interpretation and predictive performance.

Images (Optional)

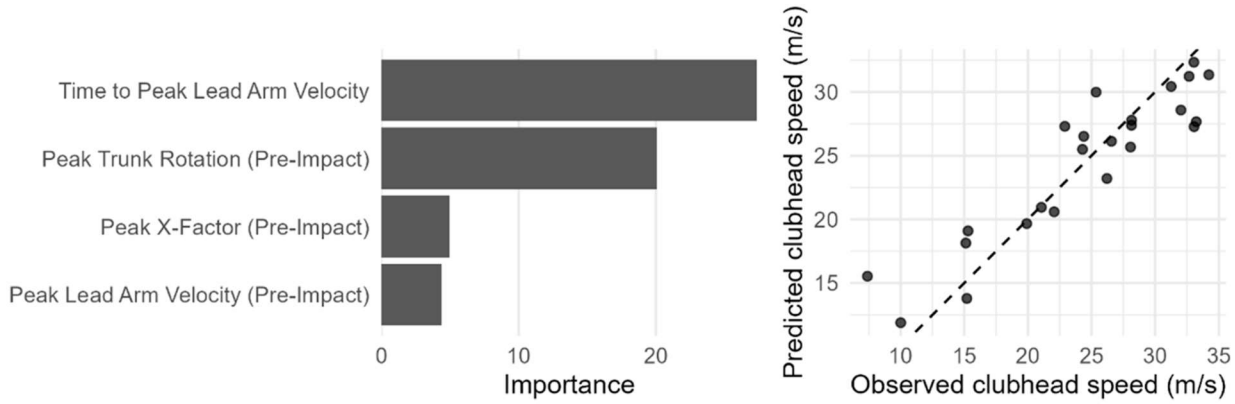


Figure 1. Left: variable importance from a random forest model predicting clubhead speed. Right: observed versus predicted clubhead speed using leave-one-subject-out cross-validation.

References (Optional)

Session Category

Human Motion and Performance: Sports

OA132-02

A Novel *Reduced Order Model*-Driven Paradigm for Real-Time Predictive Modeling of TAVR and Pre-Procedural Risk Assessment of Coronary Obstruction

Dr. Imran Shah PhD[1,2], Dr. Sri Krishna Sivakumar PhD[1], Dr. Vinod Thourani MD[3], Dr. Alessandro Veneziani PhD[2], Dr. Lakshmi Dasi PhD[1,2]

[1]Georgia Institute of Technology, Atlanta, Georgia, United States. [2]Emory University, Atlanta, Georgia, United States. [3]Piedmont Heart Institute, Atlanta, Georgia, United States

Introduction

Predictive computational modeling of coronary obstruction (CO) following transcatheter aortic valve replacement (TAVR) has become critical for pre-operative risk assessment and optimized deployment of the bioprosthetic valve. However, traditional physics-based modeling approaches require extensive computational resources to simulate the entirety of the TAVR deployment process (48-96 hours), thus limiting the exploration of various procedural factors such as deployment depth or valve type. In this study, we introduce a novel *reduced order modeling* (ROM)-driven *in-silico* paradigm for performing real-time TAVR deployment simulations, thus enabling rapid risk assessment of CO.

Methods

The ROM framework was constructed in a sequential offline-online decomposition via the Proper Orthogonal Decomposition approach to rapidly capture the structural deformation of the Evolut R valve. Interactions of the stent frame with the patient-specific native anatomy were captured via a novel surrogate contact model. The ROM-based TAVR deployment framework was applied to a cohort of patients with angiographically confirmed obstruction (n = 7), and the predictive metric DLC/d was measured for modeling the risk of CO (DLC – distance from leaflet cusp to coronary ostia, d – coronary diameter). Results from the ROM simulations were compared against traditional full order model (FOM) simulations of the deployment process, as well as post-operative CT data.

Results

Results for the ROM-based deployment simulation for a sample patient are shown in Fig. 1A. The ROM simulation required less than 20 minutes to complete, resulting in a 99% speed-up compared to the traditional FOM. The framework accurately modeled the deployment of the Evolut stent frame and its interactions with the surrounding anatomy, and strong agreements were seen between the simulation results and post-procedural

outcomes (Fig. 1B). DLC/d indices measured from the ROM-based deployment simulations were in excellent agreement with measurements obtained from traditional FOM simulations as well (Fig. 1C), with average predicted differences of 10% between the two measurements.

Discussion

The proposed ROM framework enables real-time predictive modeling of the TAVR deployment process as well as accurate mechanistic insight for post-operative risk assessment of CO via the DLC/d metric, all on local computational facilities commonly seen in the clinic (i.e., a simple laptop).

Images (Optional)

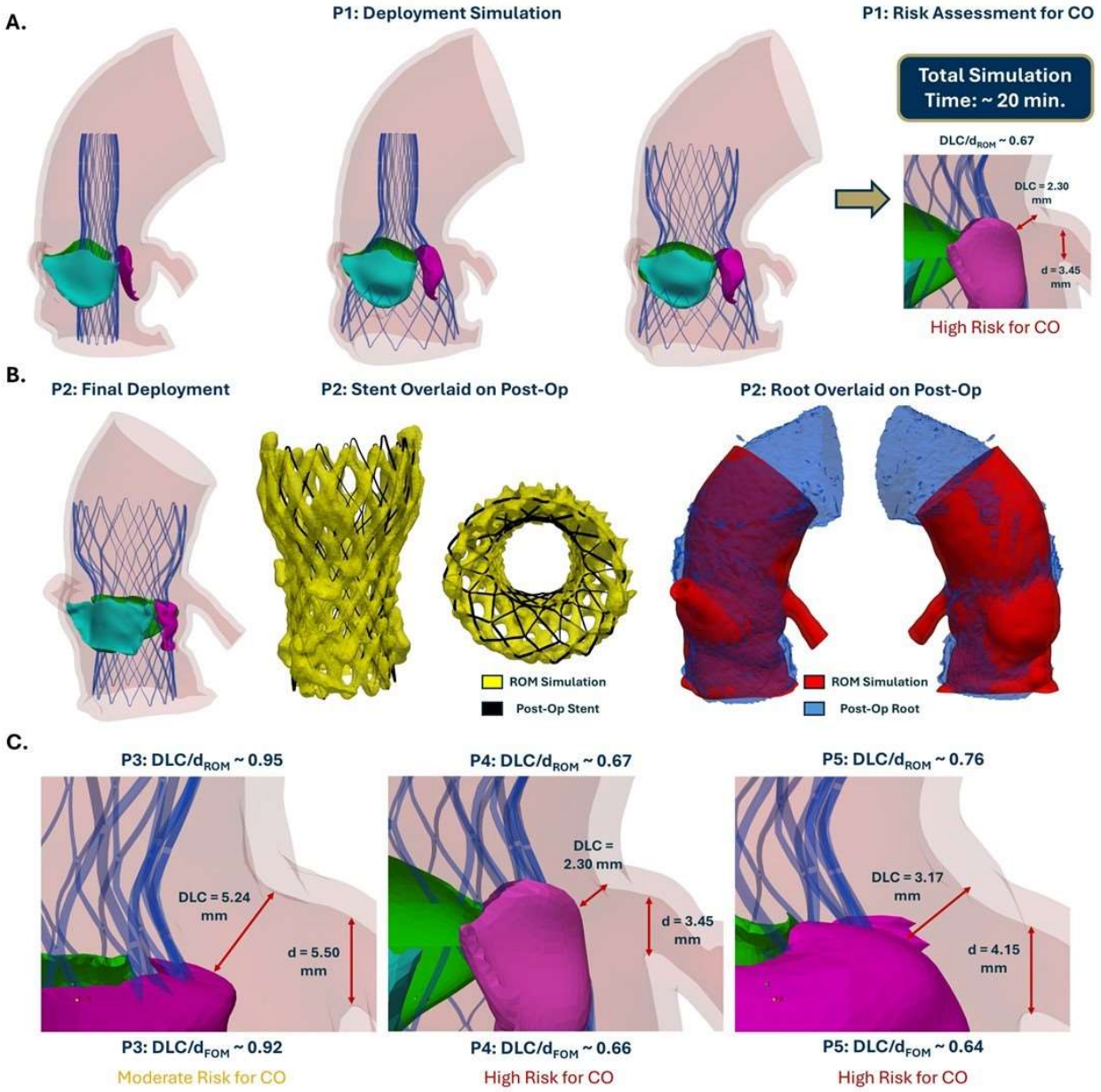


Figure 1. ROM-based computational framework for real-time predictive modeling of TAVR deployment and risk assessment of coronary obstruction (**A**). Comparisons of ROM-based deployment against available post-operative CT data for a sample patient (**B**). Risk assessment of coronary obstruction for three patients along with comparisons of the DLC/d indices obtained from both the ROM- and FOM-based simulations (**C**).

Session Category

Cardiovascular/Cardiorespiratory Biomechanics: Methods, Models and Applications

OA132-03

Relationship Between Mechanical Dispersion and T-Wave Inversion in Arrhythmic Mitral Valve Prolapse

Mr. Vahid Naeini[1], Mr. Emilio Mendiola[1], Dr. Dipan Shah[2], Dr. Reza Avazmohammadi[1]

[1]Texas A&M University, College Station, TX, United States. [2]Houston Methodist Hospital, Houston, TX, United States

Introduction

Traditionally, mitral valve prolapse (MVP) has been defined by its primary symptom, regurgitation, yet the arrhythmic type (A-MVP) presents a risk of sudden cardiac death (SCD) that persists even after surgical interventions such as mitral valve repair. In this region, mechanical instability spatially co-localizes with electrical symptoms, specifically inferior-lead T-wave inversion. A major challenge in modeling this pathology is establishing a robust quantitative link between the disparate timescales of mechanical deformation and rapid electrical events.

Methods

A patient-specific coupled electromechanical (EM) framework was used to analyze cine-CMR data from 26 MVP patients (12 A-MVP, 14 non-arrhythmic). To test the mechanistic link, 3D in-silico slabs benchmarks were extracted from the inferobasal wall of each patient. These slabs preserved patient-specific anatomical features, including local fiber angles, wall thickness, and the relative location of fibrotic tissues observed in LGE. The slab mechanical dispersion (SMD) was defined as a functional metric representing local strain heterogeneity and linking local tissue mechanics to the whole-heart mechanical dispersion (MD) observed in CMR. Simulations were performed to compare models driven by fibrosis against fully electromechanically coupled models.

Results

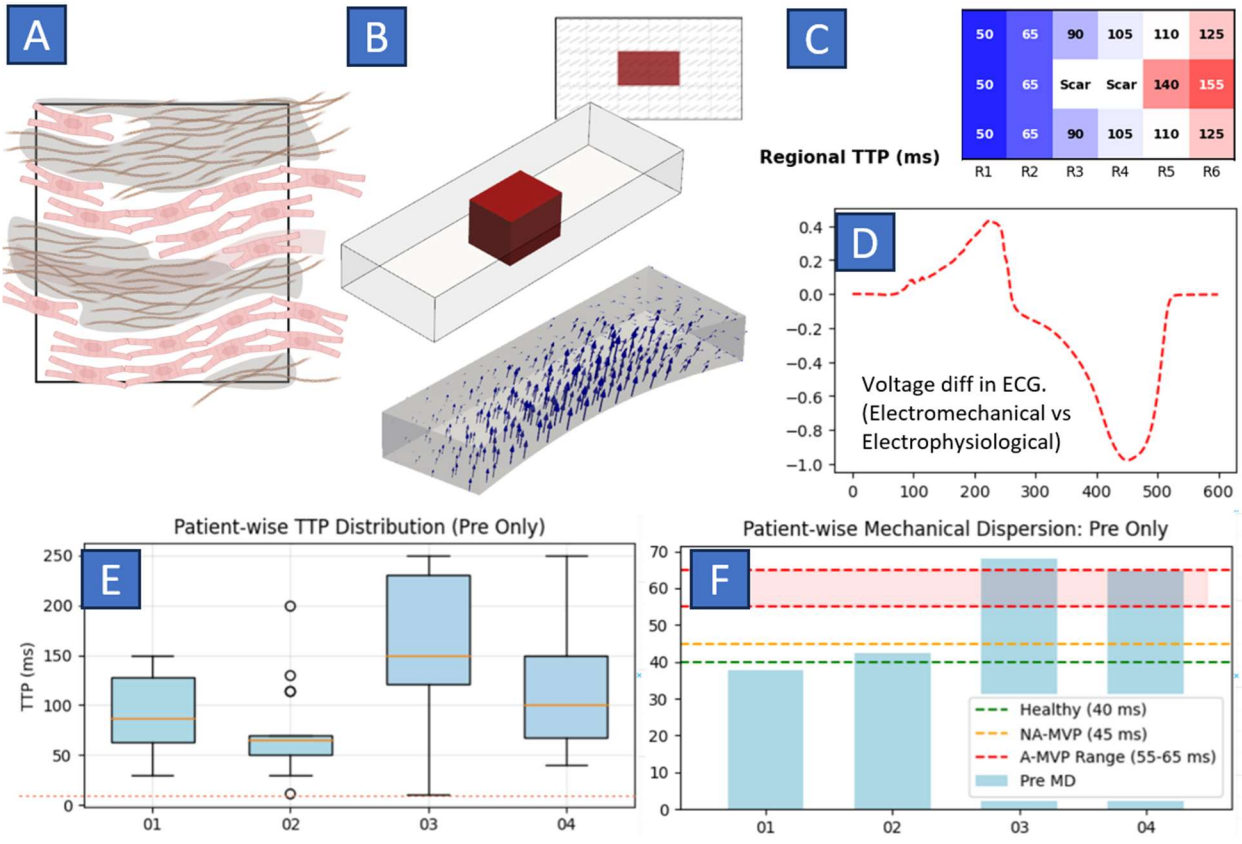
A-MVP patients exhibited a higher-dispersion category than non-arrhythmic controls. In coupled slab models, a dispersion threshold > 50 ms predicted T-wave inversion with > 85% sensitivity. This categorical agreement was unique to the coupled framework, as uncoupled models failed to reproduce the inversion morphology regardless of substrate density.

Discussion

These findings suggest that mechanical dispersion, within a fully coupled framework, can serve as a functional surrogate for underlying electrophysiological behavior. Capturing

persistent strain heterogeneity provides a constraint that allows electrophysiological properties to be estimated directly from standard cine-CMR data.

Images (Optional)



Session Category

Cardiovascular/Cardiorespiratory Biomechanics: Methods, Models and Applications

OA132-04

An In-Silico Workflow to Virtually Perform Redo-TAVI using a Balloon-Expandable Device to Assess the Risk of Vascular Injury when Varying Balloon Expansion

Miss. Sheikh Umara Zoni[1], Mr. Luis Rene Mata Quinonez[2], Dr. Sanchita Bhat[2], Dr. Lakshmi Prasad Dasi[2], Dr. Shelly Singh-Gryzbon[1]

[1]The University of Cambridge, Cambridge, Cambridgeshire, United Kingdom. [2]Georgia Institute of Technology, Atlanta, Georgia, United States

Introduction

Expanding indications for transcatheter aortic valve implantation (TAVI) in lower-surgical risk cohorts raise concerns about transcatheter heart valve (THV) durability, as patients currently outlive their initial device. Once failed, redo-TAVI can be performed by implanting a second THV within the existing prosthesis. However, experience with redo-TAVI remains limited, and early clinical studies report complications arising from device-vessel interactions but lacks mechanistic insights. This study develops a computational platform for simulating redo-TAVI, and uses the platform to investigate the structural implications of inserting a balloon-expandable valve (BEV) within an existing BEV for varying deployment strategies.

Methods

A patient-specific aortic root was reconstructed from computed tomography (CT) images, while μCT was used to define a 23 mm BEV, including its frame and leaflets. Using ABAQUS, the BEV was crimped and positioned over a compliant balloon, then nominally deployed using fluid-cavity interactions. Redo-TAVI was subsequently simulated, with modified balloon inflation to represent **under-expansion** and **over-expansion strategies**. Tie constraints were applied between the prosthetic leaflets and stent frame, and between calcifications and aortic root. The root boundaries were fixed, with balloon ends constrained in-plane and rotationally. Hard-penalty contact was enforced with a friction coefficient of 0.26. Material models included hyperelastic (aorta and leaflets), elasto-plastic (frame and calcifications) and elastic (balloon).

Results

This work presents the first computational platform for simulating redo-TAVI, from valve crimping to deployment, inclusive of THV leaflets and stent frame. It was seen that under-expansion minimised aortic root deformation, although mid-valve “dog-boning” was

observed. Over-expansion caused increased root deformation and stent dilation, representing the highest mechanical risk of vascular injury (VI).

Discussion

During redo-TAVI, reduced annular area after the initial THV combined with increased stiffness from calcifications amplifies VI risk. Although under-expansion reduces global stress, it may compromise long-term valve performance. Furthermore, inadequate sealing can cause paravalvular leakage, and residual gaps from incomplete expansion may encourage thrombosis and restenosis, further narrowing the valve. Simulations highlight the need for precise expansion strategies in redo-TAVI to balance VI with valve durability. Self-expanding valves, which exert more adaptive radial forces, may mitigate these complications, with ongoing research evaluating this possibility.

Images (Optional)

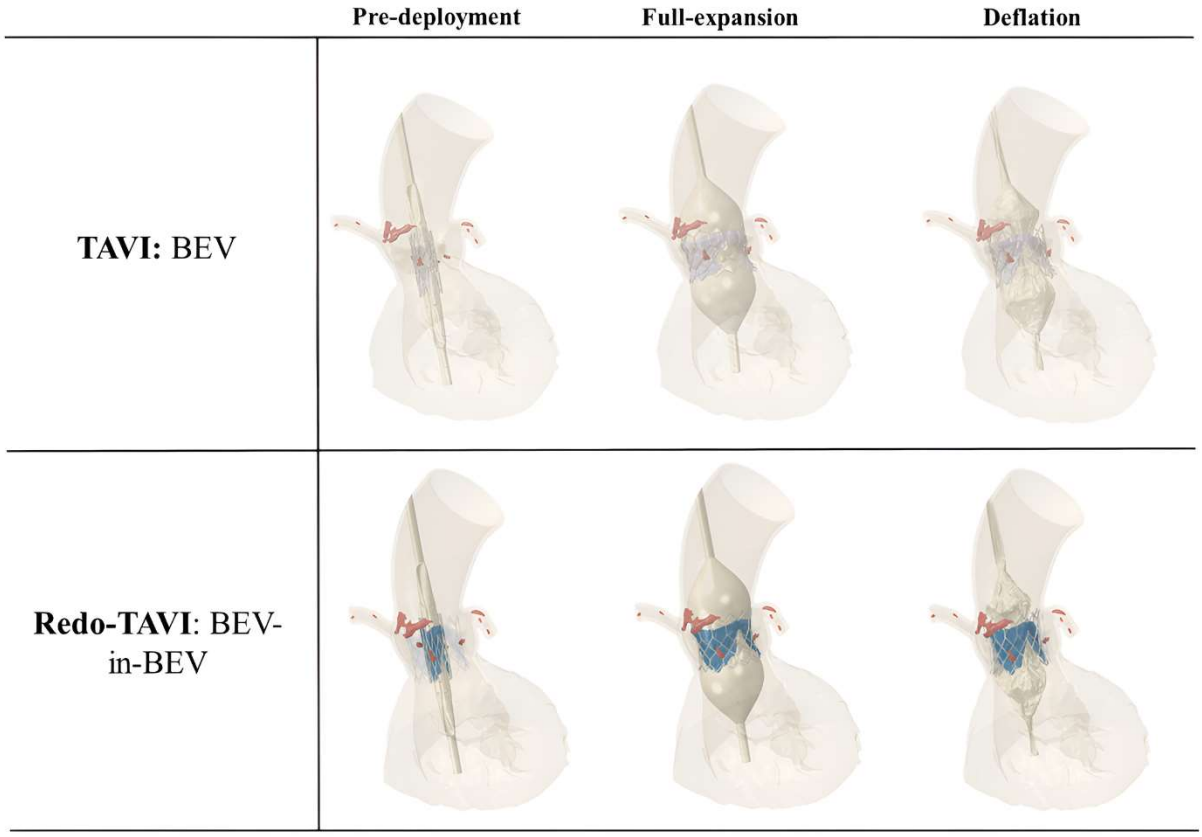


Fig.1 *Simulation pipeline for deploying the initial balloon-expandable valve (BEV; top row), followed by the second BEV (bottom row) involving valve and balloon crimping, inflation and deflation steps.*

Session Category

OA132-05

Virtual Transcatheter Repair of Atrioventricular Valve Regurgitation Using an Open-Source Finite Element Simulation Framework

Dr. Seda Aslan

Children's Hospital of Philadelphia, Philadelphia, PA, United States

Introduction

Atrioventricular valve regurgitation is a major cause of morbidity in patients with heart disease. While surgical repair remains the standard of care, many patients are poor candidates for open-heart procedures, increasing the demand for transcatheter edge-to-edge repair (TEER) and transcatheter annuloplasty. Although these approaches have shown promising outcomes, their mechanical effects on leaflet stresses, coaptation, and device–tissue interactions remain insufficiently characterized. Image-derived models aid device sizing and anatomical feasibility but cannot predict functional performance or leaflet biomechanics. To address this need, we developed an open-source finite element framework to simulate TEER, band annuloplasty, suture annuloplasty, and combined strategies under physiologic loading.

Methods

A mitral valve from a 15-year-old patient was reconstructed using SlicerHeart and 3D Slicer and modified to generate P2 prolapse and annular dilation anatomies. Virtual repairs were performed in FEBio, including four MitraClip G4, a band annuloplasty (via annular circumference reduction), and a suture annuloplasty (via targeted annular displacement). Simulations incorporated a hyperelastic model, nonlinear chordae elements, leaflet contact, physiologic systolic pressure, and a compliant annulus condition. Functional (regurgitant orifice area, ROA; coaptation area, CA) and mechanical (leaflet stress and strain) metrics were quantified for each repair.

Results

TEER restored coaptation in prolapse but increased leaflet stresses, which varied with clip geometry; larger clips produced higher stresses. Staged leaflet capture increased CA but introduced greater mechanical loading, particularly in the dilated annulus model. Band annuloplasty achieved full coaptation at ~30% annular reduction and reduced leaflet stresses relative to TEER in dilation. Suture annuloplasty produced modest annular

reduction yet generated the largest CA in prolapse. Combined TEER + band annuloplasty yielded the best overall functional outcome in dilation (ROA = 0.06 cm^2; CA = 2.57 cm^2) with reduced stresses compared to TEER alone.

Discussion

This framework demonstrates how virtual repair can differentiate biomechanical and functional performance across transcatheter strategies. With further validation and expansion to diverse patient anatomies, such simulations may support personalized device selection and procedural planning.

Images (Optional)

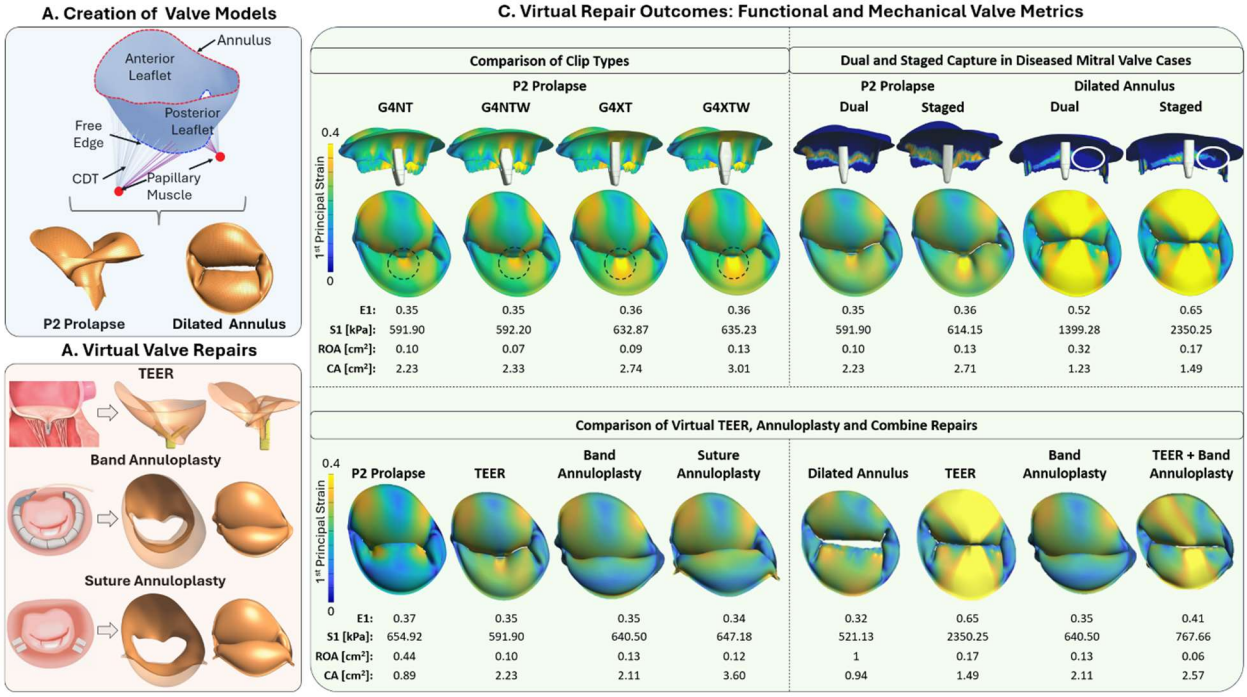


Figure 1: Workflow: (A) Creation of regurgitant mitral valve models: P2 prolapse and dilated annulus. (B) Virtual repair of TEER with explicit clip deployment, band annuloplasty, and suture annuloplasty. (C) Evaluations of functional and mechanical outcomes across repairs. Top left: Comparison of four MitraClip G4 devices in the prolapse model showing differences in strain patterns, stress (S1), coaptation area (CA), and regurgitant orifice area (ROA). Top, right: Dual vs. staged leaflet capture in prolapse and dilation cases. Bottom, left: Comparison of TEER, band, suture, and combined TEER + band repairs in the prolapse and dilated annulus models (bottom, right).

References (Optional)

Session Category

Cardiovascular/Cardiorespiratory Biomechanics: Methods, Models and Applications

OA133-02

Traumatic Brain Injury – Comparing Lateral and Sagittal Impacts with the CHIMERA Platform

Mr. Alexander Burden B.Eng, Dr. Wai Hang Cheng PhD, Mr. Luis Dias B.Eng, Dr. Jianjia Fan PhD, Dr. Mehwish Anwer PhD, Dr. Peter Cripton PhD, Dr. Cheryl Wellington PhD

UBC, Vancouver, BC, Canada

Introduction

Traumatic Brain Injury (TBI) is a heterogeneous injury in both its causes and outcomes. The direction of the initial head impact is a major source of variation, with previous studies showing that the rotational plane can have a substantial effect on brain injury severity. The Closed-Head Impact Model of Engineered Rotational Acceleration (CHIMERA) model of TBI has been used globally to produce human-like impact-acceleration injuries in a mouse model. The objective of this study is to characterize the differences between the well-established sagittal impact model with a lateral impact model of murine TBI.

Methods

Firstly, trackers were implanted onto the skull of cadaver mice, which were then impacted with CHIMERA in either the sagittal or lateral direction, at a range of energies. Phantom v1212 high speed cameras captured head motion following impact at 19000 FPS. Linear and Angular Velocities were computed for each impact.

Subsequently, live experiments were conducted on 3-month-old C57BL/6 mice, separated into 3 groups, sham (n=5), lateral (n=5), and sagittal (n=7). All animals were anesthetized and provided with analgesics according to veterinarian approval. Animals in the lateral and sagittal groups then underwent a CHIMERA TBI at 2.7 joules and were allowed to recover. At 4 hours, saphenous blood was collected for plasma biomarker (GFAP/NF-L) analysis. At 1 week, animals were perfused and brains were collected for histology.

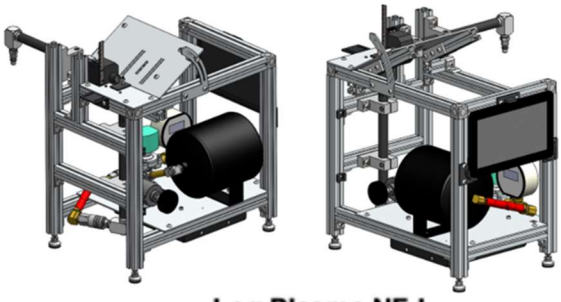
Results

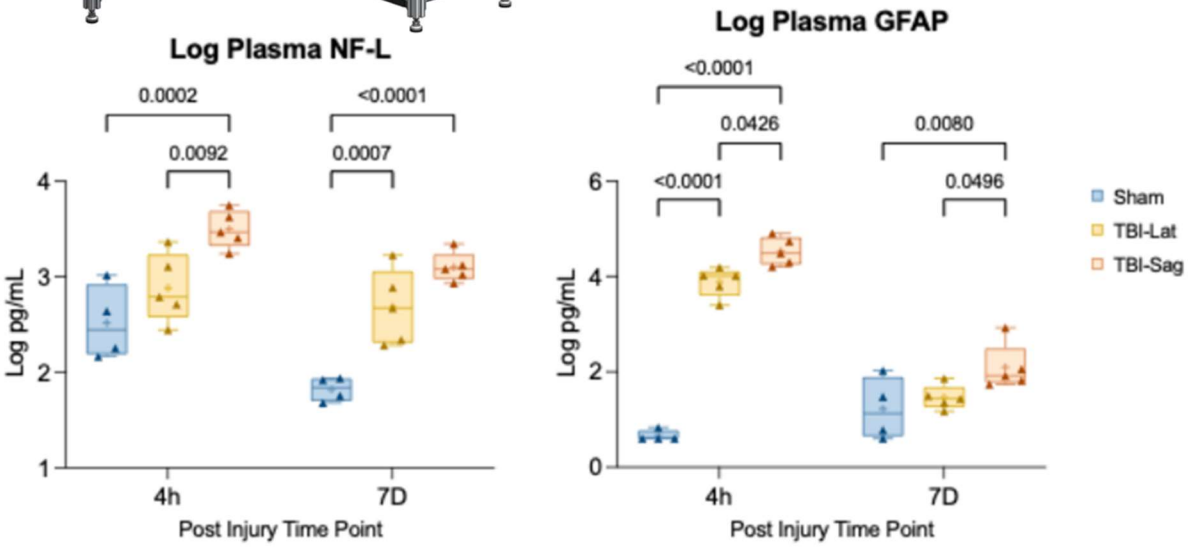
Preliminary results from the cadaver experiments indicate that lateral hits resulted in trajectories with greater velocities. Furthermore, above 2 Joules, sagittal impacts do not cause an increase in velocity, suggesting more energy is absorbed by the skull. However, initial findings from the live animal study found the sagittal group exhibited increased mortality (28% vs 0%), LRR time (120 min vs 30 min) and significantly greater GFAP and NF-L at 4 ($p<0.0426$ and $p<0.0092$) hours post-injury. Preliminary histology shows differences in affected regions as well.

Discussion

Initial results suggest that lateral impacts result in a greater dissipation of energy into head motion, while sagittal impacts cause greater direct injury to the brain. Histology indicates that sagittal impacts affect the brain symmetrically, while lateral impacts are strongly biased to the injury site.

Images (Optional)





Session Category

Injury Biomechanics: N/A

OA133-03

Factors Associated with Elevated Brain Strains in Youth American Football Players

Dr Enora Le Flao[1], Mr Chaokai Zhang[2], Dr Wei Zhao[2], Ms Samantha DeAngelo[1], Dr Adam Culiver[3], Mr Nick Shoaf[4], Mr Durshil Doshi[4], Dr Jingzhen Yang[5], Dr Sean Rose[5], Dr James Onate[1], Dr Zeynep Saygin[4], Dr Songbai Ji[2], Dr Jaclyn Caccese[1]

[1]The Ohio State University Wexner Medical Center, Columbus, OH, United States. [2]Worcester Polytechnic Institute, Worcester, MA, United States. [3]Indiana University Indianapolis, Indianapolis, IN, United States. [4]The Ohio State University, Columbus, OH, United States. [5]Nationwide Children's Hospital, Columbus, OH, United States

Introduction

American football players regularly sustain head acceleration events (HAEs). The resulting brain strain may lead to acute and long-term neurological impairments. It is essential to understand HAE exposure to design effective and targeted risk reduction strategies. The objective of this study was to identify factors affecting the magnitude of HAE-induced brain strains experienced by youth football players.

Methods

HAEs were collected from 75 American football players (8-12 years old, split into age-based teams) over two seasons using instrumented mouthguards during games and practices. True positive, high-quality HAEs with a peak linear acceleration and angular velocity over 10 g and 2 rad/s, respectively, were included for analysis. A subsequent analysis focused on video-verified game HAEs, using annotations of action (being tackled, tackling, blocking), mechanism (helmet-to-ground, helmet-to-opponent, body impact), and player position. The kinematics were used as input to a convolutional neural network based on the anisotropic Worcester Head Injury Model (WHIM) to estimate 95th percentiles of Maximal Principal Strains (MPS95). Generalized Linear Mixed Models (GLMMs) were used to assess various fixed effects on MPS95, using participant ID as random factor.

Results

A total of 2719 HAEs were included, with a median MPS95 of 6.70% [IQR: 4.75-9.47]. Games produced higher MPS95 than practices (Type III Wald χ^2 (1) = 8972.8, p <0.001; estimated means difference: +0.69%). Players in the intermediate team (5th graders) experienced higher MPS95 than those in the younger team (3/4th graders)(χ^2 (2) = 11.00, p = 0.004, +0.64%). MPS95 were similar across seasons (χ^2 (1) = 0.45, p = 0.50). Over the 403 video-verified HAEs, action, mechanism, and player position all showed a significant effect on MPS95 when tested separately. After removing collinear variables, a GLMM including

mechanism, player position, and team as fixed effects revealed a significant effect of the mechanism (χ^2 (2) = 6.38, p = 0.041). Specifically, helmet-to-ground predicted higher MPS95 than body impacts (+1.63%, p = 0.020).

Discussion

There were significant but subtle group differences in strain. Impact mechanism affected MPS95 after accounting for several factors. Helmet-to-ground impacts were a risk factor in this player cohort, and could be the focus of future risk reduction strategies.

Session Category

Injury Biomechanics: N/A

OA133-04

Defining Axonal Injury Thresholds: A Multiscale Coupling of Tissue Deformation and Molecular Damage

Ms. Maryam Majdolhosseini, Dr. Alessandra Villa, Dr. Zhou Zhou, Dr. Svein Kleiven

KTH, Stockholm, Stockholm, Sweden

Introduction

Diffuse axonal injury (DAI) is a traumatic brain injury (TBI) characterised by the deformation of axons within white matter (WM). Although the exact mechanism remains elusive, membrane disruption is hypothesised to be the initial trigger of axonal injury. However, bridging the gap between macroscopic tissue strain and these molecular events remains a significant challenge. Building on this hypothesis, we developed a multiscale approach to determine axonal injury thresholds by directly coupling tissue-scale finite element (FE) models with molecular dynamics (MD) simulations.

Methods

The developed FE model represented brain WM, including an axon composed of microtubules, neurofilaments, and a cortex layer representing the axolemma, embedded within an extra-axonal matrix. Parallel MD systems modelled a human-axolemma lipid bilayer with a voltage-gated sodium channel (Nav1.1) embedded inside. The FE model was subjected to tension, compression, and shear and the local strains of the cortex were derived. The MD models underwent uniaxial tension to monitor the structural changes of the bilayer and protein. We assumed the local strain of the cortical elements in the FE model is equivalent to the strain applied to the MD axolemma, as shown in Figure 1. Consequently, injurious strains derived from MD simulations were coupled with axonal deformation results from FE models to identify macroscopic failure thresholds.

Results

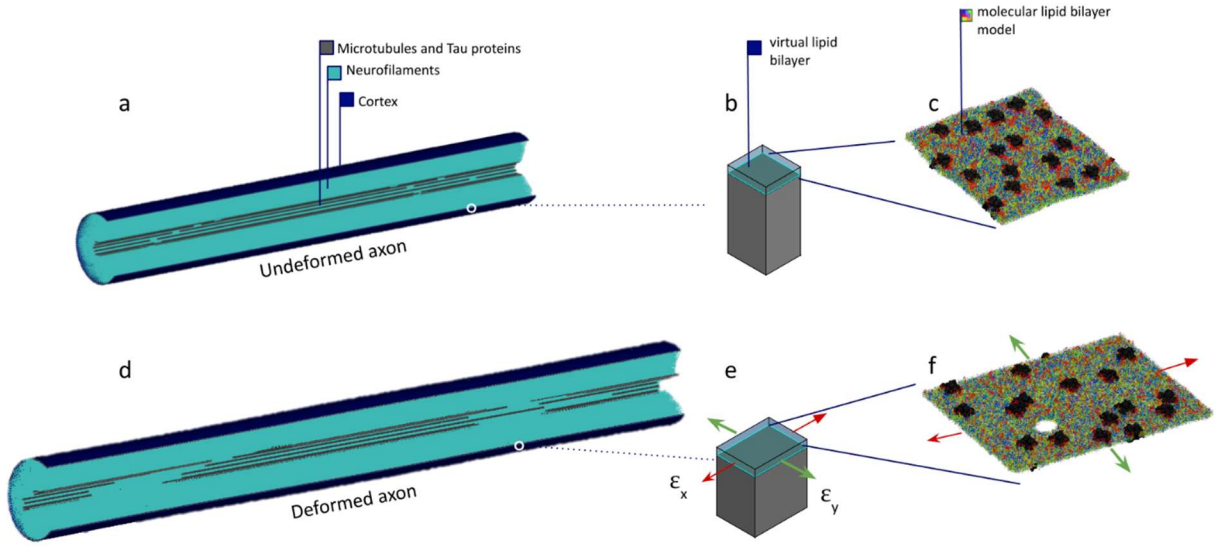
MD simulations showed bilayer mechanoporation at 41% strain, while protein conformational changes occurred earlier, at 35% strain. This suggests that functional impairment of ion channels may precede structural rupture of the membrane. Therefore, protein disruption was defined as the injury threshold at the molecular level. Preliminary results of the FE simulations indicated that the load distribution to sub-cellular elements depends on the deformation mode. By mapping the 35% molecular threshold to the FE

model, we established macroscopic axonal injury thresholds of 15% in tension, 22% in compression, and 30% in shear.

Discussion

We implemented a multiscale method to investigate axonal injury thresholds by connecting cellular deformation with axolemma disruption. This approach establishes a mechanical foundation for defining physiologically relevant injury criteria, supporting the development of more effective diagnostic and protective strategies for TBI and DAI. Future work can examine the role of cytoskeletal variability.

Images (Optional)



Acknowledgements (Optional)

This study was supported by research funds from Swedish Research Council Grants VR-2020-04496. The computational resources were provided by the National Academic Infrastructure for Supercomputing in Sweden (NAISS) through the Centre for High-Performance Computing (PDC) at KTH under Projects NAISS 2024/22-601, NAISS 2023/5-464, NAISS 2024/5-64, NAISS 2024/5-86.

Session Category

Injury Biomechanics: N/A

OA133-05

Elevated Moderate-Severe and Bleeding Brain Injury Risk in Older Adults Despite Reduced Kinematic Exposure

Dr Claire Baker, Dr Mazdak Ghajari, Professor David Sharp

Imperial College London, London, Greater London, United Kingdom

Introduction

Road traffic collisions (RTC) are a leading cause of global morbidity and often cause traumatic brain injury (TBI) [1]. Age and collision kinematics separately influence TBI outcomes, but their interaction is unstudied. UK Co-operative Crash Injury Study (CCIS) and its successor the Road Accident In-depth Studies (RAIDS) data uniquely capture collision kinematics and clinical data. We previously showed delta-V (change-in-velocity) as a key TBI determinant. We examine age-kinematics influence on TBI prevalence/type [2].

Methods

25,079 subjects were investigated (18,624 from 2000-2010 CCIS, 6,455 from 2013-2024 RAIDS data, 20,336 (81%) had known ages). 3,975 vehicle occupants additionally had valid delta-V (CCIS: 3,345, RAIDS: 630). Mayo TBI was classified as previously described [2]. Injury rates were studied in four groups (18-30/31-69/70+yrs, plus children). TBI/age/delta-V interaction was analysed with Chi-squared and Mann-Whitney statistics.

Results

20,806 injured subjects (58.1%) included 1,613 fatalities. 2,872 TBI subjects included 1,488 (51.8%) moderate-severe, 782 (27.2%) mild, 602 (21.0%) symptomatic, 674 (23.5%) skull fracture, 790 intracranial bleeding (27.5%), 599 (20.9%) subarachnoid haemorrhage, 314 (10.9%) subdural haematoma and 93 (3.2%) axonal injury.

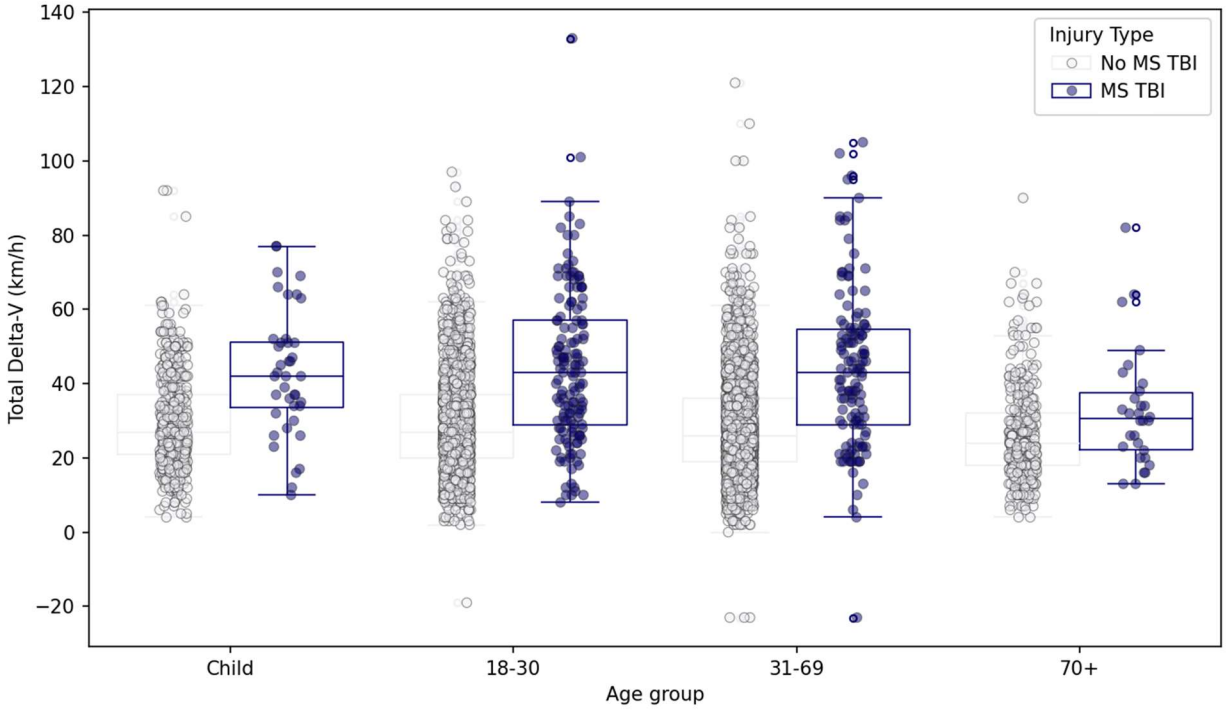
Moderate-severe TBI rate was higher in younger (18-30yrs, χ^2=48.8, p<0.00001) and older (70+yrs, χ^2=10.1, p=0.0014) adults compared to 31-69-year-olds, as was haemorrhage (SAH/SDH/non-specified intracranial bleeding) for both younger (4.0% vs 3.2%, χ^2=8.4, p=0.004) and older (4.6% vs 3.2%, χ^2=7.4, p=0.006) groups. Compared to 31-69yrs, skull fracture was not significantly higher in 70+yrs (p=0.06) but was in 18-30yrs (χ^2=35.6, p<0.00001).

Higher moderate-severe TBI rates in 70+ were not driven by higher RTC kinematics: in fact younger drivers experienced higher delta-V than those aged 70+yrs (31-69yrs versus 70+yrs: U_{MW}=501933.0, p=0.0008; 18-30yrs versus 31-69yrs: U_{MW}=2092839.0, p<0.0001). Occupants with moderate-severe TBI had higher delta-V than those who did not sustain moderate-severe TBI (children: 32.7km/h versus 29.8km/h, 18-30yrs: 44.1km/h versus 29.7km/h, 31-69yrs: 43.8km/h vs 28.3km/h, 70+yrs: 32.7km/h vs 26.2km/h).

Discussion

Older adults are more vulnerable to moderate-severe TBI/bleeding, despite being exposed to reduced RTC kinematics. This increased vulnerability has vehicle design and post-crash response implications. Further work will integrate biomechanically relevant variables (e.g. belt status).

Images (Optional)



References (Optional)

1. James et al. (2018), The Lancet, 2018.

2. Baker et al. (2022), Brain Communications.

Session Category

Injury Biomechanics: N/A

OA134-02

Experimental and Computational Models for Grey-White Interface Damage in Traumatic Brain Injury

Mr Conal Sheridan, Dr Jamie Concannon

University of Galway, Galway, Connaught, Ireland

Introduction

The mechanism of brain damage in concussion is unknown, the unvalidated hypothesis being shear delamination at the grey-white matter interface [1]. Concussion-related damage is non-visible on medical imaging, though repeated concussions contribute to aggressive neurodegeneration [2]. Regional mechanical heterogeneity in the brain is often neglected [3], despite its relevance to strain propagation in impact. This study therefore mechanically characterises ovine brain tissues regionally and describes a novel constitutive formulation for their computational modelling.

Methods

Fresh ovine grey (GM) and white matter (WM) (n=880) from the regions described in Fig.1a were isolated in dissection for unconfined compression, tension and shear to 50%, and grey, white and interface samples were subject to tensile and shear fracture to assess the clinical hypothesis detailed above. A novel bilinear formulation was developed from existing principal-stretch based bilinear models, with anatomy and experimentally informed aligned fibres, using Green-Lagrange strain to control shear behaviour.

Results

GM and WM are asymmetric between compression, tension and shear, with strain-dependent stress varying minimally regionally within the cortical GM and corona radiata (CR) WM (Fig.1a), with deep brain GM and corpus callosum WM differing from the cortex and CR. Fractures occurred in the GM and WM as well as at their interface (Fig.1b), though the interface fracture initiation stress was at least 69% lower than bulk tissues. The proposed model matches existing bilinear model performance in compression and tension (Fig.1c), while reducing shear stress prediction error by up to 62% (Fig.1d).

Discussion

Insignificant variance within the cortex and CR supports their assumed homogeneity in literature [3]. Variability in fracture initiation and propagation locations call the clinical

hypothesis into scrutiny, along with the lower nucleation stress at the grey-white interface, suggesting further mechanical heterogeneity around this interface. Significant compression-tension-shear asymmetry in both tissues highlights the importance of fitting models to multi-mode experimental data, addressed by the proposed Green-Lagrange-based model. This heterogenous and highly asymmetric behaviour is informing the design of next generation headforms for impact damage assessment.

Images (Optional)

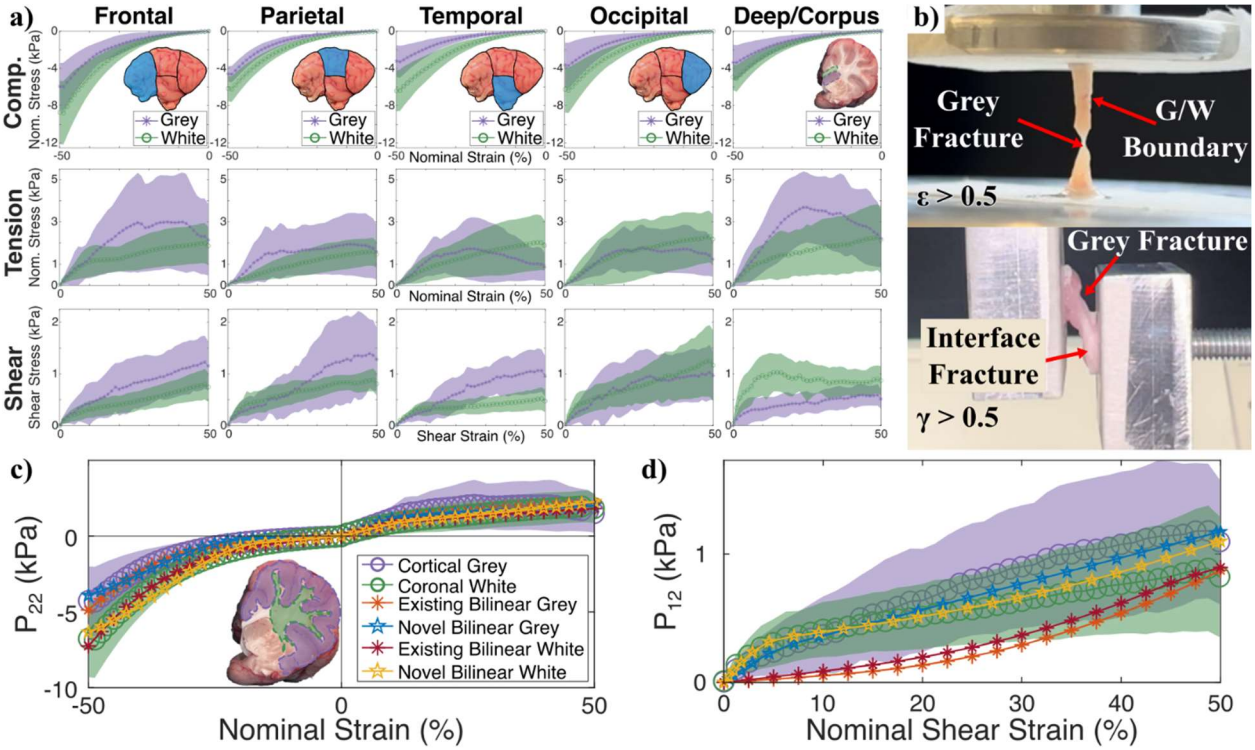


Figure 1 a) Regional mechanical behaviour of GM and WM. b) Off-interface fractures at grey-white interface in tension and shear. c) Nominal stress-strain behaviour in cortex and CR in compression and tension, with bilinear models. d) Cortex and CR in shear, comparing existing and proposed models.

References (Optional)

[1] Alisafaei et al; *Biophys. J.*, (2020).

[2] Sheridan et al., *Ann. Biomed. Eng.*, (2025)

[3] Budday et al., *Arch. Comput. Methods Eng.*, (2019)

Acknowledgements (Optional)

Session Category

Organ and Tissue Biomechanics: N/A

OA134-03

Ex Vivo Biomechanical Evaluation of Self-Expandable Metallic Stent Migration After Hepaticogastrostomy Using a Porcine Pullout Test Across the Liver Parenchyma and Gastric Wall

Prof. Hiroshi Yamada[1], Mr. Luyao Cheng[1], Prof. Yusuke Ishida[2], Prof. Takehiko Koga[2]

[1]Kyushu Institute of Technology, Kitakyushu, Fukuoka, Japan. [2]Fukuoka University, Fukuoka, Fukuoka, Japan

Introduction

Stent migration is a serious complication that can occur after endoscopic ultrasound–guided hepaticogastrostomy for biliary drainage. Although previous studies have evaluated stent mechanics using biomechanical models of the porcine gastric wall, migration involving both the gastric wall and liver parenchyma has not yet been investigated [1].

Methods

Displacement-controlled pullout tests were performed on a self-expandable metallic biliary stent (HANAROSTENT; Boston Scientific) along directions normal and oblique to the gastric wall surface. The lateral-to-normal velocity ratios were set to 0 for normal pullout and 0.25 for oblique pullout, while the pullout speed was maintained at 0.2 mm/s using two stepper motors. Three axial components of pullout force were measured with a force sensor, and stent motion was recorded on video. Relative displacement (slippage) between the stent and surrounding tissues, as well as axial stent elongation, were quantified by motion analysis of the videos.

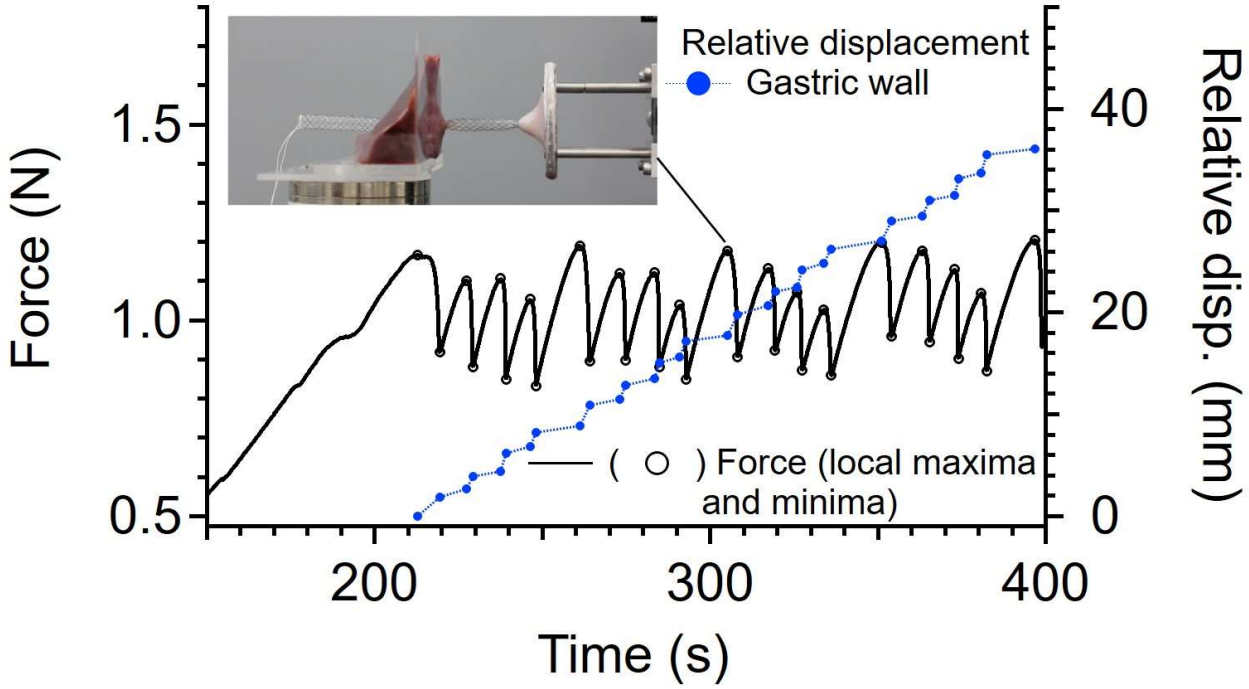
Results

The figure shows the time history of axial pullout force during pullout in the normal direction. Relative displacement is also plotted at the local maxima and minima of the force. In the gastric wall, gradual stent slippage occurred at a mean velocity of 0.2 mm/s, with periodic acceleration and deceleration occurring inversely with the cyclic decreases and increases in pullout force. In contrast, liver-side slippage was absent or less than 11% of the total slippage across tests. Mean pullout forces were 1.1 N in the normal direction and slightly lower in the oblique direction.

Discussion

Compared with our previous liver-parenchyma-only pullout tests in the normal direction, the mean pullout force in the present model in the same direction was lower by 0.2 N. Overall, these results indicate that hepaticogastrostomy stent migration is governed predominantly by slippage at the gastric wall, with little contribution from the liver parenchyma, supporting clinical observations that migration occurs primarily on the gastric side.

Images (Optional)



References (Optional)

[1] Takehiko Koga *et al*., 2024, J Hepato-Biliary-Pancreatic Sciences, 31, 840–849.

Acknowledgements (Optional)

This work was supported by JSPS KAKENHI 24K07237.

Session Category

Organ and Tissue Biomechanics: N/A

OA134-04

Lung Parenchyma Characterization Following Ventilator-Induced Lung Injury: Biaxial Tensile Experiments and Inverse Finite Element Constitutive Modeling

PhD Candidate Matthew Shankel, Dr. Arif Badrou, Dr. Mona Eskandari

University of California-Riverside, Riverside, CA, United States

Introduction

Acute respiratory distress syndrome causes heterogeneous lung damage and surfactant disruption [1]. Essential mechanical ventilation can paradoxically damage the lung. Such ventilator-induced lung injury (VILI), exhibited as collagen reorganization, suggests matrix–fiber interactions influence parenchymal mechanics [1]. To investigate these mechanisms, we employ finite element analysis and constitutive modeling to characterize the biaxial tensile behavior of the parenchyma with and without surfactant present during injury.

Methods

Sixteen male Sprague–Dawley rats were euthanized under IACUC approval; six underwent saline wash to remove surfactant. Ventilation groups included control (15 cmH_2O driving pressure, 5 cmH_2O PEEP), VILI and VILI+Surf(–) (17 mL/kg tidal volume, 0 PEEP). Distal parenchyma was stretched biaxially at 1%/s to 65% strain, and First Piola–Kirchhoff stress was computed. Cranial-caudal data are shown due to matching trends across directions. Initial and final moduli were extracted using a bilinear fit. A finite element replica in Abaqus (21,594 quadratic membrane elements, quarter-symmetry, plane stress, incompressible) applied controlled displacements at rake holes [2]. Holzapfel-Gasser-Ogden (HGO) parameters (C_{10}, k_1, k_2, κ) were optimized with MATLAB's *lsqnonlin* using multiple randomized initial guesses. Shapiro–Wilk statistical testing used $p<0.05$.

Results

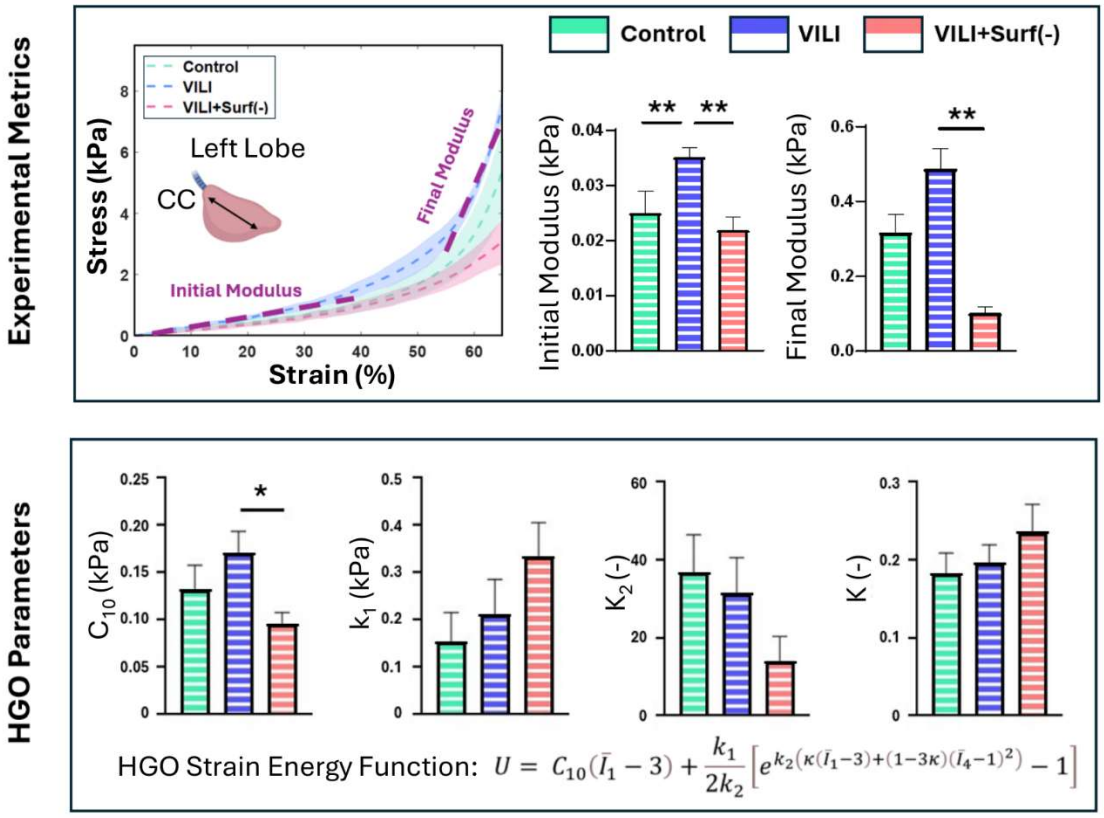
Maximum stress and modulus were greatest in VILI, while VILI+Surf(–) exhibited similar initial modulus but lower final modulus than control. HGO fits found C_{10} to be increased in VILI. k_1 and κ increased from control to VILI to VILI+Surf(–), whereas k_2 decreased across the same sequence.

Discussion

We find that VILI and VILI+Surf(–) distinctly alter parenchymal mechanics: VILI stiffens at high strain, whereas VILI+Surf(–) softens. HGO parameter shifts suggest altered matrix–fiber load sharing. Across groups, k_1 increased and k_2 decreased from control to VILI to VILI+Surf(–), indicating earlier fiber recruitment with reduced exponential stiffening as

injury increases, consistent with reported collagen elongation after VILI [1]. The high-strain softening in VILI+Surf(–) highlights that such tissue may fail when overstretched. These findings suggest injury-specific matrix–fiber interactions can advance models and ventilation strategies.

Images (Optional)



References (Optional)

[1] Richard Deyhle Jr. *et al.,* Sci. Rep., 2025

[2] Heleen Fehervary *et al.,* J. Mech. Behav. Biomed. Mater., 2016

Session Category

Organ and Tissue Biomechanics: N/A

OA134-05

Effects of Brain Tissue Preparation on Regional Biomechanics in Tauopathy Mouse Model

Dr. Mohammad Tabatabaei, Dr. Lakiesha Williams

University of Florida, Gainesville, Florida, United States

Introduction

Brain mechanobiology plays a critical role in regulating neuronal function, glial activation, and neuroinflammatory signaling in neurodegenerative diseases such as Alzheimer's disease (AD) [1]. However, brain mechanical properties can be strongly influenced by tissue harvesting and preparation methods, potentially confounding interpretation of biomechanical changes [2]. Despite widespread use of atomic force microscopy (AFM) for brain biomechanics [3], the sensitivity of regional brain stiffness to tissue preparation workflows remains poorly defined. This study establishes a framework to assess how tissue processing influences regional biomechanical measurements in a tauopathy mouse model.

Methods

Sagittal brain sections (20 μm) were obtained from PS19 transgenic mice (n = 3, 9–13 months) and age-matched C3H wild-type controls (n = 3, 9–13 months) following PBS perfusion and snap freezing. Sections underwent immunohistochemical staining for phosphorylated tau (AT8), neuronal nuclei (NeuN), and nuclear labeling (Hoechst) without chemical fixatives (Figure 1A,B). AFM nanoindentation was performed using a quadratic pyramidal probe (0.1 N/m cantilever) to quantify Young's modulus across the hippocampus, cerebellum, and cortex.

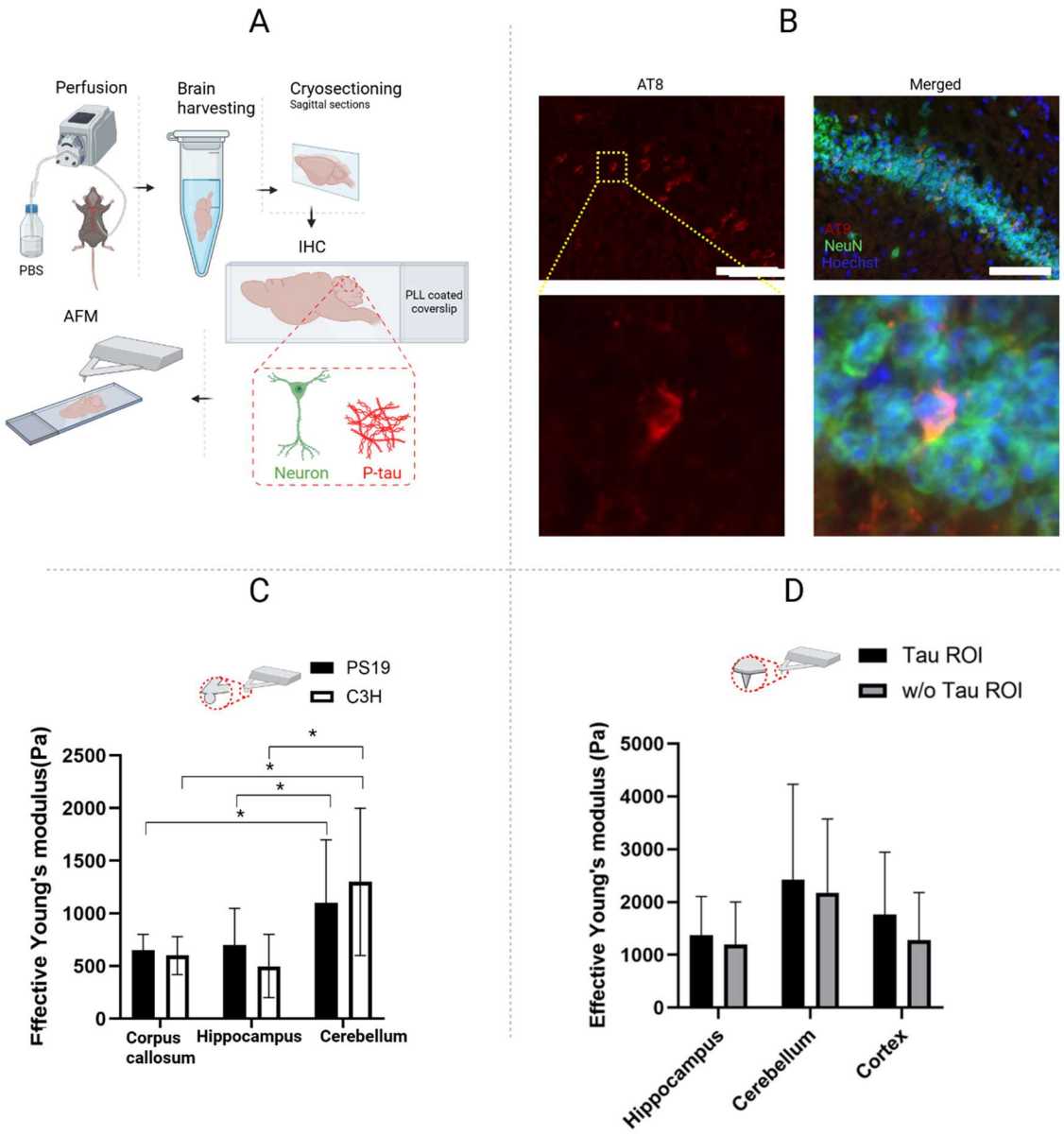
Results

Global brain tissue stiffness did not differ significantly between PS19 and wild-type mice across major anatomical regions (Figure 1C). However, pronounced regional mechanical heterogeneity was observed within both groups. Subregions with higher neuronal density, particularly within the hippocampus, exhibited elevated local stiffness values (Figure 1D). Tau-positive regions in PS19 mice frequently overlapped with locally stiffer zones, despite preserved bulk mechanical properties. These findings indicate that regional brain biomechanics are highly sensitive to microstructural organization under the current tissue preparation workflow.

Discussion

These results demonstrate that regional brain biomechanics measured by AFM are strongly shaped by tissue preparation and local microarchitecture, independent of global tissue stiffness. Spatially resolved AFM measurements integrated with neurohistology provide a robust framework for evaluating preparation-dependent biomechanical variability in neurodegeneration. Ongoing studies are extending this approach to directly compare multiple tissue harvesting and sectioning methods, including vibratome-based preparation, to establish standardized biomechanical protocols for Alzheimer's disease research.

Images (Optional)



References (Optional)

[1] Querfurth HW, LaFerla FM. *N Engl J Med*. 2010.

[2] Franze K, Janmey PA, Guck J. *Annu Rev Biomed Eng*. 2013.

[3] Moeendarbary E, et al. Nat Commun. 2017.

Session Category

Organ and Tissue Biomechanics: N/A

OA135-02

Bilateral Dynamic CT for Scapholunate Instability: Toward Personalized, Protocol-Standardized Kinematic Diagnosis

Drs. Maranda Haenen[1,2], Ir. Hanne Vries[1,3], Dr. Michelle Brinkhorst[4], Dr. Ir. Geert Streekstra[3], Dr. Stefan Hummelink[1], Prof. Ioannis Sechopoulos[1,5,6], Prof. Brigitte Van der Heijden[1,2]

[1]Radboud University Medical Center, Nijmegen, Gelderland, Netherlands. [2]Jeroen Bosch Ziekenhuis, ' s Hertogenbosch, Noord - Brabant, Netherlands. [3]Amsterdam University Medical Center, Amsterdam, Noord - Holland, Netherlands. [4]Xpert Clinics, Rotterdam, Zuid - Holland, Netherlands. [5]University of Twente, Enschede, Overijssel, Netherlands. [6]Dutch Expert Centre for screening, Nijmegen, Gelderland, Netherlands

Introduction

Dynamic CT imaging enables three-dimensional evaluation of wrist motion and is increasingly used for diagnosing scapholunate (SL) ligament injuries. However, variability in protocols across institutions restricts comparability and hinders standardization. An important consideration is whether to adopt unilateral or bilateral scanning, as unilateral approaches often rely on external reference datasets for diagnosis. This study evaluates whether contralateral referencing in bilateral dynamic CT scanning supports SL injury diagnosis by assessing (1) the influence of scan protocol variation on outcome measures; (2) similarity between wrists of healthy individuals and contralateral healthy wrists of patients; (3) wrist motion symmetry in healthy individuals; and (4) contralateral referencing in patients with a unilateral SL injury.

Methods

This retrospective multicenter study combined data from three cohorts: (1) unilaterally scanned healthy volunteers (RUMC), (2) bilaterally scanned healthy volunteers (AUMC), and (3) patients with arthroscopically confirmed unilateral SL lesions (RUMC). Dynamic CT included one static scan and multiple frames during radial–ulnar deviation (RUD) and flexion-extension (FE). At RUMC, movements were performed freehand with forearm stabilization; at AUMC, motion was guided by a custom device. Scapholunate distance (SLD) was automatically measured at five points on the SL joint during both motions (Figure 1). For each parameter, means were calculated for wrist positions achieved by ≥70% of wrists.

Results

1. **Protocol differences**: Across five SLD measurements and two motions, differences between RUMC and AUMC were greatest during RUD, with mean absolute differences of 0.32 mm (dorsal, range 0.17-0.38 mm) and 0.37 mm (volar, range 0.22-0.45 mm).
2. **Healthy vs. contralateral wrists:** Mean differences ranged from 0.04-0.20 mm (max 0.32 mm), indicating similar motion patterns.
3. **Dominant vs. non-dominant**: Mean differences ranged from 0.03-0.16 mm (max 0.26 mm), showing symmetry within individuals.
4. **SL lesions:** Complete lesions showed mean differences of 0.78-1.25 mm (max 2.08 mm) compared to the healthy side; partial lesions had smaller, localized asymmetries (mean 0.09-0.21 mm, max 0.70 mm).

Discussion

Contralateral referencing in bilateral dynamic CT scanning is both possible and justified for diagnosing unilateral SL injuries. This approach avoids the need for reference datasets and should therefore be considered.

Images (Optional)

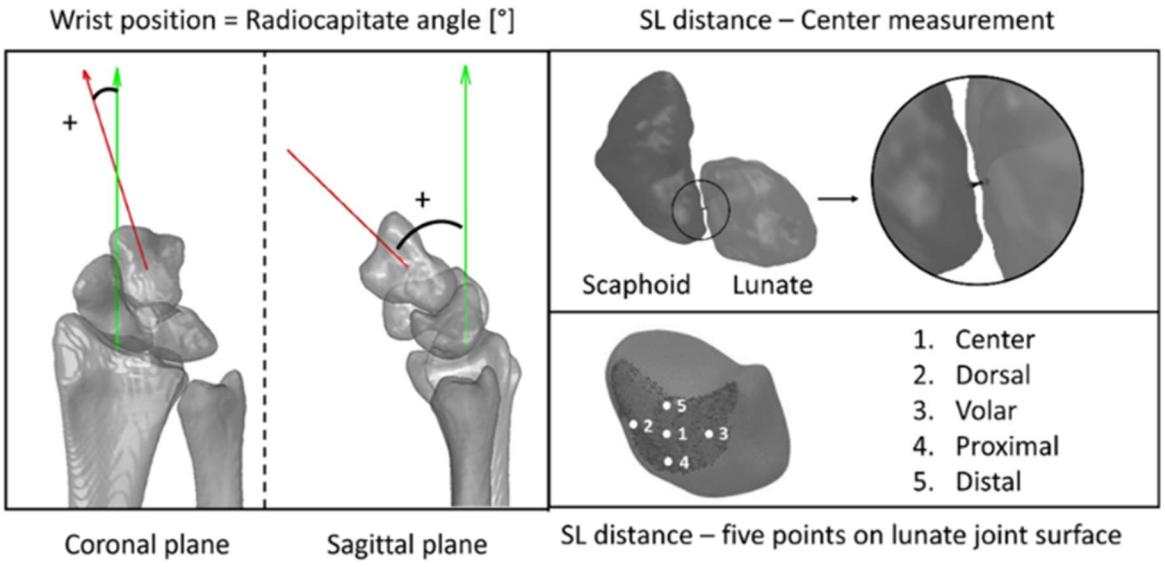


Figure 1: Visualizations of wrist position determination and automatic SLD measurements. The wrist position during RUD is defined as the angle between the radius axis and capitate axis in coronal plane. The wrist position during FE is defined as the angle between the radius axis and capitate axis in sagittal plane. The SLD is measured as the shortest Euclidean distance between the lunate and scaphoid joint surface at five pre-defined points.

Session Category

Musculoskeletal Biomechanics: Joints and Motion

OA135-03

Quantifying In-Vivo Lumbar Spine Kinematics Using Biplanar Videoradiography and MRI.

Miss Katherine Prentice[1], Miss Lauren Swain[1], Mrs Jenny Williams[1], Dr Michael Ward[2], Dr Emily Kelly[2], Professor Akbar Javadi[2], Professor Tim Holsgrove[2], Professor Jude Meakin[2], Professor Cathy Holt[1], Dr David Williams[1]

[1]Cardiff University, Cardiff, Wales, United Kingdom. [2]University of Exeter, Exeter, England, United Kingdom

Introduction

Spinal disorders are a major cause of disability, costing the UK healthcare system an estimated £3.2 [1] billion annually for back pain alone. Accurately measuring and assessing in-vivo spinal kinematics presents a significant challenge, both in improving treatments for spinal conditions and in providing a fundamental understanding of normal spinal motion. To address this, an in-vivo imaging pipeline combining Biplanar Videoradiography (BVR) and Magnetic Resonance Imaging (MRI) was developed to measure the direct movement of the vertebrae. This enables the capture of dynamic measurements of vertebral motion in the lumbar spine of healthy individuals during activities. The aim of this study is to quantify the inter-individual variability in spinal movement to establish a baseline of normal variations.

Methods

Subject-specific L2-Pelvic spinal kinematics was collected from five healthy-reporting participants. Participants underwent 3T MRI (T1-VIBE, Magnetom Prisma, Siemens) which was manually segmented into 3D bone models (Simpleware Scan IP, Synopsis). Anatomical coordinate systems were applied to each individual vertebra. BVR measurements (10Hz, 3.33ms, 85kVp, and 320mA) were obtained for three activities: stoop lift with a 10kg load, lateral bending, and axial rotation. Bone position and orientation for the lumbar vertebrae and pelvis were calculated by matching 3D bone models to BVR images (DSX Suite, C-motion, Inc.). Intervertebral kinematics were calculated (MATLAB, MathWorks, Inc.) based upon International Society of Biomechanics standards.

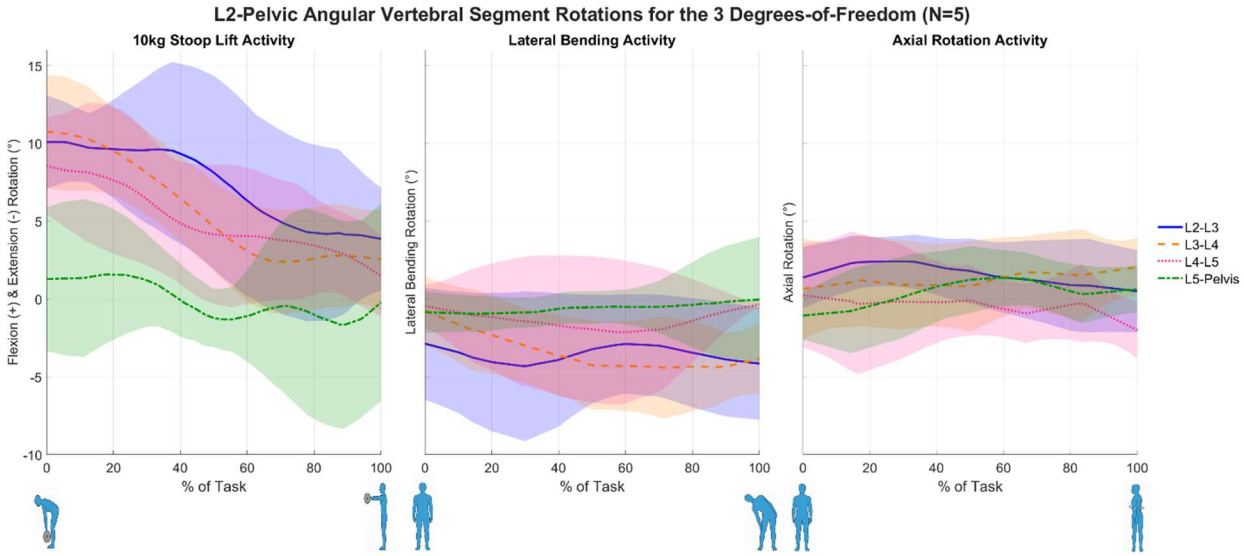
Results

As shown in Figure 1, flexion-extension angular RoM values were 6.2°, 8.2°, 7.1°, and 1.5° for levels L2-L3 through L5-Pelvis, respectively. Corresponding values for lateral bending and axial rotation were 1.3°, 3.1°, 0.1°, and 0.8° and 0.9°, 1.4°, 1.8°, and 1.7° respectively.

Discussion

Significant variability was observed between participants, as the contribution of each functional vertebral unit to overall lumbar spine motion differed for individual participants. This dataset establishes a comprehensive reference for healthy spinal kinematics, creating a baseline essential for identifying pathological deviations. These findings lay the groundwork for future clinical advancements in the diagnosis, treatment, and prevention of spinal disorders.

Images (Optional)



References (Optional)

[1] Dawit Zemedikun *et al.* British Journal of Pain, 2023

Acknowledgements (Optional)

EPSRC funded EP/V036602/1 (Meakin, Holsgrove & Javadi) and EP/V032275/1 (Holt & Williams).

Session Category

Musculoskeletal Biomechanics: Joints and Motion

OA135-04

Comparison of Hip Contact Forces Across Skin Marker and Dual Fluoroscopy Informed Musculoskeletal Models in Femoroacetabular Impingement Syndrome and Asymptomatic Controls

Ms. Brooklyn Vargas BS, Mr. Seth Kussow BS, Mrs. Lindsay Schuring MS, Mr. Rich Lisonbee MS, Dr. Jared Zitnay PhD, Dr. Scott Uhlrich PhD, Dr. Andrew Anderson PhD

University of Utah, Salt Lake City, UT, United States

Introduction

Cam femoroacetabular impingement syndrome (FAIS) has been identified as a factor in the development of hip osteoarthritis, yet specific biomechanical mechanisms driving joint degeneration remain unclear. Comparing the biomechanics of FAIS to asymptomatic cam morphology (ACM) may help us better understand the pathophysiology of FAIS. While skin marker data (SM) is widely used for biomechanical analysis, dual fluoroscopy (DF) directly captures bone motion and avoids soft tissue artifact [1]. This study investigated: (1) differences in hip joint contact forces (HCFs) between FAIS and ACM using musculoskeletal modeling during level walking and (2) the impact of motion capture modality used for scaling and kinematics on HCF estimations.

Methods

Sixteen participants with FAIS (7M/9F) and thirteen controls with ACM having similar demographics (7M/6F) performed level walking at self-selected speeds on an instrumented treadmill in this IRB-approved study. A full-body skin marker set was used, while DF data were only available for landmarks of the pelvis and the side of interest. HCFs were estimated in OpenSim [2,3]. Three simulations were performed per participant: 1) SM scaling and kinematics, 2) DF-informed scaling and kinematics, and 3) DF-informed scaling with SM kinematics (DF-SM). HCFs were compared throughout gait using statistical parametric mapping ($p \leq 0.05$).

Results

For all simulated conditions, HCFs were not significantly different between FAIS and ACM groups. For both FAIS and ACM groups, each component of HCF was significantly increased using DF and DF-SM compared to SM (Figure 1). Minimal differences were found between DF and DF-SM conditions (Figure 1).

Discussion

Individuals with FAIS exhibited similar HCFs during walking compared with ACM, regardless of the motion capture modality used. Differences between the SM and DF results may be attributed to higher accuracy in model scaling, specifically improved scale factors and pelvic tilt, when using DF data. The similarity between DF and DF-SM simulations further suggests that more accurate model scaling may yield reliable results without requiring DF data for kinematics, significantly reducing the time and labor demands of DF.

Images (Optional)

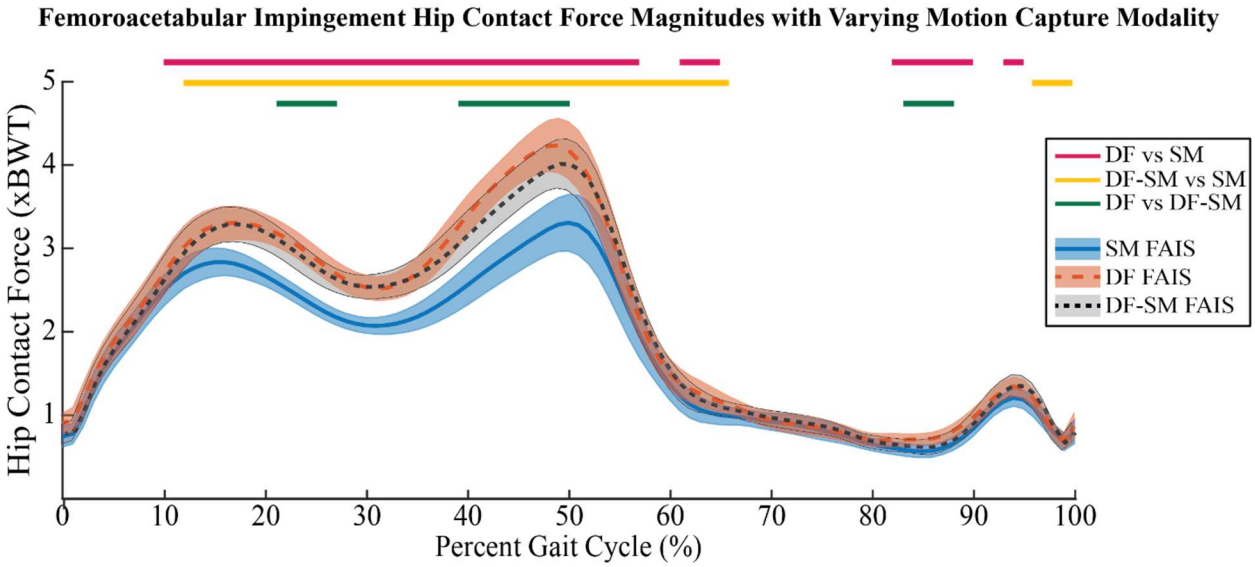


Figure 1: Hip joint contact force magnitudes during level walking in the femoroacetabular impingement syndrome (FAIS) cohort. Results were simulated under three condtions: (1) using skin marker (SM) data, (2) using dual fluoroscopy (DF) data, and (3) using DF data for scaling combined with SM data for kinematics (DF-SM). Differences detected by statistical parametric mapping ($p \leq 0.05$) are displayed above the figure.

References (Optional)

[1] Ashley Kapron et al., J. Appl. Biomech., 2014. [2] Ajay Seth et al., PLoS Comput. Biol., 2018. [3] Michael Harris et al., J. Biomech., 2017.

Acknowledgements (Optional)

This work was supported by the National Institutes of Health [R01AR077636-03] and the National Science Foundation [Graduate Research Fellowship 2139322].

Session Category

Musculoskeletal Biomechanics: Joints and Motion

OA135-05

Effect of Embedding Coupling-Curves-Based Knee Models Within Inverse Kinematics Compared to Bi-Plane Fluoroscopy-Driven Kinematics

Dr. Mehran Hatamzadeh[1], Mr. Kuan Hsien Wu[2], Dr. Tung-Wu Lu[2,3], Dr. Raphael Dumas[1]

[1]Laboratory of Biomechanics and Shock Mechanics (LBMC), University Gustave Eiffel, University Claude Bernard Lyon 1, Lyon, Rhone, France. [2]Department of Biomedical Engineering, National Taiwan University, Taipei, Taiwan, Taiwan. [3]Department of Orthopedic Surgery, School of Medicine, National Taiwan University, Taipei, Taiwan, Taiwan

Introduction

Accurate knee motion analysis requires understanding tibiofemoral and patellofemoral joints' motion, each of which is described by 6 kinematic parameters that are coupled together due to knee ligamentous constraints and articular geometry. Consequently, researchers have developed simplified knee models that estimate its 6-DOF kinematics from fewer inputs, using either flexion alone (1-DOF) or flexion and internal rotation (2-DOF). However, their performance within a lower-limb inverse kinematics (IK) framework remains unclear. Therefore, this research assesses whether or not incorporating coupling-curve-based knee models into IK improves marker-based knee kinematics accuracy compared to the gold standard bi-plane fluoroscopy.

Methods

Eleven healthy participants underwent CT imaging to generate subject-specific bone meshes. They performed functional tasks in a bi-plane fluoroscopy system while skin markers were recorded simultaneously. Ground-truth 6-DOF tibiofemoral kinematics were obtained using fluoroscopy and bone meshes (Figure 1), while marker-based kinematics were computed before and after IK using hip (spherical) and ankle (universal) models, and five published coupling-curve-based knee models [1-5]. The ensemble kinematic curves' similarities were assessed using one-dimensional statistical parametric/nonparametric (SPM/SNPM) mapping.

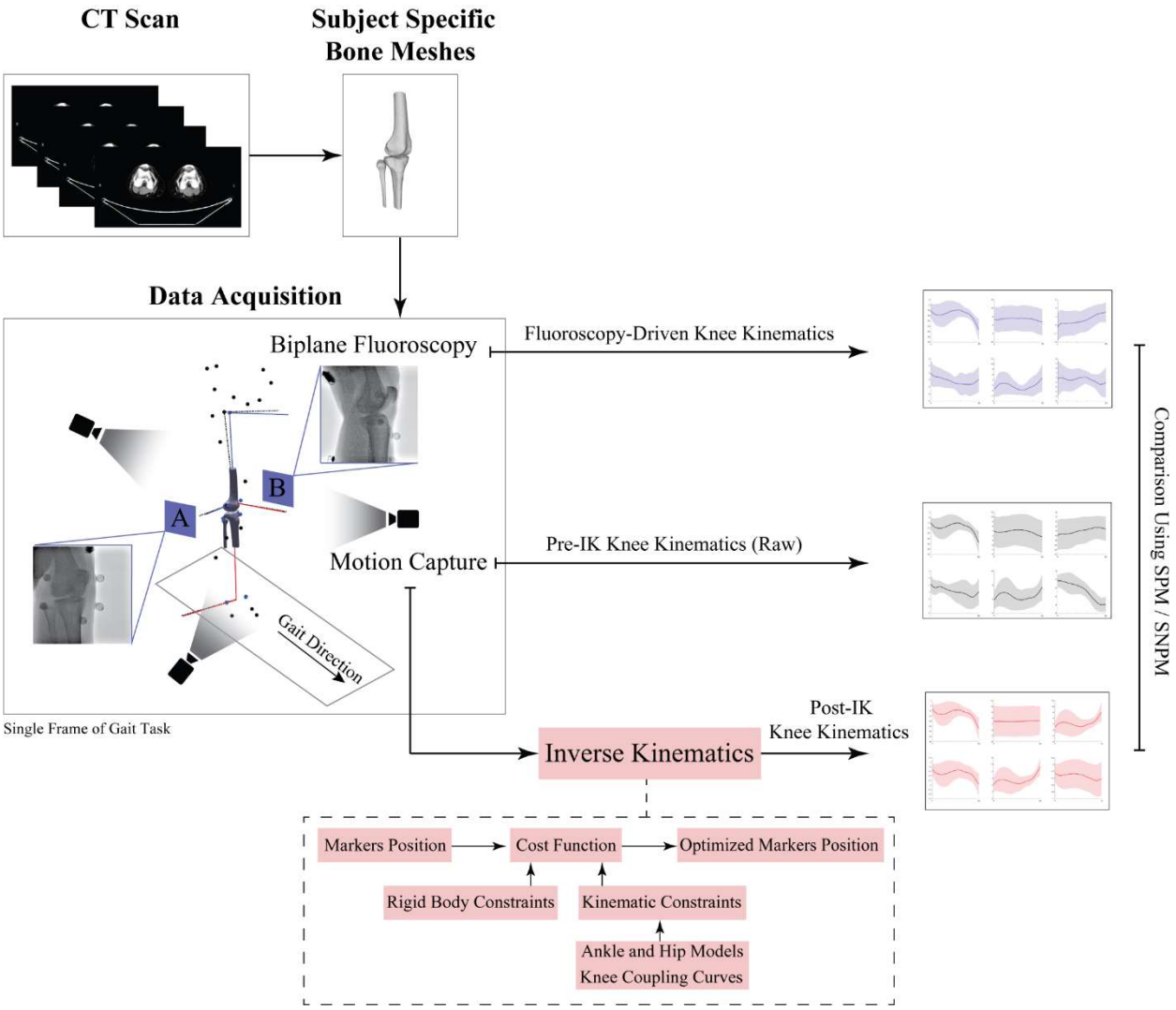
Results

During gait task, none of the coupling-curve-based models improved knee kinematics accuracy. For all three rotations, analyses show that adding coupling-curve constraints to the IK procedure significantly degrades results. For the three translations, although RMSE values differed, SPM/SNPM found no significant differences between fluoroscopic kinematics and those from raw markers (RMSE 2.4–2.9 mm) or IK using Walker-Rajagopal [1,2] (RMSE 2–3.1 mm), Guan [3] (RMSE 2–4.2 mm), or Hume [4] coupling curves. In contrast, embedding Koo's [5] coupling curves in IK significantly degraded translation accuracy, with RMSEs of 5.06 mm (lateral–medial), 6.2 mm (anterior–posterior), and 5.8 mm (superior–inferior).

Discussion

Across walking trials, the coupling-curve–based knee models (e.g., Walker [1] models implemented in OpenSim by Rajagopal [2]) did not improve accuracy, indicating that alternative methods are needed for more reliable knee-kinematics computation in musculoskeletal modeling.

Images (Optional)



References (Optional)

[1] Walker et al., Biomechanics, 1988.

[2] Rajagopal et al., Trans Biomed Eng, 2016.

[3] Guan et al., Ann Biomed Eng, 2022.

[4] Hume et al., Ann Biomed Eng, 2018.

[5] Koo et al., J Biomech Eng. 2019.

Session Category

Musculoskeletal Biomechanics: Joints and Motion

OA136-01

Biophysical Simulations Reveal the Impact of Tendon Stiffness on the Interplay Between Intrinsic Mechanics and Sensorimotor Feedback in Unsteady Movements

Dr. Hansol X. Ryu[1,2], Dr. Surabhi N. Simha[2,1], Prof. Gregory S. Sawicki[1], Prof. Lena H. Ting[2,1]

[1]Georgia Institute of Technology, Atlanta, GA, United States. [2]Emory University, Atlanta, GA, United States

Introduction

Control of unsteady movement depends on contributions from both instantaneous intrinsic mechanics of muscle-tendon unit and delayed sensorimotor feedback [1,2], with different ratio of contributions at different joints. Rapid muscle stretches due to perturbations are resisted by muscle short-range stiffness (SRS), a transient property arising from muscle cross-bridges. Joint torques in perturbed human balance rely primarily on intrinsic stiffness at the hip joint and sensorimotor feedback at the ankle [1,3]. Here we leverage a novel biophysical muscle model to systematically test the impact of tendon stiffness on the interplay between intrinsic and neural contributions to perturbation rejection. We hypothesized that tendon compliance reduces intrinsic stiffness contributions to unsteady movement control by absorbing the perturbation-induced displacement, thereby reducing the SRS contribution and increasing the reliance on feedback-driven activation.

Methods

We used a novel biophysical muscle model [4] that captures muscle SRS [5]—a property absent from standard Hill-type models [3]—in a closed-loop inverted pendulum simulation to study how muscle-tendon interactions influence control of unsteady movements. Muscle activation was modulated by feedback on simulated half-sarcomere length, velocity, and acceleration, with biologically realistic delays. Feedback gains were tuned to achieve stable steady-state after perturbation.

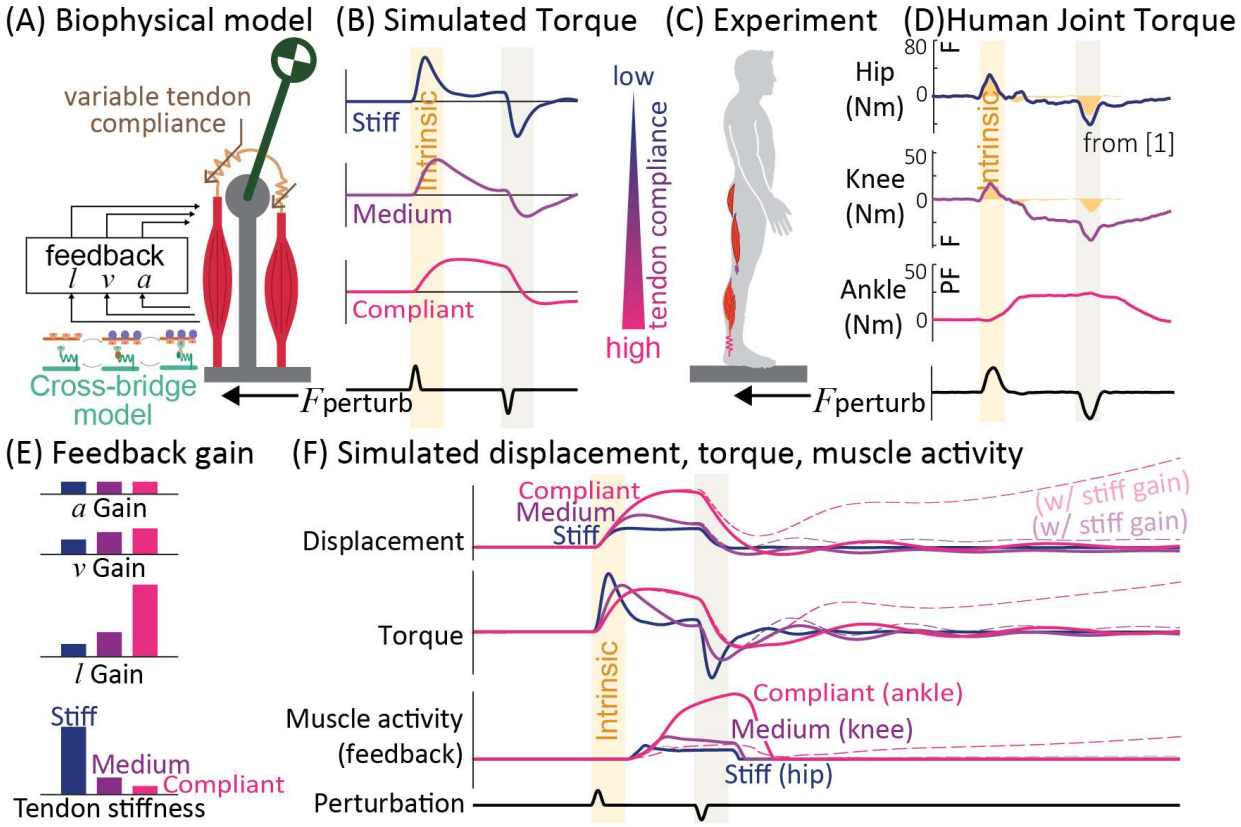
Results

Our model reproduced key trends seen in human standing balance [1]. Models with a stiff tendon (e.g. hip) had prominent and rapid increase in joint torque at perturbation onset, originating from instantaneous forces due to muscle SRS and low reliance on neural feedback. As tendon compliance increased (knee to ankle), the sharp rise in torque diminished, and more feedback-driven muscle activation (i.e. higher feedback gains) was required to stabilize the inverted pendulum.

Discussion

Our result shows that tendon compliance absorbs displacement from perturbations and reduces the SRS engagement in muscle fibers – shaping the balance between reliance on intrinsic mechanical responses and requirement for neural feedback to restore balance.

Images (Optional)



References (Optional)

[1] Jakubowski, KL, et al. *J. Neurophysiol*, 2025.
[2] Daley, MA., Voloshina, A., Biewener, AA. *J. Physiol*. 2009.
[3] De Groote F, Allen JL, Ting LH. *J. Biomech*, 2017.
[4] Campbell KS. *J. Gen. Physiol*, 2014.
[5] Horslen, BC., et al. *J. Exp. Biol*. 2023.

Acknowledgements (Optional)

This research was supported by NIH NICHD R01HD090642, NSF/DBI 2021832

Session Category

Human Motion and Performance: Balance, Posture and Control

OA136-02

Predictive Simulation of Sensorimotor Alterations to Characterize Postural Control in Parkinson's Disease

Mr. Julian Shanbhag[1], Ms. Iris Wechsler[1], Ms. Gwen Spelly[1], PD Dr. phil. Heiko Gassner[2,3], Prof. Dr.-Ing. Sandro Wartzack[1], Assoc. Prof. PD Dr.-Ing. habil. Jörg Miehling[4,1]

[1]Engineering Design, Friedrich-Alexander-Universität Erlangen-Nürnberg (FAU), Erlangen, Bavaria, Germany. [2]Department of Molecular Neurology, University Hospital Erlangen, Friedrich-Alexander-Universität Erlangen-Nürnberg (FAU), Erlangen, Bavaria, Germany. [3]Fraunhofer Institute for Integrated Circuits IIS, Erlangen, Bavaria, Germany. [4]Department of Civil and Mechanical Engineering, Technical University of Denmark (DTU), Kongens-Lyngby, Capital Region, Denmark

Introduction

Postural instability represents one cardinal symptom in Parkinson's disease (PD). However, underlying processes leading to these changes in postural control are still not fully understood. In this paper, we use predictive simulations to investigate the influence of internal sensorimotor parameters on postural control and to identify which parameter changes reproduce PD-like postural characteristics. Here, we focus specifically on alterations in motor noise and neural feedback delays as key internal parameters.

Methods

We used a previously published neuromusculoskeletal model [1] and forward dynamic simulations within the software framework SCONE [2]. The model consisted of 18 muscles and 6 degrees of freedom. Simulations were performed for quiet upright standing. We systematically increased motor signal noise and neural delays independently to assess their effects on postural control. Motor noise consisted of constant and signal-dependent Gaussian components. Additional neural delays were applied equally across all feedback pathways.

We used data from 31 PD patients and 31 age- and sex-matched healthy control participants (HCs) and applied a principal component analysis (PCA) to evaluate simulation results and to determine the simulations' agreement with experimental data. The PCA was based on kinematic outcomes, including joint angles, and sway-related center of pressure parameters. For analysis, we used the first 3 principal components, which explained over 70% of experimental data variance.

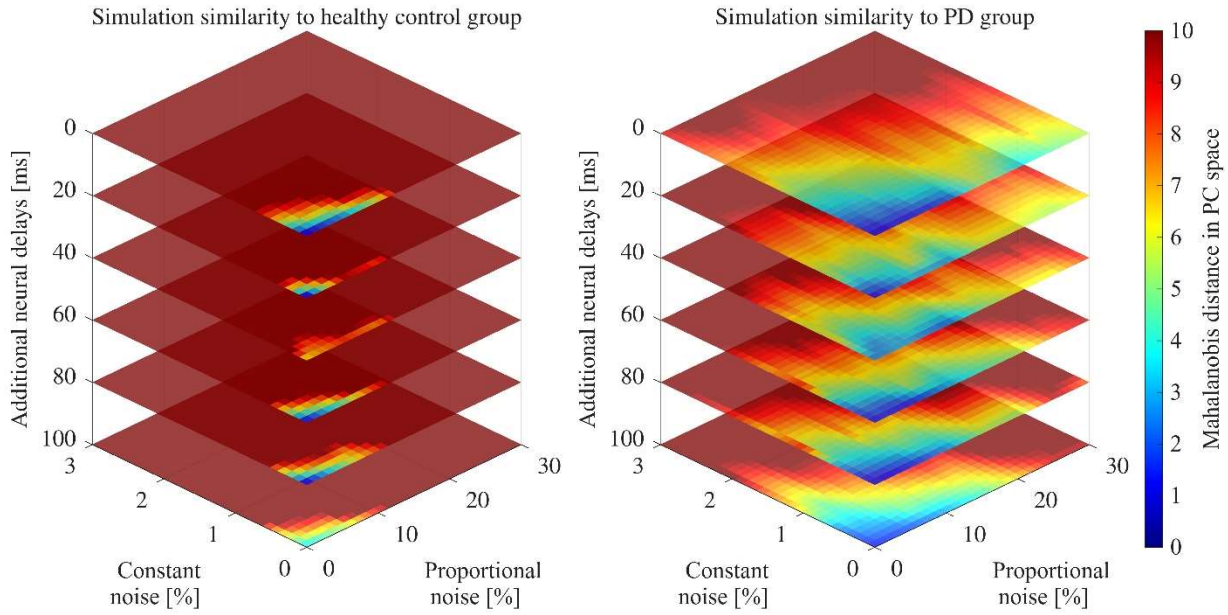
Results

Simulations showed that postural control behavior was close to HCs for small amounts of signal noise (Figure 1). Increasing motor noise and neural delays shifted simulations toward PD-like behavior, producing only minor differences in PCA projection distances compared with experimental PD data and increasingly separating them from HCs in PCA space at the same time.

Discussion

We found that simulations with small amounts of motor signal noise best describe postural control of HCs. Simulations with higher signal noise and additional neural delays showed reduced overlap to HCs but still considerably higher similarities to PD patterns. It has to be mentioned that especially variances of PD patients' sway parameters were significantly higher. Therefore, individual postural control performance is crucial for estimating personal internal parameters in future simulation work.

Images (Optional)



References (Optional)

[1] J Shanbhag *et al.*, Front. Neurosci., 2022

[2] T Geijtenbeek, JOSS, 2019

Acknowledgements (Optional)

This work was funded by the Deutsche Forschungsgemeinschaft (DFG, German Research Foundation) – SFB 1483 – Project-ID 442419336, EmpkinS.

Session Category

Human Motion and Performance: Balance, Posture and Control

OA136-03

Emergence of Ankle-to-Hip Strategy Transition in Upright Posture via Reinforcement Learning with Biomechanical and Physiological Constraints

Dr. Seongwoong Hong Ph.D.[1], Professor Joo H. Kim Ph.D.[2], Professor Sukyung Park Ph.D.[3]

[1]KAIST InnoCORE AI Co-Research & Education for innovative Drug Institute, Korea Advanced Institute of Science and Technology (KAIST), Yuseong-gu, Daejeon, Korea, Republic of. [2]Department of Mechanical and Aerospace Engineering and Center for Urban Science and Progress, New York University, Brooklyn, New York, United States. [3]Department of Mechanical Engineering, Korea Advanced Institute of Science and Technology (KAIST), Yuseong-gu, Daejeon, Korea, Republic of

Introduction

Human balance control exhibits adaptability, such as the flexible transition between ankle and hip strategies in response to environmental perturbations. Understanding these mechanisms is critical given the fall risks associated with aging and neurological disorders. However, modeling this adaptability requires a framework that integrates environmental adaptation with biomechanical and physiological constraints. While Reinforcement Learning (RL) is promising for such nonlinear tasks, handling strict constraints remains challenging. Here, we propose a constraint-based RL framework that systematically incorporates these constraints, aiming to validate its ability to accurately reproduce and predict human balance control mechanisms.

Methods

We systematically applied biomechanical and physiological constraints using both hard and soft constraint approaches to examine their effects on learned control strategies within a PPO-based framework. The model was validated against human experimental data under backward perturbations.

Results

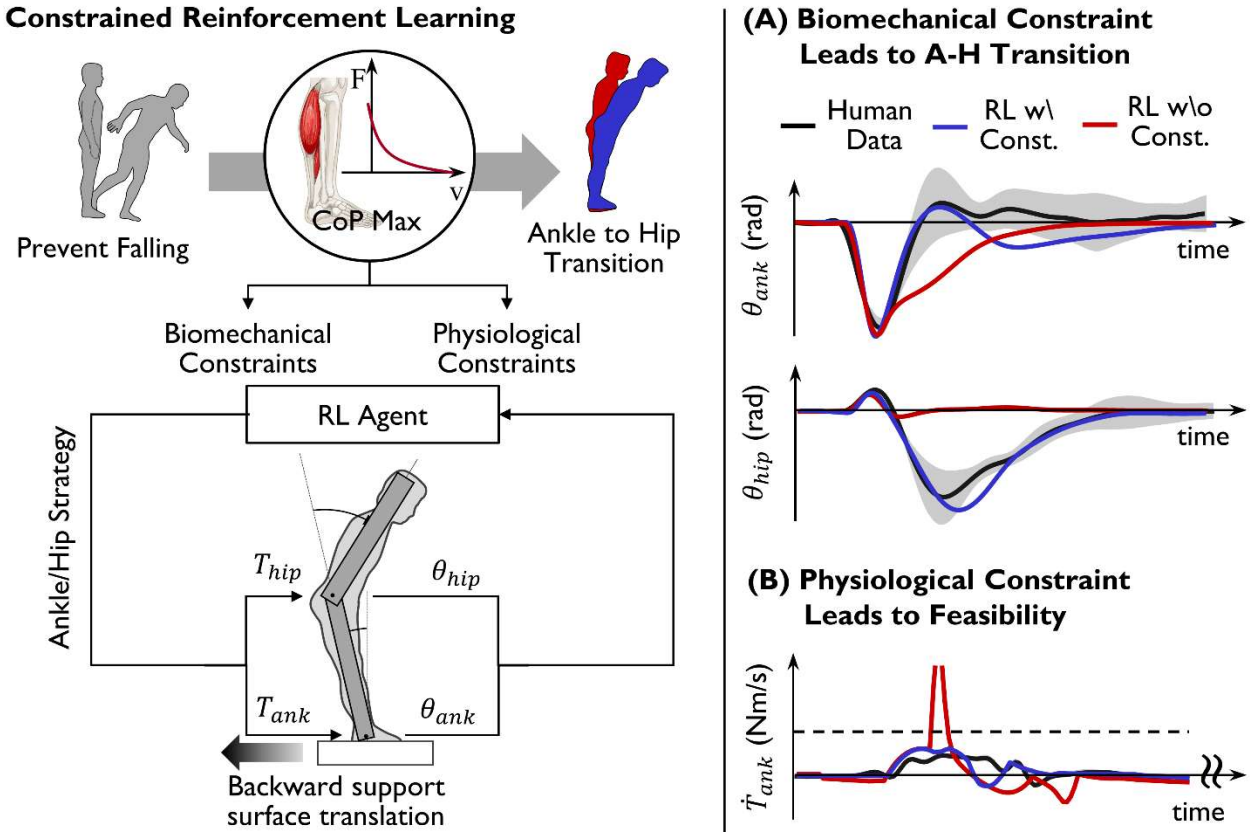
The model trained with the proposed RL framework successfully reproduced the gradual transition from ankle to hip strategy observed in humans as perturbation magnitude increased, across various initial conditions. This transition emerged only in models incorporating constraint for biomechanical ankle torque limits; unconstrained models consistently relied on ankle torque and failed to exhibit strategy transition. Furthermore, physiological torque rate constraints were essential for generating feasible torque profiles; without these constraints, joint torque rates reaching up to 20 times the physiological limits were observed. These findings indicate that biomechanical constraints act as drivers

of strategy selection in the reinforcement learning agent, whereas physiological constraints serve as execution conditions ensuring movement fidelity.

Discussion

These results demonstrate that the proposed RL model provides a valid computational approach for exploring interactions between constraints and motor control strategies. This framework can be extended to predict the effects of physical impairments, such as musculoskeletal disorders or neurological deficits, on postural stability. For instance, sensory transmission delays due to aging or neurological injury can be modeled as increased state observation latency, while muscle weakness can be represented as reduced joint torque limits, enabling predictions of how such constraint changes modify compensatory control strategies for postural maintenance. This approach is expected to contribute to understanding the stability-efficiency trade-off strategies humans adopt under various physical constraints.

Images (Optional)



Acknowledgements (Optional)

This work was supported by the InnoCORE program of the Ministry of Science and ICT(KAIST N10250153) and the National Research Foundation of Korea (NRF) grant funded by the Korea Government (MSIT) (No. RS-2024-00356657)

Session Category

Human Motion and Performance: Balance, Posture and Control

OA136-04

Impact of Age-Related Changes in Muscle Function on Postural Control Strategies in Sit-to-Stand: A Musculoskeletal Simulation with Multi-Objective Optimization

Dr. Shoma Kudo[1,2], Prof. Akinori Nagano[3], Dr. Takuma Inai[1,2], Dr. Masahiro Fujimoto[1,2]

[1]Integrated Research Center for Self-Care Technology, National Institute of Advanced Industrial Science and Technology (AIST), Takamatsu, Kagawa, Japan. [2]Health and Medical Research Institute, National Institute of Advanced Industrial Science and Technology (AIST), Takamatsu, Kagawa, Japan. [3]College of Sport and Health Science, Ritsumeikan University, Kusatsu, Shiga, Japan

Introduction

Sit-to-stand (STS) is a fundamental activity that requires balancing multiple objectives (e.g., postural stability and muscular effort), and the prioritization of these objectives is considered to change with aging [1]. Older adults often adopt a conservative strategy to ensure stability, locating the center of mass (CoM) within the base of support (BoS) before seat-off—stabilization strategy. In contrast, younger adults tend to initiate STS while the CoM is located posterior to the BoS, utilizing greater horizontal momentum to bring the CoM inside the BoS at seat-off—momentum-transfer strategy. However, it remains unclear whether the difference in STS strategy arises from age-related changes in muscular function or from different prioritization of CoM control objectives. This study aimed to clarify the impact of changes in muscle function on STS strategy.

Methods

STS was simulated using two musculoskeletal models representing the muscle functions of young adults (YA) and older adults (OA) through an evolutionary multi-objective optimization [2]. The optimization was executed to find muscle activation patterns that achieve an upright posture from sitting while considering three objectives: (1) the distance of CoM from the BoS at seat-off, (2) CoM velocity at seat-off, and (3) the sum of muscle activation during STS. For each model, the distribution of successful solutions (i.e. Pareto front) and its range were evaluated.

Results

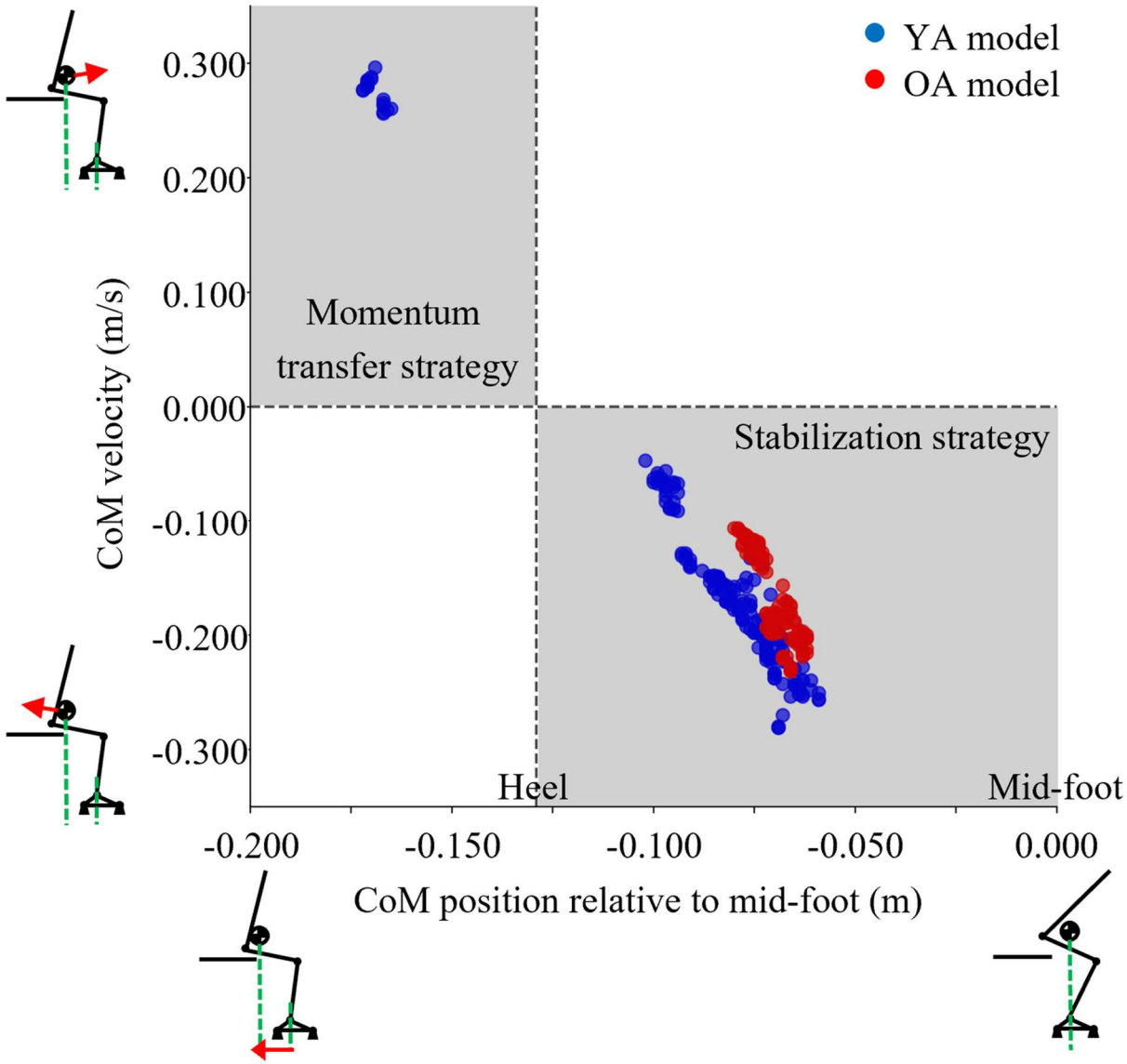
In the OA model, the CoM remained within the BoS at seat-off in all solutions, whereas the YA model located the CoM both inside and outside the BoS (Figure). For the YA model, the ranges of CoM position and CoM velocity were 0.059 to 0.172 m and −0.281 to 0.296 m/s.

For the OA model, the corresponding ranges were 0.062 to 0.080 m and −0.232 to −0.107 m/s.

Discussion

The OA model adopted only a stabilization strategy, showing narrower feasible ranges for CoM position and velocity, while the YA model demonstrated both stabilization and momentum-transfer strategies. These findings suggest that changes in muscle function limit CoM control during STS, forcing older adults to adopt strategies that prioritize stability at seat-off.

Images (Optional)



References (Optional)

[1] Papa and Cappozzo, J. Biomech., 2000
[2] Janis and Deb, IEEE Trans. Evol., 2014

Session Category

Human Motion and Performance: Balance, Posture and Control

OA136-05

Direction-Specific Muscle Force Profile During Y-Balance Test

Mr. Dongho Ha[1], Mr. Taewoong Kong[1], Ms. Hyemin Han[1], Dr. Hoon Kim[1,2]

[1]Department of Software Convergence, Soonchunhyang University, Asan-si, Chungcheongnamdo, Korea, Republic of. [2]Department of Sports Medicine, Soonchunhyang University, Asan-si, Chungcheongnamdo, Korea, Republic of

Introduction

Y-Balance Test (YBT) is a test for assessing balance while reaching a foot in three directions to evaluate joint instability in a lower limb. Previous studies have commonly utilized electromyography to muscular coordination during YBT. However, electromyography only measures superficial muscle activation and cannot fully reflect muscle functions such as muscle force [1] which is important to understand neuromuscular function during balance. Therefore, the purpose of this study was to quantify lower-body muscle forces during YBT using musculoskeletal simulation.

Methods

Eight healthy people performed three trials for each direction of YBT with barefoot, while 3D position of reflective markers, ground reaction force, and muscle activations were collected. Then, joint angles, moments, and muscle forces were calculated using inverse kinematics, inverse dynamics, and static optimization in OpenSim, respectively. We quantified muscle forces from 12 lower-limb muscles while performing YBT in three directions (e.g., anterior (ANT), posterolateral (PL), posteromedial (PM)).

Results

Figure 1 summarizes peak normalized muscle forces (N/body weight) of 12 lower-limb muscles during YBT in three directions. Vastus lateralis (ANT: 4.2, PL: 3.7, and PM: 5.0) and soleus (ANT: 3.2, PL: 2.4, and PM: 3.1) exhibited consistently high forces across all directions. Gluteus maximus generated only small forces in ANT (0.7) but much larger forces in PL (2.7) and PM (2.6). Vastus lateralis, soleus, and vastus medialis generally exhibited greater forces in PM (5.0, 3.1, and 1.7) than PL (3.7, 2.4, and 1.2).

Discussion

In general, vastus lateralis and soleus were consistently serving as primary stabilizers. The marked contrast in gluteus maximus force (Anterior vs. Posterior) indicates a fundamental

shift from a knee- to hip-dominant strategy in posterior reaches. Moreover, PM exhibited a higher mechanical demand than the PL. This high demand resulted from complex rotational stress associated with crossing the body's midline, requiring greater force generation from the vasti and soleus. Therefore, clinicians should consider performance in each YBT direction as an index of direction-specific mechanical demands. Reduced reach in a given direction may indicate insufficient contribution of the primary stabilizing muscles and guide targeted strengthening.

Images (Optional)

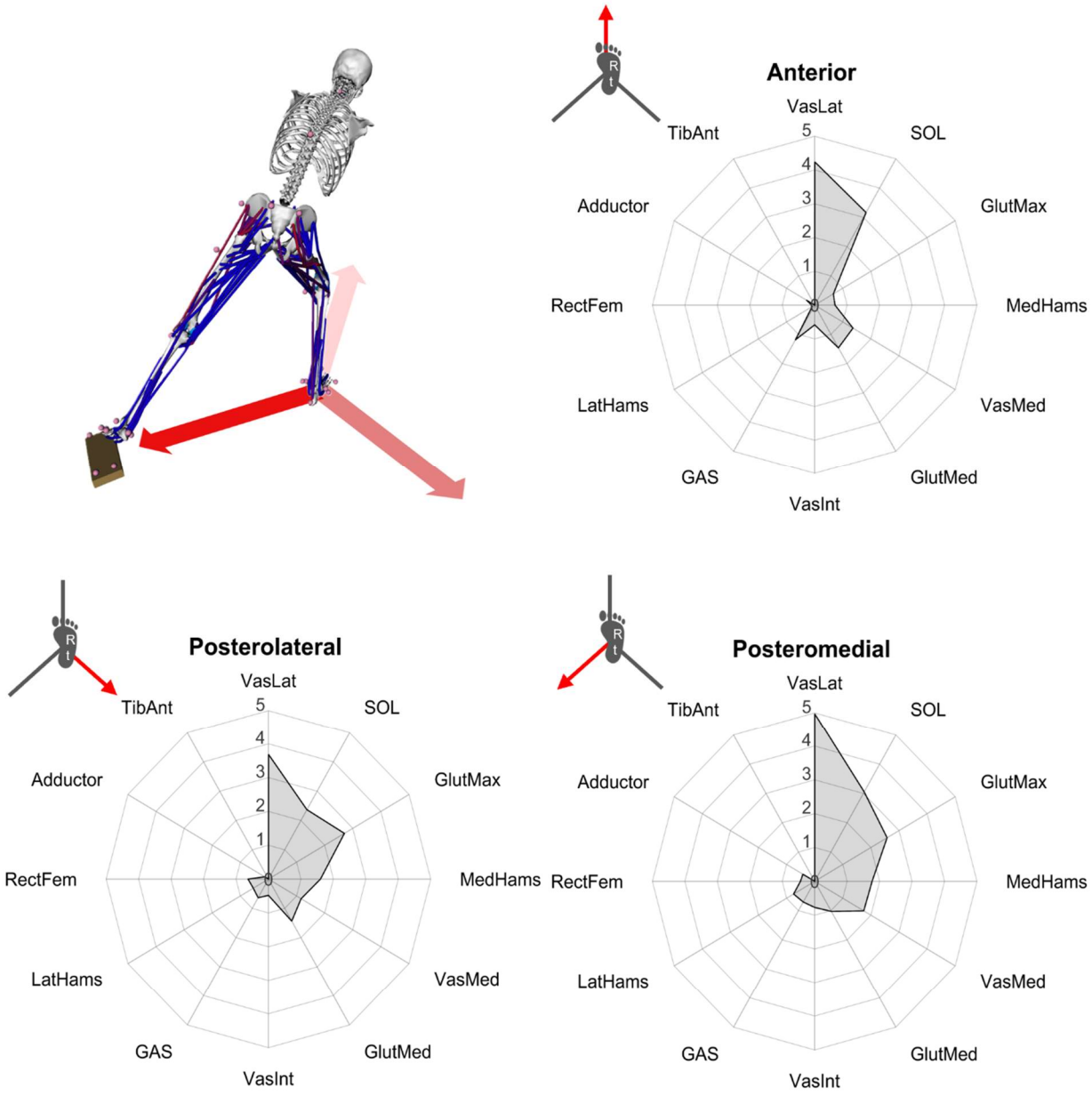


Figure 1. The spider plot for normalized peak muscle forces (N/BW) of 12 lower-limb muscles during Y-Balance Test in anterior, posterolateral, and posteromedial directions. VasLat: vastus lateralis, SOL: soleus, GlutMax: gluteus maximus, MedHams: medial hamstrings, VasMed: vastus medialis, GlutMed: gluteus medius, VasInt: vastus intermedius, GAS: gastrocnemius, LatHams: lateral hamstrings, RectFem: rectus femoris, TibAnt: tibialis anterior

References (Optional)

[1] Carlo J. De Luca, J Appl Biomech, 1997

Acknowledgements (Optional)

This work was supported by the Soonchunhyang University Research Fund and BK21 FOUR (Fostering Outstanding Universities for Research) (No. 5199990914048).

Session Category

Human Motion and Performance: Balance, Posture and Control

OA136-06

Predictive Neuromuscular Simulations Indicate That Spinal Control Does Not Solely Explain Steady-State Human Walking

Dr. Mark Price, Dr. Nidhi Seethapathi

Massachusetts Institute of Technology, Cambridge, MA, United States

Introduction

Neural control of locomotion is thought to be hierarchical, with spinal reflexes governing the steady-state rhythm and supraspinal input governing volitional control. While spinal reflex-based simulations replicate rhythmic walking patterns, it remains unclear if they replicate other aspects of steady-state walking, like foot placement control [1]. We hypothesize that supraspinal control is required for human-like foot placement control during steady-state walking.

Methods

We simulated walking with a 3D neuromuscular model implementing two controllers: (i) a Reflex-Control (RC) model using a spinal reflex network [2] optimized via CMA-ES, and (ii) a Supraspinal-Control (SC) using full-body state information [3] trained via reinforcement learning. For both models, we added sensorimotor noise to simulate variability in the locomotor patterns. We analyzed the foot placement control signatures, specifically the R^2 values for predicting the next foot placement from past CoM states, contrasted with an autoregressive baseline predicting future foot placement from past swing foot states.

Results

The RC model reproduced normative human joint kinematics. However, it did not exhibit human-like CoM-to-foot placement predictions in the fore-aft direction (~60% model vs. ~30% human) and lateral foot placement was never better predicted by CoM states than an autoregressive baseline, unlike humans [4]. In contrast, the SC model, despite poor reproduction of normative joint kinematics, better reproduced human foot placement control signatures; its CoM-to-foot placement predictions were human-like in both lateral (~85% model vs. ~80% human) and fore-aft (~40% model vs. ~30% human) directions. Like humans, its lateral foot placement was better explained by CoM states than an autoregressive baseline.

Discussion

Overall, we conclude that conventionally optimized reflex control is insufficient for explaining steady-state human walking, particularly for foot placement control. The RC

model's superior replication of normative joint mechanics suggests the importance of spinal control in regulating the rhythmic pattern of walking, while the SC model's more human-like foot placement control suggests that supraspinal control is involved in stabilizing steady state locomotion.

Images (Optional)

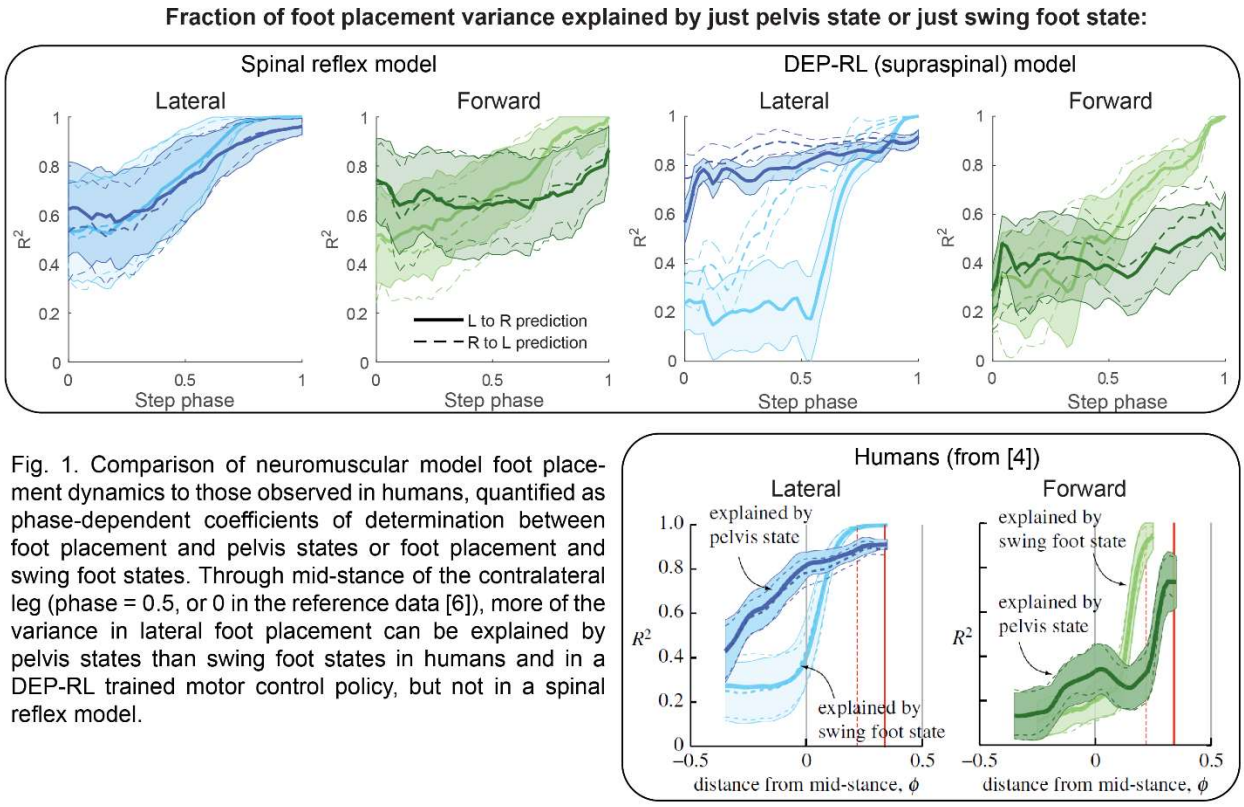


Fig. 1. Comparison of neuromuscular model foot placement dynamics to those observed in humans, quantified as phase-dependent coefficients of determination between foot placement and pelvis states or foot placement and swing foot states. Through mid-stance of the contralateral leg (phase = 0.5, or 0 in the reference data [6]), more of the variance in lateral foot placement can be explained by pelvis states than swing foot states in humans and in a DEP-RL trained motor control policy, but not in a spinal reflex model.

References (Optional)

[1] A de Comite & N Seethapathi, *PNAS*, 2025.

[2] T Geijtenbeek, J Open Source Software, 2019

[3] P Schumacher *et al.*, *arXiv*, 2023

[4] Y Wang & M Srinivasan, Biol Lett, 2014

Session Category

Human Motion and Performance: Balance, Posture and Control

OA137-02

Dose- and Time-Dependent Effects of Intramuscular Botulinum Neurotoxin on Passive Mechanical Properties of Skeletal Muscle

Dr. Albino G. Schifino PhD, Mr. Timothy McGinley MS, Dr. Benjamin Binder-Markey DPT, PhD

Drexel University, Philadelphia, PA, United States

Introduction

Botulinum neurotoxin (BoNT) is used clinically to relieve hypertonic or overactive muscles following neurological injuries. However, clinicians have begun to question the efficacy of BoNT, and recent studies have shown paradoxical increases in passive mechanics of injected muscles. However, it is unknown how dose and time affect whole muscle passive mechanics. Thus, the purpose of our investigation was to assess the dose-response of BoNT on skeletal muscle in mice at 8-weeks and 12-weeks post-injection. We hypothesize that BoNT will result in a dose-dependent reduction of muscle mass and altered *ex vivo* passive mechanics.

Methods

60 C57Bl6 mice (30M, 30F) were injected with either 2 Units (U)/kg, 4 U/kg, or 6U/kg of BoNT into the gastrocnemius. All injections were performed on the left limb, leaving the right limb as a control. The lateral gastrocnemius muscles were dissected and tested bilaterally at 8-weeks and 12-weeks post-injection. Passive muscle mechanical testing was performed *ex vivo*, muscles were attached to a 5N force transducer and incrementally stretched by 5% muscle length, to a length of 130%. All data are reported as mean ± SEM. Muscle characteristics, and stress-strain relationships were analyzed via a Mixed-Effect Model with a priori $\alpha < 0.05$.

Results

Muscle mass ratios were significantly lower following BoNT, and demonstrate a dose- and time-dependency (Fig.1A). Maximal stress was greater in muscles-injected with 2U, 4U, and 6U, respectively, compared to the contralateral control at 8-weeks and 12-weeks. Stress-strain curves indicate BoNT-injected muscles exhibited significantly higher stresses than control muscles, with a dose-response (2U<4U<6U, $p< 0.05$) (Fig. 1B).

Discussion

Our data demonstrates a dose- and time-dependent response to BoNT injection. Reductions in muscle mass support acute dose-dependent atrophy. BoNT caused alterations in passive muscle mechanics, with a dose-dependent increase in passive stresses that remained elevated after 12-weeks indicating sustained remodeling post BoNT injection.

Images (Optional)

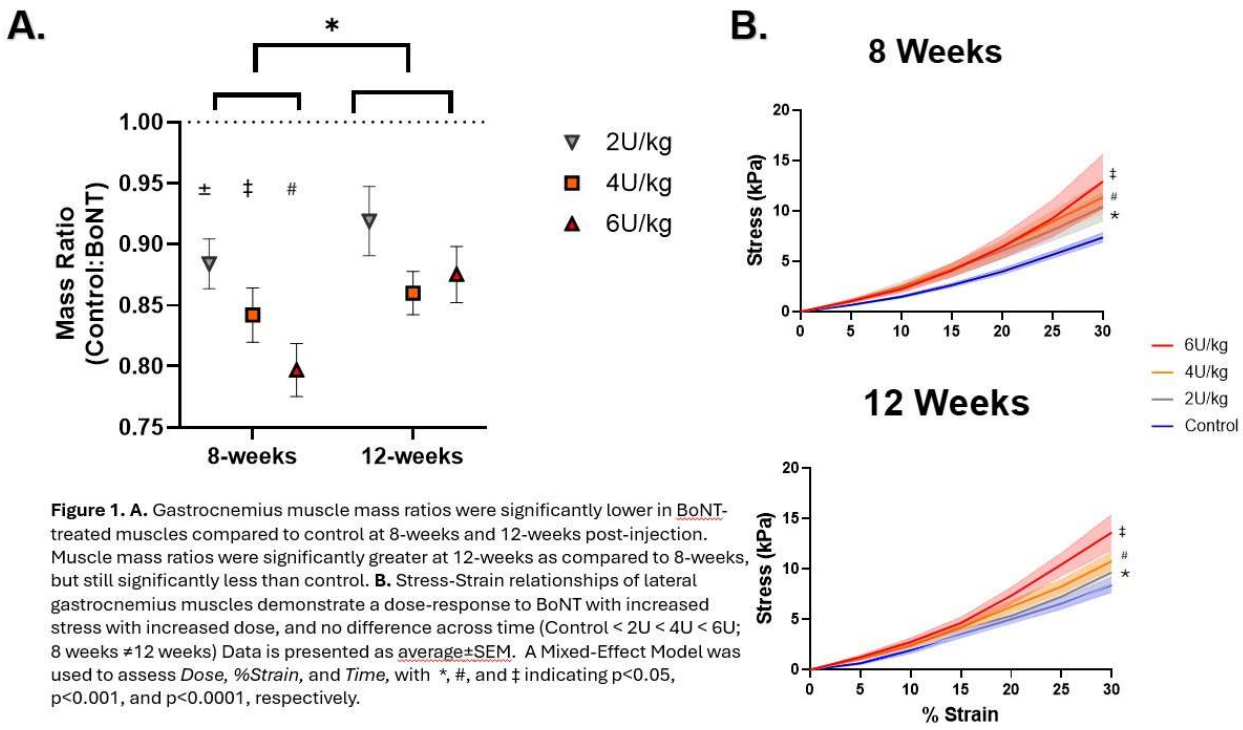


Figure 1. A. Gastrocnemius muscle mass ratios were significantly lower in BoNT-treated muscles compared to control at 8-weeks and 12-weeks post-injection. Muscle mass ratios were significantly greater at 12-weeks as compared to 8-weeks, but still significantly less than control. **B.** Stress-Strain relationships of lateral gastrocnemius muscles demonstrate a dose-response to BoNT with increased stress with increased dose, and no difference across time (Control < 2U < 4U < 6U; 8 weeks ≠12 weeks) Data is presented as average±SEM. A Mixed-Effect Model was used to assess *Dose*, *%Strain*, and *Time*, with *, #, and ‡ indicating $p<0.05$, $p<0.001$, and $p<0.0001$, respectively.

Acknowledgements (Optional)

Funding for this work was provided by The Hartwell Foundation

Session Category

Musculoskeletal Biomechanics: Tissues

OA137-03

Explaining Sarcomere Length Non-Uniformities in Single Myofibrils

Mr. Chris Tiessen, Dr. Walter Herzog

University of Calgary, Calgary, Alberta, Canada

Introduction

Sarcomere length non-uniformity (SLNU) is an inherent property of mammalian striated muscle that remains unexplained. SLNU refers to variations in sarcomere length within a given muscle preparation and can be found at all levels of muscle, including whole muscle and individual myofibrils. SLNUs in myofibril preparations are of particular interest, because in an isolated myofibril, in-series sarcomeres experience identical tensile force and yet SLNU persists. This suggests there may be inherent differences between adjacent sarcomeres within the same myofibril. Moreover, recent work from our lab suggests SLNUs in myofibrils may be deterministic; some sarcomeres are always 'long', and others are always 'short.' Thus, we hypothesize that SLNUs may be explained by inherent variation in contractile and elastic protein content in adjacent sarcomeres within the same myofibril.

Methods

We developed a unique immunolabelling system for the giant elastic protein titin that enables relative densitometric quantification of titin content in adjacent sarcomeres without compromising contractile or elastic force production in individual myofibrils (Figure 1). Isolated rabbit psoas myofibrils (n=6) were mounted on our myofibril testing system where passive and contractile forces were measured using optical nano-levers, and titin content was quantified using immunolabel densitometry relative to sarcomere length non-uniformities during isometric contraction and passive extension. Sarcomere length non-uniformities and titin content were reported as a z-score, and correlations compared using a Pearson's correlation test. Additionally, we are currently in the process of performing Volumetric Focused-Ion-Beam coupled Scanning Electron Microscopy (FIB-SEM) on tested individual myofibrils which may be able to provide absolute quantification of sarcomeric protein content in adjacent sarcomeres.

Results

We found significant inverse correlations between sarcomeric protein content and sarcomere length in both passive ($p=0.0074$) and active ($p=0.0203$) states. This confirmed

our hypothesis, suggesting sarcomeric protein content varies between sarcomeres, predicting SLNUs. Results remain in progress for FIB-SEM of individual myofibrils.

Discussion

SNLUs were recognized as early as the 1960s and have been used to explain various muscle properties including history-dependent muscle properties and descending limb sarcomere instability. For the first time, we confirm variation in sarcomeric protein content occurs within individual myofibrils and may explain this inherent property of striated muscle.

Images (Optional)

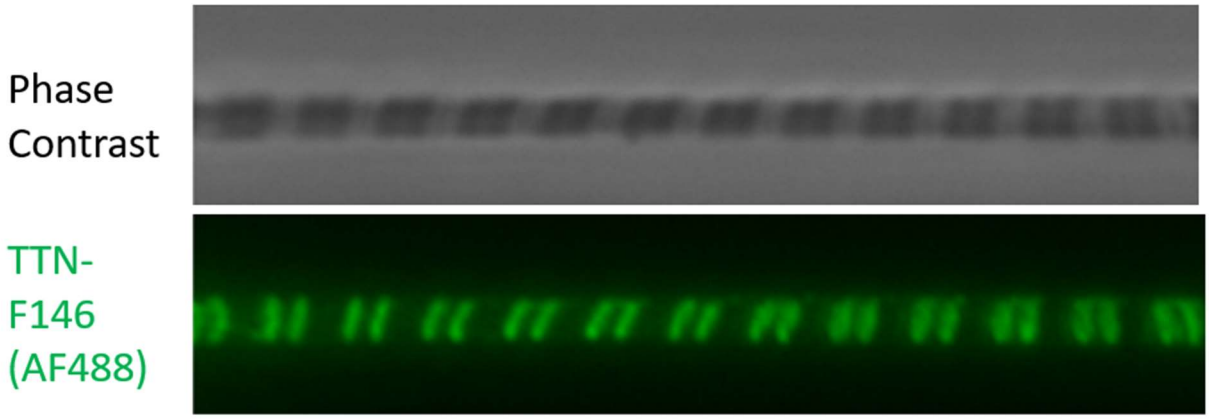


Figure 1: Single myofibril labelled using TTN-F146 for titin quantification in adjacent sarcomeres using immunolabel densitometry

References (Optional)

Session Category

Musculoskeletal Biomechanics: Tissues

OA137-04

Increasing Intramuscular Fluid Volume Increases Passive Tension in Mammalian Skeletal Muscle

Ms Samantha Falcone, Dr Richard Marsh, Mr Ofubofu Cairns, Dr Thomas Roberts

Brown University, Providence, RI, United States

Introduction

Experimental work in amphibian skeletal muscle [1] and modeling [2] have demonstrated that intramuscular fluid volume is an important determinant of passive force development during lengthening. This effect has been attributed to the interaction of intramuscular fluid and the collagenous extracellular matrix (ECM) that acts as a sleeve encapsulating muscle tissue [1]. However, this effect has not been investigated in mammalian skeletal muscle.

Methods

We exposed isolated mouse soleus and extensor digitorum longus (EDL) muscles to a graded series of hypotonic solutions to promote fluid uptake while measuring passive force development during lengthening, muscle mass, and 2D projected muscle area. We also separately investigated the effect of muscle tension on fluid uptake by comparing the masses of soleus muscles exposed to hypotonic solution and held at resting length to soleus muscles exposed to hypotonic solution and left slack.

Results

In 70%, 60%, 55%, and 50% hypotonic solutions, passive force in the soleus increased by 5.8±0.01%, 16.7±0.02%, 32.3±0.04%, and 64.8±0.06%, respectively. Passive forces in the EDL increased 8.5±0.03%, 64.3±0.19%, and 87.1±0.18% in 70%, 60%, and 55% hypotonic solutions, respectively. In both muscles, increases in passive force were accompanied by increases in mass and projected area. In our investigation of the effect of muscle tension on fluid uptake, we found that soleus muscles left slack and allowed to shorten when exposed to hypotonic solution gained much more mass than muscles held at resting length, suggesting that at resting length water uptake is limited by the buildup of hydrostatic pressure.

Discussion

These findings support the hypothesis that intramuscular fluid volume plays a key role in passive force development in mammalian skeletal muscle, consistent with previous

observations in amphibian muscle. The difference in fluid uptake and passive force development between the soleus and EDL muscles may reflect fiber-type differences in water permeability or in the ECM. Our data may be relevant for understanding *in vivo* alterations in human muscle properties resulting from exercise and passive stretching [3].

References (Optional)

[1] Sleboda & Roberts, Biol Lett, 2017.

[2] Gindre *et al.,* J Mech Behav Biomed Mater, 2013.

[3] Willwacher *et al.,* Physiol Rep, 2020.

Session Category

Musculoskeletal Biomechanics: Tissues

OA137-05

Impairments in Paraspinal Muscle Specific Force Production Following an Experimental Intervertebral Disc Injury in a Rodent Model

Dr Josh Briar PhD, Dr Alex Chan DVM, Ms Abbey Reid BSc, Ms Jana Michaud, Mr Adam Bui MSc, Ms Laura Blackburn BSc, Ms Courtney Phillips MSc, Dr Stephen Brown PhD

University of Guelph, Guelph, Ontario, Canada

Dr Josh Briar

Introduction

Paraspinal muscle dysfunction has been linked to chronic low back pain (LBP) [1], but the causative relationship between LBP and muscle dysfunction remains elusive. An experimentally induced intervertebral disc (IVD) injury animal model has been used to study corresponding structural and passive mechanical changes to the paraspinal muscles [2]. However, to date, there has been a lack of investigation into the influence of this experimental model of IVD injury on the active contractile properties of the paraspinal muscles.

Methods

31 male Sprague-Dawley rats were randomly divided into 4 groups: 15-week sham (n=8), 15-week IVD puncture (n=9), 10-week IVD puncture (n=7), 5-week IVD puncture (n=7). All rats underwent a retro-peritoneal incision and the L2-L3 and L4-L5 levels of the spine were identified. Animals in the puncture groups underwent an approximate 2mm penetration into each IVD of interest, while the sham group did not. Animals were sacrificed at different time points (5, 10 or 15 weeks) post-surgical intervention, and the contralateral multifidus and longissimus muscles were excised. Twenty fibres were isolated from each muscle and underwent active contractile testing in a pCa 4.5 solution for maximal activation. Each muscle's mean and coefficient of variation (CV) for specific force were calculated and compared between groups.

Results

A main effect of surgical group was observed for mean specific force ($F=5.284$, $df=3$, $p=0.003$, Fig 1); highlighting that it was significantly higher in the sham group than the week 5 ($p=0.018$), week 10 ($p<0.001$), and week 15 surgical groups ($p=0.002$). A main effect of

surgical group was observed for specific force CV ($F=3.77$, $df=4$, $p<0.01$); highlighting that the CV was significantly lower in the sham group than the 10-week injury group ($p=0.03$) and 15-week injury group ($p=0.04$).

Discussion

The current work highlights that following an induced IVD injury there is a significant reduction in force generating capacity of the surrounding paraspinal muscle fibres. Furthermore, the elevated specific force CV in the IVD injury groups reflects increased heterogeneity in force production capabilities of the paraspinal muscles, underscoring potential contractile impairments.

Images (Optional)

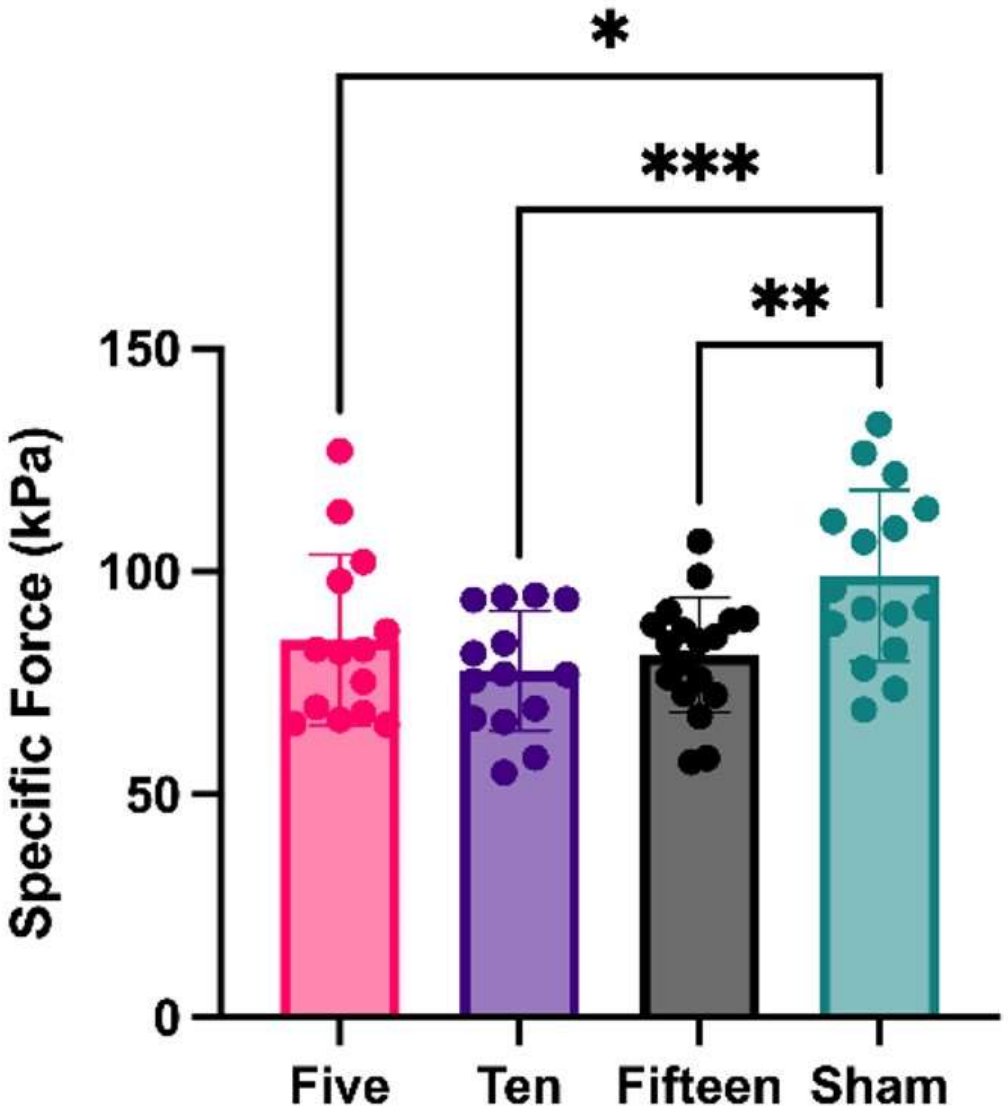


Figure 1: Mean specific force between surgical groups.

References (Optional)

[1] Noonan AM et al. (2021). JOR Spine 4, e1171.

[2] Brown SHM et al. (2011). Spine 36, 1728-1736.

Session Category

Musculoskeletal Biomechanics: Tissues

OA138-01

Curvature Regulate Cell Migration and Nuclear Dynamics

Mr. Chia-Chun Yeh, Dr. Pen-hsiu Grace Chao

National Taiwan University, Taipei, Taiwan, Taiwan

Introduction

Cells in vivo reside in complex topographies including cell-scale curvatures [1]. Recent work has identified “curvotaxis” where cells migrate in response to curvature cues [2, 3]. However, these systems often impose mixed curvature gradients, obscuring the effect of well-defined curvatures. Here, we aim to clarify the effects of curvature by confining individual cells in C-shaped microgrooves and characterize their behaviors.

Methods

Micromolded agarose walls [4] on fibronectin-coated coverslips impose curvature on mesenchymal stem cells in microgrooves. The patterns were 10 μm in width, with inner radii of 15 and 20 μm and a 270° arc span. For live-cell imaging, cells labeled with SpyDNA were seeded into the microgrooves. Time-lapse micrographs were acquired every 5 minutes for 12 hours in a stage top incubator. Nuclear shape and location were tracked and the shape changes were quantified by the dynamic nuclear aspect ratio index, which is the sum of frame-to-frame changes in nuclear aspect ratio (NAR).

Results

Cells conformed to the pattern with asymmetrical nuclear profile against the inner edge of the curve, potentially formed by the stress fibers above the nucleus (Fig. A). Live imaging found higher curvature increased cell migration speed and dynamic nuclear shape changes, which exhibit strong correlations (Fig. B & C).

Discussion

In this study, we found pattern curvature induced strong actin arcs that created asymmetric compression on the nucleus against the concave edge. Ongoing live imaging found the dynamic actin retrograde flow from the convex edge drove this nuclear movement (data not shown), which is confirmed by the dynamic nuclear shape changes. Liu et al has found inverse correlation between migration speed and curvature at a smaller scale (1/50-100 μm versus 1/15-20 μm in this study [3]). Potentially due to cell type and substrate differences, few actin fibers were observed in their system. Current studies are investigating a wider range of curvature as well as the role of actin structures on wavy cell migration.

Images (Optional)

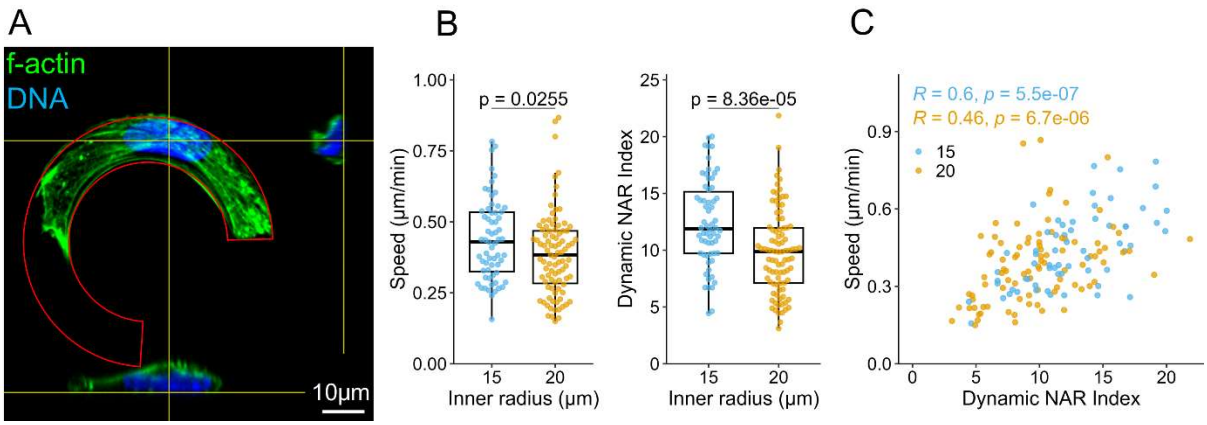


Figure (A) Confocal micrograph of MSC with 20 μm inner radius. (B) Effects of curvature on migration speed and nuclear shape dynamics. (C) Migration speed correlate with nuclear shape changes.

References (Optional)

[1] Assoian RK+, Open Biol, 2019

[2] Callens SJP+, Biomaterials, 2020

[3] Liu Y+, ACS Applied Materials & Interfaces, 2024

[4] Joo S+, BioChip Journal, 2018

Acknowledgements (Optional)

This study was supported by the Taiwanese National Science and Technology Council (NSTC 114-2221-E-002-091-MY3, 114-2923-E-002-017-MY3, and 114-2122-M-001-002).

Session Category

OA138-02

Developing a Novel Genetically Encoded Molecular Tension Sensor

Dr. Takumi Saito

The University of Osaka, Toyonaka, Osaka, Japan

Introduction

Mechanical forces play a pivotal role in regulating cellular behavior through mechanotransduction. Although numerous molecules related to mechanotransduction have been characterized, and their signaling pathways have been identified, the mechanisms of how these molecules and molecular complexes transmit mechanical forces during cellular mechanotransduction, in living cells, are still unclear due to technical limitations. To overcome the limitations, we developed a compact and robust molecular tension sensor based on a coiled-coil structure, so-called “coiled-coil tension sensor” (1). The coiled-coil tension sensors open in all or none fashion when they are pulled by forces above a threshold pre-calibrated by optical tweezers (Fig. 1A).

Methods

To detect whether the CC sensors open or close, we used a split-GFP readout (1, 2). The CC tension sensors with the GFP11 linker were genetically inserted into several regions of formin Cdc12 by the CRISPR-Cas9 gap-repair system established by our group (4). As a representative case, the CC sensors were inserted between two formin homology domains (FH1 and FH2) (Fig. 1B).

Results

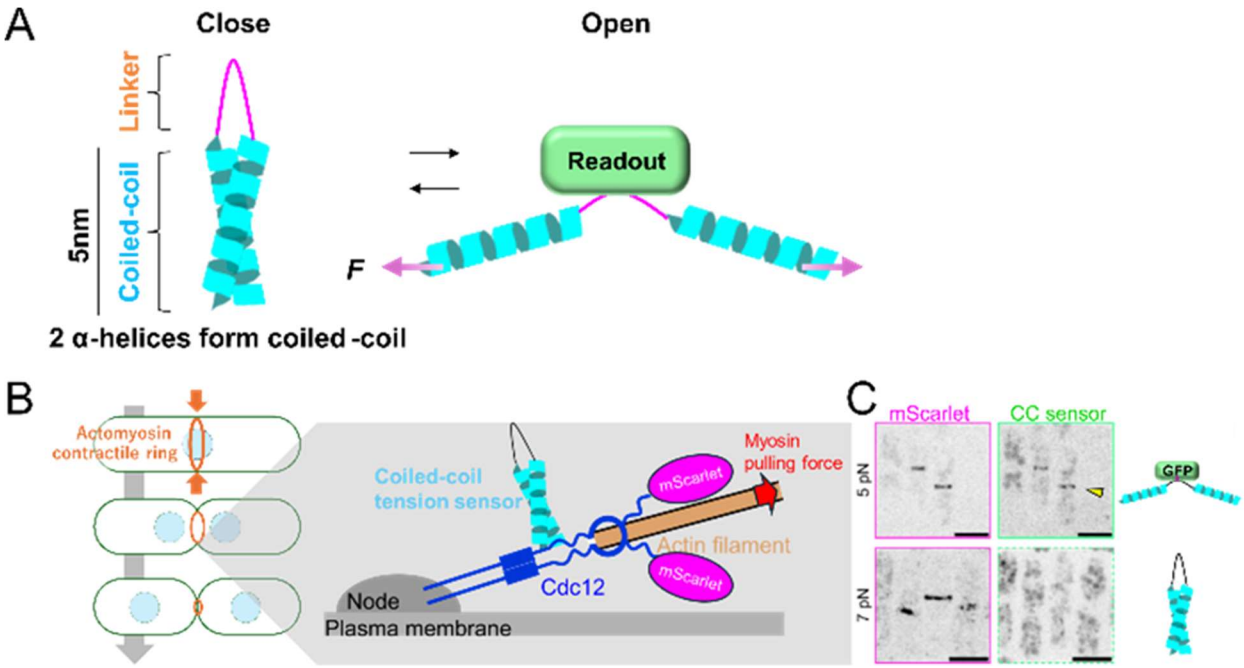
At the sensor insertion site, 5 pN sensors opened and exhibited fluorescence, whereas 7 pN sensors remained closed (Fig. 1C) (2). This result indicates that the forces between two FH domains are in the range of 5-7 pN. In addition to this insertion site, the CC sensors screened the force level along Cdc12, resulting in ~ 6 pN forces except in the dimerization domain.

Discussion

The coiled-coil force sensors revealed mechanisms of force transmission along formin Cdc12 during cytokinesis, as the representative results of force measurements on many other proteins (vinculin, spectrin, and endocytic proteins). Compared to FRET-based tension sensors, the CC tension sensors enable all-or-none binary force measurements

with a single fluorescent protein or luminescence, resulting in small, high S/N, and are capable of multiplex imaging. Thus, the CC sensors allow to quantify not only intramolecular force levels but also the fraction of molecules under tension, meaning that this approach offers a robust alternative for probing mechanotransduction at the molecular scale.

Images (Optional)



References (Optional)

1. Ren, Y., J. Yang, Saito, T. et al . 2025. *bioRxiv*. 2025.01.16.633409.

2. Saito, T. et al . 2025. *bioRxiv*. 2025.05.14.653946.

Acknowledgements (Optional)

We thank Yale West Campus Imaging core for their technical support for microscopy.

Session Category

Cell Biomechanics: Mechanobiology

OA138-03

Tomographic Shearmetry of Dynamic Flows at Cell Surfaces Using Nanoprobes

Ms Arianna Giannetti[1], Mr Marcello Bonetti[2], Ms Joni Frederick[1], Ms Alessia Castagnino[1], Mr Thierry Gacoin[2], Mr Jongwook KIM[2], Mr Abdul Barakat[1]

[1]LadHyX Ecole Polytechnique, Palaiseau, France, France. [2]PMC, Ecole Polytechnique, Palaiseau, France, France

Introduction

Mechanical forces due to fluid flow, particularly fluid dynamic shear stress, are known to play a crucial role in regulating a wide array of cellular functions. It is commonly assumed that adherent cells such as vascular endothelial cells (ECs) have no impact on the flow field. Computational simulations, however, suggest that EC topography can impact the local hydrodynamic environment, leading to significant shear stress gradients (Barbee,Am J Physiol,1995). Experimentally validating these computational predictions has remained elusive because conventional techniques such as particle image velocimetry (PIV) are very noisy due to inaccuracies in near-wall velocity measurement (Lafaurie,Biomed Microdev,2016).

Methods

Here $LaPO_4$:Eu nanorods serve as shear stress probes through their shear-induced alignment and polarized photoluminescence (Fig. 1A) (Kim,Nat Commun,2021). Spectroscopic analysis of their collective orientation enables tomographic mapping of the local shear stress on the surfaces of human umbilical vein ECs (HUVECs). In conjunction with nanorod-based shearmetry, atomic force microscopy (AFM) is used to characterize the 3D topography of ECs. To complement the nanorod-based shearmetry measurements, computational fluid dynamics (CFD) simulations are conducted on the AFM surfaces using COMSOL Multiphysics 5.6 to relate cellular topography to the local wall shear stress on the cellular surface.

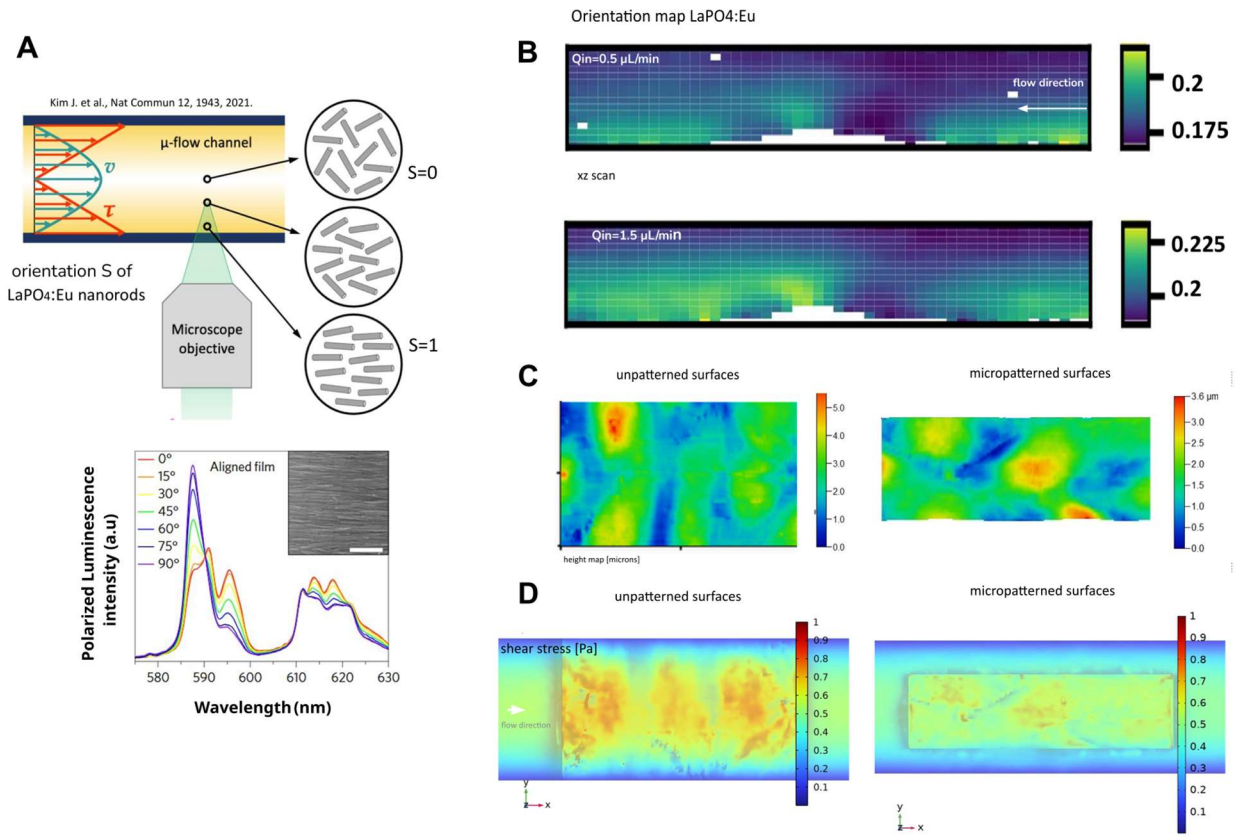
Results

Preliminary results on spatial mapping of nanorod orientations on single isolated ECs indicate increased nanorod alignment with flow and a higher nanorod order parameter (S) at the apex of the cell compared to the surrounding cell-free regions (Fig. 1B). AFM measurements demonstrate that restricting EC spreading by culturing the cells on 15 μm-wide adhesive line patterns elicits cell elongation and significant height reduction (Fig. 1C). CFD simulations on ECs cultured on either unpatterned or patterned substrates reveals that surface undulations create cell-scale shear stress variations that are attenuated by cell height reduction on the line-patterned surfaces (Fig. 1D).

Discussion

The present results suggest that nanorod-based tomographic shearmetry can potentially enable experimental mapping of shear stress levels on EC surfaces. Future work will focus on such mapping and on comparing the measurements to CFD results. Additionally, efforts will aim to correlate local shear stress distributions with functional cellular responses such as intracellular calcium mobilization.

Images (Optional)



Session Category

Cell Biomechanics: Mechanobiology

OA138-04

Magnetic Stiffening Cryogels With Hierarchical Alignment for Mechano-Modulation of Mesenchymal Stromal Cells

Dr Wen Chen

AO Research Institute Davos, Davos, Graubünden, Switzerland

Introduction

Modulation of cells *in vitro* and/or *in vivo* plays an important role in tissue engineering and regenerative medicine. In our body, cells receive biophysical cues that mimic cellular microenvironment, including but are not limited to, topography, matrix stiffness and viscoelasticity, which can manipulate cell behaviors. [1] Furthermore, cells mechanically respond to their local microenvironment through dynamic interactions shaping biological functions. These dynamic behaviors are challenging to replicate in matrices for in vitro studies. This motivated us to develop 4D anisotropic *in vitro* models with tunable stiffness for regulating cell behavior, organization and mechanotransduction (**Figure 1A**).

Methods

Anisotropic cryogels were prepared by mixing boronate-functionalized gelatin with polydopamine-functionalized magnetic-responsive nanoparticles (**Figure 1B**) under magnetic field, followed by freeze-drying. The anisotropic structures were imaged by micro-CT. The mechanical properties of magnetic-stiffening were quantified by magneto-rheometer. The human mesenchymal stromal cells (hMSCs) at passage 5 were seeded on top of the anisotropic cryogels to study the effects of anisotropy and magnetic-stiffening properties on hMSCs organization and mechanotransduction under magnetic field.

Results

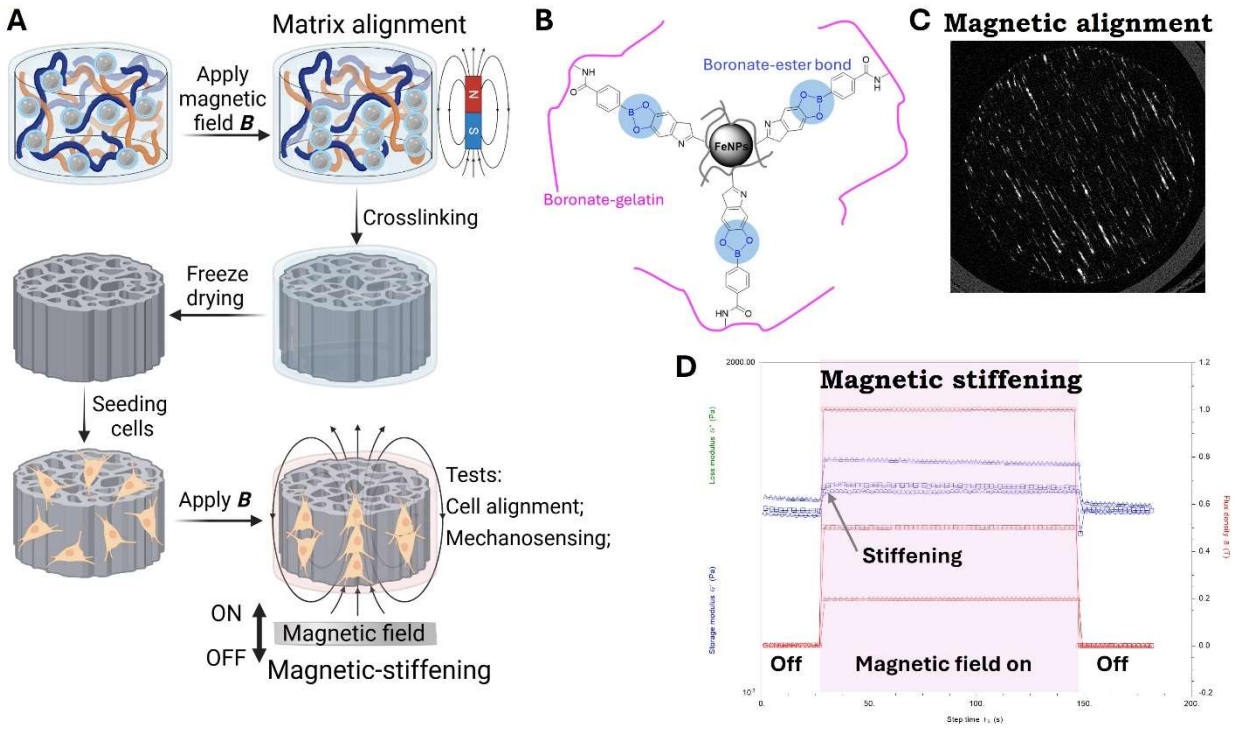
Anisotropic cryogels were prepared by aligning the magnetic nanoparticles in the hydrogel network, followed by freeze-drying. The anisotropic structures were imaged by using micro-CT (**Figure 1C**). Moreover, under magnetic field, the storage modulus *G'* of cryogels at a

concentration of 6 mg/mL magnetic nanoparticles and 30 mg/mL gelatin increased from 1600 Pa to 1700 Pa at a field intensity of 200 mT (**Figure 1D**).

Discussion

We developed anisotropic hydrogels with magnetic-stiffening properties. We are currently investigating the hMSCs behaviors in this 4D in vitro model. This approach will allow us to examine how anisotropy and magnetically tunable stiffness influence cell organization and mechanotransduction *in situ*. Insights gained from these studies will inform the design principles of scaffolds aimed at directing cell fate.

Images (Optional)



References (Optional)

[1] Wan, X. et al. Advanced Functional Materials, 2021.

Acknowledgements (Optional)

We acknowledge the MEDICI project funded by AO Research Institute Davos.

Session Category

Cell Biomechanics: Mechanobiology

OA138-05

The Role of Focal Adhesion Kinase Signaling in Response to Dynamic Cyclic Loading Changes with Hierarchical Collagen Fiber Formation in Engineered Ligaments

Dr Akshay Bhatt PhD, Dr. Jennifer Puetzer PhD

Virginia Commonwealth University, Richmond, Virginia, United States

Introduction

Hierarchically organized collagen fibers provide strength to tendons and ligaments; yet regenerate poorly after injury.[1] Understanding how cells form these fibers is critical for enabling regeneration. Mechanical cues, including passive cellular contraction and dynamic external loads, drive fiber development, but how is largely unknown. Previously, we developed a static system that guides ACL fibroblasts to produce hierarchical fibers over 6 weeks [1] and have shown that dynamic cyclic stretch improves maturation.[2] Using our static system, we found focal adhesion kinase (FAK) signaling is critical during fibril formation, but not fiber or fascicle development. Here, we evaluate whether FAK's role changes with dynamic load.

Methods

Neonatal bovine ACL fibroblasts and collagen were mixed to form constructs at 20mg/ml collagen and 5×10^6cells/ml and clamped into a tensile-bioreactor (Fig.1A).[1,2] During fibril (0-2wks), fiber (2-4wks), or fascicle (4-6wks) formation, constructs were loaded with an established intermittent cyclic loading regime (Fig.1B)[2] and FAK was inhibited with 10μM PF-573228 (FAK-I). To compare FAK's role during dynamic-load vs. passive-static cues, one group had FAK-I for 3hrs during dynamic loading only(FAK-I 3hr), and another group had FAK-I for the full 2wks to block dynamic and static signals (FAK-I ET, Fig.1C). Post-culture, collagen organization, composition, and tensile properties were evaluated.[1,2]

Results

At 2wks, FAK-I ET disrupted fibril formation, while FAK-I 3hr still formed aligned-fibrils, indicating passive cellular contraction is critical to fibril formation. By 4 and 6wks, both FAK-I groups formed fibers and early-fascicles like controls, suggesting other mechanosensors drive later maturation (Fig.1D). FAK-I reduced DNA at each timepoint, while its effect on GAG, LOX activity, and collagen varied depending on organization (Fig.1E). Particularly, FAK-I during fiber and fascicle formation significantly increased collagen concentration with loading, suggesting an injurious response or a shift in mechanotransduction. Despite increased collagen concentration and organization at 4 and

6wks, FAK-I largely reduced elastic properties (Fig.1F), but had little effect on toe-region properties.

Discussion

Collectively, this suggests integrin-mediated adhesions are critical to sensing dynamic stretch, but this role decreases as hierarchical fibers develop. Other mechanosensors may have a more prominent role beyond the fibril level.

Images (Optional)

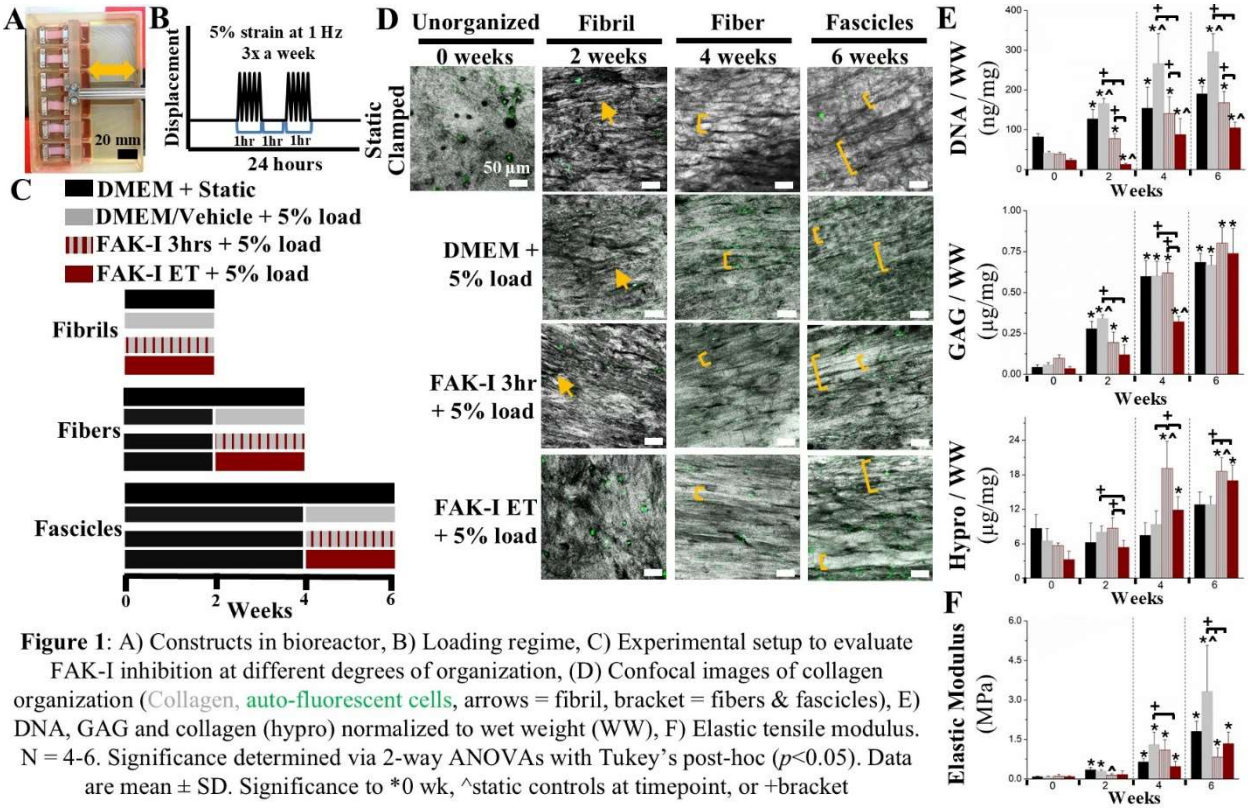


Figure 1: A) Constructs in bioreactor, B) Loading regime, C) Experimental setup to evaluate FAK-I inhibition at different degrees of organization, (D) Confocal images of collagen organization (Collagen, auto-fluorescent cells, arrows = fibril, bracket = fibers & fascicles), E) DNA, GAG and collagen (hypro) normalized to wet weight (WW), F) Elastic tensile modulus. N = 4-6. Significance determined via 2-way ANOVAs with Tukey's post-hoc (p<0.05). Data are mean ± SD. Significance to *0 wk, ^static controls at timepoint, or +bracket

References (Optional)

1.Puetzer+Biomat 2021; 2.Troop+Acta Biomater 2024

Session Category

Cell Biomechanics: Mechanobiology

OA139-02

Cell Dynamics Driven by Substrate Elasticity-Topography Interplay for Microfluidic Applications

Prof. Hiromi Miyoshi PhD[1], Dr. Tomoko G. Oyama PhD[2], Dr. Kotaro Oyama PhD[2], Dr. Mitsumasa Taguchi PhD[2]

[1]Tokyo Metropolitan University, Hachioji, Tokyo, Japan. [2]National Institutes for Quantum Science and Technology (QST), Takasaki, Gunma, Japan

Introduction

Mechanical cues encoded in the cell-substrate interface critically regulate cell adhesion, migration, and fate decisions. We developed gelatin hydrogels that retain native adhesion motifs and span physiologically relevant stiffness ranges, and previously showed that substrate elasticity and topography influence cell morphology and actin organization [1]. Here, we focus on how the interplay between substrate elasticity and topography governs cancer cell motility signatures and lineage-associated signaling responses.

Methods

We examined fibroblast lines, breast cancer cell lines, and mesenchymal stem cells to evaluate adhesion and motility. Gelatin substrates were fabricated with stiffnesses of 10–350 kPa and topographies of micrometer-scale holes, pillars, or flat surfaces. Adhesion and migration were quantified by time-lapse label-free imaging and automated tracking [2]. Because ERK regulates proliferation–differentiation switches, ERK activity under distinct elasticity–topography conditions was evaluated using a FRET sensor [3].

Results

Cancer cells exhibited lower adhesion rates on stiffer substrates, in contrast to non-cancerous epithelial cells, which adhered more strongly as stiffness increased within the physiologically and pathologically relevant 5–200 kPa range. These opposing stiffness responses enabled discrimination of metastatic versus non-metastatic cells through label-free dynamic parameters. Mesenchymal stem cells exhibited stiffness- and topography-sensitive regulatory modes relevant to differentiation control. Specifically, pillar structures promoted more dynamic motility, with this effect being more pronounced on softer 50 kPa gels than on stiffer 320 kPa gels. Correlated with these changes in motility, elasticity–topography combinations also modulated ERK signaling in mesenchymal lineage cells: pillar structures induced dynamic temporal changes in ERK activity, whereas hole structures maintained ERK activity at low levels.

Discussion

Our results demonstrate that cell dynamics relevant to cancer identification and stem-cell lineage control arise from the interplay between substrate elasticity and topography, partly via migration control. It could reflect principles shared with soft-tissue and cardiovascular biomechanics. Gelatin gels spanning physiological–pathological stiffness ranges provide mechanically instructive environments suitable for microfluidic label-free diagnostic and culture applications.

References (Optional)

[1] Oyama TG et al., Mater. Des, 2025.

[2] Endo S et al. PLoS ONE 20, 2025

[3] Lin S, Life Sci Alliance, 2021

Acknowledgements (Optional)

This work was supported by JSPS KAKENHI (JP24K01998), Tokyo Metropolitan Government Advanced Research (R2-2), and JST A-STEP (JPMJTR22U7)

Session Category

Cardiovascular/Cardiorespiratory Biomechanics: Materials and Devices

OA139-03

Tunable Soft Robotic Pulmonary Artery Banding Device for the Management of Congenital Heart Disease

Dr. Yellappa Palagani[1,2,3], Dr. Luca Rosalia[4], Mr. Amit Sharir[1,3], Dr. Perry S. Choi[1,2], Dr. Yoshikazu Ono[1,3], Dr. Masafumi Shibata[1], Dr. Sayar Munshi[1,2,3], Dr. Alexander K. Reed[1,3], Prof. Mark A. Skylar-Scott[2,3,4], Prof. Michael R. Ma[1,2,3]

[1]Department of Cardiothoracic Surgery, Stanford University, Stanford, CA, United States. [2]Maternal & Child Health Research Institute, Stanford University, Stanford, CA, United States. [3]Cardiovascular Institute, Stanford University, Stanford, CA, United States. [4]Department of Bioengineering, Stanford University, Stanford, CA, United States

Introduction

Pulmonary artery banding (PAB) is a widely used surgical technique for treating neonates and infants with congenital heart disease to limit pulmonary over-circulation and retrain a deconditioned ventricle. However, the static nature of traditional PABs often necessitates additional surgeries for readjustment as patients grow, and rely on indirect measures to assess cardiac function. To address this gap, we present a tunable pulmonary artery band (tPAB) that allows remote adjustment and provides real-time, non-invasive hemodynamic monitoring.

Methods

The tPAB was developed with a 3D-printed soft robotic actuator and a capacitive sensor, customized to fit patient-specific anatomy. The actuator regulates the narrowing of the pulmonary artery (PA) through fluidic actuation, while a capacitive sensor continuously monitors the pulmonary hemodynamics. First, we characterized the actuation and sensing abilities of the band via *ex vivo* testing using a patient-specific pediatric cardiac simulator. *In vivo* experiments were then conducted in three- and six-month-old porcine models to evaluate tPAB effectiveness across various degrees of actuation. PA pressure changes measured by the tPAB were confirmed with Edward pressure transducer and apical epicardial echocardiography.

Results

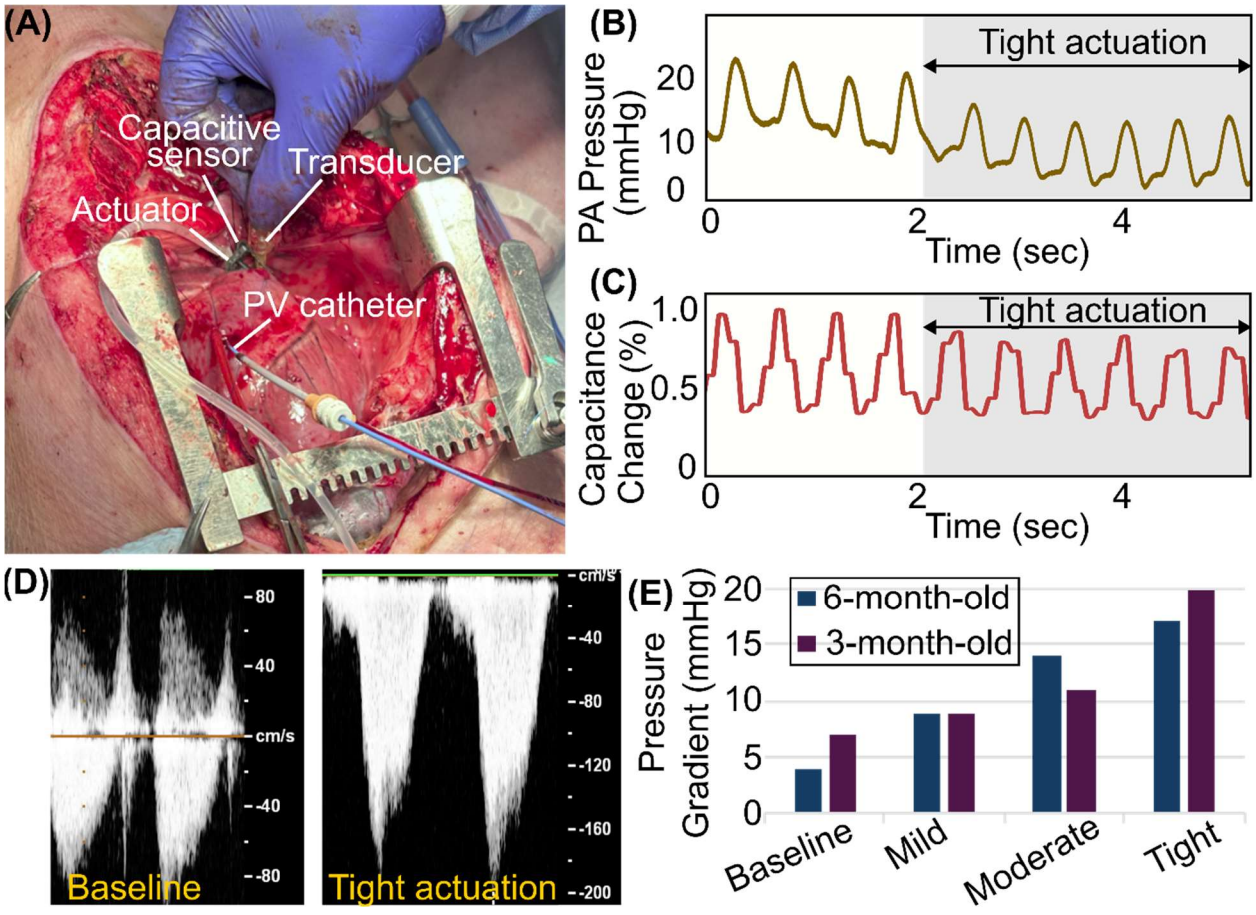
In vivo pressure gradients increased with tPAB actuation. Pressure gradients measured 4, 9, 14, and 17mmHg in the 6-month-old porcine model and 7, 9, 11, and 20mmHg in the 3-month-old porcine model at baseline (0mL), mild (0.50mL), moderate (0.75mL) and tight

(1.0mL) actuation levels, respectively, as confirmed via continuous wave Doppler imaging. These findings demonstrate the significant impact of band actuation on arterial dynamics. Capacitive sensor readings from tPAB closely matched transducer measurements, showing decreased distal PA pressure during actuation. *Figure (A)* shows the tPAB procedure; *(B, C)* show distal PA pressure changes at baseline and tight actuation via transducer and capacitive sensor; and *(D, E)* show pressure gradients in porcine models.

Discussion

The results indicate that precise actuation of the tPAB enables accurate constriction of the PA, while band effectiveness and pulmonary pressure can be monitored non-invasively. By integrating remote adjustment with continuous hemodynamic monitoring, tPAB offers a novel approach to PA banding that aims to reduce the need for repeat surgeries and improve outcomes in congenital heart disease.

Images (Optional)



Acknowledgements (Optional)

This work was supported by the Stanford Maternal & Child Health Research Institute (MCHRI).

Session Category

Cardiovascular/Cardiorespiratory Biomechanics: Materials and Devices

OA139-04

Understanding Extracorporeal Membrane Oxygenation and Impella Synergy Through a Patient-Specific Hybrid Mock Circulatory Loop

PhD Gasparotti Emanuele[1], PhD Emanuele Vignali[1], MD Dorela haxhiademi[2], Prof Simona Celi[1]

[1]BioCardioLab, Bioenegineering Unit, Fondazione Monasterio, Massa, Tuscany, Italy. [2]Anesthesiology and Intensive Care Unit, Fondazione Toscana Gabriele Monasterio, Massa, Tuscany, Italy

Introduction

Cardiogenic shock is a life-threatening condition marked by a severe reduction in cardiac output, often caused by myocardial or coronary dysfunction. The resulting hypoperfusion critically limits oxygen delivery to supra-aortic vessels, compromising cerebral circulation. Mechanical circulatory support devices such as ExtraCorporeal Membrane Oxygenation (ECMO) and the transvalvular Impella pump can temporarily restore systemic flow [1], yet their hemodynamic impact, including increased left ventricular loading, remains to be clarified. To investigate these mechanisms, this work presents in-vitro experiments designed to investigate the performance of ECMO, Impella, and their combined configuration (ECMella) under different shock conditions.

Methods

A hybrid-mock-circulatory-loop (hMCL) (Fig_a) was developed to reproduce physiological and pathological aortic hemodynamics [2]. A piston pump generated aortic flow profiles, while hybrid pressurized chambers implemented systemic boundary conditions. A patient-specific aortic phantom, including ascending aorta, supra-aortic branches, descending aorta, and iliac arteries, was manufactured from CT imaging. An ECMO pump delivered arterial return through the right iliac, and an Impella device was positioned across a biological aortic valve prosthesis. An experimental campaign (63 configurations) was performed by varying shock severity (30–70% stroke-volume reduction), ECMO flow (0–6 L/min), and Impella speed (Off, P2, P4). Hemodynamic metrics included supra-aortic flow restoration, afterload and left ventricular (LV) loading.

Results

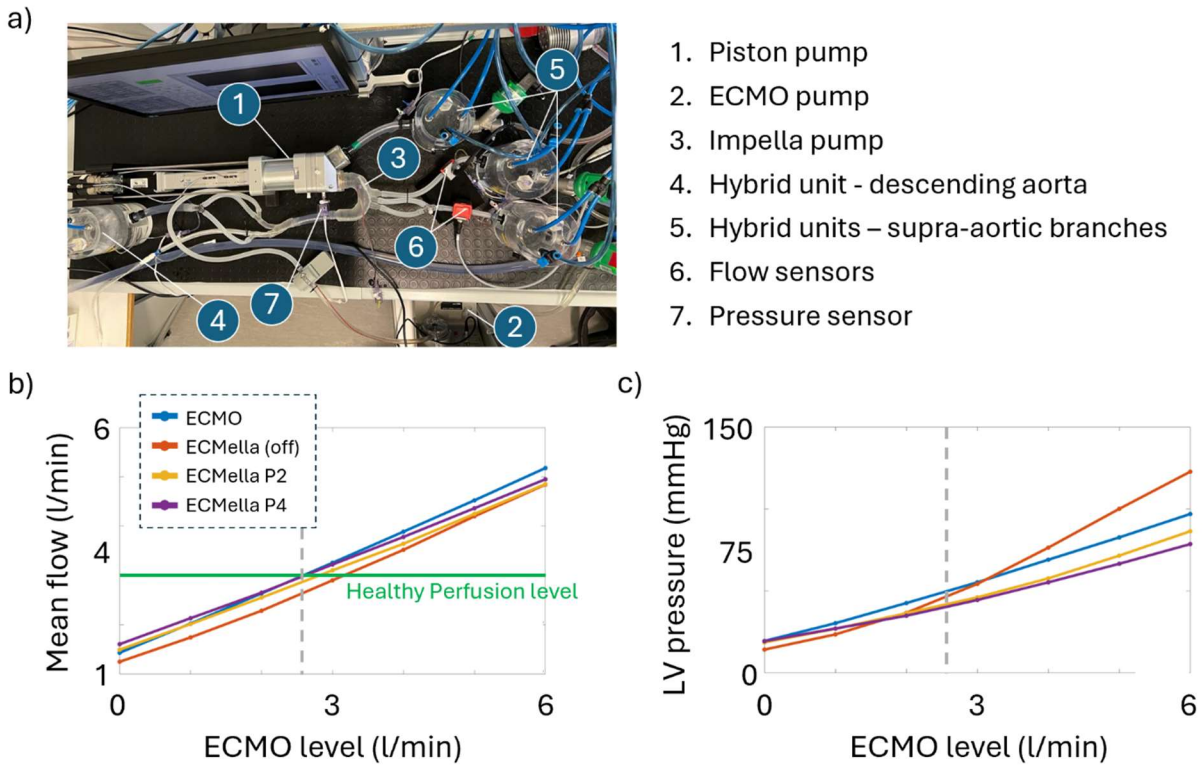
ECMO alone restored supra-aortic healthy perfusion (Fig_b) in all shock conditions, but produced afterload elevation and increased LV pressure (Fig_c). Impella alone reduced LV pressures but was unable to restore physiological supra-aortic flow at any shock level. The ECMella configuration showed synergistic behavior: perfusion restoration occurred at

lower afterload than ECMO alone, and LV unloading depended on Impella speed. At P4, Impella compensated cannula-induced regurgitation and prevented LV overload even at high ECMO flows.

Discussion

The hMCL enabled controlled, reproducible assessment of ECMO-Impella interactions under cardiogenic shock. ECMO ensured perfusion recovery but increased ventricular loading, whereas Impella provided unloading without adequate systemic flow. ECMella offered the most balanced performance, restoring perfusion while mitigating afterload and LV pressure. The platform supports optimization of ECMella strategies and informs clinical decision-making in shock management.

Images (Optional)



References (Optional)

[1] Emanuele Vignali et al., Phys. Fluids, 2023

[2] Emanuele Gasparotti et al., Biomech. Model. Mechanobiol., 2025

Session Category

OA139-05

A Data-Informed Growth and Remodeling Framework for Vein Graft Adaptation Following Coronary Artery Bypass Graft Surgery

Mr. Lazaros Papamanolis[1,2], Ms. Divya Adil[1,2], Dr. Ruizhi Wang PhD[3], Dr. Guoxiang Grayson Tong PhD[1,2], Dr. Elbert E. Heng MD[2,4], Dr. Jay Humphrey PhD[3], Dr. Alison Lesley Marsden PhD[1,2]

[1]Department of Bioengineering, Stanford University, Stanford, CA, United States. [2]Stanford Cardiovascular Institute, Stanford University, Stanford, CA, United States. [3]Department of Biomedical Engineering, Yale University, New Haven, CT, United States. [4]Department of Cardiothoracic Surgery, Stanford University, Stanford, CA, United States

Introduction

Coronary artery disease is a leading cause of mortality worldwide. Coronary artery bypass graft (CABG) surgery is the gold standard treatment for patients with diffuse, multi-vessel disease. However, saphenous vein grafts used in CABG occlude at high rates post-surgery, with the underlying immuno-mechanobiological mechanisms still unclear. In this work, we develop a modular growth and remodeling (G&R) computational framework based on longitudinal experimental rabbit data with the goal of characterizing the vein arterialization process and predicting tissue (mal)adaptations after CABG surgery.

Methods

Using a rabbit vein graft model of CABG surgery (carotid artery to jugular vein end-to-end anastomosis[1]), a total of 30 vein grafts were harvested over a period of 7 months following surgery. Biaxial mechanical testing was performed on excised grafts, followed by immuno-histological examination to quantify vessel mechanical properties, composition and inflammatory burden. Experimental data was used to inform and validate a novel G&R computational framework[2], which was developed in-house based on a modular solver architecture. G&R parameters were determined with the surrogate management framework, using training timepoints for model calibration and withholding validation timepoints for evaluating predictive performance (Fig. 1).

Results

Histological analysis revealed significant time-dependent structural remodeling of vein graft tissue, with substantial variability in collagen content over time. Mechanical testing data showed that vein grafts generally exhibit greater stiffness compared to control veins, with noticeable variability across samples. Simulated inner radius, thickness, and vessel composition (elastin, smooth muscle cells and collagen) showed good agreement with

experimental data, highlighting the model's ability to appropriately capture the main mechanobiological processes that drive growth and remodeling of venous tissue.

Discussion

These findings constitute a significant step in mechanobiologically characterizing vein graft failure after CABG surgery. Calibrated using longitudinal experimental data, the proposed modular G&R framework has the potential to accelerate identification of novel CABG treatment strategies. Future work will focus on utilizing the framework's predictive capabilities to optimize a medical device for mitigating vein graft failure.

Images (Optional)

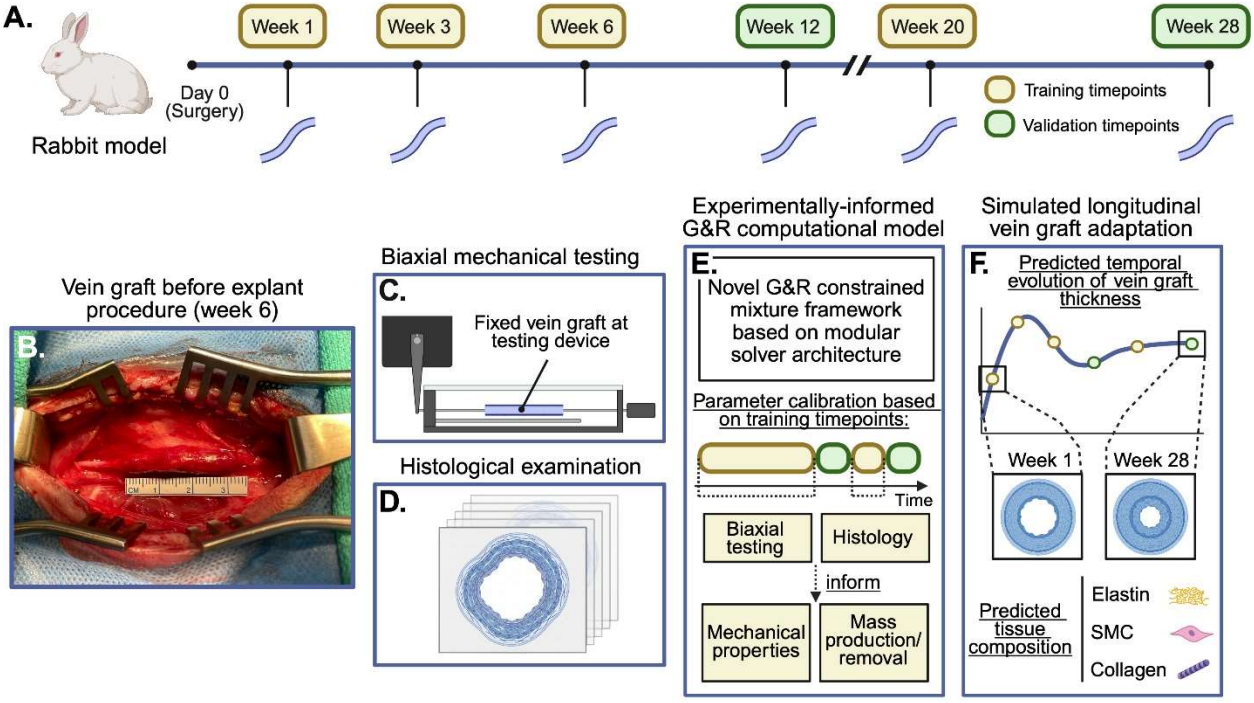


Figure 1: Illustration of end-to-end pipeline from (**A, B**) longitudinal vein graft tissue collection and (**C, D**) experimental data to (**E**) computational G&R model calibration and (**F**) prediction of vein graft adaptation (inner radius, thickness, structural composition) over time.

References (Optional)

[1] Deirdre EJ Anderson *et al.* , Tissue Eng Part C-Methods, 2018

[2] Abhay B Ramachandra *et al.* , J Biomech Eng, 2015

Session Category

Organ and Tissue Biomechanics: N/A

OA140-01

Using a Values Self-Assessment to Encourage Engagement in an Undergraduate Exercise Science Biomechanics Class

Dr. Ashlyn Jendro, Ms. Stephanie Cotariu, Dr. Kaitlin Gallagher

University of Arkansas, Fayetteville, AR, United States

Introduction

While instructors provide examples of the relevance of biomechanics to a student's degree and future career, students may still not engage if the examples are not personal to them. The purpose of this study was to evaluate how a values self-assessment can generate student engagement with course material.

Methods

Students in a third-year Exercise Science biomechanics course (n=138) completed a values self-assessment. During Week 1, students listed three values, explained how each matters, and described how each might intersect with the class. Students were given a list of values to get started; however, they could list anything meaningful to them. During Week 11, students revisited their reflections, writing about how the value has intersected with the course, and added a new value they did not initially list or think would apply to biomechanics. During the last week of the course, students read an information form stating that the instructors wanted to evaluate the values self-assessment. Tabulating values can be evaluated without students' informed consent; however, their open-ended responses cannot be used as research data without student consent. We will know who consented on December 16th, after grades are submitted. For this abstract, the de-identified value lists were downloaded, cleaned for spelling errors, and grouped into themes.

Results

The attached table lists the top five values, which account for two-thirds of responses. During Week 1, the top two values were "Family & Friends" and "Religion/Spirituality/Faith." By Week 11, students' top two values added were 'Athletics/Exercise/Health', and 'Learning & Gaining Knowledge."

Discussion

While Exercise Science students are assumed to value athletics, exercise, and health, they bring diverse values for instructors to relate to. In a different Exercise Science class taught by one of the authors and with the same assignment[1], students discussed passing on

knowledge to family/friends, direct experience with how the content affects their family/friends, ethics/morality related to their spiritual values, and finding creative solutions. Our final presentation will include direct quotes as evidence of the detailed responses regarding the intersection of their values with the course.

Images (Optional)

Table. Top 5 values shared by students during the Week 1 and Week 11 self-assessments. In Week 1, each student listed three values. In Week 11, students added one more value.

Week 1 (n=396)	Percent	Added Value Week 11 (n=131)	Percent
Family & Friends	29.6%	Athletics/Exercise/General Health	19.9%
Religion/Spirituality/Faith	13.4%	Learning & Gaining Knowledge	18.3%
Learning & Gaining Knowledge	9.6%	Being Creative/Artistic	11.5%
Independence	6.6%	Scientific Reasoning	9.2%
Athletics/Exercise/General Health	6.3%	Belonging to a Group	8.4%

References (Optional)

[1] Gallagher, Kaitlin. et al., *Work*, 2025

Session Category

Biomechanics Education, Knowledge Translation and Outreach: N/A

OA140-02

Faculty Engaged Graduate Recruitment Effort from Primarily Undergraduate Institutions

Dr. Liang Zhu

University of Maryland Baltimore County, Baltimore, Maryland, United States

Introduction

Recent restrictions on international applications for US graduate programs have shifted our focus to domestic applicants. Unfortunately, the current practice of graduate recruitment is often passive, with minimal involvement of research faculty in STEM departments. The objectives of this study were to evaluate whether engaging research faculty in primarily undergraduate institution recruitment activities inspired students' interests in applying for graduate school in engineering.

Methods

In this study, a research faculty member visited 3 primarily undergraduate institutions to give a seminar to students. The seminar presentation included not only the traditional recruitment components, such as a description of the mechanical engineering graduate program and financial assistance, but also ongoing research projects conducted in the faculty's research lab at UMBC. The research projects were focused on bioengineering, especially in applications in medicine. A survey was designed by the faculty member, and it consisted of questions about their demographic background, their previous exposure to research, the influence of the seminar on their interest in applying for graduate programs in 4-year universities, and their satisfaction with the event.

Results

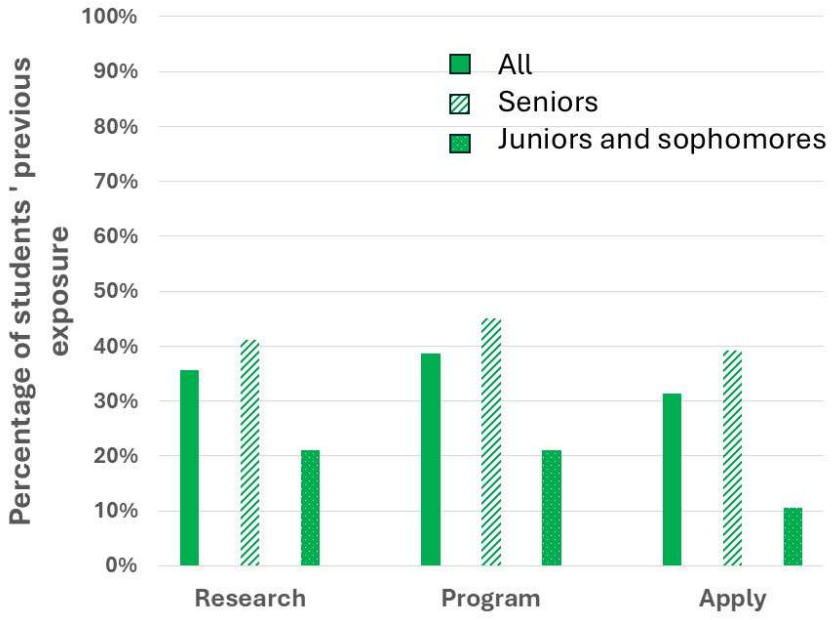
We collected 70 surveys from four visits. Results showed that prior exposure to research was low for the participants, around 36% before the faculty's visit. However, the exposure to research was much lower in juniors and sophomores than in seniors. More than 97% of the participants stated that they understood more of the technical content of research than before the seminar. 98% of them stated that they acquired more information on graduate programs. Although the majority stated "neutral", 34% or 23% of the students felt that they are more interested in applying for the graduate program at UMBC or other 4-year universities, respectively. One encouraging thing is that 82% of the students were satisfied

with the visit. 69% of them would like to attend future seminars offered by research faculty, with a higher percentage in juniors and sophomores.

Discussion

Faculty-engaged recruitment addressed the lack of research and program information among college students. Our visits had a positive impact on elevating students' interests in graduate schools. Future visits should target undergraduate students in their early college years.

Images (Optional)



Acknowledgements (Optional)

This research was supported by NSF (DUE-2518774).

Session Category

Biomechanics Education, Knowledge Translation and Outreach: N/A

OA140-03

The use of Biomechanics for a Course-Based Research Experience in a Large Class

Assistant Teaching Professor Val Sawiccy PhD, Student Taylor Wilson MS, Student Saliem Hatsey, Student Julia Wu Student, Professor Andy Karduna PhD

University of Oregon, Eugene, OR, United States

Introduction

Traditional research experiences in undergraduate biomechanics programs can be limited, leaving many students without access and widening equity gaps. Course-based Undergraduate Research Experiences (CUREs) address this by embedding research into coursework. This removes barriers like competitive selection and faculty resource constraints, allowing students to engage in original research and develop professional skills. [1] The goal of this project was to develop a scalable, sustainable CURE model iterated across terms.

Methods

We used a previously developed iPhone app for assessing proprioception. [2] Subjects were prompted to attain a target shoulder flexion angle (50, 70, or 90 degrees) via audio feedback from the phone, which was attached to their arm. Subjects attempted to replicate the target position in the absence of audio cues. Joint position sense errors were calculated as the difference between the angle at the repositioned and target positions. Students worked in pairs and were given an instructional video on using the app. Each group then recruited a subject, resulting in 71 subjects over the span of a week. Additionally, we collected survey data from the students about science self-efficacy and scientific identity. [3]

Results

Despite limited training, a sample of convenience, and scheduling complications, JPS errors followed a very similar pattern as we have seen in numerous lab-based students, with errors highest at the 50 degree target (3.4 degrees) and decreasing as target angles increased to 70 degrees (2.4 degrees) and 90 degrees (0.8 degrees). Survey results showed that students demonstrated an increased sense of belonging in the scientific community and were more likely to view themselves as scientists by the end of the course (Table 1).

Discussion

By integrating CUREs into large classrooms, this project creates a scalable model for embedding research into foundational courses. Outcomes include stronger research skills,

greater science self-efficacy, and increased STEM persistence across disciplines. Early research engagement builds transferable critical thinking and data analysis skills, while student contributions support faculty scholarship, strengthening the link between teaching and research.

Images (Optional)

Table Statistically significant post–pre changes on Likert scale 1-5, showing strong increase in scientific self-efficacy and scientific identity.

Survey Question	Construct	Likert Score Change (Post–Pre)	p-value	Direction
I am confident I can generate a clear, testable research question.	Self-Efficacy	**+0.224**	**0.0347**	**Increase**
I am confident I can use scientific literature and reports to guide research.	Self-Efficacy	**+0.326**	**0.000884**	**Increase**
I am confident I can integrate findings across studies to develop broader conclusions.	Self-Efficacy	**+0.356**	**0.000536**	**Increase**
I have a strong sense of belonging to the community of scientists.	Scientific Identity	**+0.258**	**0.000416**	**Increase**
I think of myself as a scientist.	Scientific Identity	**+0.342**	**0.001229**	**Increase**
When I am failing, my future seems uncertain.	Fear of Failure	**+0.306**	**0.001204**	**Increase (a rise in uncertainty about the future when failing)**

References (Optional)

[1] Auchincloss LC, *et al.*, CBE Life Sci Educ, 2014.

[2] Edwards *et al.*, J Biomechanics, 2016.

[3] Shortlidge and Brownell, J Microbiol Biol Educ, 2016.

Session Category

Biomechanics Education, Knowledge Translation and Outreach: N/A

OA140-04

Student Travel Awards Paired With Professional Development Programming Led to Broad Benefits for Early Career Travel Grant Recipients at a National Biomechanics Conference

Dr. Kurt E. Beschorner Ph.D.[1], Dr. Vani Sundaram Ph.D.[2], Ms. Paula Kramer[3], Dr. Christopher Wilburn Ph.D.[4], Dr. Allison Altman-Singles Ph.D.[5]

[1]University of Pittsburgh, Pittsburgh, Pennsylvania, United States. [2]Max Planck Institute for Intelligent Systems, Stuttgart, Baden-Württemberg, Germany. [3]University of Utah, Salt Lake City, Utah, United States. [4]Auburn University, Auburn, Alabama, United States. [5]Penn State Berks, Reading, Pennsylvania, United States

Introduction

Attending a scientific conference can be transformative for early-career scientists [1], enabling their integration into a research community and creating professional opportunities. High conference costs limit participation from students who are not part of well-funded research groups, hindering their development of conference-specific skills. This study measured the combined impact of funding and targeted programing on early-career scientists at the 2025 American Society of Biomechanics Annual Meeting.

Methods

Twenty-three awardees were selected from 107 applications; evaluations prioritized barriers to participation and potential career impact. Awardees received travel funding and participated in pre-conference programs on presenting research, planning conference activities, and networking (Figure 1). Impact was measured across surveys administered pre-conference (n=22), after the networking workshop (n=11), and post-conference (n=18). Surveys used a mix of choice- and free-response questions to assess perceived skills, goals, and behaviors. Paired t-tests were used to compare pre- and post-conference responses.

Results

Awardees reported high conference satisfaction (4.78/5.0). They also indicated that they met (12/18) or exceeded (5/18) their top goals, which were networking, pursuing career opportunities, and improving biomechanics skills (Figure 1B). Perceived ability significantly improved for the categories targeted in the three pre-conference programs (Figure 1E). Workshop attendees reported plans to spend more time preparing for network interactions

and introduce themselves with more intentionality. For conference skills that were not targeted with programming (e.g., asking questions after a research talk), no meaningful improvements in were observed.

Discussion

This study demonstrates that funding combined with targeted programming can lead to strong positive outcomes for early-career scientists. Awardees reported accomplishing their top goals and improved skills that were the subject of pre-conference programs. Their improved perceived ability aligns with findings from the prior year [2]. The lack of perceived improvement for other conference skills suggests that conference attendance alone might not be sufficient for gaining conference skills, further supporting the value of pre-conference programming. A key limitation of this study is the lack of a control group with randomized trials. Future conferences should emphasize pairing travel grants with development programming for early-career scientists.

Images (Optional)

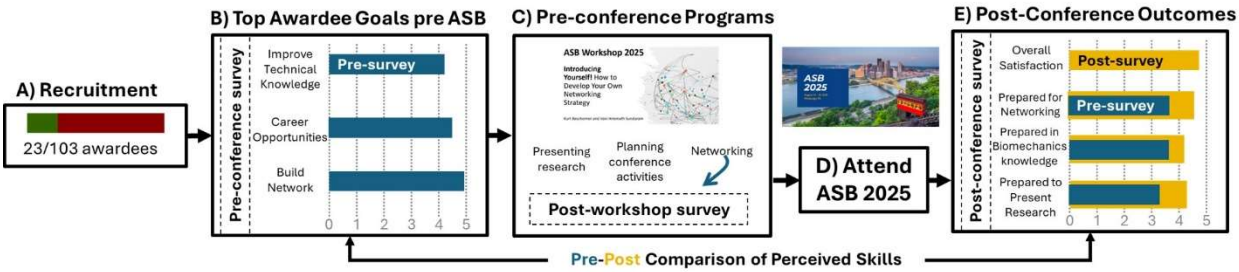


Figure 1: Research activities: A) recruitment/selection of awardees; B) pre-conference survey; C) pre-conference programs, D) attending the conference, and E) a post-conference survey, showing pre-post comparisons (all p<0.05).

References (Optional)

[1] Little, Educational Research, 2020.

[2] Beschorner et al. ASB, 2025.

Acknowledgements (Optional)

This research was funded by NIH (National Institute on Aging and Eunice Kennedy Shriver National Institute of Child Health and Human Development) R13AG096983 and NSF (Division of Civil, Mechanical and Manufacturing Innovation) Grant #2524744.

Session Category

Biomechanics Education, Knowledge Translation and Outreach: N/A

OA141-01

Video-Derived Asymmetry Enhances Prediction of Long-term Patient-reported Outcomes after ACL Reconstruction

Mr. Zhixiong Li MSc[1], Miss Sijia Li BS[1], Mr. Soyong Shin MSc[1], Dr. Evy Meinders PhD[1], Dr. Andrew Sprague PT, PhD, DPT[2], Dr. James Irrgang PT, PhD, FAPTA[2], Dr. Volker Musahl MD[2], Dr. Eni Halilaj PhD[1]

[1]Carnegie Mellon University, Pittsburgh, PA, United States. [2]University of Pittsburgh, Pittsburgh, PA, United States

Introduction

Early identification of individuals at risk of poor recovery after anterior cruciate ligament reconstruction (ACLR) is critical yet challenging. Patient-reported outcomes (PROs), such as the International Knee Documentation Committee Subjective Knee Form (IKDC-SKF) score and the Knee Injury and Osteoarthritis Outcome Score (KOOS), are subjective, while biomechanical and strength testing assess functional capacity but are challenging to collect clinically. Recent advances in markerless motion capture now allow objective quantification of kinematic asymmetry during functional testing without specialized laboratories. This study examined whether integrating video-derived asymmetry at 3 months improves prediction of nine-month IKDC-SKF outcomes.

Methods

Twenty-four participants were assessed at three and nine months post-ACLR. Participants performed three lateral step-down exercises per leg in a clinical setting while six RGB cameras (Sony RX0 II) recorded movement. DeepGaitLab [1], a markerless motion tracking tool, was used to estimate kinematics and extract hip, knee, and ankle asymmetry. Strength asymmetries in knee flexion/extension torque and hip abduction, extension, and external-rotation force were assessed using a Biodex and handheld dynamometers. PROs were assessed using all the KOOS sub-scores and the IKDC-SKF. LASSO, Ridge Regression, and Partial Least Squares models with leave-one-out cross-validation were used to predict nine-month IKDC-SKF scores from four three-month feature sets: PROs only, PROs + strength asymmetries, PROs + video-based asymmetries, and all features.

Results

Video-derived asymmetries improved prediction of nine-month IKDC-SKF scores. Using PROs alone yielded moderate predictive accuracy (Figure 1; $\rho = 0.61$, $p = 0.0008$), and strength measures provided modest gains ($\rho = 0.66$, $p = 0.0004$). PROs and video-derived asymmetries led to better performance ($\rho = 0.70$, $p < 0.0001$), while the combined model

using all the predictors performed the best ($\rho = 0.77$, $p < 0.0001$). The three-month KOOS pain subscore, IKDC-SKF score, hip abduction strength asymmetry, and knee and hip flexion/extension asymmetries were the most influential features.

Discussion

Markerless motion tracking provides clinically meaningful information that enhances prediction of long-term patient outcomes. These passive, scalable assessments could enable timely and low-burden monitoring in homes and clinics, supporting personalized rehabilitation and potentially improving long-term outcomes.

Images (Optional)

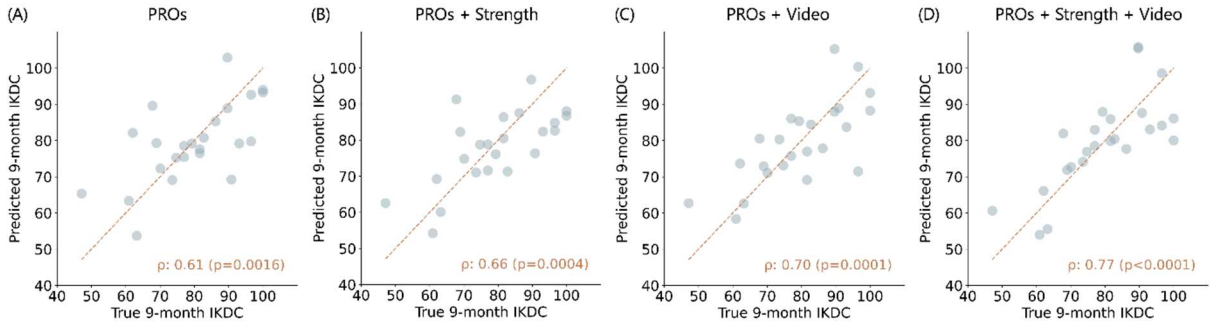


Figure 1. Predictive Model Performance. On left-out participants whose data were not used to train the models, IKDC-SKF scores at nine months could be predicted moderately well with data from the three-month visit. Models were trained using: (A) PROs, (B) adding strength asymmetry, (C) adding video-derived kinematic asymmetry, and (D) all features combined. Integrating video-derived kinematic asymmetry notably improved prediction accuracy compared with PROs alone or PROs combined with strength measures, supporting the clinical utility of scalable motion-tracking solutions.

References (Optional)

[1] Shin et al., ASB, 2025.

Acknowledgements (Optional)

This project has been funded by NIH R01AR080310.

Session Category

Clinical Biomechanics: N/A

OA141-02

The Effect of Meniscal Damage and Demographic Factors on Gait Biomechanics After ACL Injury

Mr Harry Battersby, Mr Alan Getgood, Mrs Dianne Bryant, Mr Ryan Evans, Mr Neil Wills, Mr Max Smith, Miss Jillian Neufeld, Mr Derek Pamukoff

Western University, London, Ontatio, Canada

Introduction

Gait biomechanics are altered following ACL injury, and are associated with knee osteoarthritis progression. Concomitant meniscal injury, may further influence gait impairment. The purpose was to compare sagittal plane gait mechanics between limbs and between those with and without meniscal injury.

Methods

151 individuals with unilateral ACL injury participated (78 Females, 73 Males, Meniscus injury: n=96, Age:18.95±3.09 years, time-since-injury: 8.25±12.51 months). Five overground gait biomechanics trials were recorded for each limb at a self-selected speed (1.25m/s±0.14m/s) using force plates (1200Hz) and a 12-camera motion capture system (60Hz). The peak internal hip extension moment (HEM), knee extension moment (KEM), and ankle plantar flexion moment (PFM) were extracted and normalized to a product of body weight (N) and height (m). A 2 (meniscal or no meniscal injury) by 2 (limb) ANCOVA compared gait outcomes, and sex and time since injury were included as covariates.

Results

There were no significant limb × meniscus interaction effects for any gait variable. There was a significant main effect of limb for HEM and KEM. HEM was higher in the injured compared to uninjured limb ($F_{1,147}$=12.12, 0.032 vs. 0.029BW·ht, p<.01,η^2=0.08), but KEM was lower in the injured compared to uninjured limb ($F_{1,147}$=11.84, 0.030 vs. 0.036BW·ht, p<.01, η^2=0.08). There was a main effect of meniscal injury for KEM, and KEM was lower in those with compared to without meniscal injury ($F_{1,147}$=4.73, 0.032 vs. 0.036 BW·ht, p<.01, η^2=0.03). Longer time-since-injury was associated with higher KEM (β=0.001, $F_{1,147}$=7.23, p<.01, η^2=.047), with. Sex was associated with PFM, and females had higher PFM than males (β=0.006, $F_{1,147}$=12.01, p<.01, η^2=.076).

Discussion

Lower KEM and higher HEM in the injured limb suggest both inter- and intra- limb compensatory strategies to offload the knee joint. Lower KEM in those with meniscal injury

indicates additional quadriceps avoidance. In contrast, longer time since injury may reflect progressive restoration of loading capacity. Higher PFM in females indicates sex-specific compensatory strategies to mitigate knee loading. These results emphasize the importance of considering concomitant injuries, sex and recovery timelines when interpreting and managing gait biomechanics after ACL injury.

References (Optional)

Acknowledgements (Optional)

- Canadian Institutes of Health Research (CIHR)

Session Category

Clinical Biomechanics: N/A

OA141-03

Female Athletes Exhibit Higher ACL Force than Males in Response to Valgus Moments Due to Increased Coupled Internal Tibial Rotation: A Sex-Specific Computational Modeling Study in 168 Young Athletes

Dr. Andrew Pechstein PhD[1], Ms. Isabella Gomez Hjerthen BS[1], Mr. David Shamritsky MS[1], Dr. Mitchell Wheatley PhD[1], Dr. Mark Amirtharaj MD[1], Dr. Danyal Nawabi MD[1], Dr. Thomas Wickiewicz MD[1], Dr. Michael Parides PhD[1], Dr. Andrew Pearle MD[1], Dr. Bruce Beynnon PhD[2], Dr. Carl Imhauser PhD[1]

[1]Hospital for Special Surgery, New York, New York, United States. [2]University of Vermont, Burlington, Vermont, United States

Introduction

Young female athletes are at higher risk of noncontact anterior cruciate ligament (ACL) injury than their male counterparts. Whether sex-based differences in ACL loading and tibiofemoral kinematics exist due to loads experienced during cutting and pivoting sports, namely compression, valgus, and anterior loads, remains unknown. We investigated (1) whether any of these loads disproportionately increased ACL force in females and, if differences emerged, (2) which tibiofemoral kinematic (internal tibial rotation (ITR), valgus angulation, or anterior tibial translation (ATT)) was most strongly associated with this increase.

Methods

MRI data from 120 female and 48 male high school and college athletes (half sustained noncontact ACL tear, half matched controls) were analyzed. Three-dimensional renderings of bone, cartilage, and meniscal geometries were extracted. Ligament attachments were identified and soft-tissue properties standardized. Knee models were sequentially loaded with axial compression (100N), a valgus moment (8Nm), and an anterior tibial force (30N) at 15° of flexion. ACL force and tibiofemoral kinematics were recorded during each loading step. Potential sex-differences in ACL force at each step were examined using unpaired t-tests. After identifying loading step(s) with male–female ACL force differences, relationships between ACL force increases and changes in ITR, valgus angulation, and ATT were quantified using linear regression.

Results

The valgus moment resulted in a larger increase in ACL force for females than males (72±27N vs 58±24N, p=0.002). ACL force increases were not different for axial compression and anterior tibial force (p>0.05). During the applied valgus moment, ACL force increases were most strongly associated with ITR (R^2=0.60), then ATT (R^2=0.40) and valgus angulation (R^2=0.17).

Discussion

A larger increase in ACL force from valgus moments applied after compression in females is not from increased valgus angulation. Rather, coupled ITR is most strongly associated with increased ACL force. Using subject-specific geometries with standardized soft tissue properties revealed that knee geometry increases ACL force in females. Integrating a clinical dataset with physics-based simulation revealed a distinct ACL loading mechanism in young athletes. Prevention and rehabilitation programs and surgeries that reduce valgus loads or control coupled ITR may reduce ACL loading, especially in females.

Session Category

Clinical Biomechanics: N/A

OA141-04

Longitudinal Evaluation of Sex Differences in Knee Loading During Gait After ACL Reconstruction

Dr. Alexa Johnson PhD[1], Ms. Reagan Recchia[1], Mr. Ryan Mahoney[1], Ms. Olivia Sunderlik[1], Ms. Fiona Conway[1], Mr. Michael Angelini[1], Dr. Beyza Tayfur PT, PhD[1,2], Dr. Riann Palmieri-Smith ATC, PhD[1]

[1]University of Michigan, Ann Arbor, MI, United States. [2]Kırşehir Ahi Evran University, Kırşehir, Kırşehir, Turkey

Introduction

Knee loading following ACL reconstruction is one critical component contributing to long-term joint health and the risk of subsequent ACL injury. Altered knee loading during gait can contribute to the development of post-traumatic knee osteoarthritis if not properly addressed in rehabilitation. After ACL reconstruction, females reported lower patient reported outcomes and decreased quadriceps strength compared to males, though there is limited information assessing sex differences in knee loading post-surgery. Identifying sex differences in knee loading trajectories longitudinally may help improve ACL reconstruction rehabilitation programs. Therefore, the purpose of this project was to determine differences in knee loading biomechanics between females and males throughout the rehabilitation process following ACL reconstruction.

Methods

Fifty-four individuals (27 males, 27 females; 21.4±6.7yrs; 1.73±0.9m; 78.7±17.7kgs) had undergone ACL reconstruction (45 bone patellar tendon bone, 6 hamstring tendon, 3 quadriceps tendon grafts) completed gait biomechanics testing three times, 4.4±0.5months, 9.1±0.5months, and 18.0±0.6months post-surgery. Individuals walked overground at their self-selected speed and three-dimensional motion capture and force plates were used to collect lower extremity kinetic data. Joint moments were calculated using inverse dynamics and reported as internal knee joint moments. A 2x3 (sex by time) repeated measure analysis of variance utilizing statistical parametric mapping compared the waveform of the knee moment during stance phase on the ACL limb, with posthoc t-tests run for significant main effects. Significance was set a priori at $p<0.05$.

Results

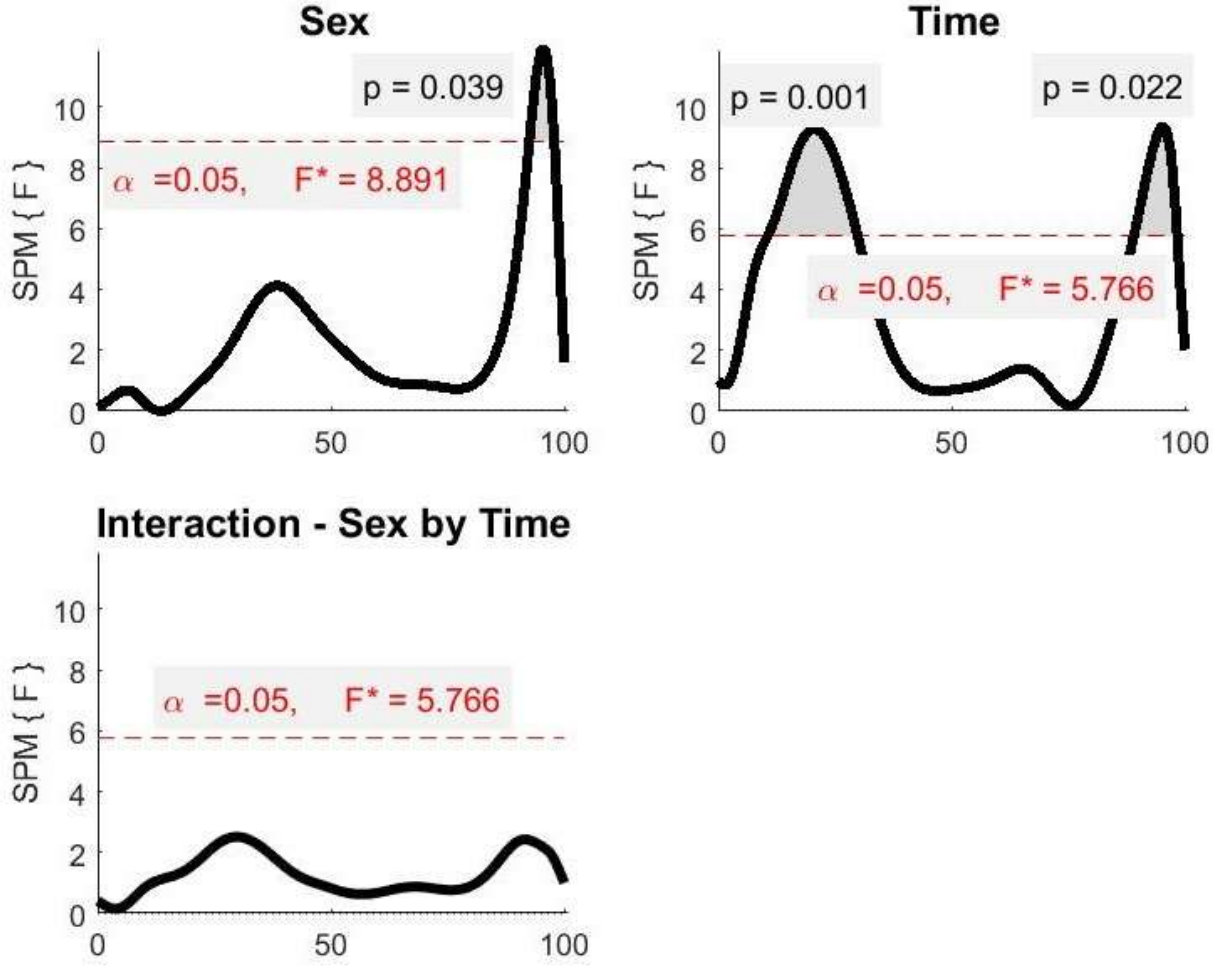
Statistical parametric mapping identified a main effect of sex between 92-97% ($p=0.039$) of stance (Figure 1), posthoc t-tests identified females had greater knee extension moments on the ACL limb during 92-97% ($p=0.017$) of stance, compared to males. There was also a

main effect for time between 10-30% (p=0.001) and 89-98% (p=0.022) of stance (Figure 1), where posthoc paired t-tests identified no differences in knee moments on the ACL limb across time points.

Discussion

We identified females increased knee loading during terminal stance on the ACL limb during gait, suggesting knee loading may be a contributing factor to sex differences following ACL reconstruction. Further analysis warrants assessing loading differences between females and males, between limbs, as well as during more functional tasks.

Images (Optional)



Acknowledgements (Optional)

This study was funded by the Eunice Kennedy Shriver National Institute of Child Health and Human Development of the National Institutes of Health under award number R01HD093626.

Session Category

Clinical Biomechanics: N/A

OA141-05

Knee Asymmetry Three Months After ACL Reconstruction Is Indicative of Poor Function at Nine Months

Dr. Evy Meinders PhD[1], Mr. Zhixiong Li MSc[1], Mr. Vu Phan MSc.[1], Dr. Andrew Sprague PT, MS, PhD, DPT[2], Dr. Volker Musahl MD[2], Dr. James J. Irrgang PT, PhD, FAPTA[2], Dr. Eni Halilaj PhD[1,2]

[1]Carnegie Mellon University, Pittsburgh, PA, United States. [2]University of Pittsburgh, Pittsburgh, PA, United States

Introduction

Many individuals continue to show asymmetric loading at follow-up visits after anterior cruciate ligament reconstruction (ACLR) [1], and this sustained asymmetry has been associated with poor clinical outcomes. While prior work has focused on linking gait asymmetry at six months following surgery to long-term outcomes [2], earlier risk identification could have greater impact on personalized rehabilitation. We aimed to determine if movement patterns three months post-ACLR provide early insight into knee function at nine months post-ACLR.

Methods

Thirty-six participants at three months post-ACLR walked on an instrumented treadmill and performed a lateral step-down exercise. Marker trajectories (OptiTrack) and ground reaction forces (Bertec) were synchronously recorded. Inverse kinematics and dynamics were performed in OpenSim. Asymmetries in peak joint kinematics and kinetics were used as inputs for a dimensionality reduction task, followed by k-means clustering. The silhouette approach was used to identify the number of clusters. Timeseries asymmetries between clusters were compared using an unpaired t-test with statistical parametric mapping ($p<0.05$). The International Knee Documentation Committee Subjective Knee Form (IKDC-SKF) was completed at three- and nine-months post-ACLR. To date, 22 participants completed the nine months IKDC-SKF. Scores were compared between clusters using an unpaired t-test ($p<0.05$).

Results

Two clusters were identified. Participants in the first cluster (N=15) were more symmetric at the knee (Figure 1A) but less symmetric at the hip (Figure 1B) compared to those in the second cluster (N=21). There were no significant differences in IKDC-SKF scores between clusters at three months (Figure 1C; Median[Q1-Q3]: 56[49-61] vs 56[47-60], p=0.83), but the first cluster had better scores at nine months (91[83-95] vs 75[69-82], p=0.005).

Discussion

We identified two movement patterns in individuals three months post-ACLR that may be more indicative of their long-term function than the IKDC-SKF score. The difference in IKDC-SKF scores at nine months surpassed the minimal clinically important difference [3], showing clinically meaningful differences in knee function between groups at nine months. Early identification of these movement patterns may enable early personalization of post-operative rehabilitation.

Images (Optional)

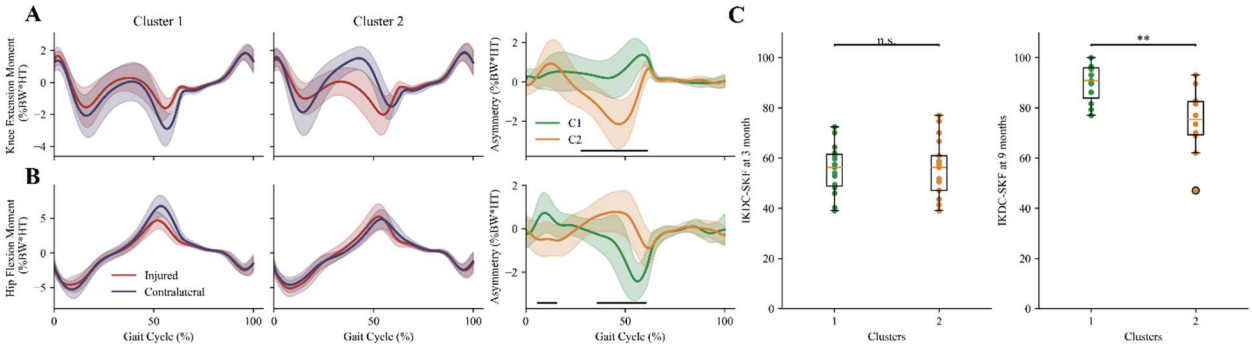


Figure 1. Knee (A) and hip (B) flexion moment during treadmill walking for two identified clusters (C1 and C2). Horizontal black bars show significant differences in asymmetry between clusters. C) IKDC scores at three and nine-months for both clusters.

References (Optional)

[1] Saxby, *et al*. MSSE, 2016. [2] Pietrosimone, *et al*. JOR, 2018. [3] Migliorini, *et al*. ESTES, 2025.

Session Category

Clinical Biomechanics: N/A

OA141-06

Associations Between Medial Tibiofemoral Contact Forces in Walking and Femoral Cartilage Health Over the First Year Following Anterior Cruciate Ligament Reconstruction

Mr. Justin Dennis M.S.[1], Dr. Thomas Birchmeier PhD, ATC[2], Dr. Beth Bacon PhD[1], Dr. Brian Pietrosimone PhD, ATC[1], Dr. Jason Franz PhD[1,3], Dr. Troy Blackburn PhD, ATC[1]

[1]University of North Carolina at Chapel Hill, Chapel Hill, North Carolina, United States. [2]University of North Carolina at Greensboro, Greensboro, North Carolina, United States. [3]North Carolina State University, Raleigh, North Carolina, United States

Introduction

Smaller medial tibiofemoral contact forces (MCF) in the anterior cruciate ligament reconstructed (ACLR) limb <12 months post-ACLR precede radiographic post-traumatic osteoarthritis (PTOA). Femoral cartilage is generally compromised before tibial cartilage, but it is unclear if MCF is associated with cartilage health over the first year post-ACLR and if these associations differ from the contralateral limb.

Methods

Walking biomechanics and magnetic resonance imaging (MRI) (i.e., T1ρ relaxation times indicating proteoglycan density) were assessed 1 and 12 months post-ACLR (Female:45%, age:23±6years, height:1.73±0.933m, mass:74.88±15.01kg). We used a full-body musculoskeletal model with a multi-compartment knee and static optimization to estimate MCF normalized to body weight, and segmented MRIs into femoral weight-bearing regions based on locations of the anterior and posterior horns of the meniscus. Linear mixed-effects models that included both limbs and time points were used for each femoral region to determine the association between peak MCF and T1ρ relaxation times while controlling for gait speed, and whether relaxation time differences exist between limbs and across time.

Results

ACLR and contralateral limb MCF were not associated with T1ρ relaxation times in the posterior, middle, or anterior femur 1 or 12 months post-ACLR ($p \geq 0.183$ for all associations). T1ρ relaxation times did not differ in the ACLR limb from 1 to 12 months in the posterior, middle, or anterior femur ($p \geq 0.472$ for all comparisons). T1ρ relaxation times were longer in the contralateral limb than the ACLR limb in the middle femur 1 month post-ACLR ($\Delta = 3.37$ms, $p < 0.001$), but did not differ between limbs in the posterior or anterior ($p \geq 0.125$) femur. T1ρ relaxation times decreased in the contralateral limb from 1 to 12

months in the middle femur (Δ=3.33ms, p=0.004), but no other limb×time interactions were observed in the posterior (p=0.119) or anterior femur (p=0.632).

Discussion

MCF was not associated with T1ρ relaxation times in either limb 1 or 12 months post-ACLR. However, contralateral limb middle femoral cartilage health was worse than the ACLR limb 1-month post-ACLR but improved from 1 to 12 months. The contralateral limb may experience increased loading demands post-ACLR, which the cartilage adapts to by remodeling (i.e., increasing proteoglycan density).

Images (Optional)

Table 1: Descriptive Statistics

Variable	ACLR	Contralateral
1 month post-ACLR (n=47)		
Posterior Medial Femur T1ρ Relaxation Times (ms)	53.48±4.73	54.44±3.49
Middle Medial Femur T1ρ Relaxation Times (ms)	50.46±4.23*	53.82±4.39
Anterior Medial Femur T1ρ Relaxation Times (ms)	53.71±7.91	52.09±5.38
Medial Tibiofemoral Contact Force (xBW)	1.20±0.72	1.37±0.65
Gait Speed (m/s)	0.96±0.30	0.96±0.30
12 months post-ACLR (n=29)		
Posterior Medial Femur T1ρ Relaxation Times (ms)	53.11±3.88	51.89±4.16
Middle Medial Femur T1ρ Relaxation Times (ms)	51.63±3.98	50.49±4.69#
Anterior Medial Femur T1ρ Relaxation Times (ms)	54.21±6.05	51.36±6.18
Medial Tibiofemoral Contact Force (xBW)	1.30±0.59	1.47±0.50
Gait Speed (m/s)	1.23±0.14	1.23±0.14

ACLR: Anterior Cruciate Ligament Reconstruction. BW: body weight. *Difference between ACLR and contralateral limbs 1 month post-ACLR $p<0.001$. #Difference between contralateral limb 1 and 12 months post-ACLR.

Acknowledgements (Optional)

This study was supported by the Department of Defence Award Number W81XWH21C00490011582719.

Session Category

Clinical Biomechanics: N/A

OA142-01

Knee Cartilage Thickness and Knee Mechanics in Walking Not Associated with Sport History in Young Runners and Swimmers

Ms. Zoey Kearns[1], Ms. Maliheh Fakhar[1], Dr. Gauri Desai[1,2], Dr. Ross Miller[1]

[1]University of Maryland, College Park, College Park, MD, United States. [2]Stanford University, Stanford, CA, United States

Introduction

Exercise in general is an effective measure to prevent initiation and development of knee osteoarthritis (OA). All forms of exercise involve some level of joint loading, but evidence is conflicting as to whether loading is beneficial or detrimental. Loading induced by recreational running participation does not seem to increase knee OA risk, but it is unknown if sports with low levels of loading, like swimming, affect the risk of developing knee OA. Generally, thinner knee cartilage and higher knee adduction moment (KAM) are associated with a greater risk of developing knee OA. Examining these variables in young athletes while cartilage is still adaptable can inform exercise recommendations for athletes to maintain joint health. The purpose of this research was to identify the relationship between sport induced loading, knee cartilage thickness, and biomechanical differences related to sport induced-loading exposure, particularly risk factors for developing knee OA.

Methods

24 young athletes with 11±4 years of experience focusing on their sport (18-29 years, 12 runners, 12 swimmers) walked and ran at three set speeds and had tibiofemoral knee cartilage thickness imaged using ultrasound (Fig. 1). Mann-Whitney non-parametric t-tests were used to identify differences between runners and swimmers in dominant leg cartilage thickness, and in lower limb gait mechanics.

Results

There were no differences between runners and swimmers in medial or lateral cartilage thickness. Swimmers ran with greater knee net work than runners, and runners walked with greater hip extensor moment and hip-to-ankle positive work ratio than swimmers. Swimmers exhibited greater peak ankle plantarflexion than runners in both gaits. There were no group differences in either gait in KAM or knee flexion moment.

Discussion

Swimmers vs. runners did not differ in knee cartilage thickness, or in biomechanical factors associated with knee OA risk, suggesting running vs. swimming history, at least at this age, has not appreciably affected knee joint health, positively or negatively. More sport-based differences were visible at the hip and ankle, which are more affected by age, suggesting that sport history could impact the age-related gait changes, and age is a demographical risk factor for OA.

Images (Optional)

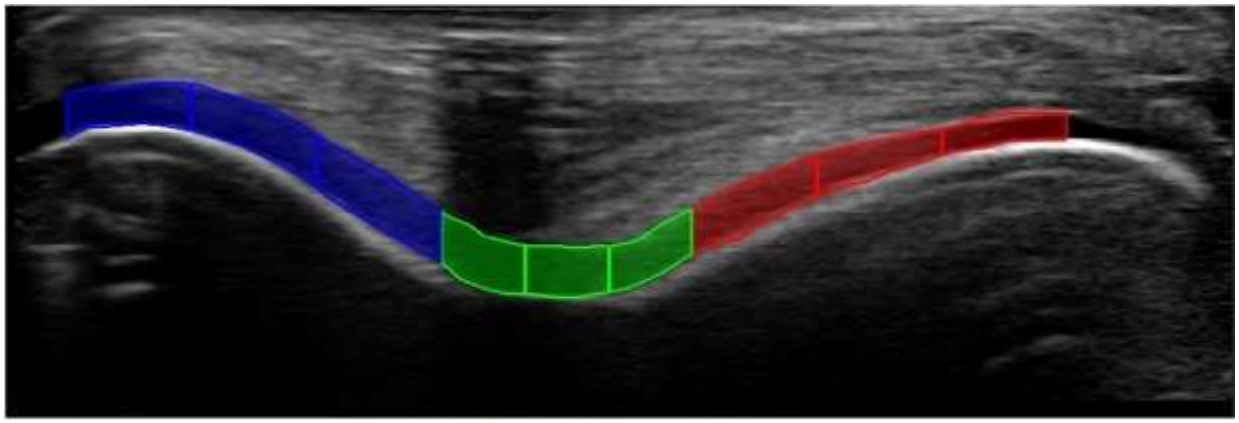


Figure 1. Ultrasound image of knee cartilage. The medial epicondyle is on the right side of the image and medial cartilage thickness is indicated by the red boxes. Lateral cartilage thickness is indicated by the blue boxes.

Session Category

Human Motion and Performance: Locomotion/Gait

OA142-02

Stroller Running Slightly Attenuates the Stride Length–Speed Relationship

Dr. Joseph Mahoney Ph.D.[1], Ms. Abby Miller[2], Dr. Allison Altman-Singles Ph.D.[2]

[1]Alvernia University, Reading, PA, United States. [2]Penn State Berks, Reading, PA, United States

Dr. Joseph Mahoney

Introduction

Pushing a jogging stroller alters running mechanics [1- 3], but its effect on the relationship between running speed and stride length is not well characterized. Overstriding or understriding may influence injury risk and performance, so quantifying stroller effects on stride length is important. Prior work reported either no change in stride length at matched speeds [1, 2] or shorter strides when runners chose slower stroller speeds [3]. However, these analyses compared conditions in aggregate rather than modeling subject-specific speed and stride relationships. The purpose of this study was to determine how jogging strollers influence the relationship between running speed and stride length.

Methods

Thirty-eight adults ran overground with and without a jogging stroller at self-selected speeds. Data collection followed previously published methods for this cohort [1]. Each participant contributed multiple strides across a range of self-selected speeds in each condition. Stride length and speed were normalized by stature. Normalized stride length was modeled as a function of normalized speed, condition (stroller or control), and their interaction using a linear mixed-effects model with subject-specific random intercepts and random slopes for speed. This approach accounted for repeated measures and individual differences.

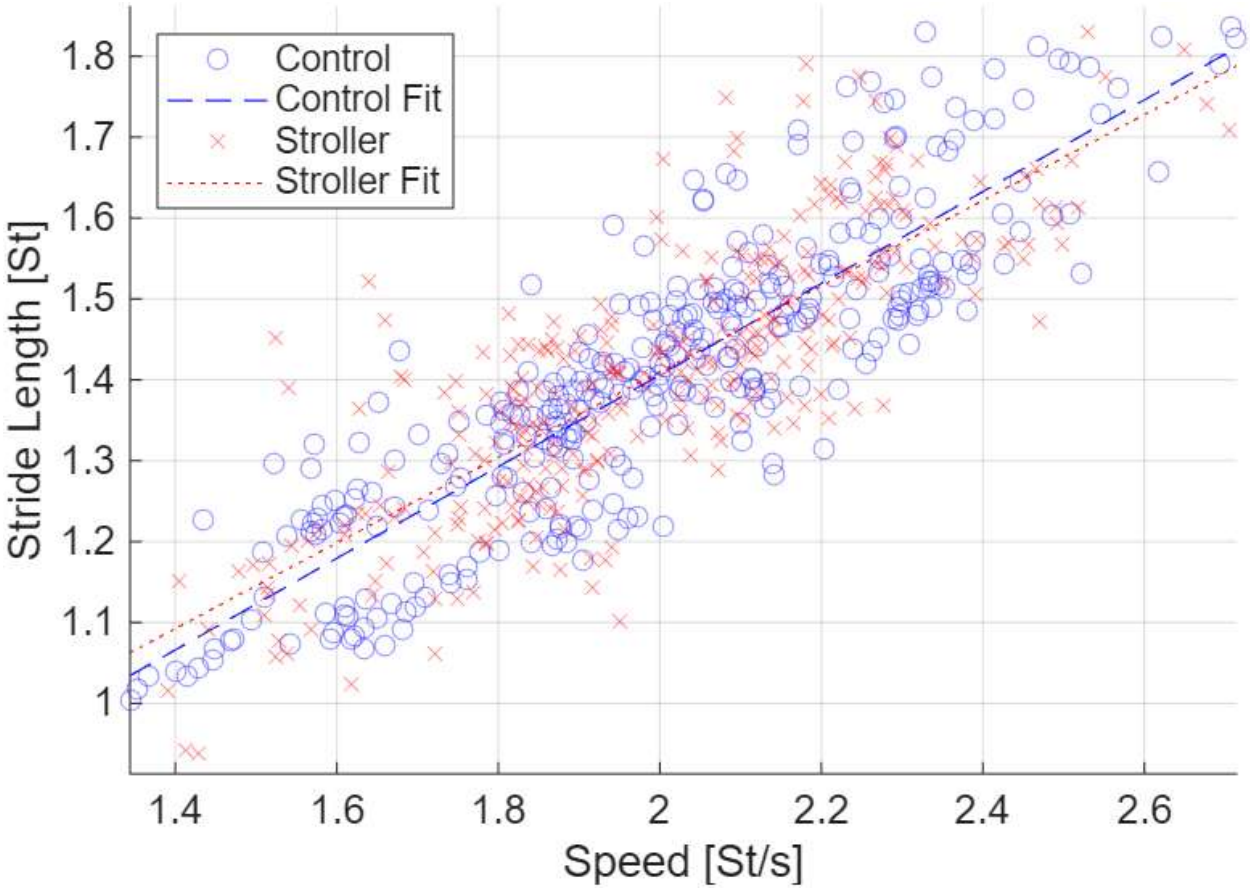
Results

Normalized stride length increased with normalized speed in both conditions ($p<0.001$). The speed-by-condition interaction was significant ($p<0.001$), with the stroller condition showing an approximately 11% lower stride length–speed slope (95% CI: 5–17%). This corresponded to a slightly compressed stride length range in the stroller condition relative to control, consistent with the fitted lines in the figure.

Discussion

Stride length increased with speed in both conditions, consistent with prior work on running mechanics. Pushing a stroller produced a small but statistically significant reduction in the stride length–speed slope, indicating a subtle change in how runners scale stride length with speed. This effect appears modest over the tested speed range but may still be relevant when interpreting running mechanics in frequent stroller users.

Images (Optional)



References (Optional)

[1] Mahoney et al. PLoS One, 2025

[2] O'Sullivan et al. G & P, 2016

[3] Alcantara and Wall-Scheffler, PLoS One, 2017

Acknowledgements (Optional)

This work is supported by funding from Penn State Berks and Alvernia University.

Session Category

Human Motion and Performance: Locomotion/Gait

OA142-03

Climbing to Lower Loads: Ground Reaction Force Adaptations in Incline Running

Dr Karen Mickle PhD

University of Newcastle, Newcastle, NSW, Australia

Introduction

Uphill running research accounts for a relatively small proportion of the overall biomechanics literature — most studies focus on level running, with fewer dedicated to uphill conditions. However, interest is increasing as participation in trail and mountain running rises. Trail running participation has seen a growth rate of 15% each year for the past decade, with current estimates at 20 million trail-runners worldwide. Current research lacks systematic investigations into different gradients, particularly those over 10%. This study aimed to investigate alterations to ground reaction forces (GRF) during uphill treadmill running.

Methods

Sixteen recreational runners (9 males and 7 females; mean (± SD) age 41.3 ± 9.4 y, height 170.7 ± 8.0 cm, weight 72.6 ± 10.1 kg) participated in this study. Long-distance runners who run at least 3 times per week, with no injuries in the previous 12 months, were eligible for the study. Following a warm-up, participants self-selected a running pace they could sustain for 1 minute on a 12% gradient. Participants were fitted with an instrumented insole (Loadsol Pro, Novel$_{gmbh}$) and data were recorded for 30s at 0, 3, 6, 9, 12 and 15 degrees in a counterbalanced order. Differences in peak vertical GRF, loading rate, cadence and contact time for the right foot were determined using a repeated measures ANOVA (SPSS, V30).

Results

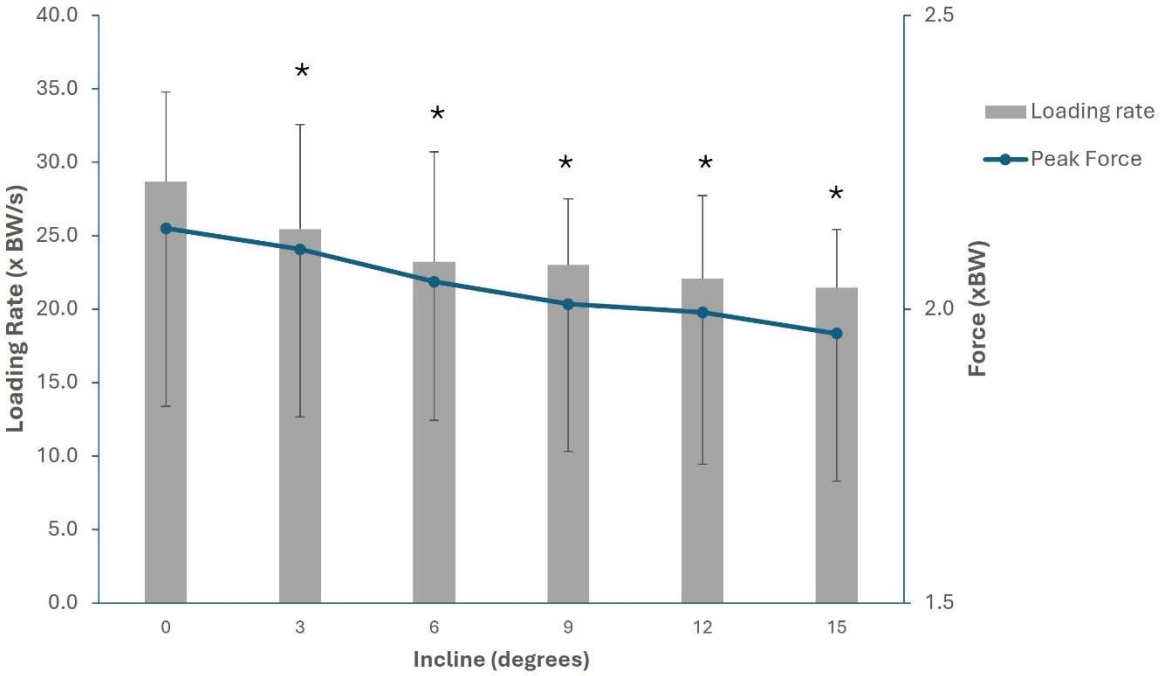
There was no significant main effect of incline on ground contact time; however, there was a significant main effect of incline on peak GRF, loading rate, and cadence ($p < 0.001$). Peak VGRF and loading rate were significantly lower at all inclines (3-15°) compared to level running (see Figure 1). Conversely, the cadence increased at every incline from level running (167.0 ± 8.5 steps/min) to 15° (176.6 ± 8.2 steps/min).

Discussion

Despite maintaining constant running speed, incline running significantly reduced peak vertical ground reaction forces and loading rates, with slopes above 6° most effective. This aligns with prior evidence that graded running alters loading mechanics and suggests that

uphill running may benefit individuals with load-related injury histories. However, findings are limited to treadmill conditions; future research should examine natural surfaces to confirm ecological validity and inform practical injury-prevention strategies.

Images (Optional)



Session Category

Human Motion and Performance: Locomotion/Gait

OA142-04

The Effect of Foot Progression Angle on Tibiofemoral Joint Contact Forces in the Medial and Lateral Compartments During Running

Ms Amber S Van Nes B.Eng, Ms Katelyn M Roe B.Eng, Dr Stephen FE Mattucci Ph.D, P.Eng, Dr Scott CE Brandon Ph.D, P.Eng

University of Guelph, Guelph, ON, Canada

Introduction

Alterations in foot progression angle (FPA) modification is a simple, non-invasive approach for modifying knee joint loading and may reduce knee osteoarthritis risk. While toe-in (TI) and toe-out (TO) gait patterns alter medial knee loading during walking, their effects on compartment-specific tibiofemoral joint contact forces (JCFs) during running remain unclear. This study quantified the effects of TI and TO gait modifications on medial and lateral tibiofemoral compartment JCFs during running. It was hypothesized that TI and TO gait would respectively shift JCFs more medially and laterally.

Methods

Eleven healthy young adults (26.1 ± 2.2 years, 1.76 ± 0.10 m, 70.8 ± 13.7 kg) completed five to eight trials of baseline (BL), TI, and TO running. FPA was modified ±10° from BL measured with a goniometer. Peak tibiofemoral JCFs, normalized to bodyweight, were estimated in the medial and lateral compartments of the right knee using OpenSim (v4.2) with the Bedo-Catelli knee model. A musculoskeletal modelling workflow was applied, including scaling, inverse kinematics, inverse dynamics, static optimization, and joint reaction analysis. Statistical comparisons performed in JASP (v0.95.4.0) between conditions were performed using a two-way repeated-measures ANOVA and Holm post-hoc tests.

Results

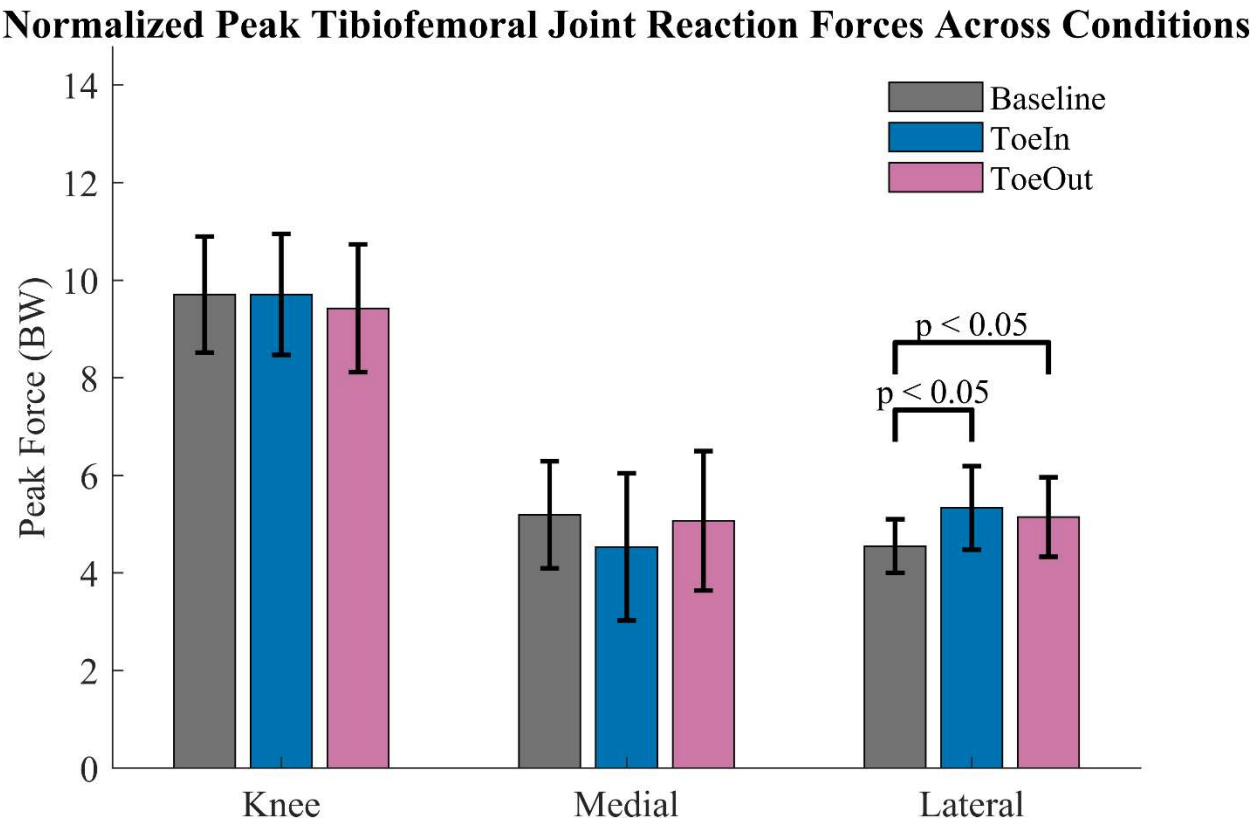
Peak tibiofemoral JCFs differ significantly across compartments, with condition-dependent changes in lateral loading. No overall effect of gait condition was present ($p=0.812$); however, a significant condition/compartment interaction was present ($p=0.003$). Post-hoc analyses showed no differences between conditions within the medial compartment (all $p>0.05$). In contrast, lateral compartment forces were significantly higher during TI compared to BL and TO compared to BL ($p<0.05$). Variability across participants was

greater in the medial than lateral JCFs across all conditions, reflecting less consistent load distribution in the medial compartment.

Discussion

FPA modifications during running altered compartmental tibiofemoral joint loading without affecting overall joint force. Contrary to expectations, both TI and TO increased lateral compartment loading, suggesting that medial-lateral compartment load redistribution during running differs from walking and may be constrained by the higher mechanical demands of running. These findings highlight the importance of evaluating gait interventions within the task context and suggest that FPA represents a modifiable parameter for influencing knee joint loading during running when appropriately applied.

Images (Optional)



Session Category

Human Motion and Performance: Locomotion/Gait

OA142-05

Classification of Running Movement Patterns in Service Members with Knee Pain

Mr Adam Bunn MS[1,2], Dr. Madeline Grosklos PhD[1,2], Dr Marisa Pontillo PhD[1,2]

[1]Extremity Trauma and Amputation Center of Excellence, San Diego, CA, United States. [2]Naval Medical Center San Diego, San Diego, CA, United States

Introduction

Understanding movement strategies in runners with knee pain is crucial for developing targeted interventions. Traditional analyses often focus on discrete variables or isolated joint patterns, potentially overlooking coordination across multiple joints and planes of motion. This study hypothesized that distinct movement strategies exist among runners with knee pain and that multivariate functional principal component analysis (MFPCA) combined with Dirichlet Process K-means (DP-means) clustering [1] could identify these strategies.

Methods

Running gait data were collected from 50 active-duty Service members (35 male/15 female; age: 32.3±8.0 years; height: 1.75±0.10 m; mass: 79.5±14.8 kg) with unilateral, non-operative knee pain using an optical motion capture system and an instrumented treadmill. Participants ran at self-selected speeds. Bilateral sagittal plane hip/knee moments, sagittal/frontal plane hip/knee/pelvis angles, and sagittal ankle angles during stance phase [2] were analyzed in Visual3D. MFPCA captured coordination patterns across all variables simultaneously, retaining principal components (PC) to explain 90% of total variance. DP-means clustering was applied to PC scores, stability assessed through bootstrap resampling, generating silhouette coefficients.

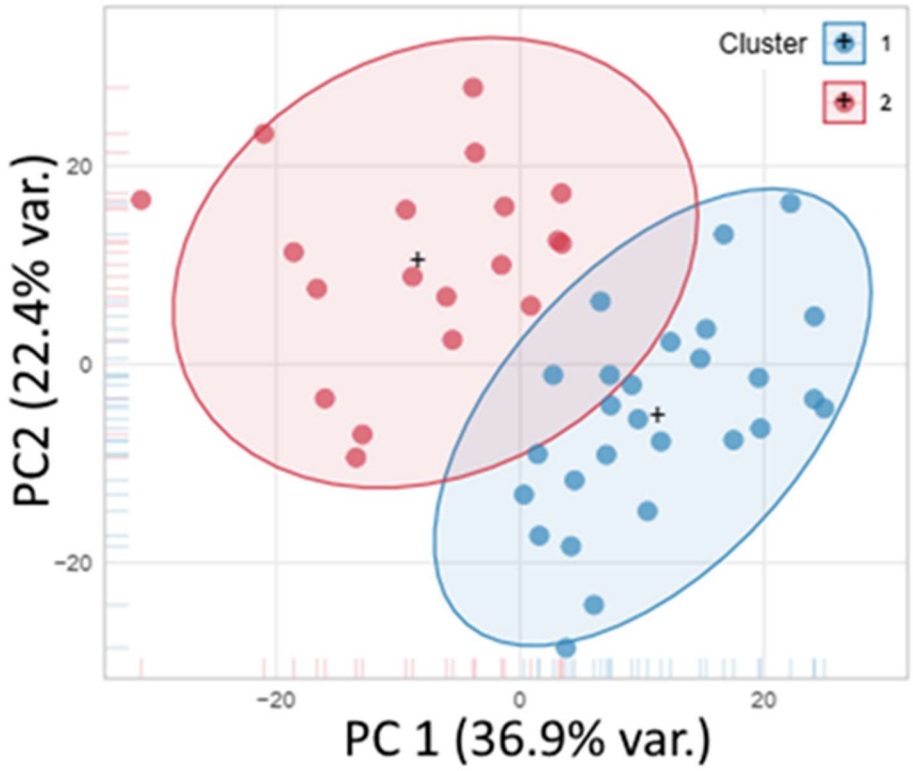
Results

DP-means clustering (lambda=1700) revealed that 92% of participants fell into two distinct movement patterns with strong cluster stability (stability score=0.765) and reasonable separation (average silhouette width=0.232). These patterns were distinguished primarily through three PCs, explaining 72.7% of total variance. The primary cluster (n=27) demonstrated a movement strategy characterized by greater frontal plane hip motion with increased sagittal plane flexion throughout the lower extremity, while the secondary cluster (n=19) showed reduced frontal plane hip motion and moments and a more extended posture across hip, knee and ankle joints.

Discussion

This study identified two stable movement patterns among runners with knee pain using MFPCA and DP-means clustering. The emergence of distinct extended versus flexed movement strategies suggests that runners may adopt consistent biomechanical adaptations in response to knee pain. These findings provide an objective foundation for developing targeted rehabilitation approaches based on movement pattern classification.

Images (Optional)



References (Optional)

[1] Dugan EL et al. (2024). Gait Posture, **113**: 40-45.

[2] Doyle E et al. (2022). J Orthop Sports Phys Ther, **52**: 192-A5.

Acknowledgements (Optional)

The views expressed herein are those of the author(s) and do not reflect the official policy or position of the Naval Medical Center San Diego, the Defense Health Agency, the Department of Defense, or any agencies under the U.S. Government.

Session Category

Human Motion and Performance: Locomotion/Gait

OA142-06

Tibial Bone Load, Strength, and Dynamic Balance in Initial Return to Run Phase Following Tibial Bone Stress Injury

Ms Megan Peach DPT, Ms Lailah Rosario, Dr. James Becker PhD

Montana State University, Bozeman, MT, United States

Introduction

Tibial bone stress injuries (BSI) are common running related injuries with a one in five recurrence rate. A possible risk factor for recurrent BSI is increased tibial loads in the early return to run phase. Altered strength and balance post injury have potential to influence running mechanics and therefore contribute to variations in tibial load during running. The purpose of this study was to compare tibial forces, strength, and dynamic balance between runners who have recently returned to running following tibial BSI and healthy controls.

Methods

Three runners diagnosed with tibial BSI (2F, 1M, age 25.0±6, BMI 22.5±0.7, speed 2.9±.7 m/s) with an average of 2.67 weeks since returning to running were matched for sex, age, BMI, and self-selected treadmill speed to three healthy controls (2F, 1M, age 22.0±3.5, BMI 21.9±.1, speed 2.9±.4 m/s). Participants ran on an instrumented treadmill for five minutes while kinematic and kinetic data were collected via motion capture. Clinical measures of dynamic balance (Y-balance test), single leg heel raise endurance, and ankle strength assessed via hand-held dynamometry (HHD) were also collected. Ankle joint angles, reaction forces, and moments were used as inputs to a musculoskeletal model to calculate tibial axial force as the sum of Achilles tendon and vertical ankle joint reaction forces. Welch's t-test was used to determine differences in peak tibial force and clinical variables between healthy and injured groups while Hedges' *g* tested for effect size.

Results

Peak tibial force, single leg heel raise endurance, and all other strength measures were not different between injured and healthy runners. However**,** Y-balance composite score was worse in the injured group compared to the healthy controls with a large effect size (Hedges' $g = 3.04$, CI: .83-5.25).

Discussion

Based on preliminary results, runners who recently returned to running after tibial BSI have decreased dynamic balance compared to healthy runners. This deficit has potential to alter running mechanics and therefore tissue load. Additional participants and further investigation are necessary to determine if differences in clinical measures are persistent and if these differences contribute to an increased risk of subsequent BSI.

Images (Optional)

Table 1 Variable Results

		Injured	Healthy	*p* value	CI
Peak Tibial Force (BW)		9.80 ± 2.22	8.08 ± 1.40	0.25	-5.08 - 1.63
Y-balance composite (% leg length)		0.88 ± 0.03	0.99 ± 0.04	<0.01*	0.06 - 0.18
Single leg heel raise (# repetitions)		21.25 ± 4.27	27.25 ± 4.86	0.11	-1.94 - 13.94
HHD (N/kg)	Dorsiflexion	1.82 ± 0.27	1.74 ± 0.21	0.71	-0.61 - 0.46
	Plantarflexion	2.23 ± 0.65	2.42 ± 0.76	0.72	-1.20 - 2.23
	Inversion	1.21 ± 0.18	1.39 ± 0.35	0.42	-0.36 - 0.72
	Eversion	1.34 ± 0.11	1.44 ± 0.41	0.68	-0.52 - 0.72

*Denotes significant difference between injured and healthy groups ($p < .05$)

Session Category

Human Motion and Performance: Locomotion/Gait

OA143-01

Menstrual Cycle Effects on Breast Acceleration During Running

Ms Ine Mylle PhD, Mr Ephrem Mekonnen MSc, Ms Jessica Yeoman BSc, Ms Sophia Wisotzki BSc, Mr Christopher Napier Prof

Simon Fraser University, Department of Biomedical Physiology and Kinesiology, Burnaby, British Columbia, Canada

Introduction

Female athletes experience cyclic changes in performance, mood, and injury risk across the menstrual cycle (MC) which also affects breast tissue composition and stiffness, yet its influence on breast biomechanics remains unexplored. During running, breasts move substantially and can cause pain, discomfort, and reduced participation, yet it is unknown whether these cyclic changes modulate breast acceleration.

Methods

Ten naturally menstruating, well-trained female runners (age: 27 ± 5.6 y, BMI: 21.6 ± 1.5; bra size range: 32A-34D) completed three treadmill-running sessions matched to the early follicular (EF), late follicular (LF), and mid-luteal (ML) phases, confirmed by 3-months of MC tracking and ovulation test kits. Participants ran at incremental speed intervals (starting at 50% of the 5k best: 23.83 ± 2.42 min) until failure while capturing accelerations of bilateral breast (nipple), sternum, and sacrum with inertial measurement units (Plantiga Technologies, Vancouver, Canada). Thirty-second sacral sensor recordings were cropped to the middle 30 running steps [Day et al., 2021] and synchronized to the other sensors to calculate mean peak resultant acceleration per speed level. All participants underwent 3D surface scanning (Artec Leo, Artec, Luxembourg) to quantify breast volume [Coltman et al., 2017] per visit. Linear mixed-effects models examined peak resultant acceleration (fixed effects: speed level, menstrual phase, and breast volume; random intercepts: subject). Significance was set to $p<0.05$.

Results

Breast acceleration significantly increased bilaterally with running speed ($p<0.001$; Figure 1). Interestingly, the left breast acceleration decreased significantly during LF and ML phases (−0.13g, $p=0.021$, $d=0.34$ for both phases) relative to EF, while the right breast showed no phase effect (LF: -0.03g, $p=0.555$, $d=0.09$; ML: 0.01g, $p=0.818$, $d=0.03$). The sternum acceleration was not different in LF (0.06g, $p=0.114$, $d=0.23$) but increased in ML (0.10g, $p=0.013$, $d=0.37$). Breast volume contributed minimally to these effects (left: -

0.0003cc, p=0.58; right: -0.0015cc, p=0.01) and left-right breast volumes were highly correlated (r=0.95), indicating asymmetry is unlikely to explain the side-specific response.

Discussion

Breast motion asymmetry during running is common and relates to differential tissue compliance. Menstrual-cycle-dependent changes in breast mechanical properties, rather than volume, may modulate these asymmetries, although hormonally influenced biomechanical factors not captured by the breast IMUs may also contribute.

Images (Optional)

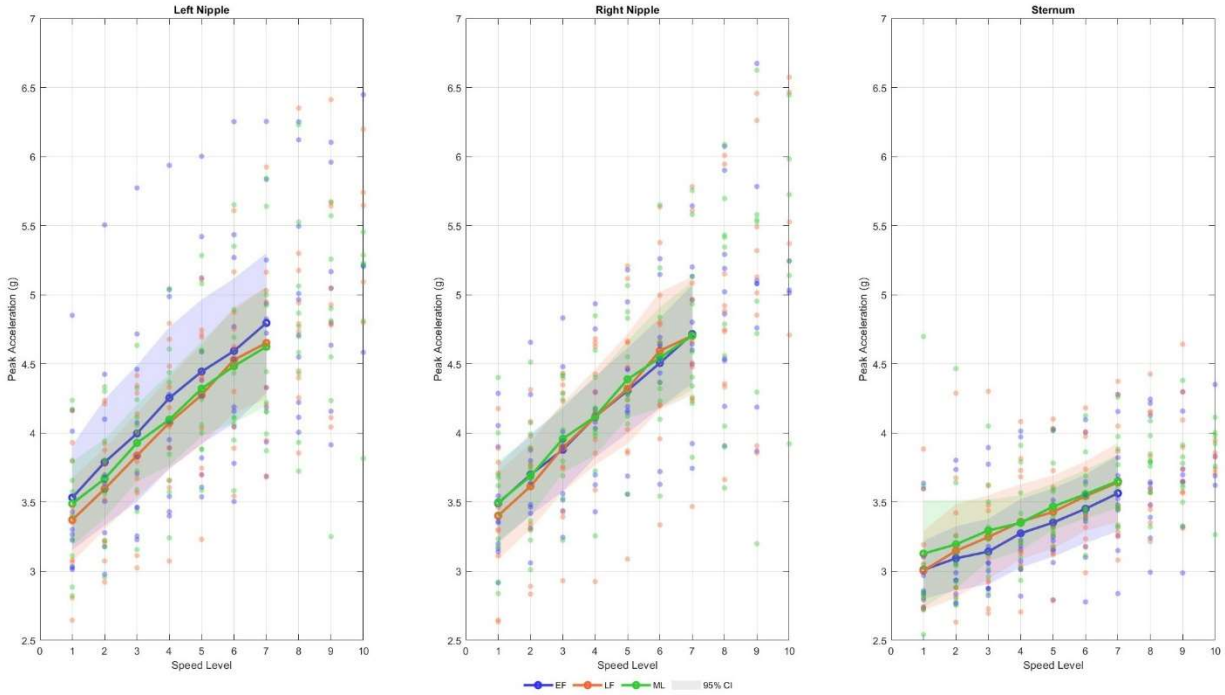


Figure 1. Phase-specific peak resultant acceleration of the left breast (left), right breast (middle) and the sternum (right) during the early follicular (EF; blue), late follicular (LF; orange), and the mid luteal (ML; green) phases. Data are shown as individual data points (faded), mean values, and 95% confidence intervals (shaded area).

References (Optional)

Session Category

Human Motion and Performance: Sports

OA143-02

Quantifying the Temporal Delay between Breast and Torso Acceleration Data Obtained From Inertial Measurement Units

Ms. Tarini Rajasekar[1,2], Dr. Ine Mylle[1], Ms. Jessica Yeoman[1], Dr. Sian Allen[3], Dr. Christopher Napier[1]

[1]SFU Run Lab, Department of Biomedical Physiology and Kinesiology, Simon Fraser University, Burnaby, BC, Canada. [2]School of Biomedical Engineering, University of British Columbia, Vancouver, BC, Canada. [3]lululemon Athletica, Vancouver, BC, Canada

Introduction

Due to the limited internal support provided to breast tissue, its motion lags the underlying thorax. Previous work using motion capture has described this breast-torso time lag during running (Williams, 2024). Quantifying this during a vertical jump with inertial measurement units (IMUs) would extend current knowledge on the breast–torso relationship, improving the understanding of soft tissue dynamics.

Methods

Ten women (31±4.74y) completed five repetitions of a 30cm vertical jump wearing a low support bra (size 6-10) with IMU sensors (iMeasureU,Vicon,Oxford,UK) placed on the sacrum, sternum, left breast (LB), and right breast (RB). An algorithm was developed to detect start/end (S/E) times for the acceleration data from each sensor after applying a 4^{th} order Butterworth filter with a 6Hz cut-off frequency. The S/E times of the breast were defined as the first instance of acceleration magnitude between 0.05-0.9m/s^2. Ground reaction force (GRF) data was estimated from vertical acceleration of the sacral IMU. First instances when GRF reached the respective stead-state standing force within a ±0.15-5N range were used to define S/E and applied to the torso (sternum) IMU. The time lag was defined as the absolute difference in S/E times between the LB/RB and sternum sensor. Coefficient of variance (CV) of LB/RB time lags within each participant were calculated.

Results

The mean time lags across S/E times and participants were LB:0.532±0.131s and RB:0.572±0.114s. Relative time lag for start times yielded negative values, LB:-0.543±0.183s and RB:-0.567±0.229s; while end times yielded positive values, LB:0.452±0.224s and RB:0.529±0.165s. Mean CV over participants for LB:0.432 and RB:0.480.

Discussion

This framework quantifies the breast-torso time lag of acceleration data and yields a larger lag in comparison to a previously reported vertical 0.05s lag during running (Haake, 2010). This is expected, as the algorithm utilizes acceleration magnitude, taking 3 planes of movement into account. Earlier start times and later end times indicate that breast and sternum motion are unsynchronized and exhibit a nonuniform relationship, as supported by higher CV values. Limitations stem from the inability to distinguish noise levels within breast acceleration.

Images (Optional)

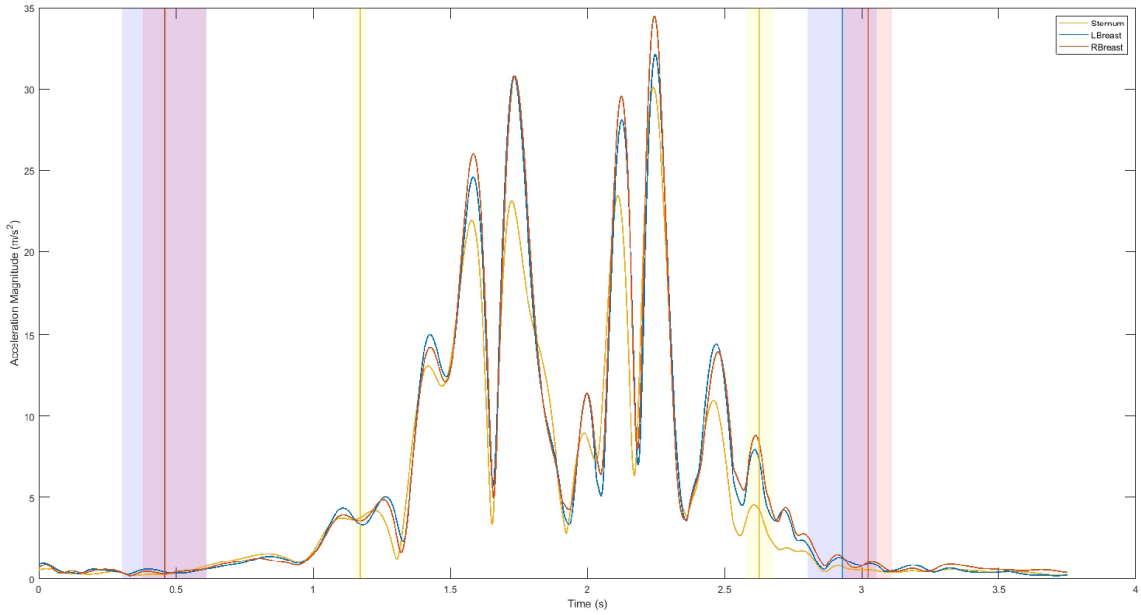


Figure 1. Example IMU acceleration data from one participant for sternum (yellow), left breast (LB; blue), and right breast (RB; red) averaged over three jumps, with mean and standard deviations of Start/End (S/E) times for each sensor (vertical lines).

Session Category

Human Motion and Performance: Sports

OA143-03

Frequency and Coherence Analysis of IMU-Derived Breast Motion Across Increasing Running Speeds

Ms. Kaylee White MSc, BSc[1], Mr. Ephrem Mekonnen[1], Dr. Ine Mylle[1], Mr. Amin M. Nasrabadi[2], Dr. Christopher Napier[1]

[1]Simon Fraser University, Burnaby, British Columbia, Canada. [2]University of British Columbia, Vancouver, British Columbia, Canada

Introduction

Female breasts lack anatomical support, resulting in passive multiplanar movement during running [1]. Running-induced fatigue and higher speeds may reduce soft-tissue shock-attenuating properties under repeated foot-strike impacts. As tissue damping capabilities are frequency-dependent, specific impact frequencies may contribute to tissue damage [2]. These concerns may also be applied to the breasts, increasing stress on the tissues and contributing to pain and damage [3]. This study aimed to assess changes in frequency distribution of breast acceleration signals and sternum-to-breast coherence as running speed increased.

Methods

Highly trained, healthy female runners were recruited from a larger study. Five inertial measurement units (Plantiga Technologies, Vancouver, Canada) were attached to the tibias, breasts, and sternum. Participants completed three-minute running intervals at increasing speeds on a treadmill until failure. The first trial and the final trial completed before failure served as the slow and fast trials, respectively. Vertical breast and sternum accelerations were extracted, trimmed to 30-second intervals, stride-segmented, and analyzed with Morlet Wavelet transform [4, 5].

Results

A subset of nine participants (age 25.6 ± 3.9, mass 64.6 ± 8.1 kg, breast volume 365.0 ± 155.6 cm^3) were analyzed. Running speeds for the slow and fast trials were 2.1 ± 0.2 and 3.2 ± 0.3 m/s, respectively. Signal features can be observed at approximately 10 Hz in both slow and fast trials, however the amplitude was higher in the fast trial, and extended later into the stride (Figure 1). Low-frequency (<5Hz) sternum-to-breast coherence was higher early in stride in the fast trial.

Discussion

This exploratory methodology revealed speed-related changes in the breast impact spectral profiles across running strides. Increased sternum-to-breast coherence in the faster trial may be due to increased cadence at faster running speeds, and therefore shorter time-lag between transmitted impacts. However, the higher-frequency spectral changes observed in the faster trial may be due to fatigue-related reductions in damping capabilities, which could contribute to breast tissue stress and pain.

Images (Optional)

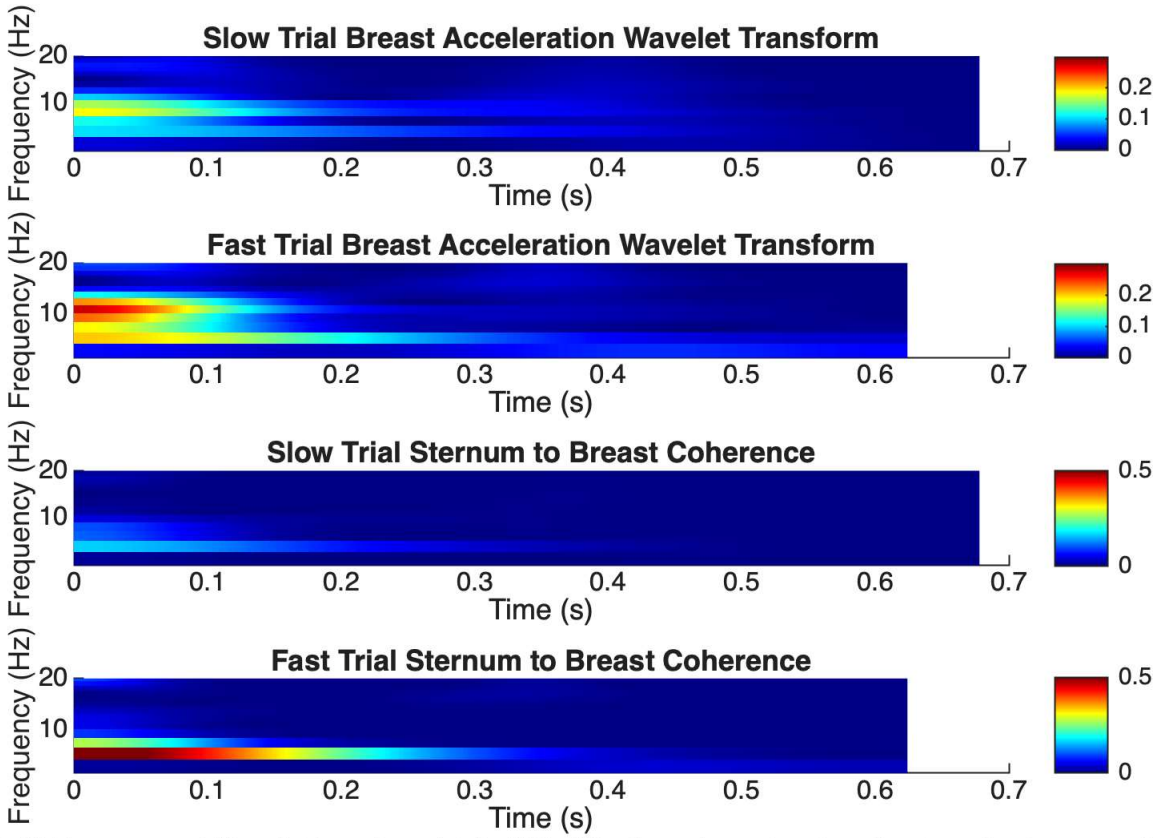


Figure 1. Stride-averaged Wavelet transform (plots 1/2) of the breast acceleration signal, and coherence of sternum-breast (plots 3/4). Increased coherence can be observed at the beginning of stride in the fast trial.

References (Optional)

[1] McGhee & Steele, Physiology, 2020

[2] Khassetarash et al., Human Movement Science, 2015

[3] Chen et al., Scientific Reports, 2025

[4] Foulger et al., Frontiers Human Neuro., 2024

[5] Purcell et al., BioMEMS Nanotech. II, 2006

Session Category

OA143-04

An Exploratory Analysis of Cut-Off Frequency Methodologies for Breast Motion IMU Data During Multiplanar and Uniplanar Movements

Ms Jessica Yeoman[1], Ms Ine Mylle Dr[1], Ms Sian Allen Dr[2], Mr Christopher Napier Dr[1]

[1]Simon Fraser University, Vancouver, BC, Canada. [2]lululemon Athletica, Vancouver, BC, Canada

Introduction

Excessive breast motion during physical activity can contribute to breast pain and discomfort, affecting female performance and participation [1]. Accurately quantifying breast motion is critical for understanding breast biomechanics and designing supportive apparel [1]. While inertial measurement units (IMUs) offer a portable method for capturing breast acceleration in ecologically valid environments, noise and error often affect the raw data [2]. Without a standardised, validated filtering methodology, accurate analysis of breast motion using IMUs remains a challenge.

Methods

Seven female athletes (age: 29.9 ± 6.0y, BMI: 22.0 ± 1.1; bra sizes: 32B-36C) performed five dynamic movements: jogging, vertical jumps, 180-degree jumps, skater jumps, and diagonal cutting. Acceleration was recorded using an IMU adhered to the left nipple. To identify cut-off frequencies, a power spectral density (PSD) analysis using Welch's method [3] was performed on each trial's raw resultant acceleration signal. Cut-off frequencies were determined for each participant and trial using the PSD elbow method [4] and the 95% cumulative power method [5], then averaged across participants. Raw signals were filtered using a zero-lag, fourth-order low-pass Butterworth filter with identified cut-offs. Filtering error was quantified by root mean square error (RMSE) and signal-to-noise ratio (SNR) between raw and filtered signals.

Results

Across all movements, the 95% cumulative power method showed lower RMSE and higher SNR compared to the elbow method, a direct result of higher cut-off frequencies (Table 1). This discrepancy was most pronounced during the vertical jump, where the elbow method produced an SNR 51% lower and an RMSE 222% higher than the 95% cumulative power method.

Discussion

These findings suggest the elbow method may over-filter movements, resulting in signal loss and reduced signal quality. Conversely, the 95% cumulative power method provides a more reliable and conservative approach for determining cut-off frequencies. Establishing a standardised processing protocol based on this method may help future research better inform apparel design, reducing a barrier to activity for women.

Images (Optional)

Table 1: Mean ± SD movement summary statistics: cut-off frequencies, root mean square error (RMSE), and signal-to-noise ratio (SNR).

Movement	Elbow Cut-off (Hz)	95% Power Cut-off (Hz)	RMSE Elbow (m/s^2)	RMSE Power95 (m/s^2)	RMSE % Difference	SNR Elbow (dB)	SNR Power95 (dB)	SNR % Difference
180 Jump	6.92 (± 0.83)	20.09 (± 5.66)	3.80 (± 1.71)	1.56 (± 0.44)	144%	11.35 (± 3.08)	18.96 (± 0.91)	-40%
Diagonal Cut	8.70 (± 2.53)	18.52 (± 4.55)	3.54 (± 1.02)	1.74 (± 0.59)	103%	12.39 (± 2.24)	18.88 (± 1.31)	-34%
Jog	11.60 (± 3.48)	30.36 (± 8.31)	8.44 (± 1.20)	3.69 (± 0.97)	129%	8.04 (± 2.28)	16.05 (± 0.45)	-50%
Skater Jump	7.81 (± 1.56)	15.18 (± 5.16)	1.85 (± 0.81)	0.96 (± 0.33)	93%	16.66 (± 3.24)	22.17 (± 2.18)	-25%
Vertical Jump	6.92 (± 0.83)	32.59 (± 13.99)	4.98 (± 2.84)	1.55 (± 0.62)	222%	9.65 (± 4.33)	19.72 (± 1.77)	-51%

Note: Percent difference represents how much the elbow method differs from the 95% cumulative power method, calculated as (elbow − 95% power) / 95% power × 100.

References (Optional)

[1] McGhee DE et al., Exerc Sport Sci Rev, 2020

[2] Kamstra H et al., Sensors (Basel), 2022

[3] Welch P, IEEE Trans Acoust, 1967

[4] Antunes M et al., IEEE, 2018

[5] Sinclair J et al., Hum Mov, 2016

Session Category

Human Motion and Performance: Sports

OA143-05

Sports Bra Support Modulates Breast-Torso Coupling and Soft-Tissue Oscillation During Dynamic Activities

Ms. Meng Pei BASc[1], Dr. Sian Allen PhD[2], Dr. Nicole Kelp PhD[2], Dr. Adrian Lai PhD[2], Dr. Christopher Napier PhD[3], Ms. Genevieve Bonnor BASc[1], Dr. Calvin Kuo PhD, P.Eng[1]

[1]University of British Columbia, Vancouver, British Columbia, Canada. [2]lululemon, Vancouver, British Columbia, Canada. [3]Simon Fraser University, Burnaby, British Columbia, Canada

Introduction

Exercise-induced breast pain affects up to 72% of active women and can reduce athletic performance [1]. Sports bras help reduce pain by limiting excessive breast motion, typically characterized using time-domain metrics. However, the mechanism by which sports bras reduce breast motion by coupling the breast to the torso is understudied. This pilot study aims to use frequency-domain analysis to assess movement coupling between the torso and breast when using sport bras.

Methods

A healthy participant (25F) completed five vertical jumps under no bra and high support bra (lululemon Energy Bra High-Support) conditions while instrumented with IMUs (1000Hz) on the left nipple and sternum. We extracted two-second windows around each vertical jump, centered around the landing impact, and low-pass filtered (fourth-order Butterworth, 100 Hz) vertical acceleration signals. We then computed time-domain peak acceleration gain between nipple and sternum sensors. Wavelet analysis was performed on the windows, and time-varying frequency-domain coherence and gain were computed.

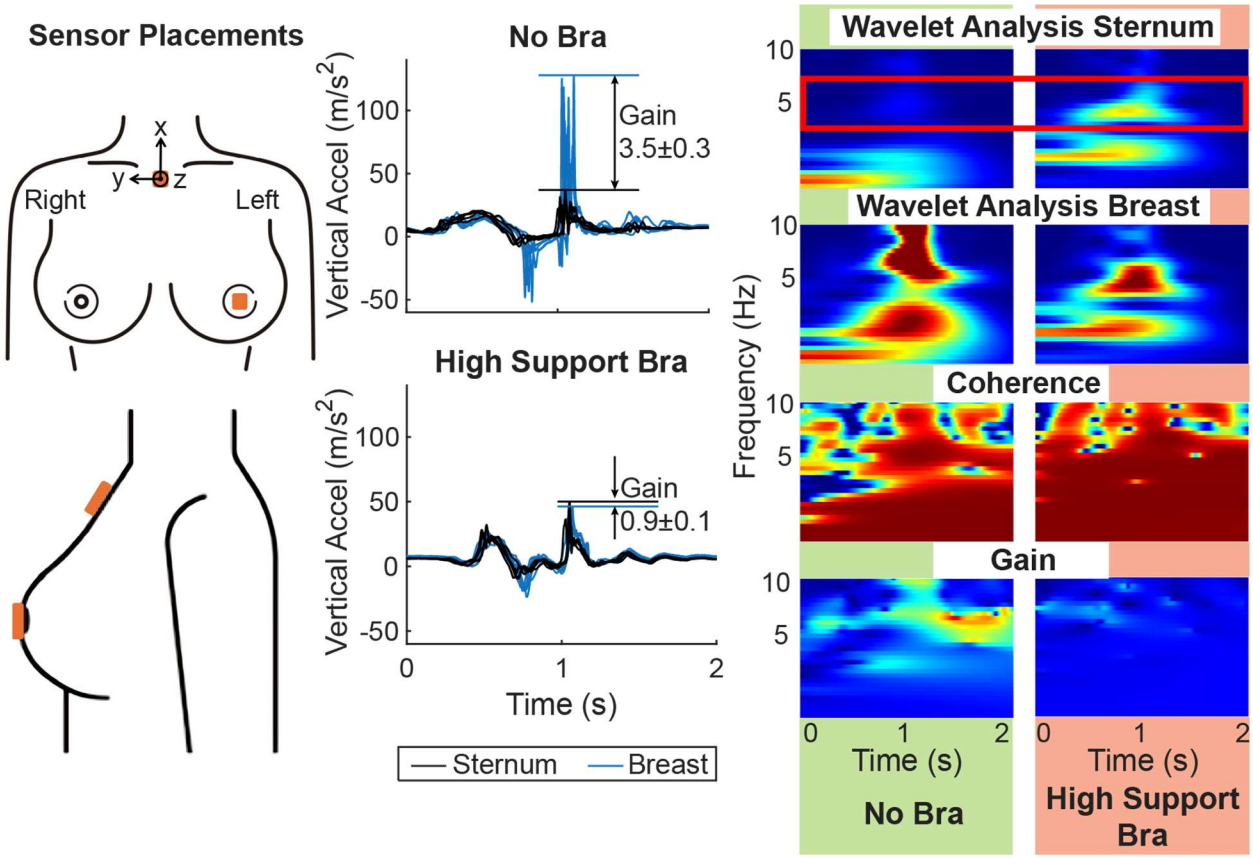
Results

Peak gain dropped from 3.5 (no bra) to 0.9 (high support), indicating the sports bra reduced excessive breast motion relative to the sternum. Wavelet analysis in the no bra condition showed a distinct 4-10Hz oscillation in the left breast not present in the sternum. With the high support bra, this breast-specific oscillation was reduced, whereas a 4-6Hz oscillation was introduced in the sternum. A coherence increase and uniform gain in the 3-10Hz range in the high support bra condition suggests the bra effectively coupled the breast and sternum movements.

Discussion

Breast-torso interaction changed relative to bra conditions during jumps. With no bra, the breast underwent large and independent motion relative to the sternum. The high support bra created more coupled motion between the breast and sternum. However, the bra does not solely restrict breast motion to the baseline sternum, but also causes the relatively large breast mass to introduce greater movements in the sternum. Soft-tissue coupling patterns may vary across individuals, particularly with different breast sizes. However, our frequency-domain analyses show the mechanism of breast-torso coupling through sports bras, where the breast also influences torso movement.

Images (Optional)



References (Optional)

[1] Brooke R. Brisbine et al., J Sci Med Sport, 2021

Session Category

Human Motion and Performance: Sports

OA143-06

The Effects of Breast Volume Reduction Surgery on Lower-Limb Kinematics in Running

Mr. Charles-Edouard Jarry, Dr. Jill Emmerzaal, Dr. Philippe C. Dixon

McGill University, Montreal, Quebec, Canada

Introduction

There is a complex interplay between breast motion, breast support, and running biomechanics in healthy women. Recent work showed that reducing breast motion increases exercise comfort and improves running efficiency [1]; however, only limited knowledge exists on the effect of breast volume reduction surgery (BVRS) on running biomechanics. Thus, the aim of this study is to compare lower-limb kinematics in running pre- vs post-BVRS.

Methods

Sixteen healthy females (18–45 years) are being recruited for this repeated-measures study (n = 4 to date). Each participant completed two testing sessions: one pre-surgery and one post-surgery. During each visit, kinematics were captured during 2 mins of treadmill running using markerless video-capture [2]. Data were processed using the opencap-processing repository [3] and custom scripts. Ankle, knee, and hip sagittal plane joint angles normalized to 100% of a running cycle were extracted. Given current sample size, visual analysis of the graphs is conducted. Analysis of gait waveforms using statistical parametric mapping paired t-tests is planned once sample size has been obtained.

Results

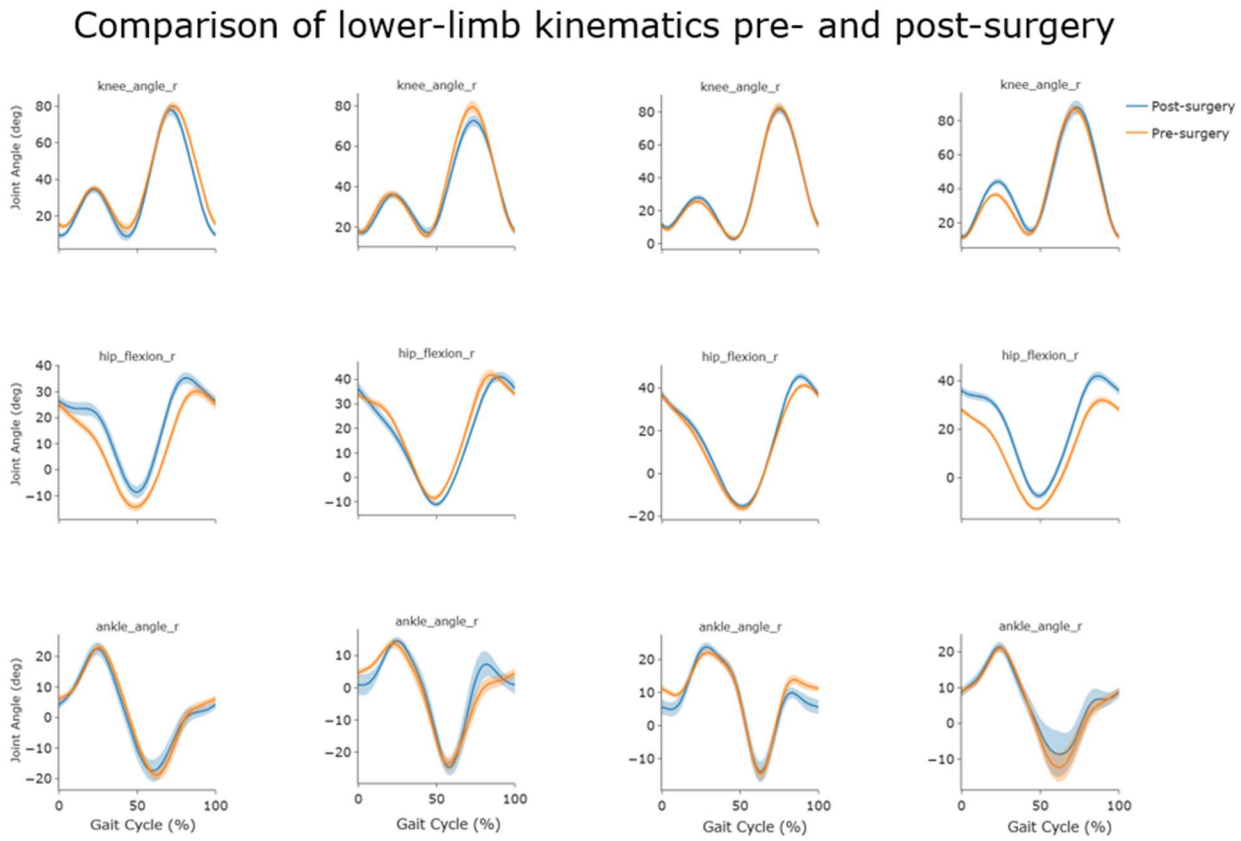
The mean breast mass was reduced from 2047.5g ±870.7 to 933.8g ±177.6. Preliminary findings suggest distinct compensatory patterns following BVRS. When differences emerge at the ankle, hip and knee kinematics appear visually similar. Conversely, when changes are observed at the hip and/or knee, ankle kinematics tend to remain visually similar (Fig. 1).

Discussion

Adaptations indicate potentially localized or segment-specific compensatory strategies. The study limitations are as follows: (i) participants differed in baseline physical activity levels and breast sizes, factors that may influence gait mechanics and (ii) small sample size, making generalization via statistical analysis difficult. Further work is needed

to fully characterize the effect of BVRS on running biomechanics. Future work will quantify breast kinematics and determine their relationship with running kinematics, spatio-temporal parameters, and dynamics to better understand the impact of BVRS on joint loading, stability, and movement efficiency. The results may assist clinicians in providing more informed guidance regarding postoperative exercise expectations and individualized rehabilitation planning.

Images (Optional)



References (Optional)

[1] Powell, et al., Front Sports Act Living, 2023

[2] Ulrich et al., PLOS Computational Biology, 2023

[3] Stanford Neuromuscular Biomechanics Laboratory. github.com/stanfordnmbl/opencap-processing

Acknowledgements (Optional)

This study was sponsored by Lululemon, Inc. via the Mitacs accelerate program.

Session Category

Human Motion and Performance: Locomotion/Gait

OA144-02

Sub-Voxel Vascular Segmentation from Coarse Resolution Medical Imaging

Dr. Numi Sveinsson Cepero[1], Dr. Julie DiCarlo[1], Prof. Shawn Shadden[2], Prof. Charles Taylor[1]

[1]University of Texas, Austin, Austin, Texas, United States. [2]University of California, Berkeley, Berkeley, CA, United States

Introduction

Patient-specific hemodynamic simulations require construction of blood vessel geometries from medical imaging. These models must be single unified bodies that are easily meshed and accurate, as geometry significantly impacts simulation results. Current workflows are cumbersome, require hours of manual input with subjective choices, and lead to inter-user differences. This bottleneck hinders scalable clinical solutions.

Deep learning (DL) offers automated, standardized, and potentially more reproducible model construction. However, most DL segmentation methods produce voxel-based predictions on the image grid. Converting these to surface models creates 'stairstep artifacts' proportional to the image resolution, especially when resolution is non-isotropic. Post-processing smoothing reduces artifacts, but changes volume and results in non-physiologic features, e.g. collapse of small vessels. This is particularly important for coronary modeling where image-based hemodynamic simulations are routinely used in clinical practice.

Methods

We produce finer-mesh ground truth segmentations by resampling training images using zero-padding interpolation. To address the substantial computational cost of processing fine-resolution volumetric data, we utilize the localized segmentation method SeqSeg[1]. By combining upsampled ground truth data with localized segmentation, we train and run inference more efficiently: only a subset of the total volume is processed. This enables the use of lower spacing than most state-of-the-art methods.

Results

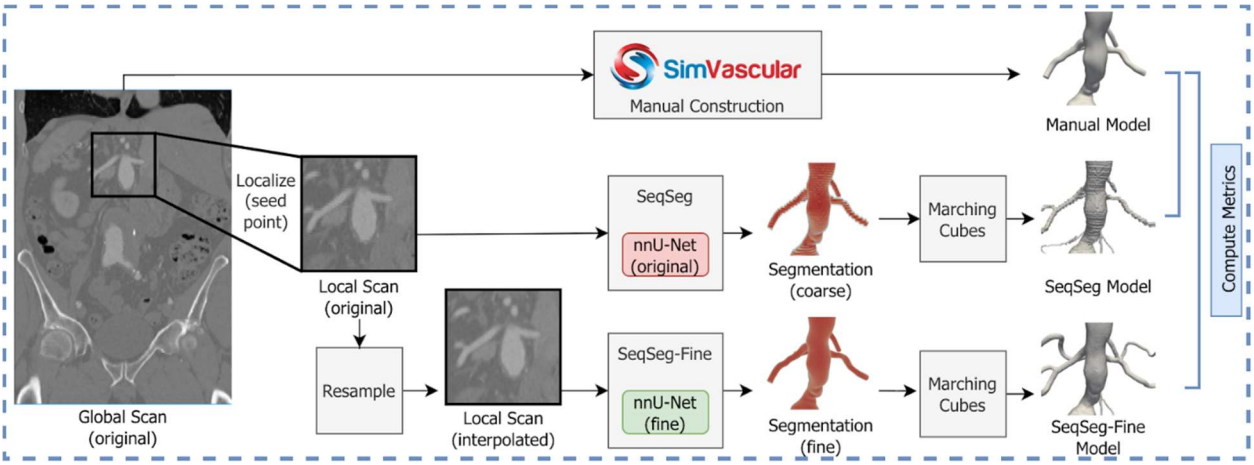
We compared abdominal aortic aneurysm vascular models created using both SeqSeg and our novel SeqSeg-Fine method with six manually-constructed ones. SeqSeg-Fine segmentations required less smoothing, allowing minimal loss of smaller vessel features while removing artifacts. Qualitatively, SeqSeg-Fine captured more branches with greater detail. Quantitatively, SeqSeg-Fine achieved superior performance: average surface

distance decreased from 0.444mm to 0.276mm, and 95th percentile Hausdorff distance decreased from 2.04mm to 1.42mm.

Discussion

By enabling sub-voxel training mesh data and local prediction, our deep learning models predicted vascular segmentations that better matched manual segmentation. These models learn to correlate image features with both voxel classification and sub-pixel vascular features. Similar to expert manual construction, surface meshes are built in higher detail than the underlying image resolution based on underlying knowledge of smoothness. Our method enables automated, expert-quality vascular reconstructions at scale, removing a critical bottleneck in patient-specific simulation workflows.

Images (Optional)



References (Optional)

[1] Sveinsson Cepero N, Shadden SC, *Ann Biomed Eng,* 2025

Acknowledgements (Optional)

We acknowledge the Savio High Performance Computing Cluster at University of California, Berkeley. This research is funded in part by a philanthropic gift from the Marakovic family to the Taylor lab at University of Texas, Austin.

Session Category

Cardiovascular/Cardiorespiratory Biomechanics: Methods, Models and Applications

OA144-03

Distinctive Coronary Tree-Level Haemodynamic Features in Spontaneous Coronary Artery Dissection: A Case–Control Imaging Study

Dr Mingzi Zhang[1,2], Dr. Lucy McGrath-Cadell[3], Dr. Stephanie Hesselson[3], Dr. Chi Shen[1], Dr. Ramtin Gharleghi[1], Dr. Nicholas Collins[3], Dr. David Muller[3], Prof Jason Kovacic[3], Prof Robert Graham[3], A/Prof Susann Beier[1]

[1]University of New South Wales, Sydney, NSW, Australia. [2]Torrens University Australia, Sydney, NSW, Australia. [3]Victor Chang Cardiac Research Institute, Sydney, NSW, Australia

Introduction

Spontaneous coronary artery dissection (SCAD) is a major cause of acute coronary syndrome in young women. While genetic predisposition is recognised, the biomechanical environment—particularly endothelial shear stress—has been implicated in arterial remodelling and disease states, such as aneurysm and plaque vulnerability. However, its role in SCAD remains unproven, as prior studies lacked controls and were limited in scope. We hypothesised that SCAD-affected coronary trees exhibit distinctive anatomical and haemodynamic signatures compared to healthy controls.

Methods

Thirty-six women with angiographically confirmed SCAD and 75 controls underwent coronary computed tomography angiography (CTCA). Three-dimensional coronary reconstructions were generated using validated segmentation pipelines. Vessel curvature, torsion, and diameter were quantified, and computational fluid dynamics simulations assessed time-averaged endothelial shear stress (TAESS) and topological shear variation index (TSVI). Tree-level comparisons employed independent t-tests, with effect sizes calculated via rank-biserial correlation. Receiver operating characteristic (ROC) analysis evaluated diagnostic performance.

Results

SCAD-affected coronary trees demonstrated significantly higher curvature (left: 0.45 ± 0.25 vs. 0.19 ± 0.02 $\times 10^3$ mm^{-1}; $p<0.001$) and TAESS (1.80 ± 1.20 vs. 0.99 ± 0.37 Pa; $p<0.001$) compared to controls. TSVI was also elevated (0.17 ± 0.07 vs. 0.13 ± 0.03 mm^{-1}; $p<0.001$), indicating greater variability in shear forces. Diameter and torsion showed no significant differences. Diagnostic accuracy (AUC 0.95–0.97) was high when curvature, TAESS and TSVI were combined, with SCAD trees rarely exhibiting zero adverse features.

Discussion

This study provides the first controlled evidence that SCAD-affected coronary trees are defined by adverse biomechanical conditions—elevated and variable shear stress coupled with geometric complexity. These findings establish a novel haemodynamic fingerprint for SCAD and support the integration of computational modelling into diagnostic workflows. We are currently extending this work to vessel- and segment-specific analyses to identify localised biomechanical biomarkers that predict SCAD occurrence. Such insights will inform predictive modelling and personalised risk stratification.

Session Category

Cardiovascular/Cardiorespiratory Biomechanics: Methods, Models and Applications

OA144-04

Analysis of ATAA Microstructure With Clinical 3T MRI Scanner via Diffusion Tensor Imaging

PhD Emanuele Vignali[1], PhD Emanuele Gasparotti[1], MSc Francesca Frijia[2], PhD Giulio Ferrazzi[3], MD Angelo Monteleone[4], MD Giulio Pellegrini[5], PhD Simona Celi[1]

[1]BioCardioLab, Bioengineering unit, Fondazione Monasterio, Massa, Tuscany, Italy. [2]Bioengineering unit, Fondazione Monasterio, Massa, Tuscany, Italy. [3]Philips Healthcare, Milan, Lombardy, Italy. [4]Radiology unit, Fondazione Monasterio, Massa, Tuscany, Italy. [5]Adult cardiac surgery unit , Fondazione Monasterio, Massa, Tuscany, Italy

Introduction

The microstructural analysis in Ascending Aortic Thoracic Aneurysms (ATAAs) remains a relevant aspect in analyzing the pathology evolution. It is well-established that the microstructure is at the basis of ATAAs progression [1]. The Diffusion Tensor Imaging (DTI) is a magnetic resonance (MR) technique providing information on the fibrous structure of tissues, with the potential of in-vivo applications. Recently, we demonstrated the feasibility of DTI analysis with a clinical 3T scanner on ATAAs [2]. This work aims to apply the established pipeline for the analysis of a population of ATAA specimens. The specimens were analyzed in terms of microstructure by assessing the curvilinear tractography and the corresponding fiber angles distributions.

Methods

A total of 20 ring-like ATAA specimens were collected from patients undergoing surgical repair. Before scanning, each specimen was mounted in a container filled with ecographic gel for mechanical support. A 3T clinical MR scanner was adopted with a multi-shot echo planar sequence. The processing workflow foresees segmentation, diffusion tensor estimation, curvilinear tractography and fiber distribution analysis. The resulting fiber angles (ϕ) (ϕ= 0°,180° and ϕ= 90° corresponding to circumferential and longitudinal directions respectively) distributions were discussed.

Results

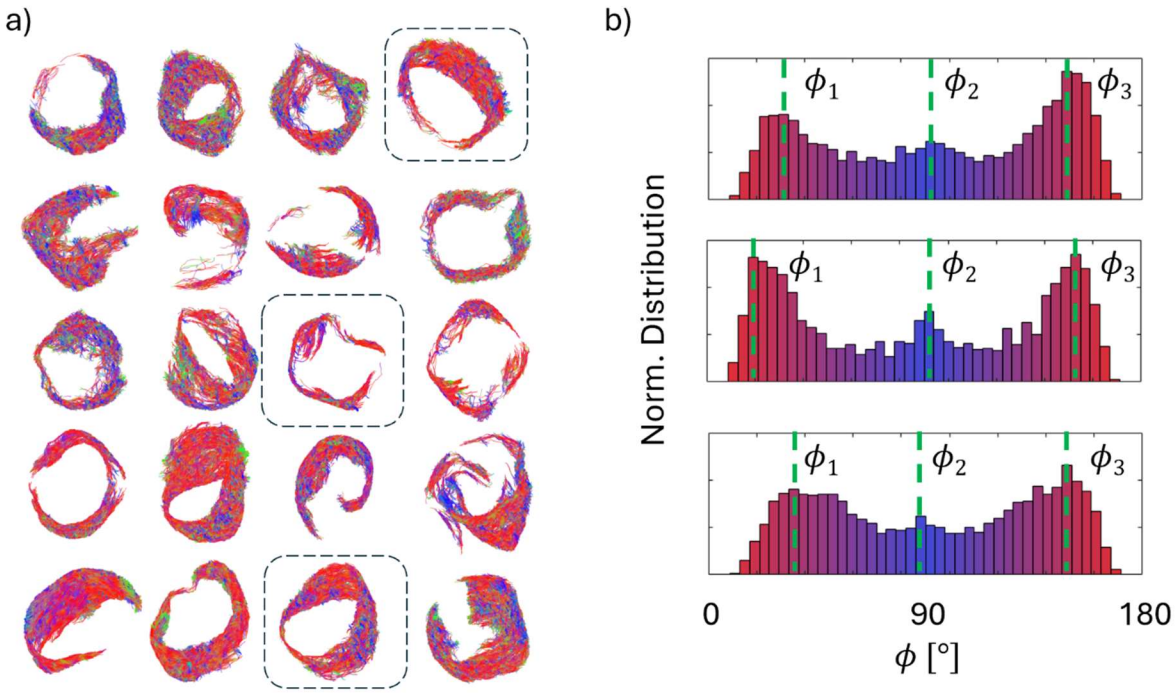
Figure1a represents tractography reconstructions for the ATAAs population. From the analysis of fiber distributions, it emerges that 80% of the cases revealed three peaks ($\phi_{1,2,3}$), as reported in the examples of Figure1b. The side peaks are always leaning towards circumferential direction and symmetric (19.2° < ϕ_1 < 39.4°, 132.5° < ϕ_3 < 160.8°), while the

central peak is parallel to longitudinal direction ($87.9° < \phi_2 < 92.1°$). The peaks are predominant in most cases, confirming the existence of two symmetric fiber families contributing mainly to the circumferential stiffness of the ATAA [3].

Discussion

We successfully applied our DTI pipeline to analyze a population of ATAAs. The microstructural characterization produced significant results in terms of fiber angle distributions, revealing that ATAAs fibers exhibit predominant circumferential orientations. It was shown that clinical MRI scans can provide reliable information about fiber architecture and ATAA pathology inferring.

Images (Optional)



References (Optional)

[1] Emanuele Vignali *et al.*, Med Eng Phys, 2020

[2] Emanuele Vignali *et al.*, J Biomechanics, 2025

[3] Xiaochen Wang *et al.*, J Mech Behav Biomed Mater, 2023

Acknowledgements (Optional)

Session Category

Cardiovascular/Cardiorespiratory Biomechanics: Methods, Models and Applications

OA144-05

Aortic Microstructure and Suture Pullout Variability

Ph.D. Candidate Gabrielle X. Lohrenz M.Eng.[1,2], Ph.D. Student Bianca Pourmussa B.A.[1,3], Professor and Vice Chair of Medicine Education, Neurobiology & Anatomy; Assistant Dean, Phase 1 Curriculum Haviva M. Goldman Ph.D.[1], Assistant Professor Brooks A. Lane Ph.D.[4], Associate Professor John F. Eberth Ph.D.[2]

[1]Drexel University, Philadelphia, PA, United States. [2]Virginia Tech, Blacksburg, VA, United States. [3]University of Pennsylvania, Philadelphia, PA, United States. [4]University of Kentucky, Lexington, KY, United States

Introduction

Aortic graft sutures experience multidirectional, dynamic loading, and interfacial failure can cause dissection or rupture. Accordingly, suture retention is defined within ISO 7198:2016 as a required test method for demonstrating the safety of vascular prostheses, grafts, and patches. While useful, these tests fail to capture the complex, anisotropic, and regionally heterogeneous properties of the aortic wall necessary for evaluating novel suture-strategies or emerging tissue-treatment technologies. In this study, we used a commercially-sourced porcine model to reveal the critical macro- and micro-structural factors contributing to large artery suture retention/failure.

Methods

Suture pullout tests were conducted on 1x3 cm strips of male and female porcine aortas in the axial or circumferential directions (ISO7198:2016). Strips were cut and grouped by proximity to small descending thoracic (DTA) and suprarenal abdominal aorta (SRAo) branches (n=4 ea; N=106), where axial samples were further separated by local region (anterior/lateral). The lower edge was clamped and 3-0 polypropylene suture inserted 2 mm from the top and pulled to failure at 50 mm/min on a Mark-10 tensile tester. Peak stresses were estimated from the maximum force and initial cross-sectional area. Elastin and collagen were evaluated using VVG and PSR staining with cross-polarization for fiber alignment. Data was analyzed using linear mixed-effect models and Tukey's post-hoc tests.

Results

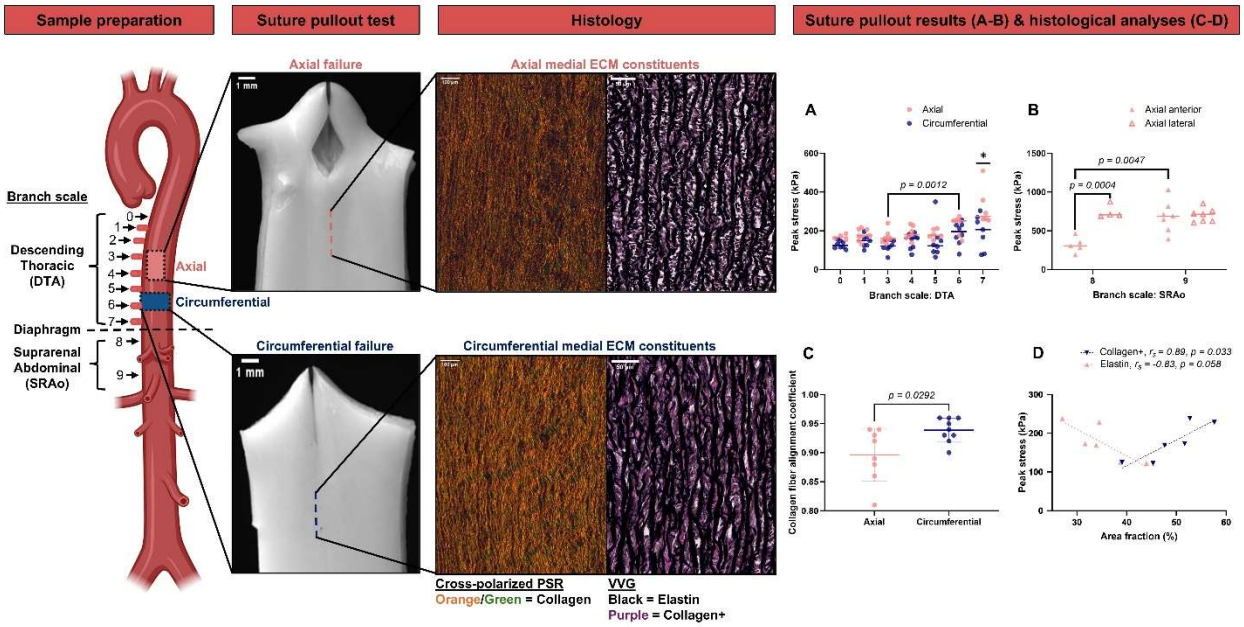
Sex had no mechanical effect (p=0.404), so male/female data were pooled for greater statistical power. Peak stress (p=0.0197) and strain (p=0.005) were notably higher in the axial than circumferential directions. Longitudinal position influenced peak stress

(p=0.0012), with higher values distally. Anteroposterior position revealed abdominal lateral sections had higher peak stress than anterior sections (p=0.0004). Elastin area fraction trended negatively with peak stress (r_s=-0.83, p=0.058), whereas collagen correlated positively (r_s=0.89, p=0.033). Medial collagen also exhibited better circumferential alignment (p=0.029).

Discussion

Our findings indicate both location and direction, but not sex, significantly influence suture pullout from porcine aortas. Peak stresses were noticeably lower when loaded parallel to the fiber direction (circumferential), where videographs suggested intrafiber slip as a mode of failure. In contrast, transverse tears were produced under perpendicular (axial) fiber loading. Our simplified findings highlight the inherent complexity of soft tissue failure.

Images (Optional)



References (Optional)

Acknowledgements (Optional)

Funding Sources: NIH2R01HL133662

Session Category

OA145-01

Where Do Single Impacts Deform the Brain Most Across Sports? a Voxel-Wise Finite-Element Study

Ms Emily Yik Kwan Chan[1], Mr Isaac Siy[1], Ms Elena Koumantou[1], Dr Chris Jones[2,3], Dr Kieran Austin[2], Prof Mike Loosemore[2,3], Dr Mazdak Ghajari[1]

[1]Imperial College London, London, London, United Kingdom. [2]Sports and Wellbeing Analytics, Swansea, Swansea, United Kingdom. [3]Institute of Sport, Exercise and Health, London, London, United Kingdom

Introduction

Head impacts in sports can cause traumatic brain injury (TBI). The nature of each sport contributes to variability in head-impact characteristics and consequent brain biomechanical responses. We aim to elucidate how the biomechanical responses of single impacts differ across sports.

Methods

Kinematic data of a total of 3139 head impacts from four sport contexts during competitions (Figure 1A) were collected using the validated Protecht instrumented mouthguards with identical post-processing [1]. These sports include professional boxing, professional and amateur mixed martial arts (MMA), and professional rugby (RFU). Each impact was simulated using the anatomically detailed Imperial College finite element brain model [2]. The brain biomechanics response was represented by the 90th-percentile maximum principal strain per element and extracted as neuroimages. Differences between sports were assessed using voxel-wise general linear modelling with 5000 permutations, including the 90th-percentile strain as a covariate to control overall magnitude. We report mean strain distributions and threshold-free cluster enhancement (TFCE)–corrected *p*-values for pairwise comparisons.

Results

Boxing and MMA-P exhibited higher strain than MMA-A and RFU, with strain concentrated cortically (Figure 1B). MMA-A versus RFU showed proportionally higher strain in sulcal and brainstem regions (Figure 1C-i). MMA-P versus MMA-A showed elevated strain in deep white matter, including corpus callosum (1C-ii). Boxing versus MMA-P showed minimal, scattered clusters (1C-iii). Boxing versus RFU showed widespread significance across inferior frontal and temporal cortices, insulae, thalamus, brainstem, and cerebellum (1C-iv).

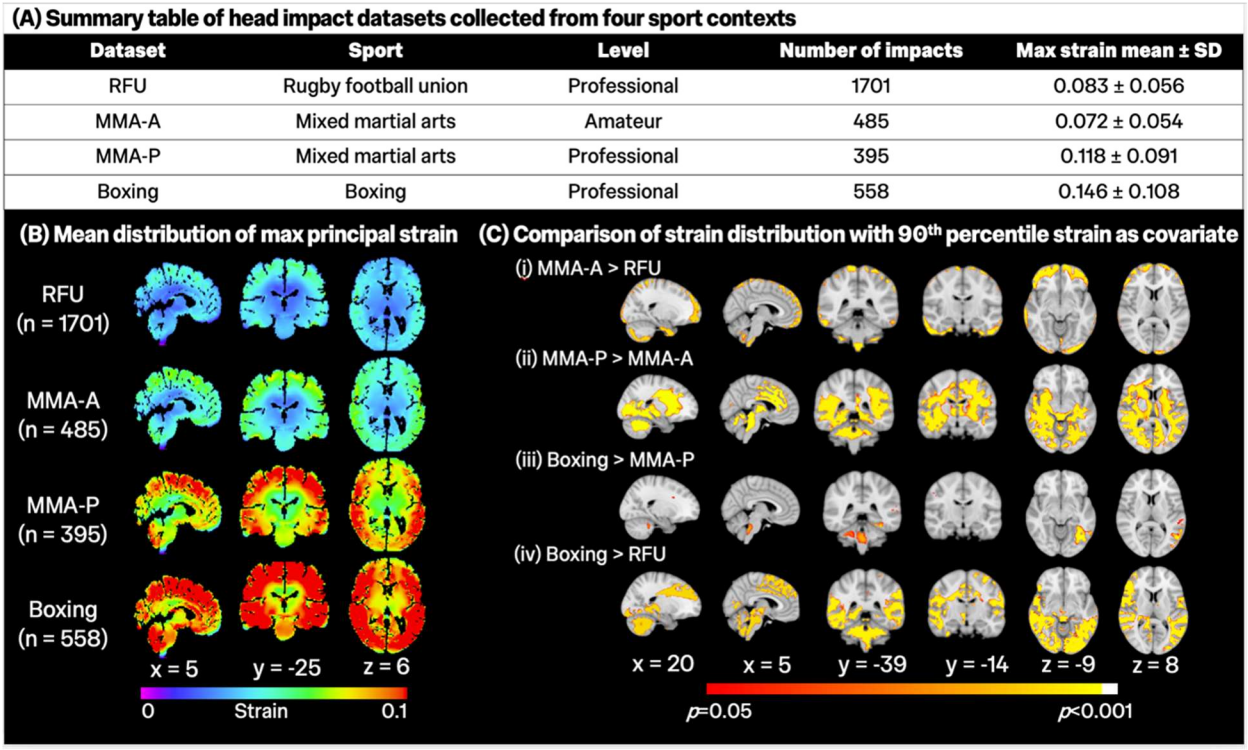
Discussion

We found that combat sports, especially professional levels, induced higher and more widespread brain strain. Professional MMA showed significantly higher strains than amateur in deep white matter, indicating professional level may increase brain deformation. To achieve this, we used a detailed brain model for strain predictions and a single mouthguard system for data collection, which minimised device-related confounding. Limitations include the absence of clinical diagnostics. Also, the study focuses on single-impact analysis without accounting for cumulative exposure; higher strain in single impact does not indicate higher injury risk of sport considering inter-impact rest periods. These findings demonstrate sport-dependent brain deformation patterns, which can inform sport-specific TBI thresholds and pitch-side surveillance.

Images (Optional)

(A) Summary table of head impact datasets collected from four sport contexts

Dataset	Sport	Level	Number of impacts	Max strain mean ± SD
RFU	Rugby football union	Professional	1701	0.083 ± 0.056
MMA-A	Mixed martial arts	Amateur	485	0.072 ± 0.054
MMA-P	Mixed martial arts	Professional	395	0.118 ± 0.091
Boxing	Boxing	Professional	558	0.146 ± 0.108



References (Optional)

[1] Jones et al., Sensors, 2023

[2] Ghajari et al., Brain, 2017

Session Category

Injury Biomechanics: N/A

OA145-02

Age-Dependent Intracranial Volume Redistribution and Its Biomechanical Implications for Traumatic Brain Injury: A Multi-Scale Analysis

MSc Claudia Sbriglio, Associate Professor Mariusz Ptak, MD-PhD Artur Kwiatkowski

Wrocław University of Science and Technology, Wrocław, Lower Silesia, Poland

Introduction

Traumatic brain injury (TBI) remains a leading cause of mortality and morbidity in adults over 60. Current computational biomechanics models, widely used to predict injury thresholds, employ static anatomical representations that fail to account for age-related brain atrophy and compensatory cerebrospinal fluid (CSF) accumulation. This 'one-size-fits-all' approach may potentially misassess injury risk in aging populations, where altered intracranial fluid-structure interactions fundamentally modify the biomechanics of impact response.

Methods

This study conducted high-resolution 3-Tesla MRI scanning with automated segmentation (Matlab and FreeSurfer) across 280 healthy subjects. Preliminary statistical modeling was performed on an initial cohort (N=130, age 7-90 years, 60 males, 70 females) using parametric distribution models, with model selection via Akaike Information Criterion. Tissue volumes (gray matter, white matter, CSF) and derived metrics (intracranial volume [ICV], CSF ratio) were quantified. Age division was defined into three groups: Young Adults (<40 years), Middle-Aged Adults (40–60), and Older Adults (>60). These anatomical data are being integrated into subject-specific finite element (FE) head models to simulate impact biomechanics and quantify how volumetric changes alter strain/pressure distributions under loading conditions.

Results

Preliminary analysis revealed CSF ratio exhibits the strongest age correlation. Older adults (>60) demonstrated 92.6% higher CSF volume compared to young adults (<40): 146.8±51.6 ml versus 76.2±24.2 ml. Proportionally, CSF comprised 11.99±4.08% of ICV in older versus 5.93±2.01% in younger cohorts, a 102% increase in fluid capacity. Sex differences in absolute volumes existed ($p<0.032$), but CSF ratios were sex-independent after head-size normalization ($p=0.517$). Complete 280-subject statistical analyses results will be presented at the conference.

Discussion

The near-doubling of intracranial CSF with aging fundamentally alters brain-skull coupling during impact. Increased fluid volume modifies viscous damping, brain displacement kinematics, and time-to-contact with cranial boundaries-mechanisms inadequately represented in generic models assuming static ~120 ml CSF across all ages. This discrepancy potentially overestimates CSF volume by 37% in young adults and underestimates by 22% in older adults, critically affecting injury threshold predictions. Age-specific finite element modeling integrating these anatomical variations is essential for establishing accurate injury tolerance curves and developing targeted protective strategies for vulnerable elderly populations.

Session Category

Injury Biomechanics: N/A

OA145-03

The Peculiar Property of Pia Mater on the Prediction of Acute Subdural Hematoma

Mr. Chengbin Li, Professor Svein Kleiven, Dr. Zhou Zhou

Neuronic Engineering, KTH Royal Institute of Technology, Huddinge, Stockholm, Sweden

Mr. Chengbin Li

Professor Svein Kleiven

Introduction

Acute subdural hematoma (ASDH) is a catastrophic injury often associated with the disruption of bridging vein (BV) or BV-superior sagittal sinus (SSS) secondary to cortical motion. Finite element (FE) models have been used to predict the ASDH risk. However, the mechanical role of the pia has been largely overlooked. This study investigates how different pia mater modelling strategies influence cortical responses and ASDH prediction.

Methods

The baseline FE head model was developed by Kleiven [1], including 11 pairs of major parasagittal BVs, originally approximated the pia mater as a linear elastic membrane (Young's Modulus 11.5 MPa; Fig.1A). In this study, we modified the pia mater as a nonlinear simplified rubber with the stress-strain curve derived from pial tension test [2] (Fig.1A). Both models were exposed to an impact loading from published post-mortem human subject experiments known to induce ASDH [3].

Results

Pia mater material modelling substantially affected the cortical motion and BV responses (Fig.1B-D). With the linear elastic pia mater, the cortical motion and maximum BV strain were predicted as 2.0 mm and 0.10, respectively. With nonlinear modelling, the cortical motion increased to 8.8 mm and BV strain to 0.16. When compared with the BV-SSS ultimate strain range (0.29 ± 0.13) [4], a possible ASDH occurrence was only predicted when the pia mater was simulated as nonlinear material. Neither of the predicted BV strains fell within the range of the BV ultimate strain (0.50 ± 0.16) [5].

Discussion

This study highlighted the mechanical role of pia mater on brain responses and the necessity of modelling pia mater with nonlinear material for reliable ASDH prediction. The majority of existing FE head models use a linear elastic material model, representing a higher stiffness than the nonlinear model adopted in this study (Fig.1A). Results indicated such an over-stiffening pia mater modelling approach constrain the brain cortical motion and thereby underestimated the BV response and interpreted ASDH risk.

Images (Optional)

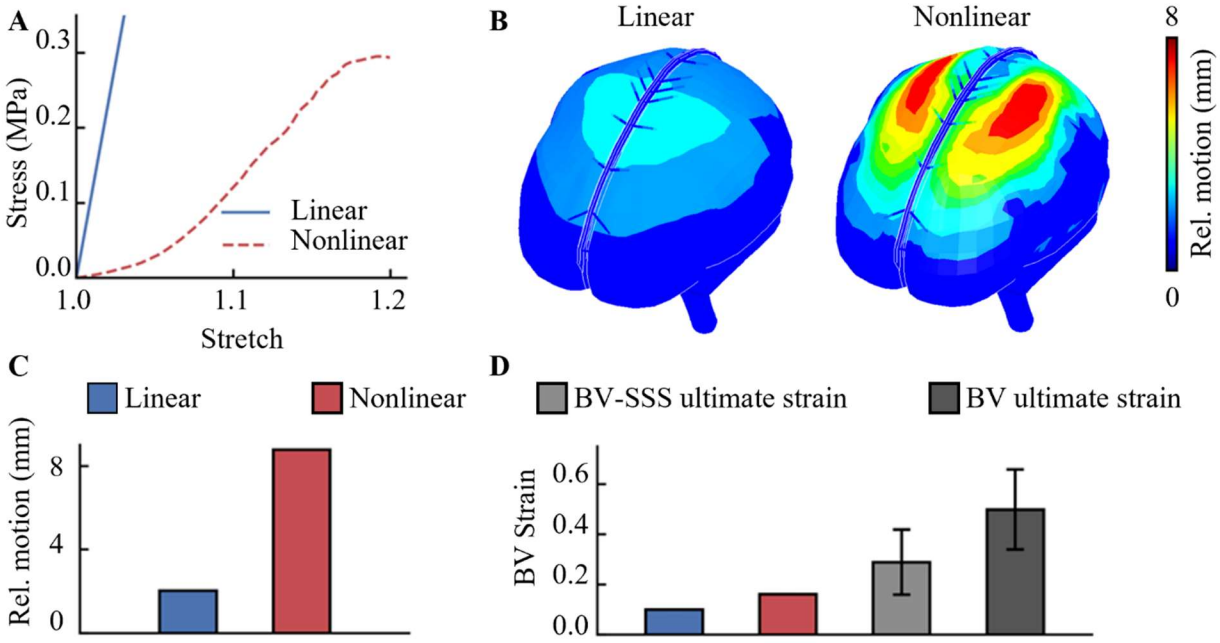


Figure 1. (A) Stress-stretch response of pia mater: linear elastic model (E=11.5 MPa) and nonlinear model [1, 2]. (B) Cortical relative motion captured at the maximum value occurring time. (C) Maximum value of the cortical relative motion. (D) Maximum BV strain plotted together with the BV- superior sagittal sinus (SSS) ultimate strain and BV ultimate strain [4, 5].

References (Optional)

[1] Svein Kleiven. Stapp Car Crash Journal, 2007.

[2] Patrick Aimedieu et al. , J Neurosurgery, 2004.

[3] Bart Depreitere et al. , J Neurosurgery, 2006.

[4] Aida Georgeta Monea et al. , J MBBM, 2013.

[5] Maw-chang Lee et al. , J Biomechanics, 1989.

Acknowledgements (Optional)

This research has received funding from KTH Royal Institute of Technology (Stockholm, Sweden), the Swedish Governmental Agency for Innovation Systems (VINNOVA) (no. 2023-00753 and no. 2024-03635), Swedish Research Council (VR-2024-05848 and VR-2024-02782), Skyltfonden from the trafiksäkerhet (TRV 2024/23811 and TRV 2024/50301). The content of this article is solely the responsibility of the authors and does not necessarily represent the official views of funding agencies. The computational simulations were enabled by resources provided by the National Academic Infrastructure for Supercomputing in Sweden (NAISS) at the center for High Performance Computing (PDC) partially funded by the Swedish Research Council through grant agreement no. 2022-06725. The authors declare that they have no known competing financial interests or personal relationships that could have appeared to influence the work reported in this paper.

Session Category

Injury Biomechanics: N/A

OA145-04

In Vivo Brain Deformation Response to Rapid Head Rotation in a Large Animal Model

Mr. Charlie Magarey[1], A/Prof. Mark Plummer[1], Prof. Peter Cripton[2], A/Prof. Claire Jones[1]

[1]Adelaide University, Adelaide, South Australia, Australia. [2]The University of British Columbia, Vancouver, British Columbia, Canada

Introduction

Synchronous measures of head kinematics and *in vivo* brain deformation during rapid head rotation could advance understanding of traumatic brain injury (TBI) mechanisms, inform protective equipment design, and provide data for validating computational models. Brain deformation has been measured in cadaveric tissue (high rate), or *in vivo* participants (low-rate); however, brain tissue strain response is rate dependent and changes rapidly postmortem. The aims of this study were to develop sonomicrometry methods to measure *in vivo* multipoint brain motion in a sheep model of rapid head rotation, assess the repeatability of brain displacement measurement, and quantify the *in vivo* brain deformation during rapid head rotation.

Methods

Three anaesthetised female adult sheep were instrumented with a skull mounted kinematics sensor array (sampled at 51.2 kHz). Up to 14 sonomicrometry transceivers (~3mm diameter, sampled at 1034 Hz) were implanted into the cerebral hemispheres, 10 were rigidly attached to the inner cranial vault (Fig. 1B-C). A custom apparatus produced repeatable rapid sagittal plane head rotation (without head impact) about the second cervical vertebra (Fig. 1A); two to five rotations were completed per animal. Head kinematics, three-dimensional brain displacement, and strain, were quantified and assessed for repeatability. Relative motion between transceivers and brain tissue was assessed with computed tomography imaging before/after each rapid head rotation.

Results

Brain displacement was tracked at up to 13 locations in each of 11 head rotations. Maximum brain displacement and strain were 2.47 mm and 18%, respectively. Brains displayed decaying rotational oscillation in the sagittal plane at 37.3±3.7 Hz (Fig. 1E), and associated oscillating tension-compression waves throughout the cerebrum, for ~100 ms from head acceleration initiation. Head kinematics and brain displacement had good-to-

excellent (CORA>0.86), and excellent (CORA=0.99) repeatability, respectively. The brain transceiver position change from pre- to post-test was negligible (mean=0.024 mm).

Discussion

Sonomicrometry was successfully applied in live anaesthetised sheep to provide repeatable measurements of brain displacement and deformation during rapid head rotation. The sheep brain rotational oscillation resembled that observed in rapid human cadaver head rotation, although the magnitude was lower and frequency was higher. These data may be used to improve validation of computational models of TBI.

Images (Optional)

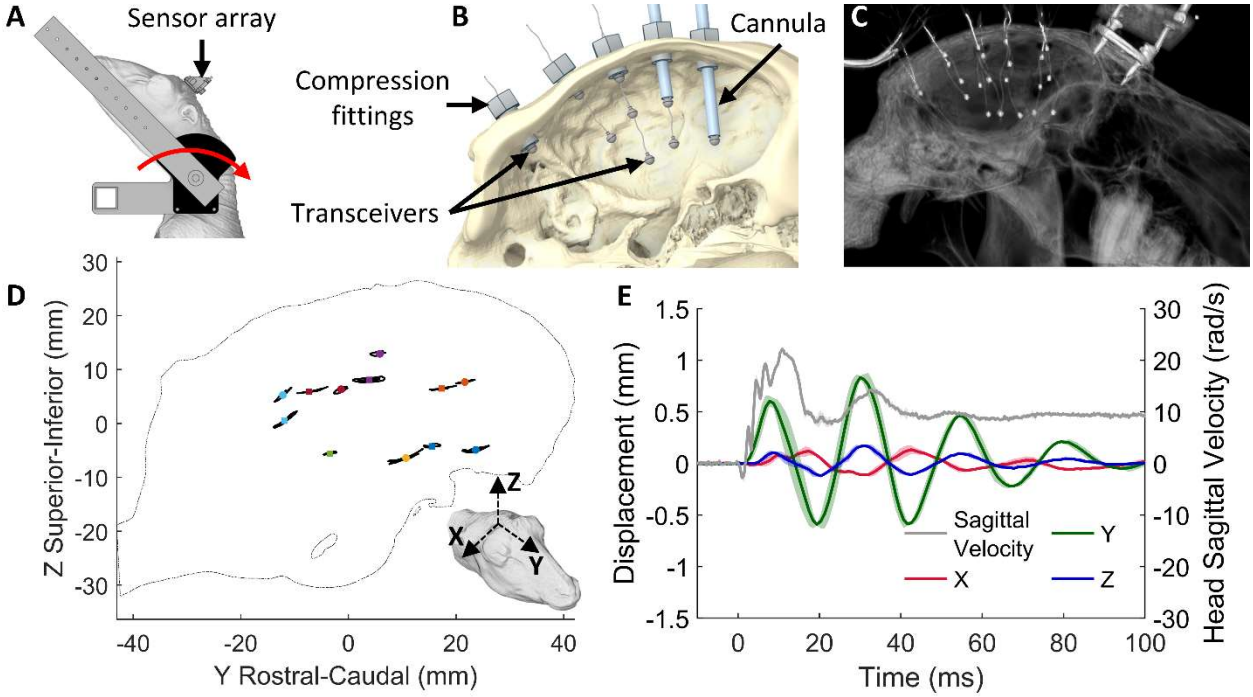


Figure 1A: Head rotation apparatus and sensor array placement. **B:** Transceivers inserted into the brain (not shown) and inner skull table via a retractable canula. **C:** CT image of instrumented head. **D:** Sagittal 2D view of brain motion amplified by 3x for clarity, insert shows head coordinate system. **E:** Head angular velocity and brain displacement versus time for single brain transceiver.

Session Category

Injury Biomechanics: N/A

OA145-05

The Influence of Angular Acceleration Versus Deceleration Ratio on Regional Brain Strain Response

Dr. Tyler F. Rooks PhD, Dr. Narayan Yoganandan PhD

Medical College of Wisconsin; Department of Neurosurgery, Milwaukee, WI, United States

Introduction

Brain injury remains a concern in sports, military training, and vehicle crashes. Brain injury simulations are used to understand injury mechanisms and mitigation approaches using model-based whole-brain injury metrics, such as cumulative strain damage measure (CSDM) and maximum principal strain (MPS). Research using simplified two-dimensional brain models or whole-brain models has shown that exposure duration and the ratio of acceleration versus deceleration affects brain strain responses. The objective of this study was to investigate the effect of exposure parameters on regional brain strain distribution using an anatomically accurate model.

Methods

The study used an existing model with 12 regions of interest (ROI). ROIs are symmetric about the midsagital plane with separate components for left and right sides. Material properties were obtained from literature. Head rotations were simulated about primary axes of motion (coronal [Rx], sagittal [Ry], and axial [Rz]) and combined axes (Rxy). Sagittal rotations included positive and negative directions (Ry and -Ry, or Rxy and -Rxy). Idealized angular acceleration exposures used a sine wave with varying duration for acceleration versus deceleration (i.e., acceleration:deceleration ratio). Duration ratios included 1:1, 1:2, and 1:3. Multiple severities were assessed. Regional CSDM (rCSDM) was calculated for strains >0.25 for each ROI. Regional MPS (rMPS95) was calculated for each ROI.

Results

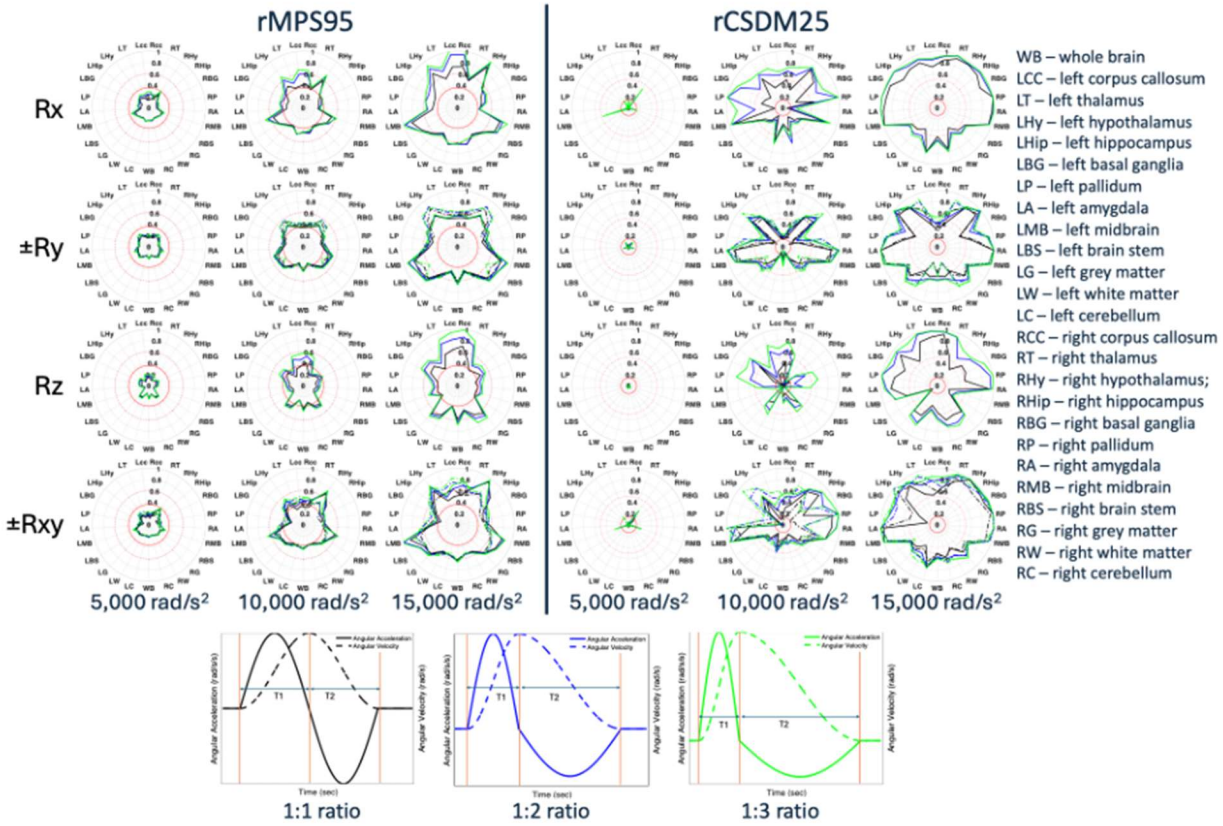
Increasing deceleration duration resulted in increases in both rCSDM25 and rMPS95 for many ROIs. The deeper structures (e.g., basal ganglia, corpus callosum, pallidum, amygdala, hypothalamus, thalamus, hippocampus) were most affected by changes in the duration ratio with large changes in response. The effect of rotational direction was inconsistent with some directions resulting in large changes (Rx) while others had smaller effect (Ry and -Ry). The rCSDM25 metric was more susceptible to changes with large

increases in many regions compared with rMPS95. The largest increases occurred when increasing the duration ratio from 1:1 to 1:2 at a peak angular acceleration of 10k rad/s^2.

Discussion

The study showed that regional brain strain response was sensitive to changes in the acceleration:deceleration duration ratio and to rotation direction. Understanding the relationship between brain strain distributions and exposure parameters may inform how exposures can influence symptoms of concussion.

Images (Optional)



Session Category

Injury Biomechanics: N/A

OA145-06

MRI to Head Model: A Reproducible Pipeline for Study-Specific Finite Element Head Model Generation From MRI for TBI Studies

Mr. Christian John Saludar[1,2], Dr. Maryam Tayebi PhD[1,3], Mr. Jacob Mathew[1], Mr. Chun Kiet Vong[1], Dr. William Schierding PhD[3,4], Mātai mTBI Group[3], A/Prof. Alan Wang PhD[1,3,5], A/Prof. Samantha Holdsworth PhD[3,5], Prof. Justin Fernandez PhD[1,3], Dr. Joshua McGeown PhD[3,5,6], Dr. Eryn Kwon PhD[1,3], Dr. Vickie Shim PhD[1,3]

[1]Auckland Bioengineering Institute, University of Auckland, Auckland, Auckland, New Zealand. [2]University of the Immaculate Conception, Davao, Davao del Sur, Philippines. [3]Mātai Medical Research Institute, Gisborn, Gisborne, New Zealand. [4]Vision Research Foundation, University of Auckland, Auckland, Auckland, New Zealand. [5]Faculty of Medical and Health Sciences & Centre for Brain Research, Auckland, Auckland, New Zealand. [6]Brain Health Research Insitute, Auckland University of Technology, Auckland, Auckland, New Zealand

Introduction

Traumatic brain injury (TBI) is a global health concern. Despite high prevalence and substantial socio-economic impact, the biomechanical mechanisms underlying TBI remain poorly understood. Accurate quantification of strain propagation within brain tissue is critical for improving our understanding of injury mechanisms. Finite element (FE) models have been widely used for this purpose, and several laboratories have developed detailed head models with high biofidelity. However, generating study-specific models that accurately reflect cohort-specific neuroanatomy, tissue properties, and geometry remains challenging. Addressing this, we developed a pipeline capable of generating a study-specific FE head model directly from structural and diffusion MRI.

Methods

Seventy-eight male high-school rugby players underwent T1-weighted and multi-shell diffusion MRI (dMRI) brain scan. T1-weighted images were denoised, corrected for N4-bias field, and skull-stripped. dMRI data underwent denoising and corrections for B1-field nonuniformity, Gibbs ringing, and susceptibility distortions. Fractional anisotropy (FA) maps and fibre orientation distributions (FODs) were estimated, and a cohort-specific template was generated using ANTs and MRtrix3 from the T1 images, FA maps, and FODs. The template T1 and FOD maps were automatically segmented to derive cortical parcellations and major white-matter tracts. Due to the difficulty of segmenting the falx

and tentorium, these structures were obtained from an open dataset by Bayly et al. and registered to our study template. A whole-brain hexahedral mesh was generated using Polycube, and an in-house script assigned each element to anatomical structures using the segmented maps. Material properties were assigned in FEBio Studio based on our previous work, and fibre orientations were incorporated from the FOD map (Figure 1).

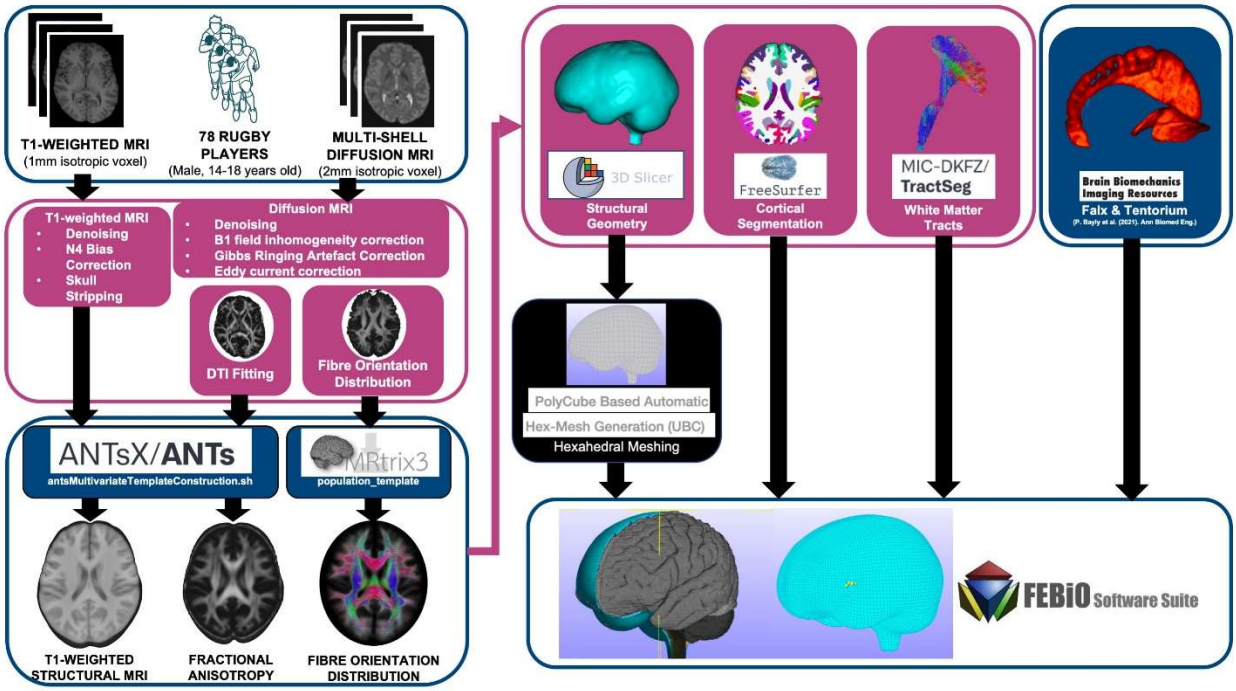
Results

The pipeline successfully produced a study-specific FE head model comprising 92,712 elements. The brainstem, cortex, cerebellum, falx, and tentorium were represented as distinct anatomical parts.

Discussion

This pipeline demonstrates a feasible approach for generating MRI-derived, study-specific FE head models that better capture cohort-specific geometry and neural structure. Ongoing work focuses on validating the model and simulating head impacts recorded through instrumented mouthguards worn during the playing season. The broader aim is to integrate FE-derived strain predictions with machine learning to link real-world impact exposure with localized structural changes, ultimately improving biomechanical understanding of TBI injury.

Images (Optional)



Acknowledgements (Optional)

We sincerely thank all participants, Gisborne Boys High School, and Mātai Ngā Māngai Māori for their engagement. Support for research: Kānoa – Regional Economic Development & Investment Unit; Trust Tairāwhiti; NZ MBIE Catalyst Strategic Fund; Neurological Foundation; Fred Lewis Enterprise Foundation; Hugh Green Foundation; JN & HB Williams Foundation; Health Research Council of New Zealand; Anonymous Donation; NZ Rugby Foundation; and Te Tītioki Mataora. We also thank GE Healthcare for MRI protocol assistance and acknowledge use of the eResearch Infrastructure Platform hosted by REANNZ Ltd. Support to researchers: C.J. Saludar – DOST-SEI Foreign Graduate Scholarship; W. Schierding – Vision Research Foundation Fellowship; J. McGeown – Neurological Foundation Philip Wrightson Fellowship; M. Tayebi and E. Kwon – Hugh Green Foundation Senior Fellowships.

Session Category

Injury Biomechanics: N/A

OA146-01

Polyphenol-Eluting Sutures to Improve Vascular Mechanostability

Ph.D. Candidate Gabrielle X. Lohrenz M.Eng.[1,2], Assistant Professor Brooks A. Lane Ph.D.[3], Advanced Cardiac Surgery Fellow Yuta Kikuchi M.D., Ph.D.[4], Professor, Hunter Endowed Chair Naren Vyavahare Ph.D.[5], Associate Professor John F. Eberth Ph.D.[2]

[1]Drexel University, Philadelphia, PA, United States. [2]Virginia Tech, Blacksburg, VA, United States. [3]University of Kentucky, Lexington, KY, United States. [4]Thomas Jefferson University, Philadelphia, PA, United States. [5]Clemson University, Clemson, South Carolina, United States

Introduction

Stress concentrations occur around permanent sutures in tension, increasing a tissue's susceptibility to inflammation and tearing. For large arteries, microtears can progress to dissection, pseudoaneurysms, intimal-medial hyperplasia, or even rupture; complications associated with significant morbidity and mortality [1]. Pentagalloyl glucose (PGG), a non-toxic, naturally occurring polyphenolic tannin, binds both collagen and elastin, strengthening structural proteins and reducing their susceptibility to proteolysis. PGG is an antioxidant, anti-inflammatory, anti-calcific, and antimicrobial small molecule, making it a compelling adjunct for the repair of aortopathies. Delivery of PGG at therapeutically effective concentrations can be challenging given the thick and heterogeneous large-artery wall, and the high-tension, blood-facing environment. Here, we report on a novel, suture-based, aortic PGG delivery system.

Methods

ISO 7198:2016 suture pullout tests were conducted on 1Í3 cm axial strips of porcine descending aorta from age/sex-matched pigs (n~10). Experimental groups include: (i) untreated controls, (ii) PGG-suture, from plasma-treating 3-0 polypropylene and attaching calcium-crosslinked PGG (1 mg) in alginate, and (iii) PGG-immersed, by incubating aortic strips in 0.15% PGG at 37°C for 24-hours. To model damage (n~3), strips were incubated in 0.25M NaOH for 24-hours and (iv) tested directly (NaOH damage), or (v) immersed in PGG (Damage+PGG). PGG release was quantified with Folin-Ciocalteu, and drug delivery confirmed by FeCl3 staining. Group differences were assessed by one-way ANOVA with Tukey's post-hoc.

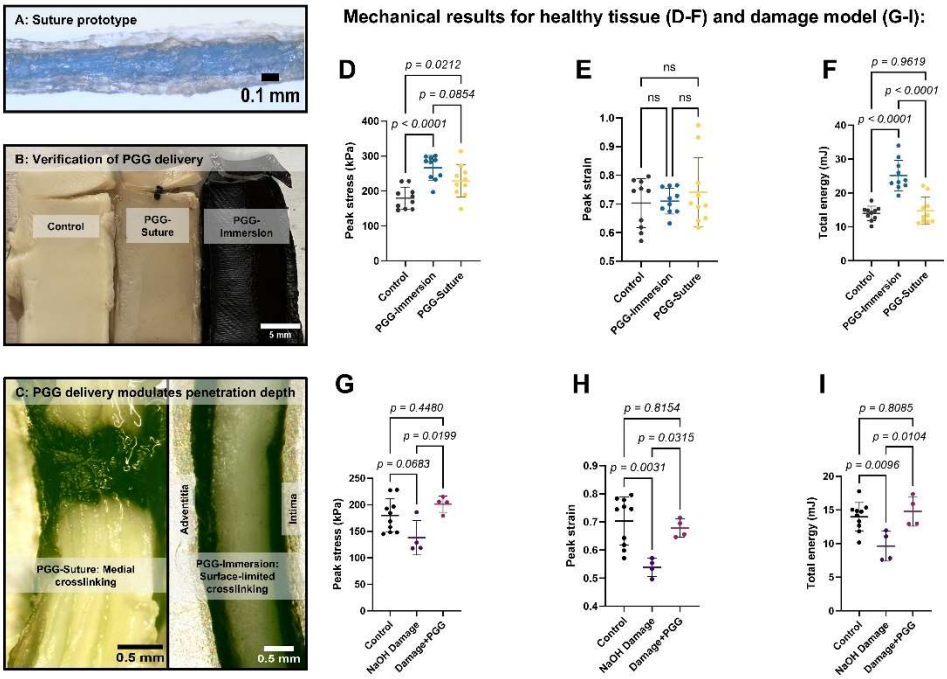
Results

70% of PGG was released from coated sutures in 1-hour with the PGG-suture (p=0.0212) and PGG-immersed (p<0.0001) samples exhibiting higher peak stresses than controls. Similar peak strains were observed across groups in the non-damage model. For NaOH damage, PGG significantly increased peak stress (p=0.020), strain (p=0.032), and energy (p=0.010).

Discussion

Suture-based delivery of PGG represents a promising strategy to strengthen the anastomotic junction, especially in structurally compromised tissue, by delivering the drug directly to key structural proteins, evenly distributing tension across the wall. While the long-term biological effects of this application, especially in bloodstream circumstances, are currently under investigation, our study reveals immediate mechanical benefits that are likely to improve postoperative outcomes without increasing procedural complexity.

Images (Optional)



References (Optional)

[1] Coselli, *Ann Thorac Surg*, (2002),73(4):1107-1116

Acknowledgements (Optional)

Funding Sources: NIH 2R01HL133662

Session Category

Cardiovascular/Cardiorespiratory Biomechanics: Methods, Models and Applications

OA146-02

Gestational Hypobaric Hypoxia Induces Long-Term Biomechanical Remodeling of the Thoracic Aorta

Mr. Álvaro Navarrete PhD[1], Mr. Adolfo A. Paz[2], Mr. Claudio García-Herrera PhD[1], Mr. Carlos Godoy-Guzmán PhD[1], Mr. Emilio A. Herrera PhD[2], Mr. Andrés Utrera MSc[1]

[1]Universidad de Santiago, Santiago, Metropolitana, Chile. [2]Universidad de Chile, Santiago, Metropolitana, Chile

Introduction

High-altitude gestation exposes the fetus to chronic hypobaric hypoxia, a condition known to impair vascular development and increase long-term cardiovascular risk [1]. Despite extensive evidence of pulmonary and systemic functional alterations, the long-term biomechanical consequences for large elastic arteries remain poorly defined. Given that arterial stiffness and residual stress are key mechanobiological markers of cardiovascular disease [2], this study tested the hypothesis that gestational hypobaric hypoxia induces persistent biomechanical and structural remodeling in the descending thoracic aorta (DTA) of adult offspring.

Methods

Pregnant guinea pigs were exposed to normoxia (N, n=6) or hypobaric hypoxia (H, n=6; equivalent to 3,800 m) throughout gestation. Offspring matured under normoxia until one year of age. DTA specimens were evaluated through:

Biomechanics: ring-opening test (residual strain), axial pre-stretching, and planar biaxial tensile testing.
Ex-vivo function: dose–response curves for K^+-induced vasoconstriction and methacholine-induced vasodilation using wire myography.
Histology: elastin and collagen quantification, smooth muscle nuclei density, endothelial cell linear density.
Appropriate parametric or non-parametric statistics were applied ($p \leq 0.05$).

Results

Hypoxic DTA exhibited greater circumferential residual strain and a significant reduction in physiological axial pre-stretch in the proximal thoracic region. Planar biaxial testing showed higher mean stiffness at low and high deformation levels (E_1, E_2) in hypoxic tissue. Functionally, hypoxic arteries showed greater maximal K^+-induced contraction and reduced methacholine-mediated vasodilation. Histologically, hypoxic DTA displayed wall

thickening, higher elastin content, and reduced endothelial cell density, consistent with outward hypertrophic remodeling.

Discussion

The combination of increased stiffness, elevated residual strain, reduced endothelial cell density, and impaired vasodilation demonstrates that gestational hypobaric hypoxia produces persistent maladaptive arterial remodeling into adulthood. These findings align with prior reports linking developmental hypoxia to vascular dysfunction and future cardiovascular risk [1,3]. The observed outward hypertrophic remodeling and functional impairment support a mechanobiological shift toward a pro-hypertensive phenotype, suggesting altered set-point regulation of wall stress. Further studies integrating computational analysis may help determine whether these remodeling patterns are adaptive or maladaptive long-term.

References (Optional)

1 González-Candia, A. et al, Frontiers in Physiology, 2021.

2 Holzapfel, G.A., & Ogden, R.W. American Journal of Physiology – Heart and Circulatory Physiology, 2018.

3 González-Candia, A. et al., Life Sciences, 2023.

Acknowledgements (Optional)

- FONDECYT Regular grants N° 1201283, 1220956 & 1241502.
- Álvaro Navarrete thanks ANID FONDECYT Postdoctorado N° 3250249.
- Andrés Utrera thanks ANID PFCHA/DOCTORADO NACIONAL BECAS CHILE (2023-21231932).
- Adolfo A. Paz thanks ANID BECA DOCTORADO NACIONAL 21230893.

Session Category

Cardiovascular/Cardiorespiratory Biomechanics: Methods, Models and Applications

OA146-03

Indentation Size Effects Dominate Aortic Tissue Nanoindentation and its Dynamic Mechanical Analysis

Prof Michele Conti, Dr. Gabriele Greco, Eng. Giulia Formenton

University of Pavia, Pavia, IT, Italy

Introduction

Nanoindentation is a powerful technique for probing the local mechanical properties of biological materials; however, its application to cardiovascular tissues remains limited and often inconsistent. Existing studies on aortic tissue employ highly heterogeneous protocols, which differ in indentation depth, tip geometry, loading conditions, and surface preparation. This makes results difficult to compare and frequently incompatible with classical analytical models. The intrinsic structural complexity of aortic tissue, characterized by irregular surface topography and heterogeneous composition, further complicates the interpretation of nanoindentation data.

Methods

In this work, we carried out an extensive nanoindentation campaign on porcine aortic tissue from multiple animals, employing 80 different experimental conditions. By systematically varying key parameters—including indentation depth (1–15 μm), indenter tip radius (25–100 μm), loading rate (0.1–10 μN/s), indentation speed (1–10 μm/s), and surface preparation—we identified the main sources of variability that compromise the validity of the Hertzian model and strongly influence the extracted Young's modulus.

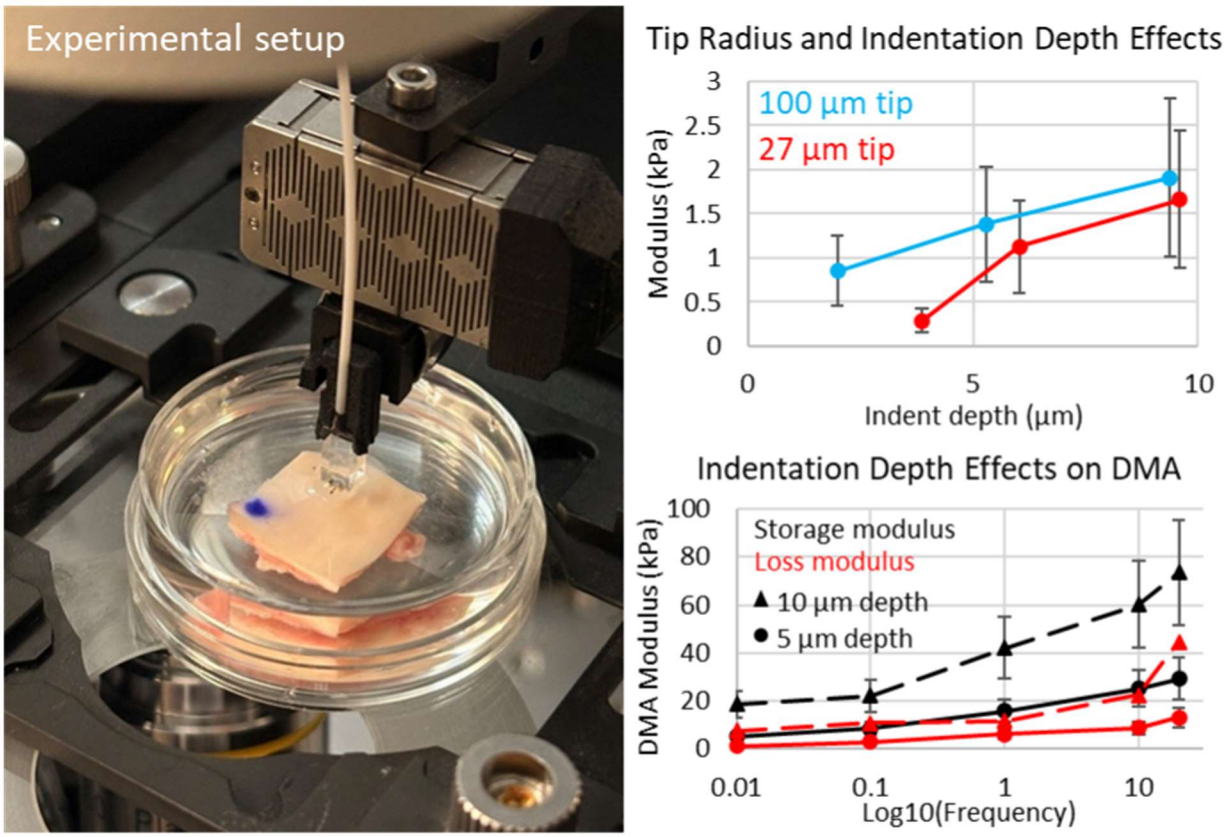
Results

Our results demonstrate that even modest deviations from standard protocols can lead to large discrepancies in measured mechanical properties, underscoring the urgent need for methodological standardization. The strongest effects arise from indentation depth and tip radius, known as indentation size effects, which profoundly influence the scaling of the tissue's mechanical response. For instance, using a 27 μm indenter tip yields apparent Young's moduli ranging from 0.3 to 1.7 kPa when the indentation depth is varied between 4 and 10 μm.

Discussion

Building on these findings, we propose a robust and reproducible nanoindentation protocol tailored to cardiovascular soft tissues. This protocol minimizes violations of model assumptions, reduces experimental variability, and improves the comparability of data across studies. We further extended our analysis to dynamic mechanical nanoindentation, testing different combinations of indentation depth (5–10 µm), frequency (0.01–20 Hz), and oscillation amplitude (0.3–2.5 µm). Again, we observed a strong dependence on indentation size effects, which dominated the mechanical response. Overall, our study provides a solid foundation for the future standardized mechanical characterization of aortic tissue. These insights open new opportunities for multiscale mechanical modeling and facilitate the data integration into advanced in-silico frameworks.

Images (Optional)



Session Category

Cardiovascular/Cardiorespiratory Biomechanics: Methods, Models and Applications

OA147-02

Hamstring Muscle Strain During Accelerated Sprints Following Repeated Sprints

BSc Leon Lobe[1,2], PhD Evy Meinders[3], Associate Professor David John Saxby[4], Professor Rod Barrett[4], Associate Professor Laura Diamond[4], Professor Arnold Baca[1], Associate Professor Hans Kainz[1,2], PhD Basílio Gonçalves[1,2]

[1]Centre for Sport Science and University Sports, University of Vienna, Vienna, Vienna, Austria. [2]Neuromechanics Research Group, University of Vienna, Vienna, Vienna, Austria. [3]Musculoskeletal Biomechanics Lab, Mechanical Engineering, Carnegie Mellon University, USA, Pittsburgh, Pennsylvania, United States. [4]Australian Centre for Precision Health and Technology, Griffith University, Australia, Gold Coast, Queensland, Australia

Introduction

Hamstring strain injuries (HSI) happen frequently during repeated sprinting with increasing incidence [1]. Hamstring strain peaks during late swing in sprinting [3] with repeated sprints exacerbating muscle fatigue [4]. Here we investigate the effects of repeated sprinting on hamstring strain. We hypothesized hamstring strain during sprinting would increase following repeated sprints.

Methods

Forty-three active recreational athletes completed 12x30m maximal sprints on a non-motorized treadmill while 3D body motions, ground reaction forces, and electromyographic signals from 12 muscles were recorded [5]. Joint angles, moments, and muscle-tendon kinematics were calculated using Opensim [6] and served as input to a calibrated electromyography-informed neuromusculoskeletal model to estimate muscle dynamics for biceps femoris long head (bflh), semitendinosus, and semimembranosus [7]. We applied statistical-parametric-mapping to test for within-participant differences in angles, moments and forces, and paired t-tests for running speed and peak strain ($\Delta l/l_0$) between pre- and post-sprint protocol.

Results

After repeated sprints, we observed a significant ($p<0.01$) reduction in running speed (16%±9%), magnitude of sagittal plane joint angles and moments, as well as semimembranosus muscle force, but no significant change in forces of bflh and semitendinosus. Peak strain significantly decreased ($p<0.01$) for bflh (17%±26%) and semitendinosus (20%±15%), but not semimembranosus (2%±39%). Peak strain increased for 5(12%), 4(9%), and 11(26%) participants in their bflh (38%±33%), semitendinosus (12%±2%), and semimembranosus (45%±49%), respectively.

Discussion

The average reduction in peak muscle strain may reflect a change in motor control, which may prevent excessive strain under fatiguing conditions. However, in some individual an increases in muscle strain occurred, which in line with previous research [3], may contribute to an increased HSI risk. Applying the workflow of this study to sprint-related sports could help identify athletes at higher risk of HSI.

Images (Optional)

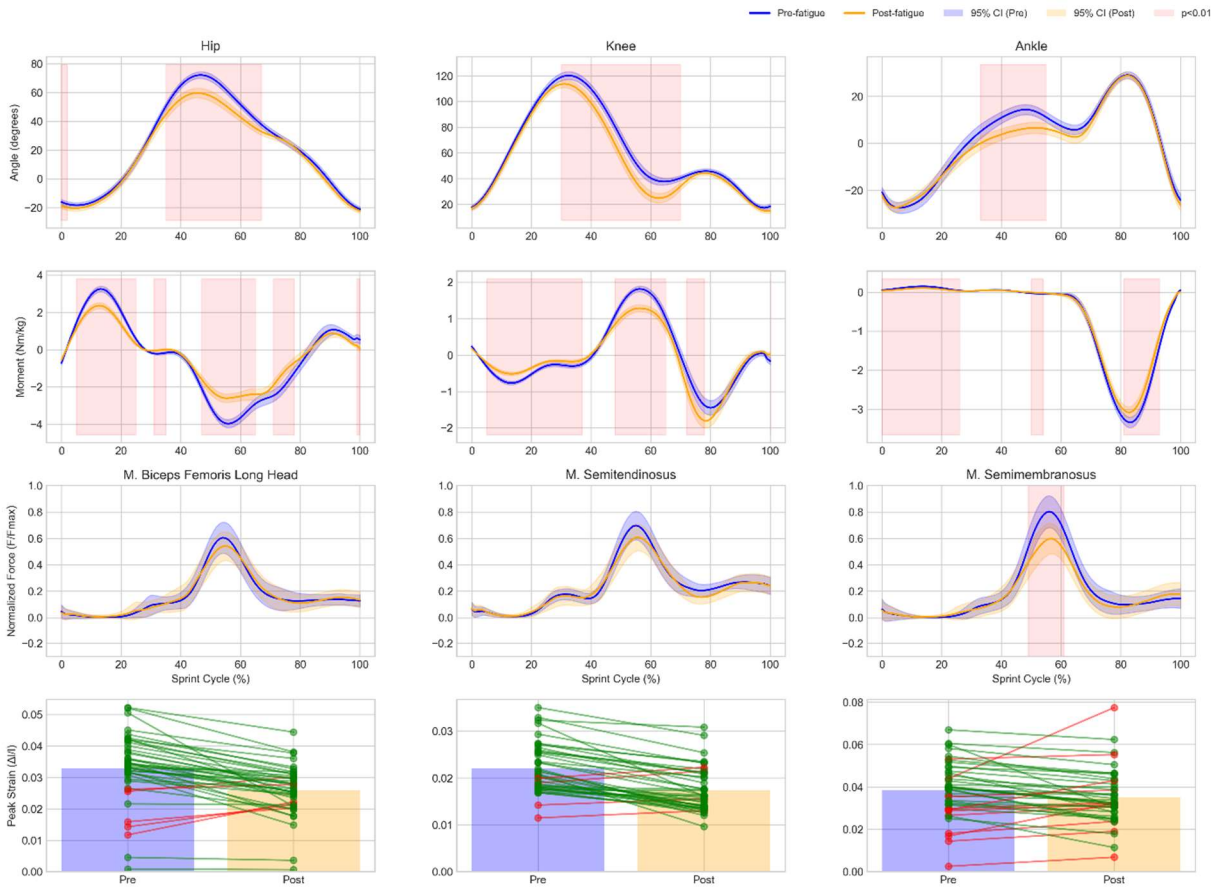


Fig. 1: Ensemble averages (n = 43) of hip, knee, and ankle angles, moments, normalized muscle forces, and peak muscle strain for a sprint cycle pre (solid blue) and post (solid orange) a repeated sprints protocol. Shaded regions indicate 95% confidence intervals. Red shaded regions denote statistically significant differences (p<0.01, Statistical Parametric Mapping). The bottom row shows individual participant responses (connecting lines) and group means (bars) for peak muscle strain. Green connecting lines indicate a decrease in peak strain, while red lines indicate an increase. Sprint cycles are defined from toe-off to toe-off and all data were normalized to 101 points (0-100%).

References (Optional)

[1] J. Ekstrand et al. Br. J. Sports Med, 2023

[2] H. Liu et al., J. Sport Health Sci., 2012

[3] R. Pimenta et al., Sci. Rep., 2023

[4] B.A.M. Gonçalves et al., Sports Health Multidiscip. Approach, 2023

[5] S.L. Delp et al., IEEE Trans. Biomed. Eng., 2007

[6] M..J. Hambly et al., IEEE Trans. Biomed. Eng., 2025

Session Category

Musculoskeletal Biomechanics: Joints and Motion

OA147-03

Influence of a Demanding 10 Km Run on Multi-Segment Foot Joint Kinetics and Kinematics

Professor Hannah Rice[1], Mr. Jonatan Riise[1], Mr. Patrick Mai[1], Ms. Naomi Frankston[1], Dr. Robert Schuster[2], Assoc. Prof. Luke Kelly[2]

[1]Norwegian School of Sport Sciences, Oslo, Oslo, Norway. [2]Austrialian Centre for Precision Health and Technology (PRECISE), Gold Coast, Queensland, Australia

Introduction

Humans are suited to endurance running, facilitated in part by the function of the foot, which can store and return energy and stiffen during the push-off phase of running stance. Running-induced fatigue has been shown to alter the distribution of vertical forces under the foot and may also influence the mechanics of the joints within the foot. There is limited understanding of how within-foot joint kinetics change as a result of prolonged or demanding running. This study aimed to quantify how the biomechanical function of the foot is influenced by completion of a demanding 10 km run.

Methods

Twenty-eight male and female runners ran barefoot at a self-selected speed over a runway pre- and post- a 10 km shod treadmill run conducted at 105% of estimated race time. Kinematic, ground reaction force and plantar pressure data were collected during the barefoot running trials. The foot and shank were modelled in OpenSim as six rigid segments. Three independent forces acting on the rearfoot, midfoot and forefoot regions were obtained from the force and pressure data; these were used for inverse dynamics analyses to quantify ankle and within-foot joint moments. Peak joint moments, the forces under each foot region and stance phase time-series kinematics were compared statistically between pre- and post-10 km run.

Results

Peak ankle plantarflexor and internal rotation moments were reduced post- compared to pre-10 km run but there were no differences in peak moments generated about any of the joints within the foot. Total vertical ground reaction forces were lower post- than pre-run, despite a consistent average running speed. Vertical forces under the forefoot region were also reduced post- compared with pre-run. There were no changes in within-foot kinematics post- compared with pre-run.

Discussion

The biomechanical function of the foot appears to be robust to running-related fatigue, in contrast to the ankle joint, perhaps due to the greater degrees of freedom available within the foot.

Session Category

Musculoskeletal Biomechanics: Joints and Motion

OA147-04

Sex Difference in Peak Hip Adduction and Its Association With Symptoms and Function in Runners With Heightened Osteoarthritis Risk: 2-Year Follow-Up Analysis of the TRAIL Prospective Cohort Study

Dr Marcella Pazzinatto[1,2], Miss Stephanie Tamer[1,2,3], A/Prof Danilo De Oliveira Silva[1,2], Prof Kay Crossley[1,2], Dr Prasanna Sritharan[1,2], Miss Melissa Haberfield[1,2], Dr Michael Girdwood[1,2], MSc Brody McCarthy[1,2,3], Miss Fernanda Serighelli[1,2], Dr Benjamin Mentiplay[1,2,3]

[1]La Trobe Sport & Exercise Medicine Research Centre, La Trobe University, Melbourne, VIC, Australia. [2]Australian International Olympic Committee (IOC) Research Centre, Melbourne, VIC, Australia. [3]Department of Sport, Exercise and Nutrition Sciences, School of Allied Health, Human Services and Sport, La Trobe University, Melbourne, VIC, Australia

Dr Marcella Pazzinatto

Introduction

Increased peak hip adduction during running has been consistently observed in runners with knee pain and is thought to increase patellofemoral joint loading and symptom development. Despite well-established sex differences in the incidence of knee pain and lower-limb running biomechanics, it remains unclear whether increased hip adduction is prospectively associated with worse symptoms in males and females with a history of knee surgery.

Aim: To compare peak hip adduction during running between males and females with a history of knee surgery and to evaluate its association with knee symptoms at baseline and 2-year follow-up.

Methods

One hundred eight runners (53 females, aged 35 (8) years, body mass index 22.6 (2.7) kg/m^2; and 55 males, aged 36 (7) years, body mass index 24.2 (2.3) kg/m^2) with a history of knee surgery were included. Three-dimensional running biomechanics were assessed during overground running at 3-3.5m/s. Peak hip adduction during stance was extracted for the surgical limb. Knee symptoms and function were assessed using the combined four-

subscales Knee injury and Osteoarthritis Outcome Score (KOOS4) at baseline and 2-year follow-up. Independent t-test was used to compare peak hip adduction between males and females. Unadjusted linear regression models were performed to evaluate associations between peak hip adduction and KOOS4 for: all participants, females only, and males only.

Results

Females had higher peak hip adduction compared to males (mean difference [95% confidence interval]= 3.64° [2.35; 4.94]). At baseline, no associations were observed between peak hip adduction and knee symptoms (KOOS4). At the 2-year follow-up, greater baseline peak hip adduction was associated with worse knee symptoms (KOOS4) in all participants (R^2= 0.123, β= −1.25, [−2.3 to −0.2]; p= 0.017) (Table 1). Although the magnitude of association was larger in females (R^2= 0.131, β= −1.77 [-3.83; 0.30]), sex-stratified analyses did not reach statistical significance in either females or males.

Discussion

Greater peak hip adduction during running at 3-3.5m/s was associated with worse knee symptoms at 2-year follow-up in runners with a history of knee surgery, regardless of sex. This finding suggests that altered frontal-plane hip mechanics during running may be clinically relevant to longer-term symptom outcomes.

Images (Optional)

Table 1. Relationship at baseline and 2-year follow-up between peak hip adduction angle and KOOS4, for all participants, females only, and males only

	R square (p-value)	**β [CI 95%]**	**R square (p-value)**	**β [CI 95%]**	**R square (p-value)**	**β [CI 95%]**
Baseline	**All** (n=108)		**Females** (n=53)		**Males** (n=55)	
KOOS4	0.01 (0.357)	-0.30 [-0.95; 0.35]	0.01 (0.599)	0.29 [-0.82; 1.40]	0.01 (0.531)	-0.31 [-1.29; 0.67]
2-year follow-up	**All** (n=46)		**Females** (n=23)		**Males** (n=23)	
KOOS4	0.123 **(0.017)**	-1.25 [-2.27; -0.24]	0.131 (0.089)	-1.77 [-3.83; 0.30]	0.003 (0.806)	0.24 [-1.77; 2.25]

Session Category

Musculoskeletal Biomechanics: Joints and Motion

OA147-05

Knee Cartilage Structure Before and After Running in Habitual Masters Runners With and Without Knee Osteoarthritis

Dr Jesse Charlton PhD[1], Ms Michaela Khan MSc[1], Ms Natasha Krowchuk BSc[1], Dr Anthony Gatti PhD[2], Dr Jean-Francois Esculier PT, PhD[3,1], Dr Michael Hunt PT, PhD[1]

[1]University of British Columbia, Vancouver, British Columbia, Canada. [2]Stanford University, Stanford, California, United States. [3]The Running Clinic, Lac-Beauport, Quebec, Canada

Introduction

More older adults than ever before are participating in running, but data are lacking to inform the appropriateness of running in this population, especially those with knee osteoarthritis. Prospectively, higher joint loads during walking are related to cartilage degradation, but it is unclear if this holds true for running. Therefore, we explored associations between running biomechanics and knee cartilage outcomes before and after a 30-minute run.

Methods

We used the baseline data (NCT04325334) of 70 runners with (KOA) and without (CON) painful radiographic knee osteoarthritis. We recorded the final 30 seconds of a 5-minute run on an instrumented treadmill (markers trajectories: 200 Hz, forces: 2000 Hz), applied a scaled 6DOF musculoskeletal model, and performed inverse dynamics. For biomechanical predictors, we calculated the instantaneous vertical loading rate (IVLR) and the time integral of the knee adduction (KAMi) and flexion moments (KFMi). Our cartilage outcomes were mean thickness and T2 relaxation times for the medial tibial and patellar regions acquired with magnetic resonance imaging (3-Tesla, 16 channel coil) before and after a 30-minute, self-paced treadmill run. We fit linear models (α=0.05) to cartilage outcomes (pre-run, post-pre change) predicted by biomechanics, group (KOA, CON), and running speed. The KAMi-by-group interaction was also assessed for cartilage thickness.

Results

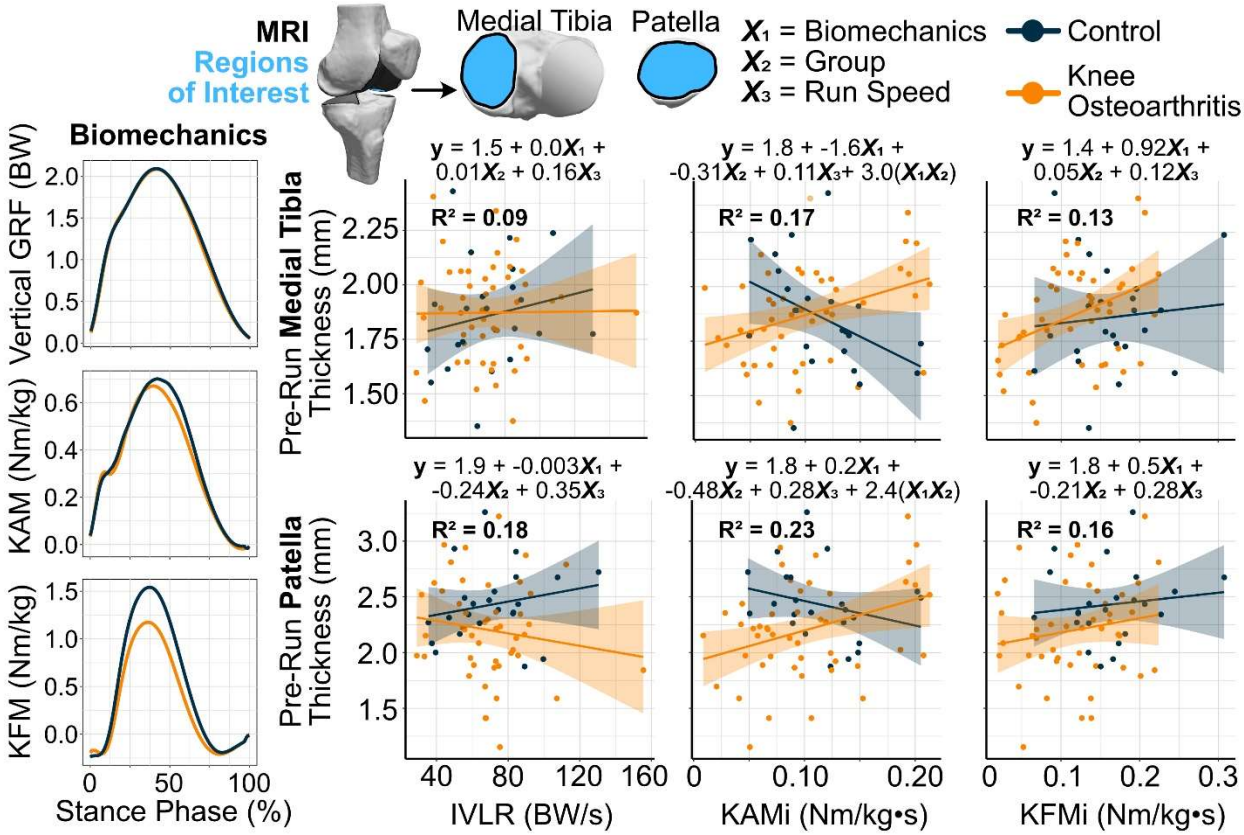
The runners had a mean±sd age=56±9 years, body mass=66.3±12.6 kg, and the KOA group had mild (n=37) and moderate (n=10) structural signs of osteoarthritis. Few biomechanical predictors were associated with cartilage outcomes (Figure). The KAMi-by-group interaction for the medial tibia (p=0.042) showed KOA and CON had opposite associations with tibia thickness (positive vs negative, respectively). Speed was a significant predictor in

most thickness models (all $p<0.022$). No predictors were associated with T2 in either compartment (all $p>0.165$) or any post-pre cartilage change (all $p>0.071$).

Discussion

Running biomechanics were poorly associated with cartilage outcomes; however, KAMi had a differential effect on pre-run thickness between groups. An acute running bout did not generate changes in cartilage that were associated with biomechanics or group. Together, these results indicate that habitual masters-aged runners generally show positive knee cartilage adaptations to loading, lending support for running continuance in this population.

Images (Optional)



Session Category

Musculoskeletal Biomechanics: Joints and Motion

OA148-01

Effects of Unisensory and Multisensory Augmentation on Standing Balance in Chronic Stroke Survivors

Ms. Isabelle Museck[1], Dr. Jesse Dean PhD[1,2]

[1]Medical University of South Carolina, Charleston, South Carolina, United States. [2]Ralph H. Johnson VA Health Care System, Charleston, South Carolina, United States

Ms. Isabelle Museck

Introduction

People with chronic stroke (PwCS) often experience mediolateral balance deficits that increase fall risk and reduce quality of life. The delivery of artificial sensory feedback in response to real-time body movements, known as sensory augmentation, has potential to improve balance outcomes and reveal sensory mechanisms underlying balance control [1]. Our preliminary work demonstrated that vibrational feedback scaled to mediolateral center of pressure (CoP) velocity can influence postural control in control participants [2]. However, it remains unknown whether similar effects occur in PwCS and whether augmenting multiple feedback sources provides additional benefits. This study applied real-time vibrational feedback to PwCS to evaluate whether augmentation delivered at single (unisensory) or multiple (multisensory) locations reduced mediolateral sway.

Methods

PwCS (>6 months post stroke) completed unisensory (n=35) and multisensory (n=34) augmentation sessions. Participants wore vibrating tactors at the lateral trunk, hip abductors, medial/lateral ankle tendons, and foot sole – locations at which vibration can elicit mediolateral sway. During 1-minute trials, participants stood on a force plate undergoing unpredictable mediolateral translations in a sum-of-sines pattern (0.1-0.9 Hz). Translation amplitude was individualized to evoke a 20 mm/s mediolateral CoP RMS velocity, standardizing difficulty. Tactor feedback was scaled to real-time CoP velocity and participants completed three sessions. The first two sessions assessed unisensory augmentation using randomized trials with five non-vibration and five vibration trials at each location. The third session evaluated multisensory augmentation, using six randomized trials with either non-vibration or simultaneous vibration at all locations. Mediolateral sway was quantified using CoP standard deviation (CoPstd). Paired t-tests

compared no-vibration and vibration conditions within the unisensory and multisensory sessions.

Results

For unisensory vibration, CoPstd did not differ significantly from non-vibration conditions ($p>0.27$), (**Fig. 1**). In contrast, multisensory augmentation significantly reduced CoPstd relative to non-vibration conditions ($p=0.003$).

Discussion

These findings indicate that simultaneous vibrotactile feedback from multiple body locations is more effective than single-site feedback for improving postural stability during dynamic balance challenges in PwCS. Future work will develop wearable multisensory augmentation devices that deliver real-time predictive feedback to improve clinical balance training outcomes.

Images (Optional)

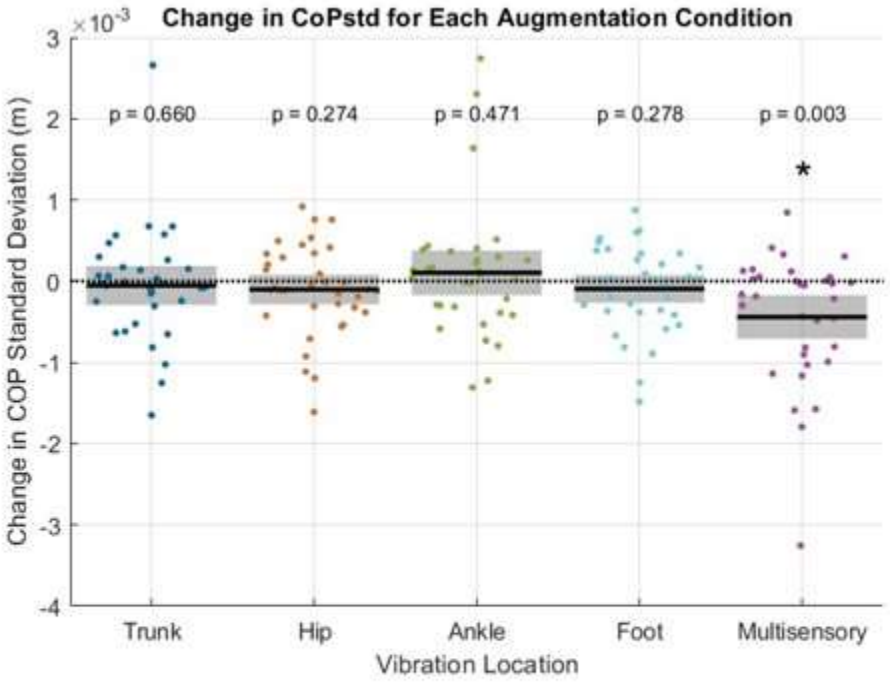


Figure 1. Change in CoP displacement relative to non-vibration conditions per participant for each sensory augmentation condition. Dots indicate individual participants, horizontal bars are mean values, and shaded areas are 95% confidence intervals.

References (Optional)

[1] Schonhaut et al. , J Biomechanics, 2024. [2] Laird et al. , ASB Annual Meeting, 2025.

Session Category

Human Motion and Performance: Balance, Posture and Control

OA148-02

Discordance Between Video-Based Measures of Balance Ability and Perception Is Associated With Fall History in People With Diverse Balance Abilities

Ms. Hannah Heigold MS, Ms. Ariana Rodrigues, Mr. Parker Ruth BS, Dr. Scott Delp PhD

Stanford University, Stanford, California, United States

Introduction

Alignment of perceived and true balance ability is important for reducing falls. Longhurst et al. quantified this by defining "discordance" as the difference between an individual's reported Activities-Specific Balance Confidence Scale (ABC) and their predicted ABC based upon their Timed Up and Go score, demonstrating it related to retrospective falls in people with Parkinson's disease [1]. To further examine discordance, we developed the StaBLE (Stanford Balance Level Evaluation) performance score, an 18-activity balance assessment using smartphone video. We then (1) computed discordance for a sample with varying balance abilities using the novel StaBLE performance score; and (2) evaluated if StaBLE-based discordance is related to functional outcomes, including fall risk and self-reported retrospective falls.

Methods

We had 153 participants with varying balance abilities complete StaBLE and the ABC. We computed discordance using the predicted ABC from StaBLE performance scores instead of TUG. We performed logistic regression to predict a fall risk label (true if ABC < 67, CDC Stay Independent 12-question tool > 3, or worried about falling) and self-reported 1-year retrospective falls using StaBLE-based discordance, StaBLE performance score, age, and sex.

Results

The StaBLE performance score ($p = 0.001$) and StaBLE-based discordance ($p < 0.001$) were both significant predictors of fall risk. The logistic regression model had a fall risk prediction accuracy of 85% (sensitivity 80%, specificity 86%) in a held-out test set. StaBLE-based discordance was the only significant predictor ($p = 0.017$) of retrospective falls, with a prediction accuracy of 67% (sensitivity 50%, specificity 72%). Density plots of discordance demonstrate individuals with fall risk had more extreme discordance magnitudes compared to the no-risk group (KS test, $p<0.01$), while individuals with a reported fall had more negative discordances (KS test, $p<0.001$).

Discussion

Since the StaBLE-based discordance was computed from a diverse cohort with an objective balance assessment, the regression line likely approximates concordance better than linear regression in a high fall risk cohort. Discordance was the only significant predictor of retrospective falls. This emphasizes the important interplay between perceived and measured abilities for real-world outcomes and suggests that StaBLE-based discordance may have clinical utility for fall reduction.

Images (Optional)

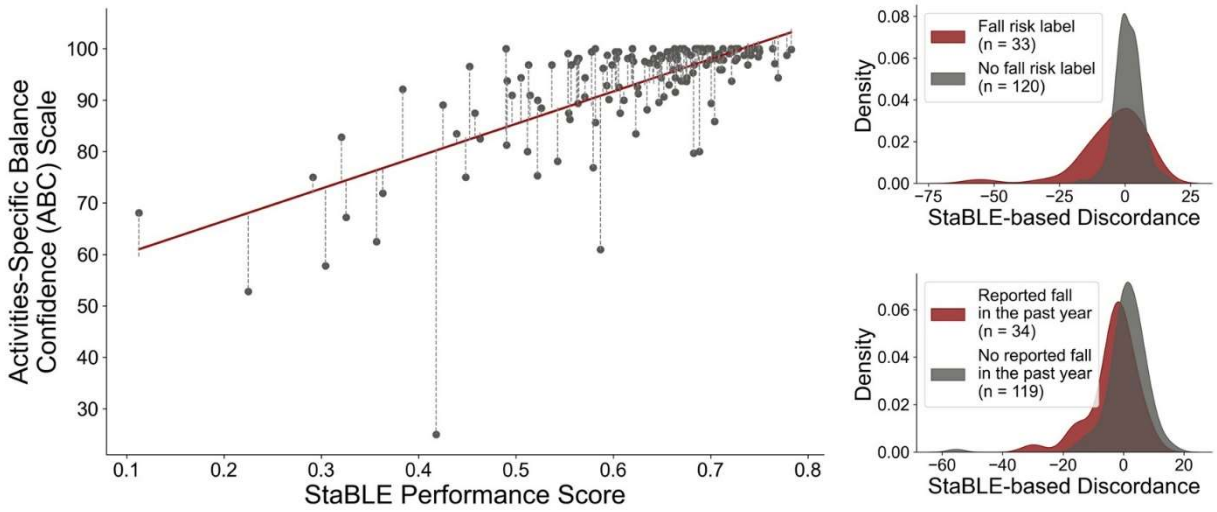


Figure 1: (Left) Linear regression of StaBLE performance score and Activities-Specific Balance Confidence Scale (ABC), with discordance computed as the residual vector from the line of best fit to the data point (min=16.1, max=-55.3, mean = 0.00, std =7.71). Underconfident participants (negative discordance) are below the regression line, and overconfident participants are above the line. A participant with a shorter residual line is more concordant (smaller magnitude of discordance). (Right Top) Discordance density across the dataset with participants identified as having fall risk in red. (Right Bottom) Discordance density across the dataset with participants who reported a fall in the past year in red.

References (Optional)

[1] Jason Longhurst *et al.*, Neurorehabil Neural Repair, 2025

Session Category

Human Motion and Performance: Balance, Posture and Control

OA148-03

User-Independent, Deep-Learning Estimates of Center of Mass Kinematics to Enable Autonomous Exoskeleton Control for Balance Augmentation

Dr Kristen Jakubowski[1,2], Dr Aaron Young[2], Dr Gregory Sawicki[2], Dr Lena Ting[1,2]

[1]Emory University, Atlanta, GA, United States. [2]Georgia Institute of Technology, Atlanta, GA, United States

Introduction

Maintaining balance in response to perturbations requires precise control of center of mass (CoM) kinematics, accomplished by modulating joint torques based on CoM state [1]. Real-time estimation of CoM kinematics could be used to autonomously control a lower-limb exoskeleton designed to assist balance. However, predicting CoM kinematics in real-time outside the lab remains challenging. Here, building on a similar approach for real-time exoskeleton control [2], we developed a deep learning model to estimate CoM kinematics from wearable sensor data during multidirectional standing balance perturbations. We evaluated whether the predicted CoM kinematics could reconstruct ankle torques using a previously developed delayed CoM feedback model [3].

Methods

Fourteen healthy young adults maintained standing balance during randomized support surface translations in 8 directions (every 45°) at 3 magnitudes (5, 10, 15cm). Participants wore a “Sensor Suit” with 6 six-axis IMUs and two pressure insoles (Fig-1A). Using data from a lab-based motion capture system, we quantified CoM kinematics relative to the base of support, joint kinematics, and joint kinetics using OpenSim. We trained a leave-one-subject-out temporal convolutional network (TCN) that used Sensor Suit data to estimate CoM kinematics. To test the feasibility of this approach for controlling an ankle exoskeleton, the TCN-predicted CoM kinematics were used to estimate ankle torque via a delayed CoM feedback model (Fig-1B).

Results

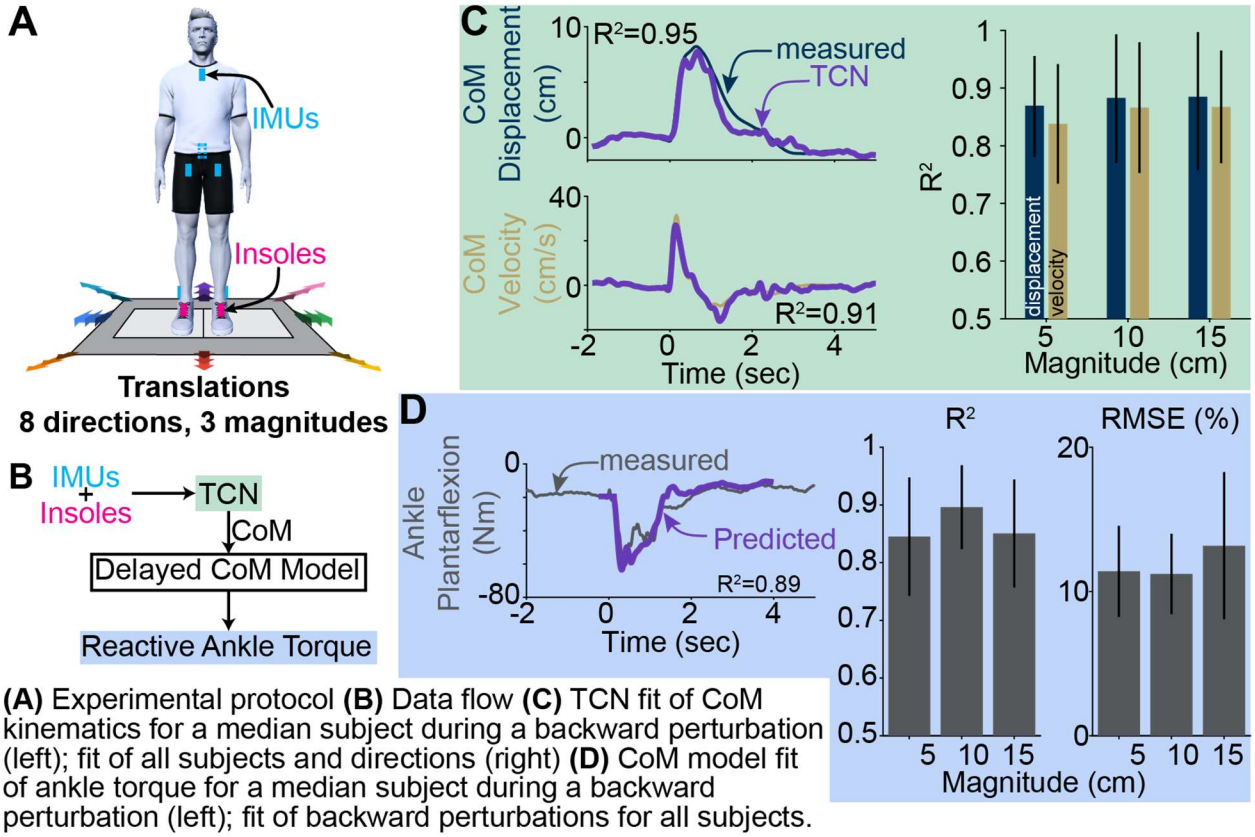
Our user-independent deep learning model accurately predicted CoM kinematics and, more importantly, the TCN-predicted CoM kinematics reconstructed ankle torques with high fidelity. Across all directions, a 14-fold leave-one-subject-out deep learning model accurately predicted CoM kinematics with high R2 (Fig-1C; Displacement: 0.88±0.11; Velocity: 0.86±0.11). Using the TCN-predicted CoM kinematics as input into a user-

independent delayed CoM feedback model, we accurately reconstructed the ankle torque response (Fig-1D; R2=0.89±0.11; RMSE=12±4% of total torque).

Discussion

Using deep learning, we can turn wearable sensor data into balance-correcting joint torques that work across multiple users. If implemented on an exoskeleton, this could enable real-time control of a fully autonomous user-independent exoskeleton for balance augmentation, a capability that has not yet been realized.

Images (Optional)



(A) Experimental protocol **(B)** Data flow **(C)** TCN fit of CoM kinematics for a median subject during a backward perturbation (left); fit of all subjects and directions (right) **(D)** CoM model fit of ankle torque for a median subject during a backward perturbation (left); fit of backward perturbations for all subjects.

References (Optional)

[1]Welch & Ting. J Neurophys, 2009

[2]Molinaro et al., Nature, 2024

[3]Jakubowski et al., J Neurophys, 2024

Session Category

OA148-04

Human-in-the-Loop Optimization of Postural States Between Sensory Conditions

Mr. Amin M Nasrabadi M.Sc.[1], Dr. Calvin Kuo Ph.D.[2], Dr. Jean-Sébastien Blouin Ph.D.[1]

[1]The School of Kinesiology, University of British Columbia, Vancouver, BC, Canada. [2]The School of Biomedical Engineering, University of British Columbia, Vancouver, BC, Canada

Introduction

Given its simple dynamics, the control of standing balance is an ideal model for uncovering sensorimotor integration principles underlying bipedalism. As we face distinct environments, it has been argued that the reliability of sensory signals and statistics of motion may explain modulations in control gains needed to remain upright. Unfortunately, the distinction between these mechanisms remains difficult because the statistics of balance motion often covary with the availability of sensory cues. Here, we present a human-in-the-loop optimization method to modulate and control the statistics of balance motion.

Methods

Sixteen participants (8 female) stood on a robotic platform reproducing the dynamics of their upright stance. Negative viscosity was used as a tunable parameter to modify the statistics of whole-body motion [1], i.e. SD of Centre-of-Mass (CoM) angle and velocity, from an initial Eyes Opened (EO) state towards a target Eyes Closed (EC) state while keeping EO. The iterative procedures were guided by a gradient-descent optimization: we computed the error between the current and target states after each trial to estimate a numerical gradient to adjust the viscosity parameter. The process continued until the statistic of balance with EO converged to those observed with EC. The stop criteria were defined as either 10 steps of optimization or <0.5 viscosity change for 2 successive steps.

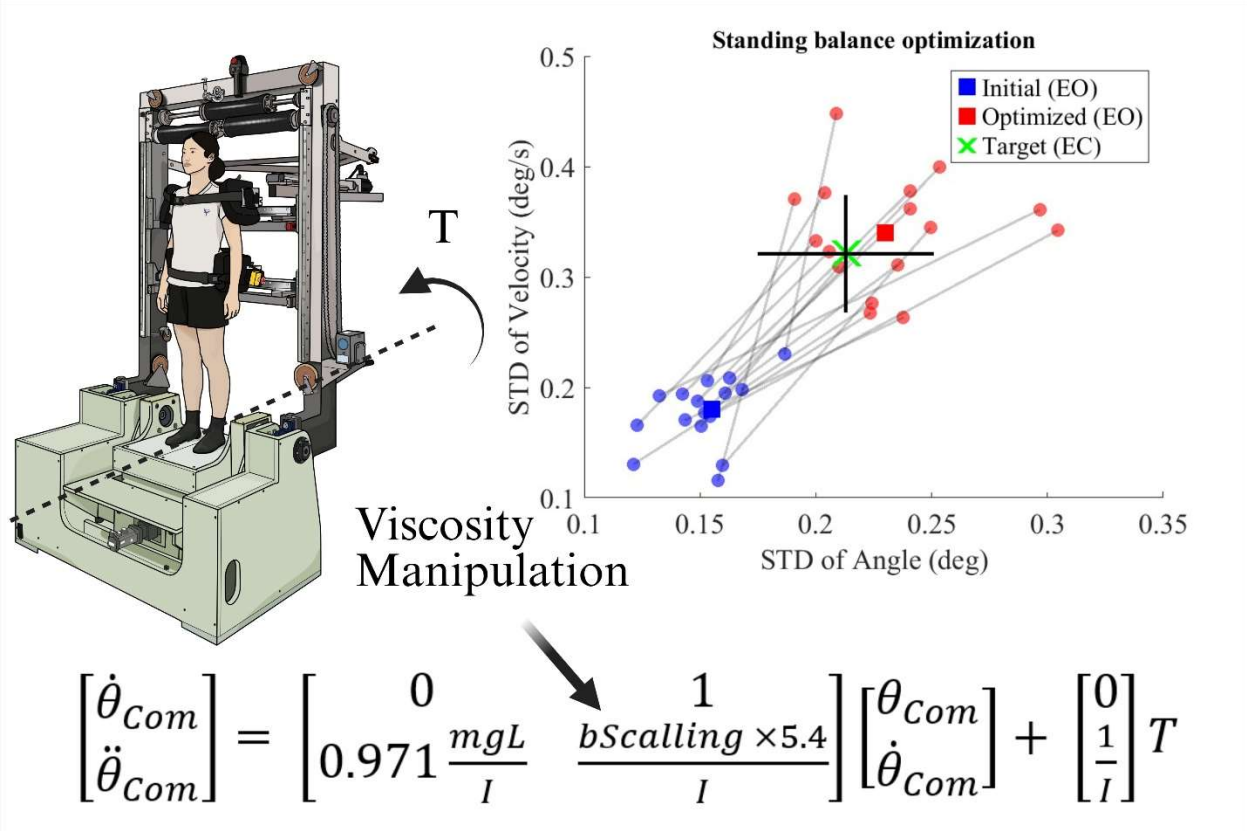
Results

The optimization algorithm matched the statistics of the standing balance of EO to EC when participants had EO. The error to the target CoM angle SD reduced from 0.11±0.02 deg to 0.02±0.03 deg, and for CoM velocity SD from 0.16±0.04 to 0.04±0.05 deg/sec. On average, the process to optimize took 8 optimization steps.

Discussion

Our findings demonstrate a method to control the statistics of balance through manipulations in body viscosity via gradient-based optimization. This framework provides a powerful tool to test neuromechanical hypotheses.

Images (Optional)



References (Optional)

[1] Paul Belzner et al., Sci. Robot 2025

Acknowledgements (Optional)

Funded by NSERC

Session Category

Human Motion and Performance: Balance, Posture and Control

OA148-05

A Privacy-Preserving, Device-Free Fall Detection System via Wi-Fi Channel StateInformation

Mr Nathaniel Im

Portsmouth Abbey School, Portsmouth, Rhode Island, United States

Introduction

Falls in the aging population represent a critical public health challenge, often leading to severe injury or mortality. Current monitoring solutions, such as optical cameras or wearable devices, suffer from privacy intrusion and low user compliance. To address these limitations, we propose "WiSafe," a novel, low-cost system utilizing Wi-Fi Channel State Information (CSI) to detect falls without on-body sensors or cameras.

Methods

The system utilizes two ESP32 microcontrollers configured as a transmitter and receiver to capture fine-grained CSI data. Unlike Received Signal Strength Indicator (RSSI), CSI provides amplitude and phase information across multiple subcarriers, enabling the detection of subtle human movements. We implemented a data acquisition pipeline that logs CSI packets at a high sampling rate. The raw signal is processed using a Butterworth low-pass filter to eliminate high-frequency noise. We designed a protocol to capture signal patterns for "Fall" events (simulated onto soft mats) versus "Activities of Daily Living" (ADL), including walking, sitting, and standing. Feature vectors, including variance, standard deviation, and interquartile range (IQR), are extracted from 5-second sliding windows to train k-Nearest Neighbors (k-NN) and Support Vector Machine (SVM) classifiers.

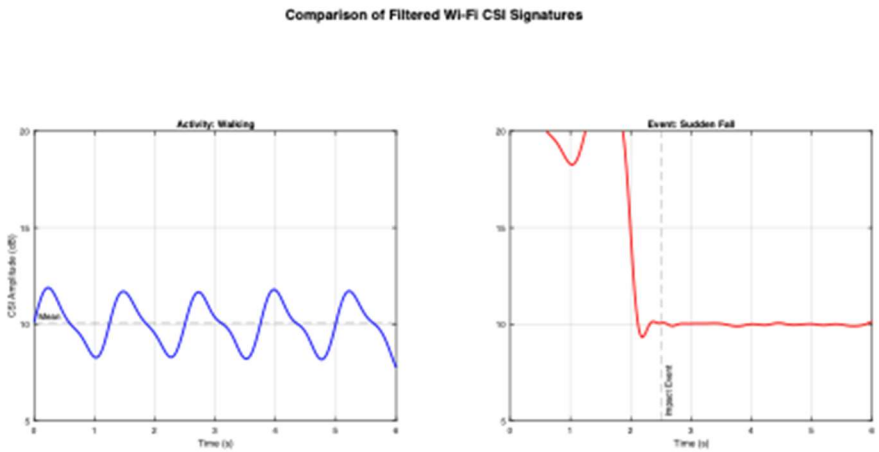
Results

Initial validation of the hardware pipeline confirms the successful extraction of stable CSI streams in a 4m x 4m controlled environment. Preliminary signal analysis demonstrates that fall events generate a distinct high-amplitude transient signature followed by a static period, contrasting sharply with the rhythmic, periodic fluctuations observed during walking. Feature extraction analysis indicates that the variance and IQR of the CSI amplitude are significantly higher during the impact phase of a fall compared to ADLs. These distinct kinematic signatures suggest that the proposed machine learning models can achieve high classification sensitivity.

Discussion

WiSafe demonstrates the feasibility of using commodity Wi-Fi hardware for robust, privacy-preserving health monitoring. By leveraging the ubiquity of Wi-Fi signals, this system offers a scalable solution to support aging-in-place while overcoming the limitations of current invasive or wearable technologies.

Images (Optional)



Session Category

Human Motion and Performance: Balance, Posture and Control

OA148-06

Balance Assessment via Markerless Motion Capture: Evaluating Center of Mass and Center of Pressure Estimations Against Gold-Standard Measurements

Dr. Milad Nazarahari

University of Alberta, Edmonton, Alberta, Canada

Introduction

Clinical characterization of balance in clinical settings currently relies on observational tests such as the Berg Balance Scale; however, outcome metrics are inherently subjective and prone to ceiling effects. While instruments, like force platforms and marker-based systems, provide ground-truth measurements, their use is restricted by high costs, limited availability, and the need for expert operators. Open-source markerless motion capture systems (MMCS) have emerged as an easy-to-use, accessible alternative This study introduces a multi-view MMCS framework utilizing OpenPose to estimate the center of mass (COM) and center of pressure (COP). This approach facilitates objective balance quantification by estimating the COM and deriving the COP via inverse dynamics.

Methods

The introduced MMCS was validated through an experimental study with twelve healthy individuals. The protocol included five balance tasks: quiet standing under varying sensory conditions (hard and soft surfaces under eyes open and eyes closed) and a weight-shift task. To establish concurrent validity, COM and COP were compared against gold-standard measurements from a marker-based system and a force plate, respectively. The study systematically investigated the influence of model complexity on COM and COP estimations by comparing performance across single-, three-, six-, and eight-segment biomechanical models.

Results

COM trajectories estimated via the MMCS demonstrated good agreement with the marker-based gold standard across all models (Pearson's correlation coefficient: CC>0.90; root-mean-square error: RMSE<3.0 mm in quasi-static tasks). For the COP estimation, the six- and eight-segment models showed the highest performance with force plate data (CC=0.95–0.98, RMSE=2.2–8.5 mm in the anteroposterior (AP) direction using eight segments). A consistent directional trend was observed across all models, wherein AP correlations generally exceeded those in the medio-lateral (ML) direction, except for the weight-shift task. Fig. 1 shows COP trajectories from the MMCS, the marker-based system, and the force plate for one participant.

Discussion

Across all tasks, increasing model complexity from a single segment to six segments showed significantly improved performance, evidenced by higher correlation coefficients and reduced RMSE, underscoring the necessity of multi-segment modelling for accurate COM and COP estimation within the MMCS framework. These results validate the MMCS as a valuable, cost-effective tool for quantitative balance assessments.

Images (Optional)

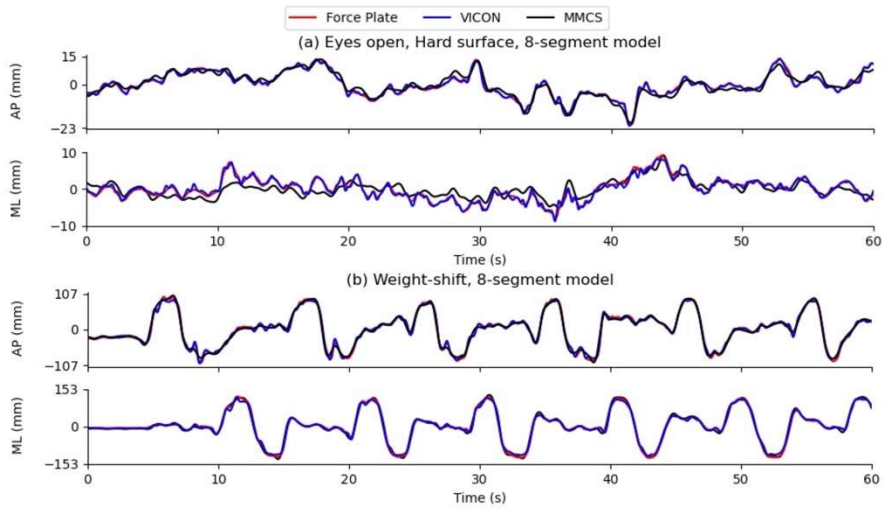


Fig. 1: Comparison of COP trajectories derived from marker-based and markerless (MMCS) systems against force plate measurements for a single participant. Both systems utilized an eight-segment model via inverse dynamics. **(a)** Results for a quiet standing trial (eyes open, hard surface). Marker-based results: RMSE (AP = 0.6 mm, ML = 0.5 mm), CC (AP = 0.99, ML = 0.98); MMCS results: RMSE (AP = 1.7 mm, ML = 1.7 mm), CC (AP = 0.96, ML = 0.80). **(b)** Results for a weight-shift task. Marker-based results: RMSE (AP = 3.9 mm, ML = 4.8 mm), CC (AP = 0.99, ML = 0.99); MMCS results: RMSE (AP = 6.0 mm, ML = 7.0 mm), CC (AP = 0.99, ML = 0.99).

References (Optional)

Session Category

Human Motion and Performance: Balance, Posture and Control

OA149-01

Osteoarthritis Progression Alters Collagen Network Reorganization in Cartilage upon Mechanical Loading

MSc Yixuan Zhang[1], Dr Seyed Ali Elahi[1], Dr Olga Shebanova[2], MSci James Rowe[3], MSc Joudi Altaleb[3], Dr Nick Terrill[2], Prof. Alexander Liddle[3], Prof. Richard Abel[3], Prof. Ilse Jonkers[1]

[1]KU Leuven, Leuven, Vlaams-Brabant, Belgium. [2]Diamond Light Source, Didcot, Oxfordshire, United Kingdom. [3]Imperial College London, London, Greater London, United Kingdom

Introduction

Cartilage load-bearing capacity relies on an organised collagen network, which is progressively disrupted in osteoarthritis (OA) [1]. This study applied synchrotron small-angle x-ray scattering (SAXS) to quantify collagen orientation and alignment under varying compressive loading in human OA cartilage, providing structural perspectives on collagen degeneration in OA.

Methods

SAXS measurements were performed at the Diamond Light Source beamline I22 [2]. Osteochondral plugs (n=24) with different OA severity were collected from 6 donors (IRAS 337246, REC 24/YH/0194) and subjected to unconfined compression–relaxation at 20%, 40%, and 60% strain, encompassing physiological to injurious levels. SAXS images were acquired at the articular surface and at ¼, ½, and ¾ cartilage depth during loading. Azimuthal intensity profiles around the 5th-order diffraction peak were extracted via radial integration in DAWN. Each profile was fitted with a two-peak Gaussian model in MATLAB to derive preferred collagen orientation (mean) and degree of disorganization (standard deviation) [3]. To determine depth-dependent alterations in collagen network alignment (alignment factor) changes in organization under load were quantified relative to the unloaded state.

Results

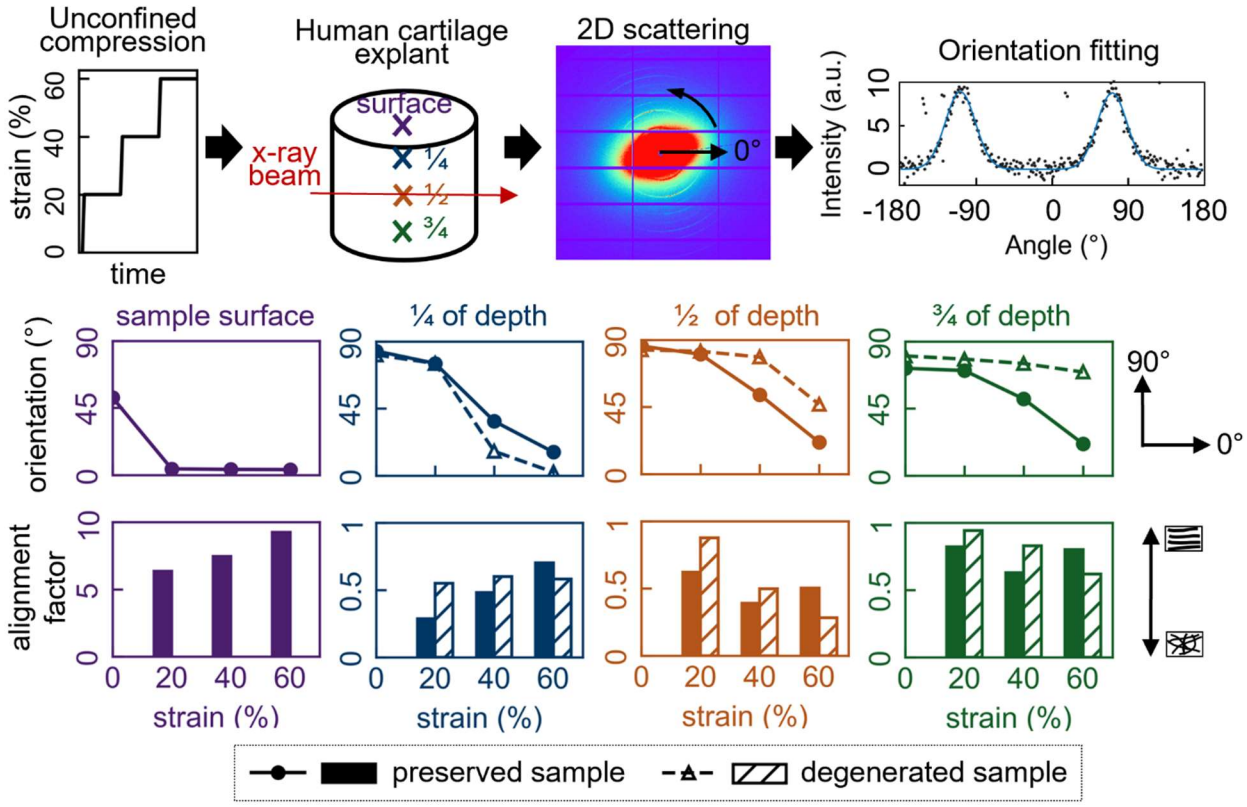
Figure 1 shows data of osteochondral plugs from the same donor in preserved (thickness=2.1mm) and degenerated (thickness=1.3mm) hip cartilage. In the preserved sample, collagen at the articular surface was oriented parallel to the surface and became more aligned (>1) upon 20% strain, while deeper zones showed minimal orientation change but reduced alignment (<1). With increasing strain, reorientation propagated through the full depth, extending surface-parallel alignment into deeper zones. In the degenerated sample, similar behaviour was presented in the proximal tissue (surface data missing,

confirmed up to ¼-depth), but deeper zones exhibited little reorientation even at 60% strain.

Discussion

These findings highlight depth-dependent collagen reorganization in cartilage under load. Orientation changes up to 90° occur under high compressive loading, potentially resisting lateral expansion. Under supra-physiological loading, preserved cartilage reorganizes collagen throughout its depth, whereas degenerated tissue shows less reorientation, which does not extend into the deep zone, confirming that collagen network disruption altered load-bearing behaviour in OA cartilage.

Images (Optional)



References (Optional)

[1] S.A. Elahi et al, Osteoarthritis Cartilage, 2023

[2] A.J. Smith et al, J Synchrotron Radiat, 2021

[3] S.R. Inamdar et al, Acta Biomater, 2021

Acknowledgements (Optional)

This work is supported by FWO PhD fellowship fundamental research (11PK924N), FWO travel grant for long research stay (V462924N), and beamtime granted by I22 at Diamond Light Source (SM37779).

Session Category

Musculoskeletal Biomechanics: Tissues

OA149-02

Knee Joint Loading Differences Affect the Mechanoregulation of Cartilage Gene Expression and Distinguish Healthy, Non-Progressor, and Progressor Knee OA Subjects

Dr. Seyed Ali Elahi[1], Dr. Satanik Mukherjee[2], PhD Candidate Yixuan Zhang[1], Dr. Bryce Killen[1], PhD Candidate Ikram Mohout[1], Dr. Miel Willems[1], PhD Candidate Ali Abedi[1], Prof. Liesbet Geris[1], Prof. Ilse Jonkers[1]

[1]KU Leuven, Leuven, Flemish Brabant, Belgium. [2]Washington University in St Louis, St. Louis, Washington, United States

Introduction

Osteoarthritis (OA) progression is driven by changes in cartilage mechanobiology, yet patient-specific mechanoregulatory patterns remain poorly defined. This study integrates tissue- and cell-scale mechanics with a gene regulatory network (GRN) to test whether mechanically driven anabolic and catabolic signalling differs among healthy controls, knee OA non-progressors, and progressors.

Methods

3D gait analysis was performed for 10 controls, 10 knee OA non-progressors, and 8 knee OA progressors, classified using 2-year changes in Kellgren–Lawrence scores. Subject-specific gait data were used in a generic musculoskeletal modeling workflow to estimate medial compartment contact pressures, which served as boundary conditions for fibril-reinforced poroelastic finite element models of medial tibial cartilage (Abaqus) [1]. The mean deformation gradient of the top 10% most-loaded elements was transferred to a cell-scale representative volume element (Abaqus) [2], and the resulting chondrocyte total force was used as input to a stochastic GRN (MATLAB) [3] for ACAN, COL2, SOX9, RUNX2, COL10, and MMP13. Pro-inflammatory cytokine exposure was modeled for both OA groups. Gene expression was normalized to the unloaded, control baseline, and group differences were assessed using Kruskal–Wallis tests with post-hoc comparisons.

Results

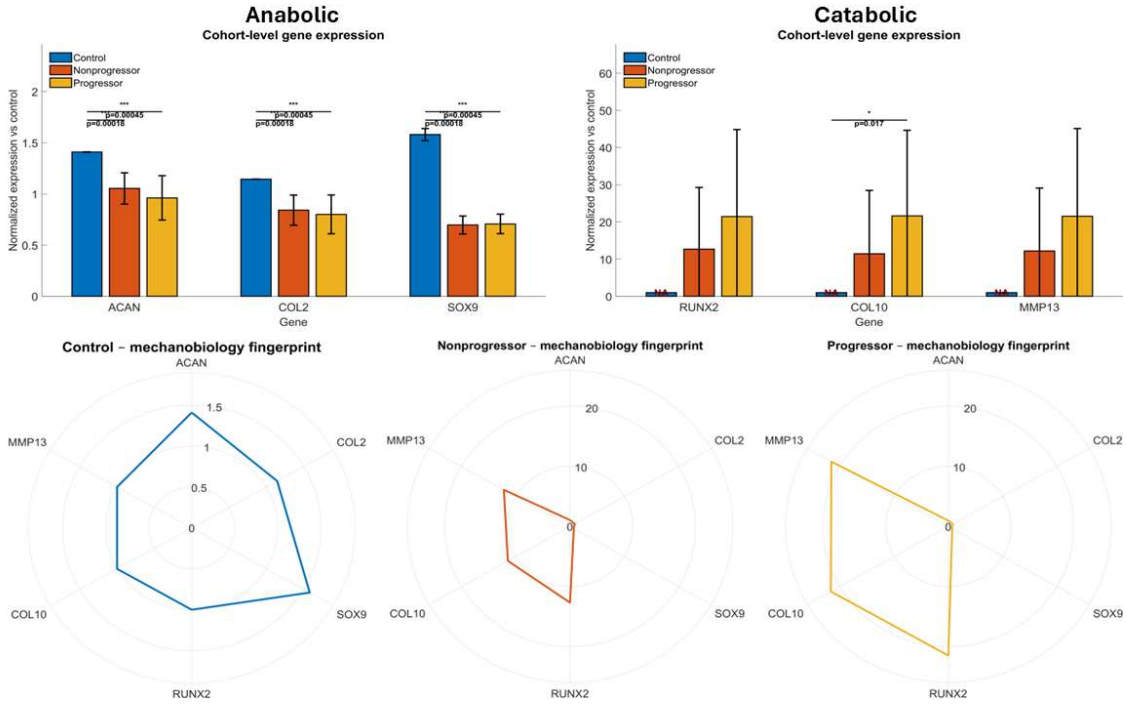
Controls consistently upregulated all anabolic genes, indicating a robust protective response to mechanical loading. OA non-progressors showed selective ACAN upregulation, accompanied by COL2 and SOX9 downregulation; whereas progressors downregulated all anabolic markers. Variability in anabolic responses increased in both

OA groups. Catabolic genes remained inactive in controls but exhibited substantial, heterogeneous upregulation in OA, most prominently in progressors. Spider plots highlighted a near-homeostatic, mildly anabolic profile in controls versus a strongly catabolic profile in both OA subgroups.

Discussion

This multi-scale tissue–cell–GRN framework reveals distinct mechanobiological signatures across knee OA phenotypes, characterized by diminished anabolic activity and variable catabolic activation in OA, particularly in progressors. These mechanoregulatory patterns may support phenotype-specific OA stratification and inform the development of targeted mechanobiological interventions.

Images (Optional)



References (Optional)

[1] Zhang and Killen et al., Scientific Reports, 2025.

[2] Sibole and Erdemir, PLoS One, 2012.

[3] Mukherjee et al., ORS Annual Meeting, 2023.

Acknowledgements (Optional)

This work is supported by ERC Advanced Grant (OA-CONNECT; 101200916), KU Leuven (C14/24/117), and FWO Happy Joints project (G045320N).

Session Category

Musculoskeletal Biomechanics: Tissues

OA149-03

Combining Raman Spectroscopy and Nanoindentation to Correlate Changes in both Mechanical Properties and Molecular Structure during Osteoarthritis Progression

Dr Sarah Davis, Dr Jurgita Zekonyte, Dr Priyanka Dey, Professor Gordon Blunn, Dr Katerina Karali

University of Portsmouth, Portsmouth, Hampshire, United Kingdom

Introduction

Osteoarthritis (OA) is linked to progressive, depth-dependent molecular and microstructural changes across the cartilage-bone interface that may alter tissue micromechanics before gross structural degeneration is observed. This study aimed to explore how compositional changes in OA influence the mechanical behaviour throughout hyaline articular cartilage (HAC), calcified cartilage (CC) and subchondral bone (SB). This may allow the early detection of OA-related tissue degeneration and contribute to the development of targeted treatments for preserving joint health.

Methods

Tibias from female Dunkin-Hartley (DH) guinea pigs at 2, 4, and 24 months of age (n = 4), representing pre-OA, early-stage OA and severe OA respectively [1], were cut longitudinally using a previous method [2]. Load-controlled quasi-static nanoindentation and Raman spectroscopy were performed across the osteochondral unit (Figure 1A) whilst submerged in PBS at room temperature. Reference markers around the central region of the medial tibial plateau ensured that measurements were performed on the same X-Y coordinates (Figure 1A). The medial condyle of the contralateral hindlimb was used for histology and modified-Mankin scoring.

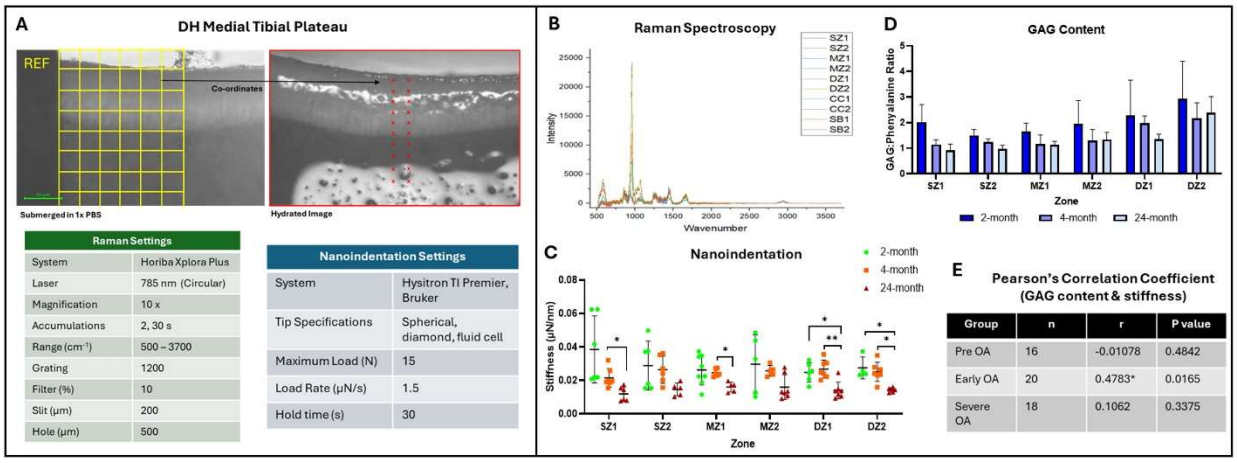
Results

24-month specimens had a significant reduction in stiffness across all zones of HAC (SZ *p = 0.0107; MZ p = 0.0281; DZ **p = 0.0048, compared to 4-month specimens, Figure 1C). GAG content increased throughout the depth of HAC from the superficial zone (SZ) to the deep zone (DZ) and was reduced in both early and severe OA (Figure 1D). Pearson's Correlation Coefficient suggested that the decrease in stiffness during OA progression is related to a reduction in GAG content during the early stages of the disease only (r = 0.04783, *p = 0.0165, Figure 1E).

Discussion

Ongoing work will include correlating immunohistochemical analysis, histology and Micro-CT to assess the microstructure of osteochondral tissues during OA progression. By combining these techniques, this study offers a multimodal strategy for investigating the relationship between molecular composition, local mechanical properties and characteristic features of OA progression, to yield deeper insights into the complex mechanisms underlying the onset of OA.

Images (Optional)



Raman Settings	
System	Horiba Xplora Plus
Laser	785 nm (Circular)
Magnification	10 x
Accumulations	2, 30 s
Range (cm^{-1})	500 – 3700
Grating	1200
Filter (%)	10
Slit (μm)	200
Hole (μm)	500

Nanoindentation Settings	
System	Hysitron TI Premier, Bruker
Tip Specifications	Spherical, diamond, fluid cell
Maximum Load (N)	15
Load Rate (μN/s)	1.5
Hold time (s)	30

Group	n	r	P value
Pre OA	16	-0.01078	0.4842
Early OA	20	0.4783*	0.0165
Severe OA	18	0.1062	0.3375

Figure 1: Depth-dependent mechanical and molecular measurements across the cartilage–bone unit in Dunkin-Hartley (DH) guinea pigs (n = 4 animals per age group) during osteoarthritis (OA) progression: (A) Schematic of the depth-oriented experimental setup for quasi-static nanoindentation and Raman measurements including the instrument configuration and acquisition settings. B) Representative Raman spectra from the 2-month group acquired through the depth of unmineralised hyaline articular cartilage (HAC) and mineralised regions (calcified cartilage CC; subchondral bone SB) (*p < 0.05, **p < 0.01). C) Indentation stiffness (μN/nm) across the HAC during OA progression. Statistics: mixed-effects model (ANOVA) with Tukey multiple comparisons tests. D) Depth-wise profile of raman-derived glycosaminoglycan (GAG) quantified as the integrated area of the 1063 cm^{-1} GAG band and expressed as a ratio normalised to the integrated area of the 1003 cm^{-1} phenylalanine band. E) Pearson's correlation coefficient between GAG content and stiffness for each age group, (n = paired points per group). Data presented as mean (± SD) where statistical significance α = 0.05.

References (Optional)

[1] Sarah Davis *et al.,* VIEW, 2025.

[2] Sarah Davis *et al.*, Bioengineering, 2023.

Session Category

Musculoskeletal Biomechanics: Tissues

OA149-04

Diet-Induced Obesity Contributes to Biochemical Changes in Cartilage in Older Rats Without Decline in Mechanical Properties

Mr. Rasmus K. Hiltunen MSc[1,2], Dr. Antti Aarnio PhD[2], Asst. Prof. Jaqueline Lourdes Rios PhD[3], Prof. Walter Herzog PhD[4], Prof. Heikki Kröger MD, PhD[1,2], Dr. Mikael J. Turunen PhD[1,2], Dr. Mikko A.J. Finnilä PhD[5], Prof. Mikko J. Nissi PhD[2], Dr. Juuso T.J. Honkanen PhD[1], Dr. Petri Tanska PhD[1,2]

[1]Kuopio University Hospital, Wellbeing Services County of North Savo, Kuopio, North Savo, Finland. [2]University of Eastern Finland, Kuopio, North Savo, Finland. [3]University Medical Center Utrecht, Utrecht, Utrecht, Netherlands. [4]University of Calgary, Calgary, Alberta, Canada. [5]University of Oulu, Oulu, North Ostrobothnia, Finland

Introduction

Obesity is a risk factor for osteoarthritis. High-fat and high-sucrose (HFHS) diets in rodents mimic human metabolic syndrome. Obesity-induced effects on cartilage and bone may differ on the obesity-onset age. Here, we investigated how diet-induced obesity, initiated in weanling and adult rats, affects patellar articular cartilage mechanics and T_1-relaxation time – a biomarker for cartilage composition.

Methods

Male Sprague-Dawley rats were assigned a chow or a HFHS diet (Fig. 1A). Cohorts consisted of two age groups: 3-week-old weanlings ($WEAN_{14}$; diet maintained for 14 weeks; N_{HFHS} = 5, N_{CHOW} = 6) and 12-week-old adults ($ADULT_{24}$; diet maintained for 24 weeks; N_{HFHS} = 6, N_{CHOW} = 6). For the first seven weeks the HFHS weanlings received a protein-supplemented diet. After the diet interventions, animals were sacrificed, and the patellae harvested. Patellar cartilage biomechanics were tested in an indentation setting (Fig. 1B) via stress-relaxation (4 steps, 5% amplitude, 20%/s ramp rate, 200 s relaxation) followed by a sinusoidal test (2 Hz, 2% amplitude, 4 cycles) at final strain. Cartilage equilibrium modulus, dynamic modulus, and phase difference were analyzed. Subsequently, the patellae were magnetic resonance imaged at 11.7 T with variable flip angle zero echo time sequences (flip angles 2°, 5°, 13°; voxel size 25 μm^3). T_1-relaxation time was estimated using non-linear fitting. Depth-wise T_1-relaxation time profiles (0–100% cartilage depth) were analyzed from a 1 × 1 mm^2 region (Fig. 1C), and the profiles were then interpolated to 10 points. Statistical analyses were done with a linear mixed model (LMM).

Results

The cartilage equilibrium modulus, dynamic modulus, and phase difference were similar between the $WEAN_{14}$ and the $ADULT_{24}$ rats in the CHOW and HFHS groups (Fig. 1D). In the HFHS group, the $ADULT_{24}$ group rats had a longer cartilage T_1-relaxation time than the $WEAN_{14}$ group rats (Fig. 1E).

Discussion

Cartilage mechanics did not differ between the $WEAN_{14}$ and $ADULT_{24}$ rats, indicating similar mechanical properties regardless of diet. Longer T_1-relaxation times in the older HFHS-fed rats, but similar T_1-relaxation times in the CHOW-fed rats, suggest that HFHS-induced obesity has an increased effect on cartilage molecular composition in aged rats without corresponding mechanical deterioration.

Images (Optional)

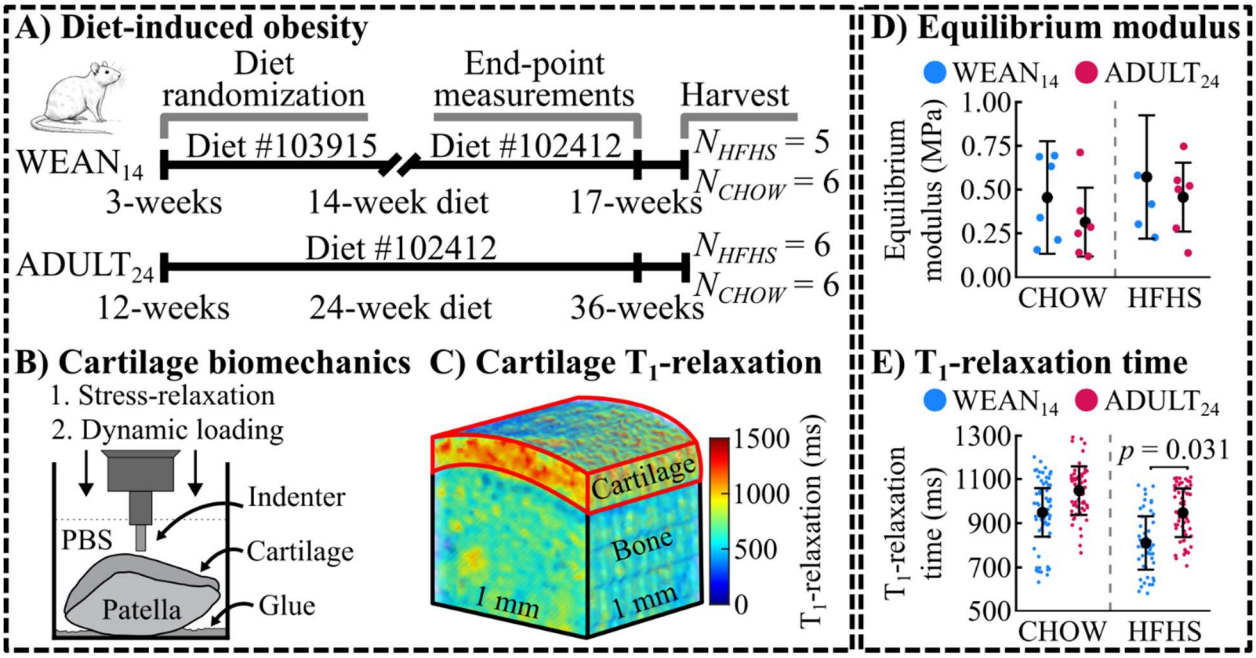


Figure 1. A) a high-fat/high-sucrose (HFHS) diet or a normal chow (CHOW) diet was maintained on 3-week-old weanling ($WEAN_{14}$) and 12-week-old adult ($ADULT_{24}$) male Sprague-Dawley rats. B) Stress-relaxation and dynamic loading were done under indentation. C) T_1-relaxation time was measured using micro-magnetic resonance imaging. D) Equilibrium modulus for the $WEAN_{14}$ and $ADULT_{24}$ groups. E) T_1-relaxation time for the $WEAN_{14}$ and $ADULT_{24}$ groups. Data is shown as mean ± 95 % CIs from LMM.

Session Category

Musculoskeletal Biomechanics: Tissues

OA150-02

Validating a Force Measuring Glove for Use in Distal Upper Limb Ergonomic Assessment Tools

Mr. Tyler Brown MSc Candidate[1], Mr. Daniel Cousins PhD Candidate[1], Mr. Ryan Porto[2], Dr. Michael Holmes PhD[1]

[1]Brock University, St. Catharines, Ontario, Canada. [2]General Motors, Warren, MI, United States

Introduction

Despite advances in ergonomics, hand and wrist injuries still constitute a significant portion of workplace injuries. Evaluating force, posture, and repetition are common inputs for distal upper limb assessment tools, such as the revised strain index (RSI). Obtaining accurate hand force measurements is one of the most challenging assessment tool inputs for ergonomists. As a result, it is common to rely on subjective ratings of exertion as a surrogate for force in assessment tools when evaluating gripping tasks. The purpose of this study was to validate a force sensing glove against a laboratory-grade load cell.

Methods

Fourteen participants were fitted with a force sensing glove which offers a novel solution containing seven embedded sensors that continuously record forces at the fingertips and palm. Participants completed various isometric finger flexion and palm push contractions (10 second duration) against a load cell (Sunrise Instruments, Ann Arbour, MI) while wearing the glove. For each of the seven glove sensors (four fingers, three palm), participants completed three trials at each of five force conditions (20, 40, 60, 80 and 100% MVC). Force levels were randomized, and rest was provided between contractions.

Results

When considering all force levels and sensors, the glove consistently overestimated forces (3.8 ± 0.6N; $p < 0.001$). The glove significantly overestimated forces at all force levels except for 20% MVC, and the largest differences were seen in the 60% (5.7 ± 1.4N) and 80% (4.5 ± 1.4N) MVC conditions. The mean difference ranged from 0.6 ± 1.7N for the distal palm to 7.9 ± 1.7 N for the index finger sensor.

Discussion

The mean absolute error across all conditions was significantly different than the load cell, however, this difference was only 3.8N. Considering most assessment tools work in ranges/bins, this error appears to be within acceptable limits and is likely more accurate than subjective methods. The glove reliably overestimated forces which may be corrected with offset values. Further research is needed to identify how to integrate these forces into current ergonomic assessment tools.

Session Category

Rehabilitation Biomechanics and Human Factors: Occupational Biomechanics

OA150-03

Multimodal Physiological Monitoring of E-sports Gaming

Ms. Yookyeong Sa, Ms. Subin Kim, Prof. Gwanseob Shin

UNIST, Ulju-gun, Ulsan, Korea, Republic of

Introduction

Esports involves a high level of cognitive and physical activity despite its outward appearance as a static task. Professional and casual players are repeatedly exposed to prolonged static posture, sustained concentration, rapid perceptual·cognitive processing demands, and acute stress. These increase the risk of musculoskeletal strain and mental fatigue. However, quantitative research on physiological changes during gameplay is limited. This study aims to establish a foundational framework for multimodal physiological monitoring during esports by examining how various physiological signals correspond to in-game events and whether these physiological patterns are consistent across individuals

Methods

15 participants in their twenties who played the target game for over 100 hours were recruited. Four sensors were attached to subjects: bilateral trapezius EMG, ECG (for HR, HRV), respiration, and skin conductance(SC) sensors on the right thumb and ring finger. Participants performed two rounds each of League of Legends and Overwatch 2 in randomized order, with rest and recovery periods between tasks.

'Events' were segmented with rest-engagement-rest phases based on the kill/death log by allies and enemies. Then, the physiological signal peaks exceeding surrounding values were matched to the events. Signal-event concordance rates were calculated as the proportion of detectable physiological signal peaks to whole engagement events

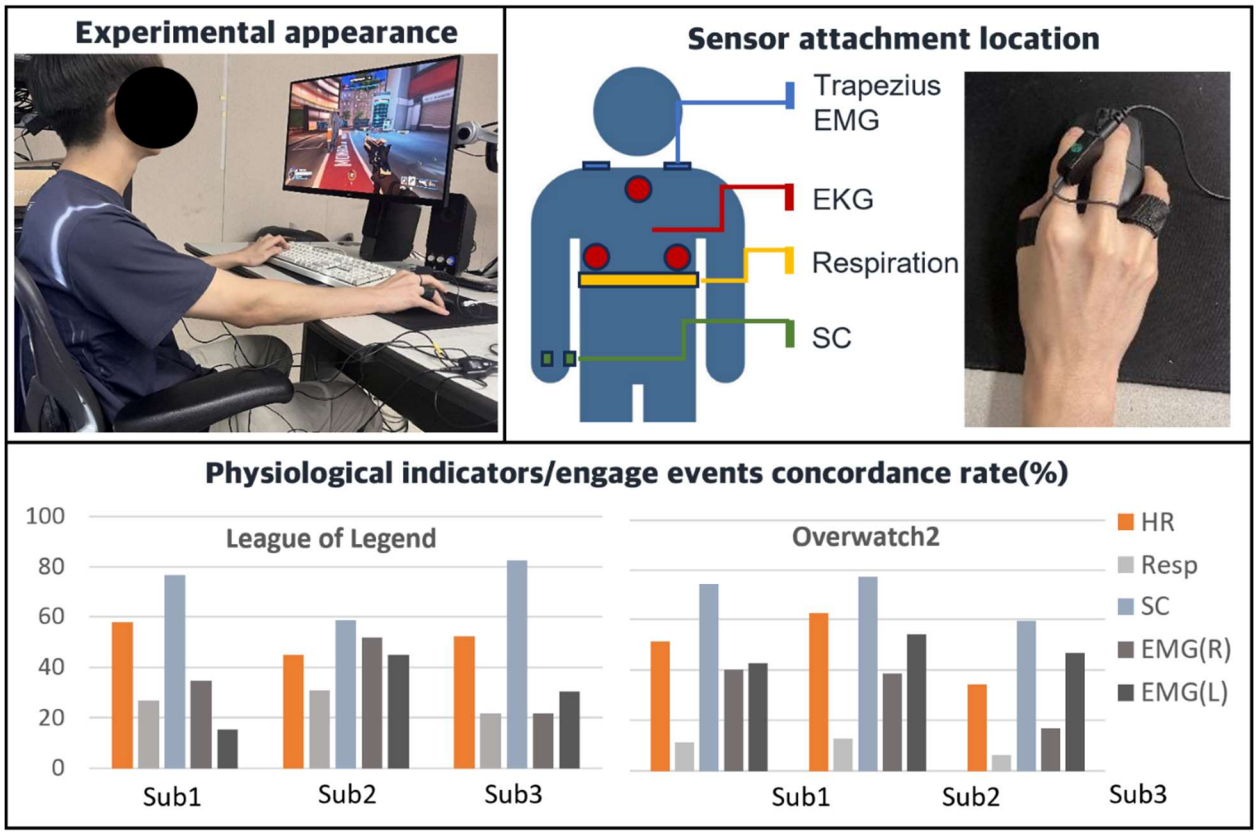
Results

In both games, SC showed the highest concordance with engaged events, followed by HR. Trapezius EMG responses varied by game: right EMG concordance was higher in Overwatch, whereas left was higher in League of Legends. Respiration showed the lowest concordance across all conditions. HRV (RMSSD) changes did not show a clear pattern across pre-, mid-, and post-task periods.

Discussion

This study demonstrates HR and SC are the most reliable indicators for monitoring physiological responses during gameplay. EMG responses influenced by game characteristics (POV, control method) and Respiration were less sensitive to the event. Physiological signals show consistent patterns within individuals. RMSSD had limitations in detecting rapid state changes during gameplay due to temporal resolution and individual variability. This study provides fundamental data for the development of a multimodal monitoring framework that can be utilized for workload management and real-time feedback for professional players, stress prevention in general gamers.

Images (Optional)



Session Category

Rehabilitation Biomechanics and Human Factors: Occupational Biomechanics

OA150-04

Identifying and Quantifying Manual Wheelchair Propulsion Patterns in the Wild

Ms. Kathylee Pinnock Branford[1], MSPH Meegan G. Van Straaten[2], PhD Omid Jahanian[2], PhD Hannah Houde[3], PhD Melissa M. B. Morrow[3], PhD Stephen Cain[1]

[1]West Virginia University, Morgantown, WV, United States. [2]Mayo Clinic, Rochester, MN, United States. [3]University of Texas Medical Branch, Galveston, TX, United States

Introduction

Poor manual wheelchair (MWC) propulsion mechanics can increase shoulder strain and the risk of overuse injuries. Clinical Practice Guidelines recommend a semicircular pattern, which reduces overuse risk by producing fewer strokes per distance traveled, decreasing wrist impact, and increasing push time [1]. Because of the importance of propulsion patterns in reducing injury risk, the objectives of this study were to develop a wearable sensor-based approach to identify MWC propulsion patterns in the real-world and to demonstrate the utility of our approach by quantifying propulsion patterns used during daily mobility in a small sample of MWC users.

Methods

Two MWC users with spinal cord injury (SCI) wore three inertial measurement units (IMUs; Axivity AX6; ±16 g, ±2000°/s; 100 Hz) placed on the dominant wrist, upper arm, and wheel for seven consecutive days of daily life. We identified steady-state propulsion cycles using the upper arm elevation angle, requiring steady-state cycles to exhibit similar arm excursion and cycle duration compared to at least one adjacent cycle. For steady-state cycles, we integrated linear acceleration from the wrist IMU to calculate wrist position (Fig1) using an approach similar to a zero-velocity update to remove integration drift. For each cycle, we calculated the duration and distance traveled and classified the propulsion pattern as either arc (not recommended), semicircular, or other.

Results

Steady-state cycles represented less than ~17% of the total time each participant spent moving (Fig1). Participant 1 primarily used an arc pattern, whereas Participant 2 primarily used a semicircular pattern.

Discussion

Calculating wrist position trajectories from IMUs during MWC propulsion enables classification of propulsion patterns outside laboratory settings. Our findings reveal that participants only utilized steady-state propulsion cycles ~17% of total mobility time,

suggesting that knowledge from laboratory-based studies of propulsion, which utilize analyses of steady-state propulsion on a treadmill or ergometer, may have limited use for understanding the demands of real-world MWC mobility. Personalized measurement of propulsion patterns in daily life could guide interventions aimed at improving propulsion mechanics and promoting long-term upper-extremity health in wheelchair users.

Images (Optional)

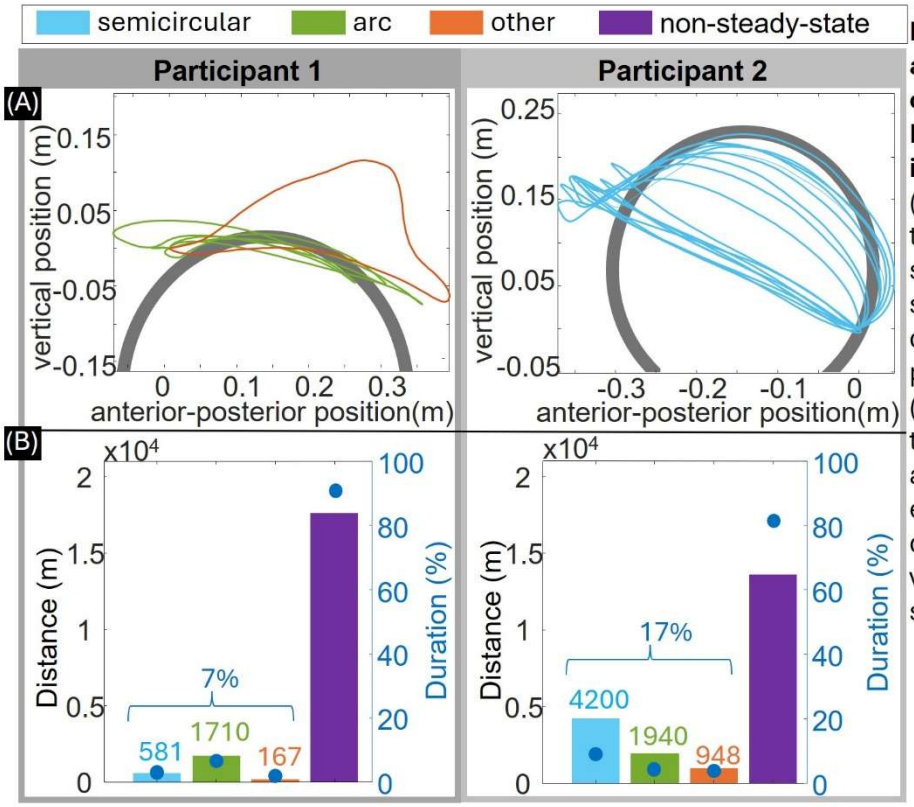


Figure 1. Wrist position and propulsion characteristics during MWC use for two individuals with SCI. (A) Wrist position trajectories in the sagittal plane during steady-state propulsion, demonstrating distinct propulsion techniques. (B) Weekly distance traveled by MWC user and time spent using each propulsion style during steady-state versus non-steady-state.

References (Optional)

[1] PVA Consortium for Spinal Cord Medicine et al., *J Spinal Cord Med*, 2005.

Acknowledgements (Optional)

NIH Eunice Kennedy Shriver National Institute of Child Health and Human Development (R01HD084423)

Session Category

Rehabilitation Biomechanics and Human Factors: Occupational Biomechanics

OA150-06

The Effects of Mental Fatigue on Movement and Muscle Activity During Cyclic Pushing

Ms. Molly Malette BSc, Mr. Ryan Chhiba MSc, Dr. Peter Keir PhD

McMaster University, Hamilton, Ontario, Canada

Introduction

Mental fatigue can impair physical performance resulting in elevated muscle activity and reduced task accuracy, leading to increased injury risk in the workplace [1]. Modern work environments often require sustained attention, multitasking, and fast-paced work, yet the combined impact of cognitive demands and physical effort on task execution and muscle activity is not well understood. This study aimed to quantify the influence mental fatigue has on task accuracy and upper-extremity muscle activity during four dynamic pushing tasks.

Methods

Twenty-two participants completed four pushing tasks following a control condition (watching a documentary) and a mental fatigue task (Stroop test). Tasks required pushing handles from 10% to 80% of maximum reach with 4 kg resistance. The tasks were (i) 15 cycles/minute, (ii) 30 cycles/minute, (iii) 15 cycles/minute with 30% handgrip, and (iv) 30 cycles/minute with 30% handgrip. Participants were instructed to reach targets accurately without over or undershooting. EMG was collected from seven upper-extremity muscles bilaterally, along with right hand grip force, displacement, and ratings of both physical and mental fatigue.

Results

Higher mental fatigue and exertion ratings were reported across all tasks in the Stroop condition. Changes in muscle activity after the Stroop task were observed for many muscles, however, variability was quite high. Muscle activity for the right forearm flexors and extensors rose from less than 10%, to over 20% when handgrip was added to the 15 and 30 cycles/minute push trials. The left forearm flexors and extensors remained around 10% with an increase in the extensors in the Stroop condition. The anterior deltoids had the highest activities across all muscles but decreased with mental fatigue.

Discussion

A brief (12 minute) mentally fatiguing task elevated activity in some muscles but reduced it in others, suggesting that some muscles may be more susceptible to mental fatigue. Preliminary analyses have not shown an increase in errors, suggesting that there may not be visual signs of impairment. These findings highlight a potential interaction between mental fatigue and dual tasks, which can have implications in risk for both acute and chronic occupational injuries.

References (Optional)

[1] Marcora, SM et al. J Appl Physiol, 2009

Acknowledgements (Optional)

Natural Sciences and Engineering Research Council of Canada (NSERC Discovery Grant RGPIN-2023-05473)

Session Category

Rehabilitation Biomechanics and Human Factors: Occupational Biomechanics

OA151-02

MRL/MpJ Inspired Therapeutic Protein Panel Restores Material Properties in Fully Torn Rat Supraspinatus Tendon

Mrs. Ellen Garner, Mr. Chinmay Mangalgi, Dr. Nelly Andarawis-Puri

Cornell University, Ithaca, NY, United States

Introduction

Supraspinatus tendon (SST) tears are common and heal with mechanically and structurally inferior scar tissue.[1] The Murphy Roths Large (MRL/MpJ) mouse strain heals tendon injuries, including SST, more effectively than canonical strains.[1] Patellar tendon healing in canonically healing mice is improved by treatment with 29 proteins of interest (POIs) that are highly upregulated in MRL/MpJ healing.[2] In vitro, these POIs similarly shift rat and mouse tenocyte behavior,3 suggesting cross-species efficacy yet to be shown in vivo. We hypothesize that POIs will retain therapeutic impact and improve mechanical properties of rat SST following acute injury wherein there is a need to reconstitute the tendon-to-bone enthesis.

Methods

Under IACUC approval, left SSTs of 10-month-old female Sprague-Dawley rat were surgically fully detached from their insertion and an osmotic pump was placed subcutaneously delivering POIs (n=6) or PBS carrier control (n=10) for 3 days. Additional rats (n=9) received injury without a pump. Injured and contralateral uninjured limbs were mechanically tested under tensile loading after euthanasia on day 42. Paired t-tests compared injured limbs to contralateral controls.

Results

Injured and uninjured limbs typically failed at the enthesis or midsubstance, respectively. Treated limbs had significantly increased cross sectional area (CSA) (Fig 1A) and decreased maximum stress (Fig 1B) and Young's modulus (Fig 1E) compared to contralateral controls. POI treatment restored hysteresis (Fig 1D), maximum force (Fig 1C), and linear stiffness (Fig 1F) to uninjured levels, while PBS-treated and no pump controls did not.

Discussion

Injured limbs in all treatment groups increased tissue deposition in an attempt to improve function. Only POI treated limbs restored material properties of linear stiffness and maximum force, allowing healed tendons to meet normal physiological demands. Hysteresis restoration shows POIs also promote recovery of protective viscoelastic

properties which was not observed in PBS or no pump treatment groups. MRL/MpJ inspired POIs are a promising therapeutic across species for healing acute tendon injuries. Future work will consider sexual dimorphism of response and optimize dosing to improve structural properties of the healed tendon.

Images (Optional)

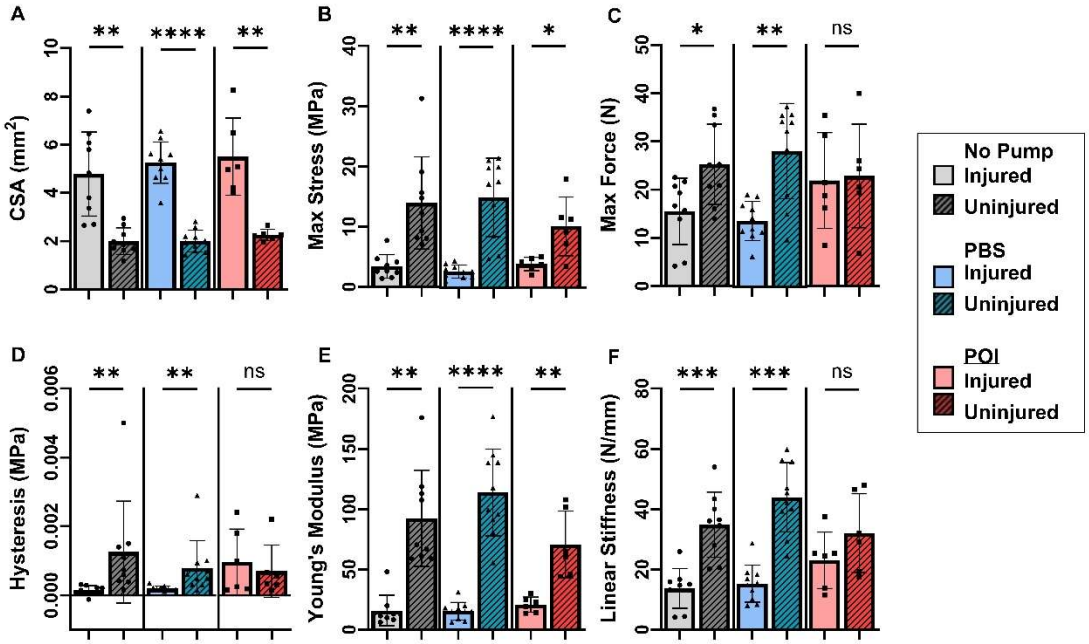


Figure 1: Mechanical properties of injured and contralateral SSTs for treatment groups. (* p<0.05, ** p<0.001, *** p<0.0001)

References (Optional)

[1]: Chatterjee *et. al.*, *JSES,* 2022 [2]: Pacheco *et. al.,* Acta Biomater., 2025 [in review] [3]: Marvin *et.al.*, bioRxiv, 2024

Acknowledgements (Optional)

NSF DGE 2139899

Session Category

Orthopaedic Biomechanics: Trauma and Repair

OA151-03

Biomechanical and In-Vitro Testing of Braided, Long-Term Biodegradable Scaffolds for Anterior Cruciate Ligament Tissue Engineering

Dr.-Ing. Caroline Emonts[1], Dr.-Ing. Benedict Bauer[1], M.Sc. Saskia Hesse[1], M.Sc. Viktoria Kiaulehn[2], Dr.-Ing. Max Praster[2], Prof. Dr. rer. nat. Mersedeh Tohidnezhad[3], Prof. Dr. Thomas Gries[1]

[1]Department of Medical Textiles, Institut für Textiltechnik of RWTH Aachen University, Aachen, NRW, Germany. [2]Department of Orthopaedic, Trauma and Reconstructive Surgery, RWTH University Hospital, Aachen, NRW, Germany. [3]Department of Anatomy and Cell Biology, RWTH University Hospital, Aachen, NRW, Germany

Introduction

Anterior Cruciate Ligament (ACL) injuries are a common sports injury. Tissue engineering offers a new approach by using scaffolds that provide temporary mechanical stability and promote cell ingrowth. Braided scaffolds offer a reproducible, scalable three-dimensional structural design with high strength and sufficient porosity. This study investigates the biomechanical properties and cell-ingrowth on long-term degradable scaffolds for ACL replacement.

Methods

The scaffolds were fabricated using round, hexagonal, and linear braiding with melt-spun PCL monofilaments [1]. Uniaxial tensile testing was performed corresponding to the length of the ACL. A cyclic tensile test with the load of walking was performed for 500000 cycles with 1,6 Hz. Porosity and pore size were quantified using µCT imaging. In addition, rat tenocytes were cultured on the scaffolds for 14 days to evaluate cell adhesion, proliferation and viability.

Results

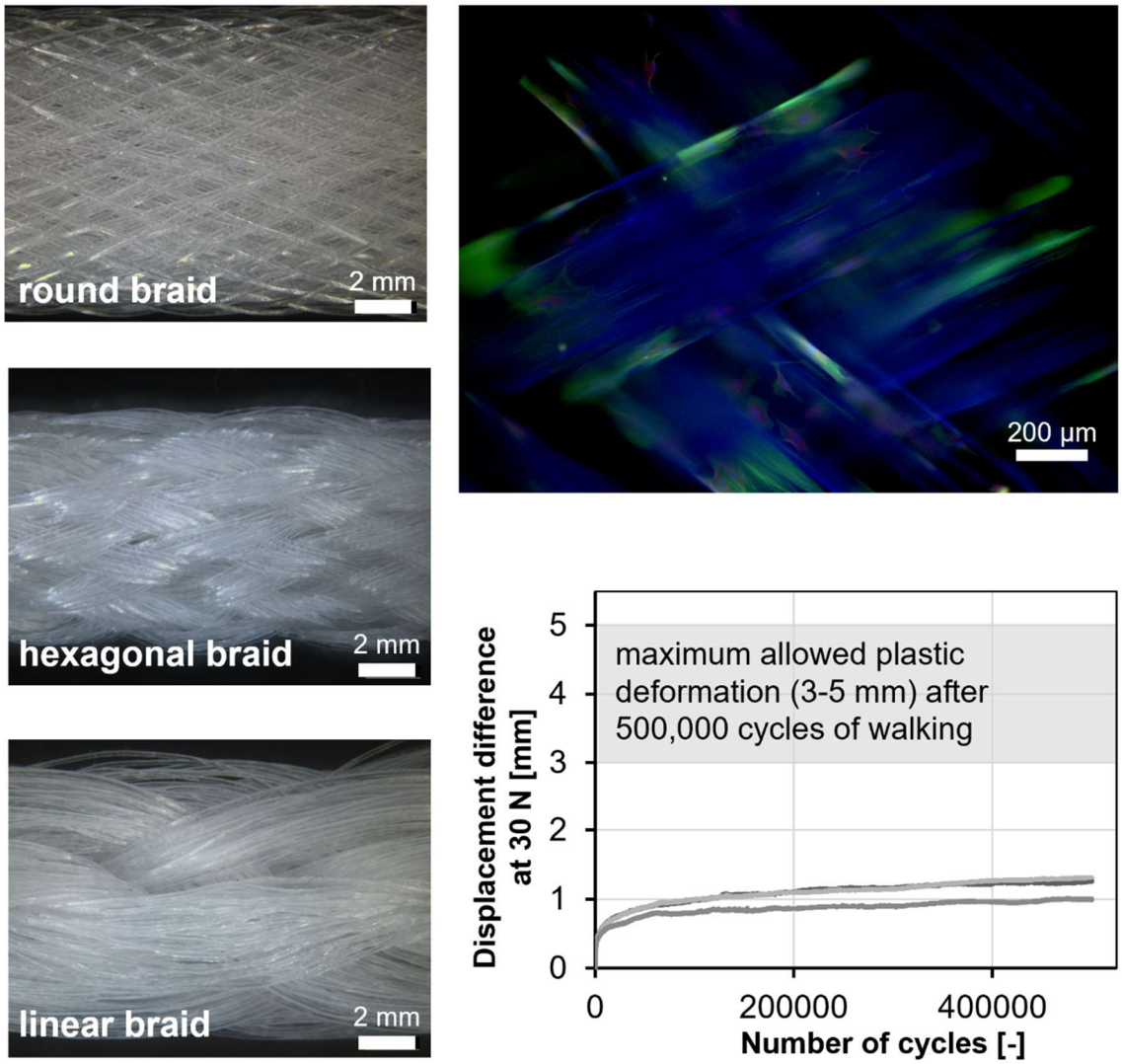
The braided scaffolds exhibited tensile strengths between 3460 - 4110 N, substantially exceeding the tensile strength of the native ACL (734–2160 N) [2,4]. The stiffness within the linear region (186–212 N/mm) corresponded closely to the physiological stiffness values of the ACL (180–242 N/mm) [2,4], indicating that the constructs fulfill the primary mechanical requirements for initial ligament substitution. Regarding cyclic loading, the laxity of the synthetic ACL caused by creep must not exceed 3-5 mm. [3] The plastic deformation is below 1.3 mm for all tested scaffolds [4]. In-vitro analyses confirmed that rat tenocytes were able to attach, proliferate, and remain viable on all scaffold types. Expression of tenogenic markers was detectable across all conditions. Cellular orientation along the

fiber axis was observed, suggesting that the scaffold topography provides appropriate cues for alignment.

Discussion

The results demonstrate the suitability of the scaffolds in terms of initial mechanical properties and cyclic loading within the physiological range. In addition, cell compatibility with relevant cell types was demonstrated. Next, the scaffolds will be tested in ex-vivo porcine knees and subsequently in in-vitro animal models.

Images (Optional)



References (Optional)

[1] Bauer et al., Fibers, 10(3), 2022

[2] Noyes, F. R. et al., J of Bone and Joint Surgery, 1976

[3] Vieira, A. C., et al.: J of Biomechanics, 2009

[4] Emonts, 2023, https://doi.org/10.18154/RWTH-2024-08389

Acknowledgements (Optional)

This project is partially funded by: Federal Ministry of Research, Technology and Space (LigaBraid 2, 16LW0632K).

Session Category

Orthopaedic Biomechanics: Trauma and Repair

OA151-04

Assessing Efficacy of Systemic Tacrolimus Immunosuppression to Improve Tendon Reconstruction: A Pilot Study

Mr. Trent Hardwick[1], Mr. Atharva Bhagwat[1], Ms. Sonia Patel[1], Ms. Jaclyn Brendenkamp[1], Ms. Elena Woo[1], Mr. Evan Fry[1], Mr. Brady Huggins[1], Mr. Alvin Patel[1], Mr. Fuad Bin Enam[1], Ms. Eeshana Bhuvanesh[1], Dr. Jeremy Eekhoff[2], Dr. Brian Mailey[1], Dr. Koyal Garg[1], Dr. Alex Reiter[1]

[1]Saint Louis University, St. Louis, Mo, United States. [2]University of Pennsylvania, Philadelphia, PA, United States

Introduction

Tendon ruptures risk poor healing and adhesion formation, often resulting in long-term deficits despite surgical advances.[1,2] Tacrolimus, a calcineurin inhibitor, exhibits anti-inflammatory and anti-fibrotic effects. Previously, tacrolimus has been shown to improve functional outcomes in a flexor tendon repair case study.[3] In a murine model of Achilles tendon rupture, tacrolimus has improved histological outcomes.[4] This pilot study examined the effects of tacrolimus on functional, mechanical, and histological outcomes in a rat model of Achilles rupture.

Methods

Forty-two female Sprague Dawley rats (10-12 weeks old, 200-275g, Inotiv) were divided into three groups: Achilles rupture with systemic tacrolimus treatment, Achilles rupture with vehicle, and naïve control. Following rupture and repair, limbs were immobilized in a cast for two weeks, and tacrolimus (2mg/kg+DMSO+saline) or vehicle (DMSO+saline) were injected intraperitoneally daily. Passive ankle range of motion (ROM) (n=5-12/group) was assessed via manual manipulation and goniometer immediately following euthanasia. Tendons were prepared for mechanical (n=10/group) and histological analysis (n=4/group). Mechanical testing consisted of preconditioning, 10-minute stress relaxation at 6% strain, and a quasistatic ramp-to-failure. Data were analyzed in MATLAB. One-way ANOVAs with Tukey post-hoc tests assessed group differences (p<0.05). Histological analysis is ongoing.

Results

Tacrolimus treatment significantly improved ROM compared to vehicle but remained reduced from control (Fig. 1A). Maximum force, stiffness, cross-sectional area, maximum

stress, tangent modulus, and percent relaxation in both injury groups were significantly different from control but not each other (Fig. 1B-G).

Discussion

While ROM data suggests tacrolimus had a modest improvement on function following injury, mechanical testing revealed no differences between injury groups. The substantial mechanical deficits in rupture groups at 2 weeks post-injury compared to controls are consistent with previous work showing a ~85% reduction in force and ~80% reduction in stiffness[5]. It is possible the early 2-week post-injury time point with full immobilization may mask any potential long-term benefits of tacrolimus treatment on tendon mechanics.

Images (Optional)

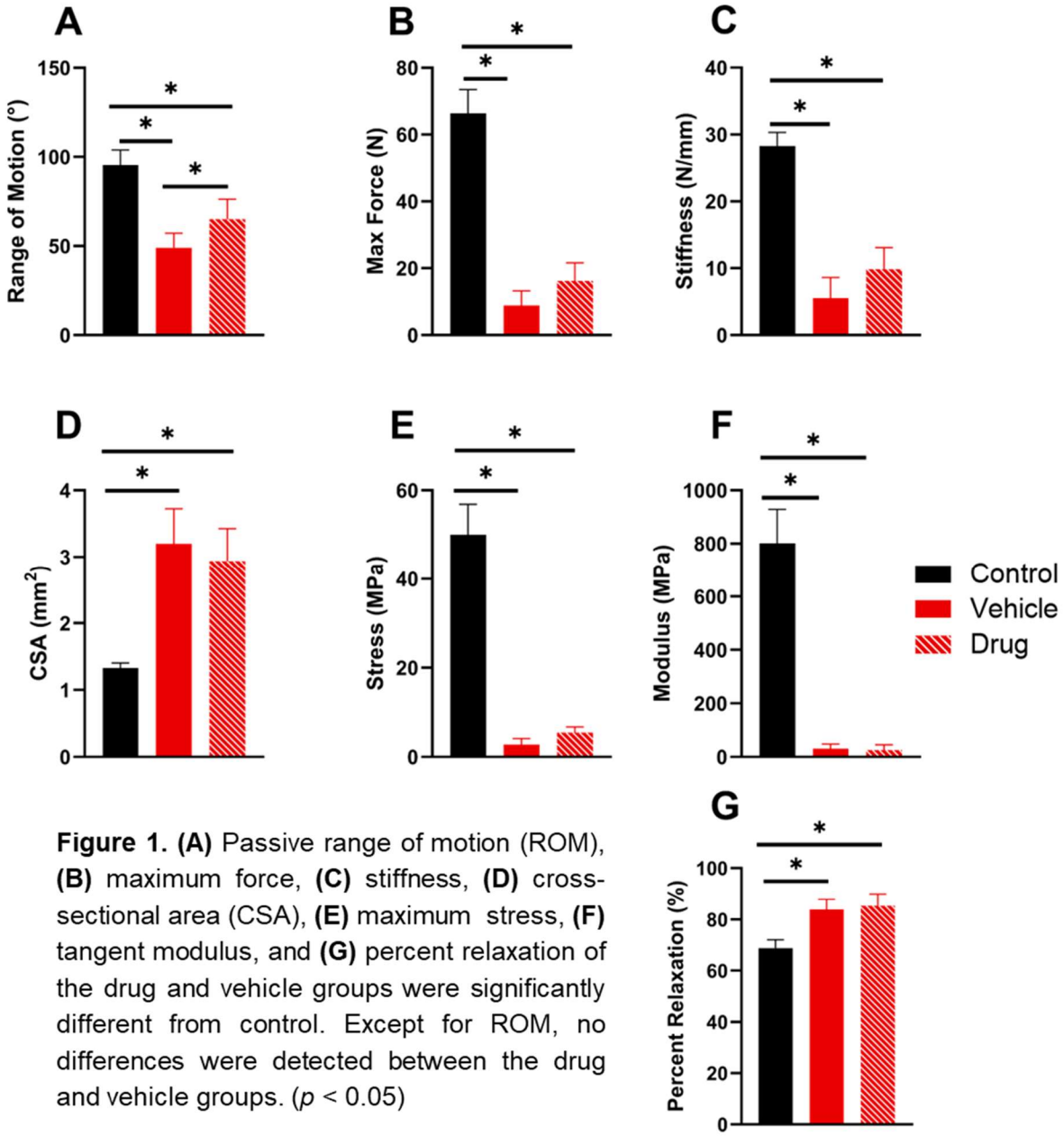


Figure 1. (A) Passive range of motion (ROM), **(B)** maximum force, **(C)** stiffness, **(D)** cross-sectional area (CSA), **(E)** maximum stress, **(F)** tangent modulus, and **(G)** percent relaxation of the drug and vehicle groups were significantly different from control. Except for ROM, no differences were detected between the drug and vehicle groups. ($p < 0.05$)

References (Optional)

[1] Carmont, *SSTA*, 2022. [2] Titan*, Plast Recon Surg, 2019.* [3] Mailey, *Plast Rec Surg Glob Open*, 2021. [4] Nazari, *Iran J Med Sci*, 2025. [5] Leahy, *AJSM*, 2022.

Acknowledgements (Optional)

Funding from the Saint Louis University Research Institute and Department of Surgery.

Session Category

Orthopaedic Biomechanics: Trauma and Repair

OA151-05

Implant Cross-Sectional Profile Affects Tendon-Implant Interactions Over Initial Cycles of Tendon Loading

Ms. Gabriella Justen, Dr. Michael Pavol, Prof. Ravi Balasubramanian

Oregon State University, Corvallis, Oregon, United States

Introduction

Tendons may bend and slide across orthopedic implants, such as volar plates at the distal radius. Tendon damage from these interactions can lead to impaired function or rupture. To better prevent these consequences, this study investigated how "implant" cross-sectional profile affects its interactions with a tendon over the initial cycles of tendon tensile loading.

Methods

Twenty-four extensor digitorum communis tendon bundles from New Zealand white rabbits were wrapped 160° around a submerged titanium rod with one of three profiles of equal contact length: blunt, circular, or knife. The circular profile was of radius 1.5 mm. The blunt profile had an 80° central section of 2.7-mm radius with 50° sections of 0.3-mm radius to either side. For the knife profile, these radii were reversed. One end of the bundle was attached to an anchor point via a cord, spring (stiffness: 1.44 N/mm), and load cell in series. The other end was attached to a linear actuator via a cord and load cell in series. Slow (2.5 mm/s) triangle-wave motion of the actuator exposed the tendon bundle to repeated cyclic tensile loading over an actuator-side force excursion from 0.5–4.5 N. Anchor-side force excursion was analyzed as a measure of force transmission and tendon sliding across the rod, and its rate of change across cycles was used to determine the transition cycle at which a near-steady-state excursion was reached.

Results

One minute into loading, the circular profile exhibited a larger anchor-side force excursion than the other profiles (Table). Anchor-side force excursion rapidly decreased thereafter until tendon failure (n =2) or transition to a near-steady-state excursion that did not differ between profiles (p =.24). This transition occurred after more cycles for the circular profile (Table).

Discussion

Regardless of rod profile, anchor-side force excursion rapidly dropped to a near-steady-state of ~6% of actuator-side excursion, with minimal (~0.2 mm) tendon sliding. However, the circular profile maintained a larger anchor-side excursion for ~1300 more loading cycles. The results suggest circular profiles should be used over blunt or knife profiles in implant designs involving tendon-implant interactions, but other measures to reduce tendon damage are likely needed.

Images (Optional)

Table. Mean ± SD anchor-side force peak-to-peak excursion and median [interquartile range] transition cycle as a function of rod profile.

	Rod Profile		
Variable	Blunt (*n* = 8)§	Circular (*n* = 8)	Knife (*n* = 7)
Anchor-side force excursion (N)			
At 1 minute	0.84 ± 0.58*	2.33 ± 0.42	0.44 ± 0.20*
At transition cycle	0.20 ± 0.09	0.30 ± 0.13‡	0.22 ± 0.10‡
Transition cycle	580 [354 – 989]†	1945 [1553 – 4102]	768 [562 – 1559]†

* $p < .001$ vs. Circular; † $p < .05$ vs. Circular; ‡ $p < .05$ vs. at 1 minute; § $n = 6$ at transition cycle.

Session Category

Orthopaedic Biomechanics: Trauma and Repair

OA152-02

Intracellular Basal Coupling Modulates Coordination in Computational Models of Autonomously Beating Cilia

Ms. Alexis Rivera BS, MS, Dr. Louis Woodhams PhD, Dr. Philip Bayly PhD

Washington University in St. Louis, St. Louis, MO, United States

Introduction

Cilia are slender organelles which oscillate to propel surrounding fluid. Cilia arrays exhibit metachronal behavior: beating with the same frequency but a spatially varying phase. Metachronal beating enhances propulsive efficacy but the mechanism is incompletely understood; hypothesized mechanisms include hydrodynamic coupling and elastic coupling between subcortical striated fibers. This computational study explores the effects of oscillation mechanism and elastic coupling on the metachronal and synchronous behavior of cilia arrays.

Methods

Arrays of 10 autonomously beating cilia were modeled (Fig. 1A,D,G,J). Each cilium was represented as a discretized Kirchoff filament with non-local hydrodynamic coupling applied between spheres on each discretized link using Rotne-Prager-Yamakawa theory [1]. Oscillatory beating was generated by two different mechanisms: (1) a dynamic flutter instability generated by follower force (Fig. 1A-F) [2]; (2) switching between a power and recovery stroke based on base-link angle (Fig. 1G-M). The intrinsic beating frequency varied between cilia by 26%. Nonlinear elastic coupling components (torsional springs) were added between adjacent filament bases. Coordination was quantified by magnitude and lag of cross-covariance between tip angles.

Results

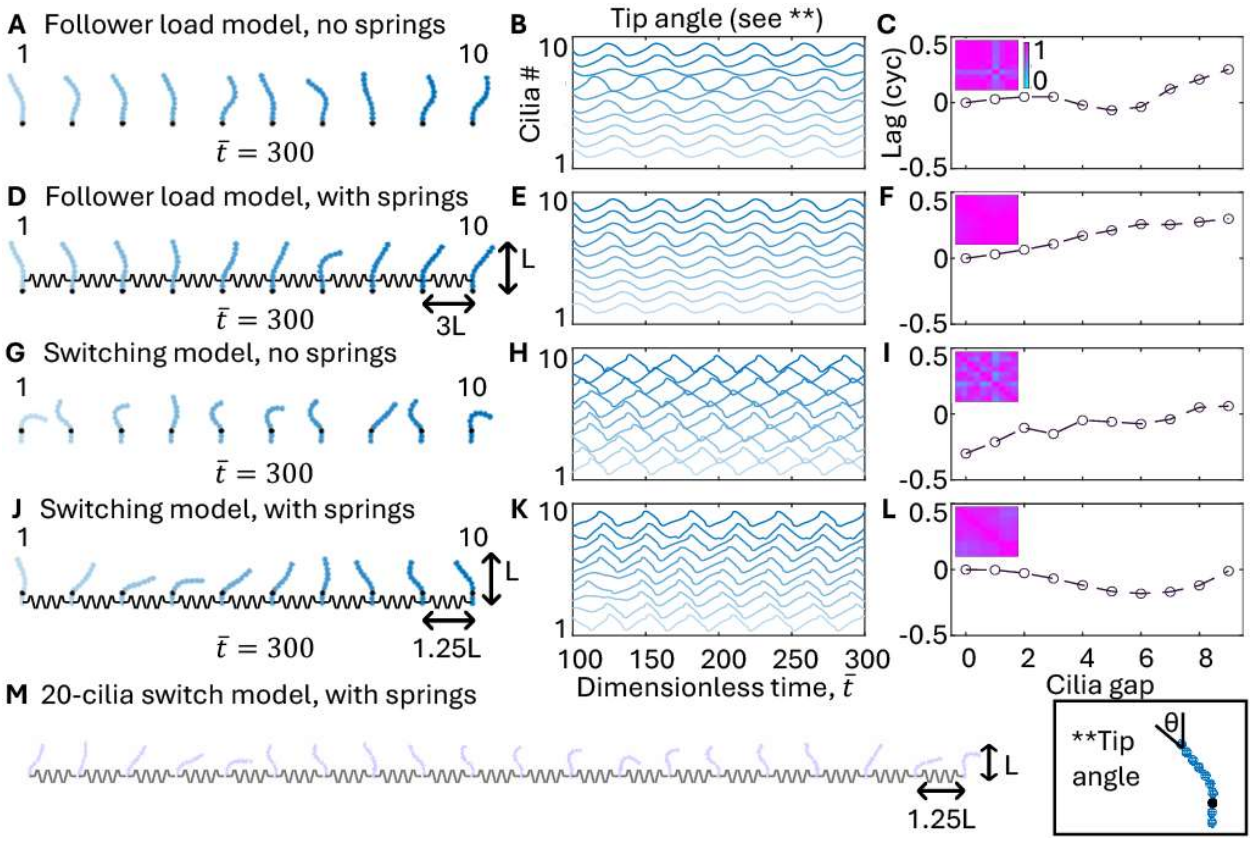
Filament tip angle traces from time domain simulations (Fig. 1B,E,H,K) revealed three general behaviors: unsynchronized beating (low covariance), highly synchronized beating (high covariance with small phase lag), and metachronal beating (high covariance with spatially increasing lag). For flutter-driven beating, fluid coupling alone highly synchronized cilia except when widely separated (Fig. 1C). Elastic coupling strengthened synchronization (Fig. 1F). Switching-driven cilia were unsynchronized by fluid coupling even when closely spaced (Fig. 1I), but elastic basal coupling induced graded metachrony (higher covariance

and spatial phase gradients) (Fig. 1L). Larger cilia arrays showed clearer metachronal behavior (Fig. 1M).

Discussion

Simulated cilia arrays of spontaneously beating filaments exhibited different patterns of coordination depending on the assumed beating mechanism and the type of inter-filament coupling. Fluid coupling alone may not be sufficient to produce robust metachronal cilia beating. Future work will compare model predictions to observations of cilia coordination in ciliated microorganisms (*Tetrahymena*) to clarify mechanisms of beating and coordination.

Images (Optional)



References (Optional)

[1] Fuchter P, Bloomfield-Gadêlha H. *J R Soc Interface,* 2023.

[2] Woodhams LG et al. *J R Soc Interface,* 2022.

Acknowledgements (Optional)

NSF2421872

Session Category

Cell Biomechanics: Methods and Models

OA152-03

A Comprehensive Thermodynamic Eshelby-informed Model for Sarcomere Growth

Mr Thomas Hayes, Prof. Patrick McGarry, Dr. Giuseppe Zurlo, Dr. Eoin McEvoy

University of Galway, Galway, Connacht, Ireland

Introduction

Mechanical loading and active contraction play a central role in regulating skeletal muscle mass [1], but the mechanisms by which these processes drive tissue-level growth and atrophy remain unclear. We develop a thermodynamically consistent continuum framework for skeletal muscle in which cross-bridge micromechanics and sarcomere structure drive growth and force generation

Methods

Skeletal muscle generates active stress via cross-bridge kinetics, where activation alters myosin chemical potential initiating cycling and force generation [2]. We develop a novel activity-associated free energy expression that is directly informed by cross-bridge micromechanics and sarcomere structure and incorporate it into a continuum description of skeletal muscle. This continuum model is formulated in a finite-growth setting, in which the tissue is free to respond to mechanical loading and activity through growth. Imposing the Second Law of thermodynamics yields a dissipation inequality which depends on the passive Eshelby stress, arising from strain-energy, stress, and the deformation. This is compounded by an active energy contribution, associated with the fraction of force-generating cross bridges, their associated energy, a function representing sarcomere geometry. Finally, the addition of new mass counters the entropic tendency toward protein dilution in the cytoplasm. From the dissipation inequality, we derive a growth evolution law as dependent on these key energetic contributions, and we analyse sarcomere growth arising from extension and force-based loading conditions.

Results

Myosin attachment lowers their high chemical potential (Fig. 1A), and maximal attachment produces a peak in force generated (Fig. 1B). The resulting sarcomere free-energy landscape, set by actomyosin overlap drives growth (Fig. 1C). Under extension-controlled loading, the energy minimum shifts toward states with increased axial growth, whereas under force-controlled loading, it shifts toward increased radial growth (Fig. 1D,E). The axial-to-radial growth ratio varies with load and protein availability (Fig. 1F).

Discussion

This framework provides a thermodynamic basis for the phenomenology of stretch and stress driven growth processes, whereby muscle grows to maximise active force generation. Understanding this mechanism has tremendous potential for uncovering treatments for muscle-wasting diseases such as sarcopenia and ALS

Images (Optional)

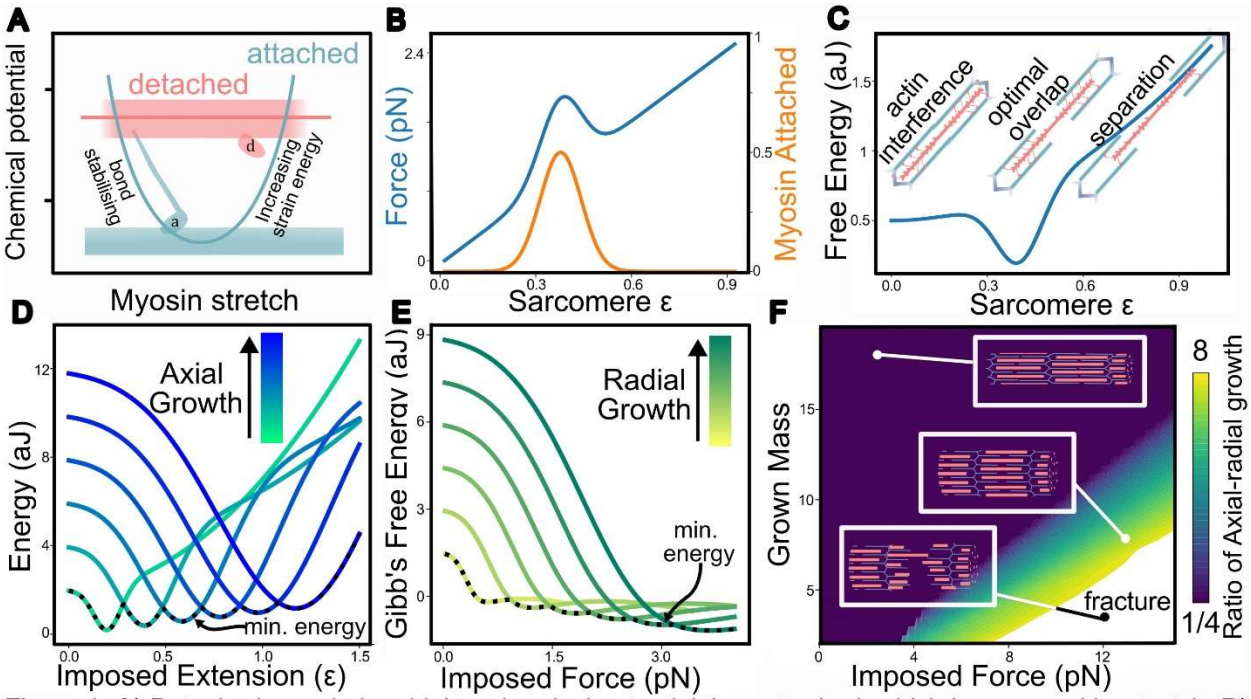


Figure 1: **A**) Detached myosin has higher chemical potential than attached, which is governed by stretch; **B**) Number of attached myosin and associated generated force, which also include passive contribution; **C**) Strain-dependent sarcomere free energy depends on actomyosin overlap; Imposed extension favours axial growth (**D**), whereas imposed force favours radial growth (**E**) by shifting energy minima; **F**) The axial-to-radial growth ratio depends on protein mass and applied load.

References (Optional)

[1] Philips, SM *et al.* , Am J Physiol, *1997*

[2] McEvoy, E *et al.* , BMMB, *2019*

Acknowledgements (Optional)

Funding from the Irish Research Council

Session Category

Cell Biomechanics: Methods and Models

OA152-04

A Thermodynamic Framework to Predict Coupled Cross-Bridge Remodeling and Deformation Dynamics

Dr Ryan Coleman, Dr Patrick McGarry

University of Galway, Galway, Galway, Ireland

Introduction

We propose a novel thermodynamic landscape to describe the mechanics of cross-bridge remodeling. This implicitly couples cross-bridge turnover with myosin tail deformation, inducing interdependent remodeling. To our knowledge this mechanism has not been described in any previous methodology and provides a novel extension to the classical Huxley-Simmons model [1]. We demonstrate that our framework provides improved prediction of experimentally measured tension generation and dynamic relaxation.

Methods

With our proposed thermodynamic landscape, we predict the rate of cross-bridge attachment, and detachment via the transition state theory (Fig.1A,B), including a bi-stable state between pre-power-stroke (pre-PS) and post-PS myosin heads reflecting tension induced via the configurational change of myosin head pivoting. Deformation rate of myosin tails is determined from dynamic force equilibrium between active tension generated by attached myosin heads with (i) externally imposed deformation, (ii) dynamic addition of new cross-bridge attachments, and (iii) loss via passive detachments.

The mechanism by which cross-bridge turnover is affected by myosin deformation is as follows. Myosin extension causes enthalpy of cross-bridges to decrease due to applied work (green dash Fig.1A). Simultaneously, extension of pre-PS myosin causes internal strain energy to increase, magnifying the barrier for pre-PS to post-PS cross-bridge transition (red dash Fig.1A).

Results

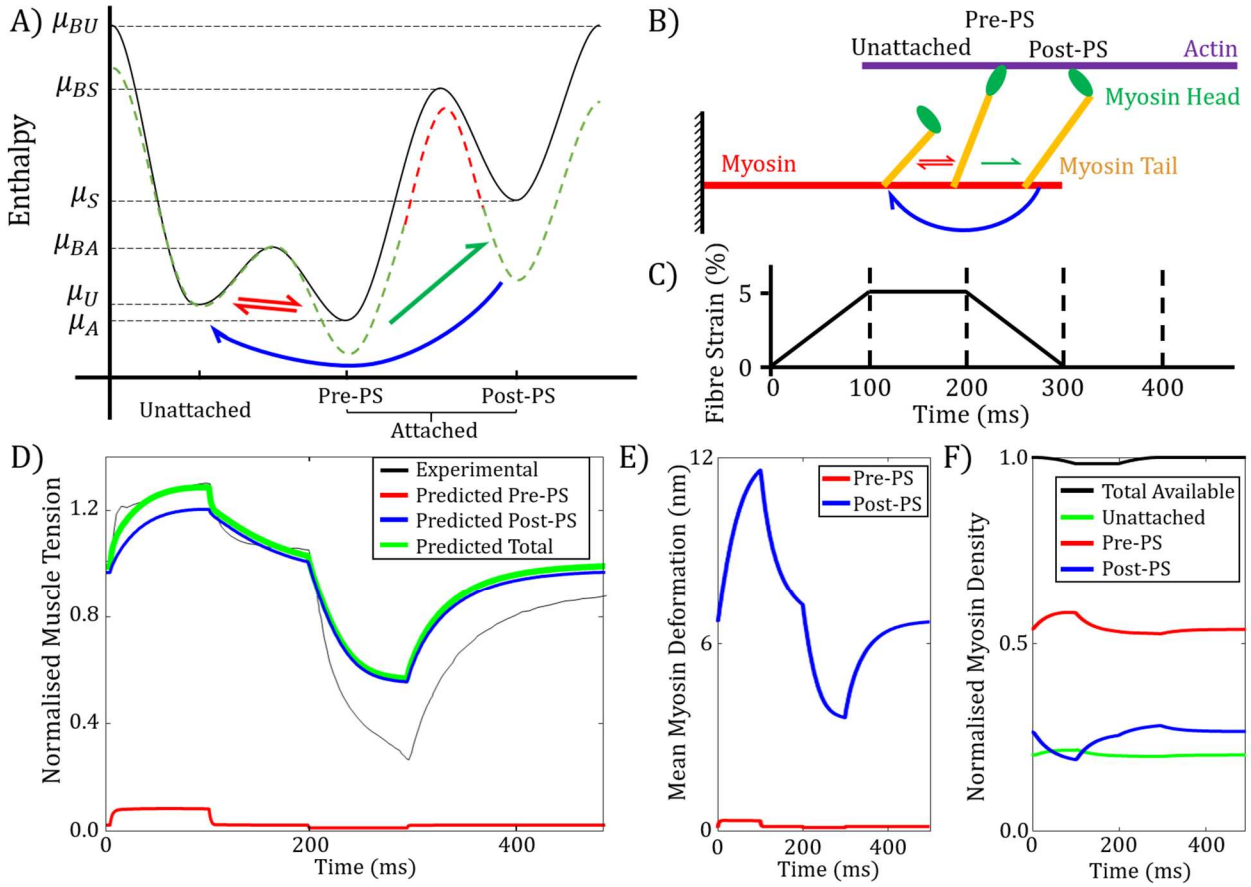
We simulate the response of muscle fibers subjected to the applied strain history shown in Fig.1C, and we compare our predictions with experimental measurements [2]. During fiber extension, tension rapidly increases and then plateaus (Fig.1D), explained by rapidly increasing deformation of the pre-PS myosin (Fig.1E). This inhibits post-PS turnover,

balancing post-PS density and deformation (Fig.1.E,F). During static stretch, tension reduces towards isometric conditions as cross-bridge concentrations self-modulate by passive turnover, regulating myosin deformation to equilibrium (Fig.1E,F). Muscle shortening reduces deformation of post-PS myosin tails (Fig.1E), facilitating tension loss.

Discussion

This framework has important implications in understanding and modelling tension dynamics in skeletal muscle, contractile smooth muscle cells, and cardiac myocytes. We will further utilize this framework to predict long term cyclic loading [3], investigating the effect of cross-bridge dynamics on sarcomere remodeling.

Images (Optional)



References (Optional)

[1] Huxley A.F., Simmons R.M., Nature, 1971.

[2] Bickham D.C. et al., Biophys.J., 2011.

[3] Wille J.J. et al., Ann.Biomed.Eng., 2006.

Acknowledgements (Optional)

GEMINI Horizon Europe Research Grant (101136438).

Session Category

Cell Biomechanics: Methods and Models

OA152-05

A Thermodynamically Consistent Biophysical Model for Stress-Dependent Cell Growth and Division

Mr Matteo Simeone[1], Mr Irish Senthilkumar[1], Dr Enda Howley[1], Dr Bart Smeets[2], Dr Eoin McEvoy[1]

[1]University of Galway, Galway, Ireland, Ireland. [2]Ku Leuven, Leuven, Belgium, Belgium

Introduction

Cell proliferation within stiff or confined tissues generates growth-induced pressures (GIP), which restrict division and alter protein expression. However, the sub-cellular mechanisms underlying this mechanosensitive response remain unclear and, in particular, its dependency on biosynthesis, ATP hydrolysis, and osmotic volume control. In this work, we propose a thermodynamically consistent model for protein synthesis and amino acid turnover, which directly promotes cell cycle growth and provides new insight into stress-dependent growth.

Methods

Biophysical growth model: We consider ATP-driven protein synthesis arising from free energy differences and Boltzmann distributions. Amino acids are replenished through active uptake and protein degradation. Alongside active and passive ion exchange from the environment, these solutes govern osmotic pressure and cell cycle growth, in competition with hydrostatic fluid pressure and external loading.

Multicellular simulation: We implement our growth model with the discrete cell framework Mpacts [1] where cells are described as pressurised deformable triangulated shells with bending stiffness and active cortical tension. In analysing yeast expansion, the probability of cell division is considered to increase with dilution of Whi5 protein concentration.

Results

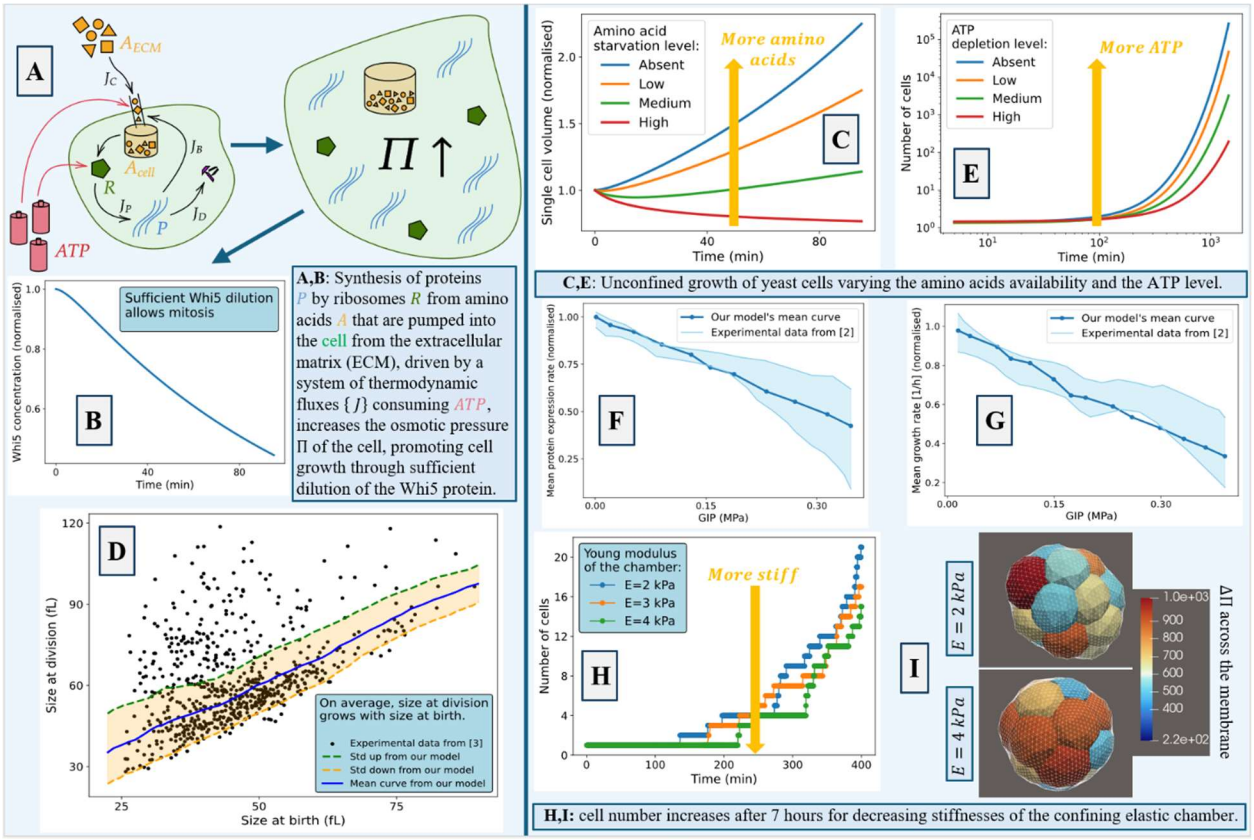
Our model predicts that biosynthesis drives cell growth, but ATP limitation reduces such synthesis (Fig 1E) and restriction of external amino acids drives a nutrient-limited regime (Fig 1C). The framework accurately predicts the influence on division (Fig 1D), arising from dilution of checkpoint inhibitors. Simulations of yeast growth inside a confined elastic chamber (Fig 1H,1I) reproduced key experimental observations in [2,3]: with GIP increasing over time, protein synthesis is suppressed (Fig 1F) and thus proliferation inhibited. The

relationship between growth rate and GIP showed a monotonic decrease (Fig 1G), without imposing phenomenological pressure-dependent growth laws.

Discussion

Our results indicate that GIP-driven growth arrest arises from energetic constraints on biosynthesis, osmotic regulation, and pressure generation. Impaired Whi5 dilution due to reduced cell growth under compression delays cell-cycle progression and lowers the probability of division. Cell behaviour under ATP depletion and amino acid starvation highlights distinct energy-limited versus substrate-limited regimes of pressure-dependent protein repression.

Images (Optional)



References (Optional)

[1]: Odenthal (et al.), *PLOS Computational Biology, 9(10),* 2013.

[2]: Alric (et al.), *Nature Physics, 18,* 2022.

[3]: Schmoller (et al.). *Nature, 526,* 2015.

Acknowledgements (Optional)

This work was supported by the European Research Council (Grant number 101116234).

Session Category

Cell Biomechanics: Methods and Models

OA153-01

Biokinetic Risk Factors in Young TKA Patients: A Gait Analysis of 88 Knees With Implications for Sports Participation and Implant Survivorship

Dr. Felipe F. Gonzalez MD[1,2], Dr. Carolline P. Nunes MD[1,2], Ms. Vibhav A. Prabhakar Student[3], Ms. Lord J. Hyeamang MD Student[4], Ms. Joshua M. Samaniego MD Student[4], Dr. Leonardo Metsavaht PhD[2], Dr. Gustavo Leporace PhD[2], Dr. Markus Wimmer PhD[1], Dr. Jonathan Gustafson PhD[1]

[1]Department of Orthopaedics, Rush University Medical Center, Chicago, Illinois, United States. [2]Instituto Brasil de Tecnologias da Saúde (IBTS), Rio de Janeiro, Rio de Janeiro, Brazil. [3]University of Illinois at Chicago, Department of Biological Sciences, Chicago, Illinois, United States. [4]Rush University Medical College, Chicago, Illinois, United States

Introduction

Total knee arthroplasty (TKA) is increasingly performed in younger patients who maintain higher functional demands. Biomechanics are central to their management, yet no in vivo data exist to guide return-to-sport decisions for individuals under 60. The objective of this study was to characterize gait kinematics and kinetics in young patients (≤60 years) and older patients (>60 years) treated with TKA and to compare them with healthy controls.

Methods

Eighty-eight knees from a motion analysis database were evaluated: older TKA (n = 50), young TKA (n = 21), and healthy controls (n = 17). All TKA procedures were performed at a single institution by fellowship-trained surgeons. Gait analysis was completed using a marker-based three-dimensional motion capture system and force plates. Primary outcomes included knee joint kinematics and kinetics. Statistical non-parametric mapping was used to compare groups across the gait cycle. Post hoc pairwise SnPM t-tests with permutation inference and Bonferroni correction addressed multiple comparisons. Significance was set at $p<0.05$.

Results

Knee extension moments (%BW·ht) were substantially higher in young patients. At initial contact, young patients demonstrated 1.4 ± 1.4, which was roughly five times higher than older patients (0.2 ± 0.8) and four times higher than controls (0.3 ± 0.8, $p < 0.05$) (Fig. 1). During terminal stance, young patients showed 0.5 ± 0.6 compared with 0.2 ± 0.5 in older patients and 0.0 ± 0.3 in controls ($p < 0.05$). Young individuals also walked with greater

varus alignment throughout the gait cycle (3.2 ± 7.8°), while controls (–7.0 ± 4.3°) and older patients (–3.6 ± 5.8°) demonstrated valgus alignment. No additional significant differences in knee kinetics or kinematics were detected.

Discussion

This study provides the first in vivo gait analysis focused on young TKA recipients. These patients showed elevated knee extension moments and persistent varus alignment, both of which increase tibiofemoral loading. Such loading patterns raise concern for long-term implant durability and may influence return-to-sport decisions. Interventions that reduce excessive extension moments and varus alignment should be prioritized to support implant longevity and allow young, high-demand individuals to safely resume higher levels of activity.

Images (Optional)

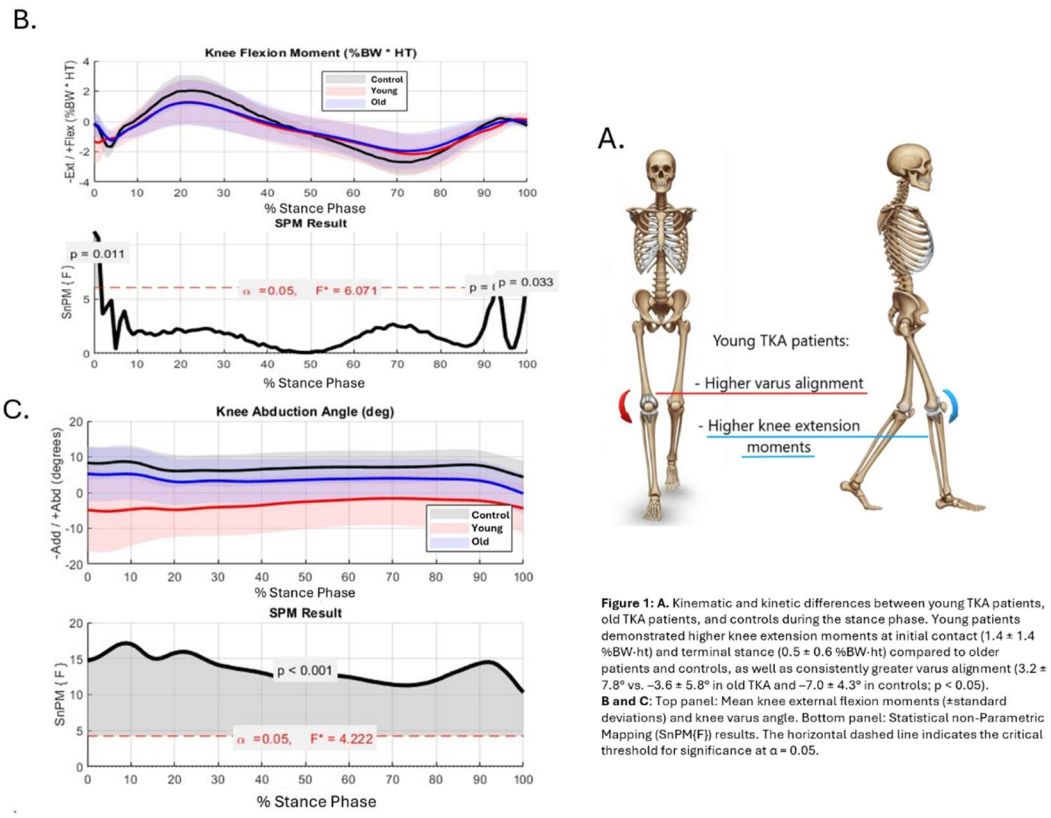


Figure 1: A. Kinematic and kinetic differences between young TKA patients, old TKA patients, and controls during the stance phase. Young patients demonstrated higher knee extension moments at initial contact (1.4 ± 1.4 %BW·ht) and terminal stance (0.5 ± 0.6 %BW·ht) compared to older patients and controls, as well as consistently greater varus alignment (3.2 ± 7.8° vs. –3.6 ± 5.8° in old TKA and –7.0 ± 4.3° in controls; $p < 0.05$). **B and C**: Top panel: Mean knee external flexion moments (±standard deviations) and knee varus angle. Bottom panel: Statistical non-Parametric Mapping (SnPM{F}) results. The horizontal dashed line indicates the critical threshold for significance at $\alpha = 0.05$.

Session Category

Clinical Biomechanics: N/A

OA153-02

3D Modelling Approach to Optimize Mini-Plate Configurations for High Predicted Bone Union Propensity for Mandibular Reconstruction Surgery

Ms. Cassidy Tizzard BASc, Mr. Hamidreza Aftabi PhD Candidate, Dr. John E. Lloyd, Dr. Eitan Prisman, Dr. Sidney Fels, Dr. Antony Hodgson

University of British Columbia, Vancouver, British Columbia, Canada

Introduction

Mandibular reconstruction is essential for restoring form and function of the jaw following tumor-related resection by replacing the removed segment with a donor bone graft (typically the fibula). Achieving bony union is critical; however, mechanisms affecting union rates remain poorly understood. In recent work, Aftabi et al. used a biomechanical Finite-Element simulation of the chewing cycle to demonstrate that changes in bone cut angle significantly alter predicted bone union propensity (BUP) based on strain-energy-density-based metrics (SED) [1].

Methods

We built on this proof-of-concept study by using the same 3D biomechanical modeling framework to evaluate the effect of mini-plate configuration on BUP. This study consisted of three stages: plate design, virtual reconstruction, and biomechanical simulation using the model developed by Aftabi et al. [2]. 2-hole mini-plates were designed in SolidWorks and positioned at high, middle and low placements on a body (B) defect reconstruction segment. Reconstruction was done using mandible and fibula CT segmentations which were imported into the Artisynth biomechanical modeling package to virtually reconstruct the mandible [3]. Chewing forces were applied to the reconstruction model, and bone healing was assessed using the resulting SED at each bone interface. Bone healing is likely to occur when SED exceeds a certain threshold, based on remodeling principles [1]. BUP was therefore defined as the percentage of elements with a normalized SED above this threshold.

Results

Figure 1 shows the predicted BUP for the left- and right-side mandible-fibula interfaces over one chewing cycle. Preliminary results show a ~6% difference in apposition (BUP) across the 3 configurations analyzed.

Discussion

These results demonstrate that plate placement affects predicted BUP, with results showing that lower placement configurations increase predicted BUP. We hypothesize that this approach, once generalized and validated, could be used to optimize not only plate placement, but also a broader range of surgical decisions including plate type and bone cut angle, to ultimately improve bone union outcomes in mandibular reconstruction.

Images (Optional)

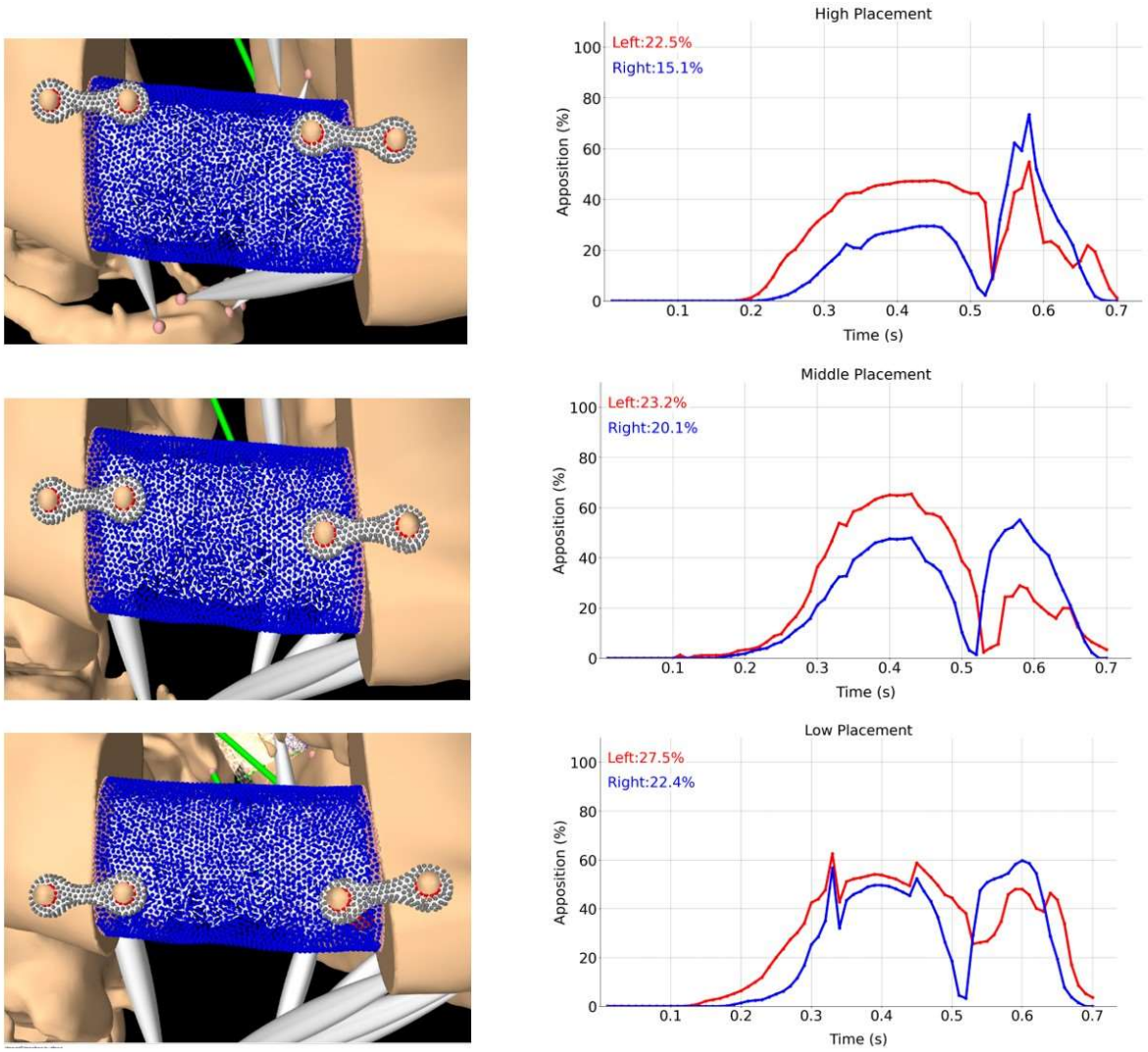


Figure 1: ***BUP Across Mini-Plate Configurations:*** *This figure shows the resulting BUP for the left and right-side mandible-fibula interfaces over one chewing cycle for high, middle, and low plate placements. The values at the top left corner of each plot are the average BUP (apposition %) for each interface.*

References (Optional)

[1] Hamidreza Aftabi et al., *Proc. IEEE ISBI*, 2025.

[2] Hamidreza Aftabi et al., *Computer Methods and Programs in Biomedicine*, 2024.

[3] John E. Lloyd et al., *Soft Tissue Biomechanical Modeling for Computer Assisted Surgery*, 2012.

Acknowledgements (Optional)

Session Category

Clinical Biomechanics: N/A

OA153-03

Biomimetic Meninges-On-a-Chip to Model Cerebrospinal Fluid Drainage and Subarachnoid Space Solute Exchange at the Temporal Bone Ear–Brain Interface in Hearing Loss and Dementia

Dr Giorgia Pistelli[1], Prof Federica Boschetti[1], Prof Claudio Conci[1], Prof Carmen Giordano[1], Prof Emanuela Jacchetti[1], Prof Manuela T Raimondi[1], Dr Diego Albani[2], Dr Simone Perottoni[1]

[1]Department of Chemistry, Materials and Chemical Engineering "Giulio Natta", Politecnico di Milano, Milan, Lombardy, Italy. [2]Department of Neuroscience, Istituto di Ricerche Farmacologiche Mario Negri IRCCS, Milan, Lombardy, Italy

Introduction

Hearing loss (HL) is a major risk factor for dementia [1]. Impaired cerebrospinal fluid (CSF) clearance of metabolic waste has been associated with both HL and cognitive impairment [2]. Although cochlear fluids communicate with CSF through narrow aqueducts in the temporal subarachnoid space (SAS), their fluid-dynamic properties and their role in solute exchange remain poorly characterized. To address this gap, the EAR2BRAIN project is developing patient-specific in silico and in vitro models of the inner-ear/brain fluidic interface. Here, we present a biomimetic meninges-on-a-chip reproducing SAS geometry, pulsatile CSF flow, intracranial pressure, and real-time molecules transport analysis in the cochlear–brain communication relevant to HL and neurodegeneration

Methods

A multi-chamber organ-on-a-chip, with a collagen-based parenchyma model, sustaining CSF-like flow and intracranial pressure (ICP)-like pulsatility was fabricated by transparent high-resolution SLA 3D printing. FITC-dextran tracers (4–500 kDa) will quantify solute transport via fluorescence microscopy and spectrofluorimetry. A cochlear aqueduct-like microchannel will be connected to the SAS channel.

Results

Collected design parameters from clinical literature led to the fabrication of the SAS–parenchyma prototype (Figure 1) enabling stable confinement of a collagen hydrogel. The system represents a simplified 1 mL flat portion of the SAS. Tracer experiments demonstrated diffusion from the hydrogel toward the SAS outlet, confirming measurable

inter-compartment transport. Anatomical data provided realistic operating ranges for CSF pressures, volumes, and flow rates.

Discussion

To date, no studies have quantitatively modeled pressure or solute exchange at the inner-ear/brain fluidic interface. While still simplified, this SAS-on-a-chip establishes the foundation for a future patient-specific biomimetic model, enabling targeted investigations of how pressure, pulsatility, and molecular size shape solute transport, to clarify fluid communication in the temporal bone under conditions characteristic of HL, impaired CSF drainage, and neurodegeneration.

Images (Optional)

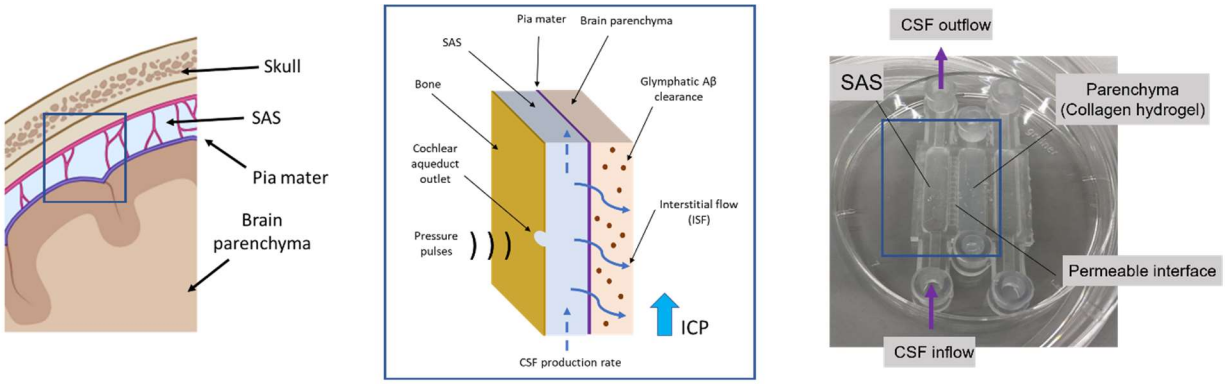


***Figure 1**. Schematic representation of the meningeal subarachnoid space (SAS)-brain parenchyma interface at the temporal auditory interface with a picture of the starting SAS-on-a-chip prototype.*

References (Optional)

[1] G. Livingston et al., “Dementia prevention, intervention, and care: 2020 report of the Lancet Commission,” The Lancet, vol. 396, no. 10248, pp. 413–446, Aug. 2020, doi: 10.1016/S0140-6736(20)30367-6.

[2] K. Xu et al., “Evaluation of glymphatic system activity by diffusion tensor image analysis along the perivascular space in presbycusis,” CNS Neurosci Ther, vol. 30, no. 3, Mar. 2024, doi: 10.1111/CNS.14458.

Acknowledgements (Optional)

This work has been supported by Fondazione Cariplo, grant n° 2024-1070 "EAR2BRAIN: A biomimetic MRI-compatible artificial cochlea to unravel the role of inner ear-brain fluids exchange on amyloid-beta clearance in dementia".

Session Category

Clinical Biomechanics: N/A

OA153-04

Lower Extremity Joint Loading During Squatting Differs Across Hemophilic Arthropathy Severity in Persons with Hemophilia

Dr. Danielle Siegel PhD[1], Mr. Caden Robertson MS[1], Dr. Joanna Roybal PT, DPT[1], Mr. Joseph Mah[1], Dr. Laura Singer-Fox PT, DPT[1], Ms. Niamh Mah[1], Dr. Sharon Funk PT, DPT[1], Dr. Marilyn Manco-Johnson MD[1], Dr. James Carollo PhD[2], Dr. Brecca Gaffney PhD[1,3], Dr. Beth B. Warren MD[1,2]

[1]University of Colorado Anshutz, Aurora, Colorado, United States. [2]Children's Hospital Colorado, Aurora, Colorado, United States. [3]University of Colorado Denver, Dever, Colorado, United States

Introduction

Persons with hemophilia (PwH) experience recurrent joint bleeding that can lead to progressive hemophilic arthropathy (HA), which shares characteristics with both osteoarthritis and inflammatory joint disease. While previous work has identified altered joint mechanics in the general PwH population compared to healthy individuals, it remains unclear how joint loading changes across HA severity. Characterizing these differences may reveal biomechanical adaptations associated with disease progression. Therefore, this study aimed to determine how hip, knee, and ankle joint loading during bilateral squatting differs across HA severity in PwH compared to healthy individuals.

Methods

Motion capture data were collected from eighteen PwH with mild (6M, age: 30.3±7.0y), moderate (5M/2F, age: 38.1±16.4y), and severe (5M, age: 30.2±7.3y) HA and seven healthy controls (6M/1F, age: 23.7±5.4y) during a bilateral squat to a self-selected depth. Joint reaction forces (JRF) at the hip, knee, and ankle were estimated in OpenSim and the JRF impulse was calculated to represent the total joint load for each limb over the squatting task. HA severity was classified using the Hemophilia Joint Health Score (HJHS), a validated physical exam where higher scores indicate greater impairment. For PwH, the JRF impulse from the more affected limb (determined by HJHS) were compared to the mean of both limbs in controls. Group differences were evaluated using Cohen’s d effect size.

Results

Knee and hip JRF impulse decreased with increasing HA severity, while no differences in ankle JRF impulse were observed (Figure 1).

Discussion

PwH exhibited reduced knee and hip joint loading during squatting with increasing HA severity. These differences highlight that HA severity-specific adaptations emerge with disease progression, reinforcing the importance of studying PwH in subgroups rather than aggregating the population, as important biomechanical differences may be obscured. Monitoring joint loading across HA severity may help identify when offloading begins to accelerate functional decline and increases bleeding risk. Additionally, squatting is a knee-dominant task, likely explaining why differences were most pronounced at the knee and hip, while ankle loading remained unchanged. Future work should examine more ankle-dominant tasks given the ankle's high incidence of bleeding events, to further understand joint loading across HA severity.

Images (Optional)

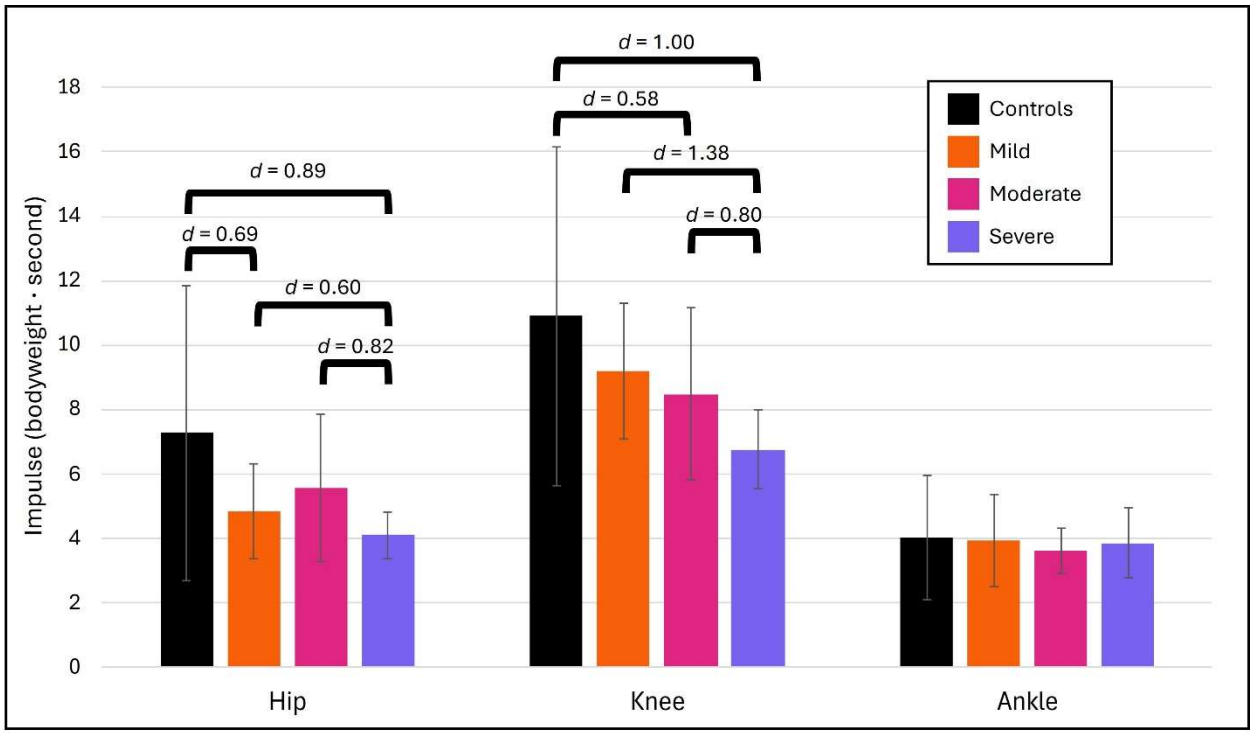


Figure 1: Impulse of the joint reaction forces (mean and standard deviation) at the hip, knee, and ankle representing the total load over time during a bilateral squatting activity for healthy controls compared to persons with hemophilia with mild, moderate, and severe hemophilic arthropathy. Cohen's d effect size is indicated for comparisons with a medium ($0.5 \geq d < 0.8$) and large ($d \geq 0.8$) difference.

Session Category

Clinical Biomechanics: N/A

OA153-05

Sweep-Frequency Impedance (SFI) for Middle-Ear Pathology Classification With Machine Learning

Dr. Michio Murakoshi[1], Dr. Teruki Toya[2], Dr. Di Zhou[1], Dr. Manabu Inaba MD[3], Dr Hisashi Sugimoto MD[3]

[1]Kanazawa University, Kanazawa, Ishikawa, Japan. [2]University of Yamanashi, Kofu, Yamanashi, Japan. [3]Kanazawa University Hospital, Kanazawa, Ishikawa, Japan

Introduction

Tympanometry is widely used to assess conductive hearing loss although its diagnostic accuracy is limited. Our group has developed a sweep frequency impedance (SFI) meter that measures middle-ear dynamic characteristics with a swept-frequency stimulus and demonstrated its clinical utility [1]. However, the required 10-second stimulus posed challenges for older adults and infants. This study aimed to implement a shorter stimulus and evaluate a machine-learning approach for classifying middle-ear pathologies [2,3].

Methods

Data were collected from 42 ears of 25 normal-hearing adults, 18 ears of 14 patients with ossicular fixation and 10 ears of 10 patients with ossicular separation. A 2-second chirp stimulus was delivered and recorded sound pressure at the ear canal was Fourier-transformed to obtain a sound-pressure-level (SPL) curve (Fig. 1). From this curve, RF (resonance frequency) and ΔSPL (related to tympanic membrane vibration amplitude) were extracted and plotted in two dimensions. Probabilistic distances from class-specific distribution centers were used to compute P_F (fixation index) and P_S (separation index), enabling classification of middle-ear status (Fig. 2).

Results

Tympanometry was evaluated using static compliance (SC), while SFI classification used P_F and P_S. For tympanometry, sensitivity, specificity and AUC for fixation were 0.61, 0.41 and 0.50; for separation, 0.88, 0.92, and 0.88 (Fig. 3). For SFI, fixation values were 0.64, 0.88, and 0.86, and separation values were 1.0, 1.0, and 1.0. These findings show that SFI outperformed tympanometry in identifying middle-ear disorders (Fig. 4).

Discussion

SFI provided more accurate classification than tympanometry, particularly for fixation. Previous wideband tympanometry (WBT) studies reported AUCs of 0.95 and 0.88 under different pressure conditions [4], and 0.81 in another study [5]. Despite measurements being made at ambient pressure, SFI achieved comparable performance using only two features, RF and ΔSPL. The reduced 2-second stimulus and machine-learning framework enabled efficient and accurate assessment of middle-ear conditions, demonstrating diagnostic capability similar to WBT.

Images (Optional)

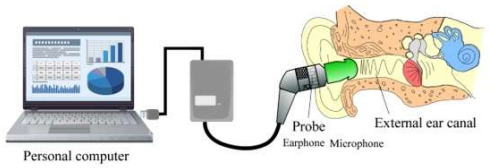


Fig. 1. Structure of the SFI meter. Sound pressure change in the ear canal in response to the short chirp stimulus is measured, termed sound pressure level (SPL) curve.

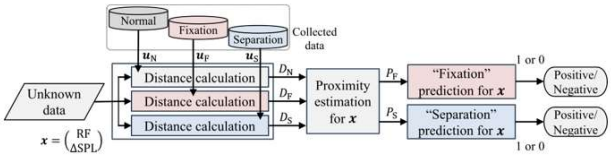


Fig. 2. Classification of middle ear status using machine learning. The middle ear status is classified based on the features RF and ΔSPL extracted from SPL curves.

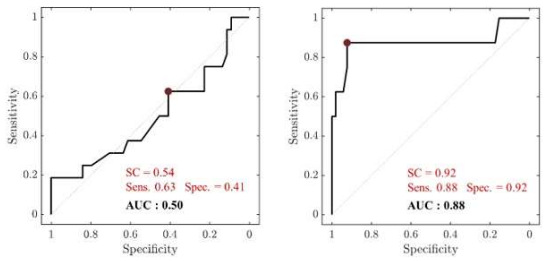


Fig. 3. ROC curves of tympanometry. Left: fixation; right: separation.

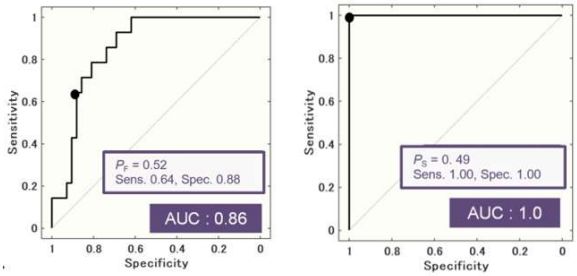


Fig. 4. ROC curves of SFI measurement. Left: fixation; right: discontinuity.

References (Optional)

[1] Wada *et al.*, Audiology, 1989. [2] Toya *et al.*, J Acoust Soc Am, 2025. [3] Zhou *et al.*, J Acoust Soc Am, 2025. [4] Keefe *et al.*, J Am Acad Audiol, 2017. [5] Feeney *et al.*, Ear Hear, 2021.

Acknowledgements (Optional)

This work was supported by AMED JP24hma322027.

Session Category

Clinical Biomechanics: N/A

OA153-06

A 3D Goal Equivalent Manifold Approach to Detecting Season-Long Post-Concussion Motor Deficits in Female Soccer Players

Dr. Xiong Zhao, Mr. Reza Rahimi, Dr. Allison Clouthier, Dr. Janie Cournoyer, Dr. Ryan Graham

University of Ottawa, Ottawa, Ontario, Canada

Introduction

Athletes with a history of concussion often display lingering motor control alterations that are not captured by conventional clinical evaluations. Studies show that these athletes are at a higher risk of sustaining musculoskeletal injuries. However, the mechanisms underlying these persistent deficits remain unclear. Traditional biomechanical analyses typically examine joint angles or peak forces, overlooking how variability is structured. The Goal-Equivalent Manifold (GEM) framework decomposes variability into goal-relevant and goal-equivalent components, but most applications are two-dimensional and exclude timing error, a key component of rhythmic tasks. This study extends GEM into three dimensions, displacement, velocity and timing error, to evaluate whether a 3D approach can capture motor control differences between athletes with and without concussion history.

Methods

Twenty-five female varsity soccer players (11 with history of concussion) performed 35 metronome-paced squats during pre-, mid-, and post-season sessions. Whole-body kinematics were captured using markerless motion capture. The center of mass served as the primary execution variable. In 2D GEM, the goal was represented as $f(D,V) = D/V - T_{target} = 0$. To incorporate temporal precision, the 3D goal was defined as $f(D,V,T_{err}) = D/V - (T_{target} + T_{err}) = 0$. A task-consistent operating point was calculated for each athlete, and variability was decomposed into goal-relevant (delta_P) and goal-equivalent components (delta_T1, delta_T2). A 3D performance index (PI_3D) was computed as $sqrt(std(deltaT1)^2 + std(delta_T2)^2) / std(delta_P)$. Group × Time effects were evaluated using Generalized Estimating Equations.

Results

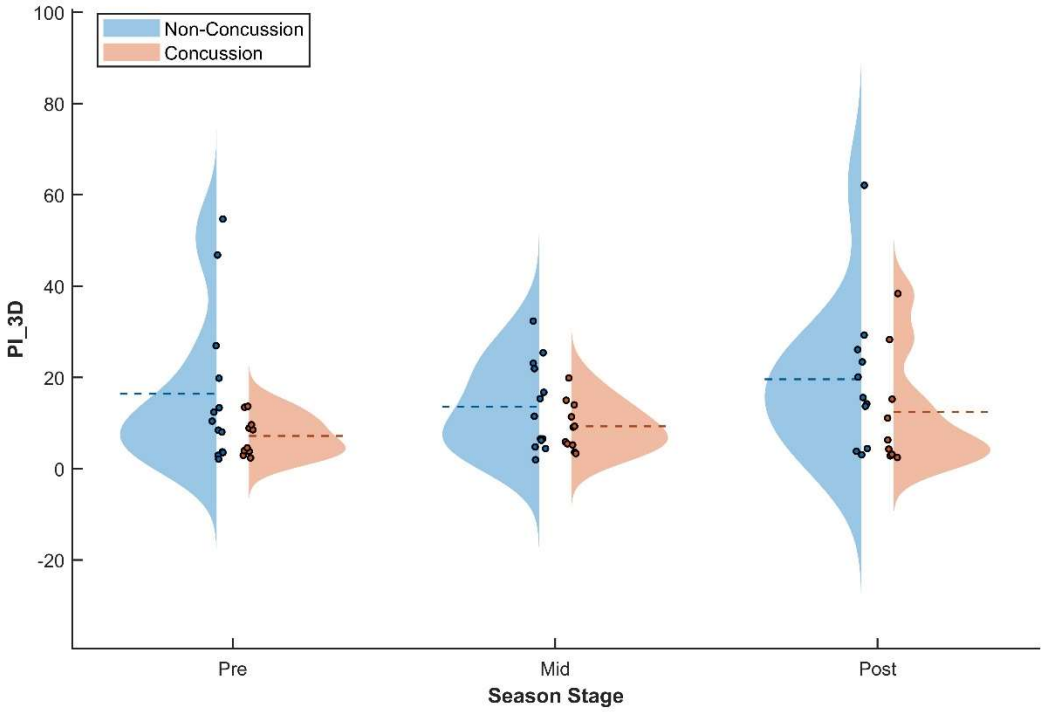
Timing error contributed 12.2% of total variability across the season. No significant group differences were detected in 2D metrics. In contrast, athletes with concussion history exhibited consistently lower PI_3D as shown in Figure 1 (pre: 7.17 vs 16.40; mid: 9.28 vs

13.59; post: 12.44 vs 19.60), with a significant main effect of concussion (p = 0.017). These findings align with prior evidence of persistent neuromuscular and sensorimotor deficits following concussion.

Discussion

The 3D GEM framework demonstrated its sensitivity for identifying subtle, persistent motor control alterations. Incorporating spatio-temporal variability into athlete monitoring may enhance return-to-play decisions and guide targeted neuromuscular rehabilitation.

Images (Optional)



References (Optional)

Session Category

Clinical Biomechanics: N/A

OA154-01

Proprioception Enables Gravity-Dependent Reorganisation of Gait

Dr Alessandro Santuz[1], Dr Francesco Luciano[2], Dr Valentina Natalucci[2], Dr Dario Cazzola[3], Dr Steffi Colyer[3], Dr James Cowburn[3,4], Prof Kirsten Albracht[5,6], Dr Bjoern Braunstein[5,7], Dr Verena Schuengel[6], Prof Jörn Rittweger[8], Dr Nolan Herssens[9], Dr Tobias Weber[9], Dr David A. Green[9,10,11], Dr Niccolò Zampieri[1], Prof Alberto E. Minetti[2], Dr Gaspare Pavei[2]

[1]Max Delbrück Center for Molecular Medicine, Berlin, Berlin, Germany. [2]Department of Pathophysiology and Transplantation, University of Milan, Milano, Lombardia, Italy. [3]Department for Health, University of Bath, Bath, England, United Kingdom. [4]School of Engineering, University of Cardiff, Cardiff, Wales, United Kingdom. [5]Institute of Movement and Neuroscience, German Sport University, Cologne, North Rhine-Westphalia, Germany. [6]Department of Medical Engineering and Technomathematics, Aachen University of Applied Sciences, Aachen, North Rhine-Westphalia, Germany. [7]Centre for Health and Integrative Physiology in Space, Cologne, North Rhine-Westphalia, Germany. [8]Division of Muscle and Bone Metabolism, Institute of Aerospace Medicine DLR, Cologne, North Rhine-Westphalia, Germany. [9]Space Medicine Team, European Astronaut Centre, European Space Agency, Cologne, North Rhine-Westphalia, Germany. [10]Centre of Human and Applied Physiological Sciences, King's College London, London, England, United Kingdom. [11]Institute for Risk and Disaster Reduction, University College London, London, England, United Kingdom

Introduction

Adults rarely adopt unilateral skipping, yet astronauts spontaneously adopted this gait on the Moon, reportedly due to improved stability [1, 2]. Future space missions will require mobility preservation in lower gravity [3], raising the question of why hypogravity enables otherwise latent gait solutions. Gravity affects mechanical loading and sensory input. Of the various sensory systems, proprioception – which provides information regarding limb position, movement and load – is a promising candidate for the control of gait modes. Here, we combined simulated hypogravity experiments in humans and transgenic mice to investigate whether proprioception is necessary for the emergence of gravity-dependent gait modes.

Methods

Twelve adults performed treadmill walking, skipping, and running at 1.00 g and under simulated Mars (0.38 g) and Moon (0.17 g) gravity using an elastic unloading system [3]. Muscle synergies, composed of time-dependent muscle activation patterns and time-invariant muscle weights, were extracted from twelve lower limb muscles using non-negative matrix factorisation [4]. Eight adult transgenic mice [5] were tested with a similar setup at 1.00 g and 0.17 g; four underwent selective ablation of muscle spindles and Golgi tendon organs. Locomotion was recorded with high-speed videography and analysed using markerless motion capture and principal component analysis. All analyses employed linear mixed-effects models.

Results

In each human gait mode, reduced gravity affected the muscle synergy temporal activation patterns, whereas the time-invariant muscle weights remained largely unchanged. Skipping and running showed similar activation patterns, but different order of otherwise similar muscle weights. Control mice exhibited a consistent hindpaw-unloading strategy at 0.17 g, forming a distinct state-space cluster that, following proprioceptive ablation, was absent.

Discussion

Our findings suggest that the nervous system possesses latent gait strategies that emerge when gravitational loading changes. The data indicate that proprioception acts as a gateway to awaken latent gait modes. As we venture into environments with reduced gravity, it will be fundamental to understand how sensory feedback unlocks these hidden strategies to predict how locomotion adapts far from Earth.

References (Optional)

[1] Kubis *et al.,* NASA, 1972

[2] Cernan, NASA, 1996

[3] Herssens *et al.,* PLoS ONE, 2022

[4] Santuz, JOSS, 2022

[5] Oliver *et al.,* Nature Communications, 2021

Session Category

Human Motion and Performance: Locomotion/Gait

OA154-02

Muscle Activation During Hypogravity Running

Ms. Lina Yu BN, RN, Ms. Hannah G. Yesuf BN, RN, Mr. Dawson S. Sheehan BN, RN, Dr. Jared R. Fletcher PhD

Mount Royal University, Calgary, Alberta, Canada

Introduction

Running in hypogravity reduces lower limb muscle activity because less force is required to support and propel the reduced body weight [1]. The energy cost of running (E_{run}) is also reduced, together or independent of changes in joint kinematics and lower-limb muscle (co)activations. This study therefore examined the relationship between E_{run} and muscle (co)activation as a function of running speed and body weight unloading.

Methods

Sixteen healthy adults ran at 80%, 100%, 120%, and 140% of their preferred running speed under three simulated gravity levels (100%, 86%, and 82% body weight) using a *Lever Up* harness system. Ultrasound imaging of the gastrocnemius medialis (GM) was used to quantify MG shortening, while surface EMG recorded and quantified average integrated EMG per stride (iEMG/stride) from the MG, soleus, tibialis anterior, and fibularis longus.

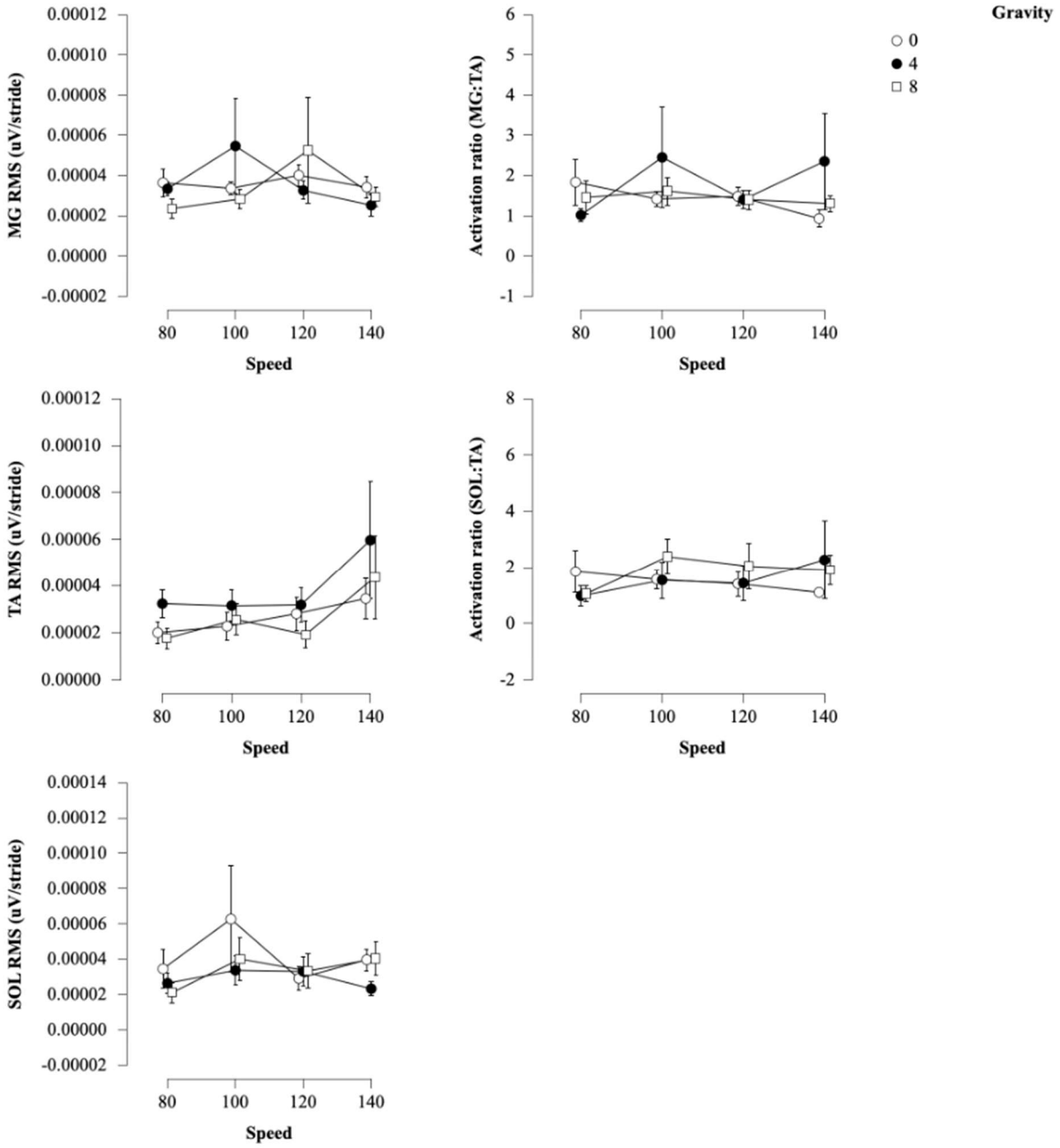
Results

CoT decreased significantly with increasing running speed ($p< 0.001$) and was further reduced with greater unloading. Across all muscles, iEMG/stride was similar across all speeds and gravity levels (all $p>0.09$, Figure 1). MG:TA coactivation also showed no significant effects of speed ($p=0.697$; gravity: $p=0.540$; speed x gravity: $p=0.425$), and SOL:TA coactivation similarly demonstrated no significant interactions ($p= 0.25$) nor main effects (speed: $p=0.122$; gravity: $p=0.638$).

Discussion

Despite significant reductions in E_{run} with speed and unloading, lower limb muscle activation and co-activation remained unchanged. suggesting changes in active muscle volume of the lower limbs is not a primary factor in an elevated metabolic cost. Rather, neuromuscular control is preserved during unloaded running which may help guide exercise countermeasures by emphasizing mechanical rather than neural factors when targeting energy expenditure during prolonged space flight.

Images (Optional)



References (Optional)

[1] Liebenberg *et al.,* J Sports Sci, 2011.

Acknowledgements (Optional)

This project was supported by The Canadian Space Health Research Network and NSERC.

Session Category

OA154-03

Do Astronauts Need to Run Faster? Achilles Tendon Loading Across Running Speeds and Simulated Reduced Gravity

Ms. Hannah G. Yesuf BN, RN, Mr. Dawson S. Sheehan BN, RN, Ms. Lina Yu BN, RN, Dr. Jared R. Fletcher PhD

Mount Royal University, Calgary, Alberta, Canada

Introduction

Exercise is used to limit rapid musculoskeletal and tendon deconditioning during prolonged space flights [1]. The Achilles tendon (AT) stores and returns elastic energy during running, contributing to a low metabolic cost, but elastic energy storage incurs a metabolic cost [2]. It remains to be seen how AT elastic energy storage and the accompanying muscle metabolic cost are affected by unloading. Our objective was to estimate AT elastic energy storage in relation to muscle metabolic cost across running speeds and gravities.

Methods

16 participants (5 male, 11 female) completed running trials on a *Lever Up* unloading system under three simulated gravity levels (100%, ~86%, and ~82% body weight), and four speeds (80%, 100%, 120%, and 140% of preferred running speed). AT force during stance was estimated from vertical ground reaction forces and location using a force-instrumented insole [3]. AT elastic energy was calculated from AT force and a fixed AT stiffness [4]. Metabolic cost was measured via indirect calorimetry, and medial gastrocnemius (MG) positive muscle work (W^+) and power (P^+) was calculated from muscle force estimates and MG fascicle shortening (ΔL_f) using ultrasonography, respectively.

Results

Peak AT force (and thus AT elastic energy storage) increased significantly with running speed ($p < 0.001$) and decreased with increased body weight unloading ($p = 0.043$). MG ΔLf and W^+ were not altered by speed ($p>0.48$) or gravity ($p>0.18$) whereas P^+ was significantly lower during intermediate unloading ($p<0.05$).

Discussion

These findings support that running speed is the primary stimulus for Achilles tendon loading. Thus, faster running speeds are required to achieve similar unloaded AT forces and maintain tendon health in reduced gravity. In contrast, the MG muscle is placed under similar mechanical demands across hypogravity levels. The nonlinear pattern across

unloading levels may reflect different neuromuscular strategies as effective body weight decreases.

Images (Optional)

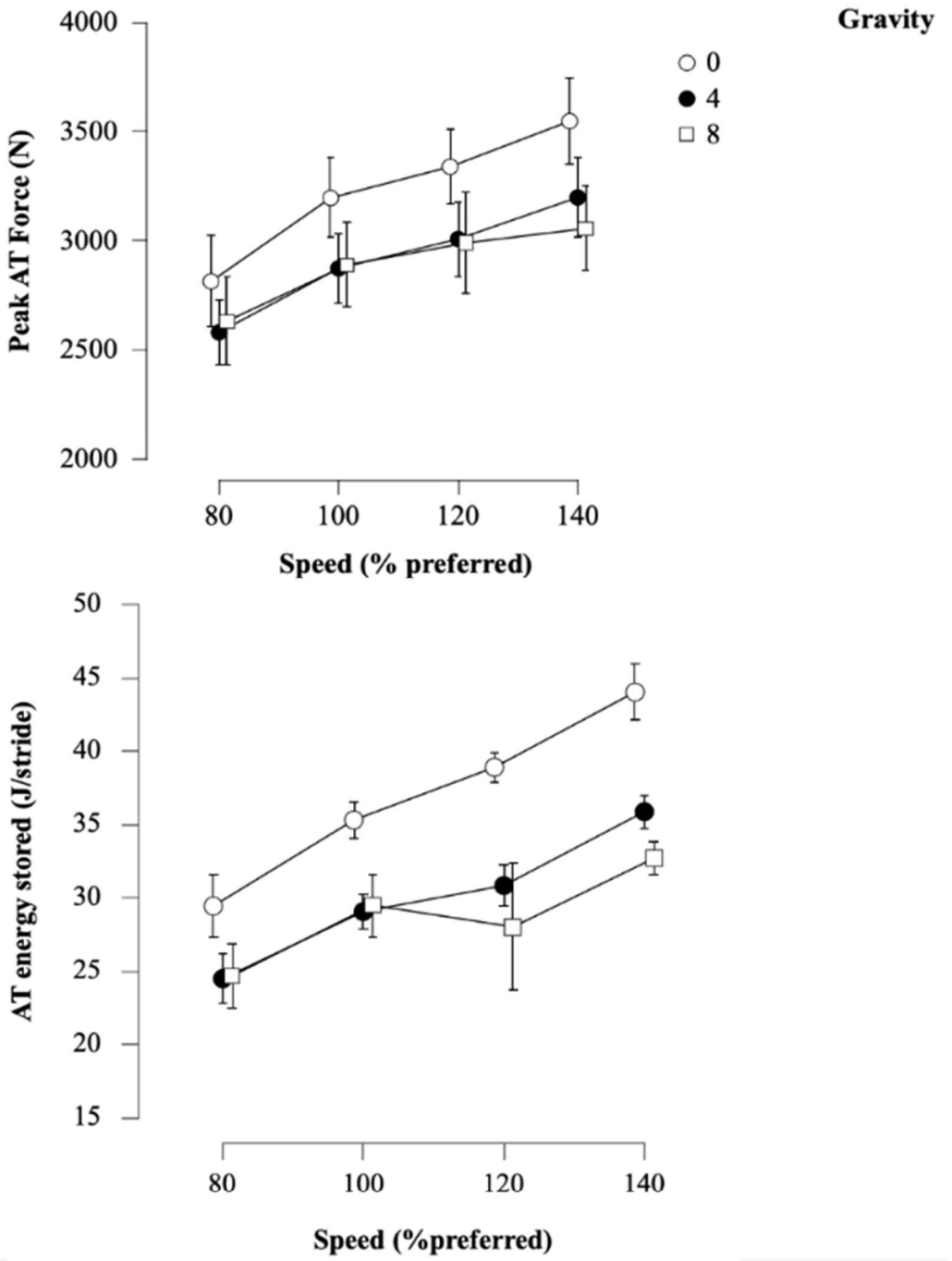


Figure 1: AT force and AT energy stored related to speed and gravity

References (Optional)

[1] Liphardt et al., NPJ Microgravity, 2023.

[2] Fletcher et al., J Appl Physiol, 2015.

[3] Hullfish and Baxter., Gait Posture, 2020.

[4] Lichtwark and Wilson., J Biomechanics, 2007.

Acknowledgements (Optional)

This project was supported by The Canadian Space Health Research Network and NSERC.

Session Category

Human Motion and Performance: Locomotion/Gait

OA154-04

Why Do Astronauts Bounce on the Moon? Mechanical Work of Walking, Running, and Skipping in Simulated Low gravity.

Dr. Francesco Luciano[1], Dr. James Cowburn[2,3], Dr. Valentina Natalucci[1], Prof. Dario Cazzola[2,3], Prof. Steffi Colyer[2], Prof. Kirsten Albracht[4,5], Dr. Bjoern Braunstein[4,5], Dr. Verena Schuengel[5], Prof. Jörn Rittweger[6], Dr. Nolan Herssens[7], Prof. Tobias Weber[7], Prof. David A. Green[7,8,9], Prof. Dominic J. Farris[10], Prof. Alberto E. Minetti[1], Prof. Gaspare Pavei[1]

[1]University of Milan, Milan, Lombardy, Italy. [2]University of Bath, Bath, England, United Kingdom. [3]Forcetek, Bath, England, United Kingdom. [4]German Sport University, Cologne, Germany, Germany. [5]Aachen University of Applied Sciences, Aachen, Germany, Germany. [6]Institute of Aerospace Medicine DLR, Cologne, Germany, Germany. [7]European Space Agency, Cologne, Germany, Germany. [8]King's College London, London, England, United Kingdom. [9]University College London, London, England, United Kingdom. [10]University of Exeter, Exeter, England, United Kingdom

Introduction

Humans typically walk or run, but occasionally employ unilateral skipping, an asymmetric gait combining double-support and aerial phases. Adults rarely skip on Earth, yet astronauts frequently did it on the Moon. Why do humans avoid skipping on Earth whereas readily adopt it in hypogravity? Skipping may reduce lower-limb muscle activation [1] and improve stability [2], but such benefits appear offset on Earth by its high metabolic cost [3]. In hypogravity, the metabolic cost of skipping decreases – even without wearing spacesuits [3] – making it more favourable. Thus, we tested the hypothesis that hypogravity alone reduces joint- and limb-level mechanical work during skipping, and compared these effects to those during walking and running.

Methods

Five adults (3 females; 31.2±6.2 years; 61.4±5.1 kg) skipped at 1.39, 1.94, and 2.50 m/s, walked at 1.39 m/s and ran at 2.50 m/s on an instrumented treadmill. Participants ambulated at Earth (1.00g), Mars (0.38g) and Moon (0.17g) gravities simulated via body-weight suspension [3], while 24 cameras tracked 68 bilateral markers. Inverse kinematics and dynamics were computed in OpenSim 4.4 using a scaled Rajagopal 2016 model. Instantaneous joint power was calculated from joint moments and angular velocities; stride-averaged positive hip, knee, and ankle powers were summed to obtain total power.

To allow comparisons across gaits and speeds, mass- and distance-normalised work (W_{mech}) was calculated from total limb power divided by speed.

Results

Gravity modulated the magnitude and between-limb distribution of W_{mech}. At Earth gravity, skipping's W_{mech} was greater than walking; although smaller than running, W_{mech} was asymmetrical between skipping limbs. As gravity decreased, W_{mech} declined more in skipping and running than walking, and work was evenly generated between skipping limbs (Fig.1).

Discussion

As gravity decreases, the mechanical demands of skipping approach those of walking and running. On Earth, skipping's benefits are offset by its high work demands. However, at Moon gravity, generated work converged across gaits and between skipping limbs, allowing humans to exploit skipping's biomechanical advantages without energetic penalties.

Images (Optional)

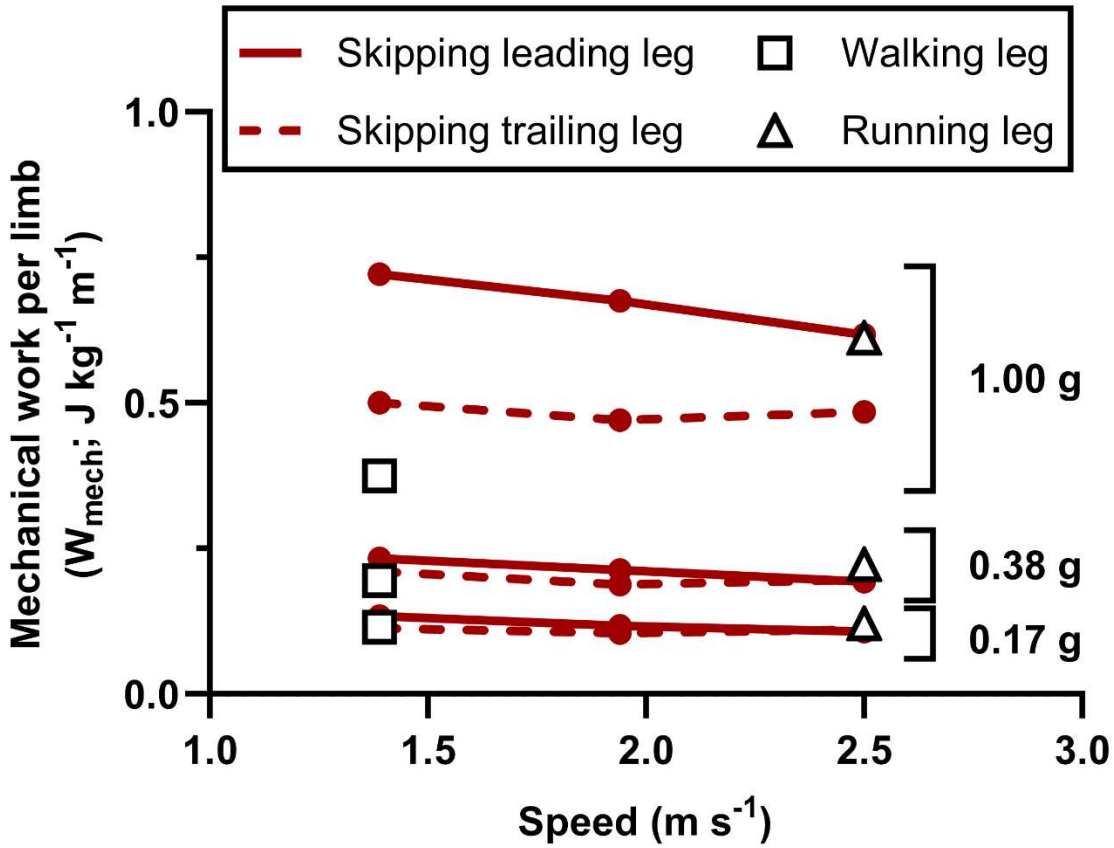


Figure 1. *Mass- and distance-normalised mechanical work per limb (W_{mech}) across gravities, gaits, and speeds.* For clarity purposes, lines and dots show across-participant averages, and standard deviations are omitted.

References (Optional)

[1] Ackermann and van den Bogert, J Biomechanics, 2012

[2] Andrada *et al.,* Royal Society Open Science, 2016

[3] Pavei *et al.,* J Applied Physiology, 2015

Session Category

Human Motion and Performance: Locomotion/Gait

OA154-05

Cost of Transport in Reduced Gravity: Optimizing Astronaut Exercise Prescriptions

Mr. Dawson Sheehan BN, Ms. Lina Yu, Ms. Hannah Yesuf, Dr. Jared Fletcher PhD

Mount Royal University, Calgary, Alberta, Canada

Introduction

There is a curvilinear relationship between cost of transport (CoT) and running speed [1]. In simulated microgravity, unloading reduces CoT, because the cost to support body weight is reduced [2]. Thus, in reduced gravity, a higher than optimal running speed is required to induce a similar CoT as on Earth. The energetics and mechanics of running at faster speeds in simulated microgravity has not yet been explored.

Methods

16 trained runners ran at 80%, 100%, 120%, and 140% of their self-selected (preferred) running speed under three simulated gravity levels (100%, ~86%, and ~82% body weight) using a series of pulleys to reduce body weight (Lever Up, Lever Movement, Boulder CO, USA) . Each condition consisted of a 6-minute run with 2-minute rest. CoT was calculated during the steady-state via indirect calorimetry. Gait kinematics and kinetics were calculated from in-shoe force sensors (LoadSol, Novel GmbH, Munich, DEU).

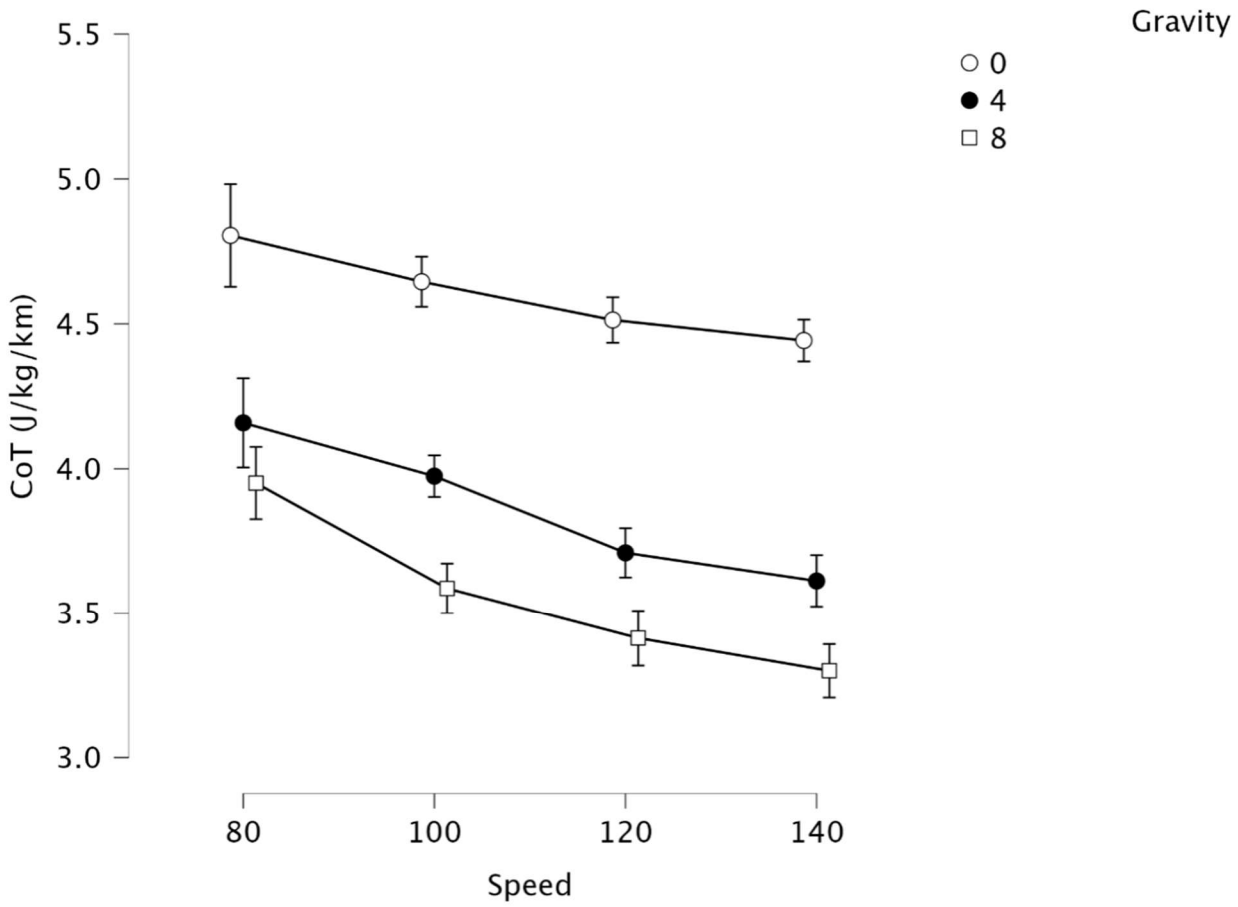
Results

CoT decreased significantly with increasing running speed ($p < 0.001$) and was further reduced with greater unloading ($p < 0.001$ Figure 1). Stance time increased with speed ($p < 0.001$) but decreased with unloading ($p < 0.001$); stride frequency increased with speed ($p < .001$) and decreased with unloading ($p < 0.001$); and duty cycle (%) increased with both speed and unloading ($p < 0.001$). Impulse per stride decreased significantly as unloading increased ($p < 0.001$).

Discussion

CoT decreased with increasing running speed and greater unloading, making locomotion more economical in simulated hypogravity. A lower CoT may reduce the metabolic stimulus needed to maintain aerobic capacity and cardiorespiratory fitness during spaceflight. A lower CoT is largely attributed by the reduced cost of generating force against body weight in simulated hypogravity.

Images (Optional)



References (Optional)

[1] Steudel-Numbers, K. L., et al., J. Hum. Evol., 2009.

[2] Barnes, K. R., et al., Sport Medicine - Open, 2017.

Acknowledgements (Optional)

This project was supported by The Canadian Space Health Research Network and NSERC.

Session Category

Human Motion and Performance: Locomotion/Gait

OA155-01

IMU-Based Measures of Trunk Movement Variability Are Not Sensitive to Fatigue in Female, Varsity Rowers During a 2000m Rowing Time-Trial

Dr Matthew Slopecki[1], Mr Paul Lucas Spagnuolo[1], Dr Julie N. Côté[2]

[1]McGill University, Montreal, Quebec, Canada. [2]University of Ottawa, Ottawa, Ontario, Canada

Introduction

Female rowers experience high lifetime incidence rates of back pain [1]. Furthermore, females have been shown to have greater electromyographical indices of fatigue during a 2000m rowing ergometer time trial (2kTT) at the thoracic and lumbar erector spinae muscles [2]. However, it is unclear if this leads to measurable effects on trunk movement patterns. Increases in cycle-to-cycle movement variability, using Sample Entropy (SampEn), are common compensatory strategies to maintain cyclical movement performance when fatigued [3]. Furthermore, detrended fluctuation analysis (DFA) can quantify long-term power correlations, or coordinated kinematic patterns. If these indices are sensitive to fatigue, affordable wearable systems could detect the onset of fatigue-related trunk kinematics. The aim of this study was to determine if changes in SampEn and DFA were observed in trunk kinematics during a 2kTT in competitive female rowers.

Methods

6 female collegiate (U-Sports) rowers completed a 2kTT. Inertial measurement units (Xsens Dot; 120 Hz) were placed on T7 and L3 vertebrae. Tri-axial angular velocity data were collected. SampEn and DFA were applied to raw angular velocity signals in the sagittal plane at each quarter of the 2kTT. Two ANOVAs compared differences in 1) SampEn and 2) DFA Alpha between each quarter of the 2kTT. Bonferroni corrected significance was set to $P < 0.025$.

Results

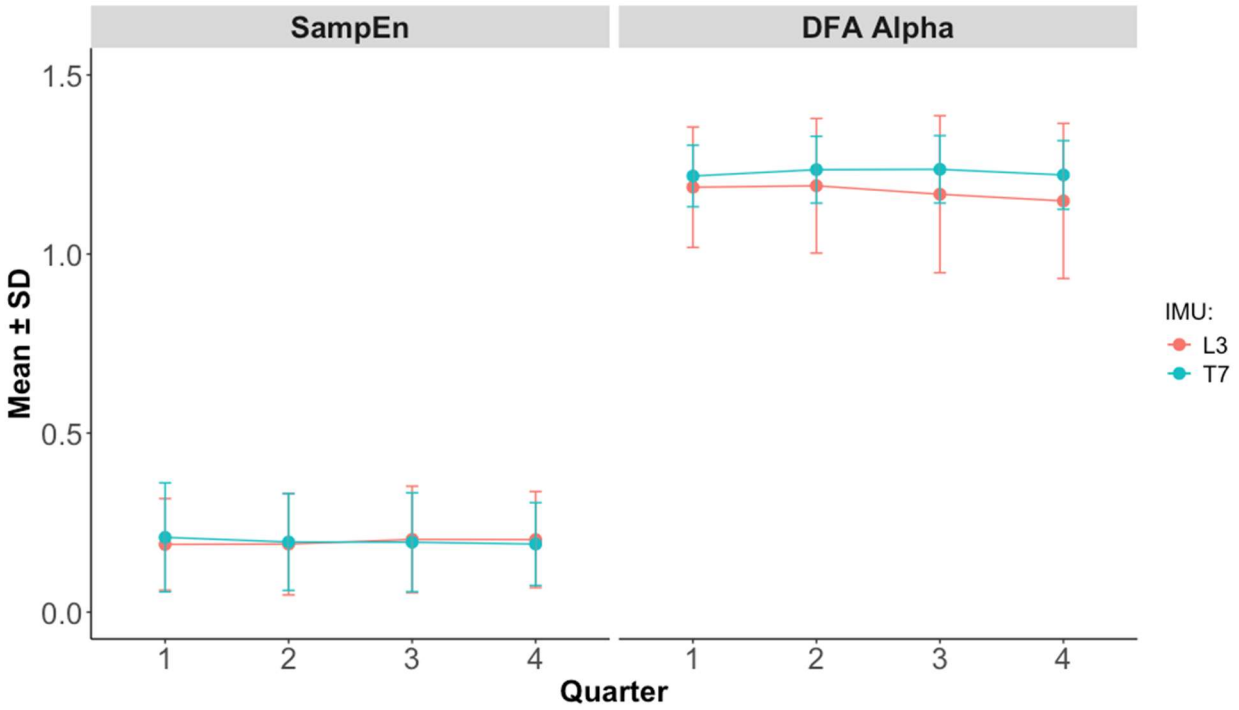
Mean (± SD) SampEn and DFA Alpha values at T7 and L3 are presented in Figure 1. No main effects of Quarter were observed at T7 or L3 vertebrae for SampEn or DFA Alpha.

Discussion

Both thoracic- and lumbar-spine kinematic patterns showed low irregularity (SampEn) or high levels of long-term power correlations (DFA Alpha) in angular velocity patterns. No differences were detected across the 2kTT, including in the later phases where muscle fatigue has been observed [2]. As such, these variables were not sensitive indicators of

trunk-muscle fatigue during the 2kTT. Future work should explore alternative kinematic measures that better capture fatigue-related changes and identify injury-risk predictors.

Images (Optional)



References (Optional)

1. Ng et al. (2014). *J Sci Med Sport,* **17**(3).
2. Spagnuolo et al. (2023). *McGill University.*
3. Slopecki et al. (2025). *Sensors*, **25**(11).

Session Category

Human Motion and Performance: Sports

OA155-02

Assessing Symmetry in Sweep Rowers: Comparison of Muscle Activation in Port, Starboard, and Bisweptual Female Collegiate Rowers on the Ergometer

Miss Madeleine Enns, Dr. Hunter Bennett

Old Dominion University, Norfolk, Virginia, United States

Introduction

Sweep rowing is an inherently asymmetrical activity. Research on sweep rowers' (a)symmetry on the ergometer is limited: one study among elite sweep rowers found asymmetric leg activation to be correlated to rowing side [1], while another found asymmetric back activation to be uncorrelated to side [2]. Symmetry on the ergometer among female collegiate rowers has not been assessed. Thus, the purpose of this preliminary investigation was to compare the muscle activation of port, starboard, and bisweptual female collegiate rowers on the ergometer.

Methods

Nine female collegiate rowers participated in this study: three port rowers, three starboard rowers, and three bisweptual rowers (with side allocation defined as greater than 75% of practice time on that side in the past two years). Each subject performed a 1000m-ergometer piece at 30 strokes per minute. Muscle activation was collected bilaterally via electromyographic (EMG) sensors on the rectus abdominis, external obliques, transverse abdominis, erector spinae, latissimus dorsi, and rectus femoris. Inertial measurement units (IMUs) were placed on upper extremities to visualize stroke phase. EMG signals were linear enveloped and normalized to the peak value recorded during warmup. Maximum voluntary contraction (MVC) was calculated during the stroke phase. Bilateral symmetry (right / left EMG) were compared using nonparametric t-tests ($alpha<0.05$).

Results

Bilateral asymmetry mean and standard deviation data are in Table 1. Despite rowing predominately on different sides, groups did not differ on symmetry index (all $p>0.05$) within this preliminary investigation. However, port rowers displayed greater left-side activation in the eternal obliques, transverse abdominis, erector spinae, and latissimus dorsi. Bisweptual and starboard rowers had a greater mix of asymmetry towards both right and left sides.

Discussion

This preliminary study did not find statistically significant differences in symmetry indexes in relation to rower's side. Nevertheless, asymmetry among all groups warrants further research with larger sample sizes, and investigating how to address female collegiate rower's muscle imbalances. Future studies should also consider repeating the data collection process on the water and analyzing symmetry in regards to a rower's years of experience.

Images (Optional)

	R/L Rectus Abdominis	R/L External Obliques	R/L Transverse Abdominis	R/L Erector Spinae	R/L Lat	R/L Rectus Femoris
Bisweptual (n=3)	1.23 ±0.10	1.18±0.76	0.86±0.76	1.03±0.52	1.35±1.78	0.98±0.09
Port (n=3)	1.61 ±0.88	0.91±0.52	0.92±0.42	0.56±0.45	0.91±0.18	1.76±1.47
Starboard (n=3)	1.18 ±0.56	0.86±0.48	1.06±0.05	0.91±0.25	1.26±0.98	1.06±0.51

References (Optional)

[1] Lars Janshen *et al.*, J Applied Biomechanics, 2009

[2] N.G. Readi *et al.*, Scand J Med Sci Sports, 2015

Session Category

Human Motion and Performance: Sports

OA155-03

Assessing the Effect of Inter-Athlete Spatiotemporal Coordination on Pairs Rowing Performance Times

Mr. Ian Doctor BSc (Honors), Mr. Daniel Brickman MSc, Miss Aurora Battis MSc, Mrs. Katie Bruggeling-Lavoie MEd, Dr. Shawn Beaudette PhD

Brock University, St. Catherines, Ontario, Canada

Mr. Ian Doctor

Introduction

Biomechanical analysis to maximize multi-athlete crew performance has been limited to use of force measurement devices with high potential error and poor reliability in intra-athlete contexts [1]. Prior research on inter-athlete coordination has utilized relative oar angles and subjective perception of coordination from athletes [2]. With the advent of 3D markerless motion capture, it is now feasible to analyze multiple athletes to assess the effect of inter-athlete spatiotemporal coordination on pair rowing performance times.

Methods

14 competitive rowers have so far been recruited (10M/4F); all are same-sex pairs with documented 2-kilometer race times on the Henley Rowing Course (Port Dalhousie, CAN). Pairs completed a 1-minute indoor rowing tank trial at race pace in matching pair combinations to the race data. Eight Miqus (Qualisys AB, SE) cameras captured concurrent video data for the duration of the trial. Post-processing utilized THEIA3D (Theia Markerless inc.), Visual3D (V3D LLC.), and MATLAB (v. R2025a MathWorks Inc.) to model and analyze the variability of oar kinematics and athlete center of mass, lower (ankle, knee, hip), and upper (shoulder, elbow, wrist) extremity joint and lumbar spine kinematics. 3D kinematics and movement timing variability were compared with on-water time trial data of 2-kilometer race segments for each athlete pair.

Results

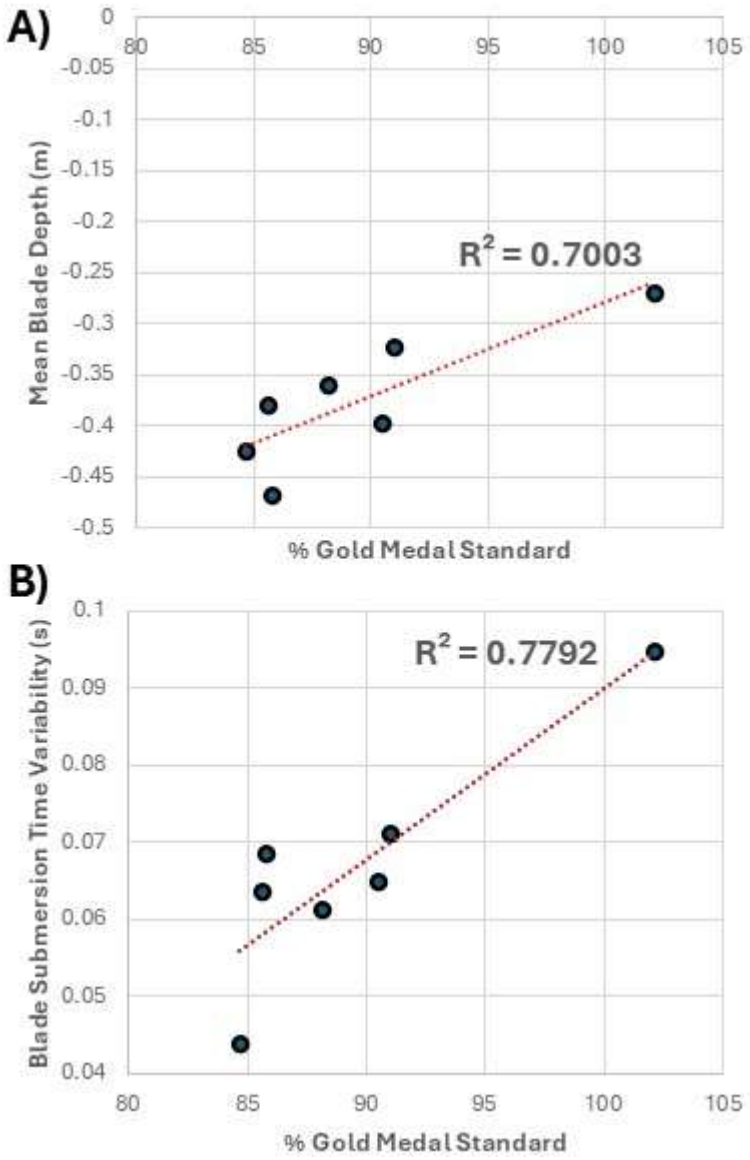
Bivariate linear regression analysis compared on-water times with kinematic outcomes. Results were precented absolute and normalized to % Gold Medal Standard (%GMS) time for age, sex, and weight class. Significant results for normalized data were Mean Blade

Depth (MBD) (R^2=0.7003, p=0.004) [Fig1a] and Blade Submersion Time Variability (BSTV) (R^2=0.7792, p=0.008) [Fig1b].

Discussion

An increase in MBD is correlated with an increase in %GMS, alluding to full blade contact and engagement with the surface of the water being a strong indicator of performance. The significant relationship of BSTV to %GMS indicates potential presence of enhanced response to changes in stroke dynamics (i.e. ratio between drive and recovery phases), where faster pairs might adapt to tempo changes at critical stroke stages (blade entry to water, early drive phase) [1] within the sampled data more effectively than slower pairs.

Images (Optional)



References (Optional)

[1] Holt et al. (2021). Front. Physiol., 12.

[2] Seifert et al. (2017). Front. Psychol., 8.

Session Category

Human Motion and Performance: Sports

OA155-04

Recognition of Front-Crawl Stroke Phases Using an Inertial Measurement Unit and Deep Learning

Master's Student Mathilde MONTEL[1,2], Assistant Professor Antoine BOUVET[1]

[1]M2S Laboratory (ENS Rennes/University of Rennes), Rennes, Bretagne, France. [2]ENS Rennes Sports Sciences & Physical Education Department, Rennes, Bretagne, France

Introduction

Monitoring intra-cyclic kinematics during daily training is crucial to support swimming performance. Gold-standard methods (i.e., manual video analysis) are time-consuming and impractical for coaches, making the use of Inertial Measurement Units (IMUs) to automate sports monitoring promising. However, intra-individual (e.g., speed, fatigue) and inter-individual (e.g., technique, expertise) kinematic variability restrict the validity and reliability of traditional IMU-based classification algorithms in ecological conditions. Thus, a generalizable human activity recognition method is needed for practical swimming phase monitoring. This study presents a deep learning model for intra-cyclic front-crawl analysis using a wrist-mounted IMU.

Methods

IMU and video data were collected at 60 Hz from 10 regional-to-national swimmers (5 male, 5 female) swimming 800 m of front-crawl at varying intensities, from warm-up to sprint. The video data were manually labeled with four phases (entry, pull, push, recovery) and used to train, validate, and test a Bi-LSTM neural network based on acceleration and angular acceleration, using a hold-out subject validation. After probabilistic post-processing of the model's predictions using a sliding window, classification performance was assessed using precision, recall and F1-score. Phase durations were also computed for user-friendly intra-cyclic monitoring.

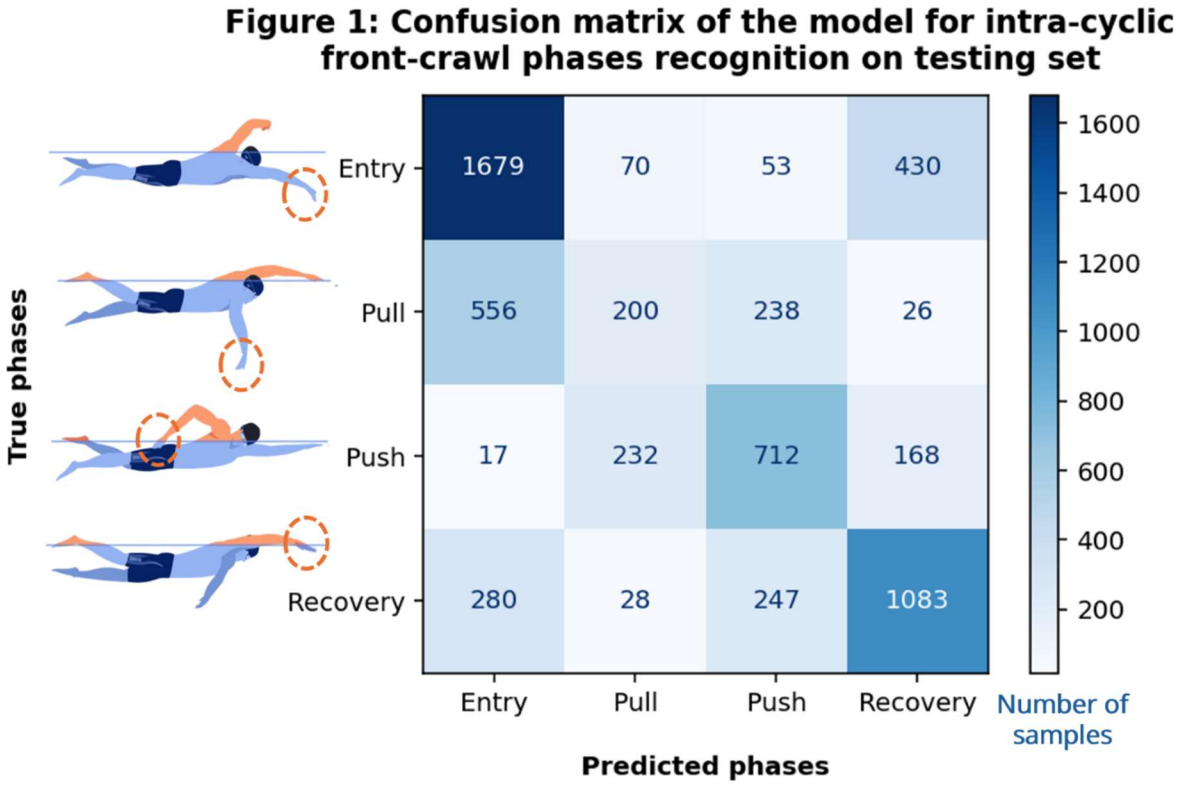
Results

The model achieved an average F1-score of 0.62 for phase recognition on the testing set: 0.69 (entry), 0.26 (pull), 0.60 (push) and 0.65 (recovery). Most errors occurred between adjacent phases (see Figure 1). The difference in duration between the predicted and true phases was 3.2% (entry), 25% (pull), 2.4% (push), and 7.6% (recovery).

Discussion

Predictions were more accurate for entry and recovery, but weaker for the pull phase, likely because it is the dataset's shortest and the one with the highest inter-individual variability. Adding more swimmers with distinct techniques and exploring hybrid architectures (e.g., CNN-Bi-LSTM) could help the model generalize and reduce errors. The model can nonetheless estimate overall time spent in each phase with low uncertainty, offering performance monitoring insights. As a preliminary study, this work is a first step toward developing a powerful training assistant to automatically analyze swimmers' intra-cyclic kinematics across skill levels during in-situ training monitoring.

Images (Optional)



Session Category

OA155-05

Quantifying Changes in Coordination Patterns in Adolescents with Cerebral Palsy Following a Learn to Row Program

Ms Ali Hawkins[1,2], Ms Karen Davies[1,3,4], Ms Farah T. Azim[1], Dr. Tim Bhatnagar[1,5,6], Ms. Diane Wickenheiser[1], Dr. Lise Leveille[1,5,6], Dr. Courtney L. Pollock[3,4]

[1]The Motion Lab at Sunny Hill Health Centre at BC Children's Hospital, Vancouver, BC, Canada. [2]School of Biomedical Engineering, UBC, Vancouver, BC, Canada. [3]Department of Physical Therapy, Faculty of Medicine, UBC, Vancouver, BC, Canada. [4]Rehabilitation Research Program, Centre for Aging SMART, Vancouver Coastal Health Research Institute, Vancouver, BC, Canada. [5]Research Institute, BC Children's Hospital, Vancouver, BC, Canada. [6]Department of Orthopedics, Faculty of Medicine, UBC, Vancouver, BC, Canada

Introduction

Rowing has been observed to improve function for adolescents with cerebral palsy (CP). Quantifying changes in range of motion (ROM) may not sufficiently describe motor skill acquisition during rowing for adolescents with CP. Coordination, a primary motor impairment of CP, has been suggested to provide a better understanding of biomechanics of movement. Recently, nonlinear analysis methods such as vector coding have been applied to rowing kinematics, providing further detail regarding coordination patterns and variability between joints. This analysis may provide an opportunity for increased understanding of potential changes in lower extremity coordination in adolescents with CP. This study investigates changes in lower extremity kinematics during the rowing stroke in adolescents with CP following a 3-month rowing program.

Methods

Participants were identified during routine clinical appointments at BC Children's Hospital. Training included 3-months of on-water rowing (90mins/session, 1-2 sessions/week). Rowing kinematics were collected pre- and post- learn-to-row program (12-camera Qualisys marker-based system, modified Helen Hayes marker set). The indoor rowing machine was instrumented with a load cell (4448N, Omega Engineering), measuring force at the handle. Participants rowed for 500m; five consecutive rowing cycles where consistent force was generated were extracted for analysis. Hip, knee, and ankle ROM was calculated. Coordination was evaluated through vector coding, comparing proximal to distal instantaneous joint positions (hip-to-knee, knee-to-ankle, hip-to-ankle) through calculating a coupling angle. Data is presented using descriptive statistics.

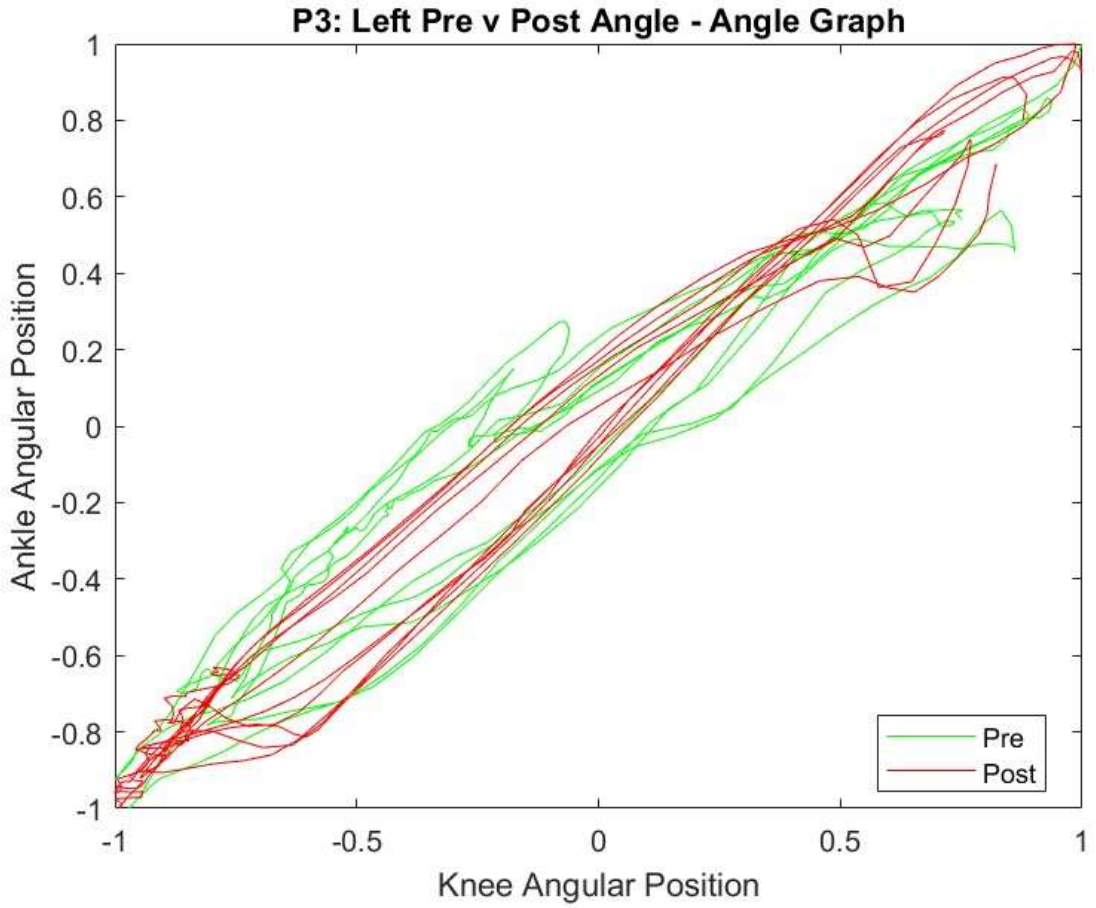
Results

Thirteen participants (ages 12-18yrs, females=4; hemiplegia=5, diplegia=7, quadriplegia=1; gross motor function classification scale, I=4, II=6, III=3). Stroke performance measures showed increased peak force development (mean:155N, range:38-510N) and stroke-rate (1.2, 5.8-0.3strokes/min). Changes in mean ROM were more variable- hip; increase 2.5degs, range:-15.5-24.5, knee; increase 3.5degs, range:-24-72, and ankle; increase 0.5degs, range:-17.5-13.5. Due to the variable changes in ROM, the vector coding technique may present a metric able to describe changes in motor performance. Vector coding analysis completed for 3/13 participants. (Fig1) shows smoother trajectory of movement post-training, with less alternating between ankle and knee dominancy.

Discussion

Vector coding applied to rowing kinematics may provide further detail regarding skill acquisition and coordination patterns between lower extremity joints, associated with improvements in motor performance in adolescents with CP.

Images (Optional)



Session Category

Human Motion and Performance: Sports

OA155-06

Effects of Pool Depth on Swimming Performance: Application to the 200-m Freestyle

Mr. Junsik Oh M.S.Student[1], Mr. Beomsu Jang[2], Professor Jooeun Ahn Ph.D[1], Professor Keunhwan Park Ph.D[2]

[1]Seoul National University, Seoul, Seoul, Korea, Republic of. [2]Gachon University, Seongnam, Gyeonggi, Korea, Republic of

Introduction

Wave drag, accounting for 3–50% of total resistance in freestyle swimming, is an important determinant of performance [1]. Given the depth dependence of wave drag, performance should vary accordingly, but this relationship has not been quantified. To quantify this depth effect, we developed a simplified depth-scaling model of hydrodynamic resistance and applied it to race results from the 2024 Paris Olympic Games (pool depth: 2.15 m) to assess its relevance in elite competition.

Methods

The model estimates total drag—including friction, form, and wave drag—as a function of depth (H) and the wave-drag fraction (α) [2]. Using the official World Aquatics database, we obtained the final race results of the men's 200-m freestyle at the 2024 Paris Olympic Games. From each athlete's race time, we calculated the mean swimming velocity, and, assuming constant mechanical power output, used our model to estimate their predicted performance if the pool depth had been 3 m [3,4].

Results

Under average race-speed conditions (V = 1.90 m/s) and α = 0.4, previously reported measurements within V ± 0.05 m/s fell within the model's prediction bounds [3,4]. Based on these conditions and assuming constant power output, the model estimates a 1.38–1.59% reduction in race time when pool depth increases from H = 2.15 m to H = 3 m.

Discussion

Our findings provide quantitative evidence that pool depth can influence freestyle performance and confirm the relevance of this effect in elite competition. However, the present model has been evaluated primarily near a race speed of 1.90 m/s, and its behavior at other velocities will be addressed in future work. Overall, these results suggest that pool depth should be considered in both training and competition planning.

Images (Optional)

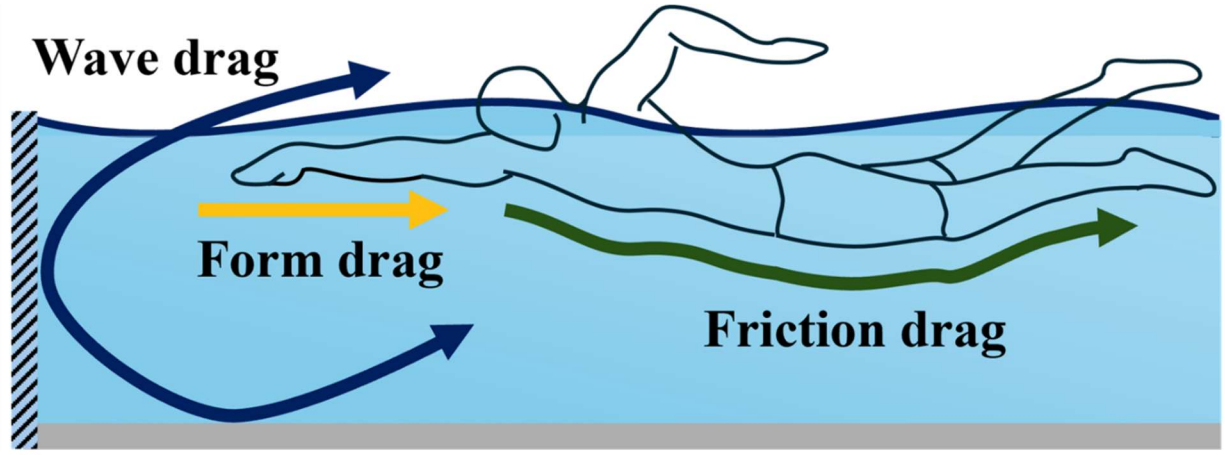


Figure 1: Schematic illustration of wave, form, friction drag acting on a swimmer

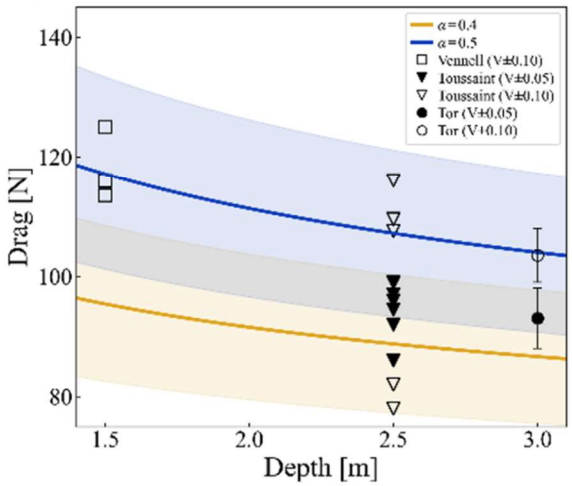


Figure 2: Depth-dependent swimming drag at the average speed of the Paris 200-m final, compared with previous experimental data

References (Optional)

[1] Vennell et al., J Biomechanics, 2006, [2] Tuck, E. O., J Fluid mechanics, 1966 [3] Toussaint et al., J Biomechanics, 2004 [4] Tor et al., J Applied Biomechanics, 2015

Acknowledgements (Optional)

Supported by KHIDI, funded by MOHW (No. HK23C0071).

Session Category

Human Motion and Performance: Sports

OA156-01

Regional Strain in Human Acute Respiratory Distress Syndrome: Mechanical Response of Focal and Non-Focal Phenotypes to Recruitment Maneuvers

Mr. Nibaldo Avilés-Rojas PhD(c)[1,2], Mr. Agustín Pérez PhD(c)[1,2], Mr. César Santis MD[2,3,4], Dr. Guillermo Bugedo MD[4], Dr. Ellen Roche PhD[5,6], Dr. Jaime Retamal MD,PhD[4,7], Dr. Daniel Hurtado PhD[1,2,6]

[1]Department of Structural and Geotechnical Engineering, School of Engineering, Pontificia Universidad Católica de Chile, Santiago, RM, Chile. [2]Institute for Biological and Medical Engineering, Schools of Engineering, Medicine and Biological Sciences, Pontificia Universidad Católica de Chile, Santiago, RM, Chile. [3]Unidad de Cuidados Intensivos,Hospital Barros Luco-Trudeau, Santiago, RM, Chile. [4]Departamento de Medicina Intensiva del Adulto, Facultad de Medicina, Pontificia Universidad Católica de Chile, Santiago, RM, Chile. [5]Institute for Medical Engineering and Science, Massachusetts Institute of Technology, Cambridge, MA, United States. [6]Department of Mechanical Engineering, Massachusetts Institute of Technology, Cambridge, MA, United States. [7]Center of Acute Respiratory Critical Illness (ARCI), Santiago, RM, Chile

Introduction

Acute respiratory distress syndrome (ARDS) exhibits morphological heterogeneity, which may influence regional mechanical behavior during recruitment maneuvers (RMs). Although focal and non-focal phenotypes show distinct radiological patterns, quantitative in-vivo evidence of their differential regional deformation remains limited. We aimed to characterize and compare regional volumetric-strain and dorsoventral linear-strain in human focal and non-focal ARDS during RMs using image-based biomechanical analysis.

Methods

We retrospectively analyzed CT scans from 11 adults with moderate-to-severe ARDS. Breath-hold CT images were acquired at airway pressures of 5, 15, and 45 cmH_2O. Lungs were segmented and meshed, and image registration (NiftyReg) was used to compute regional deformation relative to 5 cmH_2O. Gas fraction (FGAS) and aeration compartments were quantified at each pressure. Volumetric-strain and dorsoventral linear-strain were computed on tetrahedral finite element meshes, and regional values were analyzed across four gravitational regions (ventral, mid-ventral, mid-dorsal, dorsal) for focal (n=4) and non-focal (n=7) phenotypes.

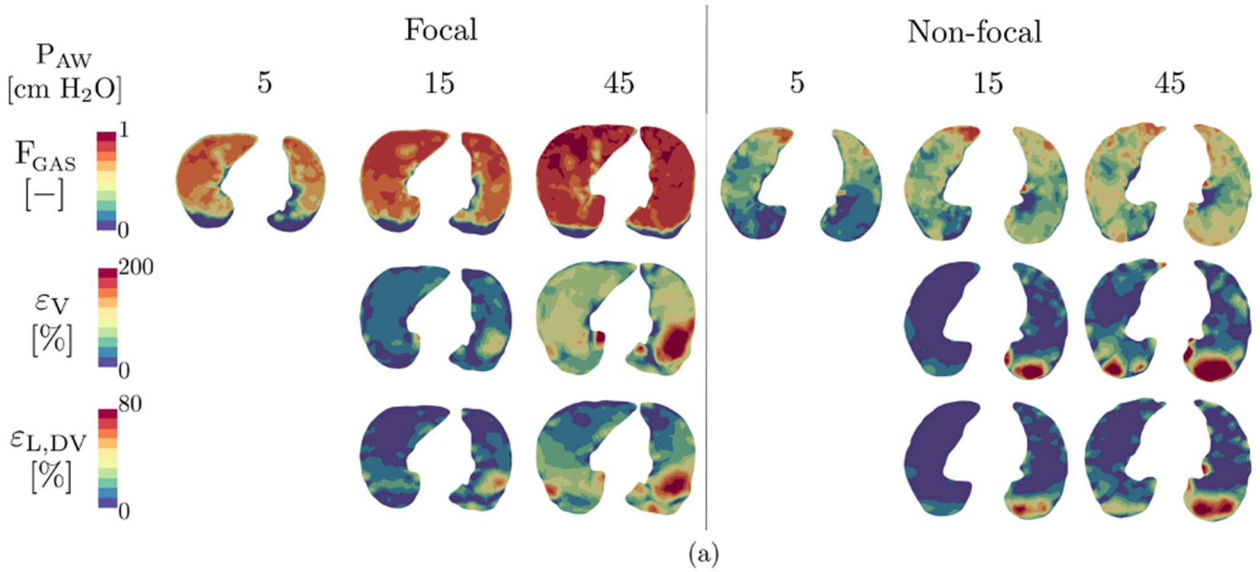
Results

Strain distributions were heterogeneous in both phenotypes but exhibited distinct spatial patterns. In focal ARDS, the initially normally aerated mid-ventral and mid-dorsal regions, the anatomical location of the “baby lung”,showed the highest deformation during RMs. At 45 cmH_2O, volumetric-strain in these regions exceeded 150–200%, with a peak of dorsoventral linear-strain in the mid-dorsal region. These high-strain zones occurred adjacent to persistently collapsed dorsal tissue. In contrast, non-focal ARDS demonstrated strain elevations predominantly in dorsal regions, corresponding to recruitment of previously poorly or non-aerated tissue. Ventral and mid-ventral strain remained significantly lower than in focal ARDS

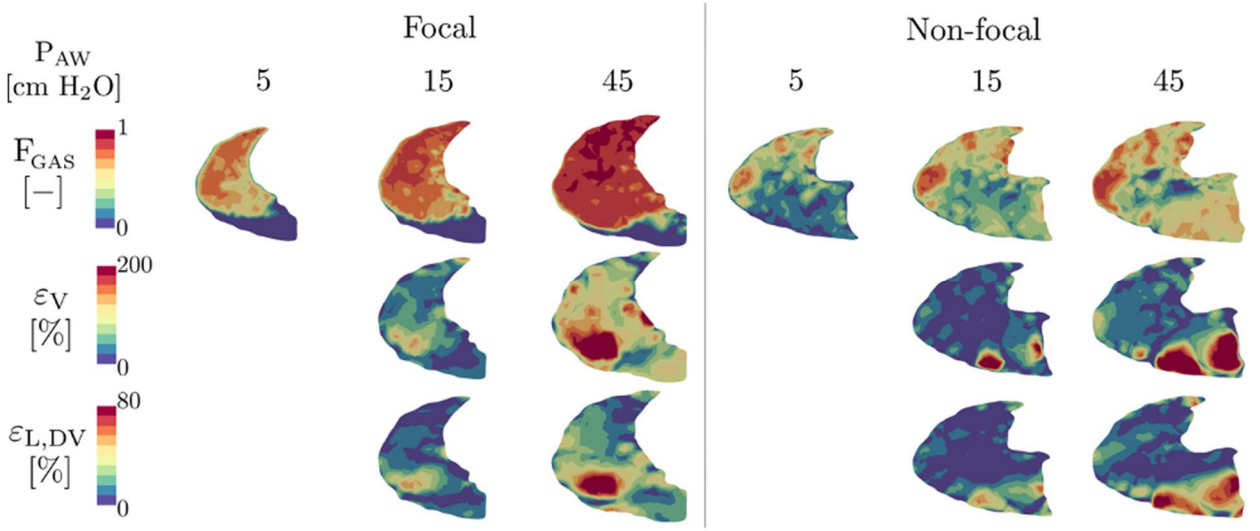
Discussion

This study provides the first quantitative in-vivo evidence that focal and non-focal ARDS exhibit different patterns of regional mechanical deformation during recruitment. In focal ARDS, the baby lung is exposed to disproportionately high volumetric and linear strain, particularly at interfaces between aerated and collapsed regions, mechanistic “stress raisers” consistent with interdependence theory. These findings offer a biomechanical explanation for the poor response and higher risk of overdistension previously reported in focal ARDS during RMs and high PEEP. Conversely, in non-focal ARDS, elevations in strain largely reflect beneficial recruitment rather than injurious deformation of already aerated tissue. These results support morphology-based personalization of ventilation strategies

Images (Optional)



(a)



(b)

Session Category

Cardiovascular/Cardiorespiratory Biomechanics: Methods, Models and Applications

OA156-02

Exploring V/Q Distribution in Children With MRI-Informed Personalised Computational Lung Models

Ms Megan Soo, Prof Merryn Tawhai, Dr Ho-Fung Chan

Auckland Bioengineering Institute, University of Auckland, Auckland, Auckland, New Zealand

Introduction

Novel lung MRI techniques are promising clinical tools for guiding paediatric lung disease management and can provide regional structure-function lung biomarkers to inform computational physiology lung models. Here, we developed an MRI-to-model framework that integrates novel MRI biomarkers to generate personalised lung models of ventilation and perfusion in healthy children. The predicted ventilation/perfusion (V/Q) distributions could potentially facilitate new strategies for managing respiratory conditions.

Methods

Three healthy children were imaged with a novel structure and function lung MRI protocol. Personalised anatomical lung models were generated using 3D ultra short echo-time (UTE) MRI [1] (Fig 1a). To account for gravitational tissue deformation, acinar tissue units were spatially and volumetrically distributed across both lungs based on MRI-derived approximate tissue density distribution at functional residual capacity (FRC). Phase resolved function lung imaging (PREFUL) MRI [2] maps of ventilation and perfusion from 2D dynamic MRI were used to identify acinar tissue units with ventilation/perfusion defects (Fig 1b). A ventilation model simulated tidal flow via pressure-driven expansion/contraction of tissue units (Fig 1c). A perfusion model simulated blood flow across extra- and intra-acinar tissue units at FRC (Fig 1d).

Results

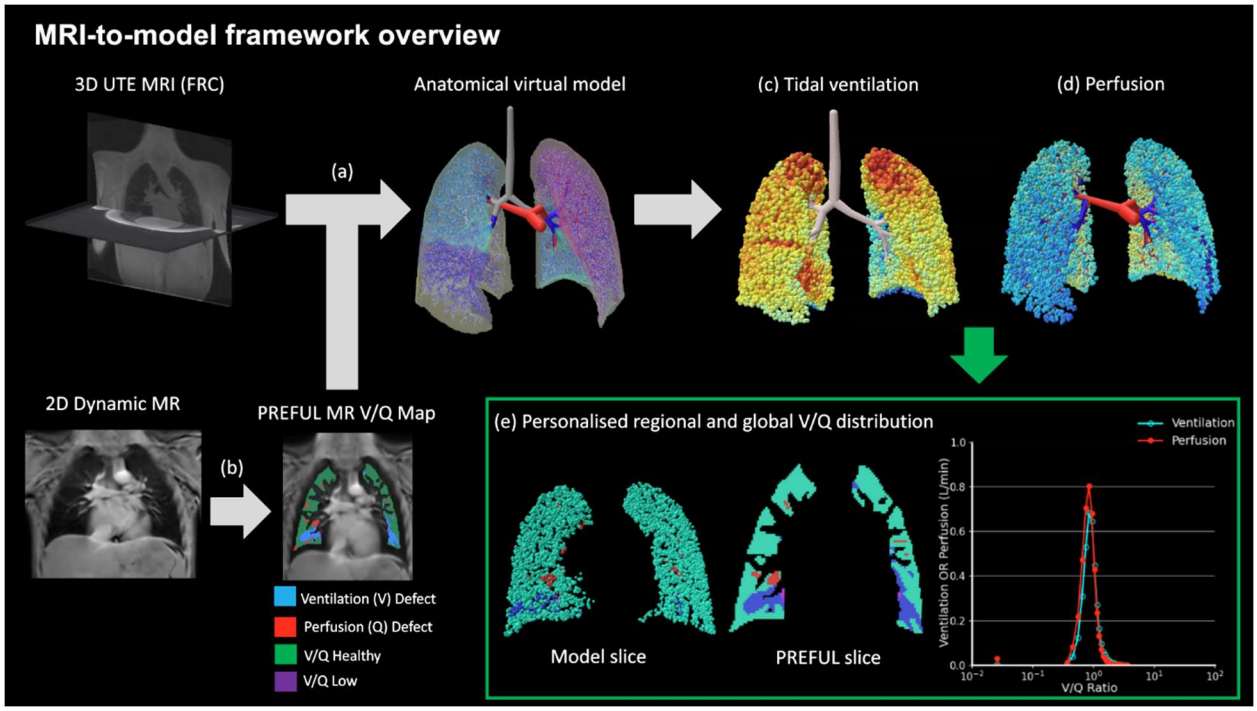
Simulated global ventilation and perfusion measurements, lung compliance (101±13 mL/cmH_2O), specific compliance (72.3±7.2 mL/cmH_2O/L-FRC), work per litre (0.53±0.02 J/L), and mean pulmonary artery pressure (15.8±0.2 mmHg), were within the normal reported range for healthy children. Simulated regional ventilation and perfusion defects in the lung models demonstrate good spatial agreement with corresponding PREFUL ventilation and perfusion maps (Fig 1e). Furthermore, the simulated VQ ratio plot, across

all acinar tissue units, was homogenous and centred around one, indicative of healthy gas exchange and VQ matching.

Discussion

MRI-informed computational lung models can provide simulations of regional ventilation/perfusion matching distribution that could facilitate novel personalised insights into gas exchange efficiency. This novel MRI-to-model framework will be further implemented in a larger cohort of healthy children, and in future work, the framework will be applied to children with asthma who have ventilation heterogeneity.

Images (Optional)



References (Optional)

[1] Johnson, K.M., et al., *Magn Reson Med*, 2013.

[2] Voskrebenzev, A., et al., *Magn Reson Med*, 2018

Acknowledgements (Optional)

This work was supported by the Aotearoa Foundation Postdoctoral Fellowship

Session Category

Cardiovascular/Cardiorespiratory Biomechanics: Methods, Models and Applications

OA156-03

Effects of Respiratory Heart Rate Variability on Cardiac Biomechanics: Experiment and Modelling Investigations

Mr Chamal Kohombakadawala[1], Dr Toan Pham[1,2], Dr Kenneth Tran[1], Prof Andrew Taberner[1,2], Dr June-Chiew Han[1]

[1]Auckland Bioengineering Institute, University of Auckland, Auckland, Auckland, New Zealand. [2]Department of Engineering Science and Biomedical Engineering, University of Auckland, Auckland, Auckland, New Zealand

Introduction

Heart rate variability (HRV), a naturally occurring phenomenon in healthy individuals, is closely synchronised with respiration. Inhalation and exhalation, respectively, inhibit and restore vagal outflows, leading to increased and decreased heart rates within each breathing cycle. This cardiopulmonary phenomenon, termed 'respiratory heart rate variability' (RespHRV), has recently been shown to improve cardiac output when externally reinstated via a pacemaker. This finding led to the hypothesis that RespHRV pacing increases cardiac work and, also energy expenditure.

Methods

We tested the hypothesis experimentally using left-ventricular muscles (n = 10) isolated from the rats and studied using the work-loop calorimeter. Simultaneous measurements of mechanics (force, length, work) and energetics (heat) were made across wide ranges of preloads and afterloads. Each muscle was paced with and without RespHRV. We also tested the hypothesis using a six-compartment computational model of human pulmonary and systemic circulations (PMID: 8238596) to simulate RespHRV effects on cardiac pressure-volume dynamics. RespHRV was modelled by alternating inter-beat intervals (two beats at 100.8 beats per minute, four beats at 63 beats per minute), compared with fixed pacing at 72 beats per minute.

Results

Experimentally, average muscle force, work, heat, and mechanical efficiency were not different between the two pacing protocols. However, RespHRV pacing elicited twitch-by-twitch variations in force magnitude and shortening, which was absent without RespHRV. Model simulations across varying cardiovascular loads, including elevated peripheral resistance and blood pressure, cardiac pressure-volume work did not differ between RespHRV and fixed pacing. Similar results were obtained when contractility was modelled as heart-rate dependent.

Discussion

In conclusion, both experimental and computational findings reject the hypothesis that RespHRV pacing alone directly augments cardiac work or efficiency under acute conditions. We speculate that chronic adaptations or additional mechanisms such as changes in cellular ionic activity, protein expression, and/or structural remodelling may underlie the improved cardiac output observed with external RespHRV pacing. Chronic experiments and models integrating excitation-contraction and subcellular remodelling are warranted to fully test the hypothesis.

Session Category

Cardiovascular/Cardiorespiratory Biomechanics: Methods, Models and Applications

OA156-04

Applying Adaptive Boundary Conditions to Improve Biomechanical Modeling of the Pulmonary Vasculature Post Lung Transplantation

Mr. Jonathan Ibinson[1], Mr. Alexander Barr MS[1], Dr. Jorge Mallea MD[2], Dr. Jason Szafron PhD[1]

[1]Carnegie Mellon University, Pittsburgh, PA, United States. [2]Mayo Clinic, Jacksonville, Florida, United States

Introduction

Optimal lung transplantation (LT) outcomes remain limited by inflammatory pathways with a mechanobiological component [1] . After transplant, hemodynamics change with the combined cardiopulmonary system of the donor and recipient. In LTs, two main shifts occur: decreased afterload in the recipient right-heart from removing diseased, often narrowed pulmonary vessels and changed flow through the donor vessels with a heart potentially adapted to high pressures. We aim to build a LT simulation pipeline that accounts for these mechanical shifts to improve predictions of post-LT vascular remodeling.

Methods

We created post-LT 3D CFD simulations using SimVascular [2]. Donor and recipient pulmonary vasculatures were joined for in silico representations of LT. We paired morphometric trees with vessels of varying sizes to outlets for detailed simulations of the distal vasculature. A 0D right heart model was created for both the donor and recipient that included the right-heart chambers, valves, and the pulmonary system. We simulated a 0D LT to get the new cardiac input, using the heart from the diseased patient and the pulmonary system parameters from the healthy patient. We simulated adaptive distal pulmonary vessels by adjusting order diameters to minimize differences from order-averaged healthy wall shear stress (WSS) [3].

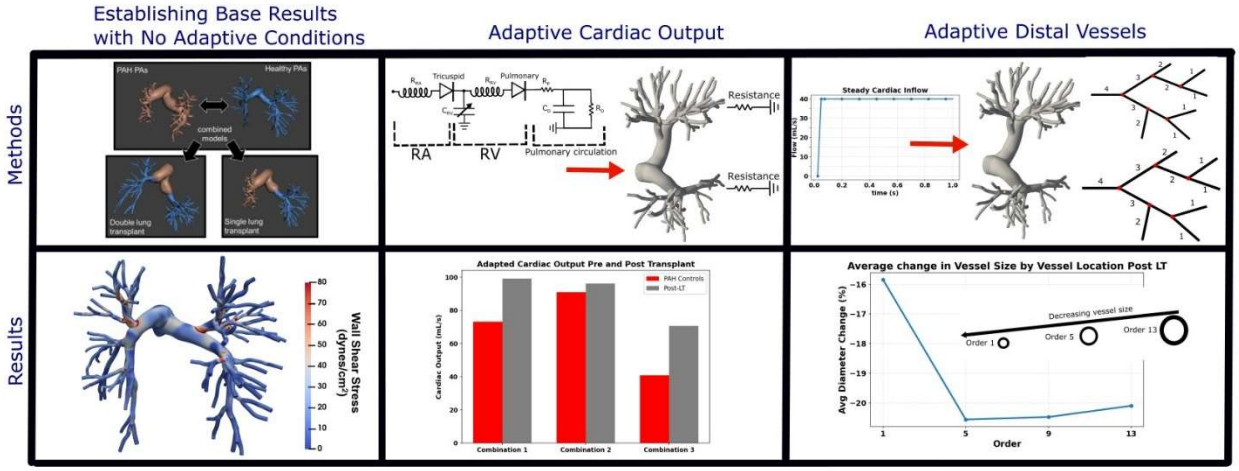
Results

We modeled a healthy donor with three different PAH vasculature combinations, simulating donor organ procurement. The PAH heart post-LT saw an average increase of 20.3 mL/s in cardiac output. When exposed to decreased flow, distal vessels saw constriction of the vessels, example shown normalized to the size of the distal vessel in the bottom right figure panel.

Discussion

Both adaptive results matched expectations of system behavior with cardiac output increasing from reduced afterload and distal resistance increasing to restore WSS towards the pre-operative level in the healthy patient. These shifts change the long-term mechanobiological stimuli experienced by donor lungs, which drive vascular remodeling and immune cell infiltration. Future work will focus on iterative coupling until both cardiac output and distal resistance reach a steady state to reflect joint feedback from both mechanisms.

Images (Optional)



References (Optional)

[1] Betty Allen *et al.*, JAHA 2023.

[2] Adam Updegrove *et al.*, Ann Biomed Eng., 2017.

[3] Axel Pries *et al.*, Hypertens., 2005.

Session Category

Cardiovascular/Cardiorespiratory Biomechanics: Methods, Models and Applications

OA157-02

Quantifying Microvascular Topology of the Myocardium with Synchrotron X-ray Phase Contrast Micro-tomography to Investigate Microthrombi Occlusions

Mr. Ross Straughan MSc[1], Dr. Anne Bonnin PhD[2], Dr. Nikola Cesarovic Med. Vet, PhD[3], Prof. Dominik Obrist PhD[1]

[1]ARTORG Center for Biomedical Engineering Research, University of Bern, Bern, Bern, Switzerland. [2]Swiss Light Source, Paul Scherrer Institute, Villigen, Aargau, Switzerland. [3]Department of Health Sciences and Technology, ETH Zurich, Zurich, Zurich, Switzerland

Introduction

Approximately half of patients that receive percutaneous coronary intervention to treat myocardial infarction suffer from Microvascular Obstruction (MVO) [1]. In cases of MVO, large thrombi are believed to be broken up, flow downstream and occlude small vessels (< 200μm diameter) of the coronary microcirculation, preventing sufficient reperfusion [2].

Despite its frequent occurrence, there is a lack of adequate diagnosis and treatment of MVO, which significantly worsens the clinical outcome after myocardial infarction. Improving diagnosis and treatment requires a better understanding of the microvascular architecture of the myocardium including the location of occluding microthrombi (MT).

Methods

A porcine model was adapted to mimic clinically observed MVO by the infusion of MT directly into the coronary circulation [2]. Six samples from six pigs were extracted and imaged with Synchrotron X-ray Phase Contrast micro-tomography with a voxel resolution of 1.625 μm. Deep-learning tools were utilized to segment myocardial layers, microvasculature and microthrombi.

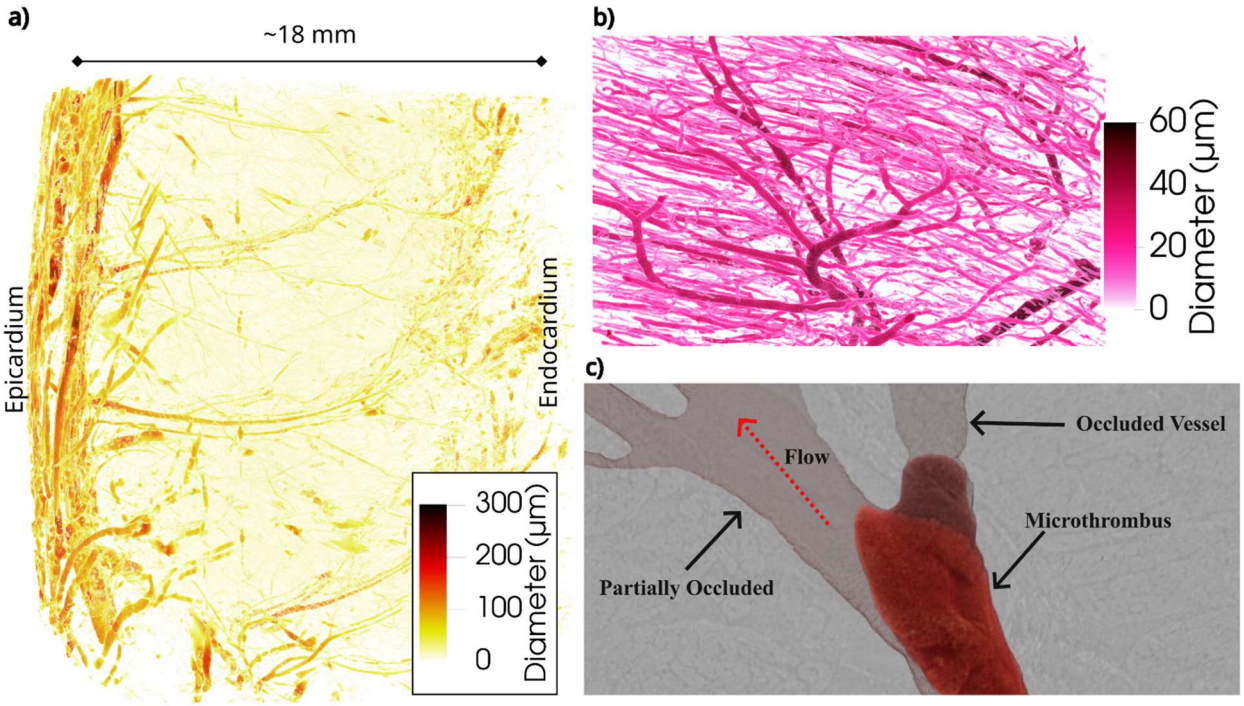
Results

Preliminary topological analysis of the segmented microvascular architecture reveals large vessels (>50μm) transversing the myocardium (figure a) and smaller vessels (<50μm) aligning circumferentially and orientated anisotropically (figure b) alongside myocytes. Collateral vessels, which may provide an important role in mitigating the impact of MVO, have also been observed. MT segmentations reveal their hierarchical location within the microvascular network, allowing for a better understanding of MVO pathology mechanisms.

Discussion

To our knowledge, these are the first three-dimensional segmentations of the myocardial microvasculature approaching the capillary level (~10 μm in diameter) for the entire thickness of the myocardium. Future efforts will be spent quantifying how MT-specific occlusions (such as in figure c) reduce or maintain the mass transfer of blood within the myocardium. By improving our understanding of these mechanisms, we hope to improve the development of targeted therapies and validate emerging diagnostic technologies.

Images (Optional)



References (Optional)

[1] Matthijs van Kranenburg et al., JACC Cardiovasc. Imaging, 2014

[2] Nikola Cesarovic et al. Circulation research, 2023

Session Category

Cardiovascular/Cardiorespiratory Biomechanics: Methods, Models and Applications

OA157-03

Real-Time Risk Stratification for Coronary Artery Thrombosis using Machine Learning

Mr. Kyle Tennison[1], Dr. Aurele Goetz PhD[2], Dr. Pablo Jeken Rico PhD[2], Dr. Kirsten Dummer MD[3], Dr. Jane Burns MD[3], Dr. Alison Marsden PhD[4], Dr. Elie Hachem PhD[2], Dr. Karthik Menon PhD[1]

[1]Georgia Institute of Technology, Atlanta, GA, United States. [2]Mines Paris - PSL, Paris, Paris, France. [3]UC San Diego School of Medicine, San Diego, CA, United States. [4]Stanford University, Stanford, CA, United States

Introduction

Kawasaki Disease (KD) is an acute vasculitis that predominantly affects children under 5 years of age. Without timely treatment, 25% of patients will develop coronary artery aneurysms (CAAs) that may cause thrombosis and subsequent myocardial infarction. Current treatments are purely guided by CAA diameter normalized for body surface area [1]. While previous work has shown that hemodynamics potentially predicts risk better than CAA diameter [2], hemodynamics cannot be measured using standard clinical tools. Computational models can quantify hemodynamics but are expensive and not feasible in clinical settings. Moreover, machine learning methods are hampered by the lack of large datasets for this relatively rare disease.

Methods

We develop a combined computational modeling and machine learning pipeline for real-time non-invasive risk stratification. Using data from patient-specific imaging, we develop techniques for learning features of real aneurysms to create a library of anatomically realistic synthetic aneurysms. We use computational fluid dynamics to compute thrombosis risk in the dataset of real and synthetic aneurysms, and build convolutional neural networks (CNN) for real-time predictions of thrombosis risk.

Results

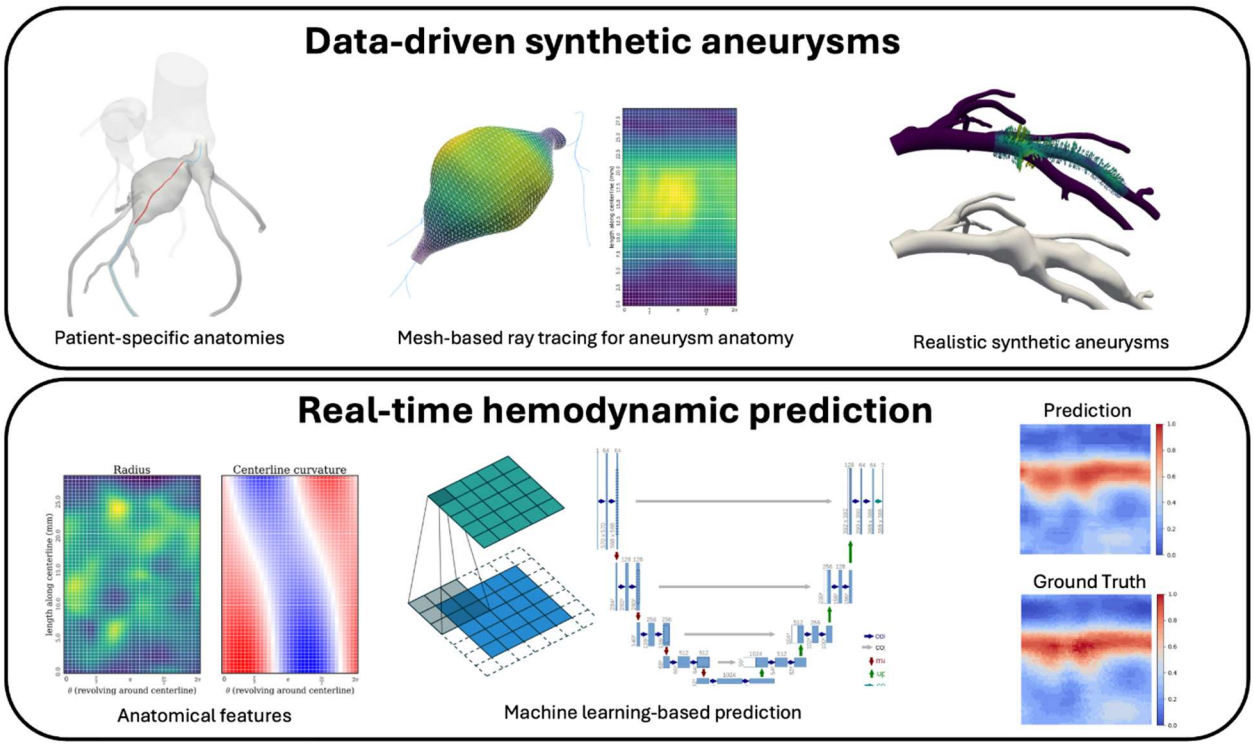
The creation of synthetic aneurysms consists of identifying local coordinate systems along aneurysm centerlines, ray-tracing for creating 2D feature maps of aneurysms, and registration to implant synthetic aneurysms on healthy vasculature. The pipeline has been tested with clinicians using a dataset of real and synthetic aneurysms. The rates of identifying real and synthetic aneurysms as real aneurysms were roughly equal, indicating the pipeline generates realistic anatomies.

The prediction of hemodynamics was performed on 810 vascular samples using a U-Net architecture. The inputs were vessel radius, curvature, distance from coronary ostium, and location of branches. The proof-of-concept was performed on predicting spatial distributions of time-averaged wall shear stress (TAWSS). The results show we are successfully able to predict patient-specific TAWSS distributions using CNNs.

Discussion

We are developing a framework for real-time and non-invasive prediction of thrombosis risk for KD patients that can be performed in clinically-realistic timeframes. The results are promising, both in terms of learning anatomical features of aneurysms, and predicting hemodynamics.

Images (Optional)



References (Optional)

[1] McCrindle, B. W. *et al. Circulation,* 2017.

[2] Menon, K. *et al. J. of Cardiovasc.Transl. Res.* , 2023.

Acknowledgements (Optional)

This work was supported by Georgia Institute of Technology Startup Funds and the Hooper Family Trust.

Session Category

Cardiovascular/Cardiorespiratory Biomechanics: Methods, Models and Applications

OA157-04

Cannula-Driven Hemodynamics and Embolic Transport During Cardiopulmonary Bypass Using Validated Patient-Specific CFD-LPT Modeling

Dr. Nafis Arefin PhD, Dr. Bryan Good PhD

University of Tennessee, Knoxville, Tennessee, United States

Dr. Nafis Arefin

Introduction

Cardiopulmonary bypass (CPB) enables life-saving cardiac surgeries, but the high-velocity jet from the aortic cannula disrupts native hemodynamics, dislodges plaques, and affects emboli transport, elevating the risk of stroke, renal, and hepatic complications. While cannula angle has been studied to some extent, prior work did not quantify how cannula orientation, age-dependent anatomy, and CPB parameters collectively dictate embolic pathways. This study addresses these gaps using validated CFD coupled with Lagrangian Particle Tracking (LPT) across patient-specific aortic anatomies representing multiple age groups. We quantitatively assessed how cannulation strategy and CPB operating conditions influence embolic transport into the full aortic and cerebrovascular anatomy, with the hypothesis that these parameters would significantly modulate embolic trajectories.

Methods

In-vitro validation used silicone-based mock circulatory loops replicating CPB cannulation and perfusion conditions. Four patient-specific aortic geometries were simulated with two cannula orientations (30° and 90°) and six CPB conditions (μ = 1.5, 2.5, 3.5 cP; Q = 3, 5 LPM). Physiological outlet boundary conditions were manually implemented in *OpenFOAM,* and embolic transport quantified using LPT, tracking 1000 collision-free emboli (0.5–2.5 mm) per simulation. Post-processing was performed in *ParaView*.

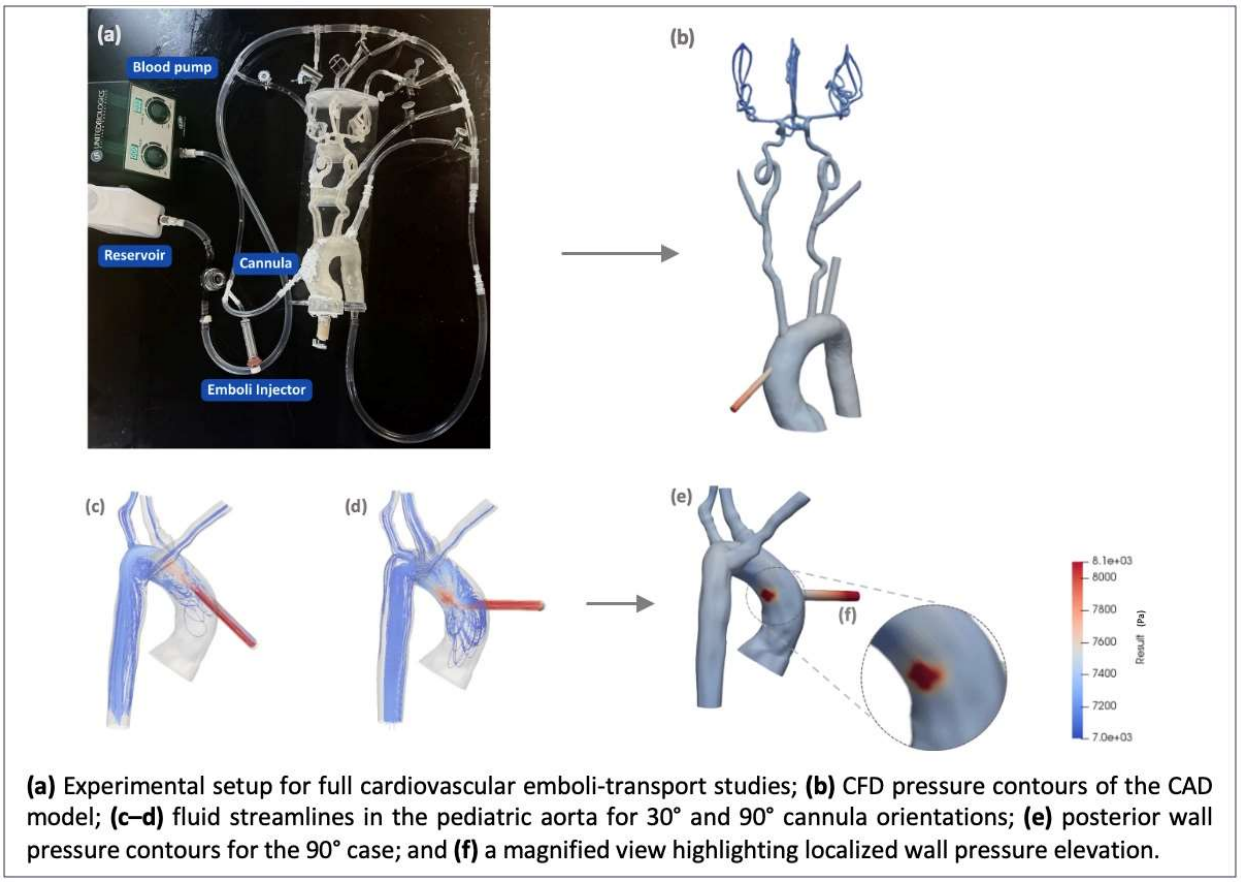
Results

Notably, the 30° angled cannula consistently reduced emboli escape by 36% on average, while decreasing posterior wall pressure by 24%. Increasing flowrate from 3 to 5 LPM raised cerebral and renal emboli by 45% and 27%. At low viscosity (1.5 cP), emboli exit into the external carotid and hepatic arteries increased by 35-55%.

Discussion

This study presents the first validated, patient-specific, multi-age embolic transport model spanning the full cardiovascular system. Angled cannulation reduced embolic transport, whereas perpendicular jets increased turbulence, elevated wall stress, and promoted embolus formation and dispersion. Higher flow rates and lower viscosity intensified turbulence, driving emboli toward slow-moving near-wall regions and increasing branch exit. Age-specific geometric differences, particularly sharper arch curvature and smaller diameters in the pediatric model, further shaped transport pathways. Limitations include rigid walls and spherical emboli, and future work will incorporate compliant walls with more realistic embolus properties. Overall, these findings provide a quantitative foundation for optimizing cannulation strategies and CPB management, enabling safer perfusion approaches that minimize stroke and organ-injury risk.

Images (Optional)



(a) Experimental setup for full cardiovascular emboli-transport studies; **(b)** CFD pressure contours of the CAD model; **(c–d)** fluid streamlines in the pediatric aorta for 30° and 90° cannula orientations; **(e)** posterior wall pressure contours for the 90° case; and **(f)** a magnified view highlighting localized wall pressure elevation.

Session Category

Cardiovascular/Cardiorespiratory Biomechanics: Methods, Models and Applications

OA157-05

Lysis Of Microthrombi in a Multi-Scale In-Vitro Model of Coronary Microvascular Obstruction

Dr. Yannick Rösch[1], Dr. Anastasia Milusev[2], Ms. Petra Wolint[3], Dr. Sabrina Frey[2], PD Dr. Nikola Cesarovic[3], Prof. Dr. Dominik Obrist[1]

[1]University of Bern, Bern, BE, Switzerland. [2]CorFlow Therapeutics AG, Bern, BE, Switzerland. [3]ETH Zurich, Zurich, ZH, Switzerland

Introduction

Coronary microvascular obstruction (MVO) affects more than 50% of all patients after successful percutaneous treatment of ST-elevation myocardial infarction (STEMI) [1]. MVO leads to impaired perfusion of the myocardium and may be caused by microthrombi (MT) obstructing vessels with a diameter of 200µm or smaller. Today, there exists no effective therapy for MVO. In this study, we test a novel therapeutic approach in which thrombolytic drugs are directly infused into the coronary vessels via catheter while the local perfusion is temporarily interrupted by a balloon.

Methods

We developed a multi-scale in-vitro model comprising a left-heart mock loop (macro), a coronary phantom (meso), and a chip modeling the microvasculature (micro) [2]. This setup reproduces physiological flow in the microchip, including effects of pulsating arterial pressure and the intramyocardial pumping effect due to myocardial contraction. The infusion of MTs into the microfluidic chips leads to an obstruction of the smaller vessels. A microdose (1.5mg) of alteplase (rtPA) is then infused into the coronary phantom and the microchip while the coronary circulation is blocked by balloon occlusion for 90 seconds. For the following 15.5 minutes, the chip is perfused with human plasma while the position and lysis of the MTs are captured by a camera with LED-backlight illumination.

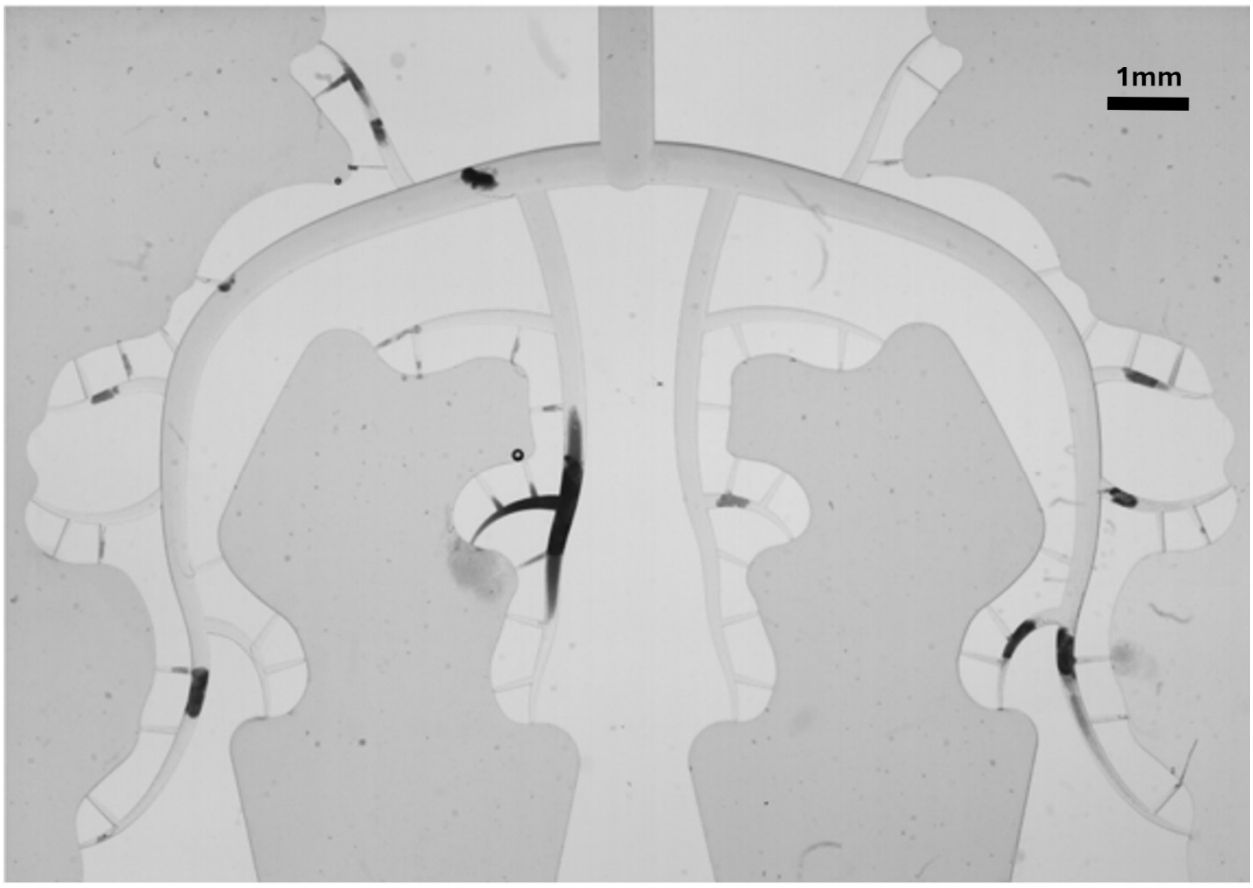
Results

Alteplase infusion resulted in a 3.5x (on average) faster reduction of the thrombus burden compared to control experiments without alteplase. Some MTs remained unchanged throughout the experiment because they were located in vessels that could not be reached by alteplase due to the absence of local flow, while others were mobilized after partial lysis and were transported to smaller vessels, resulting in new obstructions. Finally, a significant number of MTs were completely dissolved during the experiment.

Discussion

The results show that the novel therapeutic approach leads to a significant and enhanced reduction of the thrombus burden. This is remarkable as the total dose of infused alteplase was 60x lower than the recommended dose for intravenous drug infusion [3].

Images (Optional)



Microfluidic chip with infused microthrombi (black) causing local occlusions

References (Optional)

[1] De Waha *et al.*, Eurp Heart J, 2017
[2] Rösch *et al.*, Bioend & Transl Med, 2024
[3] Milusev *et al.*, Sci Rep, 2025

Acknowledgements (Optional)

This study was financed through the grants 25390.2PFLS-LS, 31010.1IP-LS, and 104.947 IP-LS from the Innosuisse – Schweizerische Agentur für Innovationsförderung.

Session Category

Cardiovascular/Cardiorespiratory Biomechanics: Methods, Models and Applications

OA158-02

Evaluating Posterior Boundary Conditions in Patient-Specific Finite Element Models of the Optic Nerve Head

Ms. Patricia M. Sabin MS[1], Dr. Brandon K. Zimmerman PhD[1], Ms. Kelly A. Clingo BS[1], Dr. Cameron A. Czerpak PhD[1], Dr. Manuel Lucas Sampaio de Oliveira PhD[1], Dr. Harry A. Quigley MD[2], Dr. Thao D. Nguyen PhD[1,2]

[1]Johns Hopkins University, Baltimore, MD, United States. [2]Johns Hopkins School of Medicine, Baltimore, MD, United States

Introduction

Eye-specific modeling of optic nerve head (ONH) biomechanics is important for understanding individualized glaucoma risk factors. A major limitation is the inability to directly measure the retrolaminar tissue pressure (RTP) acting on the posterior boundaries of the ONH. Recently, we employed digital volume correlation (DVC) of optical coherence tomography (OCT) to map the ONH deformation response in patients with normal pressure hydrocephalus (NPH) undergoing extended cerebrospinal fluid (CSF) drainage [1]. Intraocular pressure (IOP) and CSF pressure (CSFP) were measured before and after treatment. We seek to apply this unique dataset to assess approaches for using CSFP to model RTP boundary conditions.

Methods

Three eyes from 3 NPH patients (45-81 years) were imaged by spectral domain OCT. The retina, choroid, sclera, and lamina cribrosa (LC) were segmented using an automated algorithm and reviewed by a trained observer. Parameterized posterior shells with optic nerve and sheath were generated, and segmented volumes were converted into eye-specific ONH geometries and embedded within the shells. For each eye, we investigated three models for applying CSFP to the posterior tissues (Fig. 1) to evaluate the sensitivity of the deformation field to the posterior boundary conditions. A 12.3 mmHg CSFP decrease and 2 mmHg IOP increase were assumed for all eyes to compare the effect of geometry across models. Material properties were chosen from the literature.

Results

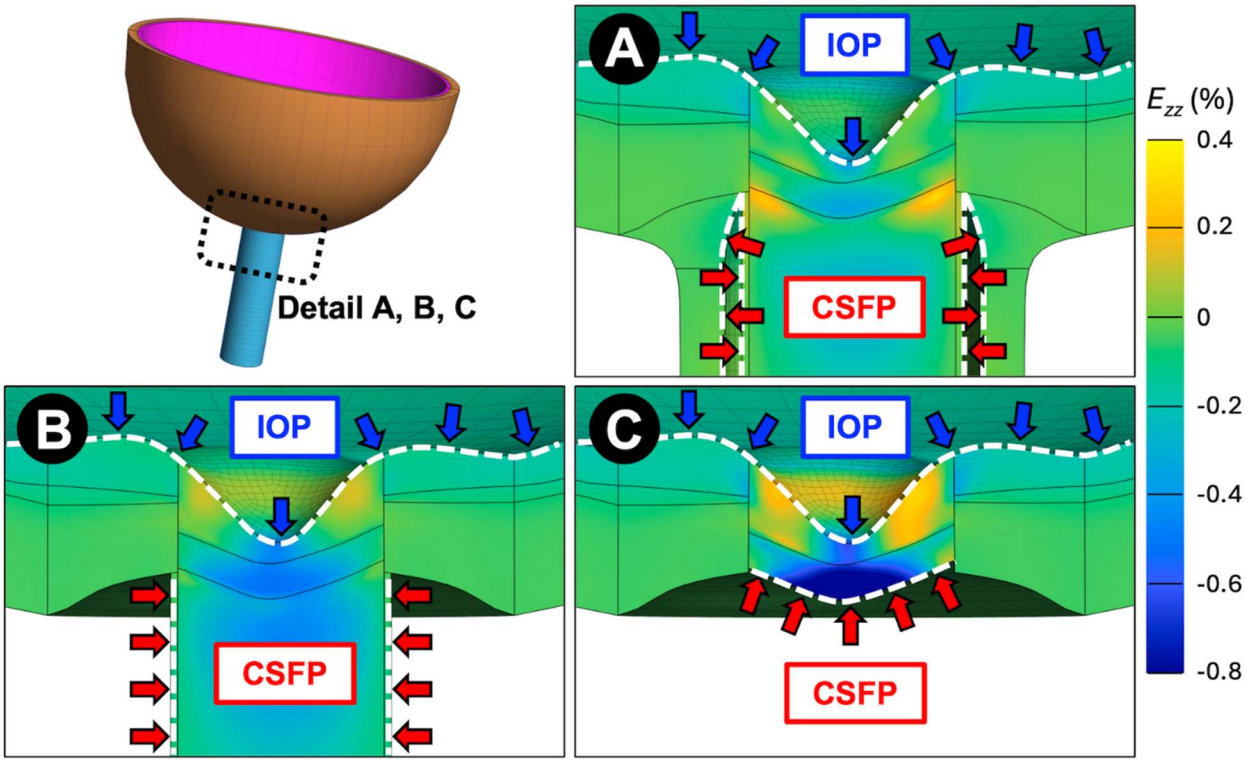
Applying CSFP in the subarachnoid space (Fig. 1A) produced less compressive LC axial strain (E_{zz} = -0.10 ± 0.01%) and smaller maximum principal strain (E_{max} = 0.28 ± 0.03%) than applying only on the pia mater (Fig. 1B; E_{zz} = -0.23 ± 0.04%, E_{max} = 0.30 ± 0.03%). Strains

from applying CSFP directly on the LC were varied (Fig. 1C; E_{zz} = -0.11 ± 0.21%, E_{max} = 0.60 ± 0.15%).

Discussion

Preliminary results indicate that LC strain predictions are sensitive to CSFP loading configuration, and incorporating the full optic nerve sheath may be important for modeling despite added computational cost. Future work will extend the dataset to 7 eyes and leverage known IOP/CSFP changes and DVC-derived strain fields to further evaluate posterior boundary conditions and refine ONH material properties.

Images (Optional)



References (Optional)

[1] KA Clingo *et al.*, J Biomech Eng, 2025

Acknowledgements (Optional)

NIH NEI R01 036042 (Dr. Thao D. Nguyen); NIH NEI R01 02120 (Dr. Harry A. Quigley)

Session Category

Organ and Tissue Biomechanics: N/A

OA158-03

Mechanical Softening of the Lamina Cribrosa Drives a Pro-Inflammatory Astrocyte Activation and Retinal Ganglion Cells Loss in a Rat Model of Chronic High Intraocular Pressure

Prof Xiuqing QIAN[1,2], Ms Yuqing WANG[1], Ms Jingxi ZHANG[3], Ms Zihan XI[1], Ms Dong MA[1], Ms Xinmiao HAN[1]

[1]Capital Medical University, Beijing, Beijing, China. [2]Beijing Key Laboratory of Intelligent Diagnosis Technology and Equipment for Optic Nerve-Related Eye Diseases, Beijing, Beijing, China. [3]Beijing Friendship Hospital, Beijing, Beijing, China

Prof Xiuqing QIAN

Introduction

In glaucoma, microstructure and mechanical properties alterations in the lamina cribrosa (LC) are primary drivers of optic neuropathy. However, the precise cascade linking altered tissue mechanics in the LC to astrocyte activation and subsequent retinal ganglion cells (RGC) loss remains incompletely defined. This study aims to investigate the relationship between biomechanical changes in the LC, activation of LC astrocytes, and structural/functional damage to the optic nerve.

Methods

A rat model with chronic high intraocular pressure (IOP) was established, maintaining high IOP for1, 4, 8weeks(n=6). We used a method combining atomic force microscopy (AFM) with image processing to segment and determine the mechanical properties of the LC and optic nerve. Optic nerve injury was comprehensively assessed via in vivo optical coherence tomography (OCT), axonal staining, immunofluorescence staining for RGCs, and rhodamine-based axonal transport assays. The activation of LC astrocytes was evaluated by detecting glial fibrillary acidic protein (GFAP) via immunofluorescence and its corresponding mRNA expression levels via qPCR. Expression of key inflammatory factors was quantified by qPCR, and their causal role in RGC injury was investigated.

Results

With duration of elevated IOP, the elastic modulus of the LC and optic nerve significantly decreased, indicating tissue softening. This mechanical degradation coincided with severe

structural and functional impairments: OCT revealed retinal nerve fiber layer thinning, axonal staining showed profound disorganization and loss, and axonal transport was significantly blocked. Immunofluorescence and qPCR confirmed activation of astrocytes, evidenced by upregulated GFAP. Crucially, this activation was coupled with marked upregulation of neuroinflammatory factors (IL-1α, TNF-α, C1q), whose presence was spatiotemporally associated with significant RGC apoptosis.

Discussion

Chronic high IOP causes LC softening and reduced load-bearing capacity. This altered mechanical microenvironment effectively triggers astrocyte activation, leading to a destructive neuroinflammatory response characterized by release of IL-1α, TNF-α, and C1q. This study reveals that LC astrocytes-driven neuroinflammation constitutes a critical intermediary step in the glaucomatous pathology, acting to amplify RGC damage after the initial biomechanical injury. Therefore, modulating the mechano-inflammatory axis linking tissue softening and astrocyte activation represents a potential strategy for mitigating secondary neurodegeneration.

References (Optional)

[1]Liu Liu *et al.*,J Mech Behav Biomed Mater. 2022

Acknowledgements (Optional)

The authors would like to thank financial supports from the National Natural Science Foundation of China (project no. 12472309)

Session Category

Organ and Tissue Biomechanics: N/A

OA158-04

Scleral Collagen Uncrimping Amplifies Nuclear Strain Relative to Fiber Strain

Dr. Xuehuan He[1], Mr. Qi Tian[1,2], Ms. Hannah Schilpp[1], Ms. Annika Oberdorfer[1,2], Dr. Xinyue Wang[1], Dr. Po-Yi Lee[1,3], Ms. Yingzhe Han[1,2], Dr. Yuankai Lu[1], Dr. Ian A. Sigal[1,2]

[1]Ophthalmology, University of Pittsburgh, Pittsburgh, Pennsylvania, United States. [2]Bioengineering, University of Pittsburgh, Pittsburgh, Pennsylvania, United States. [3]Massachusetts General Hospital WellmanCenter for Photomedicine, Boston, Massachusetts, United States

Introduction

Tissue mechanical behavior varies across scales. To understand how cells (predominantly fibroblasts) respond and drive scleral remodeling under abnormal intraocular pressure (IOP), it is important to examine mechanics not only at the tissue level but also at the collagen fiber and nuclear levels. Collagen fiber uncrimping and recruitment are established drivers of nonlinear tissue mechanics, but their effects at these smaller structural levels remain unclear. We quantified tissue, fiber, and nuclear strains under biaxial loading to determine how uncrimping and recruitment influence nuclear deformation within the scleral microenvironment.

Methods

Coronal sections (16 μm) from six sheep optic nerve heads were mounted on a custom biaxial stretcher and imaged at each stretch step with instant polarized light microscopy for collagen orientation and DAPI fluorescence for nuclei (Fig. 1A–B). Using previously reported methods we measured collagen fiber bundle length and waviness [1]. From these, we determined % fiber recruitment, and the stretch step corresponding to normal IOP (earliest step with 60% or higher fiber recruitment) (Fig. 1B). Nuclei were segmented and tracked using Cellpose [2]. Three measures of strain were computed at the final stretching step: local tissue strain (fiber bundle length changes), true fiber strain (post recruitment strain of the same bundle), and nuclear strain (nuclear major axis length changes). Each measure was calculated relative to both Step 0 and Normal IOP (Fig. 1C). We used the Wilcoxon signed rank test to compare tissue and fiber strains, and the Wilcoxon rank sum test to compare fiber and nuclear strains.

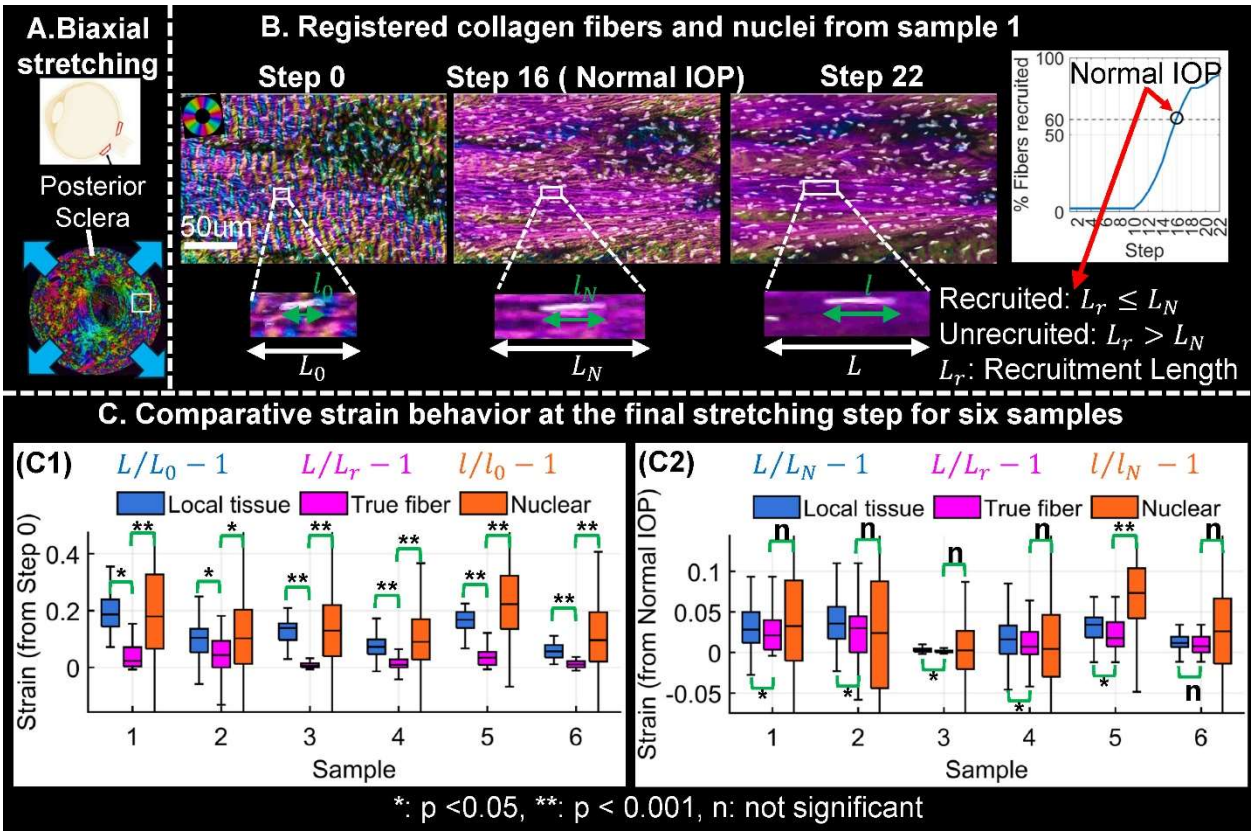
Results

Using Step 0 as reference, tissue and nuclear strains exceeded fiber strain in all samples (Fig. 1C1). When Normal IOP was used as reference, a configuration in which 60% or more fibers are already recruited, nuclear and fiber strains did not differ significantly in five samples (Fig. 1C2).

Discussion

These results suggest that nuclear strain amplification arises during collagen uncrimping at lower IOP and disappears after fiber recruitment. Thus, fiber recruitment emerges as a key regulator of the nuclear mechanical environment, with implications for scleral remodeling and glaucoma progression.

Images (Optional)



References (Optional)

[1] Lee P-Y et al., Acta Biomater., 2024.

[2] Pachitariu M et al., bioRxiv, 2025.

Acknowledgements (Optional)

This work was funded by NIH R01-EY023966, P30-EY008098 and T32-EY017271 (Bethesda, MD), Research to Prevent Blindness (unrestricted grant to UPMC ophthalmology, and Stein innovation award to Sigal IA) and BrightFocus Foundation.

Session Category

Organ and Tissue Biomechanics: N/A

OA159-03

Early Post-Injury Gait Deviations Predict Long-Term Hindlimb Kinematic Impairment After Medial Meniscal Transection in Rats

Dr. Seyed Mohammadali Rahmati PhD[1], Dr. Jarred M. Kaiser PhD[2,3], N/A Morgan Daly BS[4], N/A Kaylee Lowe BS[4], N/A Austin Moyer BS[4], Dr. Liang-Ching Tsai PhD[4], Dr. Young-Hui Chang PhD[1]

[1]Georgia Institute of Technology, Atlanta, Georgia, United States. [2]Emory University, Decatur, Georgia, United States. [3]Atlanta VA Medical Center, Decatur, Georgia, United States. [4]Georgia State University, Atlanta, Georgia, United States

Introduction

Altered knee biomechanics after injury increase osteoarthritis (OA) risk, suggesting that gait deviations may reflect pathways to degeneration and provide prognostic information. The ability to predict late-stage gait deviations based on early post-injury changes may enable targeted interventions to reduce long-term impairments. To characterize the temporal relationships among gait deviations, we quantified bilateral 3D joint angles in rats with medial meniscal transection (MMT) at Pre-surgery and at 2-, 4-, 6-, and 8-weeks (W) post-surgery. The MMT model induces detectable early-stage OA by 3W post-injury and progresses to moderate-to-late-stage OA by 8W. We hypothesized early kinematic changes predict 8W deviations, with differing strengths among stages. We also hypothesized a nonlinear recurrent neural network (RNN) would enable earlier and more accurate predictions than linear regression.

Methods

Thirty-one rats underwent MMT of the left hindlimb, with 26 used to train linear regression and RNN models and 5 held out for RNN evaluation. Biplanar X-ray fluoroscopy was processed with deep-learning key point detection and singular-value-decomposition–based bone registration to reconstruct joint kinematics (Figs. 1(a),(b)). Linear regression and the RNN used identical inputs and outputs, mapping Δ2W-Pre, Δ4W–Pre, or Δ6W-Pre joint-angle deviations to Δ8W-Pre.

Results

Experimental joint kinematics diverged markedly from Pre-surgery patterns at 2W, showed partial recovery at 4W, and diverged again at 6W. By 8W, deviations were pronounced and similar across rats, reflecting a characteristic OA gait. Consistent with the first hypothesis, the predictive strength of early post-surgery deviations for 8W gait deviations varied across stages. For linear regression, 6W inputs produced the strongest correlations with 8W

outcomes (Fig. 1(c)), whereas the RNN achieved lowest errors with 4W inputs (Figs. 1(d),(e)).

Discussion

Our data reveals that the non-linear structure of RNN can predict moderate-to-late stage OA gait by 4W post-injury in the MMT model, which is earlier than linear regression that was most predictive at 6W. Our preclinical approach enabled a repeatable model for measuring gait progression during post-traumatic OA in a controlled, accelerated timeline, but suggests that a similar approach could be adapted to provide early clinical prognosis to enable effective management through rehabilitation.

Images (Optional)

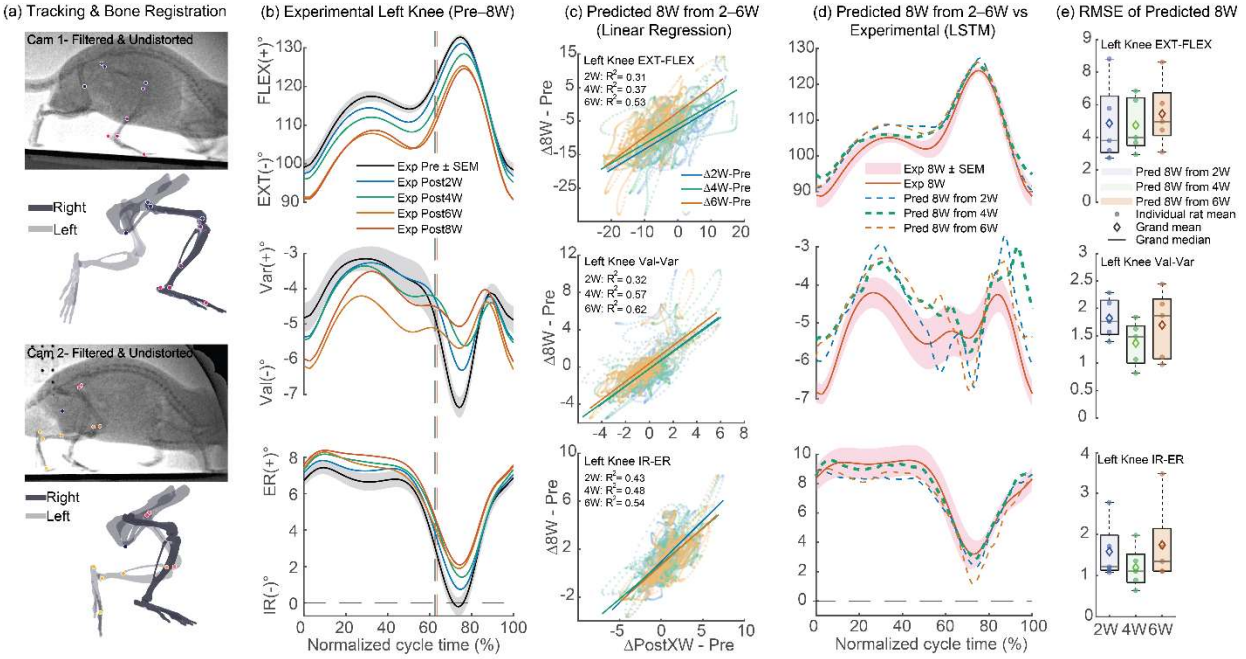


Figure 1. Experimental and predicted hindlimb kinematics following medial meniscal transection. (a) Biplanar X-ray fluoroscopy and model-based tracking pipeline using deep-learning keypoints and extended SVD registration for 3D joint reconstruction. (b) Experimental left knee extension-flexion (EXT-FLEX), valgus-varus (Val-Var), and internal-external rotation (IR-ER) at Pre, 2W, 4W, 6W, and 8W (mean ± SEM) for 26 training rats. (c) Predicted Δ8W-Pre using linear regression with Δ2W-Pre, Δ4W-Pre, and Δ6W-Pre as inputs for 26 training rats. (d) Predicted 8W trajectories from the LSTM model using 2W, 4W, and 6W deviations as inputs, compared with experimental 8W for 5 evaluation rats. (e) RMSE for predicted 8W left-knee angles across evaluation rats.

References (Optional)

Acknowledgements (Optional)

This research was supported by the National Institutes of Health, National Institute of Arthritis and Musculoskeletal and Skin Diseases (NIH R01 AR080154).

Session Category

Musculoskeletal Biomechanics: Joints and Motion

OA159-04

Kneeformatics: Deriving Knee-Specific Motion Signature from Static Medical Imaging

Dr. Ahmet Erdemir PhD, Ms. Snehal Chokhandre MS

Cleveland Clinic Research, Cleveland, Ohio, United States

Introduction

Knee injuries and disorders are significant burdens on quality of life. Since each knee has unique mechanics that affect mobility, pathology and recovery, it is imperative that individualized movement patterns of the knee are taken into consideration for diagnosis, risk assessment, and planning of interventions. However, determination of movement metrics is mostly a research endeavor that requires sophisticated biomechanical experimentation or physics-based computational modeling that are neither comprehensive nor clinically proven. Recently, we have developed Kneeformatics to deliver knee-specific movement qualities directly by processing static clinical imaging data such as MRI or CT [1]. In this study, we will demonstrate how we use Kneeformatics to determine the knee-specific motion signature.

Methods

Kneeformatics leverages bone, cartilage and meniscus geometries obtained from clinical imaging. A combinatorial contact location sampling pairs points on medial and lateral articulations of tibia against those of the femur. For each point set, optimization aligns contact locations to calculate tibiofemoral translations and rotations. Resulting kinematic configurations are further reduced by removing poses with non-physiological penetration of articulating surfaces (including menisci). Bone quality is also mapped on each point on the articular surfaces by determining the average of image intensity across a kernel volume attached to the articular surface point and oriented towards the subchondral region. High bone quality regions are indicators of frequent and high mechanical loading and thus their alignment across opposing articular contact surfaces denote frequented joint kinematic configurations where joint loads are transmitted, i.e., motion signature.

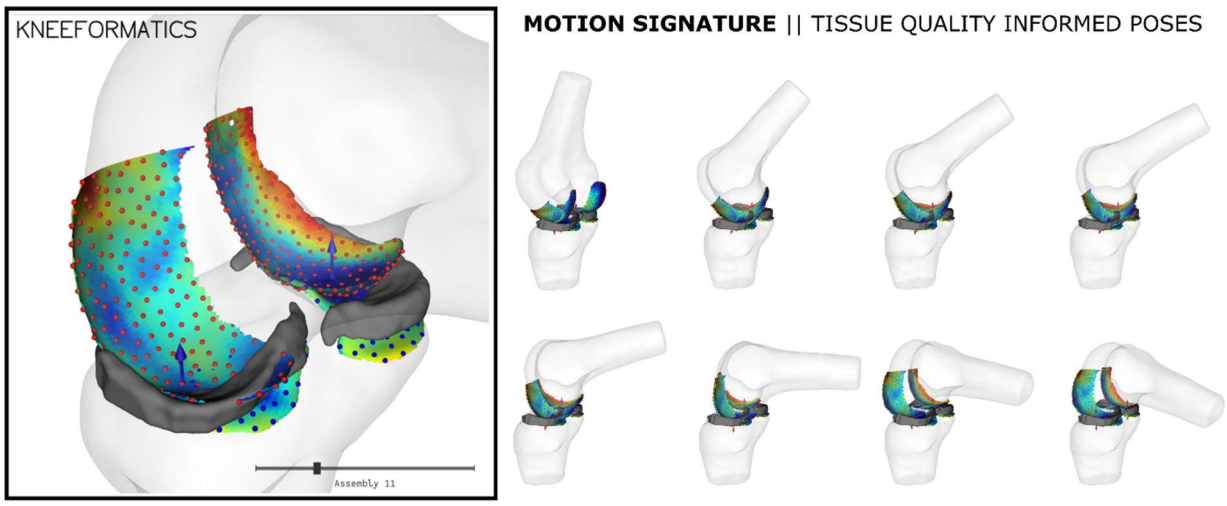
Results

Determination of motion signature was demonstrated by using data from Open Knee(s) [2]. A sample set of poses are shown for oks003, that were determined by filtering and ranking poses that align high intensity locations of femoral and tibial contact (e.g., blue areas).

Discussion

Knee-specific motion signature can be useful for individualized assessment of injury risk or disease progression. It can support personalization of implant surgery and rehabilitation. This advancement provides a pathway for comprehensive characterization of knee biomechanics compatible with existing clinical workflows where imaging is readily collected.

Images (Optional)



References (Optional)

[1] Erdemir et al., USPTO, Pub. No. US 2024/0090825 A1.

[2] Chokhandre et al., Ann Biomed Eng, 2023.

Acknowledgements (Optional)

Kneeformatics, Cleveland Clinic, Lerner Research Institute, Spark Program.

Session Category

Musculoskeletal Biomechanics: Joints and Motion

OA160-02

Adaptation to Repeated Slip-Like and Trip-Like Perturbations During Walking in Older Adults With Mild Cognitive Impairment

Ms. Jessica Pitts, Dr. Tanvi Bhatt

University of Illinois at Chicago, Chicago, IL, United States

Introduction

Older adults with mild cognitive impairment (OAwMCI) show impaired reactive balance control and 2x higher fall risk compared to cognitively intact older adults (CIOA). In CIOA, repeated perturbation exposure induces rapid, trial-by-trial motor adaptations that improve reactive balance responses. However, it is unknown if OAwMCI can acquire similar adaptations due to pathological deficits in sensorimotor integration/motor learning. Therefore, this study examined trial-by-trial adaptations to slip-like and trip-like perturbations in OAwMCI vs. CIOA.

Methods

25 OAwMCI (Montreal Cognitive Assessment (MoCA): 18-25) and 25 CIOA (MoCA: 26-30) experienced 8 slip-like (S1-8) and 8 trip-like perturbations (T1-8) during treadmill walking. Slips and trips were induced by sudden belt deceleration (-6 m/s^2) or acceleration (5 m/s^2) to induce a backward or forward loss of balance (respectively). An overhead load cell detected falls (>30% body weight), and 2x8 GLMs examined the effects of group (OAwMCI, CIOA) and trial (1-8) on fall rate. Similar 2x8 ANOVAs assessed margin of stability (MOS), recovery step length, hip height, and trunk angle at first and second recovery touchdowns (TD1, TD2).

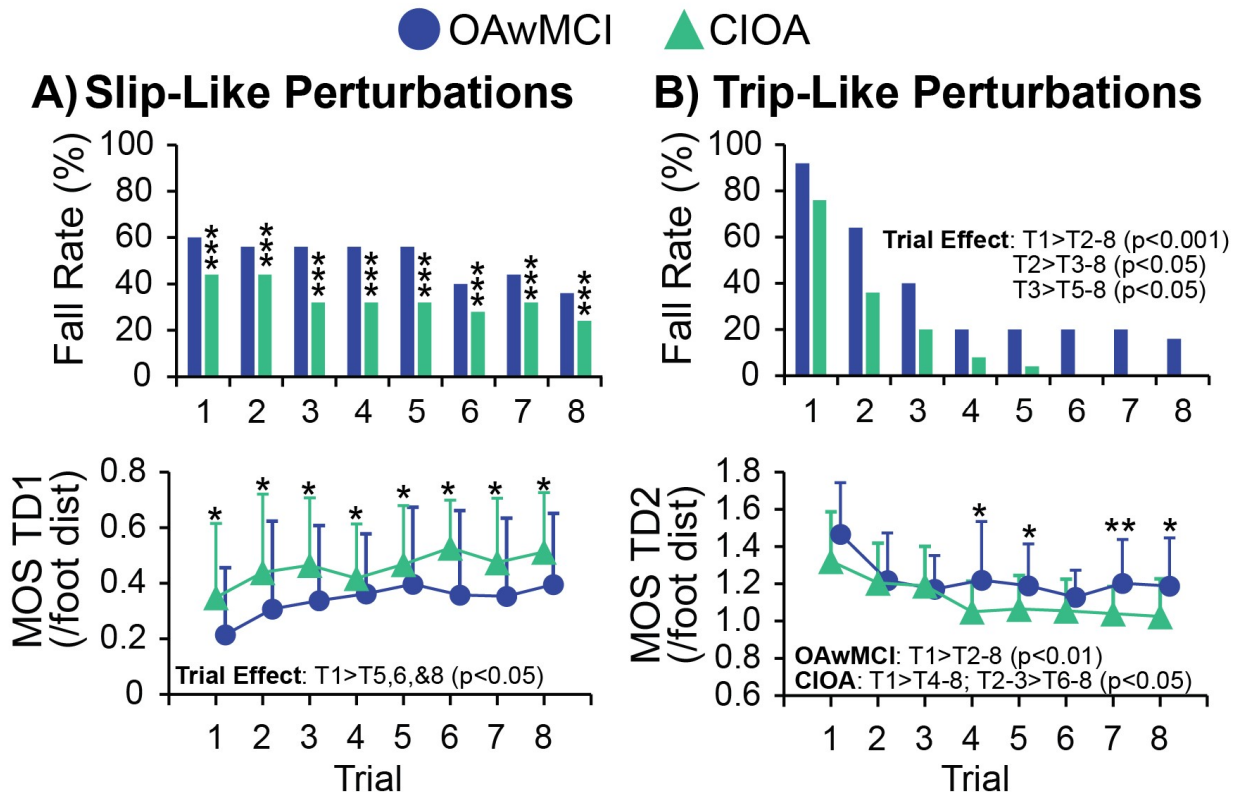
Results

For slips, fall rate was higher in OAwMCI vs. CIOA ($p<0.001$), although did not significantly change across trials ($p>0.05$). MOS at TD1 was more stable on S5-8 vs. S1 in both groups ($p<0.05$), although lower overall in OAwMCI ($p=0.018$). Step length at TD1 was longer in both groups on S5-6 vs. S1 ($p<0.05$). For trips, fall rate showed no group differences, although decreased significantly across T1-5 ($p<0.001$). MOS at TD2, step length at TD1, and trunk angle at TD2 had significant group*trial interactions ($p<0.05$), with CIOA showing greater improvements than OAwMCI (improved stability, longer step length, less trunk flexion).

Discussion

Both groups acquired adaptive improvements which improved reactive COM stability and/or reduced fall rate, including longer recovery step length (backward for slips, forward for trips) and decreased trunk flexion (for trips). However, OAwMCI improved less than CIOA and could not reach the same performance level, which could be attributed to issues updating/accessing the internal model (plans for future responses based on prior sensorimotor feedback). Thus, reactive balance training for OAwMCI may benefit from tailored dosages/adjunct approaches.

Images (Optional)



Session Category

Human Motion and Performance: Balance, Posture and Control

OA160-03

Older Adults Demonstrate Altered Biomechanical Control of Their Lateral Center of Mass Trajectory in Response to Weighted Vest Walking

Ms. Nancy Nguyen[1], Dr. Carrie Earthman[1], Dr. Jocelyn Hafer[1], Dr. John Jeka[1], Dr. Noah Rosenblatt[2], Dr. Jeremy Crenshaw[1]

[1]University of Delaware, Newark, DE, United States. [2]Rosalind Franklin University of Medicine and Science, North Chicago, IL, United States

Introduction

Individuals with obesity have altered frontal-plane gait mechanics and impaired walking balance. We have developed methods to quantify how lead- and trail-limb mechanics contribute to the changes in the lateral center of mass (COM) velocity during gait. In our previous cross-sectional study, increased body size was associated with increased trail-limb contributions. It is unknown if this relationship was due to greater non-muscular mass or other concomitant factors associated with obesity. The purpose of this study was to determine the effects of added mass alone on lead- and trail-limb contributions to lateral COM motion.

Methods

Fifteen adults with healthy-weight (8F/7M; Age: 63.6 (3.1) years; BMI: 23.4 (2.3) kg/m^2) walked on an instrumented treadmill (speed=1.12 (0.3) m/s) with and without a weighted vest (15% body weight) at the same speed in each condition. The weighted vest was placed around the torso, with mediolateral symmetry prioritized as weight was added. We implemented a novel, force-plate-only approach to calculate lead- and trail-limb contributions to the lateral COM acceleration, based on the vertical projection of the COM and center of pressure (COP) positions and the vertical ground reaction force (GRF) (see Figure 1). To account for gait phase duration, acceleration curves were integrated over time to estimate a change in velocity for each limb contribution phase. Between-condition comparisons of these contributions were assessed with paired t-tests.

Results

Compared with unweighted walking, during weighted walking participants increased trail-limb contributions ($p=0.04$, $d=0.57$, Figure 1) by increasing relative GRF ($p<0.01$, $d=1.01$) and prolonging double support time ($p<0.001$, $d=1.12$). Additionally, participants decreased lead-limb contributions ($p=0.001$, $d=-1.07$, Figure 1) due to smaller relative GRF ($p=0.04$, $d=-0.59$) and smaller lateral distance between the COM and COP ($p=0.001$, $d=-1.04$).

Discussion

During weighted walking, individuals demonstrated altered biomechanical control of their lateral COM trajectory. The results for trail-limb contributions align with what we observed in our cross-sectional study of those with and without obesity. However, in our cross-sectional study, we observed no relationship between lead-limb contributions and body size. Therefore, we cannot rule out the influence of concomitant factors associated with obesity such as thigh circumference, musculoskeletal diseases, or proprioception deficits on lead-limb mechanics.

Images (Optional)

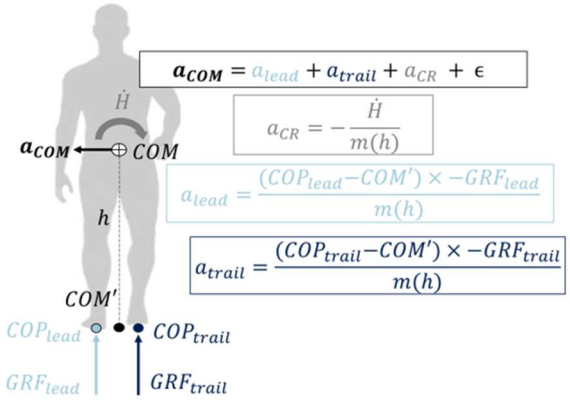
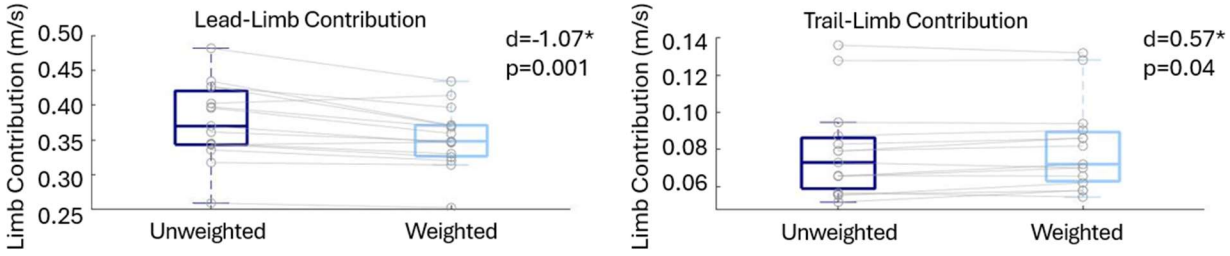


Figure 1. Representation of limb contributions to center of mass acceleration. Limb- and phase-specific contributions to lateral COM trajectory was assessed through lead- (light blue) and trail- (dark blue) limb contributions to mediolateral (ML) center of mass acceleration (a_{COM}), based on center of pressure location ($COP_{lead/trail}$), mediolateral COM position (COM'), vertical ground reaction force ($GRF_{lead/trail}$), body mass (m), and COM height (h). All measures were derived from force-plate recordings.



Session Category

Human Motion and Performance: Balance, Posture and Control

OA160-04

Not All Movements Are Equal: Balance Recovery Across Daily Movements in Older Adults

Ms Nikita Sharma MSc Biomedical Engineer[1], Dr. Marko Ackermann[2], Prof. Dr. Simon Steib[1], Dr. Lizeth H. Sloot[3]

[1]University of Heidelberg, Heidelberg, Baden-Württemberg, Germany. [2]Karlsruhe Institute of Technology, Karlsruhe, Baden-Württemberg, Germany. [3]Newcastle University, Newcastle, North East England, United Kingdom

Introduction

Older adults fall during different daily movements [1]. These movements impose different balance challenges – e.g. turning requires more lateral than forward control in walking, potentially affecting someone's ability to recover balance after a destabilizing perturbation. However, balance is mostly assessed during steady-state walking, and not at someone's maximum recovery ability. This study evaluated whether an individual's maximum balance recovery ability depends on movements and age.

Methods

Twenty non-frail (72±5 yrs), 15 pre-frail (84±5 yrs; basis fried frailty scale, [2]) older and 23 younger adults (25±3yrs) underwent unexpected treadmill belt accelerations of increasing magnitude (until >3 recovery steps or stop requested) during standing, walking, in-place turning, and bending forward. An IMU suit recorded full-body kinematics. Balance recovery was quantified as the peak centre of mass velocity excursion during the highest magnitude perturbation window and compared between movements (relative within the group) using Spearman's rank-order correlations, which were compared between groups using Fisher's r-to-z transformation.

Results

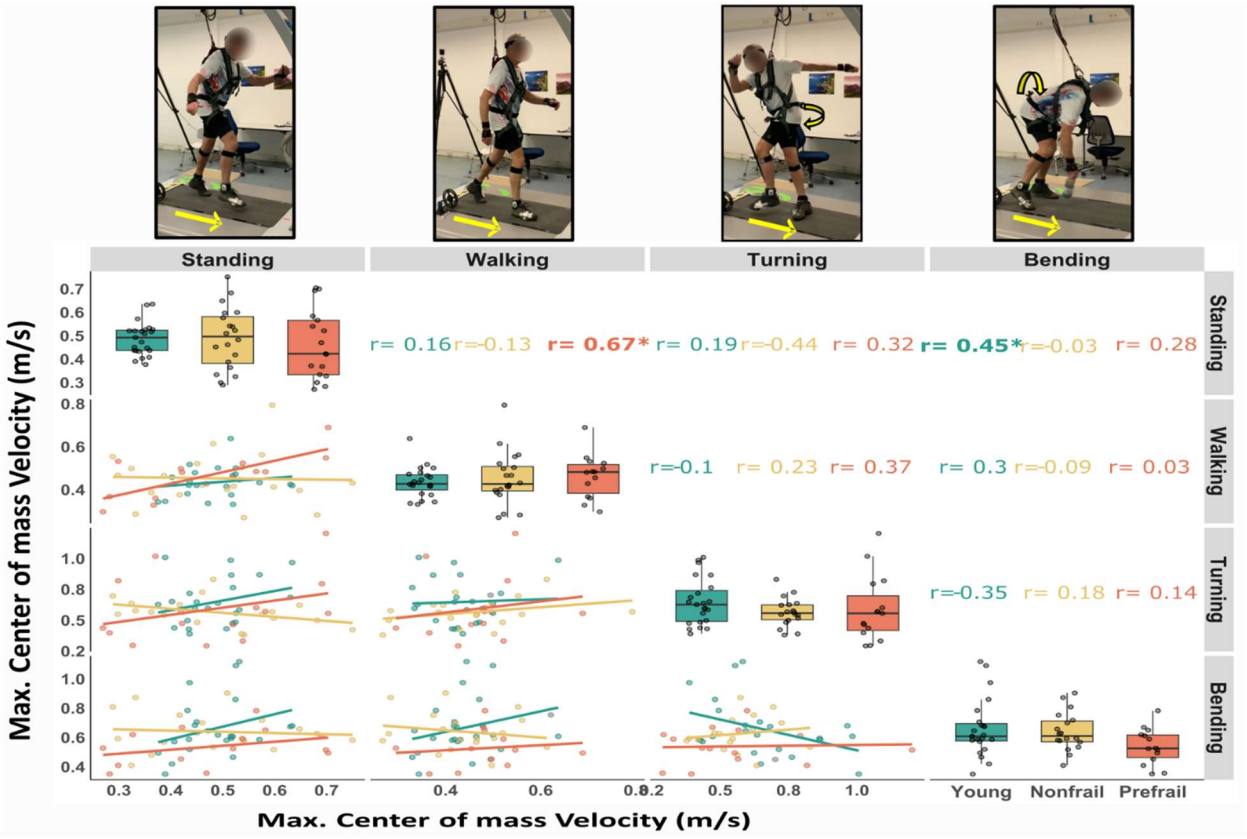
As expected, pre frail reached lower magnitudes for each movement compared to non-frail ($p_{friedman}<0.0001$) and young ($p_{friedman}<0.0001$), but still had comparable COMvel excursions ($p_{Kruskal\text{-}Wallis} \geq 0.1$). Individual balance recovery ability was not correlated between movements (each group, all movements: $r<0.5$, $p>0.5$; Fig 1), except turning and bending ($r=0.45$, $p<0.05$) in young and standing versus walking ($r=0.67$, $p\leq0.01$) in the pre-frail. This correlation did not differ between groups except for a stronger standing-walking

association in prefrail adults versus young (z=2.12, p<0.05) and non-frail (z=2.19, p<0.05) adults.

Discussion

Our unique approach exploring balance recovery at an individual's limit and across daily movements revealed that balance recovery is movement-specific, with balance issues in one movement (eg. walking) not predicting issues in another (eg. turning). We found movement-specificity for both young and older adults, although we didn't measure frail older adults. Next, we will analyse balance recovery strategies underlying these differences between movements using angular momentum. These results indicate we need to rethink our focus on balance recovery during gait and tailor balance training to an individual's movement-specific balance deficits.

Images (Optional)



References (Optional)

[1] Robinovitch et al., The Lancet,2013
[2] Fried et al., J Gerontol A Biol Sci Med Sci, 2001

Session Category

Human Motion and Performance: Balance, Posture and Control

OA160-05

Advanced Age Alters Joint-Level Planning for and Response to Walking Perturbations

Dr. Emily Eichenlaub[1], Dr. Jessica Allen PhD[2], Dr. Vicki Mercer PT, PhD[3], Dr. Jeremy Crenshaw PhD[4], Dr. Jason Franz PhD[1]

[1]University of North Carolina at Chapel Hill and North Carolina State University, Chapel Hill, NC, United States. [2]University of Florida, Gainesville, FL, United States. [3]University of North Carolina Chapel Hill, Chapel Hill, NC, United States. [4]University of Delawar, Newark, DE, United States

Introduction

When preparing for and responding to a walking balance challenge, lower extremity joint moments are used to regulate angular momentum to mitigate instability and prevent a fall [1]. Age-related deficits in motor planning and execution may elicit altered joint angular impulse control strategies to mitigate that instability, potentially increasing the risk of falling. Compounded by diminished muscle strength and power, we would further suspect that these age-related differences are disproportionately larger following unanticipated perturbations. This study investigated age- and anticipation-related differences in lower extremity joint-level proactive and reactive balance strategies via joint angular impulses. We hypothesized that older adults would exhibit greater reactive responses to balance challenges than younger adults, particularly when unanticipated.

Methods

15 younger adults (10F; age: 22.3±3.3 years; walking speed: 1.41±0.14 m/s) and 15 older adults (9F; age: 73.6±5.5 years; walking speed: 1.28±0.20 m/s) responded to treadmill belt perturbations delivered at the instant of heel-strike in which the belt accelerated or decelerated over 200 ms at 6 m/s^2 delivered either unexpectedly (i.e., unanticipated) or at the end of a 3-s verbal countdown (i.e., anticipated) in a randomized order. We calculated hip, knee, and ankle joint angular impulses during the preceding, perturbed, and recovery strides and compared between groups, focusing here on age × anticipation interaction effects.

Results

We found no age × anticipation interaction effects during the preceding stride for either perturbation direction (p-values>0.05). Compared to anticipated accelerations, unanticipated accelerations elicited larger (older adults) and smaller (younger adults) ankle dorsiflexion angular impulses during the perturbed stride (interaction, p=0.038) (**Fig. 1A**). Compared to anticipated decelerations, unanticipated decelerations elicited larger

(older adults) and smaller (younger adults) knee extension angular impulses during the recovery stride (interaction, $p<0.001$) (**Fig. 1B**).

Discussion

Anticipation-related difference in proactive lower-extremity angular impulses did not differ with age. The same is not true for reactive responses, which are fundamentally altered compared to younger adults. These findings elucidate aging effects on dynamic strategies to plan for and respond to walking balance challenges, which may inform roadmaps for prioritizing targeted interventions to decrease older adults' risk of falling.

Images (Optional)

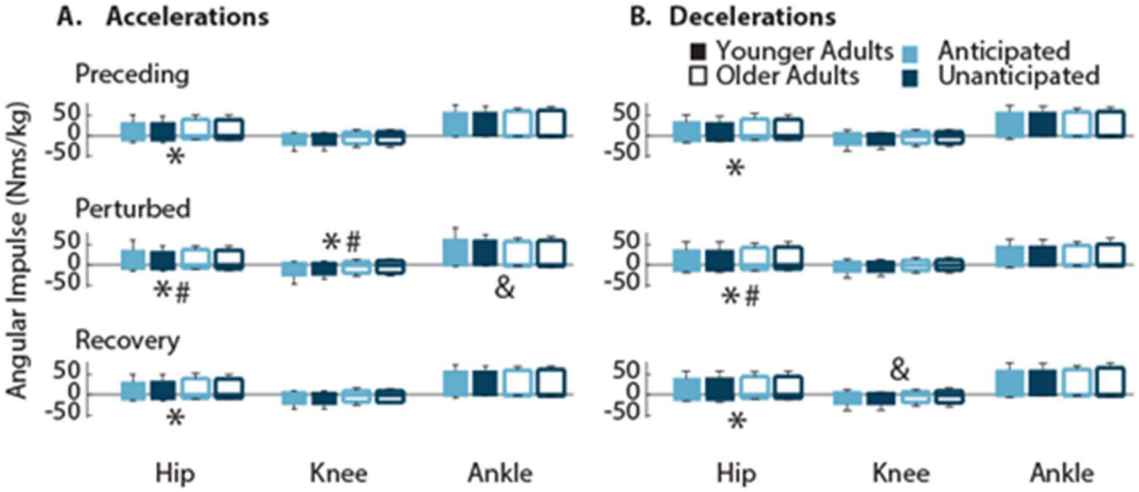


Figure 1. Hip, knee, and ankle joint angular impulses for (A) accelerations and (B) decelerations during the preceding, perturbed, and recovery strides. Statistical significance is denoted by * (age effects), # (anticipation effects), and & (age × anticipation) interaction effects.

References (Optional)

[1] Mathiyakom et al., JRRD, 2008

Acknowledgements (Optional)

Supported by the National Institutes of Health (F31AG084241).

Session Category

Human Motion and Performance: Balance, Posture and Control

OA161-02

Dynamic Compression Moderates Rate Dependent Tensile Mechanics in the Annulus Fibrosus

Mr Craig Almeida, Dr. Jill Middendorf, Ms Victoria Allen, Mr Shunyu Tan

Johns Hopkins University, Baltimore, MD, United States

Introduction

The annulus fibrosus (AF) experiences multiaxial loading. Thus, constitutive models that accurately predict multiaxial mechanics are important for understanding disc degeneration. Prior biaxial experiments showed that constant high-magnitude axial compression alters AF tensile mechanics, but AF mechanics under a more physiological dynamic low-magnitude compression with simultaneous tension remain unknown[1]. This loading is clinically relevant, especially as degeneration shifts compressive load from the nucleus pulposus to the AF[2]. This study examines how increasing dynamic axial compression influences circumferential tensile mechanics in the AF and how this loading alters parameters from existing constitutive models.

Methods

Rectangular porcine AF samples were prepared (Fig.1a,N=3). Control data consisted of three uniaxial tensile tests in the circumferential direction at 0.02%/s, 0.01%/s, and 0.0067%/s up to 10% strain magnitude. Biaxial tests added simultaneous axial compression of 10%, 20%, or 30%. Compression was applied at 0.02%/s, while tensile rate was adjusted to match total loading time. Percent changes in toe modulus, linear modulus, and peak stress relative to the 0.02%/s uniaxial case quantified differences between uniaxial and biaxial loading. Material parameter differences were obtained by fitting all data to a fiber-matrix-interaction constitutive model[3].

Results

Reducing the tensile loading rate from 0.02%/s to 0.0067%/s reduced the toe modulus, linear modulus and peak stress across all samples (Fig1:b-d). During simultaneous biaxial loading, the percent decreases in tensile properties (toe modulus, linear modulus and peak stress were smaller than those observed under rate-controlled tension alone, indicating that a simultaneous axial compression reduces the influence of tensile loading rate (Fig1:b-d). Increasing compression further reduces this influence. Constitutive modelling revealed that parameters fit to rate-controlled data do not fit well to the biaxial data (Fig1:e-g).

Discussion

Unlike prior work showing reduced tensile stress under constant high compressive preload, the low-magnitude dynamic compression used here did not reduce tensile stress. Although the mechanism is unclear, the authors believe poro-viscoelastic effects to reduce the influence of tensile loading rate during simultaneous compression. However, uniaxial coefficients still failed to predict multiaxial behavior, underscoring the need for multiaxial experiments to improve AF mechanical models and enhance predictions of spinal degeneration.

Images (Optional)

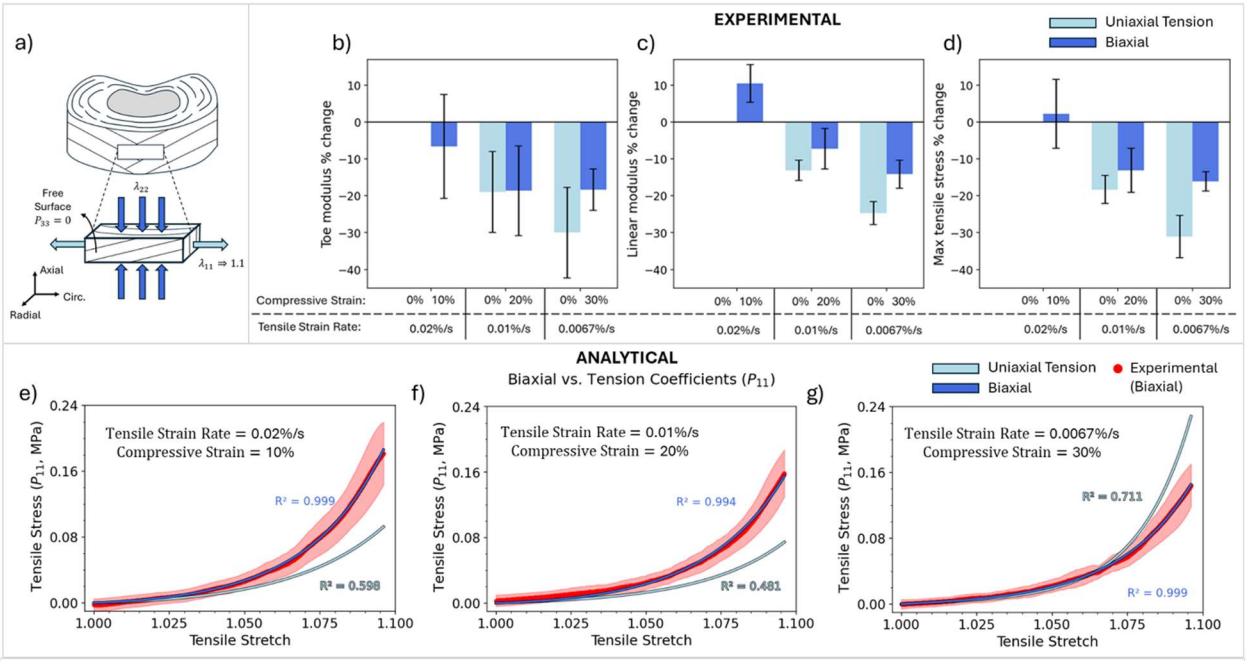


Fig.1: Schematic shows sample preparation and boundary conditions (a). Simultaneous compressive load reduces the influence of tensile strain rate on the tensile subfailure mechanics (b-d). Coefficients fit to biaxial experimental data fit well. However, those fit to the uniaxial tensile data do not fit well to the biaxial data (e-g).

References (Optional)

[1] Almeida,J.BMech.Eng.,2025; [2] Adams,JBJS,1994; [3] Nerurkar,J.BMMB,2011

Session Category

Musculoskeletal Biomechanics: Tissues

OA161-03

Quantitative Magnetic Resonance Imaging of Age-Related Adaptations to Glenoid Labrum Health

Ms. Colleen Vogel[1], Dr. Kwan-Jin Jung PhD[1], Ms. Denali Hutzelmann[1], Dr. Heath Henninger PhD[2], Dr. Caleb Cordes PhD[3], Dr. Matthew Hanks PhD[1], Dr. Joshua Leonardis PhD[3]

[1]University of Illinois at Urbana-Champaign, Urbana, IL, United States. [2]University of Utah, Salt Lake City, UT, United States. [3]The Ohio State University, Columbus, OH, United States

Introduction

The glenoid labrum is a fibrocartilaginous structure essential for shoulder stability, yet it is prone to degeneration and injury over the lifespan. Age-related collagen loss may influence labral integrity, but quantitative *in vivo* assessments remain limited. Ultrashort echo time magnetic resonance imaging (MRI) with magnetization transfer (UTE-MT) enables measurement of macromolecular fraction (MMF), a biomarker for collagen content [1], offering a novel approach to evaluate labral health. This study quantified the effects of age, sex, and arm dominance on glenoid labrum MMF using UTE-MT.

Methods

Forty-five healthy adults (25 females, 20 males; mean age 45.3 ± 16.9 years) underwent bilateral shoulder MRI on a 3T scanner using double echo steady state (DESS) and custom UTE-MT sequences. Labral segmentation was performed in 3D Slicer using DESS images, and voxel-wise MMF was computed in MATLAB from UTE-MT images (Figure 1A). Linear models tested the primary hypothesis that MMF decreases with age and differs by sex, and the secondary hypothesis that arm dominance affects MMF.

Results

Males exhibited significantly higher mean MMF than females (40.4 ± 7.3% vs. 39.6 ± 7.2%; $p = 0.031$) (Figure 1B). Age alone did not significantly impact MMF ($p = 0.759$), but a sex-by-age interaction was observed ($p = 0.033$), with males showing a steeper decline across the lifespan (Figure 1C). Dominant arms demonstrated greater MMF than non-dominant arms (41.1 ± 7.6% vs. 38.8 ± 6.9%; $p = 0.008$), independent of sex (Figure 1D).

Discussion

UTE-MT imaging revealed sex-specific and arm dominance-related differences in labral collagen content, with males exhibiting higher MMF and greater age-related decline. This

may be driven by known sex- and age-related differences in sex hormones like estrogen, which play important roles in musculoskeletal tissue health and integrity [2]. Dominant arms demonstrated greater MMF, perhaps reflecting an adaptive response to repetitive use. These findings highlight UTE-MT as a promising tool for the early detection of labral degeneration and for understanding normative and pathological adaptations across the lifespan, supporting its potential role in preventive care and the personalized management of shoulder health.

Images (Optional)

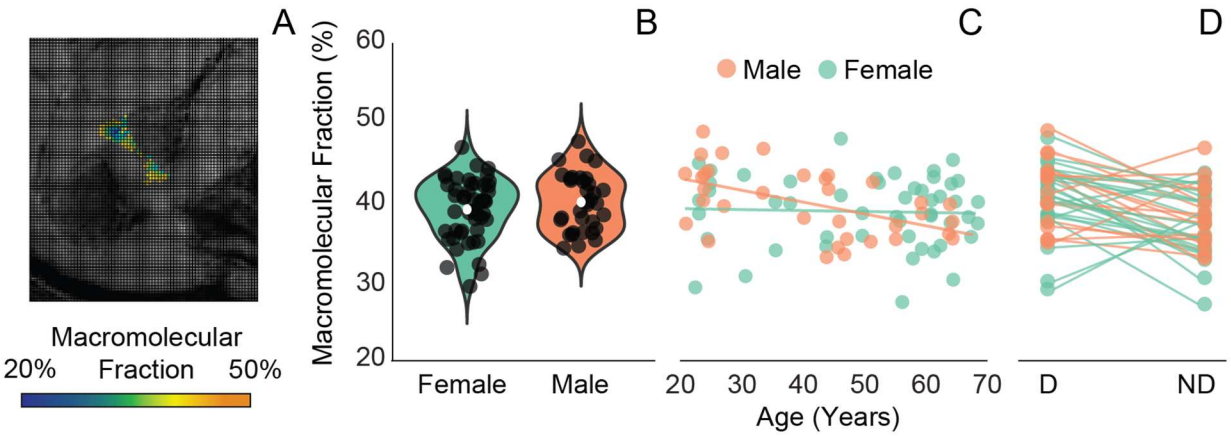


Figure 1. (A) Representative transverse view of UTE-MT scan at the midpoint of the glenoid with segmented labrum is overlaid by voxel-wise macromolecular fraction (MMF) map. The effect of (B) sex, (C) age × sex, and (D) arm dominance on glenoid labrum MMF with least squares trendlines when applicable. Dots represent individual participant arms.

Session Category

Musculoskeletal Biomechanics: Tissues

OA161-04

Trunk Tissue Asymmetry and Its Association with Aging, Disc Degeneration, and Physical Activity in Asymptomatic Adults

Dr. Soumyadip Sen, Dr. Orod Gharibi, Dr. Lichun Lu, Dr. Robert Pignolo, Dr. Asghar Rezaei

mayo Clinic, Rochester, MN, United States

Introduction

Aging is linked to the loss of muscle mass, increased fatty infiltration, and asymmetries in body composition, which collectively contribute to functional decline and disc degeneration (DD). These asymmetries arise from habitual daily activities and are evident in various domains, including muscle strength and movement patterns. Such asymmetries hold significant clinical relevance. Nevertheless, asymmetrical patterns of lean and fat mass within the trunk remain insufficiently investigated. This study seeks to examine the associations among mass asymmetry, age, DD, and physical activity levels in individuals without symptoms.

Methods

Clinically asymptomatic adults who had undergone magnetic resonance imaging (MRI) of the lumbosacral spine within the preceding three years were enrolled in the study. Participants underwent whole-body DXA scans to assess body composition, including lean mass, fat mass, and bone density. Degenerative disc disease (DD) was evaluated using the modified Pfirrmann grading system. Physical activity levels were measured using the International Physical Activity Questionnaire (IPAQ) short form. Subjects were stratified into two age groups—those younger than 55 years and those aged 55 years and older—to facilitate comparison of asymmetry between the groups.

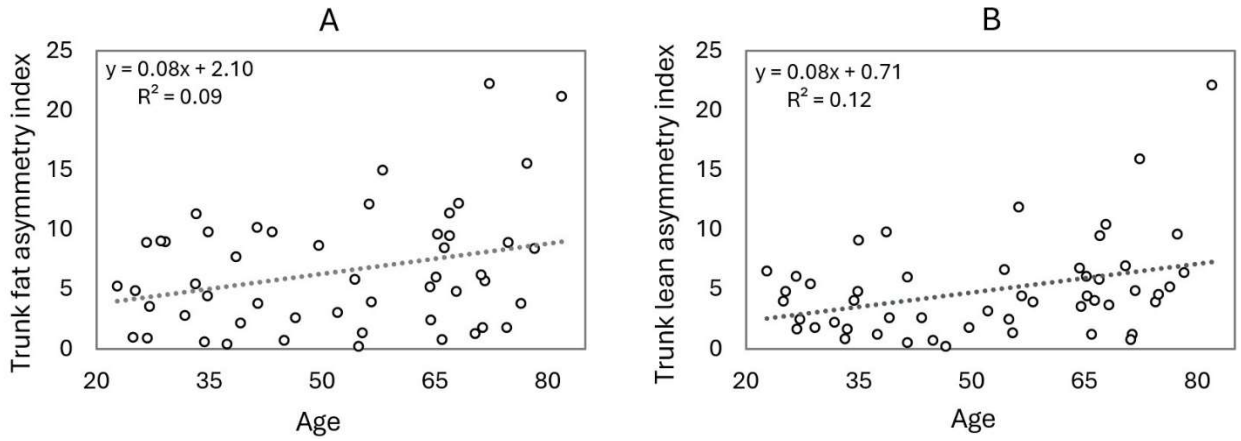
Results

A study of 51 adults (19 men, 32 women; mean age 52.3 years) found significant left-sided dominance in trunk lean and fat tissue ($p<0.0001$), while legs were mostly symmetrical except for lean mass in those over 55 ($p=0.0094$). Trunk tissue asymmetry increased with age (Figure 1), but leg asymmetry did not. Mean DD grade correlated with age ($R^2=0.48$, $p<<0.0001$), but not with tissue asymmetry. In younger adults, combined models showed only age was significant. No link was found between patient-reported physical activity level and asymmetry, but trunk fat mass index varied between medium and high activity groups ($p=0.0251$).

Discussion

Trunk asymmetry is present in asymptomatic individuals across all age groups and becomes more pronounced with aging, but leg asymmetry appears only in older adults. Physical activity influences the amount of trunk fat but does not have any association with asymmetry. These findings highlight the need for early preventive strategies to maintain musculoskeletal balance and spinal health.

Images (Optional)



Acknowledgements (Optional)

This project was supported by NIH grants UL1TR002377, K25AG068368, and the Mayo Clinic Robert and Arlene Kogod Center on Aging.

Session Category

Musculoskeletal Biomechanics: Tissues

OA161-05

Labral Mechanics After Femoroacetabular Impingement (FAI) Related Surgery: An Integrated In Vitro Imaging Study

Mr. Mohammadreza (Hooman) Kheshti[1,2], Dr. Luke Beaton[1], Mr. Minh Khoi Doan[1], Dr. Matthew G. Teeter[1,2], Dr. Louis Ferreira[1], Dr. Ryan M. Degen[1], Dr. K.C. Geoffrey Ng[1,2]

[1]Western University, London, Ontario, Canada. [2]Robarts Research Institute, London, Ontario, Canada

Introduction

Cam-type femoroacetabular impingement (FAI) is a major cause of labral and cartilage injury and may progress to early osteoarthritis. Because the acetabular labrum plays a central role in joint stability, force distribution, and the suction seal, understanding how hip preservation procedures influence its deformation is critical. This study quantified labral strain across key surgical stages for FAI using a CT-integrated testing system, and imaging across multiple joint positions.

Methods

Twenty paired cadaveric hips (age 61 ± 9 years; 10 male, 10 female) without prior pathology were mounted on a CT-compatible positioning rig after removal of soft tissues. Each hip was CT imaged (Canon Aquilion ONE) in nine combined positions of flexion (0°, 60°, 90°)and axial rotation (neutral, internal, external rotation). Following capsulotomy, eight 0.8 mm titanium beads (4 labral, 4 acetabular) were placed in a curvilinear pattern. Paired hips were randomized to two surgical sequences: Protocol A**:** cam over-resection, labral tear, repair, and reconstruction with posterior tibial tendon; Protocol B**:** labral tear, repair, reconstruction, and cam over-resection, where the capsule was repaired after each stage. A custom MATLAB workflow extracted bead coordinates and calculated radial strain at each stage, where statistical analyses were assessed with Friedman tests and post-hoc Wilcoxon comparisons ($\alpha = 0.05$).

Results

In Protocol A, labral reconstruction consistently produced greater radial strain than the native and repaired states in all positions ($P < 0.01$; Figure 1.B1). In Protocol B, reconstruction with an open capsule increased strain at 90° flexion in internal rotation compared with native ($P = 0.03$; Figure 1.B2). With capsular closure at 0° flexion in external

rotation, reconstruction also generated higher strain than both the native and repaired labrum ($P < 0.05$).

Discussion

Labral reconstruction showed the highest strain, whereas cam over-resection and labral tears did not substantially change deformation compared to native hip. These findings also suggest the native labrum can keep the strain low after tissue changes. This work advances our understanding of how specific surgical steps alter labral mechanics and helps clarify whether increases or decreases in labral strain may place the hip joint at risk.

Images (Optional)

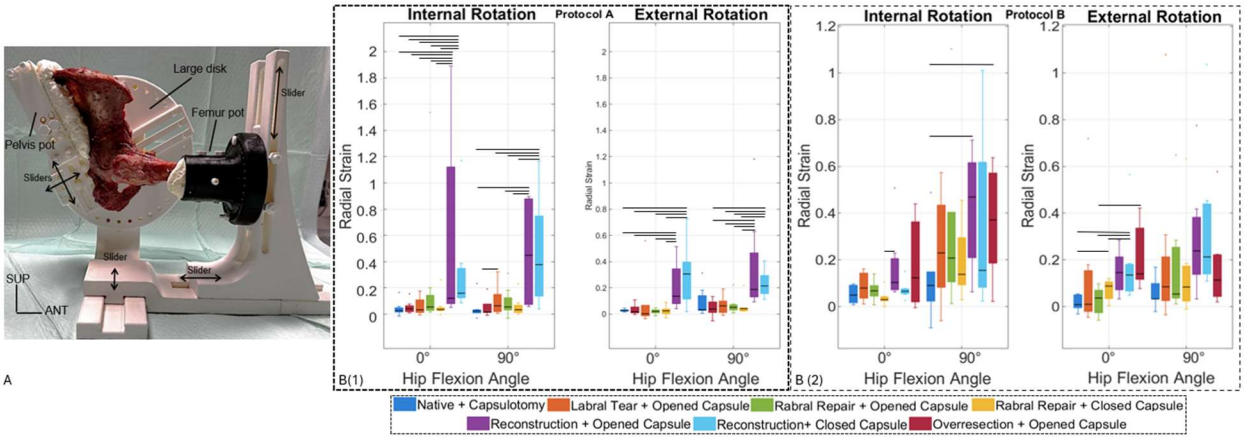


Fig 1. (A) Testing device compatible with clinical imaging with mounted cadaveric hip specimen in sagittal view (60° flexion and neutral rotation). (B) Box-and-whisker plots of radial strain under external rotation (ER) at 0°, 60°, and 90° flexion for Protocol A (B(1)) and Protocol B (B(2)). Different colors represent the tested conditions. Significant differences are denoted by asterisks: Protocol A with 2 asterisks ($P < .01$) and Protocol B with 1 asterisk ($P < .05$).

Session Category

Musculoskeletal Biomechanics: Tissues

OA162-01

Sex-Differences in Vertical and Cross-Axis Vibration Transmissibility to the Sacrum and Head During Seated Whole-Body Vibration Exposure

Mr. Ian Scagnetti PhD (Candidate), Ms. Eliza Cazzola MASc., Dr. Megan Govers PhD, Dr. Michele Oliver PhD, PEng

University of Guelph, Guelph, ON, Canada

Introduction

Seated whole-body vibration (WBV) exposure is associated with musculoskeletal injuries (MSKI), including low-back and neck pain. Women are at increased risk during WBV exposure, but research to understand underlying factors is limited. Risk can be estimated by measuring vibration transmissibility (TR) where higher TR to the spine may indicate higher compression and/or shear forces. The objective of this work was to quantify sex-differences in vertical and cross-axis vibration transmissibility at the head and sacrum for eight discrete frequencies and two accelerations.

Methods

17 males (28 ± 6 yrs) and 22 females (26 ± 6 yrs) were exposed to 3 trials of seated vertical WBV including 16 combinations of acceleration (0.25 or 0.5 m/s2 RMS) and frequency (1,3,5,7,9,11,13, or 15Hz). Exclusion criteria included: back and/or pelvis injury and/or current pregnancy. Exposure orders were counterbalanced. Vertical acceleration was measured at the input, and triaxial accelerations were measured at the sacrum and head using ICP accelerometers. Accelerations were corrected to the basicentric coordinate system defined in ISO 2631-1 using motion-capture. Adjusted vertical and cross-axis TR were calculated using the RMS method (ISO 2631-1). Vertical and cross-axis TR were compared between participants using a repeated-measures MFANOVA including within-subject effects of acceleration and frequency, and a between-subject effect of sex. When appropriate, differences between means were assessed using Bonferroni-corrected pairwise comparisons.

Results

Females had significantly greater ($p<0.05$) vertical TR than males at the sacrum (7 Hz) and head (3, 13, 15 Hz). Approaching statistical significance, females had greater cross-axis TR than males in the fore-aft ($p = 0.066$) and lateral ($p = 0.057$) directions at the sacrum (7 Hz), and fore-aft direction at the head (5 Hz, $p = 0.053$).

Discussion

Females experience greater vertical and cross-axis TR than males at the sacrum and head, which may indicate increased compression and/or shear forces in the spine. Intervertebral joints have lower tolerance for shear forces associated with fore-aft and lateral TR, which may be contributing to increased injury risk for females. Sex-differences in regional body composition may contribute to TR sex-differences due to differing tissue properties and should be further investigated.

Session Category

Rehabilitation Biomechanics and Human Factors: Occupational Biomechanics

OA162-02

Predicting Sex Differences in Seated Whole-Body Vibration Transmissibility Using Body Composition and Anthropometric Measures

Mr. Ian Scagnetti PhD (Candidate), Ms. Eliza Cazzola MASc., Dr. Megan Govers PhD, Dr. Michele Oliver PhD, PEng

University of Guelph, Guelph, ON, Canada

Introduction

Mobile machine operators are exposed to whole-body vibration (WBV) which is associated with back and neck injuries, with women at increased risk. WBV risk can be estimated by quantifying vibration transmissibility (TR). TR characterizes how vibration travels through the body where increased TR may indicate higher spine compression and/or shear forces. Work investigating sex-differences in WBV exposure risk is limited; however, understanding sex-specific TR may help inform vibration mitigation strategies. Exposing participants to vertical vibration, the objective of this work was to predict vertical (z-axis) and cross-axis (x- and y-axes) TR at the head and sacrum between males and females using regional anthropometric and body composition measurements.

Methods

17 males (28±6 yrs) and 22 females (26±6 yrs) were exposed to 0.25 m/s 2 seated vertical sinusoidal WBV at eight discrete frequencies (1,3,5,7,9,11,13,15Hz). Exclusion criteria included: back and/or pelvis injury within the past 4 years and/or current pregnancy. Vertical acceleration was measured at the input, and triaxial accelerations were measured at the sacrum and head. Vertical and cross-axis TR were calculated using the RMS method (ISO 2631-1). Anthropometric measurements (mass, height, seated height, and chest/waist/hip circumferences) were taken using a scale, stadiometer, and measuring tape. Body composition measurements (bone-mineral density, lean mass% and body fat%) were determined using dual-energy x-ray absorptiometry. Vertical and cross-axis TR were predicted using multiple stepwise linear regression models for anthropometric and body composition measures. Lean mass% was omitted to avoid multicollinearity with body fat%.

Results

Significant results ($p<0.05$) are presented in table 1.

Discussion

Males with greater chest, hip and waist circumference and greater body fat%, and females with greater hip circumference and mass may be at increased injury risk due to vertical and cross-axis vibration TR during vertical WBV exposure. Greater cross-axis TR is associated with increased shear forces at the spine, where tolerance for shear forces is much lower than for compression. The most important cross-axis TR predictors for males were hip and waist circumference and body fat% whereas for females they were hip circumference and mass. Vibration mitigation strategies that consider sex-specific TR predictors may reduce injury risk.

Images (Optional)

Table 1: **Transmissibility predictors for males and females**. Results from multiple stepwise linear regression models predicting vertical (z-axis) and cross-axis (x- and y-axes) transmissibility by anthropometric and body composition measurements for males and females. Predictors were included if $p<0.05$ and adjusted $R^2>0.4$.

Sex	*Location (axis)*	*Variable*	*p-value*	*Adj. R^2*	*Unstandardized β*
Male	Head (x)	Hip Circumference	<0.001	0.608	0.012
	Head (z)	Waist Circumference	<0.001	0.625	0.059
		Hip Circumference	0.009	0.768	-0.38
	Sacrum (x)	Waist Circumference	<0.001	0.529	0.050
	Sacrum (y)	Seated Height	0.040	0.577	-0.010
		Body Fat %	0.002	0.479	0.012
	Sacrum (z)	Chest Circumference	0.025	0.522	0.017
Female	Head (x)	Chest Circumference	<0.001	0.434	-0.046
		Mass	<0.001	0.562	0.019
	Head (z)	Mass	<0.001	0.457	-0.024
		Seated Mass	<0.001	0.496	-0.026
	Sacrum (x)	Hip Circumference	<0.001	0.412	0.065
		Height	0.032	0.517	-0.048

Session Category

Rehabilitation Biomechanics and Human Factors: Occupational Biomechanics

OA162-03

Effects of Accelerometer Orientation and Sex on Transmissibility During Seated Whole-Body Vibration Exposure

Ms. Eliza Cazzola B.Eng, MASc[1,2], Mr. Ian Scagnetti MSc, PhD Candidate[1], Dr. Megan Govers[1], Dr. Michele Oliver P.Eng[1]

[1]University of Guelph, Guelph, Ontario, Canada. [2]HumanSystems Inc., Guelph, Ontario, Canada

Introduction

Whole-body vibration (WBV) exposure from heavy mobile machinery operation can result in back injuries, with females at greater injury risk than males. Transmissibility (TR) is one way to quantify injury risk associated with WBV exposure. It is measured using accelerometers and defined in a basicentric coordinate system (BCS) according to ISO 2631-1. The internal axes of accelerometers attached to the sacrum (S1) and thoracic spine (T6) have been shown to deviate from the BCS dependent on participant sex, however, the effects on TR measurements are unknown. The objectives of this work were to determine the effect of correcting accelerometer orientation on TR at S1 and T6 and to investigate sex differences in original and corrected TR.

Methods

17 males (28.6±6.2 years) and 22 females (26.0±6.5 years) were exposed to 16 vertical sinusoidal vibrations (1,3,5,7,9,11,13, and 15Hz at 0.25 and 0.50m/s^2) while sitting upright on a rigid seat with no backrest. Four orthogonal motion capture markers were attached to a tri-axial accelerometer at S1 and a uniaxial accelerometer at T6. Acceleration data were corrected to the BCS using motion capture data. Vertical and cross-axis TR to S1 and vertical TR to T6 were calculated using original and corrected accelerations. Differences in TR between orientations and sexes were examined using a mixed factorial ANOVA (p<0.05).

Results

At T6, females had significantly greater vertical TR than males, and the differences were greater with the corrected accelerations. At S1, female vertical TR at resonance (7Hz) was significantly larger by 1.5 times than males. Females had greater cross-axis TR at S1 at all frequencies and sex differences were greater in the corrected orientation. Cross-axis TR at S1 was significantly larger with the corrected accelerations.

Discussion

Accelerometer orientation had different effects on TR between males and females highlighting the importance of correcting acceleration to accurately measure TR for both sexes. Larger cross-axis TR with corrected accelerations suggests that fore-aft spine motion is underestimated when acceleration data are not corrected. Moreover, despite exposure to the same vertical input vibration, females experienced greater vibration transmission through the spine which may be associated with higher compressive and shear forces.

Session Category

Rehabilitation Biomechanics and Human Factors: Occupational Biomechanics

OA162-04

Investigation of an Objective Measurement of Lumbar Spine Segmental Stiffness

Dr. Erinn McCreath Frangakis BSc, DC, Dr. Jack P. Callaghan PhD

University of Waterloo, Waterloo, Ontario, Canada

Introduction

Clinical assessment of the lumbar spine commonly includes manual segment palpation via a posterior-to-anteriorly directed force. This test results in an inference of spinal stiffness, informing target treatment [1]. Because this methodology is subjective, devices have been developed to reduce clinician-based variability and objectify findings. The purpose of this study was to ascertain the variability of stiffness measurements across consecutive lumbar spine segments using such a device. It was hypothesised that there would be no difference in stiffness measurements.

Methods

Participants (n=9) were recruited from the University of Waterloo graduate student population. Individuals were included if they had no low back pain or injury in the last 12 months, no known deformity, malignancy, or inflammation of the lumbar spine, no history of spinal surgery, and were not currently pregnant. Participants were randomly assigned to two groups, which determined the starting order of spinal stiffness testing: cranial-caudal (e.g., L1-L5) or caudal-cranial. A spinal indentation device [2] applied known preloads (8 N) and forces (80 N) to each lumbar spinal segment through the spinous process. Load-displacement values were measured, and lumbar segmental stiffness was calculated. Stiffness values were averaged (three per segment) and smoothed using a 6^{th}-order polynomial function.

Results

Average smoothed stiffness curves demonstrate an increased stiffness at the level of L3 (5.54 N/mm ±1.7), with a descending trend in values cranially (4.94 N/mm ±1.6) and caudally (4.99 N/mm ± 1.16) *(Figure 1)*. Initial results suggest that while there is variability of lumbar spinal stiffness at the joint level, no significant differences were found between segmental levels ($F_{(4,28)}$=1.52; P=0.255).

Discussion

This study is the first to assess a spinal indentation device on multiple segmental lumbar spinal stiffness measurements. Preliminary data suggests that in healthy populations, this stiffness is consistent across the lumbar spine. Further work should look to establish

normal stiffness curves in healthy individuals and how these may deviate in a clinical population.

Images (Optional)

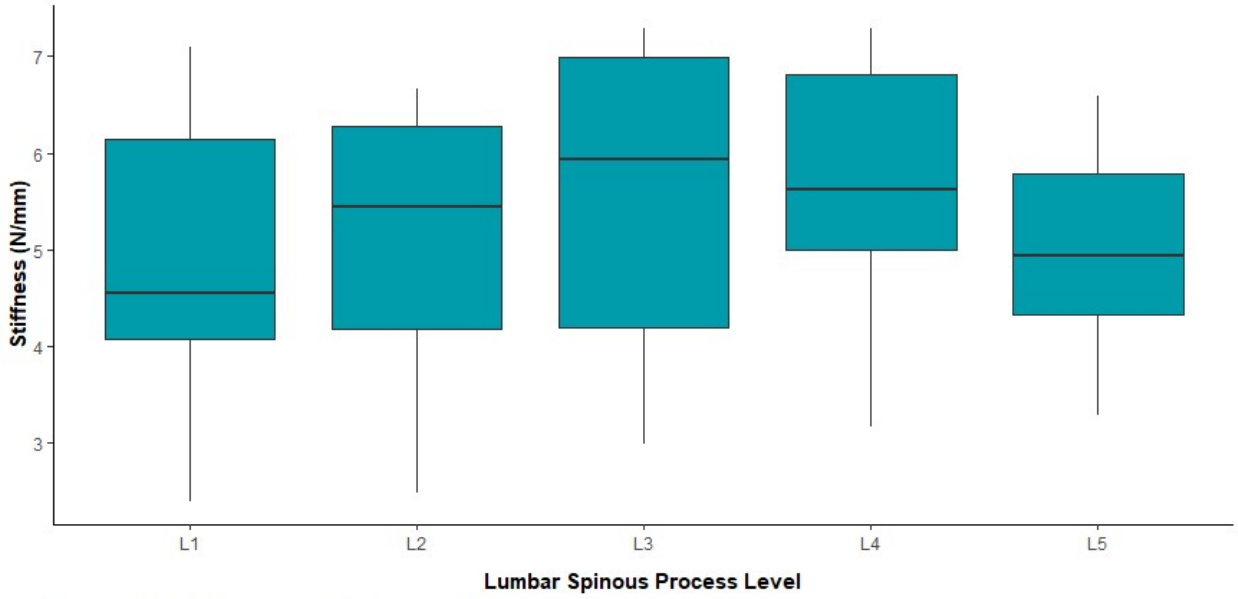


Figure 1: Variability of Lumbar Segment Stiffness

References (Optional)

[1] Tennant *et al.,* J Hum. Kinet., 2020

[2] Wong *et al.,* Man Ther., 2013

Acknowledgements (Optional)

The authors acknowledge funding from the Natural Science and Engineering Research Council of Canada and the Ontario Graduate Scholarship. JPC is further supported as the Canada Research Chair in Spine Biomechanics and Injury Prevention.

Session Category

Rehabilitation Biomechanics and Human Factors: Occupational Biomechanics

OA162-05

Powered Back Exoskeleton Reduces Epaxial Electromyography and Lumbar Moments During Lifting With Some Redistribution of Effort to the Lower Limbs

Dr. Grace Hunt[1], Dr. Tommaso Lenzi[1,2]

[1]HGN Lab for Bionic Engineering, Salt Lake City, UT, United States. [2]Rocky Mountain Center for Occupational and Environmental Health, Salt Lake City, UT, United States

Introduction

Powered back exoskeletons have the potential to prevent workplace injuries among manual material handlers by providing assistive torques as needed to reduce back strain [1,2,3]. However, powered back exoskeletons may have unintended consequences, like increasing joint and muscle effort in the lower limbs [1]. Unfortunately, no previous study has simultaneously evaluated lumbar and lower-limb muscle and joint effort with powered back exoskeletons. Therefore, the objective of this study is to assess the impact of a powered back exoskeleton on lumbar and lower-limb biomechanics during lifting. We hypothesize that a powered back exoskeleton can lower EMG activity in lumbar muscles and reduce lumbar moments with minimal impact on the lower limbs.

Methods

Three able-bodied subjects (2M/1F) lifted weighted boxes (10.8 kg) with and without a powered back exoskeleton (Volton, SuitX). We recorded full-body motion capture, forces, and electromyography (EMG) from bilateral epaxials (iliocostalis, longissimus), quadriceps (vastus medialis), and hamstrings (biceps femoris) [FigureA]. The biological lumbar moment was calculated by subtracting the exoskeleton moment from the net lumbar moment. Percentage changes in peak metrics (EMG and joint moments) from NoExo to Exo were calculated per side, then averaged across sides per subject. In time-domain figures, sides were averaged per subject. Cross-subject averages and standard deviations are reported.

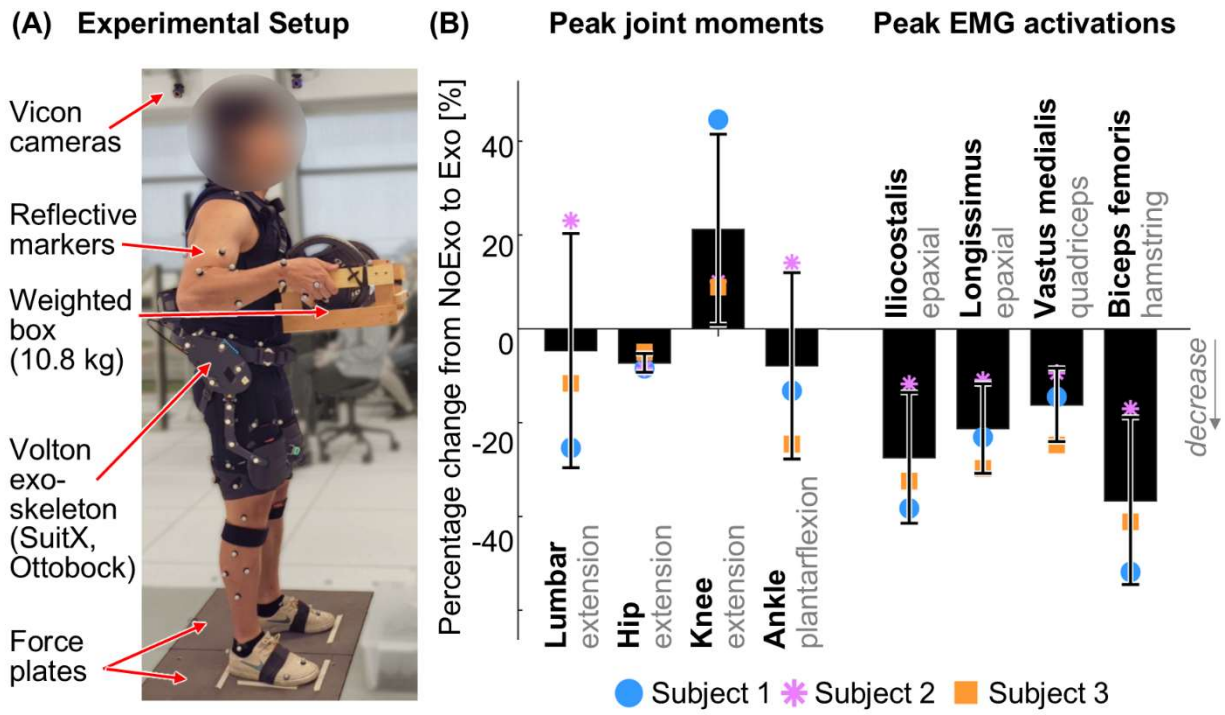
Results

EMG peaks decreased in all measured muscles for all subjects with the exoskeleton (iliocostalis: 27.5±13.9%; longissimus: 21.3±9.6%; quadriceps: 16.2±7.8%; hamstring: 36.7±17.8%) [FigureB]. The exoskeleton decreased the lumbar moment (4.7±25.0%), hip moment (7.3±2.0%), and ankle moment (7.9±19.9%) on average, although it increased the knee extension moment (21.2±20.3%). Subject 2 responded to the exoskeleton with increased lumbar and ankle moments.

Discussion

The powered back exoskeleton reduced the average biological moments at the lumbar, hip, and ankle joints, while reducing the peak muscle effort of the lumbar and lower-limb muscles. However, knee extension torque increased with the exoskeleton. This study suggests that powered back exoskeletons can reduce workplace injuries and overuse by reducing lower back strain.

Images (Optional)



References (Optional)

[1] Athar Ali *et al.,* Front Bioeng Biotechnol, 2021

[2] Niels Brouwer *et al.,* Wearable Technologies, 2024

[3] Jasper Johns *et al*, J Biomechanics, 2024

Acknowledgements (Optional)

We thank SuitX for providing the exoskeletons for this project and Dr. Minerva Pillai for input on fitting and experiment design. This work was funded in part by NSF grant 2046287.

Session Category

OA162-06

The Effects of Height and Sex on Two-Person Team Lifting

Ms. Joanna M. Misquitta[1], Mr. Ryan Chhiba[1], Mr. Ryan V. Hogan[1], Dr. Daanish M. Mulla[2], Dr. Peter J. Keir[1]

[1]McMaster University, Hamilton, Ontario, Canada. [2]York University, Toronto, Ontario, Canada

Introduction

Team lifting is used to handle heavy objects that exceed individual lifting capacity [1]. Despite its frequent use in the workplace, current guidelines and research are lacking. The purpose of this study was to examine the effects of height and sex on kinematics and kinetics during several two-person lifting tasks when pairs of lifters were matched and unmatched for height.

Methods

Twenty-three female and eighteen male participants made 19 unique height-matched (≤5cm) and unmatched (≥10cm) pairs and performed four manual materials handling tasks (knee-to-waist and chest lifts, left-right and forward-backward carries) using a 42.6kg apparatus. Upper body motion and hand forces were captured using marker-based motion capture and four 6-DOF force transducers affixed to each corner of the apparatus. Joint angles and moments for the shoulder, elbow, and trunk were determined in Visual3D.

Results

During knee-to-waist lifts in the matched condition, taller participants had greater trunk flexion, while shorter participants had greater shoulder extension and elbow flexion. These observations were amplified in the unmatched condition. During height matched knee-to-chest lifts, shorter participants had greater elbow flexion and trunk extension than taller participants. Shoulder extension was not significantly different between participants. In the unmatched condition, shorter participants had greater shoulder extension, while elbow flexion and trunk extension did not differ significantly between participants. During the carries, shorter participants had greater shoulder extension and elbow flexion, particularly in the unmatched condition. Taller participants had a more neutral trunk posture compared to shorter participants in both conditions. These posture changes were also noted in hand forces and internal joint moments. Further analyses will examine sex-based differences.

Discussion

Depending on the lifting task, height differences during two-person team lifting result in unique postural requirements for each lifter. Taller participants tend to adjust their shoulder posture, while shorter participants adjust using their elbows and trunk. These postures lead to differences in joint loading and injury risk, between both shorter and taller individuals as well as males and females. These findings provide evidence for the role of height differences in two-person team lifting to formulate guidelines for team lifting in the workplace.

Images (Optional)

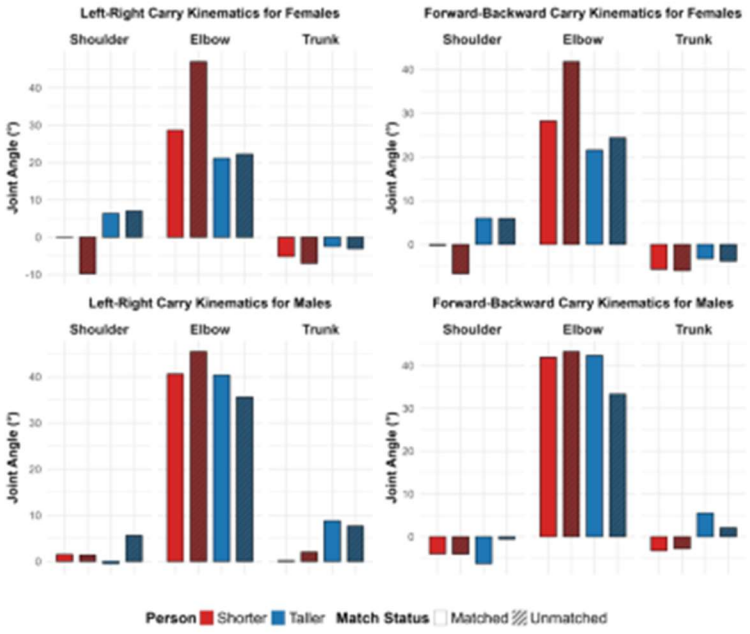


Figure 1: Mean joint angles of the shoulder, elbow, and trunk during the left-right and forward-backward carries for the relatively shorter (red) and taller (blue) lifter in the matched (solid bar) and unmatched (striped bar) conditions.

References (Optional)

[1] Barrett, RS & Dennis, GJ. HFEMSI (2005)

Acknowledgements (Optional)

This project was funded by the Natural Sciences and Engineering Research Council of Canada (NSERC Discovery Grant RGPIN-2023-05473)

Session Category

Rehabilitation Biomechanics and Human Factors: Occupational Biomechanics

OA163-02

A Non-Invasive Rat Model of ACL Rupture-Induced Osteoarthritis: Progression and Treatment Response Assessed by Mechanical and Histological Analysis

Ms. Jasmine Doan, Dr. Colleen Mathieu, Dr. Sotcheadt Sim, Dr. Eric Quenneville, Dr. Martin Garon

Biomomentum Inc, Laval, Quebec, Canada

Introduction

Osteoarthritis (OA) is a progressive joint disease causing cartilage loss, pain, and reduced mobility. Its prevalence—7.7% globally in 2021—is rising with aging and obesity. Animal models are essential for studying OA and testing therapies. Unlike traditional surgical ACL transection, non-invasive ACL rupture better mimics post-traumatic OA without surgical trauma. This study uses a refined non-invasive ACL rupture model in rats to track OA progression and evaluate intra-articular treatment.

Methods

Forty-four female Lewis rats (14-week-old) were assigned to Control(N=12), ACL Rupture Non-Treated(N=24), and Treated(N=8) groups. ACL rupture was induced mechanically using a custom fixture and Mach-1 tester, confirmed by anterior drawer test and necropsy. Treated rats received weekly Hyaluronan injections during weeks 4-6. Cartilage thickness and instantaneous modulus (IM) were measured at 4-, 7-, and 10-weeks using automated indentation mapping (~30 sites/surface). Histology included SafO/FG staining with OARSI and modified Mankin scoring. Data were analyzed by linear model.

Results

All injured joints showed complete ACL rupture with intact surrounding ligaments. In Non-Treated joints, significant thinning of the medial anterior condyle appeared by 4-weeks (p<0.001 vs. Control) and persisted through 10-weeks (Fig.1A). IM initially increased at 4- and 7-weeks before declining at 10-weeks (Fig.1C). The lateral condyle swelled between 4- and 7-weeks, then thinned at 10-weeks (Fig.1B), with IM stable until a final increase at 10-weeks (Fig.1D). Hyaluronan treatment mitigated these changes: Treated joints showed no significant differences in thickness or IM compared to Controls, though localized erosion was observed histologically. Non-Treated joints exhibited severe OA changes, including cartilage denudation in the medial anterior condyle by 7-weeks and bone remodeling by

10-weeks (Fig.1E). The lateral anterior condyle remained intact at 4-weeks but developed focal defects by 10-weeks.

Discussion

This non-invasive ACL rupture model reliably induces post-traumatic OA, revealing progressive structural and mechanical changes. Degeneration was most pronounced in the medial anterior condyle, consistent with increased load after ACL injury. Posterior and tibial regions also showed changes, indicating widespread biomechanical disruption. Treatment slowed mechanical deterioration but did not fully prevent structural damage. Overall, this model provides a clinically relevant platform for studying OA progression and testing potential treatments.

Images (Optional)

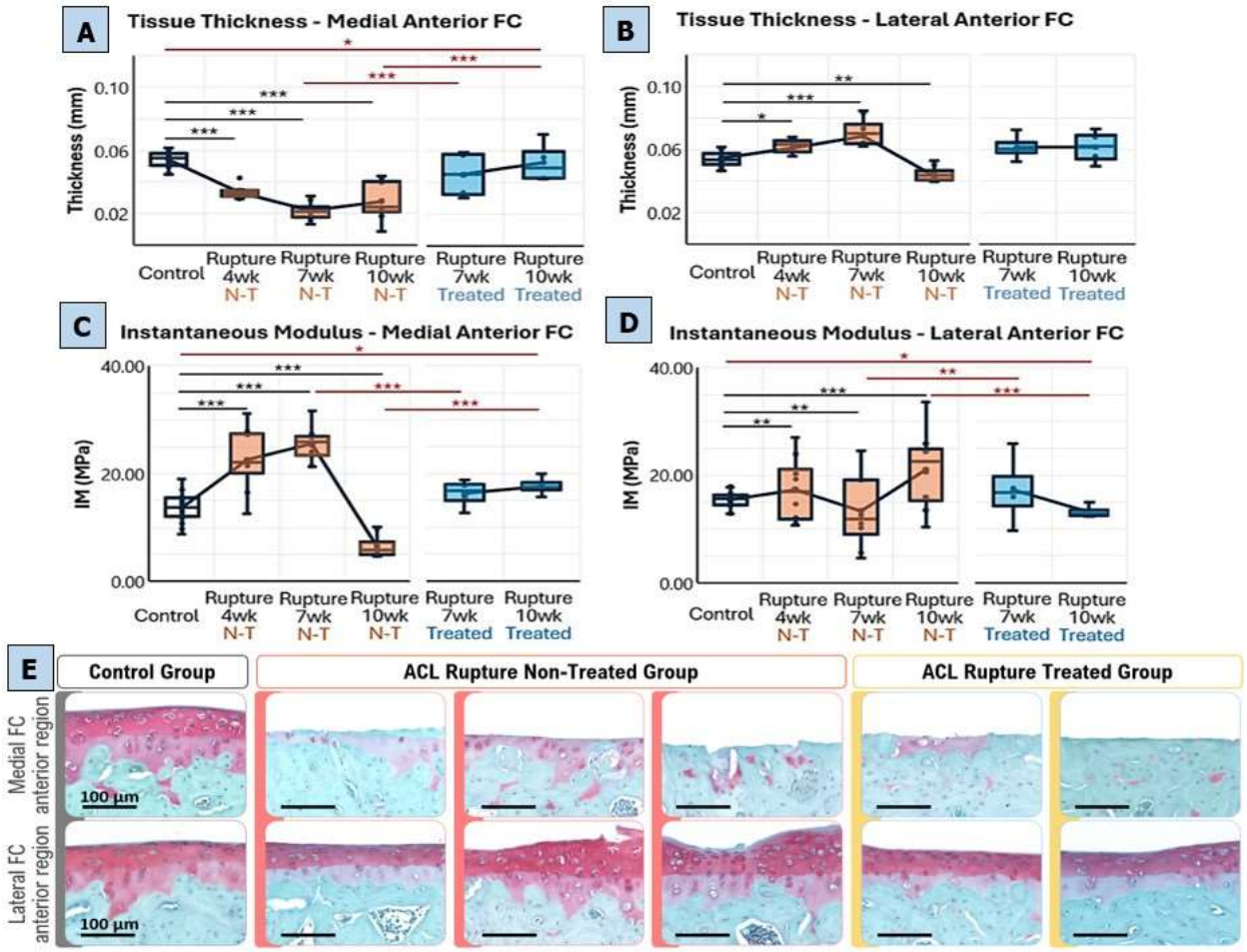


Figure 1 – (A-D) Cartilage thickness and instantaneous modulus boxplot graphs for medial and lateral anterior femoral condyles. * p<0.05; ** p<0.01; *** p<0.001. (E) Representative histological SafO/Fast Green-stained sections of femoral condyles.

References (Optional)

Session Category

Orthopaedic Biomechanics: Trauma and Repair

OA163-03

Development of an *In Vitro* Knee Model for Dynamic Biomechanical Evaluation of Meniscus Allograft Positioning

Dr Aiqin Liu PhD CEng MIMechE[1], Dr Blake McCall[2,3], Dr John Brewster[3], Dr Sanjeev Anand[4], Prof. Louise M Jennings[3]

[1]School of Biomedical Sciences, University of Leeds, Leeds, Yorkshire, United Kingdom. [2]School of Biomedical Engineering, University of New South Wales, Sydney, New South Wales, Australia. [3]Institute of Medical and Biological Engineering, School of Mechanical Engineering, University of Leeds, Leeds, Yorkshire, United Kingdom. [4]Leeds Teaching Hospitals NHS Trust, Leeds, Yorkshire, United Kingdom

Introduction

Meniscus allograft transplantation (MAT) can restore meniscal function and alleviate symptoms, but graft extrusion remains common and may accelerate osteoarthritis progression. Extrusion is associated with root positioning, and can alter tibiofemoral contact mechanics; however, most previous studies examined biomechanical changes under static conditions rather than dynamic loading during gait. Therefore, we developed an *in vitro* knee model to evaluate how MAT root positioning influences joint kinematics, shear forces, and contact mechanics under dynamic loading.

Methods

Six human cadaveric knees were tested under four conditions: intact meniscus, anatomic MAT root position (original position), and two non-anatomic positions (5 mm medial or posterior shift; Fig. 1a). For each specimen, the native root was detached and refixed in these positions using validated techniques. A force-controlled gait profile was applied on a knee simulator to measure joint kinematics and shear forces, while contact mechanics were assessed under specimen-specific displacement-controlled profiles. Data were analysed using one-way repeated measures ANOVA ($p < 0.05$) to determine the impact of root positioning on knee biomechanics.

Results

Kinematic analysis showed no significant differences among conditions for anterior–posterior displacement, internal-external tibial rotation, or shear forces ($p > 0.05$; Fig. 1b–d). All MAT root positions significantly reduced contact area compared to the intact meniscus ($p < 0.05$; Fig. 1e), with the anatomic position (OgPos) restoring only 61–64% of

intact values. Average pressures were significantly higher for all root conditions compared to intact ($p < 0.05$; Fig. 1f), and peak pressure was significantly elevated for the anatomic and medial positions, while the posterior position did not show statistically significant increase (Fig. 1g). Peak pressure locations shifted posteriorly ($p>0.05$) and medially ($p < 0.05$) for all root conditions (Fig. h-i).

Discussion

MAT root positioning within ±5 mm of the anatomic site maintained knee stability but did not fully restore native contact mechanics, with all positions shifting contact pressure posteriorly and medially. These findings are consistent with previous evidence indicating MAT cannot fully replicate native knee biomechanics, and that altered load distribution remains a biomechanical challenge following transplantation. As this study used time-zero cadaveric models, future research should incorporate healing and remodelling effects and evaluate long-term clinical implications.

Images (Optional)

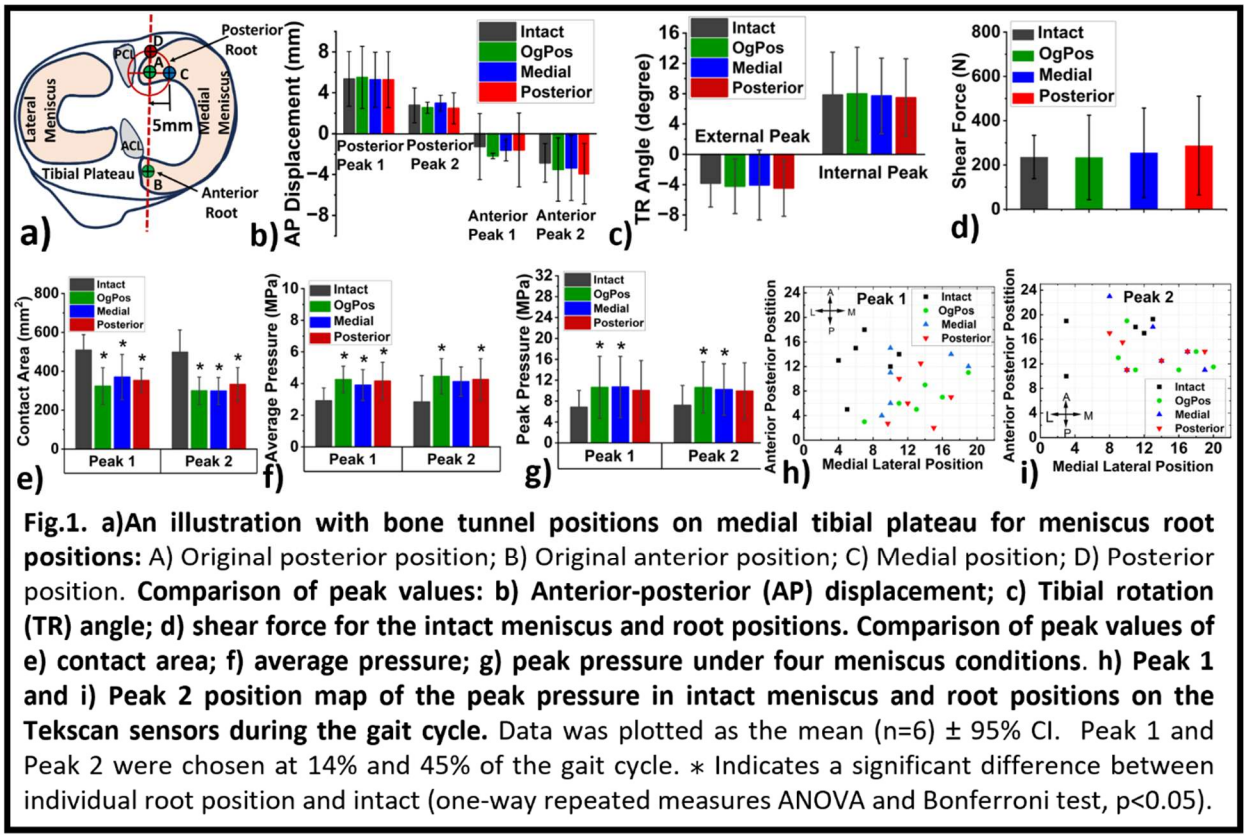


Fig.1. a)An illustration with bone tunnel positions on medial tibial plateau for meniscus root positions: A) Original posterior position; B) Original anterior position; C) Medial position; D) Posterior position. **Comparison of peak values: b) Anterior-posterior (AP) displacement; c) Tibial rotation (TR) angle; d) shear force for the intact meniscus and root positions. Comparison of peak values of e) contact area; f) average pressure; g) peak pressure under four meniscus conditions. h) Peak 1 and i) Peak 2 position map of the peak pressure in intact meniscus and root positions on the Tekscan sensors during the gait cycle.** Data was plotted as the mean (n=6) ± 95% CI. Peak 1 and Peak 2 were chosen at 14% and 45% of the gait cycle. ∗ Indicates a significant difference between individual root position and intact (one-way repeated measures ANOVA and Bonferroni test, $p<0.05$).

Session Category

Orthopaedic Biomechanics: Trauma and Repair

OA163-04

Acute Functional Instability and Long-Term Structural and Behavioral Changes in Mice After Medial Meniscus Destabilization

Ms. Olivia Dyer, Ms. Haylie Silbernagel, Mr. Ethan Stoecker, Dr. Stephanie Cone PhD

University of Delaware, Newark, Delaware, United States

Introduction

Medial meniscus destabilization (DMM) is used in mice to study disease progression, risk factors, and healing responses of post-traumatic osteoarthritis (PTOA) [1]. Prior rodent research has assessed changes *in vivo* gait, imaging, and *ex vivo* biomechanical testing [1,2]. Recent innovation in multiaxial robotic testing and movement tracking can improve research precision in the acute effects of DMM on knee function. The objective of this work was to measure immediate functional effects and long-term structural and behavioral changes in mice after DMM.

Methods

Female C57BL/6J mice underwent unilateral DMM (n=5) or SHAM surgery (n=5) [3]. During weeks 2 and 5 post-injury, animals were placed in a custom-built gait arena and activity was recorded for 10min. The total number of rearings was counted and total distance traveled was calculated via custom Python script. At week 6, animals were imaged, and trabecular bone properties were recorded (Bruker SkyScan 1276 Micro-CT). For preliminary robotic testing, a single knee was prepared, loaded with a 1.5N anterior drawer force in intact and DMM states, and resultant tibial translation was calculated [2]. Statistics included ANOVAs and t-tests.

Results

Both DMM and SHAM rearing counts decreased from week 2 to week 5. SHAM animals traveled significantly less distance per trial compared to DMM animals ($p=0.014$). On average, DMM tibiae had a bone mineral density of 0.39g/cm^2 and trabecular thickness of 0.066mm compared to 0.34g/cm^2 and 0.062mm in SHAM tibiae respectively. There were increases of 0.27mm resultant tibial translation, 0.25mm anterior tibial translation, and 0.19mm medial translation after DMM (Figure 1).

Discussion

The immediate effects of DMM injury increase both anterior and medial tibial translation. There were differences in activity between groups suggesting that the injury induces behavioral changes. Our microCT results found structural differences in tibial trabecular

bone in the DMM and SHAM mice potentially due to changes in loading and activity levels. Future work will include analyzing specific spatial-temporal gait changes in the mice as well as extending the injury development period from 6 to 8 weeks.

Images (Optional)

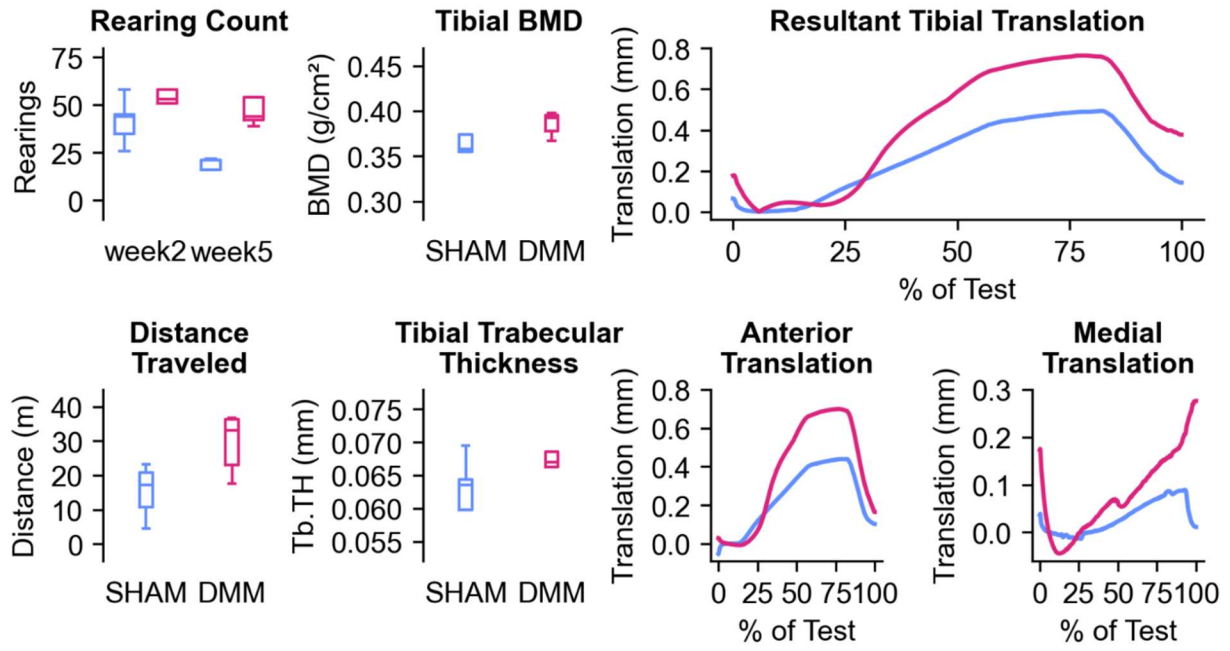


Figure 1. Number of rearings, distance traveled, tibial bone mineral density, tibial trabecular thickness were collected from SHAM (blue) and DMM (pink) injured mice. A representative resultant translation, anterior translation, and medial translation curve for a mouse knee in an intact (blue) and DMM (pink) state.

References (Optional)

[1] Allen+, Arthritis Res Ther, 2012, [2] Dyer+, J Biomech. 2025, [3] Glasson+, Osteoarthritis Cartilage, 2007

Acknowledgements (Optional)

Funding from NIH P20GM139760.

Session Category

Injury Biomechanics: N/A

OA163-05

Eccentric Contraction Improves Functional Outcomes in a Rat Model of Traumatic Muscle Injury

Mr Fuad Bin Enam, Mr Michael Borovik, Mr Trent Hardwick, Mr Patrick Hinkle, Dr Koyal Garg, Dr Alex Reiter

Saint Louis University, Saint Louis, Missouri, United States

Introduction

Volumetric muscle loss (VML) is the irrecoverable loss of muscle resulting in functional impairment [1]. Rehabilitation, including treadmill and wheel running, has shown modest to no functional improvement following VML in animal models [2-3]. Recently, eccentric contraction (EC) has been effective in restoring function of injured tibialis anterior in rats [4]. This study explored the effects of EC on improving function in gastrocnemius injured muscle. A secondary purpose was to assess the capacity of tensiometry [5] adapted for rodents to capture improvements.

Methods

Twelve female Sprague Dawley rats (10-12 weeks old, 200-275g, Inotiv) were divided into three groups: control, VML, and VML+EC. VML groups received a gastrocnemius traumatic injury [6]. Two weeks post-injury, VML+EC received EC training twice per week for four weeks [4]. Both anterior and posterior crural muscles were stimulated while the ankle rotated from plantarflexion to dorsiflexion (±20°); animals received four sets of five stimulations with two-minute rest. At six weeks, muscle function was assessed via ankle torque and a tensiometer, which measures Achilles tendon wave speed, a surrogate for gastrocnemius force. Animals were anesthetized, the right foot secured in the pedal of the torque device, and the knee fixed in a clamp; the tensiometer was placed over the Achilles tendon. Isometric contractions were induced with varying frequencies to record peak torque and wave speed.

Results

Similar trends were captured in torque and wave speed with varying stimulation frequencies (Fig 1). VML had significantly lower torque and wave speed compared to control, but VML+EC showed non-significant reductions from control. VML was significantly reduced from VML+EC in ankle torque at 100Hz but not wave speed.

Discussion

These results highlight the potential for EC to improve function in gastrocnemius injured muscle following VML, building on the previous work in tibialis anterior. They also demonstrate the capacity for tensiometry to capture VML injury deficits and functional recovery. Future work will further optimize the EC protocol and the tensiometer and assess longitudinal recovery.

Images (Optional)

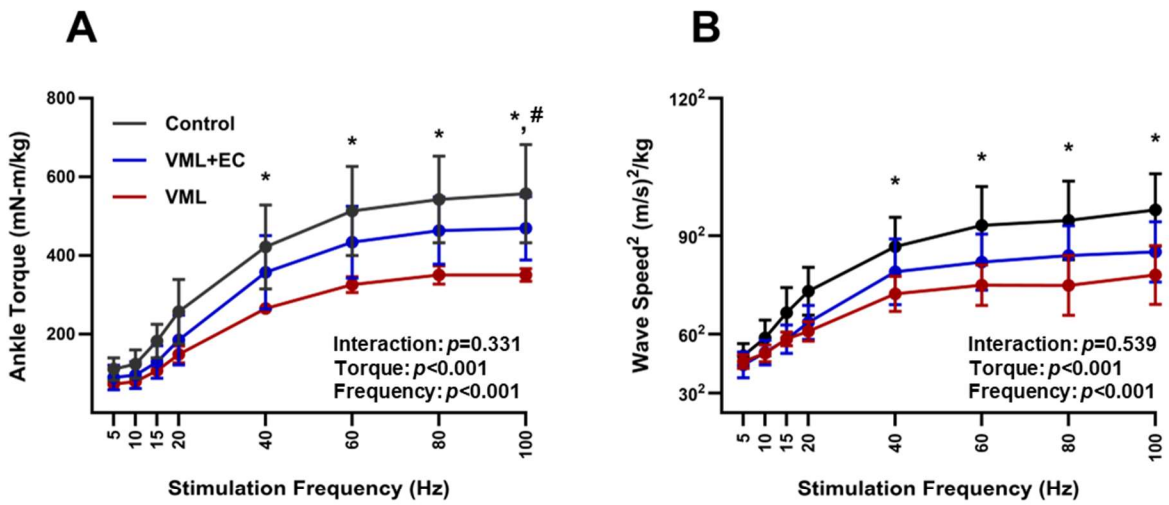


Figure 1. (A) Ankle torque and **(B)** squared wave speed showed similar trends across stimulation frequency. VML was significantly reduced (*) from control in both outcomes at 40-100Hz. VML was significantly reduced (#) from VML+EC in ankle torque at 100Hz but not wave speed. Statistical significance was assessed with two-way ANOVAs for functional outcome and frequency. When significance was detected, post-hoc Sidak's test compared groups within frequency. ($p < 0.05$)

References (Optional)

[1] Testa, *Biomedicines*, 2021. [2] Aurora, *BMC SSMR*, 2014. [3] Quarta, *Nat. Commun.*, 2017. [4] Ziemkiewicz, *JOR*, 2023. [5] Martin, *Nat. Commun.*, 2018. [6] Patel, *JBMR*, 2020

Acknowledgements (Optional)

Funding from the NIH (R03HD115731 and 1R15GM129731-02)

Session Category

Orthopaedic Biomechanics: Trauma and Repair

OA164-02

Stiffness Perceived by Cells Inside Microporous, Bio-Combatible Scaffolds: An *in Silico* 3d Modelling Approach for Quantitative Biomechanical Analysis

Mr Oliver Santos-Lopes[1], Dr Dimitrios Tzeranis[2], Dr Vasileios Vavourakis[1,3]

[1]University of Cyprus, Nicosia, Nicosia, Cyprus. [2]University of Crete, Heraklion, Heraklion, Greece. [3]University College London, London, London, United Kingdom

Introduction

Cells can sense and respond to the stiffness of their insoluble microenvironment [1]. Yet, quantifying the stiffness perceived by cells inside 3D matrices is challenging. Here we present an efficient *in silico* approach for modelling biologically relevant microporous scaffolds, a specific type of 3D matrix, with pore diameter within 30-200μm, and utilize it to quantify how cells perceive matrix stiffness when seeded inside them.

Methods

We developed an efficient finite element procedure, using ANSYS, to model two important kinds of cell-seeded microporous biomaterials of physiologically relevant sizes: Porous Collagen-based Scaffolds (PCS) utilized in regenerative medicine grafts, and scaffolds fabricated by 3D-printed methods [2]. Assuming each cell attaches and contracts with force on two points of the scaffold, a relevant approximation for spindle-like cells in microporous biomaterials [3], we calculated the matrix stiffness perceived by each cell ($k_{ce}=\delta F_c/\delta l_c$) by numerically approximating the gradient of their force-displacement (F_c-l_c) relationship.

Results

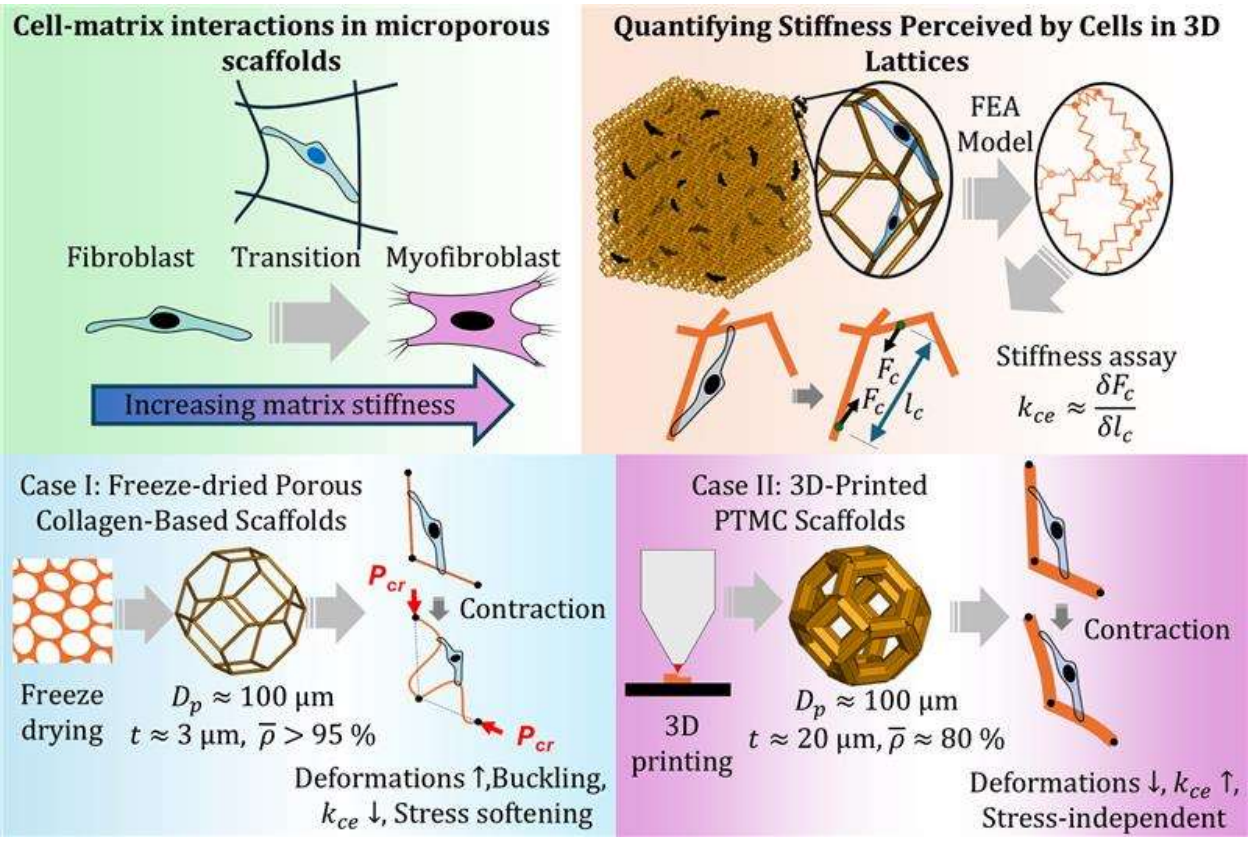
We quantified the distribution of matrix stiffness perceived by cells as a function of scaffold parameters (material properties, pore diameter, relative density) and cell parameters (contractility F_c, density, orientation). Cells seeded in PCS sensed k_{ce} in the 5--50nN/μM range, which depended on PCS structural parameters, attachment location, and contractility. Cells seeded inside 3D-printed PTMC scaffolds perceived ~3 orders of magnitude higher than cells seeded in PCS and independent of contractile force.

Discussion

Our model revealed that k_{ce} in a PCS depends strongly on both PCS parameters (pore size, relative density) and cell contractility, due to the nonlinear mechanics of open-pore biomaterials. In contrast, cells grown in 3D-printed scaffolds sense a much higher stiffness that is independent of cell contractile force. These force-dependent effects, arising from

the large deformations of PCS struts, may influence cell mechano-responsive pathways and explain reported down-regulation of wound contraction during skin regeneration in PCS. Our model provides novel insights into the mechanical interactions of cells with 3D biomaterials, which can be used to optimize biomaterials or probe phenomena that are difficult to investigate experimentally.

Images (Optional)



References (Optional)

[1] Yiu et al., Bioactive Materials, 2022

[2] Harley et al., Acta Biomaterialia, 2007

[3] Freyman et al., Experimental Cell Research, 2001

Acknowledgements (Optional)

This work was supported by the European Innovation Council through the Pathfinder Open project 'SoftReach' (Grant ID: 101099145).

Session Category

OA164-03

Effect of Mechanical Alterations in Diabetic Red Blood Cells on Their Partitioning Patterns at Microvascular Bifurcations

Ms. Xin Zhou, Prof. Xiaobo Gong

Shanghai Jiao Tong University, Shanghai, Shanghai, China

Introduction

Nonproportional red blood cell (RBC) distribution is a critical feature of the microcirculatory system. Compared to healthy RBCs, diabetic RBCs exhibit increased shear modulus, elevated intracellular viscosity, and morphological alterations, which could contribute to microvascular complications. Current research lacks numerical studies on the partitioning of RBCs with distinct mechanical properties at vascular bifurcations under multicellular interactions. This study investigates the partitioning patterns of healthy and diabetic RBCs in bifurcated vessels to elucidate how cellular mechanical properties influence RBC dynamics in microcirculation.

Methods

The immersed boundary method was employed to simulate fluid-structure interactions between cell membranes and flow fields. The effects of RBC deformability, morphology, and intracellular viscosity on cell partitioning were analyzed under varying branch diameter ratios and hematocrit levels. Subsequently, different proportions of diabetic RBCs were added to normal RBCs to investigate the distribution patterns under their mutual interactions.

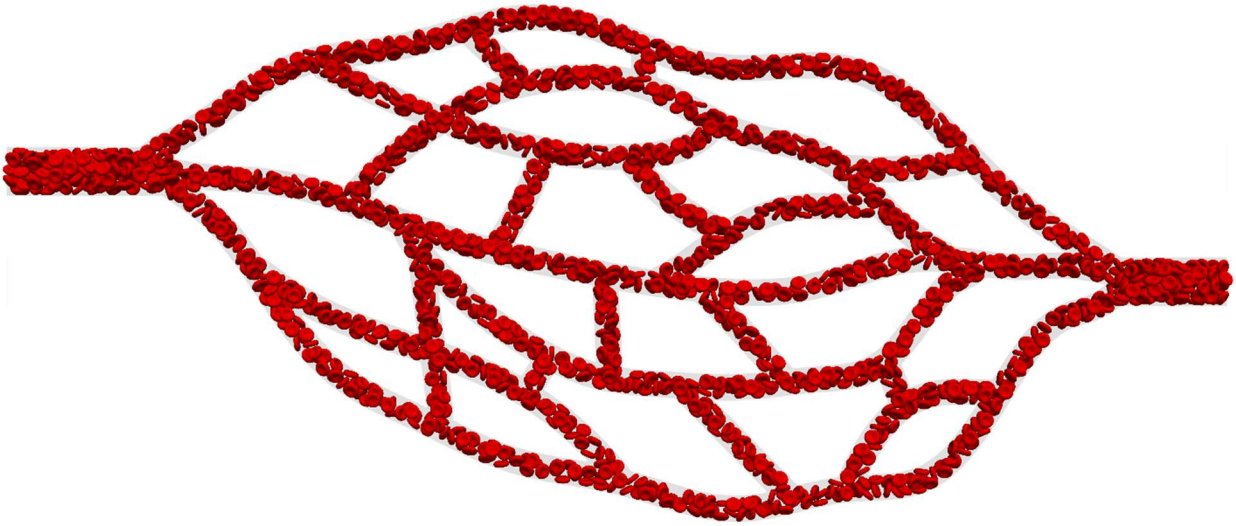
Results

The results demonstrate that the scale effects of RBCs lead to more pronounced nonproportional partitioning when branch radius differences increase. At hematocrit levels below 10%, its impact on RBC distribution is negligible; above 10%, higher hematocrit increases RBC preference for low-flow branches. Elevating shear modulus and swelling ratio enhances RBC partitioning into high-flow branches, whereas intracellular viscosity shows negligible influence. When the proportion of diabetic RBCs added to healthy RBCs is less than 20%, healthy RBCs are more likely to flow into high-flow branches than diabetic RBCs. When the proportion of diabetic RBCs exceeds 30%, diabetic RBCs are more likely to enter high-flow branches.

Discussion

Diabetic RBCs demonstrate greater propensity to enter higher-flow branches compared to normal RBCs, consistent with physiological observations. This phenomenon helps elucidate how cellular mechanics contribute to microcirculatory dysfunction in diabetes. Observed distribution patterns of diabetic-normal RBC mixtures provide valuable references for developing microfluidic chips that sort cells by mechanical properties. Future work could incorporate realistic capillary networks reconstructed from imaging data, combined with experiments to investigate cellular distribution patterns involving RBCs and nucleated cells in microcirculation.

Images (Optional)



Acknowledgements (Optional)

We acknowledge support from Key Project of the National Natural Science Foundation of China (NSFC, No. 12432014) and the National Key Research and Development Program of China (No. 2025YFE0107500).

Session Category

Cell Biomechanics: Methods and Models

OA164-04

Dynamic Astrocyte Volume and Force Modulation as Mechanisms to Regulate Interstitial Flow in the Brain

Ms. Jacqueline van Zyl[1], Professor Seunggyu Kim[1,2], Professor Ming Guo[1], Professor Roger Kamm[1]

[1]Massachusetts Institute of Technology, Cambridge, MA, United States. [2]Korea University, Sejong, Sejong, Korea, Republic of

Introduction

A common hallmark of dementia is the aggregation of protein waste, which is exacerbated when the brain's waste clearance, or glymphatic, system is compromised [1]. Despite its importance, the mechanisms regulating glymphatic or interstitial flow, including dynamic flow rate changes across the sleep-wake cycle, remain unknown or contested. Astrocytes, as the brain's primary homeostatic regulators, are well-positioned to influence these flows through two potential mechanisms: generating driving pressures through contractile forces or altering tissue hydraulic permeability through volume-dependent changes. Here, we developed quantitative *in vitro* models to assess how astrocyte mechanics respond to physiologically relevant ionic and neurotransmitter cues and evaluate their potential roles in regulating interstitial transport.

Methods

To investigate contractile mechanics, we used micropillar deflection assays in which pillar displacement was imaged and converted to force using known pillar stiffnesses. We perturbed tissues with myosin II/ROCK inhibitors to assess the mechanisms of force generation and applied ionomycin to investigate calcium-driven modulation of contraction. In parallel, astrocyte volume responses were quantified by confocal imaging of spheroid areas following increased glutamate or potassium concentrations, two stimuli that fluctuate with behavioral state and have been implicated in cell swelling.

Results

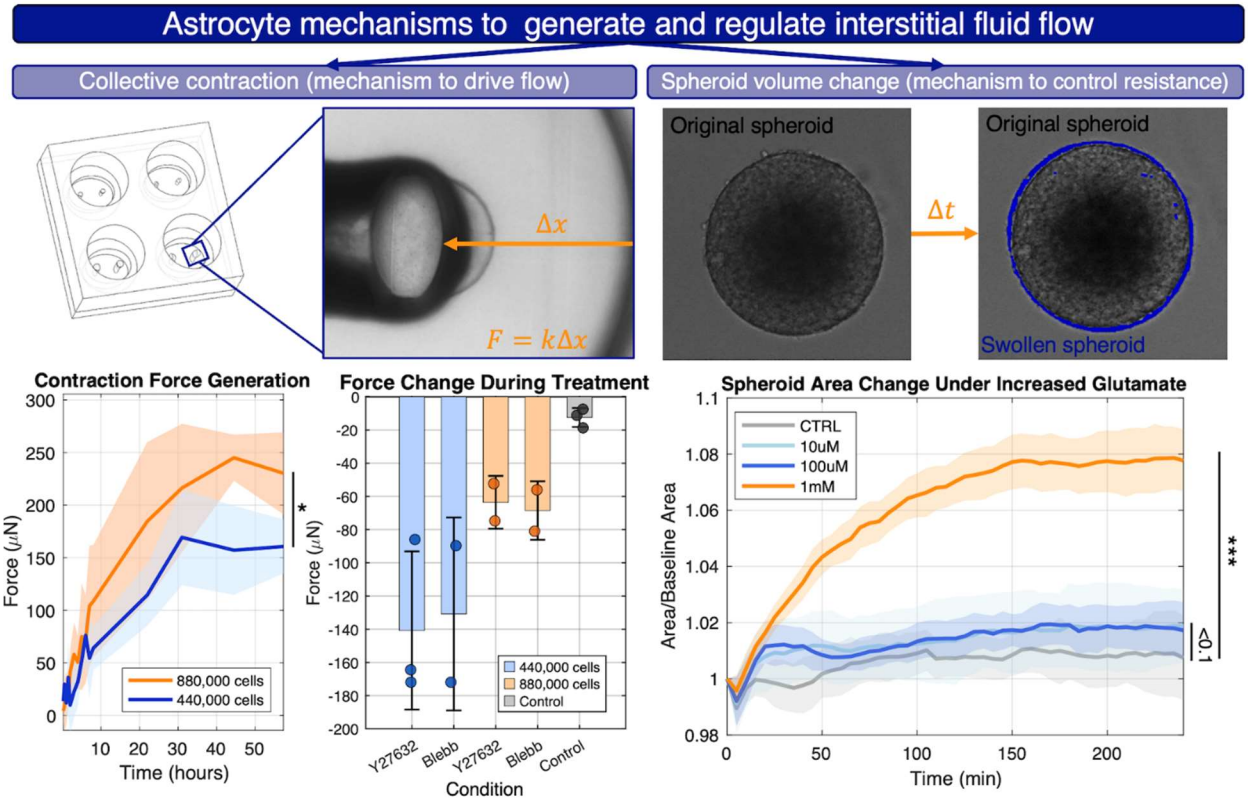
Our results show that astrocytes generated substantial collective forces, reaching hundreds of micronewtons. Inhibition by blebbistatin and Y-27632 reduced contraction by more than 50 μN, confirming active, cytoskeleton-driven forces, while ionomycin increased contraction by about 25 μN within 30 minutes, demonstrating a rapid ionic response. Volume responses differed in both magnitude and time scale, providing insight into how astrocytes may alter the extracellular space and ultimately hydraulic resistance. Potassium induced fast, transient spheroid swelling within 20 minutes, while glutamate

triggered sustained swelling over several hours, with pathological levels producing 8% swelling by 4 hours ($p<0.001$).

Discussion

These findings demonstrate that astrocytes dynamically respond to ionic and neurotransmitter cues characteristic of sleep-wake states. Coordinated modulation of contractile forces and volume suggests astrocytes may help regulate interstitial flow by modulating both driving pressures and fluidic resistances. Future work will incorporate neuron-astrocyte co-culture models to directly investigate the impact of neural state on astrocyte mechanics.

Images (Optional)



References (Optional)

[1] Maiken Nedergaard *et al.,* Science, 2020

Session Category

Cell Biomechanics: Methods and Models

OA164-05

Structural Determinants of Internal Cellular Force Balance Under Different Mechanical Stimuli

Ing. Lucie Jadrna[1,2], doc. MUDr. Jaromír Gumulec Ph.D.[3], Assoc. Prof. Eoin McEvoy Ph.D.[4], prof. Ing. Jiří Burša Ph.D.[1]

[1]Dept. of Biomechanics, Faculty of Mechanical Engineering, Brno, Czechia, Czechia. [2]European Society of Biomechanics, Brno, Czechia, Czechia. [3]Dept. of Pathophysiology, Faculty of Medicine, Brno, Czechia, Czechia. [4]School of Engineering, Biomedical Engineering, Galway, Galway, Ireland

Introduction

Cellular stiffness is a key determinant of how cells sense and respond to the mechanical properties of their environment. The ability of cells to maintain internal force balance and adapt their internal structure to the mechanical environment clearly underlies disease progression. Despite extensive experimental evidence from manipulations targeting cytoskeletal network, high resolution imaging and stiffness mapping methods, e.g., Atomic Force Microscopy (AFM) and shear flow, the role of the cellular microstructure in mechanical response remains incompletely understood.

Methods

Utilizing the Finite Element Model of a living cell comprising major cytoskeletal constituents (actin bundles, intermediate filaments, microtubules) together with the nucleus, membrane and cytoplasm (Figure, A), we previously demonstrated the impact of cytoskeletal protein density on the mechanical response of the cell [1]. Here, we investigate the contribution of intracellular components under two distinct stimuli: compressive load related to AFM through a low-strain setup and shear. We additionally focus on the impact of prestress, i.e., active contractility, and adhesion on the mechanical response, which are mechanisms facilitating the cell-substrate interaction, supposedly determining the cell internal structure but also prominent phenomena in experimental measurements.

Results

Simulations confirm the predominant role of actin, namely its contractility and elasticity. The impact of internal structure is more pronounced in global shear loading compared to

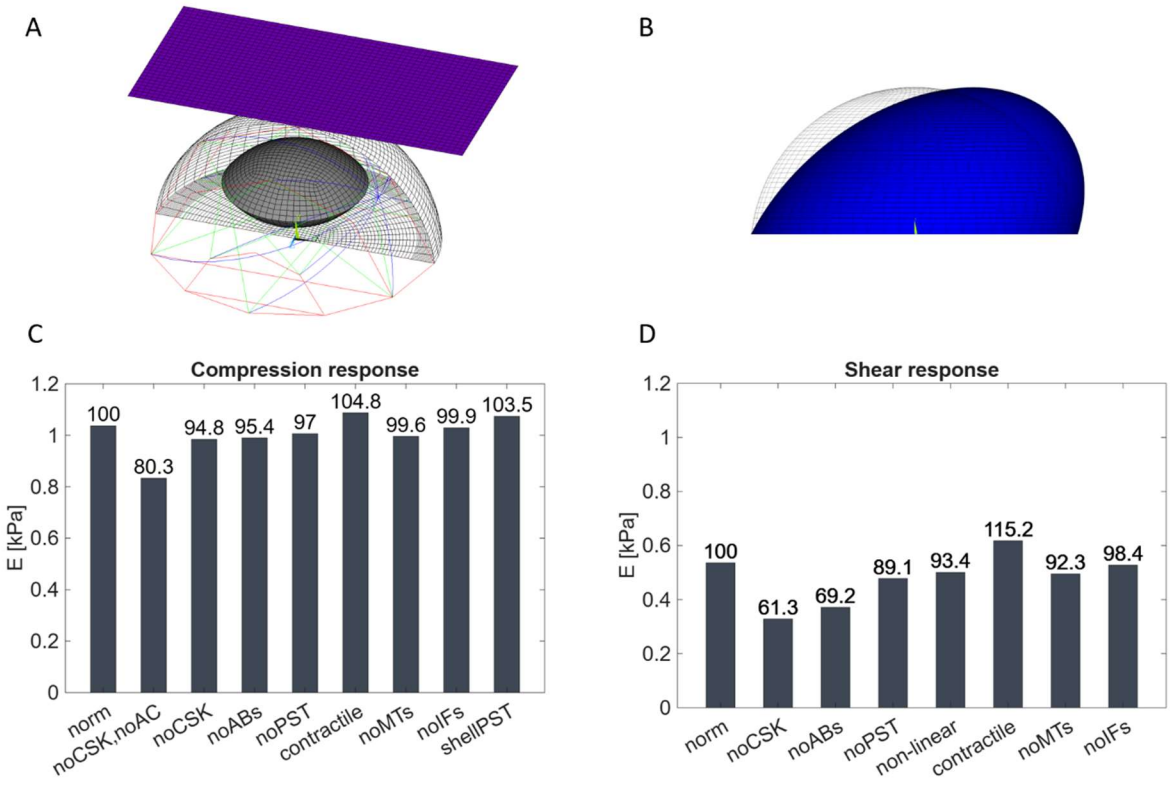
indentation typical in AFM, where the continuum properties predominate (details in the Figure).

Figure: (A) Structural model with red ABs, blue MTs and green IFs in compression by blue-magenta plate, (B) mesh deformed by low shear values, (C, D) sensitivity study results with percentual change indicated above the bars in both compression and shear.

Discussion

This study reflects on structural modulators related to force sensing to provide insight into stiffness change in diseased cells using computational modelling supported by experimental measurements. Since pathological states disrupt the internal force balance, they can be observed as internal reorganization mainly due to excessive cellular forces. The assumption of internal reorganization being driven by establishing the internal force optimum (homeostasis) calls for adjustment of internal properties of the model, such as focal adhesion count linked with underlying substrate stiffness.

Images (Optional)



References (Optional)

[1] Navratil *et al.* Cancer Cell Int, 2024

Acknowledgements (Optional)

This work was supported by Czech Science Foundation project No.26-20714S.

Session Category

Cell Biomechanics: Methods and Models

OA165-01

Dynamic Balance Declines With Age Across the Stride Cycle

Dr Lizeth Sloot[1], Dr Matthew Millard[2]

[1]Newcastle University, Newcastle, Tyne and Wear, United Kingdom. [2]University of Stuttgart, Stuttgart, Baden-Württemberg, Germany

Introduction

We fall more as we get older. Mechanical balance looks at how we coordinate our body relative to our foot's base of support (BOS). We recently showed that the functional BOS, which can exert balancing forces, is much smaller than the foot sole [1,2]. Studies have not yet accounted for this or body angular momentum. Therefore, we evaluated age-related changes in dynamic mechanical balance throughout the stride in the largest full-body motion dataset of 207 adults covering 21-90 years of lifespan ([3] and unpublished).

Methods

For body coordination, we calculate the novel foot-placement-estimator (FPE) model that uses both the body's linear and angular momentum to solve for the stepping location, which represents a balanced pose [4]. Our young fBOS model [1,2] was fitted to the foot markers, and the floor contact area was adapted throughout the stance phase. Dynamic balance was calculated as the margin-of-stability (dMoS), the distance between the stepping location and the nearest BOS edge. Age and gender differences were assessed throughout the stride using SPM analysis.

Results

The stepping point is in front and medial of the lead foot at foot contact and moves further ahead and towards the other foot throughout the stance phase (Figure 1).

dMoS decreased with age across almost the whole stride in the travel direction ($p<0.002$; Figure 1). Post-hoc analysis shows that balance declined from 70 years and above compared with those aged 20-60 years. There was no age effect for the cross direction, except for a short difference between 40-50yrs and 80-90yrs.

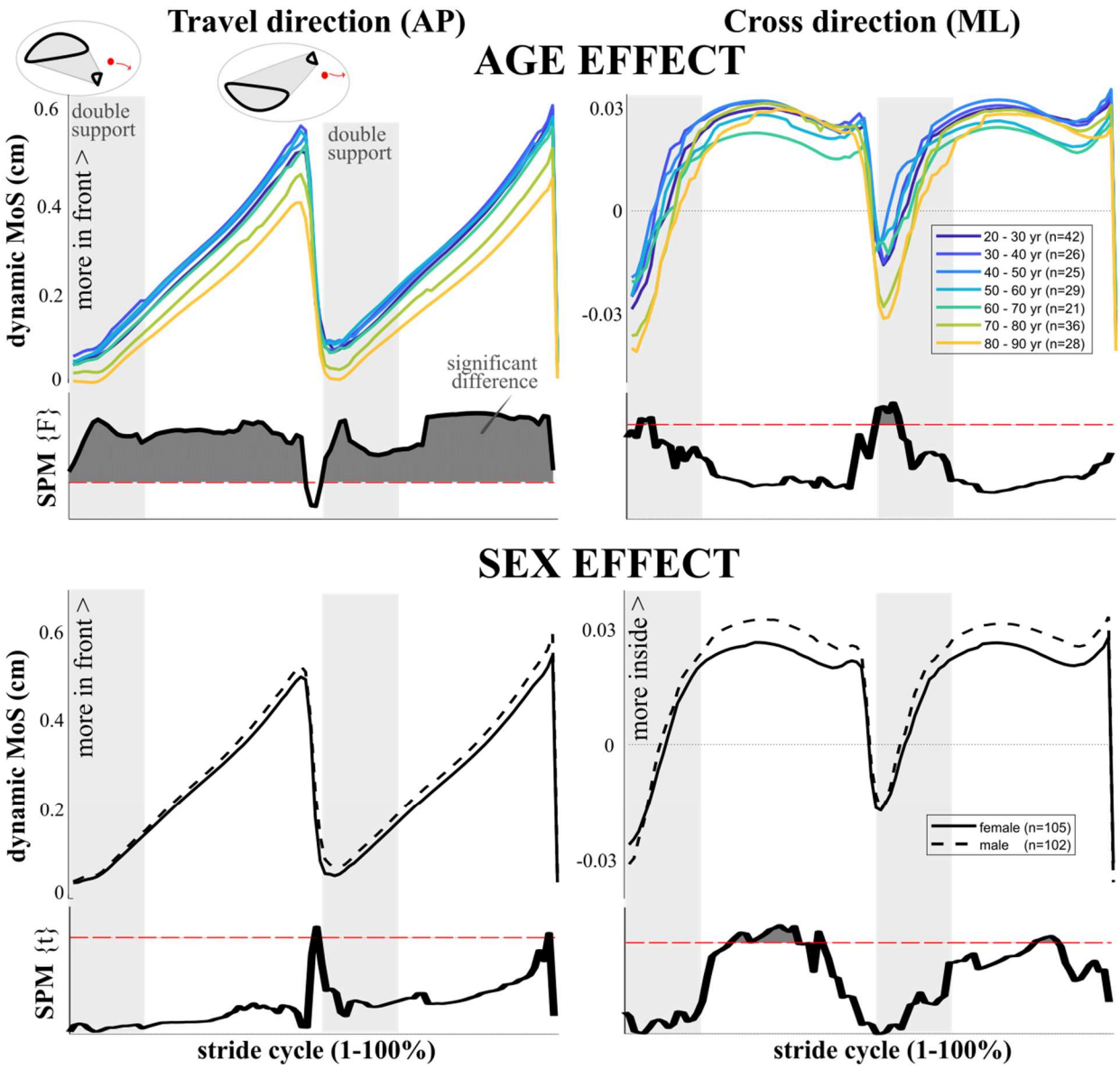
dMoS was lower in females compared to males during single stance in the cross direction ($p<0.03$), but not the travel direction.

Discussion

This large mechanical balance dataset shows that older adults and females are more cautious, staying closer to being dynamically balanced. Next, we will create age-specific

fBOS models and account for declining walking speed. Generalizability is limited to non-frail and pre-frail adults-no frail adults were measured. This detailed analysis helps us better identify people at risk of falling.

Images (Optional)



References (Optional)

[1] Millard&Sloot, JBiomechanics, 2025

[2] Sloot+, SciReports, 2025

[3] vanCriekinge+, SciData, 2023

[4] Millard+, JComputNonlinDys, 2012

Acknowledgements (Optional)

Carl-Zeiss Stiftung; Rosetrees & Stoneygate Trusts

Session Category

Clinical Biomechanics: N/A

OA165-02

Working Harder to Walk Slower: Treadmill-Based Gait Assessment Systematically Underestimates Overground Performance in Older Adults

M.Sc. Keven Santamaria-Guzman[1], Ph.D. Tyrone Loria-Calderon[2], Ph.D. Mynor Rodriguez-Hernandez[2], M.Sc. Brandon Peoples[1], M.Sc. Bria Smith[1], M.Sc. Damaris Cifuentes[1], M.Sc. Silvia Campos-Vargas[1], M.Sc. Kenneth Harrison[1], Ph.D. Jaimie Roper[1]

[1]Auburn University, Auburn, Alabama, United States. [2]University of Costa Rica, San Ramon, Alajuela, Costa Rica

M.Sc. Keven Santamaria-Guzman

Ph.D. Tyrone Loria-Calderon

Ph.D. Mynor Rodriguez-Hernandez

M.Sc. Brandon Peoples

M.Sc. Bria Smith

M.Sc. Damaris Cifuentes

M.Sc. Silvia Campos-Vargas

M.Sc. Kenneth Harrison

Introduction

Although treadmill-based gait assessments offer controlled analysis, most comparisons focus on level walking in young adults. Real-life ambulation involves slopes, yet treadmill–overground equivalence on inclines is largely unknown. Older adults remain underrepresented despite likely using different strategies. This study evaluates whether laboratory-determined self-selected speeds mirror real-world walking across inclinations.

Methods

Twenty-six older adults (70±6 years) completed six randomized 2-minute walking trials: treadmill (TR) and overground (OG) conditions across flat, uphill, and downhill terrain (5.2°, 9.1% grade) at comfortable speed. TR speeds were determined using a bidirectional protocol: incremental (0.5 m/s baseline, +0.05 m/s every 3 seconds) and decremental (1.5 m/s baseline, −0.05 m/s every 3 seconds) tests; averages determined TR speed. Kinematics were captured using six IMUs; GRF via pressure-sensing insoles. Heart rate (HR) and perceived exertion (RPE) was recorded. Participants rested until baseline HR between trials. Sensory integration was assessed via CTSIB. Paired t-tests compared conditions (α=0.05).

Results

TR systematically underestimated OG gait speed: flat (1.04±0.20 vs 1.37±0.15 m/s; Δ=24.1%), uphill (0.94±0.20 vs 1.23±0.16 m/s; Δ=23.6%), downhill (1.06±0.22 vs 1.30±0.18 m/s; Δ=18.5%; all $p<.001$) (Figure 1). TR also underestimated peak force (Δ=11–23%) and loading rate (Δ=31–41%; all $p<.001$). Paradoxically, HR was higher: flat (111±15 vs 101±13 bpm), uphill (118±14 vs 105±12 bpm), downhill (106±15 vs 99±13 bpm; all $p\leq.002$), and RPE followed the same pattern (all $p<.05$). CTSIB sensory ratios (visual, somatosensory, vestibular) showed no correlation with speed discrepancy across inclinations (all $p>.05$).

Discussion

TR underestimated OG speed by 18.5–24.1%, while simultaneously eliciting higher HR and RPE, indicating that participants worked harder to walk slower. This paradox suggests TR imposes demands beyond the absent optic flow, potentially including postural stabilization costs and altered motor control strategies. Individual sensory reliance did not correlate with discrepancy magnitude, suggesting a broad effect in older adults. Critically, the ~0.3 m/s underestimation in this sample exceeds thresholds for meaningful change in gait speed, suggesting that TR-based assessments may misclassify functional mobility status in older adults.

Images (Optional)

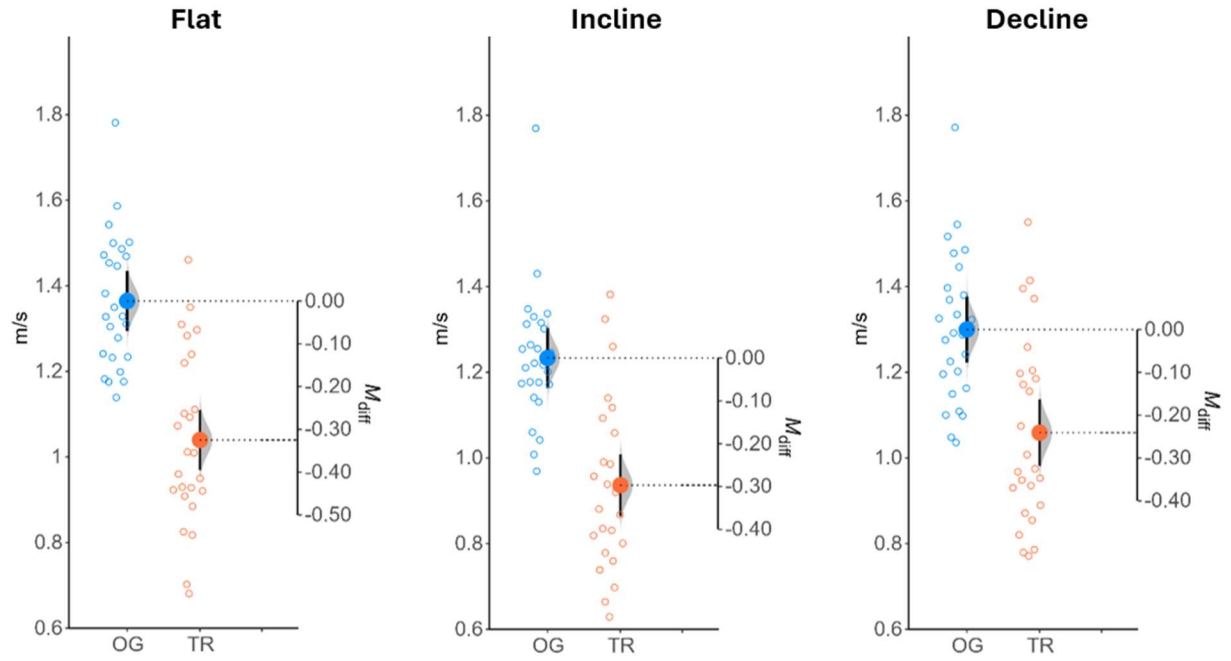


Figure 1. Gait speed comparison between overground (OG; blue) and treadmill (TR; orange) across terrain inclinations. Open circles represent individual participants; filled circles indicate group means. Difference scores (M_{diff}) reflect the speed discrepancy: flat (−0.33 m/s), incline (−0.29 m/s), decline (−0.24 m/s); all $p<.001$.

References (Optional)

Session Category

Clinical Biomechanics: N/A

OA165-03

Beta- and Gamma-Band Cortical Connectivity During Destabilizing Pivoting Stepping Movement on a Robotic Elliptical Trainer

Ms Soyoung Lee PhD, Ms Peiwen Fu, Mr Matteo Pergami-Peries PhD, Mr Li-Qun Zhang PhD

University of Maryland Baltimore, Baltimore, Maryland, United States

Introduction

Off-axis instability during stepping contributes to lower-limb injury and post-traumatic joint degeneration, yet the cortical networks supporting control of off-axis motion are poorly understood. Using a robotic off-axis elliptical stepping paradigm, we examined how beta- and gamma-band directed connectivity reorganizes when participants stabilize pivoting under destabilizing conditions.

Methods

Eight healthy adults (three female, age=32.0±3.5, BMI=22.8±2.3) stepped on a robotic elliptical trainer with adjustable pivoting. Three modes were presented in random order: (1) normal stepping; (2) free mode, in which transverse friction was removed ("walking on ice") from the right foot; and (3) perturbation mode, in which 3 Nm internal rotation torques were applied while participants resisted. Visual feedback instructed participants to maintain a zero position. Each mode lasted 10 s with 10 s rest, repeated for 15 blocks. Pivoting instability was quantified as root-mean-square pivot angle (RMSAngle) during free mode. High-density EEG (128 channels) was source-reconstructed to frontal eye fields, dorsolateral prefrontal, primary motor (MC) and somatosensory (S1) cortices, superior parietal lobule, temporo-parietal junction (TPJ), and visual cortex. Directed connectivity in beta (15–29 Hz), low-gamma (30–59 Hz), and high-gamma (60–90 Hz) bands was estimated using Phase Transfer Entropy (PTE); net PTE outflow and inflow were derived for each region. Linear mixed-effects models tested effects of mode (free, perturbation vs normal), and Pearson correlations between regional PTE outflow and RMSAngle were computed during free mode.

Results

In beta and low-gamma, perturbation (vs normal) reduced PTE outflow from left MC and right VC and increased outflow from bilateral TPJ (all $p < 0.05$), whereas free mode showed no significant changes. In high-gamma, perturbation decreased outflow from left S1 and

increased outflow from right TPJ ($p < 0.05$), with a trend toward reduced left-VC outflow. PTE outflow correlated moderately with RMSAngle, particularly in beta band.

Discussion

Pivoting perturbations during robotic elliptical stepping reconfigure cortical PTE connectivity across beta and gamma bands, shifting influence from primary sensorimotor-visual cortices to temporo-parietal association regions. Positive TPJ–RMSAngle correlations in beta and low-gamma indicate that individuals with greater pivoting instability recruit TPJ more strongly, highlighting TPJ-mediated multisensory integration as a potential target for neuromechanically informed balance rehabilitation.

Images (Optional)

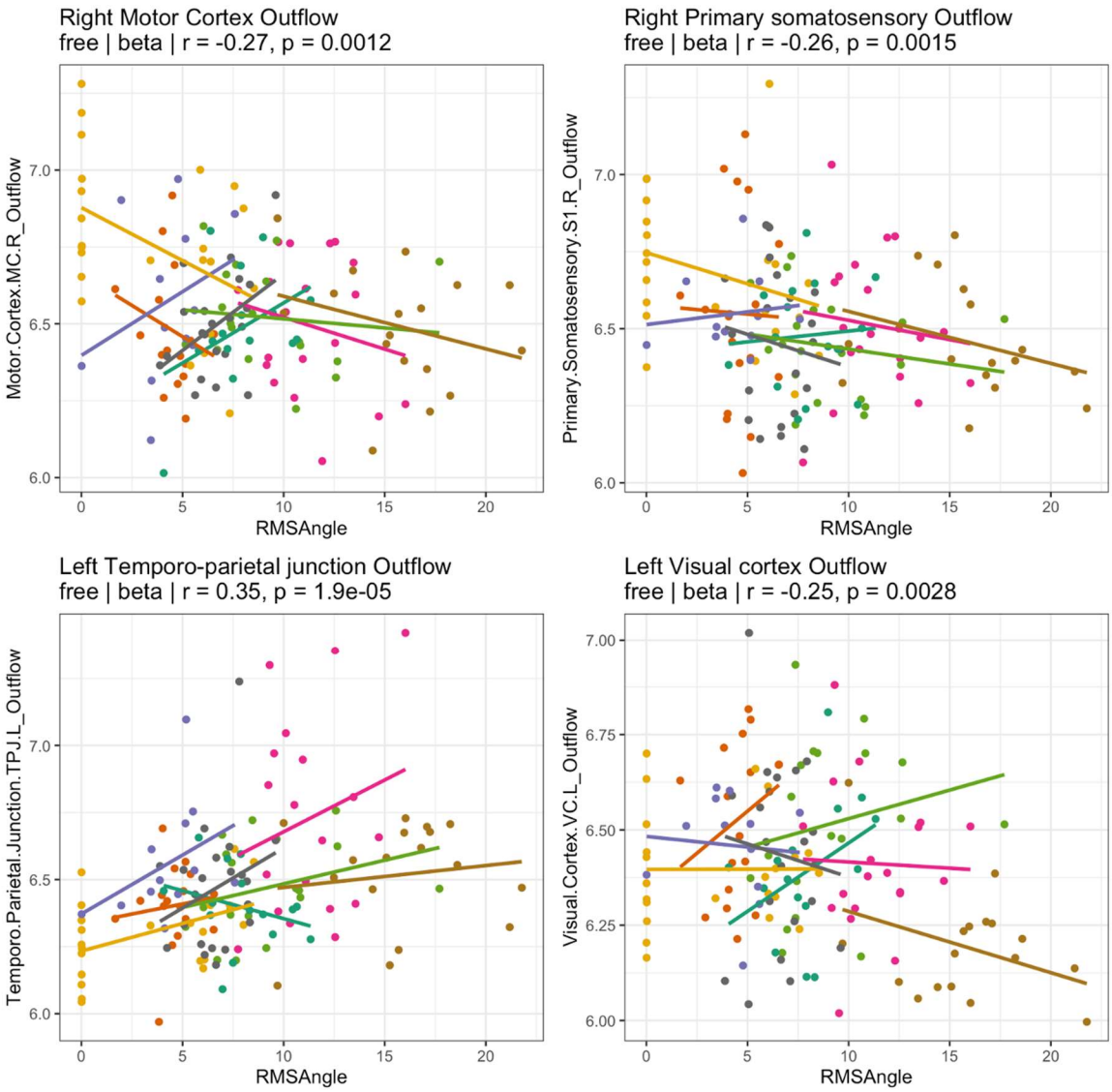


Figure 1. Scatter plots showing the relationship between PTE outflow and RMSAngle in four cortical regions during free mode. Each point represents one block and colors indicate individual participants. All four regions showed moderate, significant correlations with RMSAngle, with the strongest and most consistent associations in the temporo-parietal junction, suggesting greater engagement of this multisensory area with increasing pivoting instability.

Session Category

Clinical Biomechanics: N/A

OA165-04

Objective Gait Performance Does Not Predict Mobility Satisfaction in Older Adults

MSc Damaris Cifuentes[1], MSc Silvia Campos-Vargas[1], MSc Eduardo Santiago[2], Ph.D. Francisco Siles[2], Ph.D. Jaimie Roper[1]

[1]Auburn University, Auburn, Alabama, United States. [2]University of Costa Rica, San Jose, San Jose Province, Costa Rica

Introduction

Aging involves considerable variability in independent functional ability. Clinical guidelines have established objective ranges in spatiotemporal gait parameters (GPs) to define "healthy" mobility in older adults [1,2]; however, it remains unclear whether these objective ranges align with perceived functional adequacy and satisfaction in older adults. This study investigated the relationship between objective GPs and self-rated mobility satisfaction to determine whether normative metrics represent perceived functional health within this population.

Methods

Forty-four older adults (age: 69±9 years) performed a 40-meter walk test at their self-selected walking speed. Gait parameters (GPs) were collected using IMU sensors. Participants rated their mobility satisfaction on an analog scale from 0 to 100 (0= very poor; 100= excellent). Responses were categorized into low (0-33), medium (34-66), and high (67-100) satisfaction groups. MANOVA was conducted to examine differences in GPs across mobility satisfaction levels in older adults. GPs were compared to normative values for older adults aged 70-79 years [1].

Results

MANOVA revealed significant differences in gait speed and stride length across satisfaction groups ($p=.004$; $\alpha=0.05$). The high satisfaction group closely aligned with the normative values (gait speed: 1.23±0.12 vs. 1.10±0.19 m/s; stride length: 1.21±0.11 vs. 1.22±0.19 m). The low mobility satisfaction group demonstrated the fastest gait speed (1.31±0.19 m/s) and longest stride length (1.31±0.15 m) across all groups and exceeded the normative values. The medium mobility satisfaction group showed reduced performance in both measures (1.07±0.19 m/s, 1.14±0.16 m) compared to normative values.

Discussion

These findings suggest that mobility satisfaction relates more closely to gait consistency than to normative performance metrics, with the low mobility satisfaction group paradoxically exceeding normative values despite reporting dissatisfaction in mobility. This discrepancy highlights the importance of integrating patient-centered outcomes into clinical mobility assessments to capture perceived effort and efficiency, components overlooked by objective measures alone, to fully understand mobility capacity. Future work should explore how to best incorporate patient perspectives into clinical assessments to provide a more holistic evaluation of mobility in older adults.

Images (Optional)

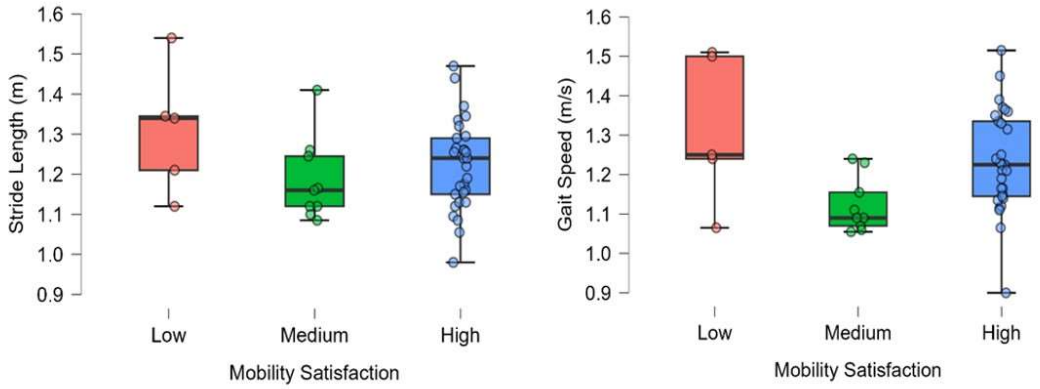


Figure 1. Box plots depicting stride length (m) and gait speed (m/s) across three levels of self-rated mobility satisfaction: low, medium, and high. The low satisfaction group demonstrated the fastest gait speed (1.31±0.19 m/s) and longest stride length (1.31±0.15 m) across all groups. The medium satisfaction group showed the slowest gait speed (1.07±0.19 m/s) and shortest stride length (1.14±0.16 m) across all groups. The high satisfaction group exhibited the lowest variability in both metrics (gait speed: 1.23±0.12 m/s; stride length: 1.21±0.11 m).

References (Optional)

[1] John H. Hollman et al., Gait and Posture, 2011 [2] Ulrike Dapp, BMC Geriatrics, 2022

Session Category

Clinical Biomechanics: N/A

OA165-05

Differences Between Young and Older Adult Knee Kinematics Can Inform Knee Arthroplasty Prosthesis Design and Selection

Ms. Emelia Krakora, Mr. Tom Gale, Dr. Malcolm Dombrowski, Dr. Alan Wilson, Dr. Johannes Plate, Dr. Kenneth Urish, Dr. William Anderst

University of Pittsburgh, Pittsburgh, PA, United States

Introduction

Total knee arthroplasty aims to restore native knee kinematics, guiding prosthesis design and surgical technique. Most existing native knee kinematics data come from cadaver studies or skin-mounted motion capture which can introduce measurement error [1]. This study used dynamic biplane radiography (DBR) to characterize knee kinematics, symmetry, center of rotation (COR), and femoral rollback during gait in younger and older asymptomatic adults. We hypothesized that older healthy knees would be less extended and less symmetric than younger healthy knees and that there would be no differences in older and younger healthy knees in COR location and femoral rollback.

Methods

Bilateral knee kinematics during treadmill gait were measured using DBR in 19 younger (31±6 years) and 20 older (65±9 years) adults. A validated tracking system matched digitally reconstructed radiographs of the femur and tibia, created from CT scans, to the biplane radiographs to track tibiofemoral motion [2]. Statistical Parametric Mapping assessed differences in kinematics waveforms and symmetry, while generalized estimating equations assessed differences in COR and lowest point locations.

Results

Older knees were more flexed at foot strike and less flexed during early stance with significant differences from 0% to 3% and from 24% to 49% of stance. The tibias in younger knees were more anterior compared to the older knees with significant differences at 1-47% and at 82-100% of stance (Figure 1). The COR was more proximal in stance extension (0.1 vs -13.42% of condyle height) and terminal stance (6.39 vs -1.19 %) in older knees (Figure 1). The lowest point in the medial compartment was more anterior at initial peak flexion (8.6 vs -1.4% of tibia depth) and toe off (5.4 vs -2.5%) in older knees. No differences in symmetry were observed.

Discussion

This study provides evidence demonstrating there are differences in *how much* the knee moves and *how* the knee moves in young and older healthy knees. These insights may be useful for guiding implant design as well as a serving as a reference standard for assessing if healthy kinematics have been restored after surgery.

Images (Optional)

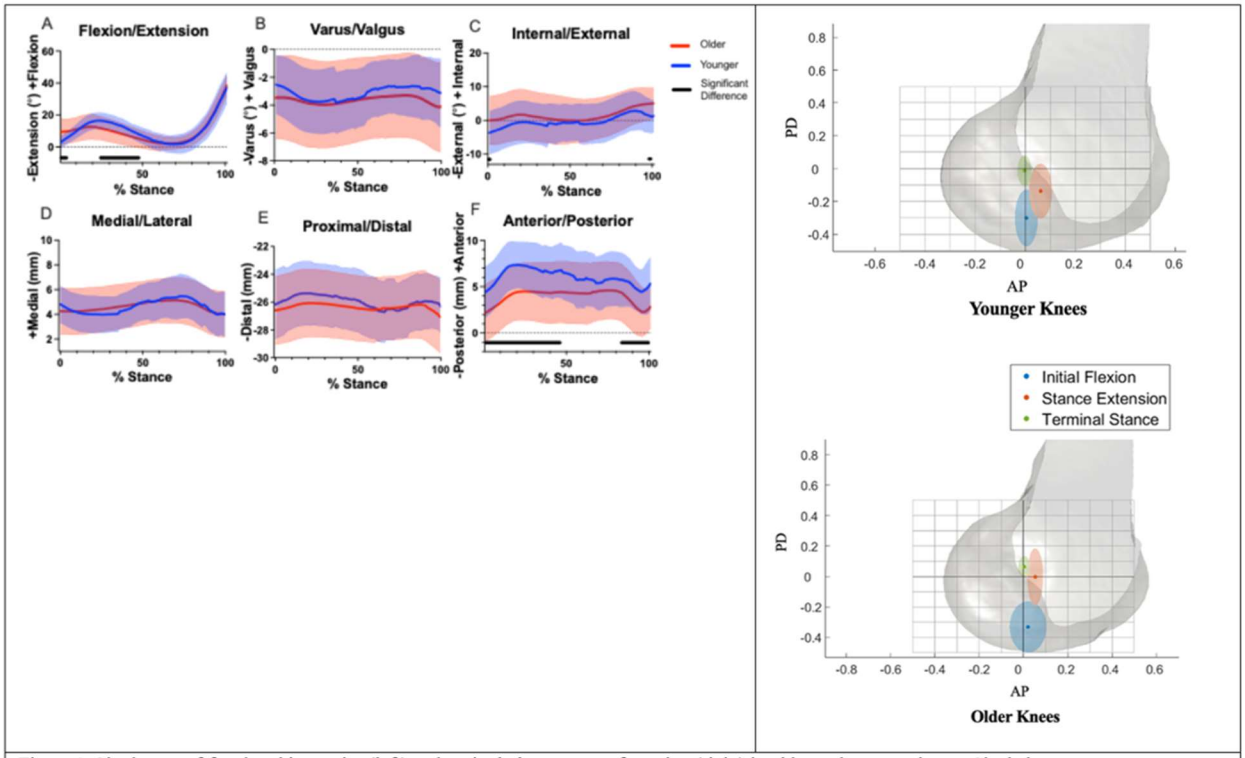


Figure 1: Six degree-of-freedom kinematics (left) and sagittal plane center of rotation (right) in older and younger knees. Shaded areas represent one standard deviation from the mean.

References (Optional)

[1] Tamaki et al., *The Knee,* 2023. [2] Anderst et al., *Med. Eng. Phys.*, 2009.

Acknowledgements (Optional)

This work was supported by a research grant from Smith & Nephew.

Session Category

Clinical Biomechanics: N/A

OA165-06

Step Variability Is Linked to Yaw Vestibular Sensitivity

Dr. Shawanee' Patrick Ph.D, Ms. Shauntelle Cannon, Ms. Sophia Chirumbole, Dr. Daniel Merfeld Ph.D, Dr. Ajit Chaudhari Ph.D

Ohio State University, Columbus, OH, United States

Introduction

Age-related vestibular decline contributes to mobility loss and fall risk, with one-third of adults over 65 falling each year [1]. Vestibular perceptual thresholds quantify sensory noise and increase with age [2], and roll-tilt thresholds relate to postural sway [3]. However, the link between vestibular perceptual sensitivity and gait is unclear, even though most falls occur during walking [4]. This study examined whether spatiotemporal gait measures and dynamic stability during a 6-minute walk test (6MWT) relate to vestibular perceptual thresholds in healthy adults.

Methods

Vestibular thresholds were measured using validated direction-recognition procedures for roll-tilt (0.5, 2 Hz), yaw rotation (2 Hz), and y- and z-translation (1 Hz) [2]. Participants completed a self-paced 6MWT along a 35.7 m hallway. Inertial measurement units (IMUs) were placed on both ankles, the pelvis, neck, and head. Straight-walking segments were extracted for spatiotemporal analysis. Step and stride metrics were derived from ankle IMUs, and short-term Lyapunov exponents were estimated from trunk motion. Linear models tested associations between gait outcomes and vestibular thresholds, adjusting for age.

Results

Thirty-nine adults (mean age = 44.77 ± 18.20 years) completed testing. Of all thresholds evaluated (roll 0.5 Hz, roll 2 Hz, yaw 2 Hz, y-translation 1 Hz, z-translation 1 Hz), only yaw 2 Hz was significantly associated with gait variability. Significant relationships were found for Step Time Coefficient of Variation (Step CoV; $R^2 = 0.19$, $p = 0.00062$), Step Time Standard Deviation (Step SD; $p = 0.00352$), and Step Frequency ($p = 0.0401$). No other threshold showed significant associations with Step CoV, Step SD, stride metrics, or short-term Lyapunov exponents ($p > 0.05$). Thus, yaw 2 Hz sensitivity was the only vestibular variable linked to gait variability.

Discussion

Findings demonstrate a selective link between 2-Hz yaw perceptual noise and step-level gait variability during prolonged walking, indicating an axis-specific vestibular contribution to locomotor control. Yaw sensitivity may influence foot placement consistency and the ability to maintain stable forward progression over time.

References (Optional)

[1] Orces (2014). J Community Health. 39(1): 1. [2] Bermúdez Rey (2016). Front Neurol. 7: 162. [3] Wagner (2023). Front Neurol. 14: 1184146. [4] Ihlen (2016). J Neuroeng Rehabil. 13: 94.

Session Category

Clinical Biomechanics: N/A

OA166-01

Mechanisms for Maximal Leaping Across a Wide Range of Locomotion Speeds

Dr Kat Daniels PhD[1], Dr J.F. Burn PhD[2]

[1]Manchester Metropolitan University, Manchester, Greater Manchester, United Kingdom. [2]University of Bristol, Bristol, Avon, United Kingdom

Introduction

Leaping is a locomotor manoeuvre that enables traversal of terrain regions that cannot safely support body weight or facilitate foot placement. The performance limits of this manoeuvre reveal how the sensorimotor system coordinates force production and momentum redirection to preserve stable locomotion near the limits of adaptive gait. Research into athletic long jump has shown a positive relationship between approach speed and jump distance but the mechanisms enabling maximal-distance leaping across everyday gait speeds are not well understood. Thus, the aim of this study was to investigate whole-body dynamics during maximal leaping across a range of speeds, from walking to high-speed running.

Methods

Fifteen healthy adults (8F/7M, aged 18-31) walked or ran along a level runway at five prescribed speeds. Each trial incorporated one maximal-length leap, taking off from one foot and landing on the other. Whole-body kinematics were recorded using optical motion capture and used to calculate the dynamics of the body centre of mass (CoM).

Results

Net mechanical energy change during leap take-off stance was positive at low approach speeds but decreased with speed, becoming negative at the fastest speeds. High-speed trials showed no net energy addition; instead, longer leaps arose from redirecting momentum vertically. Horizontal momentum increased at low speeds but decreased at approach speeds Fr>1.1 (Fr = Froude number). A decrease in net kinetic energy occurred above Fr=1.3. Across all speeds, gravitational potential energy increased during stance, primarily due to the more-upright leg angle and greater effective leg length at toe-off. Leap length increased with approach speed; however, the length increase from the penultimate step to the leap step remained constant.

Discussion

The observed mechanical energy changes suggest that two mechanisms contribute to maximising leap distance. At low speeds, muscular work increases CoM mechanical energy, although this capacity diminishes with speed due to shorter stance durations and increased requirement for lost energy replacement. At high speeds, leap length is increased by redirecting momentum, analogous to long-jump take-off dynamics and consistent with spring-mass model behaviour. The interaction between these two mechanisms results in a capacity to increase step length that is remarkably invariant across diverse locomotion speeds.

References (Optional)

Session Category

Human Motion and Performance: Locomotion/Gait

OA166-02

Ultrasound-Derived Leg Blood Flow Associates with the Metabolic Cost of Human Walking

Mr. Jose Anguiano-Hernandez MS[1], Dr. Jenna Burnett PhD[1], Mr. Cody Anderson BS[2], Dr. Song-Young Park PhD[2], Dr. Kota Takahashi PhD[1]

[1]University of Utah, Salt Lake City, UT, United States. [2]University of Nebraska at Omaha, Omaha, NE, United States

Introduction

The metabolic cost of walking ($\dot{V}O_2$) is often a key outcome of locomotion studies. However, gold-standard methods like indirect calorimetry describe whole-body metabolic cost and cannot parse out what portion is attributed to the legs. One method of parsing out the leg's contribution to the whole-body metabolic cost is measuring leg blood flow (LBF). While LBF has been measured using Doppler ultrasound during dynamic tasks like cycling [1], such a technique has not been used to quantify LBF in response to walking. The purpose of this study is to use an ultrasound-based method to determine whether walking-induced LBF reflects whole-body $\dot{V}O_2$ during walking.

Methods

Seven healthy young adults walked on a treadmill at a 0° slope, followed by a -5° and 5° slope in random order for 10 minutes at 1.2 m/s. A Doppler ultrasound probe was fastened over the dominant-side common femoral artery to measure LBF during quiet standing immediately before walking. Indirect calorimetry measured breath-by-breath $\dot{V}O_2$ before and during each walking condition. After walking, LBF was recorded for 5 minutes while participants stood quietly. Walking $\dot{V}O_2$ was calculated by averaging $\dot{V}O_2$ measurements during the final two minutes of each walking condition. Post-walking LBF was calculated by averaging LBF during the first ten seconds of each post-walking period. A linear mixed model was used to determine the association between post-walking LBF and walking $\dot{V}O_2$ at $\alpha = 0.05$.

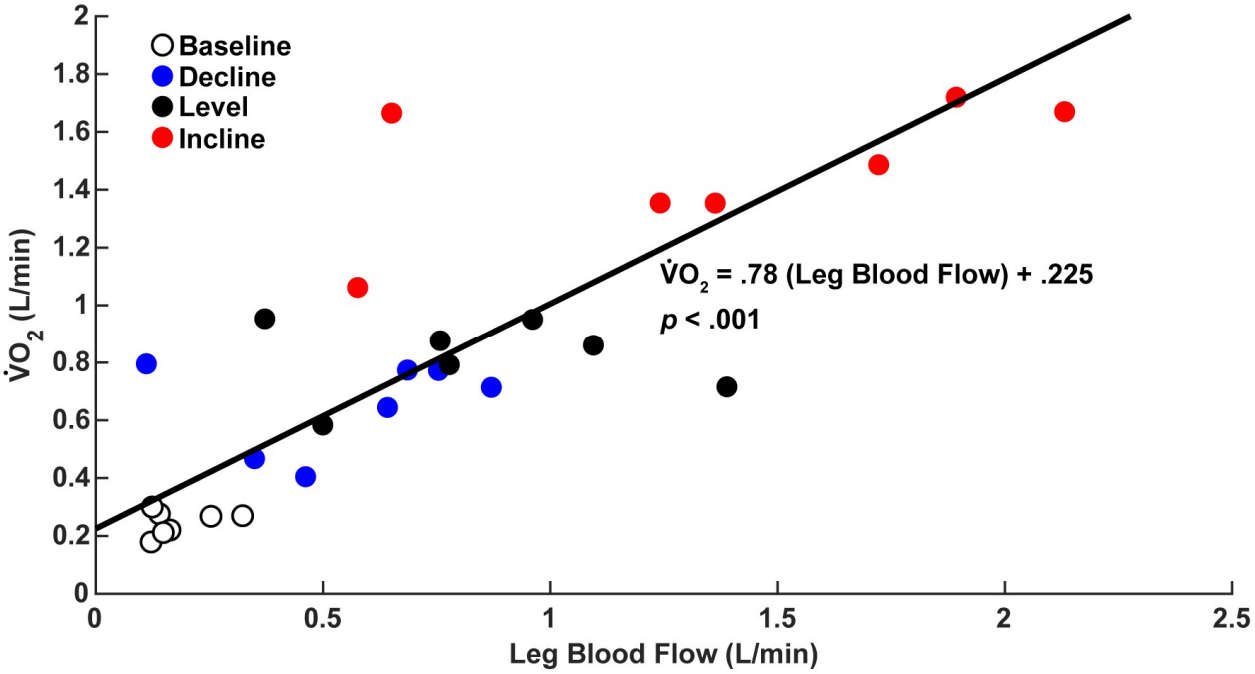
Results

Post-walking LBF associated with walking $\dot{V}O_2$ ($p < .001$), where a 1 L/min increase in LBF associated with a .78 L/min increase in whole-body $\dot{V}O_2$ (Figure 1).

Discussion

Our ultrasound method showed that leg metabolic demands may drive whole-body $\dot{V}O_2$ during walking, supporting our experimental framework to study mechanisms underpinning changes in walking $\dot{V}O_2$. This framework could also elucidate metabolic contributions of individual legs in those with gait asymmetry (e.g., stroke, amputation) or vascular impairments (e.g., diabetes, peripheral artery disease). This ultrasound technique could also measure changes in LBF when using interventions like exoskeletons or assistive devices to improve walking.

Images (Optional)



References (Optional)

[1] Cohen et al., J Appl Physiol, 2025

Session Category

Human Motion and Performance: Locomotion/Gait

OA166-03

Birds of a Feather *Walk* Together: A Simple Model Predicts Energy-Optimal Phase during Entrainment

Assistant Professor Ryan Schroeder PhD, Undergraduate Researcher Ryan Anderson

Brock University, St. Catharines, Ontario, Canada

Introduction

Human gait entrainment occurs when walking is synchronized with external oscillations from wearable robots or periodic forces at the center of mass (CoM) [1,2]. During entrainment, gait frequency is matched to the external oscillation, but phase is unknown *a priori*. Here we propose an energy minimization model to predict optimal phase during entrainment. Two walkers on separate treadmills are coupled by a spring pulling upward near the CoM. We hypothesize energy is minimized with in-phase walking such that peak spring forces reduce leg work done during the step-to-step transition. This work demonstrates a novel entrainment-based rehabilitation strategy to be applied in human experiments.

Methods

We developed a trajectory optimization model with JuMP and InfiniteOpt in Julia. Two inverted pendulum-like walkers comprise point masses (CoM) and massless legs that actively extend. The model's states are position and velocity of the CoM and controls are the leg extension forces. The objective function sums absolute mechanical work and force rate costs to model energy. Upward spring force is proportional to vertical displacement of the CoM. The optimization produced energy cost with variable spring stiffness and phase between walkers.

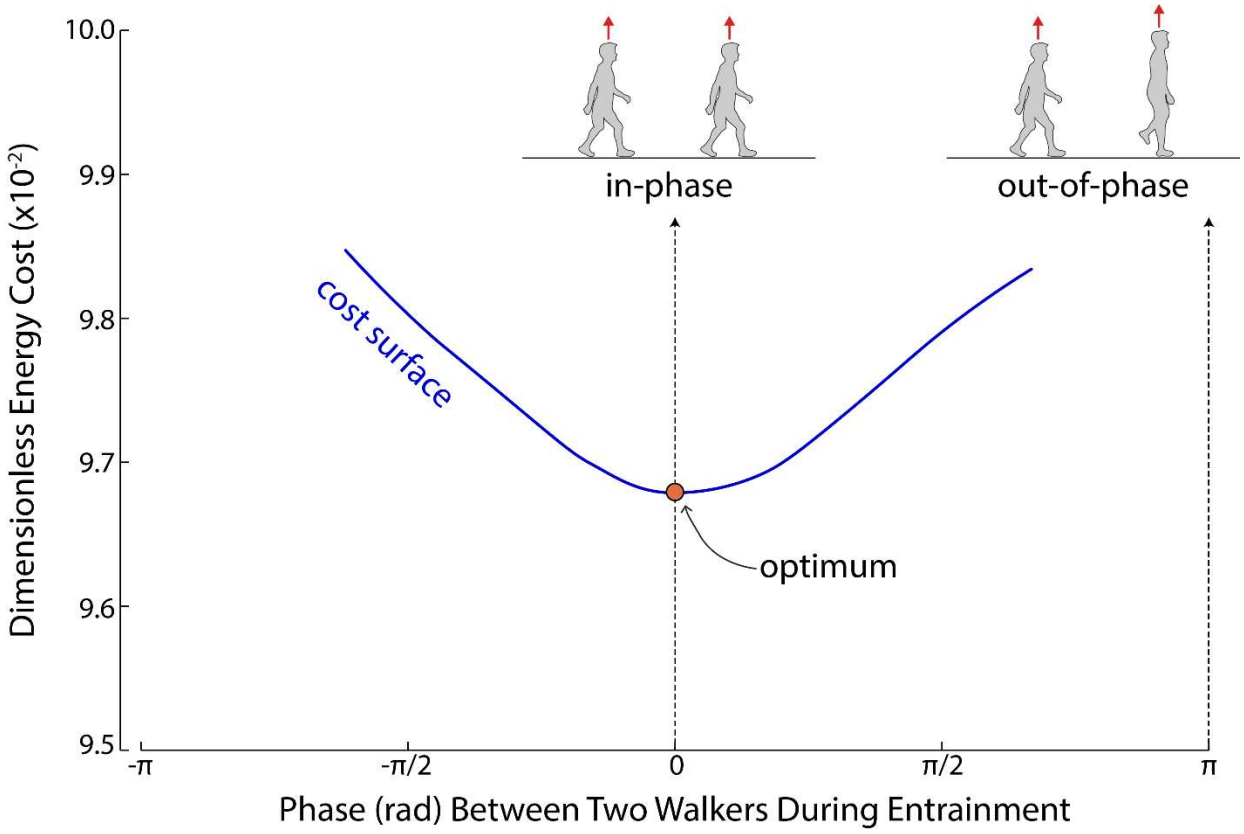
Results

Energy cost decreased by 10.7% as peak upward force increased from 2.8 to 13.8% body weight force from a stiffer spring. Decreased cost was primarily due to reduced leg work at the step-to-step transition. Energy cost was minimal during in-phase walking and increased toward out-of-phase walking (see Figure). Specifically, in-phase walking led to maximal peak upward forces occurring at the step-to-step transition, helping to reduce the leg work required to redirect the CoM from falling to rising.

Discussion

The results suggest that spring coupling could have strong potential for gait rehabilitation in clinical and healthy populations, given evidence of human energy minimization [3], but empirical validation is still needed. Future work could pair healthy and rehabilitating individuals in an entrainment protocol to motivate increased walking cadence and improved gait regularity in individuals recovering from stroke and other neuromotor injuries.

Images (Optional)



References (Optional)

[1] J Ahn & N Hogan, Dynamic Systems and Control, 2008

[2] RT Schroeder *et al.*, Sci Rep. 2021

[3] J Selinger *et al.*, Curr Biol, 2015

Session Category

Human Motion and Performance: Locomotion/Gait

OA166-04

Importance of Considering the Metabolic Cost of Walking in Gait Retraining Interventions

MSc Ellen Hellman[1], MD Jari Arokoski[2], PhD Rami Korhonen[1], PhD Lauri Stenroth[1]

[1]Department of Technical Physics, University of Eastern Finland, Kuopio, Finland, Kuopio, North Savo, Finland. [2]Department of Internal Medicine and Rehabilitation, Division of Rehabilitation, Helsinki University Hospital and University of Helsinki, Helsinki, Uusimaa Region, Finland

Introduction

Real-time electromyography (EMG) feedback has been proposed as a method for gait retraining to modify knee joint loading [1, 2], a common target in non-surgical knee osteoarthritis treatments [3]. In natural locomotion, humans tend to select muscle activation and kinematic patterns that minimize the energy cost of transport (CoT) [4]. This may be in contrast with the targets of gait retraining, limiting the feasibility or effectiveness of interventions. Here, we investigated the effects of EMG-based calf muscle modification intervention on the walking CoT in older adults.

Methods

Twenty-nine healthy adults (65–75 y) participated in an 8-week intervention including weekly gait retraining sessions on an instrumented treadmill and pre- and post-intervention outcome assessments. The training aimed at modifying the activation ratio of the soleus (SOL) and medial gastrocnemius (MG) muscles, ideally by increasing SOL and decreasing MG activation. As feedback, the ratio of the root mean square of the SOL and MG EMG signals during push-off, normalized to baseline walking, was shown on a monitor. In the pre- and post-intervention sessions, EMG and respiratory gases were measured during 5-minute walking trials (1.25 m/s). CoT (last-2-minute average) and SOL-to-MG activation ratio (last-minute average) were analyzed.

Results

There was a significant shift in the SOL-to-MG activation ratio toward a more soleus-dominant pattern, both before and after intervention. CoT increased under the feedback condition by 43% (d_z:2.073, $p<0.001$) compared to normal walking in the pre intervention measurements and by 35% (d_z:1.862, $p<0.001$) in the post measurement (Fig. 1). From pre to post, CoT decreased 8% in the normal condition (d_z:0.816, $p<0.001$) and by 13% in the feedback condition (d_z:0.764, $p<0.001$).

Discussion

The gait retraining intervention reduced the energy cost of producing intended changes in muscle activity, suggesting that training improves the feasibility of implementing an altered coordination strategy. Still, the energy cost of walking was 35% higher during modified muscle activations compared to normal walking, highlighting that energetics should be considered when designing new locomotor interventions.

Images (Optional)

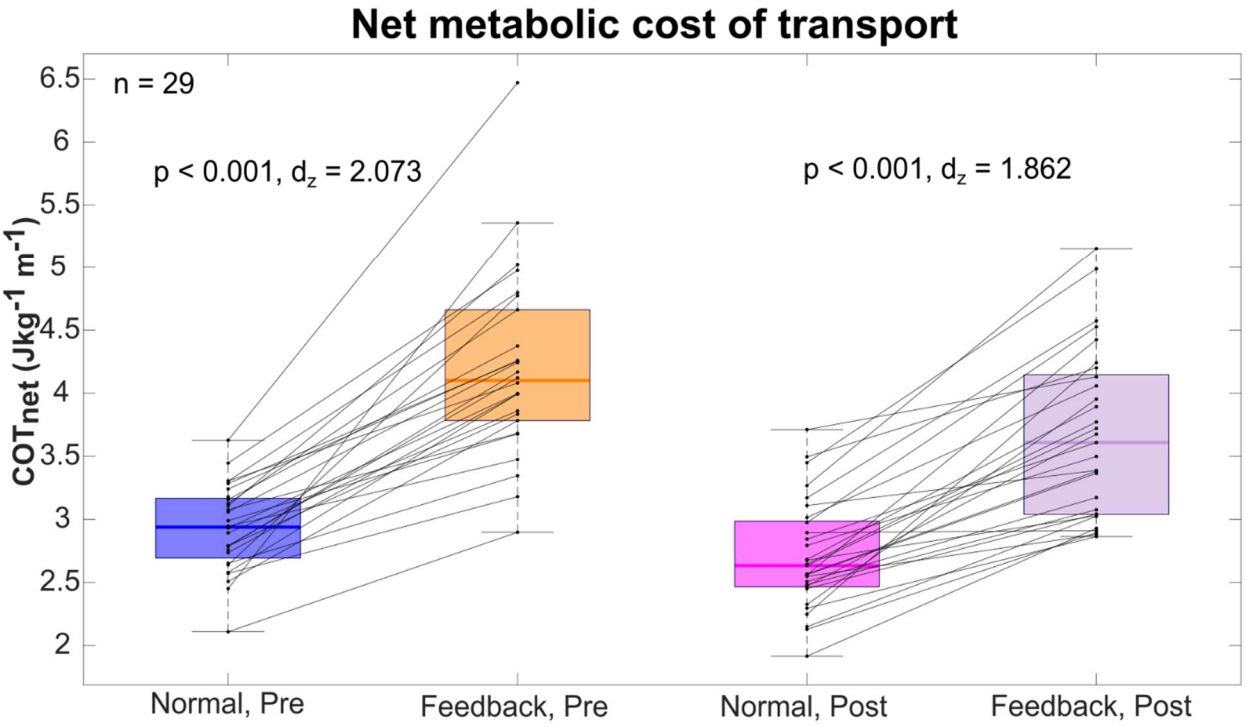


Figure 1: Net metabolic cost of transport during normal walking and during walking with modified calf muscle activations guided by real-time EMG feedback.

References (Optional)

[1] Uhlrich *et al.* Sci. Rep, 2022

[2] Hellman *et al.* J. Biomech, 2025

[3] Andriacchi *et al.* ABME, 2004

[4] McAllister *et al.* JEB, 2025

Session Category

OA166-05

Sequencing Leg Forces Drives the U-Shaped Metabolic Cost-Speed Relationship in Walking Across Adulthood

Ms. Elham Alijanpour M.Sc., Ph.D. (ABD), Dr. Ashwini Kulkarni PT, Ph.D., Dr. Hunter Bennett Ph.D., Dr. Patrick Wilson Ph.D., Dr. Heather Hamilton DPT, Ph.D.

Old Dominion University, Norfolk, Virginia, United States

Ms. Elham Alijanpour

Dr. Ashwini Kulkarni

Dr. Hunter Bennett

Dr. Patrick Wilson

Introduction

Redirecting the center of mass is a key contributor to walking energy costs. Theoretical models propose that humans decrease redirection cost either by sequencing push-off and collision forces (walking) or by using elastic leg mechanics (running). The Sequence index (S-index) quantifies the overlap between push-off and collision forces during redirection phase, ranging from 0 (complete separation, running) to 1 (simultaneous forces, standing). S-index decreases with increases in walking speed until it reaches a ceiling point. Contrarily, metabolic cost of walking (MCoW) has a U-shape relationship with walking speed. We aimed to test whether the U-shaped relationship between walking speed and metabolic cost is driven by changes in force sequencing (S-index). We hypothesized that at slower speeds, improved force sequencing (lower S-index) would reduce MCoW despite increasing speed; however, at faster speeds, when force sequencing reaches its biomechanical ceiling, further increases in walking speed would lead to increased MCoW.

Methods

Fifty healthy adults (18-79 years) walked on an instrumented treadmill at three speeds (80%, 100%, and 120% of preferred walking speed). S-index and MCoW were calculated from the last three minutes of each trial. Linear mixed models examined S-index, age, and speed as predictors of MCoW across: (M1) all speeds, (M2) speeds <1.4 m/s, and (M3) speeds ≥1.4 m/s (selected as critical threshold based on prior research).

Results

Across all speeds (M1), S index, age, speed, and S index × speed interaction significantly predicted 83% of the MCoW variation (Figure 1D). At speeds below 1.4 m/s (M2), S index, age, and S index × speed interaction significantly predicted 86% of the MCoW variation (Figure 1E). At speeds above 1.4 m/s (M3), only speed significantly predicted 93% of MCoW variation (Figure 1F).

Discussion

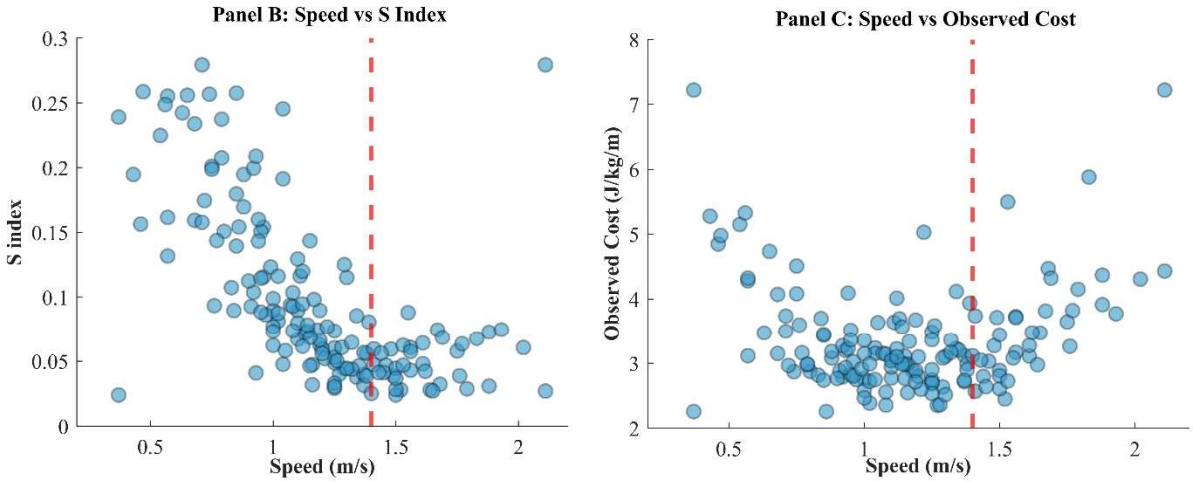
We experimentally validated Ruina et al.'s force sequencing theoretical model: improved force sequencing reduces MCoW for speed <1.4 m/s. These results have meaningful implications for gait rehabilitation in individuals who walk slower. Interventions targeting improved force sequencing can be effective to improve MCoW in these populations. The S index is a sensitive metric for identifying changes in gait efficiency at speeds relevant to daily function.

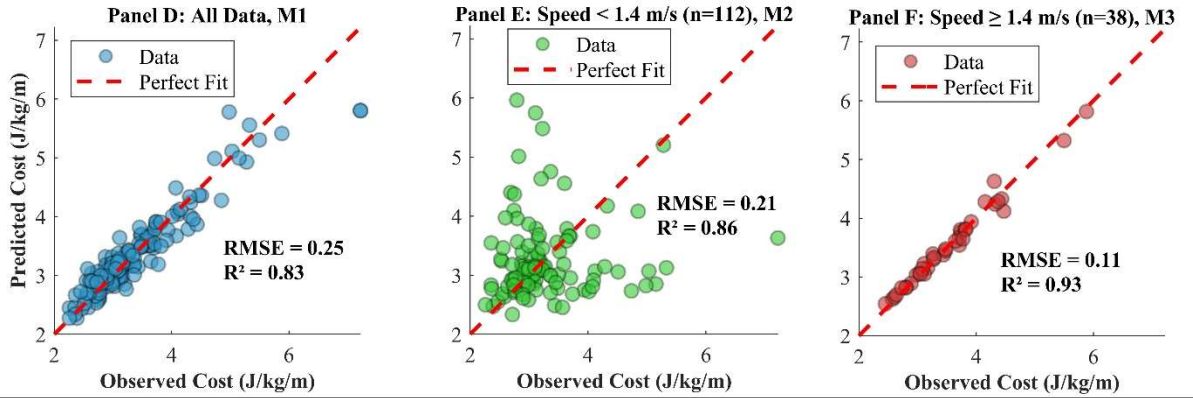
Images (Optional)

Figure 1. Mixed-effects model predictions of metabolic cost during walking. (A) Descriptive statistics of the study sample. (B) S index versus walking speed, (C) Metabolic cost versus walking speed, at speeds below 1.4 m/s as walking speed increases S index decreases, (sequencing leg forces improves) and metabolic costs decreases, however, at speeds above 1.4 m/s, S index reaches a saturation point and increases in walking speeds leads to increase in metabolic cost. (D) Model 1 (M1, all speeds): Predicted versus observed metabolic cost (RMSE = 0.25 J/kg/m, $R^2 = 0.83$). Cost = 0.95 + 0.017×Age + 12.58×S index + 1.27×Speed − 11.98×S index×Speed. Main effects significant: Age ($p<0.001$), S index ($p<0.001$), Speed ($p<0.001$), S index×Speed interaction ($p<0.001$). Age×S index interaction was not significant ($p=0.845$), indicating sequencing leg forces effects on metabolic cost are age-independent. (E) Model 2 (M2, speeds <1.4 m/s): Predicted versus observed metabolic cost (RMSE = 0.21 J/kg/m, $R^2 = 0.86$). Cost = 2.75 + 0.018×Age + 7.06×S index − 10.38×S index×Speed. Significant effects: Age ($p<0.001$), S index ($p=0.009$), S index×Speed interaction ($p<0.001$). Speed effect was not significant ($p=0.766$), indicating age and S index are critical predictors at slower speeds. (F) Model 3 (M3, speeds ≥1.4 m/s): Predicted versus observed metabolic cost (RMSE = 0.11 J/kg/m, $R^2 = 0.93$). Cost = −1.99 + 3.05×Speed. Speed was the only significant predictor ($p<0.005$). Age and S index effects were not significant (p's>0.10), indicating biomechanical constraints limit sequencing leg forces optimization at faster speeds.

Panel A: Descriptive Statistics

Variable	M1 (All)	M2 (<1.4)	M3 (≥1.4)
Age (year)			
Mean ± SD	49.49±19.21	49.51±19.63	49.47±17.61
Min-Max	18-79	18-79	18-75
n (participants/observations)	50/150	49/112	28/38
Speed (m/s)			
Mean ± SD	1.17±0.36	1.01±0.24	1.62±0.18
Min-Max	0.37-2.11	0.37-1.39	1.40-2.11
S index			
Mean ± SD	0.10±0.07	0.12±0.07	0.05±0.02
Min-Max	0.02-0.28	0.03-0.28	0.02-0.09
Cost (J/kg/m)			
Mean ± SD	3.36±0.82	3.27±0.75	3.54±0.76
Min-Max	2.26-7.22	2.26-7.22	2.45-5.88





Session Category

Human Motion and Performance: Locomotion/Gait

OA166-06

Effects of Aging on Lower Extremity Joint Loading and Energy Cost of Walking at Different Gait Speeds and Step Rates

Mr. Dante Goss, Dr. Siddhartha Angadi, Dr. Jay Hertel

University of Virginia, Charlottesville, Virginia, United States

Introduction

The distal-to-proximal shift in joint kinetics from the ankle and knee towards the hip has been proposed as a mechanism for the worsening of walking economy associated with aging, but it is unknown how manipulating gait speed and step rate influence this trend as well as walking economy. The purpose of this study was to examine how changes to gait speed and step rate influence walking economy and lower extremity sagittal plane kinetics between adults in three age groups.

Methods

Fifty-two healthy adults were classified into three age groups: Young (18-39 yrs), Middle (40-59 yrs), Old (60-75 yrs) completed nine trials of gait analysis on an instrumented treadmill while oxygen uptake was measured from indirect calorimetry. Walking trials were completed under three gait speed conditions: preferred gait speed, 10% below preferred gait speed, and 10% above preferred gait speed, and three step rate conditions: preferred step rate, 5% above preferred step rate, and 10% above preferred step rate. Linear mixed effects models were used to test the effect of gait speed, step rate, and age group on peak and impulse values for hip flexion, knee flexion, and ankle plantarflexion, as well as energy expenditure and cost of walking.

Results

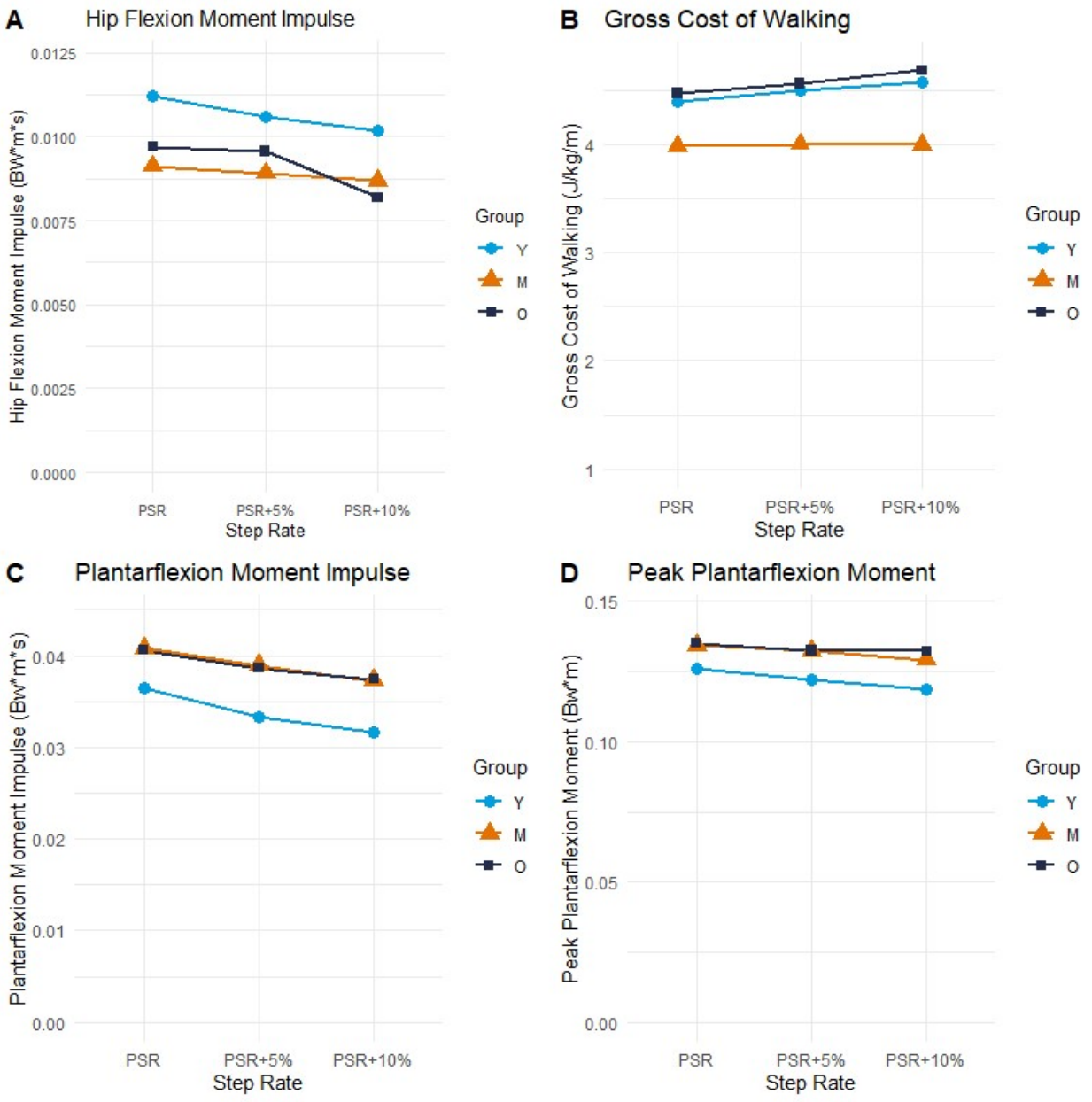
Significant interactions existed between age group and step rate for hip flexion moment impulse ($p = 0.05$), gross cost of walking ($p = 0.05$), peak plantarflexion moment ($p = 0.005$), and plantarflexion moment impulse ($p = 0.03$). The middle and old age groups had significantly higher plantarflexion moment impulse values at both 5% above preferred step rate ($p=0.026$) and 10% above preferred step rate ($p=0.018$) compared to the young group. The middle age group had significantly lower gross cost of walking values compared to the old group at 10% above preferred step rate (0.013).

Discussion

This sample did not exhibit changes consistent with age-related distal-to-proximal shift in joint kinetics and showed largely consistent changes across gait speeds with increased

step rate. Older adults may decrease cumulative plantarflexion moment loading with increased step rate less than younger and middle-aged adults, but this change is not reflected in their walking economy.

Images (Optional)



Session Category

Human Motion and Performance: Locomotion/Gait

OA167-02

Left Ventricular Deformation and Strain Reconstruction from Limited CT Frames Using Physics-informed Inverse Modeling

Mr. Weiqiang Liu[1], Dr. Hristo Valtchanov[2], Mr. Sadaival Singh[2], Dr. Francois Guibault[2], Dr. Rosaire Mongrain[1]

[1]McGill University, Montreal, Quebec, Canada. [2]Polytechnique Montreal, Montreal, Quebec, Canada

Introduction

Reconstructing left-ventricular (LV) deformation and strain is essential for biomechanical assessment and patient-specific cardiac modeling, as these metrics reveal regional contractile dysfunction and lack of perfusion. Hypokinetic wall motion often indicates impaired myocardial viability due to ischemia, necrosis, or microvascular dysfunction[1]. Quantifying such abnormal 3D deformation is crucial to clinical decision-making. Conventional finite-element analysis (FEA) requires high-quality imaging, segmentation, meshing, and computationally intensive solvers—tools rarely combined in clinical routine CT protocols. To address these limitations, we present a meshfree, physics-informed inverse-modeling framework that reconstructs volumetric LV deformation and strain from only a few CT frames.

Methods

The framework uses a hierarchical Gaussian radial basis function (RBF) representation. Surface RBFs first control the vertices' movements during elastic registration between the undeformed LV mesh and multiview CT projections, using mutual information as the optimization objective. The registered surface then provides boundary conditions for an inverse problem solved directly with volumetric RBF interpolation. Two volumetric RBF layers, a coarse layer for global deformation and a fine layer for local variations, are used to interpolate the full displacement field. A combined loss enforces surface displacement matching, fixed base boundary condition, continuity, and constitutive behavior. To evaluate performance, a forward FEA simulation of a truncated-ellipsoid LV (E = 0.5 MPa, 10 kPa endocardial pressure [2]) deformation was conducted in ANSYS as reference values.

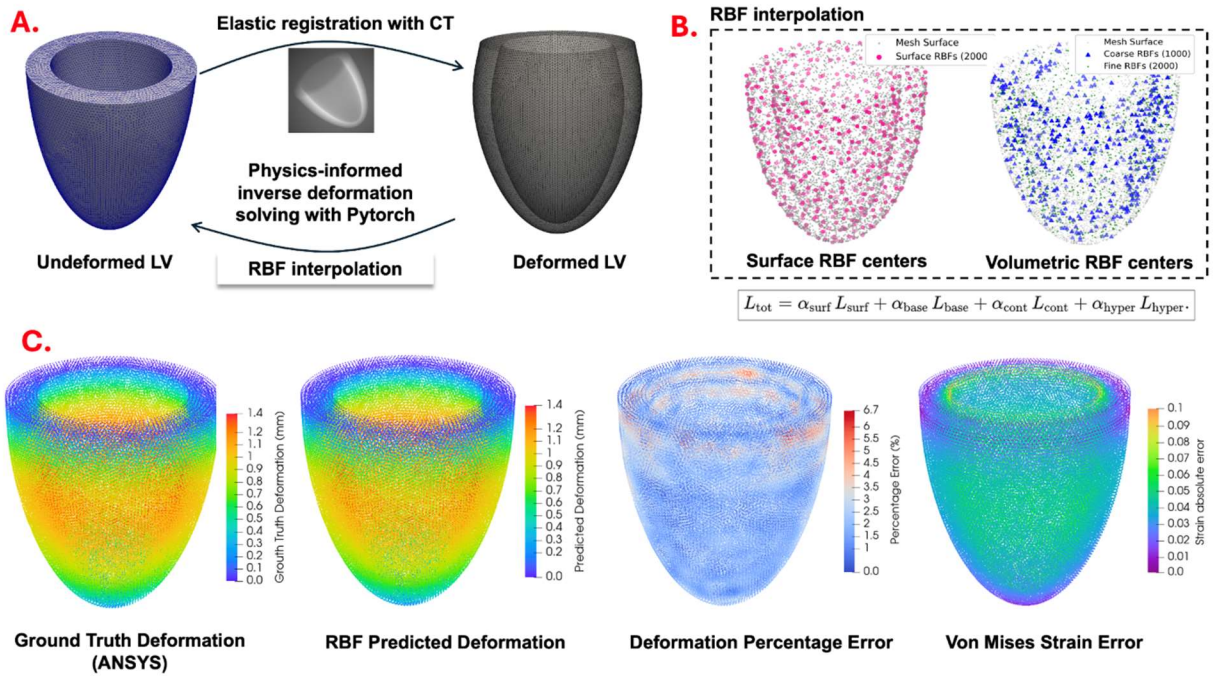
Results

On the LV dataset used for validation (~100k nodes), the hybrid RBF reconstruction achieved a mean deformation error of 3.1% and a maximum error of 6.7% relative to the finite-element reference values from ANSYS (Figure 1C).

Discussion

This physics-informed, mesh-free approach enables fast and fully automatable LV biomechanics reconstruction without segmentation or volumetric meshing. The entire pipeline runs in ~10 minutes on an NVIDIA RTX 4070, making it suitable for clinical workflows that rely on sparse CT imaging. As a proof of concept, this study adopts a simplified physical model but the framework already provides clinically meaningful deformation estimation and has potential for extension to patient-specific fiber architecture, multiscale 0D-3D hemodynamics, full heart geometries, and transient simulations.

Images (Optional)



References (Optional)

[1] R. F. Leighton et al., *Circulation*, 1974.
[2] K. Meyers et al., *Gels*, 2021.

Session Category

Cardiovascular/Cardiorespiratory Biomechanics: Methods, Models and Applications

OA167-03

Bayesian Inference of Lumped Cardiovascular Models Reveals Sex Differences in Ventricular–arterial Function

Ir. Beatrice Moscoloni[1,2,3], Prof. Dr. Ernst Rietzschel[4], Dr. Ir. Mathias Peirlinck[2], Prof. Ir. Patrick Segers[1]

[1]Institute of Biomedical Technology - BioMMedA, Ghent University, Ghent, East Flanders, Belgium. [2]Department of BioMechanical Engineering, TU Delft, Delft, South Holland, Netherlands. [3]Division of Cardiovascular Medicine, UPenn, Philadelphia, PA, United States. [4]Department of Cardiovascular Diseases, Ghent University Hospital, Ghent, East Flanders, Belgium

Introduction

Sex differences in cardiovascular disease are increasingly recognized, yet several questions about sex-specific vascular aging and ventricular–arterial coupling remain pending. Understanding these differences requires robust, mechanistic quantification of cardiovascular model parameters across large populations. Lumped parameter network models (LPNs) offer fast and interpretable estimates of cardiovascular function, yet traditional fitting strategies might fail to resolve parameter uncertainty or practical identifiability, particularly in noisy experimental data. To overcome this, we explore Bayesian inference of an open loop heart–arterial interaction model, using non-invasively recorded central pressure and flow waveforms from the 1st round of the Asklepios study, a longitudinal population study focused on healthy cardiovascular ageing.

Methods

Our LPN consists of a normalized time-varying elastance representing ventricular contraction coupled to a three-element Windkessel arterial system model representing the time-varying arterial afterload (Figure 1A). We estimate five parameters: peak ventricular elastance (Emax), peripheral resistance (R), aortic compliance (C), characteristic impedance (Zc), and timing of the elastance peak (tp)- while holding all others fixed. We work in two stages; we first perform (i) deterministic gradient-based optimization to design weakly informative priors, followed by (ii) subject-specific Markov-chain Monte Carlo sampling to obtain full posterior distributions and credible intervals of the parameters. We deploy the pipeline on a subset of 734 subjects (387F/348M) balanced for covariates.

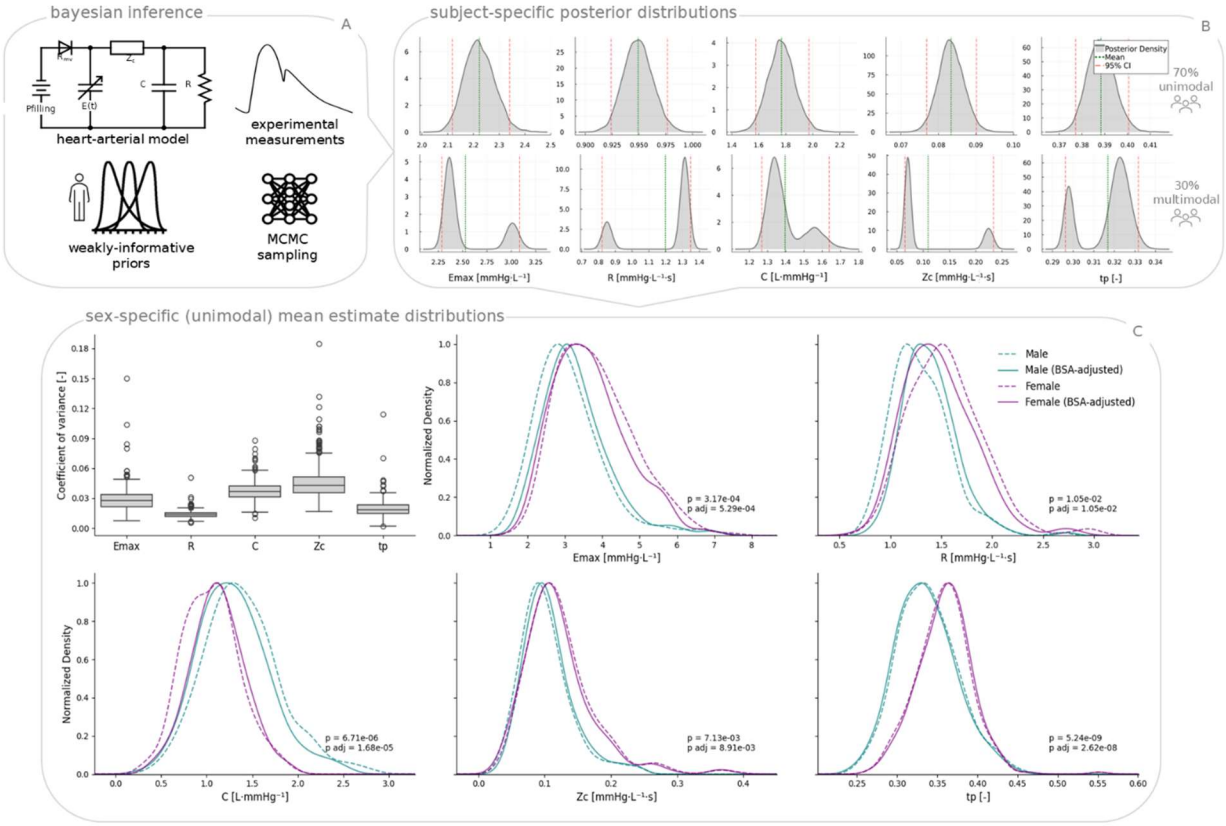
Results

We found that approximately 30% of subjects exhibited multimodal posterior distributions, indicating distinct parameter combinations capable of reproducing the observed hemodynamics (Figure 1B). Characteristic impedance (Zc) showed the greatest uncertainty, with a median normalized coefficient of variation of 0.046, followed by aortic compliance (0.037), peak elastance (0.028), and timing and resistance parameters (0.019 and 0.014 respectively – Figure 1C). Bayesian inferred model performance remained acceptable given model assumptions, with average R^2 values of 0.82 for aortic flow and 0.87 for aortic pressure. Finally, after adjusting for body surface area, we observed statistically significant sex differences in the posterior mean estimates of all (unimodal) parameters (Figure 1C).

Discussion

Our results highlight the need for uncertainty quantification to obtain reliable parameter estimates from experimental hemodynamic data and demonstrate the potential of Bayesian LPN modeling for mechanistic characterization of sex-specific ventricular–arterial function.

Images (Optional)



References (Optional)

Acknowledgements (Optional)

We thank Research Foundation Flanders (Grant no: 1PS524N) and the European Union's Horizon Europe research and innovation program (VITAL – Grant No.101136728).

Session Category

Cardiovascular/Cardiorespiratory Biomechanics: Methods, Models and Applications

OA167-04

CardioGraphFENet: A Rapid Deep-Learning Surrogate for Cardiac Myocardial Finite Element Modelling

Mr Siyu Mu, Dr Wei Xuan Chan, Miss Niimura Ai, Dr Choon Hwai Yap

Imperial College London, London, Greater London, United Kingdom

Introduction

Finite element modelling (FEM) is a foundational tool for cardiac biomechanics investigations but often requires hours for a full-cycle simulation, discoursing clinical adoption [1]. Deep learning (DL) offers a faster alternative. However, PINN-FEM require reduced-order modelling that reduces accuracy, and still need many minutes for inference, while existing one-shot networks have succeeded in modelling only passive diastolic mechanics and not systolic contractions [2]. Here, we introduce CardioGraphFENet, a DL graph-based surrogate enhanced with a cycle-consistency framework, for full-cycle FEM left ventricle (LV) modelling with any arbitrary LV 3D mesh input.

Methods

CardioGraphFENet functions as a unified surrogate for both forward FEM (predicting pressure and displacement fields) and inverse FEM (predicting the zero-pressure load-free configuration). The architecture integrates a graph fusion encoder to extract mesh features and used GRUs to encode time-dependent mechanics. It trained with a self-supervised cycle-consistent strategy, where the predicted forward FEM step is enforced to match the predicted reversal of the step. The framework was trained on a synthetic dataset of over 1.8 million LV states, generated from a range of LV shapes from a statistical shape model [3] and varying physiological conditions.

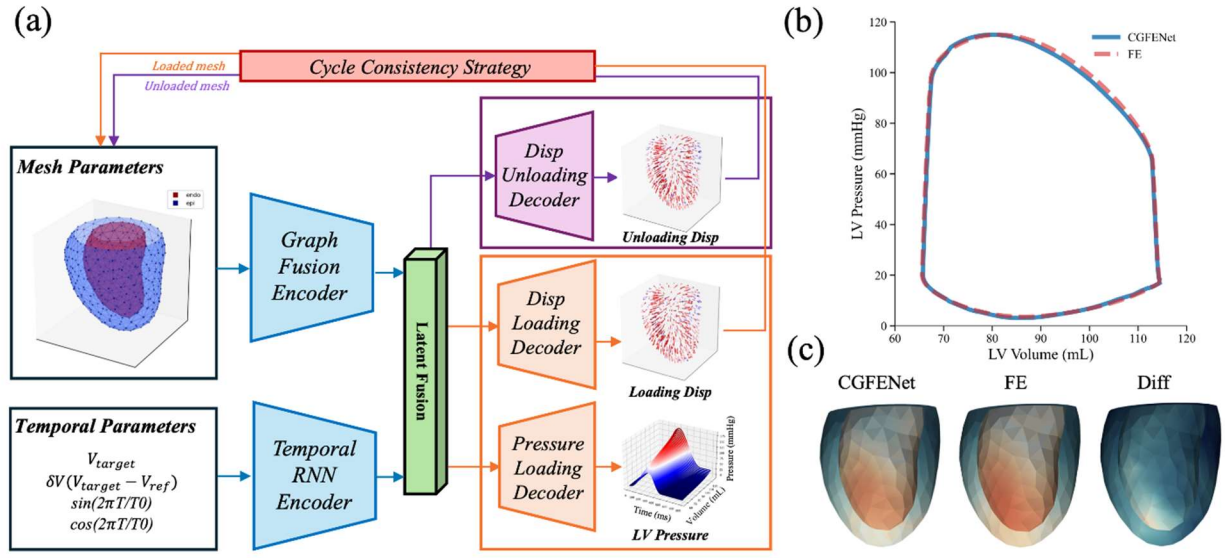
Results

CardioGraphFENet was benchmarked against GraphUNet and MeshGraphNet and demonstrated the best performance. For loading displacement prediction, the model achieved an accuracy of 90% of nodes having <1mm error and 99% <2mm error, and R^2>0.98 for pressure prediction. When combined with a lumped parameter model, the predicted P–V loop closely matched the FEM ground truths. For a full cycle simulation of 50 time points, CardioGraphFENet reduced computation time from several hours to under one minute, a 70-fold acceleration.

Discussion

CardioGraphFENet is fully supervised by mass FEM simulations. This is more effective than PINN, which incurs very high computational costs, unless reduced order is utilized, but which reduces accuracy. CardioGraphFENet allows anyone without FEM skills to perform FEM very quickly, potentially encouraging clinical adoption and enabling large clinical trials. Being robust, fast and flexible, it can be used in various secondary optimization loops.

Images (Optional)



(d)

Model	Displacement			Pressure	
	RMSE (mm)↓	Vertex Acc. < 1mm ↑	HD (mm)↓	R^2↑	RMSE (mmHg)↓
GraphUNet	0.42 ± 0.02	0.85 ± 0.01	3.30 ± 0.11	0.95 ± 0.01	5.83 ± 0.22
MeshGraphNet	0.44 ± 0.02	0.81 ± 0.03	4.88 ± 0.24	0.98 ± 0.01	3.63 ± 0.10
CardioGraphFENet (ours)	$\mathbf{0.39 \pm 0.01}$	$\mathbf{0.90 \pm 0.01}$	$\mathbf{1.89 \pm 0.15}$	$\mathbf{0.98 \pm 0.01}$	$\mathbf{1.70 \pm 0.17}$

References (Optional)

[1] C. Rodero et al., Front. Phys., 2023.

[2] D. Dalton et al., CMAME., 2023.

[3] P. Medrano-Gracia et al., JCMR, 2014.

Session Category

Cardiovascular/Cardiorespiratory Biomechanics: Methods, Models and Applications

OA167-05

Aneurysm Forecasting Studio: A Machine Learning Based Tool for Time-Series Prediction of Wall Growth and Lumen Remodeling in Abdominal Aortic Aneurysms

Ph.D. Candidate Juan Restrepo[1], Ph.D. Amanda Fernandez[1], Ph.D. Seungik Baek[2], M.D. Satish Muluk[3], M.D. Mark Eskandari[4], M.D. Vikram Kashyap[5], M.D. Eanas Yassa[5], Ph.D. Ender Finol[1]

[1]The University of Texas at San Antonio, San Antonio, Texas, United States. [2]Michigan State University, East Lansing, Michigan, United States. [3]Allegheny General Hospital, Pittsburgh, Pennsylvania, United States. [4]Northwestern University, Chicago, Illinois, United States. [5]Corewell Health, Grand Rapids, Michigan, United States

Introduction

Artificial Intelligence in cardiovascular medicine has advanced segmentation, surveillance, and risk prediction, yet time-series models for full-geometry forecasting remain limited. Most prior work predicts scalar measures such as maximum diameter or volume, overlooking spatial heterogeneity of aneurysm remodeling. This work introduces a patient-specific framework for forecasting 3D wall and lumen remodeling in Abdominal Aortic Aneurysm (AAA), enabling anticipatory surveillance and future anatomical estimations.

Methods

We modeled the AAA wall and lumen independent evolutions using local linear heterogeneity via patient-specific linear mixed-effects modeling applied in a standardized cylindrical grid within follow-ups enabling node-wise estimation of local linear trends and regional variability. We used data from 79 patients under surveillance in a multicenter cohort totaling 249 computed tomography exams. Performance was assessed using per-patient means of spatial similarity (HD95) across centerline, cylindrical, and cartesian domains, and geometric errors in maximum diameter and volume. The resulting models were integrated into an interactive forecasting interface that generates future geometries, enabling rapid visualization, threshold timing, and patient-specific monitoring.

Results

Forecasts achieved sub-millimetric spatial similarity in the cylindrical representation (HD95 wall: 0.7 mm; HD95 lumen: 0.9 mm) and low geometric errors in maximum diameter and volume (≤ 2%). Model fitting required 7–15 seconds per patient and inference produced real-time predictions, significantly reducing computation compared to growth-

and-remodeling alternatives. Predicted geometries remained anatomically coherent and captured regional remodeling patterns for diverse temporal intervals and anatomical layers. A representative evaluation case and interface output are shown in the figure.

Discussion

Our findings demonstrate that patient-specific mixed-effects modeling can accurately forecast short-term AAA wall and lumen remodeling, capturing both global trends and localized heterogeneity without requiring complex biomechanical simulations. The approach is fast, interpretable, and driven solely by past imaging and time, enabling real-time estimation of future morphology, threshold timing, and trajectory exploration. Integration into an interactive forecasting interface supports clinical use by providing instant 3D geometry previews at any prospective time point. A key limitation is the absence of clinical covariates, which may restrict physiological interpretability. Broader, globally representative datasets will be essential to validate robustness and ensure applicability across diverse patient populations.

Images (Optional)

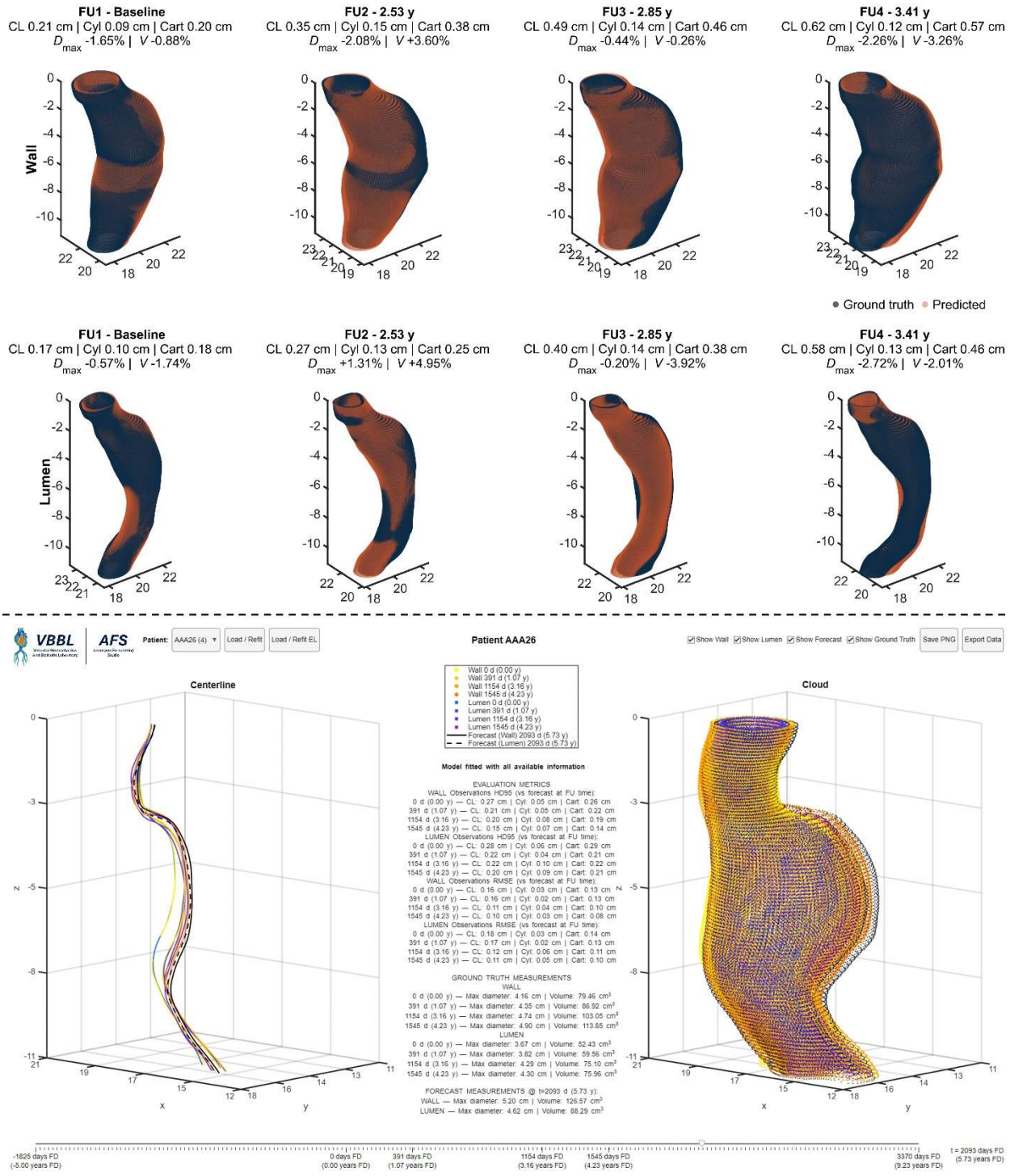


Figure. Top: Reconstruction example for a patient with four follow ups. Navy clouds show ground truth wall (top) and lumen (bottom) surfaces, and orange clouds show their corresponding predictions. Reported values are HD95 centerline (CL), cylindrical (Cyl), and Cartesian (Cart) with relative deviations in maximum diameter (D_{max}) and volume (V). Bottom: Aneurysm Forecasting Studio (AFS) display for a different patient, including a forecast 18 months beyond the last scan. Wall colors progress yellow to orange and lumen blue to purple by time, with forecasts in black. The evaluation panel reports HD95, RMSE, and forecasted D_{max} and V at a prescribed time in the future. AFS supports visibility toggles and data export for analysis and reuse.

Acknowledgements (Optional)

NIH #R01HL159300 funded this work.

Session Category

OA168-01

Semi-Automated Subject-Specific Foot Modeling for Efficient and Accurate Plantar Pressure Analysis Across Arch Types

Ms. Olamide Hassan BSc, MSc Student, Ms. Jungeun Gwon BSc, MSc Student, Prof. Jeicheong Ryu PhD, Prof. Taeyong Lee PhD

Ewha Womans University, Seoul, Seoul, Korea, Republic of

Introduction

Excessive plantar pressure is linked to pain and deformity and is strongly influenced by foot geometry, particularly arch type, and by plantar soft-tissue mechanics. Finite element analysis (FEA) can provide detailed insight into plantar loading, but existing models are time-consuming to build and typically rely on generic soft-tissue properties and manually defined ligaments, fascia, and tendons, limiting scalability. Scalable foot analysis is essential for population studies and mass-personalized insoles. This study presents a semi-automated, subject-specific foot modeling framework that integrates individual geometry, indentation-derived plantar soft-tissue properties, and semi-automated connective tissues to analyze plantar pressure across normal, flat, and high-arched feet.

Methods

Twenty adults (10 normal, 5 flat, 5 high-arched feet) underwent 3D foot scanning, weight-bearing imaging, and quiet-standing plantar pressure measurements. An X-ray–driven parametric pipeline reconstructed rigid bones from geometric primitives and embedded them in the scanned foot surface. Plantar soft tissue was represented by an indentation-calibrated visco-hyperelastic model with hyperelastic loading and viscoelastic relaxation.

Connective tissues were added semi-automatically: ligaments and plantar fascia as truss elements between bony attachments, and the Achilles tendon as a tensile connector from the calcaneus to a reference node generated with an Abaqus node-mapping script. The tibia was fixed, a rigid plate applied 50% body weight beneath the foot and 25% body weight transmitted through the Achilles connector; plantar pressure was evaluated at the plate–soft tissue interface.

Results

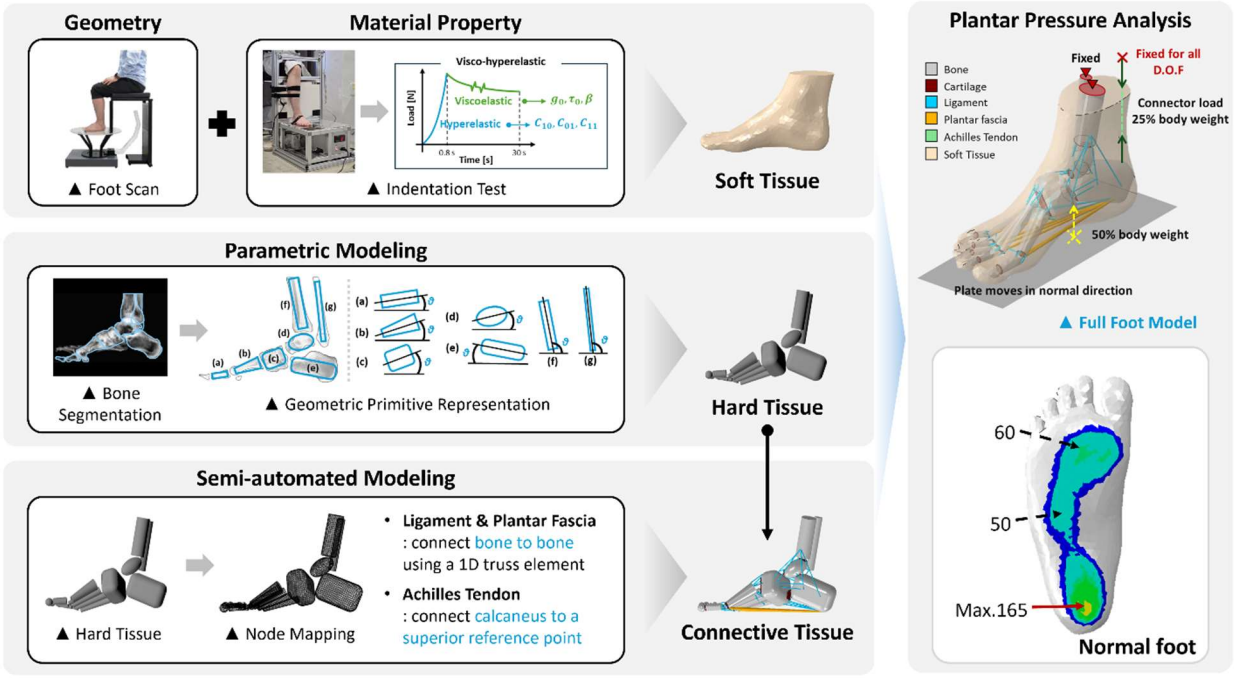
All 20 cases were successfully simulated using the proposed framework. Compared with a previously studied high-fidelity CT-based model, the X-ray–based parametric bones reduced computation time from about 5 hours to 30 minutes and preprocessing from 7

days to 3, while the proposed semi-automated connective tissue module further reduced preprocessing to under 1 hour per subject. Across subjects, simulated plantar pressure distributions showed arch-type-dependent patterns and remained within 15% error of experimental measurements.

Discussion

These findings indicate that combining subject-specific plantar soft tissue mechanics with semi-automated connective tissue generation enables scalable, biomechanically plausible plantar pressure analysis across arch types. The framework substantially reduces modelling time while preserving accuracy, providing a basis for large cohort in silico studies and future evaluation of orthotic or footwear interventions.

Images (Optional)



Acknowledgements (Optional)

Session Category

Musculoskeletal Biomechanics: Methods, Models and Applications

OA168-02

Novel Human Skeletal Muscle Biopsy Approach Allows Integration of Biomechanics and Biological Analysis

Miss Addison Barber[1,2], Miss Amber Willbanks[1], Miss Guadalupe Meza[1], Dr. Jeremie Ferey[3], Dr. Gretchen Meyer[3], Dr. Sudarshan Dayanidhi[1,4], Dr. W. David Arnold[5], Dr. Ishan Roy[1,4], Dr. Richard Lieber[1,2,4]

[1]Shirley Ryan AbilityLab, Chicago, IL, United States. [2]Hines VA Medical Center, Maywood, IL, United States. [3]Washington University School of Medicine, St. Louis, MO, United States. [4]Northwestern University, Chicago, IL, United States. [5]University of Missouri, Columbia, MO, United States

Introduction

Human muscle biopsies are often required to study or diagnose diseases, offering insights into muscle fiber mechanics, fiber composition, and molecular pathways. However, traditional biopsy approaches are limited by sample size, inconsistent fiber orientation, and patient discomfort. Fine-gauge needle biopsies (≥14-gauge) reduce invasiveness but frequently yield insufficient tissue for multidimensional and simultaneous analyses of biomechanical, biochemical, and histological properties. To address these limitations, we developed an ultrasound-guided, vacuum-assisted, single-insertion multiple-sampling technique capable of providing high-quality muscle samples suitable for integrated analysis.

Methods

In 19 healthy subjects (mean age: 30.1 years±10.6 (SD), 42% male) we collected 2-3 muscle samples from a single needle insertion into the vastus lateralis (VL) and tibialis anterior (TA) muscles. Fiber cross-sectional area (fCSA), fiber number, and satellite cells were histologically quantified. Portions of each biopsy were allocated for mitochondrial respirometry, RT-PCR, and collagen content. Permeabilized single fibers were isolated from biopsy-derived bundles for measurement of active force and passive elastic modulus. Pain ratings and adverse events were recorded immediately and 24 hours post-procedure.

Results

Ultrasound-guided biopsy allowed visualization of vasculature and nerves, preventing adverse events, and optimal needle orientation parallel with muscle fascicles. Summed VL and TA sample masses from a single needle insertion averaged 148±38mg and 166±64mg,

with dimensions of 15.83±8 x 2.9±0.6mm^2 (VL) and 15.07±7 x 3.1±0.9mm^2 (TA). VL had a mean fCSA of 4,347±1,931µm^2, with 221±86 fibers quantified. Samples were of sufficient size and quality for thorough analyses from a single biopsy procedure, including mitochondrial respirometry, RT-PCR, collagen content, satellite cell quantification. Single-fiber mechanics were successfully performed in permeabilized fibers, yielding typical isometric stress values of 187kPa with a passive modulus of 239kPa (peak) and 79kPa (stress-relaxed). This procedure was well tolerated, with mean pain ratings of pain rating of 1.5±1 (range:0-4, scale: 1-10) immediately and 1.7±1 (range:0-4) at 24-hours.

Discussion

This biopsy approach consistently yielded high-quality muscle samples suitable for integrated structural, molecular, metabolic, and single-fiber mechanical analyses. By overcoming key limitations of traditional biopsy approaches, this minimally invasive, fascicle-aligned method now provides a scalable platform for multidimensional biomechanical research and translational human studies.

Session Category

Musculoskeletal Biomechanics: Methods, Models and Applications

OA168-03

Full-Field Quantification of Anisotropic Elasticity in Skeletal Muscle During Contraction

Dr. Roberto Pineda Guzman[1], Dr. Melissa Hooijmans[1,2,3], Ms. Carly Lockard[1], Dr. Crystal Coolbaugh[2], Ms. Evelyn Bombard[4], Dr. Bruce Damon[1,2,4], Dr. Callan Luetkemeyer[4]

[1]Carle Foundation Hospital, Urbana, Illinois, United States. [2]Vanderbilt University, Nashville, Tennessee, United States. [3]Amsterdam University Medical Center, Amsterdam, North Holland, Netherlands. [4]University of Illinois Urbana-Champaign, Urbana, Illinois, United States

Introduction

Skeletal muscle has anisotropically-organized microstructural components, which may contribute to complex mechanical behavior. Disease-related microstructural disruptions alter elasticity, impair function, and increase susceptibility to damage during contraction. Microstructure-informed characterization of muscle elasticity during contraction is therefore essential for understanding disease-induced functional changes. Currently, anisotropic elasticity during contraction is measured with ultrasound-based elastography (USE) [1], which assumes mechanical linearity, provides only local 2D measurements, and does not account for fiber orientation changes during contraction. In contrast, MRI-based methods enable full-field measurements of whole-muscle fiber orientation and strain during contraction 2], enabling more comprehensive assessment. This study quantified anisotropic mechanical properties of contracted skeletal muscle using MRI-based data and the Virtual Fields Method (VFM), a microstructurally-informed and full-field inverse approach [3].

Methods

Seven healthy participants performed isometric ankle dorsiflexion at 40% maximum voluntary contraction force during 3T MRI. Full-field strain and fiber orientation data from the tibialis anterior (TA) were obtained [2]. TA force was estimated following published methods [4]. The VFM was implemented to identify parameters of the non-linear and anisotropic Holzapfel-Gasser-Ogden (HGO) model that best matched the MRI-based measurements. A non-linear cost function () incorporating three virtual fields –targeting longitudinal, transverse, and shear deformation – was minimized to obtain optimal HGO parameters. Along-fiber elastic modulus (k_1) and shear modulus (C_{10}) and the mechanical anisotropy ratio (k_1/C_{10}) were computed. For comparison, an apparent elastic modulus (E)

was computed using mean end-to-end displacement and maximum transverse cross-sectional area.

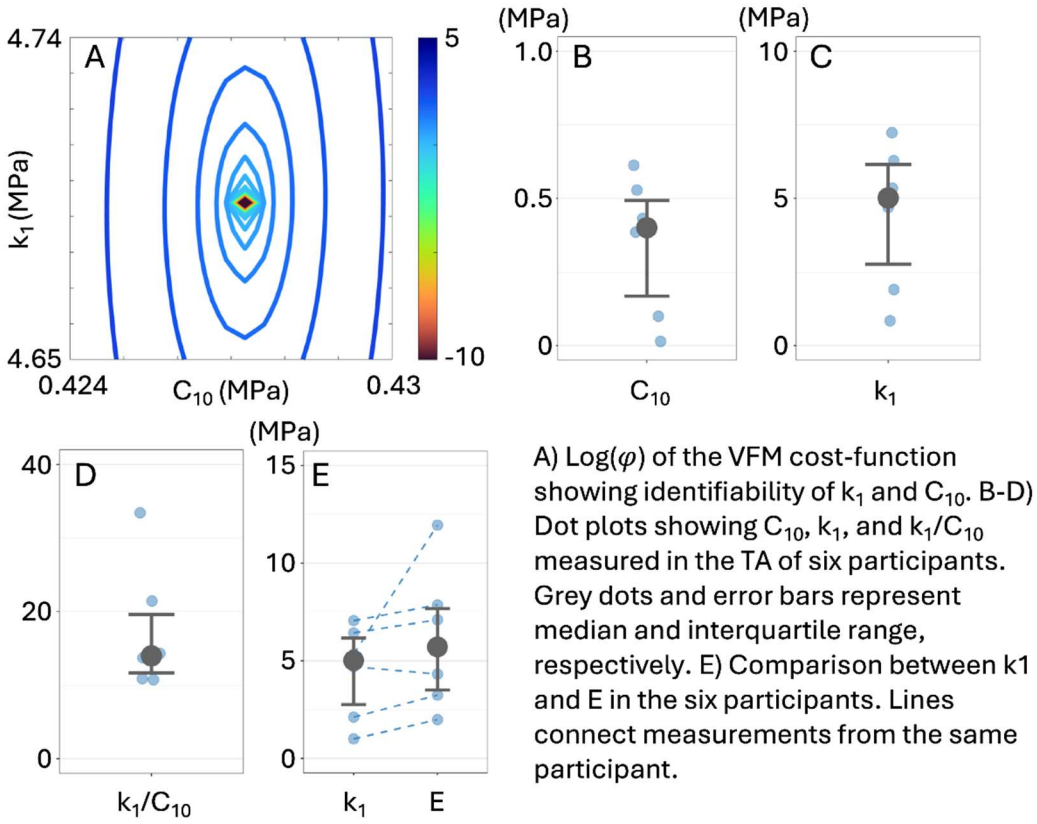
Results

The VFM cost function () was successfully minimized in six participants, yielding stable estimates of k_1 and C_{10} with well-defined local minima (Fig. 1A). Participant-specific values are shown in Figures 1B-D. Estimates of k_1 were consistent with E, while exhibiting a lower coefficient of variation.

Discussion

We demonstrate that the VFM can quantify the elasticity of skeletal muscle during contraction using the passive HGO model. The resulting k_1/C_{10} ratios align with previously reported USE measurements [1], and the agreement between k_1 and the apparent Young's modulus (E) supports using k_1 to describe along-fiber elasticity. Future work will apply this framework to diseased muscle and incorporate active contraction into constitutive models.

Images (Optional)



A) Log(φ) of the VFM cost-function showing identifiability of k_1 and C_{10}. B-D) Dot plots showing C_{10}, k_1, and k_1/C_{10} measured in the TA of six participants. Grey dots and error bars represent median and interquartile range, respectively. E) Comparison between k1 and E in the six participants. Lines connect measurements from the same participant.

References (Optional)

[1]Andrade+,ActaBio,2025 [2]PinedaGuzman+,JBiomech,2025
[3]Luetkemeyer+,JMechPhysSolids,2021 [4]Raitieri+,PeerJ,2023

Acknowledgements (Optional)

NIH/NIAMS R01 AR073831 and the Stephens Family Clinical Research Institute

Session Category

Musculoskeletal Biomechanics: Methods, Models and Applications

OA168-04

Female Pelvic Floor Muscle Strength Measured by Intravaginal Dynamometry Is Impacted by Arm Design and Protocol

Ms Olena Klahsen MSc, Dr Marina Petter Rodrigues PhD, Dr Linda McLean PhD

University of Ottawa, Ottawa, Ontario, Canada

Introduction

Intravaginal dynamometry (IVD) is the gold standard for measuring pelvic floor muscle (PFM) strength, however, the impact of variation in IVD arm designs among studies is unknown. Further, intra-abdominal pressure (IAP) may influence force outcomes. To reduce IAP crosstalk, authors have suggested using asymmetric arms to protect the measurement arm from the influence of IAP and having participants gently bear down (BD) while adjusting the arm position to ensure that IAP does not influence output force [1]. We sought to determine how IVD outcomes are impacted by arm design and device adjustment using the BD maneuver.

Methods

Four IVD arm styles were generated based on published literature: flat, rounded and saddle-shaped (symmetrical and asymmetrical) [2,3]. Twenty-two adult females attended a single laboratory session. Using each design in a random order, and using the same aperture, three trials of maximum voluntary contractions (MVCs) were performed with and without the arm position adjusted using a BD protocol. Baseline, maximum and relative peak (maximum – baseline) forces and rate of force development were computed. Separate generalized linear mixed models were used to determine the effect of arm design and BD adjustment on each outcome (α=0.05).

Results

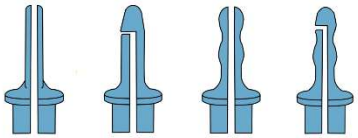
Force outcomes are presented in Table 1. There was no interaction between arm design and BD adjustment for any outcome. Arm design and BD adjustment independently influenced baseline, maximum and relative peak forces, but not the rate of force development. The highest baseline, maximum and relative peak forces were observed using the flat arms. Maximum force was lower when recorded using rounded arms than symmetrical saddle-shaped arms. In comparison to unadjusted trials, the BD adjustment resulted in lower baseline and maximum forces, and higher relative peak forces but no difference in rate of force development.

Discussion

Measures of PFM strength are not comparable among studies where different IVD arms have been used. The significant impact of BD adjustment, independent of arm design, suggests that this approach may indeed limit IAP crosstalk.

Images (Optional)

Table 1. Effect of intravaginal arm design and device adjustment on IVD measures

IVD Arm Designs  A B C D		*IVD Measures of PFM Strength*			
		Baseline Force (N)	*Maximum Force (N)*	*Relative Peak Force (N)*	*Average RFD (N/s)*
Arm Design	A. Flat	4.02 (1.40)[a]	7.63 (2.77) [a]	3.59 (2.21)[a]	8.45 (8.76)[a]
	B. Rounded	2.74 (1.00)[b]	4.92 (1.80)[b]	2.20 (1.35)[b]	6.06 (5.99)[a]
	C. Saddle Sym.	3.14 (1.09)[b]	6.08 (2.28)[c]	2.95 (1.73)[b]	7.44 (6.45)[a]
	D. Saddle Asym.	2.69 (1.15)[b]	5.51 (2.14)[b,c]	2.78 (1.50)[b]	6.90 (5.99)[a]
BD Adjust.	MVC	3.52 (1.24)[d]	6.25 (2.37)[d]	2.70 (1.81)[d]	7.29 (6.93)[d]
	BD-MVC	2.31 (1.33)[e]	5.34 (2.30)[e]	3.03 (1.47)[d]	7.05 (5.89)[d]

Data are presented as mean (standard deviation). Prior to generating means, values were collapsed by averaging across the other factor. Paired letters indicate similarity ($p \geq 0.05$).
Acronyms: BD = Bearing Down, IVD = Intravaginal Dynamometry, MVC = Maximum Voluntary Contraction, RFD = Rate of Force Development.

References (Optional)

[1] James Ashton-Miller *et al.*, Clin Biomech, 2014

[2] Chantale Dumoulin *et al.,* Neurourol Urodyn, 2003

[3] Marie-Ève Bérubé *et al.,* Neurourol Urodyn, 2018

Session Category

Musculoskeletal Biomechanics: Methods, Models and Applications

OA168-05

Novel 3-D Characterization of *in Vivo* muscle Properties Illustrates Directional Dependence in Resistance to Stress

Dr Ridhi Sahani[1,2], Dr Qifeng Wang[1], Dr Amr Mahrous[1], Research Assistant Professor Matthieu Chardon[1], Professor Kenneth Shull[1], Research Assistant Professor Daniel Ludvig[1,2], Professor Eric Perreault[1,2]

[1]Northwestern University, Chicago, Illinois, United States. [2]Shirley Ryan AbilityLab, Chicago, Illinois, United States

Introduction

Skeletal muscle injuries have debilitating impacts on daily function. The material properties of muscle govern its ability to resist stresses during injury and *in vivo* measures of these properties would help explain how and why injuries occur during physiological conditions. To characterize the full material properties of living muscle (i.e. shear (u) and Young's (E) moduli in the planes parallel (II) and perpendicular (T) to muscle fibers) we coupled micro-indentation and uniaxial extension in cat soleus muscles, with finite-element modeling. We hypothesized that Young's (E_{II}, E_T) and shear (u_{II}, u_T) moduli would increase with stress and vary between active and passive muscle, suggesting that muscles' resistance to loading is dependent on stress and activation.

Methods

In vivo material properties were measured in the soleus muscles of anesthetized cats (n=4; 2M, 2F) at active and passive lengths corresponding to 25-100% of optimal force. At each length, the short-range stiffness of the muscle-tendon-unit was used to calculate the Young's modulus parallel to muscle fibers (E_{II}) [1]. The mid-belly of the muscle was indented parallel and perpendicular to muscle fibers, using an ultrasound for visual guidance. The remaining moduli were estimated using the force-displacement data from indentation, E_{II}, and a finite-element modelling-based optimization [2].

Results

The shear modulus was greater in the parallel (u_{II}) compared with the perpendicular (u_T) plane at stress above ~50% of optimal force. u_{II} increased with both active and passive stress while u_T only increased with passive stress (Fig 1 A-B). The Young's modulus was greater in the parallel (E_{II}) compared with the perpendicular (E_T) plane at all levels of stress. E_{II} increased with both active and passive stress while E_T only increased with passive stress (Fig 1 C-D). Similar trends were observed in another cat and will be evaluated across animals.

Discussion

Our approach is the first to determine the full material properties of living muscle. Shear and tensile moduli were greater parallel than perpendicular to muscle fibers at higher stresses, suggesting a directional dependence in *in vivo* material properties and thus injury susceptibility.

Images (Optional)

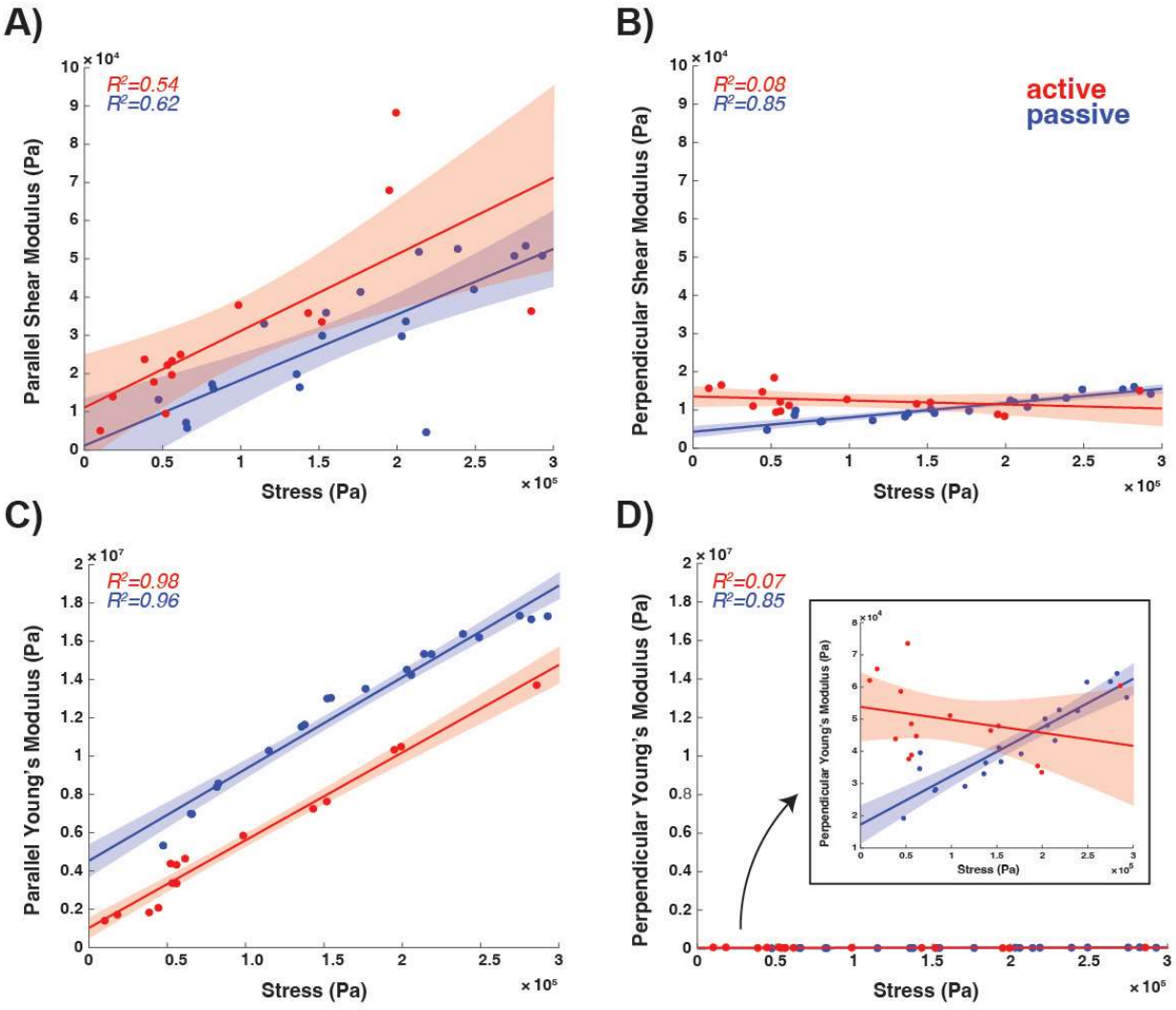


Figure 1. Data from one representative cat. Individual trials (o) in passive (blue) and active (red) muscles at approximately matched stresses. Trends from linear regression (solid line) with 95% confidence intervals (shaded region). Relationships between stress and shear modulus parallel (**A**) and perpendicular (**B**) to muscle fibers. Relationships between stress and Young's modulus parallel (**C**) and perpendicular (**D**) to muscle fibers.

References (Optional)

[1] Bernabei, M et al. J. Appl. Physiol. 2023.

[2] Wang Q et al. Acta Biomaterialia. 2025.

Acknowledgements (Optional)

Thank you to our funding: NIH R01AR071162 and NIH T32HD07418.

Session Category

Musculoskeletal Biomechanics: Methods, Models and Applications

OA169-01

Vessel Softening from TBI Increases Brain Vulnerability to Subsequent Head Trauma

Mr. Farshid Shojaeianforoud PhD Candidate[1], Mr. Alexander Venezie[1], Dr. Jose Rubio[2], Dr. Jaques Reifman[2], Dr. Brittany Coats Professor[1], Dr. Ken Monson Associate Professor[1]

[1]University of Utah, Salt Lake City, Utah, United States. [2]Department of Defense Biotechnology High Performance Computing Software Applications Institute, Fort Detrick, Maryland, United States

Mr. Farshid Shojaeianforoud

Mr. Alexander Venezie

Dr. Brittany Coats

Introduction

Repeated traumatic brain injury (TBI) is a significant concern among military personnel, athletes, and abuse victims, but little is known about the mechanisms that drive the brain's apparent increase in injury susceptibility with repeated loading. One critical factor may be the softening of cerebral blood vessels, which are significantly stiffer than brain tissue and influence its mechanical response during trauma. In this study, we employed a finite element model of a Göttingen minipig head to investigate how progressive vascular softening influences strain changes in brain tissue during both repeated blast and rapid rotation (coronal and sagittal directions).

Methods

The model, previously validated for single blast exposure, incorporated pig-specific anatomical detail and material properties, including detailed cerebral vasculature. Simulations included six repeated exposures of either blast overpressure or coronal or sagittal rotations at three severity levels (18 simulations). Additional "no-vasculature" (NV) cases were included for each loading condition (3 more simulations; 21 simulations in total) to benchmark the mechanical contribution of blood vessels. Vessel softening was

applied after each exposure based on previous experiments on Göttingen minipig cerebral arteries.

Results

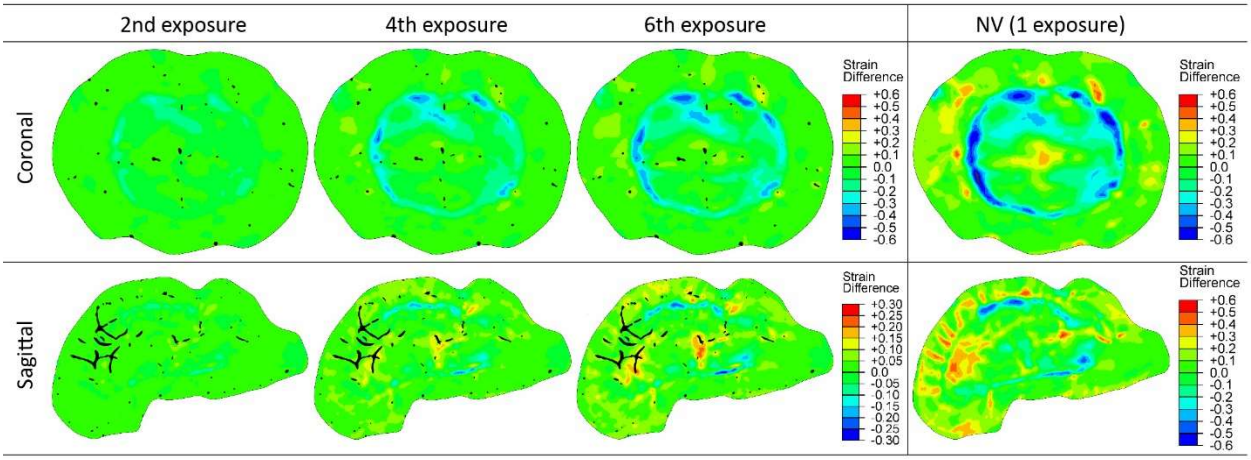
While blast exposures did not generate sufficient strain to induce vessel softening and accumulation of damage, rotational events led to progressively increasing brain strain with repetition, especially in regions adjacent to softened vessels (Fig. 1). These increases progressed toward the NV condition with repetition, consistent with diminishing structural support by softened vessels. Results also showed increasing risk of vessel rupture and axonal injury with repetition.

Figure 1: Distribution of strain difference, relative to the baseline simulation (1st exposure), in brain tissue during severe coronal and sagittal rotations. Results for coronal and sagittal rotations are shown on mid-coronal and mid-sagittal sections, respectively.

Discussion

Results demonstrate an overall increase in brain tissue strains as vessel damage accumulated with repeated loading. These findings provide novel insight into how vessel damage can amplify local brain tissue strain in repeated TBI. Progressively increasing brain tissue strain elucidate the biomechanical role of vessel softening in repeated TBI and suggest that even sub-failure vessel damage may exacerbate brain strain in repeated exposures and elevate injury risk.

Images (Optional)



Session Category

Injury Biomechanics: N/A

OA169-02

A Biomechanical–Mathematical Model Linking Brain Impact Biomechanics to Tau Protein Accumulation in Chronic Traumatic Encephalopathy

MSc Jose González Cabrero[1], MSc Carlos G.S Cardoso[1], PhD Inés Moreno González[2], PhD Ricardo J. Alves de Sousa[1]

[1]University of Aveiro, Aveiro, Aveiro, Portugal. [2]University of Málaga, Málaga, Málaga, Spain

Introduction

Chronic traumatic encephalopathy (CTE) is linked to repetitive traumatic brain injury (TBI) and long-term cognitive decline [1]. Post-mortem studies show hyperphosphorylated tau around small vessels and in cortical sulci, implicating biomechanics. Axonal strain during head impacts can damage white matter and trigger tau aggregation that later spreads through vulnerable networks [2,3]. However, most computational models describe large-scale propagation and do not quantify how impact mechanics set the initial pattern of tau pathology. Here we present a biomechanical–mathematical framework that links impact-induced brain strain to the spatiotemporal evolution of tau burden, providing a quantitative bridge between head-impact biomechanics and progressive tau pathology in CTE.

Methods

Tau-percentage measurements from controlled TBI tauopathy mouse models at early, intermediate and late stages [3] were used to calibrate a deterministic kinetic equation for the growth of tau-affected regions. A head finite-element (FE) model reconstructed from MRI data [4] was subjected to a short frontal impact to compute maximum principal strain (MPS), a marker of axonal vulnerability [2]. The normalized strain field weighted the kinetic law so that highly strained regions accumulated tau faster.

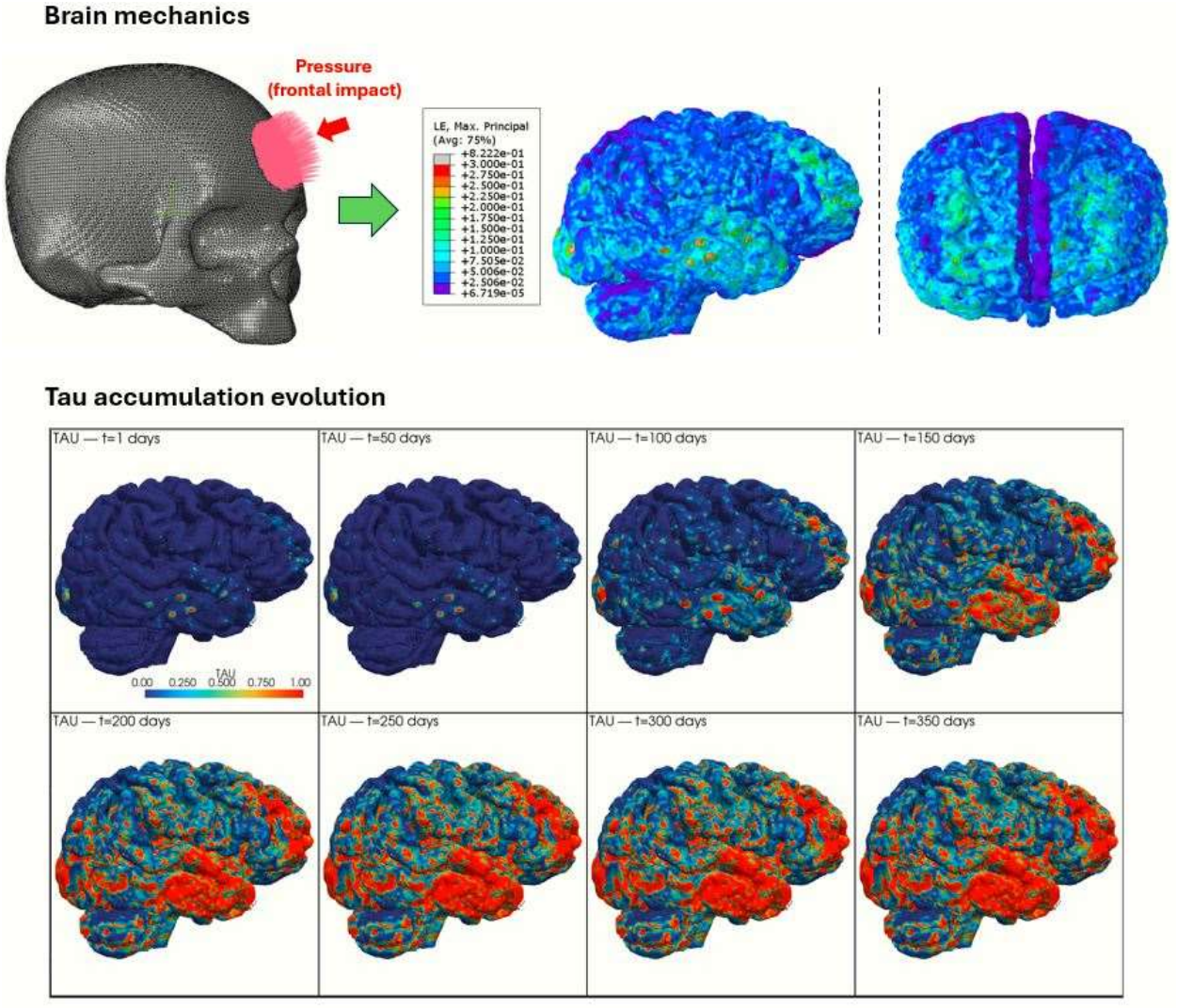
Results

The calibrated parameters of the equation reproduced the experimental tau time course, with a slow early phase, accelerated accumulation at intermediate times and later saturation [3]. FE simulations showed elevated MPS in frontal and sulcal cortex, which subsequently developed the highest predicted tau levels. Spatiotemporal maps revealed early tau clusters in high-strain areas that expanded and merged over several months.

Discussion

This framework helps explain why CTE lesions often appear in regions exposed to the largest impact-induced strains [1]. By combining FE-derived strain fields with biologically constrained kinetics, the model links acute mechanical loading to long-term tau accumulation and provides a quantitative basis for integrating head-impact biomechanics with progressive neurodegeneration. Although simplified, it can be extended to repeated impacts, anisotropic propagation and subject-specific brain mechanics.

Images (Optional)



References (Optional)

[1] A.C. McKee et al. , J Neuropathol Exp Neurol, 2009
[2] A.C. Bain et al. , J Biomech Eng, 2000
[3] G.E. Edwards III et al. , J Neurotrauma, 2019
[4] G.P. Carmo et al. , Comput Methods Programs Biomed, 2023

Session Category

Injury Biomechanics: N/A

OA169-03

Development and Validation of Physics-Informed Neural Networks for Rapid Prediction of Brain Strain in Traumatic Brain Injury Modeling

Dr. Inyani Keri MD, MSc[1], Ms. Pippa Kolking BSc[2], Dr. Kesava Reddy MD[1], Dr. Christopher R. Dennison PhD[2]

[1]Division of Neurosurgery, McMaster University, Hamilton, Ontario, Canada. [2]Department of Mechanical Engineering, University of Victoria, Victoria, British Columbia, Canada

Introduction

Finite element analysis (FEA) has advanced modeling of traumatic brain injury (TBI) **[1]**, but long run-times limit real-time use and studies with large throughput requirements. Physics-Informed Neural Networks (PINNs) blend machine learning with physical laws **[2,3]**, enabling rapid predictions grounded by mechanics. This study evaluates whether a PINN can accurately reproduce maximum principal strain (MPS)—a validated injury metric **[1]**—across parenchymal regions and do so more rapidly than a legacy FE model.

Methods

The bespoke PINN model was trained using legacy kinematic data drawn from football impacts, spanning 10–120g severity, both centric and oblique, with SIMon-predicted MPS (i.e., the FE model **[1]**). A bespoke set of region-specific tissue mechanics loss functions were implemented to anchor model predictions in material physics. For PINN training, inputs were head impact kinematics (n=300) recorded using j211-compliant methods/equipment and spatiotemporal MPS data computed from SIMon for the cerebrum, cerebellum, and brainstem. The PINN was constructed to allow prediction of spatiotemporal MPS from supplied head impact kinematics. Accuracy between the PINN and FEM was quantified using RMSE (PINN versus FEA) and inference time, using a single GPU.

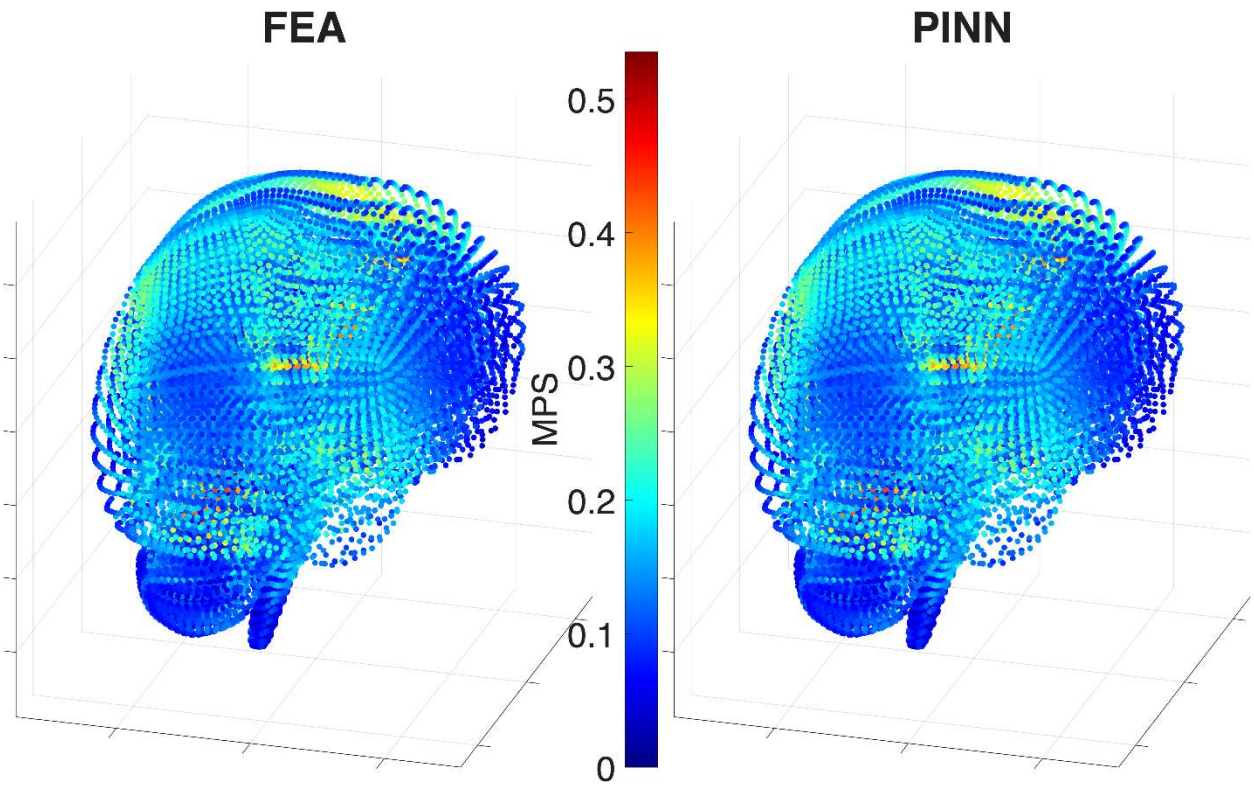
Results

Focusing on data on which it had no *a priori* training upon, the PINN accurately reproduced SIMon-derived MPS across all three parenchymal regions, with the cerebrum and cerebellum achieving mean strain RMSE < 0.01 (n=45). A graphical means of conveying this finding is shown by PINN-produced spatiotemporal MPS distributions relative to SIMon (Figure 1). Average inference time was 0.35 s per impact simulation.

Discussion

Using legacy data and a brain FEM, we have demonstrated the ability of a bespoke PINN to accurately predict brain MPS with sub-second simulation times. The trained PINN, requiring only head kinematics as inputs, could allow more rapid estimation of brain tissue strain, thereby enabling inferences on brain injury in research settings where time and throughput prevent widespread application of finite elements (e.g., sports settings, helmet assessment with large experimental datasets, etc.).

Images (Optional)



References (Optional)

1. Takhounts et al. *Stapp Car Crash J*. 2008;52
2. Haghighat E et al. *Comput Methods Appl Mech Eng*. 2021;379:113741.
3. Herrmann et al. *Comput Mech*. 2024;74

Acknowledgements (Optional)

Session Category

Injury Biomechanics: N/A

OA169-04

Predicting Mechanical Strain Relative to Axonal Orientation in Normal Pressure Hydrocephalus: A Biomechanical Model for Understanding Axonal Injury

Mr. Vahid Darvishi[1], Mrs. Martina Del Giovane[2,3], Dr. Michael C. B. David[2,3], Dr. Magdalena A. Kolanko[2,3], Prof. Paresh A. Malhotra[2,3,4], Dr. Chris Carswell[2,3,4], Prof. David Sharp[2,3], Dr. Mazdak Ghajari[1]

[1]HEAD Lab, Dyson School of Design Engineering, Imperial College London, London, London, United Kingdom. [2]Department of Brain Sciences, Imperial College London, London, London, United Kingdom. [3]UK Dementia Research Institute Care Research and Technology Centre, Imperial College London and the University of Surrey, London, London, United Kingdom. [4]Department of Neurology, Imperial College Healthcare NHS Trust, London, London, United Kingdom

Mr. Vahid Darvishi

Mrs. Martina Del Giovane

Dr. Michael C. B. David

Dr. Magdalena A. Kolanko

Prof. Paresh A. Malhotra

Dr. Chris Carswell

Prof. David Sharp

Introduction

Mechanical loading of brain tissue can cause axonal injury, a key determinant of clinical outcome, but investigating their relationship remains a challenge due to limited data. Normal pressure hydrocephalus (NPH), characterised by ventricular enlargement and white matter damage, provides a clinically relevant context to investigate links between mechanical loading and axonal injury. Our aim is to determine the distribution of mechanical strain with respect to axonal orientation after ventricular expansion, using a detailed finite element brain model.

Methods

MRI scans of 22 NPH patients (14 males, age=71.91±7.06) and 30 healthy controls (HC) (16 males, age=73.80±5.71) were acquired. T1-weighted images were averaged to create templates, from which a finite element brain model was generated[1]. The ventricular linings were loaded with displacement fields derived from registering images of HC to NPH ventricles. Changes in brain morphology and maximum principal Green-Lagrange strain (MPS) distribution were predicted (Fig1.A).

HC diffusion-weighted images were averaged to generate a template. This template was used to extract voxel-wise axonal orientations and construct local coordinate systems and corresponding rotation matrices (Fig1.B). These matrices were used to project global strain tensors into axon-based coordinates, yielding strain components parallel and perpendicular to axons.

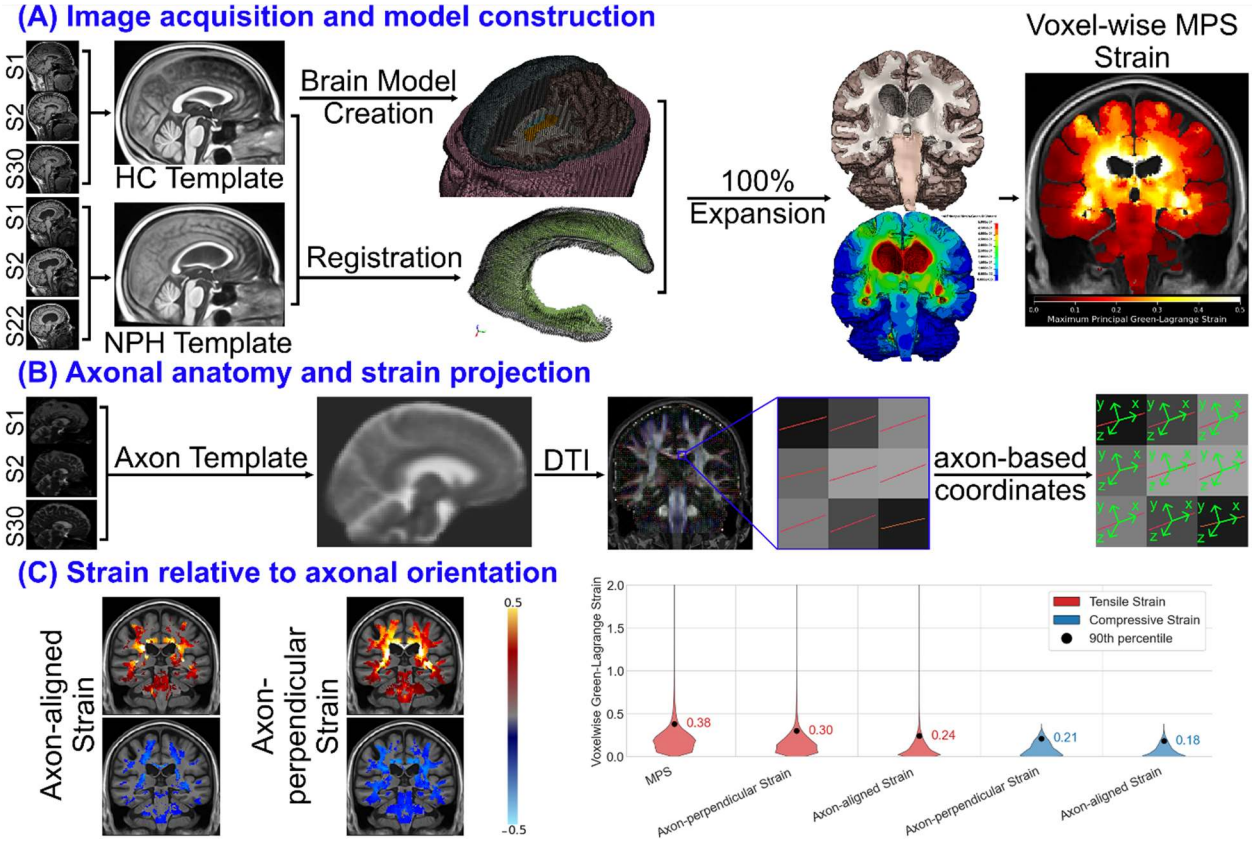
Results

The brain model accurately reproduced imaging measures of brain morphological changes, including the callosal angle and Evans Index, with 0.7% and 4.4% relative errors respectively. The model predicted strain concentration in periventricular regions, e.g. the corpus callosum. Both tensile and compressive strains parallel and perpendicular to axons were predicted in white matter tracts. Notably, the 90^{th} percentile tensile and compressive strains were higher in the direction perpendicular to axons than parallel to them (Fig1.C).

Discussion

The model predicts large strain in corpus callosum, a tract where white matter abnormality in NPH has been reported in several studies. Despite large MPS values, strain projection into axon-aligned coordinates reveals some fibers experience tension while others experience compression, both parallel and perpendicular to their orientation. Future work will use voxel-based diffusion imaging data to investigate how these loadings relate to axonal injury. These studies can advance our understanding of biomechanics of axonal injury.

Images (Optional)



References (Optional)

[1] Duckworth H *et al.*, Front_Bioeng_Biotechnol, 2022.

Acknowledgements (Optional)

Vahid Darvishi acknowledges support from the Design Engineering Department, Imperial College London, through a PhD scholarship.

Session Category

Injury Biomechanics: N/A

OA169-05

Rapid Atlas-Based Predictions of Regional Brain Strains From Wearable Head Kinematics Using Diffusion MRI-Informed Machine Learning

Mr Jacob Mathew[1], Mr Christian Saludar[1,2], Dr Maryam Tayebi[1,3], Associate Professor Alan Wang[1,4], Dr Ted Yeung[1], Professor Justin Fernandez[1], Associate Professor Samantha Holdsworth[3,4], Dr Eryn Kwon[1,3], Dr Josh McGeown[3], Dr Vickie Shim[1,3]

[1]Auckland Bioengineering Institute, Auckland, Auckland, New Zealand. [2]University of the Immaculate Conception, Davao, Davao, Philippines. [3]Matai Medical Research Institute, Gisborne, Gisborne, New Zealand. [4]Faculty of Medical and Health Sciences, Auckland, Auckland, New Zealand

Introduction

Sports-related injuries are the second leading cause of hospitalization for traumatic brain injury. Although FE simulations can provide important clinical insights by predicting brain deformation patterns from head impacts, they are computationally expensive and impractical for clinical use. Deep learning models can rapidly approximate FE-derived brain strains, but these they require thousands of impacts for training. This study aims to accelerate brain strain prediction using machine learning that requires only 15 impacts per athlete and extend these predictions to anatomical regions defined by the Desikan–Killiany (DK) and Automated Anatomical Labelling (AAL) atlases.

Methods

Twenty male high school rugby players (age 16 ± 0.6 years) were recruited for a longitudinal study over a single rugby season. Exclusion criteria included self-reported mTBI prior to study enrolment and any neurological conditions. Subject-specific anisotropic, viscoelastic FE brain models were generated from T1-weighted and diffusion MRI using our validated pipeline. Head kinematics were measured using instrumented mouthguards (HitIQ Nexus), recording angular accelerations for all head acceleration events (HAE). Brain strains for each HAE were computed by running each athlete's FE brain model with the specific HAE using FEBio. The resulting strains were parcellated to both DK and AAL atlases (containing 84 and 116 parcellations respectively) using a nearest-neighbour mapping between FE elements and voxel-wise atlas labels. Total of 15 paired parcellated average strain curves and corresponding kinematics recording per athlete were used to train multi-output nonlinear regression models using Random Forest, with TsFresh-based feature extraction applied to the angular acceleration time series.

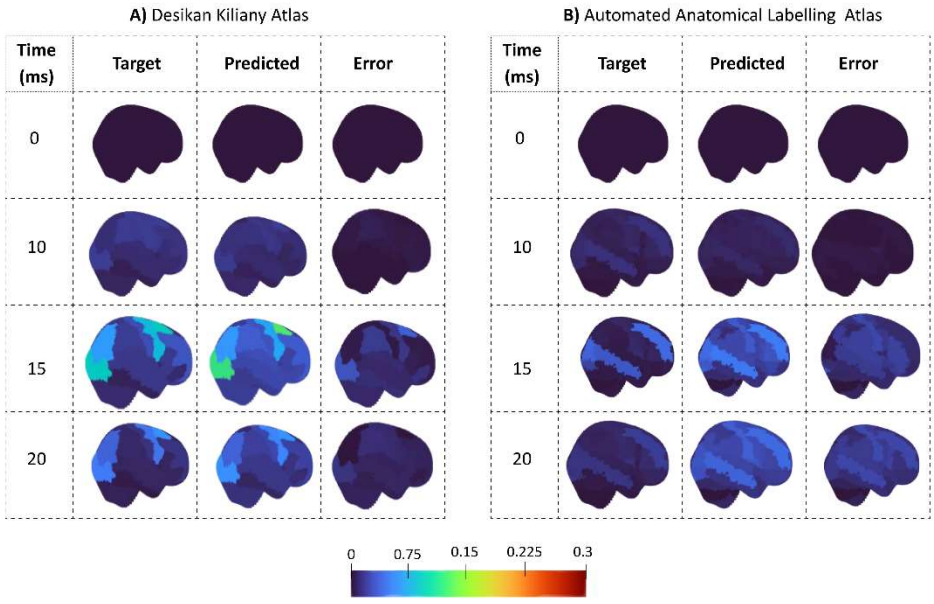
Results

Across both parcellation schemes, the median root-mean square error (RMSE) for predicted time-dependent parcellated strain profiles ranged from 0.002 to 0.007, indicating high accuracy despite the small training set. Representative visualisations of predicted strain across DK and AAL regions for an unseen impact are shown in Figure 1.

Discussion

We present a framework that integrates atlas-based brain parcellations with machine learning to predict regional brain strain directly from wearable sensor kinematics. This work captures location of injury as well as magnitude of strain. Ongoing work focuses on extending the approach to more subjects and elementwise strain predictions to improve spatial resolution and anatomical detail.

Images (Optional)



Acknowledgements (Optional)

We are grateful to Mātai Ngā Māngai Māori for their guidance, to researchers and staff from Mātai Medical Research Institute and to our research participants for dedicating their time towards this study. We acknowledge the support extended by the Mātai mTBI Research Group, composed of Leigh Potter, Paul Condron, Davidson Taylor, Daniel Cornfield, Patrick McHugh, Taylor Emsden, Helen Danesh-Meyer, Gil Newburn, Tuterangi Nepe-Apatu, and Graeme Bydder.

Session Category

Injury Biomechanics: N/A

OA169-06

Associations of Repetitive Head Impact Exposure With Brain Myelin Imaging and Multidomain Neurological Function

Dr Adam Clansey[1], Dr Rebecca Kenny[1], Mr Zaryan Masood[1], Mr Daniel Bondi[1], Mr David Luke[1], Mr Alexander Jaffray[1], Dr Songbai Ji[2], Mr Chaokai Zhang[2], Dr Shambhu Adhikari[3], Dr Alexander Rauscher[1], Dr Paul van Donkelaar[3], Dr Lyndia Wu[1]

[1]University of British Columbia, Vancouver, BC, Canada. [2]Worcester Polytechnic Institute, Worcester, MA, United States. [3]University of British Columbia, Kelowna, BC, Canada

Introduction

Repetitive head impacts in contact sports such as ice hockey are associated with changes in brain structure and impairments in neurological function, yet evidence remains limited. The corpus callosum has been shown to be vulnerable to rotational forces experienced during head impacts, with previous reports showing a disruption in myelin in the splenium of the corpus callosum following concussion. This prospective investigation aims to investigate the association between cumulative subconcussive impacts sustained across ice hockey seasons to changes in myelin and neurological functional outcomes.

Methods

Thirty-four male ice hockey players (22.06 ± 1.46 yrs) and 18 age-and sex matched controls (21.26 ± 2.00 yrs) were recruited. Players wore instrumented mouthguards (iMG) across a span of two varsity ice hockey seasons (2021-2023). Missing iMG head acceleration events (HAEs) were imputed to determine cumulative head impact outcomes. All participants completed pre- and post-season MRI brain scans for myelin water fraction (MWF) calculations and a full neurological test battery assessing neurocognitive function, sensorimotor function, symptoms and mood. Linear regression was used to examine the relationship between head impact exposure and pre- to post-season outcome changes in players. Linear mixed effects models examined group by time interactions comparing players and controls, with participant as a random effect.

Results

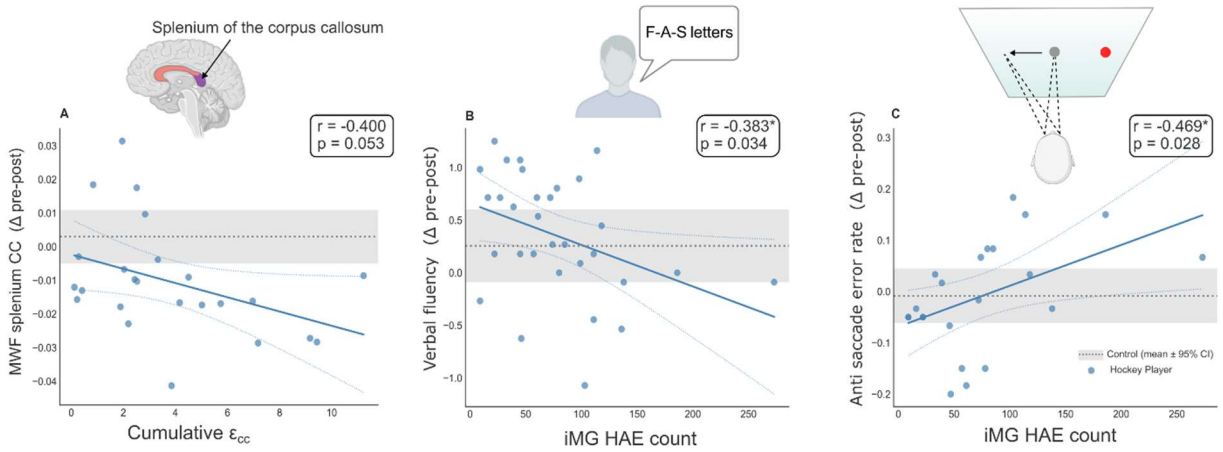
Players demonstrated a significant decrease in posterior corpus callosum MWF over the season compared to controls (Fig 1; $\beta = -0.013$, $p = 0.009$). Greater cumulative corpus callosum strain showed a trend toward reduced MWF in splenium region of brain ($r = -0.400$, $p = 0.053$). Higher iMG HAE counts were significantly associated with decreased

verbal fluency (r = -0.382, p = 0.034) and greater anti-saccade error rate (r = 0.469, p = 0.028). No other outcome parameters showed significant associations with HAE exposure.

Discussion

Preliminary results indicate cumulative head impact exposure was associated with a disruption in myelin structure in corpus callosum and worsening of verbal fluency and oculomotor function in hockey players across season of ice hockey. These findings highlight the importance of monitoring cumulative head impacts in contact sports and warrant further longitudinal investigations to determine whether such changes persist, accumulate, or recover across multiple seasons of play.

Images (Optional)



Session Category

Injury Biomechanics: N/A

OA170-02

Estrogen Regulates Stiffness of Murine Cervical Extracellular Matrix

Ms. Serena Russell ScM[1], Mx. Bex Pendrak MS[1], Dr. Camilo Duarte PhD[1], Mr. Tobias Funk[1], Dr. Priyya Madhukaran PhD[2], Dr. Mala Mahendroo PhD[2], Prof. Kristin Myers PhD[1]

[1]Columbia University, New York, NY, United States. [2]UTSW Medical Center, Dallas, TX, United States

Introduction

Molecular studies have established that estrogen regulates collagen turnover in the cervix [1,2]. This study employs a ramp-hold-to-failure test to describe cervical extracellular matrix (ECM) of control (WT), ovariectomized (OVX), and estrogen treated mice (OVX+E) to elucidate estrogen's role in cervical function.

Methods

Whole cervix was collected from wildtype C57BL6/129sv mice (WT, N=3), from OVX mice (N=3), and from OVX mice that were administered 2 μg estrogen for 15 days after surgery (OVX+E, N=3). Each specimen was subjected to a tensile ramp-hold-to-break biomechanical test. The equilibrium loading behavior was characterized by a material model (Fig. 1A) in FEBio utilizing an inverse finite element modeling approach. The biomechanical parameters in this model characterize the load-bearing ECM: waviness of collagen fibers [locking stretch, LS], initial fiber network stiffness [ξ], and ground substance bulk stiffness [κ]. Rupture stress of the tissue was calculated at the point of highest stress before break. An ANOVA with post-hoc Tukey test compared the material parameters of OVX, OVX+E, and WTs.

Results

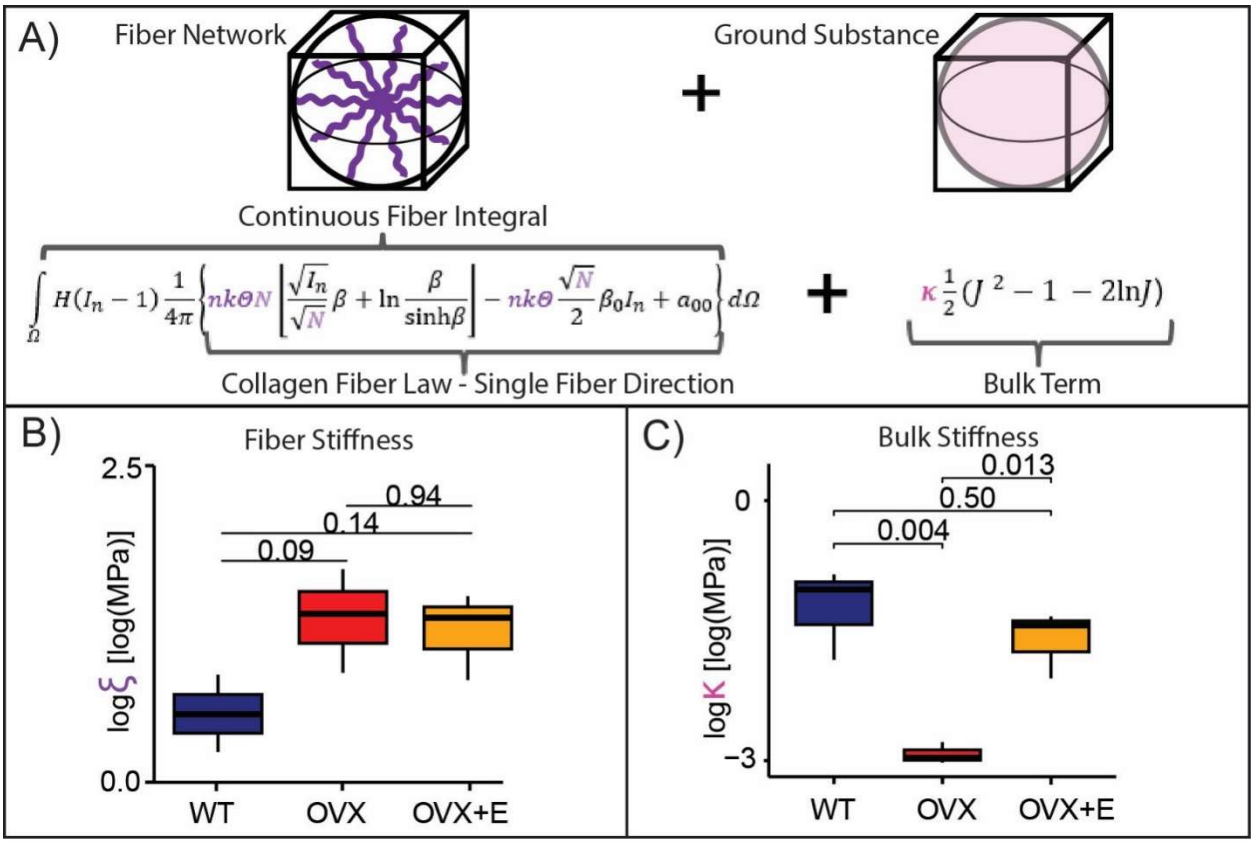
LS did not change significantly between treatment types. ξ increased in OVX and OVX+E cervix compared to WT ($p = 0.09, 0.14$, Fig. 1B). κ decreases significantly in OVX cervix compared to WT cervix, however OVX+E samples do not differ from WT ($p=0.02, 0.39$, Fig. 1C). Rupture stress was significantly lower in OVX samples than WT samples ($p=0.03$).

Discussion

Lack of estrogen negatively affects biomechanical function of the cervix. Results show that without the presence of estrogen, the initial stiffness of fibers (ξ) increases and the bulk stiffness (κ) and rupture stress decrease, leading to an overall softer cervix with less ability to stretch and handle stress. The OVX+E model recovers the lost bulk stiffness in the OVX model, displaying that estrogen regulates the bulk stiffness, while fiber stiffness may be

due to another missing factor, like progesterone. This work suggests that bulk modulus is influenced by estrogen, and replacement of missing estrogen can recover this feature.

Images (Optional)



References (Optional)

[1] Shanmugasundaram Nallasamy *et al.*, Endocrinology, 2017

[2] Mala Mahendroo *et al.*, Reproduction, 2012

Session Category

Organ and Tissue Biomechanics: N/A

OA170-03

Towards a Uterine Electromechanical Digital Twin during Late Pregnancy

Ms. Olivia Mergler, Mr. Parker Mixon, Dr. Kristin Myers, Dr. Vijay Vedula

Columbia University, New York, NY, United States

Introduction

The onset of uterine contractions is a highly regulated yet poorly understood process. Labor contractions have been found to be driven by a complex convergence of stretch-mediated inflammation and hormonal regulation. Uterine digital twins enable analyzing the sensitivity of contractions to different mechanical and electrophysiological properties and identifying the risk factors that may contribute to preterm labor.

Methods

We developed a novel digital twinning workflow for modeling uterine electromechanics. Our workflow begins with a previously developed parameterized model of the uterus and cervix, with rule-based fibers oriented longitudinally in the uterus and circumferentially in the cervix. The passive material response is characterized using the anisotropic hyperelastic GOH constitutive model, with parameters tuned to match mechanical testing data. Spatially varying Robin boundary conditions are applied to efficiently simulate interactions with the surrounding fetal membrane and abdominal organs. Active contraction is modeled using a phenomenological active stress model (Figure 1a) [1], with parameters tuned to match literature for a pre-labor single spike and plateau-type stimulus (Figure 1b) [2, 3], and spatially varying activation times based on physiological action potential propagation velocities (Figure 1c). The model is used to evaluate the effect of variable active stress waveforms on the contraction patterns (Figure 1d).

Results

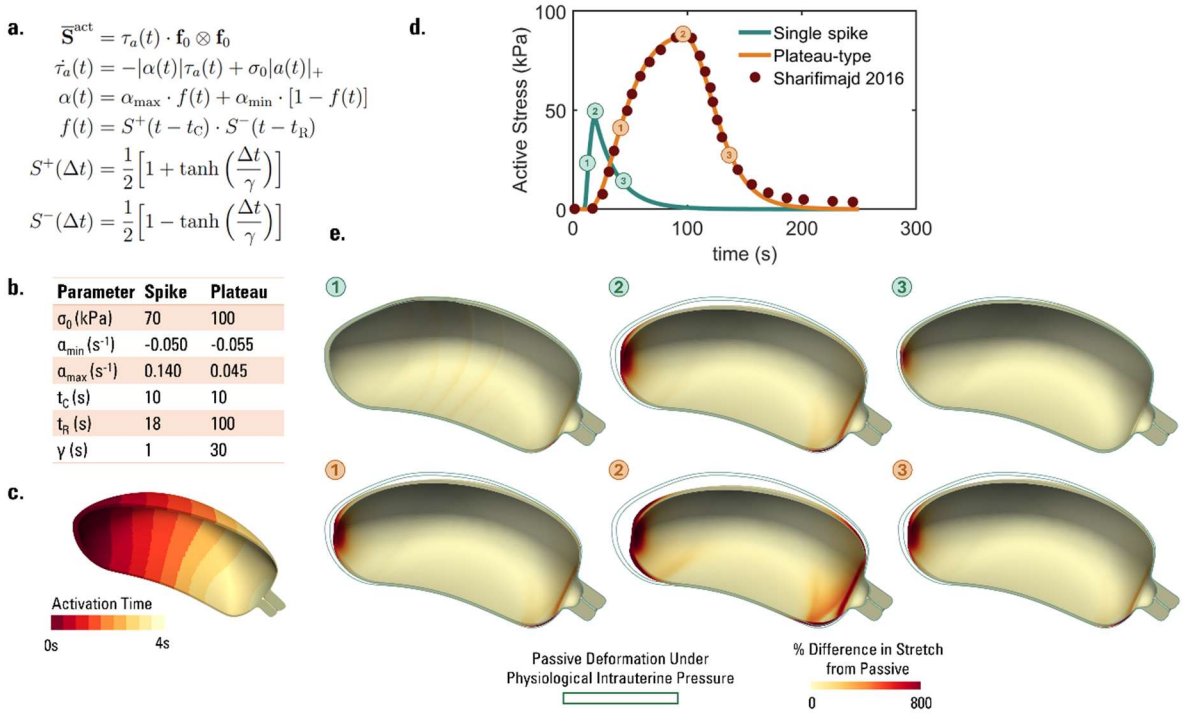
Simulated uterine contractions using tuned material parameters and active stress waveforms reveal increased uterine deformations and induced stretches upon prolonged contractions. For both single spike and plateau-type stimuli, stretches were highest at the uterine fundus and lower uterine segment during maximal contraction (Figure 1e).

Discussion

Our results are consistent with physiological labor patterns and highlight the role of progressive recruitment during labor. Uterine contractions are stretch-mediated [3]; thus, stretch concentrations can inform sites of future contraction stimuli. Stretch concentrations at the lower uterine segment may impact cervical effacement and dilation,

consistent with clinical understanding. Next steps will focus on developing a coupled excitation-contraction model, enabling further investigation into the hormonal regulation of the excitation pathways that lend to the transition between different contraction patterns.

Images (Optional)



References (Optional)

[1] Lei Shi *et al.* CMAME, 2026.

[2] Babak Sharifimajd *et al.*, Biomech Model Mechanobiol, 2016

[3] Susan Wray *et al.*, Adv Exp Med Biol, 2019

Acknowledgements (Optional)

We thank NSF and computing resources from ACCESS (SDSC Expanse) and Columbia Ginsburg HPC for supporting this work.

Session Category

Organ and Tissue Biomechanics: N/A

OA170-04

Assessing the Influence of Maternal Pelvic Geometry on Birth Simulations Using Pelvimetry-Based Models

Dr. Morgane Devismes[1], Dr. Marine Lallemant[2], Dr. Michel Cosson[1,2], Dr. Chrystèle Rubod[1,2], Dr. Olivier Mayeur[1]

[1]Univ. Lille, CNRS, Centrale Lille, UMR 9013 LaMcube Laboratoire de Mécanique, Multiphysique, Multiéchelle, Lille, 59000, France. [2]Service de Chirurgie Gynécologique, Hôpital Jeanne-de-Flandre, Centre Hospitalo-Universitaire, Lille, 59000, France

Introduction

In France, emergency cesarean sections (C-sections) represent approximately two-thirds of all cesarean deliveries [1]. These unplanned procedures are often more challenging for patients and medical teams [2,3]. A major cause for emergency C-sections is cephalopelvic disproportion (CPD), which impedes the fetal descent. Although not used in routine, pelvimetry can help assess the risk of CPD and provides valuable input for personalized birth simulations. This study aims to use pelvimetry-based imaging to develop maternal pelvic models for birth simulations, in order to investigate how variations in pelvic geometry influence simulated delivery outcomes.

Methods

Pelvimetry scans from 63 patients (age: 34 ± 7 years; BMI: 22.5 ± 6.7) were acquired at Lille University Hospital, 2 to 36 days before delivery. Maternal and fetal geometries were segmented using 3D Slicer. Then, patient-specific soft-tissue models were automatically reconstructed, including 10 key perineal structures such as the Levator Ani Muscle and the Perineal Body (Figure 1). The fetal head was simplified to its external envelope using an alpha-shape algorithm. Maternal and fetal models were then imported into Abaqus, and vaginal delivery scenarios were simulated using a prescribed fetal trajectory.

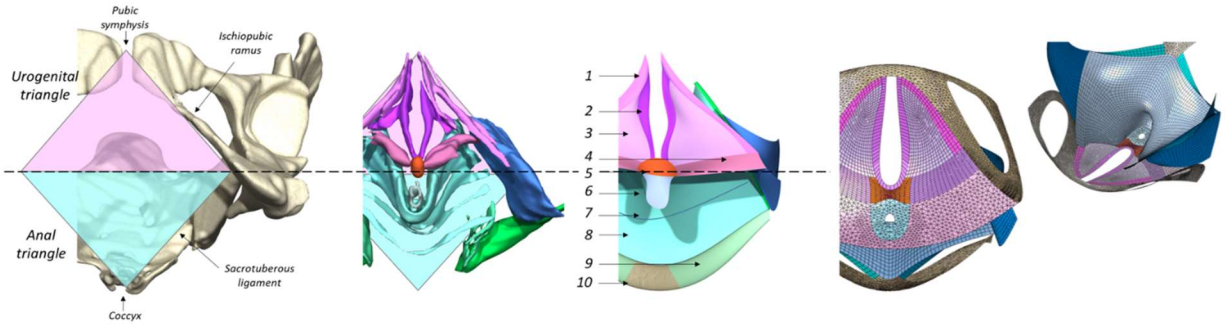
Results

All 63 maternal pelvic models were successfully reconstructed and used to build an average maternal model suitable for generic birth simulations. At this preliminary stage, simulations were conducted using a simplified ellipsoidal parametric fetal head, allowing evaluation of the differences in simulation outcomes due to the sole variations in maternal pelvic geometry. Perineal strain magnitudes peaks up to 4 approximately, with marked variability across patients, suggesting a measurable influence of pelvic shape on mechanical response during simulated fetal descent.

Discussion

This study contributes to bridging clinical practice and computational birth simulation by grounding simulation models in pelvimetry-based anatomy. Future work will include patient-specific simulations incorporating individualized fetal head geometries and presentations, comparison of simulation results with actual clinical outcomes and expansion of the cohort for improved statistical significance.

Images (Optional)



References (Optional)

[1] DREES, La naissance : caractéristiques des accouchements, 2024

[2] Pandey, S. et al, Journal of Neonatal Surgery, 14, 531-542, 2025

[3] Orovou, E. et al, BMC Psychology, 2025

Acknowledgements (Optional)

The authors would like to thank the European project PELVITRACK (HORIZON-EIC-2024-PATHFINDEROPEN-01) for its support

Session Category

Organ and Tissue Biomechanics: N/A

OA170-05

Linking Collagen Microstructure to Uterine Mechanics Using Inflation and Inverse Finite Element Analysis

Ms. Mahmuda Arshee, Ms. Adira Safar, Dr. Ayelet Ziv-Gal, Dr. Jodi Flaws, Dr. Indrani Bagchi, Dr. Callan Luetkemeyer, Dr. Amy Wagoner Johnson

University of Illinois Urbana-Champaign, Champaign, Illinois, United States

Introduction

The uterus is a mechanically dynamic organ whose function depends on collagen microstructure, which can be altered by environmental toxicant exposures such as propylparaben [1]. While our prior work showed disrupted collagen and increased local tissue stiffness, the impact on whole-organ mechanics remains unknown. Here, we address this gap by combining physiological inflation tests with inverse finite element analysis to estimate anisotropic constitutive parameters. Our approach is novel in its use of organ-level inflation testing with simultaneous microCT-based imaging and computational modeling.

Methods

Uteri from six 6-month-old diestrus control mice were inflated ex vivo using a custom balloon-catheter setup with continuous pressure–volume recording (Fig. 1A). Samples were preconditioned through several inflation–deflation cycles to ensure repeatable mechanical response. MicroCT-segmented boundaries were used to build a symmetry-constrained quarter FE model with the Gasser-Ogden-Holzapfel (GOH) formulation, with fiber families in the circumferential and longitudinal directions. As uterine cross-sections vary in thickness, we selected a representative quarter by aligning the geometry and choosing the 90° sector whose mean thickness was closest to the overall average. Material parameters were identified by minimizing the mismatch between experimental and simulated radial displacements across pressures. Local sweeps were used to assess parameter identifiability.

Results

Inflation tests showed nonlinear stiffening, with more compliant behavior at low stretch (Fig. 1B). Variability across samples in the high-stretch region (corresponding to 0.10–0.20 mL of fluid injected into the balloon) was ~8%, indicating consistent behavior suitable for modeling. The inverse framework converged reliably with low mismatch between simulated

and experimental boundary deformations (Fig. 1C). Parameter sweeps revealed a clear low-error region around the best-fit values, suggesting that the solutions are unique. Full parameter analysis across all uteri is in progress.

Discussion

The inflation response reflects progressive collagen fiber recruitment, supporting the use of a microstructure-based model such as GOH. This framework provides a quantitative basis for evaluating how environmental exposures, ageing, or hormonal cues influence uterine mechanics.

Images (Optional)

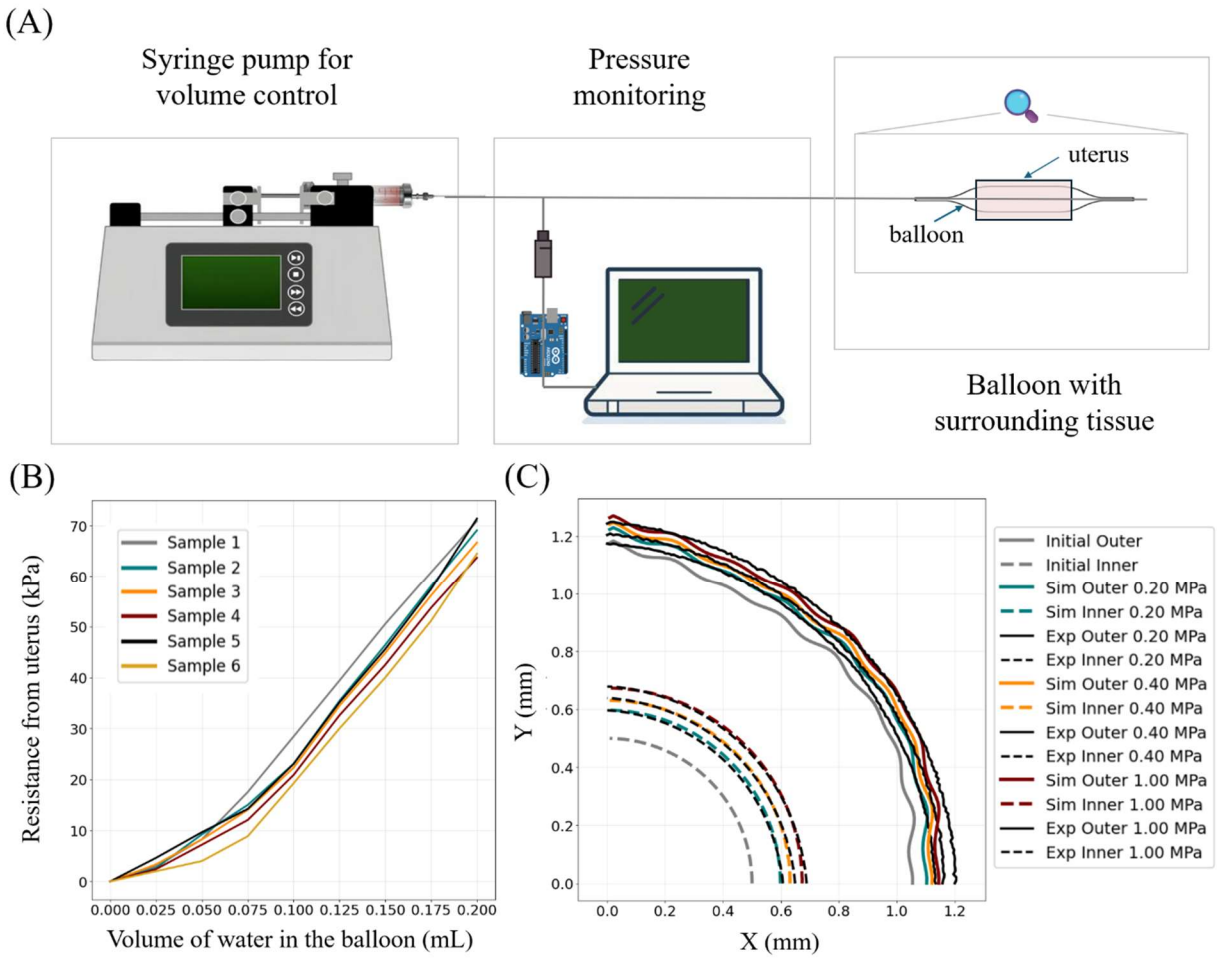


Figure 1. (A) Custom inflation apparatus consisting of a syringe pump for controlled volume input, Arduino-based pressure monitoring, and a balloon catheter positioned inside the excised uterus. (B) Measured resistance from the uterine wall as a function of balloon volume for six independent samples showing consistent nonlinear stiffening across samples. (C) Comparison of experimental and simulated inner and outer boundary profiles at multiple pressure levels, demonstrating close agreement, with <2% error between model predictions and measured deformation.

References (Optional)

[1] M. R. Arshee et al., JMBBM 165, 106926 (2025)

[2] T. C. Gasser et al., J. R. Soc. Interface. 3, 15 (2006)

Acknowledgements (Optional)

T32 HD108075, Mitul Patel Fellowship

Session Category

Organ and Tissue Biomechanics: N/A

OA171-02

Automated MRI-Based Quantification of Femoral Growth Plate Orientation in Healthy Children

Dipl.-Ing. Kevin Kitir[1], PhD Willi Koller[1], Dipl.-Ing. Clara Egner[1], BSc Laura Rathmair[1], Assoc. Prof. Wolfgang Bogner[2], Dr. Tim Emmenegger[2], Assoz.-Prof. Janina Patsch[2], Assoc. Prof. Hans Kainz[1]

[1]Universit of Vienna, Vienna, Vienna, Austria. [2]Medical University of Vienna (Austria), Vienna, Vienna, Austria

Introduction

The orientation and morphology of femoral growth plates are key determinants of longitudinal bone development [1]. Aberrant physeal alignment contributes to atypical femoral torsion [2], yet quantitative 3D reference data in typically developing children remain scarce partly due to the impracticality of manual MRI segmentation.

This study presents an automated pipeline combining multi-contrast MRI, 3D nnU-Net–based segmentation [3], and scripted geometric analysis to characterise femoral growth plate shape and orientation in healthy children. The aim is to establish normative metrics supporting future biomechanical assessments and comparisons with pathological cohorts.

Methods

Whole-limb Dixon MRI scans of 53 healthy children (5–16 years) were analysed. Manual segmentations from 15 participants trained a four-channel 3D nnU-Net model, which subsequently generated automated femur and physis segmentations for the complete cohort.

Physeal masks were converted into surface representations using moving least squares, and a second-order polynomial surface was fitted to derive continuous geometric descriptors. Femoral shaft axes were obtained via multi-subset Principal Component Analysis (PCA).

A fully automated workflow extracted physeal surface area, normal vector orientation, curvature measures, surface irregularity (RMS deviation from the polynomial fit), and the Physeal–Diaphyseal Angle (PDA). Age-dependent patterns were evaluated across the cohort.

Results

The trained nnU-Net achieved high segmentation accuracy for femora and physes (Dice 0.86–0.96). Proximal femoral growth plates showed clear developmental trends: Surface area increased with age, reflecting expected skeletal growth. Curvature radius decreased, and surface irregularity rose, indicating greater morphological complexity. The PDA showed a modest age-related reduction, implying slightly decreasing alignment with the femoral shaft-axes during maturation.

Discussion

This automated MRI-based approach enables reliable large-scale quantification of femoral physeal geometry, with results consistent with prior observations [4]. The identified trends enhance understanding of normal physeal maturation and provide critical reference data for comparisons with pathological torsional profiles or growth disorders. The modular workflow is compatible with advanced in-silico modelling [5] and supports continued research within the INSIDE-BONE project.

Images (Optional)

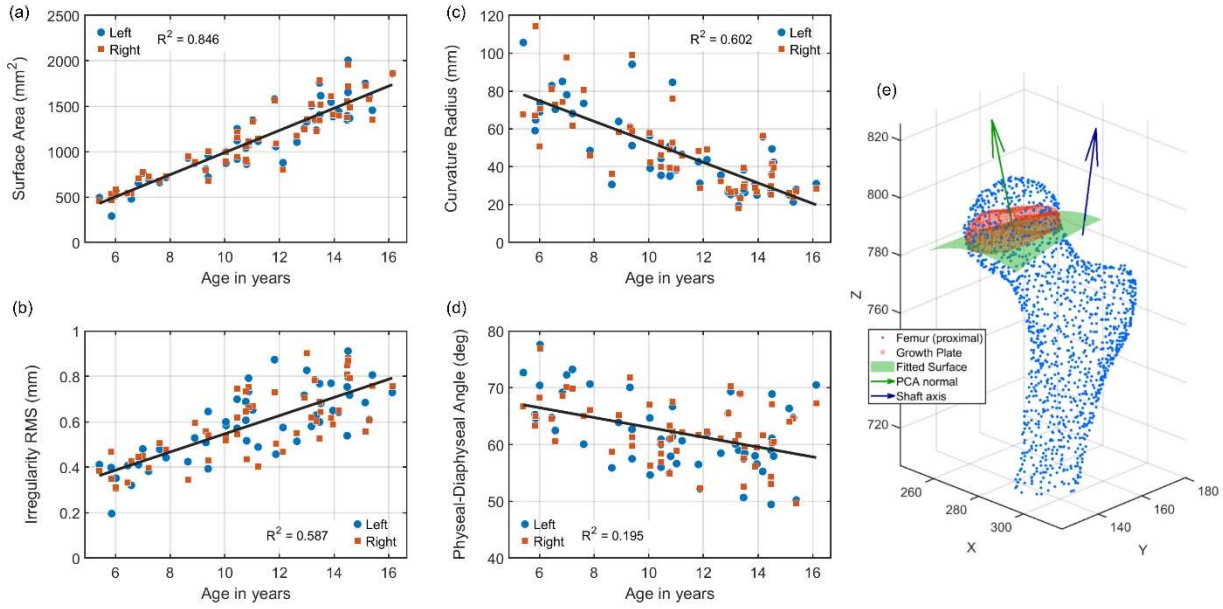


Figure 1: Left: 2×2 subplots showing an overview of growth-plate metrics over age. (a) surface area from the calculated midsurface, (b) irregularity as deviation of the midsurface from the poly-2 surface (e.g. RMS), (c) curvature radius derived from the poly-2 surface, and (d) physeal–diaphyseal angle between the femoral shaft axis and the growth-plate plane. Blue dots = right side, orange squares = left side; a common OLS regression (line) and R² are shown in each subplot. Right: (e) nnU-Net segmentations overlaid with the poly-2 surface, green arrow = growth-plate normal, blue arrow = femoral shaft axis.

References (Optional)

[1] Villemure et al., J Biomechanics,2009 [2] Koller et al., Biomech Model Mechanobiol,2025 [3] Isensee et al., Nat Methods,2021 [4] Castro-Abril et al., Comput Biol Med,2016 [5] Kainz et al., PLoS ONE,2020

Acknowledgements (Optional)

This research was funded by the European Research Council (ERC-2024-COG, 101170218, INSIDE-BONE). We would like to thank the Medical University of Vienna for their help with the MRI data collection.

Session Category

Musculoskeletal Biomechanics: Joints and Motion

OA171-03

Measuring Changes in Femoral Shape During Growth: Reliability of Methods in Paediatric Data

BSc Dipl.-Ing. Clara Egner[1], BSc MSc PhD Willi Koller[1], BSc Kevin Kitir[1], BSc BEd Laura Rathmair[1], Dr. rer. nat. Nathalie Alexander[2], Ing. Dr. Andreas Kranzl[3], Assoc. Prof. PhD Wolfgang Bogner[4], Dr. rer. nat. Tim Emmenegger[4], BSc MA Katharina Greiner[4], Assoz.-Prof. Priv.-Doz. MD PhD Janina Patsch[4], Dr. Gabriel Mindler[3], Assoc. Prof. Mag. MSc PhD Hans Kainz[1]

[1]University of Vienna, Vienna, Vienna, Austria. [2]Ostschweizer Kinderspital, St. Gallen, St. Gallen, Switzerland. [3]Orthopedic Hospital Speising, Vienna, Vienna, Austria. [4]Medical University of Vienna, Vienna, Vienna, Austria

Introduction

Lower-limb bone deformities are associated with several health conditions, often treated at a late stage, requiring extensive treatment [1]. Studying the development of deformities during growth is crucial for moving towards preventive interventions.

However, quantifying bone-shape is not straightforward: the common clinical measures for femoral geometry, Neck-Shaft-Angle (NSA) and Anteversion-Angle (AVA), have been questioned regarding inter-observer-reliability [2]. Automatic-angle-measures are available [3,4,5] but often developed on radiation-exposing CT-images or not tested on paediatric data. The aim of this study was to analyse reliability of several measurement-methods based on MRI-images.

Methods

MRIs of n=7 typically developing children were captured twice (at age 10y and 12y, 3T-T1-vibe-0.8×0.8×0.7mm). Clinical angle-measures were performed as described by Sangeux [6] by two experienced researchers (Clinical1/Clinical2). Each femur (N=28) was segmented twice (Segmentation1/Segmentation2). Difference between segmentations was calculated using dice-score (tolerance=1mm).

Three automatic angle-measures were applied to the segmented femurs: 3D-surface-model (3DSurfFCS) [3], cylinder-fitting (CylFit) [4] and a combination of MSK-staple [5], inertia-axes and refined geometry-fits (MSKsInertiaGeom). These methods are purely deterministic, leading to identical results for the same input. Therefore, robustness of such methods depends solely on segmentation.

Reliability was measured by Intraclass Correlation Coefficient (ICC).

Results

Dice-score between segmentations was 0.94±0.05. Reliability of all three automatic-angle-measures was comparable to or better than clinical measures (Fig.1). Based on MSKsInertiaGeom (overall performing best with ICC>0.8 for both angles), mean change over two years in the study population was 0.2±3.2° in NSA and -3.9±5.4° in AVA.

Discussion

While performing well compared to ICCs reported in literature [2], automatically-measured angles show maximum errors between segmentations of 10° (AVA-MSKsInertiaGeom) and 6° (NSA-MSKsInertiaGeom) - still large in relation to individual changes during growth.

Our results highlight the need for advanced automatic-MRI-segmentations, which together with consistent MRI-sequences may allow a fully reliable angle-measurement. Automatic-MRI-segmentation attempt using TotalSegmentator [7] failed for ~20% of bones for this MRI-sequence. We are currently developing an automatic-segmentation workflow using a U-Net-framework, based on a newer dataset with Dixon-decomposed MRI-images. Preliminary results are promising, indicating that fully reliable NSA- and AVA-measurements are achievable.

Images (Optional)

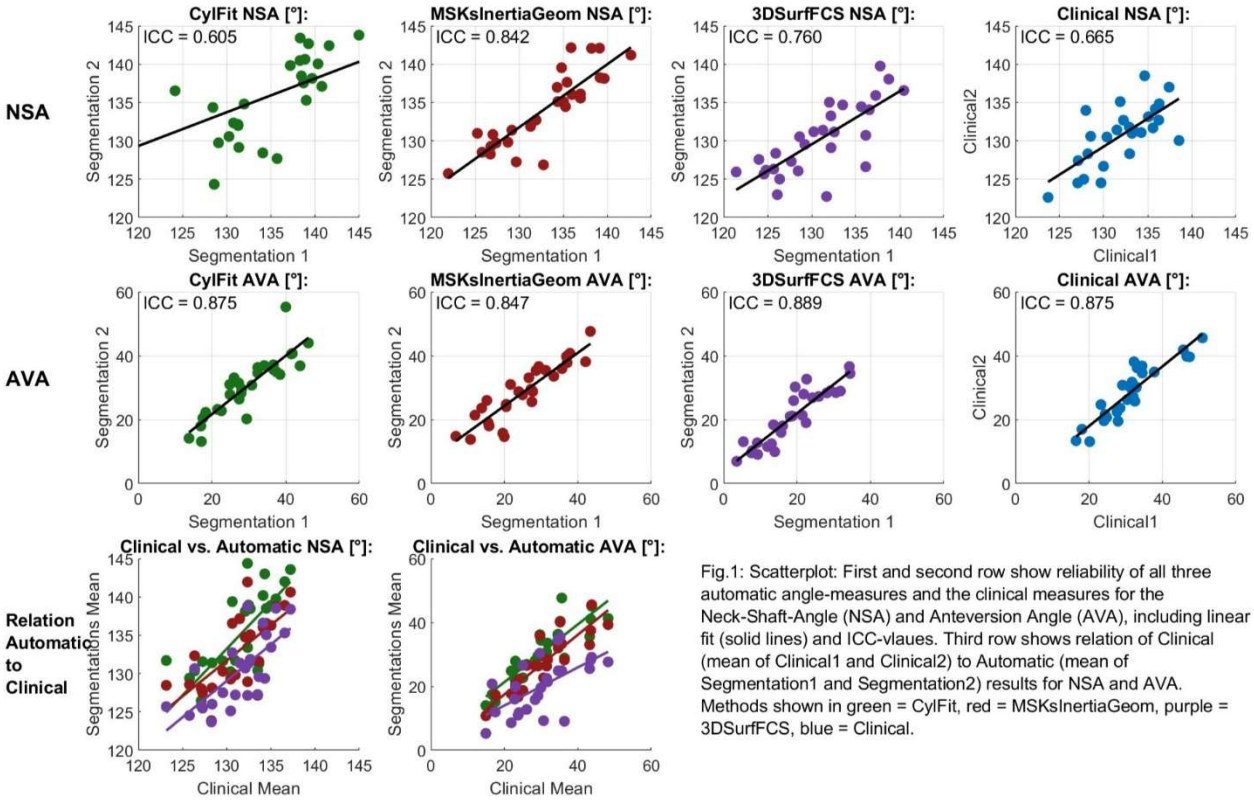


Fig.1: Scatterplot: First and second row show reliability of all three automatic angle-measures and the clinical measures for the Neck-Shaft-Angle (NSA) and Anteversion Angle (AVA), including linear fit (solid lines) and ICC-vlaues. Third row shows relation of Clinical (mean of Clinical1 and Clinical2) to Automatic (mean of Segmentation1 and Segmentation2) results for NSA and AVA. Methods shown in green = CylFit, red = MSKsInertiaGeom, purple = 3DSurfFCS, blue = Clinical.

References (Optional)

[1]Alexander,et.al.,J.Biomechanics,2019,[2]Boese,et.al.,SkeletalRadiol,2016,[3]Fischer,et.al.,*SciRep,2020,[*4]Casciaro&Craiem,ComputMethodsBiomechBiomedEng,2014,[5]Modenese,et.al.,J.Biomechanics,2021,[6]Sangeux,et.al.,JComputAssistTomogr,2015,[7]Wasserthal,et.al.,RadiolArtifIntell,2023

Acknowledgements (Optional)

This research was funded by the European Research Council (ERC-2024-COG, 101170218, INSIDE-BONE). We would like to thank the Medical University of Vienna and Bundesamt für Sport Switzerland (BASPO) for their help with data collection.

Session Category

Musculoskeletal Biomechanics: Joints and Motion

OA171-04

The Importance of Neuromusculoskeletal Model Personalisation: A Paediatric Case Example of Extreme Femoral Deformity

Miss Matilda Krywanio[1], A/Prof Nicole Williams[1,2], A/Prof Claire F. Jones[3], Prof Dominic Thewlis[1]

[1]Adelaide Medical School, The University of Adelaide, Adelaide, South Australia, Australia. [2]Department of Orthopaedic Surgery, Women's and Children's Hospital, North Adelaide, South Australia, Australia. [3]School of Electrical and Mechanical Engineering, The University of Adelaide, Adelaide, South Australia, Australia

Introduction

Developmental Dysplasia of the Hip (DDH) causes abnormalities in bone and muscle development. However, the effect of neuromusculoskeletal model personalisation for gait analysis in this condition has not been investigated. This study aimed to determine the change in estimated hip joint contact forces (JCFs) in neuromusculoskeletal models with incrementally personalised anatomy and neural solution, in one child with DDH.

Methods

The participant's affected hip (Fig. 1a) was superolaterally displaced, and the greater trochanter positioned posteriorly to the femoral head, causing abnormal muscle lever arms. Model geometry was progressively personalised: Model 1 was a linearly scaled gait2392 model. Model 2 incorporated femoral anteversion and neck shaft angles. Model 3 was fully personalised from segmented bilateral lower limb bones with magnetic resonance imaging-informed muscle pathways, in NMSBuilder [1]. For all, maximal isometric forces and musculotendon unit parameters were further scaled.

Muscle forces were estimated using static optimisation in OpenSim v4.4, or by electromyography (EMG) informed methods (Calibrated EMG-Informed NMS Modelling Toolbox v0.30.6), following which JCFs during walking were calculated. Intra-model comparisons were made using statistical parametric mapping.

Results

Compared to Model 1 with a max hip JCF of 4.5 body weight (BW), Model 2 produced higher hip JCFs (10.5BW) and Model 3, smaller (1.5BW). JCFs from EMG-informed muscles forces were not significantly different between Model 1+EMG and Model 2+EMG (5.4BW) but were lower in Model 3+EMG (2.5BW). JCFs were significantly different between Model 1 and

Model 3+EMG for 95% of stance phase ($p<0.001$, Fig. 1b). Abnormal muscle lever arms of gluteus medius in Model 3 resulted in lower forces when estimated using static optimisation, compared to Model 1 (max 0.0092BW vs. 0.77BW). When EMG signals were incorporated, the muscle force produced increased to 0.86BW, contributing to the higher JCFs estimated in Model 3+EMG compared to Model 3.

Discussion

In the presented case of significant femoral deformity, scaled generic models produced greater JCFs than the fully personalised model. Additionally, static optimisation in Model 3 misrepresented muscle forces, particularly of the gluteal muscles. With significant deformity, both personalisation of bony anatomy and incorporation of control signals should be strongly considered.

Images (Optional)

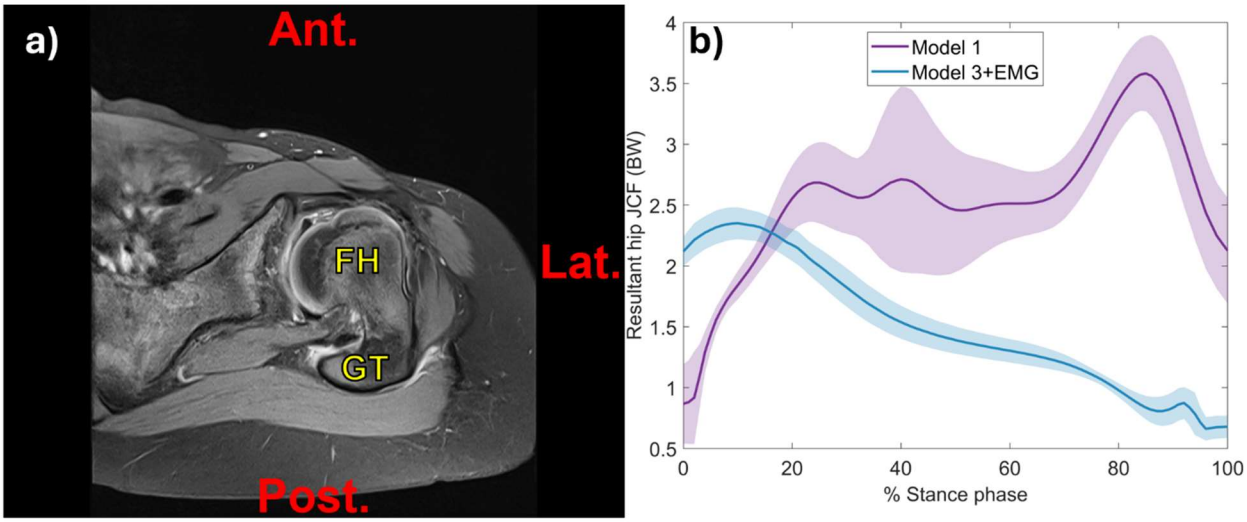


Fig. 1: a) Axial oblique proton density weighted MR image showcasing bone deformity. Ant. = Anterior, Post. = Posterior, Lat. = Lateral, FH = femoral head, GT = greater trochanter. **b)** Resultant hip JCF as mean (thick line) ± 1 standard deviation (shaded region) for Model 1 (i.e., the minimal level of personalisation) and Model 3+EMG (i.e., the maximal level of personalisation).

References (Optional)

[1] Modenese *et al.* , J Biomech., 2018

Session Category

Musculoskeletal Biomechanics: Joints and Motion

OA171-05

Quantification of 3D Trabecular Texture in the Femoral Head and Condyles Reveals the Locomotory Pattern in Humans and Sheep

Mr. Benjamin Zvi Rudski, Dr. Natalie Reznikov

McGill University, Montreal, Quebec, Canada

Introduction

Trabecular bone is abundant in the articulating ends of long bones. Stress trajectories observed in trabecular bone mirror mechanical forces through *functional adaptation* [1]. Thus, trabecular texture can serve as a proxy for loading history. In the hip, the femoral head articulates in a ball-and-socket joint with a broad range of movement. In the knee, the femoral condyles articulate in a hinge-like joint, moving primarily in the sagittal plane. We expected these movement ranges to be reflected in the trabecular texture of the femoral head and the condyles [2].

Methods

We examined human (n=3) and sheep (n=1) distal and proximal femora using microcomputed tomography. To visualise trabecular texture, we computed anisotropy vector fields using Dragonfly 3D World [3]. To quantify predominant trabecular textures, we constructed spherical orientation histograms and computed directional statistics using *VectoRose* [4].

Results

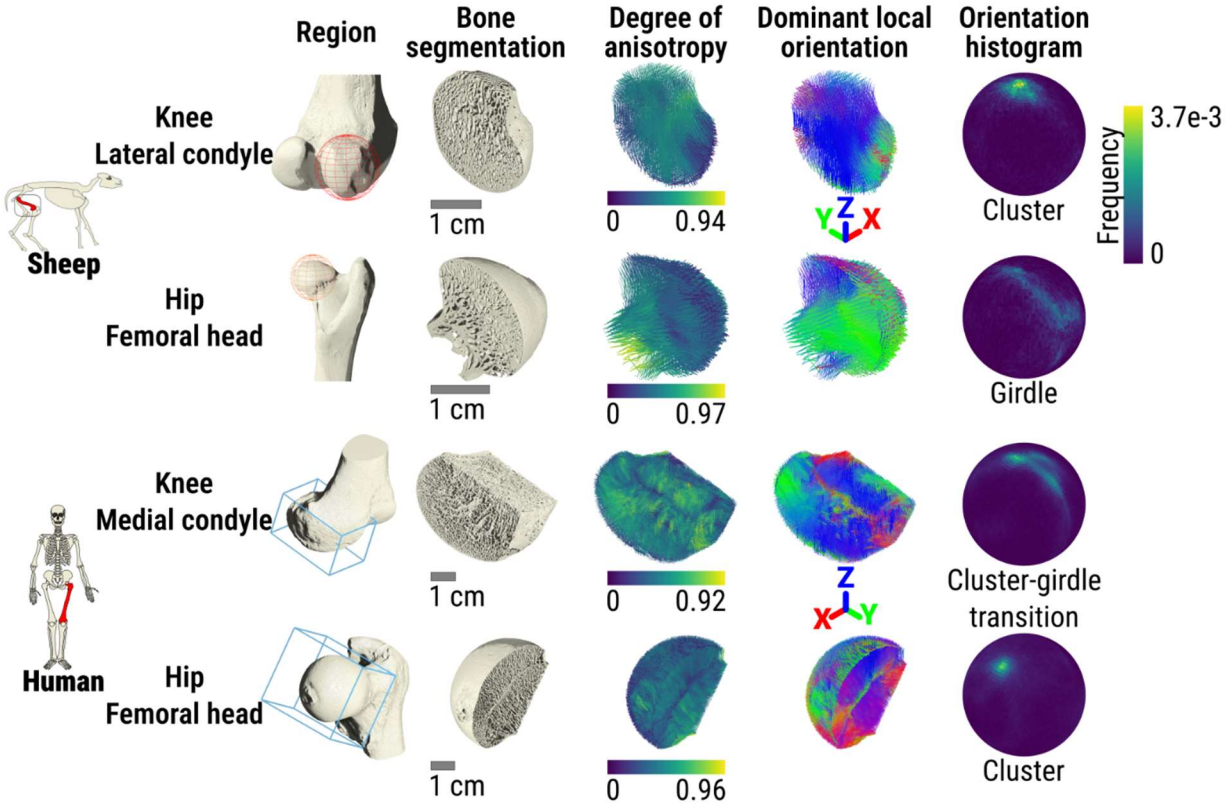
In the human femoral head, predominant trabecular orientations were clustered around an axis, instead of covering diverse orientations. In the human medial condyle, predominant trabecular orientations were indeed confined to the sagittal girdle. However, the angular range comprised 52%, 45% and 48% of the knee physiologic range of movement. In the sheep femoral head, predominant trabecular orientations were confined to the sagittal girdle rather than diverse orientations. In the sheep lateral condyle, predominant trabecular orientations were confined to a narrow cluster, rather than a girdle.

Discussion

In the proximal and distal femur, in humans and sheep alike, the range of predominant trabecular orientations is much narrower than the physiologically possible range of joint movement. This indicates that the range of habitual loading directions is also narrower than the physiologic range of movement. The extent of such restriction varies amongst individuals. Quantifying the extent of habitual utilisation of the maximal range of joint

movement opens new possibilities to explore the effects of loading history on trabecular adaptation in health and its maladaptation in disease.

Images (Optional)



References (Optional)

[1] Tracy L. Kivell, J Anat, 2016

[2] Lorna J. Gibson and Michael F. Ashby, *Cellular Solids*, 1997

[3] Natalie Reznikov *et al.*, Am J Biol Anth, 2022

[4] Benjamin Z. Rudski *et al.*, J Open Source Softw, 2025

Acknowledgements (Optional)

Both authors are supported by the Natural Sciences and Engineering Research Council of Canada (NSERC; BZR: PGS D-589427-2024, NR: RGPIN-2021-02658). Human skeleton diagram modified from Wikimedia Commons (https://commons.wikimedia.org/wiki/File:Human_skeleton_front_no-text_no-color.svg).

Session Category

Musculoskeletal Biomechanics: Joints and Motion

OA172-02

Comparison of Ankle Muscle Activation Patterns During Self-initiated Versus Motor-induced Falls From Standing Height

Mr. Donggeon Kim PT, Dr. Kitaek Lim PT, PhD, Dr. Seyoung Lee PT, PhD, Mr. Junwoo Park PT, M.S., Mr. Sungmin chun PT, Ms. Soyeon Yoon PT, Prof. Woochel Joseph Choi PT, PhD

Injury Prevention and Biomechanics Laboratory, Yonsei University, Wonju, Gangwon-do, Korea, Republic of

Introduction

To study falls, researchers employ two laboratory approaches: having participants fall voluntarily or inducing falls through external perturbations [1,2]. These two methods create fundamentally different conditions, and the resulting biomechanical responses are therefore expected to differ. However, no study has examined the impact of fall method on these responses. In particular, no information is available on how ankle muscle activation patterns vary depending on the type of fall. This study aims to address this gap.

Methods

Eight young adults participated in falling experiments that included self-initiated falls (SIF) and motor-induced falls (MIF) in forward, sideways, and backward directions. Fall kinematics were recorded using a motion capture system at 200 Hz, and muscle activity was collected using surface electromyography (EMG) at 2,000 Hz from the lateral and medial gastrocnemius (LGCM, MGCM) and tibialis anterior (TA) muscles bilaterally. Fall initiation was defined as a 10% drop in the pelvis marker. The 200 ms preceding this point was designated as the pre-fall phase, and the subsequent descending phase until body contact was time-normalized to 100%. The outcome variable was the reference voluntary contraction (%RVC), which was compared between fall types using one-dimensional statistical parametric mapping paired t-tests (SPM{t}).

Results

During the pre-fall phase, MIF exhibited greater bilateral ankle muscle activation than SIF across all directions. Sideways falls showed significant differences in every muscle, with MIF exhibiting on average about 5.3 times greater muscle activity than SIF (Figure 1a). During the descending phase, forward falls exhibited a significant cluster only in the right MGCM. In contrast, sideways falls showed multiple distinct clusters in left TA, MGCM, and LGCM, indicating different muscle activation patterns between MIF and SIF (Figure 1b). Backward falls revealed no significant differences across all muscles.

Discussion

Differences between MIF and SIF varied by fall direction and phase, suggesting that ankle responses to unexpected perturbations rely on context-specific neuromuscular strategies. These findings imply that fall-prevention or perturbation-based training may require multidirectional and unpredictable challenges rather than single-direction, predictable tasks.

Images (Optional)

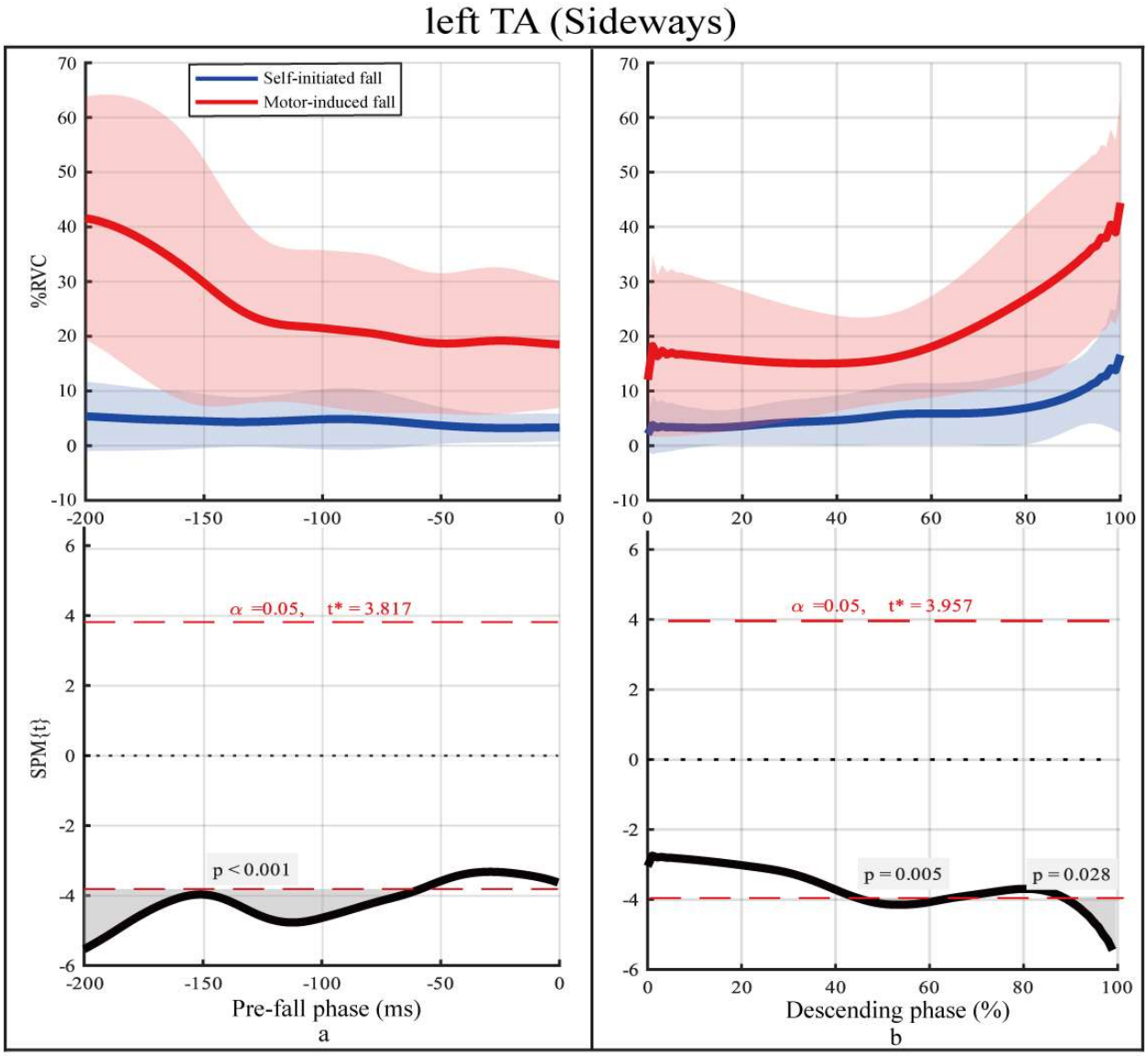


Figure 1. %RVC and corresponding SPM{t} results of the left TA muscle during (a) pre-fall and (b) descending phase of sideways falls. Differences existed between MIF and SIF

References (Optional)

[1] Lim and Choi. Osteoporos Int, 2020; [2] Hsiao and Robinovitch. J Biomech, 1998

Acknowledgements (Optional)

This work was supported by the “Brain Korea 21 FOUR Project” (F21SH8303039), Basic Science Research Program (RS-2023-00270689), National Research Foundation of Korea (NRF) grant funded by the Korea government (MSIT) (RS-2025-16071808), and by the Regional Innovation System & Education (RISE) program through the Gangwon RISE Center, funded by the Ministry of Education (MOE) and the Gangwon State (G.S.), Republic of Korea (2025-RISE-10–006).

Session Category

Human Motion and Performance: Balance, Posture and Control

OA172-03

Not All Falls Result in Injury in Older Adults: Distinct Risk Factors for Falls and Fall-Related Injuries

Mr. Junwoo Park PT, MSc, Dr. Kitaek Lim PT, PhD, Ms. Soyeon Yoon PT, Mr. Donggeon Kim PT, Mr. Sungmin Chun PT, Prof. Woochol Joseph Choi PT, PhD

Injury Prevention and Biomechanics Laboratory, Department of Physical Therapy, Yonsei University, Wonju, Gangwon-do, Korea, Republic of

Introduction

Falls can be prevented by identifying risk factors and implementing proactive strategies. However, a critical limitation is that most studies have focused only on risk factors for falls, neglecting the differences between injurious versus non-injurious falls [1]. A clear understanding of these differential risk factors should help improve fall prevention strategies.

Methods

We utilized data from the National Survey of Older Koreans 2023. We extracted the comprehensive potential risk factors, including demographics, the number of chronic disease conditions (comorbidity), assistive devices (aids), required assistance for activities of daily living (ADL), and home modifications [2,3]. Binomial logistic regression with stepwise selection was used to identify risk factors for falls (non-fallers versus fallers) and fall-related injuries (non-injurious versus injurious fallers). Falls were defined by fall history within the last year, and fall-related injuries were categorized by whether the fall required medical treatment.

Results

Characteristics of participants were presented in Table 1a. Our results suggested that height, gender, drinking, cognition, comorbidity, aids, and required assistance for ADL were significant risk factors for falls (Table 1b). Whereas, age and installation of handrails in bathrooms were significant risk factors for fall-related injuries (Table 1c).

Discussion

Our results indicated that the risk factors associated with falls differed from those associated with fall-related injuries. Interestingly, age presented as a risk factor for fall-related injuries, suggesting a marginal decrease in the odds of injurious falls as age

increases. This counterintuitive finding may be attributed to our definition of injurious falls, and it is plausible that younger older adults exhibit higher injury perception or are more likely to seek medical care following a fall. Furthermore, the installation of home modifications was associated with fall-related injuries, indicating that while home modifications are effective in preventing falls, they may not sufficiently mitigate fall-related injuries. Therefore, more considerate and injury-preventive design in home modifications is needed to develop effective fall and injury prevention strategies.

Images (Optional)

(a)

	Non-fallers (9,338)	Non-injurious fallers (249)	Injurious fallers (363)
Age (years)	73.9 (6.7)	77.2 (7.2)	75.8 (6.6)
Gender (Female)	5657 (60.6%)	198 (79.5%)	272 (74.9%)
Height (cm)	161.1 (8.1)	157.8 (6.9)	158.1 (7.4)
Cognition (points)	24.6 (4.7)	22.4 (5.7)	23 (5.2)
Drinking (Yes)	1182 (12.7%)	25 (10%)	42 (11.6%)
Comorbidity	2.1 (1.5)	3.2 (2)	3.3 (1.8)
Number of aids	0.8 (0.9)	1.5 (1.1)	1.3 (1.1)
Number of required assistance for ADL	0.7 (2.2)	1.9 (3.5)	2.3 (4.1)
Installation of handrails in bathrooms (Yes)	7755 (83.1%)	211 (84.7%)	285 (78.5%)

(b)

	Non-fallers vs. fallers			
	OR	CI		p value
Height	0.98	0.97	0.999	0.0374
Gender	1.62	1.21	2.16	< 0.01
Drinking	1.48	1.12	1.96	< 0.01
Cognition	0.98	0.97	0.998	0.0322
Comorbidity	1.3	1.24	1.37	< 0.001
Number of aids	1.31	1.20	1.42	< 0.001
Number of required assistance for ADL	1.07	1.04	1.1	< 0.001

(c)

	Non-injurious vs. injurious fallers			
	OR	CI		p value
Age	0.97	0.94	0.99	< 0.01
Installation of handrails in bathrooms	0.61	0.4	0.94	0.026

ADL: activities of daily living; OR: Odds ratio; CI: 95% confidence interval

Table 1: (a) characteristics of participants, (b) binomial logistic regression model between non-fallers and fallers, (c) between non-injurious and injurious fallers

References (Optional)

[1] Tinetti et al., N Engl J Med, 1988; [2] Sibley et al., BMC Geriatr, 2014; [3] Nguyen et al., Int J Public Health, 2022

Acknowledgements (Optional)

This work was supported by the “Brain Korea 21 FOUR Project” (F21SH8303039), the National Research Foundation of Korea (NRF) grant funded by the Korea government (MSIT) (RS-2025-16071808), and by the Regional Innovation System & Education (RISE) program through the Gangwon RISE Center, funded by the Ministry of Education (MOE) and the Gangwon State (G.S.), Republic of Korea (2025-RISE-10–006).

Session Category

Human Motion and Performance: Balance, Posture and Control

OA172-04

Asymmetrical Step Initiation Strategies and Fall Risk in Individuals with Unilateral Lower Limb Amputation: Insights from the Choice Stepping Reaction Time Test

Dr Victoria Spartacus[1], Dr Romain Tisserand[2], Dr Mathieu Gueugnon[3,4,5], Dr Louis Riglet[6,4], Ms Lauranne Claquesin[6,4], Mr Baptiste Orliac[6,4], Dr Anais Gouteron[4], Dr Clément Duraffourg[1], Ms Laurine Calistri[1]

[1]PROTEOR, 6 rue de la Redoute, CS 37833, CEDEX, Dijon, Bourgogne-Franche-Comté, France. [2]Université de Poitiers, Université de Tous, CNRS, CERCA, Poitiers, Poitou, France. [3]. INSERM, CIC 1432, Module Plurithématique, Plateforme d'Investigation Technologique, Dijon, Bourgogne-Franche-Comté, France. [4]CHU Dijon-Bourgogne, Centre d'Investigation Clinique, Module Plurithématique, Plateforme d'Investigation Technologique, Dijon, Bourgogne-Franche-Comté, France. [5]INSERM, UMR1093-CAPS, Univ. Bourgogne Franche-Comté, UB, Dijon, Bourgogne-Franche-Comté, France. [6]INSERM, CIC 1432, Module Plurithématique, Plateforme d'Investigation Technologique, Dijon, Bourgogne-Franche-Comté, France

Dr Victoria Spartacus

Dr Romain Tisserand

Dr Mathieu Gueugnon

Dr Louis Riglet

Ms Lauranne Claquesin

Mr Baptiste Orliac

Dr Anais Gouteron

Dr Clément Duraffourg

Introduction

Falls are frequent among individuals with lower limb amputation (LLA), leading to reduced mobility, independence, and quality of life. Although fall prevention research has addressed prosthetic design, risk factors, and balance assessment, the ability to initiate a step in an unpredictable context—involving compensatory mechanism crucial to maintain stability and assess fall risk—remains largely underexplored in this population. The choice stepping reaction time (CSRT) test evaluates this capacity, integrating neuropsychological, sensorimotor, and musculoskeletal control, yet it remains uncharacterized in LLA. This study examines the timing of stepping phases in a CSRT test performed by individuals with LLA, comparing the prosthetic and sound limbs.

Methods

Participants stood on two force platforms and stepped as quickly as possible onto central or lateral targets following LED cues, using either the sound or prosthetic limb (Figure 1.A). Four trials were performed for each target, resulting in 16 randomized trials. From vertical Ground Reaction Force (GRF) components, three temporal phases were defined as in [1]: Reaction Time (RT), Anticipatory Postural Adjustment (APA), and Swing Phase (SP); their sum yielded the total CSRT duration (Figure 1.B). For analysis, central and lateral targets were pooled by side (sound or prosthetic). Wilcoxon tests compared outcomes between limbs.

Results

Eleven individuals with unilateral LLA (9 transtibial and 2 transfemoral) completed the CSRT test. Initiating steps with the prosthetic limb produced significantly longer total movement durations, resulting from shorter APA and longer SP duration (Figure 1.C).

Discussion

These results reveal biomechanical asymmetry in step-initiation strategies according to the stepping side. Stepping with the prosthetic side produced longer CSRT durations, comparable to values reported in older adults at risk of falling, suggesting increased susceptibility to falls. Differences in APA and SP suggest that participants use adaptation strategies to increase reliance on the sound leg, potentially to limit landing velocity and mechanical load on the prosthetic side. Overall, the CSRT test appears suitable for

assessing balance and fall risk in individuals with LLA. It ensures high participant safety, particularly compared with other balance assessments involving external perturbations, while effectively distinguishing between the sound and prosthetic limbs.

Images (Optional)

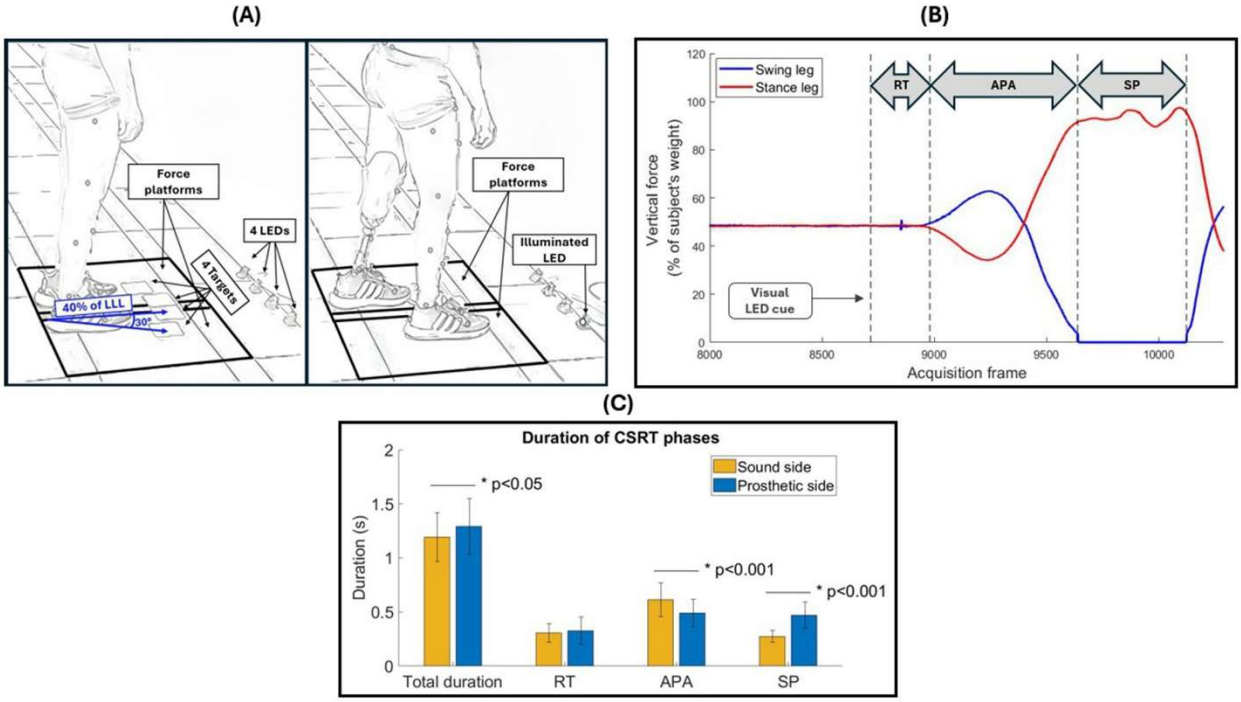


Figure 1: (A) Experimental step-up with initial position and final position, landing on a lateral target. The distance from the foot heel and the center of the target was 40% of the participant's lower limb length (LLL). (B) Example of raw vertical GRFs of one participant, under swing and stance legs, with temporal phases. (C) Mean and standard deviation of total and each phase duration. Results on central and lateral targets were pooled.

References (Optional)

[1] Tisserand et al. Front Hum Neurosci. 2016

Session Category

Human Motion and Performance: Balance, Posture and Control

OA172-05

Anticipatory and Reactive Balance Control During Walking Entry and Exit on a Moving Platform

Dr Genki Hisano[1], Dr Romain Bechet[1], Dr Helene Pillet[1], Dr Raphael Dumas[2], Dr Thomas Robert[2]

[1]Institut de Biomecanique Humaine Georges Charpak, Arts et Metiers Institute of Technology, EPF Engineering School, Universite Sorbonne Paris Nord, Paris, Île-de-France, France. [2]Univ Lyon, Univ Gustave Eiffel, Univ Claude Bernard Lyon 1, LBMC UMR_T 9406, Lyon, Auvergne-Rhône-Alpes, France

Introduction

Moving platforms such as escalators and moving walkways are common in daily life. Changes in velocity during transitions onto and off these surfaces may provoke imbalance and lead to falls, yet the underlying balance control strategies remain unclear. This study investigated anticipatory and reactive balance control during walking entry and exit on a moving walkway by examining changes in antero-posterior CoM velocity (V_{ap}) and whole-body angular momentum (WBAM) [1].

Methods

Sixteen healthy adults completed three conditions at preferred speed: steady-state walking, walking from overground to a moving walkway (entry), and the opposite condition (exit). During entry and exit, the treadmill belt moved at 0.5 m/s in the walking direction. Each trial included one stride, with the transition occurring during the second step (**Fig. 1A**). A 42-marker set defined a 13-segment full-body model. Center of mass (CoM) was computed as the barycenter of segmental mass and WBAM as the sum of segmental angular momenta about the CoM. V_{ap} (relative to the fixed ground) and WBAM waveforms were compared across conditions using non-parametric, permutation-based SPM one-way ANOVA with post hoc tests where main effects occurred ($\alpha = 0.05$).

Results

V_{ap} differed significantly across the conditions (**Fig. 1B**), increasing before the transition in entry and not returning to steady-state in the post-transition step of exit. In entry, sagittal WBAM (**Fig. 1C**) was significantly lower than steady-state during pre-transition swing, then showed a larger negative (forward-rotation) peak at the transition and a positive (backward-rotation) shift after foot contact. In exit, sagittal WBAM was significantly more positive

(backward-rotation) during pre-transition swing and more negative (forward-rotation) after the transition.

Discussion

Changes in V_{ap} indicate anticipatory preparation and a need for additional post-transition steps to stabilize. During entry, V_{ap} and sagittal WBAM patterns indicate anticipatory modulation of forward WBAM to match the moving platform's belt speed, followed by a reactive braking response after foot placement. During exit, V_{ap} and sagittal WBAM adjustments suggest anticipatory deceleration before belt assistance is withdrawn and rapid re-engagement of self-generated propulsion on the stationary surface. These findings may support applications in safety guidance or gait training.

Images (Optional)

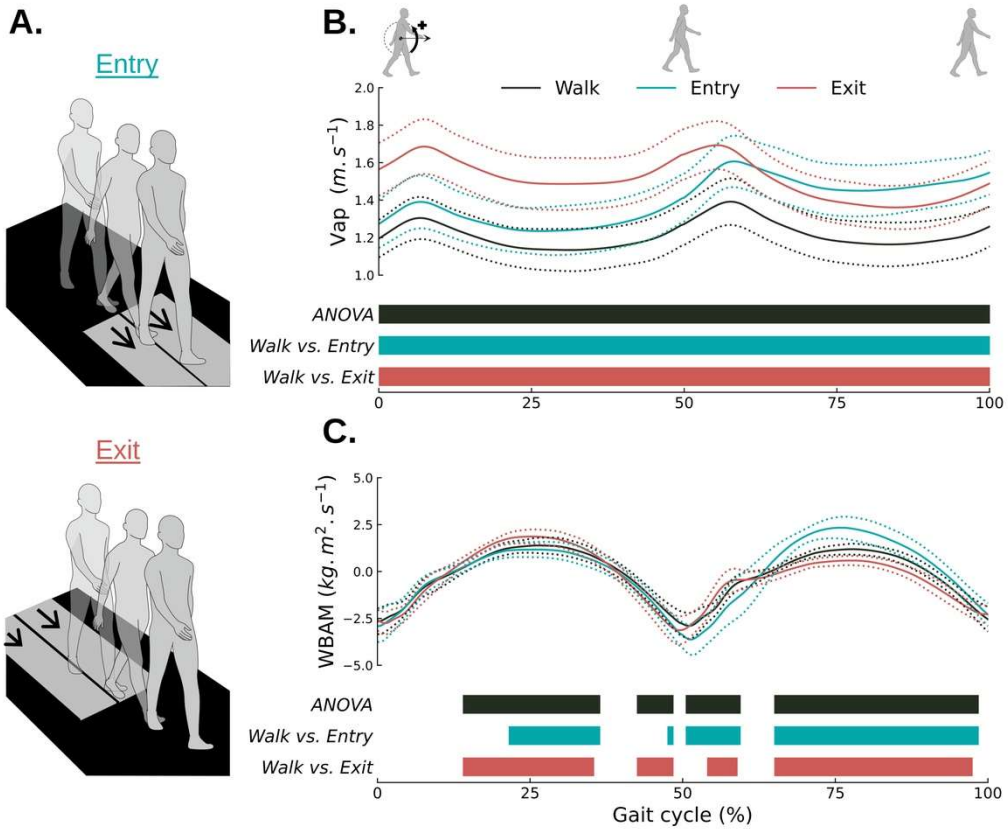


Figure 1: Task schematics for the entry and exit conditions (A.). Antero-posterior CoM velocity (V_{ap}) (B.) and sagittal whole-body angular momentum (WBAM) waveforms (C.) for three conditions: steady-state walking (black), entry (green), and exit (red). Each panel shows one stride time-normalized to 0–100%; with the transition occurring during the second step. For entry/exit conditions, the treadmill belt translated at 0.5 m/s in the walking direction. Significant one-way SPM ANOVA results ($\alpha = 0.05$) are shown by thick black bars for main effects, and by colored overlays for post hoc comparisons.

References (Optional)

[1] Bechet et al., *Gait Posture*, 2025

Session Category

Human Motion and Performance: Balance, Posture and Control

OA173-02

Dynamic Muscle Coordination Analysis Using Wearable Ultrasound: Advancing Biomechanical Assessment of Recovery

Dr. Erica L. King PhD, Dr. Qi Wei PhD, Dr. Siddhartha Sikdar PhD, Dr. Margaret T. Jones PhD, Dr. Parag V. Chitnis PhD

George Mason University, Fairfax, VA, United States

Introduction

Conventional musculoskeletal ultrasound provides high-resolution imaging but is limited to static, single-site assessments using handheld probes[1]. These constraints hinder dynamic biomechanical monitoring during rehabilitation, where multi-muscle coordination is critical for understanding recovery. This study introduces a compact, wearable ultrasound (WUS) system designed for real-time, multi-site imaging of muscle mechanics during movement.

Methods

A custom four-channel Time Delay Spectrometry Ultrasound (TDS-WUS) system[2] was developed to capture M-mode data during bilateral countermovement jumps (CMJs) on a split force platform. The system transmitted 20-ms frequency sweeps (3–5 MHz) and recorded echo signals at 50 lines/s from transducers placed over the vastus lateralis (VL) and vastus medialis oblique (VMO) bilaterally. Automated processing using Composite Factorization Principal Component Analysis (CF-PCA) extracted contraction dynamics without manual annotation, enabling quantification of intra-limb coordination and timing precision through cross-correlation analysis. Twenty NCAA Division I female athletes were categorized into two groups: prior knee injury (n = 8) and no injury (n = 12). Jump performance metrics (jump height and reactive strength index-modified) were compared alongside ultrasound-derived coordination indices.

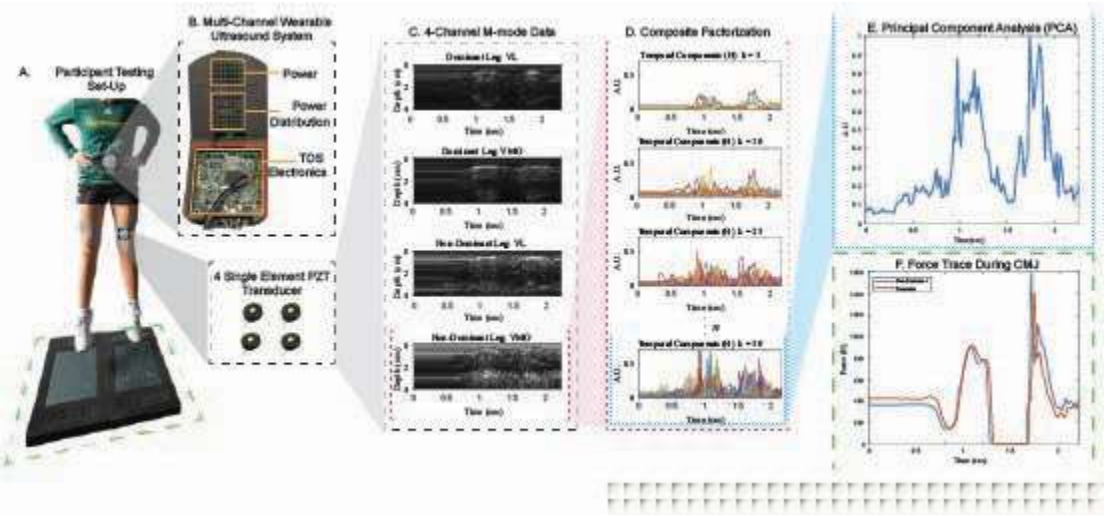
Results

While CMJ performance did not differ significantly between groups, CF-PCA revealed biomechanical disparities in muscle coordination. Athletes with prior knee injuries exhibited reduced VL–VMO synchrony ($p = 0.039$) and increased activation time-lags ($p = 0.013$), indicating persistent neuromuscular adaptations despite medical clearance. These findings align with functional survey scores ($p = 0.001$), suggesting that conventional performance metrics may mask underlying deficits in muscle recruitment and timing.

Discussion

Wearable multi-site ultrasound combined with automated analysis provides a novel biomechanical approach for assessing neuromuscular recovery. By capturing real-time coordination patterns during dynamic tasks, this technology offers clinicians and researchers objective indicators of muscle function beyond traditional performance measures. Integration into rehabilitation workflows could improve readiness-to-return assessments, reduce re-injury risk, and advance individualized recovery strategies. This work highlights the importance of synchronized, multi-muscle imaging for understanding complex biomechanical adaptations in sports medicine and rehabilitation.

Images (Optional)



References (Optional)

[1] Shah S *et al.* , *Crit Ultrasound J*. 2015

[2] Bashatah A *et al.* , IEEE Trans Biomed Eng. 2024

Acknowledgements (Optional)

Effort sponsored by the Government under Other Transactions Number W81XWH-15-9-0001

Session Category

Imaging and Biomedical Devices: Imaging Fundamentals and Applied Research

OA173-04

In-Vivo Radiation Dose During Dynamic Fluoroscopic Analysis of Knee Joint Motion

MSc Raphael Surbeck[1], Dr. Roland Zemp[1], Dr. Mirko Kaiser[1], MSc Stefan Plüss[1], Dr. Dr. Peter Cossmann[2], Prof. Dr. William R. Taylor[1]

[1]ETH Zürich, Zürich, Zürich, Switzerland. [2]MedTechConsulting, Zug, Zug, Switzerland

Introduction

Dynamic fluoroscopy enables high-accuracy in vivo assessment of joint kinematics by avoiding soft-tissue artefacts inherent to optical motion capture. However, participant exposure to ionizing radiation imposes ethical and practical limits on trial duration and frequency, potentially reducing the ecological validity of measured movements. Accurate quantification of effective radiation dose is therefore required to optimize imaging protocols and ensure participant safety. This study experimentally quantified in vivo X-ray dose during representative lower-limb motion tasks using a tracking biplanar fluoroscopy system.

Methods

A single participant (male, 46 years, 192cm, 103kg) diagnosed with knee osteoarthritis, scheduled for total knee arthroplasty and participating in an ongoing fluoroscopy study was included for this analysis. Imaging of the right knee was performed using a novel tracking biplanar videoradiography system (Fig. 1a) comprising two X-ray tubes (G1082, Varian Medical Systems, USA) and image intensifiers arranged at a 110° angle. X-ray acquisition parameters were 65 kV and 100 mA, using 30 Hz pulsed radiation with a pulse length of 1ms.

Radiation dose was measured during six functional activities with 3-4 repetitions each: level walking, stair ascent, stair descent, ramp ascent, ramp descent, and a forward lunge. For each task, four thermoluminescent dosimeters were placed 2 cm above the medial and lateral femoral epicondyles on both legs (Fig. 1b).

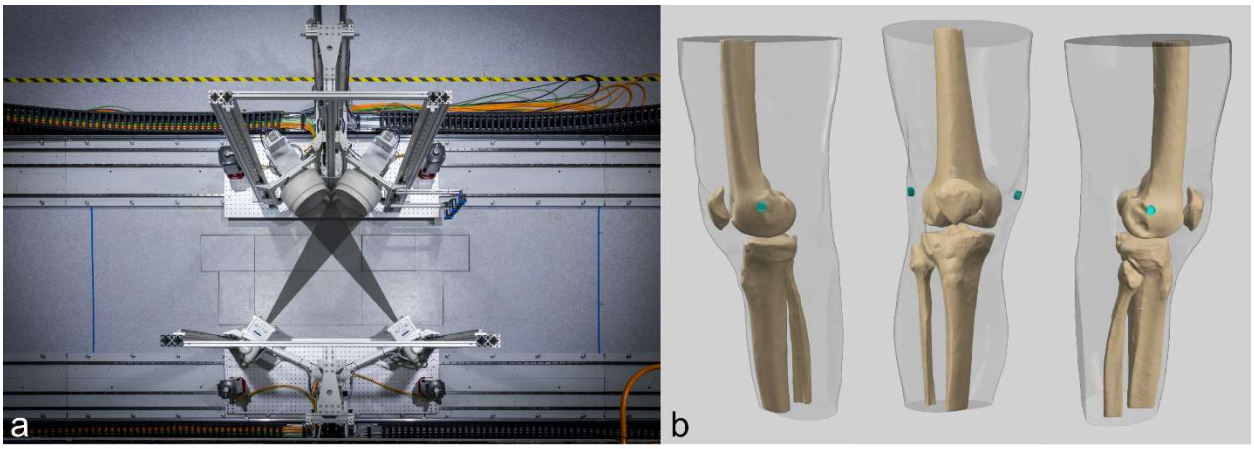
Results

A total effective dose of 0.181mSv was measured. Detailed results can be found in Fig. 1c.

Discussion

Radiation dose was substantially higher in the right (tracked) leg compared to the contralateral side for most tasks (Fig. 1c). Differences in doses between limbs and tasks could be attributed to task-specific kinematics and spatiotemporal parameters influencing the dose distribution; for example, prolonged leg crossing during stair descent increased exposure to the left leg while reducing exposure to the tracked right knee.
The cumulative dose of 0.181mSv measured during the fluoroscopic motion-analysis study was comparable to the natural background radiation accumulated over a few weeks. The estimated additional lifetime cancer risk was approximately 0.001%, indicating a negligible contribution relative to baseline population risk, consistent with ICRP Publication 103 (2007). These findings demonstrate that high-fidelity data using dynamic fluoroscopy can be obtained with minimal radiological risk.

Images (Optional)



c

Task	Level Gait	Ramp Ascent	Stair Ascent	Stair Descent	Ramp Descent	Lunge
Right Knee: Equivalence dose – Entry [mSv]	0.695	0.583	0.528	0.279	0.669	1.87
Right Knee: Equivalence dose – Exit [mSv]	0.0014	0	0.003	0	0.084	0.093
Left Knee: Equivalence dose – Entry [mSv]	0.501	0.208	0.124	0.333	0.439	0.145
Left Knee: Equivalence dose – Exit [mSv]	0.008	0.013	0	0.027	0.008	0.09
Right Knee: Entry-Exit difference [mSv]	0.694	0.583	0.525	0.279	0.585	1.77
Left Knee: Entry-Exit difference [mSv]	0.493	0.195	0.124	0.306	0.431	0.055
Right Knee: Entry-Exit sum [mSv]	4.44					
Left Knee: Entry-Exit sum [mSv]	1.60					
Both knees sum [mSv]	**6.04**					
k-factor	**0.03**					
Effective dose whole body [mSv]	**0.181**					
Frames	678	612	462	436	556	1362
Total Frames	4106					
Effective dose/frame total [mSv]	4.416×10^{-5}					
Right Leg: Effective dose/frame per task [mSv]	3.07×10^{-5}	2.86×10^{-5}	3.41×10^{-5}	1.92×10^{-5}	3.16×10^{-5}	3.91×10^{-5}
Left Leg: Effective dose/frame per task [mSv]	2.18×10^{-5}	0.956×10^{-5}	0.805×10^{-5}	2.11×10^{-5}	2.33×10^{-5}	0.121×10^{-5}
Both Legs: Effective dose/frame per task [mSv]	5.25×10^{-5}	3.81×10^{-5}	4.21×10^{-5}	4.03×10^{-5}	5.48×10^{-5}	4.03×10^{-5}
Dose-Area product [$\mu Gy*m^2$]	66.37	66.35	50.14	47.12	60.52	146.37

Figure 1. a) Tracking dual-plane fluoroscope of the Laboratory for Movement Biomechanics b) Thermoluminescent Dosimeter placement on the knee c) Results from the dosimeter measurements (equivalence doses) at entry and exit points of the radiation and calculated effective doses using a k-factor of 0.03.

Acknowledgements (Optional)

Session Category

Imaging and Biomedical Devices: Imaging Fundamentals and Applied Research

OA173-05

Stretching the Limits: Visualizing Epithelial Cell Behavior Under Cyclic Mechanical Load

M.Sc. David Jaworski[1,2], M.Sc. Lara Hundsdorfer[3,4], M.Sc. Yetong Wu[1,2], Dr. Effie Bastounis[5,3,4], Prof. Dr. Iordania Constantinou[1,2]

[1]Institute of Microtechnology (IMT), Technische Universität Braunschweig, Braunschweig, Lower Saxony, Germany. [2]Center of Pharmaceutical Engineering (PVZ), Technische Universität Braunschweig, Braunschweig, Lower Saxony, Germany. [3]Interfaculty Institute of Microbiology and Infection Medicine (IMIT), University of Tübingen, Tübingen, Baden-Wuerttemberg, Germany. [4]Cluster of Excellence "Controlling Microbes to Fight Infections" (CMFI), EXC 2124, University of Tübingen, Tübingen, Baden-Wuerttemberg, Germany. [5]Institute for Biology – Microbial Infection Biology, Humboldt-Universität zu Berlin, Berlin, Berlin, Germany

Introduction

Dynamic tissue stretching critically affects various cellular processes, from drug uptake to regeneration, and influences pathologies. The involved spatiotemporal dynamics remain largely unknown, partly due to the lack of cell stretching platforms compatible with videomicroscopy [1]. We introduce StretchView, a first-of-its-kind in vitro platform integrating cyclic cell stretching with automated, long-term videomicroscopy.

Methods

StretchView is a PDMS-based cell culture device enabling uniaxial, biaxial, or radial stretching of cells on an elastic membrane actuated by surrounding vacuum chambers. StretchView supports inverted microscopy, features a removable lid for top access, and allows automated videomicroscopy in relaxed and stretched states via an integrated ring-shaped spacer that limits vertical membrane movement to keep cells in focus (Figure a–c). As proof-of-concept, MDCK cell monolayers were grown on collagen I-coated StretchView membranes, imaged by time-lapse microscopy under radial cyclic loading (5% strain) for several hours, and analyzed for cell shape/kinematics via segmentation (Figure d) and particle image velocimetry [2]. Displacements and strains were quantified by digital image correlation for device calibration and post-experimental validation (Figure e,f).

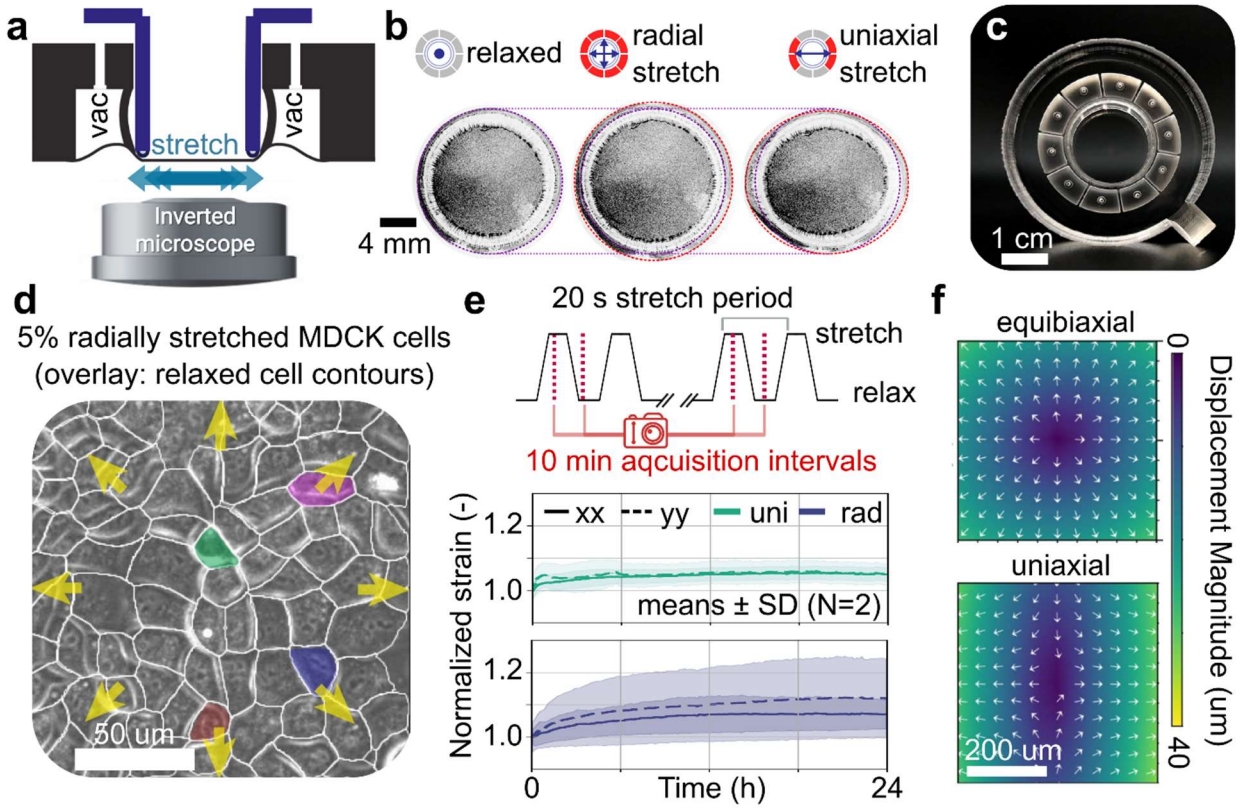
Results

Long-term stability of focus and strain fields (6% radial, 9% uniaxial strain) was confirmed through 24 h of videomicroscopy of cyclically stretched membranes, as depicted in Figure e, with mean relative strain drift of +0.05 (uniaxial) and +0.1 (radial) compared to the baseline (t=0). Long-term imaging (12 h) of cells under stretch was shown for the first time without the need for human intervention (snapshot: Figure d, full video: Supp. Movie 2 in [2]). Remarkably, alternating stretch patterns (radial, bi-/uniaxial) were demonstrated in a single experiment [2].

Discussion

Our videomicroscopy cell-stretching experiments yielded spatiotemporal data volumes exceeding prior studies limited to manual acquisition, endpoint analysis, or static stretch. As a powerful in vitro tool, StretchView enables diverse applications: multi-cell-type cultures, biomechanical measurements, FRET-based signaling dynamics monitoring, and stretching protocols with altering directions and waveforms. In our ongoing work, we analyze stretched cells by traction force microscopy, integrate membranes with tuned substrate stiffness, and enhance throughput by a multi-well design.

Images (Optional)



References (Optional)

[1] Iordania Constantinou and Effie E. Bastounis, Trends in Biotechnology, 2023

[2] David Jaworski et al. , Adv. Science, 2025

Acknowledgements (Optional)

This research was supported by the Deutsche Forschungsgemeinschaft (DFG, German Research Foundation) under Germany's Excellence Strategy – EXC 2124 – 390838134 (E.B., L.H.), and by the DFG project 490839690 (E.B, I.C., L.H., D.J.).

Session Category

Imaging and Biomedical Devices: Imaging Fundamentals and Applied Research

OA174-01

A Predictive Model for Trips on a Ladder: Groundwork to Create a Ladder Climbing Safety Tool

Dr Sarah Griffin PhD[1,2], Dr. Eni Halilaj PhD[3], Dr. Mark Redfern PhD[2], Dr. Kurt Beschorner PhD[4]

[1]University of Washington, Seattle, WA, United States. [2]University of Pittsburgh, Pttsburgh, PA, United States. [3]Carnegie Mellon University, Pittsburgh, PA, United States. [4]University of Pittsburgh, Pittsburgh, PA, United States

Introduction

Falls from ladders are a common cause of serious occupational injuries. Trips, characterized by the climber's foot inadvertently contacting the rung during swing phase, contribute to these falls. Although prior laboratory studies have not characterized these events, they likely result from poor moving quality, which can be characterized by the symmetry, stability, and smoothness of their movement.

This study developed a predictive model for ladder trips using gait quality metrics collected from a single wearable sensor. This represents a first step towards a system to monitor ladder climbing safety on a jobsite.

Methods

Twenty-five (16 F; 1.7 ± 0.09 m; 40.8 ± 12.7 years; 25.0 ± 3.7 kg/m^2) individuals who climb ladders regularly climbed up and down a series of ladder configurations (four rung designs at two different angles).

Optical motion capture data was used to identify trips during climbing, and participants were classified based on whether they experienced a trip.

An IMU attached to the pelvis collected acceleration data during ascending trials (Figure 1A). Root mean squared (RMS) acceleration (in three dimensions and overall magnitude) and harmonic ratio (in three dimensions) were calculated for one stride of each trial. These measures, as well as climbing speed, were regressors for the predictive model.

Least absolute shrinkage and selection operator (LASSO) regression generated a predictive model for trips. A nested leave-one-out approach tuned the model and evaluated its performance on left out data using the area under the receiver operating curve (AUC).

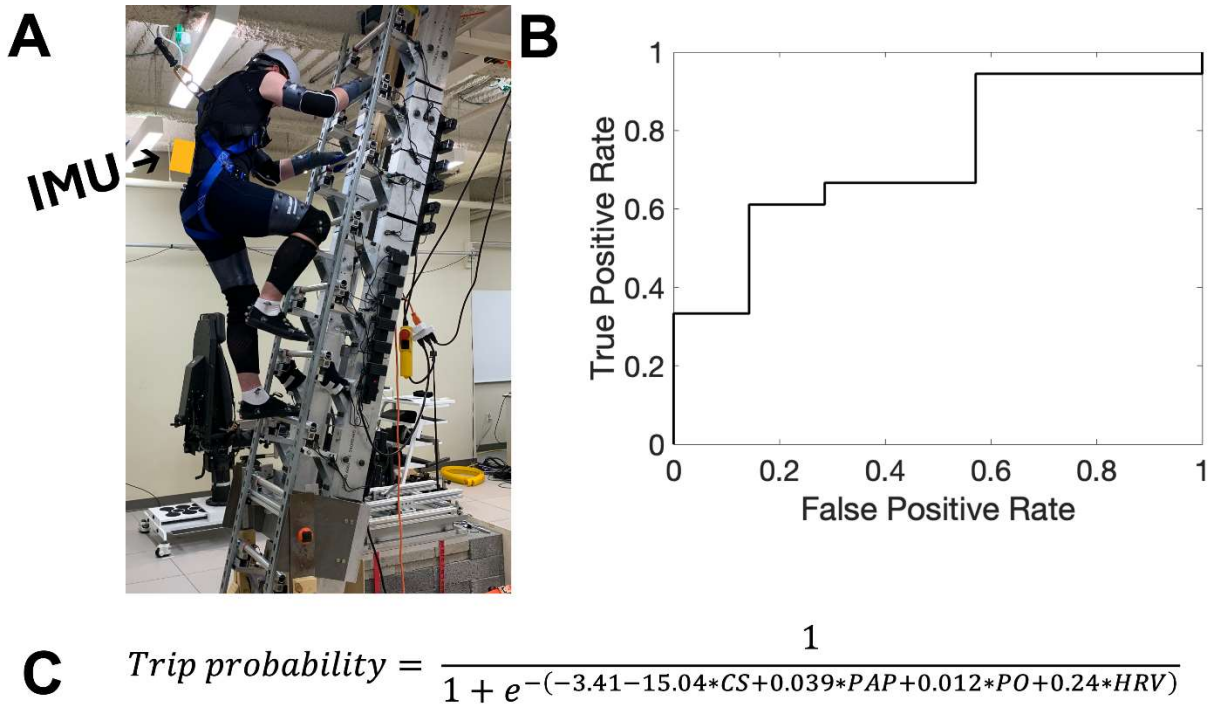
Results

The resulting model included the following predictors: climbing speed (*CS*), RMS acceleration in the AP direction (*PAP*) and of its overall magnitude (*PO*), and the vertical harmonic ratio (*HRV*) (Figure 1C). This model was moderately predictive with AUC = 0.73 (Figure 1B).

Discussion

This work suggest that whole body stability and smoothness are relevant to trip risk during climbing. In contrast, no single metric was predictive of trips (supplemental analysis). This work lays the groundwork for the development of a safety monitory tool using a combination of factors measured by a single sensor on their waist (e.g., smart phone in pocket).

Images (Optional)



C $$Trip\ probability = \frac{1}{1 + e^{-(-3.41 - 15.04 * CS + 0.039 * PAP + 0.012 * PO + 0.24 * HRV)}}$$

Figure 1: A) the testing apparatus and IMU placement location, **B)** the ROC curve for the predictive model, and **C)** the equation for the predictive model

Acknowledgements (Optional)

This research was funded by NIOSH R01OH011799 and NSF GRFP 2139321. Special thanks to Ricky Smith and Jenna Trout for their assistance with this project.

Session Category

Rehabilitation Biomechanics and Human Factors: Occupational Biomechanics

OA174-02

An Opensource Toolbox for Ergonomic Analysis using Xsens Awinda

Dr. Matthew Russell Ph.D., A.E., Mr. Justin Davidson M.Sc., CSCS, Ms. Julia Li M.Sc., Mr. Jameson Vanstone, Dr. Steven Fischer Ph.D, C.C.P.E., R.Kin

University of Waterloo, Waterloo, Ontario, Canada

Introduction

Inertial Measurement Unit (IMU) based motion capture offers a balance between traditional optical systems and publicly available computer vision models. IMUs are more portable and accessible than optical systems and do not suffer sensitivity to viewing angle and occlusions like computer vision methods. These advantages have increased their use in workplace and in-field applications, including occupational assessment and virtual task design. Despite offering a portable, detailed kinematics solution, the ability to integrate such rich data into streamlined ergonomic assessment workflows is still nascent and may benefit from opensource solutions. Thus, this study aimed to (1) develop an MSD risk assessment toolbox compliant with Xsens (Movella) data formats and (2) compare MSD risk assessment measures between IMU, optical, and computer vision motion capture systems.

Methods

Twelve participants lifted a 5.4 kg box from floor to shoulder height while collecting full body kinematics using (1) Xsens Awinda IMU-based system, (2) a 11-camera optical system (Vicon, Oxford, UK), (3) an 8-camera video-capture system (Qualisys AB, Gothenburg, Sweden). IMU data were subsequently exported to Movella's .mvnx format and processed in a custom Python (Ver. 3.11.8) toolbox.

Results

Our toolbox provides both a programmatic object-oriented interface and a graphical user interface (GUI) for interfacing with Xsens kinematic data (Figure 1.A.). Lift 'start' and 'stop' markers can be set manually or custom lift-detection algorithms can be called to identify single or multiple lift start and end times, and optionally infer the lifting frequency, by locating hand displacement minima and maxima surrounding the peak vertical hand velocities during the trial (Figure 1.B.). NIOSH recommend weight limit (RWL) and Liberty Mutual maximal acceptable load (MAL) calculations [1,2] are currently supported by

extracting relevant sex (Xsens Analyze 2025 only) and kinematic data, including horizontal and vertical lift distances, and asymmetry angle.

Discussion

Presented is an opensource toolbox to streamline analysis and dashboarding of Xsens IMU-augmented MSD risk assessments. Comparisons between IMU-, optical-, and computer vision-based MSD risk assessment measurements and coefficients are forthcoming.

Images (Optional)

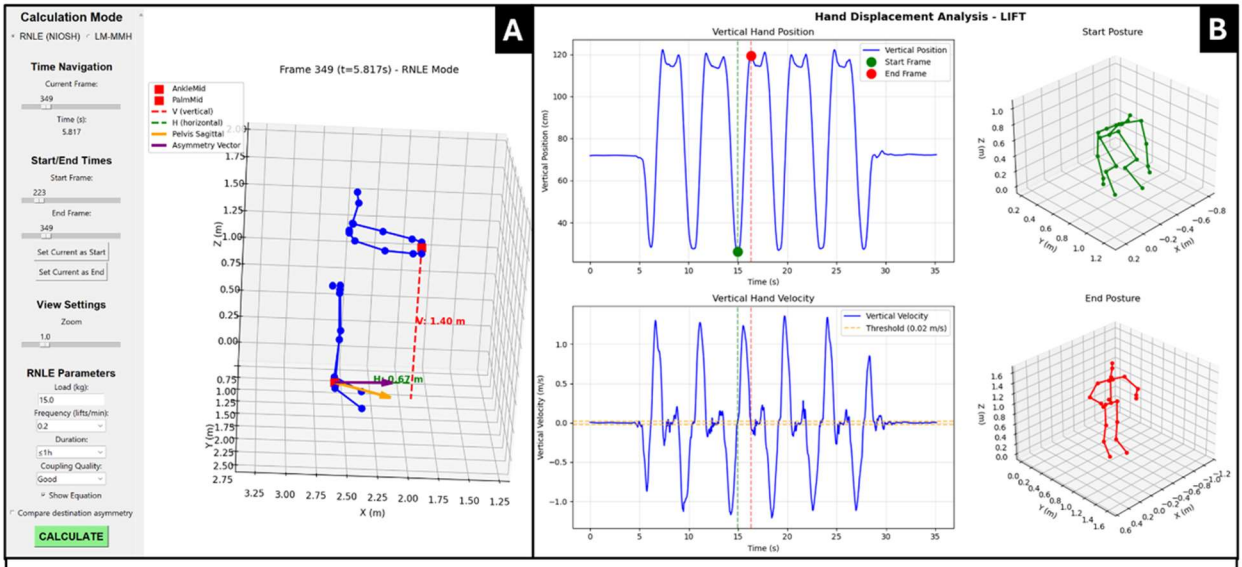


Figure 1.
Pane A: Toolbox User Interface.
Pane B: Lift Detection Algorithm Tracking Vertical Displacement and Velocity of the Midpoint Between Both Hands during the Box Lift Task (5 Lifts Performed).

References (Optional)

[1] Jim Potvin, et al. *Ergonomics*, 2021

[2] Thomas Waters, et al. Applications manual for the revised NIOSH lifting equation, 1994

Acknowledgements (Optional)

We would like to acknowledge the support of the Movella engineering team for advising on technical aspects of this project.

Session Category

Rehabilitation Biomechanics and Human Factors: Occupational Biomechanics

OA174-03

Influences of Anti-Fatigue Mat Stiffness on Self-Reported Pain During Prolonged Standing and Biomechanical Metrics of Balance Control

Ms. Alyssa M. Tondat, Mr. Taylor B. Winberg, Dr. Andrew C. Laing

University of Waterloo, Waterloo, ON, Canada

Introduction

Anti-fatigue mats (AFMs) decrease underfoot surface stiffness towards reducing musculoskeletal pain (MSK-P) [1]. However, this design principle has differential effects across competing biomechanical demands/pathways (e.g. pain, balance control). This multi-study project investigated these biomechanical pathways towards determining an optimal AFM stiffness for reducing MSK-P whilst minimizing balance impairments.

Methods

An industry partner generated AFMs (identical polyurethane foam materials and geometry) at five distinct stiffness levels characterized by CF durometer (higher CF is stiffer).

Study 1: Eleven participants completed 75-minutes prolonged standing on four separate days: three AFMs (CF 26, 34, 41), and a rigid control (RC) surface. Pain ratings were recorded for the low back (LB), shanks, and feet. Pain after 75-minutes was compared across AFM conditions. Subset analysis explored AFM effects for LB pain (LBP) developers [1].

Study 2: Ten participants completed static (standing) and dynamic (reaching, sit-to-stand) balance tasks on five AFMs (CF 24,29,32,36,40) and a RC surface. IMUs (APDM Opal) measured whole-body kinematics. Outcomes included sway velocity, RMS, and path length for standing tasks, and reach distance and trunk lean angle for dynamic tasks.

Results

Study 1: AFM stiffness effects on pain were body-part specific (Figure 1). The stiffest AFM (CF 41) decreased foot pain by 43.3% compared to RC ($p=0.022$). AFM effects were non-significant for shank pain ($p=0.403$) and LBP ($p=0.406$). For pain-developers, the stiffest AFM reduced LBP by 72.6% ($p=0.008$).

Study 2: AFMs had minimal effects on balance control. Compared to RC, there were no AFM effects on dynamic balance measures, or 4/7 static tasks (all $p>0.05$). In the three tasks with AFM effects, differences were least pronounced on the stiffest AFM (CF 40).

Discussion

This multi-study, industry-relevant project explored potentially competing demands of AFM stiffness on biomechanical outcomes. The stiffest polyurethane foam AFM produced the largest effects on MSK-P whilst minimizing effects on balance control (aligning with anecdotal reports of plywood flooring's benefits in manufacturing settings). Continued work is exploring underlying biomechanical mechanisms (muscle activation, blood oxygenation) towards developing application-specific design criteria (e.g. prolonged standing vs. impact attenuation).

Images (Optional)

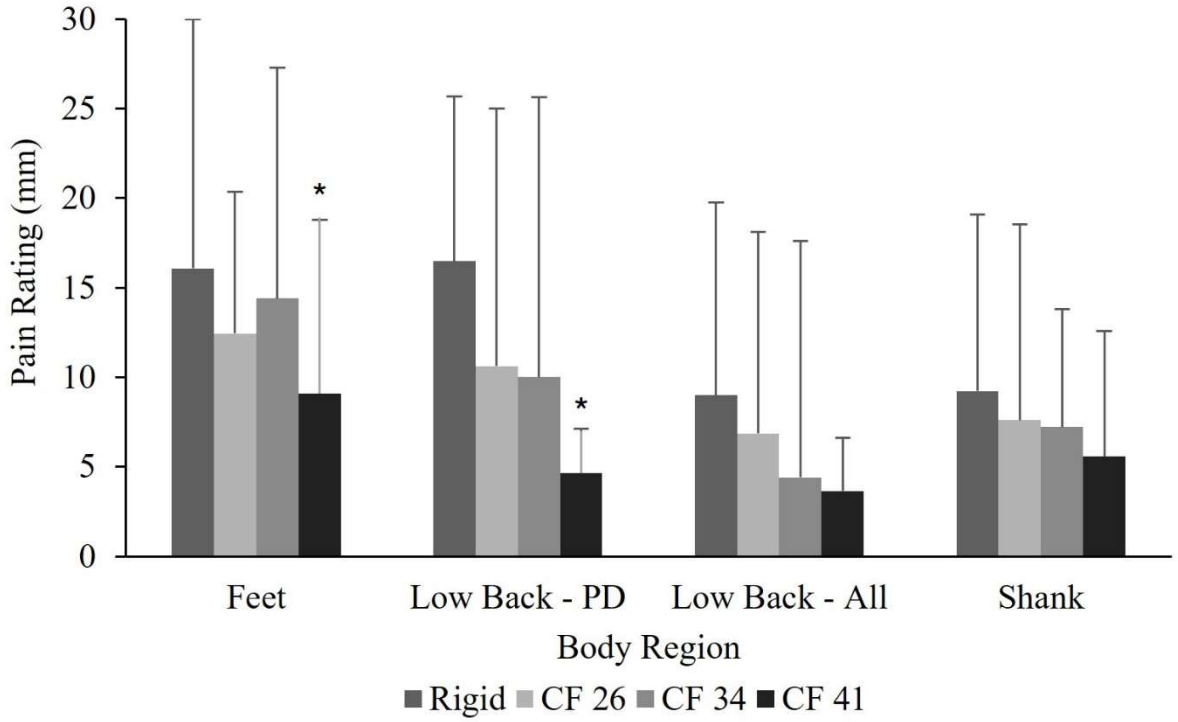


Figure 1: Pain ratings after 75-minutes of prolonged standing across body regions. PD = Pain-developer subgroup; All = all participants combined. The highest durometer AFM (CF 41) was most effective at reducing pain across all body regions. * indicates significant difference from the rigid control condition.

References (Optional)

[1] Winberg et al., Appl. Ergon., 2022

Acknowledgements (Optional)

NSERC, Ontario Centre of Innovation, Custom Foam Systems Ltd.

Session Category

Rehabilitation Biomechanics and Human Factors: Occupational Biomechanics

OA174-04

Concurrent Validity of Markerless Motion Capture for Assessing Manual Lifting Kinematics

Ph D Candidate Mengjie Zhang[1], Professor Mark Boocock PhD[2], Senior Lecturer Arne Nieuwenhuys PhD[1], Associate Professor Yanxin Zhang PhD[1]

[1]School of Exercise, Sport and Rehabilitation Sciences, Faculty of Science, University of Auckland, Auckland, Auckland Region, New Zealand. [2]Ergonomics and Human Factors Group, School of Allied Health, Auckland University of Technology, Auckland, Auckland Region, New Zealand

Ph D Candidate Mengjie Zhang

Professor Mark Boocock

Senior Lecturer Arne Nieuwenhuys

Introduction

Work-related musculoskeletal disorders (WMSDs) are a leading cause of occupational disability. Although markerless motion capture (MMC) offers low-cost, scalable alternatives to laboratory systems, validation studies have focused primarily on gait and sports, leaving complex manual handling tasks with load-induced occlusion and multi-planar movements underexplored. This study evaluated the concurrent validity of two MMC systems (OpenCap and MediaPipe) against a marker-based system (Vicon) as the gold standard for two-handed lifting tasks.

Methods

Twenty healthy participants (12 females/8 males; age 28.2 ± 2.19 years; height 1.68 ± 0.07 m; mass 60.8 ± 11.27 kg; BMI 21.43 ± 2.77) performed three tasks with increasing complexity: two-handed vertical lifting (VL), performed symmetrically in the sagittal plane; transverse lifting (TL), involving trunk rotation and frontal-plane motion; and rotational walking-and-lifting (RWL), combining lifting with short-distance walking and rotation. Full-body kinematics were captured simultaneously using Vicon (100 Hz, 39-marker Plug-in

Gait full-body model), OpenCap (60 Hz, three iOS devices), and MediaPipe (60 Hz, single-camera custom pipeline). Joint angles across all three planes were compared using Root Mean Square Error (RMSE, °), normalized RMSE% (relative to Vicon peak-to-peak range), and coefficient of determination (R^2) over the complete lifting cycle.

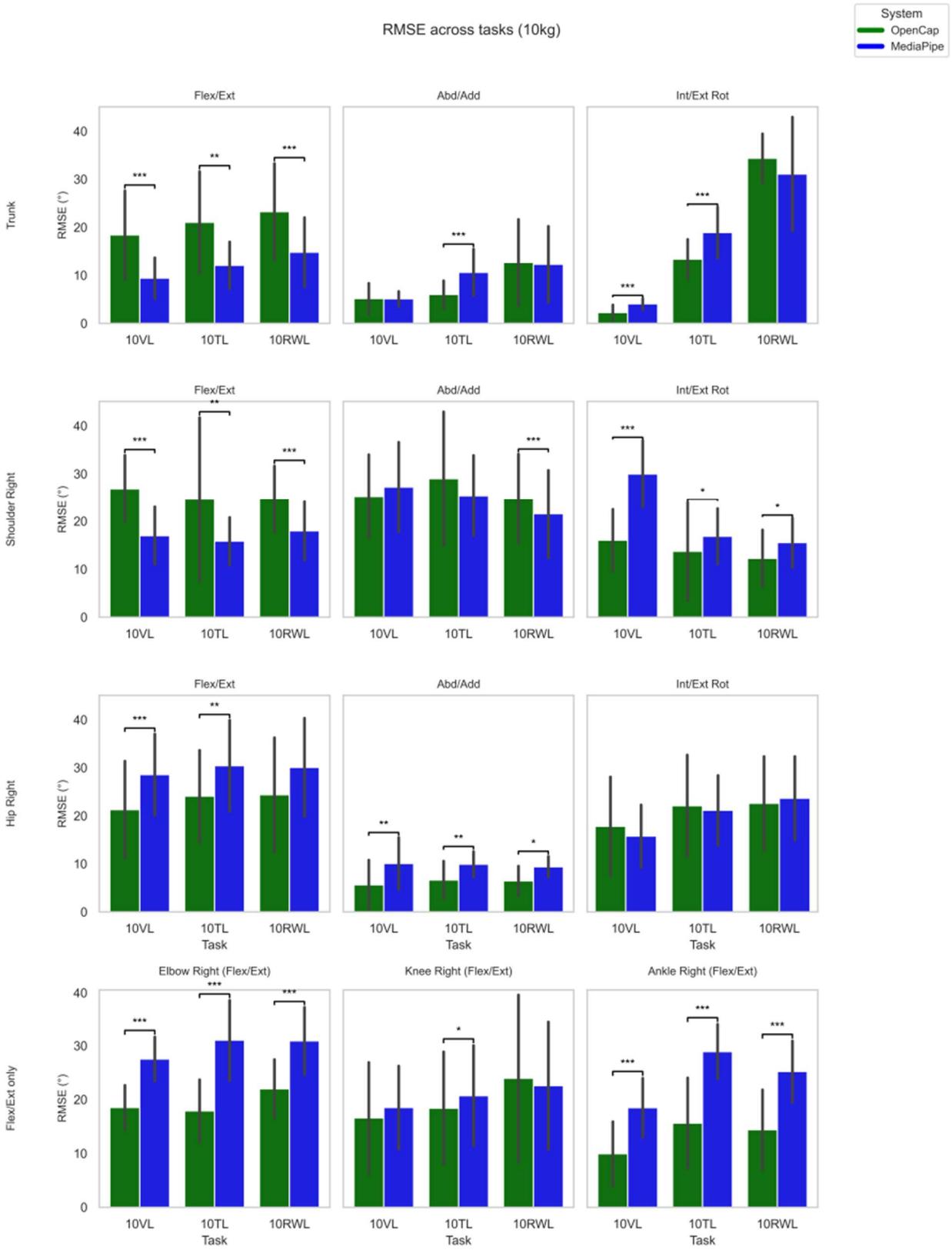
Results

Concurrent validity varied substantially by task, plane, and joint (Fig.1). For OpenCap, RMSE ranged from 4° to 67° (12-121%), with R^2 from 0.07 to 0.88. For MediaPipe, RMSE ranged from 6° to 60° (13-150%), with R^2 from 0.07 to 0.89. In the sagittal plane, RMSE% ranged from 12% to 42% across joints in VL tasks, with R^2 values up to 0.89. Accuracy decreased in the frontal and transverse planes with increasing task complexity, with RMSE% increasing approximately 15-30% from VL to RWL.

Discussion

MMC demonstrates potential for sagittal-dominant ergonomic assessment but remains substantially limited in frontal/transverse planes due to persistent landmark occlusion and depth ambiguity, challenges that persist even in optimized multi-view systems. Future work should address real-world occlusions, include diverse populations, enhance deep learning and optimization-based models, and validate hybrid approaches integrating biomechanical constraints or RGB-D fusion for robust WMSDs risk assessment.

Images (Optional)



Session Category

OA174-05

A Hybrid Two-Phase Framework for Posture Prediction of Manual Material Handling Tasks

PhD Candidate Mengjie Zhang[1], Professor Mark Boocock PhD[2], Senior Lecturer Arne Nieuwenhuys PhD[1], Associate Professor Yanxin Zhang PhD[1]

[1]School of Exercise, Sport and Rehabilitation Sciences, Faculty of Science, University of Auckland, Auckland, Auckland Region, New Zealand. [2]Ergonomics and Human Factors Group, School of Allied Health, Auckland University of Technology, Auckland, Auckland Region, New Zealand

PhD Candidate Mengjie Zhang

Professor Mark Boocock

Senior Lecturer Arne Nieuwenhuys

Introduction

Digital human models are efficient tools for simulating human postures and movements in specific work environments. Given the human body is a highly complex nonlinear system, predicting a virtual human's joint configurations under given tasks and constraints is a challenging task. Current 3-dimensional (3D) posture prediction models include redundant degrees of freedom (DOFs) that create a high-dimensional ill-posed optimization problem. On the other hand, 2-dimensional (2D) solution models consist of fewer DOFs in the sagittal plane, which are computationally efficient but lack DOFs in the frontal and transverse planes. This study developed a hybrid two-phase framework combining efficient 2D sagittal-plane optimization with 3D upper-limb reconstruction, delivering both accuracy and efficiency across diverse manual handling tasks.

Methods

Given fixed hand/foot positions, external load, and anthropometrics, Phase I performed constrained nonlinear optimization (5 DOFs) by minimizing joint torques subject to biomechanical constraints. Sequential Quadratic Programming was applied to solve the

optimization problem. During Phase II, the 3D upper-limb posture was predicted by applying inverse kinematics to compute the shoulder and elbow angles while adhering to biomechanical and performance criteria (Fig. 1). To validate the model, twelve participants (7 females/5 males; 28.5±2.19 years) performed two-handed vertical lifting (10 kg), shoulder-height drilling, and overhead drilling tasks. Vicon motion capture (100 Hz, 39 markers) provided ground truth, with validation performed using Root Mean Square Error (RMSE) for 7 joint angles.

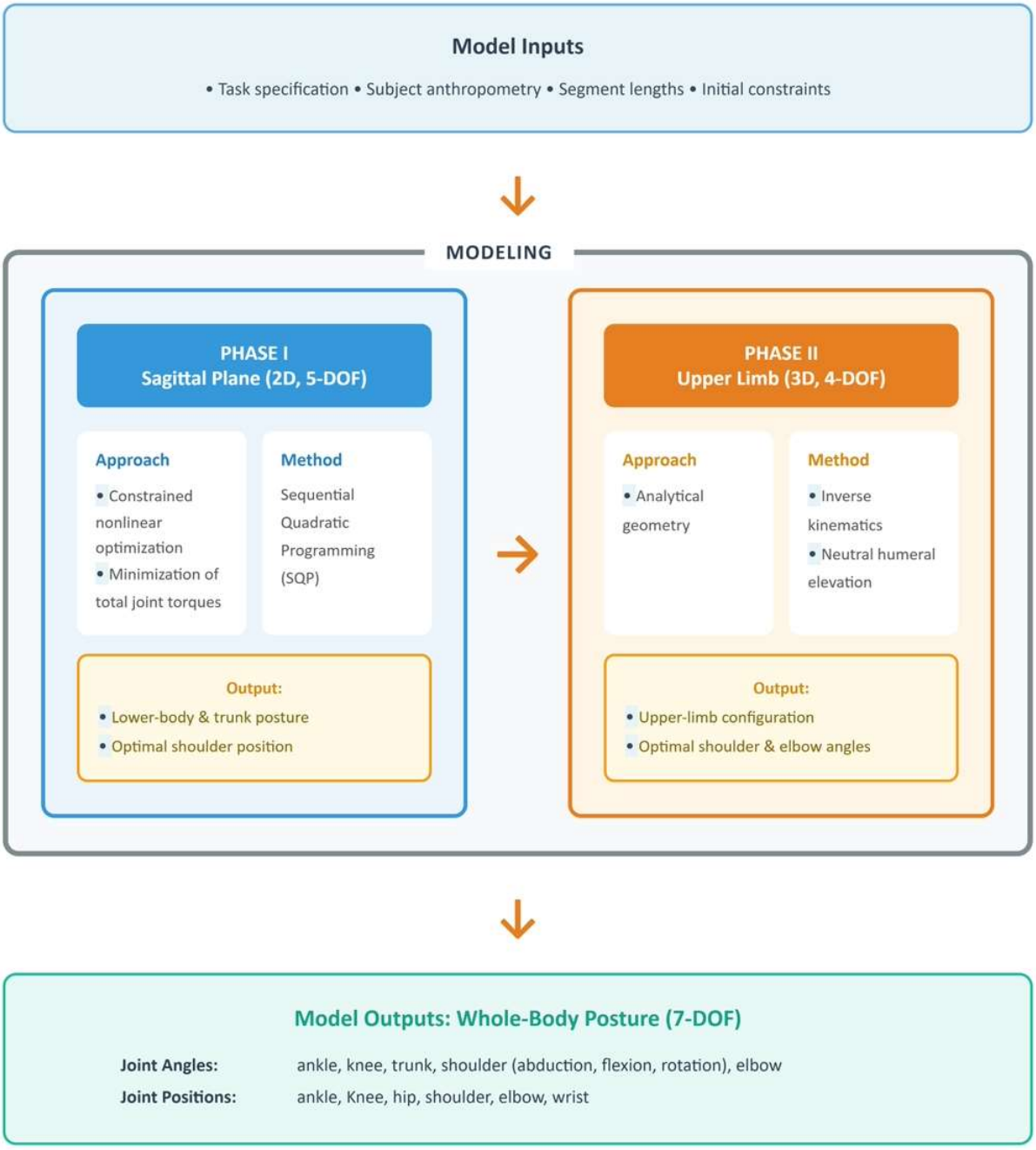
Results

Across lifting and drilling tasks, the model achieved joint angle RMSEs of 4.21°-37.32° with 65-85 ms computation time per posture. The upper-limb predictions showed shoulder flexion/extension RMSE of 5.56°-7.56°, shoulder abduction/adduction RMSE of 6.97°-11.27°, and elbow flexion RMSE of 7.25°-18.63°. The lower-body and trunk flexion/extension angles showed RMSEs of 4.21°-7.06° (ankle), 6.86°-7.55° (knee), and 10.47°-12.39° (trunk).

Discussion

By combining efficient 2D optimization for the lower body and trunk with analytical 3D reconstruction for the upper limbs, the model provides a practical tool for predicting postures in diverse manual tasks. Validation confirms its reliability in simulating both reaching and lifting activities. The model has potential to be integrated into workflows for human-machine interface design.

Images (Optional)



Session Category

Rehabilitation Biomechanics and Human Factors: Occupational Biomechanics

OA174-06

Exploring the Efficacy of Different Field-Based Kinetic Measurement Approaches for the Calculation of Peak and Cumulative Low-Back Moments.

Mr. Justin Davidson MSc., Dr. Dennis Larson PhD, Ms. Julia Li MSc, Dr. Steven Fischer PhD

University of Waterloo, Waterloo, Ontario, Canada

Introduction

Accurately estimating peak and cumulative low-back exposures in the workplace is critical for assessing low-back injury risk [1]. In lab, force plates are the standard input for bottom-up inverse dynamics; however, their high cost and limited portability make them impractical for field measurements. Hand force estimates have been used as an alternative, but accurately measuring hand forces and identifying when to apply them to a kinematic model remains difficult. Recent innovations in force-estimating insole technology offer a potential solution [2]; however, their validity in computing low-back moments has not been evaluated. This study aimed to compare three kinetic measurement approaches for estimating peak and cumulative low-back extensor moments during occupationally relevant tasks.

Methods

Forty participants (20F, 20M) performed three occupational tasks: floor-to-shoulder lifting, box packaging, and above-shoulder work sorting. Kinematics were capturing using a Qualisys video capture system and processed through Theia3D. Kinetics were measured with force plates (gold-standard), force estimating insoles (Loadsol, Novel), and hand forces estimates derived from known weights applied at the center of mass of the hand. Peak and cumulative low-back extensor moments were computed in Visual3D for each measurement approach (bottom-up for force plate and insoles, top-down for hand force estimates). Two-way repeated measures ANOVA's evaluated differences between peak and cumulative low-back extensor moments across tasks and measurement systems.

Results

Significant interactions between measurement systems and tasks existed for both peak and cumulative moments (Figure 1). Differences in peak moments between measurement systems were most pronounced during the above-shoulder work sorting task, while cumulative moments varied most during the packaging task. Moments during lifting remained similar overall between kinetic measurement approaches.

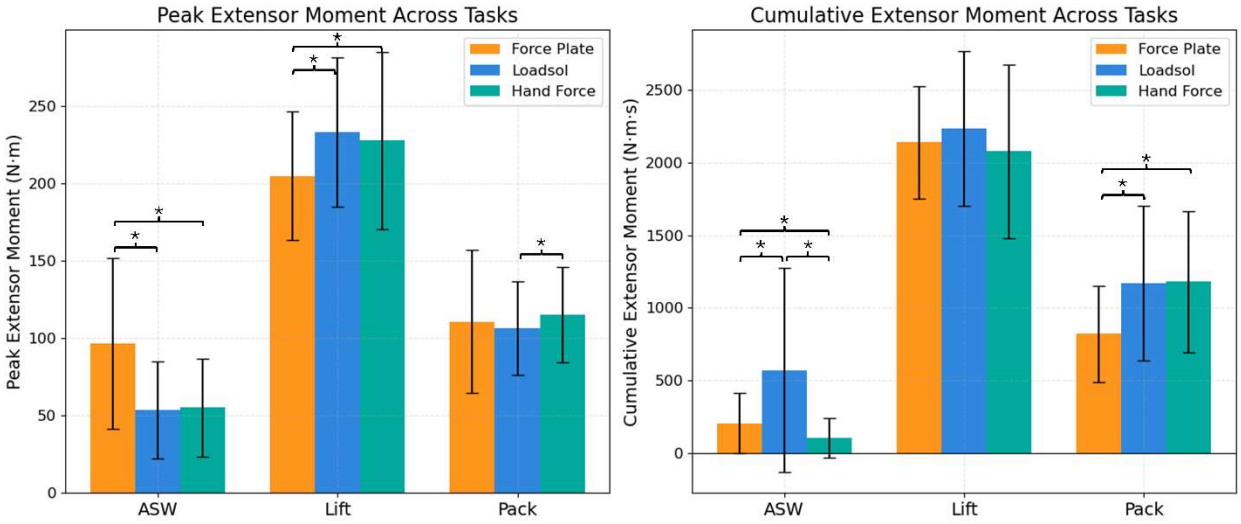
Discussion

Estimating moments via hand force and via force-estimating insoles were comparable to estimates using gold standard force plate data. Considering the practical challenges of estimating hand forces and when they should be applied in the field, force-estimating insoles may provide a viable alternative for detailed time-series low-back moment calculations. Improving the accuracy of field-based kinetic measurement can enhance our understanding of occupational low-back injury risks and inform better prevention strategies long-term.

Images (Optional)

Figure 1

Peak and cumulative low-back extensor moments for three occupational tasks measured by three unique kinetic measurement approaches. Significant interactions of task and measurement approaches were found for peak and cumulative moments. Post-hoc pairwise comparison revealed significance is indicated by an *.



References (Optional)

[1] Vieira & Kumar *J. Occup. Rehabil.*, *2004*

[2] Davidson et al., Ergonomics, 2025

Session Category

Rehabilitation Biomechanics and Human Factors: Occupational Biomechanics

OA175-02

Monitoring Longitudinal Healing in Ovine Large Defect Reconstruction using Virtual Mechanical Testing

Ms. Kylie Frew[1], Dr. Madeline Boyes[2], Dr. Thomas Schaer[2], Dr. Hannah Dailey[1]

[1]Lehigh University, Bethlehem, Pennsylvania, United States. [2]University of Pennsylvania, Department of Clinical Studies New Bolton Center, School of Veterinary Medicine, Kennet Square, Pennsylvania, United States

Introduction

Virtual mechanical testing is an image-based, noninvasive *in vivo* approach for evaluating bone rigidity. This study focused on monitoring healing in an ovine model of large-defect limb salvage. The objective of this study was to validate a new approach methodology (NAM) that can capture mechanical healing progression over time using longitudinal *in vivo* scans – data that cannot be obtained any other way – and thereby support the reduction, refinement, and replacement (3Rs) of animal use.

Methods

Thirty-three adult female sheep received either 30-mm (N=24) or 50-mm (N=9) tibial defects with autograft. *In vivo* computed tomography scans were obtained at sacrifice (18 weeks for the 30-mm, 26 weeks with 4-weekly scans for 50-mm). *Ex vivo* torsion testing was performed on the 30-mm cohort and was used to validate the virtual mechanical test. Models created from the scans in Materialize Mimics were assigned elementwise materials using a piecewise function (Fig 1A) and virtual torsional rigidity (VTR) was analyzed in ANSYS (Fig 1B). A repeated k-fold cross-validation (k = 4) procedure encompassing ~1700 simulations was used to optimize the material model parameters for the piecewise function of Fig 1A using the 30-mm cohort (N = 14 test/train, N = 10 validation). The objective of the optimization was to match VTR to physical torsional rigidity (GJ). The optimized material model was then applied to the 50-mm cohort for longitudinal healing analysis. Statistical analysis was performed in R.

Results

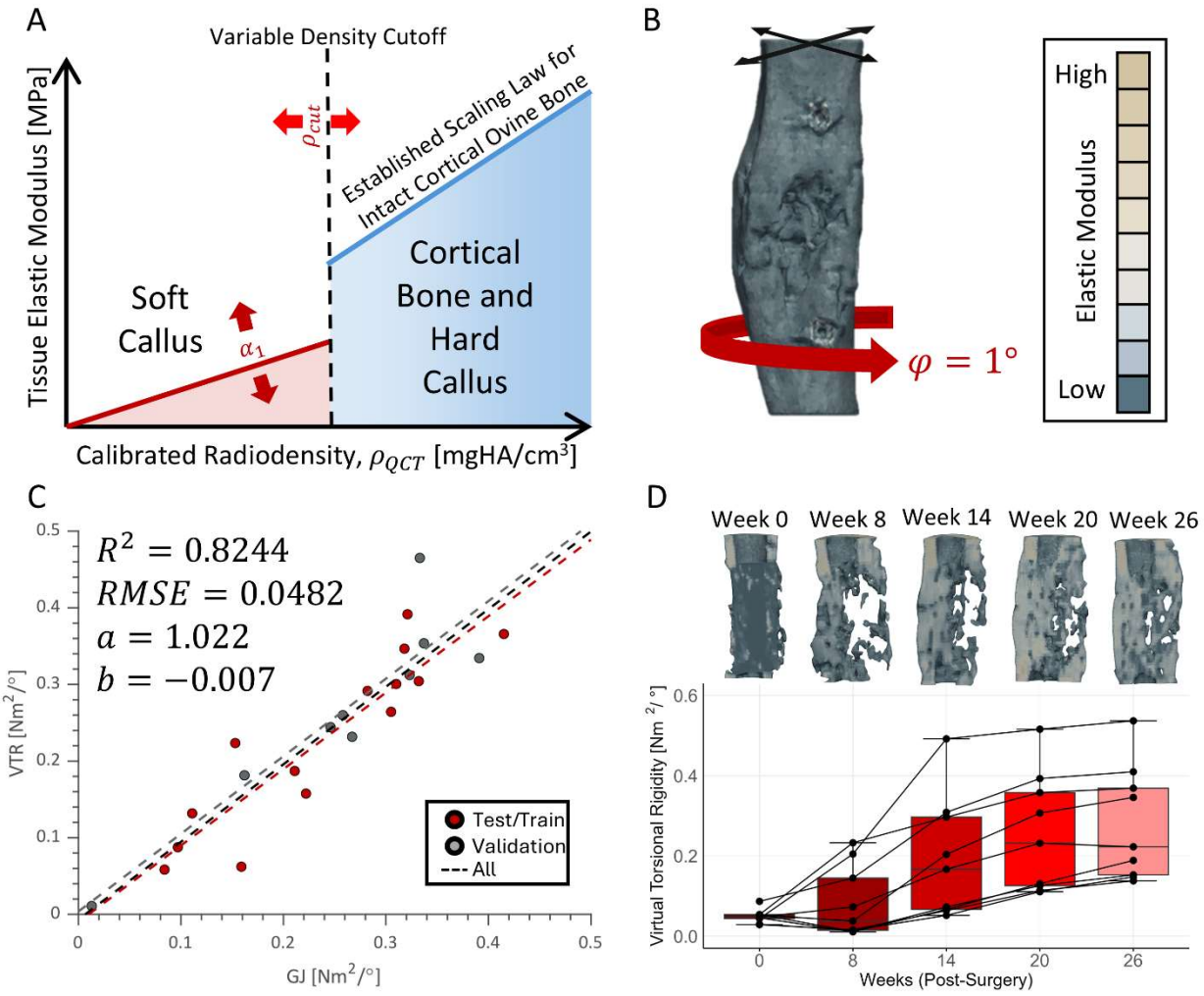
The optimized material model yielded strong, significant agreement between VTR and GJ for all optimization animals (N = 24) (Fig 1C). For the longitudinal scans in the 50-mm cohort, rigidity began to substantially increase after week 8 (significant differences vs. weeks 14, 20, 26) with callus formation plateauing around 20 weeks (non-significant

difference vs. week 26) (Fig 1D). Substantial within-week VTR variability emerged after 8 weeks, suggesting individual divergence in healing trajectories between animals.

Discussion

Virtual mechanical testing reliably quantified mechanical healing and is a validated surrogate for postmortem physical testing in this large-defect model. This method also provided nondestructive longitudinal outcomes assessment leading to clinically relevant insights that are unobtainable by other means.

Images (Optional)



Session Category

Orthopaedic Biomechanics: Trauma and Repair

OA175-03

Efficient and Validated Finite Element Analysis for Quantitative Assessment of Fracture Healing

Dr. Peter Schwarzenberg, Ms Giulia Minikus, Dr. Peter Varga

AO Research Institute Davos, Davos, Grisons, Switzerland

Introduction

Fracture-healing decisions currently rely on qualitative radiographs that potentially miss subtle mechanical deficits, contributing to tibial shaft nonunion rates near 15%. CT-based finite element (FE) modeling can quantify virtual torsional rigidity (VTR), yet current workflows involve demanding meshing and solver tools (Abaqus) and expertise that limit throughput [1]. We evaluated whether a simplified voxel-based FE pipeline involving a parallel multigrid solver (ParOSol) maintains diagnostic alignment with a high-fidelity reference model and *in vivo* strain-sensor measurements while enabling rapid, automation-ready analyses.

Methods

Data from eight sheep with tibial osteotomies fixed with locked plates including the implantable AO Fracture Monitor sensor and CT scans at eight timepoints were used. The cohort included a delayed-healing and a nonunion case. FE simulations were performed at 4 levels of sequential simplifications: L0 utilized whole-bone quadratic tetrahedral meshes with kinematic couplings solved in Abaqus; L1 simplified embedded boundary conditions; L2 used linear hexahedral mesh; L3 exchanged coupling to direct node-based displacements; L4 solved in ParOSol. Virtual torsion tests yielded VTR. Healing was determined from longitudinal VTR data using a threshold and a plateau. Strain-sensor-based relative implant load (RIL) provided ground truth. Agreement was evaluated using correlation analysis.

Results

All FE-levels reproduced the monotonically advancing healing trend for healers and identified the delayed-healing and nonunion cases seen by sensors. Cross-level VTR comparisons showed excellent correlation between L4 versus L0 ($R^2 \geq 0.980$; Figure 1A). L4 achieved similar accuracy as L0 ($R^2 = 0.769$ versus $R^2 = 0.788$; Figure 1B,C) in predicting sensor-based healing time. L4 was solved three times faster versus L0.

Discussion

Voxel FE modeling derived directly from segmented CT volumes retained diagnostic fidelity despite stepwise simplifications to geometry, mesh, loading, and solver choice. Concordance with both the reference model and the sensor-based ground truth indicates that longitudinal VTR consistency, not intricate meshing, governs clinical usefulness. The accelerated solver workflow and standardized load application reduced manual labor and positions the pipeline for automation once segmentation is scripted. Next steps include automated segmentation, extension beyond torsion, and validation in clinical fracture cohorts.

Images (Optional)

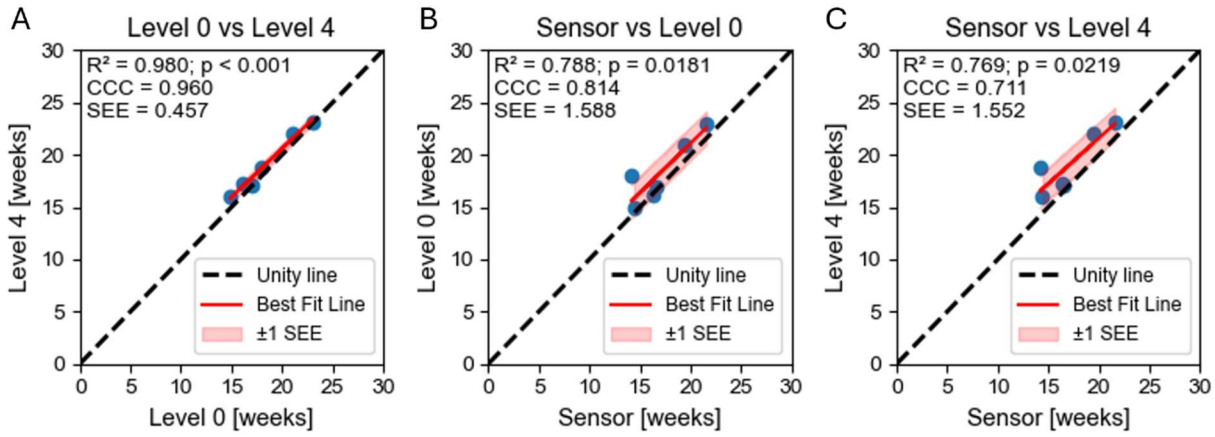


Figure 1: Agreement between simulated models and sensor-derived measurements of fracture healing. (A) Level 0 vs. Level 4. (B) Level 0 vs. Sensor. (C) Level 4 vs. Sensor.

References (Optional)

[1] Carla Hetreau *et al.*, J Orthop Res, 2024

Session Category

Orthopaedic Biomechanics: Trauma and Repair

OA175-04

A Tissue-Differentiation Framework to Predict Bone Formation Following Lumbar Interbody Fusion

Mr. Davide Ninarello MSc.Eng.[1], Professor Hanna Isaksson PhD[2], Associate Professor Luigi La Barbera PhD[1]

[1]Deptartment of Chemistry, Materials and Chemical Engineering “G. Natta”, Politecnico di Milano, Milan, Italy, Italy. [2]Department of Biomedical Engineering, Lund University, Lund, Sweden, Sweden

Introduction

Pseudoarthrosis after lumbar interbody fusion (LIF) is often linked to inadequate mechanical stimulus of tissues around the intervertebral cage. LIF technique, implant stiffness and biological factors strongly influence the surgical outcome. This study applied a tissue-differentiation algorithm to enable objective assessment of postoperative LIF biomechanics and healing process over time, across various scenarios.

Methods

An iterative ABAQUS-Python framework was implemented, where cell activity and tissue formation occurred under suitable mechanical stimuli [1], following Claes & Heigele’s theory [2]. A validated thoraco-lumbar model [3] was reduced to T12–S1, and two surgical techniques (namely, XLIF and PLIF) were simulated at L4–L5 with long posterior fixation (titanium pedicle screws and 5.5 mm rods, Fig.1A). Both Ti (E=110 GPa) and PEEK (E=4.5 GPa) cages were modelled, accounting for PEEK hydrophobicity by down-scaling parameters linked to osteoblast-specific activity.

Results

Most of bone formation occurred in the posterior disc region for both LIF techniques, independent of cage material. XLIF and PLIF showed comparable mean bone concentrations in the posterior region (38% vs 36%), though only XLIF achieved bony bridging through the cage holes (Fig.1B). Regarding cage materials, Ti produced up to 42% higher bone concentration than PEEK at day 25, a difference that fell to 3% by day 100 (Fig.1C). Ti also prevented bridging within the cage holes, whereas the more compliant PEEK cage supported a continuous bridge.

Discussion

Minor differences in bone formation were seen between XLIF and PLIF, consistent with retrospective clinical findings [4]. PEEK's hydrophobicity reduced osteoblast activity and limited bone formation near the cage (Fig.1D), potentially increasing the risk of micro-movements, in line with clinical observations [5]. Future analyses will include longer follow-ups and alternative fixation and fusion strategies. This study demonstrates the potential of tissue-differentiation algorithms to evaluate long-term outcomes of complex LIF approaches while providing relevant clinical insights.

Images (Optional)

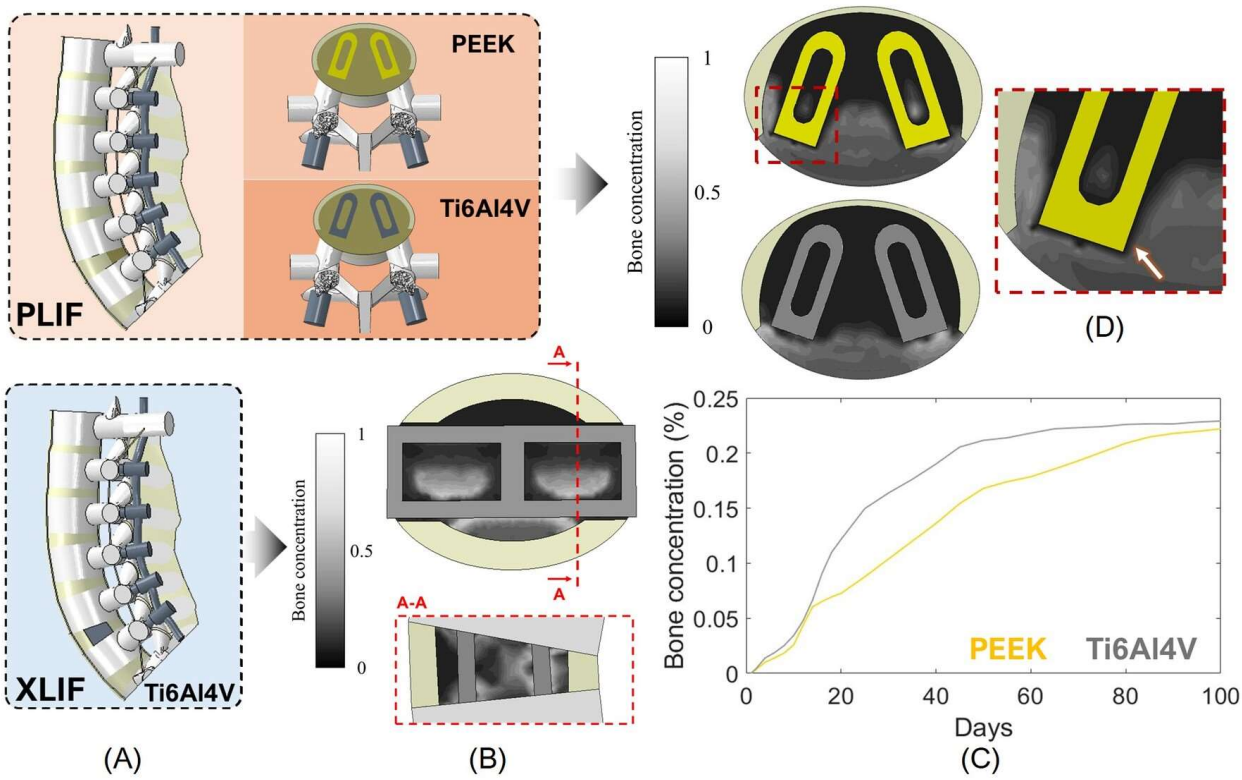


Figure 1: LIF models and bone concentration over time.

References (Optional)

1. Isaksson et al., J Theor Biol, 2008
2. Claes & Heigle, J Biomech, 1999
3. Bellina et al., J Biomech, 2024
4. Tirawanish et al., Int. J. Spine Surg, 2024
5. Chahlavi et al., Global Spine J, 2025

Session Category

OA175-05

Optimal Strength for Mandibular Reconstruction With Low Bone Stock

Dr Hans Gray[1], Mr Adrian De Angelis[2], Mr Anand Ramakrishnan[1,2], Dr Peter Lee[1]

[1]The University of Melbourne, Melbourne, Victoria, Australia. [2]The Royal Melbourne Hospital, Melbourne, Victoria, Australia

Introduction

Surgical resection of the mandible may be required as treatment for tumours involving the lower jaw. When the resection leads to a defect in continuity, reconstruction with a bony flap held together with a reconstruction plate and screws is required. When the available proximal bone stock is limited to only the mandibular condyle and neck, there may be insufficient bone for attaching a standard reconstruction plate. To design a plate for situations with low bone stock, the current study aimed to determine the optimum screw positions on the condylar neck for maximum fixation strength.

Methods

A geometric model comprising the mandibular condyle and neck was resected from a mean model of a mandible created using statistical shape modelling. The geometry represented a typical low bone stock case (Fig. 1A). A genetic optimisation algorithm coupled with finite element modelling was used to find the optimum number and positions of screws to provide maximum fixture strength. Failure envelopes were used to evaluate the efficacy of the optimised solution. A failure envelope was constructed considering 1536 unique force directions spread out in 3D space applied on the condylar head (see [1] for details on failure envelopes). A second similar failure envelope was constructed for a case with adequate bone stock and typical screw positioning (Fig. 1B) as per the current practice using existing reconstruction plates.

Results

The low bone stock case with four optimally placed screws resulted in a failure envelope (Fig.1, red envelope) that almost entirely encapsulated the failure envelope representing the current practice when sufficient bone stock is available (Fig. 1, green envelope). Only in 24 of the 1536 directions was the predicted fracture load greater for the current practice than for the optimised fixture proposed for the low bone stock case.

Discussion

The results demonstrated that the optimised solution for the low bone stock case was superior in strength to the typical current practice in mandibular reconstruction surgery when sufficient bone stock is available. Further work is underway using patient-specific models derived from CT data to understand if the results are consistent across patients.

Images (Optional)

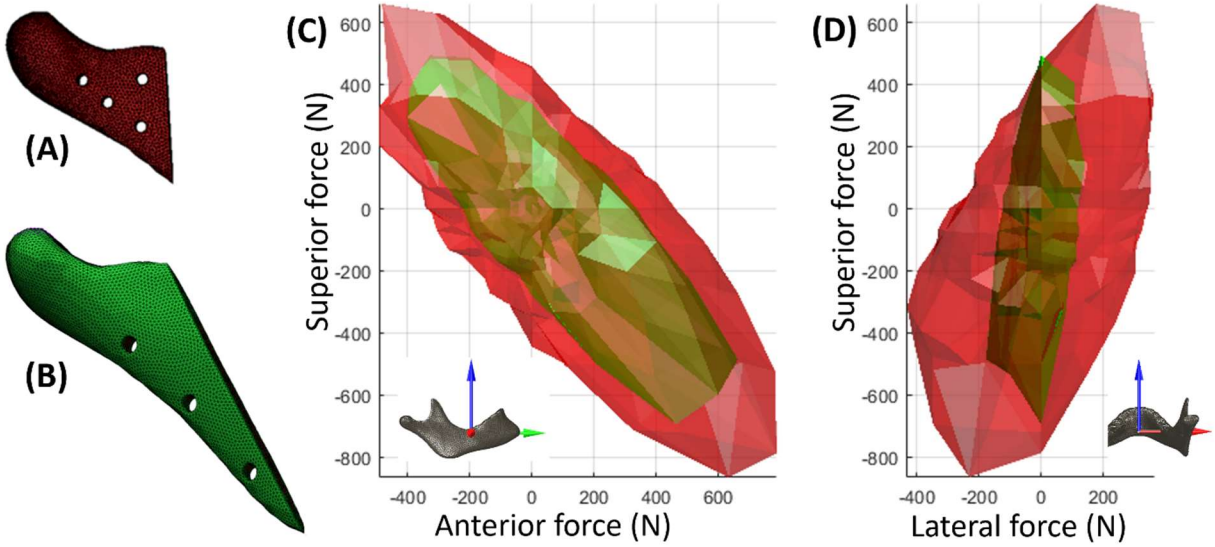


Figure 1: (A) Optimum screw configuration for low bone stock case. (B) Current practice with adequate bone stock. (C) Lateral view and (D) posterior view, of force envelopes for low bone stock (red) and current practice with adequate bone stock (green). The green envelope was almost entirely encapsulated by the red envelope, indicating the superior strength of the optimised solution compared to the typical current practice.

References (Optional)

[1] Gray et al., Sci. Rep., 2024 (10.1038/s41598-024-78421-3).

Session Category

Orthopaedic Biomechanics: Trauma and Repair

OA176-01

Development of an Automated Cell Differentiation System Integrating AI-Based State Recognition and Precision Environmental Control for Scalable Neural Cell Production

Dr. Seongwoong Hong Ph.D.[1], Dr. Chan-Beom Park Ph.D.[2], Mr. Sangyeong Park[3], Mr. Doyeon Kim[3]

[1]InnoCORE AI Co-Research & Education for innovative Drug Institute, Korea Advanced Institute of Science and Technology (KAIST), Yuseong-gu, Daejeon, Korea, Republic of. [2]InnoCORE AI Co-Research & Education for innovative Drug Institute, KAIST, Yuseong-gu, Daejeon, Korea, Republic of. [3]the Department of Mechanical Engineering, KAIST, Yuseong-gu, Daejeon, Korea, Republic of

Introduction

Stem cell-derived neuronal in-vitro models serve as essential tools for pre-clinical screening of neurological drug candidates. These systems are gaining significance for their potential to replace animal testing and improve clinical trial success rates. While basic differentiation protocols are well established, subtle variables that protocols alone cannot control inevitably arise during differentiation. Assessing cell density heterogeneity, morphological changes, and batch variations still relies on skilled researchers' experience and intuition, resulting in low reproducibility and labor and time costs limiting mass production scalability. To overcome these limitations, we propose an AI-based automated differentiation system that recognizes cellular states in real-time and adaptively controls the culture environment. As an initial step, we established a robot-based culture system with precise environmental control and developed a preliminary deep learning model using public datasets.

Methods

For environmental control, we developed a microfluidic robot driven by a stepper motor and ball screw mechanism, incorporating a Peltier cooling system, an environmental chamber, and a high-resolution microscope. For state recognition, we trained an Xception classifier on a public neuronal dataset (~100,000 images). An augmentation pipeline reflecting differentiation-associated morphological changes was also developed for future application with in-house data.

Results

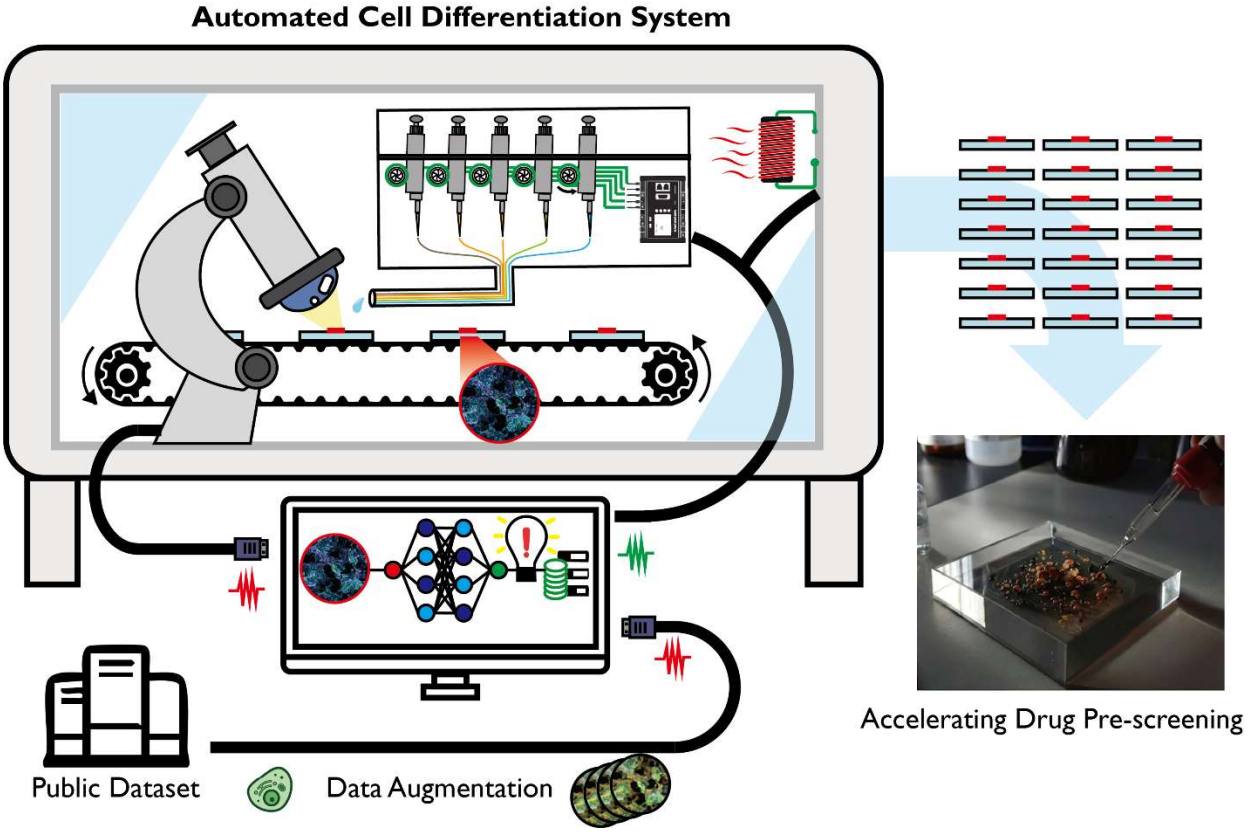
The microfluidic delivery robot was designed to achieve a fluid injection resolution of 0.05 μL. The Peltier cooling system maintained 4°C, while the integrated chamber enabled precise regulation of temperature, humidity, and gas concentrations, facilitating real-time

image acquisition. In validation on the public dataset, the Xception model achieved an overall accuracy of 98.3%. Astrocytes had the highest recognition rate (99.4%), and neurons achieved 99.0% despite being the largest sample group. Oligodendrocytes showed relatively lower accuracy (92.5%); misclassification as neurons were attributed to morphological similarities shared during specific differentiation stages.

Discussion

This study established a precision environmental control robot and a high-accuracy cell state recognition AI as an initial framework for automated cell differentiation systems. Future work will implement a real-time AI-robot feedback loop through transfer learning with in-house data and time-series-based state prediction models. This automated system is expected to enable mass production and quality standardization of brain cells, ultimately contributing to a high-throughput screening platform for neurological disease therapeutics.

Images (Optional)



Session Category

Cell Biomechanics: Methods and Models

OA176-02

Synchronized and Metachronal Coordination in Macro-Scale Physical Models of Coupled, Autonomously Beating Cilia

Ms Naomi Hsieh, Ms Jeslyn Gao, Ms Alexis Rivera BS, MS, Dr. Louis Woodhams PhD, Dr. Philip Bayly PhD

Washington University in St. Louis, St. Louis, Missouri, United States

Introduction

Motile cilia are slender organelles that project from cells and beat rhythmically to propel the cell or move fluid. In multiciliated cells or microorganisms, arrays of cilia can enhance their propulsive efficacy via metachronal coordination, in which adjacent cilia beat with a consistent phase difference. The mechanisms responsible for establishing metachronal beating are not clear. In theory, hydrodynamic coupling is sufficient to produce metachronal waves in arrays of autonomously beating cilia [1]. However, experiments in *Tetrahymena* [2] show that altering intracellular connections between cilia basal bodies disrupts metachrony. To explore the effects of mechanical coupling on cilia coordination we built physical models of autonomously beating filaments and quantified the similarity and phase of their oscillations.

Methods

Filaments exhibiting spontaneous, base-to-tip, oscillatory waveforms were constructed by connecting Hexbug™ vibrating toys (hexbug.com) by short segments of flexible rubber (Fig.1A). Each “cilium” beat autonomously with a period between 10-20 sec. Video recordings (30 fps) of arrays (5-cilia) or pairs (2-cilia) were analyzed using a custom optical flow-based tracking algorithm to measure tip displacement. Coupling was introduced by attaching 3D-printed elastic “spring” elements between basal links (Fig.1E,F,H); in some cases “free-play” nonlinearity was added by introducing a slot in the link (Fig.1J,L). Coordination was characterized by the maximum cross-covariance (C_{max}) and phase lag (ΔT, cycle fraction) between tip displacements.

Results

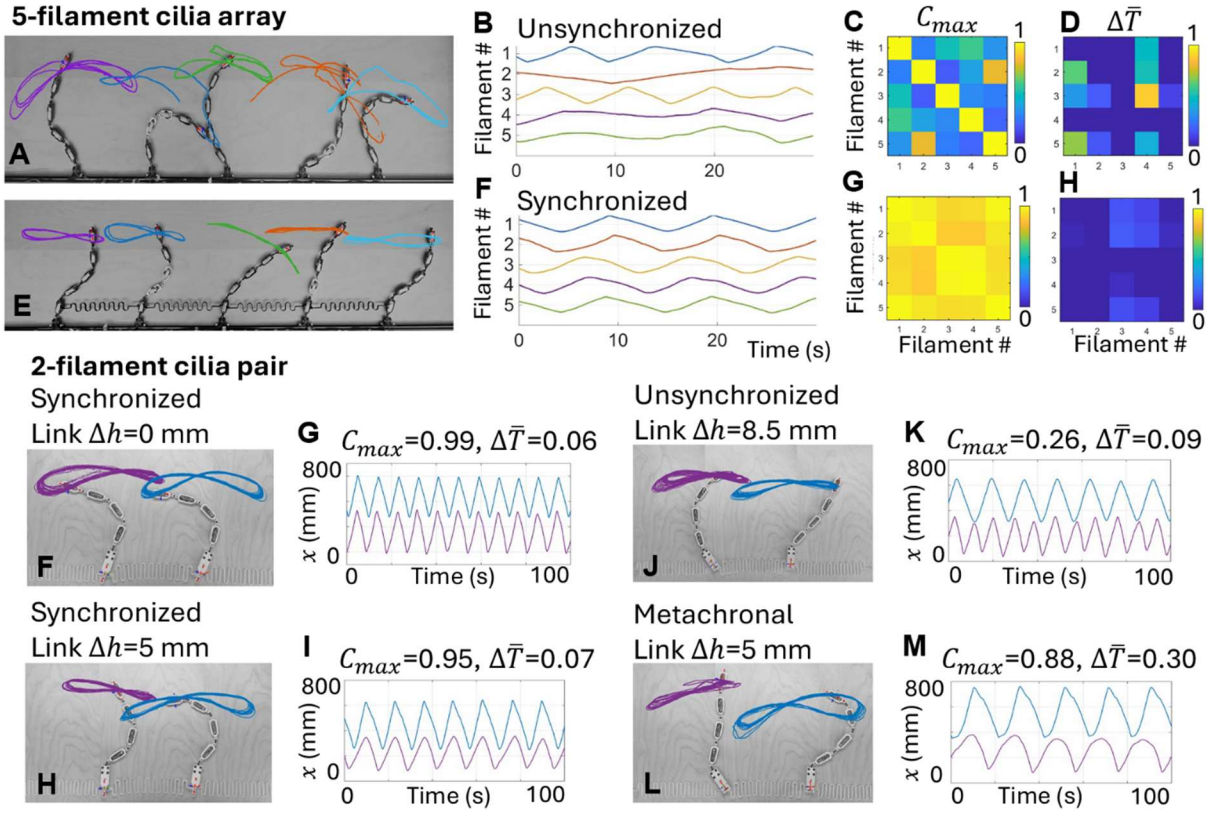
Arrays of 5 cilia were uncoordinated ($C_{max}<0.5$; Fig.1A-D) when uncoupled and synchronized ($C_{max}>0.9$, $\Delta T<0.1$; Fig.1E-H) with spring coupling. Pairs of cilia were synchronized ($C_{max}>0.9$, $\Delta T<0.1$; Fig.1F-I) with spring coupling, but when free-play was introduced, cilia were uncoordinated when intrinsic frequencies differed ($C_{max}<0.5$; Fig.1J-

K) or metachronal, beating out-of-phase (C_{max}~0.9, ΔT=0.3; Fig.1L-M) when intrinsically similar.

Discussion

Physical models of autonomously beating cilia arrays exhibited varying levels of coordination when coupled elastically at their bases. The coupling elements in these macro-scale models are analogous to intracellular links such as striated fibers that connect basal bodies of adjacent cilia in *Tetrahymena*. Experimental investigations in these physical models, including quantitative measurements of metachronal coordination, can illuminate the behavior of cilia on cells and microorganisms.

Images (Optional)



References (Optional)

[1] Elgeti J, Gompper G. PNAS, 2013.

[2] Soh AWJ et al. Mol Biol Cell, 2022.

Acknowledgements (Optional)

NSF2421872

Session Category

Cell Biomechanics: Methods and Models

OA176-03

A Mechano-Osmotic Coupling Drives Stress-Dependent Growth in Breast Cancer Spheroids Revealed Through AI-Accelerated Discrete Cell Modelling

Mr Irish Senthilkumar[1], Mr Jef Vangheel[2], Dr Vatsal Kumar[1], Prof Laoise McNamara[1], Dr Bart Smeets[2], Dr Enda Howley[1], Dr Eoin McEvoy[1]

[1]University of Galway, Galway, Galway, Ireland. [2]KU Leuven, Leuven, Leuven, Belgium

Introduction

Mechanoresponsive cell proliferation is a feature of growing tumours, despite the suppression of other regulatory checkpoints in cancer, but the underlying cell-scale mechanisms driving this behaviour remain unclear. We propose a biophysical model for cell growth as governed by actively controlled osmolarity, integrated with a discrete particle framework to simulate growth and remodelling of breast cancer spheroids.

Methods

We describe volumetric growth as dependent on biosynthesis-driven increases in osmolarity, which promotes water intake, and hydrostatic pressure generated by cortical tension and matrix-induced compression [1] (Fig1A). This formulation is implemented within MPacts (Fig1B) [2], where each cell is described as a deformable, pressurised viscoelastic shell that may divide subject to surpassing a recently identified sizing checkpoint [3]. Mechanical feedback from the extracellular matrix is implemented through a custom neural network (NN) surrogate finite element (FE) model.

Results

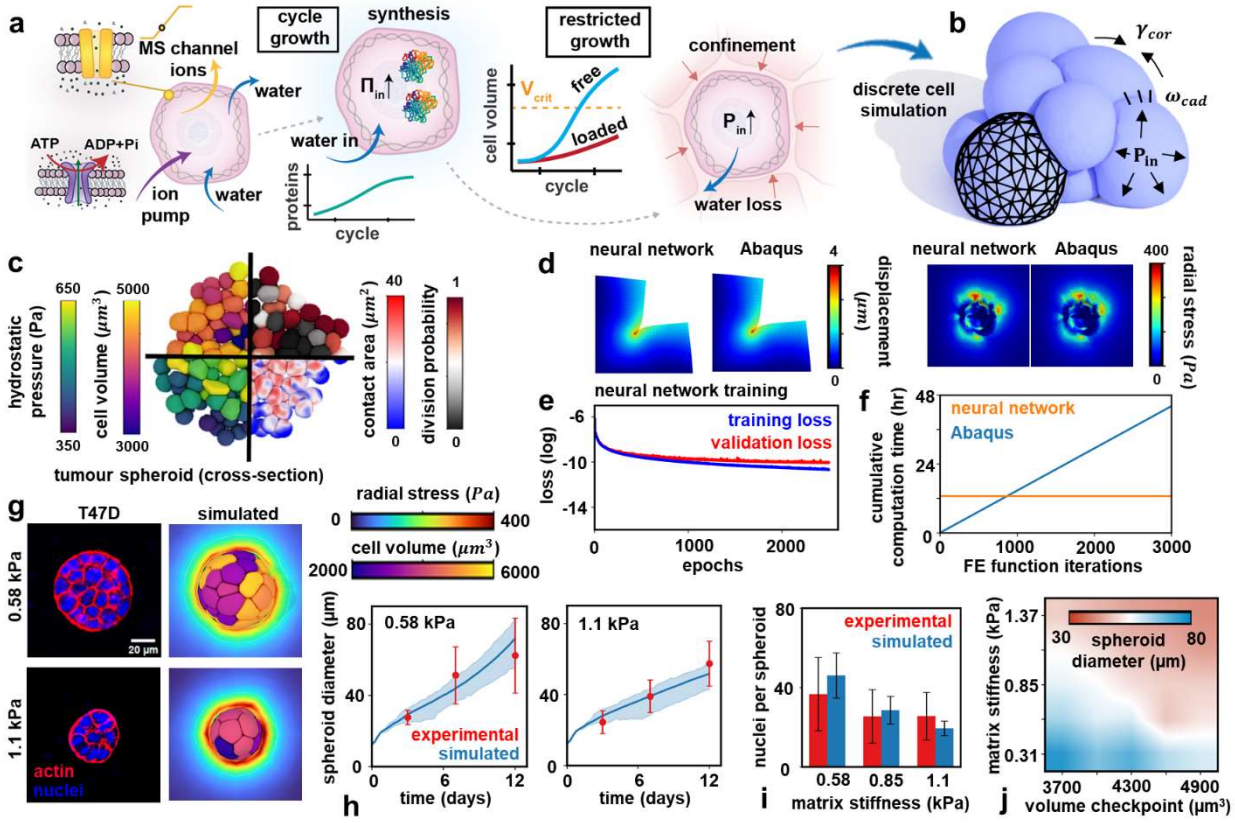
Simulations demonstrate that biosynthesis increases intracellular osmotic pressure, promoting volumetric growth, while confinement increases hydrostatic pressure to limit cell division (Fig1C). The NN-FE surrogate accurately predicts ECM deformation in both 2D and 3D (Fig1D-E) while enabling a substantial reduction in computational cost at a higher number of FE iterations (Fig1F). Extending this model to cell-matrix interactions reveals an ECM stiffness-dependent response: spheroids in softer hydrogels attain larger volumes with a higher cell division probability, while stiff hydrogels impose sufficient growth-induced stress to limit expansion (Fig1G-I) as per our experimental measurements. Increasing the volume checkpoint or matrix stiffness promotes smaller spheroids (Fig1J).

Discussion

Our models and experiments identify a mechano-osmotic mechanism for stress-dependent growth in which synthesis-driven cell swelling competes with confinement-mediated increases in intracellular pressure. This computationally efficient tool could readily be extended for analysis of patient-derived tumouroids and mechanoresistance.

Figure 1: a) Synthesis-driven cell growth in confinement; b) discrete cells modelled as pressurised viscoelastic shells; c) spatial changes in cell behaviour; d) validation of NN predictions; e) network loss during training; f) computational cost of FE vs NN-FE; g-i) comparison of predicted spheroid growth with experiments; j) predicted influence of stiffness and volume checkpoint on growth.

Images (Optional)



References (Optional)

[1] McEvoy et al. Nat.Commun, 2020

[2] Cuvelier et al. BiophysJ, 2023

[3] Varsano et al., Cell Reports, 2017

Acknowledgements (Optional)

The authors would like to acknowledge financial support from the Irish Research Council (GOIPG/2022/910), the European Research Council (Starting Grant: 101116234 and Consolidator Grant: 863795), and Research Foundation Flanders (11D9923N).

Session Category

Cell Biomechanics: Methods and Models

OA176-04

Full-Field Elastography of the Cell Nucleus Reveals Peripheral Stiffening in Response to Strain

Mr. Kurt Winkler, Dr. Stephanie Schneider, Dr. Emily Miller, Dr. Corey Neu

University of Colorado Boulder, Boulder, CO, United States

Introduction

The cell nucleus senses and responds to mechanical stimuli, making nuclear mechanics important for understanding how cells interact with and respond to their mechanical environment. While methods such as AFM and micropipette aspiration measure bulk nuclear stiffness, subnuclear stiffness resolution has remained largely unknown. Here, we introduce an image-based full-field elastography pipeline that utilizes deformable image registration and inverse modeling to determine nuclear stiffness. We demonstrate its accuracy with forward models and apply it to live cells subjected to mechanical strain.

Methods

Finite element forward models were generated from microscopy images of DAPI- and H2B-eGFP-labeled nuclei, with element stiffness correlated to pixel intensity. Equiaxial strains were applied to these models in FEBio (4.5.0) [1] to produce pairs of undeformed and deformed images. These images were registered using MATLAB's imregdemons algorithm [2] to generate displacement fields which served as inputs to an iterative inverse solver to determine full-field relative stiffness maps. To generate real data, mouse embryonic fibroblasts (MEFs) were subjected to biaxial strains of 5% or 10% for 30 minutes followed by 30 minutes of recovery. Microscopy images of cell nuclei were acquired at various timepoints to track temporal stiffness changes.

Results

Our elastography method accurately reconstructed ground truth stiffness maps in DAPI- and GFP-based forward models, achieving correlation coefficients >0.8 for physiologically relevant strains. Case examples of MEF's subjected to 5% or 10% biaxial strain showed localized hot spots of increased stiffness in the nuclear periphery, with recovery toward baseline stiffness within 20min of unloading, demonstrating dynamic and reversible alterations in nuclear stiffness.

Discussion

Our elastography method is an effective tool for mapping full-field nuclear stiffness, addressing a significant methodological gap in mechanobiology research. The ability to

measure relative stiffness under controlled strain reveals that the nucleus experiences load-dependent and region-specific changes in stiffness, highlighting its sensitivity to external stimuli. This method could be further used to study how nuclear stiffness influences cell mechanics, mechanotransduction pathways, and mechanical adaptation of cells to their environment.

Images (Optional)

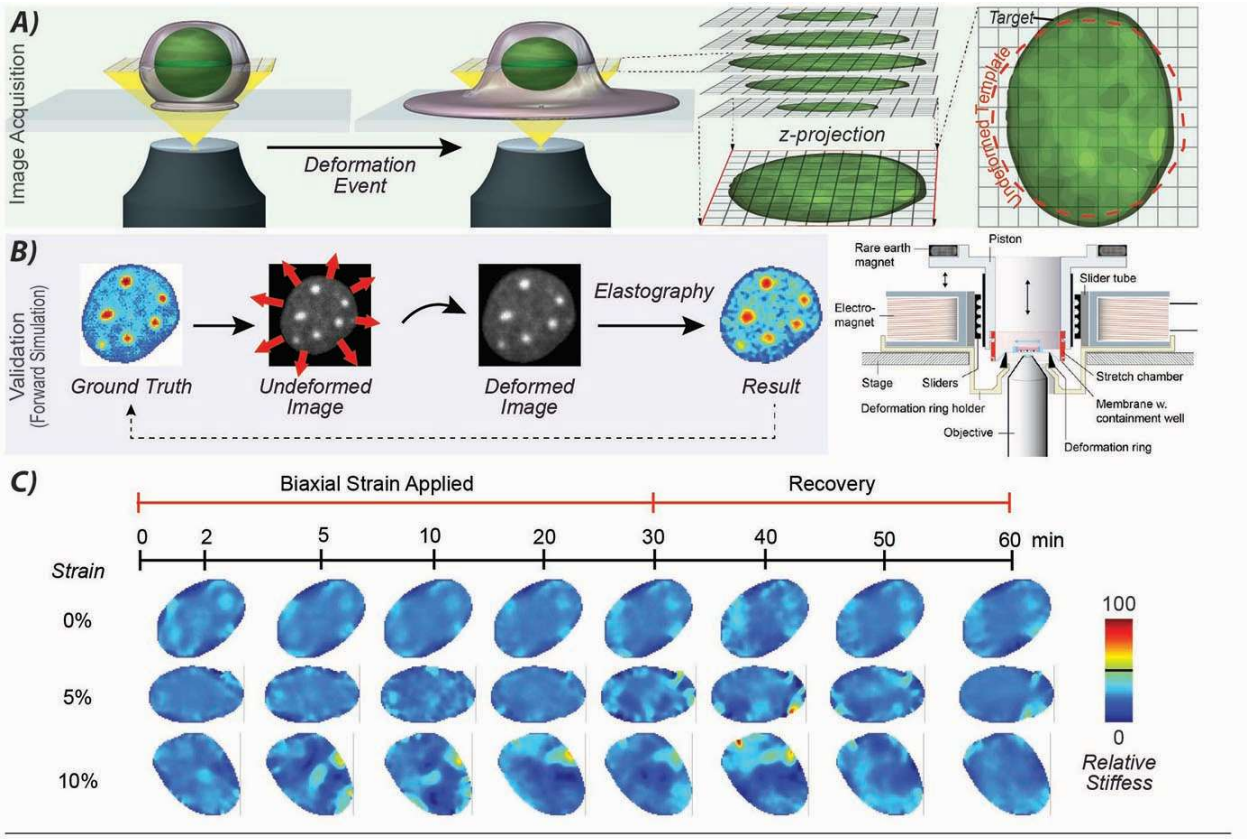


Figure 1. Intra-nuclear elastography, using image-based mechanics, enables measurement of the time-evolving stiffness in stretched cells. *(A-B)* Optical acquistion of nucleus images is used in combination with deformable image registration and inverse modeling to reveal intra-nuclear stiffness patterns. Forward simulations confirm our ability to reconstruct ground truth patterns. *(C)* Mechanical stretch of mouse embryonic fibroblasts shows a strain-dependent peripheral enrichment and recovery of stiffness over time.

References (Optional)

[1] Maas SA et al., Ellis BJ, J Biomech Eng, 2012

[2] Thirion JP., Med Image Anal, 1998

Acknowledgements (Optional)

The authors would like to thank the National Science Foundation (CMMI/BMMB 2212121) for providing financial support to this project.

Session Category

Cell Biomechanics: Methods and Models

OA177-01

Effects of Running-Related Fatigue on Hip and Knee Muscle Synergies Among Male and Female Endurance Runners

Ms Cinthuja Pathmanathan PhD candidate[1], Dr Leonardo Gizzi[2], Professor Deborah Falla[3], Professor Caroline Paquette[1], Professor Julie N Côté[4]

[1]1Department of Kinesiology and Physical Education, McGill University, Montreal, Quebec, Canada. [2]Department of Biomechatronic Systems, Fraunhofer Institute for Manufacturing Engineering and Automation, Stuttgart, Baden-Württemberg, Germany. [3]Centre of Precision Rehabilitation for Spinal Pain (CPR Spine), School of Sport, Exercise and Rehabilitation Sciences, University of Birmingham, Birmingham, England, United Kingdom. [4]School of Human Kinetics, University of Ottawa, Ottawa, Ontario, Canada

Introduction

Previous studies have shown that muscle fatigue affects some indicators of multi-muscle coordination in runners, such as the relative contributions of leg muscles. Muscle activation coefficients and areas are measures used in synergy analysis to assess motor control strategies. However, little is known about whether these fatigue-related changes are the same or different between males and females during Running Induced Fatigue (RIF). We aimed to quantify sex-specific effects of RIF on patterns of lower limb synergies.

Methods

Twenty-one healthy endurance runners (12 males, 25.0±6 years; 9 females, 23±2 years) were recruited. The activity of 10 hip and knee muscles was measured bilaterally using surface electromyography (EMG) before and after an incremental fatigue protocol performed until exhaustion (confirmed via the Borg 6-20 scale). A tridimensional motion capture system was used to measure lower limb kinematics and partition the EMG data. Non-negative matrix factorisation was applied to muscle activities to extract synergies. The best matched pairs of synergies, determined using cross-correlation, were compared between trials. Statistical parametric mapping (SPM) and generalised estimating equations were performed.

Results

Five synergies (Variance accounted for [VAF] global = 0.97±0.01) during pre-fatigue and six synergies (VAF global = 0.99±0.02) during post-fatigue status explained the neuromuscular control in both sexes. RIF resulted in a significant reduction in the activation area of all synergies (p <0.001, coefficient (β) ranges from -0.481 to 2.805) in both sexes. However, in synergy 6, which explained pelvic stability, the activation area showed a sex × fatigue

interaction effect (p <0.001, β=4.758), with the RIF-related reduction being higher in females compared to males. Sex-specific SPM analysis showed that there was no statistical difference in activation coefficients in pre- and post-fatigue statuses in all five synergies (p >0.05).

Discussion

Results suggest that runners adapt to RIF by decreasing voluntary activation of some muscles and reallocating load to other muscles (i.e. 6th synergy). A higher synergy 6 reduction in females suggests less efficiency in coordinating pelvic stabilizing muscles with fatigue, and that they may benefit from coordination training of pelvic muscles to prevent RIF-induced injuries.

Session Category

Clinical Biomechanics: N/A

OA177-02

Older Adults Exhibit Savings of Adapted Motor Patterns from Repeated Exposure to Virtually-Induced Fall-Related Anxiety

Dr. Kelly Poretti[1], Dr. Toby Ellmers[2], Dr. Quentin Sanders[3], Dr. Nathalia Peixoto[3], Dr. Christopher Rhea[4], Dr. Tiphanie Raffegeau[1]

[1]George Mason University, Manassas, VA, United States. [2]Imperial College London, London, London, United Kingdom. [3]George Mason University, Fairfax, VA, United States. [4]Old Dominion University, Norfolk, VA, United States

Introduction

Evidence-based interventions that use virtual reality (VR) to administer 'exposure therapy' for anxiety disorders combined with laboratory-based methods of inducing a postural threat that elicits fall-related anxiety may serve as a multi-dimensional fall intervention for older adults. However, it remains unknown how older adults might adapt differently to repeated immersion to postural threat compared to young adults. The purpose of this study is to determine age-related differences to gait habituation in response to repeated immersion in virtual anxiety-inducing settings.

Methods

Participants (N = 30, 14 older adults) experienced two five-minute immersions in anxiety-inducing VR settings (i.e., high elevation), with a one-minute washout period walking at ground level. Visualization of the absolute distance between the headset and ankle trackers (HTC Vive Pro Eye) was used to extract and calculate steady state gait parameters (speed, step length and width, percent double support). To determine gait habituation across trial time and immersion the first (T1) and last (T2) six steady state steps were extracted for the first (I1) and second (I2) immersion. Linear mixed-effect regression compared gait across Age (2 levels: Older vs. Young Adults), Time (2 levels: T1 vs. T2), and Immersion (2 levels: I1 vs. I2).

Results

In the first immersion, young and older adults walked with longer steps ($F = 15.50$, $p < .001$), and faster speeds ($F = 7.05$, $p = .013$) at T2 compared to T1 at I1. Demonstrating savings between immersions, young and older adults walked with longer ($F = 21.17$, $p < .001$), and faster ($F = 16.50$, $p < .001$) steps at T1 of I2 compared to T1 of I1. No savings were observed in step width or double support.

Discussion

Young and older adults preserve locomotor balance, not altering step width or double support time, while demonstrating savings of step length and increasing gait speed, likely due to the constrained walkway width. Across immersions, participants appear to gain confidence in their ability to preserve locomotor balance at high VR settings, saving habituated motor patterns. Our results provide evidence to support the potential use of the VR paradigm as a habituation intervention to reduce fall-related anxiety in older adults.

Images (Optional)

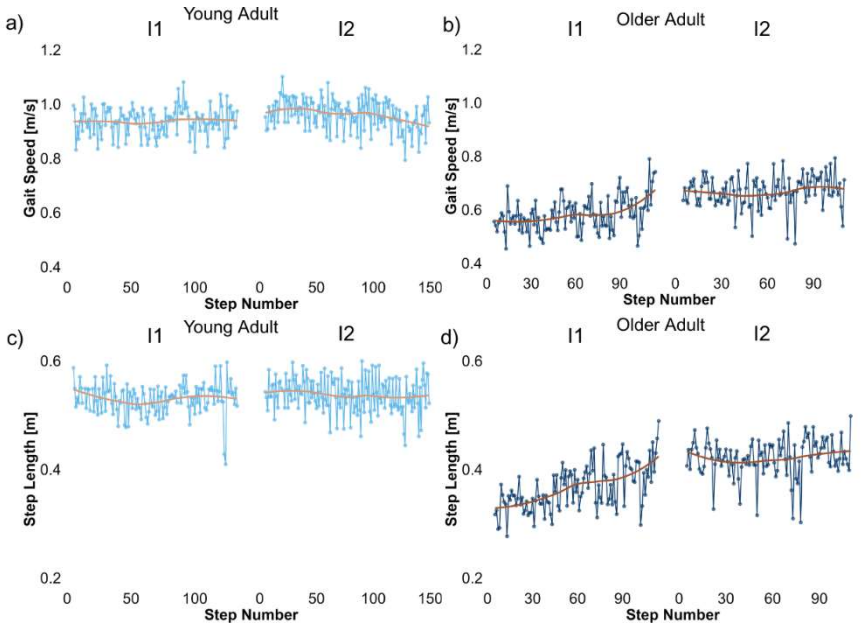


Figure 1(a-d): Sample adaptation time-series graph in representative young adults and older adults. Each graph depicts all steady state steps across time and exposure for a representative participant from each age group. (a) Young adults do not adapt gait speed over time. (b) Older adults increase their gait speed over time. (c) Young adults do not adapt step length over time. (d) Older adults adapt their step length over time.

Session Category

Clinical Biomechanics: N/A

OA177-03

Eliminating the Distal-to-Proximal Redistribution in Older Adult Joint Mechanics Improves Walking Economy

Ms. Ningzhen Zhao[1], Dr. Ross Miller[2], Dr. Lisa Griffin[1], Dr. Owen Beck[1]

[1]University of Texas at Austin, Austin, TX, United States. [2]University of Maryland College Park, College Park, Maryland, United States

Introduction

During walking, older adults push-off the ground less with their ankles than young adults, compensating by producing more work at their hip. The implications of this age-related redistribution in joint mechanics are strictly hypothetical because no intervention has restored youthful, preferred walking mechanics in older adults – until now. Here, we temporarily restored youthful joint mechanics in older adults following a brief functional electrical stimulation (FES) paradigm, uncovering the metabolic consequence of walking like an older adult.

Methods

Twenty adults (10 young: 5 F; 21 ± 2 yrs; 10 older: 5 F; 77 ± 5 yrs; Avg ± SD) performed treadmill walking trials at 1.25 m/s. Five minutes after a familiarization trial, participants performed a 5-minute baseline walking trial. Next, participants walked for 10 minutes with FES applied bilaterally over user soleus muscles during late stance [1]. Following a 20-minute rest, participants performed a final 5-minute walking trials *sans* stimulation.

Results

At baseline, older adults exhibited a greater ratio of hip-to-ankle work versus young adults ($p=0.042$). After walking with FES, older adult preferred ankle mechanical output increased versus baseline (peak power: $p=0.013$; work: $p<0.001$), with a concomitant 22% reduction in hip work ($p=0.035$). After walking with FES, older adults walked with a 21% decrease in their baseline hip-to-ankle ratio of mechanical work ($p=0.004$), yielding nearly identical relative joint work production compared to young adult at during baseline walking ($p=0.788$). Moreover, post-FES walking elicited a 4% lower gross metabolic power compared to baseline in older adults ($p=0.021$).

Discussion

The short-term carry-over effects of pairing FES with voluntary drive eliminated the distal-to-proximal redistribution in older adult preferred walking mechanics. The findings further suggest that the age-related distal-to-proximal redistribution contribute to the greater

metabolic cost of walking in older versus young adults. Overall, intervening on the nervous system is sufficient to restore youthful, preferred walking joint mechanics in older adults and reduce whole-body metabolic rate.

Images (Optional)

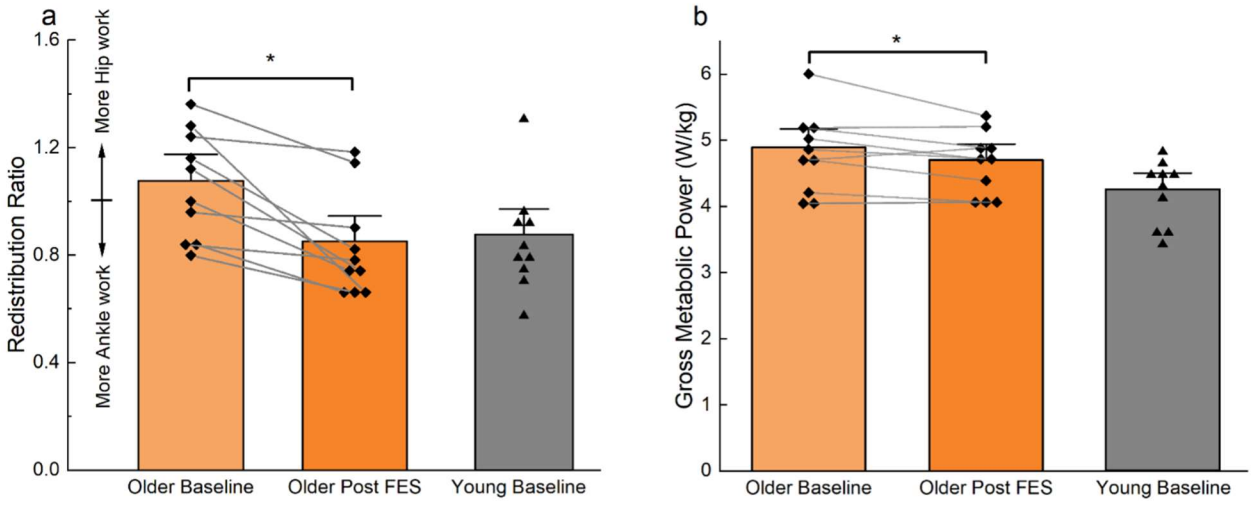


Figure 1. Redistribution ratio and metabolic power at baseline and post-FES conditions. Bar graphs represent group average (±SE) with individual data represented for each participant. a) Redistribution ratio and b) gross metabolic power. Data represents older adults baseline (light orange), older adults post-FES (dark orange), and young adults baseline (gray). Asterisks (*) indicates that p value < 0.05.

References (Optional)

[1] Zhao *et al.*, J. Appl. Physiol., 2025

Session Category

Clinical Biomechanics: N/A

OA177-04

Changes in Duty Factor in Response to Three Running Retraining Cues in Military Runners

MAJ Jennah Bulen PT[1], MAJ Gregory Freisinger PhD[1,2], Dr. Mikel Joachim PhD[3], Dr. Erin Florkiewicz PhD[4,1], LTC Jamie Morris PT, DSc[1]

[1]Baylor University - Keller Army Community Hospital Division 1 Sports Physical Therapy Fellowship, West Point, NY, United States. [2]United States Military Academy, West Point, NY, United States. [3]University of Wisconsin-Madison, Madison, WI, United States. [4]Rocky Mountain University of Health Professions, Provo, UT, United States

Introduction

Duty factor (DF) represents the proportion of ground contact time (GCT) within the step cycle and serves as a key temporal descriptor of running mechanics, capturing how runners distribute stance and flight time across each step [1–3]. Although gait retraining can modify step rate and GCT, components of DF, it remains unclear whether different cueing strategies produce distinct DF adaptations. This study examined how verbal, metronome, and visual cues independently influence DF in military runners.

Methods

Twenty-nine military runners (21 men, 8 women; mean age 25 ± 6.9 years) completed treadmill running at a consistent self-selected speed under four conditions: baseline, metronome cue set at 10% above their baseline step rate, verbal cue of pulling the foot off the ground as quickly as possible, and a visual cue set at 5% below their baseline contact time. Step rate and GCT were collected using RunScribe inertial measurement units. DF was calculated as GCT divided by stride time, with stride time estimated from step rate using established wearable-sensor methods [3]. A one-way repeated-measures ANOVA assessed cue effects on DF, with Bonferroni-adjusted pairwise comparisons.

Results

Cue type significantly affected DF ($p < .001$, partial $\eta^2 = .28$). The verbal cue produced the lowest DF, significantly lower than baseline ($p = .011$), metronome ($p < .001$), and visual cues ($p = .009$). Metronome feedback produced a small but significant increase in DF compared with baseline ($p = .039$). Visual feedback did not differ from baseline or metronome ($p = 1.000$).

Discussion

The cueing strategies produced distinct effects on DF. The verbal cue elicited the greatest reduction, the metronome produced a small but significant increase, and the visual cue showed no significant change. Overall, the verbal cue produced the most substantial shift in stride timing. Assessing DF using wearables may help clinicians monitor retraining responses and identify cues that most effectively target temporal adjustments to reduce running-related injury risk in military runners.

Images (Optional)

Table 1. Mean (± standard deviation) for step rate, ground contact time, and duty factor during running across cues.

Condition	Step Rate (spm)	Ground Contact Time (ms)	Duty Factor
Baseline	160.5 ± 8.0	308.6 ± 36.6	0.411 ± 0.042
Visual	172.8 ± 14.1	288.8 ± 35.7	0.414 ± 0.047
Metronome	173.6 ± 8.3	290.5 ± 33.5	0.419 ± 0.042*
Verbal	174.0 ± 16.4	273.0 ± 37.3	0.393 ± 0.047*

*$p < 0.05$

References (Optional)

[1] Lennert der Meulen et al., J human kinetics, 2024

[2] Anouk Nijs et al., PLOS ONE, 2023

[3] Aurélien Patoz et al., Sports, 2019

Session Category

Clinical Biomechanics: N/A

OA178-01

The Effects of Carbon Fiber Insoles on Plantar Intrinsic Foot Muscle Fatigability During Prolonged Walking

Ms Megan Spencer BS[1], Ms Sydney Menendez[1], Dr Ross Smith PhD[2], Dr Kota Takahashi PhD[3], Dr Jason Franz PhD[1]

[1]University of North Carolina and North Carolina State University, Chapel Hill, NC, United States. [2]University of Memphis, Memphis, TN, United States. [3]University of Utah, Salt Lake City, UT, United States

Introduction

The plantar intrinsic muscles (PIMs) function as a coordinated unit to support the medial longitudinal arch and regulate foot mechanics during locomotor activities such as walking. However, no studies to date have examined how PIM excitation changes during prolonged walking, an important requisite to understanding the onset and progression of walking-related fatigue ability. Further, carbon fiber insoles (CFIs) have the potential to offload PIMs and may promote fatigue resistance. Here, we used indwelling EMG time-frequency analyses to quantify intrinsic foot muscle fatiguability and the modifying influence of increased footwear bending stiffness via CFIs. We hypothesized that PIM excitations would shift toward slower frequencies with prolonged walking, indicative of fatigability, which would be mitigated when wearing CFIs.

Methods

16 young adults (9M/7, age:23.6±3.1 years) completed a two-day protocol in randomized order, each involving 30 minutes of prolonged walking at 20% faster than preferred speed. On one day, participants wore standardized shoes; on the other day, they wore the same shoes with 1.6-mm CFIs. We recorded continuous right leg indwelling electromyography (EMG) signals from the abductor muscles (AH, n=16 analyzed) and the flexor digitorum brevis (FDB, n=12 analyzed). EMG mean frequency and EMG time-frequency analyses examined spectral shifts in those muscle excitations across time.

Results

Independent of footwear condition, AH and FDB both exhibited time-dependent decreases in EMG mean frequency across time ($p<0.001$). Time-frequency analyses added that a shift toward slower-frequency excitations over time for both muscles occurred particularly during mid-to-late stance – a change indicative of fatigability that was mitigated when walking with CFIs (Fig. 1) and that would have been otherwise missed using mean frequency alone, which did not differ significantly between conditions.

Discussion

Supporting our hypothesis, prolonged walking elicited measurable changes in PIM excitations (i.e., slower mean frequencies) indicative of fatiguability. We also find evidence that CFIs promoted fatigue resistance for both AH and FDB; these PIMs exhibited a lesser shift towards slower-frequency excitations compared to walking in standardized footwear. Cumulative findings suggest that increasing footwear bending stiffness may mitigate PIM fatigue, likely by offloading the biological structures, with implications that include preserving gait function among older adults.

Images (Optional)

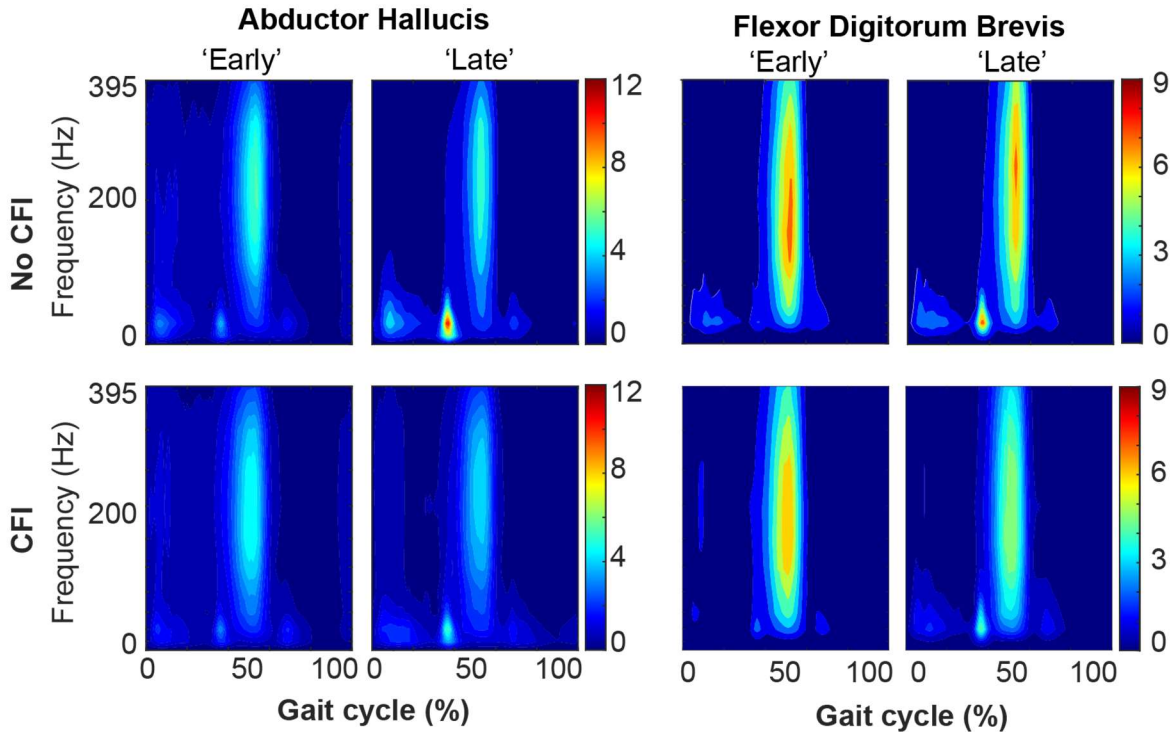


Figure 1. Time-frequency analysis of AH and FDB during the first ('early') and last ('late') minute of the prolonged 30-minute walking task.

Acknowledgements (Optional)

This work was supported by a grant from the National Institutes of Health (R01AR081287) and an NSF GRFP.

Session Category

Human Motion and Performance: Locomotion/Gait

OA178-02

Physiological, Biomechanical, and Perceptual Effects of Mass Placed Anteriorly vs Laterally on the Shank to Inform the Design of Powered Footwear Systems

Ms Kristin Quah, Ms Kristin DeHart, Dr Julia Butterfield, Dr Alison Sheets-Singer

Nike, Inc., Beaverton, Oregon, United States

Introduction

Nike is creating a powered footwear system (PFS) for running and walking. The PFS structure can introduce penalties that actuation must offset to provide athletes with enjoyable experiences. While physiological penalties from total system mass have been modeled [1,2] and can be overcome when powered [3], the biomechanical and perceptual effects of mass placement are less known. Therefore, this experiment simulates the effects of PFS mass distributions on athletes' metabolic cost, biomechanics, and perception of running by placing 1kg masses anteriorly or laterally on the proximal shank.

Methods

Fourteen athletes gave informed consent and completed familiarization and testing visits. In familiarization, athletes ran for 10 minutes with each mass location. Testing visits included six, 5.5-minute submaximal trials. The three conditions (shoes, shoes+1kg lateral mass, shoes+1kg anterior mass) were pseudo-randomized and tested in ABCCBA order. Metabolic data (COSMED K5), RPE (9-point scale), "ease of running" (100-point scale), and heel-mounted IMU data (Vicon Blue Trident) were measured. Metabolic cost (Brockway equation) and biomechanical differences (sum of angular velocity differences squared in 30–100% of stride) were compared between shoes and mass conditions in the final 1.5 minutes of each trial. Significant differences were identified using linear mixed effects models (fixed effect: condition, random effect: participant) with Tukey's post-hoc tests.

Results

While there were no metabolic differences between running with lateral and anterior masses (Figure 1A), and both increased metabolic power compared to shoes ($p<1e-6$), athletes perceived the lateral condition to be more difficult than anterior. Lateral RPE values were larger, "ease of running" scores were lower ($p<0.001$, Figures 1B/C), and all athletes preferred the anterior placement. Biomechanical differences from shoes were also larger when mass was placed laterally ($p=0.03393$, Figure 1D).

Discussion

Although the metabolic cost of adding lateral and anterior mass were not significantly different, athletes universally preferred the anterior placement and had the smallest biomechanical changes. This suggests that anterior mass distributions should be used in future PFS designs to minimize penalties introduced by the structure.

Images (Optional)

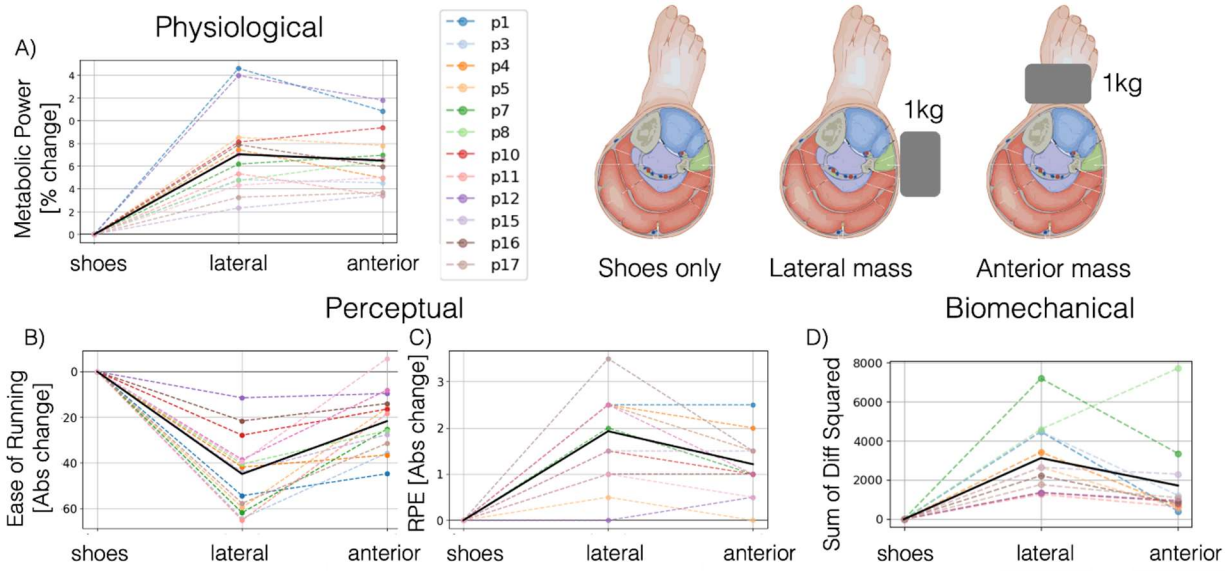


Figure 1: (A) While participants' metabolic power were larger when running in both mass conditions compared with shoes, there was no significant difference between the lateral and anterior positions. (B) Using a sliding scale of 0 (hardest) to 100 (easiest), athletes perceived running in the lateral condition to be more difficult than the anterior position. (C) Using a 9-point RPE scale, athletes perceived the lateral condition to require more effort to run in compared to the anterior position. (D) The lateral condition had a significantly larger sum of difference squared metric from the shoe condition compared to the anterior condition. Each colored point and dotted line represents data from a single athlete while the thick black line represents the mean across all athletes.

References (Optional)

[1] I. Coifman et. al., Appl. Ergon. 2024

[2] D. Catlin et. al., Med. Sci. Sports Exerc. 1979

[3] D.E. Miller et. al., J. NeuroEngineering Rehabil. 2022

Session Category

Human Motion and Performance: Locomotion/Gait

OA178-03

Spatiotemporal Plantar Pressure Differences Between Individuals with CMT and Healthy Controls

Mr. Tyce Marquez MS, Mrs. Lauren Crowe BS, Dr. Bopha Chrea MD, Dr. Jason Wilken PT, PhD, Dr. Donald Anderson PhD

University of Iowa, Iowa City, Iowa, United States

Introduction

Charcot-Marie-Tooth (CMT) disease is the most common inherited neuromuscular disease [1]. It is characterized by progressive distal muscle imbalance and often results in pes cavus feet [2], contributing to altered gait mechanics and abnormal pressures on the plantar foot surface [3]. Altered plantar pressures have been demonstrated along the lateral column in CMT patients using discrete region-of-interest analysis, an approach that fails to capture differences in load progression. This study evaluated spatiotemporal plantar pressure differences between individuals with CMT and healthy controls.

Methods

Twenty-six individuals with CMT (14M/12F, 47.2±19.9 years) and 26 healthy controls (12M/14F, 41.8±12.4 years) each completed three walking trials per foot across a Novel-EMED plantar pressure platform [4]. Time series plantar pressures sampled at 10 ms intervals were linearly interpolated to 5% intervals over stance and rotated based upon the foot progression angle [5]. Values within a bounding box defined by the maximum pressure distribution were extracted and scaled to a standard size for sensor-level comparisons. Sensor-level plantar pressure mean differences were compared between CMT and control participants.

Results

During the loading response phase of stance, CMT participants experienced decreased loading in the hindfoot relative to controls (Figure 1). In mid- and terminal stance, CMT participants had increased loading in the lateral hindfoot and midfoot, with minimal forefoot loading. During pre-swing, CMT participants had limited load progression through the toes while experiencing increased pressures at the first/fifth metatarsal heads.

Discussion

Individuals with CMT were unable to propel load progression from the hindfoot through the forefoot. This led to minimal toe loading, limiting toe-off power. Altered spatiotemporal plantar pressures were most prominent along the lateral column, potentially increasing injury risk in that region. Utilizing spatiotemporal plantar pressure assessment between healthy and deformed feet provided insight into loading features associated with pes cavus deformity. This knowledge can inform surgical interventions aimed at restoring the foot tripod to effectively reduce loading deficits.

Images (Optional)

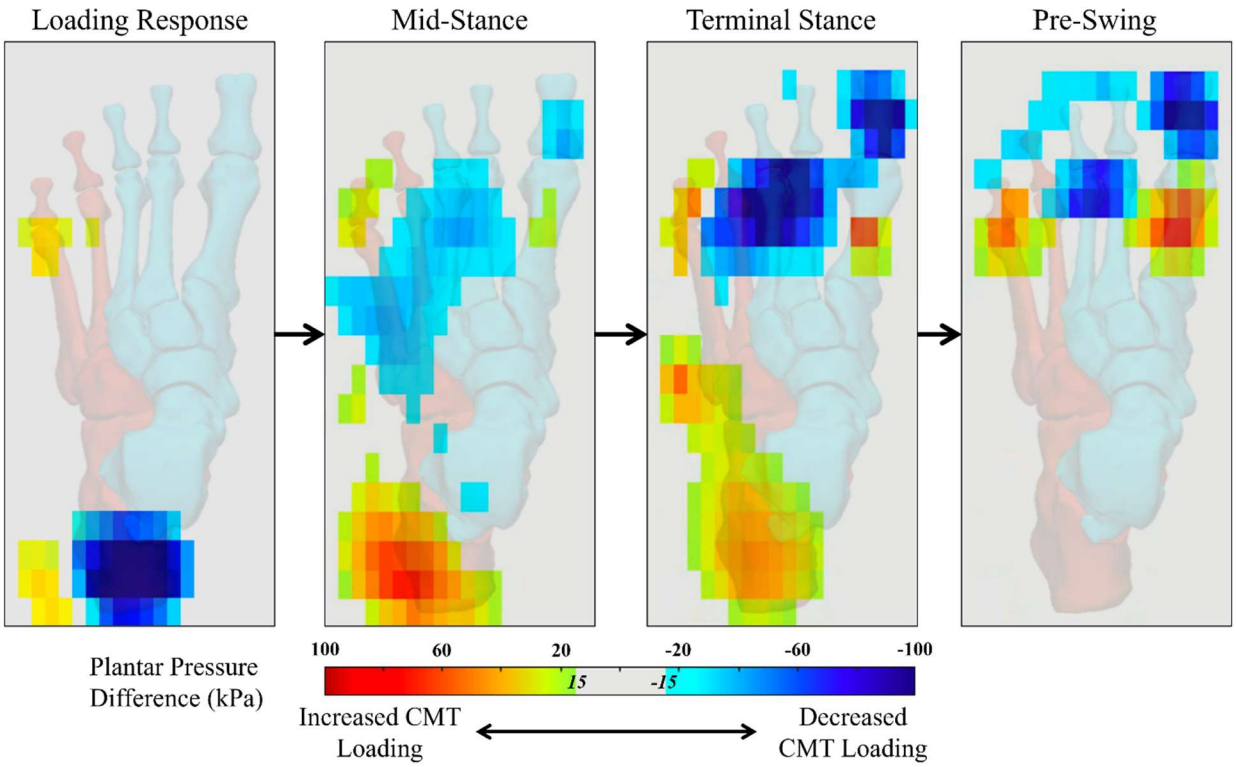


Figure 1: Mean plantar pressure differences (kPa) on a sensor-level between CMT and healthy control participants at the four phases of stance are shown here as representative distributions selected from each phase. Bony foot model is overlaid for anatomical reference with red bones representing the lateral column.

References (Optional)

[1] Laura M, et al., Muscle Nerve, 2018 [2] HH T. 1886 [3] Burns J, et al., Neurology, 2010 [4] McPoil TG, et al. J Am Podiatr Assoc, 1999 [5] Keijsers NL, et al., J Biomech 2009

Session Category

Human Motion and Performance: Locomotion/Gait

OA178-04

The Terrain Not Taken: The Effects of Trail and Road Running on Ankle Injury Predictors

Dr Key Nahan BPodMed, MSc, PhD[1], Mr Malicki Diallo BSc[1], Mr Adam Grimmitt MSc[1], Mr Aidan Watts[2], Dr Wouter Hoogkamer BSc, MSc, PhD[1]

[1]University of Massachusetts Amherst, Amherst, Massachusetts, United States. [2]SUNY College of Environmental Science and Forestry, Syracuse, New York, United States

Introduction

Trail running introduces unique mechanical challenges (e.g., uneven surfaces), which may increase the risk of ankle injuries as compared to road running. While trail running is difficult to study in a laboratory, inertial measurement units (IMUs) can overcome this barrier. IMUs can measure peak eversion velocity, which has been used assess shin splints risk [1], and peak inversion velocity, which has been used to assess ankle sprain risk [2]. Based on the uneven terrain, we hypothesize that trail running will be associated with greater peak eversion and inversion velocities during the loading phase as compared to road running.

Methods

Six participants (4M, 2F) ran on a flat road and an uneven trail at their easy pace. We collected vertical acceleration and frontal-plane angular velocity data using bilateral heel-mounted IMUs (1125 Hz; Blue Trident, IMeasureU, NZ). We segmented strides using the peak jerk squared and extracted maximum and minimum angular velocities during the loading phase (first 20% of each stride). We concatenated left and right strides and matched stride number across terrains. We used LMEMs to assess maxima and minima over all strides (dependant variable~Terrain+(1|Participant). We classified strides with inversion velocities below −300°/s as at risk for an ankle sprain [2]. The number of risky strides was assessed with a one-tailed Wilcoxon signed-rank test.

Results

Maximum angular velocity was lower on the trail (341°/s [195,488]; EMM [95%CI]) than the road (459°/s [312,605]; Δ=-117°/s [-211,-24]; p=0.021). Minimum velocity did not differ between terrains (trail:-73°/s [-121,-25], road :-50°/s [-98,-2]; Δ=-23°/s [-61,15]; p=0.201). Participants took 683±130 (mean±SD) strides, with more risky strides on the trail (18±30) than the road (1±2; Δ=17±29; p=0.016).

Discussion

Due to the higher maximum angular velocities, road running may increase eversion-related injury risk as compared to trail running. Minimum angular velocity did not differ between terrains, yet trail running had more risky strides, suggesting a higher risk of inversion ankle sprains. This may guide terrain specific footwear design.

Images (Optional)

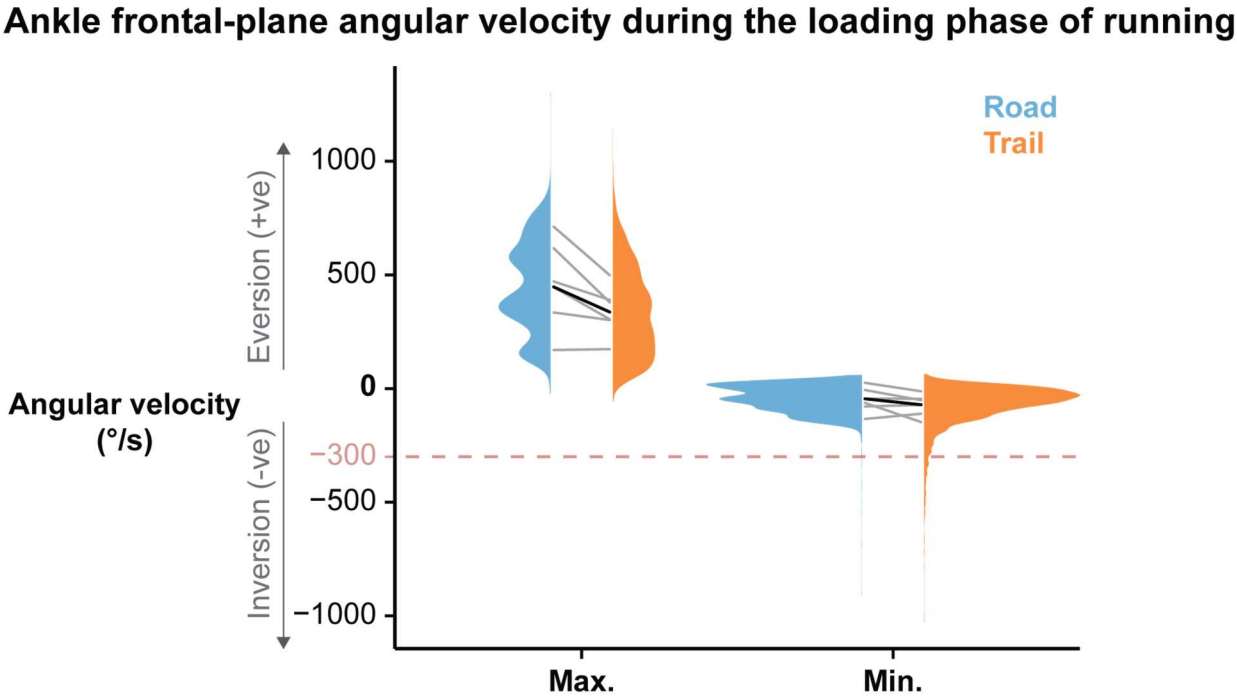


Figure 1. Ankle frontal-plane angular velocity maxima and minima during the loading phase (first 20% of a stride) of road and trail running. Black bars are group means, grey bars are participant means, and the red dotted line is the ankle sprain risk threshold.

References (Optional)

[1] Stephen Messier *et al.*, *Med Sci Sports Exerc,* 1988

[2] Vikki Wing-Shan Chu *et al.*, J Biomechanics, 2010 ial

Session Category

Human Motion and Performance: Locomotion/Gait

OA178-05

Mass Distributions of Powered Footwear Systems Affect Swing Leg Biomechanics

Dr. Julia Butterfield, Ms. Kristin Quah, Ms. Kristin DeHart, Ms. Hannah Frame, Dr. Alison Sheets-Singer

Nike, Inc., Beaverton, Oregon, United States

Introduction

Nike is creating a powered footwear system (PFS) for walking and running. Previous Nike research [1] demonstrated that mass added laterally to the shank could induce biomechanical changes during swing that were associated with negative sensations and higher perceived effort. This suggests that metabolic benefits would be harder to perceive in a PFS that changes swing-phase kinematics. In this meta-analysis, we compared swing-phase biomechanics when running in shoes and three unpowered PFS prototypes with different mass distributions.

Methods

During three experiments, 3-6 athletes gave informed consent and ran at least two 90-second 6-mph trials on a Bertec treadmill: in shoes, and an unpowered PFS. Toe position in the pelvis reference frame (VICON) and heel angular velocity (VICON Blue Trident) during swing were compared to shoes across three systems and within a system with an anterior or lateral battery placement. Metrics to compare systems included the difference in concavity of the toe position in the PFS and shoes, and the sum of the differences from shoes squared of angular velocity about the heel's vertical axes (internal/external rotation).

Results

In System 1 with primarily lateral mass, the swing-phase concavity of the toe position was significantly different than running in shoes (Figure 1), and athletes described negative sensations. Moving System 2's battery anteriorly resulted in the toe position becoming more like running in shoes. In System 3 with both an anterior battery and a smaller motor located closer to the leg, toe position was closest to running in shoes and athletes did not describe negative swing-phase sensations. Angular velocity differences about the heel's vertical axis exhibited a similar trend to the toe position concavity, demonstrating the promise of IMUs to capture this phenomenon without motion capture.

Discussion

Kinematic changes in the swing phase of running can produce negative sensations and higher perceived efforts [1] for athletes. When navigating the myriad of design goals for a

PFS, both total mass and mass distribution should be considered. Moving mass anteriorly or bringing mass closer to the leg can improve the athlete experience during straight-line locomotion by allowing natural swing-phase motion.

Images (Optional)

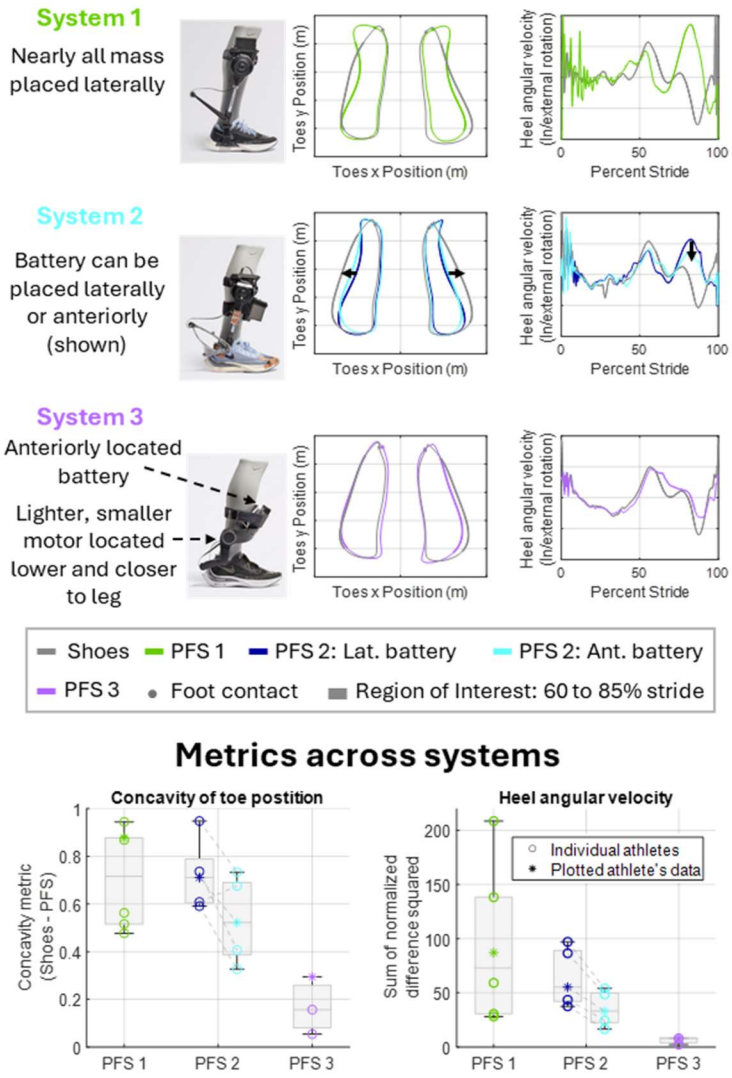


Figure 1. In System 1 (top row), nearly all of the mass is placed laterally on the leg. Toe position in the pelvis reference frame during swing (middle column, thick line corresponds to 60-85% stride) exhibits a different shape when running in the PFS (colors) compared to running in shoes (gray). Similarly, angular velocity about the heel vertical axis (foot internal/external rotation) differs between the PFS and shoe conditions during swing (right column, approximately 40% stride and later). In System 2 (second row), the battery (~250 g) can be placed on top of the motor in a lateral position, or anteriorly as shown. Moving the battery from lateral to anterior made the toe position curve of the PFS more like running in shoes. In System 3 (third row), the battery (~200g) was placed anteriorly, and the motor was lower and closer to the leg. Toe position during swing with System 3 is most like running in shoes, and heel angular velocity matches that of shoes throughout most of stride. Plots are shown for a representative athlete in each study, and all lines indicate the average across the final 20 seconds of each 90-second trial. Toe position differences were compared across athletes and prototypes using the difference in concavity during swing (bottom left). Angular velocity differences were compared using the sum of the squared differences from shoes during swing (bottom right). Stars represent metrics from the athletes whose individual data are plotted in the first three rows. Dashed lines for System 2 connect the lateral-battery and anterior-battery trials for each athlete.

References (Optional)

[1] Kristin Quah *et al.*, WCB, 2026

Session Category

Human Motion and Performance: Locomotion/Gait

OA178-06

Influence of Textured Insoles on Footstrike Characteristics and Joint Moments During Running

Mr. Nicolas Silon[1], Mr. Ryan Evans[1], Ms. Kelly Robb[2], Mr. Micheal Ryan[2], Mr. Derek Pamukoff[1]

[1]Western University, London, Ontario, Canada. [2]Kintec Footlabs Inc., Surrey, British Colombia, Canada

Introduction

Forefoot compared with rearfoot striking contributes to lower knee loading during running. Heel-textured insoles provide a tactile cue to shift the center of pressure anteriorly, which may influence footstrike pattern and lower extremity joint loading. We investigated the influence of a textured insole on footstrike characteristics and lower limb joint moments.

Methods

48 healthy recreational rearfoot strike runners participated (25 Males, 23 Females, Age: 22.8±3.7 yrs, weekly running amount: 37±20.4km). Gait biomechanics were recorded at a self-selected speed using a split-belt force-instrumented treadmill (2000Hz) and 8-camera motion capture system (200Hz). Participants were instrumented with laboratory standard footwear and reflective markers. Participants completed three running conditions (**Fig 1**): textured insole (INS), non-textured insole (SHAM), standard footwear (CON) in a random order for 10 minutes each at the same speed (average running speed: 2.92±0.38m/s). The peak internal knee extension moment (KEM), peak internal ankle plantar flexor moment (PFM), and footstrike angle (FSA) were extracted and averaged across all footstrikes. A repeated measures ANOVA compared peak KEM, peak PFM, and footstrike angle between conditions, and a Bonferroni adjustment was used for post hoc comparisons.

Results

There was an effect of condition for KEM ($F_{2,94}$=7.451, p<0.001, partial η^2=0.137) and PFM ($F_{2,94}$=5.789, p=0.004, partial η^2= 0.110). Peak KEM was lower in CON (171.5±44.5 Nm) compared to INS (175±44.8 Nm, p <0.001) and SHAM (174.3±45.2 Nm, p = 0.009). Similarly, the peak PFM was higher in CON (-172.9±42.2 Nm) compared to INS (-171±40.6 Nm, p=0.019) and SHAM (-170.5±41.3 Nm, p=0.003). No difference was found in FSA between conditions ($F_{2,94}$=0.839, p=0.436, partial η^2=0.18).

Discussion

The textured insole did not alter footstrike angle. The peak KEM was higher but the peak PFM was lower in both insole conditions compared with standard running footwear. Insoles may contribute to differences in spatiotemporal parameters of running gait, such as step length or step frequency that are known to influence net joint moments. Similarly, insoles may influence proximal muscle activation patterns that contribute to differences between conditions in net joint moments.

Images (Optional)



Figure 1: Insole conditions from left to right: sham, texture, standard footwear

Acknowledgements (Optional)

This project was funded by Kintec Footlabs Inc. (Surrey, BC).

Session Category

Human Motion and Performance: Locomotion/Gait

OA179-02

CoronaryFlow-Diffusion: A Physics-informed Conditional Diffusion Model for High-fidelity 3D Coronary Flow Field Reconstruction

Ms. Yang Yang PhD Candidate[1,2], Prof. Bao Li Ph.D.[1], Prof. Liyuan Zhang Ph.D.[1], Prof. Leo Hwa Liang Ph.D.[2], Prof. Mingai Li Ph.D.[1], Prof. Youjun Liu Ph.D.[1]

[1]Beijing University of Technology, Beijing, Chaoyang District, China. [2]National University of Singapore, Singapore, Singapore, Singapore

Introduction

Experimental blood-flow measurement techniques play a critical role in understanding cardiovascular diseases. Particle image velocimetry (PIV) is widely regarded as the gold standard for blood-flow assessment. However, it remains limited in medium-sized coronary arteries due to the small vessel diameters and the intrinsic spatial resolution constraints of PIV. Consequently, the resulting velocity fields tend to be sparse, noisy, and subject to missing data, making high-fidelity flow-field reconstruction a key challenge for advancing coronary hemodynamic analysis.

Methods

In this study, we propose CoronaryFlow-Diffusion, a physics-informed conditional diffusion model built within a stochastic differential equation (SDE) framework. It employs a PointNet-based architecture to reconstruct high-fidelity 3D coronary flow fields. Meanwhile, we constructed a dataset of 1,311 coronary computational fluid dynamics (CFD) simulation samples. Each sample includes low-resolution inputs, simulating PIV measurements, along with the corresponding high-fidelity velocity and pressure fields. By embedding the Navier–Stokes equations into the diffusion process, the model enforces physical consistency while reconstructing high-fidelity coronary flow fields.

Results

The proposed method enables high-fidelity reconstruction of flow fields in medium-sized coronary arteries and accurately captures local hemodynamic features. Quantitative evaluation on the test set shows a mean relative error of 3% in the reconstructed pressure fields and a mean squared error (MSE) of 2% in the velocity fields, indicating that the model can reliably and faithfully reconstruct coronary flow fields.

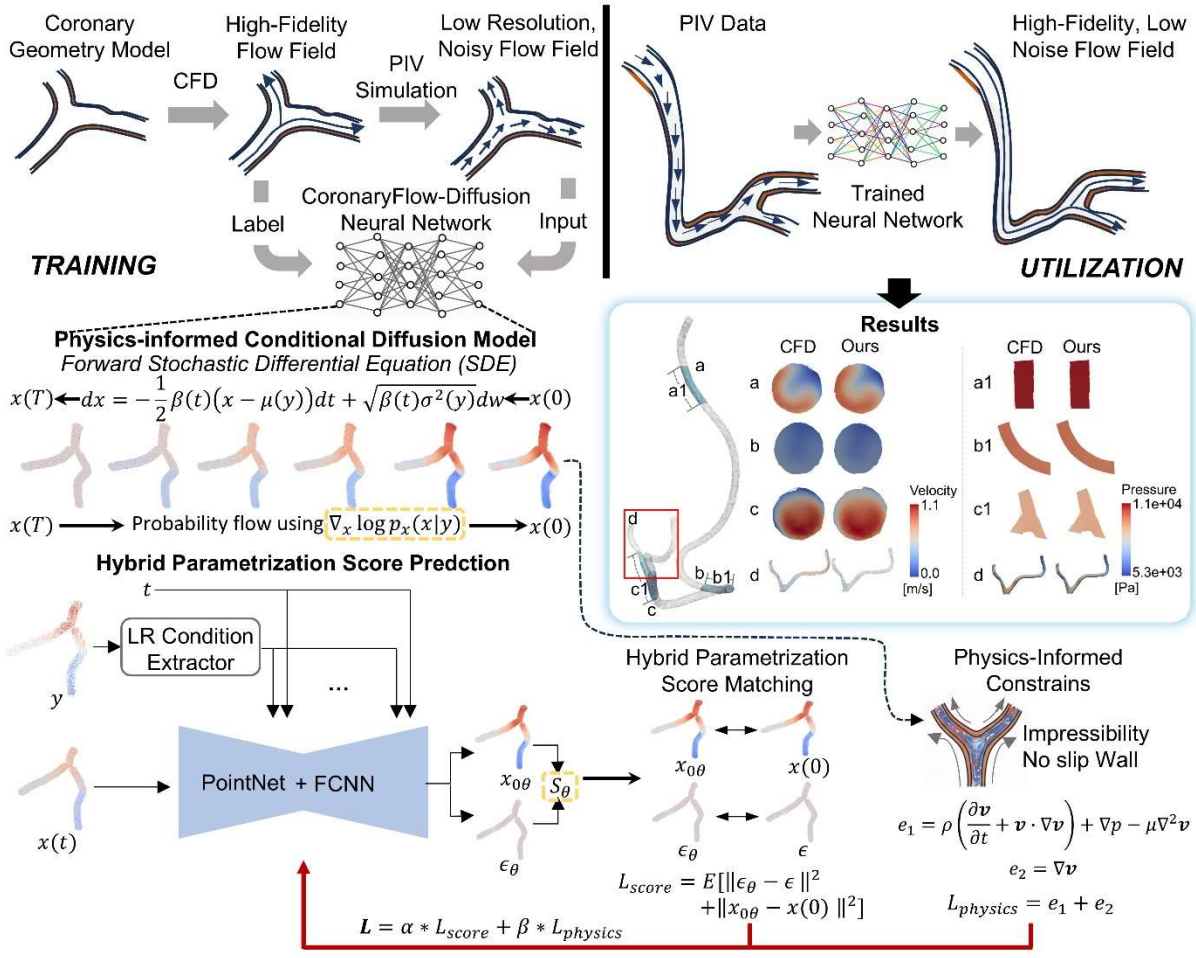
Discussion

The CoronaryFlow-Diffusion model enhances experimental flow measurements (e.g., PIV) by providing high-fidelity coronary hemodynamic information. Through the incorporation of physical equations, the method ensures physical consistency while achieving accurate flow-field reconstruction. This framework offers a promising tool for cardiovascular research and contributes to a more comprehensive understanding of coronary hemodynamics.

Images (Optional)

CoronaryFlow-Diffusion: A Physics-informed Conditional Diffusion Model for High-fidelity 3D Coronary Flow Field Reconstruction

Yang Yang[1,2], Bao Li[1], Liyuan Zhang[1], Leo Hwa Liang[2], Youjun Liu[1,*]
[1]Department of Biomedical Engineering, College of Chemistry and Life Science, Beijing University of Technology, Beijing, China
[2]BioFluid Mechanics Lab, Department of Biomedical Engineering, National University of Singapore, Singapore



Session Category

Cardiovascular/Cardiorespiratory Biomechanics: Methods, Models and Applications

OA179-03

Modeling the Evolution of Constitutive Response of Vein Grafts in Coronary Artery Bypass Graft Procedure Using Constitutive Artificial Neural Networks

Ms. Divya Adil[1], Dr. Marisa Bazzi[1], Dr. Ruizhi Wang[2], Prof. Ellen Kuhl[1], Prof. Jay Humphrey[2], Prof. Alison Marsden[1]

[1]Stanford University, Stanford, CA, United States. [2]Yale University, New Haven, CT, United States

Introduction

Coronary artery disease affects >315 million people globally and can cause myocardial infarction. Coronary artery bypass grafting commonly uses a saphenous vein graft, which experiences a venous-to-arterial pressure shift that triggers remodeling and contributes to high graft failure rates. Better characterization of graft mechanics is needed for developing failure-mitigation strategies.

Vessel walls are typically modeled as hyperelastic using a strain energy function (SEF). Arteries have been well characterized, whereas veins are structurally distinct and understudied[1], and vascular graft studies remain scarce. Constitutive artificial neural networks (CANN) provide a compact framework to discover interpretable hyperelastic constitutive laws from experiments while embedding prior knowledge[2].

Here, we perform inflation-biaxial testing on vessels explanted from a rabbit jugular-to-carotid graft model at multiple post-grafting time points to quantify evolving mechanics, and apply CANNs to discover control-vein and vein graft constitutive models from the biaxial data.

Methods

Pressure-diameter tests were run at fixed axial stretches (95%,100%,105%) of in-vivo length (veins: 5-30mmHg; grafts/arteries: 10-140mmHg)[3]. Force-length tests measured axial response at fixed pressures (veins: 10-15-20-25mmHg; grafts/arteries: 10-60-100-140mmHg). Arteries were fit using a 4-fiber family; veins were fit using quadratic 4-fiber or Fung-type models for comparison. Circumferential and axial stretches served as CANN inputs. The architecture contains invariant, fiber-recruitment, and strain-polynomial branches that can be selectively activated, and outputs an SEF. Training minimizes bi-directional RMS stress error, normalized by max stress.

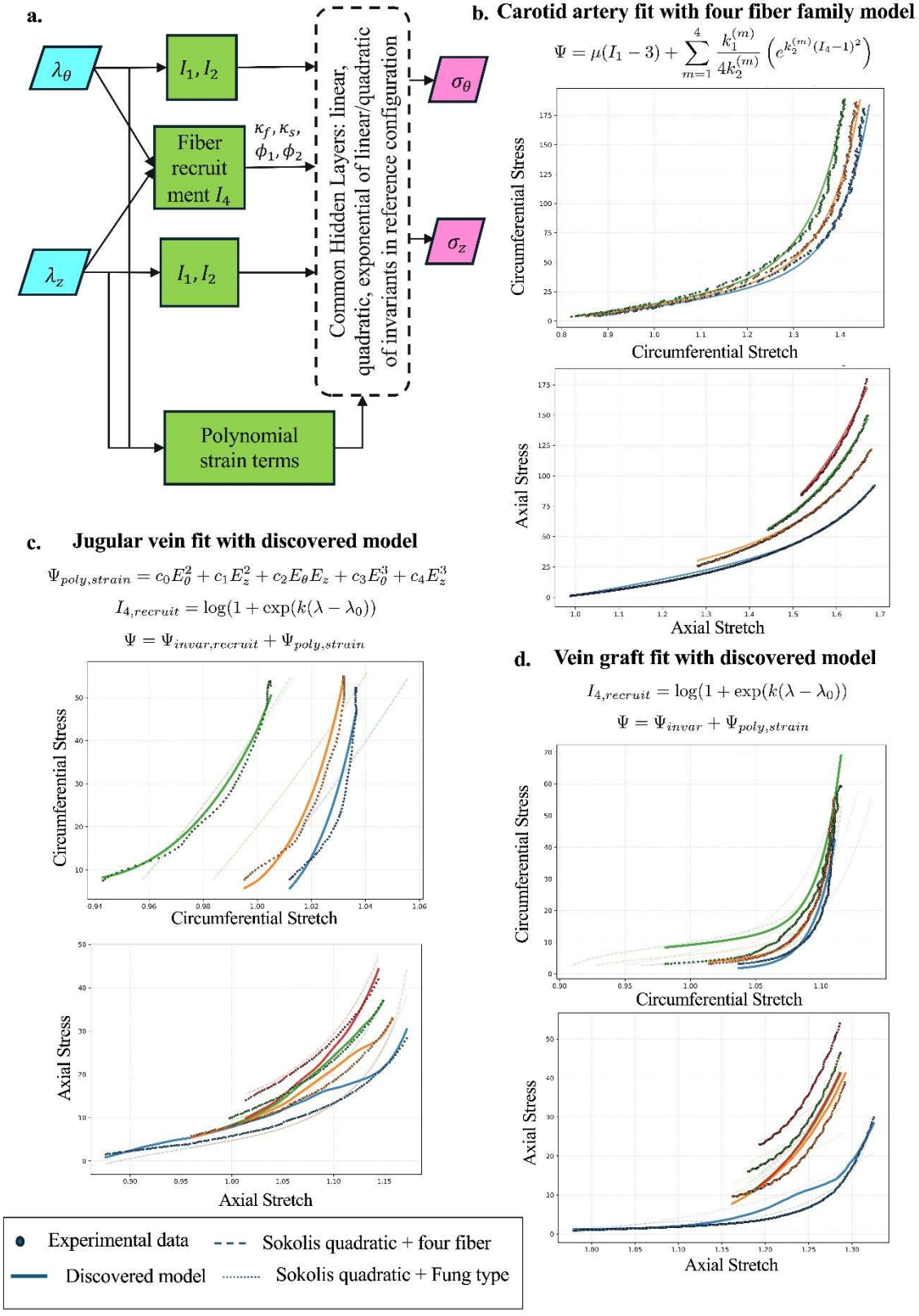
Results

The vein SEF uses a fiber-recruitment gate plus strain-polynomial terms, reducing RMSE to 0.106, > 50% improvement vs. quadratic 4-fiber and Fung models (0.223). The week-6 graft SEF incorporates the gate on a base invariant model (0.245), improving on 4-fiber (0.275,11%) and Fung (0.338,27%).

Discussion

The four-fiber model fits arteries well (RMSE 0.060072), consistent with organized collagen structure. CANN-discovered models for veins and grafts incorporate fiber-recruitment gating and additional strain terms, capturing behaviors absent in prior formulations. The week-6 graft shows intermediate mechanics between veins and arteries, indicating partial arterial adaptation. Future work will scale model discovery to multiple samples and time points.

Images (Optional)


a.
λ_θ
λ_z
I_1, I_2
Fiber recruit ment I_4
I_1, I_2
$\kappa_f, \kappa_s, \phi_1, \phi_2$
Common Hidden Layers: linear, quadratic, exponential of linear/quadratic of invariants in reference configuration
Polynomial strain terms
σ_θ
σ_z
b. Carotid artery fit with four fiber family model
$\Psi = \mu(I_1 - 3) + \sum_{m=1}^{4} \frac{k_1^{(m)}}{4k_2^{(m)}} \left(e^{k_2^{(m)}(I_4-1)^2}\right)$
Circumferential Stress
Circumferential Stretch
Axial Stress
Axial Stretch
c. Jugular vein fit with discovered model
$\Psi_{poly,strain} = c_0 E_\theta^2 + c_1 E_z^2 + c_2 E_\theta E_z + c_3 E_\theta^3 + c_4 E_z^3$
$I_{4,recruit} = \log(1 + \exp(k(\lambda - \lambda_0))$
$\Psi = \Psi_{invar,recruit} + \Psi_{poly,strain}$
Circumferential Stress
Circumferential Stretch
Axial Stress
Axial Stretch
d. Vein graft fit with discovered model
$I_{4,recruit} = \log(1 + \exp(k(\lambda - \lambda_0))$
$\Psi = \Psi_{invar} + \Psi_{poly,strain}$
Circumferential Stress
Circumferential Stretch
Axial Stress
Axial Stretch
Experimental data
Sokolis quadratic + four fiber
Discovered model
Sokolis quadratic + Fung type

References (Optional)

[1] Sokolis. Biomech. Model. Mechanobiol., 2013.

[2] Linka, Kuhl. Comput. Methods Appl. Mech. Eng., 2023.

[3] Ferruzzi et al. J. Biomech. Eng., 2015.

Session Category

Cardiovascular/Cardiorespiratory Biomechanics: Methods, Models and Applications

OA179-04

AI-Based Ensemble Approaches to Anticipate Symptom Progression in Patients with an Abdominal Aortic Aneurysm

Ph.D. Candidate Juan Restrepo[1], B.Sc. Archer French[1], Ph.D. Amanda Fernandez[1], M.D. Satish Muluk[2], M.D. Mark Eskandari[3], M.D. Vikram Kashyap[4], Ph.D. Ender Finol[1]

[1]The University of Texas at San Antonio, San Antonio, Texas, United States. [2]Allegheny General Hospital, Pittsburgh, Pennsylvania, United States. [3]Northwestern University, Chicago, Illinois, United States. [4]Corewell Health, Grand Rapids, Michigan, United States

Introduction

When an Abdominal Aortic Aneurysm (AAA) shows symptoms of impending rupture, the mortality rate can be as high as 90%. Early predictions of symptom onset could allow clinicians to intervene before a catastrophic event, thereby improving patient outcomes. This work evaluates tree-based ensemble machine learning models trained on hierarchical clinical, biomechanical, and morphological data to predict future symptom onset within a 6-month interval.

Methods

We trained three tree-based models-Random Forest, AdaBoost and XGBoost-on hierarchical datasets, combined with three pre-processing strategies, namely Principal Component Analysis (PCA), Recursive Feature Elimination (RFE), and no pre-processing, which yielded 93 different combinations. Biomechanical (B) features were generated using finite element analysis simulations that estimated wall stress and rupture potential index (RPI), while morphological (M) features were derived from established geometry quantification procedures. We used a sample of 200 patients (100 asymptomatic and 100 symptomatic within 6 months of imaging) from which CTA exams and clinical (C) records were collected. Model performance was evaluated using area under the curve (AUC), and false-positive and false-negative ratios for fair comparisons.

Results

The ensemble models achieved an average AUC = 0.87. Key predictors included C and B features consistently present for the nine top-performing models. Integrating all data hierarchies produced the best model: XGBoost [C + B (RFE) + M (PCA)], AUC = 0.95. Feature-importance analyses identified RPI, smoking status, and systolic blood pressure

as significantly associated with symptom progression. The second-best model, Random Forest [C + B (PCA)], minimized both false positives and false negatives (F1 = 0.93).

Discussion

Ensemble methods can meaningfully improve short-term prediction of symptom onset in AAA patients, offering a potential tool for preemptive clinical decision making. By integrating biomechanical, clinical and morphological features, the models capture complementary information beyond maximum diameter alone, consistent with reported literature. Notably, the Random Forest model shows clinical translation potential, as minimizing missed early-progression cases is critical for individualized surveillance and timely intervention planning. However, generalizability remains limited by the modest sample size. Future work should validate these models in larger, globally representative cohorts including broader demographics and assess their real-time utility within routine clinical workflows.

Images (Optional)

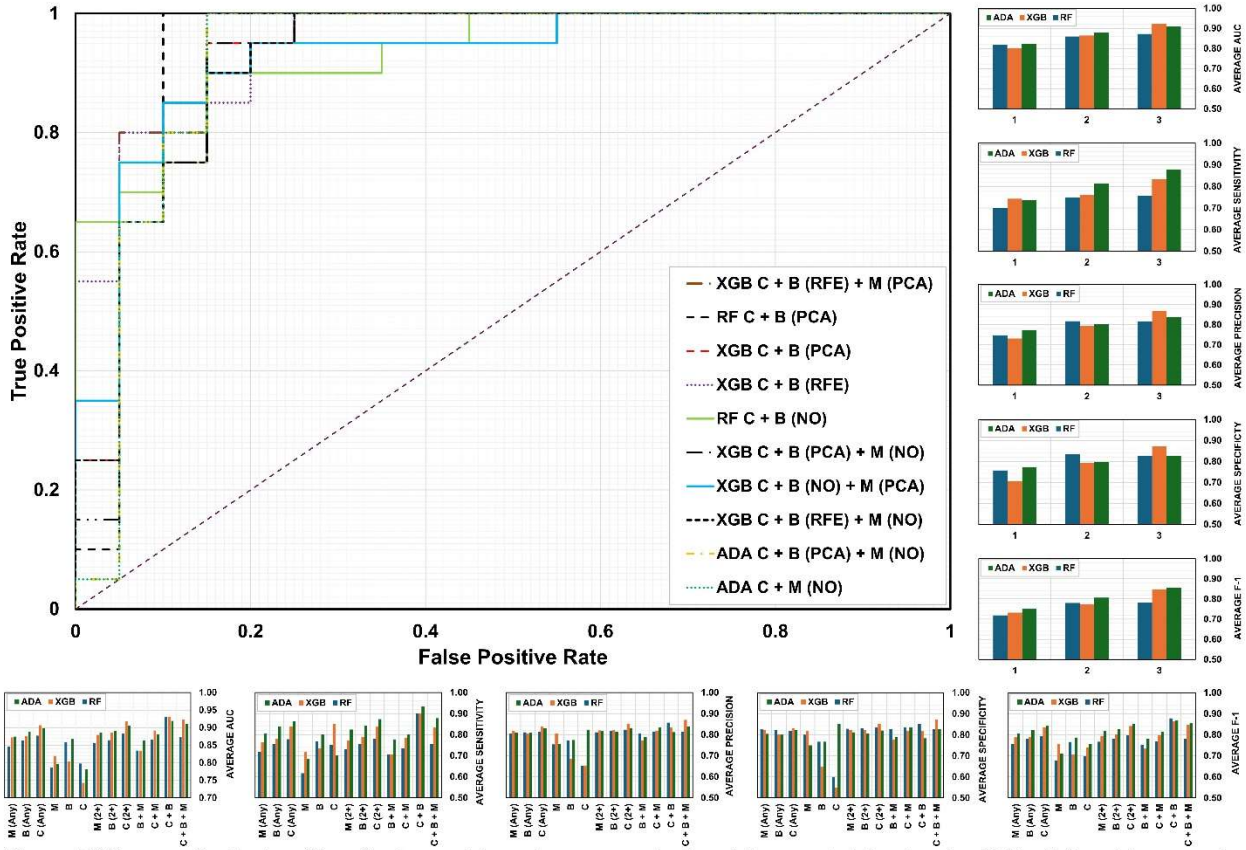


Figure. ROC curves for the top 10 performing models and average evaluation plots separated by domains (right side) and by surrogate combinations (bottom) for the three model architectures.

Acknowledgements (Optional)

NIH #R01HL159300 funded the study.

Session Category

Cardiovascular/Cardiorespiratory Biomechanics: Methods, Models and Applications

OA179-05

AI-Driven Estimation of Patient-Specific Aortic Wall Mechanical Properties for Improved Biomechanical Simulation

Ms. Ione Ianniruberto MSc[1,2], Mr. Davide Astori MSc[1], Dr. Jonathan Weinsaft[3], Prof. Emiliano Votta PhD[1], Prof. Alberto Redaelli PhD[1]

[1]Politecnico di Milano, Milano, Italy, Italy. [2]European Society of Biomechanics (ESB), Milano, Italy, Italy. [3]Weill Cornell College, New York, New York, United States

Introduction

Finite element analysis (FEA) is widely used to estimate aortic wall stress in pathological conditions, with the main goal of assessing rupture or dissection risk[1]. However, patient-specific FEA is still hindered by the lack of non-invasive measurements of aortic wall mechanical properties. Because these properties can only be obtained from excised tissue, most simulations rely on generic material parameters derived from literature data, despite pronounced inter-patient variability[2].

To address this, we introduce a new framework that estimates patient-specific material behaviour by leveraging a database of human aortic tissue mechanics and a generative AI model, a conditional variational autoencoder (CVA).

Methods

Through a literature review, we assembled 100 equibiaxial tensile tests on human aortic samples processed under consistent preservation protocols. This dataset includes paired circumferential and axial stress–stretch curves categorized according to four clinical factors: i) anatomical region, ii) pathology (thoracic aneurysm, dissection, Marfan syndrome, or healthy control), iii) valve morphology, and iv) age group (young, middle, old).

For a given patient, the method first extracts the appropriate subgroup of the database based on these factors. Within this tailored subset, the curve that best matches the patient's circumferential mechanical behaviour, estimated from systolic/diastolic pressures and aortic compliance, is selected. Once the closest circumferential curve is identified, the corresponding paired axial curve from the same tissue sample is automatically included, ensuring a consistent biaxial representation. To automate this process, we trained a CVA capable of generating stress–strain curves conditioned on patient-specific attributes.

Results

Validation was performed using tissue samples from 10 patients for whom both clinical data and ex vivo equibiaxial tests were available. A permutation test based on the L2 norm showed no significant difference between predicted and experimental curves in 8 out of 10 cases ($p < 0.001$). Preliminary analysis further demonstrates that the CVA successfully learns and reproduces the statistical characteristics inherent to each clinical subgroup.

Discussion

This approach offers a promising pathway toward integrating patient-specific mechanical surrogates into aortic biomechanics simulations, potentially improving risk stratification and personalized treatment planning.

Images (Optional)

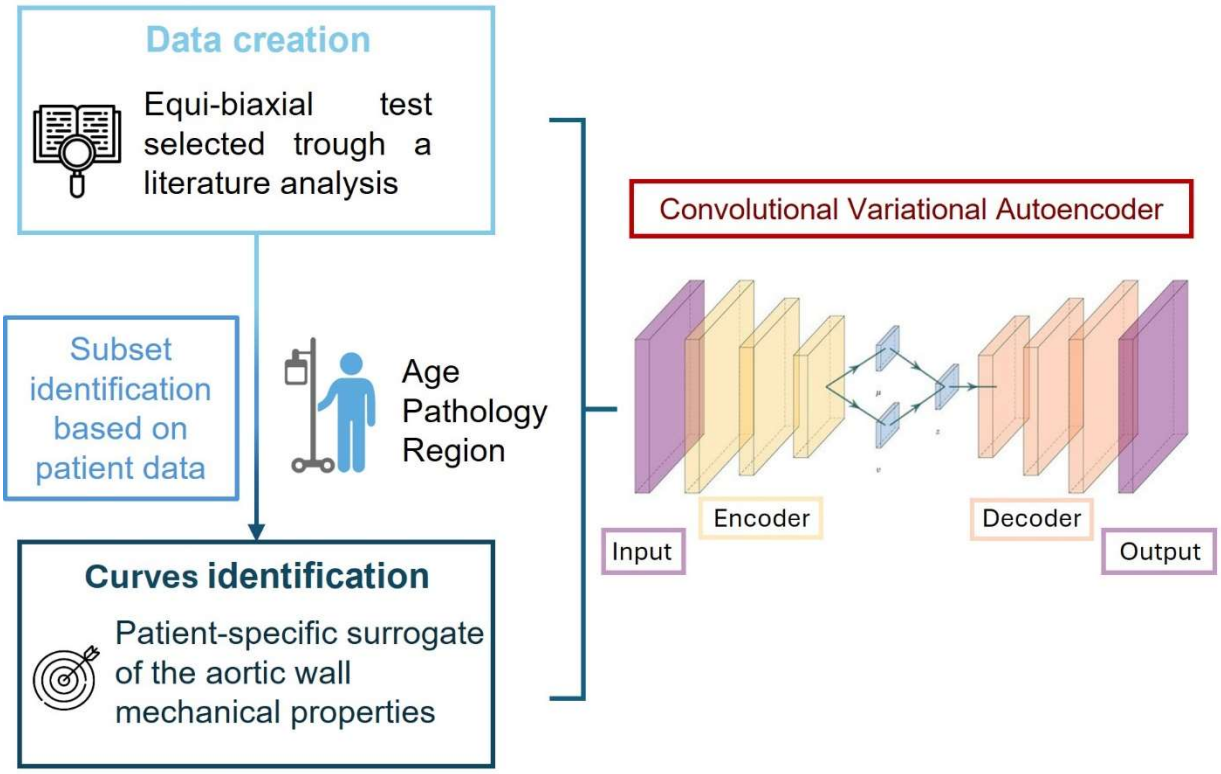


Figure 1: Algorithm implement for the curve identification starting from the database;

References (Optional)

[1] Zhu, Y et al,.*Cardiovasc Eng Tech*, 2025

[2] Roccabianca et al, *JMB of Biomedical Materials,* 2014

Acknowledgements (Optional)

This paper is funded by NIH project #1R01HL170570-01 “Towards Personalized Prosthetic Graft Replacement for Genetically Triggered Thoracic Aortic Aneurysms”.

Session Category

Cardiovascular/Cardiorespiratory Biomechanics: Methods, Models and Applications

OA180-01

C57BL/6N Mouse as a Model of the Age-Related Decline in the Matrix Quality of Bone

Ms. Emily Berestesky BS[1], Mr. Sasidhar Uppuganti MS[2], Ms. Elizabeth Hennen BS[1], Dr. Jeff Nyman PhD[2]

[1]Vanderbilt University, Nashville, TN, United States. [2]Vanderbilt University Medical Center, Nashville, TN, United States

Ms. Emily Berestesky

Introduction

To validate a model of aging for treatment strategies that target the bone matrix as way to prevent age-related declines in the fracture resistance of bone, we hypothesized that both post-yield displacement, a marker of brittleness, and fracture toughness of cortical bone are lower in aged female mice than in adult female mice because of age-related declines in bone matrix hydration.

Methods

Six- and 24-month-old, female, C57BL/6N mice from the US National Institute on Aging were euthanized to collect both femurs. We measured bone matrix hydration as bound water per bone volume (BW/BV) of the right femur using ^{1}H nuclear magnetic resonance relaxometry [1]. Next, we measured crack initiation toughness ($K_{Ic,ult}$) based on the ultimate force from monotonic, three-point bending tests and linear fracture mechanics for a micro-notch on the posterior surface of the mid-diaphysis [2]. Following μCT scans of the left femur to determine cortical tissue mineral density (Ct.TMD) and structural parameters, we loaded these hydrated bones to failure in three-point bending to determine ultimate moment (M_u), post-yield displacement (PYD), and work-to-fracture (W_f) per cross-sectional bone area (Ct.Ar from μCT) [1]. Significant differences in properties between age groups were determined based on $p<0.05$ from unpaired t-test, Welch's t-test, or Mann-Whitney U test.

Results

From 6-months to 24-months of age, bound water and cortical thickness (Ct.Th) decreased while Ct.TMD and polar moment of inertia (J) increased (Table). The ultimate stress ($\sigma_S = M_u \times c_{min} / I_{min}$), PYD, and toughness ($W_f$/Ct.Ar), experienced by the un-notched femur were

lower with age, while ultimate moment did not significantly differ between the age groups. For a given section modulus however, the ultimate moment was less in young than old mice (Fig). Lastly, crack initiation toughness significantly decreased with age.

Discussion

The effect of aging on the mechanical properties of cortical bone in C57BL/6N female is more than just a decline in strength; it involves a loss in the ability to resist post-yield crack formation with less bound water. Thus, this aging model can be used to test treatments that target the matrix.

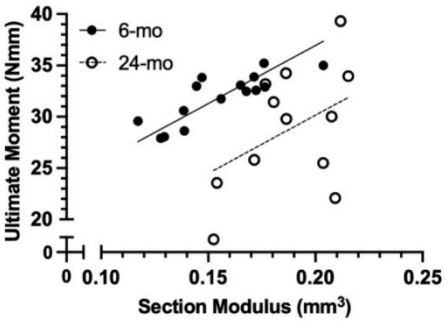
Images (Optional)

Table. Age-related differences in selected properties of C57BL/6N mouse cortical bone.

		6-month-old (n=15)		**24-month-old** (n=15)		6 vs. 24
Property	Units	Median	(1st, 3rd quartile)	Median	(1st, 3rd quartile)	p-value
BW/BV	%	7.96	(7.66, 8.53)	6.18	(5.81, 6.63)	<0.0001*
Ct.TMD	mg·HA/cm^3	1294	(1282, 1298)	1306	(1299, 1314)	0.0077*
Ct.Th	μm	0.172	(0.170, 0.183)	0.136	(0.131, 0.145)	<0.0001*
J	mm^4	0.290	(0.250, 0.322)	0.348	(0.331, 0.394)	0.0029*
Ct.Po	%	3.75	(3.57, 4.11)	4.11	(3.73, 4.43)	0.2284^
σ_S	MPa	203	(196, 220)	155	(140, 177)	<0.0001*
M_u	mm^4	32.57	(30.08, 33.44)	29.90	(25.02, 33.38)	0.1297#
PYD	1/mm	0.117	(0.091, 0.168)	0.037	(0.027, 0.041)	<0.0001^
W_f/Ct.Ar	MJ/m^3	5.10	(4.21, 6.68)	1.64	(1.21, 1.97)	<0.0001
$K_{Ic,ult}$	MPa·m$^{0.5}$	4.36	(4.28, 4.94)	3.92	(3.61, 4.07)	0.0109^

*Unpaired t-test; ^Mann-Whitney U, #Welch's t-test

Figure. For given femur size, cortical bone was weaker with age of the C57BL/6N mouse



References (Optional)

[1] Creecy et al. Bone, 2020, [2] Ritchie et al. Bone, 2010

Acknowledgements (Optional)

This study was supported by NIAMS (AR063157) and the VA Office of Research and Development (BX005866).

Session Category

Musculoskeletal Biomechanics: Methods, Models and Applications

OA180-02

Activity-Dependent Cortical Stress and Proximal Femur Stress Recovery After Total Hip Replacement

Dr. Wissal Mesfar, Dr. Mohamed Z. Bendjaballah

King Saud University, Riyadh, Riyadh, Saudi Arabia

Introduction

Preventing stress shielding after total hip replacement (THR) requires accurately predicting how cortical stresses evolve locally along the femoral shaft. Yet, most evaluations remain limited to regional averages, masking critical site-specific stress decay. This study introduces a multi-path cortical stress-tracking methodology, enabling direct comparison of pre- and post-THR stresses along anatomically matched ventral, medial, dorsal, and lateral tracks during both walking and stair climbing.

Methods

A 3D FE model of an intact femur was reconstructed from CT data and used to generate a prosthetic model hosting a cementless Ti–6Al–4V stem. Both models were meshed with hexahedral elements and assigned orthotropic/isotropic bone properties. Musculoskeletal loading for walking and stair climbing followed Heller et al. (2001). Muscle and joint loads were scaled to a 700N body weight. Twelve cortical paths— inner, middle, and outer layers at four cardinal sites lateral, ventral, medial, dorsal— were sampled for nodal von Mises stresses.

Results

Across all conditions, stresses peaked on the outer cortex, reaching ~40–50MPa during walking and ~60–80MPa during stair climbing, representing a 20–50% stress amplification depending on location. Stair climbing increased distal stresses by 35–60% relative to walking, particularly ventrally (Figure 1) and dorsally. Proximally, however, THR induced substantial stress decay—most notably on the medial path , where post-THR stresses dropped by 45–65%. Importantly, stair climbing did not reverse proximal stress loss on the medial track.

Discussion

Results reveal a clear dichotomy: stair climbing enhances distal cortical loading but fails to restore proximal stress transmission, especially medially where shielding risk is highest.

Medial proximal stress deficits exceeding 50% indicate that stem design, fixation, and stiffness—not activity modulation—govern the shielding mechanism in this region. Conversely, pronounced distal stress gains during stair climbing (up to +60%) highlight the influence of hip muscle recruitment, suggesting targeted rehabilitation strategies could exploit muscle-driven loading to stimulate regions unaffected by the prosthesis. Overall, this multi-path approach exposes highly localized stress-transfer patterns that traditional regional analyses overlook, offering a more precise framework for evaluating implant performance and optimizing post-THR rehabilitation.

Images (Optional)

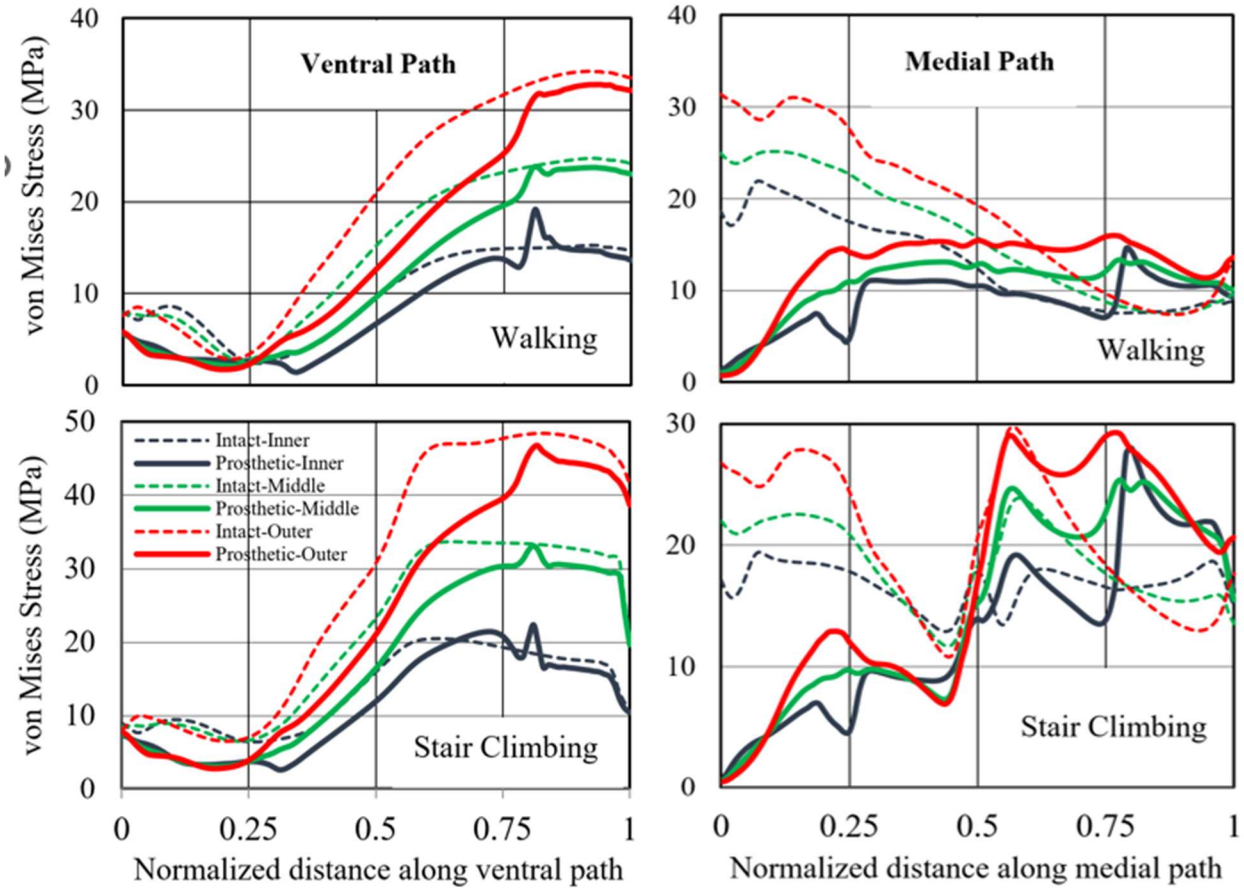


Figure 1: von Mises stresses in the intact and implanted cortical bone during walking and stair climbing activities. Two femoral paths are shown; the ventral and medial (dorsal and lateral not presented here).

References (Optional)

[1] Heller et al., J Biomech, 2001

Session Category

Musculoskeletal Biomechanics: Methods, Models and Applications

OA180-03

Prediction of Bone Loss Due to Altered Mechanical Stimulation in Transfemoral and Through-Knee Amputees

Dr Andrew Phillips[1], Dr Linjie Wang[2], Dr Louise McMenemy[3], Prof Alison McGregor[4]

[1]Structural Biomechanics, Department of Civil and Environmental Engineering, Imperial College London, London, London, United Kingdom. [2]Institute of Medical and Biological Engineering, School of Mechanical Engineering, University of Leeds, Leeds, West Yorkshire, United Kingdom. [3]Academic Department of Military Surgery and Trauma, The Royal Centre for Defence Medicine, Birmingham, West Midlands, United Kingdom. [4]Department of Surgery and Cancer, Imperial College London, London, London, United Kingdom

Introduction

Bone mineral density (BMD) reduction occurs in the femur of lower limb amputees, observed in an active military veteran cohort [1], with transfemoral amputees more severely affected than transtibial and through-knee amputees. We propose localised osteopenia is due to reduced mechanical stimulation. We used a combined musculoskeletal and finite element bone adaptation framework [2] to compare the mechanical stimulation of the femur for a body matched control subject (CS), unilateral transfemoral (TFA), and through-knee (knee disarticulation) (TKA) amputees.

Methods

Musculoskeletal models were developed to derive joint contact and muscle forces for walking, stair-ascent, stair-descent, sit-to-stand, and stand-to-sit, for control and amputee subjects. Corresponding finite element models were developed, and forces derived from the musculoskeletal models used as input, with the resulting mechanical stimulus (strain) in the femur compared between subjects. Bone adaptation simulations were run using a strain-based algorithm for CS to establish a baseline model, and for amputees to predict BMD changes.

Results

Compared to CS, BMD reduction of 32% for TFA and 8% for TKA was predicted in the proximal femur (Figure 1). For CS stair-ascent and stair-descent provided the highest levels of stimulation. For TFA reduced stimulation was observed for all activities, while for TKA stair-descent provided stimulation close to that for CS. Both amputees descended stairs using a reciprocal motion. Both amputees favoured their intact leg in sit-to-stand. Maximum hip joint contact force (HJCF) was similar between CS and both amputees, suggesting HJCF is not a suitable proxy indicator of bone health.

Discussion

Physiological load transfer was not achieved between prosthetic socket and distal femur for either amputee. Retention of the cortex in TKA resulted in a more physiological mechanical environment in the proximal femur than in TFA, suggesting knee disarticulation compared to femoral resection is beneficial for maintaining bone health. Insights as to the most beneficial activities to maintain bone health in the CS as well as amputees were established. Further work will assess the role of novel exercise regimes, socket design, and direct fixation for TFA, in maintaining and improving amputee bone health.

Images (Optional)

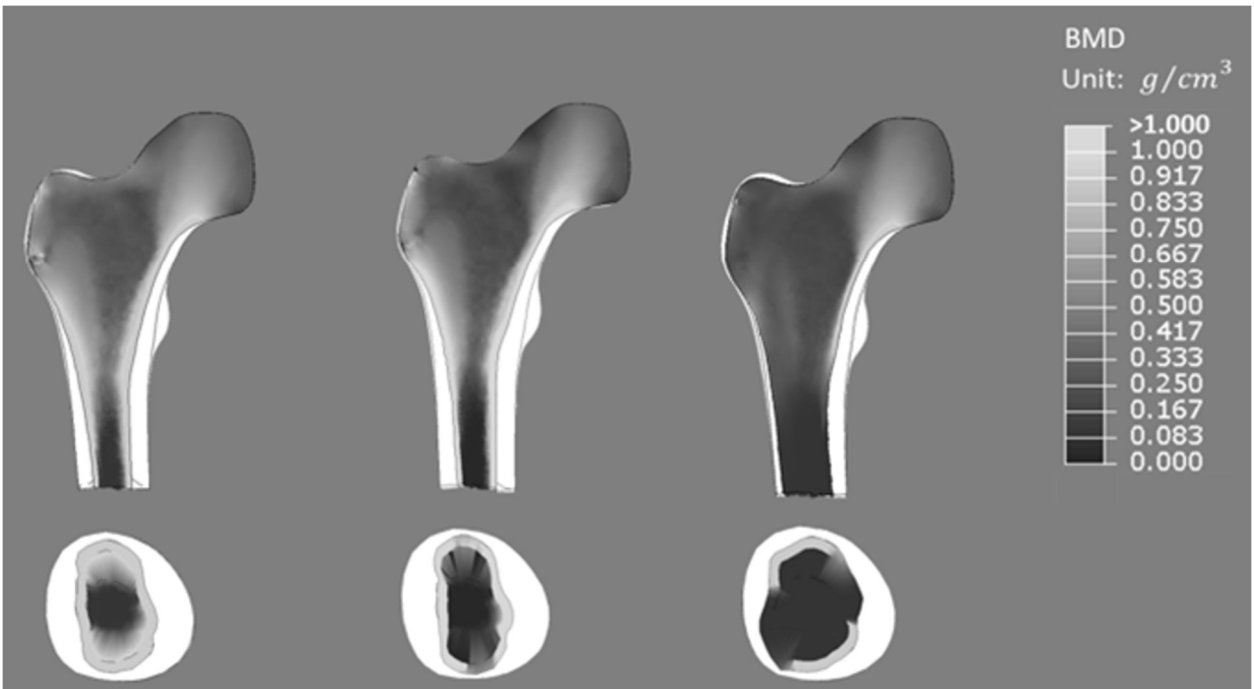


Figure 1: Predicted trabecular BMD and cortical thickness for the (left) control subject (CS), (middle) transfemoral (TFA), and (right) through-knee (TKA) amputees.

References (Optional)

[1] McMenemy et al., JBMR, 2023
[2] Phillips et al., IntBiomech, 2014

Acknowledgements (Optional)

We are thankful to the UK Office for Veterans' Affairs for providing funding through the Health Innovation Fund.

Session Category

Musculoskeletal Biomechanics: Methods, Models and Applications

OA180-04

A Bone Remodeling Model Integrating Calcium–Phosphate Homeostasis and Mechanical Loading

Prof. DDr. Gudrun Schappacher-Tilp[1], Dr. Peter Kotanko[2,3]

[1]FH JOANNEUM - University of Applied Sciences, Graz, Styria, Austria. [2]Renal Research Institute, New York City, NY, United States. [3]Icahn School of Medicine at Mount Sinai, New York City, NY, United States

Introduction

Bone adaptation is governed by the interaction of mechanical loading, cellular remodeling processes, and systemic calcium–phosphate homeostasis. Existing models typically address these components separately, limiting the ability to study their combined effects on bone behavior. The aim of the study is to develop a unified, open-source computational framework that integrates mineral balance, osteoblast–osteoclast dynamics, biochemical regulation, and mechanical stimulus into a single extensible formulation. The platform is intended as a flexible exploration environment in which users can adjust loading histories, biochemical inputs, and parameter sets to examine how systemic and local factors jointly shape bone adaptation.

Methods

The model couples population-based osteoblast and osteoclast dynamics with whole-body calcium and phosphate mass balances and a general biochemical regulatory input. Mechanical loading enters via a lumped daily strain stimulus that modulates formation and resorption rates using a lazy-zone mechanoregulation law. Bone formation/resorption fluxes are directly linked to systemic mineral concentrations, ensuring consistent mineral exchange. Apparent mechanical properties (e.g., stiffness) are derived from bone volume fraction through a standard structure–property relationship. All governing equations, parameterizations, and simulation scripts are publicly available in a dedicated GitHub repository, enabling complete reproducibility and interactive experimentation.

Results

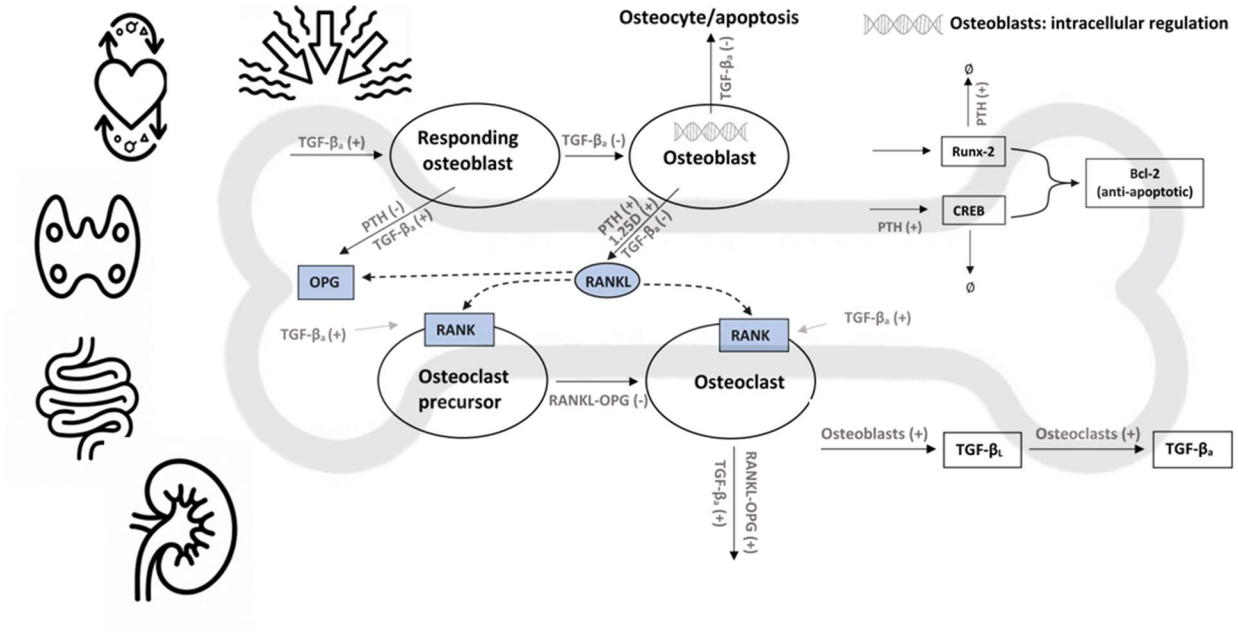
The framework is demonstrated using several qualitative validation examples. The model captures the contrasting skeletal outcomes of continuous versus intermittent PTH input: continuous exposure produces net bone loss, whereas intermittent pulses generate a net anabolic response under identical mechanical loading. The model also reproduces the expected increase in bone formation following vitamin D supplementation through its mineral-homeostasis pathways. In addition, the system naturally expresses qualitative

Wolff's-law behavior, with reduced mechanical loading leading to progressive decreases in bone volume and stiffness.

Discussion

The proposed framework consolidates mechanoregulation, cellular remodeling dynamics, and whole-body calcium–phosphate homeostasis into a single open-source computational platform. By providing a reproducible and extensible codebase, it offers a general tool for examining how mechanical loading and systemic biochemical signals interact to determine bone adaptation and mechanical competence.

Images (Optional)



Session Category

Musculoskeletal Biomechanics: Methods, Models and Applications

OA180-05

Structural Dependence of Damage Evolution and Remodeling in Trabecular Bone

Master's student Yusei Akachi[1,2], Assistant Professor Young Kwan Kim[2], Doctoral student Tsuyoshi Muto[1,2], Professor Taiji Adachi[1,2]

[1]Department of Micro Engineering, Kyoto University, Kyoto, Kyoto, Japan. [2]Institute for Life and Medical Sciences, Kyoto University, Kyoto, Kyoto, Japan

Master's student Yusei Akachi

Assistant Professor Young Kwan Kim

Doctoral student Tsuyoshi Muto

Introduction

Bone remodels its structure to adapt to the mechanical environment. When assessing bone strength, the current clinical indicator—bone mineral density—reflects only bone quantity, underscoring the need for metrics capturing bone quality. In cancellous bone, trabecular architecture and microdamage, both influencing bone quality, interact to alter mechanical behavior [1]. This study aims to develop a mathematical model that simultaneously incorporates bone adaptation and damage repair via remodeling, and to investigate how trabecular arrangements influence damage evolution.

Methods

The complex cancellous structure was modeled as a series or parallel trabecular arrangement composed of two elastic cylindrical elements (Fig. 1), each assigned a time-varying radius and a damage variable. A damage-evolution equation incorporating damage accumulation, damage repair, and bone adaptation was formulated by considering continuum damage mechanics [2] and mechanoregulation of remodeling. The initial damage values and remodeling rates were systematically perturbed. For each parameter set, trajectories of the damage variables (D_1–D_2) were analyzed in phase space to characterize failure and non-failure regions.

Results

In the series arrangement (Fig. (a)), non-failure trajectories converged toward homogenized damage states, whereas highly damaged elements exhibited transient recovery followed by rapid damage progression to failure (Fig. (b)). Increasing the remodeling rate enhanced the contribution of the repair term and expanded the non-failure region. The parallel arrangement (Fig. (c)) exhibited cyclic alternation of damage between elements (Fig. (d)), indicating a complementary damage-evolution mechanism associated with stress redistribution.

Discussion

This study demonstrates that damage-evolution mechanisms differ essentially between structural arrangements. Damage behavior is governed primarily by the local balance between accumulation and repair in each element. In the parallel arrangement, damage is additionally influenced by stress redistribution, generating complementary alternation of damage evolution. Future work will extend this framework to complex trabecular models to develop next-generation indicators of bone quality.

Images (Optional)

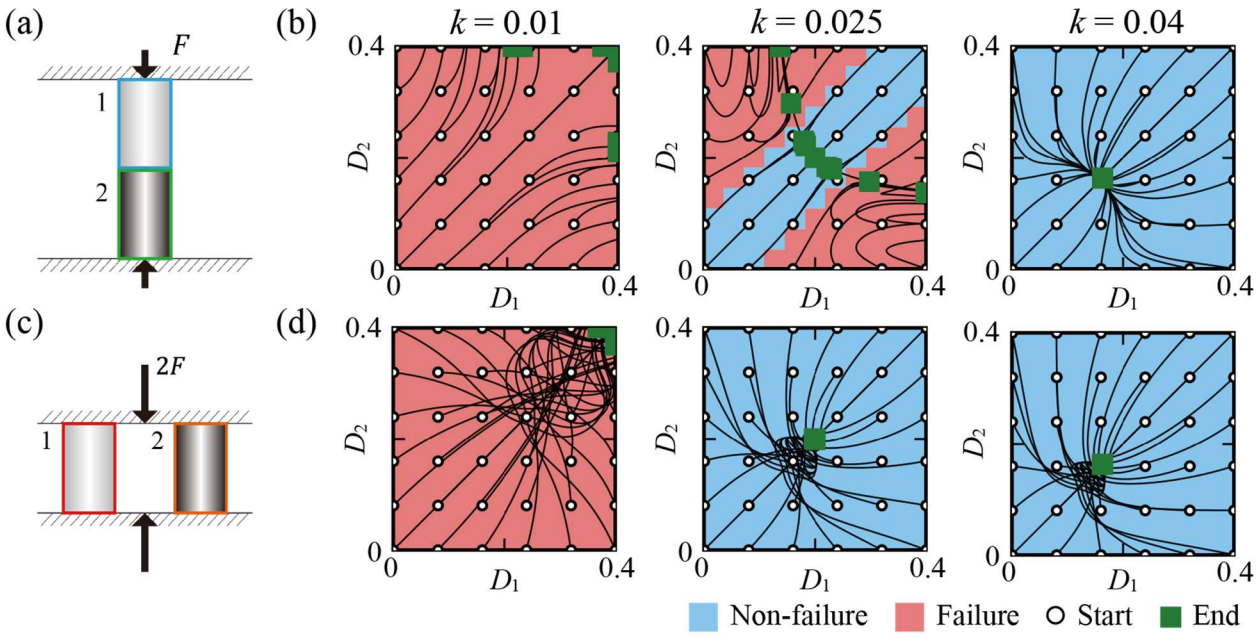


Figure 1. Damage evolution of trabecular members under load in series and parallel arrangements. (a) Series arrangement under load F. (b) Phase diagrams of (D_1,D_2) for the series model at different remodeling rates k. (c) Parallel arrangement under total load $2F$. (d) Phase diagrams of (D_1,D_2) for the parallel model at different k.

References (Optional)

1. Kreipke TC. et al., J. Biomech., 2016

2. Lemaitre J. et al., Int. Conf. Mech. Behav. Mater., 1971

Acknowledgements (Optional)

This study was supported by Grants-in-Aid for Scientific Research (KAKENHI) from Japan Society for the Promotion of Science (JSPS) (JP25H01219), Core Research for Evolutional Science and Technology (CREST) from Japan Science and Technology Agency (JST) (JPMJCR22L5)

Session Category

Musculoskeletal Biomechanics: Methods, Models and Applications

OA180-06

Improved Trabecular Microarchitecture Representation in a Whole Bone Adaptation Model: A Preliminary Study Using a Voronoi Network With Beam and Shell Elements

Mr. Muhammad Yusril Sulaiman, Dr. Andrew Phillips

Structural Biomechanics, Department of Civil and Environmental Engineering, Imperial College London, London, England, United Kingdom

Introduction

Accurate representation of trabecular bone is crucial in bone adaptation studies seeking to understand its role resisting forces during daily living and extreme activities, investigating mechanical origins of osteoporosis and osteoarthritis, and in long-term outcomes following orthopaedic surgery. A previous predictive approach modelled trabecular bone as a high-connectivity truss network (HCT) within a model of the femur, with results corroborated by trajectory identification [1] and fracture load prediction [2]. However, imaging studies suggest trabecular topology is closer to a low-connectivity Voronoi network [3], and inclusion of plates (shells) alongside rods (beams) is important [4]. In the present study, the predictive structural approach [1] is extended for a model of the femur by incorporating a Voronoi network comprised of beam and shell elements representing trabecular microarchitecture.

Methods

We implemented a rod-to-plate transformation algorithm, where beam elements forming the edges of Voronoi faces with a final diameter-to-length ratio exceeding a threshold are converted into shell elements forming the faces. A beam model (VB) is adapted, prior to the diameter-to-length ratio being used to define a beam-and-shell model (VBS) which is further adapted. Bone adaptation was driven by a target strain, adjusting either beam diameter or shell thickness. Investigated output includes predicted trabecular topology and bone mineral density (BMD).

Results

All models predicted the five main trabecular trajectories in the proximal femur (Figure 1). Plates in the VBS model were localised in the femoral head and the region where principal tensile and secondary compressive trajectories intersect, with an overall plate-to-rod ratio of 0.265:1. For BMD, the VBS model was closest to reported values [5], while other models overpredicted in the femoral head.

Discussion

The results indicate the Voronoi network and rod-to-plate algorithm provide an improved representation of trabecular bone, although the HCT model predicted clearer trabecular trajectories. Future work will focus on model calibration, mesh adaptation, and application of multiple load cases from a range of activities.

Images (Optional)

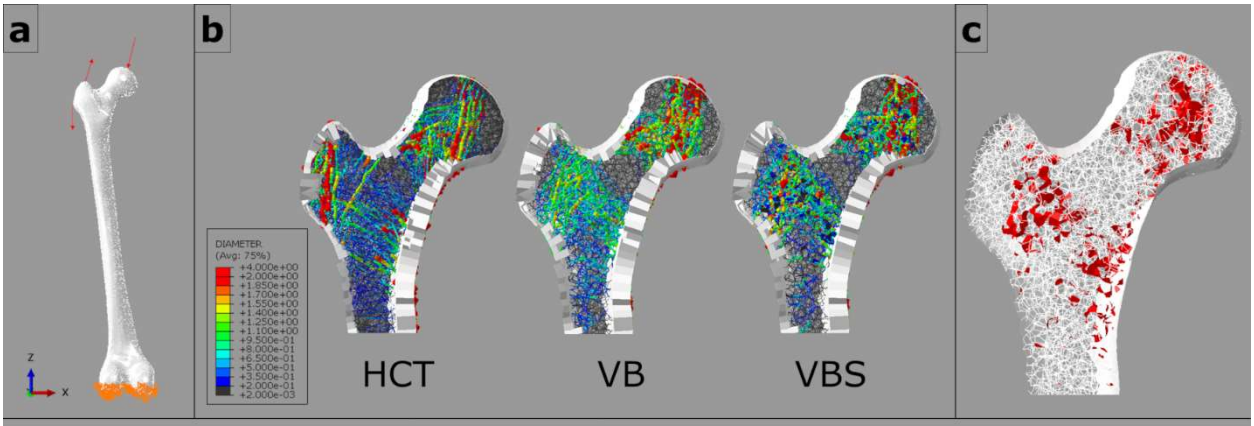


Figure 1: (a) Loading and boundary conditions for all models; (b) contour plots of beam diameter or shell thickness for a 10 mm slice through the proximal region of all models; (c) plate distribution in the VBS model.

References (Optional)

[1] Phillips et al., Int. Biomech., 2015

[2] Villette and Phillips, PloS One, 2024

[3] Reznikov et al., Acta Biomater., 2016

[4] Vanderoost et al., J. Biomech., 2011

[5] Baum et al., Osteoporosis Int., 2010

Acknowledgements (Optional)

We are thankful to The Indonesian Endowment Fund for Education (LPDP) for supporting the doctoral studies of the first author.

Session Category

Musculoskeletal Biomechanics: Methods, Models and Applications

OA181-03

A Microstructure-Based Material and Failure Model for Finite Element Simulation of Skin Lacerations Under Blunt Impact

Dipl.-Ing. Felicitas Lanzl[1], Prof. André Berger[2], M.Sc. Matthias Clermont[3], M.Sc. Jan Zimmermann[3], Prof. Steffen Peldschus[1]

[1]Biomechanics and Accident Analysis, LMU Munich, Munich, Bavaria, Germany. [2]School of Mechanical Engineering, University of Applied Sciences Stralsund, Stralsund, Mecklenburg-Western Pomerania, Germany. [3]Institute for Occupational Safety and Health of the German Social Accident Insurance (IFA), Sankt Augustin, North Rhine-Westphalia, Germany

Introduction

Despite its relevance in injury biomechanics, the onset of lacerations under blunt impact remains insufficiently understood. Experimental evidence indicates that lacerations initiate parallel to Langer's Lines (LL), reflecting the underlying collagen fibre orientation in the dermis. To capture this behaviour, this work presents a microstructure-based anisotropic material and failure model for finite element simulation of skin lacerations under blunt impact.

Methods

Skin was modelled using the anisotropic microstructure-based Gasser-Ogden-Holzapfel formulation in LS-DYNA. Failure was incorporated through a threshold in the first principal strain. Model development and validation were performed using experimental data across different loading scenarios: uniaxial compression [1], uniaxial tension parallel and perpendicular to LLs [2], and in-house drop-tower experiments. A sensitivity analysis was conducted for both the material parameters and the failure threshold. The material model was first validated for all setups, followed by a second validation of the coupled material-failure model for each setup.

Results

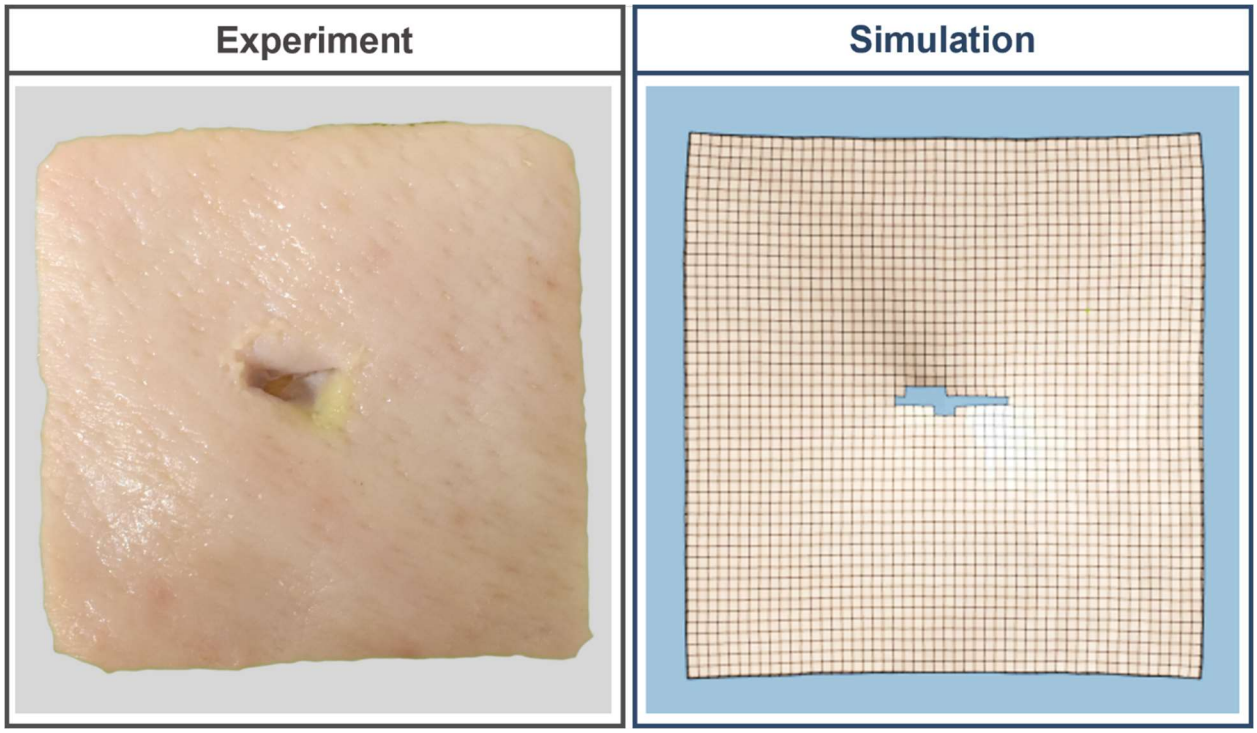
The model reproduced the experimental stress-deformation response in compression and tension, as well as the impactor acceleration in the drop-tower tests. Incorporating failure yielded consistent behaviour across the loading scenarios: no premature rupture occurred in compression, and failure characteristics in tension along the LLs agreed with the experimental values. In tension perpendicular to the LLs, failure occurred earlier than

experimentally, although the resulting failure pattern was comparable. Under blunt impact, the model predicted direction-dependent laceration formation at similar energy levels to the drop-tower tests. Thickness-dependent variability in injury onset and differences in injury shape for two impactor geometries were also qualitatively reproduced.

Discussion

The developed material-failure model captured both the onset and qualitative shape of lacerations under blunt impact (see Figure 1). These results suggest that microstructure-based modelling can contribute to a more realistic representation of injury mechanisms. Remaining discrepancies, particularly in tension perpendicular to the LLs, indicate the need to extend the approach with a damage model. As validation was limited to isolated porcine skin samples, further validation – especially against data on human tissue and tests involving intact anatomical structures – is required.

Images (Optional)



References (Optional)

[1] Shergold *et al.*, Int J Impact Eng, 2006

[2] Doerfel, Dissertation, LMU Munich, 2013

Acknowledgements (Optional)

This study was funded by the German Social Accident Insurance.

Session Category

Injury Biomechanics: N/A

OA181-04

Lung Injury Risk Curves for Behind Armor Blunt Trauma

Professor Narayan Yoganandan[1], Professor Lewis Somberg[1], Mr Jared Koser[2], Mr Alok Shah[2], Professor Brian Stemper[3], Dr. Valeta Chancey[4], Mr. Joseph McEntire[4]

[1]Medical College of Wisconsin, MIlwaukee, WI, United States. [2]Medical College of Wisconsin, MIlwaukee, wi, United States. [3]Medical College of Wisconsin, MIlwaukee, Wi, United States. [4]USAARL, Fort Rucker, AL, United States

Introduction

The Abbreviated Injury Scale (AIS) is used to score injuries i and testing standards i. While studies have been conducted to determine the biomechanics of lung injuries for behind armor blunt trauma (BABT) applications, AIS-based injury risk curves are not available. Establishing these curves is the objective of the present study.

Methods

Impact loading was applied to the lung region of live swine using a custom indenter. The design of the indenter was based on backface deformations from human cadaver tests with hard body armor [1]. The animal was positioned supine on the laboratory table to accept the indenter-induced BABT impact to the lung region. An accelerometer (model Slice Pro, Diversified Technical Systems, Inc., Seal Beach, CA) was attached to the indenter on its back face to record acceleration signals. The viscous response was calculated from the velocity and normalized deflection signals, and peak magnitude was obtained. This was termed as the viscous criterion [2]. Parametric survival analysis was used to develop risk curves [3].

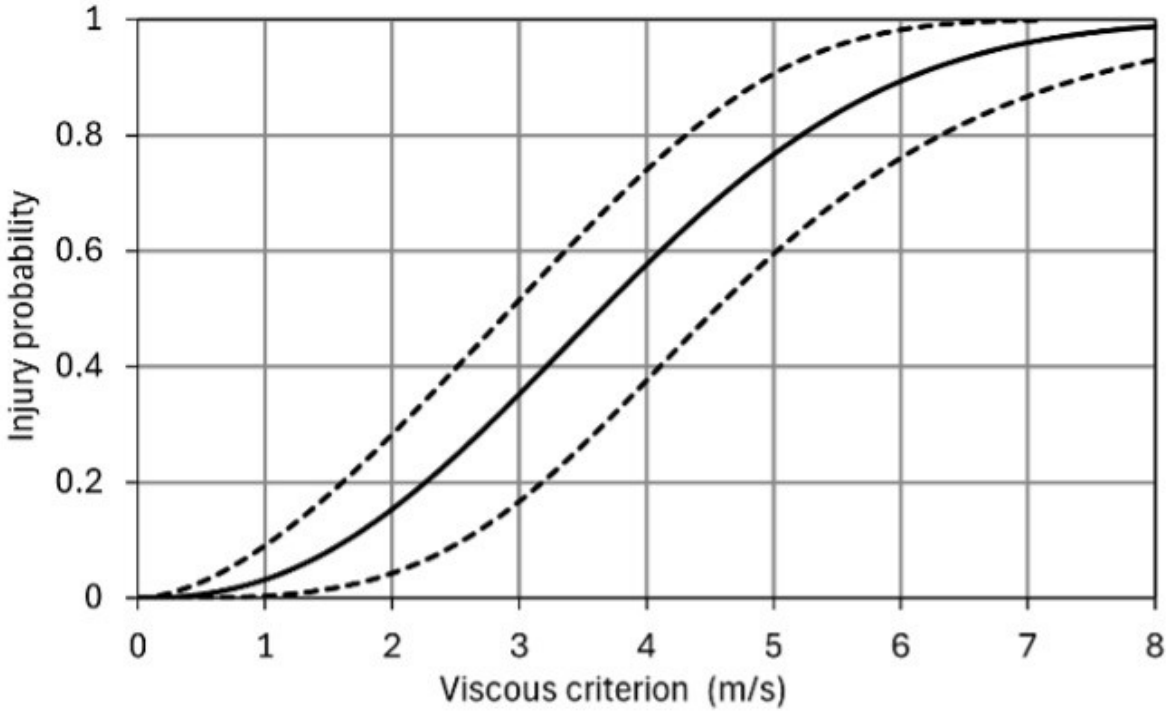
Results

There were 19 AIS2+ and 12 AIS3+ injuries, and 5 animals has no injuries. Viscous criterion at 10, 25, and 50% risks for AIS2+: 1.6, 2.5, and 3.7 m/s. For AIS3+: 2.9, 3.8, and 4.7 m/s. AIS2+ risk curves are shown (Figure 1).

Discussion

The Weibull distribution best fit the biomechanical results at AIS2+ and ASI3+ levels. Risk curves form a set of preliminary data for advancing safety from lung injuries in combat environments.

Images (Optional)



References (Optional)

1. Bass et al., *Int J Occup Saf Ergon*, 2006

2. Lau I. and Viano, D.C., *J. Biomech*, 1988

3. Yoganandan et al., *Mil Med*, 2025

Acknowledgements (Optional)

This research was supported by the U.S. Army Medical Research and Development Command contract W81XWH-21-9-0015 and the Department of Veterans Affairs Medical Research.

Session Category

Injury Biomechanics: N/A

OA181-05

Computational Model of Shock Tube Loading on the Mouse Eye

Ms. Kelly A. Clingo BS[1], Dr. JiangYue Zhang PhD[2], Dr. Thao D. Nguyen PhD[1]

[1]Johns Hopkins University, Baltimore, MD, United States. [2]Johns Hopkins University Applied Physics Laboratory, Laurel, MD, United States

Introduction

This study developed a three-dimensional finite element model of a mouse head with deformable eyes, orbital tissues, and brain, and a shock tube to simulate blast-wave interaction and characterize the elastodynamic stress and deformation fields in the ocular tissues and brain.

Methods

The 25-mm-radius cylindrical shock tube, consisting of a 25-mm-long driver and 975-mm-long driven section, had a closed boundary condition on all walls except the driven section end, which was non-reflecting. An ideal gas equation of state described the air in the shock tube, which was discretized using an Arbitrary Lagrangian-Eulerian (ALE) mesh. A deformable eye was constructed from measurements for a 3-month-old C57BL/6 mouse found in the literature and included the following structures: cornea, limbus, sclera, choroid, retina, lens, anterior and vitreous chambers, optic nerve head, and extraocular tissue, all meshed using linear brick elements and placed within a rigid skull shell model created using the 3D Digimouse Atlas [1] and meshed using quadrilateral elements (Fig. 1A-B). The ALE shock tube and Lagrangian mouse head meshes were coupled using LS-DYNA's penalty-based fluid-structure interaction.

Results

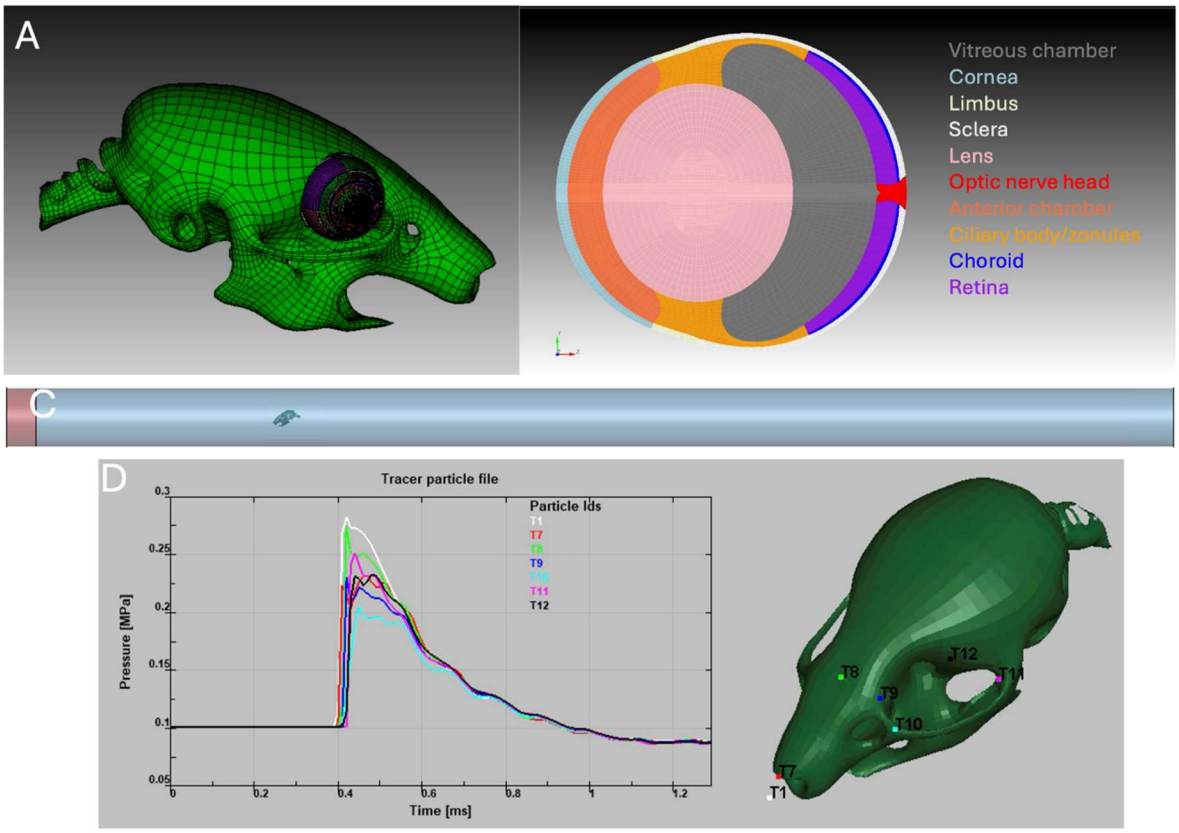
A 25-mm-long driver filled with 0.64 MPa air yielded a planar wave with 0.14 MPa peak overpressure, 0.5 ms positive and 0.8 ms negative durations, selected to simulate blast injuries produced by [2]. At this driver length, the Friedlander blast profile was achieved 215 mm from the driver, where the head was placed (Fig. 1C-D). Lengthening the driver increased the positive duration and distance where the correct blast profile was achieved. The eye model with all tissue structures was created and will be incorporated into the shock tube simulation to characterize intraocular tissue deformations and stress fields.

Discussion

The characterization of the effect of driver length on positive duration, target location, and tube length enables guidance to experimental testing and greater model efficiency. Future

work includes incorporating a deformable brain model and evaluating stresses experienced by specific tissues due to blast overpressure. This model contains more tissues and greater anatomical accuracy than previous FE models of the murine eye.

Images (Optional)



References (Optional)

[1] Belma Dogdas *et al.* , Phys Med Bio, 2007

[2] Matthew Harper *et al.* , Exp Eye Res, 2024

Acknowledgements (Optional)

Session Category

Injury Biomechanics: N/A

OA182-02

Effects of Preservation on Tensile Properties and Structure of the Meniscus

Mr. Chester Jar, Ms. Abbi Oguchi, Dr. Mohammadhamed Shahsavari PhD, Dr. Nadr Jomha PhD, Dr. Lindsey Westover PhD, Dr. Gail Thornton PhD

University of Alberta, Edmonton, Alberta, Canada

Introduction

Meniscus transplantations commonly use fresh-frozen tissue [1]. However, ice formation can disrupt meniscal microstructure [2] and the structure-function relationship is not well understood. The objective was to determine whether structural and tensile properties of menisci differ following clinical preservation methods (freezing and fresh storage). Freezing is hypothesized to negatively affect tensile properties through voids left by ice crystals which disrupt the internal collagen microstructure.

Methods

Medial and lateral menisci were obtained from porcine hindlegs the day of slaughter and allocated into four groups. Menisci were either processed immediately (Ctrl), preserved in cell culture medium (Frsh: 4 °C, 21 days), or frozen with (FrzC: -140 °C, 21 days) and without cryoprotectant (Frz: -80 °C, 21 days). Ultimate tensile strength (UTS), strain, and elastic modulus were measured from uniaxial failure tests (0.2% strain/s) in the circumferential direction (n=8). Mechanics were supplemented with scanning electron microscopy (SEM) images of the femoral surface and circumferential fibres (n=5). Linear contrasts (α=0.05) were used to compare the Ctrl with each preservation method, FrzC and Frz groups, and Frz and Frsh groups.

Results

Compared to the Ctrl, other groups had a significantly lower UTS and modulus for the lateral meniscus (p<0.002) and lower UTS for the medial meniscus (p=0.023). Compared to the FrzC group, the Frz group had a significantly lower UTS and modulus for the lateral meniscus (p<0.026) and lower modulus for the medial meniscus (p=0.010). No differences in ultimate strain were found (p>0.096). SEM revealed voids on the femoral surface of the Frz and Frsh groups, but not the Ctrl and FrzC groups. Fibre disruption and separation were also observed in the Frz and Frsh groups but were not apparent enough to be conclusive.

Discussion

Cryoprotection may benefit meniscus preservation. As transplantation is generally for younger patients, optimizing mechanical properties could improve long-term survival. Most

biomechanical studies use frozen tissue [3], leading to incorrect conclusions if treated as a reference standard. Future work should include quantitative structural analysis and viscoelastic behaviour.

Images (Optional)

Table 1: Summary of mechanical test data for medial and lateral menisci (mean ± standard deviation).

(n=8 per group)	Ctrl	FrzC	Frz	Frsh
Medial				
UTS (MPa)	47.4 ± 4.7	41.3 ± 3.2	31.1 ± 6.9	34.6 ± 5.0
Elastic Modulus (MPa)	157.7 ± 22.1	138.9 ± 19.2	111.2 ± 35.0	103.6 ± 11.5
Ultimate Strain (mm/mm)	0.52 ± 0.09	0.50 ± 0.08	0.49 ± 0.09	0.55 ± 0.05
Lateral				
UTS (MPa)	44.2 ± 7.4	34.3 ± 5.2	32.0 ± 3.9	28.3 ± 4.3
Elastic Modulus (MPa)	126.3 ± 13.1	103.3 ± 11.3	84.8 ± 12.1	80.8 ± 16.9
Ultimate Strain (mm/mm)	0.54 ± 0.08	0.56 ± 0.09	0.59 ± 0.14	0.65 ± 0.19

References (Optional)

[1] Getgood *et al.* , Am J Sports Med 2017.

[2] Gelber *et al.* , Knee Surg Traumatol Arthrosc 2008.

[3] Schwer *et al.* , Acta Biomater 2023.

Session Category

Organ and Tissue Biomechanics: N/A

OA182-03

Kneeview: An Open-Source Repository of Patient-Specific Knee Geometries and Structured Meshes

ms. Renate Janssen[1], mr. Sai Natarajan[1], mr. Francis Chemorion[1], mr. Igor Radalov[2], mr. Jordi Monfort Faure[3,4], mr. Miguel A. González Ballester[1,5], mr. Jérôme Noaílly[1]

[1]Universitat Pompeu Fabra, Barcelona, Barcelona, Spain. [2]Department of Radiology, Hospital del Mar, Barcelona, Barcelona, Spain. [3]Rheumatology service, Hospital del Mar, Barcelona, Barcelona, Spain. [4]Hospital del Mar Research Institute, Inflammation and Cartilage Research Group, Barcelona, Barcelona, Spain. [5]ICREA, Barcelona, Barcelona, Spain

Introduction

The exploitation of finite-element modeling to understand knee biomechanics is often constrained by data availability. While the osteoarthritis initiative (OAI) [1] provides invaluable imaging data, converting these images into finite-element meshes is time-consuming. Open models such as OpenKnee [2] are valuable but restricted by unstructured meshes and low subject count (n=8). To address this, we present a repository of 80 patient-specific bone geometries of the femur, tibia, patella and fibula that is being expanded with personalized structured finite-element models through mesh morphing.

Methods

The dataset included T2, fat saturated, knee MRI scans from 93 patients (38 male, 55 female) acquired at Hospital Del Mar, Barcelona. An nnUNet neural network was trained on 35 expert annotations verified by a musculoskeletal-specialized radiologist. We created a webservice, Kneeview (https://knee.view.upf.edu), to host the repository. Subjects with missing demographics were excluded and 80 subject segmentations were reported. We customize the Bayesian Coherent Point Drift (BCPD) algorithm to treat tissues distinctively: bones undergo object-specific morphing, while soft tissues are automatically interpolated.

Results

The nnUNet achieved high segmentation accuracy on a hold-out test dataset of 15 volumes with an average Dice coefficient of 0.986 ± 0.001 and IOU of 0.971 ± 0.002. The average Hausdorff Distance (HD95) was 14.464 ± 12.727. This variance was driven exclusively by distal tibial artefacts (Tibia HD95: 16.49 ± 14.22) while femur, patella and fibula gave an average HD95 of 1.46 ± 0.242. All annotated 3D models were successfully incorporated in Kneeview, in STL format. The finite-element mesh included the whole knee joint with ligaments, bones and menisci without distorted or zero-volume elements.

Discussion

A collection of 80 patient-specific models were successfully created and accessible through the new Kneeview service. The high Dice scores confirm that our automated pipeline produces geometries comparable to manual segmentation. As kneeview continues to grow, it shall address the shortage of open-source simulation-ready knee geometries. Future work will include the structured FE meshes for all subjects after these meshes have been successfully tested against finite element simulations of full gait cycles.

Images (Optional)

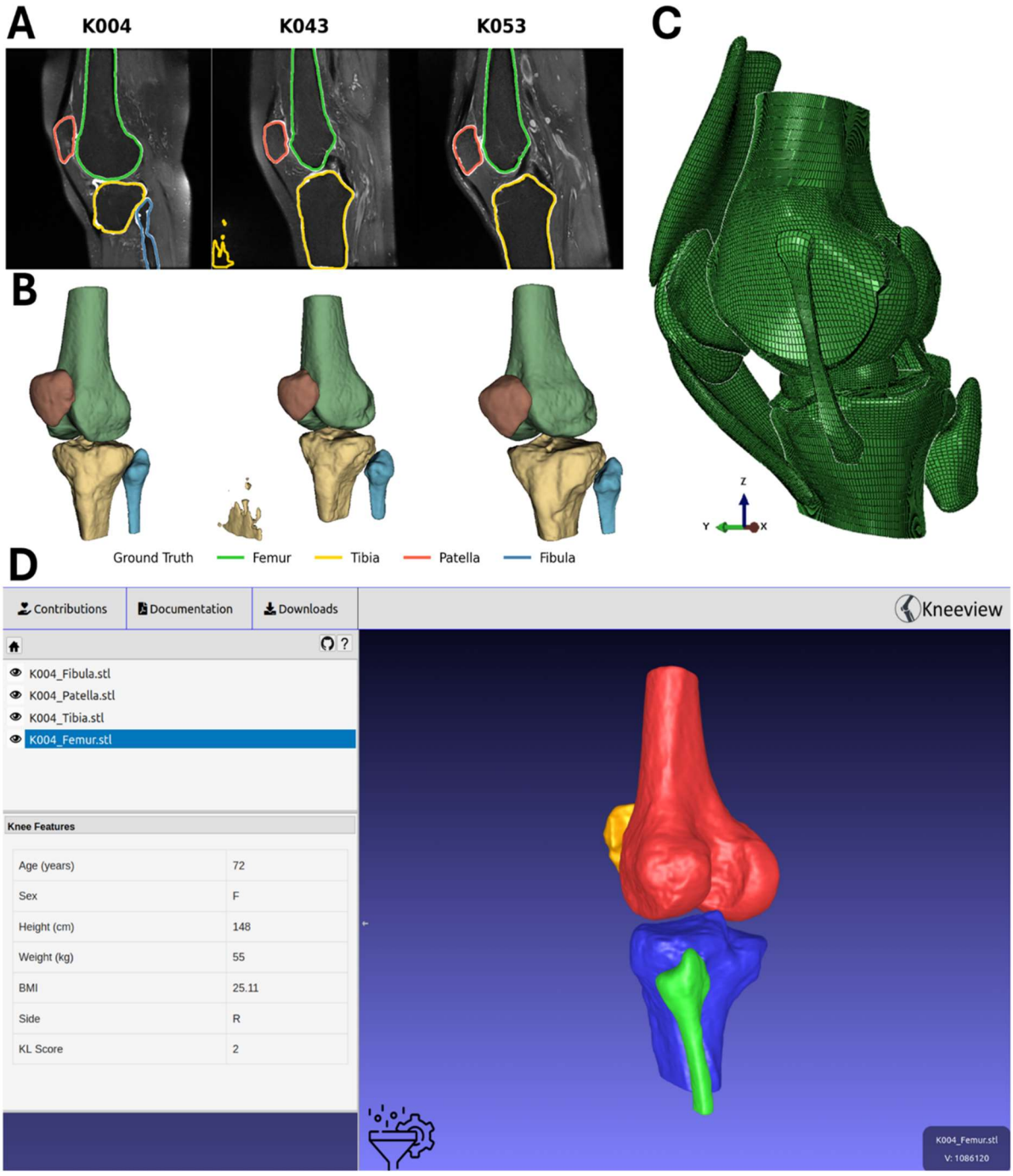


Figure 1. nnUNet segmentations and Kneeview interface. a) nnUNet segmentation versus ground truth. b) 3D visualization of segmentations. c) FEM model. d) Example of kneeview interface.

References (Optional)

[1] Lester, HSSJ, 2012

[2] Chokhandre et al., Ann Biomed Eng, 2023

Acknowledgements (Optional)

This research study was co-funded by the European Union under the Horizon Europe MSCA Joint doctoral network inSilicoHealth with grant No.101169278, by the European Research Council (ERC-2021-CoG-O-Health-101044828), and by the Spanish Ministry of Science, Innovation, and Universities project STRATO - PID2021-126469OB-C21. Views and opinions expressed are those of the author(s) only and do not necessarily reflect those of the European Union or the European Research Executive Agency (REA). Neither the European Union nor the REA can be held responsible for them.

Session Category

Organ and Tissue Biomechanics: N/A

OA182-04

Gait and Tibial Cartilage Contact Pressure in Children with Cerebral Palsy vs. Typically Developing Peers: A Musculoskeletal–Finite Element Approach

Mr Dongfei Huo[1], Professor Junyan Li[2,3], Dr Xijin Hua[1]

[1]University of Exeter, Exeter, Devon, United Kingdom. [2]Shanghai University of Medicine & Health Sciences, Shanghai, Shanghai, China. [3]Shanghai University of Medicine & Health Sciences Affiliated Zhoupu Hospital, Shanghai, Shanghai, China

Introduction

Cerebral palsy (CP) is associated with abnormal gait patterns that alter joint loading and predispose individuals to early-onset degenerative changes. This study developed an integrated musculoskeletal–finite element (MSK–FE) modeling framework to investigate differences in knee joint kinematics, knee joint reaction forces (KJRFs) and tibial cartilage stress distributions between children with CP and typically developing (TD) peers, allowing a multiscale description of knee joint loading that directly links abnormal gait patterns to cartilage-level mechanical responses.

Methods

Gait data from 13 children (5 TD, 4 hemiplegia (HP), 4 diplegia (DP)) were analyzed using OpenSim to obtain knee kinematics (Fig. 1a) and KJRFs (Fig. 1b). A scaled 3D FE knee model (Fig. 2) based on the OpenKnee(s) was implemented in FEBio with biphasic cartilage, menisci, and ligaments. Knee kinematics and KJFRs at first peak (FP), mid-stance (MS), and second peak (SP) were applied as loading inputs. Inter-limb symmetry was quantified using symmetry index (SI).

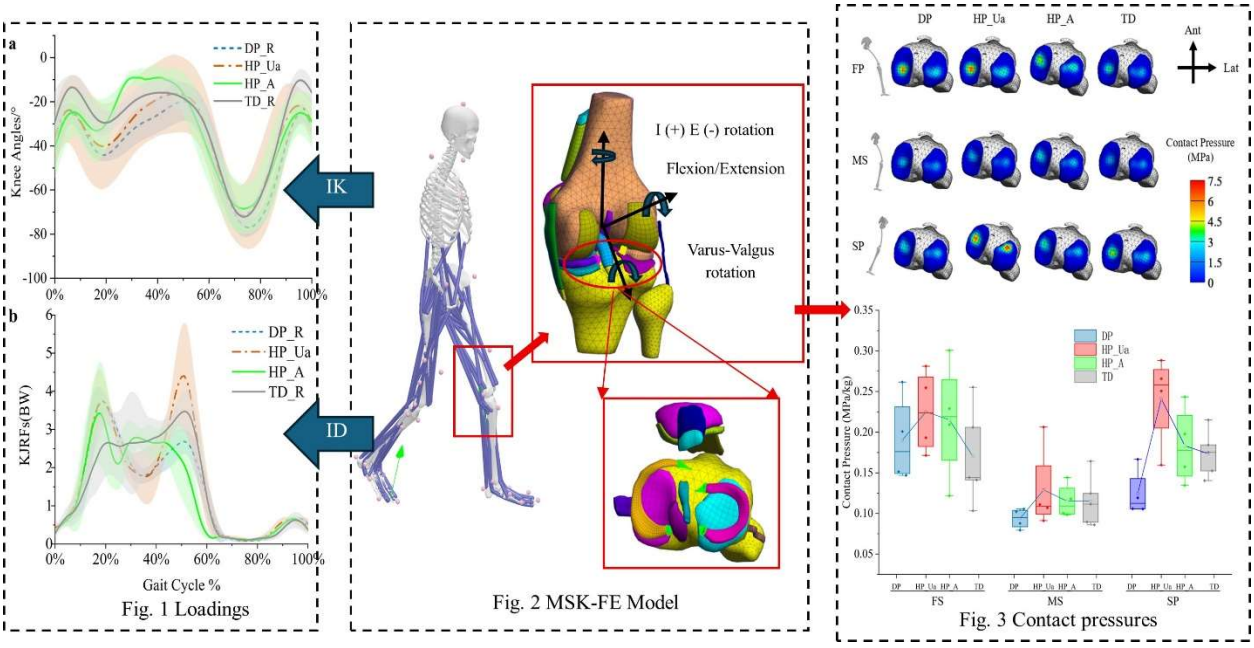
Results

All groups exhibited double-peak KJRFs and flexion–extension patterns. DP showed reduced mid-stance loading (1.8 BW vs. 2.5BW in TD) and lower late-stance peaks (2.5 BW vs. 3.5 BW in TD), despite near-symmetric SI. HP demonstrated the greatest asymmetry: the affected limb (HP_A) exhibited reduced early-stance loading and excessive flexion, while the unaffected limb (HP_Ua) generated the highest late-stance force (4.5 BW). Peak pressures in HP_A and DP occurred at FP (5.8–6.5 MPa), whereas TD and HP_Ua peaked at SP, with HP_Ua reaching the highest value (7.3 MPa). MS showed the lowest pressures across all groups (Fig. 3).

Discussion

The DP group showed globally reduced knee loading while maintaining good inter-limb symmetry. In contrast, the HP group exhibited marked biomechanical asymmetry, with reduced loading and excessive knee flexion in HP_A and compensatory overloading in HP_Ua. This abnormal asymmetric joint loading pattern has been demonstrated in existing studies to be closely associated with early-onset knee osteoarthritis. These findings reveal subtype-specific biomechanical adaptations in CP that may guide early screening and targeted rehabilitation to mitigate long-term knee OA risk. Limitation includes the small cohort size. Future work will incorporate subject-specific pediatric imaging and neuromuscular-informed modelling to improve clinical translation.

Images (Optional)



Session Category

Organ and Tissue Biomechanics: N/A

OA182-05

Synovial Molecule Diffusion into the Articular Cartilage Contributes to Knee Osteoarthritis: Patient-Specific Multiscale Simulations

Mr. Andreu Pascuet-Fontanet MSc[1], Ms. Katie Gallagher MSc[2], Dr. Stephanie E Schneider PhD[2], Dr. Laura Tio PhD[3], Dr. Jordi Monfort MD, PhD[3,4], Prof. Corey P Neu PhD[2], Prof. Jérôme Noailly PhD[1]

[1]Department of Engineering, Universitat Pompeu Fabra, Barcelona, Catalunya, Spain. [2]Paul M. Rady Department of Mechanical Engineering, University of Colorado, Boulder, Colorado, United States. [3]Hospital del Mar Research Institute, Barcelona, Catalunya, Spain. [4]Department of Rheumatology, Hospital del Mar, Barcelona, Catalunya, Spain

Introduction

Knee osteoarthritis (KOA) pathogenesis involves a complex interplay of mechanical, biochemical, and genetic factors at the cell and tissue levels, with inflammatory mediators and abnormal mechanics being critical drivers [1]. Current *in vitro* and computational models lack the biological complexity to reproduce *in vivo* observations [2, 3]. We developed a validated multiscale computational model of the knee joint to predict whether patient-specific synovial protein concentrations drive KOA.

Methods

Soluble mediators from an existing semiquantitative chondrocyte network model [4] were coupled with an articular cartilage (AC) finite-element multispecies diffusion model. Bidirectional communication was achieved using protein structure-based diffusion and degradation rates, literature-driven receptor kinetics for chondrocyte stimulation, and data-driven secretion rates. Experimentally, bovine AC explants (n=4) were stimulated (±10 ng/ml IL-1β) for 14 days, and mRNA expression was measured by qPCR. Simulations replicating experimental conditions were run (Fig. 1a). Additionally, severe KOA patient-specific simulations (n=23) were performed by fixing synovial protein concentrations for 14 days in an initially healthy AC phantom.

Results

IL-1β stimulation induced AC degradation and inflammation. The computational model's chondrocyte activity matched the mRNA expression trends, except for collagen and PIEZO (Fig. 1b). However, collagen downregulation was observed experimentally at day 7 IL-1β stimulation (not shown). Patient-specific calculations with synovial proteins diffusing into

the cartilage also shifted to KOA over the 14 simulated days, with increased network predictions of inflammatory and pro-catabolic chondrocyte activity and hypertrophy (Fig. 1c).

Discussion

The presented computational framework translates cell activity into tissue concentrations (and *vice versa*) and is validated against gene expression under IL-1β stimulation. Nevertheless, failing to increase PIEZO expression upon IL-1β stimulation suggests the necessity to incorporate mechanoreceptor biochemical regulation into the network [5]. Patient-specific results confirm the critical role of synovitis in driving KOA through diffusion [1]. Whether mechanical forces can modify this behavior is being explored, through AC mechanical loading finite-element simulations feeding the chondrocyte network.

Images (Optional)

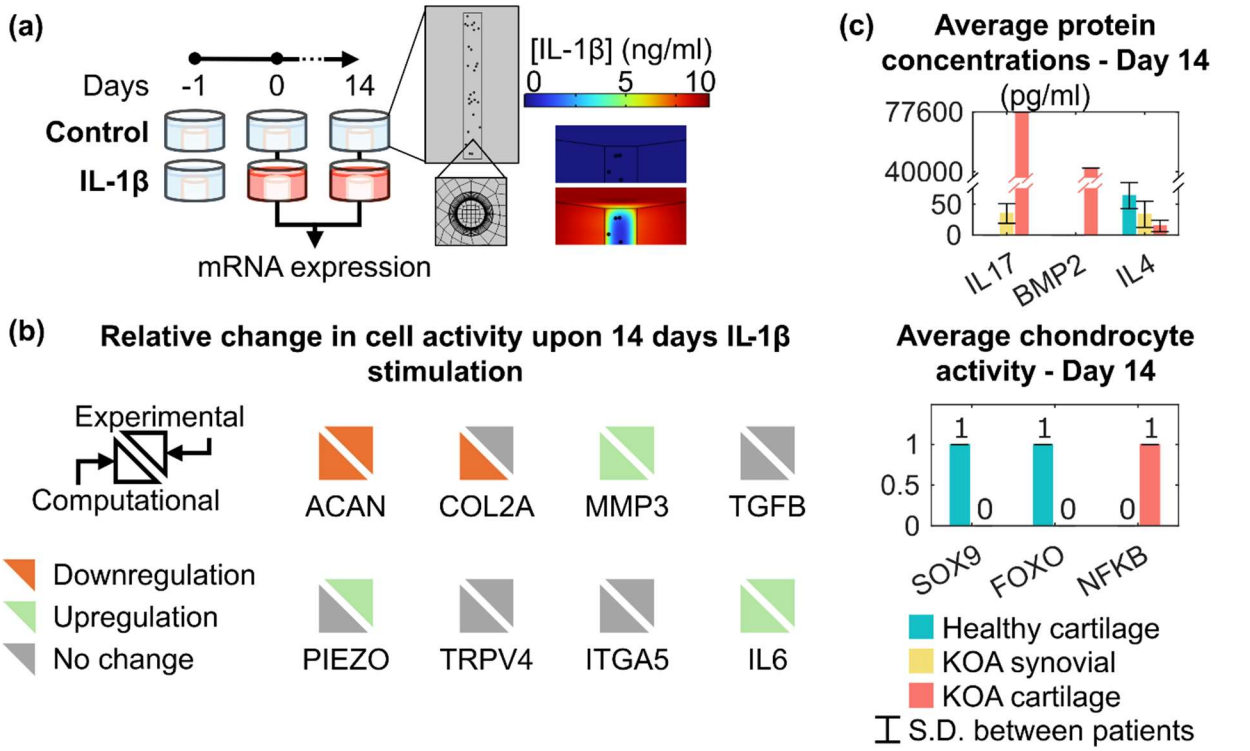


Figure 1. (a) Experimental and computational set-up. **(b)** Experimental validation results. **(c)** Patient-specific simulation results.

References (Optional)

[1] Françis Berenbaum, Osteoarthritis Cartilage, 2013

[2] Hasmik Samvelyan, *et al.*, Calcif Tissue Int, 2021

[3] Satanik Mukherjee, *et al.*, Front Bioeng Biotechnol, 2020

[4] Maria Segarra-Queralt, *et al.*, Front Bioeng Biotechnol, 2023

[5] Maria Segarra-Queralt, *et al.*, Phys Life Rev, 2024

Acknowledgements (Optional)

The author APF acknowledges the support provided by a PRE2022 Pre-Doctoral contract (Grant PRE2022-102101) funded by the Science, Innovation and Universities Spanish Ministry, associated with the project STRATO (PID2021-126469OB-C21-2). This work is part of a project that has received funding from the European Union's European Research Council Executive Agency Grant (O-Health project, Nº GA 101044828). Views and opinions expressed are however those of the author(s) only and do not necessarily reflect those of the European Union or the granting authority. Neither the European Union nor the granting authority can be held responsible for them.

Session Category

Organ and Tissue Biomechanics: N/A

OA183-02

Statistical Shape Modeling Reveals Sex-Specific Relationships Between Three-Dimensional Combinations of Tibiofemoral Bony Geometry and Knee Kinematics and ACL Force in Adult Cadaveric Knees

Presenter Lexie Bae, Submitter David Shamritsky, Submitter Isabella Gomez Hjerthen, Submitter Erin Berube, Submitter Carl Imhauser PhD, Submitter Danyal Nawabi MD, Submitter Andrew Pearle MD, Submitter Thomas Wickiewicz MD

Hospital for Special Surgery, New York, New York, United States

Introduction

Sex-specific combinations of knee bony geometric features are risk factors for sustaining non-contact anterior cruciate ligament (ACL) rupture. However, limited studies have linked these variations in bony geometry to altered knee mechanics. Moreover, previous work has typically ignored sex as a variable and focused on geometric features measured in a single anatomic plane. Our objective was to identify sex-specific relationships between variations in three-dimensional (3D) tibiofemoral geometry and knee kinematics and ACL force (ACLF) in a cadaveric model.

Methods

Thirty-seven intact adult cadaveric knees (46±16 years, 17F/20M) were tested using a 6 degree-of-freedom robotic manipulator. Tibiofemoral kinematics (internal tibial rotation (ITR), valgus angulation, anterior tibial translation (ATT)) and ACLF were measured in response to a simulated pivot shift exam (serially applied compression (100N) and valgus moment (8Nm) at 15˚ of flexion). Each specimen's 3D tibiofemoral geometry was segmented from magnetic resonance imaging. Variations in bony geometry were quantified via statistical shape modeling. Principal component analysis identified the 10 principal components (PCs) with the largest contributions to total geometric variation. For the male and female subgroups individually, these ten PCs were related to ACLF and kinematics using stepwise multiple regression (α=0.05). To quantify the relative effect of each significant PC, the change in ACLF and kinematics corresponding to a 2-standard deviation (SD) change in each PC was reported.

Results

In females, PC1 and PC6 were associated with ACLF (p=0.001 and p=0.03, respectively). A 2-SD change in PC1 and PC6 corresponded to 32 N and 17 N increases in ACLF,

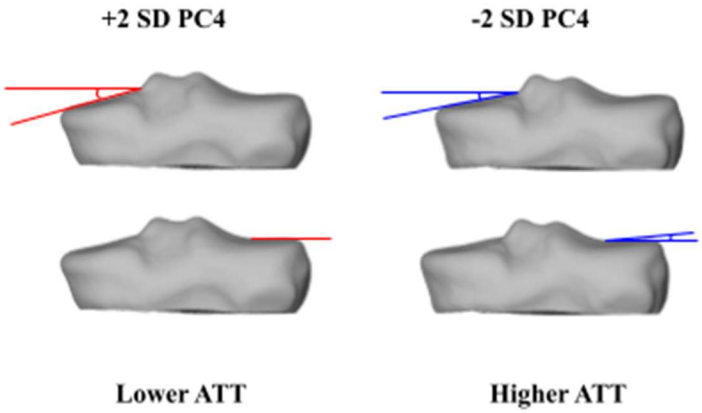
respectively. Additionally, PC2 was associated with ITR (p=0.01), and a 2-SD change corresponded to a 19.0˚ increase in ITR.

In males, PC4 was associated with both valgus angulation (p=0.02) and ATT (p=0.005). A 2-SD change in PC4 corresponded to a 1.0˚ decrease in valgus angulation and a 2.9 mm decrease in ATT.

Discussion

We identified sex-specific relationships between certain combinations of 3D bony geometric features and knee mechanics. Understanding the female-specific mechanisms that may result in increased ACL force in response to pivoting loads could lead to improved injury screening and prevention protocols.

Images (Optional)



Geometric variations captured by significant principal components were qualitatively assessed by visualizing tibiofemoral geometry spanning ±2 standard deviations for each PC. Shown is an example of bony shape variations of the tibia for PC4.
Row One: Medial-lateral tilt capturing concavity of the medial plateau
Row Two: Medial-lateral tilt capturing concavity of lateral plateau
The combination of shapes shown in the left column correspond to a lower ATT with serially applied compression and valgus loads, with the shapes in the right column correspond to higher ATT

Session Category

Musculoskeletal Biomechanics: Joints and Motion

OA183-03

Influence of Hip Joint Center Location and Walking Patterns on Hip Joint Contact Forces in Females with Acetabular Dysplasia

Ms. Ria Rao BS, Ms. Avery Kratzer BSE, Prof. Cara Lewis PT, PhD, FAPTA

Boston University, Boston, MA, United States

Introduction

Acetabular dysplasia, characterized by reduced acetabular coverage over the femur, is associated with abnormal hip joint loading and pain [1]. Joint loading in females with dysplasia is influenced by hip geometry, including a lateralized hip joint center location [2], and altered movement patterns during walking [3]. However, the individual contributions of the joint center location and movement are unclear. The purpose of this study was to assess the individual effects of typical and dysplastic hip joint center locations and movement patterns on hip loads.

Methods

Walking data were collected from five females with dysplasia (mean 24.8 years; 60.2kg; 1.66m) and five pain-free females (mean 26.4 years; 60.7kg; 1.67m) using motion capture and an instrumented treadmill (1.25 m/s). We created four model-movement combinations by pairing musculoskeletal models – representing typical or dysplastic hip joint centers – with group-specific walking patterns. The typical model used OpenSim's Gait2392, and the dysplastic model shifted its hip joint center 13.5mm laterally, 2.7mm anteriorly, and 5mm superiorly [2]. Models were then scaled, and walking data were applied. Percent differences in peak mean hip contact forces in each direction were calculated.

Results

Compared to the typical model and movement combination, the dysplastic model and movement combination had 14%, 26%, and 11% higher peak superior, medial, and resultant forces, respectively. Compared to the typical model, using the dysplastic model increased peak superior, medial, and resultant forces by 16-30% for dysplastic movement and by 20-28% for typical movement. Compared to typical movement, simulating dysplastic movement decreased the anterior, superior, and resultant forces by 12-23% for the typical model and by 8-15% for the dysplastic model **(Figure 1)**.

Discussion

Displacing the hip joint centers alone greatly increased contact forces. However, when both the model and movement were dysplastic, forces increased by a smaller percentage, suggesting that altered movement may partially offset the elevated loading associated with lateralized joint centers. This pattern may reflect an adaptive strategy used by females with dysplasia to reduce joint loading, and potentially alleviate pain, during walking.

Images (Optional)

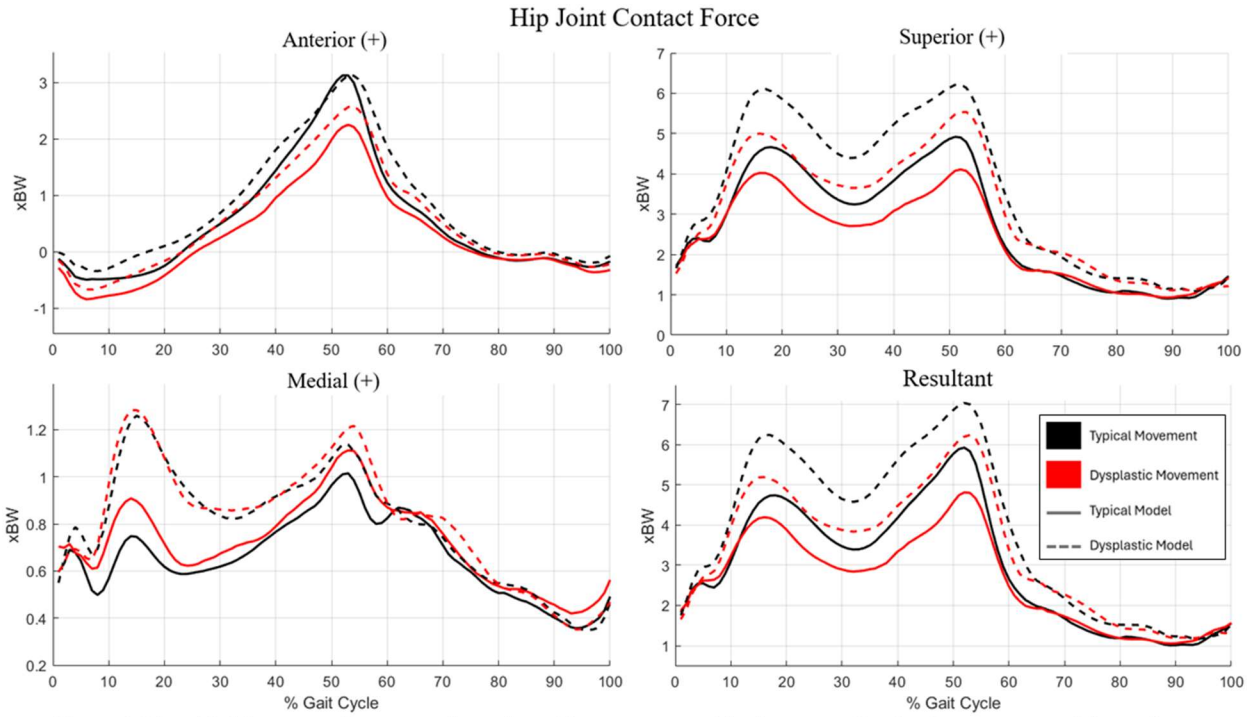


Figure 1. Mean hip joint contact force curves for each model-movement combination across directional components and the resultant. Forces are expressed in the femur-on-acetabulum reference frame.

References (Optional)

[1] Hosnijeh *et al.*, Arthritis Rheumatol, 2017; [2] Fujii, *et al.*, J Orthop Sci, 2017; [3] Rao, *et al.*, Clin Biomech, 2024

Acknowledgements (Optional)

Session Category

Musculoskeletal Biomechanics: Joints and Motion

OA183-04

Cam Femoroacetabular Impingement Surgery Partially Restores Hip Motion and Balance One Year Postoperatively

Mr. Mohamad El Fateh Shatila, Mr. Etienne Joulin, Dr. Trevor Birmingham, Dr. Ryan Degen, Dr. Geoffrey Ng

UWO, London, ON, Canada

Introduction

Cam-type femoroacetabular impingement (FAI) is characterized by an abnormal femoral head–neck junction, disrupting joint mechanics and leading to early hip osteoarthritis. While arthroscopic surgery aims to restore joint morphology, its long-term impact on joint stability and postural control remains unclear. This study examined hip and pelvic kinematics and hip kinetics during the hurdle-step and reach distances in the star excursion balance test (SEBT), comparing preoperative, 1-year postoperative, and control hips.

Methods

Eleven FAI patients (m:f = 5:6; age = 27 ± 9 years; BMI = 24 ± 4) were assessed before and 12 months postoperatively. Eleven age- and sex-matched healthy controls (m:f = 5:6; age = 25 ± 9 years; BMI = 24 ± 4) were recruited. 3D hip kinematics and kinetics were captured using a 12-camera motion capture system (60 Hz; Motion Analysis, USA) and two force plates (1200 Hz; AMTI, USA). The hurdle-step was performed by stepping over a hurdle bar (at knee height), performing a toe-tap, and returning to a double-leg stance. For the SEBT, single-leg reach distances were measured in eight directions and normalized to leg length. Data were processed in MATLAB to compute joint angles and moments. Statistical nonparametric mapping compared the three groups using 1D waveforms.

Results

During the hurdle-step stance phase, postoperative hips showed decreased internal rotation after hurdle clearance compared to controls (42-43%, $p = 0.02$). In the SEBT, preoperative hips showed reduced reach in the anteromedial (74% leg length) and medial (81% leg length) directions compared to controls (81%, $p = 0.01$; 88%, $p = 0.046$).

Discussion

The most important finding was that cam FAI patients demonstrated partial recovery in hip motion and balance 12 months after surgery. Persistent reductions in hip internal rotation, along with trends toward limited flexion and increased posterior pelvic tilt during the

hurdle-step, may reflect subtle pelvic compensation when hip mobility remains constrained. SEBT performance showed medial reach improvements but continued posterior limitations, indicating that dynamic balance deficits also remain. Overall, while surgical correction improves movement control, these residual motion and balance limitations highlight the need for rehabilitation targeting hip flexion, rotation, and coordinated lumbopelvic control to optimize recovery.

Images (Optional)

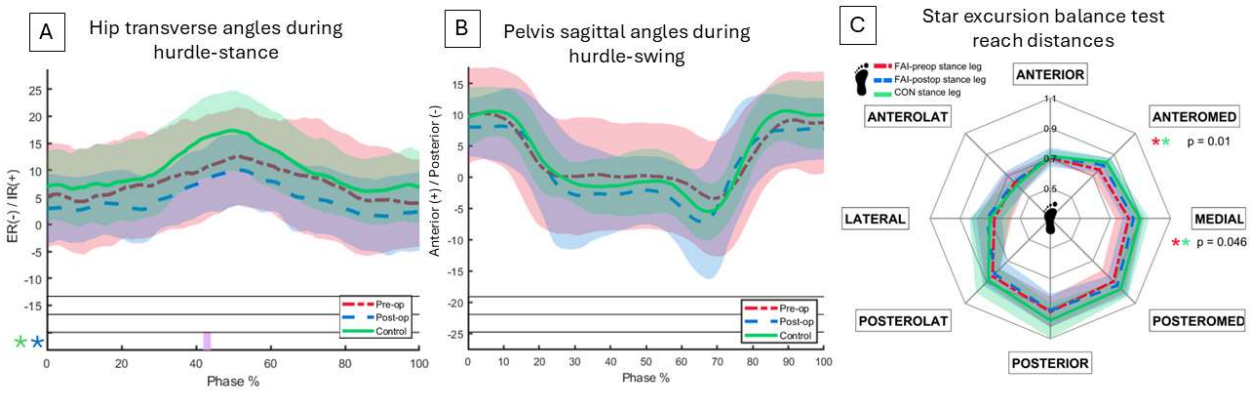


Figure. Group comparisons during the hurdle-step and star excursion balance test (SEBT).
(A) Hip rotation angles during hurdle-stance.
(B) Pelvic tilt during hurdle-swing.
(C) SEBT reach distances normalized to leg length.
Mean curves are shown with shaded standard deviations.

Session Category

Musculoskeletal Biomechanics: Joints and Motion

OA183-05

Increased Muscle Synergy and Activity in Post-Operative Cam FAI

Mr. Etienne Joulin[1], Mr. Mohamad Shatila MESc[1], Dr. Trevor Birmingham BA, BSc, MSc, PhD[1], Dr. Ryan Degen MD, MSc, FRCSC[1,2], Dr. Geoffrey Ng BScEng, MASc, PhD[1]

[1]Western University, London, Ontario, Canada. [2]London Health Sciences Centre, London, Ontario, Canada

Introduction

Cam-type femoroacetabular impingement (FAI) is characterized by an enlarged femoral head that damages the protective soft tissue in the hip joint, leading to early hip osteoarthritis. Pre-operative patients have shown altered kinematics and neuromuscular behaviour to avoid impingement, but it remains unclear if these muscle recruitment patterns recover or change after surgery. The aim was to determine the core and lower-limb muscle synergies between the pre- and post-operative hips of cam FAI patients during the hurdle step.

Methods

Seven symptomatic cam FAI patients (n = 7, m:f = 5:2, age = 8 ± 8 years, BMI = 24 ± 3) were tested before and 1-year after surgery. Surface electromyography (EMG) electrodes (Trigno, Delsys; USA) were positioned to the left and right lower-limb (gluteus maximus, biceps femoris, tensor fasciae latae, rectus femoris) and core muscles (erector spinae and rectus abdominus). Participants performed hurdle steps (Figure 1A) and maximum voluntary isometric contractions (peak EMG signals for normalization). Using a custom MATLAB script, EMG signals were aligned by movement phase (0% = start, 25% = initial step, 50% = toe tap, 75% = return step, 100% = end), filtered (20-500 Hz bandpass), and smoothed (6 Hz lowpass) using a dual-pass, zero lag fourth order Butterworth filter. The variance accounted for (VAF) was computed for each muscle and globally for all muscles to evaluate the synergies' ability to reconstruct the original signals. The pre- and post-operative VAFs and muscle activities were compared using the Wilcoxon signed-rank test ($P < 0.05$), where significant movement phases were identified using statistical non-parametric mapping.

Results

Global reconstruction improved post-operatively ($P = 0.02$) during the hurdle swing. Patients saw greater tensor fascia latae (TFL) activity post-operatively during both the swing ($P = 0.001$; Figure 1C) and stance phase ($P = 0.001$) of the hurdle step.

Discussion

The key finding was that cam FAI patients demonstrated greater muscle organization post-operatively, which may suggest improved neuromuscular coordination during impinging tasks. Greater TFL activity may help to control the swinging leg and improve hip-pelvic stability when reaching over the hurdle bar. A clearer understanding of muscle recruitment strategies could guide prehabilitation/rehabilitation protocols to improve surgical outcomes.

Images (Optional)

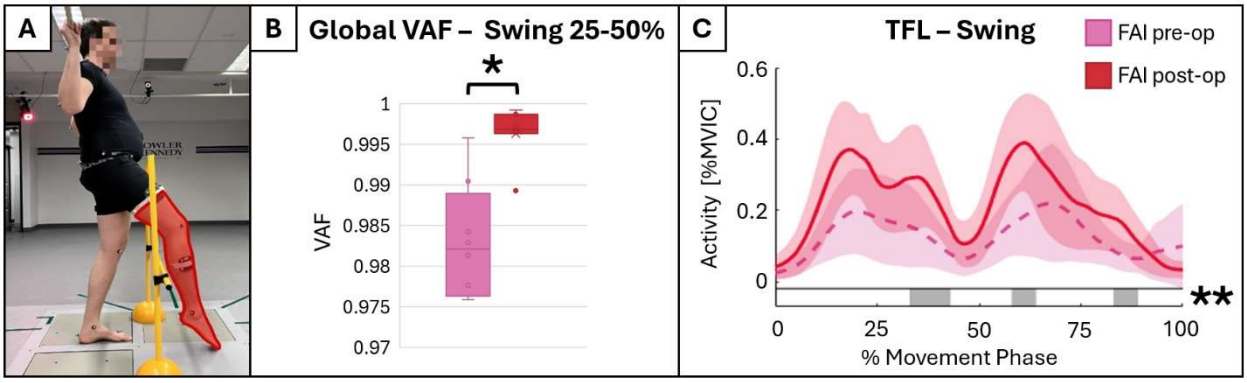


Figure 1. (A) Toe tap of the hurdle swing (50% movement phase) during the functional assessment. **(B)** Global variance accounted for (VAF) of the pre-operative and post-operative FAI patient muscle synergies during 25-50% movement phase of the hurdle swing (*$P < 0.05$). **(C)** Tensor fascia lata (TFL) activity during the hurdle swing, where significant movement phases are shaded in grey (**$P < 0.01$).

Session Category

Musculoskeletal Biomechanics: Joints and Motion

OA184-02

Influence of Ankle Exoskeleton on Human Joint Level Force Responsiveness and Control

Mr. Amro Alshareef, Mr. Shu Gong, Dr. Gregory Sawicki

Georgia Institute of Technology, Atlanta, GA, United States

Introduction

Although exoskeletons have been developed to achieve certain energetic or stability outcomes, their interaction with our sensorimotor control system is not fully understood. Recent work has investigated human force responsiveness [1]. Here we measure human force control with exoskeleton assistance in isolated joint, torque matching tasks.

Methods

Ten young adults wearing an ankle exoskeleton completed isometric torque matching tasks in a dynamometer (Fig 1A). Participants were given an auditory metronome, a visual torque target (40% of Maximum Voluntary Contraction), and visual torque feedback. Exoskeleton condition order was randomized between no assistance and Proportional Myoelectric Control (PMC). The task was to step to the target torque for 4 seconds for ten steps per trial. Conditions were repeated eight times. The step responses were quantified using controls metrics including bandwidth (BW), overshoot (OS), and steady-state error (SSE) and variability (SSV). Higher BW indicates higher responsiveness, and a lower SSE, SSV, and OS indicates greater accuracy.

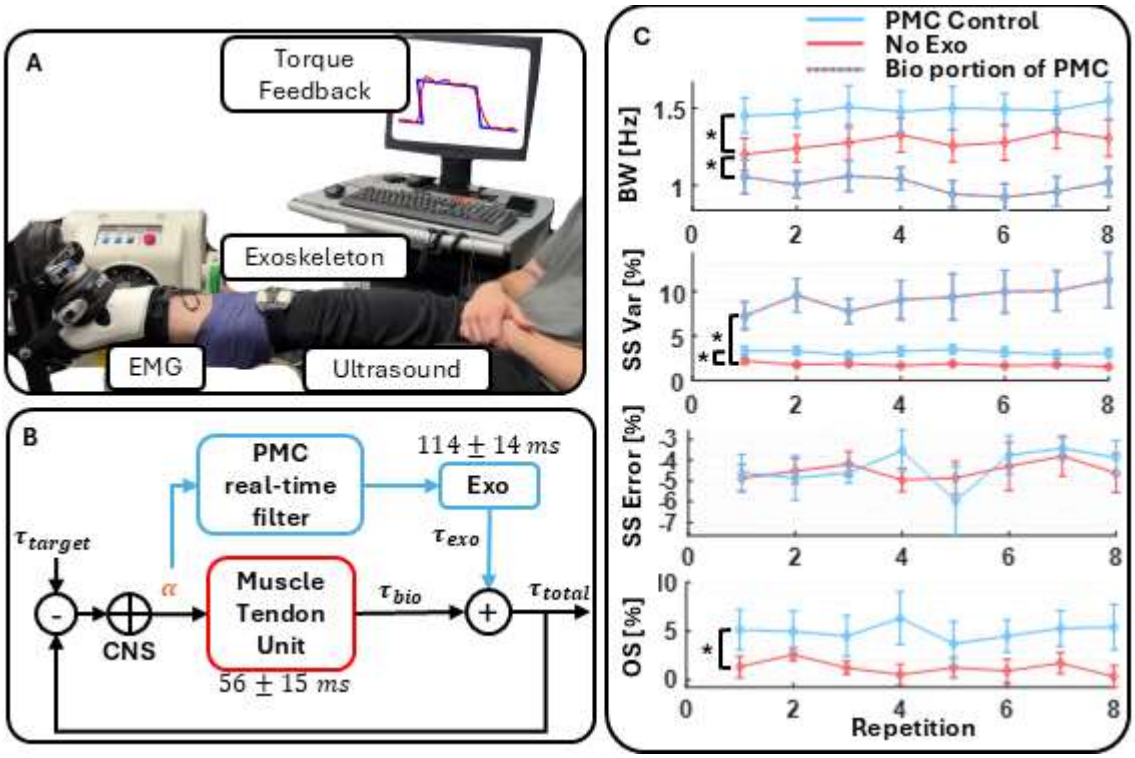
Results

The exoskeleton contributed 40 ± 17% of total torque output in the PMC condition. The exoskeleton increased total system (muscle tendon unit (MTU) + exoskeleton) BW by 0.25 ± 0.05Hz ($p<.004$) but decreased the MTU component BW by 0.23 ± 0.08Hz ($p<.007$) on average. The total system OS and SSV increased by 4.47 ± 0.8% ($p<.03$) and 1.17 ± 0.24% ($p<.005$) with the exoskeleton, respectively, whereas the MTU response SSV increased by 4.64 ± 0.59% ($p<.04$). Total system SSE was not affected by added exoskeleton assistance ($p>0.5$) (Fig 1C). The number of repetitions did not significantly affect outcomes, indicating no motor adaptation to the task or exoskeleton.

Discussion

Although the exoskeleton increased total system responsiveness, the MTU responsiveness decreased despite having a shorter onset delay than the exoskeleton (Fig 1B). This may reflect the size principle of motor unit recruitment. The exoskeleton acts fast, causing a larger overshoot, negating the need for fast motor unit recruitment after engagement of the slow motor units. The MTU's steady state variability increase seemed to largely counteract the PMC variability. Steady state error was also not affected, suggesting that an exoskeleton can increase responsiveness without compromising steady state accuracy.

Images (Optional)



References (Optional)

[1] Kudzia *et al.*, Sci Rep, 2022

Session Category

Human Motion and Performance: Balance, Posture and Control

OA184-03

Effects of Passive Heel Vibration on Gait and Postural Stability in Older Adults

Effects of Passive Heel Vibration on Gait and Postural Stability in Older Adults Hyesu Son Master's degree

Ewha Womans University, Seoul, -, Korea, Republic of

Introduction

Human balance control relies on sensory feedback, which is essential for postural stability. Age-related deterioration of sensory feedback impairs this control, increasing fall risk. Previous studies revealed suprasensory vibration can enhance postural stability by providing haptic feedback. However, the underlying sensorimotor mechanisms, including the influence of vibration on the relationship between muscle activity and postural sway, remain unclear, and prior work has mainly focused on acute vibration effects. This study investigates whether long-term vibration affects balance measured by Center of Pressure (CoP) sway metrics, and gait parameters. It further explores the relationship between ankle-foot muscle activity and CoP sway metrics.

Methods

Twenty healthy females (64.1 ± 4.1 years) completed pre- (PRE) and post- (POST) tests. They were assigned either vibration (n=10) or non-vibration shoes (n=10) for 10-week intervention. The vibration shoes contained permanent magnet modules generating 20–25 Hz vibration in response to heel strikes. PRE/POST assessments include gait and single-leg stance test to evaluate postural stability. Kinematic data were captured using 3D motion capture system. During single-leg stance test, CoP data were recorded using a force plate, and ankle–foot muscle activity was simultaneously measured via surface EMG. Data were analyzed using a two-way mixed ANOVA.

Results

Both groups showed significant improvements in single-leg stance test after 10-week intervention. However, the vibration group exhibited greater PRE to POST reductions in CoP path length (-53.9%, p=0.001), medio-lateral sway velocity (−49.6%, p=0.025), and antero-posterior sway velocity (-57.9%, < 0.001) compared to the non-vibration group. Ankle–foot muscle activity decreased by approximately 16–17% in both groups across the intervention period. Notably, the vibration group showed larger reduction in soleus activation (-13.9%,

p=0.03) than the non-vibration group. For gait analysis, step width decreased and cadence increased over time in both groups ($p < 0.05$).

Discussion

This study suggests that 10-week vibration intervention may have capacity to reduce CoP sway and ankle-foot muscle activity during challenging tasks. The vibration group had greater reductions in postural sway and muscle activation, suggesting heel vibration may enhance balance control by stabilizing postural sway. These findings imply that passive heel vibration could serve as a potential rehabilitation strategy for older adults.

Images (Optional)

	Vibration Group		Non-Vibration Group		P-value		
Variables	PRE	POST	PRE	POST	Interaction effect	Main effect for time	Main effect for group
Path length [mm]	1571.0± 417.4	725.1±2 40.0	1145.4± 385.6	809.7±2 57.7	**0.001**	**< 0.001**	0.236
Medio-lateral velocity [mm/s]	107.8± 27.9	54.3± 19.1	88.0± 29.1	59.2± 16.6	**0.025**	**< 0.001**	**0.077**
Antero-posterior velocity [mm/s]	89.4± 24.0	37.6± 11.2	54.9± 21.3	42.2± 16.4	**< 0.001**	**< 0.001**	0.451
Sway Area [mm^2]	2871.7± 1314.1	1808.8± 1246.7	6332.8± 6112.0	2685.3± 2559.5	**0.064**	**0.002**	0.161

Session Category

Human Motion and Performance: Balance, Posture and Control

OA184-04

Increasing Footwear Bending Stiffness Does Not Change Direction-Specific Functional Base of Support in Older Adults

PhD Student Paula Kramer MS[1], Associate Professor Kota Takahashi PhD[1], Professor Jason Franz PhD[2], Associate Professor Peter Fino PhD[1]

[1]University of Utah, Salt Lake City, Utah, United States. [2]University of North Carolina at Chapel Hill, Chapel Hill, North Carolina, United States

Introduction

Standing balance is achieved by maintaining the center of mass within the base of support defined by the boundaries of the feet [1]. However, less than 30% of the anatomical footprint is typically available for balance control [2]. This available area is known as the functional base of support (fBoS) and represents how far the center of pressure (CoP) can move beneath the foot [2]. The fBoS can decrease with age [3], and smaller fBoS values are associated with a higher risk of falls [4]. Because the strength of intrinsic foot muscles can influence the fBoS [5], we hypothesized that increasing footwear bending stiffness could increase the fBoS.

Methods

Twenty-one healthy older adults (mean [range] age: 64 [61–86] years, 10F/11M) provided informed consent. Participants “leaned maximally with both feet together in one of four directions (forward, backward, right, left) without stepping”. Heels, toes, and feet could lift freely to allow full ankle range of motion. Footwear stiffness was manipulated using standardized shoes (S00), S00 with a 1.6-cm carbon-fiber insole (S16), and S00 with a 3.2-cm insole (S32). Foot boundaries and CoP data were recorded from motion capture and force plates, respectively. The directional fBoS was defined as the minimum distance between the max CoP excursion point and direction-specific foot boundary landmarks (Fig.1). Linear mixed-effects models tested whether the fBoS varied by foot stiffness for each direction.

Results

There were no differences in fBoS between S00 and S16 (all p-values > 0.068) or between S00 and S32 (all p-values > 0.398) (Fig.1).

Discussion

Contrary to our hypotheses, increasing bending stiffness did not increase the fBoS. Older adults may be unable to take advantage of the increased stiffness due to weak plantarflexor muscles [5], unwilling to risk a fall by extending further than normal.

Images (Optional)

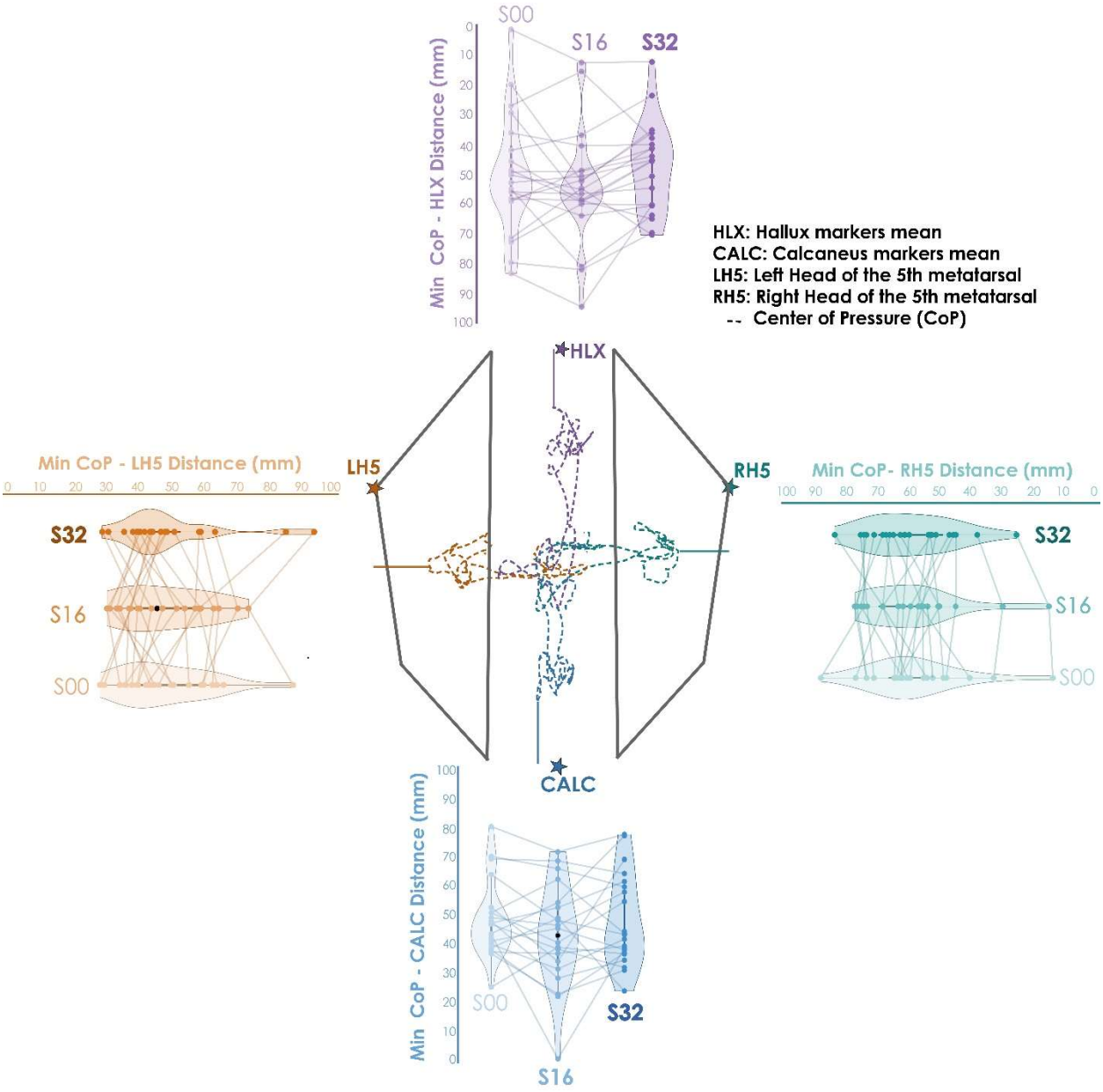


Figure 1. Comparison of minimum distance between the CoP and the corresponding foot landmark (forward=HLX, backwards=CALC, right=RH5, and left=LH5).

References (Optional)

[1] Hof et al., *J. Biomechanics, 2022*.[2] Hof & Curtze, *J. Biomechanics, 2016*. [3] King et al., *J. Gerontology ,*1994 [4] Johansson, J. et al., *Front. Aging Neuroscience, 2019* [5] Quinlan et al., *Gait & posture,2020*.

Acknowledgements (Optional)

R01AR081287, R01AR081287-03S1

Session Category

Human Motion and Performance: Balance, Posture and Control

OA184-05

Plantar Intrinsic Muscle Control of Postural Stability and Functional Sway Capacity: The Effects of Sway Direction and Footwear Bending Stiffness

Dr. Kavya Katugam-Dechene PhD[1,2], Ms. Megan Spencer BS[1,2], Dr. Kota Takahashi PhD[3], Dr. Jason Franz PhD[1,2]

[1]University of North Carolina at Chapel Hill, Chapel Hill, NC, United States. [2]North Carolina State University, Raleigh, NC, United States. [3]University of Utah, Salt Lake City, UT, United States

Introduction

Maintaining balance during standing and voluntary leaning requires precise neuromuscular coordination to regulate the body's center of pressure (CoP). While the role of large lower-limb muscles in postural control is well described, the contribution of plantar intrinsic muscles (PIMs), such as the abductor hallucis (AH) and flexor digitorum brevis (FDB), remains less well understood. Our primary objectives were to (1) characterize AH and FDB excitation in regulating postural stability and functional sway capacity, and (2) determine whether footwear bending stiffness modulates requisite PIM excitation. Here, functional sway capacity (FSC) refers to one's capacity to volitionally shift and control their body's center of gravity without losing balance.

Methods

Seventeen healthy young adults (18-35 years) completed a series of forward, rightward ("ipsilateral"), and leftward ("contralateral") functional sway capacity tasks under two footwear conditions – namely, a control shoe with/without custom 1.6-mm carbon fiber insoles (CFIs). Ultrasound-guided indwelling EMG electrodes recorded right-foot AH and FDB excitations at 1000 Hz. Each trial included a 10-s quiet standing phase followed by a maximal voluntary lean held for ~15 s. EMG were demeaned, filtered (bandpass 20-450 Hz), rectified, and normalized to a toe-flexor maximum voluntary isometric contraction (MVIC).

Results

There were no differences between footwear conditions in CoP metrics. Both muscles showed strong task-dependent modulation, with significant direction, phase, and direction × phase interaction effects (all $p<0.001$) that showed maximal excitation during the maximum forward lean. CFI effects were muscle- and direction-dependent. Specifically,

condition × direction interactions revealed that, compared to control shoes, wearing CFIs averaged 15% greater AH excitation during forward leaning (statistical trend, p=0.082) and 16% lesser FDB excitation during contralateral leaning (p=0.042).

Discussion

CFIs altered the neuromuscular strategies used to control the foot-ground interface. With CFIs, AH excitation increased during forward leaning, suggesting greater reliance on medial PIMs to modulate arch and forefoot stiffness and/or greater excitability from better sensory perception. Conversely, FDB excitation decreased during contralateral leaning, consistent with passive forefoot stiffness from CFIs partially offloading PIM demands. Direction-specific changes suggest that CFIs may redistribute how PIMs contribute to postural stability, revealing motor-equivalent solutions that preserve performance while reshaping local control.

Images (Optional)

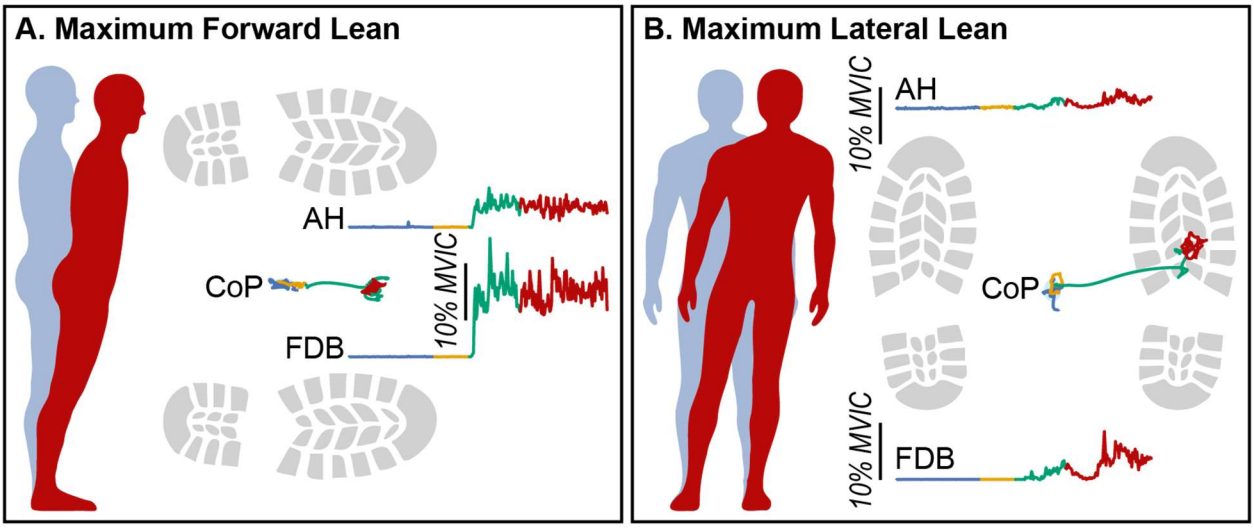


Figure 1: Illustration of functional sway capacity tasks showing **(A)** maximum forward and **(B)** maximum lateral lean. Corresponding examples of center-of-pressure (CoP) trajectories relative to feet position, and abductor hallucis (AH) and flexor digitorum brevis (FDB) excitation responses, are shown from the no CFI condition. Colors correspond to 10 seconds of still-standing (blue), countdown to lean (yellow), motion to achieve maximal lean (green), and maximal lean hold (red).

References (Optional)

Acknowledgements (Optional)

The authors would like to thank Dr. Ross Smith for his technical guidance on indwelling electromyography. Supported by NIH Grant R01AR081287.

Session Category

Human Motion and Performance: Balance, Posture and Control

OA185-01

Brain Vascular Age and Generative Modeling of Cerebrovascular Aging

Dr. Kaveh Laksari PhD[1], Dr. Aditi Deshpande PhD[1], Mr. Amin Ebrahimzadeh[1], Dr. Pouya Tahsili-Fahadan MD, MBA, FAHA[2,3], Dr. Greg Ver-Steeg PhD[1], Dr. Amit Roy-Chowdhury PhD[1]

[1]University of California, Riverside, CA, United States. [2]Inova Fairfax Medical Campus, Falls Church, VA, United States. [3]University of Virginia, Falls Church, VA, United States

Dr. Kaveh Laksari

Introduction

Cerebrovascular morphology evolves across the healthy adult lifespan, yet deviations from normative aging patterns are among the earliest indicators of neurovascular disease and cognitive decline. Existing brain-age models focus on tissue atrophy, overlooking the vasculature, despite evidence that vascular alterations often precede neuronal & tissue loss. We introduce a framework for quantifying cerebrovascular aging using (1) a Brain Vascular Age Index (BVAI) using vascular morphology and topology, and (2) a generative AI model to forecast individualized vascular networks across age. This provides a mechanistically interpretable approach to vascular aging and a foundation for vascular biomarkers of cognitive impairment.

Methods

Time-of-flight MRA scans from 915 healthy adults (ages 20–90) were segmented using our validated CNN-based cerebrovascular segmentation algorithm. The resulting 3D vascular trees were skeletonized to extract morphological and graph-network features. An Elastic Net regression model was trained to predict chronological age and derive BVAI as the difference between predicted biological and chronological age (Fig. 1). Subsequently, to model longitudinal vascular aging, we developed a diffusion-based generative model that maps subject-specific vascular networks into a latent template space (Fig. 1) conditioned on age groups. This enables counterfactual inference—i.e., generating how an individual's vasculature would look at older ages—without longitudinal data. Anatomical constraints learned from baseline modeling are incorporated for biological plausibility.

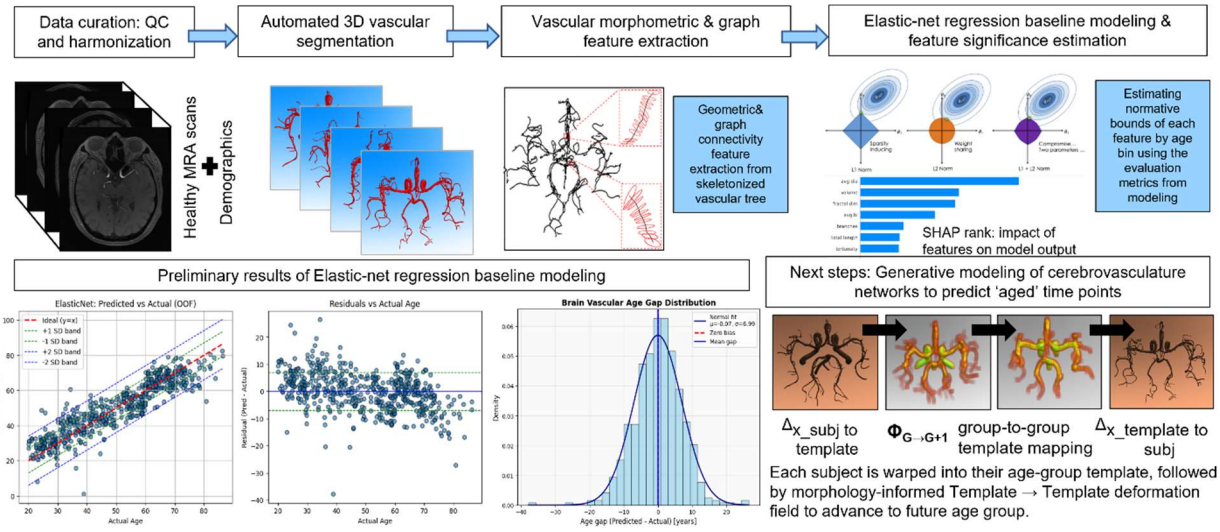
Results

The regression model achieved prediction performance of (MAE ≈ 6–8 years; R^2 ≈ 0.70–0.78) and identified tortuosity, diameter, branch count, and fractal dimension as the most predictive aging markers. BVAI successfully distinguished early vascular deviations in out-of-distribution subjects, showing sensitivity to vascular patterns associated with disease. The generative diffusion model produces topologically coherent age-progressed 3D vascular networks (given specific age values), capturing age-related increases in tortuosity and branch loss. Phantom experiments with controlled morphology will be implemented to confirm alignment of generated trajectories with empirical aging trends.

Discussion

This work introduces the first regression-generative framework for cerebrovascular aging. BVAI provides a quantitative, interpretable metric of aging, while the generative model produces subject-specific aging trajectories revealing vascular evolution over time. Together, these tools establish a foundation for vascular biomarkers of cognitive decline, neurodegeneration, and cerebrovascular disease.

Images (Optional)



Session Category

Imaging and Biomedical Devices: Imaging Fundamentals and Applied Research

OA185-02

Deep Learning Super-Resolution for Preclinical Bone Imaging: Reconstructing Trabecular and Cortical Microarchitecture from MicroCT Imaging

Mr. Amine Lagzouli[1,2], Prof. Alice Othmani[3], Dr. Kim Harrison[4], Prof. David Cooper[4], Prof. Peter Pivonka[1], Prof. Vittorio Sansalone[2]

[1]School of Mechanical, Medical, and Process Eng., Queensland University of Technology, Brisbane, Queensland, Australia. [2]Univ Paris Est Creteil, Univ Gustave Eiffel, CNRS, UMR 8208, MSME, Creteil, Ile de France, France. [3]Université Paris-Est Créteil (UPEC), LISSI, Vitry-sur-Seine, Ile de France, France. [4]Department of Anatomy, Physiology, and Pharmacology, University of Saskatchewan, Saskatoon, Saskatchewan, Canada

Introduction

High-resolution micro-computed tomography (microCT) and synchrotron radiation-based microCT (Sr-microCT) are widely used in preclinical bone research to characterize bone microarchitecture and assess remodeling and therapeutic responses. Despite their excellent spatial resolution, there are several limitations in their use, especially in *in-vivo* settings, including radiation exposure, imaging artifacts, scan-time limitations, and high storage requirements. These challenges are particularly relevant in preclinical animal studies, where accurate characterization of fine bone microstructure is essential.

Super-resolution (SR) aims to recover anatomical details that are unresolved in lower-resolution acquisitions. Deep-learning SR approaches have gained traction in biomedical imaging for both clinical and preclinical applications. In this work, we evaluate several state-of-the-art SR architectures and propose an improved variant of SwinIR [1] that incorporates spectral channel attention within the encoder to amplify frequency components critical for preserving minute bone microarchitectural features.

Methods

To evaluate SR performance for recovering bone microstructure, we trained several benchmark deep-learning SR models, along with our proposed spectral-attention model, on two high-resolution *ex-vivo* microCT datasets. The mouse dataset comprised 10 proximal tibiae acquired at 5 µm voxel size targeting trabecular bone. The rabbit dataset comprised 5 distal tibiae acquired at 7 µm voxel size targeting cortical porosity. Low-resolution (LR) inputs were simulated by downsampling the high-resolution scans and attenuating high-frequency components in the Fourier domain. Three SR scales (×5, ×6, ×7; 25-35 µm) were generated for the mouse dataset and four (×2, ×4, ×6, ×8; 14-56 µm) for the rabbit dataset.

Results

Deep-learning models demonstrated strong SR reconstruction performance, with our proposed model outperforming all state-of-the-art baselines. It successfully recovered fine trabecular structures in mice (Fig. 1a) and cortical pores in rabbits (Fig. 1b), closely matching ground truth (GT). Regional analyses showed consistent performance across distinct anatomical zones.

Discussion

The proposed model showed robust SR performance across anatomically distinct *ex-vivo* datasets, effectively reconstructing fine microarchitectural features even at coarse input resolutions. Future work will apply the model to real low-resolution *in-vivo* microCT and match it to corresponding high-resolution *ex-vivo* scans, enabling reduced radiation exposure and improved recovery of microstructural features typically lost to imaging artifacts.

Images (Optional)

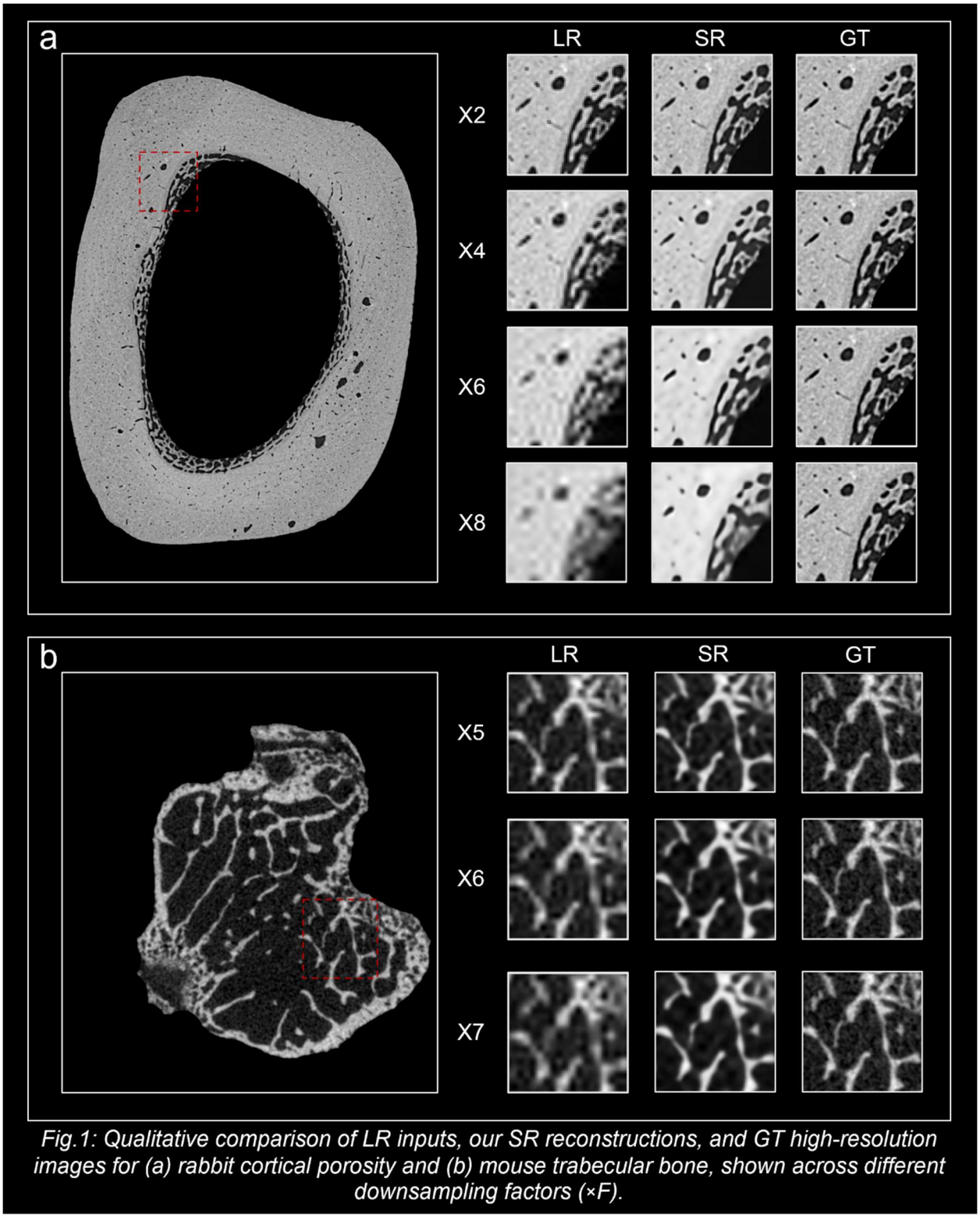


Fig.1: Qualitative comparison of LR inputs, our SR reconstructions, and GT high-resolution images for (a) rabbit cortical porosity and (b) mouse trabecular bone, shown across different downsampling factors (×F).

References (Optional)

[1] J. Liang et al., IEEE/CVF, 2021

Session Category

Imaging and Biomedical Devices: Imaging Fundamentals and Applied Research

OA185-03

AI-Based Automatic Tool for the Recognition of Coronary Anomalies

Mr Marco Magliocco[1], Dr Alessandro Caimi[2], Mr Antonio Rosato[3], Dr Chiara Catalano[4], Ms Serena Anglese[3], Prof Ferdinando Auricchio[2], Prof Salvatore Pasta[4], MD Mauro Lo Rito[3], Prof Michele Conti[2,3]

[1]University of Genova, Genova, Liguria, Italy. [2]University of Pavia, Pavia, Lombardy, Italy. [3]IRCCS Policlinico San Donato, San Donato Milanese, Lombardy, Italy. [4]University of Palermo, Palermo, Sicily, Italy

Introduction

Anomalous aortic origin of the coronary arteries (AAOCA) is a rare congenital disease in which one of the coronary arteries may originate from the aorta but in an abnormal position. Often the diagnosis of AAOCA is incidental during examinations for other medical reasons, although in a significant proportion of the cases, the first manifestation of the disease, especially in young athletes, may be a sudden cardiac death event or a myocardial infarction [1]. So far, the recognition and the classification of the coronary anomaly is deeply operator-dependent and there is no a clinical standard practice. Hence, the aim of the current work is to develop an automatic AI-based pipeline able to standardize and optimize the diagnosis and screening process of the AAOCA pathologies.

Methods

A total of 274 patients underwent contrast-enhanced coronary CT angiography at two clinical centers. Expert operators manually segmented the resulting 3D images, which were then used to train a 2.5D neural network [2] for multi-class segmentation of the ascending aorta, the left ventricle, the pulmonary artery and the coronary arteries. To ensure robust and unbiased performance evaluation, a 5-fold cross-validation procedure was implemented. Leveraging the automated segmentations, a geometry based algorithm was developed to classify coronary anomalies. The pipeline consists in: i) analysis of the different components connected to the aorta; ii) recognition of left or right coronary artery and its originary sinus; iii) identification of the anomalous coronary course; iv) classification of the anomalous type.

Results

Segmentation performance is summarized in Table 1 and reported in terms of Dice Score, expressed as the median and interquartile range (IQR) of the results obtained across the five test sets of the cross-validation. While the performances of the geometrical-based classification algorithm are reported in Table 2

Discussion

The AI-based developed pipeline can reconstruct all the anatomy for a proper classification of the pathology. Moreover, the fully automatic geometrical algorithms proved to be able to classify properly the different kind of pathology, making the proposed tools very useful in clinical practice.

Images (Optional)

Table 1

Class	Dice Score Median (IQR)
Aorta	0.95 (0.1)
Lef Ventricle	0.96 (0.04)
Pulmonary Artery	0.61 (0.24)
Coronary Arteries	0.74 (0.12)

Table 2

	Accuracy	Precision	Recall	F1-score
Control vs. Pathology	0.99	0.98	1	0.99
Right vs. Left Coronary Artery	0.99	0.97	1	0.98
Classification	0.97	0.97	0.93	0.94

References (Optional)

1. Taylor AJ, et al. Am Heart J,1997

2. Fantazzini A, et al., CVET, 2020

Acknowledgements (Optional)

The project is funded under the PNRR by the European Union – Next Generation EU – PNRR M6C2, Investment 2.1: Enhancement and Strengthening of Biomedical Research within the National Health Service (SSN).

Session Category

Imaging and Biomedical Devices: Imaging Fundamentals and Applied Research

OA185-04

Hierarchical Deep Reinforcement Learning Coordinates I*n Silico* Agent-Based Cellular Functions of Bone Remodeling from Time-Lapsed I*n Vivo* Imaging

Ms. Sorour Khadivi, Mr. Jack J. Kendall, Dr. Gisela A. Kuhn, Dr. Friederike A. Schulte, Prof. Dr. Ralph Müller

Institute for Biomechanics, ETH Zurich, Zurich, Zurich, Switzerland

Introduction

A self-adaptive framework that enables *in silico* models to learn temporal behavior patterns and simultaneously adapt to subject-specific bone remodeling dynamics as assessed from time-lapsed *in vivo* imaging would greatly enhance computational modeling. Our previous micro-multiphysics agent-based (micro-MPA) bone remodeling model [1] successfully encoded biological rules for individual cell behaviors. However, it lacked a mechanism to coordinate the frequency and sequence of concurrent biological processes to simulate subject-specific remodeling. We employ a Hierarchical Deep Reinforcement Learning (HDRL) framework to precondition and optimize the coordination of cellular processes to enhance *in silico* remodeling rates.

Methods

The HDRL framework takes decisions at two levels of hierarchy; a top-level q-value function (meta-controller) identifies the remodeling phase, and learns a policy that maximizes expected extrinsic reward, while a lower-level network (controller) activates the optimal cellular functions to achieve the chosen phase goal [2]. This process iteratively trains the model to reach the target state. Extrinsic rewards are defined based on target bone formation rate (BFR), bone resorption rate (BRR), bone volume fraction (BV/TV), and spatial alignment of *in vivo* remodeling patterns, measured from time-lapsed *in vivo* micro-computed tomography (micro-CT) of the sixth caudal vertebrae of four ovariectomized (OVX) C57BL/6 mice [3]. *In vivo* measurements started at week 15 to simulate five weeks of bone loss (week 20).

Results

The HDRL-enhanced micro-MPA model reduced iterations by 66% to reach target bone structures (Figure 1a) through a more efficient preconditioning and dynamic switching between optimal cellular functions. As shown in Figure 1b, the HDRL-enhanced model improved BFR (by 65%) and BRR (by 21%) compared to the non-HDRL-enhanced *in silico* model. Additionally, inter-subject variation increased, indicating successful adaptation to subject-specific remodeling.

Discussion

This self-adaptive HDRL framework enabled the micro-MPA model to adapt to subject-specific remodeling dynamics while adhering to underlying biological rules. This adaptability paves the way for personalized treatment and drug development, allowing the *in silico* model to learn patient-specific remodeling responses and optimize therapeutic strategies, thereby improving *in vivo* imaging capabilities.

Images (Optional)

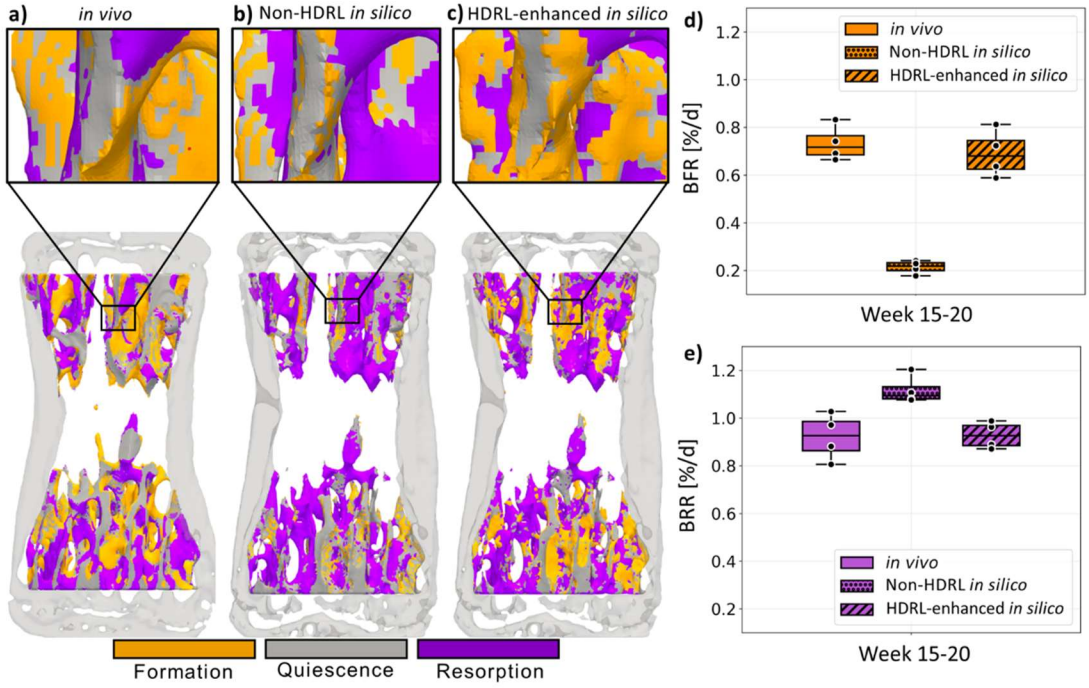


Figure 1: Visualizations of formation, quiescence, and resorption regions at week 15–20 of **(a)** the *in vivo* micro-CT, **(b)** the non-HDRL-enhanced *in silico* micro-MPA model, and **(c)** the HDRL-enhanced *in silico* micro-MPA model. The HDRL-enhanced *in silico* model shows improved alignment with *in vivo* **(d)** BFR and **(e)** BRR.

References (Optional)

[1] Boaretti D. et al., Frontiers in Bioengineering and Biotechnology, 2023.

[2] Kulkarni TD et al., CoRR, 2016.

[3] Schulte FA et al., bioRxiv, 2024.

Session Category

Imaging and Biomedical Devices: Imaging Fundamentals and Applied Research

OA186-01

The Influence of Cashier Workstation Arrangement on Muscular Demands in the Upper Extremity

Dr Clark Dickerson, Ms. Oliva Szczepanek, Mr. Aidan Armitage, Ms. Alexandra Blandford, Mr. Alireza Karimi, Dr. Alan Cudlip

University of Waterloo, Waterloo, ON, Canada

Introduction

Occupational disease is common in environments that feature repetitive work. Grocery cashiers are susceptible as they often experience repetitive strain injuries due to the awkward postures and poor workstation design encountered in their work.[2] These overuse injuries are often affect the upper extremities, where up to 51% are shoulder disorders.[3] While previous research indicated high workstation height, bagging plastic or reusable bags and high workstation intensity contribute to shoulder disorders,[1] little research has been conducted on upper extremity loading related to input device use in cashiers. The purpose of this study was to 1) identify differences in postures, muscle activation strategies and perceived effort and discomfort across emulative workstation setups and 2) quantify kinematic and activation changes between planar and oblique keyboard orientations.

Methods

40 healthy, right handed university-aged individuals (20M, 20F) completed scanning and keypad entry tasks in two workstation orientations (keypad in front of the participant, keypad to the right of the participant), two keypad heights (low, high) and four keypad angles (5/15/75/85° from horizontal). Activity of 16 upper extremity muscles was collected through surface electromyography (sEMG) electrodes, sampled at 1500 Hz. Perceived exertion was also recorded for each task condition. An analysis of variance (ANOVA) evaluated the influence of task conditions on muscle activation and perceived discomfort and exertion scores.

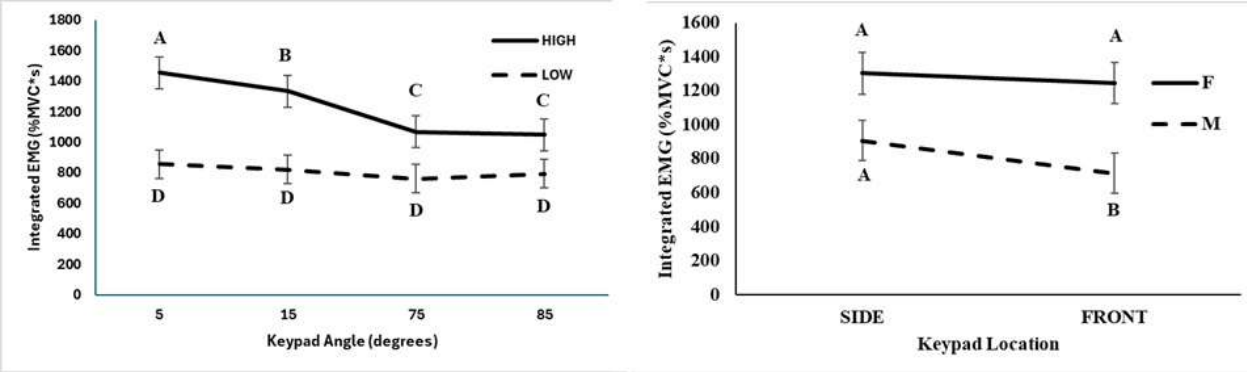
Results

Keypad height and location interacted to influence upper trapezius activity (Figure), and females generally had higher middle deltoid requirements, particularly for higher keypads (Figure). Higher discomfort was generally reported (2-3x) for the shoulder than other body regions, and for right keypad orientations (1.5-2x).

Discussion

The placement of keypads within the cashier workstation had profound influences on muscular demands, and these demands were influenced by interactions with sex for several muscles. Generally, high keypad placements combined with more horizontal orientations increased muscular demands, and females experienced overall more muscular demands for the same task. Adjustability should be considered in workstation design, particularly for those occupational environments with many female workers.

Images (Optional)



References (Optional)

[1] Maciukiewicz et al., *International Journal of Industrial Ergonomics*, 2017. [2] Niedhammer et al.,. *International Journal of Occupational and Environmental Health*, 1998. [3] Silva et al, *Safety*, 2024.

Session Category

Rehabilitation Biomechanics and Human Factors: Occupational Biomechanics

OA186-02

Effects of Hand Dominance, Sex, and Fatigue on Shoulder Muscle Synergies During a Repetitive Overhead Task: A Preliminary Study

Dr. Yiyang Chen[1,2], Dr. Erika Renda[1], Dr. Julie Côté[1,3]

[1]McGill University, Montreal, Quebec, Canada. [2]The University of Memphis, Memphis, Tennessee, United States. [3]University of Ottawa, Ottawa, Ontario, Canada

Introduction

Previous studies have shown arm- and sex-specific effects of fatigue on shoulder muscle electromyography (EMG). However, no previous studies have quantified how muscles coordinate into synergies as a function of arm and sex. This study aimed to investigate how hand dominance, fatigue and sex influence shoulder muscle synergies during a repetitive overhead fatiguing task.

Methods

Thirty right-handed healthy young adults (15 females) performed a repetitive overhead shoulder flexion task until fatigue, as determined by the Borg CR-10 scale, using the dominant arm in one session and the non-dominant arm in the other. Surface EMG signals were recorded using the Delsys system (2000 Hz) from the upper and lower trapezius, the anterior, middle and posterior deltoid, pectoralis major, latissimus dorsi, and biceps brachii muscles, and intramuscular EMG signals were collected from the supraspinatus, infraspinatus, and subscapularis.

Non-negative matrix factorization method was used to extract muscle synergies. K-means clustering was applied to functionally classify synergies based on the center of activity and full width at half maximum of the activation coefficients and synergy structures. Cosine similarity analysis was performed to compare synergy structures.

Results

In the dominant arm, females showed an unchanged number of synergies with fatigue, while males showed increased synergies with fatigue. In the non-dominant arm, females showed increased muscle synergies, while males showed a decrease. The functional clustering rate of each synergy was below 80% across all groups (Table 1).

Discussion

The overall low clustering rate suggests that the extracted synergies did not converge into consistent patterns and therefore could not be reliably clustered into the same functional roles. Future work should incorporate larger samples, consider more functionally constrained tasks (e.g. load-bearing overhead reach), and explore other clustering approaches. Results also suggest the presence of sex differences in how laterality impacts the formation of arm synergies and how they respond to fatigue. Although these results are consistent with known sex differences in mechanisms of shoulder fatigue and injury, these interpretations should be made with caution, as the functional roles of each synergy must be established first.

Images (Optional)

Table 1. Synergy clustering rate and extracted synergy number across hand dominance and fatigue conditions in both sexes.

Group	Synergy clustering rate	Synergy number
Non-dominant arm_Female_Fatigued condition	Synergy 1 = 40% Synergy 2 = 53% Synergy 3 = 53% Synergy 4 = 27%	4
Non-dominant arm_Female_Non-fatigue condition	Synergy 1 = 20% Synergy 2 = 40% Synergy 3 = 53%	3
Dominant arm_Female_Fatigued condition	Synergy 1 = 50% Synergy 2 = 43% Synergy 3 = 50%	3
Dominant arm_Female_Non-fatigue condition	Synergy 1= 43% Synergy 2 = 43% Synergy 3 = 79%	3
Non-dominant arm_Male_Fatigued condition	Synergy 1 = 36% Synergy 2 = 50% Synergy 3 = 29%	3
Non-dominant arm_Male_Non-fatigue condition	Synergy 1 = 57% Synergy 2 = 57% Synergy 3 = 57% Synergy 4 = 29%	4
Dominant arm_Male_Fatigued condition	Synergy 1 = 47% Synergy 2 = 40% Synergy 3 = 47% Synergy 4 = 33%	4
Dominant arm_Male_Non-fatigue condition	Synergy 1 = 73% Synergy 2 = 60% Synergy 3 = 33%	3

Session Category

Rehabilitation Biomechanics and Human Factors: Occupational Biomechanics

OA186-03

Interaction Forces at the Pelvis–Belt Interface of a Passive Shoulder Exoskeleton and Their Effect on Lumbar Joint Loading

Dr Chris Hayot[1], Mr Olivier Morel[1], Mr Etienne Ricard[1,2], Dr Kévin Desbrosses[1], Dr Charles Pontonnier[2]

[1]French National Research and Safety Institute for the Prevention of Occupational Accidents and Diseases, Vandoeuvre-lès-Nancy, Grand Est, France. [2]ComBO research team, Université de Rennes, Inria, CNRS, IRISA-UMR 6074, Rennes, Bretagne, France

Introduction

The increasing use of industrial exoskeletons aims to reduce workers' exposure to biomechanical risk factors associated with musculoskeletal disorders. Passive upper-limb exoskeletons effectively decrease shoulder loading during overhead work [1], yet recent studies report unintended mechanical consequences linked to their passive structures and force-transmission pathways [2]. Because assistance is generated distally but transmitted proximally through the pelvic belt, additional loads may arise at the lumbar spine. While shoulder assistance mechanisms are well described [3], proximal load redistribution remains poorly understood [4]. This study therefore measured interaction forces at the pelvis–belt interface of a passive shoulder exoskeleton and evaluated their contribution to lumbar joint loading.

Methods

Eight healthy adults performed ten cycles of shoulder flexion without and with the exoskeleton, which included four assistance levels presented in randomized order. Whole-body kinematics were captured using a 16-camera motion-capture system with 59 body markers and 32 exoskeleton markers. Belt interaction forces were recorded via two six-axis load cells, and pressure sensors identified contact locations. Lumbar joint moments were estimated using OpenSim 4.5 [5] from kinematics and external forces, including modeled humeral forces. Statistical Parametric Mapping assessed condition and assistance-level effects on force measures and lumbar moments.

Results

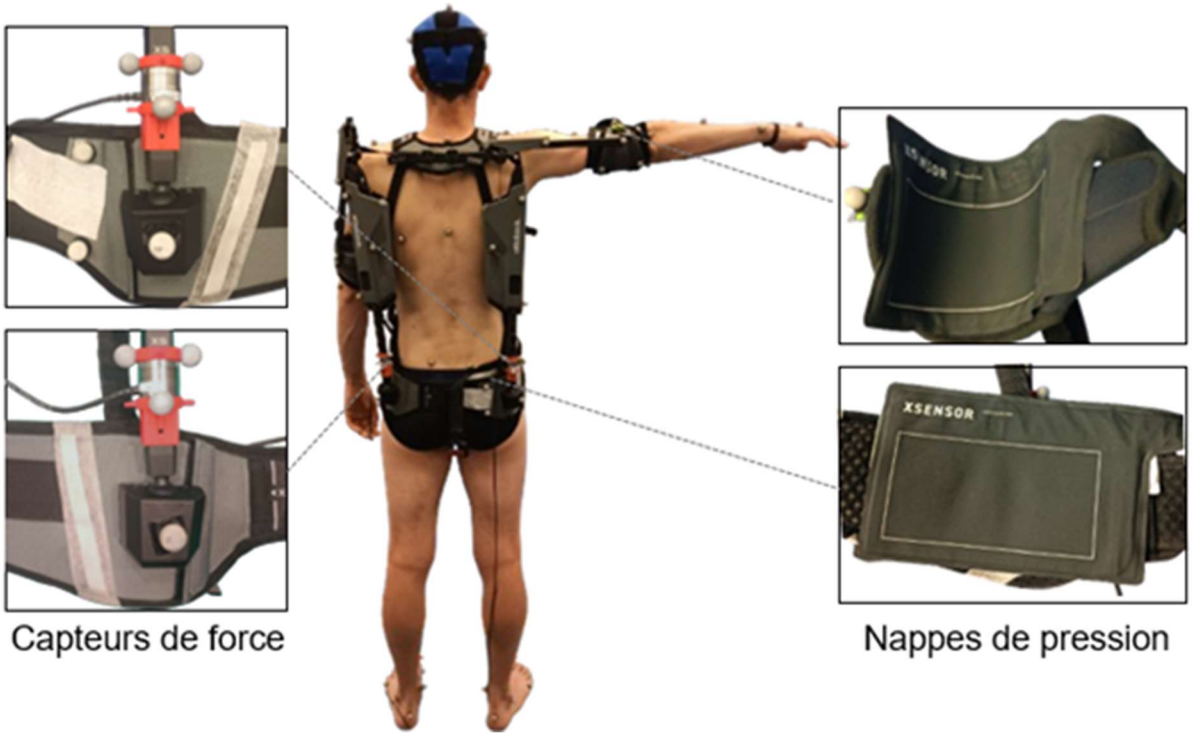
Belt interaction forces increased with exoskeleton arm opening and assistance level, while pressure center remained stable. Belt forces significantly altered lumbar loading, reducing flexion moments and progressively increasing extension, lateral bending, and axial rotation

moments across most of the movement cycle, indicating substantial assistance-dependent redistribution of lumbar joint mechanics.

Discussion

This study quantified pelvis–exoskeleton interaction forces during dynamic arm elevation and showed that belt forces increased with arm opening and assistance level, reflecting the device's torque-generation mechanism. These measurements provide the first full three-dimensional description of pelvic loading for this type of passive exoskeleton. Exoskeleton use also altered lumbar joint moments, with higher assistance levels progressively increasing extension, lateral bending, and axial rotation moments, indicating compensatory trunk loading. These findings align with reports of increased proximal joint moments due to reaction forces at support interfaces. Overall, the results highlight the need for models that integrate realistic interface forces to better predict mechanical side effects.

Images (Optional)



References (Optional)

Session Category

Rehabilitation Biomechanics and Human Factors: Occupational Biomechanics

OA186-04

The Long & Short of It: Vertical Range & Load Impact Effort Durations of Lifting & Lowering Tasks

Miss Gillian Slade MHSc Candidate[1], Mr Michael Watterworth PhD Candidate[1], Miss Hayley Janes BHSc[1], Dr Jim Potvin PhD[2], Dr Nicholas La Delfa PhD[1]

[1]Ontario Tech University, Oshawa, Ontario, Canada. [2]Work(s) Ergo Inc, Tecumseh, Ontario, Canada

Introduction

Shoulder injuries are one of the most costly workplace musculoskeletal injuries, yet few ergonomics assessment tools evaluate shoulder risk in manual materials handling. One approach uses estimates of arm strength with corrective equations to control for the fatiguing effects of task repetition. To utilize this approach, both task frequency (e.g., lifts/min) and the effective duration of each effort (seconds/lift) must be known. Task frequency is straightforward to determine, but effective duration is difficult to measure in applied settings, and limited empirical data are available for lifting and lowering. As such, this study investigated how vertical range and load influence effective duration during two-handed lifting and lowering tasks.

Methods

Twenty-one healthy adults (12F, 9M; aged 18–30) with no recent upper/lower extremity injury completed 72 bilateral lifting and lowering trials (3 loads × 6 vertical ranges × 2 directions × 2 repetitions). A custom-built box with an embedded force transducer recorded force–time histories. Trials were block-randomized by vertical range, with rest periods to mitigate fatigue. Effective duration was calculated by dividing the impulse of the force–time curve by the smoothed peak force. A four-way ANOVA examined effects of vertical range, hand load, trial number, and action type (lift vs. lower). Tukey post hoc tests identified significant pairwise differences ($\alpha = 0.05$).

Results

Heavier loads produced significantly longer effective durations across all conditions (Figure 1). Lowering required slightly longer durations than lifting (~3% on average). This effect increased at higher vertical ranges. For example, in the knuckle-to-overhead condition, lowering the 23-lb load required 22% longer effective duration than lowering the 8-lb load, whereas the corresponding lifting difference was 10%.

Discussion

Vertical range influences effective duration, and therefore the duration of muscular effort. Interestingly, lifting in the shoulder-to-overhead range (51cm) took slightly longer than the 102 cm floor-to-shoulder range, particularly with heavier box weights. This is possibly due to less favourable joint postures associated with elevated arm positions. Load magnitude further amplified differences across ranges, indicating prolonged upper-limb mechanical loading at higher elevations. These findings provide needed empirical force-time data and effort-duration values to improve analysis of upper-limb manual materials-handling tasks.

Images (Optional)

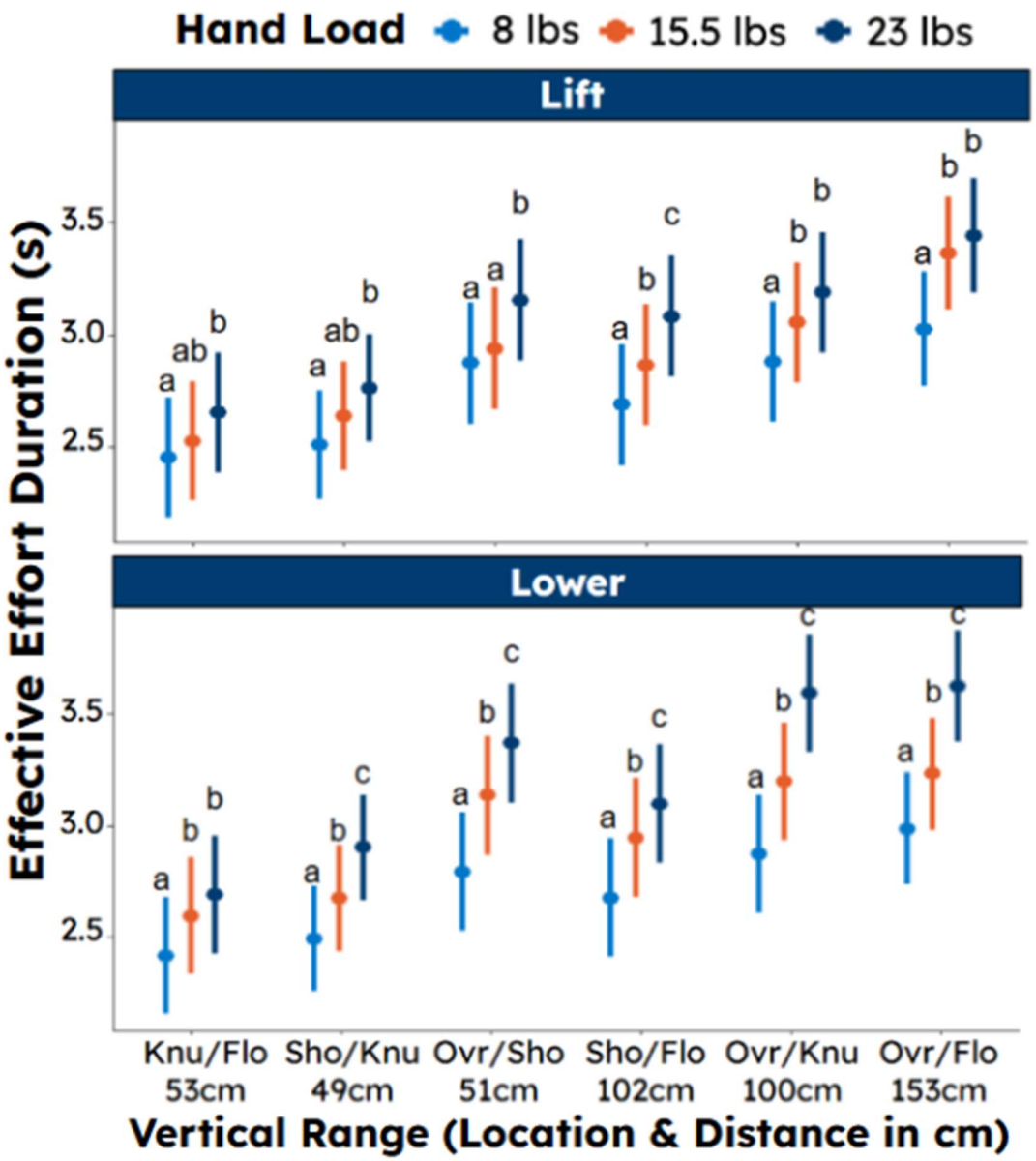


Figure 1: Effective effort duration at different vertical ranges.

Session Category

Rehabilitation Biomechanics and Human Factors: Occupational Biomechanics

OA187-01

Implanted Microscaffolds Can Control the Mechanobiology of Fibrotic Progression

Prof. Claudio Conci[1], Dr. Alberto Bocconi[1], Mr. Leonardo Cherubin[1], Dr. Chiara Martinelli[1], Ms. Giada Mainieri[1], Ms. Giulia Lodola[1], Prof. Emanuela Jacchetti[1], Mr. Matteo Vicini[1], Dr. Alessandra Nardini[2], Dr. Rebeca Martinez-Vazquez[2], Prof. Manuela Raimondi[1]

[1]Department of Chemistry, Materials and Chemical Engineering "Giulio Natta", Politecnico di Milano, Milan, Lombardia, Italy. [2]Istituto di Fotonica e Nanotecnologie (IFN)-CNR, Milan, Lombardia, Italy

Introduction

While genetic mutations initiate breast cancer, tumor progression is mostly influenced by changes in tissue mechanical microenvironment, related to fibrosis. Its progression promotes tumor stiffening. The embryonated avian egg chorioallantoic membrane (CAM), a unique alternative model, allows for real-time imaging of fibrosis in an in-vivo organism. In this work, we used a CAM model to recreate three different progression states of a foreign-body reaction, at a single timepoint and implantation site. We used nonlinear microscopy to quantify in-vivo matrix stiffness and vascularization within the fibrotic microenvironments, consisting of implanted microscaffolds, repopulated by the host cells and blood vessels (Fig1a).

Methods

We produced three sets of microscaffolds on the same glass coverslips (Ø=12mm), shaped as grids with a pore size of 10x10μm^2,30x30μm^2,50x50μm^2, 80μm height, by using two-photon polymerization of SZ2080. We implanted this array in live chick embryos, and we conducted the CAM assay 7 days post-implantation, as previously described by our group [1]. Ex-ovo inspection of the imaging window was performed using two-photon microscopy and second harmonic generation (SHG) imaging.

Results

Microscopy analyses at the implantation sites in chick embryos (Fig.1b,c) revealed tissue infiltration inside and around the microscaffolds. Neo micro vascularization inside the scaffolds highlighted capillaries 10 times shorter, 1.4 times thinner from the inner to the outer part of the scaffold and 200 and 17 times shorter and thinner, respectively, compared to unimplanted samples, (Fig.1d). In the 50x50μm^2 microcapillaries had a vascular density 2.9-fold greater compared to the ones in the 30x30μm^2, and 200-fold greater than in the

10x10μm^2. SHG revealed the presence of a collagen-I layer that was preferentially orientated and had a density significantly lower than in peri-implant areas, and greatly varying with scaffold type.

Discussion

Microscaffolds successfully reproduced different levels of fibrotic progression, mimicking tumor-associated stroma by regulating collagen synthesis and revascularization. The differences in vascular density and collagen content, across scaffold types, replicated microenvironments with three increasing levels of fibrosis, likely driving breast cancer progression. This study validates the embryonated avian egg as a versatile platform for modeling fibrosis, allowing real-time, ethical, and cost-effective imaging compared to in-vitro and mammalian models.

Images (Optional)

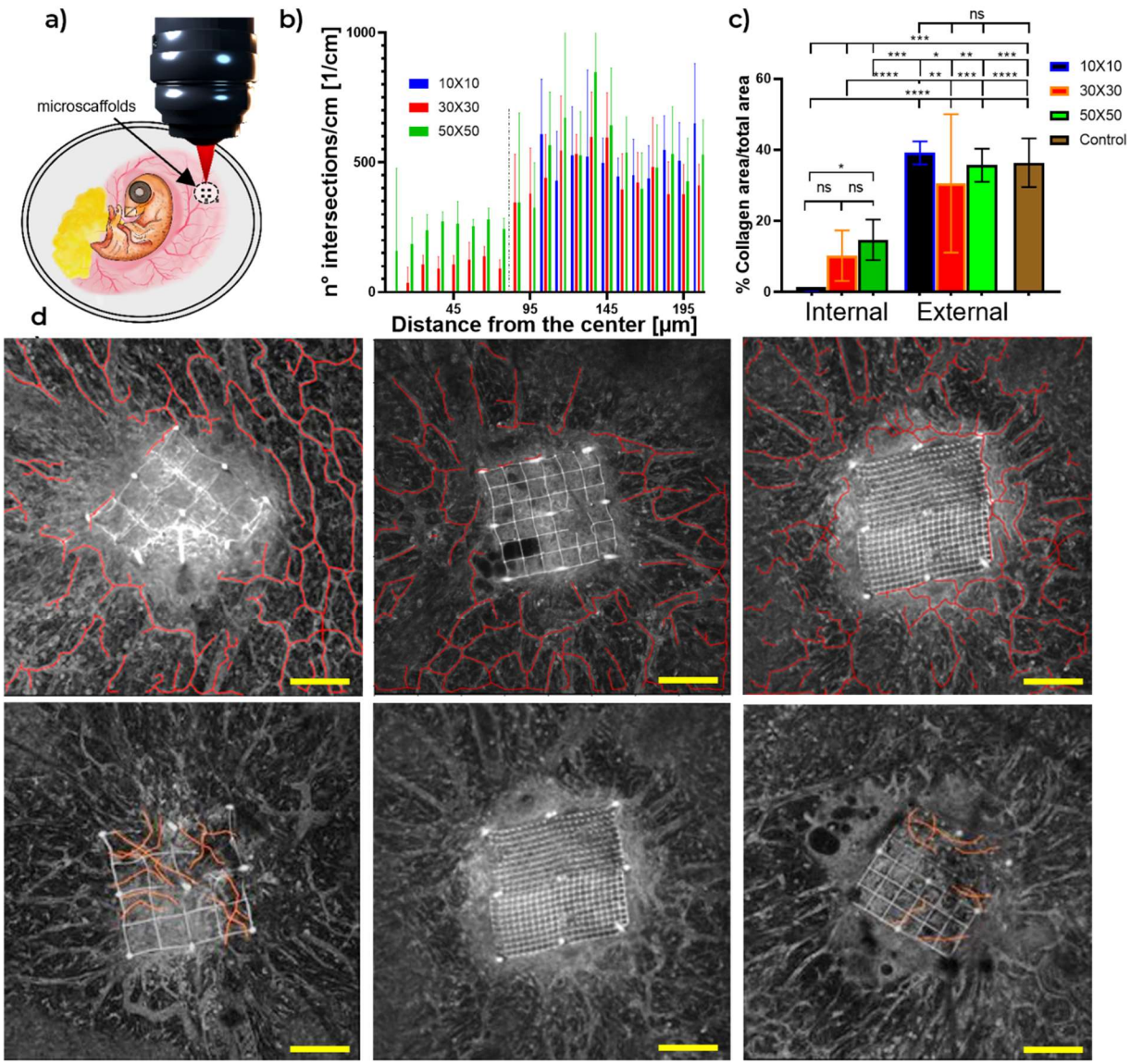


Fig.1. (a) Representation of the assay. (b) Blood vessels density in the microscaffolds and surrounding tissue (number of intersections per test line). (c) Inspected volume occupied by collagen fibers (SHG). (d) Microscaffolds implanted in the CAM taken under TPEF (λ_{Ex}= 910 nm, λ_{Em}:535/50 nm) at EID14 (scalebar = 100 µm).

References (Optional)

[1] Conci et al. AplBioeng, 2023

Acknowledgements (Optional)

ERC-BEACONSANDEGG,G.A.101053122, ERC-ALFRED 101221323

Session Category

OA187-02

Microneedles Patch With Tunable Stiffness Regulates wound Scar-Free Repair

PhD Candidate Danli Chen, Professor Xufeng Niu

Beihang University, Beijing, Beijing, China

Introduction

The application of microneedles (MNs) as a mechanotherapy strategy to modulate mechanical microenvironment of wounds has garnered increasing attention. However, the influence of mechanical properties of MNs on wound healing and fibrosis remains underexplored.

Methods

In this study, we developed a MNs patch composed of genipin cross-linked carboxymethyl chitosan (CMCS) and examined how variations in patch stiffness influence wound healing and fibrosis. To assess mechanical environment improvement, we constructed a finite element model of MNs patch-closed wounds (n=4). Additionally, *in vivo* wound-healing experiments (n=4) and *in vitro* co-culture studies (n=3) were performed to elucidate the mechanisms by which MN-mediated modulation of the mechanical microenvironment influences wound repair.

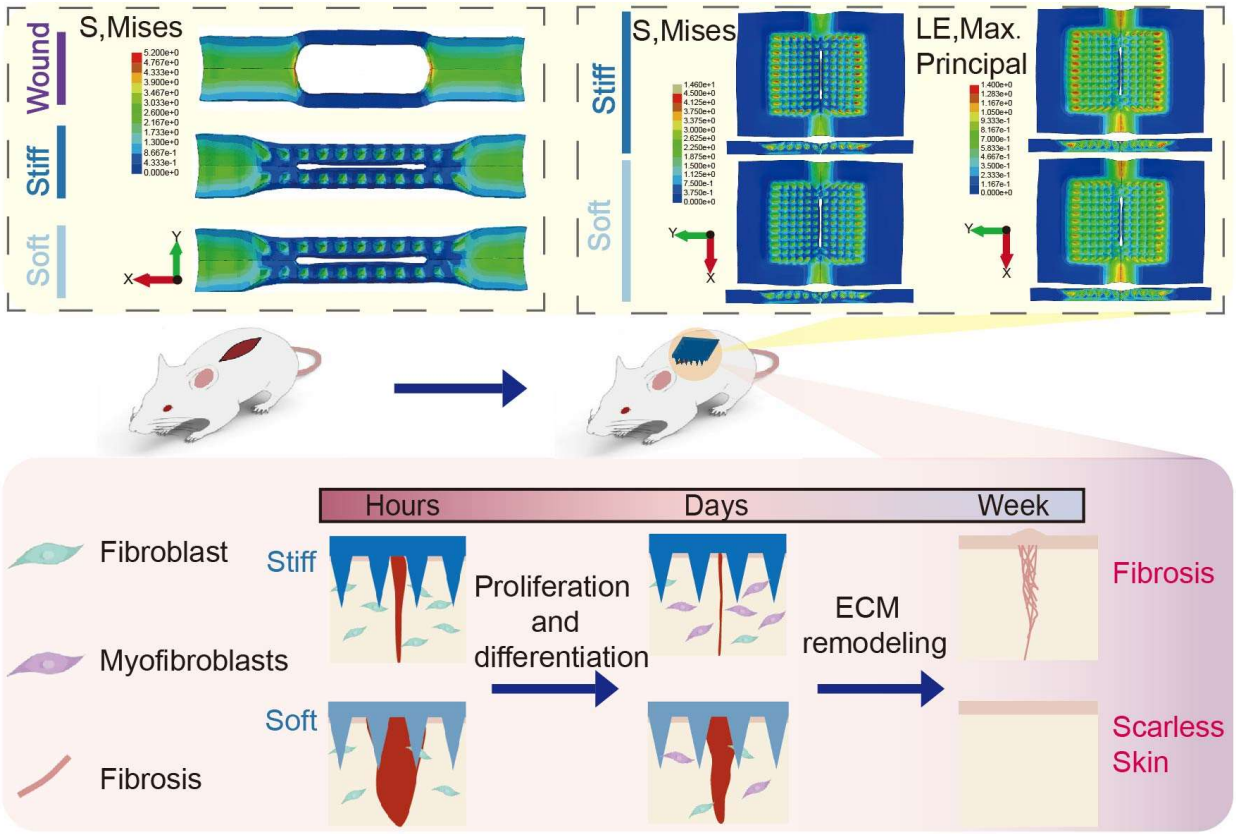
Results

MNs patches were fabricated through mold casting. The mechanical properties varied with the degree of crosslinking. In the dry state, stiff MNs exhibited a Young's modulus of 499.45 ± 61.73 MPa, compared with 255.36 ± 77.55 MPa for soft MNs. Results from the finite element modelling simulations revealed that stiff MNs patch better reduced wound area but also elevated stress in peri-wound area. Via *in vivo* experiments and co-culture experiments with fibroblasts, we confirmed that stiff MNs patch accelerated wound closure ($3.55 \times 10^{-2} \pm 8.81 \times 10^{-3}$) than soft MNs patch ($5.38 \times 10^{-2} \pm 3.68 \times 10^{-3}$, $p=0.029$), but promoted fibroblast proliferation ($8.70 \times 10^{-1} \pm 9.32 \times 10^{-2}$ for stiff MNs and $6.60 \times 10^{-2} \pm 2.28 \times 10^{-3}$ for soft MNs, $p<0.0001$) and myofibroblast differentiation ($0.58 \pm 6.85 \times 10^{-3}$ for stiff MNs and $0.44 \pm 1.14 \times 10^{-2}$ for soft MNs, $p<0.0001$), contributing to fibrosis. In contrast, soft MNs patch facilitated scar-free repair, and the height of wound applied with soft MNs patch achieved comparable thickness to normal skin (h_{MNsoft}=1493.24 ± 74.70 μm, h_{normal}=1581.58 ± 57.88 μm, $p=0.528$).

Discussion

In conclusion, MNs patches promote wound healing, stiffer MNs patches are more effective during initial stages of wound healing, whereas softer patches are preferable for minimizing fibrosis in later stages. These findings underscore that MNs' mechanical properties must be carefully tailored to balance early-stage repair efficacy with long-term goal of scar-free healing.

Images (Optional)



References (Optional)

[1] Danli Chen *et al.*, J Biomechanics, 2025

Session Category

Tissue Engineering: Mechanobiology

OA187-03

Nanovibrational Control of Chondrogenic Differentiation

Miss Ioanna Rigou PhD Researcher, Dr Rosalia Cuahtecontzi Delint Research Associate, Dr Monica Tsimbouri Research Technologist, Prof Manuel Salmeron-Sanchez Professor of Biomedical Engineering, Prof Mathew Dalby Profesor of Cell Engineering

University of Glasgow, Glasgow, Scotland, United Kingdom

Introduction

Osteoarthritis (OA) is a prevalent degenerative joint disease, and current treatments cannot restore the structure or mechanical function of damaged articular cartilage. Its limited repair capacity means that both surgical and TGFβ-based tissue-engineering approaches often produce fibrocartilage and induce hypertrophy. These limitations highlight the need for personalized, growth factor-free strategies capable of generating durable hyaline tissue. This study investigates nanoscale vibrational mechanostimulation (Nanokicking) as a clinically scalable approach to promote collagen II while suppressing collagen X in OA-derived BMMSCs.

Methods

The study followed an engineering-driven comparative design evaluating how nanoscale vibrational stimulation (30 nm, 1 kHz) modulates the mechanobiological behaviour of STRO-1^+ osteoarthritic BMMSCs. Donors ranged from 21-year-old males to 90-year-old females. Micromass responses were quantified by qPCR across ten donors, with mechanobiological characterisation integrating nanoindentation measurements with collagen II, collagen X and aggrecan expression profiles. Immunofluorescence imaging further revealed the spatial distribution of collagen within the constructs, completing the mechanobiological assessment. Bulk RNA sequencing on six donors (three male, three female) profiled the transcriptional pathways engaged under nanovibrational stimulation. Data were analysed using statistical approaches suitable for multi-donor mechanobiology studies.

Results

Across multiple OA donors, nanovibration increased SOX9, ACAN, and COL2A1 expression while suppressing COL10A1 at days 7, 14, and 21, confirmed at both the gene and protein level. Histology showed markedly enhanced proteoglycan deposition under NK stimulation. The mechanobiological behavior of the micromasses reflected these

molecular changes: NK cultures displayed a more compliant, hyaline-like viscoelastic profile than non-stimulated controls and remained significantly less stiff than TGFβ-treated micromasses ($p < 0.05$), consistent with a non-fibrocartilaginous phenotype. RNA sequencing revealed dynamic ECM-organisation changes and implicated BMP and Wnt signaling as potential regulators of the COL2A1-dominant, non-hypertrophic program. Together, these findings demonstrate that nanoscale vibration drives BMMSCs towards a mechanically and molecularly stable hyaline-like phenotype, supporting its use as a growth-factor-free chondrogenic strategy.

Discussion

These findings support nanoscale vibrational stimulation as a promising biophysical strategy for generating stable, non-hypertrophic cartilage, aligning with the broader clinical need for growth factor–free and mechanically informed approaches to cartilage repair. In our next steps, inhibitors will be used to identify the possible mechanism that activates the chondrogenic phenotype.

Acknowledgements (Optional)

I would like to express my gratitude to the Engineering and Physical Sciences Research Council (EPSRC) (Project Reference: 2795762) and the MVLS college for their support of my funding and to thank my colleagues from the CeMi group.

Session Category

Tissue Engineering: Mechanobiology

OA187-04

Wireless Mechanical Stimulation Upregulates the Foreign Body Response to Biomedical Implants Through Immune Cell Pathways

PhD Student Emily Galvin MS[1], Associate Professor Kellen Chen PhD[1], Medical Student Hudson Kussie BS[1,2], PhD Graduate Eamonn McKenna PhD[1], MD/PhD Canadite Kayleigh Berthaimue Fox MS[1], Surgery Resident Erika Kness-Knezinkis MD[1], PhD Student Vaishnavi Narayanan BS[1], Medical Student Dharshan Sivaraj MS[1,3], PhD Student Abdelrahman Alsharif BS[1], Post Bach Researcher Fidel Saenz BS[1], Medical Student Ethan McNew BS[1,4], Masters Student Alyssa Clausen BS[1], Research Assistant Lulejeta Latifi BS[1], Surgery Resident Andrew Hostler MD[1], PhD Student Katharina Berryman MD[1], Post Doc Maria Mora-Pinos MD[1], Associate Professor Phillip Gutruf PhD[1], Chair, Department of Surgery Geoffrey Gurtner MD, FACS[1]

[1]University of Arizona, Tucson, Arizona, United States. [2]Tufts University, Medford, Massachusetts, United States. [3]Standford University, Palo Alto, California, United States. [4]UT Southwestern, Dallas, Texas, United States

Introduction

Implantable biomedical devices are a hundred-billion-dollar industry [1]. These devices often fail after implantation due to the foreign body response (FBR), in which the body's immune reaction creates a fibrotic encapsulation of the device. Although we have demonstrated that external tissue mechanical forces promote severe FBR in mice and humans, the underlying cellular mechanisms remain incompletely understood [2].

Methods

We engineered a novel, wirelessly powered mechanically stimulating implant (MSI) to increase extrinsic tissue mechanical forces and promote human-like FBR in mice. 30 wild type (WT) and 6 Rac2 knockout (KO) mice received devices with no-stimulation (NS) or MSI, and fibrotic capsules were collected at postoperative day (POD) 10, 28. We performed single cell RNA sequencing (scRNA-seq) on mild and severe FBR (n=3) human breast implant capsule tissue. We compared these samples to previously published murine data. We virtually screen small molecule drugs that could specifically target RAC2. MSI WT mice were injected subcutaneously with 10 mg/kg dose of RAC2-specific inhibitor (RAC2i) daily for 10 days.

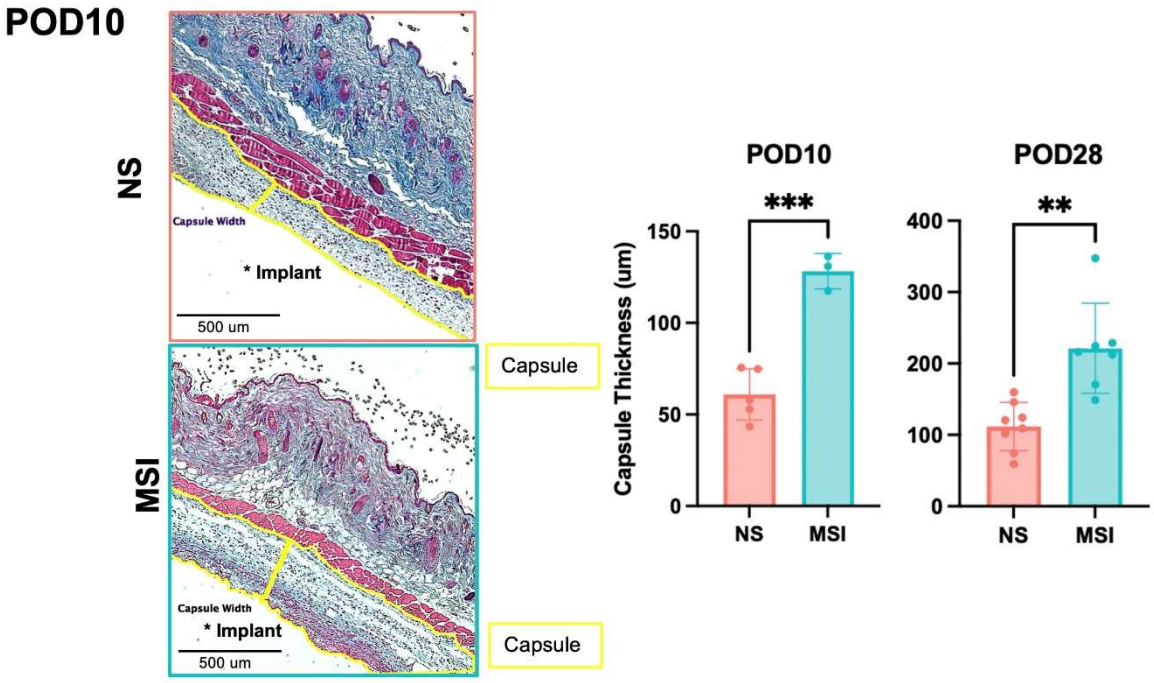
Results

MSI WT mice at POD10 caused a 110.5% increase in capsule thickness from 60.90 um to 128.2 um (p = 0.0007) between NS and MSI. At POD28, MSI WT mice showed capsule thickness increasing by 97.9% compared to NS, from 111.8 um to 221.3 um (p = 0.0027). MSI Rac2KO mice decreased the capsule thickness by 45.0% compared to WT mice (p = 0.0016) at POD28. ScRNA-seq revealed that both severe human FBR and MSI murine capsules upregulated RAC2+ mechanoresponsive myeloid cells, with an increase in inflammatory and fibrotic pathways. MSI + RAC2i caused a 55.9% decrease in capsule thickness at POD10 (p = 0.001) and 43.4% decrease at POD28 (p = 0.014) compared to MSI treated with only saline.

Discussion

Our results demonstrate that wireless mechanical stimulation activates mechanosensitive immune pathways and exacerbates FBR. We identified a potential RAC2 specific inhibitor that is effective in reducing severe FBR. By uncovering the important genes and pathways we open new avenues for treating and preventing this reaction to biomedical implantable devices.

Images (Optional)



References (Optional)

[1] Dolan, E.B. et al., Sci. Robot., 2019.

[2] J. Padmanabhan et al., Nature Biomedical Engineering, 2023.

Session Category

Tissue Engineering: Mechanobiology

OA188-01

Two-Year Sheep *In Vivo* Study Of Porous Calcium Phosphate Implant Anchored By Ultrasonically Liquefied Polymer, For Sports Medicine Applications: Short-Term Micro-CT Bone Ingrowth Analysis

M.Sc. Alice Della Casa[1,2], med.vet. Benedikt Schluse[3], Dr. Marina Rubert[2], Prof.em. Dr.med.vet. Brigitte von Rechenberg[3], Dr. Jörg Mayer[2], Dr.med.vet. DVM, PhD Karina Klein[3]

[1]Swiss Federal Laboratories for Materials Science and Technology, St. Gallen, St. Gallen, Switzerland. [2]Surgical Fusion Technologies, Schlieren, Zurich, Switzerland. [3]Musculoskeletal Research Unit, University of Zurich, Zurich, Zurich, Switzerland

Introduction

Anterior Cruciate Ligament (ACL) tears are one of the major injuries in Sports Medicine, with common complications in reconstruction surgeries linked to poor osseointegration. A new graft fixation concept, consisting of a porous 3D-printed Calcium Phosphate (CaP) implant press-fitting the graft, is securely anchored to the cancellous bone with an ultrasonically liquefied polymer pin (SupraFusion®). An *in vivo* study to test the osseointegration in a pelvic model [1] in sheep is underway, and micro-CT data at early timepoints is evaluated in terms of bone ingrowth inside the structure.

Methods

Fourteen sheep were operated. Different material combinations were implanted in both iliac bones: a porous CaP implant (PC, Ø7x10mm: LithaBone™, Lithoz, Austria) made of beta-Tricalcium Phosphate (TCP) or Hydroxyapatite (HA), was anchored by SupraFusion using a polylactide pin (PLDLLA, Ø2.4x24mm: LR 706S Resomer®, Evonik, Germany). One sheep per survival group (at 8 (8w) and 26 (26w) weeks) was selected, and the HA and TCP implants (n=1) from a single pelvis side were imaged by micro-CT. Cross-sections at 9 different heights (Fig.1A, spaced by 1mm) were extracted, smoothed (median filter, σ=10) and segmented using python scripts. The average amount of ingrown bone in each PC, as fraction of the masked cross-section, was calculated (mean±SD%, n=9).

Results

Analysis of the cross-sections showed 16.64±2.55% bone ingrowth in TCP at 8w, and 20.03±8.23% at 26w. In the HA samples, the bone ingrowth was 7.98±2.24% at 8w and 22.5±3.58% at 26w.

Discussion

In both HA and TCP, there was an increase in the average bone fraction at 26w, compared to 8w. At 8w, there was more average bone in the TCP, and slightly more bone at 26w in HA, in which the bone fraction almost tripled. These data are supplementing bone morphometric analysis from histological sections by providing a qualitative 3-dimensional representation of bone ingrowth that can otherwise not be achieved. Further analysis at timepoints 52 and 104 weeks will be carried out to verify whether porous HA and TCP show promising osseointegration, making them candidates for graft fixation in ACL Reconstruction.

Images (Optional)

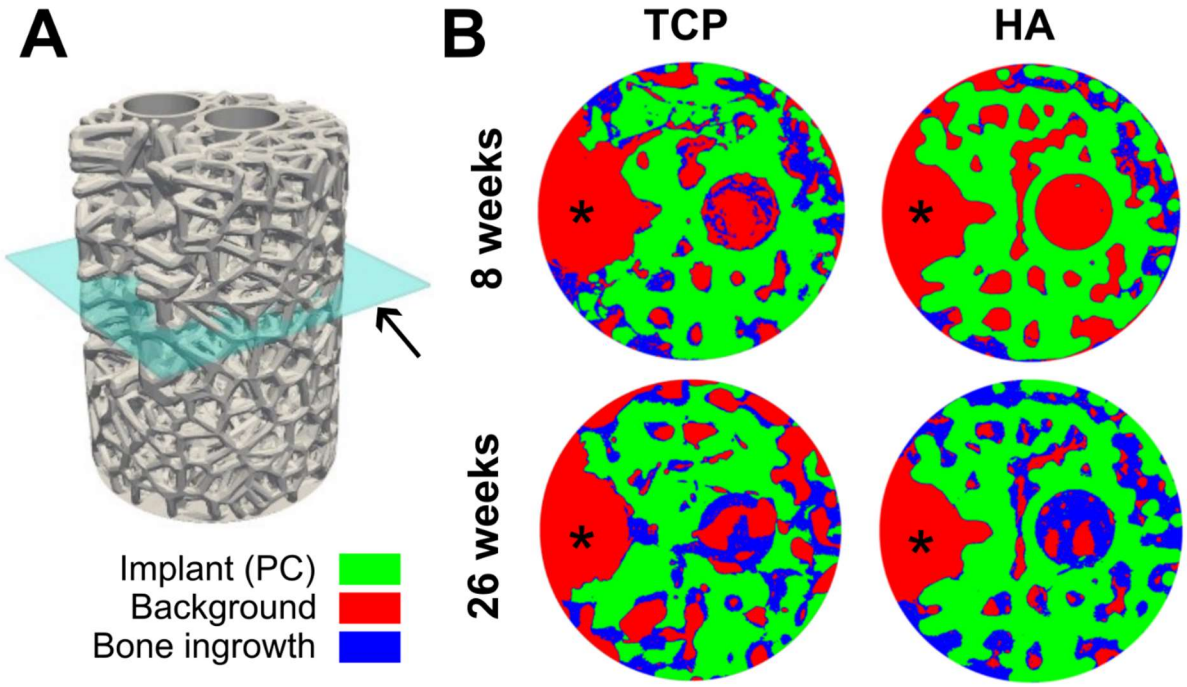


Fig. 1: (A) Porous implant design, with example cross-section plane (arrow); (B) segmented cross-sections at 7mm, with PLDLLA in the groove on the left (*) appearing as background.

References (Optional)

[1] Sabrina Ernst *et al*, Clin. Oral Implants Res, 2015

Acknowledgements (Optional)

This study was supported by the Swiss Innovation Agency (Innosuisse grant 103.715 IP-LS), and Surgical Fusion Technologies.

Session Category

Orthopaedic Biomechanics: Sports Medicine

OA188-02

ACL Reconstruction is Associated with Significant Differences in Contralateral Tibial Morphology Compared to Controls

Mr. Matthew Milcsik BSE[1], Dr. Kareem Omran MD[1], Dr. Matthew Tao MD[1], Dr. Elizabeth Wellsandt PT, DPT, PhD[1], Dr. Kevin Dibbern PhD[1,2]

[1]University of Nebraska Medical Center, Omaha, NE, United States. [2]Children's Nebraska, Omaha, NE, United States

Introduction

Posterior tibial slope (PTS) is a commonly accepted risk factor for primary anterior cruciate ligament (ACL) injury and ACL reconstruction (ACLR) graft failure. Traditional single-parameter PTS measurements may inadequately capture complex 3D morphological variations influencing biomechanics and outcomes. Statistical shape modeling (SSM) quantifies anatomical variation and may aid understanding of morphological variance within PTS toward improving ACLR and PTS correction. The objective of this study was to apply SSM to evaluate contralateral limb morphology in ACLR patients compared to uninjured control morphology.

Methods

A total of 30 participants with knee MRI were analyzed: 10 unilateral ACLR (5 adolescent, 5 adult) and 20 controls (10 adult, 10 older adult). Contralateral limbs of individuals after ACLR were segmented to approximate premorbid tibial geometry. Iterative back projection was used to obtain super-resolution images from coronal and sagittal plane proton density scans (0.3mm isotropic). ShapeWorks was used to create SSMs of all tibiae and automated 3D measures of both medial and lateral PTS were computed in Matlab. Morphological variation was evaluated with principal component analysis (PCA) of correspondence particles and Horn's parallel analysis to identify significant shape modes. Normality checks and Student’s t- or Wilcoxon tests evaluated differences between ACLR and healthy knees.

Results

Parallel analysis retained 2 significant PCA modes explaining 67% of variance between tibiae. Mode 1 demonstrated subtle lateral PTS while mode 2 demonstrated more medial PTS and deepening of condyles (Figure 1). Mode 1 demonstrated no differences between ACLR and control component scores, while mode 2 identified significant differences between ACLR and control groups. No differences were found in medial or lateral PTS between groups but mode 1 was significantly correlated with lateral PTS.

Discussion

Significant 3D morphological variation beyond traditional PTS measurements was identified in ACLR patients versus controls. Differences included condylar depth, tibial spine position, and subtle PTS variations (<6°). Articulation size and depth may be associated with age-related changes in older controls, while PTS values were lower than previous reports. Future studies with larger sample sizes may aid stratification of graft failure risk and guide surgical corrections using SSM and automated 3D PTS measures.

Images (Optional)

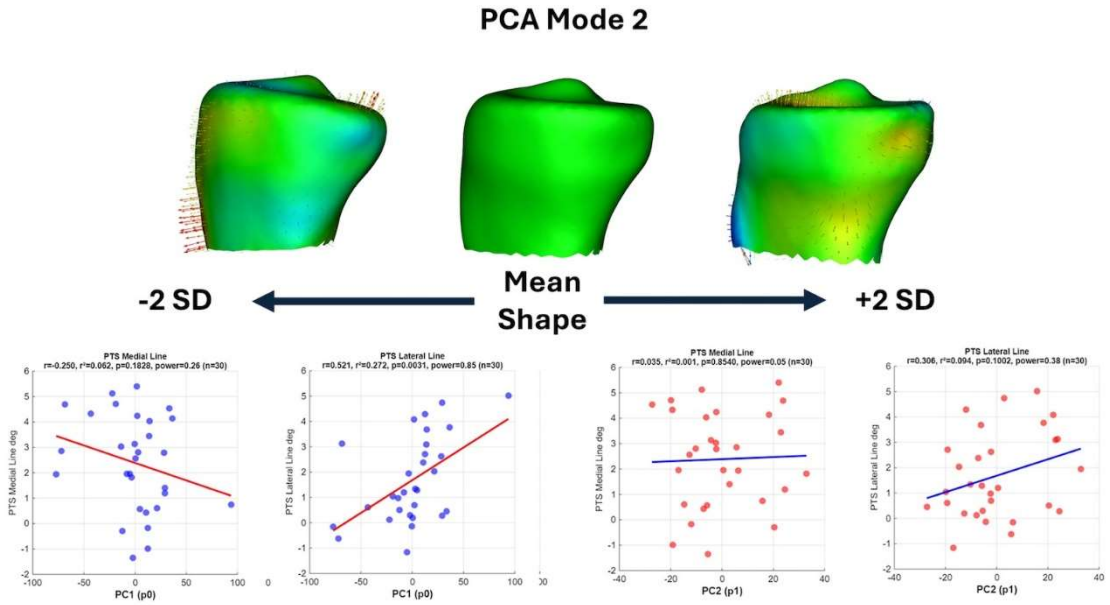


Figure 1. (Top) PCA mode 2 demonstrated posterior tibial slope (PTS) but was not significantly correlated with 3D PTS scores (bottom right, red dots with blue lines). PCA mode 1 was significantly associated with lateral but not medial PTS (bottom left, blue dots with red lines).

Session Category

Orthopaedic Biomechanics: Sports Medicine

OA188-03

Meniscal Kinematics Following Posterior Medial Meniscus Root Repair with Adjustable All-Suture Anchor Aperture Fixation: A Cadaveric Biomechanical Evaluation

Dr. Clayton Nuelle MD[1], Dr. Garrett Jackson MD[1], Mr Will Bezold BS[1], Mr. Benjamin Smith MS[2], Dr James Cook DVM, PhD, OTSC[1]

[1]University of Missouri, Columbia, MO, United States. [2]Arthrex, Inc., Naples, FL, United States

Introduction

Recent biomechanical evidence has demonstrated that, in the setting of posterior medial meniscus root (PMMR) tears, adjustable all-suture anchor (ASA) aperture fixation better restores native meniscal function compared to the gold-standard transtibial pull-through repair. However, these studies are limited to isolated meniscotibial loading models, and meniscal kinematics through loaded knee range of motion have not been investigated. It was hypothesized that ASA PMMR repair would restore meniscus translation similar to the native meniscus and maintain those parameters through a loaded cyclic knee flexion arc.

Methods

8 fresh-frozen human cadaveric knees (4 male, 2 female; mean age = 44.9) were tested. Meniscal translation was evaluated in each knee under 1) Intact, 2) PMMR release, and 3) PMMR repair conditions. Repairs were performed by one board-certified orthopedic surgeon and fixed with a knotless adjustable ASA device in a Mason-Allen configuration. In each condition, knees were axially loaded with 30 N of force through range of motion to test meniscus excursion, extrusion, and hoop strain at 0°, 30°, 60°, 90°, and 100° of flexion after 10 cycles. A 6-degree-of-freedom robotic testing platform was utilized. Statistical analysis utilized repeated-measures ANOVA or one-way ANOVA with Tukey post-hoc tests ($p<0.05$).

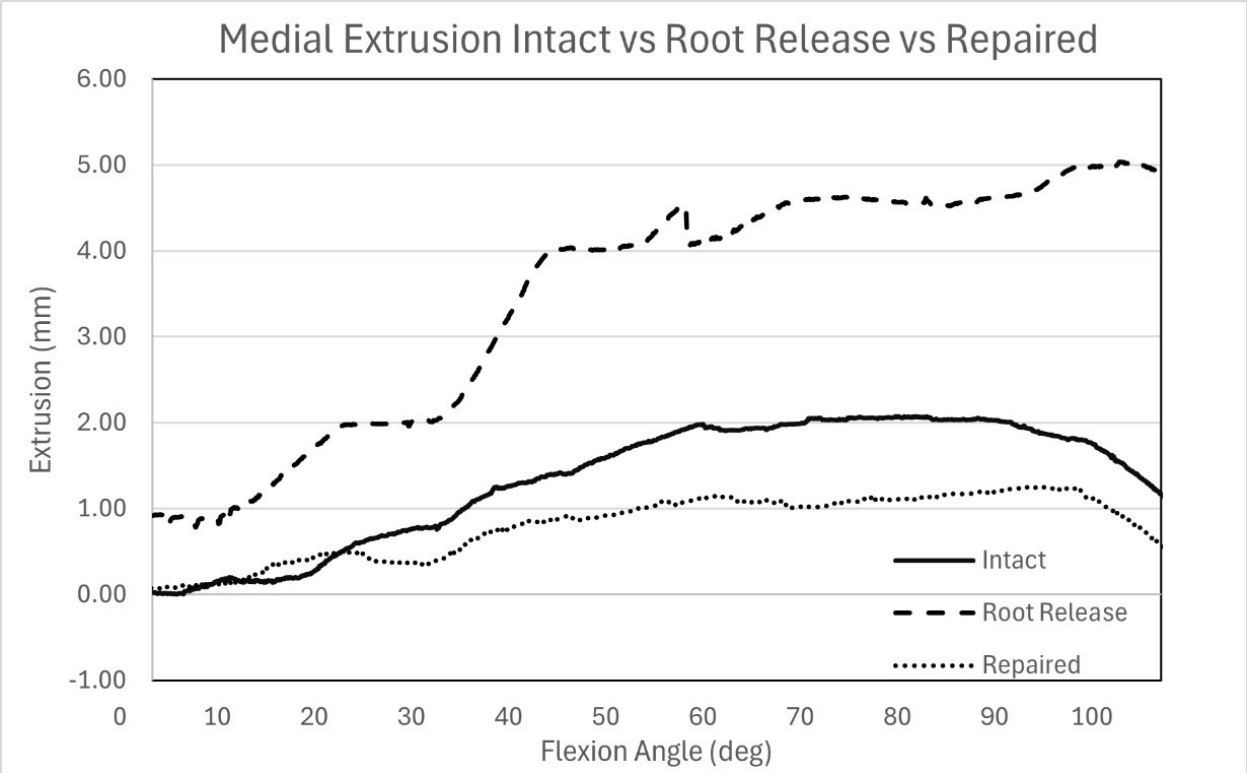
Results

Meniscal extrusion was significantly greater with PMMR release compared to the intact and repair conditions at 0° ($P<0.001$), 30° ($P=0.007$), 60° ($P<0.001$), 90° ($P<0.001$), and 100° ($P<0.001$). Extrusion in the repair condition was similar to, or less than, the intact condition across every flexion angle. Meniscus hoop strain in the repaired and intact conditions was significantly greater than in the PMMR release condition ($P<0.001$). Meniscal excursion was significantly greater with PMMR release compared to intact and repair conditions at 30° ($P=0.001$). However, excursion was significantly lower in the intact state at 60° ($P=0.021$) and 100° ($P=0.018$) compared to PMMR release and repair states.

Discussion

The results confirm the hypothesis that PMMR repair with adjustable ASA aperture fixation restores intact meniscal translation following a PMMR tear. This study provides clinically relevant full-construct evidence that builds upon existing in vitro models supporting novel aperture PMMR fixation. The findings could potentially afford accelerated post-surgical rehabilitation in pair with clinical evidence.

Images (Optional)



Session Category

Orthopaedic Biomechanics: Sports Medicine

OA188-04

Integrating Computational Modeling and Quantitative MRI to Relate Knee Instability and Longitudinal Changes in ACL Graft Composition: A Framework to Understand Mechanisms of Early Graft Failure

Ms. Isabella Gomez Hjerthen BS, Ms. Erin Berube BS, Mr. Jack Consolini MS, Ms. Elizabeth Koretsky MS, Mr. David Shamritsky MS, Ms. Deborah Jones PT, OCS, SCS, Dr. Theresa Chiaia PT, DPT, Dr. Andrew Pearle MD, Dr. Thomas Wickiewicz MD, Dr. Scott Rodeo MD, Dr. Danyal Nawabi MD, FRCS, Dr. Hollis Potter MD, Dr. Matthew Koff PhD, Dr. Carl Imhauser PhD

Hospital for Special Surgery, New York, NY, United States

Introduction

Graft failure is a devastating complication that occurs in up to 18% of young athletes undergoing primary anterior cruciate ligament reconstruction (ACLR). Instability of the ACL-deficient knee, graded via subjective clinical pivot shift exam, is related to graft failure two years after ACLR. However, it is unclear whether pre-operative instability influences the graft's post-operative remodeling process, which may affect tissue quality and likelihood of failure. Our goal was to objectively assess pre-operative knee instability via computational modeling and relate it to post-operative changes in graft structure and composition from quantitative MRI.

Methods

Fifteen subjects (9 female; age: 23±7 years) undergoing primary ACLR were enrolled in this longitudinal study. To date, data have been collected for ten subjects at 6-weeks and six subjects at 6-months post-operatively. Ultra-short echo (UTE) images of the ACLR were acquired on a clinical 3T system: TEs/TR: 0.03-25ms (ΔTE=2.5ms) / 256.6ms; voxel size $0.31x0.31x1.5mm^3$. A mean T2* of graft voxels was calculated. Subject-specific bone, cartilage, and meniscus geometries, as well as ligament insertions, were integrated into an established computational knee modeling pipeline. Tissue properties were standardized. The tibia was flexed to 15°, and a pivot shift exam was simulated by sequentially applying compression (100N), valgus (8Nm), and anterior (30N) loads. Anterior tibial translation (ATT) and internal tibial rotation (ITR) were estimated at the peak applied loads. T2* values at 6-weeks and 6-months post-operative were compared using unpaired t-test (α=0.05). Changes in T2* from 6-weeks to 6-months post-operative were related to ATT and ITR using simple linear regression (R^2; α=0.05).

Results

Mean T2* increased by 4.3±1.8ms from 6-weeks to 6-months ($p<0.05$) (Fig. 1A). Interim analysis revealed a negative trend in the relationship between change in T2* and ATT ($p=0.064$), but not ITR (Fig. 1B, 1C).

Discussion

Our finding of increased T2* between 6 weeks and 6 months after ACLR is corroborated by previous imaging studies. Continued follow-up will clarify the potential relationship between change in T2* and pre-operative pivot shift instability, particularly ATT. Relating objective and quantitative measures of instability with noninvasive measures of graft structure and composition may help clarify why pre-operative instability affects risk of ACLR failure.

Images (Optional)

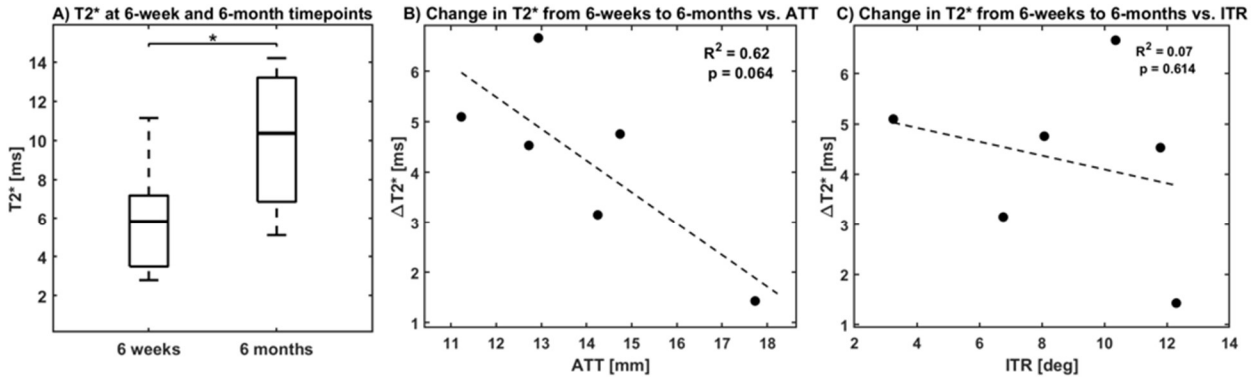


Figure 1: ACL graft T2* at 6-weeks and 6-months (A), and the relation between change in T2* and ATT (B) and ITR (C) in the preoperative knee during a simulated clinical pivot shift exam.

Acknowledgements (Optional)

HSS Kellen Scholars Grant, Clark and Kirby Foundation, HSS Surgeon-in-Chief Fund. HSS has an institutional research agreement with GE Healthcare.

Session Category

Orthopaedic Biomechanics: Sports Medicine

OA188-05

Risk of Lateral Extraarticular Tenodesis Graft Slippage Is Highly Sensitive to Femoral Anchor Location and the Flexion Angle at Which the Graft Is Anchored

Mr. Herman Feller MS, Dr. Molly Day MD, Dr. Joshua Roth PhD

University of Wisconsin-Madison, Madison, WI, United States

Mr. Herman Feller

Dr. Molly Day

Introduction

Adding a lateral extraarticular tenodesis (LET) graft to mitigate instability and anterior cruciate ligament (ACL) graft failure after ACL reconstruction (ACLR) is becoming more common. However, there is not wide spread agreement of key surgical parameters, including (1) the location the LET graft is anchored to the femur and (2) the flexion angle at which the graft is anchored. Prior literature has largely focused on how graft engagement varies when the joint is loaded, but it is possible that the combination of these two surgical parameters may lead to intraoperative graft slipping during a passive range of motion assessment. Thus, our objective was to determine which combinations of these two modifiable surgical parameters increase the risk of intraoperative LET graft slippage.

Methods

Using our established probabilistic modeling framework, we generated a virtual cohort of 3000 ACLR+LET patients with differing knee mechanics. We modelled an LET graft using the mechanical properties of the iliotibial band and randomly varied both the femoral attachment with respect to the LCL, and the knee flexion angle at which the LET graft was anchored. We then performed forward dynamic simulations of passive flexion from 0° to 90° to determine LET graft tension throughout flexion. Using the probability distributions previously reported for the failure load of common LET graft anchors, we computed the probability of graft slippage for each combination of femoral anchor location and flexion angle of LET graft anchoring.

Results

We found LET grafts anchored posteriorly to the LCL attachment with the knee in 30° to 90° flexion were at the highest risk of slippage. All LET grafts anchored at flexion angles between 0° and 30° had minimal risk of slippage (Figure).

Discussion

Our key finding that the risk of LET graft slippage was highly sensitive to both femoral anchor location and knee flexion indicates surgeons must consider these important decisions when planning and executing an LET to mitigate the risk the graft slippage that undermines the intended contribution of the LET. Slippage alters the engagement of the LET graft, which limits its ability to contribute to knee stabilization and offloading of the ACLR graft.

Images (Optional)

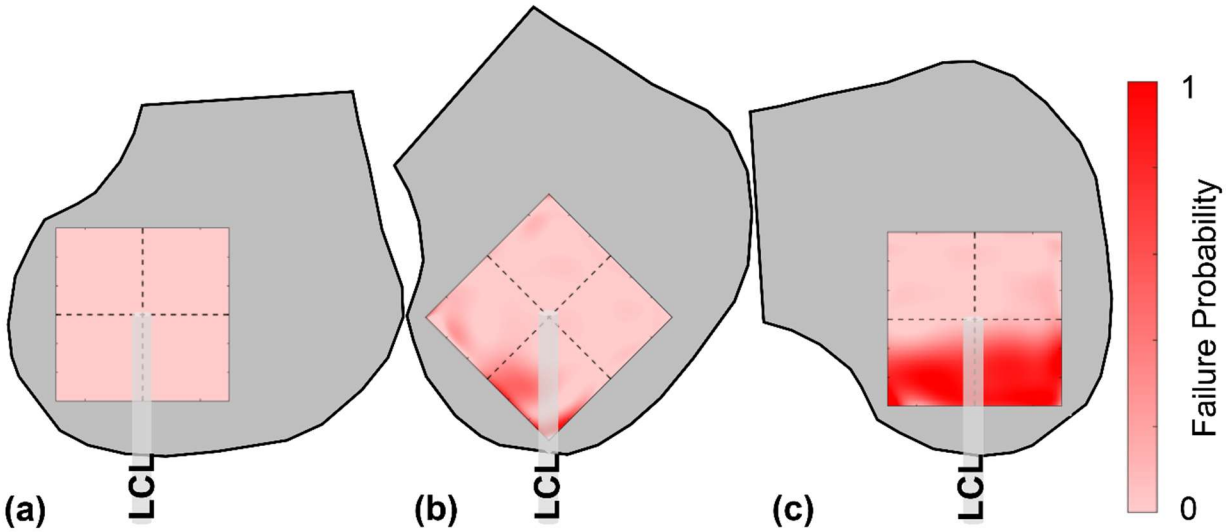


Figure 1: Heatmaps show the probability of LET graft slippage intraoperatively during passive flexion between 0° and 90° flexion for attachment locations spanning a 30 mm x 30 mm area centered on the attachment point of the LCL at fixation angles of (a) 0°-30° of flexion, (b) 30°-60° of flexion, and (c) 60°-90° of flexion.

References (Optional)

Session Category

Orthopaedic Biomechanics: Sports Medicine

OA188-06

Bonenet: Rapid and Clinically Feasible Femoral Neck Load Prediction Using Neural Network

Dr Zainab Altai[1,2], Dr Jason Moran[3], Dr Xiaojun Zhai[4], Dr Andrew T M Phillips[5], Dr Bernard X.W. Liew[3]

[1]School of Sport Rehabilitation and Exercises Sciences, , University of Essex, COLCHESTER, ESSEX, United Kingdom. [2]Institute of Public Health and Wellbeing, , University of Essex, COLCHESTER, ESSEX, United Kingdom. [3]School of Sport Rehabilitation and Exercises Sciences, University of Essex, COLCHESTER, Essex, United Kingdom. [4]School of Computer Science and Electronic Engineering, University of Essex, COLCHESTER, Essex, United Kingdom. [5]Department of Civil and Environmental Engineering, Imperial College London, London, London, United Kingdom

Introduction

Methods

Thirty-seven healthy, active participants (age 40.3 ± 13.1 y; height 1.7 ± 0.08 m; mass 68.4 ± 11.7 kg) were recruited with ethical approval. Motion-capture used 14 vicon cameras and 38 lower-limb markers, while seven IMUs on the trunk, shanks, thighs, and feet recorded accelerations and angular velocities. Participants performed walking, running, countermovement jump, squat jump, unilateral hopping, and bilateral hopping at three intensity levels.

MSK-FE models were generated in OpenSim and ANSYS to predict peak tensile and compressive FN strains. BoneNet, an eXplainable Convolutional Neural Network [3] in Python (Numpy v1.20.3, Pandas v1.3.4, Scipy v1.7.1), was trained on IMU data to predict these strains, using a 75/25% train/test split over 500 epochs with learning rates 0.1–0.2. MSK-FE strain data were outcomes; IMU signals were predictors. Peak strains were ranked and compared to walking to assess osteogenic potential, and BoneNet accuracy was evaluated via Pearson's correlation (r) and RMSE.

Results

Running at all intensities and low-intensity unilateral hopping produced significantly higher FN strains than walking (up to 47%, $p < 0.001$), whereas all other exercises generated lower peak strains (up to 175%) (Figure 1). BoneNet predicted strains with high accuracy, showing

strongest correlations during walking (r = 0.96) and lowest for squat jumps (r = 0.80), with a RMSE range of 145-551 με across exercises.

Discussion

Running at any speed and low-intensity unilateral hopping effectively stimulate FN osteogenesis, whereas bilateral jumps may not. Additionally, BONENET provide a practical, cost-effective method to monitor bone strain and support interventions to enhance bone health.

Images (Optional)

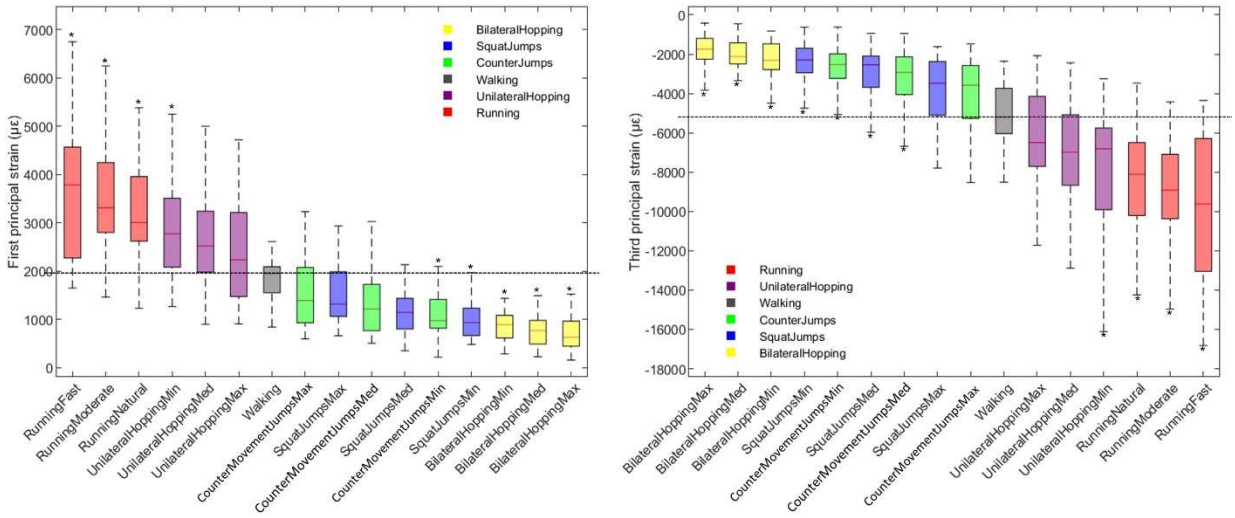


Figure 1. Box plot of large significant difference of peak first principal strain (left) and peak third principal strain (right) of the femoral neck under different levels of various dynamic exercises compared to walking at a self-selected speed indicated by the horizontal line. Asterisks denote the exercises with significant difference (*p < 0.05) compared to walking.

References (Optional)

[1] Allison et al, J Bone Miner Res, 2015.

[2] Martelli et al, Curr Osteoporos Rep, 2020.

[3] Fauvel et al, Mathematics, 2021.

Acknowledgements (Optional)

This work was supported by The Academy of Medical Sciences (SBF006\1019).

Session Category

Orthopaedic Biomechanics: Sports Medicine

OA189-01

Postpartum Biomechanical Adaptations of the Linea Alba in a Rat Model: Implications for Diastasis Recti Abdominis in Women

Ms Mya Lax BSc, Ms Mary Morgan BSc, Ms Sabrina Sinopoli MSc, Dr Diane Gregory PhD

Wilfrid Laurier University, Waterloo, Ontario, Canada

Ms Mya Lax

Ms Sabrina Sinopoli

Introduction

The linea alba (LA) is a fibrous connective tissue that joins the rectus abdominis muscles and plays a critical role in abdominal wall integrity. Physiological changes, particularly during pregnancy, have been shown to disrupt this structure. As fetal growth increases the intra-abdominal pressure, the inter-rectus distance widens due to LA stretching. If this widening is substantial, it can result in the diagnosis of diastasis recti abdominis (DRA). This study aimed to identify these changes by evaluating LA tensile strength in abdominal tissue of rats at two time points postpartum.

Methods

Twenty Sprague-Dawley rats were tested: five 3-day postpartum, five 8-week postpartum, and 10 age-matched nulliparous. Three 7.5x7.5mm LA samples were dissected from the abdominal wall of each animal: one from the level of the umbilicus, one just cranial, and one just caudal to the umbilicus. These samples underwent tensile mechanical testing at a rate of 0.5%/sec until failure. An additional six animals (three nulliparous and three 3-days postpartum) were used for histological analysis of the LA.

Results

Yield point stress (p=0.0003) and maximum stress (p=0.001) of the LA were found to be higher in the 3-day postpartum compared to both nulliparous and 8-week postpartum animals. Stiffness was also found to be higher in the 3-day postpartum animals, though not significant (p=0.062). In corroboration of this finding, histology indicated greater connective

tissue between the rectus abdominis muscles of the 3-day postpartum animals compared to nulliparous (Figure 1).

Discussion

The elevated yield and maximum stress values in the 3-day postpartum samples indicate that the LA may adapt to withstand increases in abdominal wall tension late in gestation. The corresponding histological evidence of increased connective tissue further supports the idea that structural reinforcement occurs during this period. However, as the mechanical properties returned closer to nulliparous levels by 8-weeks postpartum, this suggests the remodelling is temporary and may serve a protective role by helping maintain abdominal wall integrity during and immediately after pregnancy. It is possible that individuals who experience DRA do not undergo the same degree or timing of this remodeling response, making the LA more susceptible to separation when mechanical demands are high.

Images (Optional)

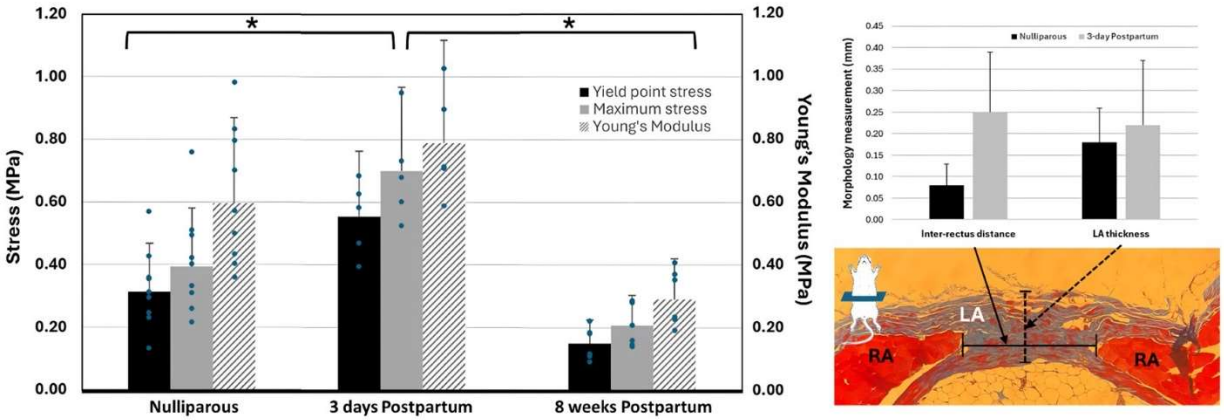


Figure 1. Left: Mean (±SD) yield point stress, maximum stress, and Young's modulus determined from tensile testing of the linea alba from control (nulliparous), 3-days postpartum, and 8-weeks postpartum animals. For all each variables, 3-days postpartum was higher than both nulliparous and 8-weeks postpartum. Right top: Mean (±SD) inter-rectus distance and linea alba thickness in the nulliparous (grey bars) and 3-day postpartum (black bars) sections. Right bottom: The inter-rectus distance and linea alba thickness measurements are shown in the representative histological image, with the rectus abdominis (RA) and linea alba (LA) labelled.

Session Category

Clinical Biomechanics: N/A

OA189-02

The Impact of Pregnancy on Hip, Knee, and Ankle Strength

Ms Kaitlyn Kleeman BS, Mrs. Maryam Golmohammadi MS, Dr. Amanda Paluch PhD, Dr. Sarah Roelker PhD

University of Massachusetts Amherst, Amherst, MA, United States

Introduction

Physiological and musculoskeletal changes occur during pregnancy, including increased body mass (1), fatigue (2), and joint laxity (3,4), which may contribute to falls. Muscle forces regulate balance during walking (5), however pregnancy-related changes in strength have only been evaluated in abdominal (6) and hip adductor (7) muscles, for which absolute strength decreased during pregnancy. This study aims to determine the effect of pregnancy on hip abductor and knee and ankle extensor strength. We hypothesized that strength at each joint would 1) decrease from the 2nd (P-T2) to 3rd (P-T3) trimester, and 2) be lower in pregnant (PREG) than age-matched nulligravida (NG) individuals, particularly in P-T3.

Methods

Isometric hip abductor, knee extensor, and plantarflexor strength was collected on a Biodex dynamometer in PREG (n = 17, 34 ± 4.3 yrs) at P-T2 and P-T3 and once in NG (n = 8, 34 ± 4.6 yrs). Participants performed three 5s contractions (15s rest between trials). Absolute strength was quantified as the maximum torque produced across all trials and relative strength was calculated by dividing absolute strength by body mass. For absolute and relative strength at each joint, paired t-tests assessed for differences between P-T2 and P-T3, while separate two-sample t-tests assessed for differences between NG and P-T2 and NG and P-T3 with Bonferroni Corrections.

Results

Relative knee extensor strength decreased from P-T2 to P-T3 (Fig. 1A). Compared to NG, PREG had significantly lower relative hip abductor strength at both timepoints (Fig. 1B). Despite no significant differences, large effect sizes (Fig. 1B) suggest PREG have potentially meaningfully lower normalized knee extensor strength than NG at both timepoints. Absolute strength did not differ between groups or timepoints at any joint.

Discussion

Decreased relative knee strength from P-T2 to P-T3 and lower relative hip strength in PREG compared to NG may influence balance regulation during pregnancy.

Images (Optional)

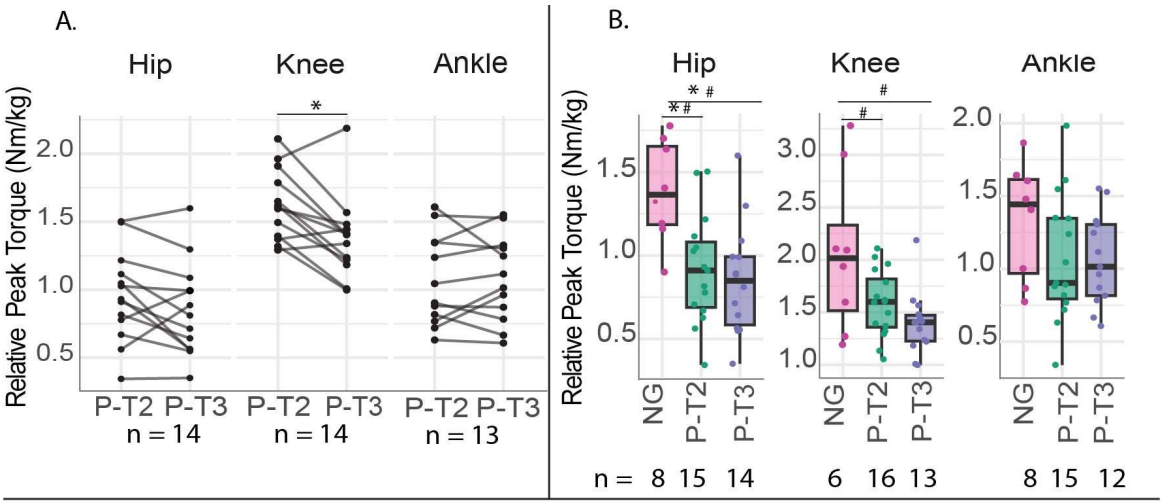


Figure 1: Body mass relative hip abductor, knee extensor, and ankle plantarflexor peak torques in nulligravida and pregnant individuals. (A) Within participant changes in relative peak torque form P-T2 to P-T3. A significant decrease in knee strength was observed from P-T2 to P-T3 ($p = 0.042$, Cohen's $d = 0.649$). (B) Boxplots of relative peak torque for NG, P-T2, and P-T3. Filled circles represent individuals. Compared to NG, hip strength was significantly lower in P-T2 ($p = 0.021$, Cohen's $d = 1.469$ and P-T3 ($p = 0.009$., Cohen's $d = 1.659$). Compared to NG, large effect sizes suggest lower knee strength in P-T2(Cohen's $d = 0.956$) and P-T3 (Cohen's $d = 0.739$). * denotes a statistically significant difference. # denotes a large effect size.

References (Optional)

(1) Krkeljas, Hum. Mov. Sci. 2018. (2) Wang & Apgar, Am Fam Physician, 1998. (3) Calguneri, Ann. Rheum. Dis, 1982. (4) Schauberger, Obstet Gynecol, 1996. (5) Neptune & McGowan, J Biomech. 2011. (6) McCrory, BJOG, 2010. (7) Santos, PLOS ONE, 2024.

Acknowledgements (Optional)

Funding: UMass Amherst IALS Midi Grant

Session Category

Clinical Biomechanics: N/A

OA189-03

High-Functioning Older Adults Use Greater Muscle Contributions to Whole-Body Angular Momentum than Younger Adults to Regulate Balance

Mr. Nikolaj Freschlin M.S., Dr. Sarah Roelker Ph.D., Dr. Katherine Boyer Ph.D.

University of Massachusetts, Amherst, Amherst, MA, United States

Introduction

Balance is maintained by regulating the whole-body angular momentum (*H*) about the center-of-mass [1]. Older adults (OLDER) often have larger peak-to-peak ranges of *H* than younger adults (YOUNG), which indicates poorer balance control [2] and increased fall risk. Muscles regulate *H* by contributing to the net external moment (NetExtM) about the center-of-mass [3]. Identifying age-related changes in muscle contributions to the NetExtM may provide insight into balance mechanisms in OLDER. The purpose of this study was to compare individual muscle contributions to *H* regulation between YOUNG and OLDER.

Methods

Motion capture data of 5 YOUNG (37.4±3.2 years) and 5 OLDER (71.8±1.6 years) walking at their preferred speed (YOUNG: 1.4±0.2 m/s; OLDER: 1.5±0.1 m/s) were used to generate simulations in OpenSim [4]. OpenSim MoCoInverse [5] estimated muscle forces while tracking electromyography from 10 muscles. Muscle forces were used to calculate muscle contributions to NetExtM [3] in frontal and sagittal planes. The *H* range and integral of each muscle's contribution to NetExtM over stance were normalized to height, weight, and speed and compared between age-groups using independent samples t-tests ($\alpha<0.05$).

Results

H range did not differ in the sagittal plane; yet, OLDER had larger contributions to forward *H* from the medial hamstrings and gastrocnemius, and larger contributions to backward *H* from the rectus femoris, vasti, and tibialis anterior than YOUNG (Fig. A-B; $p<0.05$). OLDER had lower frontal *H* range than YOUNG ($p=0.043$) and larger contributions to *H* towards the contralateral leg from the gluteus maximus, vasti, and gluteus medius (Fig. C-D; $p<0.05$).

Discussion

Compared to YOUNG, OLDER used greater muscular effort to regulate similar sagittal plane and greater frontal plane H range. This greater muscular effort may be a cautious strategy to avoid falls by more tightly controlling balance regulation and may contribute to greater energy cost of walking in OLDER.

Images (Optional)

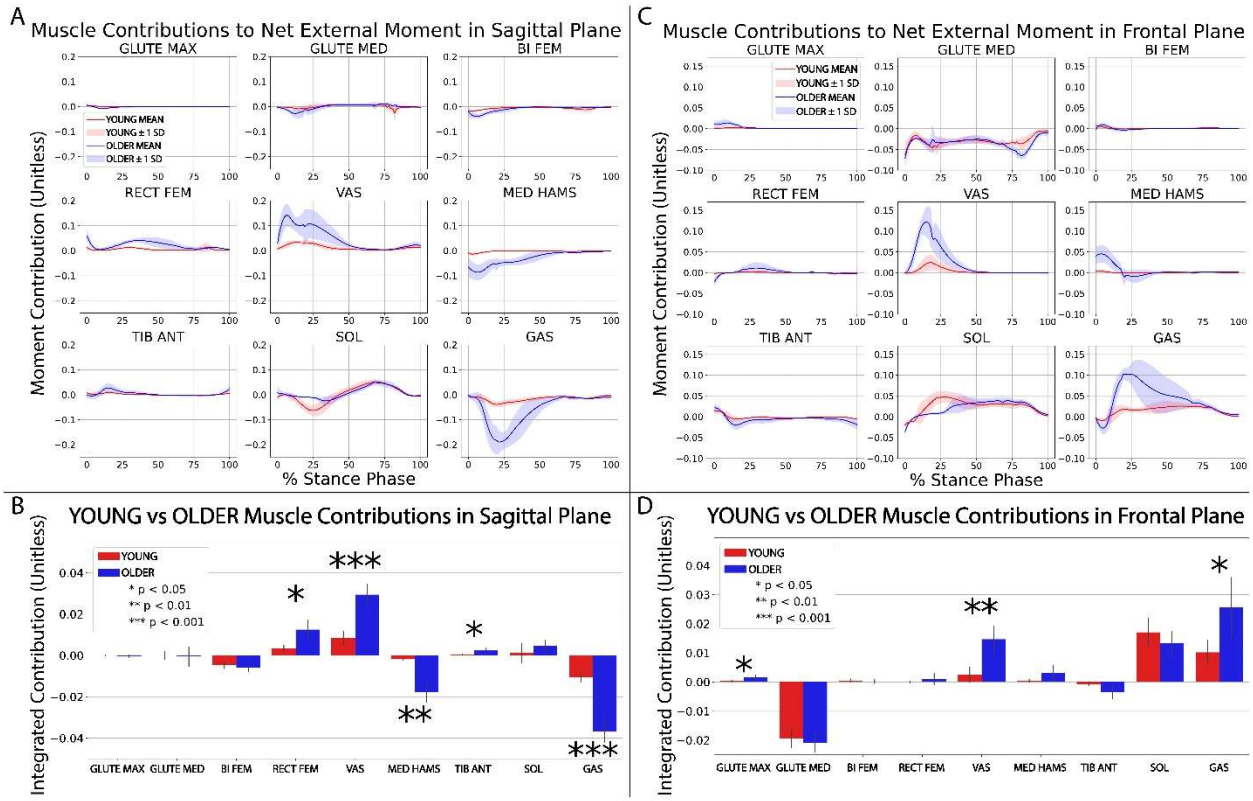


Fig. 1: Muscle contributions to balance regulation in younger and older adults. A) Muscle contributions to the sagittal NetExtM. B) Integrated muscle contributions to the sagittal NetExtM. C) Muscle contributions to the frontal NetExtM. D) Integrated muscle contributions to the frontal NetExtM. In the sagittal plane, positive (negative) values indicate the muscle is producing backward (forward) H. In the frontal plane, positive (negative) values indicate the muscle is producing H toward the contralateral (ipsilateral) limb. Muscle contributions from gluteus maximus and gluteus medius lines of action were summed in GLUTE MAX and GLUTE MED, respectively. Muscle contributions from semimembranosus and semitendinosus were summed in MED HAMS, from medial and lateral gastrocnemius were summed in GAS, and from vastus medialis, lateralis, and intermedius were summed in VAS. BI FEM (biceps femoris long head), RECT FEM (rectus femoris), TIB ANT (tibialis anterior), and SOL (soleus) each represent contributions from one muscle.

References (Optional)

[1] Herr & Popovic, *J Exp Biol*, 2008. [2] Neptune & Vistamehr, *J Biomech Eng*, 2019. [3] Neptune & McGowan, *J Biomech*, 2011. [4] Delp, *IEEE Trans Biomed Eng*, 2007. [5] Dembia, *PLoS Comp Bio*, 2020.

Acknowledgements (Optional)

Funding: NIH 5R01AG068102

Session Category

Clinical Biomechanics: N/A

OA189-04

Age-related Differences in Locomotor Response to Fall-Related Anxiety in Virtual Reality Settings Across Time

Dr. Kelly Poretti[1], Dr. Toby Ellmers[2], Dr. Quentin Sanders[3], Dr. Nathalia Peixoto[3], Dr. Christopher Rhea[4], Dr. Tiphanie Raffegeau[1]

[1]George Mason University, Manassas, VA, United States. [2]Imperial College London, London, London, United Kingdom. [3]George Mason University, Fairfax, VA, United States. [4]Old Dominion University, Norfolk, VA, United States

Introduction

Up to 60% of older adults report a fear of falling, and while certain levels of concern serve adaptive purposes, excessive fall-related anxiety can disrupt movement planning when balance is threatened. Due to age-related differences in stepping pattern adaptation, differences might also exist adapting to virtually-induced fall-related anxiety environment (e.g. simulated high elevations). The purpose of this study was to determine age-related differences in response to virtually-induced fall-related anxiety across time.

Methods

Participants (N = 30, 14 older adults) experienced one minute of self-paced walking at virtual low elevations (ground) followed by five minutes at virtual high elevations (~15m) on a walkway adjusted to allow ~6 steps per pass based on individuals' step length. Visualization of the absolute distance between the headset and ankle trackers (HTC Vive Pro Eye) was used to calculate gait parameters (gait speed, step length and width, and double support). The first (T1) and last (T2) six steady state steps were extracted to determine changes across time. Linear mixed-effect regression compared parameters due to Age (2 levels: Older, Young Adults), Height (2 levels: Low, High), and Time (2 levels: T1, T2).

Results

Both groups adapted similarly, walking with longer steps over time at low [$F = 10.25$, $p = .001$] and high [$F = 83.78$, $p < .001$] elevations. However, neither group altered step width, gait speed, or percent time in double support over time in low or high settings ($p > .179$).

Discussion

Both young and older adults habituate gait similarly with exposure to virtual anxiety-inducing settings, taking longer steps over time. In this paradigm, step lengths are not mechanically limited and are orthogonal to the direction of postural threat, thus both

groups adapted by decreasing cadence to maintain speed and take longer steps. However, neither group adapted the percent time in double support, indicating they adapt locomotion under threat by lengthening steps while sustaining the time spent in stable phases of the gait cycle.

Images (Optional)

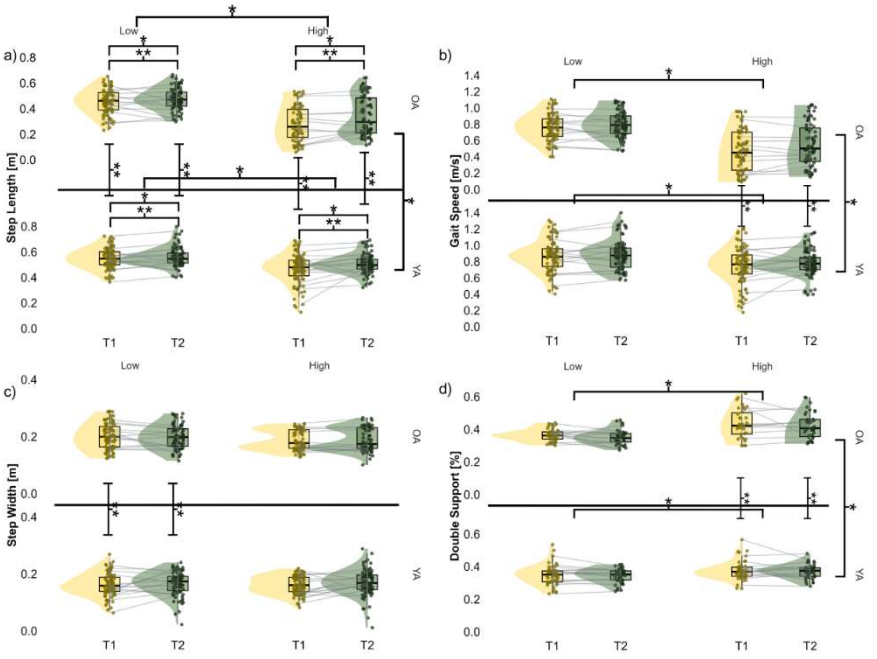


Figure 1(a-d): Age-related differences in adaptations of (a) step length, (b) gait speed, (c) step width, and (d) double support to fall-related anxiety across repeated exposures. Compensatory changes to gait parameters from the beginning of a five-minute exposure (T1) and the end of an exposure (T2) as well as between the first five-minute exposure (E1) and the second exposure (E2) to anxiety-inducing virtual settings. Older adult (OA) data is represented in the figures above the horizontal line, while young adult (YA) data is represented in the figures below. Scattered dots represent subject means, while variability is represented by the violin plots. T1 is represented by the yellow-colored violin plots, while T2 is represented by the green-colored plots. Significant main effects of group, exposure, and/or time are indicated with a single asterisk and brackets, while significant interaction effects of exposure and time are indicated with a double asterisk.

Session Category

Clinical Biomechanics: N/A

OA189-05

Does Prefrontal Cortex Activation Predict Decision-Making Performance on a Reactive Jump Landing Task?

Dr. Fatemeh Aflatounian[1,2], Ms Alexandra Lynch[1], Dr. Keith Hutchison[1], Dr. James Becker[1], Dr. Corey Pew[1], Dr. Scott Monfort[1]

[1]Montana State University, Bozeman, Montana, United States. [2]Virginia Commonwealth University, Richmond, Virginia, United States

Introduction

Anterior cruciate ligament (ACL) injuries happen often without contact in sport and are frequently linked to interruptions in cognitive–motor control during unanticipated movements. Although biomechanical risk factors have been widely studied, growing evidence suggests neural processes underlying visuomotor coordination and attention control as risk factors. Functional near-infrared spectroscopy (fNIRS) enables non-invasive measurement of cortical activation during dynamic tasks. This study examined whether prefrontal cortex activation (PFC) during an attention control task relates to decision-making performance through unanticipated jump-landings associated with ACL injury risk.

Methods

Thirty-one healthy recreational athletes (15F/16M; 23.1±2.6years) completed a computerized attention-control battery[1] while wearing an fNIRS cap targeting Brodmann areas (BA) 46 and 9. Neural activation (t-statistics) was derived using an autoregressive iterative reweighted least squares general linear model with short-separation channel regressors. Participants performed unanticipated conditions that included a simple task (Simple) of landing on the limb towards an image on one side of the screen, and a complex task (Complex) of landing on the limb towards a picture of the basketball or away from a simulated opponent. Failed trials involved incorrect cue responses and landing on the wrong limb(s). Failed trial percentage (Failed%) was calculated for each cognitive condition. Pearson correlations tested associations between fNIRS activation and Failed%.

Results

PFC in BA46 and BA9 showed no significant correlations with Failed% in either challenging condition ($p > 0.05$, Figure 1). Small-to-moderate effect sizes ($|r| \approx 0.3$) suggested a nonsignificant trend toward fewer failed landings with greater prefrontal activation.

Discussion

PFC measured during isolated cognitive testing was not associated with decision-making accuracy during dynamic jump-landings, suggesting that landing errors were not explained by baseline cognitive activation. Instead, failures likely reflected task-specific cognitive–motor demands during reactive movement. This aligns with behavioral work showing that attention-control tests typically demonstrate only small–moderate associations with task accuracy (r≈0.20–0.40), underscoring the challenge of capturing cognitive variability through isolated tasks alone. Future work should incorporate real-time neural measures and refined task designs to better characterize rapid cognitive load fluctuations preceding movement errors.

Images (Optional)

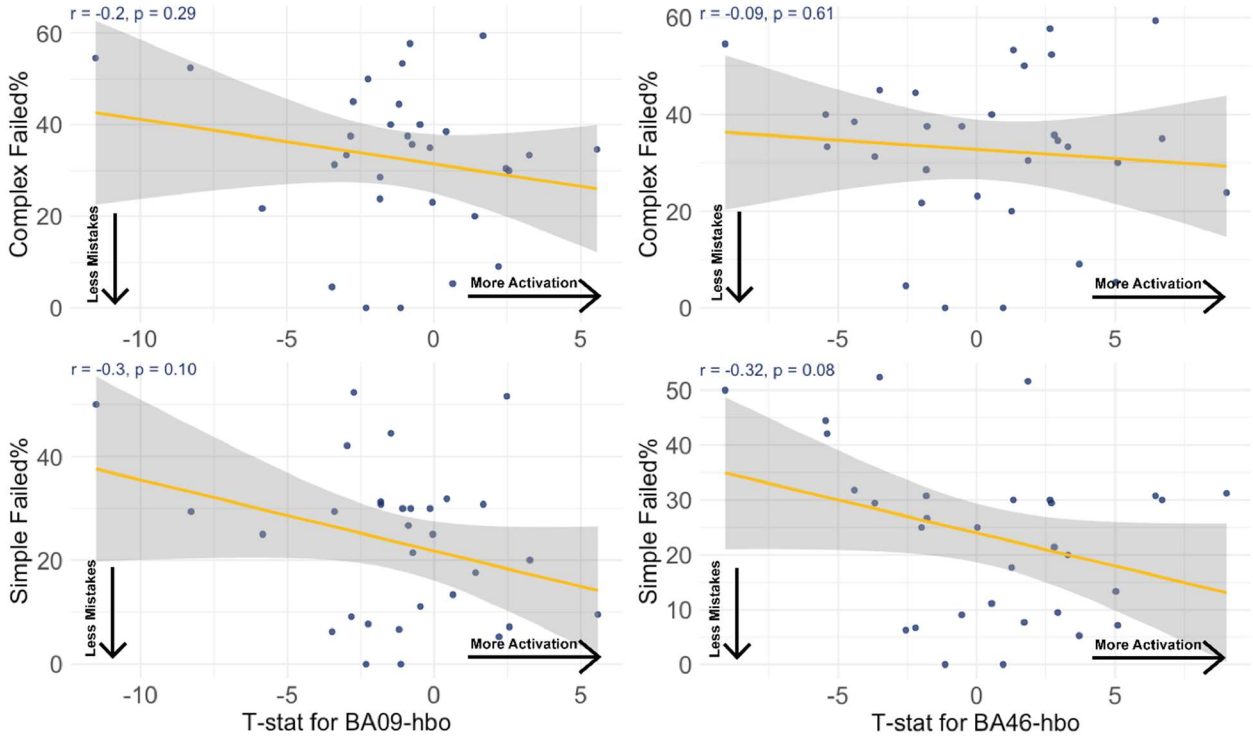


Figure 1: Scatterplots of T-stats for BA9 and BA46 and Failed% of simple and complex jump-landing conditions

References (Optional)

[1] Burgoyne et. al. (2023) J Exp Psychol Gen 152(8)

Session Category

Rehabilitation Biomechanics and Human Factors: Occupational Biomechanics

OA189-06

Arm Swing As A Mediator Of Age-related Slip-Fall Risk

Mr Shilin Wang, Feng Yang

Department of Kinesiology and Health, Georgia State University, Atlanta, Georgia, United States

Introduction

Slip-induced falls lead to injuries in older adults. Upper-extremity reactions, especially the arm swing strategy, may help restore balance after a slip by redirecting whole-body momentum. Aging appears to reduce protective arm responses [1], yet it is unclear to what extent the arm-swing strategy explains age differences in slip-induced fall risk. This study quantified age-related differences in protective arm use and slip-fall and tested whether arm swing mediates the association between age and slip-fall.

Methods

Secured by a harness connected to a loadcell, 61 young and 64 older adults (Table 1) experienced a standing-slip on an ActiveStep treadmill. Slips were induced by a 0.36-m forward belt translation over 0.6 s. A slip was deemed a fall if the peak loadcell force exceeded 30% bodyweight [2]. Motion data was used to classify each trial as arm swing (shoulder flexion≥45° post-slip) or no arm swing (shoulder angle<45°). Associations between age, arm use, and falls were quantified with χ^2 tests and generalized linear models. Single-mediator models estimated direct and indirect effects of age on fall risk through arm use. SPSS 29.0 with α of 0.05 was used.

Results

60.9% of older and 34.4% of young adults fell (odds ratio (OR)=2.97, p=0.003). Significantly fewer older adults swung their arms than younger adults (71.9% vs 91.8%, OR=0.23, p=0.007). Slips with arm swing exhibited a lower probability of falling than slips with no arm use after adjusting age (41.2% vs 78.3%; OR=0.19, p=0.003). Mediation analysis indicated that reduced arm use in older adults led to an indirect increase in fall risk of 6.0%, accounting for about 22.8% of the overall association between age and falls.

Discussion

Our results indicated that the ability to use arm swing as a protective strategy responding to a standing-slip is a fall risk factor. Aging could compromise such an ability. Findings

highlight protective arm swing as a potential training target to improve older adults' balance recovery after perturbations. Future work should test other perturbation types and high-fall-risk populations.

Images (Optional)

Table 1 Demographic information in mean ± standard deviation and distribution of participants grouped by age, the use of arm swing, and slip outcome.

Group	Arm use	Faller status		Age (years)	Sex (F/M)	Body height (cm)	Body mass (kg)
		Faller	Non-faller				
Older	Yes	26	20	64.9 ± 5.7	34 / 12	166.8 ± 10.5	65.8 ± 13.6
	No	13	5	70.3 ± 8.8	16 / 2	162.1 ± 7.7	66.3 ± 12.9
Young	Yes	16	40	23.6 ± 4.4	45 / 11	165.3 ± 8.1	64.4 ± 11.5
	No	5	0	23.0 ± 0.0	2 / 3	173.4 ± 9.1	65.3 ± 15.1

References (Optional)

[1] Lee-Confer, Front Sports Act Living, 2024; [2] Yang & Pai, J Biomech, 2011.

Acknowledgements (Optional)

The authors thank all volunteers.

Session Category

Clinical Biomechanics: N/A

OA190-02

Female Hip Joint Contact Differences in Table Tennis Are Associated With Anatomical Shape and Not Mechanical Loading

Ms Xiaoyi Yang[1], Associate Professor Qichang Mei[2], Dr Vickie Shim[1], Professor Justin Fernandez[1]

[1]University of Auckland, Auckland, CBD, New Zealand. [2]Ningbo University, Ningbo, Zhejiang, China

Introduction

Female table tennis athletes experience higher rates of hip joint injury, however, it is not fully understood if this is associated with mechanical differences or anatomical variations between the biological sexes [1]. The objective of this study was to investigate hip joint loading between female and male elite level table tennis players integrating motion analysis, finite element modelling, and statistical shape analysis to elucidate the contribution of mechanics and shape variation to hip joint loading.

Methods

Following ethical approval and player consent, 18 females and18 males (aged 20-29) performed the widely used chasse-step table tennis movement. Kinematics, kinetics, and EMG were collected and processed in OpenSIM. In parallel, a statistical shape model was created from 60 aged-matched geometries from the Victorian Institute for Forensic Medicine using GIAS3. A finite element model was constructed in Abaqus to match the OpenSIM model for a mean male and mean female. The maximum transverse loading side-step movement was simulated using each players hip orientation. Firstly, we evaluated kinetic differences (muscle and joint contact forces) on hip loading, and secondly, we evaluated shape differences using statistical shape analysis.

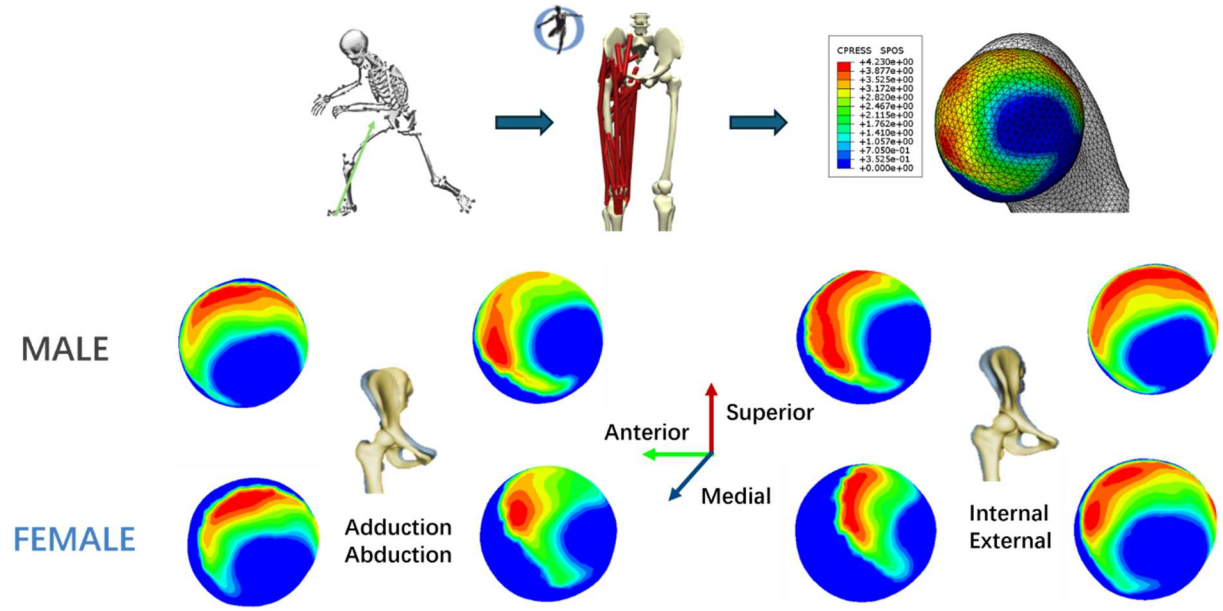
Results

Our models supported a finding that maximum hip contact pressure was similar in both males and females, despite males having larger hip joint forces and having significantly higher muscle forces across the hip. In contrast, adduction-abduction hip shape variation highlighted that hip contact zones were superior-medial in females and superior-anterior in males. Further, internal-external hip shape variation revealed hip contact zones were medial-superior in females, but anterior-superior in males. Hence, despite peak pressure being similar in range, the contact zones were significantly different.

Discussion

Our study findings suggest that hip loading differences between sexes may be associated with joint contact zone differences linked to biological sex anatomical shape and not due to mechanical loading. This highlights that shape models considering biological sex differences are important when considering dynamic sports, like table tennis, and investigating sports performance and injury prevention.

Images (Optional)



References (Optional)

[1] Yang et al., Bioengineering, 9(6), 246, 2022.

Acknowledgements (Optional)

The authors acknowledge the athlete participants in this study.

Session Category

Human Motion and Performance: Sports

OA190-03

Interlimb Strength and Loading Characteristics During Dynamic Tasks in Female Special Operation Forces Personnel

Ms. Tatiana Djafar[1], Dr. Nicholas Heebner[1], Mr. Tyler Cardinale[1], Dr. Benjamin Cuddy[1], Mr. Brad Lambert[2], Dr. Jeremy Ross[1], Dr. Joshua Winters[1]

[1]University of Kentucky, Lexington, KY, United States. [2]United States Marine Forces Special Operations Command, Camp Lejeune, NC, United States

Introduction

Female military personnel have high rates of reported injury, often associated with the rigorous nature of their tactical training. Lower limb strength and loading symmetry are commonly used for return to activity criteria following an injury. The purpose of this study was to examine the relationship between strength symmetry and functional loading during dynamic tasks in female Special Operations Forces (SOF) support personnel.

Methods

Sixteen female SOF support personnel (age: 26.25±4.54yrs; height: 164.70±5.28cm; mass: 64.78±6.08kg) who were cleared for unrestricted duty underwent a functional performance assessment (vertical jump (VJ: peak concentric and landing force), isometric mid-thigh pull (IMTP: net peak force)) on bilateral force plates and completed a running mechanics evaluation using a markerless motion capture system (peak vertical ground reaction force, impulse, average loading rate). Isometric quadriceps and hamstring strength were also measured. Paired-samples t-tests ($\alpha = 0.05$) with Hedges' g effect sizes determined limb differences. Pearson correlations were used to assess relationships between strength and dynamic tasks.

Results

Mean absolute asymmetries are presented in Table 1. VJ peak concentric force was the only statistically significant interlimb difference (6.24%, p=0.021, g=0.610). Quadriceps strength, but not peak concentric force, correlated with VJ height (dominant: r=0.508, p=0.045; non-dominant: r=0.498, p=0.050). Dominant limb quadriceps strength also moderately correlated with IMTP net peak force (dominant: r=0.574, p=0.020; non-dominant: r=0.329, p=0.213).

Discussion

Female SOF support personnel only demonstrated a statistically significant interlimb asymmetry during VJ take-off. Though there were no statistical differences in strength, the average asymmetry in the quadriceps was 12.05%, and 7/16 participants exceeded 10% asymmetry, a threshold commonly used for return-to-sport-criteria. Peak VJ landing force also exceeded this threshold with 12.39% asymmetry. However, only VJ height was correlated to quadriceps strength. From a clinical standpoint, strength may be a stronger indicator of functional performance but not necessarily of shock attenuation strategies during dynamic tasks. Though female SOF support personnel demonstrated strength and landing asymmetries greater than clinical thresholds, a lack of relationship between these metrics as well as minimal interlimb differences among other characteristics of these dynamic tasks suggest consideration for a different approach to limb symmetry evaluation.

Images (Optional)

	Vertical Jump		IMTP	Running Assessment			Isometric Strength	
	Peak Concentric Force*	Peak Landing Force	Net Peak Force[a]	Peak Vertical GRF	Impulse	Vertical Average Loading Rate	Quadriceps	Hamstrings
Asymmetry	6.24%	12.39%	5.11%	3.31%	2.62%	9.54%	12.05%	10.01%
p-value	0.021	0.083	0.414	0.308	0.171	0.127	0.811	0.866
Hedges' g	0.610	0.441	0.220	0.250	0.342	0.384	0.058	0.041

Table 1. Mean absolute asymmetries of variables of interest. GRF=Ground Reaction Force
*: $p<0.05$; [a]: statistics were run on 13/16 subjects due to data integrity

Acknowledgements (Optional)

Disclaimer: The content is solely the responsibility of the authors and does not necessarily represent the official views of the Office of Naval Research, the US Navy, or the US Special Operations Command. Supported by the Office of Naval Research N0004-21-1-2682.

Session Category

Human Motion and Performance: Sports

OA190-04

Sex-differences in Preparatory Step Biomechanics During a 90° Cutting Task

Ms. Katherine Batista MSc, Dr. Robin Trama PhD, Ms. Meghan Rogers, Ms. Emily Dittmer BSc, Dr. Zi Xiang Gao PhD, Dr. Darren Stefanyshyn PhD, Dr. John Wannop PhD

The University of Calgary, Calgary, Alberta, Canada

Introduction

Lower-limb biomechanics during cutting maneuvers have been extensively studied to gain insight into injury mechanisms and performance determinants in sport. Although research often focuses on the final change-of-direction step, emerging evidence suggests that the preceding steps prior to the change of direction may influence performance and potential injury risk variables [Jones et al., 2016; Dos'Santos et al., 2019, 2021]. Although studies have examined these preceding steps in male and female athletes separately [Dos'Santos et al., 2019; Mulligan, 2022;], no studies have directly compared sex differences. Therefore, the purpose of this study was to compare lower extremity biomechanics of the antepenultimate, penultimate, and ultimate steps between male and female athletes during a 90° cutting task.

Methods

Fifteen soccer players (5 female, 10 male) performed five maximal effort 90° cutting trials in standardized soccer cleats on artificial turf. Three-dimensional ground reaction force data were collected via three in-series force platforms for the antepenultimate, penultimate, and ultimate steps during the cutting task. Kinematic data were also collected, but only ground reaction force (GRF) data is presented in the current study. Sex differences in time-normalized vertical (vGRF) and horizontal (hGRF) ground reaction force waveforms (normalized to body weight, BW) were compared using Statistical Parametric Mapping (SPM; $a = 0.10$).

Results

Significant sex-differences were present in hGRF and vGRF across all steps. Females exhibited lower hGRF than males in the penultimate (8-32% and 73-95% stance) and ultimate (58-96% stance) steps. Conversely, females exhibited higher vGRF during the antepenultimate (23-58% stance) and penultimate (8-27% stance and 32-82% stance) steps.

Discussion

Females displayed greater vertical and lower horizontal body weight normalized GRF during the preparatory (antepenultimate and penultimate) steps, compared to male athletes. These results highlight sex-specific cutting strategies, potentially reflecting different braking or load-distribution patterns prior to the final change-of-direction step. Future work will examine accompanying kinematic (joint angles) and kinetic (joint moments) variables to provide a better understanding of these sex differences.

Images (Optional)

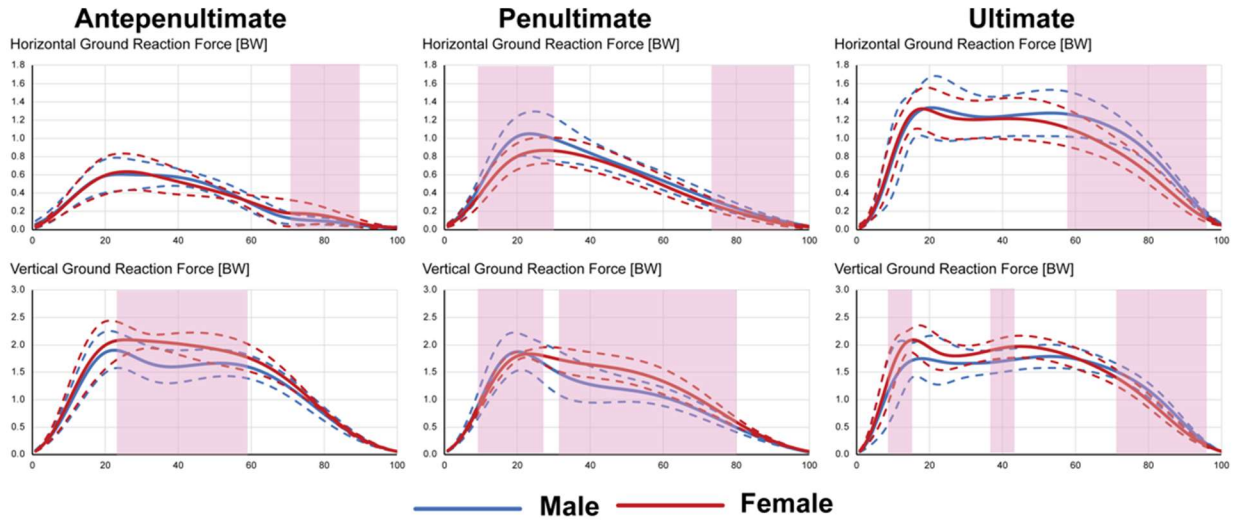


Figure 1. Vertical and horizontal ground reaction force curves of the antepenultimate, penultimate, and ultimate steps of a 90° cutting task for males (blue) and females (red). Highlighted red regions represent significant differences in stance.

Acknowledgements (Optional)

The authors would like to thank adidas for providing the footwear.

Session Category

Human Motion and Performance: Sports

OA190-05

Neuromuscular Activation Patterns During Dual Task Cutting in NCAA Soccer Players with and without Ankle Sprains

Ms. Abigail McCarthy B.S., Dr. Susan D'Andrea Ph.D.

University of Rhode Island, Kingston, RI, United States

Ms. Abigail McCarthy

Introduction

Lateral ankle sprains (LAS), one of the most common injuries in soccer, accounts for approximately 15% of non-contact injuries in collegiate soccer. [1,2] LAS has a high rate of recurrence, with the potential to develop into chronic ankle instability.[3] Traditional rehabilitation focuses on sensorimotor control, dynamic posture and functional exercises, but often lacks cognitive components common in gameplay. Research on dual-task interference in athletes with LAS during sport specific tasks remains limited. This study will investigate neuromuscular responses during cutting movements under cognitive load in NCAA Division I soccer athletes, focusing on differences between healthy individuals and those with a history of lateral ankle sprains.

Methods

Sixteen male and female soccer players aged 18–24 were recruited, eight participants reporting at least one unilateral LAS in the past 12 months and eight sex-matched healthy controls. Following a standardized warm-up, 34 reflective markers and six electromyography (EMG) sensors were placed bilaterally on the lower extremity. A modified flanker task was used and participants were instructed to perform a 45° cutting maneuver in the direction indicated by the middle arrow leading with the ipsilateral foot (Figure1A). Sixteen randomized trials (eight congruent, eight incongruent) were collected with 5–12 seconds of rest between trials.

Results

Six female soccer players are included in the analysis. To understand reaction time, the point at which the flanker arrows appear was determined by video. EMG data were filtered, rectified and enveloped. Latency was determined as the time from flanker initiation to the

onset of muscle activity on the contralateral limb. Peak EMG amplitudes from foot strike to toe off were determined for the cutting leg (Figure 2:B/C).

Discussion

Data show trends that indicate decreased peroneus longus (PL) activity in the stance phase and decreased PL latency for participants with recent ankle sprains. The alteration in PL activation may be indicative of functional instability at the ankle. Further exploration of the data will correlate kinematics to muscle activation and make comparisons between males and females.

Images (Optional)

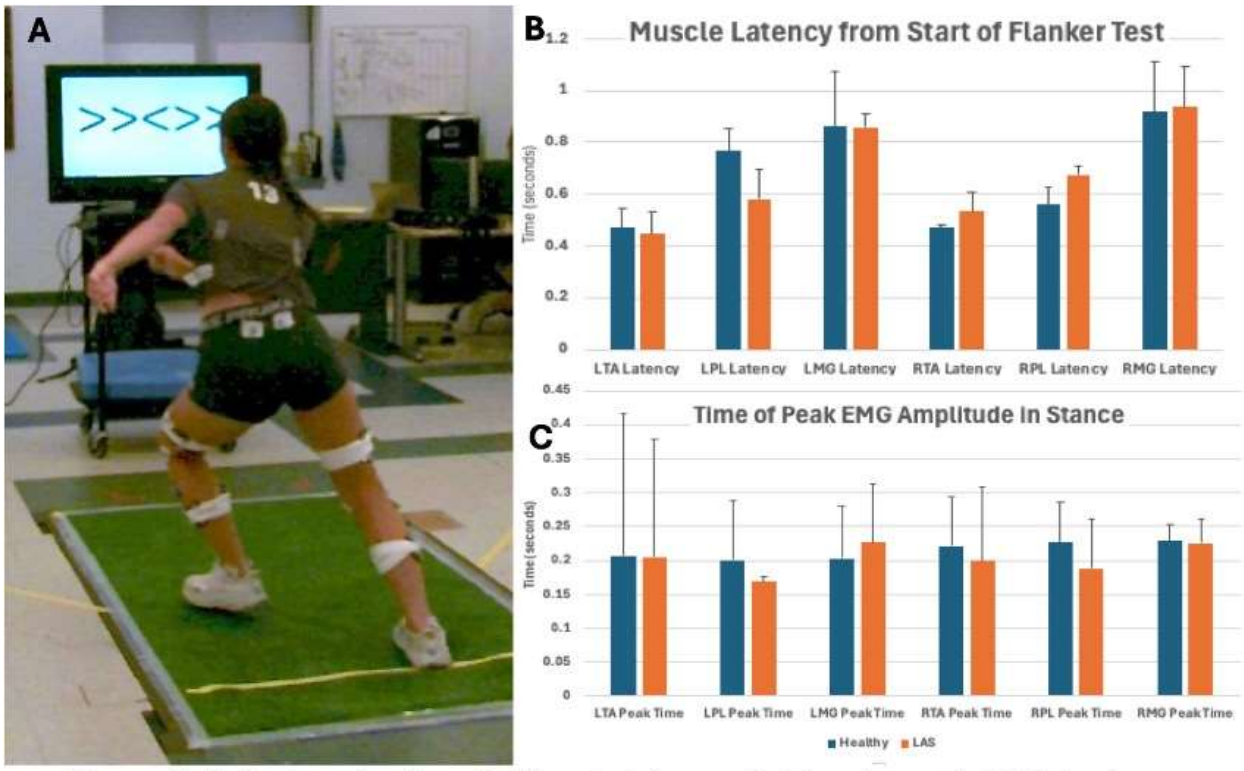


Figure 1: **A**. Data collection; **B**. Muscle latency; **C**. Time to peak EMG in stance. L/R TA- Tibialis Anterior; L/R PL – Peroneus Longus; L/R MG – Medial Gastrocnemius

References (Optional)

1. Chandran *et al*. J Athletic Training, 2021.
2. Gulbrandsen *et al*. J Athletic Training, 2019.
3. Flore *et al*. J Sports Physical Therapy, 2024.

Acknowledgements (Optional)

The authors would like to acknowledge the University of Rhode Island Men's and Women's soccer teams for volunteering their time to participate in the study.

Session Category

Human Motion and Performance: Sports

OA191-02

Non-Invasive Estimation of Pulmonary Vascular Pressure Using In-Vivo Imaging, In-Silico Modeling, and Physics-Informed Neural Networks

Mr. Rana Raza Mehdi[1], Dr. Sunder Neelakantan[1], Mr. Emilio Mendiola[1], Dr. Kyle Myers[1], Dr. Peng Zhang[2], Dr. Gaurav Choudhary[2], Dr. Reza Avaz[1]

[1]Texas A&M University, College station, Texas, United States. [2]Brown University, Providence, Rhode Island, United States

Introduction

Accurate estimation of pressure in terminal pulmonary vessels is essential for diagnosing and managing pulmonary hypertension (PH), yet current methods such as right heart catheterization are invasive and cannot resolve pressures in small distal vessels. Non-invasive modalities (ultrasound, MRI) offer indirect flow-derived measures but lack the spatial resolution needed to characterize pressures across the pulmonary vascular tree. To address this gap, we developed a physics-informed neural network (PINN) framework that integrates in-vivo CT-based vascular imaging with in-silico 1D fluid–structure interaction (FSI) modeling to predict vessel-level pressure distributions non-invasively.

Methods

Pulmonary vascular geometries were reconstructed from high-resolution CT imaging in control (n=7) and Sugen–hypoxia (n=7) rat models of PH. These geometries were used to generate high-fidelity pressure–flow simulations via a 1D FSI model under physiologic inflow and boundary conditions (Fig. 1A,B). To increase geometric diversity beyond the available animals, a set of low-fidelity synthetic vascular trees (n=2000) was generated by perturbing vessel lengths, radii, and branching angles (Fig. 1C). The combined dataset was used to train a PINN model that incorporates vessel geometry, flow inputs, and boundary specifications while embedding governing conservation laws directly into the loss function (Fig. 1D). This hybrid training strategy enabled the PINN to learn pressure fields consistent with vascular mechanics across a broad anatomical range. Model performance was evaluated by holding out real rat geometries as independent test cases.

Results

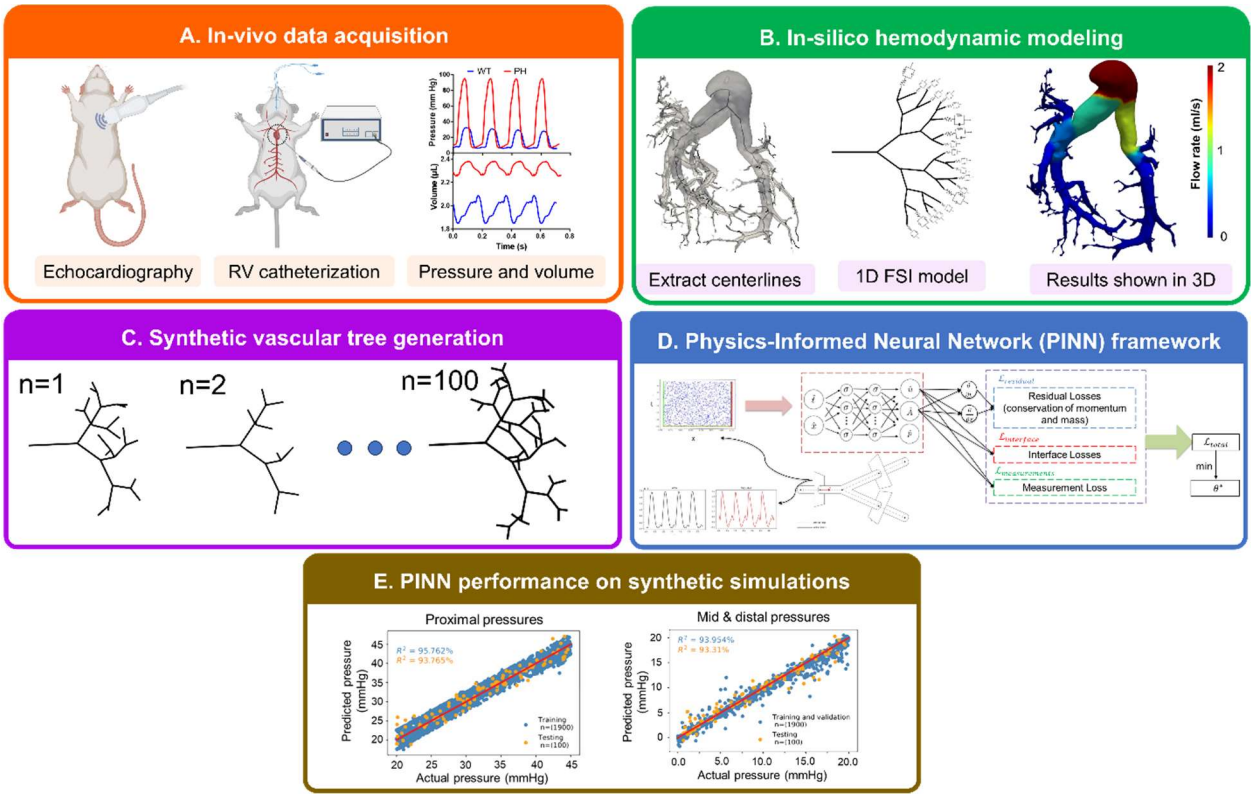
The PINN accurately reproduced pressure distributions across synthetic trees, showing strong agreement with simulated pressures (Fig. 1E). When applied to held-out real rat vasculature, the model demonstrated robust generalization, with predicted pressures closely matching high-fidelity FSI ground truth. The method remained stable in highly

asymmetric and deeply branched regions, successfully capturing distal pressure drops that conventional imaging-based approaches cannot resolve.

Discussion

This study presents a unified, non-invasive framework that couples in-vivo CT imaging, in-silico biomechanics, and physics-informed learning for accurate pulmonary vascular pressure estimation. By combining low-fidelity synthetic data with high-fidelity rat simulations and enforcing physics constraints, the approach achieves high accuracy and strong generalizability. This framework shows promise for future translation using patient-specific CT geometries to rapidly assess pulmonary vascular load without catheterization.

Images (Optional)



Session Category

Cardiovascular/Cardiorespiratory Biomechanics: Methods, Models and Applications

OA191-03

Graph Neural Networks for Classification of Abdominal Aortic Aneurysms from CTA-derived Surface Graphs

PhD Candidate Julian Carvajal Rico[1], PhD Candidate Juan C. Restrepo[1], M.D Satish C. Muluk[2], M.D Mark K. Eskandari[3], PhD Ender A. Finol[1]

[1]Department of Mechanical, Aerosp., and Ind. Engineering, UT San Antonio, San Antonio, TX, United States. [2]Department of Cardiothoracic Surgery, Allegheny Health NetworkHealth Network, Pittsburgh, PA, United States. [3]Division of Vascular Surgery, Northwestern University School of Medicine, Chicago, IL, United States

Introduction

Diameter and growth rate remain the dominant surrogates for assessing abdominal aortic aneurysm (AAA) rupture risk, yet rupture reflects localized imbalances between wall stress and wall strength. We hypothesize that graph neural networks (GNNs) operating on surface meshes derived from computed tomography angiography (CTA) images can leverage spatially distributed geometric and biomechanical features to improve rupture risk classification.

Methods

We used a multi-institution cohort of 147 AAA CTA exams (76 ruptured/symptomatic within 6 months of last exam and 71 unruptured/asymptomatic). After U-Net assisted segmentation and mesh reconstruction, each aneurysm was represented as a connectivity graph whose nodes (mesh elements) carry seven primary features: wall thickness (*WallTHK*), thrombus thickness (*ILTTHK*), Gaussian and mean curvatures (*K*, *M)*, wall stress, wall strength, rupture potential index (*RPI*=stress/strength), and radial distance to the centerline (r_L) as spatial descriptors. We benchmarked GNN variants (GCN/GraphSAGE) with stratified 5-fold cross-validation, early stopping, and feature-set ablations to identify parsimonious, high-performing combinations. Performance was evaluated with accuracy, area under the curve (AUC), precision/recall, and calibration; class imbalances were handled with stratification and loss re-weighting.

Results

Experiments on the independent 147-patient cohort trained 127 GNNs across feature subsets. The best fold achieved **96.55%** accuracy and AUC = 0.9762 using *WallTHK*, *K*, and *M* as shown in Table 1. When averaging across folds, the top configuration reached **83.0%** accuracy, indicating robust generalization beyond single-fold performance.

The features recurring in the top 10 models included *WallTHK*, *K*, *M*, and *RPI*, suggesting a complementary value from biomechanical and geometric descriptors.

Discussion

Representing AAAs as surface graphs enables GNNs to exploit local heterogeneity that is lost in global or diameter-based metrics. Early findings support the importance of combining geometric (curvature, thickness) and biomechanical (stress, strength, RPI) features. Future work should be focused on (i) completing a compact feature set, (ii) assessing alternative edge/positional encodings and weighted graphs, and (iii) exploring multimodal extensions (local graph features + global graph features, such as sex and maximum diameter). If validated, this approach could provide a scalable, anatomy-aware classifier to support patient-specific rupture risk stratification in routine CTA workflows.

Images (Optional)

Table 1. GNN feature combinations ranked by accuracy and AUC.

Rank	Number of features	Features	Accuracy	AUC score
1	3	$WallTHK, K, M$	96.55%	0.9762
2	5	$WallTHK, ILTTHK, Stress, K, RPI$	93.33%	0.9643
3	3	K, RPI, r_L	93.33%	0.9777
4	3	$ILTTHK, M, RPI$	93.33%	0.9241
5	4	$ILTTHK, Stress, K, r_L$	93.33%	0.9375
6	2	$WallTHK, M$	93.10%	0.9714
7	4	$WallTHK\ K, M, RPI$	93.10%	0.9571
8	5	$WallTHK, ILTTHK, M, RPI, r_L$	90.00%	0.9598
9	4	$WallTHK, Stress, RPI, r_L$	89.66%	0.9000
10	3	$ILTTHK, RPI, r_L$	89.66%	0.9000

Acknowledgements (Optional)

NIH award R01HL159300 funded this work.

Session Category

Cardiovascular/Cardiorespiratory Biomechanics: Methods, Models and Applications

OA191-04

Non-invasive Quantification of Left Ventricular Myocardial Stiffness In Vivo using DENSE MRI and a Physics-Informed Constitutive Model

Mr. Tawfik Hussein, M.S.[1,2], Dr. W. Robert Taylor, M.D., Ph.D.[2,3], Dr. John Oshinski, Ph.D.[2]

[1]Georgia Institute of Technology, Atlanta, GA, United States. [2]Emory University School of Medicine, Atlanta, GA, United States. [3]Joseph Maxwell Cleland Atlanta VA Medical Center, Decatur, GA, United States

Introduction

Heart failure with preserved ejection fraction (HFpEF) is a complex syndrome with poor long-term prognosis. A key feature is increased myocardial stiffness, yet current clinical tools to assess stiffness are invasive or indirect. The Criscione–Hussein model (CHM) has the potential to capture local, microstructural myocardial stiffness *non-invasively* using pixel-wise displacements from high-resolution displacement encoding with simulated echoes (DENSE) [1]. The goal of this study was to combine DENSE and CHM to quantify local mean *fiber strain α_2, stress σ_{ff}, and stiffness Λ*, and mean *laminar thickening strain α_3, stress σ_{rr}, and stiffness Φ* in human myocardium. We hypothesized that combining DENSE and CHM could capture local myocardial stiffness, and that fiber stiffness would exceed laminar thickening stiffness.

Methods

Ten healthy adults (6 males, 4 females, ages 22–59 years) underwent ECG-gated cine DENSE imaging in short-axis and long-axis views of the LV. Displacements from both views were combined to compute α_2 and α_3 in each segment of the AHA bullseye. Using published diastolic pressure values for healthy myocardium, CHM was used to fit pressure–strain relationships for each subject, producing subject-specific stiffness parameters. From these parameters, σ_{ff} and σ_{rr} were computed. Mean and standard deviation of all metrics were calculated across subjects, with the segmental means visualized as AHA bullseyes.

Results

Shown in **Figure 1**, α_2 and α_3 indicated greater laminar thickening than fiber shortening, with the lateral wall deforming more than the septal wall. The spatial distributions of σ_{ff} and σ_{rr} were largely homogeneous; σ_{ff} values were negative while σ_{rr} values were positive, consistent with fiber shortening and radial thickening, respectively. For stiffness, Λ exceeded Φ, with both showing higher magnitudes in septal regions compared to lateral regions.

Discussion

The strain patterns align with prior findings that laminar thickening exceeds fiber shortening due to sheetlet shear. This implies *greater stiffness along fibers than in the radial direction*, as well as negative σ_{ff} and positive σ_{rr}. Quantifying stiffness along material directions reveals microstructural physiology and may offer mechanistic insight into LV remodeling. These stiffness measures may ultimately serve as predictive markers of adverse remodeling in HFpEF.

Images (Optional)

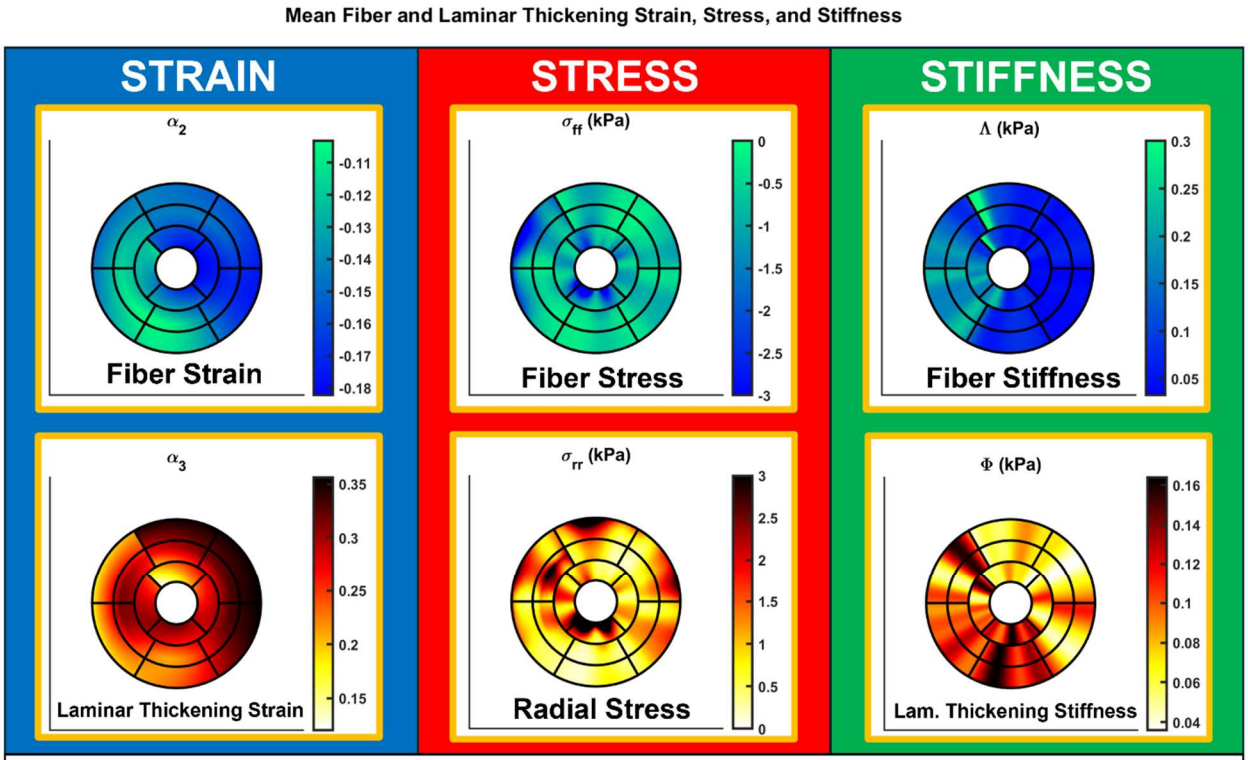


Figure 1. *AHA bullseyes for the mean α_2 (fiber strain) top left panel, mean fiber stress (top middle panel), and fiber stress (top right panel), α_3 (laminar thickening strain) bottom left panel, radial stress (bottom middle panel), and laminar thickening stiffness (bottom right panel).*

References (Optional)

[1] Hussein *et al.*, JBME, 2023.

Acknowledgements (Optional)

The authors would like to acknowledge the NIH/NHLBI training grant T32HL166146 and individual predoctoral grant 1F31HL172683.

Session Category

Cardiovascular/Cardiorespiratory Biomechanics: Methods, Models and Applications

OA191-05

Aortic Wall Biomechanics in Marfan Versus Non-Marfan Patients: Linking FE Simulations and Geometric Deep Learning

MsC Davide Astori[1,2], MsC Ione Ianniruberto[1], MsC Sofia Di Filippo[3], MsC Davide Milesi[1], Prof Alberto Redaelli[1], PhD Simone Saitta[4], Prof Emiliano Votta[1]

[1]Department of Electronics, Information and Bioengineering, Politecnico di Milano, Milano, Milano, Italy. [2]European Society of Biomechanics (ESB), Milano, Milano, Italy. [3]3D and Computer Simulation Laboratory, IRCCS Policlinico San Donato, San Donato Milanese, Milano, Italy. [4]Department of Biomechanical Engineering, TU Delft, Delft, South Holland, Netherlands

Introduction

Ascending aortic aneurysm is a leading cause of mortality in Marfan patients [1]. Optimal surgical correction timing is crucial for preventing acute dissection; however, current geometry-based clinical guidelines fail to accurately stratify risk in 60% of cases [2]. Stress-based risk assessments derived from finite element (FE) simulations have shown promise in predicting aortic dissection, but are time-expensive [3]. Here, we compare aortic wall biomechanics in Marfan *vs.* non-Marfan (Control) subjects, and investigate geometric deep learning (GDL) as a faster alternative to FE.

Methods

400 CT scans of ascending aortas were processed automatically to implement aortic wall FE models as in [2].

320 anatomies were used to generate the training dataset for a PointNet++-based GDL model aimed to infer axial and circumferential wall stresses (t_z, t_θ) from geometry, intraluminal pressure, and condition label. For each geometry, FE simulations were run using Marfan-specific and physiologic material properties to compute t_z and t_θ for pressures between 50 and 180 mmHg.

For the remaining 80 subjects with known clinical history (40 Marfan, 40 Controls), GDL model predictions were tested *vs.* FE simulations with condition-specific properties, for pressures ranging from 50 to 180 mmHg.

Results

FE simulations in the training set indicated that, on the same geometry, Marfan material properties were associated with increased t_z and t_θ *vs.* physiological properties (11.9% and 23.5% at 120 mmHg). In the test set, Marfan patients showed higher t_z and t_θ than controls at 120 mmHg (t_z=15.4±4.5 *vs.* 13.2±7.0 kPa, p<0.01; t_{circ}=55.7±13.0 *vs.* 43.9±9.8 kPa, p<0.0001), but not in hypertensive conditions. The GDL model reproduced FE-derived stresses with a 5.30±2.51% normalized mean absolute error on the test set, requiring ~3 seconds/case *vs.* ~40 minutes/case for FE analyses.

Discussion

Marfan-specific material properties substantially affect aortic wall stresses, revealing significant differences between Marfan patients and Controls at physiological pressures. The proposed pathology-aware GDL model well reproduces FE stresses with drastically reduced computation time, supporting fast, patient-specific biomechanical risk assessment.

Images (Optional)

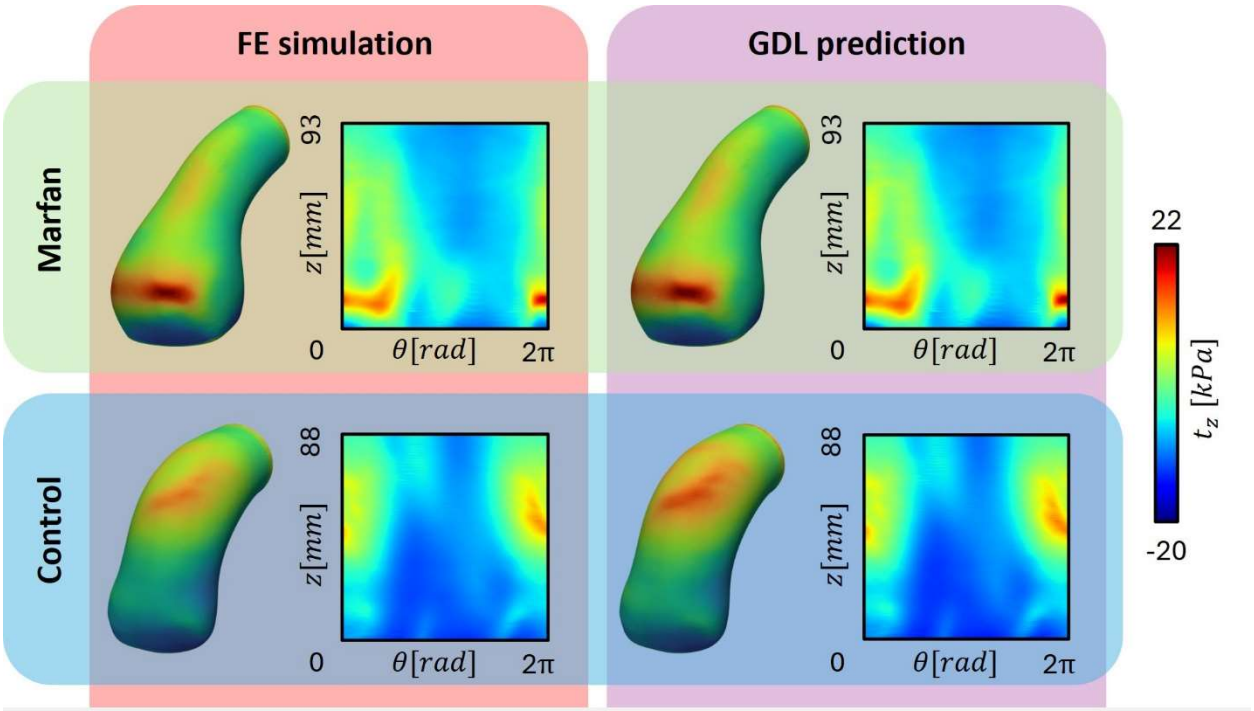


Figure 1: Overview of the FE simulations (red) and GDL predictions (purple) for the Marfan (green) and Control (blue) subjects for axial stresses (t_z) at 120 mmHg. t_z is represented on the aorta and on a patch within a cylindrical reference frame (axial – z; circumferential – θ)

References (Optional)

[1] Milewicz DM *et al.*, Circulation, 2005

[2] Wang Z *et al.*, J Thorac Cardiovasc Surg, 2021

[3] Ianniruberto I *et al.*, Eur J Cardiothorac Surg, 2025

Acknowledgements (Optional)

Simone Saitta acknowledges the support of the Marfan Foundation through the Victor McKusick Grant

Session Category

Cardiovascular/Cardiorespiratory Biomechanics: Methods, Models and Applications

OA192-01

Long-Term Implantable Sensor System for High-Resolution In Vivo Spinal Kinematics in Large Animal Models

Dr. med. vet. Sandra Reitmaier, Mr Marcel Simon Reich, Prof. Dr. Hendrik Schmidt

Charite - Universitätsmedizin Berlin, Berlin, Berlin, Germany

Introduction

Accurate long-term monitoring of spinal kinematics is essential for understanding postoperative biomechanics and evaluating interventions in preclinical models. While large animal models, such as sheep, mimic human spinal anatomy and loading [1-3], existing methods lack sufficient precision, durability, and biocompatibility for extended in-vivo measurements. To address this gap, we developed an implantable sensor capable for capturing multi-planar-motion over prolonged periods, enabling detailed assessment of vertebral biomechanics in a clinically relevant setting.

Methods

We engineered a biocompatible sensor module integrating accelerometers, gyroscopes, and magnetometers to record flexion/extension (FE) and axial rotation (AR) of individual vertebrae. The device is encapsulated in silicone with epoxy-reinforced electronics, ensuring mechanical stability. A low-power circuit and high-capacity Li-Po battery enable continuous operation for up to 24 days, controlled via magnetic switch. System performance was evaluated in laboratory calibration experiments and implanted in one sheep to assess signal fidelity, robustness under physiological loading, and long-term stability.

Results

Laboratory testing confirmed that the system achieved angular accuracy well within the targeted resolution. For FE, mean squared error (MSE) was 0.013°, root mean squared error (RMSE) 0.115°, with a mean deviation (MD) of 0.044° and a standard deviation (SD) of 0.108°. For AR, MSE was 0.011°, RMSE 0.104°, with a MD of 0.064° and a SD of 0.083°. Magnetic field characterization showed near-linear sensor behavior, enabling reliable reconstruction of angular motion using a two-point calibration. In vivo, the implanted system operated consistently throughout the monitoring period, maintaining stable signal quality (Fig.1). No degradation of sensor performance was observed, confirming the mechanical robustness and feasibility of long-term implantation.

Discussion

This study presents a robust, biocompatible, and accurate implantable system for long-term spinal kinematic monitoring in large animals. By enabling multi-planar, continuous in-vivo measurements, the system allows objective evaluation of spinal interventions and provides a foundation for translational research linking preclinical biomechanics to clinical outcomes. This technology offers a novel approach to assess post-surgical adaptations, tissue mechanics, and neuromuscular responses in a controlled, physiologically relevant environment.

Images (Optional)

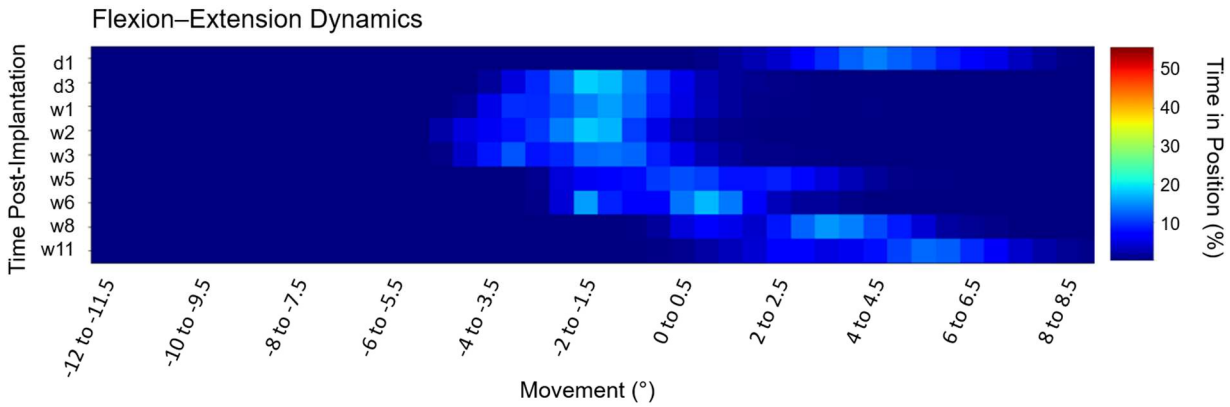


Fig. 1 Temporal profile of flexion-extension (FE) angles recorded by two implanted sensors (L2, L4). After sensor implantation, movement amplitudes are confined to a narrow, low-magnitude range (d3 to w2), likely reflecting postoperative discomfort. Thereafter, a progressive increase in the occurrence of larger-amplitude movements is observed.

Negative values indicate extension, positive values indicate flexion.
Abbreviations: d = day; w = week; d1 = day of sensor implantation.

References (Optional)

1. Reid et al., Clinical biomechanics, 2002
2. Reitmaier et al., J Bone Joint Surg Am, 2017.
3. Lussier et al., European Surgical Research, 2025.

Acknowledgements (Optional)

Funded by the German Research Foundation (FOR 5177 - GZ RE 4292/3-1; SCHM 2572/11-1; SCHM 2572/13-1).

Session Category

Musculoskeletal Biomechanics: Methods, Models and Applications

OA192-02

Sensitivity of a Soft Tissue Kalman Filter to Material Parameters

Ms. Genevieve Bonnor BASc, Dr. Calvin Kuo PhD, P.Eng

University of British Columbia, Vancouver, British Columbia, Canada

Introduction

Inertial measurement units (IMUs) are a popular tool to measure human motion outside the lab. However, in applications such as impact characterization, dynamic soft tissue artifacts (dSTAs) introduce IMU measurement errors through overestimation of peak skeletal kinematics (upwards of 100%) and post-impact oscillations [1]. We developed a soft-tissue Kalman filter (sKF) that utilizes a spring-mass-damper (SMD) system to model the effect of dSTAs and improve kinematic estimates. SMD parameters can be optimized to minimize error from a skeletal ground truth, but if no ground truth is available (as in *in vivo* testing), parameter identification becomes difficult. Since the sKF relies on these parameters to accurately model soft tissue movement, we wanted to explore the sensitivity of the sKF to variabilities in the parameters.

Methods

The sKF's SMD model uses stiffness (k), mass (m), and damping coefficient (b) parameters to estimate behaviour of dSTAs. We first optimized a generalizable set of parameters that minimized ground truth skeletal errors across 270 impacts in silicone rubber phantoms with different material properties, sensor placements, and impact severities. We then performed a Monte Carlo (10,000 iterations) on one representative impact, varying SMD parameters within a log-normal distribution (log of SMD parameters obtained when minimizing error for individual impacts). We computed the vertical acceleration normalized root mean square error (nRMSE) and peak percent error compared to the ground truth for each iteration.

Results

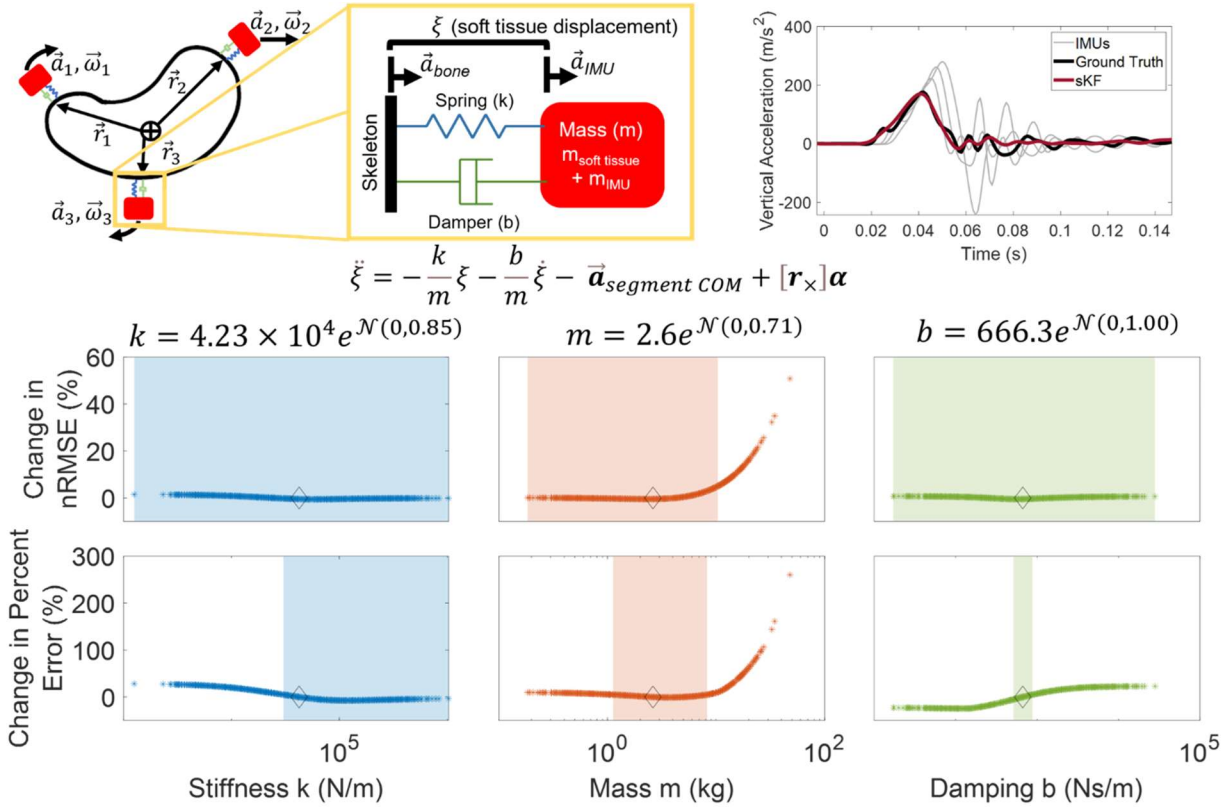
The vertical acceleration nRMSE and peak percent error were most sensitive to mass parameter changes. However, the damping parameter has a smaller range with acceptable (≤5% change) peak percent error. The sKF is most robust to stiffness parameter changes.

Discussion

We found that the sKF is robust to variations in stiffness, and that the mass parameter can be estimated within an order of magnitude. However, the damping parameter must be finely tuned to the sensor location and tissue type, and would benefit from further *in*

vivo testing to identify a setpoint. This methodology shows promise to improve impact estimation, and with future parameter adjustment, may be applied *in vivo*.

Images (Optional)



References (Optional)

[1] R. Rong and C. Kuo., IEEE Trans. Biomed. Eng., 2024

Acknowledgements (Optional)

Session Category

Musculoskeletal Biomechanics: Methods, Models and Applications

OA192-03

IMU Misalignment Correction and Calibration Methods for Patient-Placed IMUs in Telemedicine Segmental Symmetry Gait Analysis

Mr. Joseph Redmond, Mr. Kuper Banghart, Prof. Corey Pew

Montana State University, Bozeman, MT, United States

Introduction

Inertial Measurement Units (IMUs) provide a low-cost option for accessible gait analysis. For clinicians, IMUs can provide an objective measure of gait asymmetry using sagittal plane gyroscopes [1]. For patients in remote regions, IMUs could be self-placed for a virtual visit to forgo travel to the clinic. IMU alignment to anatomical segments is critical for accurate measures. While an experimental protocol partially constrained IMU self-placed misalignment, longitudinal axis rotation persisted, producing artificial asymmetry in readings. We hypothesize an algorithmic calibration can mitigate effects of misalignment on asymmetry score repeatability.

Methods

Four IMUs were self-placed by participants using a removable pin aligning the vertical axis of thigh and shank sensors. Participants were recorded treadmill walking. Optical motion capture (MoCap) quantified sensor misalignment. Placement was done twice to evaluate repeatability. IMUs misalignment was corrected using 3 methods: 1) An ideal correction computed using MoCap, 2) A 3-axis magnitude, 3) Optimized correction, orienting maximum gyroscope variance between the thigh and shank to one axis, assuming hinge-like knee behavior [2]. Asymmetry scores were computed by average Euclidian difference of sequential sagittal gyroscope cycles on the left and right sensor [1]. Method inter-trial variance was compared using Pitman-Morgan tests.

Results

MoCap generated Shank asymmetry scores on 9 Healthy Controls (6F; 53±19yrs.) produced a Minimal Detectable Change (MDC) of 2.55 points exceeded by 4% of repeated trials. Uncorrected IMU had higher variance than MoCap (Variance Ratio=3.7; p=0.001); 30% MDC exceedance. Ideally Corrected IMU was statistically the same as Mocap (Ratio=1.4; p=0.263); 15% MDC exceedance. A 3-axis magnitude showed increased variance (Ratio=2.13; p=0.038); 18% MDC exceedance. Optimized corrections had marginally equivalent variance (Ratio=1.9; p=0.056); 11% MDC exceedance.

Discussion

Realigning IMUs using a MoCap-dependent correction improves score variability under repeated conditions to match MoCap. Optimization did not depend on MoCap; while corrections were not exact, score variance improved over no correction. Additional analysis will evaluate thigh data, quantify misplacement impacts on intra-trial scoring error relative to MoCap, and discuss acceptable margins of misalignment for score reliability.

Images (Optional)

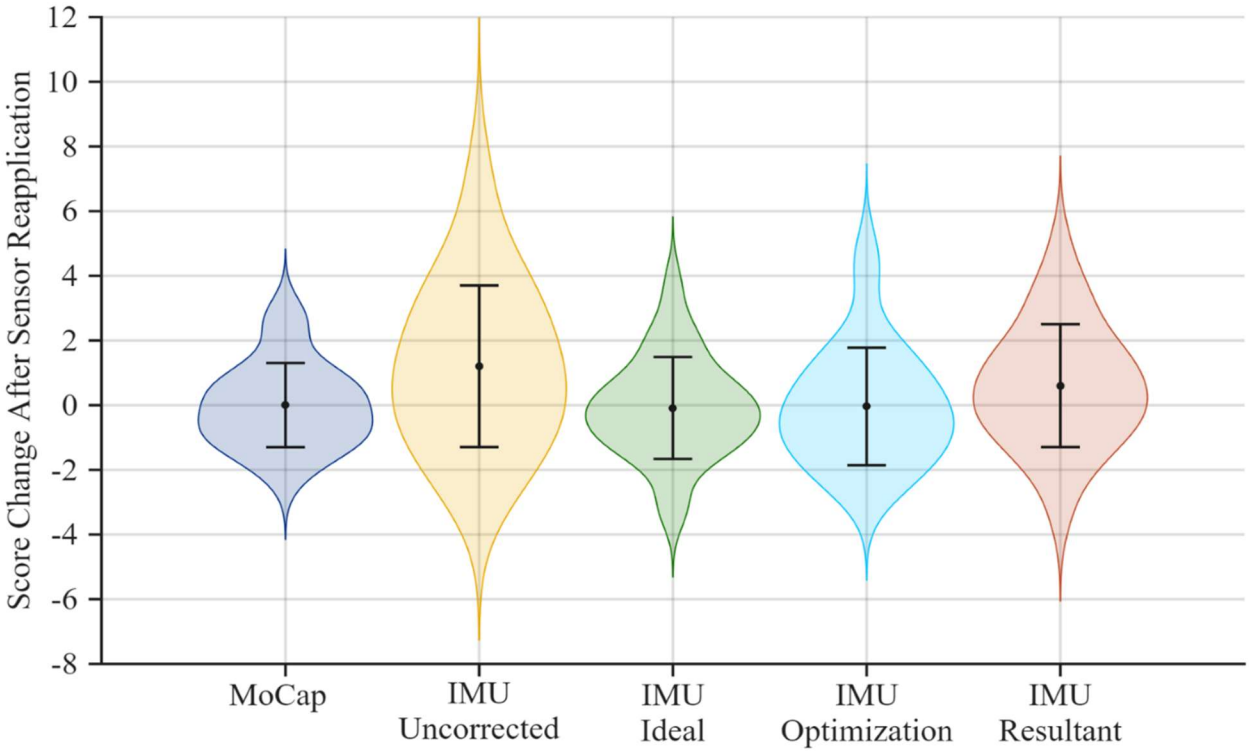


Figure 1: Violin plot of score changes in repeated trials with 2 different self placements, compared between Mocap and methods of correcting IMU misalignment (Mean ± 1 SD)

References (Optional)

[1] Sheila Clemens et al. *Clinical Biomechanics* 2020. [2] Thomas Seel et al. *IEEE CCA* 2012.

Session Category

Musculoskeletal Biomechanics: Methods, Models and Applications

OA192-04

Obtaining Dynamic Soft Tissue Model and Mechanical Properties In-Vivo Using Wearable Inertial Measurement Unit Sensors

Mr Vishak Nandan Aathresh BEng, Dr Calvin Kuo PhD, PEng

University of British Columbia, Vancouver, British Columbia, Canada

Introduction

Characterizing soft tissue material properties has applications across computer vision, medicine, and biomechanical research. Material properties such as soft tissue stiffness can be used to indicate health or help develop realistic simulations of injury. Currently, soft tissue material properties are obtained in-vivo using low-deformation rate quasi-static indentation testing or low-deformation rheometric analysis. However, it is difficult to obtain high-deformation and high-deformation rate material properties using these methods. Impacts to the body can excite soft tissue, producing dynamic high deformations and deformation rates. This study presents a method to measure soft tissue during impacts with inertial measurement units (IMUs) to obtain dynamic material properties in-vivo.

Methods

We previously collected mild leg impact data from a participant at 1000Hz using an IMU at the posterior shank with dynamic soft tissue deformations and an IMU behind the ankle representing a reference. The shank was dropped from a height of 21.6cm onto a foam pad to generate vertical impacts along the shank. The IMU mass was adjusted between 5-37grams, which was necessary to solve for all material properties.

Shank IMU vertical inertial acceleration was plotted against soft tissue deformation from double-integration of vertical acceleration difference between the IMUs. This produced a mass-normalized force-deformation curve, to which five polynomial spring models were fit. We selected the polynomial spring model with the highest r-squared and performed a forward optimization to obtain material properties that best simulate soft tissue response across mass conditions.

Results

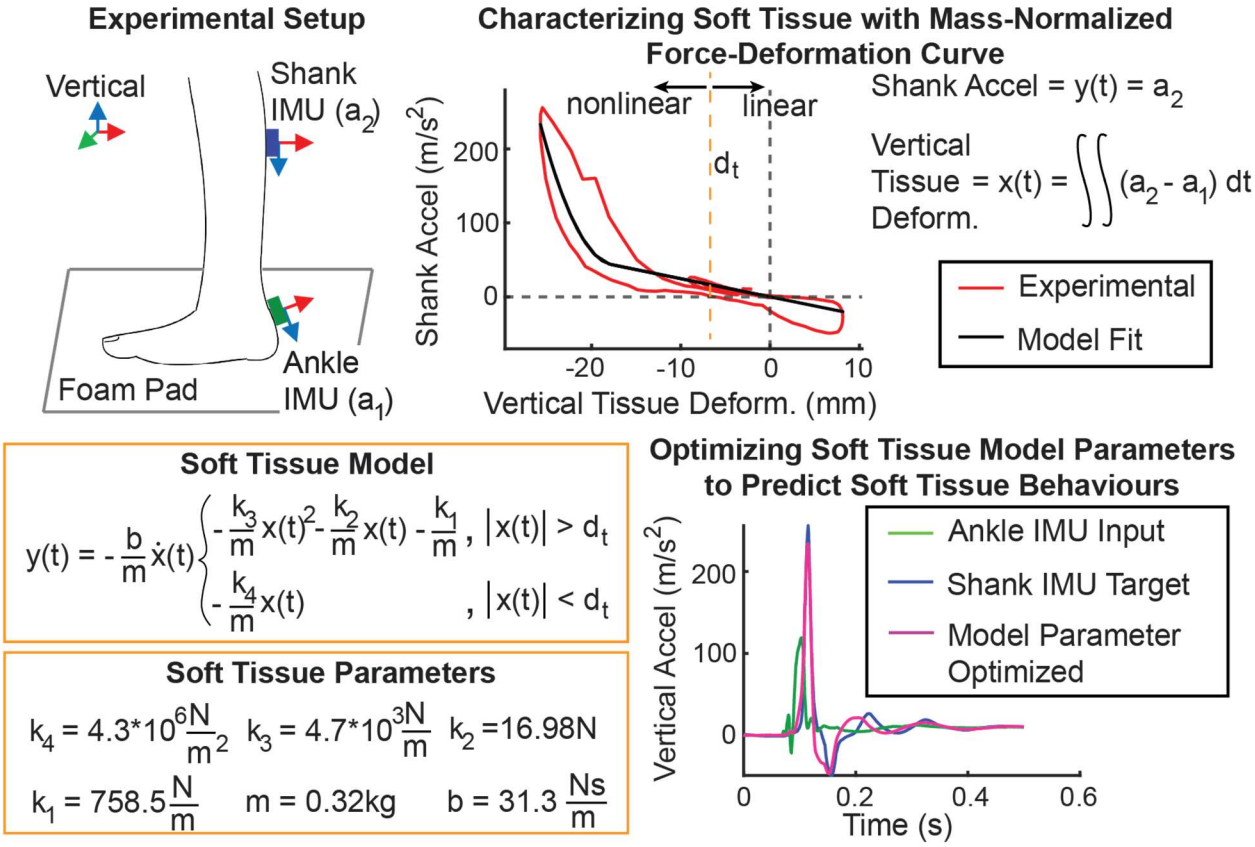
The quadratic-linear piecewise model best represented the mass-normalized force-deformation curves, detailing a low-deformation region that behaves like a linear spring-mass system with increased stiffening at high deformations. The fit mass was 0.32kg and

the linear stiffness was 758.5N/m, which falls within previous work modeling natural soft tissue oscillations [1].

Discussion

This study presents a method to obtain dynamic soft tissue model and material properties in-vivo by measuring soft tissue response during impacts with IMUs. This methodology expands tissue characterization to high-deformation and high-deformation rate scenarios, which are relevant particularly in injury modeling and assessment. Future work will expand this to other movement directions to obtain 3D dynamic material characterization.

Images (Optional)



References (Optional)

[1] Rong et al., IEEE TBME, 2024

Session Category

Musculoskeletal Biomechanics: Methods, Models and Applications

OA192-05

A Tightly Coupled IMU-to-Model Method for Estimating Shoulder Kinematics and Kinetics

Mr. Hassan Osman, Dr. Manon Kok, Dr. Ajay Seth

Delft University of Technology, Delft, Zuid-Holland, Netherlands

Introduction

The demand for portable motion capture systems is growing with the rising number of mobility disorder patients due to their ability to provide quantitative motion analysis for medical practitioners that helps them in diagnosis and treatment [1]. Sports applications further contribute to this demand, as motion capture systems provide quantified measurements that can optimize athlete performance and help prevent injuries [2]. Upper extremity movement from IMU-estimated orientations is challenging due to ferromagnetic disturbances [3] and orientations are estimated independent of the musculoskeletal dynamics. In this work, we extend a tightly-coupled IMU-based motion capture algorithm [4], to estimate shoulder movements directly from IMU-measured angular-velocities and linear-accelerations.

Methods

We formulate an iterated extended Kalman filter (IEKF) with a subject-scaled shoulder dynamical model [4,5] implemented in OpenSim [6] with its outputs coupled to IMU-measurements to estimate scapula and glenohumeral joint angles and torques. To test our approach, virtual IMU-measurements of angular velocity and linear acceleration were generated from ground truth shoulder kinematics derived from bone-pins [5]. Four virtual IMUs were attached on the acromion, thorax, humerus and radius. Scapular motion was represented by a 4-coordinate scapulothoracic joint and subject to an acromioclavicular constraint. Initial joint angles and sensor locations were assumed to be known, and initial joint torques were obtained from inverse dynamics when static in the starting pose.

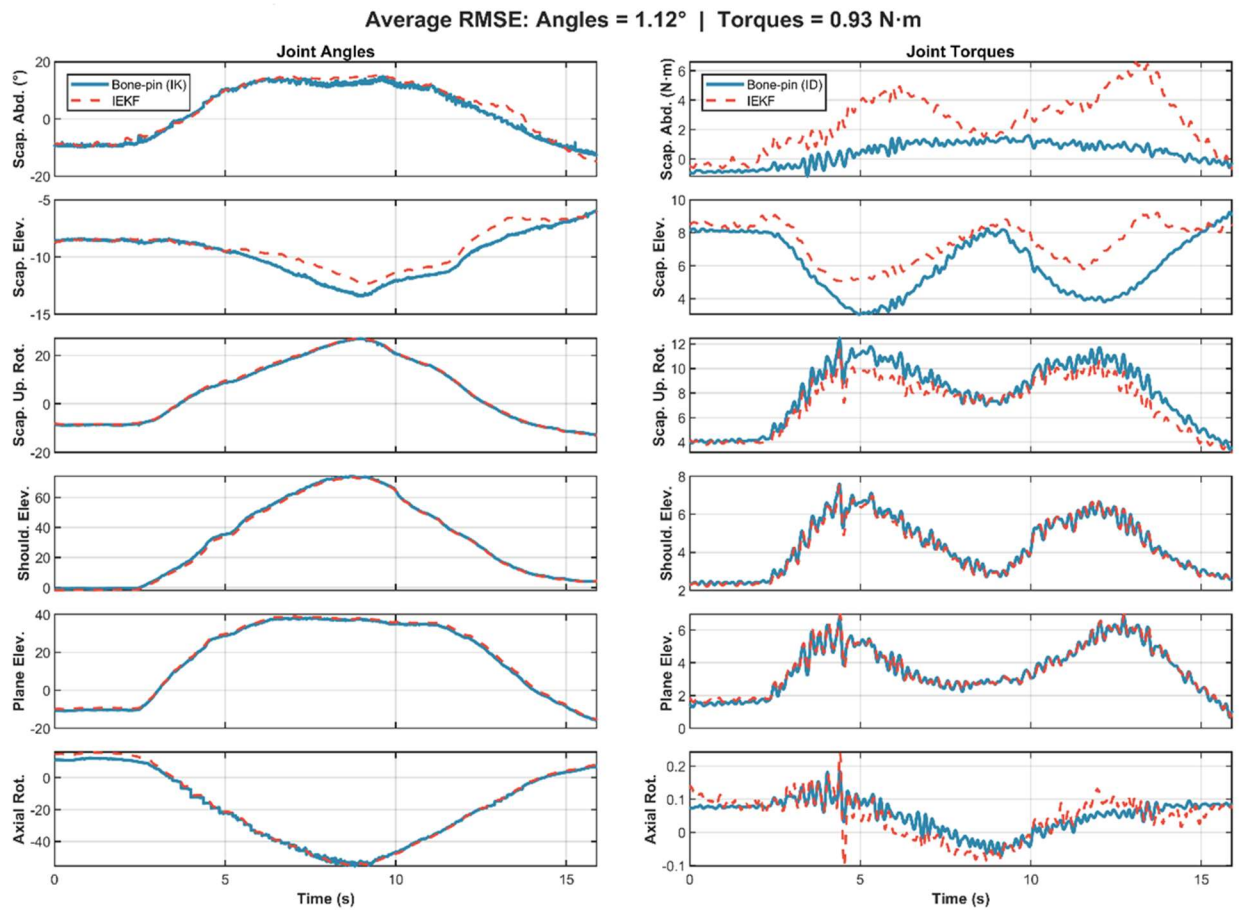
Results

We tested our algorithm on shoulder flexion and abduction movements involving different scapular movements. The figure shows joint angle and torque estimated from our tightly-coupled IEKF approach and compared against bone-pin Inverse Kinematics (IK) and Inverse Dynamics (ID) derived estimates for a shoulder flexion task.

Discussion

Our approach demonstrates the ability to estimate the kinematics and kinetics of the shoulder that includes the scapula from IMU-measurements without the magnetometer and estimates of sensor orientation. Future work will evaluate the algorithm over a broader range of upper-extremity movements, from real IMU data.

Images (Optional)



References (Optional)

[1] Salisu S et al., Diagnostics, 2023.

[2] Suo X et al., Sensors, 2024.

[3] Antonacci C et al., Sensors, 2023.

[4] Osman H et al., arXiv, 2025.

[5] Seth A et al., PLoS ONE, 2016.

[6] Seth A et al., PLoS ONE, 2018.

Acknowledgements (Optional)

The authors received financial support from the Convergence Human Mobility Centre, a flagship initiative funded by the Convergence Alliance (TU Delft, Erasmus MC, Erasmus University Rotterdam).

Session Category

Musculoskeletal Biomechanics: Methods, Models and Applications

OA192-06

Reconstructing Intermediate Spinal Segment Positions Using Two Inertial Measurement Units: A Proof-of-Concept Study

MSc. Roelien Smit-Russcher, MSc. Raymond Zandbergen

Movella Technologies B.V., Enschede, Overijssel, Netherlands

Introduction

The accurate measurement of spinal motion is critical for biomechanics research, motion analysis, and ergonomic assessment, as spinal range of motion (ROM) directly influences whole-body kinematics including arm reach and postural stability. Most studies rely on three or more inertial measurement units (IMUs) to capture gross spinal movements, yet cannot resolve intermediate vertebral motions without dense instrumentation [1]. The present model extends beyond prior approaches by reconstructing intermediate spinal segment positions using only two IMUs. This enables the model to capture the natural spinal rhythms in healthy subjects, characterized by the transition from an S-shape in standing to a C-shape during flexion.

Methods

The continuous orientation model is driven by two IMUs placed at the pelvis and sternum (projected onto T8), with positions derived from orientations. The model extends spherical linear interpolation (SLERP) to incorporate spinal rhythm through two parametrized basis functions, defined independently for the sagittal and frontal planes.

The proof-of-concept was evaluated on one healthy male subject performing five repetitions of standardized spinal movements. IMUs were placed at pelvis and sternum segments. A Qualisys optical motion capture system with 12 markers along the spinal column served as reference. Model parameters were optimized using one rotational motion, then applied to all movements to evaluate generalization. Movement-specific optimization assessed maximum achievable accuracy. Metrics included RMSE averaged over all segments and Pearson's correlation.

Results

See Table 1.

Discussion

The two-IMU model achieved RMSE below 4 cm with generalized parameters and showed strong correlations ($r = 0.80–0.98$, $p < 0.001$). Movement-specific optimization reduced errors to 1.07–2.32 cm ($r \geq 0.97$). Performance was optimal for rotation with pelvis motion (1.07 cm) and lower for fixed pelvis movements (3.97 cm), improving substantially with tuning (1.17 cm). While multi-IMU systems achieve slightly higher accuracy [1], this minimal two-sensor approach offers practical advantages for whole-body analysis. High correlations demonstrate that biomechanically-informed modelling can compensate for reduced sensor density.

The rhythmic spine model successfully reconstructs intermediate spinal segment orientations with sub-4 cm accuracy. Future work will extend the validation to a larger, more diverse cohort to establish generalizability across populations and movement patterns.

Images (Optional)

Recording	RMSE gen.	RMSE opt.	Pearson gen.	Pearson opt.	p-value gen.	p-value opt.
Rotation right side - pelvis motion*	1.07 cm	1.07 cm	0.98	0.98	< 0.001	< 0.001
Rotation left/right - pelvis fixed	3.97 cm	1.17 cm	0.80	0.98	< 0.001	< 0.001
Lateral flexion	3.12 cm	1.38 cm	0.94	0.99	< 0.001	< 0.001
Flexion - right hand to ground	3.73 cm	2.32 cm	0.96	0.97	< 0.001	< 0.001

Table 1: Root Mean Square Error (RMSE), Pearson Coefficient, and p-value between model-reconstructed spinal segment positions and reference marker data for various spinal motions.
** Generalized parameters tuned on Rotation right side.*

References (Optional)

[1] Florian Michaud *et al.*, Sensors, 2022

Session Category

Musculoskeletal Biomechanics: Methods, Models and Applications

OA193-01

Variations in Cervical Muscle Morphology: Implications for Parametric Human Models and Ergonomic Safety Design

Student Jaron Larson[1,2,3], Assistant Research Scientist Sujata Khandare[3,2], Professor Jingwen Hu[3,2]

[1]Northwestern Michigan College, Traverse City, MI, United States. [2]University of Michigan, Ann Arbor, MI, United States. [3]University of Michigan Transportation Research Institute (UMTRI), Ann Arbor, MI, United States

Student Jaron Larson

Assistant Research Scientist Sujata Khandare

Introduction

Neck muscle forces are critical for head stabilization and injury (e.g., whiplash), yet cervical morphology remains poorly represented across the population, including the midsize male model used in most crash injury assessment models. Limited empirical data on cervical muscle structure restricts our ability to represent demographic variability in injury biomechanics. Cervical muscle cross-sectional area (CSA), a key determinant of force-generating capacity, varies widely, but existing datasets are small and demographically narrow. This study quantifies how sex, stature, BMI, and age influence muscle CSA based on a large CT cohort to support development of parametric human models and population-representative ergonomic design.

Methods

Neck CT scans from 636 adults (294 Male, 342 Female; 18–79 years) were processed using TotalSegmentator [1], an AI-based segmentation tool. Levator Scapulae, Prevertebral, and Sternocleidomastoid muscles were analyzed. A custom workflow generated 3D muscle geometries and longitudinal centerlines, and applied perpendicular slicing to compute CSA for selected muscles. A targeted quality control (QC) subsample showed 89% segmentation accuracy. During CSA computation, autofiltering algorithms removed subjects with potential errors (e.g., disconnected meshes, truncated centerlines). After CSA extraction, outliers were reviewed; invalid anatomies were excluded. Demographic

effects were modeled using Analysis of Covariance (ANCOVA) with sex, stature, and age; a supplementary model substituted BMI.

Results

Mean CSA was 1049 ± 224 mm^2 (M) and 755 ± 157 mm^2 (F). In the primary ANCOVA (controlling for stature and age), sex was a significant predictor ($F=206.0$, $p<0.001$); males maintained 264 mm^2 higher CSA than females. Stature ($F=11.5$, $p<0.001$) and age ($F=52.3$, $p<0.001$) were statistically significant (Model $R^2=0.48$). A supplementary model substituting BMI for stature confirmed these effects ($F=183.5$, $p<0.001$; $R^2=0.43$), indicating sex differences in neck CSA persist regardless of body size and shape.

Discussion

Automated CT-based analysis confirms sex is a significant determinant of cervical muscle CSA independent of stature, age, or BMI. Crucially, males exhibit consistently larger CSA, suggesting current scaling methods may overestimate female capacity without considering sex effects. This scalable, QC-verified pipeline enables large-cohort morphometry, providing population-representative inputs for parametric human models to support more equitable injury-risk assessment and crash-dummy design.

Images (Optional)

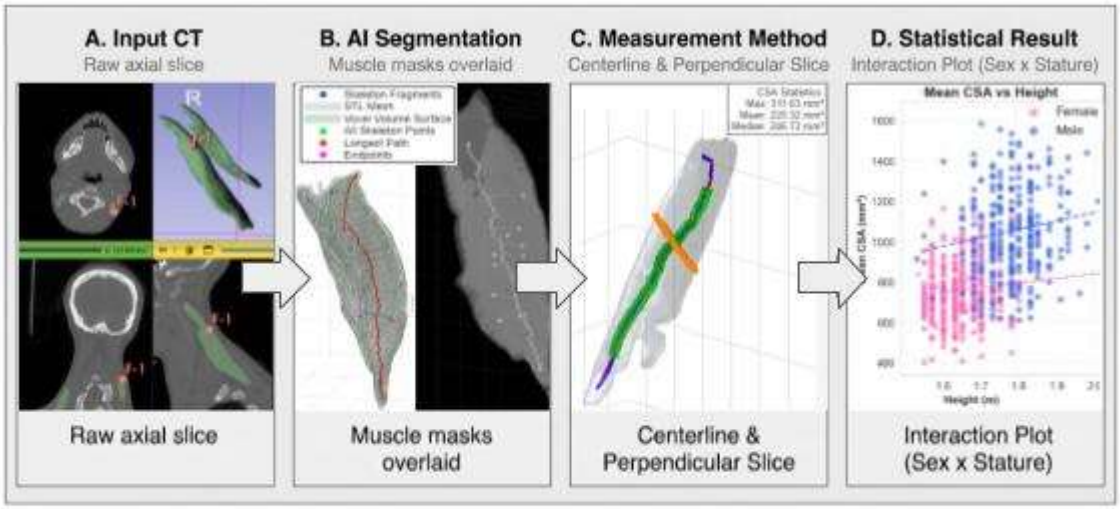


Figure 1: Automated pipeline for cervical muscle CSA quantification. (A) Raw CT input is processed to generate (B) AI-based muscle segmentations. (C) A custom workflow computes 3D centerlines and cross-sectional areas. (D) Statistical analysis reveals significant sex differences independent of body size.

References (Optional)

[1] Wasserthal et al., Radiol Artif Intell, 2023

Acknowledgements (Optional)

Undergraduate Research Opportunity Program at the University of Michigan, Andrew Mellon Foundation Research Scholarship, Yang-shen Lin from the University of Michigan Transportation Research Institute (UMTRI), Northwestern Michigan College Experiential Learning Institute.

Session Category

Injury Biomechanics: N/A

OA193-02

Associations Between Muscular Strength and Shock Exposure at the Head and the Lumbar Spine During Downhill Mountain Biking

Ms Barbara Halmai, Professor Timothy P Holsgrove, Dr Genevieve K R Williams

University of Exeter, Exeter, Devon, United Kingdom

Introduction

Downhill mountain biking (MTB) athletes are exposed to high-magnitude shocks during descents, even in the absence of crashes. While advances in bike suspension and wheel configurations can reduce shock exposure, substantial impacts are still transmitted to the head and lumbar spine, raising concerns about musculoskeletal and neurological health. Skeletal muscles play a key role in energy absorption during impacts, suggesting that stronger athletes may be better equipped to attenuate trail-induced shocks. The study aimed to investigate whether greater whole-body and neck strength are associated with reduced head and lumbar acceleration exposure during downhill MTB.

Methods

Twenty experienced downhill riders (36.0±13.6 years; 1.80±0.1m; 81.7±10.9kg; 15.4±12.8 years of experience) participated in the study. Maximal whole-body strength was evaluated using the isometric mid-thigh pull, and maximal isometric neck strength was assessed using a custom-built apparatus. Riders completed four downhill runs wearing inertial measurement units attached to the head and the lumbar spine. Peak linear acceleration was identified for the head and the lumbar spine, and peak rotational acceleration was calculated for the head. Acceleration events exceeding daily activity thresholds were also counted (linear head >3g, rotational head >400rad.s^{-2}, lumbar >8g). Multiple linear regression models were used to examine whether maximal strength predicted acceleration exposure, while controlling for age, body mass and experience.

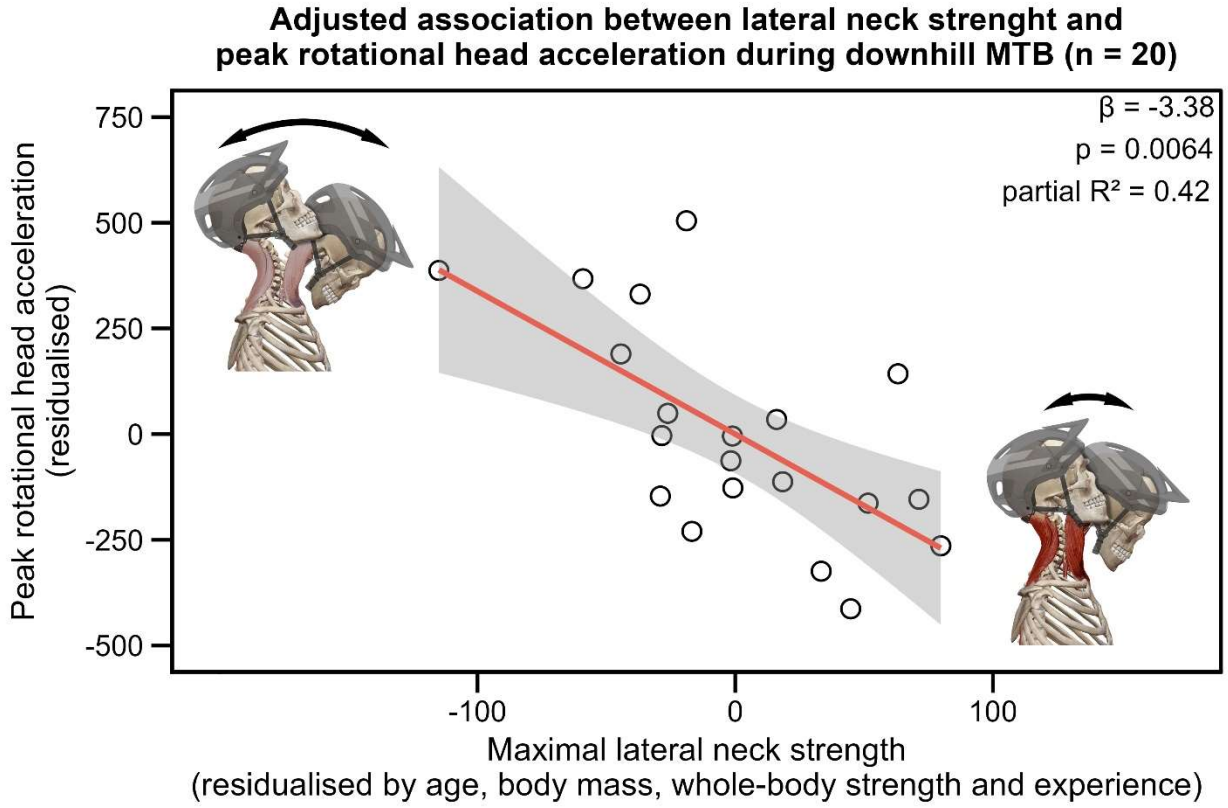
Results

Greater lateral neck strength was associated with lower rotational head accelerations during downhill riding ($t=-3.79$, $p<0.01$), with every 1N increase in strength predicting a 3.38rad.s^{-2} reduction. Whole-body strength did not significantly influence head or lumbar acceleration exposure. However, higher body mass was associated with greater lumbar acceleration peaks ($t=2.41$, $p<0.05$) and a higher number of peaks exceeding normal thresholds ($t=2.38$, $p<0.05$).

Discussion

Findings indicate that lateral neck strength contributes to rotational stabilisation of the head under transmitted shocks, potentially via an enhanced capacity for synchronous force production by cervical flexor and extensor muscles. Targeted neck strengthening and bodyweight management may represent strategies to reduce cumulative head and lumbar loading in downhill MTB athletes. This work provides the first field-based evidence that neck strength influences head accelerations under shock exposure, with important implications for injury prevention and long-term brain health.

Images (Optional)



Session Category

Injury Biomechanics: N/A

OA193-03

A Novel Neck Surrogate that Recreates Buckling Mechanics in Head Compressive Loading

Mr. AJ Hinman, Ms. Sophie Beauchesne, Mr. Aaron Brice, Dr. Christopher Dennison

University of Victoria, Victoria, BC, Canada

Introduction

In the field of experimental headgear assessment, automotive head-neck surrogates are typically applied. Scrutiny is often leveled at the necks, as they are not typically validated for head impact studies. We have previously reported on a bespoke surrogate developed for biofidelic headgear assessment [1]. The present study is an extension of this past work because it tests the hypothesis that our neck exhibits a biofidelic kinetic response in a previously untested impact scenario; vertex head loading leading to neck axial compression [2], that can lead to both head-brain and neck injury.

Methods

A custom inverted drop experiment using SAE j211 compliant equipment and post processing techniques was applied (Figure 1.A). Impact speeds were 3m/s onto a rigid surface (n=10, $m_{carriage}$=11-12kg simulating following torso). Axial force and sagittal bending moments were collected at the neck base. Data was processed to identify key kinetics, including axial force at neck buckle, peak sagittal moment, and time to buckle.

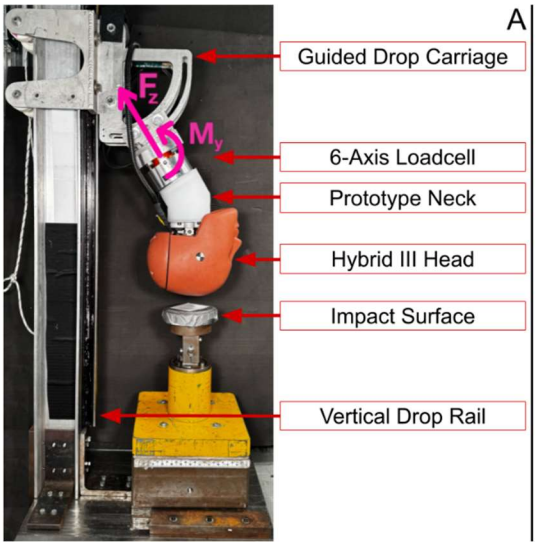
Results

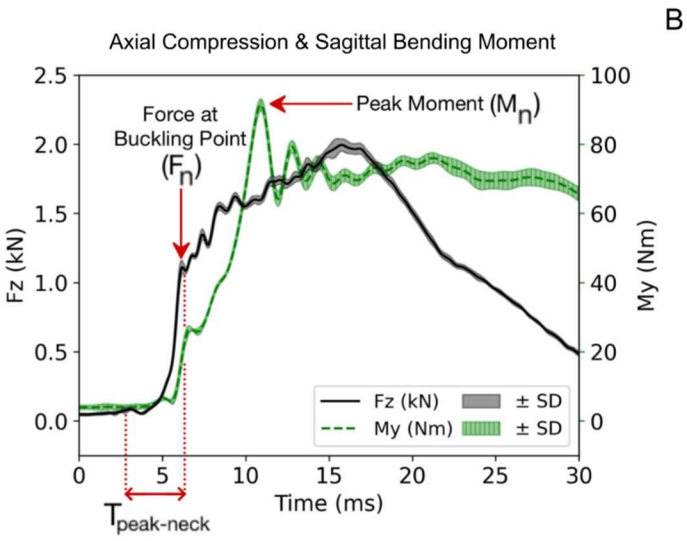
Referring to the nomenclature in Figure 1.B, peak compression force was 1.11±0.05kN (F_n), with buckling occurring at ~3.2ms ($T_{peak\text{-}neck}$). Buckling was followed by a sagittal moment maxima to 91.3±1.8Nm (M_n).

Discussion

Saari et al. [2] and Nightingale et al. [3] previously published cadaveric data from impacts we recreated in our study, and it is to this data we contrast. Saari et al. F_n were 1.91±0.73kN occurring ~4.2ms after carriage release, followed by M_n of 126.0±22.3Nm in 2.8m/s impacts (n=6, $m_{carriage}$=15kg) [2]. Select data from Nightingale et al. matching our impact parameters (n=2, $m_{carriage}$=16kg) showed F_n 1.90±0.06kN ~4.4ms after carriage release with M_n 124.9±26.9Nm (note: we equate T-injury to $T_{peak\text{-}neck}$ for the purpose of this comparison) [3]. We interpret these findings to suggest our neck can exhibit realistic buckling relative to cadavers, and offer an alternative to the Hybrid III neck that is known to be excessively stiff axially.

Images (Optional)





References (Optional)

[1] MacGillivray *et al.* 2021, JBME v49

[2] Saari *et al.* 2013, JBME v135

[3] Nightingale *et al.* 1996, JBME v29

Session Category

Injury Biomechanics: N/A

OA193-04

Velocity of Spinal Cord Injury Matters – Comparing Contusion and Dislocation in a Cervical Rat Model

MMr. Alexander Burden B.Eng, Dr. Jie Liu MD, Mr. Min Liu, Mrs. Nicole Janzen MSc, Mrs. Elizabeth Raffaele MSc, Ms. Haley Briggs BSc, Mr. Aidan Loong BSc, Dr. Oscar Seira PhD, Dr. Ward Plunet PhD, Dr. Thomas Oxland PhD, Dr. Wolfram Tetzlaff MD, PhD

UBC, Vancouver, BC, Canada

Introduction

Clinically, spinal cord injuries (SCI) are heterogeneous, occurring through various physical mechanisms, with different velocities, and depths of impingement. Cervical SCI are most common, with the majority of injuries occurring due to burst-fracture (9-35%) or dislocation (45-58%). Past pre-clinical experimental work has established that increasing velocity of contusion injuries results in greater functional deficits; however, the effect of velocity on dislocation injuries has not been clearly established. Additionally, while previous work has compared these injuries, relative severity of injury has not been controlled for, potentially conflating mechanism differences with differences in overall injury severity.

Methods

160 Sprague-Dawley rats were divided into six total groups; four contusion cohorts and two dislocation cohorts. Half of the cohorts were assigned low velocity (55mm/s) and the other half high velocity (550mm/s). Contusion cohorts (n=20) were further differentiated by two displacements; low (1.35mm depth) and high (1.45mm depth). Dislocation injuries (n=40) were conducted at 1.6 mm displacement of the C5/6 vertebrae, which were matched with the high displacement contusion groups (of low and high velocity) using the Martinez Open Field Locomotor scale. All SCI were conducted under aseptic surgery conditions using the UBC Multi-Mechanism Impactor and animals were kept for 6 weeks' post-injury for behavioral analysis, before being sacrificed and perfused for histological analysis.

Results

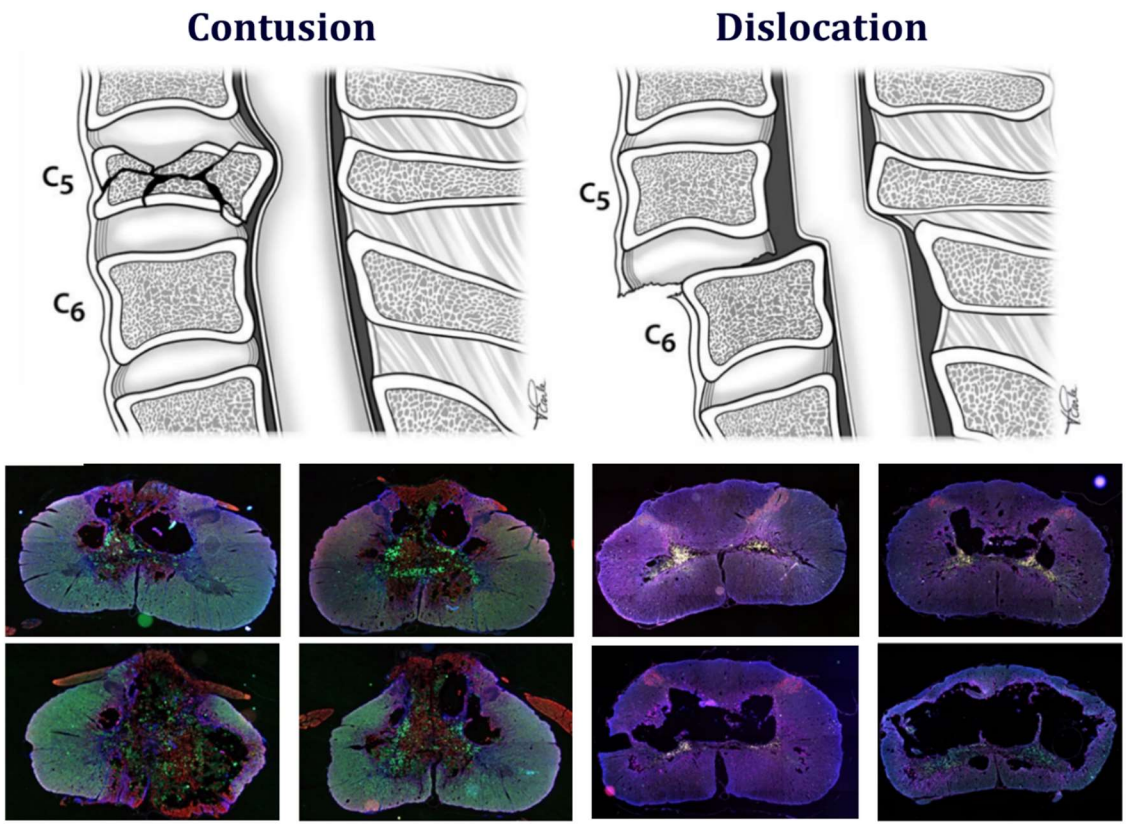
The Martinez Open Field, Irvine, Beatties, and Bresnahan (IBB) forelimb scale test showed significant differences ($p<0.001$) between mechanism and velocity cohorts, while the Grip Strength and Horizontal Ladder tests only showed differences between mechanisms ($p<0.001$). Motor Neuron counts at the injury epicentre were significantly lower in dislocation ($p<0.001$) than contusion, but were significantly higher in adjacent sections (-

1200μm and +600μm) indicating a more localized zone of injury. Myelin debris was significantly higher in dislocation ($p<0.001$) and showed an interaction effect with velocity.

Discussion

This is the largest study to directly compare contusion and dislocation injuries, and supports past work showing the differences in functional and histological outcomes between physical injury mechanisms. Velocity appears to affect injury severity in dislocation in a similar way and magnitude as it does in contusion, having significant effect on some behavioral tasks but not others.

Images (Optional)



Session Category

Injury Biomechanics: N/A

OA193-05

A User-Centered Biomechanical Approach to Reduce Low-Back Load in Circus Russian Bar Porters

M.Sc.A. Pierre Schmidt[1,2,3], PhD Marion Cossin[1], PhD Eric Wagnac[4], PhD Anne-Laure Ménard[5], M.Sc.A. Gerald Parent[5], M.Sc.A. Flavie Gilet[4], M.Sc.A. Yves Mathieu[6]

[1]Centre HUPR, Montréal, Quebec, Canada. [2]Ecole nationale de cirque, Montréal, Québec, Canada. [3]École de technologie supérieure, Montréal, Quebec, Canada. [4]ETS, Montréal, Québec, Canada. [5]INEDI, Terrebonne, Québec, Canada. [6]CDCQ, St-Jérôme, Québec, Canada

Introduction

In 2019, Cirque du Soleil reported chronic low-back pain among Russian bar artists, leading to substantial off-stage time and economic impact. Russian bar acts involve two porters supporting a flexible bar assembled with pole vaulting poles. A third artist, the flyer, performs acrobatic maneuvers by jumping on the bar. To address Cirque's concerns, a multidisciplinary transversal project involving five academic institutions and three industrial partners was conducted. This project demonstrates a new method for addressing biomechanics-related injury phenomena in the acrobatic community.

Methods

From 2019 to 2024, a multi-stage protocol was implemented after broader group of artists confirmed the prevalence of low-back pain among porters. Data were collected on two porters using motion capture, EMG, and force platforms to quantify spinal loads during typical Russian bar performances using a newly validated full-body musculoskeletal model [1]. Modeling data and iterative input from artists guided the development of several novel Russian bar concepts and ultimately, a Y-shaped prototype was selected. A fiberglass prototype was built with mechanical properties comparable to traditional bars. Using the validated model and a second data collection, spinal loads generated by the traditional and prototype bars were compared [2].

Results

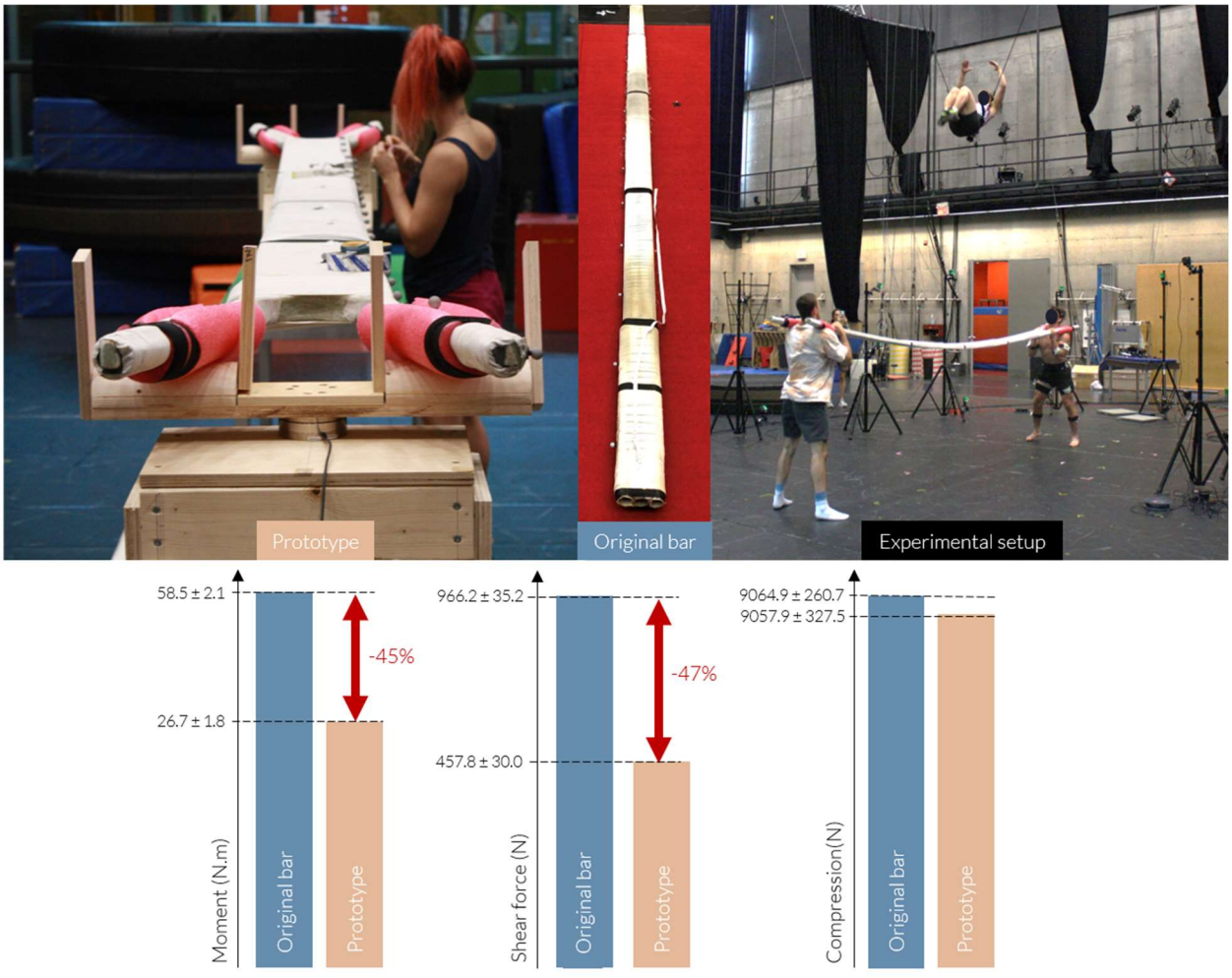
The prototype significantly reduced lumbar loading, particularly in the frontal plane with a decrease in moments of about 45% and a decrease in shearing forces of about 47%. The new prototype did not reduce compression force on the lumbar column. Artists reported

improved comfort and perceived safety when using the Y-shaped bar, notably due to reduced slipping risk.

Discussion

Despite the small sample size, these results support the notion that design thinking along with biomechanical analysis can help reduce lower load on porters back. The findings open the door to evidence-based equipment design in the performing arts. Furthermore, to our knowledge, this is the first full-body musculoskeletal model developed specifically for circus artists, a population subject to high mechanical demands. This project demonstrates how a biomechanical protocol might, in the future, support injury mitigation in the circus and/or acrobatic community.

Images (Optional)



References (Optional)

[1] Schmidt, P. *et al*., *Circus: Arts, Life, and Sciences,* 2025

[2] Cossin, M. *et al*., *Sports Biomechanics*, 2025

Session Category

Injury Biomechanics: N/A

OA193-06

Influence of Intervertebral Disc Proximity on Hemorrhagic Severity in Porcine Spinal Cord Injury: A Biomechanical and Semi-Automated Imaging Assessment

Mr. Amirhossein Borjali PhD Candidate, Biomedical Engineering, Ms. Kitty So, Ms. Aysha Allard Brown PhD Candidate, Ms. Neda Manouchehri, Ms. Juliana Mitchell, Dr. Femke Streijger PhD, Dr. Brian Kwon MD, PhD, FRCSC, Dr. Peter Cripton PhD, P.Eng.

University of British Columbia, Vancouver, BC, Canada

Introduction

Animal models of spinal cord injury (SCI) are essential for understanding SCI biomechanics and evaluating therapies, yet substantial variability persists in the severity metrics in porcine SCI despite standardized impact parameters. One potential contributor is the stiffness of the anatomical region beneath the impact site. At the vertebral body, the ventral surface of the spinal canal is concave, providing more space beneath the spinal cord, whereas impacts over the intervertebral disc (IVD) interact with a protrusive surface formed by the endplates, annulus fibrosus, and posterior longitudinal ligament (PLL). These geometric differences may influence injury severity.

Intraparenchymal hemorrhage (IPH) is a recognized marker of injury severity, but the effect of impact proximity to the IVD has not been quantified. Manual IPH segmentation also introduces operator variability. This study evaluates whether injury–IVD distance predicts hemorrhage magnitude in a porcine SCI model and assesses a semi-automated ultrasound-based pipeline for IPH quantification.

Methods

SCI was induced at T2 using a weight-drop model while varying the distance between the impact epicenter and the nearest IVD, with impact energy held constant. Ultrasound imaging provided real-time visualization of acute IPH. A semi-automated segmentation pipeline was used for IPH quantification. Hemorrhage volume was normalized to spinal cord (SC) volume, and correlation analyses examined associations with injury–IVD distance.

Results

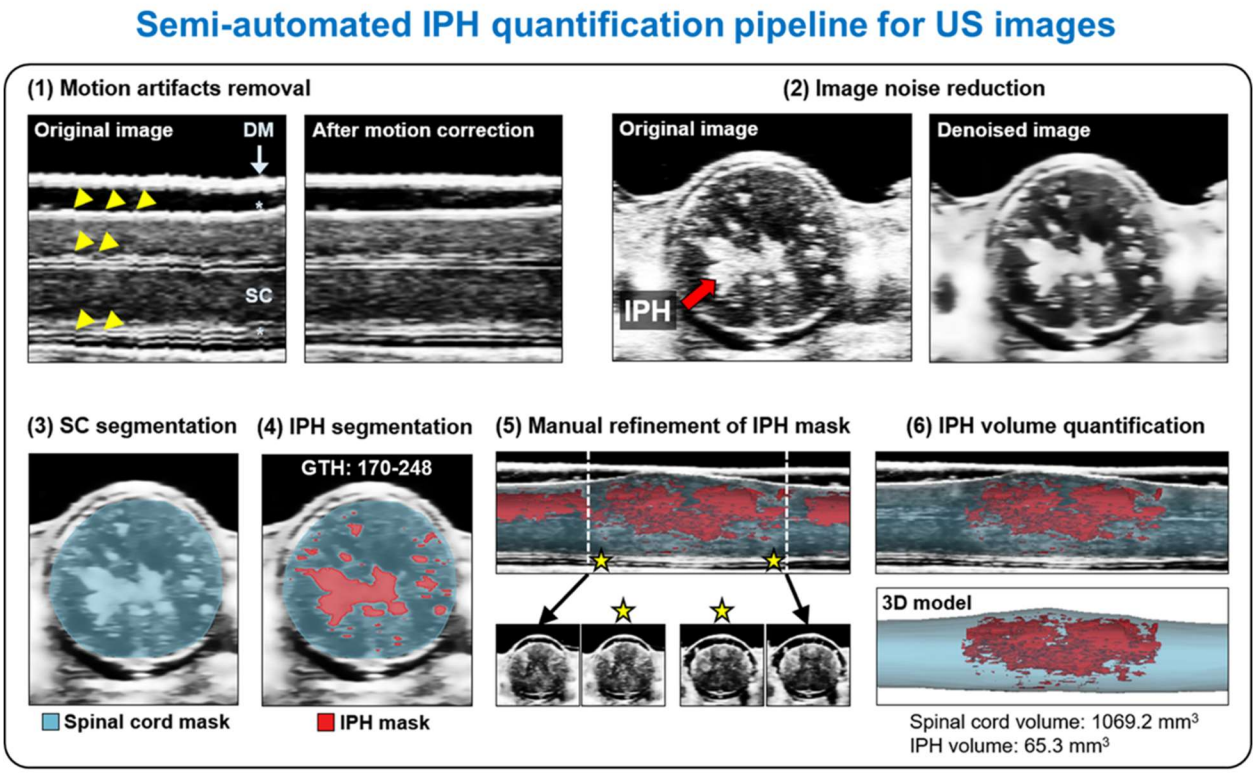
Injury–IVD distance showed a significant inverse relationship with absolute IPH volume (R^2 = 0.3181, $p < 0.01$). Injuries closer to the disc produced larger hemorrhage. Normalization to SC volume strengthened this relationship (R^2 = 0.5441, $p < 0.01$), indicating that relative hemorrhage severity increases consistently with greater IVD proximity and with greater cord size.

Discussion

The elevated hemorrhagic response near the IVD aligns with anatomical differences. The protrusion created by disc structures reduces available space and likely increases local strain in the spinal cord during impact compared with the concave ventral surface over the vertebral body. Accounting for injury–IVD distance may therefore reduce variability in porcine SCI studies.

In conclusion, proximity to the IVD significantly increases hemorrhagic severity in porcine SCI. Additionally, integrating anatomical context and objective imaging methods may improve reproducibility and translational relevance in large-animal contusion models.

Images (Optional)



Session Category

Injury Biomechanics: N/A

OA194-02

More Bone, More Problems: Compromised Microarchitecture of Osteosclerotic Matrix in Prostate Cancer Bone Metastasis

Ms. Naomi Jung BASc[1,2], Dr. Felipe Eltit PhD[2], Dr. Qiong Wang PhD[1], Ms. Robyn Birch MASc[1], Ms. Bita Mojtahedzadeh BSc[1], Mr. Dennis Xie BSc[1], Mr. Samuel Xu MEng[1], Dr. Danmei Liu PhD[1], Dr. Eva Corey PhD[3], Dr. Colm Morrissey PhD[3], Dr. Lawrence True PhD[3], Dr. Rizhi Wang PhD[1], Dr. Michael Cox PhD[1]

[1]University of British Columbia, Vancouver, British Columbia, Canada. [2]Vancouver Prostate Centre, Vancouver, British Columbia, Canada. [3]University of Washington, Seattle, Washington, United States

Introduction

1 in 8 men will be diagnosed with prostate cancer (PC), and ~15% progress to an incurable metastatic state that primarily affects the bone. Patients with PC bone metastasis (PCBM) have three-fold higher fracture risk yet the biomechanical basis for this fragility remains unknown. We hypothesize that PCBM-affected bone has altered microarchitecture and organization which contributes to lower local mechanical properties and poorer fracture resistance.

Methods

We analyzed cadaveric vertebral trabecular bone samples from the thoracic/lumbar spine of patients who died of PC (n=12) and non-cancer donors (n=3). Quantitative backscattered scanning electron microscopy (qBSE) was used to quantify calcium weight percent (CaWt%) and lacunar density/shape using a custom MATLAB pipeline (5-9 ROIs per sample per bone type). We evaluated collagen organization with picrosirius red staining and polarized light imaging, and performed nanoindentation in matched ROIs (5 indents per ROI) to measure local elastic modulus and hardness. Bulk mechanical behavior was assessed by uniaxial compression to failure (7 PCBM; 3 non-cancer). Groups were compared using t-tests or one-way ANOVA with Tukey post-hoc testing (α=0.05).

Results

PCBM samples were predominantly osteosclerotic with elevated bone volume/total volume (BV/TV; Figure 1). Peak CaWt% did not differ between control, trabecular, and sclerotic regions, but CaWt% width was greater in PCBM (p=0.026). From nanoindentation, mean elastic modulus and hardness were not different between control (E =12.96 GPa, H=0.46 GPa) and PCBM sclerotic (E=11.47 GPa, H=0.46 GPa). BV/TV explained 77% of variance in elastic modulus from compression testing. PCBM osteosclerotic bone

exhibited poor collagen organization compared to trabecular regions with elevated lacunar density, area, and circularity, and poor lacunar alignment (all $p<0.001$).

Discussion

PCBM osteosclerotic bone demonstrates collagen disorganization and abnormal lacunar morphology despite similar peak mineralization and indentation metrics. Since bulk stiffness was largely explained by BV/TV, the elevated fracture risk in PCBM may reflect tissue-level damage accumulation and impaired toughening mechanisms that are not captured by modulus or hardness alone. Notably, increased mineral density heterogeneity in osteosclerotic regions may promote local strain concentrations that facilitate microdamage. Ongoing work will quantify crack initiation and propagation following compression to define PCBM-specific fracture mechanisms.

Images (Optional)

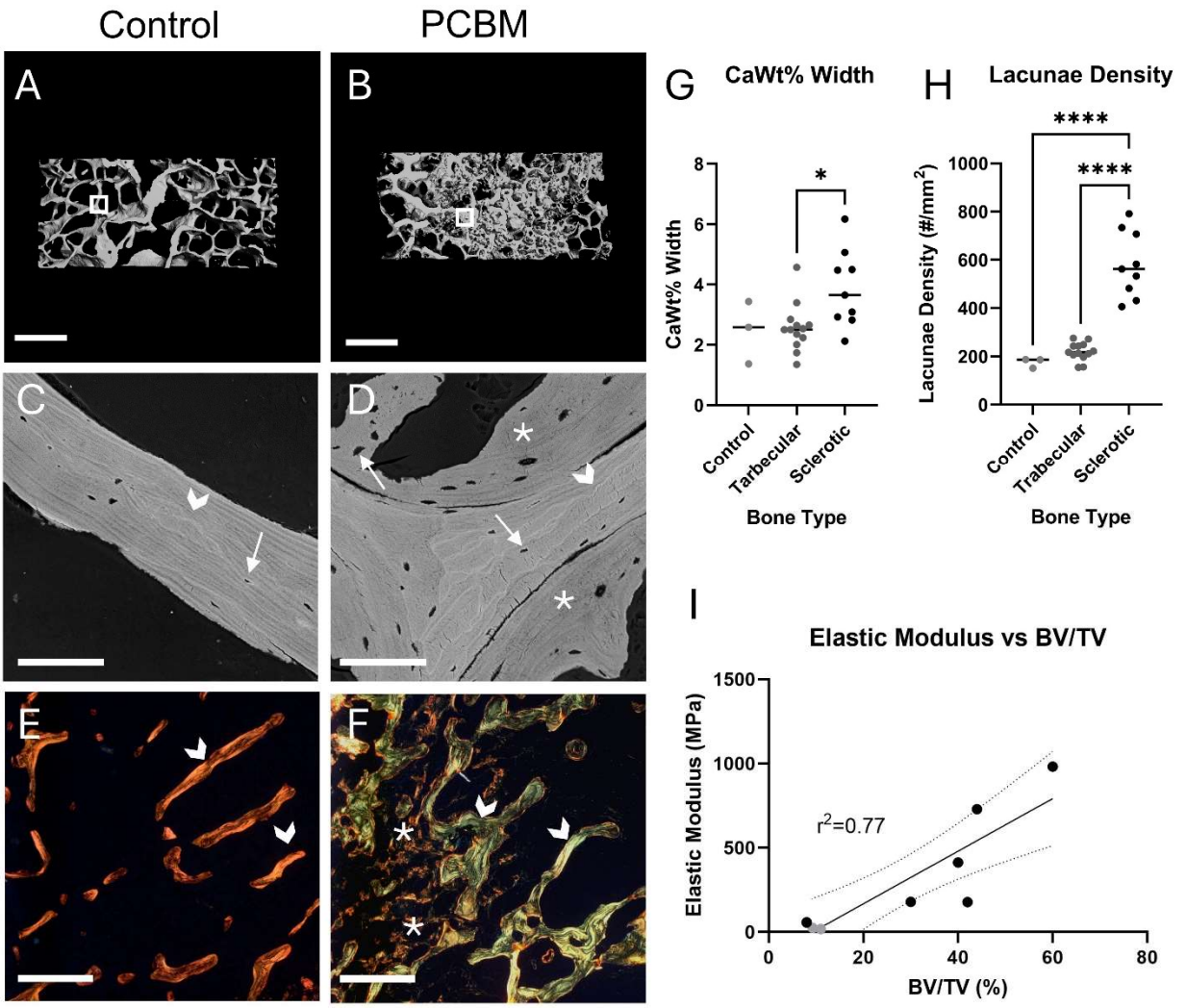


Figure 1: Prostate cancer bone metastasis (PCBM) alters bone microarchitecture and mineral density distribution. (A, B) image renders obtained from microCT (scale bar = 2 mm), **(C,D)** quantitative backscattered scanning electron microscopy (qBSE) images of boxed areas in A,B (scale bar = 100 μm), and **(E,F)** picosirius red staining and polarized light imaging of cadaveric vertebral trabecular bone samples (scale bar = 1 mm). **(G)** Mineral density heterogeneity quantified as the width of the calcium weight percent (CaWt%) distribution from qBSE. **(H)** Lacunar density quantified from qBSE images (bars show mean). **(I)** Apparent elastic modulus from compression testing plotted against BV/TV measured by microCT. Arrows indicate lacunae; arrowheads indicate trabeculae; asterisks indicate sclerotic bone. MicroCT renderings were reconstructed from 10 μm slices over a total thickness of 4.5 mm. $p < 0.05$; ****$p < 0.001$.

Session Category

Organ and Tissue Biomechanics: N/A

OA194-03

Ageing Increases Stiffness and Disrupts Strain Distribution in Human Lumbar Intervertebral Discs: Implications for Constitutive Modelling and Boundary Conditions Definition

Miss Margherita Pasini, Miss Gaia Youssef, Mr Davide Alberti, Prof Luca Cristofolini, Dr Marco Palanca

University of Bologna, Bologna, Italy, Italy

Introduction

Intervertebral discs (IVDs) undergo structural degeneration throughout life, leading to alterations of their biomechanical behaviour[1]. Yet, most available IVDs datasets come from the elderly, who exhibit marked age-related degeneration, and focus on apparent properties (stiffness, ROM, neutral zone). It remains challenging to determine how and to what extent degeneration affects IVDs mechanical behaviour, as well as to define credible specific boundary conditions for computational models across different ages.

A comprehensive biomechanical characterisation of the IVD across ageing is still missing. We aimed to provide an evaluation of age-related IVD mechanical changes to support the definition of constitutive laws.

Methods

Twenty-three lumbar IVDs were harvested from human donors and divided into age groups: young (n=11,33±2 years), adults (n=5,44±3 years), and old (n=7,63±1 years). Specimens underwent 3T-MRI and qCT to assess IVD degeneration[2] and exclude pathologies. The specimens were axially compressed within the elastic regime (up to 0.5% body weight) using a spine simulator (MIB4.0-MAS2-S) with a 6-axis load cell. A 3D-DIC system (Aramis Adjustable, Zeiss) was used to measure the full-field maximum and minimum principal strains (Eps_max, Eps_min) on the IVD surface.

The stiffness was obtained as the load-displacement slope between 20-80% of the maximum load. Strain variability was quantified using the Coefficient of Variation(CV) over the IVD surface. The age groups were compared (Kruskal-Wallis Test).

Results

Old IVDs were significantly stiffer than both young (+48%,p=0.025) and adults (+68%,p=0.050). They also showed larger Eps_min compared to young (+49%,p=0.012), and larger strain variability. Principal strains were consistently aligned over the surface of young IVDs, old IVDs showed scattered and irregular strain directions.

Discussion

The optimized architecture of the young IVDs enabled an efficient and homogeneous load transfer across adjacent vertebrae. In contrast, degenerated IVDs demonstrated strain concentrations and unpredictable mechanical responses. Age-related changes increased disc stiffness and impaired the capacity to distribute strain uniformly, thereby accentuating the mechanical difference between healthy and degenerated tissues. These findings highlight the limitations of relying on apparent material properties derived from a partially representative population and provide essential data for the development and validation of accurate vertebral computational models.

Images (Optional)

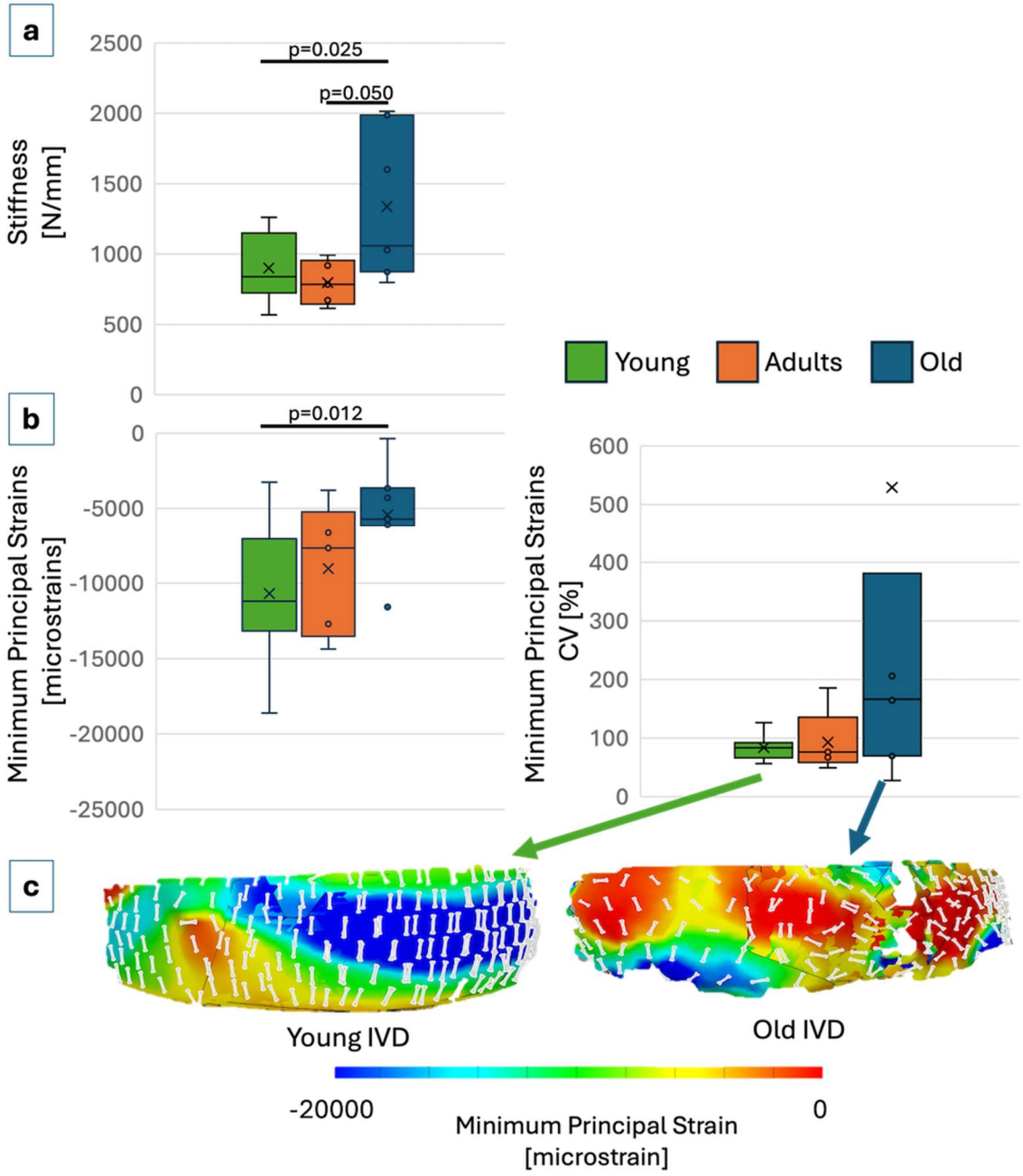


Figure: Stiffness (**a**) and Eps_min (**b**), including its CV for the Young, Adult, and Old specimens. 3D colour maps of Eps_min and theis principal strain directions for representative young and old specimen (**c**).

References (Optional)

[1] Pasini, JMBBM, 2025

Acknowledgements (Optional)

METASTRA project funded by the European Union, HEU topic HLTH-2022-12-01, grant 101080135

Session Category

Organ and Tissue Biomechanics: N/A

OA194-04

Lytic Lesion Size and Location Affect the Compressive Failure Load of Human Metastatic Vertebrae Calculated With Subject Specific Finite Element Models

Mr Robert Roger[1], Dr Rajdeep Ghosh[1], Dr Áron Lazáry[2], Dr Lingzhong Guo[1], Professor Damien Lacroix[1], Professor Enrico Dall'Ara[1]

[1]University of Sheffield, Sheffield, England, United Kingdom. [2]National Center for Spinal Disorders, Budapest, Central Hungary, Hungary

Mr Robert Roger

Dr Rajdeep Ghosh

Dr Áron Lazáry

Dr Lingzhong Guo

Professor Damien Lacroix

Introduction

Approximately 16% of cancer patients are clinically diagnosed with vertebral metastases [1], which present in different types of lesions depending on the primary tumour. Lytic lesions reduce bone mineral density and increase fracture risk. Lytic lesions form in a variety of locations and volumes, yet the biomechanical impact of these factors remains poorly quantified and is not considered in current clinical stability scores. Finite element (FE) modelling provides a means to systematically evaluate these effects. This study aimed to assess how location and volume of simulated lytic lesions influenced vertebral failure load using FE models derived from computed tomography (CT)-images.

Methods

Three radiologically healthy lumbar vertebrae from three cancer patients with spine metastases were semi-automatically segmented from CT-images. Heterogeneous isotropic elasto-plastic homogenised FE (hFE) models were created from each vertebra. Material properties were assigned from bone mineral density distributions of densitometrically calibrated CT-images. Spheroidal lesions with volume of 10%, 20%, or 30% of the vertebral body volume (VBV) were simulated by assigning an elastic modulus of 0.01 MPa. Lesion's centres are shown in Figure-1A. Compressive ultimate force (FU) was calculated for each hFE model at 1.9% of apparent axial deformation. Normalised FU was calculated with respect to intact control vertebra.

Results

The range of normalised FU was 7.3±1.7%-24.3±2.3%, 14.9±2.1%-37.8±1.4%, and 22.0±1.8%-48.8±4.1% for lesions occupying respectively 10%, 20%, and 30% of the VBV (Figure-1B).

Discussion

Both lesion size and location influenced the FU of the vertebra and should be considered in scoring systems to estimate vertebral stability. Larger lesions produced greater FU reduction. Substantial variability across locations indicates position is equally important for assessing vertebral stability. Lateral regions located close to the cortex were most detrimental, suggesting these areas represent biomechanically vulnerable regions.

Images (Optional)

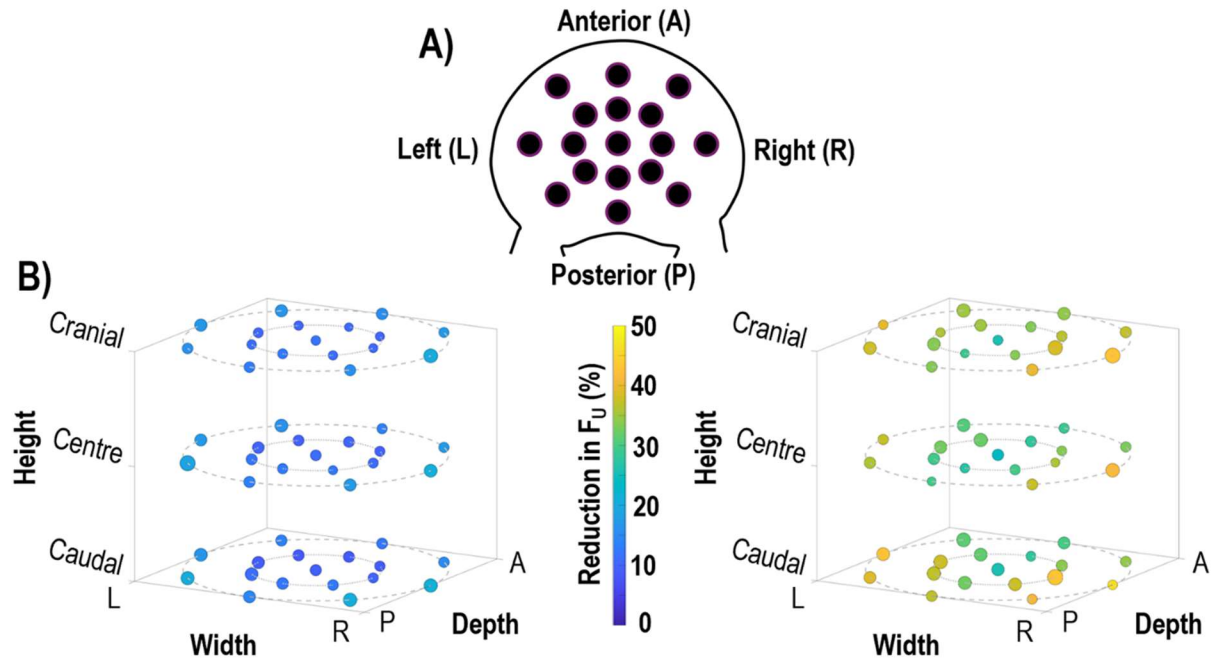


Figure 1: A) Cross section of a vertebral body displaying the location of the centre of virtual lesions at one axial location. B) Mean reduction in failure load across patients of simulated lesions with a volume of 10% (left) and 30% (right) of the vertebral body volume. Markers represent the location of the centre of the lesion, and the size of the marker represents the standard deviation of failure load reduction across patients.

References (Optional)

[1] Van Den Brande et al., J Bone Oncol. ,2022

Acknowledgements (Optional)

Supported by the METASTRA project (EU H2022 grant ID:101080135; UK Horizon Europe Guarantee Extension ID:10075325).

Session Category

Organ and Tissue Biomechanics: N/A

OA194-05

Examining the mechanical contribution of elastin in the bovine annulus fibrosus

Ms Sabrina Sinopoli MSc, Ms Amber Swent BSc, Dr Diane Gregory PhD

Wilfrid Laurier University, Waterloo, Ontario, Canada

Ms Sabrina Sinopoli

Introduction

Low back pain, a common concern for the expanding aging population, emerges from various biomechanical disruptions of the spine often a result of damage to the intervertebral disc (IVD). It is therefore important to understand the mechanical contribution of the various structural components in the IVD. One such component is the protein elastin. Research has shown that elastic fibres are present in all parts of the IVD, but that their organization varies [1]. Elastic fibres are found between lamellae (perpendicular cross-bridges) and within lamellae (orientated parallel to collagen fibres) [1]. This study examined the mechanical contribution of elastin to the properties of the annulus fibrosus via enzymatic digestion of elastin.

Methods

Six bovine lumbar spines were used to obtain 18 IVDs. Following removal of the nucleus pulposus, samples were washed in PBS and randomly assigned to one of three conditions: 1) PBS only; 2) PBS+buffers which included protease inhibitors; 3) PBS+buffers+elastase (3U/mL). The submerged samples were then placed on a rocker plate at 40 rotations/minute and incubated for 36 hours (at 37°C). Following incubation, samples were washed with PBS and dissected to obtain two T-peel test samples to quantify lamellar adhesion and two bilayer test samples to quantify annular tensile properties.

Results

No significant effect of enzymatic digestion of elastin was observed. However, the group containing PBS+buffer required significantly less stress to reach 15% strain in the bilayer tests compared to samples in the PBS only group ($p=0.04$).

Discussion

The lack of mechanical effects following enzymatic digestion suggests elastin may not play a major role in overall IVD mechanical integrity, potentially due to its limited composition (less than 5% dry weight) [2]. The intact remaining collagen fibres may have had a greater responsibility for maintaining IVD strength in the absence of elastin. Additionally, as the mechanical tests performed measured overall annular tensile mechanics and lamellar adhesive mechanics, it is possible the intralamellar matrix (the connective matrix found within single lamellae), was independently affected by elastin digestion, which may have been overlooked.

References (Optional)

[1] Jing Yu et al., J Anatomy, 2002

[2] Jing Yu, Biochem Soc Tran, 2002

Session Category

Organ and Tissue Biomechanics: N/A

OA195-02

Longitudinal Joint Mechanics in a Post-Traumatic Osteoarthritis Mouse Model Using I*n Vivo* image-Guided Mechanical Evaluation.

Ms Emma C. Boersma, Ms Annunzia M. Cagnoni, Dr Han Liu, Prof Kathryn S. Stok

The University of Melbourne, Melbourne, Victoria, Australia

Introduction

Image-guided mechanical evaluation combines mechanical testing with micro-computed tomography (microCT) to provide insight into joint loading at microstructural level [1]. Cross-sectional studies have shown that mechanical data can describe joint disease and serve as a fundamental basis for *in silico* models [1]. Longitudinal data would permit assessment of joint adaptation over time. The aim of this study was to longitudinally examine joint mechanics using *in vivo* image-guided mechanical evaluation of healthy and diseased mouse knee joints.

Methods

Destabilisation of the medial meniscus (DMM) or Sham surgery was performed on fourteen-week-old C57Bl/6 mice (n=10/group). The Mouse Actuating X-ray Imaging System (MAXIS) was used to perform stress-relaxation compression on the right knee during microCT scanning (10.4 µm, 70 kVp, 57-114 µA; vivaCT80, Scanco Medical) at three timepoints: before surgery (0-), 14- and 28-days post-surgery (Figure 1A). At each timepoint, two images were acquired during relaxation phases of the mechanical test. Steps were held at constant actuator displacement when the load cell reached (i) preload 200 mN, and (ii) loaded 300 mN. Images were processed as previously described, and joint space width (JSW), volume (JSV) and lowest voxel count (LVC) were calculated [2]. Actuator displacement at step ii (d_a) was analysed, and the effect of disease and time on imaging and mechanical measures were assessed using a mixed-effects model.

Results

Preliminary results show that following surgery, the actuator displacement required to reach the loads are smaller in DMM than Sham, with a significant difference at 4 weeks post-surgery (Figure 1B). Joint space data (not shown) suggests applied actuator displacements are larger than those experienced in the joint.

Discussion

In this first *in vivo* study using MAXIS, displacement in Sham and DMM knee joints was observed over time, demonstrating the sensitivity of MAXIS to joint health and disease progression. Displacements within the knee joint were only 1-2 voxels compared to those measured at the actuator. Further validation considering partial volume effects, must be conducted. This research leads to exciting possibilities, providing data for *in silico* models to explore links between material properties, tissue strain and cellular responses.

Images (Optional)

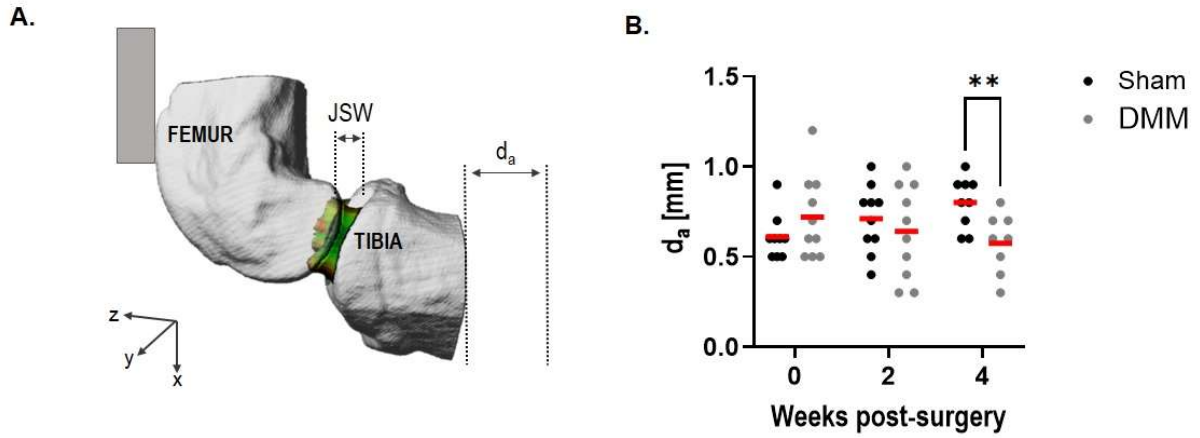


Figure 1. (A) Femur and tibia in sagittal plane and the direction of actuator displacement (d_a), along the z-direction, compared to joint space displacement, JSW and (B) showing the difference in actuation displacement over time in each group.

References (Optional)

[1]Madi,K *et al*.,Nat.Biomed.Eng.,2020

[2]Stok,K.S. et al.,Quant.Imaging.Med.Surg.,2020

Acknowledgements (Optional)

Funding received from the Australian Research Council DP180101838, FWO and F.R.S.-FNRS (Excellence of Science programme, No. 40007553) and KU Leuven – University of Melbourne International Research Training grant. We thank the engineering team behind MAXIS, the staff from the Animal Facility of The University of Melbourne and Prof Christopher Little from Kolling Institute, University of Sydney.

Session Category

Musculoskeletal Biomechanics: Joints and Motion

OA195-03

Ultrasound Evaluation of Acute Knee Cartilage Response After Walking in Patients with Knee Osteoarthritis

Dr. Derek Pamukoff PhD[1], Mr. Harry Battersby MSc[1], Dr. Richard Magony PhD[1], Dr. Hayden Atkinson PhD[1], Ms. Tamara Tompkins MSc[1], Dr. Richard Willy PT PhD[2], Dr. Tom Appleton MD PhD[1], Dr. Trevor Birmingham PT PhD[1]

[1]Western University, London, ON, Canada. [2]The Ohio State University, Columbus, Ohio, United States

Introduction

Articular cartilage degradation is a primary feature of knee osteoarthritis (OA). Ultrasound imaging is used to evaluate cartilage outcomes that may be sensitive to loading paradigms. We evaluated acute knee cartilage response to a walking bout using ultrasound imaging.

Methods

35 patients with mild-to-moderate knee OA (19 male, 16 female; Age=62.8 (12) years; BMI: 26.6 (4.3) kg/m^2; Kellgren-Lawrence Grades 1-3 (n): 12, 10, 13) completed bilateral ultrasound imaging of the femoral trochlea and medial femoral condyle before and after 30 minutes of walking on a force-instrumented treadmill with motion capture at a self-selected speed (1.13 (0.14) m/s)). Gait biomechanics were sampled for 10 seconds at the end of every fifth minute. Peak patellofemoral (PFJF) and medial tibiofemoral contact force (TFJF) were derived and averaged across stances (Fig 1A-B). Thickness and echo-intensity (EI) were extracted from ultrasound images (Fig 1C-D). Participants self-reported their more symptomatic knee. 2 (limb) x 2 (time) ANOVA with repeated measures evaluated the change in cartilage thickness and EI. Multiple stepwise regression evaluated the association between absolute gait (TFJF and PFJF) and cartilage outcomes (thickness and EI) adjusting for age, sex, BMI, and prior injury in the symptomatic knee.

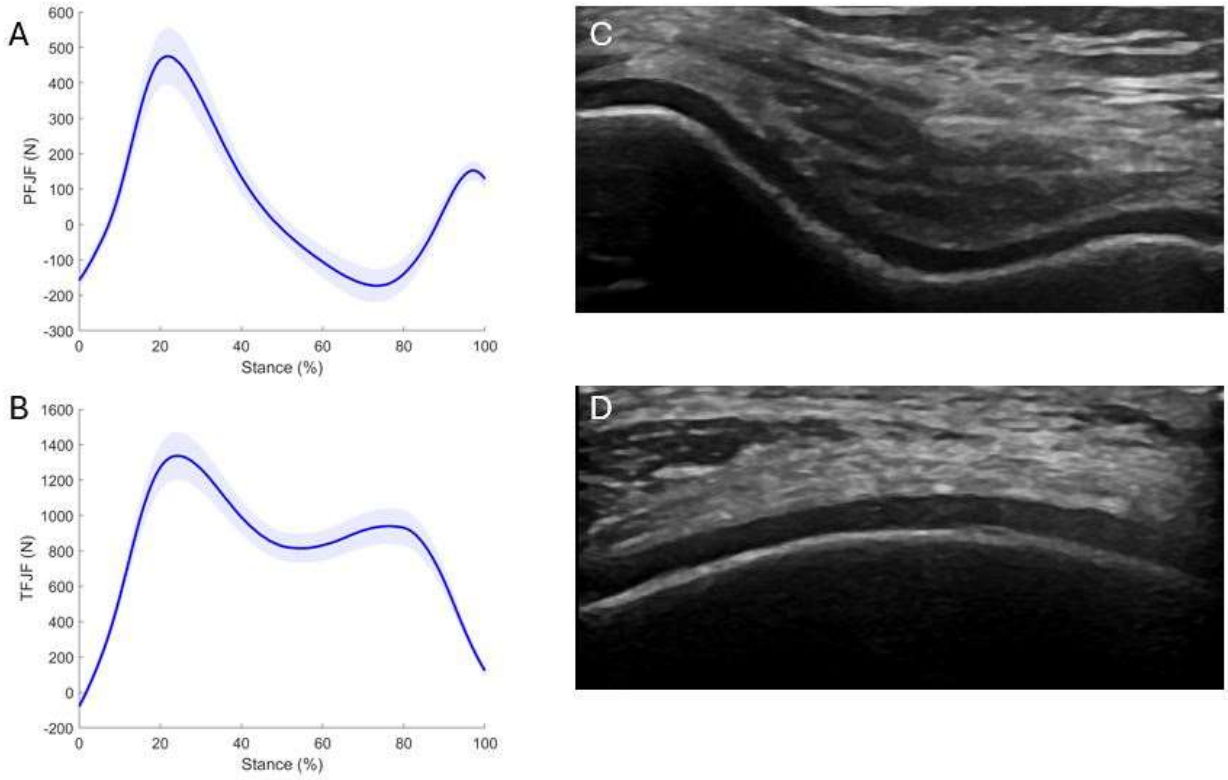
Results

There was a limb by time interaction for medial condyle cartilage thickness ($F_{1,33}$=4.94, p=0.03). Post hoc comparisons found thinner cartilage after walking in the more symptomatic knee (Mean Difference=-0.15 (-0.08, -0.21) mm, p=0.001), and cartilage was thinner in the more versus less symptomatic knee after walking (Mean Difference=-0.16 (-0.02, -0.30) mm, p=0.024). There was a main effect of limb indicating higher EI in the more symptomatic knee in the medial condyle ($F_{1,33}$=8.40, p=0.01; Mean Difference=4.34 (1.30, 7.40)) and trochlea ($F_{1,33}$=4.09, p=0.05; Mean Difference=3.22 (0.02, 6.42)). A larger medial TFJF (β=0.01, ΔR^2=0.15, p=0.021) was associated with higher medial condyle cartilage EI.

Discussion

There was an acute reduction in medial condyle cartilage thickness, but not within the trochlea. Patients with knee OA walk with less knee flexion, likely limiting patellofemoral loading. Higher medial TFJF was associated with higher cartilage EI on the medial condyle, which may provide a surrogate of cartilage composition that contributes to greater deformation in response to loading.

Images (Optional)



Acknowledgements (Optional)

The study was supported by the Western Bone and Joint Institute Catalyst Grant Program (PI: Pamukoff), Canadian Foundation for Innovation (Project ID: 42110, PI: Pamukoff)

Session Category

Musculoskeletal Biomechanics: Joints and Motion

OA195-04

In Vivo Dynamic Stereo X-Ray Analysis Shows Medial and Lateral Tibial Slope are Correlated with Knee Mechanics after Anterior Cruciate Ligament Reconstruction

Ms. Kristen Seballos BS, MS[1], Mr. Austin Carcia BS[1], Dr. Armando Vidal MD[1,2], Dr. Jonathan Godin MD, MBA[1,2], Dr. Thomas Hackett MD[1,2], Dr. Matthew Provencher MD, MBA[1,2], Dr. Peter Millett MD, MSc[1,2], Dr. Johnny Huard PhD[1], Dr. Scott Tashman PhD[1], Dr. Colin Smith PhD[1]

[1]Steadman Philippon Research Institute, Vail, Colorado, United States. [2]The Steadman Clinic, Vail, Colorado, United States

Introduction

It is widely thought that anterior cruciate ligament (ACL) strain is increased by greater posterior tibial slope (PTS), which can contribute to ACL injuries and retears [1]. However, a recent study found peak ACL strain measured during single leg jumps with Dynamic Stereo X-ray (DSX) had no significant correlation with medial and lateral PTS [2].

Methods

Twenty-six patients (15 Female, 28.3±6.3 years) received unilateral bone-patellar tendon-bone ACL reconstruction (ACLR) in an IRB-approved clinical trial investigating the impact of orthobiologics on healing (IRB#2019-13, NCT04205656). All treatments groups are combined for this analysis. DSX assessments were performed during downhill running at 6- and 12-months post-surgery. CT-based bone models were registered to the DSX images to calculate knee kinematics from 0-30% of stance. Statistical Parametric Mapping (SPM) was used to analyze correlations for anterior tibial translation, internal tibial rotation, and ACL strain to medial, lateral, mean, and difference in PTS.

Results

At 6 and 12 months for all of early stance in downhill running, anterior translation was significantly correlated with medial, lateral, and mean PTS, and internal rotation was significantly correlated with PTS difference. At 6 months, ACL strain was correlated to medial (R=0.17–0.49, p=0.03), lateral (R=0.37–0 .61, p=0.005), and mean PTS (R=0.3–0.59, p=0.008) for 5-30% of stance. No significant ACL strain correlations were found at 12 months.

Discussion

Correlations with ACL strain were present at 6 months, but not 12, suggesting healing ACL grafts remodel and gain stiffness which reduces strain. Knee kinematics were still affected by PTS and lateral-medial differences at 12 months. Our results may differ from the prior DSX study because we included running, studied ACLR patients instead of healthy, and PTS was calculated in 3D instead of 2D [2]. Future studies will be needed to evaluate potential osteotomy patients with larger PTS. We will also perform PTS measurements on clinical X-rays to increase relevance in a clinical setting.

Images (Optional)

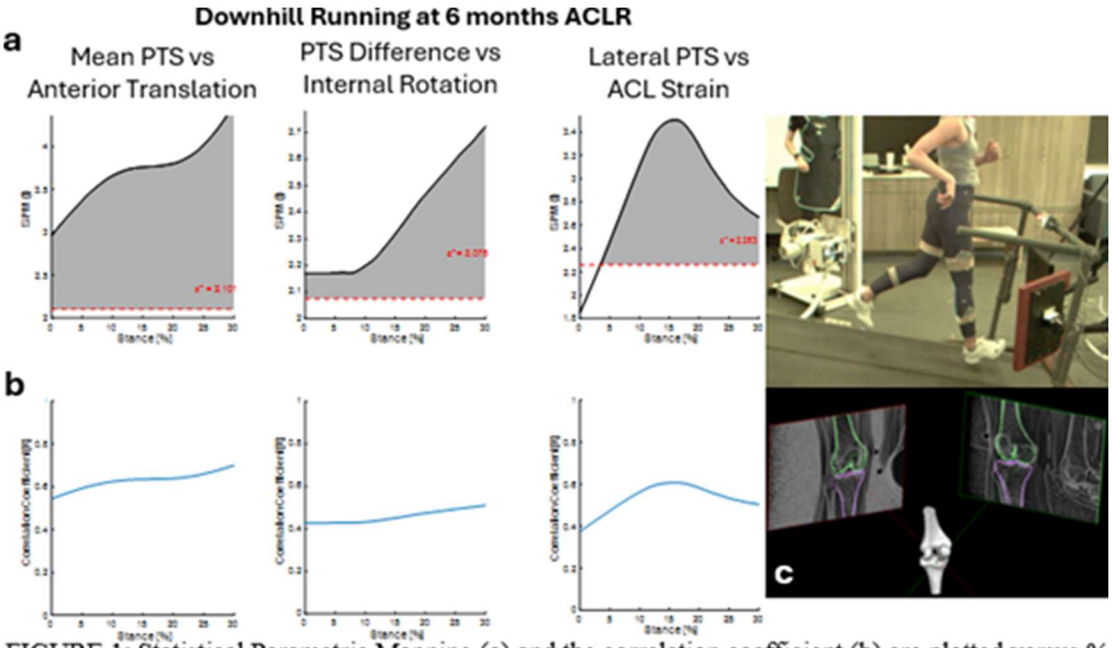


FIGURE 1: Statistical Parametric Mapping (a) and the correlation coefficient (b) are plotted versus % stance phase for downhill running at 6 months post-ACLR for PTS metrics and anterior translation, internal rotation, and ACL strain. (c) Participants performed downhill running while DSX imaging was collected to precisely measure knee kinematics.

References (Optional)

[1] Matthias Feucht *et al.*, Knee Surg Sports Traumatol Arthrosc, 2013

[2] Jacqueline Foody *et al.*, Orthop. J. Sports Med, 2024

Acknowledgements (Optional)

Office of Naval Research, Contract #N00014-19-C-2052.

Session Category

Musculoskeletal Biomechanics: Joints and Motion

OA195-05

The Effectiveness of Robotic Total Knee Arthroplasty on Restoring Knee Motion and Improving Clinical Outcomes

Dr. Shawn Robbins BscPT, PhD[1,2], Mr. Gabriel Zaccara BSc[1], Dr. David Zukor MD[3], Dr. Olga Huk MD[3], Dr. Adam Hart MD[4], Ms. Isabella Sierra BSc[1], Dr. John Antoniou MD[3]

[1]McGill University, Montreal, QC, Canada. [2]Centre for Interdisciplinary Research in Rehabilitation of Greater Montreal, Montreal, QC, Canada. [3]Jewish General Hospital, Montreal, QC, Canada. [4]Montreal General Hospital, Montreal, QC, Canada

Introduction

Total knee arthroplasty (TKA) is an end-stage treatment for patients with knee osteoarthritis. However, 20% of patients report unfavourable outcomes post-surgery.[1] Robotic-arm assisted TKA (r-TKA) can improve the accuracy of implant positioning compared with conventional, manual TKA (m-TKA).[2] There is limited research evaluating newer generation robots and it is not clear if r-TKA improves knee motion during functional activities. The objective was to compare knee motion during gait and step up/down tasks between patients that underwent r-TKA and m-TKA at 1 year post-surgery.

Methods

This cross-sectional study recruited patients that underwent m-TKA (n=24) and r-TKA (n=12) for osteoarthritis and were assessed 1 year post-surgery. One surgeon performed r-TKA with the ROSA Knee System (Zimmer Biomet), while three other surgeons performed m-TKA using conventional manual techniques. Participants completed overground gait, and step up and down tasks on a 20 cm step. Kinematic data were recorded with an eight camera motion capture system (Qualisys) at 100 Hz and a cluster-based marker system. Knee angles were calculated using a Carden XYZ order of rotation and speed was determined from pelvis markers. Speed was compared using two sample t-tests. Knee flexion and internal rotation angles throughout the tasks were compared between groups using statistical parametric mapping (SPM).

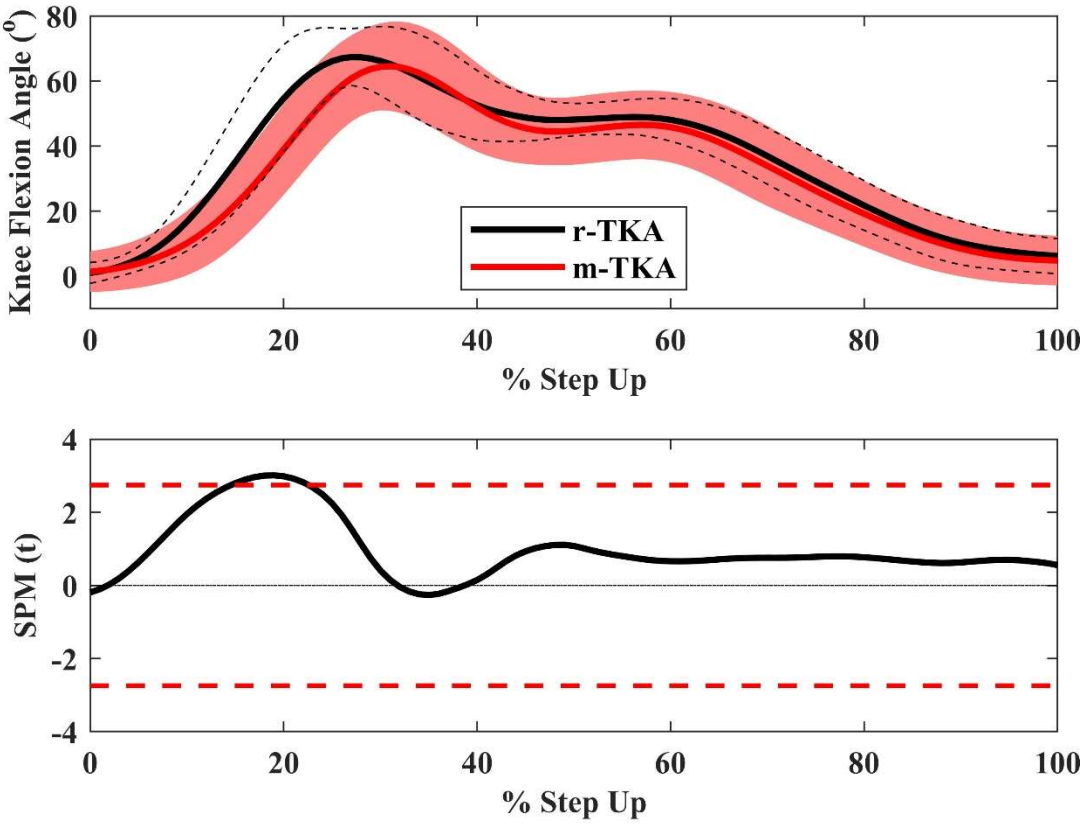
Results

There were no significant between-group differences in speed during gait (mean difference=-0.09 m/s, p=0.190), step up (mean difference=-0.06 m/s, p=0.094), and step down (mean difference=-0.05 m/s, p=0.378). There were no significant differences (p>0.050) in knee flexion and internal rotation angles during gait and step down. The r-TKA group had greater knee flexion during the early stages of the step up task (15-23%, p=0.032) compared to the m-TKA group (Figure).

Discussion

Although the r-TKA had greater knee flexion angles during step up, differences between groups were small and there were no significant findings for gait and step down. Thus, there is no clear evidence that r-TKA leads to enhanced knee motion during functional activities. Future studies should enroll larger samples and consider pre-operative function.

Images (Optional)



References (Optional)

[1] Beswick AD *et al.,* BMJ open, 2012.

[2] Zhang J *et al.,* Knee Surg Sports Traumatol Arthrosc, 2022.

Acknowledgements (Optional)

The Arthritis Society and the Centre for Interdisciplinary Research in Rehabilitation of Greater Montreal provided funding to support the project.

Session Category

Musculoskeletal Biomechanics: Joints and Motion

OA196-01

Effect of Bone-Anchored Limb Use on Segmental Angular Momenta during Walking

Ms Grace Georgiou BS[1], Mr Mitchell Ekdahl BS[2], Mr Peter Thomsen-Freitas PT, DPT, MS[1], Dr Cory Christensen PT,PhD[1], Dr Jason Stoneback MD[1], Dr Brecca Gaffney PhD[2,1]

[1]University of Colorado-Anshutz, Aurora, CO, United States. [2]University of Colorado-Denver, Denver, CO, United States

Introduction

Transfemoral socket prosthesis users have a higher fall risk than able-bodied individuals. Bone-anchored limbs (BALs) are a promising alternative to socket prostheses shown to improve static and dynamic balance. However, past comparisons have mostly been limited to pre-implantation failed-socket use. Additionally, the mechanisms driving improved balance remain unknown. Segmental angular momenta (SAM) describe individual segment's contributions to body center of mass regulation during movement, providing mechanistic insight into dynamic balance. The objective was to determine how unilateral transfemoral BAL use affects SAM compared to successful socket users and healthy control participants without amputation (HC). We hypothesize: 1) HC will have the lowest range of SAM and 2) BAL users will have lower SAM than socket users

Methods

Whole-body kinematics were collected from 30 participants during level-overground self-selected walking (BAL: 7F/3M; 49.2±14.3 y/o; 26.2±4.3 kg/m^2; Socket: 2F/8M; 59.1±10.2 y/o; 30.2±4.7 kg/m^2; HC: 7F/3M; 24.9±3.6 y/o; 23.4±3.7 kg/m^2). Link-segment models for each participant were developed with differences in prosthesis mass and center of mass accounted for. Range of SAM during the amputated-limb gait cycle (dominant-limb for HCs) were compared across groups using an ANCOVA (covariate: gait speed) with a post-hoc Bonferroni correction.

Results

Frontal plane contralateral-limb SAM range was lower in HC (nondominant-limb) and BAL users compared to socket users (sound-limb) (Figure 1). Frontal plane head/trunk, sagittal plane pelvis, and transverse plane pelvis and contralateral-limb SAM range were larger in BAL and socket users compared to HC. Sagittal head/trunk SAM range was larger in socket users than HC.

Discussion

Larger frontal/transverse lumbopelvic SAM ranges in individuals with transfemoral amputation as compared to HC collectively indicates worse dynamic balance regardless of prosthesis type. Additionally, sagittal plane head/trunk SAM ranges were lower in HC than socket users but were not different from BAL users. This may indicate BAL users have some improvements in SAM regulation compared to socket users, although future work is needed to further explore this. Nonetheless, as SAM was more regulated (lower range) in HC than BAL and socket users, these results indicate the need for continued rehabilitation following transfemoral amputation.

Images (Optional)

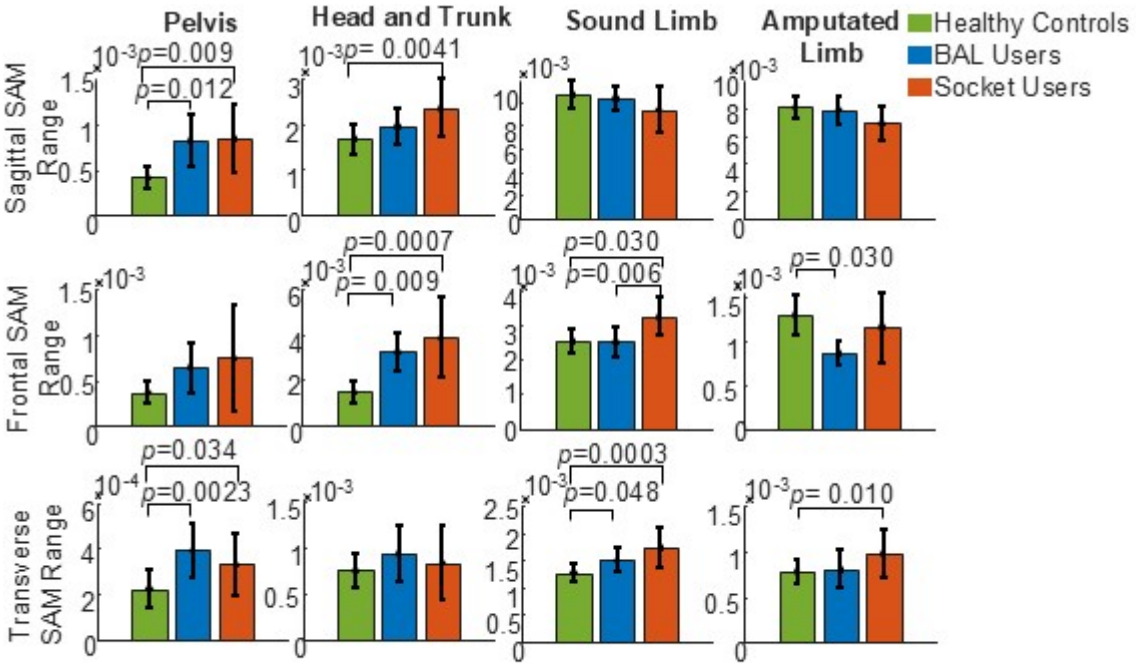


Figure 1. Mean ± 1 SD range of SAM in all planes during self-selected walking for the head and trunk, pelvis, and both legs (thigh, shank and foot).

Session Category

Human Motion and Performance: Balance, Posture and Control

OA196-03

Motor Module Generalization Across Walking and Standing Perturbations is Associated with Walking Balance Performance in Older Adults

Mr. Reece Lawrence, Mr. Grant Maddox, Ms. Kaitlyn Downer, Dr. Jessica Allen PhD

University of Florida, Gainesville, Florida, United States

Introduction

Balance ability is essential for safe walking, yet age-related declines in balance control increase the risk of falls among older adults. In relation to this risk, recent work demonstrates that neuromuscular control of walking and balance may share common structure. For example, we previously found that recruiting a common set of motor modules across walking and balance behaviors (i.e., motor module generalization) is associated with walking balance performance in both young adults and stroke survivors [1,2]. Based on these results, we hypothesize that motor module generalization represents a general control strategy for the maintenance of balance while walking. However, this shared structure has yet to be linked to walking balance performance amongst healthy older adults, which is the purpose of this study.

Methods

Motor modules were found using nonnegative matrix factorization from lower-limb electromyography while walking at self-selected speed and during a standing reactive balance task in 20 older adults (76.9±5.24 yrs). Motor module number for each behavior was chosen such that overall variance accounted for was >90%. The number of motor modules common to both behaviors were identified using Pearson's correlations. The relationship between the number of common modules and two metrics of walking performance were analyzed: walking speed (self-selected and fastest-comfortable) and distance walked on a narrowing beam.

Results

The median number of modules was 3.5 for walking (range:3-4), 3 for reactive balance (range:2-5), and 2 common between the two behaviors (range:0-3). The number of common modules correlated significantly with beam walking distance ($r=0.55$, $p=0.01$) but not with self-selected ($r=0.28$,$p=0.229$) or fast ($r=0.27$, $p=0.254$) walking speeds.

Discussion

The number of motor modules common between walking and standing reactive balance was positively associated with walking performance in older adults, but only when balance was specifically challenged. These findings are consistent with previous studies [1,2], further supporting the hypothesis that recruitment of reactive balance motor modules during walking may be a general neuromuscular strategy contributing to maintaining balance while walking and may serve as an effective target for design and/or prescription of gait rehabilitation.

Images (Optional)

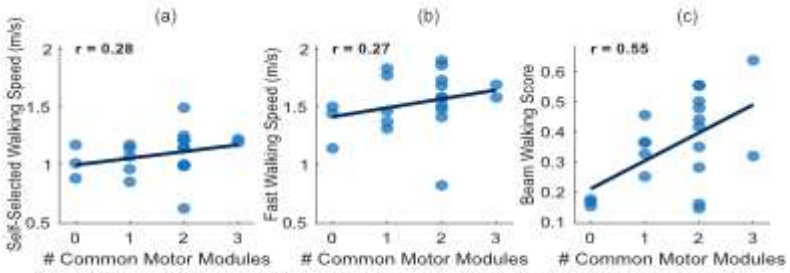


Figure 1: Relationships between the number of common motor modules between walking and standing reactive balance and (A) self-selected walking speed, (B) fast walking speed, and (C) beam-walking performance in older adults. Regression lines and Pearson correlation coefficients are shown.

References (Optional)

[1]J.L. Allen, et al., *Gait & Posture*, 2020

[2]J.L. Allen, et al., *Journal of Neurophysiology*, 2019

Acknowledgements (Optional)

This research was supported by the Claude D. Pepper Older Americans Independence Center at the University of Florida (P30 AG028740).

Session Category

Human Motion and Performance: Balance, Posture and Control

OA196-04

The Mechanical Boundaries of Upright Standing Shape Our Preferred Posture

Mr. Amin M Nasrabadi M.Sc.[1], Dr. Calvin Kuo Ph.D.[2], Dr. Jean-Sébastien Blouin Ph.D.[1]

[1]The School of Kinesiology, University of British Columbia, Vancouver, BC, Canada. [2]The School of Biomedical Engineering, University of British Columbia, Vancouver, BC, Canada

Introduction

Standing is possible over a range of angles without losing balance. Although maintaining the centre of mass (CoM) above the ankle joint requires no moment, people typically prefer to stand with a 1-2° forward lean. Biomechanical and physiological factors, such as the size of the feet (determining the base of support) or the asymmetrical moment characteristics from the ankle-flexors, could contribute to preferred upright posture. Here, we used a novel robotic platform reproducing the dynamics of upright stance to manipulate the mechanical boundaries of standing balance.

Methods

Sixteen participants (8F, 64.9±9.6 kg, 169±7 cm, 26.9±5.3 years) stood on the robot for five 1-minute trials to establish their preferred posture (i.e. CoM average and SD of sway). Based on each participant's baseline, we changed the natural -3° backward to 6° forward balance boundaries (i.e. the foot base of support) to altered ones: −3° to $CoM_{preferred\ angle}$+0.25SD for participants who maintained a forward lean or $CoM_{preferred\ angle}$−0.25SD to 6° for those having a backward lean. In subsequent trials, participants had a 1.5° forward or backward free fall when they reached the altered boundary; and passively returned to a 0° upright posture to start the next trial. We hypothesized that exposure to the new boundaries would shift the participants' preferred posture away from the altered boundary. After participants successfully balanced for 60s in three consecutive trials with new boundaries or for up to ten minutes, we restored the natural boundaries and quantified whether participants' balance returned to their natural baseline preference.

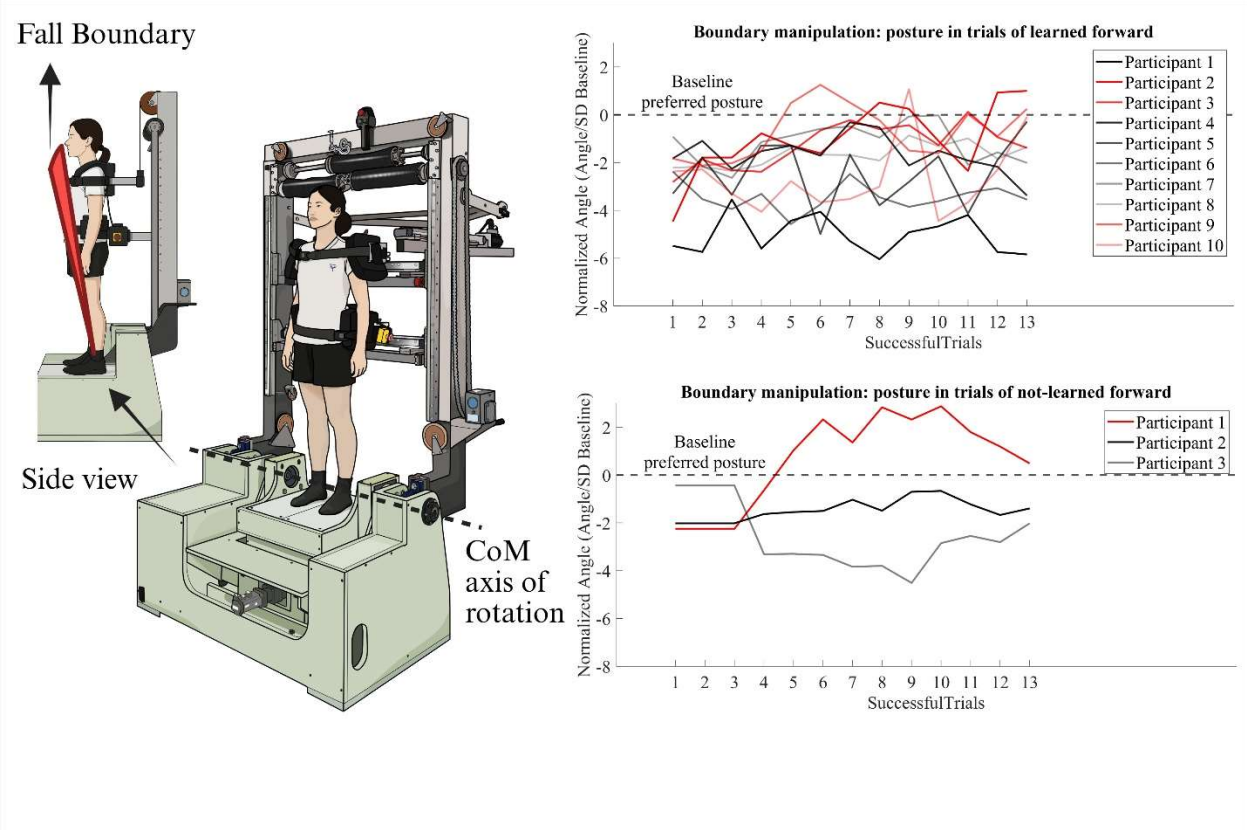
Results

13/16 participants shifted their preferred posture, on average by 1.3°±0.3°, when exposed to the altered boundaries. Their new preferred posture was significantly different from the natural preferred posture (t-test, p-value < 0.001). When restoring their natural balance boundaries, only 4/13 participants returned to their initial preferred posture, on average after 391±22 seconds.

Discussion

Using a unique balance robot, our results showed that the mechanical boundaries of upright balance alter our preferred posture. Instead of aligning their CoM with their natural posture, participants preferred to stand away of their mechanical limits of stability.

Images (Optional)



Acknowledgements (Optional)

Funded by NSERC

Session Category

Human Motion and Performance: Balance, Posture and Control

OA196-05

Cognition–Perception Interplay in Postural Control Among Individuals with Diabetes Mellitus

Dr. Kai Cheng PhD[1], Dr. John Miles MD[1], Dr. Carl Luchies PhD[2], Dr. Hen-Yu Lien PhD, PT[3], Dr. Li-Ling Chuang PhD, PT[3], Dr. Chun-Kai Huang PhD, MS, PT[1]

[1]University of Kansas Medical Center, Kansas City, KS, United States. [2]University of Kansas, Lawrence, KS, United States. [3]Chang Gung University, Taoyuan City, Taiwan, Taiwan

Introduction

Diabetes Mellitus (DM), affecting over 11% of adults globally, is associated with balance deficits and cognitive impairments, particularly executive dysfunction, which heightens fall risk. Executive function is essential for managing cognitive workload and postural control. Under dual-task (DT) conditions, individuals with DM often exhibit greater postural instability and difficulty switching attention. The Sensory Organization Test (SOT) evaluates balance by challenging somatosensory, visual, and vestibular systems. Prior research suggests the impaired central processing observed in DM considered compromised sensory integration. This study examines the interaction between cognition and perception in regulating balance under sensory conflicts using a DT-SOT paradigm, hypothesizing that DM will exhibit degraded central processing and executive function.

Methods

Seventeen individuals with DM and 17 age-matched controls completed a virtual reality–based SOT under single-task and DT conditions. The DT included an auditory Stroop test. Postural sway was decomposed into rambling (central) and trembling (peripheral) components. Cognitive workload was assessed via pupillary dynamics using the Index of Pupillary Activity (IPA).

Results

DM participants exhibited significantly greater rambling and trembling components under sensory conflicts, independent of cognitive workload. Non-linear analysis using Sample Entropy indicated increased rigidity and predictability of postural control in DM with higher cognitive demands. Individuals with DM showed a tendency for higher IPA under sensory-conflict conditions, particularly during single-task trials. Both cognitive task performance and IPA did not differ significantly between groups.

Discussion

This study demonstrated impaired central processing in DM under sensory-conflict conditions by showing the increased rambling component in postural sway and its rigidity/predictability. The elevated IPA during sensory conflicts in DM suggests the increased cognitive workload. These findings underscore the complex interplay between perception and cognition in DM-related balance deficits. Future research should include larger cohorts and additional workload measures to validate these results.

Acknowledgements (Optional)

2024 American Society of Biomechanics Research Travel Grant

Session Category

Human Motion and Performance: Balance, Posture and Control

OA196-06

Uneven Beginnings: Anticipatory Postural Adjustments and Muscle Quality Asymmetry During Gait Initiation at a Self-Selected Speed

Ms. Isabella Helm, Mr. Brandon Peoples MS, Ms. Bria Smith MS, Mr. Keven Santamaria-Guzman MS, Mr. Kenneth Harrison MS, Ms. Damaris Cifuentes MS, Ms. Silvia Campos-Vargas MS, Dr. Jaimie Roper PhD

Auburn University, Auburn, AL, United States

Introduction

Gait initiation relies on coordinated feedforward and feedback mechanisms to maintain posture as the brain prepares the body to transition from standing to stepping, known as anticipatory posture adjustments (APAs)[1, 2]. Longer APA durations can signal reduced postural control, increasing the risk of instability and impaired dynamic balance[1]. Because APAs require contributions from both limbs to stabilize the body before single-leg support, asymmetries in muscle quality may disrupt this process. Discrepancies in fat-to-muscle ratio (FMR) across the quadriceps, hamstrings, and gastrocnemius may compromise balance, neuromuscular response, and gait efficiency[3]. Although asymmetry in muscle quality has been linked to poor functional performance, its specific role in gait initiation and postural control remains poorly understood. Therefore, the purpose of the study is to evaluate the relationship between quadriceps, hamstrings, and gastrocnemius FMR asymmetry and APAs outcomes during walking.

Methods

Seven participants (2 males, 25 ± 6 years) underwent body composition assessments using dual-energy X-ray absorptiometry, with custom lower-leg segmentation to isolate the gastrocnemius, hamstrings, and quadriceps. FMR of the gastrocnemius, hamstrings, and quadriceps was determined to evaluate muscle quality. APAs were measured using inertial measurement units across two trials of the 40-meter walk test at a self-selected speed. Pearson correlation analyses were performed to examine the relationships between regional muscle compositions and APAs.

Results

Quadriceps FMR asymmetry showed strong negative correlations with first-step duration ($r = –0.911$) and first-step range of motion ($r = –0.832$), indicating that greater asymmetry may

constrain step execution and reduce movement amplitude. Hamstrings FMR asymmetry was positively correlated with APA duration (r = 0.780) and lateral acceleration (r = 0.779), suggesting that greater asymmetry in hamstring muscle quality may prolong postural preparation and increase lateral instability. No significant correlations were found between calf asymmetry and APA outcomes.

Discussion

In this pilot sample, our findings suggest that asymmetry in muscle quality influences postural control during gait initiation. These results underscore the importance of evaluating regional muscle composition when assessing balance and gait initiation strategies in populations at risk for muscle quality imbalances.

Images (Optional)

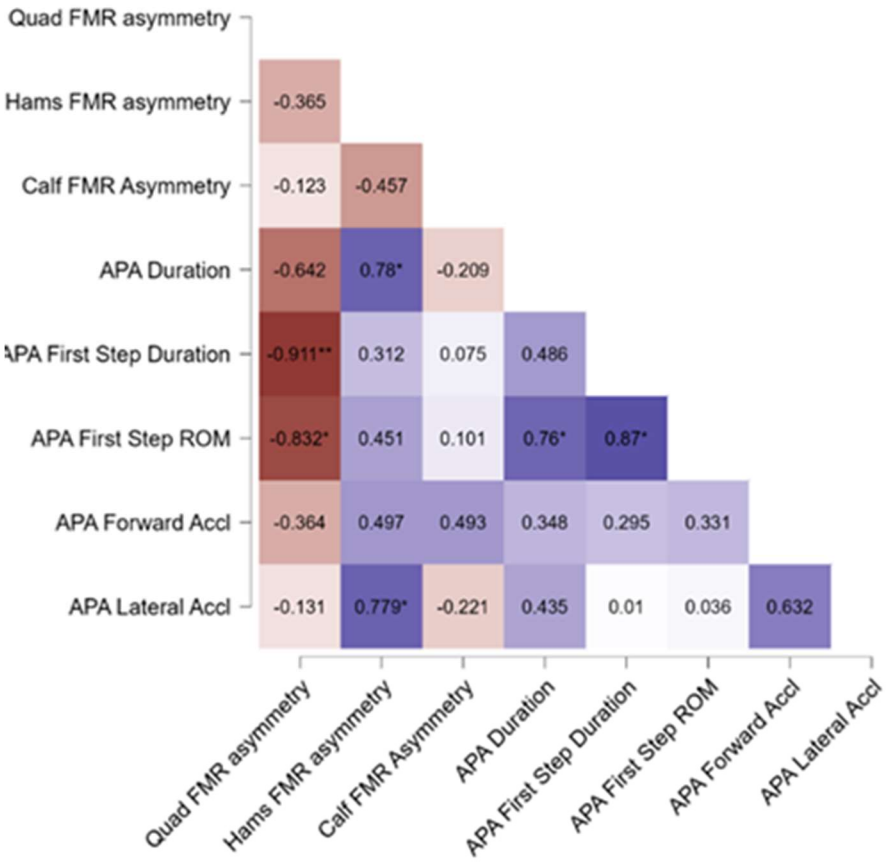


Figure 1: Correlation Heatmap Indicating the Association Between Muscle FMR Asymmetry and Anticipatory Postural Adjustment Outcomes. APA duration is the period from starting to the first measurable change in lateral acceleration and its return to baseline. APA first step duration is period between the of the APA duration to the initial contact of the first step. APA first step range of motion (ROM) is the angular displacement from the end of the APA to initial contact of the first step. APA forward acceleration (Accl) is the peak forward lumbar acceleration. APA lateral acceleration (Accl) is the peak lateral lumbar acceleration.

References (Optional)

[1]Aruin, A.S., J Nov Physiother,2016

[2]Massion, J., Progress Neurobiology,1992

[3]Storniolo, et al., Frontiers Physiology,2025

Session Category

Human Motion and Performance: Balance, Posture and Control

OA197-01

BD-Net: Bidirectional Distance Loss Function for Enhancing Vascular Structure Connectivity

Ms. Luyao Fan, Professor Bao Li, Professor Liyuan Zhang, Professor Youjun Liu, Professor Mingai Li

Beijing University of Technology, Beijing, Chaoyang District, China

Introduction

Accurate segmentation of vascular structures in medical imaging is a crucial step in diagnosing cerebrovascular diseases and enabling precision medicine, particularly for downstream hemodynamic analysis. However, vascular segmentation often faces challenges due to the complexity of vascular anatomy and the low contrast between vessels and surrounding tissues, leading to over-segmentation and under-segmentation. These issues can reduce vascular connectivity, decrease segmentation accuracy, and ultimately affect subsequent analyses and diagnoses. To address these challenges, this study introduces BD-Net for cerebral artery segmentation, aiming to enhance vascular connectivity and improve segmentation accuracy.

Methods

To improve vascular connectivity, we propose an innovative bidirectional distance loss function. Specifically, this function predicts skeleton points and label skeleton points through bidirectional nearest-neighbor connections, quantifying the distances for each direction to compute over-segmentation and under-segmentation losses. This strategy promotes high consistency in both the number and spatial positioning of skeleton points, guiding the model to enhance vascular connectivity. Given the multi-scale features of vascular structures, we incorporate an axial dynamic convolution module based on the U-Net architecture, which adjusts the receptive field of the convolution kernels to capture fine details of vessel segments. Additionally, a multi-axis attention mechanism is embedded into the model to enhance its focus on spatial, channel, and temporal features, further improving the accuracy of cerebral artery segmentation. Finally, BD-Net was trained and tested on a dataset of 141 cerebral artery images.

Results

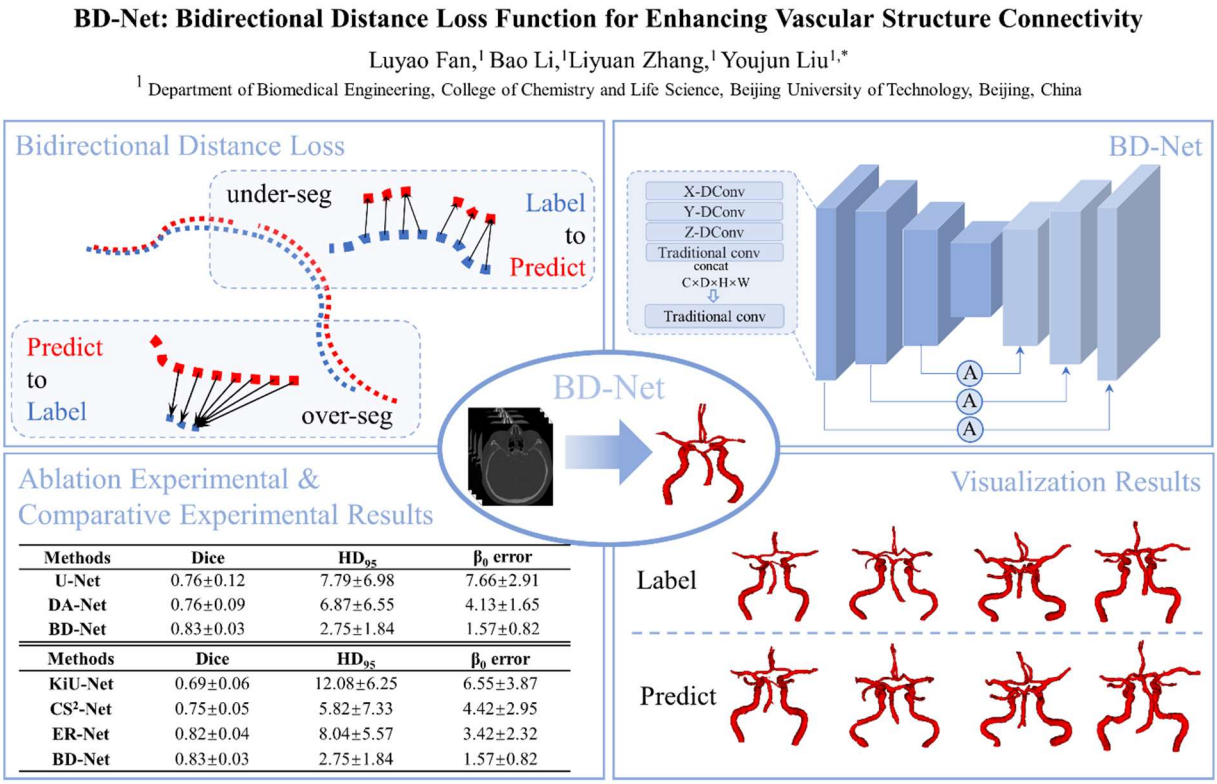
Ablation experiments demonstrated that incorporating bidirectional distance loss increased the Dice score to 0.83, reduced HD_{95} to 2.75, and decreased β_0 error to 1.57.

Comparative experiments showed that BD-Net outperformed ER-Net (Dice=0.82, HD_{95}=8.04, β_0 error=3.42) and CS2Net (Dice=0.75, HD_{95}=5.82, β_0 error=4.42).

Discussion

BD-Net effectively addresses the over-segmentation and under-segmentation issues, achieving precise cerebral artery segmentation and significantly enhancing vascular connectivity. This provides a solid foundation for subsequent hemodynamic analysis and plays a crucial role in the clinical diagnosis and precision medicine of cerebrovascular diseases.

Images (Optional)



Methods	Dice	HD_{95}	β_0 error
U-Net	0.76±0.12	7.79±6.98	7.66±2.91
DA-Net	0.76±0.09	6.87±6.55	4.13±1.65
BD-Net	0.83±0.03	2.75±1.84	1.57±0.82
Methods	**Dice**	**HD_{95}**	**β_0 error**
KiU-Net	0.69±0.06	12.08±6.25	6.55±3.87
CS^2-Net	0.75±0.05	5.82±7.33	4.42±2.95
ER-Net	0.82±0.04	8.04±5.57	3.42±2.32
BD-Net	0.83±0.03	2.75±1.84	1.57±0.82

Session Category

Imaging and Biomedical Devices: Imaging Fundamentals and Applied Research

OA197-02

Making the Most of 3D Ultrasound Data to Improve DDH Detection: Identifying the Posterior Lip and Greater Trochanter

Mrs Chloë Stiles MSc, BSc, Mr Adam McArthur BSc, Dr Abhilash Hareendranathan PhD, Dr Jacob Jaremko MD, PhD, FRCPC

University of Alberta, Edmonton, Alberta, Canada

Introduction

Developmental dysplasia of the hip (DDH) is more reliably detected by 3D ultrasound (3DUS) than conventional ultrasound (US) because image stacks more fully assess anatomy than single images, and analysis can be automated. Identifying consistent anterior-posterior slice order is a crucial initial step in automating hip US analysis since DDH indices vary significantly between anterior versus posterior hip. However, whether an image stack begins anteriorly or posteriorly depends on how the user performed the scan. Image orientation can be inferred based on the location of the Posterior Lip (PL) view within the stack relative to the Standard Plane (SP) view, which requires an awareness of the location of the Greater Trochanter (GT). We developed an AI model to correctly orient US image stacks antero-posteriorly for DDH by locating the PL and GT.

Methods

In 476 DDH 3DUS image stacks, a radiologist manually selected a central SP image and segmented ilium and femur. Retuve, an open-source framework for multi-modality DDH analysis, developed in-house, was used to segment the apex and PL (https://github.com/radoss-org/retuve). Stack orientation was inferred from relation of anatomic landmarks in images relative to the SP. Specifically, if the AI model detected the PL before SP, the stack was flipped. For automated localization of the GT, we developed a two-stage approach using the YOLO object detection model. Relevant GT-containing frames were identified before applying augmentation strategies to improve detection during training. The model then generated a video output.

Results

The AI model correctly oriented 98% of the remaining images antero-posteriorly with only one true fail. With the applied augmentations, the YOLO-based model achieved a Dice score of 0.997, indicating strong agreement with GT segmentations.

Discussion

The AI model reliably orients DDH US image stacks anterior-to-posterior through PL detection. The YOLO-based augmentation model successfully located the GT. These basic processing steps are needed to automate AI image analysis of DDH 3DUS. This novel approach opportunistically uses 3DUS images with minimal expert input. Future work will focus on completing automation by integrating GT detection with orientation for SP selection.

Images (Optional)

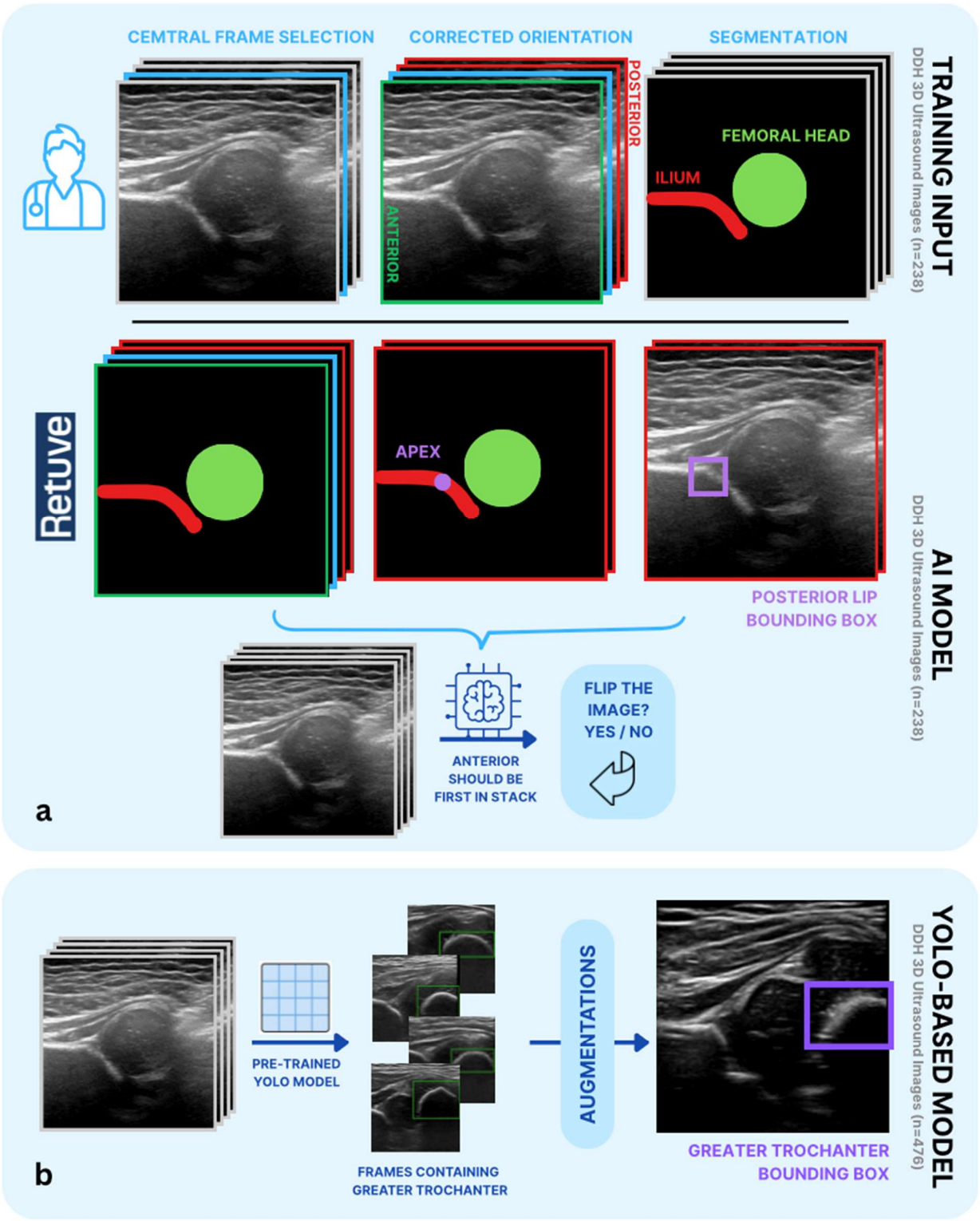


Fig. 1 Outline of methods (a) Image stack orientation using posterior lip (b) Greater trochanter detection

Session Category

OA197-03

Quantitative Multimodal and Longitudinal Characterization of Fibrotic Response: An Approach Integrating MRI and Digital Histopathology in a Chicken Embryo Model

Ms. Giulia Lodola[1], Mr. Guangchen Wang[2], Dr. Chiara Martinelli[1], Dr. Alberto Bocconi[1], Prof. Emanuela Jacchetti[1], Dr. Domenico Aquino[3], Dr. Federica Mazzi[3], Dr. Cristina Chirizzi[3], Prof. Michael G. Monaghan[4], Prof. Claudio Conci[1], Prof. Manuela T. Raimondi[1]

[1]Department of Chemistry, Materials and Chemical Engineering "Giulio Natta". Politecnico di Milano, Milano, Lombardia, Italy. [2]School of Computer Science and Statistics. Trinity College Dublin, Dublin, Dublin, Ireland. [3]Neuroradiology Unit. Fondazione IRCCS Istituto Neurologico "Carlo Besta", Milano, Lombardia, Italy. [4]Department of Mechanical, Manufacturing and Biomedical Engineering. Trinity College Dublin, Dublin, Dublin, Ireland

Introduction

The development of biomedical devices is hindered by the limitations of destructive animal models and the challenge of assessing material biocompatibility (ISO 10993-6) and foreign body reaction (FBR). To overcome this, we developed the EGGS&BEACON platform, an ex ovo system, which utilizes the avian chorioallantoic membrane (CAM) assay, offering a model for advanced imaging. Our aim is to establish the link between macro-scale Magnetic Resonance Imaging (MRI) and micro-scale cellular analysis through digital histopathology for quantitative characterization.

Methods

Intravitally, multimodal MRI was performed at embryonic incubation day (EID) 8-9-11-14 to reconstruct full embryonic volumes and major organ volumes using 7T Bruker Biospec (T2-TurboRARE sequence, 200x200x700 μm^3, voxel size) (Figure 1a, b). For *ex vivo* analysis, organs and CAMs were excised at EID 11 and 14 and processed for digital histopathology (formalin fixed, paraffin-embedded, FFPE). Sections were cut, hematoxylin–eosin (H&E) stained [1], and whole slide images (WSI) were digitalized (D-sigh 2.0, A. Menarini Diagnostic). A Machine Learning (ML) workflow, employing active learning, was used for automated cell segmentation, recognition and quantification.

Results

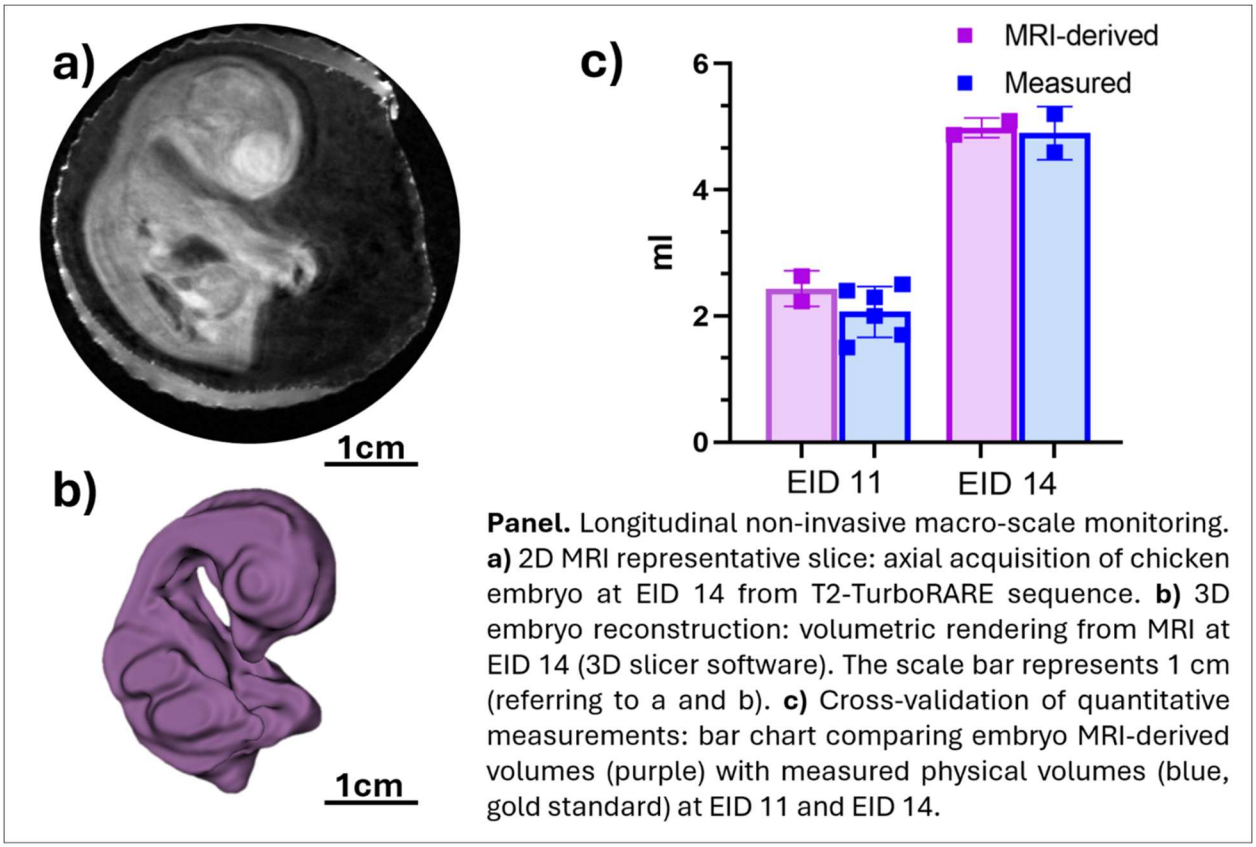
outcomes. Embryonic weight (5.82 ± 0.31 g) and measured volume (4.90 ± 0.42 ml) served as gold standards for non-invasive monitoring. A strong correlation was found between these measurements and full embryo MRI-derived volumes (5.09 ± 0.43 ml) at EID14, confirming the macro-scale acquisition's high accuracy (Figure 1c). CAM histopathology provided compartments' precise morphometrics (ectoderm: 9.49±1.3 μm; mesoderm:

68.61±9.5 µm; endoderm: 4.45±1.3 µm). The ML workflow classified and quantified cell types (red blood cells, fibroblasts, endothelial cells, and granulocytes), as cellular densities, establishing metrics for local innate immune activity [1]. Furthermore, we demonstrated the potential for recognizing organ volumes in longitudinal MRI of chicken embryos, and performing histological analysis on organs themselves, for systemic biocompatibility assessment, linking macro- and micro-scale.

Discussion

The EGGS&BEACON platform demonstrates high biocompatibility, and it is optimized for non-invasive monitoring, enabling repeated MRI acquisitions without compromising embryonic viability. The established integrated methodology (macro-scale MRI and micro-scale digital histopathology) provides robust multimodal and longitudinal characterization to assess the innate immune response and tissue mechanics for both systemic and local evaluation.

Images (Optional)



Panel. Longitudinal non-invasive macro-scale monitoring. **a)** 2D MRI representative slice: axial acquisition of chicken embryo at EID 14 from T2-TurboRARE sequence. **b)** 3D embryo reconstruction: volumetric rendering from MRI at EID 14 (3D slicer software). The scale bar represents 1 cm (referring to a and b). **c)** Cross-validation of quantitative measurements: bar chart comparing embryo MRI-derived volumes (purple) with measured physical volumes (blue, gold standard) at EID 11 and EID 14.

References (Optional)

1. Conci C., APLBioeng, 2024

Acknowledgements (Optional)

ERC, project BEACONSANDEGG, G.A.101053122

Session Category

Imaging and Biomedical Devices: Imaging Fundamentals and Applied Research

OA197-04

Classification of Bone Demineralization Patterns with HR-pQCT Texture Metrics and Derived Scores: Bone Microarchitectural Phenotypes as Indicators of Metabolic Disease?

Mr. Johannes Bereiter-Payr[1,2], Mr. Thomas Ausserer[1], Ms. Sonja Wagner[3,4], Ms. Martina Saretto[3,4], Dr. Heinz Zoller[3,4], Mr. Gerald Degenhart[1]

[1]Core Facility Micro-CT, University Hospital for Radiology, Innsbruck, Tirol, Austria. [2]VASCage - Centre on Clinical Stroke Research, Innsbruck, Tirol, Austria. [3]Medical University of Innsbruck, Department of Medicine I, Gastroenterology, Hepatology and Endocrinology, Innsbruck, Tirol, Austria. [4]Christian Doppler Laboratory on Iron and Phosphate Biology, Innsbruck, Tirol, Austria

Introduction

We report ongoing work to quantify distinguishable patterns of bone demineralization in patients with metabolic and/or cardiovascular disease. This effort was motivated by (1) the consistent visual observation of distinct microarchitectural differences in HR-pQCT images of distal extremities within our study cohorts, and (2) previously published HR-pQCT phenotype classifications related to fracture risk by Whittier, Boyd and colleagues [1].

Methods

High-resolution peripheral quantitative CT (HR-pQCT) images of the distal radius were acquired in 192 patients from two clinical cohorts using an XCT-2 system (Scanco Medical AG), with 4–6 scans per patient over 12 months. Bone texture analysis (TA) was performed according to a standardized protocol provided by the manufacturer. For each patient, mean texture parameters across all examinations were normalized for age and sex using statistical models described by Warden et al. [2]. Normalized metrics were evaluated using principal component analysis (PCA) and fuzzy c-means clustering (FCM) to identify distinct (de-)mineralization patterns. Data were cross-referenced with areal BMD (aBMD) from DXA when available, or with projected mineral density derived from HR-pQCT.

Results

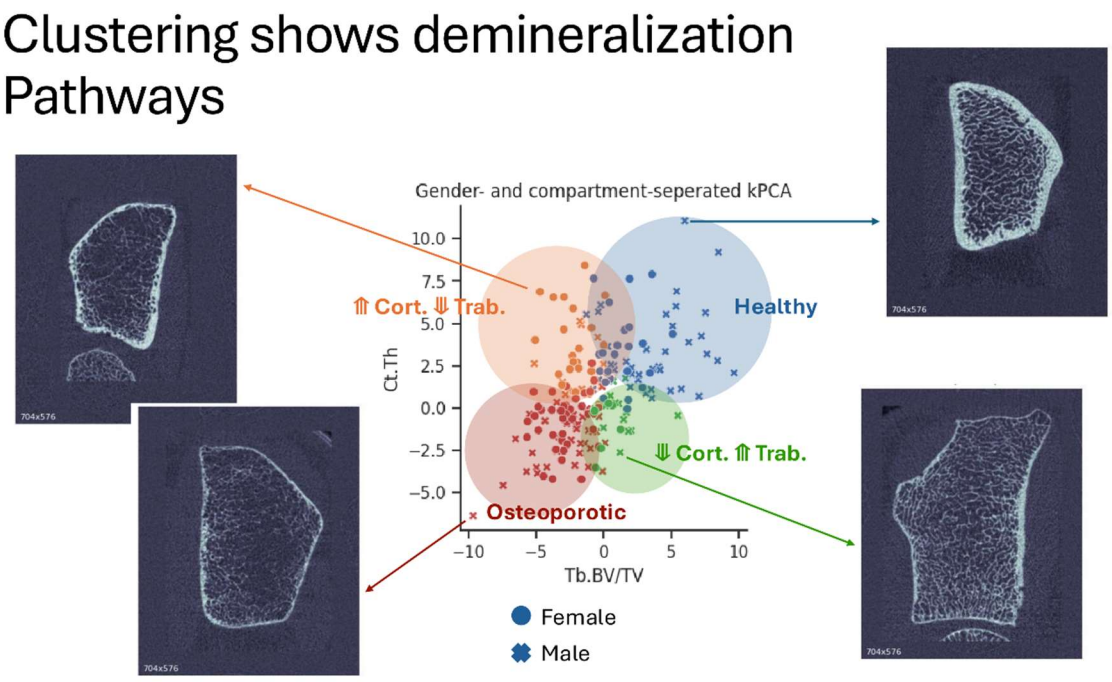
Among patients with aBMD values in the osteopenic range or showing early signs of demineralization, three potential phenotypes can be described:
(1) generalized demineralization,
(2) predominant trabecular deterioration, and
(3) selective thinning of the distal cortical compartment with relatively preserved trabecular structure.

Based on these findings, we propose a preliminary compartment-specific composite score to quantify individual demineralization patterns.

Discussion

HR-pQCT-derived structural markers can detect early alterations in bone mineralization prior to substantial changes in fracture risk. Some metabolic diseases appear to exhibit characteristic demineralization signatures. Accordingly, classification by the proposed scoring tool may serve as an indicator of bone involvement or may be useful to support the diagnosis suspected disease.

Images (Optional)



References (Optional)

[1] Whittier DE et al., J Bone Miner Res, 2020.
[2] Warden SJ et al., Osteoporos Int, 2022.

Session Category

Imaging and Biomedical Devices: Imaging Fundamentals and Applied Research

OA197-05

Robust Hip aBMD Measurement From Photon-Counting CT Projections: Overcoming DXA Positioning Constraints

Ms. Elena Paravisi[1], Dr. Jilmen Quintiens[1], Mr. Matthias Opsomer[2,3], Dr. Thomas Anijs[1], Prof. Kristl Claeys[2,3], Mr. Walter Coudyzer[4], Prof. Harry van Lenthe[1]

[1]Biomechanics Section, dept. Mechanical Engineering, KU Leuven, Leuven, Flanders, Belgium. [2]Lab. for Muscle Diseases and Neuropathies, dept. of Neurosciences, KU Leuven, Leuven, Flanders, Belgium. [3]Department of Neurology, University Hospital Leuven, Leuven, Flanders, Belgium. [4]Department of Radiology, University Hospital Leuven, Leuven, Flanders, Belgium

Introduction

Dual-energy X-ray absorptiometry (DXA) is the standard for diagnosing and monitoring osteoporosis. However, DXA measurements vary across manufacturers and depend heavily on patient positioning, potentially affecting T-score accuracy. This limitation is particularly problematic in patients with musculoskeletal contractures that prevent correct positioning in the DXA scanner. We hypothesized that 2D projections from digitally rotated 3D Photon-Counting CT (PCCT) scans can quantify areal BMD (aBMD). To test this hypothesis, we developed a semi-automated Python-based pipeline to compute hip aBMD from PCCT and evaluate its user-dependency.

Methods

Femoral PCCT and DXA scans from ten facioscapulohumeral muscular dystrophy (FSHD) patients were analysed. Three independent raters processed the PCCT scans ten times per patient over ten days. The pipeline automatically aligned the femur in the coronal plane, followed by user-guided placement of four anatomical landmarks to segment standardized DXA regions: femoral neck, intertrochanteric region, and trochanter, with total hip as their union. Correlation with DXA-derived aBMD was calculated. Intra-rater precision was assessed using root-mean-square standard deviation (RMS-SD) and coefficient of variation (RMS-CV), while inter-rater agreement was determined using the intraclass correlation coefficient (ICC) from each rater's final trial. The effect of DXA positioning errors on PCCT comparisons was tested by recomputing aBMD after applying rotations of 0–20° to the PCCT images.

Results

PCCT-derived aBMD showed strong correlation with DXA ($R^2 \geq 0.88$, Figure 1). No significant effect on the correlations was observed across the tested angles. Short-term

precision was excellent (maximum RMS-SD = 0.0121 gHA/cm^2, RMS-CV = 1.4%), and inter-rater reproducibility was high (ICC > 0.98).

Discussion

PCCT-based aBMD measurements demonstrated excellent precision and reproducibility, supporting PCCT as a robust alternative for patients unsuitable for DXA scanning as well as for opportunistic bone assessment with PCCT. However, PCCT consistently underestimated aBMD relative to DXA, as reported for other CT-based modalities[1,2]. This underestimation persisted across all tested angles, indicating that imprecise patient positioning does not fully explain the bias. Further investigations are required to determine how modality-specific imaging characteristics contribute to this systematic offset.

Images (Optional)

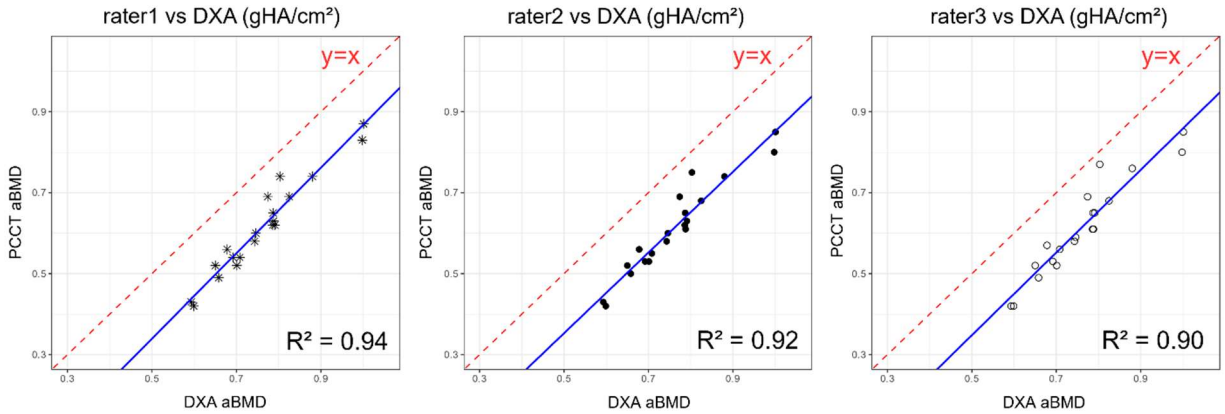


Figure 1. Scatter plot of femoral neck areal bone mineral density (aBMD) derived from PCCT scans using the proposed Python-based pipeline (final trial) compared with DXA measurements. Each plot represents one rater versus DXA. All raters demonstrate strong correlation with DXA.

References (Optional)

[1] Khoo, B. C. C. et al., Osteoporosis International, 2009.

[2] Cann, C. E. et al., PLoS ONE, 2014.

Acknowledgements (Optional)

This research was funded by the Flanders Research Foundation (FWO), grant 1SA3H26N and from the KU Leuven Industrial Research Fund (IOF) for project C24E/21/030.

Session Category

Imaging and Biomedical Devices: Imaging Fundamentals and Applied Research

OA197-06

Accuracy of a Customized Biplane Radiography with Dynamic Flat Panel Detector and Instrumented Treadmill in Multiple Joints

Dr. Minghe Yao[1], Dr. Junqing Wang[2], Prof. Kang Li[3], Prof. Yong Nie[4]

[1]Department of Orthopedic Surgery, West China Hospital, Sichuan University, Chengdu, Sichuan, China. [2]Department of Orthopedic Surgery, Orthopedic Research Institute and West China Biomedical Big Data Center, West China Hospital, Sichuan University, Chengdu, Sichuan, China. [3]Department of Orthopedic Surgery and West China Biomedical Big Data Center, West China Hospital, Sichuan University, Chengdu, Sichuan, China. [4]Department of Orthopedic Surgery and Orthopedic Research Institute, West China Hospital, Sichuan University, Chengdu, Sichuan, China

Introduction

Dynamic biplane radiography (DBR) is a gold-standard technique for measuring *in vivo* three-dimensional skeletal kinematics. Conventional image intensifier-based DBR systems are constrained by suboptimal image quality and limited imaging fields. We developed a customized DBR system equipped with large-format dynamic flat panel detectors capable of acquiring high-quality images over an extensive imaging area. Therefore, the objective of this study was to validate the accuracy of our customized DBR system across multiple joints.

Methods

Our customized DBR system is characterized by the following features: (1) a large-format dynamic flat panel detector providing an extensive high-quality imaging field with a maximum sampling rate of 90 Hz; (2) synchronization capability with an instrumented treadmill for simultaneous acquisition of images and ground reaction forces during walking; (3) an X-ray tube with a minimum pulse duration of 2 ms, effectively minimizing motion artifacts during high-speed movements. Three to six 1.6 mm stainless steel beads were embedded into each bone segment of three cadaveric specimens (one knee and two ankle specimens) and one synthetic cervical spine model. The DBR system was calibrated using a LEGO cube following the protocol developed at Brown University. Joint motion was simulated for each specimen within the imaging field of view. Marker-based tracking was performed using XMALab, whereas model-based tracking was executed using SlicerAutoscoperM. The accuracy of model-based tracking against marker-based tracking was assessed using root mean square error (RMSE).

Results

For translation, the mean RMSEs were 0.47 mm (knee), 0.21 mm (ankle), and 0.63 mm (cervical spine). For rotation, the mean RMSEs were 0.91° (knee), 1.50° (ankle), and 1.36° (cervical spine). The achieved accuracy is comparable to that reported in prior validation studies in all the three joints.

Discussion

The measurement errors of our customized DBR system of multiple joints are comparable to those reported in previous literature, demonstrating the high accuracy of our system. Critically, the capability of our customized DBR system to continuously capture images and ground reaction forces over multiple gait cycles enables more comprehensive biomechanical analysis, thereby supporting its future application in *in vivo* clinical research.

Images (Optional)

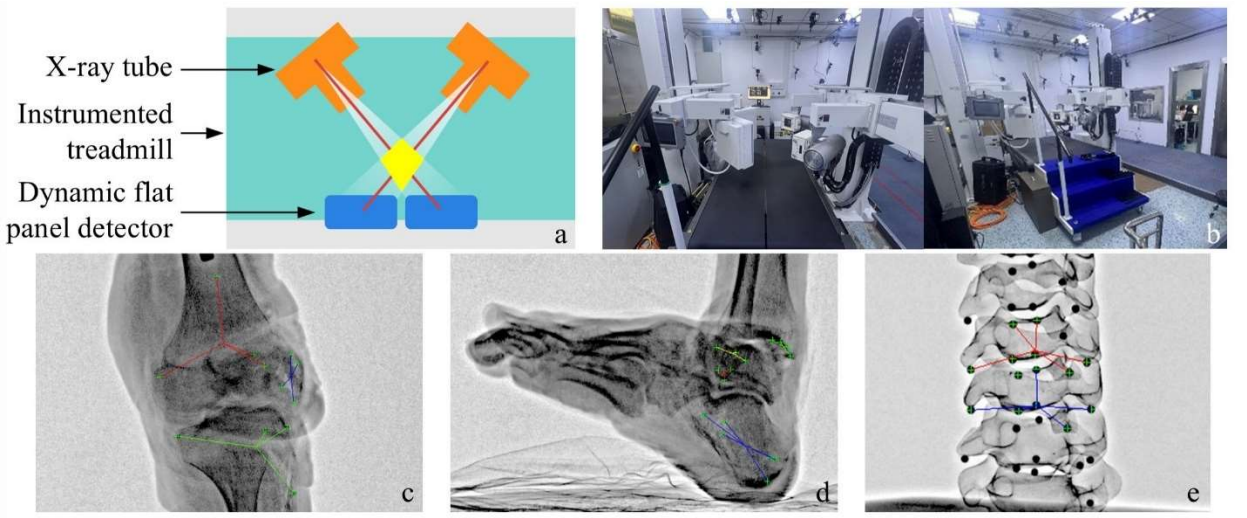


Figure 1 a: Schematic top-view diagram of system; b: System arrangement; c-e: Marker-tracking images

Table 1 Root mean square error (RMSE) for kinematic measurements in three joints

Translation/Rotation	Tibiofemoral (knee)	Tibiotalar (ankle)	Cervical spine
ML trans (mm)	0.47	0.17	0.63
AP trans (mm)	0.46	0.21	0.27
SI trans (mm)	0.29	0.21	0.25
FL/EX (deg)	0.91	1.50	0.96
AB/AD (deg)	0.80	1.40	0.86
IR/ER (deg)	0.38	0.35	1.36

Session Category

Imaging and Biomedical Devices: Imaging Fundamentals and Applied Research

OA198-01

Advanced Humanised and Vascularized Bone Model Recapitulating Molecular and Functional Signatures of Osteoporotic Bone for Therapeutic Research

Mr. Muhammad Munam Mustafa Bukhari, Dr. Syeda Masooma Naqvi, Prof. Laoise McNamara

University of Galway, Galway, Galway, Ireland

Introduction

Postmenopausal osteoporosis causes bone loss, but also alters bone tissue composition, osteocyte activity and vascularisation. Anti-sclerostin therapy induces bone formation, decreases resorption and reduces fracture risk, but the effects are transient, and the mechanisms require further investigation. Animal and in vitro models of osteoporosis cannot reproduce human multicellular responses, limiting their potential for mechanistic and therapeutic studies. Thus, the objectives of this study are to 1) develop 3D multicellular vascularized and humanized bone mimetic models for studies of osteoporosis, 2) validate the transcriptomic profiles of the models against human bone and 4) apply the model to study anti-sclerostin therapy.

Methods

Vascularised bone-like models were developed by chondrogenic and osteogenic priming [1] and cultured in osteogenic media with estrogen (17 β-estradiol) until day 42, followed by estrogen withdrawal until day 49. Next, human mononuclear cells (pre-osteoclasts) were incorporated and the models were cultured until day 63 under continued estrogen (E), estrogen withdrawal (EW), or EW+sclerostin antibody (EWS) (Fig. 1 A). Immunostaining, ELISA and rt-PCR were conducted for validation and compared to human bone samples.

Results

We have successfully developed the first humanized 3D bone mimetic model that accounts for osteocyte differentiation, mineralization and vascularization over extended culture. By inducing estrogen deficiency within the model, we recapitulated the osteoporotic phenotype with respect to sclerostin production (WNT inhibitor), mineral heterogeneity, hypertrophy (collagen X) and vascularization (CD31) (Fig.1 A). Metabolic markers separated the estrogen group (E) from the estrogen withdrawal (EW). Our models captured transcriptomic features of healthy osteogenesis (TNFRSF11B (OPG), RUNX2, ALPL) and recapitulated osteoporotic catabolic gene expression, which was validated

against human osteoporotic bone (TNFSF11, MMP1) (Fig.1C), supporting the physiological relevance of the model. Treatment with sclerostin inhibitory antibody restored WNT/β-catenin signalling and reduced osteoclastogenic signalling (Fig.1 D, F).

Discussion

This study provides a humanized bone model that recapitulates key molecular and functional signatures of osteoporosis, which are necessary for evaluation of therapies. The model was applied to reveal that sclerostin inhibition could partially restore WNT signalling under estrogen deficiency.

Images (Optional)

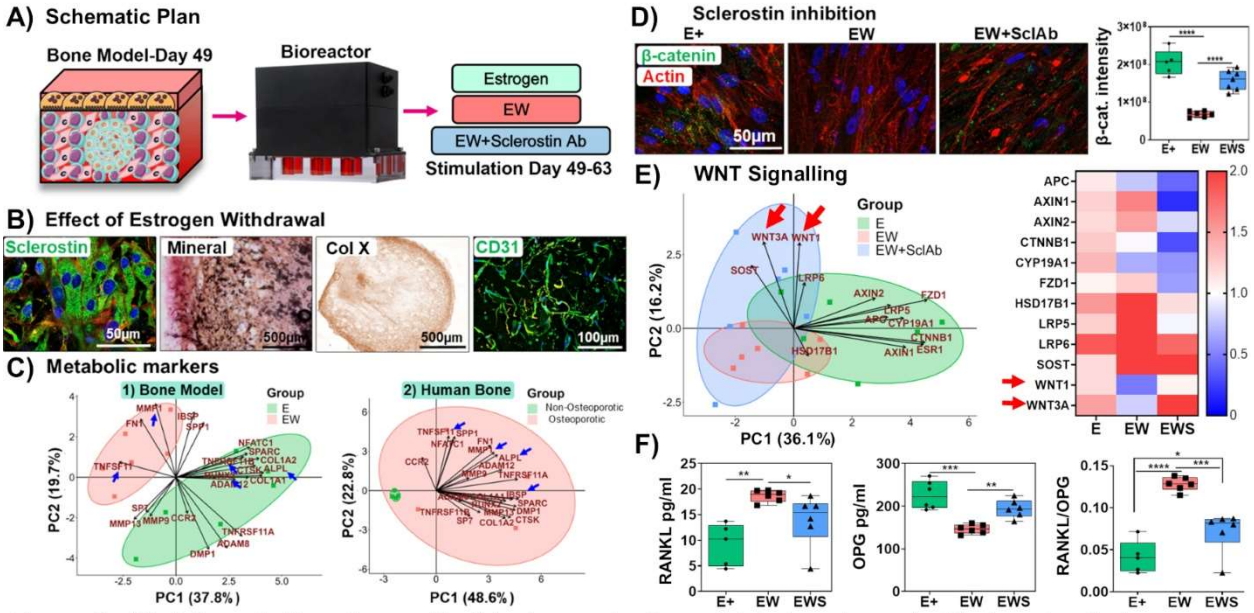


Figure 1: (A) Schematic flow plan, multicellular bone mimetic model (osteocytes, osteoblasts, osteoclasts, vascular cells), mechanical stimulation applied with bioreactor (Mechanoculture TX) (~0.5% strain, 1 Hz, 1 hour/day). (B) Histology confirming osteoporotic phenotype due to estrogen withdrawal (C) Principal component analysis (PCA) plots for metabolic markers comparing bone models (E, EW) to human bone (osteoporotic, non-osteoporotic), (D, E) Increased β-catenin and partially restored WNT signalling after Sclerostin inhibition (F) ELISA for RANKL and OPG, showing reduced osteoclastogenic signalling (RANKL/OPG) due to sclerostin inhibition. Statistical analysis, one-way Anova, * = p<0.05, **=p<0.005, ***=p<0.0005.

References (Optional)

[1] Bukhari MMM *et al.*, *Am J Physiol Cell Physiol*, 2025; **328**(3):C743–C756.

Acknowledgements (Optional)

The research was funded by ERC consolidaotro grant (ERC-863795)

Session Category

Tissue Engineering: Methods, Models and Applications

OA198-02

Investigation of Long-Term Culture of a Placental Organoid-on-a-Chip for Modeling Pregnancy Hypertension

Ms. Kinoka Kubo[1], Prof. Kenichi Funamoto PhD[2], Prof. Daisuke Yoshino PhD[1]

[1]Tokyo University of Agriculture and Technology, Koganei, Tokyo, Japan. [2]Tohoku University, Sendai, Miyagi, Japan

Introduction

Pregnancy hypertension is closely linked to maternal vascular dysfunction and impaired placental morphogenesis. Although elevated blood pressure is known to disrupt endothelial barrier integrity, the biomechanical mechanisms connecting hypertensive stress to placental and fetal vascular impairments remain unclear. To address this issue, we developed a placental organoid-on-a-chip capable of long-term culture and mechanical stimulation. This platform is designed to model the biomechanical progression from maternal hypertensive loading to pathological placental villus and umbilical vascular development.

Methods

A microfluidic device was fabricated by bonding polydimethylsiloxane to a glass substrate. The microchannels were coated with poly-D-lysine and type I collagen to enhance cell adhesion and mechanical stability. A fibrin hydrogel containing Matrigel, fetal endothelial cells, and trophoblast-derived cells was polymerized within a central gel compartment. Maternal and fetal endothelial cells were seeded into the perfusion channels located on the periphery of the tissue sample. The continuous perfusion generated by using a peristaltic pump maintained a steady flow rate, shear stress, and hydrostatic pressure. The behavioral patterns of the cultured cells were assessed by live imaging, and the structural organization and marker expression were evaluated by immunofluorescence microscopy.

Results

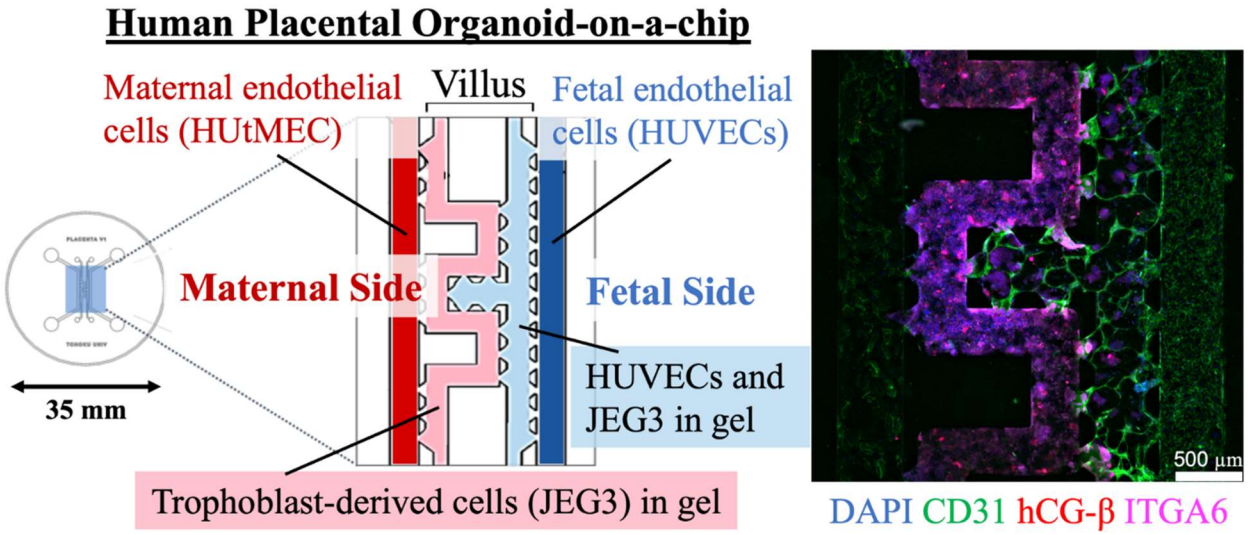
The system successfully reconstructed an in vitro placental villus unit under biomechanically relevant conditions. The endothelial cells formed a three-dimensional vascular network in the hydrogel and a confluent monolayer on the channel under shear flow. Trophoblast-derived cells demonstrated fusion and exhibited pregnancy-associated markers, thereby demonstrating functional differentiation within the engineered microenvironment. The optimization of gel stiffness, matrix composition, and seeding density has enabled the stable, long-term culture without structural collapse of the gel–channel interface. The implementation of continuous perfusion ensured the preservation

of vascular integrity, thereby facilitating real-time observation of cell–cell and cell–matrix interactions.

Discussion

The application of controlled hydrostatic pressure within the perfusion circuit provides a unique platform for modeling hypertensive loading on maternal–fetal interfaces. This system establishes a foundation for biomechanically driven disease modeling of pregnancy hypertension, enabling quantitative analysis of endothelial barrier disruption, villus deformation, and vascular morphogenesis. The platform also has the potential to facilitate mechanobiology-based therapeutic screening targeting hypertensive placental dysfunction.

Images (Optional)



Session Category

Tissue Engineering: Methods, Models and Applications

OA198-03

Optimizing A Novel Tissue-penetrating Hydrogel for Mechanical Reinforcement of Degraded Cartilage

Research Assistant Amélie Dufeil[1,2], PhD Ali Ahmadi[1], Postdoctoral Researcher James L. Martin Robinson[3], Research Assistant Erin Shapiro[1], Associate Professor Andrew Speirs[1], Assistant Professor Andrew Harris[1], Assistant Professor Irina Garces[1], Professor Jos Malda[3], Assistant Professor Eng Kuan Moo[1]

[1]Carleton University, Ottawa, Ontario, Canada. [2]CY Cergy Paris University, CY TECH, Cergy, Ile de France, France. [3]UMC Utrecht University, Utrecht, Utrecht, Netherlands

Research Assistant Amélie Dufeil

Introduction

Articular cartilage is important for load-bearing and pain-free joint articulation. In osteoarthritis (OA), cartilage quality is degraded. Medical intervention is required to restore cartilage functional properties. Low molecular weight methacrylated HA (HAMA) has been shown to penetrate cartilage and produce intra-tissue mechanical reinforcement after photo-polymerisation, a process requiring a photoinitiator. The Ru/SPS photoinitiator system is preferred as it uses visible light that reduces cytotoxicity and improves crosslinking depth. Previous studies have used high light intensity (25–30mW/cm^2) for photocrosslinking, casting doubts on its phototoxicity. This study aimed to determine a photocrosslinking protocol that minimizes cell death and evaluate the effect of HAMA on the viscoelastic properties of healthy and degraded cartilage.

Methods

Porcine cartilage samples were assigned to one of the four groups: (1) healthy, (2) OA simulated by collagenase treatment, (3) healthy+HAMA, and (4) OA+HAMA. A 4% HAMA solution (25kDa, 40% substitution) with Ru/SPS (0.5/5mM) was applied for 10min, then photocrosslinked under 400nm light. For phototoxicity test, healthy+HAMA samples were photo-crosslinked by 20 or 25mW/cm^2 for 3 or 10min. For mechanical tests, samples from Group 3–4 were photo-crosslinked by 20mW/cm^2 for 3min. Cell viability in the top 100µm tissue was assessed by confocal imaging. Tissue mechanical properties were measured by a three-step unconfined stress relaxation compression test. A 2% cyclic loading was

applied at 100–0.1Hz during the hold phase. Force-displacement data were processed for mechanical properties.

Results

Photocrosslinking at 25mW/cm^2 for 10min caused a 50μm-deep zone of death (region with >50% dead cells). This depth was reduced to 20μm at a lower dosage (20mW/cm^2, 3 min). Collagenase treatment decreased equilibrium, instantaneous and storage moduli by 55–73% compared with healthy controls. In OA-like tissue, HAMA restored all moduli to healthy levels; whereas HAMA stiffened healthy cartilage by 44–77%.

Discussion

High light intensity caused significant cell death. A reduced photo-crosslinking dosage improved cell viability while recovering the viscoelastic properties of degraded cartilage. However, off-target over-stiffening of healthy tissue was observed. This suggests a narrow photocrosslinking window balancing mechanical reinforcement and biocompatibility. Future studies will focus on further optimisation using longer wavelengths and lower photoinitiator concentrations.

Images (Optional)

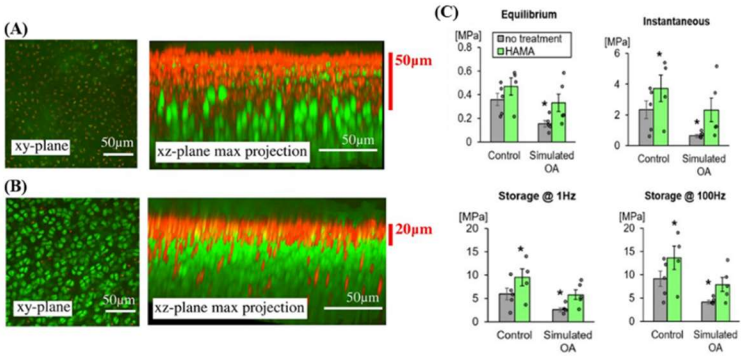


Fig1. *(A-B) Live (green)/dead (red) cells assay of HAMA-treated healthy cartilage using (A) 25 mW/cm² for 10 min and (B) 20 mW/cm² for 3 min. (C) Mechanical properties (equilibrium, instantaneous, and storage moduli) of healthy and simulated OA cartilage with or without HAMA treatment. *p<0.05 compared with control, no treatment group.*

References (Optional)

Session Category

Tissue Engineering: Methods, Models and Applications

OA199-02

Mechanobiological Response of Human Periodontal Ligament Stem Cells to Intermittent Stretch in 2D and 3D Cultures

Dr. Beatrice Masante[1,2], Eng. Mafalda Santos[3], Dr. Giovanni Putame[1,2], Dr. Joao Silva[3], Eng. Marta Tosini[1,2], Dr. Lugas Andrea[1], Dr. Ilaria Roato[4], Dr. Stefano Gabetti[1,2], Prof Federico Mussano[4], Prof Alberto Audenino[1], Prof Diana Massai[1,2]

[1]Dept. of Mechanical and Aerospace Engineering and PolitoBIOMed Lab, Politecnico di Torino, Torino, Piemonte, Italy. [2]Interuniversity Center for the Promotion of the 3Rs Principles in Teaching and Research, Torino, Piemonte, Italy. [3]Dept. of Bioengineering and iBB -Institute for Bioengineering and Biosciences, Instituto Superior Técnico, Universidade de Lisboa, Lisbon, Lisbon, Portugal. [4]Bone and Dental Bioengineering Lab, CIR-Dental School, Dept. of Surgical Sciences, University of Torino, Torino, Piemonte, Italy

Introduction

In vivo, the periodontal ligament (PDL) undergoes combined compression, tension and shear, fundamental for regulating cell growth, differentiation and tissue development [1]. Reproducing these cues *in vitro* through biomimetic materials and controlled mechanical stimulation is essential to elucidate stem-cell mechanobiology. Here, we developed and validated a bioreactor platform to study cyclic uniaxial stretch on human PDL stem cells (hPDLSCs) cultured on 2D and 3D substrates.

Methods

A previously developed stretch bioreactor [2,3] (Fig.1A) was employed to apply controlled tensile strain to hPDLSC cultures. To evaluate the influence of the environment structure, hPDLSCs were seeded either on 2D polydimethylsiloxane (PDMS) flexible substrates or on 3D electrospun polycaprolactone (PCL) aligned nanofibrous scaffolds. PDMS substrates were designed to provide homogeneous deformation to cell monolayers [4], while 3D PCL scaffolds were fabricated to reproduce the fibrous and anisotropic architecture of the native extracellular matrix. Cells were cultured under intermittent uniaxial stretch regimes (strain up to 15%, frequency = 1 Hz, applied with different intermittent protocols: 90s every 6h, 5min every 6h and 5 min every 1h) and compared to static controls.

Results

Intermittent stretch stimulation did not affect cell viability and induced hPDLSC alignment along the stretch direction in both configurations (Fig.1B). On PDMS substrates,

intermittent stretch promoted the expression of osteogenic (*ALP*) and ligament-related (*COL XII*) markers. This effect was markedly amplified when intermittent stretch stimulation was applied to 3D cell-seeded PCL constructs: enhanced alignment, improved matrix organization, and increased expression of key PDL-associated genes and proteins (*COL XII, Decorin, Periostin, OCN, and COL I*) were observed (Fig.1C), indicating a synergistic influence of mechanical stimulation and 3D microarchitecture.

Discussion

Overall, the study demonstrates a synergistic interplay between intermittent stretch and 3D microenvironment in directing hPDLSC organization and differentiation, paving the way for further mechanobiology investigations.

Images (Optional)

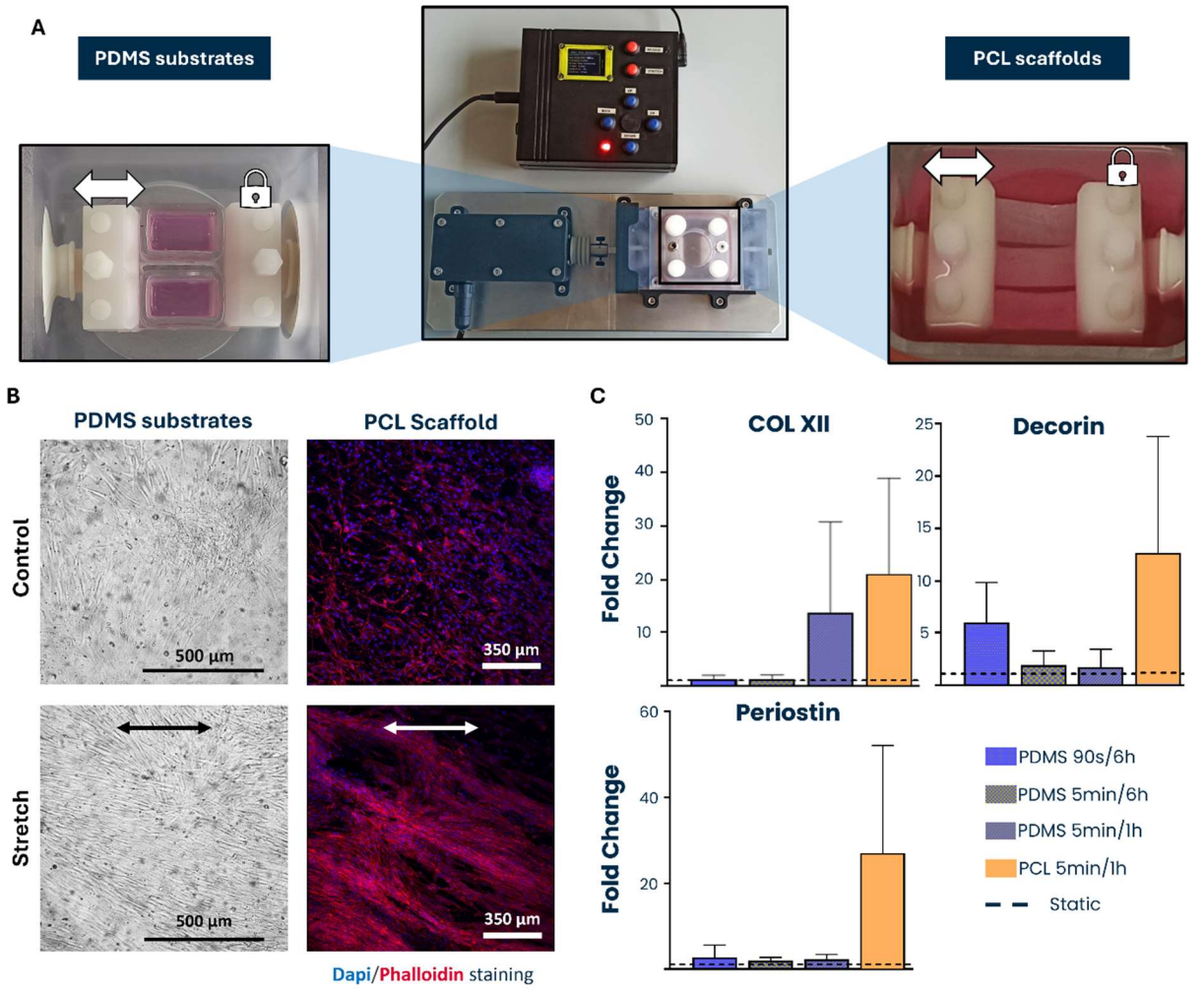


Figure 1. **A)** Overview of the stretch bioreactor, including a close-up of the PDMS substrate (left) and the PCL scaffolds (right) within the culture chamber. **B)** Bright-field images and DAPI/phalloidin staining of cells cultured on PDMS substrates and PCL scaffolds, respectively, under static (top row) and stretching (bottom row) conditions; arrows indicate the direction of the applied strain. **C)** Gene expression profiles presented as fold changes relative to the static condition (dashed line). The graphs depict comparisons among the different intermittent stretching protocols and between cultures grown on PDMS substrates and those on PCL scaffolds (n = 3).

References (Optional)

[1] Roato et al, Nanomaterials, 2022

[2] Putame et al, Med Eng Phys, 2020

[3] Massai et al, Front Bioeng Biotechnol, 2020

[4] Putame et al, Front Bioeng Biotechnol, 2025

Session Category

Tissue Engineering: Mechanobiology

OA199-03

Breast Cancer Fibrotic Microenvironment Architecture Controls Doxorubicin Diffusion: A Multiphysics Computational Study in an Avian Chorioallantoic Membrane Model

Dr. Alberto Bocconi, Dr. Claudio Conci, Mr. Leonardo Cherubin, Dr. Chiara Martinelli, Ms. Giada Mainieri, Mr. Marco Vigneri, Dr. Emanuela Jacchetti, Dr. Manuela T. Raimondi

Department of Chemistry, Materials and Chemical Engineering "Giulio Natta", Politecnico di Milano, Milano, (MI), Italy

Introduction

In breast cancer, progressive collagen deposition stiffens the tumor microenvironment, imposing physical barriers to drug penetration and reducing therapeutic efficacy. To reproduce this progressive fibrotic remodeling in vivo, a chick embryo chorioallantoic membrane (CAM) model was implanted with three micro-scaffold architectures with distinct pore sizes, each generating different levels of vascularization and collagen deposition [1]. On this basis, a three-dimensional multiphysics model was built and calibrated on imaging-derived geometric parameters, blood flow velocities and experimentally measured transport coefficients from the CAM platform. The model is used to test how changes in fibrotic microenvironment architecture modulate doxorubicin distribution and efficacy within the platform.

Methods

COMSOL Multiphysics simulations coupling Computational Fluid Dynamics and Transport of Diluted Species were used to model doxorubicin transport within SZ2080 micro-scaffolds (10×10×15, 30×30×20, 50×50×20 μm^3 pores) implanted on the CAM. For each architecture, vascular morphology and density were quantified by two-photon intravital microscopy and used to define the three-dimensional vascular geometry and inlet flows, together with blood velocities from red blood cell tracking. Fibrotic architecture, including collagen density and fiber orientation, was quantified by second-harmonic generation imaging, and CAM stiffness was measured by atomic force microscopy. Doxorubicin transport coefficients were measured experimentally and used as inputs to the model.

Results

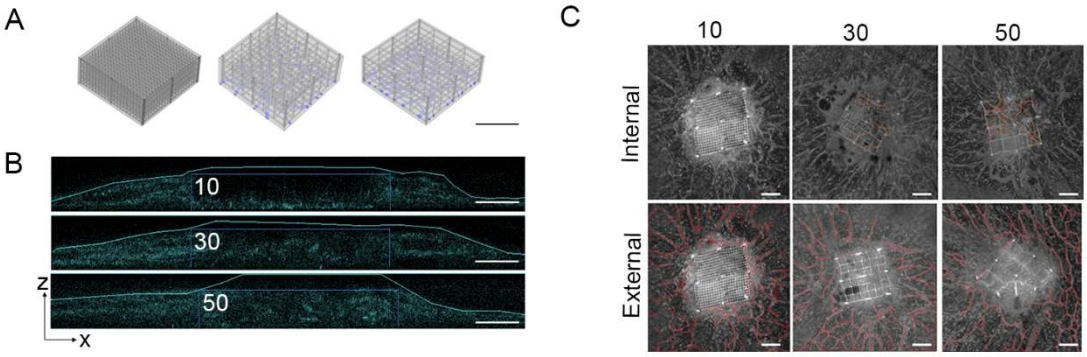
Doxorubicin concentration profiles were predicted over 120 minutes post-injection using an experimentally measured diffusion coefficient of 7.85×10^{-11} m^2/s in CAM tissue. Pore size distinctly modulated drug diffusion: 50×50×20 μm^3 scaffolds exhibited ~1.5-fold higher accumulation compared to 30×30×20 μm^3 pores, whereas 10×10×15 μm^3 pores showed

substantially reduced delivery throughout the scaffold region. Spatial concentration gradients revealed geometry-dependent diffusive resistance within the fibrotic compartment, with steeper gradients and extended low-exposure zones in the most fibrotic condition.

Discussion

This combined computational and experimental method shows that scaffold geometry regulates fibrotic microenvironment architecture by modulating vascularization and collagen deposition, hence affecting doxorubicin distribution across three fibrotic stages mimicked in the platform. By evaluating multiphysics predictions across three different pore topologies, the platform quantifies how fibrosis influences drug diffusion and may ultimately impact therapeutic efficacy.

Images (Optional)



(A) Schematic representation of the three SZ2080 micro-scaffold architectures implanted on the CAM, showing pore geometries with dimensions of 10×10×20 μm^3, 30×30×20 μm^3 and 50×50×20 μm^3. Scale bar: 100 µm (B) Orthogonal reslicing of a second-harmonic generation (SHG) z-stack of collagen, illustrating the fibrotic capsule surrounding the scaffold implantation site, the projected area occupied by a single scaffold is superimposed to delineate the scaffold. Scale bars: 50 µm. (C) Representative two-photon microscopy images of the vasculature of the implant and corresponding segmented vascular networks in the internal (top) and external (bottom) regions, used to reconstruct the three-dimensional vascular architecture and quantify vessel morphology and density. Scale bars: 50 µm.

References (Optional)

[1] Conci et al., AplBioeng, 2023

Acknowledgements (Optional)

ERC, project BEACONSANDEGG,G.A.101053122

Session Category

Tissue Engineering: Mechanobiology

OA199-04

Elucidating Mechanical Mechanisms of Alzheimer's Disease With Human Brain Models

Dr Xun Wang[1,2,3], Dr. Zhengyu Zhang[1], Ms. Annabel Tiong[1], Dr. Seunggyu Kim[1], Dr. Maria Proestaki[1], Prof. Zhengpeng Wan[1], Prof. Rudolph Tanzi[2,3], Prof. Ming Guo[1], Prof. Sehoon Choi[2,3], Prof. Roger Kamm[1]

[1]MIT, Cambridge, MA, United States. [2]Massachusetts General Hospital, Boston, MA, United States. [3]Harvard Medical School, Boston, MA, United States

Introduction

Alzheimer's disease (AD) involves the dysfunction of the blood–brain barrier (BBB) and meningeal lymphatics (ML), the brain's vascular system, which accelerates toxic protein buildup, including amyloid β (Aβ) accumulation, driving AD progression. Yet how BBB and ML interact and break down in AD remains unclear due to limited human tissue access and poor translation of animal models. Emerging evidence suggests that physical forces and mechanical properties of cells and tissues also play a role in AD, but tools to study these factors in human systems are scarce. Microfluidic engineered living systems offer a transformative solution to these limitations and reveal mechanical mechanisms of AD in the human environment.

Methods

We developed a novel 3D in-vitro human brain model that integrates perfusable BBB microvasculature, sprouting ML vessels, and AD-mimicking neurons within a single microfluidic platform. Our model recapitulates key structural and functional features of the human brain, enabling quantitative assessment of BBB permeability, ML drainage, and Aβ clearance under AD conditions. Built on top, we incorporated mechanical tools to explore therapeutic targets, including Piezo1, a mechanosensitive channel, and employed optical tweezers and force-spectrum microscopy to assess cellular mechanical changes during AD progression.

Results

Using our unified 3D human brain model, we showed increased BBB permeability, disrupted ML sprouting, reduced ML drainage, and abnormal Aβ accumulation in the AD condition. ML sprouts exhibited impaired growth and reduced clearance capacity. Mechanical measurements showed that Aβ exposure increased astrocyte stiffness and altered intracellular mechanical activity. Ongoing work is mapping similar mechanical

changes across other brain cell types, including microglia, to define AD-associated cell mechanics.

Discussion

Our physiologically relevant human model enables simultaneous analysis of Aβ dynamics, barrier function, fluid drainage, and cellular mechanics. It provides a platform to dissect neurovascular–lymphatic crosstalk and to identify mechanosensitive pathways such as Piezo1 that may regulate AD progression. Future efforts include developing fully stem-cell-derived isogenic models to reduce variability and expanding integrated mechanical measurements to characterize biomechanical dysfunction across cell types. Together, this system offers new insights into mechanical mechanisms in AD and supports the discovery of mechano-biomarkers and mechano-therapy strategies for human brain diseases.

Acknowledgements (Optional)

We thank Georgios Pavlou and Shun Zhang for their assistance with the microfluidic platform design, Marie Floryan for training in microfluidic fabrication, and Lani Lee and Haiqian Yang for support with optical tweezers and force-spectrum setup and training. This work was supported by the Cure Alzheimer's Fund and NIH R01 grant NS121078 (to R.D.K. and S.H.C.).

Session Category

Tissue Engineering: Mechanobiology

OA199-05

Numerical Simulation of Atherosclerosis Development Following the Outside-in Hypothesis

Dr. -Ing. Meisam Soleimani[1], Prof. Peter Wriggers[1], Prof. Axel Haverich[2], Prof. Christian Gasser[3], Prof. Philipp Junker[4]

[1]Leibniz University Hannover, Hannover, Lower Saxony, Germany. [2]Medical School Hannover, Hannover, Lower Saxony, Germany. [3]KTH Royal Institute of Technology, Stockholm, Stockholm, Sweden. [4]Leibniz University Hannover, Hannover, Lowersaxony, Germany

Introduction

Atherosclerosis remains the leading cause of cardiovascular disease, yet its initiation and progression are poorly understood. Emerging evidence suggests a key role of the vasa vasorum (VV), whose impaired perfusion may trigger inflammation and plaque formation through an outside-in mechanism. We present a multi-field computational model that couples tissue turnover, inflammation, and growth [1]. Perfusion is described by a diffusion–reaction equation accounting for VV dysfunction, while inflammation is represented using a phase-field formulation that tracks the evolving inflamed region. Tissue growth results from the combination of inflammation-induced swelling with stress-regulated turnover. Simulations reveal strong coupling between perfusion deficits, inflammation, and mechanical stress, illustrating how VV impairment can initiate a pathological condition.

Methods

This work refines a previously developed multi-field model that captures deformation, perfusion, and inflammation in the arterial wall using an isotropic Yeoh hyperelastic law, diffusion–reaction–based nutrient transport, and a phase-field formulation to track inflammatory interfaces. Multiplicative kinematics govern atherosclerosis-related wall thickening through inflammation-induced swelling and stress-regulated tissue turnover. The model is extended by coupling perfusion with mechanical stress. We propose two interacting disease mechanisms: (i) reduced perfusion initiates inflammation when nutrient levels drop below a critical threshold, particularly under VV dysfunction; and (ii) chronic inflammation combined with ongoing tissue turnover leads to irreversible wall thickening and plaque formation. Simplifications include homogeneous isotropic mechanics, lumped blood-borne factor transport, constant boundary nutrient supply, and a regularized phase-field description. The framework is implemented using a fully implicit, monolithic finite element formulation.

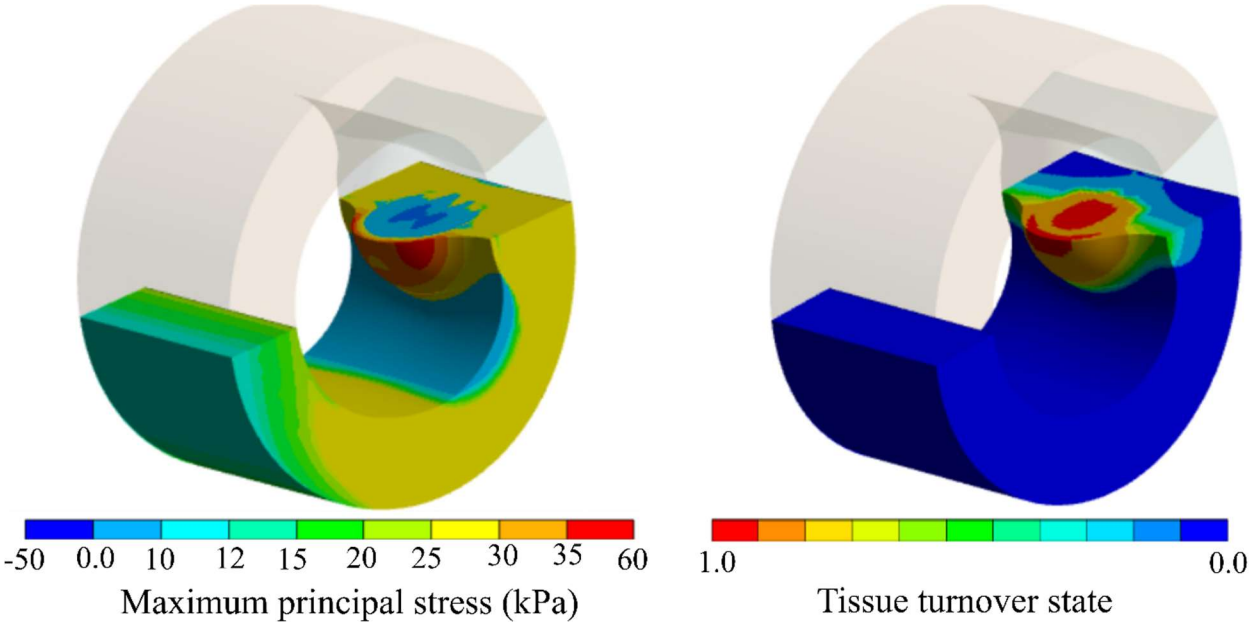
Results

One can see in Fig.1 how the model predicts artery wall thickening as a result of spreading tissue inflammation and tissue turnover. Cauchy stress in the wall (left column) and the inflamed spatial tissue domain (right column). Elevated blood pressure further amplifies peak stresses, underscoring its role in the progression of disease.

Discussion

Our model highlights the importance of VV dysfunction in driving outside-in plaque growth and reveals how mechanical, inflammatory, and perfusion processes interact during disease progression. Despite necessary modeling simplifications and the challenge of patient-specific validation, the framework provides a foundation for future AI-supported vascular simulations.

Images (Optional)



References (Optional)

[1] Soleimani et al., Archives of Computational Methods in Engineering, 2021,

Session Category

Tissue Engineering: Mechanobiology

OA200-02

Rectus Femoris Tendon as an Alternative ACL Graft: A Biomechanical Comparison with Standard Graft Configurations

MS Julian André, MS Samuel Bachmaier

Arthrex GmbH, Munich, Bavaria, Germany

MS Julian André

Introduction

Anterior cruciate ligament reconstruction (ACLR) remains the most common treatment method for ACL injuries [1], with graft choice and fixation technique being key determinants of clinical success [2]. While hamstring tendon (HT), bone-patellar tendon-bone (BTB), and quadriceps tendon autografts are commonly used [3], the rectus femoris tendon (RFT) recently gained attention due to its favorable anatomy and low donor-site morbidity [4]. However, biomechanical data on RFT grafts in ACLR remains limited. Therefore, the purpose of this study was to biomechanically evaluate the RFT as a viable graft alternative for ACLR.

Methods

Tendons were dissected from human cadaveric knees (54.9±12.6 years) and divided into four groups (n=8 per group): four-strand hamstring tendon (4HT), four-strand rectus femoris tendon (4RFT), doubled rectus femoris tendon (2RFT), and BTB graft. Specimens underwent four loading conditions (1,000 cycles each of position-controlled loading and force-controlled loading between 10-100N, 10-200N, and 10-300N), followed by a pull-to-failure (50mm/min). Residual graft force, dynamic elongation, dynamic stiffness, and ultimate failure load were evaluated. Group differences were analyzed using a one-way ANOVA with Tukey post-hoc test ($p<0.05$).

Results

The BTB group exhibited significantly greater residual graft force compared to both RFT groups ($p\leq0.046$). Dynamic elongation in the 200N load block was significantly greater in the 2RFT group compared to all other groups ($p\leq0.015$). No significant differences were observed between groups in the 100N and 300N load blocks. The dynamic stiffness of the BTB group was significantly lower compared to the 2RFT and 4HT groups ($p\leq0.019$).

Moreover, the 4HT group showed significantly greater dynamic stiffness than the 4RFT group ($p \leq 0.047$). The ultimate failure load of the 2RFT group was significantly lower than that of the 4HT and BTB groups ($p \leq 0.034$).

Discussion

This study's results confirm the RFT as a viable autograft alternative for ACLR, demonstrating comparable biomechanical performance to standard grafts. Despite increased elongation and lower failure loads, 2RFT grafts may be suitable for patients relying on preserved quadriceps function.

References (Optional)

[1] Zheng et al, BMC Surg. 2025

[2] Ostojic et al, Medicina. 2024

[3] Hart et al, Eur J Orthop Surg Traumatol. 2023

[4] Pettinari et al, Arthroscopy Techniques. 2025

Acknowledgements (Optional)

Session Category

Orthopaedic Biomechanics: Sports Medicine

OA200-03

Unicortical Quadriceps Tendon Repair With All-Suture Anchors Results In Less Gap Formation Than Traditional Hard-Body Suture Anchors

Dr. Brian Werner MD[1], Mr. Marcos Tejada BS[2], Dr. Jocelyn Wittstein MD[3], Dr. Rachel Frank MD[4], Dr. Mary Kate Evans PhD[5], Dr. Anthony Khoury PhD[2], Mr. Benjamin Smith MS[2]

[1]UVA Health, Charlottesville, Virginia, United States. [2]Arthrex, Naples, Florida, United States. [3]Duke Health, Durham, North Carolina, United States. [4]UCHealth CU Sports Medicine, Denver, Colorado, United States. [5]Artrhex, Naples, Florida, United States

Introduction

Current quadriceps tendon repair techniques following rupture include transosseous patellar bone tunnels (TO) and suture anchors (SA); however, documented failure rates range from 0-16% [1]. Adjustable all-suture anchors (ASAs) may provide better tendon footprint restoration; however, there are currently no studies that have examined ASA use for unicortical fixation. The authors hypothesized that unicortical ASA fixation would reduce gap formation and exhibit comparable stiffness, yield load, and ultimate load to the conventional unicortical hard-body suture anchor approach.

Methods

Eight matched male cadaveric knee pairs were dissected and randomized to ASA (2.6-mm) or hard-body suture anchor repairs, with medial/lateral Krackow sutures on the quadriceps tendon (1.3-mm tape). For ASA repair, two ASAs were inserted into two 2.6-mm sockets, respectively. For the control repair, two hard-body anchors were inserted into two tapped 4-mm sockets, respectively. Krackow sutures were loaded through anchors to reduce the quadriceps tendon. Knees underwent 10 native preconditioning cycles (5° to 90° of flexion) on a materials testing system, followed by 250 post-repair cycles (0.1 Hz, 150 N peak) and load-to-failure (50mm/min) [2]. Outcomes: gap formation (mm) during cyclic loading and stiffness (N/mm), 0.2% offset yield load (N), and ultimate load (N) during load-to-failure. Paired t-tests were used for statistical analyses ($p < 0.05$).

Results

ASA repair had significantly less gap formation at cycle 250 (mean Δ=4.2 mm; $p<0.001$). Mean control displacement surpassed the defined critical threshold for gap formation (5.0 mm) within the first 50 cycles; mean ASA displacement approached this threshold at cycle

200. No significant differences in stiffness or ultimate load. Yield load was significantly higher in the control group (mean Δ=54.7 N; p=0.002).

Discussion

ASA repair significantly reduced gap formation by 43%, suggesting unicortical ASA repair may lead to improved clinical outcomes. While only the yield load was significantly lower for the ASA repair, this may not result in clinical deficiencies when the post-operative healing is complete. Despite the inherent limitations of a time-zero biomechanical study, the results provide robust data to biomechanically support ASA viability for unicortical quadriceps tendon repair.

Images (Optional)

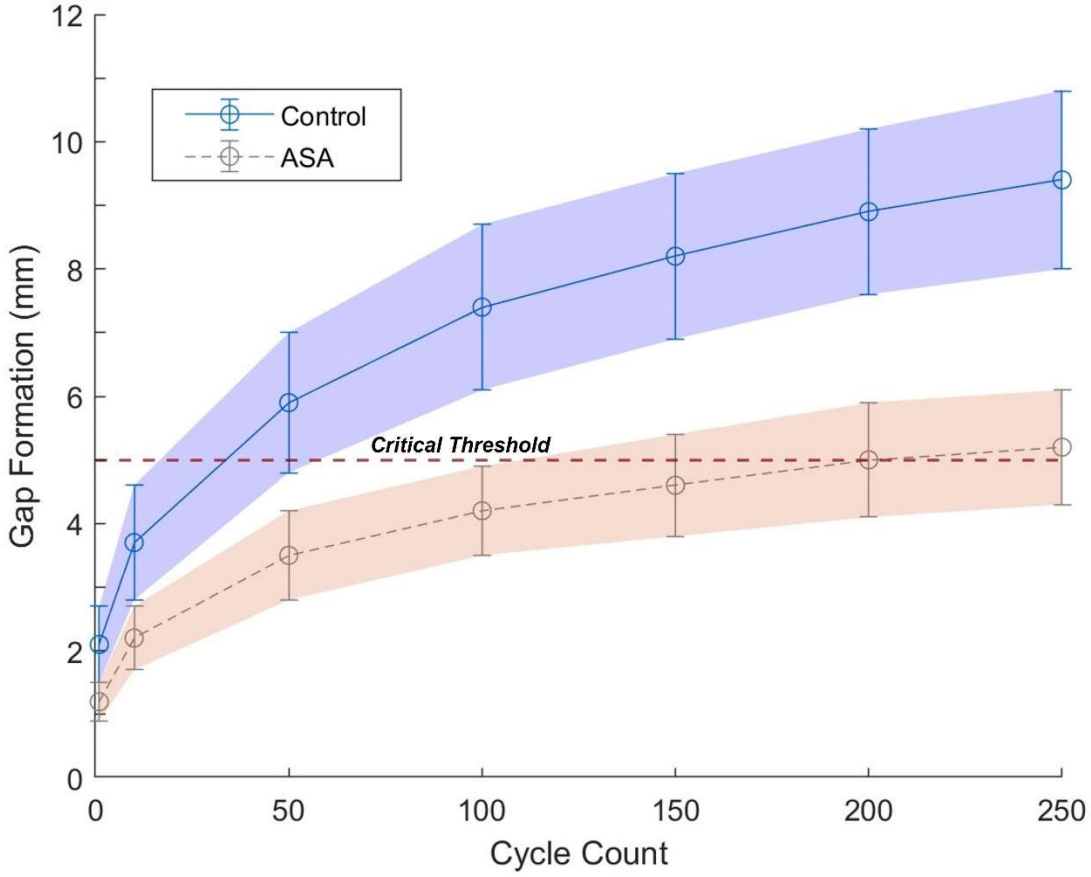


Fig 1. Gap formation at specified cycle intervals for unicortical tendon repair using control and all-suture anchor (ASA) techniques (5.0-mm critical threshold denoted). Values are shown as mean ± SD.

References (Optional)

[1] Nicholas B VanDerwerker *et al.*, Arthroscopy, 2025

[2] Jocelyn R. Wittstein *et al.*, OJSM, 2025

Session Category

Orthopaedic Biomechanics: Sports Medicine

OA200-04

Repeatability of Shear Wave Tensiometry in Tendons With and Without Pathology: A Comparison of Normalization Methods During Countermovement Jump Phases

Ms. Lucia Hockerman[1,2], Ms. Elizabeth Schmida MS[3,2], Dr. Darryl Thelen PhD[4], Dr. Bryan Heiderscheit PT, PhD, FAPTA[3,2], Dr. Naoaki Ito DPT, PhD[3,2]

[1]University of Wisconsin-Madison Department of Biomedical Engineering, Madison, Wisconsin, United States. [2]University of Wisconsin-Madison Badger Athletic Performance Program, Madison, Wisconsin, United States. [3]University of Wisconsin-Madison Department of Orthopedics and Rehabilitation, Madison, Wisconsin, United States. [4]University of Wisconsin-Madison Department of Mechanical Engineering, Madison, Wisconsin, United States

Introduction

Heavy tendon loading through exercise therapy is the recommended approach for treating patellar tendon injuries [1]. Disconnect between exercise and internal tendon loading during rehabilitation,
however, makes optimal dosing difficult. Shear wave tensiometry (SWT) is a skin-mounted sensor that measures tendon shear wave propagation speed (equivalent to axial stress [N]) [2], but its repeatability is unknown. This study aimed to assess the repeatability of SWT during propulsion and landing phases of countermovement jumps (CMJs) using different normalization methods in healthy and pathological patellar tendons.

Methods

Adults with patellar tendinopathy (n=3), anterior cruciate ligament reconstruction with a bone-patellar tendon-bone autograft (n=3), and healthy controls (n=4) participated. SWT was simultaneously recorded with (1) vertical ground reaction forces (vGRFs) during CMJs, and (2) knee extensor torque during maximum voluntary isometric contractions (MVICs) performed on an electromechanical dynamometer positioned at 60° of knee flexion. Data were collected twice within a 7-day period. The involved limb (weaker limb for controls) was analyzed. During propulsion and landing phases, peak CMJ wave speeds (WS, m/s) were identified and normalized to (1) peak WS at MVIC (%) and (2) scaled to units of body weight (BW) using a standard 4.5 cm patellar tendon moment arm. Intraclass correlations (ICCs) assessed the reliability of each normalization method and peak vGRF.

Results

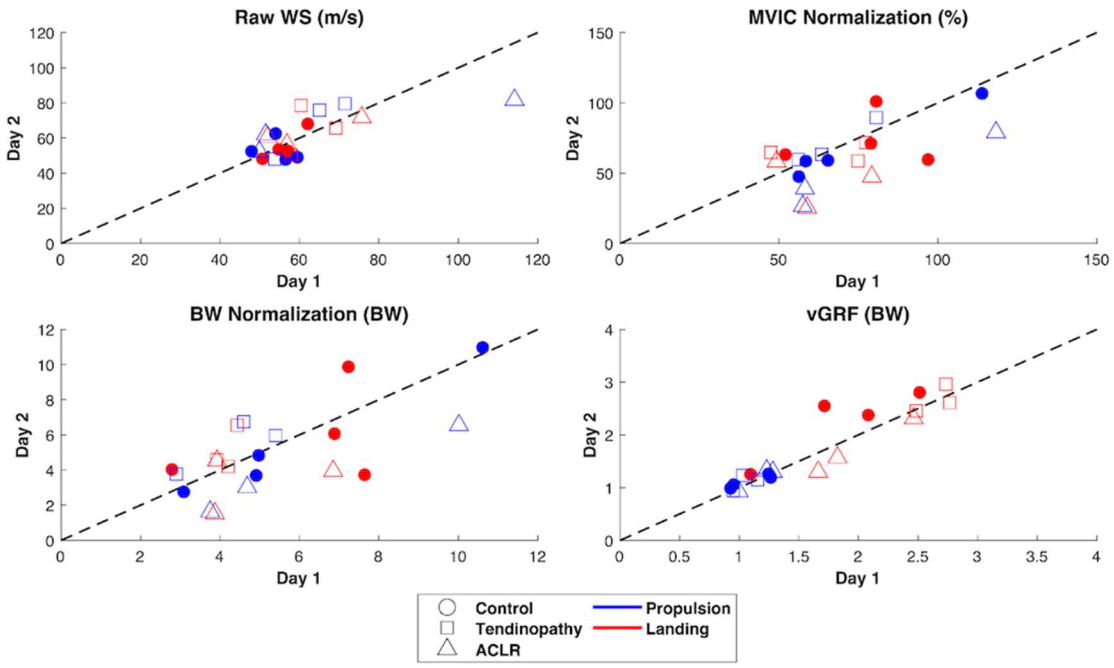
SWT ICCs during CMJ propulsion were greater than landing, with MVIC and BW normalization values comparable to vGRF. SWT ICCs during landing phase were poor (Figure 1).

Discussion

SWT was most repeatable between days during the propulsion phase of CMJ when normalization methods were implemented. Propulsion SWT was more reliable than landing, likely reflecting the propulsion phase being performed with more consistent knee biomechanics than the landing phase. Hence, the low SWT ICCs during landing may be due to normal movement variability. SWT was applied at the patellar tendon across different pathologies during CMJs with promising repeatability results. Larger cohorts with various tendon pathologies and testing in alternative movements may be needed to further determine ideal normalization methods.

Images (Optional)

(a)



(b)

Jump Phase	Variable	ICC (95% CI)	Day 1 Mean ± SD	Day 2 Mean ± SD
Propulsion	vGRF (BW)	0.84 (0.82-0.99)	1.1 ± 0.1	1.1 ± 0.1
	Raw WS (m/s)	0.68 (0.68-1.00)	62.4 ± 19.5	61.1 ± 13.4
	MVIC Normalization (%)	0.79 (0.76-1.00)	72.8 ± 24.0	63.0 ± 23.7
	BW Normalization (BW)	0.81 (0.73-1.00)	5.5 ± 2.7	5.0 ± 2.7
Landing	vGRF (BW)	0.82 (0.77-1.00)	2.1 ± 0.5	2.2 ± 0.6
	Raw WS (m/s)	0.62 (0.58-1.00)	59.7 ± 7.7	60.6 ± 10.1
	MVIC Normalization (%)	0.26 (0.22-0.99)	69.5 ± 16.5	62.2 ± 19.1
	BW Normalization (BW)	0.40 (0.23-0.99)	5.2 ± 1.8	4.9 ± 2.2

Figure 1: (a) Scatter plots of vertical ground reaction force (vGRF), raw wave speed (WS), maximum voluntary isometric contraction (MVIC) normalization, and body weight (BW) normalization between Day 1 and Day 2. The dashed line indicates line of equality. **(b)** Table showing corresponding intraclass correlations (ICCs) with confidence intervals (CIs), means and standard deviations (SDs).

References (Optional)

[1] Magnusson SP, et al. Nat Rev Rheumatol, 2010

[2] Martin JA, et al. Nat Commun, 2018

Acknowledgements (Optional)

Research reported in this abstract was supported by the National Institute Of Arthritis And Musculoskeletal And Skin Diseases of the National Institutes of Health under Award Number K99AR085752 and by the UW ICTR, grant 1UL1TR002373, from the Clinical and

Translational Science Award of the NCATS/NIH. The content is solely the responsibility of the authors and does not necessarily represent the official views of the National Institutes of Health. UW-NMBL and funding source DOD Clinical and Rehabilitative Medicine Research RESTORE program grant # W81XWH2120006 contributed to this work. This project was also supported by the University of Wisconsin Department of Orthopedics and Rehabilitation Freedom of Movement Fund and the UW School of Medicine and Public Health from the Wisconsin Partnership Program. Author LH was supported through the Hilldale Undergraduate Research Fellowship.

Session Category

Orthopaedic Biomechanics: Sports Medicine

OA200-05

Preliminary Data Suggest that Human Tendinopathic Tendons Do Not Contain More Denatured Collagen than Healthy Controls

Mx. Margaret Capalbo[1], Dr. Spencer Szczesny[1,2]

[1]Pennsylvania State University, University Park, PA, United States. [2]Penn State College of Medicine, Hershey, PA, United States

Introduction

Despite tendinopathy accounting for 30% of all musculoskeletal disorders, its pathogenesis is unclear. We previously found minimal collagen damage (i.e., denaturation) in mouse Achilles tendon (AT) explants cyclically loaded to failure, suggesting that collagen denaturation may not initiate a degenerative cellular response leading to tendinopathy. However, it is unclear whether collagen denaturation occurs in human tendinopathic samples. Additionally, HIF-1a has been measured in higher quantities in human tendinopathic tissue, suggesting a role for hypoxia as well. However, the relationship between collagen damage and hypoxic signaling is unknown. Therefore, the purpose of this study was to measure the amount of collagen denaturation and HIF-1a in tendinopathic and healthy human tendon samples. We hypothesize that both markers will be greater in tendinopathic samples than in healthy controls.

Methods

Tendinopathic tissue from the long head of the biceps tendon (LHBT) and AT were collected during surgical repairs with IRB approval. Healthy tissue was obtained from the National Disease Research Interchange. Cryosections (10um) were incubated with a collagen hybridizing peptide (CHP) to measure collagen denaturation or a HIF-1a anti-body. Fluorescence images were used to determine the percentage of tissue positively stained by CHP and HIF-1a. tatistical significance was determined using a Wilcoxon test.

Results

In the LHBT (n=3), percent area of CHP was not statistically significant between healthy (5.3% ± 4.0%) and tendinopathic (0.7% ± 1.2%) tissue (Fig. 1A,B). For the AT (n=1), the percent area of CHP was 25.8% in the healthy and 1.0% in the tendinopathic sample. For the LHBT stained for HIF-1a (n=2), the staining in healthy (0.4% ± 0.3%) and tendinopathic (0.6% ± 0.002%) samples was similar (Fig. 1C,D).

Discussion

While no statistical difference was determined between the healthy and tendinopathic samples for either tendon and marker, the amount of collagen denaturation tended to be higher in healthy tissue. This unexpected trend may be explained by ambiguous determination of the healthy and tendinopathic portions of the LHBT tissue or differences in collection methods for the AT samples. Still, our preliminary data suggest that human tendinopathic tendons do not contain substantial collagen denaturation and, therefore, may not be characteristic of tendinopathy.

Images (Optional)

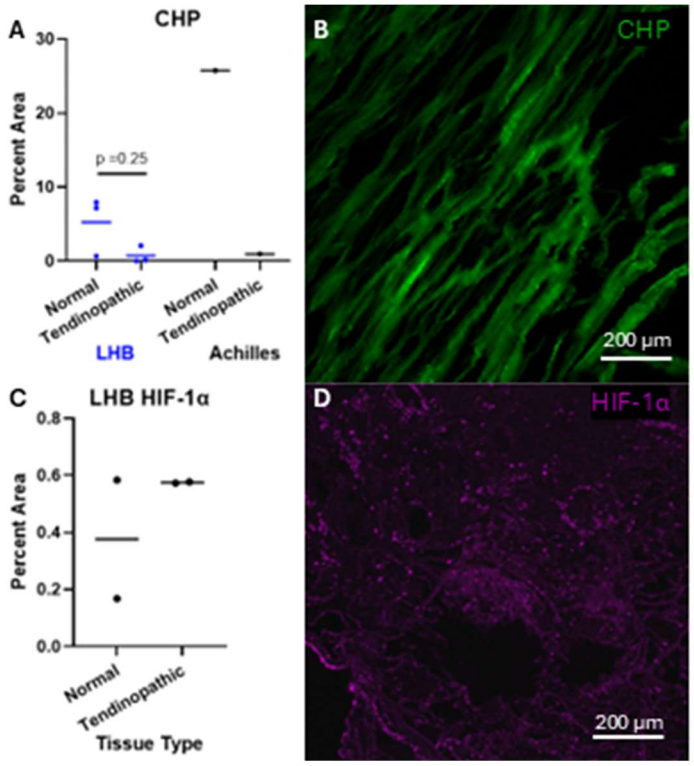


Figure 1: (A) Percent area of collagen denaturation (CHP) LHBT and AT. (B) Representative image of healthy AT for CHP staining. (C) Percent area of HIF-1α staining in LHB tendons. (D) Representative image of diseased LHBT for HIF-1α staining.

Session Category

Orthopaedic Biomechanics: Sports Medicine

P1-001

Evaluating Animated and Interactive Learning Tools for Strength Training Biomechanics Education

Assistant Teaching Professor Breanne Carlson MS[1], Associate Professor Erich Petushek PhD[1], Research Associate Oliver Faul MS[2], Professor Tron Krosshaug PhD[2]

[1]Michigan Technological University, Houghton, MI, United States. [2]Norwegian School of Sports Sciences, Oslo, Oslo, Norway

Introduction

Teaching biomechanics of strength training requires students to integrate anatomy, force vectors, moment arms, and joint moments within applied resistance-exercise contexts. Traditional lecture approaches may inadequately support this applied conceptual learning. Interactive digital platforms that combine animated demonstrations and hands-on manipulation tools may enhance understanding, yet research examining student perceptions, usability, and potential motivational bias remains limited. This study evaluated student perceptions of an instructional platform designed specifically for strength-training biomechanics and examined whether platform endorsement was related to baseline enjoyment of strength training.

Methods

Eighteen undergraduates in an exercise assessment course completed a mixed-methods survey evaluating the Muscle Animation instructional platform (see Figure 1 for example screenshots). Quantitative measures included likelihood of recommending the platform to a peer (modified Net Promoter Score; 1–5 scale) and enjoyment of strength training (1–5 scale). Descriptive statistics and 95% CI were calculated, and correlations tested associations between enjoyment and endorsement ($\alpha = .05$). Qualitative item responses assessing platform likes, dislikes, and improvement suggestions were analyzed using content analysis. Two researchers independently coded responses and resolved themes by consensus. Frequency counts estimated thematic prevalence.

Results

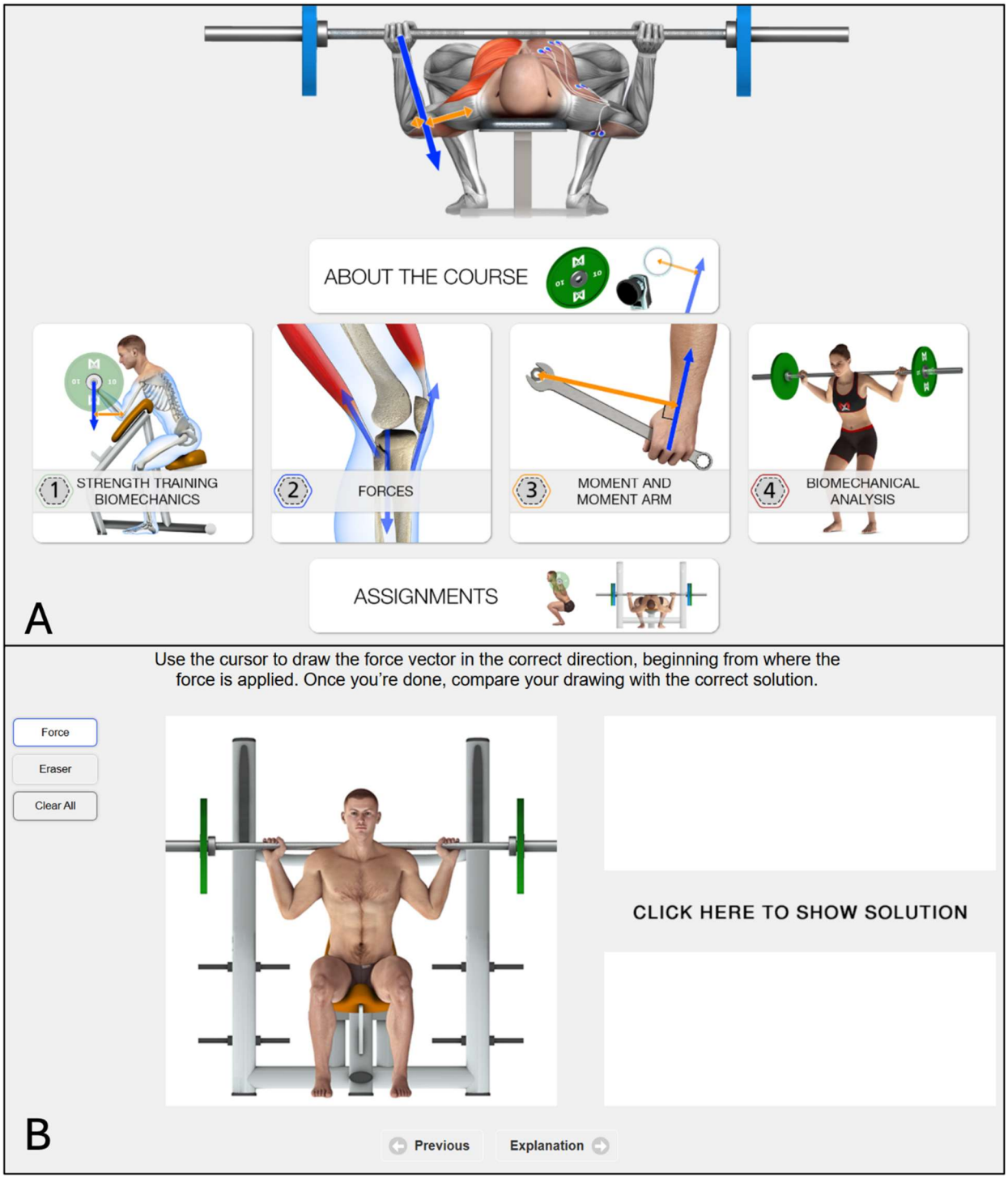
Mean likelihood of recommending the platform was 3.56 (95% CI: 2.92–4.21). Students reported high enjoyment of strength training (M = 4.06, 95% CI: 3.53–4.59). No significant association was found between enjoyment and endorsement ($r = .30$, $p = .26$). Thematic analysis identified animated visualizations of joint forces and moment arms as the most valued feature (≈50%). Interactive vector manipulation during exercises was noted by 33% as enhancing active learning and conceptual understanding. Modular lesson structure and

quiz practice were cited by 20–30%. Usability concerns were most common, including navigation difficulties (25–30%), lack of progress tracking (22%), and quiz formatting issues (22%). Approximately 28% reported no dislikes or suggestions.

Discussion

Results indicate that animated and interactive tools are highly valued for teaching strength-training biomechanics and that endorsement is independent of students' intrinsic interest. Findings emphasize usability refinements—particularly navigation workflows and progress monitoring—while retaining strong visual and interactive design elements. Future work will evaluate learning outcomes and conduct usability testing to optimize training-specific biomechanics instruction.

Images (Optional)



Session Category

Biomechanics Education, Knowledge Translation and Outreach: N/A

P1-002

FA.RE.MO: A Non-profit Platform to FAcilitate REsearch MObility in Biomechanics

Dr Cecilia Monoli[1], Dr Monika Colombo[2]

[1]Department of Health and Kinesiology, University of Utah, USA, Salt Lake City, Utah, United States. [2]Department, Aarhus, Jutland, Denmark

Introduction

International research mobility is a cornerstone for scientific and career development, fostering knowledge exchange, innovation, and personal growth. Globally, 6.9 million students engaged in international mobility in 2022, with graduate students forming the largest share in programs like Erasmus+ and U.S. exchanges [1]. For example, the U.S. hosted nearly 488,000 international graduate students in 2024/25, while NSF's IRES program supported 5,000 graduate researchers since 2006. International students are particularly concentrated in doctoral programs and STEM fields, highlighting the relevance for graduate-level mobility [1]. Despite this demand and impact, accessing international research opportunities remains challenging.

Methods

Addressing current limitations in accessing international research opportunities, we are developing **FA.RE.MO** [2], a web-based platform designed to centralize and streamline research mobility in biomechanics. As illustrated in **Fig. 1**, the platform is structured into several key components. It introduces users to the mission and provides curated information on research opportunities organized through a keyword-based system. A dedicated section compiles funding and fellowship programs. The platform hosts a growing network of international biomechanics labs, including details on research focus, equipment, contacts, and openness to hosting students. A story-sharing space, and a resources and contacts section offers templates for emails, application materials, and cultural/practical guides. FA.RE.MO is currently in active development and will be available for use at the time of the congress.

Results

FA.RE.MO aims to increase engagement by creating a dynamic, user-friendly environment for research mobility planning. Expected outcomes include:

i) A growing database of researchers and institutions across disciplines.

ii) Outreach through social media and academic channels to reach graduate students globally.

iii) Improved matching accuracy, reducing administrative burden and accelerating collaboration setup.

Discussion

By connecting researchers and institutions, FA.RE.MO is positioned to transform how research mobility is managed. The platform promotes inclusivity, transparency, and efficiency, addressing current limitations in fragmented systems. Ultimately, FA.RE.MO supports career development for graduate students and strengthens international collaboration networks, contributing to a more interconnected scientific community.

Images (Optional)



References (Optional)

[1] https://www.migrationdataportal.org
[2] http://www.faremo.carrd.co

Session Category

Biomechanics Education, Knowledge Translation and Outreach: N/A

P1-003

Integration of Quantitative Biomechanical Analysis in Non-Research Settings via an Automated Pipeline

Ms Kaley Pagnotta, Dr. Cherice Hill

University of Rochester, Rochester, NY, United States

Introduction

Biomechanical analysis is increasingly desired in athletic settings, but the necessary expertise creates a barrier to broad utilization; automated pipelines can reduce the expertise necessary, decreasing this barrier. Collaborating with coaches and athletic trainers to create a system for motion analysis that, after development, can be used independently of a biomechanics expert would allow for biomechanical analysis to be integrated in routine injury prevention and training. This study aimed to develop and pilot such a system for motion analysis in a non-research setting by non-experts.

Methods

Following consultation with an athletic program, a Qualisys Track Manager PAF pipeline was coded to automate marker-less motion capture and force plate data processing through Theia3D and Visual3D (Figure 1A). A coach was trained (~2 hours) to set up and calibrate a marker-less motion capture system and portable force plates, follow a collection protocol, process data (automated), and interpret the generated report. After training, the coach independently used the protocol and pipeline to collect and interpret data from 8 athletes at 3 timepoints across 3 months. The coach completed surveys reflecting their perception of and comfort with the biomechanical data and collection method before training, after training, and after each data collection session.

Results

The developed pipeline automated processing comparably to manual processing. The coach consistently viewed motion analysis data as “very important”. Before training, the coach had low confidence in using the equipment and collecting data, but confidence improved and remained high after training (Figure 1). All data collected by the coach was research-grade quality, with appropriate lighting and all 8 cameras having the athlete in full view. Over time, the coach set up more quickly, and the coach only had questions for the monitoring researcher at the initial data collection session.

Discussion

These findings demonstrate the potential for integration of an automated biomechanical pipeline for use in an athletic training space by a coach. Coaches demonstrated increased comfort after training and consistently expressed importance of incorporation of this data relative to training goals. As interest in biomechanical data continues to grow, future work should continue to explore ways to improve accessibility of robust biomechanical analysis.

Images (Optional)

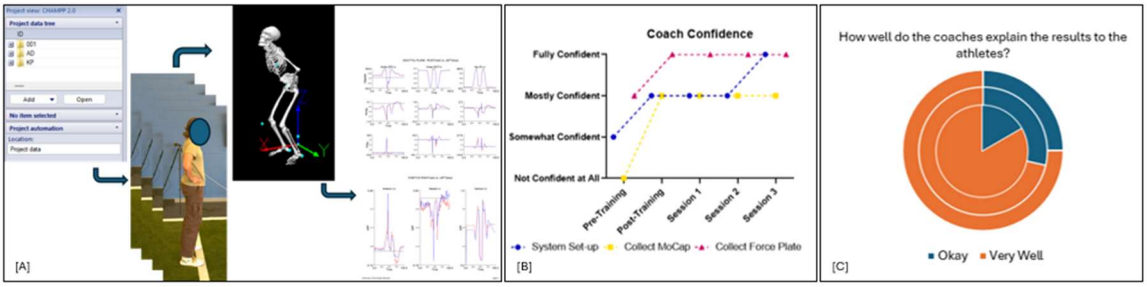


Figure 1: [A] Pipeline steps including adding a participant, collecting data, building the skeletal model, and generating a report. [B] Coach confidence in system set-up, collection of motion capture data, and collection of force plate data across time. [C] Athlete perception of how well the coach explained reports.

Session Category

Biomechanics Education, Knowledge Translation and Outreach: N/A

P1-004

Transferring Anatomical Models From Medicine to Engineering: Derivation of Requirement Categories for Anatomical Models Supporting the Development of Medical Devices Using the Example of the Lumbar Spine

Ms. Marisa Ritter M.Sc., Dr.-Ing. Robin Remus, Dr.-Ing. Marc Neumann

Biomedical Engineering Lab, Department of Mechanical Engineering, Ruhr University Bochum, Bochum, NRW, Germany

Introduction

Developing medical devices, such as spinal implants, requires a deep understanding of anatomy and biomechanics [1]. Physical models can enhance this understanding by providing visual and tactile insights into complex structures [2, 3]. This study reviews anatomical spine models used in educational settings to derive requirement categories for a physical anatomical model to impart anatomical and biomechanical knowledge and to support the development of medical devices.

Methods

A literature review was conducted in PubMed to identify publications on the educational applications of physical lumbar spine models published between 2020 and 2025. The articles were screened by title and abstract, followed by full-text assessment of eligible studies (Figure 1a). Studies were included if they described a physical spinal model and reported details on its design, fabrication, and educational application.

Results

The literature review identified six spinal teaching models used primarily in surgical training (Figure 1b). The models varied in anatomical extent, ranging from single spinal segments (L4/5) to multi-segment constructs (L1–S1). Extended versions included the pelvis and rib cage. Five of the six models targeted novice learners, typically surgical residents. All models featured clearly defined applications and learning outcomes. They were manufactured using cost-effective approaches, with reported costs not exceeding $500 per model.

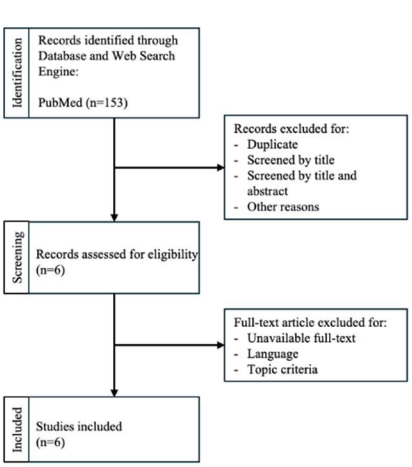
Discussion

The results indicate that existing models are primarily designed for medical residents, raising the question of whether they can be directly transferred to use in the development of medical devices. Identifying engineers' specific needs is essential to determine which anatomical or functional features require modification, simplification, or expansion.

Integrating engineers' feedback into a subsequent development phase could help ensure that the resulting requirement categories reflect actual needs. Overall, the findings provide an initial foundation for a structured requirements framework that balances anatomical realism with functional biomechanical representation and supports the design of effective anatomical models to enable engineers to gain deeper insights into anatomy and biomechanics knowledge and, later on, transfer this knowledge to degree programs of engineers for the development of medical devices.

Images (Optional)

a)



b)

Author	Year	Model	Material	Spinal Segments	Soft Tissue	Level	Cost
Koh et al.	2021	3D-Printed Phantom	PLA PU Foam Ecoflex 0030 Silicone	Lumbar spine Sacrum Pelvic bone	Intervertebral discs Muscles Skin layer	Resident	-
Pullen et al.	2022	3D-Printed Simulation Model	ABS PVC Synthetic Fibre	L1-L5 Pelvis Partial rib cage (T8-T12)	Psoas muscle Intervertebral discs Outer torso skin	Resident	Approximately $500 per model
Ozturk et al.	2024	3D-Printed	ABS PLA Polyol and Isocyanate Foam	Lumbar spine	-	Resident	Approximately $12 per model
Delgado et al.	2024	3D-Printed Simulation Model, Proof of Concept	PLA	3 spinal segments	-	Resident	Approximately $40 per model
Akbulut et al.	2024	Anatomical 3D-Printed Model	PLA TPU	L4/5	Intervertebral disc Dura mater Spinal cord roots Ligamentum flavum	Resident	Approximately $1 per model/training session
Bogdanov et al.	2025	Anatomical 3D-Printed Model	PLA PolyFlex TPU95	L1-S1	Intervertebral discs	Neurosurgical Training	-

Figure 1 – a) *Flow diagram of the literature research screening process. b) Overview of the results of the literature review.*

References (Optional)

[1] Hanna et al. (2024), Heliyon:10.4, e26154

[2] Akbulut et al. (2024), Asian spine J.:18(5), 630-638.

[3] Alam et al. (2024), World Neurosurg.:189, e61-e68.

Session Category

Biomechanics Education, Knowledge Translation and Outreach: N/A

P1-005

Leveraging Game-based and Blended Learning to Support Students with Heterogeneous Linguistic, Cultural, and Academic Backgrounds in a Lecture Series on Traffic Accident Biomechanics and Polytrauma Pathophysiology

M.Ed. Raphael Grau[1], M.A. Ann-Kathrin Steiner[2], Dr. Luke West[2], M.Ed. Matthias Mann[1], Dipl.-Ing. Katharina Bause[1], Univ.-Prof. Dr.-Ing. Tobias Düser[1]

[1]IPEK – Institute of Product Engineering, Karlsruhe Institute of Technology (KIT), Karlsruhe, Baden-Württemberg, Germany. [2]Eberhard Karl University of Tübingen, Tübingen, Baden-Württemberg, Germany

Introduction

A new international Master's program in Biomedical Engineering, brings together students from diverse linguistic, cultural, and academic backgrounds with varying prior knowledge and learning needs. To support their entry into the sensitive topics of biomechanics and pathophysiology of injured patients, a serious game was developed and implemented within a teaching course. It enables students to grasp fundamental mechanisms of traffic accidents and related injuries while learning at their own pace and focusing on individual interests. Embedded in a blended learning framework, the course bridges a research gap by combining serious gaming, adaptive learning, and inclusive access for diverse learners.

Methods

This study develops and evaluates a media-pedagogical intervention through a serious game. The learning environment follows the Technological Pedagogical Content Knowledge (TPACK) framework to ensure meaningful integration of digital tools. Principles of situated learning, complete action, and the Four-Component Instructional Design Model (4C/ID) guide the design of competence-oriented, practice-relevant tasks. Using a qualitative approach, learning processes are explored through continuous reflection, a research journal, and structured feedback with instructors and peers. Standardized questionnaires, including the User Experience Questionnaire, the Questionnaire on Learning with Serious Games, and the Questionnaire for Assessing Current Motivation, are used for student evaluation. The data collection is ongoing, but will be completed before WCB.

Results

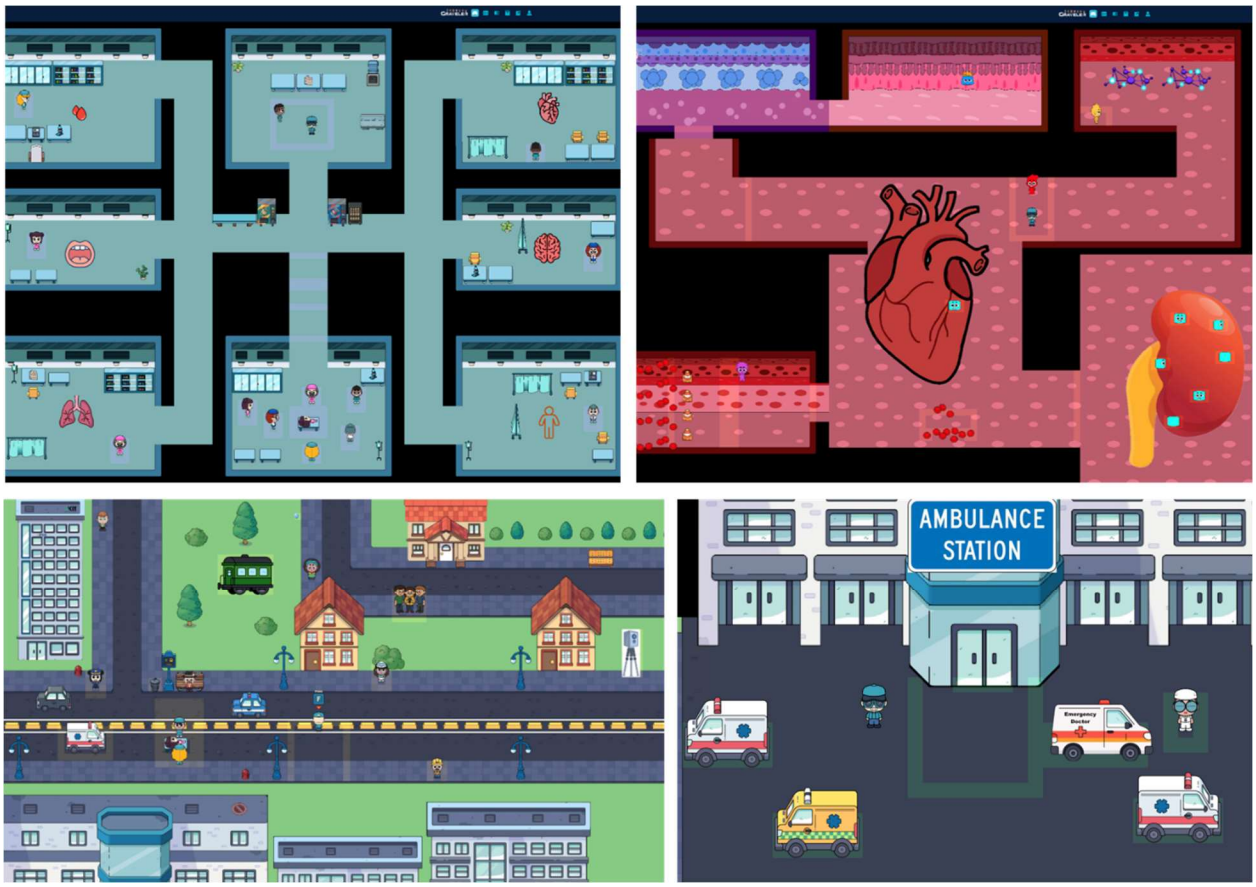
A two-dimensional online multiplayer role-playing game with integrated collection and problem-solving elements was developed, comprising six interconnected game worlds.

Students assume the role of a trainee and progress through scenarios addressing biomechanics and accident research, preclinical and clinical trauma management, and the pathophysiology of injuries. Preliminary data analysis indicates positive outcomes across all applied questionnaires. Results suggest that participants experienced enhanced motivation, engagement, and perceived learning effectiveness through the serious game intervention.

Discussion

The preliminary findings suggest that the developed serious game offers a promising approach to supporting learners with heterogeneous disciplinary backgrounds in acquiring core competencies in trauma biomechanics and emergency care. However, the ongoing evaluation will be essential to more precisely determine the magnitude of these effects and to identify design components that contribute most strongly to learning outcomes. Further iterations may refine usability, narrative integration, and alignment with curricular learning objectives.

Images (Optional)



Session Category

Biomechanics Education, Knowledge Translation and Outreach: N/A

P1-006

Does Stiffness Really Matter?The Role of Substrate Stiffness in the Mechanoresponse of Dermal Fibroblasts In Vitro

Ms. Daniela Kromer[1], Dr. Costanza Giampietro[2], Prof. Dr. Edoardo Mazza[1,2]

[1]ETHZ, Zurich, Zurich, Switzerland. [2]Empa, Duebendorf, Zurich, Switzerland

Introduction

Fibroblast mechanotransduction is widely studied using engineered substrates, yet the stiffness contribution relative to other microenvironmental factors remains unclear(1). Here, we investigate how substrate stiffness, material, surface treatment, and cell density shape the mechanoresponse of dermal fibroblasts compared with endothelial cells.

Methods

Human dermal fibroblasts and human umbilical vein endothelial cells were cultured on collagen-coated substrates of varying materials and stiffnesses. Substrates included soft (0.2kPa) and stiff (64kPa) polydimethylsiloxane (PDMS), and tissue-culture-plastic (TCP). In selected experiments, cells were activated with TGF-β1. Samples were analyzed by qPCR for mechanoregulated gene expression and immunofluorescence for morphology, cell-substrate adhesion, stiffness-responsive nuclear YAP and smooth muscle actin (α-SMA) expression.

Results

Fibroblasts displayed similar morphology, adhesion and low α-SMA levels (<2% of all cells) across all substrates. Gene expression indicated that fibroblasts respond only mildly to stiffness. Matrix-remodeling genes showed no significant stiffness-dependent changes. ACTA2 and YAP-target genes trended towards upregulation with increasing stiffness, while comparison between stiff PDMS and TCP showed a threefold upregulation, highlighting the influence of substrate material composition over stiffness.

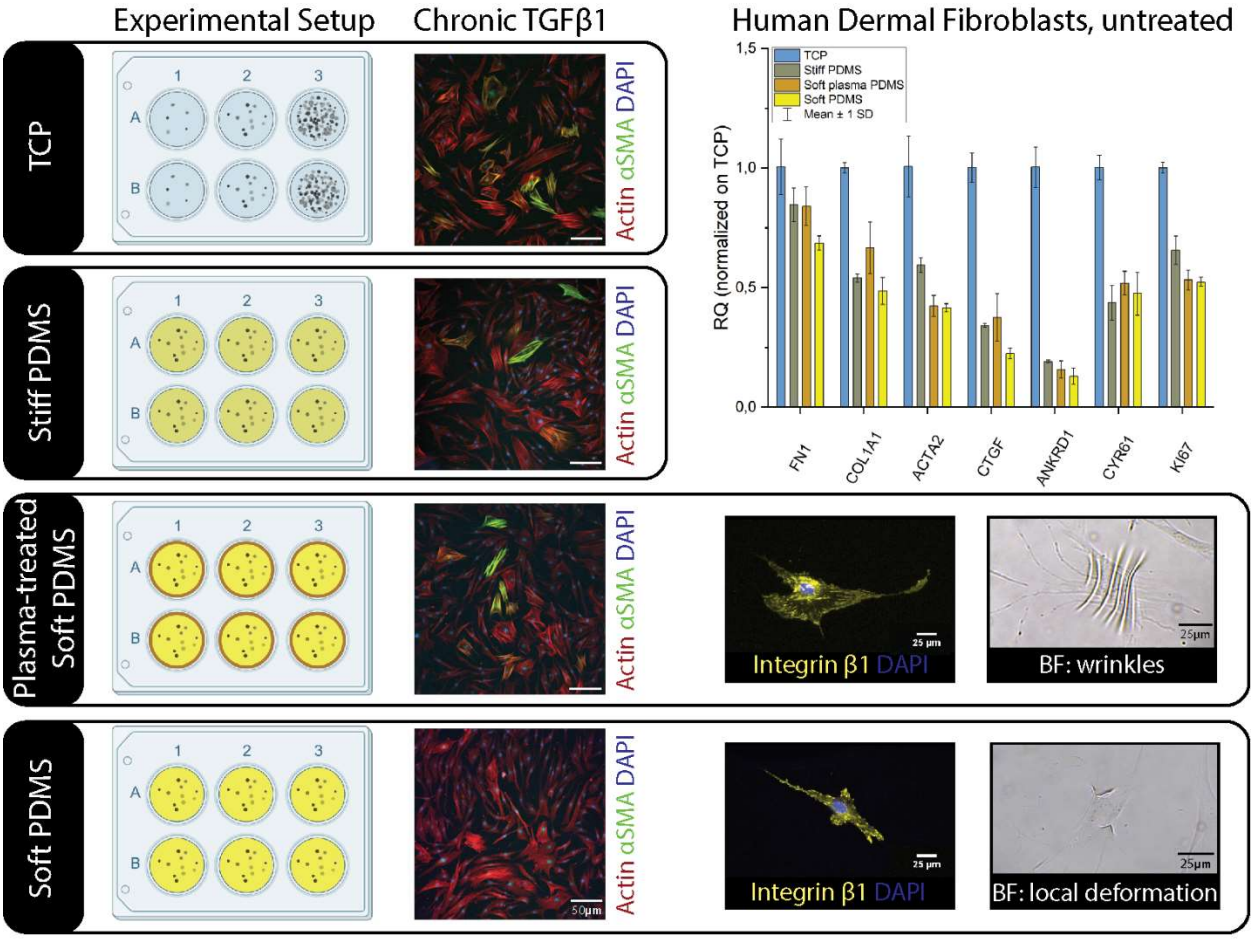
To potentiate the mechanoresponse, fibroblasts were treated with TGF-β1. Chronic TGF-β1 increased α-SMA stress fiber assembly to ~20% on TCP and ~10% on stiff or plasma-treated soft PDMS, whereas no α-SMA was assembled on soft PDMS. This suggests that under supraphysiological conditions, the stiffness-dependent response is amplified. Apart from this, fibroblasts were still able to locally deform the soft PDMS which was shown further through wrinkle formation of a stiffer surface layer added by plasma functionalization.

Compared to fibroblasts, sparse and confluent endothelial cells induced smaller mechanically deformations of soft PDMS yet displayed a faster and stronger transcriptional response to substrate stiffness. Studying sparse and confluent fibroblasts revealed cell density as a strong regulator. Together, these results reveal distinct stiffness-sensing sensitivities between fibroblasts and endothelial cells.

Discussion

Matrix stiffness plays a major role in skin pathophysiology including tissue stiffening during wound healing or fibrosis. Our results show that in vitro, substrate stiffness does not robustly activate dermal fibroblast mechanotransduction. Instead, substrate material, surface functionalization, and cell density exert stronger effects, suggesting that fibroblasts mechanoresponse in vitro is multifactorial.

Images (Optional)



References (Optional)

(1)Achterberg *et al.*, J.Invest.Dermatology,2014

Session Category

Cell Biomechanics: Mechanobiology

P1-007

Plastin-3 Influences Chondrocytes Force Transmission in a Stiffness-Dependent Manner

Ms. Daniela Maehlich[1], Ms. Franziska Busse[2], Mr. Maxim Vovchenko[3,4], Ms. Nele Vaes[3], Dr. Nils M. Kronenberg[2], Ms. Maren Dreiner[1], Dr. Miriam Weyers[1], Prof. Dr. Hans Van Oosterwyck[3,5], Prof. Dr. Malte C. Gather[2], Prof. Dr. Anja Niehoff[1,6]

[1]Institute of Biomechanics and Orthopaedics, German Sport University Cologne, Cologne, North Rhine-Westphalia, Germany. [2]Humboldt Centre for Nano- and Biophotonics, Department of Chemistry and Biochemistry, University of Cologne, Cologne, North Rhine-Westphalia, Germany. [3]Biomechanics Section, Department of Mechanical Engineering, KU Leuven, Leuven, Flanders, Belgium. [4]Laboratory for Soft Matter and Biophysics, Department of Physics and Astronomy, KU Leuven, Leuven, Flanders, Belgium. [5]Prometheus Division of Skeletal Tissue Engineering, KU Leuven, Leuven, Flanders, Belgium. [6]Cologne Center for Musculoskeletal Biomechanics, Medical Faculty, University of Cologne, Cologne, North Rhine-Westphalia, Germany

Introduction

Mechanotransduction enables cells to convert physical forces into biochemical signals, a process dependent on both the organization and dynamics of the actin cytoskeleton. Actin networks not only generate contractile tension but also transmit forces to the extracellular matrix (ECM) through focal adhesion complexes that couples stress fibers to the cell-matrix interface [1]. In articular cartilage, the ability of chondrocytes to sense and transmit mechanical forces directly governs cartilage homeostasis, matrix turnover, and degeneration. Here, we investigate how actin-binding and -bundling proteins such as plastin-3 (PLS3) modulate cytoskeletal architecture and force transmission.

Methods

Primary chondrocytes were isolated from newborn mice globally lacking (*Pls3*KO [2]) or overexpressing (*PLS3*OE [3]) PLS3 in comparison to C57BL/6N (WT) mice. 2D traction force microscopy (TFM) was performed on chondrocytes cultured for 48h on 5kPa polyacrylamide substrates embedded with fluorescent beads. Live-cell imaging simultaneously captured the cell body and bead positions in stressed and reference states, allowing to measure cell-induced displacements and to calculate cell tractions. To quantify cell-substrate deformation volumes on a nanometer-scale level, Elastic Resonator Interference Stress Microscopy (ERISM) [4] was applied. ERISM provides high sensitivity and enables stiffness comparison across 5kPa and 34kPa as well as measurements on two

different time-points (after 48h and 72h), offering a complementary assessment of chondrocyte force transmission.

Results

*Pls3*KO cells generated significantly ($p<0.05$) higher traction forces compared to WT chondrocytes, while displaying smaller traction foci. Cell area was similar across genotypes and stiffnesses after 48h, after 72h *Pls3*KO cells exhibited the largest reduction in cell area shifting from soft to stiff ($p=0.07$). In contrast, normalized indentation volume in *Pls3*KO chondrocytes was significantly higher than for WT and *PLS3*OE cells on soft (5kPa) substrates at both 48h and 72h, while this difference was lost on stiff (34kPa) substrates after 48h due to reduced indentation volume in *Pls3*KO cells under higher stiffness.

Discussion

PLS3 appears essential for early focal adhesion organization and initial force transmission, while compensatory mechanisms likely override its role in mature cytoskeletal states.

References (Optional)

[1] Martino *et al.,* Front Physiol,2018

[2] Ackermann *et al.,* Hum Mol Genet,2013

[3] Neugebauer *et al.*, Hum Mol Genet,2018

[4] Kronenberg *et al.,* Nat Cell Biol,2017

Acknowledgements (Optional)

This project is funded by German Research Foundation (DFG project no. 407176282/FOR 2722 and 384170921/FOR 2722).

Session Category

Cell Biomechanics: Mechanobiology

P1-008

Strain-Dependent Gene Expression and Remodeling by Tricuspid Valve Interstitial Cells

Dr. Devin Laurence Ph.D., Dr. Stanley Stachelek Ph.D., Mrs. Emily Hall M.S., Ms. Xiaoqiu Yang M.S., Dr. Matthew Jolley M.D., Dr. Robert Levy M.D.

Children's Hospital of Philadelphia, Philadelphia, PA, United States

Introduction

The tricuspid valve is the primary functioning heart valve for children with hypoplastic left heart syndrome (HLHS). These patients undergo surgical palliation to transition the right ventricle to handle oxygenated blood flow. This significantly increases the transvalvular pressure, and at least 40% of patients will develop tricuspid valve regurgitation (highly associated with heart failure) within 20 years of birth [1]. Our group has demonstrated aberrant serotonin (5-HT) receptor (HTR) signaling contributes to mitral valve degeneration [2] and mechanosensitive ion channels mediate these processes (under review). We hypothesize that the elevated pressure resulting from surgical palliation of HLHS triggers tricuspid valve remodeling via HTR.

Methods

Human tricuspid valve interstitial cells obtained with IRB approval were cultured on a commercial tension bioreactor system (FlexCell FX6000) at user-defined strain (0%, 10%, 20%) for 72 hours. Following a preliminary screening, we included an antagonist for the TRPC6 mechanosensitive ion channel. Specific endpoints included qRT-PCR of 5-HT signaling genes and pro-collagen 1 ELISA. Statistical comparisons were made via one-way ANOVA following Shaprio-Wilk normality test, with $p<0.05$ deemed significant.

Results

Our results (Figure 1) showed that elevated strain led to increased collagen gene expression and pro-collagen 1 secretion. Interestingly, TRPC6 antagonism mitigated these processes and resulted in a significant reduction in HTR2B gene expression, suggesting functionality up-stream of HTR signaling.

Discussion

This is the first investigation to demonstrate the strain-dependent response of tricuspid valve interstitial cells. Our findings have implications for children with HLHS and adults with pulmonary hypertension, in which the tricuspid valve experiences increased transvalvular pressures. Specifically, we showed larger strains elicit elevated

COL1A1/COL3A1 gene expression and pro-collagen secretion that would stiffen the leaflets and may lead to the development of tricuspid regurgitation. Furthermore, we demonstrated TRPC6 mechanosensitive ion channels contribute to these observations. This agrees with prior renal studies [3] and warrants further investigation. We are expanding this study to characterize the presence and role of TRPC6 (and other mechanosensitive ion channels) and to dissect the pro-fibrotic signaling pathways.

Images (Optional)

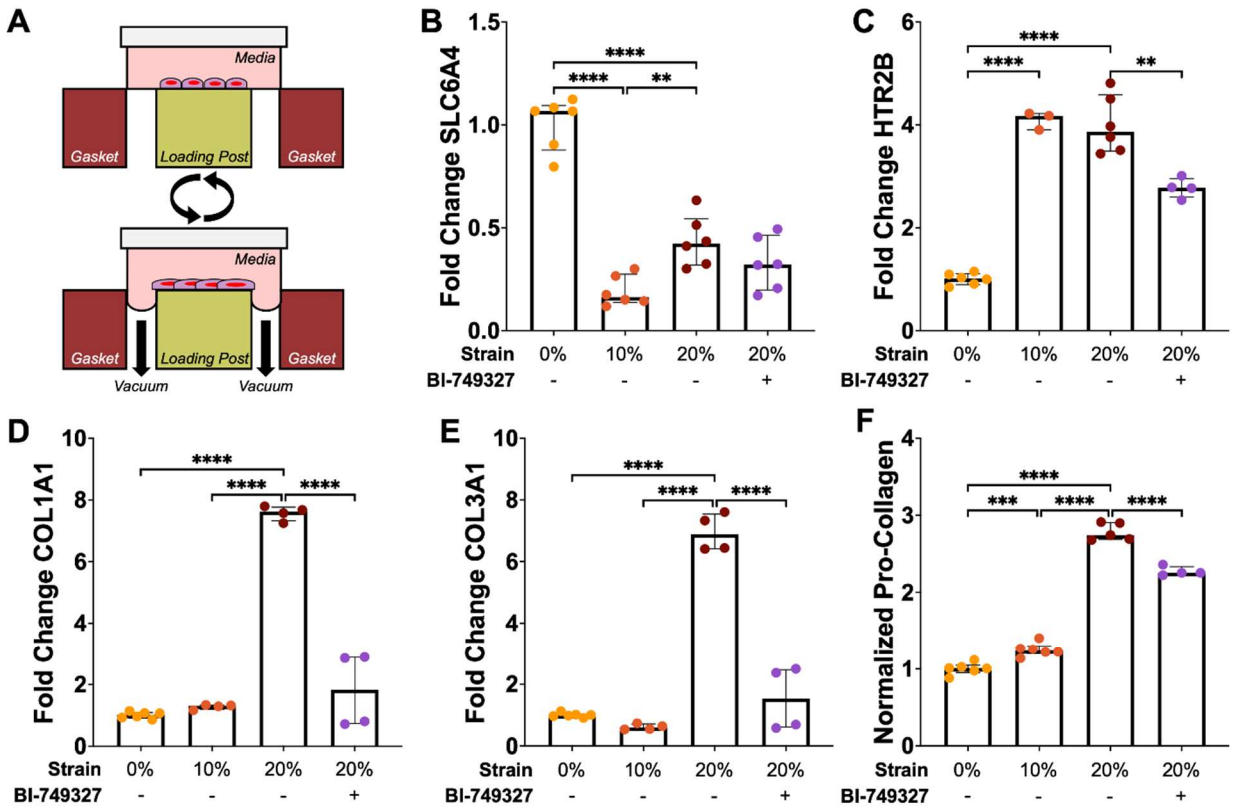


Figure 1. (A) Schematic of FlexCell FX6000 used for cyclic tension studies. (B-E) Fold change of SLC6A4, HTR2B, COL1A1, and COL3A1 gene expression at different strains with respect to static control quantified via qRT-PCR. (F) Pro-collagen 1 secretion normalized to static control quantified via ELISA. **p<0.01, ***p<0.001, ****p<0.0001.

References (Optional)

[1] King, G., et al., JACC, 2022.

[2] Castillero, E., et al., Cardiovasc. Path., 2025.

[3] Wu, Y-L., et al., Kidney International, 2017.

Acknowledgements (Optional)

This work was supported by NIH grants T32HL007915, R01HL131872, R01HL131872-S1, a CHOP Innovation Grant, the Topelowski Endowed Chair, and the CHOP Valve Center.

Session Category

Cell Biomechanics: Mechanobiology

P1-009

Calibrating Hyper-Compliant Microparticles to Quantify Microscale Forces in 3D Tissues

Mr. Dongwon Ha Ph.D. Student, Ms. Graylen Chickering Ph.D. Candidate, Professor Eric Darling Ph.D., Professor Haneesh Kesari Ph.D.

Brown University, Providence, Rhode Island, United States

Introduction

Understanding the mechanical forces that emerge within developing tissues is essential because these forces regulate how cells proliferate, migrate, and organize, ultimately shaping tissue architecture and governing key developmental and morphogenetic processes. To quantify these forces, we employed hyper-compliant microparticles (HCMPs) as force sensors to measure microscale pressure distributions [1]. To reliably use HCMPs as force sensors, it is necessary to first characterize their mechanical behavior.

Methods

HCMPs were fabricated using an inverse polymerization protocol [2]. Because the sensors are hydrogel-based, they were modeled as hyperelastic materials, and a Neo-Hookean constitutive model with two unknown parameters was selected for simplicity and parameter identifiability.

To determine these parameters, we performed two independent experiments: (1) atomic force microscopy (AFM) indentation and (2) osmotic pressure testing. AFM indentation was carried out using a spherical bead tip to compress the HCMPs, and the resulting force–displacement curves were analyzed using both the classical Hertz contact model and finite element methods (FEM). For the osmotic pressure experiments, polyethylene-glycol (PEG) solutions of varying concentrations were prepared to generate controlled osmotic pressures [3]. HCMPs were immersed in each solution and equilibrated for 12–24 hours. Following equilibration, confocal microscopy was used to measure the deformation of individual HCMPs. 3D finite element meshes were constructed by stacking 2D images. These 3D meshes used as inputs to FEM, which predicted the pressure exerted on the HCMPs. The predicted pressures were compared with the known osmotic pressures, which served as the ground-truth values for calibration.

Results

By jointly calibrating the indentation and osmotic pressure datasets, we determined that the force sensor possess a Young’s modulus of 890 Pa and a Poisson’s ratio of 0.3. The

calibrated model accurately reproduced the experimentally observed pressure–stretch behavior. Notably, the measured Poisson's ratio contradicts the common assumption that polyacrylamide hydrogels behave as nearly incompressible materials.

Discussion

These calibrated, ultra-soft force sensors enable precise quantification of cell-generated traction forces in microtissues while allowing microscale measurements with minimal disturbance to overall tissue structure.

References (Optional)

[1] Robert A. Gutierrez *et al.*, Biomaterials, 2021
[2] Nicholas R. Labriola *et al.*, Biomaterials Science, 2017
[3] Kinuko Masaki *et al.*, Biophysical Journal, 2006

Session Category

Cell Biomechanics: Mechanobiology

P1-010

Investigating Bone Cell Mechano-sensitivity in Breast and Prostate Cancer Patients

Miss Eisha Hashmi BEng[1], Dr Stefaan Verbruggen BEng, PhD, FHEA[1,2]

[1]Queen Mary University of London, London, Greater London, United Kingdom. [2]The University of Sheffield, Sheffield, South Yorkshire, United Kingdom

Introduction

Bone metastasis is a major cause of pain in advanced breast and prostate cancer. Although interactions between metastatic cells and the bone microenvironment are recognised [1], the role of osteocytes—most abundant bone cells and primary mechanosensors—remains underexplored. Osteocytes regulate mechanical environment through peri-lacunar remodelling, which may be disrupted in cancer [2] and alter osteocyte mechanics (preliminary work). Metastatic progression is also marked by dendritic loss and reduced lacuno-canalicular connectivity [2]. As dendrites are primary mechanosensory sites [3], we hypothesise that their progressive loss alters mechanotransductive signalling in cancer-altered bone.

Methods

Idealised multiphysics models were developed with osteocyte and lacuna modelled as ellipsoids (7.5×13.5μm;9×15μm), and processes and canaliculi as branching channels (Ø=0.44μm;Ø=0.6μm)–reduced by symmetry to the layout in Fig1A–B. The cell was defined as a linear elastic solid (E_{cell}=4.47kPa;ν_{cell}=0.3) and the pericellular matrix (PCM) as viscous fluid (μ_{PCM}=0.000855kg/m·s;ρ_{PCM}=997kg/m3) [4]. Metastatic deterioration was simulated by removing single, paired, triple, or all processes, with voids replaced by PCM. Interstitial flow was applied at 60μm/s, and mechanical response assessed using one-way fluid–structure interaction.

Results

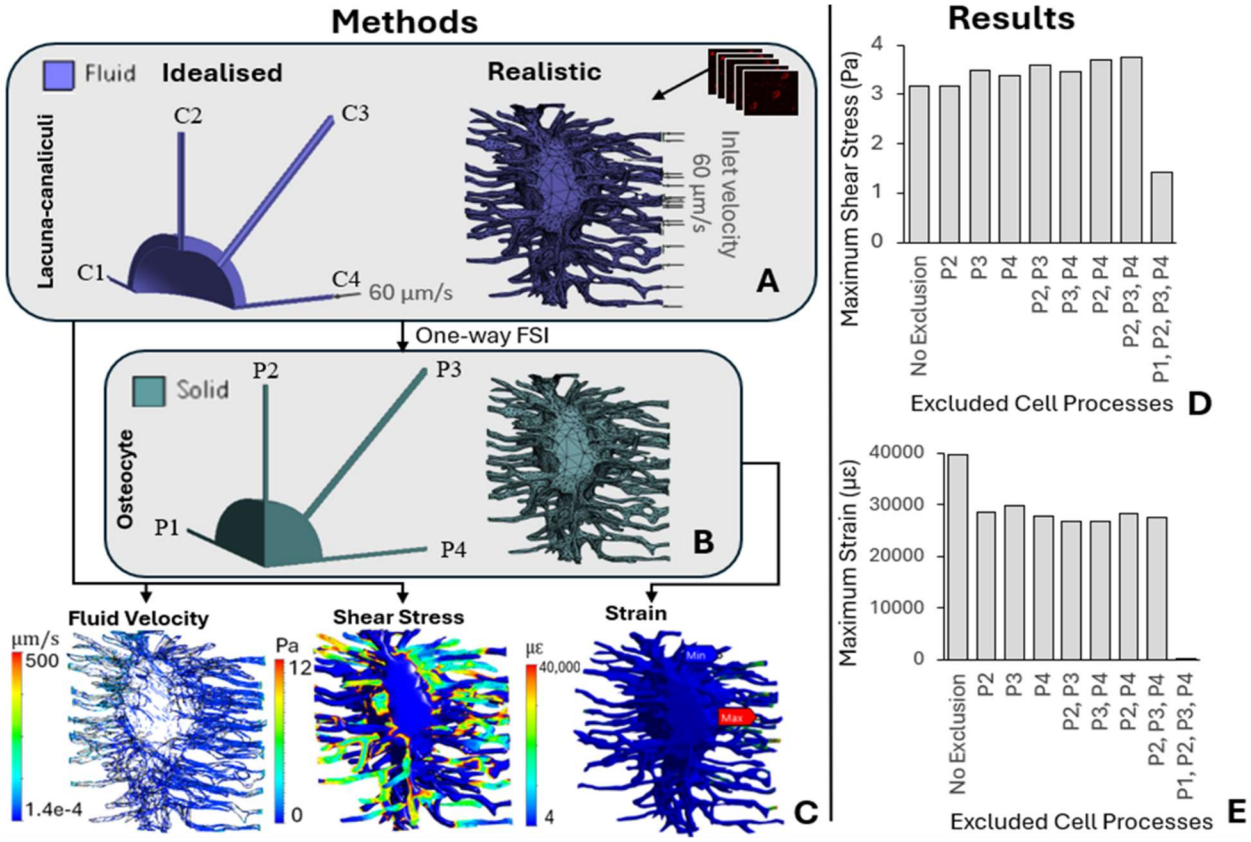
Membrane shear stress remained 3-4Pa under partial deletions but decreased to ~1.5Pa without processes. Maximum strain dropped from ~40,000 to ~30,000με after single deletion, with minimal further decline until complete removal, which reduced strain to near-zero.

Discussion

This study examined how process loss alters osteocyte mechanical cues. Shear-based mechanotransduction remained preserved—even with complete process removal—as osteogenic responses occur at ~0.8Pa [6], whereas strain-mediated signalling was

abolished; suggesting that dendrites are more critical for strain amplification than shear sensing, and osteocytes may be more mechanically robust than previously assumed. Limitations include idealised geometry and pressure-driven flow. Ongoing work incorporates realistic osteocyte geometries and two-way FSI to better predict mechanosensory failure thresholds and inform strategies to preserve osteocyte connectivity in metastatic bone.

Images (Optional)



References (Optional)

[1] James Stinson, Med Hypotheses, 1975

[2] Haniyeh Hemmatian et al., Bone, 2021

[3] Sirisha Burra et al., Proc Natl Acad Sci U S A, 2010

[4] Stefaan Verbruggen et al., Biomech Model Mechanobiol, 2014

[5] Jun You et al., J Biomech Eng, 2000

[6] Neal Chen, Am J Physiol Cell Physiol, 2000

Session Category

Cell Biomechanics: Mechanobiology

P1-011

Impact of Simulated Microgravity on Chorioretinal Cell Fate and Epithelial-to-Mesenchymal Transition

Ms. Emily Formella, Dr. Kristan Worthington, Mr. Richard Cliver

University of Iowa, Iowa City, Iowa, United States

Introduction

Spaceflight-associated neuro-ocular syndrome (SANS) is a condition seen in long-duration astronauts that is characterized by increased intracranial pressure, retina structural changes, and visual impairment. Exposure to microgravity has been identified as a primary risk factor of SANS, but the underlying cellular mechanisms are not fully understood. Microgravity is known to disrupt biomechanical signaling in many human cell types, and comparable disruptions are associated with pathological changes in retinal pigmented epithelial (RPE) cells and potentially in choroidal vascular endothelial cells (ChEC) in other ocular diseases. In this study, we aim to characterize the impact of simulated microgravity on the fate of RPE cells and investigate the role of epithelial to mesenchymal transition (EMT) in this response.

Methods

ARPE-19 cells were seeded onto Cytodex3 (C3) microcarrier beads in a low-attachment plate at a density of 200,000 cells/cm2 of C3 surface area. After allowing 24 hours for attachment, cell-coated beads were transferred to a rotating wall vessel bioreactor to simulate microgravity. Cells were cultured in simulated microgravity for a maximum of seven days with samples collected at periodic intervals to assess viability and gene expression. Viability was assessed via fluorescent staining with Calcein AM and Ethidium Homodimer-1, and gene expression was analyzed by qPCR targeting RPE genes (e.g., RPE65, CDH3, KRT18, TJP1) and mesenchymal markers (e.g., ACTA2, CDH2, SNAI1, VIM) of interest.

Results

RPE cells grown on microcarrier beads (Fig.1A) maintained high viability (>80%, Fig.1B) and cell number over seven days under standard gravity and simulated microgravity conditions. In our preliminary experiments, simulated microgravity elicited significant upregulation of RPE65 compared to standard Earth gravity (Fig.1C) but did not substantially impact EMT gene expression.

Discussion

These findings demonstrate the feasibility of using a rotating wall vessel bioreactor to study RPE cells in a mechanically altered environment. In our ongoing studies, we are replicating these conditions for additional rigor. At the same time, we recognize that the use of immortalized cells may contradict the expected biomechanical response. Thus, we are applying the same approach to iPSC derived RPE cells and expanding the study to include iPSC derived ChECs.

Images (Optional)

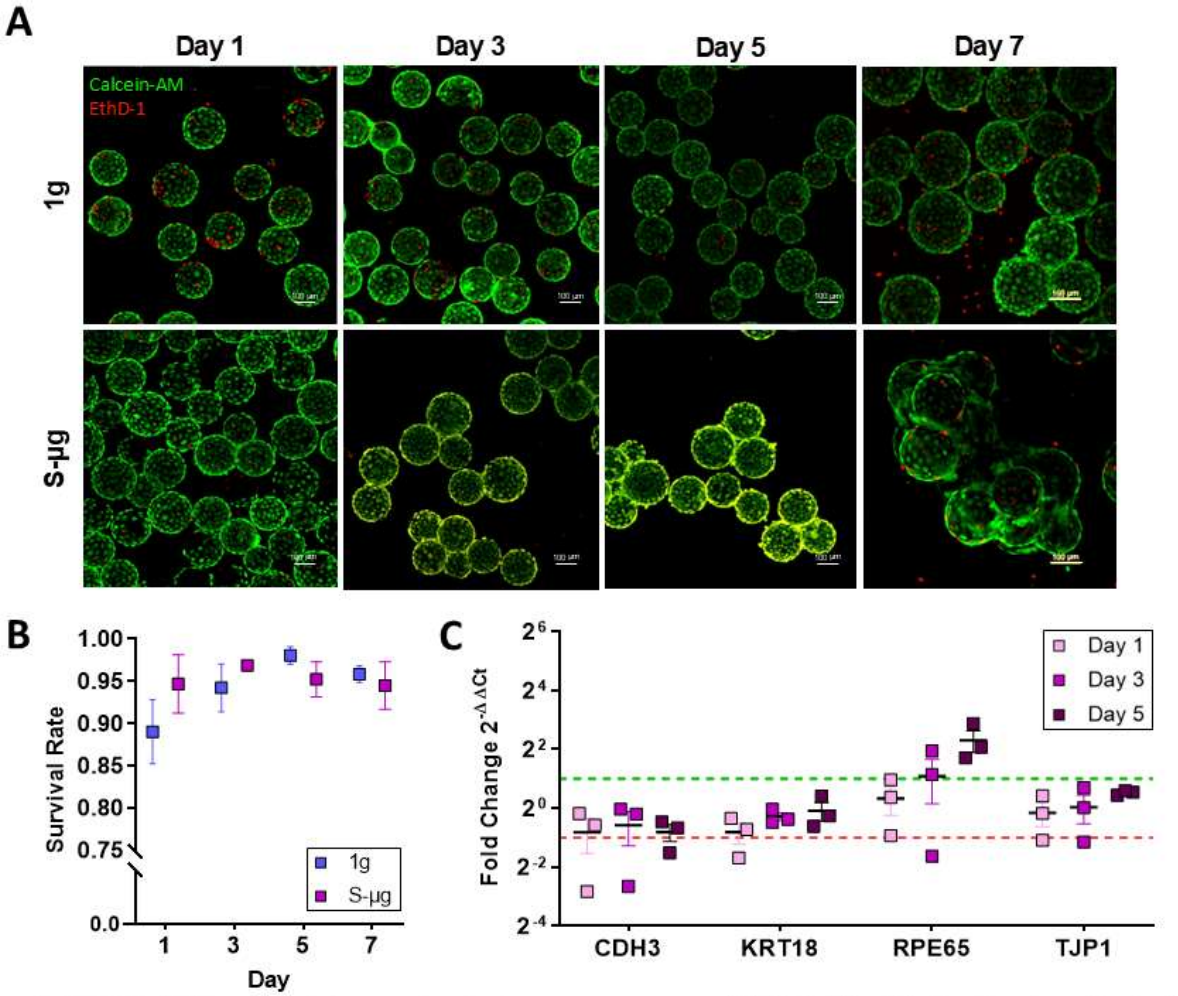


Figure 1. A) Representative confocal microscopy images of ARPE-19 cell-laden beads subjected to standard gravity (1g) and simulated microgravity (S-µg); Scale bar = 100 µm. Average cell density increased from 38.5 ± 18.5 to 172.7 ± 38.3 cells/bead across a 7-day culture period. **B)** Mean cell viability in 1g and S-µg groups (error bars show 95% CI). **C)** Relative expression of target RPE genes across five days in S-µg, normalized to 1g controls (mean ± SEM, n = 3).

Session Category

Cell Biomechanics: Mechanobiology

P1-012

Multimodal Imaging Enables Functional Characterisation of Gene Mechanoregulation During Bone Regeneration

Dr Francisco Correia Marques[1], Dr Neashan Mathavan[1], Mr Jack J. Kendall[1], Dr Amit Singh[1], Dr Dilara Yilmaz[1], Ms Denise Günther[1], Dr Gisela A. Kuhn[1], Dr Friederike A. Schulte[1], Dr Esther Wehrle[1,2], Prof. Dr Ralph Müller[1]

[1]ETH Zürich, Zürich, Zürich, Switzerland. [2]AO Research Institute, Davos, Davos, Switzerland

Introduction

Multimodal imaging approaches reveal mechanobiological processes across spatial scales. In bone, 3D micro-computed tomography (micro-CT) images can be correlated with 2D spatial transcriptomics data from the same sample using Spatial µProbe [1], linking gene expression with the mechanical environment determined by micro-finite element (micro-FE) analysis. In highly dynamic processes like bone regeneration, mechanical loading strongly influences healing outcomes [2]. However, molecular effectors involved in this response are still poorly understood. Here, we evaluate the expression of functionally-relevant genes under mechanical loading in a preclinical model of bone regeneration.

Methods

Four 12-week-old female BCR mice received mid-diaphyseal femoral defects, and individualised cyclic loading via an external fixator (n=2, Loaded) or 0N-loading (n=2, Control) from three weeks post-surgery [1-3]. Weekly *in vivo* micro-CT (10.5 µm, vivaCT80) was performed until sacrifice five weeks post-surgery. Structurally intact sections (n=1/group) were processed using the 10x Genomics Visium FFPE protocol [2-3]. 2D Visium sections were optimally positioned in 3D using Spatial µProbe and bone pixels were labelled with bone formation timepoints identified with micro-CT (Fig.1a). Time-lapsed gene expression was modelled with generalised additive models (GAM), followed by clustering per dataset. Functional characterisation was performed with g:Profiler [4] to genes that clustered together on both Loaded and Control samples (min. 3). Correlation between GAMs was assessed using Spearman coefficient ρ.

Results

Agglomerative clustering successfully identified groups of genes involved in vital musculoskeletal functions during healing. Leveraging time-lapsed information, our data suggests that muscle-related processes (e.g., aerobic respiration) are maintained

(ρ=0.837, Fig.1b) upon mechanical loading. Comparably, biological functions directly linked to bone mechanobiology showed stronger variations, including skeletal system development and oxygen transport (with lower ρ=0.687 and 0.561), and reduced cell migration from week 3 (ρ=0.475), indicating controlled remodelling activity.

Discussion

Mechanical loading targets functionally-relevant processes in multiscale bone mechanoregulation. These temporally and spatially distinct events can only be captured via multimodal imaging approaches. Spatial µProbe unlocks 2D-3D multimodal registration of time-lapsed data, enabling the quantification of these changes, inferring potential drivers and advancing our understanding of mechanical signalling and molecular biology towards novel healing therapies.

Images (Optional)

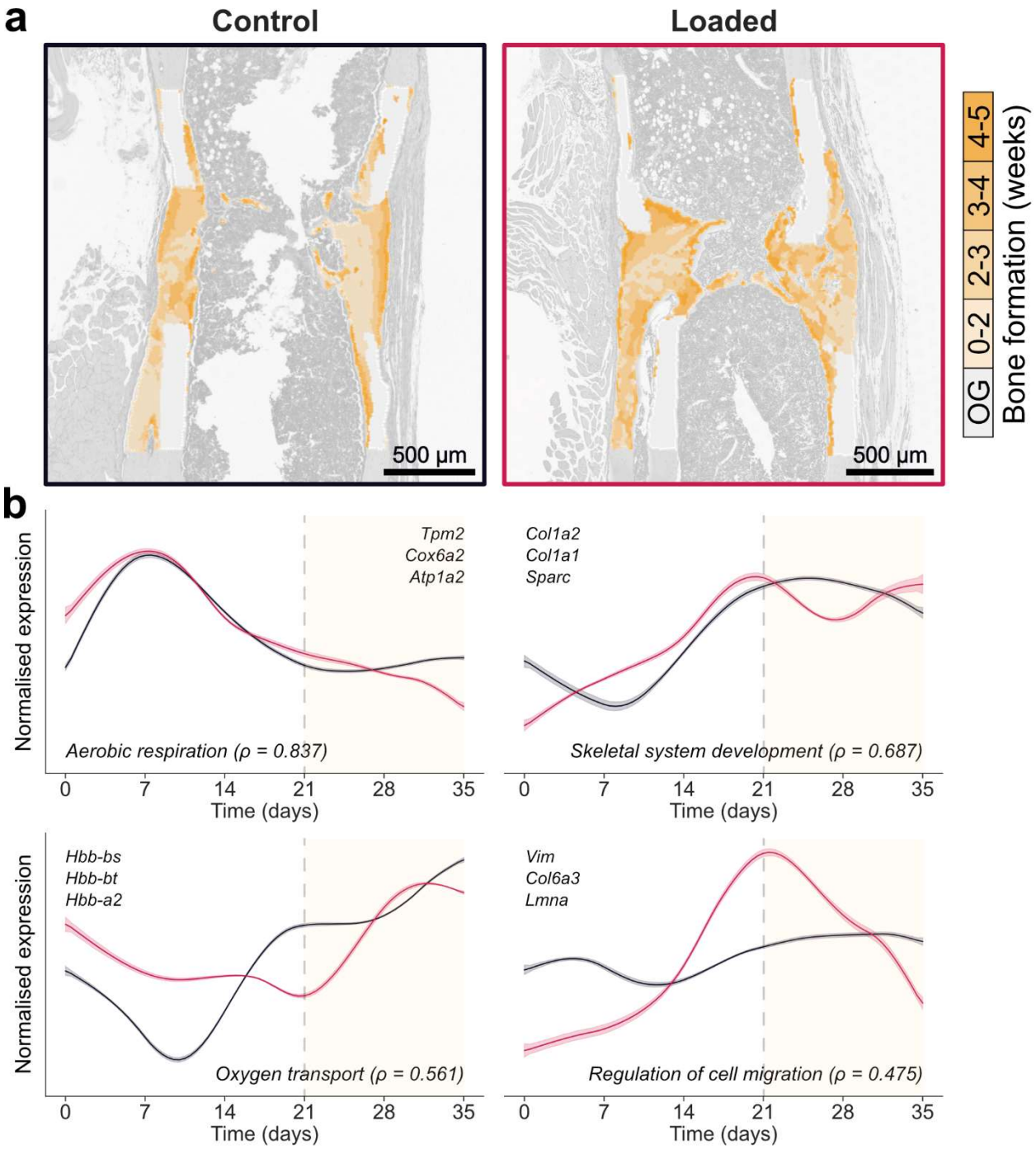


Figure 1: Functional gene mechanoregulation analysis. a) Bone formation regions identified with time-lapsed *in vivo* micro-CT and mapped to the 2D-3D registered ST section of the Control and Loaded samples. b) Comparison between the normalised expression of gene-sets between Control (black) and Loaded (red) samples. The top three most expressed genes are listed. A functionally-relevant significant enrichment term identified with g:Profiler is indicated. Spearman correlation coefficient between the curves obtained for both samples is indicated as a proxy for the change in expression trends resulting from cyclic mechanical loading.

References (Optional)

[1] C.Marques etal.,bioRxiv,2025

[2] Mathavan etal.,SciAdv,2025

[3] Wehrle etal.,STARProtocols,2024

[4] Kolberg etal.,NucleicAcidsResearch,2023

Acknowledgements (Optional)

ERC-2016-ADG-741883,MSCA-IF-2020-101029062,IZCOZ0198152

Session Category

Cell Biomechanics: Mechanobiology

P1-013

Cholesterol Depletion Disrupts Cortical Actin Organization, Rewires Metabolism, and Overcomes Drug Resistance in Cancer Cells Within 3D Microstuctured Scaffold

Mr Giovanni Buccioli[1], Ms Cristina Cortesi[1], Dr Chiara Martinelli[1], Dr Claudio Conci[1], Dr Alessandra Nardini[2], Dr Rebeca Martínez Vázquez[2], Prof Manuela Teresa Raimondi[2], Prof Emanuela Jacchetti[1]

[1]Department of Chemistry, Materials and Chemical Engineering "Giulio Natta", Politecnico di Milano, Milan, MI, Italy. [2]Institute for Photonics and Nanotechnologies, CNR, Milan, MI, Italy

Introduction

Multidrug resistance (MDR) in tumours is often sustained by efflux pumps whose activity is dictated by plasma-membrane organisation and mechanics, governed by cholesterol within lipid rafts and by the architecture of the cortical actin network [1]. Moreover, a glycolytic metabolic programme is a well-recognised hallmark of MDR, supplying the ATP demanded by these pumps. However, conventional 2D cultures fail to recapitulate native membrane structure and tumour metabolism. Here, using 2D and 3D substrates, we investigate whether cholesterol depletion disassembles the cortical actin network and thereby rewires cellular metabolism to enhance chemosensitivity.;

Methods

The custom-made 3D scaffold, named the Niche, consists of a lattice of cubic pores ($15\times15\times15\ \mu m^3$) fabricated via two-photon polymerization in biocompatible resin SZ2080 onto glass coverslip [2]. MCF7 and MDA-MB-231 cells were cultured on 2D glass coverslips and the 3D Niche. Cell viability was assessed after 24h under a Doxorubicin concentrations (4.4 μM on glass, 103.5 μM on Niche) with/without Lovastatin (1 μM). Cortical actin organization was assessed by immunofluorescence images; fluorescence-lifetime (FLIM) imaging microscopy inferred cell metabolism.

Results

Only cells cultured within the 3D microstructured scaffold and treated with Lovastatin showed a clear disassembly of the cortical actin network (Fig. 1) together with a reduced reliance on glycolysis. Under these conditions, cells displayed increased chemosensitivity to Doxorubicin, consistent with decreased efflux pump capacity in the 3D setting.

Discussion

These findings identify plasma membrane and cortex mechanics as central regulators of multidrug resistance, with cholesterol dependent membrane organisation and cortical actin integrity emerging as key control points for efflux pump function. The 3D scaffold does not simply provide a culture support, but recreates tumour relevant architectural cues that make this mechanotransduction axis measurable and drug responsive, in contrast to 2D substrates. By better approximating the structural context in which resistance is maintained, the Niche enhances the predictive value of *in vitro* testing and supports mechanistic, scaffold based screening of strategies that target cholesterol and the actin cortex to restore chemosensitivity.

Images (Optional)

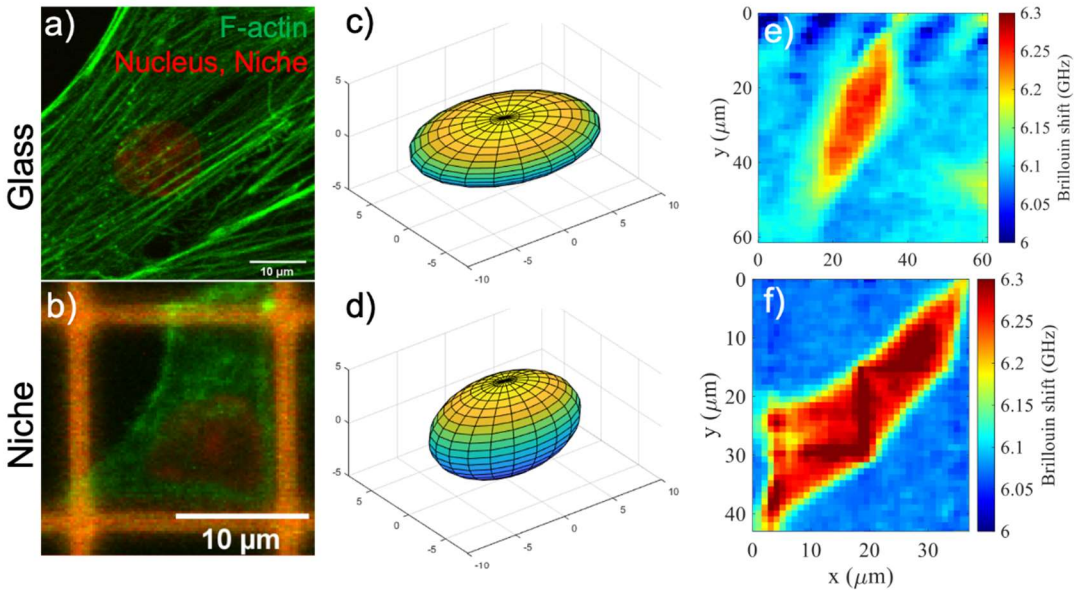


Fig. 1 Representative characterisation of MSCs on 2D glass and in the 3D Niche. (a,b) Immunofluorescence of F-actin (green), nuclei and Niche scaffold (red), showing stress fibres in 2D and predominantly cortical actin in the Niche. (c,d) Nuclear shapes modelled from morphometric parameters, flatter in 2D and rounder in 3D. (e,f) Brillouin shift maps highlighting differences in intracellular mechanical properties between 2D and 3D culture.

References (Optional)

[1] Buccioli et al, Sci Rep 14, 20298, 2024.
[2] Martinelli et al, Mater Today Bio 35, 102328, 2025

Acknowledgements (Optional)

Acknowledgements

Ministero dell’Università e della Ricerca (PRIN2022-VISION, cod. 2022FLXS8T); ERC (project BEACONSANDEGG, G.A. 101053122); European Union’s Horizon 2020 research and innovation programme (project flIMAGING3D, G.A. 101073507)

Session Category

Cell Biomechanics: Mechanobiology

P1-014

Rescue of Plasma Membrane Localization of Mislocalized Pendrin Mutants by Low-Dose Lasalocid a Sodium

Mr. Goki Nagasaki, Hisashi Sugimoto, Tomokazu Yoshizaki, Michio Murakoshi

Kanazawa University, Kanazawa, Ishikawa, Japan

Introduction

Pathogenic mutations of pendrin (SLC26A4), which is an anion exchanger expressing in the inner ear, thyroid gland and kidneys, often result in misfolding and intracellular mislocalization, being responsible for Pendred syndrome and non-syndromic hearing loss. In our previous studies, pharmacological chaperones have been proposed as a therapeutic approach; however, only limited small molecules such as salicylate derivatives have been reported, and their effective concentrations were relatively high. In the present study, Lasalocid A sodium, one of the salicylic-acid derivatives, was examined whether it can rescue plasma membrane localization of mislocalized pendrin mutants at lower concentrations and evaluated its cytotoxicity.

Methods

Human embryonic kidney(HEK)293 cells were transfected with FLAG-tagged wild-type pendrin or eight mislocalized mutants. Cells were treated with Lasalocid A sodium at 1 mM, 0.1 mM, 0.01 mM or 1 μM for 12–24 h, and plasma membrane localization was assessed by Wheat germ agglutinin (WGA) staining and FLAG immunofluorescence using a confocal microscope. Cell viability was measured by Cell Counting Kit-8 (CCK-8), and cytotoxicity was assessed by LDH release.

Results

Three responsive mutants showed relocation from the cytoplasm to the plasma membrane by treatment with 1-mM Lasalocid A sodium. Notably, 0.01-mM Lasalocid A sodium also induced plasma membrane localization in these mutants, whereas 1-μM dose did not show such changes in localization. The remaining mutants could not be restored by Lasalocid A sodium at 1mM, 0.1mM, 0.01mM and 1μM.

In toxicity assays, cell viability sharply decreased above 0.005 mM, and cell toxicity increased above 0.02 mM. Concentrations of 1-mM and 0.1-mM Lasalocid A sodium markedly reduced viability, whereas 0.01 mM maintained high viability (85–82%).

Discussion

In previous studies, differences in substituent patterns around the benzene ring and the presence of a 1,3-propanediol moiety were shown to markedly influence the activity of salicylate derivatives used to improve pendrin localization. Notably, Lasalocid also possesses a 1,3-propanediol moiety, and its enhanced potency in the present study may similarly arise from such structural features, enabling more effective interaction with partially foldable mutants. This mechanism may explain its ability to restore plasma membrane localization at substantially lower concentrations than conventional derivatives.

References (Optional)

[1] Ishihara Kenji et al., Hear Res, 2010.

[2] Michio Murakoshi et al., Auris Nasus Larynx, 2022.

[3] Wataru Nabeyama et al., Bioorg Med Chem, 2017.

Session Category

Cell Biomechanics: Mechanobiology

P1-015

Vaping-Induced Injury in Human Lymphatic Endothelial Cells

Ms. Hoda Rahimi[1], Dr. Jiwon Hong[1], Dr. Sam McCullough[2], Mr. Ben Watkin[2], Dr. Justin Rustenhoven[2], Prof. Anthony Phillips[1,3], Assoc. Prof. Kelly Burrowes[4]

[1]School of Biological Sciences, Faculty of Science, University of Auckland, Auckland, Auckland, New Zealand. [2]Department of Pharmacology, Faculty of Medicine and Health Sciences, University of Auckland, Auckland, Auckland, New Zealand. [3]Department of Surgery, Faculty of Medicine and Health Sciences, University of Auckland, Auckland, Auckland, New Zealand. [4]Auckland Bioengineering Institute, University of Auckland, Auckland, Auckland, New Zealand

Introduction

Pulmonary lymphatic endothelial cells (LECs) help maintain lung fluid balance and immune surveillance, but their response to e-cigarette aerosols is poorly understood. We developed an induced pluripotent stem cell (iPSC)–derived human LEC (iLEC) model to quantify flavor-specific toxicity and barrier disruption as a first step toward biomechanical and computational models of vaping-exposed lung lymphatics.

Methods

Human iPSCs were differentiated to iLECs using mesoderm/lymphatic induction and CD31-based sorting. iLECs were exposed for 24 h to two flavored e-liquids (Flavor A: mint berry; Flavor B: premium red) at 0.15–1.5 mg/mL nicotine, a nicotine-free PG/VG vehicle, and a negative control (no exposure). Cytotoxicity was assessed by LDH release and normalized to a positive control. Immunocytochemistry quantified VE-Cadherin junctional coverage and Hoechst nuclear counts using a standardized image-analysis threshold. In parallel, we are performing experiments using a programmable vaping machine to generate vaping aerosol condensate, exposing iLECs and measuring inflammatory activation, procoagulant signaling and barrier integrity.

Results

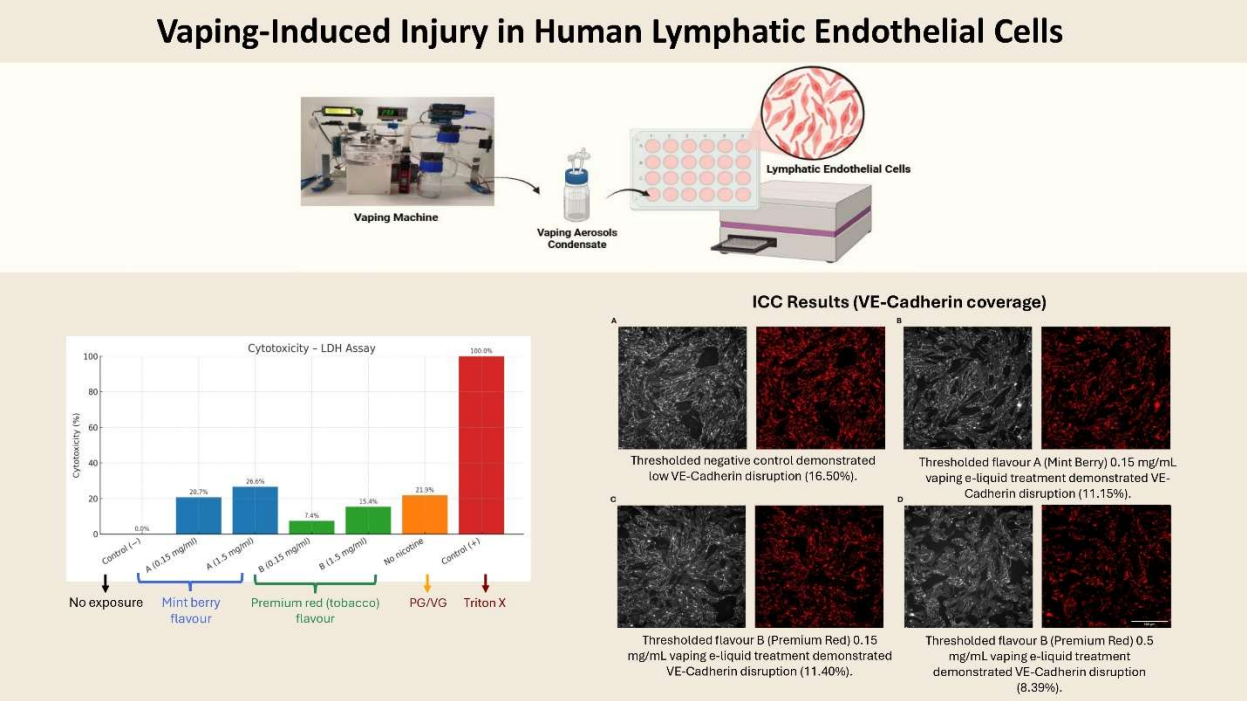
LDH assays showed a flavor-dependent toxicity profile. Mint-berry Flavor A increased cytotoxicity to 20.7% at 0.15 mg/mL and 26.6% at 1.5 mg/mL. Premium-red Flavor B caused lower toxicity (7.4% and 15.4% at 0.15 and 1.5 mg/mL, respectively), whereas the nicotine-free PG/VG vehicle produced 21.9% cytotoxicity, indicating that base components alone can damage LECs. VE-Cadherin coverage fell from 16.5% in controls to 11.15% with Flavor A (0.15 mg/mL), 11.40% with Flavor B (0.15 mg/mL) and 8.39% with Flavor B (0.5 mg/mL), consistent with junctional disruption. Hoechst nuclear counts decreased from

611 nuclei in the negative control to 548 (Flavor A 0.15 mg/mL), 523 (Flavor B 0.15 mg/mL), and 427 (Flavor B 0.5 mg/mL).

Discussion

These preliminary data show that vaping e-liquids, including nicotine-free vehicle, cause measurable, flavor-dependent cytotoxicity and junctional injury when exposed directly to human LECs. Such barrier disruption is expected to alter lymphatic transport and interstitial fluid handling. Ongoing experiments using vaping-machine–generated condensate, combined with inflammatory and coagulation readouts, will extend this platform and provide quantitative inputs for biomechanical and computational models of pulmonary lymphatic system under vaping-induced stress.

Images (Optional)



Session Category

Cell Biomechanics: Mechanobiology

P1-016

How Curvature-Driven Cell Morphology Regulates Nuclear Lamina and Chromatin Architecture

Ms I-CHIA LO, Dr. Pen-hsiu Grace Chao

National Taiwan University, Taipei, Taiwan, Taiwan

Introduction

Geometric cues are key regulators of cell phenotype [1]. Size and alignment are known to influence stem cell fate, but the effects of curvature have only recently been explored [2]. We recently found wavy structures that mimic the native collagen organization increased cell traction forces and collagen expression [3]. These changes correlate with nuclear deformation and point to potential mechanisms of phenotypic regulation. In this study, we investigate the effects of wavy morphology on actin organization and nuclear shape.

Methods

Human mesenchymal stem cells (MSCs) were cultured on micro-molded agarose grooves [4]. The grooves were 15 μm in width and the wavy structures were consisted of connecting arcs with inner radii of 15 or 20 μm. Bottom of the grooves were coverslips coated with fibronectin and MSCs were cultured in these structures for 4 hours before fixation for imaging. Wrinkling Index was calculated by binarized lamin wrinkle area normalized by nuclear area (Fig 1C left).

Results

MSCs conformed to the microgrooves and exhibited elongated and wavy morphology. The straight cells formed long stress fibers with flattened nuclei. The wavy cells had arch-like actin fibers (arrowheads, Fig 1A). Their nuclei also followed the wavy pattern, were pushed against the concave side wall, and had wrinkles that colocalized with actin fibers (Fig 1B). The increase in nuclear wrinkles was accompanied by nuclear volume decrease (Fig 1C).

Discussion

Our work provides a detailed characterization of the internal structures of wavy cells. We previously found actin to be the main regulator of nuclear shape in the wavy cells [5]. The increased traction forces and reduced nuclear volume align with previous findings that elevated forces compress the nucleus and condense chromatin [2]. We are currently employing expansion microscopy to have nanoscale characterization on cytoskeleton, nuclear membrane, and heterochromatin structures to further understand the spatial

organization in the wavy cells. Findings will clarify how curvature-dependent cytoskeletal forces reshape nuclear architecture to modulate chromatin organization and phenotype.

Images (Optional)

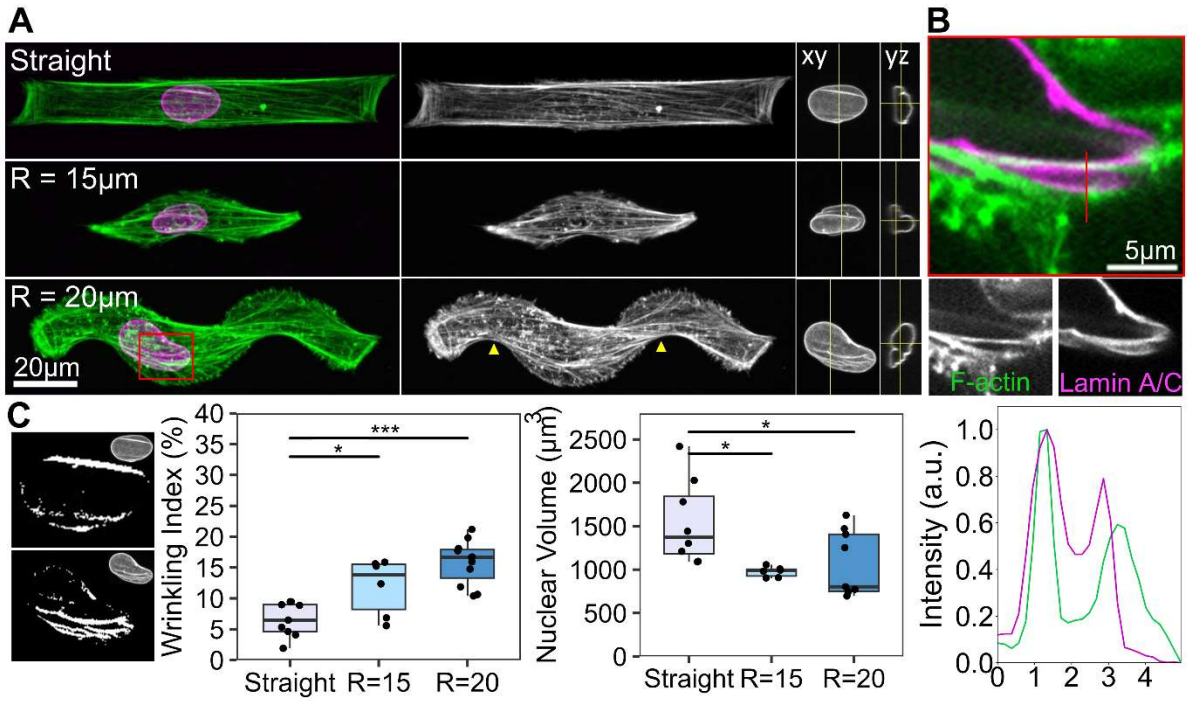


Figure 1. (A) Cells conformed to micropatterned waves. (B) Magnified region showing colocalization of actin stress fiber with nuclear membrane wrinkles. Bottom figure demonstrate colocalized intensity of actin and lamin A/C along the red line. (C) Effects of curvature on nuclear wrinkling index and volume, * $p<0.05$, ** $p<0.01$.

References (Optional)

1. Kilian KA+, PNAS, 2010
2. Versaevel M+, Nat Commun, 2012
3. Chao P-hG+, Biofabrication, 2014
4. Mercey E+, Biomaterials, 2010
5. Fu K-J and Chao P-HG. *ASCB* 2015.

Acknowledgements (Optional)

This study was supported by the Taiwanese National Science and Technology Council (NSTC 114-2221-E-002-091-MY3, 114-2923-E-002-017-MY3, and 114-2122-M-001-002).

Session Category

P1-017

Experimental Characterization and Numerical Modeling of Cell–cell Adhesion in Melanoma Using Dual Micropipette Aspiration.

Presenter Ignacio Quezada-Plaza, Presenter Aldo Abarca-Ortega

Universidad de Santiago de Chile, Santiago, Región Metropolitana, Chile

Presenter Ignacio Quezada-Plaza

Introduction

In Chile, cancer is projected to increase by 60% by 2040 [1]. Globally, the International Agency for Research on Cancer reports rising incidence and mortality for melanoma [2], highlighting the need for tools to monitor disease progression. Mechanobiology proposes stiffness and cell–cell adhesion as biomarkers; metastatic cells are softer and less adhesive than healthy cells [3]. This study quantifies cell–cell adhesion forces in melanoma using dual micropipette aspiration and explicit finite element simulations, assuming that cells with higher metastatic potential exhibit lower adhesion.

Methods

Dual micropipette aspiration tests will be performed on melanoma cells. Pairs will be selected, excluding damaged cells or aggregates. Aspiration pressure, aspirated length, deformation and detachment will be recorded to obtain force–deformation curves and cell size, from which effective stiffness, apparent viscosity and adhesion force will be estimated, considering the nuclear-to-cell diameter ratio. In parallel, an explicit quasi-static LS-Dyna model of two spherical cells with three regions (nucleus, cytoplasm, membrane) is implemented, using a Neo-Hookean solid plus Prony-series viscoelasticity. Formulations follow visco-hyperelastic models validated in previous studies [4] and will be calibrated with literature and experimental data.

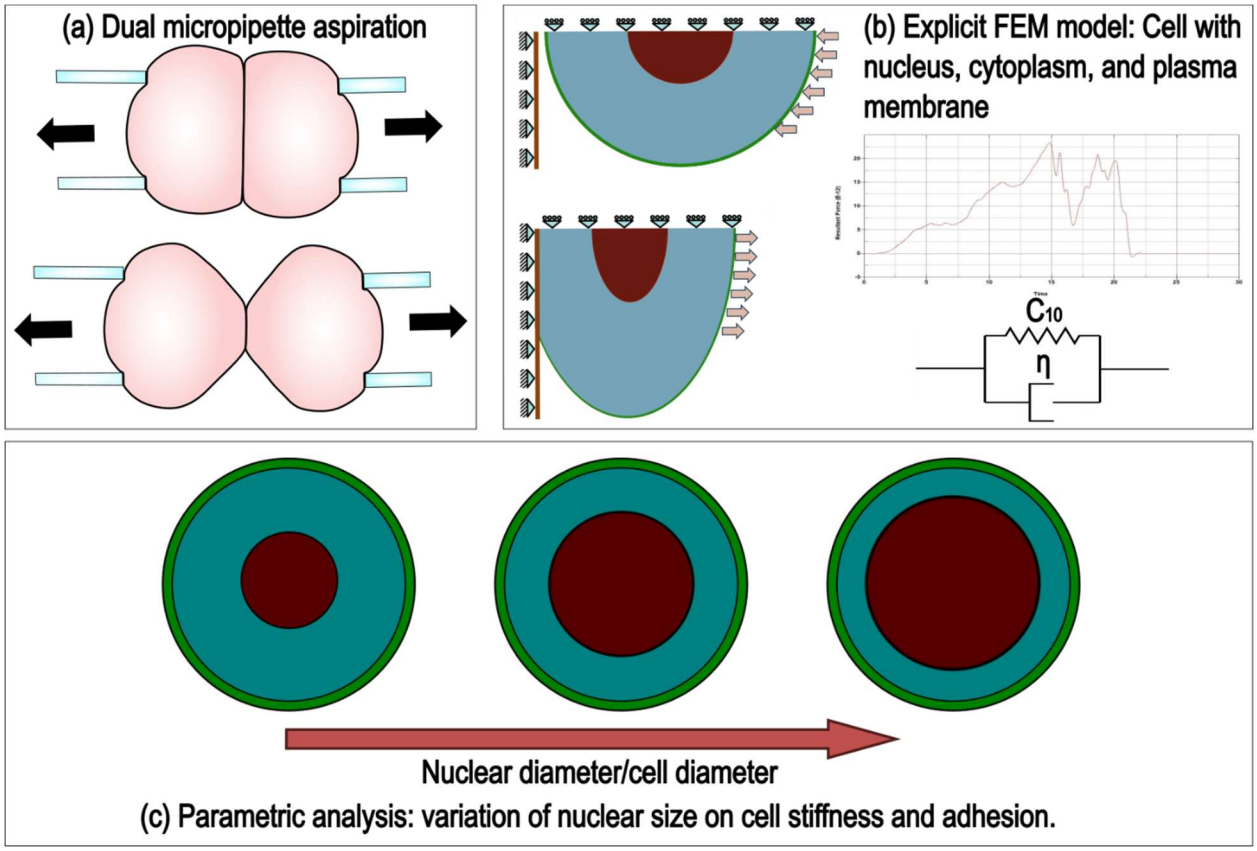
Results

Preliminary simulations predict adhesion forces comparable to reports for embryonic cells [5] and up to a tenfold reduction when melanoma-type mechanical parameters are used. The model resolves stress and strain in nucleus, cytoplasm and membrane, allowing assessment of nuclear-size effects on mechanical response and adhesion.

Discussion

These preliminary results indicate that dual micropipette aspiration with explicit finite element modeling is a feasible strategy to quantify adhesion in melanoma and relate it to mechanical parameters. Main limitations are the simplified spherical geometry and the initial use of literature-based parameters. Ongoing experiments with the dual micropipette setup will refine the models and help assess stiffness and adhesion as complementary mechanobiological biomarkers in melanoma.

Images (Optional)



References (Optional)

[1] Parra-Soto S. et al., Rev Med Chil, 2020.

[2] International Agency for Research on Cancer, Global Cancer Observatory: Melanoma, 2024.

[3] Brás M.M. et al., Front Cell Dev Biol, 2020.

[4] Abarca Ortega A.F., PhD thesis, Universidad Politécnica de Madrid, 2023.

[5] de Plater L. et al., Biophys J, 2025.

Session Category

P1-018

Assessing the Role of Syndecan-4 in Pancreatic Ductal Adenocarcinoma Cell Chemosensitivity

Mr Jan Jethro Baguyo[1,2], Dr Leah Fallon[1,2], Dr Stephen Thorpe[1,2,3]

[1]UCD School of Medicine, University College Dublin, Belfield, Dublin, Ireland. [2]UCD Conway Institute of Biomedical and Biomolecular Research, University College Dublin, Belfield, Dublin, Ireland. [3]Trinity Centre for Biomedical Engineering, Trinity College Dublin, Dublin, Dublin, Ireland

Introduction

Pancreatic ductal adenocarcinoma (PDAC) is characterised by a stiff ECM which promotes cancer cell survival, metastasis and chemoresistance. Syndecan-4 (SDC4) is a transmembrane proteoglycan upregulated in PDAC and associated with poor survival. Syndecan-4 acts as a co-receptor supporting cell adhesion and migration and has mechanosensing capabilities regulating cell contractility. However, the role of syndecan-4 in stiffness mediated chemosensitivity in PDAC is unclear. This study will address the hypothesis that syndecan-4 supports stiffness mediated chemotherapy resistance in PDAC cells in both 2D and 3D culture environments.

Methods

CRISPR gene editing was used to generate SUIT2-007 metastatic PDAC cell lines with either wild-type, knockout or overexpressed SDC4. Additionally, mutated SDC4 protein cell lines were generated to remove extracellular glycosaminoglycan chains (SDC4-ΔGAG), and to block or mimic phosphorylation of the conserved intracellular C1 domain (SDC4-Y180A, SDC4-Y180F). Western blot and immunofluorescent staining were used to confirm SDC4 expression. Cells were cultured on tissue culture plastic or on polyacrylamide gels with stiffnesses mimicking soft and stiff PDAC tissue. Substrates were coated with fibronectin or collagen type I. 3D spheroid cultures were also generated using 100 µg/mL collagen type I. Cells were subjected to gemcitabine, 5-fluoruracil or paclitaxel at IC_{50} concentrations for 48 h. Viability was assessed via metabolic activity and ATP levels.

Results

Western blot and immunofluorescent staining confirmed knockout and overexpression of SDC4 (Fig. 1A). SDC4 knockout cells had similar viability to SDC4 overexpressing cells in untreated and drug treated groups, regardless of ECM, polyacrylamide gel stiffness and drug treatment. In untreated groups, SDC4-ΔGAG exhibited higher viability than all other mutant cells (Fig. 1B). Additionally, C1 domain inhibition had lower viability than C1

domain activation. When treated with chemotherapeutics, all SDC4 mutant cells had lower viability compared to the overexpression control (Fig. 1C).

Discussion

Both SDC4-ΔGAG and phospho-null SDC4-Y180A expressing cells exhibited lower viability than SDC4-HA overexpressing and phospho-mimetic SDC4-Y180F when treated with 5-FU. This indicates that both extracellular glycosaminoglycan chains and intracellular C1 domain phosphorylation can provide therapeutic targets. Work is ongoing to investigate role of the SDC4 specific V-domain.

Images (Optional)

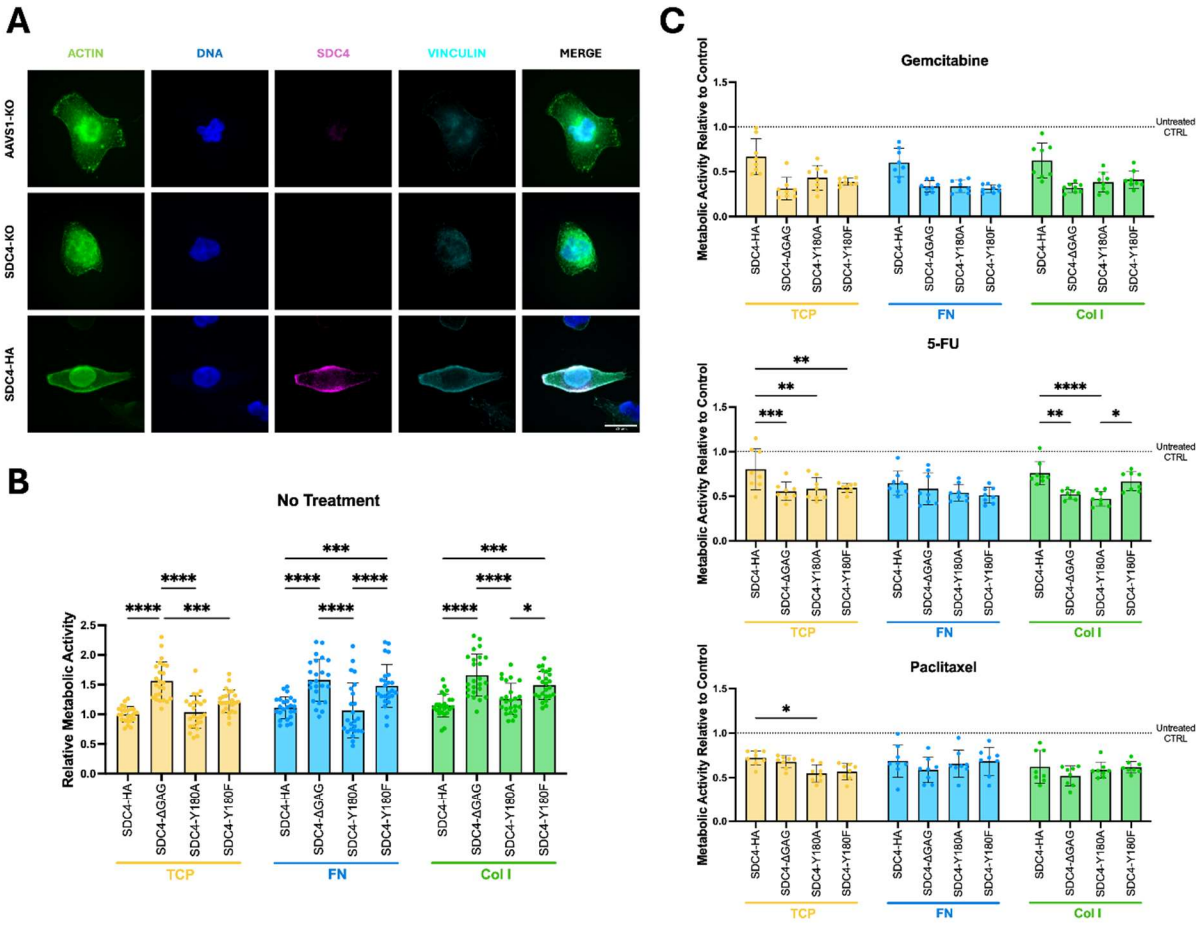


Figure 1. A Immunofluorescent imaging of SUIT2-007 cells with AAVS1-KO, SDC4-KO and SDC4-HA re-expression. Scale bar 25 µm. **B** Relative metabolic activity of untreated SDC4 mutant cells. *n* = 24. **C** Relative metabolic of activity of chemotherapy treated SDC4 mutant cells. *n* = 8.

Acknowledgements (Optional)

Funding provided by UCD School of Medicine.

Session Category

Cell Biomechanics: Mechanobiology

P1-019

Macroscopic and Microscopic Biomechanical Analysis of Scaffold-Free Bone Spheroids

Dr Jeonghyun Kim[1], Mr Takashi Inagaki[2], Dr Eijiro Maeda[2], Dr Takeo Matsumoto[2]

[1]Kyushu University, Fukuoka, Fukuoka, Japan. [2]Nagoya University, Nagoya, Aichi, Japan

Introduction

Three-dimensional scaffold-free spheroids offer a physiologically relevant model to study bone-like mineralization, yet how long-term culture alters their multiscale mechanical properties remains unclear. This study aimed to evaluate mineralization-dependent mechanical changes in human mesenchymal stem cell (hMSC) spheroids by integrating macroscopic and microscopic biomechanical measurements.

Methods

Spheroids were generated from hMSCs using U-bottom ultra-low attachment plates [1] and cultured for 2 or 35 days under osteogenic conditions in high-glucose DMEM supplemented with ascorbic acid, β-glycerophosphate, and dexamethasone. Mineralization was evaluated by Alizarin Red S staining of cryosectioned samples. Macroscale mechanical properties were measured using a customized uniaxial compression system with a glass plate to determine the apparent Young's modulus and strain-recovery behavior. Microscale stiffness and surface topography were mapped on cryosectioned spheroids using AFM indentation with spherical or conical probes.

Results

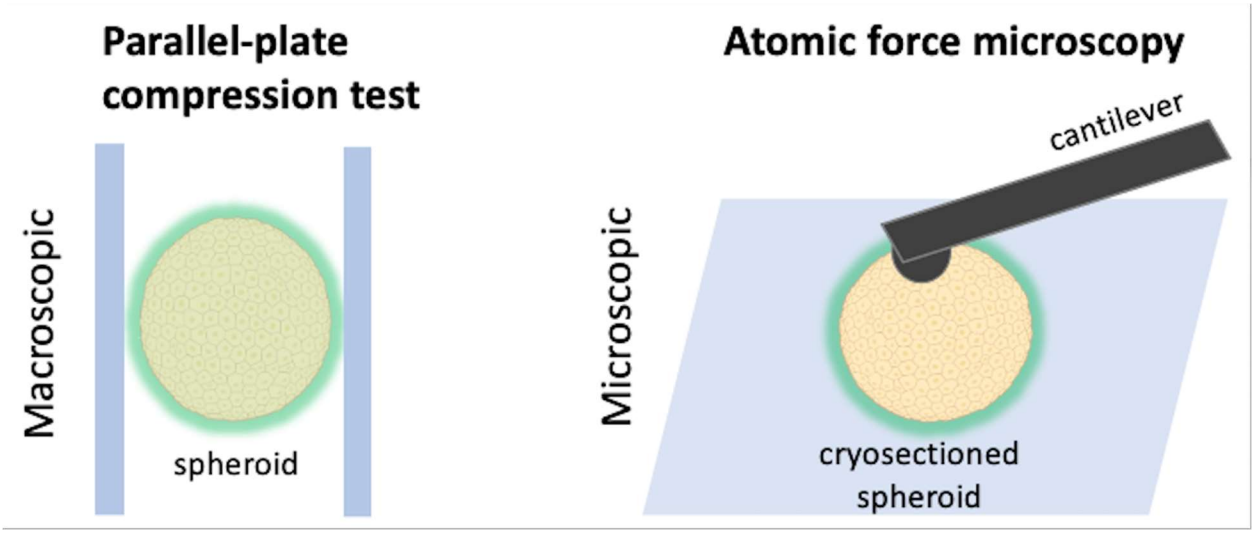
Long-term culture induced pronounced and spatially heterogeneous mineralization, primarily in the spheroid interior. Macroscopic Young's modulus increased from 17.8 to 44.4 kPa, and recovery after compression decreased markedly, indicating enhanced plastic deformation. AFM revealed a substantial rise in local stiffness from 0.7 to 15.1 kPa, with some regions exceeding 100 kPa, demonstrating strong microscale heterogeneity. Surface topography also became rougher and more complex, consistent with ECM accumulation and mineral deposition.

Discussion

Spheroids exhibited clear bone-like mechanical maturation after 35 days, characterized by increased stiffness, reduced elasticity, and greater spatial heterogeneity [2]. Agreement

between macroscopic and microscopic trends indicates that mineralization and matrix remodeling reshape tissue mechanics across scales. These findings enhance understanding of the mechanobiology of bone formation in 3D cultures and support future applications in bone tissue engineering.

Images (Optional)



References (Optional)

[1] Kim *et al.*, ***Scientific Reports***, 2021

[2] Inagaki *et al.*, ***Journal of Biomechanics***, 2026

Acknowledgements (Optional)

This work was supported by the Japan Society for the Promotion of Science (JSPS) KAKENHI [23K17193, 21H04533 and 20K20181], the Foundation of Public Interest of Tatematsu Research Grant [22A105], the Hibi Science Foundation, and the Japan Science and Technology Agency - Core Research for Evolutionary Science and Technology (JST-CREST) [JPMJCR22L5].

Session Category

Cell Biomechanics: Mechanobiology

P1-020

Adaptive Nuclear Displacement Dynamics Enable Cellular Responses to Small Accelerations

Mr. Jonathan Wadsworth[1], Mrs. Nina Nikitina[1], Dr. Sean Howard[1], Dr. Clinton Rubin[2], Dr. Gant Luxton[3], Dr. Gunes Uzer[1]

[1]Boise State University, Bosie, ID, United States. [2]Stony Brook University, Stony Brook, NY, United States. [3]University of California at Davis, Davis, CA, United States

Introduction

Small mechanical signals such as sound and vibration are ubiquitous across life, yet how unspecialized cells detect them remains unclear. We show that during low-intensity vibration (LIV), the nucleus shifts slightly out of phase with the cytoplasm, generating localized strain at the nucleo-cytoskeletal interface that can be tuned by modifying LINC (Linker of Nucleoskeleton and Cytoskeleton) complexes and cytoskeletal structure. This study therefore explores how small relative nuclear displacements act as intracellular mechanical signals that initiate adaptive responses in both cytoplasm and nucleus.

Methods

To measure nuclear motions, mesenchymal stem cells (MSCs) were labeled with calcein AM and exposed to 45 Hz, 0.2 g LIV for 30 minutes using a custom bioreactor.[1] LIV-induced nuclear and membrane motion were recorded at 1000 fps during LIV as well as after 6- and 12-hours post-LIV using un-paired samples (n=30/grp). LINC connectivity was disrupted via doxycycline-inducible mCherry-KASH[2] and MSCs were transfected with genetically encoded multimeric nanoparticles (GEMs)[3] to probe nucleo-cytoplasmic biophysical properties.

Results

At baseline, the median nucleus–membrane phase difference was 0.12 ms, corresponding to a maximum relative displacement of 0.7 μm. Disrupting the LINC complex doubled the nuclear lag, while increasing F-actin via a RhoA activator (Cytoskeleton, Inc.) suppressed most detectable baseline motion, confirming nucleo-cytoskeletal involvement. Dynamically, the phase difference increased 70% (to 0.21 ms, $p<0.05$) at 6 hours, then decreased to 0.09 ms by 12 hours ($p<0.05$).

Discussion

These findings show that even small-amplitude vibrations produce measurable, transient changes in nuclear motion relative to the cell body. The increased phase lag at 6 hours

suggests short-term cytoskeletal de-polymerization, while the return to baseline by 12 hours indicates re-stabilized nuclear–cytoskeletal coupling. Although detailed biophysical studies are ongoing, preliminary results support the idea that mechanically induced nuclear motion from low-intensity vibrations contributes to mechanosensing and mechanoadaptation independent of extracellular matrix deformation.

Images (Optional)

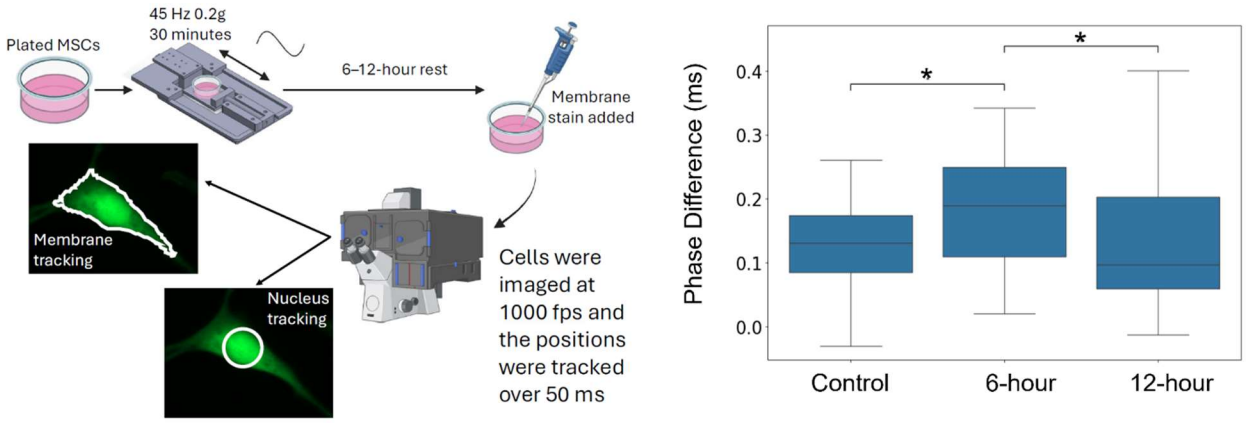


Figure 1. Nuclear phase lag increases 70% after 6 hours, returns to baseline at 12 hours

References (Optional)

[1] Nikitina, N. *et al. bioRxiv*, 2025

[2] Goelzer, M. *et al. Communications biology*, 2025

[3] Ding, X. *et al. Science advances*, 2025

Session Category

Cell Biomechanics: Mechanobiology

P1-021

Virtual framework to investigate intracellular activity in injured and inflamed articular cartilage

DSc Joonas Kosonen[1], PhD Satanik Mukherjee[2], PhD Atte SA Eskelinen[1], MSc Aya Abdelsalam[1], Prof David M Pierce[1,3], Asst Prof Petri Tanska[1,4], Prof Liesbet Geris[5,6], Prof Rami K Korhonen[1]

[1]University of Eastern Finland, Kuopio, Northern Savo, Finland. [2]Washington University, St. Louis, MO, United States. [3]University of Connecticut, Storrs, CT, United States. [4]Kuopio University Hospital, Wellbeing Services County of North Savo, Kuopio, Northern Savo, Finland. [5]KU Leuven, Leuven, Flemish Region, Belgium. [6]University of Liège, Liège, Walloon Region, Belgium

Introduction

Articular cartilage degeneration is a hallmark of post-traumatic osteoarthritis (PTOA), suggested to be triggered by excessive mechanical strains and/or pro-inflammatory cytokines [1]. Since this degeneration process remains difficult to analyze solely by experiments, earlier studies developed computational frameworks to simulate cell-driven cartilage degeneration [2]. However, most models lack intracellular signaling governing degenerative enzymes production [3], which is important for unraveling potential drug-targets. Thus, we developed a virtual framework to analyze spatially varying a disintegrin and metalloproteinase with thrombospondin motifs (ADAMTS) and matrix metalloproteinase (MMP) intracellular activity caused by injurious loading and inflammation.

Methods

We simulated cartilage shear strain (fibril-reinforced poroviscoelastic material) under injurious loading and cytokine diffusion using finite element (FE) models based on earlier experiments (Fig. 1A) [1]. Intracellular behavior was modeled with a gene–protein regulatory network (GPRN), and Monte Carlo analysis revealed two stable states: pro-hypertrophic (PH) and healthy (H) [4]. At each FE node, we determined post-injury cell state ($Z_{0,INJ+IL}$, day 0) as a weighted sum of these states. We converted cytokine concentrations (day 2) from the FE model to a non-dimensional input with a Hill-type function. The input was used to perturb GPRN, and downstream ADAMTS and MMP activity were simulated for 1000 pseudotime steps. We compared the simulated intracellular activity maps to immunohistochemical analysis (IHC) of MMP-1 and digital densitometry (DD) analysis of proteoglycans (optical density).

Results

Injurious loading with inflammation caused high ADAMTS and MMP activity across the sample (bulk avg: 0.94, scale: [0,1]), while inflammation alone limited activity near free surfaces (avg: 0.31, Fig. 1B). IHC confirmed elevated MMP in superficial regions, and DD analysis showed proteoglycan loss in areas of high ADAMTS and MMP activity (Fig. 1C).

Discussion

Our multiscale workflow with cell-tissue interactions in mechanically injured and inflamed cartilage captures experimental findings. Future calibration against gene expression remains essential. Once calibrated, the framework supports development of virtually optimized treatment strategies for PTOA drug therapies.

Images (Optional)

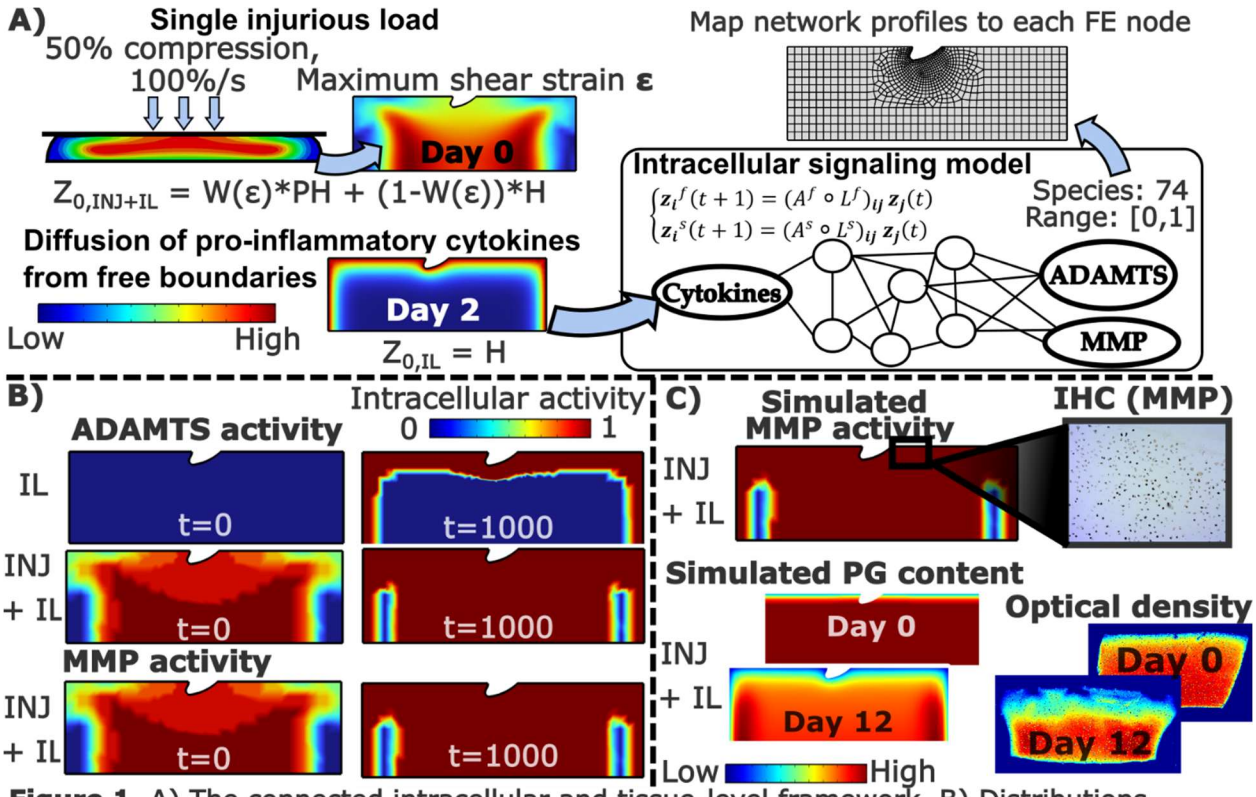


Figure 1. A) The connected intracellular and tissue-level framework. B) Distributions of the intracellular ADAMTS and MMP activity. C) Experimental comparison.

References (Optional)

[1] Yang Li *et al.*, *Osteo. Cart.,* 2013*;* [2] Atte Eskelinen *et al., PLOS Comp Biol.,* 2025; [3] Satanik Mukherjee *et al.*, *Trans Orth Res Soc*, 2023; [4] Raphaëlle Lesage *et al., BMC Biol.*, 2022

Acknowledgements (Optional)

NNF, RCF, SJF

Session Category

Cell Biomechanics: Mechanobiology

P1-022

In Vivo Fatigue Injury Transiently Alters the Capacity of Tenocytes to Interact With Aligned and Unaligned Matrix

Mr. Joseph Denisco, Dr. Nelly Andarawis-Puri

Cornell University, Ithaca, NY, United States

Introduction

Fatigue-induced tendinopathy arises from the accumulation of sub-rupture fatigue damage due to chronic overuse, ultimately impairing quality of life. Exercise post-fatigue tendon injury, akin to physical therapy, exacerbates damage at day 1 (D1) but improves healing at day 14 (D14) [1]. This differential response may reflect intrinsic changes in tenocytes, altered loading conditions created by ECM damage, or a combination of both. Examining tenocyte morphology on organized versus disorganized substrates at D1 and D14 will reveal fatigue-derived cellular responses, informing tendinopathy treatment. We hypothesize that fatigue damage induces tenocyte retraction and reduced contact area, reflecting decreased mechanosensation, with these effects amplified by unorganized ECM at D1 with properties restored by D14.

Methods

Under IACUC approval, the left patellar tendon (PT) of female 11-month old Sprague-Dawley rats (n=2) were fatigue loaded [1]. Tenocytes were harvested from PTs 1 or 14 days post-fatigue, with right PT cells utilized as a naive control. At passage 3, cells were seeded (750 cells/well) onto aligned or disorganized polycaprolactone nanofiber scaffolds (n=6-8), mimicking healthy and injured tendon structure, respectively. Cell nuclei and cytoskeletons were visualized with DAPI and phalloidin, imaged at 25X, and analyzed using ImageJ [2]. Unpaired t-tests compared fatigue-injured and naive tenocytes, and Kruskal-Wallis tests timepoint and substrate effects.

Results

Fatigued tenocytes had significantly reduced areas compared to naive control at D1 regardless of substrate type. On aligned substrates, D14 tenocytes had increased area and circularity compared to D1 tenocytes (Figure 1A,B).

Discussion

Fatigue injury directly impacts D1 tenocytes, which displayed reduced area, consistent with diminished cell–ECM contact and impaired mechanosensation. However, these fatigue-induced alterations in the cells are not sustained: by D14, differences between contralateral and fatigue-injured tenocytes largely resolve on both aligned and unaligned matrices. Results suggest that fatigue injury transiently alters tenocyte mechanosensing, with recovery occurring by approximately two weeks—a timeframe that aligns with when post-injury loading becomes therapeutic in vivo. This supports a model in which early tenocyte dysfunction normalizes as cells recover, guiding future investigation into how ECM organization and injury history jointly shape tenocyte–ECM interactions.

Images (Optional)

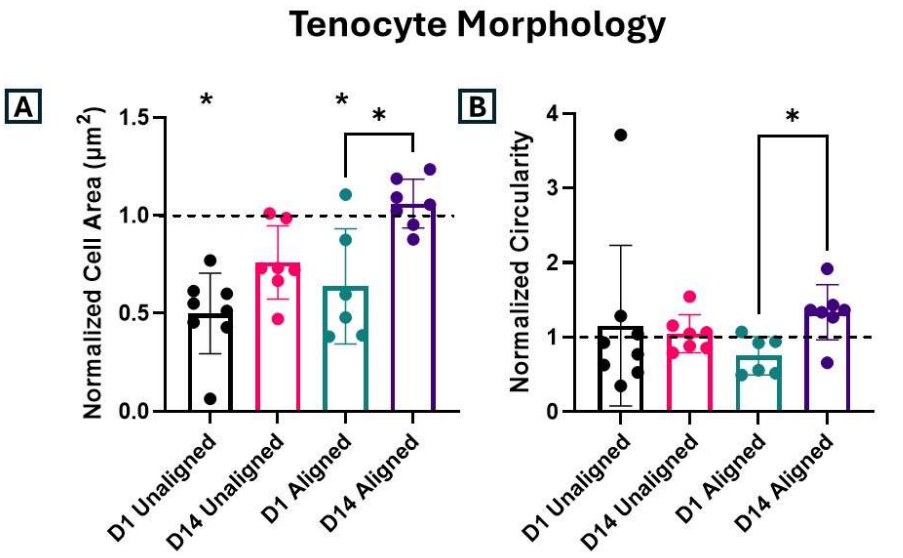


Figure 1: Cell morphology properties of fatigued normalized by naïve tenocytes on disorganized or aligned matrix. (* $p<0.05$)

References (Optional)

[1] Andarawis-Puri et al., *JOR*, 2018; [2] Marvin et al., JOR, 2023.

Session Category

Cell Biomechanics: Mechanobiology

P1-023

Preliminary Model of Hinge Epithelium Contraction in Palatal Shelf Elevation

Graduate Research Assistant Kayla Whatley BS[1], Postdoctoral Fellow Brittany M. Hufft-Martinez PhD[2], Research Assistant An J. Tran BS[2], Professor Irfan Saadi PhD[2], Professor Kenneth Fischer PhD[1]

[1]University of Kansas, Lawrence, KS, United States. [2]University of Kansas Medical Center, Kansas City, KS, United States

Introduction

Palatal shelves begin as vertical projections from the embryonic maxilla, flanking the tongue. During palatogenesis, they elevate to a horizontal position above the tongue with concurrent tongue flattening. Successful elevation and fusion forms the intact hard palate, whereas failure results in cleft palate. Elevation begins with a bulge in posterior vertical shelf hinge region that extends anteriorly to cause horizontal reorientation [1]. Hinge region contraction is considered one driver of elevation [1]. Finite element modeling can help elucidate the biomechanics and poorly understood “driving forces” of palatal shelf elevation.

Methods

Serial coronal sections (10 mm) were collected from a wildtype embryonic day (E) 13.5 mouse head (3.25 x 2.25 x 2.25 mm), histologically stained, and imaged. Images were realigned in-plane using anatomical landmarks and out-of-plane using midsagittal reference sections from a littermate. Manual image segmentation of the upper and lower jaws, tongue, Meckel’s cartilage, palatal mesenchyme, palatal epithelium, and hinge epithelium was performed in ScanIP (Synopsis), then smoothed and resampled to 10 mm on all planes (Fig 1.C-E). ScanIP generated a linear tetrahedral mesh with element edge lengths ranging between 4.8×10^{-4} mm (epithelium) to 0.28 mm and comprising of 6,881,929 elements with 1,322,124 nodes (Fig 1.A-B). Simulations were conducted in FEBio [2]. Tissues were modeled as neo-Hookean materials with relative moduli estimated from the mechanical measurements of E13.5 palatal epithelium [3]. Tongue descent was modeled using kinematic growth of 0.7. Hinge epithelium contraction was modeled as 0.7 vector kinematic growth approximating epithelial orientation.

Results

The model successfully simulated 30% tongue descent and 30% epithelial hinge contraction which drove medial rotation of the anterior palatal shelves, resulting in tongue contact (Fig 1.E-F).

Discussion

This foundational model enables future studies of the forces driving palatal shelf elevation. We are currently collecting more accurate material property data. Planned mesh convergence studies and model improvements will allow rigorous testing of biological hypotheses.

Images (Optional)

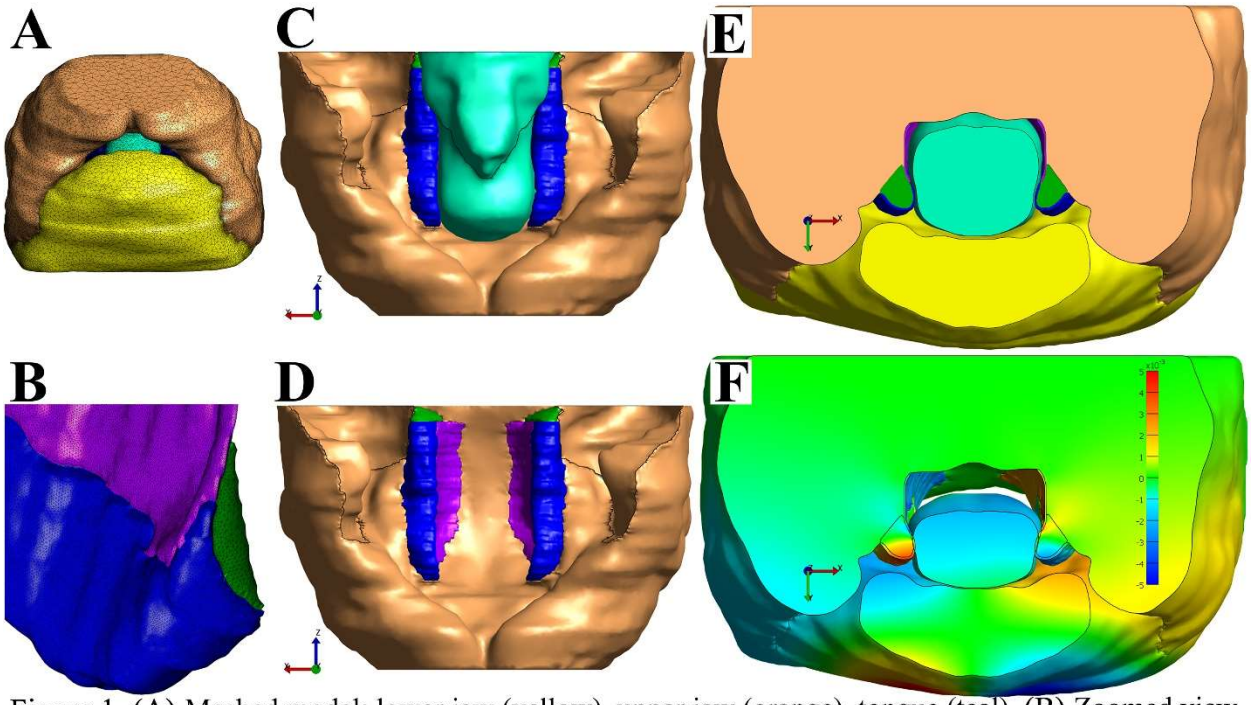


Figure 1. (A) Meshed model: lower jaw (yellow), upper jaw (orange), tongue (teal), (B) Zoomed view of fine mesh of palate epithelium (blue), palate hinge epithelium (magenta), and palate mesenchyme (green), (C) Model without lower jaw, (D) Model without tongue, (E) Anterior coronal model slice before growth, (F) Same slice after growth with plot of X (medial-lateral) displacement (mm).

References (Optional)

[1] Jeremy Georing et al., Front. Cell Dev. Biol., 2025

[2] Steve Maas et al., J. Biomech. Eng., 2012

[3] Arata Nagasaka et al., Dev. Dyn., 2025

Acknowledgements (Optional)

We thank our undergraduate research assistants Keagan Fleming, Cacia Hunnicutt, Nguyen Khuu, Jake Noonan, Macy Trease, and Miles Williamson for segmentation assistance. We thank the Madison and Lila Self Graduate Fellowship for student support. This work was funded by NIH grant R01DE032825.

Session Category

Cell Biomechanics: Mechanobiology

P1-024

Morphological characterization of smooth muscle cell phenotypic response to biophysical cues of the extracellular environment

Postdoctoral Researcher Luigi Crimaldi, Prof. Abdul Barakat

École polytechnique, Paris, Île-de-France, France

Introduction

In pathological contexts, vascular smooth muscle cells (SMCs) can switch from a contractile phenotype (elongated cell morphology) to a synthetic phenotype (more round shape). Although emerging evidence highlights the key role of extracellular matrix (ECM) biophysical cues in modulating SMC behavior, this relationship remains incompletely understood due to limited and inconsistent studies. This study aims to address this gap by characterizing SMC phenotypic response to ECM stiffness and cell density.

Methods

Bovine SMCs were cultured either on top of (2D) or embedded within (3D) collagen I hydrogels at 2, 4, and 6 mg/mL concentrations, corresponding to different gel stiffnesses. Two seeding densities were used: 100,000 cells/mL (LD) and 200,000 cells/mL (HD) in 3D, with equivalent planar densities in 2D. Cells were fixed at 24 h, stained with phalloidin, and morphological descriptors were extracted from images in Fiji. Approximately 100 cells per condition were analyzed across three independent experiments. Statistical comparisons used Kruskal–Wallis tests ($p < 0.05$*, $p < 0.01$**).

Results

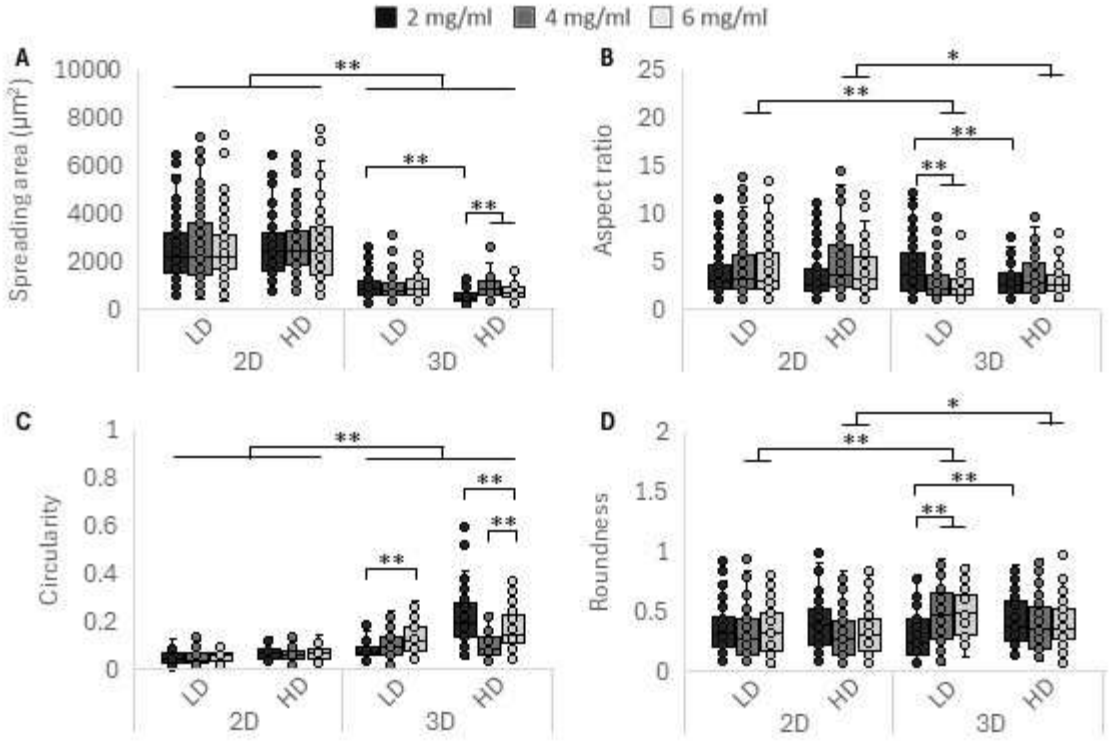
Preliminary results showed that, across all concentrations and cell densities, 2D cells exhibited significantly larger spreading areas (Fig. 1A; $p < 0.01$) and higher elongation (Fig. 1B-D) than 3D cells. While 2D morphology was insensitive to collagen concentration and cell density, cell morphology in 3D depended on both variables. LD–3D cells in 2 mg/mL gels showed significantly greater elongation (Fig. 1B,D; $p < 0.01$) than in 4–6 mg/mL gels. HD–3D cells in 2 mg/mL gels exhibited pronounced gel compaction (data not shown) and markedly reduced spreading (Fig. 1A; $p < 0.01$) than in stiffer gels.

Discussion

Consistent with previous reports, 2D cells showed a contractile-like morphology (larger spreading and higher elongation), likely due to reduced physical constraint. In 3D, LD cells in 2 mg/mL hydrogels displayed higher elongation, in agreement with studies linking lower stiffness to a more contractile phenotype. HD impaired this behavior, possibly due to cell-

mediated gel remodeling that increased local matrix stiffness. Although preliminary, these findings highlight the influence of ECM cues on SMC phenotype. Future studies will correlate morphology with molecular and functional biomarkers and explore broader density and stiffness ranges.

Images (Optional)



Session Category

Cell Biomechanics: Mechanobiology

P1-025

Integrating Mechanical and Inflammatory Cues to Predict Fibrotic Capsule Formation Around Silicone Breast Implants

PhD student Matilde Marradi, Prof. Dr. Martijn van Griensven, Assoc. Prof. Dr. Aurelie Carlier

Dept. cBITE, MERLN Institute for Technology-Inspired Regenerative Medicine, Maastricht University, Limburg, Netherlands

Introduction

The foreign body response (FBR) around silicone breast implants is a chronic reaction, involving persistent macrophage activation and the deposition of an abnormally thick and contractile fibrotic tissue capsule leading to pain and implant failure. We propose that a mechanobiological feedback loop, in which altered mechanical properties drive extracellular matrix (ECM) production and mechanosignaling, sustains the FBR. Our aim is to quantify how peri-implant mechanical conditions and early inflammatory signals influence fibrotic capsule formation around implants.

Methods

We developed a coupled computational framework consisting of a biological and a mechanical module (Figure1). In the mechanical module, an elastic model is used to compute the stress distribution in a simplified 2D breast–implant geometry under static gravity loading. The mechanical simulation is iteratively run to account for changes in tissue mechanical properties arising from ECM deposition, updating the stress field throughout the simulation (28 days, with daily time step). The biological module solves the ODEs for cytokine concentration, myofibroblast density, and normalized collagen content. The cytokine dynamics follows an early peak followed by decay; myofibroblast activation depends on local TGF-β levels and stress following a Michaelis–Menten–type kinetics; collagen deposition increases with myofibroblast density and stress. The collagen density increases the local Young's modulus, closing the mechanobiological feedback loop. Equations and parameters were adapted from [1], and solved in COMSOL-Multiphysics 6.4.

Results

The model reproduces distinct fibrotic responses under different mechanical and inflammatory inputs. Altering the implant material's stiffness generated different stresses at the implant–tissue interface, leading to distinct patterns of myofibroblast and collagen accumulation at 28. Higher initial TGF-β similarly caused an earlier, larger myofibroblast peak, with final collagen levels matching those driven by mechanical cues.

Discussion

These preliminary results indicate that both early inflammatory and interface-driven mechanical cues strongly shape fibrotic tissue development around breast implants. The model's sensitivity to mechanical cues aligns with previous reports [2], supporting the role of local mechanical conditions in the FBR progression. Future work will incorporate spatial cytokine variability and refine parameter calibration to improve the model's quantitative reliability.

Images (Optional)

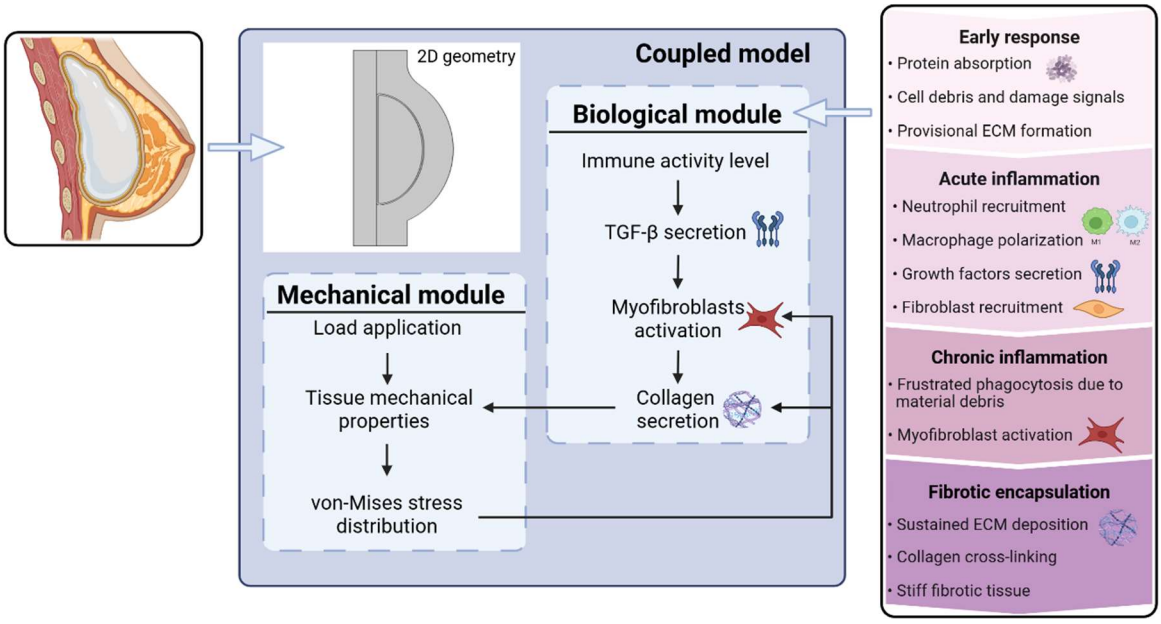


Figure 1. **Flow of infomation between the mechanical and biological module in each iteration of the simulation.** Anatomical breast anatomy is simplified to 2-D computational geometry used in the model. The mechanical module computes the stress field based on loading and material properties, while the biological module tracks four key variables representing the immune response, including collagen, which updates the mechanical properties at each time step.. A schematic of the broader immune processes illustrates how these are condensed into the four-variable biological representation.

References (Optional)

[1] Yuki Xiao *et al.*, Bulletin Mathematical Biology,2025
[2] Rishov Goswami *et al.*, Sci Signal,2021

Session Category

Cell Biomechanics: Mechanobiology

P1-026

Endothelial Dysfunction Caused by Chronic Hydrostatic Pressure: Insights Into Apoptotic Regulation

B.S. Mayuna Abe[1], Ph.D. Satomi Hirose[2], M.S. Norino Uenaka[1], Prof. Kenichi Funamoto[2], Prof. Daisuke Yoshino[1]

[1]Tokyo University of Agriculture and Technology, Koganei, Tokyo, Japan. [2]Tohoku University, Sendai, Miyagi, Japan

Introduction

Research on cellular responses to hydrostatic pressure stimulation and their mechanisms has received considerable attention in recent years. However, numerous aspects of the mechanisms by which vascular endothelial cells respond to hydrostatic pressure stimulation remain to be elucidated. This study examined the mechanism of endothelial dysfunction caused by chronic hydrostatic pressure stimulation.

Methods

Human umbilical vein endothelial cells (HUVECs) were cultured to confluence and subjected to hydrostatic pressures of 0 (control) and 50 mmHg for 24 hours. We then evaluated cell viability under each condition. The expression and localization of proteins associated with endothelial dysfunction were also analyzed based on immunoblotting and immunofluorescence staining after HUVECs were exposed to 0 (control) or 50 mmHg hydrostatic pressure for 3, 6, 12, or 24 hours.

Results

Chronic pressure application increased the proportion of HUVECs undergoing apoptosis. Concurrently, cleaved Caspase-3 expression nearly doubled in HUVECs under pressure conditions 24 hours after loading. Furthermore, GAPDH, a known inducer of apoptotic cell expression, showed substantial upregulation under pressure conditions. Expression of pro-apoptotic protein Bax remained constant regardless of pressure loading. In contrast, the expression of the anti-apoptotic protein Bcl-2 remained constant under pressure conditions, whereas it increased over time during culture in the control. These results suggest that chronic hydrostatic pressure alters pathways that suppress endothelial cell apoptosis, potentially impairing endothelial cell function.

Discussion

This study demonstrates that chronic hydrostatic pressure promotes endothelial apoptosis, as evidenced by increased cleaved Caspase-3 and upregulated GAPDH. The

lack of changes in Bax and Bcl-2 suggests that pressure does not trigger the canonical apoptotic pathway but instead disrupts endogenous anti-apoptotic regulation. Such an imbalance may reduce endothelial resilience and contribute to dysfunction under elevated pressure states, including hypertension or venous congestion. Although limited to HUVECs and apoptosis-related markers, these findings indicate that hydrostatic pressure impairs endothelial homeostasis and underscore the need to explore broader mechanotransduction mechanisms.

References (Optional)

1.

Session Category

Cell Biomechanics: Mechanobiology

P1-027

Biomechanical Modelling Suggests a Role of Vascular Smooth Muscle Cell Plasticity in Arterial Failure and Maladaptation

Ir. Yousof M.A. Abdel-Raouf[1], Dr. Ir. Lauranne Maes[1,2], Ir. Ludovica Maga[3], Prof. Dr. Julie De Backer[4,5], Dr. Patrick Sips[4], Dr. Ir. Mathias Peirlinck[3], Prof. Ir. Nele Famaey[2], Prof. Dr. Jay D. Humphrey[6,7], Prof. Ir. Patrick Segers[1]

[1]Institute of Biomedical Engineering and Technology - BioMMedA, UGent, Gent, East Flanders, Belgium. [2]Biomechanics Section, Department of Mechanical Engineering, KU Leuven, Leuven, Flemish Brabant, Belgium. [3]Department of BioMechanical Engineering, Delft University of Technology, Delft, South Holland, Netherlands. [4]Center for Medical Genetics Gent, Department of Biomolecular Medicine, Gent, East Flanders, Belgium. [5]Department of Cardiology, Gent University Hospital, Gent, East Flanders, Belgium. [6]Department of Biomedical Engineering, Yale University, New Haven, CT, United States. [7]Vascular Biology and Therapeutics Program, Yale School of Medicine, New Haven, CT, United States

Introduction

Phenotypic plasticity in vascular smooth muscle cells (VSMCs) plays a major role in extracellular matrix (ECM) turnover and the progression of arterial failure. One prevailing hypothesis is that the osteochondrocytic shift seen in synthetic VSMCs drives the accumulation and swelling of glycosaminoglycans (GAGs)—a pattern also noted in ECM disruption associated with connective tissue disorders and in cells experiencing excessive mechanical stress under hypertensive arterial pressures. It remains unclear, however, whether this phenotypic switching under non-homeostatic conditions is a contributing cause of these abnormalities or a downstream consequence of them.

Methods

We implement a cause-effect association between ECM damage, lost cell mechanosensitivity, and cell phenotype modulation using the Constrained Mixture Model [1], to predict the evolution of VSMC population over time. We modelled a cylindrical bi-layer of media and adventitia of a mouse common carotid artery as constrained mixtures *in silico*.

Results

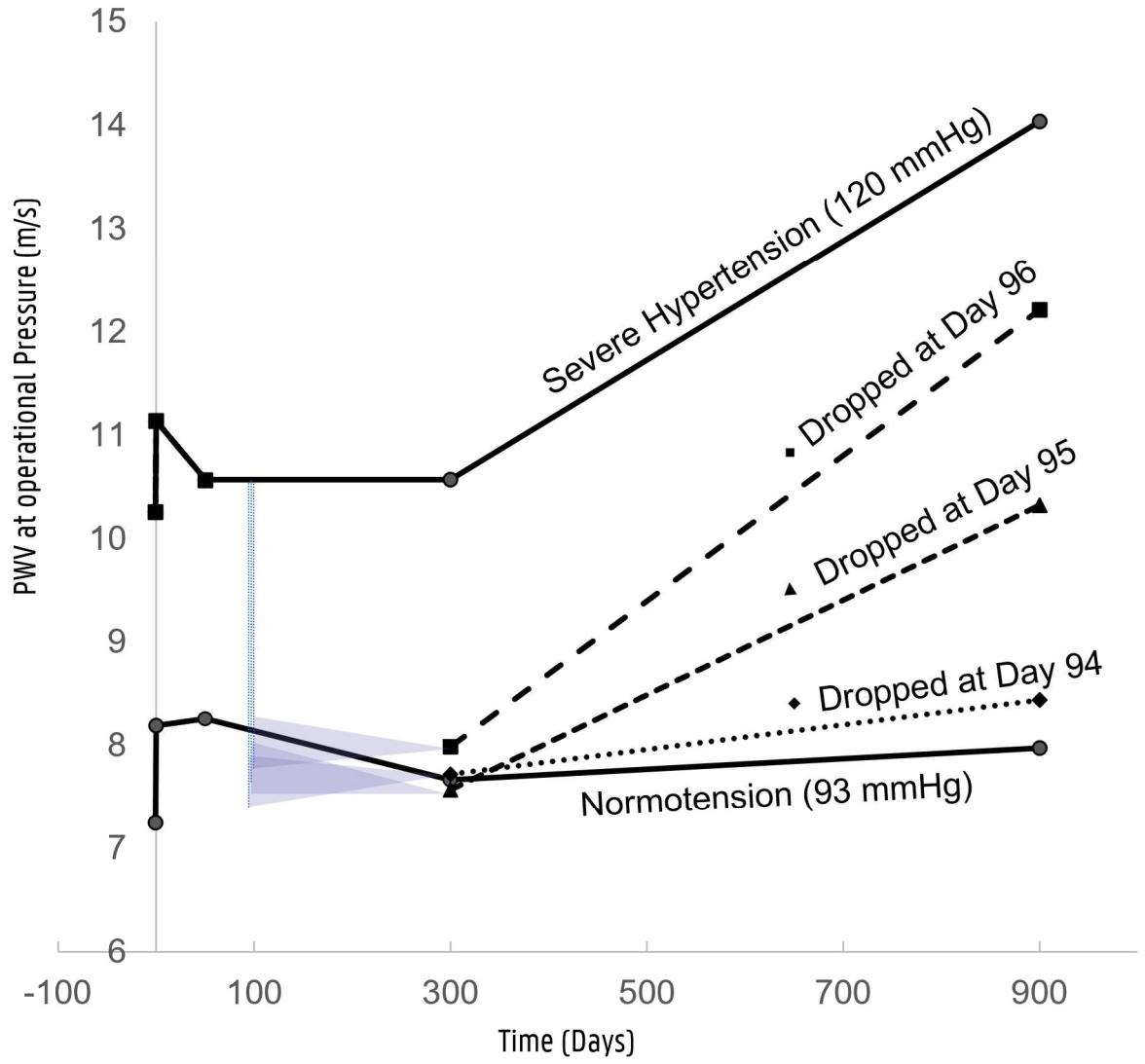
The model demonstrates that under normotensive and mildly hypertensive conditions, ECM disruption is largely corrected through physiological remodeling, which restores mechanical homeostasis to cells with only minor changes to overall mechanical

properties. Under severe hypertension, however, the model predicts complete medial degeneration when ECM damage persists. An initial rise in GAG content temporarily compensates for ECM loss, but prolonged damage triggers a VSMC phenotypic switch that accelerates structural failure. As degeneration progresses, the artery loses nearly all stored elastic energy, resulting in marked stiffening and the elevated pulse wave velocities (PWVs). The model further indicates that reducing blood pressure shortly after the initial insult prevents long-term stiffening, whereas delayed intervention fails to reverse the degenerative changes as shown in Figure 1.

Discussion

Literature suggests clear association between dense transmural GAG aggregation in aneurysmatic and hypertensive arteries [2,3], with the mechanism by which the material properties change being less understood. Our model thus offers a tool to better understand the relationship between ECM damage, arterial failure, and cell response to perturbations in their environments.

Images (Optional)



References (Optional)

[1] Sara Roccabianca *et al.*, J. R. Soc. Interface, 2014

[2] Daniella Eliathamby *et al.*, JTCVS Open, 2023

[3] LF Jensen *et al.*, Cells, 2021

Acknowledgements (Optional)

We would like to acknowledge Sara Roccabianca for sharing her previous work with us. Research was partly funded by a Concerted Action Grant of Ghent University (GOA.2021.0005.05). The work also received funding from the European Union under grant number 101136728 (VITAL project).

Session Category

P1-028

Osteoporosis Treatments and Mechanical Loading Restore Osteocyte Mechanosensitivity Measured by Osteocyte Lacunar Morphology in a Mouse Model of Osteoporosis

MSc Sara Lindenmann, Dr. Zihui Li, Dr. Friederike A. Schulte, Dr. Claudia Weigt, Dr. Floor M. Lambers, Dr. Gisela A. Kuhn, Dr. Neashan Mathavan, Prof. Dr. Ralph Müller

Institute for Biomechanics, ETH Zürich, Zürich, Zürich, Switzerland

Introduction

Common treatments for osteoporosis include anti-catabolic agents like bisphosphonates (BIS) or anabolic agents like parathyroid hormone (PTH), and effects may be enhanced by mechanical loading (ML). The lacuna-canalicular network (LCN) morphology can change with disease and may alter mechanosensitivity [1], as shown by higher mechanosensitivity of round versus flat osteocytes [2]. We investigated how ML and BIS or PTH treatment affect trabecular lacunar morphology in a mouse model of osteoporosis as an indicator of osteocyte mechanosensitivity.

Methods

Ex vivo high-resolution (voxelsize: 1.2 µm) micro-computed tomography (micro-CT) images were obtained from a 1.1 mm mid-section of the 6th caudal vertebra of 7 sham-operated and 43 ovariectomized C57BL/6JRcc mice at 24 weeks of age (license: 171/2009). Ovariectomized mice received ML (8N) 3x/week, PTH (80 µg/kg, 20-24 weeks daily) or BIS (100 µg/kg, at 20 weeks). Some animals received combined pharmacological treatment with ML. Newly formed bone from week 22-24 was identified from time-lapsed *in vivo* micro-CT and registered to the *ex vivo* micro-CT. Mean lacunar sphericity (Lc.Sr) and lacunar volume (Lc.V) was evaluated in trabecular bone and in separated formation and quiescent regions using a custom Python script [3] implemented in XamFlow. The statistical analysis is indicated in the figure caption.

Results

Approximately 70000 and 300000 lacunae were analyzed in formation and quiescent regions, respectively. Ovariectomy significantly increased Lc.Sr while ML and BIS restored it to control levels (Fig. 1A). PTH significantly reduced Lc.Sr while significantly increasing Lc.V. Lc.Sr and Lc.V in formation regions correlated with quiescent regions (Fig. 1C and 1D) but was significantly lower in formation regions for Lc.Sr (6/7 groups) and significantly higher for Lc.V (5/7 groups).

Discussion

Higher osteocyte mechanosensitivity after ovariectomy, shown by increased Lc.Sr, likely compensates for bone loss and is reversed by BIS and/or ML. PTH reduces Lc.Sr through a non-uniform increase in Lc.V and decreases variability, suggesting tighter control of its cellular effects. Osteocytes in newly formed bone show lower mechanosensitivity, independent of disease or treatment, potentially limiting excessive bone formation.

Images (Optional)

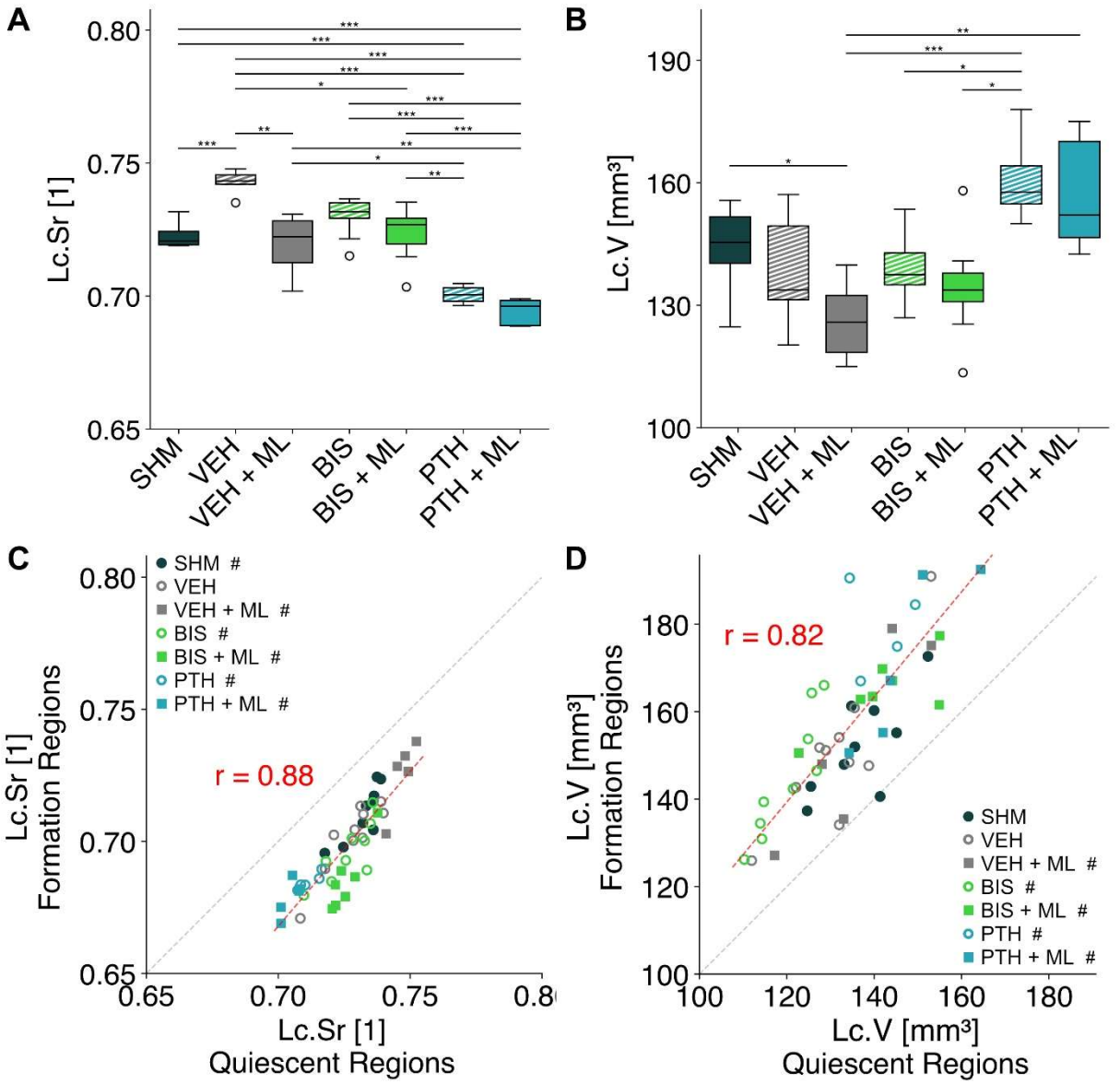


Figure 1: *(A) Mean lacunar sphericity (Lc.Sr) and (B) Mean lacunar volume (Lc.V) in trabecular bone of all groups: sham-operated (SHM), vehicle treatment only (VEH) or with mechanical loading (VEH + ML), bisphosphonate treatment only (BIS) or with mechanical loading (BIS + ML), parathyroid hormone only (PTH) or with mechanical loading (PTH + ML). Differences between groups for were tested using one-way ANOVA followed by a post-hoc analysis using Tukey's test. Significances between groups are indicated with (*) p<0.05, (**) p<0.01, (***) p<0.001. (C) Correlation between mean Lc.Sr of formation and quiescent regions. (D) Correlation between mean Lc.V of formation and quiescent regions. Data in (C) and (D) is shown with a linear fit and overall Pearson. Group-wise significant differences between formation and quiescent regions were tested using paired t-test with Bonferroni correction after confirming normality with the Shapiro-Wilk test. Significances between formation and quiescent regions per group are indicated in the legend with (#) p<0.05.*

References (Optional)

[1] Sang et al, J Mech Behav Biomed Mater, 2022

[2] Bacabac et al, J Biomech, 2008

[3] Goff et al, Bone, 2021

Acknowledgements (Optional)

Swiss National Science Foundation (Sinergia Grant 213520) and European Union (VPHOP, FP7-ICT-2008-223865).

Session Category

Cell Biomechanics: Mechanobiology

P1-029

Cell Mimic Platform Using Integrin-Targeted Emulsion Reveals Force-Dominated Apoptosis and Frequency-Dependent TRPV4 Activation in PANC-1 Cells

Mr. Sungkil Lee MS, Prof. Ryota Toyohara PhD, Prof. Toshiro Ohashi PhD

Hokkaido University, Sapporo, Hokkaido, Japan

Introduction

Mechanical forces regulate cellular functions through integrin-mediated mechanotransduction [1], yet quantitative thresholds governing fate decisions remain unclear due to limitations in delivering stable, localized mechanical inputs. We present a biofunctionalized oil-in-water cell mimic actuated by a custom hexapole magnetic-tweezer device generating precise low-frequency forces (4–20 pN, 1–6 Hz) [2]. PI control with Kalman and EWMA filtering ensured consistent outputs, while RGDS-conjugated PEG-VS-PVA microrobots [3] selectively engaged β-integrins on PANC-1 cells, enabling targeted activation of the integrin–FAK–TRPV4 pathway.

Methods

Fluorescent antibodies confirmed NHS-ester activation on the cell mimic surface. Stable RGDS–integrin attachment was observed prior to stimulation, and mechanical loading was applied only after sufficient incubation (~12 h) ensured reliable contact. Five stimulated and four control groups were analyzed at 0, 3, and 6 h using Annexin V–PI cytometry and EdU incorporation assays [1]. Ca^{2+} imaging with Fluo-4 AM and TRPV4 inhibition was performed under matched conditions to quantify ion-channel–dependent mechanotransduction.

Results

Apoptosis sharply increased at 3 h, indicating a critical decision window. Logistic regression identified a force-dependent apoptotic threshold of ~10 pN (CV-AUC = 0.833) [2,4], with force as a significant predictor. Frequency showed a positive but non-significant effect, suggesting its contribution cannot be confirmed or excluded. Ca^{2+} imaging revealed frequency-dependent TRPV4 activation: strong influx at 6 Hz suppressed by HC-067047, and negligible activation at 1 Hz. However, this rapid ion-channel response did not directly correspond to apoptosis levels at 3 h.

Discussion

These results distinguish force-dominated apoptotic commitment from frequency-dependent TRPV4 activation. Although TRPV4 gating at 6 Hz may influence early

mechanotransduction, the data do not support a direct link between Ca^{2+} influx and apoptosis under these conditions. This integrin-targeted microrobotic platform provides a quantitative basis for dissecting force- versus frequency-sensitive pathways and offers a scalable tool for precision mechanobiology and therapeutic mechanism design.

References (Optional)

[1] Matthews BD et al., Integrative Biology, 2010

[2] Lee S et al., J Bionic Engineering, 2025

[3] Raudszus B et al., International Journal of Pharmaceutics, 2018

[4] Combs JD et al., J American Chemical Society, 2024

Session Category

Cell Biomechanics: Mechanobiology

P1-030

Regulating Fibroblast Phenotype in Tissue Engineered Heart Valves

ir. Willem R. Stolk[1,2], ir. Justina Ghebryal[1,2], prof.dr.ir. Frank P.T. Baaijens[1,2], dr.ir. Sandra Loerakker[1,2]

[1]Department of Biomedical Engineering, Eindhoven University of Technology, Eindhoven, Noord-Brabant, Netherlands. [2]Institute for Complex Molecular Systems, Eindhoven, Noord-Brabant, Netherlands

Introduction

Achieving control over the regeneration of in-situ tissue-engineered heart valves (TEHVs) remains challenging, as preclinical studies report unpredictable outcomes and failures from progressive tissue deposition and leaflet retraction [1]. These complications highlight the need to understand fibroblast-driven remodeling, as fibroblasts regulate extracellular matrix production and contractility in response to mechanical and biochemical cues [2,3]. However, the spatial and temporal influence of these stimuli across valve leaflets remains poorly characterized.

Methods

This study introduces a multiscale computational framework combining finite element (FE) modeling of valve mechanics with an ordinary differential equation (ODE)-based model of intracellular signaling to investigate fibroblast phenotype regulation. FE simulations quantified strain in hinge, belly, and tip regions for two TEHV designs: Design 1, linked to leaflet retraction and failure, and Design 2, modified to prevent retraction [3,4]. Strain outputs served as inputs for the ODE model, which predicted contractility activation through intracellular signaling pathways. Knockout analyses identified key molecular targets influencing contractility, filtered for FDA-approved cardiovascular drugs.

Results

Results revealed heterogeneous strain patterns, with Design 1 exhibiting higher strains and markedly greater contractile activation in the hinge and tip region, while the belly region showed minimal activation (see figure). High-strain areas corresponded to elevated contractility, matching αSMA expression in the hinge region for Design 1. In contrast, Design 2 showed low contractility and no αSMA expression in the hinge region. Knockout simulations implicated angiotensin (AT) and endothelin (ET) signaling pathways as major

regulators. Inhibition of AT1, ETA, PI3K, mTOR, and calcium signaling reduced contractility, whereas blocking AT2 and ETB increased it.

Discussion

These findings demonstrate that mechanobiological signaling governs fibroblast phenotype and contractile behavior in TEHVs. The proposed framework provides mechanistic insight into strain-mediated remodeling and identifies pharmacological targets to modulate fibroblast activity during tissue engineering. Such strategies could mitigate leaflet retraction and improve predictability of in-situ TEHV regeneration, informing scaffold design and therapeutic interventions.

Images (Optional)

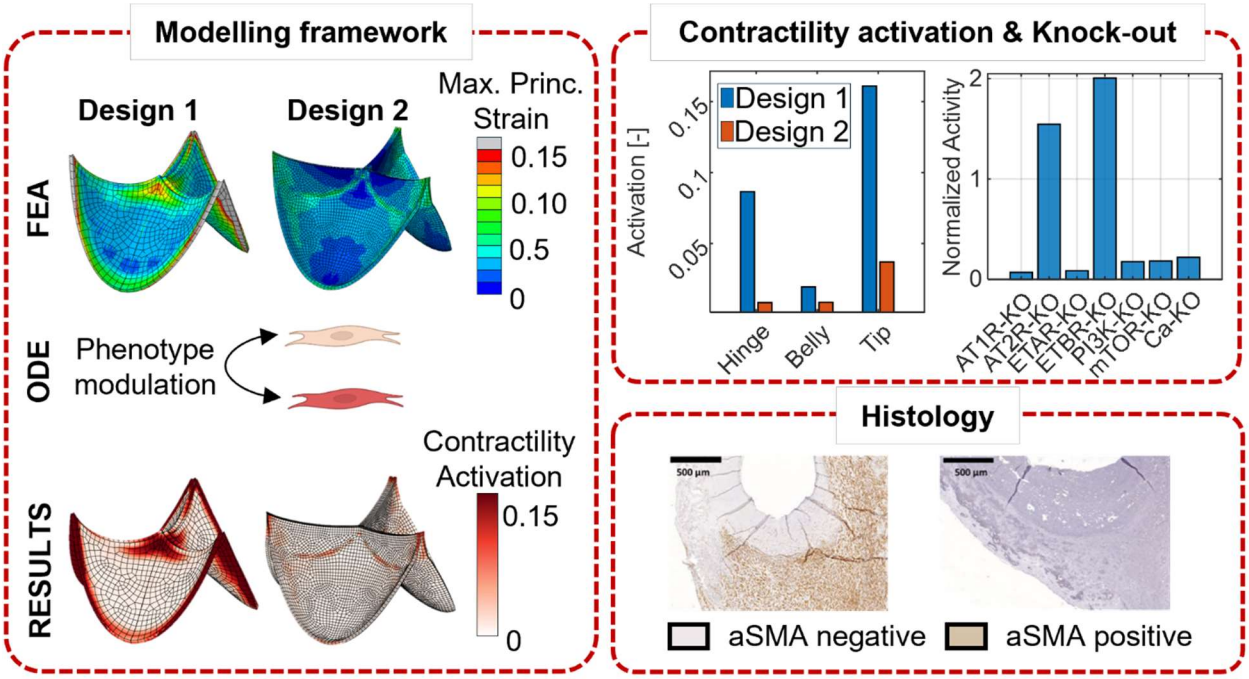


Figure: FE model predicted strain distributions for design 1 and design 2 valves, coupled to an ODE model to estimate regional contractile activation. Bar graphs show contractile activation across leaflet regions and knockout sensitivity. Histology shows αSMA expression in the hinge regions of the for design 1 (left) and design 2 (right) valves adapted from [3].

References (Optional)

[1] Fioretta et al., Nat Rev Cardiol, 2021

[2] D'Urso et al., NA. *Front Bioeng Biotechnol*, 2020

[3] Motta et al., Scientific Reports, 2020

[4] Sanders et al., Ann Biomed Eng, 2016

Acknowledgements (Optional)

This project has received funding from the Dutch Research Council (NWO), project no. 19670 of the NWO Talent Program VIDI.

Session Category

Cell Biomechanics: Mechanobiology

P1-031

Mechanical Activation of Piezo1 Drives Osteoarthritis Through Kdm5c-Mediated Epigenetic Silencing

Mr Tianyou Kan, Mr Xuran Li, Professor Zhifeng Yu

Shanghai Jiao Tong University School of Medicine, Shanghai, Shanghai, China

Introduction

Osteoarthritis (OA) remains a leading cause of global joint disability, with no disease-modifying therapy available. While pathological mechanical stress is a key driver of OA, the molecular pathways translating physical forces into persistent gene silencing in chondrocytes are poorly understood.

Methods

A mouse model with chondrocyte-specific conditional knockout of Piezo1 (*Col2a1*^{CreERT}; *Piezo1*$^{flox/flox}$). The mouse chondrocytic cell line ATDC5 was treated with small interfering RNA (siRNA), the Piezo1 agonist Yoda1. OA was surgically induced by the model of post-traumatic OA. Chondrocytes was performed with RNA-sequencing and CUT&Tag sequencing, histology, atomic force microscopy (AFM), and scanning electron microscopy (SEM).

Results

By using Piezo1 conditional knockout (*Col2a1*^{CreERT}*; Piezo1*$^{flox/flox}$) mice, we found Piezo1 activation by excessive mechanical stress caould trigger nuclear pore dilation via cytoskeletal force transmission, enabling nuclear import of the histone demethylase Kdm5c. Kdm5c in turn erases H3K4me3 marks from promoters of cartilage-anabolic genes *Col2a1* and *Runx3*, silencing their expression. Genetic ablation of and Kdm5c rescues mechanical stress induced cartilage degradation. Through drug repurposing, we identify telmisartan as a direct Kdm5c inhibitor that blocks this pathway and demonstrates disease-modifying efficacy in mouse OA models and human cartilage explants. Our results establishe the Piezo1–Kdm5c axis as a fundamental driver of OA and positions telmisartan as a mechano-epigenetic therapy with immediate translational potential.

Discussion

Here, we uncover a **previously uncharacterized mechano-epigenetic pathway** that drives OA progression and demonstrate its therapeutic targeting using a clinically approved drug. Specifically, we demonstrate:

1. **A complete signaling cascade** from the mechanosensor Piezo1 to nuclear pore dilation, facilitating nuclear import of the histone demethylase Kdm5c, which in turn erases the active H3K4me3 mark at promoters of key cartilage-anabolic genes（ *COL2A1* and *RUNX3*）.
2. **Kdm5c as a druggable epigenetic effector**, whose inhibition restores H3K4me3 levels and promotes cartilage matrix homeostasis.
3. **Telmisartan, an FDA-approved antihypertensive drug**, as a direct Kdm5c inhibitor that blocks this pathogenic axis, demonstrating robust disease-modifying efficacy in both a murine OA model and human OA cartilage explants.

Our work not only delineates a novel disease mechanism spanning from mechanosensing to epigenetic silencing, but also provides an immediately translatable therapeutic strategy by repurposing a safe, existing drug.

Acknowledgements (Optional)

Acknowledgments: T.K. and X.L. contributed equally to this work. **Funding:** This work was supported by the National Key R&D Program of China (subproject 2024YFB3814705); National Natural Science Foundation of China (12172223, 12272232, 12372308).

Session Category

Cell Biomechanics: Mechanobiology

P1-032

Regulatory Network Model of Axillary Lymph Node Metastasis in Breast Cancer

Ms. Alba Fischer-Carles[1,2,3], Dr. Carlos López[3,2,4], Ms. Tábata Sánchez-Alcántara[2,3], Dr. Laia Reverté[2,3], Mr. Mikel Relloso Ortiz de Uriarte[2,3], Ms. Esther Sauras-Colón[3,2], Ms. Noèlia Gallardo-Borràs[2,3], Mr. Alessio Fiorin[2,3,4], Dr. Marylène Lejeune[3,2,4], Dr. Ramon Bosch Príncep[3,2], Dr. Laia Adalid-Llansa[5,3,2], Dr. Daniel Mata Cano[3,2], Prof. Gemma Piella[1], Prof. Jérôme Noailly[1]

[1]BCN MedTech, Department of Engineering, Universitat Pompeu Fabra, Barcelona, Catalonia, Spain. [2]Oncological Pathology and Bioinformatics Research Group, Pere Virgili Institute for Health Research (IISPV), Tortosa, Catalonia, Spain. [3]Department of Pathology, Hospital Universitari de Tortosa Verge de la Cinta, Institut Català de la Salut, Tortosa, Catalonia, Spain. [4]Department of Computer Engineering and Mathematics, Universitat Rovira i Virgili, Tortosa, Catalonia, Spain. [5]Department of Pathology, Hospital Universitari Joan XXIII, Institut Català de la Salut, Tarragona, Catalonia, Spain

Introduction

Breast cancer (BC) is the leading cause of cancer-related mortality in women, with risk increasing once tumor cells metastasize to the axillary lymph nodes (ALN) [1,2]. Immune-tumor interactions strongly influence metastatic progression, yet mechanistic understanding remains incomplete. This study develops a regulatory network model (RNM) to examine the molecular and cellular interactions that drive ALN metastasis within the BC tumor microenvironment (TME).

Methods

The RNM was constructed using graph knowledge projection from >200 peer-reviewed publications. Nodes represented immune cells, cytokines, metalloproteinases, proteases, hormones, and tumor cells, interconnected through directional activating or inhibitory links. Node activity was computed on a continuous normalized scale using Boolean-based ordinary differential equations [3]. The model remained high-level, including a Cancer node representing ALN metastasis risk. Baseline behavior was assessed through 100 simulations, each with random node initialization to identify attractors.

Results

The RNM comprised 102 nodes and 1,001 links, being dense and highly interconnected (density 0.092, clustering coefficient 0.307). Centrality analysis identified Cancer as the

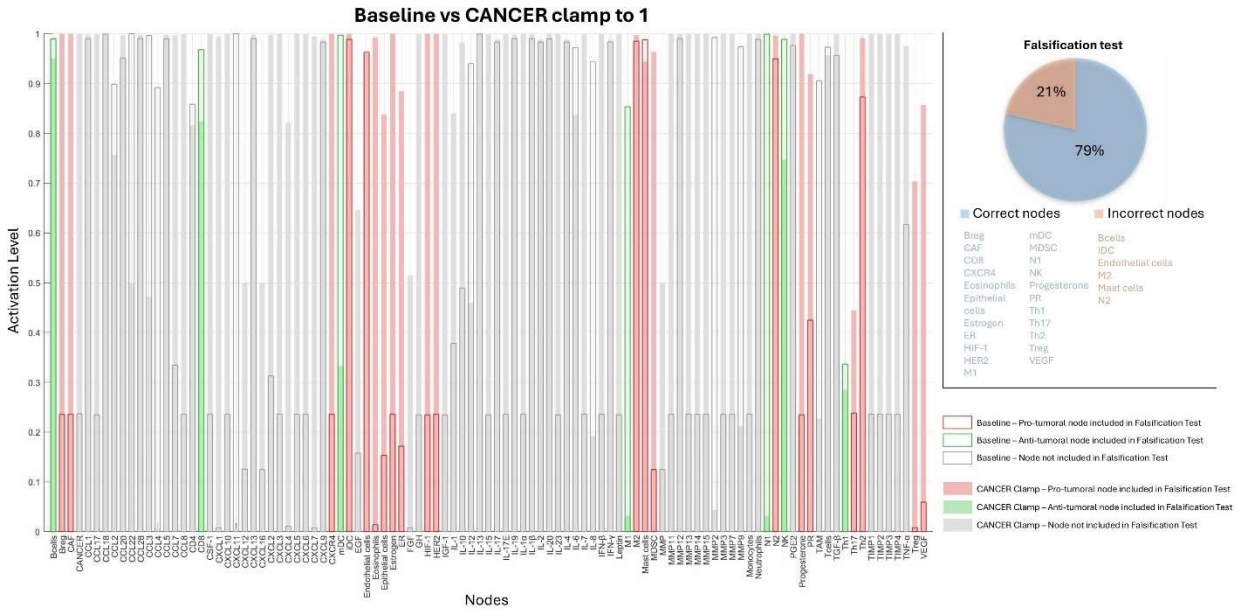
dominant hub across all metrics (MCC, EPC, degree, betweenness, closeness), verifying the mater control of this node, to explore cancer-related protein and cell regulations. Excluding Cancer, highly central nodes included endothelial cells, CAFs, CD8, Tcells, Tregs, mDCs, MDSCs, and IL-10, with endothelial cells emerging as the most influential.

Simulations with Cancer node clamped to 0 (no metastasis probability), or 1 (full metastasis probability) revealed the most functionally responsive nodes. Using a 0.05 activity-change threshold, Cancer activation increased several pro-tumoral and immunosuppressive components while decreasing several anti-tumoral nodes (Figure 1). Conversely, Cancer inhibition suppressed pro-tumoral nodes (Breg, CAF, endothelial cells, epithelial cells, hormones, hormone receptors, HIF-1, MDSC, N2, Th17, VEGF) and increased protective immune subsets (Th1, M1).

Discussion

The RNM highlights the central biomechanical drivers of ALN metastasis, reproducing ≈79% of expected early- and late-stage TME dynamics. Initial falsification test confirmed overall validity, though minor deviations suggest the need for further refinement, targeting nodes with incorrect behavior, to ensure the network accurately reflects complex tumor–immune–stromal dynamics.

Images (Optional)



References (Optional)

[1] Bray, et al., CA. Cancer J. Clin., 2024.

[2] Jana, et al., Am. J. Pathol., 2021.

[3] Mendoza, et al., Theor. Biol. Med. Model., 2006.

Session Category

Cell Biomechanics: Methods and Models

P1-033

Myosin-Driven Contraction Enables Controlled Fracture in Actomyosin Networks With Measurable Mechanical Properties.

Mr. Aniket Marne[1], Mr. Octavio Brugo[2], Ms. Sheridyn Campos[3], Dr. José Alvarado[1]

[1]The University of Texas at Austin, Austin, Texas, United States. [2]University of Miami, Coral Gables, Florida, United States. [3]Texas Christian University, Fort Worth, Texas, United States

Introduction

Cells and tissues show fracture in response to mechanical stress due to intrinsic cellular processes or external movements. Fracture can be integral part of development process such as blastocoel formation in mouse or undesired in case of mutations or diseases. Fracture is complex multiscale process and fracture we see is the outcome of molecular and then cellular level ruptures. Fracture can be triggered by passive stress or active stresses where energy consuming molecular motors generate pulling forces and then transmitted across cells through adhesion complexes. Role of active stress in fracture has been observed in multiple natural processes including leg inversion in Drosophila, asexual reproduction in Trichoplax adhaerens, loss of tissue integrity in gastrulation. Collectively, active stresses play important role in giving tissues intrinsic ability to self-rupture. However, understanding has been hindered by inability to quantitatively characterize the process of fracture.

Methods

We addressed these gaps using reconstituted actomyosin network gels composed of actin filaments, fascin crosslinks, and myosin motors. To mimic cellular adhesion, Dirichlet boundary conditions were imposed by anchoring actin filaments to fixed boundaries. A pre-defined crack front was introduced at the gel center, and its propagation was monitored under active stresses generated by myosin motor activity. We quantified crack length over time and measured the energy consumed by myosin motors during rupture. Additionally, we observed contraction both within the cracked region and in areas still attached to the boundary.

Results

Introducing controlled cracks into actomyosin gels enables directed energy relaxation within the network. This approach provides a quantitative framework for characterizing rupture behavior in active gels. We measured the coupled dynamics of crack propagation

and motor-driven contraction in reconstituted actomyosin networks, allowing extraction of key mechanical parameters, including work functions, damage evolution profiles, and effective fracture toughness.

Discussion

By resolving stress-intensity scaling, non-affine strain localization, and active energy partitioning, we present a quantitative framework for fracture mechanics in active soft matter. Our findings demonstrate that stress relaxation pathways can be guided by mimicking cellular adhesion, offering a strategy to control failure dynamics in reconstituted actomyosin networks.

Acknowledgements (Optional)

This research was primarily supported by the National Science Foundation through the Center for Dynamics and Control of Materials: an NSF MRSEC under Cooperative Agreement No. DMR-2308817. We thank the Physics Machine Shop at UT Austin for manufacturing of gel chambers.

Session Category

Cell Biomechanics: Methods and Models

P1-034

Quantify the 3D Traction Force in Different Germ Layers of Mouse Embryo Organoids

Prof. Fuxiang Wei, Miss Chenyang Ji, Miss Anqi Wang, Miss Xinman Chen, Mr Xinyu Zhang, Mr Wuhuang Liu, Prof. Junwei Chen

Huazhong University of Science and Technology, Wuhan, Hubei, China

Introduction

Mechanical force can direct regulate living cell gene expression and impact cell fate, also plays a key role in embryo development[1]. There are some reports about quantify the traction force in zebrafish embryos[2,3], but it is still elusive how to quantify the traction force during mouse embryo development and how the force impacts the germ layer patterns.

Methods

Here we present a method of quantifying the 3D traction force in mouse embryos and embryo organoids. We injected the elastin round microgels into the mouse embryos, then cultured the embryos in the living cell system compatible with confocal microscopy. The 3D images were performed every hour to record positions of fluorescence beads in the microgel. In the embryonic germ layer organoids, the elastic round microgels were co-cultured with mouse embryonic stem cells in soft 3D fibrin gels. Cytokine combinations were optimized to induce embryonic stem cell differentiation into three germ-layers structures. The microgels will be distributed to different germ layers during this process. 3D images of microgels were taken before and after treating the embryo organoids with Triton X-100.

Results

Comparing microgels deformation between different time points, we can calculate the 3D traction forces generated by the embryos and observe traction force oscillating during mouse embryo developing. The embryo development stopped when the traction force can`t oscillate. Compare the images before and after treating the Triton X-100, we can get the absolute traction force generated by germ layers and find the traction force is significal different in different layers.

Discussion

This study establishes the methods for quantifying 3D traction force in mouse embryos and organoids, reveals germ layer-specific mechanical differences.

References (Optional)

[1] Arash Tajik *et al*., Nat Mater, 2016

[2] Erfan Mohagheghian *et al*., Nat Commun, 2018

[3] Erfan Mohagheghian *et al*., Sci Robot, 2023

Acknowledgements (Optional)

NSFC Grant No. 11902122, 11902121, 32071306, 12422212 and 12572358

Session Category

Cell Biomechanics: Methods and Models

P1-035

Computational Determination of iPSC Stress-Fiber Architecture During Vasculogenesis

Mr. Gabriel Peery[1,2], Dr. Toni West[1,2], Dr. Janet Zoldan[2], Dr. Michael Sacks[1,2]

[1]Oden Institute, Austin, Texas, United States. [2]University of Texas at Austin, Austin, Texas, United States

Introduction

Induced pluripotent stem cell endothelial progenitors (iPSC-EPs) represent a promising avenue for therapeutic tissue constructs owing to vasculogenic capabilities, but achieving sufficient microvascular-network formation requires detailed insights into their biophysical behaviors [1]. We have developed an integrated 3D traction force microscopy inverse modeling pipeline to determine embedded-cell-induced hydrogel remodeling. In the present study, we extend our studies to include analysis of iPSC stress-fiber architecture at different stages of vasculogenesis.

Methods

Human iPSCs were differentiated into EPs, embedded in norbornene-functionalized hyaluronic acid hydrogels with fiducial markers, and then cultured for 4 or 7 days. Cells were stained, specimens of single cells and cell clusters (different stages of vasculogenesis) were imaged *via* 3D microscopy, treated with cytochalasin D to deactivate cellular force generation, and imaged again. Fiducial-marker displacements between states were quantified and cell meshes were generated for subsequent computational analysis.

First, we deployed our inverse finite-element model [2] to reconstruct heterogeneous material behaviors induced by cellular MMP secretion and ECM deposition. Accounting for variations in hydrogel moduli spanning orders of magnitude then allowed accurate estimation of cellular stress-fiber architecture. We adapted our previous inverse model [3] to determine stress-fiber architecture, including orientations and force generation level, to incorporate improvements in numerical stability.

Results

The stress-fiber model was extensively validated to accurately capture prescribed ground-truth fiber architectures in synthetic test cases. Inverse-model analysis revealed spatially-varying fiber orientations and force magnitudes within iPSCs that were significantly different between single and cluster specimens. Cellular protrusions near deposited ECM

exhibited high force generation. Cell-cell junctions produced signature fiber-orientation patterns.

Discussion

Differences in stress-fiber architectures may be attributable to intercellular signaling upon forming adherens junctions between adjacent cells that leads to further stages of vasculogenesis. The biophysical insights into vasculogenesis provided by our inverse modeling techniques may be extended in future work to the lumenized microvascular networks that iPSC-EPs form with longer culture time. Detailed understanding of these processes will be critical to the development of effectively-vascularized therapeutic tissue constructs [1].

References (Optional)

[1] Crosby & Zoldan, *Regen Biomater*, 2019; 6(2):61-73

[2] Peery, et al., bioRxiv, 2024; 10.1101/2025.07.03.663064v1

[3] Khang, et al., *J Biomed Eng*, 2023; 145(12):121005

Acknowledgements (Optional)

We acknowledge Janet Zoldan's group for differentiating iPSCs.

Funding: NIH-1R01HL157829, UTAUS-FA00000461, Oden Institute CSEM Fellowship

Session Category

Cell Biomechanics: Methods and Models

P1-036

Estimation of Cellular Viability Under Cold Storage Using Electrical Impedance Measurement in Cell Monolayers.

Master course of Medical Sciences Hoshito Seno CE[1], Bachelor of Clinical Engineering Kanju Katamine CE[1], Professor Masanobu Ujihira PhD[1], Professor Satoru Nebuya PhD[2], Associate Professor Kazuhiro Yoshida PhD[1], Professor Rina Sakai PhD[1]

[1]Kitasato University, Sagamihara, Kanagawa, Japan. [2]POSH WELLNESS LABORATORY, Tokyo, Tokyo, Japan

Introduction

Cold storage is commonly used for preserving cells and tissues in transplantation and regenerative medicine. However, its clinical utility is limited by short permissible preservation times and the invasive, non-real-time nature of current viability assays that require sampling of the stored material. Electrical impedance measurement has emerged as a non-invasive alternative. The purpose of this study was to examine the possibility of estimation in cellular viability under cold storage of cell monolayers using electrical impedance measurement.

Methods

Cells of rat cardiomyocytes (H9c2) were seeded on a chamber with 64 electrodes (MED probes, Alpha Med Scientific) and cultured with Dulbecco's Modified Eagle Medium (DMEM) for 24 h as a test sample. The sample was stored in DMEM and preservation solutions (ET-Kyoto, UW) at 4°C for 36 h, electrical impedance was measured at 16–200 kHz with impressed current of 10-μA at 3–36 h of storage time, and viability was independently evaluated by WST-8 following rewarming. Impedance ratios were calculated as 16 kHz/200 kHz and converted to corrected ratios (normalization correction) using an exponential fit–derived initial value and a linearly estimated convergence value. After that, estimated viability was obtained using a linear relationship between corrected ratios and actual viability.

Results

Both actual cell viability and electrical impedance ratios exhibited similar decreasing trends with storage time across all preservation conditions. Estimated viability derived from corrected impedance ratios agreed well with actual viability up to the earlier storage periods (< 12 h). Although the difference between the two measures widened slightly as

viability declined at later time points, impedance-based estimation remained applicable throughout the examined duration.

Discussion

It is considered that the slight increase of deviation in longer storage times is resulting from the decrease of change in impedance ratios in low-viability ranges (< 40%). When the temporal slope of the ratio becomes small, differences between conditions are less distinguishable. Because the deviation between estimated viability and actual viability maintained the small value even at lower viability ranges, it is thought that impedance-based estimation is applicable for assessing viability during cold storage up to this duration.

Session Category

Cell Biomechanics: Methods and Models

P1-037

Mechanotransductive Control of Nucleus Pulposus Cells: A Regulatory Network Model Analysis

Dr. Zerihun G. Workineh, Prof. Jérôme Noailly

Universitat Pompeu Fabra, Barcelona, Catalonia, Spain

Introduction

The nucleus pulposus (NP) continuously experiences mechanical forces that are converted into biochemical signals through mechanotransduction (MT). While physiological loading maintains homeostasis, excessive loading induces inflammatory and matrix-degrading responses [1]. Although individual MT pathways are known, their integrated behavior remains incomplete. To address this, we develop an integrated regulatory network model (RNM) capturing NP responses across mechanical regimes.

Methods

A systematic review of 150+ studies was conducted to classify mechanical load conditions relevant to NP cells. Literature, and Reactome and KEGG database, knowledge, was mapped in a 140-node, 353-edge RNM encompassing mechanoreceptors, intracellular mediators, transcription factors, and effectors. The RNM was formulated as a semi-quantitative ODE system consistent with Boolean logic [2], with steady states identified through >100 randomized initializations. Mechanical loading was represented through two regulatory input nodes: NL and HL reflecting normal and hyper-loading, respectively. Load regimes were: Hypo ($NL \leq 0.1$, $HL \leq 0.1$); Normal ($NL > 0.1$, $HL \leq 0.1$); Hyper ($NL \leq 0.1$, $HL > 0.1$).

Results

Hypo-loading produced a globally dampened response, with modest activation of oxidative-stress mediators (Fig. 1). Normal-loading enhanced coordinated anabolic signaling, increasing matrix proteins (ACAN, COL2A1), growth factors (TGFβ, IGF1, GDF5) (Fig. 1), and transcription factors (e.g., SOX9, PPARγ). Hyper-loading redirected the network toward a pro-catabolic–inflammatory state, elevating cytokines, proteases (MMPs, ADAMTS), oxidative-stress/apoptotic nodes (ROS, BAX, CASP3/9), and degeneration-associated transcription factors (NF-κB, AP-1). From 37 RNM falsification tests against independent cell load–response reports, about 92% passed the test.

Discussion

The RNM robustly captured load-dependent NP cell regulation by integrating dispersed MT information into a unified, interpretable framework. The NL/HL switch formulation reproduced established experimental outcomes: Hypo-loading generated slight pro-catabolic drifts, Normal-loading produced a coherent anabolic–homeostatic program, and Hyper-loading activated pro-inflammatory, oxidative, and proteolytic pathways characteristic of degenerative stress, in the modelled NP cells. The high falsification-pass rate further indicated the RNM's ability to reproduce known biological behaviors. The network inputs and outputs remain qualitative, but simulations and interpretability of the resulting node activations are an asset to explore intervention targets in disc degeneration.

Images (Optional)

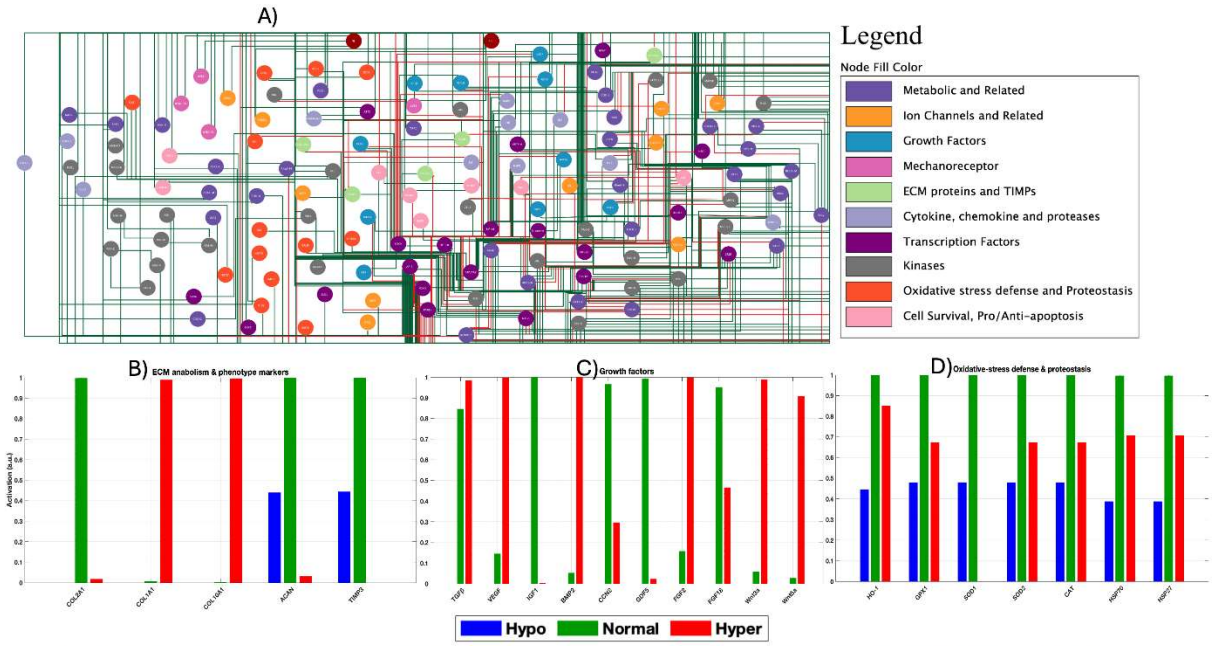


Fig. 1: Topology of NP Mechanotransductive RN (A) and activation levels of some groups of nodes (B, C, D).

References (Optional)

1. Shi S. et al., *Arthritis Res Ther* 24, 119 (2022).
2. Mendoza et al., Theor Biol Med Model. 2006

Acknowledgements (Optional)

European Research Council (ERC-CoG O-Health-101044828).

Session Category

P1-038

MATHEMATICAL MODELLING OF BONE REMODELLING TO SIMULATE $PM_{2.5}$ METAL EFFCTS ON BONE

Ms. Joudi Altaleb, Dr Ulrich Hansen, Dr Richard Abel, Dr Ian Mudway

Imperial College London, London, London, United Kingdom

Introduction

Osteoporosis poses a global health challenge. A neglected cause for osteoporosis is $PM_{2.5}$ pollution. Epidemiological evidence shows associations between long-term $PM_{2.5}$ exposure with osteoporosis [1]. One hypothesis suggests that inhaled airborne $PM_{2.5}$ associated metals impact bone cell populations affecting bone remodelling. Therefore, we developed a computational model to simulate the long-term effects of inhaled $PM_{2.5}$ associated metals on bone.

Methods

A biological algorithm of bone remodelling was constructed with a pharmacokinetic–pharmacodynamic framework for $PM_{2.5}$ metals. It includes a bone volume (BV) calculation based on cell population dynamics. Pharmacokinetics follow metals from inhalation $Dose_{metal}$,through the serum compartment $Metal_{CC}$ with both a linear and a nonlinear Michaelis-Menten elimination rate into a bone compartment $Metal_{BC}$. $Metal_{BC}$ is mapped onto functions which modulate the different bone cell types, enabling the BV calculation.

Results

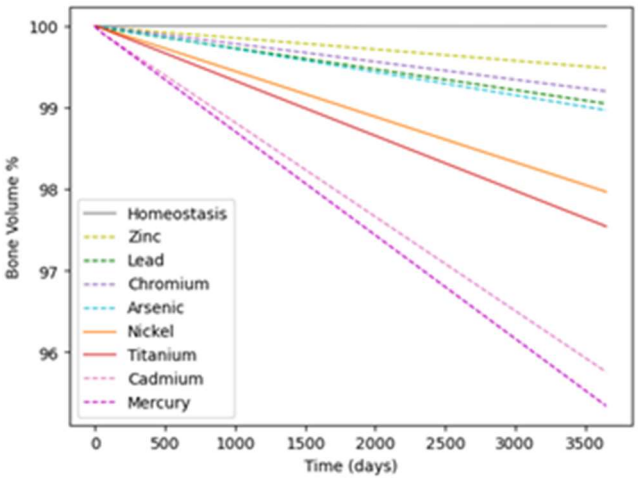
The model predicted the adverse effects of chronic exposure to Zinc, Lead, Chromium, Arsenic, Nickel, Titanium, Cadmium, and Mercury. Ten-year simulations produced bone loss values that are similar to the high levels seen in post menopause. Zn reduces BV by approximately 8.3% of overall BMD loss in post menopause [2]. Pb, As, and Cr resulted in approximately 17% of the BMD loss seen in post menopause [2]. Ni, Ti, Cd, and Hg produced BV decreases equivalent to 33%, 42%, 66%, and 76% of post-menopausal bone loss [2], respectively.

The studies used to get data on metal effects vary widely, so the units of their concentrations also vary. The figure shows the effects of Zn (300 mg/kg), Pb (5.00 μM), Cr (0.5mg/kg), As (10.00M), Ni (0.017 μM), Ti (209 μM), Cd (0.03 μM), and Hg (1.00 μM) on BV percentage over 10 years. The in-vivo and in-vitro data have been grouped for illustrative purposes.

Discussion

Simulations suggest that long-term, low-dose $PM_{2.5}$ metal exposures can meaningfully accelerate bone loss and potentially worsen osteoporosis risk. Even in a healthy baseline model without simulated postmenopausal decline, bone volume decreased by amounts comparable to those observed in menopausal women over a decade.

Images (Optional)



References (Optional)

[1] Qiao D*, et al*. Environ Res. 2020

[2] Holloway-Kew, K. L. *et al.*, J. A Calcified Tissue International, 2025.

Session Category

Cell Biomechanics: Methods and Models

P1-039

Basal Body Bending Due to Interactions of Motile Cilia in *Tetrahymena Thermophila*: Computational Modeling Reproduces Observations From Nanoscale 3D Imaging

Dr. Louis Woodhams PhD[1], Professor Phil Bayly PhD[1], Professor Chad Pearson PhD[2], Dr. Anthony Junker PhD[3], Dr. Adam Soh PhD[4]

[1]Washington University in St. Louis, Saint Louis, MO, United States. [2]University of Colorado School of Medicine, Aurora, CO, United States. [3]Emory University, Atlanta, GA, United States. [4]Duke University, Durham, NC, United States

Introduction

The single-celled organism *Tetrahymena thermophila* is propelled by an array of motile cilia structurally similar to those in human airways, making it an excellent model organism for studying ciliary beating. The approximately 400 cilia covering the surface of a *Tetrahymena* cell in a grid pattern (Fig. 1A) [1] do not beat in perfect synchrony; instead, metachronal waves of ciliary activity sweep across the cell surface much like "the wave" in a crowded baseball stadium.

In the current work, we apply computational modeling to better understand how internal forces transmitted by sub-cortical structures (Fig. 1B) cause deformations observed in *Tetrahymena* basal bodies (BBs). These forces may be responsible for ciliary coordination in a variety of organisms.

Methods

A computational model of the "9+2" ciliary axoneme and BB was built using commercial finite-element software using slender beam elements (Fig. 1C) [2]. Beating was driven by balanced internal forces and moments modeling the effects of dynein motor proteins. Sub-cortical forces between cilia were initially modeled using phase-delayed forces on the BB of a single cilium. In current work we expand this to a model of 3 interconnected cilia (Fig. 1D).

Results

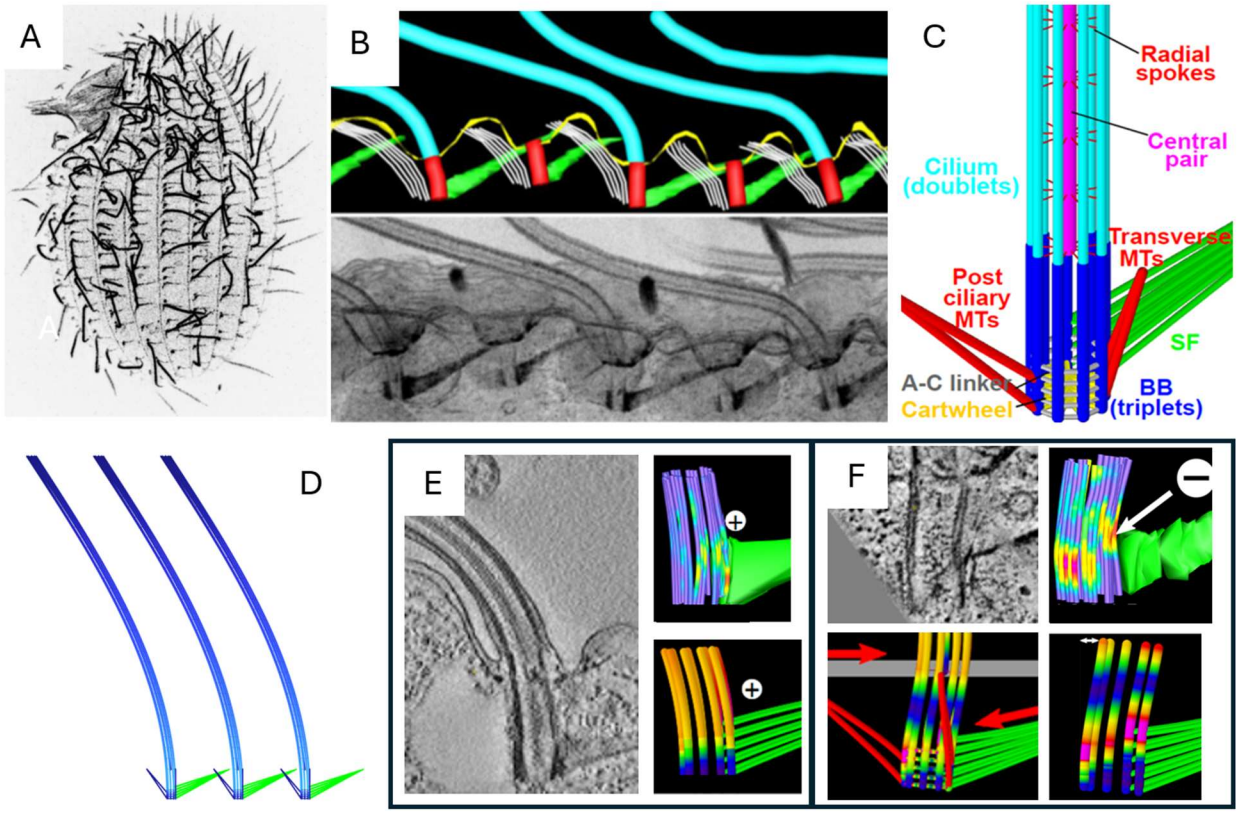
The single-cilium model matched bend patterns observed in BBs at 37 °C (Fig. 1E). Recreating the counter-bends observed at 30 °C required applying a phase-delayed force to BB connections which modeled interactions between out of phase cilia and the structural differences observed in cells grown at lower temperatures (Fig. 1F).

Perturbations to the computational model reproduced deformations observed in mutants with deficiencies in BB interconnections (disA-1) and internal BB structures (Poc1Δ).

Discussion

The current computational model helps us to understand how internal forces create deformations observed in *Tetrahymena* BBs and gives us a way to test hypotheses about the roles of structures within and connected to cilia by perturbing their properties and connections. In ongoing work, we seek to understand how ciliary beating is coordinated by expanding the model to explicitly simulate multiple beating cilia and their interconnections.

Images (Optional)



References (Optional)

[1] A.W.J. Soh et al., Mol Biol Cell, 2022

[2] A.D. Junker et al., Mol Biol Cell, 2022

Session Category

Cell Biomechanics: Methods and Models

P1-040

A Microscale Thermal Measurement for Evaluating Thermal Transport Properties Induced by Biomacromolecular Structural Transitions

Mr. Rei Nagayama, Prof. Kosei Kawai, Prof. Jeonghyun Kim, Prof. Kosaku Kurata

Kyushu University, Fukuoka, Fukuoka, Japan

Introduction

Recent studies have reported the existence of intracellular hotspots that are locally elevated by 1-2 K relative to the surrounding cytosol. However, calculations of intracellular temperature rise based on heat conduction predict an increase of only 10^{-5} K. As a potential mechanism for these localized intracellular hotspots, we focused on changes in thermal transport properties associated with temperature-responsive structural transitions in biomacromolecules. Therefore, this study aimed to establish an experimental system capable of simultaneously measuring molecular structural changes and thermal transport properties while varying temperature within a microchamber.

Methods

A fine platinum wire was suspended within a microchamber capable of holding liquid samples, allowing localized heating by applying an electric current. First, the relationship between the wire's temperature and electrical resistance was calibrated, confirming that the thin wire can also be used as a temperature sensor. Second, using air, water, and Poly(N-isopropylacrylamide) (PNIPAM) ,which undergoes a hydration-structure transition at approximately 32℃, aqueous solution as samples, the thin wire was heated stepwise under varying heat inputs. The voltage drop and current across the wire were measured using the four-terminal method, and the average temperature rise of the wire was calculated. Finally, based on the heat balance of the thin wire, the average heat transfer coefficient between the wire surface and each sample was determined from the measured temperature rise.

Results

When the thin wire was surrounded by air or water, the average heat transfer coefficient increased in a temperature-dependent manner. Furthermore, the coefficient consistently higher in water than in air. In the PNIPAM aqueous solution, the highest heat transfer coefficient was observed at 35℃, which is above the transition temperature of approximately 32℃.

Discussion

In this experiment, a 100-μm-diameter wire was used. Heat transport from the wire to the surrounding sample is considered to be dominated by thermal conduction rather than convection. Therefore, the obtained average heat transfer coefficient reflects the thermal conductivity of the sample. The increase in the average heat transfer coefficient observed at 35°C in the PNIPAM solution indicates that this experimental system is capable of detecting changes in heat transport properties associated with temperature-responsive structural transitions.

Images (Optional)

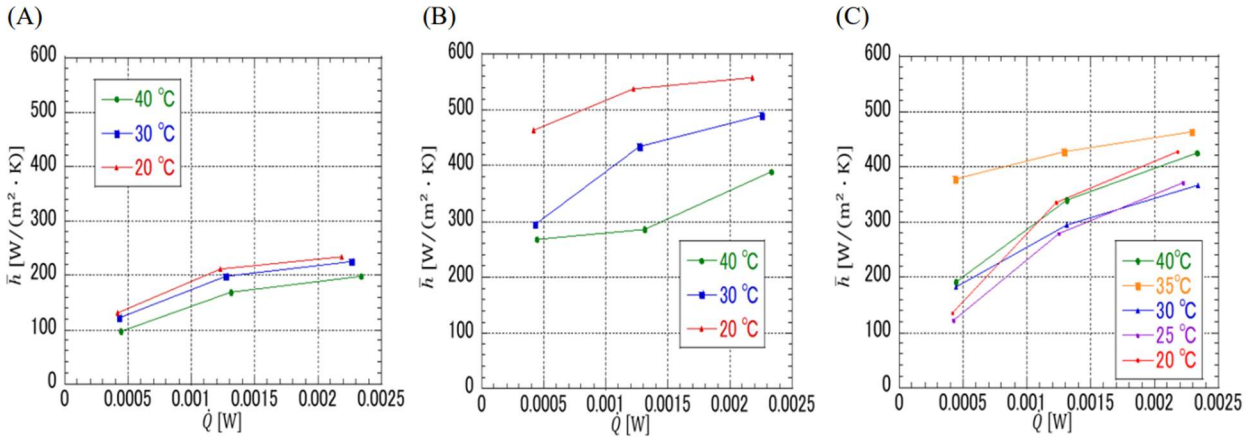


Fig. Average heat transfer coefficients of (A) air (B) water (C) PNIPAM aqueous solution.

Acknowledgements (Optional)

This work was supported by JSPS KAKENHI Grant Number 25H01385.

Session Category

Cell Biomechanics: Methods and Models

P1-041

Stress-induced Response of 3D Bioprinted Cell Filaments Under Controlled Strain Rate

Ms. Shanshan Zhang PhD student

The University of Hong Kong, Hong Kong, Hong Kong, China

Introduction

Mechanical stress not only induces deformation but also triggers morphological remodeling and functional changes within tissues. However, most existing studies have focused on cell spheroids and monolayers, which have a complicated internal stress state and a two-dimensional (2D) nature. This makes it difficult to gain precise insights into how mechanical stress affects the behavior of 3D tissues [1]. In addition, although recent studies have demonstrated that necking and rupture can occur in strip-like heart tissues formed between two micropillars or constraining boundaries, the tensile stress developed there is solely due to active contraction of cells [2]. A method that allows for precise control of external stress on tissues with predefined geometry and composition is still lacking.

Methods

A micro tensile system was fabricated using digital light 3D printing. Force-sensing pillars were created by crosslinking polydimethylsiloxane (PDMS) with a weight ratio of 20:1 for the polymer and curing agent. Different strain rates were applied to the self-organization tissue, and optical images and videos recorded real-time changes in fiber morphology, focusing on necking and fracture processes. The instantaneous force on the fibers was calculated through the displacement of the micropillar, enabling characterization of stress changes over time due to external mechanical stimuli.

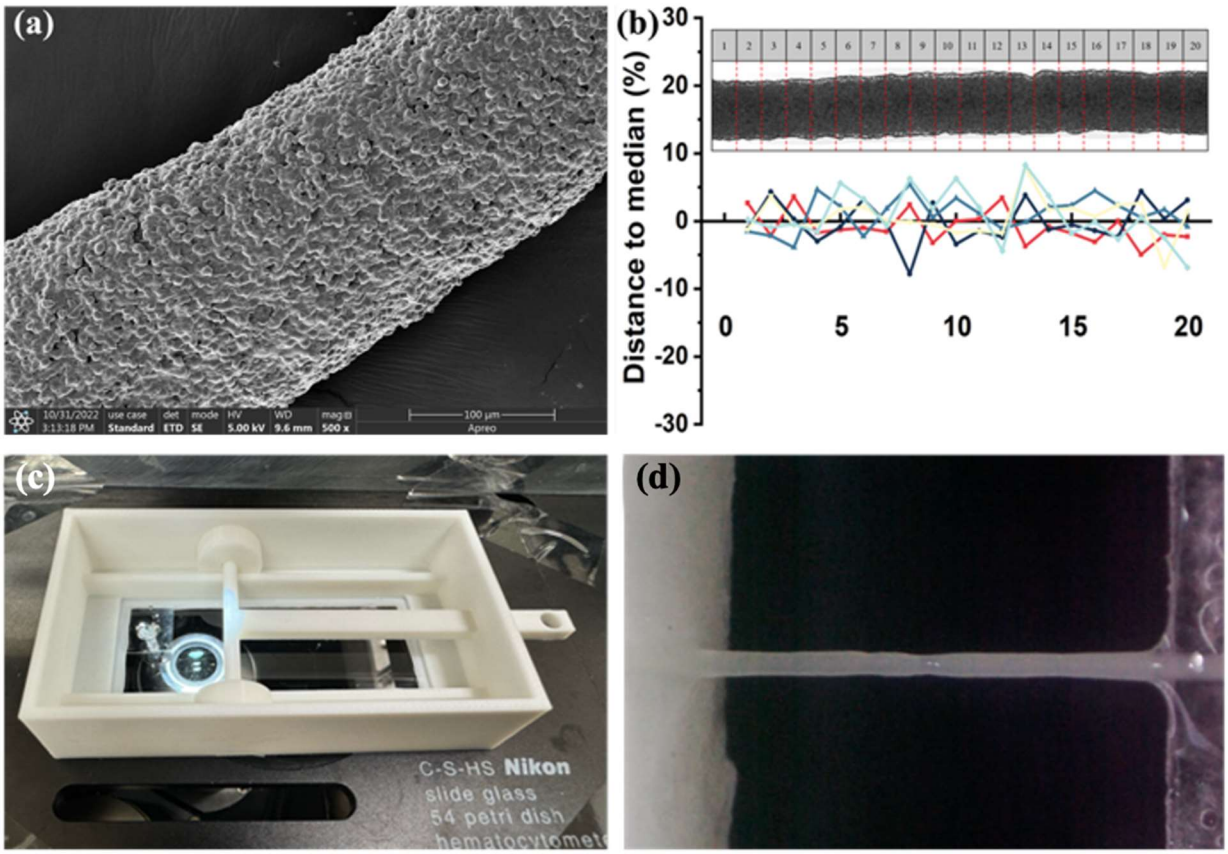
Results

The self-assembled cellular filaments have uniform diameters, providing standardized specimens for mechanical testing (Fig. 1a, 1b). The 3D-printed tensile platform delivers controllable, stable uniaxial tension (Fig. 1c), allowing uniform axial loading of the filaments. Optical imaging clearly reveals the morphological evolution of the filaments during tensile testing, including the onset of necking and its failure (Fig. 1d). By measuring the displacement of force-sensing micropillars, we can calculate the loading force on the filaments and compute the tensile stress in real time.

Discussion

Embedded bioprinting enables the systematic production of uniform cellular filaments. The tensile platform provides precise external force, allowing for the systematic investigation of stress-induced responses. This project will deepen our understanding of dynamic fracture of predefined micro-tissue and support the advancement of future theoretical models.

Images (Optional)



References (Optional)

[1] Harris A R, et al. *PNAS,* 2012, 109(41): 16449-16454.

[2] Karakan M Ç, et al. *Lab on a Chip*, 2024, 24(6): 1685-1701.

Session Category

Cell Biomechanics: Methods and Models

P1-042

Receptor-Level Modelling of OPG-Modulated RANKL Gradients in a Microscale Chemokine Diffusion Platform

Ms. Mariia Mielkozorova PhD Student, Dr. Alexandra Komrakova Associate Professor, Associate Dean, Dr. Svetlana Komarova Professor, Chair of BME Department

University of Alberta, Edmonton, Alberta, Canada

Introduction

Bone actively adapts to mechanical forces. At the cellular level, bone adaptation is actualized through the action of osteoclasts that resorb bone and osteoblasts that build bone. The key regulator of osteoclast formation and function is RANKL, a cytokine that binds to it cognate osteoclast receptor RANK. OPG is a decoy receptor that binds RANKL and prevents it interaction with RANK. We hypothesize that spatially segregated sources of RANKL and OPG can sculpt chemokine landscapes and mediate precise bone mechanoadaptation. In order to enable future experiments, we aimed to develop a quantitative framework that couples chemokine transport and interactions in experimental environments.

Methods

We engineered a 24-well plate insert with side pockets acting as RANKL and OPG reservoirs, separated from a central chamber by a rectangular window covered by a 70 kDa cut-off porous membrane. RANKL and OPG transport and interactions were simulated using coupled reaction-diffusion equations assuming experimentally suggested RANKL trimer/OPG dimer stoichiometry with Robin boundary conditions. Transport parameters were constrained using published data. Simulations were implemented in MATLAB.

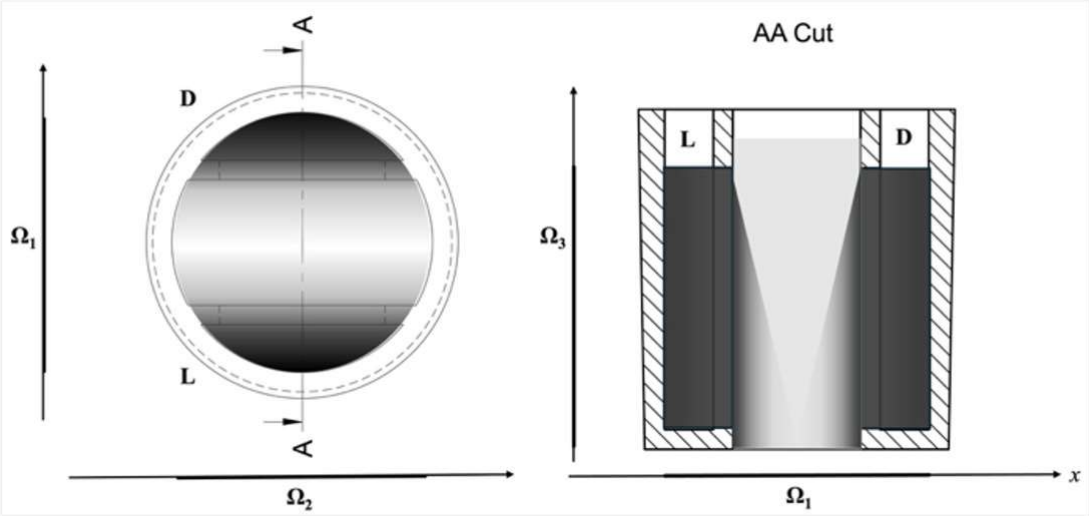
Results

Simulations predicted that when RANKL is the only chemokine present in the system, the RANKL gradient develops across the central chamber within 24 h and is sustained for approximately 72 h, after which RANKL concentration reaches equilibrium across the domain. When only OPG is present in the system, the dynamics of gradient formation was similar, although since OPG dimer is of higher molecular weight, the gradient developed slower and was sustained for longer time. When OPG was placed in the chamber opposite to RANKL, RANKL gradient was steeper, and localized sink behaviour was developed. The position of the sink within the domain depended on initial RANKL/OPG concentrations. Preliminary experiments examined the stability and persistence of RANKL gradients over 3-6 days with and without OPG loaded in the opposite pockets.

Discussion

This study builds the integrated modelling-experimental platform to study live-cell behaviour in defined RANKL/OPG fields. By reframing OPG as an active sculptor of guidance cues, rather than solely a RANKL blocker, our work suggests novel mechanism of RANKL/OPG modulation to achieve precise bone adaptation to mechanical cues.

Images (Optional)



Geometry of the culture insert used for RANKL-OPG diffusion modeling. Top view of the cylindrical insert (domain Ω_2) placed within the culture dish (domain Ω_1), showing two localized delivery compartments: RANKL source (L) and OPG source (D). Each compartment delivers ligand through an opening along the boundary. (Right) Cross-sectional view along the AA cut illustrating the vertical geometry of the insert within the culture dish (domain Ω_3). The RANKL (L) and OPG (D) compartments are positioned on opposite sides, separated by the central culture region, allowing diffusion across the experimental domain.

Session Category

Cell Biomechanics: Methods and Models

P1-043

Directional Control of Cell Division Using Wavy PDMS Substrates for Evaluating Orientation-Dependent Responses to Tumor Treating Fields

Ms. YUEYING WU, Prof. Jeonghyun KIM, Prof. Kosei KAWAI, Prof. Kosaku KURATA

Kyushu University, Fukuoka, Fukuoka, Japan

Introduction

Tumor-treating fields (TTF) are a promising cancer therapy that applies alternating electric fields to tumors. Previous studies have shown that TTF generates dielectrophoretic forces that reorient intracellular dipoles and disrupt cell mitosis, as most cells damaged after 72 hours of TTF exposure were found to divide along the electric field direction. To further elucidate the underlying mechanism, we aimed to induce the directional control of cell division and subsequently apply electric fields to cells with predefined orientation.

Methods

To regulate the orientation of cell division, we fabricated wavy wrinkle structures on PDMS substrates. Three-millimeter-thick PDMS films were stretched at ratios of 1.3–1.7 and irradiated with UV light for 20–25 min to induce surface wrinkles. A549 human lung adenocarcinoma epithelial cells were then seeded onto the wavy surfaces, where they preferentially divided along the wrinkle crest. After establishing directional control, electrodes were inserted into the cell culture dish to apply a 3 V, 300 kHz electric field. Time-lapse imaging was performed to evaluate mitosis duration, proliferation, and migration.

Results

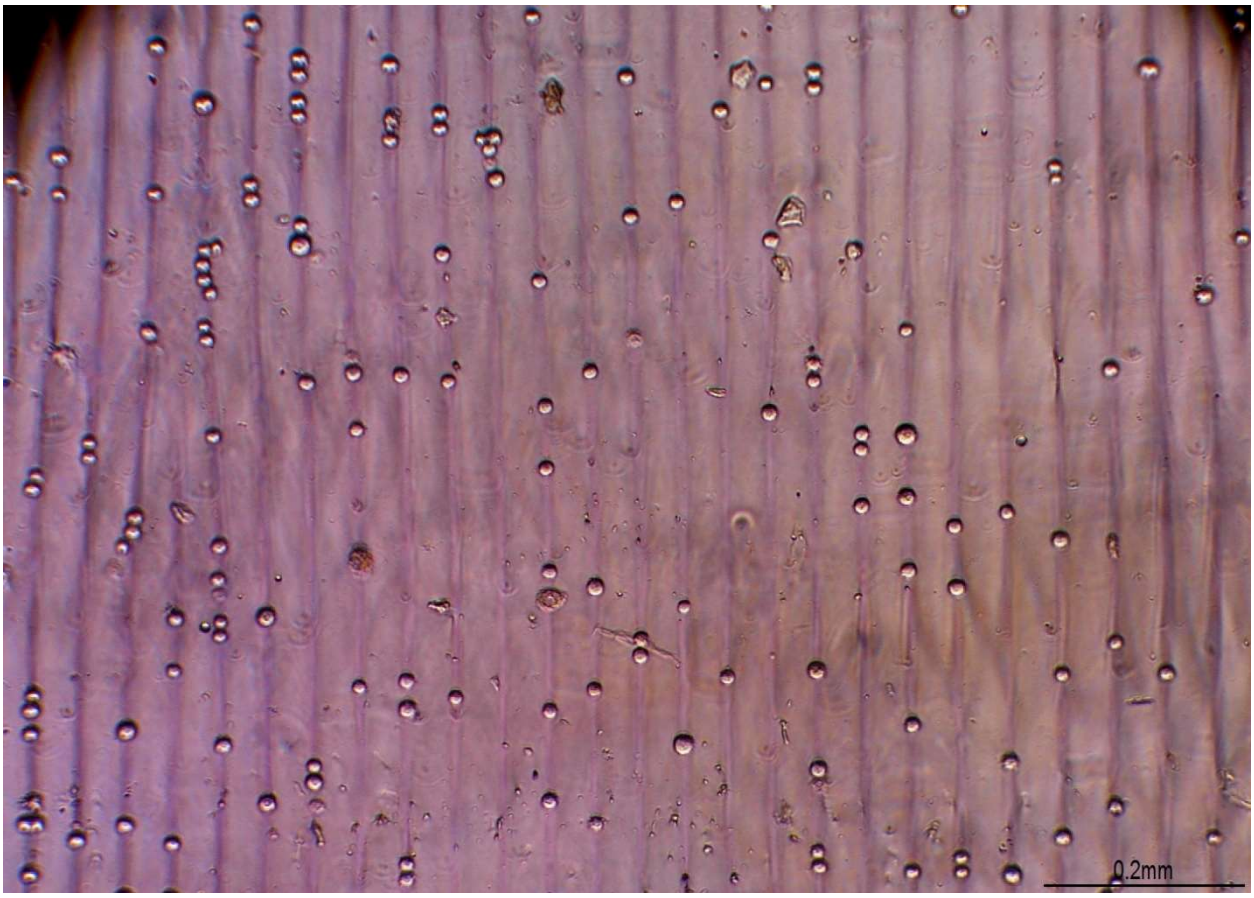
Wavy PDMS patterns with wavelengths of 35–50 μm and amplitude of 5–20 μm were successfully fabricated. More than 50% of A549 cells divided along the crest direction, and division-orientation control improved with increasing wrinkle amplitude. No significant effect of wrinkle wavelength was observed.

Discussion

We found that the effectiveness of division-orientation control depends primarily on wrinkle amplitude. It was also influenced by cell attachment and seeding density. Preliminary evidence further indicates that the direction of TTF application may influence the duration of telophase, suggesting a directional dependency in the mitotic response to alternating electric fields. As a next step, we will extend the culture duration or delay imaging onset to enhance orientation stabilization. Once stable directional alignment is

established, TTF stimulation will be applied to these cells to further elucidate how electric-field directionality modulates mitotic progression.

Images (Optional)



Session Category

Cell Biomechanics: Methods and Models

P1-044

How do the amplitudes of horse's gait affect the three-dimensional kinematics of the trunk and pelvis during riding in typically developing children?

MSc Leandra Aparecida Leal[1], PhD Andréa Gomes Moraes[2], PhD Kate da Costa Barcelos[3], PhD Amanda Piaia Silvatti[4], MSc Aline Dalfito Gava[1], PhD Ana Cristina de David[1]

[1]Universidade de Brasília, Brasília, DF, Brazil. [2]Secretaria de Estado de Educação, Brasília, DF, Brazil. [3]Universidade Federal de Goiás, Goiânia, Goiás, Brazil. [4]Universidade Federal de Viçosa, Viçosa, Minas Gerais, Brazil

MSc Leandra Aparecida Leal

Introduction

Each horse has a natural walking amplitude that generates different postural adjustments for the rider. This is an important factor in planning rehabilitation programs such as equine therapy. This study compares trunk and pelvis kinematics of typically developing (TD) children across different horse walk amplitudes: collected, medium, and extended.

Methods

The study included three TD children experienced in horse riding, aged 6, 11, and 13 years. The horse (*Crioulo* breed) measured 1.39 m at the withers and weighed 380 kg. Riders were equipped with a pad and straps without stirrups. In the collected walk, the hind limb does not overtake the forelimb; in the medium walk, it overlaps; and in the extended walk, it exceeds it. Data were collected in a closed sand arena using eight Vicon Vero v2.2 cameras at 100 Hz, positioned four cameras on each side covering a 10 m distance. The Plug-in Gait full-body protocol with 39 markers was used, and three additional markers were placed on each horse’s hooves. Data were normalized to the horse's gait cycle using forelimb strike as reference, and descriptive analyses were based on the average of three trials.

Results

The speeds (m/s) of the horse´s walk amplitudes were: collected (0.69±0.07), medium (0.97±0.05), and extended (1.54±0.06). It was observed that the pattern of trunk and pelvic

curves in children is similar across the three gait amplitudes of the horse. However, the trunk and pelvis exhibit greater amplitude in the sagittal and frontal planes during the extended equine gait (Figure 1).

Discussion

The results show that the horse's gait amplitude influences trunk and pelvic movements in children, indicating greater postural demands during extended walking. These preliminary findings may assist equine therapy professionals in selecting appropriate strategies based on therapeutic goals. Further studies with a larger number of participants and different horse breeds are needed.

Images (Optional)

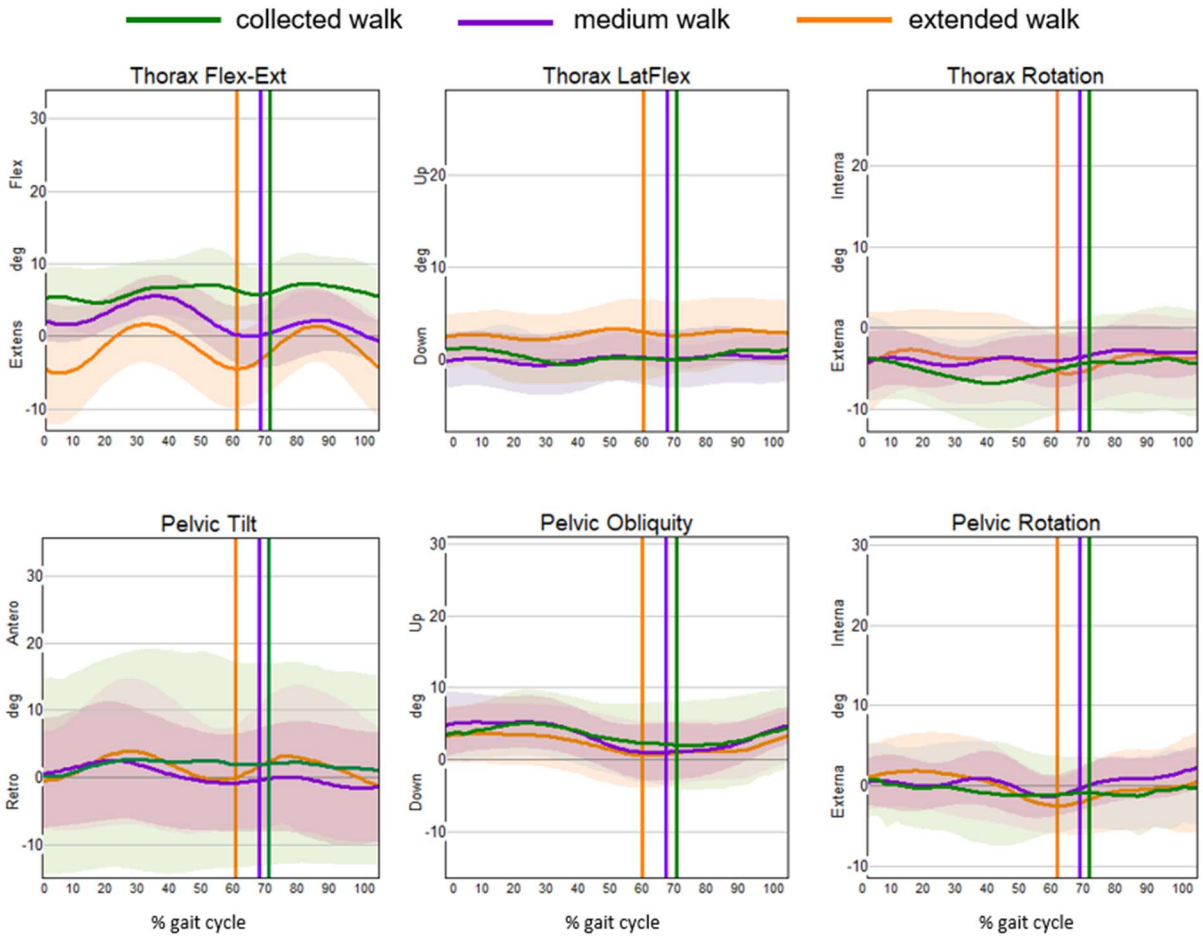


Figure 1. Angular kinematics of the trunk and pelvis on the right side of three TD children at different walk amplitudes of the horse.

Session Category

Human Motion and Performance: Balance, Posture and Control

P1-045

Emergent Behaviors in Human Compensatory Stepping Following Impulsive Torso Perturbation

Mr. Bhavya Giri Goswami MASc Student, Systems Design Engineering, Prof. Arash Arami Associate Professor, Mechanical and Mechatronics Engineering, Prof. John McPhee Professor, Systems Design Engineering

University of Waterloo, Waterloo, Ontario, Canada

Mr. Bhavya Giri Goswami

Prof. Arash Arami

Introduction

Single-step compensatory stepping is a reactive balance strategy used when large, unexpected perturbations push the center of mass (CoM) outside the base-of-support (BoS). While sagittal-plane stepping has been extensively studied[1], our impulsive torso perturbation experiments revealed some new observations.

Methods

Ten able-bodied participants (23.3±2.1yrs; 67.2±13.4kg; 1.73±0.06m; 5M/5F) received anterior–posterior impulsive torso perturbations of three magnitudes (Low <15%BW, Medium <25%BW, High <65%BW). Ten perturbations of each type were applied in random order, above the sacrum using a padded push-stick with an inline 3-axis force sensor. Participants were instructed to “balance naturally”. Whole-body motion capture, force plates, and leg EMG data (Soleus, Tibialis-Anterior, Rectus-Femoris, Bicep-Femoris) were recorded and processed to calculate stepping parameters (S*, t*) and muscle co-contraction.

Results

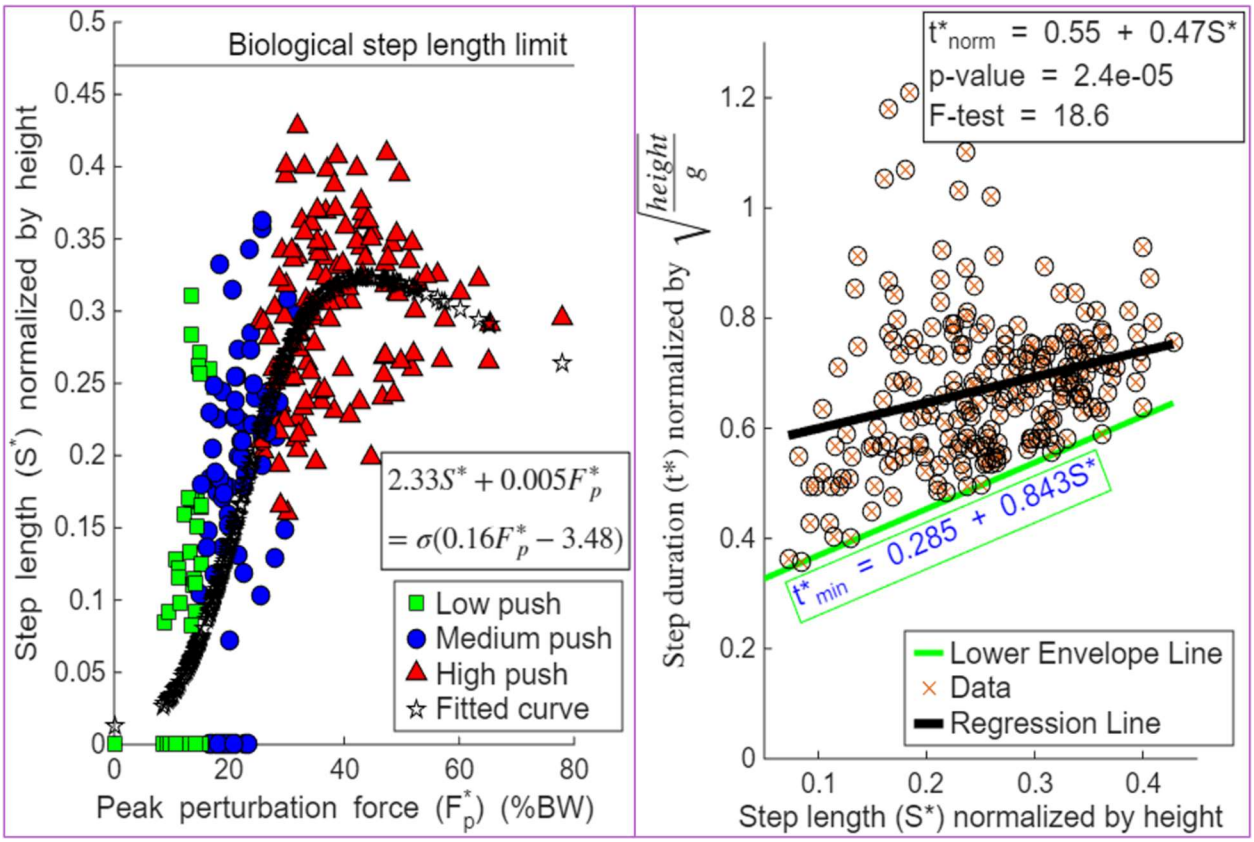
- Out of 305 trials across all participants, 228 (~75%) involved compensatory stepping; the remainder were stabilized using feet-in-place ankle strategy. Stepping probability increased with perturbation magnitude, reaching 50% at ~16.1%BW and 100% at ~25%BW peak force.

- Step length exhibited a sigmoidal(σ) relationship with peak push force, saturating at larger forces—likely due to biomechanical limits and the need for multiple steps.
- Step duration increased significantly with step length, with high variability for steps shorter than 0.25×height. Moreover, step duration appeared lower-bounded by a linear function of step length, likely reflecting muscle contraction limits.
- The inefficient hip strategy was absent, with negligible pre-toe-off bilateral hip flexion (-0.33±1.50°), minimum Rectus-Femoris activity, and a minor difference in ZMP-CMP trajectories[2] (0.0±2.8mm). This is likely due to perturbation location and induced randomness.
- 76.6% of compensatory steps used toe or mid-foot strike rather than heel strike. This pre-contact plantarflexion shifts the center of pressure anteriorly to enhance CoM deceleration.
- Swing-leg ankle co-contraction before step initiation strongly correlated with the time between CoM projection exiting the BoS and toe-off (r=0.78).

Discussion

This study identifies several new characteristics of sagittal-plane compensatory stepping, including step-force relationships, strategy selection, distinctive foot-strike, and EMG behaviors. These insights can support improved predictive models and control strategies for exoskeletons and prostheses.

Images (Optional)



References (Optional)

[1] Maki et.al., “Maintaining Upright Stance”, *Physical Therapy*, 1997

[2] Popovic et.al., “Ground Reference Points Locomotion”, *IJRR*, 2005.

Session Category

Human Motion and Performance: Balance, Posture and Control

P1-046

Balancing for Two: Inverted Pendulum Model of Pregnancy Reveals Energy/Stability Tradeoff in Adaptation to Added Mass During Standing Balance

Ms. Autumn Routt[1], Dr. Hansol Ryu[1,2], Dr. Kristen Jakubowski[1,2], Dr. Gregory Sawicki[1], Dr. Lena Ting[2,1]

[1]Georgia Institute of Technology, Atlanta, Georgia, United States. [2]Emory University, Atlanta, Georgia, United States

Introduction

Whether you are carrying a baby or a rucksack, it is important to be able to adapt to added mass. Pregnancy is an extreme example. Falls in pregnancy are common and dangerous, so pregnant people who avoid falling can be considered expert adapters. Prior literature counterintuitively shows that pregnant non-fallers (PNFs) exhibit greater center of mass (COM) displacement during perturbed standing balance compared to pregnant fallers (PFs) [1]. We developed a computational model to test whether increased COM displacement could be attributed to PNFs being better adapted than PFs to added mass. We hypothesized that this difference could be explained by PNFs prioritizing the reduction of energy costs over stability.

Methods

The dynamics-based model simulated an inverted pendulum on a cart with offset added mass (Fig.1A). A feedback controller used angle and angular velocity to create a torque at the pivot point (Fig.1B). We compared outputs from gains optimized for added mass ("adapted") and no added mass ("unadapted") based on a cost function comprised of the sum of squared muscle torques (J_{energy}), and the sum of squared angles and squared angular velocities ($J_{stability}$).

Results

The adapted model reduced stability costs relative to the unadapted model for all conditions (Fig.1C&D). With small added mass, adaptation increased J_{energy}. With larger added mass, both J_{energy} and $J_{stability}$ were reduced, but J_{energy} was reduced more than $J_{stability}$ when added mass >40kg.

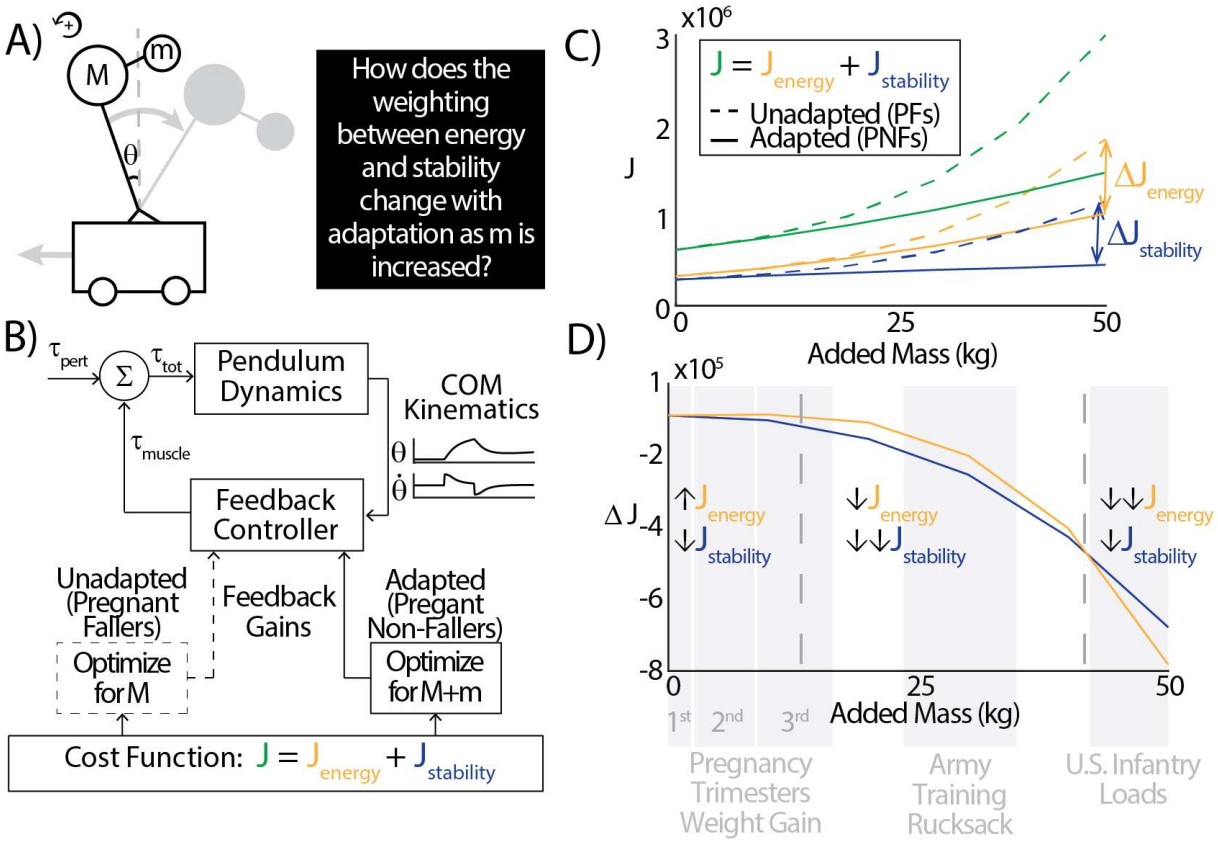
Discussion

Our adapted model did not explain increased COM excursion in PNFs. At loads similar to pregnancy, stability costs were always prioritized over energy costs. This might mean that the difference in prior literature is from musculoskeletal remodeling rather than alterations

in neural control strategy. Alternatively, some of the assumptions made in this simulation, particularly that PFs are best represented as being adapted to zero added mass and that cost function weights are fixed over the adaptation period, may be incorrect.

When loads were increased to those of a rucksack, energetic costs were sometimes prioritized over stability costs. This means for very large loads there may be a threshold past which stability is compromised because of heightened energy costs.

Images (Optional)



References (Optional)

[1] McCrory *et. al.* , BJOG, 2010

Acknowledgements (Optional)

This work was supported by the Integrative Movement Sciences Institute (IMSI) Biological Integration Institute, NSF-DBI-2319710, and the Georgia Tech Interdisciplinary Research Fellowship.

Session Category

Human Motion and Performance: Balance, Posture and Control

P1-047

Perturbation Recovery Time Detects Age-Related Changes in Balance Control of Running

M.Sc. Carlo von Diecken, M.Sc. Luca Braun, M.Sc. Bastian Anedda, M.Sc. Laila Sikeler, M.Sc. Janina Helwig, M.Sc. Sebastian Rehorst, Prof. Steffen Willwacher

Institute for Advanced Biomechanics and Motion Studies, Offenburg University of Applied Sciences, Offenburg, Baden-Wuerttemberg, Germany

Introduction

Balance control declines with age due to losses in muscle strength and sensory input, with deficits emerging at the fourth decade of life during challenging tasks. Running is a complex motor task requiring continuous and tight regulation of whole-body angular momentum (WBAM), which may be altered by age-related decline. When balance is further challenged by a perturbation (e.g., a slip), the resulting sudden shift in WBAM must be rapidly counteracted to prevent a fall. An accurate method for assessing this balance control during running would enable screening for deficits and facilitate early intervention.

Methods

Twelve young adult (26.8 ± 4.0 years; YR) and nine older adult (51.9 ± 3.8 years; OR) recreational runners completed 8 min treadmill runs at 2.78 m/s under normal running (NR) and restricted arm swing (RA) conditions, while sudden anterior-posterior slip-like perturbations were applied at pseudo-randomized time intervals. Normalized WBAM (nWBAM) in sagittal and frontal planes was computed from full-body kinematics and time-normalized to the gait cycle. Subject-specific 95% prediction bands (PB95) were constructed from unperturbed nWBAM curves (Fig. 1A). Perturbation recovery time (PRT) was defined as the duration from perturbation onset to the final time point at which either nWBAM curve exceeded PB95 bounds (Fig. 1A, B). A linear mixed-effects model assessed main and interaction effects of age group and running condition on PRT.

Results

PRT showed a significant condition–age-group interaction (p=0.004) with RA significantly increasing PRT in older runners (+0.43 s, p<0.001), but not in younger runners (+0.11, p=0.119). Further, no age-group differences were observed during NR (+0.03 s, p=0.821), but older runners exhibited longer PRT than younger runners under RA (+0.34 s, p=0.011; Fig. 1C).

Discussion

PRT increased in older adults only when perturbations were combined with restricted arm swing, indicating that age-related deficits in perturbation recovery emerge under added task constraints. This is supported by previous work showing that arm swing contributes to quick balance recovery and that subtle balance deficits become evident primarily during challenging tasks. Importantly, PRT combined with task manipulation distinguished between age groups, supporting its potential as a sensitive measure of balance control during running.

Images (Optional)

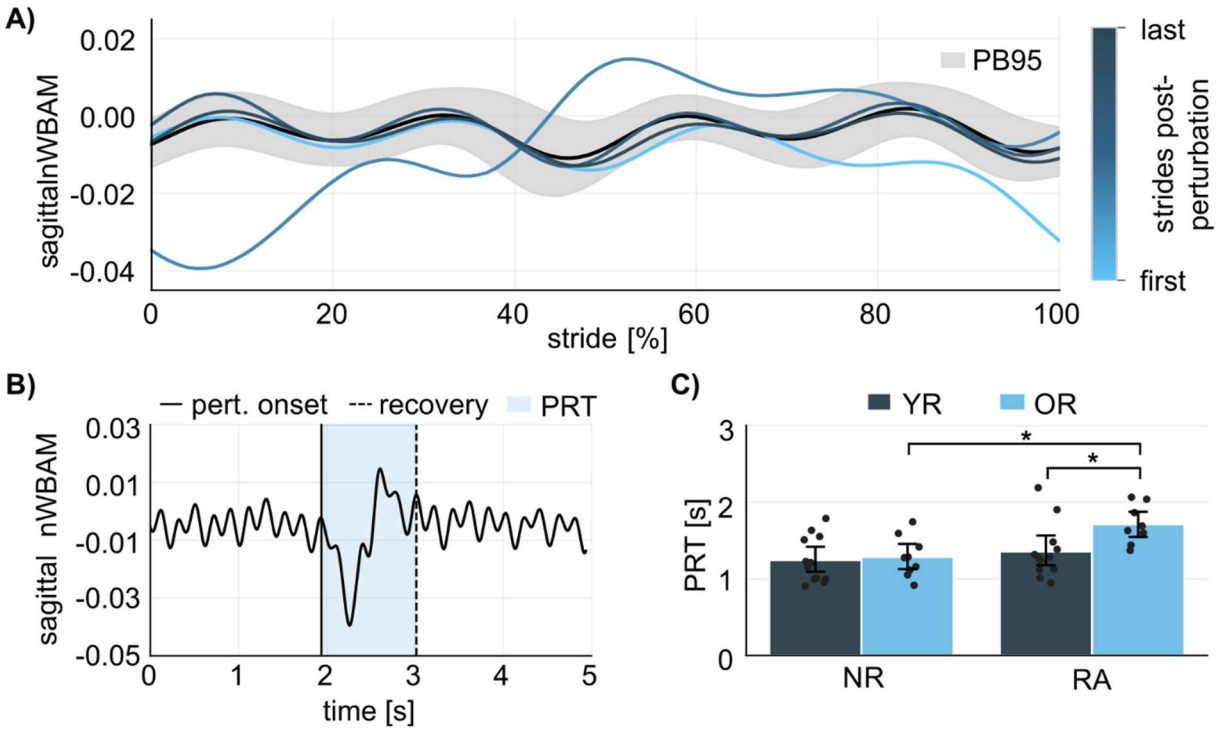


Fig. 1 A) PB95 of sagittal nWBAM and post-perturbation strides, B) sagittal nWBAM pre-during and post-perturbation, C) PRT of YR and OR during NR and RA conditions.

Session Category

Human Motion and Performance: Balance, Posture and Control

P1-048

A Novel Framework for Probing Inter-Limb Control in Standing Balance

Ms. Caroline Aitken M.E.Sc., Mr. Amin Nasrabadi M.E., Dr. Jean-Sébastien Blouin Ph.D., Dr. Lyndia Wu Ph.D., P.Eng.

The University of British Columbia, Vancouver, British Columbia, Canada

Introduction

Altered mediolateral (ML) balance is a hallmark of some neurodegenerative diseases and neural injury. Most authors quantify the centre of mass (COM) or the centre of pressure to estimate balance control under varied sensory conditions. Although this approach provides global measures of balance, it assumes inter-limb coordination is not an important aspect of balance deficits in clinical populations. To address potential deficits associated with inter-limb coordination, we developed a novel framework using two force plates to estimate bilateral torques required for standing balance control. We hypothesize that inter-limb control strategy preference varies with stance width.

Methods

Data were collected from three healthy participants standing on two force plates for 40 seconds at stance widths of 50%, 100%, and 150% of hip width (inter-hip-joint distance). The plantar/dorsiflexion and inversion/eversion axes of each foot were aligned with the anteroposterior (AP) and ML plane of the corresponding force plate (Fig. 1A). Force plate data were transformed to the ankle, and the COM's gravitational torque component – calculated using double-integration of the ground reaction forces – was removed to isolate the control signal.

Ankle inversion/eversion torques (T_i) contribute to ML motion (Fig. 1A). Plantar- and dorsi-flexion ankle torques also generate vertical forces at the ankle (F_z). When bilateral F_z have the same magnitude, pure AP torque is generated; asymmetric F_z also produces an ML torque (T_c) that increases with wider stance widths. To assess strategy preference, we compared torque variability between stance widths.

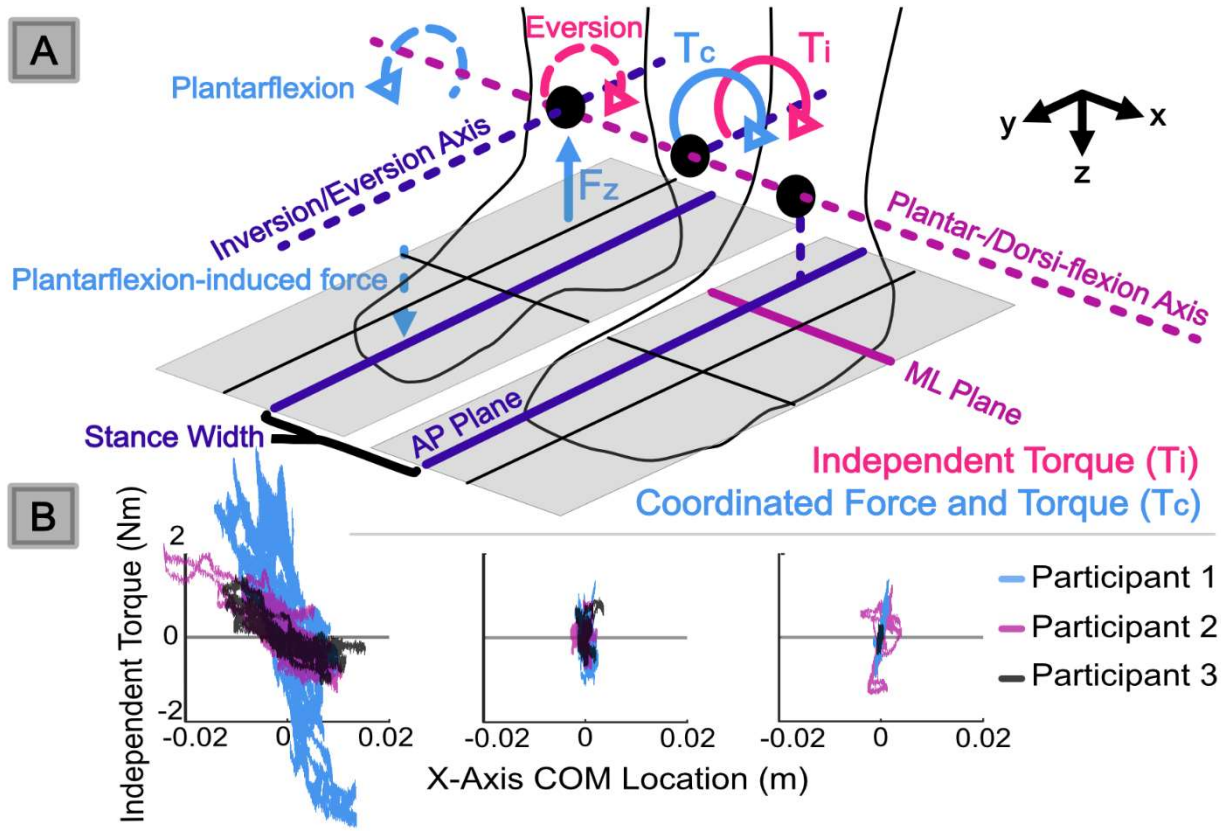
Results

T_i at 50% stance width had 8.8- and 11.4-times higher variability than at the 100% or 150% stance width (Fig. 1B). T_c variability was 12- and 8-times greater at 150% compared to 50% and 100% stance width.

Discussion

At narrow stance widths, larger T_i is likely necessary due to the smaller T_c torque arms. At wider stance widths, participants prefer the higher mechanical gain of T_c to enable the maintenance of upright balance. In future analyses, we will explore the coupling of control between the AP/ML planes, with the hope to establish a framework to reveal how neural degeneration and injury impact inter-limb coordination needed for the ML control of balance.

Images (Optional)



Session Category

Human Motion and Performance: Balance, Posture and Control

P1-049

Stable Centre of Pressure Control Is Critical for Balance in the Handstand

Dr. Charlotte Le Mouel

CNRS, Sorbonne Université, Paris, 75005, France

Introduction

During standing balance, participants control their Centre of Pressure (CoP) according to the Centre of Mass (CoM) state. This requires integrating proprioceptive, visual and vestibular information, as there is no physiological sensor of CoM state. Intriguingly, when skilled gymnasts perform the handstand, they also control their CoP according to their CoM state, indicating a novel sensorimotor coordination. We hypothesise that this sensory integration emerges over skill learning, with less accurate CoP control resulting in shorter handstands.

Methods

Sixteen intermediate-level gymnasts (inclusion criterion: being able to perform the handstand for more than 5 seconds) performed handstands during two 3-minute trials. The CoP was recorded using force plates. Full body kinematics were recorded using motion capture, and used to estimate the CoM position. The CoP was reconstructed as a linear sum of the delayed CoM position and velocity in the sagittal plane, yielding the proportional and derivative gains. The stability of the CoP controller on a given trial was determined analytically, depending on whether a controller with these gains can stabilise an inverted pendulum. We thus quantified both the accuracy with which the CoP followed the CoM (percent of CoP variance explained by CoM state) and whether the resulting controller was stable.

Results

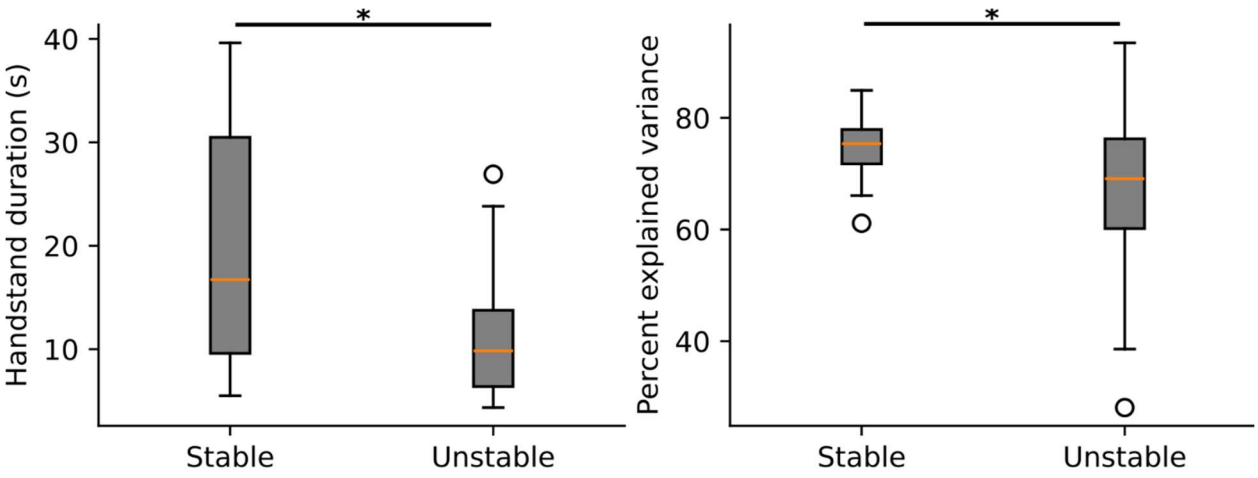
Of the 93 recorded handstands, 43 % adopted a stable CoP controller in the sagittal plane. These handstands had a significantly longer duration than those with unstable controllers (16.7 seconds versus 9.8 seconds) and more accurate CoP (75.4 % of CoP variance explained by CoM state for stable and 69.1 % for unstable trials).

Discussion

Contrary to our hypothesis, intermediate-level gymnasts have an accurate control of the CoP both for short and long handstands, suggesting that their skill is not limited by their sensory integration. Instead, their handstand durations are limited by their motor coordination, in particular their ability to adopt stable CoP controller gains. This may be

due to limited wrist flexion strength. This suggests that sensory integration of CoM state in the handstand is learned very early on in the skill acquisition process, and may be critical for achieving handstands lasting more than 5 seconds.

Images (Optional)



Influence of CoP controller stability on balance. Handstand duration (A) and Percent explained variance of the CoP in the sagittal plane (B) for trials with stable (left) or unstable (right) CoP control in the sagittal plane.

Session Category

Human Motion and Performance: Balance, Posture and Control

P1-050

Maintaining Functional Mobility: Effects of Ankle Bracing on Multi-Planar Joint Control During Landing Tasks

Dr. Clark Dickin, Dr. Henry Wang

Ball State University, Muncie, IN, United States

Introduction

Despite the use of Parachute Landing Fall techniques and Parachutist Ankle Braces, ankle injuries remain common during high-impact military landings. Extending support through the metatarsals, this study evaluated the effectiveness of an over-the-shoe External Ankle Brace (EAB) in stabilizing the ankle during landings from height. The goal was to determine whether the EAB could provide frontal and transverse-plane stability while permitting functional sagittal ankle motion without significantly altering knee or hip mechanics. We examined these effects across three landing styles: forward feet-apart, sideways feet-apart, and sideways feet-together.

Methods

Twenty healthy young adults performed landings from 20, 40, and 60 cm under two conditions: standard cross-trainer shoes (SHOD) and EAB worn bilaterally over the shoes. Each participant completed 3–5 trials per landing style and height, totaling 27-45 landings per session across two completely randomized test days (footwear, height, and jump style). A 12-camera Vicon motion capture system and two AMTI force platforms recorded three-dimensional joint kinematics and ground reaction forces, and inverse dynamics estimated joint torques for the two feet-apart landing styles.

Results

The EAB provided significant frontal and transverse plane control, reducing ankle eversion (21-41%) across all landing styles ($p < 0.001$), with the smallest eversion observed in sideways feet-together landings. EAB also reduced ankle abduction (5-16%), significantly for the sideways feet-apart landings ($p = 0.048$). While ankle dorsiflexion was reduced compared to SHOD ($p < 0.001$), sagittal mobility was only reduced by 2-6% across the landing heights and styles. Kinetic analysis for the two feet-apart styles showed a 20% reduction in plantarflexion torque and a 43% reduction in external rotation torque compared to SHOD, while frontal plane torque showed a minimal increase. Knee and hip loading patterns remained largely unchanged, indicating minimal transfer of load proximally.

Discussion

The EAB effectively provided frontal and transverse ankle stability while maintaining functional sagittal motion and not significantly altering knee or hip mechanics. While the landing heights were conservative, the general dose-response effects support the use of an EAB as a viable intervention to reduce ankle injury risk during high-impact landings, particularly in military and tactical contexts.

Session Category

Human Motion and Performance: Balance, Posture and Control

P1-051

Eye Drop Instillation Success Is Associated With Eye Drop Bottle Dynamics During Instillation

Mr. Daniel Duque Urrego[1], Dr. Stephen Cain[1], Ms. Ming-Chen Lu[2], Ms. Leslie Niziol[2], Mr. Cameron Haire[2], Dr. David Burke[2], Dr. Susan Brown[2], Dr. Paula Newman-Casey[2], Dr. Alanson Sample[2]

[1]West Virginia University, Morgantown, WV, United States. [2]University of Michigan, Ann Arbor, MI, United States

Introduction

Stability metrics derived from eye drop bottle acceleration in an inertial frame (free-acceleration) are associated with eye drop instillation success, but calculating free-acceleration from a bottle-mounted inertial sensor (IMU) requires gravity removal and frame transformations [1]. The objective of this study was to test whether stability metrics calculated from raw bottle-mounted IMU data, which do not require gravity removal or transformation, are also associated with instillation success. Simpler approaches could reduce the complexity of “smart bottle” implementations to monitor medication adherence events and instillation quality.

Methods

Ninety-nine older adults completed 18 instillation trials (three per eye in standing, sitting, and lying). A bottle-mounted IMU recorded linear acceleration and angular velocity. For each instillation attempt, we identified an instillation period using a velocity-based window. We computed stability metrics like those used for postural analysis from raw IMU data, as well as bottle tilt and instillation duration. Drop success (yes/no) was determined from synchronized video. For each posture and metric, we fitted an univariable logistic generalized estimating equation (GEE) with success as the outcome, the z-scored metric as the predictor, subject as the clustering factor, and an exchangeable working correlation. Odds ratios (ORs) with 95% confidence intervals were estimated, and adjusted p-values using the Holm method.

Results

Larger raw accelerations and angular velocities were associated with lower odds of drop success. In the lying posture, a 1-SD increase in peak planar acceleration was associated with ≈18–19% lower odds of success (ORs 0.81–0.82, adjusted $p \leq 0.002$). Lying angular-

velocity metrics showed smaller but significant effects: 1-SD increases in mean, and RMS angular velocity corresponded to ≈4–11% lower odds of success (ORs 0.89–0.96, adjusted $p<0.01$). Many remaining metrics had odds ratios near 1.0, indicating negligible effects.

Discussion

Even without gravity removal or frame transformations, stability metrics calculated using raw bottle-fixed IMU data captured consistent differences between successful and unsuccessful instillations. Compared with our earlier free-acceleration, multi-frame analysis[1], effect sizes were smaller but directionally consistent, suggesting that streamlined, on-device processing of raw signals may be sufficient for real-time feedback and integration into cloud-connected adherence systems.

Images (Optional)

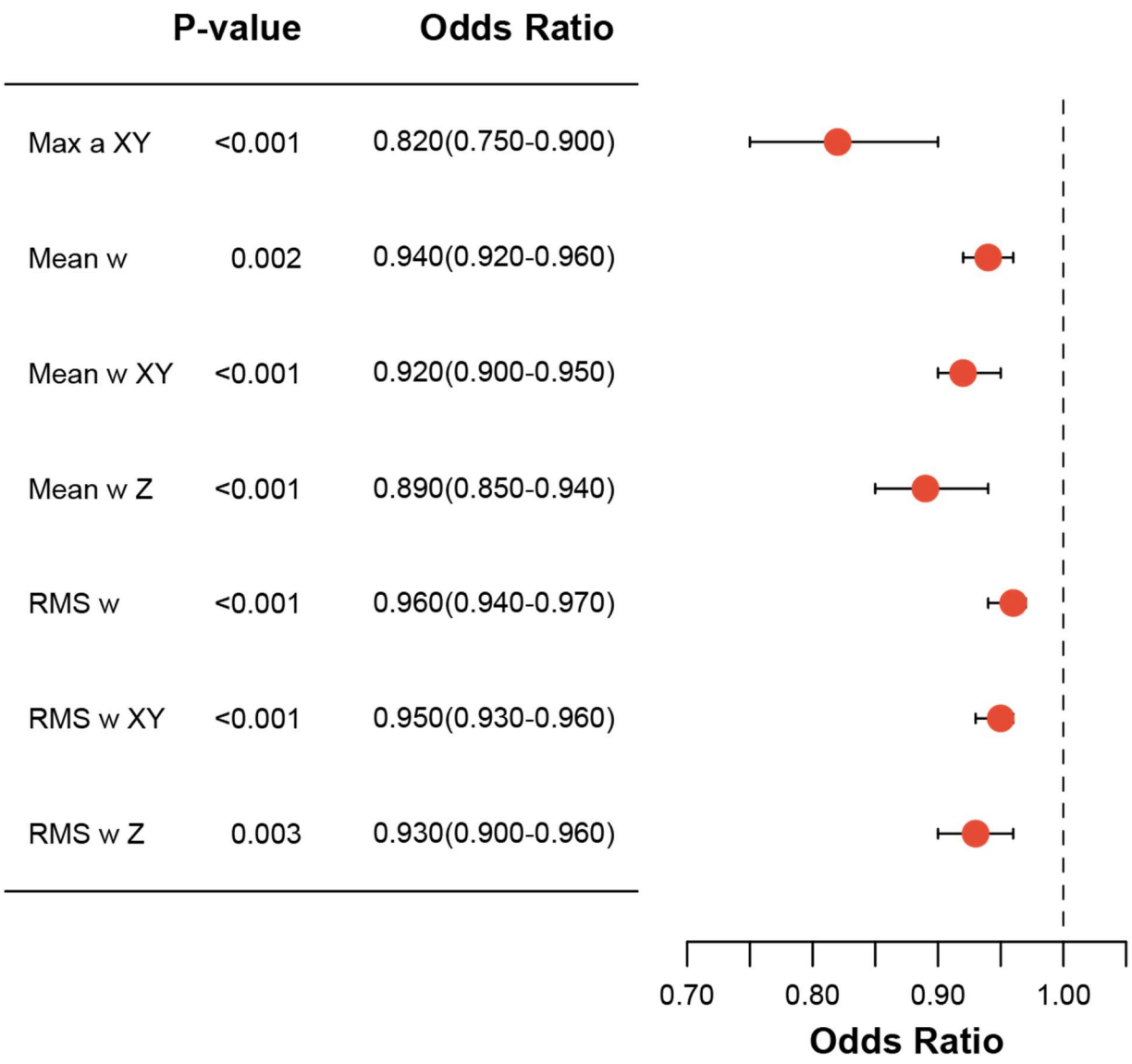


Figure 1. Odds ratios (points) and 95% confidence intervals from univariable logistic GEE models relating standardized bottle-fixed stability metrics to the odds of drop success in the lying posture. Each odds ratio corresponds to a 1-SD increase in the listed metric; the dashed vertical line indicates no association (OR = 1). All metrics shown are significantly associated with lower odds of success (Holm-adjusted p-values shown in the table; a = linear acceleration, w = angular velocity, RMS = root mean square).

References (Optional)

[1] Duque-Urrego et al. 2025. PLOSOne (In preparation)

Acknowledgements (Optional)

Grant support: National Institute of Health UM1TR004404, NIBIB R01EB03232802

Session Category

Human Motion and Performance: Balance, Posture and Control

P1-052

Phase-Specific Characterization of Human Bimanual Coordination for Dexterous Robot Hand Manipulation Strategies

Master's student En-Lin Kuo[1], Ph.D Bing-Shiang Yang[1,2]

[1]National Yang Ming Chiao Tung University, Hsinchu, Hsinchu, Taiwan. [2]Industrial Technology Research Institute, Hsinchu, Hsinchu, Taiwan

Introduction

Previous studies have examined bilateral coordination in simple tasks, but few focuses on hand interactions during naturalistic fine manipulation. Also, most existing work treats behaviors as continuous trajectories, without examining how coordination patterns change across task segments.

To address these gaps, this work will provide a data-driven segmentation method with detailed characterization of inter-hand coordination and role allocation. These findings offer a foundation for designing bimanual robotic policies that reflect human coordination patterns, interaction strengths, and role distributions, supporting generalized manipulation strategies applicable to complex, real-world tasks.

Methods

In this study, we use marker-based optical motion capture system (Vicon, 100 Hz) with seven cameras with 29 reflective markers, and four activities of daily living tasks were performed in the experiment.

Movement segmentation was performed using finger aperture and hand velocity. For each phase, four kinematic parameters (hand speed, palm speed, finger aperture, and thumb-finger angular velocity) were analyzed using a sliding-window approach to compute regression dependency (RD), Pearson correlation, and phase coupling index (PCI). All metrics were standardized using z-score normalization to allow cross-parameter comparison.

Results

Several consistent patterns were observed in the preliminary data. For symmetric bimanual tasks, all segmentation indicators exhibited a rapid increase at the reach phase. Two hands showed highly similar parameter trajectories throughout the task. During

manipulation phase, correlation and RD values for hand speed and palm speed remained close to 1. These patterns demonstrating strong temporal synchrony and biomechanical similarity between hands.

In asymmetric cooperative tasks, RD and correlation trends diverged depending on the specific object and action during manipulation phase; however, PCI consistently exceeded 0.5, indicating that both hands contributed actively through complementary rather than mirrored roles.

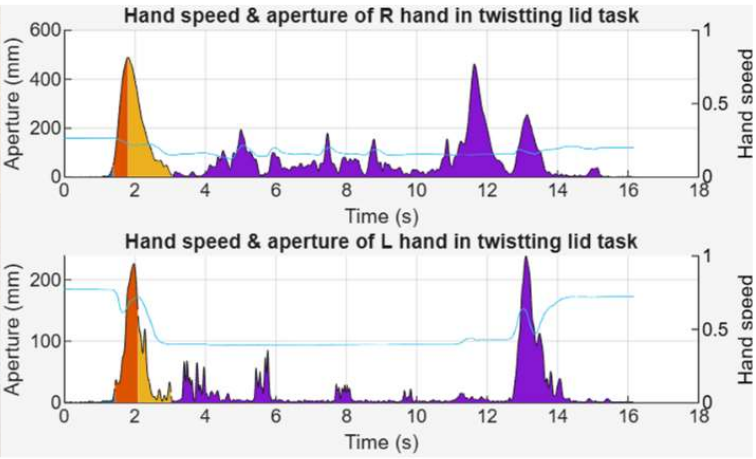
Taken together, these results providing quantitative signatures of how humans coordinate their hands across different forms of daily manipulation.

Discussion

Compared to prior work, our findings extend the understanding of bimanual coordination to more naturalistic, daily life actions. The identification of complementary control strategies expands existing frameworks, emphasizing that effective cooperation does not solely rely on synchronization but also on functional differentiation between hands. Offering a methodological foundation and guiding principles for future investigations and applications in robotic systems.

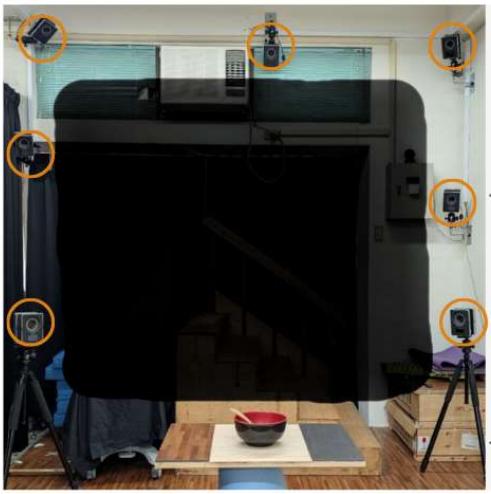
Images (Optional)

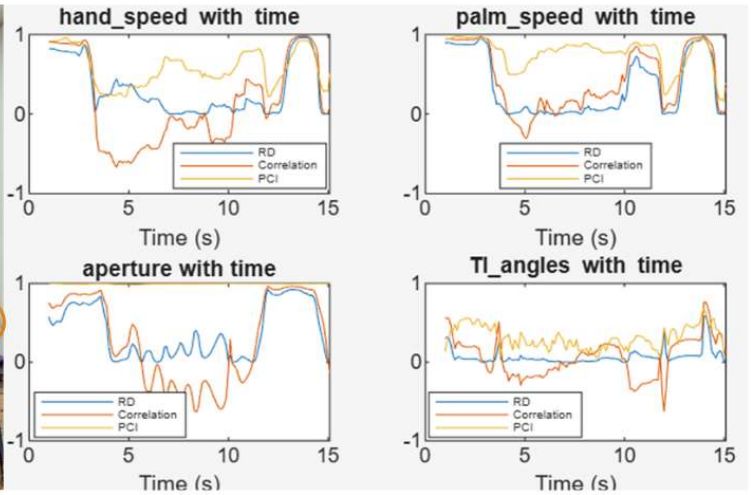




VICON marker position

Example result of phase segmentation





Experimental environment set up

Example result of four kinematic parameters

Session Category

Human Motion and Performance: Balance, Posture and Control

P1-053

Frontal Plane Peak Hip Net Joint Moments Vary With Thigh Angle During Walking and Turning

Ms. Erin Kreis, Ms. Zahava Hirsch, Dr. Jun Liu PhD, Dr. Mitchell Tillman PhD, Dr. Antonia Zaferiou PhD

Stevens Institute of Technology, Hoboken, New Jersey, United States

Introduction

Our prior research found significant differences in frontal hip net joint moments (NJM) between straight-line gait (SLG) and turns. Inspection of net joint forces and segment angles indicated the difference could stem from a whole-body strategy of leaning into the turn. The objective of this analysis was to determine whether thigh inclination angle is associated with peak NJMs during SLG and turns, and whether relationships differ by age cohort.

Methods

Healthy young adults (n=7; 20.4 ± 1.13 years) and older adults (n=16; 70.9 ± 5.58 years) completed 12 SLG and 90-degree left turn trials along a T-shaped intersection. Optical motion capture (Optitrack) and force plates at the intersection (Bertec) were used. Internal frontal hip NJM were calculated during the force plate stance phase. Turns were classified as “step” or “spin” turns based on which foot was closest to the intersection center [1]. Trials without acceptable force plate contact were excluded, leaving data from four young and six older adults.

The frontal-plane thigh angle at the time of peak NJM was calculated relative to vertical. Positive angles indicated the hip was medial to the knee. Linear mixed effects models evaluated hip frontal NJM peaks in each direction as a function of thigh angle, with age cohort, task, and foot as grouping variables. Random intercepts were used across subjects.

Results

Peak hip abductor ($p<0.001$) and hip adductor ($p<0.001$) NJM are strongly negatively associated with thigh inclination angle (Fig. 1). There was no evidence of group differences between young and older adults or right and left foot.

Discussion

Frontal plane thigh angle strongly associated with hip NJM peaks during SLG and turning. Whole-body lean into turns changes the thigh angle and its alignment with the knee net joint force, compared to SLG where the leg remains mostly upright. There were no significant differences between the cohorts, suggesting lean strategies during turns and their associated modifications in NJM could be used similarly by both groups. We are currently working on expanding the sample size. Further analysis will deepen our understanding of how turn strategies may impact joint loading and health.

Images (Optional)

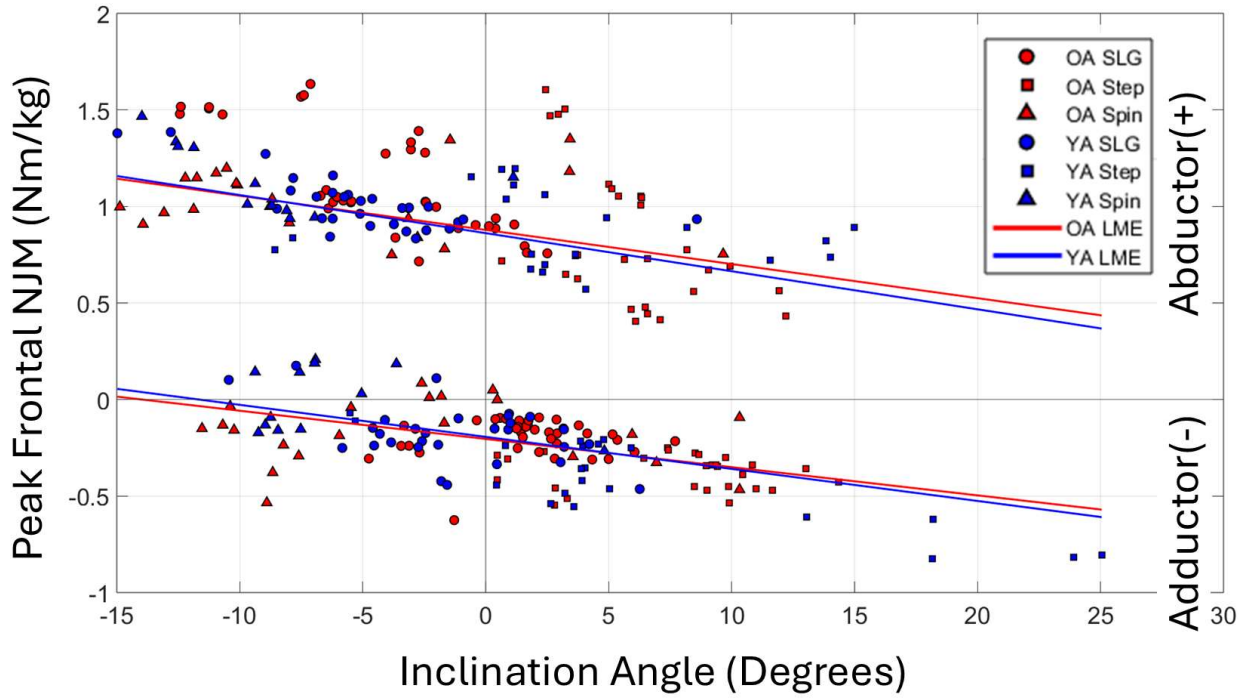


Figure 1: Relationship between thigh inclination angle and peak hip frontal-plane net joint moment (NJM) across straight-line gait (SLG) and pre-planned turning tasks.

References (Optional)

[1] Pawel Golyski et al., J Biomech, 2017

Acknowledgements (Optional)

This study was supported by NSF Award #1944207.

Session Category

Human Motion and Performance: Balance, Posture and Control

P1-054

Comparative Functional Trajectory Analysis of Gait Stability Metrics Across Sensory and Mechanical Perturbations

Mr. Francis FASUYI, Dr. Gary Heise, Dr. Abbie Ferris

University of Northern Colorado, Greeley, CO, United States

Introduction

Walking stability requires seamless integration of multiple sensory systems (visual, vestibular, and somatosensory). While stability metrics are traditionally discrete points (e.g., heel strike), full comprehension of sensory and mechanical constraints' influence on stability requires complete functional trajectory analysis of metrics over the entire gait cycle. This study quantified continuous trajectories of ten directional stability metrics (traditional-margin of stability (MOS), center-of-pressure (COP)-normalized MOS, height-normalized MOS, inclination angle (IA), and measured vs. modeled COP misalignment (dCoPmCoP)) across stance phase under seven perturbation conditions compared to normal walking (NW). We hypothesized that all perturbations would functionally alter stability metrics and that the temporal response of these perturbations would be significantly modified by age.

Methods

Fourteen (8 young: 28.9±2.0 years, 6 old: 69.6±2.9 years) healthy adults completed eight NW, including perturbations: NW-on-foam (NWF), narrow-base-walking (NBW), NBW-on-foam (NBWF), head tilt vestibular perturbations in the frontal (NWFHM), sagittal (NWSHM), and transverse (NWTHM) planes, and visual perturbation using stroboscopic glasses (NWVP). Full-body kinematic and kinetic data were recorded and lowpass filtered. Using functional linear mixed models with bootstrap inference to model the trajectory of each metric, we functionally tested (1) condition contrasts against NW with simultaneous confidence bands, (2) sensory system contributions, (3) stance phases (loading: 0-20%, mid-stance: 20-52%, terminal: 52-83%, pre-swing: 83-100%), and (4) age × condition × time interactions.

Results

NBWF caused the strongest disruptions, with the largest changes across all measures. Mediolateral stability was more affected (more significant time-points for NBWF) than anterior–posterior, especially during terminal stance (50–60%), when instability peaked. Visual challenges showed minimal effect, while vestibular challenges produced direction-specific effects, with frontal head movement improving stability, while sagittal movement

reduced it. Age*condition interactions showed older adults exhibited 35% larger responses to NBWF perturbations but attenuated vestibular effects ($p<0.05$ for age*condition functional interaction). NWF and NBW revealed moderate effects, while NBWF produced amplified rather than additive outcomes.

Discussion

Combined sensory–mechanical constraints produced the largest alterations in gait stability, with mediolateral vulnerability during terminal stance. Functional data analysis revealed compensatory temporal patterns beyond discrete-point analyses, offering mechanistic insight into sensory contributions to dynamic stability.

Images (Optional)

References (Optional)

Session Category

Human Motion and Performance: Balance, Posture and Control

P1-055

Controlling for Anticipation and Triggering the Glidiator to Elicit Experimental Slips

Doctoral student Gaspard Diotalevi M.Sc.A.[1,2], Scientific professional Chantal Gauvin ing., M.Sc.A.[3], Professor Denis Rancourt ing., Ph.D.[1,4], Professor Cécile Smeesters ing., Ph.D.[1,2]

[1]Université de Sherbrooke, Sherbrooke, Quebec, Canada. [2]Research Centre on Aging, Sherbrooke, Quebec, Canada. [3]Institut de recherche Robert-Sauvé en santé et en sécurité du travail (IRSST), Montreal, Quebec, Canada. [4]Centre for Research in Acoustics-Signal-Human of the Université de Sherbrooke (CRASH-UdeS), Sherbrooke, Quebec, Canada

Introduction

Overground experiments on true slips and falls are usually limited to a single trial per participant to prevent anticipation effects. Could a novel experimental device, the Glidiator [1], eliminate participants' anticipation of an upcoming slip event triggered automatically and thus allow us to elicit repeated unexpected slips? Much larger anticipation-free datasets on true slips could then be acquired within the same testing session, even wearing multiple pairs of shoes.

Methods

Five gait metrics influenced by the anticipation of a slip (cadence, foot angle, step length, step width and double stance time [2,3]) were monitored during repeated slipping trials. They were acquired from force platform and motion capture signals for the last 10 dry steps preceding each novel slip. The slip was induced by introducing a lubricated surface (canola oil on stainless steel) on a treadmill. Note that walking speed is immune to anticipation effects since it is prescribed by the treadmill. Triggering the Glidiator was simulated in post-processing for 20 random acquired steps to explore the feasibility of synchronising it to participant's gait so that their foot lands at the front edge of the lubricated surface, thus allowing for longer slips (Figure 1).

Results

All gait metrics fell within one SD of baseline between repeated slipping trials before participants reached the prescribed walking speed. Randomly triggering the device then blinds both participants and experimenters to the upcoming slip. Triggering simulations showed the foot landing 9.7 ± 4.9 cm from the front edge of the 133.5cm long lubricated surface (Figure 1C), proving the feasibility of targeting random heel strikes.

Discussion

Once the mechanism is made quiet enough to be imperceptible through headphones, the Glidiator will allow us to perform repeated anticipation-free slipping experiments, greatly improving data collection. Upcoming experimental trials should show greater triggering variability, since electro-mechanical delay variability will be added to the human gait variability already included in these simulation results.

Images (Optional)

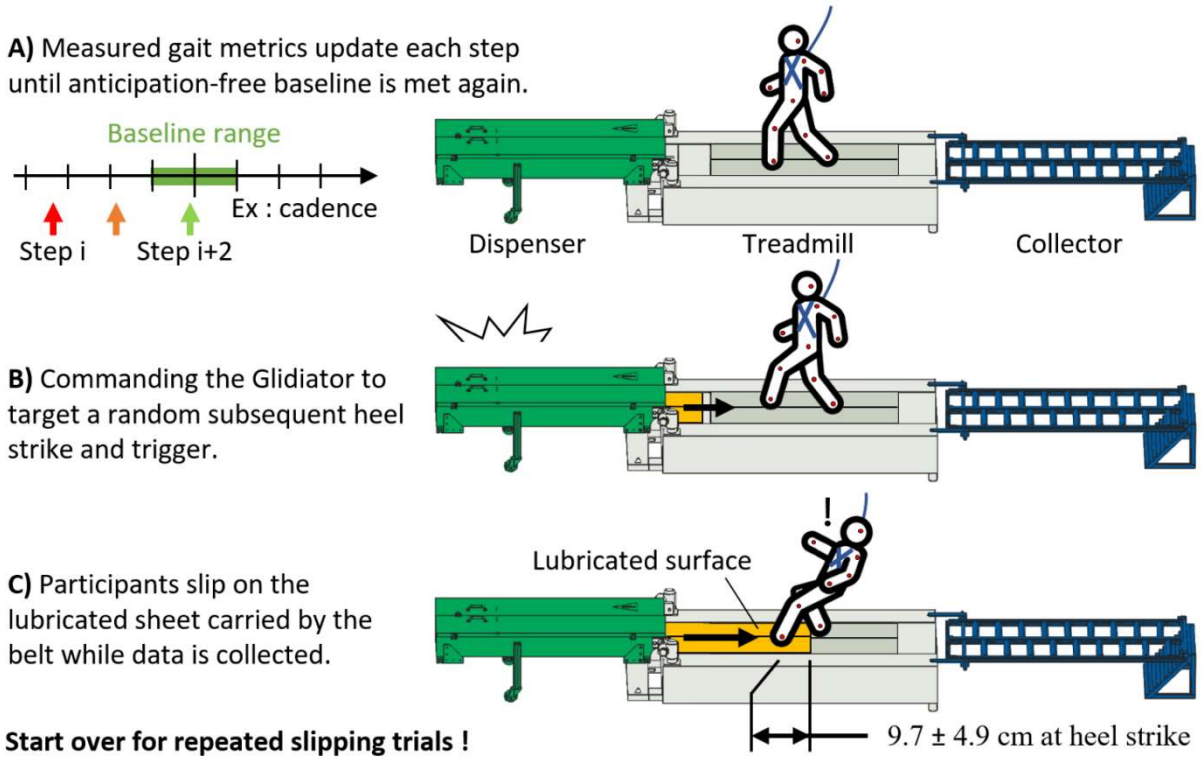


Figure 1: A hypothetical slippery trial using the Glidiator.

References (Optional)

[1] Diotalevi *et al.* , ASB2025, 2025; [2] Swart *et al.* , Scientific Reports, 2020; [3] Chambers *et al.* , Occupational ergonomics, 2003

Acknowledgements (Optional)

The FRQNT (grant 315311) and the NSERC (grant ALLRP 570347-21) for their financial support.

Session Category

Human Motion and Performance: Balance, Posture and Control

P1-056

Does Self-Motion Perception Predict Compensatory Stepping Responses in Healthy Adults?

Ms. Gracie Zimmer, Mr. Konna Respicio, Dr. Andrew Wagner PT, DPT, PhD, Dr. Corbin Rasmussen PhD

Creighton University, Omaha, Nebraska, United States

Ms. Gracie Zimmer

Introduction

Compensatory stepping is crucial for balance recovery following a perturbation, and taking multiple steps is associated with a greater fall risk. Detection of a perturbation relies on the integration of several sensory inputs including the vestibular system; however, it is unclear if the precision of vestibular signals is associated with the quality of compensatory stepping responses employed to regain upright balance. Therefore, our aim was to determine the relationship between vestibular thresholds (an assay of vestibular sensory precision) and the number of steps needed to counteract a slip-like perturbation.

Methods

Fourteen healthy adult participants (31.5±19.4 yrs.) stood with their eyes closed and arms crossed on a platform that randomly translated in one of eight directions and one of two intensities at a frequency of 1.5 Hz (Figure 1a). All participants were instructed to recover their balance without reaching for handrails surrounding the platform. Compensatory stepping reactions were recorded by high-speed cameras positioned in front and to the right of the participants. Vestibular perceptual thresholds were measured using a seated 1.5 Hz interaural translation direction recognition test to determine the smallest translation stimulus that could be accurately perceived. Video recordings were used to determine the number of steps taken to regain balance in each trial. The proportion of multistep trials (i.e., ratio between trials using > 1 step and the total trials performed) was correlated with vestibular thresholds using the Pearson correlation coefficient.

Results

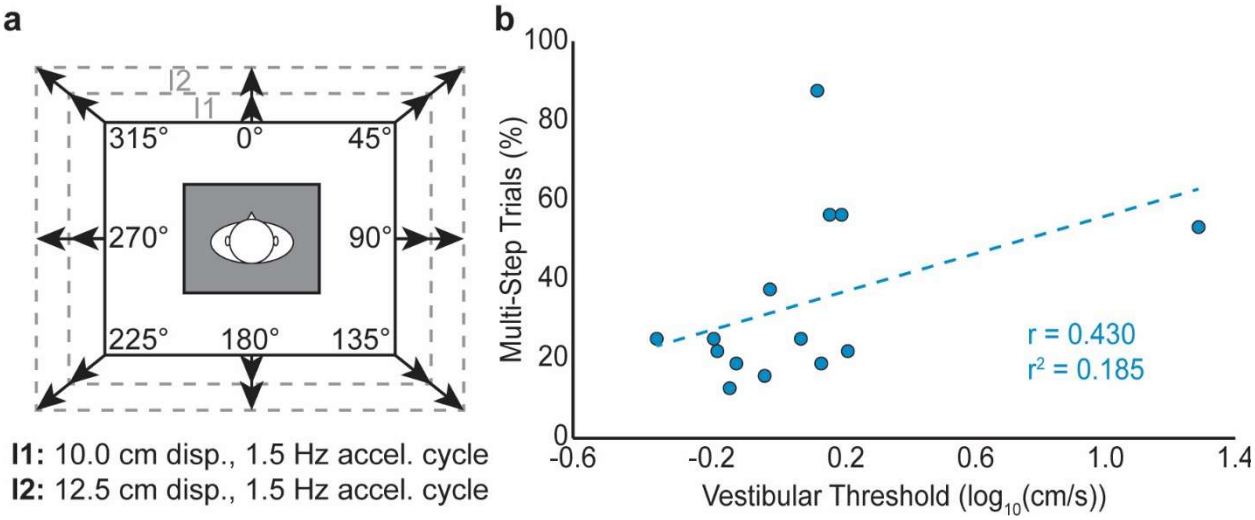
This was a preliminary analysis as data collections were ongoing at the time of submission. Vestibular perceptual thresholds were moderately associated with the frequency of multi-

step responses to balance perturbations (r(12)=0.430, p=0.125; Figure 1b), accounting for 18.5% of the variation in stepping responses.

Discussion

These preliminary analyses show a promising trend between vestibular perceptual thresholds and the number of compensatory steps needed to regain balance after a slip-like perturbation. This supports the idea that imprecision in vestibular sensory feedback contributes to a poorer quality stepping response, even in healthy adults. Future analyses will assess whether perceptual thresholds and directional biases (i.e., right vs. left) influence the specific stepping strategies selected (i.e., lateral sidestep vs. cross-over step).

Images (Optional)



Session Category

Human Motion and Performance: Balance, Posture and Control

P1-057

Stanford Balance Level Evaluation (StaBLE): Using Smartphone Videos to Assess Balance Ability

Ms. Hannah Heigold MS, Mr. Parker Ruth BS, Dr. Scott Delp PhD

Stanford University, Stanford, California, United States

Introduction

With an aging population and rising incidence of falls, objective balance metrics are needed to detect balance deficits and evaluate interventions. Current clinical balance assessments suffer from ceiling effects, lack sensitivity, and rely on subjective evaluation. Recent advances in computer vision have enabled biomechanical analysis in clinical settings using smartphones. We aim to use smartphone video to develop a freely available objective balance assessment that automatically computes balance task performance, removes ceiling effects, and is validated against age and existing balance assessments.

Methods

We designed a balance protocol with 18 tasks, derived from existing clinical scales, that challenges various components of balance. We used OpenCap, an open source platform for motion capture with smartphone video, to collect data from 153 subjects with a wide range of balance abilities from professional ballerinas and acrobats to older adults with high fall risk. We engineered the Stanford Balance Level Evaluation (StaBLE) performance score, which is computed from OpenCap data and quantifies the participant's ability to achieve the goal of each task. We validated the StaBLE performance score against age, the Activities-Specific Balance Confidence (ABC) Scale, and estimated Mini Balance Evaluation Systems Test (Mini-BESTest), 4-Stage Balance Test, and Short Physical Performance Battery (SPPB) scores.

Results

The StaBLE performance score, composed of 18 individual task performance scores, assigned a value between 0 and 1 to each subject (min=0.11, max=0.78, mean = 0.62, std = 0.12). It significantly correlated with age (rho = -0.76, $p<0.001$), Activities Specific Balance Confidence (ABC) Scale (rho = 0.61, $p<0.001$), and estimated clinical functional scores, while demonstrating a spread of StaBLE performance scores within each clinical scale scoring bin.

Discussion

The StaBLE performance score and task scores for balance tasks overcome ceiling effects seen in the ABC Scale and time metrics. It provides increased measurement resolution within each clinical score bin, and differentiates elite balancers that would otherwise be grouped together. The 4-Stage Balance and SPPB may bin high performers in lower scores due to premature stopping rules. Future work will identify a minimal subset of tasks to include in a rapid assessment.

Images (Optional)

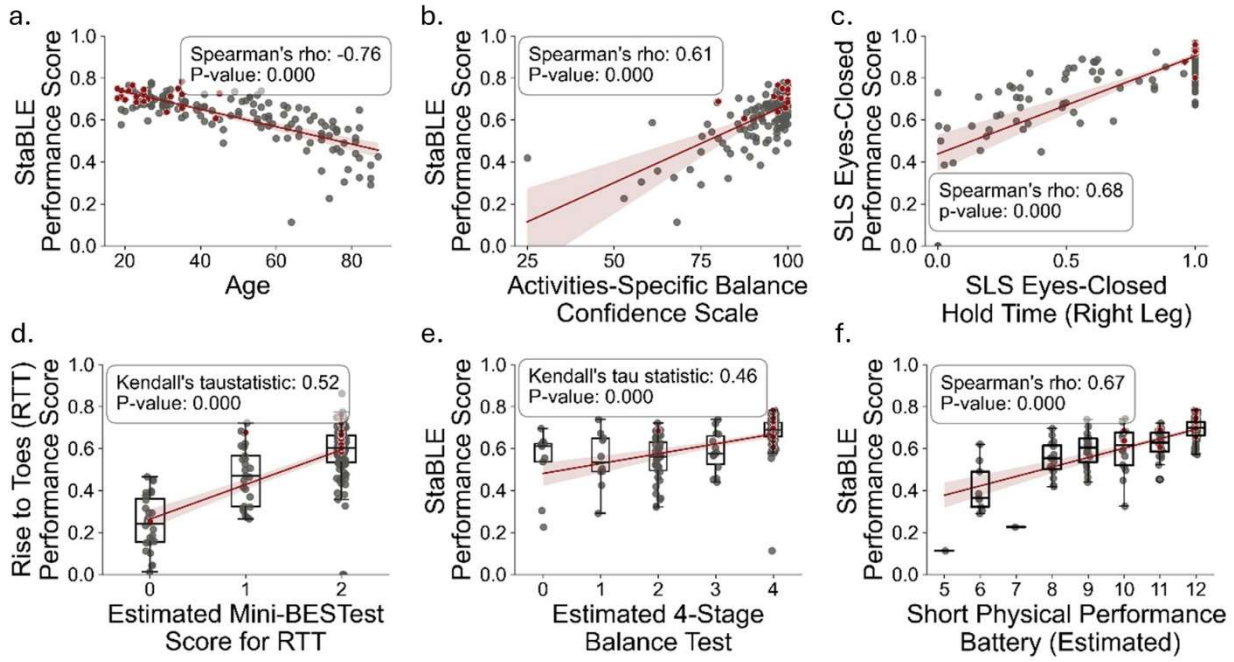


Figure 1: Linear regression and 95% confidence interval for the StaBLE performance score against age (a) and clinical scales (b, e, f); and the StaBLE task-level scores against time metrics (c) and clinical scale scores (d). Elite balancers (competitive and professional gymnasts, dancers, and acrobats) are shown in red.

SLS: single-leg stance

Session Category

Human Motion and Performance: Balance, Posture and Control

P1-058

Footedness has a Limited Relationship With Limb Preferences and Laterality Across Movement Tasks of Varying Stability/Mobility Priorities

Dr. James Tracy PhD[1,2], Dr. Jocelyn Hafer PhD[2], Dr. Thomas Buckley EdD, ATC[2], Dr. Jessica Allen PhD[3], Dr. Hendrik Reimann PhD[2], Dr. Jeremy Crenshaw PhD[2]

[1]University of Arizona, Tucson, Arizona, United States. [2]University of Delaware, Newark, Delaware, United States. [3]University of Florida, Gainesville, Florida, United States

Introduction

Limb laterality hypothesizes that limbs prioritize stability or mobility during movement. The "Waterloo Footedness Questionnaire—Revised" evaluates footedness on a continuum, rather than traditional single-limb dominance. The questionnaire also includes five "stability" and five "mobility" questions allowing for sub-scores to consider footedness within priorities. The purpose of this investigation was to explore footedness, limb preferences, and limb laterality during movement tasks with ranging stability/mobility limb priorities. We hypothesized that footedness would relate (i.e., large effects) to limb preferences and laterality across movement tasks with ranging stability/mobility requirements.

Methods

Thirty participants (15F/15M; 18-40 years; right kicking limb) completed the footedness questionnaire and movement tasks including bilateral standing, unipedal standing, gait initiation, overground walking, and treadmill-perturbation forward reactive stepping. We classified each task's preferred limb as the self-selected unipedal stance limb and the majority stepping limb during six gait initiation and six forward reactive stepping trials. When a preferred limb could not be determined (i.e., bilateral standing and overground walking) we quantified limb laterality with between-limb biomechanical differences: the contribution of each limb to anteroposterior center of pressure control during bilateral standing and the minimum lateral margin of stability (biomechanically proportional to the impulse needed to lose/regain stability) during walking. Footedness sub-scores were compared between preferred limbs (unipedal standing, gait initiation, treadmill perturbations) using Mann-Whitney tests and effect size *r*. Footedness was related to limb laterality (bilateral standing, overground walking) using Spearman-Rank tests with spearman correlation coefficient *r*. Both *r* values were interpreted using small ($r<0.3$), medium ($0.3\leq r<0.5$), and large effects ($r\geq 0.5$).

Results

Unipedal right-limb stance preferences associated with right-footed stability sub-scores (r=0.59;p<0.01;Figure). All other footedness sub-score and limb preference comparisons showed small effects (r≤0.21;p≥0.26;Figure). Footedness sub-scores and limb laterality comparisons also showed small correlations (r≤0.18;p≥0.33;Figure).

Discussion

Footedness stability sub-scores may relate to limb preferences for stability-focused unipedal standing but do not seem related to limb preferences for mobility-focused tasks where required dynamic responses increase. However, the majority of participants showed a limb preference during stepping tasks suggesting that there does exist some underlying factor(s) other than footedness influencing participant preferences to task-specific movements.

Images (Optional)

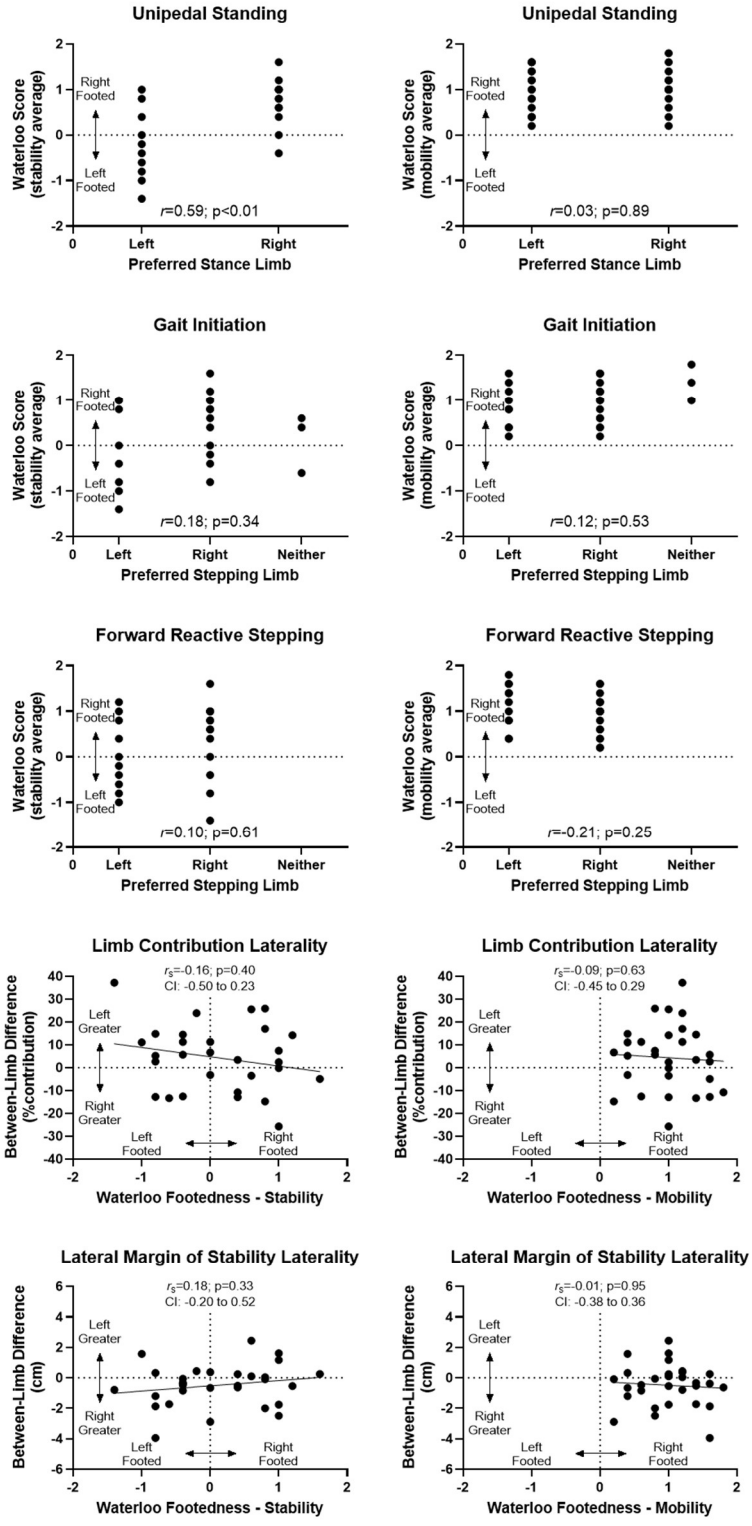


Figure – Relationships of Waterloo Footedness "stability" and "mobility" sub-scores with preferred limbs and between-limb laterality.

Session Category

Human Motion and Performance: Balance, Posture and Control

P1-059

The Effects of Hypogravity Exposure on Multisensory Integration in Posture Control

Ms. Joelle Dick M.S., Dr. Chase Rock Ph.D., Ms. Xiaoqiang Dai, Mr. David Liu, Ms. Meira Kane, Dr. Young-Hui Chang Ph.D.

Georgia Institute of Technology, Atlanta, Georgia, United States

Introduction

Posture is regulated by constant integration of sensory inputs (somatosensory, visual, and vestibular) and the selection of suitable motor adjustments within a gravitational field. To accomplish postural control, the central nervous system (CNS) dynamically reweights sensory information in response to perturbations[1]. Building on this foundation, the present study investigates how multisensory integration for postural control adapts after hypogravity exposure: a multisensory challenge to motor control. We hypothesized that updated gravity information from hypogravity jumping will alter the multisensory integration underlying postural control.

Methods

Five healthy individuals (4F/1M) participated in this IRB-approved protocol. Participants completed the modified Clinical Test of Sensory Interaction on Balance (mCTSIB)[2] following targeted jumps in normal-gravity and simulated hypogravity (0.5g)[3]. The assessment involved controlled manipulation of somatosensory (foam vs. firm surface) and visual inputs (eyes open vs. closed). Kinematics data were used to compute center of mass (COM) sway to quantify balance variability. Unimodal sensory (somatosensory, visual, and vestibular) estimates of COM trajectories were created, and resultant variance values were used to derive sensory weights in accordance with the Maximum-Likelihood Estimate Principle[4]. This approach assesses how updated gravity information influences multisensory integration. Initial analyses were performed on two participants.

Results

Our preliminary findings suggest that exposure to simulated hypogravity modified sensory integration for posture control. Following hypogravity jumping, vestibular and somatosensory mean COM variance increased, leading to inputs down-weighting from 35.8±13.0% to 27.9±23.4% and 49.6±27.6% to 44.2±9.2% respectively. Conversely, the visual input was up-weighted from 14.6±14.3% to 27.9±16.6%. This suggests that

multisensory integration for balance control responds to updates in gravitational cues from unrelated tasks.

Discussion

Our preliminary interpretation supports the hypothesis that hypogravity exposure induces multisensory reweighting as reflected by altered balance control. These initial biomechanical findings offer further insights into how the CNS controls posture. The results also highlight gravity's role in multisensory integration for coordinated actions, with relevance to spaceflight and clinical populations with balance deficits.

Images (Optional)

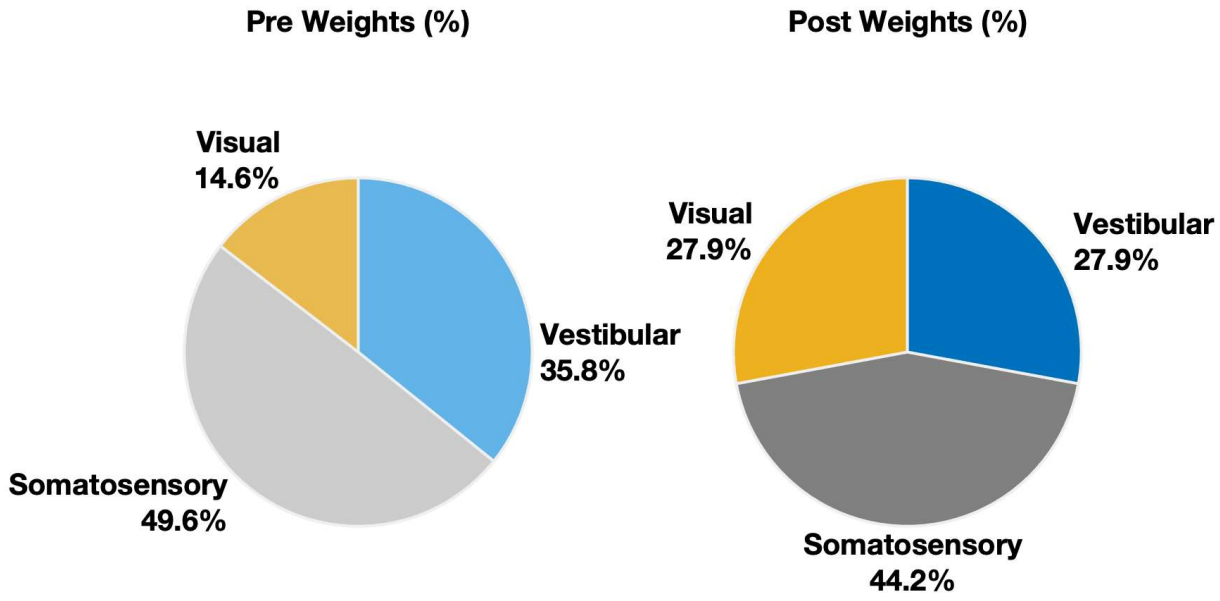


Figure 1. Mean percent sensory weights for visual, somatosensory, and vestibular cues pre- and post simulated hypogravity (0.5g). N = 2.

References (Optional)

[1] Peterka RJ. J Neurophysiol, 2002. [2] Shumway-Cook A, Horak FB. Phys Ther, 1986. [3] Rock CG et al., Front Physiol, 2024. [4] Ernst MO, Banks MS. Nature, 2002.

Session Category

Human Motion and Performance: Balance, Posture and Control

P1-060

Load Distribution and Vectorial Margin of Stability in Fundamental Karate-Do Stances: Biomechanical Insights into Postural Control

Msc. Johan Robalino[1,2], Lic. Luiz Pavani[1,2], Dra. Jacielle Ferreira[3], Dr. Márcio Goethel[1,2], Dr. João Paulo Vilas-Boas[1,2]

[1]Centre of Research, Education, Innovation and Intervention in Sport, Faculty of Sport, University of Porto, Porto, Porto, Portugal. [2]Porto Biomechanics Laboratory, Faculty of Sport, University of Porto, Porto, Porto, Portugal. [3]Postgraduate Program in Physical Education, Federal University of Mato Grosso, Cuiabá, Mato Grosso, Brazil

Introduction

Fundamental Karate-Do stances: Forward (*Zenkutsu-dachi*), Horse-riding (*Kiba-dachi*), and Back (*Kokutsu-dachi*) impose distinct patterns of vertical load distribution and center of mass (COM) control, shaping balance and postural strategies. This study evaluates intra-subject and intra-stance postural control using vectorial Margin of Stability (MoS) and vertical load measures to reveal how stance geometry governs functional stability.

Methods

Twelve elite Karate-Do practitioners (24.3 ± 8.2 y; 14.1 ± 6.5 y of training) with a mean height of 164.6 ± 9.5 cm, mass 71.3 ± 15.6 kg and body fat 25.3 ± 10.3 % were recruited. After a 5-min self-paced warm-up, three stances were performed five times each in random order, holding each for 5 s. Kinematic and kinetic data were recorded using two force plates (1000 Hz) synchronized with an eight-camera motion capture system (180 Hz) and processed via markerless reconstruction (Theia System) to generate a six-degrees-of-freedom biomechanical model.

Stability variables were computed, including rear- and front-foot load distribution, base of support area (convex hull and bounding box), COM–centroid and COP–centroid distances, relative stability radius, normalized COP–COM distance and vectorial MOS (Curtze et al., 2024). Linear mixed-effects models assessed the effects of stance and trial (fixed factors) on all variables, with participants as a random intercept to account for intra-subject variability. Post-hoc pairwise comparisons were Bonferroni-adjusted, and effect sizes are reported as partial eta squared ($\eta^2 p$), with significance set at $\alpha = 0.05$.

Results

All outcomes are summarized in Table 1.

Discussion

Karate-Do stance exhibits a distinct biomechanical profile shaping postural control and functional stability. *Kokutsu-dachi* shifted load posteriorly, with the rear foot bearing most body weight, pronounced COM and COP displacement, and the lowest vectorial MoS. *Zenkutsu-dachi* favored the front foot support, had a larger base of support, intermediate COM–COP positions, and moderate COP–COM separation. *Kiba-dachi* maintained near-symmetrical load, minimal COM–COP separation, and the highest relative stability radius and vectorial MoS. Systematic differences ($p < .001$; $\eta^2p = 0.206–0.779$) demonstrate that each stance uniquely modulates base of support, COM–COP dynamics, and neuromechanical demands, aligning with their traditional technical–tactical functions: defensive withdrawal, forward propulsion, and centralized stabilization.

Images (Optional)

Table 1. Load distribution and postural stability parameters across three Karate-Do stances (KIB, KOK, ZEN).

Variable	KIB	KOK	ZEN	LMM (F, p)	η^2p	Pairwise Comparisons
Rear-Foot Load (%BW)	50.98 ± 1.56	71.00 ± 1.56	44.90 ± 1.56	241.24, <.001	0.749	All comparisons significant
Front-Foot Load (%BW)	49.02 ± 1.56	29.00 ± 1.56	55.10 ± 1.56	241.24, <.001	0.749	All comparisons significant
Relative Stability Radius (dimensionless)	0.034 ± 0.002	0.048 ± 0.002	0.030 ± 0.002	42.94, <.001	0.346	KIB-ZEN not significant; others significant
BOS Area – Convex Hull (m^2)	0.093 ± 0.005	0.072 ± 0.005	0.090 ± 0.005	88.48, <.001	0.522	KIB-ZEN not significant; others significant
BOS Area – Bounding Box (m^2)	0.129 ± 0.029	0.244 ± 0.029	0.449 ± 0.029	286.46, <.001	0.779	All comparisons significant
COM–Centroid Distance (% half-diagonal)	4.99 ± 2.02	30.01 ± 2.02	14.30 ± 2.02	129.27, <.001	0.615	All comparisons significant
COP–Centroid Distance (% half-diagonal)	4.22 ± 2.17	31.72 ± 2.17	15.98 ± 2.17	126.52, <.001	0.611	All comparisons significant
COP–COM Distance Normalized to √BOS ($m \cdot m^{-0.5}$)	0.031 ± 0.002	0.028 ± 0.002	0.022 ± 0.002	21.02, <.001	0.206	KIB vs KOK not significant; KIB vs ZEN and KOK vs ZEN significant

Notes: Mean ± SE refers to the mean ± standard error. Linear mixed-effects models (LMMs) were used to evaluate differences, with F representing the F-statistic and p the significance level. η^2p denotes partial eta squared as a measure of effect size. KIB stands for Kiba Dachi (horse-riding stance), KOK for Kokutsu Dachi (back stance), and ZEN for Zenkutsu Dachi (forward stance). BW represents body weight, BOS indicates base of support, COM is center of mass, and COP is center of pressure. Letters (a, b, c) denote significant differences in post-hoc comparisons, with values bearing different letters considered significantly different at $p < .05$.

Session Category

Human Motion and Performance: Balance, Posture and Control

P1-061

When Jumping Hurts: A Systematic Review of Jump Biokinetics in Females With Patellofemoral Pain

Dr. Carolline P. Nunes MD[1,2], Dr. Felipe F. Gonzalez MD, MSc[1,2], Ms. Alexandre Maioli MD Candidate[2,3], Ms. Guilherme P. Saad BA[4,5], Dr. Tiago Zimerman MD[1,2], Dr. Marcos A. Barros MD[1,2], Mr. Joshua Samaniego MS[6], Dr. Eliane C. Guadagnin PhD[2], Dr. Jorge Chahla MD, PhD[1], Dr. Jonathan Gustafson PhD[7], Dr. Leonardo Metsavaht MD, PhD[2], Dr. Gustavo Leporace PhD[2]

[1]Department of Orthopaedics, Rush University Medical Center, Chicago, Illinois, United States. [2]Instituto Brasil de Tecnologias da Saúde (IBTS), Rio de Janeiro, Rio de Janeiro, Brazil. [3]Universidade Federal do Rio de Janeiro (UFRJ), Rio de Janeiro, Rio de Janeiro, Brazil. [4]Instituto Brasil de Tecnologias da Saúde (IBTS), Rio de Janeiro, Rio de Janeiro, United States. [5]Univeristy of Miami, Coral Gables, Florida, United States. [6]Rush Medical College of Rush University, Chicago, Illinois, United States. [7]Rush University Medical College, Chicago, Illinois, United States

Dr. Carolline P. Nunes

Introduction

Women experience a disproportionately high burden of patellofemoral pain (PFP) and may be up to twice as likely as men to develop symptoms in sports that involve repetitive loading, cutting, and jumping. These higher rates have been linked to biomechanical patterns commonly observed in women with PFP that increase patellofemoral joint stress. However, most biomechanical studies pool sexes, limiting the ability to identify movement patterns specific to female athletes. Sex-specific analyses are therefore essential to accurately characterize patellofemoral mechanics and guide targeted interventions for women. The objective of this study was to characterize biomechanical patterns in women with PFP during functional jumping tasks and determine whether these patterns differ from asymptomatic controls across different jump types.

Methods

A systematic search of six databases (September 2025) was conducted following PRISMA guidelines. Eligible studies reported kinematic or kinetic outcomes from jump-landing tasks in women with PFP. Studies lacking sex-specific female data, including participants

with prior knee surgery, evaluating only non-jump tasks, or focusing on other diagnoses were excluded. Standardized mean differences were pooled using random-effects models in R.

Results

Thirteen studies met inclusion criteria, including 135 women with PFP and 132 controls. Four jumping tasks were evaluated: single-leg drop jump, double-leg drop jump, single-leg vertical jump, and single-leg horizontal hop. Compared with controls, women with PFP demonstrated greater hip internal rotation (SMD = 0.53; 95% CI, 0.05–1.01; $p = 0.0063$), increased hip adduction (SMD = 1.82; 95% CI, 0.31–3.32; $p < 0.0001$), and larger contralateral pelvic drop (SMD = 1.77; 95% CI, 0.09–3.44; $p < 0.0001$), with heterogeneity ranging from moderate to very high. Other biomechanical variables showed inconsistent findings.

Discussion

Across multiple jumping tasks, women with PFP exhibited a consistent pattern of greater hip internal rotation, increased hip adduction, and larger contralateral pelvic drop relative to asymptomatic controls. These findings emphasize that proximal mechanical factors are central to the biomechanical presentation of PFP during jump-landing tasks in women.

Images (Optional)

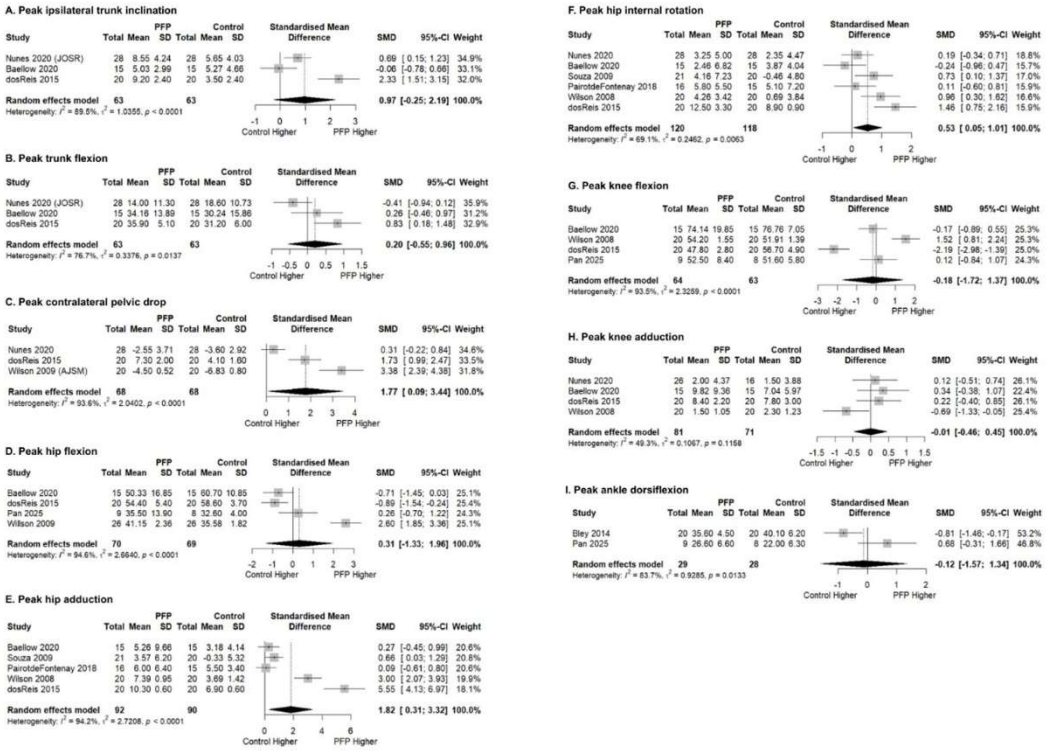


Image 1. Kinematic findings during jump tasks. Each subplot presents the Standardized Mean Difference (SMD) and 95% confidence intervals comparing women with patellofemoral pain (PFP) and asymptomatic controls for the corresponding kinematic variable across eligible studies. A. Peak ipsilateral trunk inclination; B. Peak trunk flexion; C. Peak contralateral pelvic drop; D. Peak hip flexion; E. Peak hip adduction; F. Peak hip internal; G. Peak knee flexion; H. Peak knee adduction; I. Peak ankle dorsiflexion;

Session Category

Human Motion and Performance: Balance, Posture and Control

P1-062

An Assessment of the Implications of Menstrual Cycle Phase on Upper Extremity Function, Lifting Risk, and Postural Control

Dr. Kaitlyn Armstrong, Dr. Thomas Andre, Dr. Corbit Franks, Dr. Ruaa Al Juboori, Dr. Chip Wade

University of Mississippi, University, Mississippi, United States

Introduction

Musculoskeletal injuries are the leading cause of time lost from work in the health care. The unique breakdown of female workers in this sector suggests there may be unique factors that need to be accounted for when considering injury prevention. Few studies have assessed sex disparities in healthcare-related occupational injuries, however, when assessing injury risk in other occupational settings studies have suggested consistently higher injury risks for women when compared to men. Understanding the cause behind the discrepancies could be critical to mitigating the injury rate differences. There are a few proposed explanations for the differences in injury rates. These include biomechanical differences such as higher loads that may result from lifting mechanics, ligamentous laxity resulting in lower joint stability, or potentially the strength demands of the tasks. The purpose of this study was to examine the implications of hormonal fluctuations across the menstrual cycle on lifting mechanics and injury risk.

Methods

40 females were recruited and enrolled in the study. The final sample included 26 females. The study consisted of 7 visits over two cycles. Measures included a RightEye Dynamic Vision assessment, a Proteus upper extremity function test, a balance assessment, and the Noraxon Human Factors and Ergonomics assessment. Linear mixed effects models were used to determine the effects of cycle and phase on performance. The threshold for statistical significance was set at $p<0.05$.

Results

The LMM revealed a significant phase effect on composite lifting index and lifting index at the origin for the 35lbs condition when comparing the follicular and luteal phase ($b=-0.171$, $p=0.0029$). The model revealed a significant difference between the cycles in the center of pressure path length for the eyes closed, foam surface condition when comparing the follicular and the luteal phase ($b=130.236$, $p=0.020$).

Discussion

There appear to be variable-specific effects of cycle phase; however, the effects were not consistently observed across cycles, suggesting no clear consensus can be reached on the relationship between cycle phase and performance. Future studies should focus on implementing robust methodological approaches while also considering longitudinal study designs to gain better insight into the variability in parameters across the cycle.

Session Category

Human Motion and Performance: Balance, Posture and Control

P1-063

Effects of Object Weight and Availability of Weight Information on Safety Margin Values During Precision Grip

Dr. Kazuki Hokari PhD, Associate Professor, Mr. Satoshi Ota

Nippon Bunri University, Oita, Oita, Japan

Introduction

Humans modulate grasp force to maintain stable object holding. Although using the minimum necessary force reduces muscle load, people typically apply higher forces to avoid object dropping from unexpected slippage or disturbances. This additional force, known as the safety margin, is thought to be influenced by factors such as object weight and the availability of weight information. This study examines how object weight and weight-known versus weight-unknown conditions affect safety margin values.

Methods

This study investigates grasp forces during precision grip through ongoing experiments. Twenty-three university students will participate, and preliminary results from seven are reported. The object consisted of a 3-axis force sensor fixed between aluminum plates (mass: 0.106 kg), with its weight adjusted by attaching additional masses of 0, 0.25, 0.50, 0.75, 1.00, and 1.25 kg. Two conditions were tested: weight-known and weight-unknown. Safety margins were calculated as the ratio of natural to minimum grasp force, where natural force was the peak force during each trial and minimum force was the force at slip onset.

Results

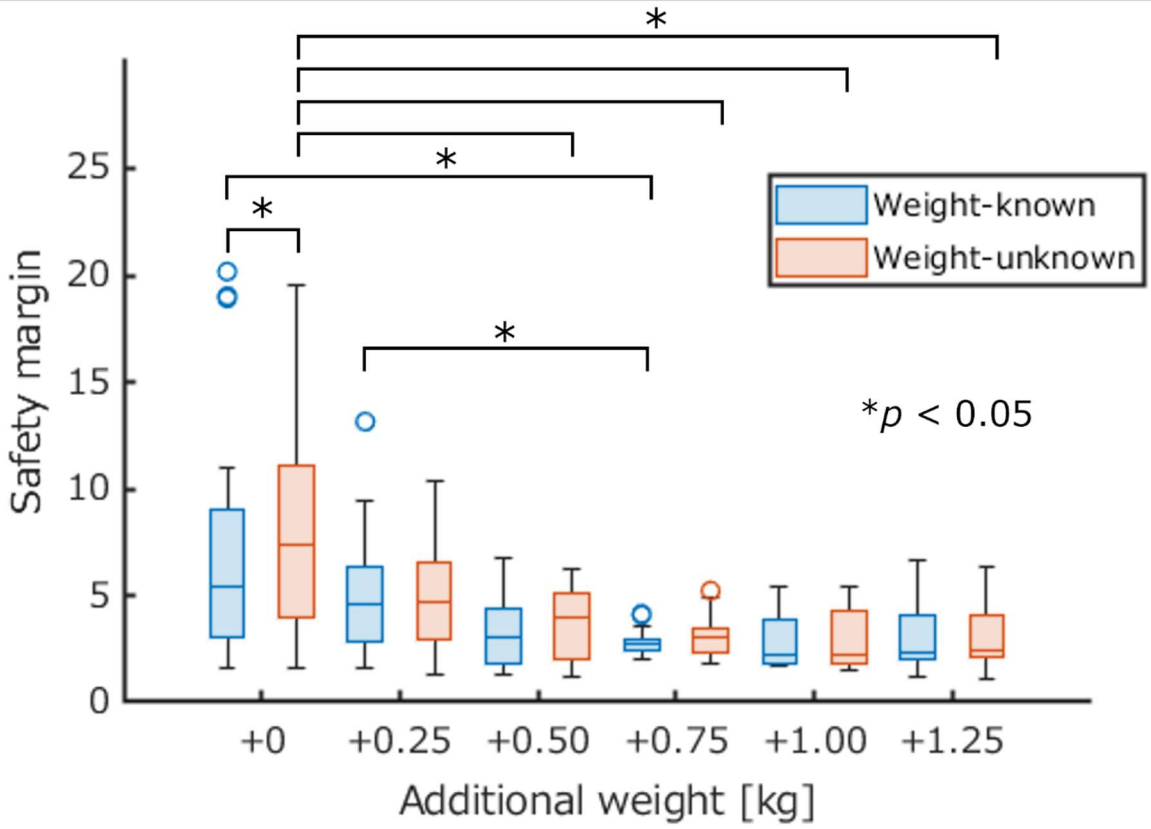
Preliminary results from seven participants showed the following safety margins under the weight-known condition: 6.9 ± 5.8 (0 kg), 5.1 ± 3.0 (0.25 kg), 3.3 ± 1.6 (0.50 kg), 2.8 ± 0.6 (0.75 kg), 2.9 ± 1.2 (1.00 kg), and 3.1 ± 1.6 (1.25 kg), with significant differences only between 0 and 0.75 kg and between 0.25 and 0.75 kg. Under the weight-unknown condition, significant differences occurred only between 0 kg and weights of 0.5 kg or greater. The safety margin for 0 kg was significantly larger in the weight-unknown than the weight-known condition, with no differences for other weights.

Discussion

The safety margins showed no significant differences under either condition except for a few weight combinations. For objects of 0.50 kg or more, participants adjusted their forces according to the weight. The 0-kg condition yielded larger safety margins than other

weights, indicating the use of force well above the minimum required. Effects of weight information appeared only at 0 kg; without weight information, participants applied much larger forces in anticipation of heavier objects.

Images (Optional)



Acknowledgements (Optional)

This study was supported by JSPS KAKENHI (grant number: JP25K21259).

Session Category

Human Motion and Performance: Balance, Posture and Control

P1-064

Effects of Jump Induced Fatigue on Unstable Seated Balance: A Pilot Study

Mrs. Kelly McGhee, Mr. Spencer Goodding, Mrs. Elyssa Bell, Dr. Abbie Ferris

University of Northern Colorado, Greeley, CO, United States

Introduction

Adults spend ~10 hours per day in a seated position [1], including on unstable surfaces (rolling chairs and vehicles). Sports such as cycling, horseback riding, and crew require athletes to maintain seated balance on a moving base of support. Yet most postural control research overlooks seated balance [2]. Further, the effects of lower extremity fatigue may have deleterious effects on seated balance on an unstable surface as fatigue affects coordination and movement control. We hypothesize that, compared to a pre-fatigue state, fatigued participants sitting on an unstable surface will demonstrate an increase in medial-lateral (ML) and anteroposterior (AP) instability and weight support through the seat.

Methods

This pilot study collected seated balance kinematic (VICON, Motion Systems Inc., Denver, CO), and ground reaction forces (AMTI, Watertown, MA) data pre- and post- fatigue protocol. Participants performed maximal countermovement jumps until volitional fatigue of the lower limbs. Participants (n=6, 1.76m$\pm$0.07, 82.11kg$\pm$14.80) sat on a wobbleboard with arms by their side for 30s. The wobbleboard consisted of a circular wooden surface 36.4cm in diameter attached to a plastic hemisphere (20 x 10.3cm) placed on a force plate.

Results

As this is a small pilot study, data are presented qualitatively. Preliminary results suggest a 114.10 $\pm$ 55.77% increase in ML and 62.18 $\pm$ 55.27% increase in AP COP excursion. Two participants demonstrated a post-fatigue increase in maximum weight support though the seat that trended towards pre-fatigue values over time. All participants increased seat reaction force variability post fatigue (Figure 1), with an increase in the coefficient of variation from 0.578$\pm$0.24% to 0.871$\pm$0.22%.

Discussion

These results suggest adaption to lower extremity fatigue includes a more unstable seat. This increased instability may hinder responses to perturbations while seated, such as in rolling chairs or accelerating vehicles. Fatigue may affect an athlete's interaction with their equipment in seated sports or their ability to maintain an effective posture. Seated sport athletes and those requiring assisted mobility devices may benefit from targeted seated balance training under fatigued conditions to counteract these effects.

Images (Optional)

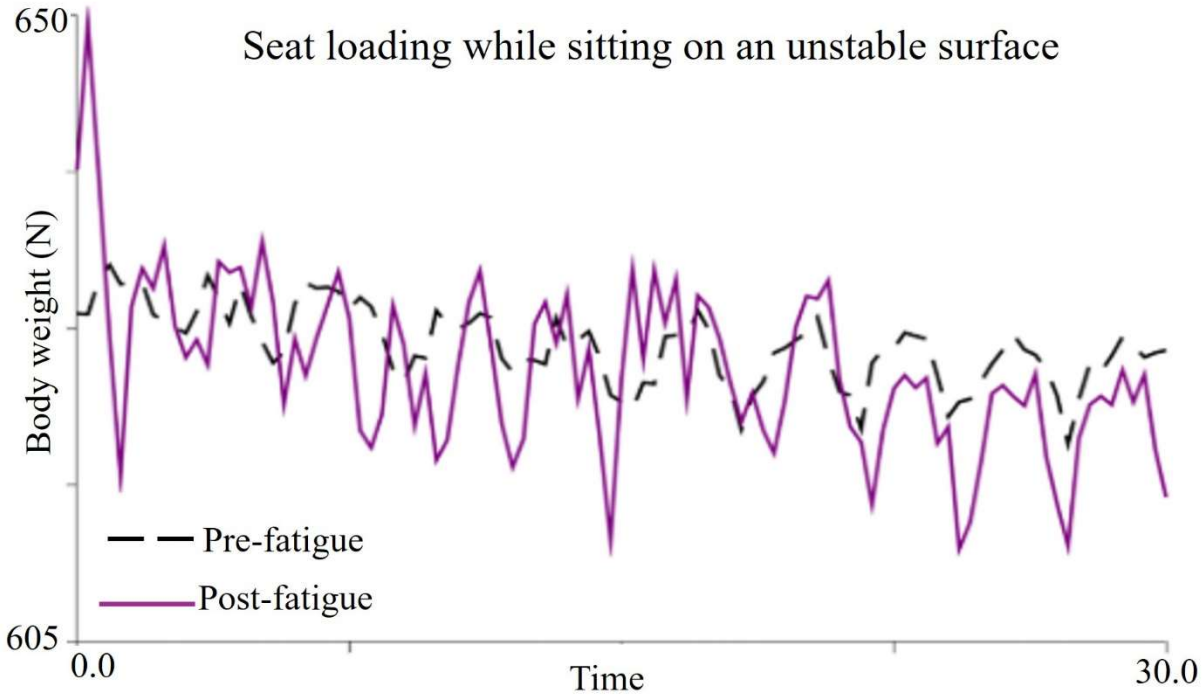


Figure 1. Representative vertical seat reaction forces from one participant over a 30-s trial. Post-fatigue shows an increased variability in seat loading compared to pre-fatigue.

References (Optional)

[1] Blodgett et al., European Heart Journal, 2003; [2] Cholewicki et al., J Biomechanics, 2003.

Session Category

Human Motion and Performance: Balance, Posture and Control

P1-065

Quantifying Performance Across Different Phases of the Timed Up-and-Go Test in Individuals With and Without Cerebral Palsy

Dr. Khushboo Verma BPT, Ph.D.[1], Dr. Michele A. Lobo PT, Ph.D.[1], Dr. Stephen DiBianca Ph.D.[2], Dr. Eman Alsaqabi PT, Ph.D.[2,3], Dr. M. Wade Shrader MD.[4], Dr. Alice Taylor BS, MACPR, MBChB[5], Dr. Jeremy Crenshaw Ph.D.[2], Dr. Laura Prosser PT, Ph.D[6,7], Dr. Stuart Binder-Macleod PT, Ph.D.[1], Dr. Samuel C.K. Lee PT, Ph.D.[1]

[1]Department of Physical Therapy, University of Delaware, Newark, DE, United States. [2]Department of Kinesiology, University of Delaware, Newark, DE, United States. [3]Department of Physical Therapy, College of Allied Health Sciences, Kuwait University, Kuwait city, Capital Governate, Kuwait. [4]Nemours Children's Health, Wilmington, DE, United States. [5]Department of Orthopedics, Alfred I. duPont Hospital for Children, Wilmington, DE, United States. [6]Division of Rehabilitation Medicine, Children's Hospital of Philadelphia, Philadelphia, PA, United States. [7]Department of Pediatrics, Perelman School of Medicine, University of Pennsylvania, Philadelphia, PA, United States

Introduction

Clinicians use various tests to evaluate motor abilities and guide intervention programs for individuals with cerebral palsy (CP). The Timed Up-and-Go Test (TUG) is a reliable, cost-effective, easy-to-implement, and safe clinical test for assessing functional mobility and fall risk. Using a single outcome measure of time to complete the TUG limits the ability to identify specific components within the TUG that may contribute to falls. With recent advancements in technology, particularly in body-worn sensors and smartphones, it is now easier to biomechanically analyze components of the TUG, providing clinicians with a broad assessment of mobility and function within a single assessment.

Methods

We evaluated and compared TUG performance of 20 individuals with spastic diplegic CP (GMFCS I-III) and 20 age- and sex-matched typically developing (TD) peers. We divided the TUG into five phases: sit-to-walk, walk-forward, turn, walk-back, and turn-to-sit. The Mann-Whitney U test examined the group differences in the time taken to complete the TUG and its phases. Z-scores were calculated for each individual, standardized to the TD group mean, for all phase-specific parameters, such as center of mass and center of pressure trajectories and spatiotemporal metrics, to explore biomechanical differences between the CP and TD groups through visual analysis.

Results

Individuals with CP took significantly longer to complete the TUG ($p = 0.0001$) and each of its phases compared to the TD group, with medium to large effect sizes. The largest difference was 4.7s for the walk-back period, and 3.6s for the turn phase. All participants with CP showed broader distributions in their z-scores and had at least one phase-time metric more than one standard deviation (SD) from the TD mean, and 11 individuals with CP had at least one metric exceeding 3 SDs (Figure). Those with CP, particularly GMFCS Levels II and III, demonstrated lower, more variable z-scores, showing shorter and wider steps, more steps, and slower COM velocities than the TD group.

Discussion

These results provide preliminary evidence that the TUG may provide useful information about mobility when segmented into its phases in individuals with CP and assist in detecting differences between individuals with mobility concerns and TD individuals.

Images (Optional)

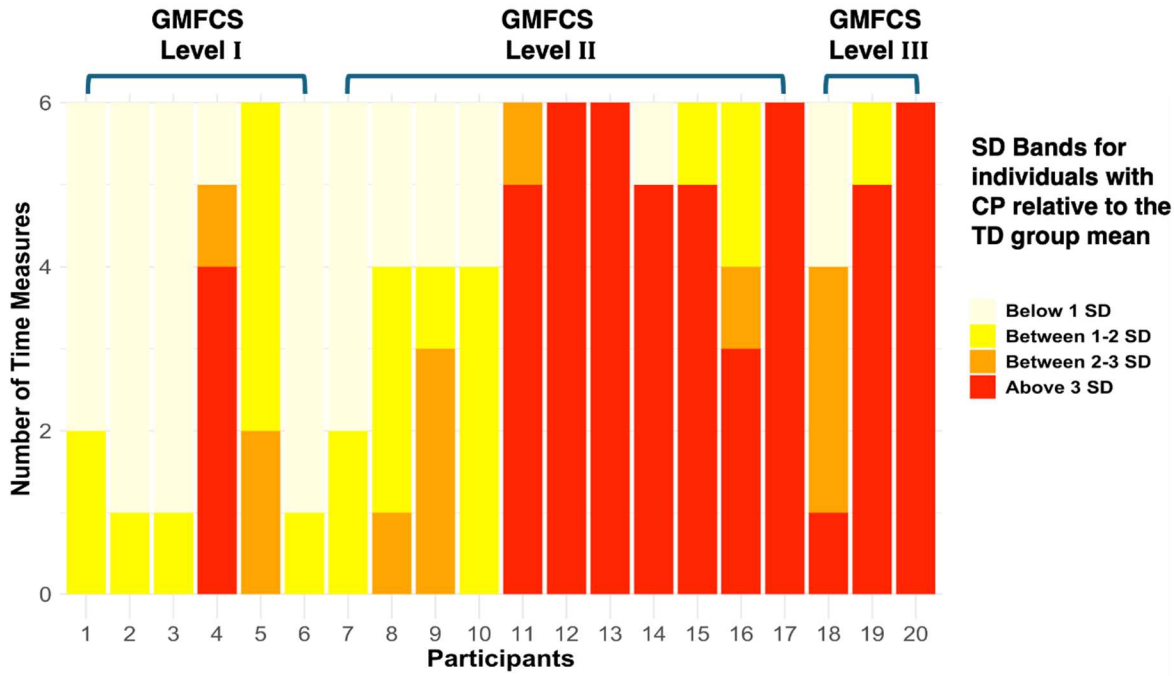


Figure: Z-score standard deviation band distributions of TUG temporal metrics in individuals with CP by Z-score deviation bands relative to the TD group. Each bar represents the proportion of individuals with metrics falling within <1 SD, 1-2 SD, 2-3 SD, or >3 SD.

Session Category

P1-066

Differential Impacts of Mental Fatigue on Gait and Cognition in Young and Older Adults

Dr. Hang Qu PhD[1], Mr. Jinfeng Li[2], Dr. Li-Shan Chou PhD[3]

[1]University of Florida, Gainesville, FL, United States. [2]Iowa State University, Ames, IA, United States. [3]Purdue University, West Lafayette, IN, United States

Introduction

Mental fatigue can significantly impair both cognitive and motor performance in daily life. Emerging evidence suggests that gait requires substantial cognitive resources and is especially susceptible to mental fatigue [1-3]. This study examined the effects of mental fatigue on cognitive performance and gait characteristics in young and older adults during single- and dual-task walking with cognitive challenges. We hypothesized that mental fatigue would impair cognitive performance in both age groups, with more pronounced effects in older adults, and alter gait characteristics, with older adults exhibiting greater changes particularly under dual-task conditions.

Methods

14 young and 14 old adults completed cognitive and gait assessments before and after a mental fatiguing protocol, which consisted of a 50-minute working memory dual-task paradigm with individualized cognitive loading. Cognitive performance was evaluated using digit span tasks (sequencing: arranging numbers in ascending order; reverse: recalling numbers in reverse order) during seated conditions and while walking. Gait performance was assessed through spatiotemporal parameters and center of mass (CoM) movement during single-task normal walking and dual-task walking with concurrent digit span tasks. A three-way mixed-design ANOVA examined effects of Age, Fatigue, and Task on the dependent variables.

Results

Both young and older adults either maintained or improved their cognitive performance post-fatigue. Young adults increased their walking speed in dual-task conditions post-fatigue (sequencing: $p=.004$; reverse: $p=.031$), while older adults walked at a similar gait velocity across conditions. Following mental fatigue, young adults exhibited significant increases in CoM velocity during normal walking ($p=.001$) and dual-task walking with reverse digit span task ($p<.001$). In contrast, older adults maintained a similar CoM movement, revealing a conservative strategy prioritizing balance control.

Discussion

Our findings revealed that older adults can effectively use compensatory strategies to sustain both cognitive performance and gait balance under mental fatigue. The interplay between mental fatigue and dual-task walking underscores the necessity of multidimensional assessments—including CoM motion control—to fully capture age-specific adaptations and inform evidence-based fall-risk management.

References (Optional)

[1] Yogev-Seligmann G, et al. Mov Disord. 2008;23(3):329–342.

[2] Shortz AE, et al. J Neuroeng Rehabil. 2015;12:115.

[3] Beurskens R, Bock O. Neural Plast. 2012;2012:131608.

Session Category

Human Motion and Performance: Balance, Posture and Control

P1-067

Improving Balance Accuracy: Effects of Motivation and Fear on the Base of Support

Ms Liyi Chen

Newcastle University, Newcastle, United Kingdom, United Kingdom

Introduction

Balance can be described in terms of how the body's centre of mass is controlled relative to the base of support formed by the feet. Recently, a 2D model of the functional base of support (fBOS), which can support forces above 40% body weight, has been published, considerably improving the BOS estimate (Millard+Sloot+2025). However, there was a large variation in the fBOS size in young people (9-36% of the foot), which could represent differences in balance ability or task execution. This study examined whether fear, motivation and human variability influence the measured fBOS area.

Methods

Ten young adults (27± 2.6 yrs) were asked to lean as far as they could in all directions in a circular motion while keeping feet in place during five conditions: baseline (repeated within the same day), a safety harness (SH), light fingertip support (PI), visual feedback (VF), and verbal encouragement (VE). Force-plates were used to calculate the fBOS area as the convex hull of the centre-of-pressure data (Figure 1A; Millard+Sloot2025). Conditions were compared using repeated-measures ANOVA; repeatability evaluated using Bland–Altman analysis.

Results

There was a significant overall effect of condition on the fBOS area ($p = 0.0097$). However, post hoc analyses showed no significant differences between Baseline and any other condition (Figure 1B). Baseline within-day repeatability showed task effect: Baseline 2 was 13.9% larger than Baseline 1 (95% LoA: −2.9% to 30.7%; Figure 1C).

Discussion

These findings show that addressing motivation or fear didn't change the fBOS area, although our study is currently limited to young adults. Next step is to compare fBOS area with balance performance. The task effect indicates that the fBOS should be assessed on a

second trial. These results contribute to a better assessment of the fBOS area, thus to a more accurate balance assessment.

Images (Optional)

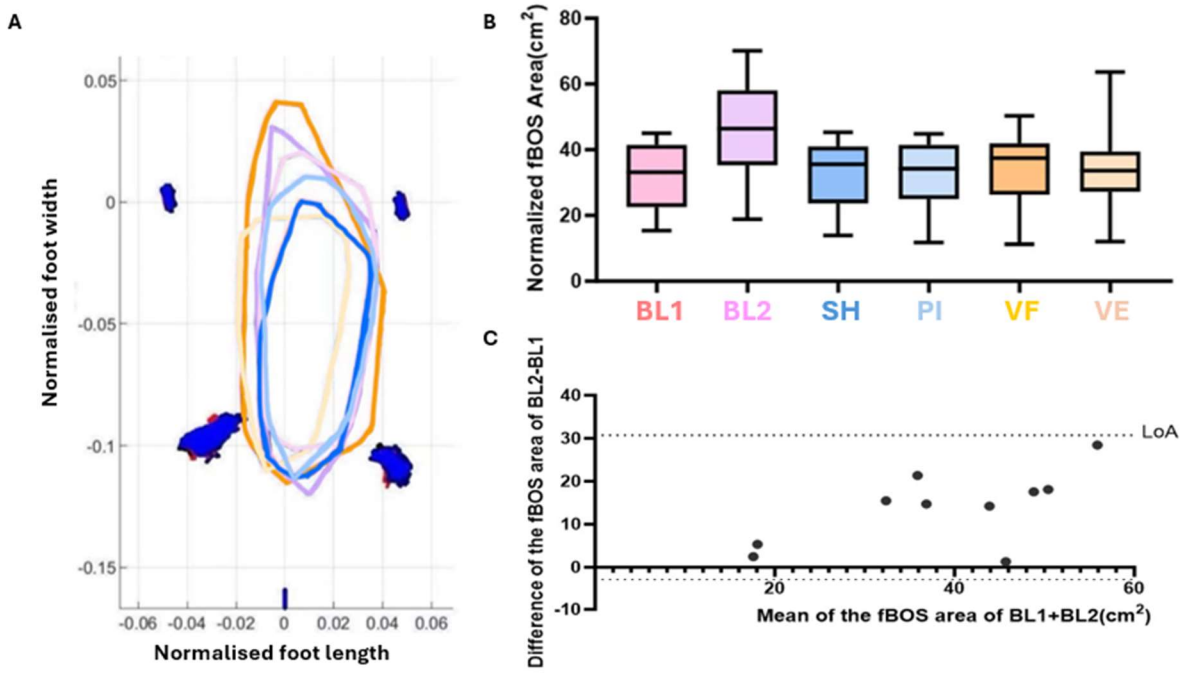


Figure 1. A). The fBOS convex hull area for the different conditions, with the heel, lateral and medial ankle, TMP1, TMP2, and TMP5 toe markers. B) boxplots of the group data of the fBOS area normalised to the 6 foot marker-based area. C) Bland-Altman plot of the baseline condition within-day repeatability.

References (Optional)

Sloot LH, Gerhardy T, Mombaur K, Millard M. The size of the functional base of support decreases with age. Sci Rep. 2025 Oct 27;15(1):37351. doi: 10.1038/s41598-025-22630-x. PMID: 41145821; PMCID: PMC12559752.

Millard, M. and Sloot, L.H. (2025) 'A polygon model of the functional base-of-support during standing improves the accuracy of balance analysis', *J Biomech*, 192, p. 112927.

Session Category

Human Motion and Performance: Balance, Posture and Control

P1-068

Does Arm Posture Influence Wrist Proprioception and Hand Tracking Performance?

Ms. Melanie Altamirano[1], Ms. Meera Sayal[1], Ms. Valentina Massone[2], Ms. Giulia Albanese[2], Mr. Jacopo Zenzeri[2], Dr. Shawn Beaudette[1], Dr. Jae Patterson[1], Dr. Michael Holmes[1]

[1]Brock University, St. Catharines, Ontario, Canada. [2]ReWing, Genoa, Liguria, Italy

Introduction

Proprioception is critical for fine motor control and is essential in occupations requiring high precision such as surgery and dentistry. While previous research has highlighted the influence of fatigue (1) and pain (2) on wrist proprioception, there remains limited understanding of how elbow position impacts wrist proprioception and movement accuracy. The purpose of this study was to investigate how elbow angle and movement direction influences proprioception and tracking accuracy at the wrist.

Methods

Twenty-one right-hand dominant adults (age: 25.5 + 4.1; 9M, 12F) completed two tasks using a 3DoF wrist manipulandum (Edusa PRO-r). Participants completed a joint position matching (JPM) task and a tracking task in three elbow postures (60°, 90° and 120° of flexion). The JPM task involved 4 trials per direction across 6 directions (flexion/extension, radial/ulnar deviation, pronation/supination), with randomized targets. Participants were blindfolded and wore noise cancelling headphones while asked to recreate a previously presented wrist angle. The tracking task required participants to trace a 3:2 Lissajous curve. Participants performed 6 laps; each lap took approximately 20 seconds to complete. JPM outcomes included matching error and error bias, while tracking outcomes included mean tracking error and percent accuracy.

Results

Elbow angle did not significantly affect JPM error, indicating robust wrist proprioception across mid-range elbow postures. Movement direction, however, significantly influenced outcomes, with flexion/extension producing greater variability ($p < .001$) and error ($p = .003$) than radial/ulnar deviation or pronation/supination. Tracking performance had a main effect of elbow angle for both percent accuracy ($p=0.11$) and tracking error ($p = .002$). Percent accuracy was significantly higher at 120° (90 ± 1.1) compared to 60° (85 ± 1.7). Tracking error was significantly higher at 60° (4.2 ± 0.26) compared to both 90° (2.3 ± 0.18) and 120° (3.03 ± 0.32).

Discussion

This study provides novel evidence that wrist proprioception is more direction-dependent than posture-dependent under static conditions, while posture plays a larger role in tracking accuracy. Findings highlight the importance of considering joint configuration and movement direction when designing ergonomic interventions, surgical training protocols, and rehabilitation strategies.

References (Optional)

[1] Albanese et al., Front Hum Neurosci, 2022

[2] Reece et al. J Manipulative Physiol Ther, 2022

Session Category

Human Motion and Performance: Balance, Posture and Control

P1-069

Neuromechanical simulations reveal how feedforward-feedback interactions shape locomotor control

Dr Naomi Chaix-Eichel, Dr Nidhi Seethapathi

MIT, Cambridge, MA, United States

Introduction

Human locomotion relies on the integration of rhythmic pattern generation and reactive, state dependent corrections. While human locomotion is often studied functionally, a mechanistic simulation-based understanding of the interaction between feedforward (rhythmic, velocity-driven) and feedback (reactive, body state-based) control is lacking. We address this gap by developing a computational framework implementing a dual-module architecture inspired by the AI-CPG architecture (Li et al., 2024) to investigate how feedforward and feedback control interact during locomotion.

Methods

Our framework comprises two modules implemented on a 27-DoF MuJoCo humanoid. The feedforward module generates target joint trajectories from a frequency input using a sequence generator followed by a Multi-Layer Perceptron, providing baseline patterns analogous to spinal central pattern generators. The feedback module employs deep reinforcement learning (PPO) to apply online, state-dependent corrections to PD-controller commands, enabling rapid adaptation to body dynamics. Critically, we parameterized the relative contribution of feedforward versus feedback control, allowing systematic study of how these components shape locomotor control.

Results

Our results demonstrate that the framework can reproduce empirically observed velocity-driven step length and state-dependent foot placement control signatures (De Comite et al., 2025). Initially, increasing feedback contribution amplified lateral foot placement corrections proportional to pelvis state, but revealed an optimal balance beyond which control amplitude decreased, suggesting a trade-off between feedforward and feedback contributions to stability.

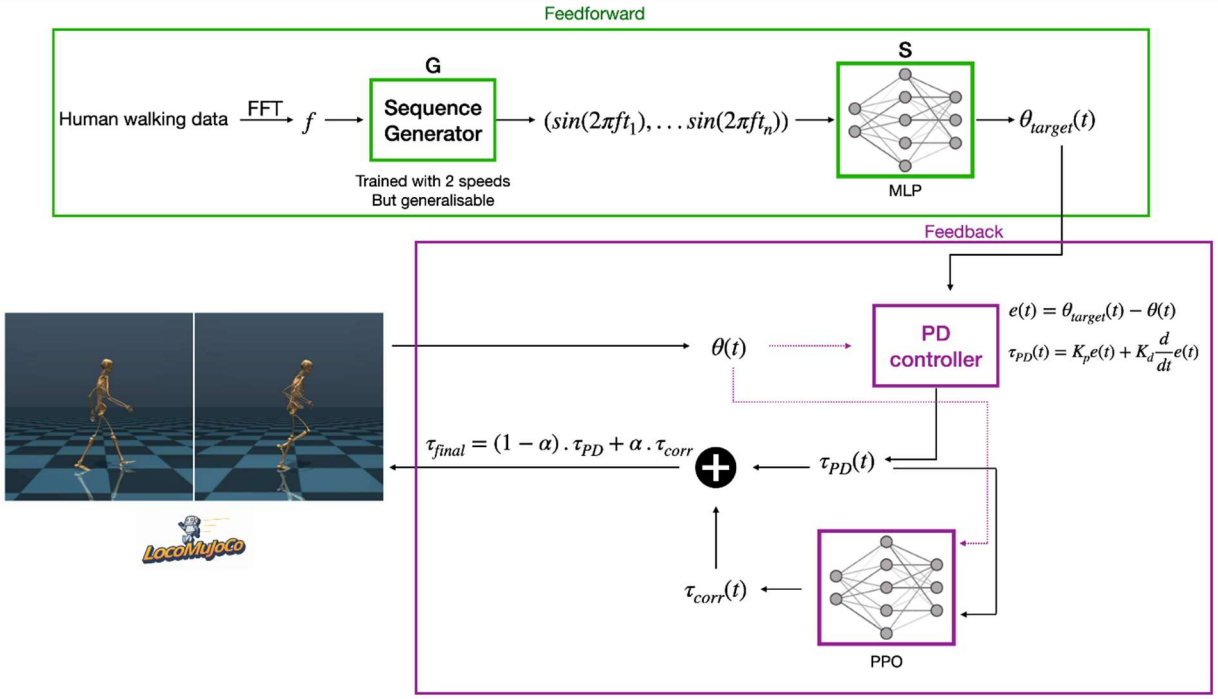
Notably, the model is presently unable to replicate the feedforward speed-step frequency relationship observed in humans, suggesting that the CPG module may need to be modified to capture this.

Discussion

These findings provide causal neuromechanical simulation evidence for the common assumption that lateral stability may preferentially utilize state-based feedback, while forward progression may be dominated by feedforward rhythmic generation (Bauby and Kuo, 2000).

This work provides a simulation-based platform for testing causal hypotheses about feedforward-feedback interactions in locomotion. By parameterizing the relative contributions of these two control modes, we can directly examine how different control strategies produce distinct biomechanical signatures. Our framework, built on open-source tools (MuJoCo, JAX), will be released to enable community extensions. Future work will test these control principles across different body morphologies, and validate whether the feedforward-feedback organization observed here reflects known neural underpinnings.

Images (Optional)



References (Optional)

Session Category

Human Motion and Performance: Balance, Posture and Control

P1-070

The Effect of Jump Distance and Jump Height Variations on Dynamic Postural Stability

Dr. Nathan Robey Ph.D., ATC[1], Dr. Otto Buchholz Ph.D., ATC[2], Ms. Harnoor Pandher[1], Mr. Sol Dehnert B.S.[1]

[1]Western Washington University, Bellingham, Washington, United States. [2]Eastern Washington University, Cheney, Washington, United States

Introduction

The dynamic postural stability index (DPSI) has commonly been used to assess an individual's dynamic stability. However, a limitation in the previous research is the lack of a consistent testing procedure for establishing jump distance and height. Therefore, the purpose of this study was to investigate the impact of various jump distances and heights on DPSI measures.

Methods

Thirty-nine healthy individuals (F = 20, M = 19, 21.2 ± 1.6 yrs, 1.7 ± 0.1 m, 74.5 ± 15.0 kg) participated in a single testing session. Participants performed a barefoot forward-jumping task using a variety of combinations of testing protocols. Participants jumped from a two-footed starting position set at one of three distances (70 cm, the participant's leg length, or 40% of their body height) and to one of three heights (6 in or 12 in hurdle, or touched an overhead target set at 50% of their maximal vertical jump height) and landed on a force platform (Watertown, MA, USA) in a single-limb position. All combinations of distance and height were tested. Condition order was randomized and counterbalanced using a custom MATLAB script. Participants remained balanced for approximately 15 seconds after landing to collect ground reaction force (GRF) data (2000 Hz). GRF data were filtered with a fourth-order Butterworth low-pass filter with a cutoff frequency of 20 Hz and used to calculate DPSI and its component measures. A doubly multivariate MANOVA ($\alpha = 0.05$) was used to compare jump distance and height conditions.

Results

The multivariate interaction was significant ($p < .001$); however, no significant univariate interactions were observed. Significant main effects for both jump distance ($p < .001$) and height ($p < .001$) were observed. Univariate testing and pairwise comparisons indicated significant differences between DPSI and its components across different protocol variables (Table).

Discussion

Leg length poses the greatest challenge to stability, with worsened dynamic postural stability in both DPSI and MLSI. Dynamic postural stability also worsens, in each directional component, as jump height increases. Interestingly, APSI and MLSI are most affected by jump height, indicating greater difficulty in controlling the GRFs during landing. Researchers should consider both factors when determining the task setup.

Images (Optional)

Conditions		1 (n = 39)	2 (n = 39)	3 (n = 39)
Jump Distance		**70 cm**	**Leg Length**	**40% Body Height**
	DPSI	0.34 ± 0.04*	0.34 ± 0.04*†	0.33 ± 0.04†
	APSI	0.03 ± 0.01	0.03 ± 0.01	0.03 ± 0.01
	MLSI	0.10 ± 0.01*	0.12 ± 0.01*†	0.10 ± 0.01†
	VSI	0.32 ± 0.04	0.32 ± 0.04	0.32 ± 0.04
Jump Height		**6 in**	**12 in**	**50% Max Vertical Jump Height**
	DPSI	0.32 ± 0.03*‡	0.34 ± 0.03*	0.35 ± 0.04‡
	APSI	0.02 ± 0.01*‡	0.03 ± 0.01*†	0.03 ± 0.01‡†
	MLSI	0.10 ± 0.01*‡	0.11 ± 0.01*†	0.10 ± 0.01‡†
	VSI	0.30 ± 0.03*‡	0.32 ± 0.03*	0.33 ± 0.04‡

Table. *indicates a significant difference between conditions 1 and 2. ‡indicates a significant difference between conditions 1 and 3. †indicates a significant difference between conditions 2 and 3.

Session Category

Human Motion and Performance: Balance, Posture and Control

P1-071

Strength, Balance, Cognition: What Works to Prevent Falls in Aging Adults

Ms. Nicole Potter MA[1], Dr. Felipe Gonzalez MD, MSc[1,2], Dr. Matheus Vilela MD, MSc[1,2], Mr. Joshua Samaniego MS[1], Mr. Nurudeen Alli BA[1], Dr. Jonathan Gustafson PhD[1]

[1]Rush University Medical Center, Chicago, IL, United States. [2]Instituto Brasil de Tecnologia da Saúde, Rio de Janeiro, RJ, Brazil

Introduction

INTRODUCTION: Falls remain the leading cause of injury among older adults, affecting one in four Americans aged ≥65 each year. Established prevention strategies (e.g., medical factors and home hazard modification) can reduce fall risk, yet the role of training-based interventions in fall prevention remains underexplored. This systematic review and meta-analysis evaluated the impact of muscle strengthening, balance, and cognitive stimulation interventions on balance and fall reduction among older adults.

Methods

METHODS: A comprehensive database search was conducted with no geographic or language restrictions. Eligible studies were randomized controlled trials (RCTs) evaluating muscle strengthening, balance, and cognitive stimulation interventions with balance as the primary outcome and falls as a secondary outcome. Inclusion criteria required a no-intervention control, participants aged ≥60 years, and no diagnosed cognitive impairment or medical conditions associated with fall risk. Two authors independently screened all studies within Covidence, with disagreements resolved by consensus or a third reviewer. Meta-analyses were performed when outcomes were comparable.

Results

RESULTS: The search identified 6,541studies; 99 of which met the inclusion criteria. The most clinically relevant outcomes – Berg Balance Scale (BBS) and Timed Up and Go (TUG) – are reported here. The pooled analysis showed that muscle strengthening (6 RCTs, 277 participants) significantly improved BBS scores (MD=2.53, 95%-CI 1.69; 3.36, $p<0.0001$, $I^2=0.0\%$). Balance training (9 RCTs, 834 participants) statistically improved BBS scores (MD=2.33, 95%-CI 0.69; 3.98, $p=0.0054$, $I^2=75.9\%$) however, cognitive stimulation (3 RCTs, 124 participants) showed no significant effect (MD=0.89, 95%-CI -0.42; 2.20, $p=0.184$, $I^2=0.0\%$). Muscle strengthening (18 RCTs, 1,702 participants) statistically improved TUG performance (MD=-1.06, 95%-CI -1.56; -0.56, $p<0.000$, $I^2=78.6\%$). Balance training (24

RCTs, 2,439 participants) also statistically improved TUG performance (MD=-0.85, 95%-CI -1.23; -0.46, p<0.000, I^2=83.5%), yet cognitive stimulation (7 RCTs, 554 participants) showed no significant effect (MD=-0.27, 95%-CI -0.80; 0.26, p=0.316, I^2=61.9%; Figure 1).

Discussion

DISCUSSION: This review found that muscle strengthening and balance interventions may reduce falls in healthy older adults, but cognitive stimulation lacks convincing support. Inconsistent outcome reporting, heterogeneous interventions, and limited long-term follow-up diminish definitive conclusions. Future research should investigate whether observed effects persist over time or require continuous intervention.

Images (Optional)

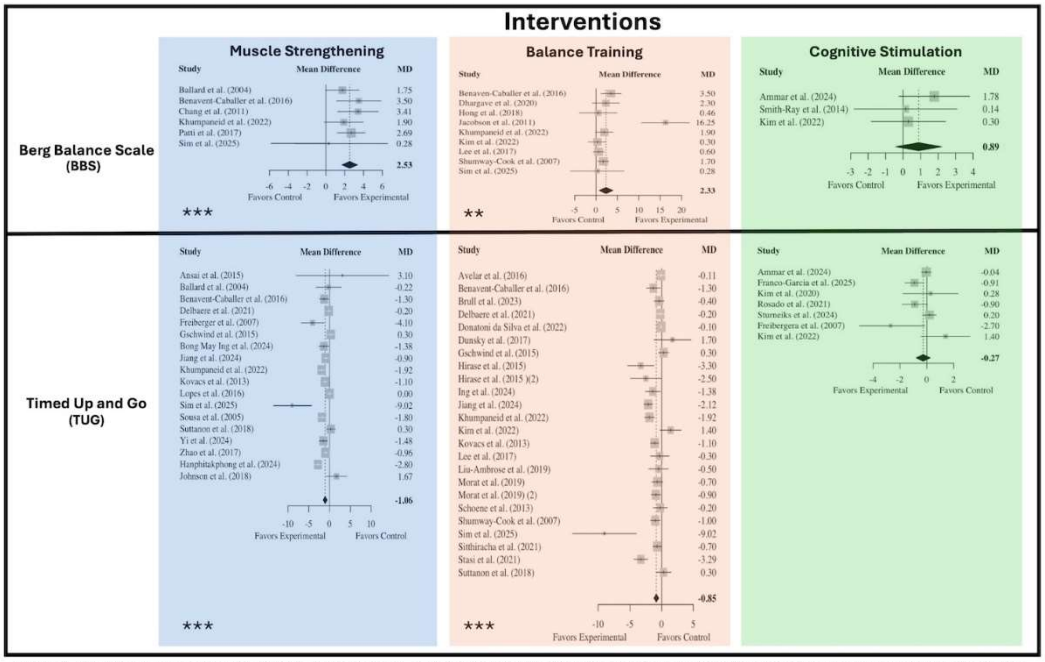


Figure 1. Effects of muscle strengthening, balance training, and cognitive stimulation interventions on Berg Balance Scale scores and Timed Up and Go performance. *** $p < 0.001$ ** $p < 0.01$

Session Category

Human Motion and Performance: Balance, Posture and Control

P1-072

Postural Responses to Forward and Backward Gait Initiation Tasks in Neurotypical Adults

Mr OLUWAFEMI ADEGBEMIGUN BPT, MSc[1,2,3], Mr Ryland Swearinger MS[3], Dr Christy Conroy[2], Miss Janki Patel MS[2], Dr Arian Vistamehr PhD[2], Dr. Clay Wauneka PhD[4], Dr. Dorian Rose PhD[1,2,3]

[1]Department of Physical Therapy, Gainesville, FL, United States. [2]Brooks Rehabilitation, Jacksonville, FL, United States. [3]Brain Rehabilitation Research Center, Malcolm Randall VA Medical Center, Gainesville, FL, United States. [4]Cook Children's Medical Center, ForthWorth, Texas, United States

Introduction

Gait initiation (GI), the transition from standing to walking, requires precise postural adjustments to maintain stability. Forward Gait Initiation (FGI) is visually guided, whereas Backward Gait Initiation (BGI) is less practiced, with limited visual feedback, and presents a greater challenge to postural control. Center of Pressure (COP) peak displacement and pathlength are two metrics that evaluate the magnitude and sway length of postural adjustment during GI. Most studies examine either peak displacement or pathlength during FGI, leaving it unclear whether one or both metrics are sensitive to gait directions. We examined both COP metrics to offer additional insight into postural control.

Methods

Eleven neurotypical adults (Age: 62.8±12.3 years old; Gender: 6M; Gait speed: 1.3m/s) participated, standing quietly, with each limb on separate force plates, for 10 seconds, and initiated gait with their dominant limb upon a verbal “go” signal. GI was repeated three times in both forward and backward directions. Data was processed in VICON and Visual 3D. Average COP peak displacement in both medial-lateral (ML) and anterior-posterior (AP) directions, and COP pathlength were calculated during the postural phase (PP) of GI. Paired t-test compared COP peak displacement of AP and ML trajectories, and pathlength during FGI and BGI

Results

In the PP, COP peak displacement during FGI and BGI were comparable in the AP (FGI: 38.3 ± 13.4mm; BGI:31.3 ± 6.9); and the ML (FGI: 53.9 ± 16.4mm; 47.6 ± 17.5)

trajectories**.** However, COP pathlength during FGI was significantly longer compared to BGI, *p=0.002* (FGI: 136.7 ± 31.2; BGI: 83.6 ± 43.5)

Discussion

Peak AP and ML COP displacement is similar for forward and backward GI, suggesting that the maximum COP excursion associated with the initial momentum is invariant to task direction, possibly due to constraints in stability margins during both tasks. In contrast, COP pathlength is greater during FGI, indicating that pathlength is direction-sensitive, implying that the initial posterior shift in FGI requires larger corrective sway than the corresponding anterior shift in BGI. Evaluation of both COP peak displacement and pathlength during GI tasks may provide a more comprehensive picture of postural control deficits in those with musculoskeletal or neurologic pathology.

Session Category

Human Motion and Performance: Balance, Posture and Control

P1-073

Effects of a Hula-Based Intervention on Balance and Fall Risk in Native Hawaiian and Pacific Islander Older Adults: A Pilot Study

Dr Patricia Young PhD[1], Ms Sheryl Yoshimura MPH, RD[2], Ms Chantelle Matagi MA[3], Dr Christopher Stickley PhD[4], Dr J. Keawe'aimoku Kaholokula PhD[5]

[1]Hawai'i Pacific University, Honolulu, HI, United States. [2]Kōkua Kalihi Valley, Honolulu, HI, United States. [3]Tagata Moana Hui Foundation, Honolulu, HI, United States. [4]University of Hawaii Mānoa, Honolulu, HI, United States. [5]University of Hawai'i, John A. Burns School of Medicine, Honolulu, HI, United States

Introduction

Hula, the traditional dance of Hawai‘i, is practiced by Native Hawaiians (NHs) and has been adopted by other Pacific Islanders (PIs), as well as by non-NHPI individuals, of all ages. The motions of Hula include stepping, shifting standing balance, turning the body and head, and upper body positioning that can shift the center of mass, challenging balance. Our goal was to determine whether regular Hula practice could be used as a culturally relevant approach to implementing balance training among NHPI older adults.

Methods

We conducted a substudy of an ongoing Hula-based clinical trial in NHPI adults ages 50-75 years with subjective or mild cognitive impairment. Forty-one participants were enrolled (mean age: 62.5 years) at two community sites: Kōkua Kalihi Valley (KKV) and Ko‘olauloa (KLL). Each site had wait-list control and Hula intervention groups with ~10 people per group. The Hula intervention comprised 2 1-hour sessions per week for 12 weeks. Balance, concern about falling and fall risk were measured pre-post intervention using the Berg Balance Scale (BBS), Falls Efficacy Scale – International (FES-I) and four-square step test (FSST). Fall history was also assessed. We conducted focus groups with the Hula groups post-intervention to determine the intervention’s acceptability.

Results

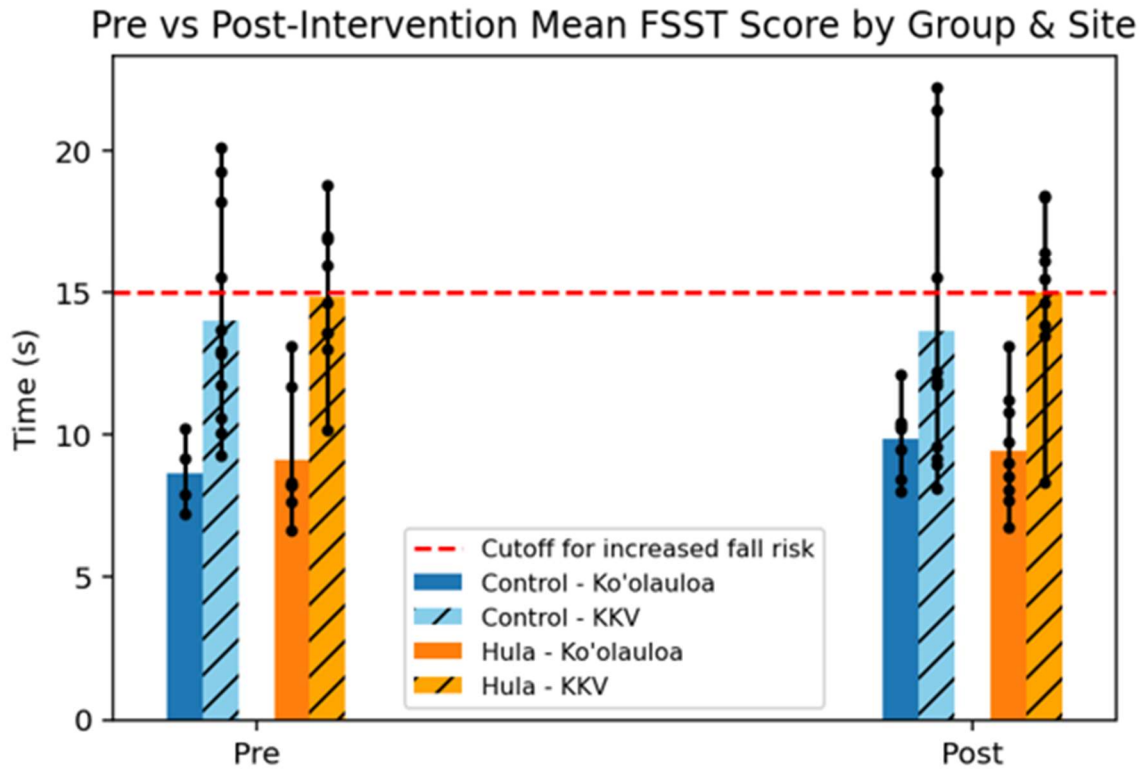
Participants had fall history rates of 45% and 27% at KKV and KLL, respectively, with an overall rate of ~39%. On the BBS, all KLL participants scored ≥48, with most scoring 56, the maximum score, pre- and posttest. A similar trend was seen on the FSST, with all participant scores <15 s. Approximately 30% of KKV participants scored between 45 and

47, indicating an increased risk of falls. Concern about falling increased pre-post among some participants. Results analyses are ongoing.

Discussion

The rate of individuals with a history of falls was higher than the state average (~22%). The balance measures employed may not have fully captured how balance indicators changed throughout the intervention. However, participants reported improved mobility and confidence in activities of daily living in the focus group followup, indicating promise in using this intervention. Camera and force plate-based measures of balance should be considered in followup studies for their increased sensitivity.

Images (Optional)



References (Optional)

Acknowledgements (Optional)

The authors would like to thank the Center for Pacific Innovations, Knowledge and Opportunities (PIKO, NIH U54GM138062) for pilot funding to P. Young for this study. We

would also like to thank the partricipants and the Kōkua Kalihi Valley, Tagata Moana Hui Foundation, and ‘IKE Kūpuna research teams.

Session Category

Human Motion and Performance: Balance, Posture and Control

P1-074

Investigating Stepping Error in Healthy Young Adults Across Task Difficulty and Divided Attention

Investigating Stepping Error in Healthy Young Adults Across Task Difficulty and Divided Attention Payton Reuter Student, Investigating Stepping Error in Healthy Young Adults Across Task Difficulty and Divided Attention Mindie Clark PhD, Professor

University of Minnesota Duluth, Duluth, Minnesota, United States

Introduction

Dual- tasking requires divided attention and can alter gait mechanics, compromising safety [1]. Even healthy young adults show reduced gait performance while texting [2]. The purpose of this study was to evaluate how task difficulty and dual-tasking affects stepping accuracy in healthy young adults using a multi-precision stepping paradigm.

Methods

Twenty young adults completed 40 trials stepping into targets during their first and third dominant footstep. For 20 trials, participants completed a concurrent simple verbal task, and for 20, the second stepping target was rotated 45°. Four combinations of ten trials were performed and participants reported mental effort after each. We calculated stepping accuracy, stepping bias, and variability. We compared within-subjects effects of target orientation and task on stepping performance (mm) and mental effort.

Results

Dual- tasking led to greater mental effort compared to single- task ($p= 0.004$). Target 1 error was not different across task in anteroposterior ($p= 0.747$) or mediolateral ($p= 0.076$) directions. Target orientation affected mediolateral stepping error in Target 2 in which single- pivot conditions were more accurate compared to single- straight conditions ($p= 0.046$), but there was no effect of task ($p= 0.423$). Stepping variability in Target 1 was significantly different across task ($p= 0.013$).

Discussion

Our findings demonstrated that even a simple verbal concurrent task can elicit greater mental effort, although its effect on stepping performance was less clear. The verbal task did not increase stepping error, suggesting that task demands did not exceed available attentional resources. Performance metrics indicate that young adults may expend greater effort to perform on tasks perceived to be more difficult and prioritize distal stepping targets that allows for more planning. Findings may not be generalizable to tasks competing for resources in the same domain (eg. two visually-guided tasks) or to populations that recruit more attentional resources for similar tasks. It is vital to evaluate safe navigation strategies in environments that strain attentional resources.

References (Optional)

[1] Pizzamiglo et al., *Frontiers, 2017*

[2] Hyeong Lee et al., J of Phys Ther Sci, 2018

Session Category

Human Motion and Performance: Balance, Posture and Control

P1-075

Force-Plate Calibration for Human Quiet-Standing Studies

Ms. Rika Sugimoto-Dimitrova, Ms. Jiajie Qiu, Professor Neville Hogan

Massachusetts Institute of Technology, Cambridge, Massachusetts, United States

Introduction

Force plates are commonly used to study human quiet standing. Traditionally, statistics of center-of-pressure (CoP) displacement have been used to describe standing behavior. More recently, horizontal foot force has also been incorporated in some balance measures, such as the intersection-point-height measure (Boehm et al. 2019). However, quiet standing involves very small movements, with CoP displacements on the order of millimeters and shear forces less than 1 N. Thus, quantifying measurement uncertainty is essential. In this study, a force-plate-calibration procedure was developed to determine the uncertainties in force-plate-derived quiet-standing measures.

Methods

A testbed was placed on the force plate being tested, and an actuator applied horizontal forces to induce shear forces and CoP displacements. Twelve 30-second trials mimicking quiet-standing data were employed to test two force plates: a portable device (Kistler 9260AA3) and a floor-mounted device (Bertec FP4060-07-1000). The data were low-pass-filtered to 10 Hz, and used to compute 10 CoP-based measures (Prieto et al. 1996) and the intersection-point-height measure. These measures were then compared against ground-truth values from a load cell to estimate error.

Results

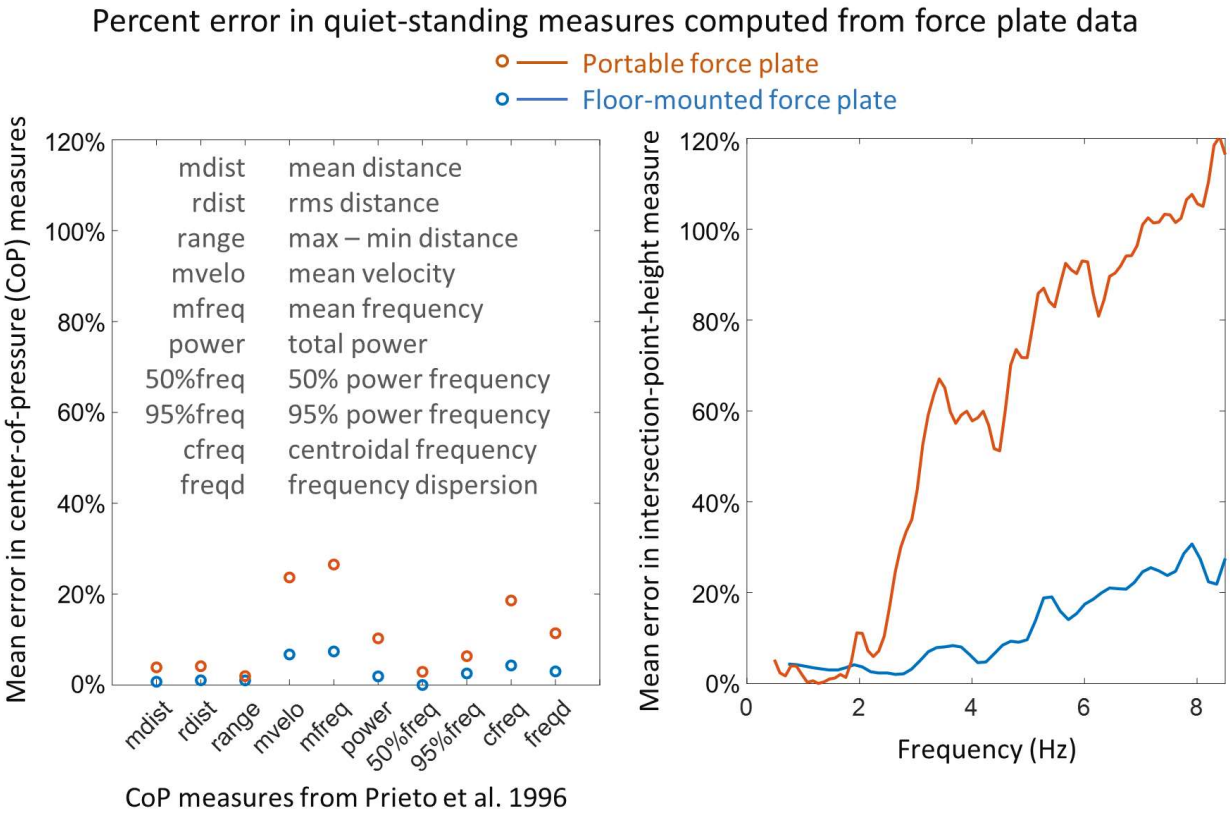
CoP data showed a larger signal-to-noise ratio than shear-force data. Measurement error was more pronounced at higher frequencies: CoP measures that depended more on lower-frequency content, such as mean or root-mean-square distance, exhibited low errors (<5%); measures sensitive to higher-frequency signals, like mean velocity, showed larger errors (up to 27%). The intersection-point-height measure showed errors less than 10% below 2 Hz, while error increased for higher frequencies: at 4 Hz, the portable force plate exhibited 60% error. The floor-mounted device generally exhibited lower errors than the portable device.

Discussion

The commonly-used CoP measures could be derived more accurately from force-plate data than the newer intersection-point-height measure that incorporates shear force and

CoP at higher frequencies. Nonetheless, accuracy depends on measurement signal strength and device noise level. Therefore, it is important to investigate data reliability for a given use-case, particularly when analyzing small-magnitude or high-frequency data.

Images (Optional)



References (Optional)

Boehm et al. (2019). Frequency-dependent contributions of sagittal-plane foot force to upright human standing. J. Biomech.

Prieto et al. (1996). Measures of postural steadiness: differences between healthy young and elderly adults. IEEE TBME.

Session Category

Human Motion and Performance: Balance, Posture and Control

P1-076

Machine Learning Framework for Optimized Wearable Sensor Detection of Gait Instability

Mr. Roshan Ragu[1], Ms. Jordan Feldman[2], Mr. Constantin Beyer[3], Dr. Jessica Allen[4], Dr. Jason Franz[1]

[1]University of North Carolina at Chapel Hill, Chapel Hill, NC, United States. [2]Harvard University, Cambridge, MA, United States. [3]Digity GmbH, Göttingen, Lower Saxony, Germany. [4]University of Florida, Gainesville, FL, United States

Introduction

Falls represent a major health risk, particularly for older adults. Remote monitoring of locomotor instability is critical for advanced diagnostics, earlier intervention, and real-world assessment of intervention efficacy. We recently discovered that inertial measurement units (IMUs) may have the potential to detect perturbation-induced instability during walking [1]. However, deploying IMUs in real-world settings requires optimization to balance feasibility and accuracy. Here, we developed a machine learning framework based on recorded IMU signals to predict the conscious perception (i.e., “yes” or “no”) of small-amplitude slip perturbations during walking.

Methods

15 healthy young adults walked at their preferred speed on a dual-belt treadmill while wearing IMUs on their posterior sacrum, wrists, anterior shanks, and dorsum of the feet (APDM, 128 Hz). 3D acceleration signals were demeaned, low-pass filtered using a sixth-order Butterworth filter (30 Hz cutoff) and converted to vector magnitudes. While walking, a custom MATLAB treadmill controller rapidly decelerated (6 m/s^2) one foot at initial contact during the stance phase every 12-15 strides at random. Eight perturbation magnitudes delivered in randomized order five times each ranged from 0.02 m/s to 0.3 m/s. Perturbations were labeled according to participant perception (yes/no), producing binary outcomes for supervised learning. A bidirectional long short-term memory (LSTM) network was combined with a Random Forest classifier in a stacked ensemble architecture, with a logistic meta-classifier integrating their predictions. Each possible combination of the seven IMU locations was evaluated to identify the minimal sensor configuration that maximized classification accuracy.

Results

The ensemble model determined that a two-IMU system (i.e., perturbed foot and unperturbed shank) maximized prediction performance (i.e., 85% accuracy); accuracy

peaked for the smallest and largest amplitude perturbations. The perturbed foot IMU appeared in all top 20 sensor combinations (81%-85% accuracy range) (Fig. 1). An important caveat is that models generally had more false negatives than false positives.

Discussion

These results demonstrate that perception of walking balance perturbations can be reliably inferred from wearable IMU data. By identifying feasible, high-performing sensor configurations, this work supports the design of lightweight, unobtrusive systems for real-world instability monitoring and fall-risk prevention.

Images (Optional)

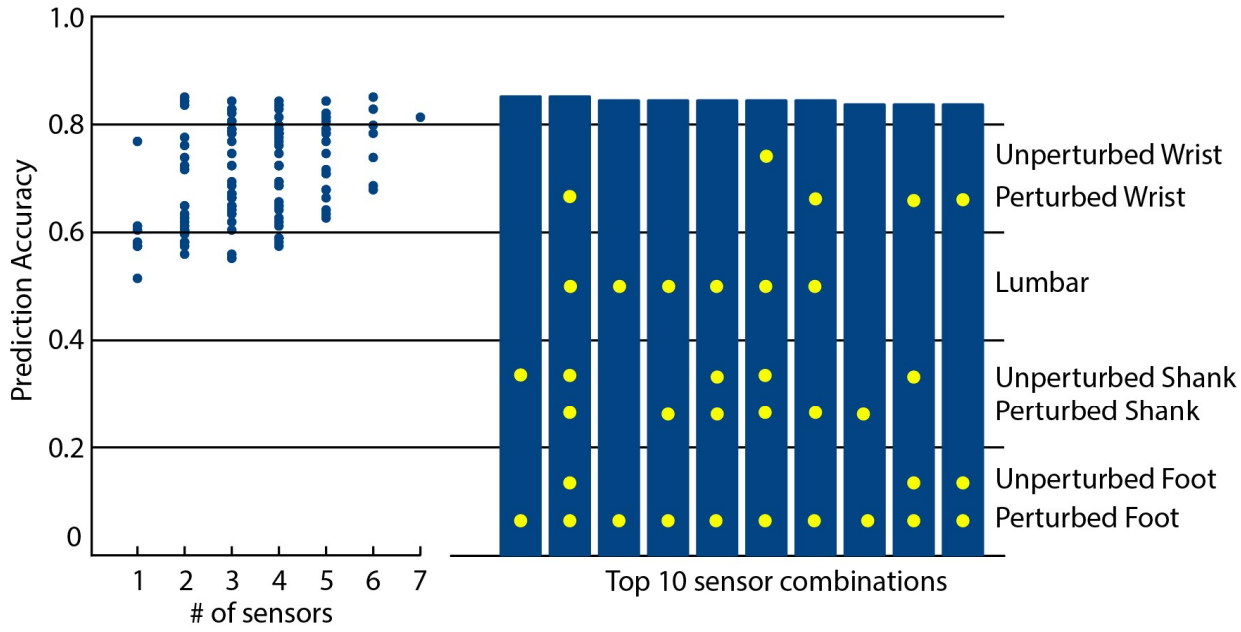


Figure 1. Results of our machine learning prediction framework, showing the prediction accuracy of all possible sensor configurations (left) and that of the top 10 sensor configurations along with their specific compositions (right).

References (Optional)

[1] Feldman et al., J Applied Biomechanics (In review)

Session Category

Human Motion and Performance: Balance, Posture and Control

P1-077

Assessing the concurrent validity and test-retest reliability of markerless motion capture for static postural control assessment

Mr. Sachitha Wijekoon BScH[1], Dr. Jereme Outerleys BEng, MASc[1], Dr. Benjamin Ritsma BS, MD[1], Dr. Kevin Deluzio BASc, MASc, PhD[1], Dr. Scott Selbie BASc, PhD[2], Dr. Vincent DePaul BHSc, PhD[1], Dr. Stephen Scott BASc, MASc, PhD[1]

[1]Queen's University, Kingston, Ontario, Canada. [2]HAS-Motion Inc, Kingston, Ontario, Canada

Introduction

Accurate assessment of impairment is essential for guiding rehabilitation in patients with postural control deficits [1]. Traditional research-grade tools provide objective precision but face practical barriers to clinical integration. Markerless motion capture systems, like Theia3D, offer a promising alternative, although their utility for measuring postural control remains unclear. To address this gap, this study evaluated the concurrent validity and test-retest reliability of Theia3D for measuring static postural control, in both laboratory and clinically relevant contexts.

Methods

Fifty-three healthy adult participants (16♂, 37♀; age=24 [18-50] years) without neurological or musculoskeletal disorders performed three quiet standing tasks across two sessions, spaced ~one week apart. Tasks were performed under two conditions: standing alone (unaccompanied), and with an individual standing nearby simulating clinical supervision (accompanied) (Figure 1). Eight synchronized cameras and a force plate recorded data simultaneously. The pelvis Centre of Mass (COM) was estimated from video using Theia3D and the Gravity Line Projection (GLP) was computed from ground reaction forces. Concurrent validity was assessed using cross-correlations and root mean square differences (RMSD) between the COM and GLP. Test-retest reliability was evaluated for common COM parameters using Intraclass Correlation Coefficients (ICCs). Spearman's correlations compared parameters across conditions.

Results

Across all tasks/conditions, COM and GLP signals showed good to excellent mean zero time-lag cross-correlations ($r=0.88$-0.99) and RMSD <0.12cm. ICCs were stronger in the unaccompanied condition across tasks, particularly for the 95% confidence ellipse area

(ICC=0.75-0.89) and mediolateral mean velocity (ICC=0.63-0.84). Significant positive correlations (r=0.37-0.81) were observed between conditions for most COM parameters.

Discussion

The COM and GLP showed strong agreement, consistent with prior work [2,3]. Several COM parameters also demonstrated good reliability. Reliability fell in the accompanied condition, likely due to occlusions and subtle behavioural changes. Nonetheless, strong validity and correlations across conditions suggest Theia3D can support comparisons between healthy and pathological postural control. Study limitations include lack of clothing standardization and using the pelvis COM as a surrogate for whole-body COM. Future work will evaluate performance in clinical populations and extend validation to dynamic tasks.

Images (Optional)

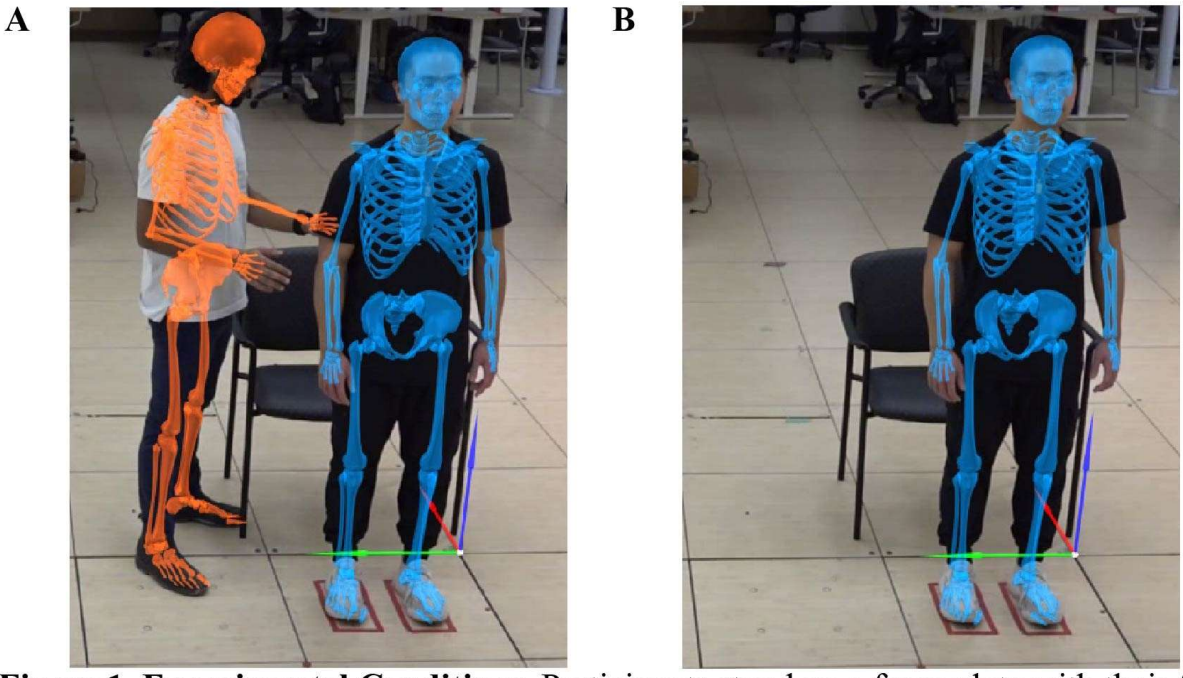


Figure 1. Experimental Conditions. Participants stood on a force plate with their feet in two boxes spaced roughly hip-width apart. **A**. The unaccompanied condition, where participants stood alone. **B.** The accompanied condition, where participants stood with an individual standing nearby, simulating clinical supervision.

References (Optional)

[1] Sibley et al., Implementation Sci, 2013

[2] Zatsiorsky and King., J Biomechanics, 1997

[3] Lafond et al., J Biomechanics, 2004

Acknowledgements (Optional)

We would like to thank K. Moore for their help in participant recruitment. We would also like to thank the members of the Human Mobility Research Laboratory, for allowing us to use their research space. This research was supported by the Ontario Research Fund (ORF RE-04-047). The funding source was not involved in the completion of this study. The authors would also like to thank the participants in this study for giving their time.

Session Category

Human Motion and Performance: Balance, Posture and Control

P1-078

Sex- and Treatment-Specific Associations Between Emotional Factors and Peripheral and Supraspinal Postural Control in Knee Osteoarthritis

Dr. Ana Filipa Durão[1], M.S. Jacopo Epifanio[1], Dr. Laura Tio[2], MD Jordi Monfort[2,3], Dr. Simone Tassani[1]

[1]Universitat Pompeu Fabra, Barcelona, Catalunya, Spain. [2]Hospital del Mar Research Institute, Inflammation and Cartilage Research Group, Barcelona, Catalunya, Spain. [3]Hospital del Mar, Rheumatology service, Barcelona, Catalunya, Spain

Dr. Ana Filipa Durão

M.S. Jacopo Epifanio

Introduction

Knee osteoarthritis (KOA) is a prevalent degenerative disease that compromises joint stability and postural control [1]. Although these are common biomechanical alterations associated with KOA, patients often exhibit heterogeneous clinical trajectories, highlighting the need for stratified analyses. Emotional and psychological factors have been shown to influence postural stability [2], yet their relationship with objectively quantified postural control parameters in KOA remains unclear. This study investigated the association between emotional factors and postural stability using advanced postural control metrics, accounting for sex and treatment type.

Methods

Eighty-three adults with KOA (Kellgren Lawrence grades 2–3; 50 women, 33 men) performed quiet standing on a force platform. Participants were stratified by sex and treatment: conservative management or total knee replacement (TKR) waiting list. Emotional factors were assessed using the Pain Catastrophizing Scale (PCS). Postural control was characterized using traditional center-of-pressure parameters, a Synchronization Index [3], and Rambling and Trembling decomposition to distinguish supraspinal (rambling) and peripheral/reflexive (trembling) contributions [4,5] in anterior–posterior (AP) and medial–lateral (ML) directions. All stability data were normalized by

height. Associations were explored using correlation-based variable selection and second-order surface fitting (adjusted R^2).

Results

Significant associations between emotional and postural stability metrics were observed exclusively in men. In conservative men, PCS was associated with the mean trembling frequency in the ML direction and peak distance (adjusted $R^2 = 0.83$), yielding a saddle-shaped response surface (Figure 1a). In men awaiting TKR, PCS was associated with AP rambling root mean square and global spectral peak maximum frequency (adjusted $R^2 = 0.83$), characterized by a surface with a maximum (Figure 1b).

Discussion

These findings strongly suggest that emotional and physical factors are interconnected in KOA through sex- and treatment-specific postural mechanisms, involving distinct peripheral and supraspinal control components. Integrating pain management strategies and a gender perspective could improve the evaluation of postural instability in KOA.

Images (Optional)

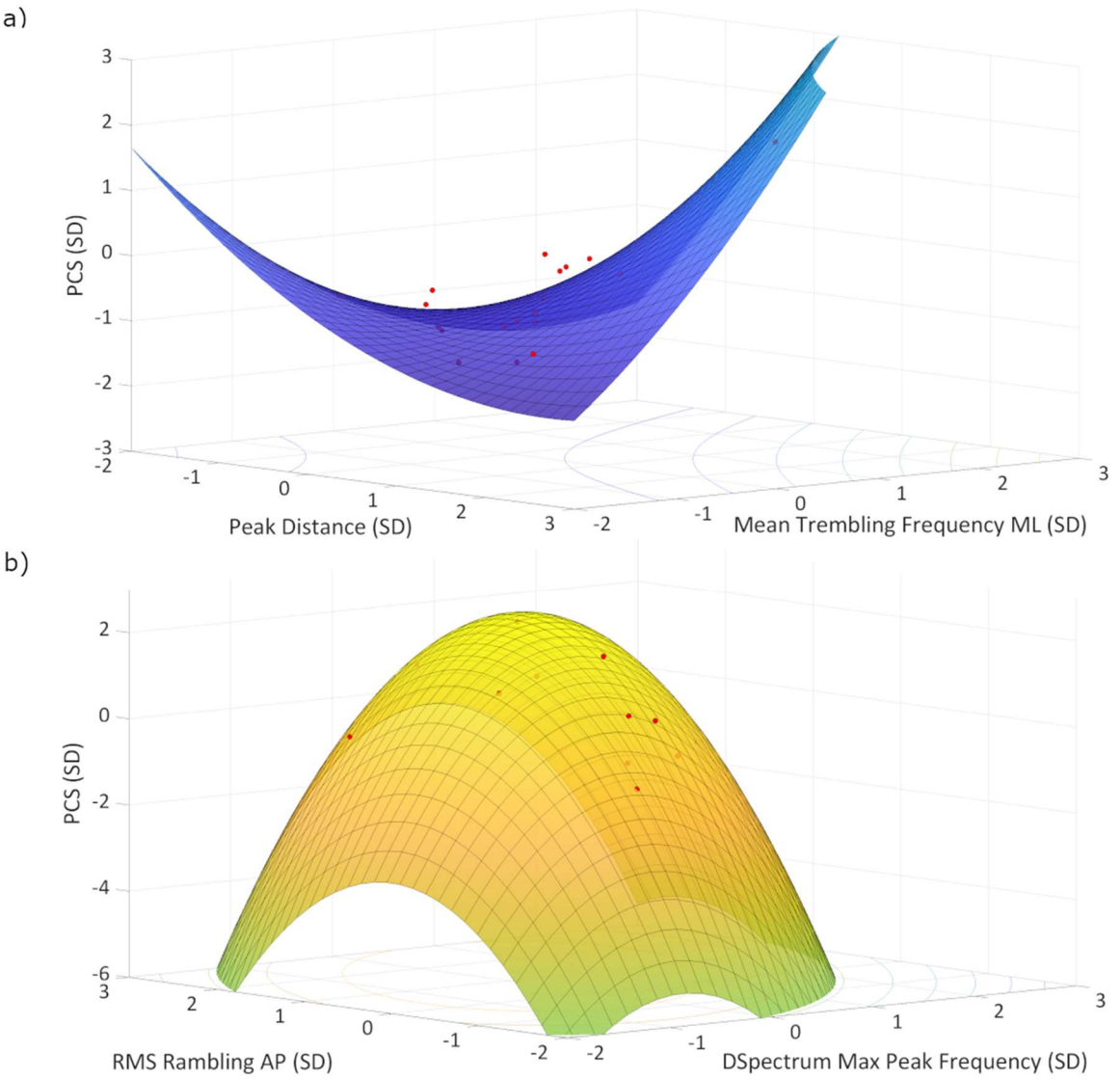


Figure 1. Second-order bivariate surface fits showing the relationship between PCS and postural stability parameters, for conservative men (a: adjusted $R^2 = 0.83$) and men awaiting TKR (b: adjusted $R^2 = 0.83$). All parameters normalized by standard deviations.

References (Optional)

1. Fitzgerald et al., Arthritis Care Res, 51:941-946, 2004
2. Brown et al., Gait Posture, 24:397-405, 2006
3. Mormann et al., Physica D, 144:358-369, 2000
4. Zatsiorsky & Duarte, Motor control, 3(1):28–38, 1999
5. Zatsiorsky & Duarte, Motor control, 4(2):185–200, 2000

Acknowledgements (Optional)

Funding: Spanish Government (STRATO PID2021-126469OB-C21); Spanish Ministry of Science and Innovation and the State Research Agency (Grant No. PID2020-118196GBI00/MICIU/AEI/10.13039/501100011033) in the MdM program (No. CEX2021-001195-M).

Session Category

Human Motion and Performance: Balance, Posture and Control

P1-079

Comparing Effects of Control Parameters on Stability and Energy in Powered Knee Prosthesis Users During Perturbed Walking

Mr. Sixu Zhou[1], Mr. Hanjun Kim[1], Mr. John Shim[1], Mr. Atli Örn Sverrisson[2], Mr. David Langlois[2], Mrs. Kinsey Herrin[1], Dr. Aaron Young[1]

[1]Georgia Institute of Technology, Atlanta, Georgia, United States. [2]Össur, Reykjavík, Reykjavík, Iceland

Introduction

Powered lower-limb prostheses restore mobility to individuals with transfemoral amputation (TFA) and reduce mechanical energy cost during walking. However, slips and falls remain a major problem for individuals with TFA [1]. While previous studies examined powered knee control parameters on energy efficiencies during steady-state walking, the impact of control parameters on stability during perturbations remains largely unexplored [2]. Thus, we evaluated the biomechanical response of individuals with TFA using the Össur PowerKnee during perturbed walking. We tested the hypotheses that an earlier swing initiation timing would 1) improve post-perturbation stability and 2) reduce biological joint work compared to a later swing initiation timing.

Methods

Nine participants with unilateral TFA consented to an IRB-approved protocol and were fit and trained on the PowerKnee. After acclimation, motion capture and force plate data were collected while participants walked on the CAREN at a self-selected speed. During each trial, perturbations were applied through the CAREN platform that included two magnitudes, four directions, and four timings, while sweeping swing initiation from 55–65% of the gait cycle with a minimum of two repetitions per perturbation condition. The biomechanical results were generated using OpenSim and the joint work is determined by the trapezium integration of the joint power. The stability is quantified using the maximum Mahalanobis distance and the recovery time of the center of mass (CoM) relative to the center of pressure (CoP) trajectory in the limit cycle.

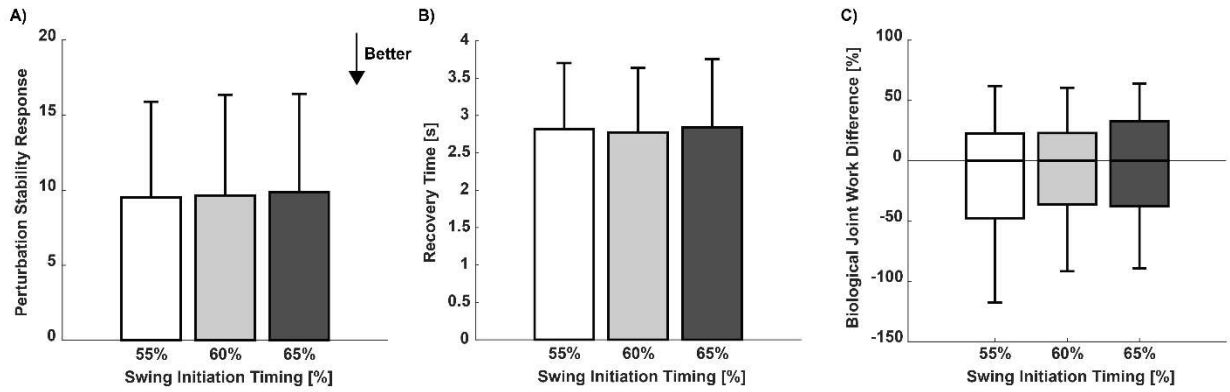
Results

As shown in Fig 1A-C, on average, an earlier swing initiation did not show a significance difference compared to a later swing initiation in both stability and energy efficiency, therefore allowing us to reject the Hypothesis 1 and 2.

Discussion

On average, an earlier swing initiation timing slightly improved stability and energy, but it was not sufficiently sensitive to detect differences in both stability and energy. However, the high subject variability emphasizes the importance of control parameter personalization. Future work should examine how biomechanical responses vary across perturbation types, magnitudes, and timings.

Images (Optional)



References (Optional)

Reference:

[1] S. T. King *et al.*, J NeuroEngineering Rehabil., 2024

[2] S. Zhou *et al.*, IEEE Trans Med. Robot. Bionics, 2025

Session Category

Human Motion and Performance: Balance, Posture and Control

P1-080

The Characterization of a Step Up, Stand Still, and Step Off Balance Assessment

Miss Sophia Chirumbole, Dr. Jessica Krok-Schoen, Dr. Shawanee' Patrick, Dr. Daniel Merfeld, Dr. Ajit Chaudhari

The Ohio State University, Columbus, OH, United States

Introduction

Falling is a concern, especially with increasing age. Falls can cause significant morbidities, such as bone fracture, traumatic brain injury, spinal cord injury [1], as well as fear of falling and self-isolation [2], so preventing falls is critically important. While quiet standing balance metrics are well-correlated to fall risk [3,4,5], dynamic balance (i.e. during stepping tasks) may be better than standing balance for predicting falls since most falls occur when someone is moving [6]. This study developed a novel step up, stand still, and step off (SUSO) task and associated analysis approach for further exploration into balance ability.

Methods

For each SUSO trial, participants were asked to step onto the force plate, stand still with their arms at their sides for approximately 3-5 seconds, then step off of the force plate. Ground reaction forces (GRF) were measured at 1000 Hz. Time to stabilization (TTSz) was calculated using the moving standard deviation (0.5 second window), with the minimum representing the most stable time window in the SUSO balance trial. The first timepoint with a standard deviation of less than five times the minimum was considered the TTSz in seconds (Figure 1).

Results

41 healthy adults participated after providing IRB-approved informed consent (36 ± 13 years old, 17M 24F). The mean (standard deviation, min-max) of TTSz was 1.44 (0.25, 1.03-2.21) seconds across all participants for the SUSO task.

Discussion

Gaining detailed information on stepping tasks could improve understanding of dynamic postural control and stabilization. The addition of force plate data and quantitative metrics like TTSz could allow for increased sensitivity and predicting balance performance. The proposed SUSO task could be easily implemented due to its familiarity for people who regularly use a weight scale. This exploratory work sets a foundation to better inform

studies of what movements contribute to falls and to design the most effective screening tools.

Images (Optional)

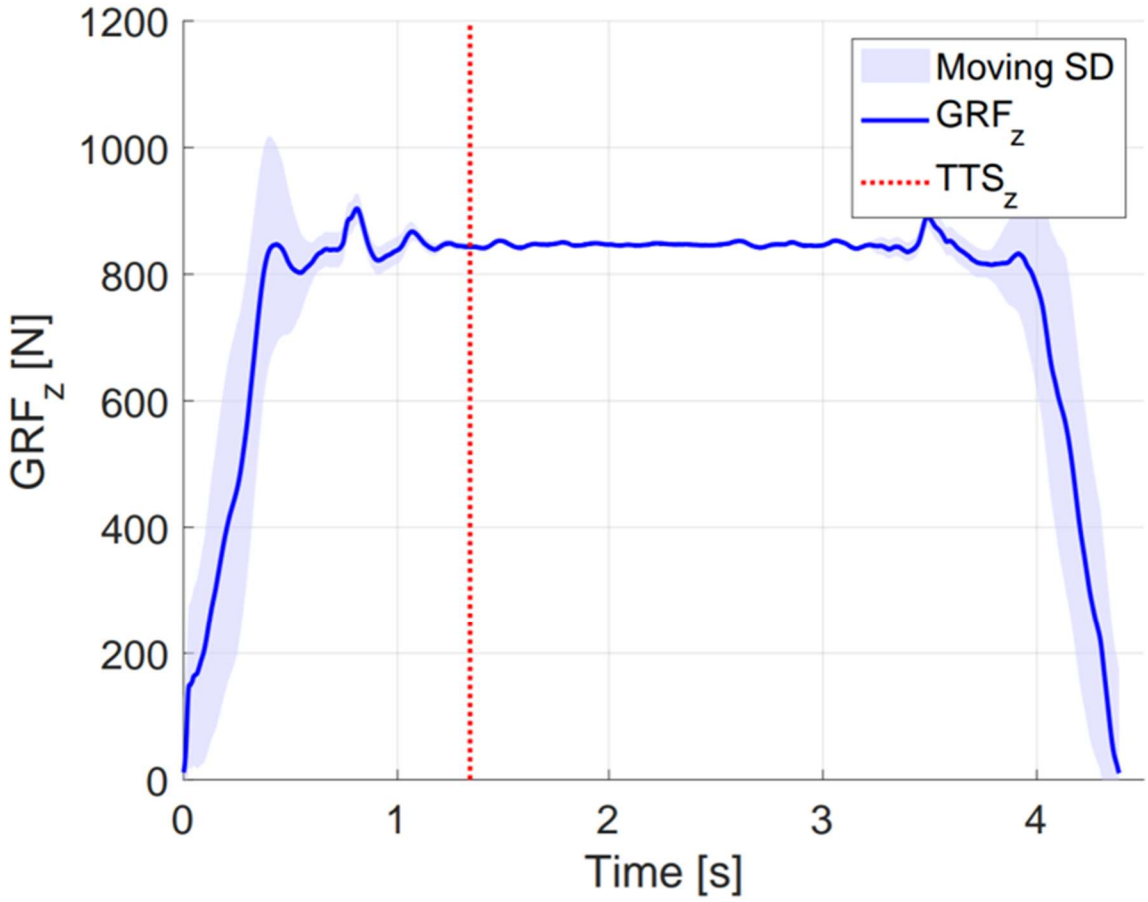


Figure 1: A single participant's SUSO trial featuring their vertical GRF trace throughout the task, with a vertical red dashed line illustrating the TTSz. Shaded area represents the moving standard deviation used to calculate TTSz.

References (Optional)

[1] James *et al.,* Inj Prev, 2020; [2] NCOA, https://www.ncoa.org/article/get-the-facts-on-falls-prevention/, 2025; [3] Maki *et al.*, J Gerontol, 1994; [4] Hewson *et al.*, Annu Int Conf IEEE Eng Med Biol Soc, 2010; [5] de Abreu *et al.,* BMC Geriatr, 2024; [6] Tideiksaar, Bull NY Acad Med, 1988.

Acknowledgements (Optional)

None.

Session Category

Human Motion and Performance: Balance, Posture and Control

P1-081

Impact of Walking Speed, Perturbation Direction, and Arm Constraints on Perceived Balance Capacity and Fall Risk

Dr. Sriram Muralidhar Postdoctoral scholar, Ms. Nkumbu Kamfwa Research Coordinator, Prof. James Finley Associate Professor

University of Southern California, Los Angeles, California, United States

Introduction

People's perceptions of their balance capacities and the risk associated with walking in different environments guide everyday walking choices. Because misjudging the relationship between one's capacity and balance-threatening features of the environment can lead to falls, it is essential to understand how task-specific estimates of perceived capacity and fall risk are influenced by factors known to modulate the risk of falls. Here, we present an experimental paradigm to quantify perceived balance capacity and fall risk, examining how they vary in response to task features known to impact actual fall risk during walking.

Methods

Participants walked on a split-belt treadmill and experienced random perturbations caused by unexpected changes in the speed of the left or right belt. In each trial, we progressively increased the change in speed until participants reported that a stronger perturbation would cause them to fall; we defined this highest tolerated perturbation as their perceived balance capacity. In addition, participants rated the riskiness of each perturbation on a 0–10 scale, with 0 corresponding to the perceived riskiness of quiet standing and 10 to a fall. They completed 28 trials each, walking at seven speeds (25–175% of self-selected speed) while experiencing forward or backward perturbations with their arms either tied or free. We fit linear mixed-effects models to determine how walking speed, perturbation direction, and arm constraint influenced perceived capacity and risk.

Results

Linear models explained trends in perceived capacity (R^2 = 44%) and risk (R^2 = 44%). Perceived capacity (Fig. 1 a-b) was higher for forward perturbations and the arms free condition ($p<0.05$). Perceived risk (Fig. 1 c-d) increased with walking speed, and was higher for backward perturbations and the tied condition ($p<0.05$).

Discussion

Our results suggest that perceived balance capacity and perceived fall risk depend on walking speed, perturbation direction, and arm constraint. This implies that fall-prevention interventions, such as perturbation training, should incorporate non–self-selected speeds, backward perturbations, and possibly physical constraints to limit the range of feasible balance recovery strategies. These perceived capacity measures may also help characterize how disease, injury, aging, or fatigue affect balance.

Images (Optional)

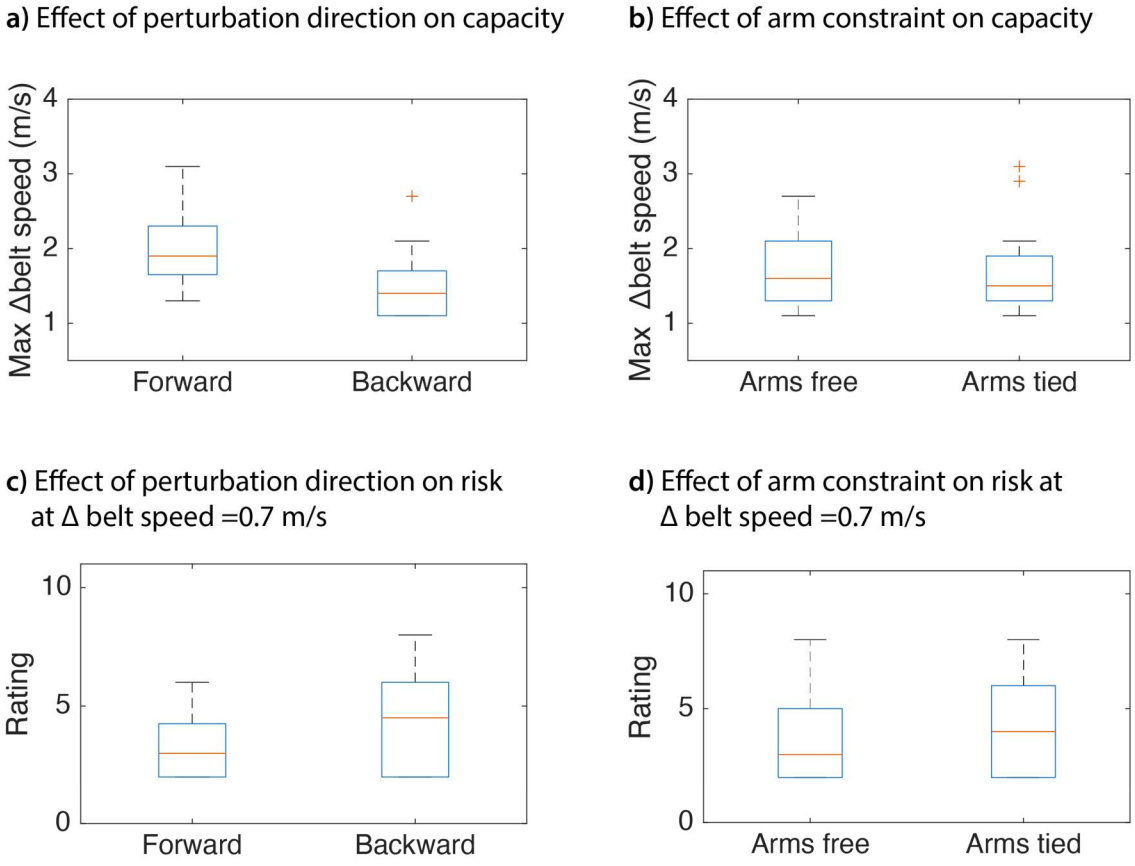


Fig 1. Perceived capacity and risk of 6 subjects walking at self selected speed. a) Perceived capacity is higher for forward perturbations than backward. **b)** Perceived capacity is higher for arms free than arms tied condition. **c)** Perceived risk is higher for backward perturbations than forward . **d)** Perceived risk is higher for arms tied than arms free condition.

References (Optional)

Acknowledgements (Optional)

This work was supported by the Integrative Movement Sciences Institute (IMSI) Biological Integration Institute, NSF-DBI-2319710.

Session Category

Human Motion and Performance: Balance, Posture and Control

P1-082

Energy Cost for Force Changes Is Nonlinear and This Nonlinearity Predicts Human Forces in Legs, Arms, Fingers, and Muscles

Dr. Sriram Muralidhar Postdoctoral scholar[1,2], Ms. Nadja Marin[3], Mr. Colin Melick[2], Dr. Hansol Ryu[4], Dr. Aya Alwan[2], Mr. Zhengcan Wang[5], Mr. Ross Baldwin[2], Prof. Kristen Heitman[2], Prof. Sam Walcott[6], Prof. Manoj Srinivasan[2]

[1]University of Southern California, Los Angeles, California, United States. [2]The Ohio State University, Columbus, Ohio, United States. [3]University of Illinois Urbana-Champaign, Champaign, Illinois, United States. [4]Georgia Institute of Technology, Atlanta, Georgia, United States. [5]University of Wisconsin–Madison, Madison, Wisconsin, United States. [6]Worcester Polytechnic Institute, Worcester, Massachusetts, United States

Introduction

A central challenge in motor control is the 'redundancy problem': how the CNS selects a specific solution from infinite possibilities. Two dominant theories propose that humans minimize either metabolic cost [1] or motor variability arising from signal-dependent noise [2]. Distinguishing these theories is difficult because they often yield correlated predictions. Here, we resolve this conflict by deriving an accurate metabolic cost function and employing novel experiments designed to disambiguate these objectives. We show that our metabolic model accurately predicts force distribution across arms, legs, fingers, and muscles.

Methods

Our study had multiple experiments, combining metabolic measurements with behavioral experiments. First, metabolic cost was modelled via two experiments: one where 19 participants tracked diverse, time-varying leg-force profiles and another involving isometric knee-flexed standing. Second, we conducted two experiments where 23 participants produced a total goal force using both arms or both legs, a redundant task allowing infinite limb-force combinations. We compared the right-left force sharing strategies predicted by minimizing our metabolic cost model with those predicted by minimizing signal-dependent error. We also applied our metabolic model to predict force sharing across fingers (unimanual and bimanual) and muscles using data from previous literature [3,4].

Results

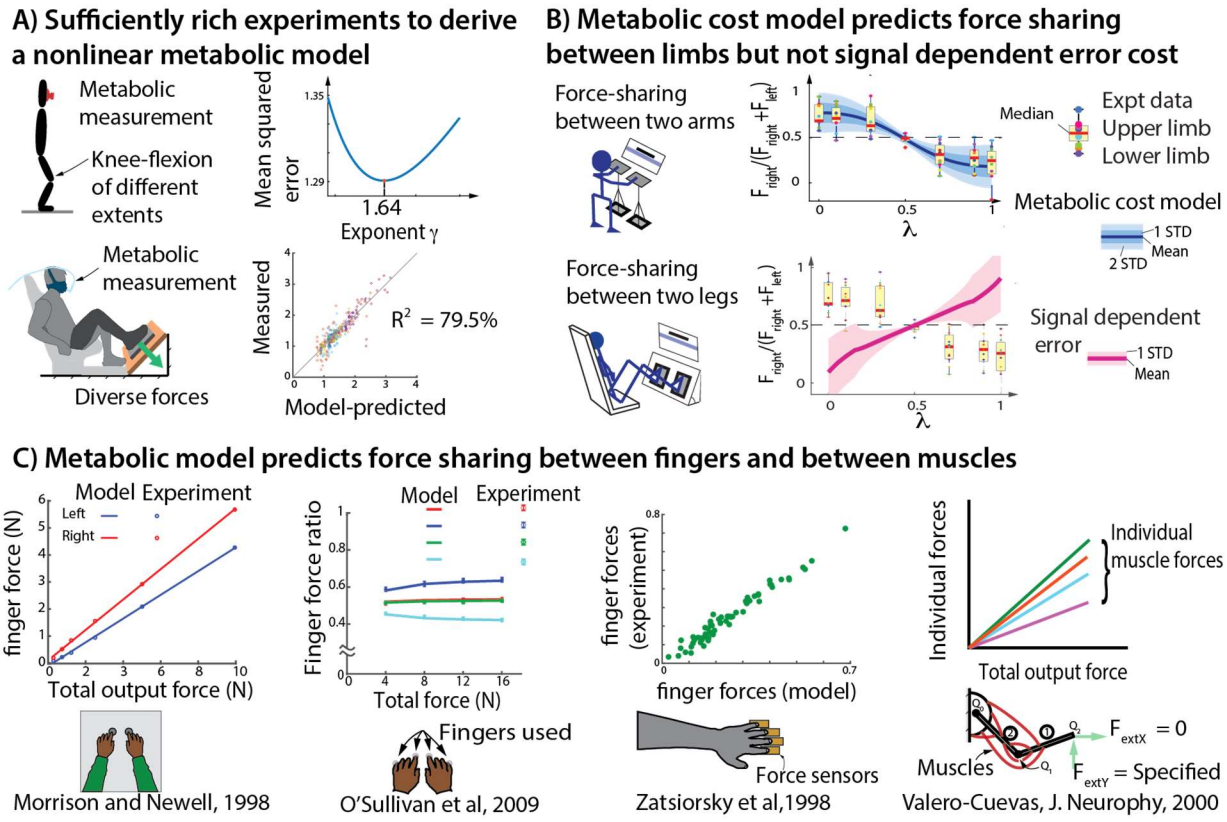
The two metabolic experiments revealed that metabolic energy scales superlinearly with force (F^{γ} with exponent $\gamma \sim 1.6$, Fig. 1a). In the force-sharing experiments, human behavior matched predictions from minimizing this nonlinear metabolic cost (Fig 1b). In contrast,

the alternative theory of minimizing signal-dependent noise predicted forces anti-correlated with the empirical data. The metabolic model also predicted force-sharing patterns between fingers and the linear scaling of individual muscle forces observed in prior literature (Fig 1c).

Discussion

Our findings demonstrate how metabolic energy scales superlinearly with force, contrasting with the common linear and quadratic models. We show that the nervous system accounts for these nonlinearities, as our model predicts force-sharing patterns across limbs, fingers, and muscles. Our findings rule out signal-dependent noise minimization, establishing metabolic energy minimization as a central driver of force sharing.

Images (Optional)



References (Optional)

[1] Brown et al, PNAS, 2021.

[2] Harris and Wolpert, Nature, 1998.

[3] Zatsiorsky et al, Biological Cybernetics, 1998.

[4] Morrison & Newell, J. Mot, Behav., 1998.

Acknowledgements (Optional)

This work was supported by NIH-R01GM135923 and NSF SCH grant 2014506. Thanks to the Ohio State CRC for access to metabolic testing.

Session Category

Human Motion and Performance: Balance, Posture and Control

P1-083

Does Balancing a Ball on the Back Change Spinal Movements During the Bird-Dog Exercise?

Dr Cathrine Feier PhD, Dr Stephen Brown PhD

University of Guelph, Guelph, Ontario, Canada

Introduction

The “bird-dog” is a commonly prescribed rehabilitation exercise for low back pain that attempts to activate spine stabilizing muscles while minimizing compressive forces. The exercise involves contralateral arm and leg extension while maintaining a neutral spine; ideally avoiding excessive rotation and flexion/extension movements. This study aimed to investigate if balancing a rubber ball on the lower back during bird-dog exercises could immediately decrease spine flexion/extension and axial rotation range of motion (RoM) in a healthy population.

Methods

Fifteen participants (mean ± standard deviation: age: 21 ± 1 years, mass: 65.4 ± 11.4 kg, height: 166.6 ± 6.9 cm) volunteered to participate in the study. Marker-based motion capture (120 Hz) was utilized to collect kinematic data for the trunk and pelvis during three trials (Pre, Ball, Post), each of 20 bird-dog repetitions. The second trial included a small rubber ball on the lower back and instructions to attempt not to drop the ball (Figure 1). A flexion-extension, lateral bend, axial rotation Cardan sequence was used to calculate the three-dimensional angles between the trunk and pelvis segments.

Results

Repeated measures ANOVAs demonstrated significant differences between trials (Pre, Ball, Post) for spine flexion/extension ($p < .001$, partial $\eta^2 = .556$) and axial rotation ($p < .001$, partial $\eta^2 = .565$) RoM. Post-hoc tests with Bonferroni adjustments revealed significantly decreased flexion/extension RoM during the Ball trial (mean ± standard error: 16.0° ± 1.0°) compared to the Pre (23.7° ± 1.8°; $p = .002$) and Post (23.2° ± 1.7°; $p = .001$) trials. Similarly, axial rotation RoM was significantly lower during the Ball trial (8.7° ± 0.9°) compared to the Pre (15.7° ± 1.6°; $p = .002$) and Post (15.0° ± 1.5°; $p = .001$) trials.

Discussion

The results indicate that attempting to balance a small ball on the lower back during bird-dog exercises can significantly decrease spine flexion/extension and axial rotation RoM. A ball could therefore be a simple facilitator for maintaining a neutral spine during bird-dog exercises. However, there was no immediate retention effect, indicating a likely need for repeated interventions to induce long term changes.

Images (Optional)

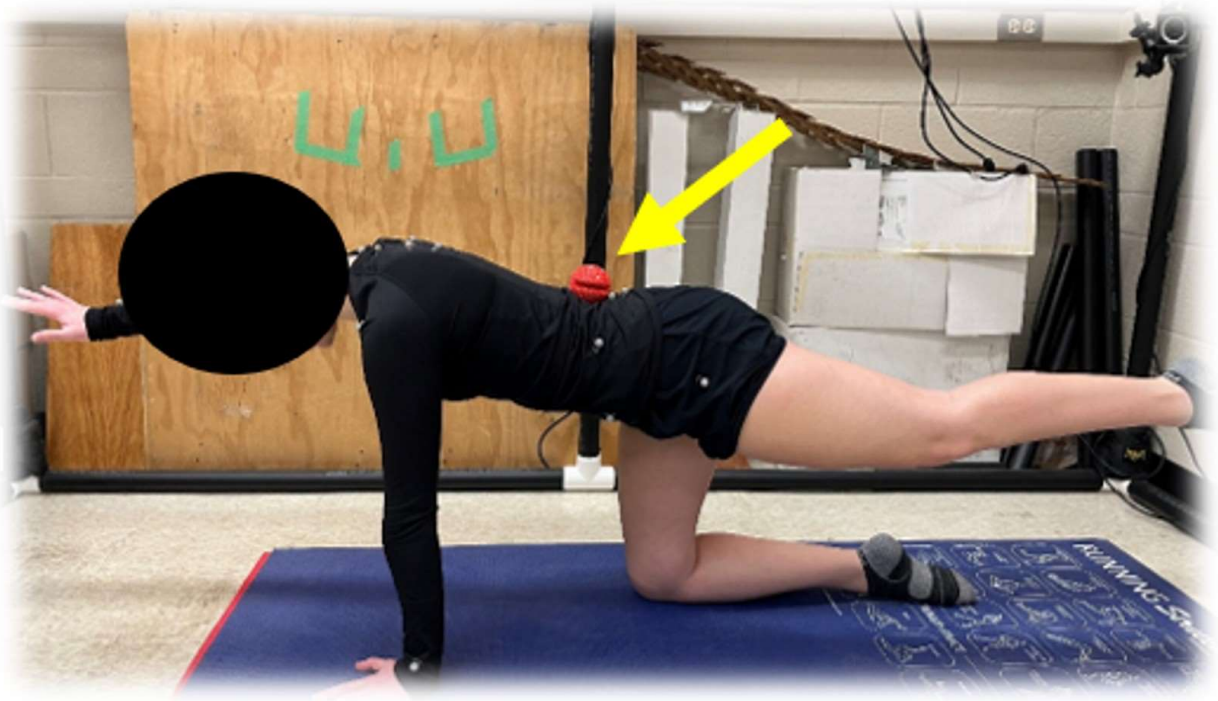


Figure 1: Lateral view of bird-dog end position with the ball.

Session Category

Human Motion and Performance: Balance, Posture and Control

P1-084

Participant Instructions During Research Studies: Open to Interpretation? a Case Study

Dr Cathrine Feier PhD[1], Ms Samantha Tsioros BSc[1], Ms Victoria Lippitt BSc[1], Dr Shawn Beaudette PhD[2], Dr Stephen Brown PhD[1]

[1]University of Guelph, Guelph, Ontario, Canada. [2]Brock University, St. Catherines, Ontario, Canada

Introduction

Clear communication is essential when providing instructions to human participants in biomechanics research studies. Underlying beliefs or experience can affect people's interpretation of instructions and lead to variable outcomes despite identical instructions. This case study explored the kinematic changes observed when clarifying instructions between movement blocks in a spine flexion study.

Methods

The participant (P12) volunteered for a study asking participants to "bend forward" with a tucked chin and arms hanging. All participants performed three blocks of 10 forward bending movements. It was deemed necessary to explain to P12 that spine flexion was preferred over hip hinging after they had completed the first block. Kinematic data were captured with marker-based motion capture (120 Hz). Flexion-extension angles and range of motion (RoM) were calculated for the lumbar (S1-T12), thoracic (T12-C7), and total spine (S1-C7). Intersegmental angles for each repetition were used in a principal components analysis and subsequent single component reconstruction (SCR) of the first principal component.

Results

P12 was the most variable participant in the study and more than doubled their mean lumbar and total spine RoM from the first to the second block (Figure 1). This can be compared to P10 who demonstrated similar values in all three blocks. The SCR plots revealed more variability in intersegmental RoM magnitude, seen as a larger separation between the 5^{th} (red line) and 95^{th} (blue line) percentiles for P12 compared to P10 (Figure 1). P12 also demonstrated different thoracic spine movement strategies between repetitions, indicated by the red and blue lines moving in opposite directions at the same point of the movement cycle.

Discussion

The change from hip hinging in the first block to spine flexion in the other blocks led to large changes in RoM and intersegmental movement strategies. The changes can be visualized by comparing the RoM for separate blocks and through SCR plots. Researchers need to be mindful of potential underlying beliefs that can affect how people move (e.g. “spine flexion should be avoided”) and previous work/exercise/injury experience.

Images (Optional)

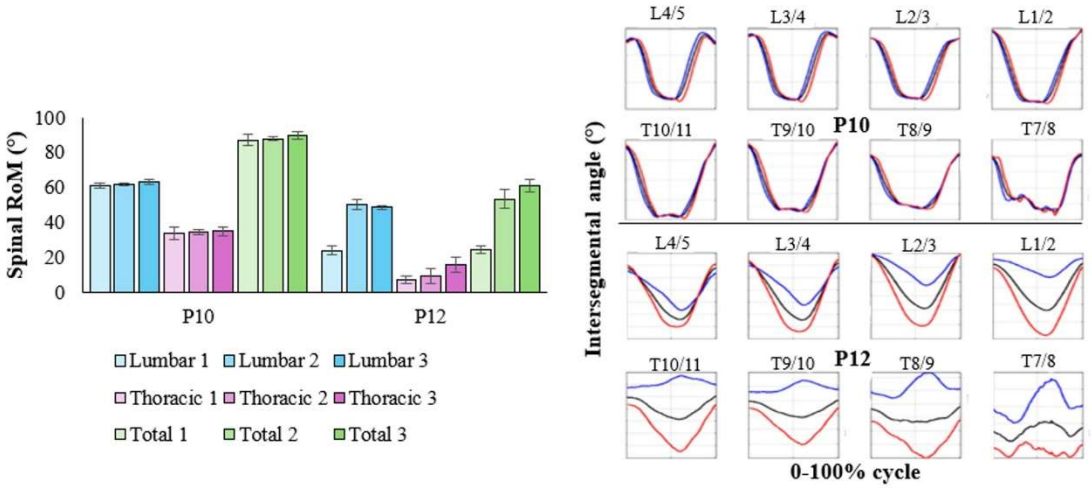


Figure 1. Left: P10 and P12’s spinal RoM by block. Right: SCR plots of intersegmental angles for P10 and P12.

Session Category

Human Motion and Performance: Balance, Posture and Control

P1-085

Strategies for Successful Balance Recovery Following Trips and Slips While Walking: A Systematic Review

Mr. Sungmin Chun PT, Mr. Junwoo Park PT, MSc, Dr. Kitaek Lim PT, PhD, Prof. Woochol Joseph Choi PT, PhD

Injury Prevention and Biomechanics Laboratory, Yonsei University, Wonju, Gangwon-do, Korea, Republic of

Introduction

One quarter of falls among older adults occur during walking, with tripping and slipping identified as primary causes [1]. Although studies have shown that individuals who successfully recover their balance following a trip or slip utilize distinct balance-recovery strategies [2–4], no comprehensive synthesis has yet outlined the most effective strategies for preventing a fall during gait [5]. This review identifies the strategies associated with successful balance recovery while walking.

Methods

Following PRISMA 2020 guidelines, PubMed, Scopus, and EMBASE were searched (1984–2025) using terms related to walking, trip, slip, and balance recovery. The search identified 1,981 records; 972 remained after deduplication. After screening and full-text review, 15 studies met inclusion criteria involving humans exposed to externally triggered, unexpected trip/slip perturbations during walking and reported strategies distinguishing successful from unsuccessful recoveries. The final dataset included sixteen studies. Data on perturbation type, strategy classification, protocols, and outcome measures were extracted.

Results

Among the six trip-related studies, elevating strategies—lifting the obstructed limb to clear the obstacle—were observed in successful recoveries in five studies (Figure 1a), whereas lowering strategies—rapidly placing the foot on the ground—were reported more frequently in three unsuccessful cases (Figure 1b). Arm movements—asymmetric retroflexion–anteflexion with abduction—appeared in two studies as secondary trunk stabilizers (Figure 1c). In the ten slip-related studies, eight identified compensatory stepping—initiating a rapid step to expand the base of support—as the primary successful strategy (Figure 1d).

Arm strategies—contralateral arm abduction—were noted in two studies but were insufficient without effective stepping (Figure 1e).

Discussion

Our results suggest that successful balance recovery following a trip-related loss of balance is primarily supported by elevating responses, whereas recovery during slip-induced falls relies on rapid compensatory stepping. Arm strategies, observed in both trip and slip scenarios, aided trunk stabilization but functioned as supplementary rather than primary recovery mechanisms. These insights can inform cause-specific, perturbation-based balance training programs to enhance fall-prevention outcomes.

Images (Optional)

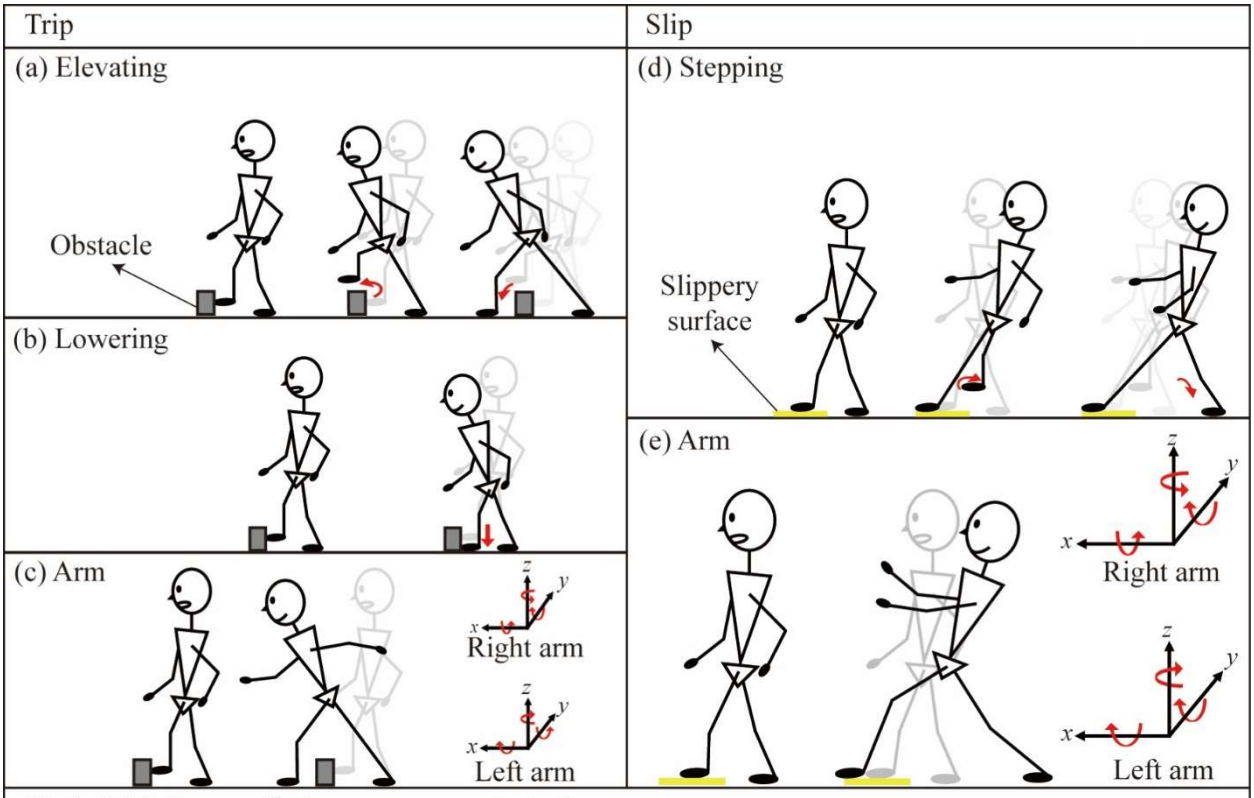


Fig 1. Stick figure of balance recovery strategies.

References (Optional)

[1] Robinovitch et al., 2013; [2] Wright et al., 2015; [3] Pavol et al., 2001; [4] Qu et al., 2012; [5] McCrum et al., 2017.

Acknowledgements (Optional)

This work was supported by the “Brain Korea 21 FOUR Project” (F21SH8303039), the National Research Foundation of Korea (NRF) grant funded by the Korea government (MSIT)

(RS-2025-16071808), and by the Regional Innovation System & Education (RISE) program through the Gangwon RISE Center, funded by the Ministry of Education (MOE) and the Gangwon State (G.S.), Republic of Korea (2025-RISE-10–006).

Session Category

Human Motion and Performance: Balance, Posture and Control

P1-086

Joint contributions to whole-body centre of mass work and muscle coordination patterns during single leg squats

Ms. Sylvia Masse BSc, Dr. Jordan Cannon PhD

University of Waterloo, Waterloo, Ontario, Canada

Ms. Sylvia Masse

Introduction

During single leg squats (SLS), changing the non-stance (NS) limb position alters kinematics and kinetics across the trunk-lower limb linkage as well as discrete activation measures for select hip muscles [1, 2]. The impact of NS limb position on relative joint contributions to whole-body centre of mass (WB-COM) dynamics and associated muscle coordination strategies is unknown. The purpose of this study was to investigate multi-joint control strategies and muscle function with relation to varying NS limb positions during SLS tasks.

Methods

3D kinematics, ground reaction forces (GRFs), and EMG of trunk and lower limb muscles were collected from 18 females during SLS tasks with NS limb positions: front, lateral, and rear. An inverse dynamics approach calculated joint power. WB-COM power was estimated as the dot product of the GRF and WB-COM velocity. Joint and WB-COM powers were integrated over time to yield work. Muscle synergy analysis is currently in progress to quantify muscle coordination and associations with joint work contributions to WB-COM work. Linear mixed effect models compared joint contributions and WB-COM work under varying NS limb positions.

Results

Results did not differ between descent and ascent phases of SLS. The hip and knee were the greatest contributors to WB-COM work, with the knee contributing significantly more than the hip (Figure 1). Despite joint contribution variability, WB-COM work was well estimated by the sum of joint work of the stance limb and lumbar joints, adding arm and NS limb joints worsened estimates.

Discussion

SLS tasks are not equal. While WB-COM work was consistent across NS limb positions, joint work contributions vary. The joint work of the NS limb and arms have opposing polarity to stance limb and lumbar spine joint work, reflecting internal work to move the segments about the WB-COM, not move the WB-COM itself. Muscle coordination is expected to change with altered magnitude and timing of muscle subsets to meet the specific demands incurred due to the NS limb position, opposed to the primary motion demands of the squat task to lower and raise WB-COM.

Images (Optional)

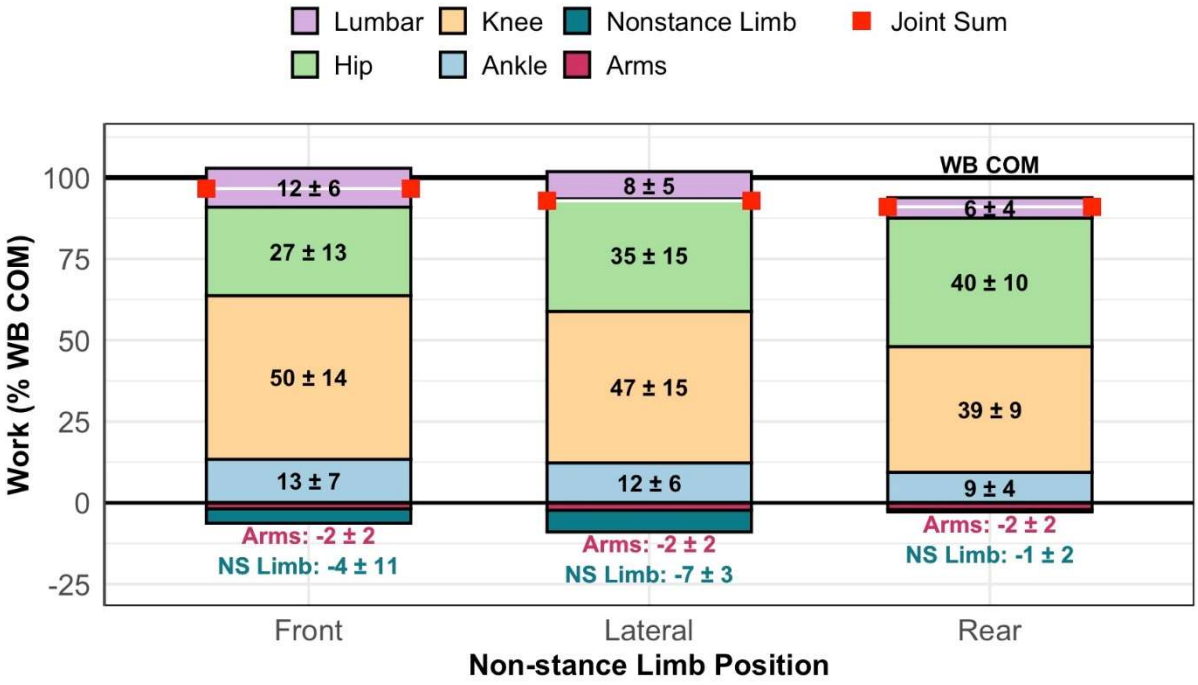


Figure 1 - Joint contributions as a percentage of WB COM work (mean ± standard deviation) during single leg squat ascent by non-stance limb position.

References (Optional)

[1] Khuu *et al.* , Hum Mov Sci, 2019

[2] Khuu *et al.* , J Ath Train, 2022

Session Category

Human Motion and Performance: Balance, Posture and Control

P1-087

Accuracy of DeepLabCut Pose Estimation Software in Extracting Whole-Body Kinematics During Falls

Ms Kylie Shlecker BSc[1], Dr Nataliya Shishov PhD[2], Teah Cribbie[2], Dr Yaejin Moon PhD[3], Dr Stephen Robinovitch PhD[2]

[1]Simon Fraser University, Burnaby, British Columbia, Canada. [2]Simon Fraser University, Burnby, British Columbia, Canada. [3]Syracuse University, Syracuse, New York, United States

Introduction

Falls are the number-one cause of injury, and a top-ten cause of death for adults over age 65. Quantifying the movements of the body during falls can provide clues on why falls occur, and how they can be prevented. In this project, our objective was to determine the accuracy of DeepLabCut (DLC), a neural network software package for markerless pose estimation, in estimating the time-varying positions of body segments during falls, when compared to manual digitization by Kinovea.

Methods

We analyzed 30 videos of sideways falls, from fall initiation to landing. Each video had a resolution of 640x480 pixels, a frame rate of 30Hz, and a duration of at least 42 frames (1.4 s). We focused on the time-varying positions of eight body parts (ankle, knee, ASIS, wrist, elbow, sternum, head, and shoulder). For DLC, 80% of the data (24 falls) were used for model training, and 20% were used for model testing (6 falls). During model training, 20 frames per video were manually annotated. Results are reported in terms of raw values of root mean square error (RMSE) in cm, and normalized values of RMSE (NRMSE), calculated as a percent of the movement amplitude for the given body part, in each of the horizontal and vertical directions.

Results

Raw errors averaged 4.1±0.2 (SE) cm, and normalized errors averaged 9.9±0.6 percent (Table 1). Overall, there was no significant difference in the accuracy of vertical versus horizontal position estimates, but this varied with body part. There was a significant effect of body part on DLC accuracy, with the wrist, ankle, and ASIS showing higher NRMSE values than other body parts ($p>0.003$). NRMSE values were affected minimally by use of a 2D (grid) versus a 1D (height) calibration.

Discussion

We found that DLC was accurate, in general, to within 4 cm in estimating the time-varying positions of the body segments during lab-based falls. This is similar to the errors reported previously for pose estimation in extracting gait kinematics. Future research should extend the analysis to real-life falls, where complex issues like occlusions of body parts may create challenges, and from 2D to 3D.

Images (Optional)

Table 1. Errors in DLC pose estimation for time-varying positions of body segments during falls from standing, based on comparison to manual digitization with Kinovea

Body part	RMSE (cm)			NRMSE (%)		
	Horizontal	Vertical	Total	Horizontal	Vertical	Total
ankle	3.5±0.5	3.1±0.3	3.3±0.3	7.1±0.8	19.7±2.4	13.3±1.8
knee	2.1±0.2	2.5±0.1	2.2±0.1	9.2±0.4	4.9±0.1	7.1±0.5
ASIS	4.8±0.9	3.2±0.2	4.0±0.5	27.1±3.0	4.3±0.2	15.7±2.8
Wrist	4.6±0.6	6.8±0.2	5.7±0.4	27.5±4.5	8.0±0.3	17.8±3.0
Elbow	2.3±0.2	5.8±0.3	4.1±0.4	8.6±0.4	6.0±0.3	7.3±0.4
sternum	2.5±0.2	5.6±0.2	4.1±0.4	6.7±0.4	5.7±0.2	6.2±0.2
Head	3.0±0.3	6.5±0.2	4.7±0.4	6.3±0.5	5.6±0.1	6.0±0.3
shoulder	1.7±0.2	6.9±0.2	4.3±0.6	4.9±0.3	6.5±0.2	5.7±0.3
TOTAL	3.1±0.2	5.0±0.2	4.1±0.2	12.2±1.1	7.6±0.6	9.9±0.6

NOTE: cell entries show average values and standard errors; ASIS = anterior superior iliac spine; RMSE = root mean square error; NRMSE = root mean square error normalized to movement amplitude

Acknowledgements (Optional)

Supported by operating grants from the Natural Science and Engineering Research Council of Canada (grant numbers ALLRP 597252-24 and RGPIN-2022-04713).

Session Category

Human Motion and Performance: Balance, Posture and Control

P1-088

Thoracolumbar Spinal Posture in Classical Ballet Dancers During Standing and Walking: The Flatter Lumbar Spine Does Not Persist Under Dynamic Conditions

Mr. Tempei Tominaga[1], Ms. Haruka Okuyama[2], Ms. Ayaka Hobo[1,3], Ms. Yoshino Shinabe[1], Dr. Natsuki Sado[4,3]

[1]Graduate School of Comprehensive Human Sciences, University of Tsukuba, Tsukuba, Ibaraki, Japan. [2]Graduate School of Human Sciences, Waseda University, Tokorozawa, Saitama, Japan. [3]Advanced Research Initiative for Human High Performance, University of Tsukuba, Tsukuba, Ibaraki, Japan. [4]Institute of Health and Sport Sciences, University of Tsukuba, Tsukuba, Ibaraki, Japan

Introduction

The spinal curve has been targeted in postural interventions because excessive curvature can lead to musculoskeletal pathologies [1]. Exercise programmes lasting up to 30 weeks are effective in reducing thoracic kyphosis (TK) but are less effective in reducing lumbar lordosis (LL) [1]. Ballet dancers, who have undergone years of ballet-specific postural training focusing on the spine, exhibit a flatter lumbar spine when standing [2]; thus, more prolonged postural training may alter LL. However, it remains unclear whether this flatter lumbar spine persists in dynamic conditions as well. Therefore, we investigated the thoracic and lumbar curves in ballet dancers under both static and dynamic conditions.

Methods

Eight female ballet dancers (DN: 16.1 ± 4.6 years of experience) and 19 female non-dancers (CON) performed 3-second quiet standing and preferred speed walking. Kinematic and ground reaction force data were collected using a motion capture system with three force platforms. TK and LL were quantified using Cobb-angle–like metrics [3] derived from markers on the T3–T10 and T12–L5 spinous processes, respectively.

Results

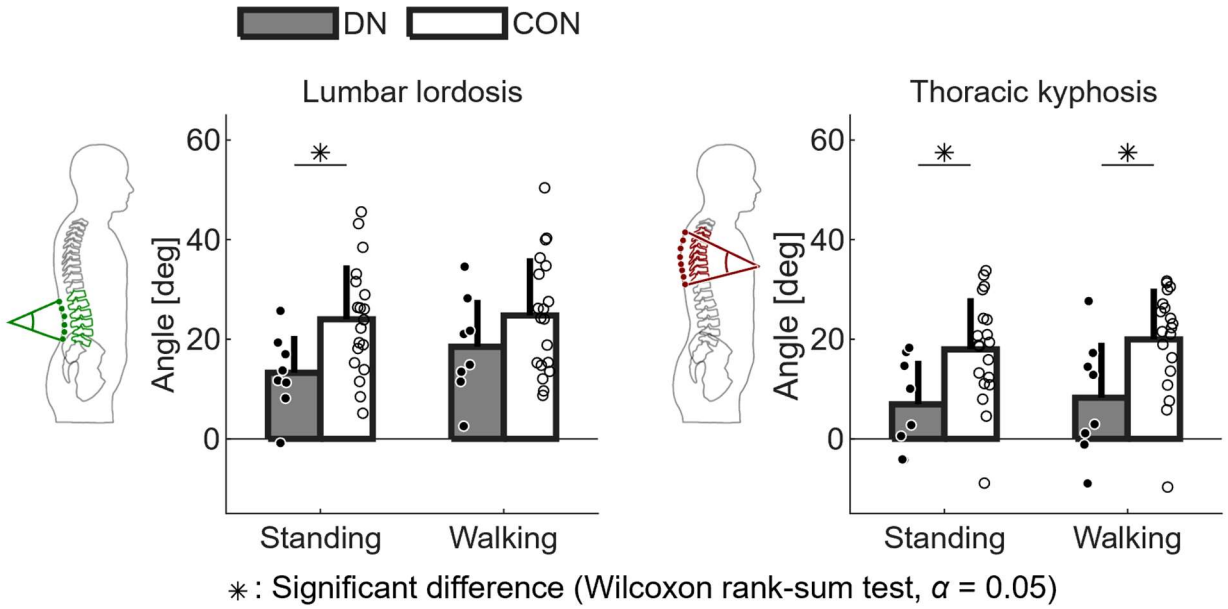
During standing, DN exhibited a flatter spine than CON, showing lower TK (DN vs. CON: 6.9 ± 8.7° vs. 18.0 ± 10.3°, $p = 0.016$) and lower LL (13.3 ± 7.4° vs. 24.0 ± 10.8°, $p = 0.028$). During walking, stride-averaged TK was lower in DN (8.3 ± 11.0° vs. 20.0 ± 10.2°, $p = 0.021$), whereas LL showed no significant difference (18.5 ± 9.4° vs. 24.8 ± 11.5°, $p = 0.232$).

Discussion

Although LL is difficult to change through exercise programmes [1], ballet dancers exhibited flatter thoracic and lumbar spines in standing. This implies that long-term training

may be effective in reducing not only thoracic, but also lumbar spinal curvature. However, the between-group difference in LL was obscured during walking, despite the consistent between-group differences in TK. These results suggest that reducing dynamic lumbar curvature may be difficult, even with long-term intervention, and this finding should be taken into account when designing postural interventions.

Images (Optional)



References (Optional)

[1] Noelia González-Gálvez et al., PLOS ONE, 2019

[2] Denise H. Iunes et al., Phys Ther Sport, 2016

[3] Tempei Tominaga et al., J Biomech, 2025

Acknowledgements (Optional)

This work was supported by Japan Science and Technology (JST) Moonshot R&D Grant (JPMJMS2295).

Session Category

Human Motion and Performance: Balance, Posture and Control

P1-089

Age-Related Changes in Lower Limb Joint Contributions During Jump Landing in Children

Mr Thibaut Toussaint[1], Dr. Clément Gambelli[1,2], Pr. Bénédicte Schepens[1]

[1]UCLouvain, Louvain-la-Neuve, ., Belgium. [2]North-West University, Potchefstroom, ., South Africa

Introduction

Landing from a jump requires coordinated control of the body segments to dissipate the mechanical energy accumulated during the aerial phase. Throughout motor development, children progressively adapt their landing strategy by increasing the mechanical contribution of their lower limb joints, while the contribution of the upper limbs remains relatively unchanged [1]. The joint-specific mechanisms underlying this increased reliance on lower limb joints remain unclear. This study aimed to quantify the contributions of the ankle, knee, and hip joints during landing across childhood.

Methods

Sixty-eight children (3–12 years) and twenty-one adults performed double-leg landings by hopping off a 30-cm box. Ground reaction forces and full-body three-dimensional kinematics were recorded. Using a bottom-up inverse dynamics approach, mechanical work performed at the ankle, knee, and hip joints was computed from touchdown to the lowest vertical position of the center of mass. A linear mixed model was used to assess the effect of age.

Results

The mass-specific amount of negative mechanical work performed by the ankle and knee increased with age (p<0.001), whereas the work performed by the hip was higher in young children and decreased throughout childhood (p=0.046; Figure). During the first instants of landing (in red), the amount of negative work performed by the lower limb joints was lower in young children and increased with age, and the ankle was the main contributor. After the force peak (in blue) the amount of negative work performed by the lower limb joints was higher in young children and decreased with age, and the knee and hip were the main contributors.

Discussion

The age-related increase of lower limb joint contribution results from modifications during the initial instants of landing, when the ankle joint dominates mechanical energy absorption. Although negative work after the force peak was higher in young children, primarily due to greater hip involvement, it did not compensate for the lower amount of work produced during the initial instants. This pattern may reflect a proximo-distal maturation of lower limb joint control.

Images (Optional)

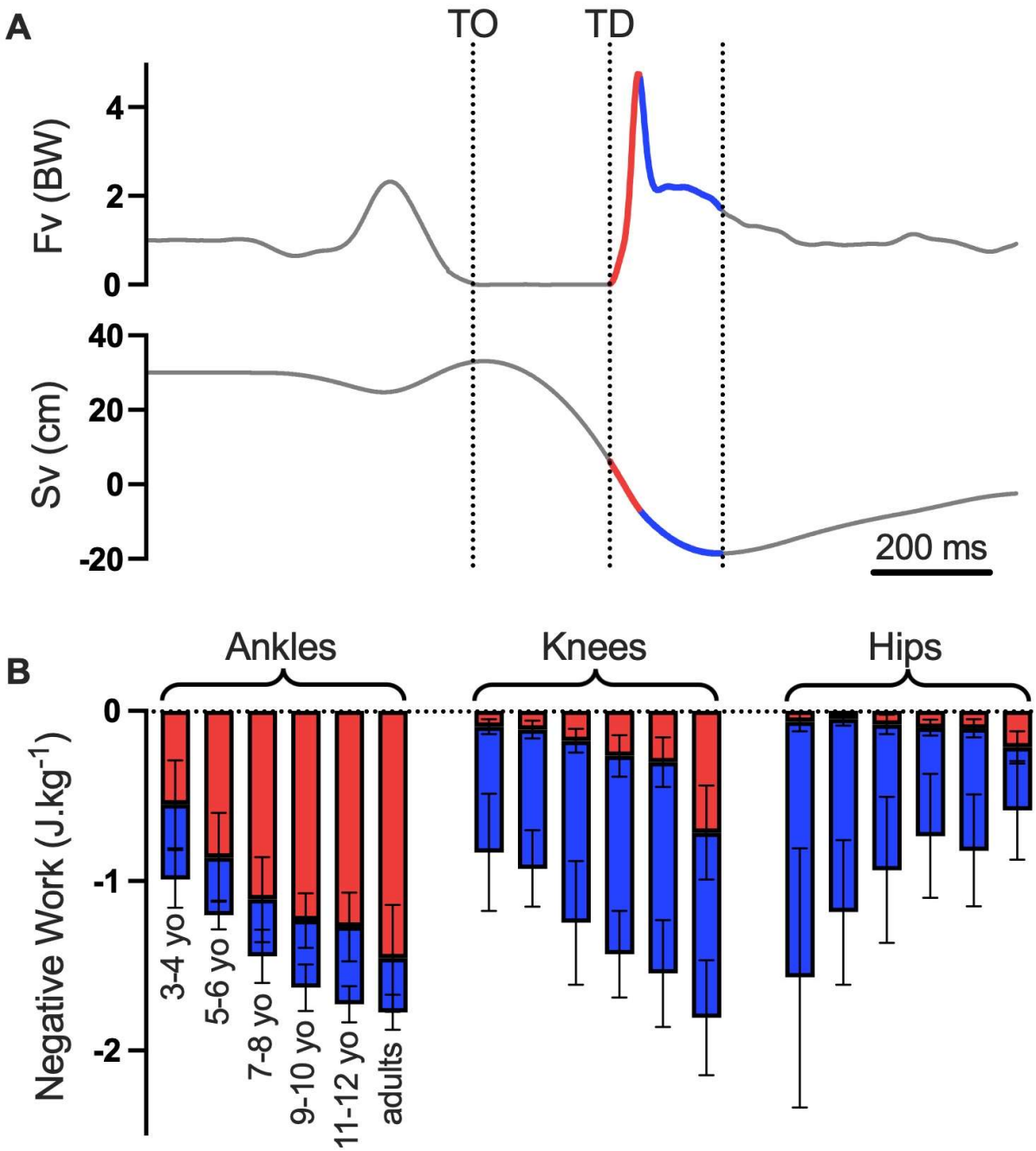


FIGURE | (A) Typical traces of the vertical component of the ground reaction force (Fv) and the vertical displacement of the center of mass of the body (Sv). Vertical dotted lines indicate the take-off (TO), the touchdown (TD) and the lowest vertical position of the center of mass of the body. (B) Negative mechanical work produced by the ankle, knee and hip joints during landing as a function of age.

References (Optional)

[1] Toussaint T. D. *et al.* , Scandinavian Journal of Medicine & Science in Sports 2025

Session Category

Human Motion and Performance: Balance, Posture and Control

P1-090

Biarticular muscle energy transfer across childhood during jump landing

Mr Thibaut Toussaint[1], Pr Bénédicte Schepens[1], Dr Clément Gambelli[1,2]

[1]UCLouvain, Louvain-la-Neuve, ., Belgium. [2]North-West University, Potchefstroom, ., South Africa

Introduction

Landing from a jump requires coordinated control of the body segments to dissipate the mechanical energy accumulated during the aerial phase. Throughout motor development, children progressively adapt their landing strategy by increasing the mechanical contribution of their lower limb joints, while the contribution of the upper limbs remains relatively unchanged [1]. From our unpublished data analysis, we found that this increased contribution of lower-limb joints with age is driven by greater mechanical work produced at the ankle and knee. Through biarticular muscles, proximal muscles can generate work that contributes to more distal joints; for example, knee extensors can contribute to the mechanical work observed at the ankle. In the present study, we aimed to investigate the potential for energy transfer through biarticular muscles to better understand the lower mechanical work performed at the ankle and knee in young children.

Methods

Sixty-eight children (3–12 years) and twenty-one adults performed double-leg landings by hopping off a 30-cm box. Ground reaction forces and full-body three-dimensional kinematics were recorded. Using ankle, knee and hip joint angles, we quantified the potential for energy transfer as the percentage of time during which adjacent joints moved in-phase (see [2] for more details). A linear mixed model was used to assess the effects of age.

Results

The potential for energy transfer between the ankle and knee, and between the knee and hip increased with age ($p < 0.001$, Figure). The percentage of time during which the ankle and knee moved in-phase ranged from 50% to 75%, whereas the percentage for the knee and hip was around 75%.

Discussion

The age-related changes in the potential for energy transfer appear to reflect adjustments in joint coordination. Throughout childhood, the increasing contribution of the ankle and knee joints, may result from a growing ability to use biarticular muscles to transfer energy. Consequently, the contribution of proximal muscles to the mechanical work observed at the ankle and knee would improve with age.

Images (Optional)

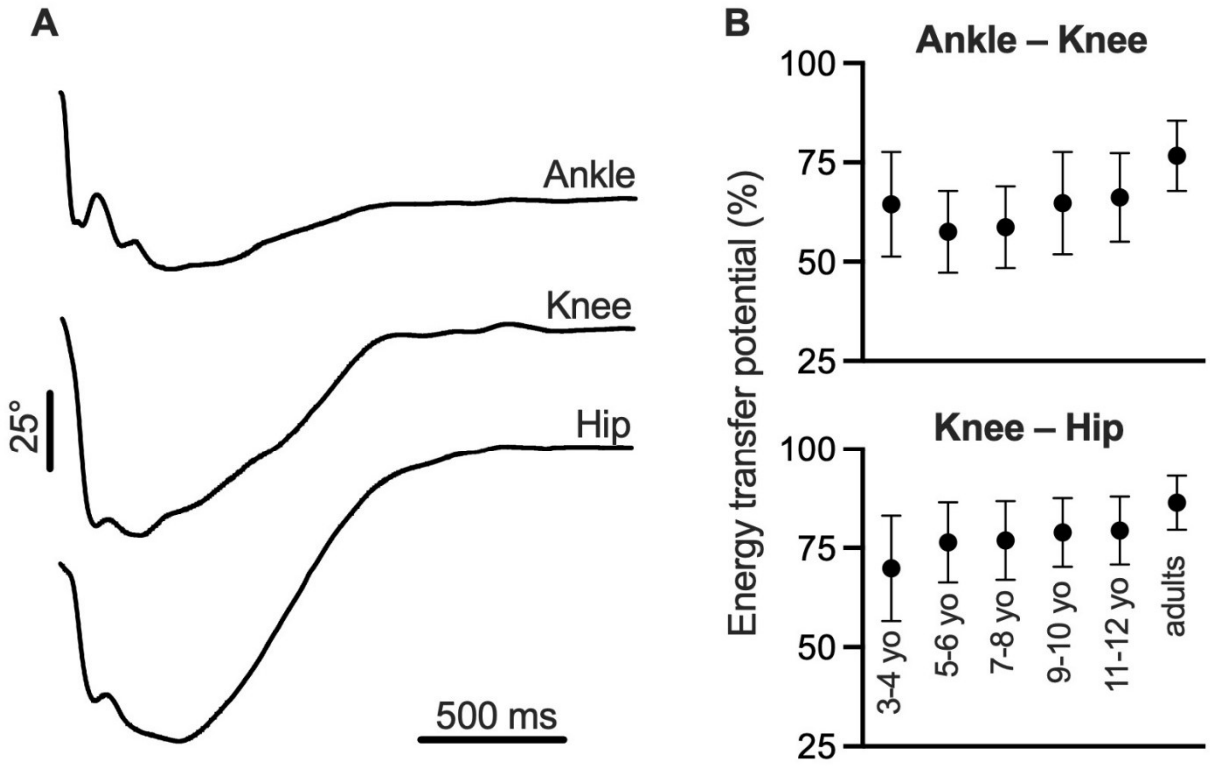


FIGURE | (A) Typical traces of the ankle, knee and hip angles during landing. (B) Energy transfer potential between ankle and knee, and between knee and hip, defined as the percentage of time during which the joints are moving in-phase.

References (Optional)

[1] Toussaint T. D. *et al.* , Scandinavian Journal of Medicine & Science in Sports 2025

[2] Bohm, S. *et al.* , Royal Society Open Science 2025

Session Category

Human Motion and Performance: Balance, Posture and Control

P1-091

Posture Control During Single-Leg Stance in Patients Before Lateral Ankle Ligament Reconstruction: A Preliminary Assessment

Ms. Wanyan Su M.S.[1], Dr. Ashley Herda Ph.D.[2], Dr. Bryan Vopat Ph.D.[3], Ms. Yu Gu M.S.[1], Ms. Sterre Van Den Anker B.A.[3], Dr. Lisa Vopat Ph.D.[3], Dr. Christopher Cleary Ph.D.[4], Dr. Yu Song Ph.D.[1]

[1]Department of Health, Sport and Exercise Sciences, University of Kansas, Lawrence, KS, United States. [2]Department of Health, Sport and Exercise Sciences, University of Kansas Edwards Campus, Overland Park, KS, United States. [3]Department of Orthopedic Surgery and Sports Medicine, University of Kansas Health System, Kansas City, KS, United States. [4]Department of Health and Human Physiological Sciences, Skidmore College, Saratoga Springs, NY, United States

Introduction

Lateral ankle sprains are the most common injury in physical activities, with a high reinjury risk. Individuals with ankle instability are associated with poor postural control performance. Therefore, this study aimed to evaluate limb differences in postural control during an eyes-closed single-leg stance task in patients with torn lateral ankle ligaments prior to surgical reconstruction.

Methods

Seven patients (5 females and 2 males, 29.1 ± 8.7 yrs, 70.9 ± 10.3 kg) performed an eyes-closed single-leg stance task on a force plate (Bertec, Columbus, OH, USA; sampling frequency=1000Hz) for both the injured and uninjured limbs. They were instructed to fold their arms across their chest and maintain a single-leg stance for up to 30 seconds. If patients were unable to continue, they were allowed to place the foot down, and the actual stance time was recorded. Center of pressure (CoP) data were collected to quantify postural control. CoP range, standard deviation, and peak velocity in the anterior-posterior and medial-lateral directions were calculated during the stance duration. The stance duration and CoP sway area were also included as dependent variables. The Wilcoxon signed-rank test was applied to identify the limb differences (p-value<0.05).

Results

Uninjured limbs showed significantly longer stance duration than injured limbs (Table 1). No significant differences were observed in the rest of the variables (Table 1).

Discussion

Although participants aimed to maintain a single-leg stance for 30 seconds, they were able to stand only about 12 seconds on the uninjured limb and approximately 6 seconds on the injured limb. The lack of statistically significant limb differences in CoP outcomes may be related to a small sample size and the data reduction. At this stage, only seven patients completed testing before their lateral ankle ligament reconstruction. In addition, the CoP outcomes were calculated based on each limb's actual stance duration. Because stance time on the uninjured limb was roughly twice that of the injured limb, the CoP metrics captured different lengths of postural control performance. Therefore, the findings suggest that the injured limb demonstrated postural control similar to the uninjured limb, but for approximately half the stance duration.

Images (Optional)

Table 1 Mean ± standard deviation and p-values of Wilcoxon signed-rank test for dependent variables during the eye-closed single-leg stance task.

	Injured leg	Uninjured leg	P-values
Stance duration (s)	5.90 ± 6.29 *	11.13 ± 8.30 *	**0.018**
Range of CoP in medial-lateral direction (cm)	6.91 ± 7.01	5.16 ± 2.69	0.499
Range of CoP in anterior-posterior direction (cm)	10.98 ± 8.65	9.58 ± 3.23	0.866
Standard deviation of CoP in medial-lateral direction (cm)	1.51 ± 1.13	1.25 ± 0.59	0.612
Standard deviation of CoP in anterior-posterior direction (cm)	2.04 ± 1.02	1.86 ± 0.52	0.499
Sway area of CoP (cm^2)	88.10 ± 154.53	37.84 ± 40.46	0.310
Peak CoP velocity in medial direction (cm/s)	70.49 ± 77.36	72.30 ± 56.69	0.866
Peak CoP velocity in lateral (-) direction (cm/s)	-82.71 ± 111.44	-51.74 ± 50.18	0.866
Peak CoP velocity in anterior direction (cm/s)	97.64 ± 95.89	77.48 ± 56.17	0.499
Peak CoP velocity in posterior (-) direction (cm/s)	-130.40 ± 113.39	-92.22 ± 79.69	0.176

Note: CoP: center of pressure. *Significant differences between injured and uninjured legs.

Session Category

Human Motion and Performance: Balance, Posture and Control

P1-092

Quantifying Sex-Specific Coordination Variability of the Inter-Segmental Center of Mass Velocity During Sidestepping

Dr. Xiaoyi Yang[1], A.P. Qichang Mei[2], Dr. Vickie Shim[1], Prof. Justin Fernandez[1]

[1]Auckland Bioengineering Institute,The University of Auckland, Auckland, North Island, New Zealand. [2]Faculty of Sports Science, Ningbo University, Ningbo, Zhejiang, China

Introduction

Sidestepping requires maintaining dynamic stability during the execution of fast lateral motion [1]. The segmental Center of Mass (sCOM), which measures the relative amplitude of movement patterns between adjacent segments, has an influence on the efficiency of the motor. Changes in segmental coordination variability may lead to biomechanical overload, ultimately compromising performance. The objective of this study was to utilize vector coding to investigate the sCOM velocity differences between males and females during sidestepping, understanding sex-specific inter-segmental coordination patterns.

Methods

Eighteen male and eighteen female national-level athletes participated in performing sidestepping with a 52-marker set attached. Data was collected using an 8-camera Vicon motion capture system and one force platform. The sCOM was analysed using OpenSim and utilized for coordination analysis. Segmental color maps were employed to provide insight into inter-segmental coordination information, including femur-tibia, pelvis-femur, pelvis-torso, torso-humerus, and humerus-forearm. The time-varying coupling angles between males and females were analysed using an independent sample t-test, with a significance threshold at 0.05.

Results

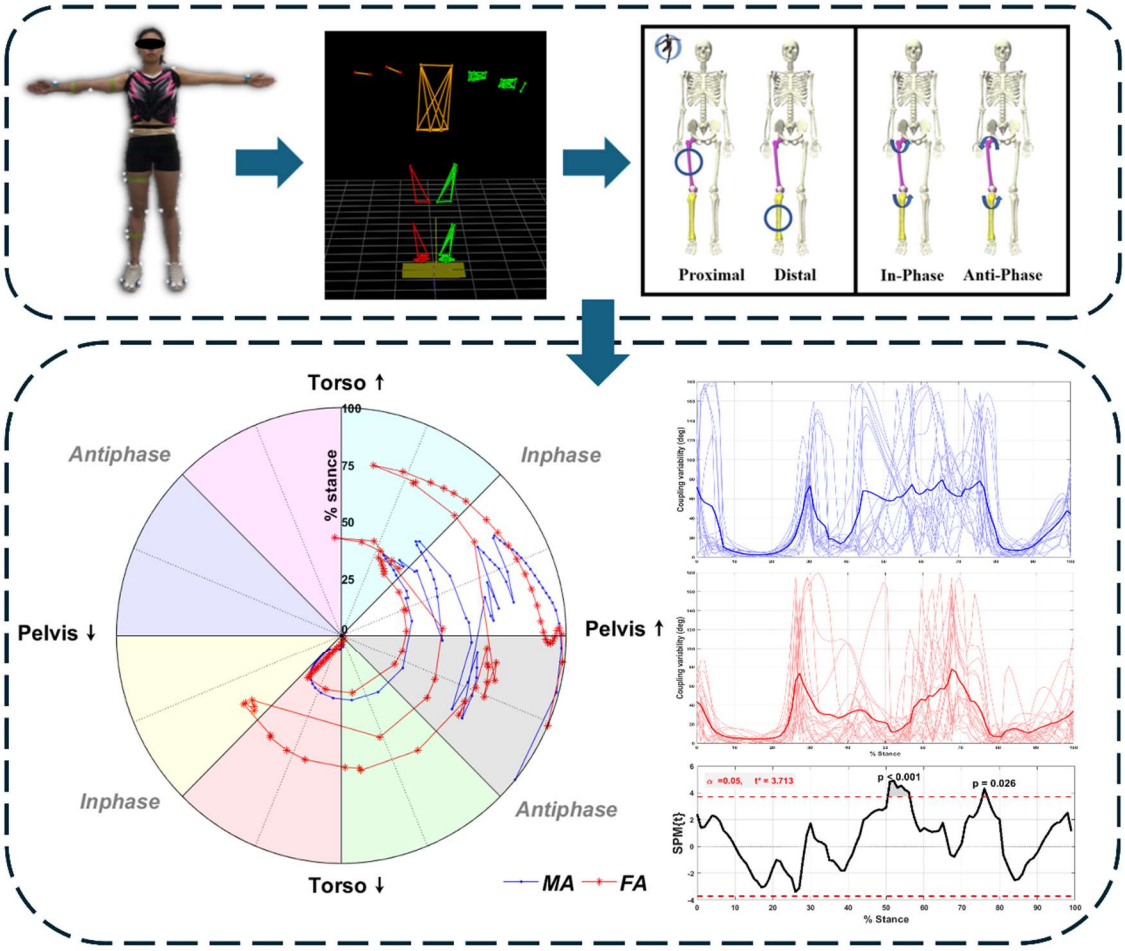
During the entire sidestepping movement, the sCOM of the whole body was faster than females ($p<0.05$). The sCOM velocity mappings of the lower extremity during sidestepping (pelvis-torso, pelvis-femur, and femur-tibia) were all in-phase with proximal dominance in males, while females were anti-phase with distal dominance. Significantly higher coordination variability was observed in the pelvis-torso ($p<0.001$) and pelvis-femur ($p=0.002$) in males. In the following phase, the upper limb's coordination (torso-humerus and humerus-forearm), exhibited distal dominance in males but proximal dominance in females, and females showed higher variability ($p=0.005$). In addition, at the end of the

following stage, the segmental velocity pattern for both males and females was characterized by forearm dominance.

Discussion

Exploring the inter-segment coordination of sex-specific would provide a better understanding of the sCOM coordination pattern in sidestepping. The profiles of inter-segmental coordination patterns and variability may practically imply the development of sex-specific training programs to control dynamic balance.

Images (Optional)



References (Optional)

[1] Sankey, Sean P *et al.* , J Biomechanics, 2020.

Acknowledgements (Optional)

The authors acknowledge the valuable contributions of all the athletes and researchers who participated in this study.

Session Category

Human Motion and Performance: Balance, Posture and Control

P1-093

Effect of Personalized Perturbation Training on Reactive Balance Skills and Perceived Balance Control in Older Adults

Ms. Celeste Thai, Dr. Noah Rosenblatt, Dr. Kristin Schneider, Dr. Ying Fang

Rosalind Franklin University, North Chicago, IL, United States

Introduction

Perturbation training has been shown to improve balance skills, and most existing protocols prescribe the same level of perturbations for all participants. However, this may undermine perceived control and cause overwhelming distress in some people. We developed an intervention that allows individuals to practice walking with perturbations at a self-selected level. This study aims to investigate the effect of this personalized intervention on reactive balance and perceived control and distress in older adults.

Methods

Preliminary data of 8 participants (4 females, age: 73±6 years, speed: 0.64±0.29 m/s) are reported. Participants completed a pre-assessment including walking trials with increasing perturbation levels, and determined the level that is challenging but manageable ($level_N$). They then completed three practice trials at $level_N$ and a post-assessment trial at $level_N$ (Figure 1A). We quantified reactive balance using recovery step length, perceived balance control using Updated Perceived Control over Falling Scale (UP-COF), and perceived distress using Subjective Units of Distress Scale (SUDS). We used paired t-tests to compare all outcomes before and after practice.

Results

There were no differences between pre- and post-practice outcomes for trip step length (pre vs. post: -0.03±0.1 m vs. -0.0042±0.14 m, p=0.672), slip step length (pre vs. post: 0.47±0.18 m vs. 0.46±0.15 m, p=0.338), UP-COF score (pre vs. post: 17±3 vs. 19±1, p=0.275), or perceived distress (pre vs. post: 2.3±1 vs. 2.2±0.9, p=0.351) (Figure 1C-F).

Discussion

Self-identified perturbation intensities ranged from level 4 to 10 out of 10 (Figure 1B). Most participants had a recovery step length that was more similar to a normal step after practice (Figure 1C-D). Although the mean UP-COP score did not change across all participants, those who had lower scores (less control over falling) during pre-assessment generally had increased scores after practice. Perceived distress did not change for most participants, likely because they chose intensities that caused no more than mild distress

(SUDS≤3). The preliminary data demonstrate the feasibility of this personalized intervention, and more participants are needed to draw stronger conclusions.

Images (Optional)

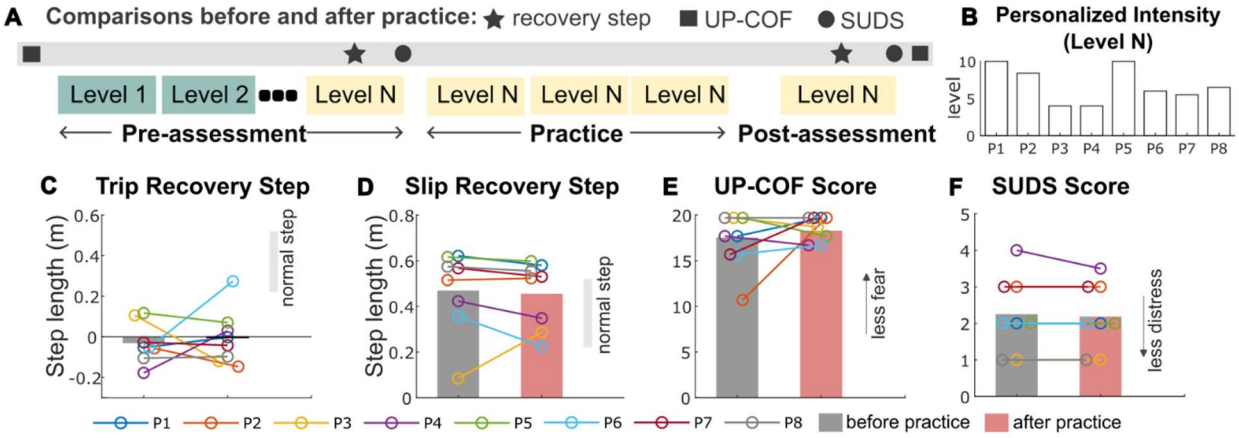


Figure 1. A) Study flow. Each box represents a walking trial with four perturbations (2 trip-like and 2 slip-like) at a given intensity. During pre-assessment, participants identified a challenging but manageable level by deciding whether to try the next level after each trial. The highest level attempted (Level N) was their self-identified level and used for practice and post-assessment. B) Self-identified perturbation level for each participant. C-F) Recovery step length, UP-COF score, and SUDS score for each participant. Bars represent the average of all participants.

Acknowledgements (Optional)

The project was funded by the ASB Junior Faculty Research Grant.

Session Category

Human Motion and Performance: Balance, Posture and Control

P1-094

Novel Cyclic-Stability Dynamics for Probing Motor Adaptation in Humans

Ms Yixin Zhang PhD Student, Dr. Calvin Kuo Assistant Professor, Dr. Jean-Sébastien Blouin Professor

University of British Columbia, Vancouver, BC, Canada

Introduction

Motor adaptation, even in tasks as simple as standing upright, engages complex neural processes, yet its underlying mechanisms remain unclear due to the lack of truly novel movement environments. To address this limitation, we introduce novel dynamics implemented on a human-in-the-loop standing balance robotic platform [1] that alters the natural physical laws of standing balance dictating the relationship between applied torques and body motion. We hypothesize that the novel dynamics will modify participant's natural standing behavior, reflected in changes in standing angle and velocity.

Methods

The robotic platform simulates and records anterior-posterior postural control as an inverted pendulum under normal dynamics, where a force plate measures ankle torques and a backboard tilts the participant forward and backward according to natural physical laws. The novel dynamics remap the relationship between ankle torques and body motion, featuring a region of cyclic stability between 1 and 3 standard deviations forward of the participant's preferred mean angle. The participant completed six 5-minute trials under randomized normal or novel balance dynamics.

Results

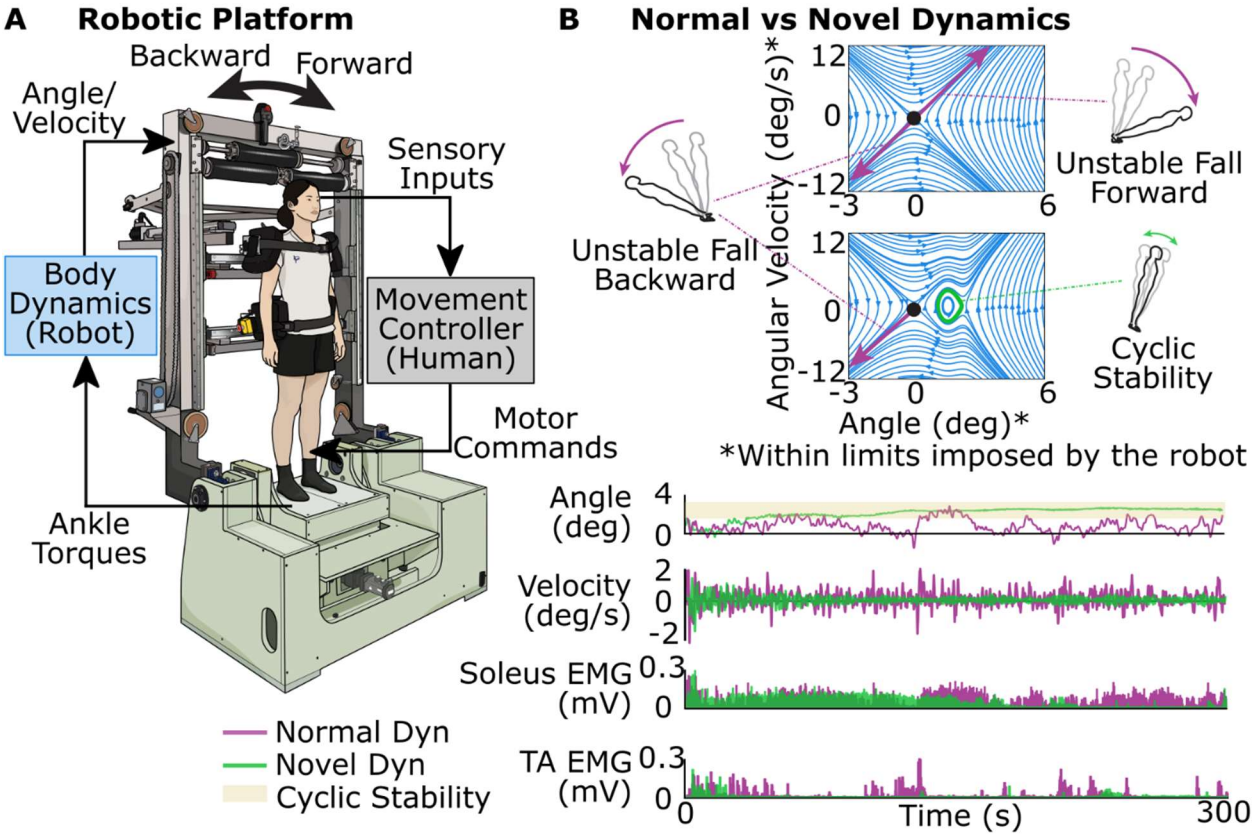
The participant's mean ± standard deviation standing angle under the normal and novel dynamics was 1.16 ± 0.26 degrees and 1.21 ± 0.20 degrees, respectively. The absolute angular velocity was 0.24 ± 0.03 degrees/second during normal dynamics and was reduced to 0.09 ± 0.004 degrees/second during novel dynamics. Root-mean-square (RMS) electromyography (EMG) of the soleus was 0.019 ± 0.007 mV during normal dynamics and was reduced to 0.007 ± 0.002 mV during novel dynamics. RMS EMG of the tibialis anterior was 0.012 ± 0.004 mV during normal dynamics and 0.011 ± 0.007 mV during novel dynamics.

Discussion

The novel dynamics enable direct probing of motor adaptation mechanisms by placing participants in a controlled environment that cannot exist under natural biomechanics. The

observed reductions in absolute velocity and soleus RMS EMG reflected adaptation to a new way of standing and exploitation of a stable and energy-efficient control strategy. Combined with reinforcement learning models, we can use the novel balance dynamics to reveal the mechanisms underlying the control of standing and probe learning deficits in varied populations.

Images (Optional)



References (Optional)

[1] Calvin Qiao et al. , IEEE robot. autom. lett., 2023

Acknowledgements (Optional)

Research funded by NFRF. Robot illustration by Julie Sugimoto.

Session Category

Human Motion and Performance: Balance, Posture and Control

P1-095

Sex-Specific Patterns of Lower-Extremity Joint Stiffness Coordination Revealed Across Drop Heights during Drop Jump

Dr. Young Min Chun

Sonoma State University, Rohnert Park, California, United States

Introduction

Lower-extremity joints play a critical role in attenuating external loads by generating joint moments in response to ground reaction forces during the weight-bearing movement. The contribution of each joint to load attenuation can vary with external demands and sex. Jumping performance may be influenced by joint coordination patterns through the use of stored elastic energy. The purpose of this study was to examine sex differences in lower-extremity joint stiffness coordination and how coordination patterns relate to jump performance across multiple drop heights.

Methods

Seventeen healthy and active college students (10 females, 7 males) performed three drop-jump trials from six box heights (10–60 cm in 10 cm increments). Joint stiffness was calculated using the joint angle and external joint moment during the eccentric phase of each jump. Left and right stiffness values were averaged for each joint and entered into a Principal Component Analysis (PCA) to identify coordination patterns using a customized R script. The primary principal component (PC1) was then used in a mixed-effects regression model to examine its relationship with jump height across conditions.

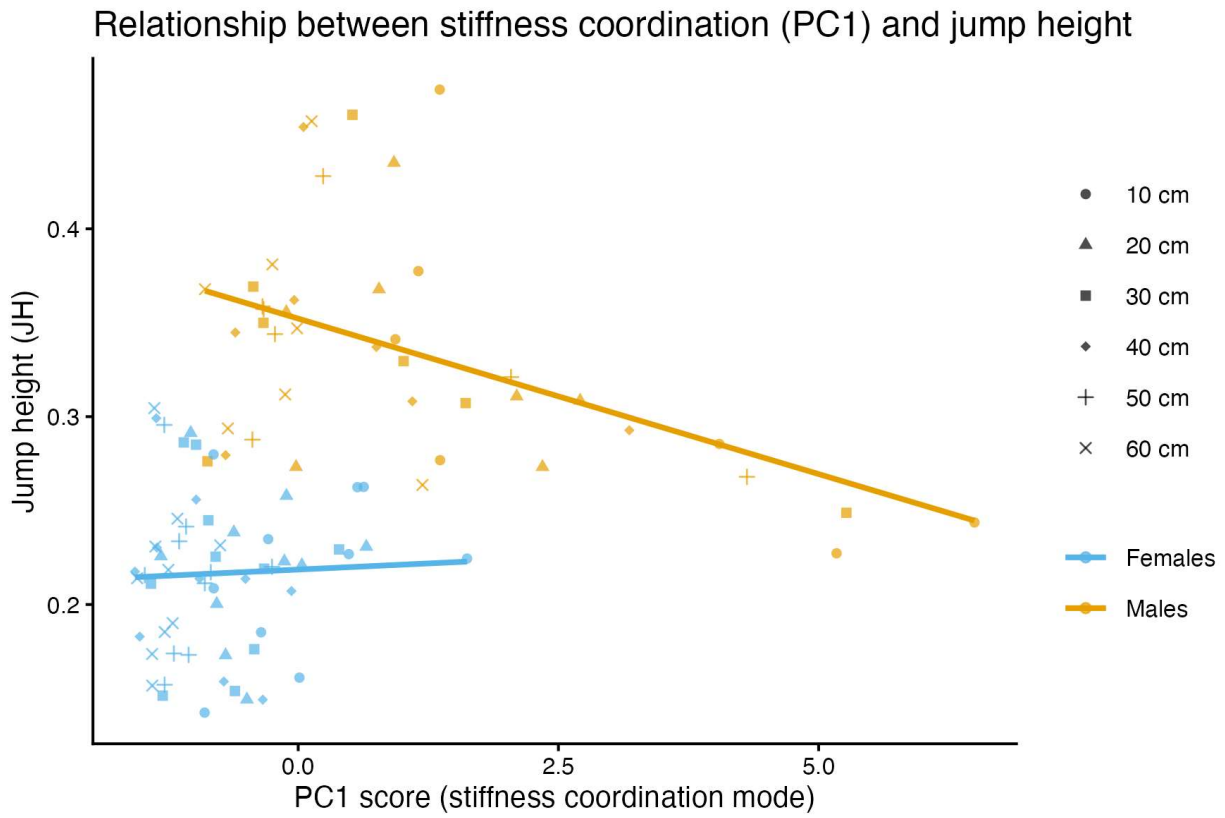
Results

PCA identified PC1 as a stiffness coordination, explaining 79% of total variance, with higher loading scores reflecting stiffer joint behavior. A significant Condition Sex interaction ($p < .001$) was observed in PC1. Post-hoc comparisons showed that males exhibited higher PC1 at lower drop heights (10–30 cm) but shifted toward lower PC1 at higher heights (40–60 cm). Females, in contrast, showed relatively small changes in PC1 across conditions and generally maintained a more compliant strategy. Mixed-effects regression indicated that the relationship between PC1 and jump height varied by both Condition and Sex (PC1 × Condition × Sex, $p < .001$).

Discussion

Males demonstrated stiff coordination at low drop heights but became more compliant as drop height increased, whereas females showed minimal modulation across conditions. This suggests that males adjust stiffness more dynamically to accommodate rising mechanical demands, while females maintain a consistent coordination strategy. Whether these differences reflect inherent sex-related neuromuscular control or arise from differences in relative loading remains unclear. Normalizing drop height or ground reaction forces to individual capacity may help distinguish these possibilities.

Images (Optional)



Session Category

Human Motion and Performance: Balance, Posture and Control

P1-096

Multi-Factorial Older-Adult Turning Strategies during 180˚ Turns

Ms. Zahava Hirsch, Ms. Erin Kreis, Dr. Antonia Zaferiou Ph.D.

Stevens Institute of Technology, Hoboken, NJ, United States

Introduction

Falls are a leading cause of injury in older-adults and are eight times more likely to result in a hip fracture during turns[1]. Previous research defines three 180˚ turn-strategies: steps (multiple steps taken), mixed (steps and pivot), and pivot[2]. Fall-risk is multi-factorial and categorized by cut-offs in assessments, including the Dynamic Gait Index (DGI), Timed Up and Go (TUG) and International Falls Efficacy Scale (FES-I). This study analyzes 180˚ turns during regular and fast speeds to elucidate the relationship between turn-strategies with frontal-plane angular momentum (H_f), gait speed, and the assessments listed. Based on previous research[3], we hypothesize that participants with "worse" measures will utilize "safer" turn-strategies (steps) and will have no difference in H_f range or gait speed between speeds.

Methods

Seven older-adults (6f, age 73.9±4.49) completed a 180˚ turning course five times at self-determined regular and fast speeds, the DGI, TUG, and FES-I. A 13-segment whole-body kinematic model was built using optical motion capture data (OptiTrack USA) and used to calculate H_f and gait speed. H_f range was normalized to a dimensionless form. Turns were visually observed and categorized. Mann Whitney U was used to compare H_f range and gait speed per participant.

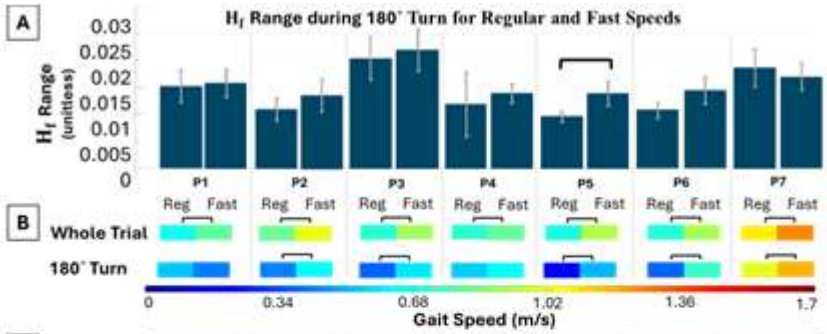
Results

Six participants had no change in H_f during the turn, indicating maintained postural control during faster speeds (Fig.1). P5 had significant difference in H_f and is the oldest participant. Five participants used the step strategy across all trials. P2 used all three strategies during regular speed, but only mixed and pivot during fast speed. P7 used only mixed and pivot across speeds and had the lowest FES-I and greatest DGI. While all participants' mean fast gait speed across the whole trial were significantly faster than regular, P1&4 did not change speeds during the 180˚ turn. P1's TUG and P4's FES-I score define them as fall-risk, indicating they may slow their gait and utilize a step strategy as a protective strategy.

Discussion

Participants with “worse” fall-risk assessments were observed utilizing conservative 180˚ turn-strategies.

Images (Optional)



C

	P1		P2		P3		P4		P5		P6		P7	
Age	74		74		68		73		82		76		70	
DGI	20		23		20		21		24		21		24	
TUG	12		9		9		10		8		10		7	
FES-I	20		19		20		62		26		21		17	
Turn Strategy	Reg	Fast	Reg	Fast	Reg	Fast	Reg	Fast	Reg	Fast	Reg	Fast	Reg	Fast
Steps	5	5	3	-	5	5	5	5	5	5	5	5	-	-
Mixed	-	-	1	3	-	-	-	-	-	-	-	-	2	2
Pivot	-	-	1	2	-	-	-	-	-	-	-	-	3	3

Figure 1: **A)** Hf range during regular and fast speeds for each participant. Brackets indicate significance regular vs. fast speeds. **B)** Gait Speed for the whole trial and the 180˚ turn across regular and fast speed per participant. Brackets indicate significance regular vs. fast speeds. **C)** Age and assessment scores, as well as 180˚ turn strategies for each trial for each participant. Red values indicate fall-risk, green indicates best scores of the cohort.

References (Optional)

[1]Nevitt & Cummings (1994), *Osteoporosis Int*. [2]Thigpen et al. (2000), *Phys.Therapy*. [3]Hirsch et al. (2025), *Sci.Rep*.

Acknowledgements (Optional)

National Science Foundation Award #1944207

Session Category

Human Motion and Performance: Balance, Posture and Control

P1-097

Simulated Pregnancy Weight Gain Increases Foot Arch Deformation and Abductor Hallucis Activation During Walking

Dr Adrienne Henderson[1], Dr Lauren Williams[2], Ms Rachel Todd[1], Dr Dustin Bruening[1]

[1]Brigham Young University, Provo, UT, United States. [2]University of Utah, Salt Lake City, UT, United States

Introduction

The foot is responsible for supporting and propelling the body during gait, commonly experiencing dynamic loads above 100% body weight. Active muscle contractions coordinate with passive bony structures to support the foot's arch as it is deformed during loading. Increased body mass as experienced in pregnancy can further increase loads on the arch which could contribute to reported pregnancy foot pain. The purpose of this study was to characterize the foot arch's response to simulated weight gain. We hypothesized increased arch range of motion (ROM), peak plantarflexion moment, negative and positive work, and increased activation of the abductor hallucis muscle (ABDH) with added weight.

Methods

Twelve healthy participants (1.69±0.07m, 66.7±9.04kg) walked at 1.0-1.2m/s under 2 randomized conditions (weighted and unweighted) while kinematic and kinetic data were measured. An anteriorly weighted vest was used for the weighted condition with mass equal to weight gained by a matched pregnant participant from a previous study.[2] A surface electromyography sensor on the right ABDH recorded peak muscle activation during stance. A three-segment foot model was used to calculate arch ROM, peak plantarflexion moment, negative work, and positive work. Moment and work metrics were normalized to mass. T-tests determined significance between conditions.

Results

Arch ROM, negative work, and peak ABDH activation significantly increased with added weight but peak plantarflexion moment and positive work remained unchanged (Table 1).

Discussion

The increased arch ROM and negative power indicate that the arch experienced greater deformation with the added mass. The ABDH seems to be attempting to attenuate this deformation with increased activation. The lack of change in normalized arch plantarflexion moment suggests that the COP remained consistent between conditions despite the center of mass moving anterior.[2] Our results contrast slightly with the prior

matched pregnant participants, who did not alter ROM or negative power across trimesters.[1] This suggests even greater muscular attenuation in pregnancy to overcome the increase in both body weight and ligament laxity. Interventions aimed at supporting the foot's arch during pregnancy may help reduce muscular discomfort.

Images (Optional)

Table 1: Group means and standard deviation for key Midtarsal metrics and peak ABDH muscle activation with p-values.

	Normal	Weighted	p-value
ROM (degrees)	8.19 ± 1.30	9.04 ± 1.52	< 0.000
Peak Plantarflexion Moment (Nm/kg)	-1.03 ± 0.11	-1.04 ± 0.14	0.663
Negative Work (J/kg)	-0.05 ± 0.02	-0.06 ± 0.02	0.001
Positive Work (J/kg)	0.07 ± 0.02	0.07 ± 0.02	0.651
Peak ABDH Activity (mV)	121.83 ± 68.53	156.40 ± 94.13	0.016

References (Optional)

1 Kern (2019) *PerrJ 7, e7487*.

2 Williams (2025) BYU dissertation.

Session Category

Human Motion and Performance: Locomotion/Gait

P1-098

Joint Contributions and Muscle Coordination During Single-Leg Lateral Jumps: Hip and Knee Joint Work Modulate Performance Despite the Ankle Being the Primary Contributor

Ms. Ainsley Durnin B.Sc., Dr. Jordan Cannon Ph.D.

University of Waterloo, Waterloo, Ontario, Canada

Ms. Ainsley Durnin

Introduction

Single-leg lateral jumps (SLJs) are complex multi-planar tasks with distinct biomechanical demands from vertical and forward jumps, yet remain under-researched [1]. Their unique demands enable exploration regarding multi-joint control and assess key aspects of athletic performance, but detailed biomechanical descriptions are lacking. Given the single-leg task demands, the hip is expected to play a key role as the connection between the trunk and lower limb. This study aimed to quantify joint contributions to whole-body dynamics and jump distance, and to examine hip muscle recruitment during maximal-distance SLJs.

Methods

Eighteen female athletes performed three maximal-distance SLJs from each limb. Full-body kinematics, kinetics, and hip muscle activation were recorded. Whole-body centre-of-mass (WB-COM) power and work were computed (dot product of ground reaction force with WB-COM velocity and its time integral, respectively). Inverse dynamics analysis calculated joint power and work (dot product of net joint moment with joint angular velocity and its time integral, respectively) across the lower limbs, trunk, and upper limbs. Linear regressions examined relationships among jump distance, WB-COM work, and joint work. Repeated-measures ANOVA compared joint contributions. Correlation analyses identified which hip muscles were recruited to meet hip joint demands.

Results

Work done on the WB-COM explained 68% of the variance in jump distance across participants. Total joint power underestimated WB-COM power by 23%. The ankle joint was the primary contributor ($p<0.001$) though only hip ($R^2=0.33$, $p=0.01$) and knee ($R^2=0.55$,

p=0.0004) work scaled with jump distance (Figure). No consistent group-level muscle coordination strategy was observed.

Discussion

Unexplained variance in jump distance by WB-COM work likely reflects unaccounted rotational kinetic energy in the WB-COM approach [2]. The inability of joint power to explain WB-COM variance likely stems from proximal-to-distal mechanical power transfer, via biarticular muscles, which the joint power approach cannot fully capture. Variability in individuals' muscle coordination strategy and relative hip joint contributions to task performance highlight limitations in relating muscle activation to joint, whole-body, and task performance at group-level. Segmental power flow and muscle synergy analyses are ongoing to better characterize multi-joint control during SLJs.

Images (Optional)

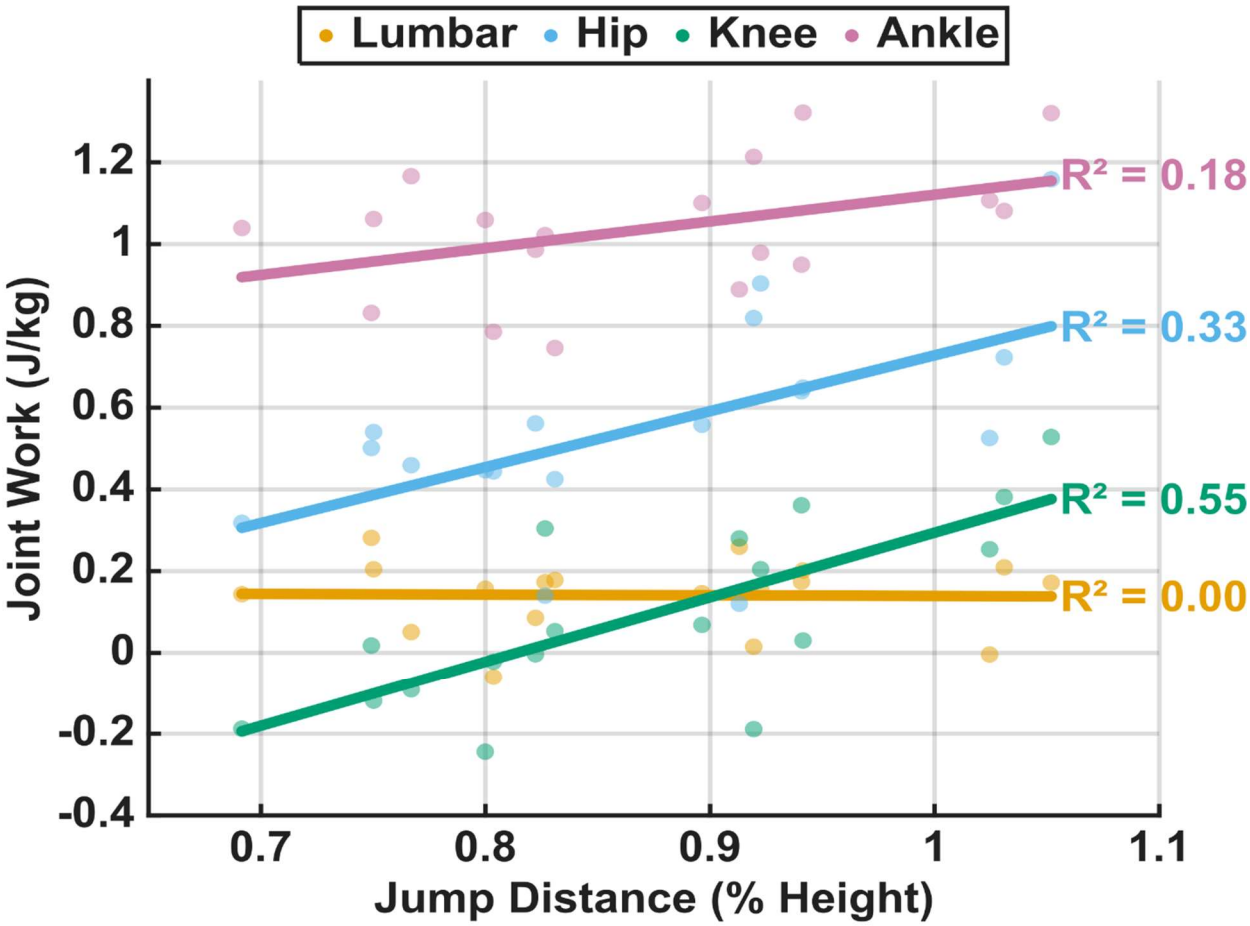


Figure: Joint work (lumbar, hip, knee, and ankle joints) during the launch phase (amount of time the single limb is in contact with and loading the force plate before takeoff occurs) normalized to bodyweight in kilograms against jump distance as a percentage of height.

References (Optional)

[1] Jeffrey Taylor *et al.*, Sports medicine, 2017

[2] Michiel de Looze *et al.*, J Biomechanics, 1992

Session Category

Human Motion and Performance: Locomotion/Gait

P1-099

Effects of Simultaneous Asymmetric Crankarm Lengthening and Shortening During Cycling on Knee Biomechanics

Mr. Alejandro Ovispo-Martinez M.S., Mr. Tsung-Lin Lu M.S., Mr. Davin Gleaves, Ms. Quinn Wilsom, Mr Jacob Rygielski, Dr. Songning Zhang PhD

University of Tennessee, Knoxville, TN, United States

Introduction

Cycling is a common modality for knee-joint injury rehabilitation. Studies have investigated the effects of symmetrical shortening and asymmetrical shortening of crankarms on lower-limb mechanics during cycling. The effect of simultaneous shortening on one side and lengthening on contralateral side has not been previously investigated. Therefore, the purpose of this study is to investigate effects of combining asymmetrical lengthening and shortening of the crankarms during cycling on knee-joint biomechanics.

Methods

The study included six healthy and recreationally active individuals (Age:25+/-5.3 yrs, Height:1.74+/0.09 m, Weight:73.68+/15.7 kg). Participants pedaled at a work rate of 70 Watts and a cadence of 70 revolution per minute in four different crankarm conditions: 170mm crankarm length both legs, 185mm crankarm length on the non-dominant leg and a 170mm crankarm length on the dominant leg, and 185mm crank length on non-dominant leg and shortened crankarm lengths of 155mm and 140mm on the dominant leg. 3D Kinematic data were collected by a 12-camera motion analysis system, and pedal reaction forces (PRF) data were collected using a pair of custom-built instrumented pedals. A 2x4 (limb x crankarm length) repeated-measures ANOVA was used to evaluate selected variables ($p < 0.05$).

Results

Significant interactions of crankarm length and limb were found in the knee-joint range of motion (KROM) and peak PRFs. Specifically, KROM decreased from C1 to C4 (excluding C2) and PRF increased in C3 and C4 in the dominant limb. The KROM was greater in conditions C2-C4 compared to C1 and for PRFs, C3 and C4 were greater in the non-dominant limb. There were no significant differences in knee-extension moments (KEM) or knee-joint power (KPOW).

Discussion

The combination of asymmetrical shortening and lengthening influenced sagittal KROM and PRFs but with minimal to no influence on KEM and KPOW. The increase in crankarm length reduced PRF requirement in the dominant limb while increasing the PRFs on the non-dominant limb without an increase in knee loading. By reducing sagittal KROM without increases in KPOW and KEM, this study provides some evidence that we can implement asymmetrical crankarm lengths in cycling intervention without increasing loading to knee joint.

Images (Optional)

Table 1. Mean peak knee extensor moment (KEM), sagittal knee-joint range of motion (KROM), peak knee-joint power (KPOW), and peak pedal reaction forces (PRF): mean± SD.

Condition	*Limb*	*Peak KEM (Nm)*	*KROM (°)*	*Peak KPOW (W)*	*Peak PRF (N)*
C1 (170/170 mm)	***D***	29.99 ± 8.35	72.67 ± 5.19	136.29 ± 35.23	213.82 ± 44.44 [cd]
	ND	29.48 ± 4.89	73.83 ± 8.57 [bcd]	137.13 ± 28.57	216.24 ± 28.59 [cd]
C2 (185/170 mm)	***D***	29.69 ± 5.34	72.97 ± 5.34 [cd]	135.10 ± 20.41	217.18 ± 24.20
	ND	28.2 ± 8.33	79.39 ± 8.04 [a]	136.18 ± 45.19	199.91 ± 44.12
C3 (185/155 mm)	***D***	31.89 ± 8.45	66.78 ± 4.84 [ab]	133.07 ± 30.18	235.09 ± 39.00 [ad]
	ND	27.06 ± 4.37	81.77 ± 10.17 [ad]	134.67 ± 26.15	199.90 ± 26.81 [ad]
C4 (185/140 mm)	***D***	30.45 ± 6.68	58.95 ± 4.28 [abc]	112.17 ± 22.84	232.68 ± 47.79 [ac]
	ND	24.55 ± 5.0	79.92 ± 9.27 [ac]	122.23 ± 34.91	187.32 ± 21.67 [ac]

[a] significantly different from C1 of same limb, [b] significantly different from C2 of same limb, [c] significantly different from C3 of same limb, [d] significantly different from C4 of same limb

References (Optional)

[1] Menke et al. 2025 Congress of ISB.

Session Category

Human Motion and Performance: Locomotion/Gait

P1-100

Running Volume and Stroller Use: Their Combined Effect on Injury Risk

Dr. Joseph Mahoney Ph.D.[1], Ms. Houn Kim[2], Dr. Andrew Friesen Ph.D.[2], Dr. Allison Altman-Singles Ph.D.[2]

[1]Alvernia University, Reading, PA, United States. [2]Penn State Berks, Reading, PA, United States

Dr. Joseph Mahoney

Dr. Andrew Friesen

Introduction

Running with a stroller allows parents to remain active while caring for young children, but postpartum runners may be vulnerable to overuse injury because of changes in lifestyle and training patterns [1]. Stroller running alters running kinetics and kinematics, which may modify musculoskeletal loading and injury risk [2]. This study examined how stroller use and total mileage are associated with overuse injury in parent runners.

Methods

Parent runners completed a retrospective survey about running from birth to 3 years after having a child. Participants reported average weekly mileage, the percentage of their total weekly miles run with a stroller, and whether they sustained an overuse injury. Responses with missing injury status or mileage were excluded. Binary logistic regression with total weekly mileage and the percentage of weekly miles run with a stroller as predictors evaluated associations with overuse injury risk.

Results

188 respondents with complete mileage data were included. Stroller users reported 18.6 ± 19.6 total weekly miles with 48.1% ± 31.0% of them being stroller running miles. Higher total mileage was associated with increased odds of overuse injury, with an odds ratio of 1.02 for each additional mile ($p = 0.039$). A higher percentage of miles run with a stroller was associated with lower estimated odds of injury, with an odds ratio of 0.62, although this effect was not statistically significant ($p = 0.45$).

Discussion

These findings suggest that stroller use may reduce overuse injury risk, although this trend did not reach statistical significance. This pattern is consistent with previous work showing that biomechanical markers linked to injury risk are reduced during stroller running [2]. The regression results affirm that increased running volume is the primary driver of injury risk in this population: each additional weekly mile was associated with a 2% increase in overuse injury risk, similar to previous running overuse injury studies [3]. Overall, these results support the safety of running strollers for parent runners while highlighting the importance of managing total training volume.

References (Optional)

[1] Kimber et al., MSSE, 2021

[2] Mahoney et al. PLoS One, 2025

[3] Correia et al., J Sport Health Sci, 2024

Acknowledgements (Optional)

Session Category

Human Motion and Performance: Locomotion/Gait

P1-101

Evaluating Feasibility of Portable Motion Capture Systems in Clinical Settings

Dr. Alyson March, Dr. Cherice Hill

University of Rochester, Rochester, NY, United States

Introduction

Biomechanics research goes hand-in-hand with clinical practice to analyze human motion and track disease presentation, progression, and rehabilitation. Integration of motion analysis into clinical settings is advantageous to enable analysis of representative populations and improve clinical outcomes. Traditionally, motion analysis is restricted to academic labs, but OpenCap enables motion tracking and evaluation of kinematics with just 2-3 iOS devices. Data can then be processed in OpenSim using muscle-driven simulations, enabling estimation of kinetics without additional equipment. However, it is currently unclear how motion analysis with OpenCap could fit into a clinical workflow. In this study, we assessed the feasibility of using OpenCap+OpenSim to evaluate walking kinetics, focusing on the time and expertise needed for data collection and processing.

Methods

Participants (n=10) completed 5 walking trials across 3 embedded force plates while data was collected using the OpenCap app on 3 iPads. Ground reaction forces (GRF) were estimated via muscle-driven simulations using OpenSim, as detailed in the OpenCap github. Each step was evaluated individually, and the time for model convergence was recorded. Maximum vertical GRF (vGRF) estimated from muscle-driven simulations was compared to peaks measured from force plates. GRFs were normalized by participant body weight.

Results

Preliminary evaluation of 40 steps has been completed (2 steps from 2 trials/participant). Three step simulations did not converge, giving the muscle-driven simulations a 93% convergence rate. The average time for simulation completion was 20±14 minutes (Figure 1A). Preliminary analysis of discrete GRF peaks for five participants demonstrates the maximum vGRF estimated by OpenCap trends greater than the measured force from force plates (Figure 1B).

Discussion

Currently, the muscle-driven simulations require significant time and expertise for completion, which would be difficult to integrate within a time-packed clinical workflow.

While use of a supercomputer may decrease the time for analysis, this requirement would reduce the accessibility of data analysis in a clinical setting. To maximize accessibility, OpenCap may be combined with portable tools to measure GRF, such as portable force plates or pressure insoles. On-going work will evaluate additional steps and complete statistical comparisons of discrete peaks and continuous curves for the measured and estimated vGRF.

Images (Optional)

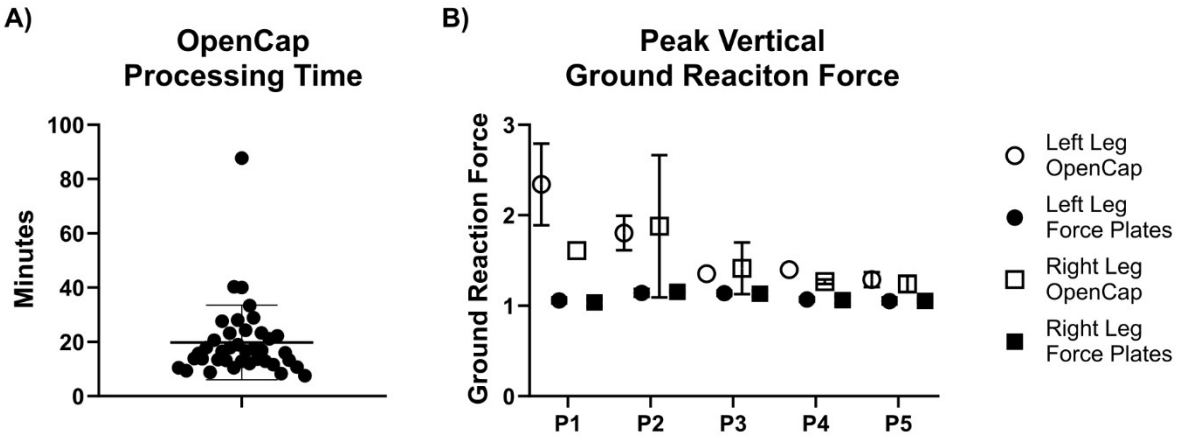


Figure 1: OpenCap kinetic estimation processing. A) Time for simulation convergence. B) Comparison of OpenCap to Force Plate vGRF.

References (Optional)

Acknowledgements (Optional)

Session Category

Human Motion and Performance: Locomotion/Gait

P1-102

A Domain-Agnostic, Frequency-Based Method for Structuring Biomechanical Signals during Cyclic Activities

Miss ChengYue Zhang[1,2], Miss Amy Coyle[1], Dr. Paula Branco[3], Dr. Richard Moulton[1]

[1]HAS-Motion Inc., Kingston, Ontario, Canada. [2]University of Toronto, Toronto, Ontario, Canada. [3]University of Ottawa, Ottawa, Ontario, Canada

Introduction

Structuring biomechanical signals for large-scale analysis on arbitrary cyclic activities is challenging as current methods require domain knowledge or labelled training data. Here, we propose a domain-agnostic, train-free cycle segmentation pipeline.

Methods

Our pipeline structures a kinematic signal given its sampling rate f_s by: (1) estimating the signal's fundamental frequency f_0 via the Harmonic Product Spectrum algorithm [1], (2) identifying recurring patterns S by seasonal decomposition, (3) extracting a template with duration $T = 1/f_0$ from S, and (4) identifying cycles with a Euclidean-distance-based similarity search to the template (Figure 1).

Public datasets used for evaluation include healthy participants treadmill-walking (Slow, Normal, Fast speeds; n=42 [2], n=10 [3]) and participants with Parkinson's Disease overground-walking (ON, OFF medication; n=26 [4]).

We compared our pipeline with domain-knowledge-based methods [5-8], deep-learning methods [9], and a peak-detection-based method [10]. Domain-agnostic approaches (our pipeline and [10]) processed 6 different signals to test generalizability. We used Linear Mixed-Effects Models (LMM) with methods as fixed effects and participants (with nested trials) as random effects, to assess each method's identified cycle counts and durations against simultaneously collected force platform data. We calculated the duration Root Mean Square Error (RMSE) on a per-trial basis.

Results

Methods with 95% confidence intervals overlapping the 0-difference line were our pipeline (all signals), [6-8], and [10] (3 signals) in counts LMM, but only our pipeline (all signals) and [8] in durations LMM.

The best and worst of our pipeline's predictions had a median RMSE of 18.7±0.7ms (Fast) and 38.6±2.3ms (OFF). Both were superior to all other methods.

Discussion

Our pipeline outperforms [5-7, 9-10] and is comparable to method [8]. Given its domain-agnostic nature, future work will expand applicability to additional cyclic activities.

Images (Optional)

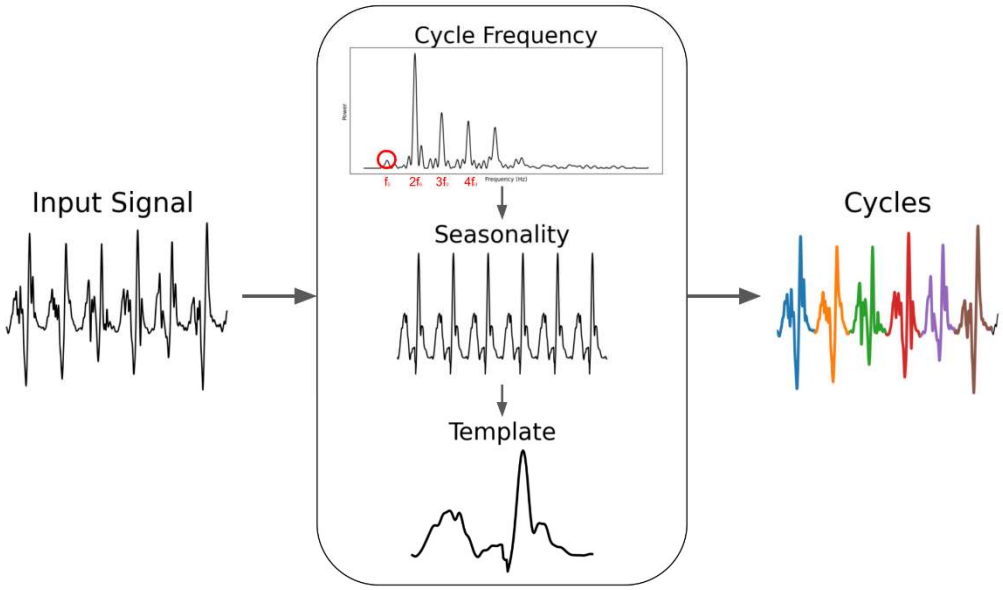


Figure 1: Overview of our pipeline. Starting from a kinematic signal and its sampling rate, the fundamental frequency f_0 (circled out in red) is detected out of its harmonics ($2f_0$, $3f_0$, $4f_0$, etc.) to estimate cycle duration. Then the signal's seasonality is identified. A cycle template is extracted from seasonality. Cycles are identified by a Euclidean-distance-based similarity search algorithm to the template.

References (Optional)

[1] Noll *et al.*, Polytechnic, 1969

[2] Fukuchi *et al.*, PeerJ, 2018

[3] Scherpereel *et al.*, Scientific Data, 2023

[4] Shida *et al.*, Front Neurosci, 2023

[5] Zeni *et al.*, Gait Posture, 2008

[6] De Asha *et al.*, Gait Posture, 2012

[7] Hreljac *et al.*, J Biomechanics, 2000

[8] O'Connor *et al.*, Gait Posture, 2007

[9] Dumphart *et al.*, PLOS ONE, 2023

[10] Jiang *et al.*, EUSIPCO, 2017

Session Category

Human Motion and Performance: Locomotion/Gait

P1-103

Co-contraction presents asymmetrically in adults walking overground

Mrs. Julie Ferrell-Olson MSc, Dr. Hannah D. Carey PhD, Mrs. Ashlyn Wormsley, Dr. Andrew Sawers CPO, PhD

University of Illinois Chicago, Chicago, IL, United States

Introduction

EMG signals during gait are often assumed to be symmetric between legs. [1,2] However, it remains unclear whether agonist-antagonist co-activation (i.e., co-contraction) [3] is also symmetric while walking, as most studies of co-contraction in unimpaired adults record EMG from a single leg. Identifying between-leg differences in co-contraction may change how we interpret differences in neuromuscular control between populations. The objective of this study was to determine if co-contraction is symmetric between legs. We hypothesized there would be significant between-leg differences in co-contraction at the ankle, knee, and hip due to lateralization of motor function.

Methods

This was a secondary analysis of EMG data in a public dataset collected from unimpaired adults walking overground at their preferred speed. [4] Co-contraction values for agonist-antagonist muscle pairs at the ankle, knee, and hip were calculated as the ratio of the less active to more active muscle multiplied by the sum of both muscles. [3] A “high” and “low” co-contraction leg was identified for each participant. Differences between high and low co-contraction values were evaluated using paired t-tests.

Results

104 participants (54 females), 21-86 years of age, were included in the analysis. Significant between-leg differences in co-contraction (mean [SD]) were observed at the ankle (0.12 [0.05] vs. 0.09 [0.04]), knee (0.22 [0.07] vs. 0.17 [0.06]), and hip (0.22 [0.07] vs. 0.16 [0.07]); all $p<0.001$) (Figure 1).

Discussion

The asymmetry in co-contraction observed in this secondary analysis of unimpaired adults may reflect motor lateralization, wherein each leg is specialized for distinct functions (e.g., stability vs. precision). Our results also suggest that some co-contraction in individuals with unilateral impairments, such as stroke or amputation, may reflect typical between-

limb asymmetries rather than purely pathological or compensatory mechanisms. To better differentiate the effects of impairment on co-contraction, future studies should collect bilateral EMG in control participants. Ongoing work will test whether kinematic and kinetic asymmetries accompany co-contraction asymmetry, helping determine if co-contraction asymmetry has a neural or mechanical origin.

Images (Optional)

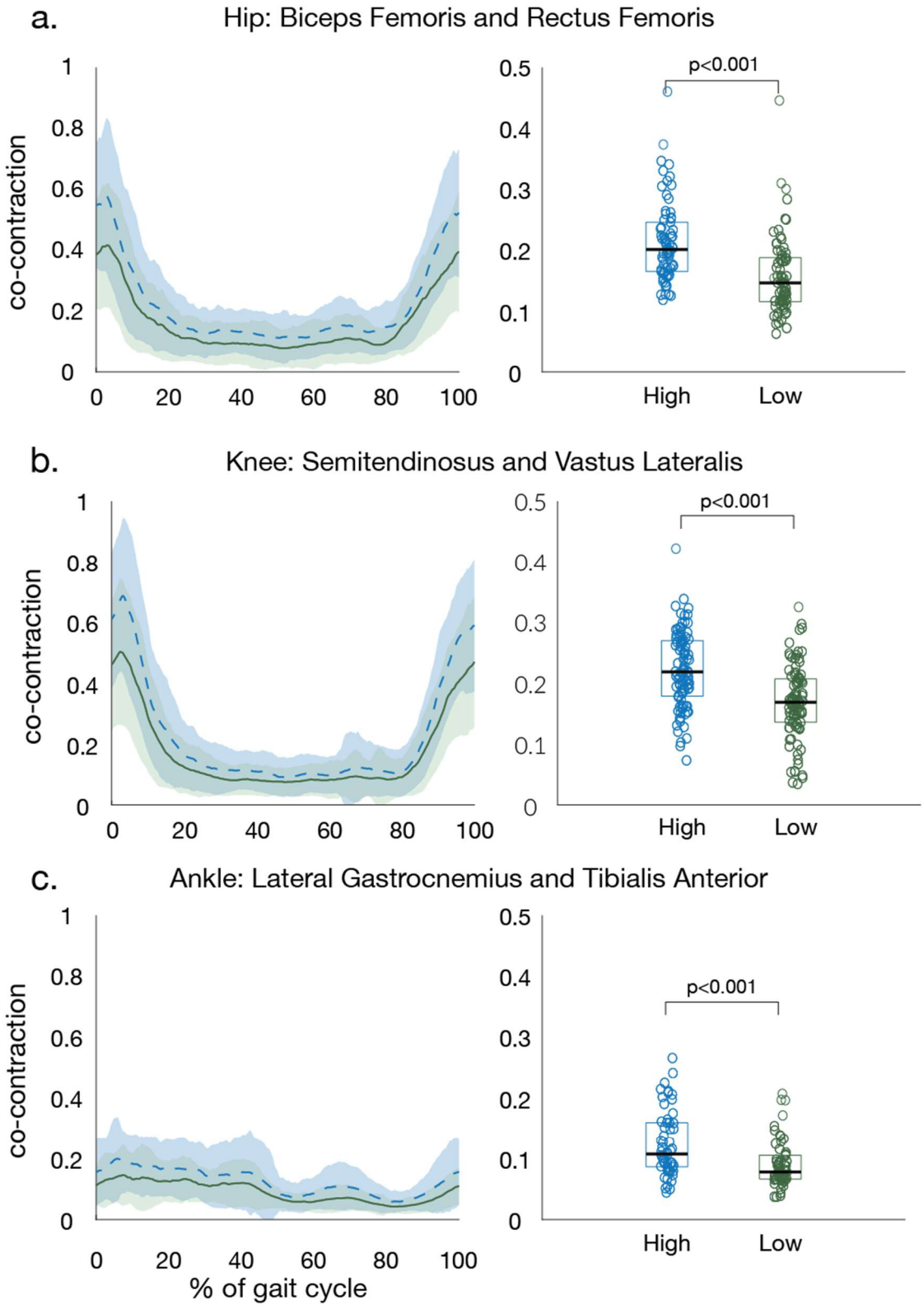


Figure 1. Co-contraction values over the gait cycle at the ankle (a), knee (b), and hip (c). Green/solid depict the 'low' co-contraction leg. Blue/dashed depicts the 'high' co-contraction leg.

References (Optional)

[1] Arsenault et al., 1986 [2] Pierotti et al., 1991 [3] Rudolph et al., 2004 [4] Van Crienkinge et al., 2023

Session Category

Human Motion and Performance: Locomotion/Gait

P1-104

Decreased Rate of Force Development in Simulated Walking Increased Double Support Times

Mr. Nicholas Yaple, Dr. Anne Martin

Pennsylvania State University, State College, PA, United States

Introduction

The rate of force development (RFD) may contribute to spatiotemporal disturbances post-stroke, such as increased time spent in double support (DS). A reduced RFD may extend the time required to complete weight transfer, leading to longer steps. It is difficult to test and isolate experimentally, so simulations may offer insight. Previously, we simulated reduced joint torques using a 2D skeletal model but found low DS times and high RFDs. We hypothesized that a lower peak RFD would increase DS time and change step length and time to better mimic post-stroke gait.

Methods

Using a 2D skeletal model (two ankles, two knees, and a shared hip joint) with ideal motor driven joints and a minimum allowable DS time of 0.15s, we generated predictive walking simulations by minimizing energetic cost while gradually reducing the RFD via torque rate limits. The RFD limit was determined using previous experimental data scaled by an RFD multiplier. For each speed (0.8m/s, 0.6m/s, and 0.4m/s), the RFD multiplier started at x10 (unconstrained) and was incrementally reduced until the optimization failed.

Results

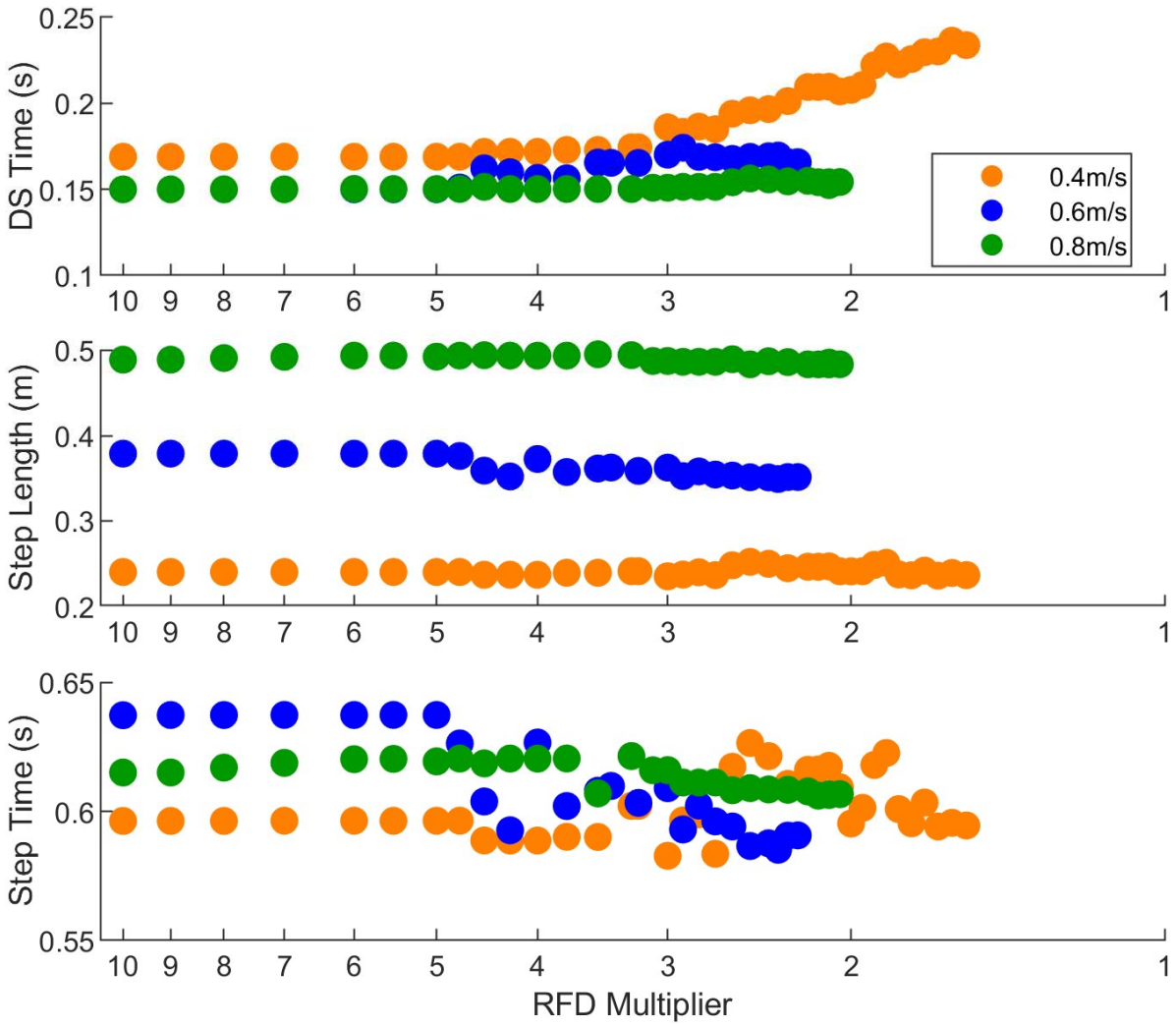
As the RFD decreased, DS times increased, particularly for the slowest speed (0.150s to 0.154s at 0.8m/s; 0.150s to 0.166s at 0.6m/s; and 0.151s to 0.234s at 0.4m/s). Step lengths slightly decreased (0.489m to 0.483m at 0.8m/s; 0.379m to 0.352m at 0.6m/s; and 0.240m to 0.237m at 0.4m/s) and step times clustered around 0.625s. The RFD limit could not be reduced to biologically observed levels (minimum of 2.05x at 0.8m/s; 2.25x at 0.6m/s; and 1.55x at 0.4m/s), which could impact findings.

Discussion

These results support the hypothesis that reduced peak RFD may increase DS time, which typically increases post-stroke. The increase was dependent on speed, where slower speeds had a larger increase in DS time. Our hypothesis of step length changing was weakly supported because while it decreased for all speeds, the difference was small. Thus, as the RFD decreases, it appears that it is energetically optimal to increase DS time

and slightly modify step length and time, indicating that limiting the RFD has an impact on gait.

Images (Optional)



Session Category

Human Motion and Performance: Locomotion/Gait

P1-105

How Competing Movement Objectives Reshape Motor Coordination

Dr. Ava Lakmazaheri[1], Ms. Jordan Feldman[1], Ms. Angeline Prasanna[1,2], Dr. Patrick Slade[1]

[1]Harvard University, Cambridge, MA, United States. [2]École Polytechnique Fédérale de Lausanne, Lausanne, Vaud, Switzerland

Introduction

Gait is modulated by multiple objectives, typically isolated in the study of motor control. Muscle synergies can reflect changes in functional complexity for motor tasks or impairments. We assessed synergy changes under competing task demands to advance understanding of real-world locomotor control.

Methods

Twelve adults walked overground at a slow self-selected speed in two-minute trials performing (i) no additional task, (ii) a “balance” task, with large mediolateral visual perturbations, (iii) an “accuracy” task, placing feet on variable-distance markers, and (iv) “balance” and “accuracy” tasks simultaneously. Electromyography was collected bilaterally from the biceps femoris (BF), rectus femoris (RF), vastus medialis (VM), soleus (SO), medial gastrocnemius (MG), and tibialis anterior (TA). Gait cycles were pre-processed and normalized to MVC. Non-negative matrix factorization extracted the minimum number of synergies to account for ≥95% of total variance per subject-trial. Hierarchical clustering identified shared synergies across subjects, with a critical value of R≥0.92 identifying similarity across tasks [1].

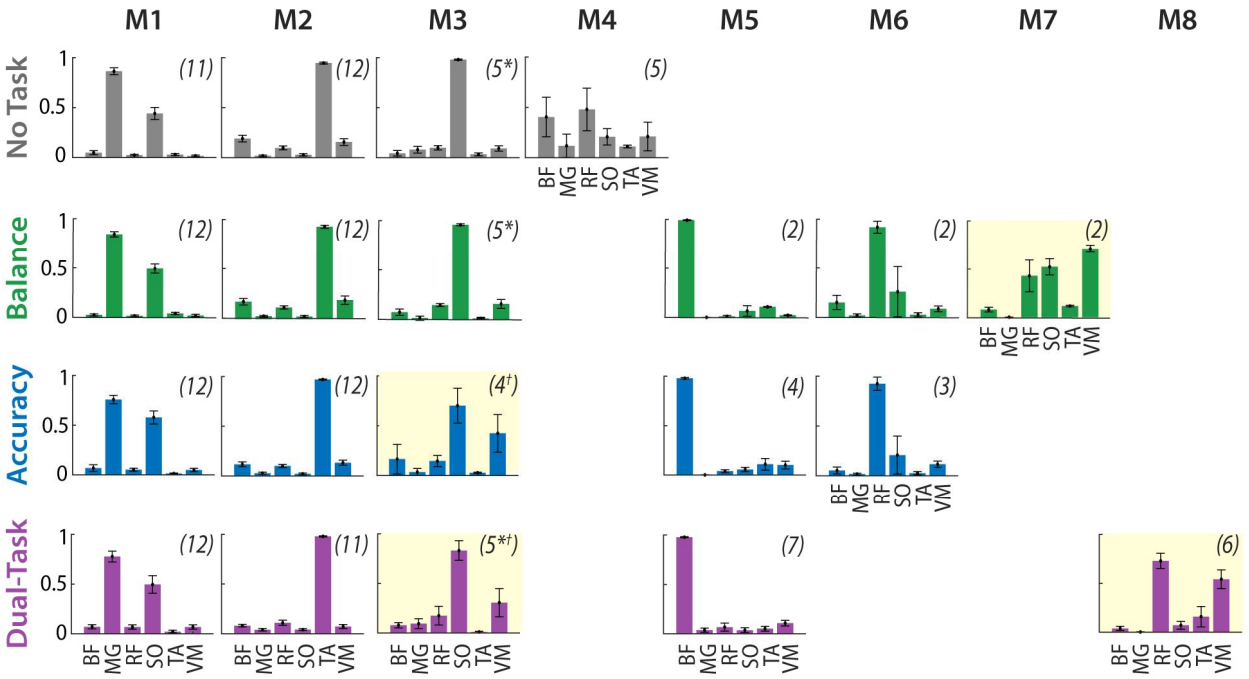
Results

All conditions included modules for propulsion (M1: MG-SO) and dorsiflexion (M2: TA). A diffuse synergy (M4) was decomposed into separable anterior (M5: RF) and posterior (M6: BF) proximal control in single-objective tasks. An additional module (M3) reflected either ankle stiffness (SO) or, when “accuracy” was included, precision shank positioning (SO-VM). A “balance”-specific synergy emerged for enhanced postural support (M7: RF-SO-VM). In the dual task, M1-M3 and M5 persisted, alongside a new hip-knee synergy (M8: RF-VM). At low (no task) and high (dual-task) complexity, many subjects were represented per module (N=5-7); motor repertoire was most varied for single-task demands (N=2-5).

Discussion

While single-task demands led to specialized motor modules, these were nonlinear in combination. Control strategies were restructured to satisfy conflicting requirements (fine vs. robust control) with minimal redundancy. As such, greater task complexity did not guarantee a higher number of motor modules. We also observed a nonlinear relationship between task complexity and inter-subject variability, suggesting smaller solution spaces with competing demands. “Accuracy”-specific synergies were uniquely preserved in the multi-objective task, suggesting a hierarchical structure of motor control. Study of additional tasks may yield further insight into this structure.

Images (Optional)



*Parentheticals indicate # subjects per cluster. All columns are similar unless similarity indicated by * or †.*

References (Optional)

[1] Jessica Allen & Jason Franz, *J Neurophysiol*, 2018.

Acknowledgements (Optional)

Session Category

Human Motion and Performance: Locomotion/Gait

P1-106

Pre- and Post-Pubertal Females Show Differences in Hip and Pelvis Kinematics During Walking

Ms. Avery Kratzer BSE, Prof. Cara Lewis PT, PhD, FAPTA

Boston University, Boston, Massachusetts, United States

Introduction

Adolescent female athletes incur hip injuries at three times the rate of their male peers, with the risk of injury increasing as females mature [1]. This increased injury risk may result from altered loading, driven by kinematic changes at the hip during adolescence. To better address hip injury risk in adolescent female athletes, it is essential to understand how kinematics change across adolescence in a repetitive everyday loading task (i.e., walking). Thus, the purpose of this preliminary study was to compare hip, pelvis, and thigh kinematics during walking in pre- and post-pubertal females.

Methods

Six pre-pubertal females (9.8±1.5 years; 1.4±0.2 m; 34.5±4.6 kg; 1.1±0.2 m/s) and 10 post-pubertal females (22.1±2.2 years; 1.7±0.1 m; 62.1±8.3 kg; 1.3±0.1 m/s) walked at a self-selected speed for two minutes on a treadmill. Kinematic data were recorded using 10-camera motion capture and processed in Visual3D. Hip, pelvis, and thigh angles in the sagittal and frontal planes were used for analysis. Peak angles were extracted for each stride, and the average across all strides of the dominant limb was calculated for each individual. Independent t-tests (α=0.05) were conducted to compare peak angles between the pre- and post-pubertal groups.

Results

The post-pubertal group demonstrated 3.2±1.0° greater peak hip abduction during swing and 3.5±1.4° less anterior peak pelvic tilt, compared to the pre-pubertal group (Figure 1). No significant differences in the remaining peak hip, pelvis, and thigh angles were detected between groups in this preliminary analysis ($p>.05$).

Discussion

The increase in hip abduction and decrease in anterior pelvic tilt during walking pre- to post-puberty in this study aligns with previous work in running [2] and standing [3], respectively. These kinematic changes may increase hip loading [4], potentially

contributing to the heightened risk of overuse injuries in female athletes during adolescence. Future work will use musculoskeletal simulations to assess the influence of these kinematic changes on hip loads.

Images (Optional)

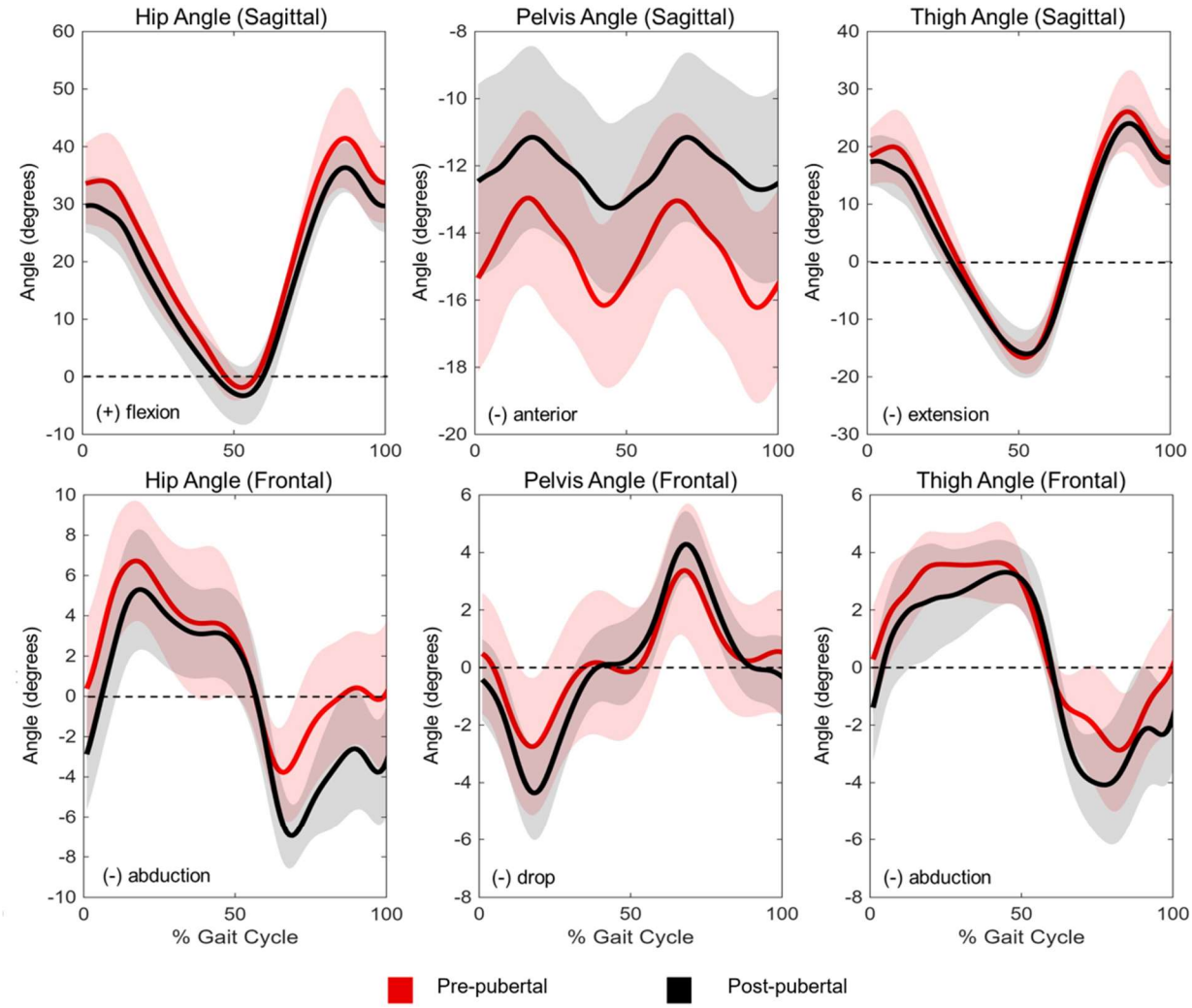


Figure 1. Hip, pelvis, and thigh angles in the sagittal and frontal planes, represented as mean ± 1 standard deviation for pre-pubertal (red) and post-pubertal (black) groups.

References (Optional)

[1] Stracciolini et al., J Pediatr Orthop B, 2016

[2] Taylor-Haas et al., J Sci Med Sport, 2022

[3] Schlosser et al., Eur Spine J, 2015

[4] Ismail & Lewis, J Biomech, 2022

Session Category

Human Motion and Performance: Locomotion/Gait

P1-107

Split-Belt Locomotor Adaptation of Inter-Limb Kinematics and Kinetics Under Different Practice Structures

Ms. Beier Lin[1], Dr. Sarah N. Kraeutner[2], Dr. William E. McIlroy[3], Dr. Courtney L. Pollock[1]

[1]University of British Columbia, Vancouver, BC, Canada. [2]University of British Columbia, Kelowna, BC, Canada. [3]University of Waterloo, Waterloo, ON, Canada

Introduction

Compared to blocked practice, random practice is suggested to decrease practice performance but enhance motor learning in upper-limb reaching tasks by increasing problem-solving demands. Single sessions of blocked split-belt lower-limb gait training have been shown with savings in kinematic and kinetic variables. However, effects of random practice on retention and transfer of locomotor adaptation remain underexplored. This study investigated whether blocked vs. random split-belt practice differentially impacted retention and transfer of between-leg gait kinematic and kinetic symmetry between testing days.

Methods

Twenty-six young adults were randomized to a Blocked (n=13; 6 female; age 24.9±5 years) or Random practice group (n=13; 7 female; age 27.2±4 years) for a single-session of split-belt treadmill walking. Fast and slow belt speeds were individualized based on the participant's fast overground gait speed. On Day 1, the blocked group completed four repeated 2.5:1 split-belt blocks (total 18.5 min) alternated with 30s tied-belt (1:1 ratio) walking. The random group experienced the same total exposure but split-belt ratios (2.5:1 and 2:1) and speeds changed every 15 or 30s. Within 24hrs post-training, both groups completed a retention test at novel split-belt 3:1 ratio and a transfer test with reversed fast leg at 1:3 ratio. Kinematic and kinetic measures of between-leg step length symmetry (SLS) and propulsive force symmetry were computed from embedded force plates. For each metric, linear mixed-effects models tested group differences in magnitude of adaptation (Day 2 first 10 strides – Day 1 first 10 strides) for each test block.

Results

The blocked group showed significantly greater magnitude of adaptation in SLS than the random group for both retention (mean difference: 0.14, $p<.05$) and transfer (mean difference: 0.15, $p<.05$) tests. No effect of Group was found on the magnitude of adaptation in propulsive force symmetry for either test block.

Discussion

Our findings suggest that blocked practice produced superior retention and enhanced transfer of SLS during split-belt walking, while SLS in the random group was largely maintained without further improvement. These results indicate the benefits of random practice observed in other motor domains (i.e., reaching adaptation) may not directly generalize to locomotor adaptation under the training parameters used here.

Session Category

Human Motion and Performance: Locomotion/Gait

P1-108

Measuring Coordination Variability with Inertial Measurement Units Using the Velocity Ellipse Method: A Pilot Study Comparing Agreement with a Motion Capture System

Mr Ben Jones[1,2], Dr Jon Wheat[3], Dr Kane Middleton[2], Dr David Carey[2], Dr Ben Heller[1]

[1]Sheffield Hallam University, Sheffield, South Yorkshire, United Kingdom. [2]La Trobe Universtiy, Melbourne, Victoria, Australia. [3]Nottingham Trent University, Nottingham, Nottinghamshire, United Kingdom

Introduction

Measures of coordination variability quantify stride-to-stride changes within the interaction between two joints or segments and have been linked to running-related injury [1]. The velocity ellipse method (VEM) quantifies coordination variability using angular velocity data, which is more robust to noise than angle-based measures [2]. However, we believe that the VEM has only ever been implemented by differentiating angular displacement data. Inertial measurement units (IMUs) measure angular velocities directly via their gyroscope and can facilitate field-based measurement of coordination variability. This study developed a method for implementing the VEM with IMUs and quantified its agreement with a motion capture system.

Methods

Twenty-seven runners completed eight minutes of running on an instrumented treadmill. Lower limb marker data were collected and used to compute thigh and shank angular velocities, whilst Blue Trident IMUs attached to these segments measured angular velocity directly. IMU data were transformed into segment coordinate systems using a functional calibration [3]. Twenty strides were identified using a vertical force threshold and peak shank resultant acceleration, for the marker and IMU data, respectively. The area of ellipses formed around the data points at each time-normalised percentage of the gait cycle on angular velocity – angular velocity plots were calculated [2]. Velocity ellipse area waveforms from the motion capture system (VEM_{MC}) and IMUs (VEM_{IMU}) were assessed for agreement using a normalised cross-correlation.

Results

The amplitude of velocity ellipse area waveforms varied between participants. Normalised cross-correlations between VEM_{MC} and VEM_{IMU} ranged from 0.859 to 0.969 (Figure 1), with a mean of 0.931.

Discussion

Normalised cross-correlations indicated high similarity between VEM_{IMU} and VEM_{MC} waveforms, although qualitative differences existed between signals from the systems. These were potentially due to the misalignment of coordinate systems and time asynchronisation. Nevertheless, our method demonstrated promise for simpler and cheaper analyses of coordination variability, particularly in field-based settings, although researchers and practitioners should make judgements on the suitability of VEM_{IMU} waveforms based on their specific context. Further research could also investigate alternative movements and segment pairings.

Images (Optional)

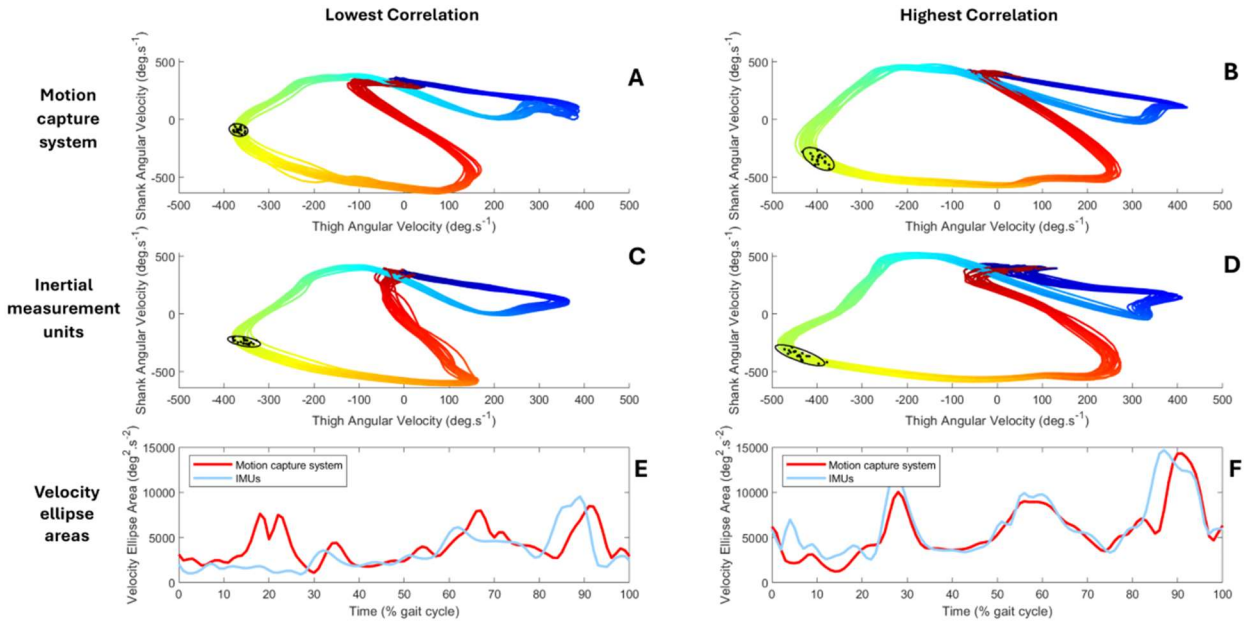


Figure 1: Comparison of angular velocity – angular velocity plots (A, B, C, D) and velocity ellipse area signals (E, F) for the pairs of signals with the lowest (left; 0.859) and highest (right; 0.969) normalised cross correlation between the motion capture system (A, B) and inertial measurement units (C, D). The jet colourmap indicates time as a percentage of the gait cycle, with dark blue indicating footstrike (0%) and dark red indicating the next ipsilateral footstrike (100%). Ellipses are drawn at 60% of the gait cycle.

References (Optional)

[1] Joe Hamill *et al.,* Sports Medicine, 2012

[2] Holly Stock *et al.,* Sports Biomechanics, 2022

[3] Stephen Cain *et al.,* Gait & Posture, 2016

Acknowledgements (Optional)

Session Category

P1-109

The Effects of Varied Step Lengths on Hip-to-Hip and Knee-to-Knee Joint Moment Ratios in Walking Lunge Exercises

Dr. Ben Meyer

Shippensburg University, Shippensburg, PA, United States

Introduction

The purpose of this project was to analyze the effects of utilizing varied step lengths during walking lunge exercises on front hip to trail hip (H/H) and front knee to trail knee (K/K) joint moment ratios. Hip-to-knee joint moment ratios have been used to analyze squats [1], but the use of H/H and K/K joint moment ratios in lunge exercises is novel. This project contributes to the literature by establishing H/H and K/K joint moment ratios during walking lunges. It was hypothesized that participants would have significantly larger H/H and K/K joint moment ratios in the walking lunges utilizing a shorter step length.

Methods

Thirty-six males and thirty-six females (age = 19 ± 2 yrs; mass = 75 ± 20 kg; height = 1.75 ± 0.10 m) performed four sets of unloaded walking lunges. Participants' movements were recorded with eight Basler cameras at 100 Hz, while ground reaction forces and moments were obtained via two AMTI force plates at 1000 Hz. The video and force plate data were processed using The MotionMonitor™ software in order to compute hip and knee joint moments for each limb. The flexion/extension joint moment values at the lowest vertical position of the entire body center of mass were used in the analysis. The relationships between joint moment ratios and lunge step lengths were assessed using two-way factorial ANOVA tests. Statistical significance was set at $\alpha = 0.05$.

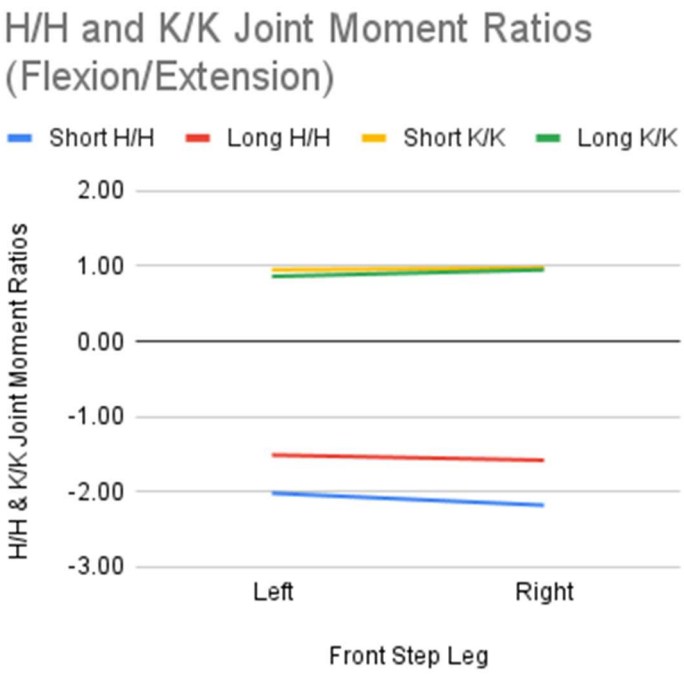
Results

Joint moment ratios did not differ between left and right limbs and were pooled together. The H/H joint moment ratio was significantly larger ($p < 0.001$) with a short step (-2.10 ± 1.05) than with a long step (-1.55 ± 0.44). The K/K joint moment ratio was not significantly different ($p = 0.060$) between short step (0.96 ± 0.31) and long step (0.91 ± 0.42).

Discussion

Results indicate that there is a significant relationship between walking lunge step length and H/H (but not K/K) joint moment ratios. The H/H and K/K ratios will provide useful insights into the mechanics of lunges.

Images (Optional)



References (Optional)

[1] Meyer, Proc Int Cong Biomech, 2005

Session Category

Human Motion and Performance: Locomotion/Gait

P1-110

The Effects of Varied Step Lengths on Front and Trail Leg Hip-to-Knee Joint Moment Ratios in Walking Lunge Exercises

Dr. Ben Meyer

Shippensburg University, Shippensburg, PA, United States

Introduction

The purpose of this project was to analyze the effects of utilizing varied step lengths during walking lunge exercises on front and trail leg hip-to-knee (H/K) joint moment ratios. Previous research has established the importance of H/K moment ratios during back squats and elevated split squats [1]. This project adds to the literature by determining H/K joint moment ratios during walking lunges. It was hypothesized that participants would have significantly larger front and trail leg H/K joint moment ratios in the walking lunges utilizing larger step lengths.

Methods

Thirty-six males and thirty-six females (age = 19 ± 2 yrs; mass = 75 ± 20 kg; height = 1.75 ± 0.10 m) performed four sets of unloaded walking lunges at their normal depth and pace. Participants' movements were recorded with eight Basler cameras capturing at 100 Hz, while ground reaction forces and moments were obtained via two AMTI force plates sampling at 1000 Hz. The video and force plate data were processed using The MotionMonitor™ software in order to compute hip and knee joint moments for each limb. The flexion/extension joint moment values at the lowest vertical position of the entire body center of mass were used in the analysis. The relationships between joint moment ratios and lunge step lengths were assessed using two-way factorial ANOVA tests. Statistical significance was set at $\alpha = 0.05$.

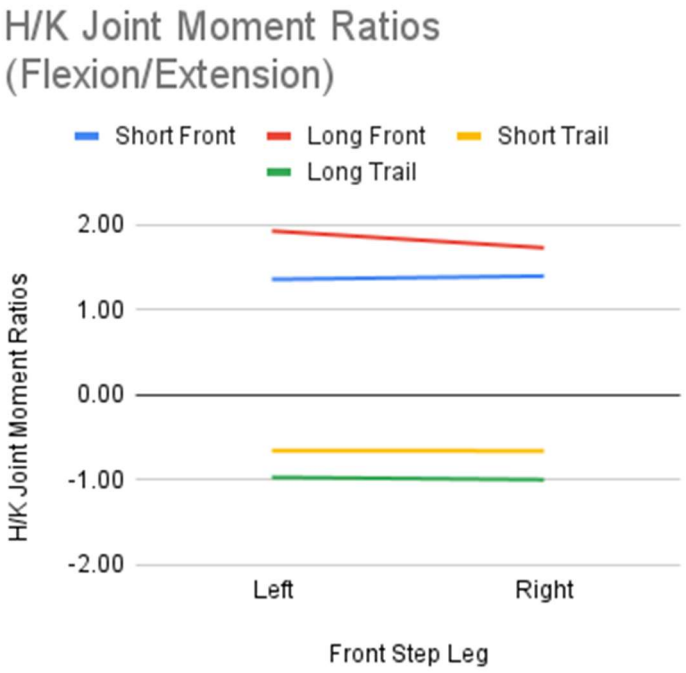
Results

Joint moment ratios did not differ between left and right limbs and were thus pooled together for subsequent analyses. The H/K joint moment ratios were significantly larger using a long step than a short step (front, $p < 0.001$; trail, $p < 0.001$) with the front leg (long, 1.83 ± 1.03; short, 1.38 ± 0.59) and the trail leg (long, -0.99 ± 0.26; short, -0.65 ± 0.23).

Discussion

Results indicate that there is a significant relationship between walking lunge step length and H/K joint moment ratios. Walking lunges performed with a larger step length have larger hip muscle utilization as indicated by the larger H/K joint moment ratios.

Images (Optional)



References (Optional)

[1] Meyer, Proc Int Cong Biomech, 2005

Session Category

Human Motion and Performance: Locomotion/Gait

P1-111

Robust Single-Camera Knee Flexion Estimation under Self-Occlusion via Semi-Supervised Non-Linear p-Laplacian Label Propagation

Mr Behnam Gholami, Dr David Hollinger, Dr Xiaojun Zhai, Dr Bernard Liew

University of Essex, Wivenhoe Park, Colchester, United Kingdom

Mr Behnam Gholami

Dr David Hollinger

Dr Xiaojun Zhai

Introduction

Introduction: Optical marker-based motion capture (MBMC) is the gold standard for gait analysis but requires multi-camera, lab-based setups. Recent single-camera, markerless Human Pose Estimation (HPE) offers a low-cost alternative, yet lower-limb applications in healthcare are limited by noise, occlusion, and gap-filling errors. We present a train-free Graph Signal Processing (GSP) framework using semi-supervised label propagation with non-linear p-Laplacian regularisation to refine single-camera markerless motion capture (MLMC) knee kinematics in frontal and sagittal views.

Methods

Methods: Four healthy adults walked along a 7 (m) walkway at self-selected speed under institutional ethical approval (ETH2425-0307). Full-body 3D kinematics were captured with Theia3D using eight Sony RX0 II RGB cameras (120 Hz) in a radial configuration. For the single-camera condition, one frontal and one sagittal view were retained per trial. 2D hip, knee and ankle positions were extracted frame-wise using OpenPose and converted to frontal- and sagittal-plane knee angles. Our method represents joint trajectories as signals on a spatiotemporal skeleton graph with temporal edges for continuity and spatial edges for segment rigidity. A non-linear p-Laplacian ($p = 1.3$), solved via Iterative Reweighted Least Squares, operates on the residual between Theia3D “ground truth” and OpenPose

estimates, with confidence-gated edge weights to handle self-occlusion. Performance was evaluated using Mean Absolute Error (MAE) and Root Mean Square Error (RMSE) against Theia3D and compared with published error benchmarks.

Results

Results: In frontal views, OpenPose knee angles showed high variability (MAE=6.23°). The proposed method reduced MAE to 0.55°, substantially suppressing jitter while preserving peak flexion. In occluded sagittal views, OpenPose errors averaged MAE=6.08° (RMSE=7.51°), consistent with (Wade et al., 2023). Our framework reduced errors to MAE=1.00° (RMSE= 3.17°), recovering plausible trajectories despite substantial self-occlusion.

Discussion

Discussion: Non-linear p-Laplacian smoothing via Iterative Reweighted Least Squares (IRLS) solver enabled the single-camera MMC pipeline to surpass the 5° clinical accuracy threshold and outperform established benchmarks for occluded tracking, while preserving sharp transitions required for gait event detection.

References (Optional)

References

Wade, L., Needham, L., Evans, M., McGuigan, P., Colyer, S., Cosker, D., Bilzon, J., 2023. Examination of 2D frontal and sagittal markerless motion capture: Implications for markerless applications. PLoS One 18, e0293917. https://doi.org/10.1371/JOURNAL.PONE.0293917

Session Category

Human Motion and Performance: Locomotion/Gait

P1-112

How Is Motivation During Gait Training Influenced by Physical Assistance and Performance Feedback?

Mr. Blake Karavas SPT, MS[1], Dr. Julia Manczurowsky PT, DPT, PhD[2], Dr. Sheng-Che Yen PT, PhD[1], Dr. Lester Leung MD, MSc[3,4], Dr. Peter Whitney PhD[1], Dr. Charles Hillman PhD[1,5], Dr. Christopher Hasson PhD[1]

[1]Northeastern University, Boston, MA, United States. [2]University of British Columbia, Vancouver, BC, Canada. [3]Tufts Medical Center, Boston, MA, United States. [4]Tufts University School of Medicine, Boston, MA, United States. [5]Institute for Cognitive and Brain Health, Boston, MA, United States

Introduction

Gait deviations are common following neurological disease, and rehabilitation often includes manual guidance by a physical therapist to improve walking function. While physical assistance, like visual feedback, is intended to enhance therapeutic outcomes, their influence together on patient motivation remains unclear. Motivation is critical in gait retraining for shaping engagement and effort, which supports the neuroplastic processes underlying motor adaptation. Here, we examine the interaction of assistance, feedback, and motivation in rehabilitation to better understand their psychological connection.

Methods

Thirty-five healthy participants walked on a treadmill and increased their right leg's mechanical work to achieve a 20% greater stride while perturbed by hamstring stimulation and mechanical resistance. A physical therapist assisted participants' right shank to achieve the stride target for 10 min (2.5 min trials x 4). Participants were randomized to see feedback of either their combined mechanical work (participant + therapist; N = 17) or comparative work (participant vs. therapist; N = 18). After each trial, they reported their perceived exertion (RPE) and pain (VAS). After training, the Intrinsic Motivation Inventory (IMI) was completed. For each group, we used Spearman rank correlations to explore how IMI subscale scores (enjoyment, choice, value, competence, relatedness, effort, pressure) relate to cumulative anterior-posterior assistance force.

Results

The control group had greater perceived competence than the comparative group ($p = 0.04$), but no significant correlations to assistance ($p > 0.05$) for either group. Though none reached significance ($p > 0.05$), controls had strongest correlations of assistance with pressure ($r = 0.36$) and effort ($r = -0.35$), and comparatives with competence ($r = 0.37$) and relatedness ($r = 0.4$). The correlation of force to RPE and VAS were small and not significant.

Discussion

Results suggest the degree of short-term manual assistance does not strongly influence motivation, exertion, or discomfort in healthy, artificially-impaired individuals during goal-directed walking. Depending on feedback type, assistance and motivation had moderate, non-significant trends that suggest participants may feel differently about their performance when their contributions are directly compared to the therapist's. However, further study is needed to determine whether these perceptions translate into positive locomotor adaptations and long-term learning benefits in clinical populations.

Images (Optional)

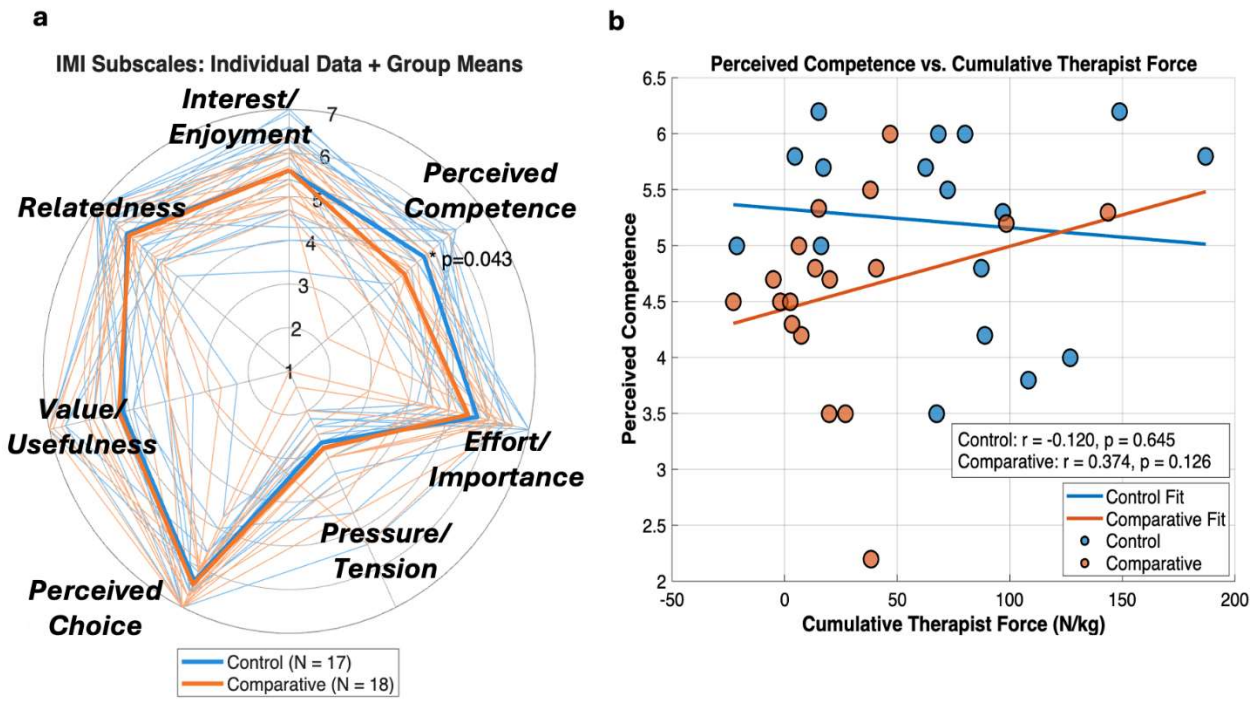


Figure 1. (a) Intrinsic Motivation Inventory subscale averages; scores range from 1 (not true) to 7 (very true). **(b)** Example correlation of cumulative applied force vs. perceived competence.

Acknowledgements (Optional)

This work was funded by NIH grants 1F31HD110254 and 1R21HD118499.

Session Category

Human Motion and Performance: Locomotion/Gait

P1-113

The Effect of Running Speed and Footwear Midsole Compliance on the Biomechanics of Sub-Elite to Elite Distance Runners Wearing Advanced Footwear Technology Spikes

Mr. Bradley Needles, Mr. Luis Morata Moreno, Dr. Alena Grabowski

University of Colorado Boulder, Boulder, Colorado, United States

Introduction

Distance runners have achieved improved race performance and running economy while wearing compliant (low stiffness) advanced footwear technology (AFT) spikes compared to stiffer traditional spikes [1], [2], which may be due to increased leg stiffness and ground contact time [1]. However, leg stiffness has been reported to increase with running speed at speeds faster than 5 m/s [3]. Based on the increased midsole foam compliance of AFT spikes, we hypothesized that distance runners wearing AFT spikes would experience increased leg stiffness and ground contact time compared to traditional spikes. Additionally, we hypothesized that the magnitude of increase in leg stiffness and ground contact time while wearing AFT spikes compared to traditional spikes would decrease as running speed increases.

Methods

8 sub-elite to elite distance runners ran at 3, 4, 5, 5.5, 6, 6.5, 7, & 7.5 m/s on a force measuring treadmill while wearing 3 custom AFT spikes (AFT A, AFT B, AFT C) and a traditional spike (TRAD) with midsole stiffness values of 170, 159, 140, & 412 N/mm, respectively. We measured ground reaction forces (1000 Hz) and compared leg stiffness and ground contact times between spike conditions and across running speeds using linear mixed models.

Results

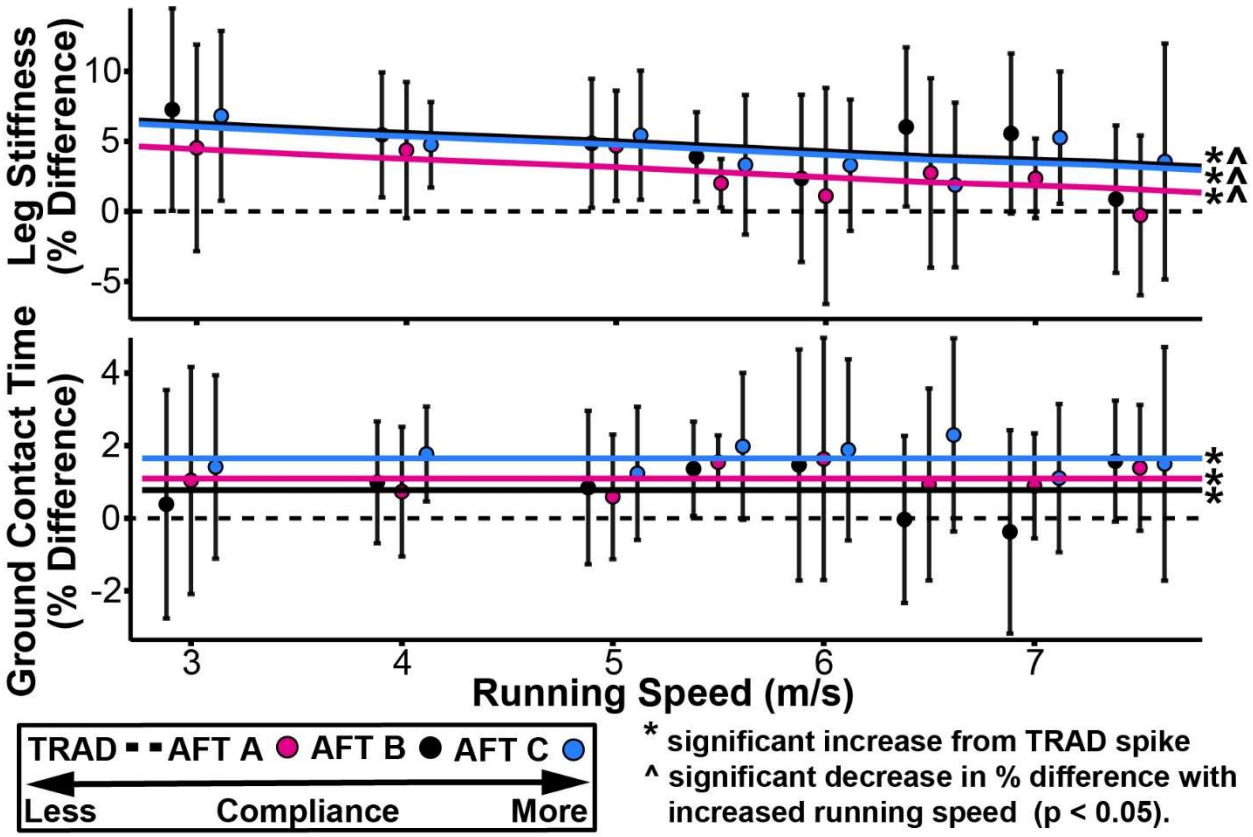
When runners wore AFT spikes, leg stiffness and ground contact time increased by an average of 3.8% and 1.2%, respectively, compared to the TRAD spikes across all running speeds ($p < 0.018$). The percentage difference in leg stiffness between the AFT spikes and TRAD spikes decreased by 0.6% for each 1 m/s increase in running speed ($p = 0.002$) while the percentage difference in ground contact time between the AFT spikes and TRAD spikes was not different across running speeds ($p=0.76$).

Discussion

The difference in leg stiffness while wearing AFT and traditional spikes may decrease as running speed increases, potentially leading to attenuated performance improvements

relative to traditional spikes as race speed increases. As a result, runners may experience race performance improvements by wearing AFT spikes with midsole stiffness values tuned for faster running speeds.

Images (Optional)



References (Optional)

[1] Needles et al., JAP, 2024

[2] Joubert et al. IJSPP, 2024

[3] Arampatzis et al, J Biomechanics, 1999

Session Category

Human Motion and Performance: Locomotion/Gait

P1-114

Hip Moments Differ by Sex at Different Walking Speeds

Ms. Caitlyn Finnerty MS, BS, Ms. Ria Rao BS, Prof. Cara Lewis PT, PhD, FAPTA

Boston University, Boston, MA, United States

Introduction

Biological sex influences movement kinematics, but its specific effects on hip moments remains understudied. As females typically have a wider pelvis, joint loading and hip moments likely differ when engaging in tasks such as walking. The altered joint loading may contribute to increased risk for hip pain in females. Based on sex-specific differences in pelvic morphology, we expect that peak internal hip moments will differ between males and females during walking.

Methods

Data were obtained from a larger dataset investigating movement and morphology in individuals with and without hip pain. This analysis included 129 females (26.7 ± 7.9 yrs; 1.67 ± 0.07 m; 65.03 ± 9.82 kg) and 59 males (26.3 ± 8.5 yrs; 1.80 ± 0.07 m; 79.35 ± 11.54 kg) who walked on an instrumented treadmill at a prescribed (1.25 m/s) and preferred speed. Females (1.29 ± 0.17 m/s) walked at faster average preferred speed than males (1.25 ± 0.17 m/s). Peak internal hip moments in the sagittal and frontal planes were calculated and normalized to body mass. Generalized linear models with Generalized Estimating Equation corrections were used to assess sex effects on hip moments in RStudio.

Results

At the prescribed speed, females walked with 8.5% lower peak hip extension ($p = .0009$) and 9.4% lower adduction ($p = .0084$) internal moments, but 7.9% greater peak hip abduction moments ($p = .0002$) than males. At the preferred speed, females produced 10.2% greater peak hip abduction internal moments compared to males ($p = .0001$).

Discussion

Hip moments differed by sex at both walking speeds, but sex-related biomechanical differences were most apparent when males and females walked at the same speed. While hip abduction moments remained higher in females than males at the preferred speed, the reduction in hip extension and adduction moment was not evident, most likely due to the faster walking speed in females. Preferred speed captures natural walking patterns and is representative of loading experienced at the hip during activities of daily living. These findings emphasize the importance of accounting for sex when interpreting gait mechanics and designing injury reduction research protocols.

Images (Optional)

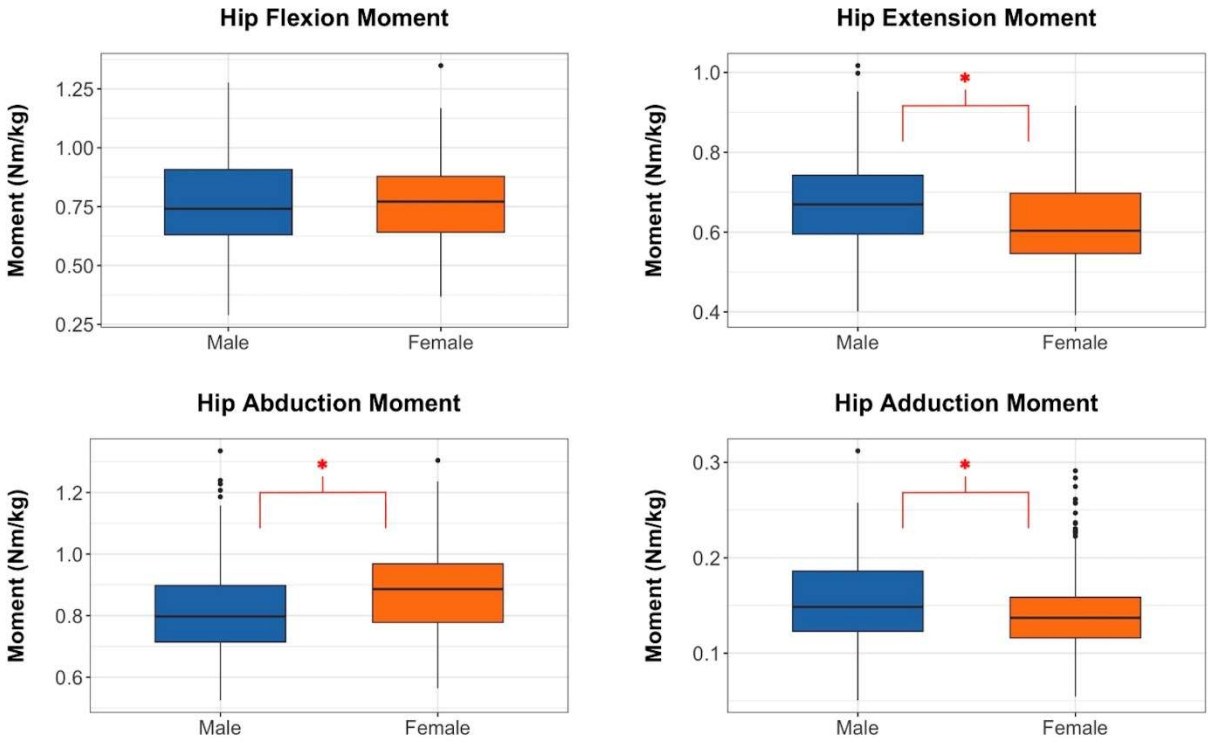


Figure 1. Boxplots of hip moments at the prescribed walking speed display the differences between males and females with the horizontal black line indicating the median moment values. The red brackets represent significance.

Session Category

Human Motion and Performance: Locomotion/Gait

P1-115

Impact of Theia3D Software Updates on Hip Kinematics and the Effectiveness of Reference Frame Realignment

Ms. Camilla Antognini[1], Dr. Ariana Ortigas-Vásquez[2], Dr. Adrian Sauer[3], Dr. Christopher Knowlton[1], Dr. Michael Utz[3], Dr. Philip Malloy[1], Dr. Markus Wimmer[1]

[1]Rush University Medical Center, Chicago, Illinois, United States. [2]ETH, Zurich, Zurich, Switzerland. [3]Aesculap AG, Tuttlingen, Baden-Württemberg, Germany

Introduction

Markerless motion capture systems are continuously updated as new algorithms are introduced, raising concerns regarding the longitudinal consistency of kinematic outputs. Recent revisions to Theia3D included updated biomechanical models and modified hip joint center definitions, but how these changes affect consistency between versions remains unclear. This study applied a reference frame alignment method, REFRAME, to hip kinematic data processed with Theia3D v2023 and v2024 to determine whether observed differences primarily reflect changes in segment coordinate system orientation or true differences in the underlying motion.

Methods

Ten healthy adults (5M/5F; age 26.8 ± 5.6 years; BMI 21.5 ± 1.8 kg/m^2) were recruited to perform five walking trials each (right side only). Markerless data were collected with an eight-camera Miqus system (Qualisys), processed in Theia3D using versions v2023 and v2024, and exported to Visual3D (HAS-Motion) for hip kinematic analysis. REFRAME was applied to reorient v2024 pelvic and femoral frames toward v2023 by minimizing hip angle root-mean-square error across planes, with femoral medio-lateral rotation constrained to maintain clinical interpretability.

Results

Greater differences between software versions were observed in the frontal and transverse planes, with v2024 producing more abducted and externally rotated hip kinematics (Figure 1). After implementing REFRAME, inter-version differences decreased across all planes, with root-mean-square error reducing from 5.6° ± 1.9° to 2.2° ± 0.5° (sagittal), 3.4° ± 0.6° to 1.0° ± 0.1° (frontal), and 4.0° ± 0.9° to 2.1° ± 0.3° (transverse). These reductions corresponded to mean rotational adjustments of 4.5° ± 2.0°, -7.6° ± 2.0°, and -3.8° ± 1.7°

about the pelvic x-, y-, and z-axes, and -4.9° ± 2.0°, and -1.4° ± 2.3° about the femoral y- and z-axes.

Discussion

Overall, this study indicates that Theia3D update from v2023 to v2024 introduced systematic hip kinematic differences primarily driven by changes in reference frame definitions. Although post-hoc alignment substantially reduced these discrepancies, residual offsets persisted, especially in the transverse plane, suggesting contributions from broader tracking-algorithm modifications, including those associated with new training datasets. Therefore, the persistence of inter-version differences, even after REFRAME, underscores the need for cautious interpretation when comparing hip kinematic data across software versions.

Images (Optional)

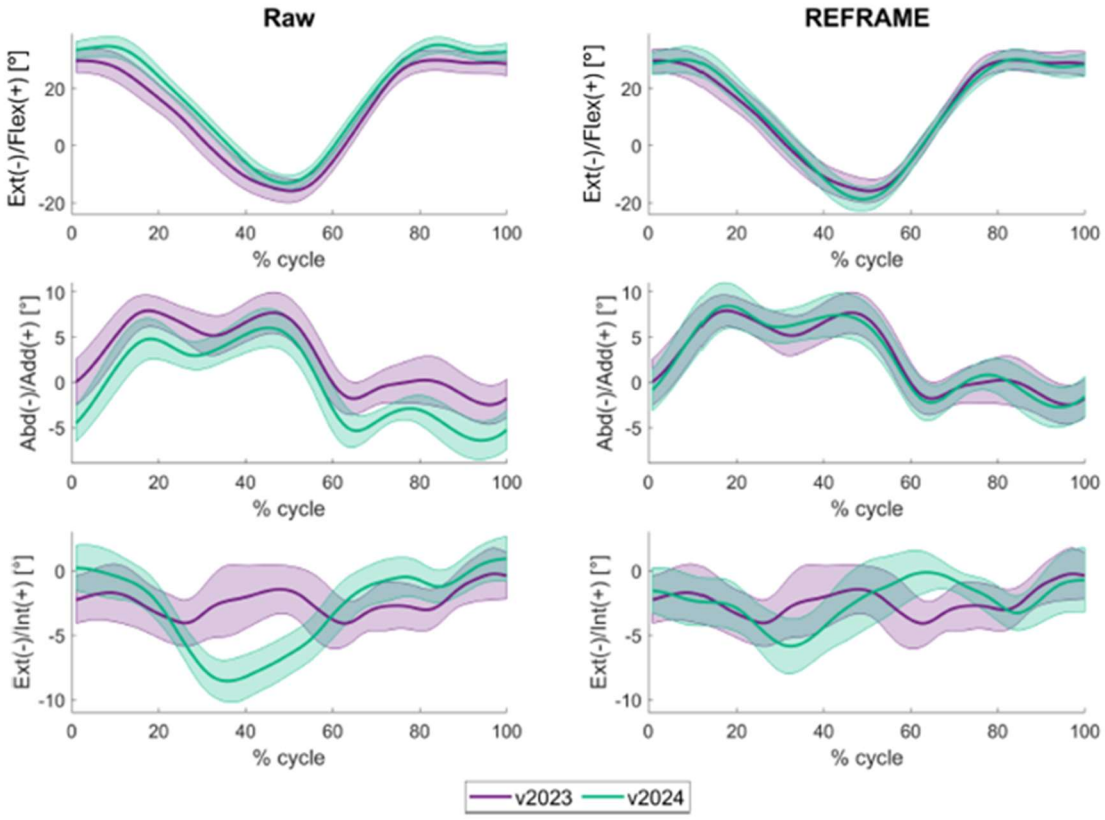


Fig. 1. Comparison of pelvis-femoral rotation signals in three dimensions between the markerless v2023 (purple) and markerless v2024 (green) data, both before (left) and after (right) REFRAME implementation to align joint coordinate systems. Mean hip joint angles in degrees (solid lines) ± standard deviation (shaded areas) across all subjects and trials are shown as a percentage of one gait cycle.

Session Category

Human Motion and Performance: Locomotion/Gait

P1-116

Gait variability reveals divergent control strategies in frontal gait disorders and Parkinson's disease

Dr. Carolin Curtze[1], Dr. Marian L. Dale[2,3], Dr. Martina Mancini[2]

[1]Montana State University, Bozeman, MT, United States. [2]Oregon Health & Science University, Portland, OR, United States. [3]Portland VA Medical Center PADRECC, Portland, OR, United States

Introduction

Human walking naturally involves small step-to-step variations in foot placement. Variability in lateral foot placement suggests the need for active control to maintain balance while walking in the frontal plane, whereas fore-aft foot placement variability reflects the extent to which humans harvest the passive dynamic properties of the leg in sagittal-plane motion [1]. These differences typically result in greater variability in step width than in step length, potentially indicating plane-specific differences in neural control demands. Unlike healthy adults, individuals with neurological gait disorders often adopt a wide-based gait [2]. However, how these gait disorders alter plane-specific control strategies remains unclear. We therefore compared step length and step width among healthy older adults, individuals with frontal gait disorders (FGD), and those with idiopathic Parkinson's disease (iPD).

Methods

Participants included individuals with idiopathic Parkinson's disease (iPD, n=72; tested OFF medication), frontal gait disorders (FGD, n=16), and healthy older adults (n=32). They completed 3 walking trials at preferred-speed on an 8-m instrumented walkway. Mean step length and width and their within-subject coefficients of variation (CV) were calculated. Group differences were examined using one-way ANOVAs with pairwise comparisons. In addition, t-tests were used to determine if step-length variability exceeded step-width variability within each group.

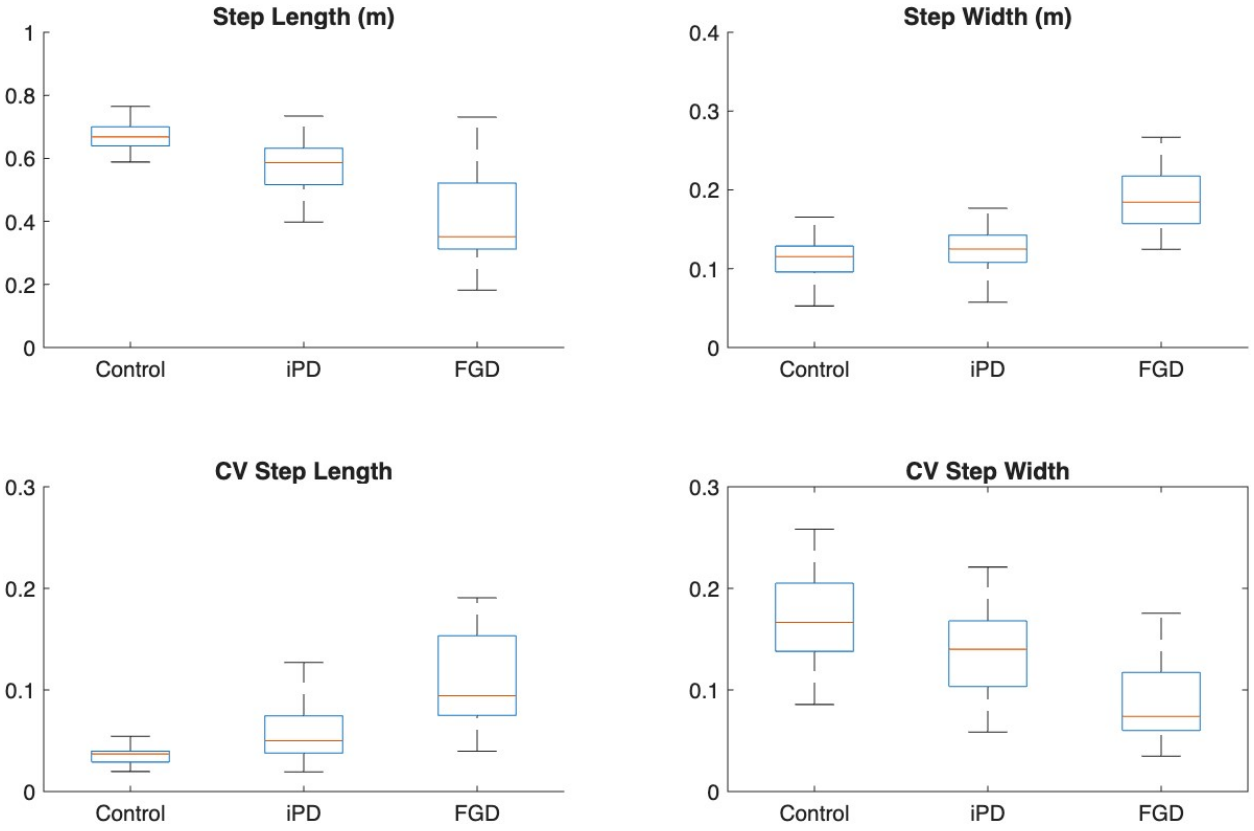
Results

The mean and within-subject CV of the step length and step width are presented in Figure 1. As anticipated, the step width variability was greater than the step length variability in older adults with and without iPD, but in FGD step length and step width variability were similar.

Discussion

Healthy older adults and individuals with iPD showed the expected pattern of greater step-length than step-width variability, consistent with typical plane-specific control in which sagittal-plane motion relies more on passive dynamics and frontal-plane motion requires active stabilization. In contrast, individuals with FGD exhibited similar variability in step length and step width, indicating a disruption of this plane-specific organization. This suggests that the wide-based, short-stepped gait of FGD reduce the need for precise active control in the frontal plane, allowing passive stability to compensate for impaired lateral balance regulation.

Images (Optional)



References (Optional)

[1] Bauby & Kuo, J Biomechanics, 2000.

[2] Curtze et al., J Neurology, 2024.

Acknowledgements (Optional)

This work was supported by NIH (2R01AG006457).

Session Category

Human Motion and Performance: Locomotion/Gait

P1-117

Step Ratio Divergence in Very Slow Walking

Dr. Carolynn Patten PhD, PT, FAPTA[1,2], Dr. Anita Bagley PhD, MPH[3], Ms. Sanjana Sivakumar BS[4], Ms. Trina Moy BS[4], Dr. Rebecca Boxer MD, MS[4], Ms. Theresa E. McGuirk MS[1,2]

[1]University of Washington, Seattle, WA, United States. [2]VA Puget Sound Health Care, Seattle, WA, United States. [3]Shriners Hospital for Children, Northern California, Sacramento, CA, United States. [4]UC Davis Health, Sacramento, CA, United States

Introduction

Human bipedal gaits (walking, running), are defined as distinct forward progression solutions along the speed continuum. Very slow walking (VSW) has been considered an extension of typical walking behavior, with heuristic speed thresholds used to predict functional decline[1]. In health, Step Ratio (Step Length/Frequency) is mostly invariant across a wide range of walking speeds revealing an heuristic value near 0.6 cm/steps/min [1]. Deviation from this ratio would therefore identify a distinct behavior. Here we sought to determine if different spatiotemporal ratios emerge at very slow speeds suggesting that VSW is distinct from habitual gait.

Methods

Participants walked across a pressure-sensing floor/mat without assistive devices at: slowest (SLx), self-selected (SS), and fastest (FAx) speeds. Multiple attempts were provided to familiarize and assure the participant achieved their slowest speed. StepRatio (step length/frequency) was calculated by stride[1], with mean and coefficient of variation (CV) calculated by gait task and examined relative to nondimensional gait velocity (Vnd)[2]. Self-reported participant health history was acquired.

Results

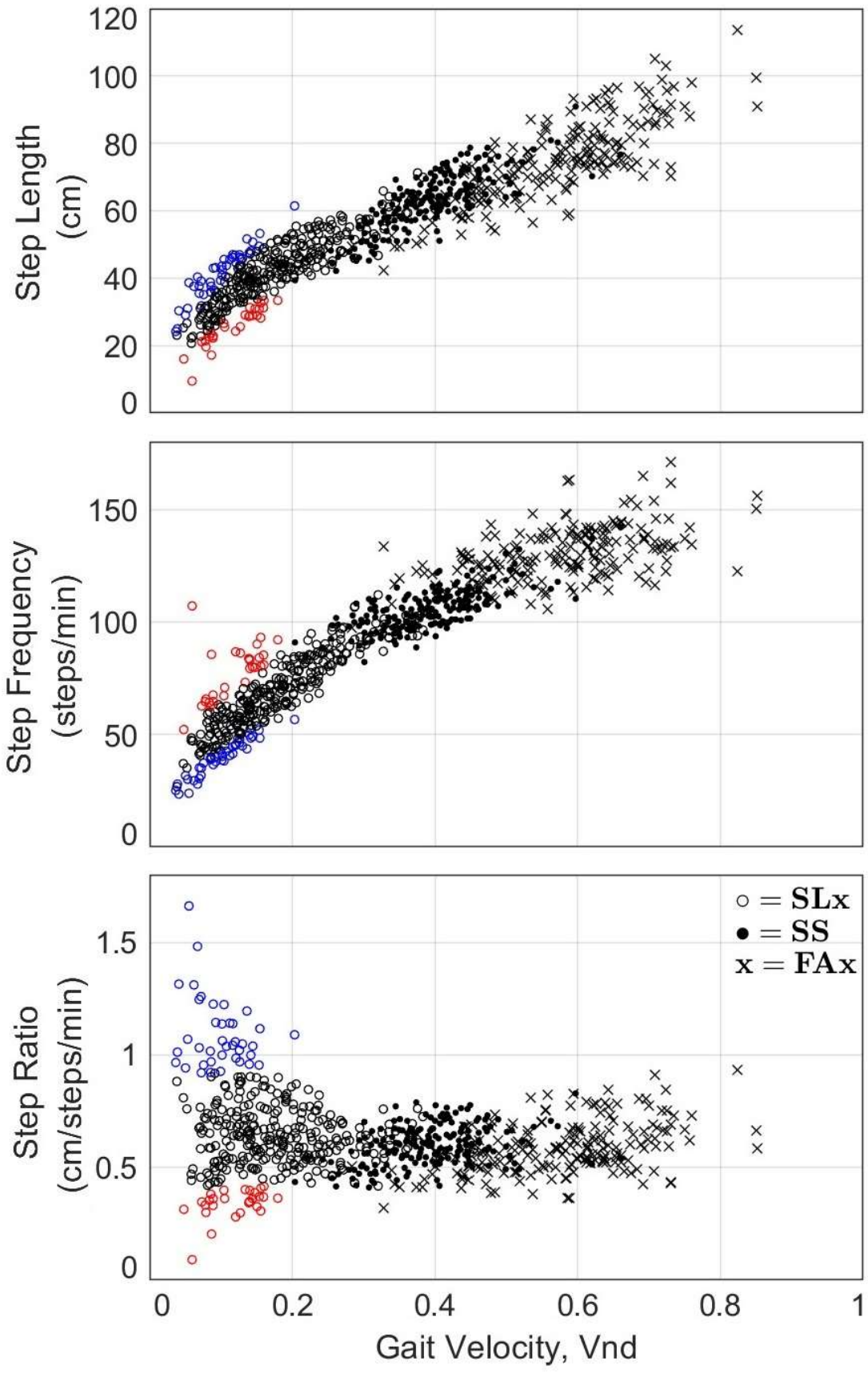
192 adults of varied health history (18-97yrs (56.68(23.98), 126F) participated, producing: Vnd mean(sd): SLx=0.169(0.078), SS=0.391(0.071), FAx=0.5672(0.109) and StepRatio mean(sd): SLx=0.656(0.048), SS=0.595(0.012), FAx=0.583(0.022). At Vnd<0.2 StepRatio revealed three distinct solutions with subsets diverging to: High (blue, n = 34, 1.077(0.16)), Low (red, n = 29, 0.343(0.045)), and Mid (black, n = 129,0.588(0.113)) values (Fig1).

Discussion

In addition to confirming StepRatio invariance of ~0.6 across typical and fast walking conditions, we observed divergence of coordination strategies among individuals able to attain speeds of Vnd<0.2 reflecting adoption of strategies distinct from habitual walking.

The High StepRatio pattern involves production of longer step lengths while maintaining lower step frequency while Low StepRatio involves shorter step lengths at higher step frequency (Fig 1). These atypical patterns suggest differences in tolerance for position of body center of mass relative to base of support. Moreover, this clear divergence in StepRatio demonstrates VSW does not involve linear scaling of spatiotemporal ratios that characterize typical walking.

Images (Optional)


Step Length (cm)
120
100
80
60
40
20
0
Step Frequency (steps/min)
150
100
50
0
Step Ratio (cm/steps/min)
1.5
1
0.5
0
○ = SLx
● = SS
x = FAx
0
0.2
0.4
0.6
0.8
1
Gait Velocity, Vnd

References (Optional)

[1] Sekiya et al., Gait Posture, 1998.

[2] Hof, Gait Posture, 1996.

Session Category

Human Motion and Performance: Locomotion/Gait

P1-118

Distance-to-Attractor Gait Anomaly Detection for Continuous Monitoring of Reactive Balance: Preliminary Validation

Dr. Cecilia Monoli, Dr. Anna C. Render, Assoc. Prof. Peter C. Fino

University of Utah, Department of Health and Kinesiology, Salt Lake City, Utah, United States

Introduction

Continuous monitoring of free-living mobility enables quantification of spatiotemporal gait and balance using wearable sensors. However, detecting reactive balance episodes, such as trips or slips, remains challenging due to high variability and noise in real-world gait. Here, we sought to apply an anomaly-detection framework that identifies deviations from an individualized gait attractor in state space (Ravi et al., 2021 *J Exp Biol*) to detect gait disruptions using wearable inertial sensors.

Methods

IRB approval and informed consent were obtained. For this validation, a single participant walked on a slip-belt instrumented treadmill at 1.0 m/s for 5 minutes. Unilateral slip-like perturbations were intermittently applied after heel strike (21 perturbations, peak 6 m/s^2, Δspeed 0.8 m/s). Two inertial measurement units placed on the sacrum (~L5) and upper thoracic region recorded triaxial acceleration and angular velocity (128 Hz). Kinematic data were processed using the anomaly-detection algorithm, which applied filtering, normalization, construction of time-delay embeddings, and generation of a phase-aligned mean attractor (Figure). Euclidean distance to the attractor was computed at each time, and anomalies were defined as values exceeding the median + 3×median absolute deviation (MAD). The algorithm was evaluated for both sensors using different input signals: vertical acceleration only or all three accelerometer axes, measuring its performance as the number of detected perturbations relative to the actual number delivered. Data collection is ongoing (1/10).

Results

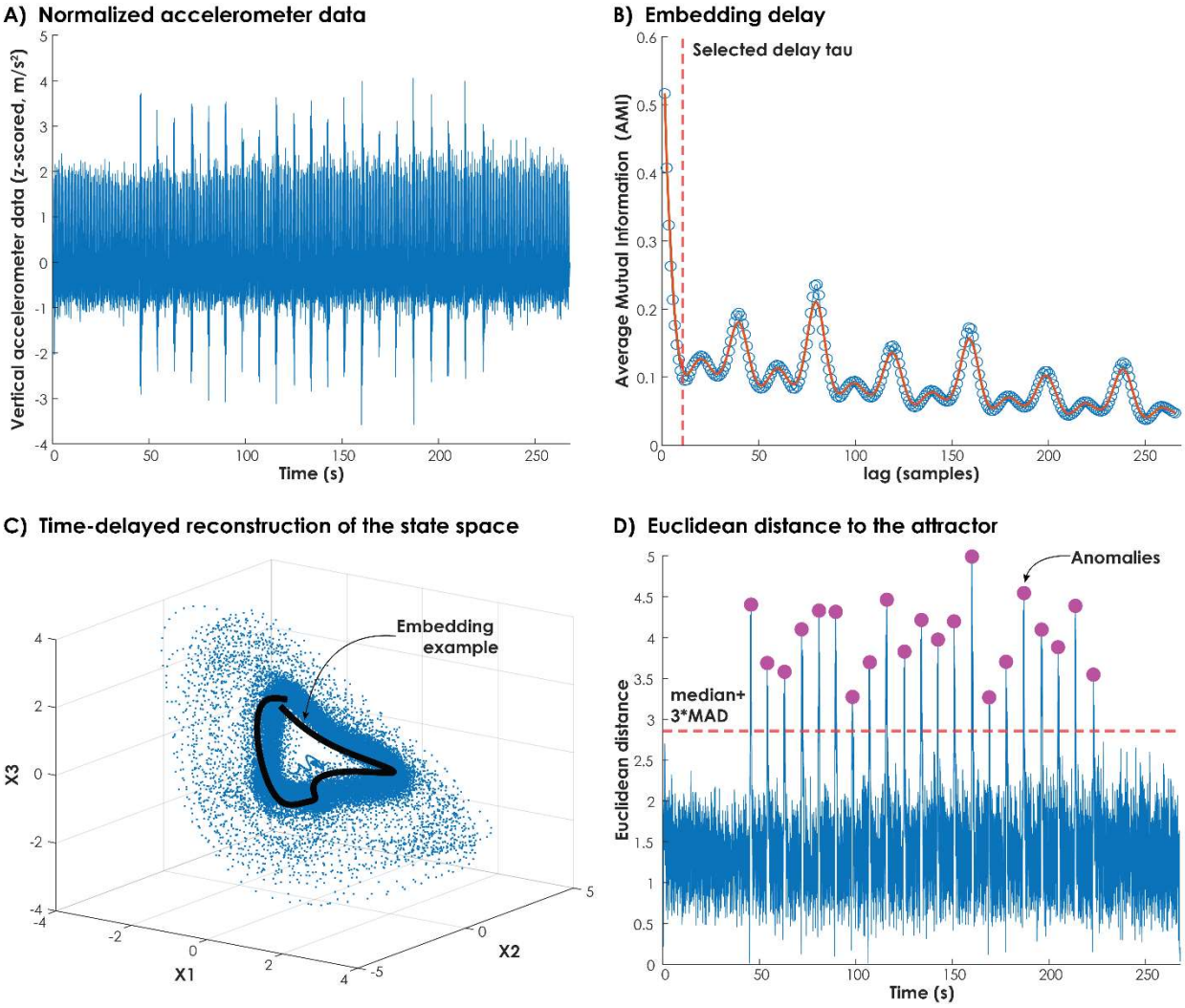
All perturbations were detected with the lumbar sensor, achieving perfect performance with vertical acceleration only (accuracy = 1.00) and slightly lower accuracy with all three axes (accuracy = 0.91). The sternum sensor detected perturbations with lower accuracy

using vertical acceleration alone (accuracy = 0.91) and worse performance when using all axes (accuracy = 0.62).

Discussion

These preliminary results show that our attractor-based algorithm can reliably detect slip-like perturbations from wearable inertial sensors, with lumbar sensors performing best. Future work will validate the identification of the anomalies and their durations against established balance-recovery metrics, evaluate algorithm robustness in daily-life environments, optimize sensor placement, and refine individualized thresholds for practical fall-risk monitoring.

Images (Optional)



Acknowledgements (Optional)

We thank Christina Geisler and the Neuromechanics and Applied Locomotion Lab for their support and help with data collection. Funding provided by NIH/NICHD (R01HD114748).

Session Category

Human Motion and Performance: Locomotion/Gait

P1-119

A Mechanical Device to Simulate Heel Strike and Early Stance Dynamics

Doctoral student Cédric Dessureault B.Ing.[1], Doctoral student Gaspard Diotalevi M.Sc.A.[1], Research assistant François Martel ing.[1], Professor Cécile Smeesters ing., Ph.D.[1], Engineer Chantal Gauvin ing. M.Sc.A.[2], Professor Denis Rancourt ing., Ph.D.[1]

[1]Université de Sherbrooke, Sherbrooke, Québec, Canada. [2]IRSST, Montréal, Québec, Canada

Introduction

Standard devices for evaluating footwear safety on slippery surfaces are not designed to replicate key gait characteristics such as heel strike dynamics, evolution of ground reaction forces (GRFs), slip initiation, changes in contact area and pressure distribution at the shoe-ground interface. In this study, an inverted pendulum was used to develop SLIPPY, a passive mechanical device with high repeatability [1] designed to simulate heel strike and early stance dynamics.

Methods

Human walking GRFs and heel strike kinematics were collected as reference data to tune SLIPPY's mechanical properties and assess its ability to reproduce participant-specific early stance GRFs. Participants walked on a dry surface wearing standardized shoes. Vertical and horizontal GRFs were recorded on force platforms at 2400 Hz, and kinematics were captured at 240 Hz. For each participant, GRFs from ten dry steps were averaged, and three representative trials were selected: one closest to the mean and two within ±1 SD. A simplified SLIPPY dynamic numerical model was used to identify the system stiffness and damping coefficients that best reproduce each participant's GRF curves. SLIPPY was then configured with these impedance values and participant-specific heel strike initial conditions. The device was launched three times per reference trial, and resulting GRFs were compared with human curves.

Results

Preliminary results show that the numerical model simulates the first 300ms of early stance GRFs with MRE of <6.37%. Estimated impedance values fall within ranges typically reported in the literature (Table 1). SLIPPY-generated vertical GRFs consistently display a heel strike transient, a feature usually absent from numerical inverted pendulum models.

Discussion

Early tests show that SLIPPY already produces human-like gait features, including M-shaped vertical GRFs [1] and a heel strike transient. Present results indicate that impedance parameters identified from human data should bring SLIPPY's GRFs closer to participant-specific reference curves. Upcoming trials will evaluate how accurately the device can simulate GRFs during heel strike and early stance across a wider range of conditions.

Images (Optional)

Table 1: Mechanical impedance ranges of our model compared to the literature.

Study	k_l (kN/m)	ξ_l (%)
Whittington, 2009 [2]	21-24	-
Kim & Park, 2011 [3]	14-23	3-8
Qin, 2013 [4]	16-23	5-8
Vega, 2022 [5]	13-34	3-13
Our model range	13-28	6.3-9.6

References (Optional)

[1] Dessureault et al., ASB2025, 2025; [2] Whittington et al., JBiomech Eng, 2009; [3] Kim & Park, JBiomech, 2011; [4] Qin et al., JSound&Vib, 2013; [5] Vega et al., Mech Syst Signal Process, 2022.

Acknowledgements (Optional)

Session Category

Human Motion and Performance: Locomotion/Gait

P1-120

Autoregressive Modeling to Evaluate Dynamic Stability During Running after Anterior Cruciate Ligament Reconstruction

Mr. Charles Eisner[1], Dr. Kristen Morgan PHD[2], Dr. Brian Noehren PT PHD FACSM[1], Dr. Meredith Owen PHD[1]

[1]University of Kentucky, Lexington, KY, United States. [2]University of Connecticut, Mansfield, CT, United States

Introduction

Asymmetries in ground reaction forces (GRFs) persist years after anterior cruciate ligament reconstruction (ACLR), which may lead to increased reinjury risk and long-term joint degeneration. Autoregressive (AR) modeling analyzes the stability of a time series through functions dependent on previous values. Research utilizing AR modeling found ACLR individuals display dynamic gait instability during running compared to a control group. This study's purpose is to characterize the dynamic stability of running in ACLR individuals throughout late stages of rehabilitation.

Methods

Fourteen individuals (5F/9M, 20±5 years, 1.8 m, 72.8 kg) completed instrumented running gait analysis at 6- and 12-months post-ACLR. Fourteen uninjured individuals matched for height and weight (5F/9M, 20±5 years, 1.8 m, 70.0 kg) participated in an identical running gait analysis. GRFs were collected at 2000 Hz and filtered with a 4^{th} order lowpass Butterworth filter at 35 Hz. Vertical GRF peaks were isolated, organized into a time series, and detrended. A second order AR model was fit to the GRF timeseries data. Model coefficients (AR1 and AR2) and stationary triangle were used to assess differences in stability between the two timepoints. The distance formula was used to calculate the total distance from the plotted coefficients to the triangle center (distance). AR1 and AR2 coefficients and distance were compared with pairwise t-tests between the 6- and 12-month data collections for ACLR participants. ACLR participants and controls were compared via independent t-tests at the 12-month timepoint.

Results

AR1 coefficients for were significantly different ($p<0.05$) between timepoints for those with ACLR. At 12-months, AR2 coefficient and distance were significantly different between groups (Table 1).

Discussion

Between 6- and 12-months, ALCR participants had significant improvements in interlimb (AR1) stability and no significant differences in intralimb (AR2) stability. However, when compared to uninjured individuals at 12-months, a common return-to-sport timepoint, intralimb instability and total distance from the most stable point of the triangle persist. These results suggest that while between limb stability improves, individuals post-ACLR still have worse intralimb stability. While much focus is placed on improving between limb symmetry (represented by AR1), improving same limb step-to-step symmetry may also be critical for long-term success.

Images (Optional)

Table 1: AR Modeling Results

	6 mo Post-ACLR	12mo Post-ACLR	6 vs. 12mo	Uninjured	12 vs. Uninjured
AR1	-0.350 (0.159)	-0.178 (0.204)	p = .04	-0.145 (0.213)	p = .68
AR2	0.441 (0.146)	0.341 (0.326)	p = .28	0.059 (0.231)	p = .01
Distance	0.586 (0.140)	0.509 (0.171)	p = .30	0.290 (0.186)	p <.01

Session Category

Human Motion and Performance: Locomotion/Gait

P1-121

Improved Accuracy of the Center of Mass Position Through Kalman Filtering of Kinematic and Kinetic Information

Dr Charlotte Le Mouel

CNRS, Paris, Ile-de-France, France

Introduction

The position of the body center of mass (CoM) is critical for evaluating balance. It can be calculated using either kinematic or kinetic methods. Each of these methods has its limitations, and it is difficult to evaluate their accuracy as there is no ground truth to which the CoM can be compared. Here, I use as ground truth the fact that, during the flight phase of running, the acceleration of the CoM is equal to gravity. I evaluate the accuracy of kinematic models of different complexity, and propose a novel method for calculating the CoM by combining kinematic and forceplate measurements.

Methods

Two open access datasets of human treadmill running were used, with a total of ten subjects running at speeds ranging from 2.5 to 4 m/s. The CoM was calculated for three kinematic models of increasing complexity. A novel method is proposed to estimate the CoM position using a Kalman filter combining kinematic and kinetic information.
For each model, the acceleration during flight was compared to gravity to determine the acceleration error. The position error was obtained by comparing the position to an indirect estimate of position obtained from kinetics.
A linear regression was used to predict foot placement from the CoM state during the previous flight phase.

Results

The error in acceleration ranges from 14 % of gravity for the most complex model to 36 % for the simplest model. The error in position ranges from 6 to 12 mm (27 % to 56 % of the CoM movement over a gait cycle).
When using the novel method, the acceleration error drops to between 1.1 and 3.1 % and position error to between 2.6 and 3.2% for all kinematic models. Moreover, the proposed method provides a more reliable evaluation of foot placement control.

Discussion

State-of-the-art kinematic models of the CoM were have poor accuracy. The novel method greatly improves the accuracy of CoM measurements. This can provide a more reliable

evaluation of balance indicators during locomotion, such as foot placement control.
The code for calculating this optimal combination is available in both Python and Matlab at: https://github.com/charlotte-lemouel/center_of_mass
The documentation is available at: https://center-of-mass.readthedocs.io

Session Category

Human Motion and Performance: Locomotion/Gait

P1-122

A Deep Learning Pipeline to Extract Clinical Gait Metrics from Single Camera Recordings

Mr. Chris Vellucci, Miss Emma Ratke, Miss Akanksha Guleria, Dr. Shawn Beaudette

Brock University, St. Catherines, ON, Canada

Introduction

Recently, open-source single camera pose estimation approaches have been adopted due to their relative ease of use and accessibility; however, data quality can be a concern. This study developed a methodology to estimate 3D lower body kinematics from multiple single camera viewpoints using deep learning.

Methods

61 participants (32 female, mean height 1.7 m, BMI: 23.6 kg/m^2) completed 10 minutes of treadmill walking. Kinematics were tracked concurrently using an IMU motion capture suit (XSENS Awinda), and 2D video cameras. 2D joint centres were extracted from video data using open-source pose estimation software (MediaPipe, Google, USA). Raw 2D pose data and the 3D lower body anatomical landmarks derived from the IMU data were processed using similar steps which included a low-pass filter (fc=6 Hz), gap-filled for missing frames, and subtracted the right ankle before being saved for training and validation of the deep learning model. A Long Short-Term Memory (LSTM) recurrent neural network was trained using these data. Data were split by participant into an 80/20 training-validation set. Hyperparameter search was completed using Bayesian Optimization with five-fold cross validation. Model performance was evaluated using leave-one-out validation (LOOV), and computed RMSE test statistics.

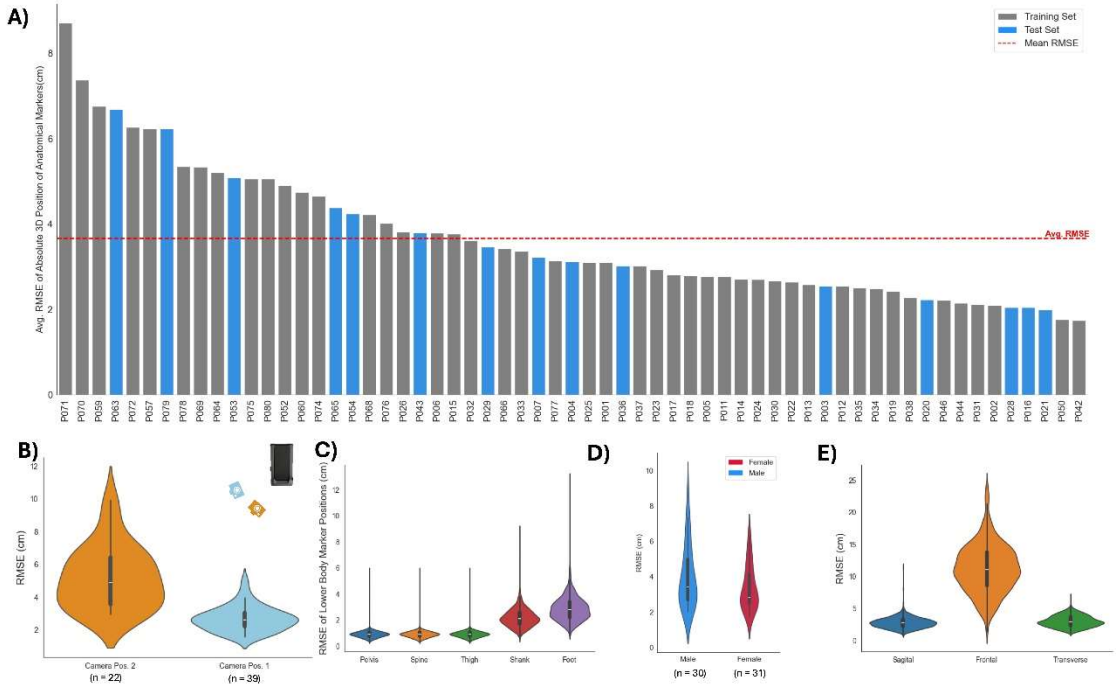
Results

Results from the LOOV demonstrated that the final model was able to predict the 3D positions of 34 landmarks with a mean RMSE of 3.21 cm +/- 2.40 (SD) (Figure 1.A). Sagittal and transverse plane segment positions showed good agreement with the research standard (Figure 1.C). The pelvis, spine, and thigh joint absolute positions showed good agreement with the research standard (Figure 1.D). Camera position 1 showed significantly lower RMSE then Camera Position 2 ($p<0.001$) (Figure 1.B). RMSE was not associated with biological sex ($p = 0.12$), or height ($p = 0.49$) (Figure 1.D).

Discussion

Results demonstrate that accurate 3D kinematics can be obtained from a single consumer grade camera. Performance can be optimized if expert models are trained for specific movements and that the camera orientation relative to the participant is optimized for both observation of the movement and the performance of open-source computer vision algorithm. Future work will evaluate the sensitivity of this approach to detect clinically relevant phenomenon.

Images (Optional)



References (Optional)

Session Category

Human Motion and Performance: Locomotion/Gait

P1-123

The relationship between toe flexor strength and positive foot work during sloped walking in older and younger adults

Mr. Christopher L. Long[1], Dr. Daniel J. Davis[1], Dr. Jason R. Franz[2], Dr. Kota Z. Takahashi[1]

[1]University of Utah, Salt Lake City, Utah, United States. [2]UNC Chapel Hill and NC State University, Chapel Hill, North Carolina, United States

Introduction

Older adults perform less positive foot work than younger adults, and these differences are more pronounced during challenging tasks such as walking uphill [1] or against impeding forces [2]. Toe flexor strength also declines with age [3] and may contribute to these task-specific energy deficits. Therefore, this study investigated whether toe flexor weakness associates with positive foot work during walking and helps to explain task-specific deficits in older adults.

Methods

Twenty-six younger (13F/13M, 24±3.3 yrs) and nineteen older (9F/10M, 70±5.9 yrs) adults walked barefoot on an instrumented treadmill at 1.2 m/s under three slope conditions: decline (−5°), level (0°), and incline (+5°). We estimated foot power distal to the calcaneus using unified deformable (UD) analysis [4], then integrated the positive portion of the power curve to compute positive foot work. Isometric toe flexor strength was measured using a toe grip dynamometer [5] and normalized to body mass. A linear mixed-effects model tested the association between toe flexor strength and positive foot work, controlling for age group, slope, and their interaction.

Results

Older adults had 33.7% weaker toe flexors than younger adults ($p<0.001$). However, toe flexor strength was not associated with positive foot work, controlling for age group and slope ($p=0.304$). Older adults generated less positive foot work during incline walking only, after controlling for toe flexor strength ($p=0.005$).

Discussion

In this sample, toe flexor strength was not associated with positive foot work during walking. Older adults still produced less positive work during incline walking, even after accounting for individual differences in toe strength. These findings suggest that task-specific deficits may be driven by factors beyond toe flexor strength, such as diminished

energy return from plantar structures (e.g., fascia, fat pads) or altered motor control strategies.

Images (Optional)

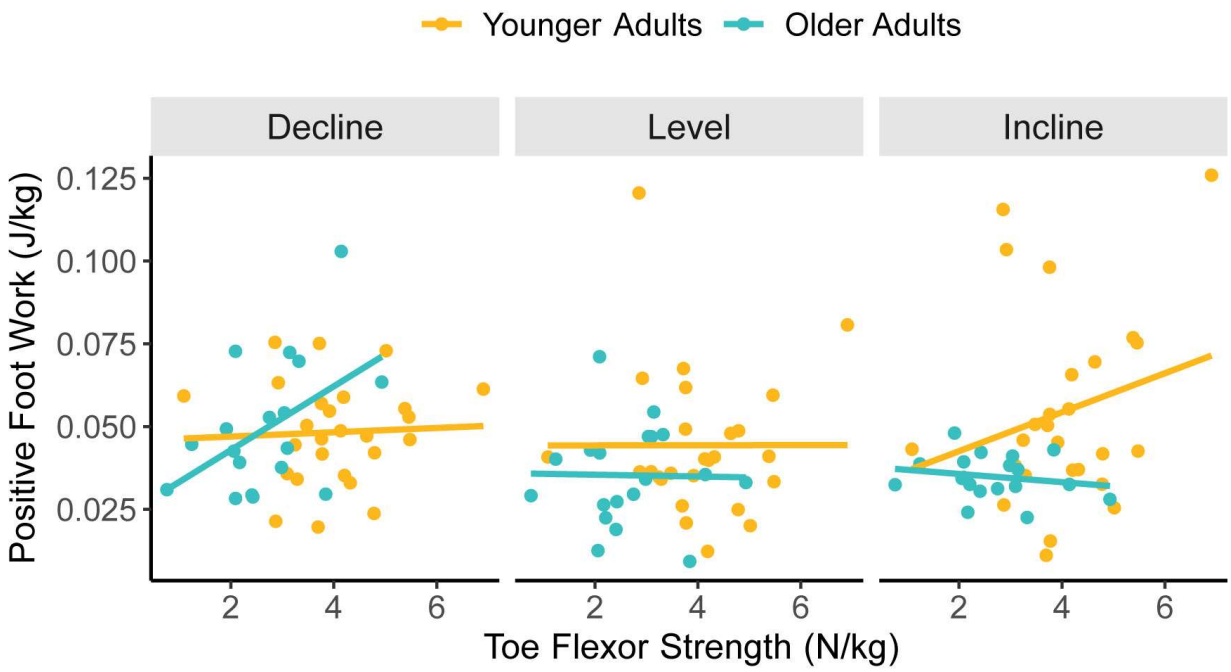


Figure 1. Relationship between toe flexor strength and positive foot work during walking at different slopes for younger (yellow) and older (blue) adults. Lines represent linear fits for each age group.

References (Optional)

[1] Long et al., ASB Conf, 2025 [2] Krupenevich et al., J Biomechanics, 2021 [3] Mickle et al., J Ortho Sports Phys Ther, 2016 [4] Takahashi et al., Sci Rep, 2017 [5] White et al., J Appl Biomech, 2025

Acknowledgements (Optional)

This work was supported by NIH R01AR081287 awarded to KZT and JRF and NIH T32TR004394 awarded to DJD

Session Category

Human Motion and Performance: Locomotion/Gait

P1-124

Evaluation of Three-IMU-Sensor Configurations for Estimating Kinematics and Kinetics of Treadmill Running using Optimal Control

Mrs. Chuyi Wang[1], Ms. Maria Camila Mejia Taborda[1], Mr. Tobias Luckfiel[2], Dr.-Ing. Marlies Nitschke[2], Prof. Dr. Anne D. Koelewijn[1]

[1]Chair of Autonomous Systems and Mechatronics, Department of Electrical Engineering, Friedrich-Alexander-Universität Erlangen-Nürnberg (FAU), Erlangen, Bavaria, Germany. [2]adidas AG, Herzogenaurach, Bavaria, Germany

Introduction

Inertial motion capture (IMC) systems using inertial measurement units (IMUs) enable natural and unrestricted gait analysis. Previous research has shown that IMU setups, e.g., with three sensors, can maintain acceptable accuracy while improving usability [1], while using a shank sensor alone has also shown good accuracy [2]. However, different combinations of three IMU sensors have not yet been compared. Furthermore, the previous study [1] evaluated overground running, whereas treadmill running differs since there is no forward body movement. Therefore, we evaluated how well sensor configuration with three IMUs can estimate running kinematics and kinetics for treadmill running.

Methods

Twenty-four healthy participants ran at a self-selected speed on an instrumented treadmill wearing three types of running shoes. We recorded the motion using an optimal motion capture (OMC) system and 7 IMUs on the pelvis and lower limbs. Three IMU setups, namely pelvis–thighs (PT), pelvis–shanks (PS), and pelvis–feet (PF), were tested. We reconstructed running motion by solving an optimal control problem with a sagittal-plane musculoskeletal model in which muscular effort and IMU tracking error were minimized [3]. We validated against processed OMC data (inverse kinematics and dynamics) by testing the agreement to the IMC results using the coefficient of multiple correlation (CMC).

Results

Results reflect preliminary analysis of five participants (Fig. 1). Joint angles showed high CMCs across all configurations, with PS and PF performing better than PT. Joint moment CMCs were lower, especially in the hip. Differences among shoe types (A–C) were small, with all three shoes exhibiting comparable accuracy trends, similar to the OMC data.

Discussion

Running kinematics and kinetics can be reconstructed with reasonable accuracy using only three IMUs, independent of shoe type. Both PS and PF configurations showed reliable accuracy, with PF recommended for ankle angle estimation, while PS provides a practical alternative where foot-mounted sensors are impractical. Overall, sparse IMU setups can effectively capture running biomechanics and reduce participant burden during gait analysis.

Images (Optional)

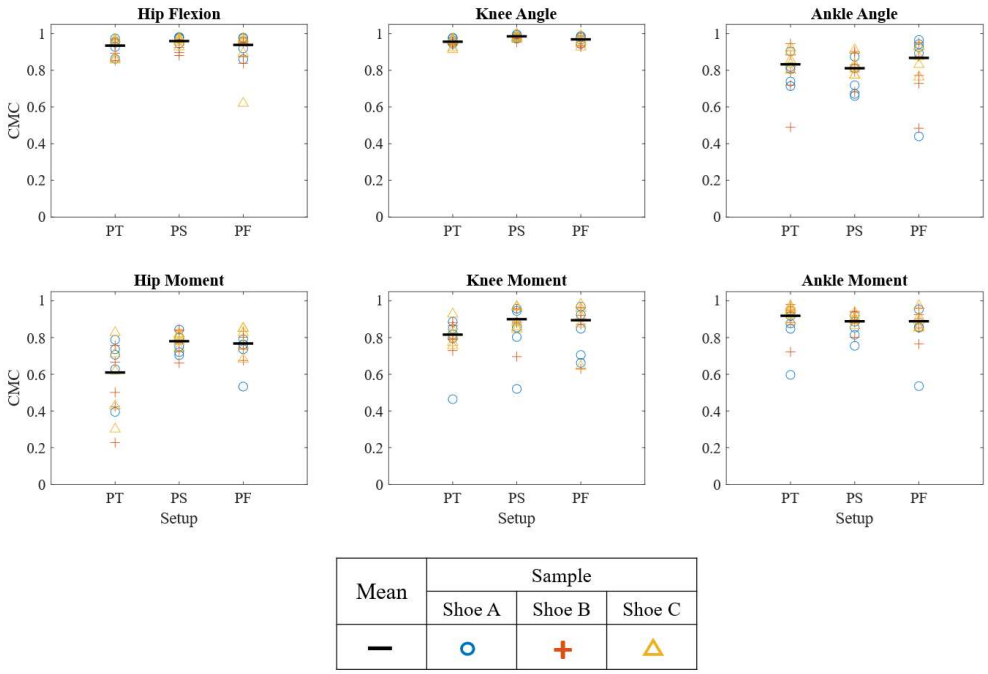


Figure 1. CMCs between joint angles and moments measured with different IMC setups versus OMC across three shoe types. Individual running cycle values for participants are shown as blue circles (Shoe A), orange plus signs (Shoe B), and yellow triangles (Shoe C). Black bars indicate the mean CMCs across all shoes and participants.

References (Optional)

[1] Dorschky, Nitschke *et al.,* Frontiers in Bioengineering and Biotechnology, 2025

[2] Yeung *et al.*, IEEE Sensors Journal, 2023.

[3] Dorschky *et al.,* Journal of biomechanics, 2019

Session Category

P1-125

Distal-to-Proximal Redistribution of Joint Work is Costly in Aging Runners

PhD student Clément Lemineur Lemineur[1], Full professor Grégory M Blain[1,2], Associate professor Pauline Gerus[1]

[1]Université Côte d'Azur, Nice, Nice, Provence-Alpes-Côte d'Azur, France. [2]Utah Valley University, Biology Department, Salt Lake City, Utah, United States

Introduction

The net metabolic cost of running (Cnet) typically increases with age and contributes to declines in endurance performance. Similar observations have been made during walking, and this might be explained by older adults relying more on hip muscles and less on the ankle for propulsion, in response to a decrease in the maximal strength of the plantar-flexors. Research question: Do age-related changes in propulsion strategy contribute to the higher metabolic cost of running?

Methods

Eighteen young adult runners (26.1±3.9 years; 63.8±10.0 kg; 60.3±6.5 $ml \cdot kg^{-1} \cdot min^{-1}$) and eighteen master athletes (63.4±2.7 years; 67.4±10.8 kg; 45.2±6.1 $ml \cdot kg^{-1} \cdot min^{-1}$) completed two experimental sessions. The first session included an assessment of maximal isometric plantar-flexion moment and a VO_2MAX test. The second session involved running at 2.5 and 3 m/s on an instrumented treadmill, with concurrent recordings of kinematics, ground reaction forces, and gas exchange. Joint mechanical work during propulsion (ankle, knee, and hip) were computed using net joint moment and angular velocity. Cnet was quantified using indirect calorimetry. Linear mixed models tested the effects of group, speed, and joint-specific mechanical work contributions on Cnet.

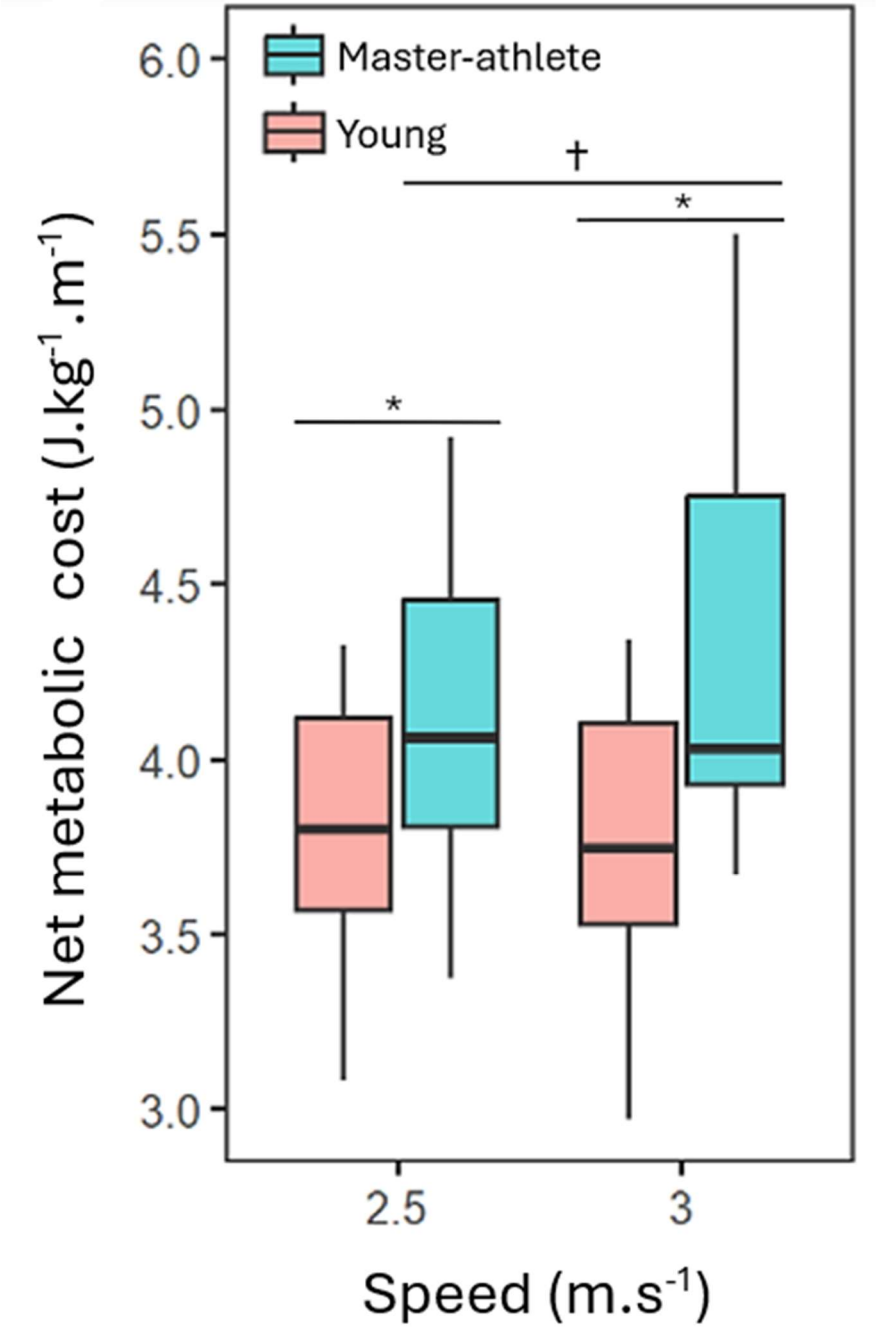
Results

Master-athletes had ~28% ($p < 0.001$) lower maximal plantar-flexion strength than young athletes. Cnet was significantly higher in master athletes ($p=0.003$) and increased from 2.5 to 3 $m.s^{-1}$ in this group, but not in young adults. In the linear mixed model, positive ankle work was significantly greater in young athletes ($p = 0.02$), whereas positive hip work was greater in master athletes and was positively associated with Cnet ($p = 0.0497$). In this model, 28% of the variance in Cnet was explained by hip work ($R^2 = 0.28$), and when individual differences were accounted for, the variance explained increased to approximately 80% ($R^2 = 0.80$).

Discussion

Master athletes showed reduced plantar-flexors strength and produced less ankle work, leading to a compensatory increase in hip work. This distal-to-proximal shift aligns with age-related neuromuscular declines at the ankle and likely contributed to the increased metabolic cost during running, as hip propulsion is less economical due to its limited ability to store and release elastic energy.

Images (Optional)



Acknowledgements (Optional)

Session Category

Human Motion and Performance: Locomotion/Gait

P1-126

Sagittal-Plane Gait Differences Between Faster and Slower Marathon Runners Captured By Markerless Motion Capture at Mile 21: Faster Runners Exhibit Greater Hip Extension During Late Stance

Dr. Colin Bond PhD, MBA

Sanford Research, Fargo, North Dakota, United States

Introduction

Three-dimensional running biomechanics are typically studied in laboratory settings, which may not reflect the mechanical demands of endurance running. Lab protocols often involve treadmills, short durations, and rested participants, limiting their relevance to the fatigue states experienced during marathons. Markerless motion capture enables high-fidelity, scalable gait analysis in natural environments. Despite widespread interest in optimizing running performance, little is known about how joint-level kinematics differ between faster and slower runners during the later stages of a marathon, when fatigue is pronounced. The purpose of this study is to compare lower-extremity sagittal-plane kinematics between faster and slower runners at mile 21 of a competitive marathon.

Methods

Data were collected using eight synchronized Qualisys Miqus Video Plus cameras that captured 50 linear feet of course at mile 21. Of 359 recorded runners, 34 (43.8±11.7y, 1.76±.09m, 75.6±11.3kg) consented to research use of their data. Markerless pose estimation was performed using Theia3D. Sagittal-plane hip, knee, and ankle joint angles were computed and gait events identified using Visual3D. Runners were stratified into fast and slow groups based on their pace and the median pace (10.0 $km \cdot h^{-1}$) for the first 21 miles. Group differences across the stance phase were assessed using statistical parametric mapping with a two-sample t-test ($\alpha = 0.05$) using Sift.

Results

There was an effect of group on sagittal-plane hip angles as faster runners exhibited greater hip extension angles during late stance, with a peak difference of 2° between groups. There was no evidence of an effect of group on sagittal-plane knee or ankle angles.

Discussion

Faster runners exhibited greater hip extension during late stance, which may reflect enhanced propulsion or greater reliance on hip musculature under fatigue. No group differences were observed in knee or ankle kinematics, suggesting that performance

differences at this stage may be more apparent proximally. This study demonstrates the feasibility of using markerless motion capture to identify gait differences in a real-world marathon setting. Future work should examine how these patterns relate to running economy, injury risk, or pacing strategy, and whether similar trends emerge at other race stages.

Images (Optional)

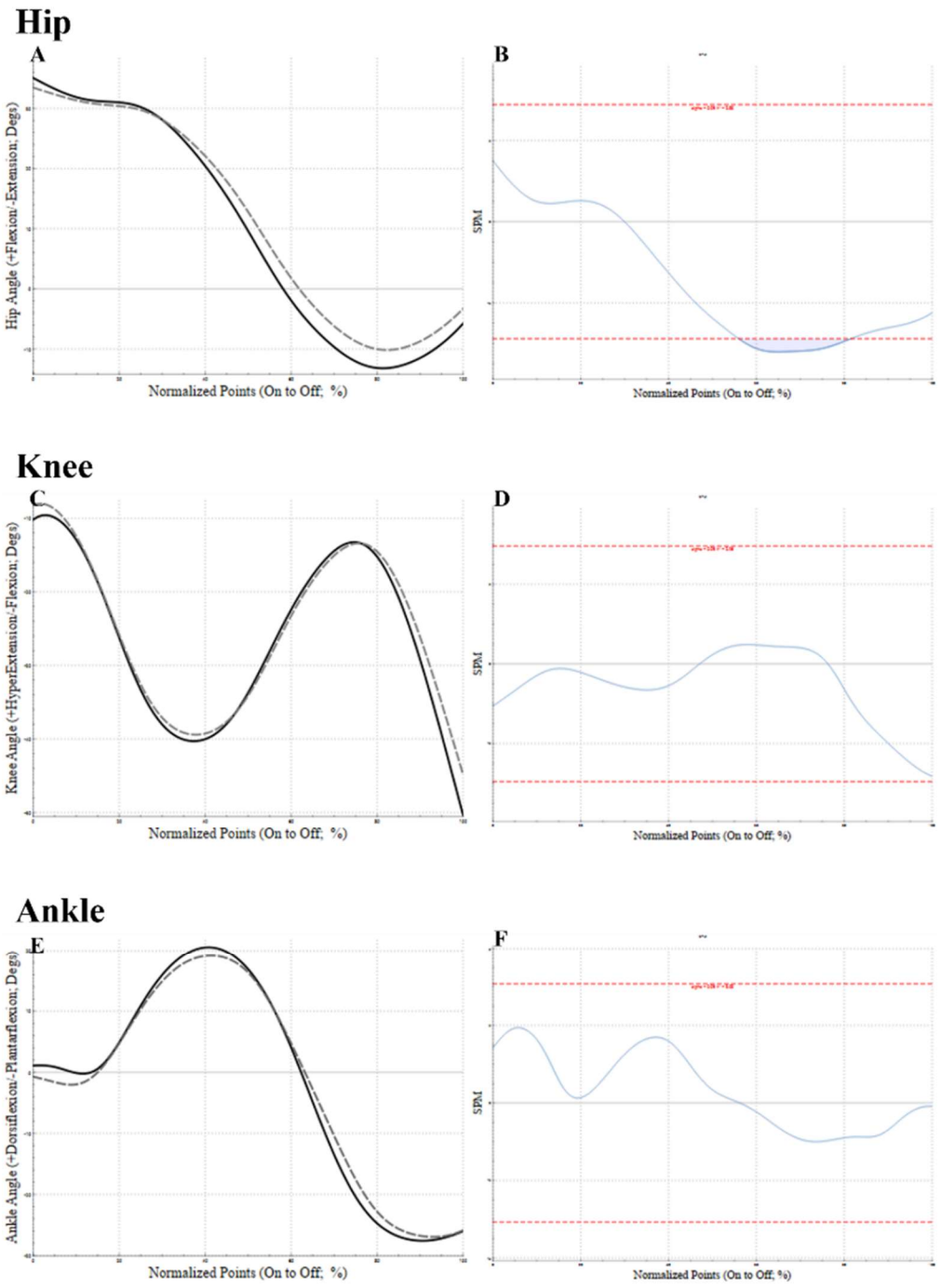


Figure 1. The general linear model (A, C, E) and statistical parametric mapping (B, D, F) for the sagittal-plane hip (A, B), knee (C, D), and ankle (E, F) comparing fast (solid black line) to slow (dashed grey line) marathon runners.

Session Category

Human Motion and Performance: Locomotion/Gait

P1-127

Classifying Marathon Runners by Lower-Extremity Compression Behavior Using Markerless Motion Capture at Mile 21: Associations With Demographics, Training History, and Injury History

Dr. Colin Bond PhD, MBA

Sanford Research, Fargo, North Dakota, United States

Introduction

Biomechanical analyses of running are typically conducted in laboratory settings, which may not reflect the demands of a competitive marathon. Markerless motion capture enables high-resolution gait analysis in natural environments. The lower-extremity can be modeled as a spring, with compression during early stance reflecting impact absorption. Compression characteristics may be linked to running performance and injury risk. The purpose of this study is to examine associations between compression and runner characteristics.

Methods

Data were collected using eight synchronized Qualisys Miqus Video Plus cameras spanning 50 linear feet of course at mile 21. Of 359 recorded runners, 34 (43.8±11.7y, 1.76±.09m, 75.6±11.3kg) consented to research use. Markerless pose estimation was performed using Theia3D. Spring length was calculated as the distance from the model's center of mass to the foot segment center of mass, then normalized to initial contact length to account for body size, and gait events were identified in Visual3D. Runners were stratified into lower-compression (LC), defined by smaller spring deformation across early stance, and higher-compression (HC) groups by applying k-means clustering to principal component scores derived from spring length waveforms during weight acceptance. Statistical analyses included two-sample t-tests (pace through mile 21, body mass index) and chi-square tests (sex, injury history, experience, weekly mileage). Significance was set at $\alpha = .05$.

Results

Out of 34 runners, 15 were classified as LC and 19 as HC. There were no significant differences between groups in pace through mile 21 ($p = .09$) or body mass index ($p = .78$). Group membership was not associated with sex ($p = .23$), injury history in the prior 12 months ($p > .99$), years of running experience ($p = .134$), or weekly running milage in the prior 3 months ($p = .361$).

Discussion

Compression-based grouping did not associate with pace, anthropometrics, sex, or injury and training history, suggesting that impact attenuation behavior may be driven more by biomechanical or neuromuscular factors than runner characteristics. This study demonstrates the feasibility of classifying runners by compression behavior using markerless capture during competition, offering new opportunities to study performance and injury risk in natural race environments.

Images (Optional)

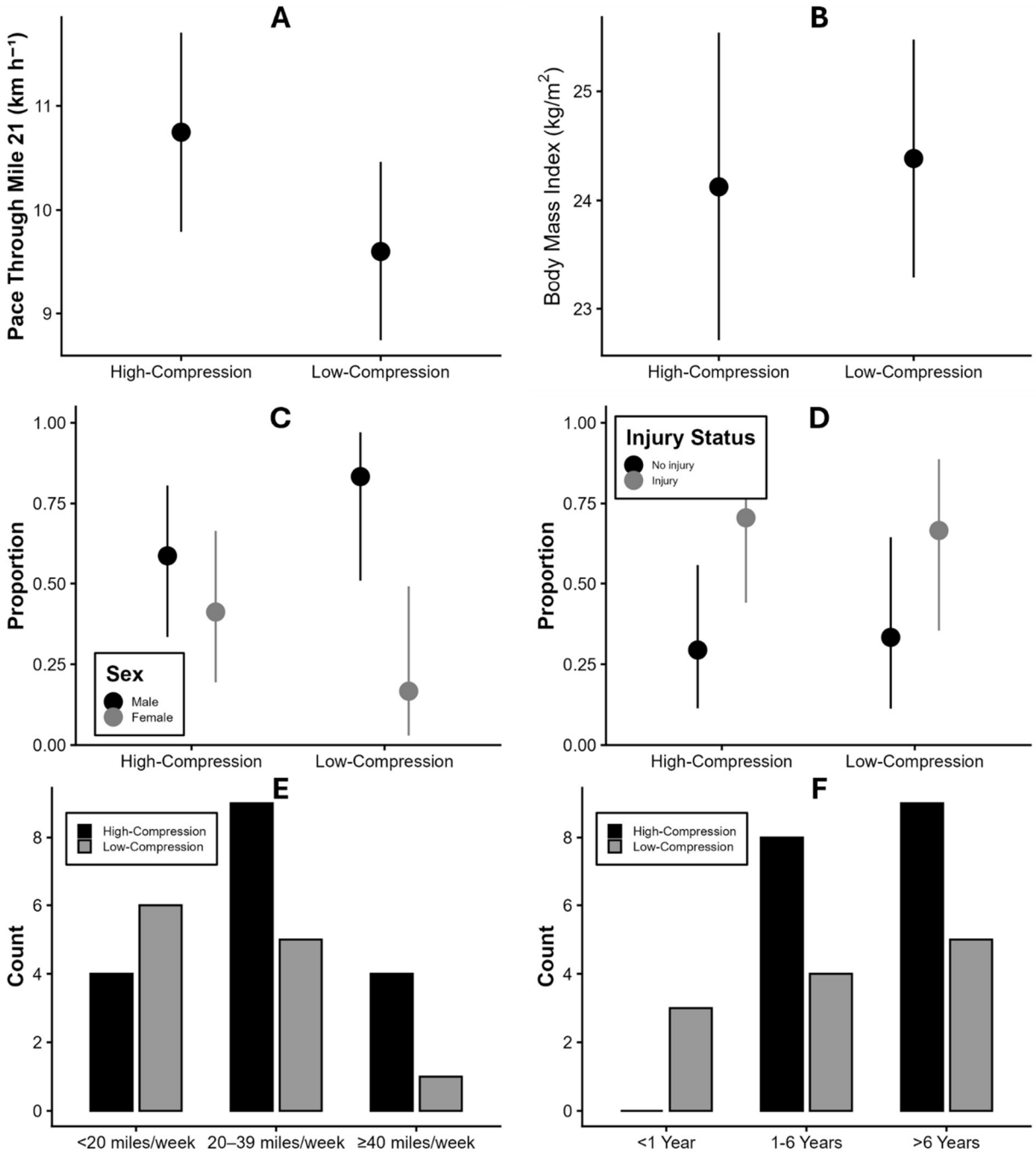


Figure 1. Mean ± 95% confidence interval for mean for pace through mile 21 (A) and body mass index (B). Proportion ± 95% confidence interval for proportion for male (black) and female (grey) (C) and for those with an injury in the prior 12 months (black) and without (grey) (D). Count for weekly running mileage (E) and years of running experience (F) for high-compression (black) and low-compression (grey).

Session Category

Human Motion and Performance: Locomotion/Gait

P1-128

Lower Extremity Acceleration Asymmetries During Running in Participants With Achilles Tendinopathy: A Case Series

Dr. Dave Heller PhD, Ms. Emily Grither, Ms Barbara Heard, Ms Kaitlyn McConnell, Ms Skylar Menner, Dr. Emily Tomlinson PT, DPT, OCS, Dr. Yaqiong Wang PhD, PT, DPT, OCS

Rockhurst University, Kansas City, MO, United States

Introduction

Achilles tendinopathy is common in runners. Previously, we noted asymmetries in acceleration during a drop landing task in a runner with unilateral insertional Achilles tendinopathy (IAT). This subsequent analysis aimed to investigate asymmetries in acceleration of the lower extremities during gait in participants with and without Achilles tendinopathy.

Methods

3 recreational runners, (M, 50y) ran on a treadmill barefoot. One with right IAT, one with left mid-tendon Achilles tendinopathy (MAT) and one healthy (H). We placed accelerometers on each thigh and leg, sampling 3D acceleration. Speed changed randomly every 30 seconds for 5 minutes. We calculated the peak, mean, standard deviation (StDev), and range of net acceleration for each segment. We analyzed data using nonparametric statistics and tests. We compared each measure for each segment without multiple-comparison correction. We hypothesized that IAT and MAT would exhibit significantly higher values for all measures on the affected segment and that H would show no asymmetry.

Results

We found asymmetries in measures of net acceleration across all participants, including, surprisingly, in the healthy participant (Table 1). For IAT at the thigh all measures were statistically significantly lower for the affected (right) limb ($p < .010$). At the leg, the affected limb exhibited statistically significantly lower mean and higher StDev and range of net acceleration ($p < .010$). For MAT, the affected (left) leg exhibited statistically significantly higher values for all measures ($p < .020$) while the affected thigh exhibited significantly lower peak and range of net acceleration but higher mean net acceleration ($p < .020$). Contrary to our hypothesis, H also exhibited statistically significant asymmetries for all measures at the thigh ($p < .008$) and for peak, mean, and range of net acceleration at the leg ($p < .004$).

Discussion

In addition to being an indicator of injury, gait asymmetries could also precede injuries. Our results raise questions about whether asymmetries in gait simply represent typical individual variability or could be early indicators of potential injury risk. A future potential longitudinal study could follow healthy individuals to determine whether those with gait asymmetries are more likely to experience injury.

Images (Optional)

Table 1.

Peak, Mean, Standard Deviation, and Range Net Accelerations (ms^{-2}) of Each Thigh and Leg During Running.

Participant		Peak	*p*	Mean	*p*	StDev	*p*	Range	*p*
IAT	LThigh	42.13 ± 5.90	*.008**	13.10 ± 0.96	*.002**	5.89 ± 0.48	*.002**	41.37 ± 5.59	*.010**
	RThigh	**34.57 ± 9.67**		**11.91 ± 0.69**		**4.75 ± 0.60**		**33.75 ± 10.21**	
	LLeg	54.77 ± 6.21	.080	16.88 ± 1.70	*.008**	6.71 ± 0.84	*.002**	51.20 ± 6.20	*.010**
	RLeg	**62.12 ± 12.72**		**16.59 ± 1.51**		**8.66 ± 0.60**		**59.84 ± 12.42**	
MAT	**LThigh**	**39.56 ± 3.60**	*.005**	**13.40 ± 1.19**	*<.001**	**6.23 ± 0.30**	.168	**38.15 ± 3.67**	*.013**
	RThigh	45.53 ± 2.79		13.05 ± 0.97		6.17 ± 0.46		43.93 ± 3.28	
	LLeg	**96.63 ± 10.29**	*<.001**	**16.81 ± 1.42**	.542	**9.93 ± 1.47**	*.017**	**89.89 ± 10.78**	*<.001**
	RLeg	84.39 ± 12.79		16.80 ± 1.64		8.92 ± 0.82		80.25 ± 12.73	
H	LThigh	60.70 ± 2.52	*.008**	16.09 ± 1.48	*.004**	8.23 ± 0.35	*.004**	58.42 ± 1.60	*.008**
	RThigh	47.10 ± 1.33		14.00 ± 1.48		7.12 ± 0.83		45.30 ± 1.23	
	LLeg	59.67 ± 1.05	*.004**	13.14 ± 0.93	*.004**	7.95 ± 0.40	.400	59.10 ± 1.08	*.004**
	RLeg	49.23 ± 2.66		15.92 ± 1.61		7.84 ± 0.83		47.99 ± 2.94	

Bold denotes affected limb

*Italics and * denote significant left/right differences at* $\alpha = 0.05$.

Session Category

Human Motion and Performance: Locomotion/Gait

P1-129

Foot Progression Angle Variability in Children with Cerebral Palsy

Ms Colina Matthews[1], Dr Kevin Dibbern[2], Dr David Kingston[1]

[1]University of Nebraska at Omaha, Omaha, NE, United States. [2]University of Nebraska Medical Center, Omaha, NE, United States

Introduction

Foot progression angle (FPA), the angle between the line of the heel and second metatarsal head with gait progression, is typically averaged over multiple steps or trials to a single directional alignment for a subject. This approach may mask step-by-step variations in clinical populations, which may misrepresent the level of impairment. The purpose of this study was to quantify step-by-step variability in children with cerebral palsy (CP) and typically developing (TD) peers to analyze the distribution and consistency of participant foot placement.

Methods

31 CP (GMFCS I and II) and 17 age-matched TD children were fitted with 54 retro-reflective markers on the lower limbs, tracked by a 20-camera motion capture system, and walked barefoot on a 10-meter level walkway over eight embedded force plates for a minimum of 8 trials(3-10 steps per trial). Data were processed in Visual3D and midstance FPA was calculated for each step. Subject-level means and the individual step-to-step absolute deviations from that mean were calculated. Linear Mixed Effects models (LMM) compared step-by-step FPA in groups and GMFCS levels.

Results

LMMs showed a large effect of group *($F(2,31.4) = 4.8$, $p = .014$, $\eta^2_p = 0.187$) and an increasing foot-placement inconsistency trend with impairment (Geometric means:* TD = 5.3°, CP1 = 8.3°, CP2 = 13.4°). Data were log transformed to correct skew. Large differences, over three times greater, in step-to-step FPA were observed for CP children at GMFCS II compared to than TD peers. Children at GMFCS I had a moderate effect.

Discussion

CP children at GMFCS II had more step-by-step variability than their TD peers; suggesting reduced foot-placement consistency. Step-by-step FPA could be used as a marker to capture fluctuations in gait and as a tool to identify children who could benefit from

stability and motor control interventions. Future work should target larger sample sizes and explore how orthoses, speed, and treadmill compared to overground walking affect FPA variability.

Session Category

Human Motion and Performance: Locomotion/Gait

P1-130

Portable Ground Reaction Force Estimation Using IMU-Based Motion Capture: A Two-Tier Trust Framework

Dr Domitille Princelle PhD

Movella Technology B.V., Enschede, Twente, Netherlands

Introduction

Ground reaction forces (GRFs) and Center of Pressure (CoP) are fundamental to clinical gait and sport performance interpretation, informing joint loading and fall risk assessment. Yet clinical and sport assessments conducted in laboratory conditions compromise ecological validity. Portable alternatives using inertial motion capture (IMC) estimate GRFs via machine learning, optimization, or Virtual Pivot Point (VPP) theory [1, 2]. However, existing VPP implementations show limited horizontal force accuracy and lack hardware flexibility. We present a two-tier trust framework with improved CoP estimation and solver, balancing portability against consistency while supporting real-time (MVN-Live) and post-processing (MVN-HD) analysis.

Methods

We validated using Wang et al. dataset's [3]: Xsens Link, Moticon insoles, and instrumented treadmill reference from 8 healthy adults across six walking speeds (0.9–5.4 km/h) and dynamic tasks (jump, land, lunge). VPP was positioned at 0.5×Body Height above center of mass per sensitivity analyses [2]. Tier 1 (IMU-only, 5/8 participants) estimates CoP from the biomechanical model; Tier 2 (IMU+Insoles, all 8 participants) incorporates direct CoP measurement. Each tier supports Live (NNLS) and post-processing (quadratic programming). Accuracy: assessed via Pearson's correlation (ρ) and RMSE (%BW).

Results

MVN-HD consistently outperformed MVN-Live across all tasks. For walking, MVN-HD achieved minimum RMSE of 0.8–6.1% BW across force components (ρ=0.8–0.99) (Table 1). For dynamic tasks, MVN-HD reduced vertical RMSE by 10 percentage points with improved correlations.

Tier 1 HD matched Tier 2 accuracy; Tier 2 enabled validation on all participants through consistent contact detection; though insole hysteresis ranked Tier 2 Live below Tier 1 Live.

Discussion

MVN-HD remained within clinically meaningful thresholds [4]; MVN-Live offers real-time feedback. Compared to Castellaz et al. [1], MVN-HD reduced vertical RMSE by 10 percentage points for walking, with improved horizontal accuracy. Tier 1 maximizes portability; Tier 2 maximizes consistency, whose accuracy depends on insole quality. This framework offers unperturbed GRF profiling in real-life scenarios for rehabilitation and monitoring, with future validation planned for Activities of Daily Living.

Images (Optional)

		Tier 1 Live	Tier 1 HD	Tier 2 Live	Tier 2 HD
		(IMU-only)	*(IMU-only)*	*(IMU+Insoles)*	*(IMU+Insoles)*
RMSE (%BW)	AP	1.6±0.2 | 5.2±0.6	1.2±0.2 | 4.8±0.7	1.4±0.03 | 4.8±1.9	1.5±0.02 | 4.0±2.5
	ML	1.4±0.3 | 2.5±0.8	0.8±0.3 | 2.1±0.7	1.8±0.5 | 3.9±2.5	1.0±0.01 | 3.3±2.5
	V	16.5±0.9 | 19.1±1.7	6.1±1.1 | 12.7±1.4	17.3±0.2 | 22.9±2.7	6.1±1.4 | 10.3±2.4
ρ	AP	0.69±0.11 | 0.88±0.02	0.83±0.12 | 0.91±0.03	0.61±0.11 | 0.87±0.03	0.86±0.15 | 0.93±0.03
	ML	0.77±0.14 | 0.85±0.07	0.84±0.09 | 0.96±0.03	0.73±0.14 | 0.85±0.14	0.80±0.03 | 0.96±0.01
	V	0.90±0.02 | 0.93±0.01	0.97±0.08 | 0.99±0.003	0.87±0.04 | 0.91±0.02	0.97±0.03 | 0.99±0.003

Table 1: RMSE (%BW) and Pearson correlation (ρ) across configurations. Values show mean ± SD across participants; minimum | maximum across the six walking speeds.

References (Optional)

[1] Castellaz, et al., IEEE Int Symp MeMeA, 2024

[2] Wagner, et al., Front Bioeng Biotech. 2024

[3] Wang, et al., Zenodo, 2022

[4] Wearing, et al., Gait Posture, 2020

Session Category

Human Motion and Performance: Locomotion/Gait

P1-131

Speed-Dependent Changes in Human Neuromotor Control Priorities During Walking

Mr. Ehsan Tahvilian, Dr. Arash Arami PhD

University of Waterloo, Waterloo, Ontario, Canada

Mr. Ehsan Tahvilian

Introduction

Human walking can be modeled using optimal control frameworks, where movement emerges from balancing multiple objectives such as stability, effort, and smoothness. Inverse optimal control (IOC) seeks to infer these objectives by estimating cost weights that reproduce observed gait patterns. However, IOC solutions are not unique, and small differences in tracking accuracy can produce different weight estimates. Here, we examine how inferred neuromotor priorities change with walking speed while accounting for ambiguity across equally valid IOC solutions.

Methods

Ten healthy adults walked on a split-belt treadmill at five speeds between 0.4 and 1.2 m/s. For each participant and speed, inverse optimal control (IOC) was run for multiple iterations, and five normalized RMSE values were computed for hip, knee, and ankle angles, as well as horizontal and vertical ground reaction forces. Each solution was represented in a five-dimensional error space, and the first Pareto front was identified. The space was divided into 0.05-wide bins, and Pareto solutions were ranked by their distance to an ideal point defined by minimum errors. All solutions within the best bin were treated as equally good fits. To assess speed effects, 1000 bootstrap samples were generated, and linear models were used to test weight-speed relationships.

Results

Three IOC weights showed clear and consistent relationships with walking speed across bootstrap samples. The CoM acceleration weight decreased with speed in 100% of iterations (linear trend, $p<0.05$), indicating reduced emphasis on regulating body acceleration at higher speeds. The foot-sliding weight increased in 95.8% of iterations ($p<0.05$) and showed a mild but significant quadratic pattern, with higher-order models improving fit ($p=0.014$). The stability-related weight increased in 100% of bootstrap fits

($p<0.05$), suggesting greater balance demands with speed. In contrast, the torso-orientation weight showed a significant trend in only 21.6% of cases ($p>0.05$), indicating no reliable speed dependence.

Discussion

As walking speed increases, neuromotor control priorities shift systematically. Reduced emphasis on CoM acceleration suggests looser regulation of body dynamics, while increased weighting of foot sliding and stability reflects greater demands for secure contact and balance. In contrast, torso orientation shows no consistent speed-dependent change.

Images (Optional)

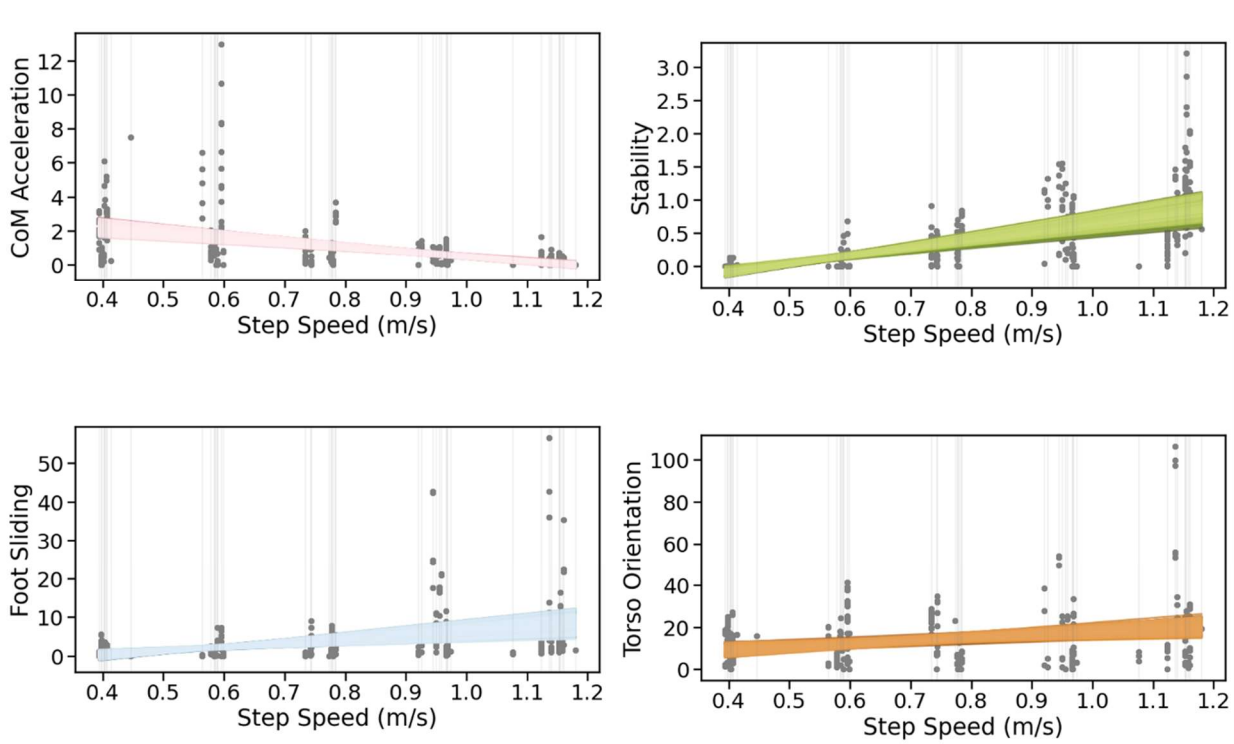


Figure 1. Pooled scatter with fitted trend lines as Speed-dependent trends in IOC-derived cost weights. Each subplot summarizes results across 1000 bootstrap fits.

References (Optional)

Session Category

Human Motion and Performance: Locomotion/Gait

P1-132

ISC3D: A Toolbox for Generalized 3D Transformation From Anatomical to Elevation Angles for Intersegmental Coordination Analysis

Mr. Elad Siman Tov, Dr. Nili Krausz

Technion, Haifa, Israel, Israel

Introduction

It is standard to present kinematic data with joint angles. However, elevation angles (measured from the global vertical axis) may reveal attributes of human motion not evident from joint angles alone. An important finding [1], is that the elevation angles of the thigh, shank, and foot in the sagittal plane form trajectories that lie on a Covariation Plane (CVP). Known as the Law of Intersegmental Coordination (ISC), this phenomenon was observed across gaits, speeds, and inclines. However, few biomechanics studies report elevation angles, and until now elevation angles had to be computed directly from surface markers. This challenges computation, bypassing established motion capture software and standard anatomical joint angle definitions, and limiting meta-analyses. To bridge these gaps, we developed ISC3d, an algorithm that directly transforms from joint angles to streamline 3D elevation angle computation. Our algorithm and code can be accessed online (https://www.mathworks.com/matlabcentral/fileexchange/182726-isc3d).

Methods

Elevation angles were reconstructed by multiplying joint angle rotation matrices with corresponding segment rotation matrices. Reference frames adhered to ISB standards. ISC3d was validated against a baseline marker-based method for 10 able-bodied (AB) subjects (n=6127 strides) [2]. Agreement between ISC3d and the baseline was quantified using RMSE and squared Pearson correlation (r^2) per segment. Outlier removal was completed using the generalized Extreme Studentized Deviate test.

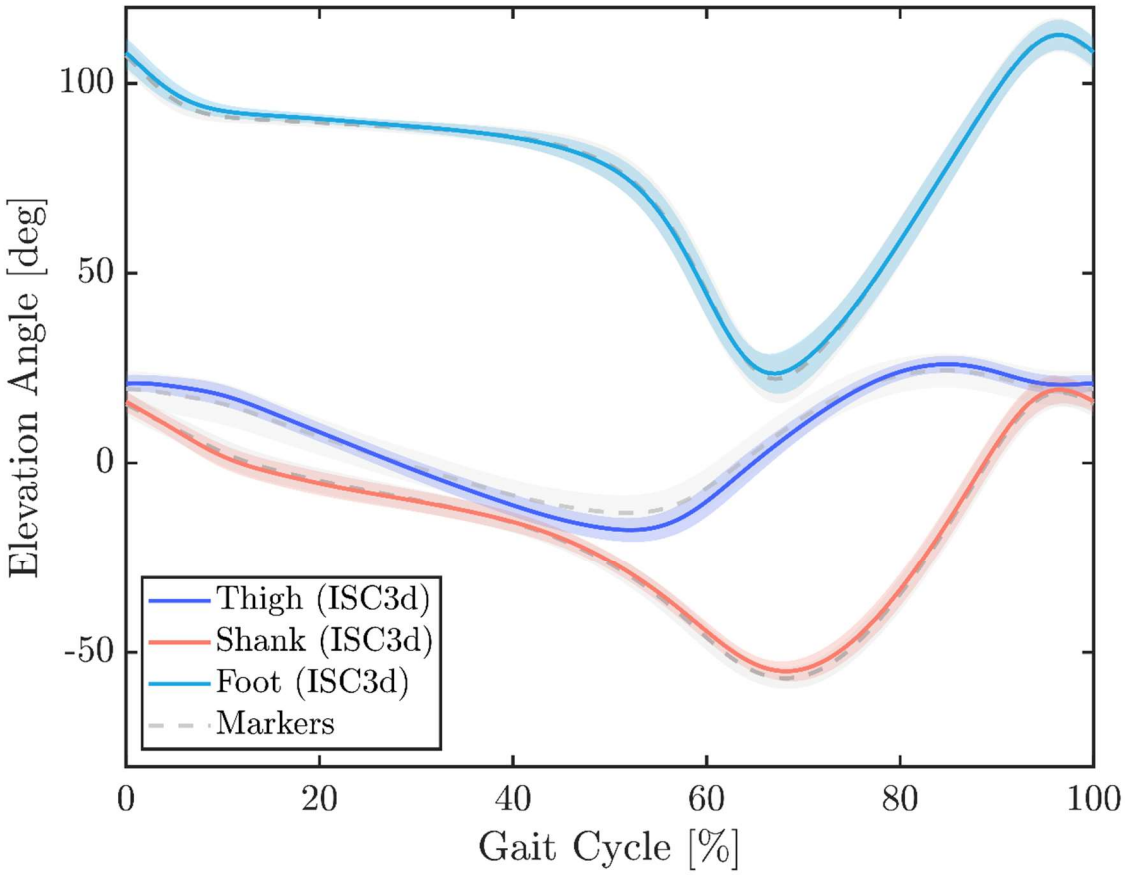
Results

The angles computed by ISC3d were correlated with the baseline (Thigh: RMSE 4.975 ± 2.121°, r^2=0.977 ± 0.024; Shank: RMSE 2.563 ± 1.163°, r^2 =0.995 ± 0.004; Foot: RMSE 1.853 ± 0.993°, r^2 =0.998 ± 0.002). The thigh elevation angles showed largest deviations between methods, perhaps since standard motion capture systems approximate joint centers. The mean and standard deviation (shaded) angles for a given AB walking condition are shown in Figure 1.

Discussion

This work provides the biomechanics community with a new, faster method for analysis, that achieved elevation angle estimation comparable with results computed from raw marker data. It also opens the door to analyze ISC in previously published datasets that only reported joint angles. Finally, it can shed light on the role of global coordinates in human movement.

Images (Optional)



References (Optional)

[1] N. A. Borghese et al., J Physiol, 1996
[2] E. Reznick et al., Sci Data, 2021

Session Category

Human Motion and Performance: Locomotion/Gait

P1-133

How Does Pushing a Cart Affect Spinal Curvature?

M.Sc. Elisa Romero Avila, Mr. Finn Jamros, Prof. Dr. Catherine Disselhorst-Klug

Institute of Rehabilitation and Prevention Engineering, Applied Medical Engineering, RWTH Aachen University, Aachen, NRW, Germany

Introduction

Repetitive manual tasks (e.g. lifting, lowering, pushing, and pulling) are recognized as potential risk factors for back pain and related musculoskeletal disorders. Although the effects of lifting and lowering have been extensively investigated, less research has focused on the biomechanical consequences of pushing and pulling activities. Video rasterstereography provides a validated method for analyzing spinal posture during such tasks by the 3D reconstruction of the spine curvature, and each vertebra's rotation.

The aim of this work is to analyze spinal curvature adaptations when pushing different external loads to simulate a cart pushing task.

Methods

Thirty healthy subjects were asked to push three different load conditions (no load, 80 N, 160 N) while walking on a treadmill at 3 km/h. For analyzing the changes in the spinal curvature, video rasterstereography was considered (DIERS Formetic 4Dmotion, DIERS International GmbH). Reflective markers were placed on the seventh cervical vertebra and on the left and right posterior superior iliac spine to define anatomical reference points. A 3D model of the spine was generated from the rasterstereography data to obtain the per-vertebra angles, as well as spine parameters. These parameters included the kyphotic and lordotic angles, trunk inclination, and kyphosis and lordosis apices.

Results

A significant increase in the trunk inclination was observed as the pushed load increased. Additionally, the kyphotic angle significantly decreased with increasing load, while no changes were observed in the lordotic angle. Analysis of the apices showed that the kyphosis apex significantly increased with increasing loads, while the lordosis apex significantly decreased. These results were supported by the per-vertebra analysis, which showed higher angle gradients between adjacent vertebrae in the loaded pushing condition compared to the no-load condition.

Discussion

The results from this study demonstrate that pushing different loads leads to adaptations in spinal posture. These adaptations include a greater forward inclination of the trunk, changes in the spine curvature in the transition between the thoracic and lumbar spine region and increases in the angle gradients between adjacent vertebrae. Although these adjustments are necessary for executing the task, repetitive performance could have implications in musculoskeletal health.

Acknowledgements (Optional)

E.R.A. would like to thank CONACYT-DAAD (57649580)

Session Category

Human Motion and Performance: Locomotion/Gait

P1-134

Gait Biomechanics Phenotypes Reflecting Bilateral Interdependence in Severe Knee Osteoarthritis

Ms Naomi Loughlin[1], Dr Elise Laende[1], Mr Jereme Outerleys[2], Dr Kevin Deluzio[2]

[1]University of Waterloo, Waterloo, Ontario, Canada. [2]Queen's University, Kingston, Ontario, Canada

Introduction

Knee osteoarthritis (OA) is a heterogeneous condition characterized by joint degeneration and altered gait patterns. Traditional radiographic assessments inadequately capture functional diversity, particularly in bilateral OA populations. This study aimed to identify distinct gait-based subgroups among individuals with severe knee OA and explore associations with clinical features, including contralateral knee OA severity.

Methods

Gait kinematics were collected from 153 participants with severe medial knee OA using a Theia markerless motion capture system during a walking task at a self-selected pace. Hierarchical clustering, incorporating gait speed, age, sagittal- and frontal-plane knee angles (principal component (PC) scores from principal component analysis of joint angle waveforms), was applied to identify subgroups. Between-cluster differences in demographics, contralateral knee OA status, and gait parameters were analyzed using ANOVA/Kruskal-Wallis and chi-squared tests ($\alpha = 0.05$).

Results

Two distinct clusters emerged. Cluster 1 (n = 93) exhibited faster gait speed (1.10 m/s) and greater range of sagittal-plane motion with a greater proportion of asymptomatic contralateral knees (28%). Cluster 2 (n = 60) showed slower gait speed (0.81 m/s), reduced flexion-extension patterns and was predominantly female (70%) with more severe contralateral OA (46.7%). Significant inter-cluster differences were observed in gait speed, sagittal-plane PC2 and PC3 scores, sex distribution, and contralateral knee OA severity ($p < 0.05$).

Discussion

Functional heterogeneity exists within radiographically uniform severe knee OA, consistent with literature of gait heterogeneity among OA patients [1]. Cluster 1's faster gait with greater range in flexion-extension suggests preserved function whereas Cluster 2's slower gait and altered flexion-extension pattern associated with stiff-kneed gait suggest greater

impairment. The association of these distinct compensatory gait strategies with contralateral knee OA severity highlights bilateral interdependence [2].

Therefore, gait-based assessment may enhance radiographic OA classification, enabling more personalized diagnostic and intervention strategies. However, the exclusion of lateral knee OA cases limits the generalizability of these findings. Future work should aim to validate the subgroups longitudinally to evaluate their prognostic relevance.

Images (Optional)

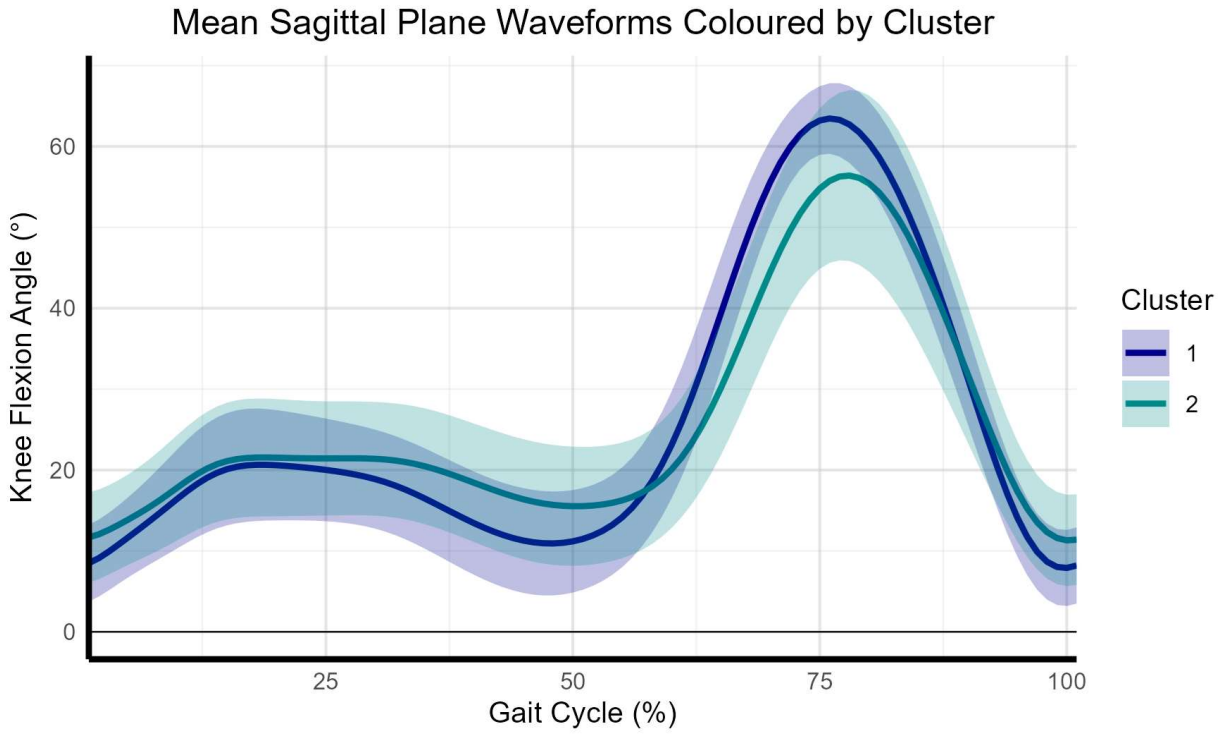


Figure 1. Mean sagittal-plane knee angles and standard deviation over the gait cycle by cluster. More positive values indicate knee flexion, near-zero values indicate knee extension.

References (Optional)

[1] K. L. Young-Shand *et al.*, J. Orthop. Res., 2023

[2] M. S. Park *et al.,* JBJS, 2010

Session Category

Human Motion and Performance: Locomotion/Gait

P1-135

Visual Environment Complexity and Cue Congruency in Virtual Reality: Impact on Gait Parameters in Young Adults

Ms Emily Marino BSc Candidate, Ms. Kristen De Melo MSc, PhD Candidate, Dr. Lori Ann Vallis PhD

University of Guelph, Guelph, Ontario, Canada

Ms Emily Marino

Ms. Kristen De Melo

Introduction

Visual information is critical for guiding safe locomotion, particularly when navigating complex environments or responding to conflicting visual cues [1]. This study used a modified Simon Task paradigm [2] to examine how spatial cues influence gait during visually guided locomotion through two different environments.

Methods

Participants with no history of impaired cognitive function or physical impairments were fitted with retroreflective markers (OptiTrack, 100 Hz; Corvallis, USA) and instructed to walk through two distinct virtual reality (VR) environments (forest vs. hallway), wearing a VR headset (HTC Vive Pro 2) while avoiding a virtual sinkhole. The direction of transient changes around the sinkhole were cued by arrows that appeared at the top of the virtual scene in one of three locations: congruent (e.g. leftward arrow on left side of screen), incongruent (e.g., leftward arrow on right side of screen) or neutral (center of the screen). It is hypothesized that more complex environments (forest) and incongruent location cues would result in more cautious gait patterns, e.g. greater step width, reduced velocity and increased time to leading edge of the sinkhole. ANOVA statistical analyses were conducted in SPPSS (Version 30).

Results

Preliminary analyses (n=3; 2M, age 22.3 ± 4.93) revealed no statistically significant differences ($p>0.05$) for either environment or cue location conditions for the gait parameters explored to date, however, study recruitment and data processing is ongoing.

Discussion

If these preliminary results do not change, it would indicate that young adults are able to integrate and interpret complex spatial visual cues and safely negotiate intricate environments with minimal disruption in ongoing gait patterns [2]. When complete, study findings will contribute to our knowledge of how visual complexity and cue congruency influence gait during VR-based navigation tasks; this information is critical for future studies involving special populations, e.g. older adults who may struggle with maintaining dynamic balance during similar locomotor tasks.

References (Optional)

[1] Matthis, J. S., Barton, S. L., & Fajen, B. R. *Proceedings of the National Academy of Sciences*, 2017

[2] Pitman, J., & Vallis, L. A. *Journal of Motor Behavior*, 2015

Session Category

Human Motion and Performance: Locomotion/Gait

P1-136

High Ground Reaction Forces Decrease Metatarsal Bone Strength in Runners

Ms. Emma Slavin[1], Ms. Julia Nicolescu[1], Dr. Adam Tenforde[2], Dr. Irene Davis[3], Dr. Karen Troy[1]

[1]Worcester Polytechnic Institute, Worcester, MA, United States. [2]Spaulding Rehabilitation Hospital, Charlestown, MA, United States. [3]University of South Florida, Tampa, FL, United States

Introduction

The metatarsals are a frequent site for bone stress injuries (BSIs), a common overuse injury in runners. Ground reaction forces load the metatarsals during running, creating metatarsal strain and stimulating bone remodeling. Remodeling facilitates bone adaptation and strengthening [1]. We hypothesized that increased vertical ground reaction forces (vGRFs) during running would be associated with improved metatarsal structure.

Methods

Participants included six healthy females (age: 20.8 ± 1.6) running ≥24 kilometers/week. Gait mechanics were collected using a ten-camera motion capture system (Vicon) while the participants ran barefoot with a forefoot strike pattern across two force platforms (AMTI) at 2.65 m/s. vGRF data were processed and normalized to body weight to identify peak vGRF during stance. High-resolution quantitative computed tomography (Scanco) images were analyzed to assess right 2nd metatarsal macrostructure. Pearson's correlations were calculated between peak vGRF and bone strength and quality measurements. Due to our small sample size, $r \geq 0.81$ were significant ($p \leq 0.05$), and $r \geq 0.7$ were considered potentially important.

Results

Peak vGRF was negatively correlated with numerous metatarsal macrostructural properties, including metatarsal principal and polar moments of inertia (Figure 1; $r = \leq -0.92$), bone mineral content, bending strength index, cross-sectional area, compressive strength index ($r = -0.84$), and bone volume ($r = -0.87$).

Discussion

The hypothesis that increased vGRFs during running would be associated with improved metatarsal structure was not supported. Runners who experienced greater vGRFs had smaller, weaker metatarsals. These results suggest that high loading magnitudes may reduce the metatarsal's ability to remodel and strengthen in response to load. Bone

remodels in response to high loading magnitudes and rates [2], and excessive turnover could impair adaptations like increased strength. Alternately, high vGRF could indicate poor running biomechanics. A combination of low bone strength and high vGRF may increase an athlete's risk for BSI.

Images (Optional)

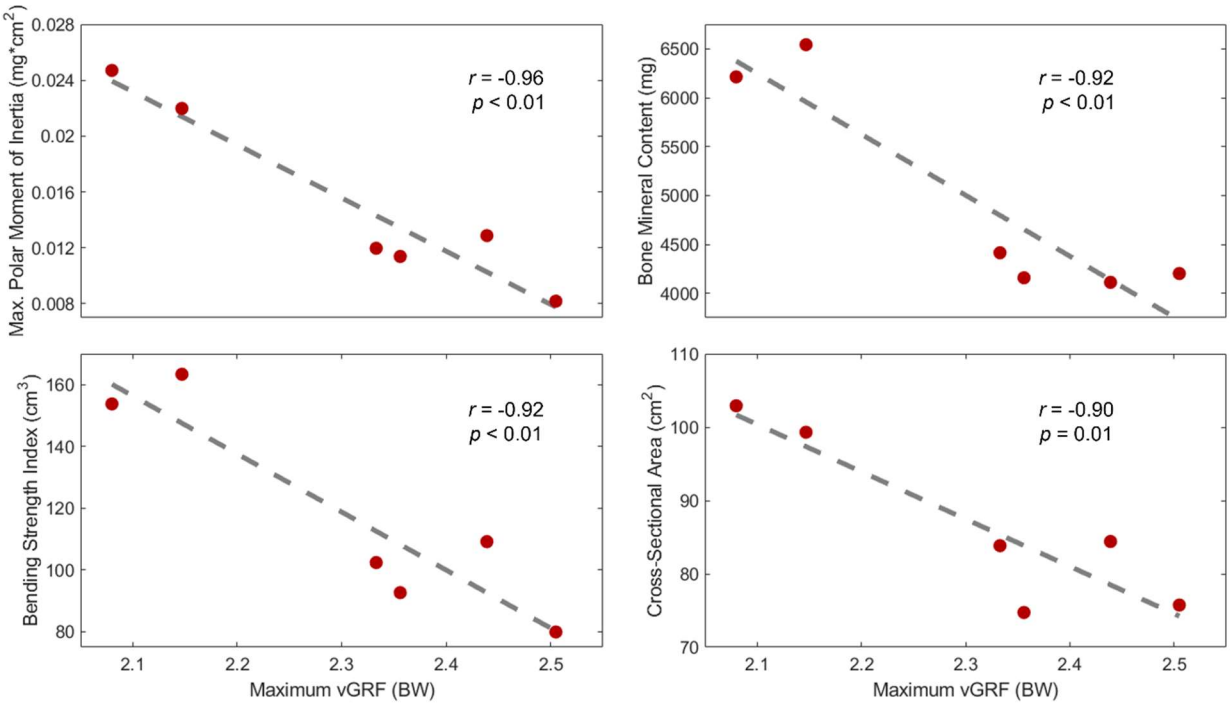


Figure 1. Maximum polar moment of inertia, bone mineral content, bending strength index, and cross-sectional area of the right 2nd metatarsal as a function of peak vGRF during running stance.

References (Optional)

[1] C. H. Turner, *Bone*, 1998. [2] K. L. Troy, et al, *JBMR*, 2020.

Acknowledgements (Optional)

The data from this work was supported by NIH R15HD104169 grant (to KLT).

Session Category

Human Motion and Performance: Locomotion/Gait

P1-137

Sex Differences in Collegiate Cross-Country Runners' Gait Patterns Across Different Treadmill Speeds

Dr. Eric Foch[1], Dr. Richard Brindle[2], Dr. Kevin Foch[3]

[1]Central Washington University, Ellensburg, WA, United States. [2]Shaw Sports Turf, Shaw Industries Group, Inc., Dalton, GA, United States. [3]High Point University, High Point, NC, United States

Introduction

To determine biomechanical differences between female and male runners, principal components analysis (PCA) with a support vector machine (SVM) classifier may separate running subgroups. Limited research exists examining running biomechanics between female and male competitive runners across different running speeds. Therefore, the purpose of this study was to determine if PCA with a SVM classifier could separate and classify collegiate female and male cross-country runners based on lower extremity biomechanics during running at different speeds.

Methods

Sixteen healthy collegiate cross-country runners (n = 8 female) participated. Runner's self-selected 'easy' pace was used to determine treadmill speeds for each one-minute condition: recovery, easy, threshold, and interval. Three-dimensional marker coordinates and ground reaction forces were collected and processed. Ankle, knee, and hip joint: angles, angular velocities, and moments were computed. Discrete values were extracted at foot-strike and at maximum during the first 60% of stance. Variables were averaged and combined into separate matrices for PCA. Principal component (PC) scores were rank ordered by effect size (d) and used as input for the linear SVM. Correlation coefficients (r) between top-ranked PCs and standardized discrete variables were calculated.

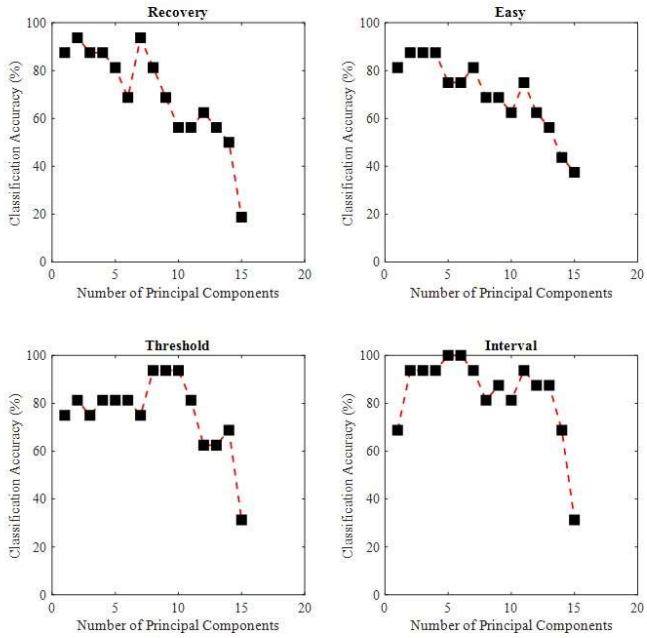
Results

Accuracy of classifying female and male collegiate cross-country runners ranged from 87.5 - 100% across the four treadmill speed conditions (Figure 1). There were high correlations ($r \geq 0.8$) between PC1 and peak dorsiflexor moment for the recovery and easy conditions. For the threshold condition, there were high correlations for all joints examined (PC1 and dorsiflexor moment, PC2 and peak knee extensor moment, PC4 and peak hip extension angle). Finally, for the interval condition, a high correlation was identified between PC1 and plantarflexion velocity.

Discussion

Sex differences in running biomechanics were found primarily in the sagittal plane which is similar with a previous multivariate biomechanical investigation. With inferential biomechanical investigations, only frontal plane hip and knee differences were reported between healthy female and male runners. Collectively, PCA with a SVM classifier can aid in explaining the complex interaction between lower extremity biomechanics and sex during running that inferential investigations may be missing.

Images (Optional)



Session Category

Human Motion and Performance: Locomotion/Gait

P1-138

Lower-Limb Joint Kinetics of Turning Gait in Young Adults

Ms. Erin Kreis, Dr. Jun Liu PhD, Dr. Mitchell Tillman PhD, Ms. Zahava Hirsch, Dr. Antonia Zaferiou PhD

Stevens Institute of Technology, Hoboken, New Jersey, United States

Introduction

Approximately 35-45% of steps are a part of turns. However, most studies focus on straight-line gait (SLG) [1]. The purpose of this study was to analyze how lower-limb net joint moments (NJM) are modulated in the "step" turn strategy [2]. We hypothesized that frontal and transverse plane NJM would be modified during turns versus SLG.

Methods

Healthy female young adults (n=7; 20.4 ± 1.13 years) completed 12 SLG and 90-degree left turn trials along a T-shaped intersection. Optical motion capture (Optitrack) and force plates at the intersection (Bertec) were used. Lower-limb internal NJM were calculated during the stance phase contacting the force plates. Turns were classified as "step" turns if the right foot was closest to the center of the intersection [2]. Trials without acceptable force plate contact were excluded. Data from four participants remained for analysis. A two-sided paired-sample t-test was used to evaluate differences in mean peak NJM between SLG and step turns (α=0.05).

Results

Frontal Plane: Turns had a larger peak ankle evertor (p=0.044) and hip adductor (p=0.049) NJM, and smaller peak ankle invertor (p=0.023) NJM than SLG (Fig.1). **Transverse Plane:** Turns had a larger peak ankle (p=0.011) and hip (p=0.003) external rotator NJM, and smaller peak knee external rotator (p=0.006) NJM than SLG (Fig.1).

Discussion

Supporting the hypothesis, young adults modified lower-limb NJM in the frontal and transverse planes during turns. Further analysis indicates differences could be due to frontal plane lean and redirection of the ground reaction force to align with the new direction of travel. Compared to prior work, ankle NJM results exhibited opposite trends, whereas knee and hip NJM were similar [3]. Data collections are ongoing to expand the sample of young and older adults. Further exploration of NJM across cohorts will improve

our understanding of turn strategies and could have implications for osteoarthritis and joint health.

Images (Optional)

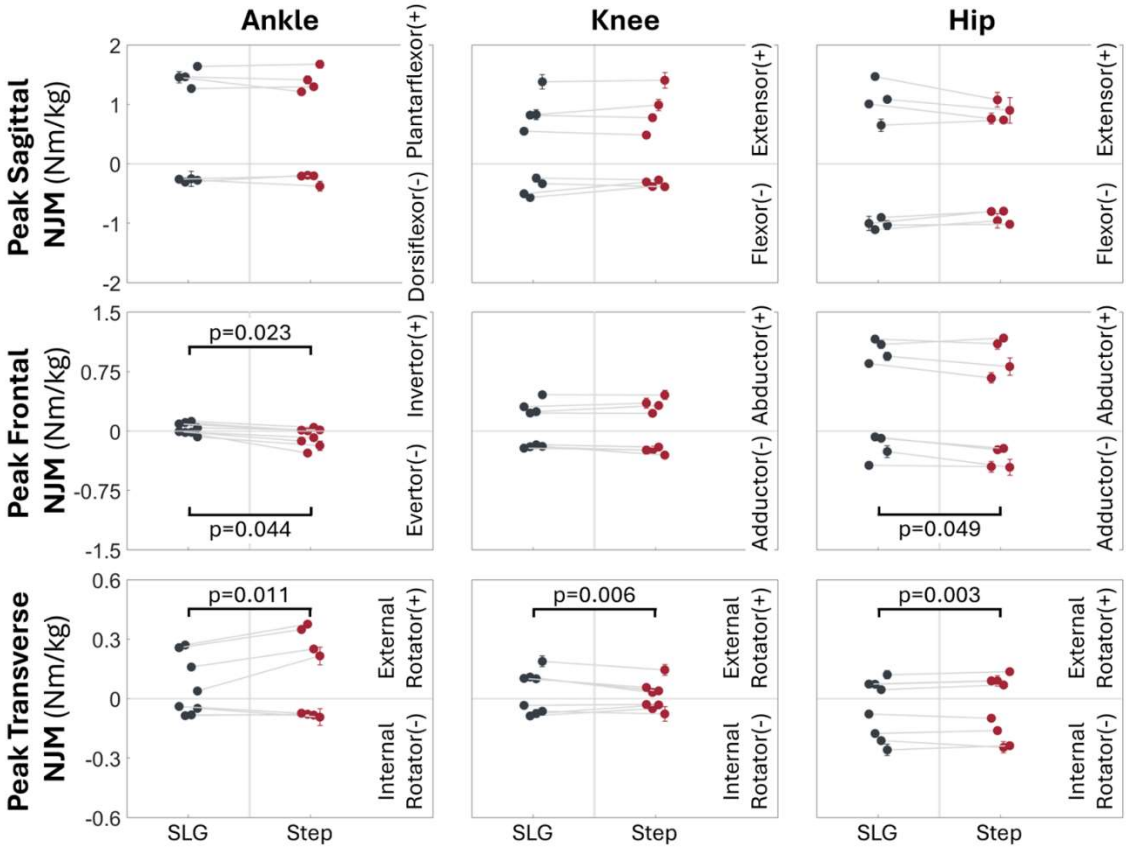


Figure 1: Peak NJM comparisons in each direction across tasks, with significant p-values.

References (Optional)

[1] Brian Glaister et al., Gait Posture, 2007

[2] Pawel Golyski et al., J Biomech, 2017

[3] Matthew Taylor et al., Hum Mov Sci, 2005

Acknowledgements (Optional)

This study was supported by NSF Award #1944207.

Session Category

Human Motion and Performance: Locomotion/Gait

P1-139

TCN Based Deep Learning Enables Task-Agnostic Ground Reaction Force Estimation Using Wearable Sensors

Mr. Ethan Baird, Mr. Matthew Lerner, Dr. Aaron Young

Georgia Institute of Technology, Atlanta, GA, United States

Mr. Ethan Baird

Mr. Matthew Lerner

Introduction

Musculoskeletal biomechanics data provide key insights for development in injury treatment, athletic performance, and disability management. This data relies on the accurate collection of ground reaction force (GRF) data with expensive stationary force plates to make joint-level calculations. Cost effective GRF estimation algorithms [1, 2] make such calculations more accessible with portable and wearable devices, but are limited in their ability to generalize predictions across subjects and tasks. Here, we translate established success in Temporal Convolutional Network (TCN) based task-agnostic joint state estimation [3] to GRF estimation with wearable sensors.

Methods

We trained a TCN on 18 unique tasks from six subjects to estimate full time series GRF: vertical (vGRF), anterior-posterior (aGRF), and mediolateral (mGRF). Features included kinematics measured with a wearable set of lower-limb inertial measurement units (IMU) and kinetics measured with pressure-sensing insoles.

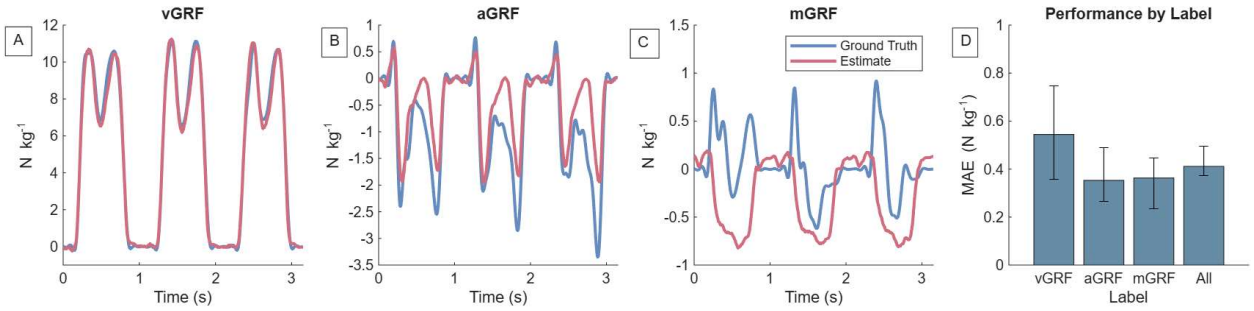
Results

Task-agnostic subject independent vGRF estimation yielded an r^2 of 0.92. Also, the model outperformed many published works in vGRF estimation during level ground walking with an r^2 of 0.98 and a mean absolute error (MAE) of 5.5% bodyweight (BW). Estimation of aGRF showed similar performance to prior works with an MAE of 3.6% BW, but the model failed to accurately track the mGRF trajectory with an MAE of 3.7% BW and an r^2 of 0.32.

Discussion

We demonstrate the feasibility of leveraging TCN-based architecture to attempt task-agnostic GRF estimation using a small dataset. Early success gives us reason to believe that changes to model architecture and size of training data could improve model performance beyond the state of the art for generalizable estimation. Improvements to mGRF estimation performance are especially important to address before this estimator can be applied in the field. One possible change is to incorporate more granular feature mapping in a “CNN-TCN” approach that analyzes a high-resolution time series pressure map of the insole. Such improvements have the potential to increase the accuracy of affordable GRF data collection methods, enabling high quality biomechanics studies in the real world.

Images (Optional)



References (Optional)

[1] Uhlrich *et al.* , PLoS Comput Biol, 2023

[2] Nurse *et al.* , TechRxiv, 2025

[3] Molinaro *et al.* , Nature, 2024

Acknowledgements (Optional)

This work is supported by the Petit Scholars Program

Session Category

Human Motion and Performance: Locomotion/Gait

P1-140

Lower-Limb Heat Flux During Walking Shows Site-Dependent Magnitude but Uniform Time Dynamics

Ms Eunbean Yang M.S., Mrs Sukyung Park Ph.D.

Korea Advanced Institute of Science and Technology (KAIST), Daejeon, Daejeon, Korea, Republic of

Ms Eunbean Yang

Introduction

Heat generated by muscle contraction during movement constitutes a major component of total energy expenditure. Conventional calorimetry-based methods are limited in applicable exercise modalities and cannot isolate muscle-specific thermal responses[1],[2]. Wearable heat-flux sensors now enable continuous monitoring of localized thermal signals, yet, the dynamic characteristics of lower-limb heat-flux responses during walking have not been systematically quantified. This study aimed to characterize the first-order response dynamics of skin heat flux at multiple lower-limb sites during walking at different speeds.

Methods

Twelve healthy adult males performed treadmill walking for 20 minutes at three speeds (1.0, 1.25, and 1.5 m/s) in randomized order. Skin heat flux was measured at four locations: the anterior and posterior aspects of the thigh and shank. GRF(Ground reaction forces) were measured by force plates. Heat flux signals were fitted to a first-order system response model to estimate the time constant and steady-state increase, and differences across speeds and anatomical sites were analyzed.

Results

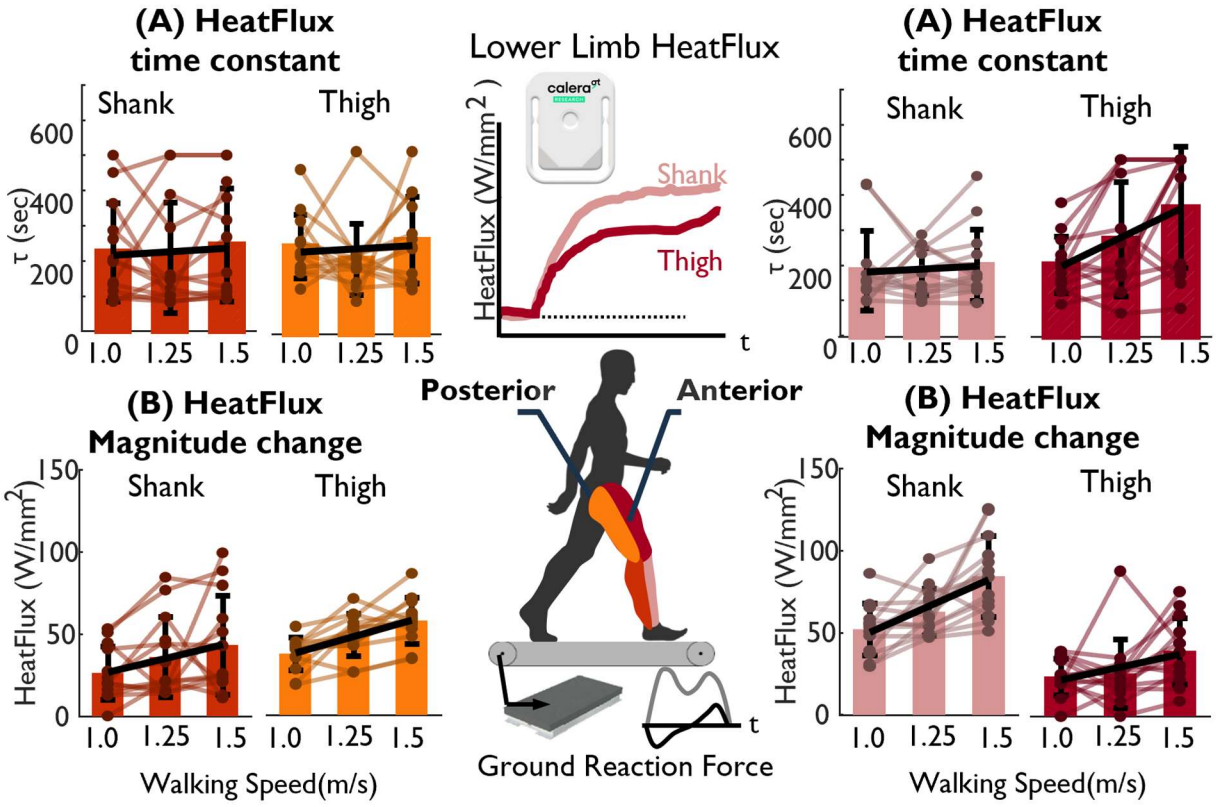
Approximately 95% of shank trials exhibited first-order response characteristics, compared to 70% for the thigh. Atypical responses such as continuous increase or superposition of dual first-order responses were observed at the thigh. The time constant remained consistent at approximately 200 seconds across all sites and speeds. Steady-state heat flux increase was significantly greater at higher speeds for all sites ($p<0.05$), with the shank showing approximately twice the magnitude of the thigh. Correlation analysis revealed

significant associations between peak propulsive GRF and heat flux increase at both of the shank (r = 0.62) and thigh (r = 0.45).

Discussion

This study quantified lower-limb skin heat flux dynamics during walking. While time constants were uniform across sites and speeds, steady-state heat flux was higher at the shank and increased with speed, likely reflecting differences in muscle activation and local thermal physiology. Correlations between steady-state increase and peak propulsive GRF suggest that skin heat flux captures mechanical output during locomotion. These findings highlight the potential of wearable heat-flux sensing for monitoring muscle-specific metabolic demand.

Images (Optional)



References (Optional)

[1] Dauncey et al., *British J Nutrition*, 1978.
[2] Cavagna et al., *J Physiology*, 1977.

Acknowledgements (Optional)

This work was supported by the National Research Foundation of Korea (NRF) grant funded by the Korea government (MSIT) (RS-2024-00356657)

Session Category

Human Motion and Performance: Locomotion/Gait

P1-141

Development and Validation of a Force-Based Self-Paced Split-Belt Treadmill to Assess Force and Speed Perception During Walking

Mr. Evan Shrier[1], Dr. Andrew Hooyman PhD, GStat[2], Dr. Natalia Sánchez Aldana PhD[2]

[1]Chapman University, Orange, California, United States. [2]Chapman University, Irvine, California, United States

Introduction

Perception of force and speed during locomotion is fundamental to balance, coordination, and gait adaptation. Humans can perceive inter-limb speed differences [1], critical for coordinating walking patterns following motor perturbations [2]. Perceiving inter-limb force differences enables targeted force production as part of interventions [1]. Speed and applied force vary concurrently [3], suggesting coupling between these variables. Despite their importance, how force and speed are perceived during locomotion remains poorly understood.

Objective: Develop and validate a novel force-based self-paced (FBSP) split-belt treadmill to assess force and speed perception during walking.

Methods

To develop the FBSP system, a dual-belt GRAIL system was programmed with a fixed speed belt while the other was self-paced based on peak propulsive force (pGRF). Participants walked at five speeds (50–150% of self-selected) with either their dominant or non-dominant leg in FBSP mode, for 10 trials of 2.5 minutes. Visual and auditory information from the treadmill was blocked. Participants were instructed to apply force with the self-paced leg to produce a treadmill speed matching the fixed belt. Validation was conducted with N=3 participants (aged 23–40; two female, one male). Speed and pGRF between fixed and FBSP legs were compared using mean and coefficient of variation (CV).

Results

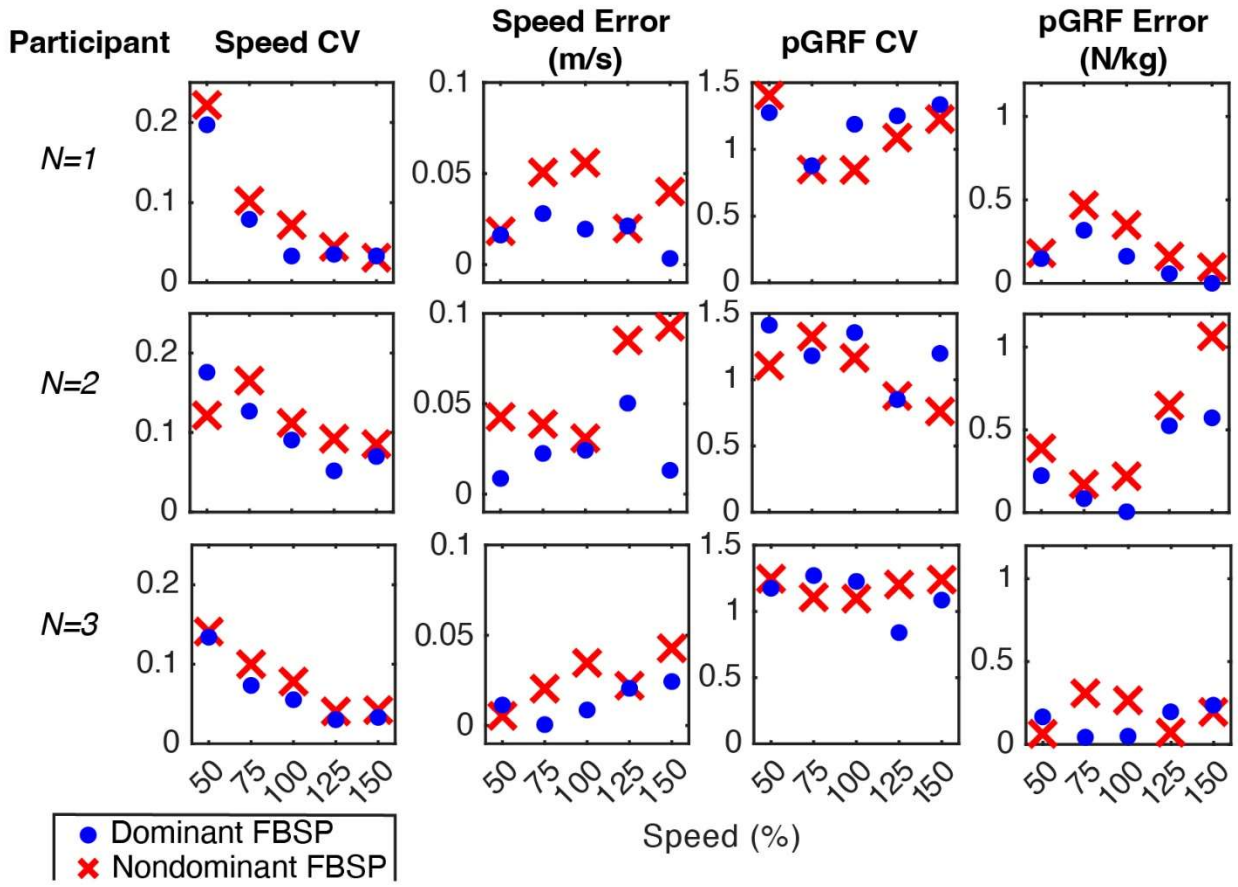
CV of speed difference ranged from 3.01% to 22.2%, showing a J-shaped pattern with greater variability at lower speeds. Speed differences between the FBSP belt and fixed belts ranged from 5.77×10^{-4} to 0.05m/s. Participants matched dominant leg speed with less error (0.017m/s difference) than the non-dominant leg (0.039m/s). No consistent performance pattern was observed across speeds. The CV of pGRF ranged from 76.1% to

141.2%, with differences between FBSP and fixed legs ranging from 2.73×10^{-4} to 1.07N/kg. No consistent effect of dominance was seen for pGRF.

Discussion

Participants perceived inter-limb speed differences during locomotion and were able to generate forces to match speeds between limbs. Preliminary findings show an effect of dominance on task performance. Further testing will assess perception across speeds, ages, and between the dominant and nondominant leg.

Images (Optional)



References (Optional)

[1] A. Vasquez, Journal of Neurophysiology, 2015

[2] N. Sanchez, Journal of Physiology, 2019

[3] M. Bonilla, Scientific Reports, 2023

Session Category

P1-142

Stride Matters: How Crocs Straps Affect Walking Velocity

Dr Fabricio Saucedo Ph.D.

Penn State Altoon, Altoona, PA, United States

Introduction

Shoes have an impact on health and quality of life. With shoes like the classic clog manufactured by Crocs® being commonplace in the food and medical industry, its significant shift to mainstream markets in recent years begs the question of whether there are benefits or risks associated with wearing this style of shoe, specifically in gait performance. Poor fit and failure to use the heel-strap properly or at all raise concerns about whether shoes like Crocs® are detrimental to walking performance. Despite growing popularity for comfort and convenience, their biomechanical impact on gait remains under-investigated. The purpose was to examine the effect of Crocs® with and without heel-strap on walking performance. We hypothesized that participants would display greater walking velocity when walking with the heel-strap, versus strapless and socked.

Methods

Randomized within-subject design was used with a convenience sample of 31 college-aged adults free of impairments. Seven Xsens MVN Awinda inertial measurement units recording at 120 Hz were used to track participants in three conditions during the timed 10-meter walking test (TMW): (i) Socked (CON): walked in socks (ii) Sports-mode (SM): Walked in Crocs® with the heel-strap, and (iii) Casual-mode (CM): Walked in Crocs® without the heel-strap. Gait events, including foot strike and toe-off, were defined by detection algorithms in the Xsens MVN Software and were used to calculate spatial and temporal parameters.

Results

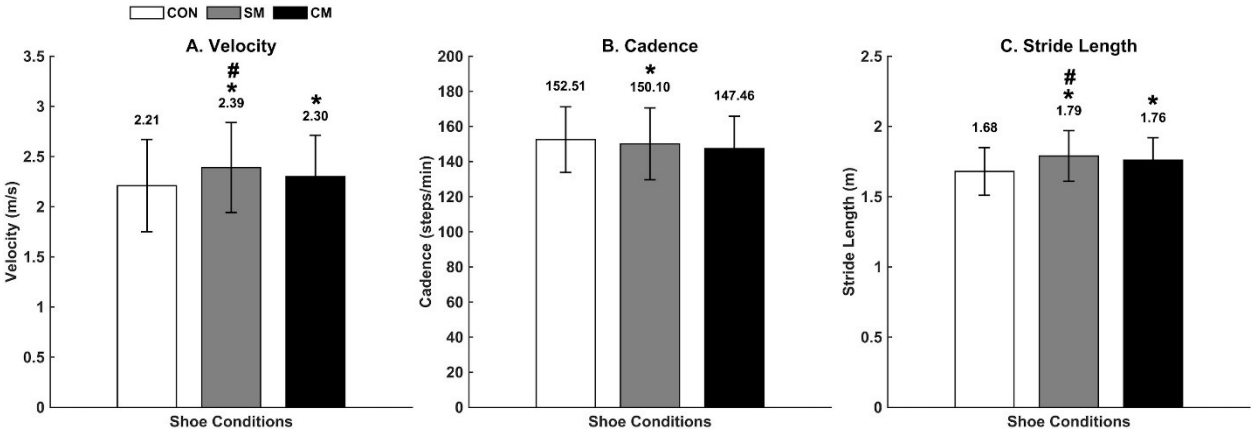
Both shod conditions resulted in improved velocity and stride length compared to the control condition. The sports-mode configuration significantly improved walking velocity and stride length compared both CM and CON conditions while walking.

Discussion

The hypothesis that participants would display better walking velocity during gait assessments while walking in Crocs® with the heel-strap, compared to walking without the

heel-strap or socked (CON) was supported. Study findings suggest that adopting footwear with a heel-strap might improve walking performance compared to a strapless option. Although further study is necessary to determine clinical significance, current findings indicate that wearing Crocs® in the SM configuration might be preferable for individuals requiring longer durations on feet and walking. Additionally, older adults or others with mobility challenges, might benefit from the more secure fit.

Images (Optional)



Acknowledgements (Optional)

The authors would like to thank Sophia Nelson, Cassandra Jane Lee, Jahdon Jerome Jaheim, Justin Hedges, Brayden Casale, Tyler Pennick, and Francois Jouan for their contributions to participant recruitment and data collection throughout the study.

Session Category

Human Motion and Performance: Locomotion/Gait

P1-143

The Influence of Sport Specialization on Movement Coordination in Female Athletes Participating in Hip-Risk Sports

Ms. Fang-Yu Syu PT, Prof. Cara Lewis PT, PhD, FAPTA

Boston University, Boston, MA, United States

Introduction

Sport specialization - intense, nearly year-round participation in a single sport - is strongly associated with lower extremity overuse injuries, particularly in female athletes participating in hip-risk sports (e.g., soccer, ice hockey, and running).

Movement coordination variability, defined as the consistency of the spatiotemporal relationship between joints, is linked to overuse injury risk. While altered knee coordination has been reported in specialized athletes during sport-specific tasks, the relationship between specialization and pelvic-thigh variability during fundamental movement tasks (e.g., walking) remains unexplored.

The purpose of this study was to investigate the relationship between levels of specialization and pelvic-thigh coordination during walking in female athletes participating in hip-risk sports.

Methods

A three-question survey was used to determine specialization level (high=3 points, low ≤ 1 point). Eight high-specialized and six low-specialized female athletes were included in this preliminary analysis. Kinematic data were collected using a motion capture system while participants walked for two minutes at a self-selected speed. Pelvic and thigh angle were processed in Visual3D.

Intersegmental coordination angles were quantified using a vector coding technique, where the coupling angle was defined as the vector orientation between adjacent points on the angle-angle plot relative to the right horizontal. Coordination variability was calculated as the circular standard deviation of the coupling angle across gait cycles. To assess phase-specific differences, coordination variability was averaged within each phase (loading response, mid-stance, terminal stance, and pre-swing).

Given the preliminary nature of the study and limited sample size, the magnitude of group differences was assessed using Cohen’s d effect sizes, interpreted as small/medium/large (0.2/0.5/0.8).

Results

High specialized athletes demonstrated substantially greater coupling angle variability in the transverse plane during loading response (d=1.01). Moderate effects (d>0.5) were also found during loading response and pre-swing (sagittal plane), mid-stance (frontal plane), and terminal stance and pre-swing (transverse plane). (Table 1)

Discussion

Greater pelvic-thigh coupling angle variability across all comparisons in the high specialized group suggests that specialization may be associated with more variable movement control during fundamental movement tasks. Thus, increased movement coordination variability may contribute to elevated overuse-injury risk in female athletes specializing in hip-risk sports.

Images (Optional)

Table 1. Demographic data and coupling angle variability

Demographic Data				
Group	**Age (years)**	**Height (m)**	**Weight (kg)**	**Preferred speed (m/s)**
High Specialized (N=8)	20.83 ± 5.67	1.65 ± 0.09	63.25 ± 15.17	1.29 ± 0.12
Low Specialized (N=6)	17.25 ± 4.71	1.58 ± 0.16	57.14 ± 6.89	1.21 ± 0.18
Pelvic-Thigh coupling angle variability				
Plane	**Sub phase**	**High Specialized Mean ± SD**	**Low Specialized Mean ± SD**	**Effect size (d)**
Sagittal				
	Loading Response	38.75 ± 7.77	34.24 ± 8.36	0.556
	Mid Stance	4.05 ± 0.67	3.95 ± 1.81	0.069
	Terminal Stance	7.48 ± 2.39	6.51 ± 1.88	0.455
	Pre Swing	23.94 ± 7.81	19.68 ± 6.23	0.612
Frontal				
	Loading Response	12.65 ± 4.54	12.65 ± 5.02	0.000
	Mid Stance	23.22 ± 5.23	18.53 ± 5.09	0.548
	Terminal Stance	33.73 ± 11.06	27.54 ± 12.47	0.286
	Pre Swing	12.8 ± 5.92	12.78 ± 6.33	0.107
Transverse				
	Loading Response	40.2 ± 12.37	36.04 ± 5.24	1.013
	Mid Stance	33.01 ± 7.76	30.33 ± 6.22	0.288
	Terminal Stance	25.65 ± 10.16	21.34 ± 6.91	0.509
	Pre Swing	28.58 ± 16.85	24.88 ± 12.73	0.565

Session Category

Human Motion and Performance: Locomotion/Gait

P1-144

Gait Responses to a Bout of Activity in Older Adults With and Without Knee Osteoarthritis

Ms. Fany Alvarado, Ms. Kathleen Downs, Ms. Millissia Murro, Ms. Nancy Nguyen, Ms. Mayumi Wagatsuma, Ms. Grace Kellaher, Dr. Jeremy Crenshaw, Dr. Jocelyn Hafer

University of Delaware, Newark, Delaware, United States

Introduction

Individuals with knee osteoarthritis (OA) have different gait mechanics compared to asymptomatic older adults. Adults with knee OA may also experience more fatigue than their healthy counterparts, potentially leading to additional gait changes. However, to our knowledge, the differences in gait between individuals with knee OA and healthy older adults under fatigue conditions have not been studied. The purpose of this study was to determine if changes in gait in response to a bout of activity differ between older adults with and without knee OA.

Methods

Nine older adults with (63.8±3.0 years) and ten without knee OA (63.5±3.3 years) walked on an instrumented treadmill for 34 minutes at self-selected speed (healthy: 1.5±0.2 m/s; OA: 1.4±0.1 m/s) with three one-minute challenge periods (50% speed increase), and underwent knee extensor dynamometer testing before and after the walk to assess muscle fatigue. A standard six-degree-of-freedom marker set was used for motion capture, and the first and last minute of the 34-minute walk were analyzed. Outcome measures included lower extremity peak sagittal and frontal joint moments and sagittal joint angles. A two-way ANOVA was used to compare gait mechanics between groups (with knee OA and without) and timepoints (pre and post 34-minute walk; α=0.05).

Results

Knee extensor muscle power decreased similarly after the 34-minute walk in both groups (without knee OA: -2.8±20.0%, with knee OA: -10.3±19.3%, p=0.2). The gait of older adults with and without knee OA did not change differently in response to the 34-minute walk (i.e., no significant interaction effects, p-values = 0.27-0.97;Figure 1). Additionally, there were no significant differences between groups or timepoints for any outcome variables (p-values = 0.17-0.94).

Discussion

Older adults with and without knee OA did not respond differently to a 34-minute walk. In contrast to previous (albeit limited) literature, our knee OA and no knee OA cohorts fatigued to a similar extent. The limited fatigue levels and corresponding lack of changes in gait may indicate that participants in both groups were relatively high-functioning. Future research may test whether adults with more severe knee OA would also respond similarly to their asymptomatic counterparts.

Images (Optional)

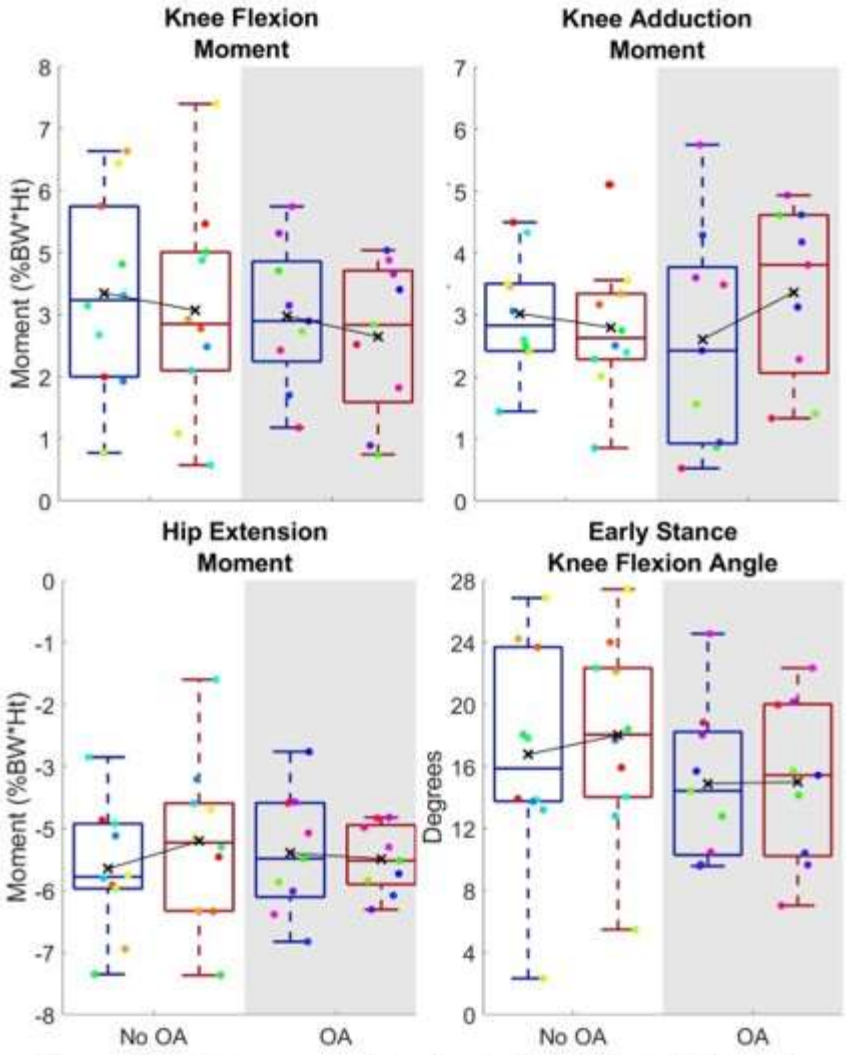


Figure 1: Boxplots represent gait mechanics before (blue) and after (red) the 34 minute treadmill walk, with colored dots showing individual results and xs denoting group means.

Acknowledgements (Optional)

Work supported by NIGMS/NIH grant U54-GM104941.

Session Category

Human Motion and Performance: Locomotion/Gait

P1-145

Comparison of Motion Capture and Pedobarography in Calculating Foot Progression Angle for Children Undergoing Clinical Gait Analysis

Miss Farah Azim BASc[1], Miss Scarlett Farrar[1,2], Ms Diane Wickenheiser BScPT[1], Ms Karen Davies MSc[1,3], Dr Lise Leveille MD, PhD[1,4,5], Dr Timothy Bhatnagar PhD[1,4,5]

[1]The Motion Lab at BC Children's Hospital, Vancouver, BC, Canada. [2]School of Biomedical Engineering, UBC, Vancouver, BC, Canada. [3]Dept of Physical Therapy, UBC, Vancouver, BC, Canada. [4]BC Children's Research Institute, Vancouver, BC, Canada. [5]Dept of Orthopedics, UBC, Vancouver, BC, Canada

Introduction

The Motion Lab (TML), BC Children's Hospital conducts clinical gait analysis (CGA) using motion capture (MoCap) for gait biomechanics and pedobarography to analyze foot pressure distribution. CGA informs decision-making for surgical/orthotic interventions. If a child cannot tolerate marker placement (hypersensitivity, cognitive challenges), only video and pedobarography are collected. Both marker-based MoCap and pedobarography calculate foot progression angle (FPA). TML is interested in comparing FPA between methods to ensure that for children who cannot tolerate markers, pedobarography's calculation of FPA is consistent with MoCap. This study will compare the FPA calculated using MoCap and pedobarography.

Methods

Thirteen participants were identified in this non-randomized cross-sectional study with a referral requesting assessment of rotational profile; both MoCap and pedobarography were collected. Physiotherapists completed a physical exam and placed markers according to the Helen Hayes marker set [1] and modified Shriners Hospital for Children Greenville multi-segment foot [2,3]. Participants completed five gait cycles and walked across the pedobarography platform, aiming for three foot-strikes per side. TML uses Qualisys MoCap system and novel emed platform for pedobarography. MoCap was processed in QTM and Visual3D. FPA was calculated as the angle between the vector from the heel to toe marker in relation to the lab, averaged across five trials. Pedobarography was processed in novel's software, which averaged FPA from three trials. Average FPA from both datasets were compared, alongside physical exam values (hip rotations, thigh/foot angles, transmalleolar angles). The right/left sides were combined.

Results

Mean difference in FPA between methods was 3.88° (SD=3.04°, range=0.15°-10.71°) across participants (mean=13.5y, 4 females), with pedobarography calculating lower FPA. Both methods measured FPA in the same direction (external/internal). Mean hip external rotation was 35° (SD=15°); hip internal rotation was 58° (SD=17°); thigh/foot angle was 15° external (SD=17°); and transmalleolar angle was 26° external (SD=10°).

Discussion

Findings show minimal differences in FPA calculated by both methods, as TML's standard of error is 3°. Future analysis will explore relationships between physical exam and FPA differences and include additional participants.

References (Optional)

[1] Kadaba et al., J Orthop Res, 1990.
[2] Maurer et al., Gait & Posture, 2013.
[3] Saraswat et al., Gait & Posture, 2012.

Session Category

Human Motion and Performance: Locomotion/Gait

P1-146

Hip Extensor EMG Frequency Patterns During Speed Increase in Stepping Tasks With Controlled Stride Parameters

Br Florencia Delfino[1], PhD Germán Pequera[1,2], PhD Carlo Biancardi[1]

[1]LIBiAM Biomechanics Lab, Dep. of Biological Sciences, CENUR Litoral Norte, Universidad de la República, Paysandú, Paysandú, Uruguay. [2]Departamento de Ingeniería Biológica, CENUR Litoral Norte, Universidad de la República, Paysandú, Paysandú, Uruguay

Br Florencia Delfino

PhD Germán Pequera

Introduction

Gait speed is used to evaluate health condition [1]. When speed increases, step frequency (F) and step length (L) increase simultaneously. The impact on muscle function of modifying F or L independently during speed augmentation has yet to be studied [2]. Knowing how adaptations work in these conditions is important for numerous applications. The objective of this ongoing research is to evaluate muscle function when legs are oscillating at different speeds by controlling F and L independently, using an airwalker as a stepping device.

Methods

Five subjects participated in three trials on an airwalker combining different target step lengths (tL) and target step frequencies (tF) to achieve two target speeds (tV), since tV = tL x tF. The University Ethics Committee approved this study. The objective was to increase speed by modifying one spatiotemporal parameter at a time. Inextensible cords linked to the airwalker platforms were used to control tL, while tF was set using an audible metronome. Trials were:

- tF=1.5Hz, tL = 0.55m achieving 3 km/h (03);
- tF = 1.5Hz, tL = 0.74m achieving 4km/h (4L);
- tF = 2.05Hz, tL = 0.55m achieving 4km/h (4F);

Data from both fifth metatarsals was registered at 100Hz (10 Vicon cameras). Electromyography (EMG) of 4 hip extensor muscles (Biceps femoris, Semitendinosus, Gluteus medius and Gluteus maximus) were collected at 2000 Hz (Delsys Trigno). F, L and velocity were calculated to validate the protocol. EMG frequency distribution (FreqDist) was estimated for each trial [3].

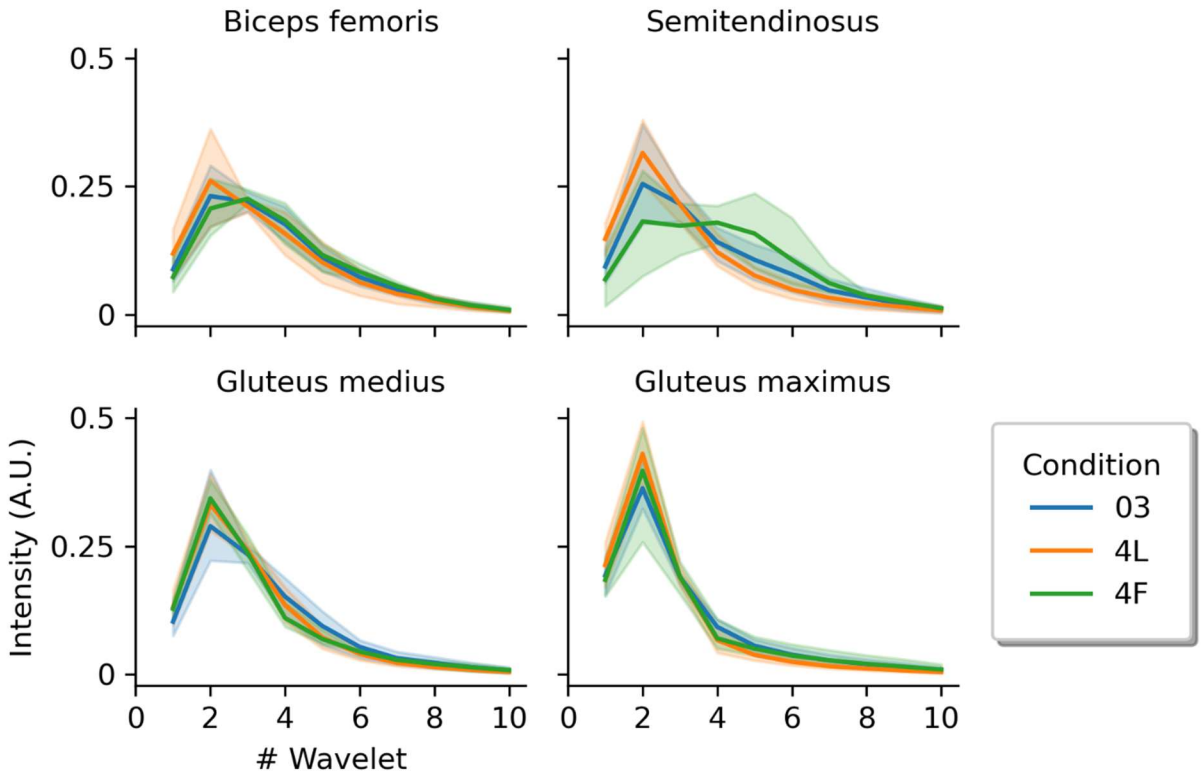
Results

Hip extensors showed different behaviors when comparing FreqDist. The most noteworthy result was observed in Semitendinosus muscle. Speed increased by L or by F modulation caused opposite changes of FreqDist. More data is needed to confirm these trends.

Discussion

Despite sharing function, hip extensors displayed different FreqDist response. F or L driven speed changes caused FreqDist shifts towards higher or lower frequency, respectively in Semitendinosus. This could indicate changes in fiber types recruitment, positioning this muscle as an important modulator of spatiotemporal parameters.

Images (Optional)



References (Optional)

[1] Fritz & Lusardi (2009). Journal of Geriatric physical therapy.

[2] Lim, et al (2017). Journal of Biomechanics.

[3] Von Tscharner (2000). Journal of Electromyography and Kinesiology

Acknowledgements (Optional)

Comisión Sectorial de Investigación Científica, Universidad de la República, Uruguay for economical support.

Session Category

Human Motion and Performance: Locomotion/Gait

P1-147

Higher Frictional Internal Work During Limb Swing in Class III Obese Adults

Dr Gaspare Pavei[1], Dr Valentina Natalucci[1], Prof Alberto Minetti[1], Dr Luca Ruggiero[2], Prof Davide Malatesta[3]

[1]University of Milan, Milan, Italy, Italy. [2]University of Konstanz, Konstanz, Germany, Germany. [3]University of Lausanne, Lausanne, Switzerland, Switzerland

Introduction

Obese class III adults [body mass index (BMI) >40 kg/m^2] showed a higher metabolic cost than lean counterparts (BMI<25 kg/m^2) [1] when walking at all speeds. The mechanical work to move the center of mass is lower in obese class III adults than lean counterparts, with no between-group differences in the work to swing the limbs [1]. Hence, the reason for the higher metabolic cost in obese class III adults is unknown. Along with the 'classical' mechanical work approach, an additional component to overcome limb friction when swinging (frictional internal work) has been recently proposed [2]. Given the higher mass of proximal segments within limbs [1], we hypothesized that obese adults would have a higher frictional work than their lean counterparts.

Methods

The lower and upper dominant limbs of 13 obese class III adults (4 female) were swung passively from an initial position of ~30° flexion, while 2D kinematics (120 Hz) was recorded. The oscillating limb was treated as a second-order pendular system with viscous damping (linear to velocity). Five trials were recorded, each yielding a damping constant. Average values were used to calculate frictional internal work [2], using spatiotemporal parameters of obese walking adults [1], and were compared with lean adults [2].

Results

In the upper limb, the damping constant was 0.52±0.19 and 0.37±0.08 Nm·s/rad in obese and lean adults, respectively. The damping constant of the lower limb was almost twice in obese than lean adults, 4.14±2.41 vs. 2.24±0.55 Nm·s/rad. These values in obese adults yielded an average frictional internal work about 30% higher than lean adults.

Discussion

The higher frictional internal work to swing limbs in obese relative to lean adults may contribute to explaining the extra metabolic cost in walking [1]. Thus, frictional internal work represents a promising parameter to be considered in future research addressing differences in locomotion between obese class III and lean adults.

References (Optional)

[1] Fernandez Menéndez *et al*., Journal of Applied Physiology, 2020.

[2] Minetti *et al.,* Proceeding of the Royal Society B, 2020.

Session Category

Human Motion and Performance: Locomotion/Gait

P1-148

Skipping vs Running Along Circular Paths: Which Is Better?

Master student Elsa Josefa Gonzalez Heit[1], PhD Valentina Silva-Pereyra[1], Master student Vanessa Yelós Tellagorry[2], PhD Gaspare Pavei[3], PhD Germán Pequera[2,1], PhD Carlo Massimo Biancardi[1]

[1]LIBiAM Biomechanics Lab, Dep. of Biological Sciences, CENUR Litoral Norte, Universidad de la República, Paysandú, Paysandú, Uruguay. [2]Departamento de Ingeniería Biológica, CENUR Litoral norte, Universidad de la República, Paysandú, Paysandú, Uruguay. [3]Physiomechanics Lab, DFPMCT, University of Milan, Milan, Lombardy, Italy

Introduction

Skipping, or bipedal gallop, is a bouncing asymmetrical gait, which cycle begins with the trailing foot strike, followed by the leading and a final, unsupported, ballistic phase. Unlike cursorial quadrupeds, humans occasionally or in specific conditions skip. Our research aims to investigate the potential advantages of skipping during asymmetric locomotor tasks, such as moving along circular paths.

Methods

Participants were asked to perform three trials along a circular path of radius 3 m: 1) Unilateral skipping with inner leading (Sk_I); 2) same with outer leading (Sk_O); 3) running (R). Auditive feedback was provided to maintain a constant stride frequency of 1.5 Hz. Ethics Committee approved the project.

Metabolic baseline was obtained during 5' upright standing before the trials, and subtracted from the average VO2 of the last minute of each trial (K5, Cosmed, Italy). The cost of transport (CT) was computed using the RER energetic equivalent. Speed was obtained by analysing videos (60 Hz).

Vertical ground reaction forces were measured with instrumented insoles (Loadsol_pro, Novel, Germany). Data were filtered (4th order zero-lag Butterworth LPF, 15 Hz cut-off). Gait events were identified using a 20N threshold. Duty factor (DF), peak vertical force and asymmetry indices were computed.

Results

The preliminary results are shown in table 1. The CT was averaged over a range of speed from 1.7 to 2.4 ms^{-1} (N=8). We have obtained kinetic data from a single subject so far. Therefore, DF and peak forces, averaged over 300 strides per condition, represent a within-subject stride variability.

Discussion

The CT was 25% higher in circular compared to linear running. Skipping did not show a similar trend, nor differences between inner and outer leading.

Preliminary single-subject kinetic data indicate a trend toward a reduction of stance asymmetry in both skipping modes, compared to linear skipping. In running, the slightly increased DF of the outer foot, if confirmed, could underline a load-mitigating strategy that counteracts the increase of the outer peak GRF and the rise in force asymmetry during circular running.

Although the metabolic cost remains high, skipping could present pros during asymmetric tasks like circular locomotion.

Images (Optional)

Table 1.

		Running	Skipping Inner leading	Skipping Outer leading
CT	J Kg^{-1} m^{-1}	5.1 ± 0.4	6.4 ± 0.8	6.1 ± 0.7
DF Leading	%	34.0 ± 2.5	52.2 ± 1.2	48.9 ± 4.9
DF Trailing	%	35.3 ± 1.4	53.1 ± 0.3	50.1 ± 2.3
Peak force Inner	N	1400 ± 15	1295 ± 59	1348 ± 43
Peak force Outer	N	1555 ± 18	1274 ± 25	1287 ± 34
Peak asymmetry	%	10.4 ± 1.0	4.3 ± 3.7	4.6 ± 2.7
Stance asymmetry	%	8.1 ± 7.5	2.6 ± 1.5	8.1 ± 7.7

References (Optional)

Acknowledgements (Optional)

This work is part of a post-graduation project supported by PEDECIBA - Program for the Development of Basic Sciences

Session Category

Human Motion and Performance: Locomotion/Gait

P1-149

Design and Preliminary Validation of a 'Modular Footwear Setup' to Test the Effect of Midsole Designs on Lower Limb Biomechanical Parameters

PhD Paolo Caravaggi[1], MEng Giulia Rogati[1], MEng Kamran Shakir[2], MPhil Hadi Sarlak[2], MEng Giorgia Sartorato[3], MS Filippo Goi[4], MD Lisa Berti[2], DPhil Alberto Leardini[1]

[1]IRCCS Istituto Ortopedico Rizzoli, Bologna, Emilia Romagna, Italy. [2]Università di Bologna, Bologna, Emilia Romagna, Italy. [3]PODARTIS srl, Treviso, Veneto, Italy. [4]Vibram, Varese, Lombardia, Italy

PhD Paolo Caravaggi

Introduction

Therapeutic footwear, often combined with insoles, is crucial for managing foot pathologies, particularly in preventing diabetic foot ulcers [1]. While various diabetic shoe designs exist, there is limited evidence on the isolated effects of midsole shape and material on lower limb kinematics and plantar pressure distribution. This study aimed to design and validate a novel, modular tool capable of assessing the isolated effect of different midsole designs and materials on relevant lower limb biomechanical parameters.

Methods

A Modular Footwear Setup (MFS) was developed, comprising a comfortable flexible upper (figure, top left), a micro-hook-and-loop-fastener layer and interchangeable midsoles (Vibram). A custom 3D-printed alignment device was designed for accurate and repeatable midsole attachment (figure, bottom left). The upper was manufactured in five sizes (EU 37-45) replicating those of a standard diabetic shoe (Botero, Podartis). Ten healthy subjects (5M, 5F; age=33±9 yrs) were asked to walk in two shod conditions: wearing the standard diabetic shoe and wearing the MFS fitted with an identical midsole. In-shoe plantar pressure was recorded using 99-sensor pressure insoles (Pedar, Novel) at 100 Hz. Lower limb kinematics were captured using seven IMU sensors (Ultium Motion, Noraxon) on the pelvis and lower limb segments. Five gait cycles were recorded per subject and per condition. The non-parametric paired Wilcoxon signed-rank test was used to compare pressure and kinematic data between the two conditions.

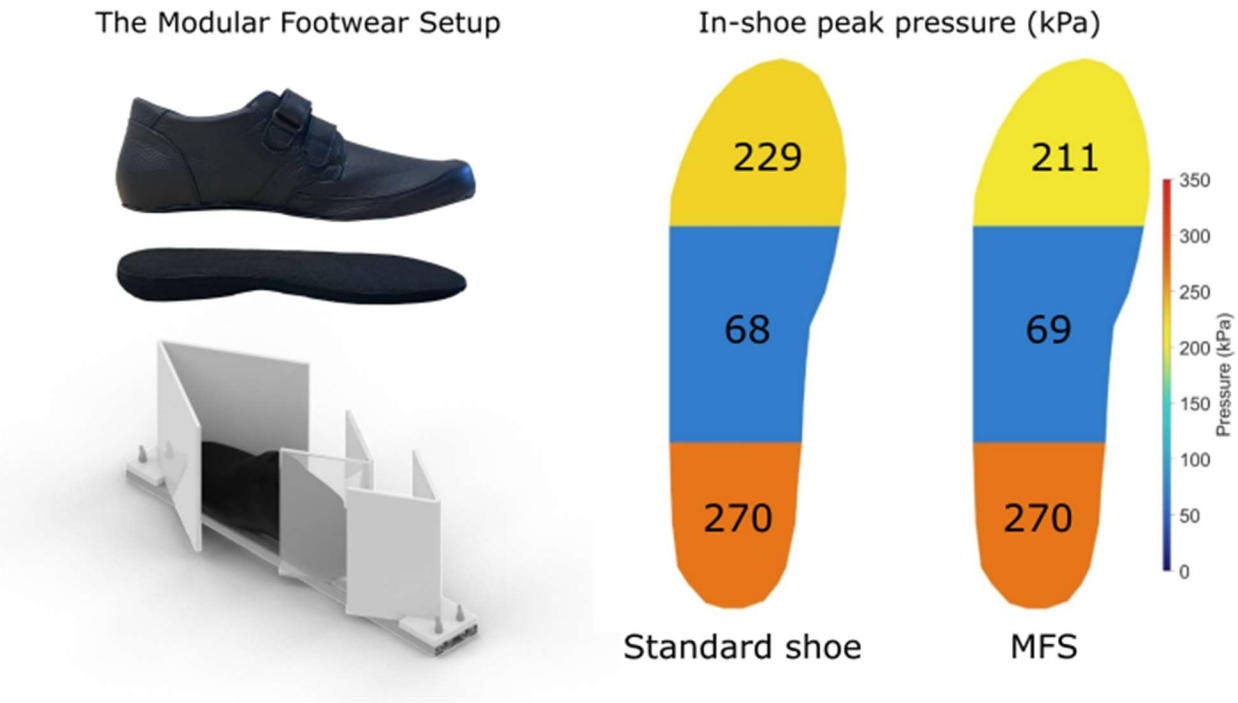
Results

Subjects maintained a consistent walking speed between the two shoe conditions ($p>0.05$). The MFS showed no significant differences in the sagittal-plane range of motion for the hip, knee, and ankle joints when compared to the standard diabetic shoe ($p>0.05$). Similarly, there were no significant differences in mean and peak plantar pressures at the forefoot, midfoot, and rearfoot regions (figure, right).

Discussion

The MFS tool appears capable of reliably replicating the kinematic and in-shoe pressure outcomes of a standard therapeutic shoe. These results suggest the MFS has the potential to be a useful and repeatable tool for testing the isolated biomechanical effects of various midsole designs and materials in large-scale clinical trials and for developing novel offloading therapeutic footwear.

Images (Optional)



References (Optional)

[1 Sicco Bus *et al.*, Diabetes Metab. Res. Rev., 2024

Acknowledgements (Optional)

This study is funded by the European Union's Horizon Europe research and innovation programme under the Marie Skłodowska-Curie Doctoral Network Grant No 101073533

Session Category

Human Motion and Performance: Locomotion/Gait

P1-150

Muscle Coordination Is More Complex In Older Adults When Walking In Real-World Conditions Versus Laboratory Conditions and Associated With Clinical Gait and Balance Scores

Mr. Grant Maddox, Mr. Reece Lawrence, Ms. Kaitlyn Downer, Dr. Jessica Allen PhD

University of Florida, Gainesville, Florida, United States

Introduction

Proper muscle coordination is essential to prevent falls while walking. While indoor straight-line walking is commonly used to assess muscle coordination complexity, it is not fully representative of the diverse range of tasks faced during real-world walking. We hypothesize that (1) muscle coordination complexity would be greater when walking in real-world settings (i.e., outdoors) than in indoor laboratory settings. Because muscle coordination complexity likely reflects underlying gait and balance capacity, we hypothesize (2) complexity would correlate with clinical gait and balance scores, and (3) correlations would be larger in outdoor walking due to higher demands. Such links may indicate that more complex environments are needed to reveal deficits in muscle coordination underlying impaired walking balance.

Methods

Seventeen older adults (76.59±5.4 years) walked at preferred speed under two conditions: laboratory-based 20-meter overground walk and an outdoor route incorporating ramps, stairs, and turning. Surface electromyography was recorded from twelve right-leg hip, knee, and ankle muscles. Muscle coordination complexity was quantified as variability not explained by one motor module (VNAF1)[1]. A paired t-test was used to identify if outdoor walking is more complex than indoor walking. We performed Pearson's correlation between each measure of complexity and four clinical test scores (Fig.1B). Steiger's z-tests were used to identify if there was a significant difference in outdoor vs. indoor correlations.

Results

Muscle coordination was more complex when walking outdoors versus indoors ($p=0.005$; Fig.1A). Although we found moderate to strong correlations between clinical tests and muscle coordination complexity in indoor ($r=0.30$-0.46) and outdoor walking ($r=0.24$–0.57), no significant differences between conditions were identified ($p=0.21$–0.73; Fig.1B).

Discussion

Outdoor walking elicited greater muscle coordination complexity, indicating higher coordination demands in real-world movement than in straight-line walking. This reinforces the importance of examining broader range of walking conditions when evaluating balance capacity. Both indoor walking and outdoor walking have similar correlations with clinical tests, suggesting that coordination complexity is likely related to gait and balance function. Future work will examine to what extent indoor vs. outdoor muscle coordination complexity relates to real-world falls, providing insight into its potential clinical relevance.

Images (Optional)

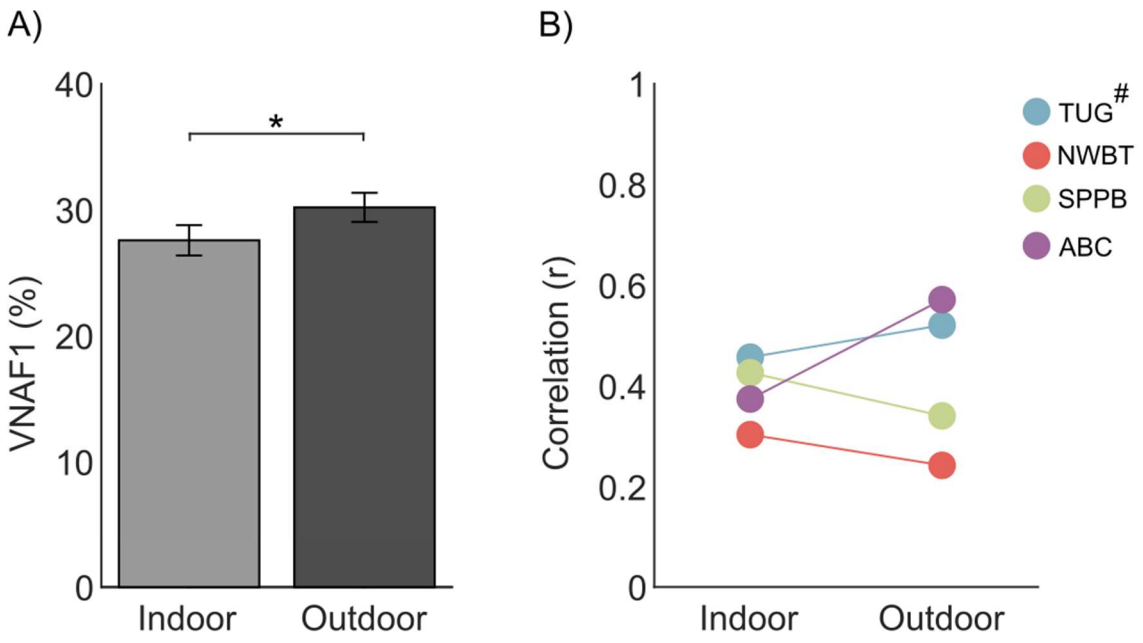


Figure 1: A) Paired t-test to evaluate the difference between indoor and outdoor muscle coordination complexity with error bars representing the standard error of the mean. B) Steigers z-test to assess differences between Pearson's correlations with clinical gait and balance tests (Timed Up and Go (TUG), Narrow Beam Walking Test (NWBT), Short Performance Physical Battery Test (SPPB), and Activity Balance Confidence (ABC) scale) and indoor and outdoor muscle coordination complexity.

#: Absolute value of Pearson's correlation

References (Optional)

[1] Steele et al., Dev Med Child Neurol, 2015

Acknowledgements (Optional)

Supported by P30 AG028740

Session Category

Human Motion and Performance: Locomotion/Gait

P1-151

Stronger Perturbations Increase the Contribution of Spinal Reflexes in Forward Dynamics Simulation of Human Walking

Mr. Gunwoo Park[1], Prof. Friedl De Groote[2], Prof. Seungbum Koo[1]

[1]KAIST, Daejeon, Daejeon, Korea, Republic of. [2]KU Leuven, Leuven, Leuven, Belgium

Introduction

Spinal reflexes are active during human walking and are widely hypothesized to enhance stability by providing rapid proprioceptive feedback [1]. Theoretical neural controller models have been proposed to explain locomotor function, yet the precise role of reflexes remains unclear, as both reflex-based and reflex-absent controllers are commonly used for walking simulations. In this study, we developed an integrated neural controller that combines supraspinal commands and spinal reflex and found that reflex-derived excitation increased if the controller is optimized under stronger pelvis force perturbation.

Methods

The neural controller comprised a reflex circuitry [2] and a multilayer perceptron (MLP) implementing a 150ms input-output delay. The MLP received the full-body state and produced both the gating variables to modulate each reflex feedback gain and the supraspinal excitation signals. Muscle excitation was the sum of the reflex-derived and supraspinal excitation from the MLP. All parameters were trained using proximal policy optimization with rewards for motion tracking and activation minimization. Training was done on a musculoskeletal model with 14 DoF and 22 Hill-type lower-limb muscles. During perturbed training episodes, anteroposterior pelvis force was applied, with its value resampled every 200ms from uniform distribution with [-Fmax, Fmax]..

Results

The neural controller achieved stable walking with a mean lower-limb joint-angle error of 1.2° relative to the reference motion when trained without perturbations. With a perturbation amplitude of 0.2BW, the controller maintained continuous walking for 20s in 88% of episodes. Reflex-derived excitation and its proportion of total excitation increased with perturbation magnitude: from 0.038 (16.6%) in the unperturbed condition to 0.073 (26.6%) with Fmax=0.1BW, and to 0.092 (29.3%) with Fmax=0.2BW.

Discussion

The increased contribution of reflex pathways observed in the perturbed training suggests that the controller adapted its policy by amplifying feedback gains to reduce falls. This

behavior indicates that spinal reflexes stabilize when the locomotor system is exposed to environmental uncertainty. Although reflex-derived excitation accounted for about 16-30% of total excitation, interpreting these quantitative values requires caution [3]. Improved models and training methods may allow more rigorous quantification of reflex contributions.

References (Optional)

[1] Zehr & Stein, Prog. Neurobiol, 1995.

[2] Song & Geyer, J. Physiol, 2015.

[3] Mrachacz-Kersting & Sinkjær, Exp. Brain. Res., 2003

Acknowledgements (Optional)

This work was supported by the IITP grant funded by the Korean government (MSIT) (No. 2022-0-00025), and the NRF grant funded by the Korean government (MSIP) (No. RS-2023-00277425).

Session Category

Human Motion and Performance: Locomotion/Gait

P1-152

Forward Dynamic Gait Simulations Considering CPGs and Spinal Reflexes

M. Sc. Gwen Spelly[1], M. Sc. Julian Shanbhag[1], PD Dr. phil. Heiko Gassner[2,3], M. Sc. Iris Wechsler[1], Prof. Dr.-Ing. Sandro Wartzack[1], Assoc. Prof. PD Dr.-Ing. habil. Jörg Miehling[4,1]

[1]Engineering Design, Friedrich-Alexander-Universität Erlangen-Nürnberg (FAU), Erlangen, Bavaria, Germany. [2]Department of Molecular Neurology, University Hospital Erlangen, Friedrich-Alexander-Universität Erlangen-Nürnberg (FAU), Erlangen, Bavaria, Germany. [3]Fraunhofer Institute for Integrated Circuits IIS, Erlangen, Bavaria, Germany. [4]Department of Civil and Mechanical Engineering, Technical University of Denmark (DTU), Kongens-Lyngby, Capital Region, Denmark

Introduction

Central pattern generators (CPGs) and reflexes are considered to contribute to the basic motor pattern of human gait at a spinal level. However, the exact mechanisms and contributions are still unclear. It is necessary to integrate such motor control mechanisms in forward dynamic gait simulations to represent healthy and pathological motor processes and to investigate the impact of various support types. The existing challenge is to map the complex motor control from supra-spinal and spinal motor functions in a physiologically plausible way.

Methods

To represent CPGs and spinal reflexes simultaneously in gait simulations, two controllers with varying amounts of feedforward and feedback signals were investigated. The simulations were conducted in SCONE using Hyfydy [1]. A two-dimensional musculoskeletal human model with 18 muscles and 9 degrees of freedom was used.

CPGs were represented by feedforward signals calculated from gait-phase-dependent interpolatory cubic splines, that aimed to mimic segment positions and orientations of a previously simulated gait movement. Spinal reflexes were adapted from previously published models [1], [2], [3].

The feedforward-dominant (FFD) controller excited all muscles based on feedforward signals. Additionally, PD-feedback was used to stabilize pelvis tilt.

The second controller calculated muscle excitations based on feedforward and feedback signals (FFB) for thigh and hip muscles. Shank muscles were solely excited by proprioception.

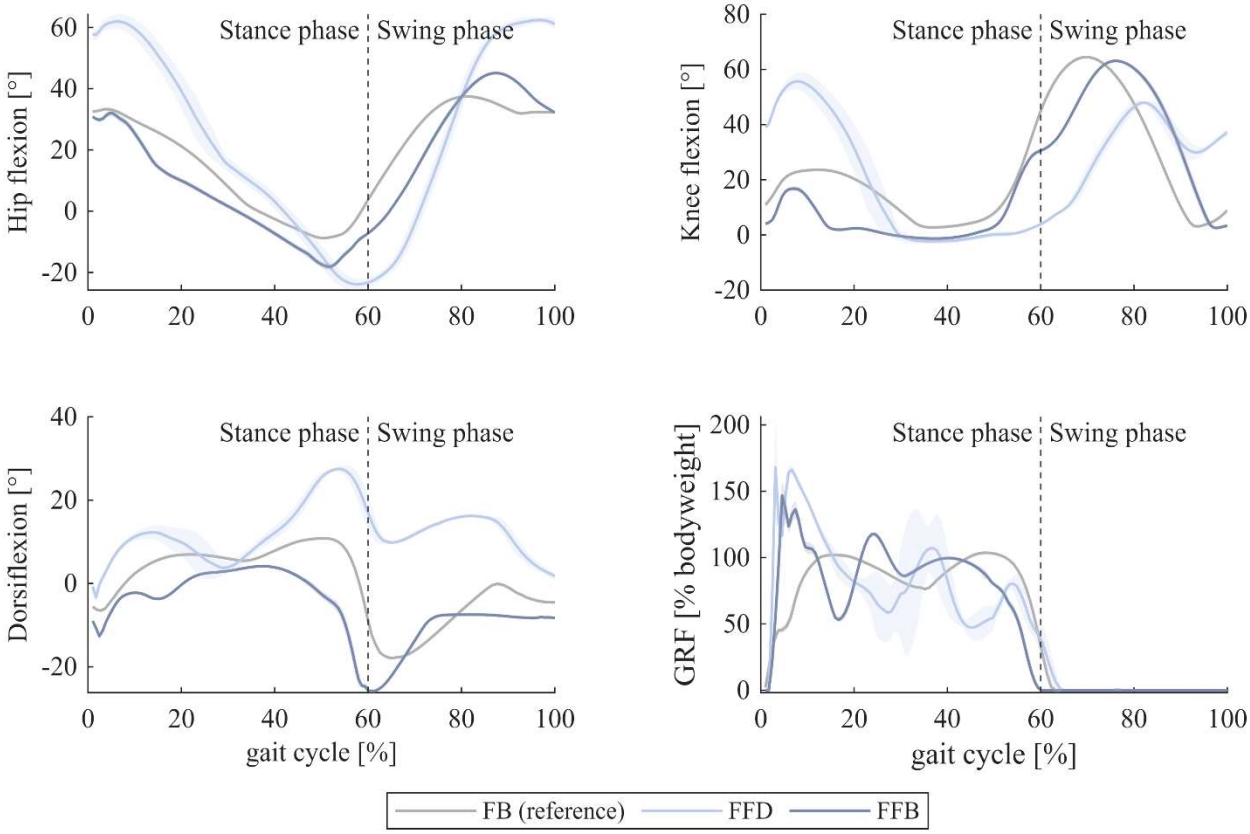
Results

Simulation results from both new controllers were compared with results from a solely reflex-based controller [1] (FB). Highly loaded initial contacts were observed. FFD led to larger step sizes, higher knee flexion during stance phase, and increased dorsiflexion. Co-contractions and maximum muscle activations were observed. FFB produced slightly increased plantarflexion during push off and higher iliopsoas activation compared to FB.

Discussion

Feedforward signals, which aim to mimic existing gait patterns, have been demonstrated to be a promising method for representing CPGs in forward dynamic gait simulations. Nonetheless, spinal reflexes, were observed to contribute to natural gait, which is in line with physiological motor control theories. Supra-spinal motor control was simplified by automatic gait-phase-detection and should be considered in the future.

Images (Optional)



References (Optional)

[1] T Geijtenbeek, *JOSS, 2019*

[2] H Geyer & H Herr, *IEEE TNSRE, 2010*

[3] CF Ong et al., *PLoS CB, 2019*

Acknowledgements (Optional)

This work was partly funded by the Deutsche Forschungsgemeinschaft (DFG, German Research Foundation) – SFB 1483 – Project-ID 442419336, EmpkinS

Session Category

Human Motion and Performance: Locomotion/Gait

P1-153

Gait Symmetry and Variability of Spatiotemporal Parameters During Treadmill Walking at the Preferred Walking Speed

Assistant Professor Haneol Kim PhD

University of Wisconsin - La Crosse, La Crosse, WI, United States

Introduction

Gait symmetry, the spatiotemporal similarity between limbs, provides a fundamental indicator of coordinated healthy neuromuscular control, while deviations are linked to pathology, injury, or musculoskeletal impairments [1]. Rhythmic auditory stimulation (RAS) has been used in rehabilitation that can induce sensorimotor entrainment and improve abnormal or pathological gait. This study aimed to examine how different RAS frequencies affect both gait symmetry and variability during treadmill walking.

Methods

Six young adults (4F/2M) voluntarily participated in this study. Each participant completed 5-minute treadmill walking trials at their preferred speed under four conditions: no auditory cueing, and three RAS frequencies set to 75, 100, and 125 beats per minute. Step length and step time asymmetry were calculated using an Asymmetry Index (AI), and variability was quantified with the Coefficient of Variation (CV) [1, 2]. A one-way repeated measures ANOVA was conducted with a significance of $\alpha = 0.05$.

Results

While AI showed no statistically significant differences across conditions, variability was significantly influenced by RAS. Young adults increased the CV of step length with RAS ($p = 0.048$). Post-hoc analysis revealed a significant difference between the no auditory cueing condition and the 125 BPM condition ($p = 0.008$). CV of step time also increased with auditory cueing ($p = 0.037$). Post-hoc analysis revealed a statistically significant difference between the no auditory cueing condition and 125 BPM ($p = 0.043$). The greatest CV was found at the metronome beats of 75 BPM, and the lowest with no auditory cueing for both parameters.

Discussion

These findings indicate healthy young adults can maintain symmetrical gait patterns even when external auditory cues disrupt likely because they can adjust to different RAS frequencies. RAS appeared to increase variability, reflecting a disruption in the consistency of their locomotor rhythm. This study contributes to understand how symmetry and

variability typically present in healthy young adults under these controlled conditions. Future research involving larger samples of young adults will be important to verify these observations and to support comparisons with children or individuals with gait impairments.

References (Optional)

[1] Cabral, S. *et al.*, J Applied Biomechanics, 2016

[2] Herssens, N. *et al.*, Gait & Posture, 2018

Acknowledgements (Optional)

We are grateful to all the participants for volunteering their participation. This study was partially supported by the University of Wisconsin-La Crosse Faculty Research Grant.

Session Category

Human Motion and Performance: Locomotion/Gait

P1-154

Video-Based Estimation of Subject-Specific Body Segment Parameters

Mr. Hariharan Sureshkumar Graduate Student, Dr. Seungmoon Song Ph.D.

Northeastern University, Boston, MA, United States

Introduction

Markerless motion capture systems are increasingly used in biomechanics and clinical assessment due to their lower cost and reduced setup time compared to marker-based systems. However, their accuracy varies across platforms and depends on camera configuration, task complexity, and environmental conditions. This study aims to evaluate the performance of three markerless systems Theia, OpenCap, and FreeMoCap across a range of gait and functional movement tasks. Theia is used as the reference system based on its established consistency in controlled laboratory environments using an eight-camera Qualisys setup. A secondary objective is to quantify how the number of cameras or iOS devices affects measurement accuracy, particularly for OpenCap and FreeMoCap.

Methods

We plan to recruit 20 healthy adults who will perform treadmill walking and running at multiple speeds, as well as overground tasks such as squats, sit-to-stand, range of motion tests, and obstacle negotiation. Data will be collected using Theia (8-camera setup), OpenCap (2–8 iOS devices), and FreeMoCap (3–4 cameras, with highercamera testing planned). Metrics include 3D joint angles, joint center trajectories, and spatiotemporal gait parameters (stride length, cadence, step time). Comparative analyses will evaluate both system-level differences and the effect of increasing camera count for OpenCap and FreeMoCap.

Results

Preliminary pilot recordings indicate that Theia provides stable and consistent joint angle estimates across treadmill walking and running. OpenCap shows minimal improvement in accuracy when increasing from one to eight iOS devices. Early FreeMoCap results suggest improved stability and reduced trajectory noise with additional cameras, though testing with more than four cameras is pending. Larger discrepancies across systems appear during fast movements and motions with large limb elevation, such as obstacle negotiation.

Discussion

Initial findings show distinct system behaviors: Theia remains reliable across conditions, OpenCap performance is relatively insensitive to additional cameras, and FreeMoCap benefits from increased camera count but requires further evaluation. The completed study will provide guidance for selecting markerless motion capture systems based on task demands, accuracy requirements, and available resources.

Images (Optional)

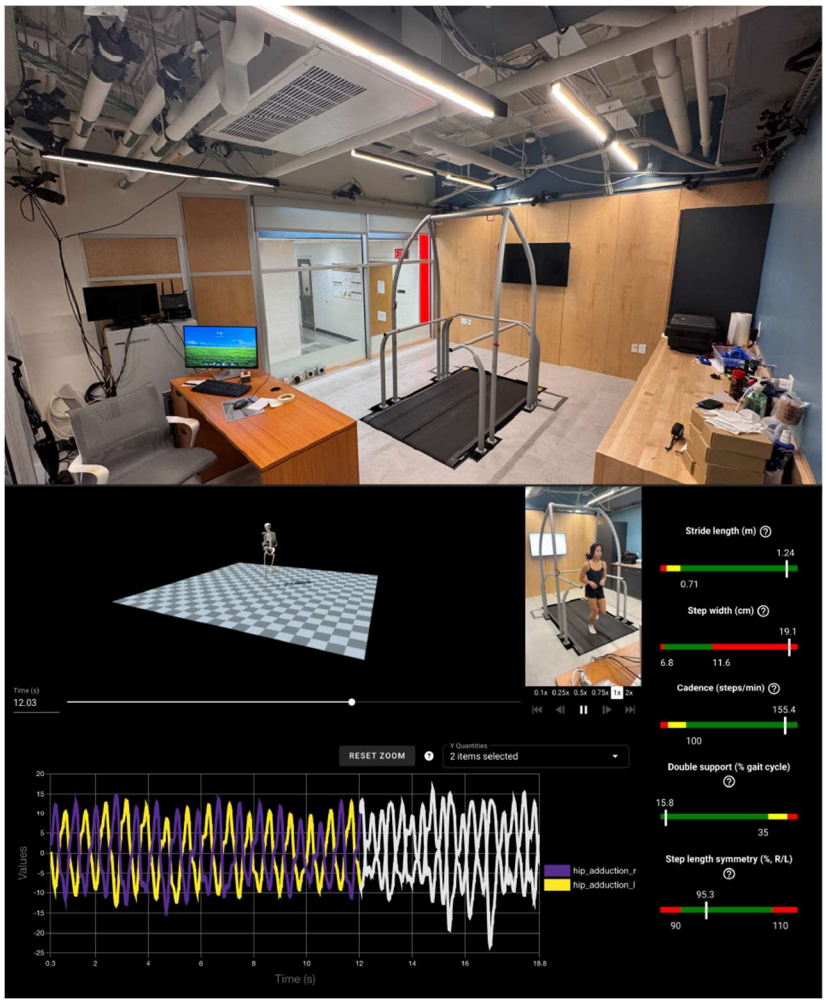


Figure 1. (Top) Qualisys Camera Setup - NeuMove Lab. (Bottom) OpenCap Software GUI.

Acknowledgements (Optional)

This work was partially supported by internal funding from Northeastern University.

Session Category

Human Motion and Performance: Locomotion/Gait

P1-155

A Sensor-Based Study of Gait Challenges in Stair Walking Among Children with Intellectual Disabilities

professor Hsin-Yi Kathy Cheng -[1], professor Wann-Yun Shieh[1], professor Yan-Ying Ju Taiwan[2], Mr. Che-Kuan Lin[1]

[1]Chang Gung University, Taoyuan, -, Taiwan. [2]National Taiwan Sport University, Taoyuan, -, Taiwan

Introduction

Children with intellectual disabilities (ID) and multiple disabilities (MD) commonly present with impaired motor coordination and balance control, which significantly affect functional mobility, especially during stair negotiation. Stair walking requires greater demands on postural regulation, muscle strength, and dynamic stability than level walking. However, quantitative analyses of stair-walking performance in these populations remain limited. This study applied wearable sensor technology to objectively analyze stair-walking gait characteristics in children with ID and MD and to explore its clinical and educational applicability.

Methods

A total of 84 participants aged 15–22 years were recruited, including 32 typically developing (TD) individuals, 32 with ID, and 20 with MD. All participants wore a lower-back Xsens inertial sensor and completed a 10-m level walking test and a stair-walking task consisting of 13 steps ascending and 13 steps descending (each step 15 cm in height and depth). One ascent–descent cycle was repeated four times. Heart rate and oxygen saturation were monitored before and after testing to ensure safety. Temporal gait parameters were analyzed using one-way ANOVA with Scheffé post hoc comparisons.

Results

During stair ascent, both the ID and MD groups demonstrated longer time per step than the TD group, with the MD group showing significantly longer total ascent time and the greatest variability. Statistical analysis revealed a significant difference only between the MD and TD groups ($p < 0.05$). During stair descent, the TD and ID groups completed the task in less than 6 seconds, whereas the MD group required approximately 1.8 times longer than the TD group (TD ≈ 4.92 s; MD ≈ 8.8 s) and exhibited greater instability and gait variability.

Discussion

Stair-walking tasks were more sensitive than level walking in revealing deficits in motor control, coordination, and stability, particularly in children with MD. Wearable sensor systems effectively quantified gait impairments and provided objective evidence to support early identification of motor dysfunction and the development of individualized rehabilitation and physical training programs in both clinical and educational settings.

Session Category

Human Motion and Performance: Locomotion/Gait

P1-156

Lower Limb and Joint Level Differences in Mechanical Demands Between Lateral and Vertical Jumps Following a Drop Land

Mr. Hua-Bin Lin BSc, Dr. Jordan Cannon PhD

University of Waterloo, Waterloo, Ontario, Canada

Mr. Hua-Bin Lin

Introduction

Drop jump tasks are complex whole-body movements requiring multi-joint control to meet the mechanical demands from landing and generate propulsion for jumping. Ground reaction force (GRF) magnitude and orientation relative to the lower limb modulates net joint moment (NJM) distribution. Unlike a drop vertical jump (DVJ), with primarily sagittal plane demands, a drop lateral jump (DLJ) requires both vertical and medial-lateral GRF components for jumping. Thus, DLJs would be expected to introduce multi-planar demands across the lower limb joints and asymmetry between limbs. The purpose of this study was to compare limb- and joint-level mechanical demands between DVJ and DLJ tasks, to gain insight into differences in multi-joint control strategies.

Methods

Eighteen female athletes performed three drop jump tasks from a 30cm box landing with each foot on a force plate before maximally jumping vertically (DVJ), laterally to the right (DLJ_R), and laterally to the left (DLJ_L). Limb-level (i.e., resultant GRF and support moment) and joint-level (i.e., resultant NJMs) mechanics were analyzed during the contact phase. Variables were averaged within each task by limb condition, such that analyses compared DVJ (average of both limbs), DLJ_I (average of ipsilateral limbs to jump direction), and DLJ_C (average of contralateral limbs to jump direction). RM-ANOVA was used to compared limb and joint levels differences across conditions.

Results

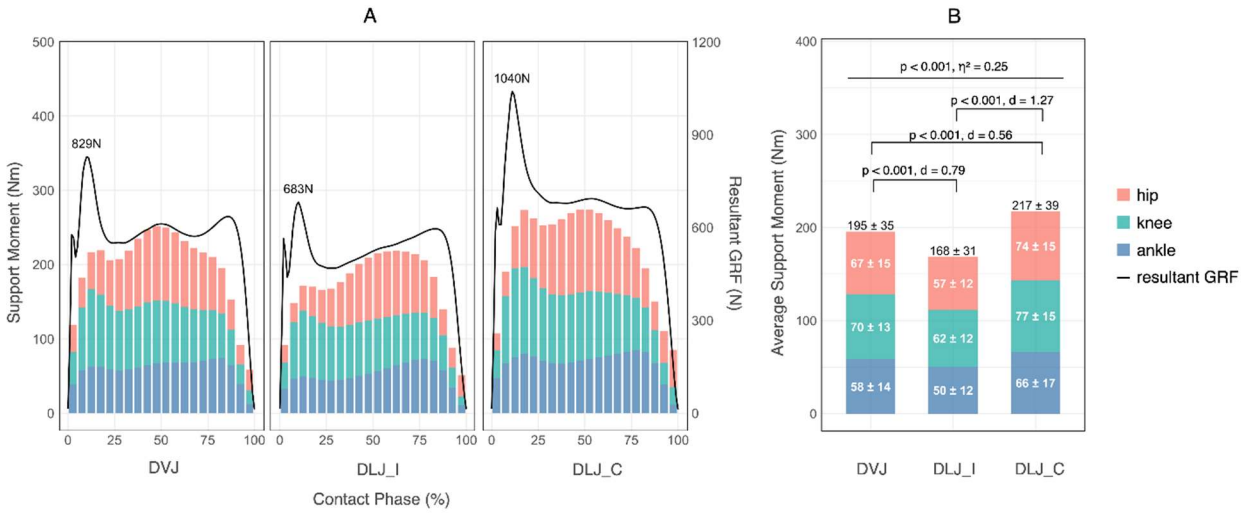
At the limb-level, the resultant GRF and support moment were greatest in DLJ_C, followed by DVJ, and then DLJ_I. Thus, the contralateral limb to jump direction had the greatest demands given its role as the “push limb.” Similarly, at the hip, knee, and ankle, joint demands were greatest in DLJ_C, followed by DVJ, and lowest in DLJ_I. Within each

condition, hip and knee resultant NJMs were similar while both were greater than the ankle.

Discussion

As expected, DLJs increased limb- and joint-level demands of the contralateral limb while reducing ipsilateral demands, compared to DVJ. However, the distribution of demands among joints was unchanged (hip: 34%, knee: 36%, ankle: 30%). Therefore, consistent multi-joint control strategies were utilized, facilitated by the relative alignment of the GRF with the lower limb despite large absolute kinematic differences across conditions.

Images (Optional)



For each task by limb condition: (A) Resultant GRF and support moment (sum of hip, knee, and ankle NJMs). (B) Average support moment and average NJMs over the contact phase (mean ± SD).

Session Category

Human Motion and Performance: Locomotion/Gait

P1-157

Running Speed Increases Movement Variability for Key Biomechanical Variables

Dr Iain Hunter PhD, Mr. Luke VanKeersbilck, Mr. Jared Ward

Brigham Young University, Provo, Utah, United States

Introduction

Experienced runners tend to have lower movement variability [1,2,3]. This lower movement variability is correlated with greater mechanical efficiency [4] which may lead to improved running economy. This study investigated how variability is influenced by running speed. We expected variability of various running mechanics variables to increase as speed increased.

Methods

Sixty-seven women and 50 men ran a 3-minute warmup followed by 20-s recordings at 3.15, 3.57, 4.12, 4.87, and 5.95 m/s for women and 3.35, 3.83, 4.46, 5.37, and 6.50 m/s for men. Theia Markerless (120 Hz) and a Bertec instrumented treadmill (960 Hz) were used to record motion and forces. Visual 3d was used to calculate peak vertical ground reaction forces, stride rate, the range of knee flexion during stance, maximum hip flexion, maximum hip extension, maximum plantar flexion velocity during stance, and center of mass vertical oscillation. The 20-s recordings allowed for at least 25 strides for each speed. Standard deviations were calculated for each speed. A mixed-model was fit predicting these movements from speed, speed^2 (for non-linear relationships), sex, and subject.

Results

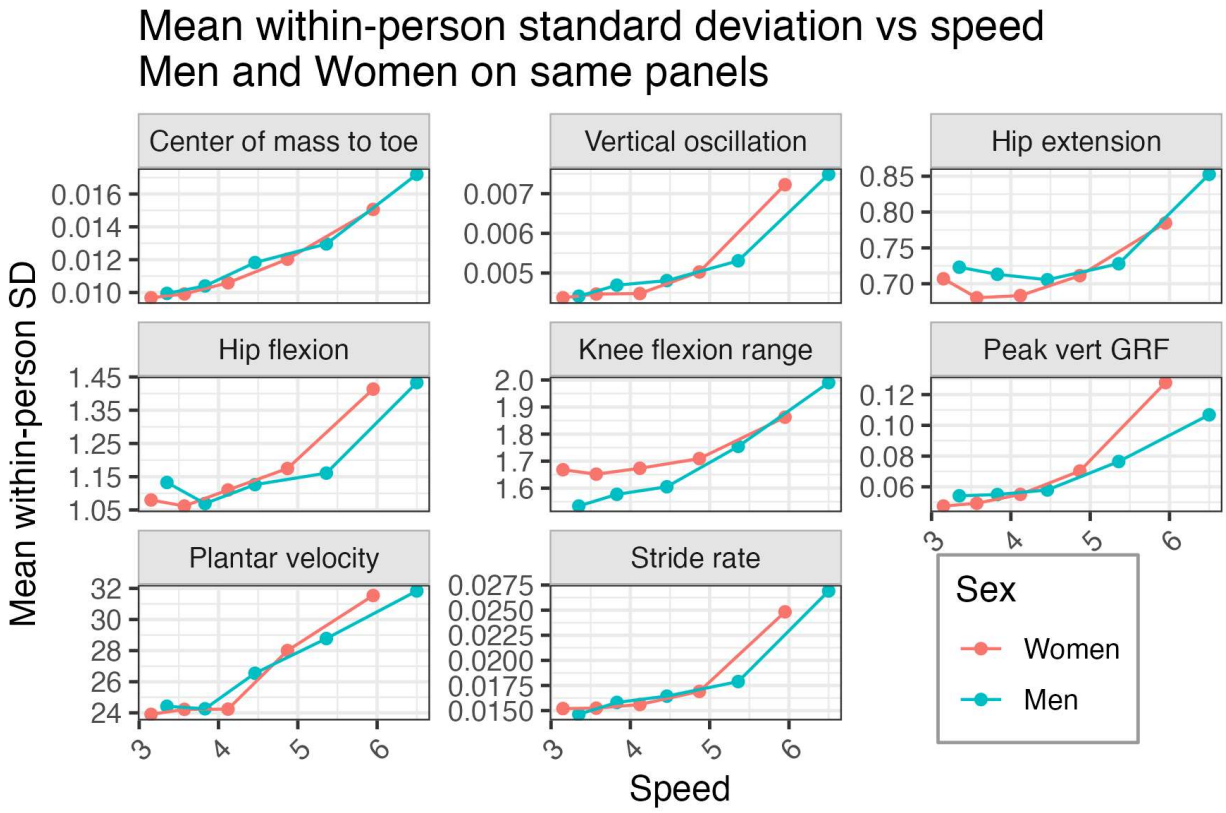
All variables showed a positive trend of standard deviations increasing with speed ($p<0.05$) and speed^2 ($p<0.001$). The only significant variable for sexes was peak force ($p=0.020$).

Discussion

Less movement variability is desirable for reducing mechanical efficiency. Variability of all running mechanics measures in this study increased with running speed. The question now becomes, what can we do to reduce movement variability when running at higher speeds to keep mechanical efficiency as low as possible. The lower variability demonstrated in trained runners suggests a likelihood that training at faster speeds could decrease variability at those speeds. Future research will investigate whether running variability

decreases as running experiences increases and correlate these changes with running economy.

Images (Optional)



References (Optional)

[1] Pablo Floría *et al.* , J Sports Sci, 2018

[2] Jared Steele. , Sports, 2022

[3] Yosuke Nakayama. , Gait & Post, 2009

[4] Francisca Melo-Fonseca. , J Biomechanics, 2020

Session Category

Human Motion and Performance: Locomotion/Gait

P1-158

Evaluating Accuracy and Confidence Intervals of a Probabilistic Multiview Markerless Motion Capture System

Ms Irina Djuraskovic BS[1,2], Dr Seth Donahue PhD[3,4]

[1]Shirley Ryan AbilityLab, Chicago, IL, United States. [2]Northwestern University, Chicago, IL, United States. [3]Shriners Hospitals for Children, Lexington, KY, United States. [4]University of Kentucky, Lexington, KY, United States

Ms Irina Djuraskovic

Introduction

Validation studies of biomechanical reconstruction from video using markerless motion capture typically report accuracy aggregated over a cohort. However, in practice, it is essential to know if markerless motion capture is accurate for an individual. While biomechanical reconstructions have been shown to perform well, they lack a measure of noise or confidence in the outputs. To be calibrated, the model's estimated 95th percentile confidence interval must contain the gold-standard data 95% of the time, and similarly for other percentiles. This study provides multi-site and validation of our probabilistic Markerless Motion Capture (MMC) model using external gold standard systems for multiple clinical populations.

Methods

Video data from 68 participants with varying diagnoses from 2 different sites, N = 41, Shirley Ryan AbilityLab (SRALab), N = 27 Shriners Children's (SC) were collected and processed as described in [1]. Clinical ground truth was obtained using the GaitRite Walkway at SRALab, and marker-based motion capture at SC. We evaluated the model's calibration using the Expected Calibration Error (ECE) metric, which is a global goodness-of-fit metric for statistical calibration. Kinematic bias was removed prior to ECE calculations. We also present the estimated uncertainty and absolute errors between the gold standard and our model.

Results

Our model showed that it is well calibrated with ECE values generally falling < 0.1. We also show that the model is fairly accurate, with the median absolute step length error of 16.22mm while joint angle errors were < 4° across all the SC participants (Table 1).

Discussion

We validate the probabilistic MMC against standard clinical tools to show we can accurately quantify body positions and joint angles and associated uncertainties with well-calibrated confidence intervals. We show that the median step length error falls within the expected bounds found in previous work [1]. Bias-removed kinematic values showed excellent calibration, and reasonable uncertainty and errors, except for pelvis rotation ECE, which showed moderate miscalibration. Future work will correct model specification differences that lead to biases and will evaluate reasons for lower confidence scores to ultimately use the confidence intervals to ensure high-quality data for its implementation in clinical analyses.

Images (Optional)

UNCERTAINTY AND ERROR METRICS

Joint	ECE	Uncertainty (°)		Error (°)	
		Med	IQR	Med	IQR
Pelvis Tilt	0.07	3.28	0.76	1.62	0.81
Pelvis Obliquity	0.06	3.23	0.67	1.52	1.27
Pelvis Rotation	0.18	1.99	0.33	2.15	1.34
Hip Flexion	0.01	4.26	0.99	2.53	1.13
Hip Abduction	0.05	3.74	0.87	1.88	1.55
Hip Rotation	0.08	4.78	1.20	3.76	1.55
Knee Flexion	0.06	3.56	0.90	2.84	1.22
Ankle Flexion	0.07	4.73	1.31	3.52	1.04
Step Length	**ECE**	**Uncertainty (mm)**		**Error (mm)**	
		Median	IQR	Median	IQR
Controls	0.08	17.55	8.30	9.08	12.29
Prosthetic	0.08	18.44	8.35	16.07	23.44
Neurologic	0.10	24.68	12.91	23.14	31.39
Pediatric	0.03	17.28	8.32	10.68	12.21

References (Optional)

[1] Cotton, R.J. ICORR, 2025

Session Category

Human Motion and Performance: Locomotion/Gait

P1-159

Does Preferred Running Speed Minimize Cost of Transport or Maintain Exercise Intensity?

Miss Isabella Shih[1], Dr. Rodger Kram[2], Dr. Jessica C. Selinger[1]

[1]School of Kinesiology and Health Studies, Queen's University, Kingston, Ontario, Canada. [2]Department of Integrative Physiology, University of Colorado, Boulder, Colorado, United States

Introduction

In humans and other animals, locomotor speed preferences tend to align with the speed that minimizes cost of transport (CoT, the *amount* of energy expended per unit distance travelled) [1, 2]. However, maintaining a given exercise intensity (*rate* of energy per unit time) is arguably more physiologically intuitive. A simple, yet untested, way to distinguish between these two objectives is to add load to the body. The speed that minimizes CoT is expected to remain largely unchanged from unloaded to loaded running [3], but exercise intensity naturally increases, allowing us to directly test which better explains PRS. The purpose of this study is to test if human PRS minimizes CoT or, instead, maintains exercise intensity using unloaded and loaded running.

Methods

Participants (n=5 of 12 planned) ran on a treadmill while metabolic expenditure and heart rate were recorded. Across three visits, runners completed a VO_2max test, PRS tests under unloaded and loaded (20% bodyweight) conditions, and ran at six speeds ranging from 70% to 120% of their PRS under both conditions. We compared runners' minimum gross CoT (J/kg/m), speed at their minimum gross CoT (m/s), PRS (m/s) and PRS exercise intensity (% VO_2max) between the unloaded and loaded conditions using paired t-tests (alpha = 0.05).

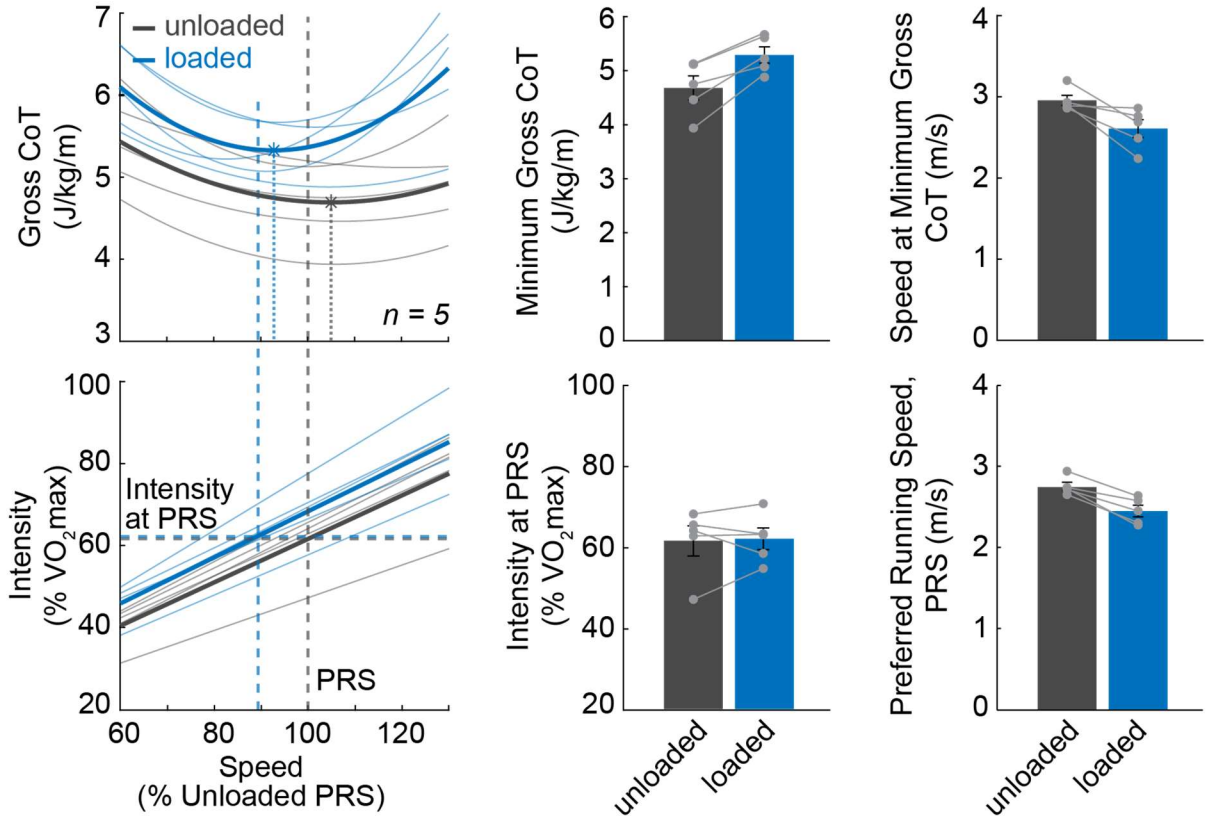
Results

PRS decreased under loaded compared to unloaded running (-11.1% ± 4.0%, p=0.0015). Unexpectedly, the speed that minimized gross CoT also decreased by a similar amount (-11.7% ± 8.5% p=0.037), although the absolute PRS tended to be slightly lower than the speed that minimized gross CoT in both conditions. PRS under unloaded and loaded conditions also resulted in very similar exercise intensities (61.7% ± 8.3% vs. 62.2% ± 6.0%, respectively; p=0.829).

Discussion

Our preliminary results suggest that human PRS may both minimize CoT and maintain exercise intensity, raising important questions about whether they are coupled or coincident objectives. The full results of this study may shed light on what fundamental objectives drive human locomotor preferences.

Images (Optional)



References (Optional)

[1] Selinger *et al.*, Current Biology, 2022

[2] Hoyt and Taylor, Nature, 1981

[3] Cureton and Sparling, Medicine Science Sports Exercise, 1980

Session Category

Human Motion and Performance: Locomotion/Gait

P1-160

Influence of Race and Motion Capture Method on Knee and Hip Kinematics during Gait

Miss Iwi Eghobamien BSc[1,2], Mr. Neil Wills MSc[1], Miss Vital Nwaokoro BSc[1], Dr. Derek Pamukoff PhD[1]

[1]University of Western Ontario, London, Ontario, Canada. [2]McMaster University, Hamilton, Ontario, Canada

Miss Iwi Eghobamien

Mr. Neil Wills

Miss Vital Nwaokoro

Introduction

Motion capture method may influence comparisons between racial groups due to differences in skin tone. This study examined the influence of race and motion capture method on knee and hip kinematics during overground gait.

Methods

Forty participants were grouped into Black (10 females, 10 males) or White (10 females, 10 males) based on self-identified race and matched on sex and body size. Two overground gait assessments along a 10m walkway were completed 2-7 days apart. Five trials were completed per session at a self-selected speed that was maintained between days using the same footwear and clothing. 14 Qualisys cameras (8 for ML and 6 for MB) recorded simultaneously (60Hz), and data were averaged between sessions. Model construction was completed using Theia 3D (ML only) and Visual 3D software. Hip and knee kinematics were time-normalized from 0-100% of the gait cycle. Kinematic waveforms were compared with statistical parametric mapping (SPM) using a 2 (race) by 2 (method) repeated ANOVA (α=0.05). Post hoc evaluations used SPM using independent samples t-tests and Bonferroni correction.

Results

There were main effects of motion capture method showing higher amplitude kinematics for MB than ML in all joints and planes of motion (all $p<0.05$). There were significant interaction effects of race and method for sagittal ($p=0.035$) and frontal ($p<0.001$) plane knee angle, and frontal ($p=0.003$) and transverse ($p=0.002$) plane hip angle. Post hoc analyses indicated larger differences in kinematic waveforms between methods in Black participants compared with White participants from ~65-90% of gait cycle. MB showed more knee adduction and hip abduction compared with ML in Black participants, and greater knee adduction in Black participants compared with White participants when evaluated with MB (Figure 1).

Discussion

Race and motion capture method influence hip and knee kinematics during swing phase, which may influence interpretations from Black participants. Findings may have stemmed from ML camera placement. Ceiling-mounted cameras may have an obstructed view of lower limb segments during swing phase, or had poor contrast between dark flooring and darker skin tones. ML methods need further evaluation to understand contributors to validity and reliability on diverse samples.

Images (Optional)

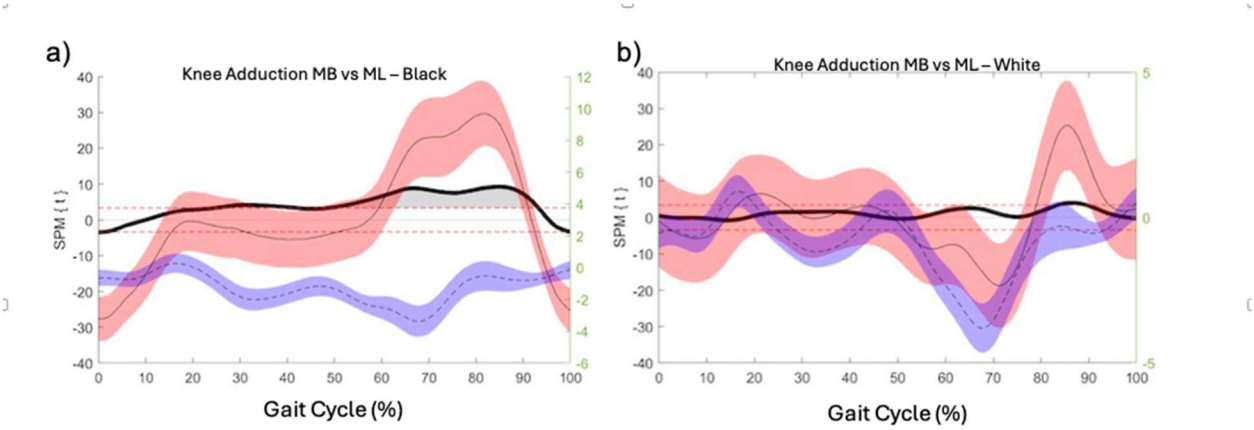


Figure 1. Post hoc comparisons of knee adduction waveforms throughout the gait cycle in Black (a) and White (b) participants. Marker-based is red, markerless is blue. Blue and red shaded regions indicate standard deviation. Gray shaded regions indicate significance.

Session Category

Human Motion and Performance: Locomotion/Gait

P1-161

Rapid Phenotyping of Unilateral Osteoarthritis via a 6-Minute Markerless Gait Stress Test

Mr Jack Clarke BEng[1], Dr Peter Ellison[1], Dr Matthew Bowes[2], Dr Nicholas Shenker[3], Mr Zijie Ren[1], Professor Adar Pelah[1,4]

[1]University Of York, York, North Yorkshire, United Kingdom. [2]York And Scarborough Teaching Hospitals NHS Foundation Trust, York, North Yorkshire, United Kingdom. [3]Cambridge University Hospitals NHS Foundation Trust University Hospitals, Cambridge, Cambridgeshire, United Kingdom. [4]Florida Atlantic University, Boca Raton, Florida, United States

Introduction

Traditional gait analysis remains confined to specialized laboratories due to high costs and complex protocols, limiting its utility for routine Osteoarthritis (OA) screening. While low-cost Time-of-Flight (ToF) cameras offer a scalable alternative, their ability to detect subtle, phenotype-specific deficits in short clinical windows remains unproven. This study aimed to validate a rapid, markerless "gait stress test" workflow for classifying Unilateral OA. We hypothesised that a 6-minute variable-velocity protocol could successfully extract robust dynamic kinematic biomarkers, unmasking the latent temporal asymmetry and maladaptive response profiles described in marker-based literature.

Methods

Gait kinematics were captured from 16 participants (9 Unilateral OA, 7 Controls) using a single Azure Kinect camera. Participants completed a 6-minute treadmill protocol (1.5–4.5 km/h staircase). Post-processing then extracted relevant spatiotemporal metrics. A Repeated Measures ANOVA was then employed to analyse the dynamic response of the left versus right limbs across velocity phases. We assessed whether the markerless data could reproduce the Speed * Group interaction (dynamic failure) and Laterality (asymmetry) patterns previously established as clinical markers of unilateral pathology.

Results

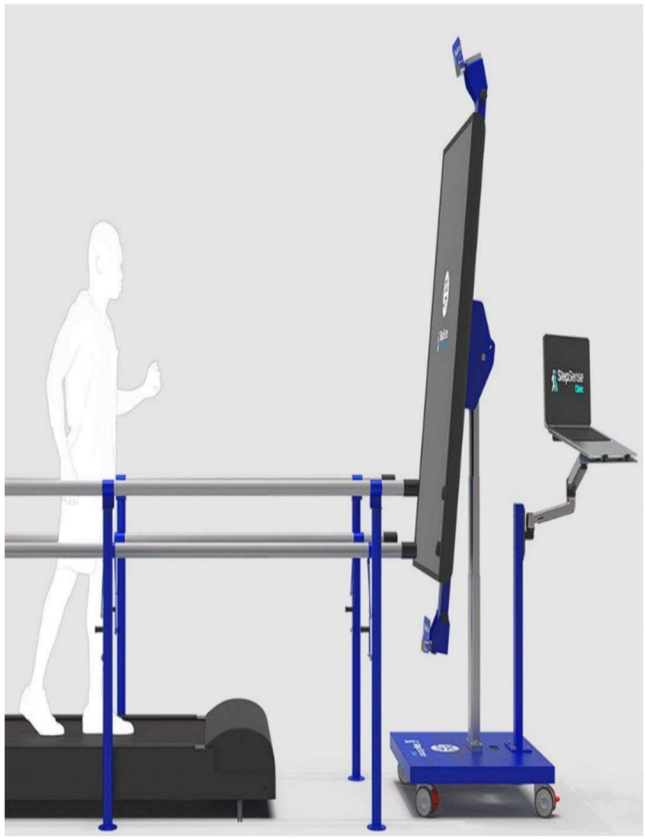
the system extracted biomarkers consistent with clinical expectations. Notably, the main effect of Group classification only approached significance ($p = 0.051$, Effect Size = 0.261), suggesting that static averages may lack diagnostic sensitivity. However, the dynamic analysis proved robust: the markerless data revealed a significant Speed * Group interaction for stride time ($p = 0.015$, Effect Size = 0.191), mirroring maladaptive responses described in marker-based studies such as Bejek et al. [1]. Furthermore, the system

reliably quantified Laterality (Left vs. Right) (p = 0.016, Effect Size = 0.373), distinguishing unilateral OA asymmetry from control symmetry.

Discussion

This study establishes the feasibility of a rapid, markerless workflow for OA phenotyping that requires no patient preparation. The successful detection of dynamic deficits (p=0.015) validates that low cost ToF Cameras can capture non-linear gait adaptations to a suitable degree of accuracy. By demonstrating that a 6-minute stress test yields asymmetry metrics consistent with established clinical pathology, this method offers a viable pathway for high-throughput screening and "functional Classification" of OA in outpatient clinics.

Images (Optional)



Repeated Measures ANOVA

Within Subjects Effects

	Sum of Squares	df	Mean Square	F	p	η^2_p
Phase	12.3717	5	2.47433	36.325	< .001	0.736
Phase ✻ Classification By Phenotype	1.0436	5	0.20871	3.064	0.015	0.191
Residual	4.4276	65	0.06812			
Side	0.0821	1	0.08213	7.737	0.016	0.373
Side ✻ Classification By Phenotype	0.0219	1	0.02192	2.065	0.174	0.137
Residual	0.1380	13	0.01062			
Phase ✻ Side	0.0205	5	0.00410	1.146	0.345	0.081
Phase ✻ Side ✻ Classification By Phenotype	0.0104	5	0.00207	0.579	0.716	0.043
Residual	0.2326	65	0.00358			

Note. Type 3 Sums of Squares

[3]

Between Subjects Effects

	Sum of Squares	df	Mean Square	F	p	η^2_p
Classification By Phenotype	2.24	1	2.241	4.60	0.051	0.261
Residual	6.33	13	0.487			

Note. Type 3 Sums of Squares

References (Optional)

"[1] Bejek, Z. et al. , *Knee Surg Sports Traumatol Arthrosc*, 2006"

Session Category

Human Motion and Performance: Locomotion/Gait

P1-162

Standing From Seat Heights Below the Popliteal Increase Muscular Demands More Than Joint Torques

Dr. Jacob Banks PhD, Dr. Neal Wiggermann PhD

Baxter Int., Batesville, Indiana, United States

Introduction

Standing from a seated posture is a common daily activity. Muscular strength and seat height can influence the success of standing[1]. While seat heights below popliteal height are more difficult to rise from; kinetic analysis has not identified differences in lower limb peak joint moment demands[2]. The aim of this work is to better understand low seat height kinetic demands.

Methods

To date, data from twelve healthy adults has been recorded and analyzed. Kinematic and kinetic data were recorded while participants stood from up to 20 seated heights ranging 18cm to 79cm. OpenSim musculoskeletal models[3] were used to estimate peak lower limb sagittal plane joint range of motion, torques, and muscle group activation levels from standing. Dependent variables were plotted relative to seat height normalized to individual popliteal height, for qualitative interpretation (Fig. 1).

Results

Hip, knee, and ankle joint ranges of motion were inversely influenced by seat height. Joint torques were also inversely related to normalized seat height, particularly for the hip and knee, however peak demands tended to plateau at heights below the popliteal. Muscle group activations resembled joint moments, though they appear more sensitive to seat height. A secondary analysis of 90-110% versus 40-60% normalized seat height indicates roughly a 15% and 22% increase for peak joint moments at the hip and knee, respectively, but a 49% and 52% increase in group muscle activation at the hip and knee, respectively.

Discussion

The phenomenon of how below popliteal level seat heights exhibiting similar kinetic demands despite more perceived effort and difficulty of standing have previously not been fully quantified. Here we applied a musculoskeletal model to demonstrate that muscle activations increase at a higher rate than joint moment demands. This discrepancy may represent reduced force-length properties of muscle and muscle moments about the joint[4]. Those with difficulty standing from low seat heights may benefit from a kinematic

strategy that optimizes muscular potential. These preliminary results will benefit from additional data and quantitative analyses.

Images (Optional)

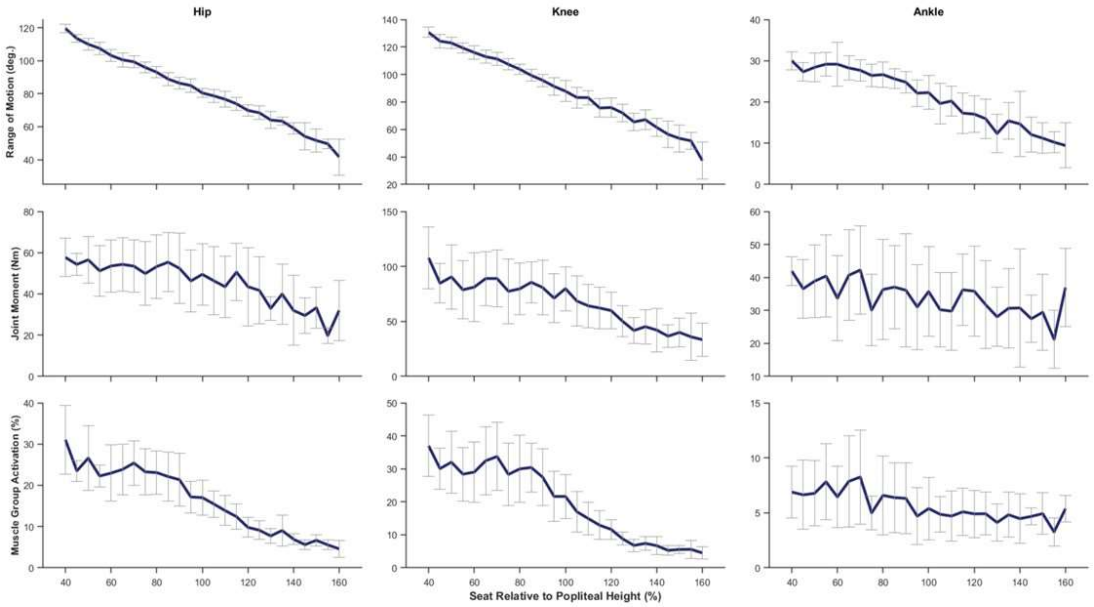


Figure 1: Hip, knee, and ankle joint ranges of motion, peak moments, and peak muscle group activations to stand from different seat heights. Seat height is normalized to each participant's popliteal height and rounded to the nearest 5%. Muscle groups represent the modeled hip extensors, knee extensors, and ankle plantar flexors. Blue line represents the mean values and grey data whiskers the standard deviation.

References (Optional)

[1]Janssen et al., PhysicalTherapy, 2002

[2]Yoshioka et al., BioMedEngOnLine, 2014

[3]Catelli et al., CMBBE, 2019

[4]Visser et al. EJAPOP, 1990

Acknowledgements (Optional)

This project was internally funded by Baxter International.

Session Category

Human Motion and Performance: Locomotion/Gait

P1-163

Attentional Adaptation and Gait Stabilization during Interactive Metronome Gait Training in Middle-Aged Adults

Jae-Won Kang M.S.[1,2], Dr. Soo-Ji Han Ph.D.[2,3], Yun-Bae Jeong M.S.[1,2], Jung-Min Yoon M.S.[1,2], Prof. Sang-Kyoon Park Ph.D.[1,2]

[1]Korea National Sport University, Seoul, Seoul, Korea, Republic of. [2]Motion Innovation Center, Seoul, Seoul, Korea, Republic of. [3]Pukyong National University, Pusan, Pusan, Korea, Republic of

Introduction

Middle-aged adults may experience age-related cognitive decline, which can lead to weakened gait ability and an increased risk of falls[1]. Interactive Metronome(IM)-based training has been proposed as an effective intervention to enhance gait stability by modulating temporal processing and attentional control in the brain through metronome beats and real-time auditory feedback. However, this dual-task condition can induce selective attentional overload and compromise gait performance, which can be resolved through sensory integration achieved by sufficient training duration[2]. Therefore, the purpose of this study was to identify the certain time interval at which selective attention adaptation occurs during IM-based treadmill gait training in middle-aged adults and to provide recommendations for a minimum training duration.

Methods

Thirteen middle-aged males (Age:57.7±3.9years; Height:170.3±5.1cm; Weight:73.8±8.1kg; K-MoCA:26.2±2.0points) without musculoskeletal disorders in the past six months participated. Treadmill walking data were collected using eight infrared cameras (Qualisys, SWE) and a treadmill (Bertec, USA), while auditory feedback was provided through an IM device (Interactive Metronome, USA). Participants walked at their preferred speeds to determine the individual cadence(109.9±6.3bpm), which was applied to the IM during a 10-minute treadmill walking session. Gait data divided into three intervals (initial:1:00–1:30 min; middle:5:00–5:30 min, final:9:00–9:30 min) were analyzed using a one-way repeated measures ANOVA followed by Bonferroni correction(α=.05).

Results

There were no significant differences in cadence and step time across intervals(Table 1). However, significant differences were shown in the ankle joint range of motion (AROM) and the coefficient of variation (CV) of AROM during the stance phase.

Discussion

Gait training using rhythmic auditory stimulation increased ankle movement and decreases variability, which improved gait consistency and stability[3]. In this study, the decrease in the CV of AROM during final suggests that the attentional control mechanisms induced by dual-task condition stabilized during the final contributing to enhanced gait stability. Therefore, it is recommended that IM-based gait training for middle-aged adults be conducted for approximately 9 minutes to achieve optimal effectiveness.

Images (Optional)

Table 1. Spatiotemporal and ankle joint kinematic variables over time

Variables	Initial[a]	Middle[b]	Final[c]	F(*p*)	Post-hoc
Cadence (step/min)	110.23(6.51)	110.79(6.78)	110.51(6.64)	2.115(.143)	-
Step Time (ms)	546.58(32.81)	543.98(34.22)	545.38(33.75)	1.395(.267)	-
Ankle ROM (deg.)	22.05(2.57)	22.97(2.80)	23.13(2.57)	**7.401(.003)***	a<b,c
Ankle ROM CV	10.17(3.52)	8.67(2.03)	8.13(1.80)	**5.650(.010)***	a>c

* Indicates significant differences between Time
Initial: 1:00 ~ 1:30 min, Middle: 5:00 ~ 5:30 min, Final: 9:00 ~ 9:30 min.

References (Optional)

[1] Moustafa, Front. Aging Neurosci., 2014.

[2] Bressler et al., *Journal of Neuroscience,* 2008.

[3] Wright et al., Fron. Neurol, 2016.

Acknowledgements (Optional)

This Study was Supported by the National Research Foundation of Korea (NRF-2022S1A5A2A01045782)

Session Category

Human Motion and Performance: Locomotion/Gait

P1-164

RPE-Based Identification of Fatigue-Related Changes in Running Spatiotemporal Variability

Ms Jaewoo Cho, Ms Hyunji Kim, Prof Jooeun Ahn

Seoul National University, Gwanak-gu, Seoul, Korea, Republic of

Introduction

Running-induced fatigue is known to increase spatiotemporal variability [1], yet conventional time-based analyses often obscure meaningful individual differences in fatigue progression [2]. The rating of perceived exertion (RPE) offers an individualized scale of internal load that may better capture fatigue-related changes in motor control [3]. This study examined how spatiotemporal variability evolves across successive RPE levels during prolonged running and explored whether specific “hard” intensity points (RPE 14–16) exhibit abrupt transitions in variability.

Methods

Seven recreationally active adults (4 males and 3 female) completed a running trial on an instrumented treadmill at a self-selected speed targeting volitional exhaustion (2.95 ± 0.32 m/s). On average, they stopped at 24.7 ± 7.0 min with a terminal RPE of 18.4 ± 1.6. 3D kinematics (120 Hz), ground reaction forces (1200 Hz) and RPE were collected. Heel-strike and toe-off were identified using a 20 N threshold, and 100 consecutive right-leg steps at each RPE level were analyzed. Cadence, contact time, flight time, stride length, and vertical oscillation were computed, and their variability was quantified using the coefficient of variation (CV).

Results

Across RPE levels, most spatiotemporal metrics showed their largest increases in variability at RPE 15. Paired t-test results comparing the absolute CV values at each RPE level with those at the preceding level indicated a significant rise in cadence variability at this point ($p < 0.05$). Vertical oscillation exhibited a significant increase at RPE 16 ($p < 0.001$), whereas other metrics showed smaller or inconsistent changes.

Discussion

RPE-based alignment accurately identified the RPE levels at which variability sharply increased, effectively reflecting individual fatigue responses. The pronounced rise in cadence variability at RPE 15 suggests a mid-fatigue transition point where step-to-step timing becomes unstable. In contrast, the significant increase in vertical oscillation at RPE

16 indicates a later-stage breakdown in whole-body motion control under higher fatigue. Together, these findings highlight that gait parameters exhibit distinct sensitivity to fatigue and that RPE-based segmentation can reveal consistent trends in spatiotemporal variability

Images (Optional)

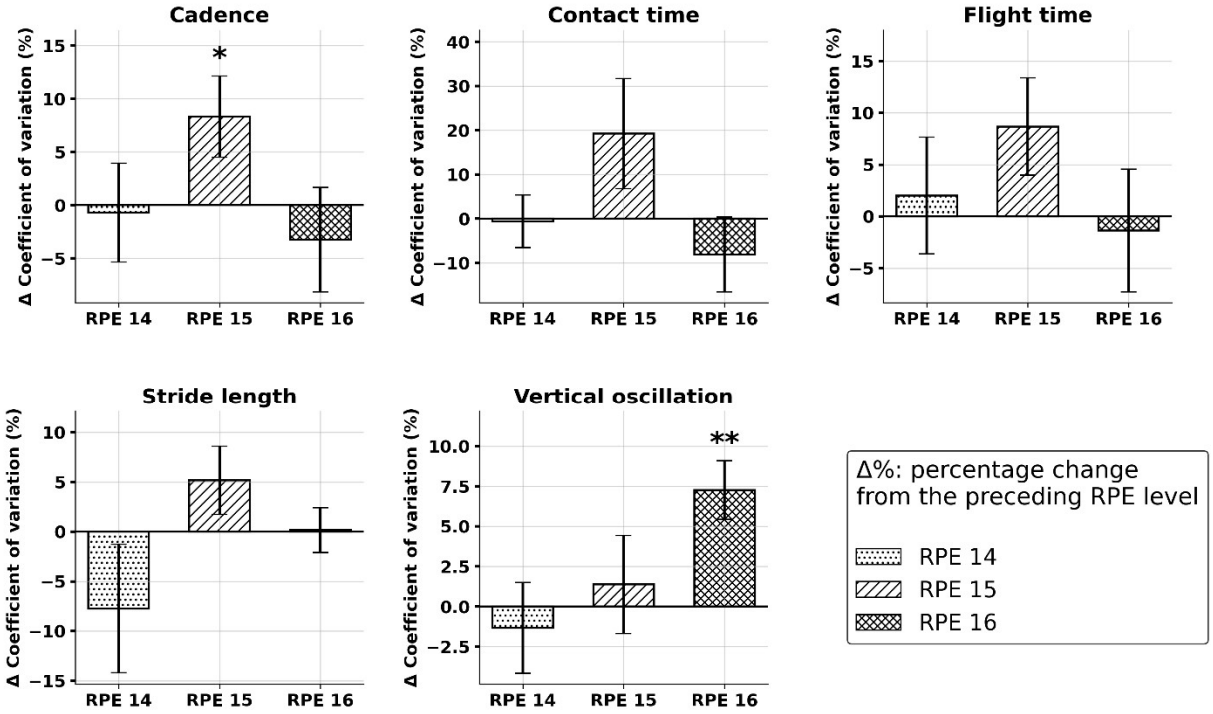


Figure 1. Changes in spatiotemporal variability across RPE levels (Mean±SEM). Δ% represents the percentage change in CV relativeto the preceding RPE level. Significance markers indicate paired t-test results. * p < 0.05, ** p < 0.001

References (Optional)

[1] García-Pinillos, F *et al.*, Gait & Posture, 2020

[2] Dimmick, H. L *et al.*, Frontiers in Sports and Active Living, 2023

[3] Bailey, Joshua P *et al.*, Sports Biomechanics, 2020

Acknowledgements (Optional)

This work was supported by the National Research Foundation of Korea (NRF) grants funded by the Korean Government (MSIT) (No. RS-2023-00208052).

Session Category

Human Motion and Performance: Locomotion/Gait

P1-165

Are Surgical Limb Knee Dynamics Altered Across the Gait Cycle Post-ACL Reconstruction

Ms. Janelle Baker, Dr. Susan Sigward PhD, PT, ATC

University of Southern California, Los Angeles, CA, United States

Introduction

Reduced knee flexion and extension excursion across stance is a prominent characteristic of altered knee gait mechanics in the surgical (Sx) limb following ACLr [1,2,3]. This, along with reduced Sx limb shank angular velocity during loading response, suggests individuals adopt less dynamic or stiffer strategies during stance. However, it is unknown if these strategies carry over to the swing phase when rapid flexion and extension are required without the demands of weight bearing.

Methods

15 individuals 113.6 ± 18.5 days post-ACLr participated. Three-dimensional kinematics (250 Hz; Qualisys, Inc. Sweden) were collected while they walked across a 10m walkway at self-selected speed. Sagittal plane knee angular velocity (extension (-) and flexion (+)) was calculated from marker trajectories using a 6 DOF kinematic model across the stance and swing phase of the gait cycle (defined as the period between subsequent heel strikes) for both limbs. Peak angular velocities were identified during loading response (LR; +), mid stance (MSt; -) and pre-swing (PreSw; +) of the stance phase and mid (MSw; -) and terminal swing (TSw; +) of the swing phase [4]. Repeated measures (limb x phase) ANOVA was used to determine whether differences exist between limbs and phases (significance $\alpha \leq 0.05$).

Results

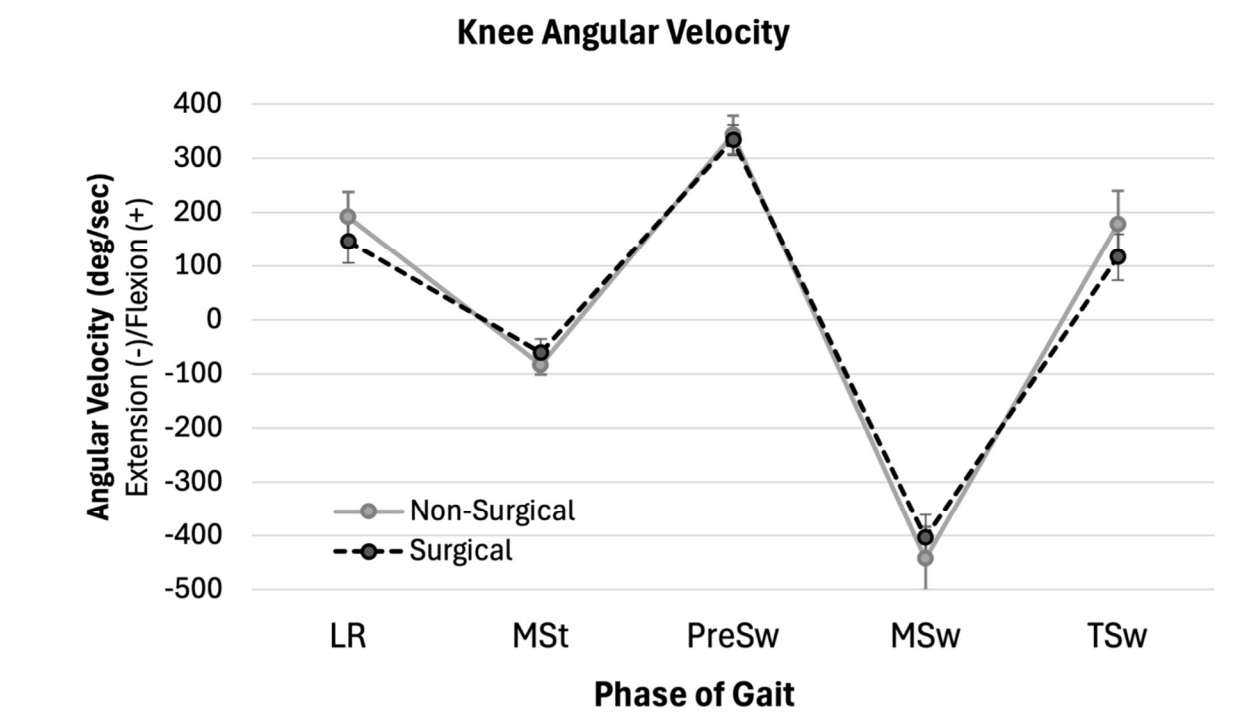
Significant main effects (limb $p=0.004$, phase $p \leq 0.001$) and interactions ($p \leq .001$) were found (Figure 1). Sx limb angular velocity was lower for LR 27.01% ($p=.001$), MSt 32.32% ($p=.001$), MSw 9.27% ($p=.032$) and TSw 41.82% ($p=.001$) but not PreSw. Extension angular velocity was greatest in MSw.

Discussion

Consistent with the characterization of less dynamic kinematics, the surgical knee exhibited reduced angular velocity across phases of stance and swing. The largest percent difference between limbs was observed in flexion velocity prior to initial contact of stance and the smallest during MSw when the angular velocity demands were the greatest. Despite the absence of weight bearing demands, it is not clear if reductions during swing

reflect an inability to achieve faster velocities or an adjustment to prepare for the demands of weight bearing.

Images (Optional)



References (Optional)

[1] M. Kaur et al., Sports Med, 2016

[2] L. Slater, J Athletic Training, 2017

[3] S. Garcia et al., J Biomechanics, 2023

[4] J. Perry, Gait Analysis, 2010

Session Category

Human Motion and Performance: Locomotion/Gait

P1-166

Effects of a Body Weight Support System on Lower Extremity Joint Kinematics During Running

Dr. Jeff Mettler Ph.D., Ms. Sasha Botsul, Ms. Josephine Cooley, Mr. Connor Rockford, Mr. Jay Clark M.Ed., ATC

Augustana College, Rock Island, IL, United States

Introduction

Body weight support (BWS) systems, which reduce the impacts experienced by a runner, have become increasingly common for both training and rehabilitation. Runners exhibit reduced hip flexion [1], knee flexion [1-2], and ankle dorsiflexion [2] when using a BWS system, although it is unknown whether a BWS system influences frontal and transverse plane kinematics. Therefore, the purpose is to investigate the effects of a BWS system on the sagittal, frontal, and transverse plane kinematics of the hip, knee, and ankle while running.

Methods

To date, pilot data from 2 adults have been analyzed. After a warmup, each participant was fitted with inertial measurement unit sensors on their pelvis and lower extremities before running at 100%, 90%, 80%, and 70% of their body weight on a BWS system (LightSpeed Lift; Duluth, MN, USA). Participants ran at a constant self-selected speed for 3 minutes during each condition with 2 minutes of walking between each condition. 30 seconds of data were collected for each condition, and peak stance phase kinematics of the right hip, knee, and ankle were analyzed for each BWS condition.

Results

Results are reported in Table 1. Participant 1 demonstrated reduced hip adduction with an increase in BWS, although participant 2 did not demonstrate the same trend. Both participants demonstrated reduced knee internal rotation and ankle dorsiflexion with increased BWS. Finally, both participants demonstrated increased ankle adduction, and participant 2 demonstrated reduced ankle eversion with increased BWS.

Discussion

Preliminary results revealed that an increase in BWS caused a reduction in ankle dorsiflexion, which is supported by previous research [2]. Furthermore, increased BWS appears to have effects on frontal and transverse plane kinematics, although the study is ongoing. An *a priori* power analysis revealed that data must be collected on at least 16

participants for the study to detect a meaningful result if it exists, and it is anticipated that sufficient statistical power will elucidate any potential effects of BWS on sagittal, frontal, and transverse plane kinematics of the lower extremity joints during running.

Images (Optional)

Table 1: Individual participant responses of peak stance phase kinematics of the hip, knee, and ankle when running at four different body weight support conditions (100%, 90%, 80%, 70%) using a belt harness system.

	Participant 1				Participant 2			
	100%	*90%*	*80%*	*70%*	*100%*	*90%*	*80%*	*70%*
Hip								
Flexion	28.4	30.9	30.6	28.3	36.2	29.8	37.3	24.9
Adduction	-21.2	-17.3	-15.3	-16.2	-9.1	-8.9	-4.1	-9.1
Internal Rotation	-7.5	-6.7	-7.9	-7.0	-9.3	-10.5	-12.7	-11.6
Knee								
Flexion	24.5	26.8	27.5	24.2	44.7	45.1	48.7	38.6
Adduction	-4.8	-6.3	-7.4	-5.0	-6.8	-10.2	-11.5	-9.9
Internal Rotation	-3.3	-1.0	-0.8	-1.0	-10.6	-8.8	-8.6	-6.2
Ankle								
Dorsiflexion	10.5	8.2	8.9	5.6	23.8	23.8	25.2	20.8
Plantarflexion	-22	-18.4	-22.2	-19.6	-5.2	-4.7	-1.8	-5.1
Eversion	-17.9	-18.8	-17.3	-17.5	-13.8	-12.3	-10.9	-10.4
Adduction	0.3	-0.9	-1.4	-2.0	-3.5	-3.4	-6.2	-5.4

References (Optional)

[1] A.V. Shpakov et al., Hum Physiol, 2021

[2] Michael Neal et al., J Orthop Sports Phys Ther, 2016

Session Category

Human Motion and Performance: Locomotion/Gait

P1-167

Evaluation and Comparison of Multiple Gait Stability Metrics for the Upper Body and Lower Body When Applied to Healthy Walking Under Graded Lateral Perturbations

Dr. Jeongin Moon Ph.D, Dr. Richard Nuckols Ph.D

University of Massachusetts Lowell, Lowell, MA, United States

Introduction

Gait stability is essential for safe locomotion and important for older adults who desire independent living. Dynamic gait stability metrics such as the margin of stability (MoS), short-term Lyapunov exponent (LE), and maximum Floquet multipliers (FM) have been used to quantify the body's ability to respond to internal or external perturbations during walking. These stability metrics have been applied to different body segments in various studies but frequently yield different interpretations of the same gait pattern. A problem may be that studies rarely analyze the various stability metrics for both the upper extremity (UB) and lower body (LB) within the same study which may lead to discrepancies and confusion. This study aimed to concurrently measure multiple dynamic stability metrics (MoS, LE, and FM) from both UB and LB during walking with progressively graded lateral perturbations.

Methods

Fifteen healthy young male adults participated in the IRB approved study (#20-057-YAN-XPD). Participants completed four 5-minute walking trials under 4 intensities of lateral perturbation on a CAREN instrumented treadmill capable of lateral translation. Marker data was recorded, and UB (trunk) and LB (limbs) kinematics were calculated. C7 marker mediolateral position was used for the UB state representation and LB joint kinematics were used for LB state representation. Dynamic stability metrics of LE, FM, and MOS were calculated from these data. We used a one-way repeated-measure ANOVA to test the effect of perturbation on stability metrics.

Results

With increasing lateral perturbation intensity, the LE significantly increased for the UB and LB which suggest reduced local stability (Figure 1). Likewise, the FM significantly increased for the UB with increasing perturbation suggesting reduced orbital stability. However, the FM decreased for the LB suggesting increasing orbital stability. The MoS had a significant correlation with the LE of the UB and LB and the FM of the LB.

Discussion

Dynamic stability metrics exhibit distinct intensity and segment dependent response patterns. By performing a systematic comparison of multiple stability metrics within a single experimental paradigm, this within-study comparison helps clarify the relationships among these measures. Future work will aim at applying this approach to better understanding clinical gait.

Images (Optional)

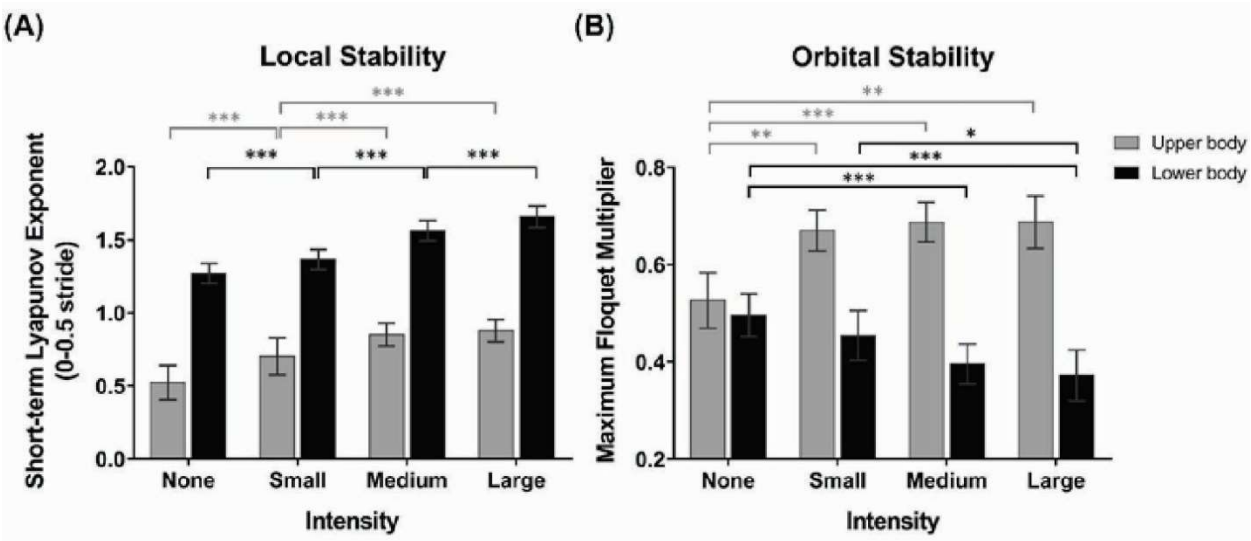


Figure 1: Gait Stability metrics across perturbation intensities. (A) Local Stability as measured by the Lyapunov exponent. (B) Orbital Stability as measured by Floquent multiplier. $p < 0.05$ (*), $p<0.01$ (**), $p< 0.001$ (***)

Session Category

Human Motion and Performance: Locomotion/Gait

P1-168

Adaptive Observation of Gait Disturbances using Central Pattern Generator Models

Mr Jesse Macht MASc, P.Eng.[1], Dr Fae Azhari PhD, P.Eng.[1], Dr Joshua Taylor PhD[2]

[1]University of Toronto, Toronto, Ontario, Canada. [2]New Jersey Institute of Technology, Newark, New Jersey, United States

Introduction

Minor gait disturbances (for example those caused by asymmetric muscle atrophy, misalignment in lower limb prosthetic systems, and pain induced adaptation) are often difficult to detect and require experienced clinical intervention to identify and correct. If left undetected, these disturbances may lead to long term health issues such as osteoarthritis. In this work, we implement an adaptive state observer that simultaneously provides estimates of state variables (joint angles) and physical parameters (muscle activity gains, limb lengths, body mass) associated with gait using a simple wearable sensor package. By providing estimates of the physical parameters as they vary over time, we present this observer as a quantitative analytical tool that can be used to measure and diagnose some physical causes of gait disturbances.

Methods

The key to rendering the musculoskeletal system as a linear time varying (LTV) state space model amenable to adaptive observation is the inclusion of a central pattern generator (CPG) model for the gait control signals originating from the central nervous system (CNS), inspired by the control model presented by Ryu and Kuo [1]. An adaptive Kalman filter is implemented to learn the LTV musculoskeletal model, thus illuminating any disturbances that may impact the gait system.

Results

We demonstrate that the gait control signal, driven in part by acceleration impulses from the motor cortex via the CPG, provides persistent excitation to the musculoskeletal system. We also provide an analysis of the observability Grammian for the LTV musculoskeletal model and the output relationship implicit in our sensor package design. To validate the proposed observer, a standard gait model in OpenSim is utilized to simulate different walking patterns with disturbances introduced in the musculoskeletal system. Simulated sensor readings (acceleration and ground reaction force) are generated from the walking simulation and passed to the adaptive observer.

Discussion

The resulting estimated states and model parameters produced by the observer are compared against the values used in simulation to discuss the effectiveness of the approach for detecting mechanical issues that lead to abnormal gait.

References (Optional)

[1] Hansol Ryu and Arthur Kuo, Scientific Reports, 2021

Acknowledgements (Optional)

We acknowledge the support of the Natural Sciences and Engineering Research Council of Canada (NSERC).

Nous remercions le Conseil de recherches en sciences naturelles et en génie du Canada (CRSNG) de son soutien.

Session Category

Human Motion and Performance: Locomotion/Gait

P1-169

Single-Camera Markerless Gait Analysis for Clinical Sagittal-Plane Assessment in Children with Cerebral Palsy

Ms. Jingwen Hu[1], Dr. Michelle Spirtos[1], Dr. Damien Kiernan[2], Prof. Ciaran Simms[1]

[1]Trinity College Dublin, Dublin, Dublin, Ireland. [2]Central Remedial Clinic, Dublin, Dublin, Ireland

Introduction

Gait analysis is critical for evaluating movement difficulties and guiding treatment in children with cerebral palsy (CP). Conventional multi-camera, marker-based motion-capture systems require dedicated infrastructure which are difficult to use in home environments. Single-camera markerless approaches that convert 2D-video into 3D-keypoints offer a more accessible alternative. However, most existing methods do not provide sufficient meaningful 3D-keypoints to define and compute clinically interpretable sagittal-plane joint angles for children with CP. This study investigates whether a transformer-based 2D-to-3D model using single-camera input can estimate 3D gait kinematics and derive sagittal-plane joint angles for children with CP.

Methods

We applied a transformer-based model to predict 3D gait motion from 2D-keypoints detected from a single-camera. The model was trained on 2000 anonymized 3D gait traces of children with CP. Using 11 input 2D-keypoints, we reconstructed 17 3D-keypoints, enabling computation of clinically relevant sagittal-plane joint angles based on the coordinate-system definitions of standard marker-set gait analysis protocols. Because real single-camera video was not yet available in the dataset, input was generated by virtual camera projection of the 3D gait data.

Results

Model performance was preliminarily examined in an independent evaluation sample of 10 children with CP, each contributing at least three gait cycles across two sessions. This evaluation indicated a substantial reduction in lower-limb joint-angle errors compared with a baseline open-source transformer pretrained on standard datasets. Mean hip-angle error decreased from 18.3° to 8.5° (left) and from 15.0° to 9.2° (right), while knee-angle error decreased from 17.7° to 4.5° (left) and from 14.2° to 5.8° (right). Using the 17 predicted 3D keypoints, sagittal-plane mean joint-angle errors were approximately 8.5°/9.7° (hip),

3.3°/3.9° (knee), and 5.5°/5.4° (ankle) for the left/right limbs, respectively. Additional offset-correction strategies are expected to further reduce hip and ankle-angle errors.

Discussion

These preliminary findings suggest that a suitably trained transformer-based, single-camera markerless approach with expanded keypoints can achieve clinically promising sagittal-plane gait accuracy in children with CP. Such a low-cost and accessible method has the potential to support gait assessment in home environments. Future work will validate this method using real mobile-device video and assess both repeatability and clinical agreement.

Images (Optional)

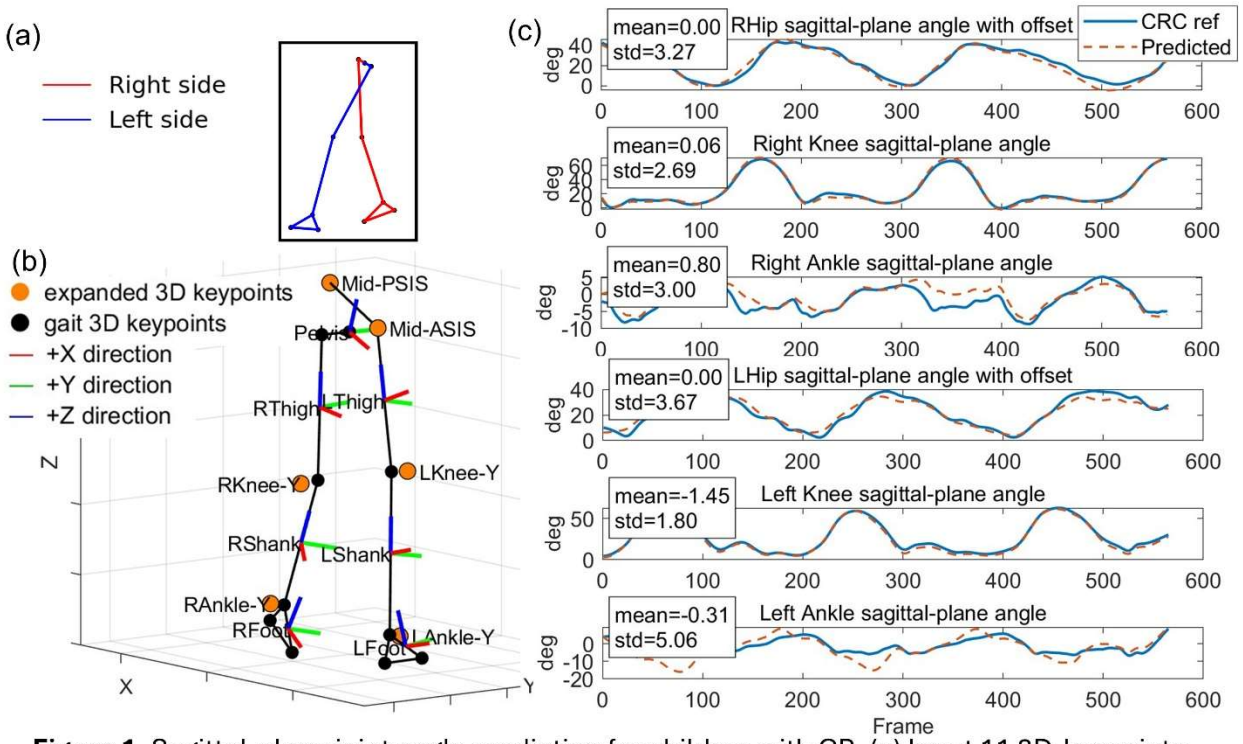


Figure 1. Sagittal-plane joint angle prediction for children with CP. (a) Input 11 2D-keypoints. (b) Estimated 17 3D-keypoints and Embedded Vector Base on lower-limbs. (c) Comparison of predicted angles with CRC reference ground-truth angles and the corresponding mean error.

Session Category

Human Motion and Performance: Locomotion/Gait

P1-170

Swing-Leg Inertia Enhances the Explanation of Ankle Contribution and Propulsive Mechanisms in Running

Dr. Jinsung Jung Ph.D[1], Prof. Hyerim Lim Ph.D[2], Prof. Sukyung Park Ph.D[1]

[1]KAIST, Yuseong-gu, Daejeon, Korea, Republic of. [2]Kumoh National Institute of Technology, Gumi-si, Gyeongsangbuk-do, Korea, Republic of

Dr. Jinsung Jung

Prof. Hyerim Lim

Introduction

The spring loaded inverted pendulum (SLIP) model has served as a fundamental representation of human gait dynamics, and extended formulations can reproduce joint level patterns. While these extensions capture ankle behavior well during walking, they diverge substantially during running [1]. Because the ankle produces the largest moment and power and governs braking and propulsion, misrepresenting its behavior leads to incorrect interpretations of stance phase mechanics. To address this, we incorporated swing leg mass to represent its inertial influence during running and its interaction with the stance leg. This addition enables more accurate representation of ankle contributions and propulsive mechanisms within a simplified framework.

Methods

The model separates the body center of mass into two point masses: one for the swing leg and one for the remainder of the body including the stance leg. These masses are connected through a pivot and a linear spring, allowing interaction between swing and stance leg dynamics. A torsional spring between the virtual torso and the swing leg generates swing related torque. Stance leg parameters such as stiffness, initial conditions, and foot geometry were adopted from prior work, while swing leg parameters were assigned based on experimental observations. To represent the flight phase required for a steady state limit cycle, the two masses were merged into one at takeoff and then allowed to follow free fall motion with appropriate initial conditions.

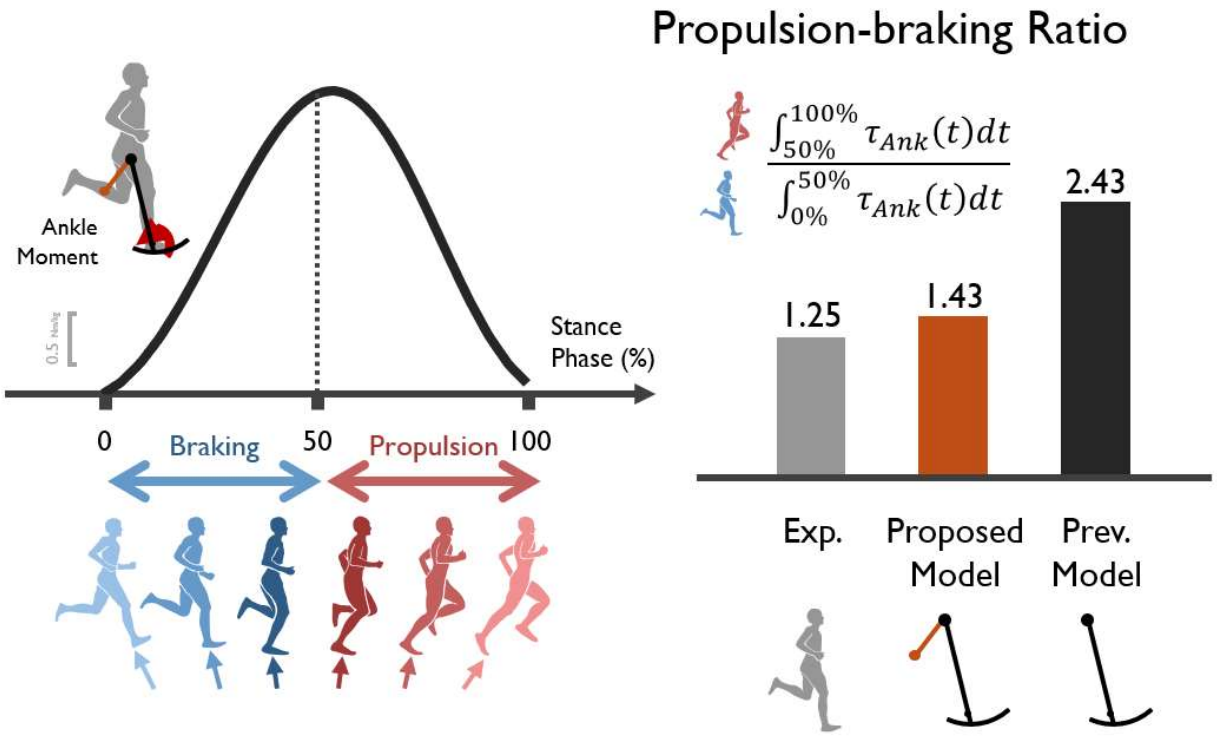
Results

The proposed model resolves the characteristic underestimation of ankle contribution in early stance and overestimation in late stance seen in previous models. It more accurately matches the ratio of the integrated ankle moment between braking and propulsion, reducing errors by over seventy percent. The model further shows that the additional kinetic energy needed at the flight transition is on the order of several tens of joules, similar to the elastic energy released from the Achilles tendon. This establishes clearer physiological relevance for the simplified propulsive mechanism.

Discussion

By more faithfully reproducing ankle dynamics in running, the model corrects major limitations of prior SLIP based approaches and provides improved insight into propulsion and stance phase mechanics.

Images (Optional)



References (Optional)

[1] H. Lim and S. Park, J Biomechanics, 2018

Acknowledgements (Optional)

This work was supported by the National Research Foundation of Korea (NRF) grant funded by the Korea government (MSIT) (RS-2024-00356657)

Session Category

Human Motion and Performance: Locomotion/Gait

P1-171

Integrated Analysis of Lower Limb Kinematics, Muscle Activation, and Plantar Pressure During Stair Ambulation in Individuals With Chronic Ankle Instability: A Pilot Study

Mr. Jongsu Kim PT, BPT, Mr. Sanghyun Cho MD, PhD, Mr. Jongwon Choi

Yonsei University, Wonju, Gangwon-do, Korea, Republic of

Introduction

Chronic ankle instability (CAI) is associated with recurrent ankle sprains and altered lower-limb biomechanics, which may contribute to secondary impairments and reduced quality of life. Nevertheless, prior studies of stair ambulation in individuals with CAI have typically been conducted under controlled laboratory settings and relied on discrete analysis, limiting their ability to characterize continuous biomechanical patterns. To address these limitations and provide more practical and clinical insights, this study conducted an integrated continuous analysis of 3D joint kinematics, muscle activation, and plantar pressure during stair ambulation outside the laboratory.

Methods

Nine young adults (4 with CAI and 5 healthy controls) participated in the study and were screened according to the recommendations of the International Ankle Consortium. Each trial consisted of 3 meters of level walking before and after a 10-step staircase. All participants completed five repetitions of stair ascent and descent at a self-selected comfortable speed. IMU-based 3D joint kinematics (pelvis, hip, knee, ankle), surface EMG (TA, PL, GCM, RF, BF, GMed), and plantar pressure were collected and synchronized using a multi-sensor system. After data processing, continuous signals were analyzed using Statistical Parametric Mapping (SPM), which enables time-series comparisons across the entire gait cycle. Hotelling's T^2 tests were used to evaluate multivariate patterns of 3D joint kinematics and muscle-coordination, followed by post hoc analyses when significant effects were detected. Independent t-tests were applied to assess differences in plantar-pressure distribution.

Results

Hotelling's T^2 tests revealed no significant group differences in 3D joint kinematics or in distal and proximal muscle-coordination patterns. Independent t-tests indicated that plantar-pressure distribution showed no clear differences between groups.

Discussion

Although no statistically significant differences were observed, differences in hip and ankle kinematics reflected characteristics in individuals with CAI, while the distal-coordination peaks suggested increased ankle strategy variability, and the proximal-coordination changes implied the use of compensatory strategies. These tendencies aligned with findings from previous SPM studies on level walking. Observed trends therefore suggest that meaningful group differences may emerge with an adequately powered sample during stair ambulation. Based on the preliminary data analysis, the main study aims to recruit at least 26 participants per group to ensure adequate statistical power.

Images (Optional)

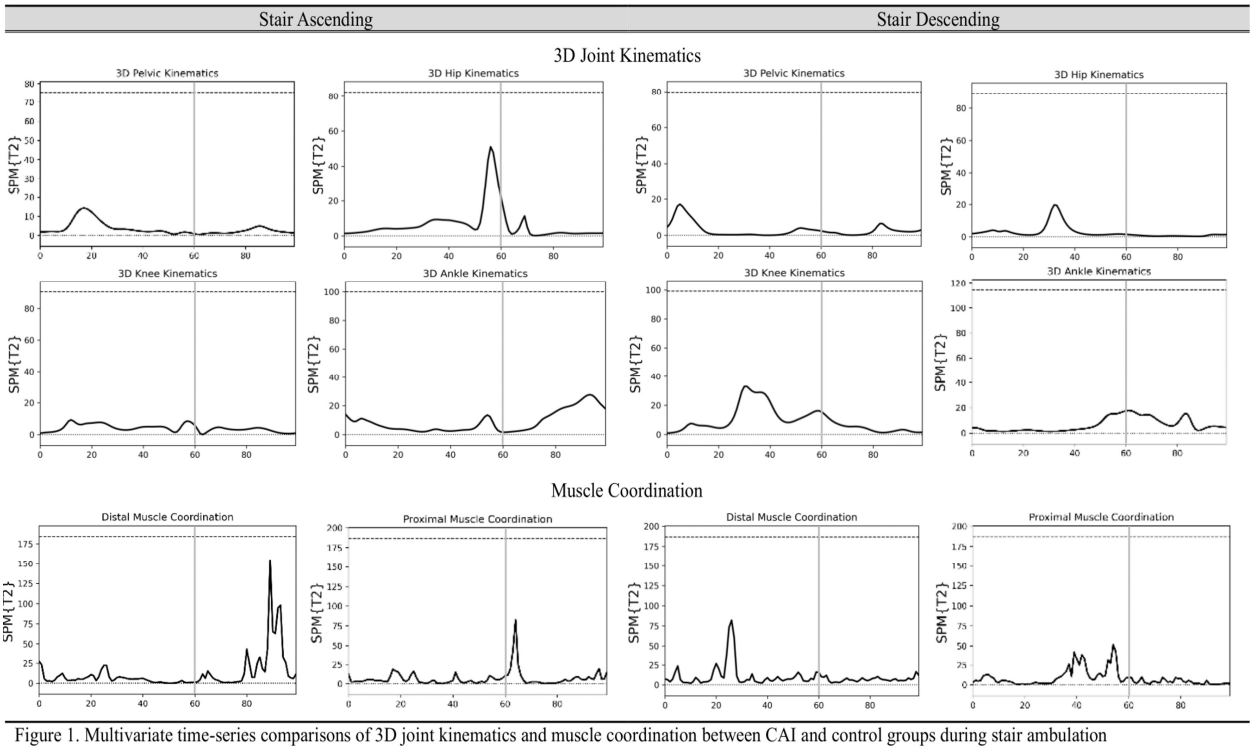


Figure 1. Multivariate time-series comparisons of 3D joint kinematics and muscle coordination between CAI and control groups during stair ambulation

Acknowledgements (Optional)

We would like to thank the participants and staff for their support during this pilot study. No external funding was received for this work.

Session Category

Human Motion and Performance: Locomotion/Gait

P1-172

Reduction of Cross-Talk in Lower Limb Secondary Joint Angles With Motion Capture Based on Dynamic 3D Scanning

Dr. Helios De Rosario[1], Dr. Juan López-Pascual[1], Dr. Mario Lamas[1], Dr. Brian Horsak[2]

[1]Instituto de Biomecánica de Valencia. Universitat Politècnica de València, Valencia, Valencia, Spain. [2]Center for Digital Health & Social Innovation, University of Applied Sciences, St. Pölten, Mostviertel, Austria

Introduction

Gait analysis with marker-based motion capture (MBMC) is the clinical standard but is time-consuming and invasive. Markerless motion capture based on RGB videos (MMC) is a convenient alternative, but often suffers from high errors, especially for secondary angles outside the sagittal plane. Alternative MMC systems based on dynamic scans measuring human shape rather than estimate poses from RGB videos may mitigate these errors. This study compared lower limb joint angles derived simultaneously from the Move4D dynamic body scanner [1] and MBMC, against true bone motion observed in previous studies with fluoroscopy.

Methods

Twelve healthy subjects underwent standard gait analysis with three repetitions. 3D kinematic data were collected simultaneously using the pose model of Move4D and with a modified Cleveland Clinic Marker Set. Hip, knee and ankle joint angles (flexion/extension, abduction/adduction, internal/external rotation) were calculated following ISB recommendations. The resulting ranges of motion (ROM) and angle profiles were compared to published in vivo fluoroscopic data, which served as the gold standard reference for actual bone motion.

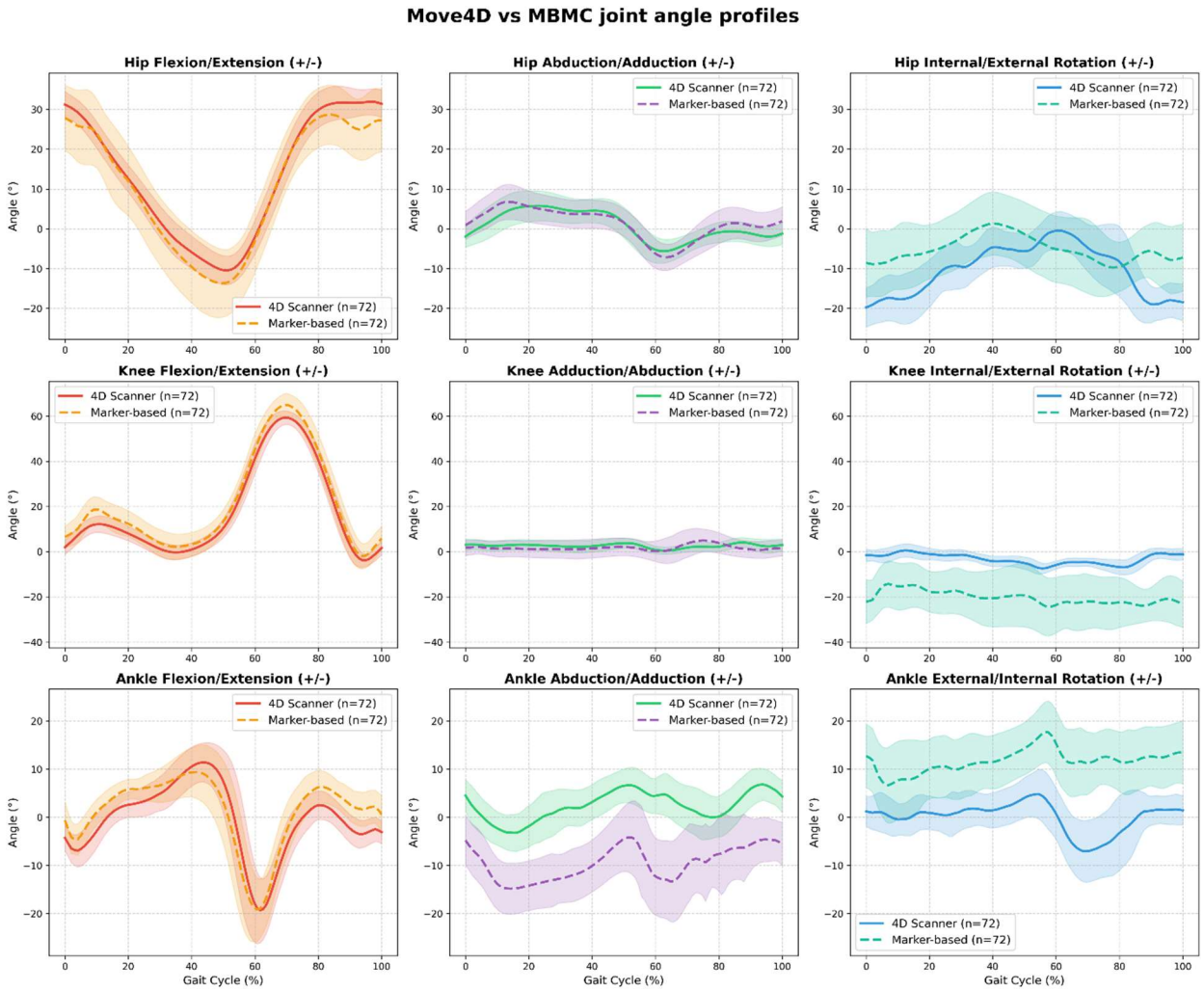
Results

The ROM of hip and ankle were consistent between both systems. The profiles of all hip angles and flexion-extension of knee and ankle were consistent, while differences emerged in secondary angles. The ROM of knee abduction/adduction was smaller in the Move4D data than for MBMC (5.1º vs 10.8º on average). While no differences were found in the ankle ROM, an offset between Move4D and MBMC was found in the secondary angles, possibly associated to the marker instrumentation error. The Move4D-derived secondary angles were closer to the published fluoroscopy values.

Discussion

The Move4D system provided convenient, non-invasive kinematic data for gait that is comparable with the results of MBMC in the main angles, and closer to the results of studies with fluoroscopy in secondary angles. The pose model derived from 3D body scans with precision < 1 mm [1] may overcome the error of soft tissue artifacts observed during standard marker-based motion capture. Therefore body scanning-based MMC seems to offer greater fidelity to true skeletal motion while providing a convenient analysis without markers or invasive methods.

Images (Optional)



References (Optional)

[1] E. Parrilla *et al.*, 3DBODY.TECH, 2019. DOI: 10.15221/19.030

Session Category

Human Motion and Performance: Locomotion/Gait

P1-173

Runners with Strong Feet Resist Arch Collapse During Loading

Ms. Julia Nicolescu MEng[1], Ms. Emma Slavin[1], Mr. Logan Gaudette MS[2], Dr. Adam Tenforde MD[2], Dr. Irene Davis PhD, PT, FAPTA[3], Dr. Karen Troy PhD[1]

[1]Worcester Polytechnic Institute, Worcester, Massachusetts, United States. [2]Spaulding Rehabilitation Hospital, Charlestown, Massachusetts, United States. [3]University of South Florida, Tampa, Florida, United States

Introduction

Runners risk developing metatarsal bone stress injuries (BSIs) due to the high impact, repetitive nature of the sport. Foot muscle strength has been identified as a modifiable risk factor for metatarsal BSI [1], but it remains unclear how strength influences arch biomechanics during running. We hypothesized that runners with stronger feet have higher arches that deflect less during loading.

Methods

Thirty-two runners (age:21.3±1.6, 16 male) who ran ≥24km/week participated in this institutionally approved study and provided written consent. Arch doming and lesser toe strengths were measured using a dynamometer and participants were divided into high and low foot strength groups. Barefoot running biomechanics data were collected to measure dynamic arch height index (dAHI), arch height deflection, and angular displacement of the midtarsal joint during stance. Maximum and minimum values and their timing were compared between groups using two-tailed t-tests. Statistical parametric mapping was used to compare dAHI throughout stance.

Results

Runners in the high strength group had flatter feet but their arches collapsed less. High strength runners had 2.9 times less negative arch deflection (Figure 1; p=0.04). They began increasing AHI earlier, so they achieved maximum dAHI and positive arch deflection 16.9% earlier in stance (p<0.01). The high strength group had 2.5º less midtarsal joint extension (p=0.04) which further suggests less arch collapse. These results suggest that the high strength group had more active muscle involvement that aided resistance to arch collapse and windlass mechanism engagement to maintain and increase dAHI.

Discussion

Our results align with the understanding that intrinsic foot muscles help regulate arch mechanics [2] and alter metatarsal loads [3]. This work offers possible explanations for

reduced injury risk seen in higher strength and lower arched athletes [1,4]. Foot strength training in runners can positively impact arch biomechanics. Decreased arch collapse may help reduce metatarsal strain and thereby reduce BSI risk. While exploratory, these results could be further substantiated in clinical trials evaluating the role of foot strengthening to modify risk for metatarsal BSI.

Images (Optional)

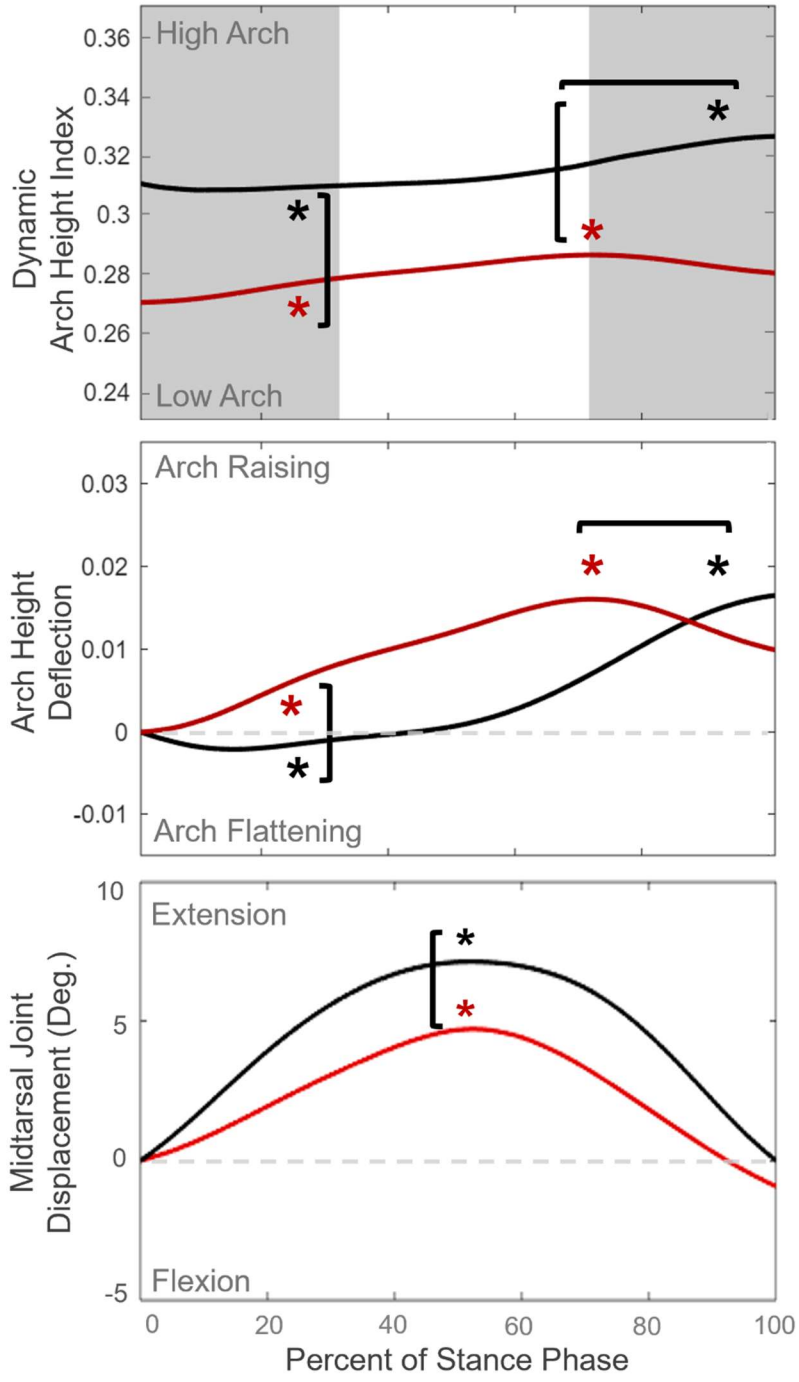


Figure 1. Dynamic arch height index, arch height deflection, and midtarsal joint displacement during running stance. High foot strength group is shown in **red**. Low foot strength group is shown in **black**. Grey-shaded regions indicate statistically significant differences between groups based on SPM analysis. Stars indicate significant differences. Vertical brackets reflect significant differences in min./max. magnitudes while horizontal brackets reflect differences in timing of those events.

References (Optional)

[1] Fujitaka *et al.*, Orthop.J.Sports.Med, 2015. [2] Kelly *et al.*, J.R.Soc.Interface, 2014. [3] Sharkey *et al.*, J.Bone.Jt.Surg., 1995. [4] Taddei *et al.*,Am.J.SportsMed, 2020.

Acknowledgements (Optional)

This research was supported by the National Institutes of Health under Award Number R15HD104169.

Session Category

Human Motion and Performance: Locomotion/Gait

P1-174

Comparison of Two Heel-Strike Perturbation Intensities on Lower Limb Kinematics in Healthy Adults

Dr. Juliane Mueller Researcher (Post-doc), B.Sc. Anne Lotte Schneider Graduate, M.Sc. Nikolai Hepke PhD Student, Prof. Dr. Jörg Lohscheller Professor, Prof. Dr. Steffen Mueller Professor

Trier University of Applied Sciences, Trier, Rhineland-Palatinate, Germany

Introduction

Understanding the biomechanical response to gait perturbations is essential for advancing sensitive diagnostic approaches and enhancing fall-prevention strategies. This study analyzed the kinematic responses of healthy adults to two perturbation intensities applied during initial heel contact, aiming to determine the minimal perturbation strength required to elicit a meaningful kinematic response.

Methods

Fifteen healthy adults (8f/7m;30±9years;174±11cm;72±17kg) walked (1m/s) on an instrumented split-belt treadmill with two separately selectable belts, while two stimuli were randomly applied five times each during initial heel contact of the right leg (S_{Strong}: acceleration/duration: -11m/s^2/0.09sec; $S_{weak:}$ acceleration/duration: -6,7m/s^2/0.055sec). Kinematics of the lower extremity were recorded during normal gait (N) and stumbling ($S_{(Strong/Weak)}$) using a 3D motion analysis system (10 cameras (Vicon),200Hz;model: HBM2). Maximal joint flexion angles (°) and their timing within the gait cycle (%GC) were extracted for the ankle and knee joint of perturbed (PL,right) and contralateral leg (CL, left). Additionally, spatiotemporal gait parameters were extracted. Multiple one-way ANOVAs for dependent samples (post-hoc Tukey-Kramer; α=0.05) were used to compare outcomes between N, S_{Strong} and S_{Weak}.

Results

The PL showed a significant increase in maximum flexion of the ankle joint ($p<0.0001$) during S (compared to N) with significant differences between stimuli ($S_{Strong} > S_{Weak}$). The timing of maximum knee flexion in the gait cycle of PL shifted significantly ($p<0.0001$) during S without differences between both stimuli. The step width ($p=0.0001$) of the PL increased significantly during S without differences between stimuli. The CL showed a significant increase of maximum flexion for both joints (ankle:$p=0.0005$;knee: $p=0.0037$) as well as a significant shift of timing of maximum flexion for both joints (ankle: $p<0.0001$;knee: $p=0.0051$) with significant differences between stimuli only for the ankle.

The stride duration of the CL increased significantly (p=0.0005) during S with significant differences between stimuli (S_{Strong}> S_{Weak}). (Tab.1)

Discussion

Both artificially induced perturbations significantly altered lower-limb kinematics and spatiotemporal gait adaptations, indicating a progressive bilateral compensation strategy. Moreover, the strong perturbation induced earlier and more pronounced compensatory responses. However, these findings validate the perturbation protocol and highlight that both stimulus levels are suitable for population-specific applications (e.g. patients, athletes, elderly).

Images (Optional)

Table 1 Knee and Ankle Joint Kinematics and Spatiotemporal Gait Adaptations during normal and perturbed walking for perturbed and contralateral leg

Outcomes	perturbed leg (right)							contralateral leg (left)						
	N	S_{weak}	S_{strong}	p values (post hoc)			p value one-way ANOVA	N	S_{weak}	S_{strong}	p values (post hoc)			p value one-way ANOVA
	Mean (± SD)	Mean (± SD)	Mean (± SD)	N vs. S_{weak}	N vs S_{strong}	S_{weak} vs S_{strong}		Mean (± SD)	Mean (± SD)	Mean (± SD)	N vs. S_{weak}	N vs S_{strong}	S_{weak} vs S_{strong}	
Kinematics														
Ankle flexion max (°; AF_{max})	11.13 ± 1.43	12.83 ± 1.07	14.88 ± 1.17	**0.0126**	**<0.0001**	**0.0025**	**<0.0001**	11.03 ± 1.16	12.22 ± 0.60	12.95 ± 1.06	**0.0278**	**0.0004**	0.2286	**0.0005**
Time of AF_{max} (%GC)	52.64 ± 3.82	50.83 ± 3.72	54.89 ± 4.92	0.6035	0.4602	0.0938	0.1122	53.21 ± 7.45	59.07 ± 5.58	68.23 ± 6.67	0.1353	**<0.0001**	**0.0118**	**<0.0001**
Knee flexion max (°; KF_{max})	64.52 ± 1.36	64.95 ± 1.25	63.97 ± 1.81	0.6914	0.7967	0.3207	0.3519	64.96 ± 1.00	65.83 0.52	66.17 ± 0.66	**0.0395**	**0.0034**	0.5724	**0.0037**
Time of KF_{max} (%GC)	76.78 ± 1.05	78.05 ± 0.62	78.97 ± 0.91	**0.0082**	**<0.0001**	0.0660	**<0.0001**	66.17 ± 2.52	74.72 2.25	71.85 ± 3.78	0.4368	**0.0051**	0.0903	**0.0065**
spatiotemporal parameters														
stride length (m)	1.21 ± 0.05	1.20 ± 0.02	1.20 ± 0.06	0.8436	0.9081	0.9895	0.8459	1.21 ± 0.03	1.21 ± 0.03	1.22 ± 0.04	0.9824	0.7274	0.8290	0.7289
stride duration (sec)	1.21 ± 0.05	1.22 ± 0.02	1.26 ± 0.06	0.9100	0.0658	0.1477	0.0591	1.21 ± 0.03	1.23 ± 0.03	1.28 ± 0.04	0.3400	**0.0005**	**0.0194**	**0.0007**
step length (cm)	61.1 ± 2.60	61.2 ± 2.90	62.1 ± 3.70	0.9977	0.7379	0.7754	0.7127	59.9 ± 1.10	60.1 ± 0.70	60.1 ± 0.90	0.8497	0.8582	0.9998	0.8262
step width (cm)	14.5 ± 0.80	15.9 ± 0.70	16.2 ± 0.70	**0.0017**	**0.0001**	0.6091	**0.0001**	14.6 ± 0.70	14.8 ± 0.40	14.6 ± 0.70	0.6311	0.9967	0.6785	0.5982

Legend: N: normal gait; S_{weak}: weak perturbation; S_{strong}: strong perturbation; AF= Ankle flexion; KF: Knee flexion, HF: hip flexion; max = maximum; %GC: Percentage of Gait Cycle

Acknowledgements (Optional)

This project was funded by the German Research Foundation (DFG) – Project No. [498061329].

Session Category

Human Motion and Performance: Locomotion/Gait

P1-175

Evaluation of Learnable Triangulation for Lower-Limb Kinematics in Osteoarthritis Patients Using a Four-Camera Markerless System

Dr. Junqing Wang, Dr. Wei Xu, Prof. Yong Nie, Prof. Kang Li

West China Hospital, Sichuan University, Chengdu, Sichuan Province, China

Introduction

Triangulation is a commonly used method for multi-view 3D pose estimation. However, when the number of cameras is limited, estimation accuracy may be compromised due to issues such as occlusion. Learnable triangulation can achieve superior estimation accuracy with fewer cameras. Nevertheless, whether this method can improve the estimation of lower-limb joint angles in patient populations remains unknown. Therefore, this study evaluated whether learnable triangulation could enhance the estimation accuracy of lower-limb joint angles compared to conventional triangulation in a dataset of patients with osteoarthritis (OA) using a four-camera system.

Methods

A total of 150 patients with end-stage hip or knee osteoarthritis were allocated to a training set (n=120) and a testing set (n=30). Kinematic data were synchronously collected at a frequency of 150 Hz as participants walked at a self-selected speed, using both a four-camera markerless system and a ten-camera marker-based system. The markerless algorithm was developed on the training set, including data preprocessing, 2D pose estimation, and 3D pose estimation (using learnable triangulation and conventional triangulation, respectively). On the testing set, the differences between the markerless and marker-based systems in terms of keypoints and lower-limb joint angles were evaluated using root mean square error (RMSE) and intraclass correlation coefficients (ICC).

Results

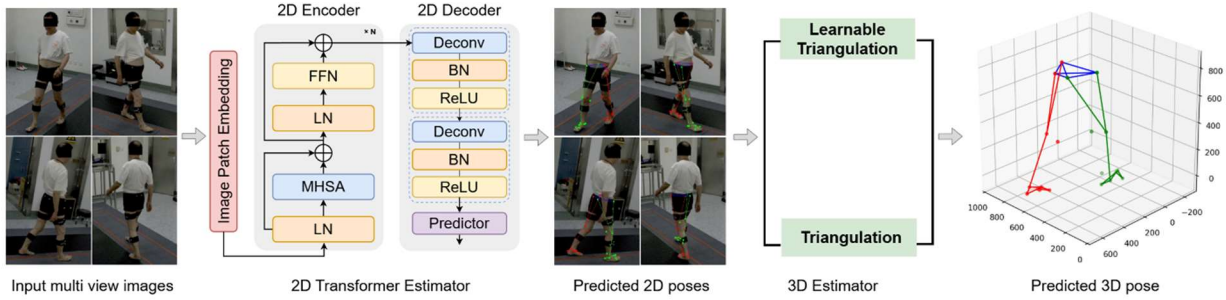
The grand mean RMSE for all keypoints predicted by learnable triangulation and conventional triangulation were 6.4 mm and 10.4 mm, respectively. The average RMSE for all joint angles using learnable triangulation and conventional triangulation were 3.79° and 4.23°, respectively. ICC values were higher in the sagittal plane (learnable triangulation: 0.96; conventional triangulation: 0.93), but lower in the frontal plane (learnable triangulation: 0.60; conventional triangulation: 0.56) and transverse plane (learnable triangulation: 0.32; conventional triangulation: 0.27).

Discussion

In a four-camera markerless system, learnable triangulation can improve keypoint prediction accuracy and subsequently enhance the accuracy of lower-limb joint angles in the sagittal plane; however, it does not improve the accuracy of lower-limb joint angles in the frontal and transverse planes. Since marker-based systems are also subject to errors due to soft tissue artifact, future studies could compare markerless results with more accurate methods such as biplane radiograph to evaluate their accuracy.

Images (Optional)

(A)



(B)

		Sagittal			Frontal			Transverse		
		Hip	Knee	Ankle	Hip	Knee	Ankle	Hip	Knee	Ankle
RMSE (°)	Learnable triangulation	3.52 (1.27)	2.90 (0.89)	2.47 (0.56)	5.47 (1.67)	3.37 (0.99)	2.21 (0.62)	6.02 (1.39)	5.40 (1.50)	2.74 (0.75)
	Triangulation	4.78 (1.77)	3.38 (1.27)	3.44 (1.36)	5.33 (1.31)	3.92 (1.67)	2.60 (0.64)	6.60 (2.37)	5.46 (2.03)	2.6 (0.79)
ICC	Learnable triangulation	0.96 (0.03)	0.97 (0.07)	0.95 (0.04)	0.68 (0.25)	0.27 (0.20)	0.81 (0.14)	0.26 (0.16)	0.26 (0.16)	0.43 (0.16)
	Triangulation	0.92 (0.07)	0.96 (0.08)	0.88 (0.06)	0.65 (0.23)	0.28 (0.19)	0.73 (0.13)	0.21 (0.14)	0.22 (0.17)	0.37 (0.16)

Figure 1: (A) The workflow of the markerless system, LN: Layer Normalization; MHSA: Multi-Head Self-Attention; FFN: Feed-Forward Network; Deconv: Deconvolution; BN: Batch Normalization; ReLU: Rectified Linear Unit.
(B) Between-system comparison of joint angle estimation errors for learnable triangulation versus conventional triangulation, RMSE: root mean square error; ICC: interclass correlation coefficient.

References (Optional)

Session Category

Human Motion and Performance: Locomotion/Gait

P1-176

Classifying Possible Sarcopenia With a Single IMU Sensor While Walking in Older Adults

Mr. Junwoo Park PT, MSc, Dr. Kitaek Lim PT, PhD, Dr. Seyoung Lee PT, PhD, Mr. Jongwon Choi PT, MSc, Prof. Woochol Joseph Choi PT, PhD

Injury Prevention and Biomechanics Laboratory, Department of Physical Therapy, Yonsei University, Wonju, Gangwon-do, Korea, Republic of

Introduction

Sarcopenia is a condition of aging-related skeletal muscle loss, and the Asian Working Group for Sarcopenia (AWGS) has suggested the clinical guidelines for identification of sarcopenia with calf circumference, muscle strength, physical performance, and skeletal muscle mass [1]. However, these are impractical for community or clinics use. We used machine learning algorithms to easily screen the possible sarcopenia with a single inertial measurement unit (IMU) sensor data collected while walking.

Methods

We recruited 57 older adults (13 males, 44 females; mean age = 78.7 years). Possible sarcopenia was defined when both of the following conditions were met based on AWGS guidelines: (1) at least one calf circumference smaller than 34 cm for men or 33 cm for women; and (2) either handgrip strength <28 kg for men or <18 kg for women, or a five-times sit-to-stand time ≥12 seconds. Twenty participants (2 males, 18 females) were classified as having possible sarcopenia. For the classification model input, IMU sensors were attached to 10 body segments, collecting kinematic data during 10 m walking. Input features included the mean and variance of IMU data per gait cycle, along with demographic information (height, weight, age, gender). Five machine learning models were developed to compare classification performance: linear/radial basis function (RBF) kernel support vector machine (SVM), decision tree, random forest, and extreme gradient boosting. Model performance was evaluated using 5-fold cross-validation.

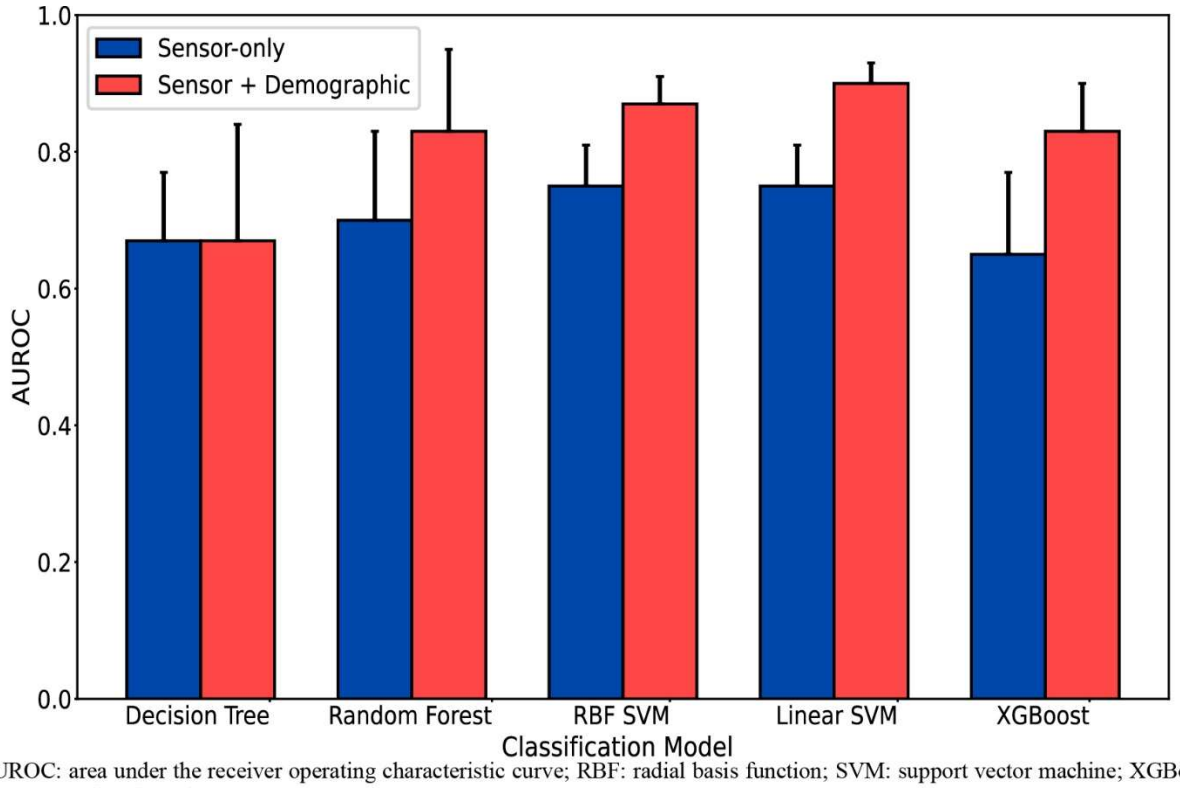
Results

The RBF-kernel SVM model using IMU data from the left lower leg demonstrated the best performance, achieving an accuracy of 0.73 (0.06) and an area under the receiver operating characteristic curve (AUROC) of 0.75 (0.06). Furthermore, the linear SVM model that incorporated both left lower leg IMU data and demographic features yielded improved classification performance, with an accuracy of 0.80 (0.04) and an AUROC of 0.90 (0.03) (Figure 1).

Discussion

Our results indicate that a single IMU sensor can classify possible sarcopenia with moderate accuracy, and that performance improves by approximately 10% when demographic information is included. These findings support the integration of wearable sensor data with clinical characteristics to enhance the detection of possible sarcopenia in older adults.

Images (Optional)



AUROC: area under the receiver operating characteristic curve; RBF: radial basis function; SVM: support vector machine; XGBoost: extreme gradient boosting

Figure 1: Model performance to classify possible sarcopenia using IMU data

References (Optional)

[1] Chen et al., 2020

Acknowledgements (Optional)

This work was supported by the “Brain Korea 21 FOUR Project” (F21SH8303039), the National Research Foundation of Korea (NRF) grant funded by the Korea government (MSIT) (RS-2025-16071808), and by the Regional Innovation System & Education (RISE) program through the Gangwon RISE Center, funded by the Ministry of Education (MOE) and the Gangwon State (G.S.), Republic of Korea (2025-RISE-10–006).

Session Category

P1-177

Lower Extremity Joint Work Redistribution After A 30-Minute Treadmill Walk Is Not Explained By Baseline Walking Mechanics, Knee Extensor Strength, Or Physical Activity In Older Adults

Mr. Justin R. Matties MS, Dr. Ross J. Brancati PhD, Ms. Zoe H. Smith PhD, Dr. Jane A. Kent PhD, Dr. Katherine A. Boyer PhD

University of Massachusetts, Amherst, MA, United States

Introduction

Older adults (O) may experience greater changes in performance in response to standardized bouts of activity (i.e., higher fatigability) than younger adults (Y) [1]. The potential interactions between altered gait mechanics, low habitual physical activity and muscle weakness in this fatigability have not been determined. Thus, we compared baseline characteristics and the responses to a 30-minute treadmill walk (30MTW) at preferred walking speed (PWS) in Y and O.

Methods

Twenty-six Y (34.7±3.2 yr, n=15 female, BMI: 24.5±3.5 $kg \cdot m^{-2}$, PWS: 1.13±0.14 $m \cdot s^{-1}$) and 29 O (73.0±2.6, n=19 female, BMI: 26.4±3.8, PWS: 1.14±0.14) wore an accelerometer (ActiGraph) to quantify minutes of weekly moderate-to-vigorous physical activity (MVPA). Overground sagittal plane joint kinematics and kinetics at PWS were calculated pre- and post-30MTW. Isometric knee extensor (KE) torque and isokinetic KE power were measured at $120° \cdot s^{-1}$ and $240° \cdot s^{-1}$ (Biodex). Changes in the relative distribution of ankle, knee and hip positive joint work were quantified as an overall redistribution score (R-score): the Euclidean distance between relative joint work distribution pre- and post-30MTW. O were bisected into high (O_{high}) and low (O_{low}) R-score groups. Group differences in baseline MVPA, KE peak torque, and gait kinematics and kinetics were assessed with ANOVAs, with Tukey HSD comparisons reported when a significant main effect was observed ($p < 0.05$).

Results

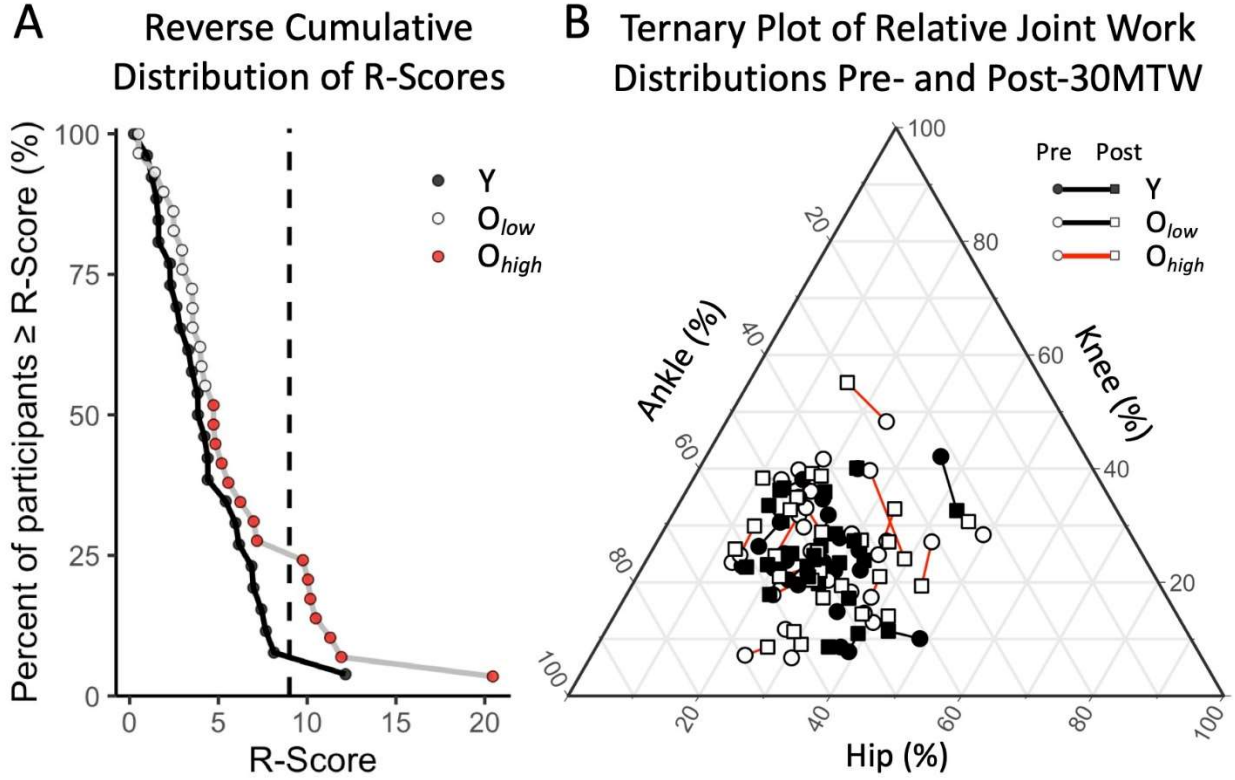
R-score >9 was observed in 24.1% of O and 3.8% of Y (Figure 1A). O_{high} exhibited a greater R-Score compared to O_{low} and Y ($p<0.001$) (Figure 1B). R-scores did not differ between O_{low} and Y ($p=0.255$). Peak isometric KE torque and power were lower in O_{low} and O_{high} than Y ($p<0.001$), but not different between O_{low} and O_{high} ($p>0.883$). MVPA ($p=0.364$), and pre-30MTW gait mechanics were not different between groups ($p\geq0.400$).

Discussion

A greater proportion of O had an altered gait strategy post 30MTW, though a common direction of change was not observed (Figure 1b). These data indicate that exercise induces gait changes independent of baseline characteristics. Future work should investigate these gait changes, captured by R-score, as contributors to fatiguability in O.

Images (Optional)

Figure 1.



References (Optional)

[1] Basil A. Eldadah, *PM&R,* 2010

Acknowledgements (Optional)

Funding: NIH R01AG058607

Session Category

Human Motion and Performance: Locomotion/Gait

P1-178

How Residual Limb Length in Individuals with Unilateral Transfemoral AmputationAffects Body Weight Transfer

Mr. Kai Kobayshi B.Sc., Mr. Shunta Kobayashi B.Sc., Assoc.Prof. Hiroaki Hobara Ph.D.

Tokyo University of Science, Toyko, Tokyo, Japan

Introduction

Weight transfer during double-limb stance is fundamental for forward progression and the maintenance of gait stability [1]. In this phase, effective weight acceptance by the leading limb is particularly critical. Among individuals with unilateral transfemoral amputation (uTFA), shorter residual limbs possess reduced musculature and leverage, potentially limiting their capacity to support body weight [2]. Although weight-transfer strategies in prosthesis users are influenced by loading/unloading responses at push-off and walking speed [3], the contribution of residual limb length to weight-transfer mechanics remains unclear. Therefore, we investigated how residual limb length influences weight transfer in individuals with uTFA.

Methods

Twenty-six individuals with uTFA and four individuals with knee disarticulation (KD) were recruited. Participants with uTFA were classified into Short, Middle and Long groups using tertile segmentation of the residual to intact femur length ratio. All participants walked on an instrumented treadmill at eight speeds (2.0-5.5 km/h), and ground reaction forces (GRFs) were collected at 1 kHz. From the vertical GRF, the first (Fz1) and second (Fz2) peaks were extracted for each step. Loading rate (LR) was calculated as Fz1 divided by the time from initial contact to Fz1, and unloading rate (uLR) as Fz2 divided by the time from Fz2 to toe-off. A three-way mixed-effects ANOVA compared prosthetic- and intact-leading conditions across limb-length groups and speeds ($P < 0.05$).

Results

No significant differences among residual limb length groups were found at any speed or leading limb condition for either parameter.

Discussion

The present findings indicate that residual limb length does not meaningfully influence body-weight transfer during gait, as neither LR nor uLR differed across limb-length groups

at any walking speed or under either leading-limb condition. These results suggest that weight acceptance on the prosthetic side may rely not on residual musculature but on compensatory hip extensor activation.

References (Optional)

[1] S M Bruijn et al., J R Soc Interface, 2013

[2] Robert Gailey et al., J Rehabil Res Dev, 2008

[3] Ryo Amma et al., Sci Rep, 2021

Acknowledgements (Optional)

This work was partly supported by JSPS KAKENHI (19K11338 and 22K11625). We appreciate all subjects who participated in this study.

Session Category

Human Motion and Performance: Locomotion/Gait

P1-179

Custom Insoles Improve Walking Efficiency in Middle-Aged Women Working in Prolonged Weight-Bearing Occupations

Mr. Kailin Xing MS[1], Mr. Zhu Fang MS[1], Mr. Zhengyi He MS[1], Mr. Joonho Um BS[1], Dr. Jong Chul Park PhD[2], Dr. Prabhat Pathak PhD[3], Dr. Siddhartha Bikram Panday PhD[1,4]

[1]Department of Physical Education, Hanyang University, Seoul, Seoul, Korea, Republic of. [2]Department of Marine Sports, Pukyong National University, Busan, Busan, Korea, Republic of. [3]Department of Sports Sciences, Seoul National University of Science and Technology, Seoul, Seoul, Korea, Republic of. [4]Department of Art and Sportainment, Hanyang University, Seoul, Seoul, Korea, Republic of

Mr. Kailin Xing

Mr. Zhu Fang

Mr. Joonho Um

Introduction

Post-menopausal estrogen loss and age-related sarcopenia reduce collagen synthesis in middle-aged and older women, increasing soft-tissue laxity and weakening the foot arch [1]. These morphological changes impair the foot's ability to store and return energy during locomotion, raising the metabolic cost of walking. This decline is particularly common among older women working long hours in weight-bearing occupations. Although foot-strengthening exercises can be beneficial, adherence is often low due to the time and effort required for women who are actively working. Considering that custom insoles (CIs) can redistribute plantar pressure and enhance sensory input to support more efficient gait [2], we evaluated the effectiveness of CIs in improving walking efficiency in middle-aged women in prolonged weight-bearing occupations.

Methods

15 women over the age of 55 working in jobs that require more than 4 hours of standing per day were recruited for this study. We used a three-dimensional (3D) foot morphology

captured using a foot scanner (MediACE Scan: MS320F) to print CIs made up of thermoplastic polyurethane (TPU) that support the medial longitudinal arch and stabilize the rearfoot to improve shock absorption and energy storage for propulsion. We compared the effectiveness of the CIs with commercially available prefabricated insoles (PIs) without medial arch support in reducing O_2 cost recorded with a portable metabolic analyzer (VO_2 Master) during 5 minutes of treadmill walking. The O_2 cost was calculated as the difference in the O_2 consumption between the last 1 minute of walking and 2 minutes of resting before walking, divided by the walking speed. We compared the O_2 cost between CIs and PIs using paired t-test ($p<0.05$).

Results

We found that wearing CIs significantly reduced the O2 cost, on average by 18.4% (Fig.1), during walking in 15 participants than PIs ($t_{[14]}=3.585$, $p=0.003$).

Discussion

In this study, CIs that are practical for use with everyday shoes effectively reduce oxygen consumption in middle-aged and older women working in prolonged weight-bearing occupations. Future studies may consider evaluating the long-term effects of using CIs on walking efficiency and muscular function.

Images (Optional)

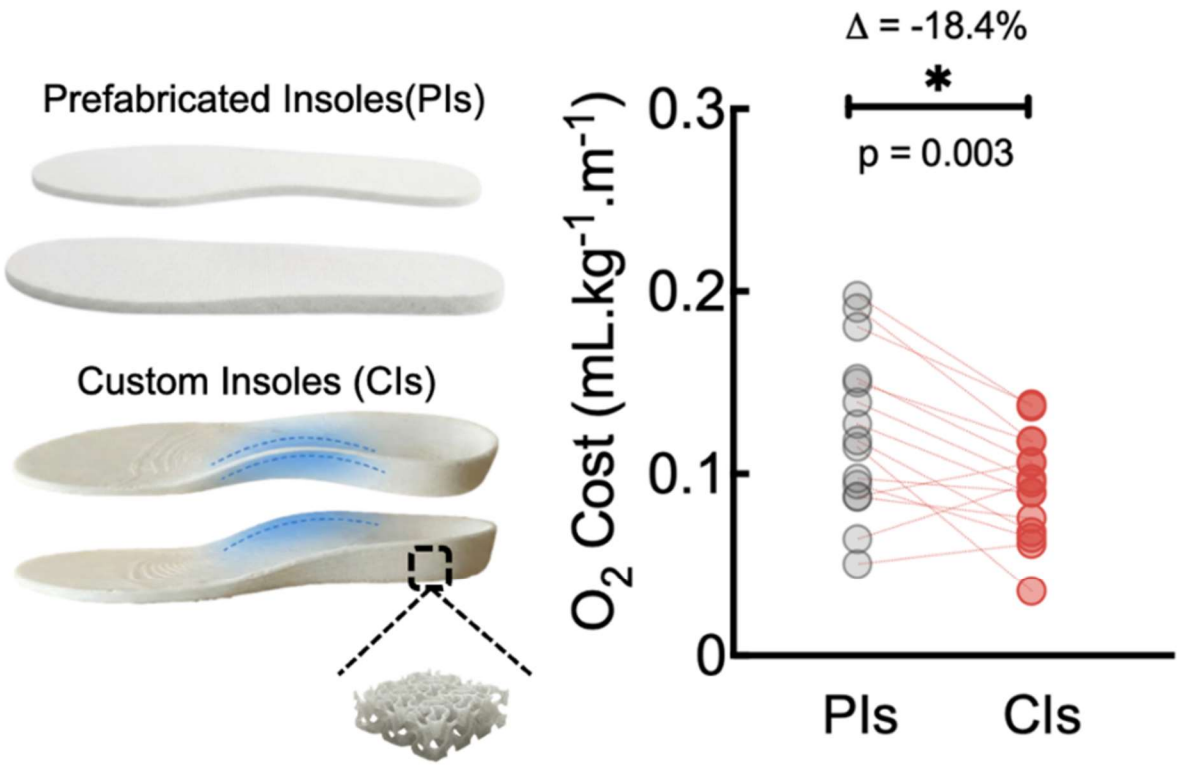


Figure 1: Pictures of prefabricated and custom insoles, and differences in O_2 cost between the two insoles for 15 participants.

References (Optional)

[1] Scott, G. et al., Gait Posture,2007; [2] Meng, Y. et al., JBBE,2020

Acknowledgements (Optional)

This work was supported by the research fund of Hanyang University (HY-202500000003787).

Session Category

Human Motion and Performance: Locomotion/Gait

P1-180

Energy Expenditure-Based Simulations Reveal Neural Contributions to Modular Control of Walking Biomechanics

Ms Kaitlyn Downer, Dr. Jessica Allen PhD

University of Florida, Gainesville, Florida, United States

Introduction

Motor modules have been proposed as a neural control strategy for complex movement, though some argue they arise purely from biomechanics [1]. We used subject-specific simulations to test whether motor modules reflect a control strategy by varying the cost function while keeping biomechanics constant. If motor modules represent an underlying control strategy, changing cost function components would influence motor module complexity and structure.

Methods

Kinematics and kinetics from seven older adults (5F; 62.7±6.3 years) walking at their self-selected speeds were used in OpenSim Moco tracking simulations. Ten gait cycles per subject were simulated to capture variability. Simulations minimized either sum of squared activations (effort) or metabolic cost of transport (CoT), with varying weights to capture different prioritization of energy expenditure. Effort weights spanned 4 orders of magnitude, while CoT simulations were dynamically weighted to achieve low (3-5 J/kg/m) and high (6-8 J/kg/m) CoT. To ensure consistent biomechanics, simulated gait cycles with solutions with RMSE >5 degrees were removed. Motor modules were extracted from simulated muscle activity and compared across simulations. Complexity was quantified as variability not explained by one module (VNAFby1). To quantify structure, four modules were extracted from each simulation [2] and compared using Pearson's correlations.

Results

All subjects had 6-10 valid gait cycles for analysis. Both motor module complexity and structure were influenced by the cost function. Increasing priority on energy expenditure generally increased complexity (higher VNAFby1; Fig. 1A). Module structure also varied across cost functions (Fig. 1B). Within model comparisons (Effort vs Effort, CoT vs CoT) were more correlated than between model comparisons (Effort vs CoT), indicating that the choice of expenditure model impacts motor modules. Variability in structure was also present within the same expenditure model, showing that the weight on the term influences module structure.

Discussion

These results support the result that motor modules reflect not only biomechanical constraints but also neural control strategies. Since clinical populations often show altered modules, rehabilitation should target neural control (e.g. EMG-guided protocols) in addition to biomechanics.

Images (Optional)

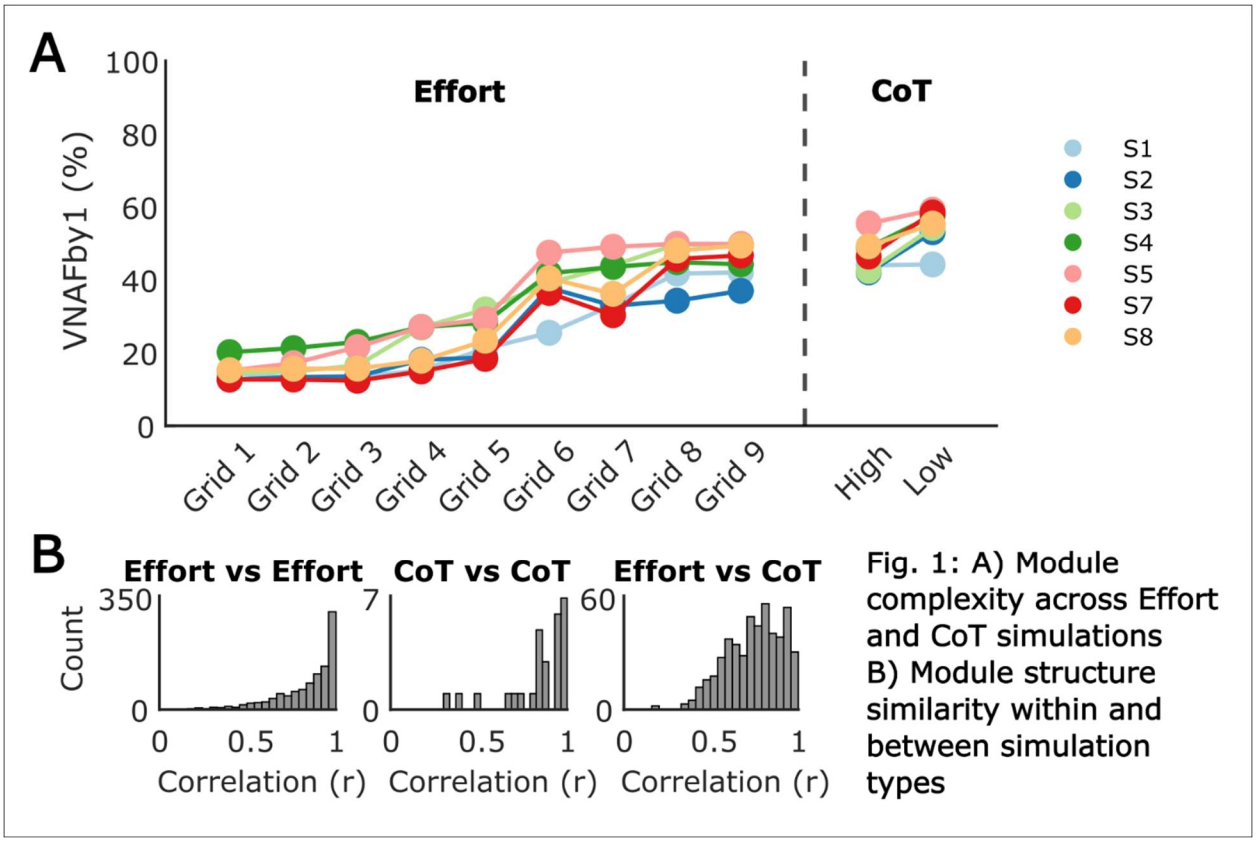


Fig. 1: A) Module complexity across Effort and CoT simulations B) Module structure similarity within and between simulation types

References (Optional)

[1] Ting and McKay, Curr Opin Neurobiol, 2007

[2] Allen *et al.*, J Neurophysiol, 2019

Acknowledgements (Optional)

NSF GRFP (to K.E.D), NSF/CBET 2339331

Session Category

Human Motion and Performance: Locomotion/Gait

P1-181

Walking Biomechanical Adaptation on an Irregular Surface in Individuals with Knee Osteoarthritis

Mr. Kai-Wen Chien[1], Ms. Jasmin Behar[1], Dr. John Antoniou[2], Dr. Bernd Grimm[3], Dr. Patrick Ippersiel[4], Dr. Philippe Dixon[1]

[1]Department of Kinesiology and Physical Education, McGill University, Montreal, Quebec, Canada. [2]Division of Orthopaedic Surgery, SMBD Jewish General Hospital, McGill University, Montreal, Quebec, Canada. [3]Department of Precision Health, Luxembourg Institute of Health, Strassen, Canton of Luxembourg, Luxembourg. [4]School of Rehabilitation Science, University of Ottawa, Ottawa, Ontario, Canada

Introduction

Knee osteoarthritis (OA) is a leading cause of disability in older adults [1]. Understanding gait and mobility in individuals with knee OA can inform interventions. Past work has shown that healthy individuals adapt their lower-extremity coordination in response to different walking surfaces [2]; however, the effects of surface on clinical populations remain unclear. This study aims to compare walking coordination biomechanics in knee OA on flat and irregular surfaces.

Methods

Ten adults with knee OA (40–75 years) were recruited. Kinematic data were collected using eight Xsens Awinda (Movella Inc., The Netherlands) Inertial Measurement Units attached to the pelvis, bilateral thighs, shanks, and feet. Participants completed ten 4-m walking trials on flat (hospital hallway) and irregular (polyurethane floor panels; Terrasensa, Germany) surfaces. Coordination amplitude and variability were quantified using Mean Absolute Relative Phase (MARP) and Deviation Phase (DP), respectively, computed from Continuous Relative Phase analysis [3] based on knee and hip sagittal-plane joint angles. Differences between surfaces were evaluated using Statistical Parametric Mapping (SPM) paired t-tests ($\alpha = 0.05$).

Results

Results from five of the participants were analyzed. Knee–hip MARP was consistently lower on the irregular surface, indicating more in-phase coordination compared with the flat surface, during the initial–mid swing phase (~70–80% of the gait cycle) (Fig. 1a, b). Knee–hip DP values appear increased on the irregular surface across the gait cycle, suggesting

greater coordination variability; however, this difference was not statistically significant (Fig. 1c, d).

Discussion

Our preliminary data indicate that irregular terrain elicits greater knee-hip in-phase coordination (lower MARP), suggesting a stability-oriented strategy. The irregular surface challenges the neuromuscular system, and this coordination pattern may help maintain upright stability and reduce fall risk. The absence of significant DP differences may reflect the small sample size. The ongoing study will recruit more participants, with future analyses examining additional kinematic measures (e.g., joint angles, range of motion) and other joint pairs (e.g., ankle–knee coordination).

Images (Optional)

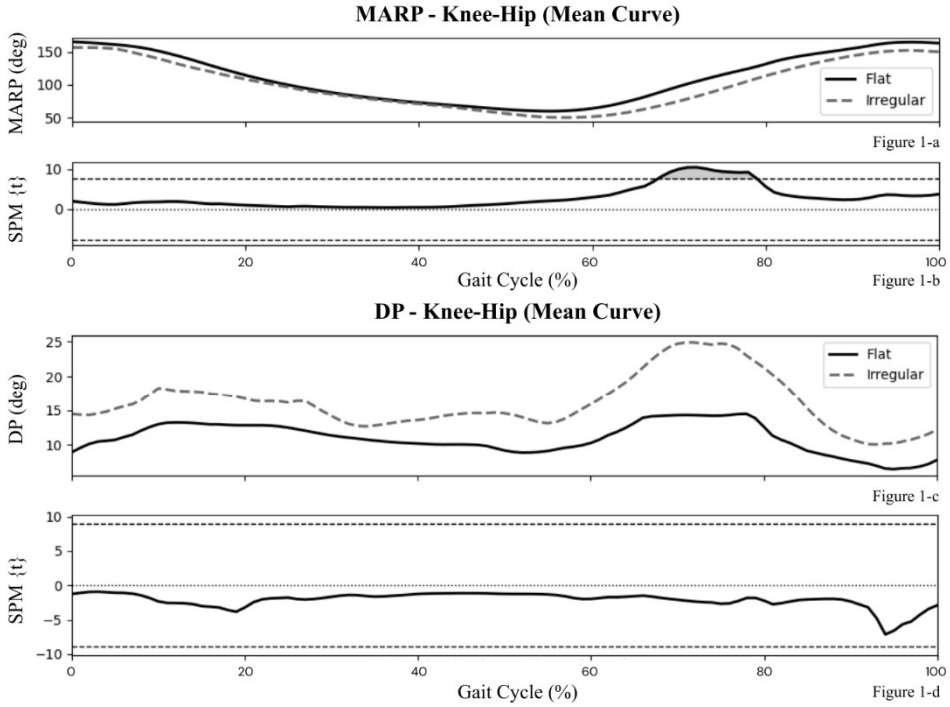


Fig. 1. Panels a and c show the mean knee–hip MARP and DP curves on different surfaces across the entire gait cycle. Panels b and d present the corresponding SPM t-tests for MARP and DP. Grey-shaded regions in the panel b indicate periods of significant difference. A positive significant region in panel c indicates that the flat surface elicited higher values.

References (Optional)

[1] Bijlsma & Knahr, Best Pract. Res.: Clin. Rheumatol., 2007 [2] Ippersiel, P. et al., Gait Posture, 2021 [3] Lamb, P.F., & Stöckl, M., Clinical Biomechanics, 2014

Session Category

Human Motion and Performance: Locomotion/Gait

P1-182

Effect of Emotional Expression on Upper Body Kinematics in Novel Movements

Ms. Katherine Elder MS, Dr. Melissa Gross PhD

University of Michigan, Ann Arbor, MI, United States

Ms. Katherine Elder

Introduction

Emotion expressed during ordinary movements like gait and sit-to-stand can be recognized by others and affects the movement kinematics. Similarly, emotion can be recognized in novel movements without a functional goal like arm gestures or dance, but little is known about the effect of emotion on the kinematics of these movements. In a study of a simple arm gesture comprising shoulder adduction from vertical to horizontal position with free movement of elbow and wrist joints, investigators found that maximum linear velocity and acceleration of the fingertips were significantly greater for anger than for sadness. The purpose of this study was to investigate the effect of emotional expression on the kinematics of a complex novel movement of the upper body.

Methods

A professional-level dancer was asked to create a short movement phrase using their upper body. The phrase was split into six gestures for analysis: gather, tilt, sweep, curl, press, and drop. Three trials were performed while expressing each of four emotions: neutral, sadness, anger, and joy, and motion capture data were collected. Visual3D was used to calculate resultant velocity and acceleration of the hands and custom Matlab code was used to extract maximum values. Significant differences were detected using ANOVA with Bonferroni post hoc comparisons.

Results

Velocity of the right and left hands was significantly affected by emotion in 3 of 6 gestures (Table 1). In general, across gestures, hand velocities decreased with sadness compared to the high arousal emotions (anger and joy). Hand acceleration was less affected by emotion, with sadness decreasing hand acceleration compared to anger in two gestures.

Discussion

We found that hand velocities and accelerations can be used to discriminate among emotions, particularly anger and sadness, consistent with previous findings for simple movements. With complex movements, however, we found that more emotions could be discriminated with analysis of only hand kinematic data, i.e., anger and joy, possibly because complex movements encode more information about emotion. Since human movement is inherently complex and often novel, future studies of emotion expression should be based on complex movement and include even more kinematic variables.

Images (Optional)

Table 1. Maximum resultant linear velocities and accelerations

Gesture	Kinematic Variable	Anger	Joy	Neutral	Sadness
Gather	Right Hand Velocity (m/s)	7.38 ± 0.98^{S}	7.35 ± 1.38^{S}	4.92 ± 0.47	$3.06 \pm 0.08^{A, J}$
	Left Hand Velocity (m/s)	$4.76 \pm 0.25^{J, N, S}$	3.69 ± 0.27^{N}	2.75 ± 0.45^{J}	$1.42 \pm 0.25^{A, J, N}$
	Left Hand Acceleration (m/s^2)	130.32 ± 50.58^{S}	67.06 ± 2.87	60.89 ± 5.21	37.28 ± 4.34^{A}
Sweep	Right Hand Velocity (m/s)	3.38 ± 1.21^{S}	3.23 ± 0.44^{S}	3.07 ± 0.38	$1.14 \pm 0.32^{A, J}$
	Left Hand Acceleration (m/s^2)	13.27 ± 5.61^{S}	5.74 ± 2.23	8.89 ± 3.43	2.51 ± 0.87^{A}
Press	Right Hand Velocity (m/s)	0.19 ± 0.06^{N}	0.22 ± 0.06^{N}	$0.04 \pm 0.02^{A, J}$	0.07 ± 0.03

All $p < .05$. Superscripts indicate values are significantly different from anger (A), joy (J), neutral (N), sadness (S).

References (Optional)

Session Category

Human Motion and Performance: Locomotion/Gait

P1-183

A Simple Resync Method for Wearable Inertial Sensors to Track Knee Flexion for 5 Days With High Fidelity

Dr. Ke Song, Dr. Josh Baxter

University of Pennsylvania, Philadelphia, Pennsylvania, United States

Introduction

Knee motion is critical for joint health, yet its real-world impact is not captured by in-lab motion analysis. While inertial measurement unit (IMU) provides a new way to track real-world knee motion, few confirmed the validity of week-long IMU data where sensor sync may be inaccurate due to device clock drift. A reliable post-hoc resync method is warranted.

Methods

5 healthy individuals (3M/2F) wore 4 IMUs on their thighs and shanks using medical tapes (**Fig. 1A**), for 5 continuous weekdays (Mon-Fri) that also included 3 in-lab markerless motion capture sessions (Mon, Wed, Fri) on walking, squat, step up/down, and sit-to-stand. Before attaching IMUs Monday and after detaching Friday, we inserted all IMUs in a custom-made "resync tool" (**Fig. 1B**) and swung it to produce a sync signal. We cross-correlated thigh/shank IMU sync signals to identify their time offsets on Mon and Fri, thereby relative clock drift over the week. We removed this drift by linearly "dilating" the faster IMU clock to match the other. After resyncing, we applied sensor-to-segment realignment to define the knee anatomical frame, then accelerometer-gyroscope fusion to calculate flexion. We compared IMU-estimated dominant-leg knee flexion to motion capture on all 3 days (Mon, Wed, Fri) using Pearson correlation and root-mean-square difference (RMSD).

Results

IMU clock drifts varied among participants (0.005–0.041 sec/hour). Our resync tool successfully removed this drift, and our IMU-estimated knee flexion strongly agreed with motion capture on all 3 days with high correlations (Mon: ≥0.948, Wed: ≥0.941, Fri: ≥0.906) and small RMSDs (Mon: ≤5.2°, Wed: ≤5.8°, Fri: ≤5.5°) (**Fig. 1C**).

Discussion

We demonstrate that leg-worn IMUs reliably track knee motion over a 5-day span, including mid-experiment (Wed) where linear drift rate was correctly assumed. This is a major advancement over single-session validations and is enabled by our simple resync method

that IMU wearers can perform at home. Our cost-friendly paradigm captures week-long data with minimal wearer interaction, which will help accelerate the translation of IMU technologies to larger clinical studies. We will leverage our novel approach to track multi-day knee mobility in osteoarthritic knees and determine how it relates to chronic disease progression.

Images (Optional)

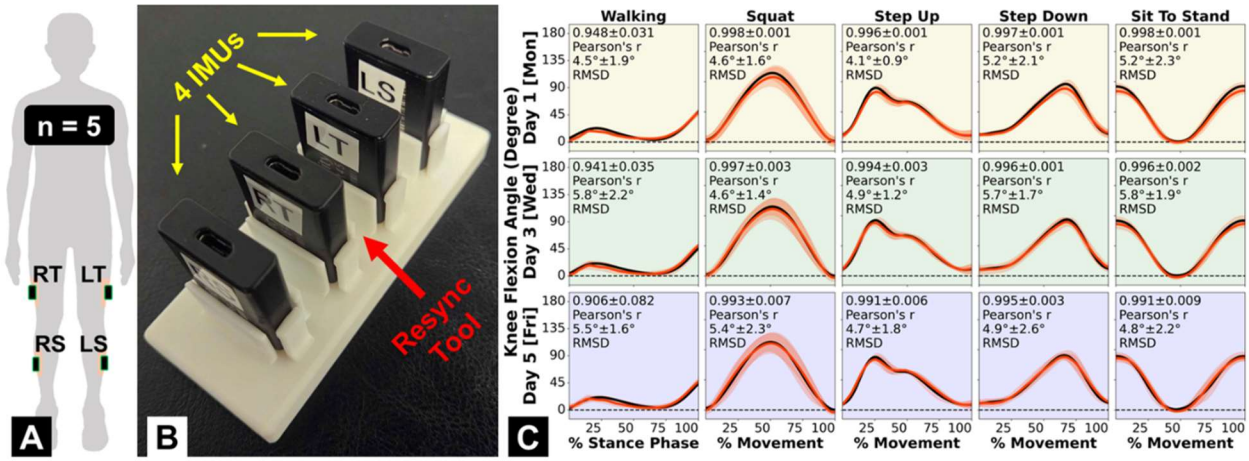


Figure 1. **(A)** IMU locations. Dominant leg was chosen for analysis. **(B)** Custom-made resync tool with all 4 IMUs inserted. L: Left, R: Right, T: Thigh, S: Shank. **(C)** IMU-estimated knee flexion (red) vs. in-lab motion capture (black) on Mon (top), Wed (center), Fri (bottom). Group mean (line) ± 1 standard deviation (shade).

Acknowledgements (Optional)

NIH R01AR078898 and VA I50RX004845.

Session Category

Human Motion and Performance: Locomotion/Gait

P1-184

Functional Electrical Stimulation of the Biceps Femoris Long Head Reduces Knee Internal Rotation Moment During Gait

PhD Candidate Koen Jongbloed MSc (Mechanical Engineering), Graduate Researcher Jacob Kok MSc (Mechanical Engineering), Professor Frans Van der Helm PhD, Associate Professor Eline Van der Kruk PhD

Delft University of Technology, Delft, Zuid-Holland, Netherlands

Introduction

Anterior cruciate ligament (ACL) injuries frequently lead to persistent gait alterations and increased risk of reinjury and osteoarthritis [1] [2]. Functional electrical stimulation (FES) applied to the biceps femoris long head (BFLH) during early stance may help reduce ACL-relevant knee loading in gait by counteracting anterior tibial translation and internal tibial rotation [3][4]**.** Repeated use may improve neuromuscular control, contributing positively to both the rehabilitation process and overall clinical outcomes. The aim of this study was to evaluate the reduction in knee joint loading during BFLH-targeted FES and to assess the after-effects of repeated FES on neuromuscular control following removal of the stimulation in healthy controls.

Methods

Nine healthy participants (24.4±1.08 years, 5M 4F) each completed two treadmill sessions after warm-up comprising 3 conditions: 4 min control, 4 min FES, and 4 min post-stimulation. FES (40 Hz, 350 µs pulse duration, 300 ms stimulation duration, Odstock FSR, intensity: max tolerable) was delivered via surface electrodes to the dominant BFLH at heel strike. Kinematic and kinetic data were collected on an instrumented treadmill (1000Hz, Motek, Vicon 100 Hz). and processed using a full-body gait model (Vicon Nexus, CGM2.5, 3-DOF joints). Statistical parametric mapping (SPM1D) identified significant differences over the gait cycle, and linear mixed-effects models evaluated changes across repeated exposure, after-effect, and retention phases.

Results

In the stimulated leg, FES significantly reduced the internal knee rotation moment (KRM) by 9.4% during 42–48% of the gait cycle compared to control ($p=0.0002$; $d=0.42$). Knee adduction moment (KAM) showed no reduction. No significant after-effects were observed.

Discussion

BFLH stimulation reduced internal rotational knee loading during gait in healthy adults. We did not observe changes in knee kinematics or kinetics after stimulation, indicating no clear evidence of lasting motor adaptation. These findings support the use of BFLH-targeted FES as an assistive strategy to modulate ACL-relevant knee loading in healthy adults. Future studies should refine stimulation protocols, and investigate effects in ACL-deficient populations.

Images (Optional)

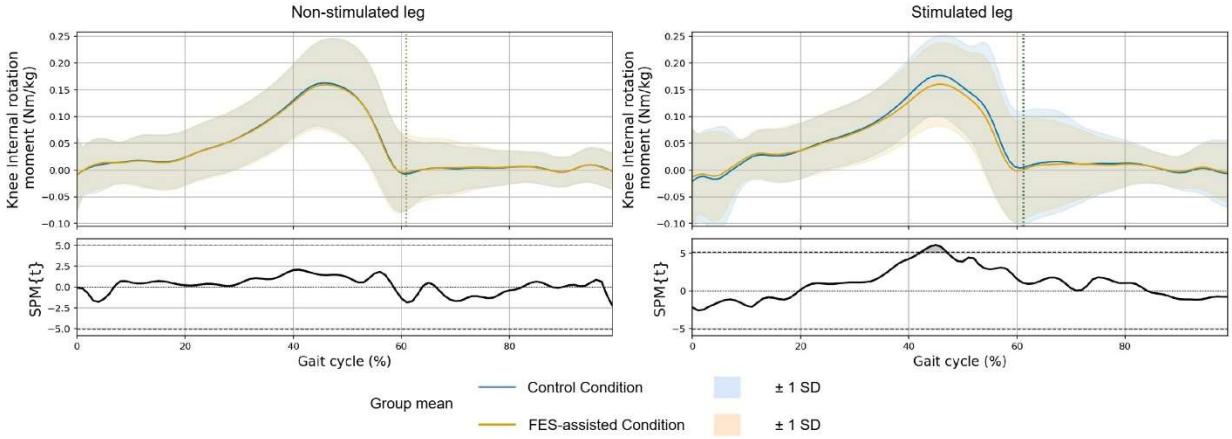


Figure 1: Mean KRM across the gait cycle for all participants during control (blue) and FES-assisted (orange) walking. Data are shown for the non-stimulated and stimulated legs, normalized to 0–100% of the gait cycle.

References (Optional)

[1] Slater et al., J Athletic training, 2017

[2] ØIESTAD et al, J Sports Medicine, 2010

[3] Amzi et al. PLOS one, 2018

[4] Xu et al., Open Science, 2019

Session Category

Human Motion and Performance: Locomotion/Gait

P1-185

Event-Specific Characteristics of Mediolateral Margin of Stability During Walking

Mr. Kouichi Suzuki B.Sc., Mr. Kai Kobayashi B.Sc., Mr. Shunta Kobayashi B.Sc., Assoc. Prof. Hiroaki Hobara Ph.D.

Tokyo University of Science, Tokyo, Tokyo, Japan

Introduction

Margin of stability (MoS) is widely used to quantify dynamic stability during walking [1]. Although the MoS was originally evaluated as the minimum value within a gait cycle, recent studies have evaluated the MoS at Heel Contact (HC) and Toe-Off (TO) [1, 2]. Event-based MoS values reflect the stability characteristics of each phase; however, the differences in the MoS between gait events have not been systematically examined. Therefore, the aim of the present study was to clarify the characteristics of MoS at multiple gait events.

Methods

Six healthy individuals were recruited. All participants walked at six speeds (2.0-7.0 km/h) on an instrumented treadmill, and ground reaction forces and moments were collected at 1 kHz. Mediolateral (ML)_Center of Pressure (CoP) position, ML_Center of Mass (CoM) position and ML_CoM velocity were calculated from these data [3]. MoS was defined as the distance between CoP and XCoM where

MoS=CoP-XCoM

$XCoM=CoM+v_{CoM}/(\sqrt{g/l})$

in which g is gravitational acceleration and l is leg length. ML_MoS at HC and TO were extracted for each gait cycle and compared across all walking speeds. Normality was assessed using the Shapiro–Wilk test. When the assumption of normality was met, a two-way repeated-measures ANOVA was performed ($p < 0.05$).

Results

There were significant main effects of speed ($p < .001$) and gait event ($p < .001$) on ML_MoS. ML_MoS at TO were significantly smaller than at HC across all walking speeds ($p < .001$). We also found a significant interaction effect on ML_MoS ($p = 0.025$).

Discussion

ML_MoS magnitude is not the same between HC and TO, indicating that these two events represent different aspects of mediolateral dynamic stability within the gait cycle. Moreover, the magnitude of the difference in ML MoS between the two events varies with walking speed.

References (Optional)

[1] A. L. Hof et al., *J. Biomech.*, 2005

[2] Carolin Curtze et al., *J. Biomech.*, 2024

[3] Tom J. W. Buurke et al., *J. Exp. Biol.*, 2018

Acknowledgements (Optional)

This work was partly supported by JSPS KAKENHI (19K11338).

Session Category

Human Motion and Performance: Locomotion/Gait

P1-186

A Young Mind vs. the Aging Brain: Age-Based Differences in a Virtual Reality Dual-Task Paradigm

Ms. Kristen De Melo MSc., PhD Candidate, Ms. Emily Marino BSc. Candidate, Dr. Lori Ann Vallis PhD

University of Guelph, Guelph, Ontario, Canada

Ms. Kristen De Melo

Ms. Emily Marino

Introduction

Maintaining the ability to dual-task (DT) is critical for functional independence; however, this ability begins to decline as early as age 40 and accelerates after age 65 [1,2]. These declines in motor-cognitive performance mirror early neurological changes, increases in fall risk, and highlight vulnerability in shared neural resources [2,3]. This study aims to explore DT interference and the role of cognition in movement control, with the long-term goal of identifying early markers and targets for non-invasive intervention.

Methods

Gait and cognitive performance were recorded (OptiTrack, 120 Hz; Corvallis, USA) as participants (18-35yrs and 60-80yrs) completed an adapted Simon effect task in virtual reality (Vive Pro 2 Headset). While walking, an arrow appeared (location: top left, right, or middle of virtual world) to indicate navigation direction around a “sinkhole” in two virtual environments (forest, hallway). This produced congruent (e.g., right-pointing arrow on the right), incongruent (e.g., right-pointing arrow on the left), and neutral trials (middle of screen). We hypothesized greater DT interference (e.g., slower gait, diminished step patterns) in older adults (OA) compared to younger adults (YA), highlighting reduced motor-cognitive integration capacity. ANOVA statistical analyses were conducted with significance set at $p<0.05$.

Results

Preliminary analyses (YA: N=3; 22.3±4.9yrs, OA: N=3; 61.7±1.2yrs) revealed variations in arrow congruency and virtual environment did not produce significant changes ($p>0.05$). However, when OA were required to transiently adapt their gait (e.g., sinkhole avoidance), they demonstrated reduced velocity and an increased time to approach the sinkhole and complete the trial compared to YA ($p<0.05$). Additionally, OA transitioned from narrow, long steps during straight walking to wider, shorter steps during gait adaptation trials, mimicking typical YA patterns ($p<0.05$). Data collection and processing are still ongoing.

Discussion

These findings highlight age-related vulnerabilities in DT and indicate that both cognitive control and movement coordination are promising targets for training. Ongoing work in this cohort will explore whether targeted cognitive and motor-cognitive training can reduce DT costs and improve functional performance, particularly in OA.

References (Optional)

[1] Ghai *et al.*, Clinical Interventions in Aging, 2017.

[2] Zhou *et al.,* The Lancet Healthy Longevity, 2023.

[3] Albrecht *et al.*, Scientific Reports, 2024.

Session Category

Human Motion and Performance: Locomotion/Gait

P1-187

Compensatory Muscle Activation Patterns of Lower Limb Muscles During Walking

Ms. Kyubin Chun, Prof. Seungbum Koo

KAIST, Daejeon, Daejeon, Korea, Republic of

Introduction

Human gait can be reproduced consistently across strides. Although joint angle variability during walking remains low [1], lower-limb muscle activation shows high variability [2]. This shows that similar gait kinematics do not necessarily result in consistent muscle activity. Motor redundancy has been reported as a potential explanation for this variability [3]. This study proposes that the ability to sustain consistent walking despite variability in muscle activation can be attributed to coordinated interactions among muscles. We hypothesize that within a muscle group with similar functions, a decrease in the activation of one muscle will be accompanied by an increase in the activation of another.

Methods

IRB approval and informed consent were obtained prior to testing. Eleven male participants walked on a treadmill for five minutes. Muscle activity was recorded from the quadriceps (vastus medialis, vastus lateralis, rectus femoris) and the plantar flexors (gastrocnemius, soleus) to investigate compensatory mechanisms. Gait cycle was divided into seven distinct phases. Mean activation values were computed for each phase. Since muscle activity may be influenced by the muscles from other functional groups, activation values were normalized using the muscle set reported in [4]. Pearson correlation coefficient was calculated between muscles within the same functional group ($p < 0.05$).

Results

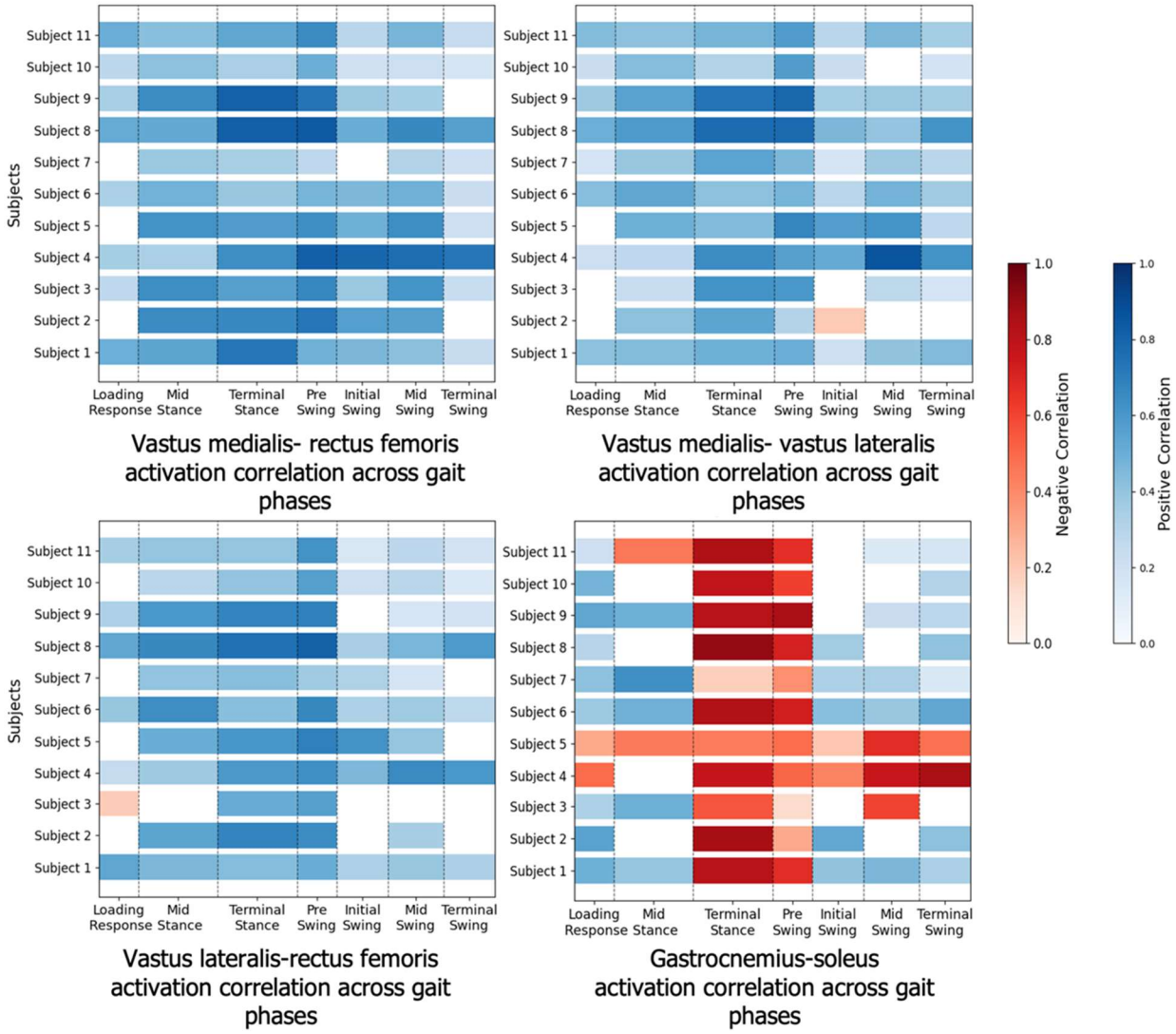
For plantar flexors, all subjects exhibited negative correlations during terminal stance and pre-swing phases. In contrast, correlations in quadriceps muscles were consistently positive. The vastus medialis–rectus femoris pair showed positive correlations across all gait phases with significant correlation. Similarly, the vastus medialis–vastus lateralis and vastus lateralis–rectus femoris pairs demonstrated positive correlations in most gait phases with significant correlation.

Discussion

Negative correlations in the plantar flexors during push-off support the presence of compensatory mechanisms. Conversely, quadriceps muscles exhibited consistently positive correlations. This demonstrates an opposite inter-muscular relationship. These

findings contradict the compensatory hypothesis for the quadriceps and instead suggest that they function as a unified group.

Images (Optional)



References (Optional)

[1]Winter DA, Biomechanics and Motor Control of Human Gait: Normal, Elderly and Pathological, 1991

[2]Yang JF *et al.*, Electroencephalography and Clinical Neurophysiology, 1987

[3]Lacquaniti F *et al.*, Physiology, 1999

[4] Van Der Krogt, M. M. *et al.*, Gait & Posture, 2012

Acknowledgements (Optional)

This research was supported by the IITP grant funded by the Korean government (MSIT) (No. 2022-0-00025)

Session Category

Human Motion and Performance: Locomotion/Gait

P1-188

Comparison of Optical and IMU-Based Gait Classification in Ankle Arthrodesis Using Machine Learning

Dr. Leandra Bauer[1,2], Dr. Andreas Brand[3,4], Prof. David Rügamer[5,6], Prof. Sebastian Baumbach[2,7]

[1]Experimental Orthopaedics, University Hospital Jena, Campus Eisenberg, Waldkliniken Eisenberg, Friedrich-Schiller-University Jena, Jena, Thuringia, Germany. [2]Department of Orthopaedics and Trauma Surgery, Musculoskeletal University Center Munich (MUM), University Hospital Munich, LMU Munich, Munich, Bavaria, Germany. [3]Institute for Biomechanics, BG Unfallklinik Murnau, Murnau, Bavaria, Germany. [4]Institute for Biomechanics, Paracelsus Medical University Salzburg, Salzburg, Bavaria, Austria. [5]Department of Statistics, LMU Munich, Munich, Bavaria, Germany. [6]Munich Center for Machine Learning (MCML), Munich, Bavaria, Germany. [7]OrthoPlus, Munich, Bavaria, Germany

Introduction

Optical motion capture (OMC) systems remain the gold standard in clinical motion analysis. Inertial measurement units (IMUs) offer a cost-effective and practical alternative. Recent developments enable multi-segmental modeling of the foot even in IMU applications, thereby expanding their clinical significance [1,2]. The aim of this study was to compare the ability of IMU and OMC systems to perform automated classification based on different ankle arthrodesis using machine learning (ML) methods.

Methods

In a prospective, bicentric study, 70 patients with tibiotalar (n = 34) or subtalar arthrodesis (n = 36) were compared. Motion analysis was performed using an IMU-based 2-segment foot model (Ultium Motion, Noraxon) and the marker-based Oxford Foot Model (Vicon). For both systems, kinematic data of the tibia–hindfoot, tibia–forefoot, and hindfoot–forefoot segments were collected over the gait cycle and processed using functional principal component analysis. Based on this, various ML algorithms (LASSO, Random Forest, SVM) were used to classify the arthrodesis (tibiotalar vs. subtalar). In addition, different input variables (such as number of steps) were compared. Model performance was evaluated based on accuracy, AUC, and F1 score; in addition, segment- and plane-specific influences on model performance were analyzed.

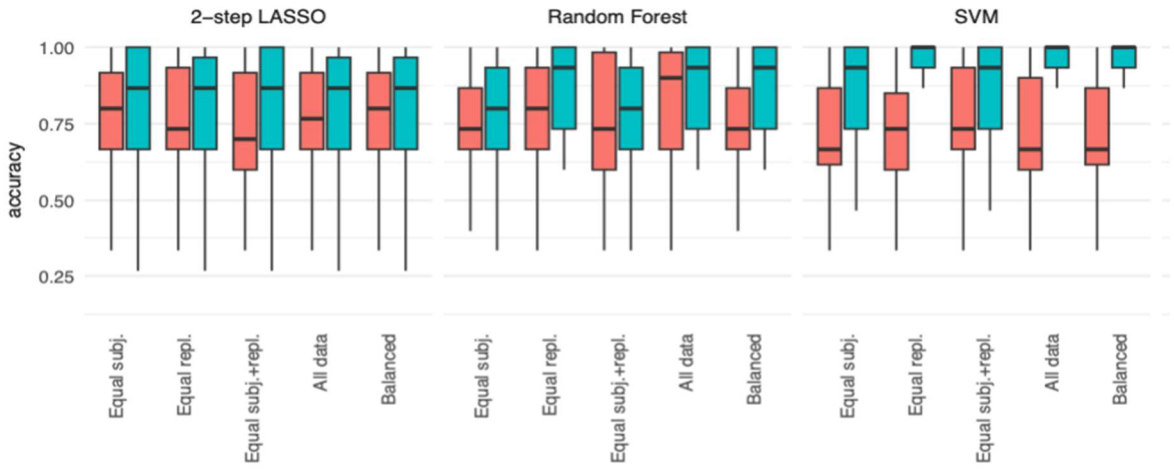
Results

All ML models achieved high classification quality with mean accuracies of 0.75–0.90 and AUC values > 0.90 (Fig. 1, IMU - red, OMC - green). The comparison showed similar results across all datasets, with IMU-based models achieving slightly lower performance values. For IMU data, sagittal movement between the rearfoot and forefoot had a significant influence on classification. For OMC data, transverse movement between the tibia and rearfoot had the strongest influence.

Discussion

The IMU-based 2-segment foot model achieved diagnostic accuracy comparable to that of the OMC system. IMU systems therefore have great potential for clinical use, particularly for objective functional assessment and follow-up after ankle arthrodesis. Future work should examine their applicability to other pathological gait patterns.

Images (Optional)



References (Optional)

[1] Leandra Bauer *et al.* BMC Musc Disord, 2024

[2] Leandra Bauer *et al.* Gait & Posture, 2024

Acknowledgements (Optional)

The study was financially supported by a local grant „Förderung Forschung und Lehre“ from Ludwig-Maximilian-University Munich (LMU).

Session Category

Human Motion and Performance: Locomotion/Gait

P1-189

A Case Study Comparing Biomechanical Variables in New Versus Old Running Prostheses Across Velocities up to Maximum Velocity

Ms. Lina Jaafar B.S.[1], Ms. Claudia Barattini M.E.[2], Dr. Alena Grabowski Ph.D[3]

[1]University of Colorado at Boulder, Boulder, CO, United States. [2]Turin Polytechnic University, Turin, Piedmont, Italy. [3]University of Colorado, Boulder, CO, United States

Introduction

Running-specific prostheses (RSPs) are passive-elastic carbon fiber devices that enable people with transtibial amputation (TTA) to run. The stiffness and energy-return of RSPs likely change with use, potentially affecting athletes' maximum velocity (vmax) and biomechanics across velocities. This case study examined an elite female athlete with a unilateral TTA using identical new and old RSPs to evaluate differences in v_{max} and biomechanics at steady running speeds.

Velocity is the product of contact length (Lc), step frequency (StepF), and stance average vertical Ground Reaction Force ($vGRF_{avg}$) [1]. Because the new RSP is likely stiffer and exhibits greater energy return versus old, we hypothesized that the new versus old RSP would result in faster v_{max}, longer Lc, higher StepF, and higher $vGRF_{avg}$ in the affected leg (AL) across velocities [1]. We further hypothesized that velocity would not have an interaction effect with RSP condition.

Methods

The athlete completed 20-step trials on a force-measuring treadmill beginning at 3 m/s and increasing by 1 m/s, with increments shrinking as she approached v_{max}: the fastest trial completed without drifting back on the treadmill. We collected GRFs for each trial and processed data in Visual3D, MATLAB, and RStudio.

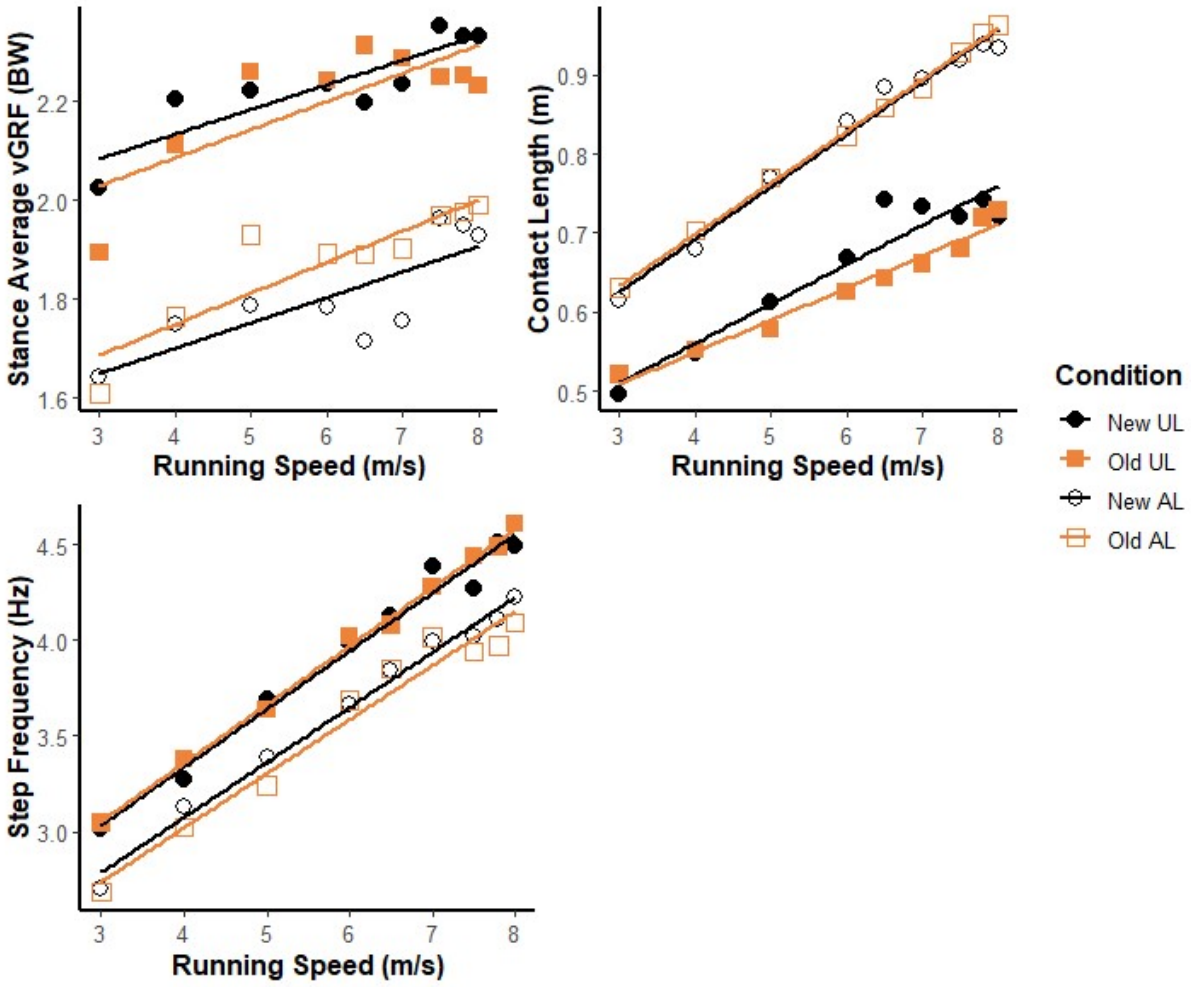
Results

The athlete achieved a v_{max} of 8.15 m/s versus 8.0 m/s wearing the new versus old RSP. Use of the new versus old RSP resulted in similar AL Lc, higher AL StepF, and lower AL $vGRF_{avg}$ across speeds. Linear regression models indicated similar AL StepF slopes for new and old RSPs across velocities (0.288 vs. 0.283), suggesting no interaction with velocity. In contrast, AL $vGRF_{avg}$ increased less with speed in the new vs. old RSP (slope 0.050 vs. 0.057).

Discussion

Our findings suggest the new RSP enabled a faster v_{max} and higher StepF, but lower $vGRF_{avg}$, potentially reflecting increased RSP stiffness that limited compression. Though limited to one participant, this study highlights the potential influence of RSP wear on sprint mechanics and performance. Future studies with larger samples and motion-capture analyses are planned to characterize human–prosthesis interactions and to evaluate UL biomechanics across speeds.

Images (Optional)



References (Optional)

[1] Owen Beck *et al.* , J Royal Society, 2017

Acknowledgements (Optional)

This study was made possible thanks to the University of Colorado at Boulder's Department of Integrative Physiology, Turin Polytechnic University's Department of Mechanical and Aerospace Engineering, and Össur hf. who provided prostheses, athletes' contact information, and funding for use in this study.

Session Category

Human Motion and Performance: Locomotion/Gait

P1-190

Dual-task Interference and Practice Related Improvements in Locomotion Among Children and Young Adults

Ms. Julia De Oliveira B.Sc. M.Sc. Candidate, Dr. Lori Ann Vallis Ph.D.

University of Guelph, Guelph, Ontario, Canada

Introduction

Adaptive locomotor behaviours permit successful navigation of the environment; however, dual-tasking (DT) can impact performance. When walking and simultaneously performing a cognitively demanding task, performance of one or both tasks can be reduced [1]. DT costs seem to be inherent across the lifespan and are observed in children and adults [2]. Past research has postulated the decline is due to interfering neural resources and has shown that practice over many sessions can mitigate DT costs [3]. The objective of the current study is to determine if *short-term practice* can also reduce DT cost in adults and children.

Methods

Participants (young adults, YA: 18-25yrs; Children, Ch: 7-9yrs) were instrumented with retroreflective markers; gait parameters were captured (Optitrack; 100Hz; Corvallis, USA) as participants stepped over an obstacle simultaneously completing an auditory Stroop task. Participants were then assigned to one of three groups: No-practice, Single task (ST) practice (single obstacle crossing followed by single auditory Stroop) or DT practice (concurrent obstacle crossing with auditory Stroop). A retest was conducted 1 hour after practice to explore consolidation effects.

Results

Preliminary statistical results for YA participants (N=3; T-test; SPSS, version 30.0) revealed reduced average antero-posterior (AP) velocity between ST (obstacle crossing) and DT (obstacle crossing + auditory Stroop; $p=0.028$) and a significant increase in standard deviation (StD) for step length, lead toe/heel and trail heel crossing distance ($p<0.001$) under DT conditions. Following short-term practice, significant reductions in StD of AP velocity ($p=0.002$) and lead heel obstacle crossing distance ($p=0.003$) were observed.

Discussion

Preliminary findings indicate that short-term practice can mitigate DT costs in YA. Previous research demonstrated similar reduction in gait variability following single locomotor

practice sessions [4]. Ongoing work includes practice with child participants; we expect that short-term DT practice will mitigate DT costs, although children may need additional practice. This research will expand our knowledge on typical locomotor and cognitive development and identify optimal practice strategies across the lifespan.

References (Optional)

[1] Iring Koch et al., Psychol. Bull., 2018

[2] Guillaume Chauvel et al., Gait & Posture, 2017

[3] Kelly Garner et al., Proc Natl Acad Sci., 2015

[4] Timothy Worden et al., J. Mot. Behav., 2014

Session Category

Human Motion and Performance: Locomotion/Gait

P1-191

Minimalist and Cushioned Footwear Interactions with Backpack Load on Children's Gait Mechanics

Prof Adriane Muniz[1,2], MSc MD Ana Silva[2], Dr Luciana Angélica Jesus[2], MSc Ana Paula Xavier[2], PT Maria Clara Gomes[2], PT Tainá Medeiros[2], Prof Luciano Menegaldo[2]

[1]Escola de Educação Física do Exército, Rio de Janeiro, RJ, Brazil. [2]Universidade Federal do Rio de Janeiro, Rio de Janeiro, RJ, Brazil

Introduction

Footwear characteristics can influence children´s gait. Minimalist shoes have been proposed as an alternative to promote foot functionality. Moreover, improper use of backpacks and inadequate footwear may impose excessive loads on the pediatric musculoskeletal system. However, few studies have investigated their combined effects on gait, particularly across different footwear types. Here, we compare gait parameters in children wearing minimalist footwear versus cushioned tennis shoes, both with and without a backpack.

Methods

Seventeen children (9.2 ± 0.8 years; 58.8% boys; 36.0 ± 4.4 kg; 1.4 ± 0.05 m) walked at 4.5 ± 0.5 km/h while their gait was recorded using a three-dimensional motion capture system (Vicon). Each participant was assessed under four conditions: cushioned tennis shoes and minimalist footwear, each with and without a backpack loaded with 10% of body mass. Pelvis, hip, knee and ankle kinematic and force plate peak parameters were compared using a two-way repeated-measures MANOVA. Significance level was set at $p<0.05$. Post hoc analyses were performed using a univariate two-way repeated-measures ANOVA with Bonferroni correction. All statistical analyses were conducted in R (R Core Team, 2025).

Results

The MANOVA revealed significant main effects of footwear ($F= 7.17$, $p=0.02$), load ($F= 42.445$, $p=0.0003$), but no footwear-load interaction ($F= 1.708$, $p=0.289$). Walking with 10% of body mass backpack increased pelvic anteversion ($p<0.001$), hip flexion ($p<0.001$), hip flexion moment ($p=0.003$), knee flexion moment ($p=0.008$), plantarflexion moment ($p<0.001$) and hip ($p=0.007$) and ankle ($p=0.005$) power generation, while reducing hip extension angle ($p<0.001$) (Figure 1). Minimalist footwear reduced ankle dorsiflexion during

stance (p<0.001) and knee abduction moment (p=0.0001) at weight acceptance. It also increased ankle plantarflexion angle (p<0.001) and propulsion power (p=0.007) (Figure 1).

Discussion

Carrying a backpack equivalent to 10% of body mass increased mechanical demands on the lower limbs during walking. Minimalist footwear reduced knee abduction moment while increasing ankle plantarflexion angle, moment, and power during propulsion, regardless of backpack use. These adaptations suggest that minimalist footwear may reduce knee load, promote the development of distal musculature, and, over time, support enhanced foot development in children.

Images (Optional)

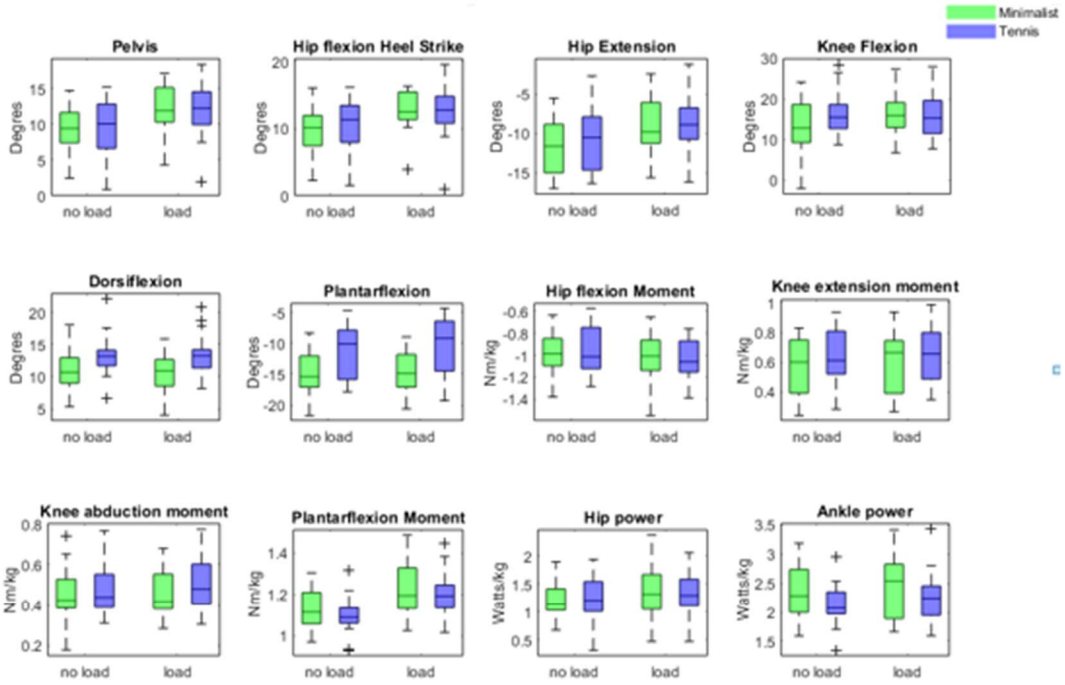


Figure 1 – Kinematic and kinetic peak parameter of gait in children wearing minimalist and cushioned tennis shoes under no-load and backpack-load conditions

Acknowledgements (Optional)

The authors thank the financial support from CNPq, CAPES, FINEP, and FAPERJ.

Session Category

P1-192

Neuromechanical Responses to Perturbations Delivered by Bilateral Ankle Exoskeletons During Human Vertical Hopping

Dr Luke Jessup, Dr Alexandra Voloshina, Dr Monica Daley

University of California, Irvine, Irvine, California, United States

Dr Luke Jessup

Dr Alexandra Voloshina

Introduction

Terrestrial locomotion is robust, even in unpredictable environments that impose frequent perturbations. Yet little is known about how mechanics across scales integrate to rapidly stabilize limb function during perturbations and how these responses may adapt. In a novel approach, we leveraged the precise, covert control of ankle exoskeletons to deliver perturbations during human hopping while measuring *in vivo* muscle and joint mechanics.

Methods

Two healthy participants hopped in place wearing bilateral cable-driven ankle exoskeletons, performing ten 45-second trials: initial unperturbed, surprise perturbation (SP; ×4), expected perturbation (EP; ×4), and final unperturbed. Hop height was prescribed; hop frequency was unconstrained. SP trials involved a single perturbation delivered at a random hop, whereas in EP trials participants were cued 5 seconds beforehand. The exoskeletons followed users' natural ankle motion throughout, except during the perturbation, when they imposed a plantarflexion motion from mid-flight through until body-weight acceptance – a phase that normally exclusively involves dorsiflexion. Kinematic, ground reaction force, lower-limb electromyographic (EMG), and soleus ultrasonographic data were collected. Data were compared between the unperturbed trials and the first SP and EP trial.

Results

There were no clear differences between the SP and EP trials. Hops immediately following the perturbation exhibited increased variability in frequency, height, and peak vertical

force. During the perturbed hop, ankle plantarflexion (-38%) and dorsiflexion (-34%) decreased, as did knee (-12%) and hip (-15%) extension, while knee (+8%) and hip (+19%) flexion increased. Consequently, joint work – particularly negative work – shifted proximally. During the same hop, peak EMG decreased for soleus (-11%) and medial gastrocnemius (-19%) but increased for all other recorded muscles, most prominently tibialis anterior (+78%), biceps femoris (+61%), and erector spinae (+42%). During the perturbation, soleus fascicles shortened 5.1 mm instead of lengthening 1.6 mm as in unperturbed hops, and in the subsequent stance phase, fascicles lengthened 5.5 mm more and shortened 1.3 mm less than during unperturbed hopping.

Discussion

Participants shifted joint work proximally and increased energy dissipation, aided by antagonist muscle activation and agonist fascicle lengthening, to recover from an exoskeleton perturbation. A larger sample will enable clearer interpretation of between-trial and between-participant differences in response timing and recovery strategy.

Images (Optional)

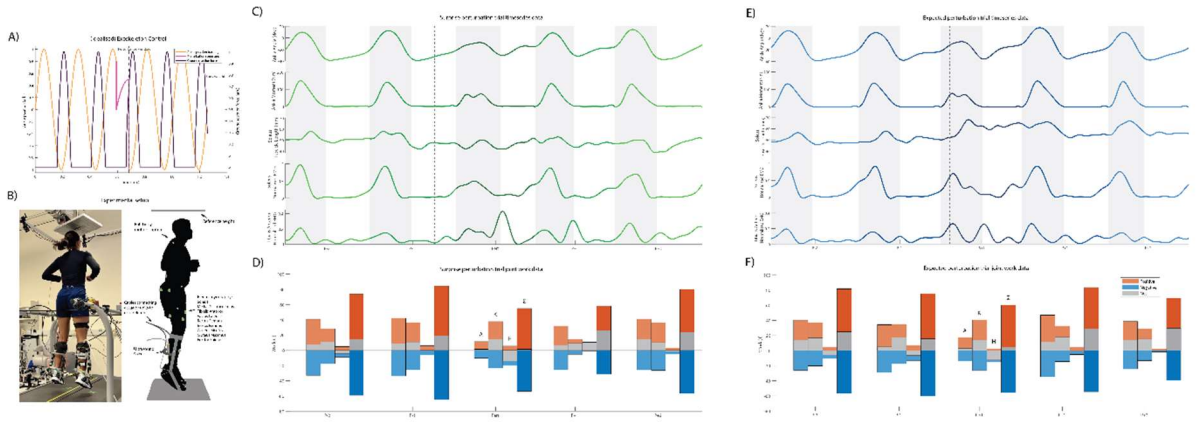


Figure. A) (Idealised) ankle exoskeleton control. In the unperturbed state, the actuators of the exoskeletons are commanded to follow ankle position. In the perturbed state, the actuators are commanded to plantarflex the ankle, from mid-flight of the hop through until the ground reaction force equals body weight during ground contact. **B) Image and illustration of the data collection.** Participants hop in bilateral ankle exoskeletons, with hop frequency unconstrained and hop height prescribed by a block suspended above their head. Motion capture, force plate, electromyography (EMG), and ultrasound data are collected simultaneously. **C) Timeseries data from the first surprise perturbation trial from participant one.** Ankle angle (positive direction = dorsiflexion), ankle moment, soleus fascicle length, soleus normalised EMG, and tibialis anterior normalised EMG. Shaded regions correspond to the ground contact phase of each hop, light regions to each aerial phase. Dashed vertical lines indicate the time over which the perturbation was applied. **D) Joint work data from the first surprise perturbation trial from participant one.** Ankle (A), knee (K), hip (H), and summed (sigma) joint work of each hop. Positive work = orange, negative work = blue, net work = grey. **E) Timeseries data from the first expected perturbation trial from participant one.** As in C. **F) Joint work data from the first expected perturbation trial from participant one.** As in D.

Acknowledgements (Optional)

Supported by NSF DBI 2319710

Session Category

Human Motion and Performance: Locomotion/Gait

P1-193

Gait on the 'GO': A Proof-of-Concept Study on Wearable Sensory Insoles for Gait Assessments

Miss Maahika Mehta[1], Mr. Adam Bradshaw[1], Mr. Sandro Nigg[1], Dr. Benno Nigg[1], Dr. Emily Matijevich[2], Dr. Maryam Hajizadeh[2]

[1]Human Performance Laboratory, Calgary, Alberta, Canada. [2]Orpyx Medical Technologies, Calgary, Alberta, Canada

Introduction

Chronic diseases like diabetes significantly impact gait characteristics, increasing risk of balance impairments and falls. Gait assessments provide a quantitative approach for characterizing these patterns. Traditionally, these utilize specialized technology or qualitative screening, reducing clinical transferability. Wearables offer accessible, objective, gait and mobility monitoring. The aim of this project is to develop a proof of concept individualized multi-task gait report, using Orpyx Motion Insight sensory insoles, providing a novel framework for quantifying motion characteristics across a diverse set of functional tasks.

Methods

This project utilized data from a previously collected dataset (REB23-0561) on individuals with diabetes and healthy controls. Plantar pressure and inertial measurement unit (IMU) data was collected during a variety of walking, stairs and standing tasks using the Orpyx Motion Insight sensory insoles. Four movement metrics were computed through custom developed algorithms: Walking Toe Clearance (cm), Stairs Stride Time Asymmetry (%), Standing Postural Sway Area (mm/s) and Standing Anterior-Posterior Peak Velocity (mm^2). Subsets of 4 individuals with diabetes and 3 healthy were selected for initial analysis; statistical group differences were not calculated at this stage. Individual data was combined into a gait report. Values were classified as healthy (green), abnormal (yellow) and at-risk (red) through a heuristic threshold method. Thresholds were determined from normative literature data if available, or from healthy participant ranges.

Results

Individuals with diabetes trended towards lower toe clearance especially in fast and cognitive walking tasks, and higher stairs stride time asymmetry (+ 5%). Postural sway area and peak velocity (anterior-posterior axis) were greater in *some* individuals with diabetes, though these metrics were subject to high variability. Comprehensive movement metric

reports revealed distinctive gait profiles, emphasizing the need for personalized, longitudinal monitoring.

Discussion

This exploratory analysis suggests that individuals with diabetes may exhibit early gait and balance changes, detectable through the Orpyx Motion Insight sensory insole metrics. By assessing multiple mobility tasks, this project aimed to capture a broad picture of functional motor performance. Future work will apply the described methodologies to a larger, generalized dataset, statistically differentiating clinical and healthy populations.

Images (Optional)

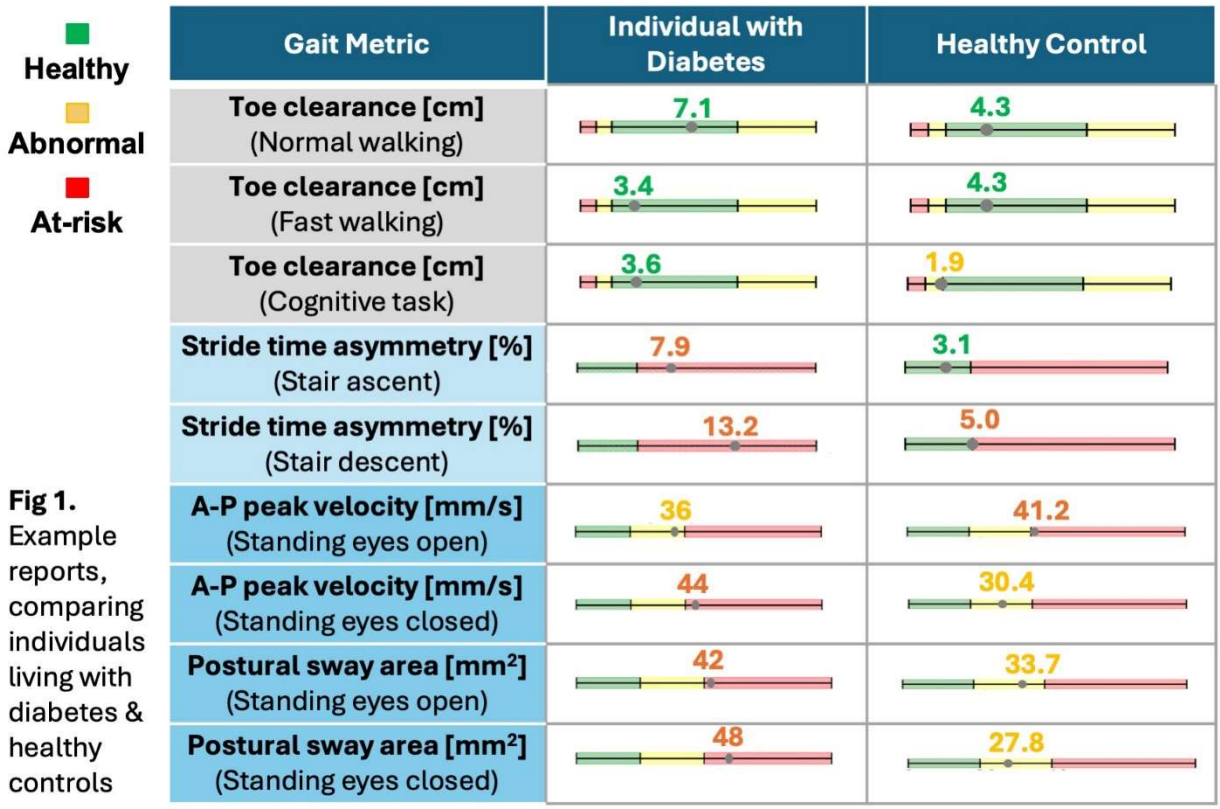


Fig 1. Example reports, comparing individuals living with diabetes & healthy controls

Session Category

Human Motion and Performance: Locomotion/Gait

P1-194

Metabolic Costs of Rhythmic Arm Swing

Ms Yilin Fu, Dr Manoj Srinivasan

The Ohio State University, Columbus, OH, United States

Introduction

Arm swing is an important part of human movement, usually studied during walking and running, where it may improve stability and reduce metabolic costs [1,2,3]. However, the energetics of independent arm swing (without being coupled to locomotion) has not been characterized. Here, we quantify the metabolic cost of rhythmic arm swing, investigating the effect of arm swing amplitude and frequency.

Methods

Participants were seated in a stable, supported position with their feet flat on the ground, performing single-arm rhythmic swings with metronome-guided frequencies from 0.25 to 1.0 Hz, amplitudes of 15° to 90°, and mean arm angles of 7.5° to 45°, totaling up to 30 trials each. Metabolic costs were measured using COSMED-K5 device and upper limb kinematics using marker-based motion capture.

Results

The data was used to quantify changes in metabolic costs across swing amplitudes and frequencies and model the relationship between upper-limb movement and metabolic costs through power-law regression. Net metabolic rate for arm swing was obtained by subtracting the mean value from a resting trial. Across all arm-swing conditions, gross metabolic rate ranged from approximately 1.014 to 1.425$W \cdot kg^{-1}$, yielding net metabolic rates from 0.054 to 0.465$W \cdot kg^{-1}$ above rest, much lower than leg swing metabolic costs at analogous amplitudes and frequencies [4,5]. Mechanical work over these frequencies ranged from 0.073 to 1.214 $J \cdot kg^{-1}$ per cycle. Fitting a power-law model to the data showed that larger amplitude and frequency movements have greater energy expenditure, with power law exponent greater than 1.

Discussion

In future work, we will seek to transform this rich data using inverse dynamics to fit a model of metabolic cost from shoulder-torque and mechanical work. This will allow us to quantify the cost of arm swing during walking. Arm swing energetics are modified by being coupled to the walking dynamics, and this modification can be understood by estimating the arm torques and mechanical work, and the consequent energy cost of such exertion.

References (Optional)

[1] Umberger, J. Biomech., 2008.
[2] Collins et al, Proc. B. Roy. Soc., 2009.
[3] Potzer et al, JEB, 2009.
[4] Doke et al, JEB, 2005.
[5] Doke & Kuo, JEB, 2007.

Acknowledgements (Optional)

Funding: NIH-R01GM135923.

Session Category

Human Motion and Performance: Locomotion/Gait

P1-195

Using Haptic Feedback to Increase or Decrease Trunk Sway

Dr. Margo Donlin PhD

Bucknell University, Lewisburg, PA, United States

Introduction

Individuals with chronic stroke often experience increased trunk sway (~10°) compared to unimpaired individuals (~5°), which can contribute to altered loading and muscle activity. Alternatively, increasing trunk sway may reduce knee adduction moments and redistribute knee cartilage load. Regardless of direction, promoting desired trunk sway may be beneficial. Previous research has used biofeedback to modulate trunk sway, but haptic feedback has rarely been used during walking.

The purpose of this study was to determine if haptic feedback can be used to modulate trunk sway during walking in unimpaired individuals. Specifically, we hypothesized that haptic feedback would result in desired increases or decreases in trunk sway.

Methods

To date, four unimpaired subjects (29±1 years; 1.60±0.04 m; 76.78±19.39 kg; 4 F) with no lower-body musculoskeletal injury in the last six months were outfitted with five inertial measurement units (SageMotion, Kalispell, MT, USA; 100 Hz) on one leg to measure real-time sagittal plane joint angles.

Subjects completed three overground walking trials at their comfortable speed. In the baseline trial, subjects walked with no feedback to measure their natural trunk sway. The two feedback trials were (1) 50% increase in trunk sway (“plus”) and (2) 50% decrease in trunk sway (“minus”). In both feedback trials, haptic feedback was provided at the upper extremity of the side that exceeded the threshold. Due to the small sample size, only visual comparisons were performed.

Results

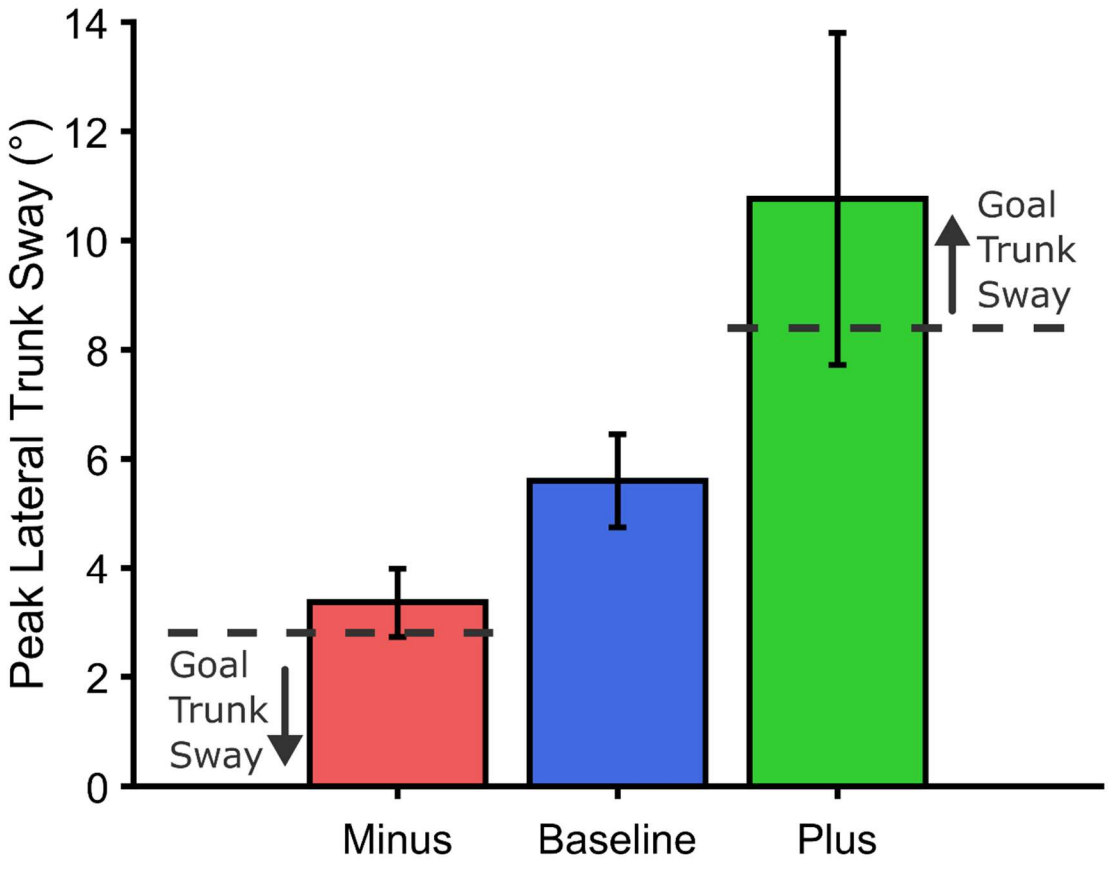
Trunk sway was smaller in the minus trial (3.4±0.6°) than baseline (5.6±0.9°) and larger in the plus trial (10.8±3.0°, Figure 1).

Discussion

Subjects were able to understand the haptic feedback and substantially alter their trunk sway in both the minus and plus trials. Therefore, haptic feedback may be a useful mechanism to promote desirable changes in trunk sway during walking, whether the goal is to decrease trunk sway in rehabilitation or increase trunk sway to reduce knee adduction moments.

This pilot study did not measure knee adduction moment, but the full-scale version will calculate this outcome measure. Future studies will include individuals with chronic stroke to determine if haptic feedback can decrease trunk sway in a clinical population.

Images (Optional)



References (Optional)

Session Category

Human Motion and Performance: Locomotion/Gait

P1-196

Musical, Visual, and Auditory Pacing Cues Produce Distinct Scaling Dynamics in Gait Entrainment

Ms. Marilena Kalaitzi Manifrenti, Mr. Vasileios Mylonas, Mr. Seung Kyeom Kim, Mr. Aaron Likens

Department of Biomechanics and Center for Research in Human Movement Variability, University of Nebraska at Omaha, Omaha, Nebraska, United States

Introduction

Human gait exhibits complex temporal dynamics that reflect interactions within the sensorimotor system. One hallmark of healthy gait is the presence of fractal patterns in step timing (pink noise), where gait features are related over time. With aging, those patterns degrade and become random (white noise). Cues are external timing signals used to influence gait timing and have been used to restore natural fractal patterns. Cueing-modalities (visual, auditory) influence gait differently; we test how cueing-modality and noise influence step-to-cue coupling (STCC) across time scales.

Methods

Eighteen healthy young adults were assigned to one of three cueing modalities: music (MUS), non-musical auditory beeps (NMA), a vertical visually oscillating bar (VIS). Participants performed 12-min walking trials pacing to pink and white noise cues, randomized. Multiscale-correlations, ρ(s), between cue and step timing were quantified using detrended cross-correlation analysis and converted to Fisher-Z (20–120 scales). A multilevel model evaluated the effects of cue-modality, noise, scale, scale^2, and their interactions, on ρ, with random participant effects.

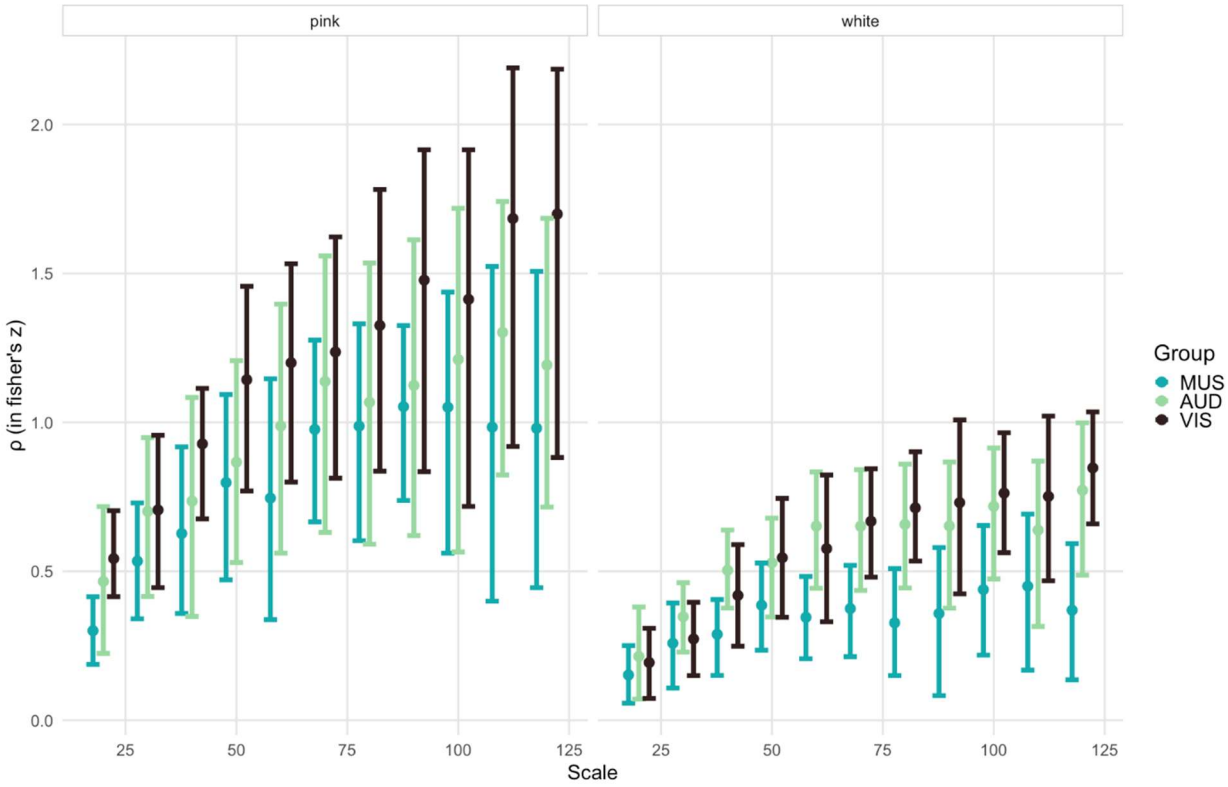
Results

Noise and scale interacted, so we don't interpret any main effects other than scale^2 which was not involved in an interaction. The model explained 80.1% of variance, with 67.2% due to individual differences. Pink noise produced steeper increases in ρ across scales compared to white noise (Fig.1), indicating stronger STCC ($\beta=2.56, t(368)=4.98, p<0.01$). Another interaction between cueing-modality and scale showed that VIS has the greatest rate of change in ρ ($\beta=5.34$, CL=(4.39,6.29)), followed by NMA ($\beta=3.69$, CL=(2.83,4.56)), and MUS ($\beta=2.70$, CL=(1.90,3.51)). Pairwise, VIS demonstrated a greater rate of change in ρ than NMA ($\beta=1.65, t(368)=2.52, p=0.033$) and MUS ($\beta=2.64, t(368)=4.17, p<0.01$).

Discussion

Findings show a quadratic relationship between ρ and scales, suggesting an STCC asymptote. Pink noise produced stronger growth in ρ across scales because its prominent low-frequency fluctuations lead to STCC. Conversely, white noise contains only unpredictable fluctuations, hence entrainment is limited to short-term corrections. Modality-wise, VIS demonstrated the strongest scale-dependent coupling putatively due to its continuous nature and vision's dominant role in locomotion. Overall, sensorimotor integration, measured through STCC, seems to improve with visual information and to be compromised when fractal dynamics are suppressed.

Images (Optional)



Acknowledgements (Optional)

NIH: P30GM159554, P20GM152301

Session Category

Human Motion and Performance: Locomotion/Gait

P1-197

Day-to-day Similarity in Muscle Fatigability and the Change in Gait Kinematics in Response to 30-minutes of Walking

Ms. Mayumi Wagatsuma[1], Mr. Julien Mihy[1], Dr. Stephen Cain[2], Dr. Jeremy Crenshaw[1], Dr. Christopher Knight[1], Dr. Jocelyn Hafer[1]

[1]University of Delaware, Newark, DE, United States. [2]West Virginia University, Morgantown, West Virginia, United States

Introduction

Older adults are susceptible to muscle fatigue in response to activity, which leads to changes in gait. Most muscle fatigue studies are conducted in lab settings with a single visit; however, self-reported fatigue in older adults fluctuates throughout and across days. A single day of muscle fatigability data might be insufficient to understand how muscle fatigue affects gait in response to activity in the real-world. It is essential to determine whether muscle fatigability and fatigue-induced gait changes vary day-to-day. Therefore, the purpose of this study was to determine whether the same bout of exercise induces similar muscle fatigue and changes in gait kinematics on different days.

Methods

Eleven adults (age 73±7yrs) completed the same protocol at two lab visits, separated by at least 9 days. The time of day was matched between visits. Participants wore five inertial measurement units and completed: (1) 10-meter walking at preferred speed (speed matched pre/post and between visits), (2) self-reported lower extremity muscle fatigue on 0-10 scales, and (3) isokinetic ($270°\cdot s^{-1}$) knee extensor dynamometer testing before and after an established 30-minute treadmill walking protocol. Stride length and knee and ankle ranges of motion (ROM) were calculated from the 10-meter walks. Dynamometer and self-reported muscle fatigability were the change in peak muscle power and the change in self-reported muscle fatigue level, respectively. Intraclass Correlation Coefficients (ICC) were used to examine the similarity of changes in gait kinematics and dynamometer and self-reported muscle fatigability between visits.

Results

There was moderate between-visit similarity for the change in ankle ROM (ICC=0.648). Self-reported muscle fatigability and the change in stride length had poor similarity (ICCs=0.40

and 0.24), while knee ROM and dynamometer fatigability had very poor similarity (ICCs=-0.06 and -0.08) between visits.

Discussion

These findings suggest that muscle fatigability and changes in gait kinematics in response to a bout of exercise may vary between in-lab visits even when the exercise is controlled to be exactly the same between visits. A traditional in-lab single visit exercise test may not be sufficient to understand muscle fatigability and gait changes in response to activity in older adults.

Acknowledgements (Optional)

We thank Millissia Murro and Fany Alvarado for helping with data collection for this study.

Session Category

Human Motion and Performance: Locomotion/Gait

P1-198

Assessing Walking Balance in Participants With Acromegaly Using Obstructed Walking

Ms Yuqi Wang MSc, Mr Gary Ohanessian MSc, Ms Michaela Title MSc, Ms Lisa Tramble RN, Dr Vicki Munro MD, FRCPC, Dr Syed Ali Imran MBBS, MRCP(UK), FRCP(Edin), FRCPC, Dr Michel Ladouceur PhD

Dalhousie University, Halifax, NS, Canada

Introduction

Acromegaly, characterized by growth hormone excess, adversely affects the patients' musculoskeletal and neural systems, consequently impairing physical function. Patients with acromegaly (PWA) experience higher rates of falls and fall-related injuries than Canadian older adults[1]. This study aims to explore the walking balance deficits in participants with acromegaly (PWA) compared to participants with non-GH-secreting pituitary adenoma (PNA), and young healthy participants (HC).

Methods

This study included two age-, sex-, BMI-matched groups (n=8 for each; PWA and PNA) and a YHC group (n=12). The kinematics of a 7 segment lower limb model was collected using an OptiTrack MoCap system and the ground reaction forces were acquired using two AMTI force plates. Participants walked without obstruction or over a 10% leg length unilateral obstacle. Inverse Dynamics were calculated using Visual 3D. A 2-way repeated ANOVA, and statistical parametric mapping was used to compare outcomes between the groups.

Results

In the crossing limb PWA's exhibited less reduction of knee extensor energy absorption in comparison to PNA and YHC participants (K3; PWA: 0.054J/kg; PNA: 0.089J/kg; YHC: 0.120J/kg; p=0.01). PWA's supporting limb generated less hip abductor energy when crossing over the obstacle in contrast to both the PNA and YHC group (PWA: -0.070J/kg; PNA: +0.122J/kg; YHC: +0.100J/kg; p=0.03).

Discussion

Our study revealed a trend of PWA adopting a different adaptation strategy during obstructed walking that is characterized by a reduction in the absorption of energy at the knee in the crossing limb and at the hip in the supporting limb. However, some of the

changes occurring with acromegaly may not be solely resulting from the GH secretion but also from the pituitary adenoma treatment as seen with the PNA group adaptations.

References (Optional)

[1]Michaela Title *et al.,* European Journal of Endocrinology, 2023

Session Category

Human Motion and Performance: Locomotion/Gait

P1-199

Kinetics Changes in Participants With Acromegaly During Walking

Ms Yugi Wang MSc, Mr Gary Ohanessian MSc, Ms Michaela Title MSc, Ms Lisa Tramble RN, Dr Vicki Munro MD, FRCPC, Dr Syed Ali Imran MBBS, MRCP(UK), FRCP(Edin), FRCPC, Dr Michel Ladouceur PhD

Dalhousie University, Halifax, NS, Canada

Introduction

Acromegaly is a multisystem disorder characterized by elevated growth hormone (GH) and insulin-like-growth factor-1 (IGF-1). Previous studies have reported a wide array of neuromuscular and skeletal abnormalities in PWA including arthropathy, bone enlargement, abnormal muscle structure and function, and central and peripheral nervous system dysfunction. In addition to the effects of elevated GH and IGF-1, mass effects of the pituitary adenoma or complications of adenoma removal surgery could potentially play a role in walking impairment. This study aims to explore the changes in the kinetics of walking in participants with acromegaly (PWA) compared to participants with non-GH-secreting pituitary adenoma (PNA), and young healthy participants (YHC).

Methods

This study included two age-, sex-, BMI-matched groups (n=8 for each; PWA and PNA) and a YHC group (n=12). The kinematics of a 7 segment lower limb model was collected using an OptiTrack MoCap system and the ground reaction forces were acquired using two AMTI force plates. Inverse Dynamics were calculated using Visual 3D. A repeated mixed linear model, and statistical parametric mapping was used to compare outcomes between the groups.

Results

Statistical parametric mapping showed that Hip and Knee moments differences during the stance phase with an increase in the hip flexor moment, a reduction in the mid-stance unloading for the hip abduction moment, the knee extension moment, and the knee abduction moment. Furthermore, the hip flexors generation of power, the knee extensors absorption of power, the ankle plantarflexors generation of power at the initiation of swing, as well as the knee flexors absorption of power at the end of swing were reduced in the PWA and PNA groups with the changes being more in the PWA group.

Discussion

Our study revealed a trend of PWA reducing their absorption of energy by muscles during walking. However, some of the changes occurring with acromegaly may not be solely resulting from the GH secretion but also from the pituitary adenoma treatment as seen with the PNA group adaptations.

Session Category

Human Motion and Performance: Locomotion/Gait

P1-200

Reconstructing the ground reaction force distribution among the foot bones

Prof Michele Conconi[1], Eng. Alexandre Naaim[2], Prof. Nicola Sancisi[3], Prof. Raphael Dumas[4], Dr Paul-André Deleu[5]

[1]Department of Industrial Engineering, University of Bologna,, Bologna, Italy, Italy. [2]2Laboratoire de Biomécanique et Mécanique des Chocs, Univ Eiffel, Univ Lyon 1, Lyon, France, France. [3]Department of Industrial Engineering, University of Bologna, Bologna, Italy, Italy. [4]Laboratoire de Biomécanique et Mécanique des Chocs, Univ Eiffel, Univ Lyon 1, Lyon, France, France. [5]Foot & Ankle institute, Brussels, Belgium, Belgium

Introduction

The use of foot models in musculoskeletal analysis is crucial to identify how ground reaction force (GRF) is distributed among the bones. The limitation of standard multi-segment foot models (MSFM) [1,2] was overcome using a new synergy-based 4-DOF foot model (SBFM) [3], which represents the kinematics of all bones as a combination of four foot motions, maintaining joint constraint consistency. In this paper, we extend the model by introducing a method for identifying contact regions and estimating the total ground reaction force for each bone, validated against experimental measures.

Methods

Twenty-four healthy subjects (50±13 years, 73±10 kg) performed gait analysis with a Footscan® pressure plate (0.5m × 0.4m, 4096 sensors) mounted over an AMTI-force plate (0.5 × 0.4 m), thus allowing the capture of both ground resultant force and pressure distribution [4,5]. A template foot, including a set of 29 contact spheres built to approximate bone eminences (Fig.1), was scaled anisotropically on each subject based on foot dimensions. Foot bone kinematics were reconstructed using the SBFM. A training set of twenty subjects at mid-stance was used to optimize the sphere radius so that sphere intersection with the ground optimally matches the measured pressure map, as well as the stiffness of the virtual spring associated with each sphere in the contact model to optimally replicate the total ground reaction force. The tuned contact model was applied to the remaining four subjects. Finally, the GRF was estimated for all subjects over the entire gait cycle.

Results

The mean RMSE between model and experimental measure was 270.8N and 209.9N for the training and the validation set respectively. Identification of the contact region was reasonable (fig. 1).

Discussion

The discrepancies between model predictions and experimental observations suggest the model should not only be calibrated at mid-stance but refined over the entire gait cycle. Nevertheless, results support the applicability of the model. The SBFM can be employed in both inverse and forward dynamics musculoskeletal models, allowing for the investigation of the foot dynamics.

Images (Optional)

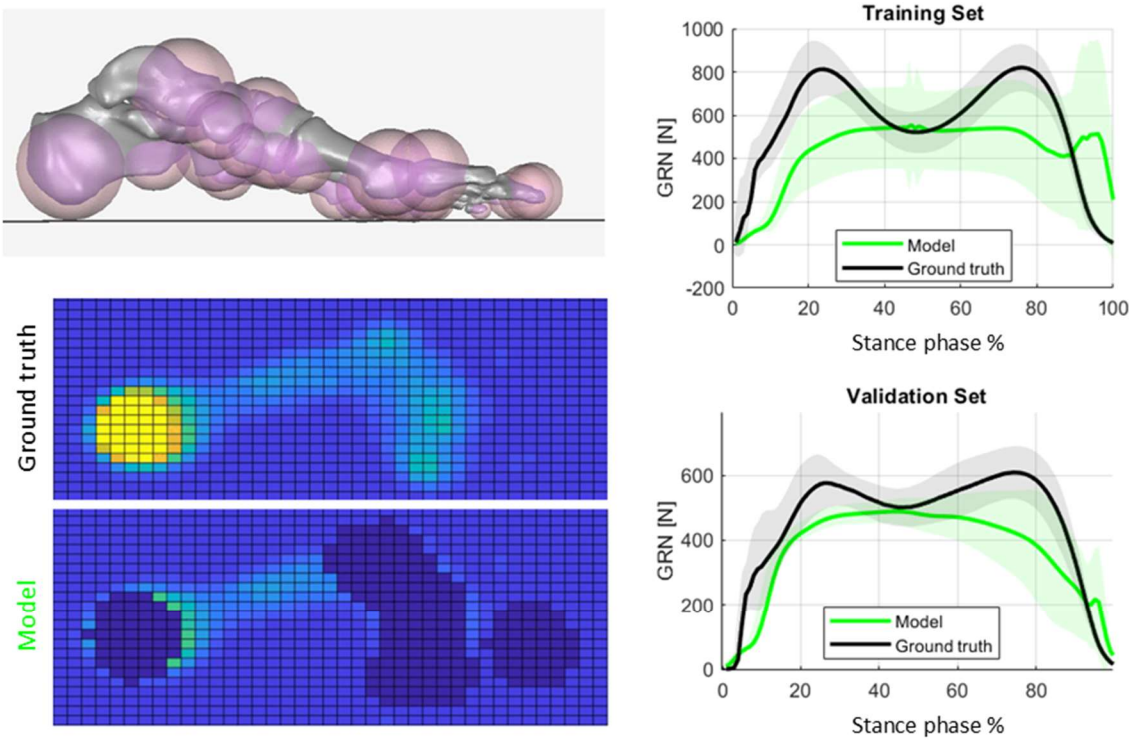


Figure 1: Distribution of the contact spheres in the model (top left); validation of the identification of the contact location (dark blue area) against pressure map (middle, bottom left). Comparison between predicted and measured GRF on the training set (top right). Comparison between predicted and measured GRF on the validation set (top right).

References (Optional)

1. Leardini (2019).*Gait&Pos.*,**69**:50-59.
2. Saraiva (2022).*Mech.Mach.Theory*,**177**,105046.
3. Conconi (2024).*Proc.ESB Congress,Edinburg*.

4. Leardini (2007).*Gait&Pos.*,**25**:453-462.
5. Deleu (2021).*Gait&Pos.*,**84**:308-314.

Session Category

Human Motion and Performance: Locomotion/Gait

P1-201

Standardized Upper-Body Joint Angle Estimation from Markerless Joint Centers

Dr. Milad Nazarahari

University of Alberta, Edmonton, Alberta, Canada

Introduction

Markerless motion capture systems provide an accessible tool to quantify upper-body kinematics. However, current non-commercial systems either lack standardized ISB-compliant joint definitions or rely on complex inverse kinematics with limited upper-limb validity. In this work, we have developed and validated a joint-center-based framework that computes standardized upper-body joint angles from the estimated joint centers using an open-source multi-view markerless system.

Methods

Six adults performed joint-focused tasks, involving single-axis movements that isolated primary upper-limb and trunk joint rotations, and a functional Pasta Box task, while an ISB-compliant marker-based system and eight smartphones recorded movements. The MediaPipe Holistic model provided 2D markerless joint centers, which were subsequently triangulated to obtain 3D joint-center positions. Thorax, humerus, forearm, and metacarpal coordinate systems were built using estimated JCs. Subsequently, shoulder angles were computed using a tilt–torsion representation with decomposition to flexion/extension (FE) and abduction/adduction (AA), and other joint angles were computed using the Grood–Suntay convention. An ISB-compliant marker-based configuration served as the gold standard. Figure 1 illustrates the segment coordinate systems for the markerless and marker-based gold standard.

Results

Markerless estimated shoulder FE, AA, and internal/external (IE) showed good-to-excellent ($r = 0.89–0.99$; RMSE = 3.0–13.3°), and elbow FE showed excellent ($r = 0.98–1.00$; RMSE = 2.7–4.0°) agreement with the gold-standard measurements. Elbow IE and wrist FE showed good-to-excellent agreement during joint-focused tasks (elbow IE $r = 0.95$, RMSE = 12.87°; wrist FE $r = 0.80$, RMSE = 12.08°); however, their accuracy decreased in the occlusion-heavy Pasta Box task (elbow IE $r = 0.56$, RMSE = 22.4°; wrist FE $r = 0.45$, RMSE = 18.2°).

Discussion

Our joint-center-based pipeline enables standardized, clinically interpretable upper-body kinematics using 3D markerless systems, with shoulder and elbow flexion/abduction

achieving accuracy that closely approaches that of the marker-based gold standard. Performance reductions were primarily limited to wrist and axial rotations during occlusion-heavy scenarios, reflecting challenges in joint-center estimation rather than limitations of the proposed approach. These findings highlight the potential of markerless systems for clinical upper-body joint angle tracking.

Images (Optional)

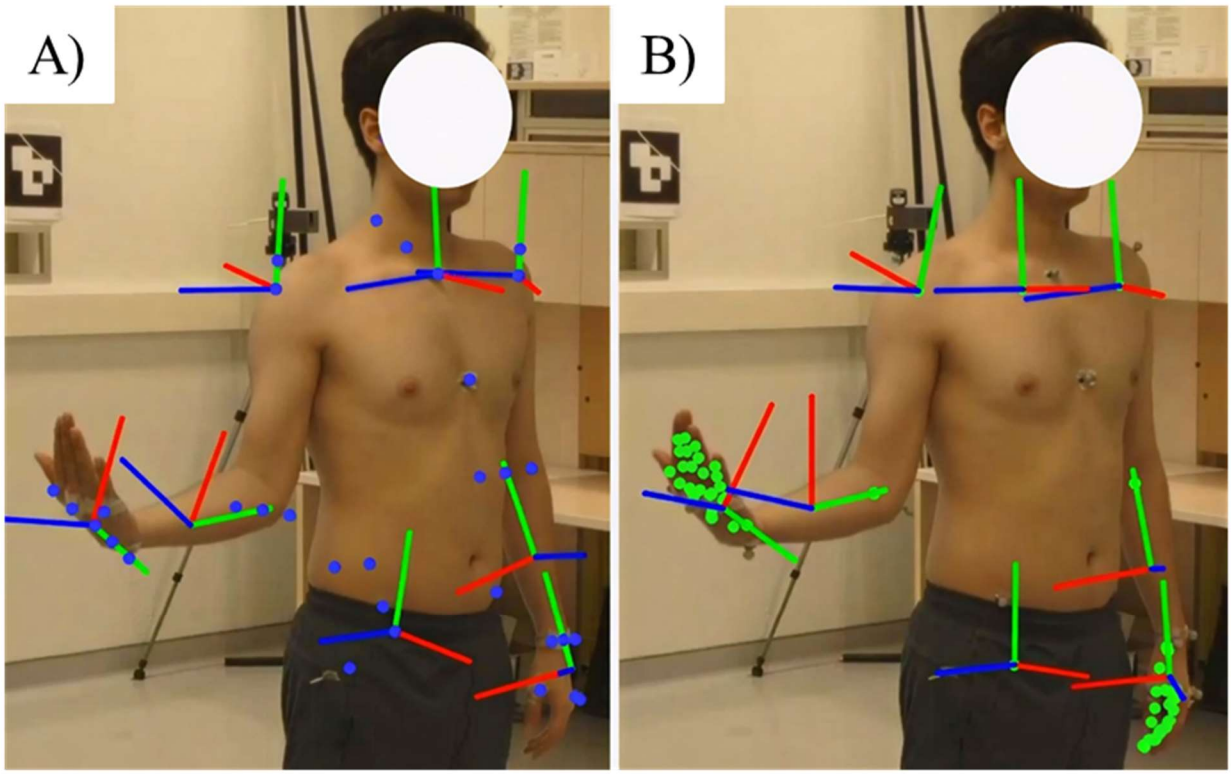


Figure 1. Segment coordinate systems constructed using A) ISB anatomical landmarks and B) markerless joint centers. X (blue), Y (green), and Z (red) axes, respectively, indicate the anterior–posterior, superior–inferior, and medial–lateral directions.

Session Category

Human Motion and Performance: Locomotion/Gait

P1-202

Muscle Latency as a Mechanism for Activity-Related Changes in Gait Mechanics

Ms. Millissia Murro, Ms. Fany Alvarado, Ms. Kathleen Downs, Ms. Nancy Nguyen, Ms. Mayumi Wagatsuma, Ms. Grace Kellaher, Dr. Jeremy Crenshaw, Dr. Jocelyn Hafer

University of Delaware, Newark, DE, United States

Introduction

Muscle fatigue (i.e., decreased muscle power following activity) can alter gait mechanics. However, the relationships between muscle fatigue and other aspects of muscle function and gait are unclear, as traditional measures such as strength and electromyography (EMG) activation do not correlate well with changes in gait. Recently, we identified that the temporal coordination between muscle activation and mechanics, *muscle latency*, changes in response to fatigue. Because latency is potentially modifiable, understanding its relationship to fatigue-induced changes in gait and muscle activation parameters may provide novel targets for intervention. The purposes of this study were to (1) examine the relationship between changes in muscle latency and changes in gait mechanics following a bout of activity, and (2) investigate factors that may explain variations in latency.

Methods

Twenty individuals (9F/11M; 63.8±3.4yrs; 11 Healthy/9 Knee OA) performed a 34-minute treadmill walk (34MTW). For the first (pre) and last (post) 4 minutes of data, we collected quadriceps and hamstrings EMG and motion capture. Variables of interest were muscle latency, peak knee flexion angle, rate of EMG rise, peak EMG activation, and quadriceps and hamstrings coactivation, all during early stance. We assessed correlations between changes (Δ=post-pre) in: (1) latency and knee flexion angle, and (2) muscle activation parameters and latency.

Results

Decreases in latency of the rectus femoris, vastus lateralis, and medialis were correlated with increases in peak knee flexion angle ($r=-0.67$, $p=0.0014$; $r=-0.63$, $p=0.0029$; $r=-0.75$, $p=0.0001$, Figure). This means that when the time between peak muscle activation and peak knee flexion angle shortened, the peak knee flexion angle increased. Increases in peak vastus medialis activation magnitude were correlated with decreases in vastus medialis latency ($r=-0.50$, $p=0.0244$).

Discussion

Our findings suggest that muscle latency may influence changes in gait mechanics following activity, and that fatigue-induced changes in latency may relate to changes in muscle activation magnitude. Latency reflects muscle activity specific to the gait mechanics of interest, whereas other commonly used measures of muscle activity lack this context. Future research may benefit from measures that combine multiple facets of movement control, such as latency, to help understand factors that influence changes in gait mechanics.

Images (Optional)

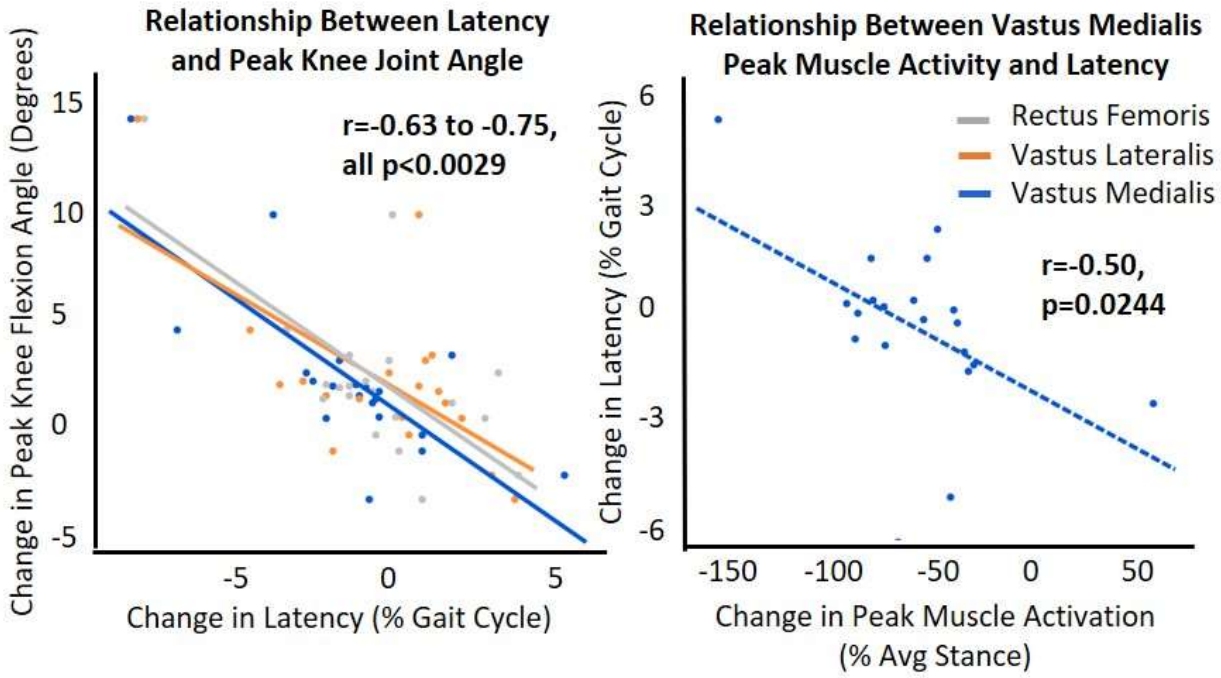


Figure. Left: Correlations between changes in quadricep muscle latency and peak knee flexion angle due to a bout of activity. Right: Correlation between changes in peak muscle activation and muscle latency of the vastus medialis muscle.

Acknowledgements (Optional)

Work supported by NIGMS/NIH grant U54-GM104941.

Session Category

Human Motion and Performance: Locomotion/Gait

P1-203

From a Single Wrist-Worn IMU to GRF Estimation via Biomechanics Informed Machine Learning

Mr. Minho Chae Ph.D. student, Ms. Guena Park Ph.D. student, Prof. Sukyung Park Ph.D.

KAIST, Yuseong-gu, Daejeon, Korea, Republic of

Mr. Minho Chae

Ms. Guena Park

Introduction

Lower limb muscle weakness caused by sarcopenia reduces gait efficiency and mobility, thereby diminishing quality of life. Even after its official designation as a disease in 2021, the absence of therapeutic drugs has made early detection and prevention increasingly important. Since muscle strength decline tends to precede changes in gait speed, indicators capable of quantitatively monitoring lower limb muscle strength are needed. Ground reaction force (GRF) is a key biomarker reflecting lower limb muscle strength, but conventional measurements are impractical for daily life use. Although IMU-based GRF estimation techniques have recently been proposed, limitations in practicality remain, including multi-sensor attachment requirements, large training datasets, and black-box modeling. This study proposes a method to estimate GRF using a single wrist-worn IMU through a machine learning approach that incorporates biomechanical domain knowledge.

Methods

To estimate GRF using only a single wrist-worn IMU signal, we leveraged the COM-GRF relationship in gait. We quantified the kinematic coupling between the forearm, upper arm, trunk linkage and the center of mass (COM), and used the estimated COM acceleration as input features for a machine learning model for GRF estimation. The performance of the proposed method was validated using GRF data collected from 19 young adults under various walking speed conditions.

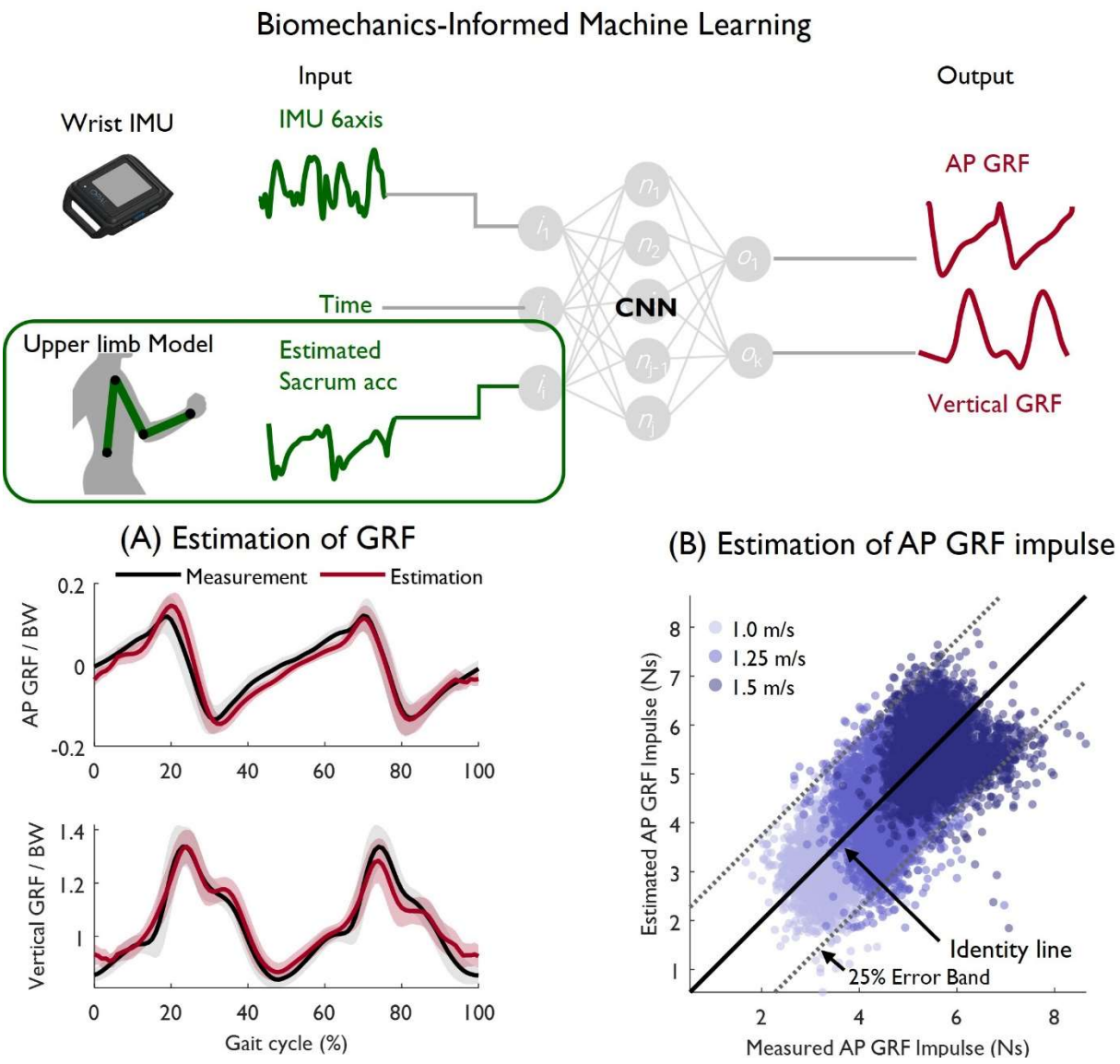
Results

The model integrating upper limb–COM kinematic coupling information as input features from a single wrist-worn IMU signal demonstrated high accuracy (nRMSE ≈ 9%) in personalized GRF estimation. Among the 6-axis IMU signals, the 2-axis acceleration and angular velocity of the forearm in the sagittal plane provided key information for GRF estimation. The movements of the upper arm and trunk exhibited speed-proportional scaling of forearm motion, indicating functionally dependent patterns. The proposed method consistently reproduced the trend of increasing forward impulse with increasing walking speed.

Discussion

This study demonstrated that GRF estimation is achievable across various walking speeds using only a single wrist-worn IMU by modeling upper limb-COM coupling and integrating it as machine learning input. The proposed method predicted GRF change trends with high linearity, suggesting the potential for long-term GRF monitoring using smartwatches and its application in early detection of lower limb muscle strength decline.

Images (Optional)



Acknowledgements (Optional)

This research was supported by Samsung Electronics Industry-Academia Research (G01250105) and the Mid-Career Researcher Program of the Ministry of Science and ICT (RS-2024-00356657).

Session Category

Human Motion and Performance: Locomotion/Gait

P1-204

The Influence of Plantar Heel Pain on Foot and Lower Extremity Walking Gait Kinematics in Middle-Aged Adults

Dr. Mohammed Alamri[1,2], Ms. Zahra Mollaei[2], Ms. Breanna Lee[2], Dr. Stephen Cobb[2]

[1]King Saud University, Riyadh, Riyadh, Saudi Arabia. [2]University of Wisconsin–Milwaukee, Milwaukee, Wisconsin, United States

Introduction

A recent study reported that 1.1% of U.S. adults were diagnosed with plantar heel pain (PHP) in the past year, with the highest prevalence among those aged 45–64. Despite intervention, PHP often persists for 6–96 months. Clinically, PHP is thought to result from mechanical overload of the plantar aponeurosis. However, the pathomechanics during gait remain poorly understood. Previous gait research has primarily examined spatiotemporal and kinetic variables, whereas investigations of kinematics have been limited and inconsistent. This study aimed to identify foot and lower-extremity walking gait dysfunction in middle-aged adults with PHP. We hypothesized that patients with PHP would demonstrate gait kinematics consistent with increased pronation in early stance and insufficient supination in mid-to-late stance.

Methods

30 middle-aged adults with PHP (54.33±4.42 years, 85.82±15.84 kg) and 30 age-matched uninjured individuals (54.53±5.69 years, 76.18±18.22 kg) participated. 3D positions of markers located on the pelvis, thigh, shank, and foot were recorded using a 14-camera system. Three force plates were used to identify stance phase events during five barefoot walking trials (1.3 m/s±10%). A MATLAB program was used to calculate 3D hip, knee, and six functional foot articulation (rearfoot, medial and lateral midfoot, medial and lateral forefoot, first metatarsophalangeal) kinematics. Group differences within three stance subphases (loading response, mid/terminal stance, pre-swing) were examined using one-way ANCOVAs, adjusting for sex and BMI.

Results

During loading response, the PHP group demonstrated decreased rearfoot complex lateral rotation ($p=0.02$), decreased medial midfoot dorsiflexion ($p=0.05$), and increased medial forefoot dorsiflexion ($p=0.03$) ROM. During mid/terminal-stance the PHP group demonstrated decreased rearfoot complex dorsiflexion ROM ($p=0.01$).

Discussion

Although the PHP group demonstrated altered foot kinematics, only the increased medial forefoot dorsiflexion during loading response was consistent with the initial hypothesis. In contrast, the decreased rearfoot complex lateral rotation and decreased medial midfoot dorsiflexion observed early in loading response, along with the decreased rearfoot complex dorsiflexion during mid/terminal stance, may represent a pain-avoidant gait adaptation aimed at reducing pain from initial impact and limiting plantar aponeurosis strain during push-off.

Acknowledgements (Optional)

King Saud University Deanship of Scientific Research, Riyadh, SA; Joseph J. Zilber Faculty Excellence Fund, UW-Milwaukee, Milwaukee, US; ASB Graduate Student Grant-in-Aid.

Session Category

Human Motion and Performance: Locomotion/Gait

P1-205

Beyond Traditional Metrics: A Waveform-Based Approach to Assessing Gait Asymmetry among Subacute and Chronic Stroke Survivors and Healthy Individual

Doctor of Physical Therapy (DPT) Muchen Ren[1], Doctor of Physical Therapy (DPT) Tangdi Lin[2], PhD Jung Hung Chien[3], MD, PhD Li Zhang[4], MD Tao Li[1], MD Jianhao Lin[5]

[1]Department of Rehabilitation Medicine, Peking University People's Hospital, Beijing, Beijing, China. [2]National Clinical Research Center for Women's Health and Obstetric and Gynecologic Diseases, Department of Obstetrics and Gynecology, Peking Union Medical College Hospital, Chinese Academy of Medical Sciences & Peking Union Medical College, Beijing, Beijing, China. [3]Life University, Marietta, GA, United States. [4]The First Affiliated Hospital of Guangxi Medical University, Nanning, Guangxi, China. [5]Arthritis Clinic & Research Center, Peking University People's Hospital, Peking University, Beijing, Beijing, China

Doctor of Physical Therapy (DPT) Muchen Ren

Introduction

Gait asymmetry is a common and disabling post-stroke sequela, frequently assessed using ratios of discrete peak values. However, this method neglects the full time-series information available in biomechanical waveforms, such as the vertical ground reaction force (vGRF) profile. Furthermore, existing literature primarily focuses on gait asymmetry in chronic rather than subacute stroke survivors, largely because the highly variable vGRF profiles in the subacute phase are difficult to compare using traditional ratio metrics. This study investigated vGRF symmetry in subacute and chronic stroke survivors during level and inclined walking using a waveform-based approach (cross-correlation, XCorr).

Methods

Fourteen subacute stroke survivors, fourteen chronic stroke survivors, and fourteen healthy age-matched controls walked on a treadmill at 0% (level) and 6% inclines. vGRF symmetry was assessed using normalized cross-correlation (XCorr), and variability was measured using the coefficient of variation. A two-way mixed measures ANOVA was used to evaluate the effects of stroke chronicity and incline angle.

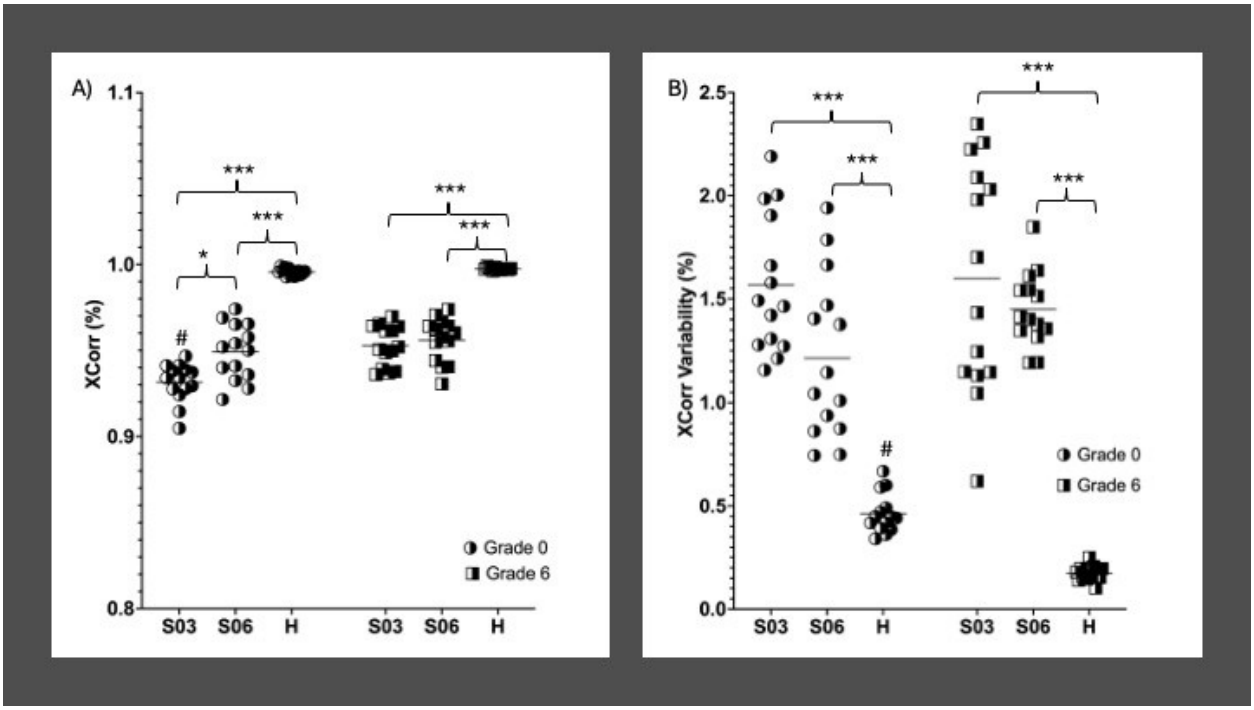
Results

Subacute stroke survivors demonstrated significantly lower XCorr values compared to chronic stroke survivors ($p<0.05$) and controls ($p<0.001$) during level walking. At the 6% incline, there was no significant difference in XCorr between subacute and chronic groups; however, both stroke groups exhibited significantly lower XCorr values than controls. Similar to XCorr, the XCorr variability was highest in subacute stroke survivors than other groups.

Discussion

XCorr effectively identifies vGRF asymmetry across different stages of stroke recovery, offering insights into whole-body mechanics that conventional peak measures often miss. Walking on a steeper grade (6%) significantly increased asymmetry and variability in stroke survivors, potentially indicating an increased risk of falls, indicating that stroke survivors need more in step-by-step adjustment during walking. Therefore, XCorr and XCorr variability are valuable clinical metrics for quantifying gait asymmetry, particularly in the subacute stage.

Images (Optional)



Session Category

Human Motion and Performance: Locomotion/Gait

P1-206

Using Instrumented Insoles During Six Minute Walk Test in Older Adults

Dr. Nicole Chimera PhD, Ms. Chyenne Neath BSc (Hons)

Brock University, St. Catharines, Ontario, Canada

Introduction

The Six Minute Walk Test (6MWT), a commonly used sub-maximal assessment of aerobic capacity, serves as a predictor of cardiovascular events; 6MWT performance decreases with age and reduced physical activity (PA). However, PA mitigates cardiac disease and may impact 6MWT performance. 6MWT is typically performed with participants walking along a 30-meter track marked at 3-meter increments to determine walking distance through manual calculation. The development of new instrumented insoles may provide a more streamlined measurement of 6MWT distance while also providing information on walking speed and gait asymmetries. Therefore, the purposes of this study were to 1) assess agreement between 6MWT distance measured manually and with instrumented insoles and 2) determine differences in walking speed, walking distance, and asymmetries during 6MWT in older adults of different PA.

Methods

A cross-sectional design assessed 6MWT in healthy individuals aged ≥55 years categorized into high, medium, and low PA via Godin-Shephard Leisure-Time Physical Activity Questionnaire. Participants were outfitted in insoles instrumented with inertial measurement units (IMU; Plantiga Technologies, Vancouver, British Columbia, Canada) to perform the 6MWT along a 30-meter indoor track. Walking distance (m) on the indoor track was recorded manually, and the IMU data included walking distance (m), walking speed (m/s), and asymmetries (%) in ground contact time and push off and impact accelerations. Agreement in 6MWT distance measured from the indoor track versus IMU was assessed with intraclass correlation coefficients (ICC); ANOVA determined differences in walking speed, distance, and gait asymmetries between older adults of different PA levels. Statistical analyses were performed in IBM SPSS (v.30; $p<.05$).

Results

Thirty older adults completed the 6MWT (Table 1); there was very strong agreement between manually measured walking distance and IMU walking distance (ICC: .998 [95%CI: .996;.999]). There was a main effect of PA for walking distance (p=.014) and speed (p=.011). Post hoc analysis indicated participants with high PA levels walked significantly

farther than moderate (p=.028) and low (p=.046) PA and significantly faster than moderate (p=.028) and low (p=.031) PA (Table 1).

Discussion

Instrumented insoles can be used to ascertain walking distance while also assessing meaningful gait parameters elucidating information otherwise unavailable with the standard 6MWT protocol.

Images (Optional)

	High PA (n=13)	Medium PA (n=11)	Low PA (n=6)
Age (years)	65.1 ± 4.3	67.0 ± 4.6	74.2 ± 5.6
Weight (kg)	73.9 ± 15.2	78.3 ± 14.8	67.5 ± 12.2
Height (cm)	169.6 ± 8.7	167.4 ± 6.5	160.1 ± 7.7
Walking Distance Measured (m)	588.9 ± 79.6	518.9 ± 47.7	507.0 ± 55.9
Walking Distance IMU (m)	594.5 ±77.2	523.3 ± 45.4	515.5 ± 58.2
Walking Speed (m/s)	1.7 ± 0.2	1.5 ± 0.1	1.5 ± 0.1
Ground Contact Time Asymmetry (%)	0.6 ± 0.5	0.9 ± 0.9	1.8 ± 2.2
Push Off Acceleration Asymmetry (%)	4.5 ± 3.7	5.5 ± 6.9	7.0 ± 8.9
Impact Acceleration Asymmetry (%)	3.4 ± 2.7	7.5 ± 6.5	4.7 ± 4.3

Table 1. Participant data (means ± standard deviation [SD]) based on physical activity (PA) level.

Session Category

Human Motion and Performance: Locomotion/Gait

P1-207

Effects of DIVA Cognitive Load on Gait Parameters in Healthy Young Women under Single- and Dual-Task Conditions

MSc Nikola Chmura, PhD Wanda Forczek-Karkosz, PhD Agnieszka Wojtowicz

University of Physical Culture in Krakow, Krakow, małopolskie, Poland

Introduction

Dual-task (DT) situations compel the central nervous system to divide limited attentional resources between simultaneous motor and cognitive processes. While DT paradigms are frequently utilized in aging research to detect fall risk, healthy young adults serve as the critical "gold standard" reference due to their optimal gait stability. However, the extent to which complex visuo-spatial tasks compromise this stability remains an important area of study. This study aimed to investigate spatiotemporal gait modifications and attentional performance across three experimental conditions: natural walking, cognitive task only, and dual-tasking - to quantify specific "dual-task costs" in a homogeneous group of healthy young women using the DIVA-gait protocol.

Methods

Fifteen healthy women (20–30 years; BMI: 18.5–24.9 kg/m^2) participated. Exclusion criteria included neurological, musculoskeletal, or visual impairments affecting gait or task performance. Three conditions were assessed: Single-Task Walking (ST-Walk), Single-Task Cognitive (ST-DIVA: standing), and Dual-Task (DT: walking+task). Motion data were captured using a 32-camera Vicon system. Spatiotemporal parameters included Walking Speed, Step Length, Step Width, Cadence, and Single and Double Support Phases. The DIVA-gait task involved rapid visual discrimination; Reaction Times (RT) and Error Rates assessed cognitive cost.

Results

Comparison of the conditions revealed only subtle gait modifications, indicating a high level of motor control preservation. Relative to ST-Walk, the DT condition resulted in a slight but significant reduction in Walking Speed and Step Length. Notably, other spatiotemporal parameters-specifically Step Width, Cadence, and Single and Double Support Phases-remained comparable to the single-task baseline, showing no signs of destabilization. Conversely, cognitive performance declined; compared to ST-DIVA, the DT condition

resulted in increased Error Rates, suggesting the dual-task cost was primarily absorbed by the cognitive domain.

Discussion

The findings demonstrate that healthy young women have sufficient attentional capacity to handle the DIVA task with minimal impact on gait stability. In contrast to clinical populations, these participants maintained spatial consistency-specifically, their Step Width remained unchanged. They simply reduced their Speed and Step Length slightly as a safety buffer. This indicates a high level of gait automaticity and a successful "posture-first" strategy, where cognitive performance drops to protect the walking pattern.

Session Category

Human Motion and Performance: Locomotion/Gait

P1-208

Shifting Preferred Joint Kinetics Distally Reduces the Metabolic Cost of Walking in Young Adults

Dr. Ross Miller PhD[1], Ms. Ningzhen Zhao MS[2], Dr. Owen Beck PhD[2]

[1]University of Maryland, College Park, MD, United States. [2]University of Texas, Austin, TX, United States

Introduction

Deviations from preferred walking mechanics tend to increase metabolic cost, suggesting that these mechanics minimize metabolic cost. Because producing joint moments at the ankle requires less metabolic energy than at the hip [1], re-distributing joint moment production from the hip to the ankle may reduce the metabolic cost of walking. The purpose of this study was to increase the voluntary kinetic output of the ankle during walking, and determine the concomitant effects on hip kinetics and metabolic cost of walking.

Methods

Fourteen young healthy adults walked on a treadmill at 1.25 m/s. After familiarization, participants performed a 5-minute baseline walking trial, then walked for 10 minutes with bilateral functional electrical stimulation (FES) of the soleus during late stance. Following a 20-25 minute rest, participant performed another 5-minute walking trial without FES. Walking neuromechanics and metabolism were compared cost pre- versus post-FES.

Results

Compared to pre-FES baseline walking, post-FES peak ankle power increased +13.9% ($p = 0.003$), peak hip power decreased -9.8% ($p = 0.015$), peak soleus electromyogram linear envelope increased +4.8% ($p = 0.047$), and gross metabolic power decreased -2.3% ($p = 0.034$). We emphasize that “post-stimulation” data are from a preferred walking trial after the removal of FES, the soleus was not being stimulated.

Discussion

These are the first data demonstrating voluntary, level-ground walking with a lower metabolic cost than pre-intervention preferred walking, and suggest that young healthy adults do not minimize metabolic cost during walking. We hypothesize that this effect is due to shifting joint-level kinetics to a more economical distribution [1] that still meets the constraint of the ground reaction force equaling body weight on average. The mechanism for these changes may be related to longer muscles with less economical fiber

characteristics at the hip versus ankle. Given that carryover effects of FES reduced the metabolic cost of walking by changing participant joint kinetics opposite those typically associated with aging [2], this paradigm may have implications for explaining the mechanics and energetics of older adult walking.

Images (Optional)

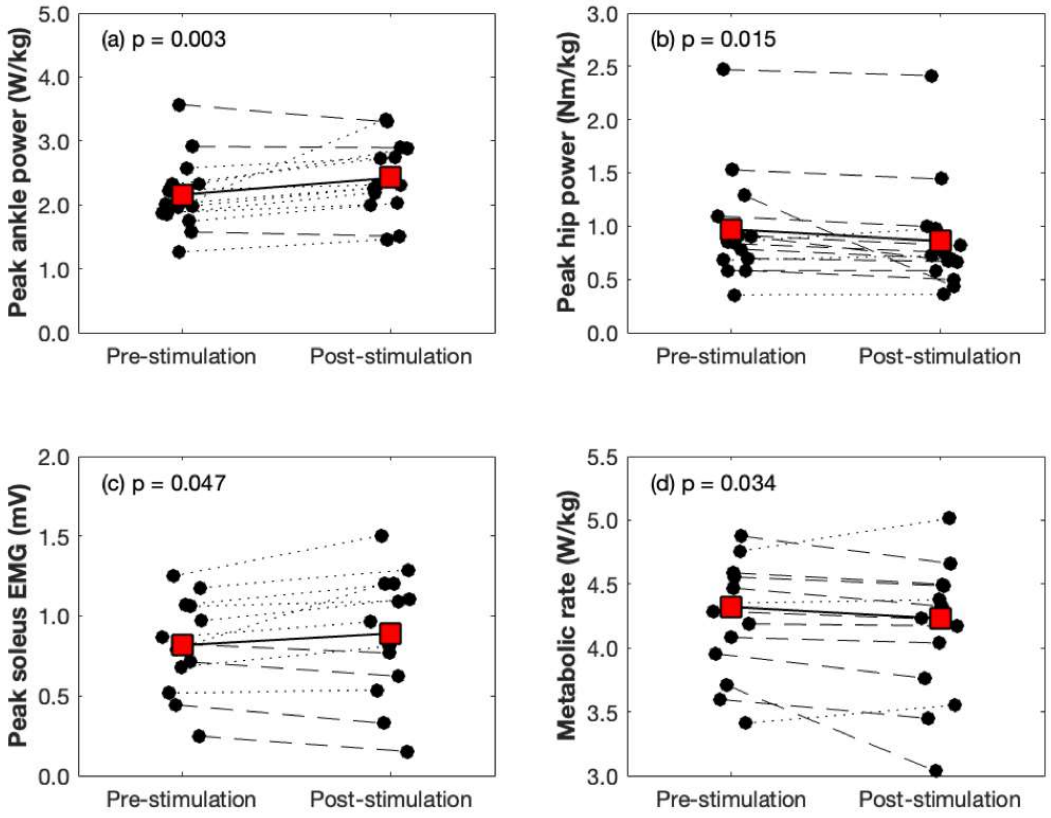


Figure 1: (a) Peak ankle power, (b) peak hip power, (c) peak soleus EMG, and (d) metabolic rate, at baseline before functional electrical stimulation (FES) of the plantarflexors, and after removal of the FES. Circles are individual participants, with dotted lines for post-stimulation increases and dashed lines for decreases. Squares are means.

References (Optional)

[1] Fallah & Beck (2025), J Exp Biol 228(2); [2] DeVita & Hortobagyi (2000), J Appl Physiol 99(5)

Session Category

Human Motion and Performance: Locomotion/Gait

P1-209

Effects of Step Rate Manipulation on Lower-Extremity Kinematics During High-Speed Running in Highly Trained Distance Runners

Undergraduate Researcher Noah Clemens, Assistant Professor Lauren Miutz PhD, Associate Professor Matthew Beerse PhD

University of Dayton, Dayton, Ohio, United States

Introduction

Running step rate (SR) is commonly manipulated to alter running biomechanics for injury prevention and performance optimization. Prior work studying elite runners at moderate running speeds has demonstrated that increasing SR leads to consistent changes in joint kinematics; however, it is unknown if a similar pattern emerges during high-speed running. Gait mechanics may differ at faster speeds; therefore, SR manipulation may not exert the same effects observed during slower running. The purpose of this study was to quantify the biomechanical changes associated with SR manipulation during high-speed running in elite male distance runners.

Methods

Twelve elite male distance runners (age: 22.5 ± 3.7 years) completed 4-minute trials under seven SR conditions ranging from 170 to 200 steps/minute. All trials were performed at 4.96 $m \times s^{-1}$ (5:24 $min \times mile^{-1}$), the average speed at anaerobic threshold identified via pilot testing. Thirty consecutive steps from the third minute of each trial were analyzed. Sagittal-plane hip range of motion (ROM), knee flexion at initial contact (IC), and peak knee flexion and hip adduction during stance phase were identified, as these variables have been linked to running-related injury and SR manipulation. Associations between SR and each variable were examined using linear mixed-effects models with participant-specific random intercepts.

Results

SR was significantly associated with peak knee flexion during stance ($p < 0.001$) and hip flexion-extension ROM ($p < 0.001$). SR was significantly but not meaningfully associated with knee flexion at IC ($p < 0.001$, $R^2_{part} = 0.009$). Partial R^2 values suggest that SR has a small to moderate association with peak knee flexion during stance ($R^2_{part} = 0.063$), and a moderate association with hip flexion-extension ROM ($R^2_{part} = 0.149$). Across participants, peak knee flexion during stance ranged from 32.7° to 62.4°, and hip flexion-extension ROM ranged from 64.9° to 91.4°.

Discussion

These findings align with results at slower running speeds, suggesting that SR manipulation influences sagittal-plane hip and knee mechanics during high-speed running in a similar manner. Thus, SR-based gait retraining strategies commonly applied at slow speeds may be similarly effective for injury mitigation and performance enhancement at faster, race-relevant velocities.

Images (Optional)

LME Model Results: Step Rate as a Predictor of Lower-Extremity Kinematics

Variable	Estimate	Std. Error	df	t-value	p-value	partial R^2
IC Knee Flexion	0.06428	0.01714	53.16431	3.751	0.000437	0.009
Peak Knee Flexion	-0.02483	0.02978	53.21068	-8.337	3.16E-11	0.063
Peak Hip Adduction	-0.00685	0.01458	55.52867	-0.470	0.640	0.000
Hip Flexion-Extension ROM	-0.37319	0.01347	54.04293	-27.700	<2E-16	0.149

Session Category

Human Motion and Performance: Locomotion/Gait

P1-210

Balancing Energy and Stability: Older Adult Fallers Modulate Step-to-Step Transitions Under Visual Cueing

Ms. Olivia Greene MS, ATC, Dr. Jacob Thomas PhD, Mr. Paul McDonnell MS, Mr. Adam Grimmitt MS, Mr. Jonaz Moreno Jaramillo MS, Dr. Douglas Martini PhD, Dr. Wouter Hoogkamer PhD

University of Massachusetts Amherst, Amherst, MA, United States

Introduction

Humans typically self-select walking patterns that minimize metabolic energy consumption, requiring coordinated redirection of the center of mass during step-to-step transitions. Minimizing overlap between push-off and collision power reduces metabolic energy cost [1], whereas greater overlap enhances stability. Age-related changes in step-to-step transitions coordination have been described, but little is known about older adults with fall history. We evaluated step-to-step transitions coordination in young adults (YA), older adults (OA), and older adults with fall history (OAF) during regular and visually cued treadmill walking to assess effects of age and fall history on step-to-step transitions coordination in typical and novel tasks.

Methods

Fourteen young adults and 22 older adults (10 OA, 12 OAF) walked on an instrumented split-belt treadmill at self-selected walking speed under two conditions: regular gait (RG) and visually cued gait (VCG). In VCG, steppingstones were projected onto the treadmill at preferred step lengths and widths. Participants targeted foot placements accordingly. Push-off and collision power overlap (Sequence Index) was calculated for ten step-to-step transitions [1], identified via center of mass velocity hodographs [2]. Sequence Index of 0 indicates push-off preceding collision, while 1 indicates push-off after collision. Group effects were tested using one-way ANOVA with Tukey's post hoc comparisons, and Bonferroni-corrected paired t-tests assessed within-group differences between conditions.

Results

In RG, YA walked with lower Sequence Index values than OA (p=0.018). During VCG, Sequence Index was lower in YA than OAF (p=0.002). Only OAF showed a significant increase in Sequence Index from RG to VCG (p=0.01).

Discussion

Older adults with fall history showed distinct adaptation of step-to-step transitions coordination when confronting a novel, visually guided stepping task. Their increased Sequence Index indicates greater push-off-collision overlap, suggesting a stability-oriented strategy when foot placement is modulated [3]. Since OA and YA maintained consistent coordination across tasks, fall history may shape how older adults modify step-to-step transitions mechanics in novel gait contexts. Modified step-to-step transition mechanics may signal fall risk in older adults, thus underscoring the need for prospective evaluation.

Images (Optional)

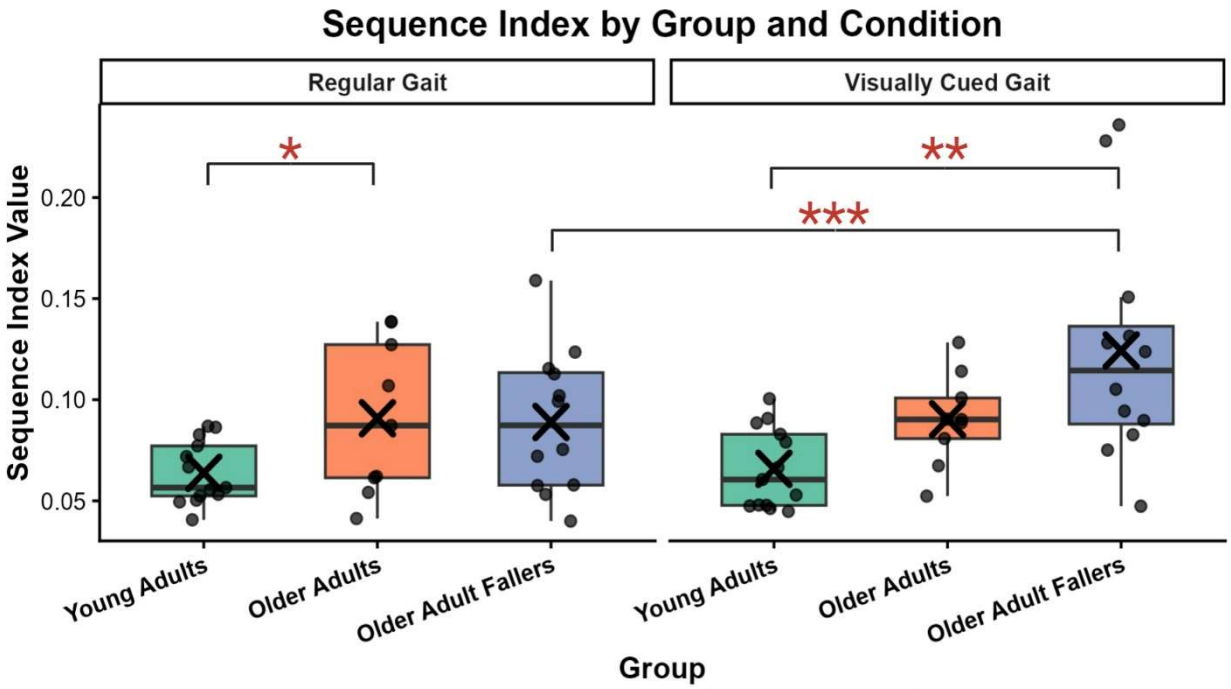


Figure 1. Box plots of push-off-collision power overlap (Sequence Index) across age groups during regular and visually cued gait. **"X"** indicates mean value. * indicates significance between groups during regular gait (p = 0.018). ** indicates significance between groups during visually cued gait (p = 0.002). *** indicates significant increase of 0.035 (p = 0.01).

References (Optional)

[1] Ruina et al., *J Theoretical Biology*, 2005; [2] Adamczyck & Kuo, *J Experimental Biology*, 2009; [3] Liu et al., *R Soc Open Sci.,* 2024.

Acknowledgements (Optional)

Supported by National Institutes of Health, award 5R21AG075489-02.

Session Category

Human Motion and Performance: Locomotion/Gait

P1-211

Factors Associated with Gait Biofeedback Accuracy in Individuals with Knee Osteoarthritis: A Feasibility Study Including Wearable Sensor Translation

Ms. Olivia Stepp[1,2], Ms. Elizabeth Bjornsen PhD[3], Ms. Anna McDermott[1], Dr. Brian Pietrosimone PhD[1], Dr. Jason Franz PhD[1,2]

[1]University of North Carolina at Chapel Hill, Chapel Hill, NC, United States. [2]North Carolina State University, Raleigh, NC, United States. [3]East Carolina University, Greensboro, NC, United States

Introduction

Knee osteoarthritis (KOA) is associated with maladaptive changes in lower-extremity loading during walking. Notably, less dynamic and more sustained vertical ground reaction force (vGRF) profiles associate with greater compressive cartilage strain[1]. Our research team has successfully used gait biofeedback to alter vGRF in individuals at risk for KOA[2]; however, the feasibility of deploying biofeedback in individuals with KOA is unknown. Our purpose was to determine whether KOA-associated factors affect the ability of individuals with KOA to augment compressive limb loading through gait biofeedback. We hypothesized that greater self-reported pain, lower self-reported function, and slower habitual walking speed would result in larger errors in achieving biofeedback targets. As a secondary objective to support translation, we assessed the accuracy of wearable sensors to estimate changes in peak vGRF with biofeedback.

Methods

13 individuals (aged 51-74) with mild-to-moderate KOA have thus far participated. Participants completed a habitual walking trial on a dual-belt, force-sensing treadmill at their habitual speed while wearing custom inertial-measurement units (IMUs) on their waist and ankles. Participants then completed four 2-minute blinded, randomized biofeedback conditions that visually-cued peak vGRF targets (-3, +3, +6, +9%body weight [BW]). Participants self-reported pain (Visual Analog Scale [VAS]) and overall joint function (Western Ontario and McMaster Universities Arthritis Index [WOMAC]). We calculated absolute error as the difference between target and measured peak vGRF, analyzed for the affected (unilateral KOA) or more symptomatic (bilateral KOA) limb. Linear regressions assessed the effect of (i) baseline pain, (ii) WOMAC score, and (iii) habitual walking speed, on absolute error. vGRF-estimate machine learning models trained on IMU signals were compared with ground-truth values.

Results

When targeting +6%BW vGRF, higher (i.e., worse) WOMAC scores and slower walking speeds associated with larger absolute errors ($p \leq 0.048$). When targeting +9%BW vGRF, higher baseline pain associated with larger absolute errors ($p=0.043$). Wearable sensor comparisons are ongoing.

Discussion

Individuals with KOA achieved significant differences in vGRF with biofeedback (*data not shown*). However, translation and prescription must consider self-reported pain, function, and walking speed, which we show here can all affect biofeedback accuracy.

Images (Optional)

Table 1: Summary of Single Linear Regression Models

Outcome	Predictor	Estimate	R^2	P-Value
-3% Target				
vGRF Absolute Error	Baseline Pain	-0.206	0.302	0.064
vGRF Absolute Error	Walking Speed	5.365	0.158	0.201
vGRF Absolute Error	WOMAC Score	-0.077	0.240	0.106
+3% Target				
vGRF Absolute Error	Baseline Pain	0.075	0.031	0.582
vGRF Absolute Error	Walking Speed	-8.095	0.281	0.076
vGRF Absolute Error	WOMAC Score	0.093	0.271	0.083
+6% Target				
vGRF Absolute Error	Baseline Pain	0.220	0.114	0.282
vGRF Absolute Error	Walking Speed	-13.605	0.338	**0.048***
vGRF Absolute Error	WOMAC Score	0.164	0.358	**0.040***
+9% Target				
vGRF Absolute Error	Baseline Pain	0.456	0.350	**0.043***
vGRF Absolute Error	Walking Speed	-3.713	0.018	0.678
vGRF Absolute Error	WOMAC Score	0.123	0.144	0.223

References (Optional)

[1] Dausch et al., *OARSI*, 2026

[2] Bjornsen et al., *J Orthop Res*, 2025

Acknowledgements (Optional)

Supported by a grant from the North Carolina Biotechnology Center.

Session Category

P1-212

Effects of Prosthesis Stiffness on Running Limb Symmetry in Persons with Unilateral Limb Amputation

Miss Paige Agnew MS, Dr. Hunter Bennett PhD

Old Dominion University, Norfolk, Virginia, United States

Introduction

The goal for individuals with lower limb loss is to achieve bilateral symmetry during locomotion. Limb and neuromuscular asymmetry can result in abnormal gait strategies and commonly lead to back pain, inefficient gait patterns, and increased loading to the unaffected limb. For runners, additional aspects must be addressed to optimize performance, such as prosthetic stiffness. As prosthetic limb stiffness increases with running speed, it is possible variations in prosthetic stiffness itself could improve running mechanics. Therefore, the purpose of this study was to assess bilateral symmetry in individuals with unilateral transtibial amputations running on two different stiffness prosthesis.

Methods

Two amputee running athletes volunteered for this study: Participant A (PA) is an endurance-trained 55-year-old female with K-4 level and Participant B (PB) is an Olympic-level sprinter 55-year-old male with K-4 level. Full body motion capture (including prosthesis), ground reaction forces (GRF), and electromyography of the glutes, rectus femoris, and biceps femoris were collected while running at a self-selected speed. Inter-limb symmetry indices for GRF loading rate, stance time, and iEMG were calculated and compared for running on prescribed and non-prescribed (i.e., stiffer/more compliant) prostheses.

Results

Due to constraints, PA used a stiffer than prescribed (mass at lowest prescription level) and PB used more compliant than prescribed (mass at highest prescription level) prosthetic. Symmetric indices are in Table. For both subjects, stance time was <10% different between prosthetics. PA had doubly greater GRF loading rate asymmetry running on prescribed prosthetic. PA demonstrated greater glute asymmetry but reduced semimembranosus asymmetry running on a stiffer prosthetic. PB demonstrated no asymmetries for rectus femoris, but doubly increased asymmetry in the glutes and vastus lateralis and reduced semimembranosus asymmetry when running on the less stiff prosthetic.

Discussion

This study found >10% asymmetry between the prosthetic limb and non-prosthetic limb for almost all lower extremity muscles. Increased GRF loading rate and muscle asymmetry within the glute maximus and the vastus lateralis could cause instability in the knee during loading. To reduce limb asymmetry, it is recommended users utilize the prescribed prosthetic based on manufacturer recommendations or opting for a stiffer prosthesis rather than a less stiff.

Images (Optional)

GRF Loading Rate		Stance Time		S1 iEMG							
Subject 1		Subject 1		Glutes		Semimembranosus		Rectus Femoris		Vastus Lateralis	
Normal	Stiff	Normal	Stiff	Normal	Stiff	Normal	Stiff	Normal	Stiff	Normal	Stiff
20.18	-11.53	3.04	5.32	49.58	74.27	-26.00	-9.00	36.00	35.00	-25.67	-23.27
GRF Loading Rate		**Stance Time**		**S4 iEMG**							
Subject 4		**Subject 4**		**Glutes**		**Semimembranosus**		**Rectus Femoris**		**Vastus Lateralis**	
Less Stiff	**Normal**	**Less Stiff**	**Normal**	**Normal**	**Less Stiff**	**Normal**	**Less Stiff**	**Normal**	**Less Stiff**	**Normal**	**Less Stiff**
5.89	7.73	-0.78	-0.74	5.33	-32.50	41.07	27.31	0.43	0.95	-28.57	-57.00

Session Category

Human Motion and Performance: Locomotion/Gait

P1-213

Plantarflexor Muscle Activity as a Surrogate for Propulsion Measurement During Treadmill Walking

Ms. Paromita Kundu[1], Dr. Sagar Doshi Research Assistant Professor[2], Dr. Jill Higginson Professor[1]

[1]University of Delaware, Newark, DE, United States. [2]Center for Composite Materials, University of Delaware, Newark, DE, United States

Introduction

Propulsion, a key biomechanical variable used to characterize walking, is widely targeted in rehabilitation strategies. It is primarily generated by the ankle plantarflexor muscles in late stance. Prior work has shown that increased plantarflexor activation is strongly associated with paretic propulsion [1]. Since plantarflexor activity is a primary contributor to propulsion during gait, it is possible that plantarflexor EMG could serve as a practical surrogate for propulsion measurement. Therefore, the purpose of this study was to quantify how accurately plantarflexor muscle activity reflects propulsion across different walking speeds.

Methods

Five healthy adults walked on a force-plate instrumented treadmill for two minutes each at three fixed speeds: slow(0.5 ms^{-1}), medium(1.0 ms^{-1}), and fast (1.5 ms^{-1}). For each trial, synchronized ground reaction force (GRF) and surface EMG were recorded from the medial gastrocnemius (MG), lateral gastrocnemius (LG), and soleus (SOL) muscles at f_s = 2000 Hz. Raw EMG and GRF signals were processed, stance phase was identified, and each stride was segmented. Mean peak propulsion and mean peak EMG activity during late stance were extracted at each speed for all subjects. Spearman correlations were computed to examine the relationship between peak EMG activity and peak propulsion.

Results

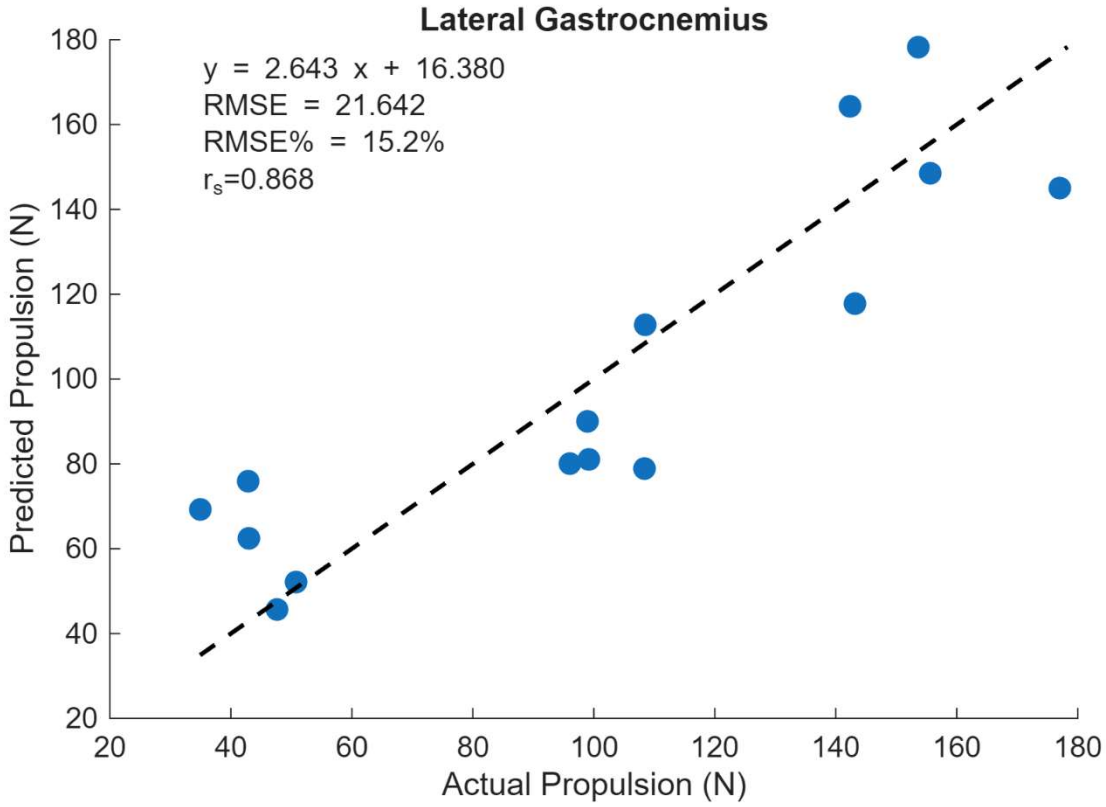
All three plantarflexor muscles showed strong correlations between peak EMG and peak propulsion. The correlation coefficients were MG: r_s = 0.73, LG: r_s = 0.87, and SOL: r_s = 0.79. Prediction accuracy based on EMG–propulsion linear models was moderate, with RMSE values of 18.8% (MG), 15.2% (LG), and 17.3% (SOL).

Discussion

Plantarflexor activity is a reliable indicator of changes in propulsion across walking speeds. Both gastrocnemius and the soleus contribute to increased propulsion, with LG showing

the highest correlation and lowest RMSE. This may indicate more consistent activation patterns and cleaner surface EMG signals for LG compared to MG, which is more variable, and SOL, which is a deeper muscle with lower signal-to-noise ratio. RMSE values in the 15–19% range are acceptable for EMG-based modeling due to inherent EMG variability [2]. Future work will focus on developing real-time EMG biofeedback based on plantarflexor activity.

Images (Optional)



References (Optional)

[1]Turns et al., APMR, 2007

[2] Daunoraviciene et al.,Sensors,2022

Session Category

Human Motion and Performance: Locomotion/Gait

P1-214

Does Bilateral Symmetry Maximize Bipedal Running Speeds?

Dr. Peter Weyand Professor, Dr. Sunil Prajapati PhD

Texas Christian University, Fort Worth, TX, United States

Introduction

Bilateral symmetry is generally considered functionally beneficial for bipedal running gaits. However, runners could theoretically meet the running gait requirement of supporting the body's weight with unequal contributions from the right and left limbs. Here, we compared the bilateral symmetry of competitive sprinters and athlete non-sprinters to test the importance of bilateral symmetry for achieving faster speeds. We hypothesized that between-limb differences in the stance-average ground forces applied during high-speed running would not differ between the two groups.

Methods

Sixteen participants, eight competitive sprinters (n=5 males, 3 females) and eight athlete non-sprinters (n=5 males, 3 females) performed a series of progressive, constant-speed runs on a force-instrumented treadmill. Stance-averaged forces for each limb were determined from the vertical ground reaction forces at 60-100% of each athlete's measured maximum speed. Bilateral symmetry was quantified on a per trial basis as the percent difference between the forces applied by right vs. left limb [{(L-R)/mean}•100)]. A total of 143 trials and 1966 steps were analyzed.

Results

The mean maximum speeds of the competitive sprinters exceeded those of the athlete non-sprinters (10.7±0.8 vs. 9.2±0.9 m/s). Between-limb asymmetries in stance-average ground forces were significantly greater for the competitive sprinters vs. athlete non-sprinters (7.90±3.5% vs. 5.30±2.8%, $p<0.01$).

Discussion

Contrary to expectation, competitive sprinters had greater differences in the stance-averaged ground forces applied by their right and left limbs than did athlete non-sprinters across the nearly 2000 high-speed running steps we analyzed. We attribute this result to: 1) some competitive sprint athletes applying greater ground forces with their left vs. right limb in nearly every trial they completed, and 2) other competitive sprint athletes running with relatively asymmetrical patterns at faster trials speeds, but without consistent

directionality from trial to trial. We conclude that faster human runners achieve their greater speeds with relatively asymmetrical patterns of ground force application.

Session Category

Human Motion and Performance: Locomotion/Gait

P1-215

Changes in mediolateral CoP dynamics, not excursion, are linked to reduced gait stability in a virtual walking environment

Miss Prachi Pisay PT, MSc, Dr. Ashwini Kulkarni PT, ACSM-EP, PhD

Old Dominion University, Norfolk, Virginia, United States

Introduction

Virtual reality (VR) provides a controlled, task-specific walking environment with real-time multisensory feedback. Because VR relies heavily on visually perceived space, and this perception can shift with different spatial dimensions, the influence of visual information may be amplified, potentially altering gait control. This secondary analysis [Simonlehner et al. (2024). Scientific Data, 11(1)] evaluates whether the environment (real vs VR), the perceived size of the environment (small vs large), alters mediolateral (ML) center of pressure (CoP) dynamics (velocity and acceleration), and ML local dynamic stability.

Methods

Participants (37.2 ± 8.7 years, 73.9 ± 15.7 kg, 170.3 ± 6.6 cm) wore HMD and walked overground across four environments: a real lab (A), virtual (VRLab (B)), small (VRLab- (C)), and a large (VRLab+(D)) virtual room. Outcome variables included step length, step width, ML CoP excursion, velocity, acceleration, and ML short-term Lyapunov exponent (λ_{ml}). Repeated-measures ANOVA compared outcome variables across conditions, and VR-induced changes were calculated using difference scores (Δ) to the real condition and correlated with λ_{ml}.

Results

VR did not change step length/width or ML CoP excursion, but increased CoP velocity ($p = 0.02$) and acceleration ($p = 0.03$). Participants who showed larger VR induced increases in CoP velocity ($r = 0.6$, $p = 0.007$, Fig.1) and acceleration ($r = 0.48$, $p = 0.04$, Fig.1) were significantly associated with higher λ_{ml} (reduced stability), and these relationships were consistent across all VR conditions (velocity: $r = 0.33$, $p = 0.01$; acceleration: $r = 0.29$, $p = 0.03$).

Discussion

VR alters the dynamics of ML control rather than the magnitude of ML control. Increased COP velocity and acceleration indicate faster and more reactive lateral weight shifting.

These were associated with higher Lyapunov exponents, indicating reduced local dynamic stability. No significant differences were observed between small and large VR environments, suggesting that the magnitude of spatial scaling was not the primary factor driving these changes. This means that even simple VR environments can meaningfully challenge balance control, offering useful opportunities for task-specific rehabilitation, particularly for individuals at risk of falls.

Images (Optional)

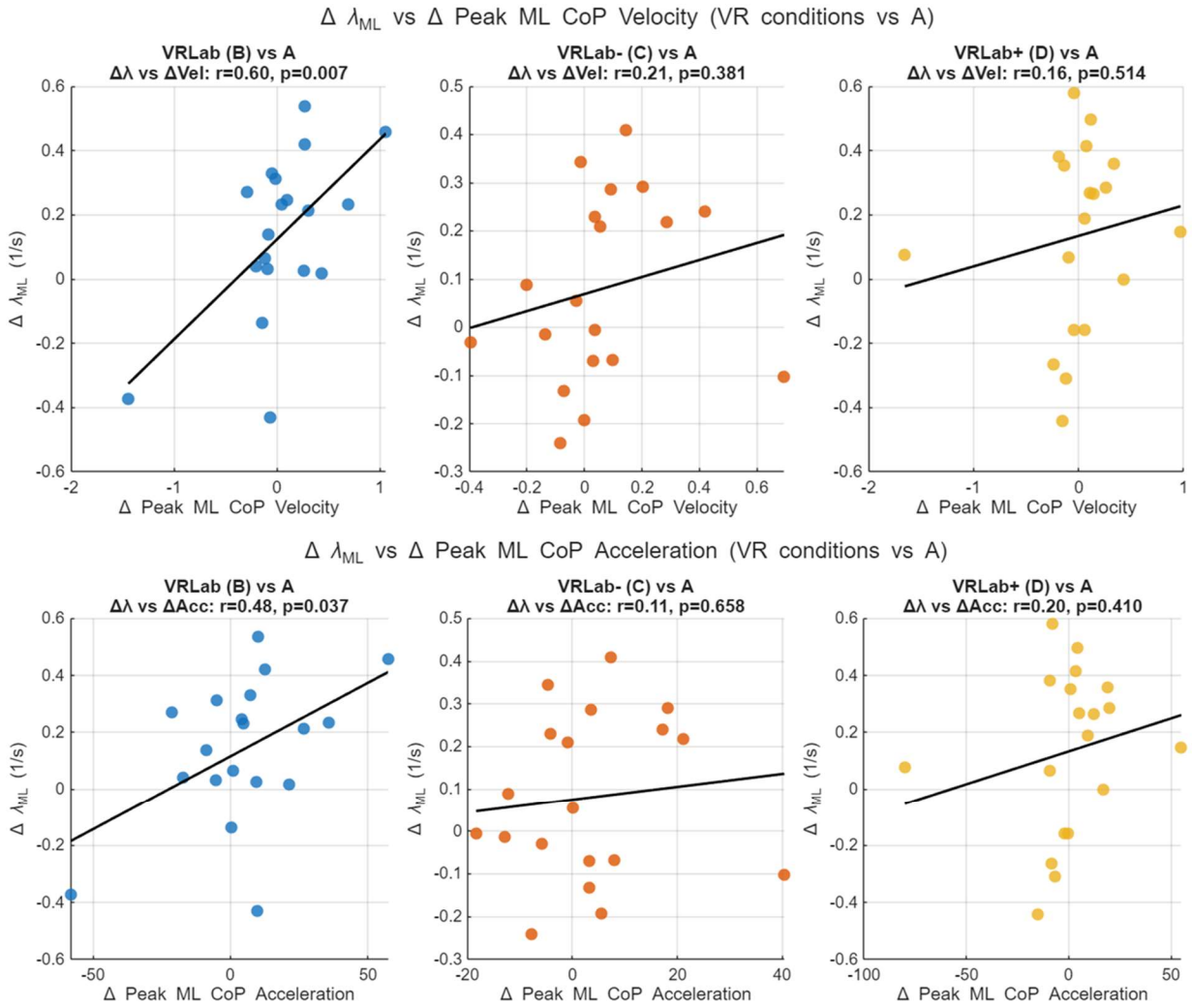


Figure 1. Scatter plots illustrating the relationship between within-subject changes in mediolateral Lyapunov exponent ($\Delta\lambda_{ml}$) and changes in peak mediolateral center of pressure (CoP) velocity (top) and acceleration (bottom) for virtual reality walking conditions (B (VR environment), C (small VR environment), D (large VR environment)) relative to real-world walking (A). Lines represent linear regression fits. Significant positive associations were observed only in the standard VR condition (B), suggesting that increases in CoP dynamics were linked to reduced local dynamic stability in VR.

References (Optional)

Acknowledgements (Optional)

This work uses data from the"Simonlehner, M., Dumphart, B., & Horsak, B. (2024). GaitRec-VR: 3D Gait Analysis for Walking Overground with and without a Head-Mounted-Display in

Virtual Reality. Scientific data, 11(1), 1099. https://doi.org/10.1038/s41597-024-03939-0". We acknowledge the authors for making it publicly available.

Session Category

Human Motion and Performance: Locomotion/Gait

P1-216

Prosthetic-Limb Mediolateral Instability Drives Functional Differences Between K2 and K3 Transfemoral Amputees

Miss Jade Carter MS student[1], Miss Prachi Pisay MSc[2], Dr Ashwini Kulkarni PT, PhD[2]

[1]Teachers College, Columbia University,, NY, NY, United States. [2]Old Dominion University, Norfolk, VA, United States

Introduction

The Medicare Functional Classification Level (K-level) guides prosthetic prescription but relies heavily on walking speed and subjective judgement, leaving its relationship to dynamic stability and its control unclear [1]. The Margin of stability in antero-posterior (MoSAP) and medio-lateral (MoSML) direction quantifies dynamic stability [2], and has been studied in amputees [3], yet how these differ by K-level, and ipsilateral/contralateral limb in transfemoral amputees remains unknown. The purpose of this study is to quantify MoSAP, MoSML, and synergies stabilizing these across prosthetic and intact limbs in K2 and K3 walkers.

Methods

This is a secondary analysis [4] where 18 unilateral transfemoral amputees (9 K2, 9 K3) walked on an instrumented treadmill at five group-specific speeds (K2: 0.4–0.8 m/s; K3: 0.6–1.4 m/s). We computed MoSAP, MoSML, and synergies stabilizing MoSAP and MoSML at heel strikes from the middle 10 steps per trial.

Results

No differences in MoSAP by K-level, limb, or speed. Δvz_{AP} was greater than 0. There were main effects of the limb. ΔVz_{AP} was weaker on the prosthetic limb ($p<0.01$). V_{UCM} and VORT were higher for prosthetic limbs ($p<0.01$) and increased with speed ($p<0.01$). In contrast, MoSML showed an interaction between K-level × Side × Speed for MoSML. The prosthetic limb had smaller MoSML ($p<0.01$) at higher speeds for K3. ΔVz_{ML} was greater than zero but no differences across factors were observed.

Discussion

The absence of differences in MoSAP suggests similar overall AP stability across K-levels and limbs, however $\Delta Vz_{AP} > 0$ indicates that MoS was actively controlled through error compensation between step length (SL) and extrapolated center of mass (XCoM). The

higher V_{UCM} and V_{ORT} for prosthetic limb indicate increased corrective effort and higher variability in SL and XCoM. In contrast, the presence of differences in MoSML suggests reduced ML stability on prosthetic limb at faster speeds, suggesting they operate closer to their ML stability limits. Although ΔVzML was > 0, indicating active stabilization of MoSML, the lack of group differences suggests similar step-to-step control strategies despite differences in average ML stability.

References (Optional)

[3]Rodrigues et al., J Biomechanics, 2021

[4] Hood et al., Scientific Data, 2020

Acknowledgements (Optional)

We acknowledge Sarah Hood and other co-authors for making this dataset public.
Hood, S., Ishmael, M.K., Gunnell, A. *et al.* A kinematic and kinetic dataset of 18 above-knee amputees walking at various speeds. *Sci Data* **7**, 150 (2020). https://doi.org/10.1038/s41597-020-0494-7

Session Category

Human Motion and Performance: Locomotion/Gait

P1-217

Stepping Into Motherhood - Teasing Out Foot Mechanical Adaptations in Pregnancy Gait

Ms. Rachel Todd[1], Dr. Lauren Williams[2], Dr. Dustin Bruening[1], Dr. Adrienne Henderson[1]

[1]Brigham Young University, Provo, Utah, United States. [2]University of Utah, Salt Lake City, Utah, United States

Introduction

During pregnancy, musculoskeletal adaptations occur including increased anterior weight and increased joint laxity from altered hormones.[1] These changes increase the load on the foot's arch which may cause pain during daily activities including walking.[2] Prior research focusing on static measures of arch height are mixed. The purpose of this study was to determine how pregnancy alters static and dynamic arch function compared to non-pregnant individuals with simulated weight gain. We hypothesize static arch height will not change, and dynamic arch height during walking will significantly decrease with added weight (pregnancy or simulated).

Methods

Thirteen pregnant participants had static arch height (AHI) and dynamic navicular height measured during walking in their 1st (TR1) and 3rd (TR3) trimesters (TR1:1.65±0.07m, 65.9±14.8kg; TR3:77.3±15.9kg). Participants walked at1.0-1.2m/s, and navicular height was defined as the lowest vertical position of a marker on the navicular tuberosity during stance. Thirteen non-pregnant controls (1.65±0.08 m, 66.2±15.7 kg) were age-, height-, and TR1 weight-matched to pregnant participants. Controls completed identical AHI and walking assessments under 2 randomized conditions: unweighted and weighted (equal to matched TR3 mass). T- tests determined significance between weight conditions and groups.

Results

There were no significant differences in any static measures but significant decreases in all dynamic measures (Table 1).

Discussion

Added weight didn't result in decreased static AHI regardless of pregnancy status, possibly because plantar loads during quiet standing may be insufficiently high or too posterior to elicit measurable arch deformation. Intrinsic and extrinsic foot muscles may also increase activation to compensate for the added load. In contrast, added weight resulted in

decreased dynamic arch height for both groups. This is likely due not only to the increased load on the foot from added weight, but increased forces needed for gait in conjunction with the anterior center of pressure in mid- and terminal stance. These results emphasize that foot mechanics should be evaluated dynamically when treating the foot.

Images (Optional)

Table 1: Group means and standard deviations for static and dynamics variables, between conditions (non-weighted vs weighted) and groups (FPG vs NFPG) with p-values.

	Comparison	Means + SD	P-Value
Static	AHI (FPG NW – W)	0.315 ±0.02 vs 0.325 ±0.03	0.098
	AHI (NFPG NW – W)	0.355 ±0.02 vs 0.352 ±0.03	0.461
	AHI (FPG -NFPG)	-0.010 ±0.02 vs 0.003 ±0.01	0.093
Dynamic	Nav (FPG NW – W)	0.036 ±0.01 vs 0.041 ±0.01	0.039
	Nav (NFPG NW – W)	0.046 ±0.01 vs 0.045 ±0.01	0.029
	Nav (FPG -NFPG)	-0.005 ±0.01 vs 0.001 ±0.00	0.022

References (Optional)

1 Pardo,et al. (2018). *Women and Birth*, 31(2).

2 Vullo,et al. (1996). *J Fam Pr*, *43*(1).

Session Category

Human Motion and Performance: Locomotion/Gait

P1-218

A Cognitive Dual Task Alters Spatiotemporal Control of Gait

Dr. Reed Gurchiek[1], Dr. William Bridges[1], Ms. Olivia Cunningham[1], Ms. Sophia Somerville[2], Mr. Harrison Nodes[1]

[1]Clemson University, Clemson, SC, United States. [2]Boston University, Boston, MA, United States

Introduction

Reduced gait speed is a well-known effect of cognitive dual-task gait, but the extent to which cognitive processes interfere with gait control beyond reduced gait speed remains unclear. A better understanding of this relationship could improve development of digital biomarkers of cognitive impairment for early detection of Alzheimer's disease.

Methods

Eighteen healthy subjects walked overground (self-selected speed) and on a treadmill (0.8, 1.0, and 1.2 m/s) with and without a cognitive dual task. We calculated stride frequency from gait events identified using shank-worn gyroscope data and overground gait speed using pelvis kinematics (via OpenCap). We fit a two-parameter power function to each subject's speed-frequency data collected in an additional 8 overground walking trials at prescribed frequencies (45-150 steps/minute) to model subject-specific spatiotemporal control strategies. Differences in the measured and model-predicted (based on speed) frequency during the overground dual-task gait were taken to indicate altered control. Frequency differences between single- and dual-task treadmill gait were interpreted similarly. We used regression analysis of these frequency differences to determine the effect of the cognitive dual-task on spatiotemporal control and cluster analysis to identify unique groups of subjects with a similar response.

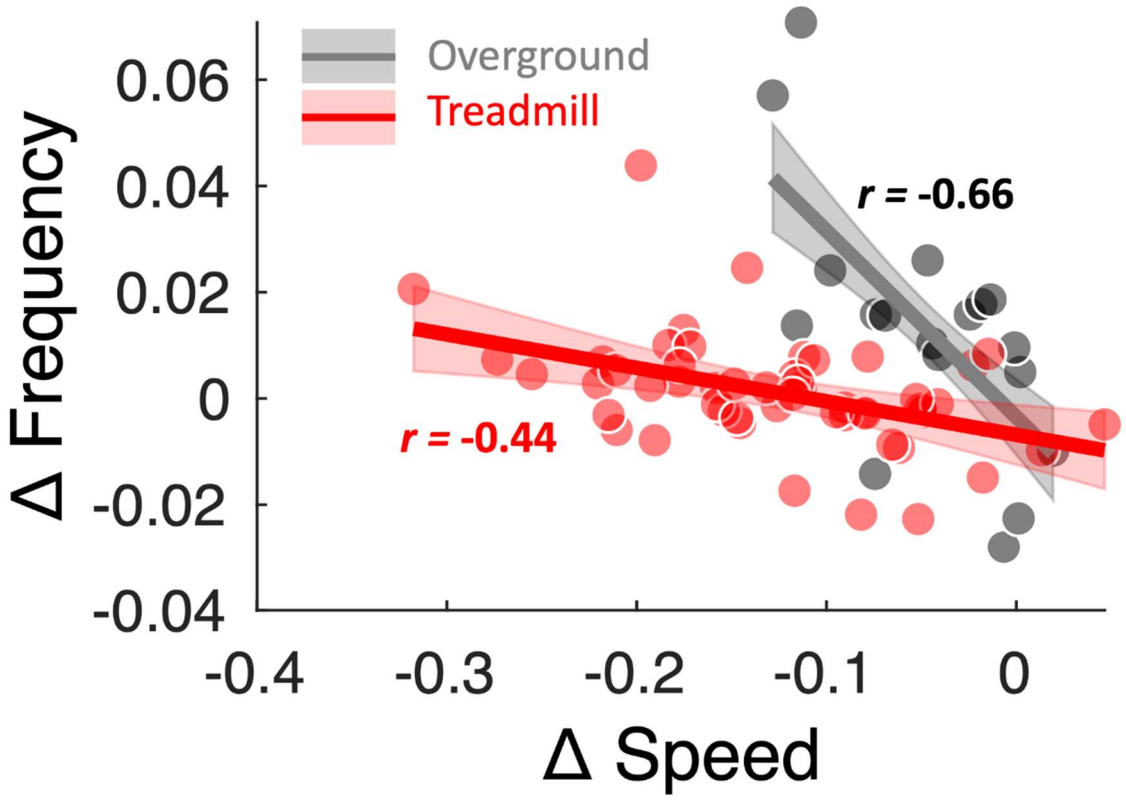
Results

Frequency deviations in the dual-task condition negatively correlated with gait speed (relative to self-selected speed) independent of goal-directedness (overground vs. treadmill) with a more pronounced effect for overground gait. The effect of the cognitive dual task on spatiotemporal control varied across people according to four unique clusters. The general negative correlation observed overall was preserved for three of the four clusters where the slope magnitude was the distinguishing factor among the three.

Discussion

Our results suggest a cognitive dual task alters spatiotemporal control of gait independent of reduced gait speed. The preferred speed-frequency relationship is thought to optimize some motor control objective. It remains unclear if the observed shift from the preferred relationship indicates an altered objective or an impediment to optimizing the original. In either case the effect varies across people, and future research should explore this phenomenon in older adults with variable cognitive abilities.

Images (Optional)



Acknowledgements (Optional)

This work was supported by the Clemson University Creative Inquiry Program and NIH (SC-INBRE DRP): P20GM103499.

Session Category

Human Motion and Performance: Locomotion/Gait

P1-219

Leveraging Ankle Foot Orthoses Kinematic Constraints to Assess Markerless Motion Capture

Mr. Riley Horn BS[1], Mr. John Collins MA, ATC[1], Dr. Heather Waters PT, DPT[1], Dr. Christine Amacker PT, DPT[1], Mr. Martins Amaechi MS[1], Dr. Rachel Thompson MD[1,2], Dr. Patrick Curran MD[1,2]

[1]Rady Children's Hospital, San Diego, CA, United States. [2]University of California San Diego, San Diego, CA, United States

Introduction

Marker-based motion capture is the clinical standard for gait analysis but is time-consuming and requires expertise for accurate marker placement. Theia3D offers a markerless alternative, though comparisons to marker-based kinematics are constrained by the inherent limitations of marker-based approximations [1]. Patients wearing ankle-foot orthoses (AFOs) present a unique opportunity to assess markerless systems, due to their predictable kinematic constraints. Hinged and posterior leaf spring AFOs restrict ankle range of motion (ROM) predominantly to the sagittal plane only [2]. We compared kinematic outputs between Theia3D and marker-based motion capture in children wearing these orthoses to determine the validity of the markerless system in capturing accurate kinematics.

Methods

Ambulatory children (Gross Motor Function Classification System (GMFCS) I-II) with cerebral palsy wearing AFOs were included for analysis (29 patients; 26 GMFCS II; age = 10.8±2.5y; 16 female). Data were collected with synchronized Qualisys systems (10 Arqus cameras, 120 Hz; 10 Miqus cameras, 85Hz; CAST 6DoF marker set) then processed in Theia3D (Theia 2025.1.2) and Visual3D (HAS-Motion). Three gait trials were averaged for each AFO-limb (n=36: 17 hinged, 19 posterior leaf spring). Ankle kinematics were compared between systems using statistical parametric mapping (SPM, spm1D.org). ROM was calculated as the difference between maximum and minimum joint angles during gait for each participant and assessed using paired t-tests.

Results

In the sagittal plane, significant between-system differences were identified during toe-off ($p=0.023$). Sagittal plane ROM differed between systems (Marker-based=14.5°; Markerless=19.3°; $p<0.001$). In the frontal plane, differences were found throughout the gait cycle ($p<0.001$), but ROM was comparable between systems. In the transverse plane,

differences were identified from initial contact to midstance (p=0.023), at pre-swing (p=0.046), and during mid-to-terminal swing (p=0.010). Transverse plane ROM differed significantly between systems (Marker-based=6.1°; Markerless=18.3°; p<0.001).

Discussion

Markerless-derived ankle kinematics showed substantial disagreement with marker-based kinematics for AFO-constrained limbs. Most notably, the markerless system reported greater transverse plane ROM relative to the marker-based system, contrary to expectations given the physical constraints of the AFOs. This disagreement between systems suggests limitations in Theia3D's foot segment definition when applied to atypical populations.

Images (Optional)

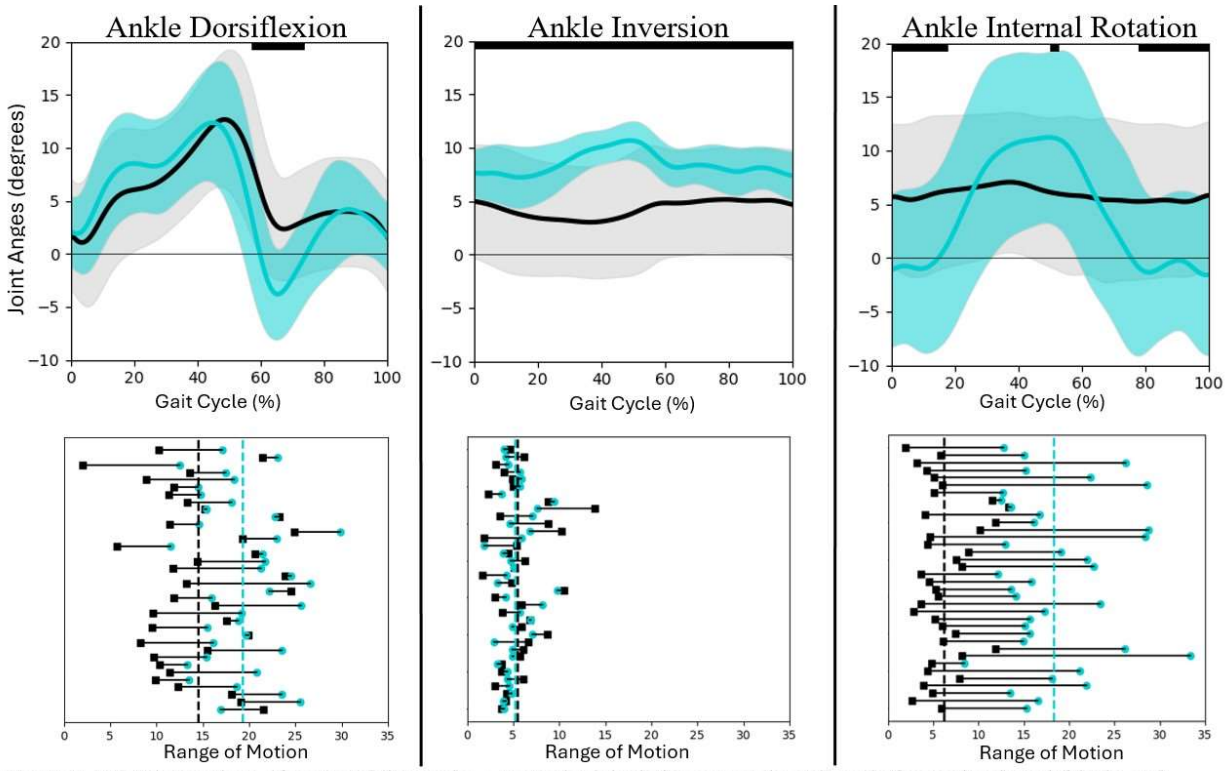


Figure 1. Top: Comparison of average joint angles ± 1 standard deviation across the gait cycle for marker-based (black) and markerless (blue). SPM analysis (upper black bar) represents percentage of gait cycle with significant differences. Bottom: Per participant range of motion values, with group means (dotted verticals lines).

References (Optional)

[1] Andreia Carvalho *et al.* , Gait Posture, 2025; [2] Diogo Ricardo *et al.* , Children, 2021

Session Category

Human Motion and Performance: Locomotion/Gait

P1-220

Are Toe Strength and Foot Compliance Predictive of Gait Speed in Older Adults With and Without Carbon Fiber Insoles?

Mr. Rohit Kundu[1], Dr. Daniel Davis[1], Dr. Jason Franz[2], Dr. Kota Takahashi[1]

[1]University of Utah, Salt Lake City, Utah, United States. [2]The University of North Carolina, Chapel Hill, North Carolina, United States

Introduction

Aging-induced structural and functional changes in the foot can alter foot mechanics and impair gait propulsion [1]. Increasing footwear stiffness with carbon fiber insoles can augment gait propulsion in young adults [2]. However, a feasibility study in older adults reported no group-level improvement in 6-minute walk distance with increased footwear stiffness [3]. Older adults with weaker toe flexors walked farther with carbon fiber insoles, suggesting that increased footwear stiffness effectiveness may depend on individual foot properties. Therefore, the purpose of this study was to examine how foot properties (toe flexor strength and passive foot compliance) modulate the effects of carbon fiber insoles on comfortable and maximum walking speeds in older adults.

Methods

Twenty-six healthy older adults (60-79 yrs) completed three overground comfortable and maximum walking speed trials over 20-m and 10-m distances, respectively, each under three randomized footwear conditions: 1) Control Shoe (S00), 2) Control Shoe+1.6 mm insole (S16), and 3) Control Shoe+3.2 mm insole (S32). Isometric toe flexor strength (N/kg) and passive foot compliance (inverse of foot stiffness; mm/kN) were assessed to characterize individual foot properties. A Linear Mixed Model (α=0.05) investigated how toe flexor strength and passive foot compliance affect comfortable and maximum walking speed across footwear conditions.

Results

There was no significant footwear × toe flexor strength or footwear × passive foot compliance interactions for comfortable (p=0.198-0.350) or maximum walking speeds (p=0.741-0.745), indicating that neither foot property modulates footwear stiffness effects on walking speed in older adults. Unlike passive foot compliance (p=0.340-0.745), toe flexor strength was positively associated with maximum (p<0.001) but not comfortable walking speed (p=0.097), independent of footwear conditions.

Discussion

Our results support previous findings that toe flexor strength contributes to overall walking performance[4, 5]. By reporting that the contribution holds independent of footwear condition, our findings further underscore the importance of strengthening toe flexor muscles to enhance walking performance in older adults.

Images (Optional)

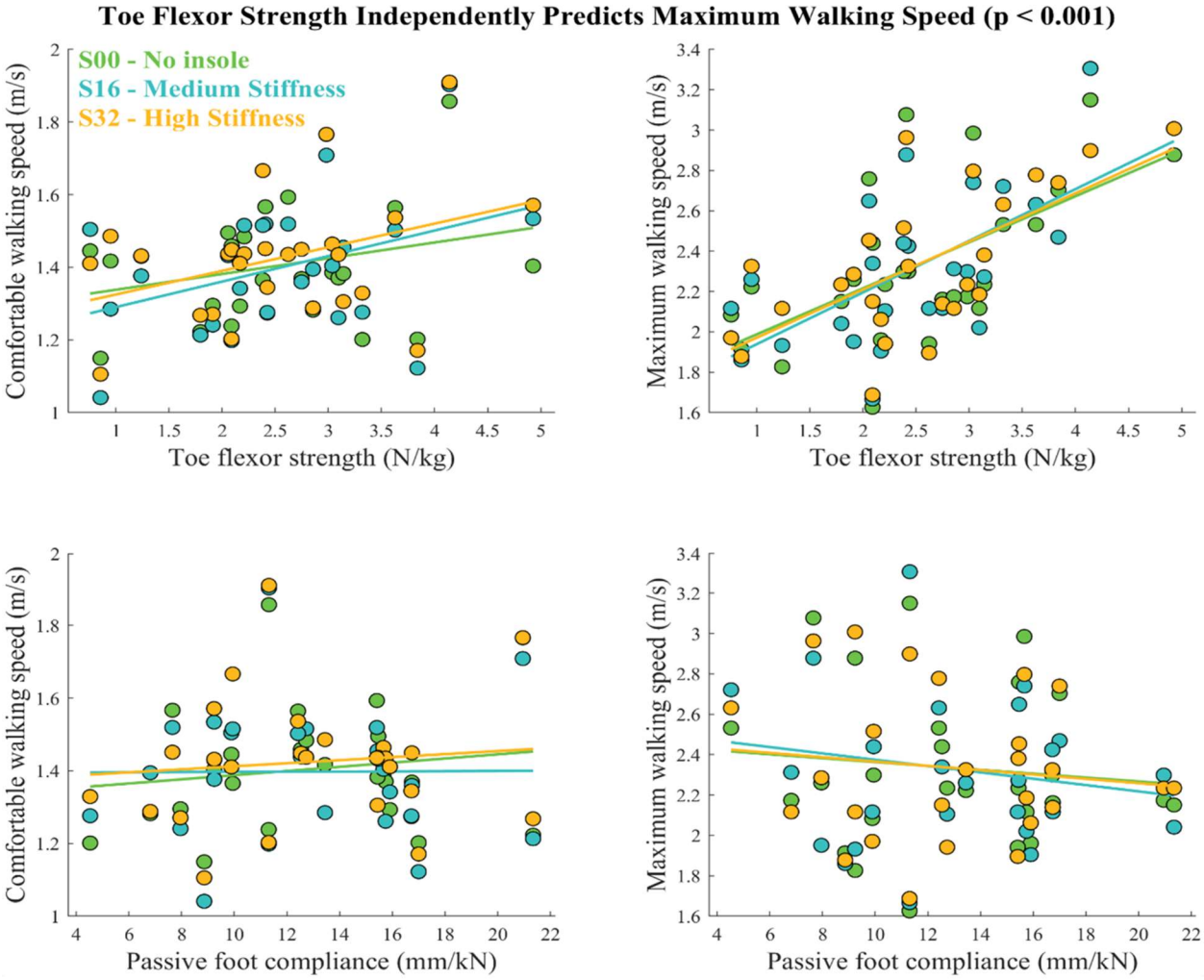


Figure 1. A Scatterplot illustrates the modulating effect of toe flexor strength and passive foot compliance on comfortable and maximum walking speed across three footwear conditions (S00 (green), S16 (blue), S32 (yellow)). Solid lines indicate condition-specific linear fits.

References (Optional)

[1] Krupenevich *et al.*, J. Biomech., 2021; [2] Ray & Takahashi, Sci Rep, 2020; [3] White et al., J Appl Biomech, 2025; [4] Misu et al., J Neuroeng Rehabil., 2014; [5] Smith *et al.,* J. Biomech., In press.

Acknowledgements (Optional)

Supported by NIH-R01AR081287 and NIH-T32TR004394.

Session Category

Human Motion and Performance: Locomotion/Gait

P1-221

The Effects of Age on Multi-Segment Foot Joint Moments During Walking

Dr. Ross Smith PhD[1], Dr. Christopher Long MS[2], Dr. Jason Franz PhD[3], Dr. Kota Takahashi PhD[2]

[1]University of Memphis Lambuth, Jackson, TN, United States. [2]University of Utah, Salt Lake City, Utah, United States. [3]University of North Carolina at Chapel Hill, Chapel Hill, North Carolina, United States

Introduction

Walking speed and metabolic economy decline with age, largely due to reduced push-off from ankle muscle–tendon units [1]. Recent work indicates walking push-off is further subverted by increased net energy dissipation at the foot in older adults, especially at faster or uphill speeds [2], potentially reflecting altered foot joint kinetics. We therefore investigated peak midtarsal (MT) and metatarsophalangeal (MTP) moments and early (0–50%) and late (51–100%) stance impulse during decline, level, and incline walking in younger and older adults (YA, OA). Prior work indicates MT moments align temporally with positive foot work and MTP moments with negative foot work; thus, we hypothesized that OA would exhibit smaller sagittal MT peaks and late-stance impulse and larger sagittal MTP peaks and early-stance impulse across slopes.

Methods

26 YA (24 y) and 19 OA (70 y) walked barefoot at 1.2 m/s on an instrumented treadmill at 5° decline, 5° incline, and level conditions. We calculated net internal joint moments for the MT and MTP joints using inverse dynamics and joint impulse as each moment's metric integral. For each participant, twenty steps from both feet were averaged and analyzed. Two-way ANOVAs assessed age and condition effects. Significant interactions were further assessed with estimated marginal means.

Results

Peak moments and impulse increased with steeper slopes ($p<.001$). Peak MT moments showed a significant interaction ($p < .001$), driven by a nonsignificant trend for YA to increase MT moment more than OA when walking uphill (trend: $p = .071$, $d = 0.57$). Late MT impulse also showed an interaction ($p<.001$) but without age differences at any slope. Older adults produced greater early MT impulse overall ($p=.049$), driven by level walking ($p=.048$). No age effects or trends were observed for the MTP joint.

Discussion

Age-related differences in MT kinetics were present during level walking, but most apparent during incline walking, which may explain previously reported gait propulsion deficits in older adults. The strength of effects shown here indicate structures not captured by inverse dynamics likely contribute to age-related changes in foot energetics.

Images (Optional)

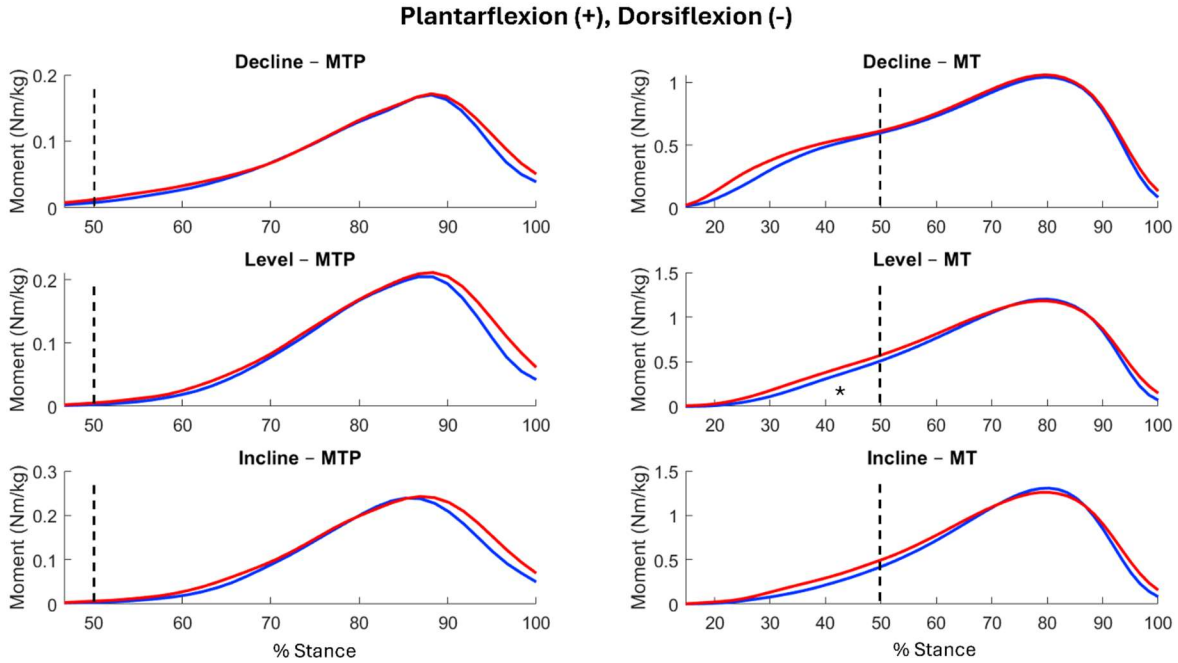


Figure 1. Group midtarsal (MT) and metatarsophalangeal (MTP) moments during decline, level, and incline walking for younger (blue) and older (red) adults. Moments were normalized to body mass and shown as percent stance. Vertical dotted lines represent mid-stance. * indicates early-phase impulse age effect.

References (Optional)

1. Franz, ESSR, 2016

2. Krupenevich *et al*. J Biomechanics, 2021

Session Category

Human Motion and Performance: Locomotion/Gait

P1-222

A Study on Human Gait Adaptation on Vertically Vibrating Surfaces

Miss Ruijie Fan

Newcastle University, Newcastle, Tyne and wear, United Kingdom

Introduction

While human bipedal locomotion evolved on stable terrain, modern environments often require walking on oscillating or deformable support surfaces. Continuous external perturbations from such surfaces increase the difficulty of balance control, necessitating constant adaptive adjustments throughout the gait cycle. Existing studies are often limited to single scenarios with scattered evidence, and a systematic understanding of human gait adaptation mechanisms in varying dynamic environments remains lacking. This study investigates gait adjustment strategies during walking under different vertical vibration conditions to systematically explore human response patterns to external vertical perturbations.

Methods

Fourteen healthy adults performed walking tasks on a treadmill mounted on a vertical vibration platform while wearing a 39-marker motion capture system. The experimental design included two acceleration levels (0.5 and 2.0 m/s^2) and three vibration frequencies relative to the individual's preferred step frequency (PSF) (0.9×, 1.1×, and 2.0× PSF). Whole-body kinematic data were recorded using a 3D motion capture system to calculate joint angles and spatiotemporal gait parameters. Statistical Parametric Mapping (SPM) and multiple comparison corrections were employed to compare each experimental condition against the baseline static walking condition.

Results

Results indicated that the displacement amplitude of the support surface was the dominant factor affecting gait behaviour. Under the low acceleration condition $0.5m/s^2$, participants adapted to vibrations primarily through rhythmic adjustments at the lower limb joint level, particularly at 0.9× and 2.0× PSF. These adjustments mainly manifested as subtle temporal changes in the hip and knee joints to maintain the intrinsic gait rhythm. Notably, the 1.1× PSF vibration condition did not induce significant gait changes under

either acceleration level, suggesting that gait remains relatively stable when the external vibration frequency approaches the human preferred step frequency.

Discussion

This study demonstrates highly selective gait synchronization to vertical vibration. Weaker vibration conditions allow individuals to maintain their natural step frequency, relying more on inertial motor control strategies to preserve stability. Furthermore, gait exhibited stronger adaptability to driving frequencies higher than the natural step frequency. These findings provide a basis for understanding whole-body coordination mechanisms and offer potential value for establishing structural vibration limits and assessing fall risks in dynamic environments

Session Category

Human Motion and Performance: Locomotion/Gait

P1-223

Evaluation of Center of Pressure Trajectories in XSensor Insoles

Ms. Sakura Herron, Ms. Chelsea Maynard, Dr. Cherice Hill

University of Rochester, Rochester, NY, United States

Introduction

The study of biomechanics is used to inform injury and disease prevention, clinical care, and athletic performance. As the use of this data continues to grow, ensuring its broad accessibility becomes increasingly important. Movement kinetics are commonly captured using force plates within gait lab settings, but in-shoe pressure insoles such as the XSENSOR X4 system have shown potential to enhance practical application and accessibility. Building on previous work validating the XSENSOR X4's force estimations during dynamic tasks, the aim of this study was to compare the center of pressure (COP) trajectories between the insoles and force plates.

Methods

30 participants completed walking and jogging tasks across an embedded force plate walkway while wearing shoes containing the XSENSOR X4 high resolution insoles. 128 walking and 116 jogging stance phases were extracted for pairwise comparison. COP excursions in the medial-lateral (ML) and anterior-posterior (AP) direction were compared between the force plates and insoles using paired t-tests in SPSS and Bland-Altman analyses in MATLAB (α=0.05).

Results

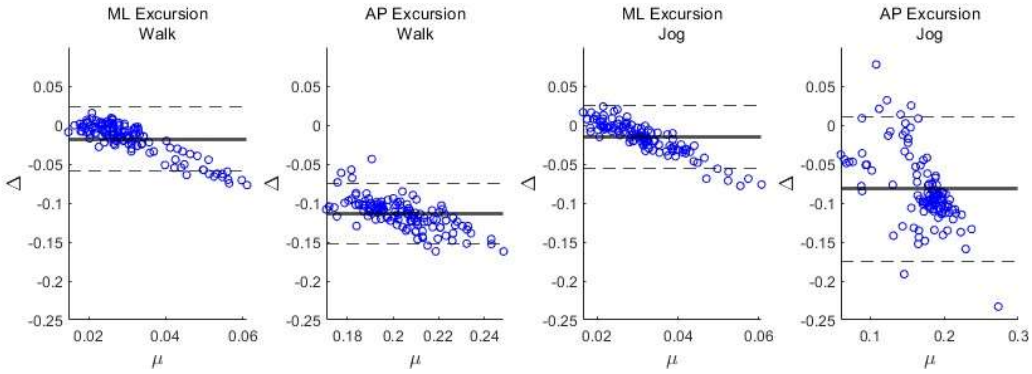
The XSENSOR insoles consistently produced shorter COP trajectories in the ML and AP directions in both tasks compared to the force plates ($p<0.001$, d: 0.74-5.83). The methodological biases were consistent across tasks. Excursion biases were smaller in the ML direction, although biases were proportionally similar considering greater AP excursion; most but not all data fell within 95% confidence intervals.

Discussion

COP trajectories measured by the insoles are shorter in both directions than those measured by force plates. While force plates capture contact between the shoe and ground, in-shoe insoles capture contact between the foot and shoe. This difference likely accounts for some of the observed biases, although additional systematic error may be present. Differences in COP trajectories should be considered when interpreting insole data compared to force plate data and when determining appropriate use cases. : The

significance of this study lies in its potential to enhance the practical application and accessibility of biomechanics research. Findings of this study demonstrate that XSENSOR Intelligent Insoles have the potential to provide a force plate alternative, given that systematic biases do not impact the question of interest.

Images (Optional)



Session Category

Human Motion and Performance: Locomotion/Gait

P1-224

Use of the Roll-Step Marching Style Gait Reduces Ground Reaction Forces at Impact

Miss Sarah Hofecker BS, Dr. Jean McCrory PhD

West Virginia University, Morgantown, WV, United States

Miss Sarah Hofecker

Introduction

The roll-step is used by members of marching bands theoretically to reduce impact load and prevent it from disputing the instrumental tone. The roll-step technique is completed by taking shorter strides and striking the ground with the heel, then rolling forward while distributing weight onto the lateral aspect of the foot until the toe hits the ground. The purpose of our study was to compare ground reaction forces (GRFs) in band members performing normal-walking and the roll-step technique.

Methods

Twenty-eight healthy experienced band members participated. After consent, subjects practiced walking at a comfortable pace through timing gates to determine average speed. GRFs were collected (1000Hz) while the band member walked at their average±5% speed in each technique. The order of conditions was randomized with three trials collected per condition. Outcome variables in the vertical forces were stance time, impact and active peaks, time to impact peak, vertical average loading rate (VALR), vertical instantaneous max loading rate (VILR), and impulse. In the shear forces, braking and propulsive peaks and impulses were calculated, as well as medial and lateral force peaks. An ANOVA was used to compare between normal and roll-step conditions (α=0.05).

Results

Data and statistical results are provided in Table 1. Speed was not different between conditions. Stance time was less in the roll-step condition. Impact peak force was lower when using the roll-step, although VIRL was greater, when compared to normal-gait. No differences were noted in VALR, active peak, and vertical impulse between conditions. In the shear forces, braking and propulsive AP peaks and medial peak were larger in normal-gait, but the lateral peak force was larger in the roll-step technique.

Discussion

As hypothesized, vertical impact force was reduced in the roll-step condition. Anteroposterior forces were also lower when using the roll-step, likely due to the shorter step length. The lateral forces were greater in the roll-step condition; however, they were only 5% BW. On-going research includes an inverse dynamics assessment of both conditions to determine if the roll-step also reduces lower extremity compressive forces at impact. If so, this may have clinical relevance for patients with lower extremity joint pain.

Images (Optional)

Table 1: Ground Reaction Forces Measures in the Roll-Step and Normal Gait Conditions

Variable	Roll-Step	Normal-Gait	p-value
Speed (m/s)	2.61 ± 0.33	2.63 ± 0.34	0.746
*Stance Time (s)	0.70 ± 0.07	0.72 ± 0.07	0.036
*Impact Peak (BW)	0.99 ± 0.08	1.03 ± 0.07	0.006
*Impact Peak Time (s)	0.21 ± 0.11	0.17 ± 0.04	0.005
VALR ($BW \cdot s^{-1}$)	7.09 ± 5.28	6.48 ± 2.62	0.344
*VILR ($BW \cdot s^{-1}$)	19.42 ± 7.44	16.24 ± 6.32	0.003
Active Peak (BW)	1.10 ± 0.07	1.11 ± 0.07	0.398
Impulse (BW·s)	0.56 ± 0.06	0.57 ± 0.05	0.310
*Braking Peak (BW)	0.14 ± 0.05	0.15 ± 0.04	0.005
*Braking Impulse (BW·s)	0.02 ± 0.01	0.03 ± 0.01	0.001
*Propulsive Peak (BW)	-0.18 ± 0.04	-0.21 ± 0.03	0.001
*Propulsive Impulse (BW·s)	-0.02 ± 0.01	-0.03 ± 0.01	0.001
*Lateral Peak (BW)	0.05 ± 0.02	0.04 ± 0.02	0.001
*Medial Peak (BW)	-0.06 ± 0.02	-0.07 ± 0.02	0.026

* Statistically significant difference between conditions

Session Category

Human Motion and Performance: Locomotion/Gait

P1-225

ANKLE JOINT INDEX AND HIP POWER CHANGES WITH INCREASING FOOTPLATE STIFFNESS

Ms. Sarah Overby[1], Dr. Adrienne Henderson[2], Dr. Dustin Bruening[2], Dr. Elisa Arch[1]

[1]University of Delaware, Newark, DE, United States. [2]Brigham Young University, Provo, UT, United States

Introduction

Joints perform distinct functions during gait, which can be described using Functional Joint Indices (FJI) that determine percentages of each joint's spring, motor, damper, and strut-like behavior[1]. FJI may aid in examining how assistive devices impact each joint's functional roles. Post-stroke, individuals commonly have reduced propulsion during walking due to plantar flexor weakness, demonstrated by a decrease in the ankle's motor role[2]. We are investigating if deformable foot orthoses (DFOs) can improve post-stroke gait by storing energy during late stance toe dorsiflexion and returning energy to improve ankle-foot energetics, including the ankle's motor role. This may reduce compensatory mechanisms at other lower limb joints, improving overall gait. This study aims to determine whether varying DFO stiffness impacted the ankle's FJI and, if so, whether other joints are affected.

Methods

Four stroke survivors walked on an instrumented treadmill under four conditions: No DFO, and three DFOs with different stiffnesses (5-ply, 7-ply, 9-ply). All trials were conducted at participant's self-selected speed, determined via a 10-meter walk test. Six degree-of-freedom kinematics and kinetic data were collected. Ankle FJI[1] and lower extremity kinematics and kinetics were calculated.

Results

Three participants showed little changes across conditions. However, for Participant 1, the ankle's motor-like behavior doubled while walking with the 7-ply and 9-ply DFOs compared to No DFO and 5-ply DFO. Late stance hip power showed a small, concomitant decrease in the 7-ply and 9-ply conditions.

Discussion

While data are preliminary, DFO use showed potential in impacting the ankle's functional role and, potentially, higher-level joint compensations in one participant. For slow gait

(0.995m/s), normalized hip powers are around 0.4w/kg in late stance[3]. For this participant (1.02m/s) while using the two stiffest DFOs, normalized late stance hip powers decrease from near 0.5w/kg to 0.35w/kg while doubling ankle motor-like behavior. This may signify improved propulsion at the ankle and reduced hip "pull-off" commonly observed post-stroke. Future work should investigate if positive impacts are seen in additional participants post-stroke, potentially with a wider range of DFO stiffnesses. Impacting FJI and joint kinetics for 25% of post-stroke participants is promising and warrants further investigation.

Images (Optional)

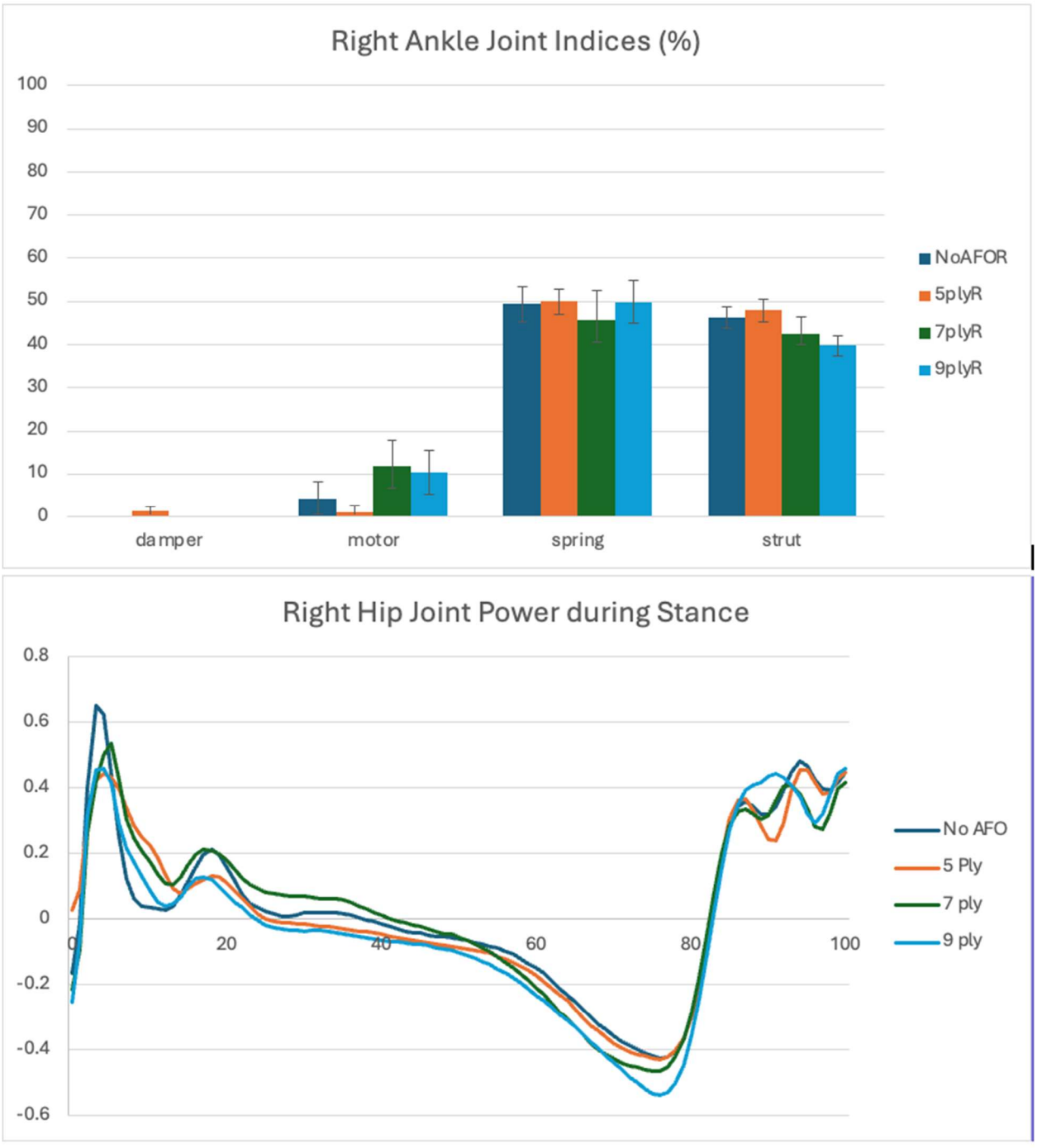


Figure 1. Participant 1's data for paretic limb. (Top) Ankle joint indices as percentage with standard error bars. (Bottom) Hip power throughout the stance phase for the same participant.

References (Optional)

[1]Qiao, 2016

[2]Nadeau, 1997

[3]Winters, 1987

Session Category

Human Motion and Performance: Locomotion/Gait

P1-226

Virtual Neuromuscular Ankle Exoskeleton Control Provides Speed-Adaptive Gait Assistance Without High-Level Modulation

Mr. Rish Rastogi M.Eng[1], Dr. Max Shepherd PhD[1,2], Dr. Seungmoon Song PhD[3]

[1]Department of Mechanical & Industrial Engineering, College of Engineering, Northeastern University, Boston, MA, United States. [2]Department of Physical Therapy, Movement, & Rehabilitation Sciences, Bouvé College of Health Sciences, Northeastern University University Department of, Boston, MA, United States. [3]Department of Mechanical & Industrial Engineering, College of Engineering, Northeastern UniversityUniversity Department of Mechanical and Industrial Engineering, College of Engineering, Boston, MA, United States

Introduction

Lower-limb exoskeletons promise to augment user mobility. However, their controllers often struggle in non-steady-state conditions. **Phase-based control (PBC)** applies torque based on predicted gait phase and can reduce the metabolic cost of transport [1], but may be ineffective or even unsafe when phase estimation is inaccurate, for instance during abrupt speed changes. A higher-level data-driven model can improve phase prediction [2], however it is unclear whether such a **machine learning estimator (MLE)** generalizes to conditions it was not trained on.

Methods

We propose **virtual neuromuscular control (VNMC)** as an alternate approach. VNMC emulates a reflex-based human locomotion model [3] by driving a virtual muscle with encoder-derived ankle kinematics to generate a virtual torque. This torque is then scaled and applied to the exoskeleton, with no need for gait phase estimation. Healthy young adults (n=10) walked through abrupt speed changes on a treadmill (B) while wearing powered ankle exoskeletons controlled in zero torque mode, PBC, VNMC, and MLE. To evaluate controller adaptability, we introduced a metric that quantifies how much the relative timing of delivered assistance during speed changes deviates from steady-state assistance.

Results

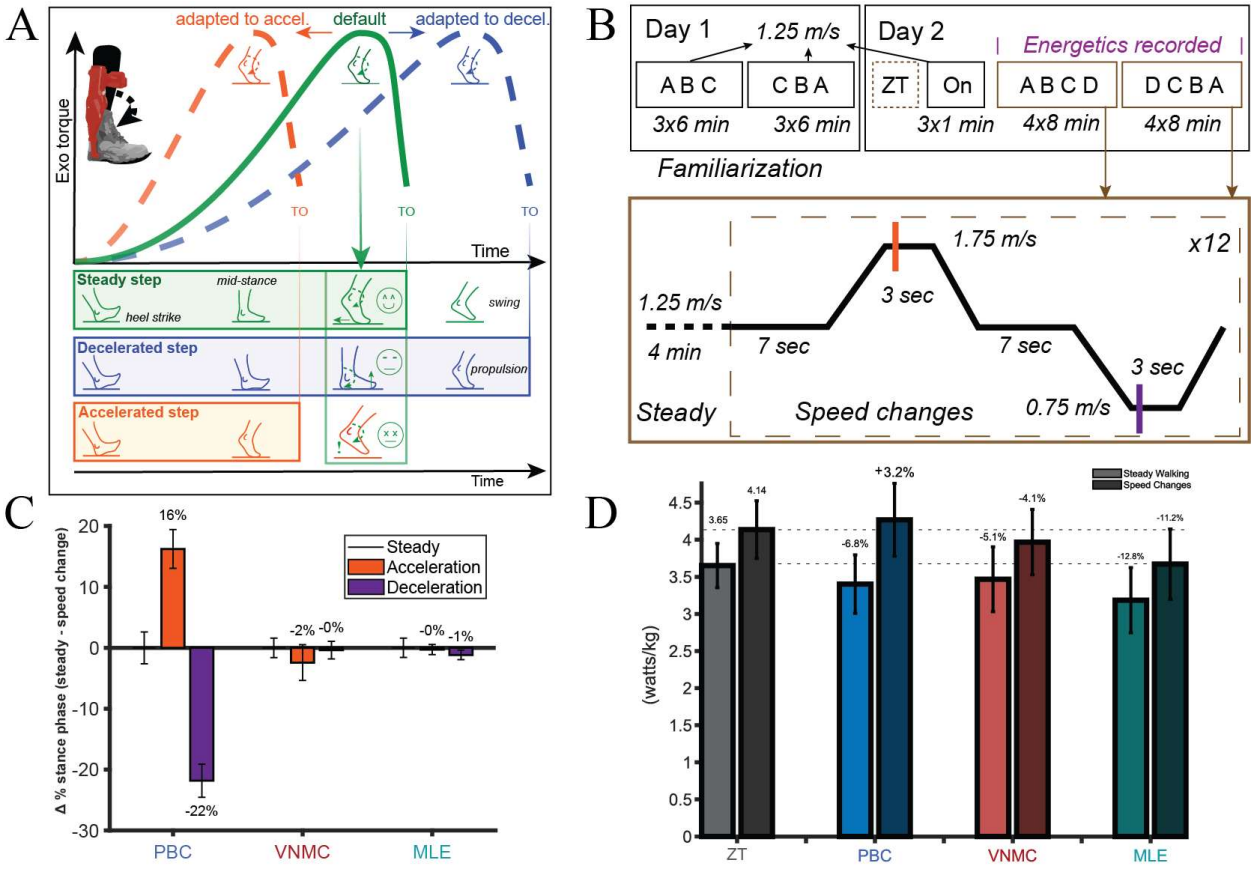
Both VNMC and MLE adapted to users during abrupt speed changes while PBC did not (C). On average, PBC deviated by **16%** ($p<0.01$) during accelerations and **22%** ($p<0.01$) during decelerations, whereas both VNMC and MLE adapted well (≤2%). While PBC, VNMC, and MLE reduced metabolic cost of transport by **6.8%**, **5.1%**, **13.8%** ($p<0.05$) in steady

walking compared to zero torque, **only PBC did not save energy during speed changes** (p<0.01) (D).

Discussion

These results highlight the importance of controller adaptability in augmenting user mobility, demonstrate VNMC's speed-adaptive nature, and support data-driven high-level control. Pairing the last with VNMC could enable the combined system to generalize beyond the machine learning model's out-of-distribution conditions because the low-level controller itself is robust. By evaluating lower-limb exoskeletons in non-steady-state conditions in the lab, we take one step closer to making exoskeletons viable in the real world.

Images (Optional)



References (Optional)

[1] Katherine Poggensee & Steve Collins, Sci Rob, 2021; [2] Pavan Shetty *et al.*, IEEE Rob. Auto. Lett., 2025; [3] Seungmoon Song & Hartmut Geyer, J Physiol, 2015

Acknowledgements (Optional)

This research is partially funded by the National Institutes of Health (R00AG065524).

Session Category

Human Motion and Performance: Locomotion/Gait

P1-227

Does PD-AFO deformation affect the mechanical cost of walking for individuals post-stroke?

Mrs. Shay Pinhey, Dr. Darcy Reisman, Dr. Elisa Arch

University of Delaware, Newark, DE, United States

Introduction

Passive-dynamic ankle-foot orthoses (PD-AFOs) can help improve cost of walking for some individuals post-stroke, but results are inconsistent [1]. This inconsistency may be because some do not appropriately engage the PD-AFO to reap its expected energetic benefits. This study's purpose was to examine if a relationship exists between degree of PD-AFO engagement and mechanical cost of transport (COT) for individuals post-stroke using a PD-AFO. If such relationship exists, future interventions could target PD-AFO engagement to increase the number of individuals post-stroke who experience the PD-AFO's energetic benefits.

Methods

17 chronic stroke participants (9F, Mass: 83.6±20.2kg, Height: 1.7±0.1m, Age: 65.9±6.4yrs, Time Since Stroke: 10.4±5.6yrs) completed the protocol so far. Participants were fit to a PD-AFO, acclimated to the PD-AFO, then completed 10-meter walk tests to determine self-selected walking speed (SSWS). Participants walked on an instrumented treadmill while 6 degree-of-freedom kinematics and kinetics were recorded. Markers were placed on the PD-AFO cuff to track deformation.

PD-AFO deformation was calculated as the peak dorsiflexion angle between the foot and PD-AFO segments during stance. COT was calculated as the sum of positive and absolute value of negative work at all lower limb joints normalized by mass and stride length. A linear regression model was run to analyze the association between COT and PD-AFO deformation when controlling for SSWS.

Results

Table 1 shows COT, PD-AFO deformation, and SSWS for each participant. Linear regression showed that PD-AFO deformation did not significantly predict COT when accounting for SSWS (R^2=0.169, F(17,14)=1.42, p=0.274). However, notably, one participant never dorsiflexed the PD-AFO (negative deformation) and had the highest COT. Additionally, data followed a visual trend that COT decreases as PD-AFO deformation increases.

Discussion

Results indicate that PD-AFO deformation is not significantly related to COT for individuals post-stroke when accounting for SSWS. We will determine if a relationship emerges with additional participants (being recruited). Understanding the effect of PD-AFO deformation on COT is an important step in determining which factors of PD-AFO use are important for improving walking energetics and ultimately improving community ambulation and quality of life for individuals post-stroke.

Images (Optional)

Table 1: PD-AFO deformation, self-selected walking speed, and cost of transport for all participants collected so far.

Subject	PD-AFO Deformation (degrees)	Self-selected Walking Speed (m/s)	Cost of Transport (J/kg/m)
1	14.5 ± 1.7	1.05	2.50 ± 0.09
2	16.2 ± 1.1	1.22	3.01 ± 0.07
3	15.8 ± 1.0	0.95	2.37 ± 0.12
4	13.4 ± 0.4	0.57	2.42 ± 0.12
5	21.9 ± 0.6	0.79	2.30 ± 0.08
6	-4.3 ± 0.6	0.22	3.23 ± 0.26
7	10.2 ± 0.9	0.49	2.69 ± 0.14
8	18.6 ± 0.2	0.97	1.42 ± 0.06
9	14.6 ± 0.9	0.47	2.32 ± 0.14
10	15.6 ± 0.7	0.98	2.63 ± 0.09
11	13.1 ± 0.3	0.89	1.58 ± 0.06
12	13.2 ± 0.6	1.11	1.91 ± 0.04
13	11.0 ± 0.5	0.89	1.61 ± 0.06
14	19.3 ± 0.6	0.60	1.98 ± 0.09
15	13.9 ± 1.0	0.31	1.89 ± 0.15
16	9.5 ± 0.9	0.50	1.99 ± 0.05
17	15.3 ± 0.6	1.73	2.28 ± 0.04

References (Optional)

[1] Skigen et al., *JNeuroEngineeringRehabil.*, 2024

Acknowledgements (Optional)

This work was supported by USAMRAA through the Orthotics & Prosthetics Outcomes Research Program under Award No. HT94252310106. Opinion, interpretations, conclusions, and recommendations are those of the author and not necessarily endorsed by USAMRAA.

Session Category

Human Motion and Performance: Locomotion/Gait

P1-228

Gait Kinematic Variability for Osteoarthritis Classification

Ms Eleonora Lubisco[1,2], Dr Marc G.Leguia[3], Dr Laura Tio[4], MD Jordi Monfort[4,5], Dr Ana Filipa Durão[2], Dr Simone Tassani[2]

[1]Alma Mater Studiorum, Bologna, Emilia-Romagna, Italy. [2]Universitat Pompeu Fabra, Barcelona, Catalunya, Spain. [3]Barcelona Supercomputing Center, Barcelona, Catalunya, Spain. [4]Hospital del Mar Research Institute, Inflammation and Cartilage Research Group, Barcelona, Catalunya, Spain. [5]Hospital del Mar, Rheumatology service, Barcelona, Catalunya, Spain

Ms Eleonora Lubisco

Introduction

Knee osteoarthritis is a degenerative condition affecting over 7% of the global population [1], resulting in the progressive deterioration of knee cartilage, leading to pain and reduced mobility. Despite the condition's prevalence, the choice between surgery and conservative treatments still relies on clinical and radiological evaluation and the surgeon's experience. Since osteoarthritis affects gait kinematics [2], this study aims to examine whether variability in parameters could distinguish patients and support clinicians in their decision-making.

Methods

Eighty-six patients with osteoarthritis (KL grade 2–3) were divided into two groups according to the suggested future treatment: conservative or total knee replacement (TKR). Gait kinematics were recorded through a motion-capture system, focusing on key parameters such as pelvis tilt, knee and hip flexion/extension [3]. The analysis employed Dynamic Time Warping (DTW), which enables robust comparison of time-series gait signals [4].

For the inter-patient analysis, a DTW Barycenter Averaging (DBA) signal was computed for each patient as their representative gait pattern, then compared across all subjects to build a distance matrix from which the mean and standard deviation of distances were extracted.

The intra-patient analysis measured individual gait variability using DTW on repeated cycles. Group differences were evaluated with a student's t-test, and binary logistic regression assessed classification performance.

Results

The conservative group showed low variability across subjects, whereas the TKR group exhibited markedly higher dissimilarity in all gait signals, except one, both in inter- and intra-patient analysis.

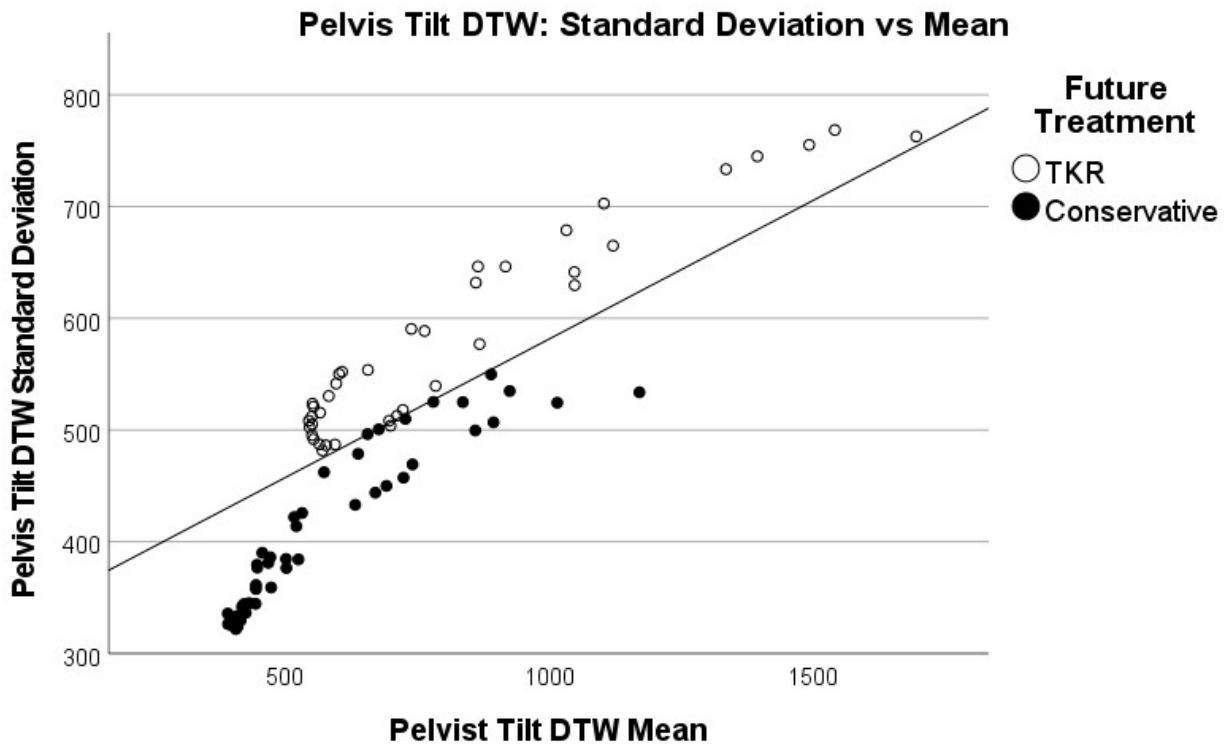
Intra-patient analysis results were significant for all parameters, especially pelvic tilt, with a p-value of 10^{-5}.

The average DTW distance and its standard deviation for pelvis tilt were sufficient to correctly classify 97.7% of the subjects (2 errors out of 86 subjects—see figure).

Discussion

The study identified clear and statistically significant gait differences between conservative and TKR patients. Pelvic tilt emerged as the most informative parameter, demonstrating strong discriminative power. The DTW-based transformation suggests the potential to build an objective decision-support model, although further validation is required for clinical application

Images (Optional)



References (Optional)

[1] J.Steinmetz et.al, National Institute of Health, 2021

[2] J.A.Zeni et.al, National Library of Medicine, 2012

[3] S.Tassani et.al, ESB, 2024

[4] F.Petitjean et.al, ELSEVIER, 2011

Acknowledgements (Optional)

The funding sources for this work were obtained from the Spanish Government (STRATO PID2021-126469OB-C21)

Session Category

Human Motion and Performance: Locomotion/Gait

P1-229

AMP: An Automated Pipeline for Marker Label Correction and Gap Filling in Motion Capture Data

Mr. Sixu Zhou, Mr. Ryan Casey, Mr. Joseph Walter, Dr. Aaron Young

Georgia Institute of Technology, Atlanta, Georgia, United States

Introduction

Marker-based optical motion capture (MoCap) is a fundamental tool in biomechanics and widely used for investigating animal or human locomotion such as biomechanical modeling and gait analysis [1]. The recorded trajectories of the markers are then used to compute joint inverse kinematics and inverse dynamics. Processing marker-based MoCap data is commonly challenging from marker tracking errors such as mislabeling, occlusion, or trajectory discontinuities shown in Fig 1A [2]. These distortions require a substantial amount of manual post-processing time and efforts from human experts. Previous studies have developed automated approaches to reduce manual interventions using deep learning techniques to gap fill the missing markers. However, there is no solution to provide a fully automated mocap processing workflow. Thus, we present an automated mocap processing pipeline (AMP) that determines the correctness of the marker labels, fixes the incorrect labels, and fills the missing marker trajectories using analytical methods. We tested the hypothesis that the AMP pipeline would reduce the processing time without human interventions compared to manual processing.

Methods

The AMP pipeline used three different approaches to infer the marker labels including using rigid body geometry, the Kalman Filter, or the patterns of the adjacent markers shown in Fig 1B. One trained human expert processed a sample trial that contains marker mislabels, swaps, jumps, drops, and missing marker trajectories using both the AMP pipeline and standard manual procedures. The processing time was evaluated in these two conditions.

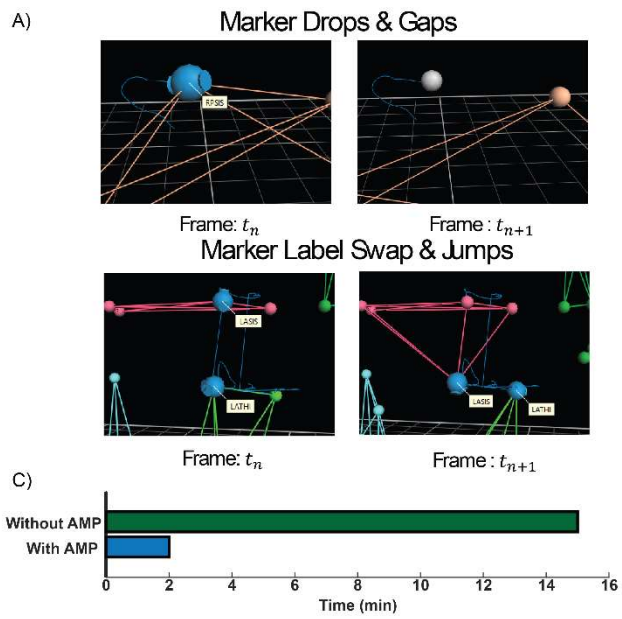
Results

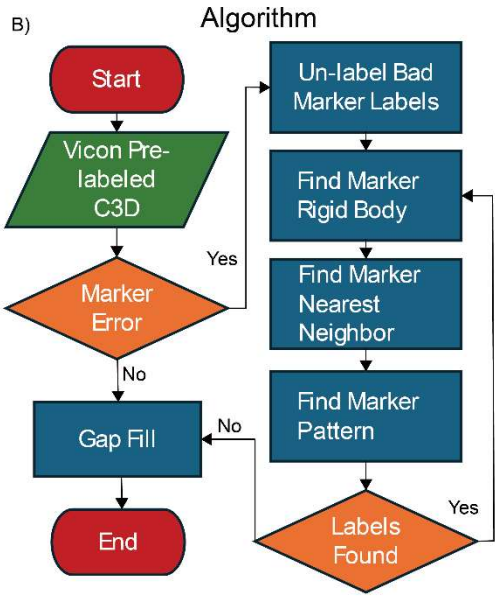
As shown in Fig 1C, the typical manual processing of a 1000-frame trial took around 15mins of manual time from an expert to fix the labels and fills the gaps while the AMP took only 2mins while maintaining the same accuracy, therefore allowing us to accept the hypothesis.

Discussion

The AMP enables a fully automated and transparent processing workflow for marker-based MoCap by simultaneously addressing mislabeling, trajectory jumps, and gap filling. The pipeline also used analytical methods without requiring any pre-trained models for applications. It substantially reduced manual processing time and showed the potential to be utilized across large biomechanics datasets.

Images (Optional)





References (Optional)

[1] A. Seth *et al.*, *PLOS Comput,* 2018

[2] P. Skurowski and M. Pawlyta., *Sensors*, 2022

Acknowledgements (Optional)

This work is sponsored by Ossur

Session Category

Human Motion and Performance: Locomotion/Gait

P1-230

Advancing a Shank-Worn Single-Sensor Approach for Measuring Stride Length in the Real World

Mr Spencer Miller[1], Mr Julien Mihy[2], Ms. Mayumi Wagatsuma[2], Dr. Jocelyn Hafer[2], Dr. Stephen Cain[1]

[1]West Virginia University, Morgantown, WV, United States. [2]Univeristy of Delaware, Newark, DE, United States

Introduction

Real-world gait analysis has become a popular approach as sensor technology and algorithms improve. Foot-mounted inertial sensors (IMU) can enable highly accurate calculations of spatiotemporal metrics using the zero-velocity-update (ZUPT) approach, which utilizes the fact that the velocity of the foot is approximately zero when the foot is on the ground. However, a foot sensor is often removed throughout the day resulting in incomplete data capture. To combat this issue, we developed a single-sensor-based approach using a shank-mounted sensor with a novel correction factor to limit the consistent underestimation of stride length when calculated from a shank sensor inertial data.

Methods

Using data from our IRB-approved study, we analyzed data from five participants, two with symptoms matching ACR clinical criteria for medial compartment knee osteoarthritis and three healthy controls. Participants wore a total of five IMUs for three consecutive days. The minimum shank angular velocity during stance defined midstance points, which were used as the start and end points of each stride. In our advanced approach, we integrate linear acceleration in a stride reference frame to calculate shank velocity and position, where we assume zero displacement in the medial-lateral direction, apply a ZUPT in the vertical direction, and apply a non-zero-velocity-update in the anterior-posterior direction using velocity estimates calculated from the angular velocity of the shank about a medial-lateral axis. In the standard shank approach, only a ZUPT is applied. Stride lengths were calculated using the change in position between midstance points using both our advanced and the standard approach and were compared to stride lengths calculated using ZUPT with foot IMU data (real-world gold-standard).

Results

Our advanced approach improves upon the standard approach by decreasing differences in stride length from -0.239±0.37m (mean±stdev) to -0.112±0.236m (Fig1). Our approach works differently depending on the participant and the terrain they walked during data collection, but in all cases improves stride length estimates compared to the standard method.

Discussion

Our approach enables accurate stride length estimates from a shank-mounted IMU, which can improve participant compliance in long-duration data collections. Future work will implement additional corrections for gait when walking up slopes or stairs.

Images (Optional)

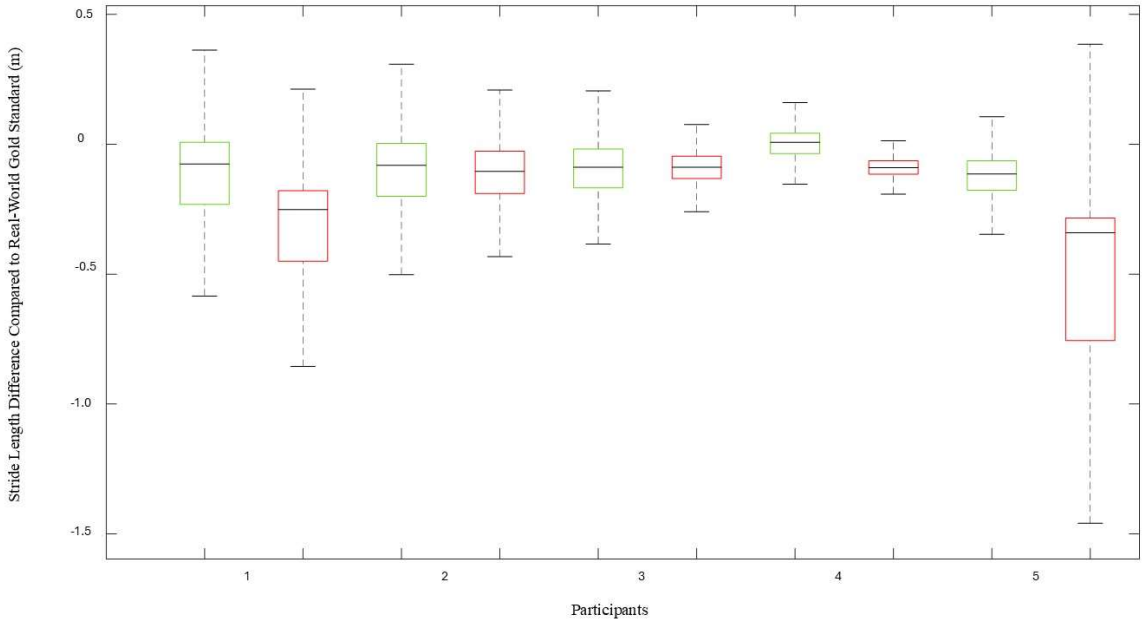


Figure 1. Differences between the standard shank-based approach for estimating stride length versus the gold-standard (red) and the advanced shank-based approach versus the gold standard (green) for all 10 participants.

Session Category

Human Motion and Performance: Locomotion/Gait

P1-231

Prolonged Standing-Induced Low Back Pain Developers Do Not Develop Low Back Pain after 45 Minutes of Walking

Ms. Stephanie Cotariu[1], Dr. Abigail Schmitt[1], Dr. Erika Nelson-Wong[2], Dr. Kaitlin Gallagher[1]

[1]University of Arkansas, Fayetteville, AR, United States. [2]Regis University, Denver, CO, United States

Introduction

Laboratory studies associate prolonged standing with low back pain (LBP), and walking breaks are beneficial for reducing standing-induced LBP. To date, it is unknown whether continuous walking, another upright task, would also elicit LBP in these individuals. Thus, this study sought to determine whether standing-induced LBP developers would also develop LBP after 45 minutes of continuous walking, and after a subsequent 30-minute standing bout.

Methods

Twenty-three adults (18-40 years) without LBP history completed two randomized testing days. On the Stand-Only day, participants stood for 75 minutes to determine their prolonged standing pain group. On the Walk-Stand Day, participants walked for 45 minutes, followed by 30 minutes of standing. Participants walked through a markerless motion capture system at 0 minutes, after 45 minutes of walking, and after 30 minutes of standing. Outcome measures were three-dimensional trunk-pelvis range of motion (ROM), trunk-pelvis vector coupling angle, and continuous relative phase deviation angles. Participants were considered pain developers (PD) if they had > 9mm increase in Visual Analog Scale (VAS) on the Stand-Only day. A McNemar's test was used to assess PD frequency on the Stand-Only and Walk-Stand days. Linear mixed-effects models were used with a between-factor of prolonged standing pain group, a repeated measure of time, and a covariate of speed.

Results

On the Stand-Only day, nine participants were classified as PDs after 75 minutes; eight reached the threshold after 45 minutes. On the Walk-Stand day, 22 of 23 participants were non-PDs after 45 minutes of walking (McNemar's test: p=.039 for 45 minutes of standing versus walking). There was a main effect of time on trunk-pelvis flexion-extension ROM (p<.001), which increased after prolonged walking and then returned to baseline following prolonged standing (see figure). There were no differences in the other outcome measures.

Discussion

LBP was not reported after 45 minutes of walking in all participants who reported standing-induced LBP. Cyclic movements in the lumbar region and observed changes in the flexion/extension angle with walking may be protective and shed light on mechanisms underlying standing-induced LBP. Future research will investigate the relationship between muscular activity and gait kinematics.

Images (Optional)

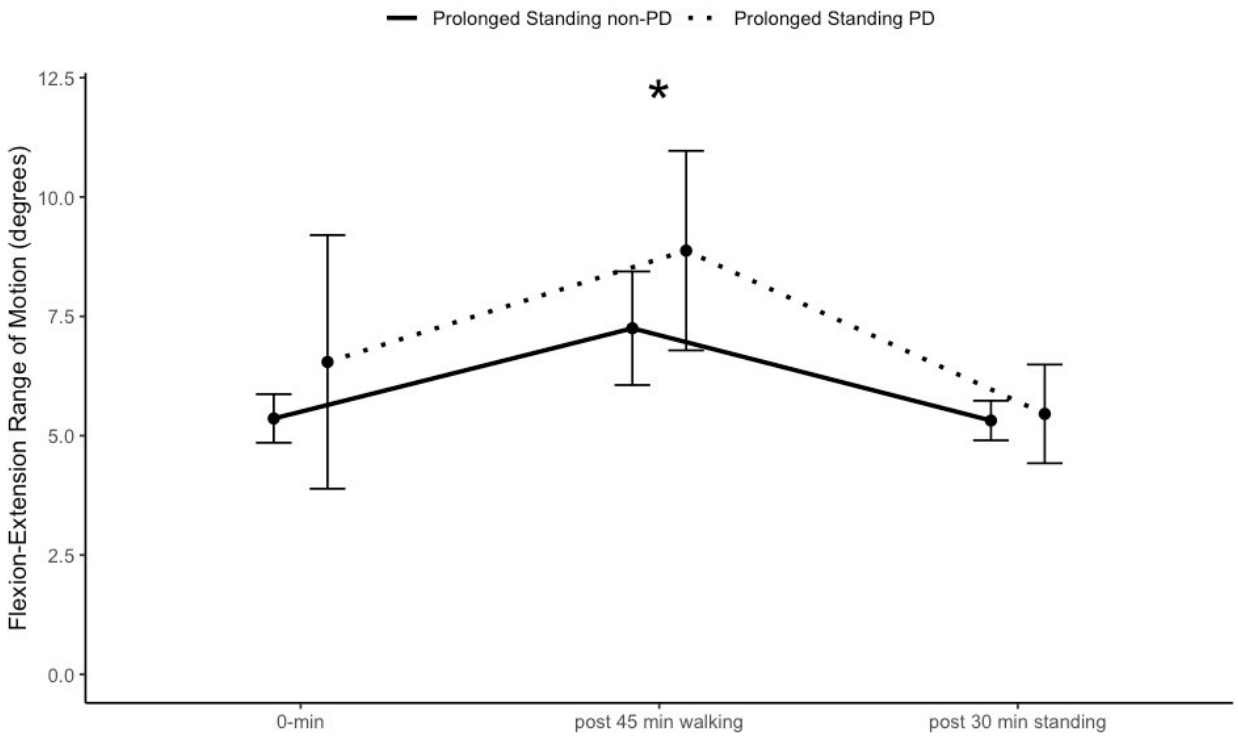


Figure. Flexion-extension range of motion when walking at the start of the trial after 45 minutes, and after standing for 30 minutes. Asterisk (*) denotes significant differences from other time points. Pain group was determined from the Stand-Only day. Data points are staggered to illustrate the full range of means and standard deviations

References (Optional)

Acknowledgements (Optional)

This project was funded by the University of Arkansas Honors College Research Grants and the Arkansas Department of Higher Education Student Undergraduate Research Fellowship.

Session Category

P1-232

Development of a Gait Pattern–Based Person Identification Algorithm under Various Footwear Conditions

Ms. Subin Kim[1], Ms. Yookyeong Sa[1], Prof. Gwanseob Shin[1], Prof. Seobin Choi[2]

[1]Ulsan National Institute of Science and Technology (UNIST), Ulsan, Ulsan, Korea, Republic of. [2]Incheon National University, Incheon, Incheon, Korea, Republic of

Introduction

Gait recognition technology has gained popularity in recent years due to its contactless nature. However, existing literature suffers from small samples and an over-reliance on either barefoot or single shoe types. As a result, current methods have failed to replicate the variability encountered in a real-world environment. Therefore, stable operation in varying environments is required. To address this, we sought to develop and test a Machine Learning-based algorithm for robust gait-based identification under varied footwear conditions, using large scale plantar pressure data of 50 subjects.

Methods

We recruited 50 healthy adults (25 males, 25 females) for the experiment. Gait data were collected using a Zebris FDM pressure mat on a 10-meter walkway. Subjects walked at their normal pace under four conditions: barefoot, running shoes (Asics Jog 100), sneakers (Vans Old Skool Low), and their own personal shoes. Five minutes of data was captured per condition. All data collected were subjected to noise removal, normalization, and sliding window preprocessing (window = 40 frames, overlap = 20 frames). Each window yielded 27 spatial and dynamic gait features to train a Random Forest classification model with optimized parameters.

Results

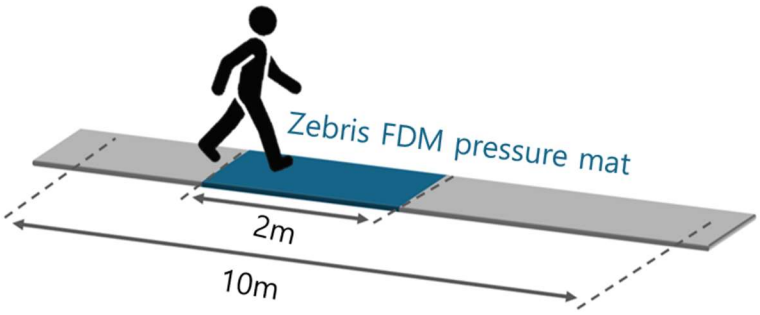
Integrated evaluation indicated that the proposed algorithm had a test accuracy of about 88.4%. The model optimization reduced the discrepancy between training and test accuracy to effectively prevent overfitting and ensure generalization. Feature importance analysis indicated that mean maximum pressure and Center of Pressure (CoP) are both key indicators. Furthermore, variables that are most strongly correlated with body weight also ranked high in importance, thus indicating that physical characteristics like weight significantly impact gait patterns.

Discussion

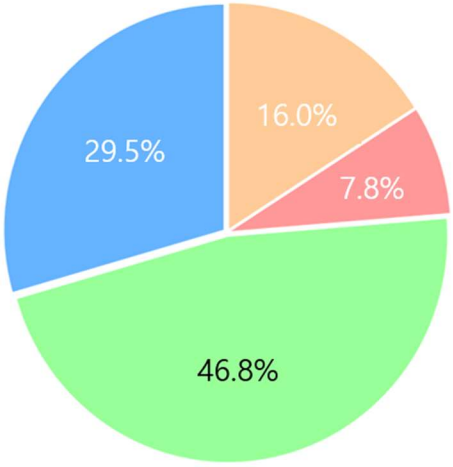
This study demonstrates the validity of plantar pressure-based gait characteristics for identification across different types of footwear in a population of 50 subjects. This is significant as prior studies were limited in their generalizability due to small sample sizes. Additionally, the results indicate that gait patterns are influenced by inherent physical traits; the application of the sliding window technique combined with an optimized model also effectively mitigated data variability. Overall, these results indicate that this methodology supports the development of effective biometric identification techniques, customized footwear design, and healthcare monitoring.

Images (Optional)

Experimental Environment



Feature Importance by Category



Top 3 Feature Importance

Rank	Feature	Importance	Type
1	max_acceleration	6.30 %	Spatial
2	max_window_force	6.19 %	Spatial
3	max_force	6.12 %	Dynamic

Acknowledgements (Optional)

This work was supported by Ulsan Metropolitan City, Korea

Session Category

Human Motion and Performance: Locomotion/Gait

P1-233

Knee Extensor Strength Correlates with Temporal Gait Parameters Derived from In-shoe Sensors in Older Women

Dr. Takuma Inai, Dr. Shoma Kudo, Dr. Wakako Tsuchida, Dr. Masahiro Fujimoto

Integrated Research Center for Self-Care Technology, National Institute of Advanced Industrial Science and Technology (AIST), Takamatsu City, Kagawa, Japan

Introduction

A decline in knee extensor strength in older women is linked to a higher risk of musculoskeletal disorders, such as knee osteoarthritis [1]. Regular assessment and maintenance of this strength are essential for disease prevention. Conventional methods (e.g., handheld dynamometers) require voluntary, sustained effort, which can be difficult for individuals with low health motivation. This study examined the relationships between knee extensor strength and force and temporal parameters measured using insole force sensors during walking. Clarifying these relationships may enable simple strength assessment by wearing sensor-equipped shoes in daily life.

Methods

Thirty-seven older women participated in the study (mean age: 78.1 ± 4.1 years). Each participant wore shoes equipped with insole force sensors (loadsol Pro, novel GmbH Inc.) and completed five round trips along a 15-m walkway at a comfortable speed. Vertical ground reaction force data were collected to calculate two force and 12 temporal parameters from 60 gait cycles per participant. Maximal isometric knee extensor strength was assessed using a Biodex System dynamometer. Each leg was tested three times, and the highest value for each leg was recorded. The mean of the right and left maximal values was then calculated for analysis. Correlation analyses were performed to examine the relationships between knee extensor strength and both force-related and temporal parameters.

Results

As shown in Table 1, knee extensor strength was significantly associated with the timing of the first peak of the vertical ground reaction force ($r = -0.58$, large), the percentage of the stance time ($r = -0.58$, large), and the percentage of the double stance time ($r = -0.59$, large).

Discussion

The findings of this study revealed that maximal knee extension strength is associated with the timing of the first peak of the vertical ground reaction force and with the percentages of stance time and double-stance time. These insights may contribute to the development of methods for evaluating and estimating maximal knee extension strength using data collected by insole force sensors during natural daily walking.

Images (Optional)

Table 1. Correlations between knee extensor strength and force and temporal parameters.

	Mean (SD)	p-value	r	Effect size	Interpretation
First peak of vGRF, N/kg	11.2 (1.2)	**0.0056**	0.45	0.45	Medium
Second peak of vGRF, N/kg	9.4 (0.7)	0.1322	-0.25	0.25	Small
Time at first peak of vGRF, sec	0.14 (0.02)	**0.0003**	-0.57	0.57	Large
Time at second peak of vGRF, sec	0.46 (0.03)	**0.0232**	-0.37	0.37	Medium
Timing of first peak of vGRF, %	14.5 (1.7)	**0.0002**	-0.58	0.58	Large
Timing of second peak of vGRF, %	47.0 (1.4)	**0.0244**	-0.37	0.37	Medium
Cadence, steps/min	123.2 (7.6)	0.1442	0.24	0.24	Small
Stride time, sec	0.98 (0.06)	0.1387	-0.25	0.25	Small
Stance time, sec	0.61 (0.05)	**0.0128**	-0.41	0.41	Medium
Swing time, sec	0.37 (0.02)	0.4217	0.14	0.14	Small
Double stance time, sec	0.11 (0.02)	**0.0003**	-0.56	0.56	Large
Stance time, % gait cycle	62.4 (1.6)	**0.0001**	-0.58	0.58	Large
Swing time, % gait cycle	37.6 (1.6)	**0.0001**	0.58	0.58	Large
Double stance time, % gait cycle	11.4 (1.5)	**0.0001**	-0.59	0.59	Large

Note: Bold values indicate $p < 0.05$. vGRF: Vertical ground reaction force.

References (Optional)

[1] Øiestad *et al.*, Osteoarthritis Cartilage, 2015

Session Category

Human Motion and Performance: Locomotion/Gait

P1-234

Dynamic Time Warping Reveals Unique Insight into Gait Symmetry Recovery Compared to Traditional Metrics in ACL-Injured Population

Scientist I Taliah Carlson MS, Assistant Professor Meredith Owen PhD, Associate Dean for Research Brian Noehren PT, PhD, FACSM

University of Kentucky, Lexington, Kentucky, United States

Introduction

Limb symmetry index (LSI) is utilized to help gauge recovery after an anterior cruciate ligament (ACL) injury; however, it only assesses a discrete time point of interlimb asymmetry during walking. LSI lacks temporal context, providing an incomplete and sometimes inaccurate measure of gait symmetry. In contrast, dynamic time warping (DTW) compares the full waveform, capturing differences in both shape and timing throughout stance. DTW may therefore provide more insight into interlimb coordination and recovery following ACL injury. To date, DTW has not yet been applied to assess knee moment symmetry in this population.

Methods

Sagittal-plane knee moments were analyzed from twenty unilateral ACL-injured participants across five standardized walking-speed steps. Data was time-normalized to 100% stance and average waveforms were compared between injured and contralateral limbs using DTW with a Sakoe-Chiba window (±12% stance, $\lambda = 0.05$). The local cost matrix, based on the absolute Euclidean difference between signals, quantified differences in waveform shape and timing. DTW normalized distance was measured as the average misfit per alignment step (raw distance/path length) to quantify waveform dissimilarity between limbs. Paired t-tests were used to compare differences between limbs at pre-surgery (PRE) and 6 months post-surgery (6MO). Pearson correlations were used to look at associations between variables.

Results

Statistical findings are summarized in Table 1.

Discussion

DTW and LSI captured different aspects of interlimb asymmetry early on following the ACL injury. Temporal symmetry (DTW) improved significantly by 6 months, indicating earlier

recovery of interlimb coordination, whereas magnitude symmetry (LSI) lagged, reflecting persistent underloading of the injured limb despite improved movement patterns shown by DTW. The strong association between DTW and late-stance peak timing at pre-surgery suggests early asymmetry was largely driven by temporal mismatches between limbs. By six months, DTW and LSI converged indicating that once coordination was recovering, both metrics reflected the same underlying asymmetry through different approaches. These findings demonstrate that coordination and magnitude recover on different timelines and that continuous waveform metrics, such as DTW, provide unique insight during early stages following injury when timing and waveform differences remain prominent.

Images (Optional)

Table 1. Paired t-tests and Correlations of Knee Internal Moment Variables at Pre-Surgery and 6 Months

	PRE (M ± SD) 6MO (M ± SD)	Statistics	Effect Size and Strength	Interpretation
Paired t-test				
DTW Norm Distance (PRE → 6MO)	PRE: 0.07±0.03 6MO: 0.04±0.02	t(19)=3.48 *p*=0.003	d=0.78 (medium)	↓ in DTW norm distance from PRE to 6MO (↑ gait waveform symmetry)
LSI (PRE → 6MO)	PRE: 93.87±55.28 6MO: 63.42±20.97	t(19)=2.94 *p*=0.008	d=0.66 (medium)	↓ in LSI from PRE to 6MO (persistent magnitude asymmetry)
Late Stance Peak Timing (%) (PRE → 6MO)	PRE: 8.3±7.44 6MO: 1.4±1.76	t(19)=4.15 *p*<0.001	d=0.93 (large)	Peaks occur closer together at 6MO (↑ temporal symmetry)
Pearson Moment Correlation				
PRE vs. 6MO DTW Norm Distance	-	r=0.506 *p*=0.023	moderate positive	↑ PRE DTW linked to ↑ 6MO DTW (persistent asymmetry)
PRE vs. 6MO LSI Moments	-	r=0.582 *p*=0.007	moderate positive	↑ PRE asymmetry linked to ↑ 6MO asymmetry (consistent LSI pattern)
6MO DTW Norm Distance vs. 6MO LSI	-	r=-0.909 *p*<0.001	strong negative	As DTW decreases, LSI increases at 6MO (↑ symmetry)
PRE DTW Norm Distance vs. PRE Late Stance Peak Timing (%)	-	r=0.727 *p*<0.001	strong positive	↑ late stance timing mismatch linked to ↑ DTW at PRE (↓ symmetry)

Acknowledgements (Optional)

Supported by the National Institutes of Health (NIH; Grant No. 5R01AR078316).

Session Category

Human Motion and Performance: Locomotion/Gait

P1-235

Spatiotemporal Parameters of Gait Reveal Very Slow Walking Is Not Walking Slowly

Ms. Theresa E. McGuirk MS[1,2], Dr. Anita Bagley PhD, MPH[3], Dr. Carolynn Patten PhD, PT, FAPTA[1,2]

[1]University of Washington, Seattle, WA, United States. [2]VA Puget Sound Health Care, Seattle, WA, United States. [3]Shriners Hospital for Children, Northern California, Sacramento, CA, United States

Introduction

Human bipedal gaits (walking, running), are defined as distinct forward progression solutions along the speed continuum. Very slow walking (VSW) has been considered an extension of typical walking behavior, with heuristic speed thresholds used to predict functional decline [1]. Paradoxically, habitual walking in some clinical populations (stroke, Parkinson's) is often limited to VSW, while others (older, sedentary females) [2] appear unable to access it voluntarily. We examined spatiotemporal gait parameters (STP) across a broad walking speed range to interrogate whether VSW is distinct from habitual walking.

Methods

Participants walked across a pressure-sensing floor at slowest (SLx), self-selected (SS), fastest (FAx) speeds. STP were calculated by stride, normalized [3], with mean and coefficient of variation (CV) calculated by task. Nondimensional velocity (Vnd) was used [3]. Linear and piecewise mixed-effects regression models with significant biological variables (Age, Sex) were applied to each STP/Vnd relationship.

Results

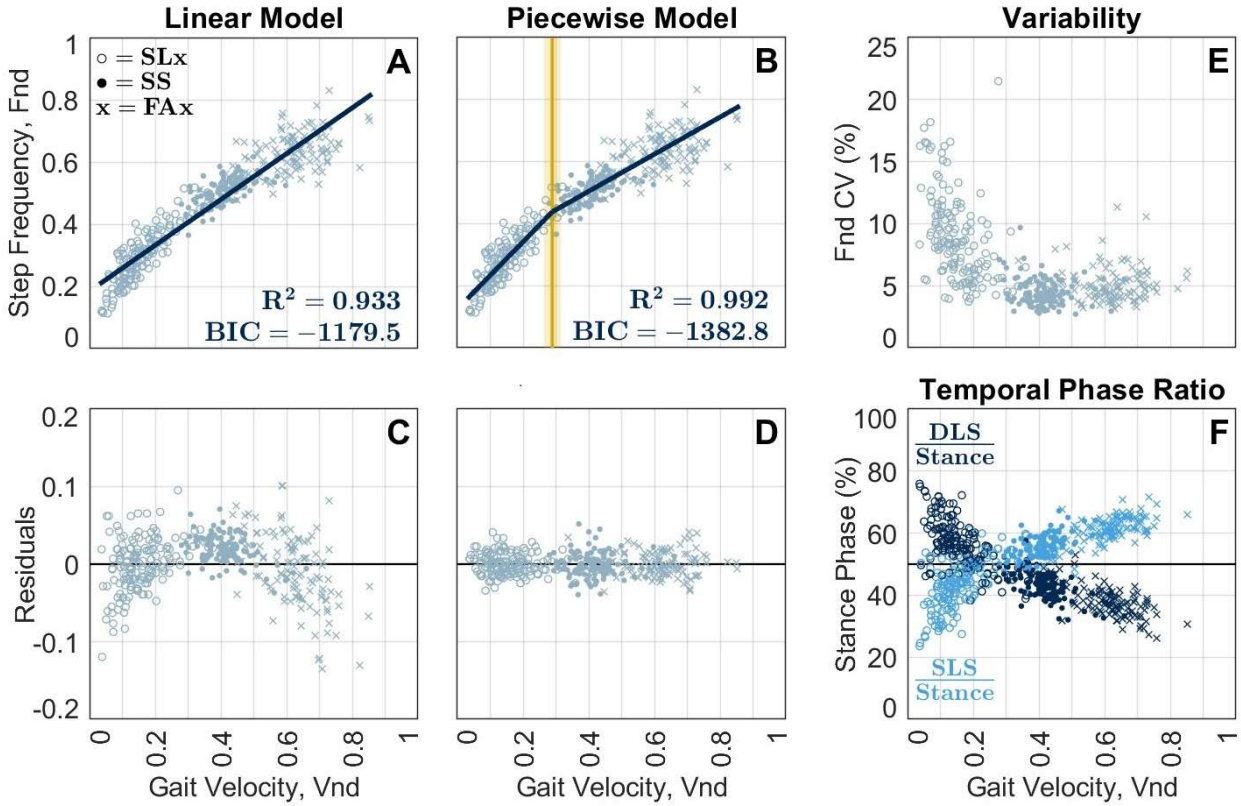
113 healthy adults (18-85yrs, 66F) participated with Vnd mean(stdv): SLx=0.141(0.067), SS=0.412(0.066), FAx=0.622(0.091). Piecewise models were preferred for all STP/Vnd relationships except Stride Width based on decreased BIC (Fig1A-D), and no 95%CI overlap between segment slopes. Piecewise models identified three similarly positioned breakpoints for temporal (Vnd=0.270), spatial (Vnd=0.235), and StepRatio (Vnd=0.185) parameters. In SLx, CV increased ($p<.001$) (Fig1E) for all STP except Stride Width, and gait cycle temporal phasing reversed to dominant double limb support (DLS) (Fig1F).

Discussion

The position of walking gait on the speed continuum, between standing posture and running gait, presupposes the presence of a walk-stand transition like the well-defined walk-run transition. Three STP characteristics differentiating VSW from walking were

identified: 1) breakpoint presence in STP/Vnd relationship, 2) increased variability, 3) DLS dominance. These characteristics (connected but not discontinuous breakpoint, increased variability, same temporal phases as walking with reversed ratios) paired with proximity to standing on the speed continuum, point to VSW as a walk-stand transition. This distinction, that VSW is not a linear extension of walking at slower speeds, redefines our interpretation of gait performance in this speed range.

Images (Optional)



References (Optional)

[1] Studenski *et al*., J Am Geriatr Soc, 2003.

[2] Leiper & Craik, J Phys Ther, 1991.

[3] Hof, Gait Posture, 1996.

Session Category

Human Motion and Performance: Locomotion/Gait

P1-236

Fourier Analysis of Vertical GRF Shape Reveals Very Slow Walking is a Distinct Behavior

Ms. Theresa E. McGuirk MS[1,2], Dr. Anita Bagley PhD, MPH[3], Dr. Carolynn Patten PhD, PT, FAPTA[1,2]

[1]University of Washington, Seattle, WA, United States. [2]VA Puget Sound Health Care, Seattle, WA, United States. [3]Shriners Hospital for Children, Northern California, Sacramento, CA, United States

Introduction

Human bipedal gaits (walking, running), are defined by distinct forward progression solutions along the speed continuum. Very slow walking (VSW) has been considered an extension of typical walking. However, when modeled simply as an inverted pendulum, kinetic energy during walking becomes insufficient to vault body mass over the stance leg at speeds <0.56m/s [1], suggesting VSW solves forward progression differently. We applied Fourier analysis to vertical ground reaction force (GRFv) curves over a broad range of walking speeds to investigate mechanistic differences between walking and VSW.

Methods

Participants walked across a pressure-sensing floor (spatial resolution=5mm; SF=100Hz) at slowest (SLx), self-selected (SS), fastest (FAx) speeds. Estimated GRFv (GRFv = Pressure x Sensor Area), was normalized to stance time (101-points) and body weight (BW) and averaged by task (Fig1B). GRFv curves were expressed as first five terms of Fourier series [2] with term coefficients (Fig1A) examined relative to nondimensional velocity (Vnd) [3].

Results

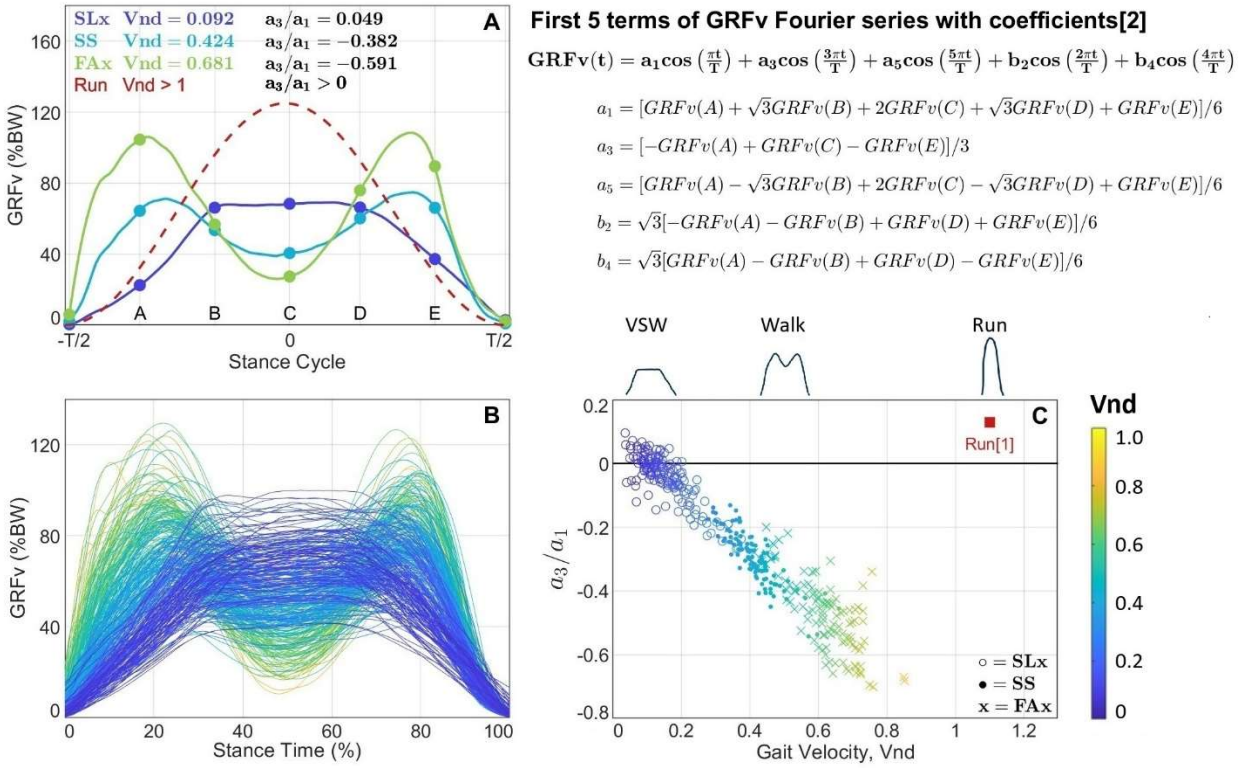
113 healthy adults (18-85yrs, 66F) participated with Vnd mean(stdv): SLx=0.141(0.067), SS=0.412(0.066), FAx=0.622(0.091). a3/a1 shifted predominantly positive at Vnd<0.2 (Fig1C). b2/a1 shifted positive near Vnd<0.5 with smaller +b2/a1 at Vnd<0.2.

Discussion

Fourier analysis has been used to distinguish signature walking and running GRFv shapes [2]. The a3/a1 sign indicates maxima quantity, where +a3/a1 captures the bell-shaped GRFv of running, and –a3/a1 the M-shaped GRFv of walking. The b2/a1 sign characterizes shape symmetry, with –b2/a1 skewed left (loading/absorption) and +b2/a1 skewed right (unloading/propulsion). Our analysis revealed +a3/a1 and +b2/a1 at Vnd<0.2. This right-skewed, bell-shaped GRFv reveals deliberate, controlled locomotion with long, shallow

loading/unloading slopes and steady plateau in single limb phase. Such behavior requires intentional, deliberate control. This finding aligns with theoretical threshold Vnd=0.18 (V=0.56m/s) [1] of the inverted pendulum model and points to the forward progression solution during VSW emerging without the automated motor control employed during habitual walking. This distinction that VSW operates by intrinsically different mechanism informs how gait performance in this speed range should be interpreted, particularly in clinical populations (stroke, Parkinson's) often limited to VSW speeds.

Images (Optional)



References (Optional)

[1] Usherwood, Biol Letters, 2005.

[2] Alexander & Jayes, J Biomechanics, 1980.

[3] Hof, Gait Posture, 1996.

Session Category

Human Motion and Performance: Locomotion/Gait

P1-237

Evaluating the Deep Learning-based Gait Event Detection Algorithm IntellEvent for Turning Tasks in Virtual Reality on an Omnidirectional Treadmill

MSc. Thiago Vidal Pereira[1,2,3], MSc. Bernhard Dumphart[4,5], Dr. Brian Horsak[4], Dr. Anouk Lamontagne[1,2,3]

[1]McGill University School of Physical and Occupational Therapy, Montreal, Quebec, Canada. [2]Feil and Oberfeld Research Centre, Laval, Quebec, Canada. [3]Centre for Interdisciplinary Research in Rehabilitation of Greater Montreal, Montreal, Quebec, Canada. [4]Center for Digital Health & Social Innovation at the University of Applied Sciences St. Pölten, St. Pölten, Niederösterreich, Austria. [5]Institute of Health Sciences at the University of Applied Sciences St. Pölten, St. Pölten, Niederösterreich, Austria

Introduction

Manually detecting gait events of walking trials is time-consuming. IntellEvent, a deep learning-based algorithm, has been validated for detecting initial contact (IC) and toe-off events during overground (OVG) straight-line walking [1]. Walking and turning on a complex setup such as an omnidirectional treadmill with virtual reality (ODTVR) involves gait adaptations [2] that may challenge automated event-detection methods. This preliminary study investigates whether IntellEvent can accurately detect IC events when executing 90° turns during OVG and ODTVR walking, compared with manual detection.

Methods

Data of five participants from a previous study [2] involving 90° turns towards the right during OVG and ODTVR walking were analyzed. A trained evaluator manually identified six IC events per trial (one gait cycle before, during, and after the turn for each leg). This process was repeated three times, with at least one week between five-hour sessions of manual IC detection. IntellEvent was then used to automatically estimate IC events within the same time window as the manual detections. Mean absolute errors were estimated to inform the consistency of manual detections and the accuracy of IntellEvent relative to the averaged manual results.

Results

Between-day differences in the manual detection of IC ranged from 0.3 ± 0.8 to 0.9 ± 1.8 frames, with lower variability in OVG versus ODTVR trials. IntellEvent closely matched averaged manual detection values, with errors of 0.3 ± 0.8 frames (OVG), 0.7 ± 1.6 frames (ODTVR), and 0.48 ± 1.3 frames overall. IntellEvent identified IC events within 3 frames in 97.8% of OVG trials and 92.2% of ODTVR trials.

Discussion

The preliminary results indicate that IntellEvent yields good accuracy of gait detection events when executing turns during OVG and ODTVR walking, with errors that fall below the threshold (20 ms or 2.4 frames) that was shown to meaningfully impact kinematic measures [3]. Importantly, IntellEvent has not yet been trained on ODTVR data, indicating a promising generalizability of the current algorithm to different walking conditions. IntellEvent processed each trial within seconds, greatly improving efficiency compared with manual detection.

Images (Optional)

Condition	D1 vs. D2	D2 vs. D3	D1 vs. D3	IntellEvent vs. Manual	≤ 3 Frames*
OVG	0.5 ± 0.9	0.3 ± 0.8	0.3 ± 0.6	0.3 ± 0.8	97.8%
ODTVR	0.6 ± 1.63	0.7 ± 1.65	0.9 ± 1.8	0.7 ± 1.6	92.2%
Sample Total	0.6 ± 1.3	0.5 ± 1.3	0.6 ± 1.4	0.48 ± 1.3	95%

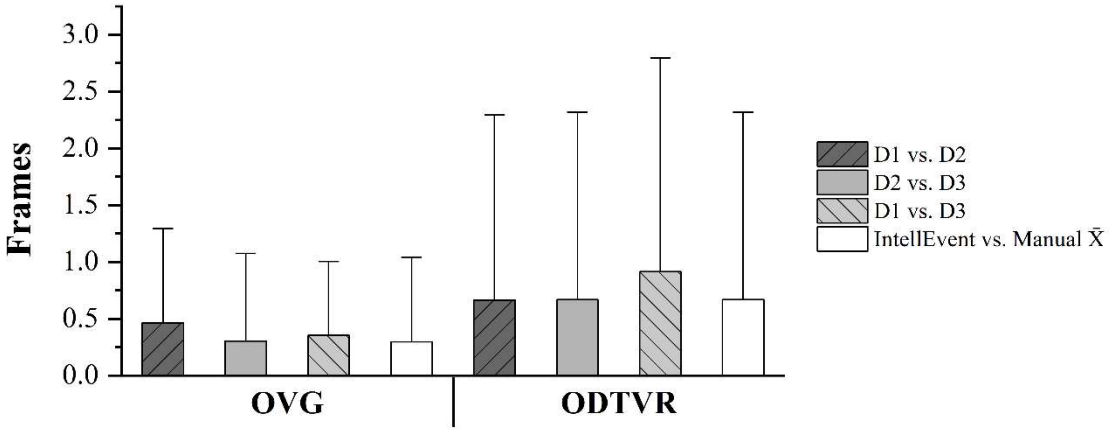


Figure 1. Mean absolute error (± 1 SD) of frame values in the OVG and ODTVR conditions. Grey bars represent comparisons of the manual event detection between days (D1 to D3). White bars represent comparisons between IntellEvent and manual detection.*Percentage of correctly identified IC by IntellEvent (difference ≤ 3 frames with manual detection).

References (Optional)

[1] B. Dumphart et al., PLoS One, 2023.

[2] T. V. Pereira et al., IEEE TNSRE, 2025.

[3] B. Dumphart et al., Gait & Posture, 2026.

Session Category

P1-238

A Framework for Robust Spatiotemporal Analysis of Dynamic Plantar Pressures Measured in Healthy and Deformed Feet

Mr. Tyce Marquez MS, Mr. Owen Kautman, Dr. Bopha Chrea MD, Dr. Jason Wilken PT, PhD, Dr. Donald Anderson PhD

University of Iowa, Iowa City, Iowa, United States

Introduction

Barefoot dynamic plantar pressure systems provide discrete pressure values over defined region of interests. This approach lacks standardization and misses important spatiotemporal features [1, 2]. Previous spatiotemporal plantar pressure analysis approaches are limited in generalizability to deformed feet. Here we present a newly developed framework for robust spatiotemporal analysis of plantar pressures in healthy and deformed feet.

Methods

Dynamic plantar pressures (3 trials per foot) were collected using the Novel-EMED platform from 10 healthy feet and 10 feet with Charcot-Marie-Tooth (CMT) peripheral neuropathy exhibiting varying deformities. Maximum pressure distributions and time series pressures sampled at 10 ms intervals were exported for analysis. The foot progression angle (FPA) was calculated on maximum pressure distributions as the average between lines tangent to the medial/lateral boundaries of the foot relative to the posterior-to-anterior platform axis [3]. Pressure distributions were rotated by the FPA, and bounding box indices collected. Time series pressures were linearly interpolated at 5% intervals across stance, rotated by the FPA, and bounding box values extracted and scaled to a standard 50x18 sensor grid. This yielded 20 aligned pressure distributions per foot for sensor-level comparisons (Figure 1). Framework reliability was assessed using intraclass correlation coefficients (ICCs) of FPA selection from two observers and the minimum detectable change (MDC) at a sensor-level from aligned maximum pressure distributions.

Results

Intra-observer ICCs from both observers were ≥ 0.94 with an inter-observer value of 0.98. The MDC across all sensors was 34.88±50.72 kPa. The maximum MDC was 355.09 kPa in the lateral forefoot, with larger MDC values generally in regions that experience increased plantar loading.

Discussion

The spatiotemporal analysis framework presented provides a straightforward and generalizable approach to analyzing healthy and deformed feet superior to prior approaches. Studies have shown altered loading in deformed feet by reporting discrete peak pressures, pressure-time integrals, and centers of pressure. However, these fail to adequately define spatiotemporal gait patterns. The new framework enables sensor-level comparisons between healthy and deformed feet, providing critical insights into load progression.

Images (Optional)

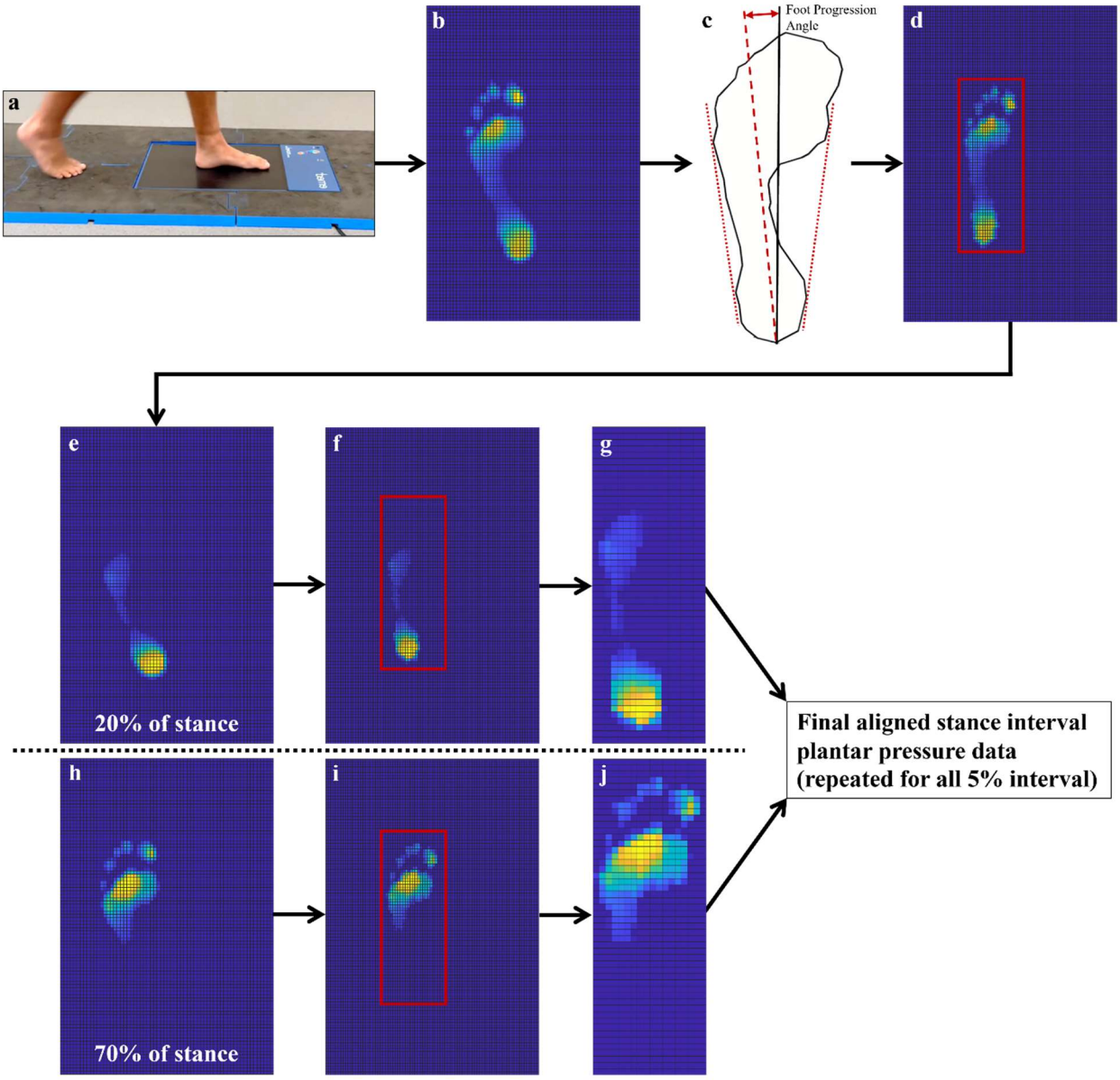


Figure 1. Flowchart for robust spatiotemporal analysis of dynamic plantar pressures. **a**) Out-of-shoe dynamic plantar pressure collection. **b)** Maximum plantar pressure distribution. **c)** Bounding contour selection from maximum plantar pressure distribution for calculating foot progression angle. **d)** Bounding box selection following rotation of the pressure distribution by foot progression angle. **e, h)** Plantar pressure distribution at e) 20% and h) 70% of stance following linear interpolation into 5% intervals. **f, i)** Plantar pressure distributions rotated by foot progression angle with bounding box indicated. **g, j)** Scaled plantar pressure distributions to compare between stance intervals at a sensor level.

References (Optional)

[1] Pataky TC, et al., J Biomech, 2008 [2] Booth BG, et al., J Biomech, 2019 [3] Keijsers NL, et al., J Biomech, 2009

Session Category

P1-239

Uneven Treadmill Terrain Weakens Gait Complexity in Low- but Not High-Functioning Older Adults

Dr. Tyler Wiles, Dr. Daniel Ferris

University of Florida, Gainesville, FL, United States

Introduction

Gait patterns are often dictated by the world around us and our level of cognitive function. The ground that we walk on is rarely perfectly flat. To dynamically respond to irregular and uneven walking surfaces in our environment, gait patterns must also contain a certain degree of irregularity and complexity. These two gait characteristics can be measured using sample entropy (SampEn) and the Hurst exponent, respectively. We hypothesized that walking over increasingly uneven treadmill terrain would increase SampEn and decrease the Hurst exponent, indicating the onset of less regular and less complex gait patterns.

Methods

A total of 26 high-functioning older adults (HFOA) and 43 low-functioning older adults (LFOA) were included in our analysis [1]. Three-minute walking trials were completed, twice, over a flat (control), low (1.3 cm pucks), medium (1.3 & 2.5 cm pucks), and high (1.3, 2.5, 3.8 cm pucks) series of treadmill terrains [1]. SampEn and the Hurst exponent were calculated from the final fifty right stride intervals. From these time series, Bayesian repeated measures ANOVAs produced Bayes Factors (BF_{10}) indicating the strength of evidence supporting a difference in the Hurst exponent or SampEn.

Results

SampEn had no evidence of a terrain or cognitive function effect at any level ($BF_{10} < 1$). Extreme evidence of an interaction and terrain main effect ($BF_{10} > 100$) suggested LFOA and HFOA should be tested independently. LFOA pairwise comparisons revealed that the Hurst exponent decreased with the onset of uneven terrain ($BF_{10} > 12$) but not increasing terrain height ($BF_{10} < 1$). HFOA Hurst exponents remained stable for all terrain ($BF_{10} < 1$).

Discussion

Reductions in the Hurst exponent, but not SampEn, suggest that LFOA adjusted their gait to become less complex, while maintaining irregularity, to overcome uneven terrain. Alternatively, HFOA appear to deploy gait patterns robust to uneven treadmill terrain. Lack of a difference in terrain height suggests that the motor strategy used to respond to

irregular and uneven surfaces is independent of terrain height, up to 3.8 cm. These results also suggest that weakening gait complexity is a feature of low-functioning older adults.

References (Optional)

Downey et al., PLoS ONE, 2022

Session Category

Human Motion and Performance: Locomotion/Gait

P1-240

Can Surface Topography of the Back Detect Surgically Fused Segments? - A Videorasterstereographic Study With Spondylodesis Patients

Dr. Ulrich Betz[1], Dr. Johanna Kniepert[2], Dr. Jürgen Konradi[1], Dr. Janine Huthwelker[1], Ms. Henriette Rönsch[1], Mr. Roman Paul[3], Prof. Philipp Drees[2]

[1]Institute of Physical Therapy, Prevention and Rehabilitation of the University Medical Center of the Johannes Gutenberg University, Mainz, Rhineland-Palatinate, Germany. [2]Department of Orthopaedics and Trauma Surgery of the University Medical Center of the Johannes Gutenberg University, Mainz, Rhineland-Palatinate, Germany. [3]Institute of Medical Biostatistics, Epidemiology and Informatics of the University Medical Center of the Johannes Gutenberg University, Mainz, Rhineland-Palatinate, Germany

Introduction

Videorasterstereography (VRS) can analyze the surface of the back and its changes during walking very accurately. However, it is not yet known whether the results reflect the movement of the spinal segment beneath the surface. To address this question, subjects were examined using VRS after surgical fusion of one or more segments.

Methods

A total of 34 subjects were analyzed who had undergone successful fusion of at least one spinal segment between C7 and L5 at least one year prior (X-ray control) and were able to walk hands-free on a treadmill at a speed of at least 2 km/h (two-minute walk test). We used a DIERS Formetric III 4D (60 Hz) VRS-system to measure the back surface at 2, 3, 4, and 5 km/h where possible. With this we obtained results for spinal rotation sum of motion per gait cycle for a total of 113 fused segments. With the target variable: observed movement a model was fitted for multiple observations per subject adjusted for sex and age.

Results

The participants had varying numbers of segments fused (1-12) and different numbers of subjects could be measured for the spinal segments (1-13). The estimated rotation for the various segments at the various speeds was between 1.39° and 5.18° with large upper 97.5%-confidence intervals up to 8.40° (L4/pelvis at 5kph). The cranial and caudal segments show more movement than the middle. Up to a margin of error of 70%, the results were significantly different from 0 (Binominal Test, adjusted lower 99.375%-confidence limit). There is a trend indicating movements above 1.5°, but this is not

significant across all speeds and segments. The speed is significantly associated with the estimated rotation ($p<0.0001$), region of the spine, number of fixed segments, age, sex, segment are not (F-Test).

Discussion

In a heterogeneous group of patients with one or more surgically stiffened segments, VRS indicates movement of stiffened spinal segments when walking. This probably reflects not a measurement error but the influence of the spine overlying soft tissue on the measurement result. The extent of the measured movement varies in the different spinal segments.

Session Category

Human Motion and Performance: Locomotion/Gait

P1-241

Humans Modulate Feedback Control to Improve Long Term Performance Through Locomotor Adaptation

Mr. Vinayak Bansal, Dr. Nidhi Seethapathi

Massachusetts Institute of Technology, Cambridge, Massachusetts, United States

Introduction

Understanding how humans adapt locomotion is central to motor control, biomechanics, and rehabilitation. Locomotor adaptation is thought to arise from interactions between fast feedback control and slow changes in biomechanical performance. However, the role of feedback control in this process is poorly understood. Existing models assume a specific feedback controller structure, such as one with equal limb angles at pushoff and heelstrike. While such choices may result in good performance in one condition, it is unclear how they affect performance across conditions. Here, we modified the controller choice across two adaptation tasks, split belt (one condition) and dynamic treadmill with sudden speed changes (four conditions) [1], examining how controller choice interacts with biomechanical performance.

Methods

Using a locomotor adaptation model [2], we studied the dynamics of asymmetry and energetics for two controllers: one that assumes equal limb angles (constrained) and one that does not (relaxed). For each condition and controller, we independently fit the model's parameters to avoid bias. We formalized the biomechanical performance metric as a weighted sum of energy, symmetry, and timing accuracy to compare the controllers.

Results

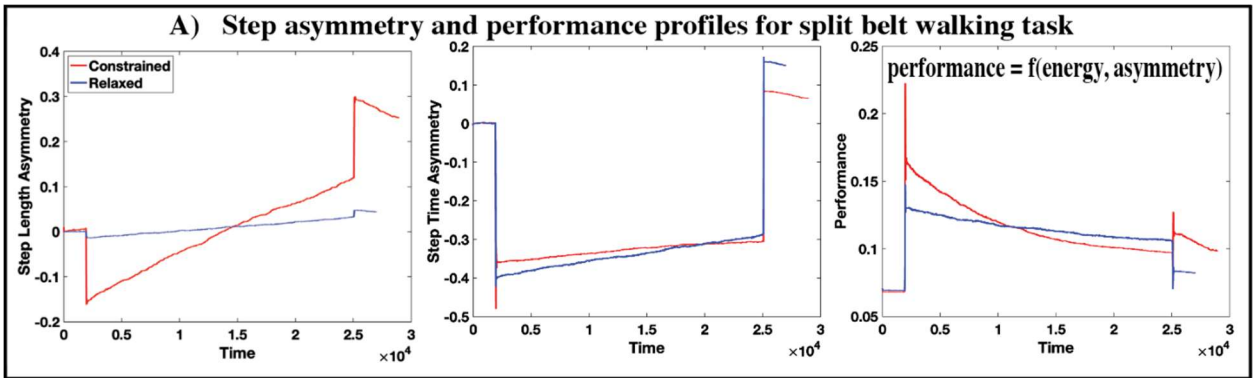
The relaxed controller better explained observed asymmetry in two conditions, the constrained controller in one, and both controllers performed similarly in the remaining two. Also, the two controllers had different energy consumptions and resulted in different timescales for asymmetry adaptation. Using the performance metric, we found that humans tend to choose a controller that maximizes long term performance. For the conditions best explained by a single controller, choosing this controller over the other

alternative resulted in long term performance benefits of 41.4 ± 24.3 %. For the conditions where both controllers explained behavior equally well, this difference was only 4.6 ± 4.7 %.

Discussion

Overall, these findings suggest that the choice of feedback controller plays an active role in how biomechanical performance changes through adaptation. We find that humans choose the feedback controller that maximizes long term performance. Rehabilitation interventions should therefore account not only for biomechanical performance, but also for which controller they engage during adaptation and learning.

Images (Optional)



A) The constrained controller has an asymmetric step length profile, which matches observed behaviour. The constrained controller is also performance optimal in the long run (t > 1.5e4). The relaxed controller does not explain behaviour and has suboptimal performance in the long run.
B) Predictions that match observed are in green. Long term performance consistently explains controller choice.

B) Asymmetry and performance results for all 5 conditions

Condition	Parameter	Observed	Relaxed	Constrained	P (Relative %)
Split Belt 1	SLA	A	A	S	
	STA	A	A	A	16
Dynamic 1	SLA	A	N	S	
	STA	S	N	S	42
Dynamic 2	SLA	A	S	S	
	STA	S	A	S	65
Dynamic 3	SLA	A	S	S	
	STA	A	A	A	1
Dynamic 4	SLA	S	S	S	
	STA	A	A	A	7
SLA : Step Length Asymmetry			A : Asymmetric		N : No trend
STA : Step Time Asymmetry			S : Symmetric		P : Performance

References (Optional)

[1] Browne et al. , Plos One 2023

[2] Seethapathi et al. , Nature Communications, 2024

Session Category

Human Motion and Performance: Locomotion/Gait

P1-242

Comparative Analysis of Locomotion Control Models in Neuromechanical Simulations

Mr. Vincent Ton, Dr. Seungmoon Song Ph.D.

Northeastern University, Boston, MA, United States

Mr. Vincent Ton

Introduction

Understanding how the nervous system generates locomotion is fundamental to movement science. Although central pattern generators (CPGs), spinal reflexes, and muscle synergies are widely discussed as key neural mechanisms, their respective roles and contributions to locomotion remain unresolved. Neuromechanical simulations with explicit control models offer a practical way to evaluate how different control hypotheses influence gait behavior. However, these proposed models have been implemented across different environments with varying musculoskeletal properties and optimization criteria, preventing direct comparison. Here, we compare four neurophysiologically-inspired control models within a unified framework to assess their diverse gait behaviors.

Methods

We investigated four representative locomotion control models: reflex-based [1], muscle-synergy-based [2], CPG-reflex-based [3], and CPG-reflex-synergy-based [4]. Using a unified neuromechanical simulation framework (MATLAB/Simulink; two-dimensional musculoskeletal model with 18 leg muscles; CMA-ES optimization), we evaluated each model's ability to: 1) produce human-like gait and 2) generate walking across speeds and slopes.

Results

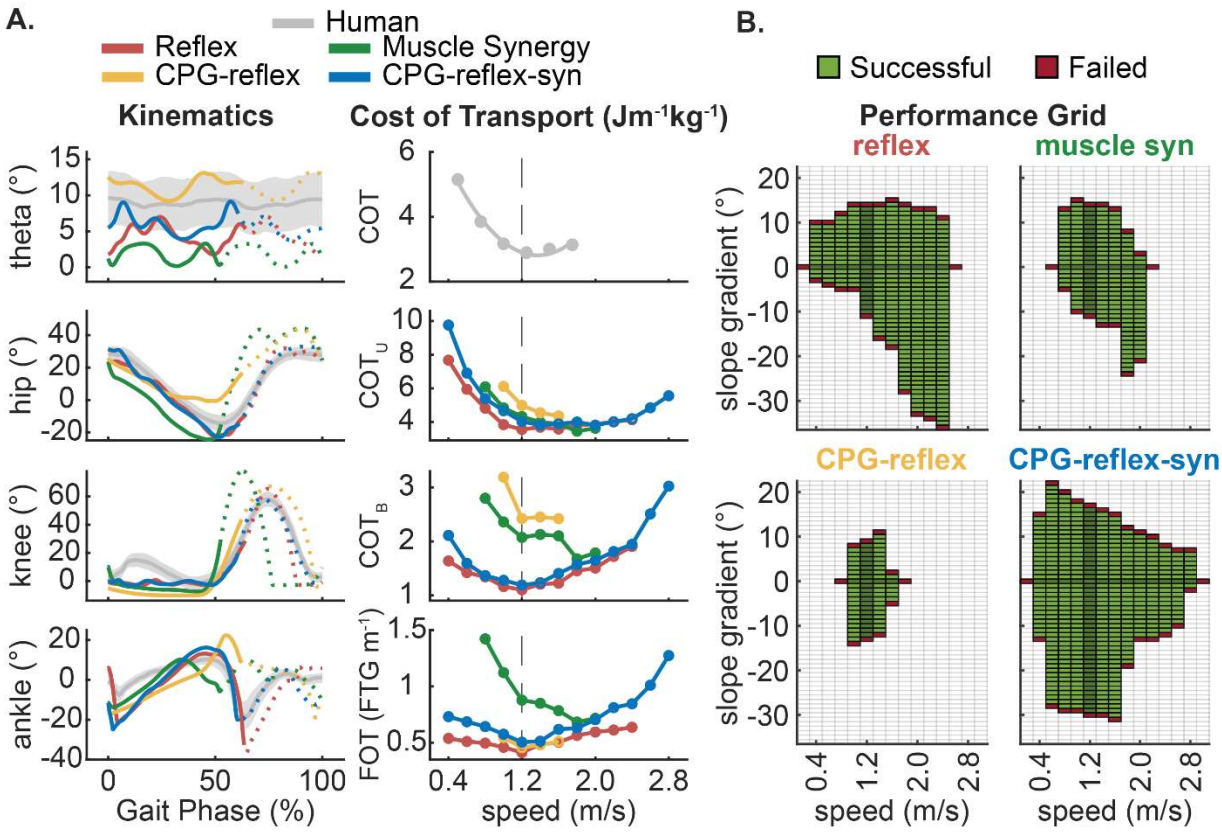
While comprehensive biomechanical analyses will be presented at the conference, the main findings are summarized here. When optimized for minimum muscle effort at normal walking speed, the reflex-based and CPG-reflex-synergy-based models generated the most human-like and efficient gait, while the muscle-synergy model showed the largest deviations (Fig. A). Across the speed–slope space, the CPG-reflex-synergy model achieved the widest range of stable walking, followed by the reflex model, with the CPG-reflex model

performing worst (Fig. B). Representative animations: https://neumove.org/project/NM4models.html.

Discussion

Although the models show clear performance differences, interpretation requires caution. These results reflect specific implementations rather than definitive judgments about underlying control hypotheses, as each strategy can be formulated in multiple ways. These models emphasize spinal mechanisms, while human walking outside nominal conditions involves supraspinal control, so performance at extreme speeds or slopes should not be over-interpreted. Additionally, other evaluations such as perturbation responses were not included. Nevertheless, this work provides the first systematic comparison within a unified framework. The codebase will be shared to facilitate further model development and hypothesis testing.

Images (Optional)



References (Optional)

[1] Song & Geyer (2015), J Physiol; [2] Aoi et al. (2019), Sci Rep; [3] Ogihara & Yamazaki (2001), Biol Cybern; [4] Di Russo et al. (2023), J Neural Eng.

Acknowledgements (Optional)

This research is funded by National Institutes of Health (R00AG065524) and National Science Foundation (DGE-2439018).

Session Category

Human Motion and Performance: Locomotion/Gait

P1-243

Dynamic Obstacle Avoidance Alters Gait Spatiotemporal Parameters and Variability During Walking

Dr. Wendi Weimar PhD, Mr Bahman Adlou MS, Mr John Grace MS

Auburn University, Auburn, AL, United States

Introduction

Obstacle avoidance is a tool required for everyday locomotion; however, too often our research is focused on navigation around stationary barriers. Yet dynamic obstacles pose a significant real-world challenge and offer valuable insight into assessing individuals with mobility impairments. Therefore, this project investigated the influence of stationary and dynamic obstacles on spatiotemporal gait parameters and variability.

Methods

Twenty-nine healthy young adults (14F/15M, age 22.7±3.1 years) completed 20 trials along a 16-foot instrumented walkway under four conditions: baseline (C1), stationary obstacle (C2), perpendicular-moving obstacle (C3), and head-on-moving obstacle (C4). Spatiotemporal gait variables including stride length, step length, and stride width were recorded, with both mean values and coefficient of variation (%CV) calculated to quantify gait variability. Linear mixed models (LMMs) with participant as a random effect were employed to compare gait parameters across conditions, using C1 as reference. Pairwise comparisons between all conditions were conducted with effect sizes quantified using Cohen's d.

Results

Linear mixed models with participant random intercepts revealed significant increases in stride length (C2: +9.4 cm, C3: +8.6 cm, C4: +4.0 cm; all $p<0.001$) and step length (C2: +5.0 cm, C3: +5.2 cm, C4: +2.9 cm; all $p<0.001$) across all obstacle conditions. Step length variability increased most dramatically with perpendicular-moving obstacles (C3: +12.3% coefficient of variation, $p<0.001$), significantly more than stationary (+6.1%) or head-on-moving (+10.0%) obstacles. Sex differences emerged, with males demonstrating greater stride lengthening in stationary and perpendicular conditions.

Discussion

This project indicates that moving obstacles, particularly those moving toward the participant regardless of direction, challenge gait stability more than stationary obstacles. The increased neuromuscular demands created by dynamic obstacles may

allow for deeper analysis of real world challenges. Dynamic obstacle performance may provide earlier detection of balance deficits and offer a more ecologically valid assessment tool. Additionally, rehabilitation programs incorporating unpredictable moving obstacles may better prepare patients for community mobility than static balance training. Future research should validate this paradigm in older adults and clinical populations to determine its predictive validity for fall risk.

Session Category

Human Motion and Performance: Locomotion/Gait

P1-244

Explainable Machine Learning Identifies Mechanisms of Gait Improvement After a Multicomponent Exercise Program in Long-Term Care

Dr. Xiaoping Zheng[1], Ms. Ziwei Zeng[1], Mr. Cheuk Yin Ho[1], Prof.dr. Junhong Zhou[2], Prof. dr. Yijian Yang[1]

[1]The Chinese University of Hong Kong, Hong Kong, Hong Kong, Hong Kong. [2]Harvard Medical School, Boston, Massachusetts, United States

Introduction

Falls are highly prevalent in long-term care (LTC) settings and nearly half (49%) of them occur during walking. Improving gait is therefore critical for fall prevention. Mobility-Fit, a 12-week multicomponent exercise program, was developed to enhance mobility in this population [1]. Given the heterogeneity in physical and cognitive function and the varied responsiveness to intervention among LTC residents, conventional analysis approaches that rely on group-level mean comparisons may be insufficient to capture meaningful changes. Facing this challenge, this study aimed to use machine learning to evaluate individual- and group-level intervention responses so as to uncover the underlying mechanisms contributing to gait improvements.

Methods

This study was a 2-arm cluster randomized controlled trial including 90 older adults from 20 LTC facilities in Hong Kong (mean age 82.2 ± 9.1 years; 64.4% female) who completed gait assessments. Participants were randomized into the intervention (Mobility-Fit; n=47) or control (standard care; n=43) groups. Gait was assessed using a 3D-accelerometer during two 5-m walking trials at baseline and post-intervention. Thirty-two gait outcomes were extracted. Unsupervised machine learning (K-means clustering) was applied to baseline gait data to identify latent gait patterns. The trained K-means clustering was then used to assign post-intervention gait patterns. Individual responsiveness was evaluated through gait pattern transitions, and group-level intervention effects were examined using chi-squared tests. Explainable AI (XAI) was employed to determine gait outcomes contributing to intervention responsiveness.

Results

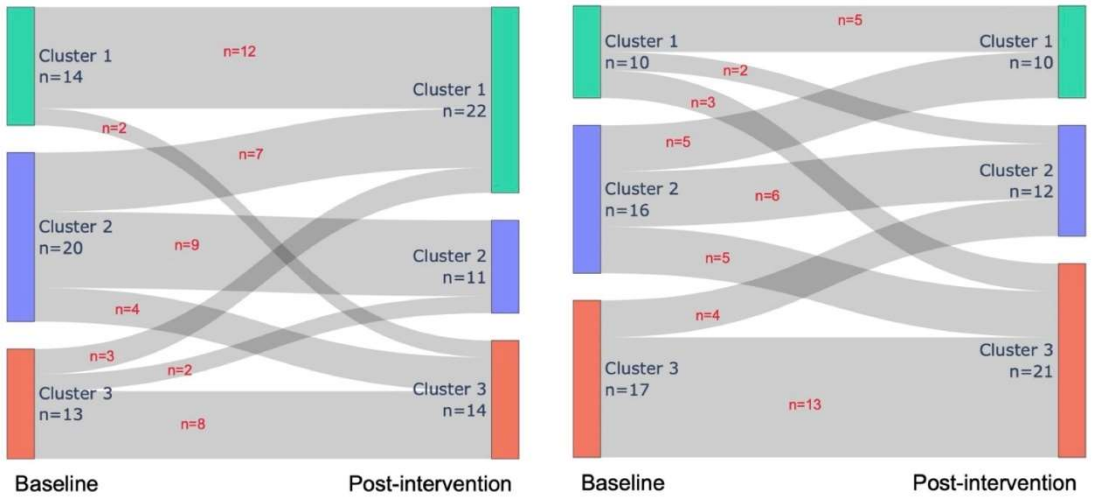
Three distinct gait patterns were identified: better-performing, moderate-performing, and poorer-performing. Gait pattern improvement was defined as: (1) transitioning improved-performing patterns (e.g., moderate to better), or (2) maintaining moderate- or better-performing patterns over time. As shown in Figure 1, the intervention group demonstrated a

higher rate of gait pattern improvement compared with the control group (70% vs. 47%, p = 0.038). XAI analyses indicated that improvements were primarily driven by enhanced gait regularity (reduced stride frequency variability; increased stride regularity) and gait smoothness (higher harmonic ratios).

Discussion

Mobility-Fit significantly improved gait quality among LTC residents, particularly in gait regularity and smoothness. Our analytic framework provides a novel approach for evaluating and optimizing exercise interventions for older adults in LTC.

Images (Optional)



(a) Intervention Group (b) Control Group

Figure 1. Gait pattern transitions from pre-test to post-test for each participant. (a) Intervention group; (b) Control group.

References (Optional)

[1] Yang Y et al., BMJ open. 2024

Session Category

Human Motion and Performance: Locomotion/Gait

P1-245

Gait Variability, but Not Gait Speed, Differ Among Older Adults With Multimorbidity

Mr. Yale Hughes M.S., Dr. Ashlyn Jendro PhD, Dr. Abigail Schmitt PhD

University of Arkansas, Fayetteville, Arkansas, United States

Introduction

Slower gait speeds are associated with reduced quality of life and often used as a clinical indicator of overall health, functional status, fall risk, and mortality risk in older adults. Likewise, multimorbidity, having one or more chronic conditions, is greatly related to decreased gait speed and quality of life, as well as increased fall risk. While gait speed and multimorbidity are independently associated with fall risk in older adults, gait variability may be a more sensitive measure in predicting falls. The Enhanced Gait Variability Index (EGVI) characterizes an individual's gait variability relative to healthy levels of gait variability. The EGVI more accurately predicts fall risk than gait speed alone, with increased EGVI indicating higher fall risk. This study sought to compare differences in EGVI and gait speed among community-dwelling older adults with multimorbidity. We hypothesized that participants with greater multimorbidity burden will exhibit slower gait speed and increased gait variability.

Methods

Data was collected from independently living older adults (n= 109, 73±6 years, 80 female) in community locations. Participants completed health history questionnaires and gait evaluations on a 6-meter instrumented pressure mat (Zeno Walkway). Gait assessments included four passes of comfortable pace walking, then EGVI and gait speed were calculated using ProtoKinetics Movement Analysis Software. Participants were grouped by number of self-reported chronic conditions (0, 1, 2, 3, and 4+), then separate analysis of variance (ANOVA) were performed to determine differences between groups for both gait parameters.

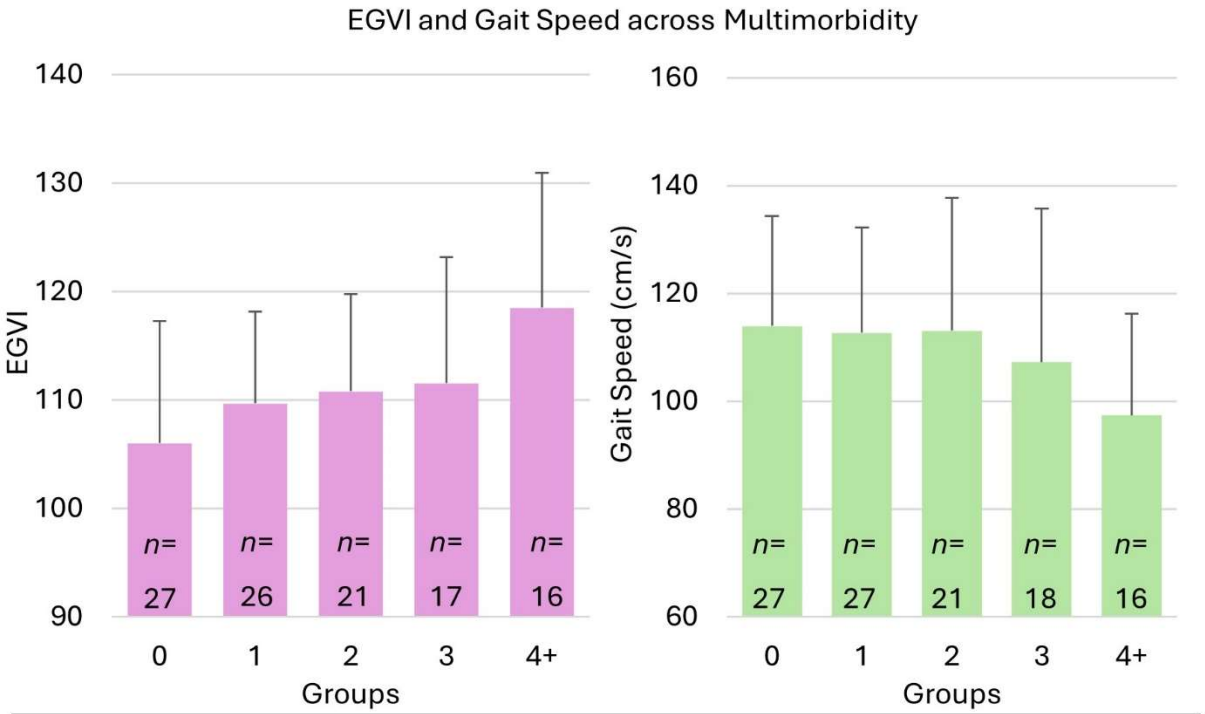
Results

EGVI differed significantly among groups (p= .008, η^2= 0.125, see figure); individuals with 4+ conditions exhibited significantly higher EGVI (M= 118.5, SD= 12.5) than those without chronic health conditions (M= 106.0, SD= 11.3), p= .002. Gait speed did not differ among groups (p= .145, η^2= 0.063, see figure).

Discussion

Higher EGVI scores reflect greater stride-to-stride variability, and our findings suggest having more chronic health conditions negatively impacts gait stability in older adults. Further, the lack of significant differences in gait speed indicates gait speed alone may not be a sensitive enough measure to evaluate multimorbidity burden on gait in older adults.

Images (Optional)



Note: Enhanced Gait Variability Index (EGVI) could not be calculated for 2 participants; thus, EGVI has 2 less participants (*n*= 107) than gait speed (*n*= 109).

Acknowledgements (Optional)

This project was funded by University of Arkansas Honors College Research Grants.

Session Category

Human Motion and Performance: Locomotion/Gait

P1-246

Frontal Plane Dynamics in Sprinting: Step Width is Determined by Center of Mass Displacement and Hip Control, Not Static Morphology

Ms Hazuki Tsubata Physical Therapis, Dr Yasuko Hirono PhD, Dr Norihisa Fujii PhD

University of TSUKUBA, Tsukuba, Ibaraki, Japan

Dr Yasuko Hirono

Introduction

Step Width, the lateral distance between consecutive foot placements in locomotion, is a critical metric resulting from complex motor control strategies that balance functional demands for stability and propulsion against inherent biomechanical constraints. Step Width variability is hypothesized to be governed by the dynamic interaction of two main factors: static morphological characteristics (e.g., pelvic width) and dynamic kinematics (e.g., hip joint angles, pelvic motion, and Center of Mass control). Understanding Step Width determinants is crucial for minimizing injury risk. The purpose of this study was to identify the morphological and/or kinematical determinants of Step Width during maximal sprinting, a key step for developing personalized intervention strategies for safer and more efficient locomotion.

Methods

Twenty-six college students performed 10 maximal running trials. Data were collected approximately 35 m from the standing start, representing the maximum velocity phase of the sprint, using a motion capture system and force platforms. Kinematic and kinetic variables were calculated using three-dimensional marker trajectories and ground reaction force measurements. The mean value of 10 trials was used as the representative value for each participant. The relationships among Step Width and the morphological, kinematic, and kinetic variables were evaluated using Pearson's product–moment correlation coefficient (significance level set at $p < 0.01$).

Results

Step Width showed significant positive correlations with lateral movement of Center of Mass displacement during flight phase (r=0.60) and lateral impulse (r=0.58). It also exhibited a significant positive correlation with the hip abduction angle at toe-off (r=0.55),

but not at touchdown. The pattern of hip adduction/abduction varied greatly between subjects. Importantly, no significant correlations were found between Step Width and static morphological variables, including pelvic width, leg length, and Q-angle.

Discussion

These findings suggest that Step Width is determined lateral displacement of the Center of Mass and the lateral impulse. However, since the generation of lateral ground reaction force cannot be solely explained by hip adduction/abduction, the results indicate that diverse, individualized motor control strategies are employed during sprinting. This finding underscores the need for coaching interventions to focus on dynamic hip and pelvic stability rather than generalized running form adjustments based on static body measurements.

Session Category

Human Motion and Performance: Locomotion/Gait

P1-247

Side-Dependent Foot Joint Power during Turning Gait

Mr. Yufan He[1], Dr. Lauren Williams[2], Mr. Jose Anguiano-Hernandez[2], Dr. Jenna Burnett[2], Dr. Kota Takahashi[2,3,4]

[1]Department of Mechanical Engineering, University of Utah, Salt Lake City, UT, United States. [2]Department of Health & Kinesiology, University of Utah, Salt Lake City, UT, United States. [3]Department of Biomedical Engineering, University of Utah, Salt Lake City, UT, United States. [4]Department of Physical Medicine & Rehabilitation, University of Utah, Salt Lake City, UT, United States

Introduction

Turning gait is a common walking pattern, requiring different power demands from the outside and inside limbs' ankle joints [1]. While ankle asymmetries are observed in turning gait, it remains unknown whether this side-dependent power pattern also holds for more distal joints of the foot (e.g., midtarsal). Because the midtarsal joint is a major source of foot energy generation, examining its behavior may reveal how energy is redistributed during turning gait and inform prosthetic design. Therefore, this study aims to compare energetics at the ankle and midtarsal joints between outside and inside limbs across different turning radii.

Methods

One healthy adult (data collection is ongoing) walked counterclockwise at 1.0 m/s along circular paths with two radii (1.0 m, 1.5 m). Motion capture and ground reaction force data were collected, and a multi-segment foot model [2] was used to compute ankle and midtarsal joint power. Power curves were integrated to obtain positive and negative work.

Results

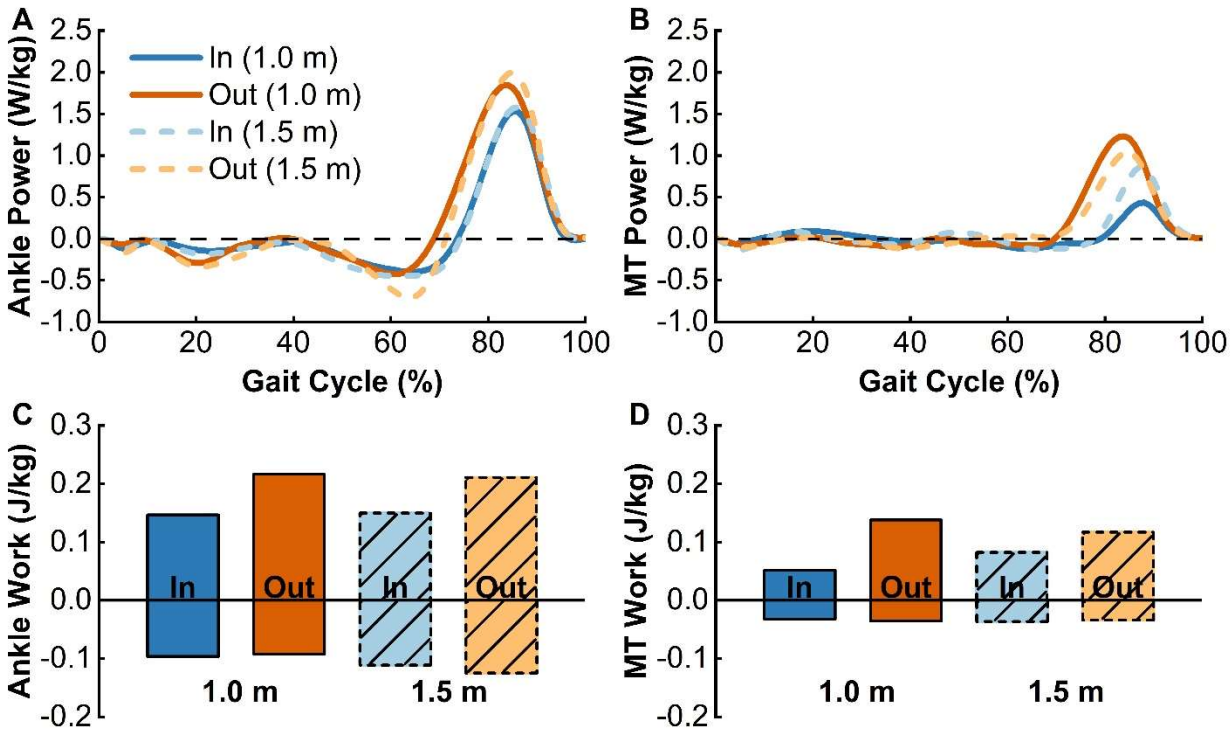
Across both radii, the outside limb generated more positive work than the inside limb at the ankle (1.0 m: 0.217 vs. 0.147 J/kg; 1.5 m: 0.211 vs. 0.150 J/kg) and midtarsal joints (1.0 m: 0.138 vs. 0.051 J/kg; 1.5 m: 0.117 vs. 0.083 J/kg). Negative work was similar between limbs. As turning radius increased, the difference in the positive work between the limbs decreased (**Figure 1**).

Discussion

Turning gait seems to rely on an asymmetric strategy of energy generation across the ankle and foot. The outside limb generated more positive work at the ankle, a pattern that also appeared at the midtarsal joint, suggesting that the midfoot may also contribute to

propulsion during turning. Negative work was similar between limbs at both joints, suggesting that energy absorption demands may not differ between the outside and inside limbs. As turning difficulty changes, energetic demands at the midtarsal joint redistribute, suggesting that the midfoot may act as a dynamic regulator of power distribution. These findings highlight the foot's contribution to turning mechanics and may guide prosthetic designs.

Images (Optional)



References (Optional)

[1] Michael S. Orendurff et al. , Gait & Posture, 2006

[2] Dustin A. Bruening et al. , Gait & Posture, 2012

Acknowledgements (Optional)

Session Category

Human Motion and Performance: Locomotion/Gait

P1-248

Evaluating Effects of Custom Insoles on Plantar Forces during Walking using Principal Component Analysis-Guided Statistical Parametric Mapping

Mr. Zhu Fang MS[1], Mr. Kailin Xing MS[1], Mr. Xinghan Li MS[1], Mr. Joohno Um BS[1], Dr. Jungho Lee PhD[2], Dr. Prabhat Pathak PhD[3], Dr. Siddhartha Bikram Panday PhD[1,4]

[1]Department of Physical Education, Hanyang University, Seoul, Seoul, Korea, Republic of. [2]Footwear Laboratory, K2 Korea, Seoul, Seoul, Korea, Republic of. [3]Department of Sports Sciences, Seoul National University of Science and Technology, Seoul, Seoul, Korea, Republic of. [4]Department of Art and Sportainment, Seoul, Seoul, Korea, Republic of

Mr. Zhu Fang

Mr. Kailin Xing

Mr. Xinghan Li

Mr. Joohno Um

Dr. Jungho Lee

Introduction

Custom insoles (CIs) are commonly used to redistribute pressure, reduce abnormal loading and cumulative stress, and improve walking comfort [1]. Statistical Parametric Mapping (SPM) is used to comprehensively evaluate the effect of CIs on plantar force (PF) by comparing its temporal changes over the stance phase [2]. However, human movement is inherently noisy, and extracting dominant features is necessary to comprehensively evaluate the effect of CIs. To this end, we present a Functional Principal Component Analysis (FPCA)-Guided SPM analysis method that first extracts dominant waveform features and then compares the temporal changes. We then use the method to evaluate the differences in temporal changes in PF using CIs.

Methods

Walking trials were collected from 16 older women (age > 55) working in prolonged weight-bearing occupations to compare the effects of CIs with control insoles (CONs). CIs were fabricated with TPU using a 25% gyroid infill printed using the foot scan of the participants captured using the MediACE3D foot scanner. PF data were recorded at 100 Hz using the Pedar system. FPCA was first applied to PF waveforms to extract dominant features from the first 2 PCs. The waveform differences between CIs and CONs were then computed, and SPM regression was used to identify statistically significant time points. These results were compared with traditional SPM applied directly to PF waveforms ($p < 0.05$).

Results

Traditional SPM detected only one brief significant interval, revealing significantly lower PF with CIs during the 0–2% stance phase. FPCA-guided SPM revealed significant differences over a larger area of the stance phase: the first two functional principal components (FPCs) showed significant differences across 2–80% of stance (Fig.1).

Discussion

Our study demonstrates that applying FPCA before SPM enabled a more comprehensive evaluation of the effect of CIs on PF. While traditional SPM detected only a brief early-stance difference, FPCA revealed significant changes across much of the stance phase, indicating broader alterations in foot–ground interaction with CIs. These findings highlight FPCA-guided SPM as a more sensitive method for capturing meaningful temporal differences in PF with CIs.

Images (Optional)

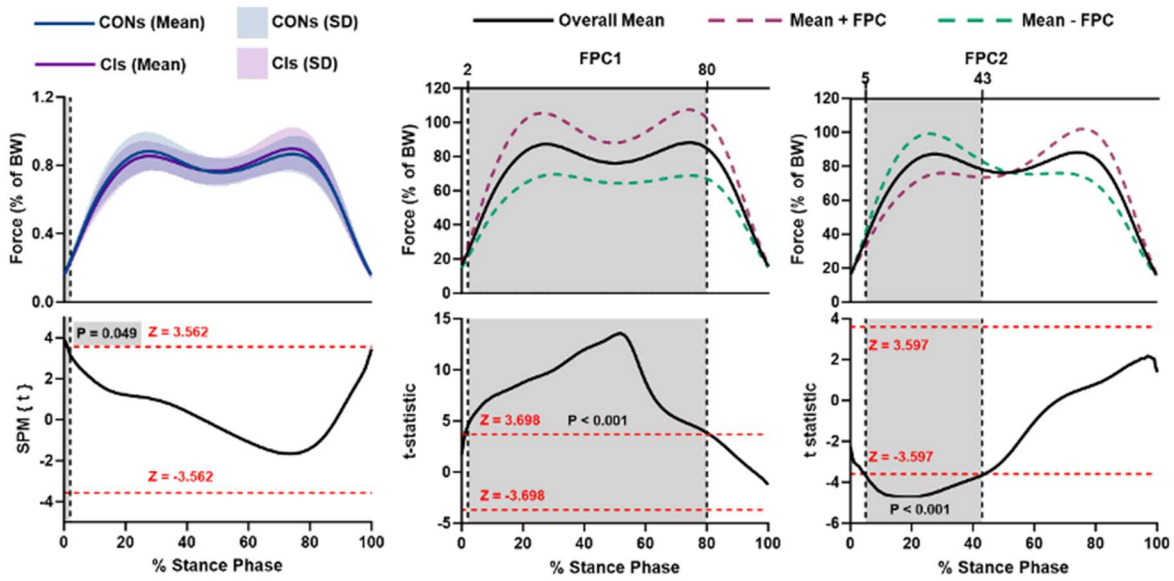


Figure 1: Comparison of plantar forces with custom insoles (CIs) and control insoles (CONs) with traditional Statistical Parametric Mapping (SPM) and Functional Principal Component Analysis (FPCA)-guided SPM analysis.

References (Optional)

[1]Harris,F. et al., App. Sci., 2021; [2]Pataky,T.C., J Biomechics, 2022

Acknowledgements (Optional)

None

Session Category

Human Motion and Performance: Locomotion/Gait

P1-249

Age-Related Increase in the Energy Cost of Walking: Metabolic Factors and Impact on Fatigability

Ms. Zoe Smith M.S., Mr. Luke Arieta M.A., Dr. Michael Busa PhD, Dr. Jane Kent PhD

University of Massachusetts Amherst, Amherst, MA, United States

Introduction

The typically greater metabolic cost of walking (CoW) in older age is generally attributed to neuromuscular and biomechanical factors [1]. However, the potential role of metabolic factors such as substrate (carbohydrate, fat) oxidation for energy production has not been evaluated. Because fat oxidation for a given task consumes more oxygen (VO_2) than carbohydrate oxidation, we hypothesized that more use of fat by older adults could contribute to their greater CoW. Further, a consequence of the greater CoW in older adults, coupled with their expected lower aerobic capacity (VO2 peak), would be a smaller "energy reserve" during walking; we examined whether a lower energy reserve might contribute to a greater perception of fatigue [2] in response to the walking task.

Methods

Seventeen young (29 ±5yr; 6F) and 15 older (72 ±5; 7F) adults completed an aerobic capacity test, followed by a 30-min treadmill walk ($1.3 m \cdot s^{-1}$) in a room calorimeter during which VO_2 and carbon dioxide production were measured. CoW (VO_2, $ml \cdot kg^{-1} \cdot min^{-1}$), carbohydrate and fat oxidation ($kJ \cdot kg^{-1}$), and energy reserve (peak minus steady state walking VO_2) were calculated. Final minus baseline Borg rating of perceived exertion (ΔRPE) was used as the measure of fatigability. Statistics: ANOVA, linear regression.

Results

CoW was ~10% greater in older than young (Figure 1A). Fat oxidation was also greater in older (44 ±9% total energy) than young (34 ±9%; $p=0.007$) and associated with CoW overall ($n=32$; $r^2=0.25$, $p=0.002$). The greater CoW and ~35% lower aerobic capacity (VO_{2peak}: older = 27.7 ±0.7 ($n=13$), young = 42.3 ±0.8; $p<0.001$), in older resulted in a lower energy reserve compared with young ($p<0.001$), which was associated with greater fatigability only in the older (Figure 1B).

Discussion

As hypothesized, these results provide intriguing new evidence that, in addition to neuromuscular and biomechanical factors, metabolic factors related to greater fat oxidation can increase CoW in older age. Additionally, the relationship between energy

reserve and fatigability in the older group only suggests that a consequence of this greater CoW is greater perceived fatigue during a standardized task in older adults.

Images (Optional)

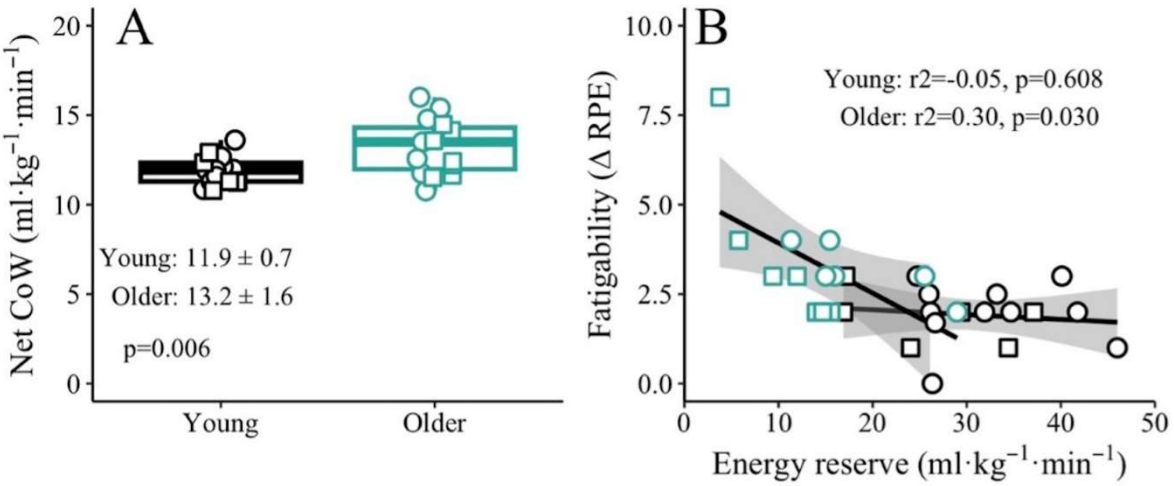


Figure 1. CoW is greater in older than young (*left*) and contributes to fatigability by lowering energy reserves (*right*). Older: outlined blue, young: outlined black.

References (Optional)

1. Boyer *et al*., ExpGerontol, 2023
2. Eldadah, PM&R, 2010

Acknowledgements (Optional)

Funded in part by a University of Massachusetts Amherst Institute for Applied Life Sciences Midi-Grant

Session Category

Human Motion and Performance: Locomotion/Gait

P1-250

Force and Kinematic Analysis of Fatigue in Collegiate Baseball Players in a Simulated Game Environment

Mr. Aaron Austin Undergraduate Researcher, BESc/BA Concurrent Program, Departments of Integrated Engineering and Kinesiology[1], Dr. Thomas Jenkyn Associate Professor, Department of Mechanical and Materials Engineering[1], Dr. Ryan Crotin Executive Vice President, ArmCare.com; Baseball Performance Research Associate, Department of Kinesiology[2,3], Dr. Emily Lalone Associate Professor, Department of Mechanical and Materials Engineering[1]

[1]Western University, London, Ontario, Canada. [2]ArmCare.com, Indialantic, Florida, United States. [3]Louisiana Tech University, Ruston, Louisiana, United States

Introduction

Major improvements in injury prevention for baseball players have occurred over the past decade via pitch-count and workload tracking. Despite this, shoulder and elbow injuries persist at all levels, highlighting the need for deeper work on fatigue management. Injury risk stems from multiple interconnected factors, but fatigue is a critical factor which contributes to injury risk. A major limitation of previous research has focused on isolated fatigue-related risk factors rather than examining how these variables interact as an integrated system. This study aims to investigate the interactions and changes between strength, coordination, and performance with the onset of fatigue.

Methods

Six collegiate pitchers (mean age: TBD) completed a simulated four-inning game consisting of 80 pitches. Full-body pitching kinematics were captured using a 12-camera 3D motion capture system, and ball velocity was recorded. Shoulder strength, range of motion, and pinch grip strength were assessed using a handheld dynamometer with shoulder strength also measured after each inning. Participants then self-reported perceived fatigue of the arms, legs, and overall exertion using a visual analog scale.

Results

Participants generally reported increasing fatigue in their arms, legs, and overall exertion as the simulated game progressed, yet individual fatigue profiles differed widely. Several pitchers reported minimal fatigue levels (<6/10 visual analogue fatigue scale score) despite measurable declines in shoulder strength, suggesting that perceived exertion may not

accurately reflect physiological fatigue. Preliminary results collected on velocity suggest that pitch velocity remains constant over the course of the simulated game.

Discussion

Our findings suggest that relying on an athlete's self-reported fatigue or coaching observations may not be a reliable way to assess fatigue as perceived exertion does not always reflect measurable declines in strength. Incorporating simple, objective strength testing during games could help identify when a pitcher is truly fatigued and therefore assist coaches in making safer substitution decisions.

Session Category

Human Motion and Performance: Sports

P1-251

Do Upper Extremity Mechanics Predict Pitch Outcome in Softball Pitchers?

Dr. Abbie E. Ferris PhD[1], Mr. Zac Bridger[2], Mr. Monte McDonald[2]

[1]University of Northern Colorado, Greeley, CO, United States. [2]Triple Crown Sports, Fort Collins, CO, United States

Introduction

Softball windmill pitching is a unique motion among competitive sports. In particular, it has received little attention in injury prevention or performance enhancement [1,2]. The windmill pitch can be used to deliver a variety of pitches designed to deceive the batter. Arguably, the two most common types of pitches are fastball (FB) and change up (CH). Yet, it is unknown how either pitch is able to produce effective changes in pitch type. Thus, we hypothesize, these two pitch types will result in significantly different upper extremity kinematics effecting ball flight trajectory.

Methods

Ten top club female softball pitchers were recruited for this study (16-18y/o, 68.18 ± 11.39kg, 1.64 ± 0.07m). Each participant threw 4 FB and CH pitches while recorded with a markerless motion capture system (Qualisys, Göteborg, Sweden). Ball flight trajectory data were simultaneously recorded for each pitch (Rapsodo, St Louis, MO). RMANOVA were preformed on joint angles and ball flight data and correlation analysis between ball flight and kinematic variables (R-Studio, Boston, MA).

Results

All participants demonstrated slower pitch speeds with a CH than FB (45.29 ± 3.88 vs 60.51 ± 2.60mph) with reduced total spin (1385.75 ± 343.68 vs 877.43 ± 206.06 deg/s). Elbow flexion velocity ($p = 0.0059$, $r = 0.796$) contributed to ball velocity during CH pitches. CH significantly reduced angular velocities at the shoulder, elbow, and wrist (Table 1). CH vertical approach angle was significantly steeper (-3.81 ± 2.37 vs -10.37 ± 3.81 deg) driven by increased shoulder flexion ($r = -0.454$). CH ball spin increased due to shoulder flexion and internal rotation. CH showed higher variability in measures than FB particularly in elbow flexion velocity (28.8% vs 42.7%CV).

Discussion

Pitchers are able to manipulate ball trajectory through the shoulder and elbow kinematics. These data support that while ball velocity can be modulated via the elbow, it is likely driven by the lower extremities and torso rotation during the launch phase of the pitch.

Given the higher variability in kinematics in CH pitches, coaches and athletes should focus on increasing consistency within each pitch type to increase ball flight trajectory accuracy.

Images (Optional)

Table 1: Kinematic variables at ball release. Data are shown mean ± SD.

	Fastball	**Changeup**
Shoulder Extension (deg)	4.99 ± 13.04*	18.81 ± 12.77
Elbow Flexion (deg)	26.04 ± 12.64	28.94 ± 5.01
Wrist Extension Velocity (deg/s)	1001.21 ± 282.73*	679.80 ± 240.43
Wrist Radial Velocity (deg/s)	726.35 ± 318.42*	641.17 ± 311.70
Elbow Flexion Velocity (deg/s)	1240.19 ± 357.62*	859.65 ± 366.94
Shoulder Internal Rotation Velocity (deg/s)	3879.56 ± 982.10*	2548.03 ± 379.04

Note: *Significant difference between pitch types ($p<0.05$)

References (Optional)

1. Werner SL et al., 2006
2. Pytiak AV et al., 2018

Session Category

Human Motion and Performance: Sports

P1-252

The Coefficient of Propulsion: A Novel Metric for Characterizing Trail Leg Ground Reaction Forces During Baseball Pitching

Mr. Adam Barrack PhD(c), CSCS, TSAC-F

University of Southern California, Los Angeles, CA, United States

Introduction

Introduction: The baseball pitch relies on coordinated ground reaction forces (GRFs) from the trail leg to initiate and transfer energy through the kinetic chain. Prior studies have described vertical and anterior shear forces independently, but forward propulsion depends on their coupled action. To capture this relationship, we introduce the coefficient of propulsion (CoPr), defined as the ratio of anterior shear to vertical force during the stride phase. CoPr provides a dimensionless index reflecting both the magnitude and timing of its GRF components, potentially offering a more meaningful representation of trail-leg propulsion than single-force measures. This study examined whether CoPr at peak anterior shear force better predicted pelvis kinetic energy (PKE) at stride foot contact compared to anterior shear magnitude alone. PKE was selected because it captures the mechanical linkage through which the trail-leg generates and transfers energy to the rest of the kinetic chain, making it a useful indicator of trail-leg propulsion efficiency.

Methods

Methods: Thirty-seven healthy collegiate pitchers threw full-effort fastballs from an instrumented mound while kinematic data (300Hz) and GRFs (1200Hz) were collected. CoPr was calculated for each trial as the ratio of anterior shear to vertical force, and its value was extracted at peak anterior shear force. PKE was computed at stride foot contact from segmental translational and rotational kinetic energy. For all variables, the average of 10 trials per pitcher were analyzed. Simple linear regression determined the proportion of variance in PKE explained by CoPr and peak anterior shear force.

Results

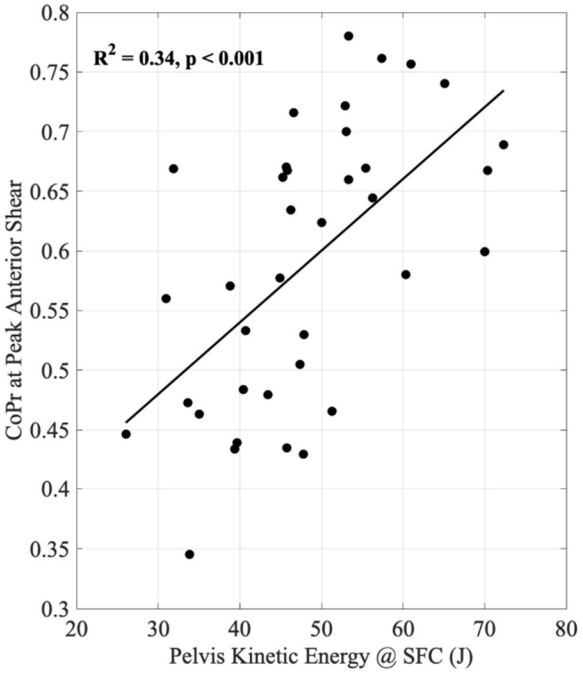
Results: CoPr exhibited substantial variability across pitchers ($\bar{x}$=0.6[0.4–0.8]). Both CoPr and peak anterior shear force significantly predicted PKE. However, CoPr explained a

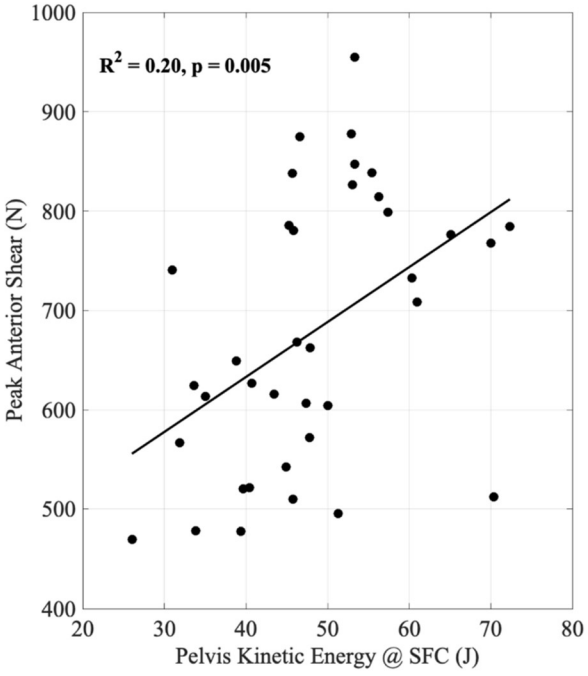
greater proportion of variance in PKE (R^2=0.34,p<0.001) than peak anterior shear force alone (R^2=0.20,p=0.005).

Discussion

Discussion: CoPr provides an integrated measure of trail-leg force production that captures the functional coupling of vertical and anterior shear forces during the stride phase. CoPr was a stronger predictor of pelvis kinetic energy than anterior shear magnitude alone, suggesting enhanced utility for characterizing propulsion strategies and energy transfer in baseball pitching. Further research should examine its implications for performance and injury risk.

Images (Optional)





Session Category

Human Motion and Performance: Sports

P1-253

Asymmetric Loading Responses to Practice and Game Demands in Male and Female Ice Hockey Players

Miss Ainsley Svetek, Dr Neal Glaviano, Dr Julie Burland

University of Connecticut, Storrs, CT, United States

Introduction

Wearable technology has emerged to quantify longitudinal athlete load during practice and competitive settings. While these metrics are becoming more common, data specific to ice hockey is limited. The purpose of this study was to examine whether asymmetric loading increases in ice hockey games compared to practice between collegiate male and female ice hockey players to provide insight needed to refine training loads and address potential injury risk.

Methods

Data were collected utilizing a tri-axial, insole embedded inertial measurement unit (Plantiga) which was placed bilaterally into the ice skates. Twenty-one female and 24 male collegiate ice hockey players wore the sensors during practices and games over the course of a 9-week period. Load asymmetry data was collected and averaged by session-type. Negative values indicated greater left limb loading, whereas positive values indicated increased right limb loading; asymmetry is expressed as percent difference between limbs. A two-way mixed ANOVA was used to quantify changes in asymmetric loading from practices and game sessions and between males and females, with significance set at $p>.05$. Post-hoc testing was performed in presence of significant effects.

Results

Across nine weeks, females had 34 practices and 14 games, while men had 31 practices and 15 games.The two-way mixed ANOVA revealed a significant sex by session interaction ($F=8.741$, $p=.005$). There was no difference in asymmetric loading between males and females for practices, however there was a significant difference in games (mean difference=4.7±1.88, $p=.016$). There was no significant effect of session type on asymmetric loading for males or females ($F=1.144$, $p=.291$). Interestingly, females had an increase in asymmetric loading from left-loaded (-1.1%) in practices to right-loaded (2.0%) in games, while males showed an increase in left-loaded in practices (-1.1%) to games (-2.5%).

Discussion

Although there was no within-group effect of session type alone, the significant interaction between session type and sex indicates the different responses from males and females to the demands of games compared to practices. Varying shifts in loading asymmetry between males and females may reflect sex-specific skating mechanics or distinct adaptations in movement strategies as game intensity increases, highlighting the importance of sex-specific responses in athlete load monitoring.

Images (Optional)

	Practice (Mean ± SD)	Game (Mean ± SD)	Sex by session interaction	Within-Subject	Between-Subject
Females	-1.46 ± 4.31	1.96 ± 7.17	p=.005	p=.291	p=.037
Males	-1.13 ± 3.40	-2.74 ± 5.42			
Between Subjects Post Hoc	p=.779	p=.016			

Session Category

Human Motion and Performance: Sports

P1-254

Three-Dimensional Motion Analysis With Minimal Calibration Process Using Omnidirectional Cameras

Dr. Akinori Nagano[1], Dr. Akitoshi Makino[1], Dr. Shoma Kudo[2], Dr. Masahiro Fujimoto[2]

[1]Ritsumeikan University, Kusatsu, Shiga, Japan. [2]National Institute of Advanced Industrial Science and Technology, Takamatsu, Kagawa, Japan

Introduction

Motion analysis is a crucial method in the field of biomechanics. The Direct Linear Transformation method (1971) and the Non-Linear Transformation method (1982) are well-established gold standards. However, a major drawback of these established methods is the requirement for a time-consuming and technically demanding calibration process. We invented a novel method utilizing omnidirectional cameras. By exploiting the unique feature that omnidirectional cameras can observe not only the points of interest (POI) but also the cameras each other, we significantly reduced the calibration time and technical demands.

Methods

The new method firstly employs a geometric approach to determine the horizontal 2D (XY) position of target objects using two omnidirectional cameras, with only two control points of known coordinates [1]. We assume that the image from the omnidirectional cameras is represented in the equirectangular projection, in which the horizontal and vertical position corresponds to the longitude and latitude within the celestial sphere, respectively. The new method is based on the geometric formation of a quadrilateral ABDC (AB: control points, CD: cameras). By applying the law of sines to the constituent triangles, proportional relationships are derived (Figure 1). This system of equations allows for determination of the XY positions of the cameras. Position of POI is determined as the intersection of camera rays. Thereafter, for 3D positions, the vertical (latitude) location of POI in the equirectangular projection image is used, applying the tangent value of the latitude. With the XY positions of cameras and POI already determined, Z position of POI is determined.

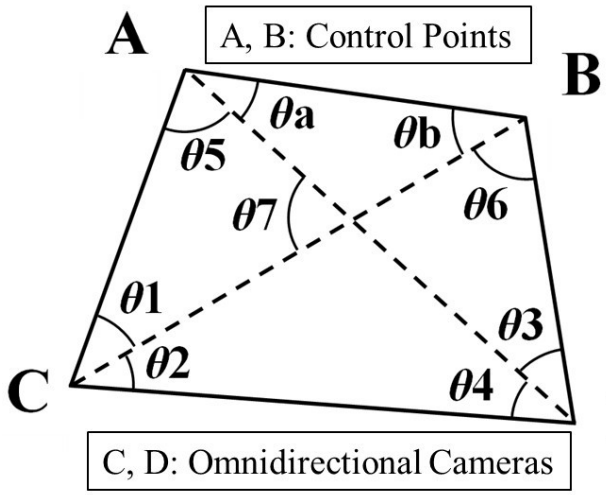
Results

The accuracy of the new 2D method was verified within a flat indoor area measuring 5mX5m. The relative error with respect to the calibrated area was <0.6%. The accuracy of the new 3D method was verified in another experiment. The relative error was <3.6%.

Discussion

This method drastically reduces the calibration time and technical demands associated with motion analysis. The achieved high precision makes this method an attractive alternative to the conventional methods.

Images (Optional)



$$\frac{\sin\theta_b}{\sin\theta_a} = \frac{AB}{BD}\cdot\frac{1}{\sin\theta_3}\cdot\frac{AC}{AB}\cdot\sin\theta_1 = \frac{AC}{BD}\cdot\frac{\sin\theta_1}{\sin\theta_3}$$

$$\frac{AC}{BD} = \frac{1}{CD}\cdot\frac{\sin\theta_6}{\sin\theta_2}\cdot CD\cdot\frac{\sin\theta_4}{\sin\theta_5} = \frac{\sin\theta_6\cdot\sin\theta_4}{\sin\theta_5\cdot\sin\theta_2}$$

$$\frac{\sin\theta_b}{\sin\theta_a} = \frac{\sin\theta_1\cdot\sin\theta_4\cdot\sin\theta_6}{\sin\theta_2\cdot\sin\theta_3\cdot\sin\theta_5}$$

References (Optional)

[1] Nagano, A. and Makino, A., in press. Journal of Trainology.

Acknowledgements (Optional)

This study was partly supported by JSPS Kakenhi.

Session Category

Human Motion and Performance: Sports

P1-255

Unilateral Achilles Tendinopathy: Comparing Muscle Strength and Range of Motion Between Symptomatic and Asymptomatic Limbs

Dr. Eliane C. Guadagnin PhD[1], Dr. Matheus M. Vilela MD, MSc[1,2], Dr. Felipe F. Gonzalez MD, MSc[1,2,3], Ms. Aleksandra Kozicka BS[2], Dr. Tiago Zimerman MD[1,2], Dr. Carolline Popovicz Nunes MD[1,2], Dr. Marcos Amstalden Barros MD[1,2], Dr. Jonathan A. Gustafson PhD[1,2], Dr. Jorge Chahla MD, PhD[2,4], Dr. Leonardo Metsavaht MD, PhD[1,3], Dr. Alexandre Godoy-Santos MD, PhD[1,5,6], Dr. Gustavo Leporace PhD[1,3]

[1]Instituto Brasil de Tecnologias da Saúde, Rio de Janeiro, RJ, Brazil. [2]Rush University Medical Center, Chicago, IL, United States. [3]Universidade Federal de São Paulo, São Paulo, SP, Brazil. [4]Midwest Orthopaedics at Rush, Chicago, IL, United States. [5]Laboratório Professor Manlio Mario Marco Napoli, Hospital das Clínicas, Faculdade de Medicina, Universidade de São Paulo,, São Paulo, SP, Brazil. [6]Hospital Israelita Albert Einstein, São Paulo, SP, Brazil

Dr. Felipe F. Gonzalez

Introduction

Achilles tendinopathy (AT) is a common overuse injury, especially among runners, and is associated with various biomechanical factors. Interlimb differences in strength and range of motion (ROM) between the symptomatic and the asymptomatic limbs may propagate symptoms, and compensations at proximal segments, such as the hip, may be important to address. This study aimed to compare ankle and hip strength and ROM between symptomatic and asymptomatic limbs in individuals with unilateral AT.

Methods

This cross-sectional study included forty-four patients with unilateral AT (36 males, eight females; mean age 47.7 ± 10.2 years). Bilateral maximal isometric strength was assessed using a handheld dynamometer for the hip abductors, extensors, external rotators, as well as ankle dorsiflexors, plantar flexors (with the knee extended and flexed), ankle inverters, and ankle evertors. ROM was measured bilaterally with a digital inclinometer for hip internal rotation and ankle movements, including weight-bearing and open-kinetic-chain dorsiflexion (with the knee extended and flexed), plantarflexion, ankle eversion, and ankle inversion. Group comparisons were conducted using paired t-tests or Wilcoxon tests

depending on data normality, and effect sizes were calculated with Cohen's d. Statistical significance was set at $P < 0.05$ for all analyses.

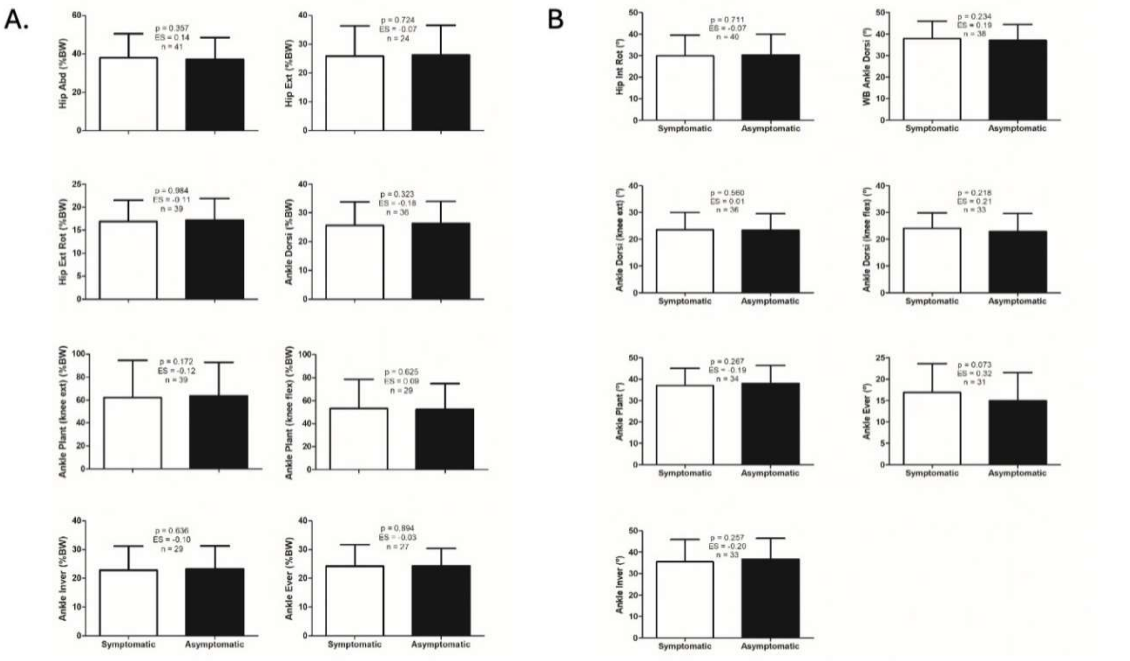
Results

No significant differences were observed between symptomatic and asymptomatic limbs for any strength or ROM measures (all $P > 0.05$) (Figure 1). Effect sizes between limbs were minimal, ranging from –0.03 to 0.32. The average differences in strength (0.5–3.0%, mean 1.8%) and ROM (0.3–11.3%, mean 3.8%) were small, indicating symmetrical static performance across joints and muscle groups.

Discussion

Individuals with unilateral AT exhibited symmetrical isometric strength and ROM at both the ankle and hip. These findings indicate that static assessments alone might not capture the complex biokinetic factors involved in AT.

Images (Optional)



A: Differences between symptomatic and asymptomatic limbs in strength tests; Abd: abductors; Ext: extensors; Ext Rot: external rotators; Dorsi: dorsiflexors; Plant: plantar flexors; Ext: extended; Flex: flexed; Ever: evertors; Inver: invertors; BW: body weight. The values presented are mean and standard deviation.

B: Differences between symptomatic and asymptomatic limbs in range of motion tests; Int Rot: internal rotation; Dorsi: dorsiflexion; Ext: extended; Flex: flexed; Plant: plantarflexion; Ever: eversion; Inver: inversion. The values presented are mean and standard deviation.

Session Category

Human Motion and Performance: Sports

P1-256

Using Wearable Data to Predict Speed and Injury Risk in Runners

Dr Sarah Johnson PhD[1,2], Dr Alex Gonzalez[2], Dr Johanna O'Day[2], Prof Scott Delp[1,2], Prof Ellen Kuhl[3], Dr Jennifer Hicks[2,1]

[1]Department of Bioengineering, Stanford University, Stanford, California, United States. [2]Wu Tsai Human Performance Alliance, Stanford University, Stanford, California, United States. [3]Department of Mechanical Engineering, Stanford University, Stanford, California, United States

Dr Sarah Johnson

Dr Alex Gonzalez

Introduction

Understanding how to manage training loads to maximize performance while minimizing injury risk is key for runners and coaches. We used longitudinal training and injury data to quantify the relationship between weekly running distance, performance, and injury risk in 203 athletes.

Methods

Athletes (age 30±6; 150 females; 43% semi-elite; 8% elite) shared 2.5 years of retrospective daily training data from their Garmin smartwatch and labelled injury and illness periods. Participants reported 58 bone stress injuries (BSIs) and 278 soft tissue injuries. We extracted athletes' average weekly running distance from time periods with no reported injury or illness. We determined best performance in the 5000m and marathon by extracting the fastest average speed during runs of sufficient length. We analyzed relationships between weekly running distance, top speed in the 5000m and marathon, and rates of BSI and soft tissue injury using statistical models that controlled for age, body mass index, and total days of training, where relevant.

Results

Speed increased with weekly running distance, with diminishing returns that occurred earlier for females than males in both the 5000m and marathon (Fig. 1A,B). The rate of BSIs

increased with weekly distance for both sexes, with nearly double the rate in females versus males (0.13 vs 0.07 yearly injuries; p=0.01; Fig. 1C) inline with previous studies[1]. Soft tissue injury rate did not correlate with weekly distance for either sex. Combining model results enabled us to compare how performance and injury risk varied with increasing weekly distance. For example, the models predict that females going from 80km to 100km per week increase their speed by 0.15 m/s (5%) in the 5000m and by 0.15m/s (7%) in the marathon, but increase their expected yearly BSI rate by 0.05 (29%) (Fig. 1D).

Discussion

Our analysis reveals relationships between weekly running distance and both speed and BSI injury risk, which differ between males and females. The rate of soft tissue injuries was not associated with weekly distance, suggesting alternative contributing factors to risk for these injuries.The observed trade-offs between performance and injury risk could help inform training plans.

Images (Optional)

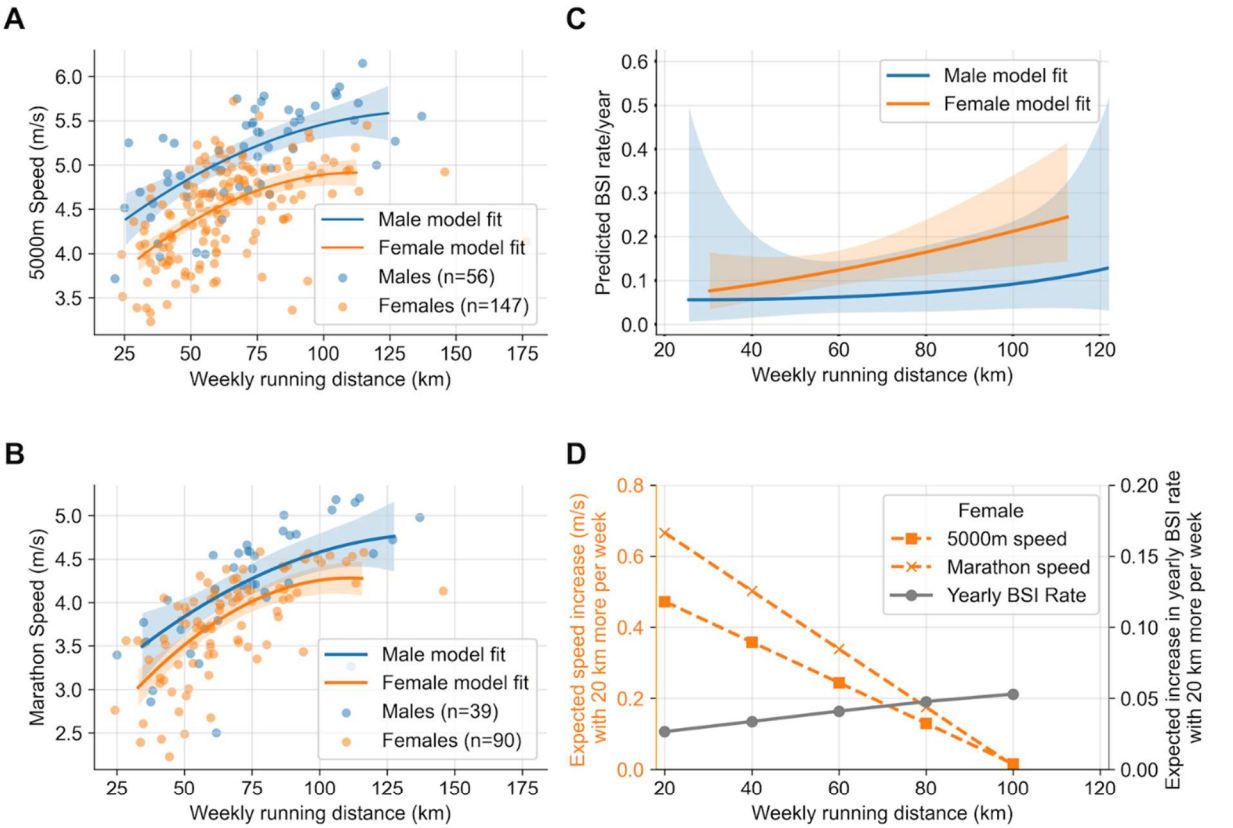


Figure 1. Speed versus weekly running distance for A) 5000m and B) the marathon. The orange and blue lines are the results of an ordinary least squares regression, controlling for age and body mass index, for females and males, respectively. The bands show 95% confidence intervals and dots the raw extracted data. C) Weekly running distance versus predicted yearly bone stress injury (BSI) rate. Lines show a Poisson regression model predicting the yearly BSI rate as a function of weekly distance, controlling for age, body mass index, and observation duration (i.e., total days of training included for a participant). D) Predicted BSI rate and speed changes if females increased their weekly distance by 20km.

References (Optional)

[1] Wolf et al., Am J Sports Med 2025.

Session Category

Human Motion and Performance: Sports

P1-257

Joint Kinematic Comparison of Telemark and Alpine Skiing Turns in Fully Certified Instructors: A Statistical Parametric Mapping Analysis

M.S. Alique Malakian[1], B.S. Tobin Arden[1], B.S. Tom Koto[2], Ph.D. John Seifert[1]

[1]Montana State University, Bozeman, Montana, United States. [2]Bogus Basin Ski Area, Boise, Idaho, United States

Introduction

Telemark turns (TT) are an alternative form of skiing characterized by the free movement of the heel compared to alpine skiing. Turns are initiated by lunging forward and differ from alpine turns (AT) due to the increased knee and hip ROM. General sagittal plane kinematics have been described previously, but specific outside and inside leg turn differences and frontal plane kinematics are not well understood. Therefore, the purpose of this study was to evaluate the kinematic differences of the hip and knee joints of a ski turn.

Methods

Two subjects (female, age: 60, male, age: 69), fully PSIA certified in both disciplines, completed four runs for each discipline. Gate distances were set to ski radius. Full-body 3D kinematics were collected using the Xsens Link IMU body suit at 240 Hz. 67 and 69 total outside and inside leg turns were selected and normalized to 100%. Kinematics were calculated using a YXZ Cardan sequence. Statistical parametric mapping paired t-tests were conducted between each subject's AT and TT.

Results

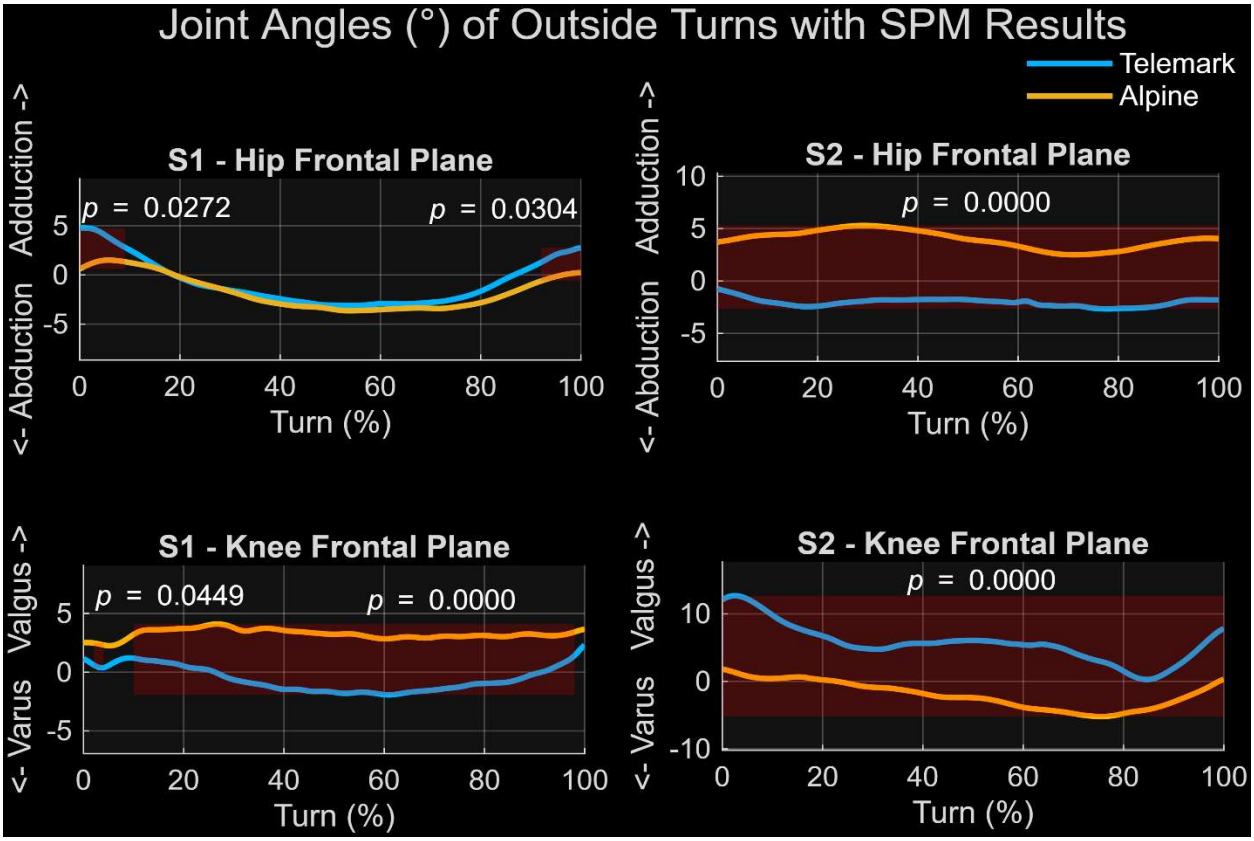
Skiers' outside leg turns were characterized by significantly increased hip and knee flexion during TT. S1 displayed significantly increased hip adduction at turn initiation and completion and significantly increased knee varus during TT. S2 displayed significantly increased hip abduction and knee valgus during TT. For the inside leg turns, both skiers displayed significantly increased hip and knee flexion during TT. S1 displayed significantly increased hip adduction and knee varus during TT. S2 displayed significantly increased hip abduction and knee valgus at turn initiation and completion during TT.

Discussion

The sagittal plane kinematic results were similar to previous TT studies; however, differentiating the outside and inside leg turns revealed contrasting frontal plane turning

strategies for each skier. Despite comparable technical expertise in both disciplines, the results indicate that complex activities, such as telemark skiing, produce great individual variability in movement execution. These data indicate that although these skiers are of expert technical level, they achieved this level by differing movement patterns. The results emphasize that a variety of strategies are possible to perform complex movements.

Images (Optional)



Session Category

Human Motion and Performance: Sports

P1-258

Neuromuscular signatures of fatigue precede kinematic changes in constant-speed treadmill running

M.A.Sc. Candidate Zachary A. Flahaut[1,2], Post-Doctoral Fellow Nicholas S. Ryan[3], Professor Pär Halje[3], Professor Allison L. Clouthier[1,4], Professor Daniel L. Benoit[3]

[1]Ottawa-Carleton Institute for Biomedical Engineering, University of Ottawa, Ottawa, Ontario, Canada. [2]Department of Mechanical Engineering, University of Ottawa, Ottawa, Ontario, Canada. [3]MoRe-Lab, Department of Health Sciences, Faculty of Medicine, Lund University, Lund, Scania, Sweden. [4]School of Human Kinetics, University of Ottawa, Ottawa, Ontario, Canada

Introduction

Neuromuscular fatigue can modify muscle activation patterns before observable changes in movement mechanics. However, most fatigue research has focused on incremental or short-duration running, and EMG fatigue analyses are typically performed under isometric or controlled laboratory conditions. It remains unclear how prolonged, constant-speed running at high metabolic strain affects neuromuscular activation patterns when joint kinematics remain preserved. This study investigated how sustained high-intensity treadmill running influences lower-limb muscle activation and joint kinematics in young adults.

Methods

Seven recreationally trained young adults completed a 30-minute treadmill run at ~85% individual VO2max on a 1% incline. Three-dimensional kinematics (200 Hz), ground reaction forces (1000 Hz), and bilateral surface EMG (2000 Hz) were recorded at three intervals: pre-fatigue, mid-fatigue, and post-fatigue. EMG metrics—mean amplitude, median frequency, power, and integrated EMG (iEMG), were quantified for eight muscles (biceps femoris, semitendinosus, gluteus medius, rectus femoris, vastus lateralis, vastus medialis, lateral gastrocnemius, medial gastrocnemius). Physiological variables (VO2, heart rate, respiratory quotient (RQ), Borg scale) were averaged across 30-second windows. Statistical parametric mapping (SPM) assessed sagittal-plane hip, knee, and ankle joint angles across the gait cycle. Repeated-measures ANOVAs evaluated fatigue-related differences.

Results

Heart rate and Borg increased significantly across fatigue stages ($p<0.01$), confirming rising physiological strain, while VO2 and RQ plateaued. SPM revealed no significant differences

in sagittal-plane hip, knee, or ankle joint angles between stages, indicating preserved running mechanics.

In contrast, significant neuromuscular alterations emerged (Figure 1). Median frequency declined in posterior thigh and triceps surae muscles, while several knee extensors and hip stabilizers exhibited reductions in iEMG across fatigue stages. These changes reflect decreased recruitment efficiency during sustained running despite unchanged kinematics.

Discussion

Despite stable kinematics, participants showed neuromuscular and physiological drift, demonstrating that fatigue alters motor unit recruitment under steady-state metabolic conditions. Unlike most fatigue studies, which rely on incremental protocols or EMG fatigue under isometric conditions, this work shows that prolonged constant-speed running induces substantial EMG-based fatigue signatures without accompanying biomechanical changes. These findings highlight the limitations of using joint kinematics alone to infer fatigue and underscore the importance of integrating neuromuscular measures for monitoring load and guiding training and injury-prevention strategies in endurance-based sports.

Images (Optional)

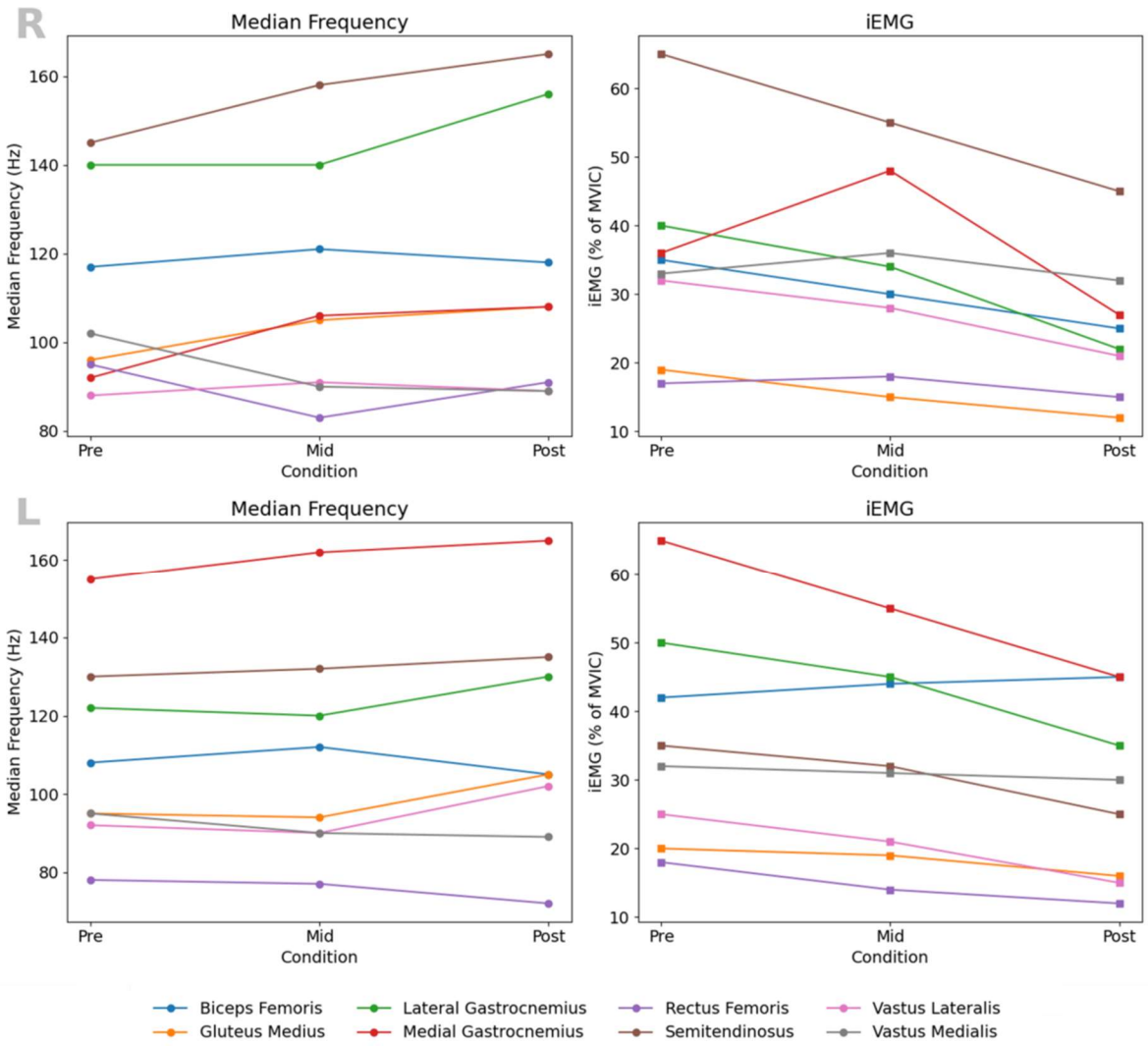


Figure 1. Mean changes in median frequency and integrated EMG (%MVIC) across Pre-, Mid-, and Post-exercise stages for eight lower-limb muscles.Right leg shown shown in the top row; left leg in the bottom row.

Session Category

Human Motion and Performance: Sports

P1-259

Evaluation of Fatiguing Effects on Grip Strength Due To Dismounted Litter Transport With and Without the Use of Assistive Devices

Mrs. Allison Robinette MS

U.S. Army Aeromedical Research Laboratory, Fort Rucker, AL, United States. Chenega Services and Federal Solutions, LLC, Chesapeake, VA, United States

Introduction

Dismounted litter transport is a physically strenuous task that is compounded by terrain, combat, and distance from the next point of care. Previously, we investigated litter carry assistive devices (LCAD) during simulated, prolonged dismounted litter transport to reduce post-carry fatiguing effects [1,2]. Our findings indicated that LCAD (shoulder harness and wrist hooks) could have many benefits to litter bearers, but further testing was needed in mass casualty (MASCAL) scenarios. As a result, we conducted field testing with the LCAD to evaluate litter carriage performance and post-carry fatigue effects in a simulated MASCAL scenario [3]. Our objective was to investigate relationships of fatigue between dominant hand and bilateral grip strength.

Methods

Following a counterbalanced design, sixteen U.S. Army Soldiers evaluated all litter carry conditions: unassisted carry (UA), shoulder harness carry (SH), wrist hooks carry (WH). For each condition, participants in two-person teams picked up, carried (50 meters), and set down a weighted litter, simulated a return to the point of injury (starting location), and repeated this process for 20 minutes. Immediately before and after each carry condition, grip strength was recorded using a VALD Dynamo Plus dynamometer with a grip strength attachment. Grip strength assessments were recorded three times for each hand, alternating between left and right. A pairwise t-tailed test was used to investigate the relationship between dominant and non-dominant grip strength. Repeated measures ANOVAs were computed for grip strength on carry condition for average change (post-carry minus pre-carry) in dominant, non-dominant, and bilateral grip strength groups ($p < 0.05$ was significant).

Results

Results did not show any significance between dominant and non-dominant hand average grip strength (p=0.697). Post-hoc analyses revealed significance in grip strength groups between UA and SH (a), SH and WH (b), and WH and UA (c) (Table).

Discussion

While all grip strength measurements were found to be acceptable measures of post-carry fatigue, variance obscured some statistical differences, but not the trends, between carry conditions. Consistent with previous findings [1,2], LCAD lessen grip strength decrements in MASCAL scenarios.

Images (Optional)

Table. Average Change in Grip Strength (Newtons) Between Carry Conditions

Grip Strength Group	UA, n=15	SH, n=16	WH, n=15
Dominant Hand	-117.2[a]	-35.7[a,b]	-67.1[b]
Non-Dominant Hand	-125.6[a,c]	-30.1[a]	-54.0[c]
Bilateral Hands	-121.7[a]	-32.7[a,b]	-60.4[b]

References (Optional)

[1] Ballard, M.T. et al. (2023), USAARL-TECH-FR-2024-06. [2] Ballard, M.T. et al. (2025), USAARL-TECH-FR-2025-23. [3] Robinette, A.M. et al (in review), USAARL-TECH-FR.

Session Category

Human Motion and Performance: Sports

P1-260

Quantifying Slip Events Using Foot Center-of-Mass (COM) Kinematics During Cutting Maneuvers in Collegiate Soccer Players

Ms. Allyson Ford[1], Dr. Brett Pexa[1], Mr. Noah Rauch[1], Mr. Garrett Hess[1], Dr. Jeffrey Taylor[1], Mr. Joseph Helseth[2], Dr. Kevin Ford[1]

[1]High Point University, High Point, NC, United States. [2]Nike Sport Research Lab, Beaverton, OR, United States

Introduction

Cleated footwear traction testing on turf surfaces often involves translational foot motion (slip events). These slip events may contribute to injury, especially if they increase joint kinetics. The purpose of this study was to develop a simplified method for objectively quantifying slip events in collegiate soccer athletes.

Methods

30 competitive soccer players (age: 20.7 ± 1.2 yrs; mass: 71.5 ± 9.9 kg; height: 171.9 ± 8.1cm, 15 male, 15 female) participated in a footwear traction study. A total of 20 trials (5 per condition) were collected from each participant performing maximum effort 180-degree cutting maneuvers across two cleated footwear conditions and two turf surface conditions. Kinematic data were collected (200Hz) on a three-dimensional motion analysis system consisting of 14 digital high-resolution cameras positioned throughout the laboratory (Qualisys AB, Göteborg, Sweden). Foot COM anterior displacement metrics (relative to running approach direction in lab coordinate system, Figure 1: minimum, maximum, mean, standard deviation) were normalized to the initial contact position and calculated through toe off. Logistic regressions were used to predict visually classified slip events. Model performance (pseudo-R^2 and AIC) and classification (accuracy, sensitivity, and specificity) were evaluated.

Results

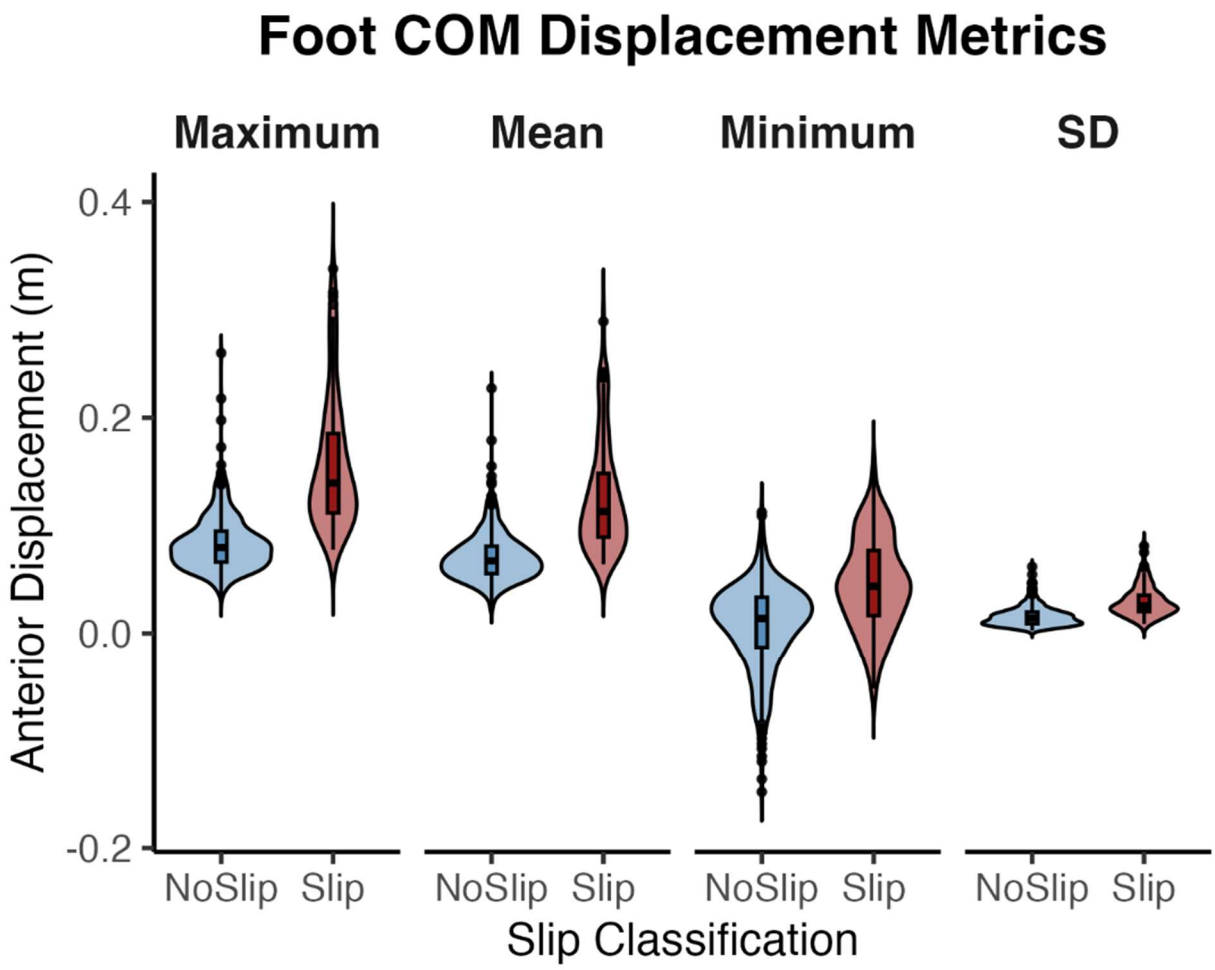
595 trials were visually reviewed by one of the authors and classified as a slip (89, 15.0%) or non-slip (506, 85.0%) based on the observed anterior translation (relative to the running direction) of the cleat during the cutting step. Logistic regression with foot COM variables predicted 91.6% of the observed slip classifications (97.8 % specificity, 56.2% sensitivity, McFadden's pseudo-R^2 = 0.48). Receiver operating characteristic (ROC) (AUC 0.946) and optimal probability threshold analyses determined Youden's index (0.13) with slightly lower

specificity (86.8%) and higher sensitivity (92.1%), resulting in correctly identifying 36% more visually observed slips. Generalization was assessed by training on 70% and testing on 30% of the sample (AUC 0.931, 88.2 % specificity, 88.9% sensitivity). A five-fold cross-validation indicated model stability (AUC 0.943 +/- 0.037).

Discussion

The optimized and validated model demonstrated high specificity and sensitivity in identifying slip and non-slip events during high-speed 180-degree cutting. This approach may reduce the need for subjective and time-sensitive visual classification of slip events.

Images (Optional)



Acknowledgements (Optional)

Funding and footwear provided by Nike.

Session Category

P1-261

The Power to Win: The Influence of Power and Playing Time as Measures of Physical Workload on Performance Error by Match Outcome and Opponent Rank in Elite Women's Rugby Sevens

Dr Amarah Epp-Stobbe[1], Dr Ming-Chang Tsai[1], Dr Marc Klimstra[2,1]

[1]Canadian Sport Institute Pacific, Victoria, BC, Canada. [2]University of Victoria, Victoria, BC, Canada

Introduction

In rugby sevens outscoring the opposition ensures a win which is influenced by individual and collective strategies and tactics[1,2]. System errors, which are deviations from strategy and tactics, reduce success[3]. While athlete physical workload affects strategic and tactical execution, the magnitude of the effect in sevens remains unclear[4]. This study investigates the influence of power and playing time as indicators of physical workload, on system errors, examining how this relationship varies according to match outcome and opponent rank.

Methods

22 female athletes (26.5±4.20years,169.5±5.90cm,70.5±6.43kg) participated in 103 international sevens matches. Athlete-worn GNSS monitors collected distance(m), speed(m/s), and playing time(mins) from which acceleration(m/s^2) was derived. Total power(W) was calculated as the cumulative sum of instantaneous absolute power (product of mass, acceleration, and velocity). Match outcome(win/loss) was recorded, and opponent rank(top-4, midrange, bottom-4) was calculated relative to the team-of-study using pre-match international rankings. System errors-per-athlete were identified using notational analysis by the team's performance analyst. A linear mixed model evaluated the relationship between fixed (power, time) and random effects (outcome, opponent) on errors by athlete.

Results

The model demonstrated a significant interaction between outcome and time, $t(997)=2.01, p<0.05$, and between power, outcome, and time, $t(997)=-2.04, p<0.05$. No other main effects or interactions reached significance. The model accounted for 18.1% of the variability in errors ($R^2_{adjusted}=0.181$).

Discussion

Errors are related to time and outcome. In wins, errors increased over time at a lower rate than losses. Further, the relationship with power, time, and errors differed depending on outcome. Higher power in wins reduced errors, suggesting a protective effect as players were highly focused, appropriately making decisions and executing team strategies[5]. Errors are equivalent across opponent, agnostic of power, inferring that additional variables such as psychological state must be considered in parallel to physical outputs when monitoring athlete workload.

Images (Optional)

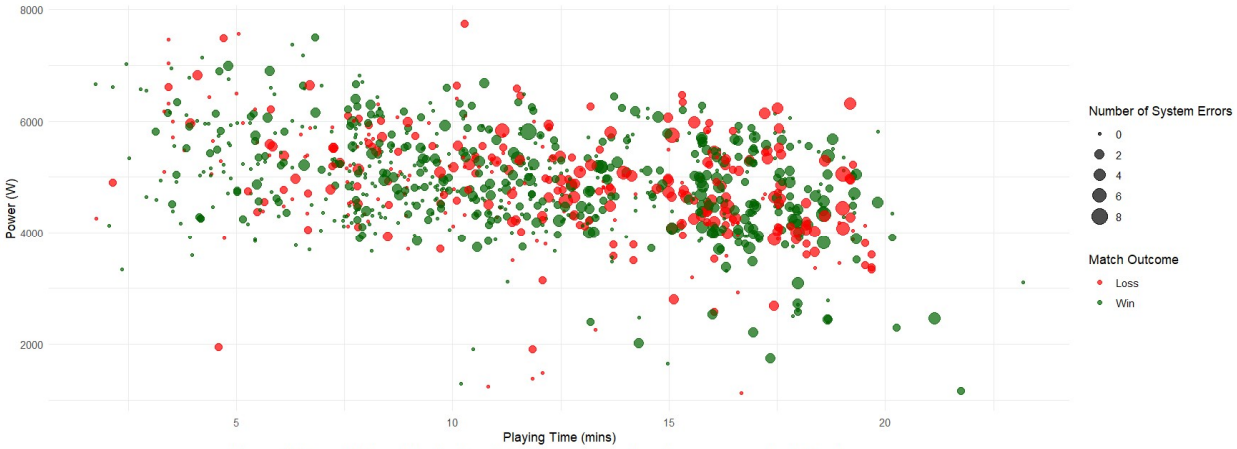


Figure 1: Power(W) and playing time(mins) by number of system errors and match outcome.

References (Optional)

[1]Higham et al.,J Sports Sci Med,2014.

[2]Lamas et al.,Int J Perf Anal Sport,2014.

[3]Colomer et al.,2020, Sports Med-Open,2020.

[4]Dambroz et al.,PLoS One,2022.

[5]Bull et al.,Eur J Sport Sci,2023.

Acknowledgements (Optional)

The authors thank Callum Morris, Rugby Canada, and Mitacs.

Session Category

Human Motion and Performance: Sports

P1-262

Shivering Magnitude Is Strongly Correlated With Temperature Recovery Following Cold Water Immersion in the Field

Dr. Amy Schwartz[1,2], Dr. Douglas Jones[1], Ms. Rebecca Weller[1,2], Ms. Rebecca McClintock[1,2], Dr. Matthew Peterson[1], Mr. Tony Duong[1,2], Dr. Amy Silder[1]

[1]Naval Health Research Center, San Diego, CA, United States. [2]Leidos Inc., San Diego, CA, United States

Introduction

After cold-water immersion (CWI), core temperature may continue to drop during early rewarming. The timing of this "afterdrop" is closely associated with shivering thermogenesis. Although core and skin temperature recovery have been well studied, their relationship to shivering cessation has not been quantified. Here, we assessed changes in shivering magnitude throughout rewarming and explored its time-dependent relationship with temperature recovery.

Methods

Active duty service members (17M; 30±7y; 163±41cm; 85.5±12.6kg) were immersed to the neck in a near-frozen outdoor pond for 10 minutes during a training exercise (water: 1.3ºC; air: -4.2ºC). After immersion, participants changed into dry clothes and began active rewarming by stair stepping in place at a predetermined frequency for 40 minutes. Shivering magnitude was estimated from an Xsens DOT accelerometer on the pectoralis. Core temperature was recorded using BodyCAP ingestible capsules. Mean skin temperature (MST) was calculated [1] from iButtons on the pectoralis, thigh, and shoulder. Data were time synchronized, with shivering magnitude averaged into 1-minute epochs to align with temperature data. Pearson's coefficient and canonical correlation analysis via statistical parametric mapping vector field analysis were used to assess the strength of correlations between variables.

Results

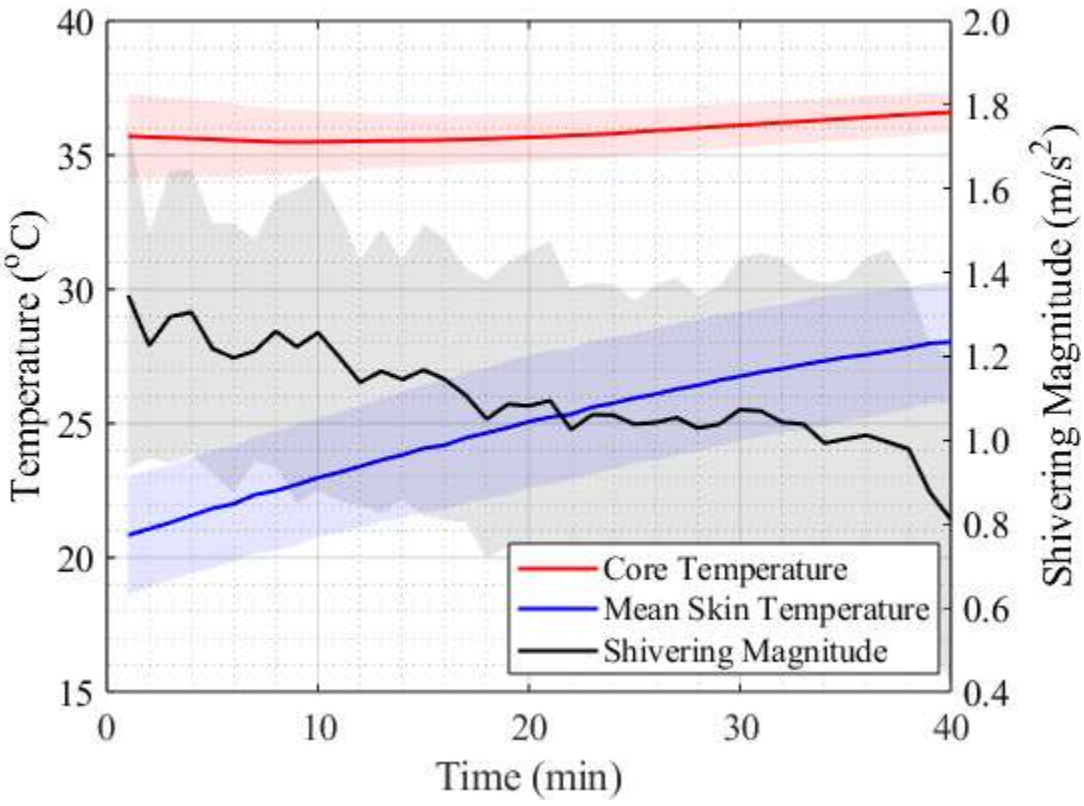
Shivering magnitude decreased from 1.35±0.41 m/s^2 to 0.81±0.39 m/s^2 across the 40-minute rewarming (Figure 1). These reductions were very strongly correlated with increasing MST ($r=-0.93$, $p<.001$) and strongly correlated with increasing core temperature ($r=-0.79$, $p<.001$). Canonical correlation revealed the rate of change in shivering magnitude was correlated with MST and core temperature from minutes 13-40 of rewarming ($p=.033$). Post hoc Pearson's correlation further revealed the rate of change in shivering magnitude

was moderately correlated with MST from 0-27 minutes (r=-0.65 to -0.50, p=.022) but not significantly correlated with core temperature.

Discussion

Shivering magnitude was strongly correlated with increasing MST and core temperature while actively rewarming following outdoor, whole-body, CWI. This association emerged shortly after minimum core temperature (minute 11.9±9.2 of rewarming), aligning with previous work relating shivering thermogenesis to afterdrop. Our findings quantify the time course of shivering cessation dynamics and may inform targeted rewarming protocols to optimize thermoregulation and reduce afterdrop risk.

Images (Optional)



References (Optional)

[1] Ramanathan. J Appl Physiol., 1964.

Session Category

Human Motion and Performance: Sports

P1-263

Investigating The Relationship between Maximal Isometric Strength and Measures of Dynamic Performance in Collegiate Female Basketball Athletes

Mr Anaikh Randhawa

McMaster University, Hamilton, Ontario, Canada

Introduction

Lower body strength is crucial for basketball performance, impacting sprinting ability, jump height, and injury risk. Traditional assessments such as one-repetition maximum testing have limitations regarding safety, fatigue, and force-time characteristics. The isometric mid-thigh pull (IMTP) is a validated alternative, providing a safer and more efficient measure of maximal isometric strength. Although IMTP-performance relationships are well established in male athletes, evidence in female basketball athletes remains limited.

Methods

The objective of this study was to determine whether IMTP-derived strength metrics correlate with dynamic performance in female basketball athletes, and to evaluate how the magnitude of these associations compares with recreational athletes. Collegiate female basketball athletes (n = 11) and recreational athletes (n = 9) completed two IMTP's on a portable force plate system to assess peak force (PF) and rate of force development (RFD). Dynamic performance was evaluated using countermovement jump (CMJ) concentric mean power (W/kg) and jump height (in), and 10-meter sprint time (s). Pearson correlations were computed within each group to examine associations between IMTP-derived strength metrics and dynamic performance outcomes.

Results

Female basketball athletes demonstrated significant correlations between RFD 0–50 ms and both jump height and sprint time, as well as between sprint time and RFD 0–150 ms and RFD 0–200 ms. Conversely, recreational athletes exhibited significant correlations between peak vertical force / BM (N/kg) and both jump height and concentric mean power, along with similar relationships using net peak vertical force (N). Detailed correlations between IMTP metrics and CMJ/sprint performance are presented in Table 1.

Discussion

These findings highlight the value of the IMTP for performance profiling in female basketball athletes, particularly through early-phase RFD, which was associated with dynamic outcomes despite no relationships with peak force. In contrast, peak force values were more strongly related to performance in recreational athletes, with no significant relationships observed for RFD, potentially reflecting reduced ability to generate rapid force. Overall, the IMTP appears useful for guiding individualized training program design. However, metric selection should be population-specific, as force expression differs across athlete groups.

Images (Optional)

Table 1: *Pearson correlations between IMTP force–time characteristics and dynamic performance metrics from CMJ and 10-Meter Sprint.*

VARIABLE	GROUP	CMJ		SPRINT
		Jump Height	Concentric Mean Power / BM	Time
PEAK VERTICAL FORCE	Basketball Athletes	0.15	0.12	0.05
	Recreational Athletes	0.81**	0.91**	-0.56
PEAK VERTICAL FORCE / BM	Basketball Athletes	0.44	0.41	-0.10
	Recreational Athletes	0.68*	0.87**	-0.37
RFD 0–50 MS	Basketball Athletes	0.90**	0.66	-0.73*
	Recreational Athletes	-0.05	0.06	-0.51
RFD 0–150 MS	Basketball Athletes	0.59	0.58	-0.67*
	Recreational Athletes	0.11	0.39	-0.39
RFD 0–200 MS	Basketball Athletes	0.61	0.68	-0.66*
	Recreational Athletes	0.20	0.57	-0.52

**Denotes $p < 0.05$, **Denotes $p < 0.01$.*

Acknowledgements (Optional)

Dr. Dylan Kobsar, Anil Palanisamy, Tamar Kritzer, Joanna Torres, and Jaden Premji.

Session Category

Human Motion and Performance: Sports

P1-264

Assessing Deep Learning Techniques for Ice Hockey Human Activity Recognition fromGame Simulated Inertial Measurement Unit Data

Mr Andrew Phillips MSc, Mr Philippe Renaud MSc, Dr Shawn Robbins PhD

McGill University, Montreal, Quebec, Canada

Introduction

The introduction of artificial intelligence (AI) has revolutionized the way sports data is collected and analyzed, opening new possibilities for what can be achieved in sports science research and performance. Human activity recognition (HAR) in ice hockey had traditionally relied on manual annotation and analysis from humans, a time-consuming task prone to error and bias. By partnering AI algorithms with movement data from wearable sensors, HAR models can be developed and implemented to provide deeper, more efficient, and more meaningful insights into hockey data. The objectives of this research were to compare three distinct deep learning neural networks in their abilities to classify eight ice hockey player events using wearable accelerometer data and to determine the optimal sensor configuration for this task.

Methods

48 hockey players performed shots and other hockey events in a game-simulated environment using 17 wearable inertial measurement units (IMU). Video footage of the participant trials was used as ground truth for labelling the IMU data. The segmented and labelled acceleration data were used to train and test three deep-learning model architectures: a traditional approach (Convolutional Neural Network (CNN)), a modern approach (Transformer Network), and a hybrid approach combining the benefits of both models (CNN-Transformer Hybrid), with three different sensors configurations (all 17 sensors (ASC), 3 sensors on the sternum and hands (SHSC), and 2 hands only sensors (HSC)).

Results

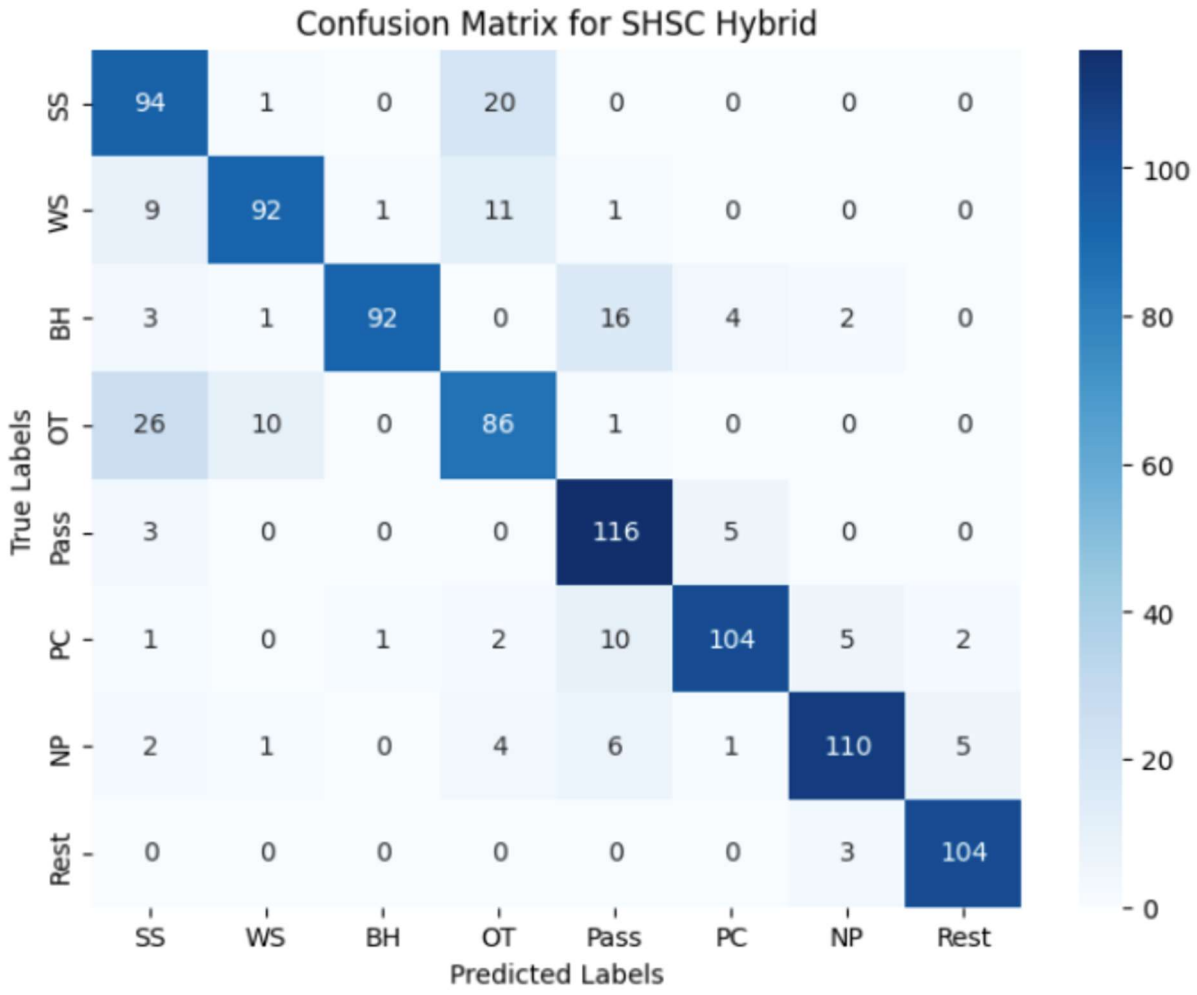
The hybrid models achieved the highest mean F1 score across all three sensor configurations (81.9%), followed by the CNN models (79.5%) and the Transformer models (74.4%). The highest-performing individual model was the 3-sensor Hybrid model, reaching an F1 score of 83.7%. The models all demonstrated their ability to differentiate between

tasks with different movements (e.g. slap shot vs pass) but struggled to differentiate between tasks with similar movement patterns (e.g., slap shot vs one-timer).

Discussion

Findings from this study can have a positive impact on the advancement of how movement data is detected and analyzed in real-game environments. These advancements have important implications for coaches, players, and analysts by supporting the development of AI technology for injury detection and rehabilitation, real-time performance tracking, and technique optimization to enhance player performance.

Images (Optional)



Session Category

Human Motion and Performance: Sports

P1-265

Neuromuscular Coherence Patterning in Female High School Soccer Athletes

Ms. Yara Izhiman[1], Ms. Annika Schaeffer[1], Dr. Vesna Novak[1,2], Dr. Michael Riley[3], Dr. Brian Grawe[4], Dr. Eric Nauman[1]

[1]Department of Biomedical Engineering, University of Cincinnati, Cincinnati, Ohio, United States. [2]Department of Electrical Engineering and Computer Science, University of Cincinnati, Cincinnati, Ohio, United States. [3]Department of Rehabilitation, Exercise, & Nutrition Sciences, University of Cincinnati, Cincinnati, Ohio, United States. [4]Orthopaedics and Sports Medicine University of Cincinnati, College of Medicine, Cincinnati, Ohio, United States

Introduction

The integration of cognitive command signals and muscle activation as biomarkers for functional performance remains under-researched yet holds potential for advancing rehabilitation strategies and enhancing athletic performance. This study aims to advance the understanding of cortico-muscular communication across functional performance in pre-professional teams such as high school soccer. To achieve this, we compared cortical and muscular correlation and coherence across different functional movements in six female high school soccer athletes. By comparing these interactions, our study aims to offer a baseline for future directions, especially in identifying indicators of injury, muscular fatigue, as well as recovery.

Methods

Data acquisition was conducted across six repetitions of two activities: calf raises and two-legged squats under a loaded and unloaded condition. Electromyography (EMG), electroencephalography (EEG), and motion capture signals were recorded concurrently to ensure synchronized multimodal datasets. The raw datasets were processed using a custom MATLAB pipeline that expanded on standardized signal processing procedures for cross-modal comparative analysis. Correlation and coherence maps describing neural, muscular, and cortico-muscular dynamics were generated for EMG, EEG, and EEG-EMG data, respectively.

Results

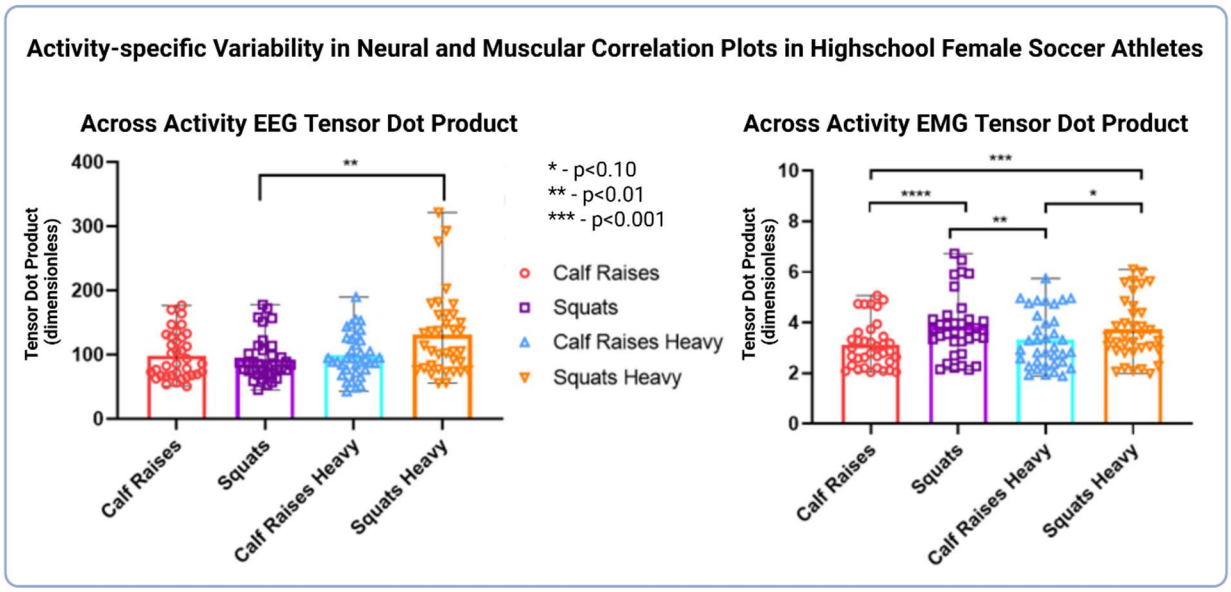
Our preliminary findings highlight statistically significant difference between functional movement, calf raises and squats, which suggests movement-dependent cortico-muscular dynamics. Furthermore, squats, which are considered complex movement as compared to calf raises, exhibited significant increases in both cortical and muscular

dynamics when loaded sets were compared to non-loaded. The increased neuromuscular dynamics in loaded squats may signify increased neuromuscular recruitment that required stabilization. In addition, the increased neural dynamics may reflect enhanced cortical drive under the loaded condition, likely required by the recruitment of higher motor strategies for neuromuscular control.

Discussion

Our preliminary results revealed that the repeatability of cortico-muscular dynamic characterization allows for utilizing cortical and muscular dynamics as markers for neuromuscular communication across functional performance in athletes. In addition, the reported activity-specific cortico-muscular dynamic variability highlights the promise of this integrated investigation in personalizing comprehensive functional performance. These findings further invite the expanded investigation of the role of athletic training in enhancing neuromuscular efficiency in functional movement. In addition, this proposed approach may allow for injury prediction, and in parallel, return-to-sport readiness following an injury.

Images (Optional)



Session Category

Human Motion and Performance: Sports

P1-266

Impact of Shoulder Fatigue on Motor Learning During High-Velocity Athletic Wheelchair Propulsion

Mr. Anthony Tremblay[1,2], Ms. Sara Havashinezhadian[1,2], Mr. Abdellah Hassar[1,2], Mr. Jason Bouffard[1,2]

[1]Université Laval, Quebec, Quebec, Canada. [2]Center for Interdisciplinary Research in Rehabilitation and Social Integration, Quebec, Quebec, Canada

Introduction

Neuromuscular fatigue emerges from sustained physical exertions and leads to diminished performance and heightened perceived effort. In the context of motor learning, it can disrupt practice quality and skill acquisition. Previous studies have shown that training under conditions of fatigue can affect motor learning, especially during precision motor tasks. However, very few studies evaluated its effects on motor learning of skills requiring important power production such as high velocity wheelchair propulsion. The objective of the study is to analyze the effects of neuromuscular fatigue on motor learning in athletic wheelchair propulsion. Fatigue is expected to impair performance and learning.

Methods

Forty healthy participants will be evaluated during three laboratory sessions. During the first session, they will complete a total of 7 blocks of 3 wheelchair propulsion trials (2 submaximal + 1 maximal). Each block will be separated by 5 minutes of fatiguing or non-fatiguing shoulder movements, depending on group assignment. Retention will be assessed in Sessions 2 and 3 during two blocks performed either with or without fatigue in randomized order. Multiple spatiotemporal (i.e. cycle frequency), velocity (average speed, within-cycle speed gains and loss) and acceleration (i.e. maximal acceleration and deceleration) metrics will be computed for each propulsion cycle and compared between blocks and groups. Subjective and objective signs of fatigue will also be assessed.

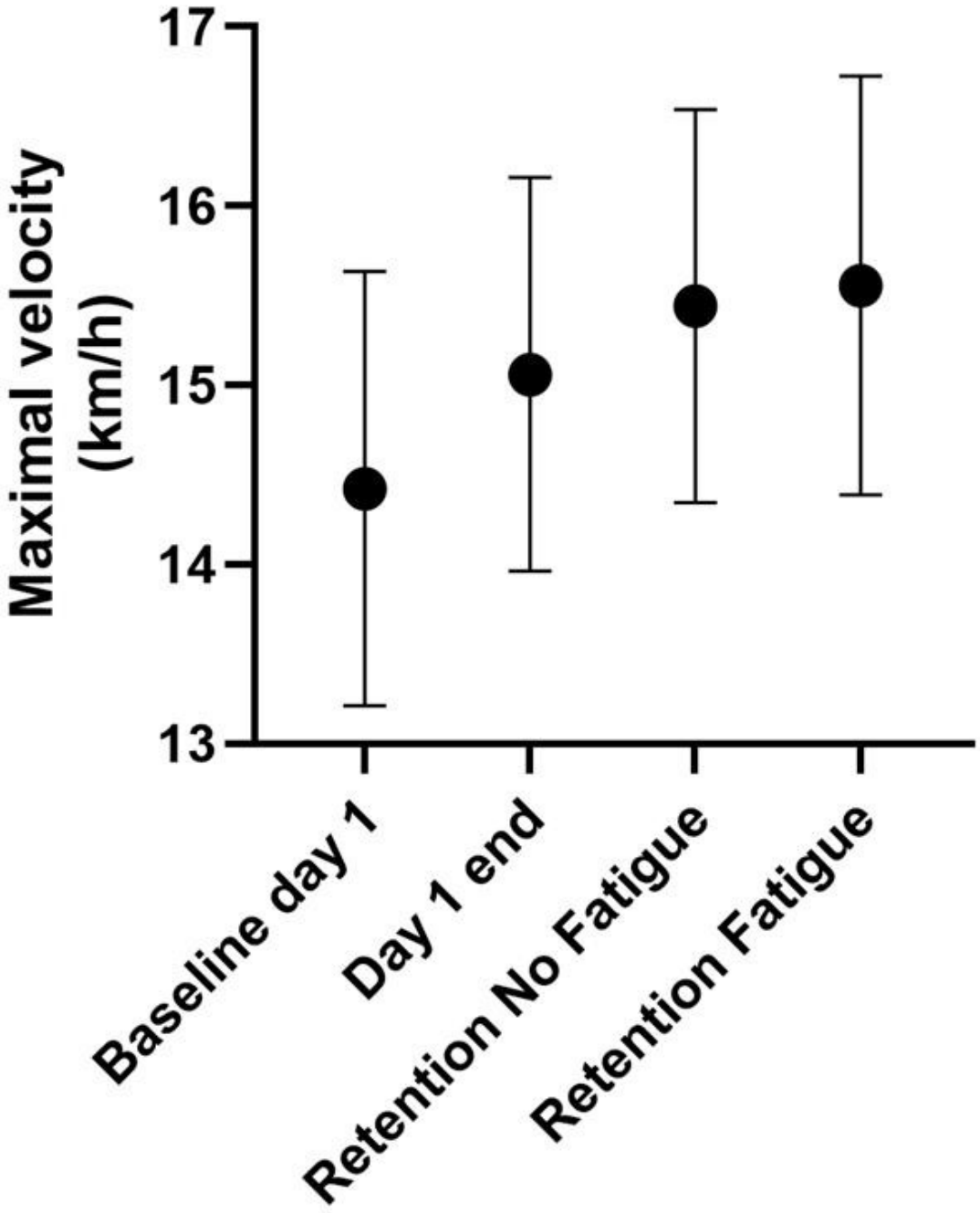
Results

Preliminary results (Control group: n=6; Fatigue group: n=4) showed a trend for improvement in maximal velocity over time when considering both groups together (Figure 1; one-way ANOVA: $p = 0.064$). Participants perceived significantly more fatigue following fatiguing (>6.5/10) than non-fatiguing contractions (<3.5 / 10), as expected. However, maximal velocity wheelchair propulsion induced significant objective (>15% decreased in maximal force) and subjective (up to 7.8 / 10) signs of fatigue in all conditions, reducing the contrast in the fatigue experienced by each group.

Discussion

Preliminary results partially confirm the validity of the protocol aiming to assess the effects of neuromuscular fatigue on motor learning. Still, results highlight challenges in finding the best balance between movement repetition and rest time to allow motor learning and prevent fatigue to advance the research field, especially in motor skills requiring important power production.

Images (Optional)



References (Optional)

Acknowledgements (Optional)

Université Laval, Center for Interdisciplinary Research in Rehabilitation and Social Integration (CIRRIS), Interactive Technologies of Engineering in Rehabilitation (INTER) and Natural Sciences and Engineering Research Council of Canada (NSERC).

Session Category

Human Motion and Performance: Sports

P1-267

Efficacy of a Frugal Inertial Sensor-based Motion Capture System in Quantifying Ankle Kinematics during Badminton Lunge

Mr. Apoorv Shrivastava PhD Student[1], Ms. Saranya Navratnarajah[2], Mr. Jeevaraaj N. Vivekanandan[3], Dr. Siew Li Goh[4], Dr. Darshan S. Shah[1]

[1]BiOME Lab, Department of Mechanical Engineering, Indian Institute of Technology Bombay, Mumbai, Maharashtra, India. [2]Institute for Advanced Studies, Universiti Malaya, Kuala Lumpur, Federal Territory of Kuala Lumpur, Malaysia. [3]Department of Biomedical Engineering, Faculty of Engineering, Universiti Malaya, Kuala Lumpur, Federal Territory of Kuala Lumpur, Malaysia. [4]Sports Medicine Unit, Faculty of Medicine, Universiti Malaya, Kuala Lumpur, Federal Territory of Kuala Lumpur, Malaysia

Introduction

Inertial sensors are an ubiquitous alternative to optical motion capture (OMC) in characterizing movement biomechanics in field applications [1]. However, issues related to measurement noise, signal distortion, sensor drift, coupled with the premium and discreet software packages of commercial sensors limit their adoption to a narrower user-base. A modular frugal inertial measurement unit (IMU)-based motion capture system was therefore, developed for more accessible, transparent and customizable biomechanical analyses. To validate this custom IMU system for high-impact, high-frequency on-field sporting tasks, this study aimed to assess the efficacy of the system in capturing ankle kinematics during badminton lunge.

Methods

The custom-IMU system consisted of a low-cost IMU (MPU9250, InvenSense, USA), a microcontroller, wireless data transmission module and on-board data storage. Data handling included signal processing, drift compensation, a Madgwick filter-based sensor fusion algorithm and a functional calibration-based sensor-to-segment alignment procedure [1]. Following institute ethics approval, 18 recreational badminton players (7F, 29±7yrs) performed three trials of forward lunges. Ankle kinematics – plantar-dorsiflexion (PDF), inversion-eversion (InvEv), internal-external rotation (IErot) – were captured using custom IMUs attached to the foot and shank segments, and an eight-camera OMC system (Qualisys, Sweden), which tracked markers attached to these segments following ISB recommendations [2]. Root mean square error (RMSE), maximum error, error in range of

motion (ROM) and paired-t test ($p<0.05$) were used to compare the accuracy of IMU-derived ankle kinematics against benchmark OMC results.

Results

RMSE and maximum error were lower for PDF (RMSE=0.89°, max. error=3.31°, ROM error=5.51%) and InvEv (RMSE=1.35°, max. error=3.76°, ROM error=15.00%) as compared to IErot (RMSE=3.62°, max. error=7.19°, ROM error=95.48%).

Discussion

RMSE results revealed 'good' accuracy of the custom-IMU system for PDF and InvEv, and 'acceptable' for IErot [3], despite higher errors near the heel-strike and foot-off events anticipated due to impact-driven movement artefacts. Large maximum and ROM errors observed for IER displayed the inefficacy of custom IMUs to track the tertiary degree of freedom. Overall, these findings for the dynamic high-impact activity showed potential of the custom-IMU system for tracking sports-related motions.

Images (Optional)

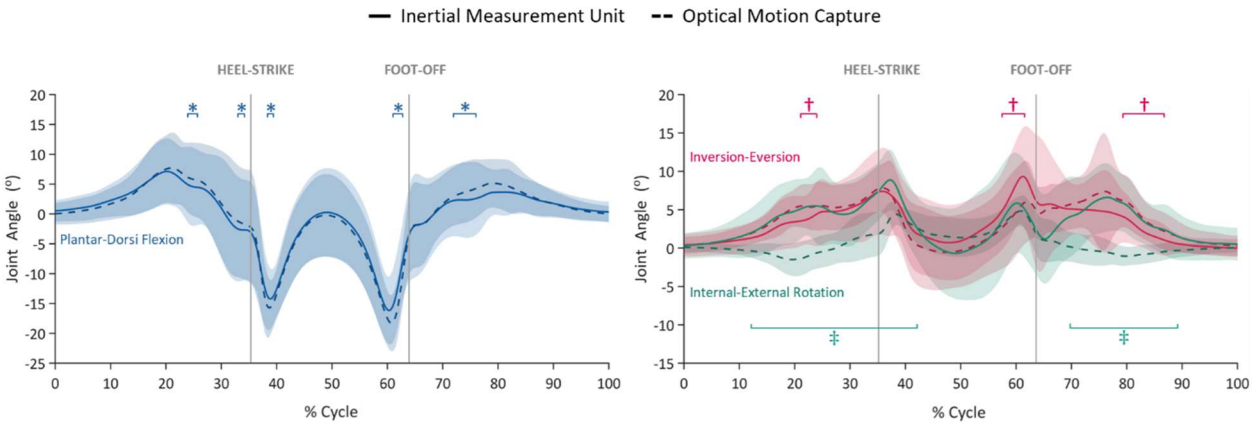


Figure 1: Ankle kinematics from custom inertial measurement unit (IMU) and optical motion capture (OMC) for badminton lunge (*, †, ‡ indicate statistically significant differences; $p<0.05$)

References (Optional)

[1] Cereatti *et al.*, J Biomechanics, 2024

[2] Wu *et al.*, J Biomechanics, 2002

[3] McGinley *et al.*, Gait Posture, 2009

Acknowledgements (Optional)

This study was supported by Seed funding for Collaboration and Partnerships Projects (SCPP), IIT Bombay. AS was supported by the Prime Minister Research Fellowship, Government of India.

Session Category

Human Motion and Performance: Sports

P1-268

A Machine Learning Pipeline to Evaluate Dive Performance

Ms. Athena Constantinou-Simek[1], Professor Jill McNitt-Gray[2], Professor Nidhi Seethapathi[1]

[1]Massachusetts Institute of Technology, Cambridge, Massachusetts, United States. [2]University of Southern California, Los Angeles, California, United States

Introduction

Several sports use automated judging systems to provide metrics of an athlete's movement or to assist referees with qualitative judgements. Springboard diving has implemented AI to measure low-dimensional features like dive height or number of revolutions, to aid judges with scoring. However, technology to automatically analyze dives directly from video is missing. Here, we create and evaluate a machine learning pipeline to track athlete movements, determining minimum labels for accurate tracking.

Methods

Our dataset consists of 126 sagittal videos from the Men's 3M Diving Preliminaries during the 2012 London Olympics. These videos were analyzed using pose estimation software (DeepLabCut (DLC)), extracting 27 keypoints using supervised learning. DLC requires several pre-labelled frames for each video, and we tested different numbers of labels to determine an optimal number for an accurately tracked video. Then, we created a Long Short-Term Memory Machine Learning (LSTM ML) model, whose inputs are the x,y coordinates of an individual video, and whose output is a single overall score, as given by the Olympic judges.

Results

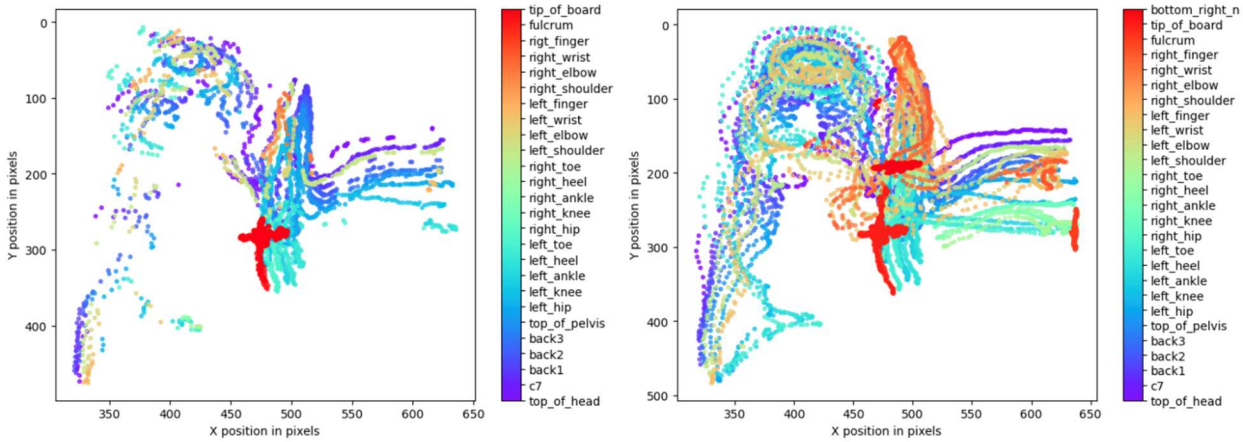
DLC generates accurate labeling on a test dataset if ~8% of the input frames are labelled. Using DLC's automatic kmeans frame extraction algorithm gives 31.99 pixels root mean squared error (rmse). When we manually extract 69 frames from the same video, the rmse is 4.6 pixels. The software performs better if the labelled frames are manually selected and concentrated around periods when the diver's position changes rapidly. We trained our LSTM ML model with 23 videos of pike dives and tested the model on 6 videos, and the rmse of the predicted judge scores is 15.2%.

Discussion

Our study clarifies the ideal method of frame selection and the number of frames needed to track a complex whole-body movement like diving. We provide preliminary evidence that such pose tracking can be used to predict the overall dive score. Going forward, we will

adjust our input movement data to determine the minimum information necessary for accurate predictions of the dive score. Overall, this data-driven approach will help advance automated scoring of sports and understand which movement features are most score-relevant.

Images (Optional)



Plots generated by DLC, graphed are x,y coordinates of 27 keypoints across all frames. Left: 20 labelled frames (2.5% of total), extracted using DLC kmeans algorithm. Right: 69 labelled frames (8.6% of total), extracted using manual selection.

Acknowledgements (Optional)

The authors would like to acknowledge the Integrative Movement Science Institute (NSF-DBI-2319710).

ACS would like to acknowledge financial support from the Paul E. Gray (1954) UROP Fund, and Eric Wang for help with computation.

Session Category

Human Motion and Performance: Sports

P1-269

Effect of Effective Mass in Lower Limb Strikes in Martial Arts Between Experience Levels

Ms. Avery Moe, Dr. Ross Miller

University of Maryland, College Park, MD, United States

Introduction

High rates of force development and deceleration just before impact are integral to martial arts striking performance. Effective mass is a measure that reflects the martial artist's ability to strike with both of these characteristics as observed in highly experienced individuals. There is little evidence on how training affects a person's ability to achieve high effective masses in the striking, or impact, leg and standing, or plant, leg upon impact. This study seeks to quantify effective mass in the impact and plant legs of a front leg round kick, and to compare effective mass between martial artists of different experience levels.

Methods

Three beginner (24±3 years old, 1±1 years of experience) and five advanced (21±2 years, 13±2 years of experience) martial artists performed five maximal effort front leg round kicks with each leg, targeting a standing 100-lb foam bag. Ground reaction forces of the participant and the target were collected. Acceleration of the participant's center of mass was calculated from the ground reaction forces, and effective mass was calculated for the striking leg and the plant leg as the ratios between the peaks of these forces and the accompanying acceleration of the center of mass. Effective mass averages were reported as absolute values in kilograms and relative values when scaled by body mass. They were then compared between groups using unpaired t-tests.

Results

No significant differences were found between groups in absolute or relative effective mass of either leg (all $p > 0.1$). Further analysis revealed that beginners had greater variance values in all outcome measures and conditions except for effective mass in the plant leg and of the sum of the forces when kicking with the right leg. No statistical significance of variances between groups was found either (all $p > 0.1$).

Discussion

Contrary to our expectation, martial artists did not differ in effective mass, regardless of experience, suggesting this skill is developed early. Advanced martial artists demonstrated more consistency in the way that they perform the kick, especially in the striking leg. This

consistency is likely beneficial for traumatic knee injury prevention when striking at higher forces.

Images (Optional)

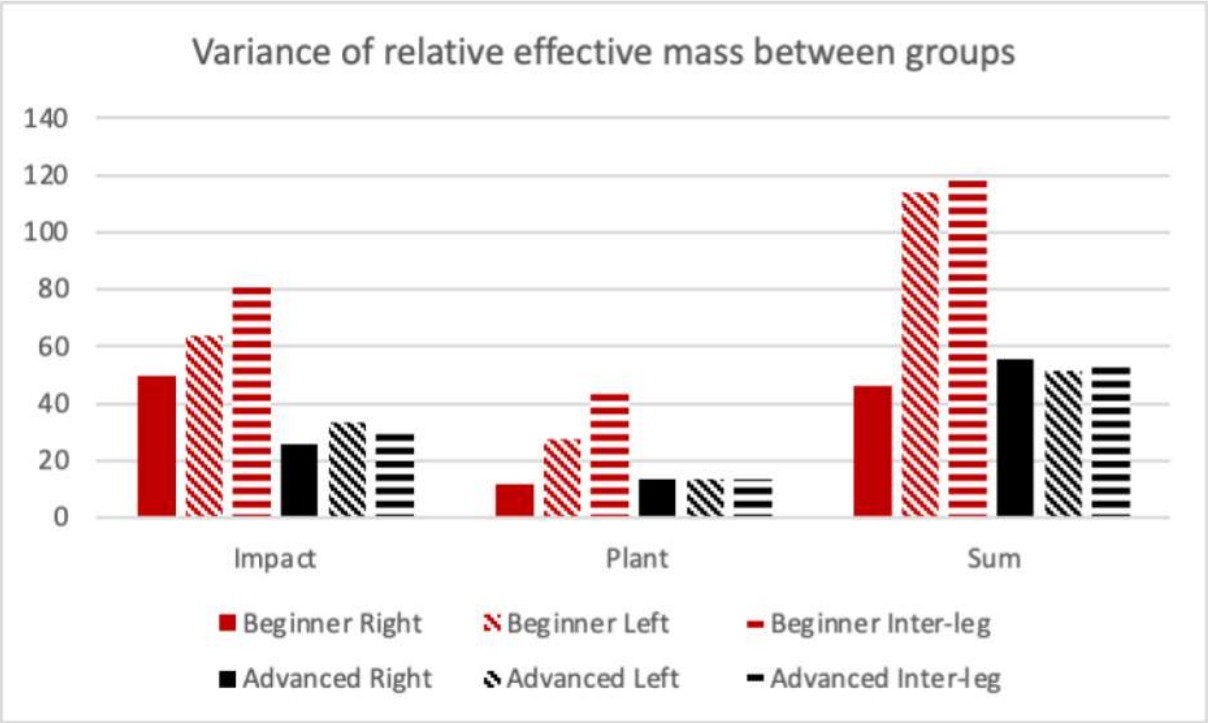


Figure 1. Average variance values of all relative effective mass measures between advanced and beginner groups across all conditions.

Session Category

Human Motion and Performance: Sports

P1-270

Effects of model personalisation on muscle and joint forces in powerlifting

Dr Basilio Goncalves[1,2], Dr Alexander Pürzel[1,2], Dr Ekaterina Stansfield[3], Dr Willi Koller[1,2], Prof Arnold Baca[1], Ass Prof Hans Kainz[1,2]

[1]Centre for Sport Science and University Sports, University of Vienna, Vienna, Vienna, Austria. [2]Neuromechanics Research Group, University of Vienna, Vienna, ViennaResearch Group, University of Vienna, Austria. [3]Department of Evolutionary Biology, University of Vienna, Austria, Vienna, Vienna, Austria

Introduction

In powerlifting squats, increasing lifting load results in heterogeneous muscle force increases particular for hip and knee muscles [1]. Powerlifting athletes have different femoral geometry compared with normal population [2] which might influence muscle and joint contact forces (JCF) [3]. Furthermore, muscle coordination strategy during squats might not aim to minimize activations, which is a common approach to calculate muscle forces [1]. We investigated how model personalisation influences muscle and JCF and hypothesised that individual bone geometry would decrease muscle and JCF while accounting for the athletes' muscle coordination would increase said forces.

Methods

Magnetic resonance image (MRI) scans of the lower limb and 3D motion capture data from seven powerlifters were collected. Generic musculoskeletal models were personalised using either marker data (linearly scaled) or using MRI derived morphology [4]. Joint kinematics and net joint moments were calculated using OpenSim and muscle forces were calculated using either Static Optimisation (SO) or a calibrated electromyography-informed neuromusculoskeletal model (CEINMS) [5]. Muscle and JCF obtained from four different simulation approaches (SO-Scaled, SO-MRI, CEINMS-Scaled, CEINMS-MRI) were compared across three different tasks (walking, bodyweight squatting, and loaded squatting).

Results

So far, data of one athlete was analysed. Personalisation of bone geometry increases knee JCF by 2% to 12% during squatting but not during walking (-8% to 19%) (Figure 1). Compared to the simplest model (SO-scaled) the most personalised model (CEINMS-MRI) resulted in similar muscle forces during walking (< 9%) but larger hip muscle forces during squatting (24 to 31%). Knee and ankle muscle forces during squatting vary largely between models.

Discussion

Personalising bone geometry and muscle coordination substantially altered muscle forces and JCF. Bone morphology increased knee JCF during squatting, while CEINMS revealed higher hip muscle forces than SO. These findings show that simplified models may underestimate key loads, highlighting the necessity of personalised musculoskeletal models for powerlifters.

Images (Optional)

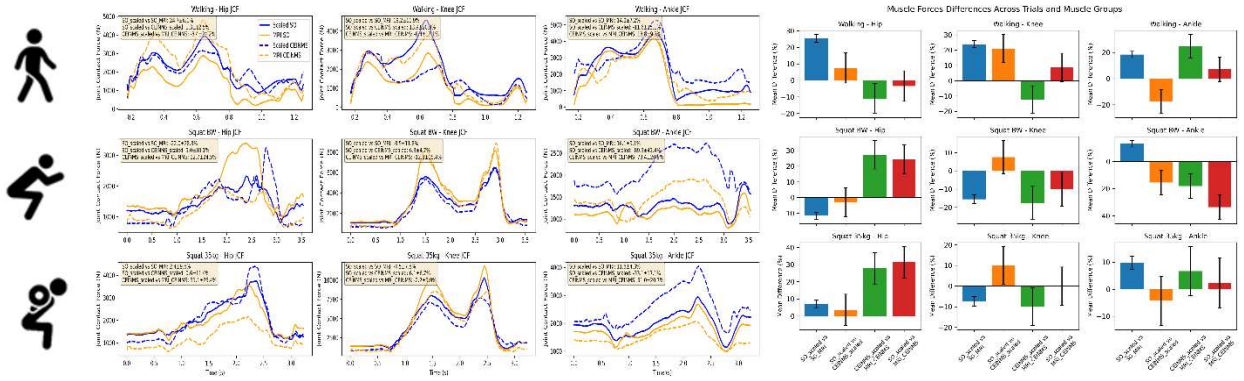


Figure 1. Effects of model personalisation on (left) joint contact forces and (right) muscle force differences between models during (top) walking, (middle) bodyweight squat,and (bottom) weighted squat in one elite powerlifter. Ensamble waveforms and standard deviations for joint contact forces were compared between a linearly scaled model (blue), an MRI-derived model (yellow), using static optimisation (solid lines) and an electromyography informed optimisation (dashed lines). Muscles forces differences are shown as mean differences (%) between the simulation approaches with standard deviation error bars. Muscles groups are shown as those crossing hip, knee, and ankle joints.

References (Optional)

[1] Pürzel et al., *Scand J Med Sci Sports*, 2025

[2] Goncalves et al., *ISBS Proceedings Archive,* 2024

[3] Kainz et al. *PLoS One*, 2023

[4] Stansfield et al., BioRxiv, 2025.

[5] Hambly et al., *IEEE Trans. Biomed. Eng.*, 2025

Session Category

Human Motion and Performance: Sports

P1-271

Midsole Rocker Geometry of Advanced Footwear Technology Affects Biomechanics but Not Running Economy or Perception in Female Runners

Mr. Ben Hazelwood, Dr. Jamie Ferris, Dr. Samuel Cheuvront, Dr. Jinger Gottschall

New Balance Sports Research Lab, Boston, MA, United States

Introduction

Midsole rocker geometry is a key feature of advanced footwear technology (AFT) and is thought to enhance endurance running performance [1]; however, its isolated effects within AFT are not well understood. This study aimed to examine effects of midsole forefoot rocker onset on running economy (RE), biomechanics, and perception in AFT.

Methods

Ten experienced female runners completed 5-minute bouts of instrumented treadmill running in three prototypes based on the New Balance FuelCell SuperComp Elite v4 of equal mass with varying midsole forefoot rocker onsets: ~50% (Early), ~60% (Mid), and ~70% (Late) of stick length. Nylon plates mirroring each prototype's rocker shape were embedded in the midsoles. RE and lower-limb biomechanics were analyzed via RMANOVA and Tukey's HSD (α=0.05). Perceived footwear attributes were rated on 7-point scales [2] and compared using Friedman tests and Dunn's post hoc pairwise comparisons.

Results

Rocker onset had non-significant effects on RE (p=0.55). Biomechanical differences occurred primarily in force, spatiotemporal, and ankle kinematic measures. These included increased peak braking force with later rocker onset and increased peak propulsion force in Late (Figure 1), as well as increased ankle sagittal range of motion in Mid (p=0.021 vs. Early; p=0.010 vs. Late). Perceived energy return (p = 0.029), ground feel (p = 0.022), and speed (p = 0.024) were different among footwear, though no pairwise differences were significant. Median values differed by less than 1 scale point out of 7.

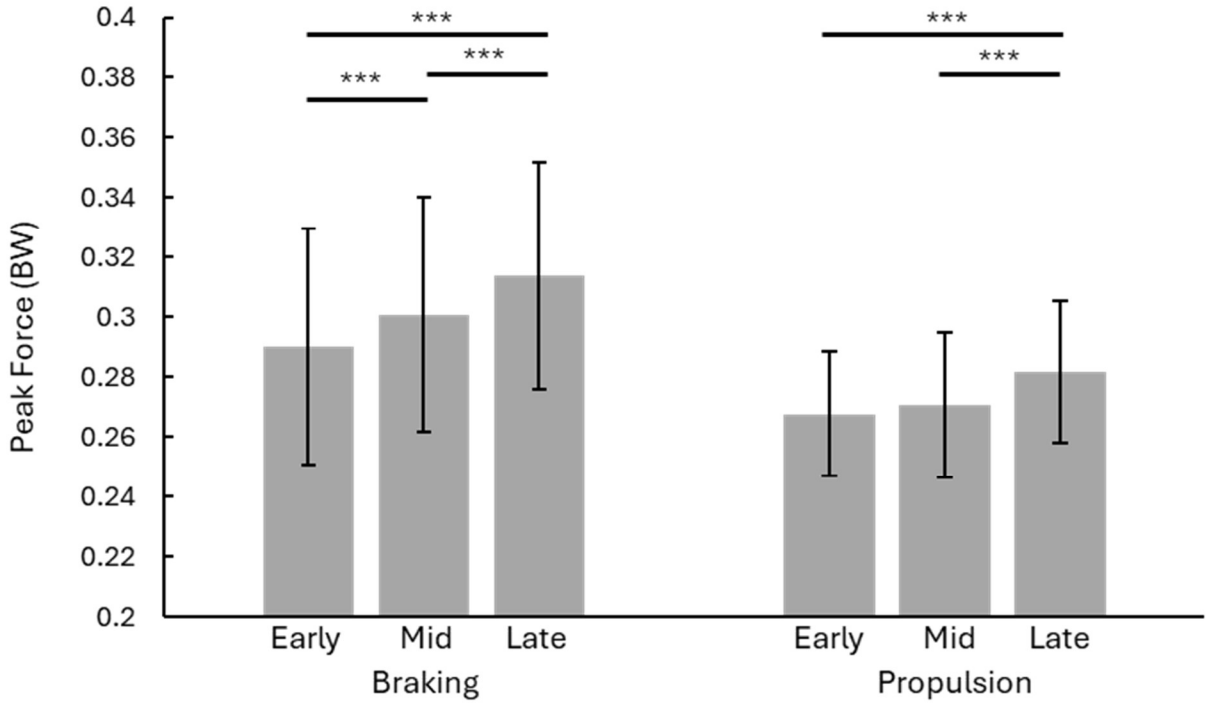
Figure 1. Average peak braking and propulsion forces across footwear conditions. ***p < 0.001

Discussion

While forefoot rocker onset in AFT affects running gait, these changes did not lead to differences in whole-body energy expenditure or footwear perception. Rocker onset in AFT

can be altered within 50-70% of stick length without impacting endurance performance or runner experience.

Images (Optional)



References (Optional)

[1] Nigg, B.M., Cigoja, S., & Nigg, S.R. (2020). Effects of running shoe construction on performance in long distance running. *Footwear Science*, *12*(3), 133–138.

[2] Agresta, C., Peacock, J., Carmichael, A., Nielsen, K.E., Zendler, J., & Gonzalez, R. (2020). The perception of ride is multidimensional for running footwear. *Footwear Science, 12*(1), 15–24.

Acknowledgements (Optional)

The authors would like to thank Jack Murphy and Long Dinh for their assistance in prototype creation.

Session Category

Human Motion and Performance: Sports

P1-272

Swinging Arms Helps Gluteus Maximus Generate More Work in the Standing Long Jump

Dr. Blake Ashby Ph.D., P.E.[1], Ms. Abigail Douglas M.S.E.[1,2]

[1]Grand Valley State University, Grand Rapids, MI, United States. [2]Thompson Surgical Instruments, Traverse City, MI, United States

Dr. Blake Ashby

Introduction

The standing long jump is a fundamental movement found in numerous sports. Prior studies using joint torque actuated models have demonstrated that arm motion improves performance in part by allowing the lower body muscles to generate more work during the takeoff phase of the movement. The purpose of the present study was to further explore this principle using muscle-actuated models to determine individual muscle contributions to performance in jumps with and without arm motion.

Methods

Three male and three female participants executed maximum effort standing long jumps: three with free arm motion and three with restricted arm motion. The motion of passive reflective markers was recorded using a 16-camera motion capture system, and ground reaction force data were recorded with two in-ground force platforms. Scaled, full-body models with 17 upper body joint torque actuators and 80 lower-body musculotendon actuators were used to analyze the longest jumps with and without arm motion for each participant. OpenSim was used to conduct inverse kinematics, inverse dynamics, residual reduction algorithm, static optimization, and muscle analyses. Muscle forces and lengths from the muscle analyses were used to calculate power and work for the takeoff phase of all jumps. Paired t-tests were performed with muscle work differences presented as mean ± standard deviation.

Results

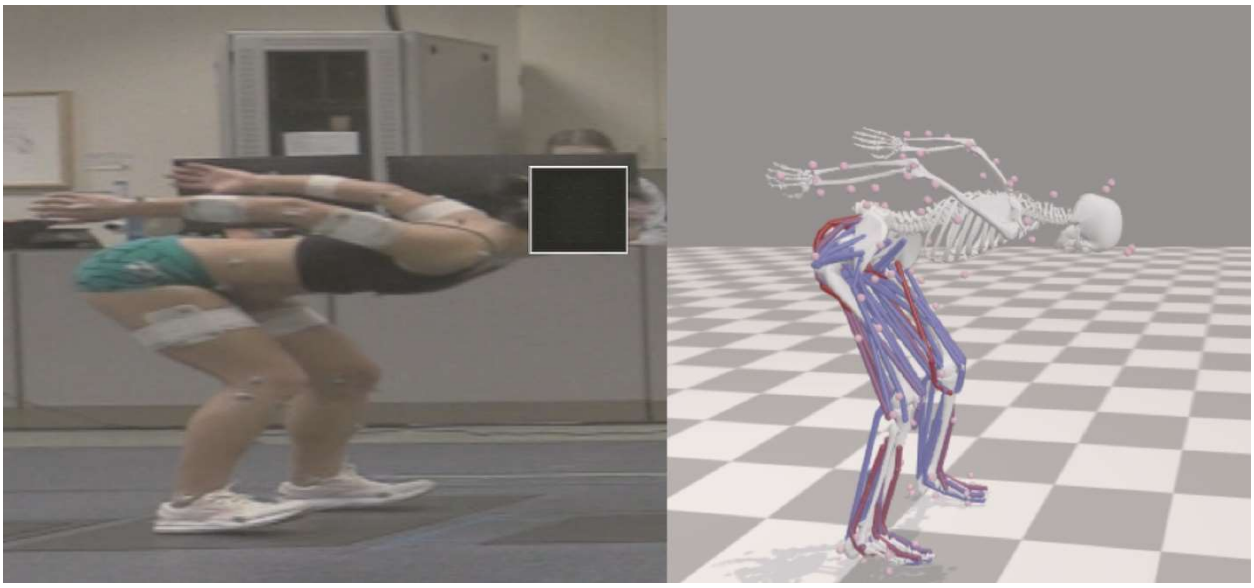
Lower body muscles generated 37.2 ± 28.2 J more work ($p = 0.02$) during the takeoff phase of jumps with free arm movement when compared to jumps with restricted arms. Over half (53%) of that work difference was due to the gluteus maximus muscles (19.7 ± 12.7 J, p =

0.01). The soleus muscles also generated significantly more work (5.0 ± 3.6 J, p = 0.02) with free arm motion.

Discussion

The largest differences in work were demonstrated by the gluteus maximus muscles, which are major hip extensors. This is consistent with the joint torque augmentation theory, which states that swinging the arms exerts downward forces at the shoulder that slow the extension of the hip allowing the hip extensor muscles to generate larger forces consistent with the force-velocity dependence of muscles. This preliminary work will be extended to include the analysis of more participant jumps.

Images (Optional)



Session Category

Human Motion and Performance: Sports

P1-273

Center-of-Mass Inclination Angle and Ski Edge Angle Influence Glide Length on Roller Skis

Mr Brandon Cabaniss, Mr Isaac Burgess MS, Mr Ethan Livingood, Dr. James Becker PhD

Montana State University, Bozeman, MT, United States

Introduction

Glide length is a critical determinant of cross-country skiing performance, with longer glide length consistently linked to faster V2 ski speed. On-snow studies show mediolateral plantar-pressure balance but not ski edge angle are strongly correlated with glide time. However this relationship has not been examined on rollerskis despite rollerskiing accounting for over half of yearly training volume. In addition to pressure balances, maintaining a stacked body position on the ski might be essential for longer glide lengths. Thus, the purpose of this study was to investigate the relationship between glide length and plantar-pressure balance, ski edge angle, and mediolateral center-of-mass inclination angles during rollerskiing.

Methods

Twenty-nine elite biathletes (15M/14F, 24±5 years) skied on a roller ski treadmill at race intensities. Ski, pole, and whole body kinematics were collected using hybrid markerless motion capture while forces applied to the ski were measured using plantar-pressure system insoles. Glide length (*GL*), mean mediolateral center-of-mass inclination angle (θ_{ML}), mean asymmetry in mediolateral pressure balance as an asymmetry index (*ASI*), and average ski edging angle (θ_{ski}) during the gliding phase were then calculated. Multiple linear regression was used to evaluate how well $\theta_{ML,}$ *ASI*, and θ_{ski} predicted *GL*

Results

Multiple regression showed that *ASI*, θ_{ski}, and θ_{ML} accounted for 30% of variance in glide length ($F_{3,52} = 7.393$, $p < 0.001$), however *ASI* was not significant ($p = 0.155$, Table 1).

Discussion

While *ASI,* not θ_{ski}, is a strong predictor of *GL* on snow, our finding suggest this is not true on rollerskis. This may be due to the differences between gliding on snow and roller skis. Less balanced *ASI* on-snow may increase ski friction and thus decrease *GL*. However, the same may not be true on a roller ski, as changing ski orientation does not have as large an impact

on the rolling speed of the ski. On a roller ski, a skiers ability to dynamically balance on the wheels, as measured by θ_{ski} and θ_{ML}, appears to be more influential than plantar-pressure balance. Skiers that maintain a more stacked body position and flatter ski across gliding phase may glide further on the skiing treadmill.

Images (Optional)

Table 1. Mean data for glide length *(GL)*, ski edge angle *(θ_{ski})*, mediolateral center-of-mass inclination angle (θ_{ML}), and mediolateral plantar-pressure balance *(ASI)* across the glide phase. Beta-coefficients *(β)* and significance for each variable in the multiple regression are shown.

Variable	Mean ± SD	*β*	*p-value*
GL (m)	3.1 ± 0.7	4.16	< 0.001
ASI (%)	4.0 ± 2.9	-0.02	0.155
θ_{ski} (°)	12.9 ± 8.2	-0.07	0.025
θ_{ML} (°)	5.7 ± 1.8	-0.05	0.049

Session Category

Human Motion and Performance: Sports

P1-274

Rate of Force Development as a Key Performance Indicator for Collegiate Golfers

Mr. Cameron Jensen MS, Dr. David Kingston PhD, Dr. Samuel Wilkins PHD, ATC, Dr. Adam Rosen PhD, ATC, Dr. Brian Knarr PhD

University of Nebraska Omaha, Omaha, NE, United States

Introduction

Peak rate of force development (RFD) is an important kinetic performance indicator for many athletic movements [1]; however, it remains unexplored during the golf swing. This study's purpose is to investigate the relationship between peak RFD during a golf driver swing with performance metrics and strength and flexibility measurements assessed by the Titleist Performance Institute (TPI) Level 1 Screen.

Methods

Twenty-six collegiate golfers (Male: 17, Right-Handed: 24, Age: 20.5 ± 1.3 years, Height: 176.7 ± 8.5 cm, Mass: 73.5 ± 10.0 kg, Handicap: +2.6 ± 1.1) completed the TPI screen and three driver swings on two force plates (AMTI, Watertown, MA, USA) in an indoor environment. Force-time and moment-time curves were derived, and the maximums and minimums were identified to determine the peak positive and negative linear and angular RFDs (angular RFD: rate of torque development), respectively. A golf launch monitor (Rapsodo, Chesterfield, MO, USA) collected clubhead speed (CHS). Spearman correlations examined relationships between average peak RFD and average CHS. Separate PCAs reduced dimensionality for TPI and kinetic variables, and a linear regression model assessed relationships between TPI-derived and kinetic-derived principal components (PC).

Results

Twenty-two RFD values had significant correlations stronger than rho = ± 0.50, with the two strongest being Back Foot Peak Angular RFD Magnitude (rho = 0.81, $p < 0.01$) and Front Foot Peak AP Angular RFD (rho = 0.78, $p < 0.01$) (Figure 1). For males, the RFD PC had a significant negative relationship ($\beta = -1.17$, $p = 0.03$) with the mobility/flexibility TPI PC.

Discussion

Golfers who can rapidly generate side-bending torque by driving the lead side downward and toward the target tend to achieve greater CHS [2]. This movement emphasizes effective weight transfer [3]. In males, peak RFD was negatively affected by mobility and flexibility, suggesting that greater flexibility may reduce the ability to generate force rapidly

[4]. Because several peak RFD measures were strongly associated with CHS, peak RFD may represent an important key performance indicator for golf performance.

Images (Optional)

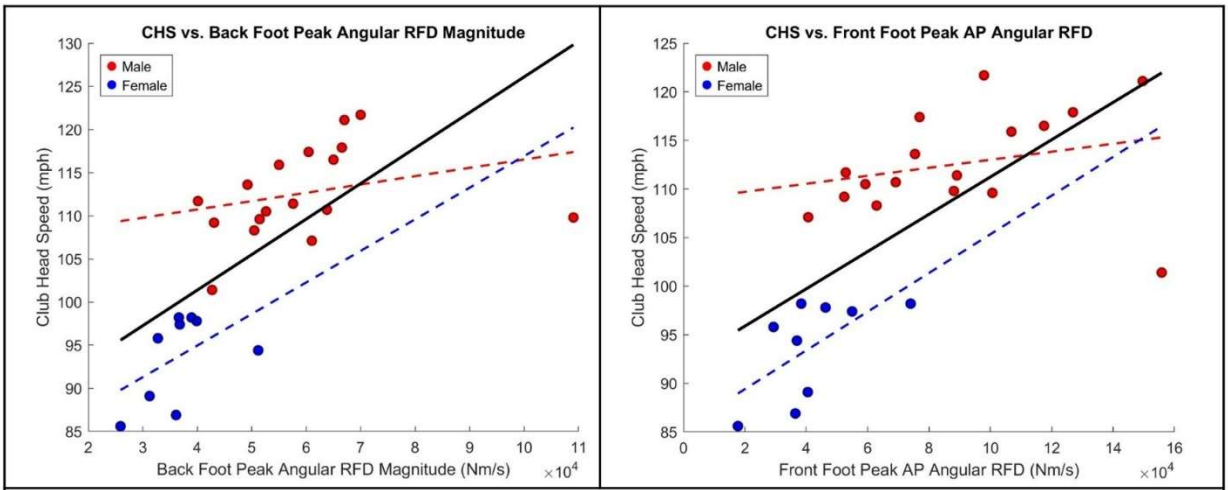


Figure 1: Correlation Plots of Back Foot Peak Angular RFD Magnitude (Left) and Front Foot peak AP Angular RFD (Right) with Clubhead Speed (CHS). Each variable has a moderate positive relationship with CHS (rho = 0.81, 0.78), with greater peak angular RFD being associated with greater CHS for both males and females, separately and combined.

References (Optional)

[1] Knudson, *J Strength Cond Res,* 2009; [2] Han et al., *Sports Biomech,* 2019; [3] Hume et al., *Sports Med.,* 2005; [4] Sheehan et al. *J. Sports Sci.,* 2019.

Session Category

Human Motion and Performance: Sports

P1-275

Comparison of Traditional Kinematics and Bidimensional Variables for Classifying Lead Leg Effectiveness in Baseball Pitchers

Mr. Brandon Doehne MS, Mr. Cameron Jensen MS, Dr. Samuel Wilkins Ph D, ATC, Dr. Adam Rosen Ph D, ATC, Dr. Brian Knarr Ph D

University of Nebraska at Omaha, Omaha, Nebraska, United States

Introduction

Previous baseball literature defines the role of a pitcher's lead leg to reduce their body's linear momentum to create a stable base for upper body rotation. While the change in lead knee angle (from stride foot contact (SFC) to ball release (BR)) and lead knee extension velocity at BR are commonly used to classify a pitcher's lead leg effectiveness, they only consider a pitcher's kinematics and lack contextual kinetic intricacies of different pitchers. This introduces the need for variables that involve kinematics and kinetics, such as joint power and work. The purpose of this study is to determine which set of variables has a greater relationship with a reduction of linear momentum.

Methods

Ninety-seven baseball pitchers (Age: 18 ± 2.1 years, Height: 183.6 ± 7.1 cm, Mass: 84.3 ± 10.1 kg) were extracted from the UNO Pitching Lab registry for preliminary analysis. Each pitcher performed maximal intent pitches on a force-instrumented mound (960-1280 Hz) while wearing a full-body marker set (240–320 Hz). The lead leg joint power, joint work, and change in linear momentum were investigated between SFC and BR. Power was calculated by taking the dot product of the proximal and distal joint angular velocities and torques. The maximum, minimum, and deltas were extracted for statistical analysis. Spearman correlation coefficients ($p<0.05$) were calculated to assess the change of linear momentum in relation to lead knee/hip power and work, along with the change in lead knee angle and extension velocity at BR.

Results

Our analysis found that traditional and bidimensional variables were significantly correlated with a pitcher's reduction of linear momentum from SFC to BR, as seen in **Table 1**. However, lead knee/hip power and work variables displayed greater correlation coefficients than the traditional ones.

Discussion

Due to the greater correlation coefficients that the joint power and work variables demonstrated, they may be potential alternative variables to traditional kinematics for quantifying the effectiveness of the lead leg. While additional research is necessary, they may serve as a standard in the future for assessing biomechanics, which could optimize a pitcher's lead leg mechanics to increase their overall performance.

Images (Optional)

Table 1. Spearman Correlation Results

Variables	Correlation Coefficient	p-value
Lead Hip Work and Change in Linear Momentum	-0.453	p<0.001
Lead Knee Angular Velocity at BR and Change in Linear Momentum	0.322	p<0.01
Max Lead Hip Power and Change in Linear Momentum	-0.322	p<0.01
Lead Knee Work and Change in Linear Momentum	-0.289	p<0.01
Max Lead Knee Power and Change in Linear Momentum	-0.267	0.013
Change in Lead Knee Angle and Change in Linear Momentum	0.247	0.022

Session Category

Human Motion and Performance: Sports

P1-276

Non-Dominant Limb Asymmetries Associate With Lower Landing Performance in Professional Soccer Players

Ms. Camilla Antognini[1], Mr. Henry Eilen[2], Mr. Matthew Varano[2], Dr. Felipe Gonzalez[1], Ms. Brittany Dowling[2], Dr. Markus Wimmer[1], Dr. Brian Forsythe[2]

[1]Rush University Medical Center, Chicago, Illinois, United States. [2]Midwest Orthopaedics at Rush, Chicago, Ilinois, United States

Introduction

Soccer requires frequent jumping and rapid directional changes that generate high lower-limb loads, making landing biomechanics central to both performance and injury risk. Although asymmetrical landing patterns have been linked to decreased performance and greater injury risk, the specific role of limb dominance in shaping performance-related landing mechanics in soccer players is not well defined. This study investigated how limb dominance and interlimb asymmetry relate to landing performance in professional male soccer players.

Methods

Twenty-six professional male players (27.1 ± 5.3 yrs, 1.83 ± 0.06 m, 80.9 ± 7.6 kg) completed pre-season testing in 2020–2021. Dominance was based on preferred kicking leg (20 right, 6 left). Only drop jumps were analyzed. Movement was recorded using marker-based motion capture (Optitrack) and dual force plates (Bertec), with kinematic and kinetic variables computed in Visual3D (HAS-Motion). Joint angles and external moments of the trunk, hip, knee, and ankle were extracted at maximal knee flexion. Performance was defined by average jump height (mean of three trials), and players were split into high- (n=13) and low-performance (n=13) groups using the sample median (49.8 cm). Analyses compared: (1) dominant-limb biomechanics between groups, (2) non-dominant-limb biomechanics between groups, and (3) dominant vs. non-dominant limbs within each group, using statistical t-tests (α=0.05).

Results

Performance groups did not differ on dominant-limb landing mechanics (Table 1). However, low-performing players showed significantly higher non-dominant knee external rotation moment (p=0.005) and ankle adduction moment (p=0.004). Within-group analyses indicated high performers displayed reduced hip abduction on the non-dominant limb relative to the dominant limb (p=0.046), whereas low performers demonstrated greater non-dominant knee external rotation and ankle adduction moments (p=0.045, p=0.05).

Discussion

Higher-performing players exhibited more symmetrical landing mechanics, while lower-performing athletes showed marked non-dominant limb asymmetries, particularly elevated frontal and transverse plane joint moments. Because such asymmetries may elevate injury risk, assessing interlimb differences can help identify athletes who may benefit from targeted neuromuscular or strength interventions.

Images (Optional)

	Dominant Side			Non-dominant Side			Dominant vs Non-dominant Sides	
	High performance (Mean ± SD)	Low performance (Mean ± SD)	p-value	High performance (Mean ± SD)	Low performance (Mean ± SD)	p-value	High performance (p-value)	Low performance (p-value)
Hip abduction angle [°]	-5.6 ± 3.6	-6.8 ± 6.6	0.585	-8,3 ± 4.1	-8.4 ± 3.7	0.907	**0.046****	0.356
Knee internal rotation moment [%BW*m]	-2.0 ± 6.9	-2.3 ± 8.5	0.758	-0.08 ± 8.3	-11.1 ± 9.7	**0.005****	0.475	**0.045****
Ankle abduction moment [%BW*m]	-3.4 ± 7.2	-4.4 ± 9.0	0.769	-1.8 ± 8.5	-13.5 ± 10.7	**0.004****	0.543	**0.05***

Table 1: Comparison of hip, knee, and ankle biomechanics between high- and low-performance groups on the dominant and non-dominant sides. Values are presented as mean ± standard deviation. The table reports group comparisons within each side (dominant vs. non-dominant) and between sides, stratified by performance level. Bold values indicate statistically significant differences ($p < 0.05$).

Session Category

Human Motion and Performance: Sports

P1-277

Intervertebral Lateral Bending Moments in the Lumbar Spine of Baseball Pitchers Across Throwing Velocities

Mr. Justin Humenay, Dr. Michael McClure, Dr. Carrie Peterson

Virginia Commonwealth University, Richmond, VA, United States

Introduction

Baseball pitching imposes substantial mechanical demands on the lumbar spine, a crucial link in the kinetic chain responsible for transferring energy from the lower body to the upper extremity. While increased pitch velocity is associated with greater trunk forces, the specific intervertebral loading patterns during high-velocity pitching remain unclear. This study investigates differences in lateral bending moments across lumbar spinal segments between collegiate pitchers throwing at high versus low velocities.

Methods

Twenty right-handed collegiate pitchers were divided into two groups: high-velocity (n = 10, 90.3 ± 1.6 mph) and low-velocity (n = 10, 81.6 ± 1.1 mph). Motion capture and external ground reaction forces from an open-access pitching dataset (Driveline Baseball [1]) were processed. A thoracolumbar model [2] and inverse dynamics analysis was used to compute lateral bending moments at six intervertebral joints. Statistical parametric mapping (SPM) was used to compare moment waveforms between groups across a time-normalized window centered at maximum shoulder external rotation. To compare the lateral bending moments of the lumbar spine between high- and low-velocity pitchers, time-series data were aligned based on the timing of maximum shoulder external rotation.

Results

We observed significant group differences at L5/S1 ($p = 0.014$) and L3/L4 ($p = 0.009$), with high-velocity pitchers showing average peak moments approximately 28% higher at L5/S1, and 24% higher at L3/L4. Additionally, the T12/L1 segment showed multiple significant intervals ($p = 0.025–0.016$) of increased loading in the high-velocity. These peaks occurred primarily during late-cocking and early acceleration.

Discussion

These findings identified high-velocity pitchers experience greater and more temporally concentrated lateral bending moments at key lumbar and thoracolumbar junctions. Our

findings may indicate enhanced spinal engagement plays a central role in generating higher pitching velocities. From a performance standpoint, these insights highlight the importance of trunk control and spinal stability in energy transfer. From an injury prevention perspective, the increased and localized loading observed in high-velocity throwers may support the emphasis on targeted strength, mobility, and recovery strategies to optimize the lumbar spine for loading.

References (Optional)

[1] Wasserberger KW et al. The OpenBiomechanics Project, 2022. [2] Bruno, AG et al. Comp Methods in Biomech Biomed Eng, 2015

Session Category

Human Motion and Performance: Sports

P1-278

Inter-joint Coordination Differences While Skiing Across Development Levels of Biathletes

Ms Charlotte Whitcomb, Mr Isaac Burgess MS, Dr. James Becker PhD

Montana State University, Bozeman, MT, United States

Introduction

Skate cross-country skiing is a complex full-body movement requiring coordinated motion across multiple joints and segments. Although previous studies have used relative timing to quantify coordination differences across development levels, this approach does not capture the continuous nature of joint interactions throughout the ski cycle. Therefore, the purpose of this study was to use a dynamical-systems approach to compare inter-joint coordination between junior (JN), national-caliber (NC), and world-class (WC) athletes during V2 skate skiing

Methods

Nine JN (18 ± 1.06 years; 4M/4F), seven NC (26 ± 3.95 years; 4M/3F), and eight WC biathletes (27.63 ± 4.50 years; 5M/3F) roller skied on a treadmill at race intensity while whole-body kinematics were recorded using markerless motion capture. A modified vector-coding approach quantified three sagittal-plane joint couplings relevant to skiing performance: torso–pole, shoulder–elbow, and hip–knee. Kinematics were time-normalized to 100% of the ski cycle, and bin counts were used in a 3x4 mixed ANOVA to determine the proportion of in-phase, anti-phase, distal-phase, and proximal-phase coordination. Statistical parametric mapping (SPM) was applied to compare differences in coordination variability (CAV) across groups.

Results

Torso-pole coordination showed a significant phase x group interaction ($F_{6,63} = 3.12$, $p = .01$) with NC athletes having more antiphase motion than either JN or WC athletes, and JN athletes having less in-phase motion than NC or WC athletes (Figure 1). SPM showed that JN athletes has less coordination variability than NC or WC athletes during the pole recovery phase for shoulder-elbow coordination ($p < .05$)

Discussion

Skill level in biathlon appears to influence both coordination of movement as well as variability of movement during V2 skate skiing. The increased antiphase movement in NC and decreased in-phase movement of JN biathletes may be indicative of inefficiency in applying force to pole and skis compared to WC biathletes. Additionally, the reduced CAV in JN athletes might show limited movement strategies to achieve efficient body positions. Future research should target whether addressing coordination patterns is one potential method for improving performance as JN athletes progress to NC and WC ranks.

Images (Optional)

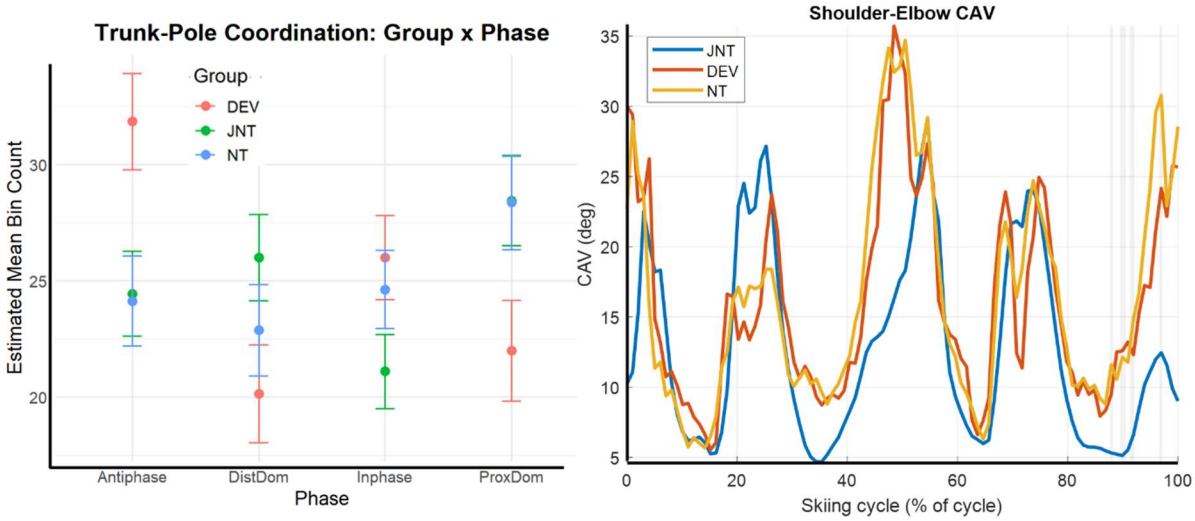


Figure 1. Bin counts for each coordination pattern across groups for the trunk-pole coordination (left) and mean CAV for the shoulder-elbow coordination (right). Shaded areas on right plot indicate where SPM reported significant differences between groups.

Session Category

Human Motion and Performance: Sports

P1-279

Ankle Strains During Ipsilateral and Contralateral Change of Direction

MSc Chi-Hsien Chen[1], PhD Timothy Derrick[1], MSc Yan-Jer Tseng[2], MSc Sung-Ting Lu[3,4], PhD Chiang Liu[2]

[1]Department of Kinesiology, Iowa State University, Ames, Iowa, United States. [2]Graduate Institute of Sports Equip-ment Technology, University of Taipei, Taipei, Taipei, Taiwan. [3]Taiwan Institute of Sports Science, Kaohsiung City, Kaohsiung City, Taiwan. [4]Graduate Institute of Athletics and Coaching Science, National Taiwan Sport University, Taoyuan, Taoyuan, Taiwan

MSc Chi-Hsien Chen

Introduction

The rapid change of direction (COD) can lead to an increase in ankle ligament strain during the ground contact phase, which may predispose an athlete to a sprained ankle. Our previous work (1) found that COD of ipsilateral direction (ipsi-COD) and contralateral direction (contra-COD) showed asymmetrical mechanisms. However, the previous study only reported the ankle joint loading in contra-COD (2). Therefore, it is necessary to confirm the differences in ankle joint ligament strain between ipsi-COD and contra-COD for understanding the risk of injuries.

Methods

Thirty-four recreational athletes (height: 176.0 ± 7.0 cm, weight: 74.8 ± 11.2 kg, age: 23.5 ± 2.7 years) performed ipsi-COD and contra-COD tasks in 60° with their non-dominant leg. A 3-D motion capture system and photocells were used to collect kinematic data. A low-pass filter with a cut-off of 6 Hz was applied to the coordinate data. Helical tibiotalar, subtalar and midfoot angles were calculated. A 3-segment musculoskeletal foot model (3) was used to estimate strain in four medial and three lateral ankle ligaments. It was assumed that there was zero strain in the ligaments while standing in the T-pose position.

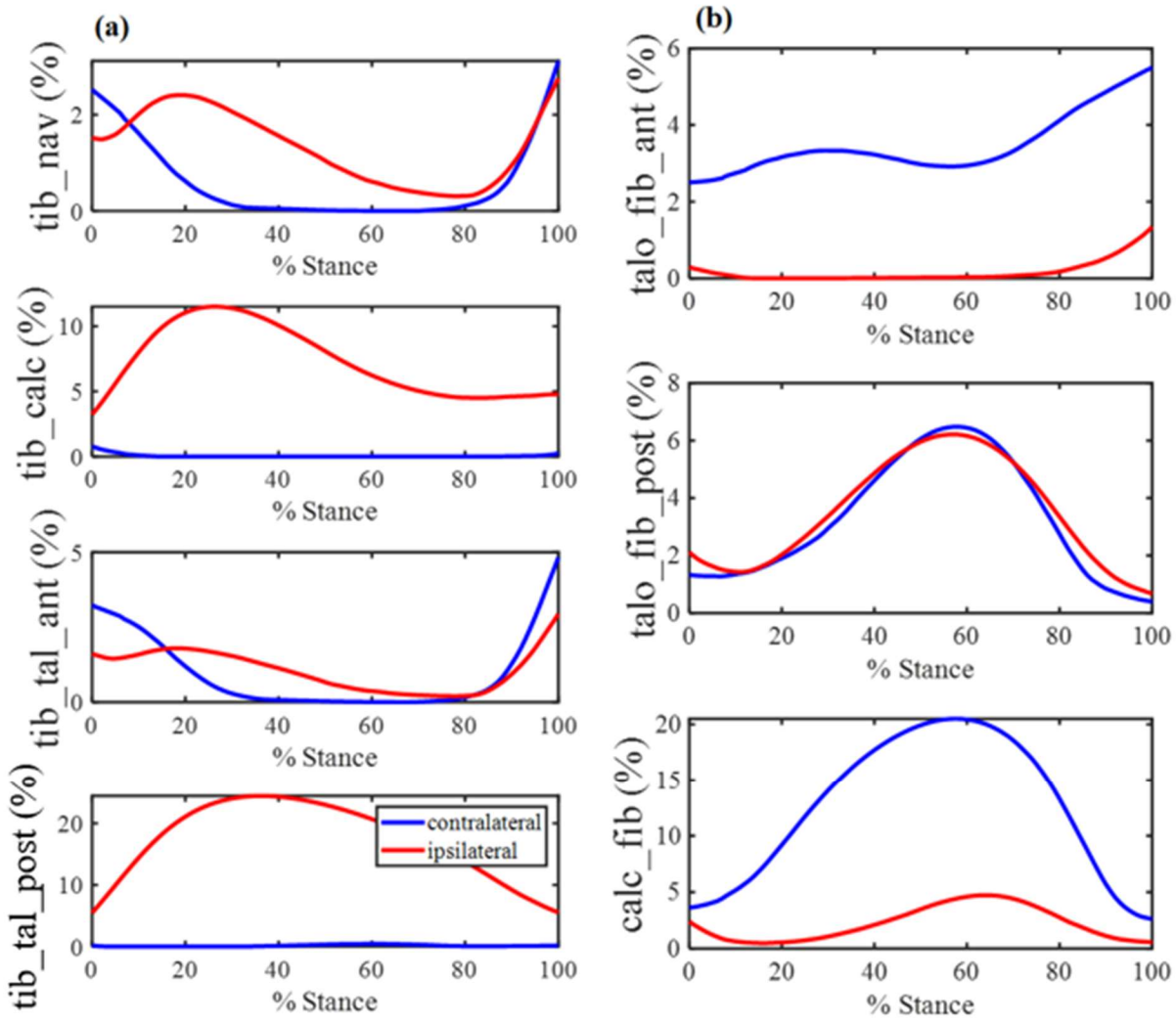
Results

The approaching speed between ipsi-COD and contra-COD showed non-significant difference. The ipsi-COD showed a significantly higher tibiocalcaneal strain (ips: 16.6 ± 6.4, contra: 1.1 ± 2.3) and higher posterior tibiotalar strain (ips: 34.4 ± 6.2, contra: 1.2 ± 3.0) compared to contra-COD. The contra-COD led to a significantly higher anterior talofibular strain (ips: 2.0 ± 1.8, contra: 7.8 ± 3.1) and higher calcaneofibular strain (ips: 8.9 ± 9.2, contra: 27.3 ± 4.9) than ipsi-COD.

Discussion

The contra-COD caused inversion at the tibiotalar and subtalar joints, while the ipsi-COD caused eversion. Inversion increased strain in the lateral ligaments, while eversion caused strain in the medial ligaments. Strains were modulated by the sagittal plane motion during midstance of the cutting motion. Dorsiflexion increased strain in the posterior ligaments while reducing strain in the anterior ligaments. Overall, the posterior tibiotalar and the calcaneofibular ligaments showed the greatest amount of stress.

Images (Optional)



References (Optional)

[1] Chi-Hsien Chen et al., J Sports Sci Med, 2025

[2] Marshall BM et al., J Strength Cond Res, 2014

[3] Malaquias TM et al., Comput Methods Biomech Biomed Eng, 2017

Session Category

Human Motion and Performance: Sports

P1-280

An Evaluation of the Functional Movement Screen and a Golf-Specific Movement Screen in Identifying Physical Limitations Related to Golf Performance

Mr. Christopher Wendt, Dr. Emma White, Dr. Courtney Crews, Dr. Brittany Gallagher, Dr. Jonathan Lind, Dr. Ellsworth Parham, Dr. William Holland, Dr. Elizabeth Nail, Dr. Mona Sajjad, Dr. Timothy Wooton, Dr. Brianna O'Connor, Dr. Sidney Rhodes, Dr. Angie Rodriguez, Dr. Landon Ward

Winston-Salem State University, Winston-Salem, NC, United States

Introduction

Over 56% of amateur golfers are at risk of sustaining a musculoskeletal injury during their lifetime, commonly due to poor swing mechanics. An effective and quick way to identify the cause of such deficits is by performing a movement screen. The Functional Movement Screen (FMS) and the golf-specific Titleist Performance Institute (TPI) Movement Screen have differing levels of evidence in the assessment of amateur golfers. The purpose of this study was to evaluate the relationship between golf swing biomechanical movement characteristics and test scores from both the TPI Movement Screen and the Functional Movement Screen, respectively.

Methods

Twenty-four amateur golfers (between ages 18-65) completed two separate sessions consisting of golf swing biomechanical analysis on one day, with FMS and TPI movement screenings on another day. Motion capture and force platform measurements provided golf swing kinematic/kinetic outcomes, such as hip rotation velocity (as shown in Figure 1), trunk/pelvis range of motion, and ground reaction force. Statistical analysis was performed to determine if there were statistically significant correlations ($p \leq .05$) between subject demographics and screening/golf swing outcomes, as well as associations between each of the TPI and FMS screening tests vs. golf swing biomechanical characteristics.

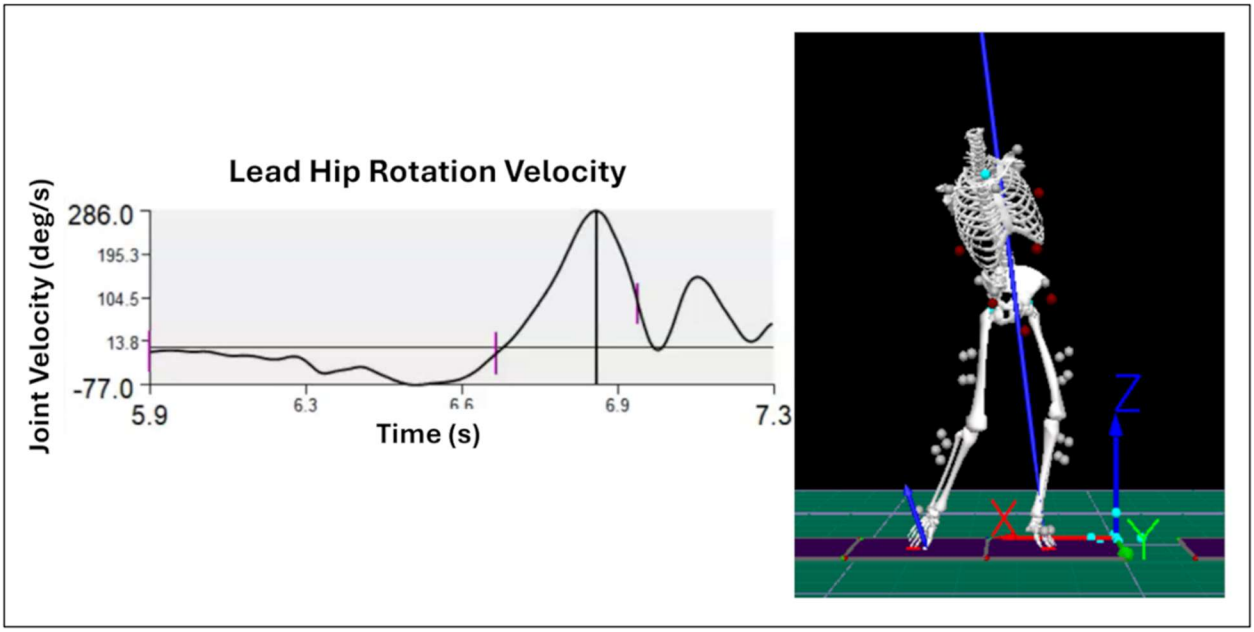
Results

Eight different TPI movement tests (50%) demonstrated a total of 11 moderate, statistically significant correlations with golf swing movement outcomes. A total of 4 significant correlations were found between 3 individual FMS movement tests (43%) and golf swing characteristics. TPI and FMS total screening scores were moderately associated ($r=.531$, $p=.008$).

Discussion

The golf-specific Titleist Performance Institute Movement Screen was positively associated with the Functional Movement Screen, suggesting agreement between the two movement screening methods. However, more statistically significant relationships were discovered between golf swing biomechanical variables and physical limitations identified using the golf-specific movement screen (TPI) vs. the Functional Movement Screen (FMS). Therefore, the golf-specific movement screen may be more useful for clinicians to assess a golfer's physical limitations, which could impact golf swing mechanics and/or risk of injury.

Images (Optional)



Session Category

Human Motion and Performance: Sports

P1-281

Whole Body Assessment of Exercise Proficiency Using a Single Camera: Application to a Sub-Academy Rugby Cohort and an Academy Gaelic Football Team

Ms Clara Mercadal MAI[1,2], Mr Robert McCarthy MAI[1], Mr Jorge Gonzalez MSc[2], Mr Leo Peyton Acct[1,2], Prof Aljosa Smolic PhD[1,3], Mr Garreth Farrell Physio[4], Mr Mark Kenneally Physio[4], Mr Des Ryan Sports Sci[5], Ms Lara Coyne PhD physio[6], Ms Giang Lam Nguyen BAI[2], Prof Ciaran Simms BA BAI PhD[1,2]

[1]Trinity College Dublin, Dublin, Leinster, Ireland. [2]KineMo, Dublin, Leinster, Ireland. [3]HLSU, Lucerne, Lucerne, Switzerland. [4]Leinster Rugby, Dublin, Leinster, Ireland. [5]Uni Galway, Galway, Connaught, Ireland. [6]Unafiliated, Galway, Connaught, Ireland

Introduction

Assessment of exercise form in large cohorts is complex and difficult. Calibrated cameras and sensors are challenging, and by-eye observation is low accuracy [1]. The single camera recording platform KineMo addresses this challenge. However, although the accuracy has been assessed [2] and the tool is available (app stores), its practical application in a large cohort has not been studied. Accordingly, we aimed to assess the practical utility of using KineMo to assess movement screening of youth athletes.

Methods

Following ethical approval, cohorts of male sub-academy male rugby and academy Gaelic football players (both mostly under 18 years old) were recorded. Rugby players performed single leg squats, overhead squats and drop jumps in two sessions. There were 109 participants in session 1 and 59 in session 2 (8 weeks later), due to logistics associated with participation. Separately, a cohort of 80 GAA football players performed single leg Romanian deadlifts and overhead squats in one session. Recording was done using mobile devices on tripods in regular gym lighting conditions, and athletes wore standard sports clothing, Figure 1a.

Results

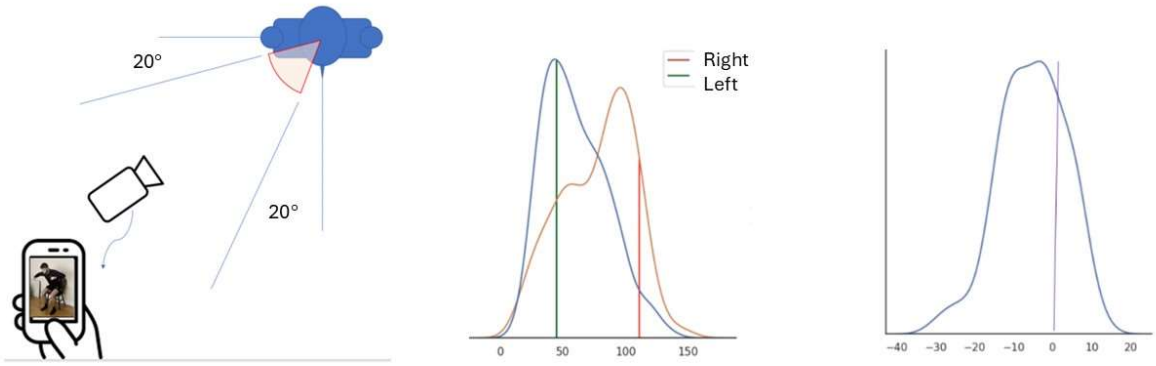
Data capture required about one minute for five repetitions of an exercise per athlete/recording station, such that whole cohorts (>30 athletes) can be readily recorded in a one-hour session in a regular gym environment. A practical requirement is that only a single athlete is visible in the camera view. Whole-body metrics such as sagittal plane ankle, knee and hip joint angles, pelvic tilt, spine flexion and shoulder flexion were

available, as well as frontal plane knee angle. These metrics were used to assess overall movement form at baseline (Figure 1b) and changes over time, for example Figure 1c.

Discussion

The results of these user trials demonstrate high throughput capabilities due to the simple nature of video data capture, and significant actionable data can be extracted. For example, the distribution across a cohort of individual metrics associated with different exercises (such as knee flexion in a squat), or the changes for large groups of individuals performing the same exercise at different time points.

Images (Optional)



References (Optional)

Abbott et al., Musculoskel Sci & Pract, 2022

Mercadal-Baudart et al., Cell Heliyon, 2024

Acknowledgements (Optional)

Research Funding from Enterprise Ireland

Session Category

P1-282

Influence of Stroke Rate and Static vs. Dynamic Rowing on Joint Kinematics Among Female Collegiate Sweep Rowers

Ms. Claudia Poehlmann, Ms. Julia Tamai, Dr. Stephanie Jones

Smith College, Northampton, Massachusetts, United States

Introduction

Training among competitive rowers includes on-land rowing using ergometers. High ergometer training loads are associated with a greater incidence of low back pain but dynamic ergometers are associated with reduced injury risk that could result from altered kinematic patterns. Understanding how stroke rate and ergometer dynamics interact to shape joint motions, could explain this discrepancy. The purpose of this study was to investigate joint kinematics in collegiate sweep rowers to determine how ergometer dynamics and pacing interact to shape rowing technique.

Methods

Ten female collegiate rowers rowed on an ergometer for 30 minutes, performing two randomized blocks of trials: Static vs. ergometer placed on slides (Dynamic). Within each block participants rowed three minutes at self-selected pace, followed by two 5 minute bouts at Low (20 strokes per minute [SPM]) and High (30 SPM) stroke rates. Ten high speed digital video cameras tracked 13 body segments to quantify 3D joint kinematics. Cycle parameters, sagittal joint ranges of motion (ROM) and peak angular velocities of lower limbs and trunk were assessed using two-way repeated measures ANOVAs (ergometer, stroke rate); significance set at $P<0.05$.

Results

Dynamic ergometry was associated with shorter cycles and drive phases, with longer recovery phases compared to static. Ankle and Knee ROM were greater in dynamic than static, while hip and trunk ROMs were unchanged across conditions. Angular motions were more invariant in dynamic, with little effect of stroke rate on ankle and knee ROM; in static, ankle and knee ROMs decreased at High stroke rate relative to Low. Knee and hip extension velocities increased at High, with similar ankle velocity across conditions. Knee and trunk flexion velocities increased during the recovery phase of dynamic rowing.

Discussion

These findings indicate that dynamic rowing consists of constant ROMs across stroke rates with reduced cycle time and drive phases. These alterations suggest rowers are leveraging

the inertia of the ergometer to assist in their transition between phases. Elevated knee and trunk velocities at higher stroke rates highlight increased mechanical demands that may affect technique and loading. Ongoing analyses will assess lower limb joint asymmetries, trunk frontal/transverse rotations and joint coordination.

Session Category

Human Motion and Performance: Sports

P1-283

Coordinated Hip, Pelvis, and Trunk Biomechanics Associated With Stride Length In Baseball Pitching

Professor Daniel Ramsey PhD[1], Dr Ryan CBaseball Consulting Services Ryan Crotin PhD[2]

[1]D'Youville University, Buffalo, New York, United States. [2]ArmCare.com, RC13 Baseball Consulting Services, LLC, Farm System Network, LLC, USA, Indialantic, Florida, United States

Professor Daniel Ramsey

Introduction

Hip and lumbopelvic coordination in pitching delivery are essential, yet frontal plane hip, pelvis and trunk biomechanics during baseball pitching in relation to stride length remans under explored.

Methods

- Nineteen collegiate baseball pitchers threw 2 randomized 80-pitch games at ±25% from desired stride length, (over-stride (OS) and under-stride (US)) then crossed over to the alternate condition after a 72-hour washout period. Conventional motion capture recorded the pitching sequence [1-3].
- Pitching cycle time normalized to 100%, from peak knee height (PKH) to ball release (BR). Hallmark events included stride foot contact (SFC) and maximal external rotation (MER) and phases were linked between hallmark events; Generation (GEN) from PKH to SFC; Brace-Transfer (BT) from SFC to MER; and Acceleration (ACC) from MER to BR.
- Paired t-tests were used for comparative analysis of joint kinematics, moments, and powers between the two stride conditions at hallmark events and phases. Statistical significance was set at $p \leq 0.05$.

Results

Figure 1: frontal plane hip and lumbopelvic dynamics.

1. OS saw drive-hip more abducted during GEN ($p < .001$) with higher adductor power generation during ACC ($p < .001$). US yielded greater negative drive-hip abductor

moments during GEN ($p < 0.001$) through eccentric work that absorbed energy and the hip more adducted during ACC ($p < .001$) that absorbed power.

2. With OS, significantly higher stride-hip adductor angular velocities concomitant with greater abductor joint power absorption during ACC ($p < .001$).
3. OS saw significantly greater upward pelvic rotation (leading hip) during GEN ($p < 0.001$), greater upward rotational velocities during BT ($p < 0.05$), but lower pelvic angle during ACC ($p < 0.001$). With US, upward (counterclockwise) pelvic rotation was higher during ACC ($p < 0.001$). Lateral trunk bending trunk displacement profiles were similar between stride conditions except at SFC ($p < 0.001$), where contralateral (non-dominant) trunk flexion was observed with OS as opposed to ipsilateral trunk flexion with US.

Discussion

Further research on optimal sequencing in response to changes in stride length for throwing arm health is warranted.

Images (Optional)

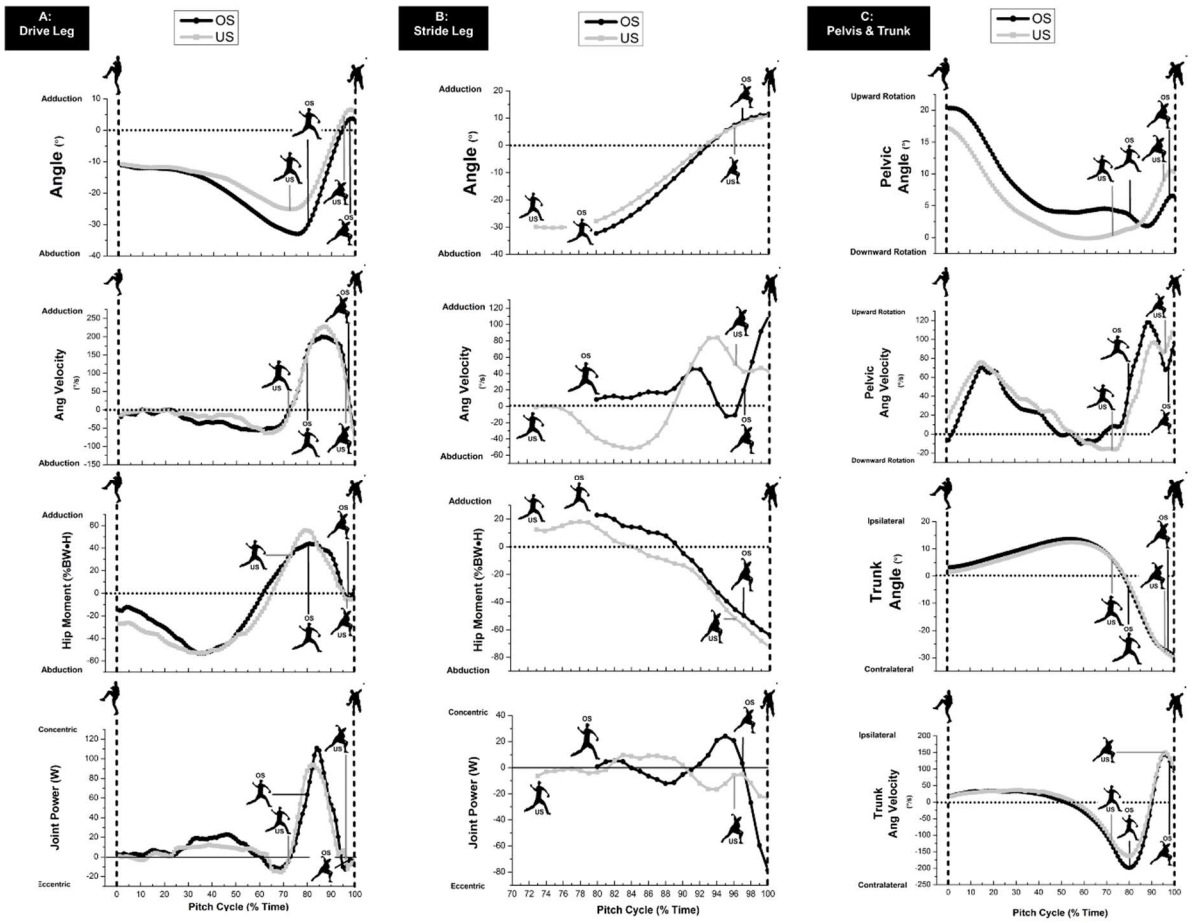


Figure 1: Frontal plane hip and lumbopelvic dynamics

A: Drive hip dynamics, Abduction (+) vs Adduction (−)

B: Stride hip dynamics, Adduction (+) vs Abduction (−)

C: Upward (+) vs Downward (−) pelvic rotation and Non-Dominant (−) vs Dominant (+) lateral trunk bending.

References (Optional)

[1] Ramsey DK et al. (2025). Life.,15(9):1440

[2] Crotin, RL. (2013). ProQuest Dissertations & Theses

[3] Crotin, RL et al. (2014). Med Sci Sports Exerc., 46(3), 565-571

Session Category

Human Motion and Performance: Sports

P1-284

The Effect of Sport and Sex on Quadratus Lumborum Musculature in Varsity Athletes

Mr Daniel Sheffield MSc, Mr Sam Vasilounis MSc, Dr Dan Desroches PhD, Dr Janessa Drake PhD

York University, Toronto, Ontario, Canada

Introduction

Asymmetry in lumbopelvic musculature and reduced lumbopelvic control have been linked to altered trunk mechanics, performance deficits, and injury risk in athletes. The quadratus lumborum (QL), a key stabilizer of the lumbar spine and pelvis, may develop side-specific differences due to repeated unilateral sport demands. This study examined QL cross-sectional area (CSA) asymmetry in varsity athletes and explored whether sex or sport influenced asymmetry magnitude, as well as whether QL CSA relates to single-leg jump performance.

Methods

Ultrasound measures of QL were collected from 116 varsity athletes (58 males, 58 females) across five sports: basketball, track and field, hockey, volleyball, and wrestling. Images were processed to quantify bilateral CSA (mm^2), and an asymmetry index assessed dominant vs. non-dominant sides. Paired t-tests examined side-to-side differences across groups. Linear regression assessed relationships between QL CSA or asymmetry and single-leg jump height.

Results

Across all athletes, the dominant QL was significantly larger than the non-dominant QL ($p < 0.001$). Significant asymmetry was present in both females ($p < 0.001$) and males ($p < 0.001$). Overall, 79 athletes (68.1%) demonstrated >10% asymmetry. All five sports showed significant side-to-side differences ($p < 0.001$).

Asymmetry was not significantly associated with single-leg jump height. However, unilateral QL CSA showed a significant contralateral relationship, with larger left QL CSA predicting greater right-leg single-leg jump height ($R^2=0.104$, $F(1,114)=13.291$, $p=0.0004$; Figure 1). No relationship was observed between right QL CSA and left-leg jump height ($R^2=0.00178$, $F(1,114)=0.2034$, $p=0.6528$).

Discussion

Varsity athletes demonstrated prevalent QL asymmetry, with over two-thirds exceeding a 10%. The presence of significant asymmetry in both sexes, and across all sports tested, suggests that unilateral adaptations in trunk musculature are a common characteristic of competitive athletic participation rather than being sport or sex-specific. This universal pattern may reflect common sport-specific unilateral loading patterns, such as repeated cutting, shooting, or skating mechanics.

Establishing normative patterns of lumbopelvic muscular asymmetry in varsity athletes provides a valuable reference for clinicians and coaches. Such benchmarks may help identify atypical asymmetry that may contribute to lumbopelvic dysfunction, performance limitations, or elevated injury risk.

Images (Optional)

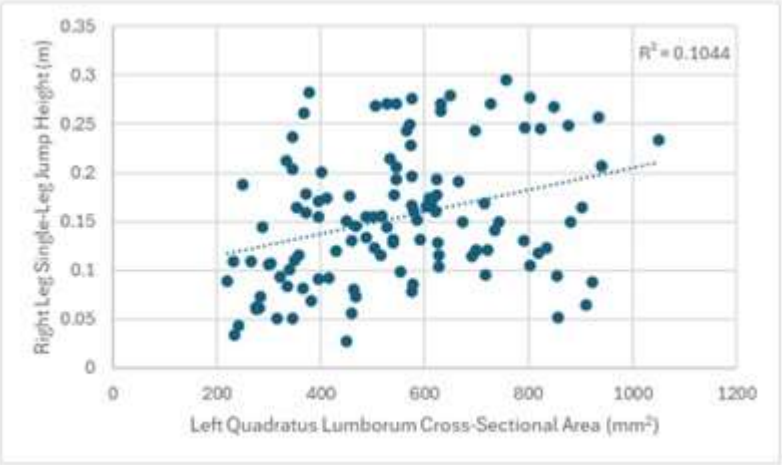


Figure 1: Plot showing the relationship between right single-leg jump and left QL CSA

Session Category

Human Motion and Performance: Sports

P1-285

How Do Head Impacts in Youth Ice Hockey Vary Based on Player Position, On-Ice Location, Score Differential, and Penalty Kills?

Mr Marco Sladoje, Mr Andrew Kotevski, Dr David Andrews

University of Windsor, Windsor, Ontario, Canada

Introduction

Concussion rates in ice hockey are nearly double those experienced in other contact sports [1], and concussions in youth athletes tend to be more severe than in adults. The frequency, mechanism of head impact, and head impact location during youth hockey games has been quantified [2], however, the effect that player position, on-ice location, score differential, and penalty kill status has on these variables has not been analyzed to date.

Methods

Seven GoPro Hero9 cameras (47° fixed lenses) captured play of U15 and U16 (13-16 years of age) boys ice hockey teams over 21 games (one season). The cameras were powered by rechargeable portable power packs. The occurrence and mechanism of 674 head impacts identified in the videos [2] were analyzed by trained observers based on player position, on-ice location, and the score differential and penalty kill (PK) status at the time of impact.

Results

61% (n=414) of head impacts were experienced by forwards and 39% (n=260) by defensemen. In terms of ice location, 62% (n=418) of impacts were board contacts and 38% (n=256) were open-ice. Nearly half the impacts occurred in the offensive zone (46%; n=308), followed by the defensive zone (36%; n=241), and then neutral zone (19%; n=125). More than 77% and 87% of the impacts occurred when the score differential was ≤ 2 points, and during even strength play, respectively. 70% (n=471) of the impacts occurred between the head and body (n=260) and head and boards (n=211).

Discussion

This analysis confirmed that the number and mechanism of head impacts varied based on player position, ice location, score differential, and PK status. More head impacts to forwards is consistent with more impacts occurring in the offensive zones. Closer scoring games resulted in more head impacts, reflecting more aggressive player interactions when the chance of winning is greater. Fewer head impacts during PK reflects more conservative

play by the PK team. Analysis of hockey games for girls and across a wider range of ages would inform age- and gender-specific interventions.

References (Optional)

[1] Canadian Institute for Health Information, 2018.

[2] Emily Roberts, Masters Thesis, University of Windsor, 2024.

Acknowledgements (Optional)

Funded by the WE-SPARK Health Institute

Session Category

Human Motion and Performance: Sports

P1-286

A Descriptive Analysis of Tackling Techniques in Youth Football

Ms Vanessa Bechard[1], Ms Claudia Graham[2], Dr Danielle Gyemi[1], Dr David Andrews[1]

[1]University of Windsor, Windsor, ON, Canada. [2]University of Waterloo, Waterloo, ON, Canada

Introduction

There is limited understanding of how youth football players respond to head impacts. Improper tackling techniques, such as leading with the head or using poor body alignment, are major contributors to the high rates of head injuries, including concussions [3]. This study aims to describe the tackling techniques used by youth football players across three age groups (9-12, 13-14 and 15-16 years).

Methods

Tackling events from video records of football games of players from three age groups [9-12 years: ATOM (A), 13-14 years: Bantam (B), and 15-16 years: Junior Varsity (JV)] were evaluated [2] based on categories including contact method, head position, balance, rib protection and anticipation. Comprehensive multi-angle views of tackling events were captured using an 11-camera GoPro system [2]. Tackling techniques were evaluated by two raters using validated frameworks [1,4].

Results

Forty-nine tackles were analyzed across the age groups [A(5), B(33), JV(11)]. Over 80% of tackles across the three age groups were in a head-up position. A head-across-the-bow technique was observed in 20.0%, 15.2%, and 45.5% of A, B, and JV tackles, respectively. There were no significant differences for any of the tackle grading categories between age groups ($p>0.05$). Interrater reliability for tackle categories ranged from fair [Cohens Kappa (k) = 0.275] for Posture Striker, to very good (k = 1.000) for Player Motion Struck [mean k = 0.668 (good)].

Discussion

Positive tackling technique execution was present across all three age levels. However, the use of the head-across-the-bow technique by all age groups is a concern, as it is associated with more frequent and severe head impacts [3]. Despite the lack of significant differences between age groups for all tackling categories, the results provide useful descriptive insights into youth tackling technique. Investigations of additional tackling

events across different ages of youth players are needed to advance this important area of inquiry.

References (Optional)

[1] Gellner et al., J Sports Engineering Technology, 2020.

[2] Gyemi et al., J Biomechanics, 2021.

[3] Schussler et al., International J Sports Physical Therapy, 2018.

[4] Stockwell et al., Orthopaedic J Sports Medicine, 2020.

Session Category

Human Motion and Performance: Sports

P1-287

Biomechanical Comparison of Deep and Shallow Squatters

Dr David Hudson PT, PhD

Western Carolina University, Cullowhee, NC, United States

Introduction

Squatting is a compound movement commonly used as a screening tool to identify deficits in mobility, force production, and motor coordination. This study seeks to improve the utility of the squat as a screening tool by understanding differences in joint coupling, kinematics and lower extremity joint mobility.

Methods

Twenty-six healthy adult subjects (12 males) were measured for maximal hip and knee flexion, and ankle dorsiflexion (weight bearing / knee flexed) using a goniometer. Squat depth and sagittal plane motions of the trunk and (right) hip, knee, ankle joints were then recorded while double limb squatting using a 14-camera motion analysis system where 6 successive squats were performed as deeply as able in preferred stance. Subjects were ranked according to normalized squat depth to form deep and shallow groups. The accompanying image shows cyclograms and their slopes of averaged group data showing movement coordination across joints and segments (trunk-shank and hip-ankle). Independent t-tests were performed to determine the presence of group differences in maximal hip, knee, ankle joint mobility (goniometer), maximal flexion angles of the trunk, hip, knee, and ankle (kinematic data), and slopes of the (individual subjects) cyclograms. Bonferoni correction was used to account for multiple comparisons and a was adjusted to 0.0056.

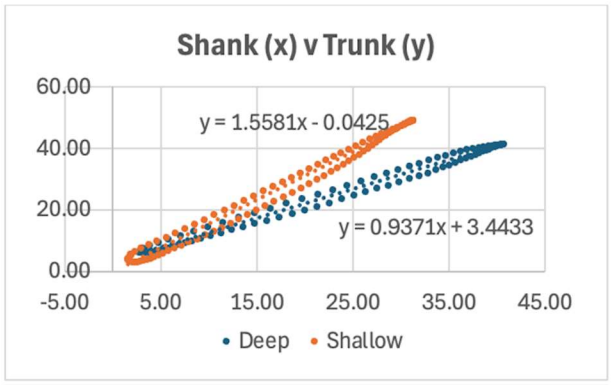
Results

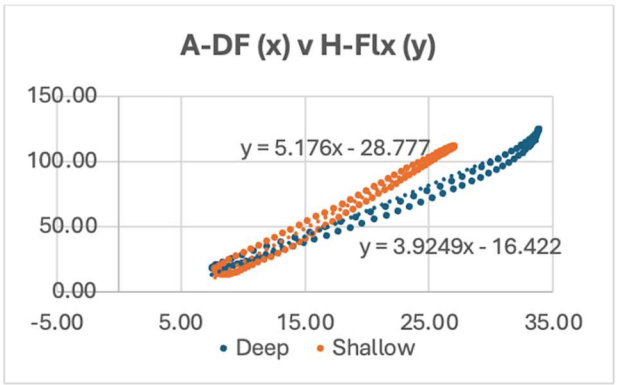
There was no significant difference in mobility of the hip, knee, and ankle measured with the goniometer. Maximal flexion angles (kinematics) were significantly different between deep v. shallow squatters; respectively: Trunk (41.5°±13.3° v. 49.3°±6.9°; $p < .004$) and Ankle (33.9°±5.2° v. 27.0°±2.3°; $p < .003$). Slopes of the shallow squatters cyclograms were significantly higher (see image for equation); Trunk-Shank ($p < .001$) and Hip-Ankle ($p < .001$).

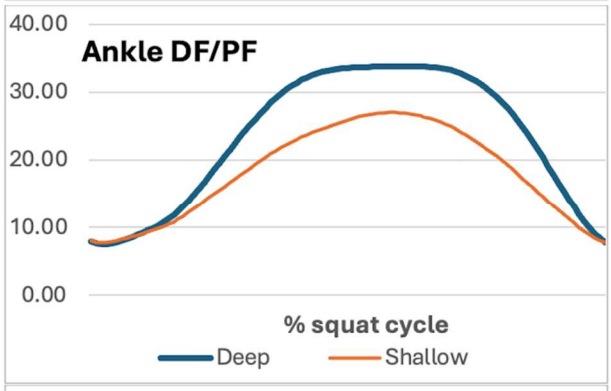
Discussion

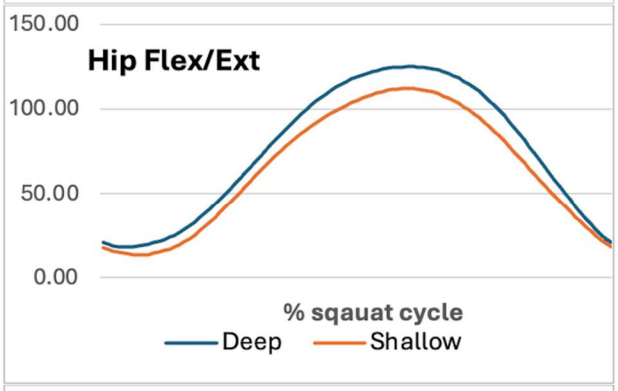
The cyclograms show shallow squatters are dominant in hip and trunk movements where deep squatters utilize greater knee and ankle movement. Despite no significant difference in goniometric mobility of the hip, knee, and ankle, there were differences in maximal kinematic angles and movement coordination between segments. This study is ongoing, the differences seen in these and additional kinematic waveforms and cyclograms will be further explored and reported on using a Statistical Parametric Mapping (SPM) approach.

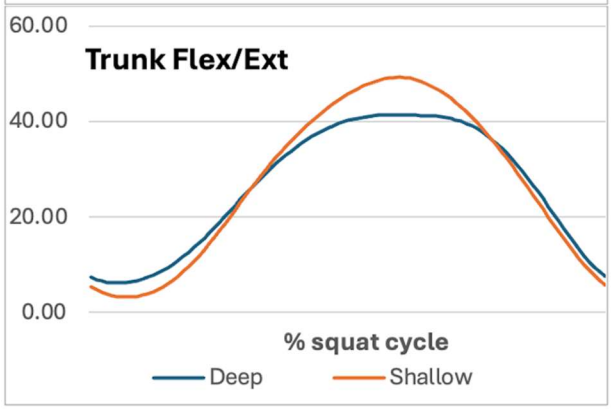
Images (Optional)

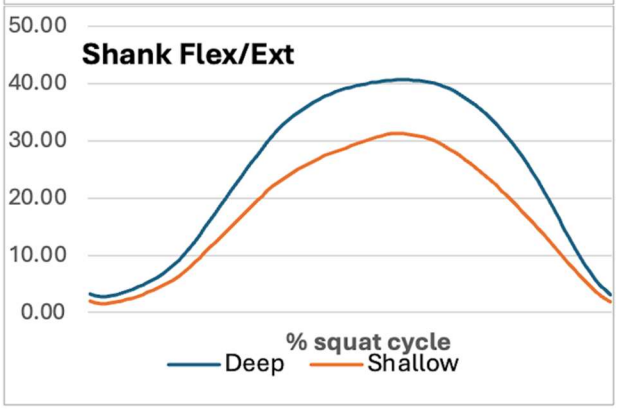












Session Category

Human Motion and Performance: Sports

P1-288

Reliability, Agreement and Waveform Differences Regarding Separate Mathematical Calculations of Knee Valgus Angles During a Land-Cut Task

Dr. Derek Dewig PhD, ATC[1], Ms. Tricia Lemasters[1], Ms. Lindsey Ulring[1], Dr. Taylor Oldfather PhD[2]

[1]Fairmont State University, Fairmont, WV, United States. [2]Auburn University, Auburn, AL, United States

Introduction

Knee valgus angles (KVAs) are frequently assessed in biomechanics research as they are associated with lower-extremity injury occurrence.[1] However, ambiguity in reported KVA calculations and definition inconsistency renders direct comparison of kinematic outcomes between studies difficult or obfuscate.[2] This ongoing study aims to evaluate the reliability, agreement and waveform differences between two mathematical methods of calculating KVAs during a single-leg, land-cut task.

Methods

Kinematics and kinetics (8-camera motion capture and forceplates sampling at 200 and 2000Hz, respectively) of 6 participants were assessed as they dropped off a 30-cm box, landed on a force-plate with their dominant leg, and cut 45-degrees towards the non-dominant leg. Two KVAs were calculated: 1) the orientation of the shank relative to thigh in the frontal plane defined by the thigh coordinate system (KVA_{knee}) and 2) the orientation of the shank relative to the vertical global axis in the frontal plane of the global coordinate system (KVA_{gcs}). Angles were evaluated from initial contact (vGRF >20N) to peak knee flexion angle. Intrasession reliability for both peak KVA measures was evaluated via Intraclass Correlation Coefficients (ICC(3,k)), and agreement between peak measurements was assessed via a repeated measures correlation and Bland-Altman Limits of Agreement (LOA)/bias. Statistical Parameter Mapping paired t-test was conducted on both ensemble waveforms to identify temporal differences in measurements.

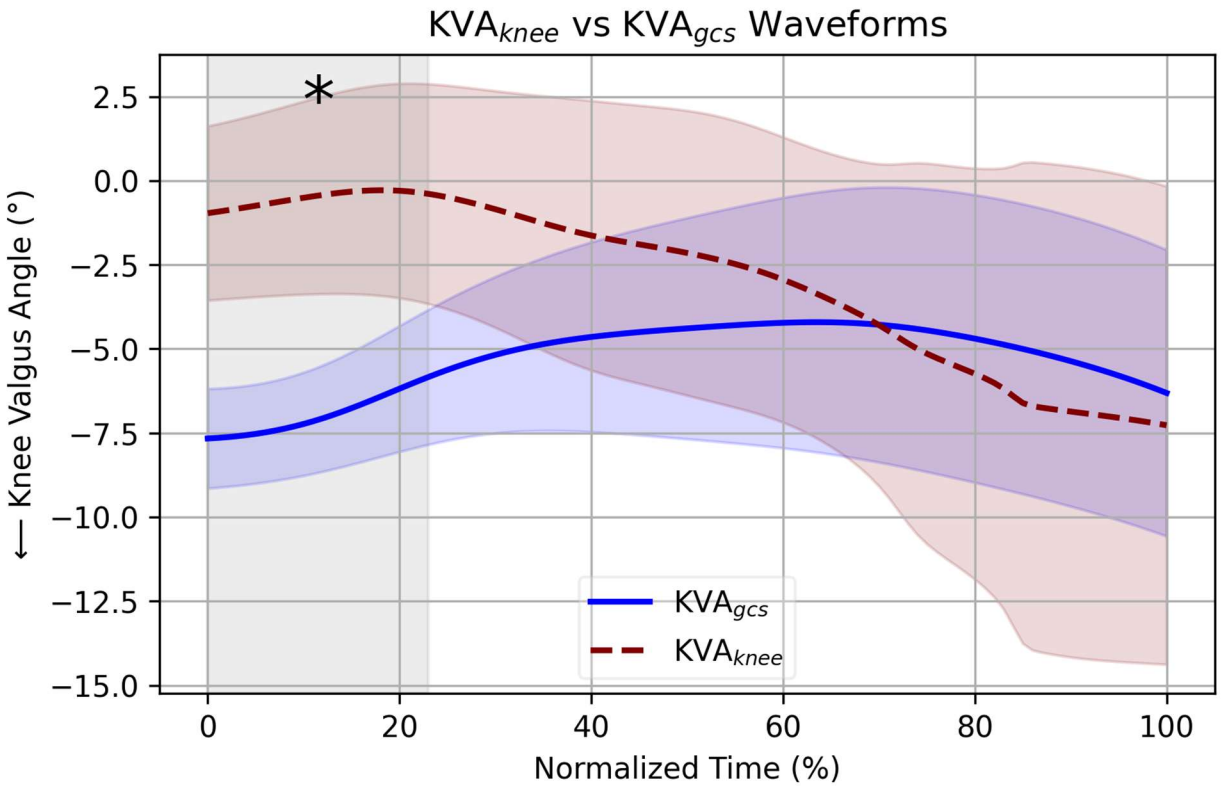
Results

Both peak KVA_{knee} (ICC=0.993) and KVA_{gcs} (ICC=0.934) had excellent intrasession reliability. The bias of difference (KVA_{knee}-KVA_{gcs}) was 1.1°, LOA were between -13.0° and 15.2° and there was no significant correlation between measures ($r = 0.218$, $P = 0.47$). KVA_{gcs} was significantly greater than KVA_{knee} during the first 23% stance (t_{max}= -6.3, t*= ±4.1).

Discussion

KVA_{knee} and KVA_{gcs} are not correlated with each other and have large LOA despite within session reliability, indicating problematic comparisons between differently calculated definitions of KVAs. Additionally, early stance rends the largest difference between measurements, which could have implications for injury risk evaluation as most non-contact injuries occur within 50ms of landing.[3]

Images (Optional)



References (Optional)

[1] Pedley *et al.*, J of Science in Sport and Exercise, 2020

[2] Oldfather *et al.*, J Biomech Eng. 2020

[3] Krosshaug *et al.*, Am J Sports Med. 2007

Session Category

Human Motion and Performance: Sports

P1-289

The Role of Minimum Pelvis Velocity in Kinematic Sequencing and Performance in Baseball Pitchers

Mr. Dimitri Haan MS

University of Nebraska at Omaha, Omaha, NE, United States

Introduction

The kinematic sequence suggests that pitchers reach peak rotational velocity of their segments in a proximal-to-distal fashion, with each subsequent segment achieving a higher velocity.[1–3] Research shows the strongest predictor of pitch velocity is trunk maximum velocity, and a strong predictor of trunk velocity is pelvis velocity.[4] Little research has investigated the effect of minimum pelvis velocity (MinPV) on trunk velocity (MTV) and pitch velocity. The segmental interaction principle states that distal segment acceleration increases when the proximal segment decelerates, resulting in a faster, whip-like motion due to the transfer of momentum.[5] For a baseball pitch, this may present as the trunk reaching a higher rotational velocity due to the pelvis reaching a lower minimum velocity. Therefore, the purpose of this study was to investigate the effect of MinPV on MTV and pitch velocity. We hypothesized that MinPV would have an inverse relationship with trunk and pitch velocity.

Methods

100 pitchers were included in this study (Age: 18.5±2.83 years, Height: 1.82±0.099 m, Mass: 82.67±14.12, Right-Handed: 74, Left-Handed: 26). Pitchers were excluded if they missed competition due to injury within the last 6 months. Pitchers threw fastballs, and motion capture data were collected (240 Hz-333 Hz). The fastest three fastballs were exported to Visual3D for analysis. Maximum and minimum pelvis velocity, maximum trunk velocity, and associated timing were exported to RStudio for analysis. Pitch velocity was collected using a Stalker Radar Gun.

A linear mixed-effects model was used to measure the effect of MinPV and time of MinPV on MTV. A second model measured the effect of MinPV and time of MinPV on pitch velocity. Significance (†) was set at t=2.00.

Results

Results of the model show that MinPV has a moderate significant effect on MTV and small, significant effect on pitch velocity. The results suggest that for every 100°/s slower a pitcher's MinPV is, MTV increases by 15.2°/s, and pitch velocity increases by 0.6mph.

Discussion

These results expand the scope of the kinematic sequence, offering more information to coaches and players on how to move in a way that optimizes segmental interaction and performance.

Images (Optional)

Table 1.

Model Design	β_{MinPV}	t_{MinPV}	β_{Time_MinPV}	t_{Time_MinPV}
MTV ~ MinPV + Time_MinPV + (1 | Subjects)	-0.152	-3.99 †	-2.33	-1.34
Pitch Velocity ~ MinPV + Time_MinPV + (1 | Subjects)	-0.0063	-3.21 †	-0.118	-1.38

Session Category

Human Motion and Performance: Sports

P1-290

The Relationship Between Energy Flow, Ball Velocity, and Upper Extremity Joint Loading in High School Baseball Pitchers

Mr. Brandon Muczynski BS, Dr. Adam B. Rosen Ph.D, Dr. Samuel J. Wilkins Ph.D, Dr. Brian A. Knarr Ph.D, Mr. Dimitri Haan M.S

University of Nebraska Omaha, Omaha, NE, United States

Introduction

In 2024/2025, over 8.2 million U.S. high school athletes participated in sports, with baseball ranked third in popularity at 472,598 participants. Among male pitchers, 46–57% experience shoulder or elbow injuries, accounting for 39.6% of shoulder and 56.9% of elbow injuries. A comprehensive energy flow analysis will be performed across multiple pitch types, measuring joint forces, torques, power, and work in the lower extremities (LE) , trunk, and upper extremities (UE). We hypothesize that different pitch types will show distinct patterns of segmental energy flow, with inefficient transfer linked to increased joint stress and decreased velocity.

Methods

Six male high-school baseball pitchers (16.6 ± 1.47 yrs, 186.94 ± 4.59 cm., 84.38± 8.02 kg) were extracted from the UNO Pitching Lab database. Kinetics and kinematics were collected using three in-mound force plates (AMTI, 320 Hz) and a 16-camera motion capture system (Qualisys, 320 Hz) using a 41-marker full-body model. Joint forces, torques and velocities were computed using inverse dynamics in Visual 3D software v2024.10.4 (Germantown, MD). Custom MATLAB code calculated torque power, work and Energy-Transfer Efficiency (ETE). ETE is defined as the ratio of distal (UE) to proximal (LE+ trunk) positive work. Data were normalized to the pitch cycle (Setup→Ball Release). Spearman/Pearson correlation ($p<0.05$) was used to evaluate relationships between ETE, work, and joint kinetics.

Results

Clear proximal-to-distal sequencing of joint kinetics was observed. The LE accounted for 75%–85% of all positive work, with sliders producing the most. The UE exhibited greater positive work than negative work, with curveballs generating the highest. Elbow varus torque was greatest in fastballs and curveballs, change-ups and sliders producing the lowest. A moderate positive correlation was found between UE positive work and shoulder torque ($r_s = 0.42$, $p = 0.05$), and a weak trend for elbow varus torque ($r_s = 0.39$, $p = 0.076$).

Discussion

High school and youth pitchers are especially vulnerable due to inadequate training and instruction as well as underdeveloped pitching mechanics. Different pitch types place varying demands on the body, emphasizing the need for efficient energy transfer to reduce arm stress and injury risk.

Images (Optional)

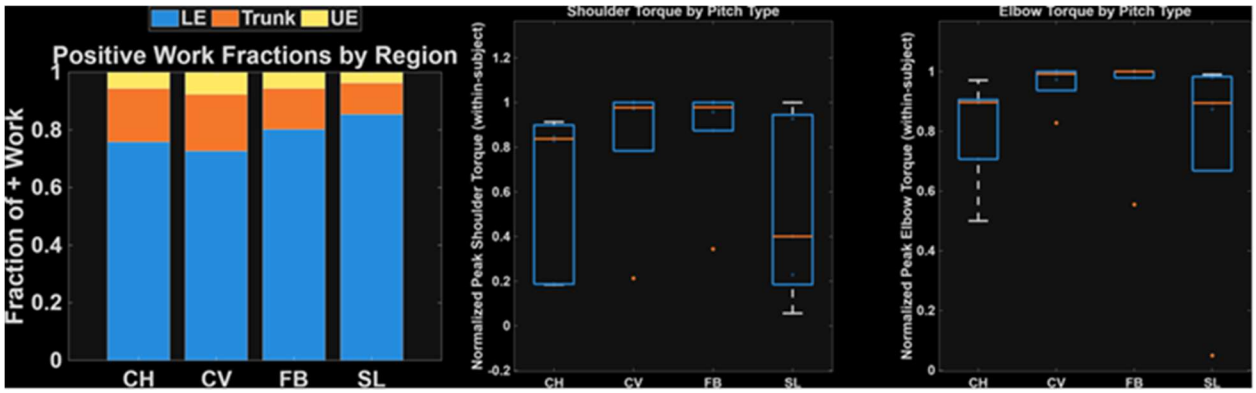


Figure 1. Positive joint work fractions for the lower extremity (LE), trunk, and upper extremity (UE) across pitch types (left). Normalized peak shoulder and elbow torques by pitch type (right).

Session Category

Human Motion and Performance: Sports

P1-291

Maximal Sprint Acceleration: Is it Better to be More Grounded?

Mr. Dominic Crisostomo, Mr. Gouresh Powar, Dr. Peter Weyand

Texas Christian University, Fort Worth, Texas, United States

Introduction

The maximal accelerations of the fastest sprinters on earth are typically substantially less than the earth's rate of gravitational acceleration of 9.81m/s^2. What factors might set this relatively modest limit? Unlike automobiles and other forms of wheeled transportation, human sprinters accelerate in a pulsatile fashion, where the body's velocity is increased during each push of the foot on the ground but remains unchanged during the aerial periods between steps. Between-step aerial periods are obviously necessary for limb repositioning, but they also introduce periods of zero force application that limit maximal rates of acceleration. Here, we hypothesized that humans minimize aerial times between steps to maximize sprint running acceleration. We tested this idea using torso weighting as an experimental tool, predicting that aerial times during maximal sprint accelerations would be unchanged in the weighted condition.

Methods

Two sprint-trained males ran five maximal sprint acceleration trials each from starting blocks under unweighted and torso-weighted conditions (+15% of bodyweight). The participants accelerated across a 5.3-meter force platform-runway system (Bertec, 1000Hz). Contact and aerial times were determined by analyzing the periods above and below a vertical force of 30N, respectively. Means were determined across the first five contact and four aerial periods. Step-by-step means were also determined for each participant

Results

Mean contact times across the first five steps were longer (1.17 vs. 1.05s) and aerial times were shorter (0.16 vs. 0.25s) in the weighted vs. unweighted condition, respectively. Corresponding percent differences were: T_c: +11.4%; T_{air}: -36%. Mean velocities were 4.0% slower in the weighted vs. unweighted condition (3.60 vs. 3.75 m/s).

Discussion

Contrary to expectation, runners decreased aerial times by more than a third in the weighted vs. unweighted condition. This occurred, at least in part, due to an elongation of the contact length (=tc•velocity) and contact times utilized to meet the additional vertical

force requirement in the torso-loaded condition. These data do not discount the possibility that the runners utilize limb repositioning strategies that maximize the time of propulsive force application when accelerating maximally.

Images (Optional)

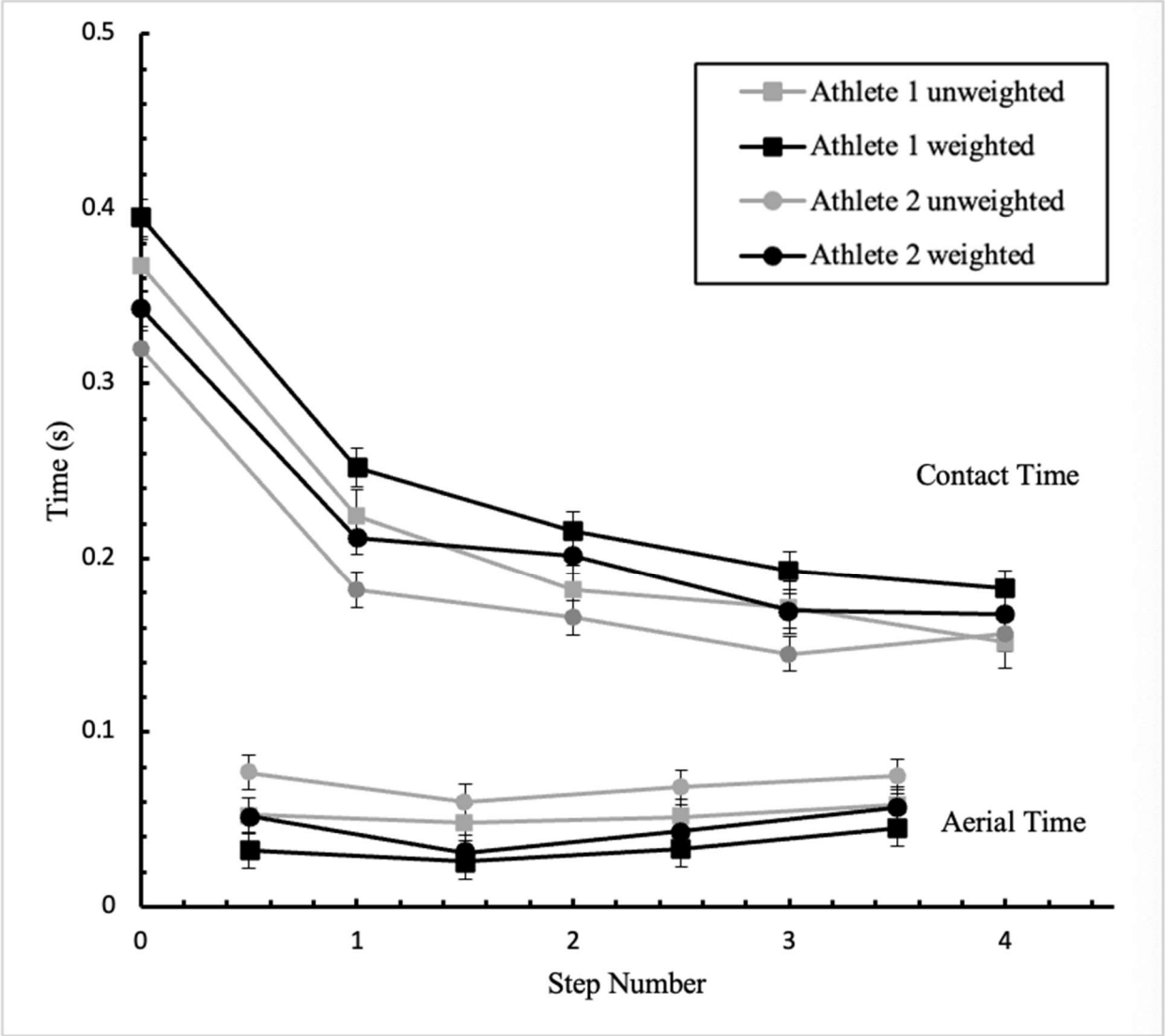


Figure 1: Contact and aerial times for the first five steps of maximal sprint trials from starting blocks.

Session Category

Human Motion and Performance: Sports

P1-292

A Biomechanical Investigation of Strike Kinematics in the Filipino Martial Art of Arnis: Use of Segmental Timing and Proximal-to-Distal Energy and Momentum Transfer to Generate Powerful Stick Strikes

Dr. Elaine Serina PhD[1,2], Dr. Eric Mockensturm PhD[1], Mr. Noah Schneider BS[1], Mr. Ellis Chiang[1,2]

[1]Talas Engineering, Hayward, CA, United States. [2]Legacy Filipino Martial Arts, Daly City, CA, United States

Introduction

The Filipino martial art of Arnis is a weapons-based defensive system where powerful, injury-producing strikes are executed using a long, lightweight rattan stick. Arnis techniques optimize stick dynamics so that even small-sized individuals can generate excessive force; however, the mechanism has not been scientifically studied. Research on limb dynamics in badminton forehand shots and baseball throws identified a proximal-to-distal sequencing that optimized energy transfer down the linkage system, enhancing distal speed. Effective execution depended on multi-joint coordination rather than isolated strength. This study investigated the applicability of this movement pattern to Arnis strikes.

Methods

Strikes by two elite Arnis practitioners were conducted in the horizontal plane using a standard 26-inch Arnis stick (1-inch diameter, ½ lbf). Overhead high-speed video (500Hz) was captured, and anatomical joint markers on the upper extremities were digitized to determine torso, upper arm, forearm, hand, and stick trajectories. Using subject anthropometric data, mass moments of inertia were calculated, adjusted to account for out-of-plane segment orientation over time. Kinematic parameters—limb velocities, angular momentum about a central-body axis, and energy—of each segment were calculated. Total momentum and energy data were compared to a simple 1-DOF model that assumes a fully extended arm/stick system with fixed joints.

Results

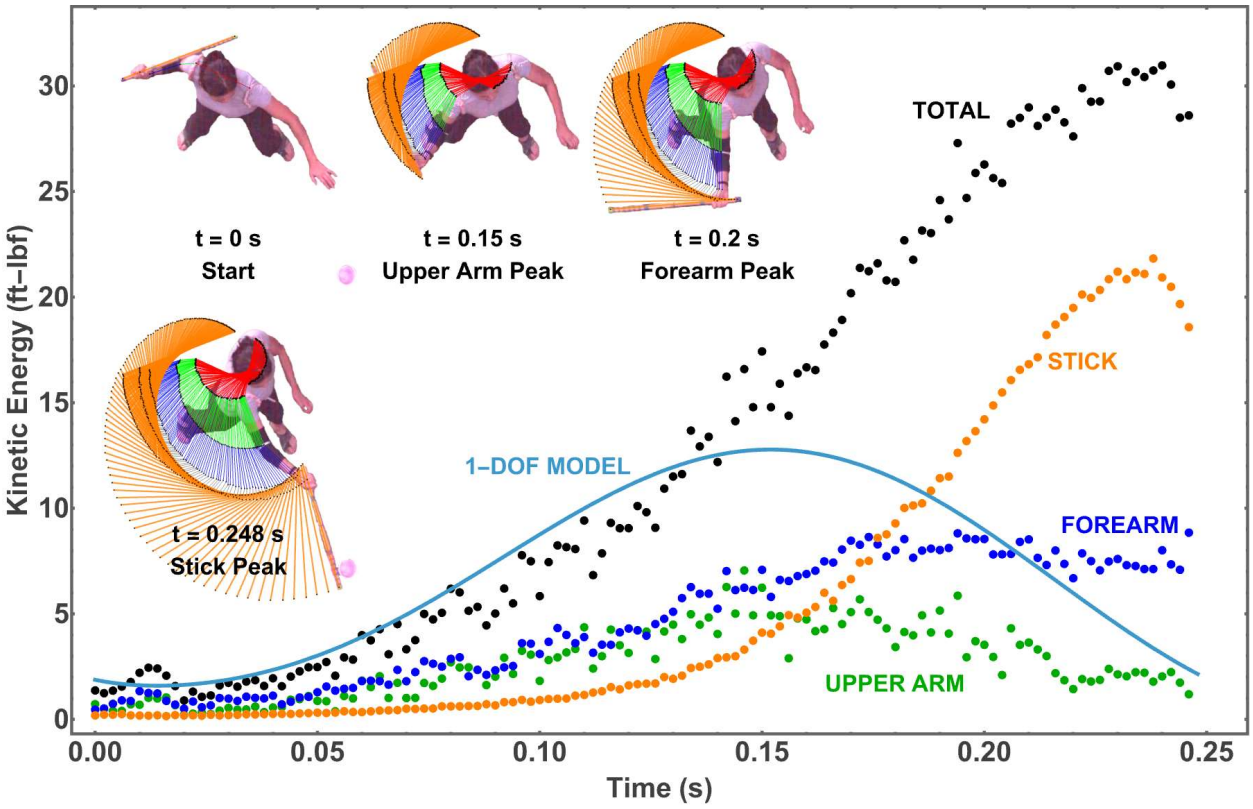
Overall, joint movements between subjects were generally consistent. Stick velocities reached 80mph over a 180-250ms duration. Kinematic parameters of the proximal body segments peaked sequentially earlier than distal segments. Torso rotation contributed

significantly to the momentum and energy due to its much greater mass moment, despite its lower speeds.

Discussion

Arnis striking techniques optimize the generation of peak momentum and kinetic energy at impact to maximize the impulse and energy transfer to the target. Coordinated sequencing within the linked-segment system was observed, where velocity, energy, and momentum are transferred from proximal to adjacent distal segments. For horizontal strikes, the elbow-joint orientation was out of plane; thus, the elbow joint primarily extends the arm, increasing the inertia of the system to impact. In comparison, kinematic values of the 1-DOF model peaked earlier in the swing at less than half the magnitude and were only a fraction of their values at impact.

Images (Optional)



Session Category

Human Motion and Performance: Sports

P1-293

The Interaction Effect of Sex and Cleat Design on the 180-Degree Cut

Mr. Garrett Hess[1], Dr. Brett Pexa[1], Dr. Jeffrey Taylor[1], Mr. Joseph Helseth[2], Dr. Kevin Ford[1]

[1]High Point University, High Point, NC, United States. [2]Nike Sport Research Lab, Beaverton, OR, United States

Introduction

Athletes' performance and injury risk are influenced by several factors. These factors include inherent biological differences and the modifiable tools used in sport, which may influence an athlete's movement both independently and collectively. Further research is still needed to understand how the interaction between biological sex and cleated footwear influences lower extremity biomechanics.

Methods

30 collegiate soccer players (15 male: age: 21.0 ± 1.2 yrs; mass: 78.5 ± 7.1 kg; height: 177.9 ± 5.5 cm; 15 female: age: 20.5 ± 1.2 yrs; mass: 64.5 ± 8.9 kg; height: 165.9 ± 5.4 cm), completed five maximal effort 180-degree cuts with a 6-meter approach in two different cleats (Nike Phantom GX II Elite Artificial Grass (AG) & Nike Phantom GX II Elite Firm Ground (FG)), in a randomized order on a slit film fiber turf, infilled with a mixture of crumb rubber and sand. A 14-camera motion capture system (200Hz, Qualisys AB, Göteborg, Sweden) synchronized with in-ground force platforms (1200Hz, Advanced Mechanical Technology Inc., Watertown, MA, USA) were used to assess the movement.

Results

There was a sex and cleat interaction effect for normalized peak knee internal rotation moment (p=.007) with both a main effect of sex (p<.001) and cleat (p=.023). Post-hoc analysis indicated that males had a greater normalized peak knee internal rotation moment in both cleat conditions (p<.01) than females. Additionally, males had a reduction in the knee internal rotation moment in FG (0.58 ± 0.16 Nm/kg) compared to AG (0.66 ± 0.16 Nm/kg; p=.008, d=0.8), while females did not differ between cleated conditions (p=.61). There was also a main effect of sex for peak knee abduction angle with females demonstrating greater peak knee abduction in both cleated conditions (p=.011).

Discussion

Both biological sex and footwear influence knee biomechanics during the 180-degree cut. The sex differences in knee moment and angle showed that individuals may perform the task differently. The firm ground cleat reduced internal knee moments in males but not females compared to the artificial grass cleat, which differed in stud configuration and shape. This is an important factor to acknowledge for both cleat design and selection.

Acknowledgements (Optional)

Funding and footwear provided by Nike.

Session Category

Human Motion and Performance: Sports

P1-294

High-Frequency Plantar TENS Enhances Jump Performance, Landing Biomechanics, and Dynamic Balance: Preliminary Evidence for Sensory-Driven Modulation of Athletic Movement

Ms. Gina Garcia MA[1,2], Dr. Jae Shim PhD[1]

[1]University of Maryland - College Park, College Park, Maryland, United States. [2]Exos Human Performance Lab, Phoenix, Arizona, United States

Introduction

Plantar sensory input directly influences motor output by modulating excitability within sensorimotor pathways. Mechanoreceptors in the foot sole provide afferent feedback to the central nervous system, shaping movement planning, force production, and joint-level loading through spinal and supraspinal integration. Transcutaneous electrical nerve stimulation (TENS) provides a practical method to augment sensory input by lowering mechanoreceptor firing thresholds and amplifying afferent signaling. Pacinian corpuscles are highly sensitive to electrical stimulation, especially >100 Hz, making them an ideal target for influencing motor output. This study examined whether high-frequency plantar TENS improves countermovement jump (CMJ) performance, jump-landing biomechanics, dynamic balance, and fatigue resistance compared with low-frequency stimulation and no-stimulation.

Methods

Five jump-trained adults (22.4 ± 3.3 y) completed three randomized conditions: no stimulation, 50 Hz TENS, and 150 Hz TENS applied bilaterally to the heel and lateral forefoot at 90% of sensory threshold (Figure 1). CMJ performance and landing biomechanics were assessed using 3D motion capture (200 Hz) and force plates (1000 Hz). Joint kinematics, kinetics, and concentric/eccentric work were calculated via inverse dynamics. Dynamic balance was assessed using the Y-Balance Test (YBT) before and immediately after a fatiguing continuous jumping protocol. Fatigue was quantified from 30 s repeated CMJs using fatigue index.

Results

Three participants achieved their greatest CMJ height in the 150 Hz condition (mean improvement: +0.65 cm vs no stimulation; +1.08 cm vs 50 Hz). High-frequency stimulation increased the proportion of ankle concentric work in four participants and reduced knee

concentric contribution in three. During landing, ankle eccentric work was greatest in the 150 Hz condition for three participants, while relative knee contribution was lowest in three. Dynamic balance favored 150 Hz for posteromedial, posterolateral, and composite YBT scores in most participants. Under fatigue, three participants demonstrated lower fatigue index values with 150 Hz stimulation.

Discussion

These preliminary findings suggest that enhancing plantar sensory input can positively influence motor output, movement strategy, and balance performance, and may help preserve performance under fatigue. Individual responses varied, indicating possible responder heterogeneity. Ongoing data collection ($n \leq 30$) will evaluate whether high-frequency TENS consistently modifies performance, landing biomechanics, and balance outcomes at the group level

Images (Optional)

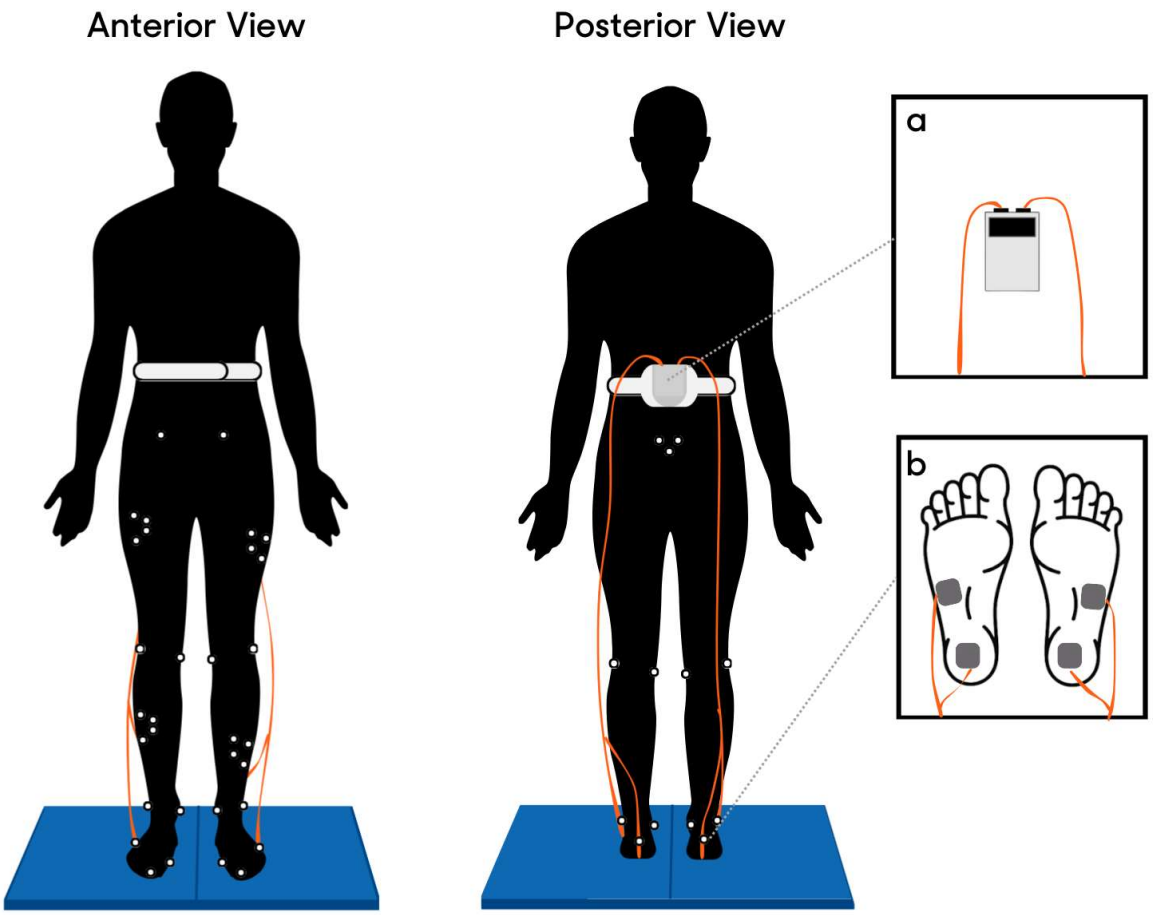


Figure 1. Placement of reflective markers, a) the TENS unit and b) TENS pads on the soles of the feet of a participant

Session Category

Human Motion and Performance: Sports

P1-295

The Influence of Sample and Filter Frequencies on Baseball Pitching Data

Dr. Glenn Fleisig[1], Ms. Brittany Dowling[2], Dr. Jonathan Slowik[1]

[1]American Sports Medicine Institute, Birmingham, AL, United States. [2]Midwest Orthopaedics at Rush, Chicago, IL, United States

Introduction

The throwing motion in baseball pitching is the fastest recorded human motion, demanding higher sample frequencies than most human movements. Previous studies have used sample frequencies from 240-500 Hz and a wide range of low-pass filter frequencies, although 13.4 and 18.0 Hz are the most common. This study examined the effects of two common sample frequencies (240 and 480 Hz) and three filter frequencies (13.4, 18.0, and 27.2 Hz) on pitching data.

Methods

Fastballs from 28 professional baseball pitchers were collected at 480 with marker motion capture, then down-sampled to 240 Hz; each data set was filtered at the three filter frequencies. Twenty-six common kinematic, temporal, and kinetic variables were computed for each pitcher across all sample-filter frequency combinations and compared using two-way repeated measures ANOVA. Differences were interpreted relative to minimal clinically important differences (MCID). Based upon recent studies,[1,2] MCID for stride length, joint angles, arm angular velocities, lower body angular velocities, torques and forces were set as 1% height, 2°, 100°/s, 20°/s, 3 Nm and 30 N, respectively.

Results

Differences for kinematic and kinetic variables are shown in Table 1. There were numerous statistically significant differences in pitching biomechanics associated with sample and/or filter frequency. However, many of these differences were less than MCID and therefore have limited clinical value.

Discussion

Pitching data were more sensitive to filter frequency (significant differences above MCID in 13 of 26 variables) than to sample frequency (4 of 26 variables). Velocity and kinetic variables were most impacted by sample and filer frequency, as sensitivity to sample and filter frequency increases with each level of numerical differentiation.[3,4] Based upon these findings and time-series inspection, we recommend a minimum sample frequency of

240 Hz and a Butterworth low-pass filter of 18.0 Hz for with marker-based motion capture pitching mechanics.

Images (Optional)

Table 1. Differences between various sample and filter frequencies

	240 Hz			480 Hz		
	13.4 Hz	18.0 Hz	27.2 Hz	13.4 Hz	18.0 Hz	27.2 Hz
Kinematics at Foot Contact						
Stride length (% height)*	80.9±5.5	80.9±5.4[f]	80.8±5.4[g]	80.9±5.4	80.9±5.4[f]	80.9±5.3[g]
Elbow flexion (°)	99.3±14.5	99.4±14.2	99.2±14.0	99.2±14.3	99.5±13.9	99.7±13.6
Shoulder external rotation (°)*	26.0±29.4	25.6±29.3[f]	25.1±29.2[g]	26.2±29.6	26.7±29.3[f]	26.7±28.7[g]
Trunk rotation (°)	39.7±9.3	39.7±9.3	39.8±9.2	39.8±9.2	40.0±9.1	40.1±9.1
Kinematics at Maximum External Rotation						
Elbow flexion (°)[b,c]	90.0±9.6	91.5±9.2	91.8±9.1	89.6±9.3	91.2±9.1	91.6±8.9
Shoulder rotation (°)*	**166.2±8.5[e,H,I]**	**168.8±8.5[H,j]**	**170.1±8.4[I,j]**	**166.3±8.4[e,k,L]**	**168.8±8.4[k,M]**	**170.1±8.4[L,M]**
Kinematics at Ball Release						
Elbow flexion (°)*	**30.5±3.8[E,H,I]**	**34.4±4.1[F,H,J]**	**37.2±4.5[G,I,J]**	**28.3±3.8[E,K,L]**	**31.6±4.0[F,K,M]**	**33.7±4.3[G,L,M]**
Shoulder abduction (°)*	**95.0±8.1[e,h,I]**	93.4±8.2[f,h,j]	**92.4±8.3[g,I,j]**	**94.0±8.4[e,k,L]**	92.3±8.6[f,k,m]	**91.2±8.7[g,L,m]**
Trunk lateral flexion (°)[b,c,d]	28.2±7.9	28.4±7.9	28.5±7.9	28.3±7.9	28.5±7.8	28.5±7.8
Trunk flexion (°)*	19.1±7.7[e]	19.1±7.7[f]	19.1±7.7[g]	18.0±7.6[e]	18.0±7.6[f]	18.1±7.6[g]
Lead knee excursion (°)[a,b,c]	17.6±12.7	18.1±12.9	18.4±13.2	16.9±12.4	17.5±12.3	17.9±12.4
Maximum Kinetic Values						
Elbow varus torque (Nm)[a,B,C]	**98.7±11.7**	**102.1±12.4**	**102.4±12.6**	**98.6±11.7**	**101.9±12.3**	**102.3±12.5**
Elbow flexion torque (Nm)*	**73.0±9.0[H,I]**	**82.1±9.2[H,J]**	**95.7±10.3[g,I,J]**	**73.3±8.8[K,L]**	**82.4±9.0[K,M]**	**96.7±10.4[g,L,M]**
Elbow proximal force (N)*	**1002±118[E]**	**992±116[F]**	**985±131[G]**	**1169±111[E,k,L]**	**1140±112[F,k,M]**	**1090±130[G,L,M]**
Shoulder internal rotation	**100.7±13.4[H,I]**	**105.8±13.6[f,H,j]**	**108.0±14.4[g,I,j]**	**100.6±13.4[K,L]**	**105.5±13.5[f,K,m]**	**107.6±14.4[g,L,m]**
Shoulder proximal force	**1076±152[E,H,I]**	**1120±164[F,H,J]**	**1225±188[G,I,J]**	**1195±131[E,L]**	**1181±143[F,M]**	**1260±178[G,L,M]**

*: Statistically significant sample frequency - filter frequency interaction effect
Statistically significant difference (no interaction effect):
a: Between 240 Hz and 480 Hz sample frequency data
Statistically significant pairwise comparison (no interaction effect):
b: Between 13.4 Hz and 18.0 Hz filter frequency data
c: Between 13.4 Hz and 27.2 Hz filter frequency data
d: Between 18.0 Hz and 27.2 Hz filter frequency data
Statistically significant pairwise comparison (interaction effect):
e: Between 240 Hz and 480 Hz sample frequency data when filtered at 13.4 Hz
f: Between 240 Hz and 480 Hz sample frequency data when filtered at 18.0 Hz
g: Between 240 Hz and 480 Hz sample frequency data when filtered at 27.2 Hz
h: Between 13.4 Hz and 18.0 Hz filter frequency data for 240 Hz sample frequency data
i: Between 13.4 Hz and 27.2 Hz filter frequency data for 240 Hz sample frequency data
j: Between 18.0 Hz and 27.2 Hz filter frequency data for 240 Hz sample frequency data
k: Between 13.4 Hz and 18.0 Hz filter frequency data for 480 Hz sample frequency data
l: Between 13.4 Hz and 27.2 Hz filter frequency data for 480 Hz sample frequency data
m: Between 18.0 Hz and 27.2 Hz filter frequency data for 480 Hz sample frequency data
Bold: Value with significant difference greater than minimally clinically important difference (MCID) of 2° or 1% height.
CAPITALIZATION of superscripted letter: Individual comparison greater than MCID

References (Optional)

[1] Glenn S. Fleisig *et al.*, Am J Sports Med, 2024

[2] Glenn S. Fleisig *et al.*, Orthop J Sports Med, 2025

[3] Georgios Christodoulakis *et al.*, 7th Int Symp CSNDSP, 2010

[4] Moreno D'Amico *et al.*, Med Biol Eng Comput, 1990

Session Category

Human Motion and Performance: Sports

P1-296

Comparison of Baseball Infielder and Pitcher Throwing Biomechanics

Dr. Glenn Fleisig, Dr. Jonathan Slowik

American Sports Medicine Institute, Birmingham, AL, United States

Introduction

While numerous studies have quantified baseball throwing biomechanics, these studies have almost exclusively focused on pitching. Establishing infielder throwing biomechanics could provide valuable, lacking information for biomechanists, coaches, and players. Furthermore, infielders in youth through collegiate baseball often pitch too, raising questions and concerns whether playing infield in addition to pitching increases risk of arm injury. Thus, the purpose of this study was to compare infield throwing and pitching biomechanics.

Methods

Throwing biomechanics were captured for 11 baseball players in a laboratory setting with a 12-camera marker-based motion capture system at 240 Hz. Each player was both a pitcher and an infielder on a youth, high school, college, or professional baseball team. After warming up, each player threw ten fastballs from a pitching mound to a strike zone over a home plate 18.44 m away. After the mound was removed, the player fielded ten groundballs rolled to him and threw the ball to a first base target. For each throw, 31 biomechanical parameters were calculated from tracking the 47 markers on the athlete as previously described. Ball velocity was captured with a radar gun. Differences between pitching and infield throwing biomechanics were analyzed with paired t-tests ($p<0.05$).

Results

Only four of the 16 upper extremity biomechanical parameters showed statistical differences. Angular velocities of shoulder internal rotation (mean 6955 vs 6613 °/s) and elbow extension (2757 vs 2676 °/s) were greater when pitching. There were no significant differences in elbow varus torque (63.9 vs 63.7 Nm) or any other elbow and shoulder kinetics.

Nearly all (13 of 16) trunk and lower extremity parameters showed significant differences. The athletes demonstrated greater lead knee height (60.4 vs 23.3 % body height), stride length (81.0 vs 72.1 % body height), lead knee extension from foot contact to ball release (8.7° extension vs 1.5° flexion), and lateral trunk tilt to the glove side at ball release (26.8 vs 11.5 °) when pitching.

Discussion

While elbow and shoulder kinetics are similar for infield throwing and pitching, full-body kinematics are significantly different. Thus, pitching and infield throws create similar elbow and shoulder stress, but different mechanics are utilized.

Session Category

Human Motion and Performance: Sports

P1-297

Mechanical Basis of Maximal Speed in World-Class Sprinters

Mr. Gouresh Powar, Dr. Peter Weyand

Texas Christian University, Fort Worth, Texas, United States

Introduction

The maximal speeds of sprint runners are determined primarily by the application of large mass-specific ground forces [1, 2]. The relationship between stance average mass-specific ground forces and velocity can be expressed as:

$V_{max} = [(F_{avg}/M_b)*L_C]*Freq_{Step}$

Where:

V_{max} = Maximum Sprinting Velocity,

F_{avg}/M_b = Average mass-specific force,

L_C = contact length,

$Freq_{step}$ = Step Frequency.

Within the heterogeneous runners the positive relationship between Average mass-specific force and maximal velocity is known [1, 2], but which of these variables differentiate performance among the world-class sprinters is not known. We hypothesize that the Average mass-specific force and contact length will have a positive relationship with maximal velocity.

Methods

We acquired running performance and body size data for 48 national and international caliber male sprinters. The maximum instantaneous velocities for two over-ground sprinting steps at international competitions (World-champs, U.S. nationals 100m final) were recorded with a high speed video (≥ 200 Hz). The minimum speed required for inclusion was 10.5 m/s.

Results

The observed mean ± standard deviation and ranges for the variables are as follows: Maximum Sprinting Velocity (V_{max}): mean ± SD = 11.42 ± 0.37 m/s; Average mass-specific force (F_{avg}/M_b): mean ± SD = 2.38 ± 0.15 W_b; Contact length (L_C): mean ± SD = 1.02 ± 0.07

meters; Step Frequency ($Freq_{step}$): mean ± SD = 4.74 ± 0.19 Hz; Leg length (L_O): mean ± SD = 0.98 ± 0.03 meters. Our analysis showed that V_{max} is not significantly related to $Favg/M_b$ or step Frequency, but it was significantly related to L_C and L_C/L_O ($R^2 = 0.1$, $p = 0.02$).

Discussion

Although all sprinters ran with high step frequency and applied large mass specific ground forces (mean of nearly 2.5 times body weight). However frequency and force application did not differentiate between faster and slower world class sprinters. Among variables examined only contact length was significantly related to max velocity. Our results imply that the maximum velocities of the world's fastest sprinters are partially attributable to an ability to sprint with relatively long contact lengths.

Images (Optional)

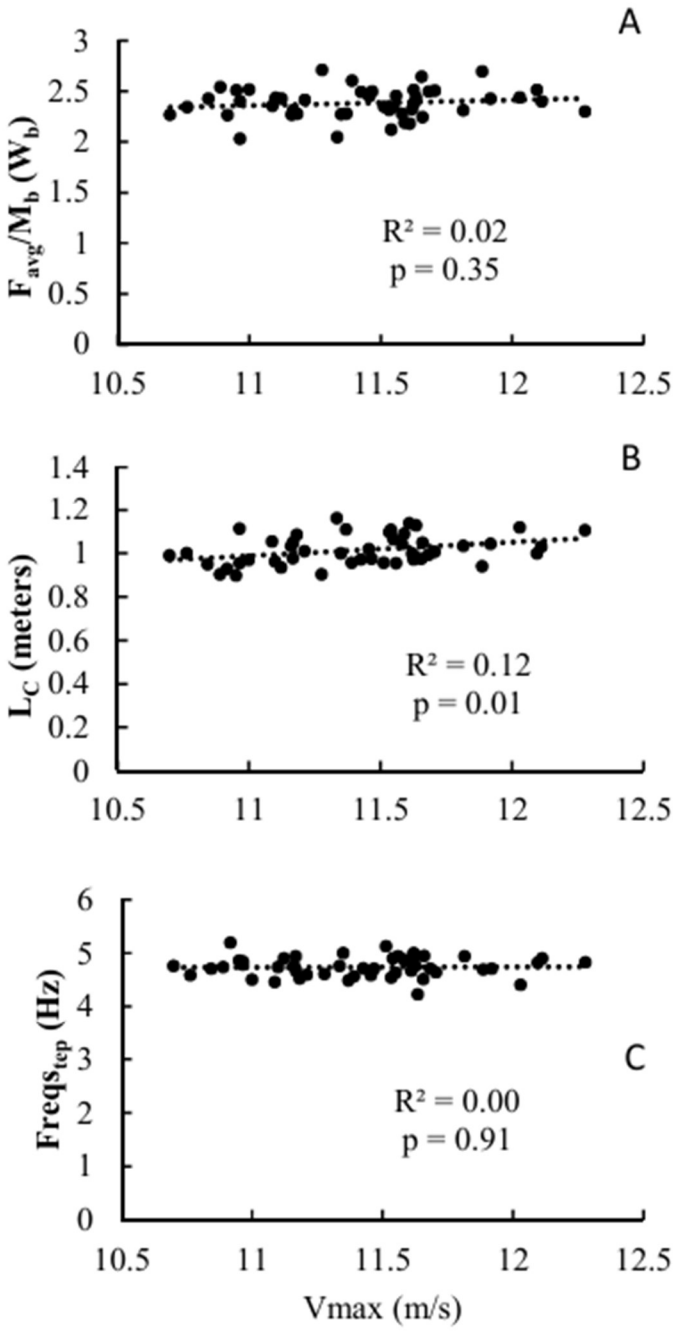


Figure 1: Average mass-specific force (Favg/M_b), Contact length (L_C), Step Frequency ($Freq_{step}$), as a function of maximum velocity (V_{max}). A: F_{avg}/M_bVs V_{max}. B: L_CVs V_{max} C: $Freq_{step}$ Vs V_{max}

References (Optional)

[1] Weyand, P. G. et al. *J Appl Physiol, 2000*

[2] Weyand, P. G. et al. *J Appl Physiol,* 2010.

Session Category

Human Motion and Performance: Sports

P1-298

Can a Smartwatch Learn My Practice Swing? IMU-Only Golf Swing Estimation via Supervised Learning Using Consumer Grade Video Labels

Ms. Guena Park Ph.D. Student, Prof. Sukyung Park Ph.D.

Korea Advanced Institute of Science and Technology, Yuseong-gu, Daejeon, Korea, Republic of

Ms. Guena Park

Introduction

Wearable devices using smartwatches and inertial measurement units (IMUs) are widely adopted in sports and rehabilitation. In golf, these devices typically provide simple low-dimensional metrics such as swing tempo or wrist angle. However, accurate 3D wrist trajectory monitoring is essential for improving swing performance. A single IMU alone struggles to estimate sensor orientation and control cumulative drift errors. A previous study [1] addressed this using machine learning with motion capture-based labels, but this approach requires large scale motion capture data and offers limited model interpretability. Recently, consumer-grade video from smartphones has become ubiquitous, facilitating synchronized IMU–video collection. This study aims to develop a supervised learning method that corrects IMU drift using video-based anchors and estimates swing trajectories from a single IMU without motion capture.

Methods

Ten amateur golfers (mean score: 87.5 ± 4.2) performed 400 driver swings. A 9-axis IMU on the left wrist was synchronized with consumer-grade video, with motion capture providing 3D wrist trajectories as ground truth. Initial sensor orientation was estimated from IMU alone at address, and displacement correction was applied, combining a prior velocity drift correction [2] with video-extracted wrist position anchors. Supervised learning models were trained on labeled IMU–video datasets and evaluated for 3D trajectory and pattern estimation using single-IMU input only.

Results

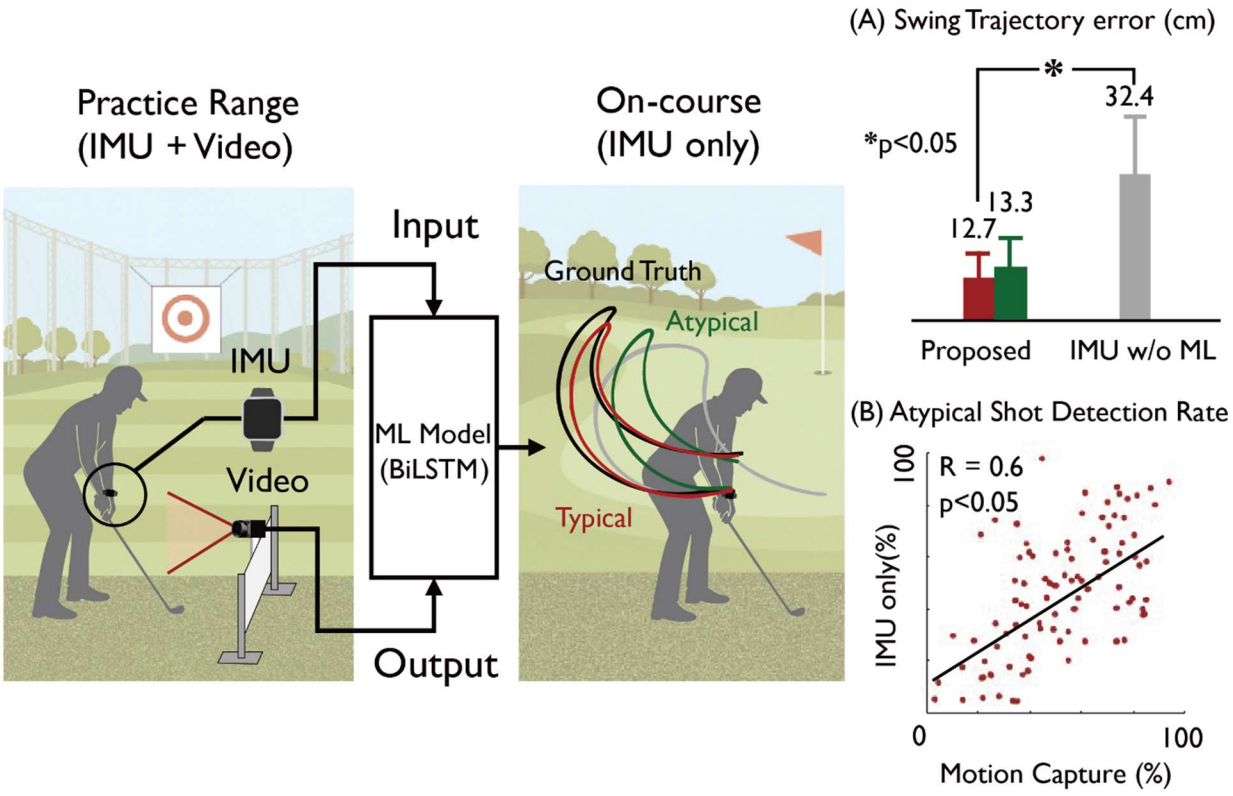
The proposed video-labeling correction reduced wrist position error by over 50% compared to raw IMU integration without machine learning. The final mean average error was 12.7 ±

3.9 cm, comparable to motion capture based supervised learning [2]. Additionally, atypical shot detection rates predicted by the model showed a positive correlation (R = 0.6) with motion capture ground truth, confirming the feasibility of single-IMU-based atypical shot detection.

Discussion

This study demonstrates that IMU-based swing trajectory estimation and supervised learning are achievable using consumer-grade video labels alone, without motion capture. The proposed method reduces data acquisition burden while achieving performance comparable to motion capture-based approaches. With long-term data accumulation, this framework could extend to personalized swing monitoring and feedback systems using a single IMU and video-labeled models.

Images (Optional)



References (Optional)

[1] Jia et al., Proc. ACM IMWUT, 2021

[2] Kim M and Park S, Sci Rep, 2024

Acknowledgements (Optional)

This work was supported by the National Research Foundation of Korea (NRF) grant funded by the Korea government (MSIT) (RS-2024-00356657)

Session Category

Human Motion and Performance: Sports

P1-299

Differences in Muscle Synergy Pattern between Satisfactory and Unsatisfactory Golf Swing: Pilot study

Prof. Hae Dong Lee PhD[1], Mr. Yoon Hyung Cho MSc[1], Mr. Jun Hyun Han BSc[1], Ms Song Yi Choi PhD[1,2]

[1]Yonsei Univeristy, Seoul, Seodaemun-gu, Korea, Republic of. [2]Yonsei Golf Science, Seoul, Jung-gu, Korea, Republic of

Prof. Hae Dong Lee

Mr. Yoon Hyung Cho

Mr. Jun Hyun Han

Introduction

To better understand the complexity of the golf swing, this study investigated how the muscle synergy pattern differs between satisfactory and unsatisfactory golf swings using a non-negative matrix factorization model [1]. Within the framework of dynamic motor control theory [2], the spatial and temporal muscle synergies were investigated during drive swing.

Methods

Young and healthy male volunteers (n = 3, handicap 15~20) performed drive swings until five bad (BS) and five good (GS) swings were collected, with classification based on both the subject's own evaluations and objective data from a ball tracker. This approach aimed to ensure consistent and reliable categorization of swing quality. For the selected swings, 3D joint kinematics and surface electromyography (sEMG) from 13 muscles across the body were obtained. During the downswing phase, using non-negative matrix factorization (NMF), the muscle synergy matrix weight (W) and a neural recruitment coefficient (C) were estimated. Within-subject comparisons of W and C between the conditions were performed using the Mann-Whitney U test and SPM1D, respectively, with a significance level of .05.

Results

For all participants, 3 synergies were found, including BS and GS. The subject-specific synergy weights are shown in Fig. 1A: in Subject 1, RRA in Synergy 1 was larger in good swings, whereas RRF in Synergy 2 was smaller in good swings; in Subject 2, RLD in Synergy 1 was lower in good swings, while RRA in Synergy 3 was higher; in Subject 3, RRA in Synergy 1 and LTB and RTB in Synergy 3 were all higher in good swings. The temporal activation coefficients (C) did not show any significant differences between BS and GS (Fig. 1B).

Discussion

In a driver golf swing, a non-repetitive, goal-directed task, differences between GS and BS were primarily expressed in the synergy weight (W) rather than in the time-varying synergies (C). Notably, all participants showed higher weighting of the right rectus abdominis during GS, suggesting that enhanced trunk stabilization may be a key component of the synergy architecture underpinning successful golf swings.

Images (Optional)

Figure. 1A

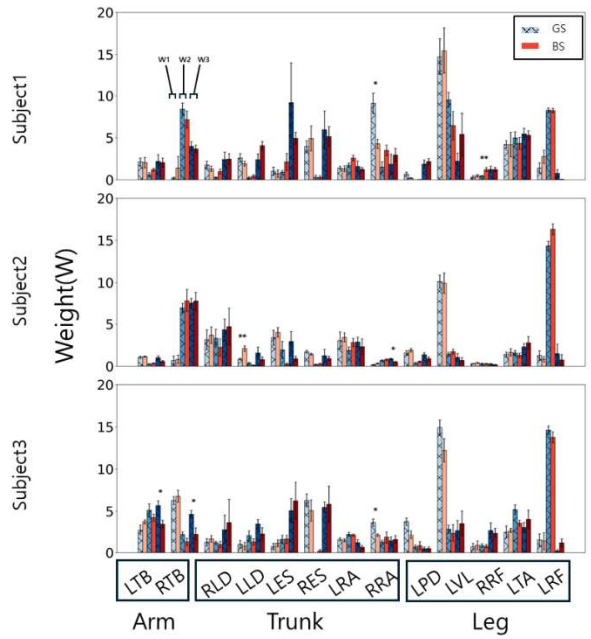
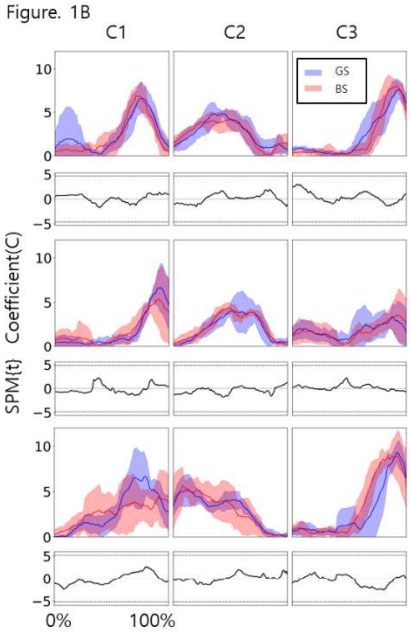


Figure. 1B



/22

References (Optional)

1. D'avella, A. T., M. C., Advances in Neural Information Processing Systems 14, 2002

2. Bernshteĭn, N. A. (1967). Pergamon Press.

Session Category

P1-300

Exploring Modeled Muscle Activation Profiles of Ballet Dancers With Different Jump Landing Techniques

Ms Hailey Wrona[1], Dr Glenna Clifton[2], Dr Kathleen Bieryla[3], Dr Shawn Russell[1]

[1]University of Virginia, Charlottesville, VA, United States. [2]University of Portland, Portland, OR, United States. [3]Carnegie Mellon University, Pittsburgh, PA, United States

Introduction

Ballet dancers are required to exhibit exceptional strength and control while they train beyond typical joint ranges. The primary mechanism of injury in over 50% of time-loss injuries for ballet dancers is attributed to jumping and landing movements. In certain training techniques, they are encouraged to keep their weight forward and maintain a heel-lifted position, landing primarily on their forefoot. In other disciplines, forefoot jump landings and strikes have been linked to increased musculotendon injury risk factors. Therefore, the purpose of this study was to investigate how ballet dance training style influences muscle activation profiles in forefoot (FR) landing and full-foot (FL) landing strategies.

Methods

Thirteen preprofessional dancers performed three sets of jumps in first position (Fig.1A), hips externally rotated with their heels touching, in the two landing styles: FR and FL. The Rizzoli marker set with Optitrak motion capture cameras (100 Hz) and a Bertec force plate (1000 Hz) covered with marley dance floor material was used for kinematics and kinetic data collection. In OpenSim 4.5, to best represent the muscles engaged in the turned-out position, the parameters of the short external rotator muscles of the hip were updated from the generic musculoskeletal (MSK) model based on updated anatomical measurements. With updated subject-specific MSK models, computed muscle control was used to estimate muscle activations.

Results

It was first established that the hip-updated MSK model produced significantly different ($p<0.05$) external rotator outputs. Statistical parametric mapping and heat map visualization (Fig.1B) then revealed that the FR condition exhibited larger muscle activations in the plantarflexion group during take-off compared to the FF condition. Simultaneously, the FF condition showed larger hip flexion muscle activation during take-off than the FR condition.

Discussion

The difference in muscle activation profiles, with the FR condition more significantly using their plantar flexor muscle groups compared to the FF condition, could be a compensation strategy. This strategy may help counteract the dancers' reduced ability to use their base of support to absorb forces through the lower extremity. The FR condition's overreliance of the plantar flexors without sufficient involvement of the hip muscles places them in a position of increased injury risk.

Images (Optional)

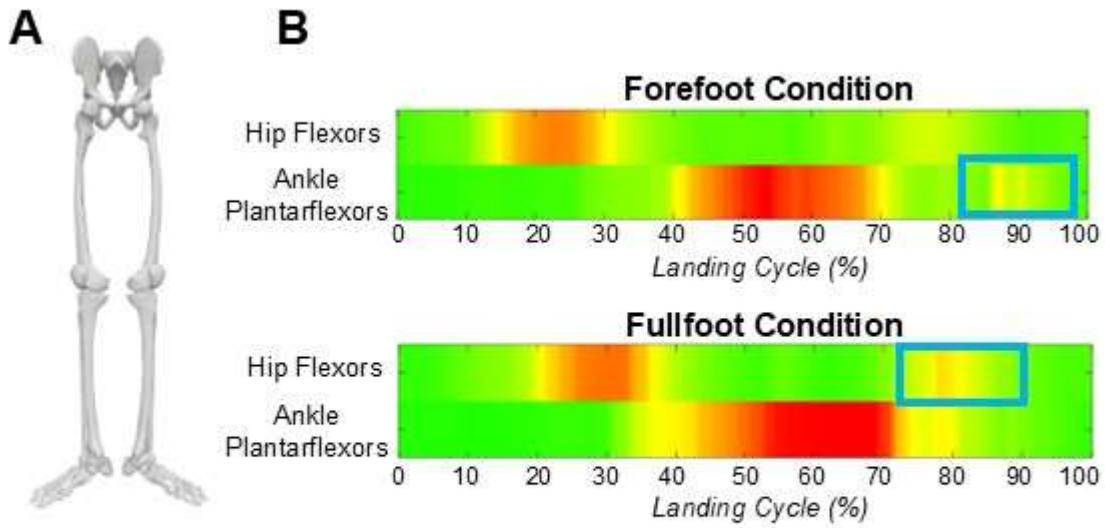


Figure 1. (A) OpenSim MSK model in ballet first position with the hips externally rotated, knees aligned in the direction of turnout, and heels touching with toes pointing outwards. (B) Heat map visualization of the muscle coordinate group activation profiles across the jump landing cycle for the forefoot (FR) and fullfoot (FF) conditions. The color intensity reflects normalized muscle activation with red (high, 1) and green (low, 0).

Session Category

Human Motion and Performance: Sports

P1-301

Comparison of Arm Positions During Double Leg Drop Landing and Their Impact on Lower Extremity Kinetics and Kinematics

Ms. Hallie Music, Ms. Madelyn LeGault, Mr. Jacob Vassar, Dr. Abbie Ferris

University of Northern Colorado, Greeley, Co, United States

Introduction

Drop landings have been used to study ACL injury mechanics [1], analyze performance metrics [2], and monitor athlete performance [3]. However, arm position has either been restricted (to standardize research protocols), unreported, or ignored [4]. Comparisons between arm placements and sport-specific arm positions have not been assessed. The purpose of this study is to determine if arm position during double leg drop landing alters lower extremity mechanics. We hypothesize lower extremity joint angles and vertical ground reaction force (GRFv) will be greater when restricting arm movement than over free arm conditions during double leg (DL) drop landing.

Methods

Four adults (2M/2F, 24±4.69 y) were asked to complete DL drop landing tasks from 30cm. Kinematic (VICON, Denver, CO) and kinetic (AMTI, Watertown, MA) data were measured during four arm conditions: free arm (FA), hands on hips (HH), arms across chest (AC), and arms overhead (AO). Peak joint angles, moments, and powers, and GRFvwere calculated during the initial landing phase. Given the small n in these preliminary data, no statistics were performed; trends are noted below and will be expanded upon in our poster as we add participants.

Results

GRF_V was reduced for AC and HH. In general, HH and AO conditions showed small, but notable differences at the ankle, knee and hip. The HH condition showed increased ankle plantarflexion and eversion and hip flexion, but reduced knee flexion and knee valgus. In contrast, the AO condition showed reduced ankle plantarflexion and hip flexion, and increased knee flexion. Further, reduced peak plantar flexor knee extensor, and hip abduction moments and less ankle power absorption were noted in the HH condition. AO consistently maintained a more extended trunk position than all other conditions.

Discussion

These preliminary data suggest that during DL landing, the lower extremity can successfully adjust to different arm positions. While we did note that HH and AO

conditions resulted in differences, they were generally not large. Coaches, practitioners, and researchers should be aware of these results to help them better direct their research goals. Although arm position does not affect DL landing, single leg landings may show different results.

References (Optional)

Session Category

Human Motion and Performance: Sports

P1-302

Lower Extremity Mechanics are Impacted by Arm Position during Single Leg Drop Landings

Ms. Hallie Music, Ms. Madelyn LeGault, Mr. Jacob Vassar, Dr. Abbie Ferris

University of Northern Colorado, Greeley, Co, United States

Introduction

Single leg drop landings have been used to identify movement deficits of the ankle, knee, and hip [1] because it has an increased load on the lower extremity than other tasks [2]. However, arm position has either been restricted (to standardize research protocols) or sport specific [3], but the impact of these conditions on the lower extremity have not been evaluated. The purpose of this study is to determine if arm position during single leg drop landing alters lower extremity mechanics. We hypothesize lower extremity joint angles and vertical ground reaction force (GRFv) will be greater when restricting arm movement during single leg (SL) drop landing.

Methods

Four adults (2M/2F, 24±4.69 y) completed SL drop landing tasks from 30cm. Kinematic (VICON, Denver, CO) and kinetic (AMTI, Watertown, MA) data were measured during four arm conditions: free arm (FA), hands on hips (HH), arms across chest (AC), and arms overhead (AO). Peak joint angles and GRFv were calculated during the initial landing phase. Given the small n in these preliminary data, no statistics were performed; trends are noted below and will be expanded upon in our poster as we add participants.

Results

Initial trends suggest GRFv was greatest for AO and lowest for HH. Generally, we noted arms constrained conditions (HH and AC) differed from unconstrained conditions (AO and FA) with HH and AO showing greater differences. HH showed a more neutral ankle while the AO condition maintained a dorsiflexed position. The arm constrained conditions showed a reduction in knee flexion. HH increased hip flexion and AO reduced hip flexion. Most interestingly, overall limb position differs between the arm conditions. The HH showed a more upright limb position, whereas the FA and AO place the foot medially creating an increased adduction limb angle.

Discussion

These preliminary data suggest arm position changes lower extremity mechanics during SL landings. This is especially true at the knee where limb position can be affected by arm

placement thus altering measures such as Q angle. Therefore, if the goal of training or rehabilitation is to evaluate limb mechanics, athletes should use an unconstrained arm position.

References (Optional)

Session Category

Human Motion and Performance: Sports

P1-303

Real-Time Markerless and Serverless Estimation of Dual-Foot Ground Reaction Forces during the Acceleration Phase of Baseball Pitching

Dr. Hiroki Tanioka[1], Mr. Masato Ueguri[2]

[1]Tokushima University, Tokushima, Tokushima, Japan. [2]Baseball Partners Tokushima Co., Ltd., Tokushima, Tokushima, Japan

Dr. Hiroki Tanioka

Introduction

Ground reaction forces (GRFs) are essential for generating pitching velocity and limiting joint loading [1][2], yet their measurement outside laboratories is difficult. Force plates are accurate but impractical, and markerless methods typically estimate only kinematics. Existing GRF models, developed for steady gait [5][6][8], do not capture pitching acceleration, especially the force distribution between both legs during double support. This study proposes a real-time, markerless, serverless method to estimate total and dual-leg GRFs [9].

Methods

One collegiate pitcher threw three fastballs recorded with a smartphone (60 fps). MoveNet provided keypoints to compute center-of-mass acceleration and estimate total and dual-foot GRFs. Foot-load distribution was derived from the CoM-acceleration vector [3][4]. Estimates were validated against FSR plate measurements using basic error metrics.

MoveNet keypoints → center-of-mass acceleration
Total and dual-foot GRFs estimated from CoM dynamics
Foot-load ratio from CoM-acceleration vector and foot positions
Validation against FSR plates using error metrics [7]

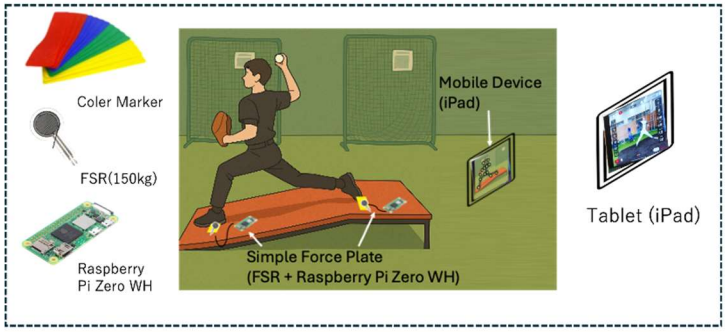
Results

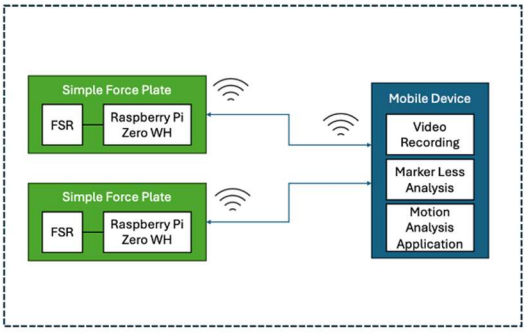
Estimated GRFs closely matched measured forces. Total vertical GRF showed RMSE values of 8–13% of body weight, with peak-force errors under 12% and correlations above 0.90. The estimated drive-to-lead load-transfer pattern replicated the measured transition during acceleration, with loading-ratio errors of 9–15%. Timing errors for key loading events were under 20 ms.

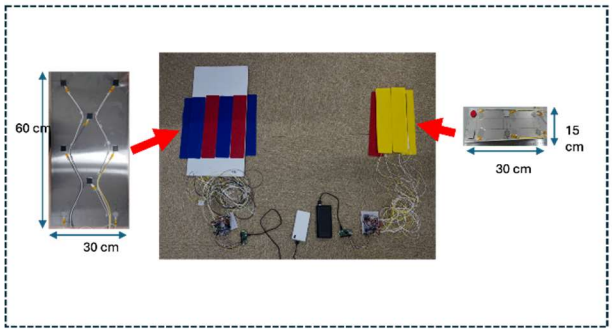
Discussion

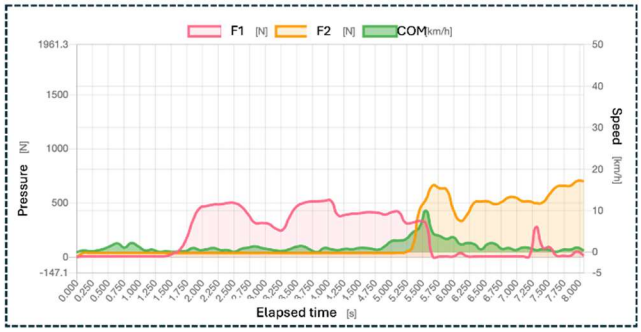
Results suggest dual-foot GRFs in acceleration phase can be estimated from markerless kinematics alone. Despite single-subject validation, the method shows on-field potential. Future work will test more pitchers and evaluate effects of handedness, camera angles, arm slots, and multi-view setups.

Images (Optional)









References (Optional)

[1] Seroyer, S. et al., Kinetic chain in pitching. Sports Health, 2010
[2] Fortenbaugh, D. et al., Pitching biomechanics. Sports Health, 2009
[3] Shimada, T. et al., Energy flow in pitching. JPE, 2004
[4] de Swart, J. et al., Lower-limb energy flow. J Sports Sci., 2022
[5] Zeni, J. et al., Two simple methods for gait event detection. Gait Posture, 2008
[6] Fellin, R. et al., Footstrike/toe-off identification. J Sci Med Sport, 2010
[7] Evans, M. et al., Video-based foot contact detection. MVA, 2021
[8] Leitch, J. et al., Gait events without force plates. Gait Posture, 2011
[9] Physics-Informed GRF Dynamics., arXiv, 2025

Acknowledgements (Optional)

This work stems from collaborative research with Baseball Partners Tokushima Co., Ltd.

Session Category

Human Motion and Performance: Sports

P1-304

Laboratory Derived Biomechanical Predictors of Biathlon Ski Speed

Mr Isaac Burgess MS, Mr Ethan Livingood BS, Mr Brandon Cabaniss, Dr James Becker PhD

Montana State University, Bozeman, MT, United States

Introduction

Previous studies have shown that physiological performance measures during laboratory tests can predict ski speed during biathlon competitions. While numerous studies have shown gross-biomechanical measures such as cycle length influence ski speed, it is unclear whether kinematic and kinetic markers of ski technique during laboratory assessments also predict ski speed in races. Therefore, the purpose of this study was to evaluate whether laboratory based biomechanical assessments of ski technique predict ski speed in elite biathletes.

Methods

Twenty-eight elite biathletes (17M/11F, 24±5 years) skied on a rollerski treadmill while body, ski, and pole kinematics were captured with hybrid-markerless motion capture while forces applied to the ski were measured using plantar-pressure insoles. Biomechanical variables that may be important for achieving higher speeds during V2 skating were then calculated for different phases of the ski cycle, which included; Poling - mean anterior-posterior inclination angle (θ_{AP}), Gliding - mean mediolateral center-of-mass inclination angle (θ_{ML}) and mean asymmetry in mediolateral pressure balance (*ASI*), Pushing - peak force applied to the ski (F_{peak}) and peak knee angular velocity (ω_{knee}), Ski placement - step-out distance (d_{step}) and V-angle (V_{θ}) at ski contact. All athletes then participated in a biathlon sprint competition on rollerskis, where average ski speed was calculated. Pearson correlation coefficients quantified relationships between each variable and ski speed. Variables correlated with ski speed ($r \geq 0.5$) entered a multiple regression to evaluate whether they explained ski speed.

Results

θ_{ML}, θ_{AP}, F_{peak}, *ASI* , and d_{step} were weakly correlated with ski speed and not considered further (Table 1). The multiple regression with the remaining variables showed a model containing V_{θ} ($\beta = -0.09$, $p = 0.008$) and ω_{knee} ($\beta = 0.08$, $p = 0.024$) accounted for 46% of ski speed ($p < 0.001$).

Discussion

The greater ω_{knee} may allow athletes to pre-load the ski more effectively. Additionally, this finding may also reflect more effective use of a stretch-shortening cycle in the leg muscles for greater force production. A lower V_θ at ski-on may improve energy transfer from the pushing to gliding ski, as the gliding ski is more aligned with skiing direction. Future research should investigate whether improving these variables can increase ski speed.

Images (Optional)

Table 1. Mean ± standard deviation for biomechanical variables and Pearson product-moment correlation coefficients (r) for average ski speed in biathlon competition and selected laboratory-derived biomechanical variables.

		Average Competition Ski Speed	
Variable	**Mean ± SD**	***r***	***p-value***
V_θ (°)	7.9 ± 3.1	-0.62	<0.001
ω_{knee} (rad/s)	146.3 ± 30.1	0.60	<0.001
θ_{ML} (°)	5.7 ± 1.8	-0.45	0.003
ASI (%)	14.5 ± 7.9	-0.35	0.03
F_{peak} (BW)	1.26 ± 0.15	0.32	0.05
θ_{AP} (°)	7.5 ± 2.8	0.27	0.09
d_{step} (cm)	1.02 ± 0.50	-0.22	0.17

Note. Pearson product-moment correlation coefficients were evaluated as very weak (0.00-0.29), weak (0.30-0.49), moderate (0.50-0.69), and strong (>0.70).

Session Category

Human Motion and Performance: Sports

P1-305

The Turnout Control During Bipodal and Unipodal Ballet Jumps: Multi-Joint Strategies Across Landing Conditions

MSc., P.T. Luciana C. Manfrim[1], PhD. Maria Isabel V. Orselli[2,1,3], P.T. Bianca M. Portela[1], P.T. Matheus O. Moutinho[1], PhD Paolo Caravaggi[4], PhD Isabel C.N. Sacco[1]

[1]School of Medicine, University of Sao Paulo, São Paulo, São Paulo, Brazil. [2]Israeli College of Health Sciences Albert Einstein, São Paulo, São Paulo, Brazil. [3]Universidade Cidade de São Paulo (UNICID), Graduate Program in Physical Therapy, São Paulo, São Paulo, Brazil. [4]Movement Analysis Laboratory, IRCCS Istituto Ortopedico Rizzoli, Bologna, Emilia-Romagna, Italy

MSc., P.T. Luciana C. Manfrim

PhD. Maria Isabel V. Orselli

P.T. Bianca M. Portela

P.T. Matheus O. Moutinho

PhD Paolo Caravaggi

Introduction

The Turnout, or external rotation of the lower limbs, is a fundamental skill in ballet. While the hip is turnout's main contributor, the coordinated roles of the knee and ankle remain unclear under aerial skills, such as jumps. Despite the importance of turnout for ballet, its understanding and biomechanical investigation during aerial movements has been overlooked[1], especially in unipodal jumps. This study aimed at analyzing kinematic contributions of hip, knee, and ankle to turnout during 3 jumps from fifth position: Assemblé Dessus (bipodal, lateral aerial body displacement), Sissone Ouvert En Avant

(unipodal, anterior displacement), and Sissone Ouvert Devant (unipodal, lateral displacement).

Methods

We accessed 30 pre-professional dancers (20.1±2.6yrs; 11.7±4.1yrs ballet experience) with a 8-camera optoelectronic system (Vicon, @100Hz) using a rigid cluster-based marker protocol[2,3]. Kinematic profile of the hip, knee and ankle joints were calculated using a 6-DOF model implemented in Visual3D. Peak rotation and its timing were extracted and compared across joints and jump phases (preparation, flight, and landing) using repeated measures ANOVA, followed by Newman Keuls post hoc ($p<0.05$).

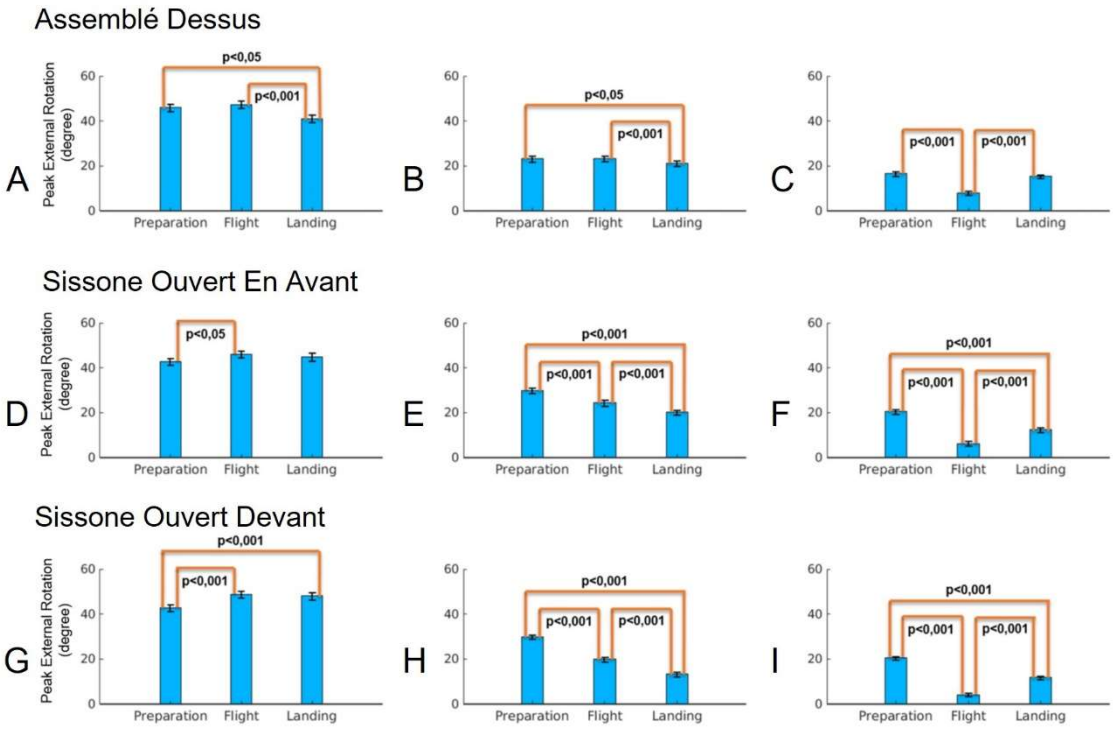
Results

The hip consistently exhibited the greatest external rotation across all jumps and phases (Fig.1, $p<0.001$). In both Sissones, hip rotation remained stable from flight to landing, whereas in Assemblé, hip and knee rotations decreased upon landing ($p<0.001$). Ankle rotation increased during landing ($p<0.001$) and was the lowest during flight. Timing of rotation peaks varied across joints: the hip peaked earlier, while the ankle reached its maximum in late flight and late landing. Fig.1:Mean (SE) external rotation peak in preparation, flight and landing of all jumps for hip (A,D,G), knee (B,E,H), ankle (C,F,I).

Discussion

The hip is the primary contributor to turnout in all jumps, whereas the knee and ankle act complementarily, with the knee reducing its contribution and the ankle increasing it from flight to landing. Jump type and landing support influence rotational contributions, reinforcing the need for training that optimises coordination and joint alignment.

Images (Optional)



References (Optional)

[1] Manfrim LC et al. *PeerJ*. 2025;13:e20263.

[2] Gontijo BA et al. *J Biomech*. 2023;147:111452

[3] Orselli MIV et al. Gait Posture. 2025. Manuscript under review.

Acknowledgements (Optional)

CNPq/Brazil (302558/2022-5; 124672/2024-8) and CAPES (Financial code 001).

Session Category

Human Motion and Performance: Sports

P1-306

Longitudinal Bending Stiffness affects Biomechanics but Not Running Economy or Perception in Advanced Footwear Technology

Dr. Jamie Ferris, Mr. Ben Hazelwood, Dr. Samuel Cheuvront, Dr. Jinger Gottschall

New Balance, Boston, MA, United States

Introduction

Evidence suggests longitudinal bending stiffness (LBS) does not independently affect running economy (RE) or ankle mechanics (Stephen, et al., 2025); however, the current data quality is limited by uncontrolled footwear differences and by methodology such as shoe-mounted markers. This study aimed to examine the effects of LBS on RE, biomechanics, and perception in advanced footwear technology (AFT) using controlled footwear and foot-mounted markers.

Methods

Twelve experienced runners (6 female; biomechanical data for 10) completed 5-minute bouts of treadmill running in four mass-adjusted prototypes based on the New Balance FuelCell SuperComp Elite v5 with carbon fiber plate variations: no plate, plate with medial-lateral cuts, lower-stiffness plate, and higher-stiffness plate. RE and lower-limb biomechanics were analyzed via RMANOVA and Tukey's HSD ($\alpha = 0.05$). Perceived footwear attributes were rated on 7-point scales and compared using Friedman tests with subsequent Dunn's pairwise comparisons.

Results

LBS had inconsistent and non-significant effects on RE ($p = 0.584$) and perception, including yield ($p = 0.822$), energy return ($p = 0.690$), and speed ($p = 0.575$) (Agresta, et al., 2020). Spatiotemporal variables were unaffected. Biomechanical changes occurred primarily at the metatarsophalangeal (MTP) joint, including reduced MTP negative work as LBS increased (Figure 1). Ankle mechanics were unchanged, and effects at the knee and hip were limited.

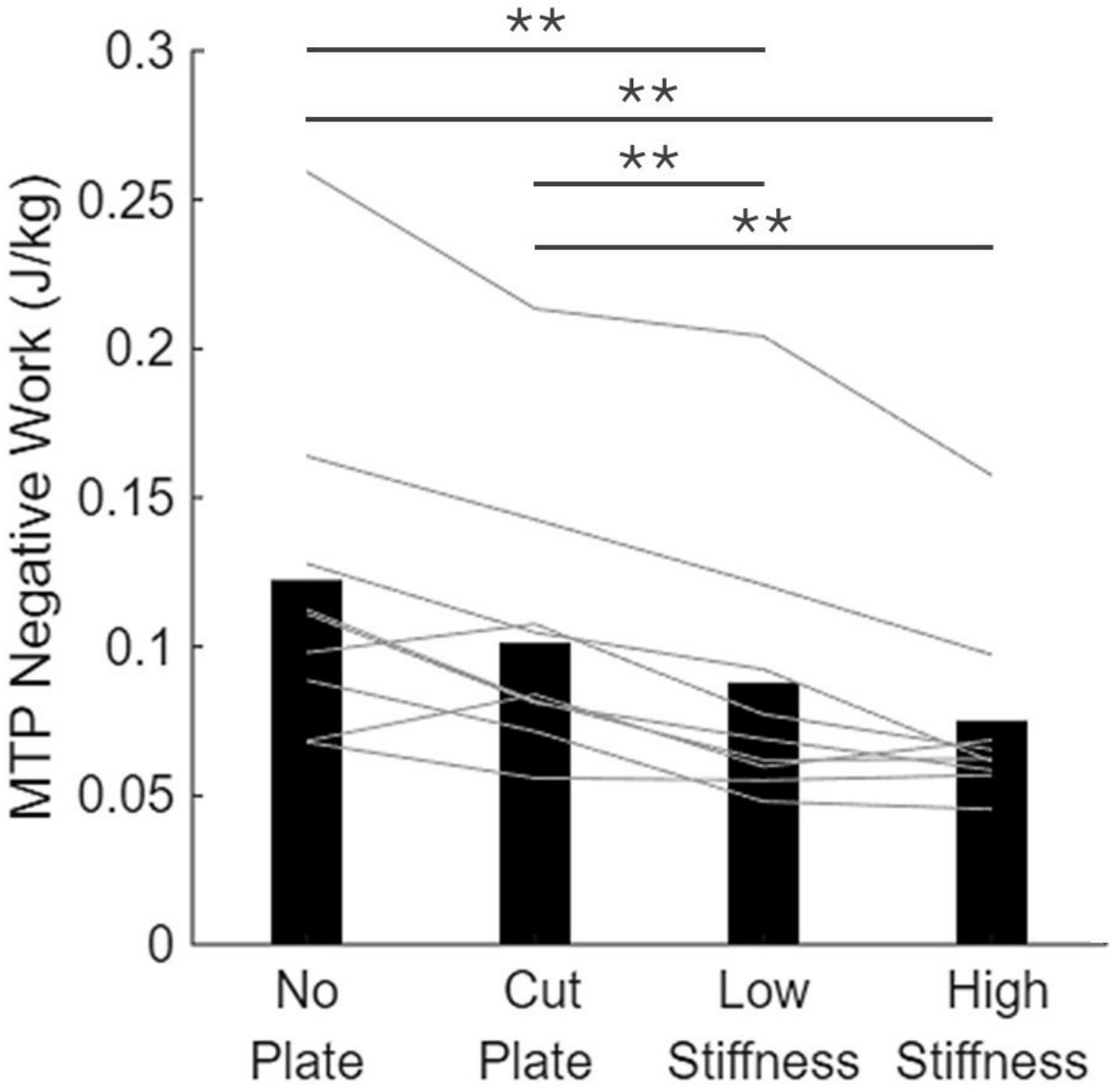
Figure 1. Average and individual MTP negative work across footwear conditions. ** $p < 0.01$

Discussion

Although lower negative work at the MTP joint may reduce local energy expenditure, this did not translate into measurable whole-body energy savings—likely due to the MTP joint's

small contribution to total energy expenditure. Racing footwear may therefore vary in LBS without performance or perceptual effects.

Images (Optional)



References (Optional)

Stephen, C., Kelly, L. A., Schuster, R. W., & Diamond, L. E. (2025). The effects of running shoe longitudinal bending stiffness and midsole energy return on oxygen consumption and ankle mechanics and energetics: A systematic review and meta-analysis. *Journal of Sport and Health Science, 14*, 101069.

Agresta, C., Peacock, J., Carmichael, A., Nielsen, K.E., Zendler, J., & Gonzalez, R. (2020). The perception of ride is multidimensional for running footwear. *Footwear Science, 12*(1), 15–24.

Session Category

Human Motion and Performance: Sports

P1-307

"Thinking Inside the Box": Ice Hockey Goaltender Glove Position Analysis

Ms. Jasmine Kwan BSc, Mr. Seth Daley MSc, Dr. Kathleen MacLean Ph.D.

Dalhousie University, Halifax, Nova Scotia, Canada

Introduction

Optimal performance for ice hockey goaltenders requires dynamic positioning of their equipment within the net's frame, including the glove, to block shots. There is no criterion standard for goaltender glove positioning. However, "box control" is a concept to teach maximum net coverage and glove positioning, highlighting how net size dynamically changes based on puck shooting location. Whether goaltenders execute box control and what factors influence their ability to optimally cover the net is not known. This study examined goaltender box control performance by investigating how three-dimensional glove position changes based on duration of play, perceived fatigue, and gender.

Methods

Fourteen experienced goaltenders' (9 men, 5 women) completed three conditions: 1) baseline, 2) short trial, and 3) long trial, while glove position was tracked at four high-shooting puck locations using Optitrak motion capture (NaturalPoint Inc.; Corvallis, USA). Baseline trials captured the static optimal glove position at each puck location. Short and long trials tracked dynamic glove position as participants moved to each puck in pre-determined patterns. A rating of perceived exertion (RPE) was obtained after each trial. Short and long trial glove position at puck locations were compared to the baseline to compute three-dimensional translational and rotational errors in box control using two-way ANOVA's. Pearson's correlation determined the association between glove position error and RPE and gender.

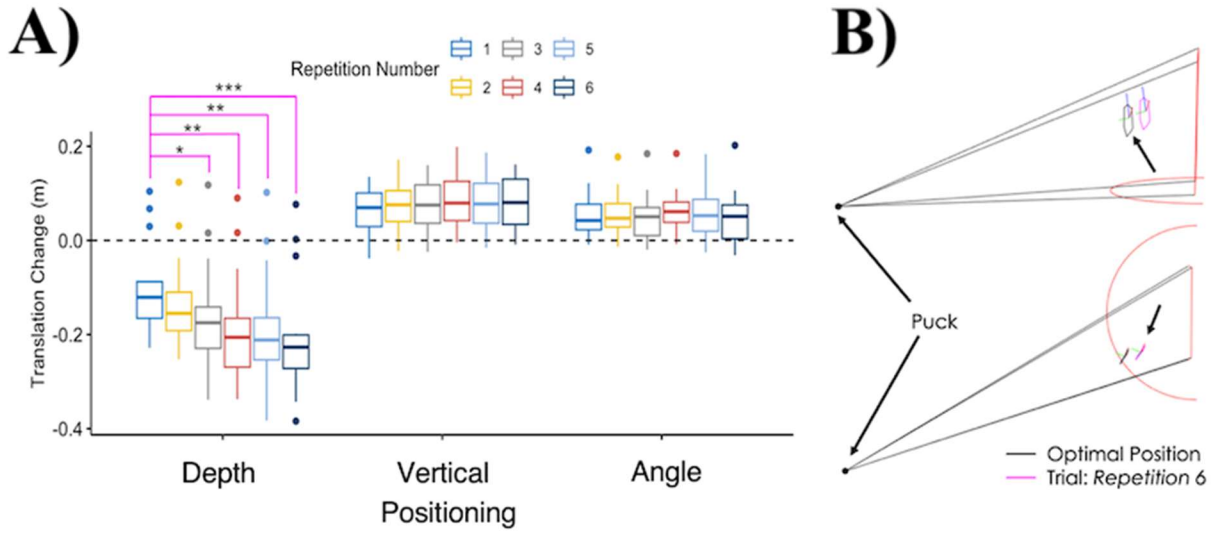
Results

In the short trial, goaltenders had significantly more translational error for pucks located on the far left ($p<0.04$) and right ($p<0.045$) and significantly higher rotational error about the vertical axis ($p<0.001$). In the long trial, goaltenders drifted back into the net with increased trial duration ($p<0.001$) (Fig. 1). Error increased with increasing RPE. No league-identified gender differences were found in the short trial, but men's league goaltenders had greater error in the long trial.

Discussion

Experienced goaltenders struggled to maintain box control in short and long bouts of simulated play. Alternative, standardized coaching methods may be needed to improve off-center glove positioning for wide shots. Greater glove position errors with duration, drift into the net, and RPE indicate a need for targeted isometric training to mitigate potential muscular fatigue and improve net coverage.

Images (Optional)



Session Category

Human Motion and Performance: Sports

P1-308

The First Line of Defense Against Head Accelerations in Wrestling

Dr. Jeffrey S. Brooks PhD[1], Mr. Rashad J. Hussain[1], Dr. Ryan T. Schroeder PhD[1,2], Ms. Princess A. Uona MSc[1], Mr. Daniel C. Anzovino MSc[1], Ms. Emma J. Ratke BSc[1], Dr. Shawn M. Beaudette PhD[1], Dr. Amanda M. Black PhD, CAT(C)[1,3]

[1]Department of Kinesiology, Faculty of Applied Health Sciences, Brock University, St Catharines, Ontario, Canada. [2]Department of Engineering , Faculty of Mathematics and Science, Brock University, St Catharines, Ontario, Canada. [3]Department of Community Health Sciences, Cumming School of Medicine, University of Calgary, Calgary, Ontario, Canada

Introduction

Wrestling has one of the highest concussion rates in collegiate sports [1]. Understanding head impact kinematics is critical to assessing concussion risk, yet few studies have quantified head accelerations in wrestling. The sequence of body segment contact with the mat may influence peak linear head acceleration (PLA). This study examined whether earlier body segment contact during takedowns reduces PLA.

Methods

Eight varsity wrestlers (4F, 18–23 years), paired by weight class, performed common takedowns in a controlled setting at submaximal intensity, completing 10 trials per maneuver (5 offensive, 5 defensive). Full-body kinematics were captured using 17 XSens Awinda IMUs (60 Hz) placed on 17 anatomical landmarks. The time between first limb contact to PLA was calculated (negative = contact after peak). A 5g threshold was applied to exclude accelerations associated with daily living. Linear mixed-effects models assessed whether contact timing predicted PLA, with takedown subtype and role as fixed effects and wrestler as a random effect.

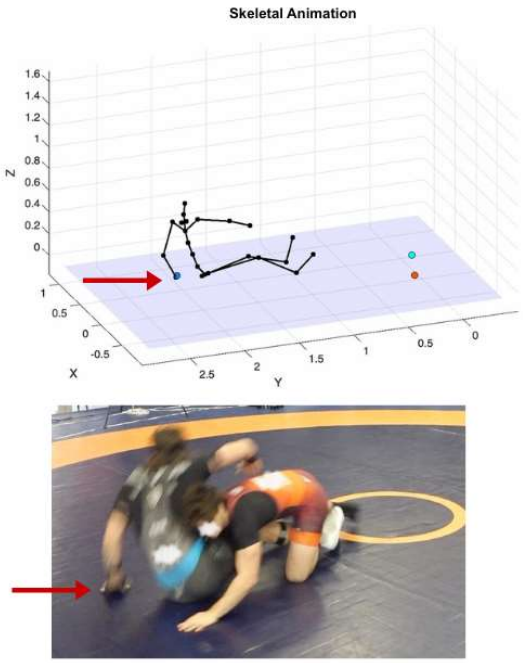
Results

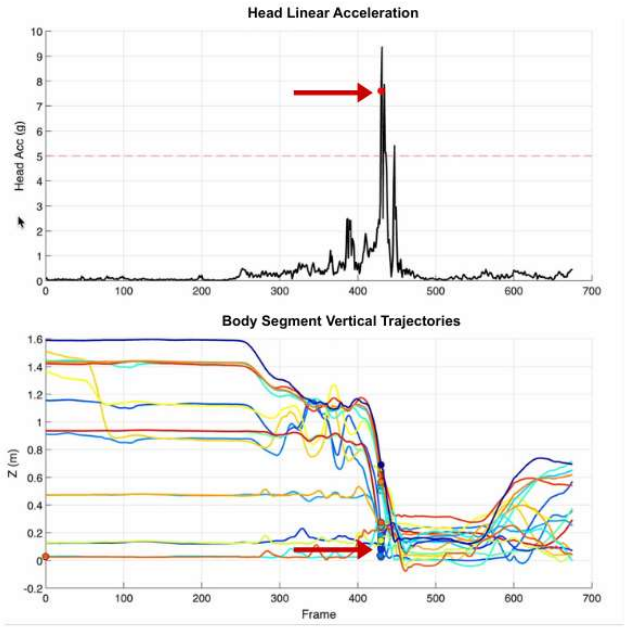
Head acceleration >5 g occurred in 42% of takedowns (157/374), distributed across subtypes (Double: 69, Throw: 66, Single: 12, Snapdown: 11). Body segment contact with the mat occurred before PLA in 18–45% of trials. For defense, preceding contact was most common at the lower leg (32%), shoulder (30%), and upper arm (30%). For offense, the lower leg (44%) and hand (29%) were most frequent. The time from first segment contact to PLA averaged 0.92 s (SD: 1.1; range: -4.93 to 3.22s). A role-specific relationship was observed: for offense, later segment contact was associated with higher PLA (β=2.83, p=0.014), whereas timing was not a predictor for defense.

Discussion

The timing of body segment mat contact relative to PLA during wrestling takedowns showed a role-specific association: for offensive athletes, later contact corresponded to higher PLA. This offensive-specific effect aligns with prior observations that offensive moves produce higher-magnitude head kinematics [3], highlighting a potential technical factor for concussion risk mitigation. This provides initial biomechanical evidence that skill execution - specifically, the sequence of ground contact - may modify injury risk in high-impact scenarios.

Images (Optional)





References (Optional)

[1] Powell *et al.*, J Ath Tr, 2021

[2] Friesen *et al.* Ann Biomed Eng, 2025

Session Category

Human Motion and Performance: Sports

P1-309

Biomechanical Determinants of Primary and Secondary ACL Injury Risk - A Comparison of Two Cases

Mr. Jeremy La Rosa, Mr. Walker Rost Kruger, Mr. Sergio Ibarra AT, MS, Dr. Santiago Ortega DPT, MS, Dr. Sara Gombatto PT, PhD

San Diego State University, San Diego, CA, United States

Introduction

Non-contact anterior cruciate ligament (ACL) injuries are common in female athletes. Nearly 1 in 29 female athletes experience an ACL injury and return-to-sport with a higher risk for reinjury [1]. Kinetic and kinematic measures have been identified as risk factors for primary or secondary ACL injury [2,3]. We retrospectively examined biomechanics screenings in two female collegiate athletes to determine presence of risk factors associated with ACL injury.

Methods

Two female collegiate athletes were examined (Vball,Bball). Vball was tested pre-season, several weeks prior to ACL injury; Bball was tested 6-months after ACL reconstruction. Drop vertical jumps (DVJ) were performed in a 3D motion capture lab with 16-cameras and two force plates. 3D lower extremity kinematics and kinetics were measured during DVJ landing. Risk factors from prior studies, including peak vGRF and the following knee joint angles were calculated: maximum abduction (MA), initial contact abduction (ICA), total abduction excursion (TAE), maximum flexion (MF). Measures were compared to average values for athletes who developed ACL injuries from prior prospective studies.

Results

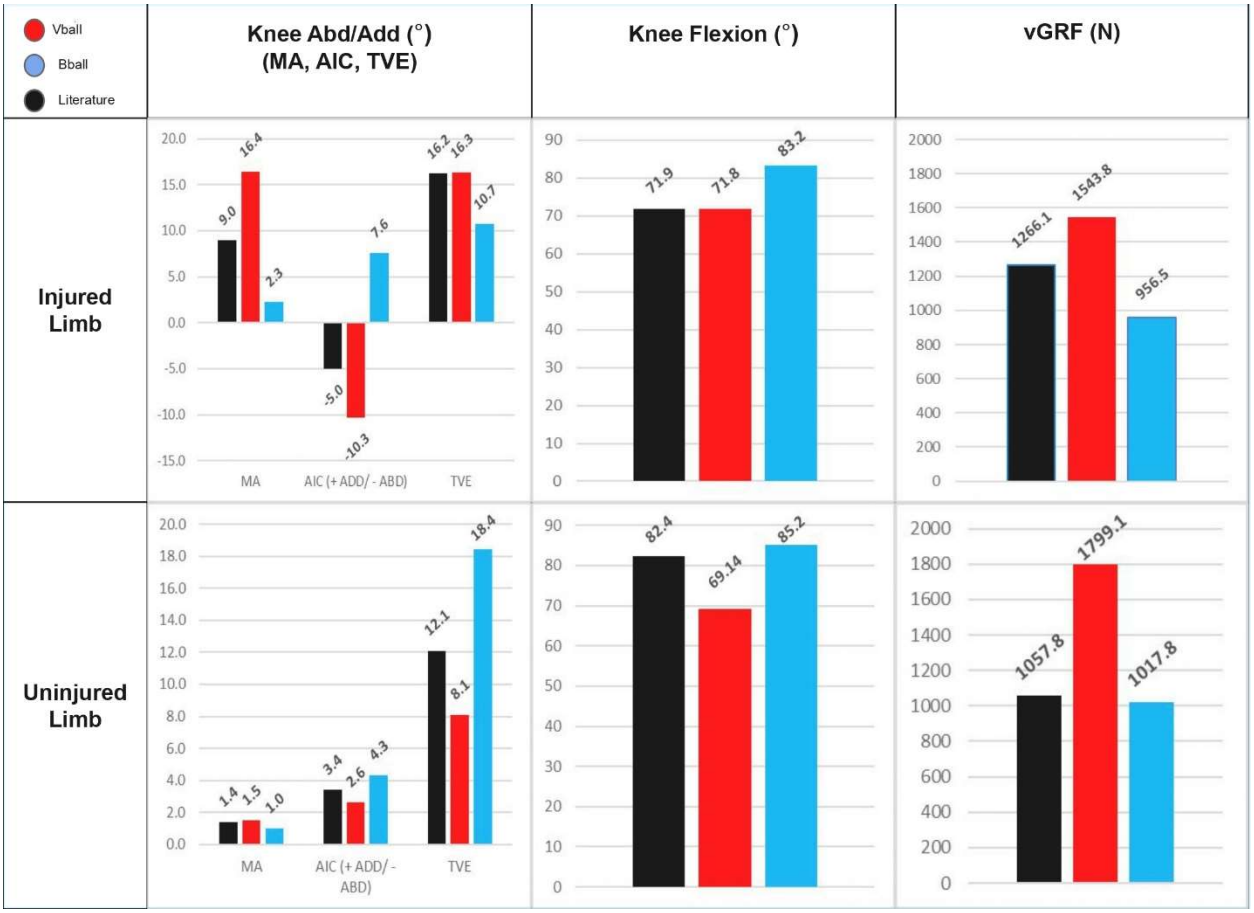
Injured limbs: Peak vGRF was greater for Vball (1544N) but less for Bball (956N) than from prior studies (1266N). MA was greater for Vball (16.4°) and less for Bball (2.3°) than prior studies (9°). ICA was greater for VBall (-10.3°) than prior studies (-5°), but Bball exhibited adduction (7.6°). TAE for Vball (16.3°) was similar to prior studies (16.2°), but Bball was less (10.7°). MF for Vball (71.8°) was similar to prior studies (71.9°), but MF was greater for Bball (83.2°). *Uninjured limbs*: Peak vGRF was greater for Vball (1799N) and TAE was greater (18.4°) for Bball in their uninjured limbs when compared to injured limbs from prior studies.

Discussion

Vball displayed movement patterns associated with increased risk of ACL injury, then suffered an ACL injury during the season. Bball did not display increased risk factors on the

affected limb. Both athletes displayed isolated risk factors on their unaffected limbs, which may increase risk of subsequent ACL injury. Integrating 3D motion analysis into screenings may help identify injury risk factors that can be targeted in ACL injury prevention programs.

Images (Optional)



References (Optional)

Acknowledgements (Optional)

Thank you to student volunteers and research assistants who supported this project, including Christopher Alfaro, Jay Barolo, Alexandra Guzzardo, Sarah Konig, and Katya Pushka.

Session Category

Human Motion and Performance: Sports

P1-310

The Effects of Kinesio Taping on Countermovement Jump Performance Before and After Fatigue in Collegiate Basketball Athletes

Dr. Po-Teng Huang[1,2], Lecturer Che-Yi Yang[3], Professor Jia-Hao Chang[1]

[1]Department of Physical Education and Sports Sciences, National Taiwan Normal University, Taipei, Taiwan, Taiwan. [2]Office of Physical Education, Fu Jen Catholic University, New Taipei, Taiwan, Taiwan. [3]Department of Physical Education, Fu Jen Catholic University, New Taipei, Taiwan, Taiwan

Introduction

Kinesio Taping (KT) is widely used in sports, but its acute biomechanical effects remain unclear in trained athletes. This study investigated the immediate effects of KT on countermovement jump (CMJ) performance before and after fatigue in collegiate basketball players.

Methods

Six male athletes completed CMJ testing under three taping conditions: non-taping, placebo taping, and KT applied with 50% tension to the both quadriceps muscles. The CMJ trials before and after fatigue procedures were recorded by a force plate in each condition. Jump height was calculated using flight time, and take-off impulse was obtained by integrating vertical ground reaction force from the lowest center of mass (COM) position to take-off. A two-way ANOVA with repeated measurement was used to evaluate the effects of taping condition, fatigue, and their interaction.

Results

The values of jump height in non-taping, placebo, and KT groups before fatigue procedure were 39.05 ± 5.04, 37.32 ± 5.27, and 36.80 ± 5.39 cm, respectively. And the values were decreased to 28.46 ± 5.21, 28.99 ± 7.19, and 27.66 ± 4.44 cm after fatigue procedure. No significant effects were noted in take-off impulse.

Discussion

These findings indicate that KT does not acutely enhance jump height or take-off impulse and does not mitigate fatigue-related performance decline. The effects observed may reflect the high neuromuscular efficiency of trained athletes, limiting the potential influence of external sensory input. Although KT may provide benefits in joint support, proprioception, or injury conditions, its acute biomechanical influence on explosive tasks appears minimal in healthy trained populations. Further research with larger samples and

additional biomechanical variables is recommended to clarify the conditions under which KT may provide functional benefits.

Session Category

Human Motion and Performance: Sports

P1-311

Does a Directional Compression Garment Alter Lower-Body Kinematics and Jump Performance?

Mr. John Grace, Dr. Bahman Adlou, Dr. Christopher Wilburn, Dr. Wendi Weimar

Auburn University, Auburn, AL, United States

Introduction

Athletes choose to wear compression garments when competing to provide support and improve performance. Previous literature has indicated that compression wear alters movement patterns [1]. Some companies are designing directional compression wear to mitigate poor mechanics and improve performance, yet their efficacy is still in question. Therefore, this study analyzed the ability of directional compression garments to alter joint angle and jump performance.

Methods

Ten healthy men (180.27 ± 7.99 cm, 85.75 ± 12.16 kg) between the ages of 18 and 40 provided informed consent and participated in this project. They completed 5 trials of two different movements: counter-movement jump (CMJ) and 30 cm drop jump (DDJ) in two conditions: wearing normal compression shorts and wearing shorts with directional compression. The directional compression shorts have a band fixed on the outside of the shorts in the sacrum area that travels around the lateral side of the thigh to the medial portion of the thigh, just above the knee. The proposed intervention is to encourage external rotation of the hip. The last 3 jumps of each set were used for analysis. Jump height and hip rotation angles for each leg were collected at their peak and at the bottom of the countermovement for each leg. Linear mixed models were used on each outcome variable, with condition and movement as fixed effects and participant as a random effect.

Results

None of the outcome variables showed significant differences between the shorts conditions. There was a significant difference in jump height between the CMJ and DDJ trials ($p<.001$), so this data was separated and reanalyzed. After further analysis, there was no significant difference in jump height between the shorts conditions in either jump trial type.

Discussion

This project indicates that directional compression garments may not be able to control specific movement pattern alterations during dynamic motions. While traditional

compression attire such as shorts and tights has been shown to alter movement patterns, including reducing hip abduction, this style of directional compression shorts was not able to provide any significant improvement over existing compression attire during functional sport-specific movements.

Images (Optional)

	Estimate	Std. Error	df	t value	Pr(>|t|)
Jump Height	-0.02802	0.006221	107	-0.450	0.653322
Right Hip Rotation at Bottom	1.9825	1.2257	107	1.617	0.109
Left Hip Rotation at Bottom	1.0246	1.4387	107	0.712	0.478
Peak Right Hip Rotation	0.7388	1.1466	107	0.644	0.52071
Peak Left Hip Rotation	-0.2122	1.3134	107	-0.162	0.872

Table 1. Results of 5 Linear Mixed Models. Each Estimate is the difference between the regular compression shorts condition and the directional compression shorts condition (regular compression shorts was the intercept).

References (Optional)

[1] Rui-Feng Huang *et al.*, J Functional Morphology and Kinesiology, 2025

Session Category

Human Motion and Performance: Sports

P1-312

Impact of Upper-Extremity Training on Shoulder Abduction Acceleration During Rapid Reactive Movements

Dr. Jonathan Lee-Confer Ph.D., Ms. Sierra Bogner B.S., Dr. James Tracy Ph.D.

University of Arizona, Tucson, Arizona, United States

Introduction

Falls impose substantial healthcare costs and remain a major public health concern. Current fall-prevention programs emphasize lower-extremity training. Recent biomechanical evidence also highlights a rapid arm movement's ability, particularly shoulder abduction, to restore stability during slips or trips. Whether individuals with targeted upper-extremity training exhibit faster abduction responses is unknown. Racket-sports athletes utilize their dominant arm for high-velocity overhead movements like serves and forehands, resulting in a disproportionate exposure and training compared with the non-dominant arm. Determining whether training influences shoulder abduction acceleration may guide development of arm-focused interventions to reduce fall risk.

Methods

To date, this study enrolled 3 male trained athletes in racket sports (mean(SD) 28 (11) y/o, 183 (5) cm, 84 (8.6) kg). An inertial measurement unit (MetaMotionRL, MBientLab, USA, 800 Hz) was secured to the middle upper arm (dominant and non-dominant). Participants stood with arms at their side and were instructed to perform shoulder abduction "as fast as possible without moving the trunk". Five maximal-effort repetitions for each arm with one minute of rest between trials were conducted. IMU-derived peak shoulder abduction acceleration served as the primary outcome. Each participant's five trials were averaged to yield a single peak acceleration value for the dominant and non-dominant arms. A paired samples t-test with Cohen's *d* effect size was conducted to compare the peak abduction acceleration between the dominant and non-dominant arms.

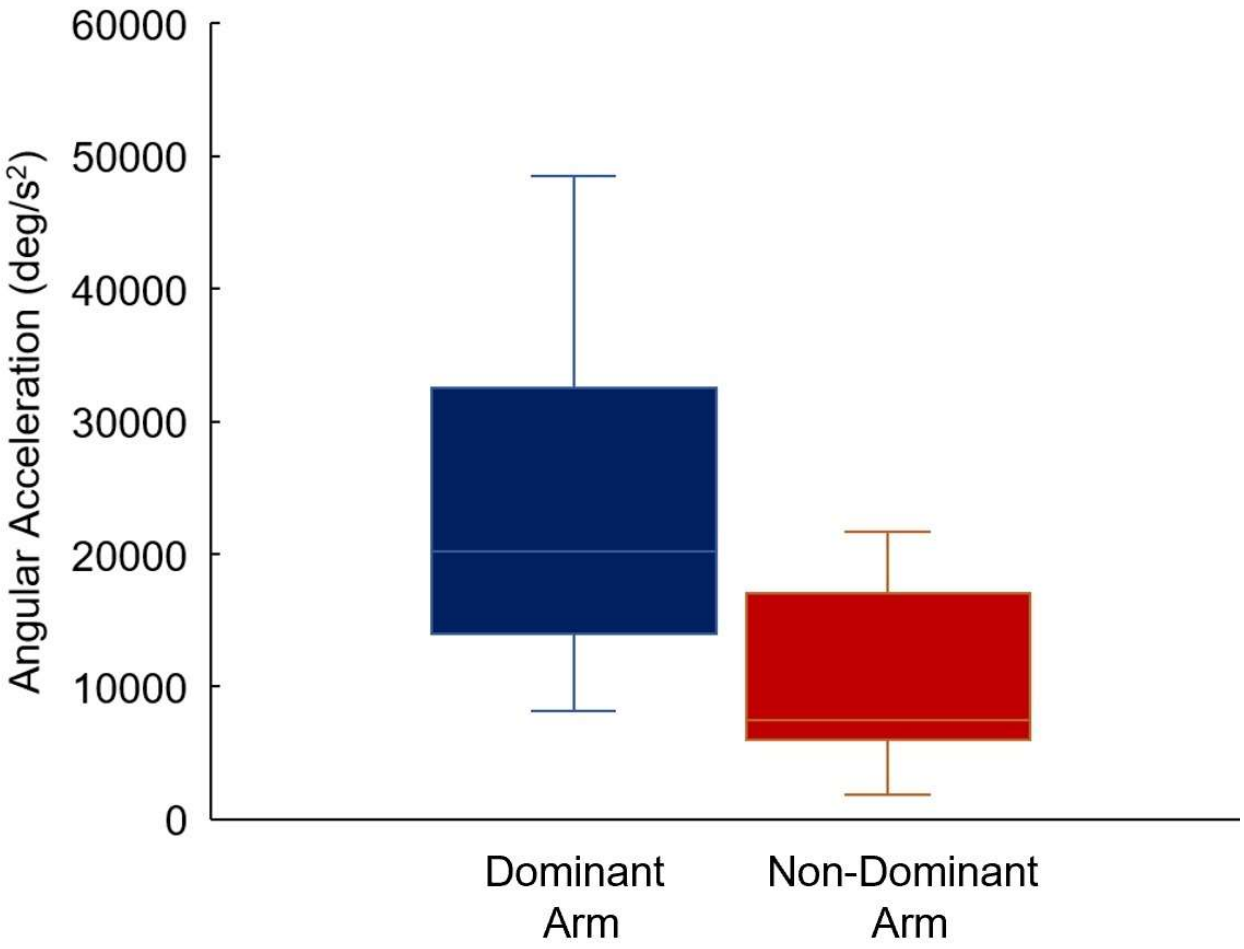
Results

Peak shoulder abduction acceleration was greater in the dominant arm compared with the non-dominant arm with a large effect size (dominant: 24667 (13295) deg/s^2, non-dominant: 13051 ± 11054 deg/s^2, $p = 0.01$, $d = 0.95$).

Discussion

These findings demonstrate that trained upper-extremity function is associated with faster shoulder abduction acceleration. This between-arm difference suggests that upper-extremity training and repeated sport-specific use may enhance the reactive capacity of the shoulder abductors. Given that rapid arm movements contribute to stabilizing the body during slips and trips, these results support the premise that arm-focused training may be a modifiable factor for improving protective arm reactions during balance disturbances. The observed acceleration asymmetry provides preliminary evidence for targeting upper-extremity strengthening or power-based training into fall-prevention programs.

Images (Optional)



Session Category

Human Motion and Performance: Sports

P1-313

Subjective and Objective Assessment of Cleated Footwear Preference

Dr. Brett Pexa[1], Dr. Jeffrey Taylor[1], Mr. Garrett Hess[1], Mr. Joseph Helseth[2], Mr. Noah Rauch[1], Ms. Isabelle Lee[1], Dr. Kevin Ford[1]

[1]High Point University, High Point, NC, United States. [2]Nike Sport Research Lab, Beaverton, OR, United States

Introduction

There is limited subjective and objective data on the preference for specific cleated footwear. The purpose of this study was to determine the differences in subjective and objective outcomes between preferred and nonpreferred cleated footwear in a collegiate soccer population.

Methods

Thirty collegiate soccer athletes (15M, 15F, age: 21.0 ± 1.2 yrs; mass: 78.5 ± 7.1 kg; height: 177.9 ± 5.5 cm) completed 180-degree cutting trials in two randomized cleated conditions (Nike Phantom GX II Elite Artificial Grass (AG) & Nike Phantom GX II Elite Firm Ground (FG)) over an infill turf surface. The footwear had the same upper and midsole, with different soleplate configurations. During the cutting tasks, kinematics were captured with 14 motion capture cameras (200Hz) and two in-ground force plates (1200Hz). After each cleated condition, participants provided self-reported data on fit, traction, and cutting ability. Participants were asked, following the completion of all trials, to indicate the shoe they preferred. Self-reported data was compared with Wilcoxon signed rank tests (W) and associated effect size (r). A paired t-test was used to compare lower extremity biomechanics between preferred and nonpreferred shoes.

Results

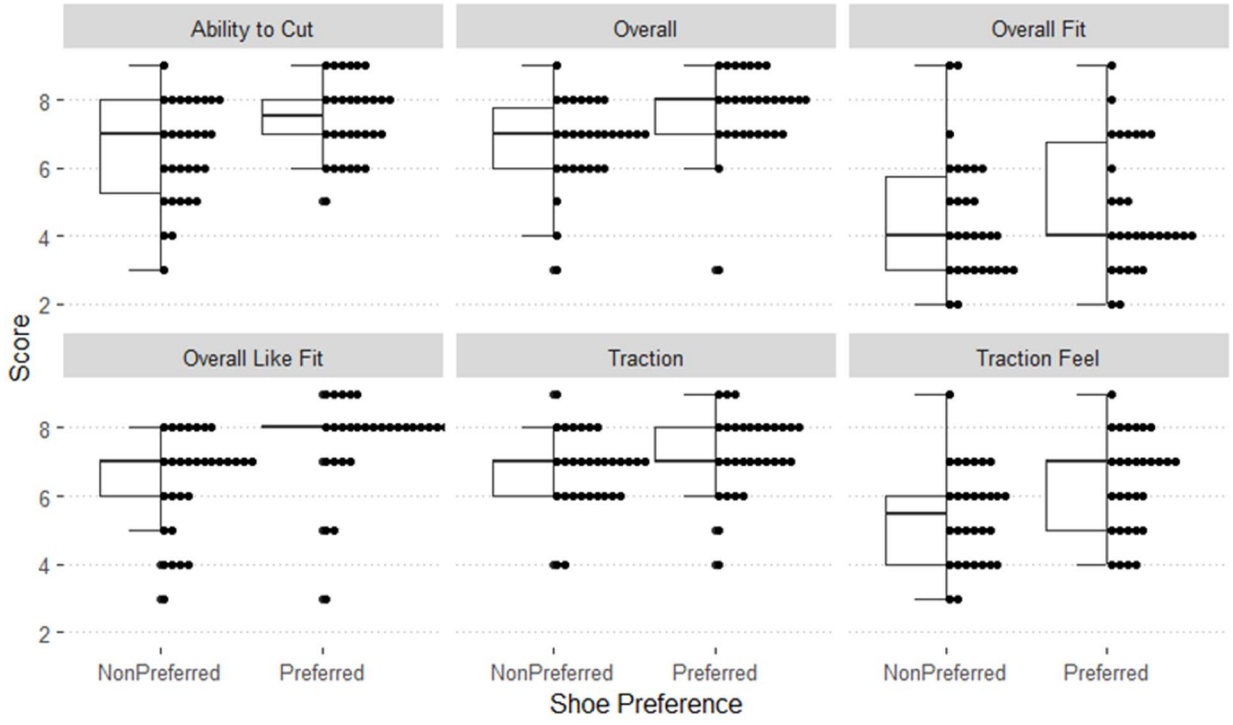
Fifteen participants preferred AG (7F, 8M) and fifteen preferred FG (8F, 7M). There was a significant difference between preferred and non-preferred shoes regarding how participants perceived the fit, the overall shoe, the ability to cut, and the feel of the traction ($p<0.05$). The preferred shoe had more favorable scores in the overall rating of the shoe ($W = 236.5$, $p = 0.001$, $r = 0.42$), ability to cut ($W = 286.5$, $p = 0.013$, $r = 0.32$), the traction feel ($W = 186.5$, $p = 0.013$, $r = 0.32$), and the overall enjoyment of the fit ($W = 192.5$, $p<0.001$, $r = 0.51$) than the nonpreferred shoe. There were no significant differences in cut performance,

ground reaction forces, or utilized traction measures between preferred and nonpreferred shoe.

Discussion

There are subjective differences between preferred footwear, however no significant differences were found in biomechanics. Future research should continue to measure subjective outcomes related to shoe preference to determine if shoe preference influences lower extremity biomechanics.

Images (Optional)



Acknowledgements (Optional)

Funding and footwear provided by Nike.

Session Category

Human Motion and Performance: Sports

P1-314

Rowers With Low Back Pain Demonstrate Altered Kinematic Patterns That May Reflect a Strategy of Trunk Restriction and Invariant Timing in Static vs. Dynamic Ergometry

Ms. Julia Tamai, Dr. Stephanie Jones

Smith College, Northampton, Massachusetts, United States

Introduction

Low back pain (LBP) accounts for up to 53% of injuries among competitive rowers, which is associated with ergometer training volume, total training hours, and fatigue. Stationary ergometers are associated with higher loads during training as the rower must contend with motions not dampened by inertia of dynamic ergometer motion. Standard rowing ergometry is also confined to sagittal movements, however, sweep rowers use one oar when on water employing asymmetric patterns of trunk rotation and side bending. This mismatch may provide a misalignment between the demands of on-water rowing and trained movements. The purpose of this study was to investigate joint kinematic patterns of rowers with and without LBP when performing static vs. dynamic ergometry at two stroke rates.

Methods

Five female collegiate rowers with LBP (rLBP) and five without (CON) rowed on an ergometer for two randomized blocks, static vs. dynamic (ergometer on sliders to allow translation); in each block, participants rowed at Low and High (20 vs. 30 strokes/min) cadence each for 5 minutes. Reflective markers were placed on 13 body segments and recorded using high speed digital cameras. 3D kinematics of trunk and lower limbs bilaterally were computed; cycle parameters, joint ranges of motion (ROMs) and peak angular velocities were computed and analyzed using mixed model repeated measures ANOVAs (ergometer modeXstrokeXgroup) with significance set at $P<0.05$.

Results

rLBP had invariant cycle times between static vs. dynamic, with trends to longer drive and shorter recovery phases; CON demonstrated reduced cycle time in dynamic vs. static. Ankle and knee ROMs were similar between groups, but rLBP demonstrated increased hip ROM and decreased trunk ROM compared to CON. Similarly, rLBP demonstrated increased hip and tended to decrease trunk peak velocities compared to CON.

Discussion

rLBP demonstrated increased hip motion and restricted trunk motion regardless of stroke rate or ergometer condition. Movement patterns were invariant among rLBP between conditions, particularly in cycle timing and trunk velocity, which may be an attempt to restrict trunk movement. Prolonged drive and shortened recovery phases among rLBP could contribute to fatigue, which may increase susceptibility to pain. Additional analyses will assess asymmetries and multi-joint coordination.

References (Optional)

Session Category

Human Motion and Performance: Sports

P1-315

Biomechanics of Slide Board Training in Sprint Speed Skaters

Jung-Min Yoon M.S.[1,2], Prof. Sukhoon Yoon Ph.D.[1,2], Prof. Sihyun Ryu Ph.D.[1,2], Prof. Sang-Kyoon Park Ph.D.[1,2]

[1]Korea National Sport Univercity, Seoul, Seoul, Korea, Republic of. [2]Motion Innovation Center, Seoul, Seoul, Korea, Republic of

Introduction

The purpose of this study was to analyze temporal changes in biomechanical variables during slide-board movements in 500m speed skating athletes and to provide various insights for improving performance and technique.

Methods

Ten elite male short-distance speed skaters in their 20s and 30s (n = 10; age: 23.5 ± 3.4 yrs, height: 174.7 ± 3.1 cm, weight: 74.9 ± 5.9 kg) participated in the study. Eight infrared cameras (sampling rate: 100 Hz), one force platform (sampling rate: 1,000 Hz), and a custom-made slide board were used for data collection. The variables analyzed included trunk segment angles, lower-limb joint angles, and lower-limb joint moments. In this study, five strokes were extracted and analyzed at 0 s, 30 s, and 55 s, and one-way repeated-measures ANOVA were conducted for statistical analysis. The level of statistical significance was set at $\alpha = .05$.

Results

The results showed that, over time, ankle plantarflexion angle and knee extension, and hip extension angles increased during the push-off phase ($p<.05$), while knee and hip extension moments decreased ($p<.05$).

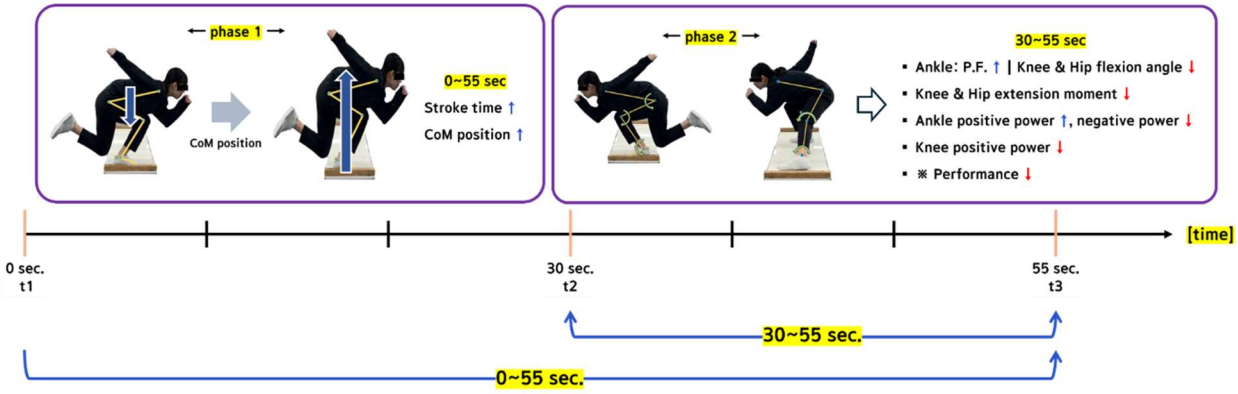
Discussion

Increased in ankle plantarflexion angle can cause the blade tip to scrape the ice during the stroke, resulting in deceleration (Ingen Schenau, De Groot, Scheurs, Meester & De Koning, 1996). Conversely, maintaining greater lower-limb flexion during the push-off phase enhances pushing force and consequently increases propulsive power. De Boer et al. (1987) reported that larger pushing forces lead to greater knee and hip extension moments during the stroke. However, if knee and hip extension angles increase while extension

moments decrease, the skating posture becomes more upright, which reduces the magnitude of pushing force and step width, ultimately impairing performance.

Therefore, athletes should aim to maintain a flexed lower-limb position throughout the push-off phase during slide-board training. This strategy is expected to positively influence key biomechanical factors and enhance on-once skating performance.

Images (Optional)



References (Optional)

[1] De Boer, R. W., et al., (1987). Biomechanical aspects of push-off techniques in speed skating the curves. *Journal of Applied Biomechanics, 3*(1), 69-79.

[2] Van Ingen Schenau, G. J., et al., (1996). A new skate allowing powerful plantar flexions improves performance. *Medicine and Science in Sports and Exercise, 28*(4), 531–535.

Session Category

Human Motion and Performance: Sports

P1-316

The Implications of the Menstrual Cycle on Upper Extremity Performance Metrics

Ms. Emma Cochran[1], Dr. Kaitlyn Armstrong[2], Dr. Thomas Andre[2], Dr. Corbit Franks[2], Dr. Chip Wade[2]

[1]University of Mississippi Medical Center, Jackson, MS, United States. [2]University of Mississippi, University, MS, United States

Introduction

There has been a significant rise in the number of female athletes participating sports. While there are a variety of studies looking at physiology in sports on performance, training methods, and injuries; this research is often generalized. When it comes to female-specific physiology concerning training and performance, there are very few high quality studies. One area of interest is the menstrual cycle in the female population. The literature suggests biological plausibility for changes in joint laxity and muscle repair throughout the various phases of the menstrual cycle, which can affect how female athletes perform and respond to training. To optimize performance, potentially reduce injury risk, and ensure better care for female athletes, a deeper understanding of the implications of these hormonal fluctuations is crucial.

Methods

16 physically active females completed the study. Saliva samples were completed at each visit to confirm menstrual cycle phase and urinary testing was completed prior to visits 2 and 5 to confirm ovulation, while the Proteus Motion was used for physical assessments. The Proteus evaluates the full range, velocity, and power of upper and lower extremity movement profiles. The participants completed a testing protocol consisting of 7 different tests. These tests include (1) chest press and pull, (2) straight arm trunk rotation, (3) PNF D2 flexion and extension. Visits were timed to occur within 96 hours of the onset of menses, within 24 hours of a positive urinary LH test, and 7 to 9 days post-ovulation.

Results

There were quantitative and statistical differences across Proteus measures. Most notably, there were significant quantitative differences within cycle 1 for visits 1 and 2 (ΔP= 12.982W), visits 2 and 3 (ΔP= 9.471W), and visits 1 and 3 (ΔP= 22.453W). While there were quantitative differences across matched phases across cycles, these differences were insignificant.

Discussion

The results of this study suggest that the luteal phase of the menstrual cycle was associated with enhanced performance in certain upper extremity tasks involving power, velocity, acceleration, and deceleration. however, there was no clear phase-specific effect. Future research should further investigate the relationship between the typical hormonal fluctuations across the cycle.

Session Category

Human Motion and Performance: Sports

P1-317

The Effect of Sex-Specific Footwear on Cutting Kinematics in Youth Female Soccer Players

Ms. Karen Chen PhD(c), PT[1,2], Mr. Ethan W.C. Wilkie PhD(c), MSc[1], Mr. Nicolas Herrera MSc[3], Dr. Shawn Robbins PhD, PT[1,2]

[1]McGill University, Montreal, Qc, Canada. [2]Center for Interdisciplinary Research in Rehabilitation, Montreal, Qc, Canada. [3]Shriners Hospitals for Children, Montreal, Qc, Canada

Introduction

Injury rates in female athletes are disproportionately higher than males. Sex differences have been identified in foot morphology and movement patterns during sport-specific movements. Yet, soccer footwear for females are commonly manufactured using a male foot template (i.e., last), overlooking distinct biomechanical sex differences. Therefore, this study examined whether sex-specific soccer cleats affect joint kinematics during unanticipated sidestep cutting, compared to unisex soccer cleats among female youth soccer players.

Methods

This cross-over study recruited 32 female soccer players, aged 13-17 years old and enrolled in the sport etude program at Soccer Montreal. Participants tested both the female-specific (IDA centra FG/AG) and unisex (Nike Tiempo Legend 10 Academy, multi-ground) cleats. Kinematic data were captured using markerless motion capture system (Miqus Video, Qualysis, 120Hz, 720p resolution) during unanticipated sidestep cuttings at $45^0 \pm 10^0$ on indoor artificial turf and processed with Theia3D. Principal component analysis extracted important features from trunk and lower extremity joint angles. Hierarchical linear model examined the impact of shoe condition on angle principal component scores (*PC-scores*).

Results

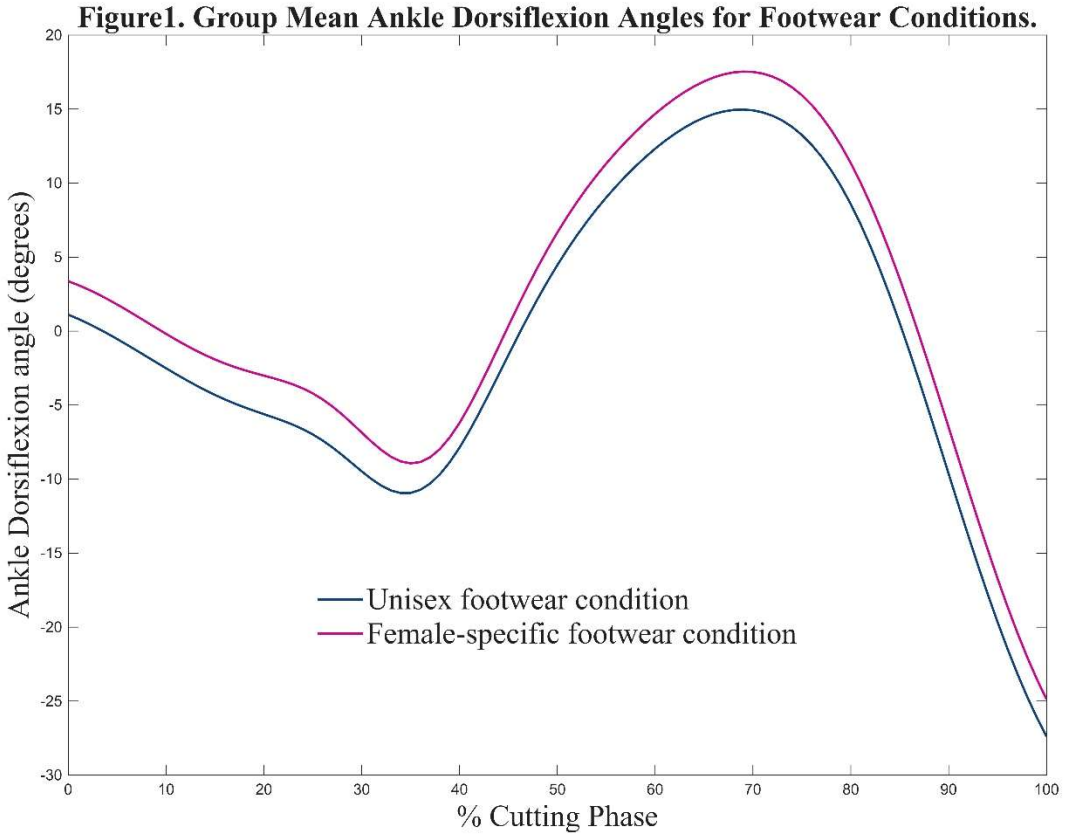
Specifically, female-specific shoe condition showed greater differences in knee flexion angles (*PC2-scores*, p=0.03) between early/mid-stance (0-50%) and late stance (60-100%) of cutting, and greater ankle dorsiflexion angles throughout cutting (*PC1*, p=0.002) and during mid/late stance (40-80%, *PC2*, p=0.04) than the unisex footwear (Figure1). Female-specific footwear showed greater ankle inversion angles throughout cutting (*PC1*, p<0.001) and greater differences in inversion angles between mid/late (50-80%), pre/early (0-30%) and late stance/foot-off (90-100%, *PC3*, p=0.002) than the unisex footwear. Additionally,

unisex footwear showed greater differences in ankle inversion angles (PC2, $p<0.001$) between early/mid (25-50%) and late stance (80-100%) than the female-specific footwear. No differences between shoe conditions were found for other joint angles.

Discussion

Female-specific footwear may allow greater mobility at the ankle. As most findings pertain to the ankle, there may be potential effects regarding stabilization of the ankle during midstance and pre-positioning the foot towards the cutting direction (ankle inversion). Although these findings may have less impact on injury. These insights may further the understanding of female adaptations during cutting and aid in the development of more targeted female-specific footwear.

Images (Optional)



Session Category

Human Motion and Performance: Sports

P1-318

The Effect of Sex and a Shortened FIFA11+ Warm-Up Program on Cutting Kinematics in Youth Soccer Players

Ms. Karen Chen PhD(c), PT[1,2], Mr. Ethan W.C. Wilkie PhD(c), MSc[1], Mr. Nicolas Herrera MSc[3], Mr. Adrien Moufflet MSc[4], Dr. Moreno Morelli MD, MSc, FRCSC[5], Dr. Shawn Robbins PhD, PT[1,2]

[1]McGill University, Montreal, Qc, Canada. [2]Center for Interdisciplinary Research in Rehabilitation, Montreal, Qc, Canada. [3]Shriners Hospitals for Children, Montreal, Qc, Canada. [4]Roses de Montreal, Montreal, Qc, Canada. [5]St. Marys Hospital, Montreal, Qc, Canada

Introduction

Injury prevention programs, such as the FIFA11+ have been proposed to decrease soccer-related injury rates. However, exercise adherence remains challenging and its ability to modify at-risk movement patterns remains unclear. This study examined the effect of sex and a shortened FIFA11+ program lasting 3 months, compared to a standard warm-up program, on joint kinematics during unanticipated sidestep cuttings in youth soccer players.

Methods

Sixty-four healthy soccer players (32 males, 32 females), aged 13-17 years old and enrolled in the sport etude program at Soccer Montreal, were recruited for this two-group parallel randomized controlled trial. The standard group (SG, n=32) followed a Brazilian warm-up, while the intervention group (sFIFAG, n=32) followed a shortened FIFA11+ warm-up consisting of five exercises from the original FIFA11+, focusing on lower-extremity alignment and cutting-specific tasks. Programs were conducted at least twice a week for 3 months. Data were captured at baseline and 3-months using a markerless motion capture system (Miqus Video, Qualysis, 120Hz, 720p resolution) during unanticipated sidestep cuttings at $45^0 \pm 10^0$ and processed with Theia3D. Principal component analysis extracted important features from lower extremity and trunk angles. An analysis of covariance examined sex and intervention effects on angle principal component scores (*PC-scores*), while accounting for baseline angle using a per protocol approach.

Results

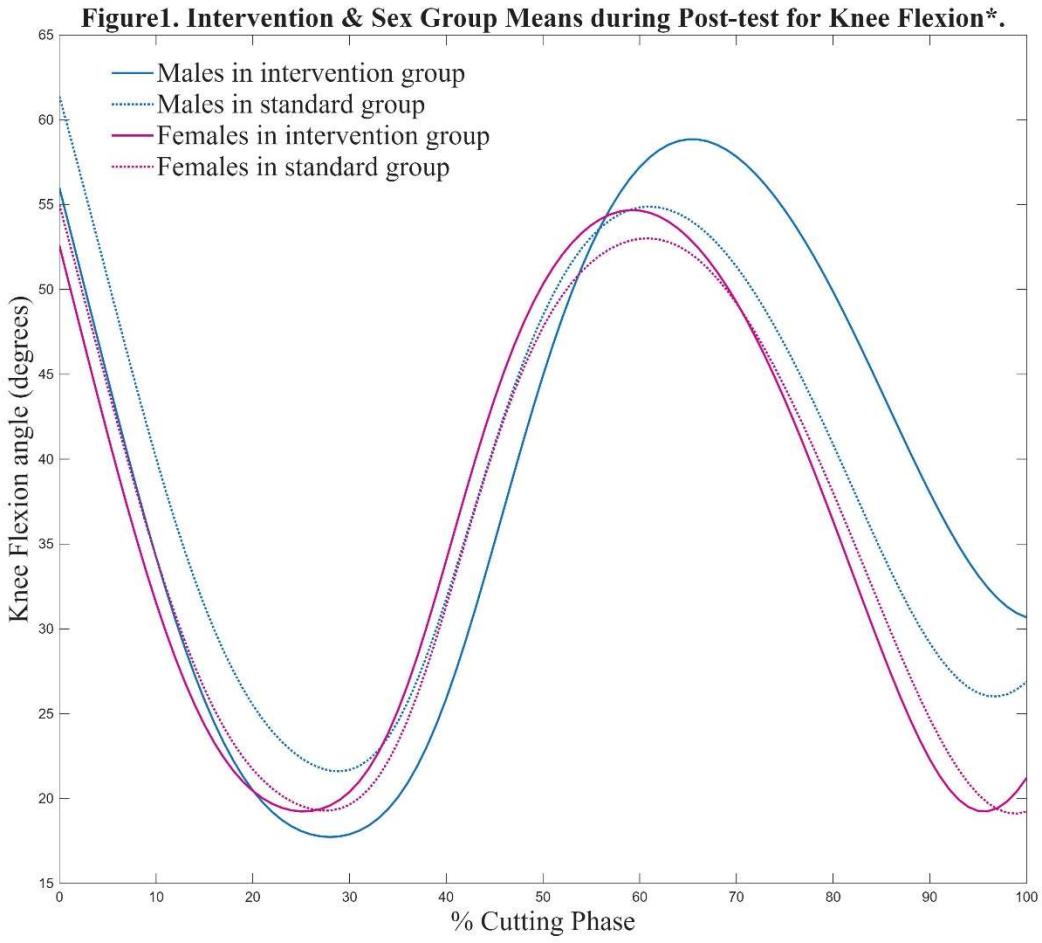
One intervention effect was found for ankle dorsiflexion (*PC3-scores*) showing greater differences in angles between pre/early stance (0-30%) and late stance (60-90%) of cutting for sFIFAG than SG (p=0.02). Intervention and sex interaction effects showed lower knee

flexion during late stance (60-100%, *PC2*, post-hoc p=0.01) (Figure 1) and greater differences in ankle dorsiflexion between mid-stance (40-75%) and late stance/foot-off (90-100%, *PC2*, post-hoc p=0.01) in males for SG than sFIFAG. Within sFIFAG, females showed greater differences in ankle dorsiflexion *PC2-scores* (post-hoc p=0.04) than males. Differences between sexes were found for hip flexion, knee adduction, and trunk rotation and side-flexion.

Discussion

A shortened FIFA program showed potential influences in cutting patterns, although at-risk patterns (e.g., excessive knee abduction) were not improved. Sex differences remained prominent, indicating potential needs of sex-specific prevention programs. Nonetheless, these insights may help in the development of more effective training programs.

Images (Optional)



*This figure pertains only to post-test results (i.e., data collected at 3-months).

Session Category

Human Motion and Performance: Sports

P1-319

Training Characteristics and Individual Variability Among Recreational Runners: Implications for Running Load Monitoring

Mr Jasper Wong MSpEx[1], Dr Hannah Wyatt PhD[1,2,3], Associate Professor Chris Whatman PhD[1], Dr Matt Cross PhD[1], Associate Professor Kelly Sheerin PhD[1]

[1]Sports Performance Research Institute NZ, Auckland University of Technology, Auckland, Auckland, New Zealand. [2]Sports, Health and Rehabilitation Research Cluster, University of Canterbury, Christchurch, Canterbury, New Zealand. [3]Biomolecular Interaction Centre, University of Canterbury, Christchurch, Canterbury, New Zealand

Mr Jasper Wong

Dr Hannah Wyatt

Associate Professor Chris Whatman

Dr Matt Cross

Introduction

Much of the running-related injury research has been lab-based, targeting specific biomechanical variables. This does not account for load accumulation or individual training preferences, both important considerations for individuals who run for long periods of time, with substantial contributions from injury risk factors, which may contribute to more injuries. Wearable technology developments allow for the monitoring of biomechanical variables and workload accumulation during normal training. The purpose of this study was to describe the training characteristics of recreational runners to better understand differences in training profiles and the implications for ongoing load monitoring.

Methods

One-hundred injury-free recreational runners were recruited. Participants' self-selected (normal) training pace was determined on a treadmill, followed by two velocity bands below and above their normal training pace, in 0.3 m/s increments. Habitual running was captured via a GPS smartwatch for 26 weeks. Data were processed to align with the five predetermined velocity bands. Weekly velocity-band totals were expressed as proportions of each athlete's total weekly distances and summarised at two levels: 1) between-individual differences, using each runner's typical weekly proportion per band (as mean and standard deviation [SD] of individual means, and coefficient of variation [CV]); 2) within-individual variability, reflecting week-to-week fluctuations (mean of each runner's SD).

Results

93,478 km of data were collected from 9776 sessions. Variability between individuals in the proportion of distance covered was greatest at the 'slowest' and 'fastest' velocity bands (CV=75-133%), while the 'slow' and 'normal' velocity bands were more consistent between athletes (CV=43-49%). Within-runner absolute variability was greatest in the 'slow' and 'normal' velocity bands (mean SD=0.155-0.156), and lowest in the 'fastest' velocity bands (mean SD=0.049-0.061).

Discussion

Training profiles differed markedly between runners, especially in the extreme velocity bands (slowest and fastest), suggesting runners accumulate volume differently. However, the greatest absolute week-to-week variation for individual runners was in moderate velocity bands, where the two fastest bands showed less (likely explained by intermittent and lower proportional volumes). These findings highlight runners differ in how they structure their training, which may not be evident from session-averaged data. Therefore, velocity-banded data provides a more informative representation for load monitoring.

Images (Optional)

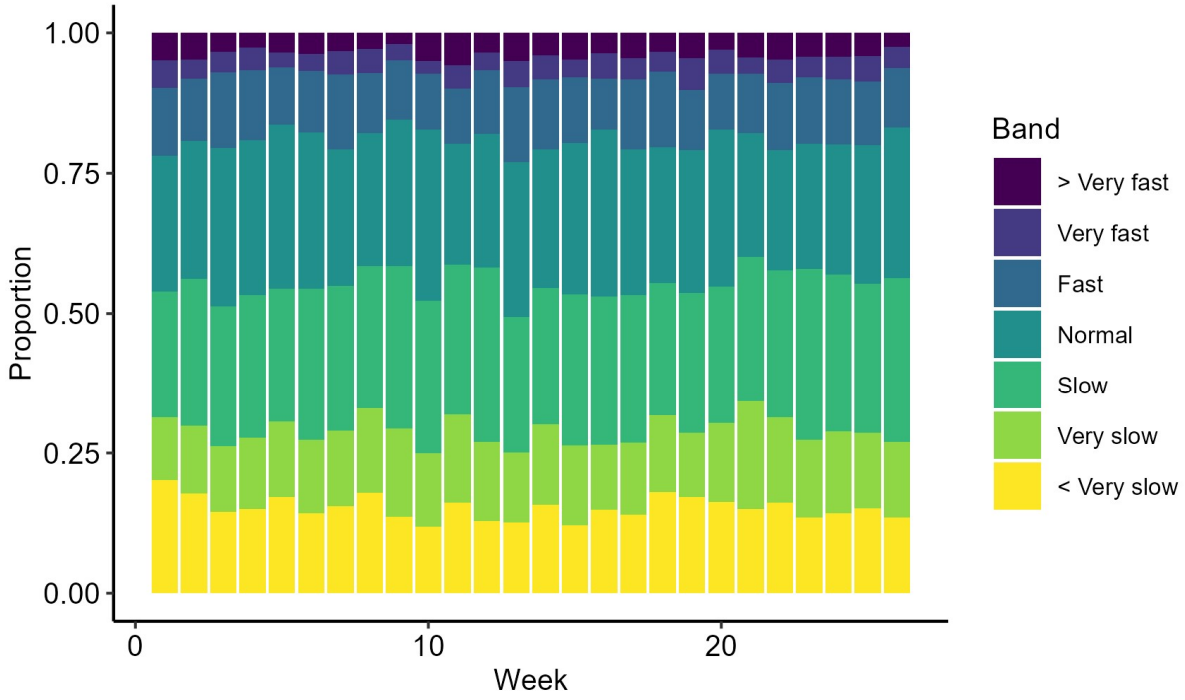


Figure 1. Overall weekly composition of distance.

Session Category

Human Motion and Performance: Sports

P1-320

Audio Versus Visual Unanticipated Stimuli on Kinetics and Kinematics in a Run-to-Cut Maneuver

Miss Kendra Graham, Dr. Joshua Weinhandl

University of Tennessee, Knoxville, TN, United States

Introduction

Anterior cruciate ligament (ACL) injuries are among the most common sport-related knee injuries, with almost 250,000 instances annually in the United States. Approximately 70% occur via non-contact mechanisms, often during rapid loading and directional changes such as sidestep-cut. These tasks elicit knee joint kinematics associated with increased ACL strain, such as an increase in knee adduction moment. During sport, athletes frequently respond to auditory and visual cues, yet the influence of stimulus modality on knee kinematics and kinetics is still unclear. Understanding these effects will inform injury prevention and rehabilitation strategies. The purpose is to determine if knee kinematic and kinetic differences exist in a sidestep-cut in response to an unanticipated audio versus visual stimulus.

Methods

16 individuals performed unanticipated sidestep-cut maneuvers in response to visual (arrow) and auditory ("right"/"left") stimuli at approach speeds of 3.0m/s–3.5m/s. Three-dimensional marker coordinate and ground reaction force data were collected for each trial. Peak knee angles and moments were extracted for analysis. Separate 2×2 repeated measures ANOVAs (limb×condition) were performed (α=.05).

Results

Significant stimulus × direction interactions were observed for peak knee adduction moment (pKAM, p=.044), peak knee abduction angle (pKAA, p=.006), and peak knee rotation angle (pKRA, p=.007). Audio cues elicited greater pKAM during left direction cuts compared with visual cues (p=.02) and with audio right direction cuts (p=.01). In contrast, visual cues produced greater pKAA (p<.001) and pKRA (p=.007) during right direction cuts compared with audio cues.

Discussion

Sensory modality differentially influences frontal and transverse plane knee mechanics in a limb specific manner during unanticipated cutting. When planting on the dominant limb and cutting to the left, auditory cues specifically resulted in increased pKAM, a variable

notably associated with ACL injury risk. Conversely, visual cues resulted in larger pKAA and pKRA when planting on the nondominant limb and cutting to the right. Results suggest auditory stimulus may have greater influence on the dominant limb while visual stimulus may have greater influence on the non-dominant limb during an unanticipated cut maneuver. Incorporating multimodal reaction stimuli into training and rehabilitation may improve adaptability and neuromuscular control during unpredictable situations that result in risky biomechanics.

Images (Optional)

Table 1. Mean ± standard deviation peak knee joint moments and angles during auditory left (AL), auditory right (AR), visual left (VL) and visual right (VR) sidestep cutting maneuvers.

	AL	AR	VL	VR
pKAM*[ac]	.71 ± .34	.53 ± .27	.61 ± .32	.53 ± .29
pKFM	3.23 ± .46	3.00 ± .55	3.10 ± .68	2.94 ± .57
pKRM[Δ]	-.16 ± .11	-.27 ± .12	-.18 ± .12	-.26 ± .14
pKAA[b]	-8.40 ± 3.92	-9.18 ± 3.56	-8.20 ± 3.59	-10.44 ± 3.52
pKFA	-57.30 ± 5.43	-57.01 ± 6.87	-58.49 ± 5.90	-56.97 ± 7.85
pKRA[b]	8.63 ± 5.04	9.48 ± 5.47	8.25 ± 5.46	10.85 ± 6.48

* indicates significant condition × leg interaction ($p<.05$)
[a] indicates condition effect within left leg
[b] indicates condition effect within right leg
[c] indicates leg effect within audio condition
[Δ] indicates significant leg main effect

Session Category

Human Motion and Performance: Sports

P1-321

The Influence of Calibration Poses on Scapular Kinematics during the Windmill Softball Pitch

Dr. Kenzie B. Friesen, Dr. Angelica Lang

University of Saskatchewan, Saskatoon, Saskatchewan, Canada

Introduction

Unique properties of the scapula make it difficult to measure, particularly during fast motions like the windmill pitch. Targeted procedures may improve the accuracy of scapular motion tracking [1], allowing for characterization of scapular motion during softball pitching. This study compared scapular and humeral kinematics during the windmill pitch using two scapular calibration procedures.

Methods

Seven youth softball pitchers (15±2 years, 167±31cm, 70±14kg) completed 5 fastball pitches (averaged for analysis) while their upper body motion was tracked. Landmarks of the scapulae were first digitized during three poses: rest, maximal humeral elevation, and 90º shoulder abduction. Scapular angles were estimated based on humeral elevation using a double calibration procedure [1] with two sets of poses: 1) rest and maximum humeral elevation, and 2) rest and 90º humeral abduction. Paired t-tests compared kinematics between the two calibrations at pitch events including “top of pitch” (peak humeral elevation), “stride foot contact,” and “ball release.” Statistical parametric mapping t-tests were conducted to compare kinematics during the pitch acceleration phase (peak push off the ground to ball release).

Results

Humeral elevation, scapular internal, and upward rotation did not differ at pitch events or during the acceleration phase of the pitch between calibration poses ($p>0.05$) (Figure 1).

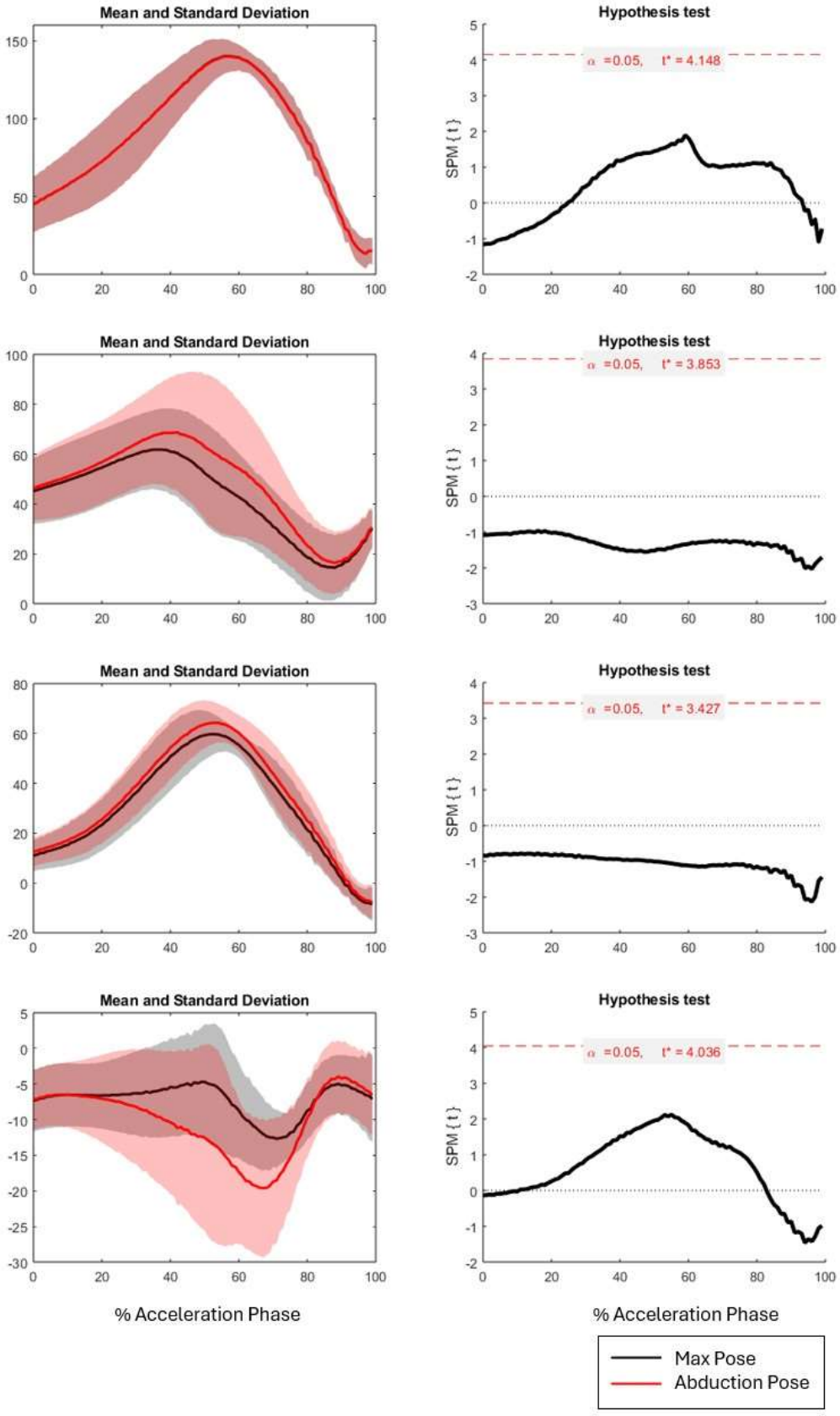
Discussion

Results indicate that double calibration methods produce similar scapular angles at discrete pitch events and during the pitch acceleration phase. Mean scapular angles from this current study report greater scapular motion than previous literature [2]. Given the double calibration procedure estimates scapular angles based on humeral elevation, and the humerus achieves near 140º humeral elevation throughout the windmill pitch, it is hypothesized that the double calibration procedure may more accurately assess scapular

angles predominantly during high range of motion tasks and should be incorporated for dynamic overhead tasks.

Limitations include the small sample size. More participants across a broader skill range are necessary to explore the influence of multiple poses on scapular kinematic calculations. Future research might seek to explore the effects of implementing multiple poses to reflect certain pitch positions.

Images (Optional)


Mean and Standard Deviation
Hypothesis test
α =0.05, t* = 4.148
SPM{t}
Mean and Standard Deviation
Hypothesis test
α =0.05, t* = 3.853
SPM{t}
Mean and Standard Deviation
Hypothesis test
α =0.05, t* = 3.427
SPM{t}
Mean and Standard Deviation
Hypothesis test
α =0.05, t* = 4.036
SPM{t}
% Acceleration Phase
% Acceleration Phase
Max Pose
Abduction Pose

References (Optional)

[1] Richardson et al., *J Biomech,* 2016

[2] Holtz et al., *Int J Sports Med*, 2025

Session Category

Human Motion and Performance: Sports

P1-322

Traction and Perception Differences During Cutting Between Female Collegiate Soccer and Lacrosse Players

Dr. Kevin Ford, Mr. Garrett Hess, Dr. Jeffrey Taylor, Mr. John Kilzi, Mr. Quinn Hopkins, Ms. Ashley Glass, Dr. Brett Pexa

High Point University, High Point, NC, United States

Introduction

Subjective ratings of cleated footwear during cutting tasks may provide distinct insights when combined with utilized traction and biomechanical analyses. Both female soccer and lacrosse athletes increasingly participate on synthetic turf surfaces. The purpose of this study was to compare the traction and perception of currently worn footwear during a cutting task between collegiate soccer and lacrosse players.

Methods

55 female collegiate soccer (n=26) and lacrosse (n=29) players (age: 20.0 ± 1.3 yrs; mass: 63.7 ± 6.8 kg; height: 165.6 ± 5.6 cm) performed left foot and right foot 180-degree cutting on an infill turf surface. Participants were asked to wear the cleats they currently use when playing on synthetic turf fields. Vertical and horizontal ground reaction forces were collected with two in-ground force plates (1200Hz). Following the completion of trials, a survey was administered. Three items assessed overall liking, fit, and traction preference using a 9-point Likert scale ranging from *Dislike Extremely (1)* to *Like Extremely (9)*. Three additional items used construct-specific anchors: overall fit feel (*Very Tight (1)* to *Very Loose (9)*), traction feel (*Very Slippery (1)* to *Very Sticky (9)*), and ability to cut (*Very Unconfident (1)* to *Very Confident (9)*). Differences between soccer and lacrosse players were evaluated for survey Likert scores (1-9) (Mann-Whitney U) and ground reaction force (independent t-test) variables.

Results

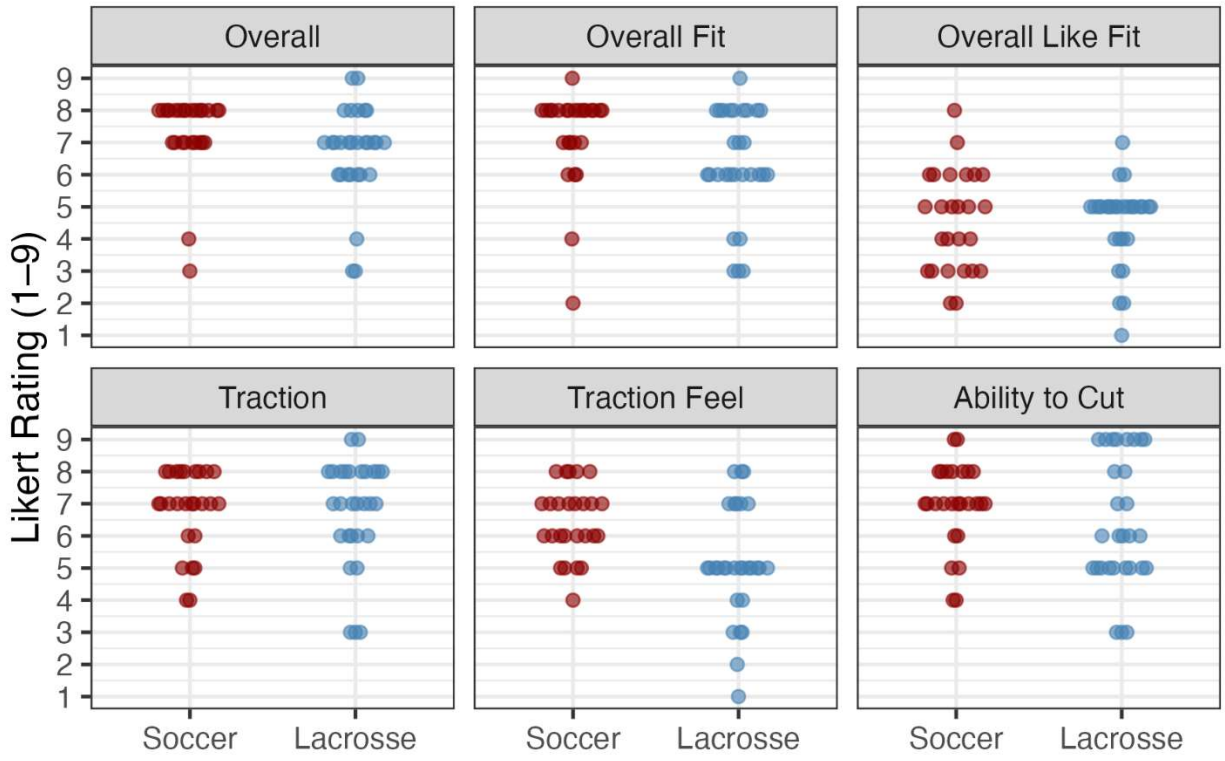
Traction feel was greater (closer to “sticky”) in soccer players compared to lacrosse players ($p=0.002$). However, there were no group differences in how much they liked or disliked the traction of the footwear ($p=0.9$). Soccer players also rated footwear higher in overall liking ($p=0.014$) and overall fit feel ($p=0.024$, closer to “loose”). Utilized translational traction was not different ($p=0.6$) between lacrosse players (0.77 ± 0.06) compared to soccer players (0.77 ± 0.04). Statistically significant differences were not found between sports for peak

vertical (Soccer 2.1 ± 0.3xBW, Lacrosse 2.0 ± 0.3 xBW, p=0.7) or braking force (Soccer 1.39 ± 0.2 xBW, Lacrosse 1.39 ± 0.2 xBW, p=0.98).

Discussion

Soccer players subjectively perceived their footwear traction to "feel" more "sticky" than lacrosse players which appears to contrast the utilized translational traction results. Additional studies should investigate the effects of varying footwear and surface conditions.

Images (Optional)



Session Category

Human Motion and Performance: Sports

P1-323

Estimating Baseball Pitch Velocity from Popular Field-Based Performance Tests

Dr. Kiara Barrett[1], Ms. Neha Kapoor[2], Dr. Lauren A Luginsland[3]

[1]Bertec Corporaation, Columbus, Ohio, United States. [2]Bertec Corporation, Columbus, Ohio, United States. [3]University of South Florida, Tampa, Florida, United States

Introduction

Baseball pitching is a multifaceted full-body movement with complex movement patterns. The countermovement jump, squat jump, isometric mid-thigh pull, hop test and plyometric push-up are often performed during pitching training sessions and utilized as quantitative measures of muscular improvement, despite differing movement profiles. While previous research demonstrated associations between pitch velocity (PV) and metrics from performance assessments [1], no studies integrated these metrics into a comprehensive predictive model. The purpose of this study was to use kinematic and kinetic metrics from standard upper- and lower-body performance assessments to predict PV in collegiate baseball players using multivariate regression analyses.

Methods

Performance and pitching data from 167 male collegiate athletes (89.28±10.09kg, 21.29±2.25yrs, 1.85±0.07m) were collected on ForceDecks and Bertec force plates, stored in Driveline's OpenBiomechanics dataset [2], and retrospectively analyzed. An elastic net generalized regression model ($\alpha = 0.99$) with BIC stopping rule-based selection was used to predict peak PV (mph) from 35 performance metrics. Model fit was evaluated using R^2 and root averaged square error (RASE), and predictor effects were assessed using Wald chi-square tests ($\alpha = 0.05$). Analyses were performed in *JMP Pro 18* (SAS Institute, Cary, NC).

Results

The elastic net regression model explained 33.6% of pitch speed variance ($R^2 = 0.336$; RASE = 4.39 mph), retaining 6 predictors shown in Table 1.

Discussion

Selected force plate-derived metrics from standard performance assessments explained 33.6% of variance in PV. Pitchers with higher peak power, peak force, jump height, and reactive strength pitched faster. Practitioners can utilize this information to develop targeted training exercises to improve relevant neuromuscular qualities.

Previous research has reported models predicting around 30% of variance in pitch velocity [3]; this low value is most likely due to the complexity of pitching movement patterns. While our multivariate approach provides marginally more insight compared to isolated testing, 67% of variance remains unexplained. The inclusion of more upper-body strength and rotational assessments may provide further insight into pitching performance.

Images (Optional)

Table 1. Regression Effect Tests

$$Pitch\ Velocity = 67.0832 + 0.0008 * CMJ\ Peak\ Power\ (W) + 2.9173 * CMJ\ RSI\ Modified\ \left(\frac{m}{s}\right) + 0.0016 * SJ\ Peak\ Power\ (W) + 0.0001 * IMTP\ Peak\ Vertical\ Force\ (N) + 0.0228 * HT\ Best\ Jump\ Height\ (cm) + 0.0143 * HT\ Best\ RSI\ \left(\frac{m}{s}\right)$$

Variable	Wald χ^2	Prob > χ^2
SJ Peak Power (W)	1.7246831	0.1891
HT Best RSI (jump height/contact time) (m/s)	0.5151404	0.4729
Avg. CMJ RSI_{mod} (m/s)	0.4230385	0.5154
CMJ Peak Power (W)	0.3329826	0.5639
HT Best Jump Height (cm)	0.0412195	0.8391
IMTP Peak Force (N)	0.0185231	0.8917

SJ: Squat Jump; CMJ: Countermovement Jump; IMTP: Isometric Mid-Thigh Pull; SJ: Squat Jump; HT: Hop Test; RSI: Reactive Strength Index; RSI_{mod}: Modified Reactive Strength Index;

References (Optional)

[1] Wong, *et al.*, J Strength Cond Res, 2025

[2] Wasserberger *et al*,, The OpenBiomechanics Project, 2022

[3] Wong, *et al.*, J Strength Cond Res, 2023

Acknowledgements (Optional)

Joseph Marsh, Driveline

Dr. Kamran Barin

Session Category

Human Motion and Performance: Sports

P1-324

Influence of Available Reaction Time on Knee Joint Biomechanics and the Implications for Anterior Cruciate Ligament Injury

Miss Lauren Crawford

University of Tennessee, Knoxville, Knoxville, TN, United States

Introduction

Anterior cruciate ligament injuries frequently occur through non-contact mechanisms during rapid, unanticipated movements which are often influenced by cognitive and reaction time demands. This study examines how varying time available to respond to unanticipated stimuli influences knee biomechanics during a run-to-cut maneuver. Findings aim to better connect laboratory research with real-world athletic maneuvers and inform targeted prevention strategies.

Methods

This study analyzed cutting mechanics of 15, right leg dominant, recreationally active college students (aged 21.6 ± 3.57 years) with no lower extremity injury history. Participants performed 20 run-to-cut maneuvers in response to visual cues displayed 1.5m (short RT) or 2.5m (long RT) from the plates front edge. 3D kinematics and GRF's were recorded using a 12-camera Vicon motion capture system and embedded force plates. Peak hip and knee angles and moments during the stance phase were extracted.

Results

Significant effects for both leg and time were observed. Significant leg effects indicate that the right leg exhibits greater peak hip extension moments, peak knee external rotation moments, and peak knee abduction angles compared to the left. Significant time effects indicate that long reaction time trials were performed with increased peak hip internal rotation moments and peak hip flexion angles, whereas short reaction time trials resulted in greater knee flexion and abduction angles at initial contact.

Discussion

Preliminary results suggest that the right limb may experience greater knee joint loading, potentially reflecting dominant-side movement strategies or uneven neuromuscular control patterns. These differences may have implications for injury risk, particularly during rapid deceleration and fast cutting movements. The time dependent effects may indicate

that movement patterns change when reaction time is limited. This altered strategy could heighten joint loading, thereby increasing injury risk. Further work should aim to quantify muscle activation patterns to verify the suggested neuromuscular control strategy.

Images (Optional)

Variable	Left leg/ long RT	Left leg/ short RT	Right leg/ long RT	Right leg/ short RT	Effect size (d)
PK Hip Exten. Mom.$^{b+}$	-1.89 ± .74	-1.78 ± .79	-1.62 ± .81	-1.49 ± .56	0.28
PK Knee Ext. Rot. Mom^{b++}	-0.40 ± .14	-0.37 ± .12	-0.20 ± .17	-0.19 ± .13	**1.01**
PK Knee Abd. Ang.$^{b+}$	-9.13 ± 5.74	-14.22 ± 13.66	-6.43 ± 3.77	-7.70 ± 3.92	**0.52**
PK Hip Int. Rot. Mom. $^{a+}$	0.29 ± .15	0.23 ± .11	0.19 ± .13	0.18 ± .10	0.26
PK Hip Flex. Ang. $^{a+}$	38.08 ± 10.91	32.38 ± 17.87	37.71 ± 7.28	35.09 ±10.11	0.29
IC Knee Flex. Ang. $^{a+}$	-21.43 ± 8.76	-26.08 ± 13.87	-22.03 ± 8.06	-29.14 ± 13.66	0.37
IC Knee Abd. Ang. $^{a++}$	-1.16 ± 3.41	-3.18 ± 4.29	0.10 ± 2.84	-1.51 ± 2.46	0.47

Table. 1 Means, SD, and bias corrected effect size by condition. PK = Peak, IC = Initial Contact, ^{b}Significant Limb Main Effect, ^{a}Significant Time Main Effect, $^{+}$ $p \leq 0.05$, $^{++}$ $p \leq 0.001$.

Session Category

Human Motion and Performance: Sports

P1-325

Motorcycle Finger Braking Techniques Affect Forearm Muscle Fatigue During a Simulated Race

Mr. Leon Lauret[1,2], Mr. Philip Maschlanka[1], Dr. Daniel Hahn[1,3]

[1]Human Movement Science, Faculty of Sport Science, Ruhr University Bochum, Bochum, NRW, Germany. [2]Biomedical Engineering Lab, Department of Mechanical Engineering, Ruhr University Bochum, Bochum, NRW, Germany. [3]School of Human Movement and Nutrition Sciences, The University of Queensland, Brisbane, Queensland, Australia

Introduction

In professional motorcycle racing, speeds nowadays exceed 360 km/h. The physical demands during races cause many drivers to suffer from chronic exertional compartment syndrome (CECS), mainly affecting the forearms [1,2]. With CECS, fascia surrounding the muscles does not expand during muscle contraction, resulting in higher compartment pressure and muscle compression. Symptoms range from the sensation of tightness to loss of forearm muscle control and strength, posing a concerning safety risk. One factor contributing to CECS in racing is the constant use of the hand-controlled front brake, which is applied hundreds of times during a race [2]. Interestingly, riders use different braking techniques (1-finger, 2-finger or 4-finger, Fig. 1B) based on personal preference. We aimed to investigate whether the specific braking techniques lead to distinct forearm muscle fatigue and could thus reduce the prevalence of CECS.

Methods

We simulated braking by a repeated braking protocol, which matched a typical sprint-race in braking numbers (81), magnitude (15 bar), and duration (3.6 sec, Fig. 1A). For this, a pressure sensor recorded and displayed the braking pressure of a motorcycle brake. Participants had to complete the protocol for each braking technique in a random order, and differences in forearm muscle fatigue between braking techniques were evaluated using electromyography (m. flexor digitorum superficialis), grip strength, and tissue stiffness measurements.

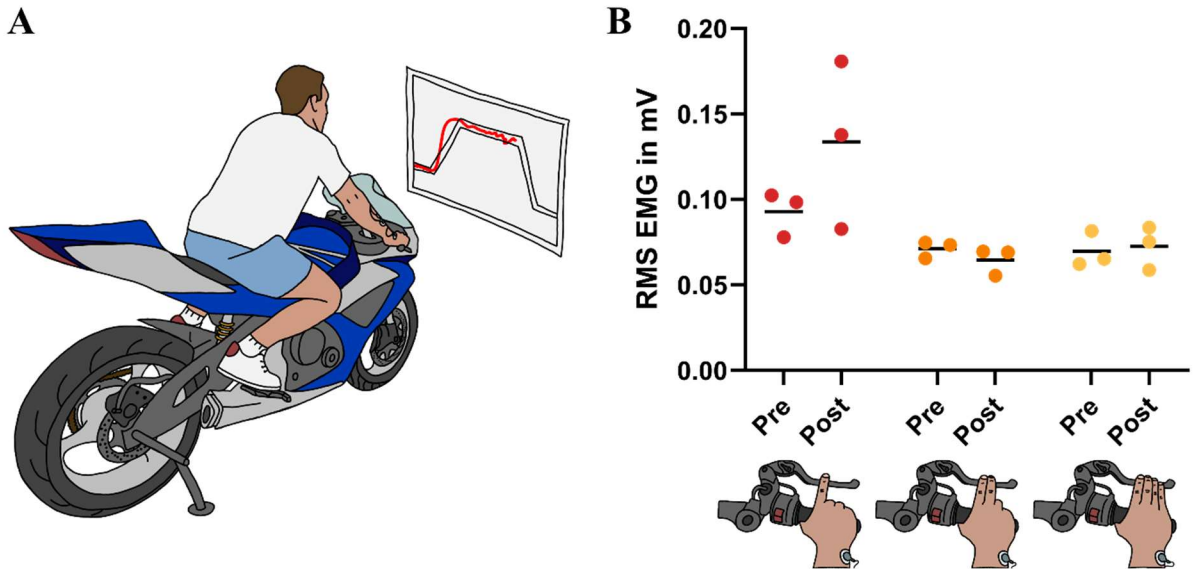
Results

Preliminary results (n=3, mean±SD: 30.5±1.9yr, 1.76±0.04m, 73.7±2.5kg) are shown in Figure 1B. Braking with one finger led to increased muscle activity and increased tissue stiffness after the braking protocol. Additionally, post grip strength was reduced by -6%, -5% and -5% (1-, 2- and 4-finger braking, respectively).

Discussion

Our preliminary data shows that the 1-finger braking technique induces fatigue during repeated braking compared with 2- and 4-finger braking. Contrary to our expectations, 4-finger braking has no additional benefit compared with 2-finger braking. These findings may help to develop preventive and rehabilitative measures for riders suffering from CECS, as reducing fatigue could help to decrease compartment pressure. Additionally, race performance of habitual 1-finger brakers could be improved.

Images (Optional)



References (Optional)

Sindhu et al. Physician Sportsmed., 2019
O'Dowd et al. J. Orthop. Surg. Res., 2021

Session Category

Human Motion and Performance: Sports

P1-326

Biomechanical Validity of the Swing Test

Dr Lindsay Carroll PT, DPT, PhD,OCS, Dr AJ Lievre PT, DPT, EdD, Dr. Dominic Nestor PT, DPT, Dr. Saige Silva PT, DPT

Shenandoah University, Winchester, VA, United States

Introduction

The swing test (ST) is a dynamic test that is used to clinically assess a runner's hip motion when a full running evaluation is not possible due to injury, time, or resources. While the ST is believed to reflect hip motion occurring during running, its relationship to running kinematics is unknown. The purpose of this study was to determine if the sagittal plane hip motion during running was related to the motion occurring during the ST. The secondary aim was to determine if static clinical tests of hip range of motion (ROM) were related to the hip motion occurring during running.

Methods

Thirty-six healthy, recreationally active participants between 18 and 45 years of age (mean age = 23.6 ± 1.5 years; 78.38% female; mean BMI = 25.78 ± 3.37 kg/m^2) participated in this cross-sectional study. Inertial measurement units measured sagittal plane hip motion during the ST and treadmill running. Static hip ROM was measured with a blinded goniometer and the modified Thomas test (mTT) and the straight leg raise (SLR). Pearson correlation coefficients evaluated the relationships between maximum hip flexion/extension and total excursion during the ST and running and between the mTT and SLR and running.

Results

Moderately strong, statistically significant correlations were found when maximum hip extension ($r = 0.688$, $p < 0.001$), maximum hip flexion ($r = 0.415$, $p = 0.012$), and total sagittal plane hip motion ($r = 0.679$, $p = 0.001$) occurring during the ST and running were compared. In contrast, the relationships between mTT and maximum hip extension during running ($r = -0.132$, $p = 0.444$) and between SLR and maximum hip flexion during running ($r = 0.121$, $p = 0.480$) were not statistically or clinically meaningful.

Discussion

The ST may be more useful for assessing running-related sagittal plane hip mobility than static clinical tests such as the mTT and SLR. Clinicians may consider using the ST to estimate sagittal plane hip kinematics when a full running evaluation is not feasible.

Further research is needed to determine if this relationship can be reliably assessed clinically and if the test is valid in individuals with injuries.

References (Optional)

Session Category

Human Motion and Performance: Sports

P1-327

Phase-Specific Whole-Body Coordination Associated With Countermovement Jump With Arm Swing Height Performance in Soccer Female Athletes

MSc, PhD Candidate Lucie Courtois, Ryan Graham

University of Ottawa, Ottawa, Ontario, Canada

Introduction

Countermovement jump (CMJ) is typically studied through lower-limb mechanics, meanwhile jumping is a whole-body task requiring coordinated motion. While lower-limb coordination has been quantified using Continuous Relative Phase (CRP), trunk and upper-body contributions remain unexplored. Understanding how whole-body coordination relates to jump performance could refine training strategies. This study investigated whether phase-specific inter-joint coordination during CMJ correlates with jump height performance.

Methods

Seventeen female soccer players performed three CMJs with arm swing. Markerless kinematics were collected using Vicon Vue and processed using Theia3D. Sagittal plane Mean Absolute Relative Phase (MARP) was computed for four joint pairs: ankle-knee (AK), knee-hip (KH), hip-thoracic spine (HT), and thoracic spine-shoulder (TS). From movement onset to jump apex, signals were time-normalized to 100%, and jump height was computed using pelvis center-of-mass displacement. Functional Data Analysis (FDA) was applied to compute pointwise Pearson correlations between MARP and jump height across the movement.

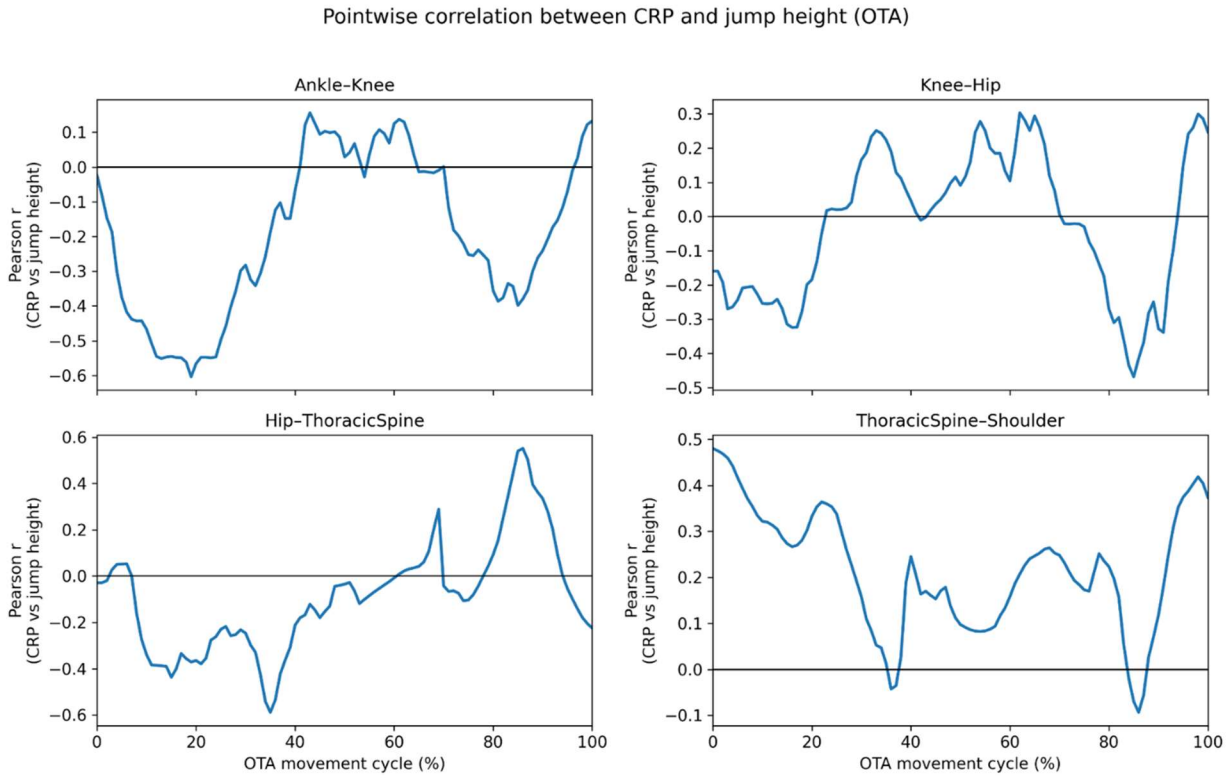
Results

Jump height ranged from 0.33-0.52 m (mean: 0.41 ± 0.05 m). FDA revealed distinct phase-specific coordination-performance correlations for each joint pair. AK showed significant negative correlations in early countermovement ($r \approx -0.55$, $p < 0.001$) and late propulsion ($r \approx -0.35$, $p < 0.01$). KH showed significant negative correlation in late propulsion phase ($r \approx -0.45$, $p < 0.01$). HT demonstrated significant negative correlations during the countermovement ($r \approx -0.50$, $p < 0.05$) and positive correlations during the propulsion ($r \approx -0.55$, $p < 0.05$). TS showed small to medium positive correlations throughout the movement, with peaks in early countermovement ($r \approx -0.45$, $p < 0.001$) and early flight ($r \approx -0.40$, $p < 0.01$).

Discussion

This study provides novel evidence that whole-body coordination is correlated to CMJ performance, with distinct joint-pair contributions varying across movement phases. Negative correlations indicate synchronized coordination, whereas positive correlations reflect out-of-phase coordination. Higher performers modulate inter-joint coupling across the kinetic chain, synchronizing lower-limb joints during countermovement and propulsion while using more out-of-phase trunk and shoulder patterns. These results suggest that training should target coordinated lower-limb triple extension, HT sequencing, and dynamic arm swing, which may lead to more effective jump-performance training interventions.

Images (Optional)



Session Category

Human Motion and Performance: Sports

P1-328

Experimental Characterisation of Wrist Biomechanics During Upper Limb Loading in Gymnastics

Miss Lucy Buchanan[1,2], Prof. Liang He[1,2], Prof. Amy Zavatsky[2]

[1]Podium Institute for Sports Medicine & Technology, University of Oxford, Oxford, Oxfordshire, United Kingdom. [2]Department of Engineering Science, University of Oxford, Oxford, Oxfordshire, United Kingdom

Introduction

Gymnastics places large physical demands on the body, and unlike in most sports, the wrist functions as a weight-bearing joint. Repetitive upper limb loading predisposes gymnasts to high risks of wrist injury. Gymnast's wrist is a stress injury to the distal radial physis common in adolescents who sustain high training volumes during periods of musculoskeletal immaturity. The injury mechanism involves repetitive wrist loading in an extended position. Understanding wrist biomechanics during loading conditions is essential for developing monitoring techniques and injury prevention strategies. This study characterises wrist motion and loading in terms of the key variables associated with gymnast's wrist: extension and force.

Methods

Ten adult participants (5M, 5F; height 1.72 m (SD 0.095); mass 65.3 kg (SD 9.2)) performed three trials of handstand, cartwheel, handstand-walk, handstand-hop. Full-body motion and ground-reaction forces (GRFs) were recorded by a sixteen-camera Vicon motion capture setup (Valkyrie 16), and force plates (AMTI). The calculated wrist extension angle was projected into the sagittal plane in the initial analysis of the data.

Results

Mean maximum wrist extension angles were Handstand: 58.7° (SD: 4.5°, max: 69.4°); Cartwheel: 61.8° (SD: 7.7°, max: 75.8°); Handstand Walk: 67.4° (SD: 4.5°, max: 77.4°); Handstand Hop: 57.3° (SD: 4.5°, max: 68.7°). Forces experienced were largest in the handstand-hop movement, with peak GRFs reaching more than three times bodyweight in some cases. Technique differences between participants were identified, most notably in the handstand hop, where wrist extension angle and the magnitude of GRF during the first-hand contact were affected by approach angle and timing of hop initiation (Figure 1).

Discussion

Results are consistent with the knowledge that gymnasts sustain forces multiple times their bodyweight at the wrist joint whilst it is in extreme extension [1]. The largest extension angles were observed in the handstand walk, with most variation between participants in the cartwheel. Differences in wrist extension and GRF patterns between movement strategies indicate that technique choice alters wrist loading; therefore, technique selection may be a key modifiable factor influencing wrist injury risk.

Images (Optional)

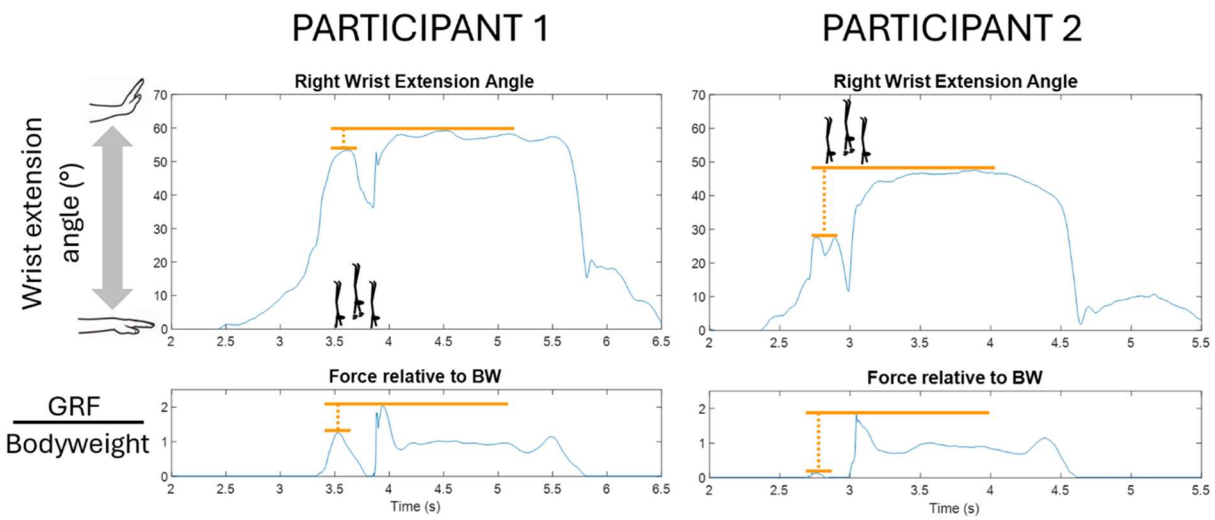


Figure 1: Wrist extension angle and magnitude of ground reaction force (GRF) relative to bodyweight for a handstand hop trial, for two different participants. Orange lines highlight the difference between maximum wrist extension angle, and peak GRF at each hand contact.

References (Optional)

[1] DiFiori *et al.*, AJSM, 2006, 34(5):840-849.

Acknowledgements (Optional)

This work is supported by the Podium Institute for Sports Medicine and Technology.

Session Category

P1-329

Effects of Lighting Conditions on Trail Running Performance Measures

Mr. Malicki Diallo BS[1], Dr. Key Nahan PhD[1], Mr. Adam Grimmitt MS[1], Mr. Aidan Watts[2], Dr. Meghan Huber PhD[1], Dr. Wouter Hoogkamer PhD[1]

[1]University of Massachusetts Amherst, Amherst, MA, United States. [2]State University of New York College of Environmental Science and Forestry, Syracuse, NY, United States

Introduction

Ultramarathon running provides a unique paradigm where runners navigate complex terrains with often varying lighting (e.g. day, night). Runners depend on wearable lighting devices during night sessions; however, it is still unclear whether this illumination allows nighttime running to match daytime performance. Previous research has found walking gait slows in older adults while navigating simple terrain in near darkness [1]. However, the effects of lighting conditions have not yet been explored for trail running. We hypothesize runners will run slower during nighttime with wearable lighting devices as compared to running in the daylight.

Methods

Five recreational runners (3M, 2F) ran four trials on a ~500m uneven trail during the day and six trials at night at their easy pace. At night, participants ran twice with a headlamp, twice with a waist lamp, and twice with both. We measured split times with a stopwatch and ground reaction forces with force insoles (LoadSol, Novel) at 200 Hz. Gait events were identified using a 20N threshold, and stride and contact time were calculated in MATLAB. Temporal measures were averaged across legs and trials, and speed was averaged across trials. A paired t-test was completed to observe mean differences across measures.

Results

Participants ran slower at night (2.04±0.36 m/s) compared to during the day (2.38±0.29; $p=0.0103$). Stride time ($p=0.0705$) and contact time ($p=0.0533$) did not differ significantly between night and day trials.

Discussion

Nighttime running with wearable lighting devices provides a greater challenge than daytime running resulting in slower running speeds. For this initial small sample differences in stride time and contact time were not significantly different. Further research will reassess

this with appropriate statistical power and also evaluate the effects of different wearable lighting devices (headlamp or waist lamp) on trail running speed.

Images (Optional)

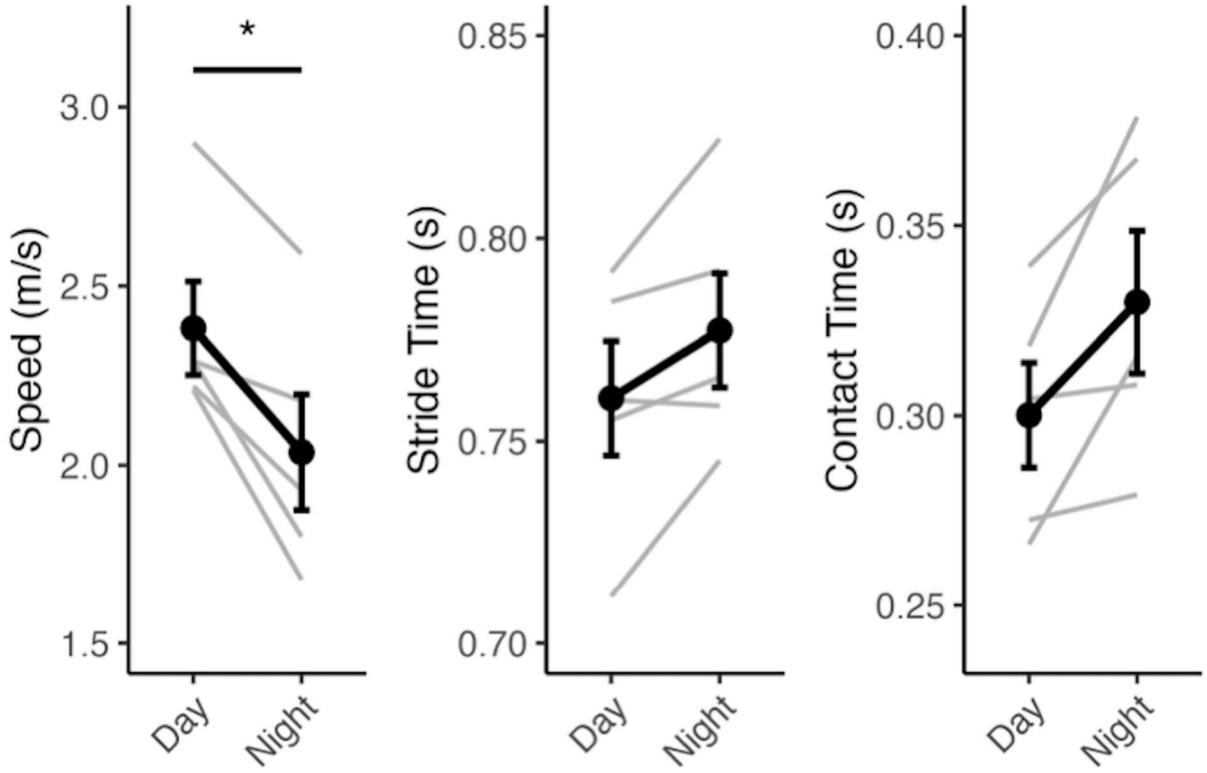


Fig 1. Comparisons of running speed, stride time, and contact time between day and night trials. Gray lines show individual participant data; black lines and points indicate group means with standard error bars. Asterisk denotes a significant difference ($\alpha = 0.05$).

References (Optional)

[1] Kesler et al. (2005) J. NeuroEng. Rehabil.

Session Category

Human Motion and Performance: Sports

P1-330

Fatigue-Related Changes in Knee Kinematics During Incremental Treadmill Running in Well-Trained Runners

M.Sc. Marco Rahner[1], B.Eng. Leah Reiter[2], Dr. Jörg Lohscheller[3], Dr. Juliane Mueller[1], Dr. Steffen Mueller[1]

[1]Trier University of Applied Sciences, Department of Computer Science – Therapeutic Sciences, Trier, Rhineland-Palatinate, Germany. [2]Trier University of Applied Sciences, Department of Engineering, Trier, Rhineland-Palatinate, Germany. [3]Trier University of Applied Sciences, Department of Computer Science, Trier, Rhineland-Palatinate, Germany

Introduction

During running, acute fatigue has been shown to increase maximal knee flexion (MKF) during swing phase and at initial contact, while stance phase MKF appears unaffected. However, few studies have examined stance phase maximal knee adduction (MKAD) and abduction (MKAB) or the effects of higher running velocities [1].

The present study aims to expand understanding of fatigue-induced acute changes in knee kinematics during incremental treadmill running in well-trained runners.

Methods

Eight male, healthy well-trained runners (31±7years; 178±2cm height; 71.8±4.3kg weight; 65±24.5km in 6.5±1.8h training per week) performed a maximal incremental test on a treadmill (incline: 0%; initial running velocity: 8km/h; increment duration: 3min; increment step: +2km/h). Blood-lactate concentration was measured between increments. Full-body kinematics were measured for each increment after 30s (A) and 150s (B) for 20s using a markerless motion-capturing system (Theia3D; Axiom v2025) with eight cameras (100Hz).

After gait events detection, knee kinematics (MKF [°], MKAD [°], and MKAB [°]) during stance phase were calculated and averaged across legs.

A two-way repeated-measures ANOVA (Measurement × Increment) was conducted to assess between-increment changes. Furthermore, within-increment changes were evaluated using a one-way repeated-measures ANOVA on absolute measurement-point differences (B-A) for each increment. Both analyses were carried out across the following increments: Start (8km/h), Aerobic Threshold (LT1; 2mmol/L), Anaerobic Threshold (LT2; 4mmol/L), and the last completed increment (Final). Holm-corrected post-hoc tests were applied where appropriate.

Results

Velocity at Start were 8.0±0km/h, at LT1 14.8±1.4km/h, at LT2 17.0±1.4km/h, and at Final 20.3±1.6km/h. Fig.1 shows distribution and individual changes between-increments (A) and within-increments differences for all outcomes.

There was a significant main effect for between-increment MKAD (p=.039; Greenhouse–Geisser corrected). However, post-hoc comparisons revealed no significant pairwise differences. No other outcomes showed significant changes within or between increments.

Discussion

The absence of significant (pairwise) within- and between-increment changes across all outcomes, suggests that maximal knee kinematics during the stance phase are not sensitive indicators of acute fatigue. Nonetheless, increasing within-increment heterogeneity appears, especially for Final. These findings align with [1] and extend prior work by adding knee ad-/abduction measures and higher running velocities.

Images (Optional)

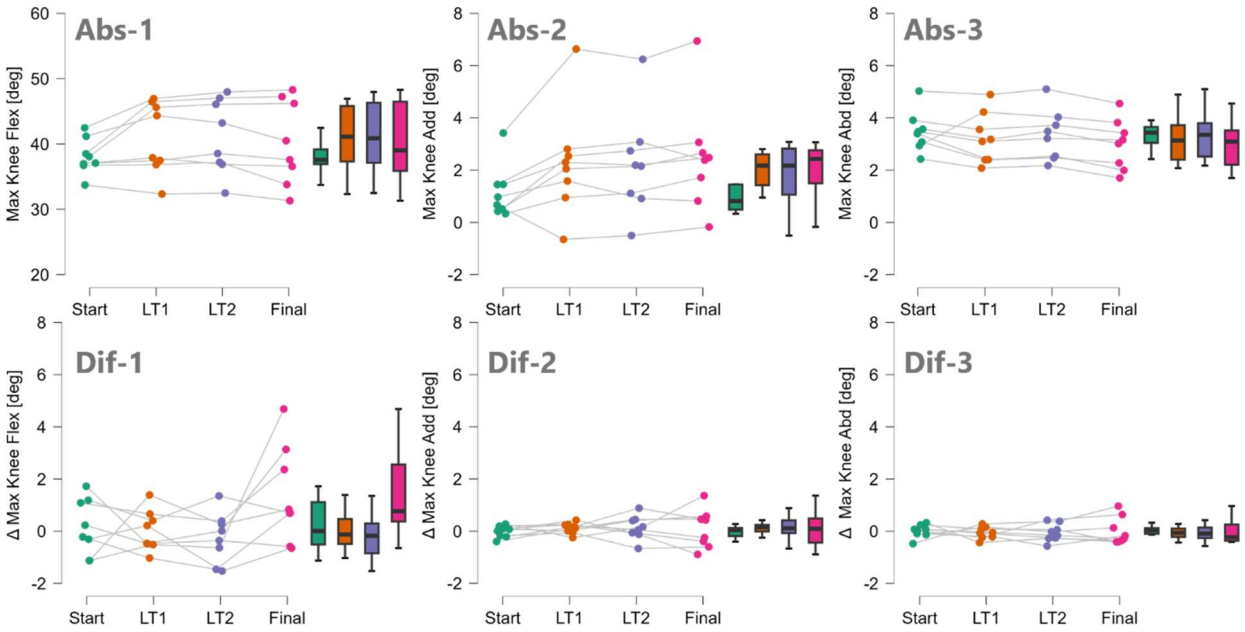


Fig. 1: Absolute between-increment changes in maximal knee flexion (Abs-1), adduction (Abs-2), and abduction (Abs-3) for the measurement A, and relative within-increment changes (Dif-1, Dif-2, Dif-3) during stance phase of an incremental treadmill test (Start, LT1, LT2, Final) in well-trained runners.

References (Optional)

[1] Zanderberg et al., Gait & Posture, 2023

Session Category

Human Motion and Performance: Sports

P1-331

Field-Based Evaluation of an ACL Injury Prevention Training Intervention on Change-of-Direction Movements

MSc Mareike Kühne, BA Semjon Schmidt, Dr. Maurice Mohr

University of Innsbruck, Innsbruck, Tyrol, Austria

Introduction

ACL injuries often occur during unplanned change-of-direction (COD) movements [1]. Injury prevention training programs have shown promising effects in improving injury-prone movement patterns while maintaining performance [2]. Previous studies have tested the effects of training programs on preplanned COD kinematics in lab-settings. We used a field-based approach to investigate whether such training effects can be observed in a more sports-specific setting with unplanned scenarios. We hypothesized to find an adaptation in COD kinematics after the intervention training and no change in COD performance.

Methods

Seventeen male soccer players (mean age = 19 years) of the third highest league in Austria participated in a six-week training intervention and completed a field-based pre- and post-assessment. The intervention focused on practicing COD techniques associated with lower knee joint loading under increasing cognitive demands. The pre- and post-test consisted of twenty COD maneuvers of different anticipatory conditions (preplanned, unplanned with equal (50:50) and unequal (80:20) probability of direction). Performance (completion time) and IMU-based kinematics at the initial contact of the sidestepping leg were assessed and statistically analyzed using linear mixed models (alpha = 0.05, fixed effect ‘time x anticipatory condition’).

Results

The kinematics of the sagittal plane (higher knee (p = 0.08) and hip flexion (p < .001), lower trunk flexion (p = 0.003)). A significant interaction effect revealed that hip abduction angles were specifically reduced in unplanned (p < 0.04) but not preplanned COD movements (p = 0.799). COD completion times significantly increased by 0.04s after the intervention (p = 0.009).

Discussion

Our field-based approach revealed adaptations in on-field COD kinematics following a six-week COD training intervention, even in unplanned scenarios. Lower-body COD kinematics

of the sagittal and frontal plane changed in a way consistent with a reduced risk of non-contact ACL injury [3], however, at the cost of a small performance decrease. Additionally, some adaptations can only be observed under cognitively demanding conditions.

Images (Optional)

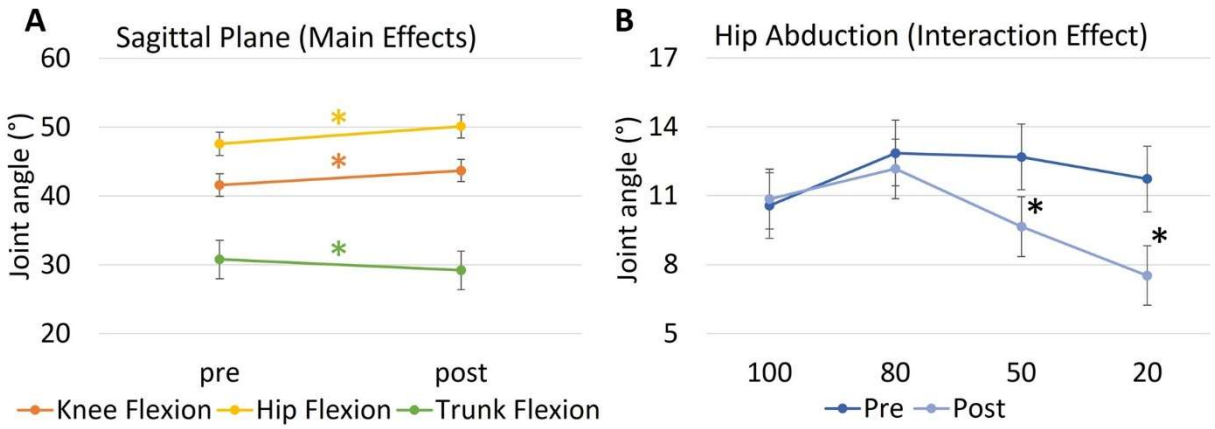


Figure 1: Kinematic outcome variables are depicted in means (with standard errors) over time (**A**) or anticipation conditions split by time point (**B**). Asterisks indicate significant pre-post changes.

References (Optional)

[1] Gokeler A *et al.*, J. Athl. Train., 2024

[2] Mohr M *et al.,* Sci Rep., 2024

[3] Donelon TA *et al.,* Sports Med. Open, 2020

Acknowledgements (Optional)

This research was funded in whole or in part by the Austrian Science Fund (FWF) [10.55776/I6547].

Session Category

Human Motion and Performance: Sports

P1-332

Application of a Single-Camera Markerless Motion Capture System to Assess Sprint Biomechanics Following Hamstring Injury: A Case Study

Dr. Margherita Mendicino[1], Dr. Stefano Di Paolo[2], Dr. Francesco Della Villa[2], Prof. Stefano Zaffagnini[1,3]

[1]2nd Orthopaedic and Traumatologic Clinic, IRCCS Rizzoli Orthopaedic Institute, Bologna, Emilia Romagna, Italy. [2]Education and Research Department, Isokinetic Medical Group, FIFA Medical Centre of Excellence, Bologna, Emilia Romagna, Italy. [3]Department of Biomedical and Neuromotor Sciences, University of Bologna, Bologna, Emilia Romagna, Italy

Introduction

Markerless motion capture systems based on artificial intelligence (AI) are emerging as practical alternatives to optoelectronic marker-based (OMB) systems for biomechanical assessment [1]. This study validates the accuracy of an AI-based single-camera markerless system, Sports2D, against a gold-standard OMB system in quantifying sagittal-plane kinematics during typical rehabilitation and return-to-sport (RTS) movements. A case study of an athlete recovering from a hamstring injury further illustrates the system's ecological applicability.

Methods

For the concurrent validation, 166 valid trials from 6 healthy athletes were evaluated using a 10-camera OMB system (Vicon Vero, 120Hz) and videos recorded with three synchronized high-speed RGB cameras and processed with Sports2D (Pagnon, 2024). Athletes performed six tasks: single-leg squat, single-leg hop, drop jump, 90° change-of-direction, forward sprint with single-leg deceleration, and sliding. Sagittal-plane lower limb and trunk kinematics were compared using peak differences, RMSE and correlation coefficients. For the case study, an athlete with a history of hamstring injury performed maximal sprint trials before and after targeted rehabilitation, recorded with a single-camera (iPhone13, Apple). Sagittal-plane kinematics was extracted from Sports2D to evaluate hamstring lengthening and lengthening velocity, hip–knee cyclograms, and joint flexion angles at key running cycle events, allowing pre-/post-training performance comparison.

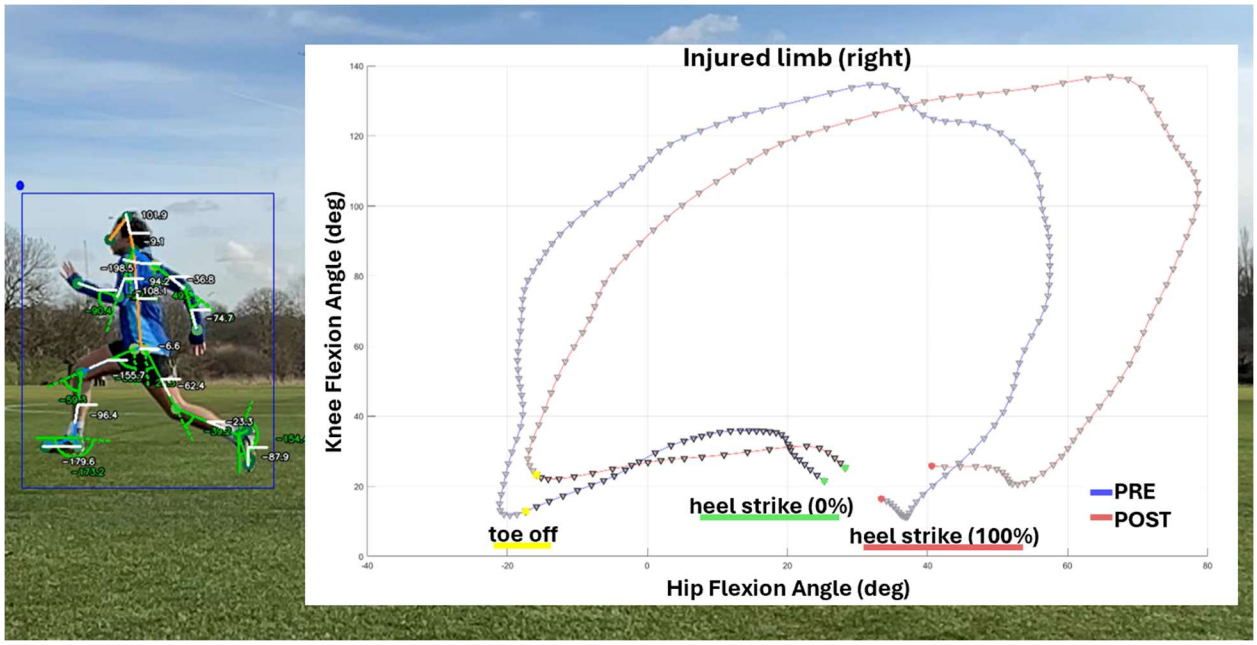
Results

Overall agreement between systems ranged from poor to excellent depending on joint and task. Trunk showed the highest consistency (r=0.76–0.80, ΔOFF<4.2°), ankle exhibited small peak differences in most tasks (ΔOFF 0.3°–4.3°). Hip and knee agreement was excellent in drop jumps (r=0.83–0.88) and for the hip joint also in single-leg squats (r=0.75). Change-of-direction tasks produced the largest discrepancies. Sports2D detected meaningful changes in pre-/post-rehabilitation sprint biomechanics (Figure 1), including improved hip flexion ROM (Δ=17°), higher hip (Δ=3-7°) and knee (Δ=4-9°) flexion at heel strike, higher peak hamstring lengthening velocity (Δ=14deg/s) and increased cyclogram area (Δ=821deg^2).

Discussion

An AI-based single-camera markerless system showed good agreement with OMB in controlled tasks, with larger discrepancies in complex multidirectional movements. The case study further highlights Sports2D as an ecological, rapid, non-invasive on-field data collection tool, that could be used to support rehabilitation and RTS decisions with near real-time data processing.

Images (Optional)



References (Optional)

[1] David Pagnon *et al.*, JOSS, 2024.

Session Category

Human Motion and Performance: Sports

P1-333

Can Footwear Affect Rope Climbing Performance?

Lead Biomechanics Researcher Marlon Rainville, Director of Footwear Biomechanics Jay Worobets

Nike Sport Research Lab, Beaverton, Oregon, United States

Introduction

Rope climbing is a common task in functional fitness competitions and training among first responders and military personnel [1, 2]. To maximize climbing speed, athletes use various foot wrap techniques to create traction between the feet and rope, allowing substantial leg forces to contribute to vertical acceleration (**Figure 1a**) [3]. Increasing available traction between the shoe and rope may also improve performance.

The purpose of this study was to quantify the effects of rope climb-specific footwear design features on rope climbing performance and perception.

Methods

Sixteen athletes completed six rounds of three repetitions (ascent and descent) of 4.5 m rope climbs as fast as possible in two footwear conditions. The NIKE Metcon 9 ("Extra Grip") shoe incorporates a textured midfoot rubber intended for enhanced grip on a climbing rope. The NIKE Free Metcon 6 ("Control") shoe has no rope climb-specific design features.

Kinematic data were collected with Theia markerless MOCAP. Metrics of interest were statistically compared between footwear using paired-sample t-tests ($\alpha < 0.05$).

After each trial, athletes were asked to rate on a 9-point intensity scale, ranging from "1 - strongly disagree" to "9 - strongly agree", their response to a statement reading "This shoe allowed me to complete rope climbs with ease."

Results

Rope climbing ascent performance was significantly faster in the Extra Grip shoe by 6.2% on average (6.60 ± 3.09 sec vs. 7.09 ± 3.65 sec; $p = 0.04$), with 13 out of 16 athletes achieving faster ascents in the Extra Grip shoe (**Figure 1b**).

Athletes perceived that the Extra Grip shoe made rope climbing easier (8.56 ± 0.79 vs 4.88 ± 2.12; $p < 0.01$) (**Figure 1c**).

Discussion

Rope climb-specific footwear design features enhanced rope climbing performance and perception. We speculate that the mechanism responsible is an increased available traction between the shoe and rope, enabling the athlete to transfer more leg force to the rope.

A limitation of this study was a lack of mechanical test methods to directly measure available traction between shoes and a climbing rope.

Images (Optional)

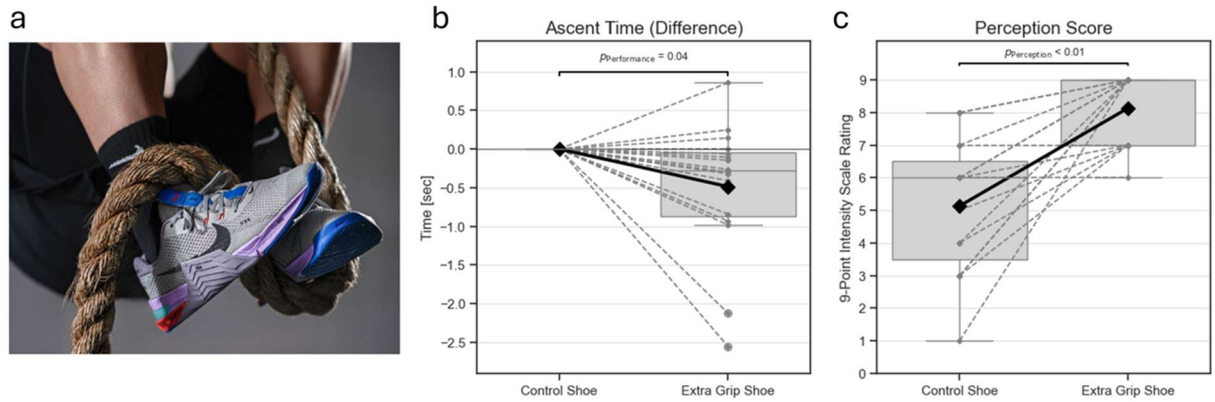


Figure 1: *(a) Example of foot wrap technique (b) Ascent time differences relative to Control shoe (c) Scores of perceived "ease of rope climbing" (black line indicates the mean values across all athletes; dashed lines represent individual athlete means)*

References (Optional)

[1] Glassman, The CrossFit Journal, 2002

[2] Paine. et al., Gen. Staff College of the U.S. Army, 2010

[3] Spence et al., Journal of NSCA, 2016

Session Category

Human Motion and Performance: Sports

P1-334

Plantar Intrinsic Muscle Excitations During Running Before and After a Locomotor Fatiguing Task

Ms Megan Spencer BS[1], Ms Sydney Menendez[1], Dr Ross Smith PhD[2], Dr Jason Franz PhD[1]

[1]University of North Carolina and North Carolina State University, Chapel Hill, NC, United States. [2]University of Memphis, Memphis, TN, United States

Introduction

The plantar intrinsic muscles (PIMs) play a critical role in supporting the medial longitudinal arch and actively regulating foot mechanics during dynamic activities such as walking [1-2] and running [3-4]. However, their contribution during high-intensity tasks such as running, to include changes therein following a locomotor fatiguing task, remains poorly understood. Beyond improving our foundational understanding of PIM and foot function, addressing this knowledge gap has the potential to inform the development of interventions designed to prevent injury. Here, we used indwelling electromyography (EMG) to test the hypothesis that, compared to baseline, PIM excitations during running would exhibit a shift toward slower-frequency intensities following a locomotor fatiguing task.

Methods

16 young adults (9M/7, age: 23.6±3.1 years) completed a one-minute run at 9:40 mile pace before and after a 30-min walk performed at 20% faster than preferred overground speed. This task was selected given its relevance to locomotion, known PIM engagement, and propensity to elicit leg muscle fatigability. We recorded indwelling EMG from the abductor hallucis (AH, a greater toe flexor) and flexor digitorum brevis (FDB, a lesser toe flexor) from which we compared EMG mean frequencies and amplitudes before and after the locomotor fatiguing task.

Results

FDB showed a significant 13.8% average decrease in EMG mean frequency following locomotor fatigue (pre-post, $p = 0.042$) whereas AH exhibited no significant difference ($p=0.258$). Conversely, EMG amplitudes were unaffected by locomotor fatigue.

Discussion

We discovered muscle-specific differences in the vulnerability to locomotor fatigue among the plantar intrinsic muscles during running. FDB, which regulates flexion of the lesser toes, showed disproportionate vulnerability to fatiguability than AH. One key implication of this discovery is in potentially helping to explain why 2nd and 3rd metatarsal stress fractures

are among the most common overuse injuries in runners. With this understanding, we may be better positioned to develop anatomically-informed interventions, such as footwear modifications or strength training, designed to promote fatigue resistance and thereby mitigate running-related overuse injuries.

Images (Optional)

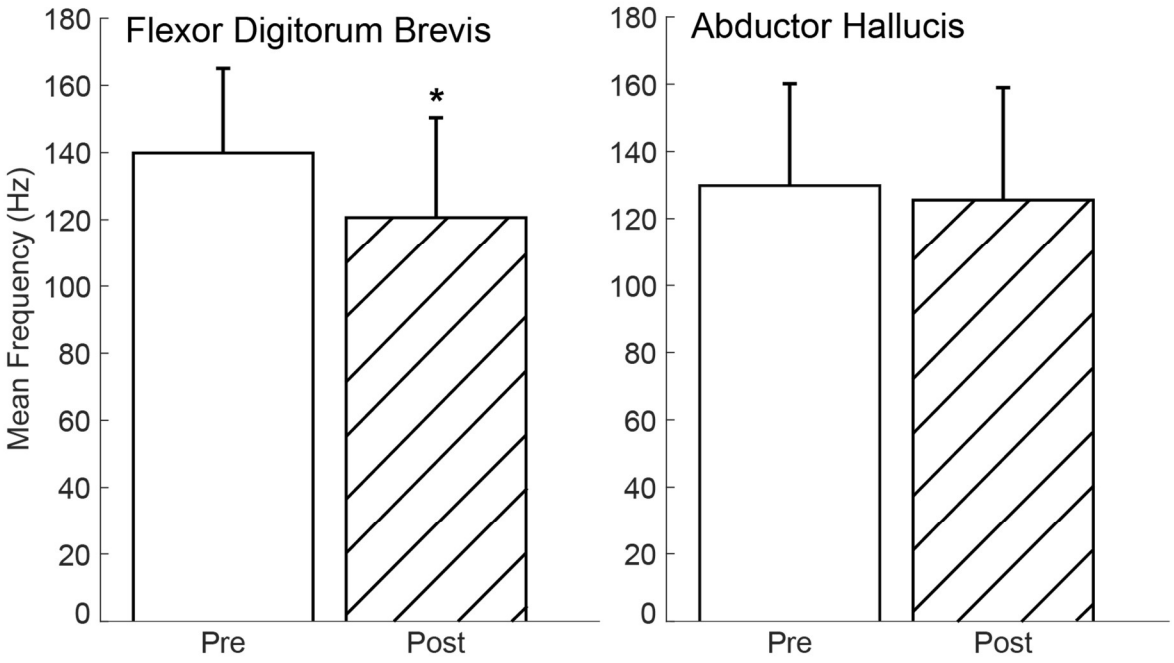


Figure 1. EMG mean frequency before (Pre) and after (Post) the locomotor fatiguing task for FDB and AH. Based on pairwise comparisons, only FDB exhibited a significant decrease in EMG mean frequency, reflecting disproportionate vulnerability to fatigue.

References (Optional)

[1]Kelly et al., J. Appl. Physiol. 2019 [2] Fiolkowski et al.,JFAS., 2003 [3] Kelly et al., JSMS, 2013 [4] Farris et al, Proc Natl Acad Sci USA, 2019

Acknowledgements (Optional)

This work was supported by a grant from the National Institutes of Health (R01AR081287) and an NSF GRFP.

Session Category

Human Motion and Performance: Sports

P1-335

Comparing Landing Ground Reaction Forces in Cushioned and Traditional Flat Ballet Shoes

Dr Michael Pohl PhD, Mr Andy Jenkins, Mr Jacob Mizrahi, Ms Katherine Podoll, Dr Karin Steere PhD

University of Puget Sound, Tacoma, WA, United States

Introduction

Overuse injuries are highly prevalent in ballet, with 66–91% affecting the lower extremities, reflecting the substantial mechanical demands of leaps such as the grand jeté, where landing forces are high. Previous research in running has shown that differences in footwear can alter ground reaction forces and loading rates. However, studies examining the biomechanical effects of non-pointe shoe footwear in ballet remain limited. A cushioned ballet shoe (ORZA, USA) has recently been developed, but its biomechanical impact has not yet been evaluated. This study aimed to compare ground reaction forces during grand jeté landings between this novel cushioned shoe and a traditional flat ballet shoe.

Methods

Four elite ballet dancers, free from pain or current injury rehabilitation, performed grand jeté leaps in both traditional (Trad) and cushioned (ORZA) shoes. Three successful trials were recorded per condition, with order randomized. Kinetic data were collected at 1000 Hz using a floor-embedded force plate (AMTI BP600600, USA) and filtered with a 50-Hz low-pass Butterworth filter. Ground reaction forces were normalized to body weight. Dependent variables included peak vertical GRF, time to peak vGRF, and vertical loading rate (peak vGRF divided by time to peak). Given the small sample size at this point, effect sizes (Cohen's d) were calculated.

Results

There were no meaningful differences between the ORZA and traditional shoes for peak vGRF, time to peak vGRF, or loading rates as indicated by the small to trivial effect sizes. Statistical data including mean (standard deviation) and effect sizes (d) are presented in the table.

Discussion

This ongoing study is the first to compare landing ground reaction forces between a novel cushioned ballet shoe and a traditional flat shoe. While cushioned footwear has been

shown to alter impact ground reaction force variables in running, these changes are often linked to significant shifts in foot-strike patterns, which are unlikely to occur during ballet landings due to aesthetic requirements. Although preliminary results from the current study showed no differences between shoe types, continued investigation as the sample size increases is warranted. Additionally, accompanying kinematic analyses may provide deeper insight into landing mechanics across footwear conditions.

Images (Optional)

	ORZA	Trad	d
Peak vGRF (BW)	3.41 (0.53)	3.57 (0.42)	0.42
Time to Peak vGRF (s)	0.068 (0.013)	0.068 (0.007)	0.03
vGRF Loading rate (BW/s)	53.1 (13.2)	54.3 (9.4)	0.12

References (Optional)

Acknowledgements (Optional)

Session Category

Human Motion and Performance: Sports

P1-336

Wrap Fit Enables Better Trail Performance

Miss Milena Singletary, Dr. Eric C. Honert PhD., Mrs. Bethany Kilpatrick, Mr. Adam Luftglass, Dr. Daniel Feeney PhD., Dr. Kathryn Harrison PhD.

BOA Technology Inc., Denver, Colorado, United States

Introduction

Improvements in shoe fit and running performance have been found in trail running with a wrap fit system compared to traditional laces [1]. Another common fit system in trail shoes is speed lace. It is unknown if there is also a performance and fit difference between speed lace and wrap fit systems.

Methods

Ten experienced trail runners ran a 1700m loop twice in two shoes in a counter balanced order: An on-market zonal speed lace shoe, and the same base shoe prototyped with a wrap fit system. The shoes were equipped with plantar pressure insoles and an inertial measurement unit (IMU) attached to the heel counter. From the IMU, peak foot eversion velocity (PFEV) and speed were computed for each stride. Peak toe pressure was computed for each step from the plantar insoles. Heart rate was also collected. Bayesian models were used to assess the effect of fit system on shoe fit and running performance. Percent of posterior above/below zero and 95% credible interval and differences between Wrap and Lace are presented.

Results

On average, Wrap decreased peak toe pressures by 1.4 kpa (98% < 0, CI: -2.7 to -0.6%) and decreased PFEV by 25.0 deg/s (80% < 0, CI: -5.2 to 1.2%). Participants ran faster, after controlling for heart rate, in Wrap by 0.03 m/s (83% > 0, CI: -0.3 to 2.1%).

Discussion

Despite having targeted closure at the midfoot and forefoot, the speed lace provided a worse fit than the Wrap. Better fit reduces the need to grip the shoe with the toes, resulting in lower peak toe pressures [1]. This has been associated with improved mechanical energy efficiency, which may help explain the improvement in running speed [2]. Further, Wrap reduced the PFEV suggesting a better fit allowing better control of the foot – this is critical in sports requiring navigation of technical terrain.

References (Optional)

[1] Honert et al., Frontiers in Sports, 2023.

[2] Honert et al., American Society of Biomechanics, 2024.

Session Category

Human Motion and Performance: Sports

P1-337

Marathon Training and Fatigue Resistance: Effects on Running Mechanics

Mr. Nate Goldcamp, Ms. Shannon Hugard, Dr. Michael Hahn PhD

University of Oregon, Eugene, Oregon, United States

Introduction

Novice runners experience running-related injuries at a disproportionate rate compared to their trained counterparts. One factor thought to contribute to the increased injury risk is altered running mechanics after fatigue. The ability to resist biomechanical changes from fatigue (joint angles, center of mass displacement, and vertical stiffness) can be described as fatigue resistance, which has been shown to be greater in trained runners compared to novice runners.[1] However, no work has investigated how a training program influences fatigue resistance. This study aims to examine the effect marathon training has on fatigued running mechanics. It is hypothesized that marathon training will improve fatigue resistance, shown by a smaller percent change in biomechanical metrics following fatigue when comparing pre- and post-training.

Methods

Three novice marathon runners (1F, 2M; height: 177.1±15.3 cm; weight: 74.1±15.2 kg) completed a 16-week marathon training plan. Prior to beginning the training plan (week 0), participants completed a biomechanical analysis consisting of three running trials. The first and third trials consisted of a 10-minute submaximal run at 80% of their speed at lactate turn point. The second trial served as the fatiguing element, consisting of a run at 105% of the participants' speed at lactate turn point until volitional exhaustion. Lower-extremity biomechanics data were collected using a force-instrumented treadmill (Bertec,1000 Hz) and an 8-camera motion capture system recorded marker trajectories (Motion Analysis Corp., 200 Hz). Running trials were repeated in week 14 of marathon training. Fatigue resistance metrics were quantified as the percent change before and after the fatiguing trials. A within-subject comparison of percent change values between weeks 0 and 14 was conducted using paired t-tests.

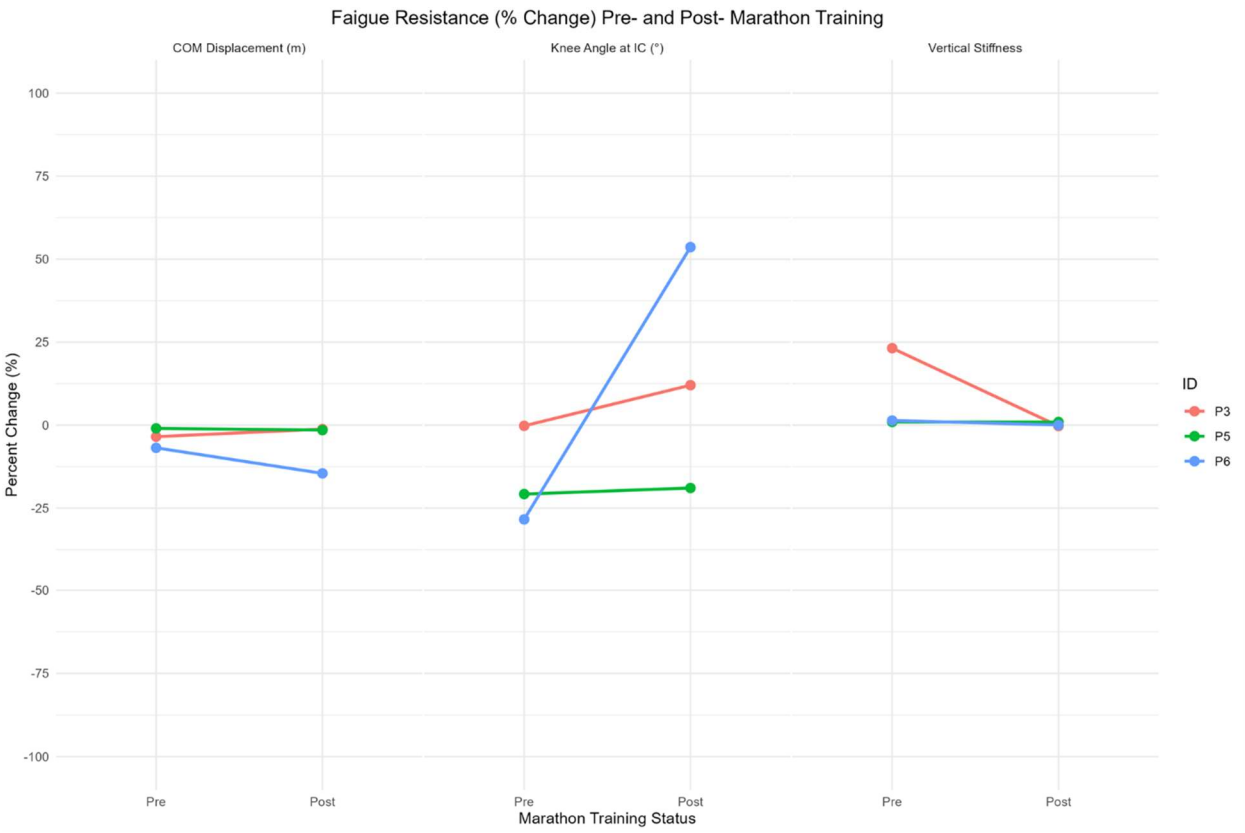
Results

No significant changes in fatigue resistance metrics were observed following marathon training ($p>0.05$). Metrics assessed included joint angles (at initial contact and maximum), center of mass displacement, and vertical stiffness during stance.

Discussion

Preliminary analysis includes data from three participants. Currently, no mechanical factors of fatigue resistance show significant change, however, no conclusions can be made at this point in the research process. The study aims to reach a sample size of 28.

Images (Optional)



References (Optional)

[1] Zandbergen et al. (2023). *Gait & Posture* ***99***: 60-75.

Acknowledgements (Optional)

This work was supported by the Wu Tsai Human Performance Alliance and the Joe and Clara Tsai Foundation.

Session Category

Human Motion and Performance: Sports

P1-338

A Model for Predicting Bat Speed from Popular Field-Based Performance Tests

Ms. Neha Kapoor[1], Dr. Kiara Barrett[1], Dr. Lauren A Luginsland[2]

[1]Bertec Corporaation, Columbus, Ohio, United States. [2]University of South Florida, Tampa, Florida, United States

Introduction

Bat speed (BS) is a critical metric for evaluating hitting performance in baseball that reflects an athlete's capacity to generate and transfer force through the kinetic chain. To better understand the physical factors that contribute to BS and assess athletic ability, performance professionals evaluate strength-based force plate assessments such the countermovement jump (CMJ), squat jump (SJ), isometric mid-thigh pull (IMTP) and hop test (HT) [1]. The purpose of this study was to determine the collective variance in BS explained by force plate-derived metrics from CMJ, SJ, IMTP, and HT assessments using multivariate regression analysis in collegiate baseball players.

Methods

Data from Driveline's OpenBiomechanics dataset was retrospectively analyzed [2]. 231 male collegiate athletes (87.84±9.95kg, 20.12±2.16yrs, 1.80±0.07m) visited a Driveline performance center and completed CMJ, SJ, IMTP, and HT protocols; kinetic data during hitting was collected with Bertec force plates (Bertec Corporation, Columbus, OH). An elastic net regression model ($\alpha = 0.99$) with BIC stopping rule-based selection was used to predict peak BS (mph) with 31 variables averaged across trials. Analyses were performed in *JMP Pro 18* (SAS Institute, Cary, NC); significance was evaluated using Wald chi-square tests ($\alpha = 0.05$).

Results

The elastic net regression model explained 49.6% of bat speed variance ($R^2 = 0.496$; RASE = 3.58 mph) and retained 5 predictors from CMJ, SJ, and IMTP as shown in Table 1.

Discussion

Force plate-derived metrics from CMJ, SJ, and IMTP explained 49.6% of the variance in BS, indicating that lower-body force and power qualities substantially contribute to swing performance. No predictors from HT were retained. Coaches can use the derived prediction equation to estimate an athlete's expected BS based on their neuromuscular profile; if an athlete's BS falls below the predicted value, this may indicate inefficiencies in energy transfer through the kinetic chain. This model therefore offers a practical tool for

identifying performance gaps and guiding individualized training. Future work should validate these relationships in broader athlete samples and examine the contribution of additional performance assessments.

Images (Optional)

Table 1. Regression Effect Tests

$$Bat\ Speed = 47.4491 + 0.0011 * CMJ\ Peak\ Power\ (W) + 0.0007 * CMJ\ Concentric\ Peak\ Force\ (N) + 0.0017 * CMJ\ Peak\ Eccentric\ Force\ (N) + 0.0012 * SJ\ Peak\ Power\ (W) + 0.0005 * IMTP\ Peak\ Vertical\ Force\ (N)$$

Variable	Wald χ^2	Prob > χ^2
SJ Peak Power (W)	3.0129578	0.0826
CMJ Peak Power (W)	2.1816166	0.1397
IMTP Peak Force (N)	1.3003148	0.2542
CMJ ECC Peak Force (N)	0.2426799	0.6223
CMJ CON Peak Force (N)	0.0327719	0.8563

CON: Concentric; ECC: Eccentric

References (Optional)

[1] Bordelon, *et al.*, J Strength Cond Res, 2025

[2] Wasserberger *et al.*, The OpenBiomechanics Project, 2022

Acknowledgements (Optional)

Joseph Marsh, Driveline

Dr. Kamran Barin

Session Category

Human Motion and Performance: Sports

P1-339

The Biomechanical Effects of Weighted Perturbed Jumps

Mr. Nicholas Tom[1], Mr. Malicki Diallo[2], Mr. Daniel Richie MS[1], Dr. Ajit Chaudhari PhD, FACSM[1]

[1]The Ohio State University, Columbus, OH, United States. [2]University of Massachusetts Amherst, Amherst, MA, United States

Introduction

The drop vertical jump (DVJ) has been demonstrated to be a useful tool in identifying injury risk factors, and past research suggests that stiffer landings increase injury risk [1]. Current DVJ protocols occur in controlled environments; however, this may not represent sporting contexts where athletes experience external perturbations. Research has begun exploring the effects of dual tasking (i.e. cognitive perturbations) on DVJs, but research is limited on the effect of physical perturbations [2,3]. The purpose of this study was to identify if weighted perturbations affect movement patterns in ways that could increase injury risk. Therefore, we hypothesized that knee flexion (KF) at initial contact (IC) and max would decrease in response to perturbations.

Methods

30 healthy adults (26.3±6.2 years, 15F) completed 9 DVJs, 3 under each condition: baseline (BW), static weight (SW), and perturbation weight (PW). The PW comprised 4.54kg of water in a Tidal Tank Hydrovest, donned across the upper back. The SW comprised 4.54 kg of metal affixed in a foam roll similarly attached to the Hydrovest. Jumps were done off a 30 cm box onto two force plates, and 3-D motion capture (9 Vicon Vero cameras, 300 Hz) was used to estimate kinematics. Mixed effects models compared differences between conditions KF at IC and max using SPSS.

Results

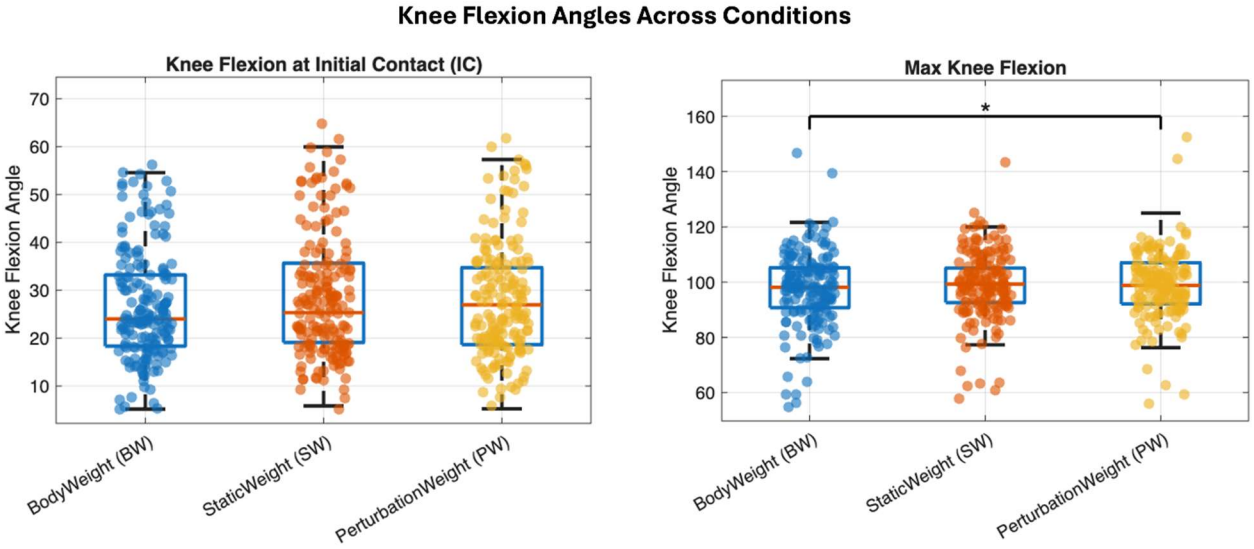
Significant effects of jump condition were found for KF max ($p=0.043$) but not for KF IC ($p=0.113$). Pairwise comparisons revealed significant differences between the BW and PW for max ($\Delta 1.7°$, $p=0.013$). KF angles increased across conditions (BW, SW, PW) for IC (26.8°, 27.9°, 28.6°) and max (97.6°, 98.6°, 99.3°).

Discussion

Previous research has linked dual tasking DVJs with stiffer landings as exhibited by decreased KF [2,3]. However, in this study we see KF increase with PW. This is the opposite of our hypothesis and may indicate that participants were anticipatorily softening their

landing in preparation for perturbations. Perturbations have promise in making DVJ testing more realistic, and future research should continue focusing on their effects.

Images (Optional)



References (Optional)

[1] Leppänen, Am J Sports Med, 2017; [2] Almonroeder, JOSPT, 2018; [3] Aflatounian, Orthop J Sports Med, 2025

Session Category

Human Motion and Performance: Sports

P1-340

Effects of Slip Events on Lower Extremity Biomechanics During Cutting Maneuvers in Collegiate Soccer Players

Mr. Noah Rauch[1], Dr. Brett Pexa[1], Mr. Garrett Hess[1], Dr. Jeffrey Taylor[1], Mr. Joseph Helseth[2], Dr. Kevin Ford[1]

[1]High Point University, High Point, NC, United States. [2]Nike Sport Research Lab, Beaverton, OR, United States

Introduction

There is limited information on lower extremity biomechanics during a slip when performing a sporting movement, such as a quick change-of-direction cut. A slip may lead to high-risk biomechanical movements, which may predispose athletes to injury. The purpose of this study was to determine the difference in lower extremity biomechanics between a slip versus a non-slip movement in collegiate soccer athletes.

Methods

Thirty competitive soccer players (15M, 15F; age: 20.8±1.2yrs), performed a 180-degree cutting task in a cleated condition (Nike Phantom GX II Elite Artificial Grass (AG)) on an infill turf surface. Kinematics were recorded with a 14-camera motion capture system (Qualisys AB, Göteborg, Sweden, 200 Hz), and kinetics were captured with two in-ground force plates (AMTI, Watertown, MA, USA, 1200 Hz). Slips were identified visually by anterior displacement of the center of gravity of the foot (relative to running approach direction in lab coordinate system) during the first 50% of ground contact time. Participants who had at least one slip and one non-slip trial were included for statistical analysis. Pairwise t-tests and Cohen's d effect sizes were used to compare the biomechanics between slip and non-slip trials.

Results

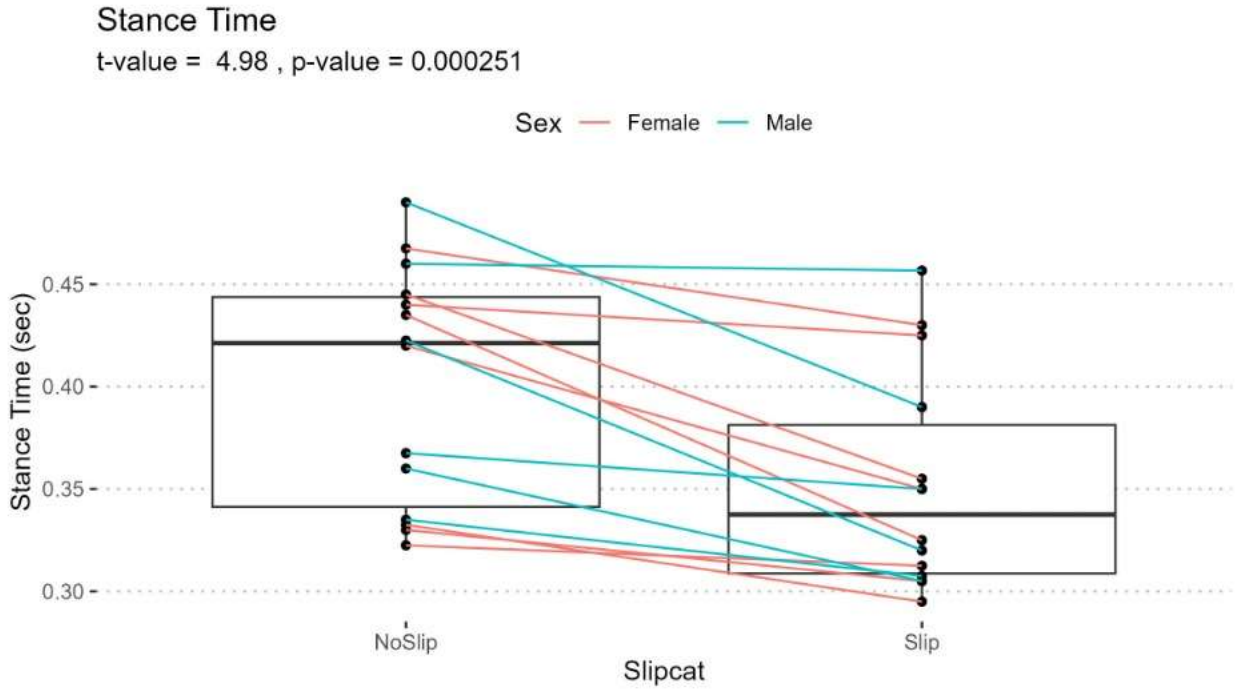
Fourteen participants had a slipping trial (8F, 6M). There was a significant difference in peak hip extension angle ($t=4.36$, $p<0.001$, $d=1.16$), peak knee extension angle ($t=-4.20$, $p=0.001$, $d=1.12$), and stance time ($t=4.98$, $p<0.001$, $d=1.33$) between slips and non-slips. Slip trials had increased hip and knee extension with a decreased stance time. When comparing kinetics, knee flexion moment at initial contact ($t=2.93$, $p=0.016$, $d=0.78$), peak hip abduction moment ($t=2.83$, $p=0.014$, $d=0.75$) and braking force ($t=2.73$, $p=0.016$, $d=0.73$) were significantly different between slips and non-slips. Slips

demonstrated decreased peak knee flexion moment at initial contact, decreased hip abduction moment, and increased peak braking force than non-slip trials.

Discussion

Slip trials significantly reduced stance time compared to non-slip trials, indicating that athletes likely adopt a rapid transition strategy to minimize potential deleterious effects. The altered biomechanics during the slip require further investigation on different surface and footwear conditions. Future footwear innovations targeting utilized traction may mitigate adverse effects during slip events.

Images (Optional)



Acknowledgements (Optional)

Funding and footwear provided by Nike.

Session Category

Human Motion and Performance: Sports

P1-341

Evaluation of Jump Height Variance in Collegiate Men Team Sport Athletes

Ms Noelle D Saine MS, CSCS, Dr Erica King PhD, Dr. Angela Miller Phd, Dr Margaret Jones PhD, CSCS*D

George Mason University, Fairfax, VA, United States

Introduction

Countermovement jumps (CMJs) are becoming more widespread in sport science settings to evaluate athlete readiness, recovery, and maximal power. There is conflicting literature in determining the best metric to evaluate athlete performance in team sport athletes. Although jump height (JH) remains the most commonly interpreted measure, limited research has examined how athletes achieve maximal performance through different CMJ phase strategies. Therefore, this study aims to quantify variance in JH across team sports and determine how phase-specific variables contribute to performance differences within each sport.

Methods

NCAA Division I men' athletes (n=201) from baseball (BASE, n=64), basketball (MBB, n=31), swimming (MSD, n=22), soccer (MSOC, n=31), volleyball (MVB, n=25), and wrestling (WREST, n=28) participated. Athletes performed routine CMJ testing over two years, where after a standardized warmup, each athlete completed 3 maximal effort CMJs on bilateral force plates. The jump with the maximal jump height (JH) from that session was recorded for analysis. To evaluate CMJ phase utilization eccentric peak power standardized by body mass (ECC) and concentric mean power standardized by body mass (CON) were analyzed in this model. On average, athletes completed 16 jump sessions, and a total of 3313 jump sessions were analyzed. Hierarchical linear modeling with random intercepts assessed the variation within and between individuals. MSOC athletes were used as the reference group as they recorded the lowest average JH. Both CMJ phase variables were grand mean centered.

Results

With average ECC and CON, MSOC had an average jump height of 39.09cm. BASE and MBB athletes did not significantly differ from men's soccer when ECC and CON were centered. As CON increases, MBB JH decreases ($\beta = -0.75$, $p<0.001$), MVB JH increases ($\beta = 0.80$, $p<0.001$), and WREST JH increases ($\beta = 0.30$, $p<0.01$). As ECC increases, MBB JH increases ($\beta = 0.16$, $p<0.001$), MVB JH decreases ($\beta = -0.30$, $p<0.05$) and WREST JH decreases ($\beta = -0.44$, $p<0.001$).

Discussion

Although jump heights may be similar, utilization of eccentric and concentric components varies across team sport athletes. These findings underscore the importance of individualized CMJ phase monitoring for optimizing training and rehabilitation in team sport athletes.

Images (Optional)

	Base Model		Model 2		Final Model	
Variable	β	SE	β	SE	β	SE
Intercept	35.01***	0.88	38.71***	0.59	39.53***	0.61
ECC_GMC			0.06***	0.02	0.09***	0.02
CON_GMC			0.88***	0.2	1.07***	0.03
BASE	5.70***	1.03	2.15**	0.69	1.34	0.72
MBB	3.66**	1.18	-2.2**	0.79	-1.59***	0.82
MSD	6.07***	1.33	3.99***	0.89	3.5***	0.92
MVB	2.68*	1.24	4.11***	0.83	7.64***	0.92
WREST	3.36**	1.29	1.46	0.87	1.33	1.09
CON_GMC X BASE						
CON_GMC X MBB					-0.75***	0.04
CON_GMC X MSD						
CON_GMC X MVB					0.8***	0.08
CON_GMC X WREST					0.3***	0.04
ECC_GMC X BASE						
ECC_GMC X MBB					0.16***	0.03
ECC_GMC X MSD						
ECC_GMC X MVB					-0.3***	0.06
ECC_GMC X WREST					-0.44***	0.09
Variance						
τ	17.37		7.41		8.76	
σ	12.80		6.45		4.76	
ICC	0.57		0.535		0.648	

Session Category

Human Motion and Performance: Sports

P1-342

Relationships Between Countermovement Jump Metrics and Fastball Pitching Metrics in Collegiate Baseball Athletes

Ms Noelle Saine MS, CSCS, Dr Erica King PhD, Dr Margaret Jones PhD, CSCS*D

George Mason University, Fairfax, VA, United States

Introduction

Countermovement jumps (CMJs) are becoming increasingly more prevalent in sport science programs to monitor sport performance and neuromuscular readiness. Previous studies have identified significant associations between CMJ performance and pitch velocity, suggesting that lower body power production can influence throwing performance. However, limited research exists examining same-day CMJ performance and fastball pitch performance.

Methods

National Collegiate Athletic Association DI baseball players (n=10 mean + SD; age: 21.35 + 1.76 years; body mass: 90.46 + 10.12 kg; height: 186.84 + 7.62 cm; body fat: 17.56 + 1.99 %) participated. Over two fall-ball weekends, the athletes had outings where they threw a minimum of 50% fastballs, and were considered to be primarily fastball pitchers. On the morning before play, all athletes completed 3 CMJs after a standardized warmup, four hours prior to the first pitch. CMJ metrics include variables derived from the eccentric and concentric phase of the jump, as well as performance outcome variables. All pitching data was recorded via radar-based tracking software. From this software, the following fastball pitching metrics were derived: spin rate, velocity, induced vertical break, and horizontal break. A Pearson correlation coefficient was conducted to determine relationships between the CMJ and the fastball metrics. Significance was set at $p < 0.05$.

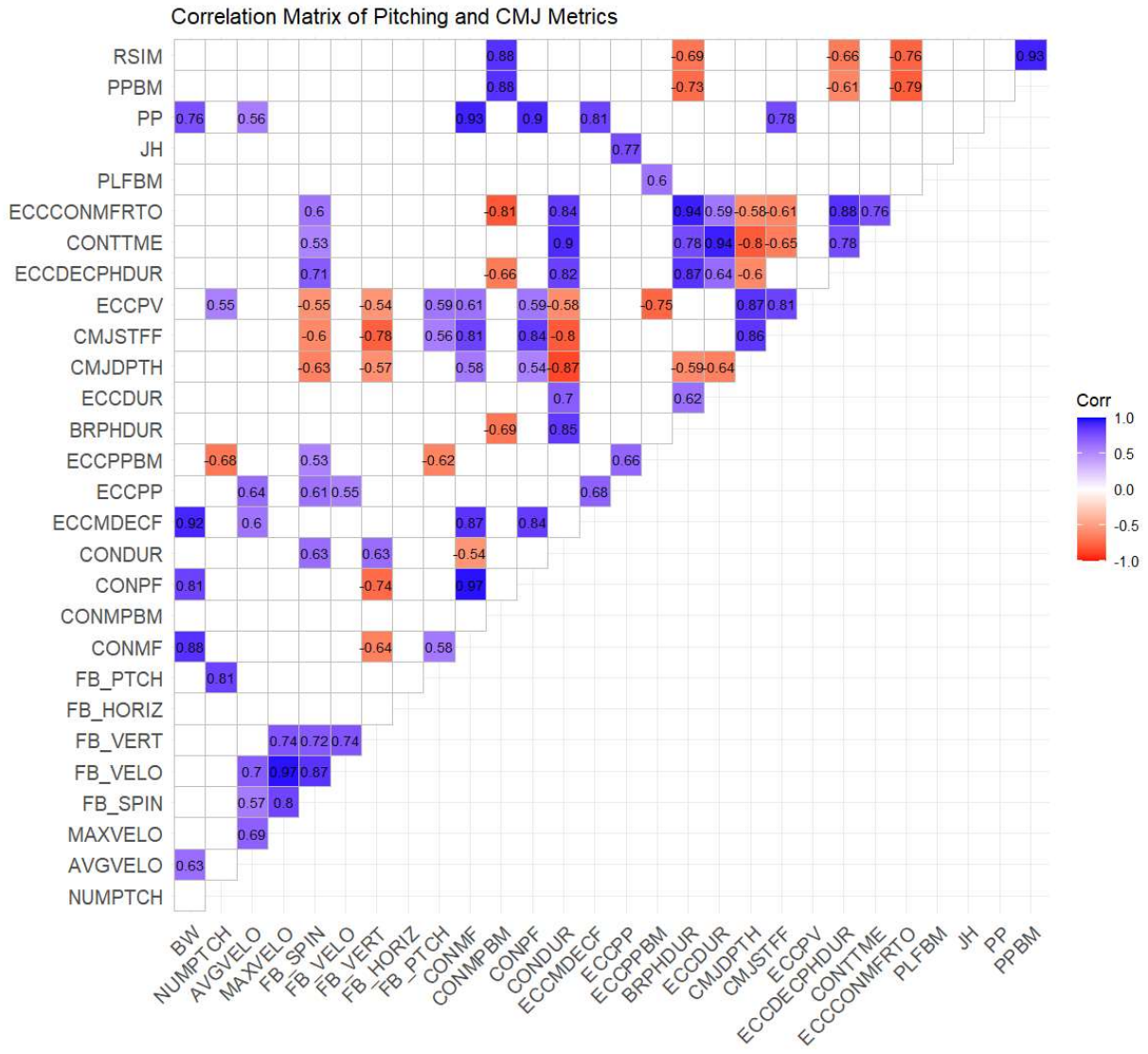
Results

Fastball velocity was significantly correlated with ECCPP (0.55, $p<0.05$). Fastball spin rate was significantly correlated with ECCDECPHDUR (0.71, $p<0.01$), CMJDPTH (-0.63, $p<0.05$), CONDUR (0.63, $p<0.5$), ECCPP (0.61, $p<0.05$), ECCCONMFRTO (0.60, $p<0.05$), CMJSTFF (-0.60, $p<0.05$), ECCPV (-0.55, $p< 0.05$), ECCPPBM (0.54, $p<0.05$), and CONTTME (0.53, $p<0.05$). Fastball induced vertical break was significantly correlated with CMJSTFF (-0.78, $p<0.01$), CONPF (-0.74, 0.01), CONMF (-0.64, $p<0.05$), CONDUR (0.63, $p<0.05$), CMJDPTH (-0.57, $p<0.05$), and ECCPV (-0.54, $p<0.05$). Horizontal break was not significantly correlated with any CMJ metrics.

Discussion

Same-day CMJ metrics are significantly correlated with fastball pitching metrics, highlighting the potential for utilization in decision-making for pitching staff outings. Future studies are needed to further explore the relationships between CMJ and fastball pitching metrics in larger samples and across competitive contexts.

Images (Optional)



Session Category

Human Motion and Performance: Sports

P1-343

In-Situ Horizontal Force Velocity Profiling in Wheelchair Rugby

Mr. Paul Lucas Spagnuolo M Sc.[1,2], Mr. Daniel Geneau M Sc.[1,2], Dr. Marc Klimstra PhD[1,2]

[1]University of Victoria, Victoria, British Columbia, Canada. [2]Canadian Sport Institute Pacific, Victoria, British Columbia, Canada

Introduction

In sport it is standard practice to assess athlete physical capacity. However, isolated testing sessions can be disruptive to training. Therefore, “invisible” or “in-situ” monitoring has emerged in recent years utilizing microtechnology.

As sprinting is important in invasion sports like soccer and rugby, horizontal force-velocity-power (hFVP) profiles, have received attention. In wheelchair sport there is evidence that hFVP can be generated from wheel-mounted IMU sensors. However, there are no studies with In-Situ FV profile development. Further, new approaches support the development of a complete sprint record from piece wise sprints during training and competition.

The goal of this project was to determine whether valid FV profiles can be derived using a single wheel-mounted IMU data collected during match and practice play from piece-wise developed sprints.

Methods

Wheelchair velocity was calculated using a wheel-mounted IMU during standalone sprints (40m) and continuous in-game and training movement from 4 national wheelchair rugby athletes. The data was then filtered using a 5th order lowpass Butterworth filter with a cutoff frequency of 0.15 Hz. A piecewise sprint was constructed using maximal onset acceleration across the entire continuous dataset at every 0.01m/s. The minimum time it would take the athlete to reach the next velocity bin was then computed. This process was repeated across an athlete's dataset. A sigmoid model was fit to both the piecewise and dedicated sprint to produce a FVP profile (Figure 1.). Interclass Correlation (2,1) (ICC) was used to compare FV outcomes.
Figure 1. Dedicated Sprint and Piecewise Sprint overlayed with respective sigmoid fits

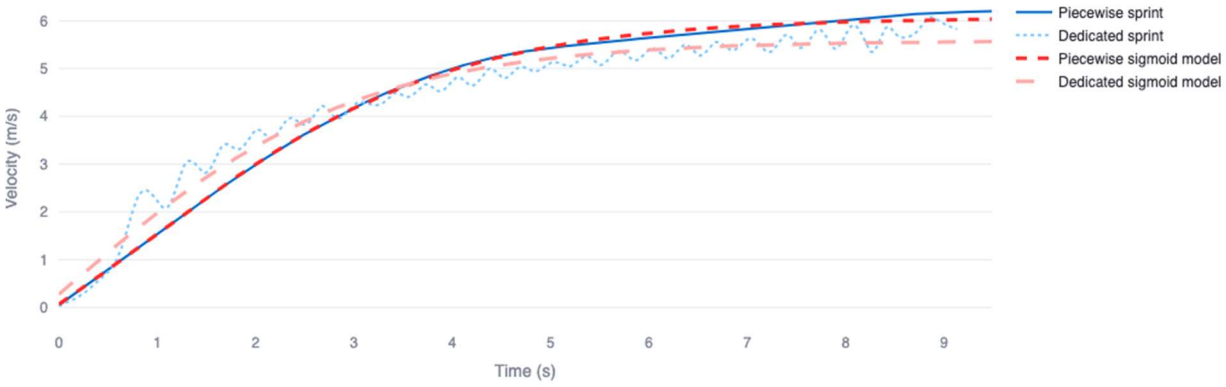
Results

Preliminary results suggest we can accurately predict theoretical maximum velocity (Vo) using these methods (R= 0.93). There was less correlation between the two methods in generating theoretical maximum force (Fo) (R = 0.65). We did not observe significant correlation between the FV Slope (R= -0.21).

Discussion

While Vo can be accurately predicted using current methods refinement of methods is required to predict Fo and FV slope. Through further development in-situ FV profiling in wheelchair sports may provide athletes and coaches accurate assessments without the need for isolated testing.

Images (Optional)



References (Optional)

Session Category

Human Motion and Performance: Sports

P1-344

Biomechanical Characteristics During High-Demand Functional Tasks in Females After Anterior Cruciate Ligament Reconstruction: A Systematic Review

Dr Peta Johnston, Dr Brodwen McBain, Professor Jodie McClelland, Professor Kate Webster

La Trobe University, Melbourne, Victoria, Australia

Introduction

Female athletes returning to sport after anterior cruciate ligament (ACL) reconstruction have a higher risk of reinjury compared to their uninjured female counterparts. Although numerous factors have been explored, the role of altered movement mechanics during high-demand functional tasks in females has received less attention.

The aims of this systematic review were to (1) identify the high-demand functional tasks most commonly studied, (2) describe biomechanical assessment methods and (3) synthesise lower limb movement patterns in females following ACL reconstruction.

Methods

A systematic review of the literature was conducted using four databases searched until 19th of March 2025 (Embase, MEDLINE, SportDiscus and PubMed). Inclusion required that participants were assessed post-operatively for at least one biomechanical variable during high-demand functional tasks, and that biomechanical data for the ACL reconstructed limb was compared with either the unaffected limb or healthy female counterparts. Meta-analysis with standardised mean differences (SMD) were performed for peak knee angles during the bilateral drop vertical jump.

Results

A total of 71 studies met inclusion criteria. Studies evaluated biomechanics during high-demand functional tasks between five months post ACL reconstruction surgery up to 13.4 years. The most frequently investigated tasks were the bilateral drop vertical jump (21 studies), followed by running/cutting manoeuvres (13 studies), and single leg forward hops (9 studies). During the bilateral drop vertical jump, studies consistently reported increased peak knee valgus angle in the ACL reconstructed limb compared with a healthy control group (SMD 0.59; 95% confidence interval [CI] 0.04 to 1.15). In contrast, no significant differences in the peak knee flexion angle were identified during the bilateral drop vertical jump between the ACL reconstructed limb and a healthy control group (SMD 0.10; 95% CI -0.70 to 0.91).

Discussion

These findings highlight persistent alterations in knee loading patterns in females after ACL reconstruction, particularly increased knee valgus during bilateral drop vertical jumps compared with healthy controls, a movement pattern repeatedly implicated in primary and second ACL injury risk. Recognising these sex-specific biomechanical characteristics may inform more targeted rehabilitation strategies to mitigate reinjury risk in female athletes.

References (Optional)

Session Category

Human Motion and Performance: Sports

P1-345

Biomechanical Modelling for Safety and Performance Enhancement of Running Footwear

Mr Pramod Yadav, Dr Arnab Chanda

Indian Institute of Technology Delhi, New Delhi, Delhi, India

Introduction

Running is one of the most widely practiced physical activities and a common entity in every sport. However, inadequate conditioning and improper technique frequently lead to injuries such as sprains and fractures. The design of footwear, particularly the insole and outsole, plays an important role in enhancing performance and preventing injuries by influencing lower limb biomechanics. While extensive research has been conducted on midsole behavior, limited studies have focused on how insole and outsole characteristics interact for traction, shock absorption, and overall injury risk. Key knowledge gaps include the biomechanics of progressive outsole wear and the combined influence of insole hardness, geometry, and thickness.

Methods

This study examines the traction performance of both worn and unworn running shoes, assesses the shock absorption during controlled jumping and gait tasks, and identifies design features that can improve running safety and performance. This study evaluated the traction performance of eighteen commonly used running shoes on two different track surfaces under controlled slipping conditions, including common surfaces such as ethylene propylene diene monomer (EPDM) and synthetic material-based track surfaces, in both wet and dry conditions. Further, to assess the impact of insoles on impact attenuation, vertical ground reaction forces (vGRF) were analyzed during jumping tasks.

Results

The results showed that footwear with modified hexagonal or block-based tread patterns and radial grooves produced the highest ACOF in both tracks and conditions. Additionally, a correlation analysis was conducted between ACOF and the apparent contact area, suggesting that these tread designs exhibit better resistance to synthetic surfaces due to their unique pattern. In Drop Jump, the maximum vertical reaction force was measured with and without cushioning (insole), and it was reduced by 12% with the insole. Similarly,

the vertical reaction force was significantly reduced by 35% in Counter Movement Jump with an insole compared to without an insole.

Discussion

Future work will incorporate real-time pressure mapping during Quattro Jump tasks to examine dynamic load distribution and cushioning performance. Overall, this work aims to support the development of novel footwear solutions that enhance traction, reduce injury risk, and improve performance, with direct applications for the athletic footwear industry.

Session Category

Human Motion and Performance: Sports

P1-346

Do Pitching Biomechanics Differ Between Windup and Stretch Pitching Deliveries from a Dirt Surface Mound In College Baseball Pitchers?

Dr Rafael Escamilla PhD, PT, CSCS, FACSM[1], Dr Jonathan Slowik PhD[2], Dr Rodney Imamura PhD[1], Dr Irwin Thompson EdD, PT[1], Dr Robert Asuncion DPT, PT[1], Dr Arnel Aguinaldo PhD, ATC, CSCS[3], Dr Glenn Fleisig PhD[2]

[1]California State University, Sacramento, Sacramento, CA, United States. [2]American Sports Medicine Institute, Birmingham, AL, United States. [3]Point Loma Nazarene University, San Diego, CA, United States

Dr Rafael Escamilla

Dr Jonathan Slowik

Dr Rodney Imamura

Dr Irwin Thompson

Dr Robert Asuncion

Dr Arnel Aguinaldo

Introduction

It's unknown how pitching biomechanics in college baseball pitchers differ between windup and stretch pitching deliveries from a dirt-surface-mound. The purpose was to assess differences in shoulder and elbow kinetics and pitching kinematics in college pitchers between windup-and-stretch pitching deliveries from a dirt-surface-mound. It was hypothesized that between windup and stretch pitching deliveries, there would be a

limited number of significant kinetic differences and a greater number of significant kinematic differences.

Methods

Eighteen college pitchers pitched from a dirt-surface-mound using windup-and-stretch pitching deliveries. Inclusion criteria included healthy pitchers who all employed both windup and stretch deliveries in baseball games, employed overhead or three-quarter pitching deliveries, and pitched exclusively on dirt mounds. All pitchers were tested using a 240-Hz, 12-camera motion-analysis-system, and 28 kinematic and 7 kinetic parameters were calculated. Paired t-tests (Benjamini-Hochberg adjusted $p < 0.05$) assessed biomechanical differences between windup-and-stretch deliveries.

Results

From Table 1, maximum shoulder horizontal adduction torque, maximum shoulder anterior force, maximum lead knee height, ball velocity at ball release, forward trunk tilt at ball release, maximum upper trunk angular velocity, maximum elbow extension angular velocity, and maximum shoulder internal rotation angular velocity were all significantly greater using a windup delivery compared to a stretch delivery, while pelvic drift at maximum lead knee height was significantly greater in a stretch delivery compared to a windup delivery.

Discussion

As hypothesized, of the 35 pitching biomechanical comparisons, just over a quarter of these (9 out of 35) resulted in significant differences between windup and stretch deliveries, with most of these kinematic differences. It can be concluded that pitching kinetics in college pitchers are more similar than different between windup and stretch pitching deliveries. More research is needed to assess if the greater shoulder force and torque generated in the windup compared to the stretch increases shoulder injury risk in the windup compared to the stretch. The kinematic differences found suggest that shoulder, elbow trunk, and pelvis pitching kinematics do differ some between windup and stretch deliveries. The results of this study are important in assessing how pitching biomechanics differ between windup and stretch deliveries from a dirt surface mound for college pitchers.

Images (Optional)

Table 1. Kinematic and kinetic significant differences* (adjusted $p < 0.05$) between windup and stretch.

	Windup (n=18)	**Stretch (n=18)**	**Unadjusted p-values**	**Adjusted p-values (*)**
Windup phase				
Max lead knee height (% height)	61±5	56±6	*p < 0.001*	**p = 0.001*
Pelvic drift at max lead knee height (cm)	14±4	18±4	*p = 0.005*	**p = 0.027*
Arm cocking phase				
Max upper trunk angular velocity (°/s)	1096±60	1084±57	*p = 0.006*	**p = 0.027*
Max shoulder horizontal add torque (N•m)	91.1±17.1	89.5±16.9	*p = 0.003*	**p = 0.019*
Arm acceleration phase				
Max elbow extension angular velocity (°/s)	2563±171	2520±183	*p =0.002*	**p =0.018*
Max shoulder internal rotation Ang vel (°/s)	6468±576	6341±614	*p = 0.008*	**p = 0.032*
Ball release				
Ball velocity (m/s)	35.1±1.1	34.8±1.1	*p = 0.001*	**p = 0.017*
Forward trunk tilt (°)	34±9	32±9	*p = 0.006*	**p = 0.027*

Session Category

Human Motion and Performance: Sports

P1-347

Knee Kinematics and Frontal Plane Habitual Motion Path Deviations Are Related to Rectus Femoris Muscle Oxygenation During a Fatiguing Run

Dr. Rebekah Pallone MS, PhD, Dr. Jake Hudgins MS, PhD, Miss Kimberly Nickerson BS, Mrs. Bridget Sopeña MS, Dr. Jennifer Sumner MS, PhD, Dr. Evan Day MS, PhD

Brooks Sports, Seattle, WA, United States

Dr. Rebekah Pallone

Dr. Jake Hudgins

Miss Kimberly Nickerson

Mrs. Bridget Sopeña

Dr. Jennifer Sumner

Introduction

Prolonged running induces muscular metabolic stress, potentially impacting neuromuscular support and increasing deviations from habitual motion paths (HMP; runner's typical joint movement patterns[1]). However, the link between muscular metabolic stress and HMP deviations during running is unknown. This study examined the relationship between running kinematics and muscle oxygenation (%SmO_2), which indicates muscle oxygen supply-demand balance. We hypothesized that during a fatiguing run, a more negative rectus femoris (RF) %SmO_2 slope (i.e., deteriorating oxygen supply-demand balance) would be associated with greater ranges of motion (ROMs) and HMP deviations at the knee.

Methods

Ten recreational runners (8M/2F; 41±12yr; 73±12kg; est. 5K: 23.4±4.0min) performed a 45-minute run at 88% of maximal metabolic steady state speed. Heart rate (HR) and RF %SmO_2 were collected continuously. %SmO_2 slope was calculated between 30% and 100% of the run to exclude exercise onset muscle oxygenation dynamics. Rating of perceived exertion (RPE), three-dimensional lower limb kinematics, and ground reaction forces were collected at the start and end of the run. HMP deviations were quantified according to Sumner et al.[1]. Start- to end-of-run changes in frontal (AbAd) and transverse (TIR) plane knee deviations and tri-planar ROMs were determined.

Results

HR rose from 139±9 to 168±11 bpm (p<0.001) and RPE rose from 9.0±1.8 to 16.3±2.1 (p<0.001), indicating increased physiological stress. Linear mixed-effects modeling revealed a more negative RF %SmO_2 slope was significantly associated with greater decreases in flexion ROM (p<0.001), and greater increases in AbAd ROM (p<0.001), AbAd deviation (p≤0.002), and TIR ROM (p=0.034), but not TIR deviation (p≥0.307).

Discussion

Reduced ability of the RF to maintain oxygen supply-demand balance (negative %SmO_2 slope) during prolonged running was related to decreased sagittal ROM, increased frontal and transverse ROMs, and frontal deviation from HMP at the knee. The observed response may indicate that muscular fatigue of the RF leads to reduced neuromuscular support of the knee joint and altered movement patterns. Though further work is needed to confirm causal relationships, these findings may provide a physiological basis for targeted interventions aimed at reducing injury risk in fatigued runners.

References (Optional)

[1] Sumner et al., Footwear Sci, 2024.

Session Category

Human Motion and Performance: Sports

P1-348

Going Out on a Limb – Effect of Limb Dominance and Sport on ACL Injury Relevant Biomechanics During Cutting and Landing Maneuvers Among Female Canadian University Athletes

Mr. Reid Vander Vleuten PhD Candidate, MScPT[1,2], Dr. Meghan Critchley PhD[3], Ms. Reyna Crawford MSc[2], Mr. Chris Rusling PhD Candidate, MSc[3], Dr. John Wannop PhD[2], Dr. Matthew J. Jordan PhD[1,2,4], Dr. Tron Krosshaug PhD[5], Dr. Kati Pasanen PhD[1,2,4,6]

[1]Integrative Neuromuscular Sport Performance Laboratory, Faculty of Kinesiology, University of Calgary, Calgary, Alberta, Canada. [2]Human Performance Laboratory, Faculty of Kinesiology, University of Calgary, Calgary, Alberta, Canada. [3]Sport Injury Prevention Research Center, Faculty of Kinesiology, University of Calgary, Calgary, Alberta, Canada. [4]McCaig Institute for Bone and Joint Health, University of Calgary, Calgary, Alberta, Canada. [5]Oslo Sports Trauma Research Center, Norwegian School of Sport Sciences, Oslo, Østlandet, Norway. [6]Tampere Research Center of Sports Medicine, UKK Institute, Tampere, Pirkanmaa, Finland

Introduction

Female athletes have a 4-6x greater risk of non-contact anterior cruciate ligament (ACL) injury than males [1], potentially due to biomechanical patterns including increased knee joint loading, greater knee valgus, and reduced flexion during cutting and landing [2,3]. How limb dominance and sport influence these biomechanics during these tasks remains understudied. Therefore, we investigated the effects of limb dominance and sport on ACL injury relevant biomechanics during sport-specific maneuvers in female university soccer and basketball athletes.

Methods

Female university soccer (n=23, age=20.07years, height=1.67m, weight=63.47kg) and basketball (n=12, age=20.23years, height=1.77m, weight=74.29kg) athletes completed four tasks: 180° pivot-turn, 90° cut, single-leg drop jump, and a sport-specific heading/rebound task with a 45° cut on landing. 3-D motion capture and force plates measured three trials per leg and task. Inverse dynamics calculated peak external knee abduction (pKAM), internal rotation (pKIRM) and flexion moments (pKFM), knee valgus and flexion angles (peak and initial contact), and peak resultant ground reaction force within 100 ms of ground contact. A 2×2 mixed ANOVA statistically analyzed the effects of limb (within-subject) and sport (between-subject) effects on all variables (a = 0.05).

Results

A main effect of sport revealed greater pKAM in soccer athletes during cutting tasks, and basketball athletes during the heading/rebound task. Limb main effects indicated greater non-dominant limb pKIRM for all tasks, and greater knee flexion at initial contact for the single-leg drop jump. Significant interaction effects in the heading/rebound task showed basketball athletes exhibited greater non-dominant pKFM and knee valgus at initial contact. Meanwhile, soccer athletes demonstrated greater non-dominant limb pKIRM and lesser knee flexion at initial contact.

Discussion

Limb dominance and sport significantly influenced ACL injury relevant biomechanics in female university athletes. Main and interaction effects highlighted riskier non-dominant limb cutting and landing mechanics associated with ACL injury. As sport also influenced biomechanics, perhaps sport-specific demands, training history, and anthropometric characteristics partially drive these differences. Future studies may consider these variables when aiming to modify ACL injury relevant biomechanics.

Images (Optional)

Table 1: Significant Main and Interaction Effects of Limb Dominance and Sport on ACL Injury Relevant Biomechanical Variables

Task	Variable	Soccer D Mean (SD)	Soccer ND Mean (SD)	Basketball D Mean (SD)	Basketball ND Mean (SD)
180° Pivot Turn	pKAM (Nm/kg)*	0.73 (0.24)	0.69 (0.15)	0.48 (0.26)	0.58 (0.24)
	pKFM (Nm/kg)*	1.95 (0.54)	1.99 (0.39)	2.25 (0.54)	2.28 (0.54)
	pKIRM (Nm/kg)†	0.14 (0.15)	0.31 (0.09)	0.22 (0.11)	0.32 (0.14)
90° Cut	pKAM (Nm/kg)*	0.70 (0.24)	0.67 (0.27)	0.50 (0.27)	0.52 (0.38)
	pKFM (Nm/kg)*	2.56 (0.48)	2.63 (0.50)	3.05 (0.52)	2.96 (0.42)
	KFA at IC (°)*	23.07 (6.59)	20.24 (5.72)	26.50 (6.45)	28.07 (4.17)
	pKIRM (Nm/kg)†	0.13 (0.17)	0.30 (0.11)	0.21 (0.11)	0.32 (0.14)
Heading/ Rebound Task	pKAM (Nm/kg)*	0.48 (0.26)	0.43 (0.29)	0.80 (0.46)	0.61 (0.45)
	pKFM (Nm/kg)*§	3.07 (0.75)	2.92 (0.82)	3.39 (0.54)	4.01 (0.47)
	KVA at IC (°)†*§	0.42 (3.32)	-4.18 (5.34)	2.94 (2.19)	2.31 (2.52)
	KFA at IC (°)*§	9.92 (6.66)	4.35 (7.38)	12.60 (5.75)	12.95 (5.89)
	pKIRM(Nm/kg)†§	0.04 (0.08)	0.22 (0.12)	0.13 (0.12)	0.20 (0.13)
SLDJ	KFA at IC (°)†*	19.91 (7.47)	21.08 (6.12)	20.33 (14.61)	26.05 (8.53)
	pKIRM (Nm/kg)†	-0.002 (0.04)	0.04 (0.04)	0.04 (0.02)	0.05 (0.05)

† = significant limb-dominance main effect, * = significant sport main effect, § = significant interaction effect. SLDJ = Single leg drop jump task, pKAM = peak knee abduction moment, pKFM = peak knee flexion moment, pKIRM = peak knee internal rotation moment, KFA = knee flexion angle, KVA = knee valgus angle, IC = initial contact. D = Dominant Limb, ND = Non-Dominant Limb
Level of significance set at $p = 0.05$ with Bonferroni-adjusted pairwise comparison.

References (Optional)

[1] Agel *et al*. *Clinical J Sports Med*, 2016

[2] Donelon *et al*. *Am J Sports Med*, 2024

[3] Dennis *et al*. *J Biomechanics*, 2023

Acknowledgements (Optional)

Thank you to the University of Calgary Women's Soccer and Basketball team for their involvement in the study.

Session Category

Human Motion and Performance: Sports

P1-349

Supporting Ankle Angle Differences During Roundhouse Kicks at Two Heights

Miss Renee Alexander, Dr Timothy Derrick

Iowa State University, Ames, Iowa, United States

Introduction

Olypmic taekwondo sparring awards additional points for kicks to the head compared to kicks to the chest. Higher roundhouse kicks have been found to increase pelvic tilt, hip internal rotation, and maximum distal knee joint flexion [1, 2]. However, there is limited research on the supporting leg during martial arts kicks to varying heights and even less on the supporting ankle during martial arts kicking. It was hypothesized that kicking higher would change tibiotalar and subtalar ankle angles at the supporting foot.

Methods

Twenty-six black belts in kicking martial arts were recruited for the study. Marker clusters were placed on both legs and on the left ankle and foot. Ground reaction forces (AMTI, 1125 Hz) and 3D kinematics (12 camera Qualisys system, 225 Hz) were collected during five trials of roundhouse kicks to a paddle held at hip height and then at neck height. Trials were trimmed based on when the kicking foot left and then returned to the ground. Subtalar and tibiotalar angles were derived based on the relative motion of their segment markers using helical angles. SPM with an alpha of 0.05 was used to statistically compare between heights.

Results

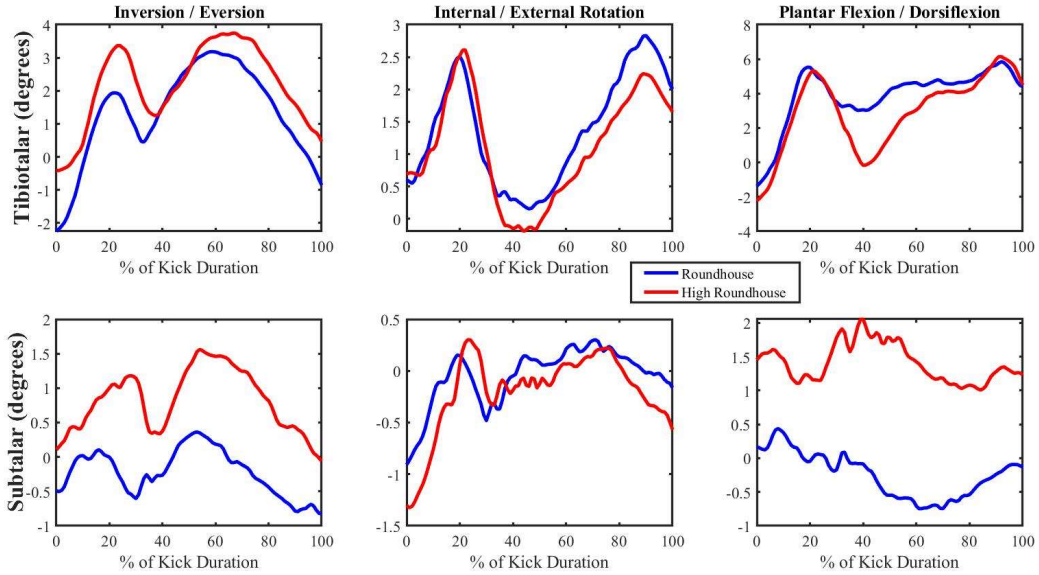
Tibiotalar inversion angles generally increased with kick height (Figure 1). Tibiotalar internal rotation increased between about 19% to 32% of the kick duration. From 32% of the kick to the end of the kick, internal rotation at the tibiotalar joint was decreased with increased height. A higher kicking target increased tibiotalar plantar flexion, but decreased dorsiflexion. Dorsiflexion and inversion angles were increased at the subtalar joint when kicking higher. Internal and external rotations at teh subtalar joint remained similar between both conditions. No statistically significant differences were found between conditions using SPM.

Discussion

Inversion/eversion and dorsiflexion/plantar flexion angles were observed to have changed at the tibiotalar and subtalar joints of the supporting ankle when the kick height was

increased, while any changes were less prevalent for internal/external rotation. Further testing and analysis is needed to evaluate differences at the supporting ankle joints.

Images (Optional)



References (Optional)

[1] Jaewoong Kim, Dissertation, 2010

[2] Tsun-Te Liu et. al., *Int J Perf Analy Spor*, 2021

Session Category

Human Motion and Performance: Sports

P1-350

Muscle Coordination Effects On Pedal-Force Direction and Mechanical Effectiveness During Incremental Stationary Cycling

Mr Reza Ahmadi, Dr Shahram Rasoulian, Dr Walter Herzog, Dr Amin Komeili

University of Calgary, Calgary, AB, Canada

Introduction

Cycling performance and joint loading depend not only on how much force is produced, but also on where and in what direction forces are applied across the crank cycle. The correlation between the ratio of the tangential component to the resultant force, or index of effectiveness (IE) [1], and muscle coordination has not been studied across different power levels.

Methods

Twenty healthy adult amateur cyclists (male/female=8/12, age 22.6±4.5 years), performed an incremental step test on a stationary bike at three intensities: the lowest power level (LPL), the middle power level (MPL), and the highest power level (HPL) at 70 RPM. EMG from 6 lower-limb muscles was synchronized with crank angle and 3D pedal reaction forces. EMG was processed to linear envelopes and normalized to a dynamic maximum. Tangential (F_t) force component was computed using standard pedal-force decomposition approaches [2], and IE = F_t / |$F_R$esultant| was calculated within crank-angle bins. Muscle coordination of the ankle joint was quantified by using the coactivation index (CI) as a ratio of agonist to antagonist pairs relevant to ankle control [3].

Results

IE increased with intensity for both limbs ($p < 0.05$). Dominant- non-dominant IE (mean±SD) was 0.32±0.14 - 0.26±0.14 (LPL), 0.59±0.07 - 0.63±0.08 (MPL), and 0.76±0.05 - 0.76±0.07 (HPL). Ankle CI also increased with exercise intensity ($p < 0.05$): 0.19±0.09 - 0.16±0.06 (LPL), 0.23±0.07 - 0.19±0.07 (MPL), and 0.33±0.11 - 0.27±0.09 (HPL). Post-hoc tests indicated significant increases from HPL compared with LPL and MPL ($p < 0.05$). Phase-specific patterns suggested that higher ankle CI coincided with relatively greater tangential force contribution and higher IE.

Discussion

These preliminary results suggest that mechanical effectiveness increased with power level. Since the ankle joint is an extensor joint in cycling, increasing CI reflects its adaptation to higher exercise intensities. Conducting the CI analysis on knee and hip

joints may provide an interpretable target for real-time biofeedback to improve effective force application while maintaining stability.

Images (Optional)

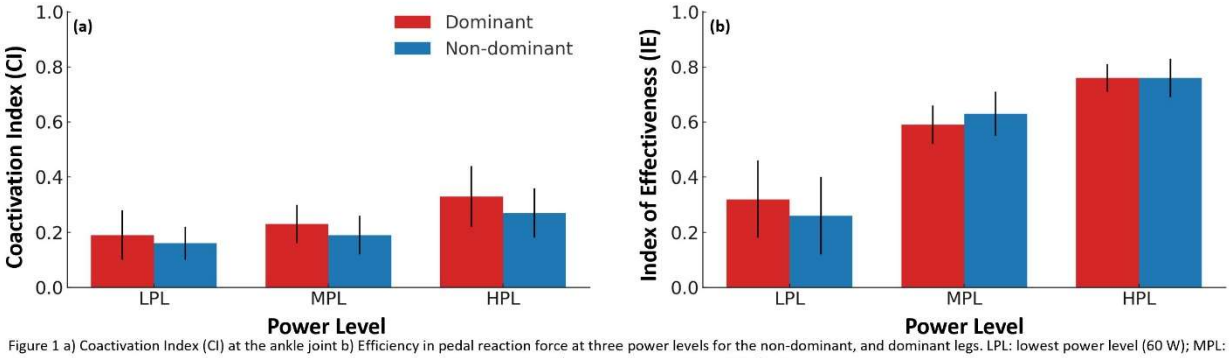


Figure 1 a) Coactivation Index (CI) at the ankle joint b) Efficiency in pedal reaction force at three power levels for the non-dominant, and dominant legs. LPL: lowest power level (60 W); MPL: middle power level (midway between LPL and HPL); HPL.

References (Optional)

[1] Bini RR et al., J Sci Cycling. 2013.

[2] Hull ML et al., J Biomech. 1985

[3] Latash et al., J Neurophysiol. 2018

Session Category

Human Motion and Performance: Sports

P1-351

Influence of Attentional Cues on Inter-Limb Biomechanics During the Rear Foot Elevated Split Squat

Mr. Ryan Burke[1], Mr. Morgan Murray[1], Dr. Stain Larsen[2], Dr. Erik Hummer[1]

[1]Rutgers, The State University of New Jersey, New Brunswick, NJ, United States. [2]AFPT, Fredrikstad, Ostfold, Norway

Introduction

INTRODUCTION: This study aimed to investigate how different attentional focus cues influence acute responses in vertical ground reaction forces (vGRF) and lower-extremity muscle action potentials measured via surface electromyography (sEMG) of resistance-trained individuals during the rear foot elevated split squat (RFESS).

Methods

METHODS: 20 individuals (10F; 23.2 ± 4.2 yrs; 169.8 ± 8.8 cm; 74.6 ± 13.7 kg) completed 2 sets of the RFESS at 10 RM load emphasizing either their front or rear limb to complete the task. Synchronous collection of vGRF data sEMG amplitudes of the rectus femoris (RF), vastus medialis (VM), vastus lateralis (VL), biceps femoris (BF), semitendinosus (ST), and medial gastrocnemius (MG) were collected. A 2 × 2 (limb × attentional focus cue) repeated-measures multivariate analysis of variance was conducted on key outcomes ($\alpha = 0.05$).

Results

RESULTS: A significant main effect of limb was observed ($F = 68.405$, $p<0.001$, $\eta_P^2=0.855$). Further statistical assessment found significant differences between limbs (Front – Rear) for average vGRF (mean difference [MD] = 779.01 N, $p<0.001$, d=4.9) and for the average normalized sEMG amplitude for the following: BF (MD = 0.392, $p<0.001$, d=1.8), MG (MD = 0.050, $p<0.001$, d=1.0), ST (MD = 0.333, $p<0.001$, d=1.4), VL (MD = 0.098, $p<0.001$, d=1.2), and VM (MD = 0.116, $p<0.001$, d=0.9) but not for RF (MD = 0.031, $p=0.116$, d=0.1).

Discussion

DISCUSSION: Directing individuals to emphasize the use of a specific limb did not elicit any statistically relevant responses in primary outcomes. More structured or objective feedback to enhance the verbal cue may be necessary for individuals to adopt significantly altered movement pattern during the RFESS. We did find a significant effect of limb on all key outcomes despite the average normalized sEMG amplitude for the RF. The average normalized sEMG for the BF, ST, MG, VM, and VL displayed decreased activation in the rear limb, supporting the notion of the rear limbs' role aiding in stabilization. The non-

significance found in the RF may be indicative of a similar degree of action potential activity in this bi-articular muscle in the rear limb compared to front limb.

Session Category

Human Motion and Performance: Sports

P1-352

Does Box Height During the Rear Foot Elevated Split Squat Impact Lower Extremity Biomechanics?

Mr. Ryan Burke[1], Mr. Morgan Murray[1], Dr. Stian Larsen[2], Dr. Erik Hummer[1]

[1]Rutgers, The State University of New Jersey, New Bunswick, NJ, United States. [2]AFPT, Fredrikstad, Østfold, Norway

Introduction

This study aimed to investigate how different rear foot heights (40 and 28 cm) impact vertical ground reaction forces (vGRF) and average normalized surface electromyography (sEMG) amplitudes in the lower extremities of resistance-trained individuals the rear foot elevated split squat (RFESS).

Methods

19 individuals (9F;23.2 ± 4.2 yrs;169.8 ± 9.0 cm;75.0 ± 13.4 kg) completed two sets of the dumbbell RFESS (40 cm and 28 cm heights, 10-RM load). Synchronous collection of 3D kinetics (1200 Hz, AMTI) and bilateral lower extremity muscle action potentials (1200 Hz, Delsys Inc.) for the biceps femoris (BF), semitendinosus (ST), medial gastrocnemius (MG), vastus lateralis (VL), vastus medialis (VM) and rectus femoris (RF) were conducted. sEMG data was processed using a linear envelope and normalized to the peak sEMG amplitude during a countermovement jump. A 2×2 (limb×height) repeated-measures multivariate analysis of variance was conducted with a *priori* alpha set to 0.05.

Results

No significant interaction ($F = 0.333$, $p=0.936$, $\eta_P^2=0.034$) or main effect of height ($F = 0.092$, $p=0.999$, $\eta_P^2=0.010$) were found but, a main effect of limb was demonstrated ($F = 84.693$, $p<0.001$, $\eta_P^2=0.900$). Further assessment found significant differences for vGRF (mean difference [MD] = 791.38 N, $p<0.001$, d=5.1) and for the average normalized sEMG amplitude for the following: BF (MD = 0.294, p 0.001, d=1.9), MG (MD = 0.052, $p<0.001$, d=1.3), ST (MD = 0.285, $p<0.001$, d=1.7), VL (MD = 0.105, $p<0.001$, d=1.0), and VM (MD = 0.099, $p<0.001$, d=1.1) but no statistical significance for the RF (MD = 0.004, $p=0.835$, d=0.4).

Discussion

The differences in height may not have been relevant enough to elicit notable changes in key variables. Additionally, rear foot heights exceeding 40cm were not assessed and merit further investigation with implications for lower extremity bi-articular musculature. The front limb displayed significantly greater average vGRF and average normalized sEMG amplitude of all lower extremity muscles apart from the RF. This may indicate that the RF plays a larger role in the stabilization of the rear limb during the RFESS. However, further

analysis is needed to draw more concrete conclusions. Future studies exploring muscle forces derived from muscle activation dynamics may provide additional insight.

Session Category

Human Motion and Performance: Sports

P1-353

Effects of Running Shoe Midsole Compliance on Running Performance

Mr. Ryan Knowles, Dr. Rachel Robinson, Dr. Alex Denton, Dr. Mike Hahn

University of Oregon, Eugene, OR, United States

Introduction

Modern running shoe parameters can enhance an athlete's biomechanical and physiological performance [1]; however, the independent and collective effects of midsole stiffness and bending stiffness remain unclear. Midsole stiffness alone [2] or the combined effect of midsole stiffness and longitudinal bending stiffness [3] can enhance running performance by improving running economy through the storage and return of elastic strain energy during ground contact. Thus, the purpose of this study was to examine the impact of running shoe midsole stiffness on running mechanics and metabolic cost of transport (MCOT) using musculoskeletal modeling and computer simulation. It was hypothesized that a more compliant midsole would lower MCOT.

Methods

Preliminary work generated predictive simulations of a stride of running (3.16 m/s) in OpenSim Moco [4] with a sagittal plane model [5]. The goal of the optimal control problem was to minimize the sum of cubed muscle excitations. Ground contact elements were calibrated to match the industry-tested stiffness of a neutral baseline running shoe and varied -75-100% of baseline. Each solution was used to estimate whole-body and muscle-specific MCOT [6].

Results

The data displayed a U-shaped relationship between midsole stiffness and MCOT (R^2 = 0.88) (Figure 1). Midsole stiffness 50% lower than baseline minimized MCOT and lowered whole-body MCOT by 1%. Lower whole-body MCOT was driven by lower hip (2.7% decrease) and knee (1.6%) extensor muscle-specific costs.

Discussion

A relatively compliant midsole was beneficial for lowering whole-body metabolic energy cost by lowering the demand on metabolically expensive muscle groups, but had no impact on more economical muscle groups, such as the plantar flexors. Running shoes with compliant midsoles should be considered for endurance efforts to enhance performance. Further investigation is required to characterize individual responses to

midsole stiffness. This work is being expanded using a 3-D musculoskeletal model paired with experimental data from a cohort of distance runners.

Images (Optional)

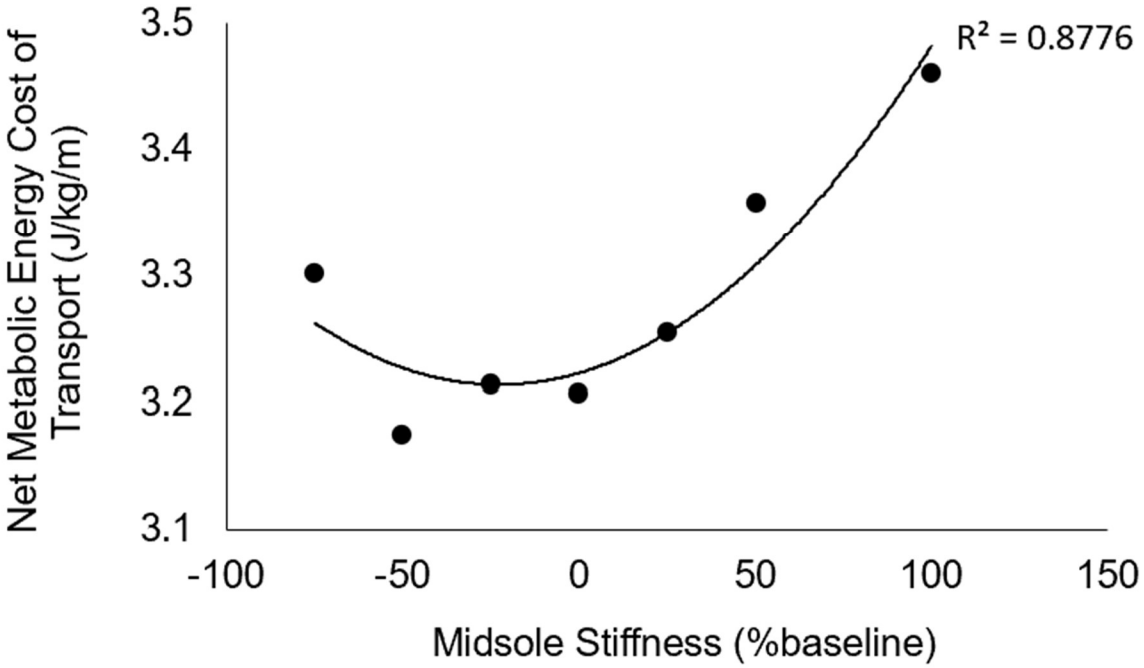


Figure 1. The net metabolic energy cost of transport during running with variable midsole stiffness (-75%-100%) relative to the baseline condition (0%).

References (Optional)

[1] Hoogkamer et al., Sports Med, 2018 [2] Healey et al., JSHS, 2022 [3] Stephen et al., JSHS, 2025 [4] Dembia et al., PLos Comput Biol., 2020 [5] Nguyen et al., IEEE TNSRE, 2019 [6] Bhargava et al., J Biomech, 2004

Session Category

Human Motion and Performance: Sports

P1-354

Competitive Level Influences Performance of Double Figure Skating Jumps

Ms. Sarah Trager Ridge PhD[1], Ms. Mia Caminita PhD[2], Ms. Elizabeth Klemm MS[3], Mr. Dustin Bruening PhD[4], Mr. Michael Jones PhD[4]

[1]University of Hartford, West Hartford, CT, United States. [2]Children's National Hospital, Silver Spring, MD, United States. [3]East Carolina University, Greenville, NC, United States. [4]Brigham Young University, Provo, UT, United States

Introduction

Success in competitive singles figure skating requires the performance of high-quality jumps. Historically, coaches and skaters have honed technique based on a combination of experience, trial and error, and the application of fundamental biomechanical principles. The current availability and quality of wearable devices now allow researchers to quantify jump performance and optimize technique for performance and injury prevention. The purpose of this study was to compare how skaters of different competitive levels perform multiple rotation jumps.

Methods

Fifty-six figure skaters wore a waist-mounted IMU as they performed 222 double rotation jumps. Synchronized high speed video was collected to identify take-off and landing events, jump type, and whether the jump was fully rotated. Key performance metrics (KPM) were calculated from the gyroscope. Groups were created based on skaters' US Figure Skating competition levels - Elite = Junior or Senior international (12 skaters/32 jumps); High = Novice, Junior, or Senior domestic (25 skaters/118 jumps); Low = Preliminary, Juvenile, or Intermediate, (19 skaters/71 jumps). KPM were compared between groups using ANOVAs followed by Tukey pairwise post-hoc tests ($\alpha<0.05$).

Results

Air time (t-air) and rotations completed (R#) increased with skater level, while peak angular velocity (ω-p) decreased (Figure 1). For these three variables, all pairwise comparisons were significant, except for R# between elite and high levels. Timing variables were not different among levels.

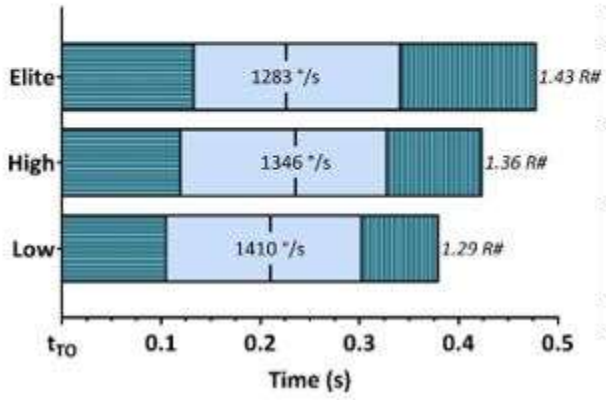
Discussion

Higher-level skaters who are able to successfully complete triple jumps performed their double jumps differently than lower-level skaters, primarily driven by their greater t-air. Theoretically, they could perform doubles either through a more open body position or by

altering timing, for instance completing the required rotations earlier to prepare for landing. Our results suggest that they typically choose the former, in line with a prior study showing similar timing control despite using a tool to increase rotation speed [1]. In contrast, lower-level skaters with lower t-air must rotate faster. This suggests that increasing t-air is a critical developmental step prior to attempting additional rotations (e.g. progressing from double to triple jumps). Using this type of objective data could increase training efficiency and, by extension, decrease injury risks.

Images (Optional)

Figure 1: Group average KPM during all double jumps (excluding Axels). The horizontal bars represent air time (t-air) and are split into intervals based on the timing of angular velocity events. The middle light shaded area includes peak angular velocity (ω-p, broken vertical line) and represents the time the skater is above 90% w-p. The darker horizontal and vertical striped areas represent periods leading up to (t+90) and dropping below (t-90) this threshold (both events expressed as % t-air). The number to the right of each bar represents the average number of rotations completed (R#) during the double jumps.



	t-air	ω-p	R#	t+90	t-90
Elite	0.48 ± 0.08	1283 ± 100	1.43 ± 0.19	27.6 ± 17.9	72.4 ± 20.2
High	0.42 ± 0.06	1346 ± 110	1.36 ± 0.18	28.9 ± 19.7	78.4 ± 21.8
Low	0.38 ± 0.06	1410 ± 127	1.29 ± 0.19	28.4 ± 18.0	80.5 ± 21.2
p	<0.001	<0.001	<0.001	0.936	0.203

References (Optional)

Sarah Ridge *et al.*, Sports Biomechanics, 2022

Session Category

Human Motion and Performance: Sports

P1-355

Comparison of Spatiotemporal Characteristics with Marker-Based and Markerless Motion Capture for Sport Motion Analysis: A Pilot Study

Miss Scarlett Farrar[1,2], Miss Farah Azim BASc[1], Ms Diane Wickenheiser BScPT[1], Ms Ayli Berson MPT[3], Ms Karen Davies MSc[1,4], Dr. Lise Leveille MD, PhD, FRCSC[1,5,6,3], Dr. Timothy Bhatnagar PhD[1,5,6]

[1]The Motion Lab, BC Children's Hospital, Vancouver, British Columbia, Canada. [2]School of Biomedical Engineering, UBC, Vancouver, British Columbia, Canada. [3]Department of Orthopedics, BC Children's Hospital, Vancouver, British Columbia, Canada. [4]Department of Physical Therapy, Faculty of Medicine, UBC, Vancouver, British Columbia, Canada. [5]Research Institue, BC Children's Hospital, Vancouver, British Columbia, Canada. [6]Department of Orthopedics, Faculty of Medicine, UBC, Vancouver, British Columbia, Canada

Introduction

The Motion Lab (TML), BC Children's Hospital conducts clinical motion analysis following anterior cruciate ligament reconstruction (ACLr) to evaluate readiness to return to sport, using parameters including spatiotemporal characteristics [1]. Comparisons of marker-based versus markerless motion capture (MoCap) quantifying gait parameters have been studied showing reliable agreement [2]. These comparisons are underexplored for sport assessments, particularly in paediatrics. This study compares marker-based and markerless MoCap for measuring spatiotemporal characteristics in paediatric sport assessments following ACLr.

Methods

For this non-randomized cross-sectional study, participants were divided into two groups: >9 months post–ACLr, referred for sport assessment; and control population with no injury history. Retro-reflective markers were placed on anatomical landmarks and participants followed the PRiSM Sports Protocol [3]. Marker-based and markerless data was collected simultaneously using Qualisys MoCap system (12 Oqus, 12 Miqus cameras). Marker-based data was processed in QTM and markerless data using Theia for the same activity trials. Data was analyzed with Visual3D to calculate spatiotemporal characteristics, including single leg hop distance normalized to height (SLHDH) and limb symmetry index (LSI). Metrics were compared between MoCap techniques and groups.

Results

Participants in post-ACLr (n=4, 3 female, 3 left ACLr) were mean 15.7y (sd=1.6) and the control (n=2, 2 female) were mean 15.9y (sd=0.7). For post-ACLr, mean LSI for marker-based and markerless, was 95.83% (sd=2.76) and 96.08% (sd=2.71) (Figure 1). For the control, mean LSI for marker-based and markerless, was 99.76% (sd=5.09) and 100.05% (sd=3.27) (Figure 1). Mean SLHDH of post-ACLr for marker-based and markerless, was 88.37% (sd=15.78) and 88.37% (sd=15.48). For the control, mean SLHDH for marker-based and markerless, was 80.49% (sd=5.25) and 80.57%(sd=4.63). Average difference between marker-based and markerless LSI post-ACLr was 0.40% (sd=0.29) and control 1.82% (sd=0.29). For SLHDH post-ACLr was 0.52% (sd=0.25) and control 0.55% (sd=0.51).

Discussion

Preliminary results show minimal differences in the LSI and SLHDH between MoCap techniques. There is a greater difference in LSI between techniques for the control compared to post-ACLr. Additional participants are required to further explore the relationship between MoCap techniques and groups.

Images (Optional)

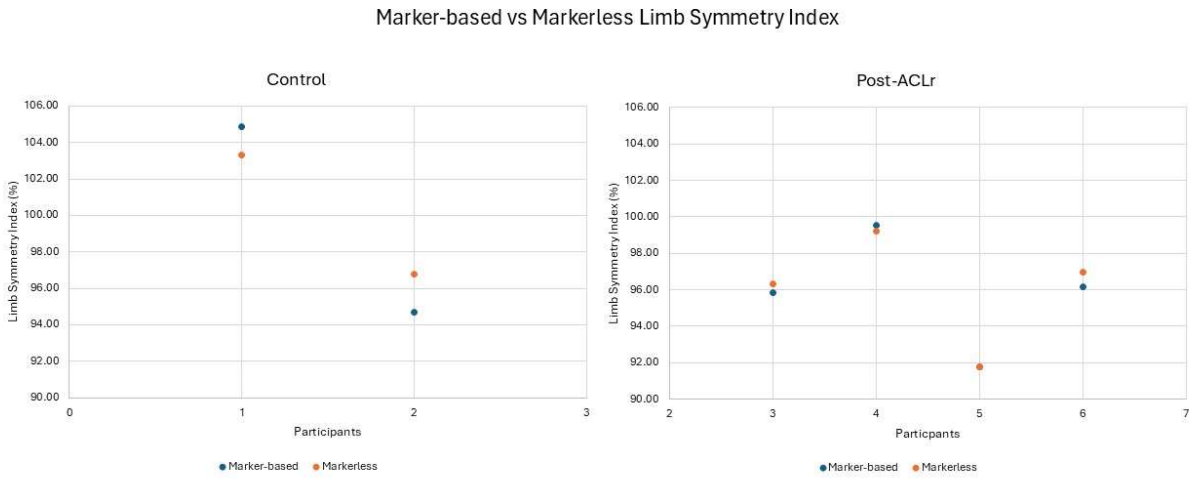


Figure 1: Marker-based and markerless LSI for participants in control group and post-ACLr group (marker-based: blue and markerless: orange).

References (Optional)

[1] Kanko *et al.*, J Biomechanics, 2021

[2] Seuthe *et al.*, J Biomechanics, 2025

[3] PRiSM, Sports Protocol, 2022

Session Category

Human Motion and Performance: Sports

P1-356

Are Failed Decisions Associated With Increased Knee Loading Under Complex Cognitive Demands?

Dr. Fatemeh Aflatounian[1,2], Dr. Keith Hutchison[1], Dr. James Becker[1], Dr. Corey Pew[1], Dr. Scott Monfort[1]

[1]Montana State University, Bozeman, Montana, United States. [2]Virginia Commonwealth University, Richmond, Virginia, United States

Introduction

Anterior cruciate ligament (ACL) injuries often occur during unplanned cutting/landing movements. Cognitively challenging jumping protocols aim to evaluate biomechanics during these scenarios by requiring participants to react to directional cues, which often produce failed or unbalanced landings. These imperfect trials are typically discarded, yet they may reveal meaningful deficits in muscle activation, joint stability, and dynamic postural control. This study examines whether knee biomechanics of unbalanced and successful jump landings vary with failure rate in response to challenging decision-making demands.

Methods

Forty-one active recreational athletes (17F/24M; 23.7±3.7yrs) completed drop-landing tasks recorded with markerless motion capture (100Hz) and force plates (1000Hz). Three conditions were tested: Baseline (anticipated direction), Simple (reactive single-leg landing toward a basketball image on one side of the screen), and Complex (reactive landing toward a basketball image or away from a simulated opponent). Trials were classified as successful, unbalanced, or failed. Unbalanced trials involved correct cue responses but inability to maintain balance for two seconds. Failed trials involved incorrect cue responses but landing on the wrong limb(s). Failed trial percentage (Failed%) was calculated for each cognitive condition. Kinematic/kinetic data were processed in Theia3D/Visual3D. Primary outcomes included changes between successful and unbalanced trials for peak knee flexion angle (ΔpKFA), peak knee abduction angle (ΔpKAbA), and peak knee abduction moment (ΔpKAbM), and their Pearson/Spearman correlations with Failed% (α=0.05).

Results

For ΔpKFA and ΔpKAbA, no significant correlations were observed. ΔpKAbM showed no association in the Simple condition; however, in the Complex condition, higher failure rates were associated with greater ΔpKAbM (ρ=-0.4,p=0.01; Figure-1).

Discussion

Differences in kinematic outcomes between successful and unbalanced landings were not associated with failure rate. However, under higher cognitive load, athletes with higher failure rates demonstrated riskier responses during unbalanced landings, which may indicate gross deficits in coordinating neuromuscular responses to directional stimuli. This result highlights the potential bias that may be introduced if isolating pKAbM estimates to only typically considered 'successful' trials (i.e., those with higher failure rates show greater deterioration in biomechanics for unbalanced trials that are often omitted). These findings support incorporating cognitively demanding tasks and unbalanced trials to reveal ACL-relevant neuromechanical vulnerabilities.

Images (Optional)

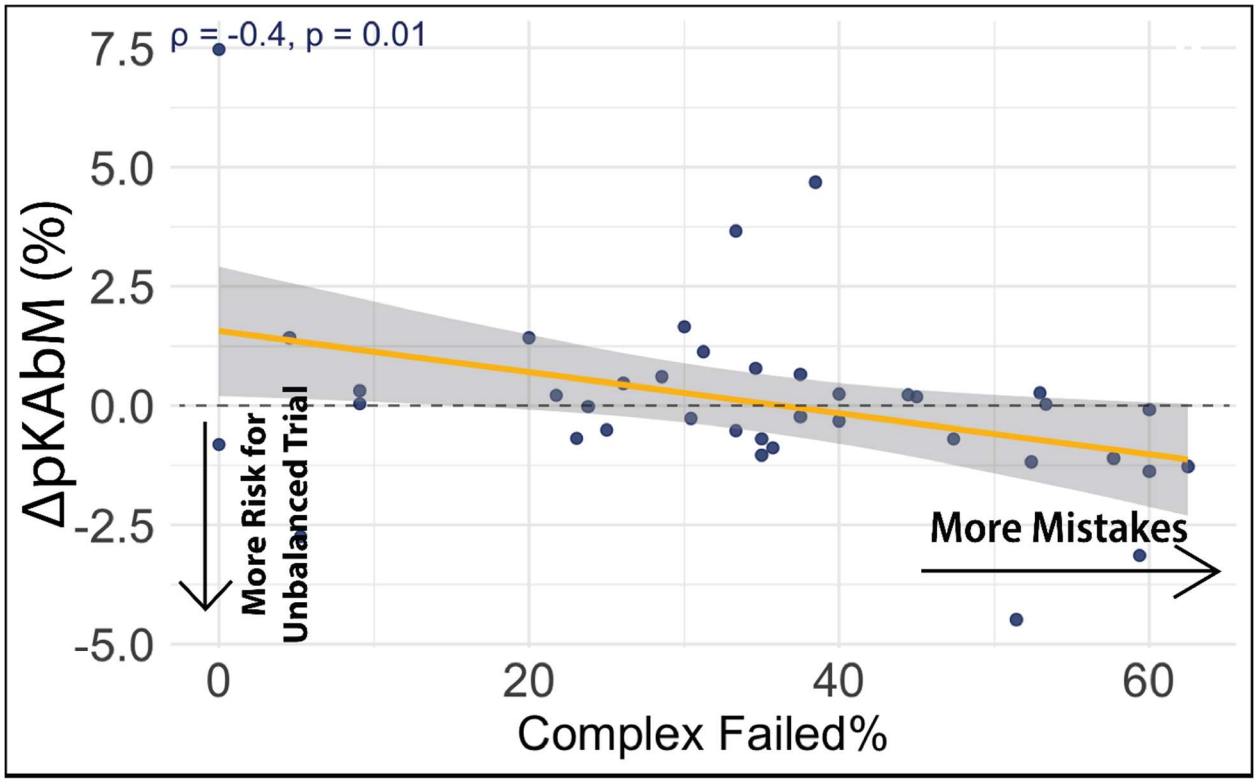


Figure 1: (A) Relationship between complex-task failure percentage and change in knee abduction moment (ΔpKAbM = Successful – Unbalanced variables, ρ = -0.4, p = 0.01).

Session Category

Human Motion and Performance: Sports

P1-357

Individualized Biomechanical Responses to Rest Duration during an Ultra-Endurance Running Event

Mr. Sean K.T. Gaiesky MSc.[1,2], Ms. Minju Kim MSc.[1,2], Ms. Jessica Yeoman[1,3], Dr. Aïda Valevicius PhD[3], Mr. Tyler Chuang MSc.[3], Dr. Christopher Napier PhD[1,2]

[1]Simon Fraser University, Burnaby, B.C., Canada. [2]University of British Columbia Okanagan, Kelowna, B.C., Canada. [3]lululemon Athletica, Vancouver, B.C., Canada

Introduction

Ultra-endurance running (UER) performance is contingent on how an athlete balances the demands of the task with adequate rest. Although athletes appear to lower their peak vertical force from pre- to post-UER [1], individualized rest strategies during multi-day races could potentially lead to altered responses throughout the event. Our objective was to determine how individual rest strategies affect biomechanics during a multi-day UER event.

Methods

Ten athletes completed a 6-day time-limited UER event. Participants wore sacral-mounted inertial measurement units (IMUs; 500Hz; Plantiga Technologies, Vancouver, Canada) and re-oriented acceleration signals were used to calculate kinetic and spring-mass biomechanical outcomes [2,3]. Mean vertical stiffness (kNm^{-1}) and peak vertical force (BW) were calculated for non-overlapping 60-second windows. Rest strategy was self-regulated and preceding rest-type defined as short (≥10 and <60 min) or long (≥60 min). Athlete-specific linear models were used to determine the effects of rest-type and running-bout (periods of running separated by >10 minutes) on the biomechanical outcomes, while controlling for speed.

Results

The top two finishers who covered the most distance were analyzed (Athlete A: 42 y, 901.7 km; Athlete B: 32 y, 643.5 km). Both athletes demonstrated significant main effects of running-bout (β: 0.27 – 0.65; η^2: 0.26 – 0.65), and rest-type (β: -0.52 – 0.34; η^2: 0.01 – 0.10) on vertical stiffness and peak vertical force ($p < 0.05$). Both athletes also demonstrated significant interaction effects on vertical stiffness (β: -0.02 – 0.01; η^2: 0.01 – 0.04); however, only Athlete A showed an interaction on peak vertical force (β: -0.001; η^2: 0.02).

Discussion

Athlete B consistently exhibited higher vertical stiffness and similar peak vertical forces following a long rest, whereas Athlete A's rest-type response was dependent on rest-type and running-bout (Figure 1). Athlete B's rest strategy, centered around longer long rests, potentially enabled them to resist the decreases in vertical peak force often adopted following UER events [1]. Although limited to the specific individuals, our results provide further insight into how in-race rest strategies could play an important role in the maintenance of running technique.

Images (Optional)

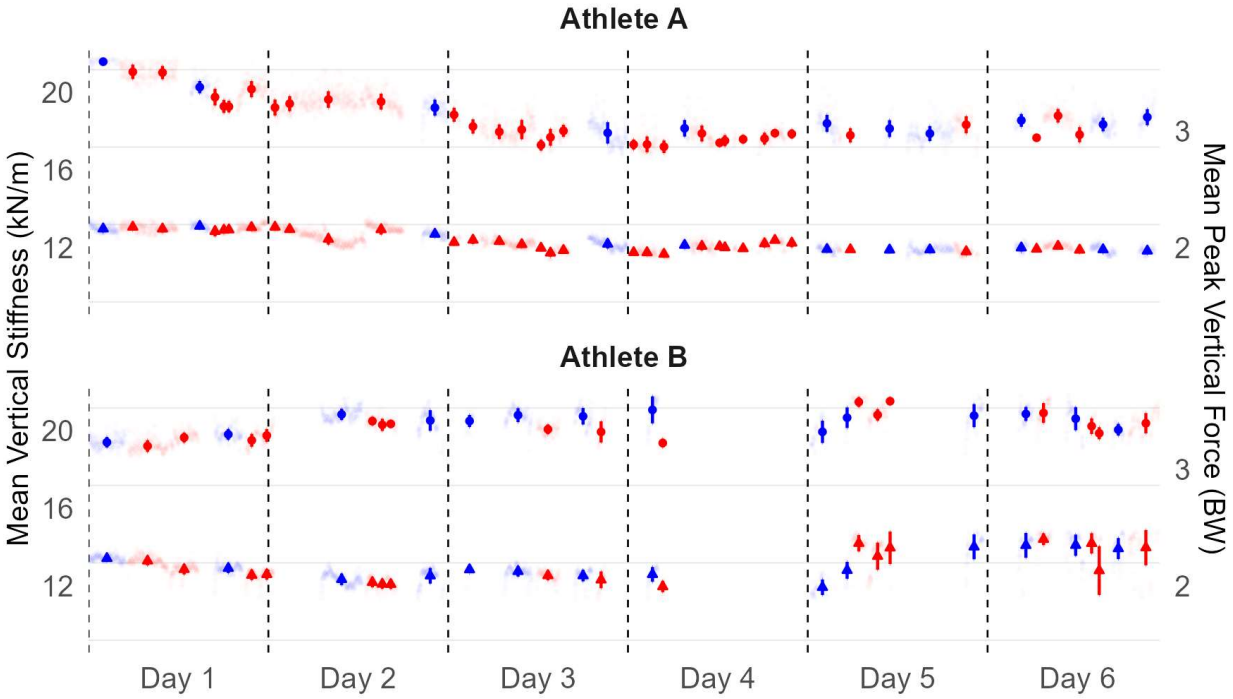


Figure 1. Running-bout and minute averaged vertical stiffness (kN/m) (●) and peak vertical force (BW) (▲) +/- 1SD following long (●) and short (●) rest-types over the 6-day UER event for Athlete A and Athlete B. Small translucent points represent individual observations.

References (Optional)

[1] Degache et al., IJSPP, 2016 [2] Patoz et al., J Biomechanics, 2021 [3] Morin et al., J App. Biomechanics, 2005

Session Category

Human Motion and Performance: Sports

P1-358

Stopping Shots: Understanding the Relationship Between Goaltender Leg Pad Construction and Over Rotation During Common Goaltending Movements

Mr Seth Daley MSc, Ms Jasmine Kwan BSc, Dr Ryan Frayne PhD

Dalhousie, Halifax, NS, Canada

Introduction

Ice hockey goaltenders adopt complex, often extreme body postures, as they attempt to stop 110–141 km/hr shots; therefore, their equipment must provide adequate protection without impeding performance or interfering with their movements. Goaltender leg pad construction typically falls into one of two designs: a stiff leg pad, and a flexible leg pad. Common player feedback is that the stiff pads may interfere with movements and apply unwanted forces to the goaltender, and flexible pads may twist (along the long axis) or over-rotate causing holes beneath the leg pad and ice surface. The purpose of this study is to understand the effect that pad construction has on their respond to forces applied during common movements.

Methods

This study recruited 13 participants ranging in skill from junior hockey to professional. Each goaltender conducted four common goaltender movements (Ready stance, T-push, Butterfly and RVH) in 5 different pad conditions varying in knee and thigh region flexibility (i.e. control, Pre-curved-Flexible, Pre-curved-stiff with thigh extension, straight-flexible and straight- stiff with thigh extension). A 14 camera (Optitrack Inc.) passive motion capture system collected rigid bodies that tracked pad rotations during the movements. Tekscan pressure sensors, located at the goaltender/equipment interface recorded goaltender applied forces.

Results

Minimal interface forces were identified for all movements except the RVH, where increased forces were located lateral and below the knee of the pad. Preliminary analyses suggest that the pre-curved pads have greater longitudinal torsion (15°) during the RVH compared to straight pads (10°). Leg pad roll, relative the ice surface, was greatest (30°) in a straight stiff pad condition compared to straight flex pads (15°) or pre-curved pads of either design (17°).

Discussion

Leg pad over torsion and over-rotation is a concern for goaltenders during blocking positions, like the RVH, as it decreases pad surface area shown to the shooter. Over rotation, additionally, causes gaps in the seal between the pad and the ice surface where a puck could get through. Therefore, from a performance perspective, the pre-curved pads "bending" but not "breaking" the seal with the ice surface during the RVH may make them the preferable pad for goaltenders.

Session Category

Human Motion and Performance: Sports

P1-359

Effects of Non-Elastic Ankle Taping on Time-Series Muscle Activation and Joint Mechanics During Landing in Individuals With Chronic Ankle Instability

Dr. Seung-Min Baik[1], Prof. Heon-Seock Cynn[1], Prof. Chung-Hwi Yi[1], Prof. Woochol Choi[1], Prof. Jae-Hun Shim[2], Prof. Ji-Hyun Lee[2], Ms. Kyung-Eun Lee[1], Mr. Seok-Hyun Kim[1]

[1]Department of Physical Therapy, College of Software and Digital Healthcare Convergence, Yonsei University, Wonju-si, Kangwon-do, Korea, Republic of. [2]Departement of Physical Therapy, Baekseok University, Cheonan-si, Chungcheongnam-do, Korea, Republic of

Introduction

Individuals with chronic ankle instability (CAI) commonly exhibit altered neuromuscular control during landing, potentially increasing mechanical demands on the ankle [1, 2]. Although non-elastic ankle taping is frequently applied to enhance functional stability, its time-series effects on muscle activation and ankle joint mechanics across different landing tasks remain unclear. This study examined whether non-elastic ankle taping reduces neuromuscular demands and ankle joint loading during multiple landing conditions in individuals with CAI.

Methods

Twenty-nine participants with CAI were recruited using the International Ankle Consortium criteria [2]. Exclusion criteria included lower-extremity surgery or fracture, recent injury, and musculoskeletal or neurologic disorders. Participants completed single-leg drop landings on flat, foam, and laterally inclined surfaces, with and without taping. Surface EMG was collected from the biceps femoris, peroneus longus, tibialis anterior, and medial/lateral gastrocnemius. External ankle joint moments in sagittal, frontal, and transverse planes were computed using motion-capture and force-plate data. Time-series muscle activity and joint moments during the preactivation and landing phases were analyzed using one-dimensional statistical parametric mapping (SPM1d; paired t-tests, $\alpha = 0.05$) [2, 3]. The institutional review board approved all procedures.

Results

Across tasks, taping significantly reduced EMG activity in multiple muscles during both preactivation and landing phases. Reductions were most consistent in the peroneus longus, tibialis anterior, and gastrocnemius muscles across the flat, foam, and wedge conditions. Sagittal-plane external ankle moments were also decreased with taping during flat and foam landings. No significant differences were observed in frontal or transverse-plane moments for any task.

Discussion

Non-elastic ankle taping reduced neuromuscular activation and sagittal-plane ankle joint loading during single-leg landing in individuals with CAI, suggesting decreased neuromuscular demand when taped. However, the magnitude and timing of these effects varied by task, indicating that taping does not uniformly influence landing biomechanics across instability-provoking conditions. These findings highlight the task-dependent nature of taping effects and underscore the need to consider landing context when implementing taping strategies for CAI management.

Images (Optional)

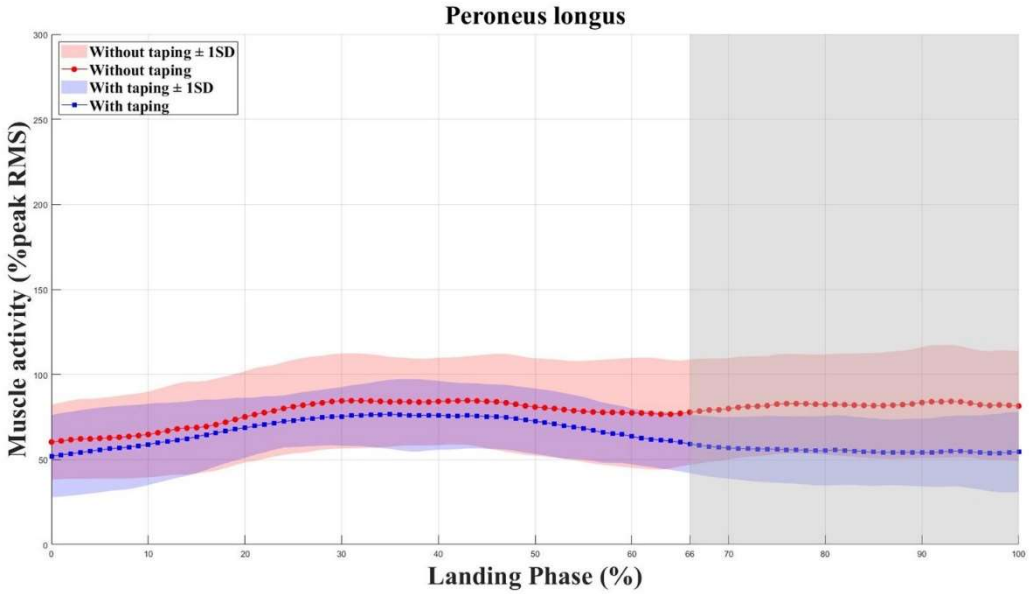


Figure. Peroneus longus muscle activity with and without non-elastic taping during the SLDL-FOAM landing phase. Shaded regions represent ±1 SD. Gray regions indicate the time periods in which significant differences were identified using SPM ($p < 0.05$).

References (Optional)

[1] Simpson J.D. et al., *Phys Ther Sport*, 2019
[2] Simpson J.D. et al., *J Athl Train*, 2020
[3] Zhou H. et al., *Int J Environ Res Public Health*, 2021

Session Category

Human Motion and Performance: Sports

P1-360

Impact of Sex and Skate Blade on Backwards Skating Kinematics and Plantar Pressure in Ice Hockey Players

Dr. Shawn Robbins BscPT, PhD[1,2], Ms. Natalie Schwarz MSc[1], Mr. Tayfun Ertekin BSc[1], Mr. Philippe Renaud MSc[1], Dr. Richard Preuss BSc, MSc, PhD[1], Dr. Dustin Bruening BSE, MSc, PhD[3], Dr. Philippe Dixon BSc, MSc, PhD[1]

[1]McGill University, Montreal, QC, Canada. [2]Centre for Interdisciplinary Research in Rehabilitation of Greater Montreal, Montreal, QC, Canada. [3]Brigham Young University, Provo, UT, United States

Introduction

Sex differences have been found during forward skating in ice hockey players,[1,2] but has not been investigated during backwards skating. New skate blade designs may impact backwards skating. The objective was to compare joint angles and plantar pressures between males and females when using different skate blades during backwards skating c-cuts.

Methods

Sixteen players (7 males, 9 females) were recruited for this cross-sectional study. They completed backwards skating c-cuts using four skate blades that had different radii of curvature (ROC): standard (10 foot radius), Quad (four different radii), Zuperior (three different radii), Ellipse (ellipse shape). Kinematics were measured with 17 inertial measurement units (Xsens) at 120 Hz. Lower extremity joint angles were calculated using Carden XYZ, and hip angles were used to segment c-cuts into push and recovery phases. Joint angle waveforms were compared between sex and blade conditions using statistical parametric mapping. Plantar pressures (Xsensor) were measured at 120 Hz, and feet were split into six regions (medial and lateral hindfoot, midfoot, forefoot). Hierarchical linear models assessed relationships between mean plantar pressure during c-cuts with sex, blade, and their interaction.

Results

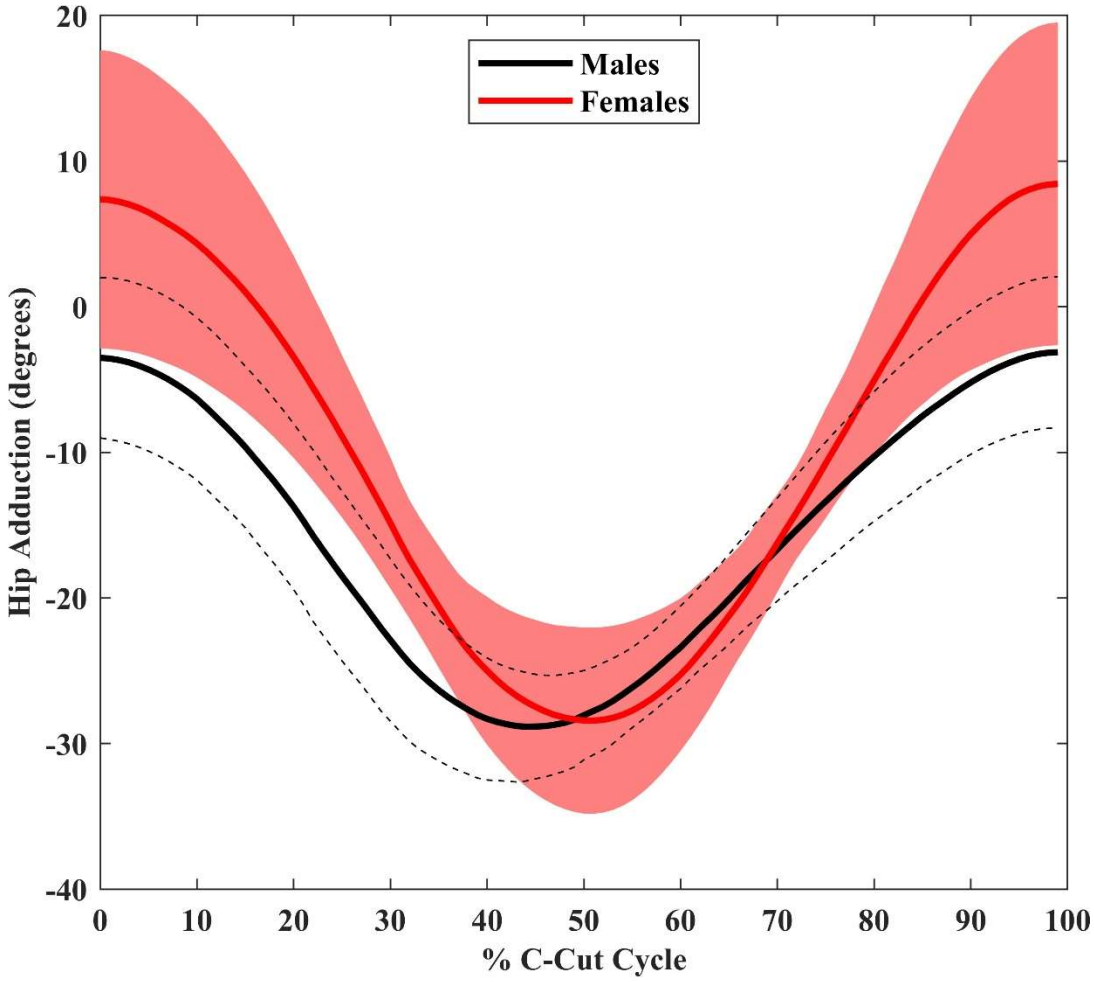
There were no significant blade effects for joint angles. However, females had greater hip adduction during push phase (Figure 1) and less knee flexion during recovery. For plantar pressures, there were significant regression coefficients ($p<0.001$ to 0.033) for blade and sex-blade interactions in all regions. Males had lower plantar pressures with the Quad (four radii) and Zuperior (three radii) blades in five and three regions, respectively, compared to

the standard blade. Plantar pressures did not differ substantially between blades for females.

Discussion

Greater hip adduction and less knee flexion during backwards c-cuts in females was consistent with forward skating studies and may be due to anatomical and strength sex differences.[1,2] Males and females had different responses to non-standard blade designs. Designs for non-standard blades were a larger departure from standard blade for males and they were unable to adapt to ROC changes. Results indicate that sex should be considered when designing equipment.

Images (Optional)



References (Optional)

[1] Budarick AR et al., *Sports Biomech*, 2022.

[2] Shell JR et al. *Sports Biomech*, 2017.

Acknowledgements (Optional)

We would like to thank Laura Holman for assistance with data collection. NSERC and Bauer Hockey Ltd. provided funding.

Session Category

Human Motion and Performance: Sports

P1-361

SHOULDER OR ELBOW: THE BETTER AXE-THROWING STRATEGY?

Graduate Student Shelby Schober, Undergraduate Student Brady Holcomb, Dr. Amber Chelette, Dr. Jeremy Stovall

Stephen F. Austin State University, Nacogdoches, Texas, United States

Introduction

Axe throwing is an increasingly popular timbersport. Due to little prior research, there is limited understanding of the upper-body biomechanics involved in effective axe throwing techniques. This study seeks to identify the most accurate axe throwing techniques and determine if throwing strategies differ by sex. An analysis of shoulder and elbow biomechanics was conduced in male and female collegiate timbersport athletes.

Methods

Ten subjects (5 females, 5 males with average age of 20.4) were recruited from a collegiate timbersports team. The axe had a head weight of 1.35 kg, an edge length of 15 cm, and a wood handle length of 52 cm. Athletes stood ~4.6 m from a wood plank target 70.5 cm wide with a 0.25 cm wide dot for a bullseye at 1.23 m above the ground.

Axes were thrown two handed and were recorded only if the axe successfully stuck in the target. Accuracy was measured as the distance between the center of the bullseye of the target to the closest point of the axe bit.

A Matlab script was utilized to calculate functional range of motion (FROM) in the sagittal plane. Spearman's Rho determined the relationship of shoulder and elbow functional range of motion with accuracy. Mann-Whitney U was conducted to analyze differences between males and females.

Results

Spearman's Rho illustrated a moderate correlation between accuracy and FROM in both shoulder (r=.28) and elbow (r=.52) flexion. Elbow FROM significantly differed between male (25.8±, 19.8) and female (10.3±, 5.78) (p = .01), but not shoulder FROM or accuracy. Examination of a shoulder and elbow FROM scatter plot demonstrates females tend to use more elbow and less shoulder compared to the male subjects.

Discussion

Males and females use different strategies for throwing an axe but their differing strategies did not affect their accuracy of throwing. This difference may be attributable to size or strength which should be studied further.

Session Category

Human Motion and Performance: Sports

P1-362

Comparison of Ankle Kinetic Estimates During Badminton Lunge Using a Custom Inertial Sensor-Based System vs. an Optical Motion Capture System With OpenSim

Mr Shifin A S[1], Mr Apoorv Shrivastava[1], Mrs Saranya Navratnarajah[2], Mr Jeevaraaj N[2], Mrs Siew Li Goh[2], Mr Darshan S. Shah[1]

[1]Indian Institute of Technology Bombay, Mumbai, Maharashtra, India. [2]Universiti Malaya, Kuala Lumpur, Wilayah Persekutuan Kuala Lumpur, Malaysia

Introduction

Inertial measurement units (IMU) have been widely used to estimate joint kinematics considering the advantages of cost-effectiveness, lower setup times and out-of-lab capabilities when compared to optical motion capture systems (OMC).[1,2] Musculoskeletal models based on custom-IMU systems could provide hardware frugality and model versatility to estimate joint kinetics; although, efficiency of custom-IMU systems in estimating kinetic parameters needs validation against benchmarked OMC-based approaches. Therefore, the current study aims to compare the ankle joint moments during badminton lunge estimated from kinematics captured using a custom-IMU system against those obtained from OpenSim using OMC-derived kinematics.

Methods

Custom IMUs (MPU9250, InvenSense, USA) and retroreflective markers were attached to the foot and shank segments of five recreational badminton players, following institutional ethical approval. Ankle kinematics were captured using an eight-camera OMC system (Qualisys, Sweden), while ground reaction forces were measured using force plates (AMTI, USA). Each subject performed five cycles of ankle plantar-dorsiflexion (PDF) for the functional calibration of custom IMUs,[3] followed by three trials of forward badminton lunges. A custom subject-specific musculoskeletal model of the lower limb was developed (MATLAB R2025a, Mathworks, USA) to estimate ankle joint moments using the custom-IMU-derived kinematics. Root mean square error (RMSE), Pearson correlation (R) and paired t-test were used to compare aforementioned normalised ankle joint moments with OpenSim estimates based on OMC-derived kinematics.

Results

Custom-IMU-based peak PDF moment and inversion-eversion moment were higher than those obtained from OpenSim ($p<0.02$) with high correlation in overall trends ($R=0.94$)

(Figure 1). RMSE for custom-IMU-derived method with respect to OpenSim was 0.06 N.m/kg.m and 0.04 N.m/kg.m for PDF and inversion-eversion moments, respectively.

Discussion

Efficacy of the custom-IMU system to estimate joint kinetics was exhibited through the good correlation of joint moments with OpenSim values; however, overestimations in ankle joint moments observed in custom-IMU-based model could be incorrectly interpreted towards injury prediction. Better functional calibration protocols of the custom-IMU sensors could improve joint kinetic estimations using custom-IMU systems coupled with custom subject-specific musculoskeletal modelling.

Images (Optional)

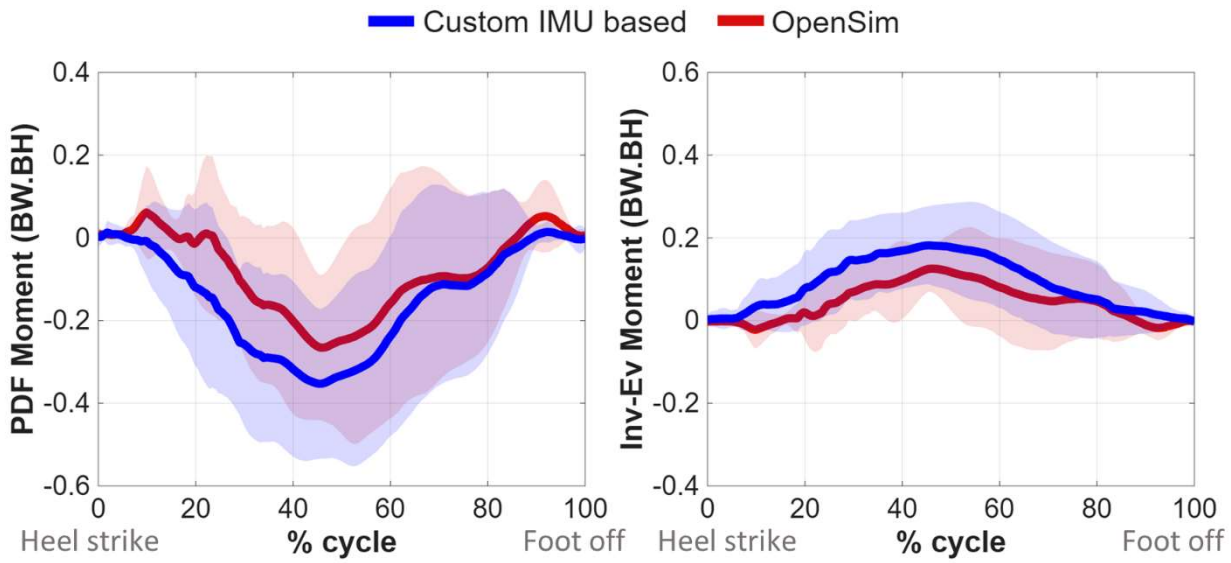


Figure 1: Inverse dynamics-based plantar-dorsiflexion (PDF) and inversion-eversion (Inv-Ev) moments derived from musculoskeletal model based on kinematics from custom inertial measurement unit (IMU) system and the OpenSim model based on kinematics from optical motion capture system

References (Optional)

[1] Lebleu et al., Sensors, 2020

[2] Kim et al., J of Sensors, 2017

[2] Cereatti et al., J of Biomechanics, 2024

Acknowledgements (Optional)

This study was supported by Seed funding for Collaboration and Partnerships Projects (SCPP), IIT Bombay. Apoorv Shrivastava was supported by Prime Minister Research Fellowship, Government of India.

Session Category

Human Motion and Performance: Sports

P1-363

Agreement between Marker-Based and Markerless Motion Capture for Knee Work Asymmetry Assessment after ACL Reconstruction

Mrs. Sierra Hastings PT, DPT, SCS[1], Ms. Katelyn Campbell MS[1], Dr. Eric Dugan PhD[1,2]

[1]Texas Children's Hospital, The Woodlands, Texas, United States. [2]Baylor College of Medicine, Houston, Texas, United States

Introduction

Markerless motion capture (Theia) offers a practical alternative to marker-based systems in sports rehabilitation, but its suitability for joint-level variables used in return-to-sport testing after ACL reconstruction (ACLr) remains uncertain. Positive knee work asymmetry during countermovement jump propulsion reflects limb loading strategy and recovery status. This pilot study evaluated whether Theia produces knee work asymmetry estimates comparable to a marker-based system after ACLr.

Methods

Six participants, 5 males and 1 female, post-ACLr (109 to 1218 days post-surgery) with mean age of 17.5 ± 3.83 years completed six countermovement jumps recorded simultaneously with marker-based and Theia systems. For each system, positive knee work during the concentric phase computed for the involved and uninvolved limbs and normalized to body mass (J/kg). Knee work asymmetry calculated using a bilateral asymmetry index that expresses the percent difference between limbs relative to their sum, consistent with recommendations for bilateral tasks [1]. Agreement between systems evaluated using a linear mixed-effects model with a random intercept for subject, ICC(3,k), and Bland Altman analysis.

Results

Knee work asymmetry ranged from approximately 2% to more than 23%, representing symmetric, moderately asymmetric, and highly asymmetric loading patterns. The mixed-effects model showed no significant difference between systems (Estimate=−1.44%, SE=1.13, p=0.21). Agreement based on subject-level values was high (ICC(3,k)=0.971, 95% CI: 0.83 to 1.00). Bland Altman analysis indicated small bias of −1.44% with limits of agreement from -1.00% to 3.88%(Figure 1).

Discussion

Knee work asymmetry measured with Theia closely aligned with values from the marker-based system across a range of recovery stages and asymmetry magnitudes. Between-system differences were small relative to a commonly used clinical target of 10% asymmetry[2] and were smaller than the asymmetry typically observed in healthy athletes[3]. Although preliminary, these findings suggest that Theia may provide clinically comparable information for knee work asymmetry after ACLr. Larger studies are needed to confirm these results and evaluate performance across a range of tasks and populations.

Images (Optional)

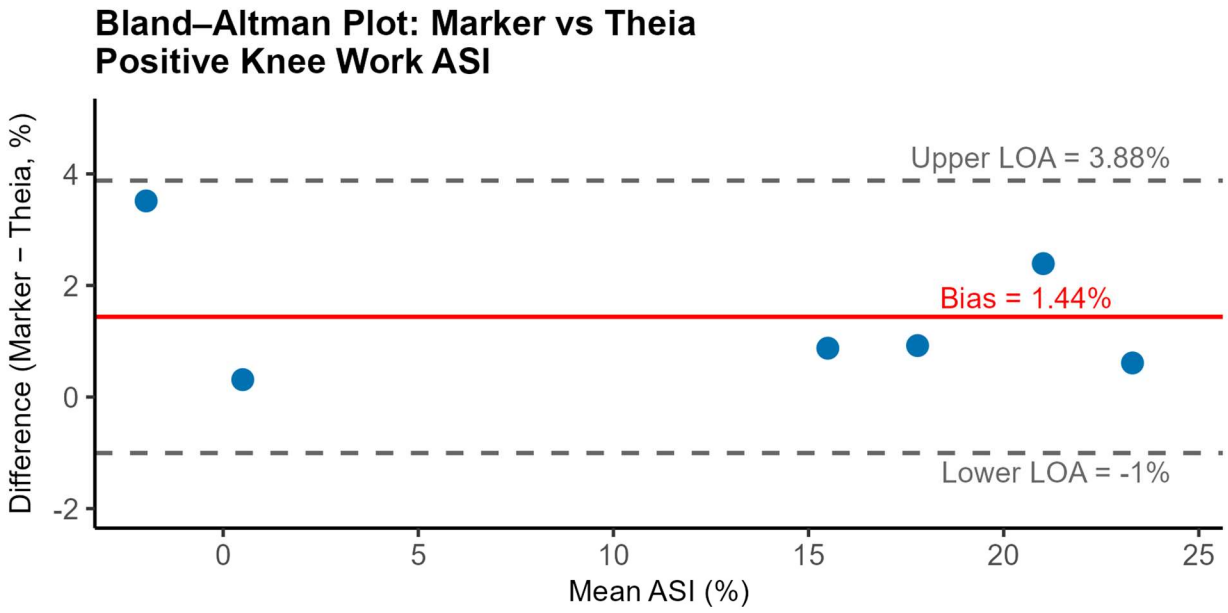


Figure 1. Bland–Altman plot comparing positive knee work asymmetry measured using marker-based and markerless (Theia) systems. Bias between systems was 1.44 percent, and the 95 percent limits of agreement ranged from −1.00 to 3.88 percent.

References (Optional)

[1] Bishop et al., Strength Cond J., 2018

[2] Szabó et al., J. Funct. Morphol. Kinesiol., 2025

[3] Joachim et al., MSSE, 2025

Session Category

Human Motion and Performance: Sports

P1-364

Accuracy of Vertical Force Estimation by DARI Marker-less Motion Capture System

Ms Silvia Zanini[1], Mr Wenpei Liu[2], Mr Mark Lenhoff[1], Mr Snehal Patel[1], Dr Howard Hillstrom[1]

[1]Hospital for Special Surgery, New York, New York, United States. [2]Philadelphia College of Osteopatic Medicine, Philadelphia, Pennsylvania, United States

Introduction

Force plates (FP) are the gold standard for measuring ground reaction forces. However, they are expensive. DARI is an 8-camera marker-less motion-capture system that acquires videos of patients. It extracts 3D volumetric silhouette of each body segment to track and scale a model representing the patient and their movements. This information, combined with body weight, is used to estimate vertical ground reaction force.

This study determined the accuracy of vertical ground reaction force estimation for DARI, to determine its utility and limitations in clinical and research evaluation of patients.

Methods

Twenty healthy individuals (10M+10F; 34.2±8.9years; 171.8±8.9cm; 74.4±13.4kg) participated in this IRB-approved validation study. Participants performed 3 trials of double-leg vertical jump on FP while simultaneously being recorded with DARI.

Accuracy was established from: (1) root mean square error (RMSE) between DARI and raw FP and (2) Pearson correlation coefficient (R) from a regression of DARI onto raw FP vertical forces at each jump frame. All variables were calculated for right leg, left leg, and combined sum.

Frame rates between systems were resampled to match and data was synchronized using the minimum RMSE.

Results

The average RMSE in vertical force (N) during the jump was 62±17, 63±17, and 100±33 for right, left, and combined force, respectively.

Linear regression of DARI onto FP vertical forces (figure-1b) shows good agreement, with discrepancies at 0 (where timing was off) and at high forces (when landing occurred), as seen on the force-time graph (figure-1a). The average R was 0.95±0.03, 0.96±0.02, and 0.97±0.01, and R^2 was 0.91±0.05, 0.92±0.03, and 0.93±0.03 for right, left, and combined force, respectively.

Discussion

DARI provides a good estimate of vertical ground reaction forces in the absence of FP.

The greatest discrepancies occurred 1) for timing of the jump possibly due to camera views and 2) at landing possibly due to DARI data processing and filtering (proprietary algorithm).

Additional exercises and synchronization and filtering techniques will be explored next.

These kinetic measures are clinically valuable and useful outcomes in performance and rehabilitation when addressing a patient's ability to load their lower limbs.

Images (Optional)

Figure 1a. Force-time curves (FP vs DARI).
Representative sample

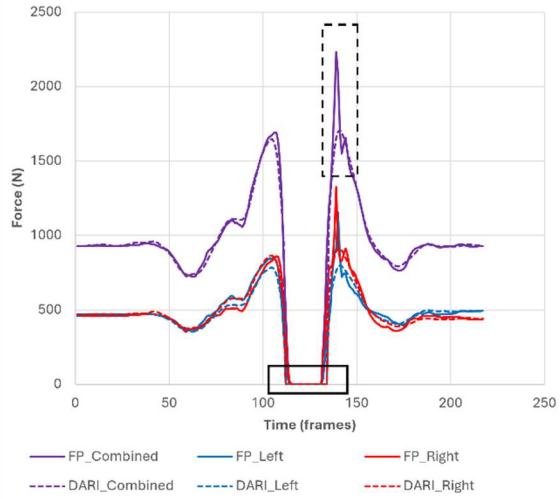
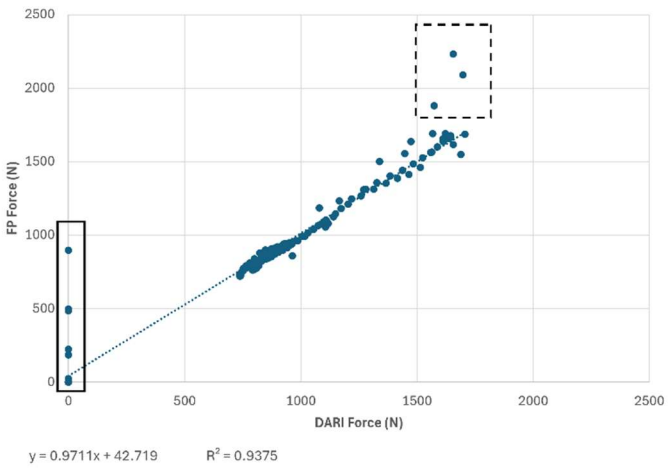


Figure 1b. Linear Regression – Combined Vertical Force - FP vs DARI
Representative sample



Acknowledgements (Optional)

This is a collaborative study between DARI and HSS. DARI is providing no funding for this study.

Session Category

Human Motion and Performance: Sports

P1-365

Neurofencing - Study of the Physiology and Biomechanics of a Fencer's Movement

Neurofencing - Study of the Physiology and Biomechanics of a Fencer's Movement Supriya Nair Undergraduate

Stanford Online High School, Redwood City, California, United States. Backyard Brains, Ann Arbor, Michigan, United States. Mount Sinai, New York, New York, United States. CoRE Lab, Seattle, Washington, United States

Introduction

Fencing is a permanent fixture at the Olympics. Agile footwork and bladework are hallmarks of a successful fencer. Based on sword fighting, fencing demands speed, patience, and good reflexes. Warm-ups improve performance. A typical fencing attack technique involves the lunge - an explosive extension of the fencer's body propelled by the non-dominant leg (ND) in which the dominant leg (D) is kicked forward. We study the physiology, underlying kinematics, and healthy range of joint movements to prevent injuries.

Methods

Six fencers, participated in Mount Sinai (STUDY2201661) over the course of two days. One day included a 15-minute warmup of predetermined exercises. All fencers performed ten lunges towards a fixed target 6ft away each day. Delsys Trigno sensors were placed on various muscle groups to collect electromyogram (EMG). Two-minute recordings of electrocardiogram (EKG) and electroencephalogram (EEG) at baseline and post-lunge timepoints was taken. EEG data w/ Neuroelectrics Enbio to assess band power across eight channels. EKG data was collected w/ Polar H10, HRVElite.

Fifty fencers participated in UW (STUDY00019084). Fencers conduct five standard lunges (SL) and five advanced lunges (AL) towards a dummy target 6ft away. These lunges were captured using VICON motion capture system w/ 60 markers on each subject. The second part of the experiment involved playing two games (G1) & (G3) on a Favero fencing target and scoring their discomfort level with nine wrist tendon injury rehabilitation exercises.

Results

A 9.4% faster touch speed was observed after 15-minute warmup (p=0.01). Biomechanics findings relate to ground reaction forces and analysis of dominant knee joint angle. During the extended lunge motion, their dominant foot lands with more force than the standard*

lunge in a shorter period of time. Both the hamstring and rectus femoris play critical roles in regulating the knee's flexion and extension, as the rectus femoris gets the dominant leg moving forward and the hamstring slows it down preventing knee over flexion.

Discussion

The rapid and repetitive fencing lunges along with rapid extension and flexion produces strenuous impact loading on the lower extremities particularly the knee, hip & ankle joints.

Images (Optional)



References (Optional)

Engstrom, Ian et al (2023) PloS one vol. 18,5 0285676.

Acknowledgements (Optional)

Mentors at {Stanford OHS, Backyard Brains, Delsys, VICON, HAS V3D, Abilities Research Center Mount Sinai, CoRE Lab, University of Washington}

Session Category

Human Motion and Performance: Sports

P1-366

Total-Body Motion and Lower-Body Power Generation Strategies in Relation to Baseball Pitching Ball Velocity

Biomechanical Analyst Takato Ogasawara, Associate Professor Brian Knarr

University of Nebraska at Omaha, Omaha, Nebraska, United States

Introduction

Pitching performance depends on efficient energy generation from the lower extremities. Stride-leg ground reaction forces often predict ball velocity (BV), but drive-leg contributions are less consistent, suggesting whole-body movement during the drive phase may better indicate performance and capture mechanical efficiency. Lower-body strength and anthropometry influence BV, highlighting the need to control body mass. This study examines whether total-body movement during the drive phase predicts BV, and how different lower-body strategies contribute to generating that movement.

Methods

Ninety-two pitchers (age 11–24) threw from a mound with force plates while 3D marker-based motion capture. Total-body drive-phase mechanics were quantified using Center of Mass (COM) motion and whole-body energy metrics (kinetic, potential, and total energy, both peak and time-integral). Pearson and partial correlations (weight as covariate) and hierarchical mixed-effects regressions tested relationships with BV, controlling for body mass and height. Lower-body strategy was quantified as time-integrated ankle, knee, and hip positive joint torque power, expressed as fractional contributions to total lower-body work. Pearson correlations assessed relationships between lower-body strategy, total-body mechanics, and BV.

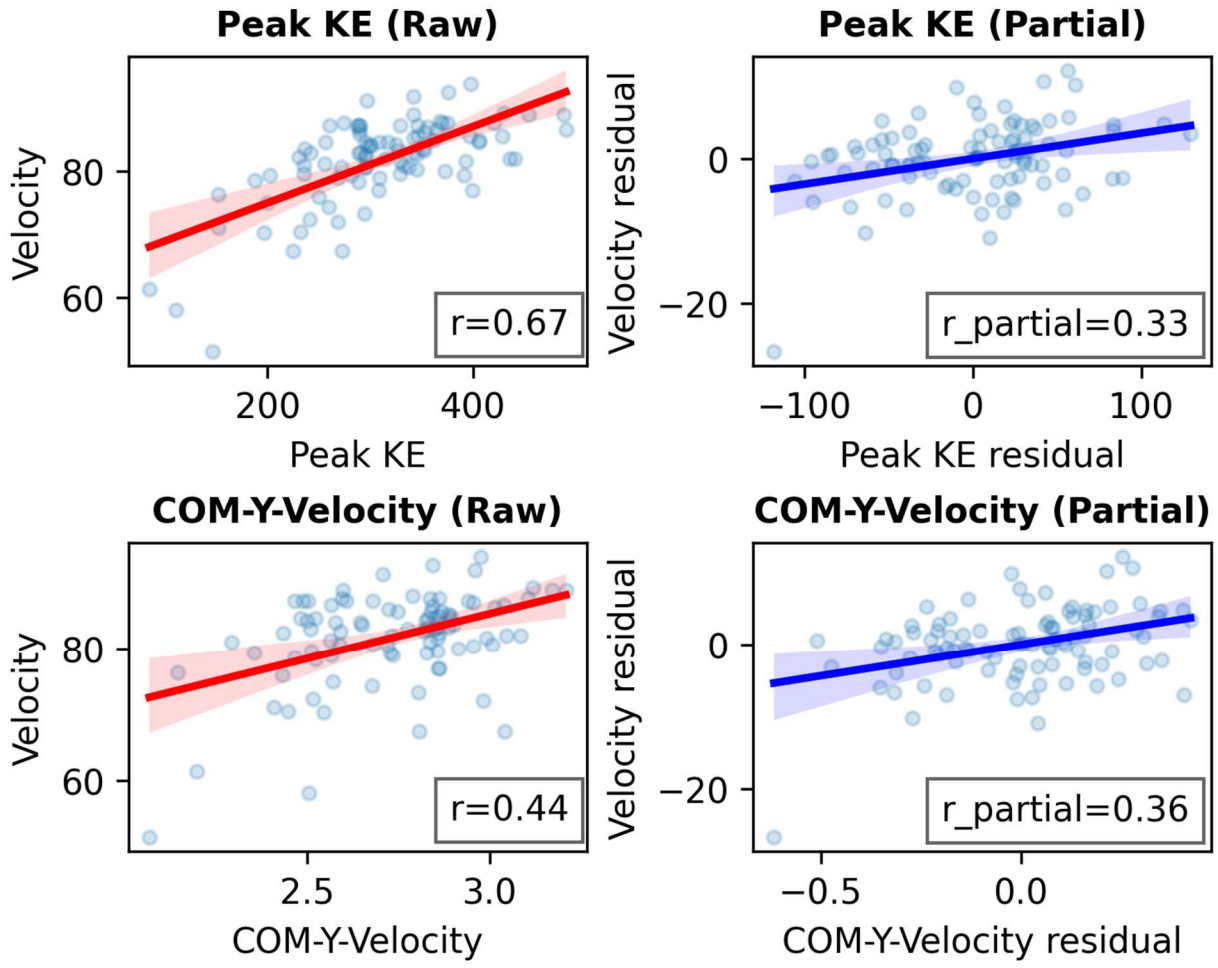
Results

Peak kinetic energy (KE) and COM-Y-velocity (forward) were strongly correlated with ball velocity ($r=0.67$ and 0.48, $p<0.01$), with correlations reduced when controlling for body weight ($r_{partial}=0.33$ and 0.39, $p<0.01$), shown in Figure. Hierarchical regression showed that adding peak kinetic energy, COM-Y-velocity, and COM-Y-acceleration to a weight/height-only model increased R^2 from 0.44 to 0.56 ($\Delta R^2=0.13$, $p<0.05$). Lower-body strategies, as fractional positive work, showed ankle negatively ($r_{partial}=–0.38$, $p<0.01$) and hip positively ($r_{partial}=0.28$, $p<0.01$) correlated with BV, while knee was not significant, and none correlated with peak COM-Y-velocity.

Discussion

Peak KE and COM forward velocity were associated with BV, indicating that greater whole-body output during the drive phase predicts faster pitches. Partial correlations controlling for body weight reduced effect sizes, highlighting anthropometry's influence, while hierarchical regression confirmed total-body motion contributes independently to BV. Lower-body strategies were related to BV, but not reflected in COM velocity, suggesting translational COM metrics alone miss rotational motion, pelvis tilt, and timing differences. Evaluating both mechanics and strategy is critical to optimizing pitching performance.

Images (Optional)



References (Optional)

Session Category

Human Motion and Performance: Sports

P1-367

Novel Inertial Sensor-Based Methods Provide Valid and Reliable Countermovement Jump Force Measures

Dr Therese Parr[1,2], Mr Leutrim Mehmeti[1,3], Dr Justin Reed[1,4], Lt Col Robert Briggs[1], Dr Peter Le[1]

[1]711th Human Performance Wing, Air Force Research Laboratory, Wright Patterson Air Force Base, OH, United States. [2]Innovative Element, Washington, DC, United States. [3]Reef Systems, Cary, NC, United States. [4]KBR, Inc., Houston, TX, United States

Introduction

The countermovement jump (CMJ) is utilized to monitor lower-body performance and guide training/rehabilitation. While force plates (FPs) are the standard to quantify CMJ metrics, they are expensive and resource intensive. Inertial measurement units (IMUs) have been shown to accurately measure CMJ height [1-2], offering a more accessible alternative to FPs. However, research remains limited regarding IMUs ability to quantify metrics that provide insight into the rate, magnitude, and strategy of muscle force production [1-2], limiting their utility in sports, military, and clinical performance monitoring. This study aims to validate IMU-based methods for computing CMJ force metrics: eccentric impulse, concentric force/power/impulse, jump height and modified Reactive Strength Index (RSI-mod).

Methods

Twenty-five participants (9F/16M, 29±6 yrs, 75.9±12.4 kg, 173.7±7.4 cm) performed three CMJs on FPs (VALD, Queensland, Australia) while wearing a sacral-mounted IMU (Movella, Enschede, Netherlands) recording at 500 and 60 Hz, respectively. IMU acceleration and orientation were filtered with a 4th order low-pass Butterworth filter with cutoff frequencies of 6.5 and 10 Hz, respectively [2]. IMU-derived metrics of force, power, and impulse were calculated over the appropriate phases based on physics principles. Jump height and RSI-mod were estimated using literature-based flight-time [1], and impulse-momentum methods [2]. Validity between systems was assessed using mean absolute percent error (MAPE), and Pearson correlation coefficient (r). Reliability was assessed with an intraclass correlation coefficient (ICC).

Results

IMUs-derived metrics demonstrated strong agreement with FPs ($r > 0.9$; $MAPE < 10\%$). Reliability was excellent across all variables for FPs and IMUs ($ICC > 0.9$).

Discussion

A sacral-mounted IMU can accurately and reliably compute force metrics captured from commercial FPs. This is a novel advancement, as previous research has had limited success in deriving force, impulse, and power metrics from inertial sensors [2]. These inertial-based methods enable more accessible and comprehensive jump performance monitoring for applied sports, miliary, and clinical settings.

Images (Optional)

	Concentric Mean Force/BM	**Concentric Mean Power/BM**
MAPE (SD)	2.12 (1.64)	5.12 (4.72)
r	0.96**	0.97**
ICC IMU//FP	0.92//0.93	0.96//0.98
	Concentric Impulse	**Eccentric Deceleration Impulse**
MAPE (SD)	4.21 (3.22)	7.99 (6.99)
r	0.97**	0.90**
ICC IMU//FP	0.98//0.99	0.91//0.90
	Jump Height (Flight Time)	**Jump Height (Impulse-Momentum)**
MAPE (SD)	4.98 (3.69)	8.43 (6.68)
r	0.98**	0.94**
ICC IMU//FP	0.99//0.98	0.96//0.99
	RSI-mod (Flight Time)	**RSI-mod (Impulse-Momentum)**
MAPE (SD)	9.24 (7.11)	9.86 (7.73)
r	0.96**	0.95**
ICC IMU//FP	0.91//0.97	0.92//0.96

**p <0.0001 for Pearson correlation coefficient

BM = body mass; SD = standard deviation

References (Optional)

[1] Miranda-Oliviero P *et al.* Sensors, 2022.

[2] Toft N *et al.* J SpMed Rehab, 2019

Acknowledgements (Optional)

The views expressed herein do not reflect official policy of the U.S. Departments of Air Force, DoD, nor the U.S. Government. Study protocols were approved by the AFRL Institutional Review Board.

Session Category

Human Motion and Performance: Sports

P1-368

Effects of Real-time Peak Impact Force-based Augmented Feedback on Running Patterns of Novice Recreational Runners

Professor Thomas Kernozek PhD, FACSM[1,2], Ms. Nora Stroh[1], Mr. Drew Rutherford MS[1,2], Mr. C. Nathan Vannatta DPT, SCS[3,2], Professor Sherwin Toribio PhD[1]

[1]UW La Crosse, La Crosse, WI, United States. [2]La Crosse Institute for Movement Science, La Crosse, WI, United States. [3]Gundersen Sports Medicine, La Crosse, WI, United States

Introduction

Running-related injuries may be related to aspects of ground reaction forces (GRF). Training to reduce GRF resulted in a lower incidence of running-related injury [1]. The purpose was to determine if novice runners lowered their peak GRF via receiving concurrent GRF feedback while running on a treadmill.

Methods

28 healthy male and female novice runners ages 19-23 years were examined. 54 retro-reflective markers were placed on selected body segments. After a standardized warmup, running data were collected on baseline peak GRF to determine 5% and 10% reduction goals. Runners received concurrent GRF-augmented visual feedback indicating whether they were above or below their 5% and 10% peak GRF reduction goals. Feedback was removed, and a short-term retention within that running bout was examined. All analyses examined the stance phase of running at a standardized running speed (3.68 m/s). 3-D kinematics (180 Hz) and kinetics (1800 Hz) on an instrumented treadmill were measured. A repeated-measures analysis of variance compared kinematic and kinetic variables at baseline, after 5% and 10% GRF reduction feedback (α=0.05).

Results

Overall, novice runners reduced their peak GRF compared to baseline ($p<0.05$). Table 1 depicts means, standard deviations, effect size, and percent change for each kinematic and kinetic variable from baseline running, 5% and 10% reduction goals. Most runners successfully reduced their GRF forces in response to feedback; 21.4% (6/28) and 42.9% (12/28) did not achieve the 5% and 10% reduction goals. A regression analysis was used to determine the kinematic or kinetic strategies used to reduce peak GRF. At 5%, foot reach explained about 15.3% of this reduction in peak GRF. At 10%, ankle plantarflexion power, hip extension moment, and hip extension angle explained about 61.1% of the reduction.

Discussion

Providing augmented feedback may be effective in reducing GRF in novice runners. Ankle and hip strategies appear to be employed to reduce GRF in some variables relevant to running injury.

Images (Optional)

Table 1. Mean, Standard Deviation, Effect Size, and Percent Change in Kinematic and Kinetic Variables

				Effect Size (Percent Change)	
Variable	Baseline	5% GRF Reduction	10% GRF Reduction	Baseline v. 5% GRF Reduction	Baseline v. 10% GRF Reduction
Peak Vertical GRF (BW)	2.22 (0.14)	2.02 (.15)	1.95 (.16)	1.38 (8.9%) *	1.83 (12.3%) *
Cadence (steps/min)	158.89 (8.11)	164.16 (10.25)	164.99 (12.18)	0.57 (3.3%) *	0.60 (3.8%) *
COM Vertical Excursion (mm)	78.51 (11.59)	68.28 (11.06)	66.24 (11.57)	0.90 (13%) *	1.06 (15.6%) *
Foot Reach (mm)	142.76 (24.96)	161.28 (38.03)	167.98 (38.88)	0.59 (13%) *	0.79 (15.6%) *
Foot Inclination Angle (°)	20.72 (6.22)	21.22 (2.34)	19.83 (8.28)	0.07 (2.4%)	0.12 (4.4%)
Peak Ankle Plantarflexion Angle (°)	-9.70 (5.72)	-9.17 (6.89)	-8.20 (5.77)	0.08 (-0.5%)	0.26 (-1.5%)
Peak Ankle Dorsiflexion Angle (°)	-28.02 (3.89)	-29.04 (4.86)	-28.51 (3.98)	0.24 (0.9%)	0.13 (0.4%)
Peak Hip Flexion Angle (°)	49.27 (4.37)	49.97 (4.96)	50.79 (5.80)	0.15 (1.4%)	0.30 (3.1%)
Peak Hip Extension Angle (°)	2.21 (9.85)	0.85 (9.31)	0.29 (8.25)	0.14 (-61.5%)	0.21 (-87) *
Peak Knee Flexion Angle (°)	48.72 (4.43)	49.08 (5.31)	50.03 (5.81)	0.07 (0.7%)	0.26 (2.7%)
Peak Knee Extension Angle (°)	16.19 (3.26)	16.39 (3.67)	17.96 (3.80)	0.06 (1.2%)	0.50 (10.9%) *
Peak Ankle Plantarflexion Moment (BW*m)	0.25 (0.03)	0.23 (0.03)	0.23 (0.03)	0.58 (-7.4%) *	0.63 (-7.8%) *
Peak Hip Extension Moment (BW*m)	0.11 (0.02)	0.11 (0.02)	0.12 (0.02)	0.38 (8.2%) *	0.66 (14.7%) *
Peak Knee Extension Moment (BW*m)	0.26 (0.04)	0.24 (0.04)	0.23 (0.04)	0.66 (-9.3%) *	0.75 (-11.1%) *
Peak Ankle Plantarflexion Power (W/BW)	0.81 (0.17)	0.71 (0.21)	0.70 (0.17)	0.56 (-13.1%) *	0.65 (-13.4%) *

Note: *p<0.05

References (Optional)

[1] Chan et al. Am J Sports Med, 2018.

Acknowledgements (Optional)

UWL La Crosse College of Science and Health, Gundersen Medical Foundation

Session Category

Human Motion and Performance: Sports

P1-369

Mechanical Hysteresis Performance of Athletics Track Spikes

Professor Todd Stewart PhD, BSc, Doctor Graham Askew PhD, BSc., Professor Andy Brown PhD, BSc.

University of Leeds, Leeds, West Yorkshire, United Kingdom

Introduction

Evidence suggests that modern track spikes with advanced footwear technology produce faster running times [1]. These spikes typically feature lightweight, compliant midsole foams and increased longitudinal bending stiffness; there is often substantial variation within a single brand. This study reports the results of biomechanical testing of midsole compliance and bending stiffness using cyclic loading to focus on mechanical hysteresis and energy losses.

Methods

Four Nike running spikes were compared: All shoes had a single Pebax spike plate outsole, Zoom MambaV6 (2023), ZoomX Dragonfly (2021), ZoomX Dragonfly (heavy use). The Air ZoomX Victory2 (2024) had a carbon insole. For the evaluation of midsole compliance a 36mm diameter cylindrical indenter was applied centrally across the MCP joint. A 0-500N force was applied sinusoidally at 4Hz replicating a 185ms ground contact [1]. Bending tests applied 16 degrees of flexion across the MCP joint.

Results

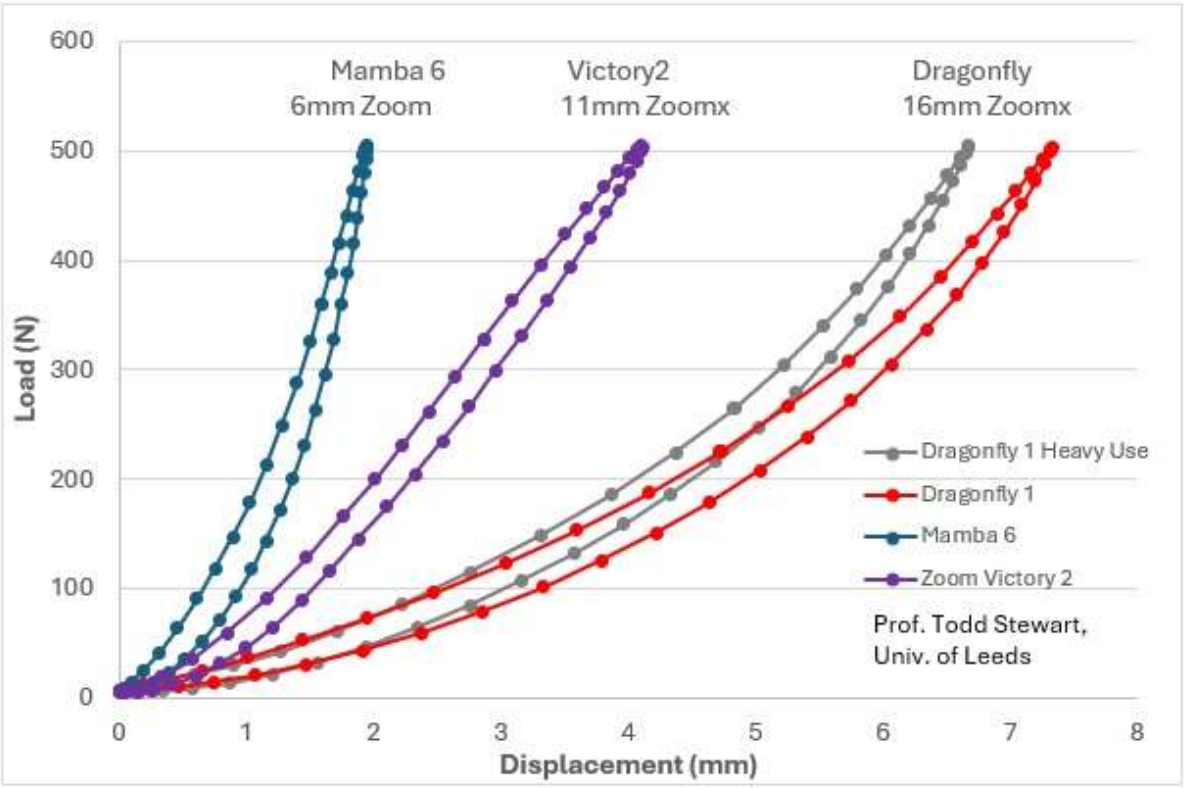
Compliance testing was validated with a steel spring producing negligible energy losses. Figure 1 shows the load/unload response of Track Spikes with the gradient giving the stiffness of the sole in N/mm. A large variation in deformation from 1.9 to 7.3mm was observed suggesting a broad range of comfort. Victory2 produced an uncharacteristically linear loading pattern. Under bending most shoes required a force of 30-40N to flex the toe to 16 degrees (stiffness 1.6N/mm), except the carbon Victory2, that required a force of 87N (stiffness 3.7N/mm).

Discussion

There was a 3-fold variation in midsole compliance across the range of spikes likely linked directly to the thickness of the foam (and shoe weight). In flexion stiffness may be more related to the number of layers within the sole than the specific layer material. A single

layer outsole spike plate shoe is only as stiff as the spike plate, whereas the addition of an internal carbon plate insole increases the moment of inertia proportional to the square of the distance between the plates. Hysteresis was inversely proportional to foam thickness. Victory2 results indicate additional potential for energy storage/return. The interaction and combination of plate layering and a resilient foam affects a shoe's performance.

Images (Optional)



References (Optional)

[1] W.Hoogkamer etal, S*ports Med. 2018.*

Session Category

Human Motion and Performance: Sports

P1-370

The Examination of Upper Body Mechanics in Women Softball Pitch Count to Prevent Arm Injury

Dr. Tong-Ching Tom Wu Professor, Ph.D.

Bridgewater State University, Bridgewater, MA, United States

Introduction

In baseball, pitch count regulations are established for pitchers to prevent overuse arm injury. In softball, the ball is pitched in an underhand motion, and research has shown that women softball pitchers also experience significant arm injury. The purpose of the study was to examine the upper body joint mechanics to establish and advocate softball pitch count regulations to prevent arm injury from fatigue due to pitching multiple games.

Methods

Three college and one elite high school female pitchers participated in the study. Each pitcher threw five fastballs, five changeups, and five curveballs. After the participant threw 15 pitches, the participant rested for 10 minutes and then threw another 15 pitches. This pitching process repeated seven times to mimic seven innings of a game. After one game, the participant rested for 20 minutes and then pitched for another game. Each participant threw a total of 210 pitches during the two games. A high-speed video camera (120 Hz) was used to capture the upper body joint kinematics. A one-way repeated measure ANOVA test was conducted at $\alpha = 0.05$ and followed by t-test with Bonferroni adjustment if a significant difference was found.

Results

The results showed there was no statistically significant difference in shoulder, elbow and wrist joint angles for all three different types of pitch. It was found that the elbow joint showed some differences, particularly for change up and curveball but not statistically significant enough, Table 1.

Discussion

Wu et al. (2019) showed pitchers started to show signs of fatigue after approximately165 pitches because a significant decrease in fastball velocity (25.4 ± 2.5 m/s decreased to 24.3 ± 2.7 m/s) was observed. In this study, the changes in upper body mechanics were not observed. Thus, this study suggested that the pitchers may experience physiological muscle fatigue, but it was not substantial enough to cause the changes in pitching mechanics. This study provides an important preliminary understanding of the effects of

pitch count on upper body pitching mechanics, and future studies are warranted with the increase of sample size and pitch count to examine the changes in pitching mechanics.

Images (Optional)

Table 1: Elbow joint angle in three different types of pitch during multiple games.

Joint Angle (°)	Game 1 (1st Inning)	Game 1 (4th Inning)	Game 1 (7th Inning)	Game 2 (1st Inning)	Game 2 (4th Inning)	Game 2 (7th Inning)
Fastball	147.4 ± 16.3	151.2 ± 14.5	154.4 ± 15.4	152.9 ± 14.7	153.6 ± 11.8	152.4 ± 16.5
Changeup	147.6 ± 20.7	153.9 ± 20.5	155.3 ± 16.1	153.3 ± 21.8	153.1 ± 17.0	150.1 ± 18.8
Curveball	153.4 ± 7.0	155.4 ± 9.0	157.3 ± 9.2	157.8 ± 4.9	159.4 ± 6.9	159.2 ± 5.7

**Statistical significant at $p < .01$*

References (Optional)

Session Category

Human Motion and Performance: Sports

P1-371

Comparison of Sagittal-Plane Knee Biomechanics Between Upright and Recumbent Cycling

Mr. Tsung-Lin Lu MS, Mr. Alejandro Ovispo-Martinez MS, Ms. Yufei Sun MS, Mr. Jacob Rygielski, Mr. Davin Gleaves, Ms. Quinn Wilson, Dr. Songning Zhang PhD

The University of Tennessee, Knoxville, TN, United States

Introduction

Recumbent bicycles have gained popularity for both exercise and rehabilitation. Several studies have reported lower or similar peak knee extension moments compared with upright bicycles; for example, a recent study discussed reductions in peak knee extension moments during recumbent cycling based on a comparison with an earlier upright-cycling study [1]. However, such cross-study comparisons may not yield meaningful results, as they involve different populations and/or work rates. To address this limitation, this study directly compared sagittal-plane knee biomechanics between upright and recumbent cycling using a within-subject design at matched power outputs.

Methods

Ten healthy participants (6 males, 4 females; age 25.1±3.8 years; height 1.75±0.07 m; weight 72.2±12.8 kg) were recruited. Participants cycled on both an upright cycle ergometer (Excalibur+Sport, Lode BV, Groningen, The Netherlands) and a recumbent ergometer (RE7, Kettler, Germany) equipped with instrumented 3D force pedals at 100 W and 80 rpm for 2 minutes. The last 10 seconds were recorded and truncated into five consecutive crank cycles. 3D Kinematic (240 Hz) and kinetic (1,200 Hz) data were collected using a 12-camera Vicon system and analyzed in Visual3D. Paired-sample t-tests ($\alpha = 0.05$) were conducted to compare knee variables between upright and recumbent cycling.

Results

Knee extension ROM (73.80±6.42° vs. 72.26±5.61°; $p = 0.26$), peak knee extension moment (32.69±5.38 vs. 33.98±7.16 Nm; $p = 0.52$), and peak knee power (167.39±25.54 vs. 161.61±37.76 W; $p = 0.62$) did not differ significantly between upright and recumbent cycling (Table 1).

Discussion

No significant differences in knee biomechanics were observed between upright and recumbent cycling. These findings contrast with prior reports that noted lower peak knee extension moments in a recumbent cycling study compared with results from a separate

upright cycling study [1], which involved different populations and work rates rather than within-subject measurements at matched power outputs. Therefore, the present controlled, within-subject study suggests that sagittal-plane knee loading is comparable between bike types, providing evidence to support the use of recumbent cycling in exercise or rehabilitation without concern for overloading the knee joint.

Images (Optional)

Table 1: *Knee Extension ROM (°), Peak Extension Moment (Nm), and Peak Power (W) across bike conditions: Mean ± SD.*

Variable	Upright Bike	Recumbent Bike	| Cohen's *d* |	*p*-value
Extension ROM	73.80 ± 6.42	72.26 ± 5.61	0.39	0.26
Peak Extension Moment	32.69 ± 5.38	33.98 ± 7.16	0.21	0.52
Peak Power	167.39 ± 25.54	161.61 ± 37.76	0.16	0.62

Note: Reported values correspond to the right limb only.

References (Optional)

[1] Lu et al., 2023. *Sports Biomech* **22**(4), 494–509.

Session Category

Human Motion and Performance: Sports

P1-372

Accuracy and Precision of Kinematic Methods for Determining Ball Release in Baseball Pitching

Dr. Tsutomu Jinji PhD[1], Dr. Glenn Fleisig PhD[2], Dr. Jon Slowik PhD[2]

[1]Kokugakuin University, Shibuya, Tokyo, Japan. [2]American Sports Medicine Institute, Birmingham, Alabama, United States

Introduction

Accurate identification of ball release is fundamental for baseball biomechanics. Standard fixed-offset methods lack validation across diverse pitch types, while emerging markerless systems rely on unvalidated assumptions. Therefore, this study determined which kinematic event most accurately and precisely identifies release without fixed offsets. We evaluated the systematic bias (accuracy) and random variability (precision) of three detection methods.

Methods

Forty-eight pitchers threw fastballs (FB) and other pitches among curveballs (CB), sliders, change-ups, and splitters. Kinematic data (1000 Hz) defined Actual Release (t_{actual}) based upon ball-fingertip separation (+0.5 cm margin). Three events were identified: wrist passes elbow (Wrist Pass), metacarpal passes wrist (MCP3 Pass), and MCP3 Peak Velocity. Time offset from actual release was calculated for each event. Differences in Accuracy (mean offset) and Precision (mean absolute deviation) were analyzed by pitch type ($p < 0.05$).

Results

MCP3 Pass showed the highest accuracy (offsets ≈ 0 ms) but lowest precision across all pitch types. Wrist Pass and MCP3 Peak Velocity exhibited systematic offsets but significantly higher precision. For FB, MCP3 Peak Velocity demonstrated the highest precision. However, for CB, its precision deteriorated, whereas Wrist Pass maintained high precision. While Wrist Pass precision was consistent, time offsets varied significantly by pitch type.

Discussion

Time offsets for Wrist Pass and MCP3 Peak Velocity varied by pitch type, necessitating pitch-specific offsets. However, precision is the critical determinant of reliability. With angular velocities reaching ~7,000 deg/s (shoulder) and ~2,500 deg/s (wrist) near release [1,2], random variability of just 1 ms may cause errors exceeding Minimal Clinically Important Difference (MCID) thresholds [2]. MCP3 Pass demonstrated low precision due to

finger variability, and MCP3 Peak Velocity deteriorated for CB. In contrast, Wrist Pass maintained high precision across all pitch types. Thus, to ensure kinematic data validity within MCID limits, we recommend using the Wrist Pass method; 7 ms after the wrist passes the elbow for fastballs, change-ups, and splitters, and 3 ms for breaking pitches (curveballs and sliders). This minimizes random timing errors and accommodates the biomechanical diversity of a pitcher's full repertoire.

Images (Optional)

Table 1. Time offsets relative to actual ball release for each method.

		Wrist Pass (ms)	MCP3 Pass (ms)	MCP3 Peak Velocity (ms)
Fastball (n=48)	**mean**	-6.8	-0.3	-6.8
	SD	1.3	1.9	1.2
Curveball (n=16)	**mean**	-2.6	-0.7	-2.2
	SD	1.2	3.2	2.8
Slider (n=27)	**mean**	-3.6	1.3	-2.6
	SD	1.6	2.1	2.5
Change-Up (n=16)	**mean**	-7.4	-0.6	-6.1
	SD	1.5	1.7	1.6
Splitter (n=14)	**mean**	-5.3	-0.6	-6.1
	SD	1.9	1.7	1.6

References (Optional)

[1] Barrentine et al., J. Appl. Biomech., 1998

[2] Fleisig et al., Am. J. Sports Med., 2024

Session Category

Human Motion and Performance: Sports

P1-373

Performance Asymmetry during a Single-Leg Jump does not Influence Performance during a Bilateral Countermovement Jump in Naval and Marine Corps Aviation Servicemembers

Assistant Professor Tyler Cardinale M.S.[1], Assistant Professor Tatiana Djafar M.S.[1], Biomechanist Andrew Plows M.S.[2], Assistant Professor Benjamin Cuddy DPT[1], Biomechanist Gaervyn Salverda M.S.[2], Lab Director Trevor Kingsbury M.S.[2], Assistant Specialty Leader Eric Infante Commander, DPT[3], Associate Professor Joshua Winters PhD[1]

[1]University of Kentucky, Lexington, Kentucky, United States. [2]Naval Medical Center San Diego, San Diego, CA, United States. [3]Naval Special Warfare, San Diego, CA, United States

Introduction

Assessing unilateral jumping tasks can expose inter-limb force production differences. However, it remains unclear whether unilateral performance asymmetries meaningfully influence bilateral jump mechanics or overall jump performance. This study examined how single-leg jump (SLJ) asymmetry relates to bilateral countermovement jump (CMJ) performance and inter-limb asymmetries across key phases of the movement. Understanding these relationships may clarify whether asymmetry expressed in isolation during unilateral tasks translates to bilateral performance deficits or reflects an independent characteristic of performance.

Methods

A total of 90 servicemembers completed a standardized biomechanical assessment using dual force plates. Testing included three SLJ's on each limb and five CMJ's. Participants were classified into two groups based on SLJ jump-height asymmetry: a low-asymmetry group ((<5%), (n=29; age=29.0yrs± 5.8)) and a high-asymmetry group ((>10%), (n=35; age=31.5 yrs±6.4)). Variables of interest derived from the countermovement jump (CMJ) included jump height, peak power, concentric impulse asymmetry, concentric peak force asymmetry, and peak landing force asymmetry. Independent T-Tests determined group differences ($\alpha = 0.05$).

Results

No significant differences were observed between SLJ asymmetry groups for CMJ performance metrics, including jump height ($p = 0.221$) and peak power relative to body weight ($p = 0.341$). The high-asymmetry group exhibited significantly greater CMJ concentric impulse asymmetry compared to the low-asymmetry group ($p = 0.008$), despite

not seeing significant differences in peak concentric force asymmetry (p = 0.245). The lower asymmetry group landed significantly more asymmetric (P = 0.041).

Discussion

Servicemembers classified in the >10% SLJ asymmetry group demonstrated clear unilateral performance deficits; however, these asymmetries did not translate to reductions in bilateral CMJ jump height. Though CMJ performance was unaffected, concentric impulse asymmetries were observed, suggesting that compensatory strategies may occur during the entire phase of concentric force production. How these asymmetries influence overall performance warrants further investigation. Interestingly, the <5% asymmetry group landed significantly more asymmetric, indicating that landing mechanics may operate independently of propulsive strategies. These findings suggest that bilateral performance may be independent of unilateral performance, highlighting the importance of utilizing a more comprehensive assessment strategy to uncover and address inter-limb differences.

Images (Optional)

Variable	Group <5 (Mean ± SD)	Group >10 (Mean ± SD)	p-value	Effect Size
CMJ Concentric Impulse Asymmetry [%]	4.53 ± 2.95	8.11 ± 6.92	0.008*	0.64
CMJ Peak Landing Force Asymmetry [%]	13.51 ± 9.79	9.10 ± 6.20	0.041*	-0.54
CMJ Concentric Peak Force Asymmetry [%]	5.95 ± 3.43	7.25 ± 5.33	0.245	0.280
CMJ Peak Power / BM [W/kg]	44.84 ± 6.12	43.16 ± 7.85	0.341	-0.23
CMJ Jump Height [in]	12.17 ± 2.42	11.36 ± 2.84	0.221	-0.30

Table 1. Between group comparison of key CMJ variables

Acknowledgements (Optional)

This analysis is part of a larger study "Restoration and Maintenance of Physical and Neurosensory Performance study (RaMP): Naval and Marine Corps Aviation" funded through the Office of Naval Research: (N00014-25-12288).

Disclaimer: The views expressed in this work are those of the author(s) and do not reflect the official policy or position of the Department of the Navy, Department of Defense, nor the US Government.

Session Category

Human Motion and Performance: Sports

P1-374

Understanding The Role of Biological Sex, Barefoot Walking and PA in Foot Core Development

Mr Umar Yousufy MSc, Mrs. Nicole J Chimera PhD

Brock University, St.Catharines, Ontario, Canada

Introduction

The foot is vital in establishing a base of support during physical activity (PA). The "foot core" (FC) system encompasses passive, active, and neural subsystems that stabilize the foot and attenuate force. The passive subsystem maintains foot arch; the active subsystem provides foot stabilization through intrinsic foot muscles (IFM). Males and those who engage in barefoot walking (BFW) exhibit greater arch height and IFM cross-sectional area (CSA), which may reflect greater foot stability and force attenuation. Additionally, the role of PA on the passive and active subsystems is less known. However, PA is important to consider since low PA correlates with ankle instability and may play a role in foot instability. The purpose of this study was to examine the relationship of biological sex, PA, and BFW on the passive and active FC subsystems.

Methods

This cross-sectional design determined whether sex, PA, and BFW were predictors of the passive and active subsystems. The predictor variables were sex, PA, and BFW, while the criterion variables were the passive and active subsystems. The Physical Activity Questionnaire-Adults (PAQ-A), a 5-point Likert scale was used to measure PA. A BFW questionnaire determined if participants were habitually barefoot, scored based on a 3-point Likert scale. To measure the passive subsystem, Arch Height Index (AHI) was assessed at 10% and 90% of total body weight in both feet; the active subsystem was measured with IFM (abductor hallicus, flexor digitorium brevis, and abductor digiti minimi) CSA (cm^2) (Clarius Ultrasound L15 HD3 probe) for both feet. A Shapiro-Wilks Test ($p < .050$) examined normality and preliminary analysis was conducted using Pearson's Correlation (r) in SPSS (v.29). Regression analysis will evaluate the variance in AHI and IFM CSA based on predictors with additional participants.

Results

A significantly strong negative correlation was observed between sex and abductor hallicus (ABH) CSA (r = - .882, *p* = .015). No other significant correlations were found.

Discussion

To date, ABH CSA is significantly larger in males, which highlights an emerging relationship between biological sex and the active FC subsystem. This study will highlight how sex, PA, and BFW relate to foot structure and IFM size.

Images (Optional)

Table 1. Preliminary data (mean ± standard deviation) for predictor and criterion variables in 7 healthy young adults.

Predictor and Criterion Variables	Mean ± Standard Deviation (n = 7)	
	Males (n = 3)	Females (n = 4)
Age	25.00 ± 0.82	26.2 ± 3.54
Height (cm)	175.33 ± 5.78	164.88 ± 5.88
Weight (lbs)	170.80 ± 8.02	163.20 ± 28.36
PAQ-A (5-point Likert scale	2.67 ± 0.47	2.80 ± 0.44
Habitual Barefoot (3-point Likert Scale)	4.66 ± 0.94	5.20 ± 1.17
AHI: 10% Body Weight	R: 0.1992 ± 0.01 L: 0.2289 ± 0.02	R: 0.1688 ± 0.04 L: 0.2340 ± 0.04
AHI: 90% Body Weight	R: 0.1768 ± 0.03 L: 0.1968 ± 0.00	R: 0.1692 ± 0.02 L: 0.2342 ± 0.05
CSA: Abductor Hallicus (cm^2)	R: 2.08 ± 0.22 L: 1.98 ± 0.30	R: 1.22 ± 0.27 L: 1.21 ± 0.27
CSA: Flexor Digitorium Brevis (cm^2)	R: 1.40 ± 0.37 L: 1.56 ± 0.09	R: 1.17 ± 0.39 L: 1.09 ± 0.20
CSA: Abductor Digiti Minimi (cm^2)	R: 0.46 ± 0.09 L: 0.64 ± 0.22	R: 0.42 ± 0.12 L: 0.48 ± 0.13

*PAQ-A = Physical Activity Questionnaire – Adults; AHI = arch height index (dorsum height at 50% of foot length/truncated foot length); CSA= cross-sectional area; R = Right, L = Left

Session Category

Human Motion and Performance: Sports

P1-375

Understanding the Role of the Foot Core System in Countermovement Jump Performance

Mr. Umar Yousufy MSc, Mrs. Nicole Chimera PhD

Brock University, St.Catharines, Ontario, Canada

Introduction

The “foot core” (FC) system encompasses passive, active, and neural subsystems that stabilize the foot and attenuate force. The passive subsystem maintains foot arch; the active subsystem provides foot stabilization through intrinsic foot muscles (IFM); thus, force attenuation, stabilization, and force production during jumping may be influenced by the FC. The countermovement jump (CMJ) examines lower limb power and neuromuscular function and may be influenced by the FC function. The purpose of this study was to determine the relationship between the passive and active FC subsystems and CMJ performance.

Methods

This cross-sectional design determined the amount of variance explained in jump height (JH), foot acceleration and stiffness during repetitive CMJs based on the passive and active subsystems. The predictor variables were the passive and active subsystems, and the criterion variables were JH, take-off acceleration (TOA), impact acceleration (IA), and qusai-joint stiffness. The passive subsystem was measured with the Arch Height Index (AHI) at 10% and 90% of total body weight in both feet, while the active subsystem was measured with abductor hallicus (ABH), flexor digitorium brevis (FDB), and abductor digiti minimi (ADM) CSA for both feet (cm^2) (Clarius Ultrasound L15 HD3 probe). Participants performed 5 repetitive CMJs in instrumented insoles (Plantiga accelerometers, Vancouver, British Columbia, Canada) to quantify JH (cm), TOA (m/s^2), and IA (m/s^2). Stiffness (N/m) was computed using body weight (lbs), flight time (secs), and ground contact time (secs). A Shapiro-Wilks Test ($p < .05$) examined normality and preliminary analysis was conducted using Pearson’s Correlation (r) in SPSS (v.29). A regression analysis will determine the JH, TOA, IA, and stiffness variance based on AHI and IFM CSA with additional participants.

Results

A significant, strong positive correlation was observed between right (r = .806, *p* = .029) and left (r = .825, *p* = .023) ABH CSA and left FDB (r = .804, *p* = .029) CSA with stiffness. No other significant correlations were found.

Discussion

To date, participants with greater ABH and left FDB CSA exhibit greater stiffness, suggesting the FC may contribute to neuromuscular function during CMJ performance. This study may inform targeted foot training interventions based on preliminary evidence.

Images (Optional)

Table 1. Preliminary data (mean ± standard deviation) for the predictor and criterion variables for 7 healthy young participants.

Predictor and Criterion Variables	Mean ± Standard Deviation (n = 7)	
	Males (n = 3)	Females (n = 4)
Age	25.00 ± 0.82	26.2 ± 3.54
Height (cm)	175.33 ± 5.78	164.88 ± 5.88
Weight (lbs)	170.80 ± 8.02	163.20 ± 28.36
AHI: 10% Body Weight	R: 0.1992 ± 0.01 L: 0.2289 ± 0.02	R: 0.1688 ± 0.04 L: 0.2340 ± 0.04
AHI: 90% Body Weight	R: 0.1768 ± 0.03 L: 0.1968 ± 0.00	R: 0.1692 ± 0.02 L: 0.2342 ± 0.05
CSA: Abductor Hallicus (cm^2)	R: 2.08 ± 0.22 L: 1.98 ± 0.30	R: 1.22 ± 0.27 L: 1.21 ± 0.27
CSA: Flexor Digitorium Brevis (cm^2)	R: 1.40 ± 0.37 L: 1.56 ± 0.09	R: 1.17 ± 0.39 L: 1.09 ± 0.20
CSA: Abductor Digiti Minimi (cm^2)	R: 0.46 ± 0.09 Left: 0.64 ± 0.22	R: 0.42 ± 0.12 L: 0.48 ± 0.13
JH (cm)	36.20 ± 3.40	18.00 ± 7.96
TOA (m/s^2)	R: 83.52 ± 6.02 L: 76.69 ± 7.10	R: 85.63 ± 13.5 L: 80.00 ± 29.78
IA (m/s^2)	R: 99.40 ± 3.52 L: 97.79 ± 11.08	R 87.51 ± 39.58 L: 80.93 ± 25.42
Siffness (N/m)	1051.18 ± 94.69	546.36 ± 187.30

* TOA was defined as the peak acceleration as the foot left the ground and IA was defined as the peak acceleration at foot contact during landing following each CMJ; AHI = arch height index (dorsum height at 50% of foot length/truncated foot length); CSA= cross-sectional area; JH = jump height; TOA = take-off acceleration; IA = impact acceleration; R = right; L = left; JH, TOA, and IA were averaged across 5 CMJs

Session Category

Human Motion and Performance: Sports

P1-376

Entry-phase biomechanics in hammer throw: differences between 3gr and 4gr techniques

Dr Gian Mario Castaldi[1], Dr Sebastiano Conci[1], Dr Filippo Goi[1], Dr Silvia Camboni[2], Dr Alessandro Di Gregorio[3], Prof. Valentina Camomilla[1]

[1]University of Rome Foro Italico, Italy, Rome, Italy, Italy. [2]Vibram Spa, Bergamo, Italy, Italy. [3]Washburn University, Topeka, Kansas, United States

Introduction

The hammer-throw entry links preliminary swings to the first turn and helps organize posture, foot support, and early implement acceleration, yet it is less quantified than later phases [1]. Two common techniques differ in preparation and initial pivot. In 3gr, there is no hammer pre-start, no right-foot displacement at the end of preliminaries, and rotation begins on the left heel. In 4gr, a hammer pre-start and right-foot displacement precede rotation initiation on the left forefoot. Kinetic and kinematic differences were compared between 3gr and 4gr during the entry phase to inform their potential impact on subsequent phases.

Methods

Six trained throwers (3 women; 21.0±4.9 years; 1.78±0.08 m; 80.7±13.5 kg) provided informed consent (CAR 194/2024) and performed three 3gr and 4gr entry trials. Data were collected using stereophotogrammetry (200–250 Hz) and force plates (1000 Hz). A CGM v2.5 marker set was used; 4-markers tracked the hammer centroid. Five instants were identified from kinematics and forces: I1 hammer farthest left (frontal plane), I2 hammer aligned with metatarsal markers, I3 hammer passing in front of the right foot, I4 hammer lowest point, I5 right toe-off. Outcomes at I1–I5 included: (1) left/right GRF components (AP, ML, VERT), normalized to body-weight; (2) ankle plantar/dorsiflexion; and (3) hammer centroid tangential velocity relative to athlete COM. Normality and variance were tested to eventually use non-parametric alternatives. Significance was set at $p<0.05$.

Results

Technique differences were mainly in left-foot GRF, with 4gr generally higher than 3gr. At I1, left-foot AP and VERT GRF were higher in 4gr; ML and VERT at I2; and AP at I4–I5. Hammer

tangential velocity modulus differed only at I3, with higher values in 4gr. Ankle plantar-/dorsiflexion showed no consistent difference.

Discussion

Overall, 4gr imposed greater left-foot kinetic demands across the entry and showed a localized velocity increase at I3, indicating phase-specific technique effects. Limitations include small sample size and entry-only analysis without performance outcomes. Future work will expand cohorts and link entry mechanics to release variables.

Images (Optional)

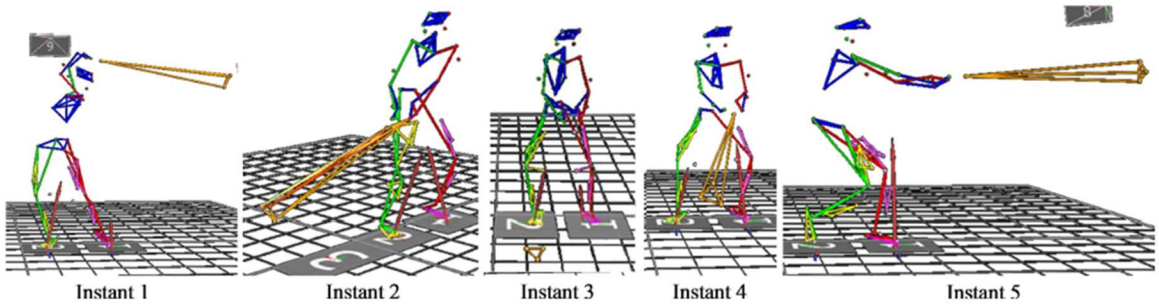


Figure 1: Key instants of the entry phase: the beginning of the active phase after the last preliminary turn Instant 1), the descending phase of the hammer on the right side of the thrower (Instant 2), the passage of the hammer in front of the thrower's right foot (Instant 3), the reaching of the low point of the hammer's path (Instant 4), and the end of the entry phase with the landing of the right foot from the ground (Instant 5).

References (Optional)

[1] Castaldi, G.M. et al. Biomechanics of the hammer throw: Narrative review. Frontiers in Sports and Active Living, 4(853536), 2022.

Session Category

Human Motion and Performance: Sports

P1-377

Functional Usability and User Satisfaction of the Optical Screening for Injury Resilience (OSCIR) System

Ms. Vianey Hortencia Ocampo[1,2], Mr. Joshua Kline[3,4], Ms. Nicole Donahue[3,4], Mr. Nikolas Lamb[3,4], Mr. Dan Clapp[3,4], Ms. Helene Huang[3,4], Dr. Serge Roy[3,4], Mr. Gianluca De Luca[3,4], Ms. Bhawna Shiwani[3,4], Ms. Amy Silder[2]

[1]Leidos Inc, San Deigo, CA, United States. [2]Naval Health Research Center, San Deigo, CA, United States. [3]Altec Inc, Natick, MA, United States. [4]Delsys Inc, Natick, MA, United States

Introduction

The Optical Screening for Injury Resilience (OSCIR) system was developed to aid in the prevention and recovery of musculoskeletal injuries. It is a portable, markerless motion feedback system that provides offline, real-time feedback on technique during commonly performed exercises. The software displays real-time body tracking (e.g., joint angles, body/equipment alignment), repetition counts, and error indicators then stores the metrics locally, without relying on cloud services. The system is portable and can be set up in ~10 minutes. In this study, the System Usability Scale (SUS) was used to understand the functional usability of OSCIR at military fitness facilities.

Methods

Active-duty participants (n=33) were recruited from local U.S. Navy and Marine Corps fitness facilities. Participants were asked to select and perform a minimum of three exercises, then complete the SUS and provide open-ended feedback. Options included plank, pushup, forward lunge, deadlift, double-leg squat, overhead press, jump squat, side hop, and single-leg balance. Questions from the usability section of the SUS (8-of-10 questions, excluding Q4 and Q10) were considered [1].

Results

Open-ended feedback was positive and the mean (SD) SUS score was 80.77 (12.93), indicating “excellent” usability (>80) [2]. Most answers suggested users would “use this system frequently”, that it “was easy to use”, and that “most people would learn to use this system very quickly.” Negative feedback included comments like, “certain exercises [worked] better than others” and comments focused on tuning the software to provide more intuitive cues like, “Keep chest up” rather than a “Trunk-tibia alignment” error.

Discussion

The mean SUS score met the universal benchmark for a good experience and suggests excellent usability. Questions related to frequency of use, complexity, and the learning curve for system usability received the highest scores. Participants noted the system was great for correcting 'technique' and posture. They appreciated the readily available quantitative movement metrics and could see this system being incorporated into their typical unit training activities. We are currently working to integrate OSCIR for clinical care and to provide feedback during normal training.

Images (Optional)

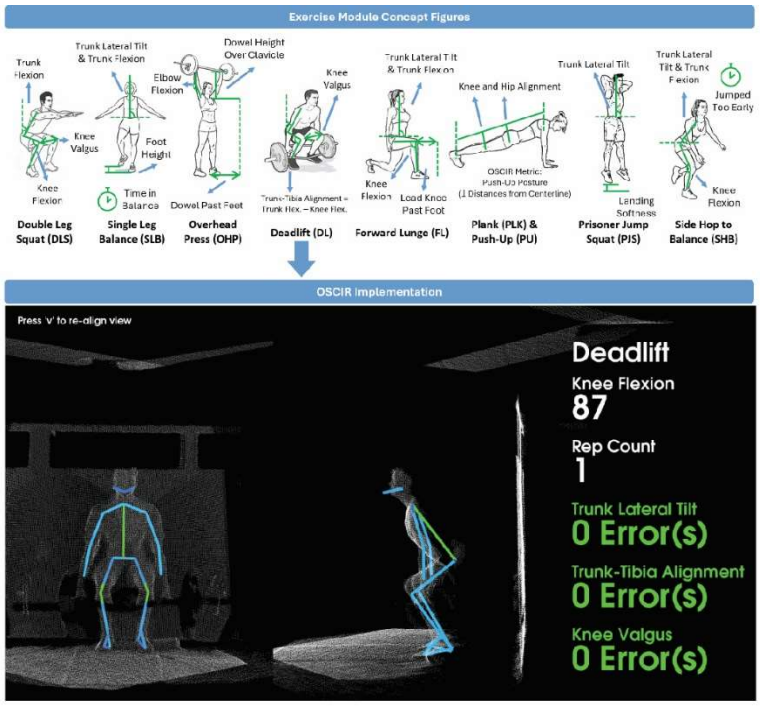


Figure 1: Sketches of the OSCIR exercise modules with subsets of spatial- and angular-based form-flagging outcome metrics (top); Example real-time graphical user interface of the Deadlift module (bottom). Top schematics courtesy of Altec Inc and bottom image courtesy of NHRC.

References (Optional)

[1] Brooke, J., Usability Evaluation in Industry, 1996

[2] Lewis, J. et. al., J Usability Studies, 2018

Session Category

Human Motion and Performance: Sports

P1-378

Concurrent Validity of an Inertial Measurement System for Evaluating Energy Fluctuation in Pole Vaulting

M Victor RESTRAT PhD student[1,2], M Guillaume Nicolas PhD[2], M Georges Dumont Full Professor[1], M Bideau Nicolas PhD[2]

[1]IRISA, Rennes, Bretagne, France. [2]M2S, Rennes, Bretagne, France

Introduction

Pole vault performance is strongly influenced by mechanical energy generated and transferred during the run-up and take-off phases [1]. While 2D video approaches are commonly used to estimate these parameters, they have notable limitations [2]. Inertial measurement units (IMUs) have emerged as alternative tools in sports biomechanics, but their accuracy in quantifying pole vault energy dynamics remains unvalidated. This study aims to assess the concurrent validity of embedded IMUs by comparing them with a reference optoelectronic marker-based system to evaluate energy exchanges under realistic, in situ conditions.

Methods

In this ongoing study, four pole vaulters (2F, 2M) each performed six vaults (soft and medium poles; bar heights: 3.30 m for females, 4.30–4.50 m for males). Kinematics were recorded simultaneously with Xsens MVN Awinda (17 IMUs, 60 Hz) and Qualisys motion capture (20 cameras, 240 Hz; 42 markers), synchronized via a SyncUnit. Kinetic, potential, and mechanical energies were computed at take-off (TO), maximal pole bend (MPB), and bar clearance (BC) using a full-body model [3].

Results

Results show excellent agreement between IMU and Marker based system for kinetic, potential and mechanical energies with mean differences consistently below 1.2 J/kg. Across all trials, RMS values for KE, EPP and EM were moderate for TO to MPB phase with respectively (1.8 J/kg, 1.1 J/kg and 1.1 J/kg) and for the MPB to BC phase (0.5 J/kg, 1.2 J/kg and 1.1 J/kg).

Discussion

The IMU system provides robust estimates of energetics variables throughout the vaulting cycle, with low absolute error in relation to the observed energy amplitude. The elevated

RMS values for KE during the TO to MPB phase may reflect the system's sensitivity to variations in segmental velocity. The limited magnitude of relative errors and inter-trial variability supports its use in quantitative in situ biomechanical analysis. A kinematic and dynamic analysis could enhance this study by establishing links between the athletes' technical qualities and energy quantities.

Images (Optional)

Technique	*KE* (J/kg)			*EPP* (J/kg)			*EM* (J/kg)		
	TO	MPB	BC	TO	MPB	BC	TO	MPB	BC
IMU	24.2 ± 0.7	6.5 ± 1.2	5.1 ± 0.7	10.2 ± 0.1	18.5 ± 0.9	36.5± 0.2	34.7 ± 0.7	25.1 ± 0.5	41.5 ± 0.9
Marker	25.4 ± 0.8	6.0 ± 0.2	4.35 ± 0.2	9.4 ± 0.3	18.5 ± 0.2	35.5 ± 0.4	34.9 ± 0.5	24.5 ± 0.2	39.8 ± 0.6
Difference	-1.2 ± 1.2	0.5 ± 1.1	0.7 ± 0.5	0.8 ± 0.3	-0.04 ± 0.7	-0.9 ± 0.4	-0.5 ± 1.1	0.5 ± 0.5	1.7 ± 0.8
%	- 4.73 ± 4.65 %	8.3 ± 18.6 %	16.2 ± 11.2 %	8.1 ± 3.2 %	0.2 ± 3.6 %	-2.8 ± 1.1 %	-1.3 ± 3.1 %	2.2 ± 2.2 %	4.2 ± 2.1 %

References (Optional)

[1] Frère et al. , Sports Biomechanics, 2021

[2] Cassirame et al., Journal of Sport Sciences, 2024

[3] Muller et al., Journal of Open Source Software, 2019

Acknowledgements (Optional)

The present study was supported by French National Research Agency under the Investments for the Future program (PIA) with the grant ANR-21-ESRE-0030 CONTINUUM project and within the framework of the (PIA) EUR DIGISPORT ANR-18-EURE-0022.

Session Category

Human Motion and Performance: Sports

P1-379

Kinematic and Kinetic Modulation of Joint Stiffness Across Sequential Landing Phases in Drop Vertical Jumps

PhD Student Victoria Vandiver MA, Dr. Changki Kim Ph.D, Dr. Timothy Lowe Ph.D

The University of Alabama, Tuscaloosa, AL, United States

Introduction

Drop vertical jumps (DVJs) are widely used to assess rehabilitation progress and sport performance. DVJs include two landings that represent distinct motor tasks with different neuromechanical demands. The first landing primarily reflects pre-planned control strategies, while the second requires adaptive regulation influenced by the preceding jump, including variable timing, trajectory, and center-of-mass dynamics. These task-dependent differences affect how athletes coordinate force attenuation and modulate joint stiffness. Comparing stiffness across landings therefore provides a mechanistic view of how neuromechanical control adapts to changing movement constraints, offering insight into joint function, loading strategies, and potential performance or injury-related compensations.

Methods

Eleven healthy adults with no injury history performed three single-leg DVJs from a 0.30-m platform using their preferred limb. Participants landed on a force plate, jumped vertically as high as possible, and returned to the same plate. Peak vertical ground reaction force (vGRF) was recorded, and peak joint angles, moments, and joint stiffness were calculated for the first and second landings. vGRF and moments were normalized to body weight. Paired t-tests compared biomechanics between landings ($\alpha=0.05$).

Results

No differences were found in max or peak vGRF or in hip, knee, or ankle stiffness between landings (all $p > 0.09$). COM height decreased from the first to second jump (1.29 ± 0.06 m vs. 1.17 ± 0.07 m, $p < 0.01$). Despite similar loading, several kinematic and kinetic variables changed. At the hip, initial angle, peak angle, and initial moment all decreased ($p \leq 0.04$). At the knee, initial angle and peak moment increased ($p \leq 0.05$), while knee excursion decreased ($p < 0.01$). At the ankle, peak angle and peak moment increased during the second landing ($p \leq 0.05$).

Discussion

Joint stiffness was unchanged, however, differences in stiffness components across landings were observed. Suggesting that landing mechanics were altered to preserve joint stiffness. Peak COM was different despite vGRF being unaffected. The observed differences in the second landing produced an increased vGRF, despite peak height differences. This suggests, that changes in landing mechanics diminish force attenuation. These findings demonstrate the importance of analyzing the second landing to offer insight into joint function, loading strategies, and illuminate performance and injury-related compensations.

Session Category

Human Motion and Performance: Sports

P1-380

Lower-Limb Intracellular Water Is Associated With Glucose Rate-of-Change During Moderate-Intensity Running

Master's Student Wooyoung Park, Professor Sukyung Park

KAIST, Daejeon, Daejeon, Korea, Republic of

Introduction

Maintaining stable glucose regulation during exercise is essential for sustaining performance, as it is tightly linked to energy metabolism. Previous studies using continuous glucose monitoring (CGM) have focused mainly on exercise-related factors such as intensity and duration. Yet glucose responses still vary considerably across individuals under identical loads, suggesting that intrinsic skeletal muscle characteristics—including muscle mass, fiber composition, and cellular hydration—may influence glucose dynamics. However, the relationship between these muscle properties and glucose change rates during exercise remains unclear. This study investigated the association between lower-limb intracellular water (ICW), a proxy for active muscle cell volume, and glucose change rate during aerobic exercise.

Methods

A total of 21 adults (20–58 years) participated. Body composition was measured before exercise using the InBody BWA 2.0 system, and glucose levels were recorded via a Dexcom G7 CGM attached to the upper arm. All participants completed a 60-minute treadmill run in a fasting state (>8 hours), maintaining 40–65% heart-rate reserve. Heart rate was continuously monitored with a smartwatch, and HRmax was estimated using the age-predicted formula (220 – age). Treadmill speed was adjusted throughout the session to ensure the target HRR range was maintained. The glucose change rate was calculated using linear regression on CGM data collected at 5-minute intervals. Each participant completed two to three sessions, and the average glucose slope was used for analysis. The relationship between glucose change rate and lower-limb ICW ratio was examined.

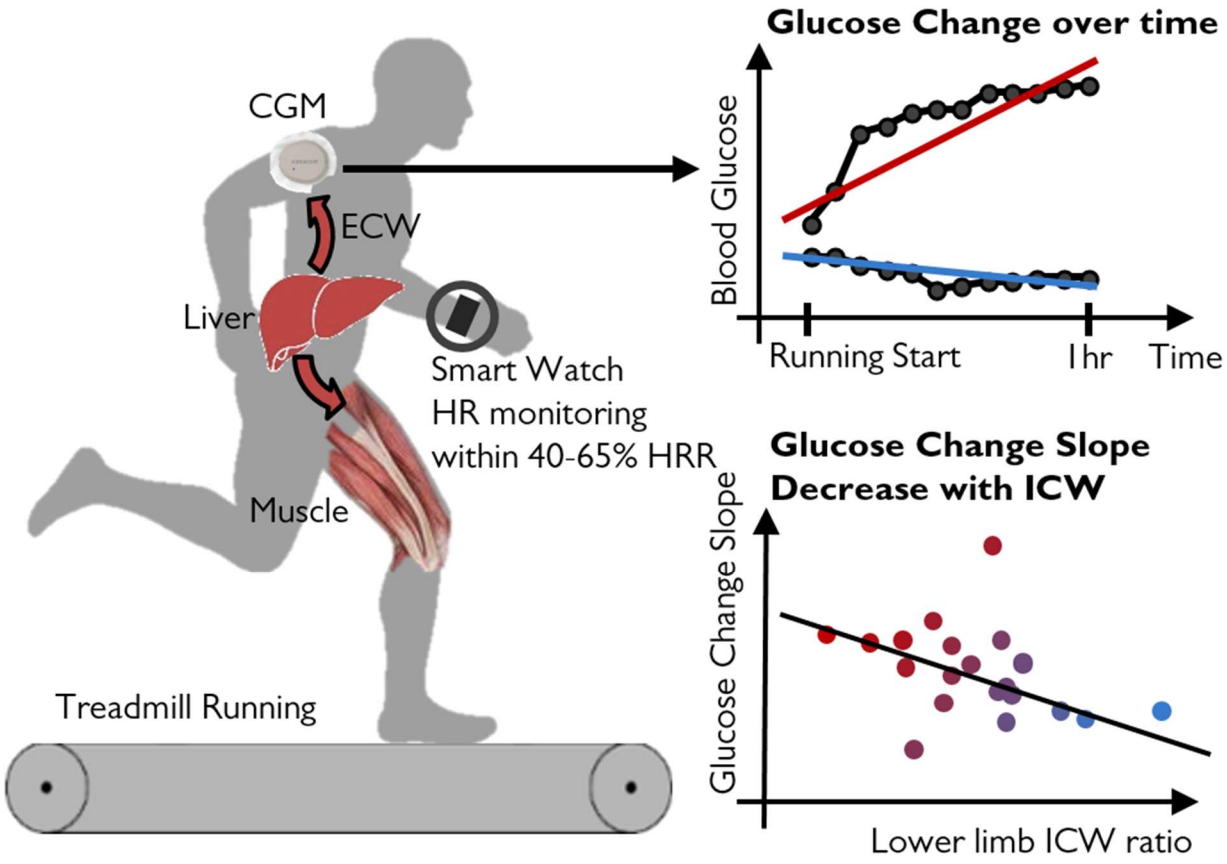
Results

Across all participants running at moderate intensity based on HRR, a weak negative association was observed between glucose slope and lower-limb ICW ratio ($R^2 = 0.120$, $p = 0.12$), suggesting that muscle cellular properties may partially contribute to individual differences in glucose responses during exercise. This relationship appeared more pronounced in recreational runners, whereas no significant association was found in more experienced runners.

Discussion

These findings indicate that intracellular hydration and muscle/body composition may be related to glucose stability during exercise. This relationship has potential implications for assessing hypoglycemia risk during physical activity, designing hydration and nutrition strategies, developing personalized exercise prescriptions that consider body composition, and improving predictive models of glucose dynamics.

Images (Optional)



Acknowledgements (Optional)

This research was supported by the Faculty Basic Research Funds for 2025 (A0601003029) of KAIST, Research Foundation of Korea (NRF) grant funded by the Korea government (MSIT) (No. N01250940)

Session Category

Human Motion and Performance: Sports

P1-381

Dynamic Foot Perception: Differences in Sensory Sensitivity Between Marathon and Basketball Athletes Under Simulated Motion States

Bachelor Rongxi Lan[1], Dortor Fan Yang[2], Associate professor Xianyi Zhang[1]

[1]SunYat-sen university, Shenzhen, Guangdong, China. [2]Li Ning Sports Science Application Research Center, Tongzhou, Bejing, China

Introduction

Research on physiological plantar perception threshold, specifically tactile, vibration, and pressure pain threshold, is largely limited to static conditions, failing to reflect the dynamic demands of active sports. This study aims to bridge this gap by quantifying sensory thresholds under static versus simulated motion states. The primary objective is to evaluate how simulated motion states affects plantar sensitivity and to determine differences in plantar sensory thresholds between marathon runners and basketball players.

Methods

Twenty male athletes (10 marathon runners and 10 basketball players) were recruited. Sensory thresholds were measured at 6 anatomical locations on the foot sole using Semmes-Weinstein filaments (tactile threshold), a neurothesiometer (vibration threshold), and a digital force gauge (pressure pain threshold). Simulated running phases (heel strike, mid-stance, and toe-off) were achieved by fixing the foot at specific joint angles using custom 3D-printed devices while participants adopted corresponding joint positions. Measurements were conducted only when participants actively replicated certain percentage of the specific muscle activation patterns associated with each motion phase, monitored via real-time electromyography (EMG).

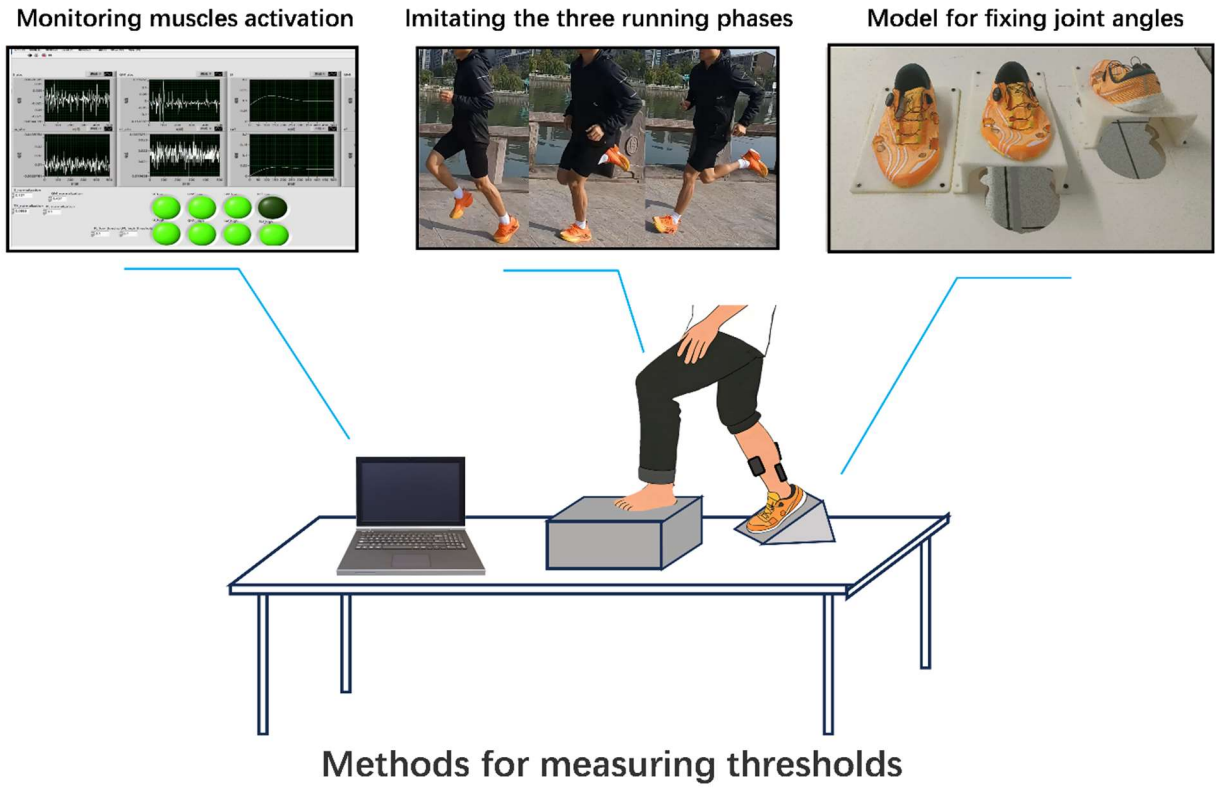
Results

Dynamic simulations revealed significant shifts in sensory thresholds. For marathon runners, plantar vibration thresholds were significantly higher in motion states compared to static conditions; specifically, the heel region showed a marked reduction in vibration threshold during the heel-strike phase ($p = 0.005$). For basketball players, plantar tactile thresholds were significantly higher in dynamic states compared to static conditions ($p < 0.001$). In inter-group comparisons, basketball players demonstrated significantly higher overall plantar pressure pain thresholds than marathon runners ($p < 0.001$).

Discussion

The findings confirm that static assessments do not accurately reflect plantar perception during athletic activity, as thresholds generally change under dynamic load, exhibiting distinct variation patterns across different plantar regions. The significantly reduced sensitivity observed in basketball players compared to runners suggests sport-specific physiological adaptations, such as callus formation. These physiological differences indicate that marathon runners may maintain higher sensory acuity for ground feedback, whereas basketball players may rely more on impact protection, providing a fundamental basis for differentiating athletic footwear design.

Images (Optional)



References (Optional)

[1]*Smith S G.V.S,et al.,* Front Bioeng Biotechnol,2021

Session Category

Human Motion and Performance: Sports

P1-382

Decreased Intra-Foot Coordination Variability on Bilateral Sides of Individuals With Unilateral Chronic Ankle Instability During Landing

Ms Xiaomei Hu[1], Ms Ziwei Zeng[1], Mr Cheukyin Ho[1], Dr Daniel Fong[2], Professor Yijian Yang[1]

[1]The Chinese University of Hong Kong, New Territories, Hong Kong, China. [2]Loughborough University, Loughborough, Leicestershire, United Kingdom

Introduction

People with unilateral chronic ankle instability (CAI) have been found to display lower limb coordination dysfunction during landing. Landing, a movement associated with the risk of ankle sprain, is widely used to detect altered motor patterns. In recent years, there were studies observed that people with unilateral CAI may present bilateral dysfunction, suggesting that the injury may influence the contralateral function. Additionally, some studies found that the ankle sprain may also affect foot function; however, little is known about the bilateral intra-foot coordination and variability in individuals with unilateral CAI. Therefore, this study aimed to investigate the intra-foot coordination and variability in bilateral sides of people with unilateral CAI. We hypothesized that individuals with unilateral CAI would exhibit decreased coordination variability in bilateral sagittal planes and increased coordination variability in bilateral frontal planes compared to healthy controls.

Methods

Forty unilateral CAI and 40 control participants aged between 18 and 40 years old were enrolled. Landing task was executed to explore the intra-foot coordination patterns and variability calculated by modified vector coding. A 2 (group) × 2 (limb) mixed-model ANOVA was applied to analyze the differences between groups and injured/uninjured sides on coordination patterns and variability.

Results

Compared to the healthy controls, participants with unilateral CAI displayed reduced coordination variability in rearfoot-midfoot (48.73 ± 2.95 vs. 50.03 ± 2.21, $p = 0.012$) and rearfoot-forefoot (49.39 ± 3.25 vs. 50.92 ± 2.29, $p = 0.005$) sagittal plane coordination bilaterally. For rearfoot-forefoot sagittal plane coordination pattens, both sides of unilateral CAI participants showed higher frequency of in-phase with proximal dominance pattern (36.24 ± 6.48 vs. 33.56 ± 6.10, $p = 0.021$) and lower frequency of in-phase with distal dominance pattern (19.35 ± 2.95 vs. 20.71 ± 3.10, $p = 0.017$) in comparison with the controls.

Discussion

Individuals with unilateral CAI exhibited an increased rearfoot-dominance coordination pattern and decreased coordination variability in sagittal planes bilaterally, suggesting a more rigid intra-foot coordination pattern. These findings also suggest that the rehabilitation regarding unilateral CAI may not only target at injured side, but also focus on contralateral side and foot. Central function evaluation and functional connectivity analysis may help elucidate the underlying mechanisms in individuals with unilateral CAI.

Session Category

Human Motion and Performance: Sports

P1-383

Running Economy and Kinetics in Rocker and Flat Carbon-Plated Shoes

Dr Yasushi Enomoto[1], Dr Yasuko Hirono[2], Ms Masako Nishihira[3]

[1]University of Tsukuba, Tsukuba, Ibaraki, Japan. [2]University of Tsukuba, Tsukuba, Ibaraki, Japan. [3]YONEX, Tokyo, Tokyo, Japan

Introduction

The purpose of this study was to compare the O_2 cost and running kinetics at faster speeds while wearing two types of carbon-plated shoes among competitive runners, and to get insight into how carbon plates contribute to improving running speed efficiently at a competitive level.

Methods

Eleven competitive distance runners belonging to a university team participated in this study. Two types of shoes equipped with a carbon plate—one with a rocker-shaped plate and the other with a flat-shaped plate (R and F) were evaluated biomechanically and physiologically. Running kinetics at 4.17, 4.76, and 5.56 m/s (low, mid, high) were measured using a motion capture system with integrated force plates on an experimental runway. In a separate experiment, oxygen uptake during treadmill running at low and mid speeds was measured using a metabolic measurement system.

Results

The results are summarized as follows. O_2 cost for F was lower than for R. Ankle torque for F was greater than for R, although no significant difference was observed in vertical ground reaction force between the two shoe types. The one of possible reason of greater ankle torque for F could be a larger anterior–posterior distance between the ankle joint center and the center of pressure (CoP) on the force plate.

Discussion

All participants exhibited a mid or fore-foot strike pattern. Their CoP shifted backward immediately after foot strike and then moved forward toward toe-off. A possible explanation is that greater ankle torque may occur concurrently with smaller knee torque

when ground reaction force remains similar, which is associated with lower energy cost during running [1]. We hypothesize that the rocker-shaped plate may not facilitate forward CoP movement once it shifts backward, compared with the flat plate, although the rocker design may assist forward CoP movement immediately after heel contact. In conclusion, flat carbon-plated shoes may reduce O_2 cost by increasing ankle joint torque in competitive distance runners.

References (Optional)

[1] Seki, K., et al., J. Sports Sciences, 2020.

Session Category

Human Motion and Performance: Sports

P1-384

Validity of IMU-based Assessment of Knee Motor Control in Difference Stance Conditions using Angular Velocity Vector Analysis

Dr. Yu Kashiwagi PhD[1], Dr. Jeffery Rankin MSE, PhD[2], Prof. Jill McNitt-Gray PhD[3]

[1]Senshu University Institute of Sport, Kawasaki, Kanagawa, Japan. [2]Pathokinesiology Laboratory and Rehabilitation Engineering, Rancho Los Amigos National Rehabilitation Center, Downey, California, United States. [3]Biological Sciences and Biomedical Engineering, University of Southern California, Los Angeles, California, United States

Dr. Yu Kashiwagi

Dr. Jeffery Rankin

Introduction

Inertial measurement units (IMUs) enable motion analysis in real-world contexts without the spatial constraints of optical motion capture. IMUs reduce preparation burden by eliminating the need for camera calibration, marker placement, and marker detection issues. Although three-dimensional joint motion reflects an individual's multijoint control strategy, its representation is dependent on global and local reference systems that are not consistently defined across platforms. We addressed these challenges by examining resultant joint angular velocity time-series, derived from adjacent segment kinematics[1], to characterize motor control during sit-to-stand (STS) tasks[2]. We hypothesized that the resultant knee angular velocity vector magnitude and direction would be comparable between measurement systems and would differentiate within-participant strategies across three STS conditions.

Methods

One adult male participated and performed ten consecutive STS movements at a self-selected tempo using three stance conditions: preferred, ankle posterior to knee, and toe-out. Movement data were collected simultaneously using a marker-based motion capture system and a seven-sensor IMU system (Vayu Technology). Forty-seven reflective markers defined the model, and each IMU was fitted with three markers to maintain spatial registration. Local segment coordinate systems were aligned to a static standing posture

and transformed into IMU frames using quaternions, which were differentiated to obtain angular velocity vectors. Five stable cycles were selected for analysis, and cross-correlation coefficients were computed for knee angles and angular velocity vectors. Three-dimensional vectors were visualized for velocity magnitudes exceeding 50% of the peak extension-phase value.

Results

Knee angular velocity vectors showed differences across stance conditions in direction, distribution, and variability, indicating altered motor strategies. Time-series patterns of quaternions and segment angles matched between collection systems (Cross-correlation coefficients: resultant angular velocity magnitude (0.925 to 0.984), direction (.158 to 0.873), knee angles (0.44 to 1.00). Correlations increased with greater rotational amplitude .

Discussion

IMU-derived angular velocity vectors demonstrated high validity compared to optical motion capture and were sensitive to differences in multijoint coordination across stance conditions. Findings support the use of IMU-based resultant angular velocity vectors to characterize joint control in diverse stances.

Images (Optional)

Table 1. Comparison of cross-correlation coefficients for knee resultant angular velocity vectors during sit-to-stand movements, measured using IMUs and motion capture across different stance conditions.

Stance	PeakCorrelation	PeakLag_sec	PeakLag_samples
Preferred	0.954	-0.010	-1.000
Ankle posterior to knee	0.984	-0.010	-1.000
Toe-out	0.958	0.080	8.000

References (Optional)

1. McNitt-Gray JL, et al. (2025) Sports Biomech Jul;24(7):1879-1898.
2. Mathiyakom W et al. (2005) Clinical Biomech 20(1),105-111.

Acknowledgements (Optional)

We would like to express our sincere appreciation to Mr. Harsh Holalad (Vayu) for his support with the data processing in this study.

Session Category

Human Motion and Performance: Sports

P1-385

Biomechanical Analysis of Compression Garment During Running

Yun-Bae Jeong M.S.[1,2], Jae-Won Kang M.S.[1,2], Jung-Min Yoon M.S.[1,2], Prof. Sihyun Ryu Ph.D.[1,2], Prof. Sukhoon Yoon Ph.D.[1,2], Prof. Sang-Kyoon Park Ph.D.[1,2]

[1]Korea National Sport University, Seoul, Seoul, Korea, Republic of. [2]Motion Innovation Center, Seoul, Seoul, Korea, Republic of

Introduction

Compression garments are widely used in sports to reduce muscle oscillation during impact without restricting movement[1]. For the lower extremities, these are typically categorized as knee sleeves (joint-targeted) and leg sleeves (muscle-targeted). While previous research has focused on vibration-dampening effects, comparative analyses of how biomechanical variables differ based on the application area remain insufficient. This study investigated the effects of joint-supporting knee sleeves and muscle-supporting leg sleeves on key biomechanical variables during running.

Methods

Fifteen healthy males participated in this study. Participants performed treadmill running for three minutes at a speed of 3.6 m/sunder three conditions: Control (C), Knee sleeve (K), and Leg sleeve (L). Kinematic and kinetic data were collected using nine infrared cameras (100 Hz) and an instrumented treadmill (1000 Hz). A one-way repeated measures ANOVA with Bonferroni post-hoc tests was used to examine differences between conditions (α=.05).

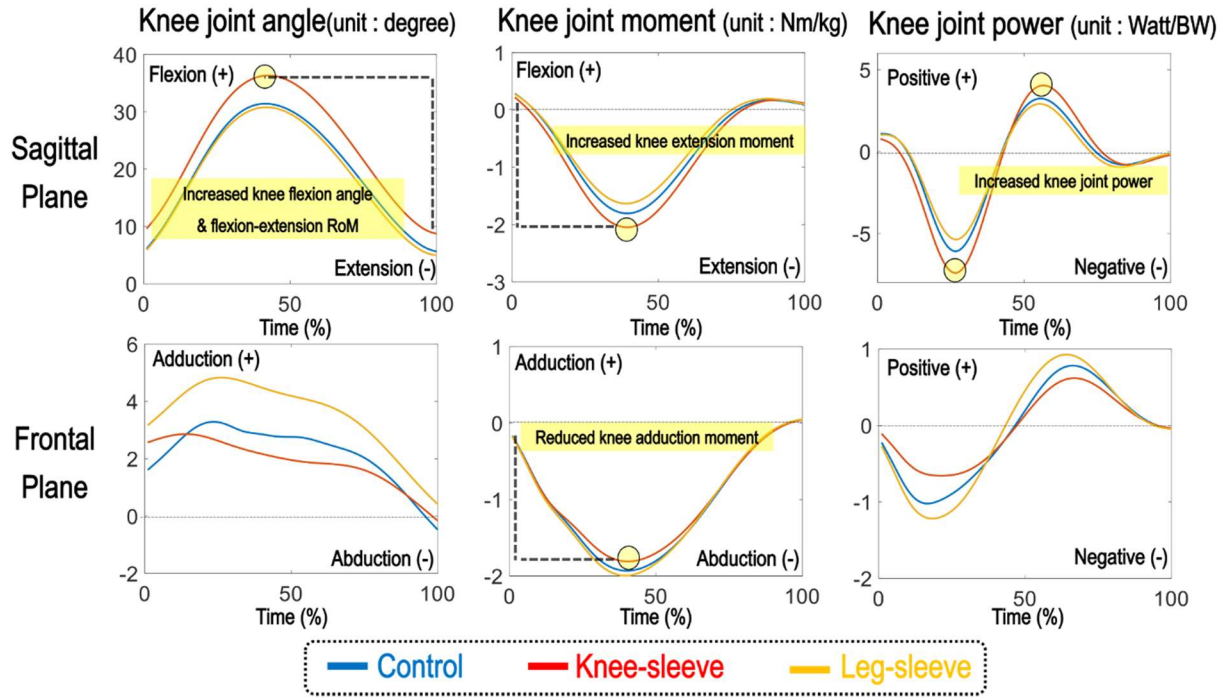
Results

No significant differences were observed in spatiotemporal variables (contact time, stride length, and cadence) among the three conditions. However, the K condition showed a significant increase in peak knee flexion angle, flexion-extension range of motion, extension angular velocity, extension moment, and negative power in the sagittal plane compared to C and L. Conversely, in the frontal plane, the K condition significantly decreased the knee adduction angle and adduction moment compared to C and L conditions.

Discussion

The knee sleeve enhanced knee frontal plane stability while increasing sagittal plane knee joint forces, whereas the leg sleeve showed no significant biomechanical changes. Given that compression garments primarily contribute to muscle protection and improved energy economy by reducing muscle oscillation during prolonged exercise, the short running duration in this study likely limited the observability of leg sleeve effects. Future studies should verify the long-term implications of increased sagittal plane loading from knee sleeves and further investigate the specific benefits of leg sleeves regarding muscle protection and energy efficiency over extended durations.

Images (Optional)



References (Optional)

[1] Deng, L., Yang, Y., Yang, C., Fang, Y., Zhang, X., Liu, L., & Fu, W. (2021). Compression garments reduce soft tissue vibrations and muscle activations during drop jumps: an accelerometry evaluation. Sensors, 21(16), 5644.

Acknowledgements (Optional)

This study was supported by the National Research Foundation of Korea (2022R1F1A1071359).

Session Category

Human Motion and Performance: Sports

P1-386

Joint Stiffness During the Landing Stage in Table Tennis Footwork

Asst. Prof. Yuqi He[1,2], Assoc. Prof. Daisuke Takeshita[2], Asst. Prof. Ping Yeap Loh[3], Prof. Guopeng Hu[1]

[1]Huaqiao Univesity, Quanzhou, Fujian, China. [2]The University of Tokyo, Tokyo, Tokyo, Japan. [3]Kyushu Universiy, Fukuoka, Kyushu, Japan

Introduction

The joint reaction force (JRF) and stiffness are important indicators to evaluate the mechanical performance of joints during movement. The purpose of this study is to explore the JRF and joint stiffness of the chasse-step (CS) and one-step (OS) footwork during the landing phase to further reveal the intrinsic mechanical mechanism of table tennis footwork and provide a theoretical basis for the prevention of joint injury.

Methods

Sixteen male table tennis athletes (height: 171.98 ± 4.97 cm; weight: 68.77 ± 7.86 kg; experience: 10.67 ± 1.86 years; age: 22.50 ± 1.64 years) performed CS and OS footwork to return the ball from the coach by topspin forehand stroke. The kinematics, kinetics, and muscle activity of the lower limb were recorded by the motion capture, force platform, and Electromyography (EMG) system. Statistical parametric mapping (SPM) analysis was used to investigate any difference between the CS and OS footwork during the stroke.

Results

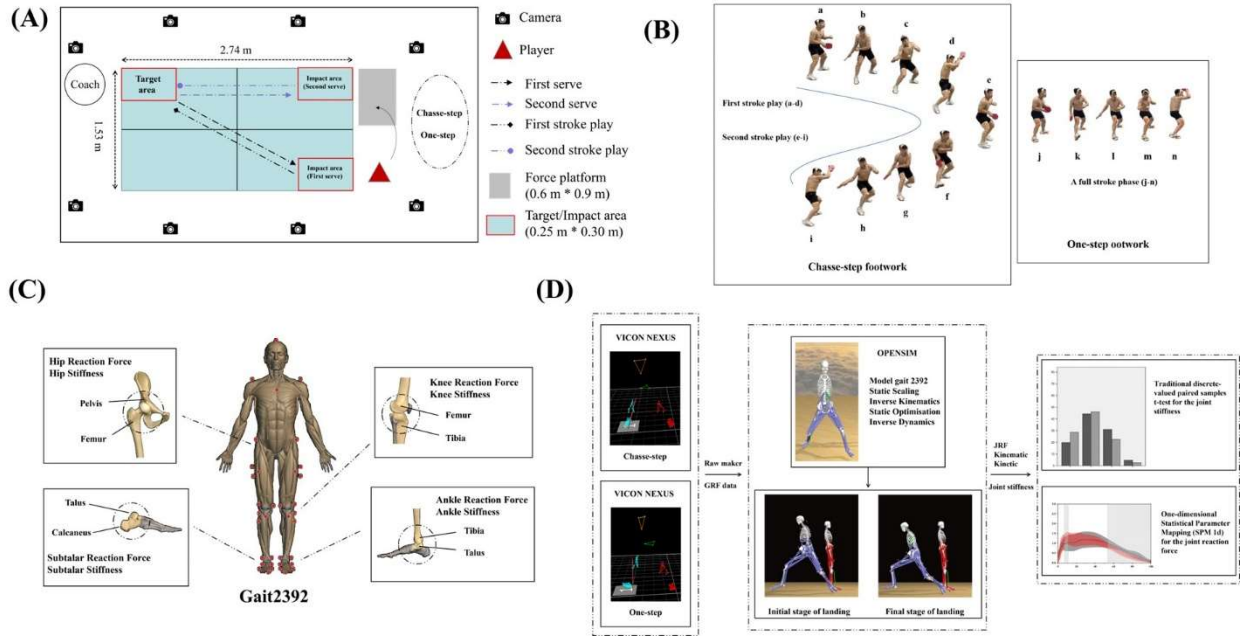
During landing, the subtalar joint exhibits the greatest joint stiffness (0.242±0.078 in CS, 0.338±0.185 in OS). Compared with OS, the stiffness of the knee and hip's transverse plane in the CS was significantly greater (Knee: CS = 0.072 ± 0.011 N·M·KG-1·Deg-1, OS = 0.038 ± 0.010 N·M·KG-1·Deg-1, $t = 9.487$, $p = 0$; Hip: CS = 0.119 ± 0.037 N·M·KG-1·Deg-1, OS = 0.073 ± 0.027 N·M·KG-1·Deg-1, $t = 3.934$, $p = 0$).

The results shows that 1) in the knee, the JRF in CS was significantly greater than in OS in the percentage of 30.89-35.83% ($p = 0.035$) and 36.19-100% ($p < 0.001$) but lower than in OS in the percentage of 8.74-14.05% ($p = 0.034$). 2) in the subtalar, the JRF in CS was significantly greater than in OS in the percentage of 24.24-30.15% ($p = 0.028$) and 41.14-100% ($p < 0.001$).

Discussion

The results of this study can be applied to movement control and injury prevention in table tennis footwork.

Images (Optional)



Session Category

Human Motion and Performance: Sports

P1-387

Leveraging Biomechanics for Rugby Player Safety: Insights from the FIR

Dott.ssa Fabiola Spolaor[1], PhD Student Federica Beghetti[1], Ing. Federica Cibin[2], Mr. Davide Bruschi[1], Dott. Giovanni Biondi[3], Associate Professor Zimi Sawacha[1]

[1]Department of Information Engineering, University of Padova, Italy, Padova, ITA, Italy. [2]BBSoF - Beyond Biomechanics Sport on Field, Padova, ITA, Italy. [3]FIR (Federazione Italiana Rugby), Roma, ITA, Italy

Introduction

Rugby is a high-contact sport with frequent collisions and rapid directional changes, leading to a high risk of lower-limb injuries, especially ACL ruptures [1]. Traditional prevention relies on general functional tests, which partially capture sport-specific mechanical demands and lack ecological validity [2]. The Italian Rugby Federation implemented a rugby-specific cutting task after an up-and-under reception, combining video and pressure-insole analysis to assess joint kinematics and kinetics. through ACL Quick Check® [3] method. Multi-technique clustering was applied to identify subgroups with similar biomechanical deficits and guide targeted exercises.

Methods

Ninety-two rugby players (17 ± 5 years, 27 ± 3 kg/m^2) were assessed on-site using seven synchronized cameras (GoPro Hero, 30–240 Hz) and a wireless plantar pressure system (X Sensor, 200 sensors, 100 Hz). Each player performed four sidestep cuts (two per side) with randomly assigned direction and the following variables were computed: hip, knee, ankle angles and torques, joint ranges of motion, vertical ground reaction forces, each variable peak occurrence within the task duration. A subgroup of athletes with no history of injuries was selected to define the normative bands. Unsupervised machine-learning analysis (K-means, Hierarchical Clustering, DBSCAN) was applied to the remaining 42 athletes, using grid-search and Silhouette scores to select optimal parameters and cluster counts. The resulting clusters were used to assign athletes to exercise groups, and an expert trainer's independent assignments served as the benchmark for validation.

Results

Results revealed four distinct clusters: two (3, 0) characterized by altered hip and knee biomechanics. Cluster 3 was characterized by increased hip adduction and reduced hip flexion moments. Cluster 0 displayed a similar pattern but with a deeper squat strategy, further accentuating these biomechanical alterations. In contrast, Cluster 2 grouped

athletes demonstrating more efficient joint coordination and overall better management of the task.

Discussion

A good agreement was found between personal trainer assignment and clustering based one. Identification of recurrent hip-driven deficits underscores the importance of proximal control in ACL-risk biomechanics. The variability in compensatory strategies highlights the need for biomechanics-based interventions.

Images (Optional)

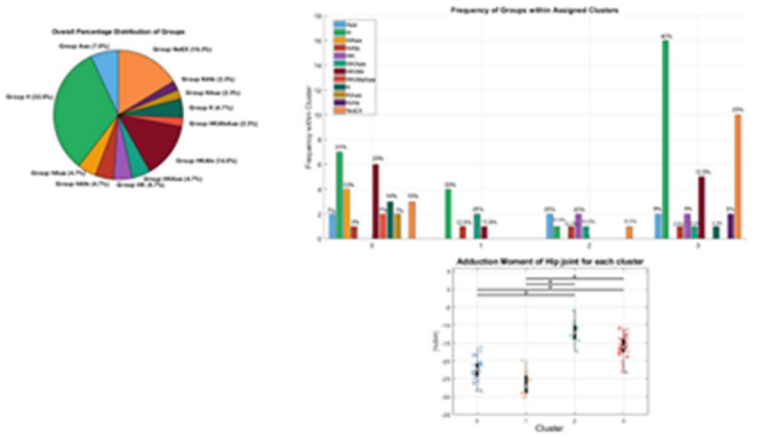


Fig. 1: *Left:* Pie chart illustrating the proportion of athletes assigned to each exercise group according to the personal trainer's classification. The NoEx group includes athletes with no detected alterations; HIP represents hip-related alterations (H); KNEE indicates knee-related alterations (K); and ANKLE corresponds to ankle-related alterations (A), with subgroups distinguishing dorsiflexion/plantarflexion issues (Afe) and adduction/abduction deficits (Aaa). Mixed groups reflect combinations of two or more of these biomechanical alterations.
Top Right: Histogram showing the distribution of athletes across the four clusters identified through the k-means analysis. The comparison provides insight into the differences between practitioner-based and data-driven groupings.
Bottom Right: Boxplot and scatter plot with all the observations of the adduction torque of the hip joint, for each cluster.

References (Optional)

[1] van Zyl S.*Phys Ther Sport*. 2024;

[2] Weir G. et al. *Sports Biomechanics*. 2021;

[3] Guiotto A. et al.,*Sensors*. 2021

Session Category

Human Motion and Performance: Sports

P1-389

Acoustic Microfluidic Confinement Elucidates the Photoshock Response of Light-Sensitive Microswimmers

Prof. J. Mark Meacham[1], Mr. Advaith Narayan[1], Dr. Mingyang Cui[1,2], Prof. Susan Dutcher[3], Prof. Philip Bayly[1]

[1]Washington University in St. Louis, St. Louis, MO, United States. [2]Massachusetts Institute of Technology, Cambridge, MA, United States. [3]Washington University School of Medicine in St. Louis, St. Louis, MO, United States

Introduction

Conventional studies of sustained cilia motion in microswimmers are laborious, time-intensive, and overconstrained as rapidly swimming cells must be immobilized to observe their behavior over time. Alternatively, acoustic tweezers are able to trap the (microscale) cell body without affecting the natural motion of the (nanoscale) cilia. This capability enables detailed investigation of photoshock in wild-type *Chlamydomonas reinhardtii* cells.

Methods

Two acoustic tweezers were developed: (i) a circular chamber with a central node for population-based trap-and-release motility assessment and (ii) a square chamber with an array of traps for studying cilia dynamics in individual cells (see figure panel **a**). Both devices used Cr/Au interdigital transducers (IDTs) on $LiNbO_3$ piezoelectric substrates to generate standing acoustic waves within fluid-filled glass channels. Photoshock was induced using a red-to-white-light illumination change. For trap-and-release experiments, ultrasound removal was synchronized with photoshock; cell trajectories were used to determine swimming speed and linearity of the cell populations. For single-cell analyses, the trap remained on during and after photoshock (panel **b**).

Results

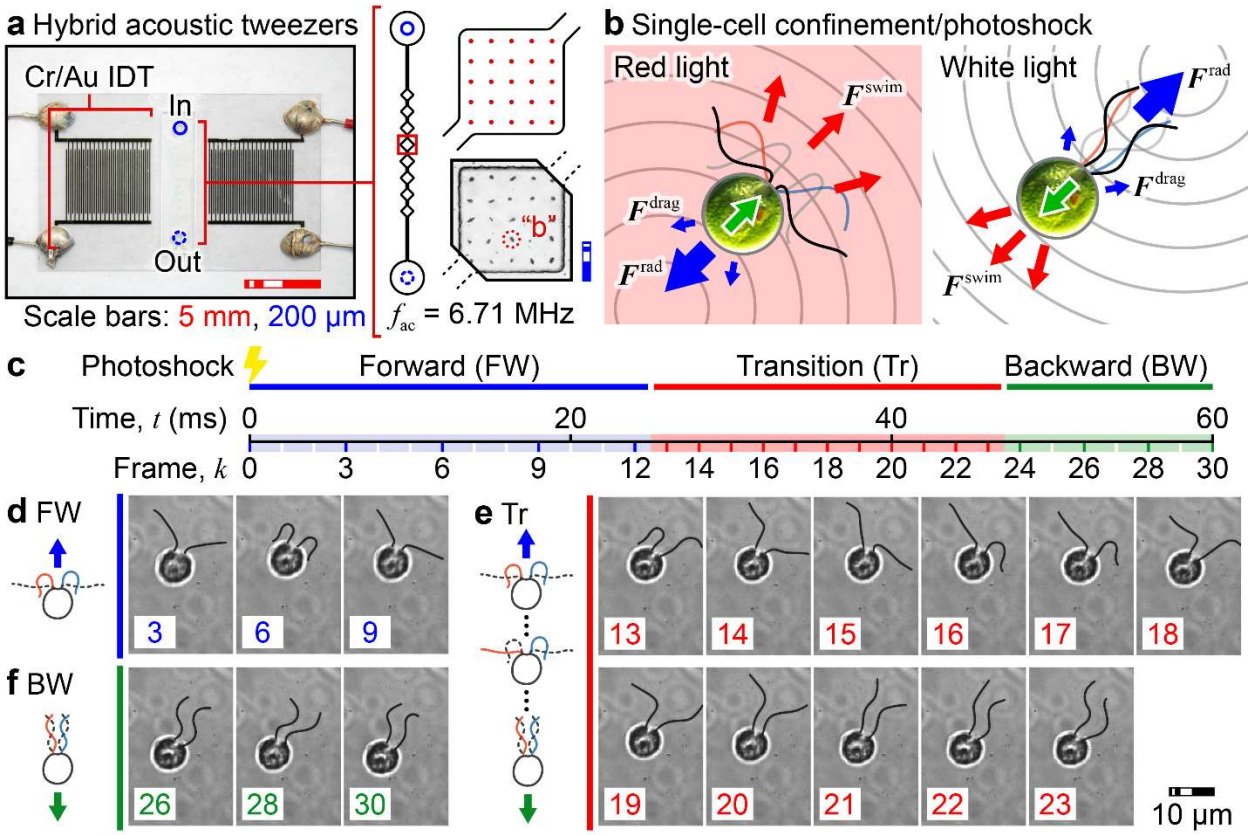
Slightly more than half of the light-treated cells (13 of 22 over two experiments) exhibited backward swimming based on a low median speed u = 26.7 μm/s. Some treated cells (4 of 22) maintained a forward swimming presentation (less linear, significantly higher u = 77.4 μm/s). The remaining cells were unidentifiable. The median speed of untreated control cells was 88.2 μm/s (12 cells). Acoustic confinement enabled high-resolution imaging of the two cilia during the transition from forward to photoshock-induced backward

swimming (panels **c-f**). The asymmetric mode that propels cells in forward swimming was observed for ~12 frames (two beat cycles at ~80 Hz) after the photoshock stimulus (panel **d**). The two cilia transitioned independently with one (right cilium, panel **e**) accelerating before both cilia extended to take on the symmetric, undulatory beat pattern indicative of backward swimming (panel **f**).

Discussion

Acoustic tweezers are versatile tools for exploring microswimmer behavior at the multi-organism-, organism-, and organelle-scales. Cilia behavior is consistent with prior studies using uniciliated mutants or cells held rigidly on micropipettes; however, acoustic tweezers do not rely on rigid immobilization, thus allowing locally free, three-dimensional swimming.

Images (Optional)



Acknowledgements (Optional)

This work was supported under National Science Foundation Grants No. CMMI-1633971 and CBET-1944063. The authors acknowledge use of the Institute of Materials Science and Engineering microfabrication facility at Washington University in St. Louis.

Session Category

Micro/Biofluidics: Experiments

P1-390

A Study on Vascular Endothelial Cell Mechanobiological Responses to Disturbed Flows Around Narrow Vessels Based on Vessel-on-a-Chip Model

Dr. Jifeng Ren, Ms. Dong Ma

Capital Medical University, Beijing, Beijing, China

Introduction

Atherosclerosis is a leading global cause of mortality and disability worldwide. This progressive condition, which leads to vascular narrow and triggers severe cardiovascular events. Narrow vessel regions existing in most atherosclerosis cases, therefore abnormal flow conditions such as disturbed flow usually occur. Since traditional cell culture methods struggle to replicate physiological functions of blood vessels, novel research methods should be applied. Vessel-on-a-chip systems not only replicate specific mechanical conditions of diseased regions but also allow real-time observation of cellular behaviors and molecular mechanisms. In this study, vessel-on-a-chip models with different cell mechanical properties were built to unveil mechanobiological clues in the progression of atherosclerosis.

Methods

Microfluidic device design and fabrication: A straight vessel containing partial narrow regions was designed to mimic the pathological condition of atherosclerosis. The microfluidic devices were fabricated by following standard soft lithography process.

Cell culture: Human umbilical vein endothelial cells (HUVECs) were used in this study. Cells were first cultured in flasks and resuspended using trypsin-EDTA before seeding into microfluidic chips.

Cell viscoelasticity measurement: Cell viscoelasticity can be quantified using a previously developed microfluidic cytometer (see *ref*[1,2]).

Abnormal viscoelasticity cell model: High viscoelasticity HUVECs can be induced by using an actin polymerization inducer Jasplakinolide.

Results

By considering cells as standard linear solid materials, higher viscoelastic parameters (i.e. viscosity, instant elasticity & relaxed elasticity) were discovered in Jasplakinolide treated HUVECs using microfluidic cytometer measurement.

Disturbed flow streamlines can be observed around narrow vessel regions, indicating abnormal flow condition is realized in our vessel-on-a-chip devices.

Epithelial mesenchymal transition marker vimentin was discovered to have higher expression level in Jasplakinolide treated vessel-on-a-chip model.

Discussion

Our current results indicate abnormal high cell mechanical property is an important factor in the progression of atherosclerosis, which is consist with the alternations of cell viscoelasticity in senescent HUVEC models (*ref*[2]). The limitation of the study is shortage of protein types to reflect HUVEC epithelial mesenchymal transition. In the future, we are planning to involve more protein types such as alpha-SMA to solidify findings in this study.

References (Optional)

[1] Jifeng Ren *et al*. , Lab Chip, 2020

[2] Dong Ma *et al*. , Cell Rep. Phys. Sci., 2025

Acknowledgements (Optional)

The authors would like to thank financial supports from the National Natural Science Foundation of China (project no. 12402380).

Session Category

Micro/Biofluidics: Experiments

P1-391

Development of Microfluidic Devices to Generate Oxygen and pH Heterogeneity

Mr. Taishi Nakamura B.Eng., Prof. Kenichi Funamoto Ph.D.

Tohoku University, Sendai, Miyagi, Japan

Introduction

Heterogeneous hypoxic and acidic (pH < 7.4) conditions are generated in cancer and inflammatory microenvironments due to massive O_2 consumption and lactate release during glycolysis. Hence, elucidation of the effects of O_2 and pH on cell dynamics and functions is essential to develop novel therapeutic strategies for these diseases. However, conventional cell culture systems have had difficulties in reproducing in vivo microenvironments with spatiotemporal changes of O_2 and pH. Here, we introduce microfluidic devices to rapidly and precisely control dissolved gas concentrations around cells.

Methods

The microfluidic devices were fabricated from polydimethylsiloxane (PDMS), a polycarbonate (PC) film, and a glass coverslip [1]. Cell culture channels were located on the glass coverslip, and gas channels were formed above them. By supplying gas mixtures with adjusted components (O_2, CO_2, and N_2) to the gas channels, O_2 and CO_2 concentrations were controlled by gas exchange through the gas-permeable PDMS layer between the channels. Subsequently, the chemical equilibrium of $NaHCO_3$ supplemented in the cell culture media was shifted by dissolved CO_2, enabling pH control. A low gas-permeable PC film was embedded in the device covering the channels to reduce infusion of ambient gas components. The steady-state and transient characteristics of dissolved gas control were investigated by numerical simulations and validated experimentally using materials that exhibited O_2-dependent phosphorescence or pH-dependent fluorescence. Device feasibility was examined by observing migratory behaviors of MDA-MB-231 breast cancer cells.

Results

The devices generated arbitrary uniform or gradient conditions (0.3%–21% O_2 and pH 6.5–7.9) in cell culture channels filled with DMEM cell culture medium. Temporal characterization revealed that steady-state conditions could be achieved within 15 min after switching gas mixtures. Cell experiments showed changes in migratory behaviors of MDA-MB-231 cells. Migration speed tended to increase under hypoxic conditions. Moreover, it increased under alkaline conditions but decreased under acidic conditions,

with cells exhibiting directional migration toward regions with pH 7.6 (5% CO_2 concentration).

Discussion

Our microfluidic devices can generate arbitrary O_2 and pH conditions covering both physiological and pathological ranges. These devices are expected to be useful tools for cell experiments and drug screening.

References (Optional)

[1] Tomita et al. Sci Rep, 14, 28730 (2024).

Session Category

Micro/Biofluidics: Experiments

P1-392

Hydrophilic Macromolecule Transport into Deep Skin via Sweat Ducts: Quantitative 3D Imaging and Diffusion Simulation

Assoc. Prof. Kenji Kikuchi Doctor of Engineering[1], Researcher Keisuke Kikuchi Doctor of Pharmaceutical Sciences[2], Researcher Sanae Hirota[2]

[1]Tohoku University, Sendai, Miyagi, Japan. [2]Maruho Co.,Ltd., Kyoto, Kyoto, Japan

Assoc. Prof. Kenji Kikuchi

Researcher Keisuke Kikuchi

Introduction

Hydrophilic macromolecules and polymers with molecular weight well above 500 Da and very low log P are generally regarded as incapable of crossing the stratum corneum barrier by passive diffusion. Yet clinical experience with mucopolysaccharide polysulfate (MPS) ointments suggests pharmacological actions in deep skin, raising the question of which pathway enables such water-soluble drugs to reach dermal targets. We hypothesised that sweat ducts provide a dominant shunt route and aimed to visualise and quantify MPS transport via this pathway.

Methods

Fluorescein-labelled MPS cream was topically applied to the plantar skin of hairless regions of C57BL/6J mice. After defined application times, tissue clearing with a high-refractive-index medium enabled three-dimensional confocal imaging of individual sweat ducts and surrounding tissue. Duct morphology was characterized and parameterized as helical segments in the stratum corneum, epidermis, and dermis. Depth-dependent fluorescence attenuation was calibrated by immersing skin in solutions of known concentration and fitting a three-layer (SC/Epi/Derm) exponential attenuation model using nonlinear least-squares optimization. Fluorescence recovery after photobleaching (FRAP) provided the diffusion coefficient of MPS in the formulation. One-dimensional finite-volume simulations of diffusion along the duct, with a Michaelis–Menten sink at the secretory portion, were used to interpret the spatial distribution of drug mass.

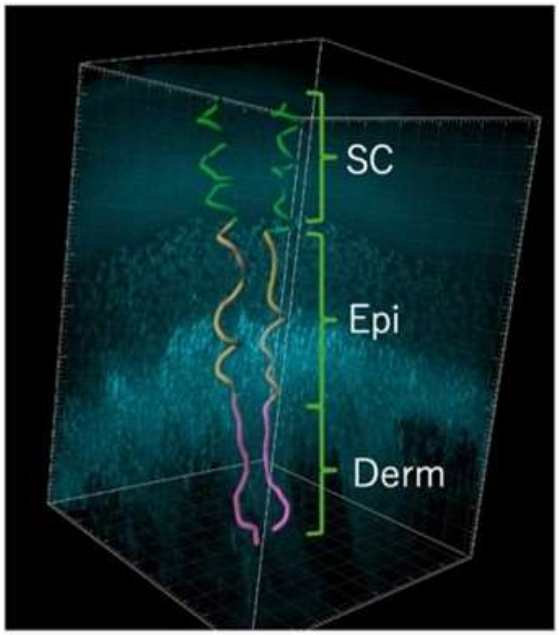
Results

Cleared-tissue imaging revealed intense MPS accumulation along the intra-epidermal duct extending several hundred micrometers below the surface. The calibrated attenuation model enabled quantitative three-dimensional maps of local drug concentration in and around sweat ducts. FRAP yielded diffusion coefficients, consistent with rheological measurements. Simulated time-evolution of duct concentration profiles reproduced the experimentally reconstructed depth-dependent accumulation and total drug amount with good qualitative agreement.

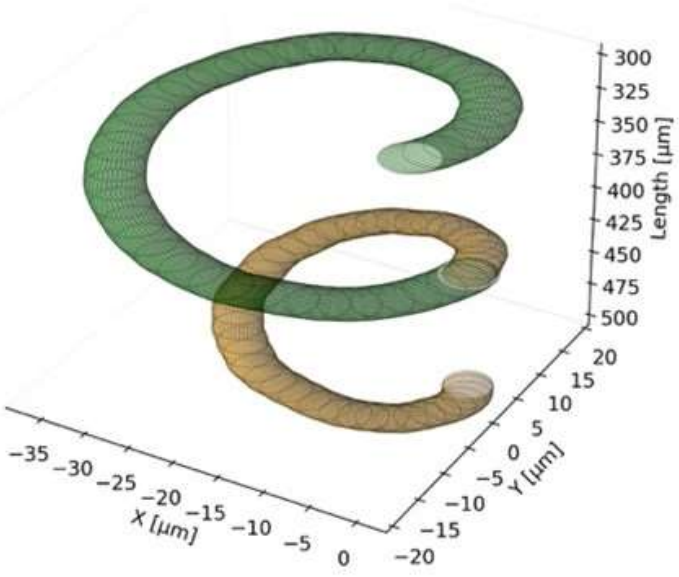
Discussion

These findings demonstrate that, in the absence of sweating, highly water-soluble, high-molecular-weight polymers such as MPS can reach deep skin layers predominantly through sweat ducts via diffusion-dominated transport. Preliminary experiments under controlled sweating conditions, which are currently ongoing, qualitatively confirm that MPS can also penetrate along sweat ducts even in the presence of outward sweat flow. The combined framework of 3D microscopic visualization, quantitative fluorescence reconstruction, and transport simulation provides a general strategy for rational design and evaluation of sweat-duct-mediated transdermal drug delivery.

Images (Optional)



Mouse sweat duct visualization and *Quantification of drug permeation*



Numerical simulation of hydrophilic drug permeation in sweat duct

Session Category

Micro/Biofluidics: Experiments

P1-393

Rheological Comparison of Resting and Stimulated Saliva in the Context of Phonation in Ectodermal Dysplasia

PD Dr.-Ing. Marion Semmler[1], Ms. Jamina Holbach[1], Dr. med. Maximilian Eckhardt[1], Dr.-Ing. Bogac Tur[1], - Sophie Wolfsteiner[1], MSc Samuel Schlicht[2], Prof. Dr.-Ing. Dietmar Drummer[2], Dr. rer. nat. Olaf Wendler[1], Prof. Dr. med. Holm Schneider[3]

[1]University Hospital Erlangen, Medical School, Division of Phoniatrics and Pediatric Audiology at the Department of Otorhinolaryngology – Head and Neck Surgery, Friedrich-Alexander-Universität Erlangen-Nürnberg, Erlangen, Bavaria, Germany. [2]Institute of Polymer Technology, Friedrich-Alexander-Universität Erlangen-Nürnberg, Erlangen, Bavaria, Germany. [3]Division of Molecular Pediatrics at the Department of Pediatrics, Friedrich-Alexander-Universität Erlangen-Nürnberg, Erlangen, Bavaria, Germany

Introduction

Patients with the rare condition Ectodermal Dysplasia (ED), a group of inherited disorders in the development of ectodermal structures, display a significant lack of skin appendages as well as a reduced function of some eccrine glands. Previous studies showed significantly reduced saliva production and impairment of the acoustic outcome in male ED patients compared to healthy male controls. ED offers a unique chance to study the fundamental role of laryngeal mucus in the phonation process. The aim of this study was a thorough rheological analysis of saliva samples serving as a non-invasively obtainable substitute for the laryngeal mucus.

Methods

This study included 36 ED patients and 96 controls. Samples of resting and stimulated saliva were obtained for a period of 5 min. The samples were measured with a plate-plate rheometer (plate diameter: 25 mm, slit width: 120 µm). Frequency was varied between f=1-10 Hz in 15 steps at τ=0.01 Pa, and the amplitude of the applied shear stress was systematically varied between τ=0.01-20Pa at 0.5 Hz in 30 steps. Storage modulus G’ and loss modulus G” were determined in both frequency and strain sweeps and were analyzed statistically with regard to differences between stimulated and resting saliva for ED patients and controls.

Results

The present study shows significantly lower values for G' und G" at lower frequencies and at lower strains for stimulated saliva compared to resting saliva in controls and female ED subjects, but not for male ED patients. With increasing frequency and strain, mean G' and G" of stimulated saliva were slightly higher than in resting saliva. Male ED subjects displayed only minor differences between resting and stimulated saliva.

Discussion

Our data suggest that resting and stimulated saliva do not differ to the same extent for male ED subjects compared to controls. The changed rheology in stimulated saliva might result from the altered concentration or molecular weight of hyaluronic acid and mucins, or overall protein concentration. The differences in the viscoelasticity between resting and stimulated saliva for the quasi-static range of lower frequencies and amplitudes indicate reduced resistance against external forces in controls, which would influence the retention rate.

Session Category

Micro/Biofluidics: Experiments

P1-394

Microfluidic-Enhanced Size-Based Cell Separation for Biomedical Applications

Mr Mohsen Hassani, Dr Amir Sanati Nezhad

University of Calgary, Calgary, AB, Canada

Mr Mohsen Hassani

Introduction

Efficient size-based separation of cells and sub-cellular particles is essential for accurate biomedical analysis and diagnostic workflows. Conventional techniques such as ultracentrifugation and precipitation method often require bulky equipment, generate shear stress, or deliver inconsistent size selectivity [1]. Microfluidic systems offer a compact, controllable alternative by leveraging laminar flow and engineered channel geometries to achieve precise, label-free separation [2]. This work presents a microfluidic-enhanced platform optimized for size-dependent cell separation, aiming to improve separation performance, purity, recovery rate, and reduce operational complexity for a range of biomedical applications.

Methods

A microfluidic platform was designed with size-selective constriction zones and a hydrodynamic filtration membrane optimized to separate cells based on their effective diameter. Devices were fabricated using Polyethylene Terephthalate (PET) film and bonded to create enclosed microchannels. Cell suspensions of defined size ranges were introduced through a single inlet under controlled capillary-driven flow, and separation was achieved as the filtration membrane selectively allowed smaller cells to pass while retaining larger ones. Outlet fractions were collected and analysed using Dynamic Light Scattering (DLS) and Nanoparticle Tracking Analysis (NTA) to quantify size distribution and recovery. Purity assessment will be conducted in the next phase of evaluation.

Results

The microfluidic platform effectively separated particles based on size using its integrated hydrodynamic filtration membrane. Filtration of ~90 µL PBS containing 500 nm particles was completed in under 5 minutes, demonstrating rapid processing capability. Tests with sweat and saliva showed consistent size-selective performance, though saliva required

slightly longer filtration due to higher viscosity. As a proof of concept, a urine sample from a cancer patient was processed, and Nanoparticle Tracking Analysis confirmed successful enrichment of particles below 100 nm with reduced larger-particle content.

Discussion

Results indicate that membrane-based microfluidic filtration provides rapid, consistent size selectivity without external pumping. Performance remained stable across fluids of varying viscosity, supporting broad applicability. Successful enrichment of sub-100 nm particles from urine highlights potential for downstream diagnostic workflows, including extracellular vesicles analysis, pathogen detection, and other size-dependent assays. The platform's simplicity positions it well for point-of-care use.

Images (Optional)

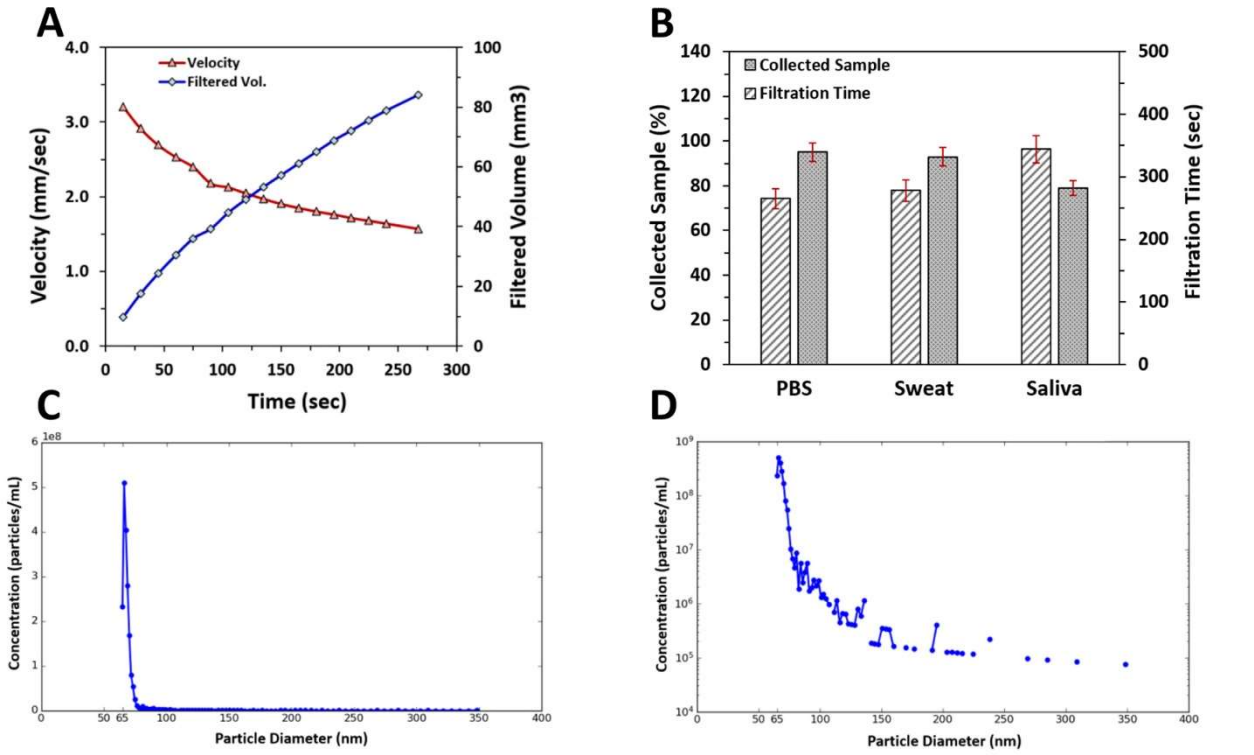


Figure 1: Performance of developed microfluidic platform; (A) Fluid velocity and filtered volume of PBS solution over the separation time, (B) Operational functionality of the microfluidic platform across various biological fluids, (C) NTA-based characterization of separated cells (extracellular vesicles) from a urine sample, (D) Magnified view of concentration and size distribution of separated cells (extracellular vesicles) in the urine sample.

References (Optional)

[1] Farshid Jaberi Ansari *et al.* , Biochemistry reports, 2024.

[2] Xudong Zhao *et al.* , ACS nano, 2025.

Session Category

Micro/Biofluidics: Experiments

P1-395

Transfection of Suspension Cells Using a Microbubble Generator That Combines Mechanical and Electrical Stimuli

Dr. Nobutoshi Ota, M.S. Kei Tateishi, Prof. Yoko Yamanishi

Kyushu University, Fukuoka, Fukuoka, Japan

Introduction

Modification of cellular functions can be achieved by delivering desired genetic materials into cells, called transfection. Physical methods of transfection shows high reproducibility due to precise control of physical parameters while one type of physical stimulation is applicable for limited cell types. To explore transfection to broader cell types, we have developed a core-shell structured microbubble generator, which performs a transfection method called electromechanical poration (EMP). EMP uses mechanical and electrical stimuli to perforate the membrane of cells. Although EMP has been applied to adherent cells [1], its capability has not been investigated for suspension cells.

Methods

Figure 1 illustrates transfection via EMP. EMP uses electric pulses, which induce electric stimulation to the suspended cells. Simultaneously, electric pulses are applied to a microbubble generator to form microbubbles at the tip of the generator. The microbubbles oscillate their volume based on applied electric pulses and provide mechanical stimulation to suspended cells.

The experimental setup is shown in Figure.2. A core-shell structured microbubble generator was consisted with a tungsten wire inserted to a glass capillary and was connected to a high-voltage power source for EMP. During EMP, target cells and plasmids were suspended in culture medium. After EMP, perforated cells were allowed to recover for 24 h. Recovered cells were evaluated by expression of a reporter gene such as green fluorescent protein (GFP), which indicates successful transfection.

Results

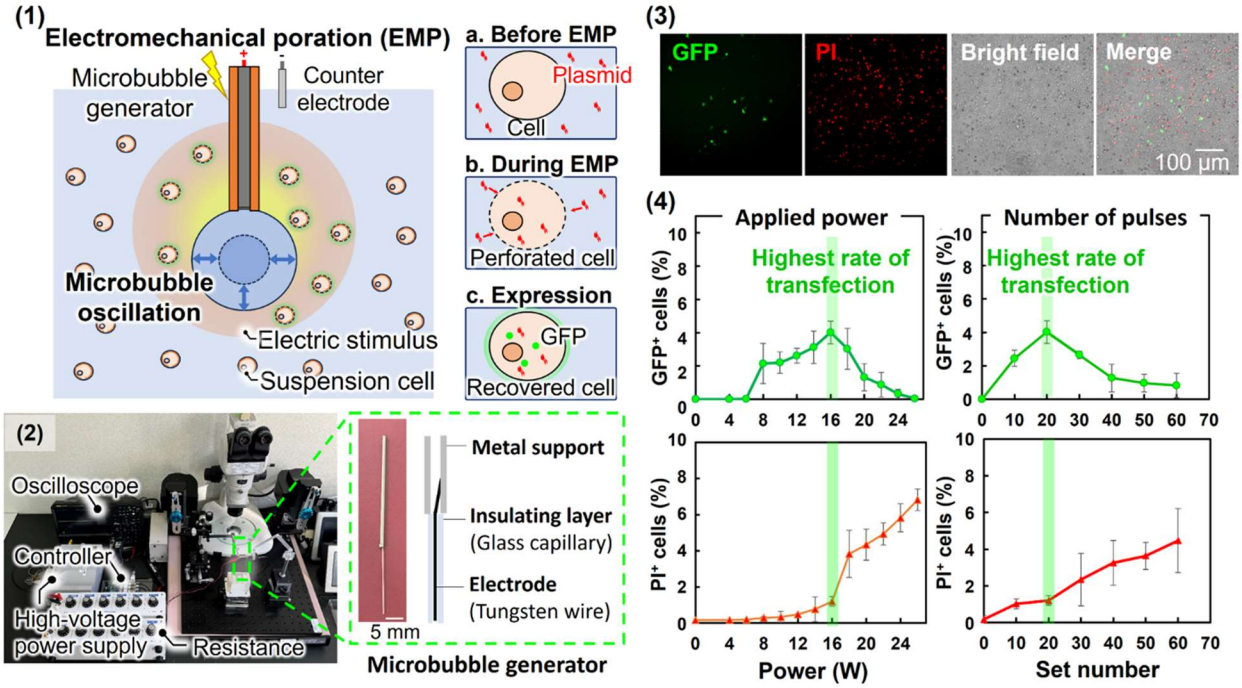
Figure 3 shows bright field and fluorescence images of transfected cells under microscope observation. Green fluorescence given by GFP indicates successful transfected cells. Red fluorescence given by propidium iodide (PI) staining indicates dead cells. Changes in physical parameters, applied power and pulse number, resulted in various rates of

transfection and cell death (Figure 4). When the cells are perforated appropriately, transfection rate was as high as 4% and cell death was kept as low as <10%.

Discussion

In this study, we have succeeded transfection of suspension cells by EMP. Further improvement of transfection can be achieved by modifying other physical parameters, such as frequency of electric pulses, for successful transfection to broader types of suspension cells.

Images (Optional)



References (Optional)

[1] Wenjing. Huang, et. al., Lab Chip, 2022.

Session Category

Micro/Biofluidics: Experiments

P1-396

Optimization of Microchannel Geometry for Efficient Sorting of Highly Motile Sperm Using a Microfluidic Device

Prof Toru Hyakutake

Yokohama National University, Yokohama, Kanagawa, Japan

Introduction

In Japan, the declining birthrate has become a serious social concern, and infertility is considered one of its major contributing factors. Current treatment methods—artificial insemination (AI), in vitro fertilization (IVF), and intracytoplasmic sperm injection (ICSI)—are selected based on the patient's condition. However, the commonly used density-gradient centrifugation method may cause DNA damage to sperm. Microfluidic devices, which use gentle microscale flow, offer an alternative approach by sorting sperm with minimal mechanical stress and in a shorter processing time. Against this background, we developed a microfluidic device composed of multiple parallel microchannels with widths comparable to sperm length. By creating flow through a hydraulic head difference between two reservoirs, the device allows sperm exhibiting rheotaxis and thigmotaxis to swim upstream, enabling selective collection of highly motile sperm. The aim of this work was to investigate how microchannel geometry affects sorting performance and to identify design guidelines for optimizing the device.

Methods

The microfluidic devices were fabricated in polydimethylsiloxane (PDMS) using standard soft lithography techniques. Each device included several parallel microchannels connected to a sorting and a semen reservoir. Japanese cattle semen cryopreserved in 0.5-mL straws was used. Flow in the channels was generated by the hydraulic head difference, and sperm swam upstream under these conditions. After incubation, sperm were collected from the sorting reservoir and evaluated for sperm concentration and motility.

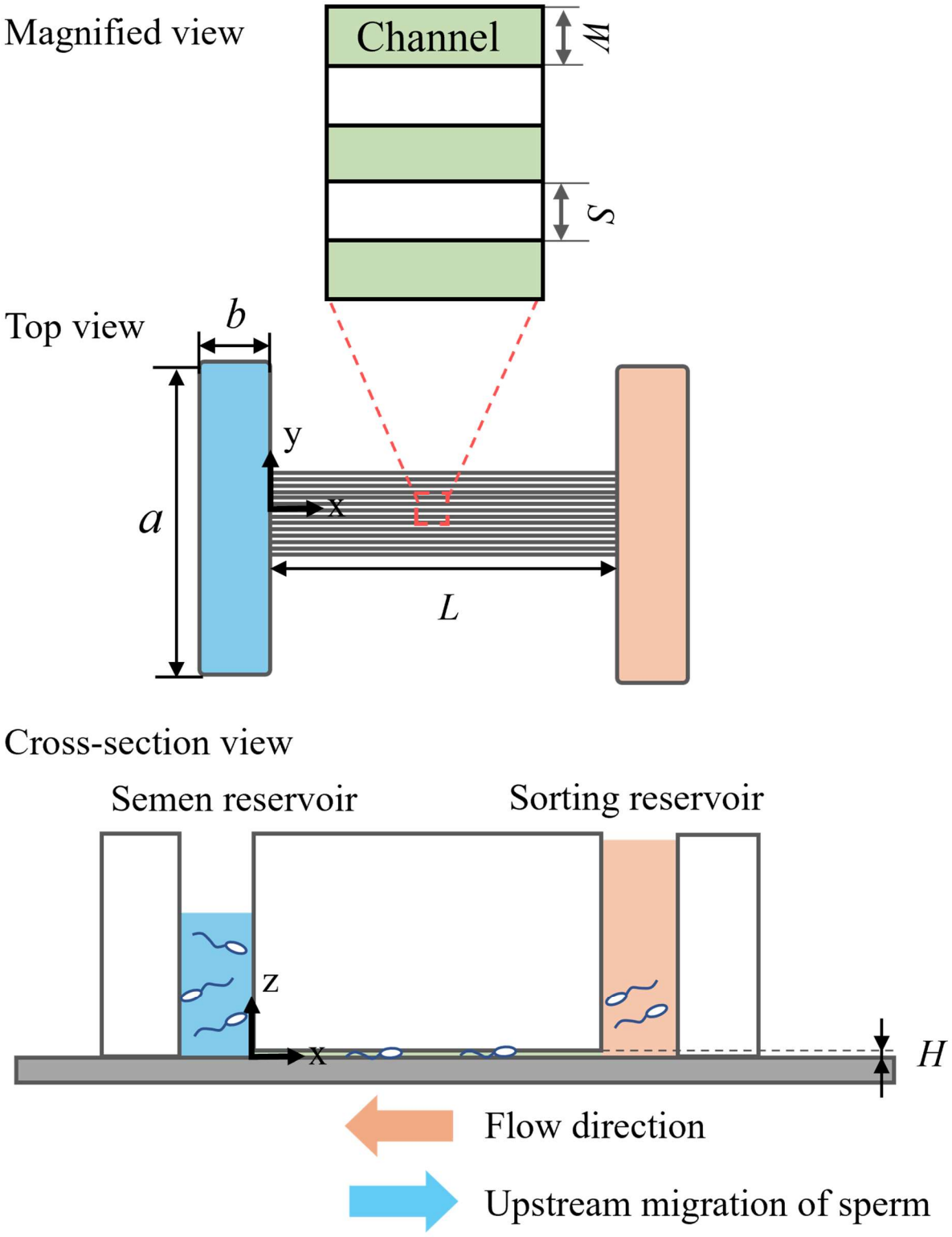
Results

The results showed that the number of sorted sperm increased as the number of channels increased. Sperm in the sorting reservoir had higher motility than those in the semen reservoir, confirming that highly motile sperm were selectively sorted. Larger channel spacing reduced the number of collected sperm, and reservoir geometry also affected sorting: devices with smaller aspect ratios showed higher sperm concentrations.

Discussion

These findings suggest that the proposed microfluidic device is a promising alternative to conventional sperm-selection methods used before IVF. In future work, we will use the sperm collected by this device for embryo transfer (ET) and evaluate the resulting conception rates. The outcomes of this study are expected to contribute to improved reproductive efficiency in both livestock production and human assisted reproductive technologies.

Images (Optional)



Session Category

Micro/Biofluidics: Experiments

P1-397

Relative Velocity of Red Blood Cells to a Surrounding Continuous Fluid in a Microchannel with an Abrupt Change in its Cross Sectional Area

Ms. Yi Li[1], Mr. Takayuki Osawa[2], Dr. Satoru Kuriu[2], Dr. Marie Shinohara[2], Dr. Soo Hyeon Kim[2], Dr. Yukiko Matsunaga[2], Prof. Yosuke Hasegawa[2]

[1]Department of Mechanical Engineering, School of Engineering, The University of Tokyo, Tokyo, Tokyo, Japan. [2]Institute of Industrial Science, The University of Tokyo, Tokyo, Tokyo, Japan

Introduction

The transport of red blood cells (RBCs) in surrounding fluids plays critical roles in nanoparticle margination, which in turn influences drug delivery. Because of the strong interaction between RBCs and the surrounding fluid, simultaneous measurement of both phases is essential for understanding their coupled dynamics. Although previous studies have reported RBC–fluid slip, most studies focus only on fluid velocities measured from nanoparticles (NPs) and cannot capture RBC velocities simultaneously with the background flow. As a result, quantitative dual-phase velocimetry in microchannels remains limited.

Methods

A dual-phase micro-PIV system was developed to measure RBC and nanoparticle (NP) velocities simultaneously using LED volume illumination and laser fluorescence. A U-Net model is developed to segment micro-PIV images. It locates RBCs from the input image, therefore segment the input images into NPs image and RBCs image separately. Then, the velocities of NPs and RBCs are calculated through particle image velocimetry and Lagrangian trajectories, respectively.

A 40-μm-high PDMS microchannel with 100 μm inlet and outlet widths and a 400 μm width middle section was fabricated, with expansion and contraction structures. A suspension consists of 0.5% hematocrit RBC and 0.05% volume fraction fluorescent NP (0.5 μm) in phosphate-buffered saline (PBS) is used with a flow rate of 1 μL/min. This condition was selected to enable simultaneous visualization of both phases while maintaining low hematocrit to prevent channel clogging.

Results

Clear cell-free layers were observed in both expansion and contraction regions, consistent with existing studies [1]. RBC velocities were generally lower than the background fluids

represented by NPs. RBC slip velocity increases both toward the channel center and toward the constriction throat, suggesting regulation by transverse velocity gradients and axial acceleration, although further investigation is required to confirm these effects.

Discussion

The observed increase in slip velocities toward the channel center and constriction throat suggests competing effects between RBC deformability, local shear gradients, and axial acceleration of the surrounding fluid. These factors can alter RBC–fluid momentum exchange, leading to spatially varying slip. Further experiments under different hematocrit and flow-rate conditions are needed to isolate each contribution.

References (Optional)

[1] Steffen M. Recktenwald *et al.*, Phys Rev Fluids, 2023

Session Category

Micro/Biofluidics: Experiments

P1-398

Quantitative and Time-Resolved Analysis of Macrophage Responses to Fine Particles Using a Continuous-Exposure Micro-Gap Chamber

Prof. Yoshitaka Nakanishi PhD, Dr. Yukio Fujiwara MD, Prof. Yuta Nakashima PhD

Kumamoto University, Kumamoto, Kumamoto, Japan

Introduction

Fine particles such as asbestos and diesel exhaust particulates are well-known health hazards, and recent concern has expanded to micro- and nanoplastics dispersed in the environment and wear debris from artificial organs. Understanding how such particles interact with biological systems remains both a longstanding challenge and an urgent issue. Macrophages internalize foreign particles and secrete pro-inflammatory cytokines, serving as key indicators of particle-induced biological effects. However, conventional well-plate exposure assays are limited by particle sedimentation, unstable local concentrations, the need for numerous independent cultures, and difficulty reproducing continuous or cumulative exposure. These limitations hinder quantitative evaluation of exposure–response relationships and long-term effects.

Methods

To address these issues, a large-area, low-ceiling Micro-gap Exposure Chamber was developed to reproduce macrophage–particle interactions under continuous, stable conditions suitable for quantitative and time-resolved analysis. The chamber incorporates a ceiling height of 50–200 μm to limit particle floating and maintain proximity to the cell layer. A 15-mm culture area accommodates 1.5–2.5 × 10^5 macrophages, enabling quantitative measurements and qualitative imaging. Particle suspensions are introduced at a constant low flow rate of 0.05–0.10 mL/h, and six inlet ports reduce flow velocity to achieve uniform circulation and sufficient phagocytosis time. A motor-driven micro-syringe ensures stable medium retention and allows periodic sampling for cytokine quantification. An integrated vertical-motion mechanism minimizes mechanical stress while maintaining homogeneous particle distribution.

Results

Using this system, particles of identical size produced distinctly different acute macrophage responses depending on polymer type. Cytokine production also varied with particle size for the same polymer. Under continuous exposure, macrophages exhibited a

characteristic temporal pattern: gradual cytokine elevation, a defined peak, and subsequent decline. This nonlinear response was not observable with conventional well-plate assays.

Discussion

The observed dynamics cannot be explained solely by mechanical stimuli related to particle size or morphology. The findings indicate that physicochemical surface properties regulate organic molecule adsorption and subsequently influence phagocytosis, intracellular degradation, and signaling pathways. The exposure platform provides a robust basis for advancing research on particle–cell interactions and supports applications in environmental science, biomaterials evaluation, and toxicology.

Acknowledgements (Optional)

This work was supported by Innovative Science and Technology Initiative for Security Grant

Number JPJ004596, ATLA, Japan.

Session Category

Micro/Biofluidics: Experiments

P1-399

Simulation of the Swimming Behavior of Magnetic Bacteria Near the Wall in a Magnetic Field

Mr. Akihiro Kawasaki, Prof. Yuji Shimogonya PhD

Nihon University, Koriyama, Fukushima, Japan

Introduction

Bacteria swim through water by rotating their flagella, which serve as motility organs. Near surfaces, hydrodynamic interactions between bacteria and surfaces cause them to trace circular trajectories. Magnetic bacteria, a type of bacterium, possess magnetic particles within their bodies and swim along the direction of external magnetic fields. However, the swimming behavior of magnetic bacteria near walls remains poorly understood. Therefore, this study aims to analyze the swimming behavior of magnetic bacteria near walls when the surrounding magnetic field is altered, using numerical simulations.

Methods

Using the same method as our previous study[1], we created a three-dimensional model of a bacterium composed of a prolate ellipsoidal cell body and elongated flagella (Fig. 1(a)). The interaction between the magnetic moment of the bacterial cell and the external magnetic field was formulated as a magnetic torque to represent the characteristics of the magnetic bacterium. In this case, the flow field has an extremely low Reynolds number, allowing the assumption of Stokes flow. Therefore, the boundary element method[1], the most reasonable and highly accurate numerical simulation technique for this case, was employed to analyze the swimming behavior near the wall.

Results

Figure 1(b) shows the swimming behavior of magnetic bacteria near a wall. The external magnetic field was applied perpendicular to the wall. The values in the figure represent how many times the applied external magnetic field strength exceeds that of the Earth's magnetic field. These results indicate that up to an external magnetic field approximately twice the strength of the Earth's magnetic field, the bacteria remain near the wall and exhibit nearly circular swimming trajectories. However, when the external field exceeds this strength, the swimming trajectories change significantly, and the bacteria swim away from the wall.

Discussion

Additional simulations revealed that controlling swimming direction parallel to the wall requires an external magnetic field over 100 times stronger than the Earth's magnetic field (figure omitted). Thus, this study clarified that while controlling magnetic bacteria to move away from the wall is relatively easy, controlling movement along the wall requires a much stronger magnetic field.

Images (Optional)

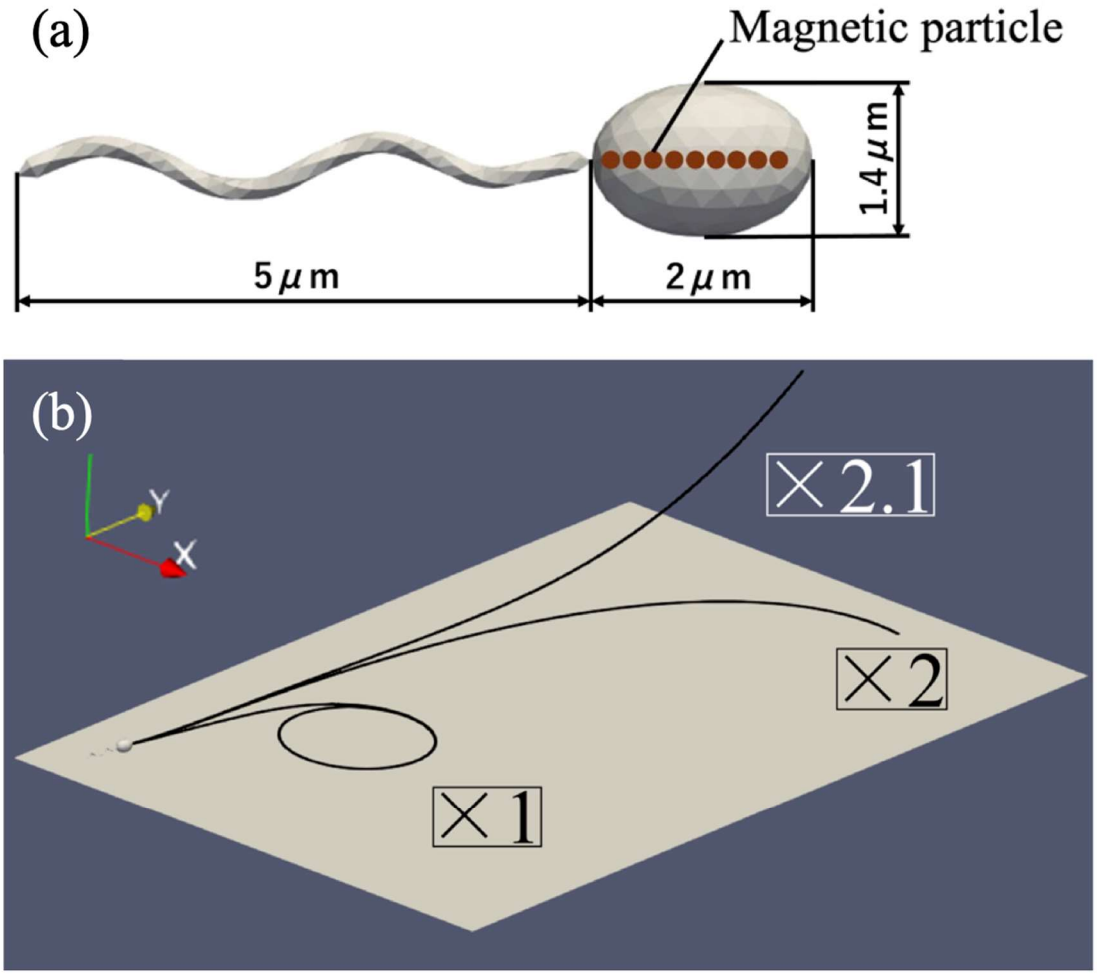


Fig. 1 (a) Bacterial model. (b) Swimming trajectories.

References (Optional)

[1] Shimogonya *et al.*, Scientific Reports, 2015

Acknowledgements (Optional)

This work was supported in part by a Japan Society Promotion of Science Grants-in-Aid for Scientific Research (JSPS KAKENHI) (Grant No. 24K07308).

Session Category

Micro/Biofluidics: In Silico Models and Simulation

P1-400

Patient-specific Spectral and Temporal Analysis of Hemodynamics Modeling of Abdominal Aortic Aneurysms

Mr Pratik Mitra PhD Candidate[1], Mr Archer A French Undergraduate Research Assistant[1], Dr. Satish C Muluk MD[2], Dr. Mark K Eskandari MD[3], Associate Professor Seungik Baek PhD[4], Professor Ender A Finol PhD[1]

[1]The University of Texas at San Antonio, San Antonio, Texas, United States. [2]Allegheny Health Network, Pittsburgh, Pennsylvania, United States. [3]Northwestern University School of Medicine, Chicago, Illinois, United States. [4]Michigan State University, East Lansing, Michigan, United States

Mr Pratik Mitra

Mr Archer A French

Dr. Satish C Muluk

Dr. Mark K Eskandari

Associate Professor Seungik Baek

Introduction

Abdominal Aortic Aneurysm (AAA) is a dilation of the abdominal aorta greater than 3 cm. Wall shear stress (WSS) is thought to play a significant role in AAA development. To this end, we investigated the use of spectral analysis and the power spectrum density (PSD) of WSS as potential hemodynamic descriptors of the AAA flow environment.

Methods

Abdominal computed tomography scans of five saccular (S1–S5) and one fusiform (F1) AAAs were collected retrospectively and segmented using MIMICS. SimVascular was used to perform pre-processing and volume meshing, while the blood flow simulations were performed using the svSolver. Dynamic mode decomposition (DMD) was performed using the linear operator $X'=AX$, where $X = [u_1,u_2,u_3,\ldots u_{n-1}]$ and $X' = [u_2,u_3,u_4,\ldots u_n]$, and u_1,u_2,u_3 are the velocity vector components. The PSD in the vicinity of the AAA sac was computed from the temporal WSS distributions.

Results

DMD yielded differences in the temporal and spatial hemodynamic signatures for S1–S5 compared to F1. For all AAAs, the mode frequency plots (Fig. 1a) showed a small number of dominant modes with larger amplitudes, indicating that unsteady sac flow is governed by strong low-frequency coherent structures. Growth/decay (real component) revealed localized regions of persistent hemodynamic phenomena, particularly along recirculation zones within the sac (see Fig. 1b). Oscillation frequency (imaginary component) highlighted concentrated high-frequency fluctuations in shear-layer regions, suggesting complex vortex dynamics (see Fig. 1c). The PSD of WSS, extracted from sac point data, showed distinct peak amplitudes (see Fig. 1d).

Discussion

The DMD and spectral analyses collectively demonstrated that AAA sac shape has a substantial impact on the underlying flow physics. The saccular AAAs (S1–S5) exhibited stronger low-frequency coherent structures and more pronounced high-frequency oscillatory content, reflecting an overall unsteady flow environment inside the sac. These features corresponded to regions of recirculation, shear-layer interaction, and vortex trapping. In contrast, the fusiform AAA (F1) exhibited fewer energetic modes and a narrower spectral bandwidth, indicating a more stable flow regime. The dominant WSS frequency range in saccular AAAs was 1–3 Hz, whereas the fusiform AAA exhibited frequencies in the range of 3–8 Hz at the lumen wall.

Images (Optional)

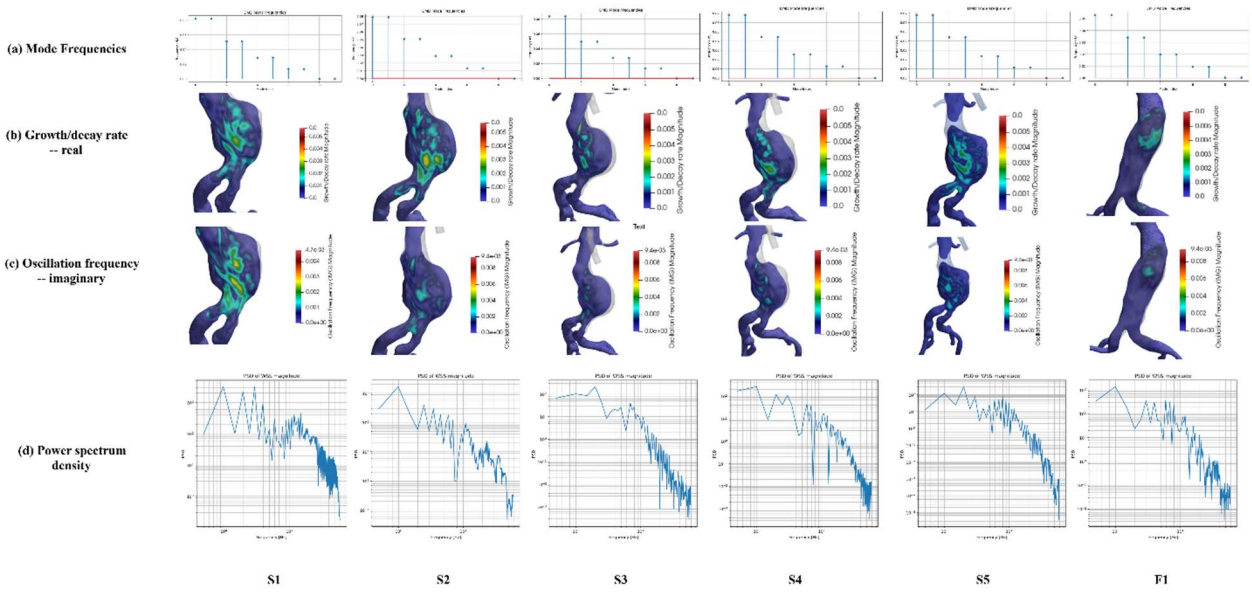


Figure 1. Dynamic Mode Decomposition (DMD) of hemodynamics in five saccular AAAs (S1–S5) and one fusiform AAA (F1). (a) Mode frequencies and associated spatial DMD modes. (b) Growth/decay rate, $Re(\omega_k)$, showing regions of flow structure and decaying recirculation. (c) Oscillation frequency, $Im(\omega_k)$, highlighting shear-layer and vortex-driven oscillations. (d) Power spectrum density (PSD) of WSS from sac wall signals, demonstrating multi-frequency content and distinct spectral peaks that reflect the underlying unsteady flow.

Acknowledgements (Optional)

NIH #R01HL159300 funded the study.

Session Category

Micro/Biofluidics: In Silico Models and Simulation

P1-401

Oxygen Transport during High-frequency Jet Ventilation using CFD with Dynamic Boundary Conditions

MSc Seyedmohsen Baghaei Oskouei[1,2], Univ.Lektor Dr.med. Alexander Aloy[3], Mr Robert Kölbl[4], Univ.Prof. Dipl.-Ing. Dr.techn. Michael Harasek[5], Univ.Prof.in Dipl.-Ing.in Dr.in techn. Margit Gföhler[1]

[1]Institute of Engineering Design and Product Development, TU Wien, Vienna, Vienna, Austria. [2]Institute of Chemical, Environmental and Bioscience Engineering, TU Wien, Vienna, Vienna, Austria. [3]Institute of Fluid Mechanics and Heat Transfer, TU Wien, Vienna, Vienna, Austria. [4]Carl Reiner GmbH, Vienna, Vienna, Austria. [5]Institute of Chemical, Environmental and Bioscience Engineering, TU Wien, Vienaa, Vienna, Austria

Introduction

In this work, a 7-generation Computational Fluid Dynamics (CFD) domain of the respiratory system is utilized to estimate the oxygen delivery efficiency during High-frequency Jet Ventilation (HFJV) at 300 pulsations per minute.

Methods

CFD is used to model the oxygen transport in the respiratory system. The domain is extracted from the dimensions provided by Weibel [1]. Unsteady Reynolds-Averaged Naiver-Stokes (URANS) k-ω SST turbulence model is used to simulate the flow field with a mesh of y+ around 1. Dynamic pressure outlet boundary conditions that include the resistance and compliance of the lung after each outlet (gen.7) are utilized in the CFD model (total lung compliance = 0.05 L/cmH_2O). The CFD model is validated against our in-house Particle Image Velocimetry (PIV) experimental results, utilizing a refractive index-matched fluid and 3D-printed test pieces.

Results

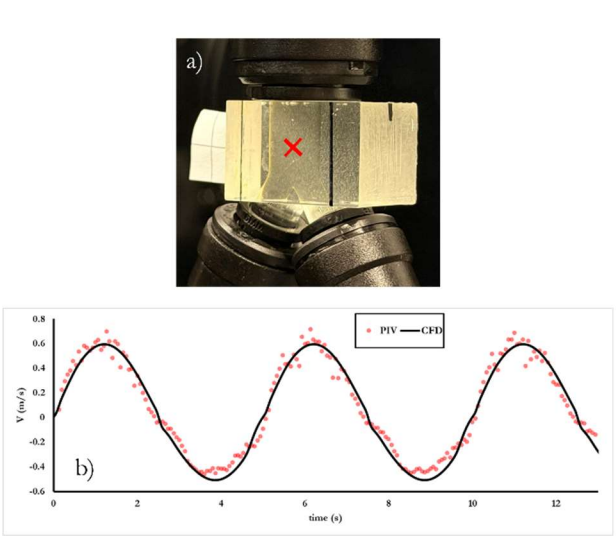
Figure 1 a and b show the test piece used in PIV measurements, with a comparison of the vertical velocities on the mid-plane 4.5 mm above the junction between the PIV and CFD. Figure 1c, d and e depict the resultant flow rate, volume and oxygen delivery behavior in the 7-generation model respectively. Each pulsation delivers some portion of the oxygen provided to the lung to the deep lung.

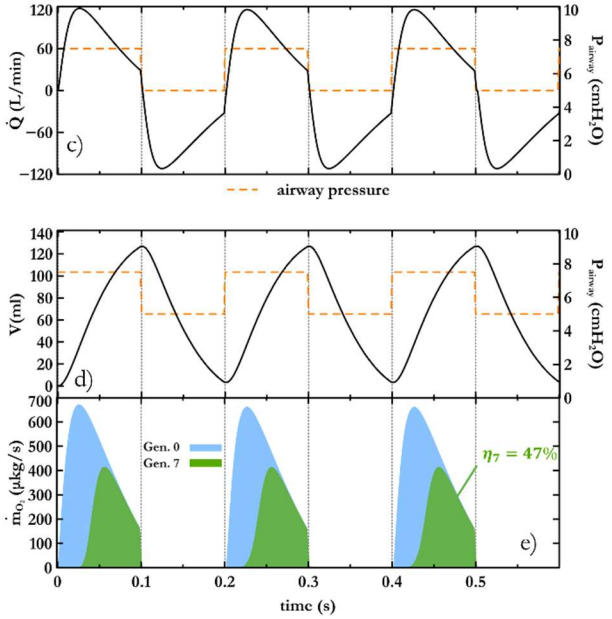
Discussion

CFD results strongly agree with the PIV (maximum Re = 1763, Wo = 3.82). At a frequency of 300 per minute, the tidal volume of around 125 ml is achieved while only 47% of oxygen

delivered to generation 7 per pulsation. In further studies, turbulent PIV will be used in validation, and different frequencies will be examined.

Images (Optional)





References (Optional)

[1] E. R. Weibel, *Morphometry of the Human Lung*. Berlin, Heidelberg: Springer Berlin Heidelberg, 1963. doi: 10.1007/978-3-642-87553-3.

Acknowledgements (Optional)

The authors state that this research was partially funded by the Austrian Research Promotion Agency (FFG). Project: HiELuVent, grant number FO999903605.

Session Category

Micro/Biofluidics: In Silico Models and Simulation

P1-402

Hemodynamic Analysis of Patient-Specific Coarctation of Aorta Model via Two-way Fluid-Structure Interaction Modeling

Mr. Mashrur Muntasir Nuhash, Dr. Victor K. Lai, Dr. Ruihang Zhang

University of Minnesota Duluth, Duluth, Minnesota, United States

Introduction

Coarctation of the aorta (CoA) is a congenital cardiovascular defect characterized by a narrowing of the aortic arch and accounts for approximately 6-8% of congenital heart disease cases at birth. Even after successful surgery, some patients will still have a high possibility of cardiovascular complications, such as hypertension. To study the hemodynamics, we developed a fluid-structure interaction (FSI) model to replicate the patient-specific coarctation of the aorta (CoA) and flow dynamics in the ascending and descending aortic wall.

Methods

Structural simulations were conducted in Ansys Mechanical APDL, and fluid dynamic simulations were performed in Ansys Fluent, with the two domains coupled through the Ansys System Coupling module. A pulsatile velocity profile is applied at the inlet, while mass-flow outlet conditions are imposed at the arch branches and descending aorta with prescribed flow percentages. The aortic wall was modeled as an anisotropic hyperelastic material to replicate realistic deformation of the aorta during the cardiac cycle. The non-Newtonian behavior of blood is replicated using the Casson model. The two-way FSI model is run for several cardiac cycles with a time step size of 1e-4 seconds, and the final cycle is used to analyze the results

Results

A high-speed jet alongside complex secondary flows was observed downstream of the coarctation segment, with pronounced recirculation during the diastole at post coarctation region. The asymmetric jet generated high helical flow, which slid along the wall of the aorta. High wall shear stress was observed at the edge of the coarctation at peak systole, and the compliant aortic model depicted large deformation of the walls downstream of the narrowed section of the geometry. Incorporating a hyperelastic model generates mechanical behavior that would be remiss in a rigid wall model.

Discussion

The localization of abnormal hemodynamics downstream of the coarctation region indicated the possibility of hypertension, dilation and aneurysm formation, which also explains why the patients may remain at risk even after reconstructive surgery. However, the current model is limited to a single patient-specific geometry. Extending this work to a larger cohort with varying CoA severities and including both repaired and healthy aortas, would provide a more comprehensive insight.

Session Category

Micro/Biofluidics: In Silico Models and Simulation

P1-403

Simulation of the Swimming Behavior of Bacteria With Two Flagella Near the Wall

Prof. Yuji Shimogonya PhD

Nihon University, Koriyama, Fukushima, Japan

Introduction

Bacteria swim through water by rotating their elongated flagella. *Escherichia coli*, a representative bacterium, swims using a single bundle of flagella and is known to trace circular paths near walls. In contrast, bacterium MO-1, which we are interested in, possesses two flagella[1], yet the swimming behavior of bacteria with two flagella near walls remains unknown. Therefore, this study aims to clarify the swimming behavior of bacterium MO-1 near the wall using numerical simulation.

Methods

A three-dimensional model was created that mimics the actual shape of MO-1, consisting of a prolate ellipsoidal cell body and two helical flagella. Based on preliminary investigations, one flagellum was set as a left-handed helix rotating clockwise, while the other was set as a left-handed helix rotating counterclockwise. Since the flow field around the swimming bacterium can be assumed to be Stokes flow, we analyzed its swimming behavior near the wall using the boundary element method code previously developed by our group[2].

Results

Swimming simulations near the wall were performed considering four flagellar conditions, including MO-1. The results are shown in Fig. 1. Condition (a) represents MO-1, (b) represents a condition where only one flagellum rotates, (c) represents a condition where one flagellum is missing, and (d) represents a condition mimicking *Escherichia coli*. Models under conditions (b), (c), and (d) exhibited circular trajectories near the wall. In contrast, the MO-1 model under condition (a) swam in a straight line without any deflection of its trajectory, even in the presence of a nearby wall surface.

Discussion

The difference in swimming trajectories can be explained by the fluid resistance acting on the cell body and flagella. In conditions (b), (c), and (d), the fluid resistance acting on the cell body and flagella is in opposite directions, causing the trajectory to bend. In contrast,

under condition (a), the presence of two flagella causes the forces bending the trajectory to cancel each other out. This study successfully demonstrated that bacteria with two flagella exhibit significantly different swimming behavior near the wall compared to bacteria with one flagellum.

Images (Optional)

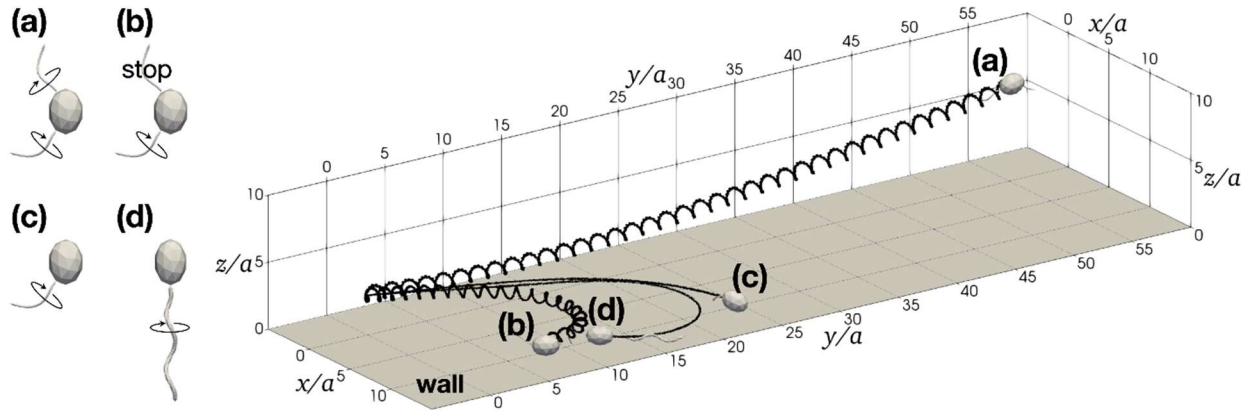


Fig. 1 Swimming trajectories of the bacterial models near a wall at $z = 0$

References (Optional)

[1] Ruan *et al.*, PNAS, 2012

[2] Shimogonya *et al.*, Scientific Reports, 2015

Acknowledgements (Optional)

This work was supported in part by a Japan Society Promotion of Science Grants-in-Aid for Scientific Research (JSPS KAKENHI) (Grant No. 24K07308).

Session Category

Micro/Biofluidics: In Silico Models and Simulation

P1-404

Characterisation of Tumour Cell Biomechanics using High-Throughput Microfluidic Devices

Ms Orlaith McSweeney[1], Prof María Ángeles Pérez Ansón[2], Prof José Manuel García-Aznar[2], Prof María José Gómez-Benito[2], Dr Eoin McEvoy[1]

[1]University of Galway, Galway, Galway, Ireland. [2]University of Zaragoza, Zaragoza, Aragon, Spain

Introduction

Personalised breast cancer treatment requires a mechanistic understanding of heterogeneous cell behaviour within a patient's tumour material, where increased cell stiffness can be a marker for chemoresistance. In this project, we develop a platform for microfluidic cell aspiration in response to pressure, which, in conjunction with computational modelling, is applied to characterise heterogeneity in active tumour cell biomechanics.

Methods

Micropipette aspiration probes cell biomechanics by aspirating the membrane. We extend this technique for high-throughput microfluidic devices, by controlling pressure gradients ΔP across microchannels. Chips with 5-15μm microchannels were fabricated by casting PDMS onto photo-patterned masks and plasma-bonding to coverslips. We developed computational fluid dynamics (CFD) models to predict how geometry and boundary conditions govern ΔP (Fig.1A). Microfluidic devices were connected to pressure controllers (Fluigent) to control microchannel ΔPs in a 0.6-1kPa range. We seeded T47D cells ($1x10^6$ cells/ml) within the device and monitored short-term aspiration into microchannels (Fig.1B). We utilised ImageJ to measure diameters of calcein-stained cells pre-aspiration, and to identify aspiration lengths, L. We subsequently developed finite element models containing active cortical, cytoplasmic and nucleic regions (Abaqus, Simulia), to derive the non-linear biomechanical behaviour of measured cells.

Results

CFD modelling revealed microfluidic chip design and experimental input conditions to ensure a gradual ΔP was achieved across microchannels (Fig.1A). Subsequently, partial aspiration of T47D cells was achieved in optimal microchannel widths of 6-9μm, where experiments showed that aspiration length increased with channel width and ΔP (Fig.1C).

Variability in results reflected heterogeneity in cell size and stiffness, confirmed by fluorescent imaging (Φ_{mean}: 12.09 ± 3.09μm). Finite element modelling uncovered the interplay between non-linear cortex and nucleus stiffness in governing aspiration length arising from heterogeneous cell biomechanics (Fig.1D). While stiff cells are more readily aspirated at smaller sizes (Fig.1E), interestingly softer cells exhibit greater aspiration lengths when larger due to a transition from an elasticity-limited to a volume-limited response.

Discussion

This study provides a platform to characterise non-linear tumour cell biomechanics using coupled experimental and computational modelling. This framework can readily be extended to provide novel characterisation and insight for biomechanisms of chemoresistance, multicellular spheroids, and patient tissue.

Images (Optional)

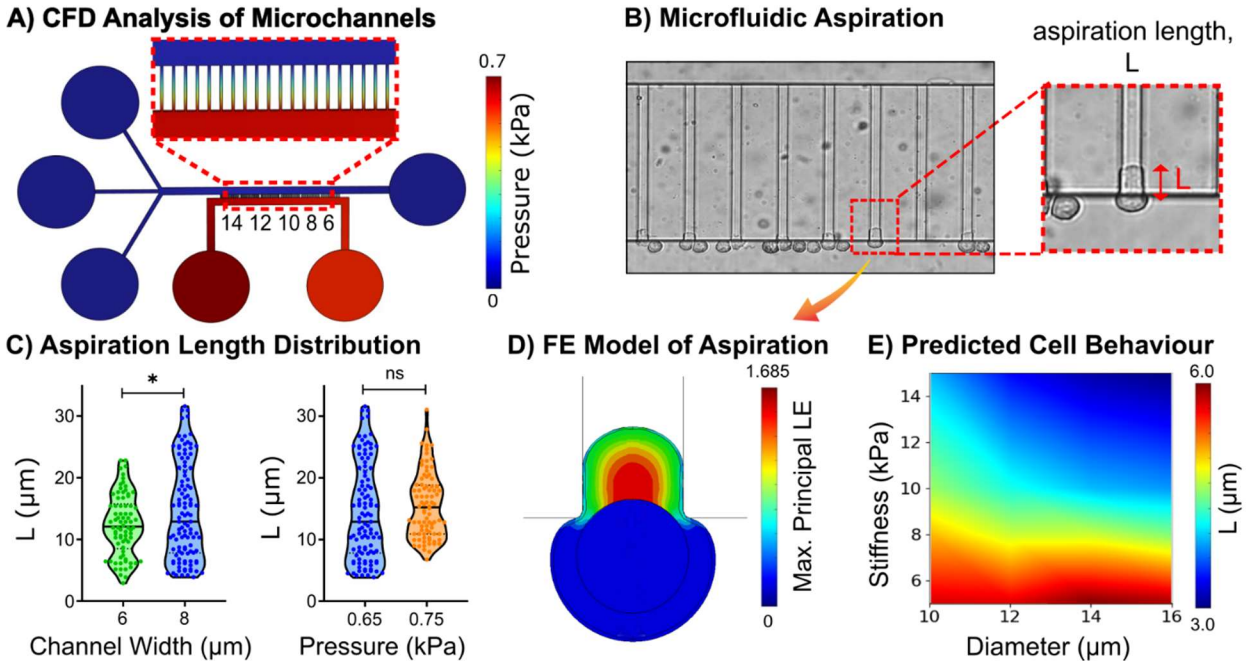


Figure 1: A) Pressure contour of experimental setup, with homogeneous ΔP across microchannels. B) Experimental data (Olympus IX51, 20x), with measured aspiration length, L. C) Data shows L increases with channel width and ΔP. Statistical analysis: unpaired t-test, * = $p<0.05$, ns = not significant. D) Max. principal strain of hyperelastic model (Abaqus). E) Phase diagram of aspiration length varying cortical stiffness and cell diameter (6μm channel).

Acknowledgements (Optional)

This work was supported by the European Research Council (Grant number 101116234).

Session Category

Cell Biomechanics: Methods and Models

P1-405

Quadratus Lumborum Asymmetry Linked to Hip Abduction Strength and Nonlinear Measures of Unilateral Postural Control

Mr. Sam Vasilounis[1], Mr. Daniel Sheffield[1], Dr. Dan Desroches[1], Dr. Janessa Drake[1]

[1]York University, Toronto, Ontario, Canada

Introduction

Single-leg stance (SLS) demands lumbopelvic coordination, with the quadratus lumborum (QL) serving as one of the critical stabilizers against lateral flexion and pelvic obliquity. Linear measures often overlook complex neuromuscular dynamics, but sample entropy (SampEn) is utilized to measure postural sway regularity. This study examined the relationship between unilateral QL asymmetry, hip abduction force, and centre of pressure (COP) SampEn during SLS. It was hypothesized that asymmetry will correlate with lower SampEn values, reflecting rigid and less adaptable postural control.

Methods

60 healthy, right-hand dominant athletes (aged 18-21y; 28M/32F, height 1.78m ± 0.22, weight 87.2 kg ± 5.4). QL cross-sectional area (CSA) was measured via ultrasound at the L3/L4 vertebral level using a LOGIQ P-series ultrasound system (GE Healthcare, USA). Asymmetry indices for QL morphology were calculated using the formula derived from previous literature. Isometric hip abduction force was quantified bilaterally with a hand-held dynamometer (Hoggan Scientific, USA) during maximum side-lying hip abduction (SLHA). Postural control was assessed during three 30s SLS trials on a force plate (AMTI OR-6 Newton, USA), from which COP and SampEn were derived to quantify sway complexity.

Results

34 (21F/13M) participants exhibited greater than 10% asymmetry. The right QL CSA was significantly larger than the left (567.8mm^2 ± 195.8, 461.6mm^2 ± 150.8; $p < 0.001$, $d = 1.38$), and SLHA force was significantly greater on the right (163.6N ± 43.1, 147.9N ± 42.0; $p < 0.001$, $d = 1.34$). There was a statistically significant main effect of sex on QL CSA (F (1,47) = 15.44, $p < 0.001$) indicating males had larger QL CSA than females. SampEn^{ML} was significantly larger on the right side (Right: 0.034 ± 0.021 vs. Left: 0.018 ± 0.028; $p = 0.004$). Pearson correlations revealed moderate positive associations between QL CSA and SLHA on both sides ($r = 0.42–0.44$), reaching statistical significance on the left ($p = 0.040$).

Discussion

Participants exhibited clear right-sided dominance in muscle size and strength. Furthermore, asymmetry was isolated to the frontal plane, where significantly lower $SampEn^{ML}$ on the weaker left side reflects a compensatory strategy. These findings imply the non-dominant side lumbopelvic-hip complex may be limited not only by force deficits but by a rigid control mechanism.

Images (Optional)

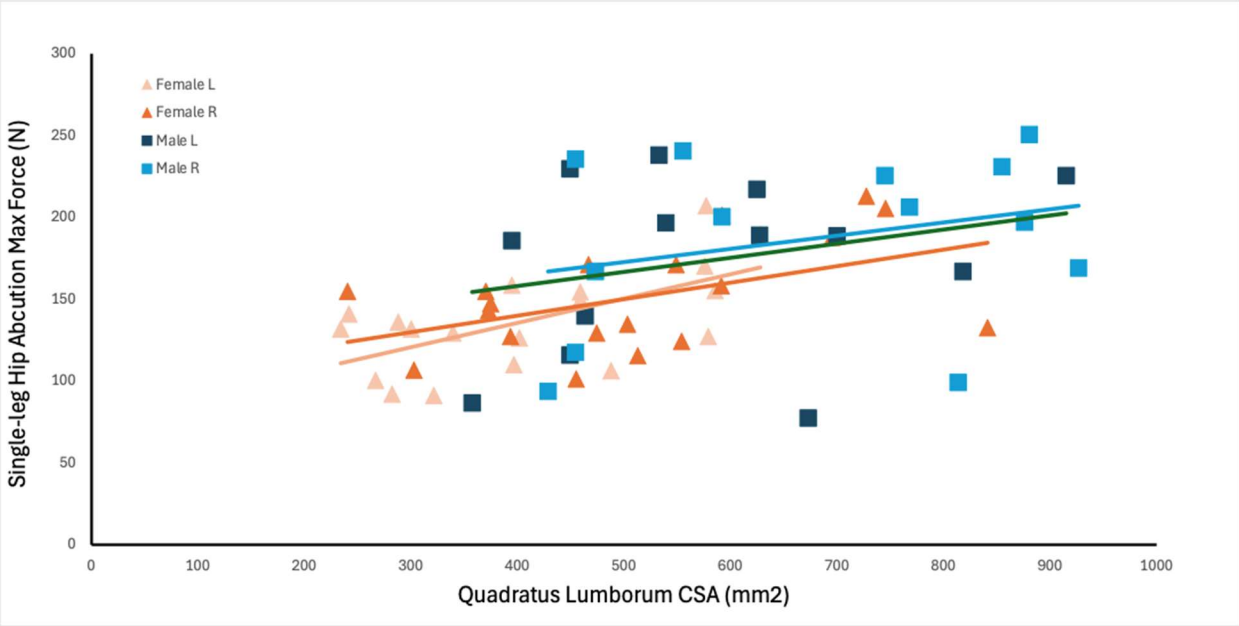


Figure 1. Relationship between quadratus lumborum cross-sectional area (QL-CSA) and single-leg hp abduction maximum force (SLHA) grouped by sex and side. Points show individual right and left measurements for females and males, with lines depicting the linear mixed model. The model indicates a modest positive association between the QL CSA and SLHA, with greater strength on the right versus left and higher SLHA in males versus females after adjusting for QL CSA.

Session Category

Human Motion and Performance: Balance, Posture and Control

P2-001

Are Distinct Lamina Cribrosa Collagen Architectures Between Species Adaptations to Different Mechanical Loading Conditions?

Dr. Adam Galloy PhD, Dr. Ian Sigal PhD

University of Pittsburgh, Pittsburgh, PA, United States

Introduction

Nerve axons are vulnerable to damage from a variety of loads as they exit the eye including translaminar pressure (the drop in pressure from inside to outside the globe) and tractions from eye rotations. The lamina cribrosa (LC) is a complex collagen network that provides protection to the nerve axons at this location. Different species exhibit distinct LC collagen architectures. For example, tree shrew LCs follow a wheel and spoke pattern, human LCs have a nasal-temporal bias in fiber direction and density, and monkey LCs exhibit mesh-like structure. We hypothesize that these diverse architectures are specializations to different loading conditions. To examine the plausibility of this hypothesis, we created topological optimization (TO) models of the LC to contrast optimal fiber architectures for different loading cases.

Methods

A truss network TO algorithm [1] was adapted with a compression penalty to create tension-only fiber networks. The network was optimized within a cylindrical domain (2 mm diameter, 0.25 mm thick) with a small cylindrical obstacle through the center representing the central vessels. Pressures of 15 mmHg and 7 mmHg were applied to the anterior and posterior surface respectively modeling the translaminar pressure. Additional models with shear tractions distributed uniformly to the posterior surface (net 8 mN) modeled eye rotation tractions. A support structure for fiber attachments surrounded the entire circumference of the domain.

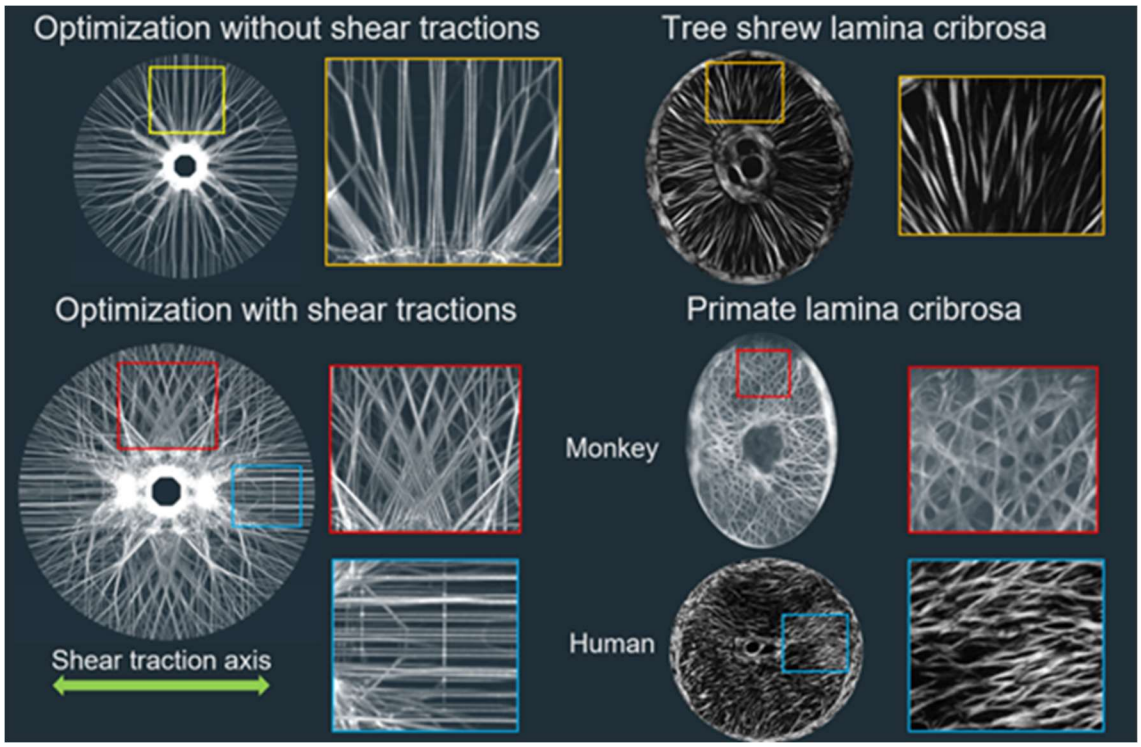
Results

When TO models only included translaminar pressure, fibers formed in a radial pattern like the collagen architecture in tree shrew LCs. When models included rotational shear tractions, the fibers skewed towards the applied shear. Super-imposing results with shear tractions pointing in opposite directions resulted in a biased collagen orientation and meshwork crossings capturing aspects of human and monkey LCs respectively.

Discussion

These results suggest that interspecies differences in LC architecture may be understood in terms of adaptations to specialized loading conditions to protect nerve axons. The nasal-temporal biased human LC collagen networks and meshwork monkey LCs could be adaptations to primates' heavy reliance on eye movements. The wheel pattern of tree shrew LCs suggests they are adapted primarily for pressure not large eye rotations.

Images (Optional)



References (Optional)

[1] Rowe and Chern, SIGGRAPH Asia, 2023

Acknowledgements (Optional)

Canadian Institutes of Health Research, NIH R01-EY023966, R01-EY031708, P30-EY008098 and T32-EY017271 (Bethesda, MD), Research to Prevent Blindness (unrestricted grant to UPMC ophthalmology, and Stein innovation award to Sigal IA), BrightFocus Foundation

Session Category

Comparative Biomechanics: N/A

P2-002

Improved Muscle Gearing in the Gastrocnemius of Pregnant and Lactating Rats and Its Implications for Locomotor Energetics

Dr. Adrien A. Arias[1,2], Ms. M. Lauren Delargy[1], Dr. Nicole Danos[1]

[1]University of San Diego, San Diego, CA, United States. [2]University of California, Irvine, Irvine, CA, United States

Introduction

Pregnancy and lactation are both energetically expensive for mammals. Basal metabolic rate increases by approximately 2- 6x during gestation and up to 7x during lactation in mammals. However, mammals operate under a 'metabolic ceiling' and cannot support these drastic increases in metabolic rate with increased food intake alone. This suggests that the high energetic demands of pregnancy and lactation may necessitate a reduction in the energetic budgets of other organ systems. Patterns of improved fuel economy in transmission systems with wider gearing ranges combined with previous work on muscle gearing and musculoskeletal remodeling in rats during motherhood suggest that pennate locomotor muscles may improve gearing ability to mitigate the large increases in energy consumption during reproduction.

Methods

We used fixed-end 'isometric' contractions and after-loaded isotonic contractions under maximal stimulation *in situ* to test our hypothesis that remodeling of the medial gastrocnemius muscle-tendon unit during motherhood in rats (*Rattus norvegicus*) leads to an improved ability to vary architectural gear ratio across force conditions (i.e. we expect a wider range of gear ratios and steeper slope across force conditions in pregnant and lactating animals compared to non-pregnant controls).

Results

We found that the medial gastrocnemius has a significantly wider range of AGRs and steeper linear relationship between AGR and muscle force during motherhood (Figure 1). Additionally, we found that pregnant and lactating rats had more compliant muscles.

Discussion

Overall, our findings show that the medial gastrocnemius of pregnant and lactating rats has improved gearing ability compared to non-pregnant animals, which is underpinned by

increased muscle compliance, suggesting a trade-off between gearing ability and maximal contractile dynamics. We propose, like engineered systems, improved muscle gearing ability may improve locomotor energetics during motherhood in rats.

Images (Optional)

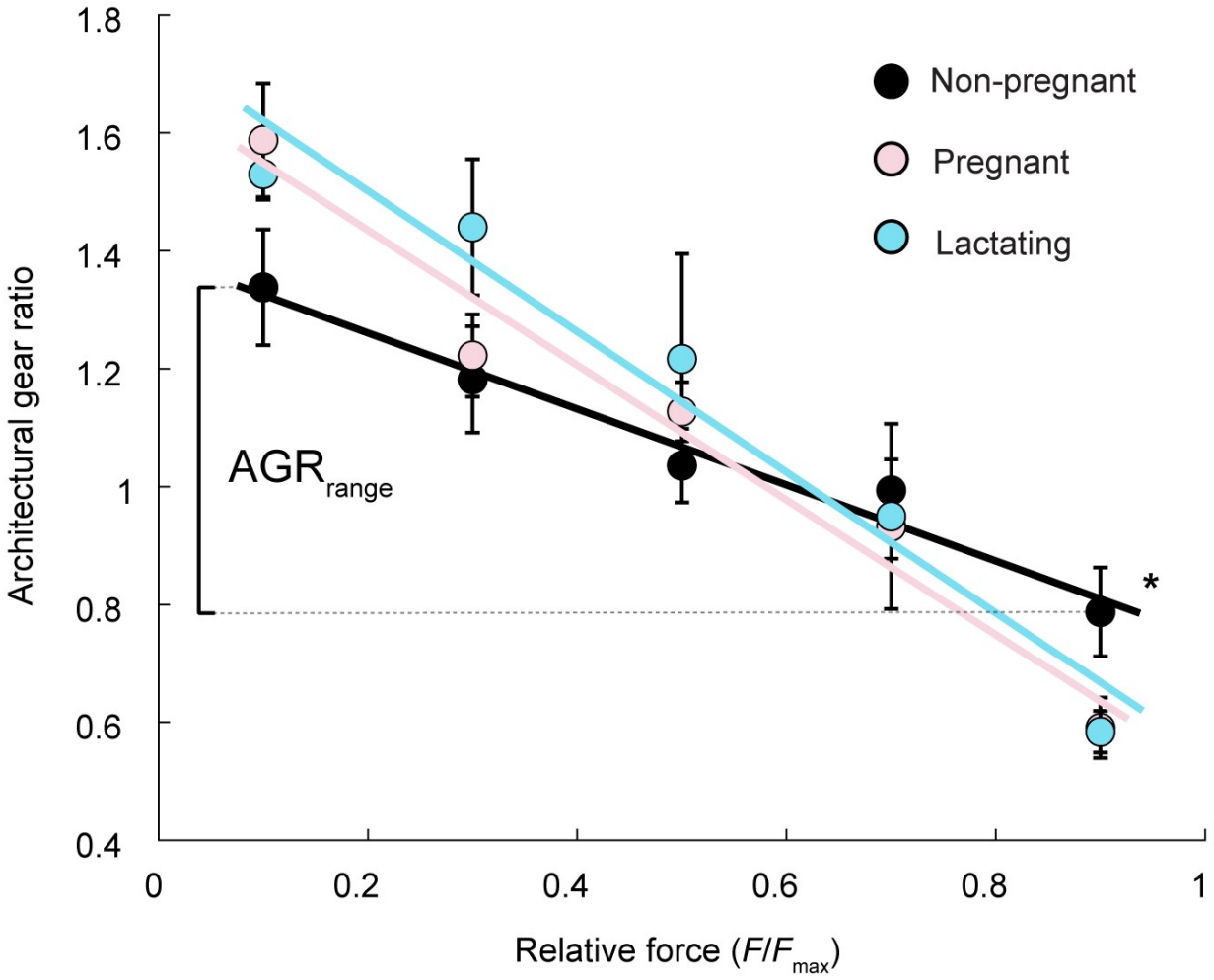


Figure 1: The effect of pregnancy and lactation on architectural gear ratio (AGR). AGR across relative muscle forces is shown for non-pregnant (black), pregnant (pink), and lactating (blue) rats. Pregnant and lactating animals had significantly wider AGR ranges (LME, $p=0.002$) and steeper slopes (LME, $p=0.001$) relative to non-pregnant controls (Tukey's post-hoc, $p<0.05$). Asterisk represents statistically significant difference in AGR slope between non-pregnant animals and the other two conditions.

Session Category

Comparative Biomechanics: N/A

P2-003

Enhanced Behavioral Control Precision of Paramecium and Realization of a Paramecium-Driven Autonomous Object Transport System

Prof. Akitoshi ITO PhD, Mr. Kenta TOKUYAMA M.S., Mr. Taisei Ohira BS

Tokyo Denki University, Adachi-ku, Tokyo, Japan

Introduction

1. Introduction

Methods

2. Control Algorithm Improvement

Results

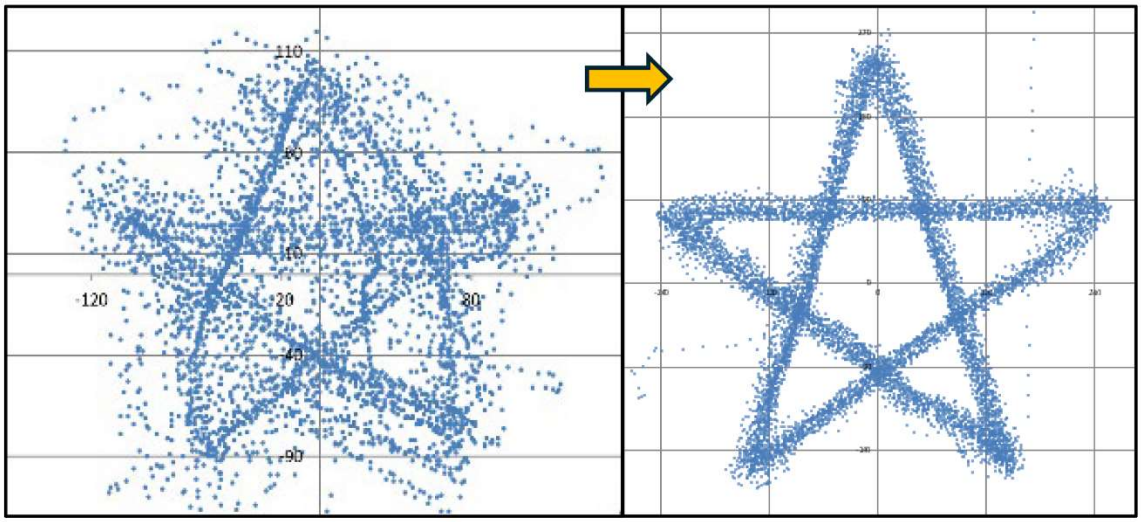
3. Autonomous Transport System

Discussion

4. Discussion

This platform enables observable-microbe-driven payload delivery in spatially constrained or cluttered micro-environments inaccessible to conventional 3-D micromanipulators. Extending analogous control strategies to gastrointestinal microorganisms could offer future potential within the digestive tract. We frame biomedical translation as a long-term engineering challenge rather than an infeasible concept.

Images (Optional)



(a) Old algorithm (b) New algorithm

Fig. Trace changes of the motion control experiment of a paramecium. Controllability is drastically improved by the new control algorithm

References (Optional)

[1] A. Itoh, IEEE/ASME, Trans. On Mechatronics, Vol.5, No.2, pp.181-188, 2000.

[2] A. Itoh and W. Tamura, Springer-Verlag Tokyo, “Bio Mechanisms of Swimming and Flying”, pp. 41-52, 2007.

Session Category

Comparative Biomechanics: N/A

P2-004

EMG-Informed Simulation of Bipedal Chimpanzee Walking

Dr. Aravind Sundararajan[1], Dr. Brian Umberger[2], Dr. Matthew O'Neill[3]

[1]Elemance, LLC, Winston-Salem, NC, United States. [2]University of Michigan, Ann Arbor, MI, United States. [3]Midwestern University, Glendale, AZ, United States

Introduction

Optimal control simulations of locomotion using musculoskeletal models allow prediction of muscle activation, but these predictions may fail to replicate some characteristics of electromyography (EMG) measurements. EMG-informed simulations can improve estimation of muscle activation, but may affect dependent quantities, such as muscle energy consumption. Here, we integrate EMG measurements from 32 pelvis and hind limb muscles into three-dimensional (3-D) tracking simulations of bipedal chimpanzee walking and evaluate its effect on the simulated metabolic cost of transport (COT).

Methods

A 3-D musculoskeletal chimpanzee model [1, Fig. 1a] tracked experimental 3-D kinematic and ground reaction force data while minimizing gross COT, determined using a muscle energetics model. For EMG-informed simulations, fine-wire EMG waveforms from 32 pelvis and hind limb muscles per limb [2] were also tracked. The EMG tracking term was iteratively weighted to account for 0 to 51% of the total cost function value (J). All simulations were generated using OpenSim Moco. Correspondence between the predicted muscle activations and EMG was assessed via zero-lag cross-correlations (r) across all 32 muscles.

Results

Excluding EMG from the optimal control problem, the simulated gross COT was 6.2 $J \cdot kg^{-1} \cdot m^{-1}$ and muscle activations agreed moderately well with experimental EMG (r=0.53). Increasing the weight on the EMG tracking term achieved an r=0.80 with only an 8.7% increase in the simulated COT. A near-maximum tracking fit increased the correspondence to r=0.91, but led to a simulated COT ~40% higher than experimental measurements [3, Fig 1b].

Discussion

Using an EMG-informed approach, a Pareto frontier exists where EMG tracking can enhance neuromuscular realism with only a modest effect on the simulated COT [Fig 1].

These results provide an avenue to gain greater insight into chimpanzee biology and important comparative context for understanding hominin walking evolution.

Images (Optional)

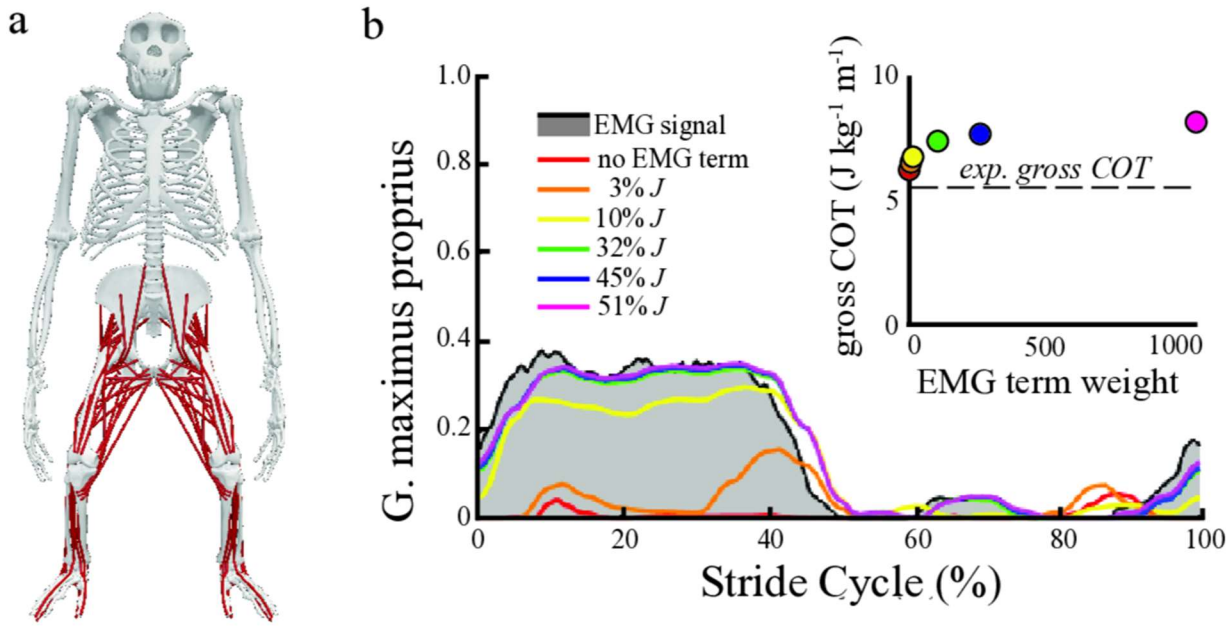


Figure 1. (a) Chimpanzee model and (b) example of EMG-informed effects on predicted muscle activations, (inset) gross COT.

References (Optional)

[1] O'Neill et al., J Experimental Biology, 2013; [2] Larson, J Human Evolution, 2025; [3] Sockol et al., Proc. Natl Acad Sci USA, 2007

Acknowledgements (Optional)

This work was funded by the National Science Foundation BCS 0935327, 0935321, 2018436, 2018523.

Session Category

Comparative Biomechanics: N/A

P2-005

Mineralized Cartilage Struts Significantly Stiffen Stingray Jaw

Mr Benjamin Flaum[1], Mr Salman Matan[2], Mr Carlos Puerta[2], Ms Kira Schmitt[3], Mr Frederik Mollen[4], Dr Fabian Wilde[5], Dr Daniel Baum[3], Dr Itai Cohen[6], Dr Lawrence Bonassar[2,7], Dr Mason Dean[1,8]

[1]Department of Infectious Diseases and Public Health, City University of Hong Kong, Hong Kong, Hong Kong, Hong Kong. [2]Meinig School of Biomedical Engineering, Cornell University, Ithaca, New York, United States. [3]Department of Visual and Data-centric Computing, Zuse-Institute Berlin, Berlin, Berlin, Germany. [4]Elasmobranch Research Belgium, Bonheiden, Antwerp, Belgium. [5]Helmholtz-Zentrum hereon GmbH, Hamburg, Hamburg, Germany. [6]Department of Physics, Cornell University, Ithaca, New York, United States. [7]Sibley School of Mechanical and Aerospace Engineering, Cornell University, Ithaca, New York, United States. [8]Centre for Nature-Inspired Engineering, City University of Hong Kong, Hong Kong, Hong Kong, Hong Kong

Introduction

Sharks and rays (elasmobranch) possess cartilaginous skeletons. Despite being made of compliant material, the hyaline cartilage cores of elasmobranch skeletal elements are wrapped by a cortex of mineralized tiles (tesserae), imparting dynamic compressive stiffness. Additional reinforcements via mineralized tubes made of tesserae coursing through skeletal elements have been described in numerous stingray species. This study seeks to understand how these mineral struts change the mechanics of cartilaginous tissue.

Methods

19 samples from three cownose ray (*Rhinoptera)* jaws were imaged via conventional μCT, then tested in confined compression. Post-testing, sample composition was analyzed and compared with mechanical properties (Pearson's r). Five samples from two additional cownose jaws were imaged on the PETRA III μCT beamline synchrotron under confined compression.

Results

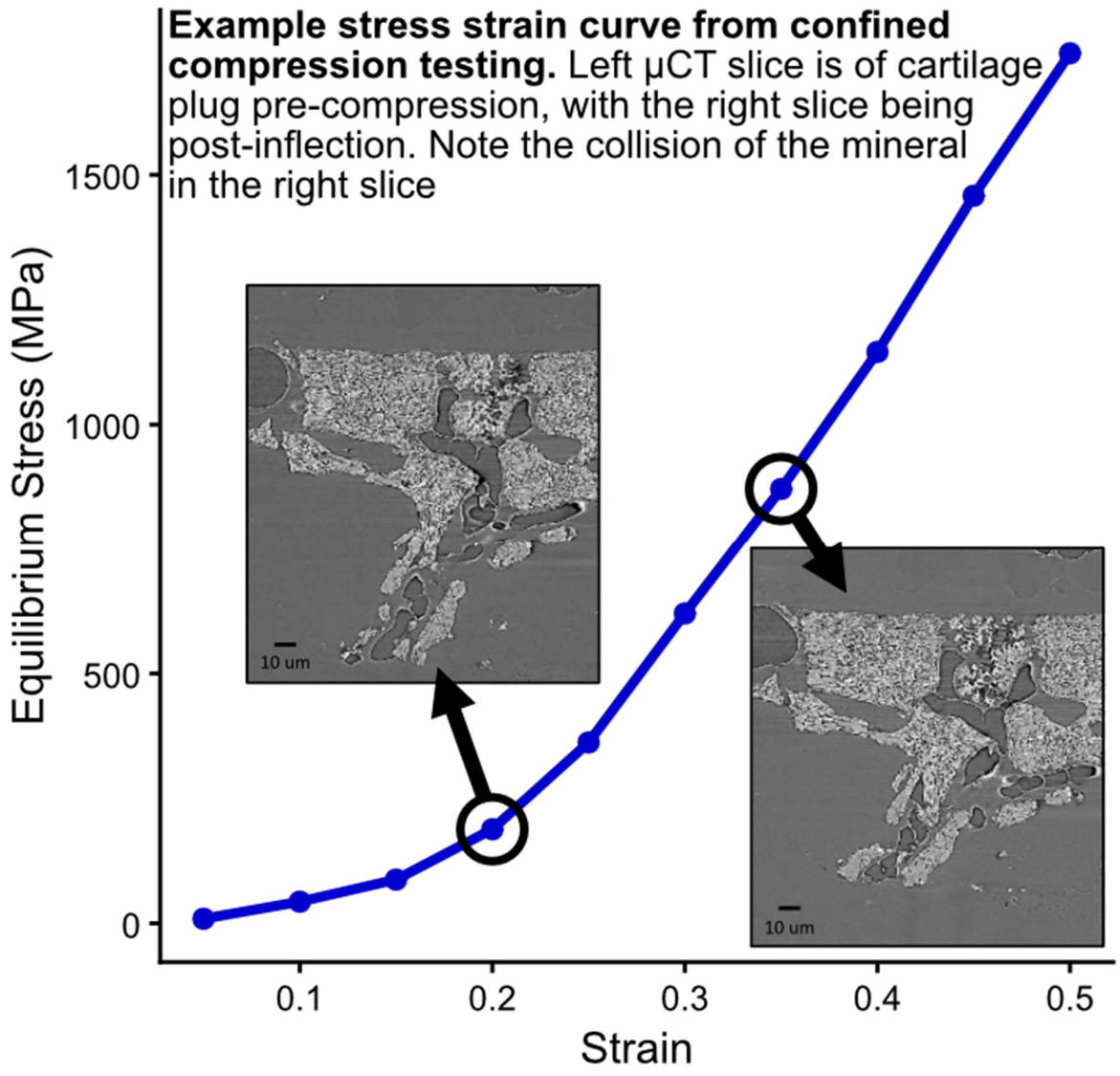
Mineral content from μCT and confined compression demonstrate that the mechanical properties of tessellated cartilage are directly tied to its mineral content, with highly mineralized cartilage (many trabeculae) having equilibrium moduli up to five times greater

than less mineralized (fewer trabeculae) cartilage. The corresponding stress-relaxation stress-stain curves had two distinct shapes depending on the level of mineralization. Highly mineralized cartilage exhibited a distinct J-shaped curve with an initial low-stiffness toe region, followed by a massive increase in stiffness after an inflection point at around 25% compression. Less mineralized cartilage had only a singular linear curve, similar to stress-strain curves from mammalian cartilage. Synchrotron μCT images showed the trabeculae collapsing under high strains.

Discussion

We hypothesize the J shaped curve is due to the soft/ hard composite nature of trabeculated cartilage, with the toe region being caused by initial compression of soft cartilage, followed by the stiffer region representing collision of tesserae. Images from the synchrotron supported this theory, showing the tesserae colliding only after the inflection point. This is the first time this phenomenon has been described in tessellated cartilage loaded perpendicular to the skeleton surface (previously only seen in parallel loading). Trabeculae therefore demonstrate an additional way that tesserae can reinforce cartilage without adding more cortex layers. These novel mechanical tests on tessellated cartilage create a foundation for future studies on the mechanics of this cartilage-only high-load system.

Images (Optional)



Session Category

Comparative Biomechanics: N/A

P2-006

Stereotypic Behaviours Affect Thoroughbred Racehorse Gait Symmetry and Stride Time

Ms Brittany Davis PhD Cand., PAS, Dr. Zoe Chan, Ms. Karelhia Garcia PhD Student, Ms. Charlotte De Bruyne PhD Student, Dr. Thilo Pfau

University of Calgary, Calgary, Alberta, Canada

Introduction

Stereotypic behaviours (STBs) are repetitive, abnormal behaviours performed for a substantial portion of the day, and are common in Thoroughbred racehorses. Some STBs do involve a significant physical aspect in the performance of those behaviours, and they are associated with clinical sequelae that may increase their risk of injury. However, STBs are typically only considered as a behavioural issue and their potential impact on equine biomechanics is not considered. Previous research has found a difference in race performance between STB horses and control horses, and this study expands more into the biomechanical effect that STB has on racehorses to further our understanding of injury risk and welfare.

Methods

A total of 29 actively racing Thoroughbreds (15 STB and 14 matched controls) were outfitted with 9 IMU EquiGait sensors. Horses were trotted up and down an aisle to analyze their symmetry and gait. All statistical analyses were performed using independent t-tests in SPSS.

Results

STB horses demonstrated a reduced stride time by 24.67ms ($p=0.05$), several head movement asymmetry was increased between 2.01mm to 5.77mm ($p=0.04$ to $p=0.028$). Withers asymmetry in STB horses nearly doubled ($p=0.039$). Pelvic movement asymmetries were higher in STB horses with increases of 2.64mm and 6.5mm ($p=0.05$ and $p=0.033$) when compared to control horses.

Discussion

Horses with STBs have increased gait asymmetry in both the front and hind end as well as an increased difference in forces produced between the left and right forelimbs when compared to matched controls. Increased asymmetries can lead to uneven joint loading and increased risk of injury. The asymmetries may also indicate that sub-clinical lameness

is present. The reduced stride time may indicate that horses are unable to fully extend their bodies, possibly indicating pain, lameness, or muscular fatigue.

Images (Optional)



Acknowledgements (Optional)

Session Category

Comparative Biomechanics: N/A

P2-007

Impact Analysis of the Hoof During Walking Using IMU Sensors

Bsc Beatrice poller, Bsc Chiara Steinwender, A. Univ. Prof. Dr. Christian Peham

University of Veterinary Medicine, Vienna, Vienna, Austria

Introduction

Lameness in horses and the condition of the surface/ground of sport arenas are a widespread problem that significantly affects the equine well-being and performance.The aim of the study was to show that accelerometers on the hoof can detect different surfaces (sandy soil, paved path, asphalt) as well as movement asymmetries.

Methods

For this purpose, a total of 30 horses were led at a walk and fitted with IMU sensors (3 axis, 16g, sample rate 833 Hz) on their front hooves. The measured data were evaluated with regard to their maximum acceleration and compared both between the forelimbs and between the different surfaces (sand soil, paved path, asphalt).The length of the 3-dimensional acceleration vector was calculated as follows: $accel3D = \sqrt{ax2 + ay2 + az2}$. The maximum acceleration values during impact and lifted off of the hoof were determined. The data were grouped and tested for normal distribution using the Kolmogorov-Smirnov test.To test the different soil types, a repeated-measures ANOVA was used; for the left-right comparison (asymmetry), a t-test (normally distributed data) or a Wilcoxon rank test (non-normally distributed data) was used.

Results

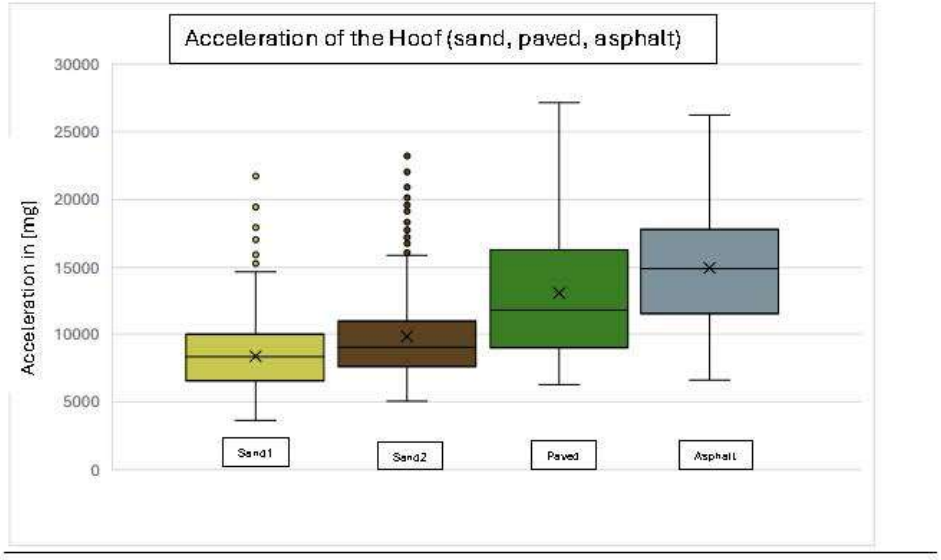
The results show partially asymmetrical movement patterns as well as significant differences in vertical acceleration values depending on the surface. The study demonstrates that IMU sensors are a suitable instrument for the objective detection of movement asymmetries and for differentiating the mechanical properties of various soils (figure 1).

Discussion

These results suggest that ground conditions play a role in lameness assessment. The results show partially asymmetrical movement patterns and significant differences in acceleration values depending on the surface. The study demonstrates that IMU sensors are a suitable tool for objectively recording movement asymmetries and differentiating the mechanical properties of various surfaces. Furthermore, it shows that combining ground properties and symmetry assessment can be advantageous. Their application thus opens

up promising perspectives for targeted use in training design, as well as in the prevention and diagnosis of musculoskeletal disorders.

Images (Optional)


Acceleration of the Hoof (sand, paved, asphalt)
Acceleration in [mg]
30000
25000
20000
15000
10000
5000
0
Sand1
Sand2
Paved
Asphalt

Session Category

Comparative Biomechanics: N/A

P2-008

How Temperature Tunes Muscle Mechanics During Active Lengthening Contractions: Implications for Muscle Models and Injury Risk

Dr Graham Askew[1], Dr Roger Kissane[2]

[1]University of Leeds, Leeds, West Yorkshire, United Kingdom. [2]University of Liverpool, Liverpool, Merseyside, United Kingdom

Introduction

Eccentric muscle contractions occur when muscles actively lengthen, dissipating energy and stabilising joints. During active stretch, muscle force rises in two phases (Figure 1): an initial rapid increase (phase-1), followed by a slower, sustained rise (phase-2). Phase-1 reflects the strain on attached cross-bridges, while the phase-2 is linked to increased strain of non-contractile elastic elements (e.g. titin). The temperature sensitivity of these responses remains poorly understood, despite its importance for musculoskeletal models that often rely on data collected at non-physiological temperatures.

Aim: to characterise the temperature dependence of the eccentric force-velocity relationship in mammalian skeletal muscle.

Methods

Mouse extensor digitorum longus muscles were subjected to ramp lengthening contractions during tetanic activation at 17, 27 and 37°C. The rate of force development during each phase was calculated.

Results

Phase-1 stiffness decreased at higher temperatures indicating faster ATP-dependent cross-bridge detachment, although mechanical strain-dependent detachment also contributes to the change in stiffness. Phase-2 stiffness increased with temperature, consistent with stronger and faster titin-actin binding. The transition between phases (muscle *'give'*) varied with temperature, with lower temperatures delaying cross-bridges detachment and engagement of the parallel elastic elements.

Discussion

These findings provide new insights into the eccentric force-velocity relationship and its temperature dependence, revealing distinct mechanisms underlying phase-specific responses. The interplay between cross-bridge kinetics and titin engagement highlights an intrinsic tuning of muscle mechanics to potentially reduce the risk of damage under

different thermal conditions. These results have important implications for musculoskeletal modelling, which often relies on data collected at sub-physiological temperatures.

Images (Optional)

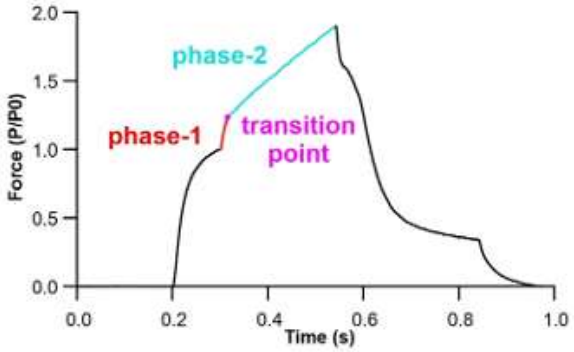


Figure 1. Eccentric lengthening of muscle. The initiation of stretch during an isometric tetanic contraction results in a rapid rise in force (phase-1), followed by a lower rate of force development (phase-2).

Acknowledgements (Optional)

This research was supported by an Early Career Researcher and Returners Fund from the University of Liverpool to RWPK and a BBSRC Project Grants (BB/R016917/1; BB/Y002466/1) to GNA.

Session Category

Comparative Biomechanics: N/A

P2-009

Morphological and Bioenergetic Adaptations to Environmental Temperature in Endotherms

Mr. Jason Cullum, Ms. Arianna Lopez, Mr. Peter Niehaus, Mr. Ali Mossayebi, Dr. Audrey Stone Ph.D., Dr. Owen Beck Ph.D.

University of Texas at Austin, Austin, Texas, United States

Introduction

Environmental temperature alters morphological and bioenergetic traits of endotherms, potentially creating a tradeoff in the ability to maintain body temperature versus producing mechanical power. In colder environments, animals typically exhibit a reduced ratio of surface-area-to-volume and fat-to-lean mass, as well as decreased mitochondrial ATP production efficiency with each of these having implications to thermoregulation and mechanical power production (1,2).

We hypothesized that endotherms from colder environments would adapt their physiology for greater heat production. To test this hypothesis, we reared rats in colder (6.5º C) and warmer (30º C) environments and predicted that the colder rats would develop relatively shorter tibias, a higher proportion of fat-to-lean mass, lower electron transport chain (ETC) efficiency, as well as high metabolic flux control though ETC complex I.

Methods

Twenty-four post-weaned Sprague-Dawley rats were equally divided into colder and hotter incubation chambers. Groups were size and sex matched at the start of incubation (85.2 ± 24.7 g for colder; 83.6 ± 26.7g for hotter; 50% female; Mean ± SD). Body composition and dimensions were analyzed using Dual X-Ray Absorptiometry scans one-month post-weaning. We isolated the soleus mitochondria of a room temperature rat and analyzed ETC characteristics.

Results

The tibia lengths of the colder (3.84 ± 0.24cm) and hotter rats (3.86 ± 0.23cm) were similar ($p=0.93$; $d=0.09$). There was no difference between the lean mass percentage ($p=0.06$; $d=1.61$), but colder rats had a lower body fat percentage ($p<0.01$; $d=2.28$) (Fig.1a,b). The coupling efficiency of the room temperature rat's ETC was 66% and synthesis of ATP depended on metabolic flux through complex I, with inhibition of the complex bringing down metabolic flux by 40% (Fig.1c).

Discussion

Our preliminary results indicate that environmental temperature exhibit some morphological adaptation, partially rejecting our hypothesis. Unexpectedly, the tibia length and lean mass percentage were unaffected, though these differences may arise at advanced ages. We expect the ETC characteristics in the colder rats to elicit greater heat production. As further data are obtained, we expect to detect tradeoffs between an animal's capacity to generate heat and mechanical power.

Images (Optional)

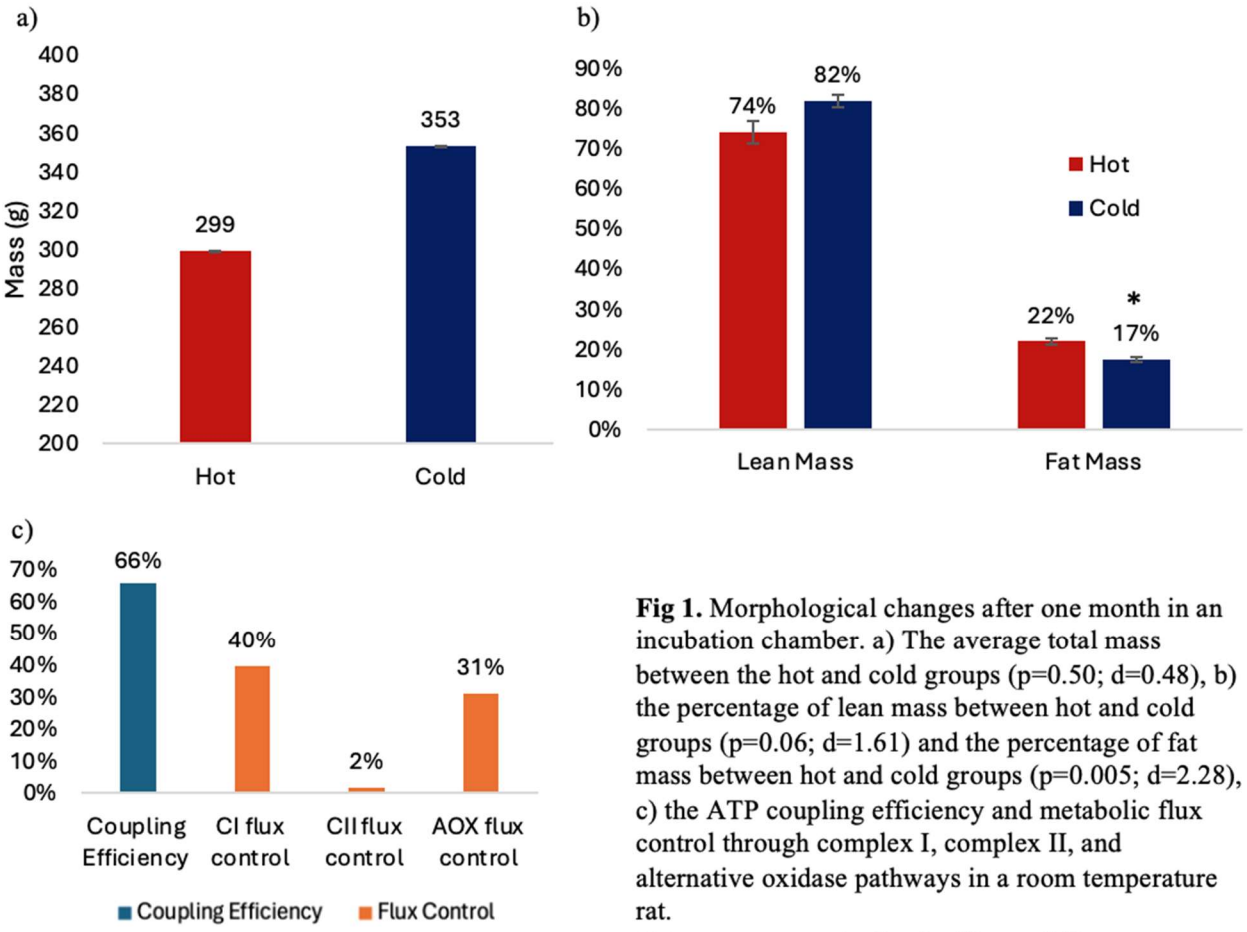


Fig 1. Morphological changes after one month in an incubation chamber. a) The average total mass between the hot and cold groups (p=0.50; d=0.48), b) the percentage of lean mass between hot and cold groups (p=0.06; d=1.61) and the percentage of fat mass between hot and cold groups (p=0.005; d=2.28), c) the ATP coupling efficiency and metabolic flux control through complex I, complex II, and alternative oxidase pathways in a room temperature rat.
* Denotes a statistically significant difference.

References (Optional)

[1] Mahalingam *et al*, J. Physiol, 2020

[2] Serrat, Compr. Physiol, 2014

Session Category

Comparative Biomechanics: N/A

P2-010

Development and Validation of a Custom Force Treadmill for Small Animal Biomechanics Research

Ms. Jessica Murawski MS, Dr. Derek Jurestovsky PhD, Dr. Stephen Piazza PhD, Dr. Jonas Rubenson PhD

The Pennsylvania State University, University Park, Pennsylvania, United States

Introduction

Force plates are widely used in biomechanics to measure ground reaction forces during locomotion performed either overground or on a treadmill. While there are commercial force plates available that are sensitive enough for small animal research, they are particularly susceptible to errors and noise when placed in the vibrating environments of a treadmill. To address this problem in ongoing studies of guinea fowl (Numida meleagris) locomotion, we built a treadmill fitted with a customized force platform specifically designed to accommodate small animals and the vibrations of the treadmill.

Methods

The Avian Force Treadmill (AFT) is equipped with a servomotor and controller with a manual dial controller and speed display. The system allows speed adjustment in real time. The AFT has an integrated custom-built high frequency force platform (AMTI; Model Number: BP400600HF-400-CTT). Sitting atop the treadmill without contacting it is an enclosure with a transparent side wall for video recording and the rear aspect open for access to the animal by the handler.

To test the ability of the treadmill to measure ground reaction forces consistent with small animal locomotion, we employed a passive dynamic elliptical cylinder rolling downhill (2.3° decline) under two mass conditions (0.91 kg and 1.18 kg) at 1.10 $m \cdot s^{-1}$. We also conducted trials with a guinea fowl (1.78 kg) running at 1.34 $m \cdot s^{-1}$ up a 6.0° incline.

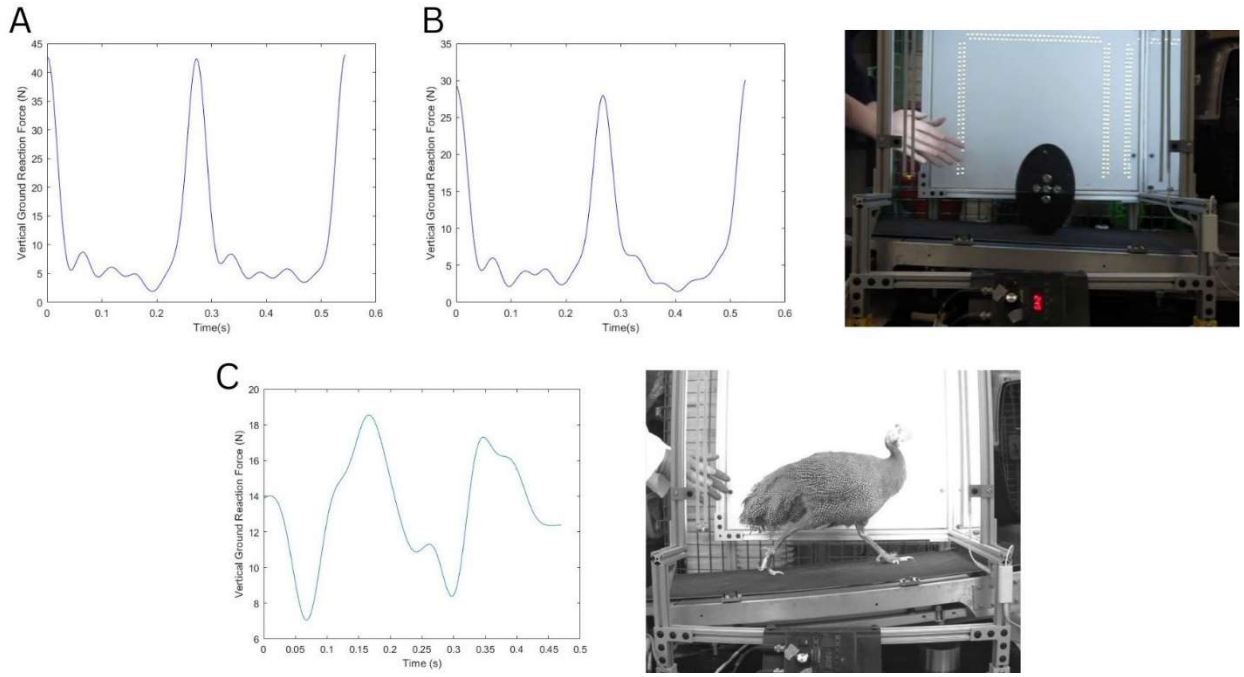
Results

The AFT was found to make measurements of ground reaction forces that discriminated between the different mass conditions despite the vibrations of the treadmill. Figure 1 shows the larger peak forces for the larger mass condition (Fig. 1A) and lower peak forces for the lighter mass condition (Fig. 1B). Figure 1 also shows representative ground reaction force data (combined from both feet) from a guinea fowl (Fig. 1C).

Discussion

The results of these tests support the ability of the AFT to measure ground reaction forces in a vibrating environment. Ongoing work will make use of additional passive dynamic walking robots to test force measurements and force-derived kinematic measures. This approach may be valuable for researchers working with small animals or where traditional calibration methods are insufficient due to environmental noise.

Images (Optional)



Acknowledgements (Optional)

This research was supported by the National Institutes of Health under grant number R01AR080711. This research study, including all procedures for animal care, was approved by the Penn State Institutional Animal Care and Use Committee (IACUC protocol PROTO202202152).

Session Category

Comparative Biomechanics: N/A

P2-011

Investigating the Role of Foot Biomechanics in Load Redistribution for Medio-Lateral Balance and Stability in Ground Birds

Mr. Junhyuck Woo[1], Ms. Alyssa Desamito[1], Ms. Samar Rana[1], Mr. Harish Saravanakumar[1], Prof. Monica Daley Ph.D.[1,2,3]

[1]Department of Ecology & Evolutionary Biology, University of California, Irvine, Irvine, CA, United States. [2]Department of Mechanical and Aerospace Engineering, University of California, Irvine, Irvine, CA, United States. [3]Department of Biomedical Engineering, University of California, Irvine, Irvine, CA, United States

Introduction

Ground birds serve as useful animal models for investigating diversity and shared features for balance and stability in bipedal locomotion. Bipedal ground birds must maintain balance in the face of mediolateral (ML) disturbances when navigating uneven terrain. Although avian bipedal locomotion has been extensively studied, most work has focused on sagittal-plane dynamics [1]. Consequently, neuromechanical strategies for frontal-plane balance remain unclear. Here we investigate the foot and whole limb mechanisms for frontal plane ML balance control in avian bipedal locomotion.

Methods

Helmeted guinea fowl (Numida meleagris, 1.50 ± 0.15 kg, n = 7) were trained to run across a runway with a 15° positive-roll ML perturbation manually triggered just before stance. We collected frontal-view kinematics and ground reaction forces (GRF). Videos were tracked with DeepLabCut [2] to extract limb, foot and body landmarks. The center of mass (CoM) was estimated as the centroid of six tracked points. We analyze the angle of the ground reaction force vector relative to virtual leg (VL) vectors between the medial and lateral toes and the CoM (Fig.1A). The angle between the medial and lateral VL components and the GRF vector was measured to estimate redistribution of load between the medial and lateral digits Stance phases were time-normalized, and angles were evaluated at 10%, 50%, and 90% of stance to represent early, mid, and late contact.

Results

Preliminary analysis suggests that smaller VL-GRF angles reflect greater mechanical contribution of that toe to weight support. Early to mid stance showed a redistribution between the toes, consistent with stabilizing against the perturbation. By end stance, both limbs shift toward greater medial toe contribution, which may reflect preparation for forward propulsion approaching takeoff rather than lateral stabilization.

Discussion

These findings suggest weight redistribution between toes to restore balance following a ML perturbation. In ongoing work, we will analyze how the foot kinematics relate to shifts in GRF over time during both the initial response and recovery from the perturbation.

Images (Optional)

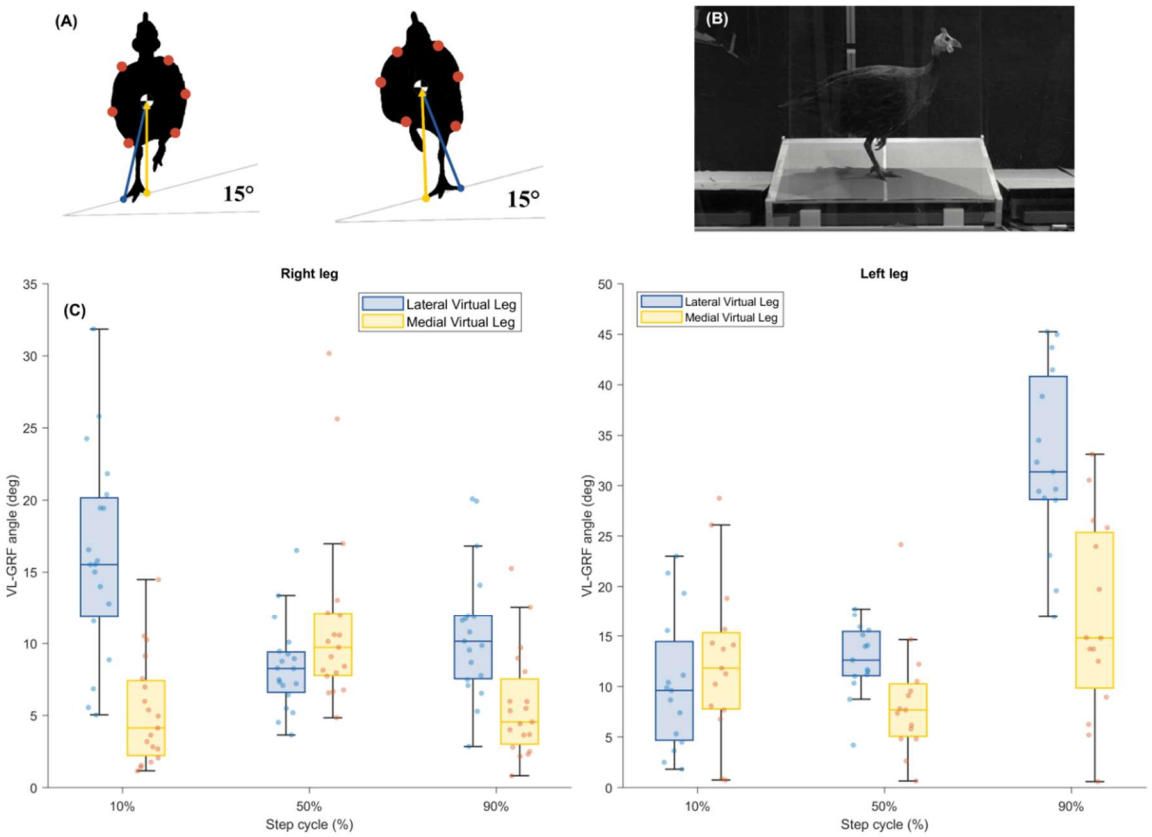


Figure 1. A) Illustraion of frontal kinematic analysis during medio-lateral perturbation, illustrating right leg and left leg contacts. The center of mass (CoM) is estimated from six tracked body points (orange). The medial VL (yellow) connects digit 2 to the CoM, and the lateral VL (blue) connects digit 4 to CoM. **B) Illustration of perturbation device (sagittal-plane view).** A sagittal-plane frame showing the bird encountering the perturbation device as it makes foot contact. **C) VL-GRF angle distributions at three timepoints in stance.** Data are from seven helmeted guinea fowl. The x-axis indicates the fraction of the step cycle, at early (10%), mid (50%), and late (90%) stance. The y-axis shows the angle between the VL vectors and ground reaction force (GRF). The right- and left-limb plots represent independent perturbation trials, illustrating how each limb responds to the perturbation. Each timepoint within stance contains paired boxplots for the medial (yellow) and lateral (blue) VL vectors.

References (Optional)

[1] M. A. Daley et al. (2007) J Experimental Biology.

[2] A. Mathis et al. (2018) Nature Neuroscience.

Acknowledgements (Optional)

NSF-DBI-2319710

Session Category

Comparative Biomechanics: N/A

P2-012

Mechanics of Bipedal Hopping on Uneven Terrain

Ms. Mary Peña[1], Dr. David Lin[2], Dr. Craig McGowan[1]

[1]Keck School of Medicine, Los Angeles, CA, United States. [2]Washington State University, Pullman, WA, United States

Introduction

For animals locomoting on uneven terrain, mitigating abrupt surface changes that can impede forward progression and cause instability can be critical for survival. The mechanisms by which the elements of the musculoskeletal system work together to enable dynamic stability under such conditions are still not thoroughly understood. This study examined how kangaroo rats *Dipodomys deserti* accommodate a decelerating perturbation – a sudden 12-degree upslope. We hypothesized that (1) pitching moments about the center of mass (CoM) would be minimized through changes in limb orientation and (2) the ankle joint would be the primary contributor to increased energy absorption demands caused by the decelerating perturbation.

Methods

Six kangaroo rats hopped bipedally at 1.77 m s^{-1} on a custom variable-terrain rotary treadmill under two conditions: level ground and perturbed. High-speed video (300 fps) and ground reaction forces (GRFs) were collected. An inverse dynamics analysis was used to quantify whole body and joint level mechanical output. A Wilcoxon signed-rank test was used to test differences between conditions. Linear regressions with ANCOVA assessed relationships between net joint work and acceleration.

Results

Peak pitching moments and the rotational impulses about the CoM did not differ between conditions. The relative orientation of the hindlimb to the GRF vector also did not differ between conditions. The perturbation was on average more decelerative than the level condition (-4.34 ± 0.73 m s^{-2}, -1.11 ± 0.79 m s^{-2}, respectively) but similar variability in acceleration was present in both conditions. Distal joint net work did not differ on average; however, for a given acceleration, the ankle absorbed less energy in the perturbed condition.

Discussion

The changes in hindlimb posture observed in accordance with GRF vector orientation support our first hypothesis by maintaining CoM rotational mechanics during decelerative

conditions. Our second hypothesis was not supported; however, the ankle exhibited a perturbation-specific response independent of deceleration. Because our inverse dynamics analysis is limited to rigid segments, it does not include the trunk, whose CoM lies anterior to the whole body CoM and likely produces an extensor moment. We propose that intrinsic ankle mechanisms help counteract the perturbation specific effects from larger body segments to preserve stability.

Acknowledgements (Optional)

This work was supported by NSF-2128546, and the Integrative Movement Sciences Institute (IMSI) Biological Integration Institute, NSF-DBI-2319710

Session Category

Comparative Biomechanics: N/A

P2-013

Kink in the Armor: The Mechanical Properties of Bony Armor in Agonidae Fishes

Ms Megan Vandenberg[1], Dr. Bart Boom[1], Dr. Adam Summers[1], Dr. Cassandra Donatelli[2]

[1]University of Washington, Seattle, WA, United States. [2]University of Washington Tacoma, Tacoma, WA, United States

Introduction

In an aquatic environment, evading predators determines survival. Many fishes use C-starts where the body bends into a tight curve before recoiling to propel away from danger [1]. Armored fishes behave as natural composite systems where added stiffness allows for greater energy storage during bending [2]. Agonidae are a family of fishes with diverse overlapping bony armor plates covering their bodies (1.A) [3]. Their armor features spines which offer protection - covering vulnerable gaps between plates, and hydrodynamic benefits - decreasing drag [4]. Below the spines, ridges provide a packing point which limits motion and potentially stores energy for C-starts. We used kinematic analysis, material testing, and micro-computed tomography to compare how different armor morphologies affect body stiffness.

Methods

We filmed C-starts for four species and extracted maximum bending angle. Specimens were euthanized and subject to cantilever bending tests at four locations to 110% of species-specific curvature. From force-displacement curves, we identified the packing point – interpreted as the onset of scale interlocking – using a linear regression (1.B). We calculated work to 100% of maximum C-start displacement and stiffness. We CT-scanned specimens to measure cross-sectional area, second moment of inertia and visualize the packing point.

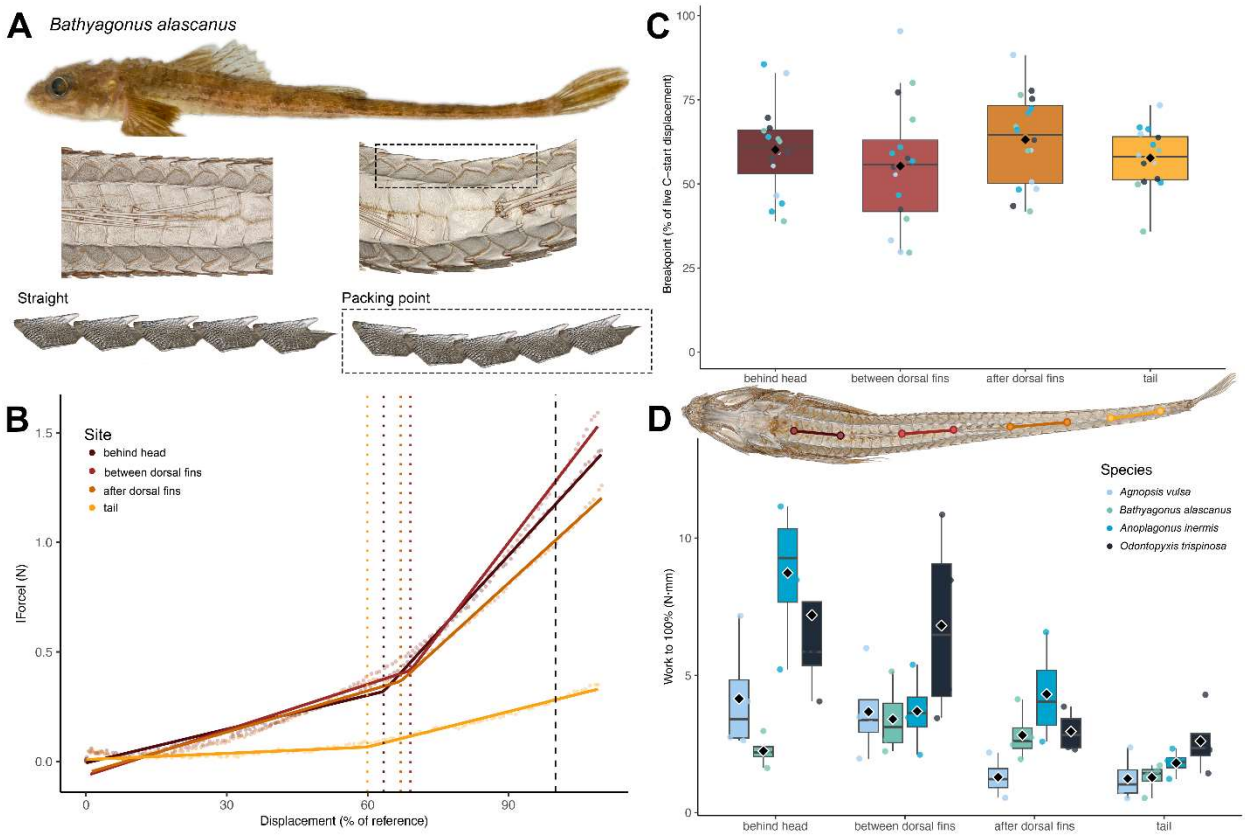
Results

Armor plates interlocked at 50%-75% of the full C-start bending showing body stiffness increases before they reach peak escape curvature (1.C). Species with more armoring require more work (2.5x-1.75x more) to bend to 100% curvature (1.D). For all species, stiffness increased after the packing point, from 2.5x stiffer behind the head to almost 5x stiffer at the tail.

Discussion

The substantial rise in stiffness after plate interlocking suggests that agonid armor acts as an energy-storage system, remaining flexible and compliant during small deflections but rapidly stiffening under larger deflections. The majority (80-95%) of the total work required to reach 100% displacement occurs after the packing point, indicating that most potential energy is stored only after reaching high curvature, allowing for rapid energy return during the final stage of the C-start.

Images (Optional)



References (Optional)

[1] Wakeling., Comp Biochem and Phys, 2001

[2] Brainerd., J Zoology, 1994

[3] Kolmann *et al.*, J R Soc. Interface, 2020

[4] Vandenberg *et al.*, Biol. J Linn. Soc., 2024.

Session Category

Comparative Biomechanics: N/A

P2-014

Understanding the roles of the active and passive components within the digital flexors of the equine forelimb

Ms Olivia Kenny, Dr Kasara Toth, Mr Joshua Mang, Dr Nigel Shrive, Dr. John E.A. Bertram, Dr Holly Sparks

University of Calgary, Calgary, Alberta, Canada

Introduction

Equine musculoskeletal overuse injuries are unfortunately common. Studying the injury mechanics and risk factors benefits horses and advances our understanding of comparable human conditions. The distal forelimb has two flexor muscle-tendon-ligament units (MTLUs) containing the superficial and deep muscles (SDFm and DDFm), tendons (SDFT and DDFT) and accessory ligaments (AL-SDFT and AL-DDFT). These MTLUs differ structurally and the SDFT is preferentially injured in racehorses [1, 2]. Identifying how active (muscles) and passive (tendons and ligaments) components function is critical, especially as fatigue increases injury susceptibility during exercise. This study aims to determine the roles and load distribution in the equine forelimb digital flexor system during mid-stance.

Methods

A novel testing frame was developed to test cadaveric forelimbs. Cyclic loads of 1000-3000N were applied vertically to the limb and 250-500N applied to each muscle to simulate active muscle engagement. Fetlock joint angle, SDFT strain, force and displacement data were measured. Four muscle engagement trials were completed (1) no muscle engagement (2) SDFm only (3) DDFm only (4) SDFm and DDFm engaged simultaneously. These trials were completed on three limb conditions (a) the intact limb [N=10] (b) single accessory ligament transected: AL-SDFT [N=5], AL-DDFT [N=5] (c) both accessory ligaments transected [N=10].

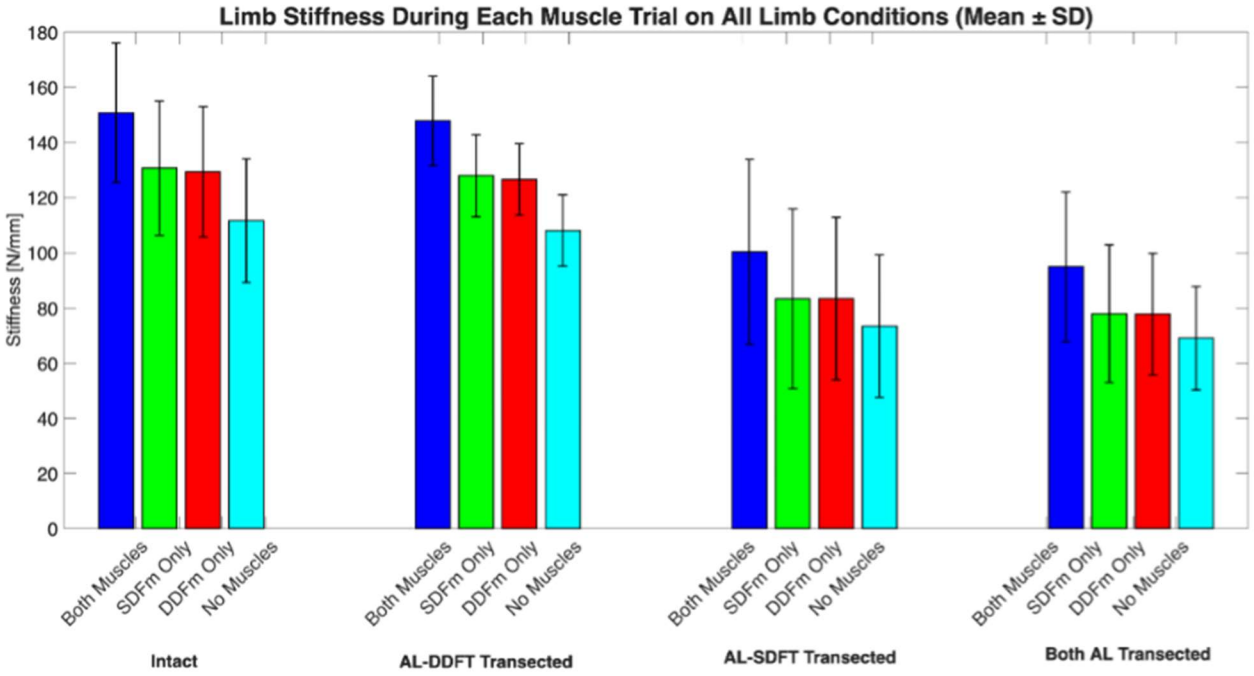
Results

Limb stiffness was calculated as force divided by displacement and group means/standard deviations are shown in Figure 1. SDFT strain and fetlock drop were greatest with no muscle engagement and lowest with both muscles engaged. Preliminary analysis indicates no statistical differences in SDFT strain or fetlock drop between individual muscle-engagement conditions.

Discussion

AL-SDFT transection reduced limb stiffness more than AL-DDFT transection, suggesting it provides greater passive support at mid-stance. Individual muscle engagement produced similar limb stiffness, SDFT strain and fetlock drop. SDFm engagement did not directly increase the SDFT strain possibly through the alteration of joint conformations and tendon moment arm reduction. This indicates the SDFT functions ambiguously, acting partly as a ligament during specific loading conditions. This information is critical in understanding the role and load distribution of the forelimb components during mid-stance.

Images (Optional)



References (Optional)

[1] Butcher *et al.*, Equine Vet J, 2007

[2] Ribitsch *et al.*, J Anatomy, 2019

Acknowledgements (Optional)

The University of Calgary Veterinary Medicine technicians and anatomy team are recognized for their assistance in obtaining samples.

Session Category

Comparative Biomechanics: N/A

P2-015

Subject-Specific CFD Characterisation of Craniospinal CSF Flow in Cavalier King Charles Spaniels with Chiari-Like Malformation and Syringomyelia

Mr Ryan Jones MEng[1], Prof. Clare Rusbridge BVMS PhD DECVN FRCVS[1,2], Dr Srdjan Cirovic PhD[1]

[1]University of Surrey, Guildford, Surrey, United Kingdom. [2]Wear Referrals Veterinary Specialist & Emergency Hospital, Bradbury, Stockton-on-Tees, United Kingdom

Introduction

Cavalier King Charles Spaniels (CKCS) spontaneously develop Chiari-like malformation (CM) and syringomyelia (SM), conditions associated with craniospinal overcrowding and disrupted cerebrospinal fluid (CSF) dynamics. Because these disorders closely parallel human CM and SM, CKCS represent a valuable comparative model for investigating their origin and treatment. This study performed subject-specific simulations of CSF flow in healthy, CM, and CM+SM CKCS and to identify flow parameters that statistically discriminate among these groups.

Methods

Thirty subject-specific CFD models of the ventricular system, cranial and spinal subarachnoid space (SAS), and central canal (CC, truncated at T3/4) were constructed from clinical MRI. The cranial SAS was modelled as a uniformly wide (0.5 mm) and the spinal SAS was created by lofting surfaces between manually defined inner and outer curves. A pulsatile velocity boundary condition was applied to ventricular and cranial SAS surfaces representing arterial-driven CSF motion; a pressure boundary condition at the caudal spinal end was implemented via a lumped dural compliance. Ten models were generated for each group (healthy, CM, CM+SM), from which velocities, pressures, impedances, and flow volumes were calculated. Principle component analysis (PCA) was then applied to identify group-specific flow patterns.

Results

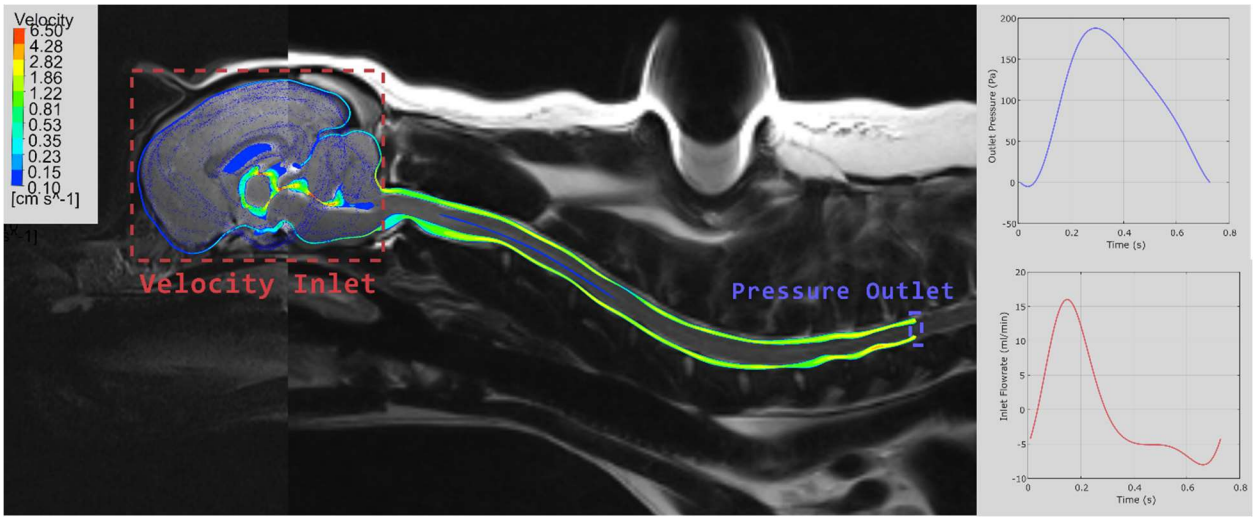
All model exhibited laminar CSF flow (Reynolds numbers <150 and Womersley numbers <5). Significant group differences were observed in craniospinal impedance; In syringomyelia cases, the integrated impedance between C2-3 was elevated in the SAS (~6 Pa/ml) but reduced in the CC (~1455 Pa/ml) compared with healthy and CM-only dogs (~1 Pa/ml in the SAS and ~2600 Pa/ml in the CC). PCA of slice-wise flow features (relative peak and mean velocities, flow rates, pressure gradients, and regional impedance) revealed distinct clustering. Several SM models exhibited focal CSF acceleration in regions where

the syrinx diameter increased abruptly. Syrinx-affected dogs also demonstrated large instantaneous pressure differences (>40 Pa) between the SAS and CC.

Discussion

These findings demonstrate that impedance and pressure patterns are altered in SM in ways consistent with proposed mechanisms of syrinx formation. Moreover, PCA reveals subtle flow abnormalities that support refined flow-based classification of CM and SM, and may offer useful parameters for postoperative assessment.

Images (Optional)



Session Category

Comparative Biomechanics: N/A

P2-016

Inverse Dynamics Analysis of a Dolphin Musculoskeletal Model During Swimming

Professor Shunichi Kobayashi Ph.D.[1], Graduate Student Taisuke Nakamura[1], Graduate Student Aoi Take[1], Professor Yutaro Motoori Ph.D.[2]

[1]Shinshu University, Ueda, Nagano, Japan. [2]The University of Osaka, Toyonaka, Osaka, Japan

Introduction

Dolphins exhibit excellent swimming performance, and the thrust generated by their tail flukes has attracted considerable attention. To develop underwater propulsion systems using fluke-inspired fins, it is necessary to understand dolphin swimming and the associated whole body motion and loading. Musculoskeletal modeling with inverse dynamics provides a noninvasive method for estimating internal forces. In this study, we built an anatomically based dolphin musculoskeletal model and used inverse dynamics with fluid forces on the tail flukes to clarify the muscle forces and tendon tensions in the caudal peduncle during swimming.

Methods

Based on anatomical data for dolphins [1], we constructed a musculoskeletal model focusing on the region from the caudal peduncle to the tail flukes of the dolphin. The model included dorsal axial tendons I and II dorsally, the ventral axial tendon ventrally, and 18 caudal vertebrae, ventral chevron bones, and ligaments (Figure 1). Inverse dynamics analysis was performed in AnyBody using the prescribed motion, mass properties, and externally applied fluid forces to compute the muscle forces (tendon tensions). The fluid forces were obtained from a numerical simulation [2] of a swimming dolphin using an immersed boundary–lattice Boltzmann method and applied from the body surface to each vertebra.

Results

The muscle length changes corresponding to the vertebrae-connected tendons tended to increase toward the leading edge of the tail fluke, and tendon tension was generated even during stretching. In dorsal axial tendon I, tension occurred during the upstroke, with particularly large forces on the trunk. In contrast, in the ventral axial tendon, tension was generated during the downstroke, with large values in the tendon attached to the trunk-side of the chevron bones.

Discussion

The tendon tension fluctuated with the hydrodynamic forces on the tail flukes, showing large peaks at the upstroke–downstroke transition. In both the dorsal and ventral axial tendons, tension increased from the caudal peduncle toward the trunk. However, the model accuracy remains limited, and tendon attachment locations require further refinement.

Images (Optional)

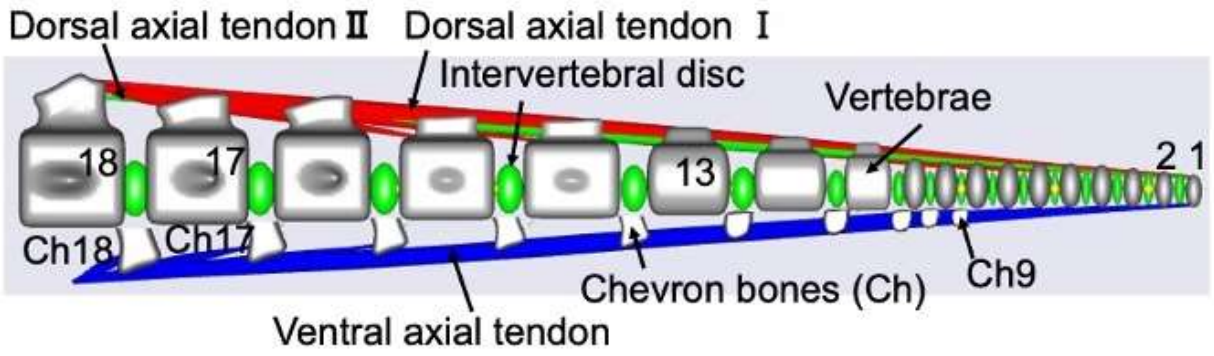


Figure 1. Musculoskeletal model of the caudal peduncle and tail flukes of a dolphin.

References (Optional)

[1] Q. Sun et al. , J Biomech Sci Eng, 2010.

[2] Y. Motoori et al., submitted to Phys. Rev. Fluids.

Session Category

Comparative Biomechanics: N/A

P2-017

Computational Modeling of YAP Phosphorylation Within Integrin Adhesions

Dr. Hamidreza Jafarinia[1], Dr. Lidan Shi[2], Dr. Haguy Wolfenson[2], dr. Aurélie Carlier[1]

[1]Maastricht University, Maastricht, Limburg, Netherlands. [2]Technion, Haifa, Haifa, Israel

Dr. Hamidreza Jafarinia

Dr. Lidan Shi

Dr. Haguy Wolfenson

Introduction

Mechanical and biochemical cues intricately activate YAP, which is pivotal for the cellular responses to these stimuli. Recent findings reveal an unexplored role of YAP in influencing the apoptotic process. It has been shown that on soft matrices YAP is recruited to small adhesions, phosphorylated at Y357, and translocated into the nucleus triggering apoptosis [1]. Interestingly, YAP Y357 phosphorylation is significantly reduced in larger mature focal adhesions on stiff matrices. Building upon these novel insights, we aimed to use stochastic modelling to delve deeper into the complex dynamics of YAP phosphorylation within integrin adhesions.

Methods

The dynamics of YAP phosphorylation within integrin adhesions is simulated using a spatially stochastic Gillespie algorithm. In each simulation step, YAP undergoes diffusion or reaction events, including binding, unbinding, phosphorylation, dephosphorylation (Figure 1). We also model adhesion formation and disassembly at varying intervals within the cell. Simulations are conducted in MATLAB version 2022.

Results

Our findings emphasize several key points: firstly, increasing the cytosolic diffusion rate of YAP correlates with higher levels of phosphorylated YAP (pYAP), secondly, increasing the number of binding sites and distributing them across the membrane surface, mimicking smaller adhesions, leads to higher pYAP levels, particularly at lower diffusion rates. Moreover, we show that the binding and release rate of YAP to adhesions as well as adhesion lifetimes significantly influence the size-effect of adhesion-induced YAP phosphorylation.

Discussion

The findings highlight the complex and dynamic interplay between adhesion lifetime, the rate of pYAP unbinding from adhesions, and dephosphorylation rates, collectively shaping overall pYAP levels. In summary, our work advances the understanding of YAP mechanotransduction and opens avenues for experimental validation.

Images (Optional)

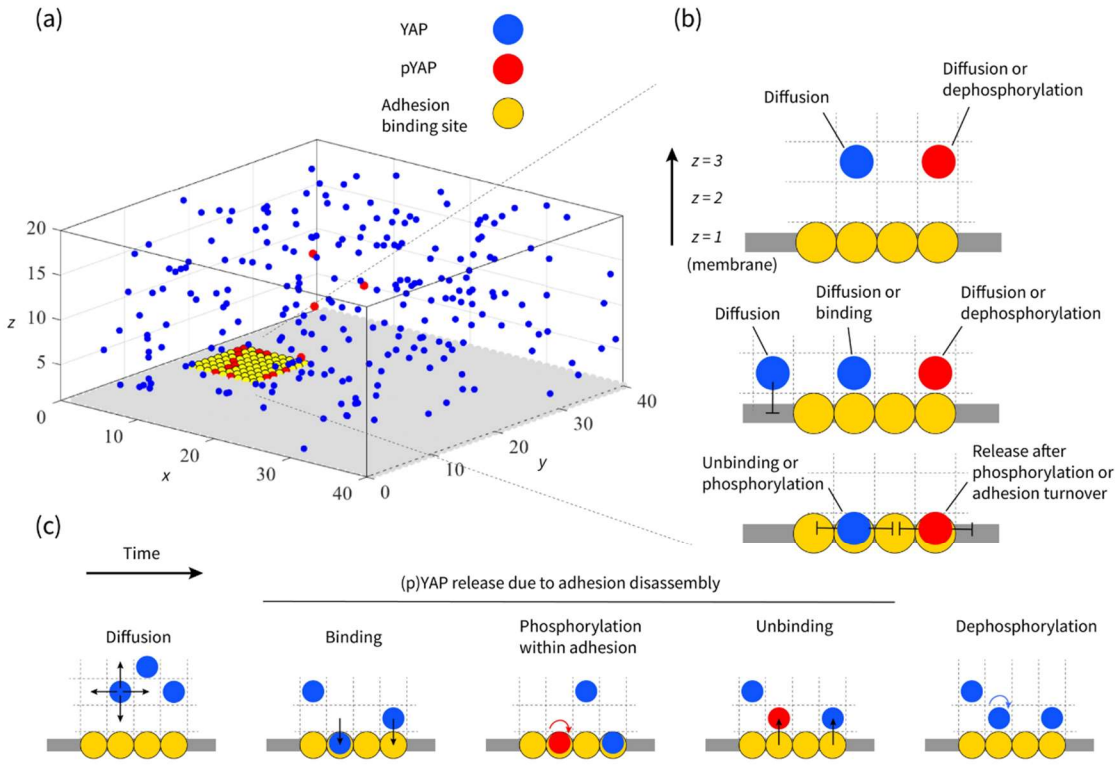


FIGURE 1: A sample snapshot of the simulation domain and schematics illustrating the simulated events. (a) 3D simulation domain for YAP phosphorylation within integrin adhesions. Integrin adhesions depicted with yellow beads on the membrane. Blue beads show YAP and red beads show phosphorylated YAP (pYAP). (b) Schematic representations of the diffusion and reaction events incorporated in the model. (c) Sequence of events in the model.

References (Optional)

[1] Shi et al. 2024. YAP mediates apoptosis through failed integrin adhesion reinforcement. Cell Rep. 43:113811

Acknowledgements (Optional)

This work was financially supported by the Gravitation Program “Materials Driven Regeneration”, funded by the Netherlands Organisation for Scientific Research (024.003.013). H.W. acknowledges support by the Rappaport Family Foundation, the John

Templeton Foundation (grant-62568; the opinions expressed in this publication are those of the authors and do not necessarily reflect the views of the John Templeton Foundation), and the German Research Foundation (DFG; grant no. GZ PO1725/13-1 AOBJ-697448).

Session Category

Molecular Biomechanics: N/A

P2-018

Relation Between Perfumes Intensity and Mechanical Tension Index Influenced by Age and Gender

Ms Emilie Khattignavong[1,2], Mrs Sophie Raviot-Derrien[2], Mr Hassan Zahouani[1]

[1]Ecole Centrale de Lyon, Ecully, Auvergne Rhône Alpes, France. [2]COTY R&D, Versoix, Geneva, Switzerland

Introduction

Perfume is a mixture of odorants and solvents whose physicochemical properties such as volatility, molecular weight, and vapor pressure can vary widely. Understanding how these properties influence the fragrance evaporation and how perfume interacts with skin surface is essential for controlling its release over time.

At the same time, intercellular lipids (ICL) in the stratum corneum (SC), the skin's outermost layer, are essential for skin barrier function and controlling the penetration of external substances. This barrier function is strongly linked to the ICL [1]. At the SC surface, the molecular organization and composition of these lipids can be altered by external factors such as cosmetic products like perfume. From a mechanical point of view, human skin is subjected to an initial tension exerted by the superficial connective tissue: the fascia. The developed model allows for the study of three parameters in the spectral domain: wavelength, spatial frequencies, and anisometry along the x and y axes. Based on a static equilibrium model of internal forces, the model quantifies three tension index.

Methods

Confocal Raman microscopy (CRM) is a technique capable of analyzing the skin structure and composition. A protocol was developed to investigate the molecular mechanisms involved in the interactions between fragrances and human skin *in vivo* using CRM. Hydration, lipid content, and lipid organization were measured on untreated skin and on skin treated with fragrance at T0h and T6h. Mechanical parameters, including skin tension index, were also assessed, and an olfactory study was conducted to establish relationships between these parameters in a panel of 20 volunteers.

Results

The results show that the fragrance leads to a decrease in hydration and disrupts lipid organization over time. Strong correlations were also identified between skin tension index and the perceived fragrance intensity at T0h, particularly among older and male participants.

Discussion

These observations suggest that the application of perfumes may increase the permeability of the SC [2]. Furthermore, the skin tension index appears to be a key parameter to consider in the perceived fragrance intensity.

References (Optional)

"[1] G.K. Menon *et al*. , International Journal of Pharmaceutics, 2012"

"[2] B.Breiden *et al*. , Biochimica et Biophysica, 2014"

Session Category

Molecular Biomechanics: N/A

P2-019

Exploring Collagen Mechanics and Protein Interactions Across Hierarchical Scales: Insights from Fluorescence Microscopy and AFM Imaging

PhD Candidate Janine Srocka, PhD Candidate Koushik Bar, Professor Nancy R. Forde

Simon Fraser University, Burnaby, BC, Canada

Introduction

Extracellular matrix (ECM) mechanics play a crucial role in cellular physiology, and maintaining ECM homeostasis is essential for proper cellular development and tissue function. Cells sense and respond to mechanical stimuli, but the role of force-induced structural changes in ECM scaffolding proteins, such as collagen, in mechanical signal transduction remains poorly understood. Collagen exists in a range of hierarchical assemblies, from individual molecules to fibrils and fascicles. Given this complexity, it is essential to assess collagen's mechanical behaviour across these different scales to fully understand how structural transitions impact force transmission and protein–protein interactions.

Methods

In this study, we explored collagen's mechanical properties and how they influence its interactions with binding partners. To investigate collagen's behaviour across different scales, we utilized both fluorescence microscopy and atomic force microscopy (AFM). A fluorescence-based stretching assay was employed to screen for proteins whose interactions with collagen are modulated by mechanical strain, offering insights into collagen's force response at the tissue scale. AFM imaging was used to visualize collagen at various hierarchical levels, from single molecules to fibrils, enabling the assessment of its mechanical properties and structural organization. Additionally, AFM imaging was employed to examine protein binding to collagen at the molecular level.

Results

In our experiments, we identified proteins whose interactions with collagen were either affected or unaffected by mechanical strain, as demonstrated by our fluorescence-based stretching assay. AFM imaging was used to observe single collagen molecules, both with and without bound proteins, providing initial structural insights into these molecular interactions.

Discussion

Our findings provide initial insights into different approaches for studying collagen across its hierarchical scales. While fluorescence-based assays and AFM imaging offer valuable perspectives on collagen's mechanical properties, these approaches present experimental challenges such as distinguishing specific from non-specific binding. These difficulties highlight the need for further optimization of experimental protocols. Moving forward, improving strain-specific assays and exploring collagen's behaviour at multiple scales will be crucial for advancing our understanding of ECM mechanics and collagen's role in mechanotransduction.

Session Category

Molecular Biomechanics: N/A

P2-020

Spontaneous Clustering of LINC Complex Units Enhances Nuclear Force Transmission

PhD Student Nya Domkam, Professor Mohammad Mofrad PhD

University of California Berkeley, Berkeley, CA, United States

Introduction

The LINC (LInker of the Nucleus to the Cytoskeleton) complex plays a pivotal role in this process. Composed of SUN proteins in the inner nuclear membrane and KASH peptides in the outer nuclear membrane, the LINC complex forms a continuous mechanical bridge across the nuclear envelope. Through this bridge, forces from the cytoskeleton can directly influence nuclear architecture and function.

Although a single LINC complex unit (LCU) is structurally capable of withstanding some level of mechanical load, the magnitude of forces generated by aligned actin bundles in the actin cap likely exceeds the capacity of an individual LCU without unfolding.

In this study, we investigate whether LCUs spontaneously form stable higher-order assemblies under minimal-force conditions

Methods

We performed all-atom molecular dynamics simulations. The SUN2/KASH2 trimeric structure served as the basis for all models. Multiple candidate cluster arrangements were constructed using complementary approaches: protein–protein docking, AI-based structure prediction, and manually oriented configurations.

Results

Analysis of interaction energetics revealed two distinct stabilizing mechanisms across models. Many were stabilized by electrostatic complementarity and hydrogen-bond networks, with a locally increased density of hydrogen bonds at the interacting interfaces. While others were stabilized predominantly by hydrophobic packing, which overcame

repulsive interactions among neighboring charged residues and produced a tightly associated interface.

To quantify relative stability, we ranked all structures by total complexation free energy. The most favorable complexation energies—and the most favorable stepwise energy profiles—were observed in protein–protein docking models.

Discussion

The emergence of multiple stable clustering modes suggests that LINC complex organization at the nuclear envelope may be driven not only by externally applied forces but also by favorable thermodynamic interactions. Distinct stabilizing mechanisms — electrostatic/hydrogen-bond networks versus hydrophobic packing — likely represent alternative assembly pathways that the cell can exploit under different mechanical environments. These modes may differentially contribute to nuclear force buffering when cytoskeletal tensions increase.

Future work will directly test the contribution of hydrophobic interactions by mutational disruption of interface residues. Experimentally, in vitro oligomerization assays such as size-exclusion chromatography can validate clustering, while FRAP studies in cells can evaluate cluster stability by comparing protein mobility between mutants and wild type.

References (Optional)

Session Category

Molecular Biomechanics: N/A

P2-021

Basic Study Using Ex-Vivo Pig Ear Skin for Connective Tissue Softening via Fractional Laser

Basic Study Using Ex-Vivo Pig Ear Skin for Connective Tissue Softening via Fractional Laser Ren Sato Doctoral Student, Basic Study Using Ex-Vivo Pig Ear Skin for Connective Tissue Softening via Fractional Laser Ippei Yagi Assistant Professor, Basic Study Using Ex-Vivo Pig Ear Skin for Connective Tissue Softening via Fractional Laser Satoshi Uchida Professor

Tokyo Metropolitan University, Hino, Tokyo, Japan

Introduction

Fibrosis causes organ dysfunction through excessive collagen accumulation and tissue stiffening. Current pharmacological treatments, such as pirfenidone, only delay disease progression and cannot reverse established rigidity or side effects. This study investigates a novel application of Fractional Laser (FL) therapy—typically used for skin tightening—to instead *soften* fibrotic tissue via controlled thermal denaturation. The hypothesis is that heating collagen above 63°C transforms it into gelatin, thereby reducing tissue stiffness.

Methods

To verify this mechanism, researchers conducted *ex-vivo* experiments using porcine ear dermis. A 1064 nm fiber laser was applied to tissue samples at four irradiation densities (150, 300, 450, and 600 dots/mm^2). The effects were evaluated using Collagen Hybridizing Peptide (CHP) staining to visualize denaturation and uniaxial tensile testing to measure changes in Young's Modulus.

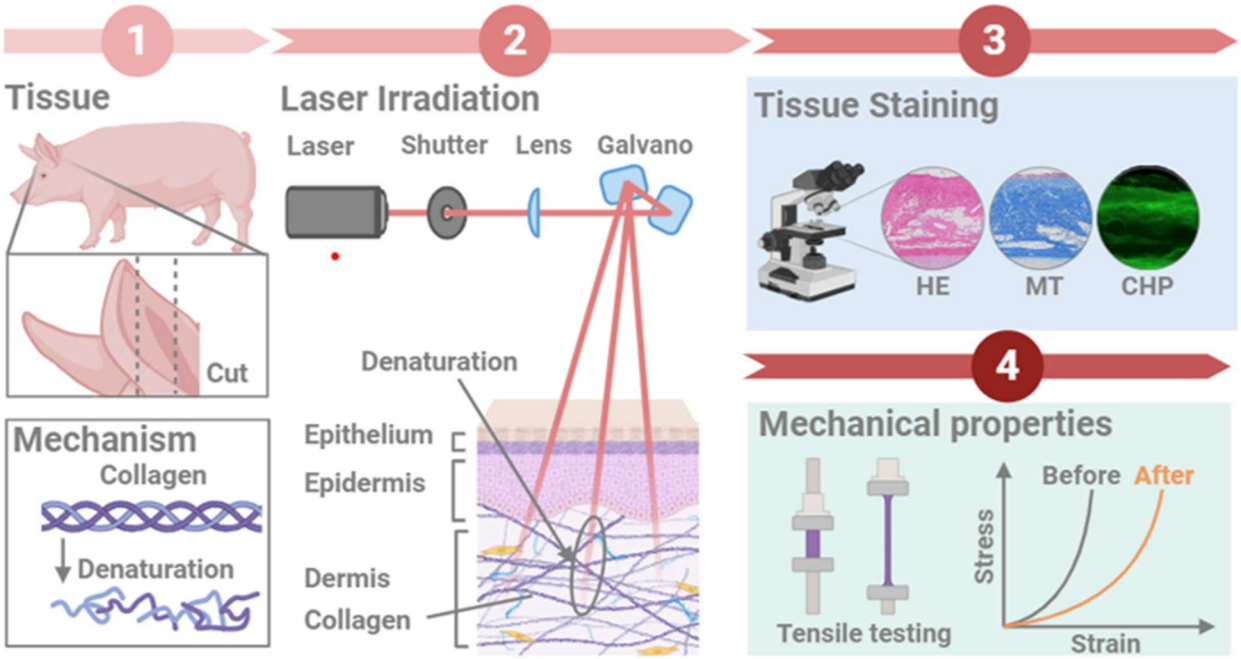
Results

Histological analysis confirmed that the laser successfully induced deep thermal denaturation. Mechanical testing revealed a significant, density-dependent response. While the lowest density (150 dots/mm^2) caused slight stiffening due to dehydration, higher densities resulted in marked softening. Specifically, irradiation at 600 dots/mm^2 reduced the tissue’s Young's Modulus to 39% of the pre-treatment value. These results indicate that at sufficient densities, the structural breakdown of collagen dominates over dehydration effects.

Discussion

This study provides fundamental evidence that FL irradiation can be tuned to reduce tissue stiffness, offering a potential alternative to drug therapy for fibrosis. However, a key limitation is the use of an ex-vivo model, which excludes biological wound healing responses. Future in-vivo studies are necessary to determine if the thermal damage triggers inflammatory re-fibrosis or if the softening effect is sustainable during the healing process.

Images (Optional)



References (Optional)

[1]Michael, Z. *et al.,* American Journal of Physiology, 2013

[2]Maria, C. *et al.,* Pharmaceuticals, 2024

[3]Marc, O. *et al.,* Journal der Deutschen Dermatologischen Gesellschaft, 2009

[4]Su, W. *et al.,* Scientfic Reports, 2018

[5]Rebecca, G. W., eLife, 2022

[6]Lucas, L. B. *et al.*, Biomaterials, 2018

Session Category

Molecular Biomechanics: N/A

P2-022

Preliminary Quantification of Hindlimb Joint Biomechanics in a Large Animal Model of Hypophosphatasia Using a Novel Inverse Dynamics Model

Dr. Aaron Henry PhD[1], Dr. Dana Gaddy PhD[1], Dr. Larry Suva PhD[1], Dr. Andrew Robbins PhD[2]

[1]Texas A&M University, College Station, Texas, United States. [2]University of Texas at Tyler, Tyler, Texas, United States

Introduction

Hypophosphatasia (HPP) is a rare genetic disorder impacting bone mineralization and development. Biomechanical investigations have focused on orthopedic symptoms, but joint biomechanics during gait have yet to be quantified in any HPP population. Large animal models provide a vital platform to understand disease progression, thus this study evaluated HPP impacts on hindlimb gait biomechanics in a sheep model.

Methods

Sixteen skeletally mature Rambouillet sheep (wildtype [WT] and HPP) were utilized, with kinematic and kinetic data collected using a Vicon Motion Capture System and AMTI force plates integrated into a custom runway. Joint centers and body segment inertial properties (BSIPs) were calculated using predictive models based on computed tomography data [1,2], while a novel inverse dynamics model calculated hindlimb joint kinetics. Primary endpoints included ground reaction forces, joint angles, intersegmental forces, and moments of the hip, stifle, hock, and metatarsophalangeal joints. A two-way Type II ANOVA test compared extrema values of all kinematic and kinetic endpoints between WT and HPP groups.

Results

Endpoints were generally similar, with exceptions primarily in the stifle joint. Significant differences were seen in joint flexion extrema of the hip, stifle, and hock. HPP sheep had significantly smaller peak stifle posterior intersegmental force. Regarding moments, HPP sheep had higher peak stifle flexion moment at early stance, reduced peak stifle extension just before swing, and a larger peak abduction moment at the stifle in early stance. No significant differences were seen in joint range of motion or non-sagittal plane joint angle extrema.

Discussion

This study provides the first quantitative analysis of joint biomechanics during gait of any HPP population. Results do not suggest substantial differences between HPP and WT hindlimb gait, though significant differences occurred primarily in the sagittal plane, particularly at the stifle joint. However, the limited sample size resulted in relatively low statistical power; inclusion of additional animals or improvement of the inverse dynamics model could identify more subtle differences.

Images (Optional)

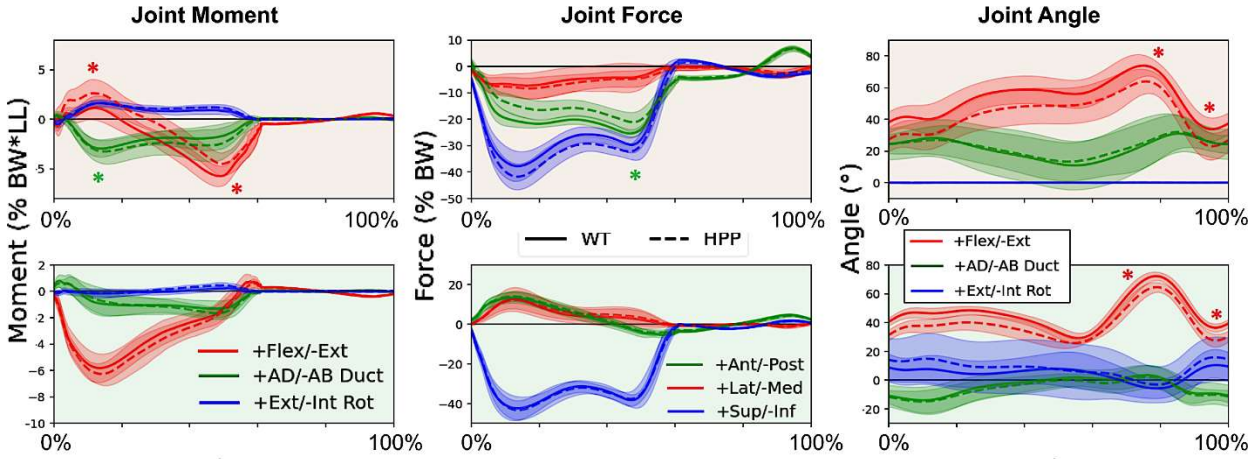


Figure 1: Intersegmental angles, forces, and moments for the stifle (top row) and the hock (bottom row) joints. (*) Indicates statistical significance ($p<.05$) for the local extreme of the matching color. X-axis is percentage of gait cycle.

References (Optional)

[1] Henry, J. Biomech., 161, 111861 (2023), 10.1016/j.jbiomech.2023.111861

[2] Henry, *J. Biomech.*, 190, 112848 (2025), 10.1016/j.jbiomech.2025.112848

Session Category

Musculoskeletal Biomechanics: Joints and Motion

P2-023

Towards Better Understanding of Trimester Specific Gait Kinematics During Pregnancy

Ms. Alyson Colpitts MASc, Ms. Heather Li Yam Nam, Dr. Martine McGregor PhD, Dr. Elise Laende PhD

University of Waterloo, Waterloo, ON, Canada

Introduction

Current understanding of biomechanical changes during pregnancy and post-partum is limited. A 2025 meta-analysis on pregnant and postpartum gait kinematics, which included only 32 viable papers, found indications that pregnant women experience increased pelvic tilt, knee flexion, and lateral foot progression angle, with decreased hip extension and ankle plantarflexion [1]. The objective of our study was to investigate kinematic changes over pregnancy and the feasibility of capturing data these changes using accessible markerless motion capture.

Methods

Data were collected using 8 synchronized Sony video cameras and processed with markerless motion capture software (Theia3D, Kingston, ON). Exercises included walking, fast walking, balance, and lifting and carrying tasks. Subjects who were pregnant were recruited to participate in 6 sessions, one at the end of each trimester of pregnancy (12, 24, and 36 weeks) and three post-partum (12-, 24-, and 36-weeks post-partum). Pose data were processed using Visual3D and subsequently MATLAB to generate 3D joint kinematics and calculate average maximum values of joint motion in the sagittal plane.

Results

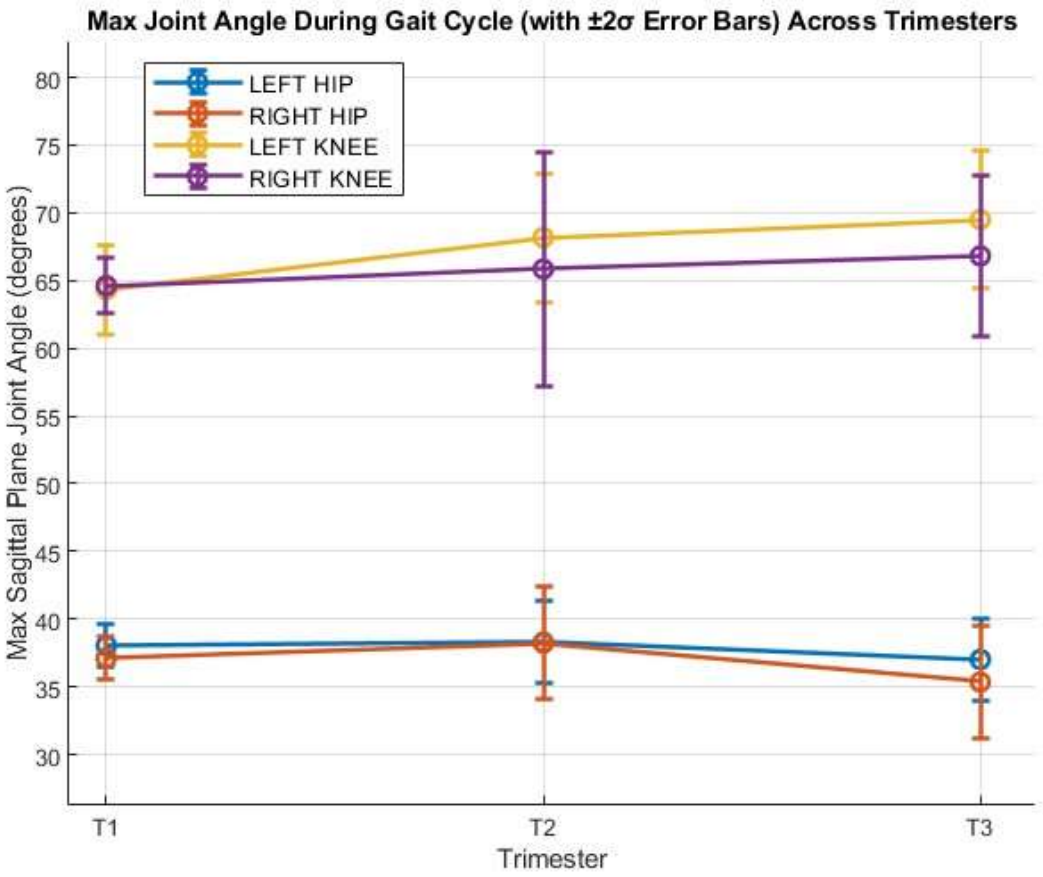
Complete kinematic data for overground walking were available for two participants over their pregnancies. Similar to existing literature, participants had decreased maximum hip sagittal plane angle between trimester 1 (37.6+/-0.9 degrees) and trimester 3 (36.2+/-2.0 degrees) and increased maximum knee flexion angle from trimester 1 (64.5+/-1.4 degrees) to trimester 3 (68.2+/-3.1 degrees; Figure 1).

Discussion

Findings from this data support current understanding of gait changes throughout pregnancy. Recruitment and analysis are ongoing with 4 additional participants currently enrolled. Variability increase from first to third trimester, as indicated by standard deviation, will be further examined. This work demonstrated initial feasibility of using a novel markerless motion capture approach to track kinematics in a pregnant population,

enabling high throughput and minimizing participant burden which will support ongoing research in this understudied area.

Images (Optional)



References (Optional)

[1] H. da C. Souza et al., “Gait and Posture, 121 (2025).

Session Category

Musculoskeletal Biomechanics: Joints and Motion

P2-024

How Muscle–Tendon Inertia Influences Neuromuscular Coordination in Cycling

Dr Ameur Latreche[1], Dr Stephanie Ross[2], Dr Taylor Dick[3], Dr James Wakeling[1]

[1]Simon Fraser University, Burnaby, BC, Canada. [2]University, Calgary, AB, Canada. [3]The University of Queensland, Brisbane, Qld, Australia

Introduction

Muscle–tendon unit (MTU) inertia is usually neglected in musculoskeletal simulations, despite its potential to affect the muscle forces and hence the coordination patterns. The purpose of this study was to assess whether coordination patterns between muscles, predicted from a musculoskeletal simulation of cycling, differ as intramuscular mass of lower limb muscles was systematically varied. We combined a mass-enhanced Hill-type muscle model, embedded into musculoskeletal simulations of pedalling, and classified the predicted activations with principal component analysis (PCA) and mixed-effects statistics.

Methods

Cycling kinematics and crank load data were used from 12 subjects. We implemented a multi-body mass-enhanced Hill-type muscle model into a muscle redundancy solver [1] linked to OpenSim [2] for 43 muscles of the lower extremity. The muscle masses were scaled from 0.01 to 125 times the mass of the nominal human-sized muscles. We simulated pedalling at a range of speeds (80, 120, 140 r.p.m.). Predicted muscle activation patterns in 43 lower limb muscles were interpolated to 100-points per pedal cycle (3 cycles analysed per trial), pooled across muscles and classified by PCA.

Results

Cadence emerged as the dominant factor that affected the PC scores. The mass-scale also produced a robust significant, non-trivial modulation of several principal components, especially PC4. For PC4, the mass-scale had a significant main effect ($F = 248$, $p < 0.0001$) such that larger muscle masses were associated with greater peak amplitudes and a systematic shift in the timing of the PC4 waveform compared with lower mass-scales.

Discussion

These findings demonstrate that muscle mass is a functionally relevant parameter that influences the organisation of neuromuscular coordination during cycling. Incorporating mass-enhanced muscle models into simulation pipelines may therefore be critical for

evaluating predictions of muscle activation and energetics, particularly for studies that consider how muscle coordination varies across animal size.

Images (Optional)

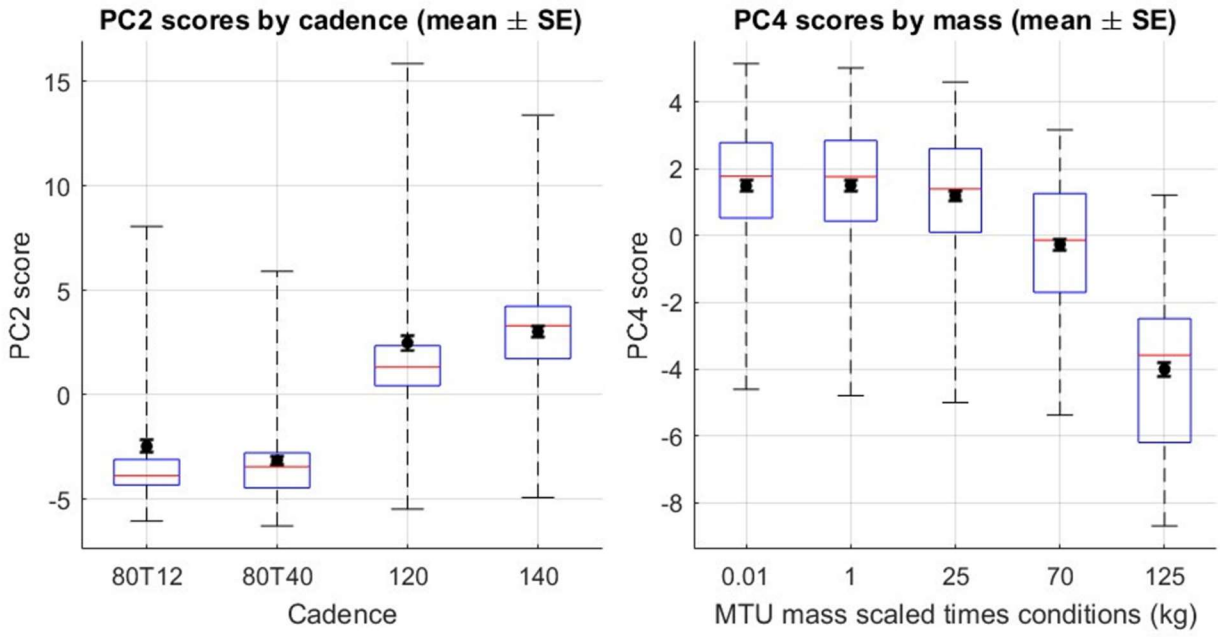


Figure: PC2 scores by cadence and PC4 scores by scaled times MTU

References (Optional)

[1] De Groote, Friedl et al., Annals of biomedical engineering, 2016

[2] Delp, Scott L., et al., IEEE transactions on biomedical engineering, 2007.

Session Category

Musculoskeletal Biomechanics: Joints and Motion

P2-025

How Do Anatomically Defined and Kinematically Optimized Coordinate Systems Differ in Knees With Osteoarthritis?

Ms Amiya Gupta BS, Dr. Lesley Lizalek PhD, Dr. Joshua Roth PhD

University of Wisconsin-Madison, Madison, WI, United States

Ms Amiya Gupta

Dr. Lesley Lizalek

Introduction

Conceptually, local coordinate systems that define the widely utilized joint coordinate system reported by Grood and Suntay should be defined based on key anatomy linked to biomechanics (e.g., articular surface of the femur); however, practically, there are a variety of approaches used for defining the local coordinate systems of the knee including palpable landmarks (e.g., femoral epicondyles), segmented articular surfaces (e.g., cylindrical or spherical axis), and kinematically optimized based on passive kinematics, which may need to changes when studying knees with osteoarthritis. Thus, our objectives in this study were to: (1) quantify differences between the coordinate systems defined using the aforementioned approaches in cadaveric knees with varying severities of osteoarthritis, and (2) determine whether these differences correlated with degree of osteoarthritis severity.

Methods

We procured 9 knees with a range of osteoarthritis severities. Using bone models created from computed tomography scans, we defined local coordinate systems based on (1) palpable bony landmarks, (2) the cylindrical axis, and (3) the spherical axis of the femur. Using a robotic testing system, we moved each knee through passive flexion and internal-external rotation ranges of motion in the coordinate system based on the spherical axis of the femur. These kinematics were input into an established coordinate system optimization algorithm to determine the coordinate system that minimized off-axis kinematics during both passive flexion and internal-external rotation trajectories.

Results

We found the femoral coordinate system based on the cylindrical axis was most similar to that based on the spherical axis (Figure 1, RMSE of difference in axis-angle = 2.7°). We also found that the differences in the optimized coordinate system were weakly correlated with osteophyte volume ($R^2 = 0.24$), but these were more strongly correlated than differences in the other two anatomically defined coordinate systems (palpable: $R^2 = 0.12$ and cylindrical: $R^2 = 0.21$).

Discussion

Our key findings were that (1) optimized coordinate systems have large differences from coordinate systems defined based on the articular surfaces, and (2) these differences became slightly larger for knees with more severe OA, which suggests that care must be taken when defining the coordinate system for knees with more and less severe OA.

Images (Optional)

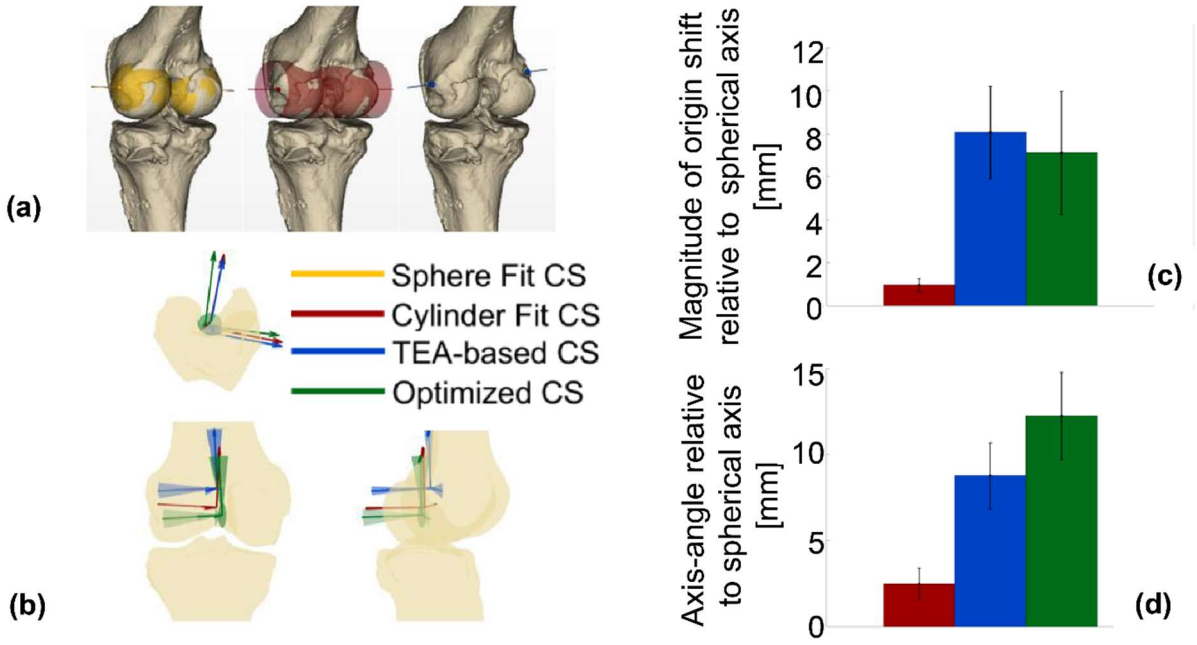


Figure 1. (a) Images show the three anatomically defined coordinate systems. (b) Plots show how the coordinate systems differ within the 9 knees. Arrows represent the mean axes and the shaded funnels represent the standard deviations of the differences between axes. (c) and (d) show these same differences between axes. TEA = Transepicondylar axis.

Session Category

Musculoskeletal Biomechanics: Joints and Motion

P2-026

Linking Ankle and Hindfoot Morphology with Kinematics in Asymptomatic Flatfoot

Mr. Andrew Peterson MS[1], Mr. Tradd Rector[1], Ms. Elizabeth Bowman[1], Dr. Kassidy Knutson PhD[1], Dr. Karen Kruger PhD[2,3], Dr. Amy Lenz PhD[1]

[1]University of Utah, Salt Lake City, Utah, United States. [2]Marquette University, Milwaukee, Wisconsin, United States. [3]Shriners Children's, Chicago, Illinois, United States

Introduction

Ankle and hindfoot morphology are presumed to influence tibiotalar and subtalar mechanics, yet quantitative studies linking 3D bone shape to dynamic motion remain limited.

Methods

Weightbearing CT scans and biplane fluoroscopy kinematics were collected for asymptomatic flatfoot (AFF, n=10) and control (CNO, n = 13) participants during walking. Two statistical shape models were generated: the tibia-talus complex and the talus-calcaneus complex. Shape scores from principal component analysis (PCA) modes of variation were correlated with stance-normalized joint kinematics using one-dimensional regression (SPM1D, α=0.05).

Results

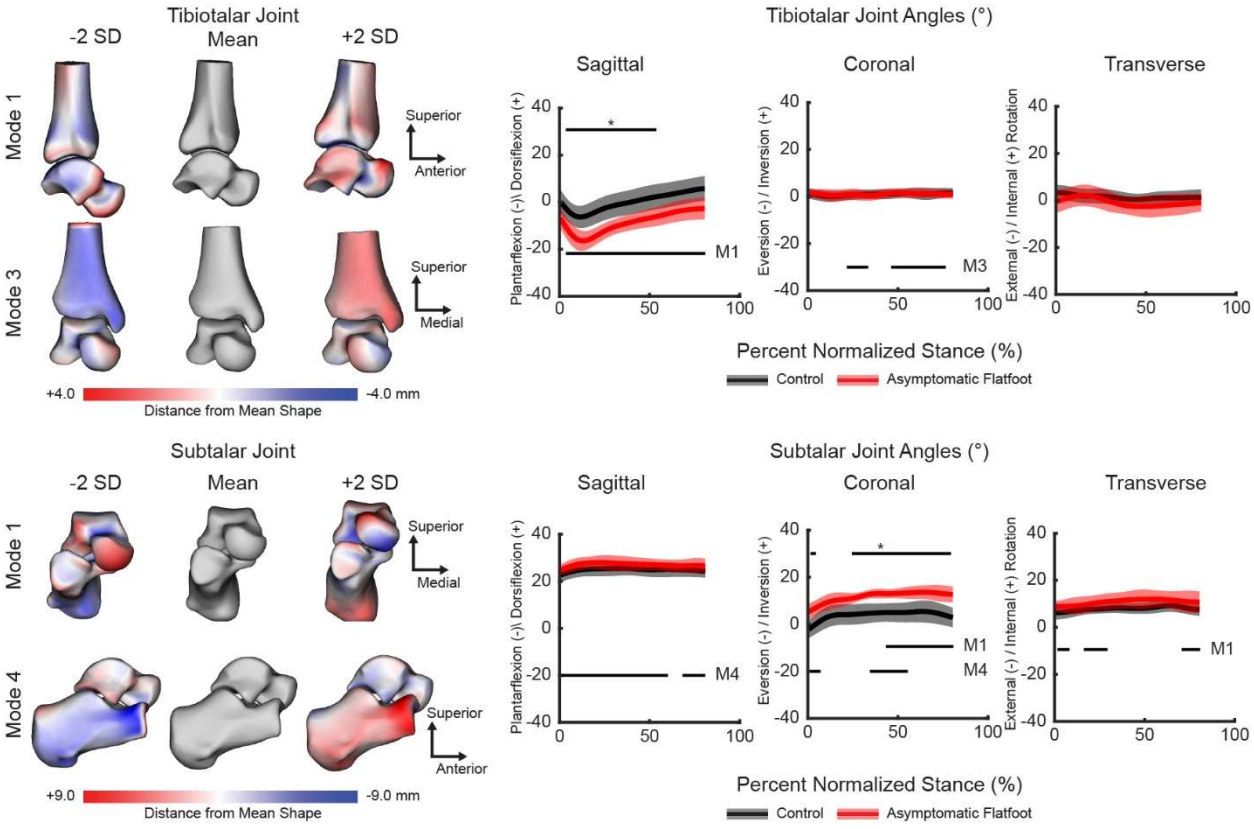
For the tibiotalar joint, the AFF group was significantly more plantarflexed in early-to-mid stance and had greater transverse-plane range of motion (ROM). Two shape modes significantly correlated with kinematics (Figure 1). PCA Mode 1 showed a plantarflexed joint related to increased plantarflexion throughout stance. PCA Mode 3 showed a flatter talar dome, broader morphology, and external-rotation related to increased inversion during mid-to-late stance. For the subtalar joint, the AFF group was significantly more inverted throughout stance and had greater transverse-plane ROM. Two shape modes significantly correlated with kinematics (Figure 1). PCA Mode 1 showed valgus alignment related to increased inversion during mid-to-late stance and internal rotation during early and late stance. PCA Mode 4 showed steep posterior facet and rounder talar dome related to greater dorsiflexion across stance and inversion during early-to-mid stance.

Discussion

Alignment-related modes (tibiotalar mode 1, subtalar mode 1) primarily influence baseline posture, whereas the curvature and facet-related modes (tibiotalar mode 3, subtalar mode 4) affect joint compliance and motion magnitude. Although group mean shape scores did

not differ, morphology predicted stance-phase kinematics, indicating continuous structure-function coupling rather than discrete group effects. Rounder, steeper articulations were associated with more inverted, compliant mechanics observed in the AFF group, while higher calcaneal pitch and neutral alignment reflected the stiffer control pattern. Subtle shape and alignment differences modulate how the bones move and interact. In some planes, AFF individuals appear to adapt functionally, maintaining near-normal kinematics despite morphological variation, while in others, distinct shape axes determine which portions of stance diverge. Such compensatory coupling between structure and motion may underlie why certain morphologies remain asymptomatic while others progress to deformity.

Images (Optional)



Session Category

Musculoskeletal Biomechanics: Joints and Motion

P2-027

Racial Differences in Knee Kinematic Outcomes in Response to Injury Prediction and Return to Activity Assessment Tasks: A Pilot Study

Ms. Anita Borhani, Dr. Kristie Liu, Dr. Timothy Burkhart

University of Toronto, Toronto, Ontario, Canada

Introduction

Race is rarely considered in biomechanical research despite documented racial differences in musculoskeletal injuries, perioperative outcomes, knee morphology, and movement mechanics [4, 5]. Hill et al. reported differences in gait, running, and landing mechanics between African Americans (AA) and Caucasian Americans (CA) [1, 2], yet no studies have examined whether similar differences exist in functional tasks used for injury-risk and return-to-activity assessment. Therefore, BIPOC groups may be under-represented in normative biomechanical benchmarks. This study aims to quantify three-dimensional knee kinematic differences between Black Canadians (BC) and White Canadians (WC).

Methods

Twenty-three healthy adults aged 18–35 (10 BC, 13 WC) performed a 90° cutting task and step up/down while markerless motion capture and ground reaction force data were collected. Three-dimensional right knee angles were extracted at movement initiation, and 200 milliseconds after in cutting and at ascent-phase peak vertical ground reaction force in step up/down, to calculate knee range of motion (RoM). Independent t-tests and Cohen's d effect sizes were used to quantify between-group differences ($\alpha = 0.05$).

Results

Knee flexion/extension RoM was significantly greater in BCs (44.39 ± 7.91) than WCs (38.33 ± 8.18, $p = .04$, $d = .75$) during step up/down. No other significant differences were found, although cutting abduction/adduction RoM showed a moderate effect size (BC: 5.34 ± 2.83, WC: 3.87 ± 1.52, $p = .08$, $d = .68$).

Discussion

BCs showed greater sagittal-plane knee RoM during step up/down, suggesting enhanced muscular shock absorption relative to passive structures [3]. Although most comparisons were non-significant, the moderate frontal-plane effect size during cutting aligns with Hill et al.'s finding that AA females exhibited greater frontal-plane knee RoM during landing than

CA females [2]. This suggests that meaningful race-related kinematic differences may exist but remain undetected in small samples. Future work should include larger, sex-stratified cohorts, and neuromuscular and morphological measures to inform more representative functional benchmarks for BIPOC groups.

Images (Optional)

Table 1. Three-dimensional knee RoM (mean ± SD) in the first 200 milliseconds of cutting and between heel-off and the first peak in vertical ground reaction force during the ascent phase of step up/down for Black Canadian (BC) and White Canadian (WC) participants.

		Mean ± SD		Group Comparison	
		BC	WC	p-value	Cohen's d
90° Cut	Flexion/Extension (°)	37.77 ± 8.04	40.16 ± 7.23	.23	-.32
	Abduction/Adduction (°)	5.34 ± 2.83	3.87 ± 1.52	.08	.68
	Internal/External Rotation (°)	7.42 ± 2.51	7.63 ± 2.92	.43	-.07
Step Up/Down	Flexion/Extension (°)	44.39 ± 7.91	38.33 ± 8.18	.04*	.75
	Abduction/Adduction (°)	7.94 ± 4.63	7.84 ± 3.64	.84	.02
	Internal/External Rotation (°)	8.91 ± 1.66	8.14 ± 2.89	.23	.32

* = significant between-group difference ($p < 0.05$)

References (Optional)

[1] Hill *et al.* , J Biomechanics, 2020

[2] Hill *et al.* , Sports Biomech, 2022

[3] Myer *et al.* , J Strength Cond Res, 2005

[4] Owens *et al.* , Int J Sports Med, 2007

[5] Stone *et al.* , J Arthroplasty, 2019

Session Category

Musculoskeletal Biomechanics: Joints and Motion

P2-028

Determination of the Subtalar Joint Axis: A Comparison of Methods

M.Sc. Anja Seeger, Prof. Dr. Wilfried Alt

Institute of Sport and Movement Science, University of Stuttgart, Stuttgart, Baden-Württemberg, Germany

Introduction

The orientation of the subtalar axis (STA) might be associated with injury mechanisms of the ankle and knee joints [1]. Therefore, a valid axis determination (deviation, inclination) is necessary. Previously described methods rely either on motion capturing of eversion/inversion movements or on analysing articular surfaces using imaging procedures. There is little literature addressing a direct comparison of these approaches. In this study, we present first results comparing function-based and structure-based STA determination methods using MR.

Methods

Three MRIs of the right foot of 13 participants were obtained: in 15° eversion, 20° inversion, and neutral foot position. Calcaneus and talus were segmented and exported as 3D-files. The structure-based STA was calculated by fitting spheres to the talar articular surfaces following Parr [2] and Montefiori [3] (fig. 1). For determining the function-based STA, an iterative closest point algorithm was used to register the bones in eversion and inversion orientation to neutral orientation. The points on the calcaneus with the least motion between eversion and inversion were identified (fig. 1). Using PCA, a best-fit straight line (the STA) through these points was estimated. Deviation and inclination were calculated with reference to an anatomical coordinate system after Manter [4], based on the neutral MRI. Spearman correlation was applied to deviation and inclination for the following comparisons: function-based vs. Parr, function-based vs. Montefiori, and Parr vs. Montefiori.

Results

Correlation was strong for deviation in all comparisons (function-based - Parr: 0.85; function-based - Montefiori: 0.75; Parr - Montefiori: 0.9). For inclination, correlation was weak between the function-based and both structure-based methods (function-based - Parr: 0.18; function-based - Montefiori: 0.36) but strong between the two structure-based methods (Parr - Montefiori: 0.65).

Discussion

The results for deviation were similar across all methods. However, for inclination, the comparison between function- and structure-based methods showed a clear difference. This abstract includes preliminary results. Data analysis is ongoing and will provide further insight, including additional participants and a comparison to STA determination based on Conconi [5].

Images (Optional)

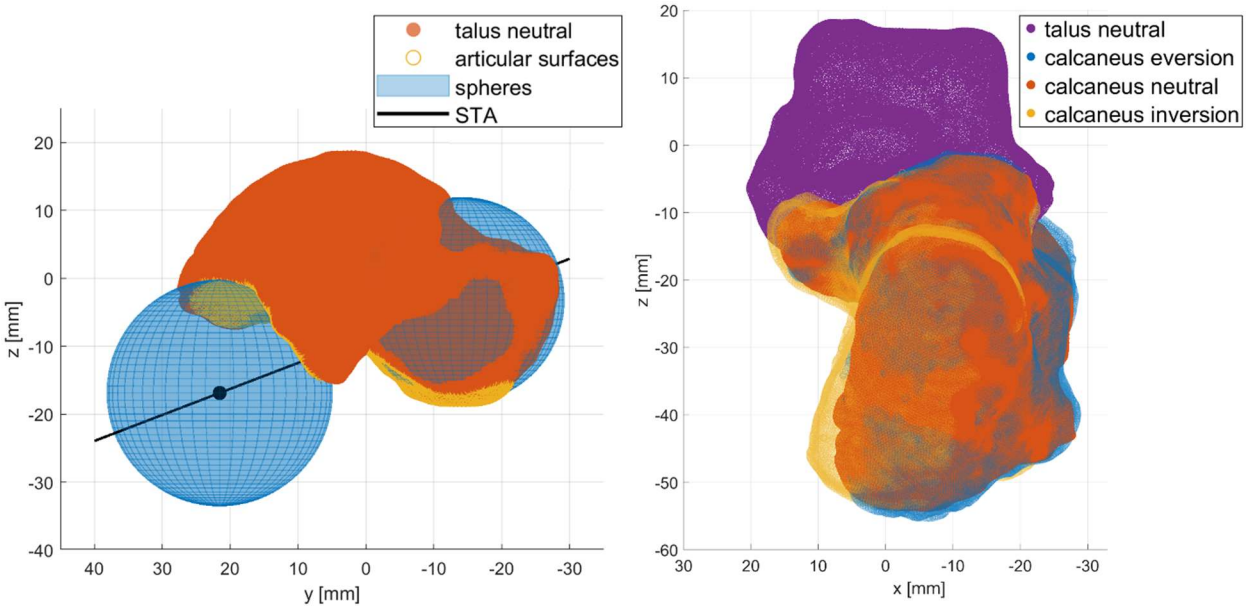


Figure 1: left: STA calculation after Parr et al., right: result of iterative closest point algorithm

References (Optional)

[1] Alt, C. Maurer, 2001
[2] Parr *et al.*, J Biomech, 2012
[3] Montefiori *et al.*, J Biomech, 2014
[4] Manter, Anat Rec, 1941
[5] Conconi *et al.*, J Foot Ankle Res, 2021

Session Category

Musculoskeletal Biomechanics: Joints and Motion

P2-029

Patellar Instability Anatomy Affects Patellofemoral Walking Kinematics: A Subject-Specific Musculoskeletal Modeling Study

Ms. Annette Chang[1], Dr. Anthony Gatti[2], Dr. Shital Parikh[3], Dr. Scott Delp[2], Dr. Seth Sherman[2], Dr. Marissa Sinopoli[1]

[1]Harvey Mudd College, Claremont, CA, United States. [2]Stanford University, Stanford, CA, United States. [3]Cincinnati Children's Hospital Medical Center, Cincinnati, OH, United States

Introduction

Patellar instability can cause pain and osteoarthritis. It is associated with atypical knee anatomy, including patellar tilt, patella alta, trochlear dysplasia, and external rotation of the tibia relative to the femur [1]. Understanding how anatomy influences biomechanics may inform surgical intervention to reduce instability. The goal of this study is to estimate how simulated patellofemoral walking biomechanics differ between knees with and without patellar instability. We hypothesized that knees with patellar instability and atypical patellofemoral anatomy would exhibit elevated measures of dynamic instability, including lateral tilt, lateral shift, and lateral trochlear constraint forces.

Methods

We retrospectively analyzed magnetic resonance images of 8 knees with patellar instability (10-18 years, 4F/4M) and 8 control knees (12-17 years, 4F/4M). We generated subject-specific 3D bone and cartilage meshes from scan segmentations and integrated them into a generic musculoskeletal model [2]. We personalized model parameters, including ligament slack lengths and muscle wrapping surfaces, based on subject-specific anatomy. Next, we ran the COMAK routine in OpenSim with generic gait data [2,3] to compute 12-degree-of-freedom knee kinematics, cartilage pressures, and muscle activations. We extracted three measures of dynamic instability: patellar tilt, patellar shift, and lateral trochlear constraint force. We used statistical parametric mapping to compare the biomechanics between the two groups.

Results

Mean patellar tilt was significantly greater ($p \leq 0.021$) in knees with patellar instability through the first half of stance and from late stance to early swing (0-33% and 50-63% of the gait cycle; Figure A). Knees with patellar instability demonstrated nonsignificant trends toward elevated patellar shift and lateral trochlear constraint force throughout the gait cycle (Figures B, C).

Discussion

These findings demonstrate that knee morphology associated with patellar instability produces elevated patellar tilt, a key measure of dynamic instability, across most of stance. This work establishes a foundation for future research to investigate specific anatomical morphologies that contribute to increased dynamic patellar tilt and to simulate personalized surgical treatments for patients with patellar instability.

Images (Optional)

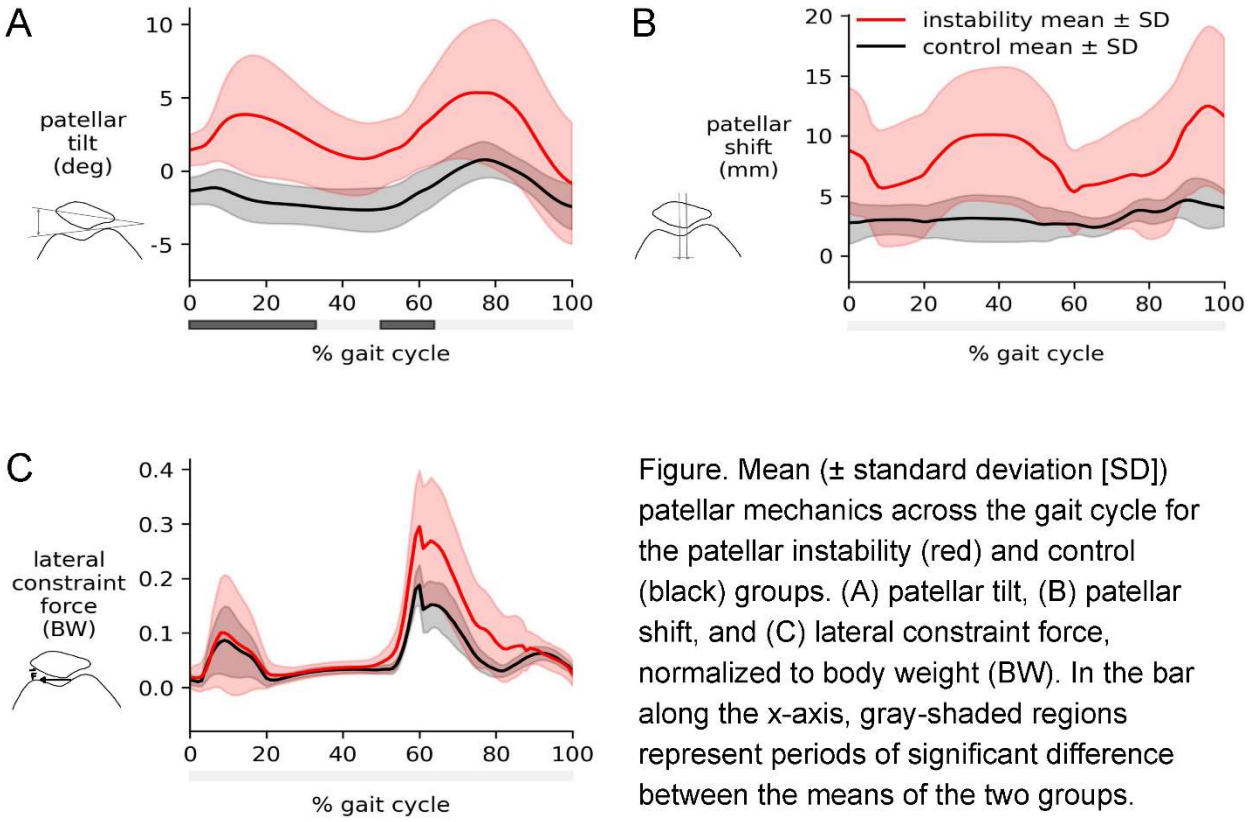


Figure. Mean (± standard deviation [SD]) patellar mechanics across the gait cycle for the patellar instability (red) and control (black) groups. (A) patellar tilt, (B) patellar shift, and (C) lateral constraint force, normalized to body weight (BW). In the bar along the x-axis, gray-shaded regions represent periods of significant difference between the means of the two groups.

References (Optional)

[1] Henri Dejour et al., Knee Surg Sports Traumatol Arthrosc, 1994

[2] Rachel Lenhart et al., J Biomech, 2015

[3] Ajay Seth et al., PLOS Computat Bio, 2018

Acknowledgements (Optional)

This work was supported by Harvey Mudd College, CONMED, the Mobilize Center (P41EB027060), and the Wu Tsai Human Performance Alliance.

Session Category

Musculoskeletal Biomechanics: Joints and Motion

P2-030

Optimizing IMU Configurations for Upper-Limb Kinematics via Regression Neural Network

Mr. Arthur Fabre[1,2], Dr. Wolbert van den Hoorn[1,2], Dr. Laith Alzubaidi[2,3], Prof. Peter Pivonka[2,3], Prof Graham Kerr[1,2]

[1]School of Exercise and Nutrition Sciences, Queensland University of Technology, Brisbane, Queensland, Australia. [2]Australian Research Council Training Centre in Joint Biomechanics, Queensland University of Techonology, Brisbane, Queensland, Australia. [3]School of Mechanical, Medical & Process Engineering, Queensland University of Technology, Brisbane, Queensland, Australia

Introduction

Inertial-measurement-units (IMUs) enable portable three-dimensional assessment of upper-limb joint orientation. Current multi-sensors configurations are burdensome and impractical for clinical or remote monitoring [1]. Reduced configurations would improve compliance, ecological validity and their adoption in multiple settings [2]. This study explored the accuracy of a regression-neural-network (RNN) in the prediction of IMU-derived upper limb and shoulder segment orientations from a single wrist sensor.

Methods

An RNN was developed to predict the orientation of the thorax, clavicle, scapula, upper arm and hand segments using the wrist. The network included two hidden layers (128 and 64 neurons) with rectified linear unit activation, L2 norm regularization and standardized predictors. Twenty participants performed clinical (e.g. internal/external rotation, humerothoracic flexion, abduction) and functional tasks (e.g. box transfer to a shelf, walking, running) while IMUs recorded segment kinematics. The predictors included segment quaternions and angular velocities of the wrist; the response was the quaternion orientation of the remaining body segments. Data were normalized, randomized, and split by participant. Model performance was assessed using root mean square of the decomposed error quaternion (RMS) and coefficient of determination (R^2) of the predicted quaternion.

Results

Using the wrist as the sole predictor yielded the highest accuracy for estimating hand orientation (RMS: 8°, see Figure 1, R^2: 0.83). Predictions for the humerus were moderately accurate (RMS: 17°, R^2: 0.42), while scapula and thorax showed similar errors and lower agreement (RMS: 14° and 9°; R^2: 0.22 and 0.20, respectively). Clavicle predictions were

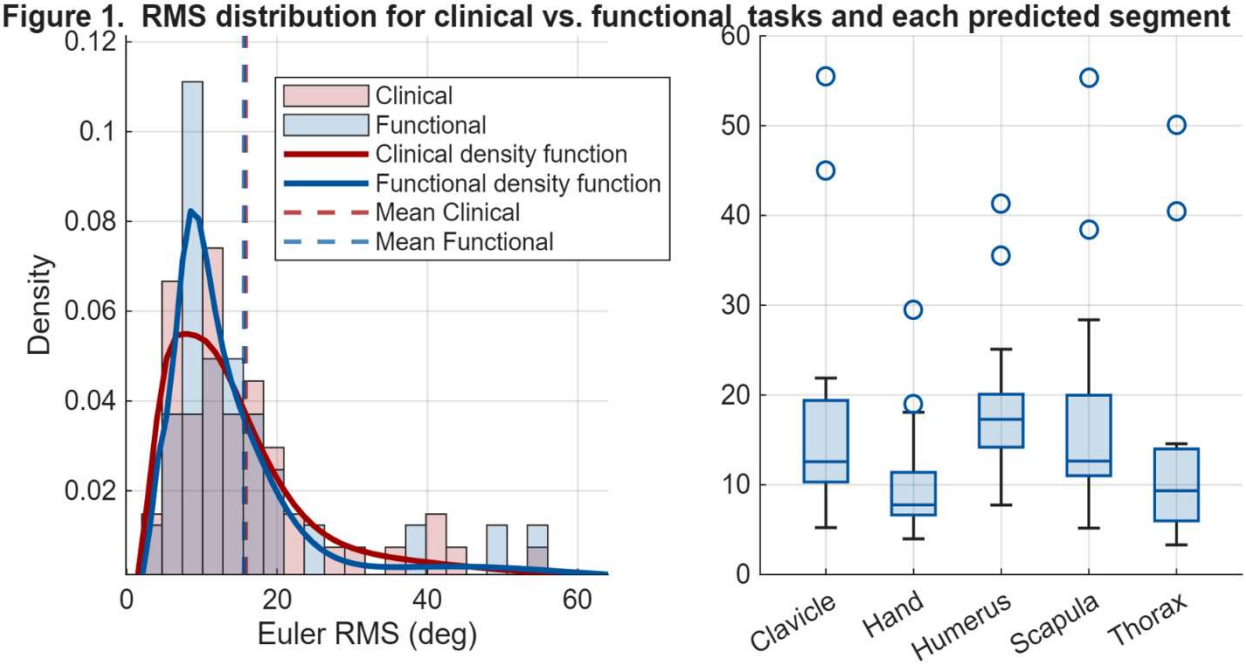
poorest, with RMS of 13° and near-zero R^2 (0.03). Overall, prediction accuracy decreased with increasing anatomical distance from the wrist, confirming its strong predictive value for distal segments and limited utility for proximal ones.

Discussion

This work demonstrates the potential for optimizing IMU configurations to simplify upper-limb motion assessment while improving wearability and remote monitoring. Future research should explore physics-informed neural networks [3] and multi-predictor strategies to enhance accuracy and generalizability across tasks, as these models can embed biomechanical constraints into learning and improve temporal coherence in the prediction of IMU-derived body segment orientation.

Images (Optional)

Figure 1. RMS distribution for clinical vs. functional tasks and each predicted segment



References (Optional)

[1] Rapp, 2021. Journal of Biomechanics, 116.

[2] Nino-Tejada, 2025. Electronics, 14(15).

[3] Golroudbari, 2024. ArXiv.or.

Session Category

Musculoskeletal Biomechanics: Joints and Motion

P2-031

Hidden Segmental Asymmetries in Lumbar Spine Motion: Implications for Spinal Pathologies and Clinical Assessment

Dr. Asghar Rezaei, Mr. Alexander Hooke, Dr. Babak Dashtdar, Mrs. Areonna Schreiber, Dr. Abdelrahman Hamouda, Dr. Kai-Nan An, Dr. Benjamin Elder, Dr. Kenton Kaufman, Dr. Lichun Lu

Mayo Clinic, Rochester, MN, United States

Introduction

The lumbar spine's multiplanar motion is vital for daily function, but segmental asymmetries may contribute to spinal pathologies such as low back pain and deformity. While global symmetry is often assumed, hidden segmental differences in torque and range of motion (ROM) may underlie uneven vertebral loading and disease progression. This study aims to quantify segmental kinematics and asymmetry in human lumbar spines, advancing understanding of spinal biomechanics and informing clinical strategies.

Methods

Six cadaveric lumbar spines were imaged and prepared for biomechanical testing. Fiducial markers enabled precise 3D tracking of vertebral motion using optical metrology. Specimens were mounted to a 6-degree-of-freedom robotic system, which applied controlled flexion-extension, lateral bending, and axial rotation. Motions were initiated from neutral and progressed to maximum ROM under quasi-static loading. Segmental torque and ROM asymmetries were calculated as normalized differences between right and left sides. Imaging findings were correlated with biomechanical data to explore associations between pathologies and asymmetry.

Results

Segmental ROM asymmetry exceeded 40% and torque asymmetry surpassed 15% in several vertebrae, even when global outputs appeared symmetrical. Asymmetry patterns varied within and between spines. Imaging revealed degeneration and deformities that partially explained subject-specific asymmetries, but no universal pattern was found. Some subjects showed compensatory adaptations between segments, suggesting complex biomechanical interplay.

Discussion

Segmental asymmetries in torque and ROM are prevalent in the lumbar spine and may contribute to uneven loading and progression of spinal disorders. The study's novel

approach highlights limitations of global assessments and underscores the need for segment-level analysis. Findings support individualized, pathology-specific interventions and suggest further research with larger cohorts is needed. Overall, segmental biomechanical analysis advances understanding of lumbar spine function and informs clinical practice.

Acknowledgements (Optional)

Scientific funding for the study was provided by the NIH grant K25AG068368 from the National Institute on Aging. The study was also supported by the NIH grant R01AR56212.

Session Category

Musculoskeletal Biomechanics: Joints and Motion

P2-032

The Functional Strength Landscape of the Human Foot-Ankle Complex

Dr. Aubrey Gray[1], Dr. Ross Smith[2], Dr. Kota Takahashi[3], Dr. Jason Franz[4,5]

[1]University of Massachusetts Amherst, Amherst, MA, United States. [2]University of Memphis, Jackson, TN, United States. [3]University of Utah, Salt Lake City, UT, United States. [4]University of North Carolina at Chapel Hill, Chapel Hill, NC, United States. [5]North Carolina State University, Raleigh, NC, United States

Introduction

The human foot and ankle are governed by form-function interactions involving active muscle force, passive series elastic structures, and joint articulations. Prior work has suggested that the sophisticated network of intrinsic and extrinsic force-generating and force-transmitting structures may yield a "strength landscape" of maximum force-generating potential for the plantar intrinsic muscles (PIM) and plantar flexors (PF). However, no study to date has characterized the functional strength landscape of the foot-ankle complex across ankle and metatarsal phalangeal (MTP) joint postures in context of walking kinematics and timing of muscle excitations. We hypothesized that MTP extension would offset declines in the force-generating potential of the foot-ankle complex (i.e., PF + PIM) with ankle plantarflexion – coinciding with late stance kinematics and peak calf and intrinsic foot muscle excitations during walking.

Methods

22 younger adults (26±5 years, 15F/7M, 74.3±13.7kg, 1.7±0.1m) participated. Participants completed PF and PIM maximum voluntary isometric contractions (MVICs) on a Biodex dynamometer (PF) and a foot dynamometer (PIM) across combinations of ankle and MTP joint postures. Specifically, at 3 ankle joint angles (20˚ dorsiflexion, 0˚ neutral, and 20˚ plantarflexion) we tested 3 MTP joint angles (0˚, 30˚ and 60˚ MTP extension) and vice versa, for a total of 9 MVIC conditions. Participants also walked at 1.4 m/s while we recorded joint kinematics and excitations of the soleus, medial gastrocnemius, and flexor digitorum brevis.

Results

An interaction (p=0.001) revealed that ankle angle (p=0.018) more than MTP angle (p=0.062) affected PF strength (Fig. 1A). The interaction also revealed that MTP extension decreased PF strength when in ankle dorsiflexion but increased PF strength when in ankle plantarflexion. Conversely, although not supported by a significant interaction (p=0.256),

we found that MTP angle ($p<0.001$) but not ankle angle ($p=0.558$) affected PIM strength (Fig. 1B). Coincident joint kinematics and muscle excitations supported the hypothesis.

Discussion

These findings demonstrate that the interaction between ankle and toe postures plays a critical role in preserving force-generating potential of the foot-ankle complex through push-off in walking. Potential explanations are that MTP extension enables favorable force-length conditions and/or removes series elastic tissue slack for biarticular extrinsic foot muscles contributing to push-off.

Images (Optional)

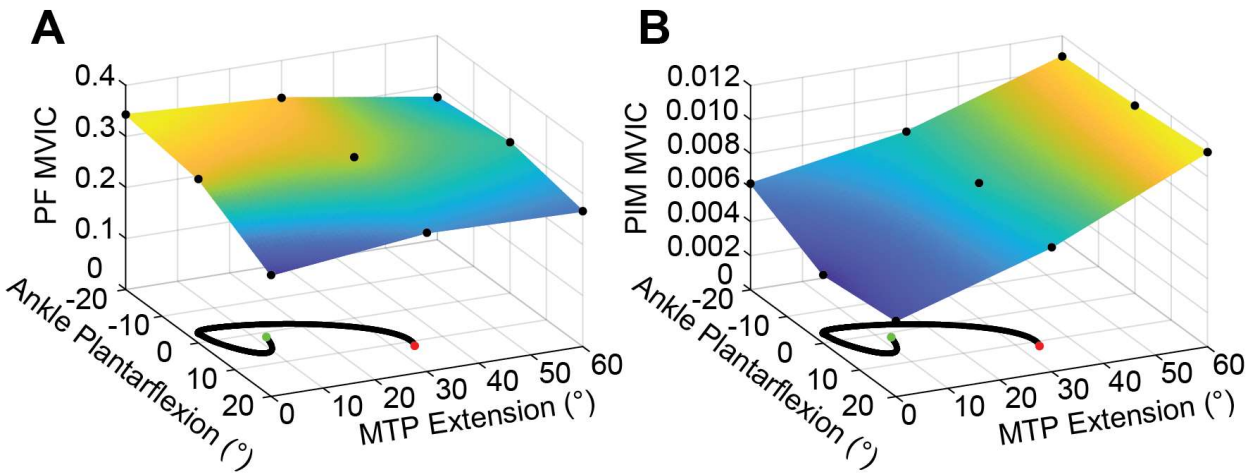


Figure 1. All data in Nm/kg. *(A)* Plantarflexor MVICs as a function of ankle plantarflexion and MTP extension angles *(B)* Plantar intrinsic muscle MVICs as a function of ankle plantarflexion and MTP extension angles. Walking angle-angle kinematics (black line) for the stance phase (green=start, red=end) shown for functional context.

Acknowledgements (Optional)

This work was supported by a grant from the National Institutes of Health (R01AR081287).

Session Category

Musculoskeletal Biomechanics: Joints and Motion

P2-033

Evaluation and Comparison of Muscle Forces Estimates from a Musculoskeletal Model with EMG during Obstacle Crossing in Soldiers

Mr Aurélien Schuster[1,2], Dr Charles Pontonnier[2], Pr Georges Dumont[2]

[1]Centre de Recherches des écoles de Saint-Cyr Coëtquidan, Guer, Britanny, France. [2]Univ Rennes, Inria, CNRS, IRISA, M2S, Rennes, Britanny, France

Introduction

The increase in load carried in military contexts contributes to onset of musculoskeletal disorders such as low back pain. Musculoskeletal analysis, particularly muscle forces estimation, can help quantify these problems and understand the injuries mechanisms. Most studies on muscle activity focus on walking or running, whereas studying other operational tasks such as obstacle crossing could improve model validation [1]. This study examines lower back muscle forces estimates during obstacle crossing using electromyography as a reference.

Methods

Five soldiers performed five obstacle-crossing trials using the same technique. Participants provided informed consent and the protocol was approved by the National Ethics Committee (CPP n°2024-A02736-41). Forty-eight reflective markers were placed on anatomical landmarks following ISB recommendations. Surface EMG were placed on each side of the iliocostalis, longissimus, and multifidus muscles, according to SENIAM guidelines. Reaction forces were measured using ground force plates and sensors on the obstacle. Using a full-body musculoskeletal model with an articulated thoracolumbar spine [2], inverse dynamics and static optimization calculations with CusToM [3], the lower trunk joint torques (L5/S1) were extracted, and muscle forces were estimated and compared to EMG via cross-correlation for each acquisition.

Results

Marker tracking errors showed a mean RMS of 1.61 ± 0.28 cm. The highest mean dynamic residuals reached 4.24 ± 1.02%peakRF for vertical forces and 2.08 ± 0.34%peakRF·hCOM for moments in the transverse plane. The means (±SD) of normalized muscle forces and EMGs are shown in Figure 1(a), with takeoff and landing indicated (Figure 1(b)).

Discussion

Strong correlation coefficients (r > 0.7) indicate good agreement between estimated muscle forces and EMG regarding activation timing. Peak forces were found in longissimus and multifidus before lift-off matching with peak extension torques. Similarly, peak lateral flexion torques between lift-off and landing matched higher iliocostalis muscle forces and EMG. Despite tracking errors consistent with the literature, the dynamics residuals call for caution in interpreting these results. Moreover, large standard deviations in EMG and muscle forces suggest important inter-individual strategies that warrant further investigation.

Images (Optional)

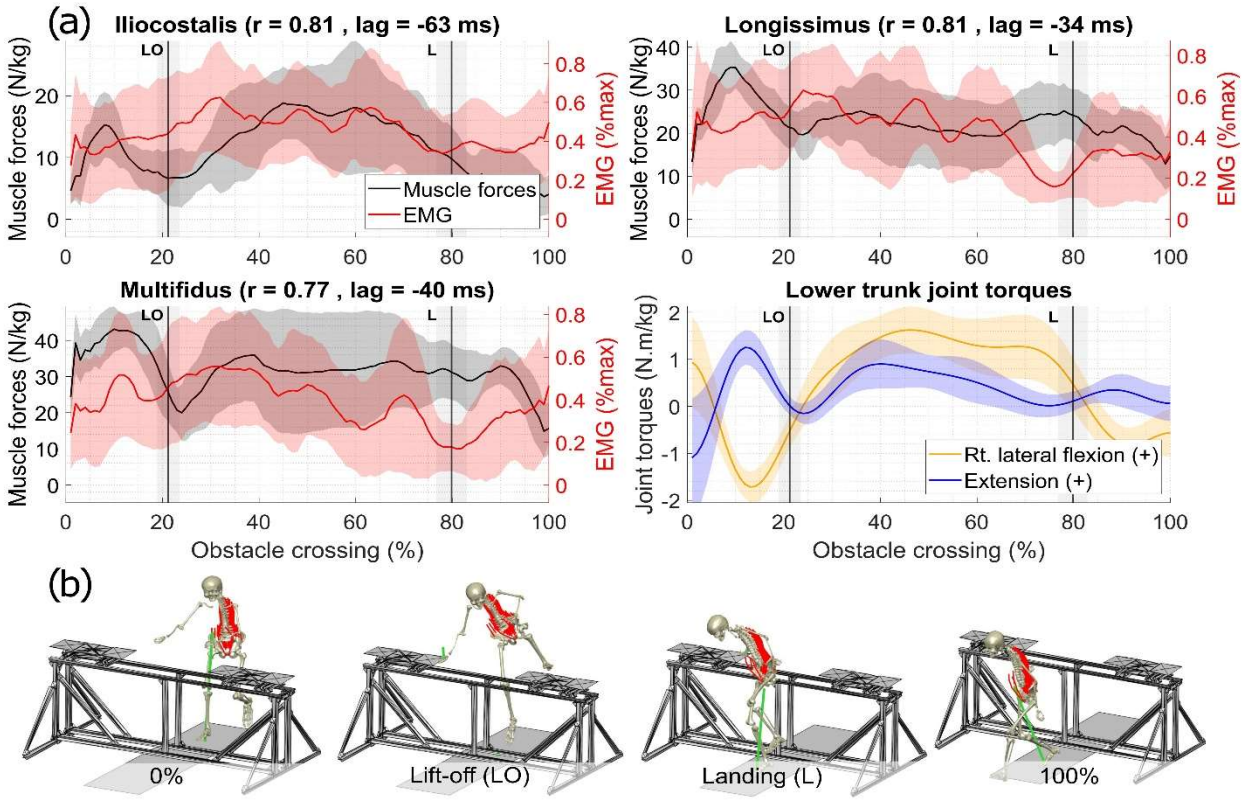


Figure 1: (a) Mean (SD) estimated muscles forces and measured EMG across all participants; (b) reported instants of obstacle crossing technique

References (Optional)

[1] Sturdy J.T. et al. , Applied Ergonomics, 2021

[2] Bruno A.G. et al. , J Biomechanical Engineering, 2015

[3] Muller A. et al. , J Open Source Software, 2019

Acknowledgements (Optional)

The present study was partly funded by the chair of the enhanced soldier in the digital battlefield from the St-Cyr Foundation and supported by French government funding managed by the National Research Agency under the Investments for the Future program (PIA) with the grant ANR-21-ESRE-0030 (CONTINUUM project).

Session Category

Musculoskeletal Biomechanics: Joints and Motion

P2-034

The Effects of Cues to Run Softly and Quietly vs. Changing to a Forefoot Strike Pattern on Kinetics and Kinematics in Healthy Individuals

Dr. Caleb Johnson, Mr. Cole Dempsey, Mr. Lucas Sarantos, Mr. David Zeppetelli

U.S. Army Research Institute of Environmental Medicine, Natick, MA, United States

Introduction

Cues to run softly/quietly (SOF) have been shown to be a viable gait modification for reducing external forces during running, even compared to shifting to a forefoot strike pattern (FFS). However, no studies have compared changes in joint kinetics/kinematics between these two modifications.

Methods

33 participants completed testing, including running with habitual gait (HAB), as well as with the SOF and FFS modifications, on an instrumented treadmill while optical motion capture was used to capture three-dimensional kinematics. Variables of interest included: a) frontal/sagittal plane peak hip/knee/ankle moments, as well as sagittal knee stiffness, b) frontal/sagittal plane joint angles and sagittal foot angles at initial contact (foot strike angle). One-way repeated measures ANOVAs (1x3) were used to compare variables between gait conditions.

Results

Full results are reported in the Table. Due to the large number of statistically significant differences found, we chose to focus on “key differences” based on those having at least a moderate effect size (Cohen’s $d \geq 0.5$). The SOF condition showed increased hip extension (vs. FFS) and flexion (vs. HAB/FFS) moments, and reduced knee stiffness (vs. HAB/FFS) and ankle plantarflexion moments (vs. FFS). The FFS condition also showed increased knee flexion and ankle plantarflexion moments compared to HAB. For kinematics, the SOF condition showed higher peak knee flexion angles (vs. HAB/FFS) and excursion (vs. HAB), foot strike angles (vs. HAB/FFS), peak/initial contact ankle dorsiflexion angles (vs. FFS), and peak eversion angles (vs. FFS), as well as lower initial contact ankle inversion angles (vs. FFS). The FFS condition also showed lower initial contact ankle dorsiflexion angles and foot strike angles (i.e., plantarflexion), and increased initial contact inversion angles, compared to HAB.

Discussion

These results provide support for the SOF modification as an alternative to FFS for reducing biomechanical loading during running, especially in reducing knee/ankle forces. However, the increases in hip joint forces lead to some caution for its use in those susceptible to hip injuries and warrant further investigation.

Images (Optional)

Table. Descriptive statistics and results of tests for mean differences between gait conditions

	HAB (Mean ± SD)		FFS (Mean ± SD)		SOF (Mean ± SD)		F	p
Hip								
Ext. Moment (Nm/kg)	1.052 ±	0.257	0.992 ±	0.215	1.144 ±	0.322*,**	7.73	<0.001
Flx. Moment (Nm/kg)	-0.521 ±	0.144	-0.505 ±	0.183	-0.631 ±	0.149*,**	11.90	<0.001
Abd. Moment (Nm/kg)	1.854 ±	0.342	1.868 ±	0.396	1.697 ±	0.355*,**	26.13	<0.001
Flx./ Ext. Angle- IC (°)	25.37 ±	8.03	25.57 ±	8.98	27.81 ±	8.05*,**	11.89	<0.001
Flx. Angle- Pk (°)	25.98 ±	7.79	25.94 ±	8.70	28.62 ±	7.79*,**	14.49	<0.001
Ext. Angle- Pk (°)	-9.96 ±	7.36	-10.10 ±	7.88	-9.47 ±	7.88	2.18	0.122
Add./ Abd. Angle- IC (°)	7.28 ±	4.06	7.19 ±	4.61	7.08 ±	4.42	0.25	0.781
Add. Angle- Pk (°)	12.47 ±	3.49	11.58 ±	4.12*	12.04 ±	3.86	5.47	0.006
Knee								
Ext. Moment (Nm/kg)	2.092 ±	0.468	1.926 ±	0.540*	2.023 ±	0.484	5.62	0.006
Flx. Moment (Nm/kg)	-0.413 ±	0.096	-0.466 ±	0.103*	-0.446 ±	0.089	7.29	0.003
Abd. Moment (Nm/kg)	0.602 ±	0.214	0.639 ±	0.226	0.539 ±	0.217*,**	12.22	<0.001
Sagittal Stiffness (Nm/kg/ °)	0.089 ±	0.013	0.091 ±	0.019	0.080 ±	0.013*,**	17.06	<0.001
Flx./ Ext. Angle- IC (°)	12.09 ±	4.48	14.02 ±	5.69*	12.62 ±	4.74**	9.10	<0.001
Flx. Angle- Pk (°)	40.58 ±	5.39	40.72 ±	6.82	44.04 ±	6.32*,**	18.29	<0.001
Flx. Angle- Exc (°)	29.27 ±	5.01	28.19 ±	5.42	31.67 ±	5.09*,**	19.35	<0.001
Add./ Abd. Angle- IC (°)	-1.49 ±	3.20	-0.88 ±	3.48*	-1.53 ±	3.36**	9.14	<0.001
Add. Angle- Pk (°)	-0.147 ±	3.21	0.388 ±	3.46*	0.181 ±	3.40	5.01	0.010
Ankle								
P.Flx Moment (Nm/kg)	2.384 ±	0.464	2.901 ±	0.448*	2.179 ±	0.472*,**	67.66	<0.001
Inv. Moment (Nm/kg)	0.542 ±	0.327	0.605 ±	0.405*	0.535 ±	0.297*,**	6.51	0.006
D.Flx./ P.Flx. Angle- IC (°)	6.35 ±	6.81	-10.20 ±	5.89*	9.89 ±	8.81**	107.35	<0.001
D.Flx. Angle- Pk (°)	24.45 ±	3.51	23.01 ±	4.12	25.81 ±	4.01*,**	24.78	<0.001
Inv./ Evr. Angle- IC (°)	6.47 ±	4.60	10.50 ±	4.13*	6.13 ±	5.61**	26.96	<0.001
Evr. Angle- Pk (°)	-7.39 ±	3.01	-5.70 ±	3.62*	-7.61 ±	3.29**	24.49	<0.001
Sagittal Foot Angle- IC (°)	9.78 ±	7.29	-8.20 ±	4.10*	15.20 ±	9.86*,**	116.56	<0.001

- Flx, flexion; Ext, extension; Add, adduction; Abd, abduction; D.Flx, dorsiflexion; P.Flx, plantarflexion; Inv, inversion; Evr, eversion; Pk, peak; IC, initial contact; HAB/FFS/SOF, habitual, forefoot strike, soft/quiet running conditions; SD, standard deviation
- All joint kinetic variables expressed as internal moments
- F/p values result of ANOVAs; for pairwise tests: * = significant difference from habitual gait condition, ** = significant difference from forefoot strike gait condition

Acknowledgements (Optional)

Opinions in this manuscript are not official policy or views of the US Army.

Session Category

Musculoskeletal Biomechanics: Joints and Motion

P2-035

Stride Characteristics in an Accelerative Figure-Eight Maneuver During Competitive Chuckwagon Racing

Ms. Camille Eamon MSc, BSc[1], Mr. Matthijs van den Broek BSc[1,2], Dr. Karelhia Garcia Alamo DVM, MSc[1], Ms. Charlotte de Bruyne MSc, BSc[1], Ms. Brittany Davis MSc, BSc[1], Ms. Maggie Fallscheer[1], Ms. Sara Frostad[1], Ms. Sara Skotarek Loch MSc, BSc[1], Dr. Edmond Pajor PhD, MSc, BSc[1], Dr. Renate Weller DVM, PhD, MSc[1], Dr. Zoe Yau Shan Chan PhD, MPhil, BE[1], Dr. Thilo Pfau Dr.-Ing, Dipl.-Ing[1]

[1]University of Calgary, Calgary, Alberta, Canada. [2]Delft University of Technology, Delft, South Holland, Netherlands

Introduction

In Chuckwagon racing, teams of four Thoroughbred racehorses pull a wagon on dirt racetracks. Each horse has a position as left or right leader (LL, RL) or wheeler (LW, RW). Races begin with a figure-eight maneuver around two barrels, which is not seen in other disciplines. Previous work has used stride characteristics to predict racehorse injury risk [1], but limited work has been done in Chuckwagon racing. Using wearable sensors, we previously showed that one Chuckwagon racehorse who sustained a catastrophic fracture while racing as a RW had highly asymmetrical movement in the days leading to the injury. Here we quantified this horse's stride characteristics in the figure-eight and compared them to other RWs and RLs.

Methods

Over ten race days, 8 RLs and 9 RWs (1 injured) wore Global Navigation Satellite Systems combined with Inertial Measurement Units (GNSS-IMUs) sampling at 25Hz on their harnesses at the midline of the back in the cranial/mid thoracic area. GNSS speed and position data were recorded during practice figure-eights (minutes before race start) and race figure-eights. Stride cycles were identified from speed plots to calculate stride frequency (SF). Linear mixed models compared SF between practice and race figure-eights with speed as a covariate and horse as a random factor ($p<0.05$).

Results

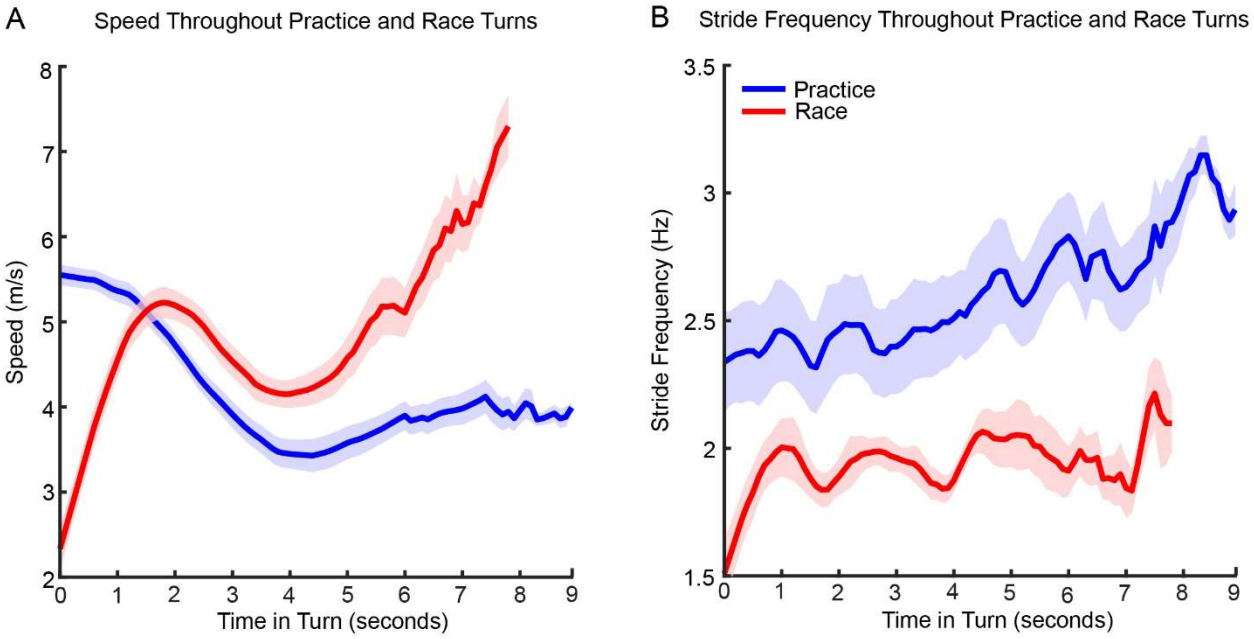
Thirty-six figure-eights (18 practice, 18 race) were analyzed. Four maneuvers were obtained for the injured horse: practice and race four days pre-injury, and on the day of injury. Mean speed was 4.23m/s in practice and 4.70m/s in race for all horses (Figure 1A). Uninjured horses showed higher SF in practice (2.60Hz) than race (1.98Hz; $p<0.001$; Figure 1B). The

injured horse had higher SFs than others four days pre-injury (practice 3.06Hz, race 1.92Hz) and on the day of injury (practice 3.18Hz, race 1.90Hz).

Discussion

SF was higher in practice figure-eights, with the injured horse exhibiting higher practice SFs than other horses. More data is needed to characterize normal stride characteristics during this unique maneuver and identify horses at an increased injury risk. GNSS-IMU devices offer a practical tool for non-disruptive monitoring to support proactive injury management.

Images (Optional)



References (Optional)

[1] Adelene Wong et al., Equine Vet J, 2023

Acknowledgements (Optional)

We acknowledge the Calgary Stampede and participating Chuckwagon drivers for allowing access to the Chuckwagon racehorses.

Session Category

Musculoskeletal Biomechanics: Joints and Motion

P2-036

Effect of Race Progression on Speed and Stride Parameters in Chuckwagon Racehorses

Dr. Thilo Pfau Dr.-Ing, Dipl.-Ing[1], Ms. Camille Eamon MSc, BSc[1], Mr. Matthijs van den Broek BSc[1,2], Ms. Charlotte de Bruyne MSc, BSc[1], Ms. Brittany Davis MSc, BSc[1], Ms. Maggie Fallscheer[1], Ms. Sara Frostad[1], Dr. Karelhia Garcia Alamo DVM, MSc[1], Ms. Sara Skotarek Loch MSc, BSc[1], Dr. Renate Weller DVM, PhD, MSc[1], Dr. Edmond Pajor PhD, MSc, BSc[1], Dr. Zoe Yau Shan Chan PhD, MPhil, BE[1]

[1]University of Calgary, Calgary, Alberta, Canada. [2]Delft University of Technology, Delft, South Holland, Netherlands

Introduction

Chuckwagon racing is a competitive horseracing event where teams of four Thoroughbreds pull a 600kg wagon around a dirt racetrack. There is a lack of fundamental knowledge about associations between speed, stride parameters and Chuckwagon race characteristics and this limits the development of predictive injury models similar to models emerging for other disciplines.

Methods

59 Chuckwagon horses competing at the 2025 Calgary Stampede Rangeland Derby were equipped with global navigation satellite system (GNSS) loggers attached to their harnesses. Average speed, stride frequency (SF) and stride length (SL) were calculated for 100m race segments using validated algorithms. Linear mixed models (random factor: horse, fixed factor: race segment) were implemented for speed, SL and SF. Additional models for SL and SF included speed as fixed covariate and track geometry information ($1^{st}/2^{nd}$ curve, $1^{st}/2^{nd}$ straight) as fixed factor. Significance was set to $p<0.05$ with Bonferroni correction for multiple comparisons.

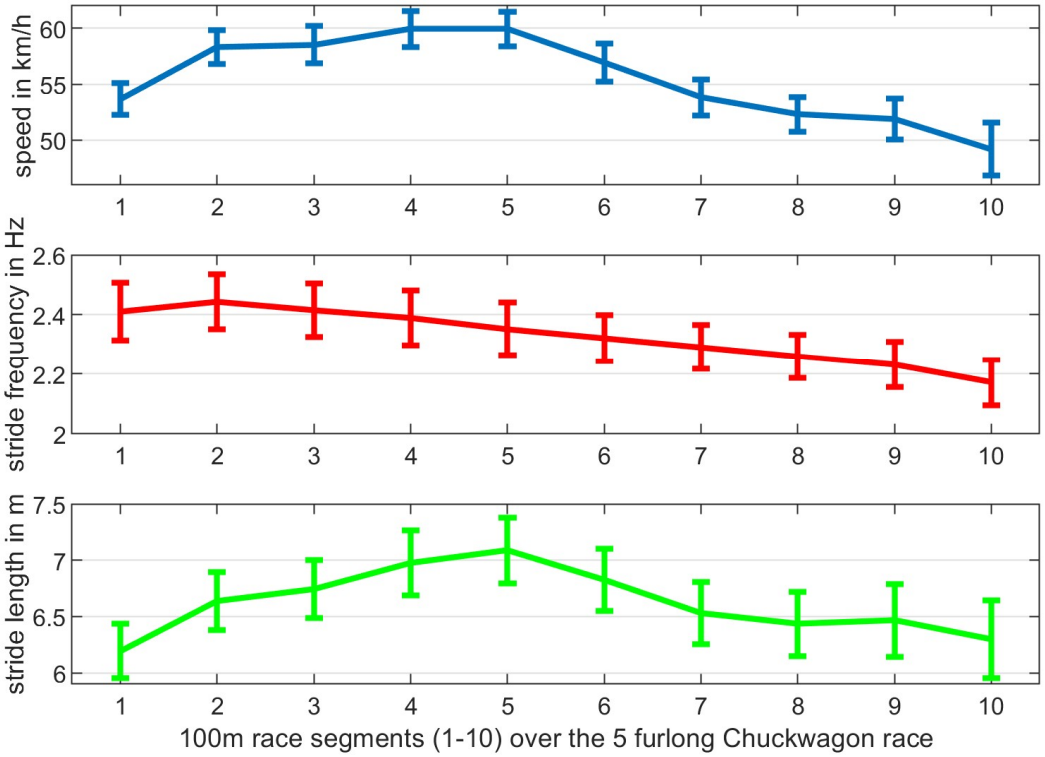
Results

Speed increased from the start and plateaued around 60 km/h towards the end of the first straight (segments 4 to 5, Fig 1A), then decreased continually. SF (Fig 1B) increased rapidly peaking in segment 2 (2.43Hz) then dropping. SL peaked later (segment 5, Fig 1C, 7.11m) before dropping in alignment with speed. Significant effects of race segment were found for all three variables (all $p<0.001$). Models including speed as covariate (mean speed of 55.5 km/h) showed a significant interaction between speed and geometry. SF was approximately 0.1Hz higher (and SL 0.3m lower) in the 1^{st} compared to the 2^{nd} curve and compared to both straights (all pairwise $p<0.001$).

Discussion

This study presents in-race speed and stride parameters for competitive Chuckwagon horseracing using a validated GNSS-logger. Speed and SL reach peak values at the end of the first straight. Consequently, the track should be monitored in this region where peak vertical ground reaction forces occur in the limbs. Changes in SL between track segments exceed the changes observed previously in the runup to injury emphasizing the need for detailed discipline-specific stride parameter models.

Images (Optional)



Acknowledgements (Optional)

With thanks to the Calgary Stampede and all the Chuckwagon teams for facilitating measurements during competitive races.

Session Category

Musculoskeletal Biomechanics: Joints and Motion

P2-037

Two Ultrasonographic Methods of Evaluating Acromio-Humeral Distance: Intra- and Inter-rater Reliability in Young, Healthy Participants

Dr. Christa Nelson PT, DPT, PhD, Dr. Lance Grunert PT, DPT, Dr. Eleni Papastratakos PT, DPT, Dr. Nate Rusk PT, DPT, Dr. Ana Maria Acosta PhD

Northwestern University Feinberg School of Medicine, Department of Physical Therapy and Human Movement Sciences, Chicago, IL, United States

Introduction

Shoulder subluxation is a debilitating condition that can significantly affect shoulder mobility and participation in daily activities. Clinically, subluxation is measured through finger breadth palpation or tape measurements, but this lacks precision and reliability. Advanced imaging methods such as MRI, CT or radiographs can quantify subluxation but are costly or expose patients to radiation. Ultrasound (US) provides an accessible alternative and has been used to evaluate humeral position in shoulder impingement, glenohumeral instability, and post-stroke, but it often requires advanced training. Two ultrasonographic measures have been described: the acromio-humeral distance (AHD) and the acromio-greater tuberosity distance (AGT), but reliability information is limited and only reported using expert ultrasonographers. No known studies have examined reliability of these measures when performed by novice raters. The purpose of this study was to evaluate intra- and inter-rater reliability of AHD and AGT measurements obtained by novice ultrasonographers.

Methods

Thirteen adults with no prior shoulder pathology (7 female, 6 male; age = 24.5 ± 2.3 years) participated. Using 2-D ultrasound (Aixplorer Multiwave), two randomly selected (out of three possible) novice ultrasonographers acquired three images per shoulder for both AHD and AGT (24 total images / participant). Images were imported into Fiji ImageJ software, where two random raters measured AHD and AGT in each image. Intra- and inter-rater reliability were calculated using ICCs with 95% confidence intervals.

Results

AHD measurements demonstrated excellent single rater reliability with ICC (95% CI) = 0.96 (0.94, 0.97) and excellent inter-rater reliability with ICC (95% CI) = 0.98 (0.97, 0.99). Results for AGT measurement demonstrated excellent single rater reliability with ICC (95%CI) =

0.98 (0.96, 0.98) and excellent inter-rater reliability with an ICC (95% CI) = 0.99 (0.98, 0.99). Intra-rater reliability for AHD was excellent with test-retest reliability ICC (95% CI) = 0.90 (0.87, 0.93), and good for AGT ICC (95% CI) = 0.86 (0.81, 0.89).

Discussion

US proved to be a repeatable, reliable method to evaluate AHD and AGT distance with good-excellent intra- and inter-rater reliability across 3 novice ultrasonographers. AHD was the most reliable between the two measures. Future work is indicated to evaluate these measures in different shoulder positions and clinical populations.

Images (Optional)

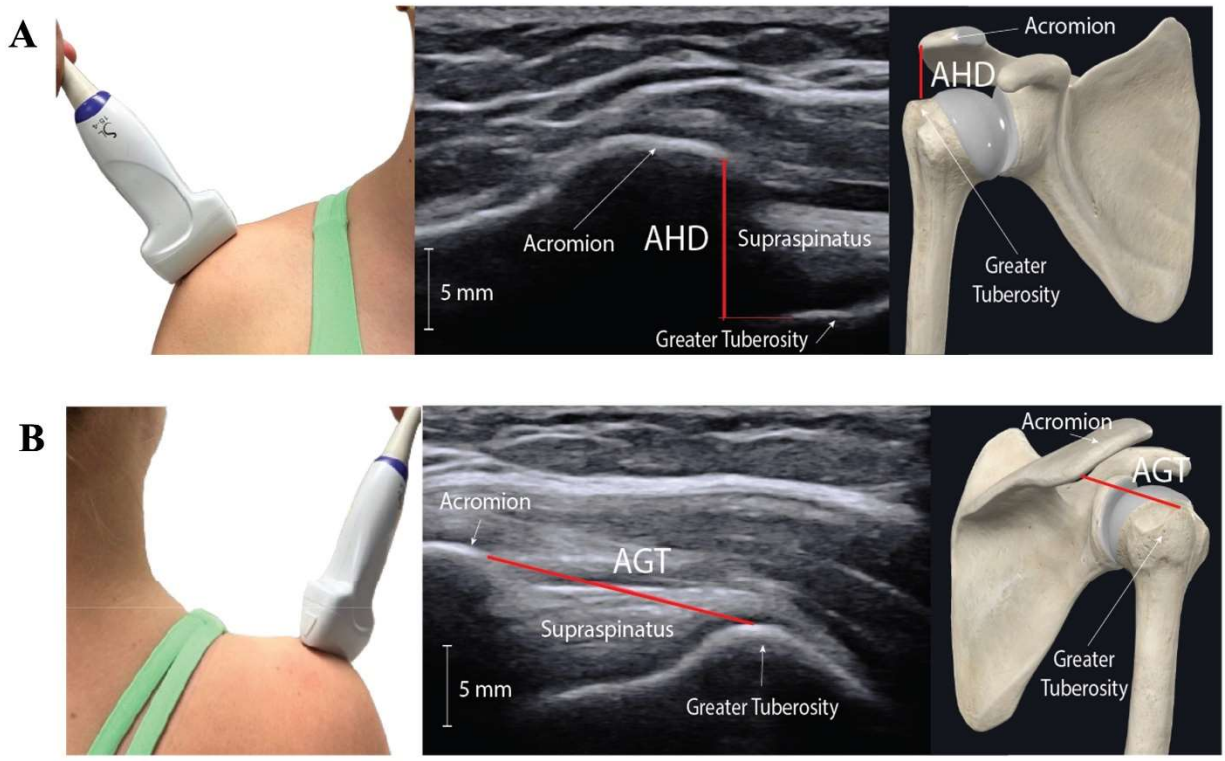


Figure 1. A) Acromion-Humerus Distance (AHD) and B) Acromion Greater Tuberosity Distance (AGT) measurements

References (Optional)

Session Category

Musculoskeletal Biomechanics: Joints and Motion

P2-038

Uneven and Loose Surfaces Challenge the Ankle Joint Complex by Increasing Frontal Plane Angles and Moments During Walking

Dr Clare Milner PhD, Mr Dylan Mulligan MS

Drexel University, Philadelphia, PA, United States

Introduction

Laboratory-based studies of gait typically measure biomechanics during walking over level ground. However, walking in the outdoor environment often includes uneven or loose surfaces that likely alter gait biomechanics. These surfaces may increase the risk of injury such as ankle sprains by increasing frontal plane movement in the ankle joint complex. The purpose of this study was to compare frontal plane ankle biomechanics during walking over level, uneven, and loose surfaces. We hypothesized that frontal plane range of motion and moments would be largest on the loose surface, then the uneven surface, and smallest during level walking.

Methods

As part of an ongoing study, 5 young healthy adults provided written informed consent to participate (4 female, 1 male, age 23.4 (0.5) years, height 1.70 (0.05) m, weight 74.4 (13.8) kg). All procedures were approved by the Institutional Review Board. Motion capture (200Hz) and force plate (1000Hz) data were collected as participants walked over level ground, a fixed uneven surface, and a loose rocks surface in sneakers. Each surface was instrumented with a force platform. Gait data were processed in Visual3D and MATLAB and frontal plane angles and internal moments extracted for three steps per condition per participant. Effect size was used to evaluate differences among conditions.

Results

Both uneven and loose surfaces had a large effect for increased frontal plane range of motion and peak inversion moment during walking (Table 1). Peak eversion moment was decreased with a moderate effect on the uneven surface, but moderately increased on the loose surface. Generally, the loose surface had greater effects compared to the uneven surface.

Discussion

Walking surface profile affects frontal plane ankle range of motion and peak internal inversion moment in young healthy adults. Effects varied according to surface type and were greater during walking on a loose surface than a fixed uneven surface, and both were

greater than during level surface walking. Investigators should consider including multiple surface types likely to be encountered in everyday life in gait assessments to better reflect the changing demand on the ankle joint complex.

Images (Optional)

Table 1: Mean and standard deviation of frontal plane angle range of motion and peak moments during walking on different surfaces.

	Range of Motion (degrees)	Peak Inversion Moment (Nm/kg)	Peak Eversion Moment (Nm/kg)
Level ground	13.5 (4.2)	0.14 (0.05)	-0.10 (0.07)
Uneven surface	18.5 (3.2)	0.21 (0.10)	-0.05 (0.06)
Loose surface	22.2 (10.3)	0.24 (0.14)	-0.20 (0.27)
Effect Size uneven vs level	1.35	0.93	-0.77
Effect Size loose vs level	1.29	1.05	0.59
Effect Size loose vs uneven	0.55	0.25	0.91

Session Category

Musculoskeletal Biomechanics: Joints and Motion

P2-039

Sex-Dependent Effects of Footwear Longitudinal Bending Stiffness on Metatarsal Strains During Running

Dr. Colin Firminger PhD[1], Dr. Sarah Manske PhD[2], Dr. W. Brent Edwards PhD[1], Dr. Michael Asmussen PhD[3]

[1]Human Performance Lab, University of Calgary, Calgary, AB, Canada. [2]University of Calgary, Calgary, AB, Canada. [3]Vancouver Island University, Nanaimo, BC, Canada

Introduction

Second and third metatarsal stress fractures are highly prevalent overuse injuries amongst runners, with females facing nearly twice the stress fracture risk as men [1]. Stress fracture development is associated with repetitive bone strain, and shoes with increased longitudinal bending stiffness (LBS) may represent an intervention to reduce metatarsal strain during running [2]. Therefore, the purpose of this research was to examine the effect of shoe LBS on metatarsal strains in female and male runners.

Methods

Sixteen athletes (8 female) ran at 3.3 m/s on an instrumented treadmill wearing a high-LBS (0.54 Nm) and low-LBS (0.28 Nm) Nike Alphafly 3 while plantar pressure and motion capture data were recorded. The high-LBS shoe was unmodified, while the low-LBS shoe had six medial-lateral cuts in the forefoot through the embedded carbon fibre plate. Musculoskeletal models of the second and third metatarsophalangeal joints were used to estimate metatarsal loading during stance [3], and weight-bearing computed tomography (WBCT) scans with concurrent motion capture were taken at different running-specific metatarsophalangeal angles to establish relationships between WBCT-measured and motion capture-estimated metatarsal orientations. Subject-specific finite element models were then created using bone geometry from the WBCT scans and solved from 30-80% of stance, with peak strain being tabulated for statistical analysis.

Results

Female runners illustrated significantly lower peak strain in the high-LBS shoe for the second ($p=0.024$) and third ($p=0.050$) metatarsals, while no significant change was observed for males ($p\geq0.262$; see Figure 1). Decreased peak second metatarsal strains in the female runners were associated with significant reductions metatarsal load ($p=0.027$) in the high-LBS condition, while metatarsal orientation remained consistent ($p=0.222$).

Discussion

This study is the first to systematically evaluate the effect of shoe LBS on metatarsal strains, illustrating significant reductions in strain for the second and third metatarsals in the high-LBS shoe amongst female runners. In terms of metatarsal stress fracture risk, this research elucidates potential benefits of using high-LBS shoes in a population of female runners.

Images (Optional)

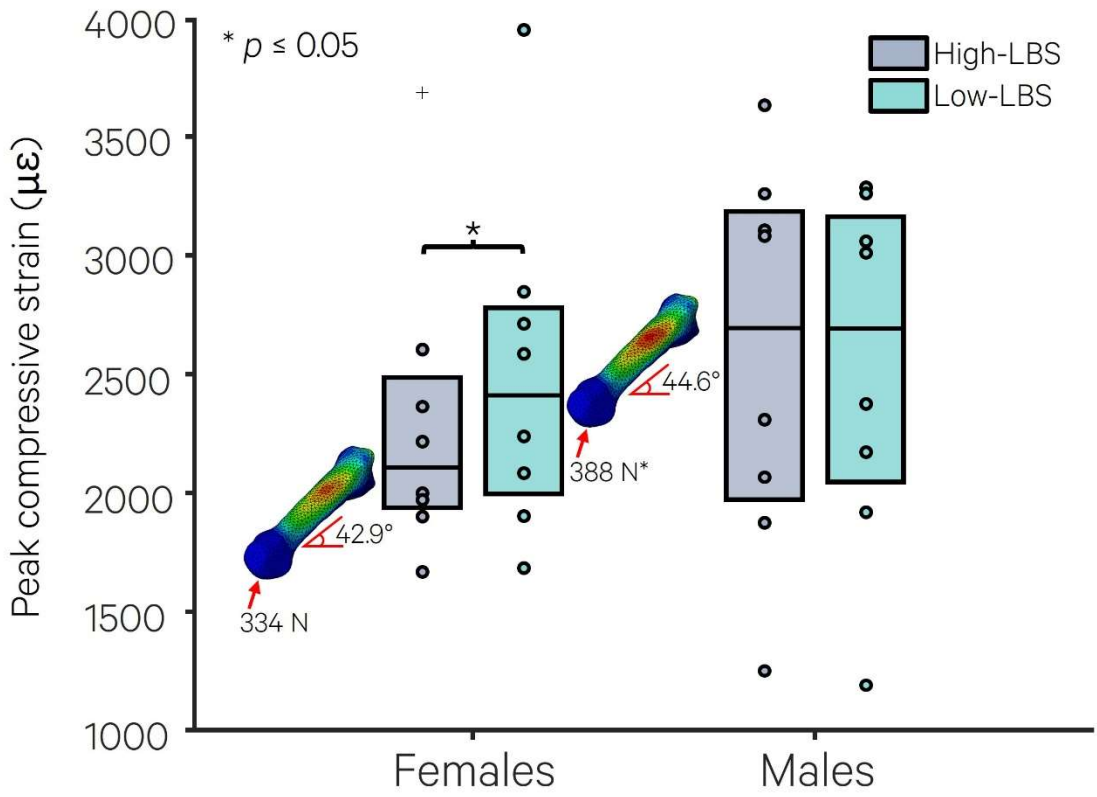


Figure 1: Second metatarsal peak compressive strains for females (n=8) and males (n=8). Finite element modelled strains are shown for a representative female subject with group-averaged metatarsal head force and orientation overlaid.

References (Optional)

[1] MacGregor *et al.*, J Women's Health, 2022

[2] Chen *et al.*, Foot Sci, 2025

[3] Stokes *et al.*, J Anatomy, 1979

Acknowledgements (Optional)

The authors would like to acknowledge Luka Dukaric and Maria Rodriguez for their assistance with data collection and processing.

Session Category

Musculoskeletal Biomechanics: Joints and Motion

P2-040

Biarticular Muscle Control for a Multi-joint In Vitro Physiological Lower-limb Simulator: A Phantom Study

Mr. R. Yogeshwar Rao, Mr. Shridhar Iyer, Mr. Eshan Kshatriya, Dr. Darshan S. Shah PhD

BiOME Lab, Indian Institute of Technology Bombay, Mumbai, Maharashtra, India

Mr. R. Yogeshwar Rao

Introduction

In vitro physiological knee simulators replicate joint kinematics and kinetics and are widely used to evaluate knee biomechanics before and after surgery [1]. Most simulators control knee flexion and apply quadriceps/hamstring loads to achieve a target vertical ground reaction force, but they typically actuate a single quadriceps tendon despite physiological activation arising from both the uniarticular vastii and the biarticular rectus femoris. This actuator mismatch reduces simulator fidelity for tasks requiring coordinated multi-muscle activation. Therefore the aim of the study was to evaluated a hybrid biarticular controller on a multi-actuator lower-limb simulator.

Methods

A two degree-of-freedom scaled sagittal-plane lower-limb model was fabricated with the linkage geometry and mass distribution chosen to femur and tibia proportions [3] (Fig. 1). Dynamic muscle forces were simulated by linear actuators (TiMotion, Taiwan) connected via steel cables to replicate lines of action of uniarticular (vasti, iliopsoas) and biarticular (hamstrings, rectus femoris) muscles. Inline S-beam load cells (Rudra sensors, India) measured muscle forces, while optical encoders (Potel, India) measured hip and knee flexion angles. A novel hybrid controller architecture consisting of position feedback controllers for the hip and knee joint angles, along with force feedback controllers for each muscle enforcing muscle-specific bounds corresponding to muscle capacity. Four input scenarios based on combinations of the following three setpoints for the hip and the knee flexion – fixed (constant), flexion-extension (FE; 0°-40°-0°), extension-flexion (EF; 40°-0°-40°) – were performed in triplicate. Mean of the root mean square errors across trials and their standard deviations were used to evaluate controller accuracy and repeatability, respectively.

Results

Repeatability improved by 74% for biarticular motions, as compared to uniarticular motions (Fig. 1). Accuracy decreased by 52% for out-of-phase biarticular motion, as compared to in-phase motion.

Discussion

The study demonstrated an accurate and repeatable biarticular controller for a multi-joint simulator, although certain motion combinations exhibited higher tracking errors that highlight actuator redundancy and biarticular coupling. These issues can be mitigated by adding biarticular load-sharing blocks with a redundancy-handling capability to the controller. Future work will validate the hybrid biarticular controller on a human-scaled physiological knee simulator with native cadaveric specimens.

Images (Optional)

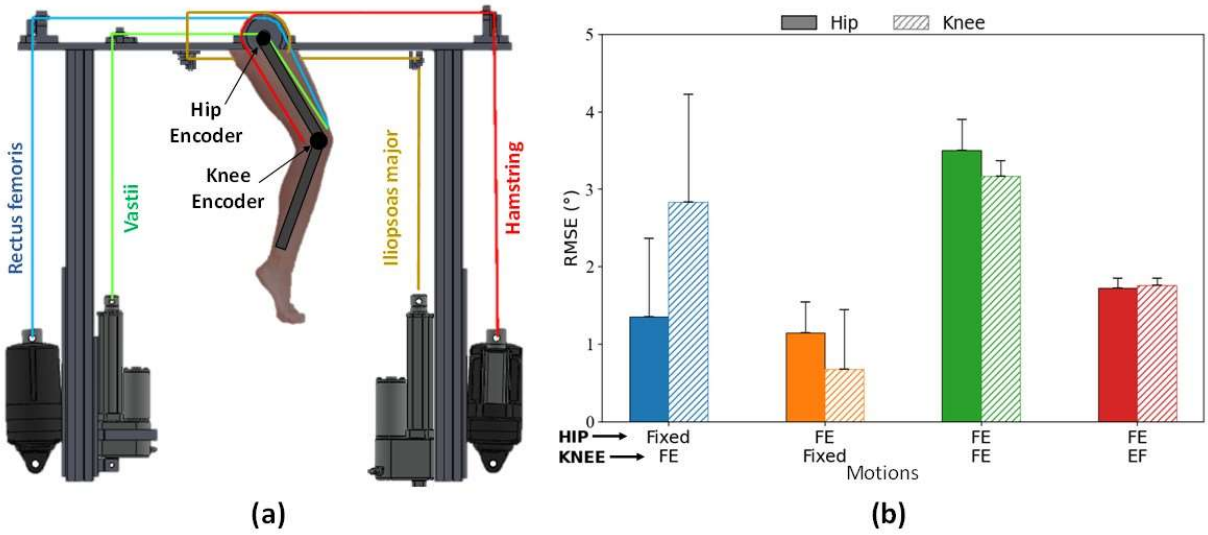


Fig. 1 (a) Schematic of the biarticular simulator setup (b) Root mean square error (RMSE) for hip and knee flexion angles with respect to desired setpoints for four conditions – pure knee flexion-extension (FE) with hip fixed, pure hip FE with knee fixed, hip FE with knee FE in-phase, hip FE with knee extension-flexion (EF) out-of-phase (data represented as mean ± standard deviation across three trials)

References (Optional)

Acknowledgements (Optional)

The study was supported by the Startup Research Grant, Science and Engineering Research Board, India. R. Yogeshwar Rao was supported by Prime Minister Research Fellowship, Government of India.

Session Category

Musculoskeletal Biomechanics: Joints and Motion

P2-041

Ankle Kinetics in Persons with Achilles Tendinopathy During Unipedal Repetitive Vertical Hopping

Dr. David Ortiz-Weissberg PhD[1,2], Dr. Kornelia Kulig PhD, PT, FAPTA[1]

[1]University of Southern California, Los Angeles, CA, United States. [2]University of San Diego, San Diego, CA, United States

Dr. David Ortiz-Weissberg

Introduction

The Achilles tendon is the largest tendon in the body and aids in propulsion during numerous tasks. Given that the Achilles is the primary plantar flexor tendon, Achilles tendinopathy may have negative consequences for movement. Investigating ankle joint kinetics is crucial for understanding how Achilles tendinopathy impacts ankle function and movement. Repetitive vertical hopping is the only multi-joint task where the joint energetics are consistently greatest at the ankle across task speeds and phases, making it the optimal task for examining ankle kinetics.

This study aimed to examine how Achilles tendinopathy impacts ankle kinetics during unipedal vertical hopping. We hypothesized that the involved limb would exhibit reduced ankle contributions to limb-level energy relative to unaffected limbs.

Methods

We recruited 27 persons with and 27 without a history of Achilles tendon pain or morphologic alterations. Participants were tasked with unipedal repetitive vertical hopping at 2.33 Hz on both limbs. The joint contribution to limb energy was the ratio of NJM work to the sum of joint work. Robust paired difference tests were used to compare the ankle contribution to limb energy between the involved limb and a matched healthy control limb. To account for the high variance, k-means clustering of all available limbs was performed (clustering variable: average power). The ankle and knee contributions were compared between clusters using robust confidence intervals.

Results

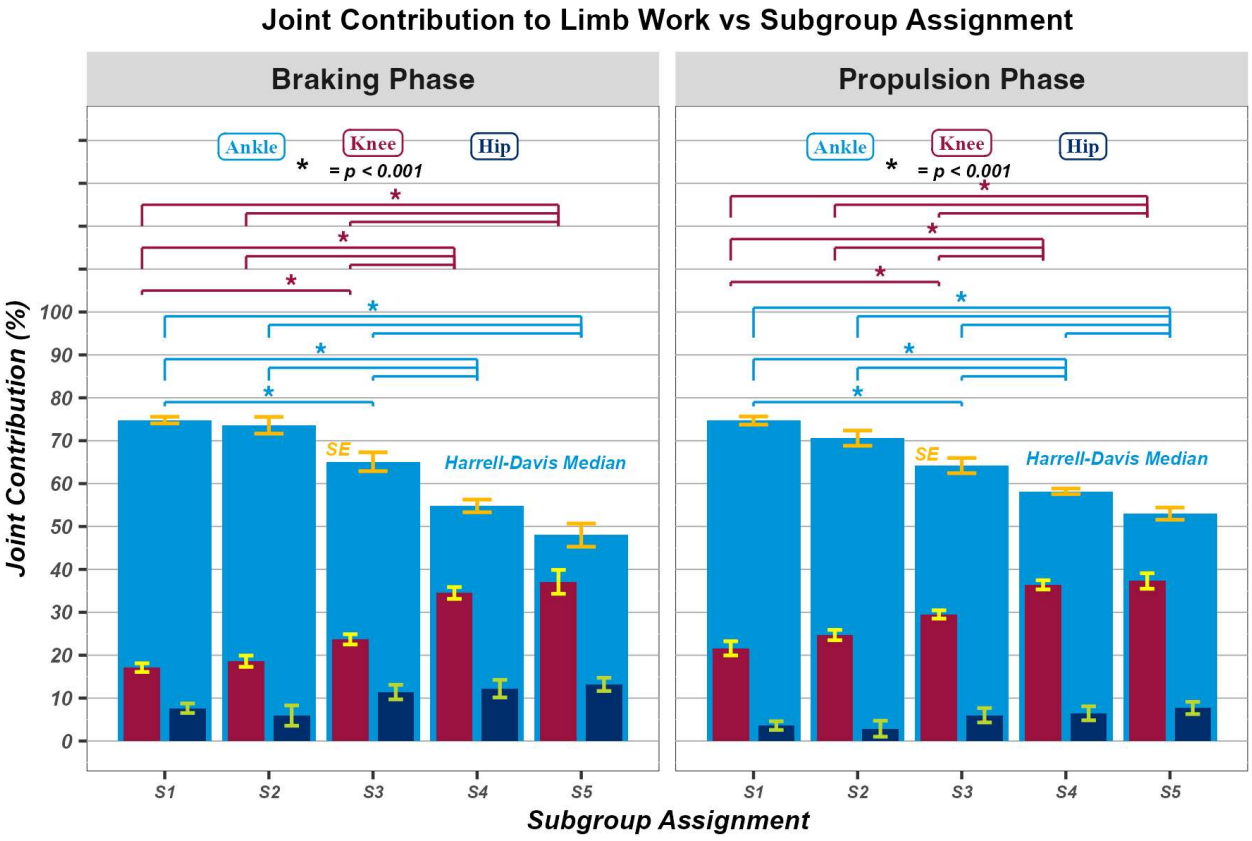
At the whole-group level, there were no significant between-group differences in ankle contributions to limb-level energy absorption and generation. The k-means clustering

identified five subgroups. Subgroups 4 and 5 displayed significantly lower ankle and greater knee contributions (both absorption and generation) than the other subgroups (Figure 1). 28 of the 37 limbs with a history of Achilles tendinopathy were assigned to Subgroups 4 and 5.

Discussion

This is the first study to characterize joint kinetics in persons with Achilles tendinopathy using a task that is dynamic and ankle-driven and thus challenges the ankle. The subgroups confirms that persons with Achilles tendinopathy frequently display impaired ankle kinetics and compensatory increases in knee kinetics. However, this is not universally true: some symptomatic limbs were placed in subgroups with high ankle kinetic magnitudes.

Images (Optional)



Acknowledgements (Optional)

This research was supported by the American Society of Biomechanics Graduate Student Grant-In-Aid and the International Society of Biomechanics Matching Dissertation Grant.

Session Category

Musculoskeletal Biomechanics: Joints and Motion

P2-042

Combinations of Three-Dimensional Tibiofemoral Geometries in Young Female Athletes Are Related to Increased Anterior Cruciate Ligament Force Estimated from Computational Models

Mr. David Shamritsky MEng[1], Ms. Isabella Gomez Hjerthen BS[1], Dr. Mitchell Wheatley PhD[1], Dr. Andrew Pechstein PhD[1], Mr. Julius Kim BS[1], Dr. Danyal Nawabi MD[1], Dr. Thomas Wickiewicz MD[1], Dr. Andrew Pearle MD[1], Dr. Bruce Beynnon PhD[2], Dr. Carl Imhauser PhD[1]

[1]Hospital for Special Surgery, New York, NY, United States. [2]University of Vermont, Burlington, VT, United States

Introduction

Features of tibiofemoral bony geometry are associated with young female athletes' risk of sustaining noncontact anterior cruciate ligament (ACL) rupture. However, the relationship between bony geometry and ACL loading in this high-risk population remains unclear. Our objective was to identify three-dimensional variations in female tibiofemoral bony geometry that are related to estimates of ACL force using physics-based computational modeling.

Methods

Three-dimensional (3D) renderings of tibiofemoral bone, cartilage, and menisci were generated from magnetic resonance imaging of 60 female athletes with a noncontact ACL tear and 60 matched uninjured athletes (mean age: 17±2 years). Computational models were constructed by mapping the cruciate, collateral, and capsular ligaments onto the 3D renderings and applying standardized properties to these ligaments. The tibia was then flexed to 15° and loaded with 100 N compression, 8 Nm valgus moment, and 30 N anterior force to simulate the clinical pivot shift exam. ACL force at peak applied load was estimated for each subject. Statistical shape modeling was used to quantify variations in bony geometry. All 120 geometries were cropped to isolate the distal femoral condyles and the tibial plateau. Then, a mesh correspondence and alignment algorithm was applied. Finally, principal component analysis identified the ten principal components (PCs) with largest contributions to total geometric variation. These ten PCs were related to ACL force using stepwise multiple regression (α=0.05). The increase in ACL force corresponding to a 2-standard deviation (SD) change in each significant PC was reported to describe their relative impact on ACL force.

Results

ACL force averaged 124±33 N across all 120 female subjects. PCs with the fourth and seventh largest contributions (PC4: 5.4% and PC7: 2.8% of total variation, respectively) were correlated with ACL force ($p<0.001$). 2-SD changes in PC4 and PC7 corresponded to 21 N and 22 N increases in ACL force, respectively.

Discussion

By integrating clinical imaging data with physics-based computational models and statistical shape modeling, we reveal that ACL loading in young, high-risk female athletes is related to unique combinations of bony geometries. Mechanistic evaluation of how bony anatomy modulates knee mechanics will allow for anatomy-based injury screening, prevention protocols, and surgical treatments.

Session Category

Musculoskeletal Biomechanics: Joints and Motion

P2-043

Estimating Scapular Kinematics During Tasks With Independent Scapular Motion Using Individualized Regression Models

Ms. Denise Balogh MSc, Dr. Angelica Lang PhD

University of Saskatchewan, Saskatoon, Saskatchewan, Canada

Introduction

Individualized linear regression (ILR) models have been proposed as an alternative to both generalized scapular regression models and the double calibrated acromial marker cluster (AMC) for the estimation of scapular kinematics [1,2]. This study examines how the number of ILR model predictor variables and training poses affects the prediction of scapular kinematics.

Methods

Reflective markers were placed on 13 healthy participants according to ISB standards to capture bilateral shoulder kinematics [3]. Participants positioned each arm in 11 static 'training' poses, and anatomical landmarks of the scapula were palpated. Scapular Euler angles, humeral helical angles, and acromial process (AP) displacements were calculated. Humeral helical angles from either 11 or 6 poses, with or without AP displacements, were used as predictor variables for the development of 4 different ILR models for each participant: Model 11, Model 6, Model 11+AP, and Model 6+AP. The ability of the ILR models to predict scapular kinematics during 7 new 'test' poses, as compared to scapular kinematics obtained from palpation and from direct tracking with the AMC, was examined. The root mean square error (RMSE) between scapular angles extracted from the AMC and ILR models and the palpated scapular orientations was calculated. Three-way repeated measures ANOVAs (method*test pose*scapular axis; a=.05) were additionally computed on the scapular angles.

Results

Mean RMSEs were below 14º for all methods except for Model 6+AA, in which large RMSEs occurred (Table 1). Model 11 consistently produced the lowest ILR model RMSEs for many of the 'test' poses, emphasizing the benefit of developing the models from a greater number of 'training' poses. However, including the AP displacements as predictor variables may not benefit the models. Significant 3-way ANOVA interactions ($p<0.05$) indicated that for certain 'test' poses and axes combinations, differences in estimates of scapular orientation were present across methods.

Discussion

The predictor variables to an ILR model impact the accuracy of static scapular kinematic estimations. Additional analysis will expand to the prediction of dynamic scapular kinematics, with the full study sample (N=20).

Images (Optional)

Table 1. Mean (standard deviation) RMSEs (palpation – AMC/ILR model) for each scapular axis across all 7 'test' poses. All values are in degrees.

	AMC	Model 11	Model 6	Model 11+AA	Model 6+AA
Internal Rot.	6.84 (1.72)	8.90 (2.55)	11.90 (1.93)	9.94 (2.17)	36.44 (17.56)
Upward Rot.	7.42 (1.93)	8.92 (2.49)	13.56 (1.73)	9.20 (2.30)	53.91 (25.56)
Tilt	10.48 (10.18)	5.25 (0.68)	8.28 (1.51)	7.77 (2.09)	44.42 (21.86)

References (Optional)

[1]Nicholson *et al.*, J Biomechanics, 2017; [2]Rapp *et al.*, J Biomechanics, 2017; [3]Wu *et al.*, J Biomechanics, 2005.

Session Category

Musculoskeletal Biomechanics: Joints and Motion

P2-044

Hyaluronic Acid Formulations Modulate the Efficacy of Lubricin in Lubricating Articular Cartilage

Graduate Student Spencer Witt B.S.[1], Undergraduate Student Dylan Shen[1], Professor Heidi Reesink PhD, DVM[2], Professor Matthew Paszek PhD[2], Professor Lawrence Bonassar PhD[1]

[1]Cornell University, Ithaca, New York, United States. [2]University of California Davis, Davis, California, United States

Introduction

Articular cartilage maintains low friction due to synergistic interactions between lubricin and hyaluronic acid (HA) within synovial fluid. Much work has been done characterizing the friction of a variety of HA and lubricin forms. The objective of this study is to characterize the interactions of eLub, a recently synthesized recombinant lubricin based on the equine PRG4 gene, with various formulations of HA using the Stribeck framework (Fig 1A).

Methods

A 20 mg/mL eLub stock was diluted with PBS and HA to yield 0.16 and 1.6 mg/mL eLub and 5 mg/mL HA. Friction was measured on a biaxial load-cell tribometer. Cartilage plugs (6 mm diameter) were punched from neonatal bovine femoral condyles, trimmed to 2 mm thick, and glued to pivots. Samples were compressed to 30% strain against glass in the lubricant bath, allowed to relax for 1 h, then slid reciprocally at 0.1–10 mm/s. The friction coefficient was computed as the shear-to-normal load ratio.

Results

In the absence of eLub, all four types of HA exhibited changes in the friction coefficient consistent with a classical elastoviscous Stribeck model (Fig. 1B). All formulations of HA lower friction when combined with 0.16 mg/ml eLub (Fig. 1C). At 1.6 mg/ml, the viscous friction was higher than boundary friction and the increase varied across different formulations of HA. (Fig. 1B, 1C).

Discussion

Without eLub, HA lowered friction compared to PBS consistent with previous work. Friction at 0.16 mg/ml eLub with HA exhibits synergy, as the viscous friction of the combined solution is lower than either eLub or HA alone. Unexpectedly, at high concentrations of eLub, the friction coefficient of the combined solution is higher than eLub alone, with

varying response based on the formulation of HA. Additionally, the effects of different HA formulations can be seen at lower eLub concentrations, with different HAs exhibiting varying reductions in friction coefficient. In sum, this study demonstrated novel interactions between a recombinant lubricin and commercially available HAs in cartilage lubrication, revealing unexpected frictional behaviors that could influence the design and optimization of therapeutic lubricants.

Images (Optional)

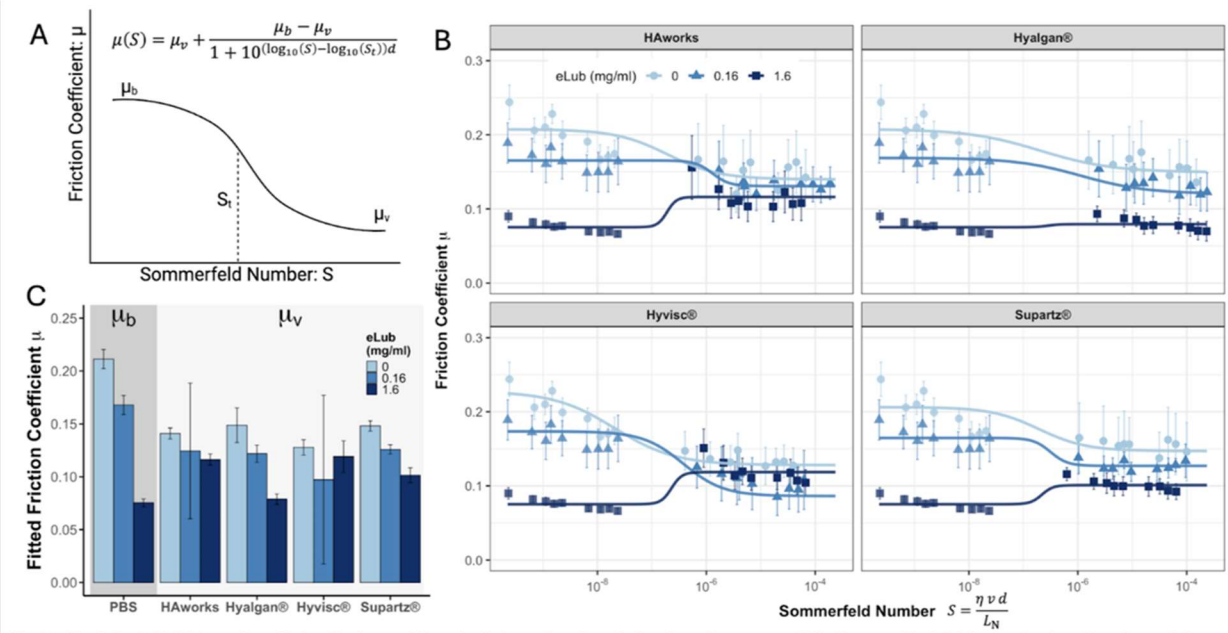


Fig. 1A: The Stribeck Model for cartilage friction. The Sommerfeld number is the product of speed, viscosity, and contact area divided by normal load. Friction is a function of boundary and viscous friction, the Sommerfeld number, and the Sommerfeld transition number. **Fig. 1B:** Friction of four formulations of HA combined with eLub, with Stribeck curves. Darker shades represent increasing eLub concentrations. Values on the left of each box represent boundary friction at different speeds, while the values on the right represent viscous friction values. **Fig. 1C:** Comparison of the boundary (PBS) and viscous (HA) friction values at various eLub concentrations.

Acknowledgements (Optional)

LEAP HI NSF CMMI 2245367

Session Category

Musculoskeletal Biomechanics: Joints and Motion

P2-045

How Do Menstrual Cycles Affect Active and Passive Modulators of Joint Level Stiffness? A Literature Review

Dr Anne Silverman PhD[1,2], Dr. Katherine Knaus PhD[1], Dr. Eline van der Kruk PhD[2]

[1]Colorado School of Mines, Golden, CO, United States. [2]Delft University of Technology, Delft, South Holland, Netherlands

Introduction

Maintaining effective torsional joint stiffness is critical to avoid injury. Active (muscles) and passive (e.g., ligaments) structures modulate torsional stiffness during movement, but their relative contributions remain unclear. High stiffness allows for rapid rates of force development, and low stiffness often results in greater tissue strains; extreme stiffnesses are likely to result in injury. Injury prevalence often differs between men and women, such as in anterior cruciate ligament (ACL) injuries and ankle sprains(e.g. [1,2]). One hypothesis explaining differential injury prevalence is changing connective tissue mechanical properties due to changing hormone levels over the menstrual cycle. Altered neuromuscular control may also change and/or compensate for changing passive mechanical properties. The purpose of this review was to investigate menstrual cycle effects on active and passive modulators of joint-level stiffness.

Methods

The following search terms were applied in Scopus to title/abstract/key words: ("menstrual cycle" OR menstruation) AND (joint) AND (strength OR stiffness OR laxity OR biomechanics) and were subject to multiple exclusion criteria (Table).

Results

The search returned 204 articles. 137 articles were removed due to the exclusion criteria (Table), leaving 55 remaining articles. 30 of these articles evaluated knee joint laxity, commonly used in studies related to ACL injury. 14 articles evaluated muscle level stiffness, and/or excitation. 19 articles presented joint level torque/angle measures during isometric (5), isokinetic (8), and/or dynamic (10) conditions, with 18/19 incorporating active contributions. 35 articles found a significant effect on outcome parameters with the phases of the menstrual cycle, most often indicating that joint laxity and muscle strength (measured by joint torque) increase during the ovulation phase. 12 studies incorporated male participants for comparison.

Discussion

The effects of the menstrual cycle on joint level stiffness and the modulators of this joint stiffness remain unclear. These results highlight the difficulty in evaluating the interacting changes in different tissues that contribute to joint level stiffness. Additionalmeasurements, especially of active muscle contributions to joint level stiffness, are needed to evaluate menstrual cycle effects on joint level biomechanics.

Images (Optional)

Table: Article Exclusion Criteria and Number of Excluded Articles

Exclusion Criteria	# Excluded Articles
1) Not in English	6
2) Did not address musculoskeletal Biomechaincs	26
3) Evaluated Disease/Impairment	34
4) No Direct Measurements	53
5) Evaluated Interventions	21
6) No Humans	2
7) Kinematics Only Without Consideration for Forces or Mechanical Properties	7
Total Excluded	**137**

References (Optional)

[1] Sutton, et al. J Am Acad Orthop Surg. 2013

[2] Ristolainen et al. J Sports Sci Med. 2009

Session Category

Musculoskeletal Biomechanics: Joints and Motion

P2-046

Inertial Tracking of Skeletal Kinematics Matches the Accuracy of Marker-Based Tracking: A Biplane Radiography Comparison

Mr. Vu Phan[1], Mr. Tom Gale[2], Dr. William Anderst[2], Dr. Eni Halilaj[1]

[1]Carnegie Mellon University, Pittsburgh, PA, United States. [2]University of Pittsburgh, Pittsburgh, PA, United States

Introduction

Despite years of advancements and growing interest, inertial tracking is still considered inferior to marker-based analysis. Based on this premise, new inertial tracking methods, from structured filtering to data-driven algorithms that use marker-based motion tracking as the ground truth, have been proposed. Our study assesses the foundational assumption that marker-based motion tracking is more accurate than inertial tracking, with the goal of informing future progress in computational frameworks for inertial data analysis.

Methods

With IRB approval and informed consent, 15 healthy athletes (8 males and 7 females; age: 20.07 ± 1.24 years; height: 173.07 ± 9.99 cm; weight: 71.88 ± 10.86 kg) performed four physical exercises while being recorded with three different systems: inertial motion tracking, marker-based motion tracking, and biplane radiography of the knee joint (as the reference ground truth for skeletal kinematics) (Fig. 1A). Marker-based kinematics were computed directly from marker trajectories using unconstrained kinematics. Inertial-based kinematics were computed using open-source filters. The primary outcome was the root-mean-square difference (RMSD) between a tracking system and the ground-truth skeletal kinematics. We used Wilcoxon signed-rank tests for comparisons.

Results

Both inertial and marker-based systems captured knee flexion/extension with a median RMSD of <4°, ab/adduction >5°, and internal/external rotation >7° (Fig. 1B). There was no significant difference between inertial and marker-based tracking, across degrees of freedom or tasks. In both approaches, internal/external rotation showed the poorest tracking accuracy. Open-source state estimation filters like Madgwick (MAD), Mahony (MAH), and the versatile quaternion-based filter (VQF) performed equally well and better than the extended Kalman (EKF) and data-driven (RIANN) filters (Fig. 1C).

Discussion

While further validation across demographics and broader activities are necessary to confirm the generalizability of our findings, these initial findings mark an exciting turning point in the field of human movement biomechanics. Wearables have been met with cautious optimism as a set of tools that will transform our field by enabling ecologically valid studies, but the evidence required to trust them as much as we have trusted marker-based motion tracking has been elusive. This is a first step toward building that trust.

Images (Optional)

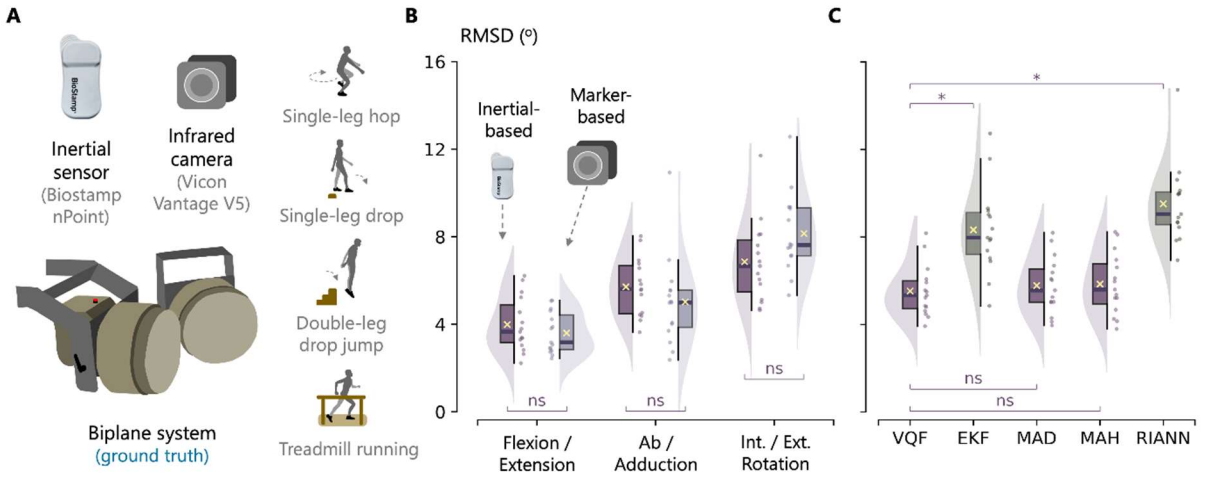


Figure 1: Comparison of Inertial and Marker-based Knee Kinematics using Biplane Radiography. A). Movement data during four functional exercises were collected with three different systems: inertial motion tracking, marker-based motion tracking, and biplane radiography (ground-truth skeletal kinematics). **B)** Inertial and marker-based kinematics showed similar agreement with skeletal kinematics across different degrees of freedom of the knee. **C)** A comparison of different open-source state estimation filters. RMSD = root-mean-square difference, VQF = versatile quaternion-based filter, EKF = extended Kalman filter, MAD = Madgwick filter, MAH = Mahony filter, RIANN = robust IMU-based attitude neural network. (B) and (C) have the same scale and unit.

Acknowledgements (Optional)

We thank the NSF (CBET 2145473).

Session Category

Musculoskeletal Biomechanics: Joints and Motion

P2-047

Lumbar Spine Biomechanical Responses to High-Velocity, Low-Amplitude Osteopathic Manipulative Treatment.

Mr. Eugene Ablordeppey[1], Mr. Jeremy Schap[1], Mr. Jakob Wolf[1], Mr. Christopher Wendt[2], Dr. Laura Lintner DO[3], Dr. Neil Sparks DO[3], Dr. Kristen Nicholson PhD[1,2], Dr. Matthew Davis PhD[1], Dr. Derek Jones PhD[1], Dr. Joel Stitzel PhD[1], Dr. Gunnar Brolinson DO[4], Dr. Philip Brown PhD[1]

[1]Center for Injury Biomechanics, Virginia Tech – Wake Forest University School of Medicine, Winston-Salem, NC, United States. [2]Orthopedic Surgery and Rehabilitation, Wake Forest University School of Medicine, Winston-Salem, NC, United States. [3]Sports Medicine, Wake Forest University School of Medicine, Winston-Salem, NC, United States. [4]Virginia College of Osteopathic Medicine and Virginia Tech University, Blacksburg, VA, United States

Introduction

High-velocity, low-amplitude osteopathic manipulative treatment (HVLA-OMT) is widely used by osteopathic physicians to manage low back pain (LBP), which affects 84% of adults and is a leading cause of disability [1]. Despite its clinical effectiveness, little is known about the internal biomechanics of HVLA-OMT. Previous studies have quantified forces applied by physicians and pre- and post-manipulation changes in facet joint gapping [2,3]. However, the mechanisms underlying HVLA-OMT remain unclear. This study aims to characterize lumbar biomechanical changes in silico using motion capture-driven computational modeling.

Methods

One participant underwent an HVLA-OMT delivered by an osteopathic physician (Fig.1a). Contact forces were recorded with load-cells mounted on the physician's forearms. 3D kinematics were captured at 120Hz using reflective markers on the participant, physician, treatment table, and load-cells. Marker trajectories were filtered using a 4^{th}-order Butterworth filter and used to drive the GHBMC 5th percentile female pedestrian human body model in LS-Dyna (Fig.1b)[4], incorporating table stiffness. Facet joint gap and intervertebral disc height changes were quantified during HVLA thrust.

Results

Manipulation started with a 50N preload, and the thrust peaked at 265N over 2.73s (impulse = 557N·s) (Fig.1c). On average, facet gapping showed a peak increase of 0.31±0.28mm (3.79min-22.96max%) over 2.80s, with moderate correlation to thrust rate

(R^2=0.59) (Fig.1d). Disc height showed a peak decrease of 0.73±0.29mm (8.26min-17.60max%) over 2.81s, showing strong correlation with thrust rate (R^2=0.96) (Fig. 1e).

Discussion

This study quantifies mechanical events of HVLA-OMT, including applied forces and internal lumbar responses such as facet gap and disc height changes. Preliminary findings demonstrate relationships between thrust forces and changes in facet gapping and disc height, with variable responses across lumbar levels. Data collection is ongoing in participants with LBP, and future analyses will examine additional biomechanical responses, including stress and strain in lumbar ligaments, muscles, and vertebral bodies, to better understand potential contributors to clinical outcomes.

Images (Optional)

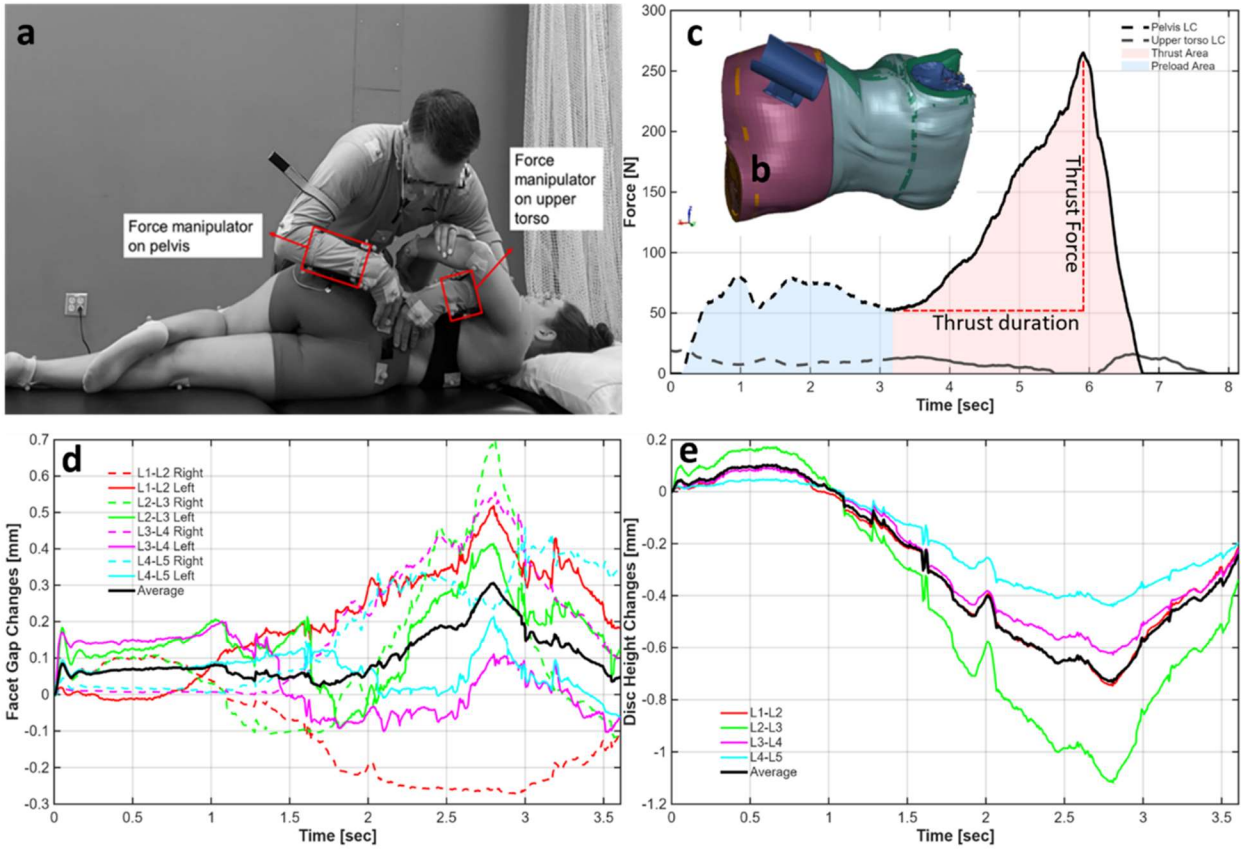


Figure 1.(a) HVLA-OMT session. (b) GHBMC 5th percentile female pedestrian human body model setup in LS-Dyna. (c) Force profile of the HVLA-OMT showing preload, thrust, and resolution phases. (d) Changes in facet gaps for both left and right sides at all lumbar levels. (e) Disc height changes for all lumbar spine

References (Optional)

[1] Licciardone JC., Osteopath Med Prim Care, 2008.
[2] Bell S *et al.*, Journal of Manipulative and Physiological Therapeutics, 2017.
[3] Cramer GD. *et al.*, Journal of Manipulative and Physiological Therapeutics, 2013.
[4] Von-Kleeck *et al.*, Traffic Injury Prevention, 2022.

Acknowledgements (Optional)

Virginia Institute for Critical Technology and Applied Science (ICTAS) and the Edward Via College of Osteopathic Medicine (VCOM); Elemance LLC

Session Category

Musculoskeletal Biomechanics: Joints and Motion

P2-048

Anteroposterior Translations of the Tibiofemoral Joint During the Forward-Lunge Activity

Mr Fengtao Zhang MEng, BEng[1], Professor Todd Stewart PhD, BSc[1], Dr Aiqin Liu PhD, MEng, BEng,[2]

[1]Institute of Medical and Biological Engineering, Leeds, West Yorkshire, United Kingdom. [2]Faculty of Biological Sciences, Leeds, West Yorkshire, United Kingdom

Introduction

Assessing anterior-posterior translations in the knee joint during rehabilitation and sports activities is vital for understanding the biomechanical interactions necessary for healing. Dual fluoroscopy and 3D CT/MRI[1] offer high imaging accuracy but are constrained by cost, limited accessibility, and small fields of view, while optical marker-based motion capture enables large-cohort dynamic analysis but lacks accuracy in anterior-posterior translation. This study aimed to develop a new OpenSim model to investigate whether anterior-posterior knee translation during forward lunge activities can be accurately estimated from 3D motion capture data.

Methods

Gait .c3d data was taken from seventeen healthy subjects (9 males, 8 females, age 20-70 years) completing a forward-lunge, and converted to OpenSim compatible .trc and .mot format. A modified OpenSim model, with six-degree-of-freedom enabled, was firstly scaled to each subject's anthropometrics.

A Euler rotation matrix was applied to obtain the anterior-posterior translation of tibia relative to femur in the global coordinate. The entire analysis pipeline, from model modification and scaling to the final application of the Euler rotation matrix for coordinate transformation, was executed using custom Python scripts interfacing with the OpenSim API.

Results

Compared to the static pose of CT/MRI/Fluro studies the forward-lunge began with the subjects moving, generating a small swing phase causing the knee to be flexed initially at 22.3°[1]. The average anterior-posterior translation (Figure 1) showed the tibia moved ~5mm posteriorly from –14.2mm(± 8.0) at flexion of 21.0° to –19.2mm (± 8.5) at flexion of 51.1°. Average tibial movement progressed anteriorly with ~13.2mm translation to –

6.0mm(± 7.8) between the flexion angle of 22.3° and 105.94°. These magnitudes were generally less than those published from past weight-bearing static pose trials.

Discussion

Marker-based motion capture with a modified OpenSim model and custom Python programming successfully enabled tibiofemoral anterior-posterior translation to be assessed during the forward-lunge. Average tibial anterior-posterior translation of 8.2mm (± 8.0) mm was observed. Future work will expand to a broader range of activities and incorporate rotation to investigate joint contact motion paths and shear towards defining movement characteristics for evaluation of cartilage substitution therapies.

Images (Optional)

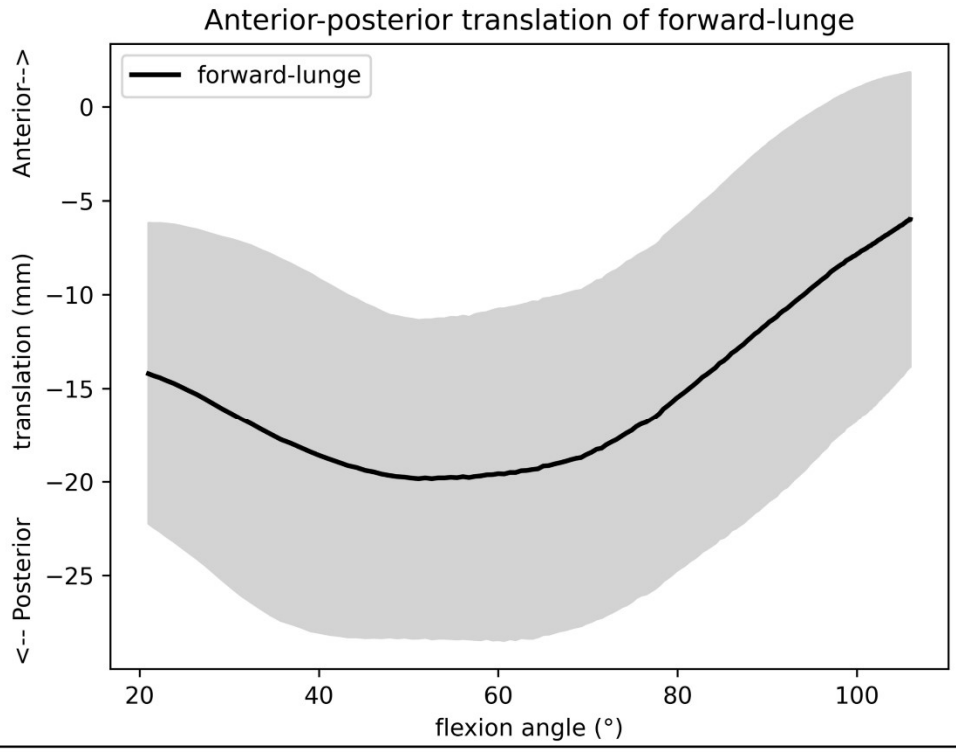


Figure [1], The Anterior-Posterior translation of the tibia relative to the femur during forward-lunge, plotted against the knee flexion angle. The solid black line represents the mean AP translation, and the grey shaded region represents the standard deviation across all subjects.

References (Optional)

[1] W. Qi, et al., J. Biomechanics, 2013.

Session Category

Musculoskeletal Biomechanics: Joints and Motion

P2-049

Developmental Remodelling of the Articular Cartilage Matrisome

Miss Giulia Giuffredi

University College Dublin, Dublin, Dublin, Ireland

Introduction

Articular cartilage (AC) is a connective tissue whose extracellular matrix (ECM) is composed mainly of type II collagen and aggrecan, providing tensile strength and resistance to compression. Due to its avascular and sparsely cellular nature, AC has limited turnover and repair capacity, making it vulnerable to degeneration. Tissue remodelling during growth is essential for long-term joint function, yet the underlying protein-level adaptations remain poorly characterised. Here, label-free mass spectrometry was used to profile the ECM proteome of goat AC, a large-animal model relevant to human joint biology, to define tissue maturation at molecular level and generate a reference for developmental and disease-related research.

Methods

AC was collected at seven postnatal stages from neonatal to adult (n=3 per stage) under UCD ethical approval (AREC-21-22). Full-thickness distal first-phalanx samples (20 mg) were cryopulverised and extracted using a guanidine-HCl protocol to separate soluble and insoluble ECM fractions. Peptides were digested with trypsin and analysed by LC–MS/MS. Data were processed in MaxQuant using the Capra hircus proteome. Label-free quantification values were filtered, log-transformed and analysed in R. Proteins were classified with MatrisomeDB; differential abundance was assessed with limma and pathway enrichment performed with Reactome and Gene Ontology.

Results

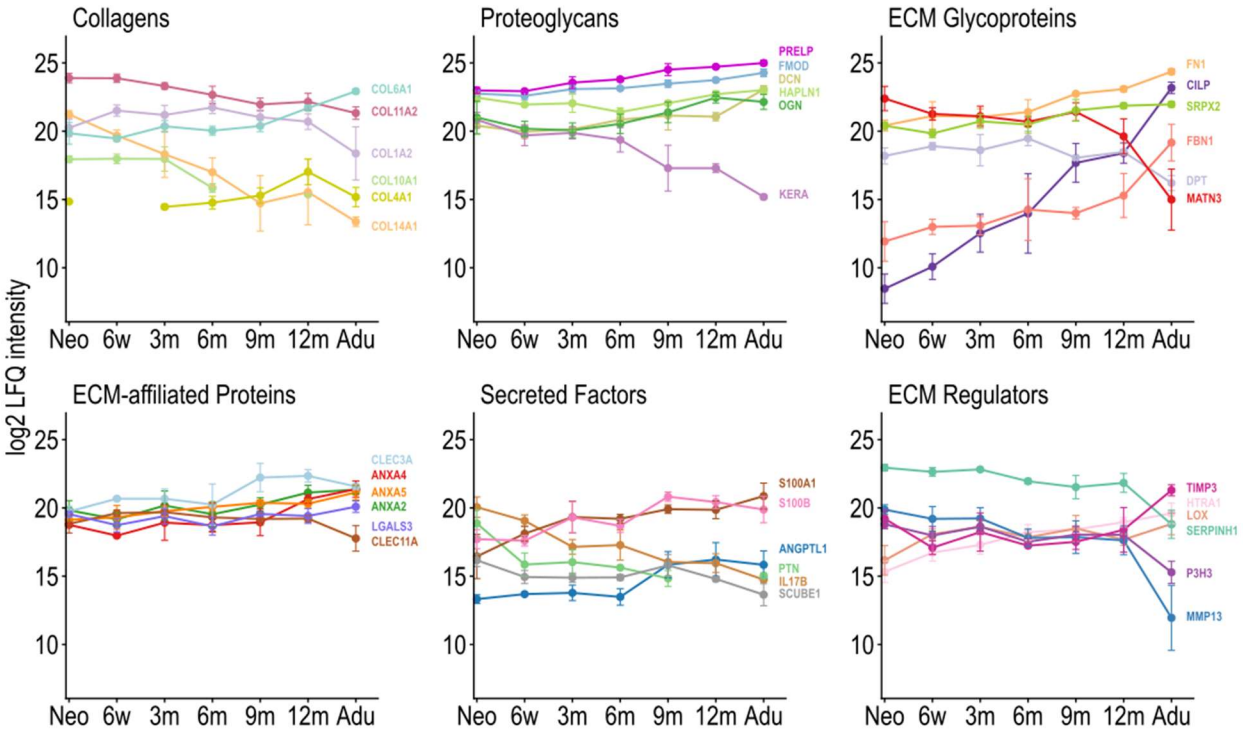
A total of 799 proteins were identified, including 157 ECM components. Early stages were enriched in collagens and proteoglycans such as COL9A1, COL11A1 and ACAN, while regulators and structural proteins including COL6A1, FN1, CILP and HTRA1 increased with age. Enrichment analysis indicated reduced collagen biosynthesis after mid-juvenile stages and increased elastic-fibre formation, crosslinking and glycosaminoglycan metabolism, marking a shift from ECM synthesis to maintenance.

Discussion

AC maturation appears to involve functional reorganisation rather than replacement of ECM components. Early development emphasises fibril assembly and collagen

modification, whereas later stages strengthen existing networks through LOX-mediated crosslinking and expansion of the pericellular matrix. Pathways linked to collagen synthesis and ECM assembly decline with age, while those related to elastic-fibre formation and crosslinking become increasingly enriched. Several proteins that rise with age (HTRA1, CILP, SPP1, FN1) are also associated with osteoarthritis, suggesting shared mechanisms between matrix maturation and degeneration.

Images (Optional)



Acknowledgements (Optional)

Session Category

Musculoskeletal Biomechanics: Joints and Motion

P2-050

Influence of Treadmill Gradient on Multi-Segment Foot Kinematics and Gait Variability in Healthy Adults

Grant Schwiebert[1,2], Matthew Parrett M.Ed.[1], Mallory Rowan M.S.[1], Jessica Lewis PT, DPT[1], Dr. Sean Tabaie MD[1], Dr. Kirsten Kirsten PhD[1]

[1]Nationwide Children's Hospital, Columbus, Ohio, United States. [2]The Ohio State University, Columbus, Ohio, United States

Introduction

Inclined and declined walking alters lower-limb mechanics, neuromuscular control, and stability demands. The influence of slope on regional foot kinematics, particularly hindfoot, midfoot, and medial/lateral forefoot coordination, remains poorly understood. Unlike single-segment models, multi-segment foot models (MSFMs) can detect changes in arch deformation and segment coordination. This study aimed to identify slope-dependent changes in segmental kinematics, spatiotemporal variability, and nonlinear dynamic stability, which is crucial for understanding functional demands in clinical populations and informing treatment strategies.

Methods

Seven healthy adults (6M, 24.1±3.9yrs, 77.0±9.8kg, 175.8±7.6cm) walked barefoot at 2.5 mph across nine grades (0°, ±3°, ±6°, ±9°, ±12°) for 90 seconds while 3D kinematics were collected using a novel MSFM. Intersegmental Euler angles of the tibia, hindfoot, midfoot and medial/lateral forefoot and hallux planar angles were computed across ≥69 gait cycles. Variability metrics (standard deviation (SD), coefficient of variation (CV), range of motion (ROM), ROM-CV), spatiotemporal metrics (stride time, stance/swing duration, cadence, step length/width), and short- and long-term Lyapunov exponents (SLE/LLE) were calculated per grade. Pearson correlation analysis evaluated the relationship between slope angle and segmental kinematics, variability, and stability.

Results

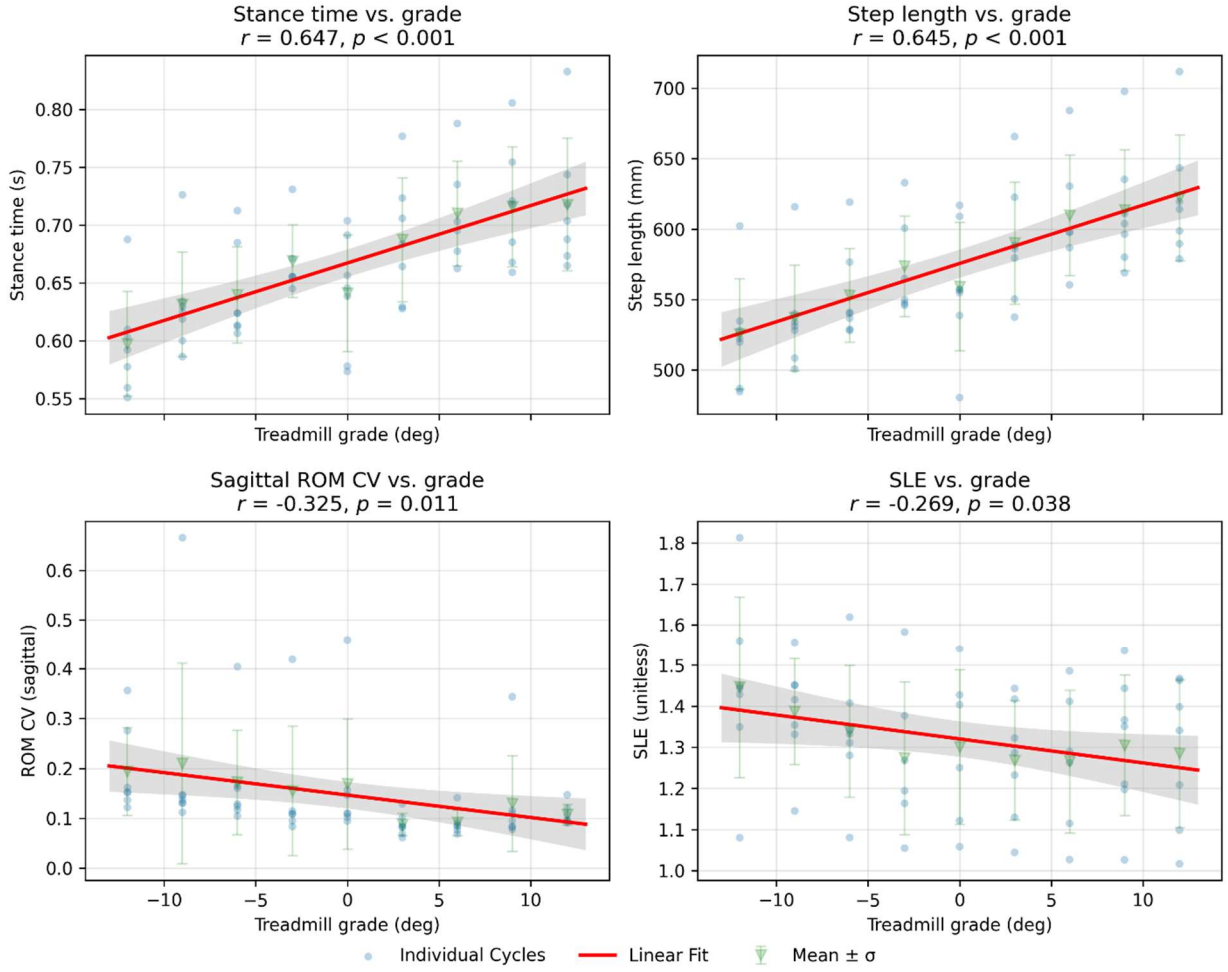
Spatiotemporal parameters displayed strong grade associations: stance-time (r=0.64), step-length (r=0.64), cadence (r=0.62), and stride-time (r=0.59). Joint-angle variability showed more modest grade effects, with sagittal ROM-CV demonstrating the strongest association (r=–0.325, p=0.011). Frontal-plane hindfoot–tibia and forefoot–tibia variability showed minimal sensitivity to grade, suggesting preserved mediolateral control. Dynamic

stability was invariant across grades: SLE showed only a small correlation (r=–0.269, p=0.038), and LLE showed no significant effect (r=–0.024, p=0.855).

Discussion

Despite spatiotemporal adaptations with changing slope, regional foot-segment kinematics and nonlinear stability metrics were largely preserved, indicating that healthy adults maintain robust intra-foot coordination under altered mechanical and neuromuscular demands. This robustness may reflect effective neuromechanical compensation mechanisms at the ankle and foot. Future work will expand sample size, incorporate pathological case studies, and integrate subject-specific foot morphology to refine interpretations of slope-dependent segmental mechanics, advancing applications in clinical gait analysis, fall-risk evaluation, and slope-based treatment strategies.

Images (Optional)



Session Category

Musculoskeletal Biomechanics: Joints and Motion

P2-051

Motor Adaptation and Perceived Exertion During Repetitive Lifting With Passive and Active Occupational Back-Support Exoskeletons

Dr. Hanjun Park[1], Dr. Maury Nussbaum[2]

[1]Texas Tech University, Lubbock, Texas, United States. [2]Virginia Tech, Blacksburg, Virginia, United States

Introduction

Back-support exoskeletons (BSEs) are increasingly used to reduce occupational physical demands during repetitive lifting, yet little is known about how users adapt their movement strategies and how perceived exertion changes with repeated use. Prior studies vary widely in task type and exposure duration, and findings have been mixed, resulting in a limited fundamental understanding of how users adapt and whether adapted behaviors are retained after a prolonged break.

Methods

Twenty-seven healthy adults were randomly assigned to a passive BSE, active BSE, or no-BSE control group (6 males, 3 females per group). Each participant completed one familiarization session and four experimental sessions. Sessions 1–3 included a pre-adaptation phase (~5 min), an adaptation phase (~15 min), and a post-adaptation phase (~5 min). Session 4 included only the adaptation phase (~15 min) to assess retention. Participants performed trials of repetitive symmetric lifting of a load equal to 15% of body mass at a fixed pace of 6 lifts/min. Lifting height, pace, and load were standardized to isolate adaptation effects rather than task-related variability. Primary outcomes were trunk, hip, and knee ROM; lower-back and leg RPE (Borg CR-10). Linear mixed-effects models evaluated Intervention, Session, and Trial effects ($\alpha = 0.05$).

Results

Intervention × Session interactions were significant for all joint ROMs. Both BSE groups exhibited greater trunk ROM than control (≈11–20°, ~23–40%). Trunk ROM decreased over time in the passive group but remained elevated in the active group (~20° greater in Sessions 2–3). Hip ROM decreased by ~15° (passive) and ~9° (active) across sessions versus <1° in control. Knee ROM in BSE users became 20–32° lower (~50%) than control by Sessions 3–4. Lower-back and leg RPEs declined by ~2 CR-10 points (≈70–75%) by Session 4, while the control group plateaued.

Discussion

Multi-session BSE use led to clear motor adaptation, characterized by increased trunk and reduced knee ROM and substantial reductions in perceived exertion. Passive BSE users showed progressive stabilization of trunk ROM, whereas active BSE users maintained larger trunk ROMs. These findings highlight the importance of structured, multi-session familiarization when integrating BSEs into practice.

Session Category

Musculoskeletal Biomechanics: Joints and Motion

P2-052

How Do Sulcus Angle and TT-TG Distance Drive Patellofemoral Contact Mechanics?A Finite Element Analysis Investigation

Ms. Carolina S. Haboba Nebel MS[1], Mr. Thomas Turinske BS[2], Mr. Edouard J. Augustin BS[1], Mr. Kofi K. Acheampong BS[1], Mr. Jay Amin[1], Mr. Cade Smelley BS[1], Mr. Divesh Sachdev[1], Dr. Adam B. Yanke MD[1], Dr. Hannah J. Lundberg PhD[1]

[1]Rush University Medical Center, Chicago, IL, United States. [2]Rosalind Franklin University of Medicine and Science, North Chicago, IL, United States

Introduction

We developed a series of patient-specific models using a semi-automated finite element analysis (FEA) computational framework to investigate how individual phenotypes influence patellofemoral contact mechanics across knee flexion. We hypothesized that subjects with a sulcus angle greater than 145 degrees and a TT-TG greater than 15 mm will have more concentrated contact pressure in the lateral condyle with higher peaks and smaller contact area, as well as abnormal patellar range of motion.

Methods

One control patient and five patellofemoral instability patients with knee 3D MRI scans from 2019-2023 were included. The patients had a variety of Dejour classifications, dysplasia, J-sign, TT-TG, and sulcus angles. Femur, tibia, and patella bones and femoral and patellar articular cartilage were segmented (Mimics, Materialize, NV). Bones were modeled as rigid bodies, cartilage as linear elastic (E = 14MPa, v = 0.45) [1], and patellar and quadricep tendons with hyperelastic material properties. Axial connectors actuate the quadricep tendon and represent the MPFL to stabilize the patella. Tibiofemoral contact was simulated with a 50N load. FEA models were built in Abaqus Explicit. Femoral contact pressure and area were compared to patient anatomical characteristics.

Results

The control patient (TT-TG: 7.6mm, sulcus angle: 139.3°, no instability) had a contact area range of 1.4-3.35 cm^2. Contact pressure peak (3.1 MPa) at 55°. Average contact pressure over the entire ROM was 2.8 MPa. Patellofemoral instability patients (TT-TG: 14.9-22.8 mm) had less contact area minimum average 0.8 (0.68-1.4 cm^2) – maximum average 1.9 (1.4-2.7 cm^2), a lateral patella at 0° of flexion, abnormal patellar tracking, and higher and lateral

peak contact pressures (4.3-5.6 MPa). Greater sulcus angle (>145°) was associated with early peak contact pressure (8-24° of flexion), compared to the peaks at 33-39°of flexion for models with sulcus angles in the standard range (134-139°).

Discussion

The previously validated computational framework shows meaningful results, visualizing how individual phenotypes influence the mechanics of the joint. TT-TG greater than 15mm led to higher contact pressure during the flexion range, and sulcus angles greater than 145° led to lateralized contact pressure, with early higher peaks and smaller contact areas.

Images (Optional)

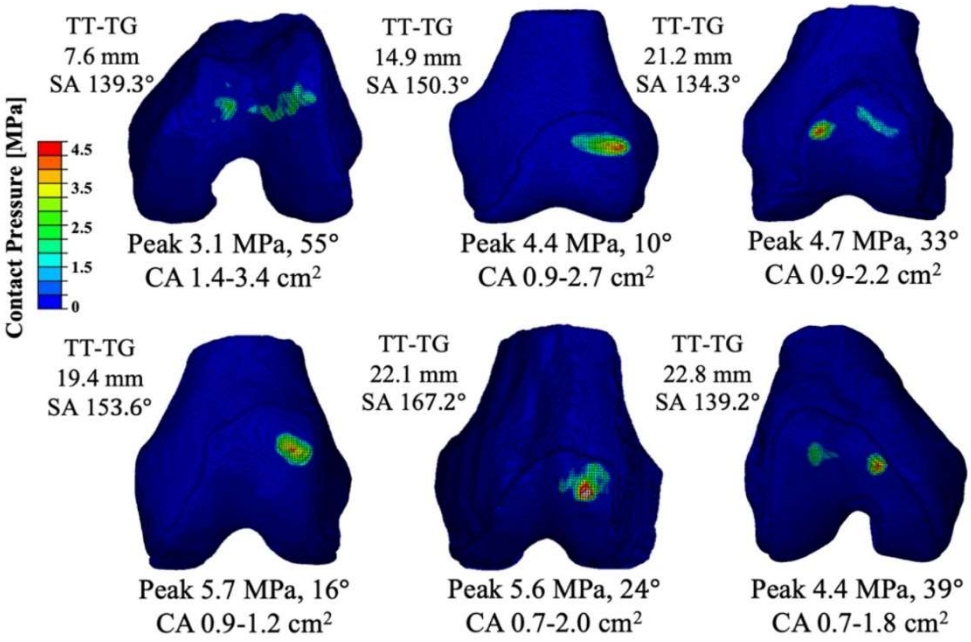


Figure 1 – Finite Element Analysis results (peak of contact pressure, flexion angle at which the peak occurs, contact area (CA)) and patient anatomical characteristics (TT-TG, Sulcus Angle (SA)). Results are shown for the flexion angle with greatest contact pressure for each model

References (Optional)

[1] Watson ND et al, Iowa Orthop J. 2015

Session Category

Musculoskeletal Biomechanics: Joints and Motion

P2-053

Validation of Theia 3D Markerless Motion Capture for Quantifying Upper Extremity Kinematics

Miss Hayley Janes BHSc, Mr. Michael Watterworth PhD Candidate, Miss Gillian Slade MHSc Student, Dr. Nicholas La Delfa PhD

Ontario Tech University, Oshawa, Ontario, Canada

Introduction

Marker-based motion capture (MoCap) systems are widely regarded as the gold-standard for quantifying human kinematics. Markerless motion capture (MoCap) offers a promising alternative that addresses several limitations of common marker-based kinematics approaches. Despite its potential, research validating markerless MoCap for upper extremity kinematics remains limited. This study aims to evaluate the validity of novel markerless MoCap technology for estimating shoulder, elbow and wrist joint angles by comparing markerless (Theia3D) outputs with those from a marker-based system.

Methods

Kinematic data from 13 (5M,7F) participants were captured simultaneously with 10 Vicon and 8 Sony HD cameras. Each participant completed three identical sessions, which consisted of a series of range of motion (ROM) trials and several dynamic functional movements. Vicon Nexus and Theia3D were used to process and calculate upper extremity joint angles for the shoulder (3 degrees of freedom), elbow (2) and wrist (2) in Visual3D. Two rotation sequences were used: XZY for shoulder flexion movements and ZXY for all other trials. RMSD and concordance correlation coefficients (CCC) were calculated between the Vicon and Theia time-series data, and ICC(3,1) was used to assess the consistency of ROM values across the three sessions.

Results

Results from nine right-arm ROM conditions are reported. Figure 1 shows the mean joint angles over time with RMSD and CCC values presented within each panel. The highest agreement between systems occurred in shoulder internal/external rotation (0.985), while the lowest correlation occurred for elbow pronation/supination (0.073). Theia showed higher ICC values for elbow flexion/extension (0.771) and shoulder plane of elevation (0.822) compared to Vicon (0.488 and 0.639, respectively), whereas Vicon produced higher ICCs for all remaining movements.

Discussion

These results show that Theia3D demonstrates strong agreement with traditional marker-based MoCap for several shoulder movements, although substantial differences remain for shoulder flexion movements (18.5°, 17.0°, 21.8°). Elbow and wrist motions also show lower agreement, indicating further refinement of markerless tracking for these joints is warranted. Advancing and validating Theia3D for shoulder, elbow, and wrist motions will be an important step in enabling markerless motion capture to play a larger role in upper extremity focused research.

Images (Optional)

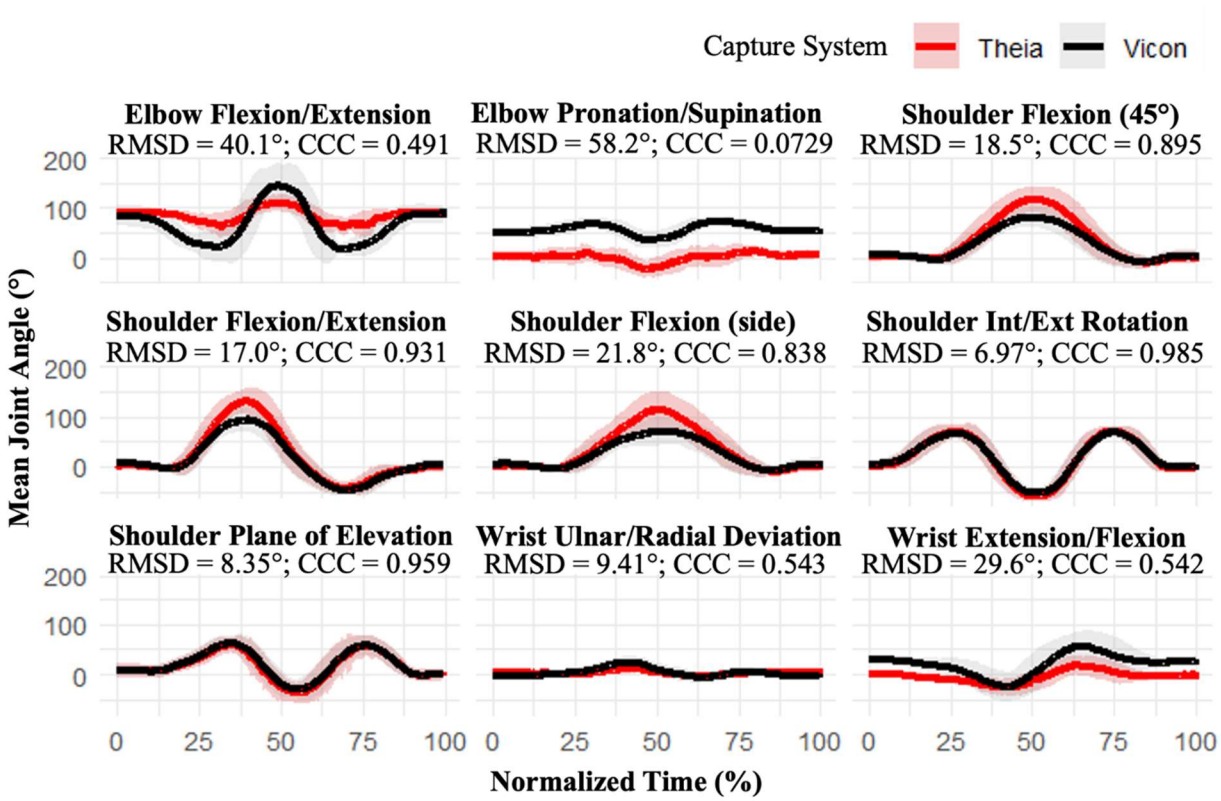


Figure 1: Mean Joint Angles of Nine Range of Motion Trials with RMSD and CCC values

Session Category

Musculoskeletal Biomechanics: Joints and Motion

P2-054

Diurnal variation in neuromuscular function in males and females

Ms. Isla R. G. MacPherson[1,2], Dr. Alexander M. Zero[1], Mr. Charlie Kanuka[2], Dr. Chris McNeil[2], Dr. Charles L. Rice[3], Dr. Brian H. Dalton[2], Dr. Geoffrey A. Power[1]

[1]University of Guelph, Guelph, Ontario, Canada. [2]University of British Columbia, Kelowna, British Columbia, Canada. [3]University of Western Ontario, London, Ontario, Canada

Introduction

Peripheral circadian clocks located within skeletal muscle may influence contractile function, as strength (i.e., maximum voluntary isometric contraction torque; MVC) is greater, and rate of torque development (RTD) is faster throughout the day [1, 3, 4], but with little data available for females [4]. It is currently unknown whether peak isotonic power is influenced by circadian rhythm and if RTD may contribute to the potential fluctuations in power throughout the day in females and males.

Methods

Healthy, recreationally active adults (n=16, 7 females, aged 25±3y) with regular sleep schedules participated. Testing occurred in the morning 1-h after waking (i.e., AM) and 12-h from this timepoint (i.e., PM). Voluntary and electrically evoked (i.e., percutaneous muscle stimulation) contractile function of the knee extensors was assessed on a dynamometer. Isometric measures at a knee angle of 80º included MVC torque, peak RTD, and evoked twitches. Peak power was determined from a range of isotonic loads (unloaded-60% MVC) throughout an 80-140º knee joint range of motion.

Results

Body temperature increased in both females and males (~0.5-1%; $P<0.05$) throughout the day. Although males were stronger (peak MVC and twitch torque), faster (RTD), and more powerful (isotonic power) as compared with females, (all $P<0.05$), twitch torque, voluntary peak RTD, and peak power were unaffected by time-of-day (all $P>0.05$). For MVC torque there was a trend towards an interaction of time × sex ($P=0.055$), such that males had a greater diurnal effect with ~10% higher MVC torque in the PM than AM. Voluntary activation decreased (~2%) for both sexes from AM to PM ($P<0.05$).

Discussion

To date, results indicate there was no diurnal-related difference in power production or RTD, which was similar between the sexes. Nonetheless, both sexes exhibited different time-of-day effects for MVC torque. From AM to PM, males showed a larger relative

increase in MVC torque, indicating greater diurnal variation in strength compared with females. However, these changes do not appear to be explained by voluntary activation or twitch contractile properties.

References (Optional)

[1] Castainghts *et al.* , Chronobiol Int, 2004

[2] Cossich & Maffiuletti , J Electromyogr Kinesiol, 2020

[3] Giacomoni *et al.* , Ergonomics, 2005

[4] Roberston *et al.* , Chronobiol Int, 2024

Session Category

Musculoskeletal Biomechanics: Joints and Motion

P2-055

Longitudinal Changes in Anterior Tibial Laxity Following ACL Injury in MRL/MpJ and C57BL/6J Mice

Mr. Jackson Gabbard[1], Ms. Olivia Dyer[1], Dr. Blaine Christiansen Ph.D.[2], Dr. Stephanie Cone Ph.D.[1]

[1]University of Delaware, Newark, DE, United States. [2]University of California, Davis, Sacramento, CA, United States

Introduction

Post-traumatic osteoarthritis (PTOA) is a debilitating disease that occurs after traumatic joint injury (i.e. anterior cruciate ligament (ACL) rupture). Using miniature 6 degree-of-freedom (DOF) robotic testing, we investigated the effects of ACL injury on *in situ* knee joint function in wild-type C57BL/6J mice and "super-healer" MRL/MpJ mice, which have shown resistance to articular cartilage degradation following injury-induced damage [1]. We hypothesized that MRL mice will exhibit no significant difference in joint mechanics between injured and uninjured limbs, while wild-type mice will have increased joint laxity in injured knees.

Methods

Female C57BL/6J (n=18) and MRL (n=16) mice (34 weeks old) underwent unilateral non-invasive right-limb ACL rupture via tibial compression. Animals were euthanized at 0-, 2-, or 4-weeks post-injury, and bilateral hind limbs were harvested for 6-DOF robotic testing (Mecademic, simVITRO). Joints were fixed at 40° flexion and loaded with 1N anterior tibial drawer force. Force-translation curves were created and anterior tibial translation, in situ joint slack and joint stiffness were calculated as previously described [2]. Statistics included ANOVA analysis.

Results

No significant difference was found in anterior tibial translation, joint slack, or joint stiffness due to injury state, mouse strain, or timepoint (Figure 1), likely related to high degrees of between-animal variability (~30-40% of means). Average anterior tibial translation for the C57BL/6J mice was 0.59mm±0.25mm (uninjured) and 0.62mm±0.19mm (injured), while MRL mice was 0.39mm±0.17mm (uninjured) and 0.58mm±0.22mm (injured). Average joint slack for C57BL/6J mice was 0.61mm±0.34mm (uninjured) and 0.61mm±0.26mm (injured). Average joint stiffness for MRL mice was greater, though these

findings did not reach statistical significance - in uninjured joints 2.03N/mm±0.75N/mm compared to injured joints 1.53N/mm±0.77N/mm.

Discussion

Contrary to our hypothesis, no significant differences were found between MRL and C57BL/6J joint function after ACL rupture. Future studies will assess specific mechanical and biological differences between mouse strains to better understand alternative mechanisms explaining the osteoarthritis resistance in MRL mice.

Images (Optional)

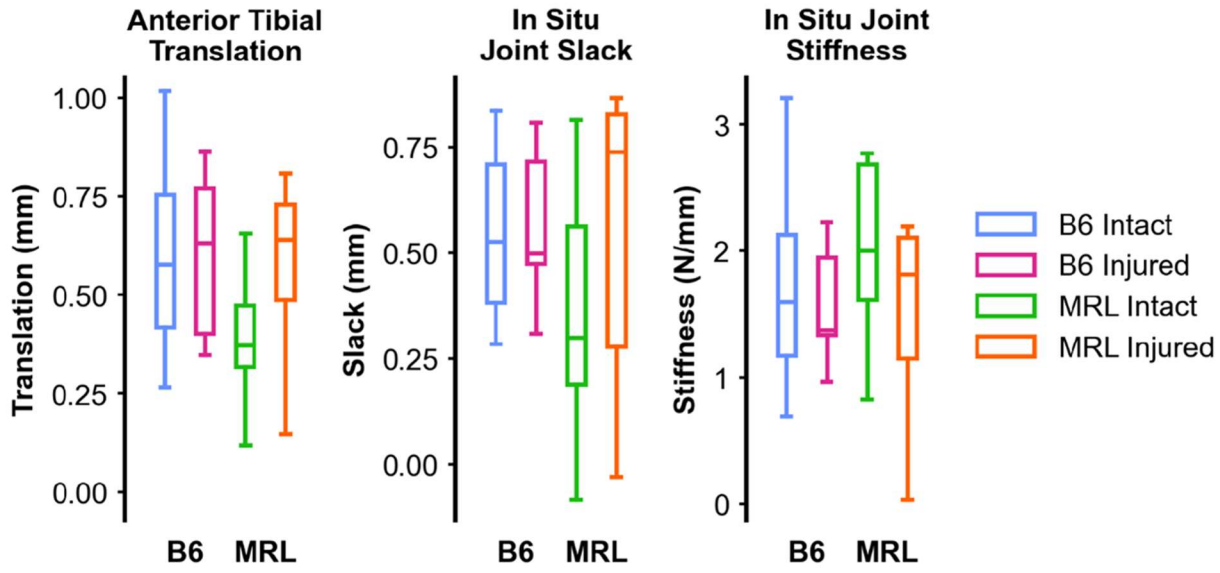


Figure 1: Injured/uninjured C57BL/6J (B6) vs. injured/uninjured MRL/MpJ (MRL) mice comparisons of anterior tibial translation (mm), *in situ* joint slack (mm), and *in situ* joint stiffness (N/mm).

References (Optional)

[1] Fitzgerald et al. (2008) *Osteoarthr. Cartil.* [2] Dyer et al. (2025) *Sci. Rep.*

Acknowledgements (Optional)

Funding from NIH R01AR075013 and P20GM139760.

Session Category

Musculoskeletal Biomechanics: Joints and Motion

P2-056

Flyband® ExoBoots™ Provide Superior Support, Comfort, and Performance During Dynamic Movements and Assessments Compared to Conventional Boots and Bracing

Ms. Jania Williams MS[1], Ms. Gabrielle Moser BS[1], Dr. Farah Fallahtafi[1], Dr. Corbin Rasumussen[2], Mr. Keith Eriks[3], Dr. Nataliya Rokhmanova[3], Mr. Mark Roser[3], Dr. Sarah A. Myers[1,4]

[1]University of Nebraska at Omaha, Omaha, Nebraska, United States. [2]Creighton University, Omaha, Nebraska, United States. [3]Results Groups LLc, Glastonbury, Connecticut, United States. [4]Omaha Veterans Affairs Medical Center, Omaha, Nebraska, United States

Introduction

Lateral ankle sprains are the most common musculoskeletal overuse injury in soldiers, likely due to training and deployments taking place on uneven terrain. Bracing is the current standard of care, but it is inadequate in rehabilitating soldiers from ankle injury. This study evaluated the impact of Flyband® ExoBoots™(FB) on ankle joint performance during dynamic movements. Conventional boots and bracing were compared to FB with carbon fiber ankle cartridges. We hypothesized that FB would allow easier movement in the anterior–posterior direction and increase comfort, while providing comparable support in the mediolateral (ML) direction.

Methods

Healthy adults (19-45 yrs) completed six experimental conditions that included a boot, conventional or FB, and standard low, mid, or high bracing for conventional boots and carbon fiber support for FB on their right ankle (Figure 1A). To evaluate dynamic movement and agility, participants performed a 55-step stair run and a three-cone shuttle drill (Figure 1B), in which completion times were recorded for each task. Peak ankle inversion and dorsiflexion angles were calculated from marker trajectories during two-foot landings on a 16° cross-sloping surface from a 24-inch. plyo box. User comfort was assessed using a Technology Acceptance Model (TAM) visual analog scale, ranging from ‘strongly disagree’ (0 points) to ‘strongly agree’ (15 points). A 2 x 3 repeated-measures ANOVA ($\alpha = 0.05$) tested the effects of boot type and bracing level on each outcome measure.

Results

Stair run and shuttle drill completion times were lower in FB compared to conventional boots ($p=0.010$, $p=0.013$; Figure1C). Peak inversion angle was greater in the low bracing

conditions compared to mid and high conditions for both boots (p=.038; Figure 1D). FB comfort ratings were higher than conventional boots, indicating increased comfort during dynamic tasks (p=0.024).

Discussion

The FB showed superior performance to the conventional boot, with faster completion times and greater sagittal mobility, indicating improved ML support and comfort. The interchangeable carbon fiber cartridges also provide comparable ankle ROM in the sagittal plane while restricting greater ROM in the frontal plane compared to conventional bracing. Future research will evaluate the effect of boots and bracing on service members with previous ankle sprains.

Images (Optional)

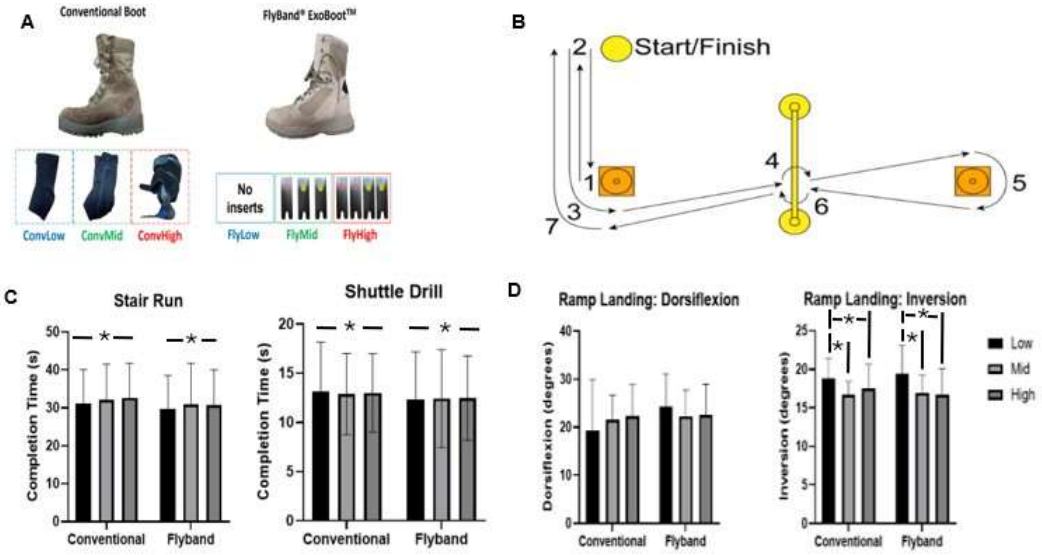


Figure 1. (A) Dynamic assessments were completed in six unique boot-brace combinations. (B) An indoor L-shaped obstacle course was completed by participants for agility assessment. (C) A significant main effect of boot was observed for stair runs and shuttle drill. (D) A significant main effect for bracing was observed between low-mid and low-high bracing conditions for inversion landing.

Session Category

Musculoskeletal Biomechanics: Joints and Motion

P2-057

Using a Combined I*n-Vivo* and I*n-Vitro* Approach to Assess Changes in Spine Mechanical Properties With Prolonged Sitting

Ms. Jessa M. Davidson MSc, Dr. Jack P. Callaghan PhD

University of Waterloo, Waterloo, Ontario, Canada

Introduction

Low back pain responses in sitting may be linked to viscoelastic adaptations in spine tissues, which are mediated by the adopted lumbar spine postures as well as frequency and amplitude of micromovements [1]. Using both *in-vivo* and *in-vitro* testing, the current analysis assessed changes in spine mechanical properties in response to prolonged sitting.

Methods

Twenty participants completed one week of seated office work. During workdays, sitting time was quantified by a thigh-worn activity monitor and seated lumbar spine flexion-extension was quantified from the relative inclination of tri-axial accelerometers on the low back. Further, lumbar passive flexion stiffness was measured at morning and evening laboratory sessions.

A mechanical testing system was utilized to apply exposures, derived from *in-vivo* data, to forty-two porcine cervical (C34, C56) functional spinal units (FSUs). Following a 15-min 300N preload and definition of the neutral zone (NZ), FSUs were loaded at 10% of their predicted ultimate compressive tolerance for six hours. FSUs were loaded in static neutral, static flexion (300% NZ), or in flexion with low (25% NZ; 60s) and high (50% NZ; 30s) amplitude and frequency shifting micromovements. NZ testing was then performed again.

Results

Daily prolonged sitting resulted in increased lumbar passive stiffness. Small decreases in angular breakpoints occurred on Monday evening and Tuesday morning (4.6% and 6.8 %PassiveFlex), then angles progressively increased to within 1.7% to 2.3 %PassiveFlex of baseline values by the following Monday morning ($p \geq 0.06$). The daily changes were correlated with sitting time ($R^2 = 0.21$ [95% CI: 0.00, 0.62]).

Main effects of *time* for the NZ flexion limit, length, and slope indicated that prolonged static loading increased joint stiffness ($p \leq 0.01$). Moreover, mean changes in the flexion

limit were smallest for static neutral (0.5°) and largest for static flexion (-2.7°; $p = 0.03$), with micromovements demonstrating a moderately protective effect (-1.6°).

Discussion

Both *in-vivo* and *in-vitro* analyses indicated that prolonged sitting resulted in increases in spine stiffness. These changes were likely attributable to time-dependent elastic adaptations in spine tissues (e.g., fluid re-distribution). Seated micromovement may attenuate these viscoelastic adaptations, potentially mitigating the risk of low back pain.

References (Optional)

[1] Dunk and Callaghan, Work, 2010

Session Category

Musculoskeletal Biomechanics: Joints and Motion

P2-058

Compensatory Movement Patterns With Symptom Presentation in Carpometacarpal Osteoarthritis

Ms. Jessica Molina, Ms. Alexis Benoit MS, Dr. Thomas Wright MD, Dr. Jennifer Nichols PhD

University of Florida, Gainesville, Florida, United States

Introduction

Carpometacarpal osteoarthritis (CMC OA) is debilitating due to pain, functional limitations, and decreased quality of life. Current treatments fail to address all aspects of CMC OA, often offering pain relief at the expense of function. To understand the multifaceted impact of CMC OA, this work aims to evaluate biomechanics and pain in tandem. Specifically, we assess to what extent radiographic and symptom severity affects motion.

Methods

Based on x-rays and the Australian/Canadian Osteoarthritis Hand Index pain subscale, 11 participants (age:66±9 years, 64% female) were categorized based on radiographic and symptom severity as Healthy (n=3), Early-Stage Pain (n=3), or Late-Stage Pain (n=5). Four range of motion (ROM) tasks [radial and palmar abduction/adduction; opposition to the base and tip of pinky] were evaluated using marker-based motion capture. ROM at the thumb [CMC flexion/abduction, metacarpophalangeal (MP) flexion, interphalangeal (IP) flexion] and pinky [5^{th} MP flexion, 5^{th} proximal interphalangeal (PIP) flexion, 5^{th} distal interphalangeal (DIP) flexion] were compared between groups using effect sizes (Cohen's d).

Results

Early-Stage Pain individuals showed consistent overcompensation along the thumb's kinematic chain for all tasks (Fig.1). For example, when comparing Early-Stage Pain and Healthy participants, large effect sizes ($d>0.8$) were consistently observed in thumb MP flexion (palmar abduction/adduction $d=0.85$, radial abduction/adduction $d=2.04$, opposition tip of pinky $d=0.90$), with the Early-Stage Pain group having greater ROM. In contrast, Late-Stage Pain individuals tended to exhibit phalangeal joint compensatory movements for all tasks (Fig.1). Notably, compared to the Early-Stage Pain group, the Late-Stage Pain group showed a dramatic increase in 5^{th} MP flexion (opposition base of pinky $d=2.59$).

Discussion

ROM was altered at different joints across cohorts, indicating that comprehensive analysis of ROM during functional tasks can delineate CMC OA disease severity. Notably, individuals with radiographic evidence of late-stage disease and pain compensated with increased flexion of their fifth digit during opposition tasks, while those with early-stage disease and pain relied upon increased motion within distal joints of the thumb. These results highlight the importance of considering how the combined effects of radiographic and symptom severity can be leveraged to further differentiate patient groupings for personalized care.

Images (Optional)

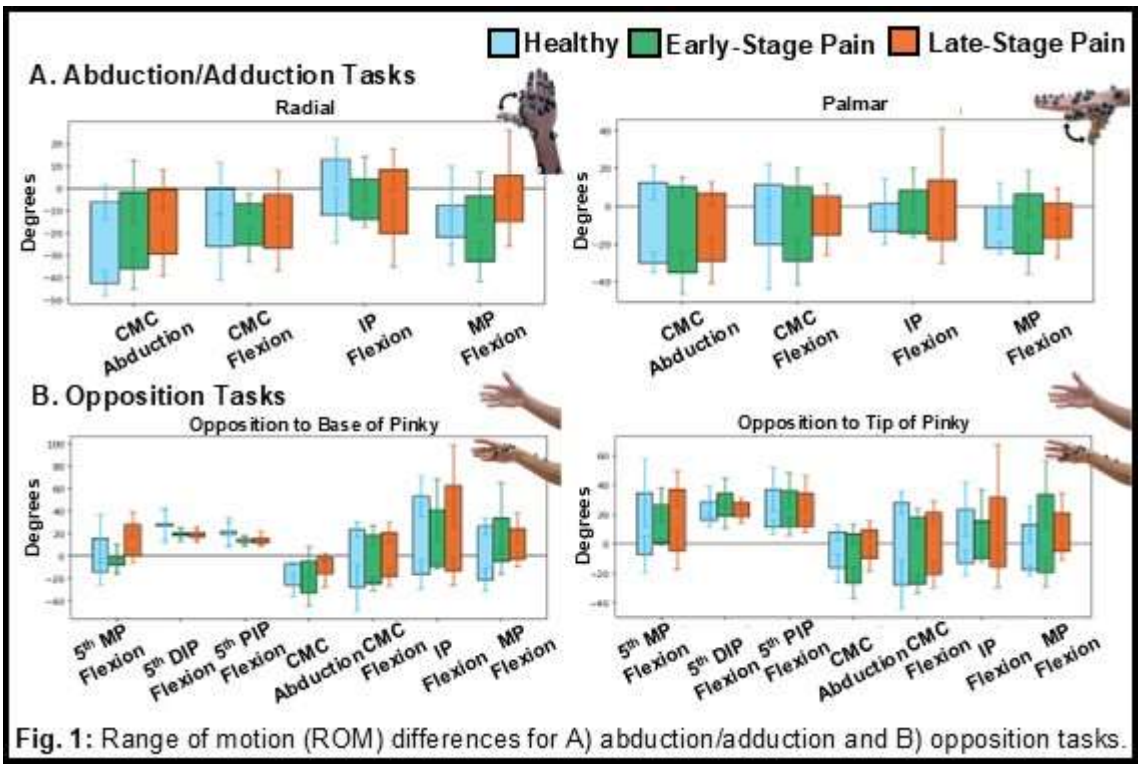


Fig. 1: Range of motion (ROM) differences for A) abduction/adduction and B) opposition tasks.

Acknowledgements (Optional)

Funding from NIH R01AR078817 and F30AR085997.

Session Category

Musculoskeletal Biomechanics: Joints and Motion

P2-059

Measurement of Real-World Changes in Pain and Gait in Adults with Knee Osteoarthritis

Mr. Julien Mihy[1], Ms. Mayumi Wagatsuma[1], Mr. Spencer Miller[2], Dr. Elisa Arch[1], Dr. Katie Butera[1], Dr. Stephen Cain[2], Dr. Jocelyn Hafer[1]

[1]University of Delaware, Newark, DE, United States. [2]West Virginia University, Morgantown, WV, United States

Introduction

Adults with knee osteoarthritis (KOA) often experience pain with movement, which may influence daily activities like walking. It is vital to understand the effect of pain on walking as gait mechanics are associated with KOA initiation and progression. To date associations between pain and gait have only been assessed in controlled, laboratory settings. Thus, there is a critical gap in evidence regarding whether established relationships between gait and KOA disease progression retain their ecological validity in real-world settings. Accordingly, the purpose of this study was to evaluate the relationship between pain and gait during real-world walking in adults with symptomatic KOA.

Methods

Sixteen participants wore 4 inertial measurement units (IMUs) on their more symptomatic thigh and shank and on each foot during three days in the real-world. Peak pain during walking (0-10) was collected via text messages 5 times per day, every 2 hours. When receiving a text, participants were instructed to complete a ~3 minute walk and report their pain during that walk. We identified bouts of walking, foot trajectories, and gait events from raw IMU data. Bouts of walking closest to the time stamped text survey responses were analyzed. Segment angular velocities were integrated about functional mediolateral axes to estimate sagittal joint excursions. Gait mechanics were averaged across all strides within bouts of interest. A random coefficients model was run to determine the relationship between pain and gait parameters (i.e., gait speed, stride length, and knee and ankle ranges of motion (ROM)).

Results

Higher pain was associated with lower knee ROM ($p=0.03$, Figure), where a 1-unit increase in pain was associated with 2.7° less knee ROM on average. Pain was not associated with any other gait parameters (all $p>0.66$).

Discussion

This was the first study to assess concomitant pain and gait mechanics in a real-world environment. Our findings suggest that a 2-unit increase in pain – a common fluctuation in real-world pain in our data – could induce meaningful (i.e., ≥5°) changes in knee ROM. Therefore, individuals may be experiencing meaningful changes in gait mechanics regularly which could influence the rate of disease progression.

Images (Optional)

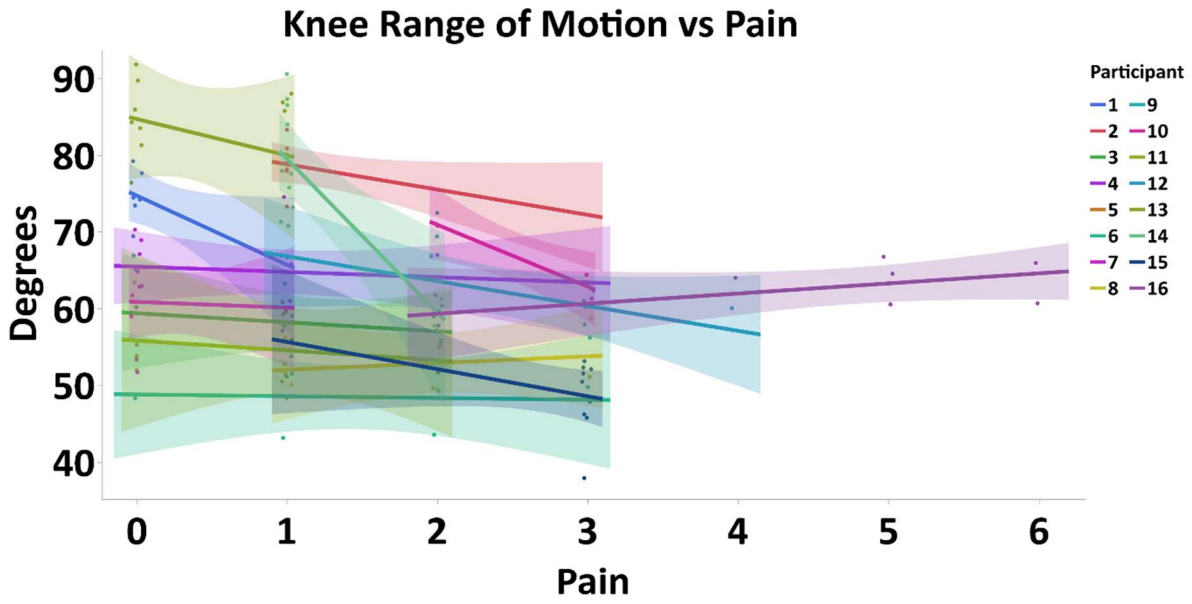


Figure Relationship between pain and knee range of motion (ROM) for all participants during three days of daily life. Lines represent the relation between knee ROM and pain for individual participants with each dot representing the pain and concurrent knee ROM at a text response timepoint. Shaded regions show the confidence intervals for each line of best fit.

Session Category

Musculoskeletal Biomechanics: Joints and Motion

P2-060

Quantification of Frailty via the Lens of Feasible Output shows That Ankle Plantar Flexors Are Most Crucial to Stair Ascent

Mr Eric Kwei[1], Mr John Kim[1], Ms Sanskriti Gurappa[1], Mr Yamato Irie[1], Mr Zijie Zhu[1], Dr Francisco Valero-Cuevas[1,2]

[1]University of Southern California, Los Angeles, California, United States. [2]Biokinesiology & PT, Los Angeles, California, United States

Introduction

Clinical measures of frailty focus on decline in physiology and mobility, but often lack neuromechanical specificity. We use a computational approach to quantify the relationship between muscle strength and the mechanical demands of stair ascent as it is an early indicator of functional decline in older adults, and may serve as a sensitive early detector of frailty. We use Feasibility Theory1 to evaluate the impact of muscle weakening on the ability to meet the vertical ground-reaction forces (GRFs) required throughout the cycle of stair ascent.

Methods

We applied published kinematic data[2] during stair ascent to a normative adult OpenSim lower-limb musculoskeletal model to predict the feasible force set (FFS) polytope at the leading foot during the ascent cycle as a function of optimal muscle fiber length, moment arms, pennation angles, tendon slack lengths, and maximum isometric force. Considering stepping as quasi-static, we computed moment-arms, Jacobians, and the maximum muscle force to calculate the FFS of the leg[3] during the step climbing cycle. This allowed us to quantify "frailty" as the distance of the GRF needed throughout in the cycle to the edge of the FFS: if the FFS shrinks below the necessary GRF at any point in the cycle, then stair climbing becomes infeasible.

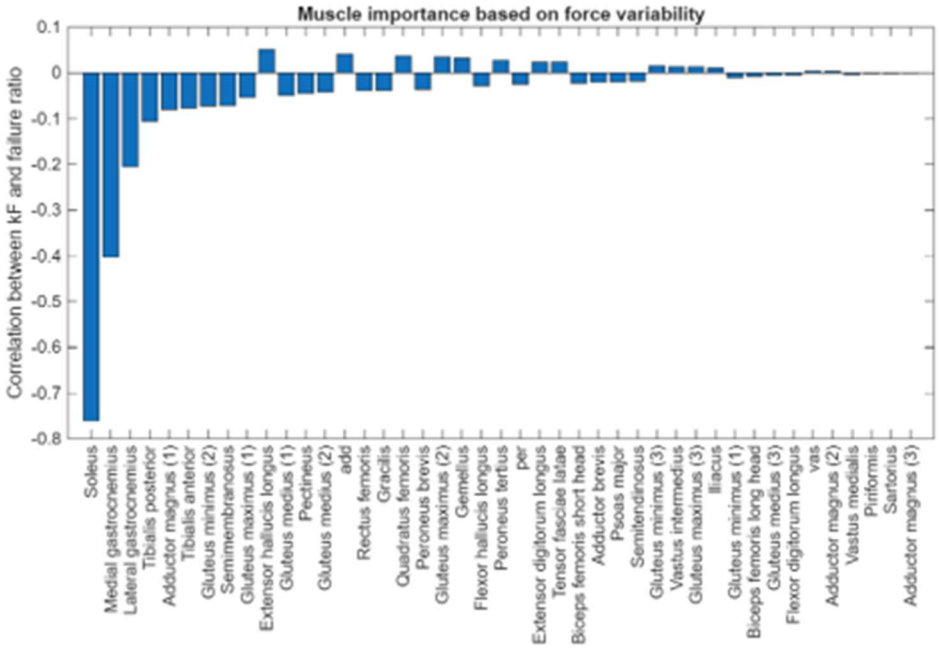
Results

The shape and size of the FFS polytope changes across the ascent cycle, and Monte Carlo simulations weakening individual muscles show some muscles are particularly critical. Even modest (10–20%) strength reductions in the plantar flexor from normative values disproportionately shrink the feasible set's vertical component below the required GRF during certain phases of the ascent, resulting in failure, and suggesting limited robustness to plantar flexor muscle weakening.

Discussion

Defining frailty as a loss of feasible mechanical output allows comparison to task demands. This can help identify specific muscles and gait phases most vulnerable to sarcopenia in healthy aging or disease. This framework offers quantifiable thresholds for frailty to inform targeted strengthening interventions for older adults.

Images (Optional)



References (Optional)

[1] *Cohn BA, et al. (2018), Front Comput Neurosci*; [2] *Reznick et al.* (2021), Sci Data 8(282); [3] *Kutch JJ, et al. (2011), Jour. Biomech.*

Session Category

Musculoskeletal Biomechanics: Joints and Motion

P2-061

Sensitivity Analysis of Soccer Kicking Motion on Eccentric Muscle Mechanics Using Markerless Motion-Capture, Sensorized Insoles and Neuromusculoskeletal Simulation

Ms. Juliette Wyatt, Mr. Javier Batista, Dr. Nick Fey

University of Texas at Austin, Austin, Texas, United States

Ms. Juliette Wyatt

Introduction

Soccer, as one of the most popular sports worldwide, accounts for 228,000 sports injuries per year and 28% are hip related. Taking up 5-6% of all adult sports injuries, hip injuries significantly impact athletes in their performance. Due to the high occurrence of hip injuries in soccer players, it is vital to explore in-game causes. Utilizing state-of-the-art dynamic analysis, a range of angles were identified for soccer instep kicking to provide a training framework that ensures accuracy and kick power while minimizing hip injury risk. We hypothesized kicking with decreased hip rotation, increased knee flexion, and decreased hip adduction would result in less eccentric loads on hip musculature, therefore lowering risk of injury.

Methods

In hip motion and injury, the adductors, psoas, and rectus femoris muscles drive body movement [1,3-4], and were isolated for analysis in the optimized model. Using markerless Motion Capture (MoCap), nominal kicking motion was tracked, utilizing pressure-sensing insoles to obtain ground reaction forces (GRF). The dataset defined the right (dominant) leg as the kicking leg and the left as planted. In OpenSim, several iterations of static optimization were performed, sweeping through kicking kinematics within known performance variability to establish an optimized model.

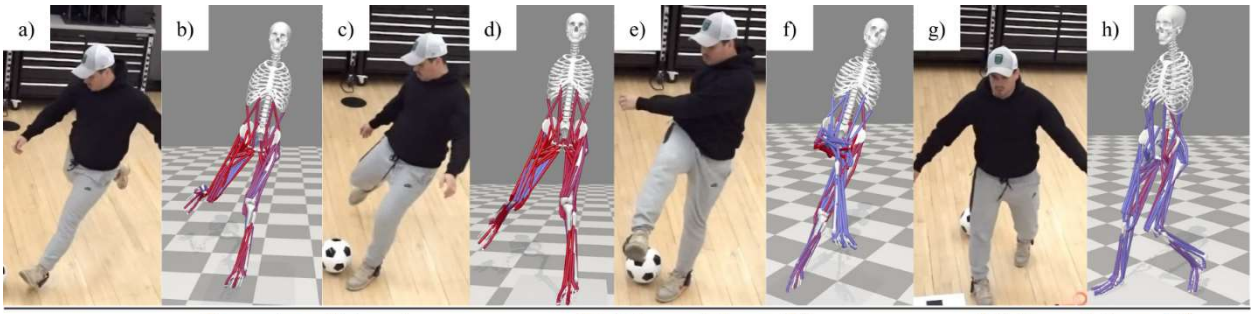
Results

The optimized values were as follows: hip adduction angle at 22°, hip rotation at 32°, and knee angle at 68°. In kicking leg models, peak forces occurred at the start of the swing phase, particularly in the adductor longus and the rectus femoris. Higher knee flexion slightly increased the psoas force but was ultimately beneficial as forces were distributed more evenly. By reducing hip adduction and rotation angles, the muscle forces were lowered, creating safe kicking mechanics. This reduction of swing leg adduction and rotation resulted in lower stance forces on the planted leg.

Discussion

This study defined the specific joint angle parameters optimal for injury prevention while maintaining kicking performance. Soccer professionals can utilize this information to train in effective, risk-reducing kicking form and prevent future hip injuries. The technical approach involving motion capture and neuromusculoskeletal modeling may not only prevent injuries but also create stronger, more technical players.

Images (Optional)



Trial	Parameters of interest			Right leg peak forces (N)			Left leg peak forces (N)		
	Hip adduction (°)	Hip rotation (°)	Knee angle (°)	Adductor longus	Psoas	Rectus femoris	Adductor longus	Psoas	Rectus femoris
Baseline	5.9	6.8	44.8	598	1925	1797	841	1770	1916
1i	30	45	60	931	1123	1910	903	1568	1885
2i	28	40	62	912	1173	1845	937	1642	2208
3i	26	38	64	943	1152	1836	983	1877	2203
4i	24	34	66	952	1136	1800	896	1511	1855
5i	**22**	**32**	**68**	**703**	**1119**	**1730**	**876**	**1541**	**1661**
6i	20	30	70	946	1363	1891	905	1489	1926

Figure 1: **Comparison of experimental and simulated soccer kick biomechanics.** The top panels display paired snapshots of the kicking motion, aligning real-world video footage with the corresponding musculoskeletal simulation view: (a) and (b) show the initial approach; (c) and (d) depict the backswing; (e) and (f) capture the ball contact phase; and (g) and (h) show the follow-through. The table below summarizes the kinematic parameters (hip adduction, hip rotation, knee angle) and peak muscle forces for the Adductor longus, Psoas, and Rectus femoris muscles in both the right and left legs across baseline and six iteration trials. **Note: Iteration 5i yielded the most favorable combination of joint angles and reduced peak muscle forces, and is therefore highlighted.**

Session Category

Musculoskeletal Biomechanics: Joints and Motion

P2-062

Estimating knee contact force in a subject with knee osteoarthritis using out-of-the lab measurement systems

MSc. Karin van Minnen[1,2], Dr. Miel Willems[1], MSc. Gloria Scanagatta[1], Dr. Bryce Killen[1], Prof. Ilse Jonkers[1]

[1]KU Leuven, Leuven, Flemish Region, Belgium. [2]Delft University of Technology, Delft, South Holland, Netherlands

Introduction

Osteoarthritis (OA) is a chronic joint condition, with knee OA (KOA) the most prevalent form (1). Mechanical loading is a key factor in KOA and can be assessed using musculoskeletal (MSK) modelling. This study investigates whether out-of-the-lab measurement systems can serve as input for an MSK modelling framework to estimate knee joint load and support accessible screening.

Methods

Kinematic and kinetic data were collected for 40 seconds of treadmill walking in a male early KOA participant (62 y, BMI 28.4) using OpenCap (2), force plates, and pressure insoles (3). Insole ground reaction forces (GRFs) were decomposed into three components using an in-house neural network (NN). A jump synchronized kinematics and GRFs, and CoPs were aligned using heel and toe markers. A scaled Lenhart model (4) was used for inverse kinematics, inverse dynamics, and COMAK (5) with NN-estimated GRFs and treadmill GRFs (using insole CoP) to compute knee contact forces across eight stance phases.

Results

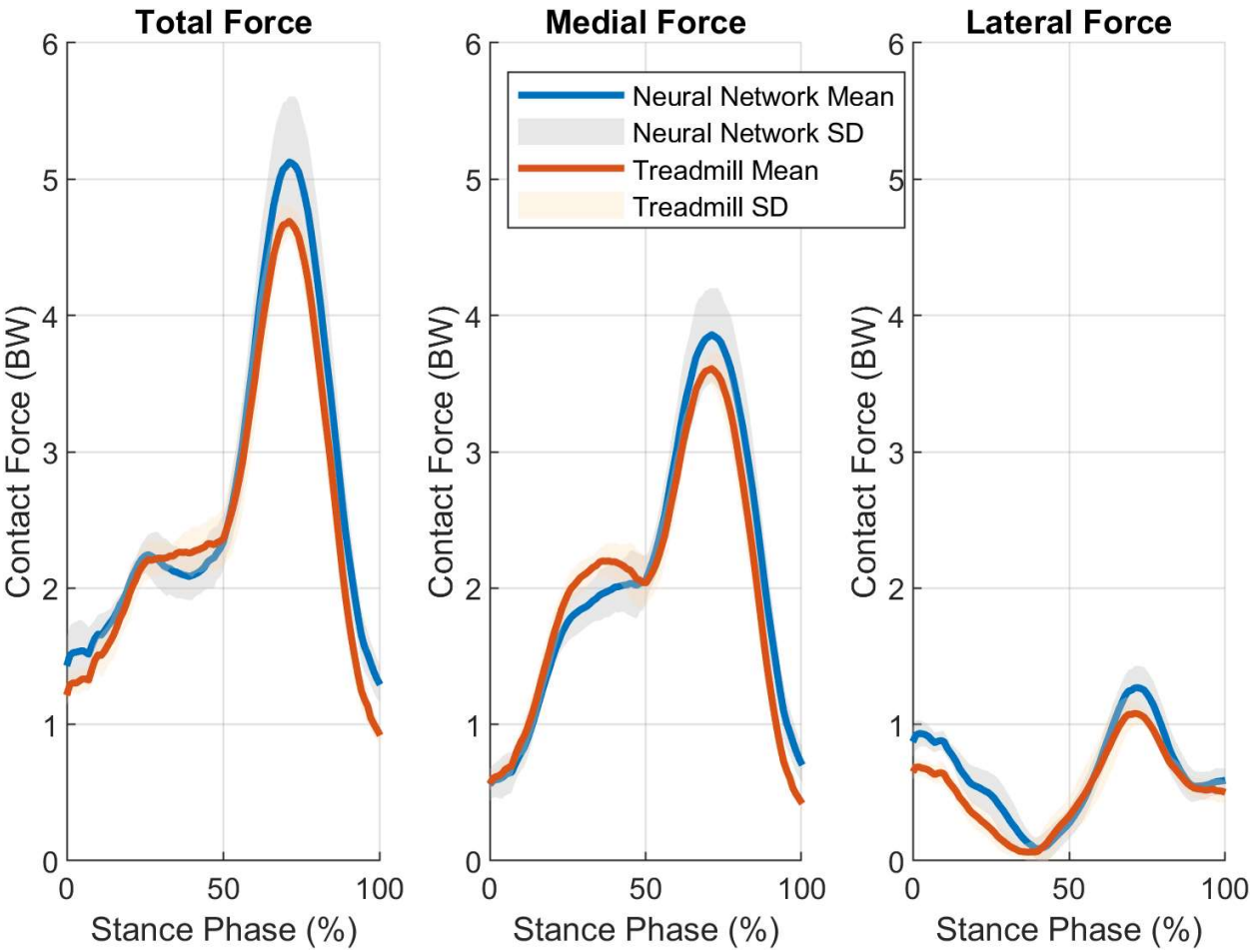
Maximum medial tibial contact force was 3.910 ± 0.345 BW for NN-predicted forces and 3.642 ± 0.105 BW for GRFs (treadmill), 7% lower. Lateral peaks were 1.299 ± 0.148 BW (NN) and 1.113 ± 0.102 BW (treadmill). The medial peak exceeded previously reported treadmill values (6), while the lateral peak for treadmill forces remained within the reported range.

Discussion

This study presents a workflow for estimating knee contact forces using out-of-the-lab systems. Previous work in our group identified a 3.16% threshold in the second peak to distinguish early KOA from non-OA. The current 7% difference exceeds this, suggesting the estimates are not yet clinically applicable. Future work will focus on optimizing insole-

based CoP and GRF alignment with video-based kinematics, leveraging Bayesian techniques to quantify the effects of positioning error. This is a critical step to maximize the use of out-of-the-lab systems for detecting clinically relevant differences in knee loading.

Images (Optional)



References (Optional)

[1] Jaimie Steinmetz et al., Lancet Rheumatol, 2023

[2] Scott Uhlrich et al., PLoS Comput Biol., 2023

[3] Leora Cramer et al., Sensors (Basel), 2022

[4] Rachel Lenhart et al., Ann Biomed Eng., 2015

[5] Colin Smith et al., J Biomech., 2019

[6] Darryl D'Lima et al., Proc Inst Mech Eng H, 2012

Acknowledgements (Optional)

This project has received funding from the European Union's Horizon Europe programme under the Marie Curie Grant Agreement No. 101169278.

Session Category

Musculoskeletal Biomechanics: Joints and Motion

P2-063

A CAD-Driven Jig Workflow for Specimen-Specific Joint Alignment Preservation

Ms. Kate Benfield, Mr. Cody Willson, Mr. Jack Holmes, Ms. Angelica Carhaus, Dr. Trevor Lujan

Boise State University, Boise, Idaho, United States

Introduction

Proper knee joint alignment is essential for accurately characterizing joint mechanics during in-vitro simulation. Standard workflows physically digitize bony landmarks to embed anatomical coordinate systems into the femur and tibia, with the bones then manually and permanently potted into the test system. However, this methodology is prone to operator error and becomes problematic when using robotic knee simulators since proper joint rotation requires the bone rotational axes to align with the simulator's mechanical axes. Here we developed a CAD-based jig workflow that allows the operator to virtually verify and correct joint alignment prior to potting.

Methods

An ovine knee joint was scanned using a Keyence 3D scanner to generate high-resolution 3D models of the femur and tibia **(Fig. 1A)**. 3D models were imported into SolidWorks, and anatomical coordinate systems were embedded using established bony landmarks [1]. Each bone was virtually oriented with the medial-lateral and anterior-posterior axes aligned with the global axes of custom jigs **(Fig. 1B)**, thus enabling the creation of specimen-specific cavities. These cavities fully constrain the position of each bone through a precise, form-fitting interface with the jig thus preserving alignment **(Fig. 1C)**. The bone-jig assemblies were then incorporated into a CAD model of the joint testing system to visually inspect alignment **(Fig. 1D)**. The process was repeated five times, and variability was quantified using landmark coordinate differences between trials and angular deviations from the SolidWorks global frame.

Results

Rotational variability across embeddings averaged 2.0° (ML), 1.0° (AP), and 1.3° (DP), while origin variability was 0.12 mm, 0.87 mm, and 0.69 mm along the x, y, and z axes, respectively. Inter-operator consistency was excellent for translations (ICC = 0.98) and rotations (ICC = 0.98). Qualitative assessment confirmed alignment between bones and test system rotational axes.

Discussion

This CAD-driven workflow provides a feasible method for defining and reproducing virtual joint alignment, allowing coordinate frames to be corrected and verified prior to physical joint potting. This work will be expanded using shape-fitting to define embedded bone axes and reduce alignment error, with future studies aimed at evaluating wear-and-tear in ovine knee joints using robotic simulation.

Images (Optional)

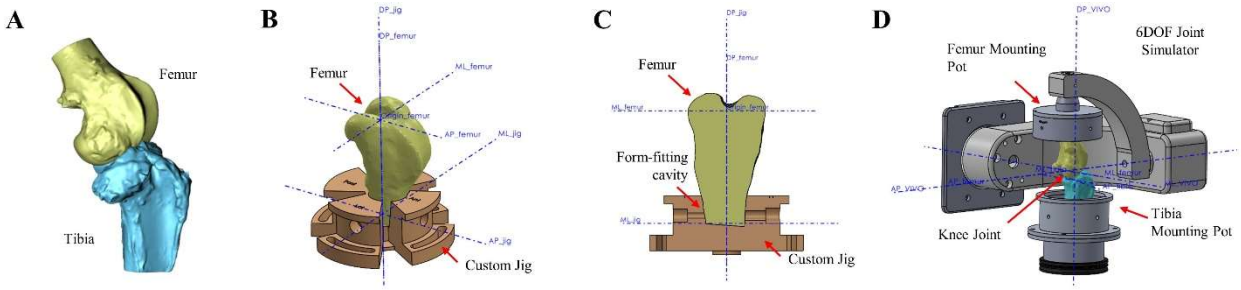


Figure 1: Overview of the CAD-driven workflow showing **A)** the 3D-scanned tibia and femur bone replicas, where **B)** axes are embedded and aligned within custom jigs that **C)** constrain the bones using form-fitting cavities (cross-section shown). **D)** Joint alignment can then be virtually evaluated prior to physical joint potting and simulation.

References (Optional)

[1] Grood and Suntay, JBME, 1983

Session Category

Musculoskeletal Biomechanics: Joints and Motion

P2-064

The Effects of a Barefoot Orthotic on Ankle Biomechanics

Dr. Kristie Liu, Ms. Dorsa Eshaghi, Dr. Timothy Burkhart

University of Toronto, Toronto, ON, Canada

Introduction

Plantar fasciitis and flat feet are estimated to affect 10% and 25% of the population, respectively. Foot orthotics are commonly used to address these conditions by correcting the foot alignment; however, they are currently designed to be worn in shoes. A novel foot orthotic, HeelSnaps®, has been developed to be worn barefoot. The objective of this study was to quantify the effect of the HeelSnaps® on ankle biomechanics.

Methods

15 healthy adults (6 male, 9 female) completed walking, change of direction (cutting), and squat tasks, barefoot and while wearing HeelSnaps®. Kinematic data were collected using an 8-camera markerless motion capture system (Qualisys Miqus; Qualisys, Gothenburg Sweden). Ground reaction force (GRF) data were collected using two force plates (BP600900; AMTI, Watertown, MA, USA).

Kinematic data were processed using Theia3D software (Theia Markerless Inc., Canada), where data were constrained to three degrees-of-freedom at the hips, knees, and ankles and filtered with a generalized cross-validatory spline smoothing and differentiation filter with an 8Hz cutoff frequency.

The walking and cutting tasks were analyzed during contact with the force place, while the squat was evaluated for the entire movement cycle. Ankle kinematics and GRFs were time normalized to 101 data points. One-dimensional paired t-test statistical parametric mapping was conducted to compare the barefoot and HeelSnaps® conditions ($\alpha=0.05$). The mean difference and standard deviation of statistically significant regions were calculated.

Results

See Table 1 for full results. During gait, significantly reduced dorsiflexion and increased plantarflexion were observed while wearing HeelSnaps®, with short durations of significantly reduced right ankle adduction and increased right ankle internal rotation.

Significant effects for cutting were limited to right-side cuts, with reduced left ankle dorsiflexion and vertical GRF. During the squat, ankle dorsiflexion was reduced bilaterally.

Table 1. Regions of statistical significance between the HeelSnaps® and barefoot conditions at the ankle and in ground reaction forces.

Discussion

Ankle dorsiflexion was reduced while wearing the HeelSnaps®; however, it is unclear whether these small differences improve foot alignment. Future work should evaluate whether foot mechanics are significantly altered in individuals diagnosed with plantar fasciitis and/or flat feet.

Images (Optional)

Task	Side	Axis	Duration	Mean Difference (SD)	p-value
Gait	Left	X	0-3%	-1.58 (0.04)	0.046
Gait	Left	X	10-85%	-2.15 (0.18)	<0.01
Gait	Right	X	0-76%	-1.71 (0.20)	<0.01
Gait	Right	X	96-100%	-2.62 (0.07)	0.045
Gait	Right	Y	77-85%	-0.64 (0.05)	<0.01
Gait	Right	Z	49-64%	0.93 (0.04)	<0.01
Cut Right	Left	X	39-62%	-2.29 (0.06)	<0.01
Cut Right	Left	GRF_Z	19-23%	-73.77 (9.88)	0.02
Squat	Left	X	7-67%	-2.61 (0.48)	<0.01
Squat	Left	X	97-100%	-1.79 (0.03)	0.04
Squat	Right	X	24-56%	-1.93 (0.37)	<0.01
Squat	Right	X	96-100%	-1.70(0.05)	0.025

References (Optional)

Session Category

Musculoskeletal Biomechanics: Joints and Motion

P2-065

Classification of Lower-Extremity Alignment Sub-types in Children with Genu Varum Using Factor and Cluster Analysis

Presenter Kyungeon Kim M

Yonsei University, Seoul, Seoul, Korea, Republic of

Introduction

Lower-extremity alignment in children results from the combined influence of pelvic position, femoral and tibial rotation, knee alignment, and foot–ankle posture. Disruptions in this kinetic chain—particularly the structural deviations observed in genu varum (GV)—can alter load distribution and compensation patterns, increasing long-term risk for musculoskeletal dysfunction. However, existing research has relied largely on isolated alignment measures, leaving the **latent multidimensional structure** of GV-related alignment patterns poorly defined. Therefore, this study aimed to identify underlying alignment factors and classify distinct structural subtypes in children with GV through a combined factor and cluster analytic approach.

Methods

Clinical and biomechanical alignment variables—including Q-angle, tibiofemoral angle, and rearfoot angle in both weight-bearing conditions; pelvic alignment; femoral anteversion; leg-length discrepancy; navicular drop; tibial torsion; tibial varum; genu recurvatum; and forefoot angle—were collected from the dominant limb of 218 participants. Principal Component Analysis was conducted to identify the latent structure of lower-extremity alignment, yielding seven core factors. These factor scores were then used to classify alignment patterns within the GV. A hierarchical cluster analysis was first performed to determine the optimal cluster solution. Based on the dendrogram, K-means clustering was applied to assign participants to final clusters. One-way ANOVA was conducted to test factor score differences across clusters. Significant factors were further examined using Bonferroni post hoc tests. This procedure enabled the identification and validation of distinct GV alignment subtypes.

Results

Factor analysis identified seven distinct alignment factors capturing both structural and compensatory characteristics of the lower extremity. Based on these factor-derived patterns, three GV subtypes emerged. Cluster 1 exhibited marked pelvic asymmetry,

pronounced arch-collapse compensation, and strong pelvic–forefoot coupling. Cluster 2 was defined by increased tibial torsion accompanied by reduced pelvic tilt, representing a rotational compensation subtype. Cluster 3 showed elevated pelvic tilt and forefoot alignment with minimal pelvic asymmetry. Collectively, these clusters illustrate heterogeneous combinations of structural deviations and compensatory strategies among children with GV.

Discussion

The findings emphasize that GV encompasses multiple biomechanical pathways rather than a single structural deformity. The identification of subtypes based on factor-derived alignment profiles offers an important step toward individualized assessment and intervention.

Session Category

Musculoskeletal Biomechanics: Joints and Motion

P2-066

Muscle Activity Patterns According to Chopstick-Holding Methods

Ms. Kyungmin Lee, Mr. Taehyung Kim, Prof. Gwanseob Shin

Ulsan National Institute of Science and Technology, Ulju-gun, Ulsan, Korea, Republic of

Introduction

Using chopsticks is a complex fine-motor skill that requires precise coordination of several hand and arm muscles. Chopsticks are widely used as an essential eating tool in East Asian cultures, and their use has recently spread worldwide. Despite this, the biomechanical characteristics according to different chopstick-holding postures and force levels have not been sufficiently examined. Especially, differences in holding styles may influence muscle activity and operation efficiency. The purpose of this study is to investigate the muscle activity patterns of hand and arm muscles under different chopstick-holding postures and force conditions.

Methods

Healthy participants in their twenties performed a task in which they maintained chopstick-holding postures under one uncontrolled preferred posture and three pre-determined controlled posture. And the task included three force conditions, and each condition was performed in a randomized order. During the task, electromyography (EMG) signals were collected from six hand and arm muscles to compare muscle activity according to the different posture and force condition. The EMG signals were normalized to maximum voluntary isomeric contraction (MVC) for analysis.

Results

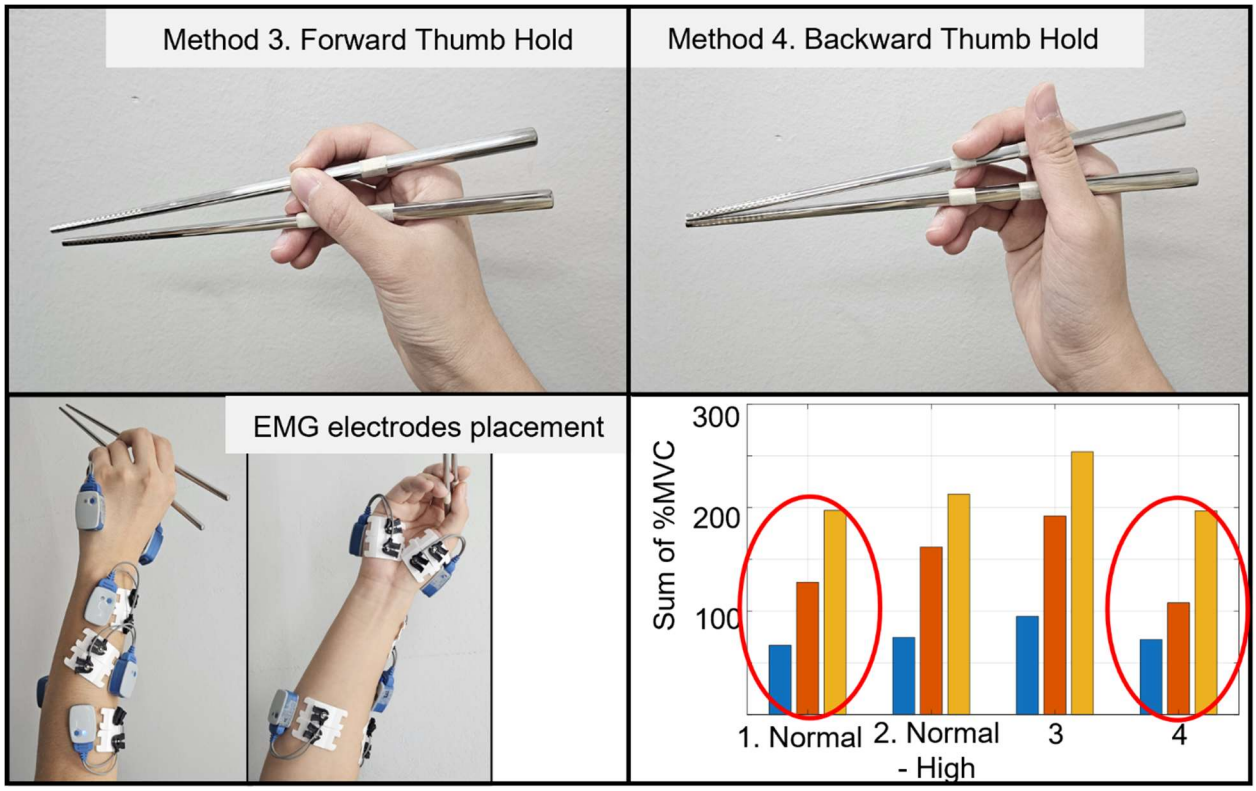
Muscle activity was different depending on the chopstick-holding posture and force level. For most patients, EMG activity tended to increase in all muscles as the force level increased. Interestingly, among the newly introduced postures, backward thumb hold posture showed muscle activity that was similar to or more efficient that the participant's usual posture. In contrast, the other posture tended to show higher muscle activity compared to the usual posture.

Discussion

This study showed that chopstick-holding posture and force level influence muscle activity. Particularly interesting thing was that one of the newly introduced postures appeared to be as efficient as, or more efficient than, the participants' usual posture. These results suggest that there may be alternative methods of using chopsticks that are more efficient than the

traditional method commonly used. Therefore, the findings of this study emphasize the importance of holding techniques in chopstick use and provide new evidence that may be useful for future chopstick training, rehabilitation exercises, and ergonomic tool design.

Images (Optional)



Acknowledgements (Optional)

This work was supported by the National Research Foundation of Korea grant funded by the Korea government (MSIT). (No. RS-2025-00556960)

Session Category

Musculoskeletal Biomechanics: Joints and Motion

P2-067

Relationship Between Lower Extremity Joint Range of Motion and Center of Mass Vertical Displacement During Running

Ms Lailah Rosario, Ms. Megan Peach DPT, Dr. James Becker PhD

Montana State University, Bozeman, MT, United States

Introduction

Higher center of mass vertical displacement (comVD) in long-distance runners has been related to overuse injuries. While cycle metrics such as stride length and step frequency have been established as interventions to reduce comVD, it is unclear if manipulating lower extremity joint range of motion (ROM) has utility as an intervention to reduce comVD. This study aims to evaluate the relationship between lower extremity joint ROM and comVD during running.

Methods

Fifteen participants (7 F, 8 M; 23.25 ± 2.32 years, height 1.77 ± 0.08 m, mass 75.96 ± 12.99 kg, weekly activity 326.56 ± 158.48 minutes) ran five trials along a 15 m runway while whole body kinematics were recorded using markerless motion capture. A 13-segment biomechanical model was used to calculate center of mass, and sagittal hip, knee, and ankle angles. Total sagittal joint ROM and comVD was calculated during stance phase. A multiple linear regression model was used to determine relationships between hip, knee, and ankle ROM and comVD during running.

Results

A model including ROM for hip, knee, and ankle accounted for 41.4% of the variance in comVD ($F = 16.49$, $p = <.001$). Knee and ankle ROM, but not hip ROM, were significant predictors of comVD, with increasing ROM resulting in greater comVD.

Discussion

An increase of a single degree of sagittal knee or ankle ROM results in ~1 mm increase in comVD during running. Reducing knee or ankle ROM during running has potential as an intervention to reduce comVD. Future studies should examine interventions that target reductions in knee or ankle ROM as a means of decreasing comVD and identify any adverse biomechanical consequences that may result from decreasing ROM.

Images (Optional)

Table 1 Variable Statistics

	Mean ± SD	β	*p* value
ComVD (cm)	7.81 ± 1.67	0.03	-
Hip ROM (deg)	44.35 ± 5.41	-0.001	0.086
Knee ROM (deg)	33.53 ± 5.94	0.001	<.001
Ankle ROM (deg)	38.50 ± 6.37	0.001	.014

Session Category

Musculoskeletal Biomechanics: Joints and Motion

P2-068

Estimating Joint Moments During Walking With a Markerless, Smartphone-Based Motion Capture System

BSc BEd Laura Rathmair[1], BSc MSc PhD Willi Koller[1], FH-Prof. Priv.-Doz. Dr. Brian Horsak Brian Horsak[2], Assoc. Prof.Mag. MSc PhD Hans Kainz[1]

[1]University of Vienna, Vienna, Vienna, Austria. [2]University of Applied Sciences St. Pölten, St. Pölten, Lower Austria, Austria

Introduction

OpenCap is a new, markerless motion capture system providing an easily accessible, low-cost alternative to marker-based motion capture. OpenCap estimates joint angles, ground reaction forces (GRF) and joint moments solely based on video recordings from at least two synchronized smartphones [1]. Several studies have examined OpenCap's accuracy regarding joint kinematics, whereas joint kinetics have only scarcely been examined. This study explored OpenCap's ability to estimate GRFs and joint moments during walking.

Methods

Walking trials of nine healthy, uninjured adults were recorded with a 12-camera marker-based system, and force plates simultaneously with OpenCap using four smartphones. Four different workflows were compared: 1) *OpenSimStandard*: standard marker-based approach in OpenSim with force plate GRF data, 2) *OpenCapOnly*: standard OpenCap configuration to estimate joint angles, GRFs and joint moments, 3) *OpenCapForcePlate*, standard OpenCap configuration using GRF data from force plates, and 4) *OpenSim+GRF*$_{est}$: combining marker-based kinematics with GRFs estimated as in OpenCap. For all workflows, average waveforms of joint angles, GRFs and joint moments were compared using Statistical Parametric Mapping (SPM) based paired t-tests [2].

Results

An overall root mean square error (RMSE) of 7.2 ± 3.4 degrees for joint angles between marker-based data and OpenCap was found. For both markerless and marker-based kinematics, GRFs were systematically overestimated by OpenCap. Peaks and zero-crossings of GRFs were more consistent with marker-based kinematics. SPM results revealed that *OpenCap+ForcePlate* was similar in waveforms to *OpenSimStandard*, while *OpenCapOnly* and *OpenSim+GRF*$_{est}$ differed significantly from *OpenSimStandard* for most of the stance phase.

Discussion

OpenCap+ForcePlate showed reasonable waveform similarity with *OpenSimStandard*, especially for joint moments in the sagittal plane. This workflow yielded both low RMSE and high coefficient of multiple correlations values, suggesting that the estimation of joint moments is primarily influenced by GRF quality rather than kinematic inputs. *OpenCapOnly* showed large deviations in GRFs and joint moments from *OpenSimStandard*, likely resulting from inaccurate GRF estimation due to imperfect markerless joint kinematics. Findings suggest that smartphone-based approaches can approximate the overall temporal patterns of gait kinetics, but caution is advised if accurate quantification joint moments is necessary.

Images (Optional)

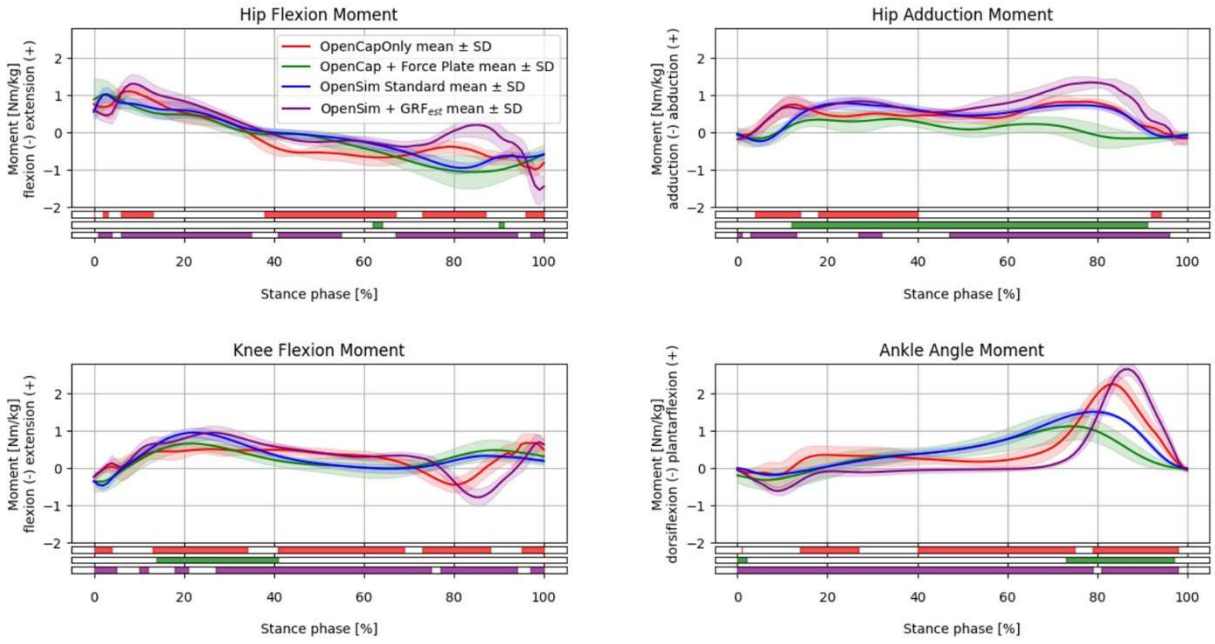


Figure 1: Mean ± 1 standard deviation of hip, knee and ankle joint moments across workflows.
Blue: OpenSimStandard; Red: OpenCapOnly vs. OpenSimStandard; Green: OpenCap + Force Plate vs. OpenSimStandard; Purple: OpenSim + GRFest vs. OpenSimStandard.
Horizontal bars underneath each subplot indicate significant differences based on the SPM analysis.
Red: OpenCapOnly vs. OpenSimStandard; Green: OpenCap + Force Plate vs. OpenSimStandard; Purple: OpenSim + GRFest vs. OpenSimStandard.

References (Optional)

[1] Scott Uhlrich et al., bioRxiv, 2022

[2] Todd Pataky, CMBBE, 2012

Session Category

Musculoskeletal Biomechanics: Joints and Motion

P2-069

Evaluating the Effect of Gait Modifications on Hip and Knee Joint Contact Forces in Children

BSc BEd Laura Rathmair[1], Dipl.-Ing. Clara Egner BSc[1], BSc Kevin Kitir[1], BSc MSc PhD Willi Koller[1], Assoc.-Prof. Mag. Hans Kainz MSc PhD[1], Dr. rer. nat. Nathalie Alexander[2], Ing. Dr. Andreas Kranzl[3], Dr. Peter Pivonka[4], Assoc. Prof. Claudio Pizzolato BSc MSc PhD[5]

[1]University of Vienna, Vienna, Vienna, Austria. [2]Ostschweizer Kinderspital, St. Gallen, Ostschweiz, Switzerland. [3]Orthopaedic Hospital Speising, Vienna, Vienna, Austria. [4]Queensland University of Technology, Brisbane, Queensland, Australia. [5]Griffith University, Brisbane, Queensland, Australia

Introduction

Gait modifications can alter joint loadings and influence the progression of degenerative diseases in adults [1]. In children with cerebral palsy, abnormal hip (HJCF) and knee joint contact forces (KJCF) have been linked to pathological growth plate stresses, which may contribute to pathological femoral development [2, 3]. However, it remains unclear whether gait modifications can change joint contact forces (JCF)- and thereby affect femoral growth- in children. This study aimed to evaluate how different gait modifications influence HJCF and KJCF in a paediatric population.

Methods

Three typically developing children underwent magnetic resonance imaging and three-dimensional gait analysis (Vicon, Oxford, UK) on a force plate instrumented treadmill (AMTI, Watertown, USA). Participants walked physiologically, and with varying degrees of in- and out-toeing, stance width, foot strike patterns and walking velocities. Personalized musculoskeletal models were created using the OpenSimCreator ModelWarper [4] which adapts bone geometries and muscle paths of a RajagopalLaiUhlrich2023 model to match the individual's anatomy obtained from imaging. Mean KJCF and HJCF of 5-7 trials per leg and condition were calculated for each participant using musculoskeletal simulations in OpenSim with static optimization. JCF were then compared across conditions

Results

So far, only modifications of the foot progression angle (FPA) have been analyzed. In all participants, the in-toeing modifications reduced peak KJCF during terminal stance at least on one leg, compared to normal walking. Effects of the gait modifications on the magnitude and orientation of HJCF varied among participants (Figure 1).

Discussion

To our knowledge, this is the first study to show that gait modifications can alter JCF in children. For participant TD03, asymmetries in KJCF may relate to differences in femoral anteversion (7° left, 13.3° right), highlighting how anatomy affects modification effects. Preliminary results showed that in-toeing can reduce peak KJCF during terminal stance. HJCF changes displayed substantial inter-individual variability with no consistent trend. These findings emphasize the need for personalized musculoskeletal models and individualized gait interventions to modulate joint loading in children.

Images (Optional)

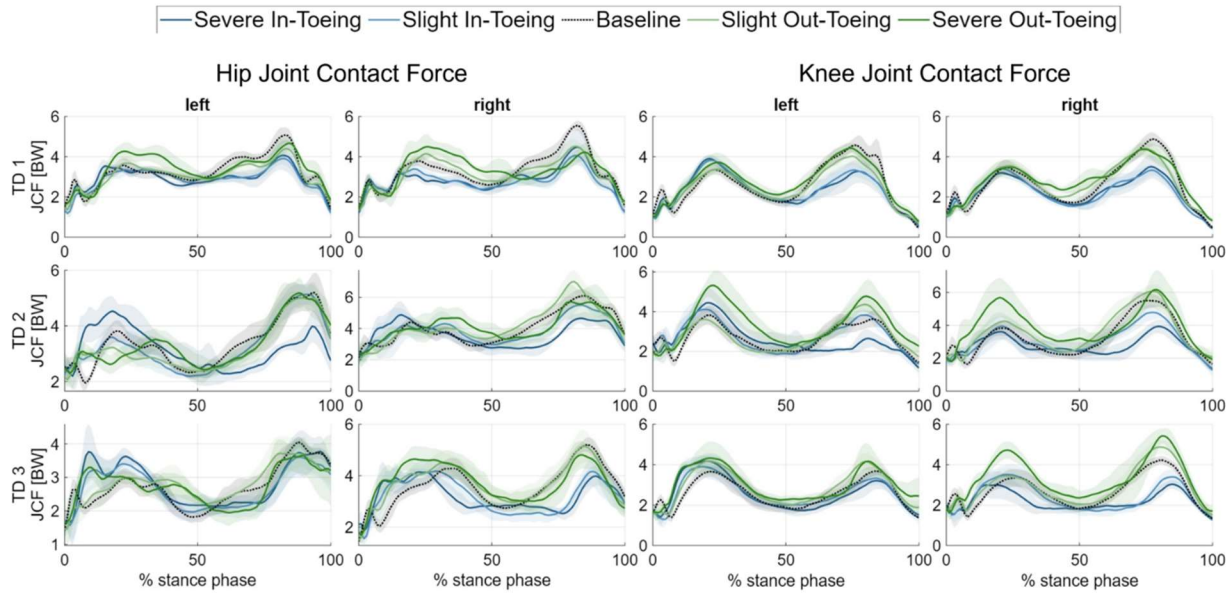


Figure 1: Hip and knee joint contact forces of the stance phase of left and right leg for three participants during baseline (physiological walking at free walking speed calculated from leg length), and varying degrees of foot progression angle

References (Optional)

[1] Diamond et al., OAC Open, 2022

[2] Koller et al., Front. Bioeng. Biotechnol., 2023

[3] Koller et al., Gait & Posture, 2024

[4] Kewley et al., Zenodo, 2025

Acknowledgements (Optional)

This research was funded by the European Research Council (ERC-2024-COG, 101170218, INSIDE-BONE). We would like to thank the Medical University of Vienna for their help with the MRI data collection.

Session Category

Musculoskeletal Biomechanics: Joints and Motion

P2-070

In-vivo Tibiofemoral Kinematics of Healthy Knees during Daily Activities Using Biplanar Videoradiography

Miss Lauren Swain[1], Dr David Williams[1], Miss Janine Flohr[1], Mrs Jenny Williams[1], Prof Andrew Amis[2], Dr Richard van Arkel[2], Prof Cathy Holt[1]

[1]Cardiff University, Cardiff, Wales, United Kingdom. [2]Imperial College London, London, England, United Kingdom

Introduction

Accurate quantification of tibiofemoral (TF) kinematics in-vivo is essential for understanding how osteoarthritis and total knee replacement (TKR) alter joint function, yet existing motion analysis methods lack the precision to resolve subtle but clinically important abnormalities. Biplanar videoradiography (BVR) combined with MRI allows direct measurement of the bones during different activities of living, enabling accurate calculation of joint kinematics. To be able to evaluate the biomechanical and functional effects of knee disease and treatments it is important to be able to quantify healthy knee function.

Methods

A range of activities were included to investigate the biomechanical function of the TF joint, including level and downhill treadmill walking, step down, stand-to-sit, pivot and knee extension. BVR, and synchronised motion capture, were collected during the dynamic activities in a cohort of healthy volunteers. Image registration was performed (SlicerAutoscoperM [1]) by matching digitally reconstructed radiographs derived from MRI segmented bone models (Simpleware, ScanIP) to BVR X-rays per frame to determine bone poses. Anatomical coordinate systems were applied to the segmented bone models [2]. Six degree of freedom kinematics were calculated (MATLAB, Mathworks) from the bone poses using Grood and Suntay's methodology [3].

Results

Figure 1 presents pilot results for three healthy participants for one activity (stand-to-sit) to demonstrate the use of the processing pipeline.

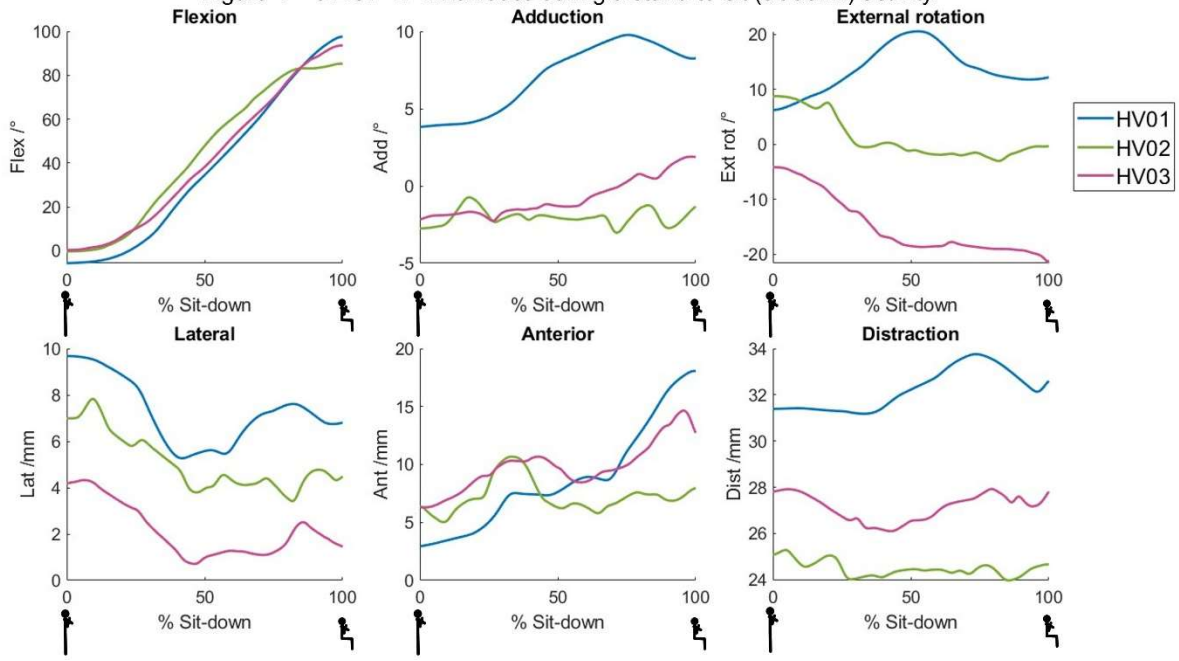
Discussion

Flexion profiles were highly consistent across participants, and anterior translation indicated a clear femoral rollback pattern in two of the three volunteers. In contrast, adduction and external rotation exhibited pronounced inter-participant variability,

reflecting the different movement strategies adopted to accomplish the stand-to-sit task. Similar flexion and anterior translation patterns have been reported previously in TKR cohorts [4]. This work will be expanded in the future to the rest of the activities, as well as to a pre- and post-TKR patient cohort. The 6 DOF TF kinematics will inform a larger study, incorporating in-vitro and in-silico methods to investigate knee joint function across these cohorts.

Images (Optional)

Figure 1 – 6 DOF TF kinematics during a stand-to-sit (sit down) activity.



References (Optional)

[1] Amy Morton *et al.*, J Biomechanics, 2025
[2] Daniel Miranda *et al.*, J Biomechanics, 2010
[3] Grood and Suntay, J Biomechanical Engineering, 1983
[4] Nigel Kour *et al.* JOR, 2022

Acknowledgements (Optional)

Funding from the Engineering and Physical Sciences Research Council (EPSRC): EP/X039870 (Holt & Williams)

Session Category

Musculoskeletal Biomechanics: Joints and Motion

P2-071

A Higher Muscle Energy Cost, Not Lower Efficiency, May Explain the Elevated Energy Cost of Joint Work Redistribution

Ms. Lisa Cozma[1], Dr. Jared Fletcher PhD[2]

[1]University of Calgary, Calgary, Alberta, Canada. [2]Mount Royal University, Calgary, Alberta, Canada

Introduction

Mechanical joint work shifts from distal to proximal joints during running, elevating the metabolic cost. It is assumed that metabolic cost increases because muscles crossing the knee are less efficient compared to muscles crossing the ankle [1]. This study compared muscle efficiency of the vastus lateralis (VL) and the gastrocnemius medialis (GM) while performing fixed mechanical joint work.

Methods

13 recreationally-active adults (23±2yrs, 177±10cm, 71.8±9.9kg) performed positive ankle and knee mechanical joint work (Wmech) targeting 50% maximal ankle plantarflexion moment over 50% of joint-specific range of motion on a dynamometer. Indirect calorimetry quantified metabolic cost of performing work (Emet). Positive muscle work (Wm) was calculated from ultrasound-measured GM and VL fascicle shortening and estimated muscle forces [2]. Mechanical (εmech) and muscle efficiencies (εm) were calculated as the ratios of Wmech to Emet and Wm to Emet, respectively. Muscle shortening velocity associated with peak (Vopt) was calculated [3].

Results

Wmech was not significantly different between ankle (24.6±11.5J/cycle) and knee (31.8±11.8J/cycle, p=0.071). Wm and Emet were significantly higher in VL compared to GM (p<0.01). Knee εmech was significantly higher (8.1±2.5%) than the ankle (5.5±2.1%, p=0.005). εm was similar across muscles (7.5±2.4% for GM and 8.9±4.1% for VL, p=0.393). VL shortened 29±12% slower than Vopt while GM shortened 14±11% faster than Vopt. A weak-to-moderate, positive correlation between Wmech and εmech was seen at the ankle (r2=0.21, p=0.25) and at the knee (r2=0.42, p=0.04, Figure1). εm was

independent of Wm for the GM, (r2=-0.11, p=0.70) which was not the case for the VL (r2=0.61, p=0.005).

Discussion

Performing Wmech at the ankle was less efficient than performing Wmech at the knee. These results refute the notion that energy cost of running increases as a result of joint work redistribution. Rather, greater muscle work and muscle energy cost to perform mechanical work in muscles crossing the knee may explain the elevated energy cost seen during running, independent of differences in εm.

Images (Optional)

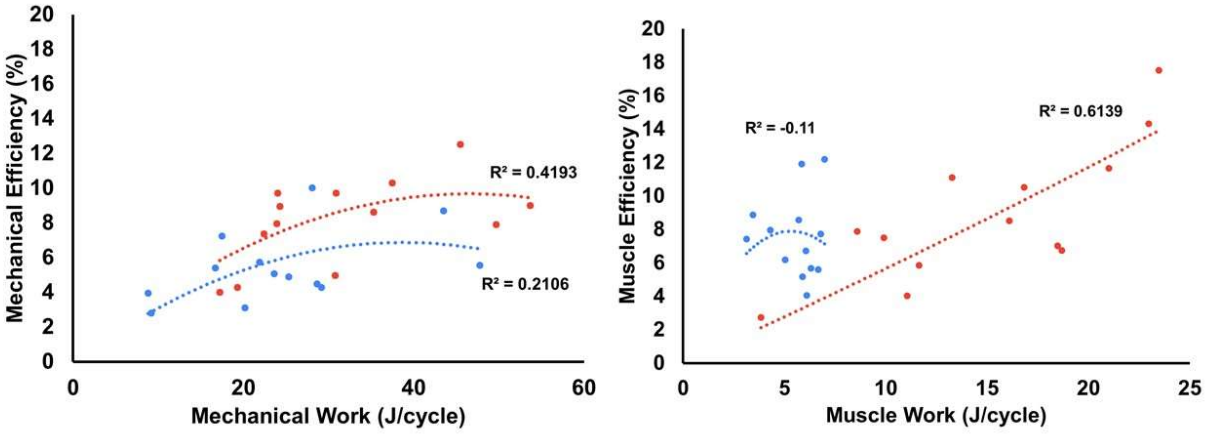


Figure 1: Relationship between mechanical efficiency and mechanical work (left) of the ankle (blue) and knee joint (red) and muscle efficiency and muscle work (right) of the gastrocnemius medialis (blue) and vastus lateralis (red).

References (Optional)

[1] Sanno et al. ,*Med Sci Sports E,* 2018

[2] Fukunaga et al. ,*J. Ortho research,* 1992

[3] Bohm et al. ,Proc R Soc B, 2021

Acknowledgements (Optional)

We acknowledge the support of the *Natural Sciences and Engineering Research Council of Canada (NSERC)* and *Sigma Xi*.

Session Category

Musculoskeletal Biomechanics: Joints and Motion

P2-072

Achilles Tendon Structure-Function Varies Across Menstrual Cycle Phases in Participants With and Without Hormonal Contraceptive Use

Ms. Madeleine Krotine, Dr. Stephanie Cone PhD

University of Delaware, Newark, DE, United States

Introduction

Females undergo changes in hormone (i.e. estrogen) levels through the menstrual cycle and hormonal contraceptive (HC) use, directly impacting the biochemical environment of the body with suspected effects on musculoskeletal health [1]. Lowered estrogen levels are thought to impact tendon mechanics and injury incidence in Achilles rupture and tendinopathy [2]. However, mechanisms behind these structure-function hormonal impacts are still poorly understood. This study aimed to compare daily hormone levels and weekly Achilles structure-function metrics across menstrual cycle phases in HC users and naturally cycling (NC) participants.

Methods

Female participants (HC=4, NC=4), aged 18-45 experiencing regular menstrual cycles (21-35 days, <10 days of inter-cycle variation), underwent 12 weeks of daily hormone testing and weekly structure-function testing. Daily at-home hormone testing was performed using commercial monitors. Weekly testing assessed ankle dorsiflexion range of motion (ROM), ultrasound measurement of tendon thickness and cross-sectional area (LOGIQe,10.0 MHz), shear wave tensiometry measurement of walking and running [3], and plantar-flexion maximum voluntary isometric contractions (MVICs) in a prone position and a neutral ankle angle (HUMAC Norm). Menstrual cycles were sorted into four phases and individual strides were segmented for gait measures. A linear-mixed effects model was used to assess statistical difference between weeks and groups.

Results

A significant effect of cycle phase in the HC user group was found for normalized plantar-flexion MVIC and normalized Achilles tendon thickness ($p=0.034$,$p=0.04$), however follow-up mean comparisons did not show phase-specific differences (Figure 1). No significant effects were found in the NC group.

Discussion

These findings indicate strength and structure changes across the menstrual cycle, potentially indicating variations in performance and tendon health. HC users exhibited greater aggregate variation between cycle phases than NC users, possibly related to HC use stabilizing hormone levels and thus cyclic patterns for improved statistical power within this cohort. Between- and within-subject variability was evident at the current sample size, motivating continued study with increased enrollment and advanced analysis of hormone concentrations.

Images (Optional)

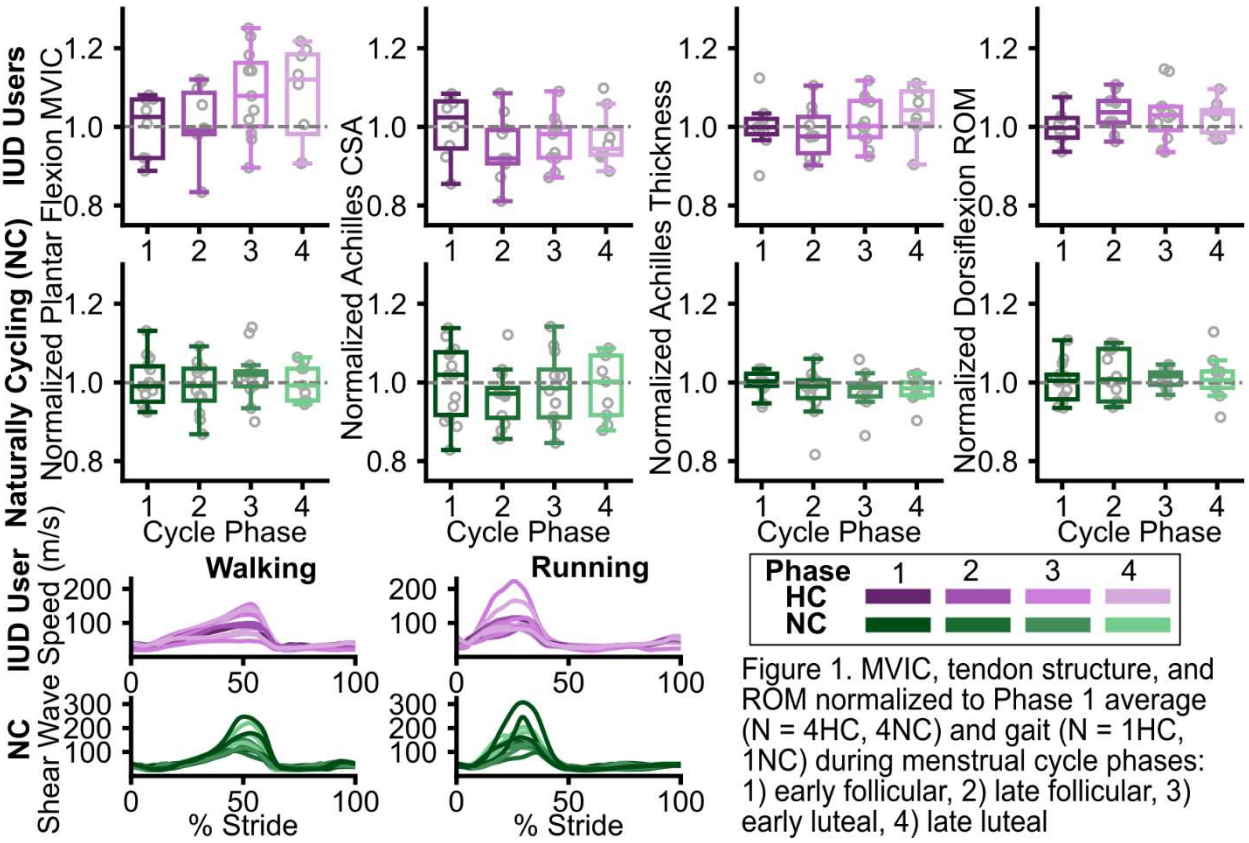


Figure 1. MVIC, tendon structure, and ROM normalized to Phase 1 average (N = 4HC, 4NC) and gait (N = 1HC, 1NC) during menstrual cycle phases: 1) early follicular, 2) late follicular, 3) early luteal, 4) late luteal

References (Optional)

[1] Maffulli *et al.*, J Orthop. Surg., 2023; [2] Hansen and Kjaer, Adv. Exp. Med. Biol, 2016; [3] Schmitz *et al.*, Sensors, 2022.

Acknowledgements (Optional)

Funding from P20GM139760.

Session Category

Musculoskeletal Biomechanics: Joints and Motion

P2-073

Sex Differences in Hip Contact Forces During Dynamic Tasks in Healthy Adults

Ms. Margaret Harrington BKin, Ms. Dorothy Zeng, Dr. Timothy Burkhart PhD

University of Toronto, Toronto, Ontario, Canada

Introduction

Hip contact forces (HCFs) may influence the risk of developing hip disorders, such as femoroacetabular impingement syndrome (FAIS), and affect treatment outcomes. Movement patterns that may result in abnormal HCFs have been shown in females with FAIS [1], but research quantifying sex-specific HCFs is limited. Therefore, the purpose of this study is to compare HCFs between healthy males and females during dynamic body weight tasks to establish normative values.

Methods

Thirty physically active adults (15 females; aged 18-40 years) with no lower extremity injuries participated in this ongoing study. Whole-body kinematics were captured using Theia3D markerless motion capture, along with simultaneous ground reaction forces, while the participants performed three trials each of squats to maximum depth, gait, forward lunges, countermovement jumps, and side-cut maneuvers. OpenSim was used to estimate joint angles and moments, muscle forces, and HCFs.

Results

Preliminary analysis of the squat task for ten participants (five females) showed sex-related differences in hip kinematics and joint loading. While the mean ± SD peak resultant HCF was the same for both sexes (2.8±1.1 N/BW), and peak hip flexion was comparable (116.1±9.0° vs. 112.3±6.2°), females displayed higher HCFs for a longer duration of the squat cycle, particularly during the descent (~0-50% of the cycle), along with higher hip flexion (Figure 1). Additionally, females demonstrated higher peak anterior pelvic tilt (27.5±10.2° vs. 15.3±3.2°) and hip internal rotation (9.1±6.2° vs. 6.0±4.2°), and less hip abduction (-13.5±5.5° vs. -21.6±6.9°) compared to males, with these patterns maintained throughout the entire time-normalized squat cycle (Figure 1).

Discussion

These preliminary findings support previous research indicating that sex-based kinematic differences may contribute to differences in HCFs [1]. This study aims to establish

normative data on hip loading patterns in young, healthy males and females, to help understand why certain hip disorders disproportionately affect females and why treatment outcomes can differ by sex. Ongoing analysis will include all participants, tasks, and additional variables (e.g., muscle forces), creating a comprehensive data set for future comparisons with individuals experiencing chronic hip pain and disorders.

Images (Optional)

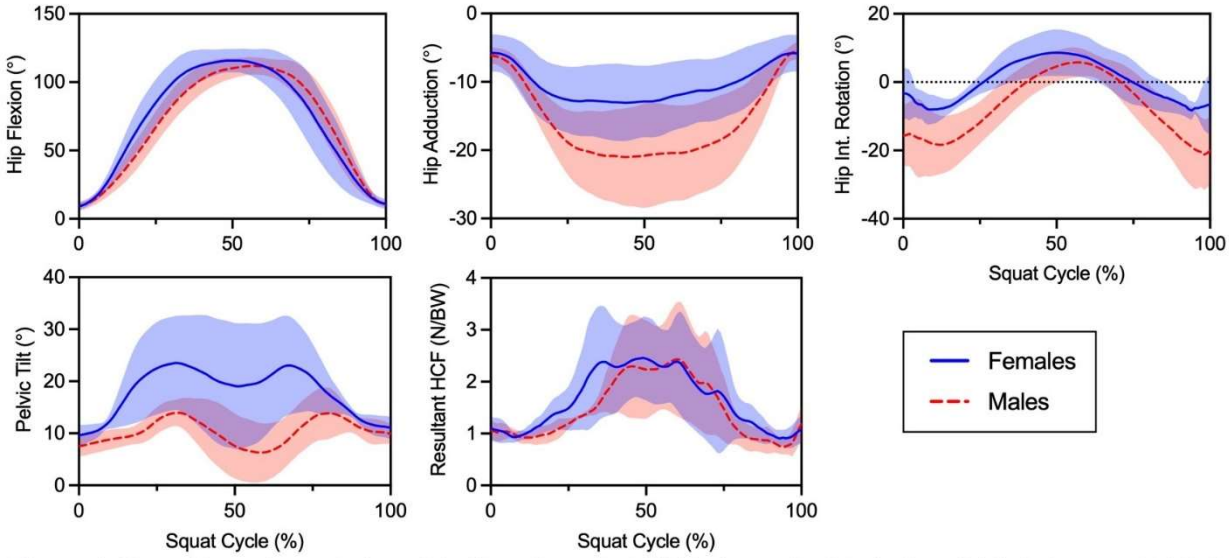


Figure 1. Mean hip angles, anterior pelvic tilt, and resultant HCFs (normalized to body weight) during squat trials for female (n = 5) and male (n = 5) participants. Data was time-normalized to 100% of the movement cycle, with averages calculated from three squat trials and both hips. Shaded areas indicate the standard deviation.

References (Optional)

[1] Brown-Taylor *et al.*, J Orthop Research, 2020

Session Category

Musculoskeletal Biomechanics: Joints and Motion

P2-074

Preliminary Assessment of Knee Joint Mechanics in Children with and without Marfan Syndrome

Ms. Mariana V. Jacobs MS, Dr. Jody L. Clasey PhD, Dr. Christopher S. Fry PhD, Dr. Mary B. Sheppard MD, Dr. Michael A. Samaan PhD

University of Kentucky, Lexington, Kentucky, United States

Introduction

Marfan syndrome (MFS) is a hereditary autosomal dominant connective tissue disorder caused by mutations in the fibrillin-1 (FBN-1) gene. Muscle dysfunction, severe joint pain, and a high incidence of early onset osteoarthritis (OA) is prevalent in adults with MFS. Additionally, adults with MFS ambulate with altered knee joint mechanics that may be associated with OA development. As MFS is a genetic disorder, these aberrant gait patterns may be present at an earlier age during the lifespan. Therefore, the purpose of this study was to compare knee joint kinematics and kinetics during walking in children with and without MFS.

Methods

This preliminary cross-sectional analysis included three children with MFS (2F; age=8.3±2.1 yrs; height=1.6±0.2 m; mass=48.7±28.5 kg) and two healthy, asymptomatic controls (2F; age=7.5±0.5 yrs; height=1.3±0.03 m; mass=24.9±0.3 kg). All participants underwent motion capture while ambulating at a self-selected walking speed. Between-group differences in sagittal, frontal and transverse plane knee joint kinematics and external joint moments were assessed using an independent t-test. Statistical significance was set at $p<0.05$.

Results

There were no significant between-group differences in age, height, mass or gait speed ($p>0.05$; Table 1). Children with MFS exhibited larger frontal plane knee joint range of motion ($p=0.02$; Table 1) and a smaller external knee adduction moment during the second half of stance ($p=0.03$; Table 1) compared to children without MFS.

Discussion

These preliminary data demonstrate that children with MFS ambulate with altered knee joint mechanics when compared to children without MFS. More specifically, children with MFS exhibit more frontal plane knee joint laxity and exhibit a reduced frontal plane knee joint load during the propulsive phase of gait. Our ongoing research will assess knee joint

muscle function (strength and rate of torque development), knee joint bone and articular cartilage health via Dual energy X-ray absorptiometry (DXA) and quantitative ultrasounds, respectively, in a larger cohort size. Our long-term goal is to determine the potential alterations that occur in knee muscle and joint function in children with MFS to help inform interventions to mitigate knee joint disease at an earlier age in the lifespan in individuals with MFS.

Images (Optional)

	Marfan (mean ± std) n=3	**Control (mean ± std) n=2**	**p-value**
Demographics & Gait Speed			
Age (yrs)	8.33 ± 2.06	7.5 ± 0.5	0.63
Height (m)	1.60 ± 0.18	1.30 ± 0.03	0.14
Body Mass (kg)	48.7 ± 28.5	24.9 ± 0.3	0.36
Gait Speed (m/s^2)	1.48 ± 0.07	1.30 ± 0.08	0.21
Joint Angles (°)			
Knee Flexion at Initial Contact	-9.50 ± 8.45	-14.24 ± 5.04	0.59
Peak Knee Flexion during Loading Response	-29.78 ± 13.72	-32.82 ± 1.95	0.79
Peak Knee Abduction Angle	-6.01 ± 3.24	-3.47 ± 0.65	0.38
Peak Knee Adduction Angle	5.63 ± 2.91	3.02 ± 0.37	0.33
Peak Knee Internal Rotation Angle	10.02 ± 4.38	9.05 ± 3.69	0.86
Peak Knee External Rotation Angle	-1.34 ± 4.87	-5.09 ± 2.94	0.47
Knee Sagittal Excursion	18.45 ± 8.32	18.58 ± 3.09	0.99
Knee Frontal Range of Motion	11.63 ± 1.18	6.49 ± 0.28	**0.02***
Knee Transverse Range of Motion	11.36 ± 2.24	14.14 ± 0.74	0.22
External Net Joint Moments ($Nm \cdot kg^{-1}$)			
Peak Knee Flexor Moment	-0.43 ± 0.10	-0.40 ± 0.03	0.75
Peak Knee Extensor Moment	0.84 ± 0.40	0.58 ± 0.06	0.46
Peak Knee Abduction Moment	0.27 ± 0.06	0.19 ± 0.03	0.18
Peak Knee Adduction Moment (1^{st} half of stance)	-0.15 ± 0.06	-0.54 ± 0.12	0.16
Peak Knee Adduction Moment (1^{st} half of stance)	-0.07 ± 0.05	-0.23 ± 0.02	**0.03***
Peak Knee Internal Rotation Moment	0.24 ± 0.12	0.10 ± 0.07	0.30
Peak Knee External Rotation Moment	-0.12 ± 0.02	-0.16 ± 0.04	0.47

References (Optional)

Acknowledgements (Optional)

Funding support via NIH (K01-AG073698, TL1-TR001997, K01-HL149984), the University of Kentucky Pediatric Exercise Physiology Lab Endowment and the 2025 American Society of Biomechanics Graduate Student Research Grant.

Session Category

Musculoskeletal Biomechanics: Joints and Motion

P2-075

Upper-Limb Joint Moments and Muscle Forces During Cup-Transport Reaching Tasks With Different Precision Requirements

Mr. Masaya Suzuki B.S., Prof. Yoshimori Kiriyama Ph.D, Prof. Katsumasa Tanaka Ph.D

Kogakuin University, Shinjuku, Tokyo, Japan

Introduction

Transporting a liquid-filled cup requires accurate control to prevent spillage, yet its effects on upper-limb joint loading and individual muscle forces remain unclear. Therefore, this study compared a water-filled cup with an exposed liquid surface (Filled) and the same cup with a lid (Covered) during a cup-transport reaching task.

Methods

Ten healthy subjects performed seated forward cup-transport reaching under two randomized conditions (Filled and Covered). Three-dimensional motion capture data were used to scale the Saul et al. upper-limb musculoskeletal model in OpenSim [1]. Shoulder and elbow joint moments were computed by inverse kinematics and inverse dynamics. Individual muscle forces were estimated by static optimization with a sum-of-squared-activations objective. For each subject and condition, waveforms were time-normalized to 0–100% of the reaching phase, and time-integrated shoulder and elbow flexion moments were computed. Condition differences were tested using Wilcoxon signed-rank tests with Bonferroni correction ($\alpha = 0.05$).

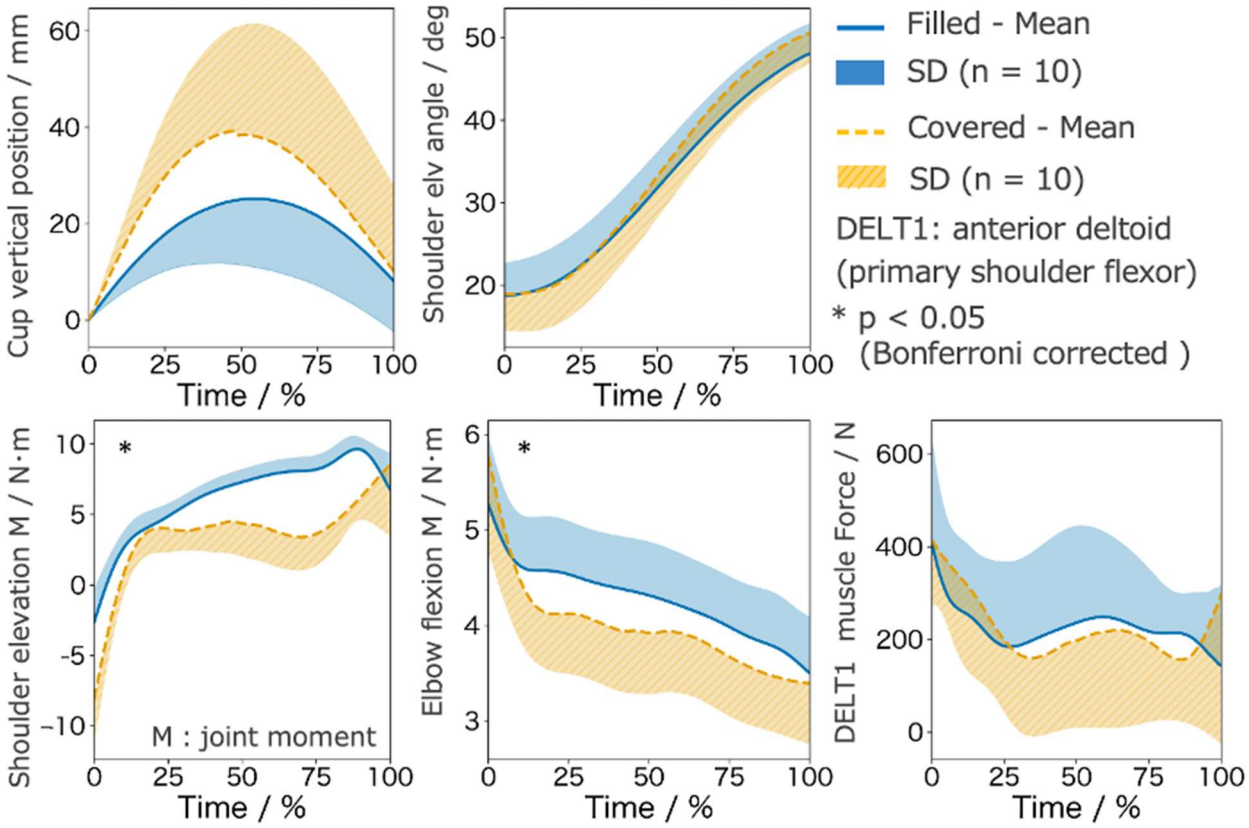
Results

Cup and upper-limb joint angle waveforms were generally similar between conditions, with no marked differences in reaching duration or end-point posture. The vertical cup trajectory tended to be lower in Filled than in Covered. Time-integrated shoulder and elbow flexion moments over the reaching phase were significantly larger in Filled ($p < 0.05$), with differences of about 1–5 N·m. Muscle force waveforms largely overlapped between conditions, and no muscle showed a significant condition effect after multiple-comparison correction, although anterior deltoid force tended to be slightly greater in Filled around mid-reach.

Discussion

Participants maintained similar reaching kinematics between conditions, but appeared to accommodate the exposed liquid by lowering the cup slightly and modestly increasing time-integrated shoulder and elbow flexion moments. This adjustment could have helped stabilize the liquid surface against sloshing or perturbations. The additional torque at the shoulder and elbow was small, indicating only limited changes in mechanical load. The trend toward higher anterior deltoid force is consistent with its role as a proximal monoarticular shoulder flexor that could fine-tune shoulder flexion torque while leaving elbow and forearm kinematics largely unchanged, suggesting that the extra torque was generated primarily by a slight increase in its activation.

Images (Optional)



References (Optional)

[1] Saul KR et al., CMBBE 2015;18:1445–1458.

Session Category

Musculoskeletal Biomechanics: Joints and Motion

P2-076

Shape and Motion of the Trapeziometacarpal Joint

Mr Matthew Oram, Dr Roberto Leonardo-Diaz, Dr Sophie Williams, Dr Marlène Mengoni

University of Leeds, Leeds, West Yorkshire, United Kingdom

Introduction

The trapeziometacarpal (TMC) joint is a saddle-shaped articulation between the trapezium and the first metacarpal that enables much of the thumb's motion and stability. Osteoarthritis is common in the TMC joint and can lead to pain and loss of function. The influence of joint surface shape on range of motion (ROM)—and how this affects surgical outcomes—remains ambiguous. This study used bone surface meshes and kinematics data from the "Open-Source Carpal Database" [1] to investigate whether curvature-based metrics of joint shape are associated with maximum active ROM in healthy TMC joints.

Methods

Wrists from healthy volunteers (n=46; 25 Females, 21 Males; age groups: 18–25 yr, 45–75 yr) were analysed in four maximum active ROM positions. The motion of the first metacarpal relative to the trapezium was quantified by computing rotations about the principal axes of flexion–extension and abduction–adduction. Articular surface regions were extracted from each mesh, and 5^{th} order polynomial surfaces were fitted, from which curvature maps were calculated. Differences in the principal curvatures of opposing points on the trapezial and metacarpal articular surfaces were used to compute a pose dependent measure of joint congruence. Correlations were assessed between ROM, surface-averaged curvatures, and congruence metrics across subjects.

Results

There were large individual differences in active ROM measurements (17°–64°), but no significant correlations were found between ROM and surface-averaged curvature or overall congruence. These trends were consistent across both primary movement directions and across age and sex groups. The strongest observed relationship was a modest positive association between ROM during flexion–extension and congruence in the 18–25 yr group (ρ=0.38), but this trend was not present in the 45–75 yr group (Fig. 1).

Discussion

The absence of a clear relationship between the investigated measures of TMC joint shape and motion, suggests that these metrics alone are not primary determinants of unloaded active ROM in healthy TMC joints. These results indicate that further research into soft tissue factors such as ligamentous constraints, capsular laxity, and muscular control may provide clearer insight into the key drivers of thumb function.

Images (Optional)

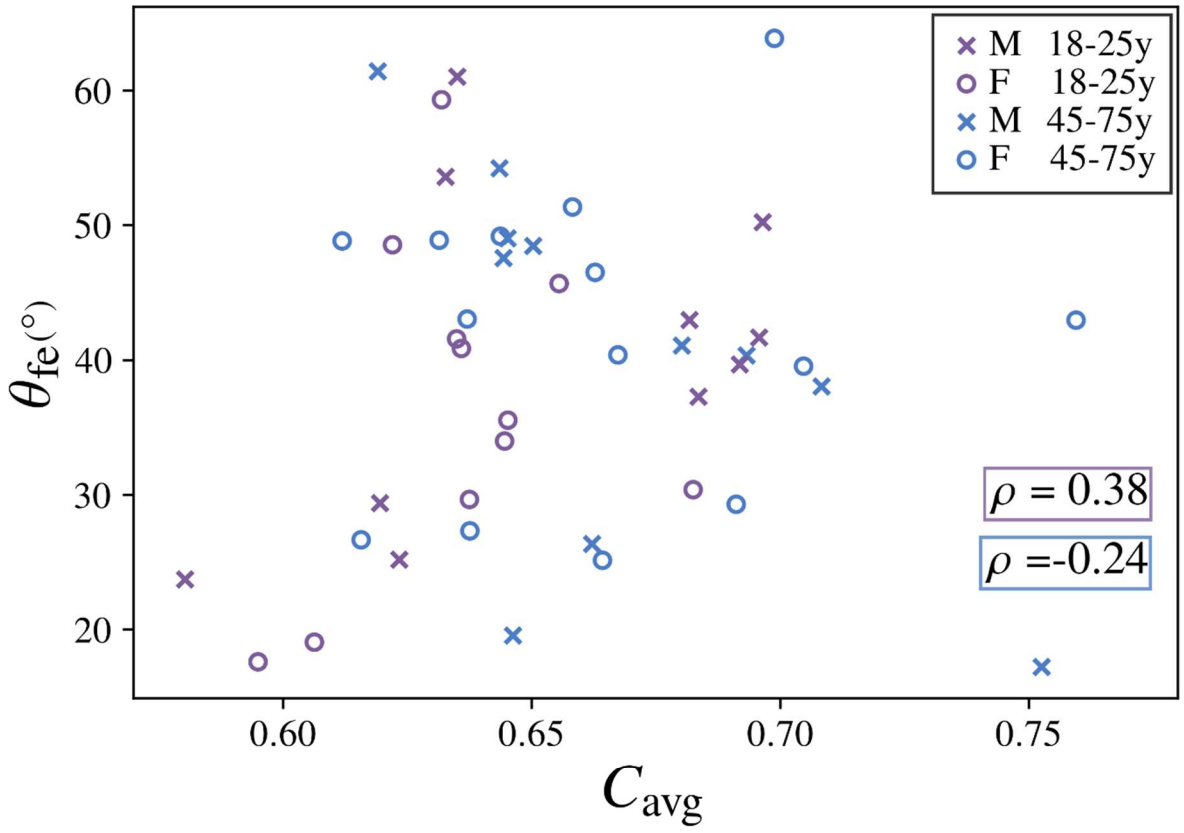


Fig. 1: Relationship between metacarpal principal rotation from the flexed to extended poses (θ_{fe}) and joint congruence averaged across all poses (C_{avg}). Pearson correlation coefficients for both age groups are labelled in the purple (18-25 yr) and blue (45-75 yr) boxes.

References (Optional)

[1] Bardiya Akhbari *et al.* , J Orthopaedic Research, 2019

Session Category

Musculoskeletal Biomechanics: Joints and Motion

P2-077

Sensitivity of Sit-to-Walk Joint Moments to Age-Related Mass Distribution

Mr. Michael Miller[1], Dr. Eline van der Kruk[2], Dr. Katherine Knaus[1], Dr. Anne Silverman[1]

[1]Colorado School of Mines, Golden, Colorado, United States. [2]Delft University of Technology, Delft, South Holland, Netherlands

Introduction

Sit-to-walk (STW) transitions place substantial mechanical demands on older adults. Generic inertial property definitions may not reflect age-related changes in body mass distribution. Older adults have greater torso and pelvic mass relative to lower limbs compared to younger adults [1], which can require greater joint moments to rise. We systematically increased the relative upper-body mass of a male and female model to determine effects on joint moments during STW.

Methods

A generic model containing 37 degrees of freedom and 22 segments was scaled in size and body mass to the heaviest older male and female participants from a larger study (Male: 53 yrs, 107.3 kg, 1.8 m; Female: 65 yrs, 115.7 kg, 1.67 m). Baseline model mass distributions were 44% in the head, arms and trunk (HAT) and 56% in the lower limbs (male), and 45% HAT/55% lower limbs (female) [2]. Relative segment masses were adjusted to match dual x-ray absorptiometry measurements for older men (47% HAT/53% legs) and women (49% HAT / 51% legs) (aged condition) [1,3]. Then, mass was shifted in 5% total body mass increments from the legs to the HAT until 25% of the mass had shifted, resulting in seven mass-distributed models per participant. Lower limb joint moments calculated using inverse dynamics were normalized to body mass.

Results

Using older segment mass distributions [1,3] increased peak hip extension moments by 4.1% (male) and 2.5% (female), and peak knee extension moments by 1.1% (male) and 1.0% (female) from baseline models (Figure). Ankle plantarflexion moments changed <1%. A 25% mass shift increased peak hip extension moments by 25.1% (male) and 24.5% (female), and knee extension moments by 4.0% (male) and 2.7% (female).

Discussion

Altering generic models to reflect older adult segment mass distributions produced the greatest changes in hip moments, but the percent change was small. Age-related mass distribution has limited influence on joint moments during low-velocity tasks like STW,

particularly at distal joints. More extreme mass shifts substantially altered joint moments at instances with high acceleration at more proximal joints.

Images (Optional)

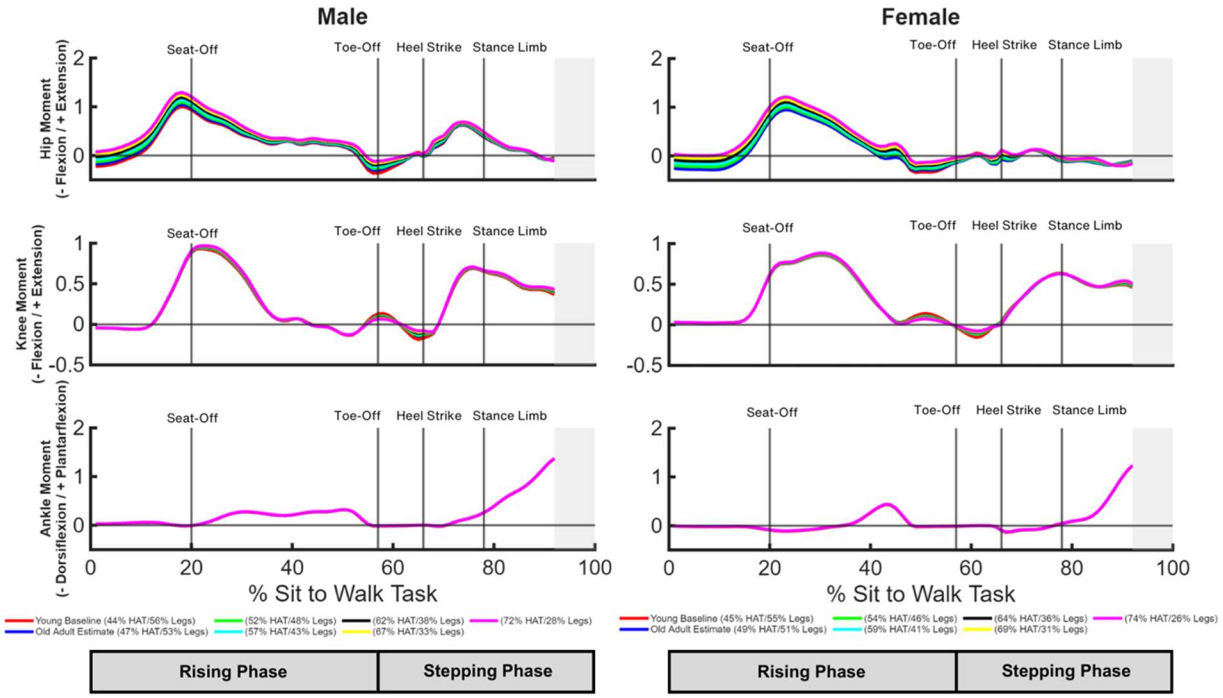


Figure: Body mass-normalized hip, knee and ankle joint moments for male and female models on the stepping limb during STW. STW began when the forward body center of mass velocity exceeded 0.15 m/s and ended when the stepping limb left the second force plate.

References (Optional)

[1] Pavol, et al., J Biomech, 2002. [2] Handsfield, et al., J. Biomech., 2014. [3] Chambers, et al., Clin. Biomech, 2010.

Session Category

Musculoskeletal Biomechanics: Joints and Motion

P2-078

Aged Muscle Parameters Affect Muscle Recruitment During Simulations of Sit-to-Walk

Mr. Michael Miller[1], Dr. Eline van der Kruk[2], Dr. Katherine Knaus[1], Dr. Anne Silverman[1]

[1]Colorado School of Mines, Golden, Colorado, United States. [2]Delft University of Technology, Delft, South Holland, Netherlands

Introduction

Musculoskeletal simulations can estimate muscle forces during movements like sit-to-walk (STW) but depend on musculotendon parameters that change with age [1]. We evaluated predicted muscle forces from aged musculotendon parameters in an older adult completing STW. Soleus (SOL), gastrocnemius (GAS), and tibialis anterior (TA) muscle forces were evaluated because of their functions to provide support, forward propulsion, and balance control.

Methods

Whole-body motion and ground reaction forces were collected for an older adult (F, 73 yrs, 51 kg, 1.66 m) performing three STW trials. Inverse kinematics solutions of a body mass-scaled, generic model containing 80 Hill-type musculotendon actuators were determined and musculotendon properties were adjusted in 7 cases: 1) baseline model (no changes), 2) -20% v_{max}, 3) +20% τ_{deact} ,4) +16.67% passive element stiffness, 5) -6% Achilles tendon stiffness, 6) F_{iso} variable muscle reduction , and 7) all property changes combined. The F_{iso} reductions were hip extensors -21%, hip flexors -23%, knee extensors -29%, knee flexors -25%, ankle plantarflexors -32%, and ankle dorsiflexors -8%. Muscle forces and activations were determined using Computed Muscle Control and compared using a repeated measured ANOVA (α= 0.05).

Results

Reducing max F_{iso} induced the largest changes from baseline, increasing SOL (37.4%, $p<0.01$), decreasing GAS (31.8%, $p=0.02$), and increasing TA (111%, $p<0.01$) peak forces. Increasing τ_{deact} increased SOL (20.4%, $p<0.05$) and TA (122%, $p<0.01$) peak forces. Combining all properties increased SOL (33.2%, $p<0.05$), decreased GAS (43.8%, $p<0.05$), and increased TA (95%, $p<0.05$) peak forces. Changes to the other properties in-isolation peak forces ($p>0.05$).

Discussion

Strong effects of F_{iso} are supported by musculotendon sensitivity studies during gait [2]; F_{iso} was the biggest driver of force changes in the combined condition. Greater SOL force

with reduced suggests greater activation, which we observed (Figure). Greater τ_{deact} causing prolonged activation increased antagonist muscle forces in SOL and TA. Aging muscle properties changed muscle force sharing, with greater SOL force and lesser GAS force. This emergent result of aging the model is consistent with plantarflexor muscle recruitment changes with aging [3].

Images (Optional)

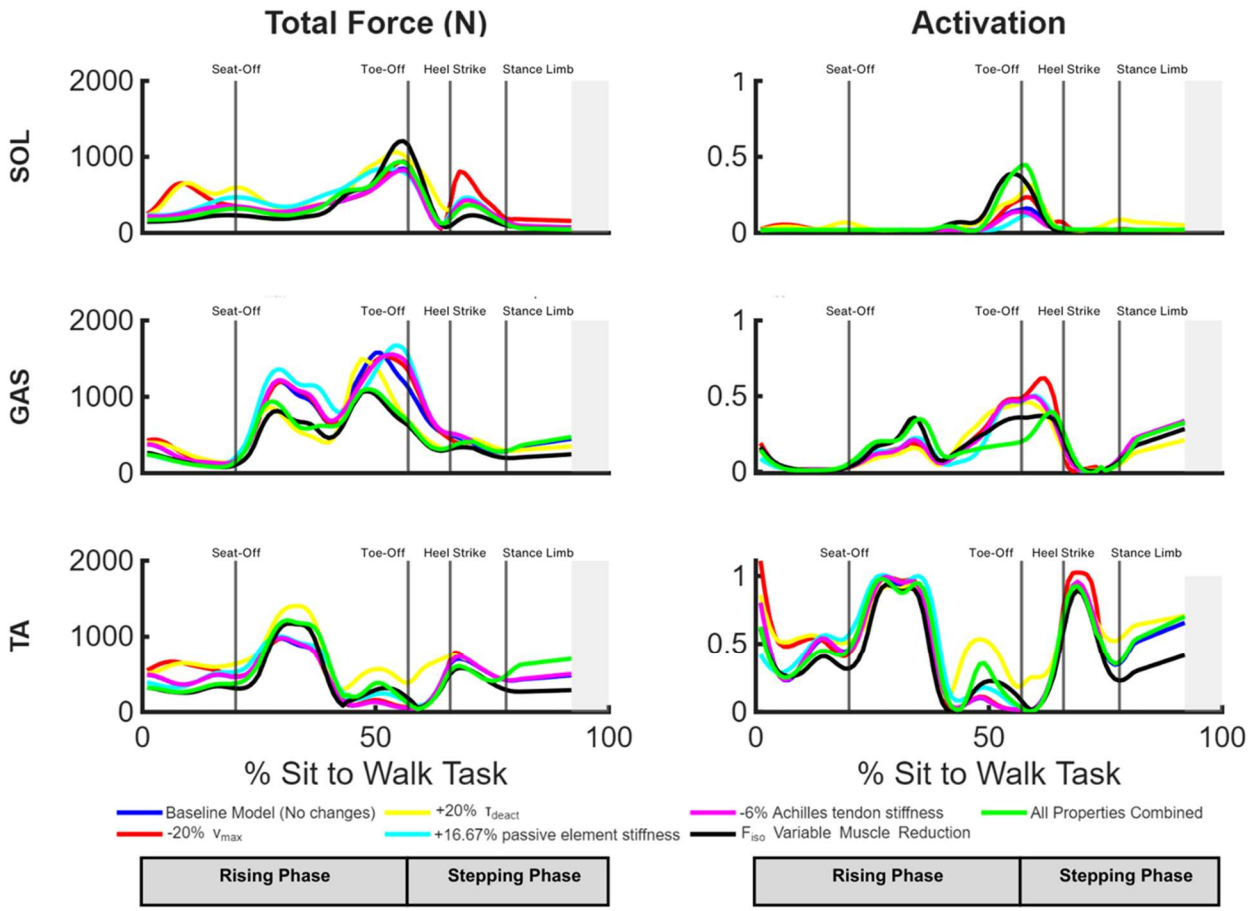


Figure: Total musculotendon force and activation for the stepping limb soleus (SOL), gastrocnemius (GAS), and tibialis anterior (TA). STW began when the forward body center of mass velocity exceeded 0.15 m/s and ended when the stepping limb left the second force plate.

References (Optional)

[1] Thelen, J. Biomech. Eng., 2003. [2] Chen and Franklin, Ann. Biomed. Eng., 2023. [3] Kim and Franz, J. Appl. Physiol., 2021.

Session Category

Musculoskeletal Biomechanics: Joints and Motion

P2-079

Comparative Analysis of Subtalar Joint Kinematics in Humans and African Great apes

Prof. Michele Conconi[1], Prof. Nicola Sancisi[2], Prof. Rita Sorrentino[3], Prof. Alberto Leardini[4], Prof. Naomichi Ogihara[5], Prof. Claudio Belvedere[4]

[1]Department of Industrial Engineering, University of Bologna,, Bologna, Italy, Italy. [2]Department of Industrial Engineering, University of Bologna,, Bologna, Italiy, Italy. [3]Department of Biological, Geological, and Environmental Sciences, University of Bologna, Bologna, Italy, Italy. [4]Laboratory of Movement Analysis, IRCCS Istituto Ortopedico Rizzoli, Bologna, Italy, Italy. [5]Laboratory of Human Evolutionary Biomechanics, Department of Biological Sciences, The University of Tokyo, Tokyo, Japan, Japan

Introduction

A detailed understanding of articular physiology is critical for elucidating the etiology of musculoskeletal disorders. This study focuses on the subtalar joint and tests the hypothesis—previously supported in the human knee and ankle [1,2]—that functional adaptation shapes the articular surfaces to optimize load transmission across the full range of motion, and that this adaptive principle is conserved between human and non-human African great apes. We infer subtalar joint kinematics in modern humans, chimpanzees, and gorillas from subchondral bone geometry using this optimization principle, and validate these predictions against *in-vitro* kinematic data obtained from sequential CT images.

Methods

Subtalar kinematics was obtained from thirty-two CT scans for three human feet [3], and from two CT scans for two chimpanzees and two gorillas [4]. The experimental poses were expressed using anatomical reference systems and the Euler sequence of rotation [5]. For each specimen, the mean subchondral bone spacing at the anterior and posterior facets of the talocalcaneal joint was measured in the unloaded neutral scan. This spacing was used to approximate a uniform cartilage layer by offsetting the subchondral bone surfaces of both the bones. Talocalcaneal kinematics were then reconstructed by congruence maximization [1,2].

Results

Predicted kinematics were compared with experimental measurements by evaluating the magnitudes of the rotational and translational error vectors. Mean errors were 0.9 ± 0.5° and 1.1 ± 0.3 mm for humans, 1.1 ± 0.6° and 1.6 ± 1.0 mm for chimpanzees, and 2.8 ± 1.7° and 3.1 ± 1.1 mm for gorillas, respectively.

Discussion

The small discrepancies between model predictions and experimental observations (Fig. 1) validate the model and support the hypothesis that cartilage and subchondral bone morphology arise from an adaptive process shared between humans and non-human African great apes. This approach provides insight into joint tissue physiology and offers a method for predicting subject-specific articular kinematics that is applicable across species, facilitating translational and evolutionary studies.

Images (Optional)

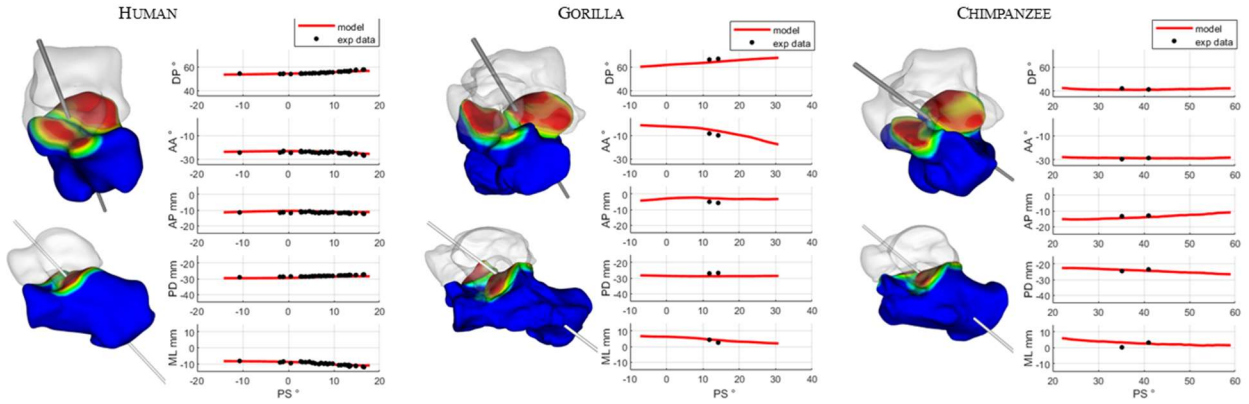


Figure 1: Comparison of predicted (red) and experimental (black dots) subtalar joint kinematics for a human (left), gorilla (center), and chimpanzee (right): the dorsi/plantar (DP) flexion, the abduction/adduction (AA), and the anterior/posterior (AP), proximal/distal (PD), and medial/lateral (ML) translations are plotted versus the pronation/supination (PS) angle. Bone models are shown in the neutral configuration, with colors representing relative inter-surface distance (red: contact; blue: >7 mm). The grey cylinder indicates the mean helical axis of maximum congruence motion.

References (Optional)

[1] Conconi et al.,2015. *J Biomech* 48:2960-2967.

[2] Conconi et al.,2020. *IEEE Trans Biomed Eng* 68:1084-1092.

[3] Conconi et al.,2024. *J Orht.Res.* 42.1:148-163.

[4] Conconi et al.,2021. *J Foot&Ank.Res.* 14.1:66.

[5] Negishi et al.,2021. *R. Soc.OpenSci.* 8.11:211344.

Session Category

Musculoskeletal Biomechanics: Joints and Motion

P2-080

Effects of Transtibial Bone-Anchored Limb Use on Bilateral Knee Cartilage Contact Pressure During Gait

Mr. Mitchell Ekdahl BS[1], Dr. Cory Christiansen PhD[2], Dr. Jason Stoneback MD[2], Dr. Brecca Gaffney PhD[1,2]

[1]University of Colorado Denver, Denver, CO, United States. [2]University of Colorado Anschutz Medical Campus, Aurora, CO, United States

Introduction

Knee osteoarthritis is nearly 18 times more common in people with unilateral transtibial amputation (TTA) using socket prostheses compared to individuals without amputation, which is largely attributed to chronically altered intra-articular joint mechanics. Bone-anchored limbs (BALs) are an alternative to traditional socket prostheses that attach directly to the residual limb bone. While early work has shown that unilateral transtibial BAL use does not change joint loading in either knee during walking, the direct effects on intra-articular joint mechanics remain unknown.

Methods

Motion capture during overground walking at self-selected speed was collected from fourteen adults (5F/9M, 53.7±13.1y, BMI: 28.5±4.6) with unilateral TTA at two timepoints: before (in socket prosthesis) and one year after BAL implantation. Musculoskeletal knee contact models were developed for each participant. A concurrent optimization approach was used to estimate knee joint kinematics and muscle forces. Cartilage contact pressure in each compartment of the tibiofemoral joint was calculated as a function of overlap depth between the femoral and tibial cartilage surfaces using an elastic foundation model. Mean contact pressure impulse in each knee during each functional phase of the stance period was compared between timepoints using repeated measures ANCOVA, with gait speed as the covariate (α=0.05).

Results

Mean pressure impulse in the medial compartment of the amputated-limb knee was increased during terminal stance after BAL implantation (1.00±0.13 MPa*s (before) vs 1.03±0.14 MPa*s (after), p=0.036). Sound-limb mean pressure impulse was not changed during any functional phase of stance with BAL use.

Discussion

Transtibial BAL use increased amputated-limb dynamic knee cartilage contact pressure during terminal stance but did not affect sound-limb contact pressure. Increased medial compartment pressure in the amputated-limb knee after BAL implantation may be attributed to the direct force transmission created by BALs. Underloading of the amputated-limb knee joint in socket prosthesis users can contribute to articular cartilage degradation. Knee osteoarthritis in people with TTA is more common in the sound-limb, which is mechanistically driven by compensatory overloading of that limb. The absence of changes in sound-limb cartilage contact pressure following BAL implantation may suggest that sound-limb knee osteoarthritis risk is not changed after BAL implantation.

Images (Optional)

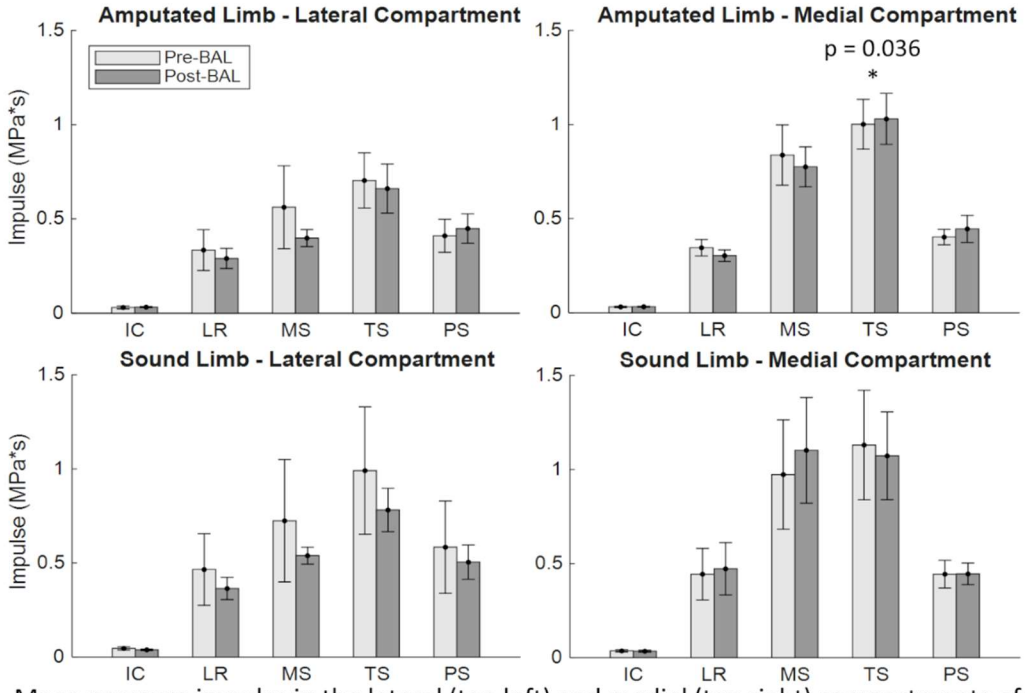


Figure 1. Mean pressure impulse in the lateral (top left) and medial (top right) compartments of the amputated-limb knee joint, and the lateral (bottom left) and medial (bottom right) compartments of the sound-limb knee joint during each functional phase of stance before (light gray) and after (dark gray) BAL implantation. (IC: initial contact; LR: loading response; MS: mid-stance; TS: terminal stance; PS: pre-swing)

References (Optional)

Session Category

Musculoskeletal Biomechanics: Joints and Motion

P2-081

Effects of Footwear Cushioning and Frequency Constraints on the Metabolic Cost of Hopping

Mr. Montgomery Bertschy, Ms. Nicole Sylvain, Dr. Wouter Hoogkamer

University of Massachusetts Amherst, Amherst, MA, United States

Introduction

Footwear cushioning can reduce the metabolic cost of running, with highly resilient materials seeming to have the greatest benefit [1]. However, since midsole materials will always return less than 100% of the mechanical energy stored, with more cushioning, more energy will be lost. If more mechanical energy is lost, athletes need to increase positive net work to compensate. The purpose of this study was to understand the effect of footwear cushioning on metabolic cost, using hopping as a model to minimize variability in gait mechanics. We hypothesized that extreme midsole cushioning would lead to increased metabolic cost due to higher energy losses in the midsole.

Methods

Across two visits, experienced runners performed eight 4-minute hopping trials in four footwear conditions (twice per condition): a minimalist shoe with negligible cushioning (0 cm), minimalist shoe with ~1 cm of resilient foam in the forefoot (1 cm), running shoe with ~2 cm (2 cm), and ~5 cm (5 cm) of foam in the forefoot. Participants hopped to a set height range (7-9 cm) at their preferred frequency (visit 1) and at a prescribed frequency (2.2 Hz metronome, visit 2). We measured net metabolic cost, kinematics, muscle behavior, and ground reaction forces.

Results

Net metabolic cost was highest in the 5 cm footwear condition, driving a significant effect of midsole thickness on net metabolic cost (0.07±0.03 W/kg per 1 cm of cushioning). Preferred frequency was 0.17±0.02 Hz higher than hopping frequency in the prescribed condition, with a 0.64±0.12 W/kg lower metabolic cost. There was no significant effect of footwear on hopping frequency

Discussion

Between the two extreme conditions (0 and 5 cm), the increase in metabolic cost was consistent between frequency conditions. These findings agree with data on the effect of surface damping on net joint work [2]. In the intermediate conditions, the results tend to

diverge between the frequency conditions. Direct analysis of muscle-tendon unit behavior for these footwear conditions may explain the differences in these results.

Images (Optional)

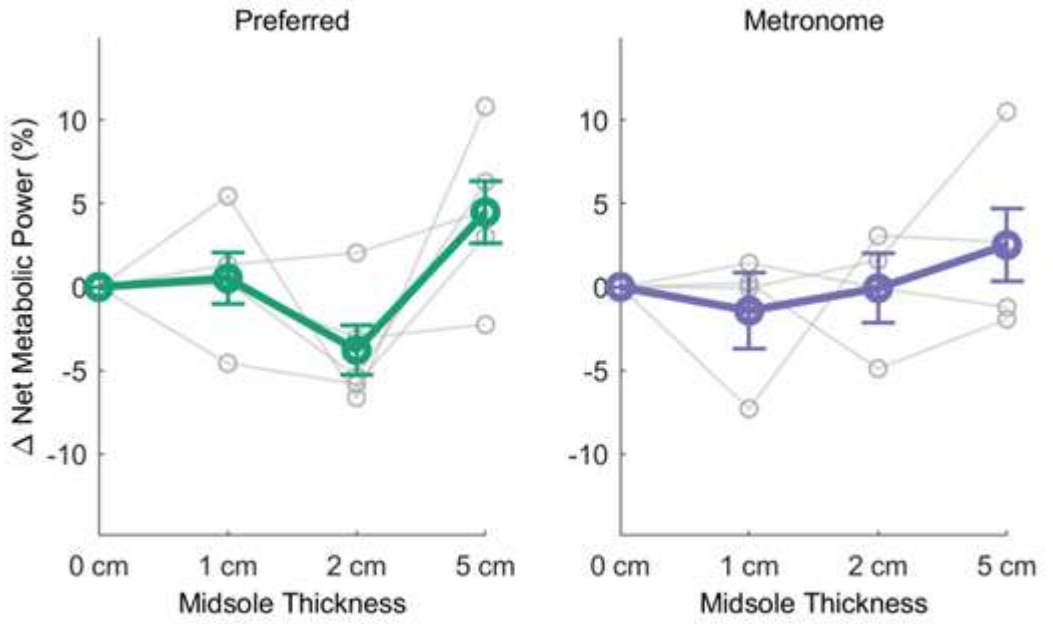


Figure 1: Change in metabolic power (W/kg) relative to the baseline condition (0 cm). Grey lines represent participant averages; colors represent group averages ± standard error.

References (Optional)

[1] Bertschy et al., J. Exp. Biol., 2025

[2] Moritz et al., J. Appl. Physiol., 2004

Session Category

Musculoskeletal Biomechanics: Joints and Motion

P2-082

Multi-Task Learning for Joint Impedance Estimation

Ms. Nana Porter-Honicky B.S., Dr. Elliott Rouse PhD

University of Michigan, Ann Arbor, MI, United States

Ms. Nana Porter-Honicky

Introduction

The inertia, damping, and stiffness of a joint, or joint impedance, characterize the body as a mechanical system, offering insight into mechanical changes in the body due to conditions like stroke or cerebral palsy [1]. However, quantifying joint impedance is prohibitively difficult due to data constraints. Such quantification requires a perturbation to the joint and unperturbed baseline trials, where the difference between the unperturbed and perturbed joint encodes the properties that make up joint impedance. This difference is parametrically modeled as a second order system. Current methods require hundreds of trials [1], limiting utility outside of research contexts. We propose a method of using a multi-task neural network to predict the unperturbed joint positions and torques and estimate joint impedance without unperturbed trials. Importantly, our model predicts the joint positions and torques needed to calculate impedance values, rather than predict them directly. This maintains the robustness of established estimation pipelines while significantly reducing data collection requirements.

Methods

The joint positions and torques are modeled as a 100^{th}-order Markov chain, where the previous 100 states are used to predict the next 100. The loss function of the model was designed to optimize for the terms in the second-order parametric impedance model. Hyperparameters were chosen via a Bayesian hyperparameter sweep. To optimize data utility, we preprocessed each phase-normalized trial using a windowing method. The model was trained on data collected during previous level-ground-walking ankle impedance estimation studies [1,2].

Results

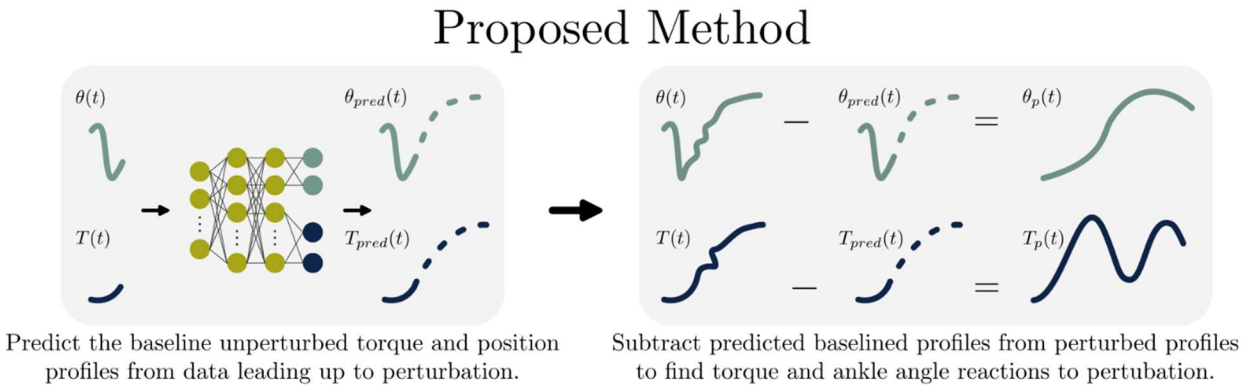
K-fold cross-validation and leave-one-out validation show torque and position errors considerably lower than the perturbation magnitudes typical in impedance estimation

experiments. Crucially, the resulting predictions account for up to 97% of the variance in the perturbed data when fit to the second-order impedance equation.

Discussion

Impedance is a critical metric for understanding and modeling the mechanical properties of biological joints. Our proposed method to quantify impedance yields similar results to current methods and reduces data requirements by as much as half. This removes barriers to evaluating more impaired populations [2], paving the way for broader clinical applications.

Images (Optional)



Predict the baseline unperturbed torque and position profiles from data leading up to perturbation.

Subtract predicted baselined profiles from perturbed profiles to find torque and ankle angle reactions to pertubation.

$$T_p = I\ddot{\theta}_p + b\dot{\theta}_p + k\theta_p$$

Find inertia I, damping b, and stiffness k with linear regression of joint reaction to perturbation.

Results

Use case	Torque Error (Nm/kg)	Angle Error (rad)	VAF (%)
Subject Dependent	$4.64 \pm 2.27 \times 10^{-4}$	$1.05 \pm 0.47 \times 10^{-2}$	97.4 ± 4.6
Subject Independent	$0.85 \pm 2.20 \times 10^{-4}$	$1.45 \pm 1.15 \times 10^{-2}$	95.7 ± 10.3

Table 1: Mean Absolute Error of torque and angle predictions in the subject dependent and subject independent use cases. Variance Accounted For (VAF) of the predictions fit to perturbation response model.

References (Optional)

[1] Shorter *et. al*, Sci Rep, 2021

[2] Rouse *et. al*, IEEE Trans Neural Syst Rehabil Eng, 2014

Acknowledgements (Optional)

This work was supported in part by the Rackham Merritt Fellowship and the NIH grant (1R01HD111567-01).

Session Category

Musculoskeletal Biomechanics: Joints and Motion

P2-083

Causal Dynamic Balance Networks as a Diagnostic Feature for Structural Hip Disease

Mr Brandon Nunley MS[1], Dr Joel Wells MD[2], Dr. Nicholas Fey PhD[1]

[1]The University of Texas at Austin, Austin, TX, United States. [2]Baylor Scott & White, Dallas, TX, United States

Introduction

Developmental dysplasia of the hip (DDH) alters the loading environment of the hip, which can lead to pain and gait compensations [1]. The system-wide effects of this local instability on dynamic balance during locomotion are not well understood. Convergent cross-mapping (CCM) offers a framework for investigating these complex, non-linear interactions [2]. Unlike traditional correlation analyses, CCM can detect causal coupling between time-series in dynamic systems. The purpose of this study was to quantify how local hip instability alters segmental coordination by applying CCM to pairs of segmental angular momentum signals in DDH and control participants.

Methods

Fifteen DDH patients who underwent PAO completed this study. Nine control participants completed a single visit. Patients performed a 1-min treadmill walking trial at self-selected speed for each of three ramp conditions: incline (+10º), level (0º), and decline (-10º). Kinetic and kinematic data were collected using an instrumented treadmill and 10-camera infrared motion capture system. Continuous, normalized segmental angular momenta of the thorax, pelvis, thighs, shanks, and feet were used to reconstruct the phase space dynamics (Figure 1a). For each signal, we constructed a "shadow manifold" using time-delay embedding. Causal coupling strength between pairs of connected segments was quantified by the correlation coefficient between the predicted and observed signals. A causal link was inferred if the prediction skill increases and converges to a stable value as the library size grows. This analysis was performed bidirectionally to distinguish between unidirectional forcing and bidirectional feedback. CCM analysis was performed using the pyEDM software package.

Results

Feature vectors derived from inter-segmental causal connectivity networks revealed distinct coordination patterns between DDH patients and controls. Clustering achieved a classification accuracy of 91.6% in distinguishing DDH subjects from controls (Figure 1b).

Discussion

These findings demonstrate that analyzing causal interactions within the dynamic balance network provides a sensitive measure of localized dynamic hip instability. The high classification accuracy indicates that DDH pathology drives distinct, non-linear compensatory strategies that persist beyond local joint mechanics. This causality-based framework offers a novel functional biomarker to complement static radiography.

References (Optional)

[1] Joshua Harris *et al.*, Clin Sports Med, 2021

[2] Sugihara *et al.*, Science, 2012

Session Category

Musculoskeletal Biomechanics: Joints and Motion

P2-084

Rearfoot and Midfoot Joint Rotations under Isolated and Combined TA-TP Tendon Force Perturbations

Miss Niharika Pathare, Dr. Anthony Le, Dr. Amy Lenz

University of Utah, Salt Lake City, Utah, United States

Introduction

Several neuromuscular conditions are characterized by altered muscle synergies that disrupt midfoot and hindfoot alignment at initial contact during gait. However, joint-level foot kinematics cannot be isolated in vivo due to neural compensation, soft-tissue variability, and measurement limitations. This study tested whether isolated and combined perturbations to tibialis anterior (TA) and tibialis posterior (TP) tendon loading produce systematic changes in passive multisegment foot alignment at heel strike in cadaveric feet.

Methods

With IRB approval, four cadaveric lower limbs (male; 58.8 ± 12.7 yrs, 78.1 ± 16.8 kg) were prepared with bone-embedded optical markers to quantify 3D joint rotations; only male specimens from the donor pool allowed occlusion-free marker placement. Each specimen was vertically loaded to 20% body weight (BW) and tested in a controlled heel-strike posture to reproduce 5% BW early-stance loading. Specimen-specific scaled baseline tendon forces for TA, extensors, peroneal brevis and longus, flexors, TP, and Achilles were derived from OpenSim. Three conditions, each with three steady-state trials, were tested by perturbing TA and TP forces relative to baseline heel strike: TA_{50} TP_{100}, $TA_{100}TP_{50}$, and TA_{50} TP_{120}; the subscripts denote the percentage of the corresponding tendon's baseline force. Joint angles were computed relative to the anatomical axes of the proximal bone via Euler decomposition. Linear mixed-effects models assessed condition effects with Tukey contrasts and Cohen's d effect size for pairwise comparisons (α=0.05).

Results

Significant synergy-dependent joint angle changes were observed across multiple joints ($p < 10^{-4}$ to 10^{-9}), with talonavicular and subtalar joints demonstrating changes across all three anatomical planes. Except for subtalar sagittal motion, $TA_{50}TP_{100}$ and $TA_{50}TP_{120}$ produce similar rotational patterns across joints, whereas $TA_{100}TP_{50}$ consistently shows larger and directionally distinct deviations. Talonavicular joint angles deviate the most from baseline across conditions, with several pairwise contrasts that involve $TA_{100}TP_{50}$ reaching large effect sizes ($|d| \approx 0.8–2.35$). Subtalar rotations show similar

patterns between conditions but with smaller angle magnitudes, while demonstrating substantial between-condition differences (|d| up to 2.1).

Discussion

These findings demonstrate that TA-TP synergy patterns significantly reorganize rearfoot-midfoot kinematics at heel strike, with talonavicular and subtalar joints showing the greatest sensitivity to coordinated tendon loading.

Images (Optional)

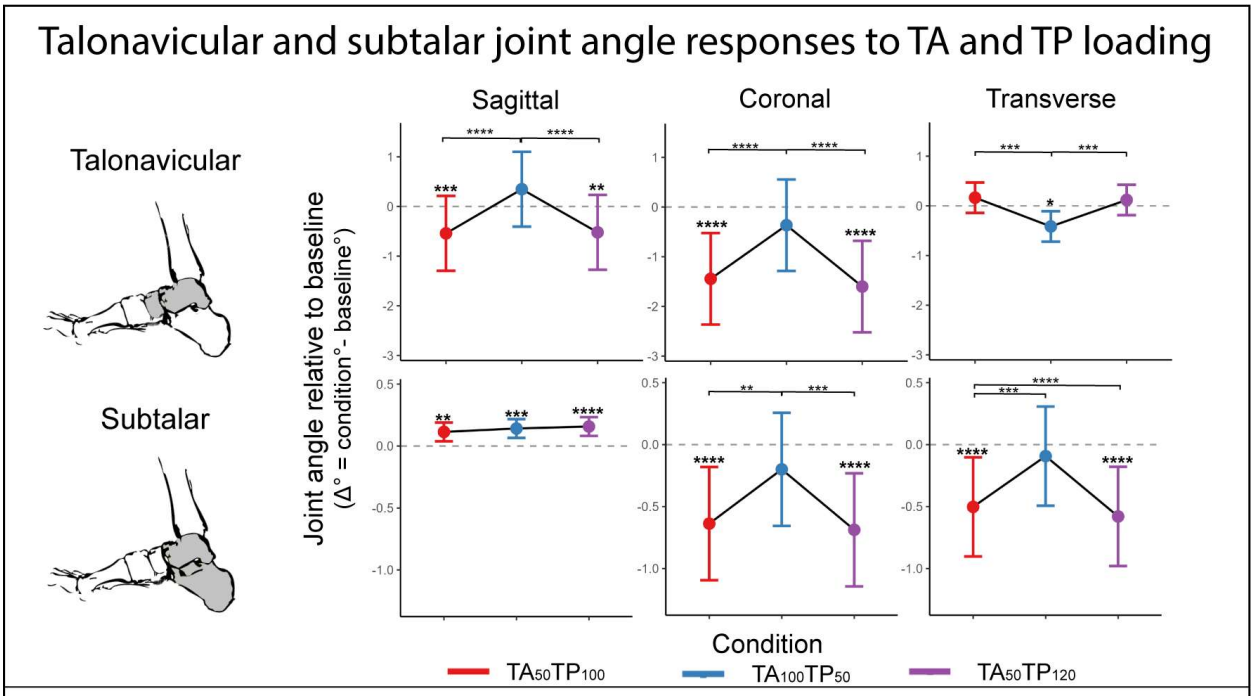


Fig. 1: Estimated marginal means (EMMs) of talonavicular and subtalar joint angle changes (Δ° ± SE) across sagittal, coronal, and transverse planes under $TA_{50}TP_{100}$ (red), $TA_{100}TP_{50}$ (blue), $TA_{50}TP_{120}$ (purple). Talonavicular rotations showed the largest deviations across conditions. Horizontal brackets indicate significant Tukey-adjusted pairwise differences; *, **, ***, **** correspond to $p < 0.05$, 0.01, 0.001, 0.0001, respectively.

Session Category

Musculoskeletal Biomechanics: Joints and Motion

P2-085

Ligament contributions to talus motion during walking and running

Mr Quinn Yetman, Dr. Michael Rainbow

Queen's University, Kingston, Ontario, Canada

Introduction

The foot and ankle coordinate their mechanics to enable efficient upright locomotion [1]. This coupling occurs at the talus, which is uniquely passive, meaning only ligaments and cartilage drive its motion. Although ligaments are essential for constraining talus motion and maintaining ankle stability, how they coordinate their mechanics to stabilize the talus across locomotor tasks has not been explored in-depth. Given the substantial variation in ligament properties [2] and articular morphology across people [3], we question whether some individuals require more ligament support than others.

Methods

We quantified the ligament contributions to talus motion using a subject-specific, biplanar videoradiography (BVR) driven model. BVR captures individual 6 degree-of-freedom bone kinematics with errors < 2°. The model, implemented in ArtiSynth, simulated talus motion with cartilage contact and ligament forces during walking and running for 5 participants (Figure 1a). Ligament contributions were assessed by comparing simulated talus kinematics with and without ligaments using root-mean-square helical-axis orientation error (RMSE) relative to BVR-measured talus motion.

Results

Removing ligaments increased the RMSE for 3 of 5 participants for walking and 4 of 5 participants for running (Figure 1b). The magnitude of this effect varied across individuals (-10% to +23%) and across subphases of stance. Removing ligaments had a large effect on error during running propulsion (average increase of +17%) with mixed responses in other subphases, including decreases in some participants. Participants with larger increases in RMSE when ligaments were removed tended to exhibit lower BVR-measured talocrural inversion, and net ankle dorsiflexion and internal rotation range of motion (ROM) during loading.

Discussion

We saw variability in how ligament removal affected talus-tracking error. Two participants showed larger increases in error, motivating the hypothesis that reliance on ligament support varies meaningfully across people. There was some correlation between increased error from removing ligaments and lower ROM, supporting this idea. The substantial increase in error during running propulsion highlights the critical role of ligaments in stabilizing the talus during this subphase. Future work will test these hypotheses and look for predictors of ligament sensitivity.

Images (Optional)

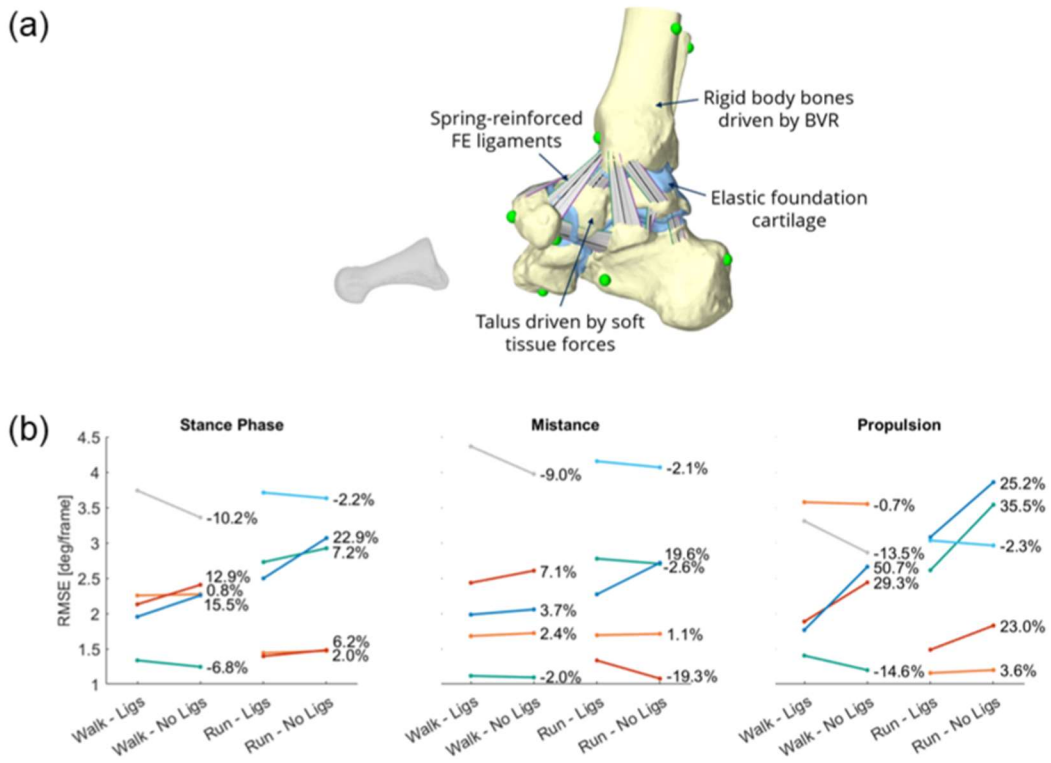


Figure 1: (a) The ankle joint complex model in ArtiSynth. Bones and cartilage were modelled as rigid bodies, and ligaments as spring reinforced finite element membranes. Kinematics from biplanar videoradiography drove bones surrounding the talus while the talus was driven by cartilage contact and ligament forces. Soft tissue material properties were found by minimizing the RMSE using a design of experiments approach using kinematics separate from those used for analysis. First metatarsal is included in the image to give context but was not simulated. (b) The effect of removing all ligaments from the simulation on RMSE over all of stance, midstance (when the entire foot is contacting the ground), and propulsion (heel rise to toe off).

References (Optional)

[1] Welte et al., Front., 2023

[2] Siegler et al., Foot Ankle, 1988

[3] Lenz et al., Sci Rep, 2021.

Session Category

Musculoskeletal Biomechanics: Joints and Motion

P2-086

The (K)need for Speed: Optimizing In Vitro Joint Testing for Speed

Dr. Tara Nagle PhD, Miss Elizabeth Pace BS, Dr. Robb Colbrunn PhD

Cleveland Clinic, Cleveland, Ohio, United States

Introduction

In vitro joint biomechanics testing requires the use of a 6-DOF joint simulator to apply loads. In some cases, when viscoelastic properties are important, achieving high speeds is crucial. The goal of this study was to evaluate how test variables contribute to 1) minimum achievable simulated gait duration and 2) % RMS load errors, when testing a cadaveric knee on a 6-DOF joint simulator.

Methods

A modified ISO-gait profile (Fig. 1A) was applied to a cadaveric knee (male, 65) using a Jupiter-3000 simVITRO system. Three variables were investigated to determine the optimal testing setup: 1. Fixturing, 2. Trajectory Interpolation, and 3. Control Method.

Fixturing included a) Standard or b) L-bracket, where the femur was mounted such that the knee's flexion axis was aligned to robot axis-6. Trajectory Interpolation included a) Linear or b) Spline. Control methods included a) Force control (F-Ctrl) or b) Position control *with* adaptive compensation (P-Ctrl), where commanded joint kinematics were iteratively optimized over five 30-second gait cycles to achieve the desired loads, and kinematics determined for the 5^{th} cycle were applied in position control over various durations. Tuning parameters remained consistent. Gait durations of 120, 60, 30, 15, 10, 6.7, 5, 4, and 3 seconds were attempted, and shortest achievable duration, % RMS-error and failure mode were recorded for each combination.

Results

The fastest achievable gait duration was 4 seconds and was completed with L-bracket fixturing, linear interpolation, and P-Ctrl. The fastest achievable duration was 15 seconds with F-Ctrl, and 10 seconds with standard fixturing and P-Ctrl. In all unsuccessful cases, failure occurred due to robot motor torque overload on axis-6.

For all DOF, % RMS-error reduced with P-Ctrl compared to F-Ctrl. For Anterior force and ER torque, % RMS-error was lower with L-bracket fixturing compared to standard (Figure 1B-D). Interpolation showed only minor effects on % RMS-error.

Discussion

Selecting L-bracket fixturing and P-Ctrl is optimal for high-speed testing. This makes sense because by aligning the flexion axis to axis-6, stress is reduced on the motor with the lowest torque rating, and robots are designed for P-Ctrl. Future work will examine other variables that affect performance, like tuning parameters, and will include additional specimens.

Images (Optional)

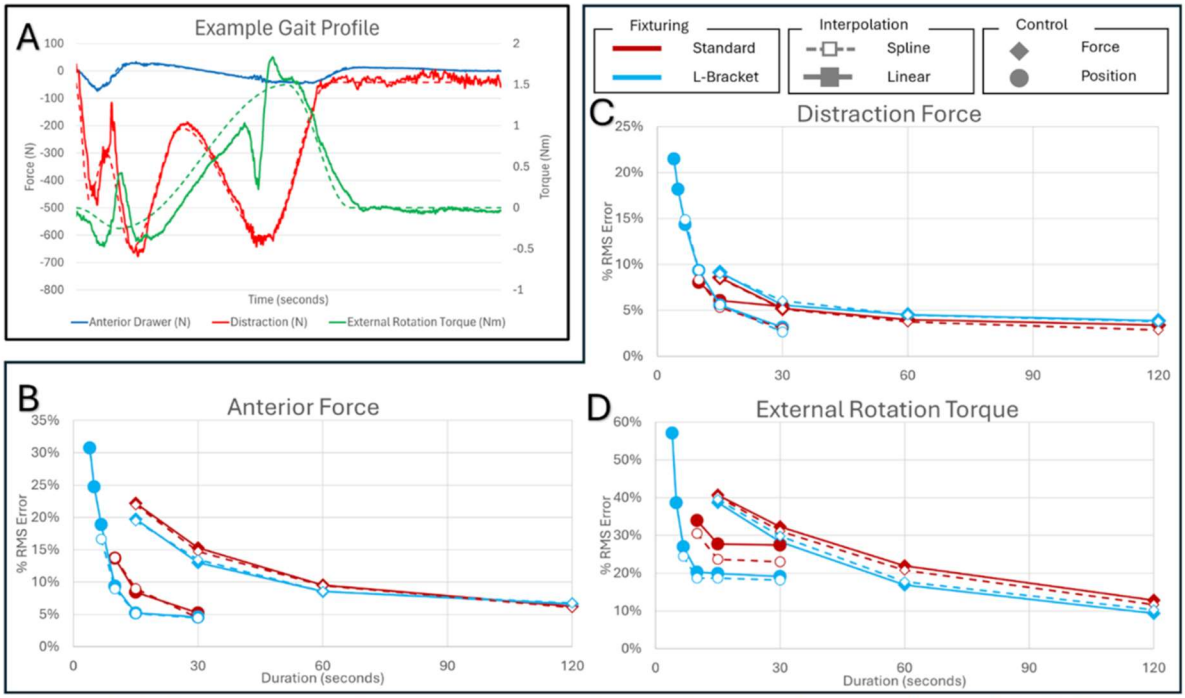


Figure 1: A) Commanded gait profile (dotted) and example actual loads (solid), and % RMS error across each gait cycle as a function of duration, fixturing, interpolation and control method for B) Anterior Force, C) Distraction Force and D) External Rotation Torque.

Session Category

Musculoskeletal Biomechanics: Joints and Motion

P2-087

Talonavicular Kinematics: Matching Healthy Controls to Clinical Populations

Mr. Robert Chauvet[1,2], Ms Emily Smith-Bregeda[1,2], Ms Janae Ruzicki[1,2], Dr. Koren Roach[1,2]

[1]McCaig Institute for Bone and Joint Health, University of Calgary, Calgary, Alberta, Canada. [2]Department of Biomedical Engineering, University of Calgary, Calgary, Alberta, Canada

Introduction

In clinical gait studies comparing pathological populations to healthy controls, participants are typically matched by age and sex [1]. Given the variability in foot shape and its potential influence on joint kinematics of the midfoot, it is worth considering whether matching for foot shape should also be standard practice [2]. This study investigates how confounding variables such as age, sex, body mass index (BMI), and foot shape affects talonavicular (TN) kinematics.

Methods

Eight healthy participants (4F/4M; age: 36.6±14.1yrs; BMI: 22.5kg/m^2; Meary's angle: 0.8±5.3°; calcaneal tilt: 23.2±2.5°), were recruited (REB19-1743). Participant feet and ankles were imaged at 120 Hz with a dual fluoroscopy system while participants performed activities of daily living: walking, step up, and step down. A computed tomography (CT) scan was acquired of the mid-tibia through toe tips. Clinical radiographs were taken and evaluated for Meary's angle and calcaneal tilt. The tibia, talus, calcaneus, and navicular were segmented on the CT images to generate 3D bone models. A 2D-3D registration process was used to align bone models with 2D DF images and determine joint angles and range of motion (ROM) throughout each activity. Joint angle ROMs were compared against demographic variables using stepwise multiple regression analysis and between age groups, split by median age, using a Wilcoxon signed-rank test.

Results

Age was the strongest predictor of TN ROM (R^2 = 0.52, p = 0.043). Younger (age: 21.1±2.68yrs) participants exhibited significantly greater (p = 0.029; Cohen's d = 1.95) TN ROM (13.15±4.50°) compared to older (5.85±0.88°) participants. No significant associations were found between TN ROM and foot shape or any other demographics.

Discussion

Age as a predictor of TN ROM may be explained by soft tissue stiffening and degenerative changes reducing midfoot flexibility [3]. These preliminary results suggest age-matching is

more important than foot shape or other demographics. However, these results encompass a narrow range of arch heights, and we are currently recruiting additional controls with low and high arches to investigate how foot shape affects TN joint kinematics.

Images (Optional)

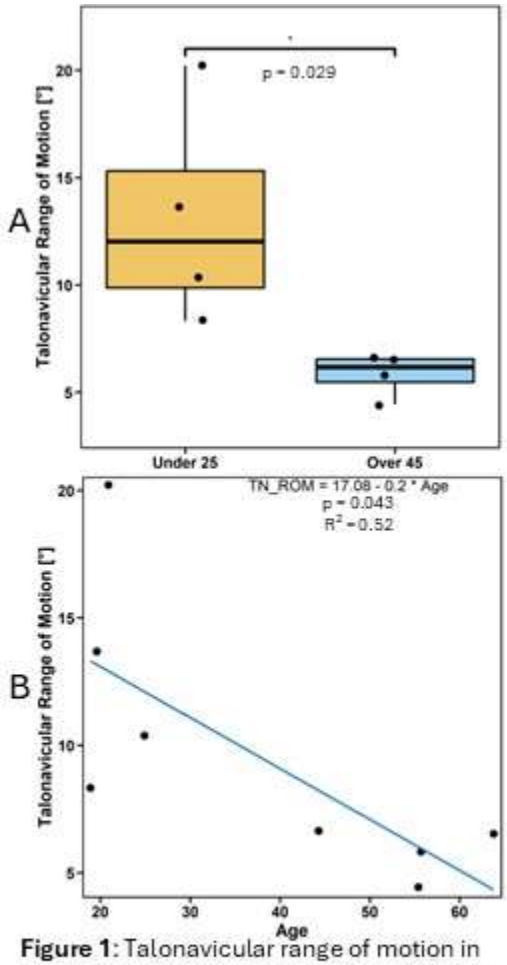


Figure 1: Talonavicular range of motion in walking (TN_ROM) (A) for the over 45 (blue) and under 25 (yellow) groups and regression analysis (B) showing the linear fit between age and talonavicular range of motion variables.

References (Optional)

[1] Rowe et al. 2021 *Gait and Posture*

[2] Louie et al. 2014 *JOR*

[3] Menz 2015 *Gerontology*

Acknowledgements (Optional)

We gratefully acknowledge funding from the University of Calgary McCaig Institute and Department of Biomedical Engineering, NSERC, and CIHR.

Session Category

Musculoskeletal Biomechanics: Joints and Motion

P2-088

Acute Medial Femoral Condyle Cartilage Response Following a Running Bout

Mr Ryan Evans MSc[1], Mr Harry Battersby MSc[1], Mr Tom Boers[1], Dr Richard Willy PT, PhD[2], Dr Derek Pamukoff PhD[1]

[1]Western University, London, ON, Canada. [2]The Ohio State University, Columbus, OH, United States

Introduction

Studies using ultrasound assessed immediate cartilage response to loading have focused on the patellofemoral joint. Tibiofemoral joint contact forces during weight-bearing activities are well documented, but their internal tissue response remains unclear. We examined medial femoral condyle cartilage deformation after running, resting thickness, and their relationship with knee loading.

Methods

Thirty-one distance runners participated. Medial femoral condyle cartilage was evaluated using ultrasound prior to and following a 35-minute run at a self-selected pace on a force instrumented treadmill while kinematic (240Hz) and kinetic (2400Hz) data were collected. Peak medial tibiofemoral joint force (TFJF) was extracted using a musculoskeletal model and normalized to body weight. A (3) region, by (2) time ANOVA assessed changes in cartilage thickness, and post hoc pairwise comparisons were made using a Bonferroni correction. Pearson's r examined associations among magnitude of deformation, resting thickness, and joint loading.

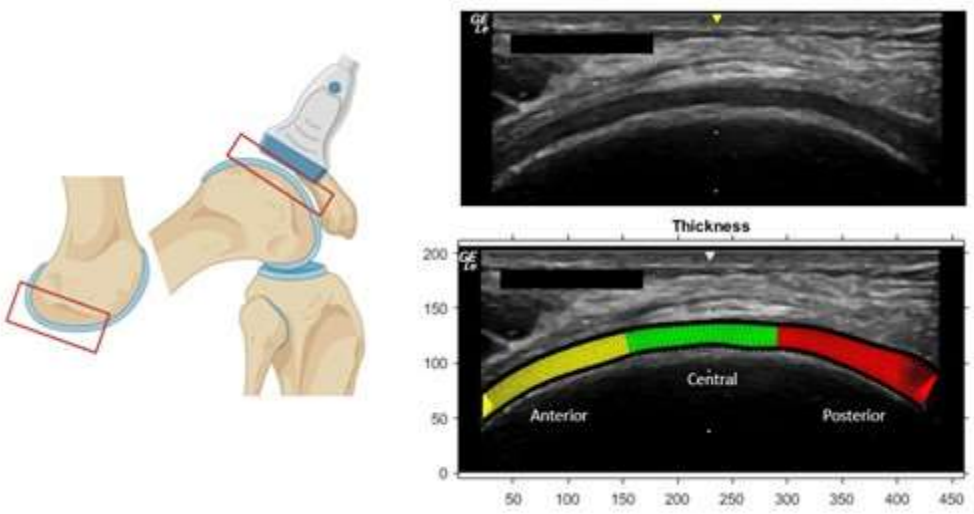
Results

There was a significant region by time interaction effect ($F_{2,28}$=8.067, p=0.005, partial η^2=0.218). Post hoc comparisons demonstrated that the anterior region decreased from pre- to post-measurement (mean difference = -0.291 (-0.169, -0.412) mm, p<0.001), but not in the central (mean difference = -0.085 (-0.156, -0.013) mm p=0.022) or posterior (mean difference = -0.024 (-0.160, 0.113) mm p=0.728, η^2=0.004) regions. Higher peak medial TFJF was not associated with cartilage deformation in the anterior (r=-0.161, p=0.397), central (r=-0.106, p=0.577) and posterior (r=0.149, p=0.433) regions. Higher peak medial TFJF was moderately associated with central (r=0.392, p=0.029), but not associated with anterior (r=-0.326, p=0.074) or posterior (r=0.005, p=0.978) resting medial femoral condyle cartilage thickness.

Discussion

The anterior region of the medial femoral condyle cartilage may respond differently following running than the central and posterior regions, likely due to joint contact patterns. Peak medial TFJF may not influence acute cartilage response following a running bout, but may contribute to thicker resting cartilage in the central region of the medial femoral condyle. External peak medial TFJF may not represent internal femoral condyle tissue response due to the number of loading cycles taken while running. However, thicker central region resting cartilage suggests peak medial TFJF during running may contribute to positive cartilage adaptation over time.

Images (Optional)



References (Optional)

Acknowledgements (Optional)

This project received funding from the Natural Sciences and Engineering Research Council of Canada (RGPIN-2022-04804, PI: DN Pamukoff), the Canadian Foundation for Innovation John R. Evans Leader Fund (Project ID: 42110, PI: DN Pamukoff) and the Ontario Graduate Scholarship 2024-2025 (RJ Evans).

Session Category

Musculoskeletal Biomechanics: Joints and Motion

P2-089

Associations Between Changes in Knee Gait Mechanics and Changes in Frontal Plane Laxity After Sustained Kneeling

Ms. Sarah Hallman B.Sc., Mr. Daniel Mines M.Sc., CPE, Dr. Stacey Acker PhD

University of Waterloo, Waterloo, Ontario, Canada

Ms. Sarah Hallman

Mr. Daniel Mines

Introduction

Sustained kneeling is a risk factor for knee osteoarthritis (KOA), resulting in altered gait mechanics [1]. Increase in frontal plane laxity (FPL), present through the progression of KOA, is a hypothesized but understudied mechanism for these gait modifications [1,2] by reducing the passive resistance of ligaments [1,3].

This study aimed to determine the relationship between changes in knee gait mechanics and FPL following an acute kneeling exposure. It was hypothesized that there would be significant correlations between FPL and all gait mechanics that exhibited significant changes post-kneeling.

Methods

15 healthy young adults (8M, 7F) underwent 3 FPL measurements in a custom sled device, followed by 3 gait trials at a self-selected pace, with right leg motion (and ground reactions, during gait) recorded before and immediately following kneeling (three 10-minute kneeling bouts alternating with 5-minute seated rest periods [1]).

Knee angles were calculated using an extension-abduction-internal rotation Cardan sequence. Net external joint moments were calculated using inverse dynamics, normalized to %BW*Ht, and expressed in the tibial coordinate system.

One-tailed paired t-tests (α=0.05) tested for significant differences (post- versus pre-kneeling) in FPL and gait outcomes, with a Holm-Bonferroni correction for multiple comparisons. For the gait outcomes (Figure 1) that exhibited significant change, Pearson

correlations (r) were calculated between the average within-participant change and the average within-participant change in FPL.

Results

Post-kneeling, there was a significant increase in the knee flexion angle at heel strike (p=0.010), peak knee flexion angle during early stance (p=0.015), and peak knee adduction moment during early stance (p=0.049). No significant differences were observed in the other gait variables or FPL (p>0.05).

Two of the significantly changed gait outcomes had significant moderate (r=0.4-0.699) correlations with the change in FPL (Figure 1).

Discussion

Associations between osteoarthritic-like changes in gait mechanics and changes in FPL were found following an acute exposure to sustained kneeling, supporting this potential mechanistic pathway. Future longitudinal research is warranted to elucidate the causal relationships between kneeling exposures and KOA.

Images (Optional)

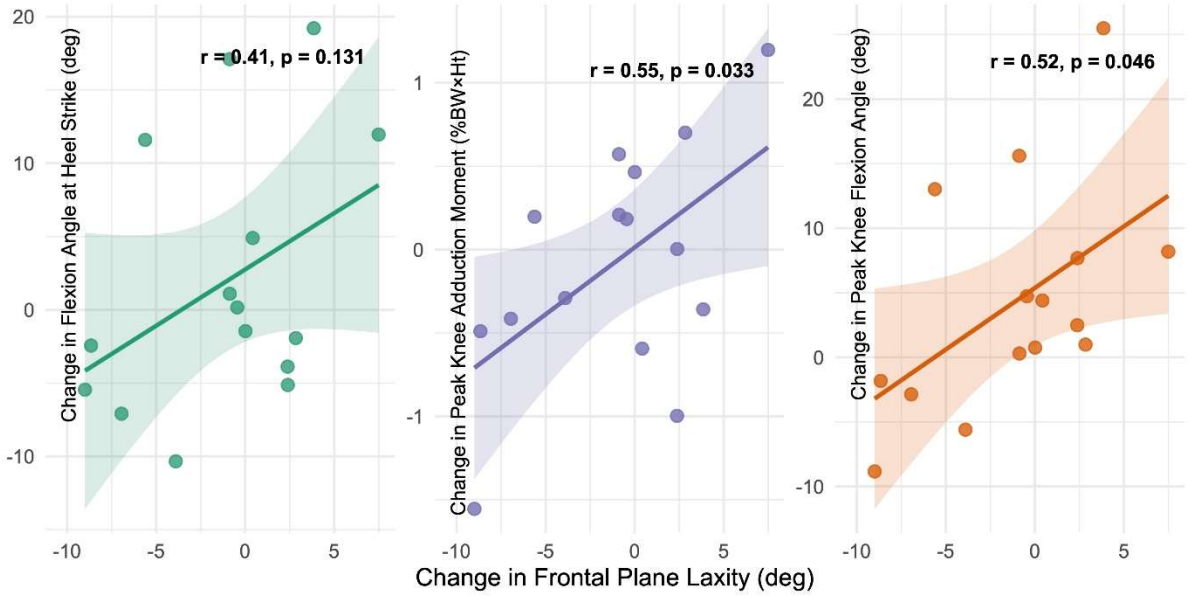


Figure 1. Correlations between the average change in FPL and average change in gait outcomes that exhibited significant changes after the kneeling exposure.

Note: The shaded region represents the 95% confidence interval and positive change indicates an increase from pre- to post-kneeling.

References (Optional)

[1] Kajaks & Costigan, *Appl Ergo, 2015*.

[2] van der Esch et al., Scandinavian J of Rheum, 2005.

[3] Park et al., *The Knee, 2006*.

Session Category

Musculoskeletal Biomechanics: Joints and Motion

P2-090

Effects of Static Stretching on Achilles Tendon Hysteresis: A Pilot Study

Mr. Simon Embaye[1,2], Mr. Jimmy Stanley[1], Dr. Jared Fletcher PhD[1]

[1]Mount Royal University - Department of Health and Physical Education, Calgary, Alberta, Canada. [2]University of Alberta - Faculty of Kinesiology, Sport, and Recreation, Edmonton, Alberta, Canada

Introduction

During locomotion, the compliant, viscoelastic Achilles tendon (AT) is stretched, storing elastic strain energy contributing to economical locomotion. AT energy storage is quantified from AT stretch and estimated AT forces. A portion of the AT strain energy is lost during AT recoil, known as hysteresis. Prolonged static stretching has been shown to increase AT hysteresis, potentially contributing to greater AT strain energy loss during running. How changes in AT hysteresis impacts the energy cost of running (E_{run}) remains to be shown. The purpose of this pilot study was to evaluate the effect of static stretching on tendon hysteresis and their impact on E_{run}.

Methods

AT hysteresis prior to and following 10-minutes of static stretching was assessed in 8 male and female participants (29±11 years, 182±9cm, 78.5±6.1 kg). AT hysteresis was calculated from AT length change from ultrasound imaging and calculated AT force from loading and unloading of the AT during a maximal voluntary contraction (MVC) on a dynamometer. E_{run} was quantified prior to and following the stretch using indirect calorimetry. Cohen's d was used to quantify the effect size.

Results

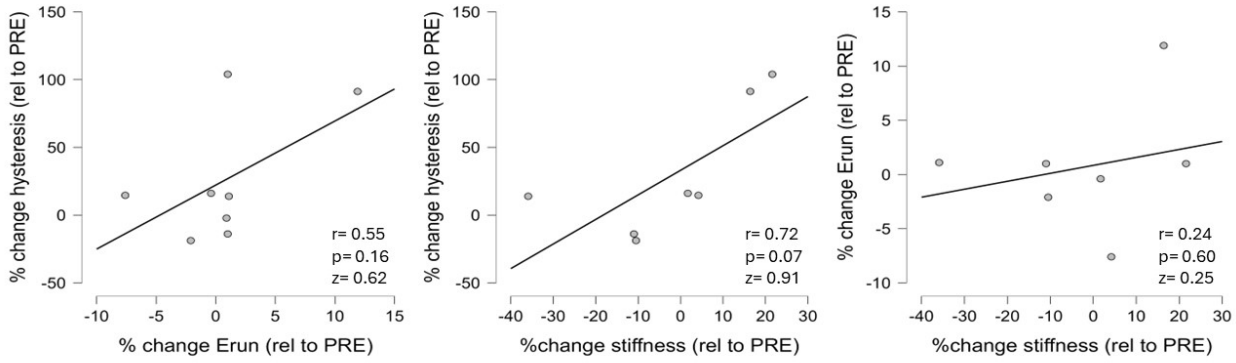
Stretching did not impact changes in MVC (Pre: 122±33 Nm vs. Post: 119±42 Nm, p=0.822, d=-0.089) nor changes in AT stiffness (Pre: 309±217 $N \cdot mm^{-1}$ vs. Post: 283±180 $N \cdot mm^{-1}$, p=0.34, d=0.39). A medium effect of stretching was seen for AT hysteresis: from 38.0±10.5% prior to stretching to 45.7±14.1% following stretch (d=0.56). No meaningful change in E_{run} (post stretch increase of 0.6%) was seen following stretching

(p=0.72, d=0.13). Moderate correlations were found between both the changes in AT hysteresis and the change in E_{run} and the change in AT hysteresis and AT stiffness (Figure 1).

Discussion

These results suggest that 10 mins of static stretching causes a moderate increase in AT hysteresis, which is moderately correlated to the increased E_{run} following stretch. This may be due to static stretching reducing AT strain energy return. If the reduced AT hysteresis persists during running, this may negatively impact the energy cost of running.

Images (Optional)



Session Category

Musculoskeletal Biomechanics: Joints and Motion

P2-091

FINITE ELEMENT MODELLING OF THE FOREARM AND WRIST TO SIMULATE GYMNASTICS-TYPE LOADING IN ADOLESCENT WRISTS

Miss Stefania DiLeo[1], Mr. Mahziyar Darvishi[1], Dr. Ryan Paul[2], Dr. Andrea Chan[2], Dr. Timothy Burkhart[1]

[1]Faculty of Kinesiology and Physical Education, University of Toronto, Toronto, Ontario, Canada. [2]Divisions of Orthopaedic and Plastic Surgery, University of Toronto, Toronto, Ontario, Canada

Introduction

Distal radius physeal stress reaction, or Gymnast Wrist (GW), is prevalent in adolescent gymnasts due to repeated high force loading at the extended wrist. Finite element (FE) modelling has proven valuable for advancing knowledge on injury biomechanics in a safe and ethical manner. However, previous FE models have neither examined gymnastics-type wrist loading nor have they modelled the distribution of loads across the open distal radius physis (DRP) of an adolescent with GW. Therefore, this study aimed to develop an FE model of the GW-affected wrist to estimate the magnitude and distribution of loads across the open distal forearm physes during a front handspring.

Methods

A CT scan of the GW-affected wrist was obtained from a single 14-year-old female gymnast. The solid 3D geometry of the distal radius, ulna, and their physes were developed using 3D Slicer (The Slicer Community, Boston, USA). Models were meshed in 3-Matic (Materialise, Leuvan, BEL) prior to assigning material properties in Mimics (Materialise, Leuvan, BEL). The peak hand impact force for a front handspring (retrieved *in vivo* from a youth gymnast) was applied in Abaqus (Dassault Systèmes, Vélizy-Villacoublay, FRA) to estimate the stresses/strains through the distal radius and ulna physes, as well as contact pressures at their epiphyseal-physeal and metaphyseal-physeal interfaces.

Results

A concentration of von Mises stress was found along the DRP volar rim (Fig. 1). The minimum principal stress (-48.1MPa) and strain (-1.15MPa) occurred within the volar aspect of the DRP. The radius experienced greater mean contact pressures than the ulna at the epiphyseal-physeal (2.94 vs 2.15MPa) and metaphyseal-physeal (2.97 vs 2.21MPa) interfaces.

Discussion

This study presents a novel FE model for estimating stresses and strains across the distal forearm physes in an adolescent with GW. The concentration of peak stresses/strains within the DRP volar rim may suggest that the continued application of gymnastics-type loads through a wrist with GW leads to their redistribution toward the DRP volar rim, though further validation of findings is necessary. Results may be crucial for identifying risk factors in the development/progression of GW in adolescent gymnasts, helping to enhance the long-term wrist health of these vulnerable athletes.

Images (Optional)

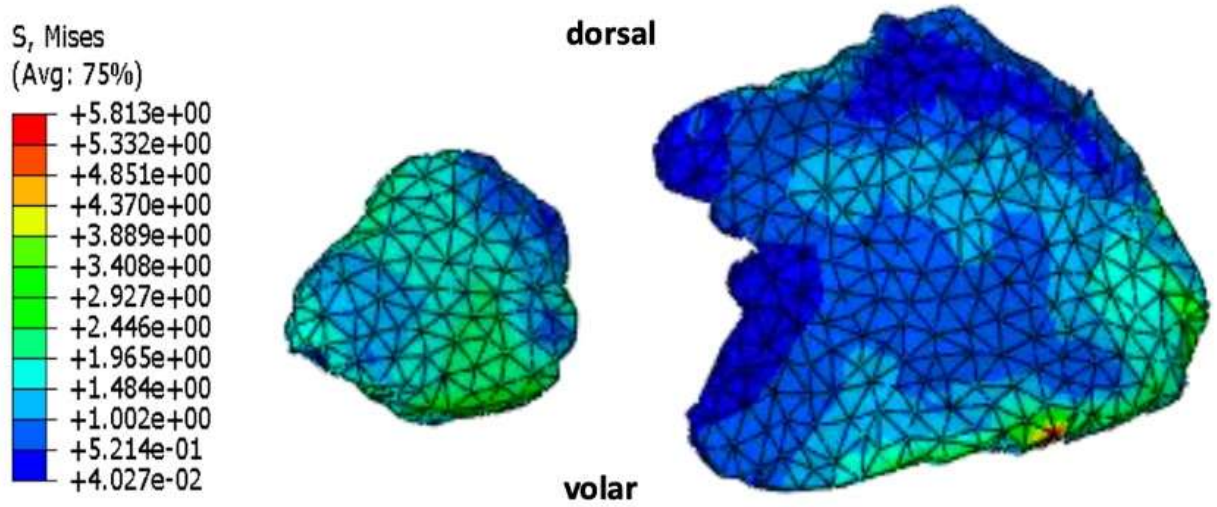


Figure 1: Distribution of von Mises stress across distal radius (right) and ulna (left) physes. Associated values given in MPa.

Session Category

Musculoskeletal Biomechanics: Joints and Motion

P2-092

EMG-Informed OpenSim Analysis to Assess Firefighter Helmet Effects on Cervical Spine Loading

Mr. Gustavo Paulon Ph.D. Student, Dr. Suman Chowdhury Associate Professor

University of Florida, Gainesville, Florida, United States

Introduction

Musculoskeletal modeling platforms, like OpenSim, are widely used to determine how external loads, such as heavyweight, unbalanced helmets, alter cervical spinal joint reaction forces (JRFs). Particularly, OpenSim generic approaches—static optimization (SO) or computed muscle control (CMC)—estimate JRFs using a cost function (e.g., minimizing the squared muscle activations). However, they do not reflect a subject's true physiological muscle recruitment and underpredict intervertebral JRFs. Therefore, this study aimed to assess individualized estimates of cervical JRFs by implementing an EMG-informed optimization approach in order to investigate the biomechanical demands of various heavyweight, unbalanced firefighting helmets.

Methods

We analyzed 12 male and 12 female firefighters' kinematics and electromyography (bilateral sternocleidomastoid, infrahyoid, upper and cervical trapezius) data acquired during dynamic neck flexion-extension movements and maximum isometric flexion and extension exertions under three helmet conditions: No-helmet, US-helmet (1.77kg; COM: (anterior, superior, left) 0.002m, 0.152m, -0.006m) and EU-helmet (2.02kg; COM: (anterior, superior, left) 0.019m, 0.094, -0.008m). We used OpenSim MASI model and the Calibrated EMG-Informed Neuromusculoskeletal Modeling (CEINMS) Toolbox to calculate subject-specific cervical JRFs in the inferior-superior (IS), anteroposterior (AP), and mediolateral (ML) directions (Figure 1) with optimal weights (alpha=1~100, beta=1~1000, and gamma=1~1000) that minimized the overall RMSE ($RMSE_{overall}$= $RMSE_{ID}$ + $RMSE_{muscles}$) for each subject, task, and helmet type. We employed Friedman's test to evaluate the effects of *helmets* on the non-normal JRFs.

Results

Helmet use significantly increased IS-JRFs during static flexion ($p<0.005$, US-helmet: 14.0%, EU-helmet: 7.70%), extension ($p>0.05$, US-helmet: 4.34%, EU-helmet: 1.39%), and dynamic flexion-extension ($p<0.014$, US-helmet: 15.16%, EU-helmet: 7.62%) across all joints. The US-helmet showed higher AP-JRFs during static flexion (6.98%) and flexion-

extension (4.70%) than EU-helmet, but decreased the AP-JRFs during static extension (37.59%).

Discussion

Despite being 250g lighter, the US-helmet's high COM (5.8 cm above the EU-helmet) increased MOI by 10% at C0-C1, leading to higher compressive and shear forces. However, US-helmets reduced JRFs across all cervical joints. Since firefighter helmets increase cervical intervertebral maximum flexion angles, prolonged helmet use can increase the risk of disc degeneration and muscle injury. Incorporating subject-specific parameters to estimate cervical loading can yield accurate estimates of injury likelihood in the cervical spine.

Session Category

Musculoskeletal Biomechanics: Joints and Motion

P2-093

Continuous Estimation of Elbow Joint Angle and Force from Surface EMG Using Machine Learning

Mr. Taehyung Kim, Ms. Kyungmin Lee, Prof. Gwanseob Shin

Ulsan National Institute of Science and Technology, Ulju-gun, Ulsan, Korea, Republic of

Introduction

Conventional methods for estimating elbow joint angles have mainly relied on motion capture systems or inertial sensors, which restrict measurement environments and make it difficult to directly obtain information on actual muscular force or external load. In addition, most previous studies using electromyography (EMG) to estimate joint kinematics have treated joint angle and force as separate targets. This study aims to develop a machine learning–based model that simultaneously and continuously estimates elbow joint angle and load using only surface EMG signals.

Methods

Surface EMG signals were recorded from four muscles—biceps brachii, triceps brachii (lateral head), brachioradialis, and anconeus—during elbow flexion–extension tasks in five subjects. After preprocessing, short-time window (0.2s)–based feature extraction was applied, and the extracted features were used as inputs to the machine learning models. Ground-truth joint angles were obtained using a motion capture system, and load was normalized as a percentage of maximum voluntary contraction (MVC). The performance of several models, including Random Forest (RF), XGBoost (XGB), multilayer perceptron (MLP), one-dimensional convolutional neural network (1D-CNN), and recurrent neural network (RNN), was compared.

Results

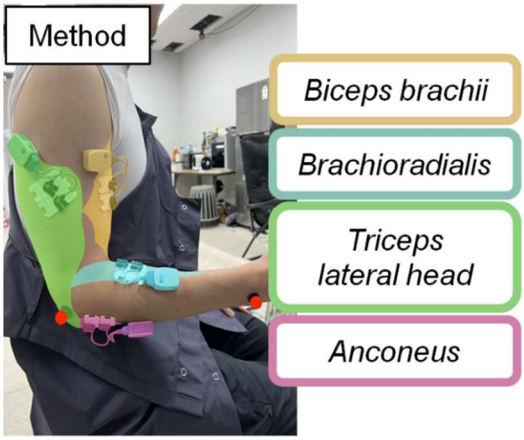
Using a temporal split evaluation in which the last 20% of each sequence was reserved as test data, the RF model achieved an RMSE of approximately 20° with a correlation coefficient of $r \approx 0.84$ for joint angle estimation. For load prediction, the model yielded an RMSE of approximately 1.4% with $r \approx 0.88$. These results indicate that continuous estimation of joint angle and load using only surface EMG is feasible.

Discussion

Although this study experimentally demonstrates the feasibility of surface EMG–based estimation of joint angle and load, several limitations remain, including the non-uniqueness of EMG signals, inter-subject variability, insufficient validation in real-time

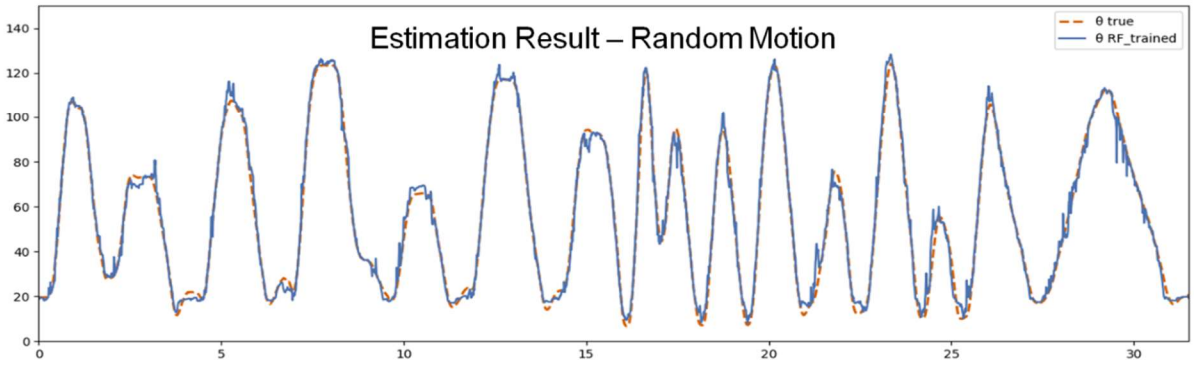
environments, and limited exploitation of temporal dynamics. Future work will focus on personalized learning strategies and the development of dynamic models that better capture the relationship between muscle activation and joint motion. Further investigation is also required to evaluate generalization performance under various loading and movement conditions.

Images (Optional)



Result

	RMSE_ theta	r_ theta	RMSE_ weight	r_ weight
RF	20.5	0.84	1.42	0.88
XGB	21.1	0.83	1.14	0.90
MLP	26.1	0.76	1.40	0.82
CNN	21.7	0.82	1.92	0.77
RNN	20.8	0.83	1.84	0.74



Session Category

Musculoskeletal Biomechanics: Joints and Motion

P2-094

Impact of Gait Modifications on Growth Plate Loads and Femoral Growth Trajectories in Children: Results from a Proof-of-Concept Study

Assoc. Prof. Dr. Hans Kainz[1], DI Clara Egner[1], BSc Laura Rathmair[1], BSc Kevin Kitir[1], Assoc. Prof. Dr. Claudio Pizzolato[2], Prof. Dr. Peter Pivonka[3], MD Gabriel Mindler[4], Dr. Willi Koller[1]

[1]University of Vienna, Vienna, Vienna, Austria. [2]Griffith University, Gold Coast, Queensland, Australia. [3]Queensland University of Technology, Brisbane, Queensland, Australia. [4]Orthopedic Hospital Speising, Vienna, Vienna, Austria

Introduction

Bone growth and shape are influenced by mechanical loads during daily activities. Torsional femoral deformities—characterized by abnormal anteversion angle (AVA)—are common and can lead to pain, altered gait, and increased osteoarthritis risk [1]. While gait modifications can alter joint loads and disease progression in adults [2], their impact on pediatric growth plate loading and subsequent bone growth is unknown. This proof-of-concept study examined whether gait modifications can change femoral growth trajectories in a child.

Methods

One typically developing child underwent lower-limb MRI and 3D gait analysis (Vicon,Oxford,UK) on a force plate–instrumented treadmill (AMTI,Watertown,USA). The participant walked with natural gait and with prescribed in-toeing and out-toeing modifications of varying magnitude. MRI of the pelvis, femur, and tibia was segmented to build a personalized musculoskeletal model using OpenSimCreator ModelWarper. Musculoskeletal simulations in OpenSim estimated muscle forces and joint contact forces (JCF) across 5–7 trials per condition; forces from one representative trial per condition were used for finite element (FE) analysis. A subject-specific FE model of the femur was generated using our previously developed workflow [3]. Muscle and JCF outputs were applied as nodal loads to compute compressive and shear stresses in the proximal femoral growth plate. The osteogenic index was derived from these stresses and input into a calibrated mechanobiological model [4] to predict growth trends, focusing on changes in AVA and neck–shaft angle (NSA).

Results

Relative to natural gait, in-toeing reduced hip JCF, modified shear stress distributions in the growth plate, and primarily influenced predicted AVA development. Out-toeing increased

hip JCF during early stance, altered shear stresses, and predominantly affected predicted NSA development (Figure 1).

Discussion

Gait modifications based on personalized multi-scale simulations may alter femoral growth plate loading, with the potential to redirect femoral growth trajectories. If validated in larger cohorts—including children with torsional deformities—early, non-invasive gait interventions could reduce the need for later de-rotation osteotomies. Future work will quantify dose–response relationships and determine the duration of gait modifications needed to achieve clinically-meaningful growth corrections.

Images (Optional)

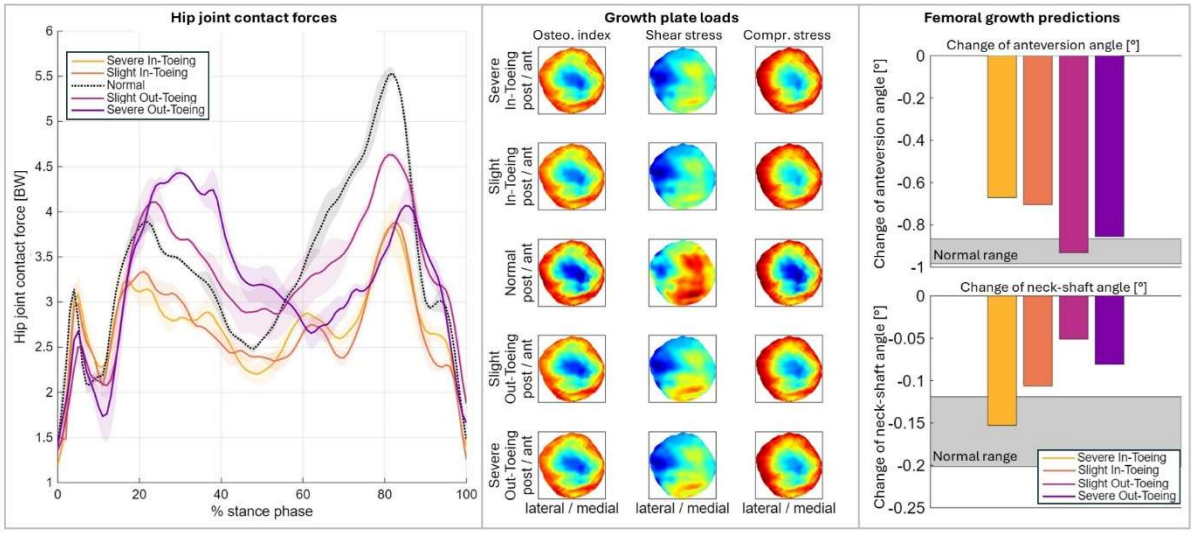


Figure 1. Hip joint contact forces, growth plate stresses and femoral growth predictions based on the normal gait pattern and the slight in-toeing, severe in-toeing, slight out-toeing and server out-toeing gait modification. Oesteo.=osteogenic, Compr.=compressive.

References (Optional)

[1]Scorcelletti et al.,J.Anatomy,2020

[2]Uhlrich et al.,LancetRheum.,2025

[3]Koller et al.,Front.Bioeng.Biotechnol.,2023

[4]Koller et al.,Biomech.ModelingMechanobiol.,2025

Acknowledgements (Optional)

This research was funded by the European Research Council (ERC-2024-COG, 101170218, INSIDE-BONE). We would like to thank the Medical University of Vienna for their help with the MRI data collection.

Session Category

Musculoskeletal Biomechanics: Joints and Motion

P2-095

Preliminary Findings Demonstrate Fatigue Induced by Unilateral Eccentric Plantarflexion Decreases Localized Muscular Capacity to Perturb Single Leg Hopping Mechanics

Mr. William Feldman[1], Ms. Caroline Turner[1], Ms. Lindsay Dietz[1], Ms. Kyle Grote[1], Dr. Luke Jessup PhD[2], Dr. Monica Daley PhD[2,3], Dr. Katherine Knaus PhD[1], Dr. Anne Silverman PhD[1]

[1]Colorado School of Mines, Golden, Colorado, United States. [2]University of California, Irvine, Irvine, California, United States. [3]Henri Samueli School of Engineering, Irvine, California, United States

Introduction

Decreased musculoskeletal capacity can lead to compensatory movements [1]. Investigating hopping elucidates relationships between muscle mechanics and human performance [2], however, changes in hopping mechanics due to localized reduced muscular capacity are not well understood. To probe this interaction, we quantified how unilateral ankle plantarflexor muscular fatigue affects single-leg hopping mechanics. We hypothesized that, after unilateral fatigue, hopping on the fatigued limb would demonstrate changes in body center of mass (COM) height and lower limb joint kinematics and kinetics from decreased force production capacity. We expected no changes in hopping mechanics in the non-fatigued limb.

Methods

Kinematics were collected and synchronized with ground reaction forces on a single participant (M, right leg dominant, 38yrs, 188cm, 92kg). Preferred hopping frequency was determined from unconstrained double-leg hopping and then prescribed for all trials of 15s single-leg hopping on each leg before and after fatigue. The fatiguing exercise consisted of isokinetic eccentric-dominant ankle plantarflexor contractions on a dynamometer until 25% decrease in maximum isometric torque was achieved. An eight-segment dynamic model was used to compute lower-limb sagittal-plane joint angles and moments, and COM height, and was normalized in time from ground contact to subsequent ground contact.

Results

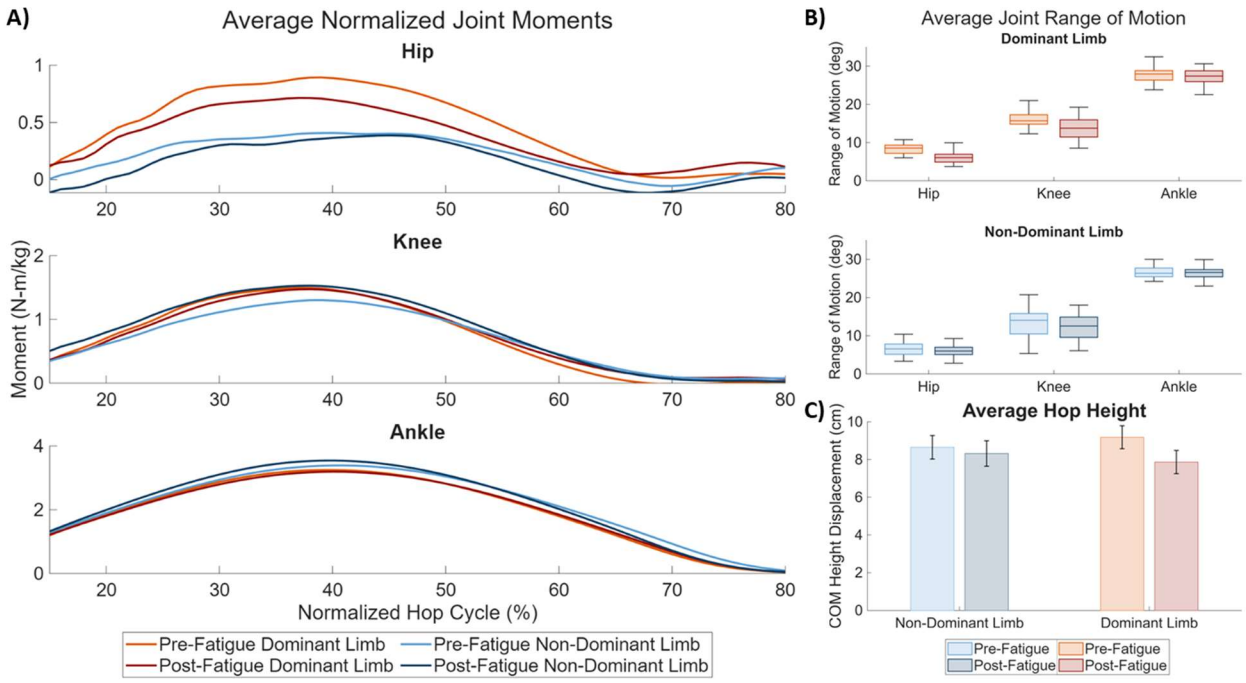
The participant had 38 ± 2 cycles per limb before and after fatigue at 2.68 ± .07 Hz. Following fatigue, the fatigued limb had 26% and 16% decreases in respective hip and knee range of motion (ROM), compared to 6.4% and 6.8% decrease in the non-fatigued limb. The

fatigued limb had 18% smaller peak hip moment and 14% decrease in hop height, compared to 5.3% and 3.8% decreases in the non-fatigued limb, respectively.

Discussion

Dominant ankle plantarflexor fatigue decreased ROM, hop height, and peak hip moment in the fatigued limb, indicating smaller force production in this muscle group. Smaller hip moments suggest altered muscle activity and movement control with fatigue. Results demonstrate fatiguing exercise as an effective perturbation of muscular capacity to investigate effects on hopping mechanics. Future work will extend to additional participants to generalize the results.

Images (Optional)



Comparison of bilateral single-leg hopping prior to and following eccentric isokinetic fatigue of dominant ankle plantarflexors **A)** Average joint moments normalized to body mass. **B)** Average total range of motion of lower limb joints. **C)** Average hop height, calculated from maximum COM height displacement from neutral static pose COM height position.

References (Optional)

[1] Eline van der kruk et al., J Biomechanics, 2021

[2] Luke Jessup et al., J Experimental Biology 2023

Acknowledgements (Optional)

National Science Foundation, Division of Biological Infrastructure

Biology Integration Institute: Integrative Movement Science Institute

Award No. 2319710

Session Category

Musculoskeletal Biomechanics: Joints and Motion

P2-096

Markerless Motion Capture to Characterize Ground Contact Time and Joint Coordination During Depth Jumps Using an OpenCap to OpenSim System

Mr. William Spradlin

Roanoke College, Salem, VA, United States

Introduction

Depth jumps are commonly used to assess reactive strength and lower-limb coordination, but typically require force plates and marker-based motion capture. Markerless systems such as OpenCap, combined with musculoskeletal modeling in OpenSim, may enable accessible assessment of jump mechanics outside of laboratory environments. This study evaluated whether an OpenCap–OpenSim workflow can differentiate intentionally varied ground contact times (GCTs) and characterize associated hip–knee coordination patterns during depth jumps.

Methods

Seven healthy college-aged athletes performed depth jumps from a 30-cm platform. After landing, participants were cued to produce low, medium, or high GCT rebound jumps. Movements were recorded using three synchronized smartphones running OpenCap. Kinematic files were exported and processed in OpenSim.

Ground contact was identified from pelvis vertical displacement (pelvis_ty), with landing defined as the local minimum preceding the downward acceleration phase. GCT was measured from landing to takeoff. Representative GCT ranges were approximately: low: 0.20–0.25 s, medium: 0.28–0.34 s, high: 0.38–0.45 s. Inverse dynamics outputs were used to refine event boundaries and reduce noise around impact and propulsion. Three participants were randomly selected for detailed coordination analysis, and one trial per GCT category was plotted. Hip flexion was mapped against knee angle to form joint coordination loops for low, medium, and high GCT jumps.

Results

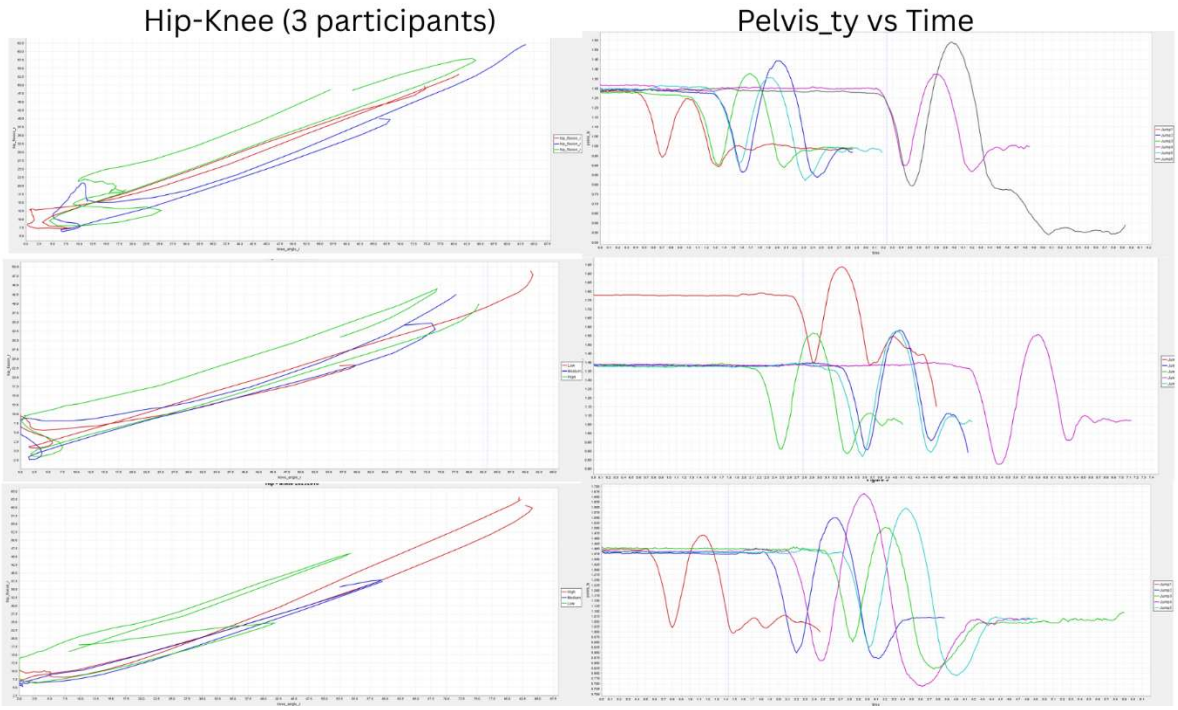
Pelvis_ty trajectories showed clear and systematic differences in contact duration across conditions, confirming that participants successfully modulated GCT in accordance with

instructions. Hip–knee coordination loops demonstrated distinct movement strategies: low-GCT jumps produced compact, rapid flexion–extension cycles; medium-GCT jumps displayed intermediate loop widths and balanced hip–knee contribution; and high-GCT jumps exhibited substantially larger loops with prolonged hip flexion and greater knee excursion. These patterns were consistent across participants.

Discussion

This study demonstrates that a markerless OpenCap–OpenSim workflow can identify changes in GCT and capture corresponding alterations in hip–knee coordination during depth jumps. The results support the feasibility of low-cost, field-deployable tools for assessing reactive strength and movement strategies. Future work will integrate force-plate validation, automated event detection, and larger participant samples.

Images (Optional)



References (Optional)

(References omitted per abstract guidelines but available upon request.)

Acknowledgements (Optional)

We thank the participants for their involvement and Roanoke College Engineering Science for equipment access.

Session Category

Musculoskeletal Biomechanics: Joints and Motion

P2-097

Knee joint contact forces in the medial and lateral compartment during cycling

Dr. Wouter Schallig[1], MSc Sabrina Hörmann[2], Ir. Joost van den Broek[1,2], prof. dr. ir. Jaap Harlaar[1,2], dr. Ajay Seth[2]

[1]Erasmus Medical Center, Rotterdam, Zuid-Holland, Netherlands. [2]TU Delft, Delft, Zuid-Holland, Netherlands

Introduction

Joint loading contributes to the development of knee osteoarthritis, with the medial compartment typically experiencing higher loads during walking. Cycling is promoted as a low-impact exercise. However, the medial–lateral distribution of knee joint contact forces during cycling remains unknown. Moreover, it likely depends on bike-fitting parameters and cycling technique, which are usually optimized for performance rather than joint health. Therefore, we aim to quantify medial and lateral knee compartment forces during cycling and evaluate their sensitivity to common bike-fitting parameters.

Methods

We modified a cycling-specific musculoskeletal OpenSim model [1] by incorporating a medial-lateral knee model [2]. Cycling motion analysis data of 5 participants was selected from an open-access dataset [1] and used in the original and medial-lateral compartment (MLC) model. Scaling, inverse kinematics, static optimization and joint reaction analysis in OpenSim were used to estimate the tibiofemoral contact forces and its medial-lateral distribution. We included 5 participants with matched characteristics who cycled at matched power output and cadence and with EMG-electrodes on seven lower-limb muscles to assess agreement between measured and estimated muscle activations with cross-correlations.

Results

Total tibiofemoral compressive force and estimated muscle activations were not different between the original and MLC model. In all participants, the tibiofemoral compressive force was larger on the lateral compared to medial compartment (Fig.1). Muscle activation agreement was high ($R>0.9$) for vastus lateralis and medialis, but lower ($0.4<R<0.8$) for the other muscles.

Discussion

These preliminary results suggest that during cycling the lateral compartment is loaded more than the medial compartment, which would be especially relevant for medial knee osteoarthritis patients. However, muscle activations may not be sufficiently representative of subject coordination. Also considering the high muscle forces and co-contraction rates during cycling, an EMG-informed model may be needed. To improve muscle activation validation, we will soon include 15 additional healthy participants to perform a marker-based cycling motion analysis including both force pedals and EMG. Adjustable bike parameters (e.g. cadence, saddle positioning, foot orientation) will be systematically varied to determine their effect on compartmental knee loads with a EMG-informed musculoskeletal model.

Images (Optional)

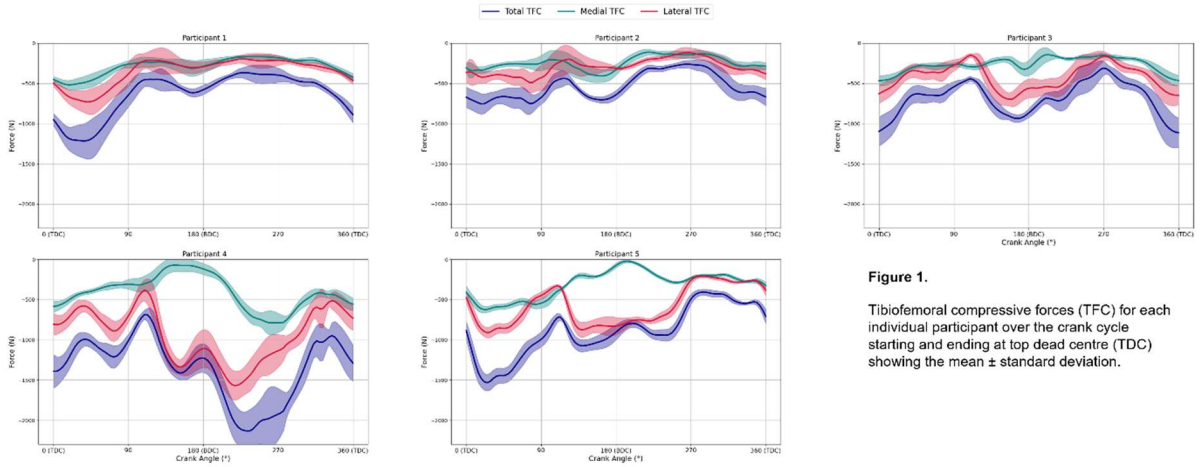


Figure 1.

Tibiofemoral compressive forces (TFC) for each individual participant over the crank cycle starting and ending at top dead centre (TDC) showing the mean ± standard deviation.

References (Optional)

[1] Clancy *et al.*, Scientific Rep, 2023
[2] Lerner *et al.*, J. Biomechanics, 2015

Acknowledgements (Optional)

This abstract is part of the project LoaD (projectnr. NWA1389.20.009) of the NWA-ORC research program, which is (partly) financed by the Dutch Research Council (NWO).

Session Category

Musculoskeletal Biomechanics: Joints and Motion

P2-098

Titanium–Hydrogel Hip Resurfacing Implant Featuring a Gyroid TPMS Fixation Stem

Dr. Xiaoyu Du, Ms. Isabelle Wüthrich, Prof. Stephen Ferguson

ETH Zurich, Zurich, Zurich, Switzerland

Introduction

Hip resurfacing arthroplasty offers a bone-sparing option compared with total hip replacement. Our earlier work introduced a titanium–hydrogel resurfacing implant designed to deliver ultra-low friction and effective shock absorption through a hydrogel-on-hydrogel interface [1]. However, a traditional solid stem can still trigger loosening and stress shielding. In this study, we explore a gyroid fixation stem, using finite-element analysis to evaluate its feasibility to reduce stem stiffness, enhance osseointegration, and enable physiological load transfer within the femoral head.

Methods

A stepwise finite-element workflow was used (Abaqus 2023). Parametric compression tests on unit-cell gyroid lattices examined how relative density and cell size affected stiffness; a 50% density, 2 mm cell design was selected. Solid and gyroid stems were then compared under displacement-controlled compression. The implant was evaluated in a femur model under two loading scenarios: axial compressive loading applied through the acetabular cup, and superior compression applied via a horizontal rigid plate with the implant aligned according to the ISO 7206-4.

Results

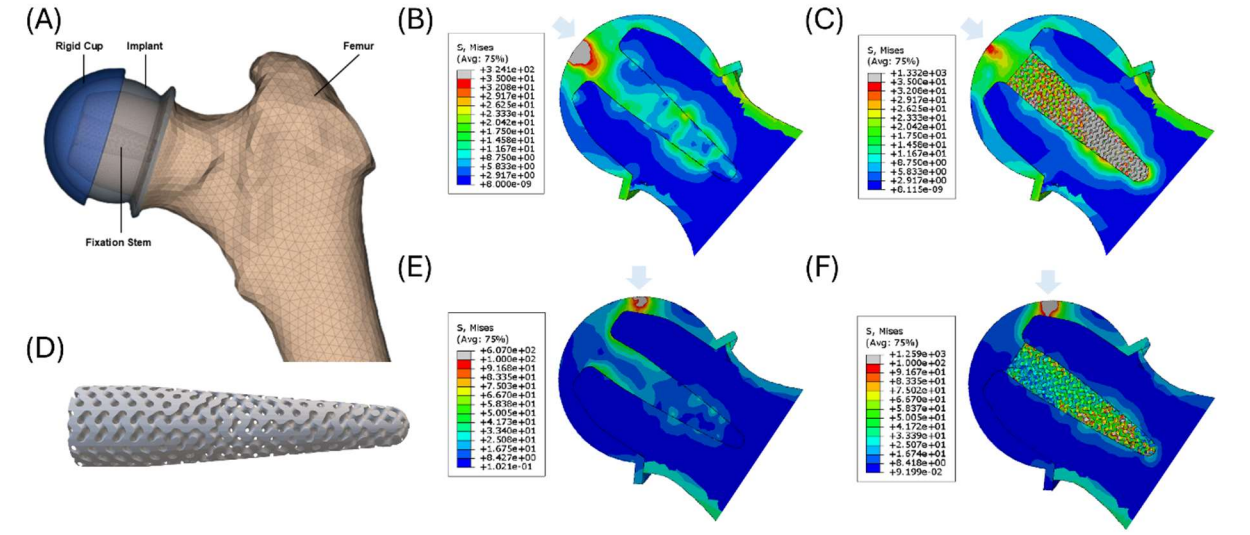
The gyroid lattice reduced unit-cell stiffness by nearly 80% compared with solid structures, with the D50U2 design selected for the final stem (25.7 GPa vs. 129.0 GPa). Under axial compression, peri-implant cancellous bone experienced higher and more uniformly distributed stresses with the gyroid stem, with peaks slightly above 35 MPa. The cancellous bone surrounding the solid stem showed similar peak stresses but in more localized regions, and principal strain followed the same trend. Under ISO-based loading, these patterns persisted, with the lattice actively contributing to internal load transmission, particularly transferring stress to the distal stem and surrounding bone.

Discussion

The TPMS fixation stem promoted a broader stress distribution within the peri-implant cancellous bone. Integrating a gyroid TPMS lattice into the fixation stem can effectively tailor implant stiffness and improve physiological load sharing, thereby reducing the risk of

stress shielding and implant loosening. However, some higher local stresses in the TPMS lattice arise from mesh artifacts and thin or highly curved regions that are more sensitive to load concentration. These areas will be optimized in future designs.

Images (Optional)



References (Optional)

[1] Xiaoyu Du *et al.* , 30th Congress of the European Society of Biomechanics (ESB), 2025

Session Category

Musculoskeletal Biomechanics: Joints and Motion

P2-099

Effects of a New Self-Guided Foot Intervention on Lower-Body Pain, Intrinsic Foot Muscles Development, and Arch Function: A Case Report.

Mr Yaron Glazer

Counterspiral, San Francisco, California, United States

Introduction

Chronic lower-extremity musculoskeletal pain can be associated with limited foot mobility, intrinsic muscle weakness, diminished arch function, and reduced proprioceptive control. These deficits may contribute to dysfunctional loading patterns, impaired gait mechanics, and persistent pain. This case report describes the experience of a 40-year-old male with chronic musculoskeletal pain who developed and implemented a self-directed foot training program after limited improvement with conventional treatments. The program targeted foot and toe range of motion, intrinsic muscle strength, toe flexor strength, arch function, stability, and proprioception.

Methods

The participant performed a progressive foot-training program 6–7 days per week for the past 10 years. The core exercise of the training program involves maximally clenching the toes of both feet, maximally inverting both ankles, and maximally externally rotating both hips. The feet are placed in contact and rotated medially against each other, engaging in symmetric and simultaneous rotations to increase the range of motion. This core exercise was performed in several variations as shown in Figure 1. Self-reported pain levels, functional capacity, perceived motor control, and qualitative changes in arch structure, proprioception, and foot grip strength were recorded throughout the training period.

Results

The participant reported progressive reductions in pain intensity and frequency, ultimately achieving complete pain resolution. Functional capacity during daily and recreational activities improved significantly. Observed biomechanical changes included increased definition and functional reconstruction of the medial longitudinal arch, enhanced activation, control and endurance of intrinsic foot muscles, proprioception, visible strengthening and elevation of the transverse arch. Toe grip strength and metatarsophalangeal joint mobility also improved significantly. These adaptations

contributed to improving balance and stability. Although self-reported and observational, the improvements were consistent, progressive, and maintained to the present day.

Discussion

This case describes how a structured, self-directed foot training program is capable of producing meaningful improvements in intrinsic muscle strength, arch morphology, foot range of motion, balance, stability, and proprioception, alongside significant reductions in chronic lower-extremity, back and neck pain. The observed outcomes highlight the potential value of foot-focused interventions and support further controlled research to investigate their mechanisms and clinical applicability in larger populations.

Images (Optional)



Session Category

Musculoskeletal Biomechanics: Joints and Motion

P2-100

The Effect of ACL Status on the *in Vitro* Mechanics of the Porcine Tibiofemoral Joint During Simulated Rehabilitation Exercise

Miss Zhané Murrell-Smith, Professor Sarah Astill, Professor Louise Jennings, Dr Aiqin Liu

University of Leeds, Leeds, West Yorkshire, United Kingdom

Introduction

Anterior cruciate ligament (ACL) injuries are among the most common knee pathologies. Rehabilitation following ACL reconstruction (ACLR) restores function and facilitates return to activity, however protocols lack a gold standard or biomechanical basis. Subsequently, ACLR patients may develop osteoarthritis at a similar rate to those who remain ACL deficient.

The aim of this study was to compare tibiofemoral kinematics and contact mechanics in an *in vitro* porcine model of the knee in ACL intact (ACLI), ACL deficient (ACLD), and ACLR conditions during simulated rehabilitation exercise.

Methods

Six porcine right hind limbs were dissected to the knee joint and mounted in a six-degrees-of-freedom knee simulator. Simulated profiles of squat and lunge exercises were developed from 3D motion capture data and verified via literature. Samples were simulated first with the native ACL intact. The anterior-posterior and internal-external tibial rotation axes were run in force control to measure kinematics. Tekscan pressure sensors were secured underneath the menisci with the axes ran in displacement control to measure tibiofemoral contact mechanics. The simulations were repeated in samples with the ACL resected and ACL reconstructed using a synthetic graft.

Results

During squat, anterior displacement
was significantly larger in the ACLD condition compared to ACLI ($p = 0.006$) and ACLR ($p = 0.010$) conditions. Larger anterior
displacements were also found during lunge between ACLD and ACLI condition ($p = 0.029$) and ACLR condition ($p = 0.021$), with no significant differences between ACLI and ACLR ($p > 0.05$). No significant differences were found for tibial rotation kinematics in between any ACL status for both exercises ($p > 0.05$).

During squat, peak contact pressure in the medial tibial compartment was significantly higher in the ACLD than following ACLR ($p = 0.017$). ACLR also significantly reduced peak

contact area in the medial compartment compared to the ACLD knee ($p = 0.005$). No significant differences in contact mechanics were found during simulated lunge ($p > 0.05$).

Discussion

In an *in vitro* porcine model, ACLR recovered kinematics and contact pressure during simulated exercise, although contact area in the medial compartment was reduced. Consistent with previous studies, ACL deficiency significantly altered both anterior-posterior displacements and medial tibiofemoral contact pressure.

Session Category

Musculoskeletal Biomechanics: Joints and Motion

P2-101

An Inverse Dynamics Model for Hindlimb Joint Kinetics in Sheep

Dr. Aaron Henry PhD[1], Dr. Dana Gaddy PhD[1], Dr. Larry Suva PhD[1], Dr. Andrew Robbins PhD[2]

[1]Texas A&M University, College Station, Texas, United States. [2]University of Texas at Tyler, Tyler, Texas, United States

Introduction

Sheep are frequently used animal models of musculoskeletal diseases, yet methods for modeling their biomechanics are significantly underdeveloped. In particular, no broadly generalizable inverse dynamics (ID) models of sheep have been presented to date. To address this shortcoming, an ID model for calculating intersegmental forces and moments of the hindlimbs in sheep was developed.

Methods

The ID model comprised five segments (pastern, metatarsus, crus, thigh, pelvis) used to estimate kinetics of hip, stifle, hock, and metatarsophalangeal joints. Marker trajectories and force plate data were used to construct the model. Body segment inertial properties and joint centers were estimated using previously reported predictive models [1,2], while intersegmental forces and moments were calculated using expanded Newton-Euler equations of motion. A preliminary sensitivity analysis evaluated shortcomings by applying random perturbations to markers defining the right hock.

Results

Kinematic and kinetic endpoints were calculated for the four bilateral joints, with occasional constant offsets between left and right joint angles observed before normalization. Stifle internal/external rotation remained at 0 degrees due to the shared flexion axis between the thigh and crus segments. Endpoint means over the gait cycle did not show substantial sensitivity to marker perturbations; however, variability clearly increased. Notably, non-sagittal plane endpoints were more sensitive to perturbations (Figure 1).

Discussion

This ID model is the first to utilize predictive equations for hindlimb joint centers and inertial properties, allowing calculation of intersegmental forces and moments without sacrificing the animal to directly measure the inertial properties. However, the model is subject to skin movement artefacts and positional errors, as confirmed by the sensitivity

analysis in which non-sagittal endpoint variability substantially increased. Although improvements are warranted, the present model provides a foundation for future work.

Images (Optional)

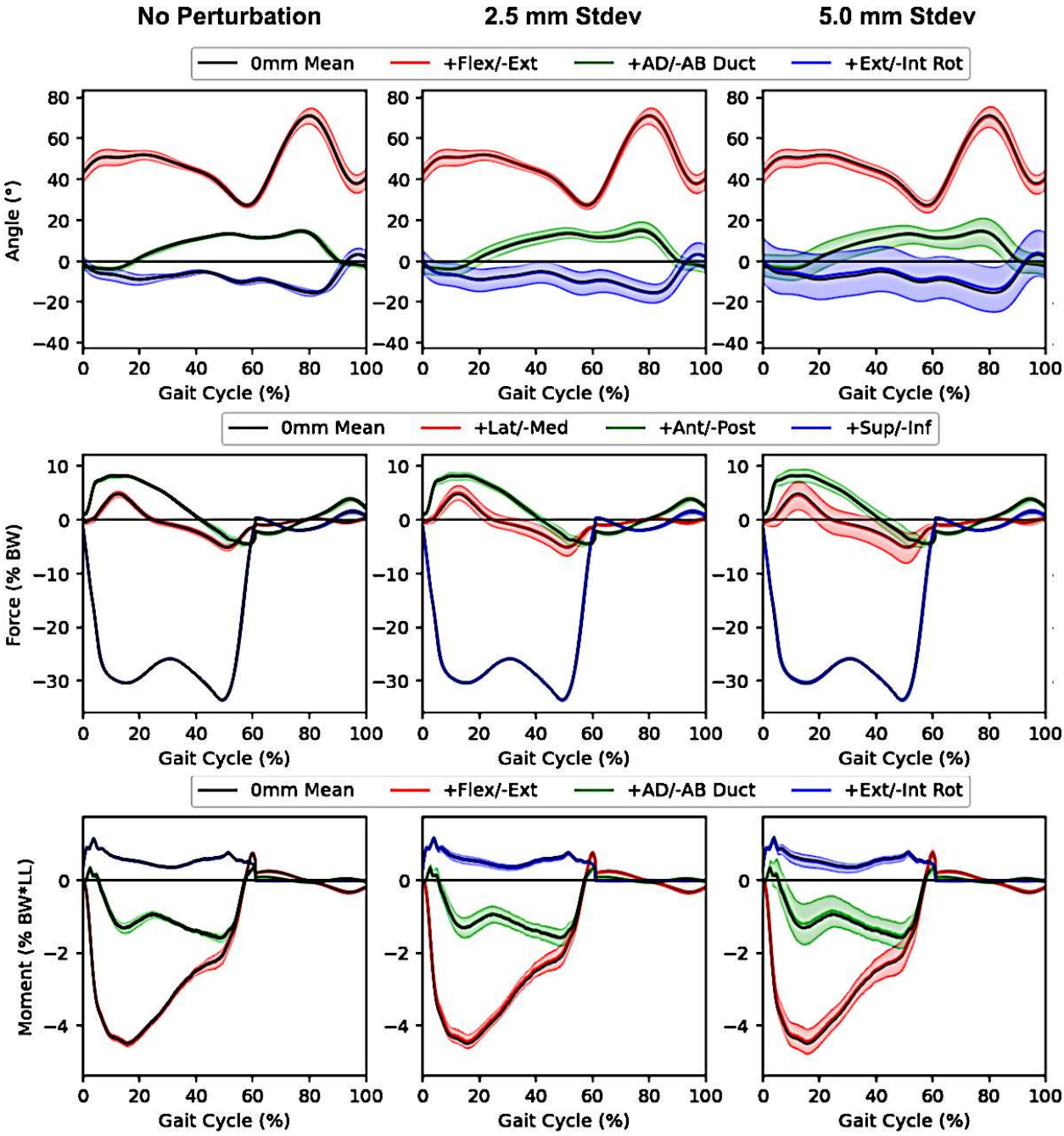


Figure 1: Model outputs for the right hock joint are shown for no perturbation, 2.5mm and 5 mm. As the perturbations increase, the variability (indicated by the standard deviation) increases.

References (Optional)

[1] A. Henry *et al.*, *J. Biomech.*, 161, 111861 (2023), 10.1016/j.jbiomech.2023.111861

[2] A. Henry *et al.*, J. Biomech., 190, 112848 (2025), 10.1016/j.jbiomech.2025.112848

Session Category

Musculoskeletal Biomechanics: Methods, Models and Applications

P2-102

Initial Development of a Probabilistic Metric of Risky Biomechanics Related to Anterior Cruciate Ligament Injury Risk

Ms. Alexandra Lynch MS[1], Dr. Fatemeh Aflatounian PhD[1], Dr. David Saxby PhD[2], Dr. Scott Monfort PhD[1]

[1]Montana State University, Bozeman, MT, United States. [2]Griffith University, Gold Coast, QLD, Australia

Introduction

Anterior cruciate ligament (ACL) injury risk factors are often assessed using single-limb drop jumps (SLDJ) with biomechanical variables averaged over several trials. However, many ACL tears appear to occur acutely rather than due to an accumulation. Thus, averaging performance across repeated trials may mask variability in performance and overlook less frequent but higher risk mechanics. The purposes of this study were to 1) develop a probabilistic metric[1] to characterize risky biomechanics (i.e. probability of injurious load (P_{INJ})[Fig.1A]) during SLDJ, and 2) determine how the number of jump landings in a dataset influence P_{INJ}.

Methods

Eight healthy participants (3F/5M;23.3±3.3years;171.7±10.6cm;71.0±8.7kg) performed reactive SLDJ. Body motions, ground reaction forces, and electromyograms (9 lower-limb muscles) were collected. Calibrated electromyography-informed neuromusculoskeletal modeling was used to estimate muscle forces[2] and linked sequentially to a model of ACL loading to estimate force in the ACL (F_{ACL}) for each SLDJ[3]. Eight SLDJ landings per participant were analyzed. For each participant, a probability density function was calculated and the probability of an injurious load (P_{INJ})[1] was estimated by integrating above a sex-, height-, and mass-adjusted estimate of ACL failure load (F_{INJ})[4]. P_{INJ} was recalculated after removing 0-5 jumps and the resulting (log-transformed) P_{INJ} estimates were compared using a mixed-effects model.

Results

P_{INJ} estimates varied by participant[Fig.1C] and were influenced by the number of jumps used in their estimate($p=0.032$).

Discussion

P_{INJ} was calculated for SLDJ landings, which aims to reflect relative risk (i.e., higher is riskier), incorporating mean and variance measures relative to ACL failure strength[Fig.1A]. Notably, P_{INJ} is not a direct probability of sustaining an injury and the clinical utility of this metric must still be established. This study provides initial development of P_{INJ} as a tool for assessing ACL injury risk. P_{INJ} varied across the number of jumps used in its estimation, with the highest number of trials (8) not yet establishing an effect size asymptote[Fig.1B]. Ongoing efforts will explore higher numbers of trials (>8), with effects expected to stabilize as more trials and participants are included.

Images (Optional)

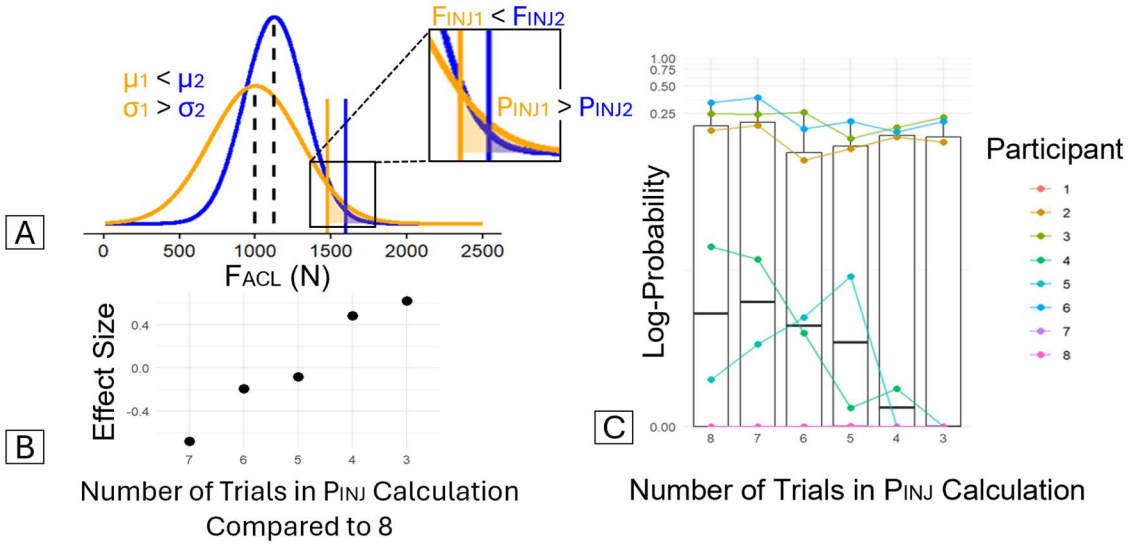


Figure 1: A) Example probability density functions (PDF) are calculated from the mean (μ_1, μ_2)and standard deviation (σ_1, σ_2) of F_{ACL} for two participants. Probabilities of injury (P_{INJ1}, P_{INJ2}) are found by integrating the PDFs above ACL failure strengths (F_{INJ1}, F_{INJ2}). Despite $\mu_2 > \mu_1$, $P_{INJ1} > P_{INJ2}$ because of greater variability and ACL failure strength, illustrating a pitfall of using mean F_{ACL} alone. B) Effect sizes on log-transformed data between n8 and all other trials were calculated using paired Cohen's d. C) Log-probability plot of raw P_{INJ} values on a log-scale. Minimum P_{INJ} values for Participants 1, 7, and 8 approach 0. A significant pairwise difference existed between n8-n3 (d = 0.62, p = 0.019).

References (Optional)

[1] Kazanski,*JBiomech*,2022

[2] Pizzolato,*JBiomech*,2015

[3] Nasseri,MedSciSportsExerc,2021

[4] Hashemi,*JOrthop,2011*

Acknowledgements (Optional)

Supported by MSU NACOE TEER and MSU NRT seed grants.

Session Category

Musculoskeletal Biomechanics: Methods, Models and Applications

P2-103

Estimating Dynamic Loads to Reduce Residual Errors in Field Environments

Ms. Alicia Kanai[1], Dr. Jazmin Cruz PhD[2,3], Dr. Felicia Davenport PhD[2,3], Dr. Peter Le PhD[2], Dr. Anne Silverman PhD[1]

[1]Colorado School of Mines, Golden, CO, United States. [2]Air Force Research Laboratory, Dayton, OH, United States. [3]Oak Ridge Institute for Science and Education, Oak Ridge, TN, United States

Introduction

Musculoskeletal modeling allows for the analysis of internal mechanics that can be indicative of injury risk. However, these approaches have rarely been applied in high-impact activities performed outside of laboratories, such as military parachute jumps.

Methods

Whole-body kinematic data from 15 wearable inertial measurement units (IMUs) and normal force data from pressure-sensing insoles were collected from a male participant (1.72m, 85.2 kg) performing a training parachute jump. A musculoskeletal model was scaled in segment length and body mass. The inverse kinematics solution was calculated in OpenSim from the IMUs by minimizing the sum of weighted squared orientations errors between the model and experimental kinematics.

Unmeasured net external forces and moments during descent were estimated using three techniques: 1) as a baseline, no external load was applied to the model, 2) external forces were estimated using center-of-mass (COM) linear acceleration data, 3) the output reaction forces and moments from inverse dynamics (ID) in OpenSim were used to define external loads at the pelvis. A residual reduction algorithm was executed to assess dynamic consistency. The root-mean-squared (RMS) residual forces and moments were compared between techniques.

Results

The ID method had the lowest errors, quantified as RMS values for residual forces and moments, in all directions, except for the transverse moment (Table 1). The greatest overall decrease in RMS values was the vertical force.

Discussion

Results indicate that the ID method effectively estimates unknown external loads in austere environments. However, a limitation to this approach is that it also incorporates

dynamic errors due to modeling assumptions and experimental errors that are not part of the physical, external loads in the system. The estimated loads agree well with expected loads during a descent [1], but these loads can vary widely due to environmental conditions. This framework applies outside the laboratory to realistic environments with limitations in data collection to drive musculoskeletal models. Future work will extend these approaches to the ground contact phase and examine the muscle recruitment solution and internal joint contact forces during these parachute landings.

Images (Optional)

RMS of Residual	FX (N)	FY (N)	FZ (N)	MX (Nm)	MY (Nm)	MZ (Nm)
No Applied External Loads	55.81	877.64	51.09	26.61	9.68	20.67
COM-based External Loads	64.59	47.27	37.14	39.72	4.49	131.53
ID-based External Loads	0.94	0.98	0.98	1.20	4.51	1.39

Table 1: RMS values of residual forces and moments from each simulation technique. The residuals are reported in the pelvis coordinate frame, where the x-axis is anterior, the y-axis is vertical, and the z-axis is to the right.

References (Optional)

[1] Airborne Systems MC-6, 2025

Acknowledgements (Optional)

Distribution Statement A: Approved for Public Release, Unlimited distribution. AFRL-2025-5204, Cleared 21 NOV 2025.

Session Category

Musculoskeletal Biomechanics: Methods, Models and Applications

P2-104

A Comparison of Maximal Rate of Force Development between Burst and Maximum Voluntary Contractions: Reliability and Neuromuscular Determinants

Mr. Andrew Nickel BSc Biomechanics, Mr. Anoush Rehmani, Mr. Zachary McClean, Mr. Nathan Boon-van Mossel, Mr. Nathaniel Morris, Mr. Matthew Zukowski, Dr. Walter Herzog, Dr. Matthew Jordan

University of Calgary, Calgary, Alberta, Canada

Introduction

Explosive strength, defined as the neuromuscular capacity for rapid force production, is critical for evaluating athletic potential, maintaining functionality, and injury rehabilitation. Knee extensor explosive strength can be quantified as the maximal rate of torque development (RTD_{max}), and is traditionally evaluated isometrically during either maximum voluntary isometric contractions (MVIC), where maximal torque is generated "as fast and as hard as possible" over a contraction lasting ~3 seconds, or rapid 'burst' contractions, where torque is developed "as fast as possible" during a ~1 second contraction to a submaximal torque target. However, the optimal approach for evaluating RTD_{max} is unclear, and neuromuscular activation between MVIC and burst contractions has not been compared. Furthermore, compliance within commercial dynamometers reduces RTD_{max} reliability, prompting recommendations for the use of custom-built devices. The purpose of this study was to compare the reliability, RTD_{max} output, and neuromuscular activation between the burst and MVIC methods using a rigid, custom-built isometric dynamometer.

Methods

Strength-trained (n = 30; females = 13) participants completed maximal effort knee extension MVIC and burst contractions. Neuromuscular activation was assessed by the rate of rise of the vastus medialis (VM) and vastus lateralis (VL) electromyography (EMG) root mean square (RMS) signal normalized to the intra-repetition peak EMG RMS amplitude (RER_{max}). RTD_{max} was computed from the numerical derivative of the torque-time curve as the average RTD around the instant of the peak knee extensor RTD using a ±25 ms window.

Results

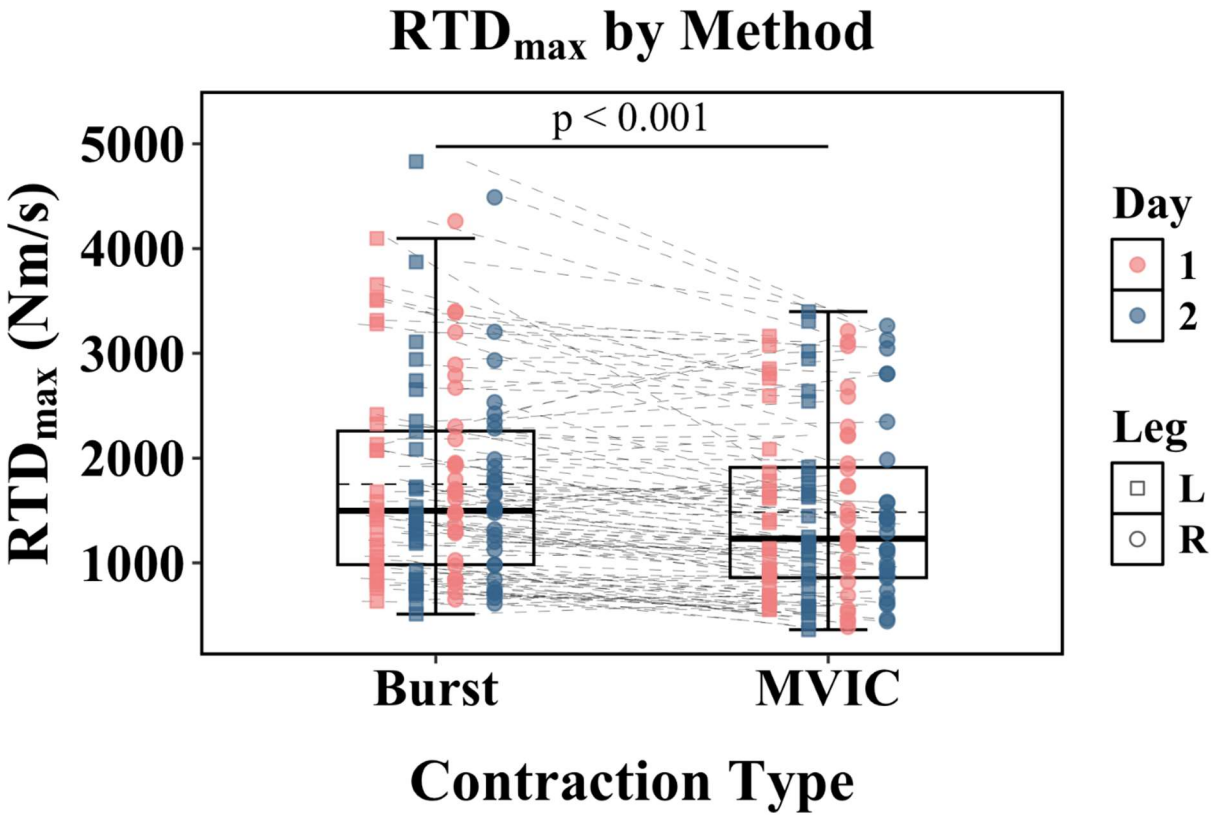
RTD_{max} demonstrated excellent reliability for MVIC (right: ICC = 0.87; left: ICC = 0.93) and burst (right: ICC = 0.86; left: ICC = 0.88) contractions. Linear mixed effects models revealed

an effect of contraction type on RTD_{max} (β = -257.80, SE = 44.58, $p < 0.01$) and RER_{max} (VM: β = -0.60, SE = 0.15, $p < 0.05$; VL: β = -0.72, SE = 0.14, $p < 0.05$), indicating that explosive strength and neuromuscular activation were higher during burst contractions.

Discussion

Explosive strength capacity is directly related to human ballistic motor performance. These findings advance scientific knowledge on reliable testing methodologies for explosive strength assessment, carrying important applications for athletic performance and healthy aging.

Images (Optional)



References (Optional)

Session Category

Musculoskeletal Biomechanics: Methods, Models and Applications

P2-105

Integration of Weight-Bearing Computed Tomography and Magnetic Resonance Imaging for Advanced Musculoskeletal Statistical Shape Modeling of the Foot and Ankle

Ms Melissa Requist BS, Mr Andrew Peterson MS, Dr Curran Reddy MD, PhD, Dr Megan Mills MD, Dr Amy Lenz PhD

University of Utah, Salt Lake City, Utah, United States

Introduction

Statistical shape models (SSM) describe three-dimensional (3D) anatomic morphology. SSM relies on accurate anatomic structure segmentation with weight-bearing computed tomography (WBCT) being used to characterize skeletal deformity in the foot and ankle. While WBCT provides satisfactory osseous segmentation it is less accurate for soft tissue structures. Magnetic resonance imaging (MRI) provides improved evaluation of the soft tissue structures but less accurate segmentation of osseous structures. This analysis describes methods for coregistration of anatomical structures from MRI and WBCT for SSM illustrated by two examples, a combined musculoskeletal model and a distal tibia growth plate model.

Methods

Bilateral WBCTs of the mid-tibia through toe-tip with 0.37mm isovoxel and bilateral T1-weighted DIXON MRIs of the knee through toe-tip with 0.1mm isovoxel were collected from 13 pediatric participants (age 8-18). 14 bones were semi-automatically segmented from WBCT (Figure 1A) and manually aligned with the in-phase MRI scan based on distal tibia and fibula outlines (Figure 1B). From this scan, muscles of the leg were segmented semi-automatically and the distal tibia growth plate was manually segmented within the previously segmented bony structure (Figure 1C). Anatomical axes of the tibia were calculated (Figure 1D) and used to crop bone segmentations and normalize the combined bone and muscle structures to leg length. 3D parts were smoothed and remeshed (Figure 1E). For each model, structures were aligned using iterative closest point alignment (Figure 1F) and SSMs were generated using a single-domain optimization for multi-domain model pipeline (Figure 1G).

Results

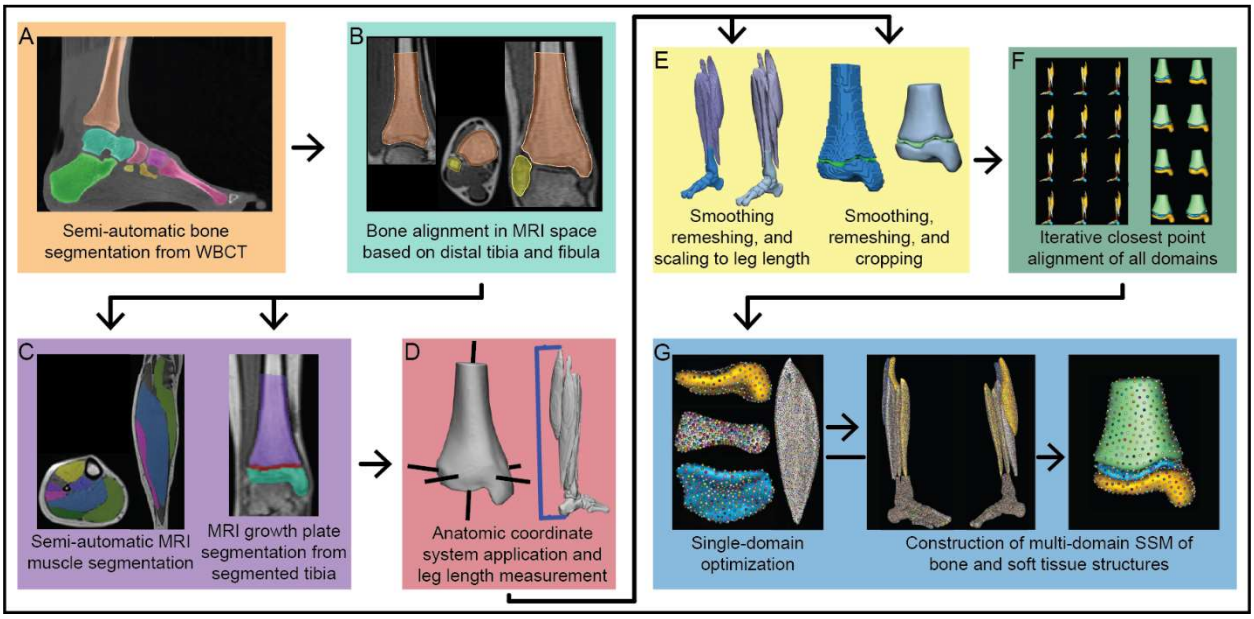
This method yielded two SSMs, one demonstrating combined bony and muscle morphology of the leg and the other showcasing growth plate anatomy in the distal tibia,

showing a decrease in growth plate thickness with age. Both models demonstrated compactness, specificity, and generalization comparable to previously published SSMs.

Discussion

Coregistration of WBCT and MRI structures allows for application of SSM to novel questions in musculoskeletal morphology. Limitations include manual registration of structures between imaging modalities and resolution constraints in MRI. This analysis presented examples of muscle and growth plate models, but other MRI sequences could allow for inclusion of ligaments, tendons, or articular cartilage in the future.

Images (Optional)



Session Category

Musculoskeletal Biomechanics: Methods, Models and Applications

P2-107

Case Study: A Novel Multi-Domain Neuro-mechanical Assessment Comparing Repeatability of Neuromuscular Communication

Ms. Yara Izhiman[1], Ms. Annika Schaeffer[1], Mr. Ethan Haight[1], Dr. Vesna Novak[1,2], Dr. Thomas Talavage[1], Dr. Brian Grawe[3], Dr. Frank Noyes[4,1], Dr. Eric Nauman[1]

[1]Department of Biomedical Engineering, University of Cincinnati, Cincinnati, Ohio, United States. [2]Department of Electrical Engineering and Computer Science, University of Cincinnati, Cincinnati, Ohio, United States. [3]Orthopaedics and Sports Medicine University of Cincinnati, College of Medicine, Cincinnati, Ohio, United States. [4]Noyes Knee Institute, Cincinnati Sports Medicine and Orthopaedic Center, Cincinnati, Ohio, United States

Introduction

This study examines differences in cortico-muscular communication across two male recreational athletes during two types of functional movements. The goal was to employ electromyography (EMG) and electroencephalography (EEG) as a joint cortico-muscular communication quantification tool. While these two tools have long been used independently, we propose an approach to examine the interactions between the nervous and musculoskeletal systems. This approach demonstrates the potential for quantifying patterns of cortico-muscular dynamics across dynamic functional movement and identifying markers of injury and state of recovery. In this study, we investigate the within-subject variability in cortico-muscular communication along with the repeatability of measures across three testing sessions.

Methods

Data acquisition involved athletes performing a series of functional movements with and without additional weights. Steady-state recordings and weighted sets served as baselines for subsequent data normalization. During each segment, EEG, EMG, and motion capture data were recorded concurrently to ensure synchronized multimodal datasets. The raw signals were processed through a custom MATLAB pipeline that expanded on standardized signal processing procedures for cross-modal comparative analysis. Correlation and coherence maps describing neural, muscular, and cortico-muscular dynamics were generated for EEG, EMG, and EEG-EMG data, respectively.

Results

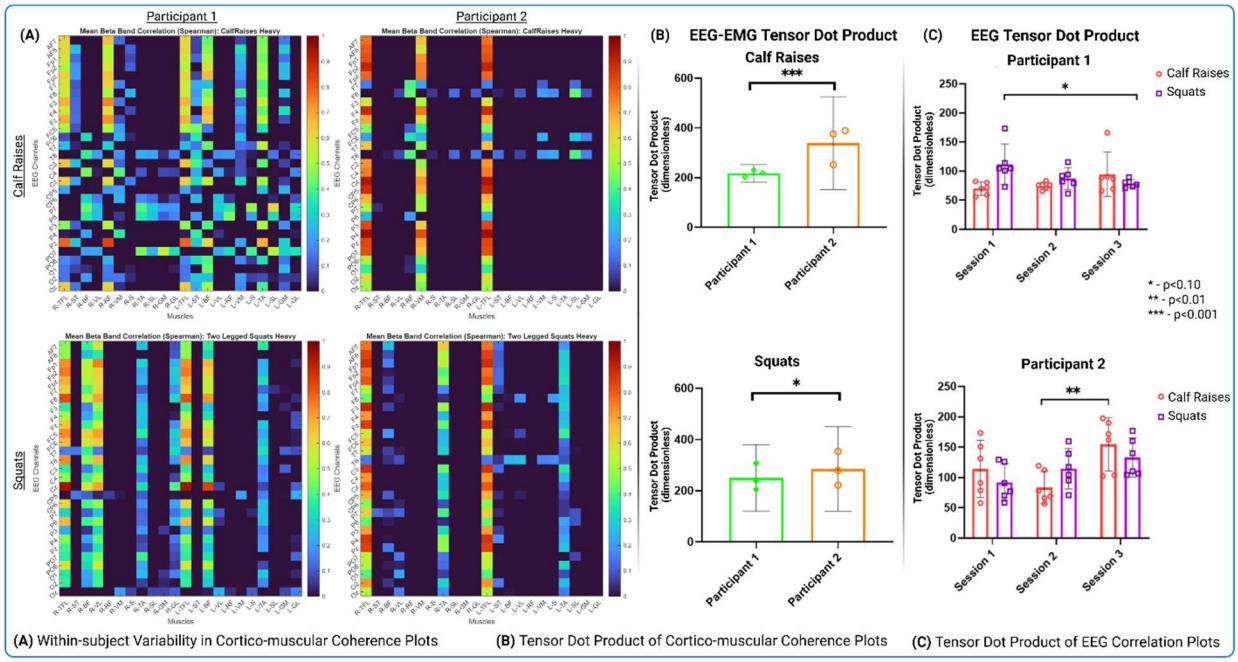
Our preliminary findings highlight the repeatability of our approach with no significant effects observed across three different experimental sessions of the same exercises. Furthermore, comparisons between individuals demonstrated statistically significant

differences, especially when comparing squats to calf raises, suggesting that variability was more pronounced at the inter-individual level than within sessions. In addition, the increased neuromuscular and cortical demands in squats, compared to calf raises may explain the greater variability observed between participants.

Discussion

The reported repeatability of cortico-muscular dynamic characterization allows for utilizing cortical and muscular dynamics as markers for neuromuscular communication across functional performance in athletes. In addition, within-subject cortico-muscular dynamic variability further highlights the promise of this approach in personalizing comprehensive functional performance characterization. These findings further invite the expansion of this investigation to evaluate performance as a function of athletic caliber, injury, and rehabilitation.

Images (Optional)



Session Category

Musculoskeletal Biomechanics: Methods, Models and Applications

P2-108

Comparing Scaling Approaches and Their Impact on Joint Kinematics in Markerless and Marker-Based Motion Capture Systems

PhD student Sandra Salvador-Lis, PhD student Andy Man Kit Lei, PhD Student Sara Oliveira, Dr Antonio P. Veloso, Dr João Brito, Dr Silvia Cabral

CIPER, Faculdade de Motricidade Humana, Universidade de Lisboa, Lisbon, Lisbon, Portugal

Introduction

OpenCap is a new open-source 3D markerless motion capture (MOCAP) system. To validate new MOCAP systems, it is essential to use the same model and data processing to identify the differences between systems. The scaling process has a high importance in musculoskeletal modelling because it can significantly impact segment lengths and, consequently, joint kinematics, moments and muscle forces. When scaling is performed using pairs of markers, identical procedures cannot always be replicated on different MOCAP systems without additional software. The goal of this study is to estimate the effect of using different pairs of pelvis markers for scaling on side-cutting kinematics.

Methods

Four female football players (aged 23±1 years) performed 90° side-cutting manoeuvres while data were acquired simultaneously using OpenCap and marker-based MOCAP system. Segments length and joint angles estimated with OpenCap were compared with those analysed in OpenSim with: 1) data collected with OpenCap and using a) the same pair of markers [hip joint center(HJC)] and b) the Anterior Superior Iliac Spines (ASIS); and 2) data collected with marker-based system using a)HJC, b)ASIS and c)the midpoint between ASIS and posterior superior iliac spines. The root mean square error (RMSE) over the full time series of joint angles was calculated.

Results

In the estimation of joint angles (Table 1), except for the pelvis tilt, pelvis list and ankle sagittal plane of motion, the RMSE exceeded more than 5°. Discrepancies were larger when comparing marker-based with OpenCap than when comparing methods within the same MOCAP system. However, within-system differences were below 2° for OpenCap and below 3° for marker-based. A similar pattern was observed for femur length and pelvis width, where the greatest differences occurred between systems.

Discussion

These findings in joint angles align with results reported elsewhere[1] when comparing marker-based MOCAP system with OpenCap. No comparable results have been found for the segment measurements. Therefore, it can be concluded that different marker pairs within the same system do not cause substantial variations (<3°) in kinematics, and any of them may be used to validate OpenCap.

Images (Optional)

Table 1: Segment lengths and RMSE joint angles between the OpenCap model and the different marker pairs on the right leg.

		OpenCap	Vs Neutral OC	Vs ASIS OC	Vs ASIS MB	Vs mSIS MB	Vs HJC MB
RMSE Joint Angles	Pelvis sagittal plane (tilt)(°)		0.6	0.5	3.2	3.2	2.6
	Pelvis frontal plane (list)(°)		0.2	0.3	1.7	1.8	1.8
	Pelvis transversal plane (rot)(°)		0.4	0.6	8.8	8.9	8.7
	Hip sagittal plane (flex/ext)(°)		0.8	0.8	7.6	7.3	5.4
	Hip frontal plane (add/abd)(°)		0.3	0.3	5.3	5.6	4.7
	Hip transversal plane (rot)(°)		0.9	3.0	9.7	10.3	9.6
	Knee sagittal plane (flex/ext)(°)		0.8	2.5	7.4	7.2	5.3
	Ankle sagittal plane (flex/ext)(°)		0.4	2.2	4.9	5.0	5.3
	Ankle frontal plane (inv/ev)(°)		2.0	3.9	13.6	14.1	11.1
Segment lengths	Femur length (mean ±std dev)(m)	0.34±0.02	0.33±0.02	0.33±0.02	0.30±0.02	0.31±0.01	0.32±0.03
	Pelvis width (mean±std dev)(m)	0.34±0.04	0.32±0.03	0.30±0.02	0.24±0.05	0.24±0.05	0.24±0.05

Abbreviations: OC= OpenCap; MB= Marker-Based; mSIS= midpoint superior iliac spine; std dev= standard deviation; rot= rotation; flex=flexion; ext= extension; add=adduction; abd= abduction; inv= inversion; ev=eversion.

References (Optional)

[1] A. Svetek, et al. , *J Biomech,* 2025.

Acknowledgements (Optional)

https://doi.org/10.54499/UID/PRR/6349/2025 (ref 2024.03647.BD)

Session Category

Musculoskeletal Biomechanics: Methods, Models and Applications

P2-109

A Novel Kinematics-Driven Muscle Force Control System Improves Biofidelity of *in Vitro* Gait Simulation

Dr Antony Crossman, Dr Angela Kedgley

Imperial College London, London, Greater London, United Kingdom

Introduction

In vitro gait simulators are important tools in surgical and implant innovation. They recreate *in vivo* gait data, giving insights into the body's internal mechanisms. Previous simulators applied average pre-calculated muscle forces, leaving kinematics unconstrained. Unconstrained kinematics resulted in linear correlations of $r_{xy} > 0.87$, between achieved and desired ankle joint kinematics, with no mention of error magnitudes [1]. The hypothesis of this study was that the biofidelity of *in vitro* gait simulators can be improved through kinematic control, eliciting trial-specific muscle forces.

Methods

A novel kinematics-driven, three-stage cascade control system, developed as a plugin for the simVITRO gait module, controlled a custom built, five-segment, nine-muscle foot and ankle model. The torque needed to achieve *in vivo* kinematics of gait was calculated using PID control and input into a muscle force minimisation algorithm, which determined trial-specific forces and actuator positions.

Ten repetitions of stance were simulated. Kinetic (vertical ground reaction force (vGRF)) and kinematic (plantar-/dorsiflexion (PD), hallux flexion/extension (Hal-FE)) accuracies were assessed through mean absolute errors between achieved and desired data. Repeatability was defined as the mean standard deviation of kinetics and kinematics between repetitions. Physiological muscle timing was assessed using phase correlation between *in vivo* EMG data and executed muscle forces for the gastrocnemius (GN), tibialis anterior (TA) and peroneus brevis (PB).

Results

The kinematic accuracy and repeatability were 0.48° ± 0.56° and 0.20° ± 0.07° for PD, and 1.78° ± 1.67° and 0.59° ± 0.42° for Hal-FE with kinematic correlations of $r_{xy} \geq 0.99$ (Figure 1a). The muscle force patterning was excellent for $P_{TA} = 0.94$, $P_{PB} = 0.88$ and $P_{GN} = 0.83$. Accuracy of vGRF was 7.7 N ± 4.8 N with a repeatability of 3.7 N ± 1.5 N (Figure 1b).

Discussion

Biodfidelity of the stance phase of gait was successfully improved using a kinematics-driven control system when compared to force control [1]. Excellent muscle patterning, high kinematic and kinetic accuracy and repeatability demonstrates the successful implementation of cascade control for gait simulation.

Images (Optional)

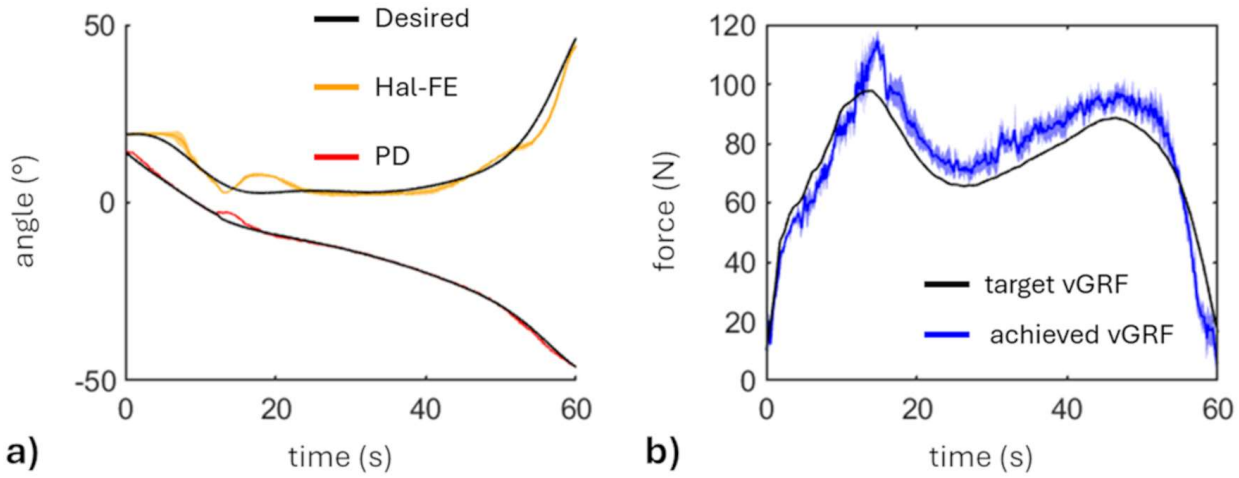


Figure 1: Desired and average (± one standard deviation) achieved stance phase kinetics and kinematics of a) plantar-/dorsiflexion (PD) and flexion/extension of the metatarsophalangeal joint at the base of the hallux (Hal-FE), and b) vertical ground reaction force (vGRF)

References (Optional)

[1] Wang D *et al*. Proc Inst Mech Eng H, 2020, **234**:1070-1082

Acknowledgements (Optional)

AJC was supported by the UK Engineering and Physical Sciences Research Council (EPSRC) grant EP/S02249X/1 for the Centre for Doctoral Training in Prosthetics and Orthotics.

Session Category

Musculoskeletal Biomechanics: Methods, Models and Applications

P2-110

Variations in the Expressed Section of the Force-Length Curve of the Human Soleus

Ms. Axelle M. Wasiak, Dr. John H. Challis

The Pennsylvania State University, University Park, Pennsylvania, United States

Introduction

The force-length relationship is well established in isolated muscle, but muscles *in vivo* do not necessarily operate over the entire range of the theoretical force-length curve. For the bi-articular gastrocnemius and rectus femoris muscles, using dynamometry, it has been demonstrated that *in vivo* the expressed section of the force-length curves can vary between individuals. The purpose of this study was to determine, *in vivo,* the properties of the human soleus muscle-tendon complex using a combination of dynamometry, ultrasound imaging, and modeling. It was hypothesized that the ratio of tendon slack length to fascicle optimum length will dictate the expressed section of the force-length curve.

Methods

Thirteen participants (6M 7F) provided informed consent for this study. The soleus moment arm was determined using the tendon excursion method, with the tendon excursion tracked using ultrasound. For strength testing, to eliminate the gastrocnemius contribution to the ankle plantarflexion moment, the knee was flexed until gastrocnemius buckling was observed in ultrasound images (40° to 70° knee angle). Participants performed maximal voluntary isometric plantarflexions at eight ankle angles (15° dorsiflexion to 30° plantarflexion). The ankle moment was recorded using a dynamometer. The soleus architecture, tendon slack length and elongation were imaged simultaneously using a dual probe ultrasound.

Results

Eight participants operated on the ascending limb of the force-length curve, two on the plateau region, and three on the descending limb. No significant differences were found between ascending and descending groups in maximum tendon extension (p=0.34), optimum fascicle length (p=0.33), and maximum force (p=0.34), but tendon slack length (p=0.013), and the ratio of tendon slack length to fascicle optimal length (p<0.001) were significantly different. Those participants whose soleus operated on the ascending limb of the force-length curve had longer tendon slack lengths and a larger ratio of tendon slack length to fascicle optimal length.

Discussion

This study successfully characterized the soleus force-length relationship *in vivo*. Variations in the expressed region of the force-length curve can be explained by individual differences in the ratio of tendon slack length to fascicle optimal length. This characterization has implications for understanding the function of the soleus *in vivo*.

Session Category

Musculoskeletal Biomechanics: Methods, Models and Applications

P2-111

Direct Comparison of GPOPS-II and CasADi for Generating Predictive Simulations of Human Movement

Prof. B.J. Fregly Ph.D., Mr. Spencer Williams B.S.

Rice University, Houston, Texas, United States

Introduction

Predictive simulations of human movement can potentially be used to design personalized treatments for movement impairments. While direct collocation optimal control solvers GPOPS-II (commercial) [1] and CasADi (open-source) [2] are commonly used to generate predictive simulations, no studies have compared solver convergence properties for identical human movement prediction problems. This study performed such a comparison within the Neuromusculoskeletal Modeling (NMSM) Pipeline [3].

Methods

A three-dimensional full-body torque-driven soccer kicking tutorial problem available with the NMSM Pipeline was modified for use in this study. The modification involved adding a deformable foot-ground contact model under the left foot. Three torque actuators controlled the sagittal plane motion of the right hip, knee, and ankle. The motion of the remaining sagittal plane joints was tracked, while the motion of all non-sagittal plane joints was prescribed.

The NMSM Pipeline works with GPOPS-II, and a limited prototype implementation of CasADi was added to permit solver comparison. Both solvers were applied to a sequence of three optimizations. First, a Tracking Optimization (two formulations) eliminated the sagittal plane residual forces and moment on the pelvis while closely reproducing the experimental motion of all non-prescribed joints and the experimental inverse dynamics moments for the right leg. Next, a Verification Optimization verified that the torque controls from the first optimization reproduced the motion of the right leg without tracking it. Finally, a Design Optimization (predictive simulation) predicted how the right leg control torques and full body motion should change to increase the anterior velocity of the right toe by 10% at ball contact.

Results

Both solvers successfully solved all three optimization problems. GPOPS-II performed better for Tracking Optimization while CasADi performed better for Verification and Design Optimization. Solutions produced by both solvers were nearly identical for Tracking and

Verification Optimization, while GPOPS-II predicted more knee flexion and less hip extension than did CasADi for Design Optimization.

Discussion

With refinements for Tracking Optimization, CasADi appears to be a viable open-source alternative to GPOPS-II within the NMSM Pipeline.

Images (Optional)

Solver	Optimization	Iterations	CPU Time (s)	CPU Time/ Iteration (s)
GPOPS-II	Tracking (Controller)	76	135.8	1.79
	Tracking (Inv Dyn)	92	151.8	1.65
	Verification	11	18.5	1.68
	Design	57	115.6	2.03
CasADi	Tracking (Controller)	145	173.6	1.20
	Tracking (Inv Dyn)	111	10,800.3	97.30
	Verification	2	4.6	2.28
	Design	23	29.3	1.27

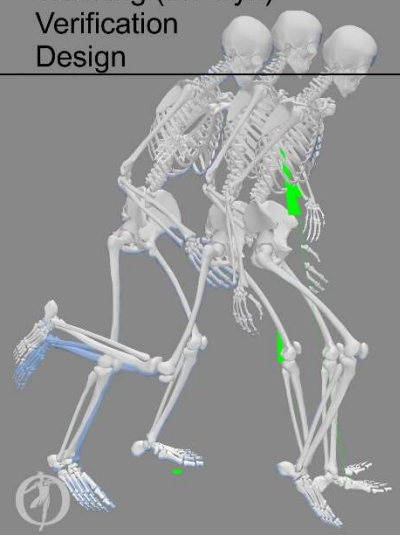


Table above: Comparison of GPOPS-II and CasAdi convergence for Tracking, Verification, and Design Optimizations.

Figure left: Comparison of experimental (blue) and optimal (white) kicking motion.

References (Optional)

[1] M. Patterson *et al.*, ACM TOMS, 2014.

[2] J. Andersson *et al.*, Math. Prog. Comp., 2019.

[3] C. Hammond *et al.*, J. NeuroEng. Rehab., 2025.

Acknowledgements (Optional)

NIH R01EB030520

Session Category

Musculoskeletal Biomechanics: Methods, Models and Applications

P2-112

The effect of triceps surae force-length behavior on jumping performance

Mr. Ben Perrin, Dr. John Challis

The Pennsylvania State University, State College, PA, United States

Introduction

In vivo it has been found that the expressed region of the force-length curve for the triceps surae varies between individuals, which introduces the possibility that this variation influences performance. For a jump, it is of interest whether the high-to-low force production potential of the ascending limb, or vice versa for the descending limb, would yield greater jump heights. The purpose of this study was to investigate this question for a jump in which the joints above to the ankle were locked. It was hypothesized that a greater jump height would be achieved when muscles were operating on the ascending limb.

Methods

A model consisting of a multi segment foot, that had been previously validated using kinematic and kinetic data from five human participants, was used in this study. Two model variations were created by altering the tendon slack length of the soleus and gastrocnemius where in Model 1 they acted on the ascending limb of the force-length curve, and in Model 2 the descending limb. Maximal vertical jump optimizations were simulated for each model, and jump performance and muscle behavior were compared. Upper body inertial properties of the models were altered, and simulations were rerun to see if this accentuated any differences.

Results

Model 2, which acted on the descending limb, jumped 10.5% higher than Model 1. A Brake-Spring-Motor index indicated that the gastrocnemius and soleus were acting almost entirely as movement producers (motors) for both models. In Model 2 the gastrocnemius did 2.4% and the soleus 13.3% more work compared with Model 1. When the mass of the upper body was increased by 50%, these differences were magnified as Model 2 jumped 20.2% higher and the soleus did 48.7% more work compared with Model 1.

Discussion

The results of this study indicate that having the triceps surae operate on the ascending limb is not optimal for maximal jumping tasks. Given that for both muscles it has been found that the majority of people operate on the ascending limb, the question is raised as to what movements they may be optimized for.

Session Category

Musculoskeletal Biomechanics: Methods, Models and Applications

P2-113

Sex-Specific Differences in Hip Abduction Moment Arms Reveal Limitations of Scaled Musculoskeletal Models

Mr. Brendan S. Shea

University of Virginia, Charlottesville, VA, United States

Introduction

Computational models of the lower limb are widely derived from male-only datasets or from sex-averaged data, despite the well-documented sex differences in skeletal morphology, muscle architecture and strength. These limitations are relevant given that women are at increased risk for musculoskeletal pain and discomfort [1]. Therefore, models that explicitly incorporate sex-specific anatomy are needed to accurately characterize movement biomechanics as the unique placements of attachment points influence moment arms.

Methods

Seventy-seven healthy adults (40F, 37M; Age 20-49 years) underwent full MRI scans of both lower limbs and motion capture gait analysis (Vicon Nexus). Lower limb muscles and bones were segmented using a trained AI algorithm with manual validation (Springbok Analytics,Charlottesville,VA).The 2016 Rajagopal model [2] was scaled in OpenSim using static motion capture data and subject mass. Gluteus medius and minimus muscle attachment points for the subject-specific models were located in a semi-automatic manner using bony landmarks, anatomical data, and visual inspection. Peak moment arms were extracted as the maximum absolute value of each muscle's moment arm curve using the OpenSim API for both the scaled Rajagopal model and the subject-specific models. Peak moment arms from the two models were compared for each subject and muscle.

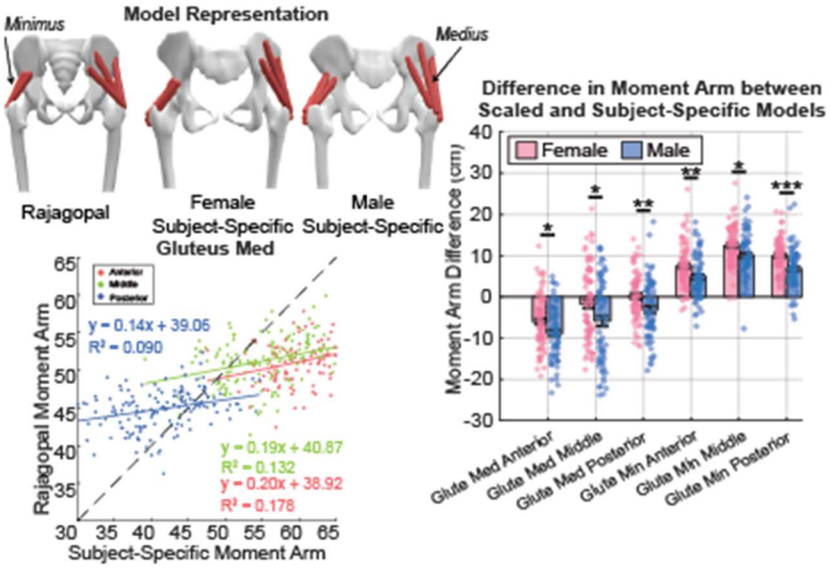
Results

Across all gluteus medius muscle compartments, the scaled Rajagopal model showed a greater magnitude of difference from the subject-specific models in male subjects compared to female subjects. In contrast, the gluteus minimus compartments exhibited the opposite pattern, with female models demonstrating larger differences across all compartments. Significant differences in moment arms were observed across all compartments and muscles, with the posterior compartment of the gluteus minimus showing the largest and significant difference ($p<0.001$).

Discussion

These findings demonstrate that current generic scaled models better represent the male anatomy than female anatomy. This work underscores the need for sex-specific muscle modeling to accurately capture anatomy and function of both sexes. Future work will investigate the relationships between moment arms and anthropometric measures to further elucidate the sources of sex-based differences in moment arm output.

Images (Optional)



References (Optional)

[1] Wolf, J.M. et al., J Am Acad Orthop Surg, 2015

[2] Rajagopal, A *et al*., IEEE Transactions on Biomedical Engineering 2016

Acknowledgements (Optional)

University of Virginia, M3 Lab, Springbok Analytics, R01AR078396

Session Category

Musculoskeletal Biomechanics: Methods, Models and Applications

P2-114

Predicting Below Knee Muscle Forces from Ground Reaction Forces in Older and Younger Populations Using Sequence- and Attention-Based Models

Mr. Brian Keller[1], Mr. Ty Lunde[1], Dr. Anthony Le[1], Dr. Scott Ulrich[2], Dr. Amy Silder[3], Dr. Bryan Heiderscheit[4], Dr. Darryl Thelen[5], Dr. Amy Lenz[2]

[1]University of Utah, Department of Biomedical Engineering, Salt Lake City, Utah, United States. [2]University of Utah, Department of Mechanical Engineering, Salt Lake City, Utah, United States. [3]University of Wisconsin-Madison, Department of Biomedical Engineering, Madison, Wisconsin, United States. [4]University of Wisconsin-Madison, Department of Orthopedics and Rehabilitation, Madison, Wisconsin, United States. [5]University of Wisconsin-Madison, Department of Mechanical Engineering, Madison, Wisconsin, United States

Mr. Brian Keller

Introduction

Increasing availability of portable force plates has enabled a broader adoption of data-driven approaches to sports training and rehabilitation[1]. Despite rapid growth and accessibility of biomechanical datasets, tools for extracting deeper physiological and clinical insight remain limited. Our project aimed to address this gap by developing generalized deep learning models that predict below knee muscle forces between younger and older adult populations according to clinical thresholds using ground reaction force (GRF) data.

Methods

Kinematic and kinetic data from prior gait studies were collected from 20 older adults[2] (OA; 14 females, 72.7±5.4 yrs old) and 10 younger adults[3] (YA; 4 females, 26.4±4.1 yrs old) during walking trials performed at various speeds. Ground-truth muscle forces were estimated in OpenSim[4] using scaled generic models[5], inverse kinematics/dynamics and custom static optimization pipeline[3]. In total, 1500 stance phases of estimated muscle force and GRF (50-50 split OA/YA) were divided into training, validation, and testing sets. Four deep learning architectures, a LSTM (LongShortTermMemory), CNN-LSTM (ConvolutionalNeuralNetwork-LongShortTermMemory), LSTM with attention, and transformer, were trained to predict stance-phase forces in 11 ankle-crossing muscles

using input GRF data. Model results were evaluated using a threshold derived from literature quantifying the difference in ankle moments between OA and YA populations (<3.03N/kg)[6].

Results

The model with lowest mean absolute error normalized by bodyweight (MAE) was the LSTM (MAE=1.20N/kg), followed by the transformer (MAE=1.23N/kg), LSTM with attention (MAE=1.26N/kg), and CNN-LSTM (MAE=1.69N/kg). All models had overall normalized MAE below our clinical threshold.

Discussion

Normalized model errors for predicted muscle forces being less than the clinically derived difference between OA and YA gait indicate these models can discriminate between those populations in a clinically relevant way. Their generalizability across healthy populations makes these models valuable tools for indirectly extracting muscle force information and establishes deep learning models as effective methods for getting more complete biomechanical data.

Images (Optional)

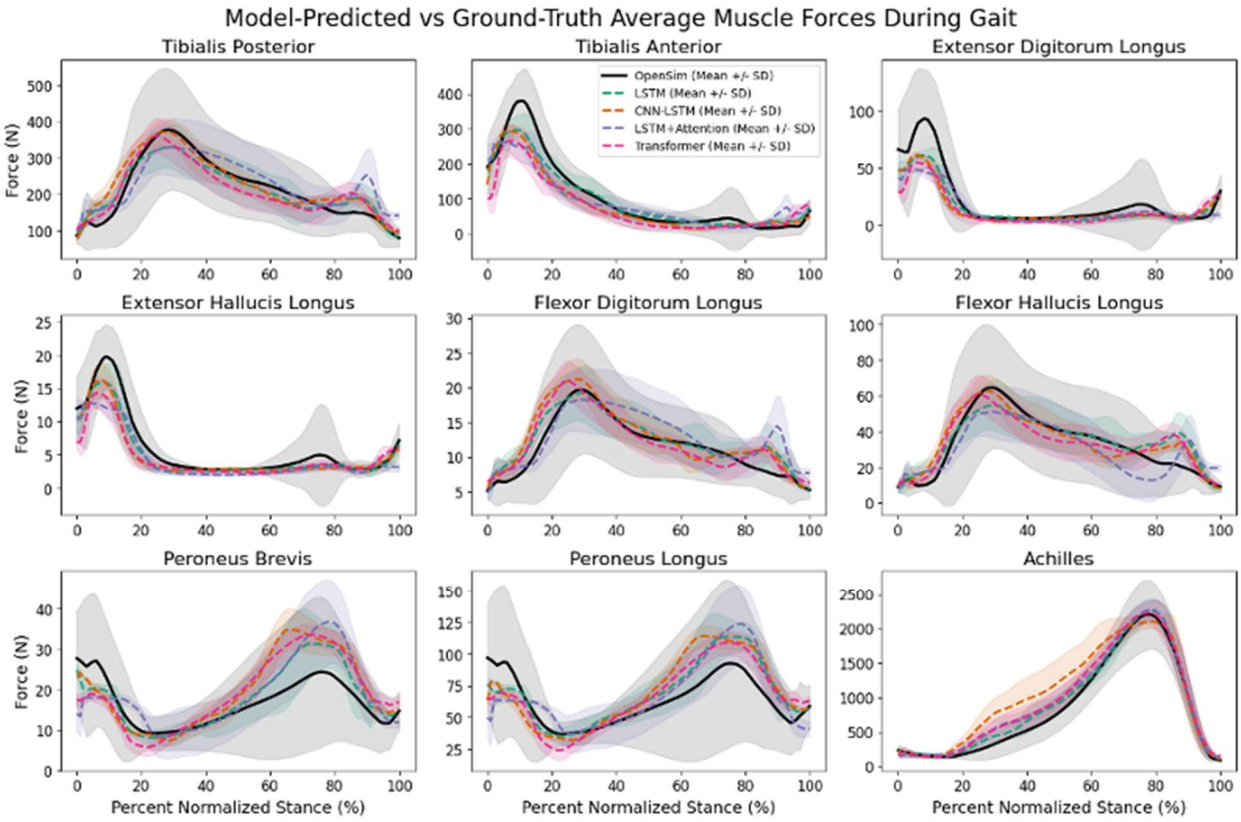


Figure 1: Mean ± 1 SD muscle force profiles for OpenSim calculated ground truth and all predictive models. Lines are mean values, while shaded regions indicate one standard deviation.

References (Optional)

[1] Jia Y, et al., BMC Sports Sci Med Rehabil., 2025.

[2] Silder et al., J Biomech., 2008.

[3] Uhlrich et al., Scientific Reports, 2022.

[4] Seth et al., Comput Biol., 2018.

[5] Rajagopal et al., Transactions on BME, 2016.

[6] Sloot et al., Gait & Posture, 2021.

Session Category

Musculoskeletal Biomechanics: Methods, Models and Applications

P2-115

Pilot Study for THUMS Spine Model in Proximal Junctional Kyphosis Investigation

Mr. Chin Rhong Koh BEng (Hons)[1], Dr. Philip Purcell PhD[1], Dr. Stephen Tiernan PhD[1], Prof. Seamus Morris MB BCh BAO MMedSci MCh FSEM AFRCSI FRCS (Tr & Orth)[2]

[1]Technological University Dublin, Tallaght, Dublin, Ireland. [2]Mater Misericordiae University Hospital, Dublin, Dublin, Ireland

Introduction

Proximal junctional kyphosis (PJK) is a major postoperative complication following spinal deformity correction, with reported incidence rates as high as 61.7% [1]. Finite element analysis (FEA) is frequently employed to explore preventative strategies. However, published FEA studies exhibit substantial methodological inconsistencies, encompassing diverse modelling approaches, boundary conditions, and loading criteria. To address this lack of standardization, the present study aims to develop and validate a standardized FEA framework using the Total HUman Model for Safety (THUMS) for quasi-static analysis in the investigation of PJK mechanisms. A pilot study was carried out using the L3-L4 functional spinal unit (FSU) model from THUMS.

Methods

The L3-L4 FSU model was imported into ANSYS Mechanical 2024R1 with ligaments and disc fiber modelled as LINK180 tension-only elements (Figure 1A). Facet joint interaction was defined by frictionless contact with pure penalty formulation. The model was validated against THUMS published data.

After validating, the model was deformed by applying remote displacement (Figure 1A), and the deformed model was exported as base model for simulation with screws and rods modelled as simplified beam element remotely attached to the vertebrae (Figure 1B).

Results

The model was validated flexion-extension, compression, and lateral bending, which showed similar trends to results published by THUMS. However, the range of motion (RoM) for flexion was underestimated by 13%.

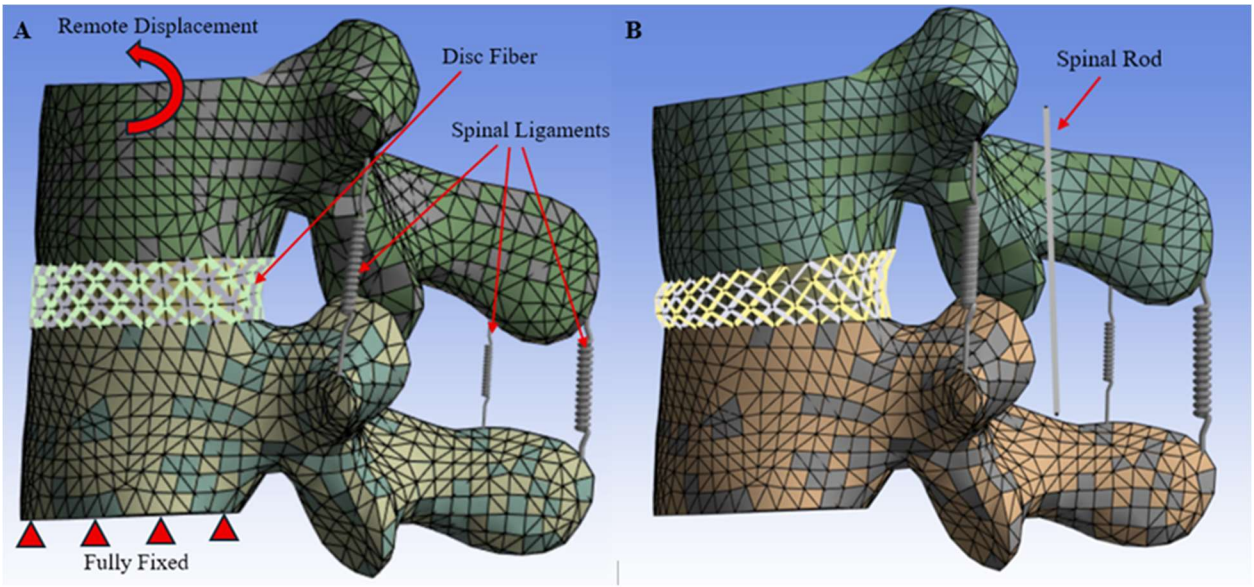
Furthermore, deformed FSU with spinal rods showed 40% reduction in RoM for flexion compared to deformed FSU without spinal rods.

Discussion

The underestimation of RoM in flexion could be partly attributed to overly stiff posterior ligaments. As the tension-only posterior ligaments play a more significant role in flexion. Simplified spinal rods modelled as circular beam elements remotely attached to vertebrae showed promising preliminary results, reducing the computational power required.

This ongoing validation framework will be carried out with longer T12-L5 spinal segment, and lastly the full spine column C1-S5 from THUMS, including rib cage. The realization of this framework will enable future investigations on optimizing spinal deformity correction surgeries to mitigate PJK risk, such as identifying the optimal fixation length and instrumentation devices.

Images (Optional)



References (Optional)

[1] Han Jo Kim et al., Journal of the American Academy of Orthopedic Surgeons, 2016

Session Category

Musculoskeletal Biomechanics: Methods, Models and Applications

P2-116

Choosing a Back Support Exoskeleton From Among Different Designs: Considerations Related to Cumulative Spinal Loading, Muscle Fatigue, Physiological Strain, and Discomfort During a Repetitive Lifting Task

Dr Christian Larivière Ph.D.[1], Dr Étienne Goubault Ph.D.[1], Dr Guillaume Durandau Ph.D.[2], M. Hakim Mecheri M.Sc.[1], Dr Denys Denis Ph.D.[3], Dr Gabriel Diamond-Ouellette Ph.D.[4]

[1]Institut de recherche Robert-Sauvé en santé et en sécurité du travail (IRSST), Montréal, Québec, Canada. [2]Department of Mechanical Engineering, McGill University, Montreal, Québec, Canada. [3]Département des sciences de l'activité physique, Université du Québec à Montréal (UQAM), Montréal, Québec, Canada. [4]TOP-MED: Recherche et innovation en santé, Québec, Québec, Canada

Introduction

Warehouse and healthcare workers frequently develop back pain due to repetitive lifting tasks, yet conventional lifting training programs often fail to prevent it. Back-support exoskeletons (BSEs) may help by reducing muscle fatigue and spinal loading, but selecting the appropriate design is challenging because it depends on multiple criteria. This study aimed to compare three BSE designs (**Table**) based on different criteria.

Methods

Nineteen male participants completed five laboratory sessions: one for task/measurement familiarization and BSE assistance adjustments and four for testing randomized conditions (no BSE, BSE1, BSE2, BSE3). The task was 60-min symmetric lifting/lowering (7 cycles/min) of a crate from floor to hip height; the load set at 10% of lifting strength. Measurements included cumulative spinal compression (spinal shrinkage), muscle fatigue (static lifting strength; perceived fatigue using a Borg CR-10 scale), heart rate, and discomfort at BSE support points (shoulders, upper back, chest, pelvis, thighs). Data were analyzed using repeated-measures ANOVA, Tukey pairwise comparisons, and Hedge's *g* effect size (ES) estimates interpreted as negligible ($g < 0.20$), small (0.20 to 0.49), medium (0.50 to 0.79) and large (≥ 0.80).

Results

Spinal shrinkage (large ES) and reduced lifting strength (small ES) occurred during the 60-minute task ($P < 0.001$), but none of the BSEs mitigated these effects compared to the control condition (negligible to small ES). However, BSE2 significantly reduced perceived lower back muscle fatigue and heart rate (by 10–13 bpm) compared to other conditions ($P <$

0.01; medium to large ES). Overall discomfort ratings were acceptable, though BSE3 caused greater discomfort at the thighs and shoulders ($P < 0.05$; medium to large ES).

Discussion

The absence of BSE impact on spinal shrinkage and objective fatigue measures may reflect that these devices do not assist trunk extensor muscles throughout the full range of motion (e.g. standing and slight flexion). Conversely, subjective fatigue ratings suggest that BSE2 reduces low back muscle forces, as further supported by the decrease in heart rate. Discomfort with BSE3 likely stems from longitudinal forces transmitted to extremity supports (shoulders and thighs). These results may not generalize to females and to static or asymmetrical lifting tasks.

Images (Optional)

Table. Characteristics of the back support exoskeletons (BSEs)

BSE model:	**BSE1: UpLift Lite**	**BSE2: Laevo FLEX**	**BSE3: Biolift**
Picture:			
Design:	Soft design (elastics on the back increasing lever arm	Rigid design (gas springs on hip sides + rods pulling the torso)	Rigid design (coil spring behind the back pulling the torso)
Weight (kg):	1.6 kg	4.0-4.4 kg	4.0 kg
Assistance (Nm):	Low (~ 10-20 Nm)	Moderate (~ 50-60 Nm)	Moderate (~ 50-60 Nm)
Force orientation: (relative to torso)	Parallel (pulling down)	Perpendicular (pulling backward)	Parallel + perpendicular (pulling down + backward)

References (Optional)

Session Category

Musculoskeletal Biomechanics: Methods, Models and Applications

P2-117

Toward Real-Time EMG-Informed Neuromusculoskeletal Modelling: Validation of a Differentiable-Physics Calibration Approach

Dr Matthew Worsey PhD, Mr Matthew Hambly Masters, BEng, Miss Yumei Sun Masters IT, AProf David Saxby PhD, AProf Laura Diamond PhD, AProf Claudio Pizzolato PhD

Griffith University, Gold Coast, Queensland, Australia

Introduction

Since the inception of calibrated electromyogram (EMG)-informed neuromusculoskeletal modelling [1], numerous calibration and execution strategies have been presented without comprehensive assessment of generalisability. We recently implemented an EMG-informed neuromusculoskeletal model using differentiable physics incorporating a Meyerhof-Hill-type muscle model and auto-differentiable elastic tendon (CEINMS-NN) [2]. We evaluated whether novel differentiable-physics calibration workflows achieve joint-moment and EMG tracking comparable to established workflows. We assessed three calibration methods: traditional CEINMS, CEINMS-NN, and CEINMS-NN-hybrid. Both traditional CEINMS and CEINMS-NN optimise excitation-to-activation and musculotendon parameters to match inverse-dynamics joint moments using recorded EMG signals; however, CEINMS-NN performs this optimization within a differentiable-physics framework. CEINMS-NN-hybrid synthesizes EMG for unrecorded muscles to improve moment tracking. All models were calibrated using identical optimization weights and executed using CEINMS EMG-assisted mode to evaluate whether the new optimization framework maintains tracking accuracy.

Methods

Fifty-two participants (n=52, 29.7±6.5 years, 45 females) performed 264 overground walking and 141 running trials while optical motion capture, ground-reaction forces, and EMG from eight knee-spanning muscles were recorded. Walking and running trials were processed to obtain joint kinematics, inverse-dynamics moments, musculotendon lengths, moment arms, and normalized EMG inputs for calibration (124 trials) and execution (281 trials).

Results

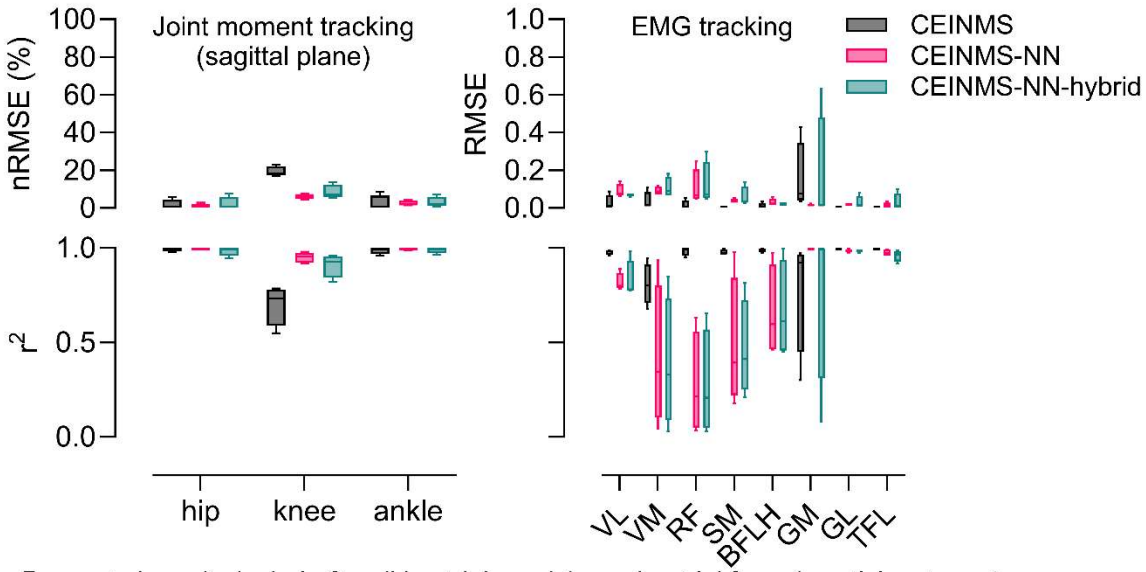
Models calibrated using the new optimisation framework achieved hip and ankle torque tracking comparable to the established CEINMS pipeline (Figure 1). Knee-moment tracking improved substantially with both CEINMS-NN variants relative to CEINMS. In contrast, EMG-tracking performance was lower for CEINMS-NN and CEINMS-NN-hybrid than for

CEINMS. Calibration times for CEINMS-NN and CEINMS-NN-hybrid were substantially reduced (21 seconds and 25 seconds respectively) compared to CEINMS (27 minutes).

Discussion

The differentiable-physics calibration improved knee moment tracking while maintaining comparable accuracy at the hip and ankle, albeit with reduced fidelity in reproducing recorded EMG. Optimisation of EMG-assisted execution weights could improve EMG tracking. Despite this trade-off, combining the novel calibration methods with traditional CEINMS EMG-assisted execution provided a practical and valid workflow. The substantially reduced calibration time supports future real-time applications and integration into CEINMS-RT, offering a fast and flexible alternative for EMG-informed neuromusculoskeletal modelling.

Images (Optional)



Presented results include 3 walking trials and 1 running trial from 1 participant; vastus lateralis (VL), vastus medialis (VM), rectus femoris (RF), semimembranosus (SM), bicep femoris long head (BFLH), medial gastrocnemius (GM), lateral gastrocnemius (GL), tensor fasciae latae (TFL)

References (Optional)

[1] D.G. Lloyd *et al.*, J Biomechanics, 2003

[2] M. J. Hambly *et al.,* IEEE Trans. Biomed Eng, 2025

Acknowledgements (Optional)

The authors would like to acknowledge Professor David G Lloyd for his continuous support, mentorship and advice given throughout this project.

Session Category

Musculoskeletal Biomechanics: Methods, Models and Applications

P2-118

The Forward-Leaning Kinematic Adaptations Seen in Older Adults During Sit-to-Stand Movements seems to Reflect a Strategy to Reduce Hip and Knee Torques

Mr. Daehoon Kwon, Ms. Xiaofan Liu, Mr. Jingcheng Shi, Ms. Yiwen Bao, Prof. Francisco J. Valero-Cuevas

University of Southern California, Los Angeles, CA, United States

Mr. Daehoon Kwon

Ms. Xiaofan Liu

Mr. Jingcheng Shi

Ms. Yiwen Bao

Introduction

Frailty in healthy aging, driven by sarcopenia, can make every day tasks such as sit-to-stand (STS) difficult. For example, older adults often adopt a forward-leaning, hip-flexed strategy during STS [1], but whether this is an adaptation to sarcopenia or to balance/vestibular comorbidities in ageing is not known. Using principles of mechanics [2], we tested whether the forward-leaning strategy reduces hip and knee joint torques, and is therefore an adaptation to sarcopenia.

Methods

We modeled the lower limb in the sagittal plane as a 3-DOF linkage with ankle, knee, and hip joints, and segment lengths followed 50th-percentile adult male anthropometry(L1, L2, L3), with the body weight, w, concentrated as a point mass on the torso [3]. This allowed us to calculate hip, knee and ankle torques as a vector τ for any posture q as $\tau = J(q)^T w$. Similar to [4] Monte Carlo simulations generated 1,000 reasonable STS joint trajectories from a same sitting posture to a target standing posture, via interpolated piecewise-cubic Hermite polynomials all within physiological limits. Those below and above the median

peak hip flexion were labeled “older-like” and “younger-like,” respectively. We then calculated hip and knee torques at maximum hip flexion angle.

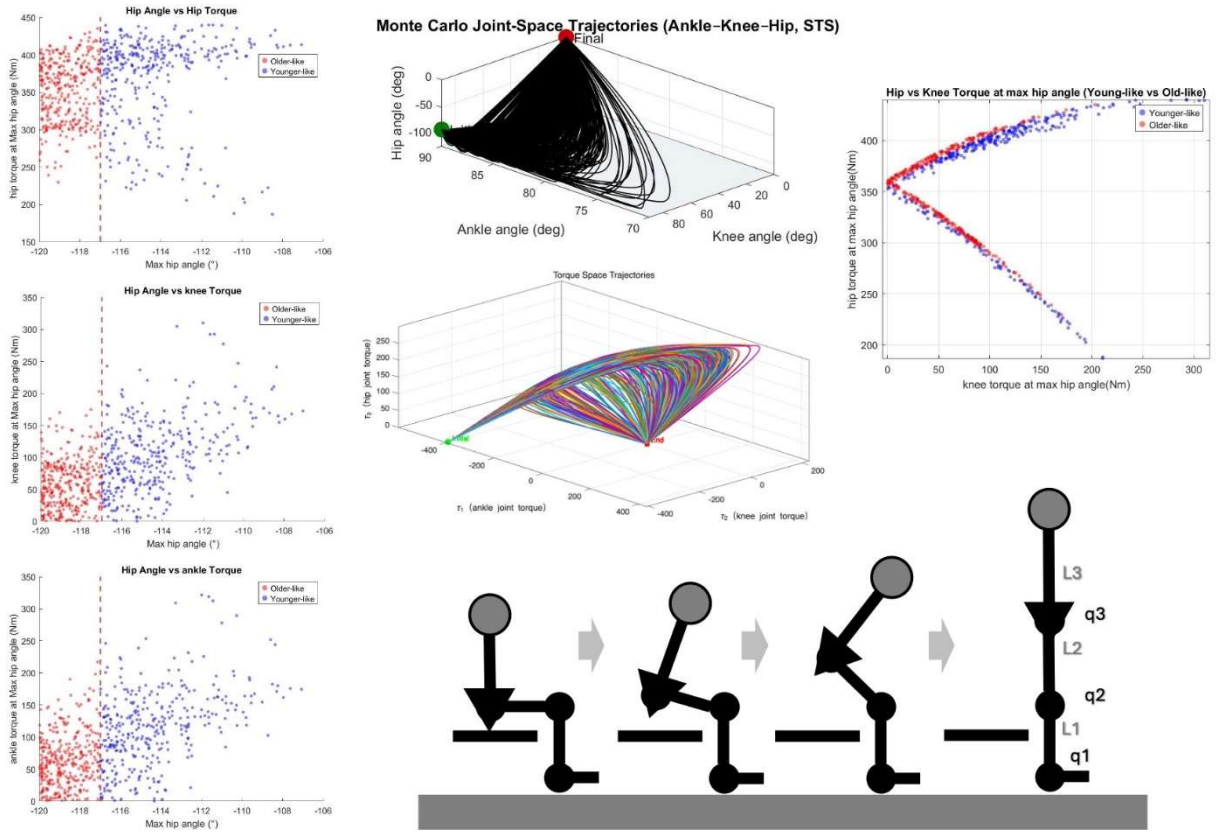
Results

The group of older-like trajectories showed lower mean torques than the younger-like trajectories (t-tests, $p < 0.01$). At maximum hip flexion, older-like trajectories exhibited significantly smaller mean hip (≈352.5±41.7 vs 368.3±59.4 N·m), knee torques (≈59.1±38.04 vs 105.4±56.4 N·m) and ankle torques (≈63.99±41.07 vs 115.68±59.80 N·m). As strength decreases, high-torque, knee-dominant trajectories are eliminated first, leaving a narrow region of low-demand, hip-dominant solutions.

Discussion

We can conclude that hip-flexion patterns observed in older adults reflect an appropriate compensation to sarcopenia independently of other comorbidities in aging . Identifying such low-torque STS trajectories and muscle weakening that drives them can guide targeted strengthening, safer training, assistive-device design, and early-warning tools for functional decline.

Images (Optional)



References (Optional)

[1] Alexander, J Gerontology Series A, 2001.[2] Valero-Cuevas, F Neuromechanics, 2016. [3] Gordon, 2012 Anthropometric Survey of U.S. Army, 2014.[4] Hagen&Valero-Cuevas, Errors in Predicting Muscle Fiber Lengths from Joint Kinematics, 2020.

Acknowledgements (Optional)

We thank Grace Niyo and our classmates in BME 504 for their helpful feedback and support.

All authors contributed equally to this work and shared first authorship.

Session Category

Musculoskeletal Biomechanics: Methods, Models and Applications

P2-119

Multi-Scale Modelling of Obesity-Driven Cartilage Degeneration in Subject-Specific Knee Joints

Mr Juntong Lai[1,2], Professor Damien Lacroix[1,2]

[1]Insigneo Institute, University of Sheffield, Sheffield, South Yorkshire, United Kingdom. [2]School of Mechanical, Aerospace and Civil Engineering, University of Sheffield, Sheffield, South Yorkshire, United Kingdom

Mr Juntong Lai

Introduction

Articular cartilage degeneration, a primary sign of osteoarthritis (OA), involves complex mechanobiological regulations at multi-scale. Excess adipose tissue resulting from obesity is not only associated with mechanical overloading but also with the regulation of OA inflammation. This subject-specific research aimed to investigate the subject-specific obesity effects on cartilage degeneration, using an advanced multi-scale modelling framework.

Methods

Three validated subject-specific finite element models [1] of the human knee joint were integrated into a multi-scale modelling framework to simulate the biomechanical and inflammatory effects of obesity on cartilage degeneration. S1-LTKN8941 and S2-LTKN1468 are two healthy left knees, in contrast to S3-RTKN0668, a right knee showing osteoarthritic changes on the lateral femoral cartilage. An axial knee force was scaled proportionally to BMI levels, representing repetitive loading at each iteration. The duration of each iteration was estimated by coupling variations in cartilage poroelasticity and inflammatory activities. To study the endotype of obesity-driven OA across subjects, cartilage degeneration was simulated for 5 years at different BMIs. The interquartile range (IQR) and distribution of the degeneration level were visualised.

Results

Obesity resulted in a more uniform distribution of the cartilage degeneration in S1, whereas degeneration in S2 and S3 was primarily localised to the lateral cartilage (Figure 1a). The median degeneration level of medial cartilage was 23.3% (IQR 23.1% - 25.3%) in S1 and 0%

in S2 at a normal BMI (Figure 1b). At a low BMI, the degeneration level was concentrated to 24.5% (IQR 23.3% - 28%) in the femoral cartilage of S3, compared to diverging degeneration in both S1 (IQR 12.8%-23.5%) and S2 (IQR 1.6%-23.5%).

Discussion

The variations in cartilage degeneration level and distribution demonstrate the subject-specificity of obesity-related OA, whereas a decrease in BMI can reduce overall degeneration. This study, for the first time, integrated the mechano-biological regulations of obesity to study the subject-specific cartilage degeneration, demonstrating a potential computational approach that can be individualised to assess the effectiveness of BMI reduction.

Images (Optional)

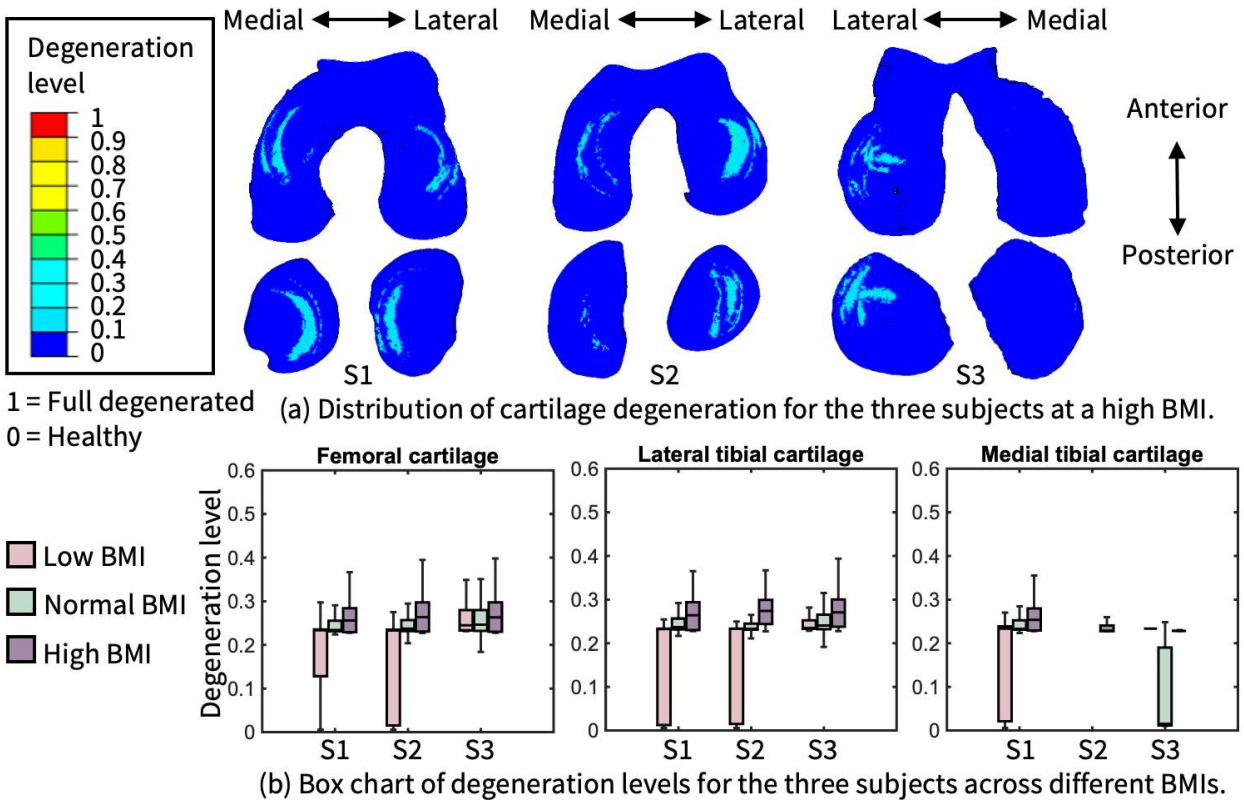


Figure 1. Distribution and IQR of cartilage degeneration levels in the three subjects.

References (Optional)

[1] Cooper et al., experimental validation and modelling dataset, 2023.

Acknowledgements (Optional)

This work was supported by the UK Engineering and Physical Sciences Research Council [EP/W524360/1/2747654].

Session Category

Musculoskeletal Biomechanics: Methods, Models and Applications

P2-120

Evaluating Automatic Tracking to Determine Tibiofemoral Kinematics From Biplane Videoradiography

Miss Janine Flohr, Dr Lauren Swain, Prof Cathy Holt, Dr David Williams

Cardiff University, Cardiff, Wales, United Kingdom

Introduction

Biplane videoradiography (BVR) is a method for deriving joint kinematics. Manual Image Registration (IR) involves aligning digitally reconstructed radiographs (DRRs) of bone geometry onto biplane radiographs and can take 20-40 hours per trial. An automated framework (Autotrack) was developed at University of Denver (DU) to register computed tomography (CT) geometry of the femur and tibia-fibula to biplane radiographs. This has been implemented at Cardiff University (CU) with magnetic resonance imaging (MRI) geometry. The current work aims to assess the accuracy of Autotrack at CU when compared to manual registration for three trials.

Methods

Autotrack's method is detailed in prior publication from DU [1]. At CU, three healthy participant's knees (PD Space) and whole leg (T1 TSE) were MRI scanned. Participants then completed BVR for a stand-to-sit (S2S) activity. Manual IR was performed using bone geometry in SlicerAutoscoperM. For Autotrack, the knee and whole leg were coregistered and merged to create one geometry with a fine resolution at the region of interest and a courser geometry at the diaphysis, proximal femur, and distal tibia-fibula. Both sets of 6-degree of freedom (6-DOF) kinematics were determined according to ISB recommendations and smoothed using a 10Hz low-pass Butterworth filter. Root-mean-square error (RMSE) was determined for the difference between the manual and Autotrack kinematics.

Results

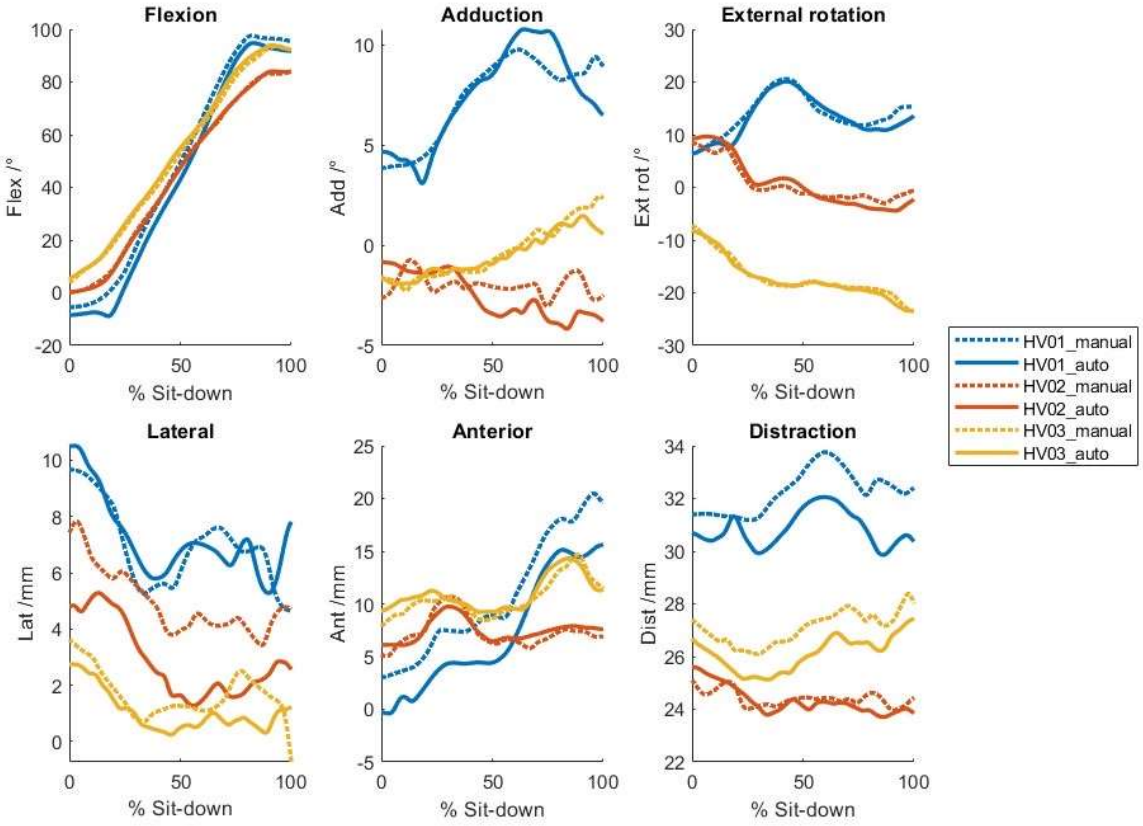
Average RMSEs across participants were: flexion-extension 2.44mm; adduction-abduction 0.90mm; external-internal rotation 1.19mm; lateral translation 1.30deg; anterior translation 1.64deg; distraction translation 0.97deg. Figure 1 shows the kinematics throughout the S2S trial for each participant using both manual IR and Autotrack.

Discussion

Flexion-extension and anterior translation had the largest RMSE, likely due to flexion-extension being the largest rotation range and tibial anterior translation having the largest

translation range in the knee. Agreement between the tracking methods somewhat diverges towards the end of the trial, due to occlusion of x-rays caused by soft tissue. Additionally, the Autotrack training data has not previously included S2S trials, and there is likely scope for improvement when the model is retrained incorporating S2S and other new activities. Future work will be to increase sample size, expand activities, and include osteoarthritic patient data.

Images (Optional)



References (Optional)

[1] William Burton *et al.*, J. Biomechanics, 2024

Acknowledgements (Optional)

The author would like to thank Dr William Burton from University of Denver for his assistance with Autotrack.

Session Category

Musculoskeletal Biomechanics: Methods, Models and Applications

P2-121

Comparison of Subjective and Objective Fatigue Responses to an Aerobic, Isometric, and Aerobic-Anaerobic Fatigue Protocol

Ms. Dveeta Lal Master's Student, Mr. Quinn Mulligan Master's Student, Dr. Timothy Burkhart Assistant Professor

University of Toronto, Toronto, Ontario, Canada

Introduction

Neuromuscular fatigue (NMF) may increase ACL injury risk by causing deleterious alterations in lower extremity kinematics that subsequently lead to increased strain on the ACL. However, there is conflicting evidence regarding this theory. Due to inconsistencies in the way fatigue has been induced and measured, drawing meaningful and consistent conclusions remains difficult. Consequently, the true role NMF plays in ACL injury risk, remains a point of contention. The purpose of this research is to assess three common methods of inducing NMF, and two methods of quantifying the onset of NMF, to determine if an optimal method exists.

Methods

26 healthy participants will be recruited and exposed to three fatigue protocols over two days: i) Aerobic – stationary bike task where participants increase resistance every five minutes (till 200W); ii) Isometric – sustained contraction (50%$_{max}$) of the quadriceps at 90º; and iii) Aerobic-Anaerobic – sets of five squat jumps and 30 seconds high-knees. Participants will continue each protocol until volitional fatigue (cannot sustain the protocol) or objective fatigue (determined through muscle activity). Bilateral sEMG data will be collected from three quadricep muscles, and the mean power frequency (MnPF) of the EMG signal, in response to a 50% MVIC contraction, will be monitored in real-time. A 10% decrease from baseline MnPF will indicate objective NMF. Participants' subjective rating of perceived exertion (RPE) will also be recorded, where a rating of 8+ indicates fatigue.

Results

Analyses from five participants revealed that objective NMF was achieved by 0%, 60%, and 60% in the aerobic, isometric, and aerobic-anaerobic protocols, respectively. Conversely, subjective fatigue was achieved by 60%, 70%, and 60% of the participants, respectively. Further analysis demonstrated that 40%, 50%, and 20% of the participants in the aerobic, isometric, and aerobic-anaerobic conditions, respectively, had matching subjective and objective fatigue outcomes.

Discussion

These preliminary findings demonstrate that fatigue responses varied quite substantially across the protocols, suggesting that fatigue protocols do vary in their ability to induce NMF. Additionally, agreement between subjective and objective fatigue measures was poor, suggesting that the RPE scale may not be a reliable measure and therefore cannot be used in place of a more objective measure like MnPF.

Session Category

Musculoskeletal Biomechanics: Methods, Models and Applications

P2-122

Rocky steps: The effect of loose surfaces on the kinetics of gait

Mr Dylan Mulligan MS, Dr Clare Milner PhD

Drexel University, Philadelphia, PA, United States

Introduction

Force plate-based studies of gait kinetics are typically conducted on level surfaces. However, different conditions may be encountered walking outdoors, such as unstable surfaces. Outdoor surfaces like loose rocks have greater force dispersal as the surface moves under the foot during walking. Determining how loose rocks affect kinetics may deepen our understanding of gait in real-world environments. The purpose of this study was to compare ground reaction forces (GRFs) while walking on loose rocks and level ground. We hypothesized that GRFs would decrease on loose rocks compared to level ground.

Methods

As part of an ongoing study, 5 healthy young adults provided written consent to participate (4 female, 1 male, age 23.4 (0.5) years, height 1.70 (0.05) m, weight 74.4 (13.8) kg). All procedures were approved by the Institutional Review Board. GRF data were sampled at 1000Hz as participants walked over level ground and loose rocks in sneakers. Level ground was instrumented with an embedded force plate. The loose rocks were instrumented with a portable force platform isolated within a 3.00x0.43x0.05 meter frame and covered with loose rocks. Data were processed in Visual3D and MATLAB, where GRFs were extracted for three steps per condition per participant. The GRF variables extracted were passive, active, braking, propulsive, medial, and lateral peaks. Vertical, braking, and propulsive impulses were also calculated. Effect sizes were used to evaluate differences, with large effects being considered meaningful.

Results

Loose rocks had a large effect on decreasing the magnitude of anterior posterior (AP) GRF variables as well as vertical impulse compared to level ground (Table 1). All other variables were similar on both surfaces.

Discussion

Loose rocks decreased GRF variables during walking particularly in the AP direction compared to level ground. GRF decreased because the applied force was dispersed through many moving loose rocks, primarily in the AP direction as the person progressed through the gait cycle. Vertical impulse also decreased as it is a summary measure representing the force dispersal over the entire stance phase. This instrumented loose rock obstacle design provides researchers with objective measurements of how loose surfaces affect gait kinetics.

Images (Optional)

Table 1: Mean and standard deviations of GRF variables on level ground and loose rocks. BW: Body Weight, SD: Standard Deviation

Variable	Level Ground (Mean ± SD)	Loose Rocks (Mean ± SD)	Effect size
Passive peak (BW)	1.10±0.17	1.16±0.07	0.50
Active peak (BW)	1.15±0.05	1.10±0.09	-0.71
Vertical impulse (BW*s)	819.05±38.65	775.37±23.30	-1.41
Braking peak (BW)	0.21±0.03	0.14±0.01	-3.26
Propulsive peak (BW)	0.21±0.02	0.15±0.01	-4.24
Braking impulse (BW*s)	100.34±10.16	68.08±8.45	-3.47
Propulsive impulse (BW*s)	108.31±11.09	74.04±4.98	-4.27
Medial peak (BW)	0.06±0.02	0.05±0.02	-0.71
Lateral peak (BW)	0.04±0.01	0.04±0.02	0.23

Session Category

Musculoskeletal Biomechanics: Methods, Models and Applications

P2-123

Allowing Metatarsophalangeal Motion Alters Intact Limb Knee Joint Loads During A Walking Simulation of an Individual with Transtibial Amputation

Dr. E. Daniel Syrett PT, DPT, PhD, OCS[1], Dr. Benjamin Darter PT, PhD[2]

[1]Central Virginia VA Hospital, Richmond, VA, United States. [2]Virginia Commonwealth University, Richmond, VA, United States

Introduction

Many researchers who perform muscle-driven simulations model the foot as a rigid lever, disallowing motion at the metatarsophalangeal (MTP) joints. However, permitting motion at this joint during simulations can alter variables which contribute to tibiofemoral joint contact force (TJCF) [1,2]. As TJCF is linked to knee OA [3], and those with lower limb amputation (LLA) have elevated intact knee OA risk [4], accurate TJCF estimates are critical. However, the effect of MTP locking on TJCF in LLA is unknown. This preliminary study examined how locking MTP joints affects TJCF in a tracking simulation of an individual with LLA.

Methods

Averaged treadmill gait data from one female with unilateral transtibial amputation (TTA, age 54, 59 kg, 1.7 m) drove two OpenSim Moco tracking simulations using a gait2392 model adapted for TTA [5]. Simulations used identical goals, weights, initial guesses, and tracking data. One allowed bilateral MTP motion (tracking 0°); the other contained welded MTP joints. Intact limb stance-phase medial TJCF (mTJCF) was normalized to body weight and compared using Pearson's *r*, RMSE, Sprague-Geers metrics, and qualitative peak/impulses differences.

Results

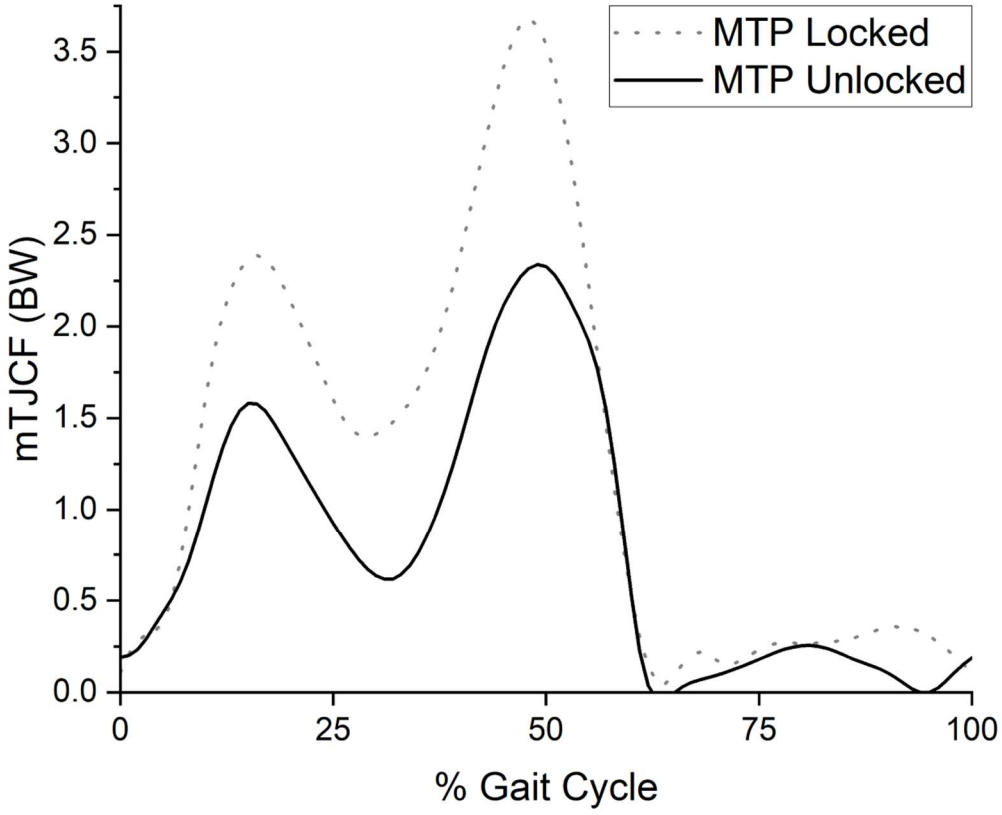
Kinematics and GRFs were similar between conditions. mTJCF patterns were also similar (Figure 1), though the locked MTP condition showed consistently higher stance-phase magnitude (r = 0.97, RMSE = 0.63 BW). Sprague-Geers: magnitude "poor" matching (0.55), phase "really good" matching (0.05). Peaks (BW): 1st - Locked 2.39 vs. Unlocked 1.58; 2nd - Locked 3.68 vs. Unlocked 2.34. Impulse (BW-s): Locked 1.15 vs. Unlocked 0.73.

Discussion

Preliminary results suggest locking the MTP increases stance phase intact limb mTJCF during walking simulations for an individual with TTA. Allowing MTP motion decreased the compressive force of the joint, likely due to power absorption occurring at the MTP joint [1]

and reduced gastrocnemius force during push-off [2]. Researchers should consider these effects when interpreting simulation-based estimates of knee joint loading.

Images (Optional)



References (Optional)

[1] Falisse et al., PLoS One, 2022

[2] Kim & Kipp, J. Orthop. Res, 2019

[3] Amiri et al., Knee, 2023

[4] Struyf et al., Arch. Phys. Med. Rehabil, 2009

[5] Syrett et al., Gait Posture, 2025

Session Category

Musculoskeletal Biomechanics: Methods, Models and Applications

P2-124

Validity and Reliability of Theia3D, OpenCap and Marker-Based Motion Capture Systems in Evaluating Joint Angles and Body Segments Trajectories

M.Sc. Eleonora Bonelli[1,2], B.Sc. Cecilia Mazzola[1,2], Dr. Anna C. Render[2], Prof. Alessandro Colombo[1], Prof. Peter C. Fino[2], Dr. Cecilia Monoli[2]

[1]Politecnico di Milano, Milano, Italy, Italy. [2]University of Utah, Salt Lake City, UT, United States

Introduction

Marker-based motion capture is considered the gold standard in motion analysis, but it is limited by soft-tissue artifacts and other factors, such as time consumption and reliance on expert operators for subject preparation, and controlled environments. Recently, markerless systems have emerged to address these limitations. While many validation studies still use marker-based systems as a reference, both marker-based and markerless systems are prone to errors. This study aims to evaluate the performance of Theia3D, OpenCap, and Vicon in controlled tasks, using fixed joint angles and body segment distances as references.

Methods

In this IRB-approved pilot study, we simultaneously used a marker-based mocap system (VICON Nexus 2.16), and two markerless mocap systems – Theia3D and OpenCap. Two participants completed a series of tasks focused on feet, hands, and pelvis displacement. Afterwards, we analyzed major joints angles using fixed angles as objective reference: shoulder (flexion, abduction, rotation), elbow (flexion), hip (flexion, abduction, rotation), and knee (flexion).

Results

Our preliminary results (see Table 1) aimed to investigate the validity of the systems, as the Root Mean Squared Error (RMSE) between the mocap system outcome and reference measure, along with the reliability (Coefficient of Variation, CV) across multiple repetitions of each task. Overall, results are consistent across systems. Particularly when multiple body segments move simultaneously, isolating and assessing a single degree of freedom appears challenging (e.g., shoulder rotation, hip abduction and rotation). In some tasks, OpenCap's low RMSE may appear to indicate better accuracy, but it could actually result from incomplete tracking of complex movements (e.g., shoulder and elbow flexion, hip rotation). This highlights the need for additional trials.

Discussion

These preliminary results provide some of the first data comparing multiple markerless and marker-based motion capture systems, especially in the novelty of assessing their performance in reference to ground-truth constraints. Indeed, each mocap system uses a different model, introducing another source of error and making system comparison more challenging. Building on the results of this pilot study, our goal is to further investigate the simultaneous evaluation of different systems aiming to improve the robustness of the evaluation.

Images (Optional)

Target segment/joint	Task description	Validity RMSE - average (SD)			Reliability CV - average (SD)		
		Vicon	Theia3D	OpenCap	Vicon	Theia3D	OpenCap
Feet distance [m]	Feet in a fixed distance (0.4m) with some steps in between	0.035 (0.013)	0.038 (0.015)	0.012 (0.008)	2.064 (1.148)	2.501 (1.641)	1.984 (1.098)
Hand distance [m]	Hand grabbing a wooden rod (0.6m) and moving in the space	0.064 (0.012)	0.055 (0.011)	0.037 (0.011)	1.738 (0.049)	1.602 (0.419)	1.625 (0.456)
Pelvis vertical displacement [m]	Sit-to-stand from a stool (0.55m height)	0.167 (0.014)	0.136 (0.029)	0.195 (0.002)	0.384 (0.332)	0.325 (0.153)	0.828 (0.556)
Shoulder angle [°]	90° flexion	17.26 (1.10)	11.37 (2.52)	5.20 (3.42)	2.196 (1.567)	1.638 (1.055)	1.825 (0.599)
	180° flexion	11.48 (4.64)	13.37 (2.84)	3.73 (1.57)	0.604 (0.309)	0.481 (0.029)	0.541 (0.063)
	90° abduction	14.46 (1.25)	13.27 (4.11)	13.54 (13.73)	1.697 (0.074)	2.382 (0.105)	1.920 (0.903)
	60° external rotation	12.84 (10.15)	13.92 (6.92)	9.91 (1.95)	11.737 (3.545)	11.666 (3.534)	8.477 (0.419)
	60° internal rotation	7.29 (4.14)	13.35 (2.42)	23.14 (4.72)	7.337 (1.049)	8.082 (1.634)	10.689 (2.725)
Elbow angle [°]	90° flexion	2.09 (0.19)	7.23 (1.20)	1.52 (1.26)	2.081 (0.351)	2.486 (1.815)	1.411 (0.743)
Hip angle [°]	90° flexion	22.03 (2.81)	2.50 (1.36)	14.38 (0.48)	1.315 (0.113)	1.629 (0.275)	0.641 (0.576)
	45° abduction	11.27 (0.14)	16.90 (2.70)	14.81 (0.92)	3.297 (1.127)	4.035 (1.406)	4.142 (3.278)
	40° rotation	28.61 (0.38)	16.40 (0.11)	1.02 (1.44)	3.313 (0.342)	1.511 (0.237)	1.589 (2.247)
Knee [°]	90° flexion	6.28 (0.42)	7.15 (1.78)	8.40 (4.22)	7.009 (0.300)	6.426 (0.461)	4.328 (1.920)

Acknowledgements (Optional)

Thanks to Christina Geisler and Shawn Robert for their support during this work, and to the Neuromechanics and Applied Locomotion Lab at University of Utah for hosting the study and providing the necessary resources.

Session Category

Musculoskeletal Biomechanics: Methods, Models and Applications

P2-125

Virtual Mouse Twin to Predict Bone Adaptation Due to Pharmacological and Biomechanical Treatments for Osteoporosis

Prof Enrico Dall'Ara[1], Dr Sara Oliviero[1], Dr Bryant Roberts[2], Dr Saira Farage-O'Reilly[1], Dr Thomas Valerio[1], Dr Hector Manuel Arredondo Carrera[1], Dr Tegid Watkin[1], Mrs Jingzhi Zhang[1], Mrs Silvia Dirstaru[1], Dr Sanjay Singh[1], Dr Vee San Cheong[1]

[1]University of Sheffield, Sheffield, Yorkshire, United Kingdom. [2]University of Adelaide, Adelaide, South Australia, Australia

Introduction

Osteoporotic patients have lower bone strength and higher fracture risk. Combined biomechanical and pharmacological treatments have great potential but testing all possible combinations in animals is too expensive and unethical. The goal of this study was to develop and validate the virtual mouse twin for skeletal applications (VMT:SK), a multiscale computational model that predicts bone adaptation over time associated with osteoporosis treatments.

Methods

We developed pipelines to create micro-Computed Tomography (microCT) based micro-Finite Element (microFE) models that predict the mechanical properties of the mouse tibia *in vivo*. The models have been validated against compressive test performed on 20 mouse tibiae [1]. We evaluated the effect of mechanical loading and/or Parathyroid Hormone treatment on the bone strength for ovariectomised female C57Bl/6 mice microCT-scanned and treated between week 18 and 24 of age (total 30 mice, 3 time-points, N=6 per group) [2]. We developed mechano-regulation models to predict bone adaptation and compared their outputs to longitudinal microCT images [3].

Results

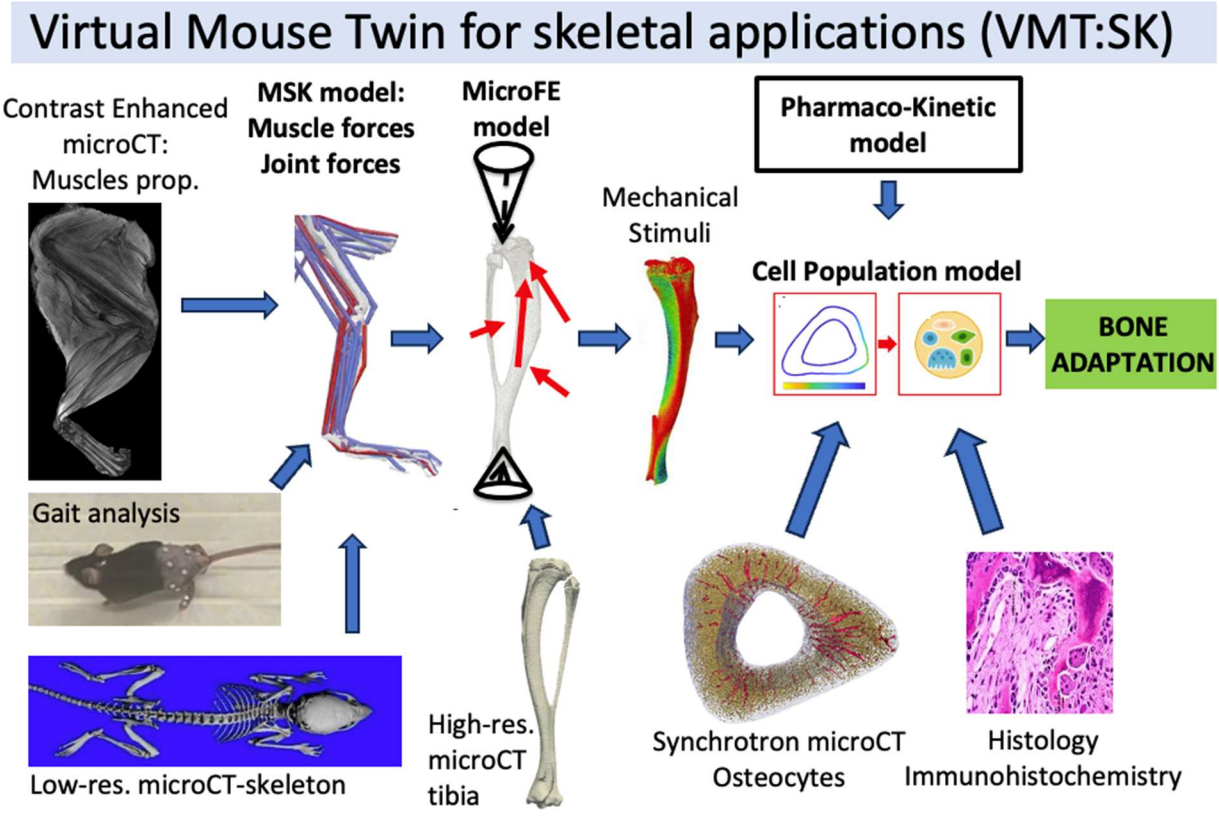
The microFE models predicted normalised compressive strength with errors of ~10-15% [1]. PTH alone or in combinations with mechanical loading increased bone strength by 15-20% and 19-31%, after 2 or 4 weeks of treatment, respectively [2]. The mechano-regulation models predicted well the tibia bone mineral content (no differences between predicted and measured values after 2 weeks of treatment; 4% differences after 4 weeks of

treatment) and the local bone formation (between 45% and 95%), but less well local bone resorption (below 40%) [3].

Discussion

The results, similar or better than those for the vertebrae, highlight that most bone formation is mechano-regulated. However, models should improve for bone resorption. The VMT:SK (Figure1) is being improved by: 1) defining realistic joint/muscle forces from multibody dynamics models informed by mouse gait analysis; 2) considering heterogeneous mechano-sensation and mechano-regulation informed by the distribution of osteocyte lacunae; 3) considering the biochemical signalling by adding cell population models informed by histology and immunohistochemistry.

Images (Optional)



References (Optional)

[1] Oliviero *et al.*, J Mechanical Behavior Biomedical Materials, 2021

[2] Roberts *et al.*, J Orthopaedic Research, 2024

[3] Cheong *et al.*, Acta Biomaterialia, 2021

Acknowledgements (Optional)

Funding from EPSRC (EP/Z000203/1) and NC3Rs (NC/R001073/1).

Session Category

Musculoskeletal Biomechanics: Methods, Models and Applications

P2-126

The Impact of Normalization Method on the Interpretation of Surface Electromyography Signals in Dynamic Tasks

Mr. Evan Curd MSc, PhD (c), Ms. Margaret Harrington BSc, PhD (c), Dr. Timothy Burkhart PhD, Ms. Claire McLaughlin

University of Toronto, Toronto, ON, Canada

Introduction

Normalization of surface electromyography (sEMG), relative to an individual's maximal voluntary isometric contraction (MVIC), is a common signal processing method to reduce inter-individual variability in sEMG magnitudes. One limitation of MVIC, is participants may not be able to produce a true maximal activation voluntarily, potentially underestimating the true magnitude. This is demonstrated in dynamic tasks where supramaximal (>100%) activation levels are observed when normalized to MVIC. The purpose of this study is to assess the effect of four EMG normalization methods on sEMG amplitudes in response to dynamic tasks.

Methods

Recreationally active participants (18-29 years) were included. Four sEMG sensors (TrignoTM wireless system; Delsys Inc. Natick MA) were affixed over the muscle bellies of the rectus femoris, vastus lateralis, biceps femoris, and semitendinosus. The participants were instructed to perform four normalization methods: i) MVIC; ii) quiet-laying trial - participants laid on a table completely relaxed; iii) activated static baseline - participants stood static with their knees in minimal flexion; iv) dynamic maximum - participants performed three maximal squat jumps. The maximal (MVIC & dynamic max) or average (quiet & activated baseline) value was extracted from the three-trial means for each task. Participants were then instructed to perform two experimental tasks: i) body-weight squat; ii) drop-vertical jump (DVJ) three times. The experimental task signals were averaged across three trials and subsequently normalized to each discreet value from the normalization tasks. Only the rectus femoris results are presented here.

Results

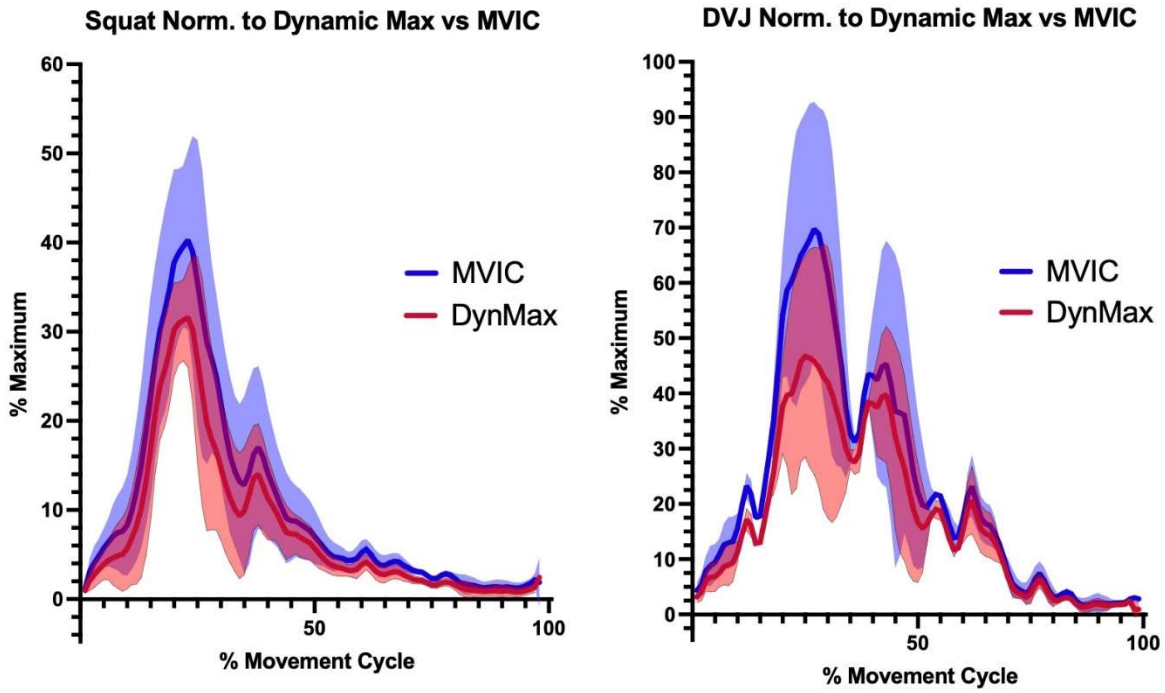
Five participants have participated in this ongoing study. Activation was lower when normalized to the dynamic maximum when compared to MVIC in both experimental tasks (mean difference across signal, Squat: 5.7% ± 3.4; DVJ: 13.0% ± 7.2) (Fig. 1). Activated baseline scaled consistently to the quiet laying trial by a factor of 9 (mean factor across signal, Squat: 9.2 ± 0.2; DVJ 9.0 ± 0.4).

Discussion

The sEMG was overestimated when normalized to MVIC compared to dynamic maximum in both tasks. This observation supports the hypothesis that MVIC may not be ideal for dynamic task normalization. Although use of the MVIC optimizes comparisons between studies, groups, and conditions, it may be limited when used as a surrogate of true maximal muscle activation.

Images (Optional)

Figure 1: Squat and Drop-Vertical Jump Normalized to Dynamic Max vs MVIC (Rectus Femoris)



References (Optional)

Session Category

Musculoskeletal Biomechanics: Methods, Models and Applications

P2-127

Exploratory Evaluation of Twitch-Based and Voluntary Fatigue Indicators During Sustained, Moderate-Load Isometric Contractions

Ms. Gahyun Lee, Ms. Jiwon Ryu, Mr. Cheoljae Lee, Prof. Gwanseob Shin

Ulsan National Institute of Science and Technology, Ulju-gun, Ulsan, Korea, Republic of

Introduction

Fatigue during sustained, moderate-load tasks reflects combined central and peripheral mechanisms, yet commonly used measures—such as MVC reductions or EMG spectral shifts—mainly capture global or peripheral changes. Electrically evoked twitch-based indices, including superimposed twitch torque, the central activation ratio (CAR), voluntary activation (VA), and potentiated twitch torque, probe voluntary drive and muscle contractile properties. Their applicability under repeated, work-like loading remains insufficiently evaluated. This pilot study examined whether voluntary and twitch-based indices can detect central and peripheral fatigue during a sustained, submaximal ankle plantar-flexion task.

Methods

We evaluated fatigue-related changes across variables representing central (superimposed twitch torque, CAR, VA) and peripheral (potentiated twitch torque, EMG median frequency) mechanisms. Electrically evoked twitches were delivered to the posterior tibial nerve during MVC (superimposed twitch) and, for one participant, at rest (potentiated twitch). Surface EMG from six lower-leg muscles quantified spectral changes.

Participants first completed a baseline MVC with twitch responses. The fatiguing task consisted of repeated >40% MVC contractions inducing gradual fatigue. After each bout, twitch responses and MVC-based voluntary assessments were collected until MVC declined to ≤70% of baseline. Twitch-derived indices were analyzed only when stimulation and EMG quality met validity criteria.

Results

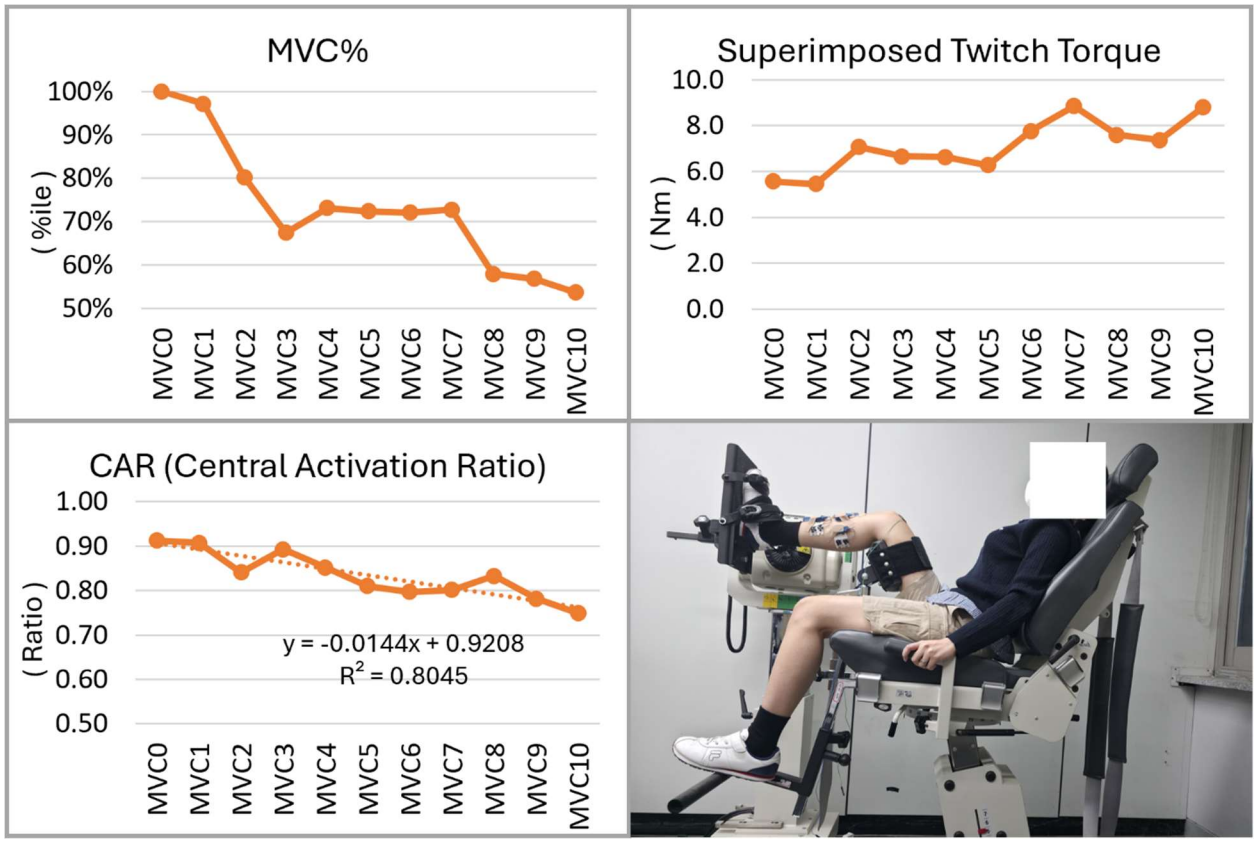
MVC torque progressively decreased in both participants, accompanied by reductions in EMG median frequency across most muscles. Participant A showed increasing superimposed twitch torque and decreasing CAR, indicating reduced central drive. Participant B exhibited inconsistent superimposed twitch and CAR responses due to unstable MVC during stimulation. Potentiated twitch torque, measured only in Participant

B, declined across cycles, suggesting peripheral contractile impairment. VA values for Participant B were unstable because of inconsistent twitch responses.

Discussion

Voluntary and twitch-based indices together captured distinct fatigue components during moderate-load, work-like plantar-flexion tasks. EMG spectral reductions and declining potentiated twitches reflected peripheral impairment, whereas increasing superimposed twitch torque and decreasing CAR suggested central fatigue when MVC stability was maintained. These findings highlight both the utility and challenges of twitch-based assessment under repeated submaximal loading. Maintaining stable MVC during stimulation is essential for reliable interpretation. Continued data collection is expected to improve feasibility evaluation and strengthen the robustness of twitch-derived indices in applied fatigue research.

Images (Optional)



Acknowledgements (Optional)

This work was supported by the National Research Foundation of Korea grant funded by the Korea government (MSIT). (No. RS-2025-00556960)

Session Category

Musculoskeletal Biomechanics: Methods, Models and Applications

P2-128

Phantomless Calibration for the Estimation of Bone Strength in Paediatric Femora: Comparing Constant and Variable Currents

Mr George Allison[1,2], Mr Salman Almutairi[3], Professor Amaka C Offiah[3,2], Dr Xinshan Li[1,2]

[1]School of Mechanical, Aerospace & Civil Engineering, University of Sheffield, Sheffield, England, United Kingdom. [2]Insigneo Institute, University of Sheffield, Sheffield, England, United Kingdom. [3]School of Medicine and Population Health, University of Sheffield, Sheffield, England, United Kingdom

Introduction

Finite element (FE) analysis of paediatric bone based on retrospective computed tomography (CT) scans is restricted by the need for a density calibration phantom, limiting the amount of CT scans available for an under-researched population as clinical scans often use variable currents. This study aims to develop and validate a phantomless calibration technique to overcome this limitation and demonstrates its application in one child with rickets scanned with variable current.

Methods

Seventy anonymised post-mortem CT scans were obtained from Sheffield Children's Hospital, including 69 children (0-15 years old) with no known skeletal pathologies scanned with two constant currents (100kVp 60mA, 100kVp 100mA), and one 10-month-old child with rickets scanned with a variable current. Offline European Spine Phantom (ESP) calibration scans were available for all. Personalised material properties were determined based on Hounsfield units through two methodologies: (a) ESP calibration (MOD1) and (b) phantomless calibration using air, fat, and muscle peaks (MOD2) [1]. Using the PyPeCT2S pipeline, each model was subjected to four-point bending simulations, utilising two equidistant forces on the diaphysis and partially fixed ends.

Results

MOD2 calibration generally performs well against the MOD1 calibration when comparing predicted FE values as seen in Figure (1). In the infant subset of children there is negligible bias and consistent agreement at the lower predicted critical moment, while looking across the entire age range there were more pronounced differences for older cases. Many outliers trended in the negative region of the plot indicating that MOD2 generally predicted

lower bone strength estimates than MOD1. When the rickets case was predicted it saw a predicted difference of 40% with an over prediction in bone strength.

Discussion

Phantomless calibrations were comparable to phantom-based calibration, especially for younger children with no skeletal pathology scanned at a constant current. This included good performance on 6 children where the peaks were visually indistinguishable from one another. The variable current case remains an outlier. The preliminary results for constant current cases suggest that phantomless calibration could be used when no ESP calibration is present, however the inconsistencies need to be investigated further.

Images (Optional)

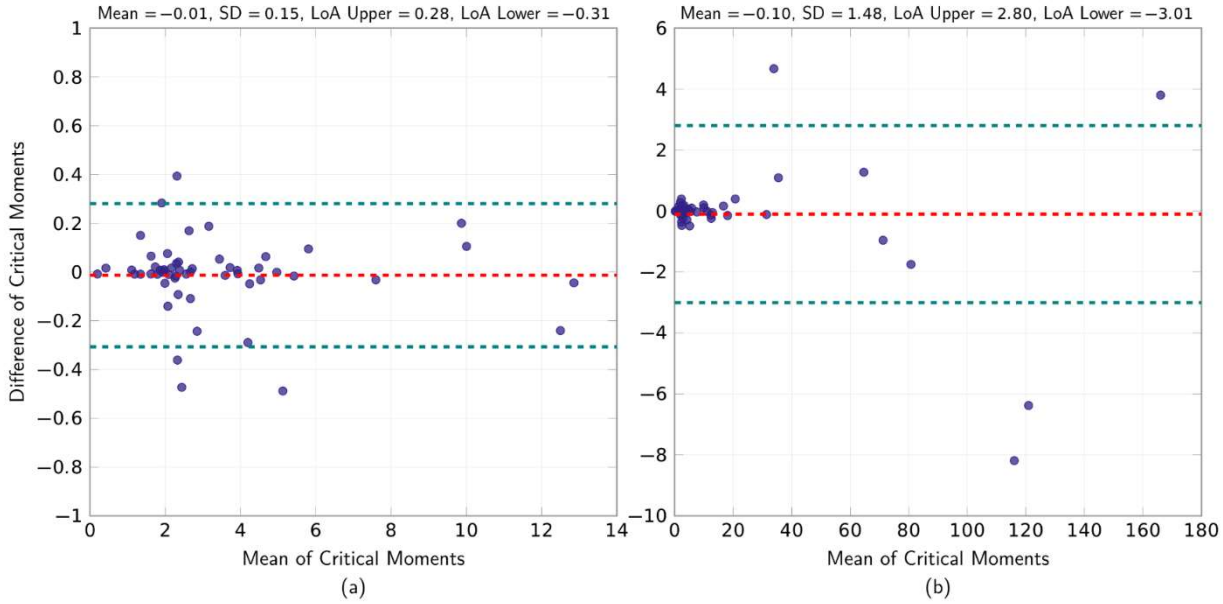


Figure 1: Bland-Altman plots showing the difference in predicted critical moment (Nm) between MOD1 (ESP) and MOD2 (Phantomless) calibration methods on the constant current cohort group. (a) Children up to 1-year-old (n=55). (b) The entire age range of the cohort (n=69).

References (Optional)

[1] Eggermont et al., 10.1371/journal.pone.0220564

Session Category

Musculoskeletal Biomechanics: Methods, Models and Applications

P2-129

Estimating Ankle Plantar Flexor Muscle-Tendon Lengths Using Simplified Subject-Specific Bone Geometry

Ms. Georgia Hidson MSc Student, Dr. Lauren Welte PhD

University of Alberta, Edmonton, Alberta, Canada

Ms. Georgia Hidson

Introduction

Modelling muscle forces requires defined muscle-tendon-unit (MTU) paths on a bone model. While isometrically scaled, generic bones are commonly used due to their accessibility and affordability, subject-specific geometries derived from medical imaging are more accurate [1]. Open-source statistical shape models (SSMs) provide an accessible alternative method to generate individualized bones, but current approaches still require partial data from medical imaging or motion capture [2]. We investigated if reconstructing the tibia and fibula from one discrete measure using an SSM is sufficient to accurately model MTU lengths.

Methods

Tibia-fibula meshes (n=35, 22M, 13F), segmented from an independent set of MRI scans, were aligned and registered to the mean of an open-source SSM using Coherent Point Drift and Procrustes analysis [1,2]. Discrete measures were investigated for a linear correlation with the first principal component (PC) of the SSM (84% variation); the identified relationship between the tibia-fibula complex length and PC1 was used to score and reconstruct the sample meshes. Soleus, tibialis posterior, peroneus longus, and peroneus brevis MTU insertions were manually selected on the SSM mean. Corresponding points on the original and reconstructed bones mapped the MTU paths using an established wrapping algorithm [3]. The Jaccard index assessed volumetric similarity between original and reconstructed meshes. Paired t-tests evaluated differences in axial bone and MTU lengths.

Results

PC1 and the tibia-fibula complex length had a strong linear correlation (r^2=0.99, $p<0.05$). The average Jaccard index (mean±1sd) for the tibia and fibula was 0.72±0.06 and

0.48±0.11, respectively. The bone lengths between the original and reconstructed complex were not significantly different ($p>0.05$), whereas MTU length was significantly different for only the soleus and peroneus brevis fibres ($p<0.05$) (Figure 1).

Discussion

Agreement between the original and reconstructed bones lengths suggests that linear-regression-based reconstructions are suitable for creating subject-specific tibia-fibula bone models. However, geometric differences affect the soleus and peroneus brevis fibres that wrap closely along the bone. Therefore, improving volumetric similarity by reconstructing from multiple PCs that describe variation for the tibia and fibula individually may improve their MTU length estimations.

Images (Optional)

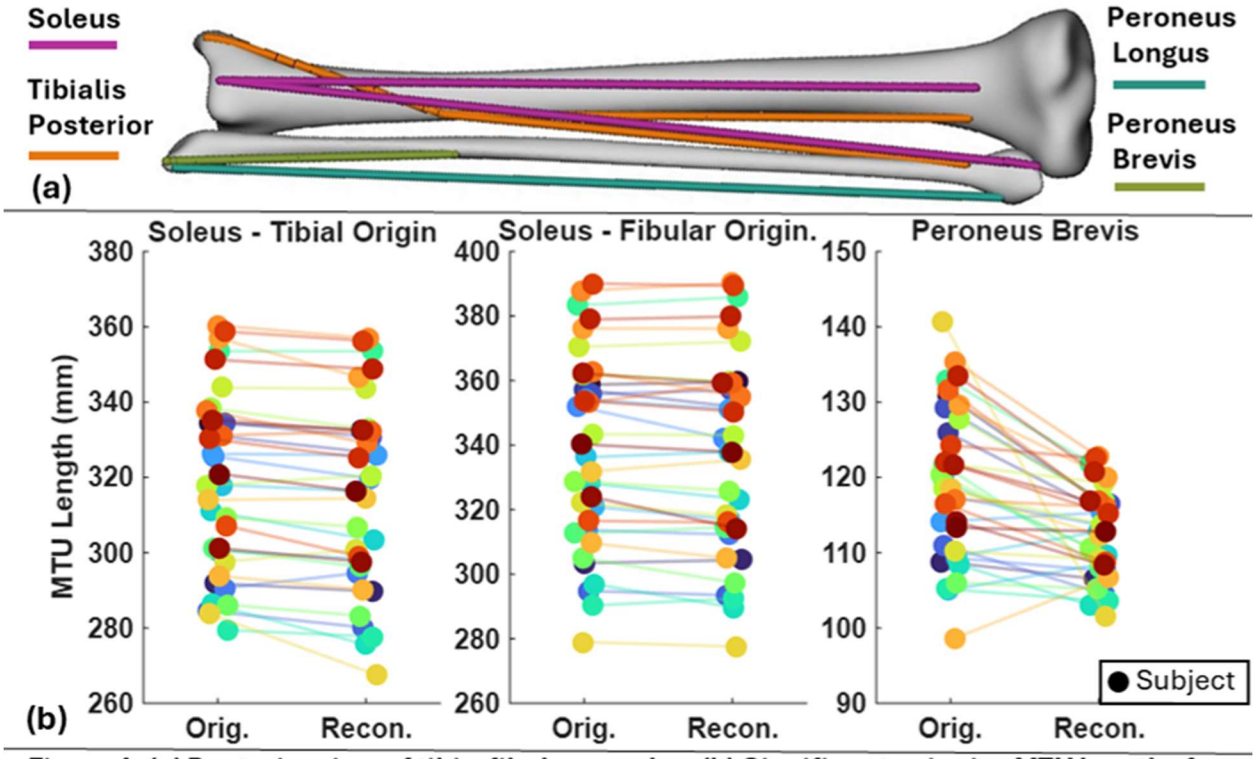


Figure 1: (a) Posterior view of tibia-fibula complex. (b) Significant pairwise MTU lengths for original and reconstructed bones.

References (Optional)

[1] Nolte. *J.Biomechanics,* 2016

[2] Keast. *PeerJ,* 2023

[3] Marai. *IEEE Trans Biomed Eng,* 2004

Acknowledgements (Optional)

This work was supported by an NSERC CGS M.

Session Category

Musculoskeletal Biomechanics: Methods, Models and Applications

P2-130

Estimating individual muscle forces during load sharing through an elastography-driven model

Dr. Gustavo Grinspan[1,2], Dr. Liliam Fernandes de Oliveira[3], Dr. Maria Clara Branda[3], Dr. Nicolás Benech[2]

[1]Biophysics and Systems Biology Section, Faculty of Sciences, University of the Republic, Montevideo, Montevideo, Uruguay. [2]Ultrasonic Acoustics Laboratory, Faculty of Sciences, University of the Republic, Montevideo, Montevideo, Uruguay. [3]Laboratory of Neurophysiology and Muscle Mechanics, Biomedical Engineering Program, Federal University of Rio de Janeiro, Rio de Janeiro, Rio de Janeiro, Brazil

Introduction

Estimating individual muscle forces is a long-standing problem in muscle biomechanics. In recent years, elastography has been proposed as a good alternative for such a purpose. By measuring the longitudinal shear elastic modulus (μ_L) at different joint torque (τ) levels, the relative longitudinal shortening (Δl) of individual muscles can be characterized by $C(\tau) = 1-(\mu_L(0)/\mu_L(\tau))$, being $C \propto \Delta l$ and $C \in [0, 1]$ [1]. Thus, this work proposes a model that, based on the $C(\tau)$ coefficients, allows the calculation of the individual muscle forces of the biceps brachii (BB), brachioradialis (BR), and brachialis (BA) muscles during their synergistic action.

Methods

We employed the $C_i(\tau)$ values reported in [1], derived from $\mu_{Li}(\tau)$ measurements in thirteen healthy volunteers using an Aixplorer ultrasonic scanner in SSI mode (i = BB, BR, BA). The protocol consisted of linear isometric elbow-flexion ramps from rest to 30% MVC over 15 s, with the elbow at 90° and the wrist supinated. The $C_i(\tau)$ coefficients were used to obtain input values for an optimization algorithm, which retrieves the corresponding $F_i(\tau)$ forces required to establish the static equilibrium across the elbow joint. Likewise, as $C_{BB}(\tau)$ described a sigmoidal curve, we calculate its inflection point ($C_{BB}^{\sim}$) through the Hill cooperative model [2].

Results

The $F_i(\tau)$ values ranged from 0 – 290.65 ± 52.99 N, 0 – 204.66 ± 37.42 N, and 0 – 211.40 ± 82.45 N, for BB, BR, and BA, respectively. These values stabilize the external elbow torque, yielding a net torque of zero. The $C_{BB}^{\sim}$ was found at 10.90 ± 4.92 % MVC.

Discussion

We found that for ~0-15% MVC, torque production is mainly due to the BA and BR, whereas for 10-30% MVC, it is mainly due to the BB. Thus, the C_{BB}~ ~10% MVC appears to be a load-sharing breakpoint between these muscles. This is in good agreement with previous studies [3], suggesting the present model can retrieve plausible $F_i(\tau)$ values regarding the load-sharing behavior between synergistic muscles.

References (Optional)

[1] Grinspan GA et al., Scientific Reports, 2023

[2] Wyman J et al., University Science Books, 1990

[3] Bouillard K et al., J Biomechanics, 2012

Session Category

Musculoskeletal Biomechanics: Methods, Models and Applications

P2-131

Impact of Helical Fibres on Soft Bodied Animals: A Computational Model

Mr Harshil Pathak, Dr. Nilima Nigam, Dr. James Wakeling

Simon Fraser University, Burnaby, British Columbia, Canada

Introduction

Skeletal muscles can undergo large deformations over short timescales, driven by the nonlinear activation of muscle fibres. In many soft-bodied organisms, such as worms, these fibres are arranged in longitudinal, circular, and cross-linked helical patterns. Understanding how these architectures influence deformation motivates the development of computational tools that can represent realistic fibre configurations.

Methods

We use a three-dimensional finite element model to simulate elastic deformations in skeletal muscle. The model was implemented in our open source **Flexodeal** code [1], a finite element framework based on the Hill-type muscle model, capable of simulating both dynamic and quasi-static muscle contractions. We extend **Flexodeal** to incorporate spatially varying fibre orientations and nonuniform activation patterns, allowing us to represent helical and circular architectures. All simulations were carried out using a fully dynamic formulation that includes inertial effects and each simulation ramps the activation of fibres from 0% to 100%. We run four simulations: helical fibres 100% active; longitudinal fibres 100% active; both helical and longitudinal fibres 100% active; and helical fibres 100% active with longitudinal fibres 10% active. Each case is evaluated for helical angles ranging from 0° to 90°. We also use the 3D model to examine how strain energy varies with fibre angle.

Results

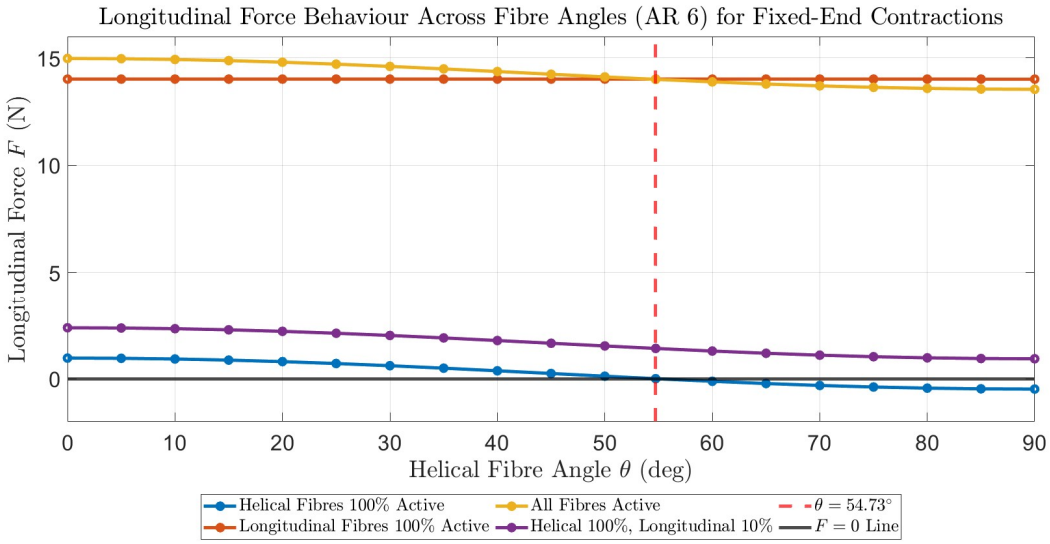
The results were insensitive to the aspect ratio (AR), defined as the ratio of cylinder length to radius. The longitudinal forces depended on the helical fibre angle ($\theta = 54.73^\circ$), and we observed a critical angle at which the longitudinal force dropped to zero for fixed-end contractions (shown in Figure).

Discussion

The numerical experiments reproduce deformation patterns that are consistent with physiological expectations for longitudinal, circular, and helical fibre arrangements. We found that the quantities we report are insensitive to aspect ratio, in contrast to the findings of Ellers et al. [2]. We also recover the same critical helical angle ($\theta = 54.73^\circ$), despite using

a nonlinear model with realistic muscle properties, consistent with the geometrical prediction of Clarke and Cowey [3].

Images (Optional)



References (Optional)

[1] https://github.com/sfu-nml/flexodeal

[2] Olaf Ellers *et al.* , Integrative and Comparative Biology, 2025

[3] R. B. Clark *et al.* , J Experimental Biology, 1958

Session Category

Musculoskeletal Biomechanics: Methods, Models and Applications

P2-132

Validation of an Innovative Kinematic Model for the Analysis of Spinal Deformations Considered as a Single Deformable Body (Case of Receiving a Right Knee Strike in Muay Thai)

Dr. Hassen LE SAGE HAKIM[1,2], Dr. Olivier NOCENT[2]

[1]ILEPS, Higher School of Sports and Teaching Professions; CY Cergy Paris University, Cergy, Île-de-France, France. [2]Performance Health Metrology Society laboratory (PSMS EA 7507), University of Reims Champagne-Ardenne, Reims, Champagne-Ardenne, France

Introduction

***Introduction*:** The aim of this study was to establish an experimental methodology to 3D movements analysis of the spine, which will be considered as a single deformable body. These analyses focus to study its local mechanical load during an impact.

Methods

***Methods*:** Two professional Nak-Muay of international level participated in this study. The receiver of the knee strike (P2) was equipped with markers placed: at the vertex, on the sixth cervical vertebra (C6), at the thoracic level (T1, T3, T5, T6, T7, T8) and at the lumbar level (L1, L3, L5). Markers were positioned on the anterior and posterior superior iliac spines to create a local landmark. A 16-camera optoelectronic system (Flex13, Optitrack; Motive Body software) was used to perform motion capture and analysis.

The most realistic polynomial reproducing the spine as a whole, from the origin of the local landmark to the vertex, is of degree 5. The plotting of the profile of the range of maximum voluntary amplitudes (MVA), describing the evolution of the so-called normal spinal curvatures, made it possible to scroll through all the curves of the curvatures of the polynomials representing the deformations of the spine following the knee strike.

Results

***Results*:** No overshoot in the cervical region. The curvatures were between K=1.3 and K=-2.4 for a range of MVA curvatures between Kmax≈5 and Kmin≈-7.5.

At the thoracic spine level, the maximum curvature obtained following the impact (K=8.13) exceeds the MVA (K=4.03) between T7 and T8.

The deformation of the lumbar region evolves outside the range of the MVA to reach its maximum value of K=22, compared to the corresponding point on the MVA, at the level of L5, K=3.74 (Fig.1a). The spine spends a total of 0.425 seconds outside its comfort zone.

Discussion

***Discussion*:** Our study allowed us to validate the biomechanical model of Ranavolo et al., (2013), representing the spine in its natural shape using a reduced number of markers. This validation enabled us to develop our own geometric reconstruction method dedicated to the three-dimensional monitoring of the entire spine as a single deformable body in order to determine its possible lesion behaviors.

Images (Optional)

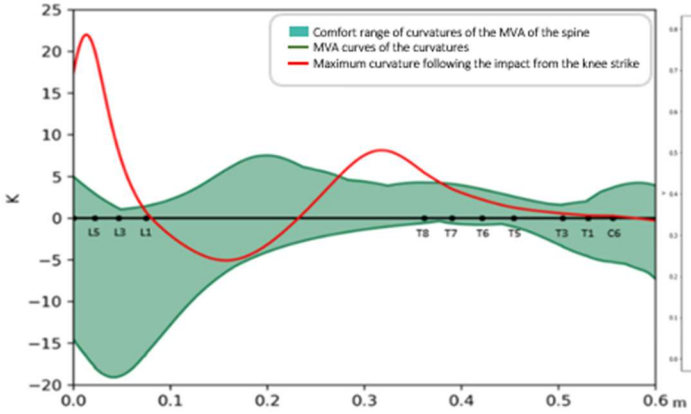


Fig1a: Maximum curvatures of the lumbar and thoracic rachis due to knee strike impact exceeding the range of MVA of movements in the sagittal plane expressed in local curvatures (K) calculated every millimeter over the different polynomials.

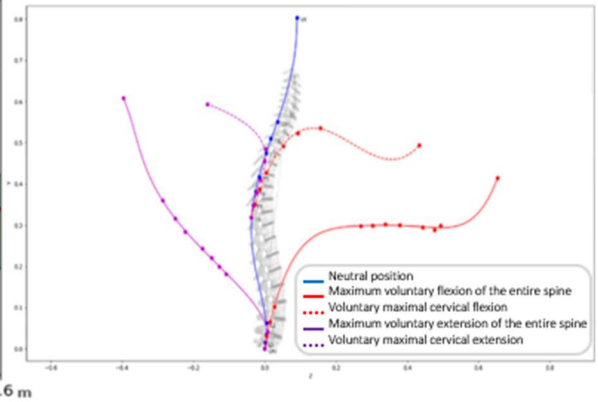


Fig1b: Allures of the polynomials representing the entire spine and the cervical region, in the pelvic landmark, during the maximum voluntary amplitudes of movements in the sagittal plane.

Session Category

Musculoskeletal Biomechanics: Methods, Models and Applications

P2-133

Impact of Viewing Volume Width on Gait Kinematics Captured With Markerless Motion Capture

Ms. Heather Li Yam Nam, Ms. Alyson Colpitts MASc, Dr. Elise Laende PhD

University of Waterloo, Waterloo, Ontario, Canada

Introduction

Markerless motion capture offers a simple and cost-effective solution to collect human kinematic data and opens up the possibility of performing motion capture in non-traditional, out-of-lab environments that may offer increased access to populations of interest but may have space limitations (e.g., narrow hallways). Site-specific differences in gait kinematics from markerless motion capture have been shown in previous work [1], but the effect of viewing volume width specifically has not been previously investigated. The objective of our study was to compare gait kinematics from two markerless motion capture configurations (narrow and wide) collected simultaneously to investigate the impact of viewing volume width on joint angles.

Methods

Two 8-camera (Sony RXOII) markerless configurations were set up to represent a narrow hallway (2.4 m wide) and wide space (7.7 m wide) in a single larger volume to permit concurrent data collections by both systems. Overground walking trials of 1 minute were collected and processed for 49 healthy participants using markerless motion software (Theia3D, version 2024.1.19). Kinematic event detection was performed in Visual3D and data were exported to R for further analysis. Mean joint waveforms were plotted for both configurations and root mean square differences (RMSD) across waveforms were calculated for all planes.

Results

Group mean knee joint angle waveforms in all planes generally show good agreement, but offsets in the sagittal plane between the narrow and wide configurations (Figure 1). RMSD values were 6.4 degrees in the sagittal plane, 3.2 degrees in the frontal plane, and 3.0 degrees in the transverse plane for the knee joint angles.

Discussion

Our results compare favourably to previously reported values for marker-based motion capture (mean offsets between multiple marker-based motion capture sites of 11 degrees in the sagittal plane and 4 degrees in the frontal plane [2]). Future work will investigate intermediate widths to identify viewing volume limits and investigate mitigation measures, such as adding additional cameras. We anticipate future outcomes will further advance the standardization of data collection protocols and reporting to facilitate high quality data for multi-centre research.

Images (Optional)

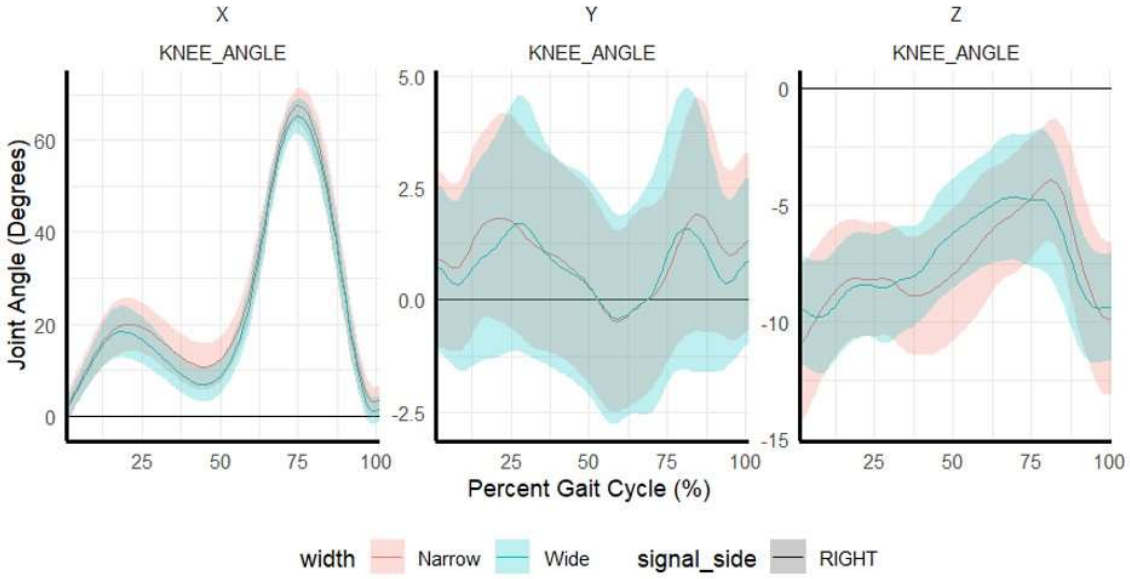


Figure 1. Knee joint angles for the narrow and wide configurations in the sagittal plane (X), frontal plane (Y) and transverse plane (Z). Mean and standard deviations for 49 participants (right knees only).

References (Optional)

[1] Outerleys JB, *JBiomech*, 192 (2025)

[2] Schrijvers JC, *The Knee*, 29 (2021)

Acknowledgements (Optional)

Michaela Wallace, Anna Klygina, Laura Madrid

Session Category

Musculoskeletal Biomechanics: Methods, Models and Applications

P2-134

A Multimodal View on Chronic Low Back Pain: Integrating Structure, Movement and Mechanics Across Disciplines

Prof. Dr. Hendrik Schmidt[1], Prof. Dr. Sara Checa[2], Prof. Dr. Matthias Pumberger[1], Dr. Ulrike Grittner[1], Prof. Dr. Adamantios Arampatzis[3], Prof. Dr. Lena Fleig[4], Dr. Özgür Celik[1], Prof. Dr. Georg Duda[1], Dr. Sandra Reitmaier[1]

[1]Charite-Universitaetsmedizin Berlin, Berlin, Berlin, Germany. [2]Hamburg University of Technology, Hamburg, Hamburg, Germany. [3]Humboldt-Universität zu Berlin, Berlin, Berlin, Germany. [4]Medical School Berlin, Berlin, Berlin, Germany

Introduction

Chronic low back pain (cLBP) remains one of the most prevalent and costly musculoskeletal disorders, yet its underlying drivers are incompletely understood, limiting the development of targeted diagnostics and individualized treatments. To address this, our Research Unit, bringing together biomechanists, human and veterinary clinicians, biologists, psychologists, computational engineers and data scientists, investigated how structural alterations, movement behavior and mechanical loading interact in cLBP onset and persistence.

Methods

Here, we summarize key insights from the first four years of coordinated research.

Results

Population-based multimodal investigations on 2,500 individuals with and without cLBP revealed consistent associations between lumbar disc degeneration, particularly at L5/S1, paraspinal muscle degeneration, reduced functional and constrained multi-planar lumbar mobility. Individuals with cLBP exhibited fewer distinct habitual postures during daily life, reduced lumbar lordosis, smaller segmental excursions and diminished movement variability, reflecting protective or pain-avoidant motor patterns. These adaptations often extended beyond the lumbar region into thoracic and pelvic regions. Psychosocial factors, including kinesiophobia and reduced physical/mental well-being, further shaped these structural–functional patterns, while inactivity amplified pain and disability. The consortium applied diverse methodologies, including linear mixed models, PCA-based movement analyses, machine learning, finite-element simulations, and controlled animal experiments, yielding heterogeneous statistical bases. Specific numerical results are omitted for clarity; detailed quantitative outcomes will be presented at the WCB. Still, two overarching trends emerged: (i) diagnostic models based solely on routine clinical

assessments achieved ~60% accuracy, whereas (ii) inclusion of dynamic measures of muscle activity, real-life motion profiles, and segmental loading increased accuracy to ~70%, highlighting the value of functional and mechanical information.

Mechanistic studies supported this interpretation. In a controlled sheep model, nucleotomy induced early hypomobility and increased neuromuscular stabilization rather than hypermobility; finite-element simulations confirmed rapid restoration of segmental stiffness under complex loading. Mouse tail-loading demonstrated that mechanical overload triggers bone and marrow remodeling and alters inflammation-related receptor patterns.

Discussion

Taken together, these four-year findings advocate a shift from predominantly structure-focused evaluation toward a dynamic, biopsychosocial understanding of cLBP. Our findings emphasize the need for diagnostic strategies that integrate muscular function, compensatory movement behavior and psychosocial variables to prevent chronification and improve clinical outcomes.

Acknowledgements (Optional)

Funded by the German Research Foundation (FOR 5177 - SCHM 2572/11-1).

Session Category

Musculoskeletal Biomechanics: Methods, Models and Applications

P2-135

An Optimized Hinge Joint Approximates the 3D Motion of the Walker Knee

Mr. Jacob Foster MS BIOE, Dr. Reed Gurchiek PhD

Clemson University, Clemson, South Carolina, United States

Introduction

The Walker knee model is commonly used in gait analysis for its ability to capture 3D knee motions (flexion, valgus, and internal rotation). However, only the flexion angle parameterizes joint configuration wherein knee valgus and internal rotation follow a prescribed relationship with flexion. Such a motion could result from rotation about a single axis. In this study, we aimed to identify said axis toward a hinge joint approximation to the Walker knee. This would reduce computational cost by removing the need to calculate knee valgus and internal rotation.

Methods

We simulated flexion of the Walker knee (1-120 degrees) using the RajagopalLaiUhlrich2023 OpenSim model. To determine the single axis of rotation which best approximated the 3D motions of the Walker knee across all configurations, we solved a constrained optimization problem. The three components of the axis and the rotation about said axis for each configuration were the decision variables and the axis was subject to a unit-length constraint. The cost function quantified the angle of the error rotation matrix. We quantified error in this approximation using the average angle of the error rotation matrix and the root mean square error (RMSE) of the flexion, valgus, and internal rotation angles.

Results

The optimal axis was slightly anterior and superior to the Walker knee flexion axis in the neutral configuration. Modeling the knee as a hinge joint using this axis approximated the 3D motion of the Walker knee to within 2.67 degrees (average rotation angle of the error matrix) and 0.49, 1.59, and 2.49 degrees RMSE for flexion, valgus, and internal rotation angles, respectively. This approximation was superior to a naïve approximation based on the flexion axis of the Walker knee in the neutral configuration which yielded over 15 degrees RMSE for the internal rotation angle.

Discussion

Our results demonstrate the feasibility of approximating the 3D motions of the Walker knee model with a hinge joint given an optimized hinge joint axis. A better approximation for gait models could be made by optimizing over a reduced knee range of motion (e.g., 90 instead of 120 degrees). Future work should assess effects on relevant muscle moment arms.

Session Category

Musculoskeletal Biomechanics: Methods, Models and Applications

P2-136

Influence of the Residuum–Socket Interface on Hip Joint Loading in Individuals with Transfemoral Amputation

Ms. Jacqueline Sammel, Mr. Mitchell Ekdahl, Dr. Brecca Gaffney

University if Colorado Denver, Denver, CO, United States

Introduction

Individuals with transfemoral amputations (TFA) have an increased risk of hip osteoarthritis (OA), commonly attributed to asymmetric joint loading. Standard methods for quantifying dynamic joint loading commonly use rigid body link-segments models. However, previously developed TFA models assume the residuum-socket interface (RSI) as rigid, ignoring soft-tissue compliance and potentially altering calculated joint loading. Recent work introduced and validated the kinematics within a musculoskeletal model permitting six degrees of freedom (6-DOF) at the RSI for individuals with transtibial amputations, but the RSI's effect on estimated muscle-driven joint reaction forces (JRFs) during walking remain unknown. Our objective was to determine the influence of modeling the RSI joint on hip JRFs in individuals with TFA during walking.

Methods

Motion capture data was collected from 13 adults with unilateral TFA (6M/7F, Age: 54±15.9 yr, BMI: 28.3±4.6 kg/m^2) during overground walking. For each participant, two subject-specific models were created: (1) a model with a 6-DOF custom femur-socket joint allowing for RSI motion and (2) a rigid model with no RSI motion. Muscle forces were computed via static optimization and used to estimate hip JRFs (normalized to bodyweight (BW)) during the stance period. Temporal comparisons of hip JRFs were made between models via one-dimensional statistical parametric mapping. Discrete comparisons of peaks and impulse JRFs (positive and negative) were compared using paired t-tests (α=0.05).

Results

There were no temporal differences for hip JRFs between model types throughout the stance phase (Figure 1). Maximum medial JRF was larger in the rigid model than the RSI model ($p<0.017$, RSI:0.78 ±0.38 xBW ; Rigid:0.82 ±0.40 xBW).

Discussion

Allowing RSI motion did not significantly influence amputated limb hip JRFs compared to the rigid model, suggesting that small interface motions at the residual limb do not alter

time-continuous hip JRFs estimated from link-segment models during level walking. These results are relevant when considering how to account for soft-tissue compliance dependent upon suspension type. For example, when examining joint loading differences with a rigid fixation prosthesis (e.g., bone-anchored limb) and a socket-prosthesis, incorporating motion at the residuum-socket interface is negligible.

Images (Optional)

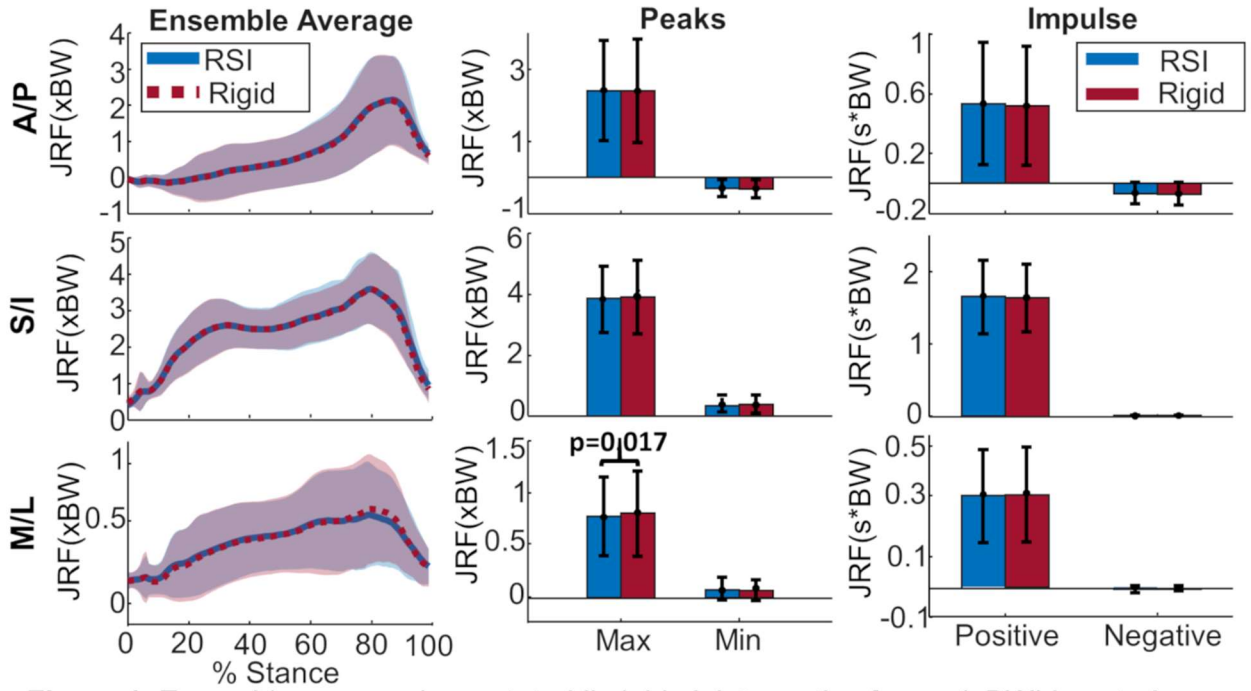


Figure 1. Ensemble-averaged amputated-limb hip joint reaction forces (×BW) in anterior–posterior (A/P), superior–inferior (S/I), and medial–lateral (M/L) directions comparing RSI (blue) and rigid (red) models during stance, with corresponding group mean (±SD) peaks and positive/negative impulses.

Session Category

Musculoskeletal Biomechanics: Methods, Models and Applications

P2-137

Finite Element Models of the Proximal Tibia Accurately Predict Internal Bone Displacements and Reaction Forces

Mr Dylan Zaluski MSc, Dr Saija Kontulainen PhD, Dr James (J.D.) Johnston PhD

University of Saskatchewan, Saskatoon, Saskatchewan, Canada

Introduction

Subject-specific finite element (FE) models of bones, with geometry and material properties measured via quantitative computed tomography (QCT), are a valuable tool for studying the role played by bone mechanics in joint diseases like osteoarthritis. Previous QCT-based FE models (QCT-FEMs) of the human tibia have been validated for surface phenomena (strain, stiffness); however, the validity of these models for internal bone deformation has not yet been reported. The objective of this study was to validate QCT-FEMs of the proximal tibia against both internal bone displacements and external reaction forces.

Methods

Five embalmed human tibiae were mechanically tested inside a high-resolution peripheral QCT (HR-pQCT) scanner during imaging (0.041mm isotropic voxel). Compressive loads were applied to individual medial and lateral tibial compartments using a Zwick electro-mechanical testing system in steps of 0.5, 1.0 and 1.5mm (max load: 10kN). Internal displacement fields were measured using LaVision digital volume correlation (DVC) software. HR-pQCT scans were down-sampled to simulate clinical CT (0.5mm voxel), segmented and meshed to create QCT-FEMs with linear hexahedral elements. Each element was assigned elastic moduli (E) (isotropic and anisotropic) proportional to its bone-mineral density (BMD) using various sets of trabecular and cortical density-modulus relationships (E-BMD) from the literature. Displacement boundary conditions were applied to the loaded surfaces by interpolating DVC measurements. A custom element-by-element solver was used to predict nodal displacements and reaction forces. Root-mean-square error (RMSE) was used to quantify the accuracy of FE-predicted compared to experimentally-measured internal bone displacements (~280,000 measures) and global reaction forces (30 measures).

Results

The accuracy of predictions of internal bone displacements was relatively insensitive to the selected E-BMD relationships (Table 1 includes a sample of min/max results). External reaction forces exhibited considerably greater variability with selected E-BMD.

Discussion

Predictions of internal bone displacements were acceptably accurate for all tested E-BMD (RMSE less than 4.3%). FE-predicted reaction forces had greater variability, with the Nazemi et al approach offering the lowest error (11.8%). The results presented here expand upon previous QCT-FE validation studies of the proximal tibia by validating predictions of internal bone mechanics, finding these models to be suitably accurate for modeling proximal tibial mechanical behavior.

Images (Optional)

E-BMD		RMSE%	
Cortical	Trabecular	Displacement	Reaction Force
Rho (1995)	Keller (1994)	4.07	14.7
Rho (1995)	Rho (1995)	4.29	248
Rho (1995)	*Cowin (1985)	3.88	12.2
Snyder (1991)	Keller (1994)	4.07	14.7
Snyder (1991)	Rho (1995)	4.38	226
Snyder (1991)	*Cowin (1985)	3.87	12.4
Nazemi (2017)	Nazemi (2017)	4.03	11.8

Table 1: Comparisons between QCT-FE predictions and experimental measurements for internal bone displacements and external reaction forces for different choice of E-BMD. RMSE are normalized to the largest experimental measurement. *Cowin approach uses anisotropic material properties; others are isotropic.

References (Optional)

Acknowledgements (Optional)

Session Category

Musculoskeletal Biomechanics: Methods, Models and Applications

P2-138

Kinematic Coupling Constraints Create Physiological Motions for OpenSim Musculoskeletal Models but Change Muscle Moment Arms Which Compromise Muscle Forces and Joint Loads

Dr. Jeffrey Reinbolt Ph.D.[1], Dr. Anita Vasavada Ph.D.[2]

[1]University of Tennessee-Knoxville, Knoxville, TN, United States. [2]Washington State University, Pullman, WA, United States

Introduction

Musculoskeletal models require physiological kinematics of multiple bodies, many of which cannot be tracked directly. Kinematic couplings between bodies (*e.g.*, "spinal rhythm" for vertebral kinematics) are implemented in OpenSim using CoordinateCouplerConstraints to effectively apply non-physiological loads constraining the kinematics to follow physiologically-based mathematical relationships. We evaluated two models, a simple double pendulum and complex cervical spine (Figure a), to determine how kinematic constraints affect computed muscle forces and joint loads.

Methods

Both models had unconstrained and constrained versions created, simulated, and analyzed in OpenSim 4.3. The double pendulum had 2 joints and 2 muscle-tendon units (uniarticular and biarticular). The cervical spine had 9 joints and 82 muscle-tendon units (uniarticular and multiarticular). For kinematic constraints, a generalized coordinate represented the overall flexion-extension angle, and each joint angle was constrained to a defined percentage of the overall angle. The coupler constraint acts as a gear ratio defining relative motion of the bodies (Figure b). The effects of kinematic constraints were compared across: net joint moments from inverse dynamics, muscle forces from static optimizations, muscle moment arms from muscle analyses, joint loads from joint reaction analyses, and constraint loads from force reporter analyses.

Results

Without constraints, joint and muscle moments were equal with uniarticular muscle forces contributing the most (Figure c). With constraints, muscle moments using geometric moment arms changed in different directions because the forces decreased in the uniarticular muscles but increased in multiarticular muscles. The moment changes were perfectly offset by their respective constraint loads so that their sum matched the net joint moments. However, muscle moments using muscle analysis moment arms increased due to greater moment arms for all muscles because of kinematic constraints, and the sum

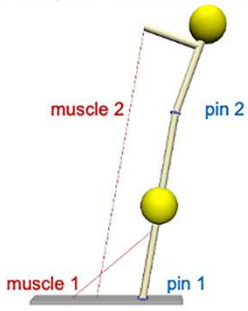
with constraint loads no longer matched the net joint moments. Including constraints changed the joint loads.

Discussion

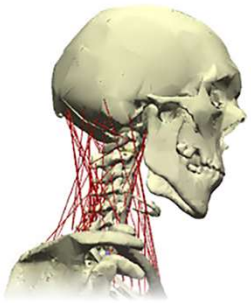
Muscle forces, moments, and joint loads changed when kinematic constraints were included in models. Constraints led to higher forces in multiarticular muscles because of kinematic couplings. These couplings increased moment arms when calculated by the "effective torque" method used in OpenSim. Kinematic constraints should only be used to define physiological motion, not when computing loads.

Images (Optional)

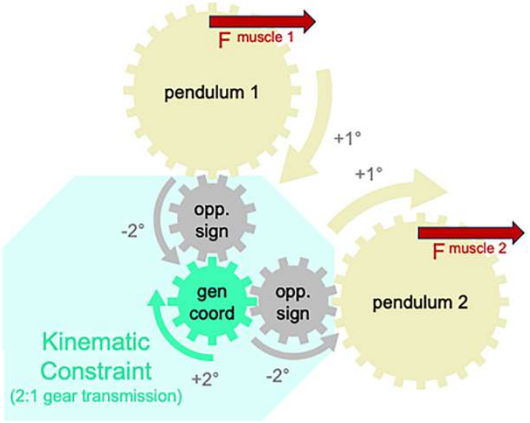
a) Simple Double Pendulum



Complex Cervical Spine



b) Couplings Between Bodies



c) Double Pendulum Results

		Pin Joint	Muscle	Model: Without Constraints	Model: With Constraints
Net Joint Moments (Nm)		pin 1		5.29	5.29
		pin 2		2.10	2.10
Muscle Forces (N)			muscle 1	26.49	12.26
			muscle 2	17.39	24.51
Geometric	Moment Arms (m)	pin 1	muscle 1	0.12	0.12
			muscle 2	0.12	0.12
		pin 2	muscle 1		
			muscle 2	0.12	0.12
	Calculated Muscle Moments (Nm)	pin 1	muscle 1	3.19	1.48
			muscle 2	2.10	2.95
			sum of both	5.29	4.43
		pin 2	muscle 1		
			muscle 2	2.10	2.95
			sum of both	2.10	2.95
Muscle Analysis	Moment Arms (m)	pin 1	muscle 1	0.12	0.12
			muscle 2	0.12	0.24
		pin 2	muscle 1		0.12
			muscle 2	0.12	0.24
	Calculated Muscle Moments (Nm)	pin 1	muscle 1	3.19	1.48
			muscle 2	2.10	5.91
			sum of both	5.29	7.39
		pin 2	muscle 1		1.48
			muscle 2	2.10	5.91
			sum of both	2.10	7.39
Joint Load Magnitudes (N)		pin 1		86.40	82.19
		pin 2		41.76	48.84
Constraint Loads (Nm)		pin 1			-0.86
		pin 2			0.86

References (Optional)

Session Category

Musculoskeletal Biomechanics: Methods, Models and Applications

P2-139

Comparing Pose Estimation Models for Reconstructing Three-Dimensional Joint Centre and Anatomical Landmark Positions in Markerless Gait Analysis

MR. Wenfeng Zhang[1], MR. Jeng-Heng Lin[1], MS. Tsai-Ling Lin[1], MR. Cheng-Hao Yu[1], Prof. Ting-Ming Wang[2], Prof. Tung-Wu Lu[1]

[1]National Taiwan University, Taipei, Taiwan, Taiwan. [2]National Taiwan University Hospital, Taipei, Taiwan, Taiwan

Introduction

Traditionally, gait analysis requires placing infrared retroreflective markers on anatomical landmarks and tracking their three-dimensional (3D) trajectories using stereophotogrammetry. Although this approach can accurately reconstruct the motions of body segments during walking, the requirement for markers restricts its use to laboratory settings and often alters natural movement patterns. With recent advances in human pose estimation (HPE) techniques, tracking anatomical landmarks from RGB videos offers a promising alternative, but their accuracy remains unclear. This study aims to compare different HPE models for reconstructing 3D joint centre and anatomical landmark positions during gait by evaluating their accuracy against the data obtained using a marker-based motion capture system.

Methods

Twelve participants walked while their movements were recorded using eight synchronised RGB cameras. Three HPE models (i.e., Mediapipe, MMPose, and OpenPose) were used to extract two-dimensional locations of lower-limb joints from videos, and the corresponding 3D joint centre positions were reconstructed using the direct linear transformation algorithm. The 3D positions of anatomical landmarks for each lower-limb segment were then estimated using a recurrent neural network [1] based on the predicted joint centre positions. The reconstruction accuracy was quantified using the root-mean-square error relative to ground truth obtained from a marker-based stereophotogrammetry system. A Kruskal-Wallis test was conducted to compare reconstruction errors across models and body parts, with Friedman tests used for post-hoc comparison.

Results

OpenPose and MMPose showed significantly lower reconstruction errors on the joint centre than MediaPipe, with the hip joints exhibiting significantly larger errors than the other lower-limb joints (Table 1). Compared to MMPose, OpenPose showed significantly lower reconstruction errors for anatomical landmarks on the pelvis, shank, and foot, with

those on the pelcis segment exhibiting significantly larger errors than those on the other segments (Table 1).

Discussion

This study provides a systematic evaluation of the accuracy of HPE models in reconstructing 3D positions of joint centres and anatomical landmarks during gait. The OpenPose models yielded reconstruction errors lower than those of MediaPipe and MMPose, but all remained at the centimetre level, indicating a continued need for more accurate HPE models for markerless gait analysis.

Images (Optional)

Table 1. Comparison of human pose estimation models (MediaPipe, MMPose, and OpenPose) using root-mean-squared errors of three-dimensional lower-limb joint center and anatomical landmark positions during walking.

Error (mm)	MMPose	OpenPose	MediaPipe	Effects	
				Model	Body
Lower limb 3D joints center positions					
Hip	35.8 (14.4)	35.6 (12.7)	51.5 (13.5)		
Knee	23.6 (5.7)	20.3 (4.5)	29.2 (7.5)	$P_M = <0.01$*	$P_J = <0.01$*
Ankle	16.2 (4.1)	20.0 (3.3)	28.4 (15.7)		
Lower limb 3D anatomical landmark positions					
Pelvis	43.6 (12.4)	36.1 (11.8)	--	$P_p = 0.03$*	
Thigh	32.9 (11.6)	27.6 (11.5)	--	$P_t = 0.11$, $P_s = <0.01$*	$P_o = <0.01$*
Shank	18.2 (3.1)	12.9 (3.2)	--	$P_f = 0.03$*, $P_m = <0.01$*	
Foot	24.9 (6.0)	19.8 (5.9)	--		

P_M: compared model effect; P_J: joint effect; P_P: model effect in pelvis; P_t: model effect in thigh; P_s: model effect in shank; P_f: model effect in foot; P_m: joint effect. P_m: p-value from Friedman test of joint-wise errors within MMPose. P_o: p-value from Friedman test of joint-wise errors within OpenPose. * indicates a significant statistical difference ($p<0.05$).

References (Optional)

[1] Antoine Falisse et al., IEEE Trans. Biomed. Eng., 2025

Session Category

Musculoskeletal Biomechanics: Methods, Models and Applications

P2-140

Assessing Cytocompatibility of 3D-Printed MED610™ Constructs

PhD Mahsa Zojaji[1], BSc Annelise Grace Pageau[1], BSc Mariya Peskova[2], BSc Teodora Maluckov[1], MSc. Eng. Johannes Eichwalder[1], PhD Corey Daniel Smith[3], MD, FRCSC George Athwal[3], PhD Maud Gorbet[2], PhD, PEng Louis Miguel Ferreira[4,3], PhD Nikolas Knowles[1]

[1]Department of Kinesiology and Health Sciences, University of Waterloo, Waterloo, Ontario, Canada. [2]Department of Systems Design Engineering,, Waterloo, Ontario, Canada. [3]Roth McFarlane Hand and Upper Limb Centre, London, Ontario, Canada. [4]Department of Mechanical and Materials Engineering, Western University, London, Ontario, Canada

Introduction

3D printing enables fabrication of highly customized, patient-specific biomedical devices [1]. MED610, a biocompatible photopolymer, may pose cytotoxic risks from residual printing materials, limiting its use in cell and tissue culture [2]. This study evaluated the cytocompatibility of 3D-printed MED610 constructs for in vitro and ex vivo applications.

Methods

Disks (n=18,Ø15×2mm) and custom bioreactor components were 3D-printed using MED610. Differentiated osteoblasts (MC3T3-OB) were seeded at 20,000 cells/mL on MED610 disks, with negative (NEG, untreated) and positive controls (POS, 2%ethanol) under osteogenic condition [2]. Human osteoarthritic trabecular bone cores (Ø9.15±0.14 × 9.5±2.0 mm, n=16) from four arthroplasty patients were cultured in bioreactors for 21 days, with negative controls cultured in 6-well plates (NEG, n=6). Osteogenic, metabolic, and genomic activity (dsDNA), along with lactate dehydrogenase (LDH) levels, were assessed to quantify differentiation, viability, proliferation and cytotoxicity of bone cells *in vitro* (Days 1, 3, 7) and *ex vivo* (Days 0, 6, 13, 21).

Results

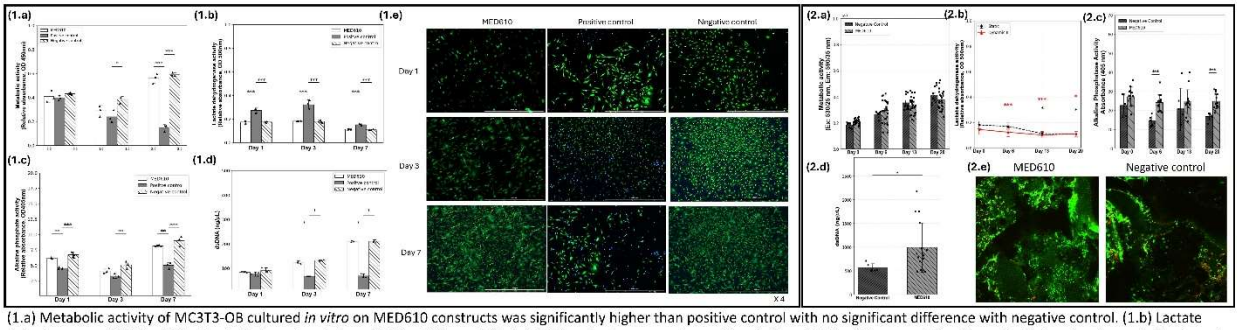
Metabolic activity of MC3T3-OB on MED610 was significantly higher than in the POS (85%viability) and lower LDH level indicating 15% cytotoxicity(fig.1.a-e). Osteogenic activity, measured via alkaline phosphatase (ALP), was significantly higher on MED610 and the NEG compared to the POS. Total dsDNA content also increased significantly on MED610 relative to the POS. Perfused bone tissue in the bioreactor exhibited a significant increase in metabolic activity over the 21-day culture period, comparable to NEG (fig.2.a-

d). ALP levels were elevated in perfused tissue, while LDH levels decreased over time and were similar to the NEG. dsDNA content was significantly higher in perfused tissue.

Discussion

These preliminary results indicate that MED610 is a cytocompatible material. MC3T3-OB cells cultured on MED610 showed enhanced metabolic and osteogenic activity as evidenced by higher ALP activity and increased dsDNA. Perfused bone tissue also showed increased viability over the 21-day of culture, supporting the biocompatibility of MED610 for tissue culture application. Future work will assess osteoclast activity and characterize the material properties of MED610 constructs to further optimize their design for cell culture applications.

Images (Optional)



(1.a) Metabolic activity of MC3T3-OB cultured *in vitro* on MED610 constructs was significantly higher than positive control with no significant difference with negative control. (1.b) Lactate dehydrogenase (LDH) activity, (1.c) alkaline phosphatase (ALP) activity, and (1.d) dsDNA content measured over Days 1, 3, and 7. (1.e) Representative live cell staining showing cell attachment, viability and proliferation of cells cultured on MED610 (Calcein AM, green: live cells; DAPI, blue: nuclei of dead cells).
(2a-e) Human trabecular bone cores *ex vivo* cultured in 3D-printable MED610 bioreactors for 21 days. Measurements of (2.a) metabolic activity, (2.b) LDH level, (2.c) ALP activity, (2.d) dsDNA content, and (2.e) representative confocal images of live (Calcein AM, green) and dead (Deep Red, Red) staining indicate that MED610 supports bone tissue viability, proliferation, and osteogenic function. Data are presented as mean ± SD. *p < 0.05, **p < 0.01, ***p < 0.001.

References (Optional)

[1] Kermavnar et al., Addit Manuf (2021).

[2] Haghpanah et al. J Biomed Mater Res (2024).

Session Category

Musculoskeletal Biomechanics: Methods, Models and Applications

P2-141

The Influence of Soleus Architecture on Muscle Efficiency During Running

Professor JOHN H Challis, Ms Axelle M Wasiak

Penn State University, University Park, PA, United States

Introduction

The Achilles tendon is a major site of elastic energy storage and return during human locomotion, and its behavior can influence the energetic cost of movement. Variations in muscle-tendon complex architecture can alter how the Achilles tendon modulates the energetic cost of force production by the triceps surae. Two key features of soleus architecture were identified for investigation: the ratio of tendon slack length to optimal fascicle length, and the ratio of tendon cross-sectional area to muscle cross-sectional area. The purpose of this study was to determine how these architectural parameters affect the efficiency of soleus force production during running. We hypothesized that there exists a combination of soleus architectural parameters that minimizes the muscle's energetic requirements during running.

Methods

Soleus muscle–tendon properties were measured in 13 participants (6 M 7 F) using dynamometry and ultrasound imaging to characterize a physiologically realistic range of architectural values.. Data were collected on seven healthy runners (3M 4F) who ran barefoot at 3.1 m/s while force plate and motion data were captured. From these data the mean kinematics and kinetics of the stance phase were determined. A muscle model driven by these experimental inputs estimated soleus behavior during stance. From model outputs - active state, fascicle length and velocity - the energetic cost of the muscle was calculated.

Results

Soleus energy cost was greatest when the ratio of tendon slack length to optimal fascicle length was low, corresponding to a relatively short tendon and long fascicles. Energy cost was also elevated when the ratio of tendon cross-sectional area to muscle cross-sectional area was high. In contrast, energy cost was minimized when participants exhibited a relatively long tendon (high tendon slack length to fascicle length ratio) and a more compliant tendon (low tendon cross-sectional area to muscle cross-sectional area ratio).

Discussion

This study demonstrates that soleus muscle architecture strongly influences the energetic efficiency of force production during running. It highlighted the value of having a long Achilles tendon relative to the optimal fascicle length and a compliant tendon on minimizing the energetic cost for the soleus during the support phase of running.

Session Category

Musculoskeletal Biomechanics: Methods, Models and Applications

P2-142

Repeatability of Segmental Symmetry Metrics using Self-Placed IMUs for Telemedicine Amputee Mobility Assessment

Mr. Joseph Redmond, Mr. Colin Kennedy, Mr. William Nash, Mr. Gregory Flynn, Prof. Corey Pew

Montana State University, Bozeman, MT, United States

Introduction

Amputees experience gait asymmetries, impacting mobility and quality of life. Clinicians currently assess amputees using Observational Gait Analysis, a subjective measure relying on clinician skill and in-person appointments. For remote populations, assessments can be infrequent and inaccessible. Inertial Measurement Units (IMUs) can provide objective metrics of gait symmetry using segmental metrics of the thigh and shank [1]. Measurements may lose accuracy if IMUs are self-placed in Telemedicine visits. This study aims to evaluate IMU measures of segmental symmetry when sensors are placed by the patient. We hypothesize that self-placed IMUs can produce reliable and repeatable segmental symmetry analysis.

Methods

Four IMUs with an alignment pin were developed to aid participants in self-placement on the anterior thighs and shanks. Participants were observed walking on a treadmill at three speeds relative to a two-minute walk test. Optical motion capture (MoCap) generated a control dataset, and markers applied to IMUs quantified misalignment. Sagittal angular velocity measurements were normalized and used to create asymmetry scores for each segment pair, computed by the mean Euclidian difference between paired gait cycles on the left and right [1]. Self-placement was done twice to assess measurement repeatability. Between MoCap and IMU generated scores, a paired t-test evaluated score changes, while a Pitman-Morgan test evaluated intertrial variance.

Results

Shank asymmetry metrics on 9 Healthy Controls (6F; 53±19yrs.) were found to be greater using self-placed IMUs compared to MoCap (11.85 vs 11.12, $p=0.021$) and showed higher variance under with sensor reapplication (Ratio=3.7, $p=0.001$). Net axial misalignment between the left and right sensors correlated with higher asymmetry scores ($\beta=0.09$ pts/deg, $R^2=0.19$, $p=0.001$; Misalignment=11.6±8.1º). Under repeated conditions, motion

capture established a minimal detectable change (MDC=2.55) that 29% of IMU score pairings exceeded.

Discussion

While score bias can be calibrated, IMU noise reduces repeatability of asymmetry measurements. Sensor alignment impacted scores, and differences between placements increased variability. Comparison of scores to clinician-placed IMUs could vary and lead to misclassification of gait changes in telemedicine translation. Future work will discuss consistency metrics, incorporate thigh scoring, evaluate amputee populations, and consider noise regression.

Images (Optional)

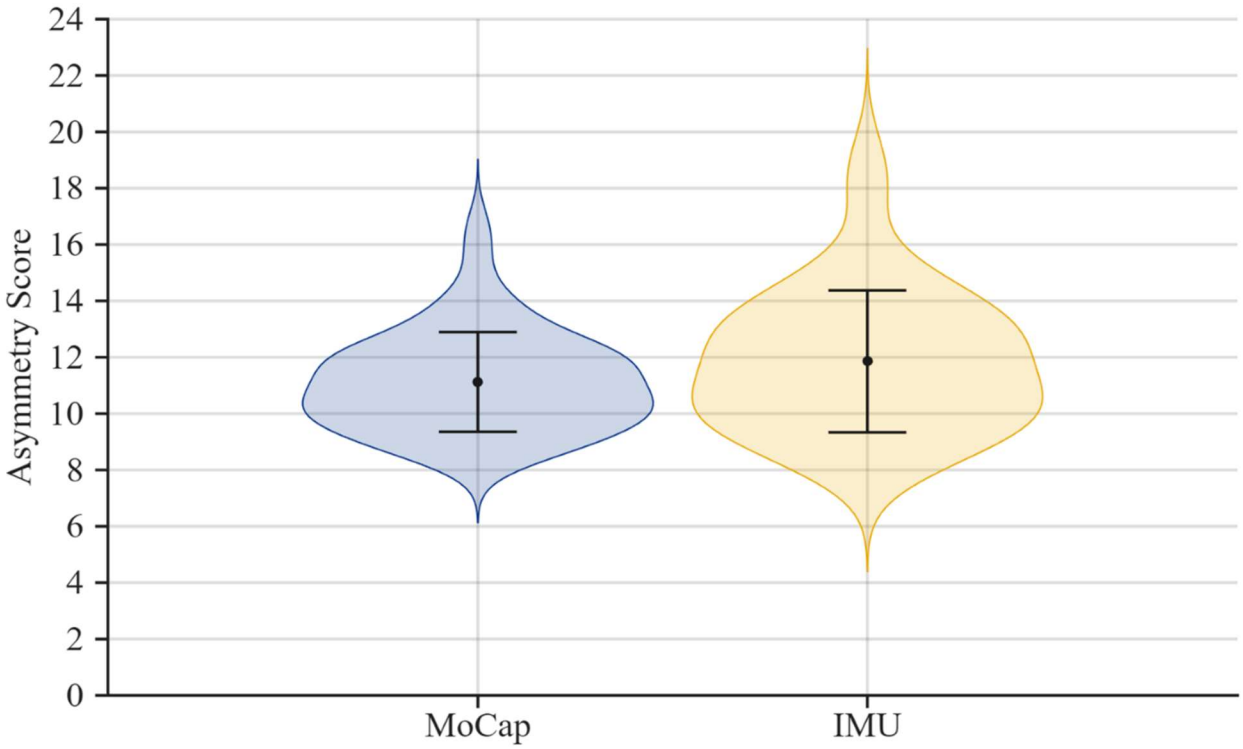


Figure 1: Violin plot of asymmetry score distributions, compared between IMU and Mocap collected data (Mean ± 1 SD)

References (Optional)

[1] Sheila Clemens et al. *Clinical Biomechanics* 2020

Acknowledgements (Optional)

Session Category

P2-143

Investigating Biomechanical Factors that Influence Power Generation in Functional Neuromuscular Stimulation Cycling via Musculoskeletal Modeling

Ms. Kanthi Karumbunathan[1,2], Dr. Musa Audu[1,2], Dr. Ronald Triolo[1,2]

[1]Case Western Reserve University, Cleveland, OH, United States. [2]Louis Stokes Cleveland VA Medical Center, Cleveland, OH, United States

Introduction

For individuals with spinal cord injury (SCI), functional neuromuscular stimulation (FNS) is an invaluable intervention used to mitigate muscle atrophy, cardiovascular deconditioning, and bone demineralization while simultaneously supporting psychological well-being through restoration of lost function. By delivering coordinated, low-level electrical pulses to motor neurons, FNS elicits muscle contractions to produce functional motion such as cycling. Despite its widespread use, FNS cycling faces two primary limitations: minimal power output and rapid-onset muscle fatigue. Understanding how biomechanical configurations influence cycling performance is critical in developing more effective therapies. This study evaluates the effect of hip height on upright, FNS cycling efficiency using musculoskeletal modeling in OpenSim with a secondary aim of identifying significant correlations between hip-height-dependent biomechanical parameters and cycling efficiency.

Methods

For each seat-height configuration, iterative forward-dynamics-based optimizations identified muscle excitation patterns required to reproduce a target pedaling motion at 35 RPM. Mechanical power output, obtained through inverse dynamics, and metabolic power consumption, determined via the Umberger muscle energetics model, were used to characterize efficiency trends.

Results

Results demonstrate a distinct optimal hip-height range, approximately 0.51–0.57 m above the crank, that maximizes efficiency, with a peak at ~0.54 m (Fig. 1). Muscle fiber lengths and contraction velocities for the gluteus maximus, vasti, and rectus femoris were extracted from the simulated muscle states as secondary effects of seat height. Among these variables, mean gluteus maximus fiber velocity squared demonstrated a significant negative correlation with gross efficiency ($p = 0.006$), characterizing it as a primary

biomechanical predictor of performance under the set conditions. Lorentzian peak analysis of instantaneous-efficiency profiles (all $R^2 > 0.89$) revealed five conserved peak clusters across seat heights; peak behavior significantly associated with gross efficiency also aligned with regions of minimized square gluteus maximus velocity, cross-validating the gluteus maximus fiber-velocity-squared–gross-efficiency relationship.

Discussion

These findings highlight the impact of hip biomechanics on FNS cycling efficiency and identify gluteus maximus fiber-velocity dynamics as a key determinant. Ongoing work includes translating this methodology into a recumbent cycling model and validating resulting correlations clinically. This study ultimately provides a potential framework for pre-clinical optimization of biomechanical variables to enhance therapeutic outcomes of FNS cycling.

Images (Optional)

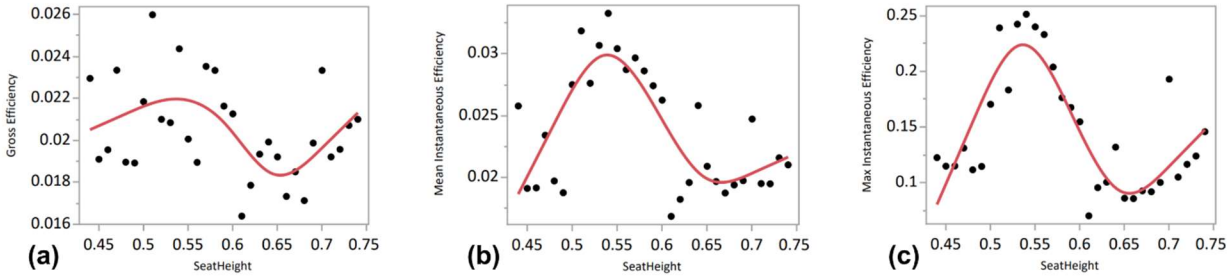


Fig 1. **(a)** Gross efficiency ($p = 0.05$), **(b)** mean instantaneous efficiency ($p = 0.00006$), and **(c)** maximum instantaneous efficiency ($p = 0.0000$) vs. seat height. All spline fit with knots at 0.48 m, 0.535 m, 0.59 m. Maximum efficiencies conserved between 0.51 m & 0.57 m with peak at ~0.54 m.

Acknowledgements (Optional)

Thank you to the Advanced Platform Technology Center & Louis Stokes Cleveland VA for supporting this research.

Session Category

Musculoskeletal Biomechanics: Methods, Models and Applications

P2-144

Effects of Fixed and Adaptive Filtering Methods on Joint Work During Countermovement Jumping After ACL Reconstruction

Ms. Katelyn Campbell MS[1], Dr. Eric Dugan PhD[1,2]

[1]Texas Children's Hospital, The Woodlands, Texas, United States. [2]Baylor College of Medicine, Houston, Texas, United States

Introduction

Joint mechanics during dynamic tasks are sensitive to signal processing choices, yet cutoff selection is rarely standardized in return-to-sport evaluation. Fixed-cutoff filters may oversuppress impact-related frequencies and alter estimates of joint loading and energy absorption used to assess readiness for sport after ACL reconstruction. Augustus et al. introduced a time-varying cutoff profile that preserves these features. This study evaluated whether filtering strategy influences joint work during countermovement jumping and whether any differences are clinically meaningful.

Methods

Twenty-two adolescents, 6 to 12 months after ACL reconstruction, completed three countermovement jump trials. Marker and ground reaction force data were filtered using three matched approaches: 10 Hz, 15 Hz, and an adaptive 10 to 50 Hz method applied identically to kinematic and GRF signals. Joint work was computed for the braking, propulsive, and landing phases. Linear mixed-effects models tested effects of Filter Type, Limb Status, and their interaction. Pairwise equivalence testing evaluated whether filters produced clinically equivalent values using bounds of plus or minus 5 percent of mean absolute work.

Results

Filtering method did not affect ankle or knee work in any phase, and it did not affect hip braking or hip propulsive work. Hip landing work was the only variable that differed across filtering methods ($p = 0.008$). Limb Status effects were significant for most joints, although there were no Filter by Limb interactions, indicating that filtering did not alter injury-related asymmetry patterns. Equivalence testing showed that joint work estimates were clinically equivalent across filters for eight of the nine joint and phase combinations. Hip landing work was the only measure that did not meet equivalence criteria.

Discussion

Most joint work variables used in return-to-sport evaluations were unaffected by filtering choices, indicating consistent interpretation across preprocessing methods. Hip landing work was the only measure sensitive to filter design. The adaptive filter produced the most negative values, the 10 Hz filter produced intermediate values, and the 15 Hz filter produced the least. Because hip landing work reflects impact attenuation after ACL reconstruction, these differences may influence interpretation in landing-focused assessments, although overall filtering effects were limited.

References (Optional)

[1] Augustus et al. (2024), J Sports Sci 42(21)

Session Category

Musculoskeletal Biomechanics: Methods, Models and Applications

P2-145

Multiscale Modeling Reveals That Offsetting the Stepping Foot During Sit-to-Walk Generates Greater and More Heterogeneous Positive Net Work by Soleus Muscle Fascicles

Dr. Katherine Knaus, Mr. Haozhixiang Li, Mr. Michael Miller, Dr. Anne Silverman

Colorado School of Mines, Golden, CO, United States

Introduction

Muscle work required for activities of daily living like sit-to-walk (STW) can be affected by selected movement strategy [1]. Multiscale modeling can reveal underlying nonuniform muscle mechanics during whole body movement. We characterized soleus muscle work in STW with different initial foot placements to determine how fascicle work varies throughout the muscle with movement strategy.

Methods

Whole-body kinematics and electromyography (EMG) were measured in young adults performing STW [1] with feet initially positioned symmetrically (**Sym**) or with anterior-posterior offset (APO). Soleus musculotendon lengths computed from musculoskeletal model [2] simulations of STW and average soleus EMG [1] prescribed varying activation and length inputs to a 3D finite element model (FEM) [3] for the **Step** and Stance limb soleus muscle in **Sym** and APO conditions. FEM explicitly defined fascicle architecture [3] to compute individual fascicle lengths and forces, which were used to calculate soleus work described by each fascicle [Figure 1].

Results

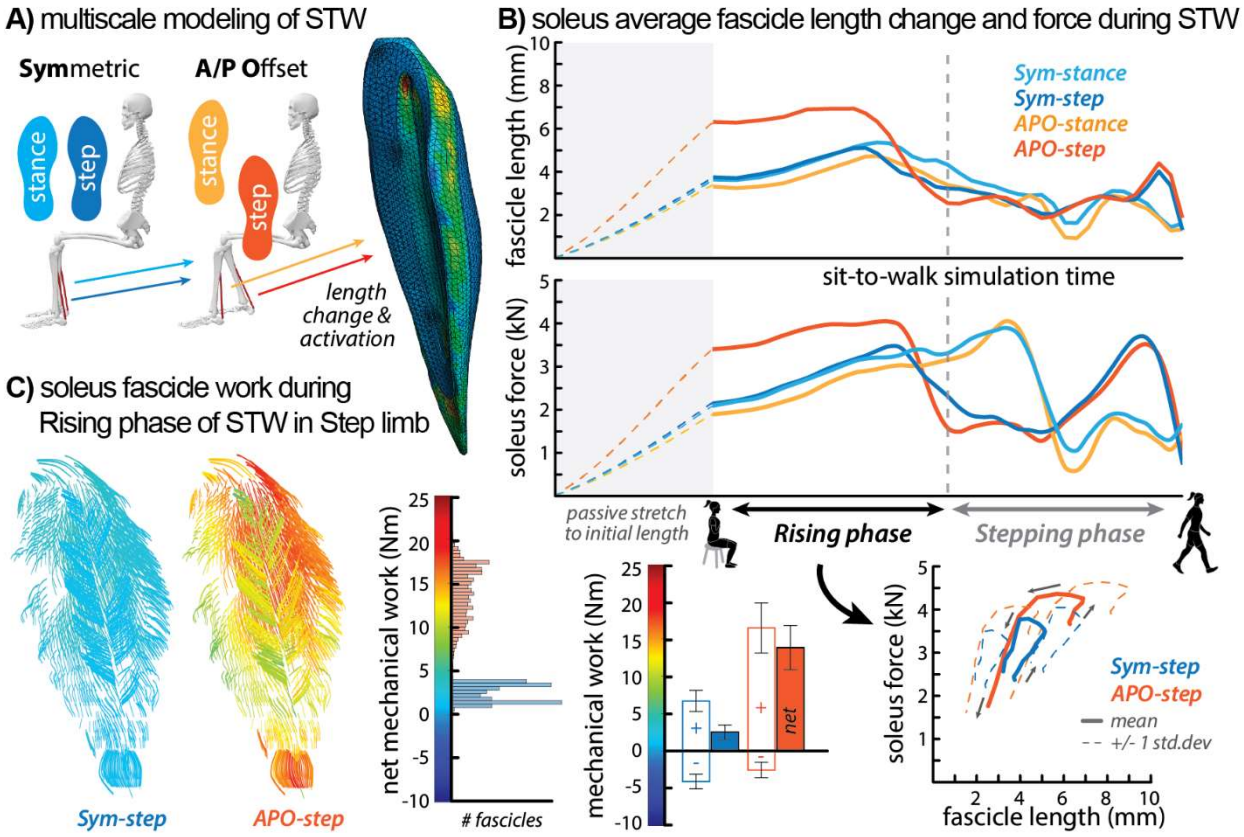
Multiscale modeling predicted nonuniform fascicle dynamics in both **Step** and Stance limb soleus during STW performed with **Sym** and APO foot placements. During **Rising**, Step limb soleus fascicles performed 140% more net work in **APO** than Sym with 85% more positive and 45% less negative work [Figure 1]. Distribution of work by **Step** limb soleus fascicles during Rising was greater in **APO** (5.4-20.5kN*m) than Sym (0.7-4.1N*m).

Discussion

Step limb soleus stores more energy (negative work) in **APO** before starting STW as the foot offsets posteriorly, allowing the muscle to perform more work to propel the body during Rising. Differences in soleus fascicle mechanics between **APO** and **Sym** persist in both

limbs into **Stepping** following initial differences in work during **Rising**. While soleus work during **Rising** is greater in **APO**, nonuniformity in fascicle work leads to a range of differences between foot placements depending on which fascicle is measured (29-188% difference). Variability in fascicle mechanics should be considered when assessing muscle work required in different strategies for movements like STW based on measurements of a specific region of muscle, like with ultrasound.

Images (Optional)



References (Optional)

[1] Miller et al., *J Biomech*, 2024

[2] Delp et al., *IEEE Trans BME*, 2007

[3] Knaus et al., J Biomech, 2022

Session Category

Musculoskeletal Biomechanics: Methods, Models and Applications

P2-146

Toward the Development of a Thumb Musculoskeletal Model With a Translational degree of Freedom at the Carpometacarpal Joint: A Preliminary Modeling Study

Mr. Keith Brennan[1], Dr. Joseph Towles PhD[2]

[1]Case Western Reserve University, Cleveland, OH, United States. [2]Swarthmore College, Swarthmore, PA, United States

Introduction

Neurological injuries result in loss of grasp function, significantly impacting activities of daily living. Biomechanical models are increasingly used to plan thumb reconstruction surgeries by predicting how tendon transfers affect thumb-tip forces in the context of restoring grasping ability [1]. Current thumb models do not replicate well the endpoint forces that thumb muscles produce [2]. We believe that the absence of a translational degree of freedom (DOF) at the carpometacarpal (CMC) joint currently limits their predictive accuracy. The goal of this work was to enhance thumb model realism by incorporating a translational DOF at the CMC joint and to evaluate its effect on individual muscle endpoint force predictions by the model.

Methods

A published, open-source upper extremity model [2] was modified in both extended and flexed thumb postures by adding a translational DOF at the CMC joint. To simulate muscle endpoint force production, we welded the thumb-tip to the environment in the postures of interest and applied 10 N of force to each of the 9 thumb muscles.

Results

In 12 of 18 instances, the discrepancy between the model-predicted and cadaver-measured thumb-tip force directions was reduced. In the extended thumb posture, endpoint force directional discrepancies were reduced in all 9 thumb muscles. In FPL, the reduction was 38° (Fig. 1), in EPL 42°, in EPB 15°, in APL 55°, in FPBr 19°, in APB 35°, in FPBu 23°, in ADP 6°, and in OPP 57°. In the flexed thumb posture, endpoint force directional

discrepancies were reduced in 3 muscles only. In FPL, the reduction was 18°, in EPL 1°, and in EPB 68°.

Discussion

The observation that the modified CMC joint had positive effects on the model's ability to replicate measured muscle endpoint force direction in multiple thumb postures speaks to the potential importance of representing translational kinematic properties in future thumb models. This work challenges long-standing approaches to model the thumb with rotational joints only.

Images (Optional)

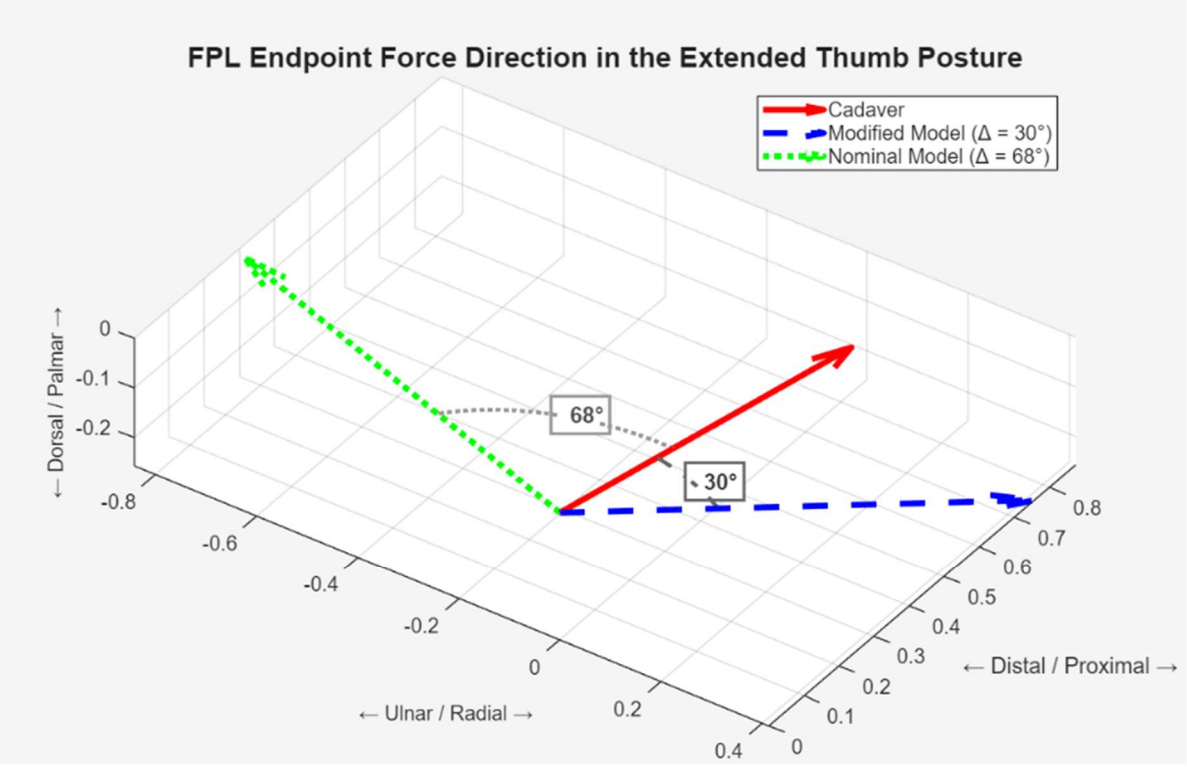


Figure 1: FPL Endpoint Force Unit Vectors in the Extended Thumb. The modified model reduced the muscle endpoint force direction discrepancy by 38 deg (i.e., 68 deg - 30 deg).

References (Optional)

[1] Garcia O and Towles JD (2025), J Biomech 191 (2025) 112882. [2] McFarland DC et al (2023), IEEE Trans Biomed Eng 70(5).

Session Category

Musculoskeletal Biomechanics: Methods, Models and Applications

P2-147

Cervical Disc Loads During Isometric Flexion, Extension and Lateral Bending

Dr Kodjo Moglo, Mr. Rizwan Arshad

Royal Military College of Canada, Kingston, Ontario, Canada

Introduction

Cervical disc loads under isometric loading conditions could vary largely due to varying muscle strengths [1]. This study investigates the variation in compressive disc load with the difference in specific muscle strength

Methods

A 50th percentile head and neck musculoskeletal model (C0-T1) was used to estimate C4C5 compressive load [2]. The cadaveric neck muscle volume was scaled up according to Zheng et al [3]. The joints considered 6 DoF (3 rotations, 3 translations). Two values (30 and 60 N/cm^2) of specific muscle strengths were considered. In total 8 simulations were performed for each direction by varying applied loads and disc compressive and shear stiffness at two levels. Ensuring that maximum muscle activity condition was achieved in one or more muscle groups, various external load in extension (Ex), flexion (Fl) and lateral bending (Lb) was applied.

Results

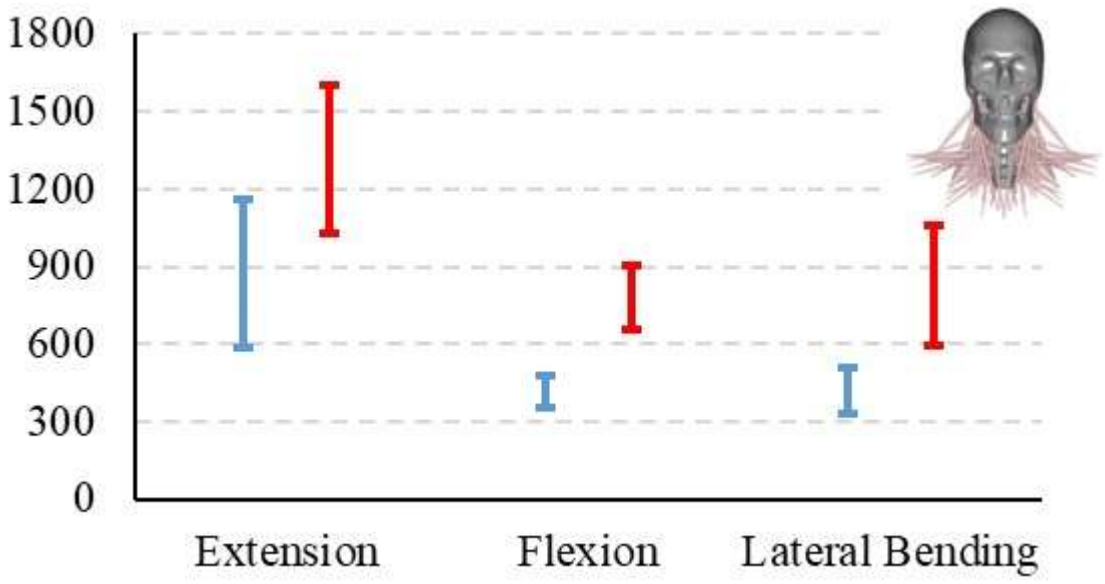
Under isometric loading conditions in extension, flexion and lateral bending, the estimated compressive loads at C4-C5 level showed large variation due to specific muscle strength (Fig. 1). The highest loads were found during extension, followed by lateral bending and flexion. For specific strength of 30 and 60 N/cm^2, the compressive loads at C4-C5 during isometric extension were between 584-1156N and 1025 to 1605N. For lateral bending, loads were between 331-506 and 591-1057N, whereas for isometric flexion, estimated loads were between 354-481N and 653-901N. Figure 1 shows C4-C5 disc loads under isometric conditions with specific muscle strength: 30 N/cm^2 (Blue) and 60 N/cm^2 (Red).

Discussion

Cervical spine loading during isometric loading conditions remains poorly understood. Many biomechanical parameters can affect the disc loads. However, neck muscle strength is key factor determining the range of maximum loads that can be endured by the cervical joints. The specific muscle strength can differ between neck flexors and extensors due to

fiber type composition and physiological demands. These estimated loads provide insights into load bearing capacity of healthy populations whose varying neck muscle strength can be measured in vivo.

Images (Optional)



References (Optional)

[1] Ikai and Fukunage, Int. Z.Angew. Physiol. Einschl. Arbeitsphysiol. 26, 26–32 (1968).

[2] Arshad et al., Front Bioeng Biotechnol; 10:751291 (2022).

[3] Zheng et al., J Biomech; 46(5):899–904 (2013).

Acknowledgements (Optional)

Sponsored by the Directorate of Aerospace Engineering Support (DTAES 7-8), DND, Canada.

Session Category

Musculoskeletal Biomechanics: Methods, Models and Applications

P2-148

Active Muscular-Contraction-Induced Knee Flexion of an Anatomically Faithful Lower Limb

Dr. Anup Pant, Dr. Lance Frazer, Dr. Daniel Nicolella

Southwest Research Institute, San Antonio, TX, United States

Introduction

Personalized Finite Element (FE) models provide unique insight into subjects' tissue mechanics [1]. Typical workflows for estimating tissue strains from physiological movement use rigid-body musculoskeletal (MSK) tools to estimate joint loads and muscle forces, which are then applied as FE boundary conditions. However, this approach requires limiting assumptions, such as mismatched geometries between the rigid-body and FE models and missing physics (internal contact, soft tissue, etc.). Direct FE modeling of the human model driven by observed motion can bypass rigid-body models and more accurately capture tissue responses. In this work, we demonstrate direct FE modeling of movement using contractile 3D musculature.

Methods

A right lower-limb FE model was generated from MRI-based bone and muscle geometry of a 21-year-old male. The MRI data lacked high fidelity soft tissue of the knee, so a height-weight matched Open Knee joint (subject 009) was blended into the model [2]. Bones were treated as rigid, muscles as Ogden rubber with active contraction, and ligaments as springs. A quasi-static FE analysis [3] was performed where hamstring activation drove knee flexion. Using an inverse-dynamics-approach, knee-flexion was prescribed, muscle activations were optimized to minimize the resulting knee moment [4], and the activations were reapplied to verify reproduction of the knee-flexion.

Results

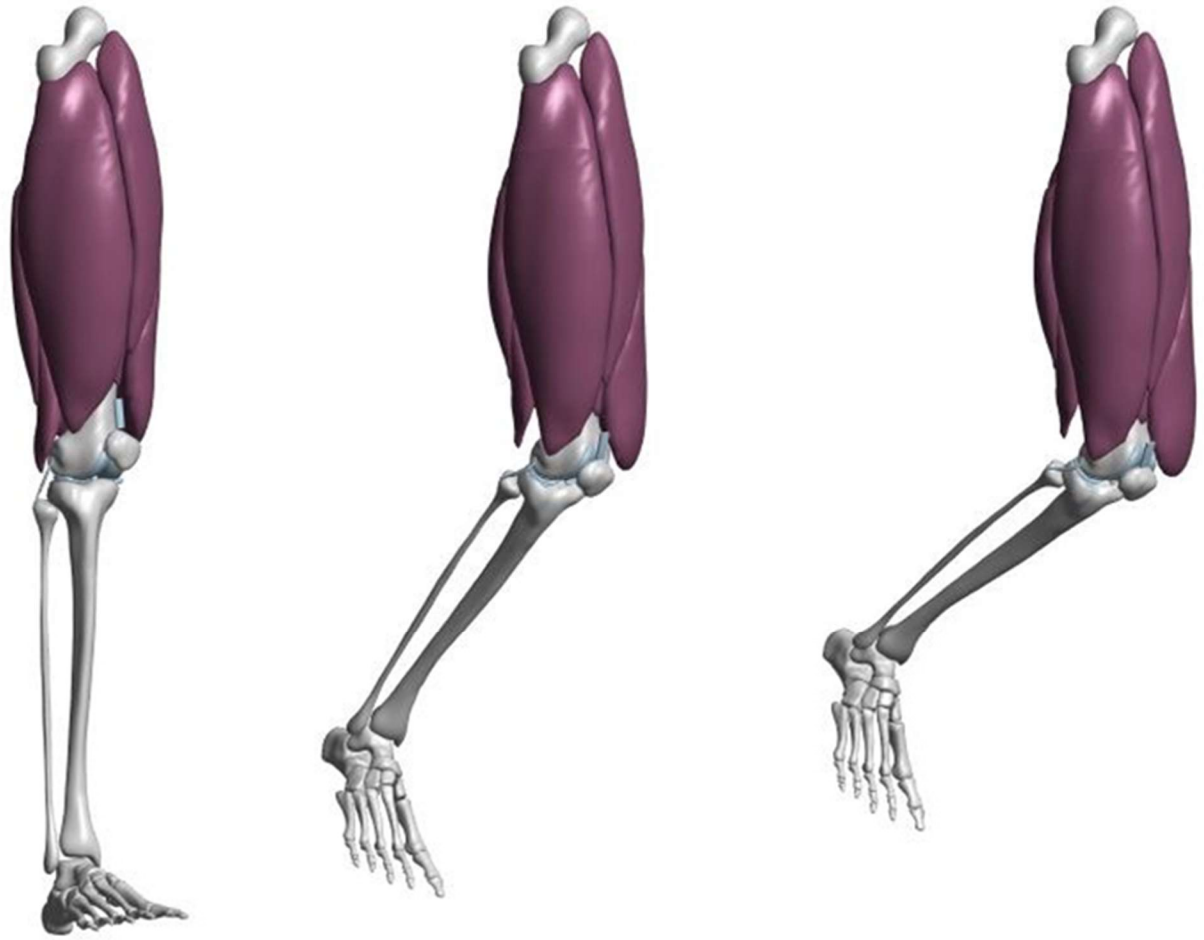
The model successfully reproduced 60° knee-flexion (Figure 1) via forward simulation. Knee contact was preserved through the full motion.

Discussion

Direct FE modeling from motion removes the need for separate rigid-body musculoskeletal analyses. Paired with motion capture data, more accurate predictions of tissues mechanics are achievable compared to using rigid-body modeling as an intermediary.

Higher fidelity FE modeling of motion can provide actionable biomechanics insights, such as identifying high-risk loading patterns, tracking rehabilitation progress, or guiding performance optimization.

Images (Optional)



References (Optional)

1. Kote, V.B., et al. *Journal of Biomechanical Engineering* 147.12 (2025): 121005.
2. Chokhandre, S., et al. *Annals of biomedical engineering* 51.1 (2023): 10-23.
3. Maas, Steve A., et al. "FEBio: finite elements for biomechanics." (2012): 011005.
4. Li, Junyan, et al. *Journal of biomechanics* 94 (2019): 230-234.

Acknowledgements (Optional)

The authors would like to thank SpringBok Analytics for providing segmented musculature from MRI.

Session Category

Musculoskeletal Biomechanics: Methods, Models and Applications

P2-149

Spring-Damper Titin Model to Improve the Estimation of Muscle Forces and Metabolic Costs

Ms Lena Kloock[1], Ms Myriam de Graaf[1,2,3], Dr. Kim Boström[1], Prof. Dr. Heiko Wagner[1,2,3]

[1]Dept. of Movement Science, Institute of Sport Sciences, University of Münster, Münster, North Rhine-Westphalia, Germany. [2]Otto Creutzfeldt Center for Cognitive and Behavioral Neuroscience, University of Münster, Münster, North Rhine-Westphalia, Germany. [3]Center for Data Science and Complexity (CDSC), University of Münster, Münster, North Rhine-Westphalia, Germany

Introduction

Hill-type muscle models are a key component of large-scale inverse dynamic models, that calculate muscle activation, joint contact forces, and, when used in conjunction with energy expenditure models, metabolic costs. However, models without the molecular spring titin [1] do not accurately reproduce relevant characteristics of eccentric movements, such as force-enhancement or metabolic costs [2]. Here, we add a spring-damper titin model to a Hill-type muscle model and evaluate the accuracy of resulting model predictions. In a next step, we will determine if the enhanced model also improves the estimation of muscle metabolic costs during eccentric phases.

Methods

We added a spring-damper module to represent titin's elastic and viscoelastic behavior to a Hill-type muscle model with force-length and force-velocity relationships. For validation, we compared the predictions of the standard and the titin model to reference data from force-enhancement experiments [3]. We used the relative root-mean-square-error (rRMSE) as performance indicator, and a repeated measures ANOVA to check for significant performance improvements.

In a later phase, muscle metabolic costs will be calculated using an inverse-dynamic musculoskeletal model (Computed MyoGraphie®, Predimo GmbH, Münster, Germany) [4] enhanced with a metabolic energy model. Titin will be added to the muscles of the inverse-dynamics model. Measuring nine subjects during walking, we used movement kinematics (XSens MVN Link, Movella, Enschede, Netherlands) as input data, and energy expenditure (MetaMax 3B, Cortex Biophysik GmbH, Leipzig, Germany) as validation data.

Results

The model with titin predicts force-enhancement significantly better than titin-less model (see Figure 1). Results of the metabolic energy prediction are not yet available.

Discussion

Adding a spring-damper titin model to a Hill-type muscle model improves muscle force prediction during force-enhancement experiments. Though being less complex than other titin models, the proposed model accurately predicts measured muscle forces. Due to its simplicity, the model can efficiently be incorporated into large-scale inverse-dynamics models used to predict metabolic cost. We expect the inclusion of titin will also improve metabolic cost predictions.

Images (Optional)

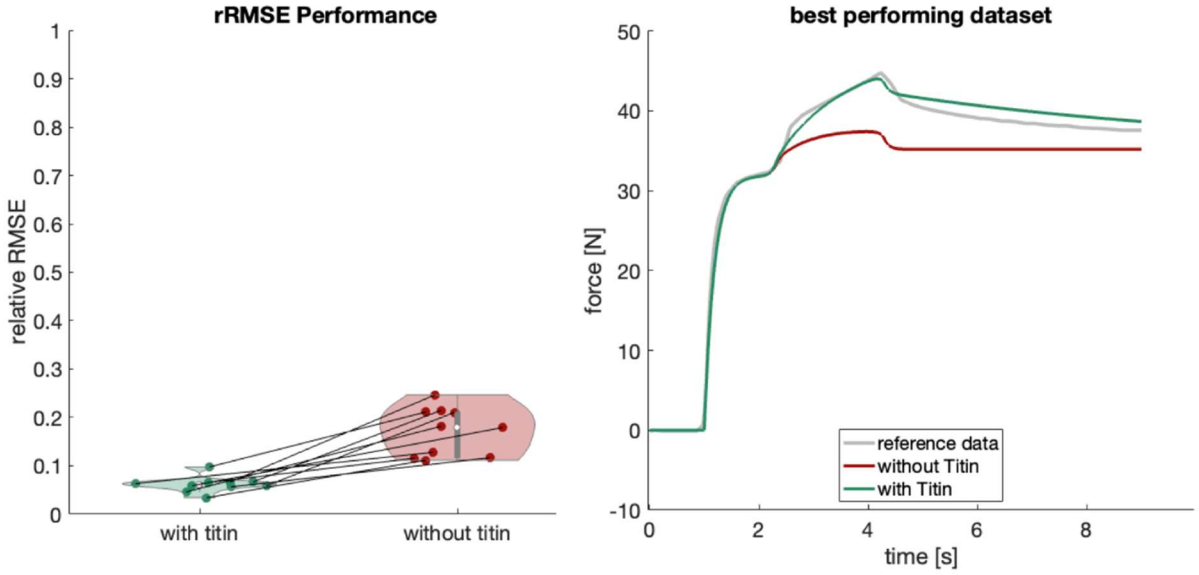


Figure 1: rRMSE (left) and time course of a Hill-type model with titin (green) and without (red) validated on force-enhancement experimental data (grey). Asterisks indicate significance (***: p<0.001).

References (Optional)

[1] Walter Herzog *et al.*, Biophys. Rev., 2018
[2] Anne Koelewijn *et al.* , Plos One, 2019
[3] Walter Herzog & Leonard T. , J Exp Biol, 2002
[4] Heiko Wagner *et al.* , Mot. Control, 2022

Acknowledgements (Optional)

We thank Predimo GmbH for providing the Computed MyoGraphie® software.

Session Category

Musculoskeletal Biomechanics: Methods, Models and Applications

P2-150

Static and Fatigue Strength of Tibiotalocalcaneal (TTC) Nail: In-silico Method Development, Verification & Validation

Dr. Lin Wang[1], Mr. Stanley Kmiec Jr.[2], Dr. Dana Coombs[2]

[1]DePuy Synthes, Leeds, West Yorkshire, United Kingdom. [2]DePuy Synthes, West Chester, Pennsylvania, United States

Introduction

Tibiotalocalcaneal (TTC) arthrodesis is a commonly used medical procedure to treat severe arthritis, deformities, and trauma in the hindfoot, by fusing the ankle and subtalar joints with an intramedullary (IM) nail. As such, the nail must withstand complex biomechanical loads and preclinical investigation of its mechanical integrity is critical. This study aims to develop an efficient and effective in-silico (computational) modelling method to answer the question of interest whether proposed TTC nails meet static and fatigue strength requirements.

Methods

A 10x150mm DePuy Synthes EXPERT™ Hindfoot Arthrodesis Nail (EX-HAN) was used for model development, and model credibility was accessed as per ASME V&V40 framework (Figure 1a). Finite Element Analysis (FEA) would be employed to simulate the benchtop testing of the TTC nails under offset bending loads (Context-of-Use), then the predicted yielding load and max. principal stress (Quantities-of-Interest) would be used for design benchmarking (Figure 1b). Based on the model influence and decision consequence, model risk was determined to be medium. Force and displacement controls were applied to the hole of the proximal block for static and fatigue analyses (with modified Goodman method) respectively, while the ball bearing near the distal block was simplified with relevant remote boundary conditions. All interactions were modelled with friction contacts except for the bonded screw-block pairs. Metallic components were modelled as elastic-plastic while Delrin blocks as elastic material.

Results

Code and Calculation activities are completed as part of the verification efforts and resulted in adequate credibility (e.g. grid discretization error < 3%). When validating the static FEA with corresponding benchtop comparator, the difference of yielding load is only 2% (Figure 1c), demonstrating sufficient credibility of this in-silico approach. Furthermore, the fatigue FEA estimates that the peak max. principal stress occurs at the middle (distal) hole, which correlates with the crack location of the testing samples (Figure 1d).

Discussion

An in-silico method has been successfully developed to evaluate the static and fatigue strength of TTC nails, offering an alternative to the traditional, costly, and iterative design-prototyping-testing. Moreover, it provides an ideal platform to benchmark TTC nail design changes/concepts exclusively, without any variability from experimental, patient, or surgical factors.

Images (Optional)

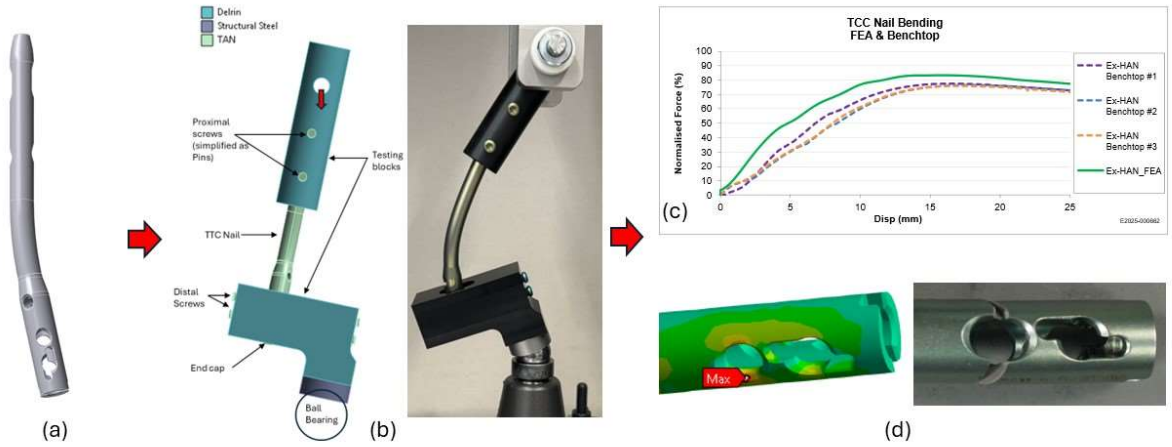


Figure 1 (a) 10x150mm DePuy Synthes EXPERT™ Hindfoot Arthrodesis Nail (EX-HAN); (b) In-silico and benchtop testing setup; (c) Force-displacement results of static FEA; (d) Peak principal stress and fatigue failure locations of EX-HAN

Session Category

Musculoskeletal Biomechanics: Methods, Models and Applications

P2-151

A Parametric CAD Model Generator for the Thoracolumbar Spine: Integration of the Muscular Architecture

Ms Linda Carpenedo, Mr Alessandro Carini, Mr Davide Joseph Pedretti, Prof. Luigi La Barbera

LaBS, Dept. of Chemistry, Materials and Chemical Engineering, Politecnico di Milano, Milan, Italy, Italy

Introduction

Spine models are essential for studying biomechanics and guiding clinical decisions. In general, both the reference morphology and the definition of loading conditions are determined by the specific goals of each study. Here, a fully parametric thoracolumbar spine CAD generator, recently extended to include pelvis and sacrum [1], is further expanded to incorporate detailed thoracolumbar musculature while preserving full parametric control for adaptable morphology and loading definitions.

Methods

A literature review identified the 11 thoracolumbar muscle groups involved in flexion–extension [2], which are implemented by discretizing each muscle into fascicles anchored to vertebral and pelvic/sacral landmarks (Figure 1a). Model reliability is assessed by comparing normalized fascicle lengths with published data and by validating insertion sites and lever arms against an external dataset [3].

Results

24 lumbar and 82 thoracic muscle fascicles per side are included in the model in a symmetric muscular architecture (Figure 1a). As all the fascicles attach to anatomical landmarks, the muscular architecture properly follows the model updates. Muscular modelling choices result in normalised muscle lengths that always match those reported by other *in vivo* and *in silico* references (median difference on 106 fascicles of 9%, with a maximal one of 90% measured for the *external oblique*) [4]. Moreover, medio-lateral and antero-posterior distances for the attachments and the lever arms are always coherent with those of an external dataset [3] (Figure 1b).

Discussion

This work developed a reliable parametric musculoskeletal model of the thoracolumbar spine. The muscular architecture is coherent with anatomical data [2,3,4]. Some discrepancies can be justified by the approximations introduced by other models and by

specific muscle configurations; for example, the oblique muscles are broad and flat, whereas we represent them as discrete fascicles. The parametric features allow tuning the model to patient-specific characteristics, and the tool may be used for further biomechanical finite element analyses. Future developments include extending the muscular architecture to muscle groups involved in other tasks (i.e., lateral bending and torsion).

Images (Optional)

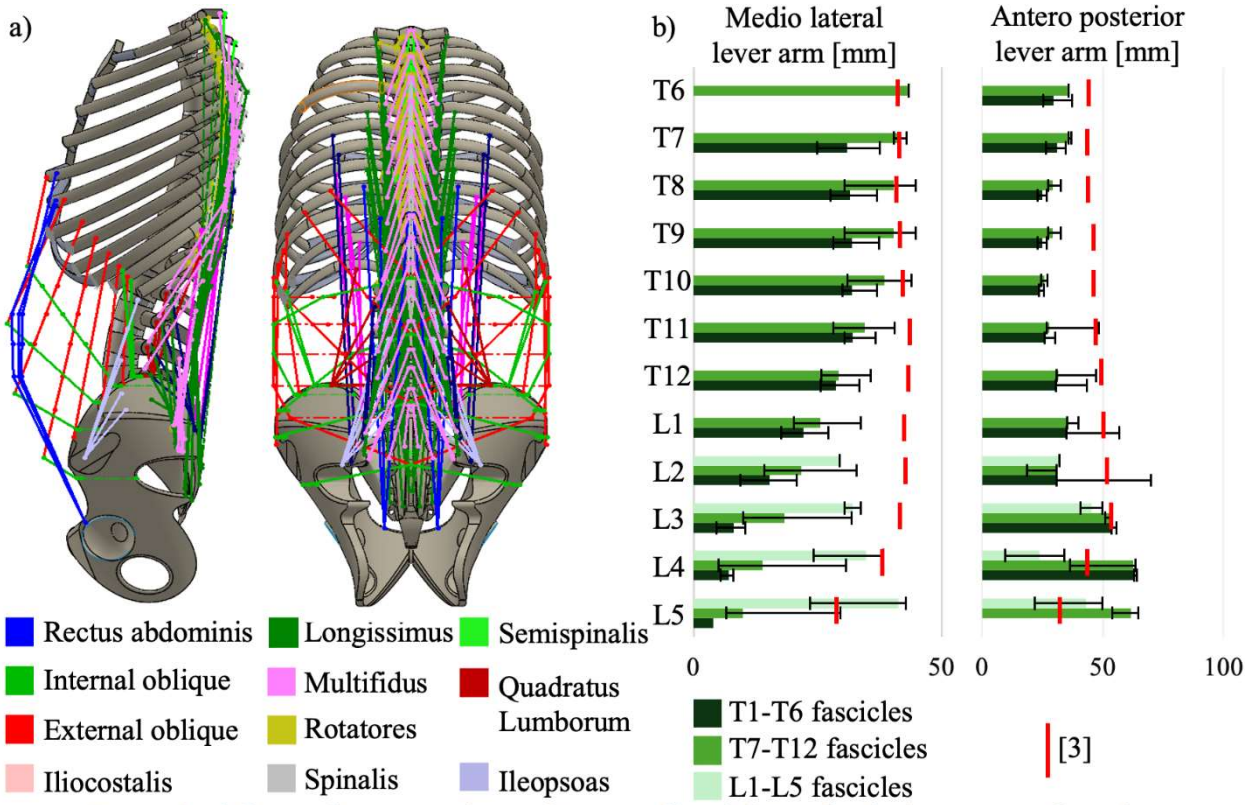


Figure 1: a) the resulting muscular architecture, b) validation for the longissimus fascicles.

References (Optional)

[1] Leoncavallo C et al. CMBBE, 2025

[2] Moore KL et al. Clinically oriented anatomy, 2017

[4] Bayoglu R et al. J Biomech, 2017

Session Category

Musculoskeletal Biomechanics: Methods, Models and Applications

P2-152

Fit Is a Safety Factor: Biomechanical Evidence Challenging One-Size-Fits-All Medical Gowns

Dr. Jingeng Li PhD[1], Professor Li-Shan Chou PhD[2]

[1]Iowa State University, Ames, Iowa, United States. [2]Purdue University, West Lafayette, Indiana, United States

Introduction

Self-contamination during medical gown doffing remains a persistent threat to healthcare worker safety, yet the influence of gown tightness on biomechanical performance and contamination risk is poorly understood. Although universal-sized gowns are widely used for cost and logistical convenience, improper fit, whether excessively tight or oversized, may alter movement patterns, increase hand–gown contact, and compromise the safety of doffing. This study investigated how three gown tightness conditions (Tight, Fit, Oversize) affect contamination risk, upper-limb kinematics, movement smoothness, and hand–gown interactions during standardized medical gown removal.

Methods

Forty healthy adults (12 Tight, 15 Fit, and 13 Oversized) performed CDC-recommended gown-doffing procedures while instrumented with five inertial measurement units (SageMotion, USA) and a marker-based optical motion capture system. Each participant doffed gowns sprayed with fluorescent solution to simulate contamination. Upper-limb range of motion, normalized zero-crossing (NZC) of angular velocity, hand-to-gown distance, and hand-gown contact time were computed. Group differences were assessed using either one-way ANOVA or the Kruskal–Wallis test, depending on whether the normality assumptions were met. Stepwise regression identified biomechanical predictors of contamination risk.

Results

Tight and Oversize gowns resulted in significantly higher contamination counts on the dominant hand and whole body compared with Fit gowns ($p \leq .015$). Range of motion was largely unaffected by gown tightness, whereas NZC values, reflecting reduced movement smoothness, were consistently higher in Oversize gowns across multiple joints ($p < .05$). Tight gowns produced significantly shorter hand-to-gown distances ($p \leq .016$), indicating forced proximity to contaminated surfaces. Stepwise regression identified elbow flexion/extension NZC as the strongest single predictor of contamination ($R^2 = 0.157$),

indicating that a decrease in motor control due to wearing an unmatched gown could be a key risk factor for contamination.

Discussion

Improper gown tightness significantly increases contamination risk by disrupting movement smoothness and altering hand–gown interactions, even when removal procedures are standardized. Both excessively tight and oversized gowns introduce biomechanical disadvantages that elevate exposure risk. These findings provide quantitative evidence supporting the need for properly fitted medical gowns and indicate that movement smoothness may be a critical biomechanical factor in explaining contamination during PPE doffing.

Session Category

Musculoskeletal Biomechanics: Methods, Models and Applications

P2-153

Validation of OpenCap-Based Estimates of Peak Knee Abduction Moments during a Drop Vertical Jump

Mr. Lucas Gaston, Ms. Sophia Stemler, Dr. Scott Monfort, Ms. Alexandra Lynch, Ms. Fatemeh Aflatounian

Montana State University, Bozeman, MT, United States

Introduction

Peak external knee abduction moments (pKAbM) have been linked to anterior cruciate ligament (ACL) injury risk.[1] However, monitoring knee kinetics using motion capture (MoCap) requires expensive equipment and is often impractical in clinical settings. OpenCap offers an affordable and easy-to-use alternative, requiring only iOS devices to collect motion data, making it more feasible for clinicians.[2] However, OpenCap-based estimates of pKAbM have scarcely been validated against MoCap data. This study aims to address this gap by simultaneously collecting MoCap and OpenCap data during the clinically significant double limb drop vertical jump (DLDJ). We hypothesized that OpenCap-based pKAbM would strongly correlate with MoCap-based pKAbM, supporting potential suitability for clinical implementation.

Methods

Eight participants (4F/4M; 22.5 ± 3.5 yrs; 1.72 ± 0.08 m; 69.5 ± 14 kg; Tegner: 4.57 ± 1.27; Marx: 6.25 ± 3.69) completed five DLDJ trials. Three iOS devices running OpenCap and the 8-camera hybrid Qualisys MoCap system recorded data. MoCap data was processed in Theia3D, and OpenCap kinetics were estimated using torque-driven OpenSim algorithmic differentiation simulations. Right leg pKAbM during the first 100ms after landing were estimated and normalized by height and weight. Eight trials were removed due to simulations not converging. Pearson correlations were found between the OpenCap and MoCap values.

Results

OpenCap and MoCap pKAbM values demonstrated a weak, nonsignificant correlation ($r = 0.245$; $p = 0.177$; Fig.1).

Discussion

The weak, nonsignificant relationship between OpenCap and MoCap estimates of pKAbM highlights the difficulty of estimating frontal plane kinetics. Ongoing data collection efforts will help to adequately power the detection of this relationship; however, the upper bound

of the 95% confidence interval of the correlation coefficient for the current sample (i.e., r = 0.55) suggests that the relationship may not reach a strong magnitude. Ongoing data collection will also include a marker-based MoCap comparison, which will provide a benchmark against 'gold-standard' MoCap.

Images (Optional)

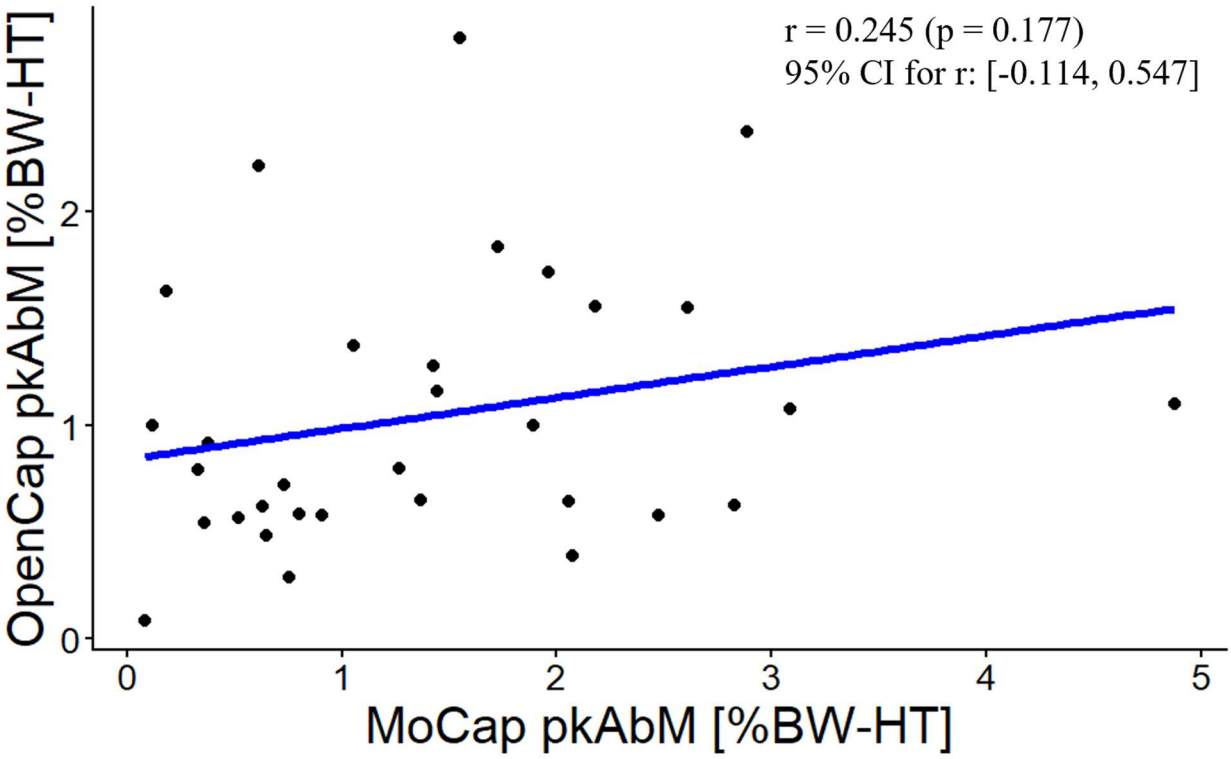


Figure 1: Correlation of pkAbM estimated from MoCap vs OpenCap plus simulation. Values are presented in units of %BW-HT: percent bodyweight-height.

References (Optional)

[1] Mark Paterno et al., Am J. Sports Med, 2010

[2] Jeffrey Turner et al., J. Biomech., 2024

Acknowledgements (Optional)

This research was supported by M.J. Murdock Charitable Trust grants and MSU USP.

Session Category

Musculoskeletal Biomechanics: Methods, Models and Applications

P2-154

Effect of Posterior Elements Removal on the Mechanical Behaviour of Thoracic and Lumbar Human Spine Segments Tested in Compression

Miss Margherita Pasini[1], Miss Gaia Youssef[1], Prof Enrico Dall'Ara[2], Prof Luca Cristofolini[1], Dr Marco Palanca[1]

[1]University of Bologna, Bologna, Italy, Italy. [2]University of Sheffield, Sheffield, United Kingdom, United Kingdom

Introduction

In-situ mechanical testing with microCT and DVC has provided unprecedented insights into spinal biomechanics [1]. However, due to the limited size of the microCT chamber, removal of the posterior elements is often required. Because thoracic and lumbar regions differ in morphology, the biomechanical effect of the posterior-element removal may also differ, jeopardising comparisons across spinal levels. This study aimed to investigate whether, and to what extent, posterior elements removal affects the biomechanics of thoracic and lumbar spine segments.

Methods

Six thoracic and five lumbar four-vertebrae segments were tested in the elastic regime using a spine simulator (MIB4.0-MAS2-S) equipped with a 6-axis load cell. Vertebral strain fields were measured with a four-camera 3D-DIC system (Aramis Adjustable 12M, Zeiss).

Each specimen was axially compressed until an average minimum principal strain (Eps_min) of 2000microstrains on the anterior vertebral surface was reached [2].

Posterior elements were removed, cutting the pedicles. The same protocol was then repeated.

The following parameters were calculated and compared (paired t-Test) before and after posterior element removal, separately for thoracis and lumbar vertebrae: 1) target load as the load required to induce Eps_min=2000microstrain on the anterior vertebral surface, 2) stiffness as the slope of the load-displacement curve between 20%-80% of the target load, 3) strain variability as the standard deviation of the maximum (Eps_max) and minimum (Eps_min) principal strains on vertebral surface.

Results

Posterior element removal did not affect the mechanical properties of the thoracic specimens (Figure 1, p>0.05). Lumbar specimens showed smaller target load (-40%, p=0.0096) and stiffness (-23%, p=0.027) together with a significantly increased Eps_max variability (+34%, p=0.004).

Discussion

Posterior element removal introduces significant mechanical alterations in lumbar specimens. The physiological lumbar lordosis, indeed, stresses the posterior elements when the spine is loaded in compression. Once removed, the segment becomes less stable. By contrast, the kyphotic curvature of the thoracic spine reduces the contribution of posterior elements under compression, making thoracic segments less sensitive to their removal. In conclusion, lumbar specimens should be tested with intact posterior elements, whereas thoracic specimens can yield reliable results even after posterior elements removal.

Images (Optional)

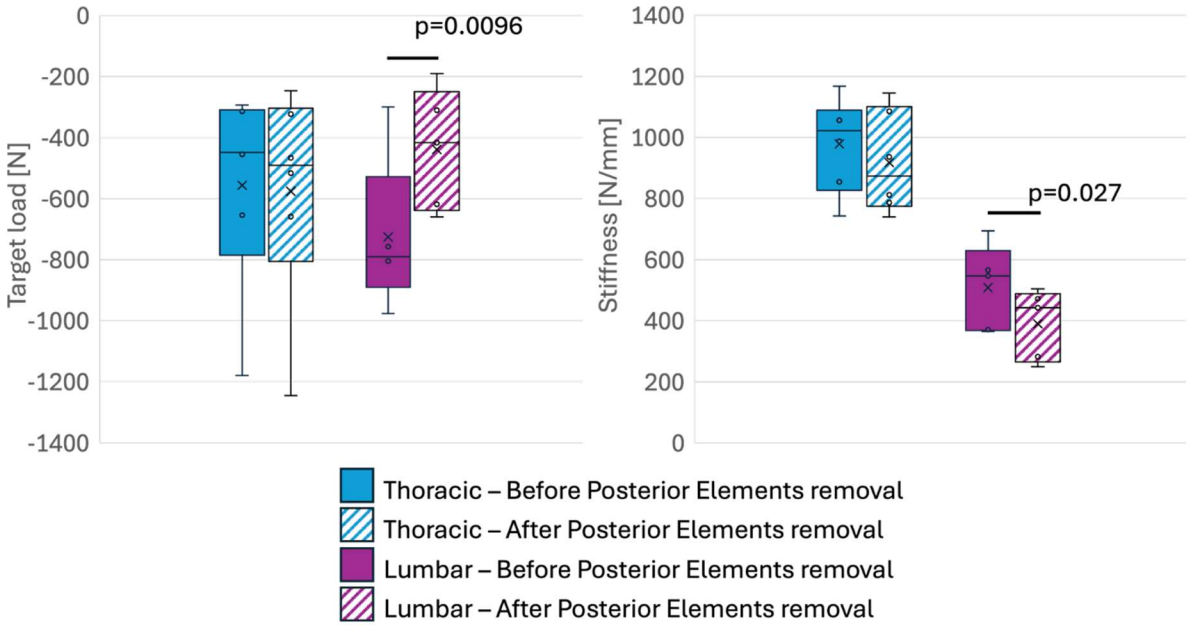


Figure 1: Target load [N] (left) and Stiffness [N/mm] (right) computed for thoracic and lumbar specimens before and after the posterior elements removal.

References (Optional)

[1] Palanca, Bone (2023)

[2] Pasini, JMBBM (2025)

Acknowledgements (Optional)

METASTRA project funded by the European Union, HEU topic HLTH-2022-12-01, grant 101080135

Session Category

Musculoskeletal Biomechanics: Methods, Models and Applications

P2-155

Toward a 8DOF Multisegment Musculoskeletal Modeling Framework for planning personalised exercise protocol for Diabetic Foot Prevention

Ms. Maria Dalle Vacche, Mr. Giulio Rigoni, Ms. Annamaria Guiotto, Ms. Fabiola Spolaor, Prof. Zimi Sawacha

University of Padova, Padova, Veneto, Italy

Introduction

Diabetes affects 537 million people worldwide, with up to 46% developing diabetic foot (DF) leading to ulcers and amputations [1]. In DF individuals, lumbrical and interosseous muscles often show atrophy and weakness, contributing to biomechanical alterations associated with plantar ulcers. Despite guidelines suggesting the adoption of customized orthoses, 34% of DF individuals develop ulcers, highlighting the need for complementary treatments such as exercise protocols targeting lumbrical and interosseous muscles [1]. However quantitative individual muscle force measurement is often unavailable in routine clinical settings. This paper aims to address this through the adoption of a 8-degree-of-freedom (DOF) EMG-informed multisegment musculoskeletal (MSM) foot model [2] in OpenSim.

Methods

The gait of 20 subjects (mean age and BMI: 55.4 ± 11.4 years, 25 ± 4.1 kg/m^2) was assessed (9 controls, 6 diabetic, 5 neuropathic subjects) through 6 BTS cameras, synchronized with two Bertec force platforms , a 12-channel surface-EMG (sEMG) system, 2 Imago Ortesi plantar pressure systems (150 Hz). The foot Padova model was adopted [3] and the sEMG activity of 6 lower limb muscles recorded bilaterally. Muscle activations and forces were estimated either through a modified version of [2] which includes an EMG-informed approach [4] and via static optimization. Activation results were compared with sEMG envelopes for validity assessment [5]. Statistical Parametric Mapping (SPM) analysis [6] was conducted to compare different subject groups.

Results

Figure 1 shows the proposed framework. Preliminary muscle activation estimates obtained through Static Optimization indicate that diabetic participants exhibit higher activation levels than both controls and neuropathic subjects, likely due to the increased stiffness of the plantar fascia.

Discussion

The proposed model allows identifying specific foot muscle impairments associated with diabetes. This methodology could be used for planning specific selective foot muscles strengthening protocols, and assessing the effect of the interventions.

Images (Optional)

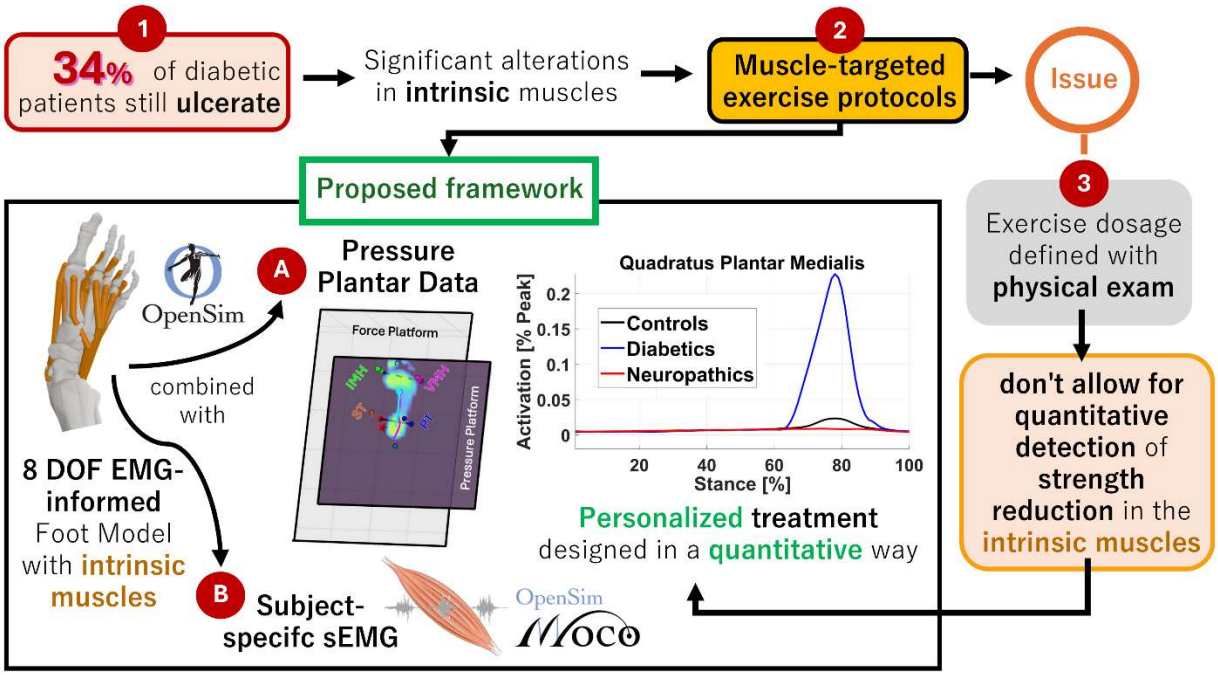


Figure 1: *Proposed Musculoskeletal Modeling Framework*. Simulations to estimate muscle activations and forces were performed in OpenSim. A) Ground reaction forces were partitioned into rearfoot, midfoot, and forefoot contributions by integrating plantar pressure data. B) Experimental sEMG signals were incorporated into Moco to perform EMG-informed simulations.

References (Optional)

[1] Bus SA, et al. Diabetes Metab Res Rev. 2024.

[2] Malaquias TM, et al. CMBBE. 2017.

[3] Sawacha Z, et al. Gait Posture. 2012.

[4] Dembia CL, et al. PLoS Comput Biol. 2020.

[5] Scarton A, et al. Gait Posture. 2018

[6] Pataky TC, et al. CMBBE. 2012.

Session Category

Musculoskeletal Biomechanics: Methods, Models and Applications

P2-156

Impact of Patient-Specific Anatomy on Muscle Parameter Calibration and Muscle Forces Estimations in Children with Cerebral Palsy

MSc Markus Astl, MSc Elias Wallnöfer, PhD Willi Koller, PhD Basilio Goncalves, Assoz. Prof. Mag. Hans Kainz

University of Vienna, Vienna, Vienna, Austria

Introduction

The importance of electromyography-assisted approaches and imaging-based musculoskeletal models for neuromuscular simulations in children with cerebral palsy (CP) has been shown [1,2]. Muscle parameter calibration represents a further step in personalization. CEINMS [3] and the Muscle Redundancy Solver (MuReSo) [4] incorporate such calibrations and have been used in CP studies [2,5]. This study evaluated how these two EMG-informed frameworks alter muscle properties and forces in generic-scaled and MRI-based models.

Methods

Retrospective data [1], including 3D motion capture, ground reaction forces, electromyography (EMG), and both a generic-scaled model [6] (GSM) and an MRI-based model [7] (MBM) of four children with CP, were analyzed. EMG from eight lower-limb muscles was normalized to maximum activations obtained by static optimization in OpenSim [8]. Muscle parameter calibration and force estimation were performed with CEINMS and MuReSo. Shared parameters were matched across tools, while tool-specific settings were optimized for validation. Calibration of optimal fibre length and tendon slack length was limited to ±5%.

Results

Preliminary results for one child showed that CEINMS and MuReSo adjusted optimal fibre lengths (OFL) in the same direction for 57% of muscles in the GSM and 61% in the MBM. Tendon slack lengths (TSL) showed higher agreement (61% and 73%) between approaches. Calibration reduced OFL and TSL differences between GSM and MBM for 39% and 68% of muscles respectively. Mean root-mean-square-differences of muscle forces between models was 14% and 7% body weight for CEINMS and MuReSo respectively.

Discussion

Limited agreement in calibration direction and muscle forces highlights that CEINMS and MuReSo respond differently to identical input data, likely due to tool-specific objective functions. The greater stability of MuReSo muscle forces across personalization levels indicates lower sensitivity to parameter perturbations. Analyses across all participant will evaluate the robustness of these findings.

Images (Optional)

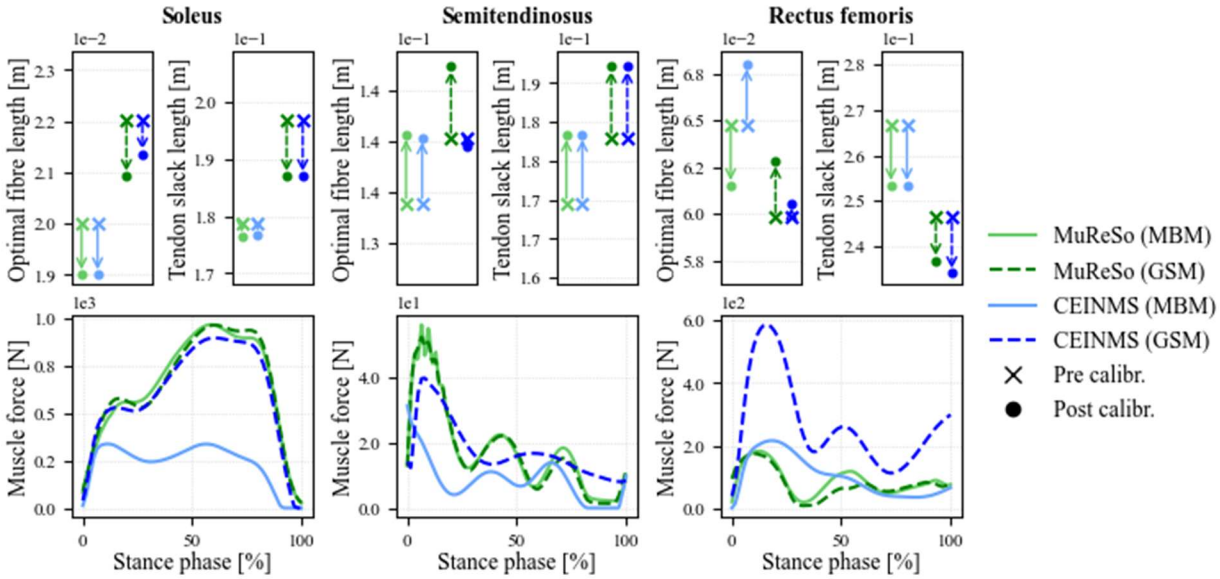


Figure 1: Calibration-induced changes in musculotendon parameters and muscle forces for three muscles of the right leg. MRI-Based Model=MBM, Generic Scaled Model=GSM, Muscle Redundancy Solver=MuReSo.

References (Optional)

[1] Kainz & Jonkers, Gait & Posture, 2023

[2] Davico et al., Clinical Biomechanics, 2020

[3] Pizzolato et al., Journal of Biomechanics, 2015

[4] De Groote et al., Ann Biomed Eng, 2016

[5] Falisse et al., Front. Hum. Neurosci., 2020

[6] Delp et al., IEEE Trans. Biomed. Eng., 1990

[7] Scheys et al., Biomedical Simulation (Springer), 2006

[8] Delp et al., IEEE Trans. Biomed. Eng., 2007

Acknowledgements (Optional)

This research was funded by the Austrian Science Fund.

Session Category

Musculoskeletal Biomechanics: Methods, Models and Applications

P2-157

Kinematic Variability Between a Single-Segment vs. Multi-Segment Foot Model During Treadmill Walking in Healthy Adults

Grant Schwiebert[1,2], Matthew Parrett M.Ed.[1], Mallory Rowan M.S.[1], Jessica Lewis PT, DPT[1], Dr. Sean Tabaie MD[1], Dr. Kirsten Tulchin-Francis PhD[1]

[1]Nationwide Children's Hospital, Columbus, Ohio, United States. [2]The Ohio State Unviersity, Columbis, Ohio, United States

Introduction

Single-segment foot models (SSFMs) remain common in clinical gait analysis despite bone-pin and fluoroscopic studies showing inter-segmental motion and violation of rigid-body assumptions. Existing multi-segment foot models (MSFMs) add anatomical detail but vary widely and rarely include medial-lateral forefoot or radiograph-analogous angles needed to assess deformity and loading asymmetry. The purpose of this study was to assess regional kinematics of a novel MSFM, and to quantify stride-to-stride variability, nonlinear dynamic stability, and waveform reliability relative to a SSFM.

Methods

Seven healthy adults (6M, 24.1±3.9yrs, 77.0±9.8kg, 175.8±7.6cm) walked barefoot on a treadmill at 2.5 mph for 90 seconds while 3D motion capture data were collected using the Shriners Children's Gait Model (SCGM) and a novel MSFM simultaneously. The MSFM included intersegment Euler angles between the tibia, hindfoot, forefoot, and medial and lateral forefoot. Across >70 gait cycles per participant, variability metrics (standard deviation [SD], coefficient of variation [CV], range of motion [ROM], ROM-CV), and nonlinear stability metrics (short- and long-term Lyapunov exponents [SLE/LLE]) were computed. Cycle-wise waveform reliability was evaluated with ICC(2,1).

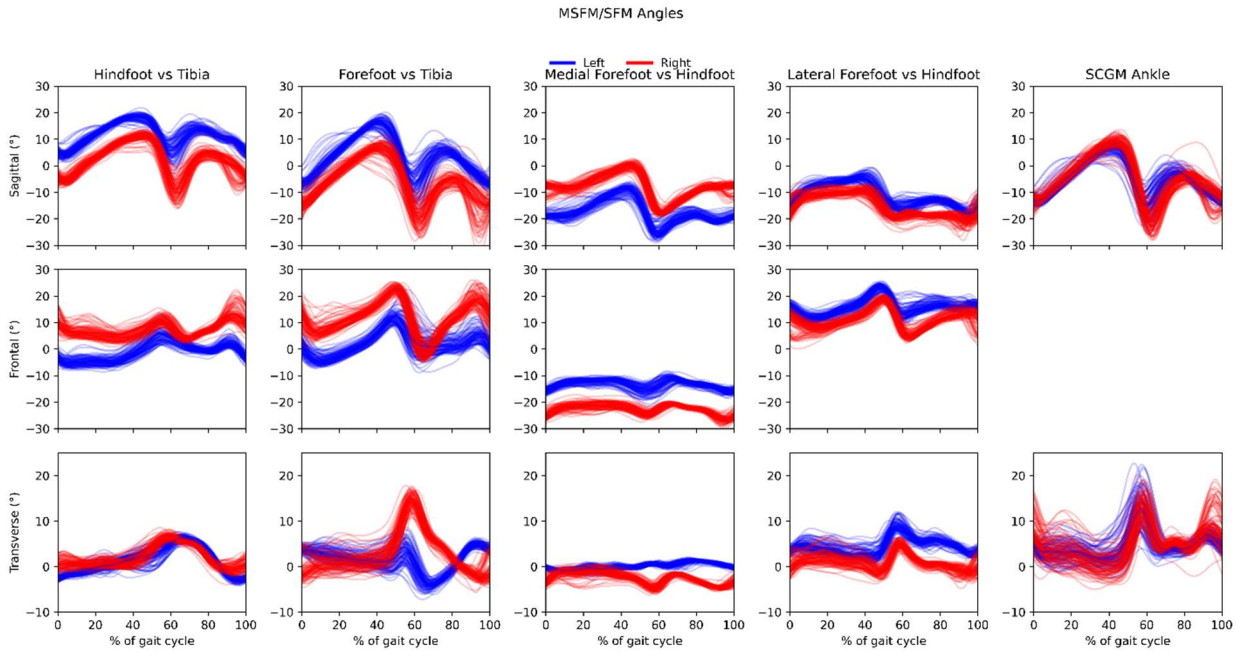
Results

The MSFM generated repeatable waveforms across all participants (Fig 1). Mean stride-to-stride ROM variability was 4.4°/1.8°/3.9° across sagittal, frontal, and transverse planes, respectively. Medial and lateral forefoot segments exhibited distinct variability signatures (1.8°/1.0°/0.7° vs 2.0°/1.3°/0.8°), demonstrating sensitivity to regional mechanics. Nonlinear MSFM stability was comparable to single-segment ankle angles (SLE: 1.29 vs 1.32; LLE: 0.067 vs 0.066). Reliability was high: ICC averaged 0.79 for Euler angles and 0.79 for SCGM ankle angles.

Discussion

This preliminary evaluation demonstrates that the proposed MSFM is stable, reliable, and sensitive to clinically important medial–lateral forefoot differences often obscured by traditional models. This framework enhances the ability to analyze deformity progression, orthotic and surgical intervention outcomes, and pathological gait using repeatable, regional kinematics. Future work will include developing normative datasets, assessing the model with a probabilistic marker-placement error and soft-tissue artifact analysis to strengthen clinical translation, and evaluating its performance in pathological feet. The intra-foot mechanics with segment-specific fidelity of this MSFM provides a strong foundation for improved diagnosis, treatment planning, and longitudinal monitoring.

Images (Optional)



References (Optional)

Session Category

Musculoskeletal Biomechanics: Methods, Models and Applications

P2-158

Inter-Site Reliability of Ankle Kinematics from Biplanar Videoradiography

Dr David Williams[1], Miss Katherine Prentice[1], Miss Lauren Swain[1], Dr Michael Rainbow[2]

[1]Cardiff University, Cardiff, Wales, United Kingdom. [2]Queen's University, Kingston, Ontario, Canada

Introduction

Accurate measurement of kinematics is essential for advancing clinical and fundamental biomechanical understanding of the foot and ankle; however, the small sample sizes typical of biplanar videoradiography (BVR) studies potentially limit the power of this accurate analysis. Multisite data collection offers a route to increase participant numbers, but only if comparable biomechanical signals can be obtained across laboratories operating separate imaging systems and processing workflows. This study presents a foundational inter-site comparison designed to inform a larger multisite initiative.

Methods

One volunteer who had previously received tantalum bead implants: five in the distal tibia, four in the talus, three in the calcaneus and four in the navicular [1] performed barefoot level walking at two separate laboratories, each using a BVR system with matched X-ray geometry parameters. CT images were captured (Resolution: 0.441 mm x 0.441 mm x 0.625 mm) and segmented to generate bone surface models and define bead location. Bone poses from each site were determined by digitising bead positions in XMALab. Kinematics were derived for the talocrural (tibia–talus), subtalar (talus–calcaneus), and talonavicular (talus–navicular) joints using anatomically aligned coordinate systems. Joint angles were time-normalised to the gait cycle and compared across sites.

Results

Hindfoot kinematics showed close inter-site agreement (Figure 1). Differences across the gait cycle were 3 ± 2°, 3 ± 1°, and 2 ± 1° for tibia–talus rotations, and −2 ± 4°, −2 ± 2°, and −6 ± 3° for talus–calcaneus rotations (Sagittal, Frontal, Transverse respectively). Larger discrepancies were observed at the talonavicular joint (−5 ± 11°, 6 ± 6°, −21 ± 5°).

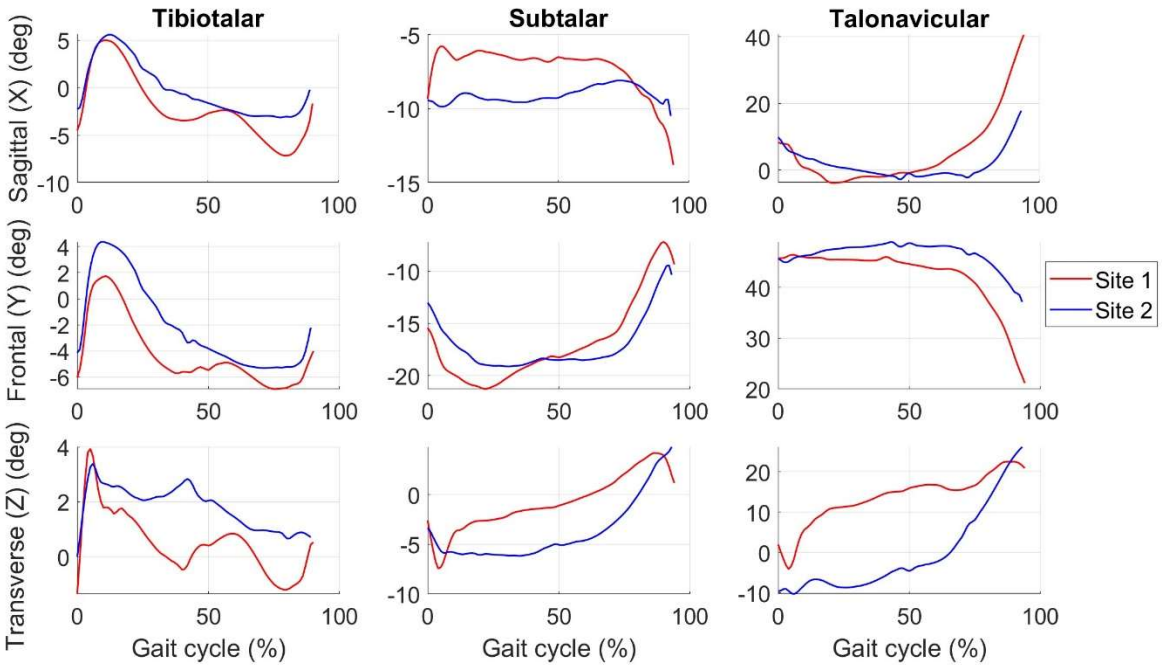
Discussion

While it is unclear whether the differences we observe are due to inter-day variation in movement patterns or to systematic differences between labs, these findings demonstrate that comparable hindfoot kinematics can be obtained across independent BVR laboratories. Biplanar videoradiography lends itself well to multi-site studies because

traditional sources of inter-lab variation [2] such as user-defined anatomical coordinate systems, replicating camera setups, and soft tissue artifact are eliminated. Future work will expand this comparison to other joints in the foot and ankle complex.

Images (Optional)

Figure 1: In-vivo rotations of the same volunteer from two BVR laboratories



References (Optional)

[1] Lauren Welte *et al.* JoVE, 2022

[2] George Gorton *et al.* Gait & Posture, 2009

Acknowledgements (Optional)

Funding provided by Engineering and Physical Sciences Research Council (EPSRC) Impact Acceleration Account award administered by Cardiff University and NSERC Discovery Grant (RGPIN/04688-2015).

Session Category

Musculoskeletal Biomechanics: Methods, Models and Applications

P2-159

Superior and Inferior Endplate Deflection in Response to Physiologic Loading Scenarios

Mr. Michael Watson MSc[1], Dr. Jackie Zehr PhD[2], Dr. Jack Callaghan PhD[1]

[1]University of Waterloo, Waterloo, ON, Canada. [2]University of Toronto, Toronto, ON, Canada

Introduction

Within a spinal joint, the vertebral endplate transmits compression force between adjacent intervertebral discs and vertebrae. Prior literature has attributed the inferior endplate's (IE) higher incidence of failure to its greater tendency to deflect compared to the superior endplate (SE) [1]. However, existing endplate deflection measures are confounded by techniques that either rely on prolonged static loading or damage the vertebral structure. This study introduces a novel method that avoids these limitations and enables the change in endplate deflection to be measured under cyclic loading conditions, providing a more physiologically relevant deflection metric.

Methods

Eighteen porcine cervical functional units (C3C4, C4C5, C5C6; N = 6 per level) were dissected into 36 vertebrae. High-resolution laser profilometry captured cranial and caudal endplate topography to enable the fabrication of custom 3D-printed indenters that both conformed to and contacted exclusively the nuclear region of the endplate. Specimens were positioned neutrally and loaded with a custom cyclic waveform ranging from 0.3 kN to 30% of predicted ultimate strength. Endplate deflection was assessed after 0, 1000, 3000, and 5000 cycles by recording indenter displacement under brief static loads of 0.3, 1, and 3 kN, totalling 12 measurements per vertebra. Linear mixed-effects models tested the effects of load magnitude, cycle count, endplate level, and the nucleus occupying proportion of endplate area on deflection.

Results

Greater IE deflection was observed across all measures with IEs of C4C5 and C5C6 joints demonstrating a significant increase in deflection rate during the first 1000 cycles. C4C5 joints exhibited the largest difference in SE and IE deflection, followed by C5C6 and C3C4 joints. Endplate deflection was not influenced by the proportion of the nucleus occupying endplate area at any spinal level.

Discussion

This study demonstrates the utility of a novel method for measuring SE and IE deflection under cyclic loading conditions. The results indicate that inferior–superior compliance differences vary by spinal level, reflecting anatomical and structural factors that influence injury susceptibility. The absence of an effect from the nucleus occupying area further supports deflection being driven primarily by localized structural weaknesses.

References (Optional)

[1] Hulme et al., Journal of Biomechanics, 2008

Session Category

Musculoskeletal Biomechanics: Methods, Models and Applications

P2-160

During 3D Center-Out Reaching Movement of the Mouse Forelimb, Fascicular Velocities Are Greatly Affected by Target Location and Can at Times Exhibit Both Eccentric and Concentric Contractions Within a Movement

Ms. Shuting Chen, Mr. Minghuan Gu, Ms. Nancy Shao, Ms. Anisa Torres, Dr. Francisco Valero-Cuevas

University of Southern California, Los Angeles, CA, United States

Introduction

The fusimotor system is critical for limb movement[3]. Murine models help understand mismodulation of stretch reflexes relevant to spasticity in neurological conditions such as stroke[1]. Therefore, there is a need to quantify fascicular velocities for the mouse forelimb to inform experimental protocols for muscle mechanics[2].

Methods

Our computational model of the murine forelimb quantifies fascicular velocities for 3D center-out movements. We extended a 3D, 6-DOF, 21-muscle forelimb model[2] by adding wrist flexion-extension and radio-ulnar deviation in OpenSim 4.5, and reading out fascicular velocities via the Java API in MATLAB. 100 Monte Carlo simulations of 500-ms center-out movements spanned the 3-D workspace via quintic minimum-jerk S-curve trajectories from reference to target. Fascicular velocities were normalized to each muscles' optimal fiber length L_0. Additionally, we randomly perturbed each S-curve and L_0 by ±10%.

Results

Most simulated peak fascicle velocities across all muscles and targets were within ±1 L_0/s, and only 5 muscles surpassed 1 L_0/s. The fastest fascicle velocities consistently occurred within *Pectoralis Major, Latissimus Dorsi, Medial Deltoid,* and Flexor Carpi Radialis.

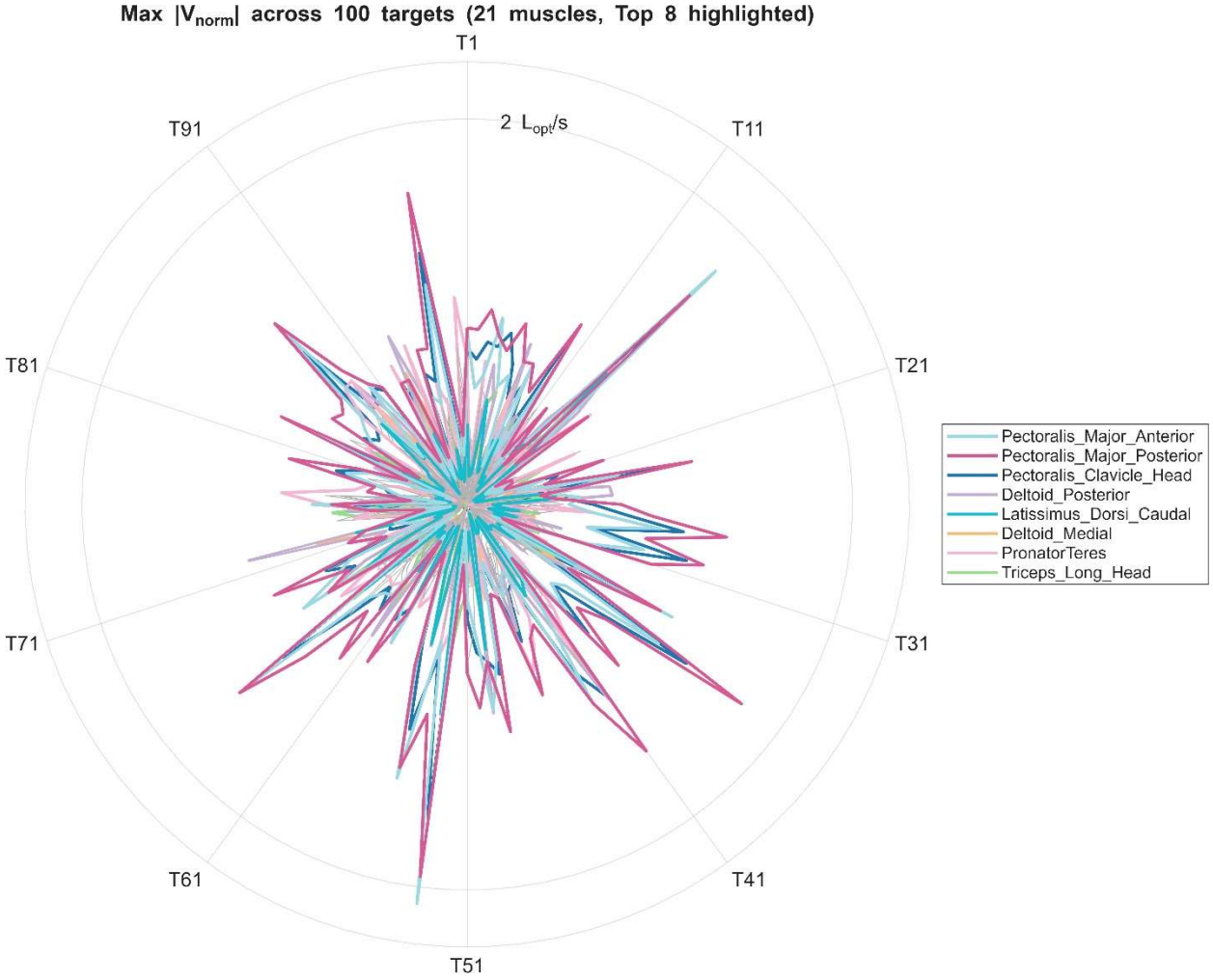
Our Monte Carlo analysis showed that <10% of perturbed trajectories exceeded 1 L_0/s. Varying L_0 by ±10% yielded modest variability in peak velocities (coefficients of variation ~6-7% for most sensitive muscles) suggesting our predictions are robust to muscle architecture.

Most importantly, we find that even center-out movements induce some muscles to have fascicular velocities that switch between eccentric and concentric velocities, as has also been predicted in humans and non-human primates[3].

Discussion

Murine experimental paradigms to understand fusimotor regulation of reflexes in the forelimb must identify both movement targets to use, and muscles to record from. Our study identifies both, and also shows that fascicular velocities are relatively slow for 500 ms movements. We also confirm predictions that 3D forelimb movements induce target-dependent complex fascicular velocities that are useful to study the fusimotor system.

Images (Optional)



References (Optional)

[1] Darvish *et al.*, Medical Hypotheses, 2025

[2] Jesse Gilmer *et al.*, J Neuro Physiology, 2025

[3] Grace Niyo *et al.*, PNAS, 2024

Acknowledgements (Optional)

This work was supported with the structure of BME/BKN 504: Neuromechanics class under USC Alfred E. Mann Department of Biomedical Engineering and USC Division of Biokinesiology and Physical Therapy, taught by Dr. Francisco Valero-Cuevas, Dean's Professor of Biomedical Engineering at USC. The authors would like to thank Grace Niyo, Ph.D. Student at the Valero Lab at the University of Southern California (USC) Viterbi School of Engineering and BME/BKN 504 Teaching Assistant, for her contribution to our simulation work.

All authors contributed equally.

Session Category

Musculoskeletal Biomechanics: Methods, Models and Applications

P2-161

Scaling Knee Kinematics: Beyond Sex and Size—Toward Shape-Based Insights

Dr. Morgan J. Dalman Ph.D.[1], Dr. Emily M. McCain Ph.D.[2], Mr. Brendan S. Shea[1], Ms. Emma R. Swartz[1], Dr. Silvia S. Blemker Ph.D.[1,2]

[1]University of Virginia, Charlottesville, VA, United States. [2]Springbok Analytics, Charlottesville, VA, United States

Introduction

Musculoskeletal models typically rely on standardized assumptions for joint positioning, limiting subject-specific accuracy. Current scaling techniques are size-based, assuming larger bones require proportionally larger shifts in positioning. Because bone size often differs by sex, these methods impose sex-related differences without accounting for actual kinematic variation. For example, tibiofemoral (TF) kinematics defined by Walker et al. (1988)[1] were derived from 23 cadaveric knees of unknown sex, while patellofemoral (PF) kinematics from Van Eijden et al. (1986)[2] were based on 10 male cadaver knees. This study investigates whether scaling factors for knee kinematics differ by sex and if they relate to size-based metrics commonly used in musculoskeletal modeling.

Methods

Subject-specific knee models (N = 69; 38F/31M; 27.5 ± 7.3 years) were generated for both limbs from three-point Dixon Sequence MRI scans. Scans were processed using an AI-based segmentation pipeline with manual validation (Springbok Analytics, Charlottesville, VA). Models incorporated Walker's tibiofemoral coordinate system and Van Eijden's patella model, which relate patella position to the angle (ϕ) between the tibial axis and patella ligament. Segmented TF and PF joint spaces were calculated at 0° flexion, and optimized scaling factors minimizing joint space differences between 0° and 120° flexion were applied to translations and ϕ_{120}, respectively. Sex differences and correlations with size-based metrics were analyzed.

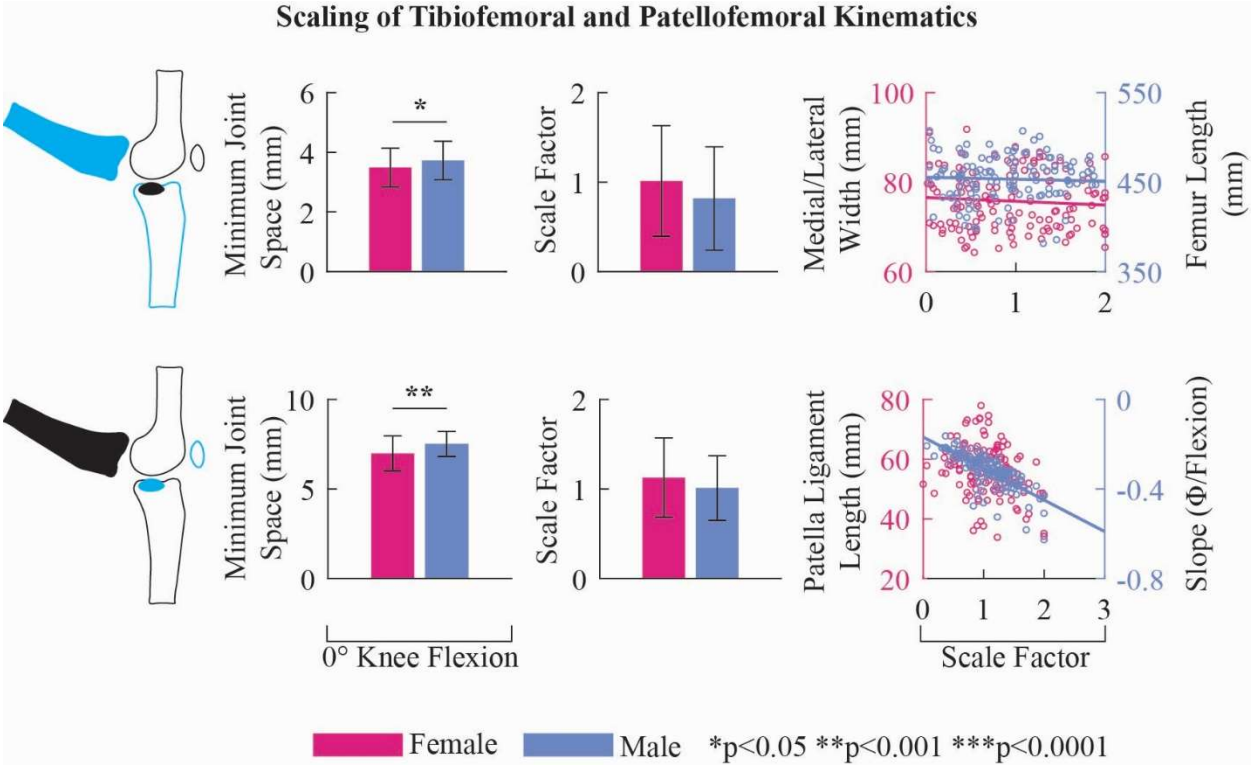
Results

Initial joint spacing differed significantly between sexes (TF: $p < 0.05$; PF: $p < 0.001$), but scaling factors did not (TF: $p = 0.06$; PF: $p = 0.09$). TF scaling factors showed no correlation with size-based metrics such as medial-lateral width ($R^2 = 0.00$; $p = 0.37$) and femur length ($R^2 = 0.00$; $p = 0.55$). PF scaling factors were weakly related to patella ligament length ($R^2 = 0.09$; $p < 0.001$), but strongly influenced by the slope of ϕ versus knee angle ($R^2 = 0.57$; $p < 0.0001$).

Discussion

These findings demonstrate that current-sized based scaling assumptions do not solely explain kinematic scaling and sex differences are not a determining factor. Instead, they highlight the need to explore shape-based drivers in future work.

Images (Optional)



References (Optional)

[1] Walker, P. S. et al. *J. Biomech.* 1988.

[2] Van Eijden, T. M. et al. *J. Biomech.* 1986.

Acknowledgements (Optional)

NIH Grant #R01AR078396a and Hartwell Postdoctoral Fellowship.

Session Category

Musculoskeletal Biomechanics: Methods, Models and Applications

P2-162

Towards a Patient-Specific Finite Element Model to Simulate 3D Orthodontic Tooth Movement During Leveling Phase

Mr. Mouhamad ABOU HAMDAN [PhD Student][1], Dr. Siham TOUCHAL [Associate Professor][1], Dr. Hamdi JMAL [Associate Professor][1], Dr. Delphine WAGNER [Associate Professor][1,2,3]

[1]ICube Laboratory, UMR 7357 CNRS, Mechanics Department, University of Strasbourg, Illkirch, Grand Est, France. [2]Pôle de médecine et de chirurgie bucco-dentaire, structure interne d'orthopédie dento-faciale, Strasbourg, Grand Est, France. [3]Faculté de chirurgie dentaire, Université de Strasbourg, Strasbourg, Grand Est, France

Introduction

During leveling phase, orthodontists use a sequence of superelastic Nickel-Titanium (NiTi) archwires chosen largely by clinical expertise for their light forces that drive bone remodeling and then teeth movement.

This study develops a patient-specific 3D FE model to simulate Orthodontic Tooth Movement (OTM) during the alignment phase and quantifies the loads applied by an initial NiTi archwire on individual teeth.

Methods

Passive self-ligating brackets and the ideal 0.016” archform were positioned on the upper right teeth reconstructed from CBCT scans. Only the lateral-incisor, canine, and first-premolar were allowed to move, while other were considered fixed. Activation was achieved by displacing the brackets already fitted in the wire to their prescribed positions on misaligned teeth, mainly characterized by 3 mm intrusion of the canine, enforcing symmetry at the wire midline.

The one-month treatment phase, automated in ABAQUS® using Python, followed two steps: first, importing the activated wire and loads to generate initial periodontal ligaments deformation within the corresponding reconstructed bone. Second, applying an external bone remodeling model [1], to update and remesh the geometry daily, repeating the process while re-importing the archwire iteratively.

Results

At treatment onset, the archwire slid through the bracket slots as the teeth began to move, resulting in a rapid decay of the initial applied forces. By around day 9, the forces reached

near stable values, remaining higher on the canine and lower but comparable on the adjacent teeth (see *Figure 1*).

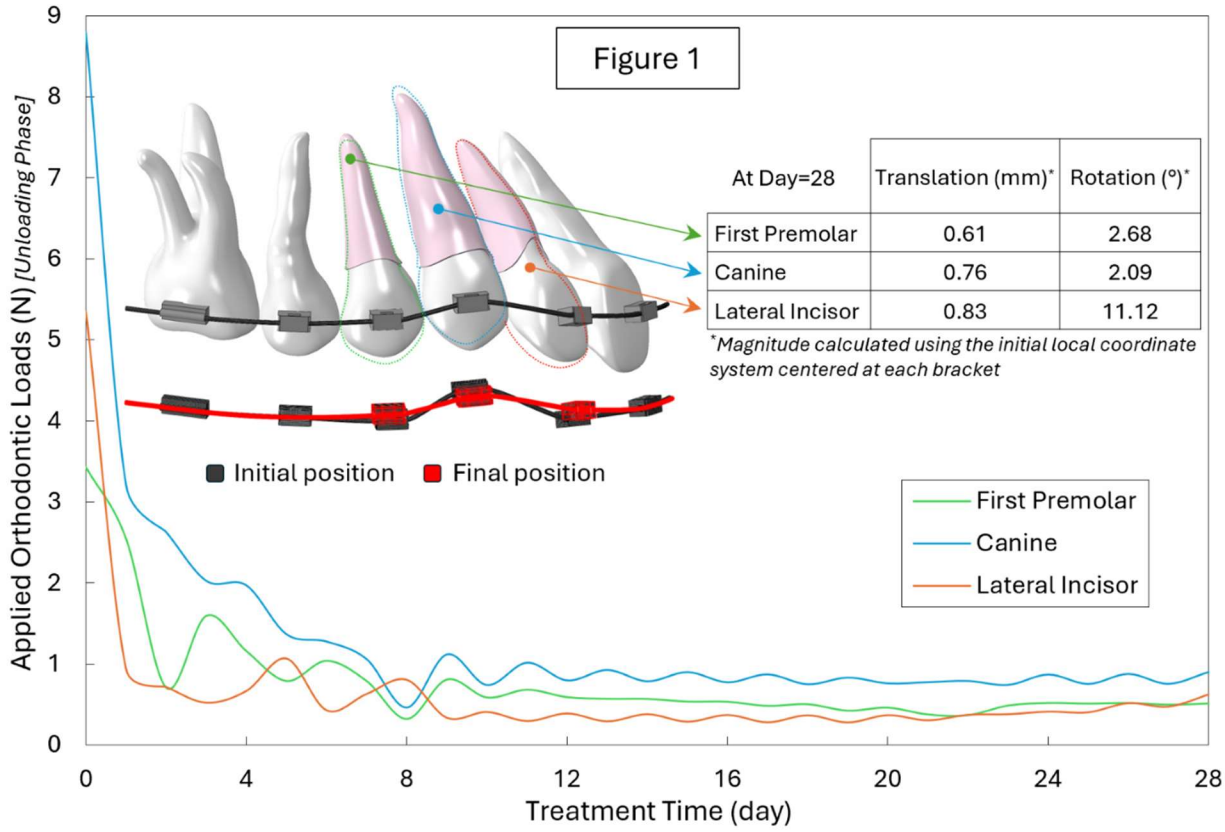
As shown in *Figure 1*, these forces resulted in extrusion of the canine and intrusion of the neighboring teeth, contributing to early arch leveling, while also generating pronounced buccolingual tipping of the lateral-incisor and a milder opposite tipping in the first-premolar.

Discussion

Despite being based on patient-specific anatomy and limited to the movement of three-teeth segment, the predicted displacement magnitudes over 28-days induced by the light and stable forces align with the lower bound of clinical OTM rates reported in [2].

Future work will investigate different NiTi archwire sequences until the teeth reach almost same vertical level to optimize treatment strategies during the leveling phase.

Images (Optional)



References (Optional)

[1] Qian *et al.*, Clin-Biomech, 2008

[2] De Pontouraude *et al*., Clin-Oral-Investig, 2021

Acknowledgements (Optional)

This work of the Interdisciplinary Thematic Institute HealthTech, as part of the ITI 2021-2028 program of the University of Strasbourg, CNRS and Inserm, was supported by IdEx Unistra (ANR10-IDEX-0002) and SFRI (STRAT'US project, ANR-20-SFRI-0012) under the framework of the French Investments for the Future Program.

Session Category

Musculoskeletal Biomechanics: Methods, Models and Applications

P2-163

Journey of Geometries: Variability of Knee Joint Segmentation in a Consensus Workflow

Ms Nancy Kim[1], Ms Kate Moyle[1], Ms Maryam Nazem[2], Mr Peter Laz[2], Mr Jason Halloran[3], Mr Carl Imhauser[4], Ms Snehal Chokhandre[5], Mr Ahmet Erdemir[5], Mr Thor Besier[1]

[1]Auckland Bioengineering Institute, Auckland, Auckland, New Zealand. [2]University of Denver, Denver, Colorado, United States. [3]Washington State University, Spokane, Washington, United States. [4]Hospital for Special Surgery, New York, New York, United States. [5]Cleveland Clinic, Cleveland, Ohio, United States

Introduction

Context-of-use and modelling decisions lead to variability in computational models of the knee. Our KneeHub project has shown that modelling decisions and methodological choices lead to divergent model outputs, reducing consistency and credibility for clinical use. Accurate representation of the joint tissues is a critical first step in generating a computational knee joint model, involving segmentation, smoothing, meshing, and defining anatomical coordinate systems. This study quantified variability across three independent groups at each step of constructing the geometries of the same knee, to support the development of a consensus workflow for computational knee model generation.

Methods

Three inexperienced modellers performed repeated segmentation of MR images of the same knee, each using different software. Smoothing and meshing was then performed by each group. For each processing step, intra- and inter-variability were quantified using the mean absolute distance, root-mean-square distance, Hausdorff distance, mean signed distance, and the corresponding standard deviation computed between two meshes of the same anatomy.

Results

All mean differences observed across the segmentation and meshing steps were below the twice the image resolution of 0.3125 x 0.3125 x 0.6 mm. Varying the number of image slices, performed by a single modeller, produced similar results, with an average absolute mean difference of 0.35 mm across slice-number conditions. The influence of smoothing was minimal, with mean absolute distances below 0.001 mm and a Hausdorff distance of

0.011 mm. The absolute mean difference between the raw mesh and the final mesh was 0.003 mm.

Discussion

Intra- and inter-modeller variability in knee joint segmentation remain within the expected range—below twice the image resolution[TB1] . However, some regions with larger differences may still influence downstream modelling outcomes (Figure 1). Clear documentation describing how each anatomical structure is segmented, along with information about the underlying algorithms and software tools, is essential for repeatable and accurate model generation. The values found from this study can vary depending on the algorithm and the degree of smoothing applied. Future work will quantify differences in coordinate systems and analyse their relationship to mesh-derived variability in computational knee models.

Images (Optional)

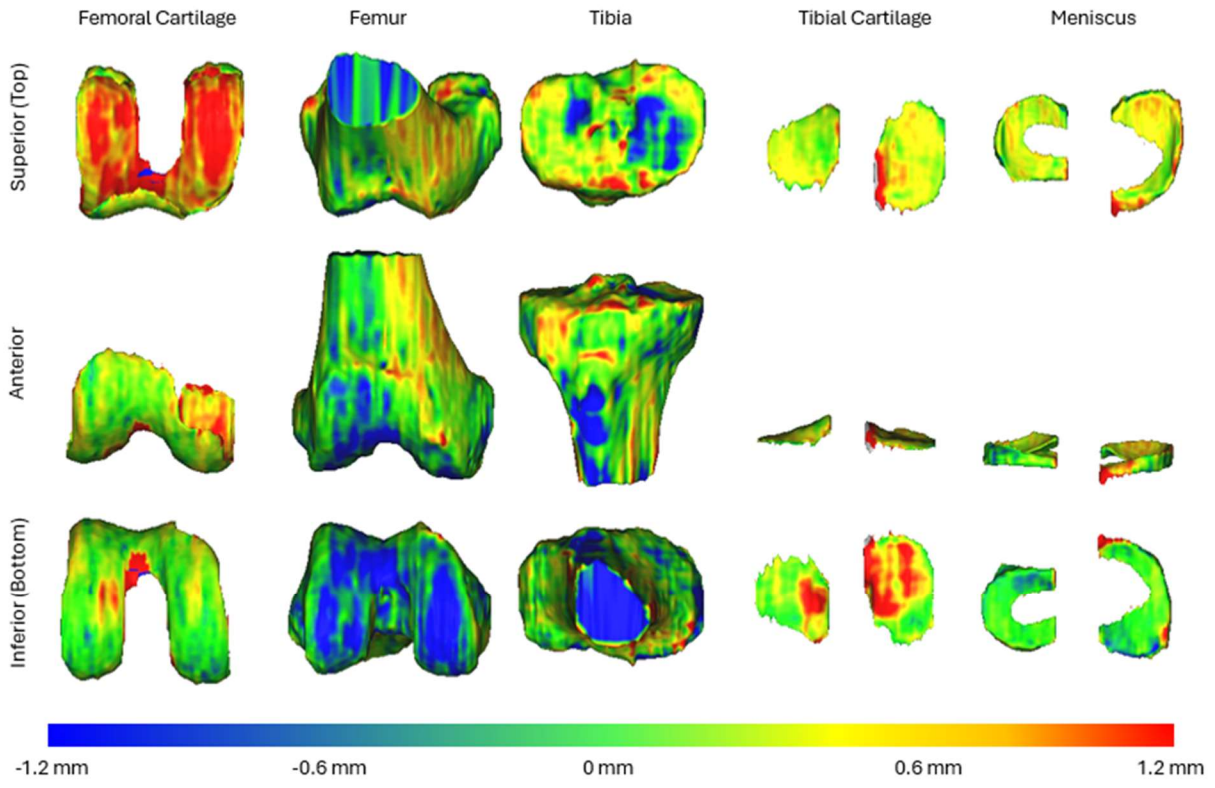


Figure 1. Signed differences between two independent knee segmentations shown across three anatomical views. Colour scale (in mm) indicates the magnitude and direction of differences, with the corresponding bar displayed at the bottom.

Session Category

Musculoskeletal Biomechanics: Methods, Models and Applications

P2-164

Within-Day Repeatability and Between-Day Reliability of Estimates of Second Metatarsal Bone Stress During Running

Ms. Naomi Frankston MS[1], Dr. Matthew Ellison PhD[2], Dr. Dominic Farris PhD[2], Dr. Hannah Rice PhD[1]

[1]Norwegian School of Sport Sciences, Oslo, Oslo, Norway. [2]University of Exeter, Exeter, Devon, United Kingdom

Introduction

Runners have a high prevalence of bone stress injuries in the foot, particularly in the second metatarsal. Quantifying internal bone stress during running is important for understanding risk of bone stress injury. Bone stress can be estimated using beam theory modeling of experimental data, but it is unclear how repeatable and reliable this approach is.

Methods

Twenty-eight female and male participants ran barefoot overground at their preferred speed while kinematics, pressure data, and ground reaction forces were recorded. At least five trials were collected at the same running speed (±5%) during laboratory visits on two different days, a mean (SD) of 21 (26) days apart (range: 1 – 139 days). Bone stress was calculated using a two-dimensional beam theory model of the second metatarsal using average bone geometries. Distances between skin-mounted metatarsal markers were calculated from static trials to allow assessment of methodological reliability independent of the reliability of running technique. Within-day trial-to-trial repeatability was assessed using an interclass correlation coefficient (ICC) and averaged over test days. Between-day reliability was assessed using ICC and standard error of measurement, defined as SD * $\sqrt{}$(1 – ICC), reported as a percentage of the mean value.

Results

Within-day between-trial repeatability was excellent (ICC > 0.9) for peak dorsal stress and peak whole body vertical ground reaction force and good (ICC: 0.75 – 0.9) for peak vertical force under the second metatarsal and second metatarsal pitch angle at the time of peak stress (Table 1). Between-day reliability was excellent for peak second metatarsal dorsal stress, peak vertical force under the second metatarsal, peak whole body vertical force, and second metatarsal pitch angle. Between-day reliability was moderate (ICC: 0.5 – 0.75) for second metatarsal length measured from skin-mounted markers, distance between the

first and second metatarsal head markers, and distance between the first metatarsal head and second metatarsal base markers.

Discussion

The experimentally obtained model inputs and peak second metatarsal stress output demonstrated excellent within-day repeatability and between-day reliability, despite moderate between-day marker placement reliability. Therefore, the model appears robust to repeat measurements of the same running condition but its sensitivity to detect true changes in stress between conditions may be limited.

Images (Optional)

Table 1: Within- and between-day intraclass correlation coefficients (ICC) for variables of interest and standard error measurement (SEM) as a percentage of the mean value.

Variable	Within-Day Mean ICC	Between-Day ICC	SEM (%)
Peak Second Metatarsal Dorsal Stress	0.923	0.934	6.2
Peak Vertical Force under Second Metatarsal	0.886	0.979	2.8
Peak Whole Body Vertical Force	0.980	0.980	2.5
Second Metatarsal Pitch Angle at Time of Peak Stress	0.892	0.936	3.1
Second Metatarsal Length	---	0.656	5.9
Resultant Distance between First and Second Metatarsal Head Markers	---	0.621	6.1
Resultant Distance between First Metatarsal Head and Second Metatarsal Base Markers	---	0.579	5.8

Session Category

Musculoskeletal Biomechanics: Methods, Models and Applications

P2-165

Can a Virtual Exoskeleton Reflect Real Use? A Musculoskeletal Modeling Comparison

Ms. Negar Riahi, Mr. Niromand Jasimi Zindashti, Dr. Ali Golabchi, Dr. Mahdi Tavakoli, Dr. Hossein Rouhani

University of Alberta, Edmonton, AB, Canada

Introduction

With the growing variety of industrial back-support exoskeletons, assessing their effects for specific users and tasks is essential. Musculoskeletal modeling enables such evaluation, including parameters difficult to measure experimentally. While most studies use motion collected with the device, some apply virtual exoskeletons to no-exoskeleton motion data of participants. This faster approach still requires evaluation to ensure it yields outcomes comparable to real exoskeleton use. This study examines that feasibility by comparing modeling outcomes from exoskeleton trials with those produced by applying a virtual exoskeleton to no-exoskeleton motion data.

Methods

Two participants performed lifts of 5, 10, and 15 kg from the ground to hip height under no-exoskeleton and BackX exoskeleton conditions, randomized and repeated three times. Motion was captured with nine Vicon cameras and ground reaction forces with two OR6-7 force plates. Motion modeling was performed in OpenSim to acquire joint reaction forces. Exoskeleton support was modeled as external forces on the chest and thighs (Method 3 in [1]). For the virtual-exoskeleton condition, no-exoskeleton motion data were used to simulate exoskeleton support. In both virtual-exoskeleton and exoskeleton conditions, supporting torque was computed from trunk and thigh angles. Total L5-S1 joint reaction forces were compared using Sprague and Geers curve magnitude (*M*), phase (*P*), and Comprehensive Error Factor (*C*) [2]. Peak L5-S1 loading errors during lifting and lowering were also computed and normalized to peak loading in the exoskeleton condition.

Results

As shown in Table 1, *C* ranged from 6.7 to 11.4% across loads. Normalized peak L5-S1 loading differed by 5.5–16.0% in lifting and 6.8–18.7% in lowering.

Discussion

Overall, the virtual exoskeleton showed small magnitude and phase differences relative to the real exoskeleton but consistently underestimated support, reflected by higher estimated loads (positive *M*). Agreement was lowest at 5 kg, with higher *C* values and larger normalized peak loading errors. While these initial results suggest reasonable agreement between virtual and real exoskeleton modeling (*M*/*P*/*C* values <20%), future studies should include more participants to permit statistical analysis and fully assess the feasibility of modeling a virtual back-support exoskeleton.

Images (Optional)

Table 1. Comparison of the virtual-exoskeleton and exoskeleton modeling approaches based on total L5-S1 joint reaction force. Metrics include curve magnitude (M), phase (P), and Comprehensive Error Factor (C), where 0 indicates identical curves. Peak L5-S1 loading errors during lifting and lowering phases are also shown, normalized to the peak loading in the exoskeleton condition. All values are presented as mean (SD).

Lifted weight	*M* (%)	*P* (%)	*C* (%)	Normalized Peak Load Error - Lifting (%)	Normalized Peak Load Error - Lowering (%)
5 kg	6.4 (5.2)	8.1 (4.6)	11.4 (0.3)	16.0 (0.3)	18.7 (5.5)
10 kg	7.2 (1.6)	6.7 (0.8)	9.9 (0.6)	5.6 (4.6)	6.8 (8.6)
15 kg	4.7 (1.0)	4.4 (2.4)	6.7 (0.9)	5.5 (7.2)	9.8 (0.3)

References (Optional)

[1]Riahi et al., AnnBiomedEng, 2025
[2]Sprague & Geers, JComputPhys, 2003

Session Category

Musculoskeletal Biomechanics: Methods, Models and Applications

P2-166

In-Silico Biomechanical Effects of Running with the Intrepid Dynamic Exoskeletal Orthosis

Dr. Nicholas Vandenberg[1], Dr. Anup Pant[1], Ms. Julia Gambill[2,3], Dr. Pawel Golyski[4,5], Dr. Lee Childers[2,4], Mr. Travis Eliason[1], Dr. Daniel Nicolella[1]

[1]Southwest Research Institute, San Antonio, TX, United States. [2]Center for the Intrepid, Brooke Army Medical Center, JBSA Fort Sam Houston, TX, United States. [3]The Henry M. Jackson Foundation for the Advancement of Military Medicine Inc., Bethesda, MD, United States. [4]Extremity Trauma and Amputation Center of Excellence, Falls Church, VA, United States. [5]Walter Reed National Military Medical Center, Bethesda, MD, United States

Introduction

Ankle-foot orthoses, such as the Intrepid Dynamic Exoskeletal Orthosis (IDEO), are commonly prescribed to overcome gait deficiencies following mild to severe lower-extremity injury. IDEO devices provide mediolateral support with rigid footplates that limit ankle range-of-motion (ROM), energy storage-and-return via posterior strut, and offload the affected limb through a proximal cuff. While physical function is restored, movement compensations are necessary while using IDEO devices. The objective of this study was to understand the biomechanical effects of altered movement strategies using an IDEO.

Methods

A baseline OpenSim model with right lower-limb musculature, reserve actuators for joints without musculature, and ground-contact was scaled to one subject. An IDEO device was additionally modeled by limiting ankle ROM and adding passive rotational stiffness to the ankle joint, defined from mechanical testing. Baseline and IDEO models tracked a running stance phase using OpenSim Moco (tracking kinematics and ground reaction forces while minimizing squared muscle activity). Kinematics and joint reaction forces (JRF) were compared from both solutions.

Results

Compared to baseline, IDEO use altered movement patterns during running stance (Figure 1a-d). Specifically, increasing hip and knee flexion, decreasing anterior pelvic tilt, and increasing forward trunk lean. The IDEO model also showed decreased resultant JRF across all joints (Figure 1e,f,h). However, mediolateral knee JRF increased using the IDEO (Figure 1g). Changes in joint loading were driven by reduced vertical JRF, no other significant JRF changes were observed.

Discussion

The simulated IDEO recreated commonly observed movement pattern adaptations, notably increasing the hip/knee flexion to act as a shock absorber due to limited ankle ROM. These preliminary results also indicate that the simulated IDEO reduced resultant joint loading in the stance limb. However, the increased mediolateral JRF could be demonstrative of increased risk for potential injury that warrants further investigation. Our future work will incorporate muscle forces, joint loading, and kinematics into a finite element modeling pipeline to determine tissue-level changes from IDEO device use during running and better understand potential deleterious effects of altered mediolateral JRF. Additionally, we will expand the IDEO model to include passive stiffness of the cuff as well as the unloading interaction between the cuff and tibia.

Images (Optional)

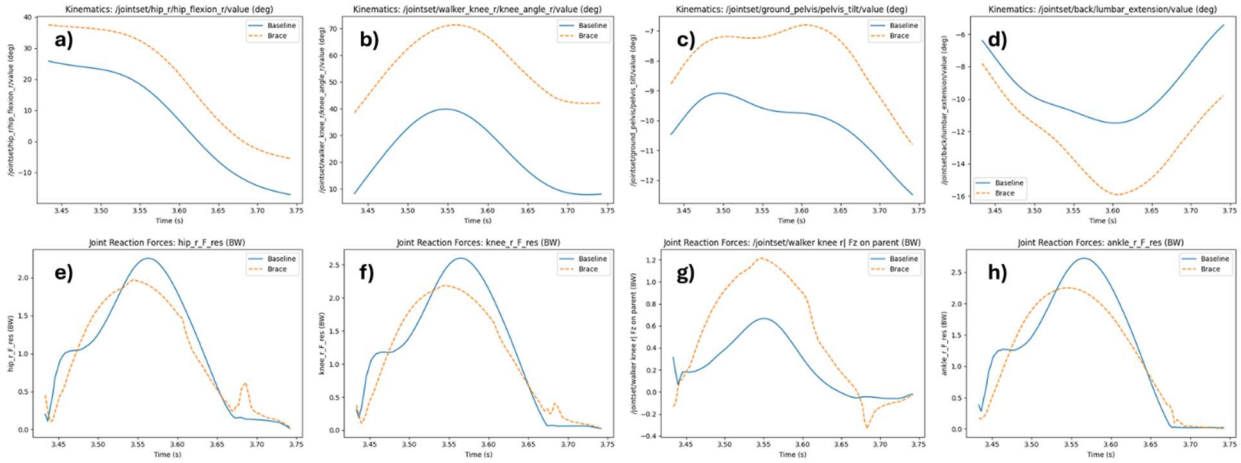


Figure 1. Stance phase kinematic (degrees) and joint loading (xBW) comparisons. a) hip flexion, b) knee flexion, c) pelvic tilt, d) lumbar flexion, e) resultant hip JRF, f) resultant knee JRF, g) mediolateral (shear) knee JRF, and h) resultant ankle JRF.

Acknowledgements (Optional)

The views expressed in this abstract are those of the authors and do not necessarily reflect the official policy or position of the Henry M. Jackson Foundation for the Advancement of Military Medicine, Inc., the Defense Health Agency, Department of Defense, nor the U.S. Government.

Session Category

Musculoskeletal Biomechanics: Methods, Models and Applications

P2-167

Quantifying the Biomechanical Effects of Muscle Strength Asymmetry during Running Using Optimal Control and Probabilistic Analyses

Dr. Nicholas Vandenberg[1], Dr. Anup Pant[1], Dr. Sarah Shaffer[1], Ms. Julia Gambill[2,3], Dr. Pawel Golyski[4,5], Dr. Lee Childers[2,4], Mr. Travis Eliason[1], Dr. Daniel Nicolella[1]

[1]Southwest Research Institute, San Antonio, TX, United States. [2]Center for the Intrepid, Brooke Army Medical Center, JBSA Fort Sam Houston, TX, United States. [3]The Henry M. Jackson Foundation for the Advancement of Military Medicine Inc., Bethesda, MD, United States. [4]Extremity Trauma and Amputation Center of Excellence, Falls Church, VA, United States. [5]Walter Reed National Military Medical Center, Bethesda, MD, United States

Introduction

Musculoskeletal overuse injuries (i.e., tibial stress fractures (TSF)) are common during military, basic training. A relationship has been observed between weak ankle plantarflexors and TSF risk, but the effects of expanded muscle strength imbalances are not well understood. The objective of this study was to determine the effects of muscle strength asymmetry on TSF risk.

Methods

A scaled musculoskeletal model with right lower-limb musculature, reserve actuators, and a ground-contact set was used for a baseline running stance solution using OpenSim Moco (tracking kinematics and ground reaction forces (GRFs) while minimizing squared muscle activity). Five asymmetry scale-factors were defined for antagonist muscle groups (hip flexor/extensors, abductor/adductors, internal/external rotators; knee flexor/extensors, and ankle plantar/dorsiflexors). 100 perturbed models were created by sampling these scale-factors using a normal distribution (mean = 1, std = 0.1) with Latin Hypercube Sampling. Perturbed models tracked the same running stance phase in Moco with 84/100 terminating normally. Variability of simulation outputs (namely: hip flexion, knee flexion, ankle angle, and knee vertical joint reaction force (JRF)) were quantified using mean ± SD trajectories and percentile envelopes, and linear regression was used to explain peak outcome variability related to asymmetry scale-factors.

Results

Knee flexion and JRF demonstrated the largest variability (Figure 1b,d). Regression analyses showed that muscle asymmetry explained 93% of knee flexion variance and 81% of knee JRF variance, which was primarily driven by asymmetry in the ankle plantar/dorsiflexor and

knee flexor/extensor musculature. Hip flexion and ankle angle were largely insensitive to muscle asymmetry (Figure 1a,c).

Discussion

Distal muscle asymmetry had the largest influence on knee kinematics and joint loading, with hip and ankle motion comparatively insensitive. These preliminary results suggest that even small functional imbalances in ankle and knee musculature can meaningfully alter knee joint loading during running, which may have implications for increased TSF risk. Future work will incorporate muscle forces from perturbed models and resulting movement and joint loading to evaluate tissue-level effects from muscle asymmetry within a finite element modeling pipeline to better understand the relationship between muscle asymmetry and risk of TSF.

Images (Optional)

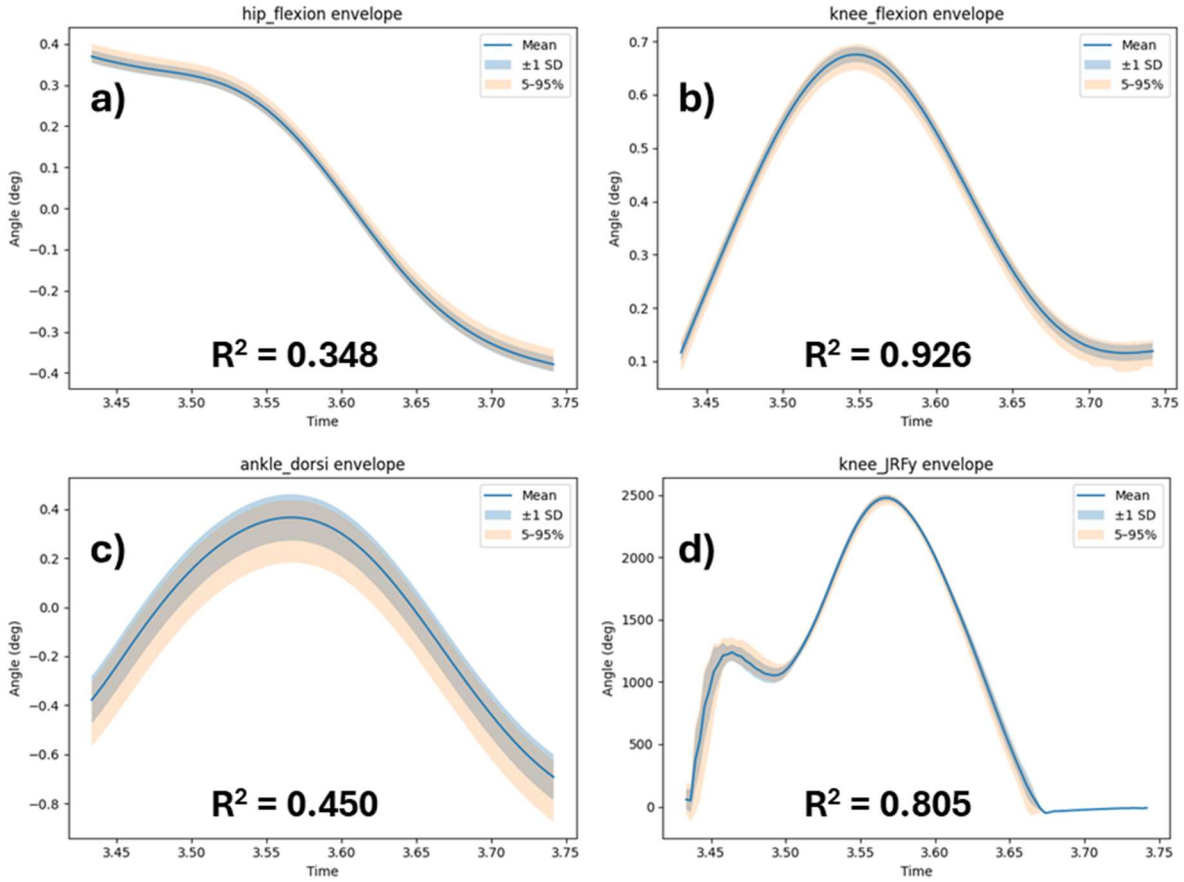


Figure 1. Variance in simulation outcomes: a) hip flexion/extension, b) knee flexion/extension, c) ankle plantar/dorsiflexion, and d) knee vertical JRF. R^2 values from linear regression are shown on respective plots.

Acknowledgements (Optional)

The views expressed in this abstract are those of the authors and do not necessarily reflect the official policy or position of the Henry M. Jackson Foundation for the Advancement of Military Medicine, Inc., the Defense Health Agency, Department of Defense, nor the U.S. Government.

Session Category

Musculoskeletal Biomechanics: Methods, Models and Applications

P2-168

Influence of Regional Thoracic Curvature on Underband Pressure in a Sports Bra

Dr Nicole Yvette Kelp PhD[1], Dr Adrian Lai PhD[2], Ms Ishi Arora[2], Ms Olga Radivojevic[2], Ms Vivian Nguyen MSc[2], Dr Michael Asmussen PhD[1]

[1]Vancouver Island University, Nanaimo, BC, Canada. [2]lululemon, Vancouver, BC, Canada

Introduction

Approximately 43–85% of women wear the wrong size bras or experience fit issues despite professional sizing [1]. This highly prevalent issue is particularly evident at the underband, where excessive or uneven pressure can cause discomfort, chafing, digging, and breathing restrictions [2,3]. Limited fit education, reliance on online sizing tools, and the assumption that the torso can be described solely by circumference, likely contributes to these persistent fit issues as female thoracic morphology is highly variable [2,4]. A mismatch exists between body geometry, bra structure, and traditional sizing metrics. This study aimed to determine how three-dimensional underbust morphology influences underband pressure distribution.

Methods

Twelve female participants (sizes 32B–34D/36C) wore a professionally sized compression sports bra with an elastic underband. Mean curvature (m-1) at fourteen standardized regions around the underbust was calculated with a neighborhood radius of 0.03 m from segmented three-dimensional body scans (Figure 1). Underband pressure (Kikuhime) was measured at peak inhalation in the same underbust regions.

Results

Using linear mixed effects models, mean curvature and underbust region were strong predictors of maximum underband pressure, with no interactions. Higher local curvature was associated with significantly greater inhalation pressure ($\beta = 0.92$ mmHg per 1 m^{-1}, $p < 0.001$), indicating that more curved regions of the ribcage experienced consistently higher loading. Pressures were highest in the lateral and posterolateral regions and lowest at anterior sites, with notable asymmetry on the anterior ribcage. Across participants, pressures varied by 8–12 mmHg depending on location, demonstrating substantial individual and regional variability.

Discussion

Curvature-driven pressure differences underscore the importance of thoracic morphology in determining underband pressure. Quantifying regional curvature adds an objective measure of shape that complements traditional size and circumference metrics and helps to explain observed differences in fit and comfort among same-size wearers [2]. Future work should include more diverse bra styles, body size, and bra regions to enhance its applicability.

Images (Optional)

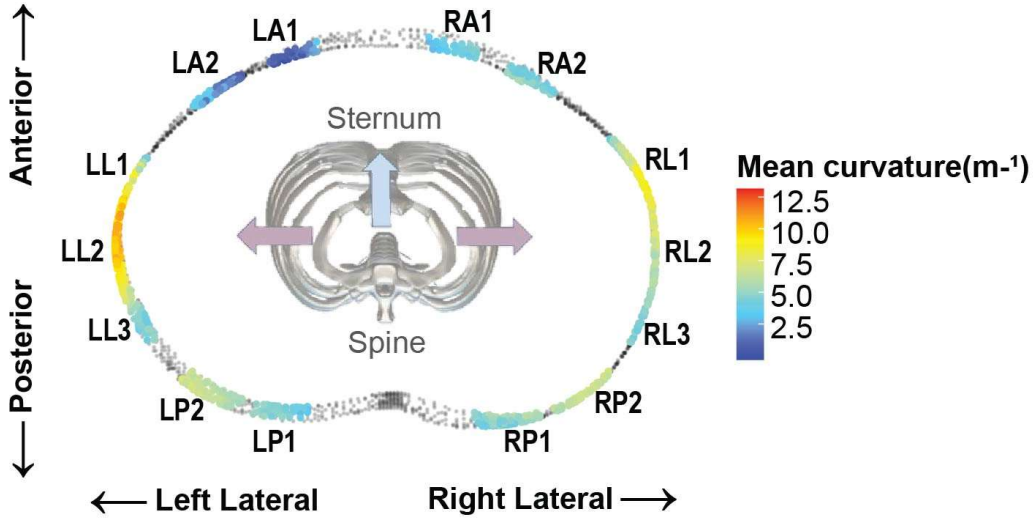


Figure 1. Superior view of a thoracic cross-section derived from 3D body scans. Scalar-field colormaps illustrate regional mean curvature across the fourteen underbust regions: left/right anterior (LA1–2, RA1–2), left/right lateral (LL1–3, RL1–3), and left/right posterior (LP1–2, RP1–2). Example shown for Subject 1.

References (Optional)

[1] Haworth et al., Int J Fashion Design, Tech, Ed, 2025

[2] Coltman et al., Clothing Textiles Research J, 2018

[3] Kipp et al., Med Sci Sports Exerc, 2024

[4] Robinson et al., Frontiers Bioeng Biotech, 2024

Acknowledgements (Optional)

Industry Partner: lululemon

Grant Funding: Mitacs

Curvature Analysis Advice: Pearson Wyder-Hodge

Session Category

Musculoskeletal Biomechanics: Methods, Models and Applications

P2-169

Beyond Anthropometric Scaling: Improving Spinal Load Prediction via Machine Learning-Derived Muscle Parameters

Mr Nima Ashjaee, Dr. Sidney Fels, Dr. John Street, Dr. Thomas Oxland

University of British Columbia, Vancouver, BC, Canada

Introduction

Subject-specific musculoskeletal (MSK) models are increasingly used to study spinal biomechanics and adult spinal deformity [1]. However, clinical adoption is limited by the difficulty of obtaining individualized soft-tissue properties. Vertebral geometry can be obtained from biplanar radiography, but muscle geometry or force capacity typically require CT/MRI. Current practice scales generic models using height and mass, which introduces substantial error [1,2]. Here, we show that machine-learning models can predict subject-specific muscle geometry and force capacity from readily available spinal geometry and demographic features, improving downstream MSK load prediction by 17%.

Methods

We used 250 subject-specific thoracolumbar models [3] in OpenSim following established research [1]. Inputs included age, sex, height, weight, and 3D coordinates of 17 vertebrae. Two muscle parameters most influencing loading [2] were targets: maximum-isometric-force (575 muscles) and geometry-path (4008 points). Two data-conditioning strategies were evaluated: a Native-Data workflow (inputs used directly) and an Anthropometrically-Normalized workflow (inputs normalized by height/weight). Within each workflow we evaluated Random Forests, Multi-Layer Perceptrons, and a Hierarchical Autoencoder. The best models were then used to generate pseudo-subject-specific MSK models. For every subject, three variants were simulated: (i) Ground-Truth (CT-derived), (ii) Baseline height/weight scaling, and (iii) our Proposed model. Ten static postures were simulated and intervertebral compression was computed with Static Optimization.

Results

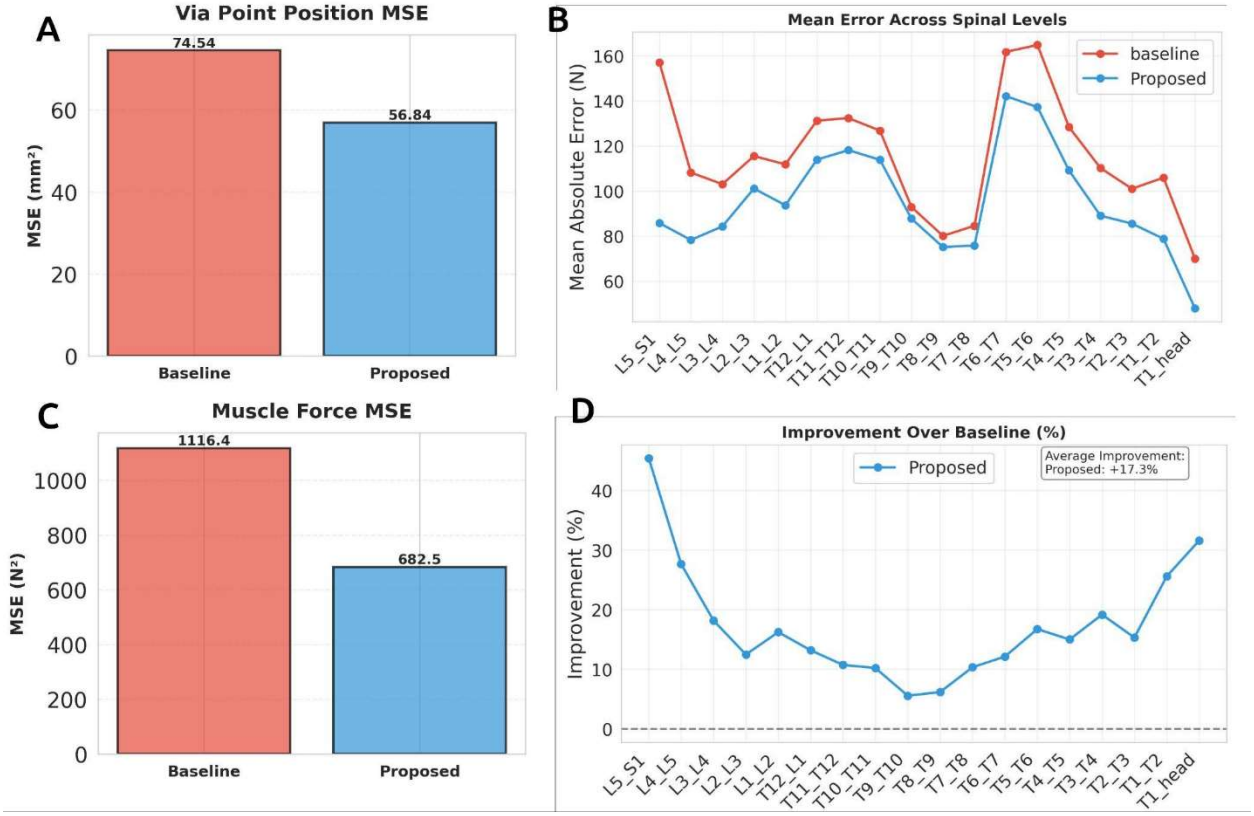
A hybrid approach performed best: Random Forests (Native-Data) for maximum-isometric-force and the Autoencoder (Normalized) for geometry-path. Compared to conventional scaling, the Proposed method reduced Mean-Square-Error in via-point positions (56.84 vs. 74.54 mm^2; Fig 1a) and maximum-isometric-force (682 vs. 1116 N^2; Fig1b). These improvements yielded more realistic spinal loads: the Proposed model reduced compressive-force error at all spinal levels (Fig 1c) and improved accuracy by 17% on

average. The largest gains occurred at the cranial and caudal extremities, with smaller but consistent benefits in the mid-thoracic spine (Fig 1d).

Discussion

Predicting subject-specific muscle geometry and force capacity from available imaging improves anatomical fidelity and downstream load prediction. This approach may enable subject-specific MSK modeling in settings where soft-tissue imaging is unavailable.

Images (Optional)



References (Optional)

[1] Bruno et al. , J Biomech Eng, 2015

[2] Ashjaee et al. , J Biomech, 2025

[3] Anderson et al. , Harvard Dataverse, 2020

Session Category

Musculoskeletal Biomechanics: Methods, Models and Applications

P2-170

Sensitivity of Hill-Type Muscle Parameters to Joint-Moment Capacity During Walking, Running, and Sprinting

Student Nozomu Tanaka MSc[1], Associate Professor Stacey Meardon PhD[2], Professor Timothy Derrick PhD[1]

[1]Iowa State University, Ames, Iowa, United States. [2]East Carolina University, Greenville, North Carolina, United States

Introduction

Musculoskeletal models with Hill-type muscles are widely used to estimate muscle forces during human movement. These models work well for walking, but several studies have noted that some muscle parameters must be adjusted to generate sufficient force for running activities. Although such modifications can reduce apparent moment deficits, the sensitivity of each parameter remains unclear. This study investigated the impact of maximum isometric force (F_{iso}), maximum contraction velocity (v_{max}), and tendon compliance (ε^{T}_{o}) on joint-moment capacity during walking, running, and sprinting.

Methods

Thirteen healthy adults performed overground walking, running, and sprinting at target speeds of 1.5, 3.5, and 5.5 $m \cdot s^{-1}$. Three-dimensional kinematics were captured using an eight-camera Qualisys system, and ground-reaction forces were recorded with six Bertec force plates embedded in the floor. Joint-moment capacities were the maximum torque a joint can produce in a given direction. They were estimated using OpenSim Gait2392 with the Thelen2003 muscle model by summing moments about the joint axes from each crossing muscle's maximum force (based on muscle length and contraction velocity) and its moment arm, assuming maximal agonist activation and no cocontractions. Functional Demand (FD) was defined as the ratio of the experimental joint moment to the modeled moment capacity. Sensitivity analyses were performed by scaling F_{iso} (1×, 2×, 6×), increasing v_{max} (10, 15, 20 $l_0 \cdot s^{-1}$), and modifying ε^{T}_{o} (1×, 2×, 3×).

Results

During walking, joint-moment capacities estimated with default parameters exceeded actual joint moments (FD < 1). During running and sprinting, the model underestimated capacity, with the largest deficit seen for ankle plantarflexion during sprinting at push-off (FD ≈ 5.5). Increasing F_{iso} reduced FD proportionally, yet achieving FD ≤ 1 at push-off required roughly a six-fold increase. Increasing v_{max} to 20 $l_0 \cdot s^{-1}$ reduced FD to about 1.7 but did not resolve the plantarflexion deficit. Changes in ε^{T}_{o} had a minimal effect at push-off.

Discussion

Sensitivity analysis revealed that parameter tuning enhanced joint-moment capacities; however, the effects were limited and often required parameter values outside physiological ranges. These results indicate that tuning alone cannot fully address the moment deficits observed during high-speed locomotion. Additional factors beyond simple parameter adjustments may need consideration to improve model performance.

Images (Optional)

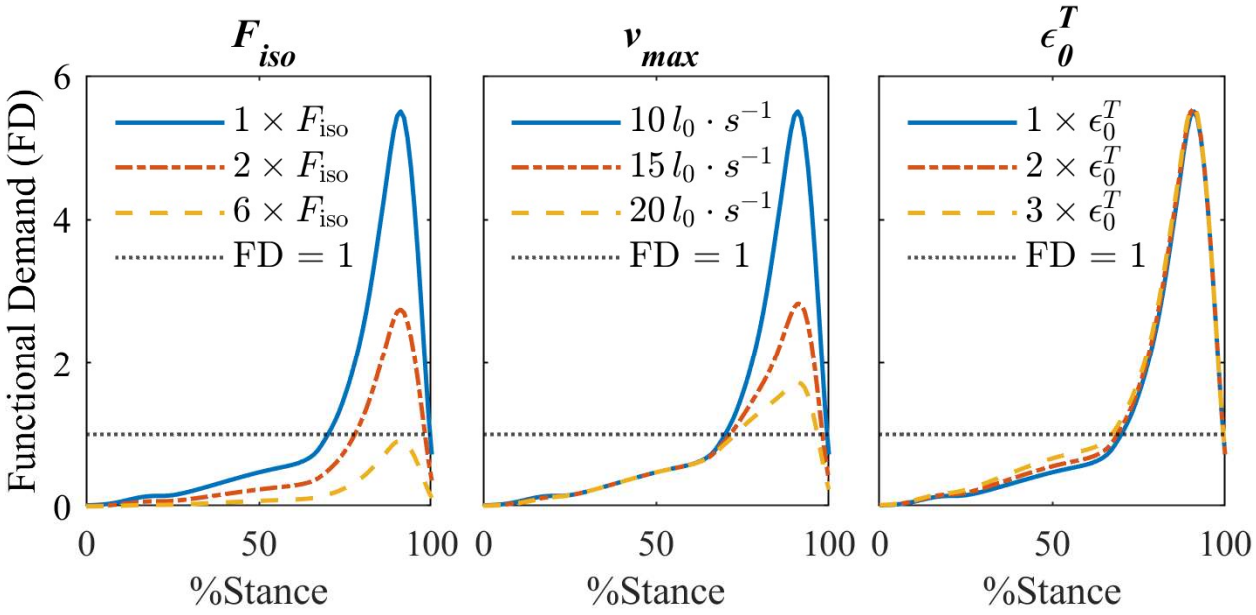


Figure 1. Sensitivity of muscle parameters on Functional Demand (FD) at the ankle joint during sprinting.

Session Category

Musculoskeletal Biomechanics: Methods, Models and Applications

P2-171

Quantitative Determination of the Sample Size Required for Modeling Anatomical Variation of the Human Knee Joint in a Population

Mr. Nurkeldi Iznat, Prof. LePing Li Ph.D.

University of Calgary, Calgary, Alberta, Canada

Introduction

Statistical shape modeling (SSM) is essential for characterizing population-level variability in knee geometry, providing insights that inform joint function. In studies involving SSM, it is common to select 6–10 principal components (PCs) to form the basis for subsequent analyses. Nevertheless, no standard procedure yet exists to evaluate the stability of modes associated with PCs and determine the sample size required to adequately represent a population. The objective of this study was to determine the number of knee samples required to characterize knee joint anatomical variation within a target population.

Methods

A published method based on left-ventricle synthetic datasets [1] was adapted for our tibiofemoral joint models, incorporating all cartilages and menisci. Sample sufficiency is indicated when the number of stable modes, m, converges as the sample size grows. We started to evaluate whether 71 knee samples were sufficient to model the male population of European ancestry by determining m for n samples (n = 31, 41, 51, 61, 69). For example, given n = 31, 500 subsets were generated from the 71 samples via bootstrapping, with each subset containing 31 knees with possible replications. Stable modes were identified by comparing the PCs from each subset with that derived from the full 71-knee dataset, using a one-tailed t-test against Gaussian noise. If m does not converge by 71 samples, the procedure must be repeated with a larger sample size to determine the required sample size.

Results

Stable modes were identified for each subset using quantitative analysis. Their number, m, failed to converge (Fig. 1a), and the high-dimensional PC directions remained divergent (Fig. 1b). Therefore, 71 knee samples were not adequate to represent the target population. A speculative curve-fit indicated that 100 or more samples may be required.

Discussion

The tested method may establish a rigorous criterion for mode retention in SSM. Subsequent analyses, including finite element simulations, should rely solely on the stable

modes. We are verifying the number of subsets required to accurately identify the stable modes. Larger sample sizes will then be used to determine the number of knees required for the population.

Images (Optional)

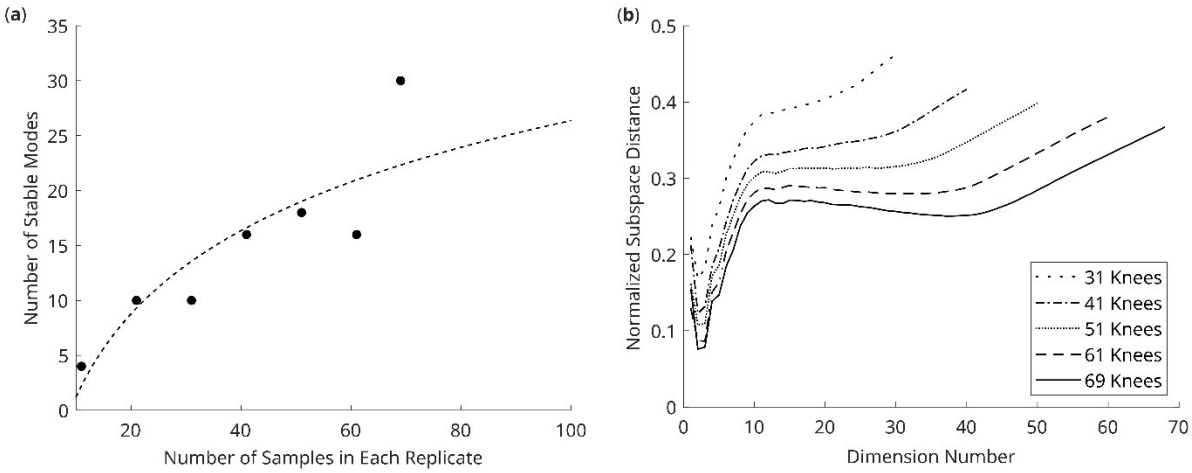


Figure 1. (**a**) Number of stable principal modes at each sample size ($p \leq 0.05$). (**b**) Average difference between the PC space of the full 71-knee dataset and the PC spaces obtained from fewer number of samples. Larger values mean the subset produces PC directions that differ more from the full dataset.

References (Optional)

[1] Mei L *et al.*, MICCAI, 2008, p425.

Session Category

Musculoskeletal Biomechanics: Methods, Models and Applications

P2-172

Body position and instruction paradigm independently influence measures of pelvic floor function obtained with ultrasound imaging and intravaginal dynamometry

Ms. Olena Klahsen MSc, Dr Linda McLean PhD

University of Ottawa, Ottawa, Ontario, Canada

Introduction

Symptoms of pelvic floor disorders (e.g., urine leakage) can be attributed to dysfunction of the pelvic floor muscles (PFMs), whereby they are unable to support the pelvic organs or stabilize the urethra. Assessment of PFM function is commonly conducted using ultrasound imaging (USI) and intravaginal dynamometry (IVD) during maximum-effort voluntary contractions (MVCs). Most studies report MVC outcomes recorded in a supine position, despite symptoms often being reported in upright postures. Instructions also vary among studies. We sought to determine how body position and an instruction paradigm involving contractile speed impact measures of female PFM function.

Methods

Fifty adult females were recruited and participated in a single laboratory session involving 2-dimenstional transperineal USI and IVD. For each modality, body position (standing vs. supine) and instruction paradigm (normal vs. rapid MVCs) were block-randomized with three trials performed under each condition. USI outcomes included baseline, peak and change in levator plate length and bladder neck height; IVD outcomes included baseline, maximum and relative peak (maximum – baseline) forces and rate of force development. Generalized linear mixed models were used to determine the effect of body position and instruction paradigm on each outcome (α=0.05).

Results

There was no interaction between position and instruction paradigm for any outcome. Main effects are presented in Table 1. Standing led to longer levator plate length and lower bladder neck height on USI, and higher baseline force, lower peak force and slower rate of force development on IVD. The rapid MVC instruction paradigm led to higher rate of force development on IVD but had no effect on other IVD or USI measures.

Discussion

Lower force and altered pelvic organ displacement on PFM contraction in the standing position relative to supine may contribute to symptoms being predominantly experienced where anti-gravity demands are higher. While efforts to contract the PFMs rapidly do not

impact organ displacement nor maximum force, instructions to perform the contraction as quickly as possible may be necessary to properly evaluate PFM power.

Images (Optional)

Table 1. Main effects of body position and instruction paradigm on pelvic floor muscle function

Outcome Measures		***Body Position***		***Instruction Paradigm***	
		Supine	*Standing*	*MVC*	*Rapid MVC*
Levator Plate Length (mm)	Baseline	**51.77 (6.76)**	**55.09 (8.30)**	53.16 (6.91)	53.70 (7.24)
	Peak	**42.64 (6.03)**	**46.56 (6.82)**	44.42 (6.05)	44.78 (6.35)
	Change	-9.22 (3.70)	-8.50 (3.86)	-8.85 (3.30)	-8.87 (3.62)
Bladder Neck Height (mm)	Baseline	**25.37 (4.84)**	**17.52 (6.24)**	21.69 (5.30)	21.20 (5.03)
	Peak	**28.35 (5.71)**	**20.00 (7.29)**	24.51 (6.11)	23.84 (5.99)
	Change	2.86 (4.03)	2.26 (3.42)	2.71 (3.43)	2.41 (4.08)
Force (N)	Baseline	**3.54 (1.26)**	**4.80 (1.47)**	**4.28 (1.16)**	**4.07 (1.32)**
	Maximum Peak	**6.88 (3.21)**	**7.06 (2.79)**	7.09 (2.64)	6.91 (3.07)
	Relative Peak	**3.67 (2.02)**	**2.66 (1.52)**	3.18 (1.53)	3.21 (1.71)
Average RFD (N/s)		**8.16 (6.41)**	**5.38 (4.49)**	**5.59 (5.25)**	**7.99 (5.77)**

Data are presented as mean (standard deviation). Bolded values indicate significant difference within main effect ($p<0.05$). MVC = Maximum Voluntary Contraction, RFD = Rate of Force Development.

Session Category

Musculoskeletal Biomechanics: Methods, Models and Applications

P2-173

Sensitivity Study of Muscle Modelling in Rabbit Masticatory Simulations

Dr Linjie Wang[1], Dr Roger Kissane[2], Prof Karl Bates[2], Dr Graham Askew[3], Prof Michael Fagan[4], Dr Peter Watson[1]

[1]Institute of Medical and Biological Engineering, School of Mechanical Engineering, University of Leeds, Leeds, West Yorkshire, United Kingdom. [2]Department of Musculoskeletal & Ageing Science, Institute of Life Course and Medical Sciences, University of Liverpool, Liverpool, Merseyside, United Kingdom. [3]School of Biomedical Sciences, University of Leeds, Leeds, West Yorkshire, United Kingdom. [4]School of Engineering, University of Hull, Hull, East Yorkshire, United Kingdom

Introduction

Computational models assist in design/evaluation of biomedical experiments, thus supporting the principles of 3Rs of animals by reducing animal use in experiments. However, their accuracy often depends on knowledge of physiological muscle mechanics, which can create barriers for their implementation. This study investigated how 1) population variance in physiological muscle properties and 2) the level of complexity in modelling muscle dynamics, influences predicted masticatory forces in rabbits.

Methods

A subject-specific model of a rabbit was developed through combining MRI data, muscle contractile properties, and jaw movements (measured using XROMM) (Figure 1). Inverse and forward dynamics, combined with Hill-type muscle modelling, were used to simulate a maximum bite, and biting during chewing. Several iterations of the model tested the influence of: 1) population variation in muscle mechanics; 2) using literature-based muscle data (species and non-species specific); 3) complexity in muscle contractile dynamics, through sequentially reducing the input data in the muscle modelling. Models were validated by comparing the outputs to experimentally measured maximum bite force and *in vivo* muscle function.

Results

Compared to experimentally measured maximum bite forces, subject-specific modelling predicted a similar force (within 12.9%), whereas incorporating population variance resulted in larger forces (max. 24% greater). Greater differences (over 50%) occurred when using literature-based muscle contractile properties and simplified muscle modelling.

When simulating chewing, incorporating population variance predicted similar muscle activity of the superficial masseter muscle, to that of subject-specific modelling. Larger deviations were observed in other models, with predictions using literature-based muscle data activating later (max. 20ms) and for a longer duration (max. 36ms), while simplified muscle modelling predicted a greater peak activation (max. 40%) and a longer time to peak (max. 48ms).

Discussion

This study shows that modelling of the rabbit masticatory system should ideally incorporate subject-specific muscle data. While population-based data does not affect the outputs, species-specific data from the literature should only be used when more specific data are not available. Modelling using simplified muscle mechanics should be use with caution, as it overestimates muscle force and activity. In conclusion, these findings provide important considerations for developing in silico skull models for implant testing.

Images (Optional)

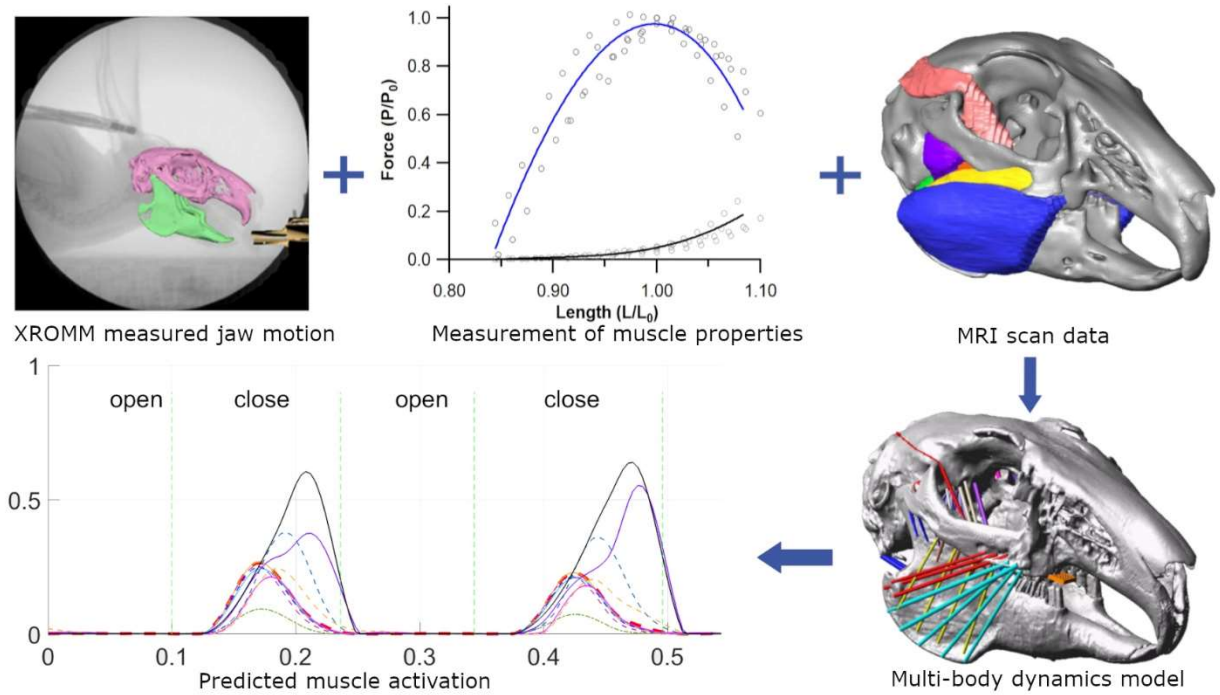


Figure 1. The experimental-computational framework used in this study: data analysis compared maximum bite forces and muscle activation profiles across several iterations of the model. The result graph shows the predicted muscle activity in model iterations, highlighting the difference in muscle activation when incorporating non-species-specific muscle contractile dynamics (dashed blue line) and when sequentially simplifying the complexity of the muscle modelling (solid purple line and solid black line).

Session Category

Musculoskeletal Biomechanics: Methods, Models and Applications

P2-174

Effects Of Changes in the Joint Center Location on Joint Biomechanics in Musculoskeletal Model Studies of Human Knee and Spine

Mr Pooya Salehi, Dr. Saeed Shirazi-Adl, Dr. Farshid Ghezelbash

Polytechnique Montreal, Montreal, Quebec, Canada

Mr Pooya Salehi

Dr. Saeed Shirazi-Adl

Introduction

Musculoskeletal (MS) model studies have emerged as viable and popular tools to estimate muscle forces and internal loads. Complex passive joints are idealized either as hinges or beams positioned at the joint geometrical center or center of rotation. The question is how sensitive are results to the joint simulation and location. We investigate the influence of changes in the joint modeling and location on detailed kinematics-kinetics and passive joint reaction moments. Both human knee and spine intervertebral joints are studied.

Methods

Finite element (FE)-MS models of the (1) lower limb, including a detailed knee and (2) trunk including deformable lumbar discs were employed. In the former, seated maximum voluntary contraction (MVIC) flexion/extension tasks at 30°, 60° and 90° knee flexion while in the latter, the trunk in the upright and flexed lifting were simulated. The position of the idealized joint was then shifted anteriorly or posteriorly to evaluate its effect on estimated muscle forces, tissue/ligament stresses, contact forces and joint passive reaction moments. In the trunk simulations, frictionless/frictional and beam idealizations were considered. Equivalent OpenSim (Gait2392) simulations were also carried out in knee MVIC extension.

Results

In all MS knee flexion/extension MVIC simulations when representing the knee with a complex FE model, passive knee (reaction) moments were highly sensitive to the location of the joint center whereas the muscle, ligament and contact forces remained unchanged

(Fig. 1). Muscle forces and internal loads, however, substantially altered at different joint centers when using an idealized joint (hinge or beam) in spine models during lifting. OpenSim also yielded high sensitivity to the joint center location (Fig. 1).

Discussion

Muscle forces and internal load distribution in knee and spine MS models substantially alter as the joint center at which moment equations are verified are altered. Results highlight the fundamental shortcomings in MS models that regularly idealize complex joints as frictionless at their center of rotation. This effect deteriorates in heavier tasks with larger reaction compression forces. As a remedy, either the joint should be represented by a detailed FE model or its passive stiffness properties be adjusted with location.

Images (Optional)

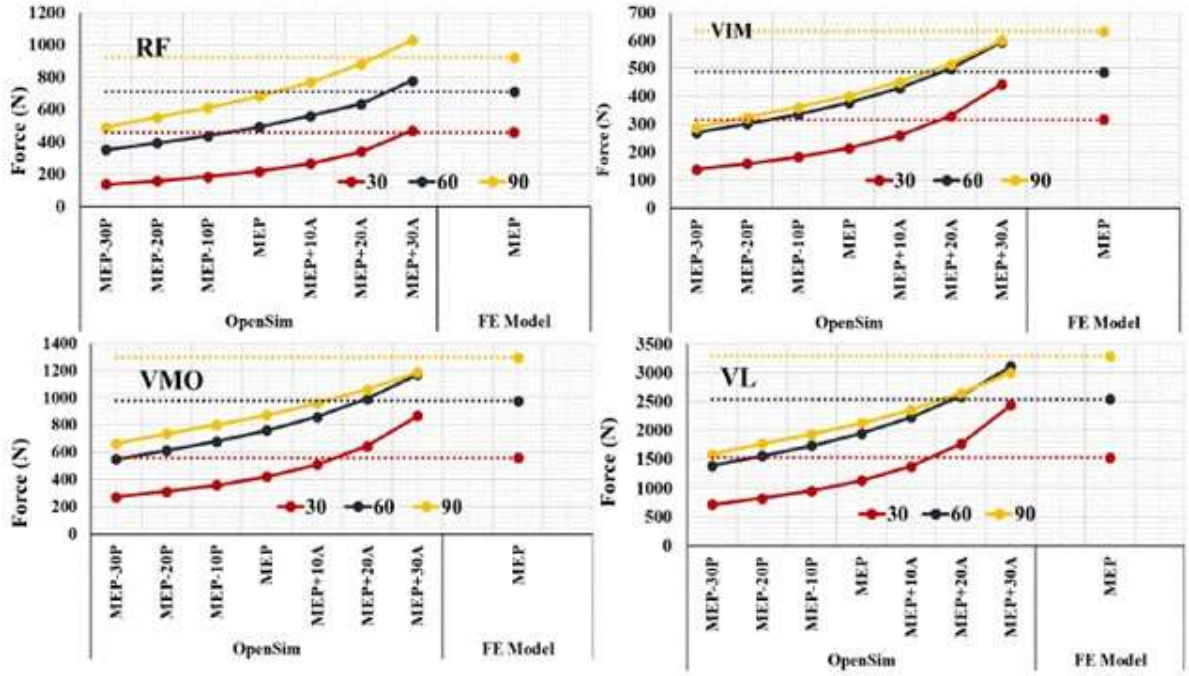


Figure 1 Comparison of quadriceps forces estimated by the OpenSim Gait 2392 model and our own FE-MS model as the joint center (placed at the mid epicondylar axis, MEP) is shifted in the anterior (A) and posterior (P) directions by up to 30 mm during MVIC extension simulations (under mean extension moments without co-activation constraints and with the resistance force applied 390 mm distal to the knee). Individual quadriceps forces in the MS-FE model remained unchanged irrespective of changes in the joint center location.

Acknowledgements (Optional)

Supported by NSERC-Canada.

Session Category

Musculoskeletal Biomechanics: Methods, Models and Applications

P2-175

Computational biomechanics of human knee joint in maximum voluntary isometric exercises: Role of muscle coordination and resistant force lever arm

Mr. Pooya Salehi, Prof. Saeed Shirazi-Adl

Poytechnique Montreal, Montreal, Quebec, Canada

Mr. Pooya Salehi

Introduction

Knee maximum voluntary isometric contractions (MVIC) in flexion and extension are widely used to assess strength and rehabilitation programs, yet the muscle, ligament, and contact forces remain mostly unknown. A coupled finite element–musculoskeletal (FE-MS) model of the lower extremity is used to perform parametric simulations of seated MVICs at 30°, 60°, and 90° knee flexion angles.

Methods

Knee MVIC flexion and extension were simulated with a detailed FE-MS model. Under MVIC moment represented by a resistant force near the ankle, a Taguchi design considered applied moment, coactivity in antagonist muscle groups, and the resistant force lever arm as variables at 4 levels each, yielding 16 cases for every knee flexion and MVIC direction.

Results

In flexion MVIC, PCL tension rose from ~20N at 30° to ~700N at 90°. In extension MVIC, ACL force peaked to ~120N at 30° and disappeared at 90°. Flexion MVIC loaded medial hamstrings and gastrocnemii to >1kN, whereas quadriceps forces peaked to ~6.3kN at 90° in extension MVIC. Tibiofemoral (TF) contact force peaked to ~4.3BW at 30° in flexion and ~3.9BW at 60° in extension MVIC. Patellofemoral (PF) contact forces were small in flexion but very large in extension MVIC (~2.0kN at 30° to ~5.6kN at 90°, ~9BW). Sensitivity analyses demonstrated the marked effects of changes in MVIC moment, muscle coactivation, and resistant force lever arm on all results.

Discussion

In MVIC flexion, PCL force increased with knee flexion, MVIC moment, and coactivity in quads but markedly dropped with greater activity in gastrocnemii. In MVIC extension, ACL force increased at smaller knee flexion angles and larger moment and resistant force lever arm. It markedly increased in extension when loading was idealized as a pure moment. While TF contact forces were slightly larger in flexion, PF contact forces along with PT and quads forces were much larger in extension MVIC, resulting in PF cartilage contact pressures >20MPa at 90° knee flexion angle. Sensitivity analyses underscored the need to control the applied moment, knee flexion angle, and testing configuration (force lever arm) to safeguard ACL, PCL, PT, and patellar cartilage in MVIC exercises.

Images (Optional)

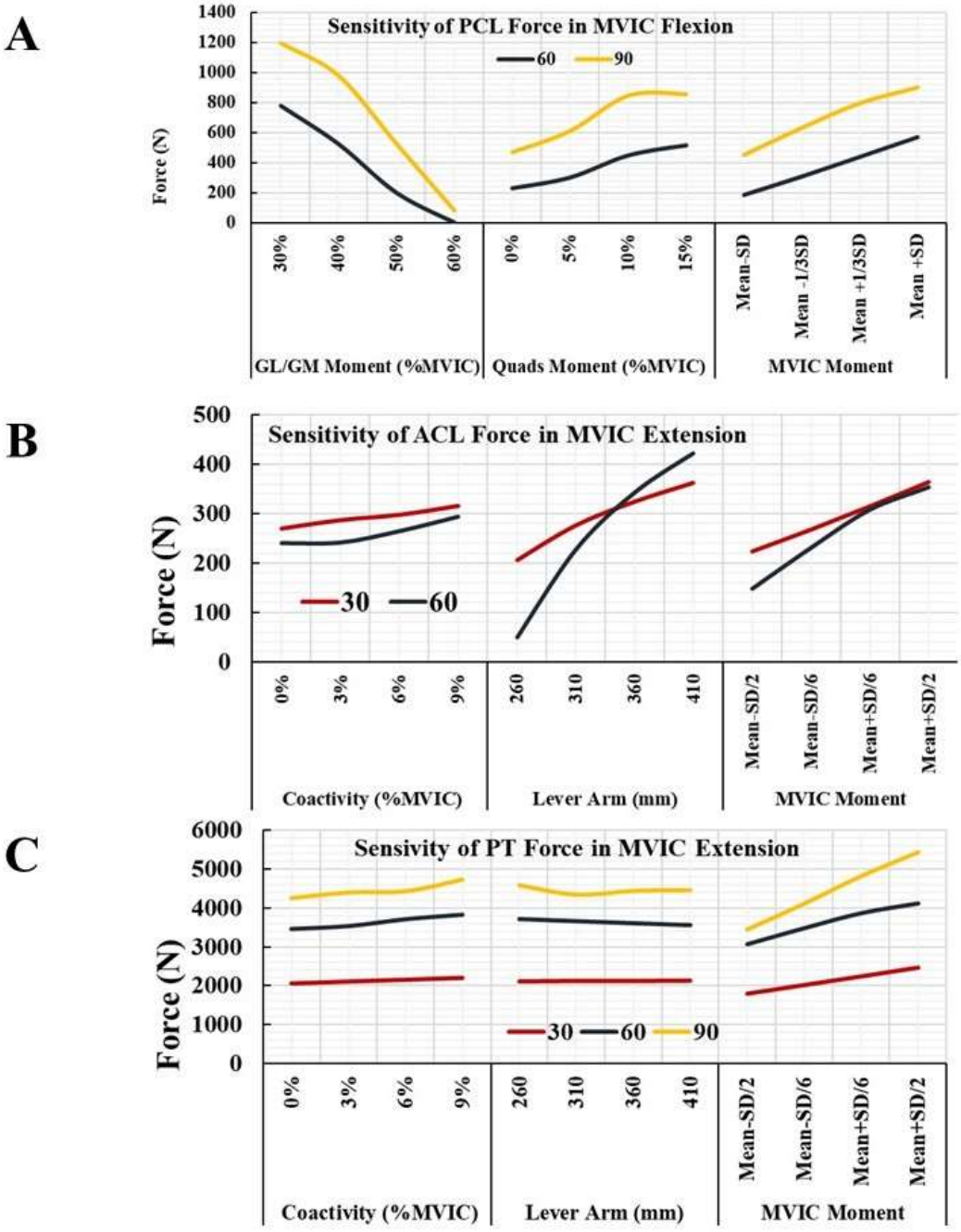


Figure 1 Sensitivity of cruciate ligaments (ACL and PCL) and patellar tendon (PT) force to various parameters each changing at 4 levels. A) PCL forces in MVIC flexion as the gastrocnemii activation level (left), quadriceps co-activation level (middle), and applied moment (right) altered. B) ACL forces and C) PT forces in MVIC extension as the co-activity in flexor muscles (left), external load lever arm (middle), and MVIC extension moment (right) altered.

Acknowledgements (Optional)

Supported by NSERC-Canada.

Session Category

Musculoskeletal Biomechanics: Methods, Models and Applications

P2-176

Biomechanics-aware Multi-view Markerless Motion Capture Reconstruction of Complex Hand Motions and Object Interaction

Mr. Pouyan Firouzabadi[1,2], Dr. Wendy Murray[1,2], Mr. J.D. Peiffer[1,2], Mr. Kunal Shah[2], Dr. Anton Sobinov[3], Dr. Lee Miller[1,2], Dr. R. James Cotton M.D. PhD[2]

[1]Northwestern University, Chicago, IL, United States. [2]Shirely Ryan AbilityLab, Chicago, IL, United States. [3]University of Chicago, Chicago, IL, United States

Introduction

Video-based motion capture has been sparingly applied for the biomechanical analysis of hand motion. Multi-view markerless motion capture (MMC) uses pose estimation algorithms to localize keypoints in individual 2D video frames [1]. Traditionally, 2D keypoints from all camera views are triangulated into 3D space and processed through inverse kinematics using a biomechanical model. However, frame-by-frame 2D errors propagate through the triangulation process, yielding non-physiological joint trajectories that require manual correction. We aim to demonstrate accurate 3D reconstruction of hand movements via a biomechanically constrained, end-to-end approach that eliminates the need for manual intervention [2], [3].

Methods

We used a custom 8-camera set-up to collect videos of six healthy participants performing hand postures and object interaction tasks. Videos were processed using publicly available pose estimation algorithms detecting 21 hand keypoints. A gradient-based optimization approach integrated a biomechanical model in the loop to produce plausible 3D joint kinematic trajectories. We directly compared performance of our workflow to the traditional approach that only applies biomechanical constraints after triangulation during inverse kinematics.

Results

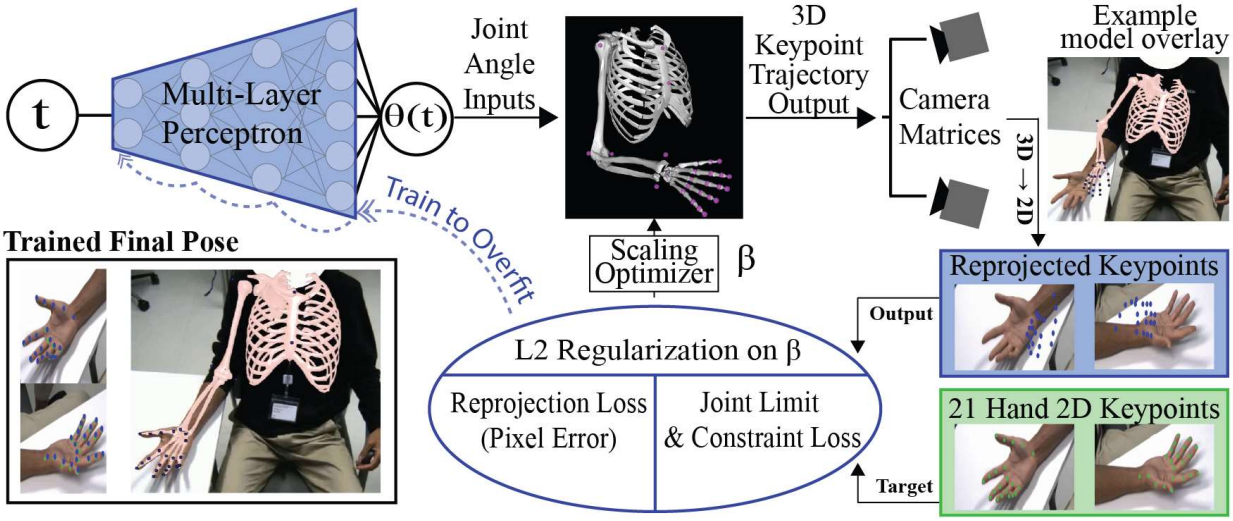
The two methods produced different joint angle estimates. Joint angle differences averaged 12.1 ± 8.8° between methods; distal joints had the largest deviations (21.2°± 8.8°). Qualitative analysis demonstrated worse performance for the traditional method. For example, for a posture with all fingers fully extended (0° flexion), average distal joint angles were 1.7° (our method) vs. 29.9° (traditional approach). Our method also improved performance when evaluated using computer vision metrics. Specifically, alignment of our keypoints with those from pose estimation was 20% better than the traditional method. For

object interaction tasks, keypoint alignment declined by 12% further for the traditional method, but did not change relative to hand posture tasks for our approach.

Discussion

These findings demonstrate that integrating biomechanical constraints into an end-to-end pipeline improves accuracy and robustness across complex hand motions.

Images (Optional)



Our end-to-end MMC reconstruction pipeline: The multi-layer perceptron (MLP), outputs arbitrary joint angles to pose the biomechanical model, which is labeled with the 3D keypoints of interest. When the model assumes the pose, the 3D keypoints are then reprojected to each of the 8 camera's 2D planes, allowing direct comparison to the 2D keypoints identified by the pose estimation algorithm for that frame. During training, the β parameter fine-tunes the marker locations as well as the scaling of the bones specific to the participant. The MLP is trained for 40000 iterations to overfit based on the defined loss functions learning a mapping from time (t) to joint angles Θ(t) producing final poses that best represent the 2D information from all 8 camera planes

References (Optional)

[1] S. Ghorbani et al., PLOS ONE, 2021

[2] R. J. Cotton, International Conference On Rehabilitation Robotics, 2025

[3] T. Unger et al., IEEE Trans. Med. Robot. Bionics 2025

Acknowledgements (Optional)

This work was funded by the National Institutes of Health (R01 NS131953; T32 HD007418), the Restore Center P2C (NIH P2CHD101913), and the Research Accelerator Program of the Shirley Ryan AbilityLab.

Session Category

Musculoskeletal Biomechanics: Methods, Models and Applications

P2-177

Developing A Novel Contact Modeling Framework; A Step Towards the Development of Dynamic Human Rolling Simulations

Mr. Rahmat Safdar, Ms. Mariam Jabr, Dr. Nils Hakansson

Wichita State University, Wichita, Kansas, United States

Introduction

Human rolling is a fundamental daily activity requiring coordinated motion of the trunk and extremities [1]. Rolling often occurs on compliant surfaces and involvescomplex contact mechanics. Currently, no framework exists for simulating rolling on a compliant mattress; therefore, developing a mattress contact model is essential for future investigations of rolling. Here, we investigate novel mattress contact models in two modeling programs, OpenSim and Simcenter MADYMOto create a contact model for human rolling simulations. Modeling dynamic contact is computationally expensive. OpenSim offers a simple contact model;MADYMO offers more complex computationally efficient contact modeling, but it lacks the musculoskeletal modeling capabilities of OpenSim.

Methods

Contact model parameters were derived from thirty bowling ball-drop trials recorded using high-speed motion capture (120 Hz) and ASTM D3574 indentation tests performed on a foam mattress. The OpenSim mattress surface was modeled as a Hunt-Crossley contact surface with stiffness and dissipation inputs. The MADYMO mattress surface was modeled using a planar finite-element surface with data-driven hysteretic and viscoelastic contact characteristics with loading/unloading and damping inputs. Experimental ball-drop trials were used to validate contact simulations. The simulation trajectories were assessed using RMS errors.

Results

The ball center of mass (COM) trajectories for experimental data and both simulations with summary results, including penetration and rebound distances andcoefficient of restitution (COR), are illustrated in Figure 1. The Hunt-Crossley model in OpenSim represented the initial contact and rebound behavior accurately, but MADYMO was able to replicate the overall trajectory of the ball.

Discussion

The simulations reproduced the main features of the experimental ball-drop test; the dynamics of initial impact and rebound behavior tracked the experimental average. The

results confirm Hunt-Crossley models are well-suited for quick impacts. The MADYMO model presented better energy dissipation and static behavior. Future work will pursue a modified contact model for OpenSim that combines the energy dissipative features of the MADYMO model with the Hunt-Crossley impact dynamics to provide a foundation for dynamic human rolling simulations using neuromusculoskeletal modeling approaches.

Images (Optional)

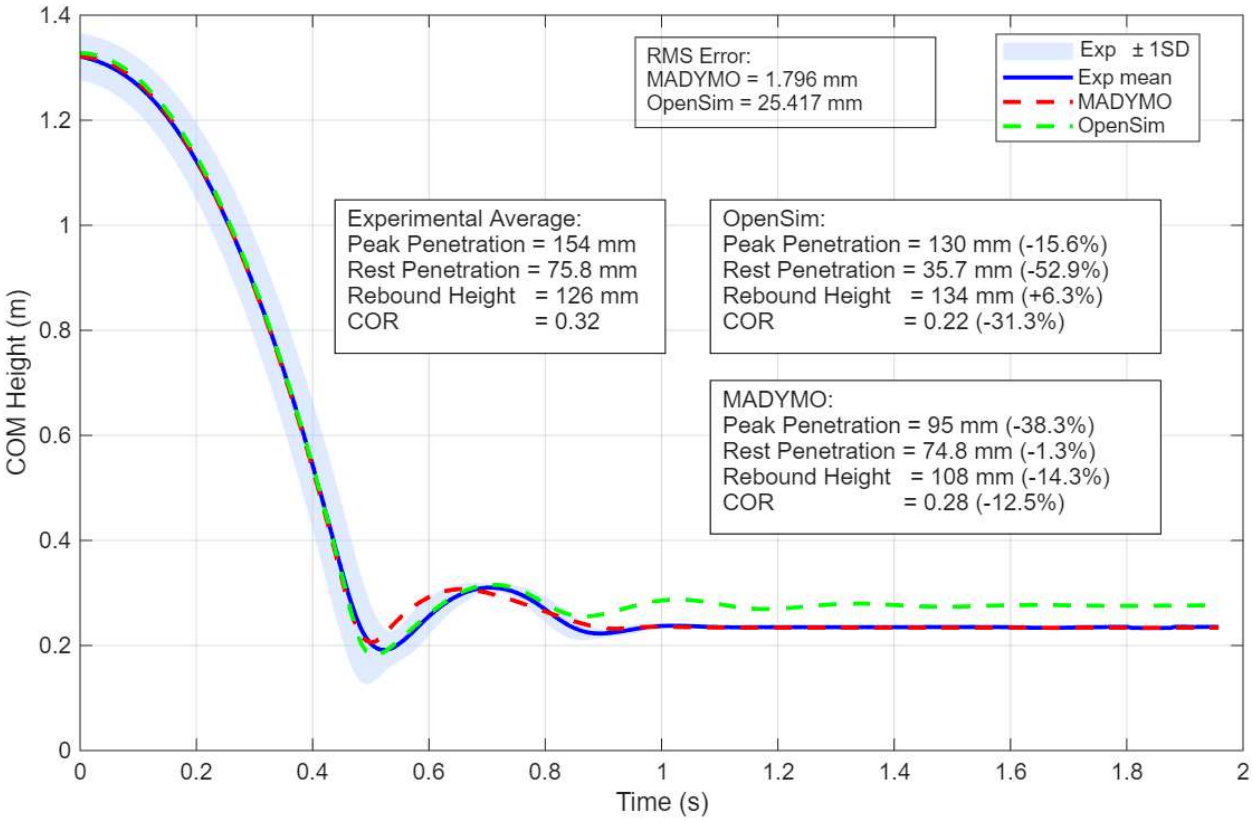


Figure 1. Bowling ball COM trajectory; experimental average and both simulations.

References (Optional)

[1] Richter et al., Phys. Ther 69:63-71, 1989.

Session Category

Musculoskeletal Biomechanics: Methods, Models and Applications

P2-178

Estimating Knee Joint Cartilage Mechanics Using Finite Element Models Driven by Video Camera-Based Kinetic and Kinematic Data

Doctoral Researcher Seyed Mahan Nematollahi Sanij[1], Postdoctoral Researcher Amir Esrafilian[1], Postdoctoral Researcher Jere Lavikainen[1], Senior Researcher Mika Mononen[1], Associate Professor Lauri Stenroth[1], Professor Jari Arokoski[2], Associate Professor David Saxby[3], Professor David G. Lloyd[3], Professor Rami Korhonen[1,3]

[1]Department of Technical Physics, University of Eastern Finland, Kuopio, North Savo, Finland. [2]Department of Internal Medicine and Rehabilitation, Helsinki University Hospital and Helsinki University, Helsinki, Helsinki, Finland. [3]Australian Centre for Precision Health and Technology (PRECISE), Griffith University, Gold Coast, Queensland, Australia

Introduction

Low-fidelity, AI-based approaches are increasingly used to estimate the kinematics and kinetics of human movement, traditionally measured by high-fidelity, marker-based motion capture (Mocap) systems [1]. However, their application to tissue-level mechanics, specifically estimating stresses and strains, remains relatively underexplored. Previously, we developed a finite element modeling (FEM) pipeline, driven by artificial neural network-based knee joint kinetics, to estimate cartilage mechanics. Here, we refined this pipeline by implementing a video camera (VC)-based method capable of extracting subject-specific knee flexion angles (KFA).

Methods

Eight healthy adults (3 females, 5 males; age 29 ± 6 years; BMI 23 ± 7 kg/m^2) were included in the study. Marker trajectories and ground reaction forces were recorded during walking in a Mocap laboratory, and magnetic resonance imaging was performed to obtain knee joint geometries. For the high-fidelity approach, Mocap data were processed in OpenSim to estimate knee joint contact forces (KJCFs) and moments (Fig. 1A), which served as inputs to a detailed FEM including cartilage, menisci, and ligaments (Fig. 1B) [2]. In the low-fidelity approach, a multiple linear regression model was used to estimate KJCF from selected subject demographic variables and knee flexion angles extracted from VC (Fig. 1A) [3,4]. The estimated KJCF and KFA from VC were applied to a simplified FEM containing cartilage layers, represented as boundary conditions (Fig. 1B).

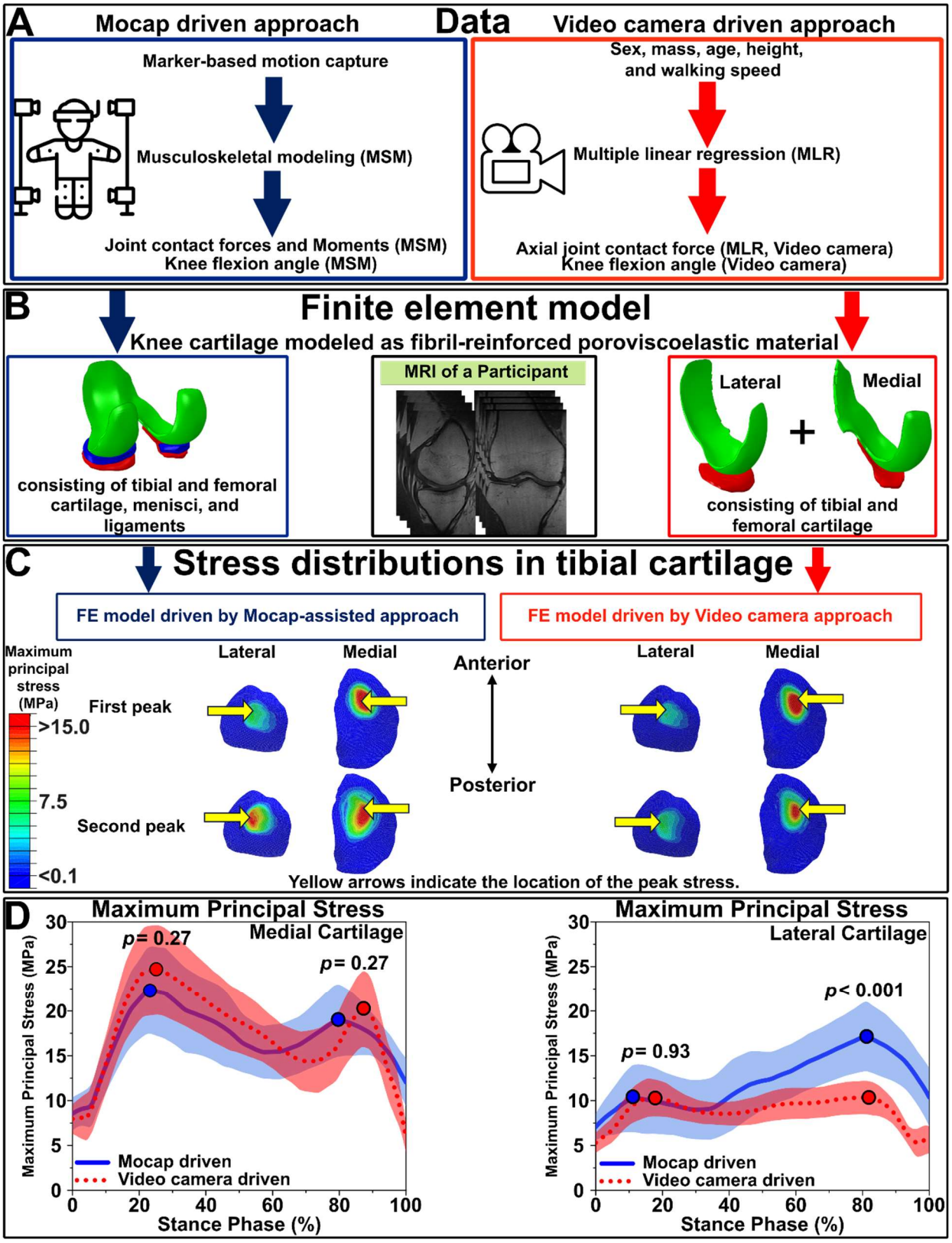
Results

In the medial tibial cartilage, average stress values were not significantly different between the approaches ($P>0.05$, Fig. 1D). The only significant differences in peak stresses were found in the lateral tibial cartilage at about 80% of stance ($P<0.05$), likely due to varying cartilage-cartilage contact areas, necessitating further model refinement.

Discussion

We present a computational modeling method to estimate knee joint cartilage mechanics using video camera-based knee kinetic and kinematic data. This enables out-of-lab estimation of knee tissue mechanics and remodeling to support rehabilitation planning and self-management of knee degenerative diseases.

Images (Optional)



References (Optional)

1] Song et al. J Biomechanics,2023

[2] Esrafilian et al. IEEE Trans Biomed Eng,2025

[3] Paz et al. Ann Biomed Eng,2024

[4] Lavikainen et al. Ann Biomed Eng,2024

Acknowledgements (Optional)

Sigrid Jusélius Foundation,Novo Nordisk Foundation,Research Council of Finland (#363459,#363854),Marie Skłodowska-Curie GA#101108335,NHMRC 2001734 inAustralia.

Session Category

Musculoskeletal Biomechanics: Methods, Models and Applications

P2-179

Evaluation of Parallel Mechanisms for Ankle and Knee With in Vivo Measured Running Kinematics

Mr Manuel Romeo MSc[1], Ms Anna Pedretti[1], Mr Michele Conconi PhD[1], Mr Nicola Sancisi PhD[1], Mr Raphael Dumas PhD[2]

[1]Department of Industrial Engineering, University of Bologna, Bologna, Emilia Romagna, Italy. [2]Univ Eiffel, Univ Lyon 1, LBMC UMR_T 9406, Lyon, Auvergne Rhone Alpes, France

Introduction

Multibody kinematics optimization (MKO) is essential for musculoskeletal modelling, but the resulting joint angles are highly influenced by the chosen kinematic model. The Twente Lower Extermity Model (TLEM2 [1]) is a comprehensive lower limb model that uses simple hinges for the tibiofemoral, subtalar, and talocrural joints. Parallel mechanisms, including rigid contacts and isometric ligaments, have been proposed as a more anatomically detailed alternative for modeling these joints.

The objective of this study is to preliminarily evaluate the joint angles derived from MKO when using the TLEM2 augmented with parallel mechanisms for the knee and ankle joints.

Methods

Parallel mechanisms (1 DoF) were synthesized based on the TLEM2 bone geometries [1] and predicted passive kinematics (using a congruence method [2]). They were incorporated into the musculoskeletal model to replace the hinges. The model was scaled and used to track skin marker trajectories during the stance phase of running using the dataset from [3]. This dataset also includes the trajectories of pin markers embedded in the femur, tibia, and calcaneus of 3 participants (5 trials each).

Results

The figure compares the knee and ankle angles estimated using skin markers (MKO) against the reference angles obtained from pin markers. Patterns were generally reproduced by the parallel mechanisms: R^2 between 0.92 and 0.99 for ankle and knee lexion/extension, with mean RMSE of 8.9° and 2.8°, respectively. Regarding the other DoFs, errors were limited for ankle and knee adduction/abduction, and ankle inversion/eversion (< 5.8°), while higher for knee internal/external rotation (< 13.2°). Values were comparable with hinges.

Discussion

The errors in the joint angles come from both the soft tissue (and shoe) artefact and the differences between the generic models and the participants' anatomy, particularly for the knee internal/external rotation. The parallel mechanisms may ensure more biomimetic output of joint angles computed by MKO. Future evaluations will include a wider quantification of the errors (bias, limits of agreements, correlations).

Images (Optional)

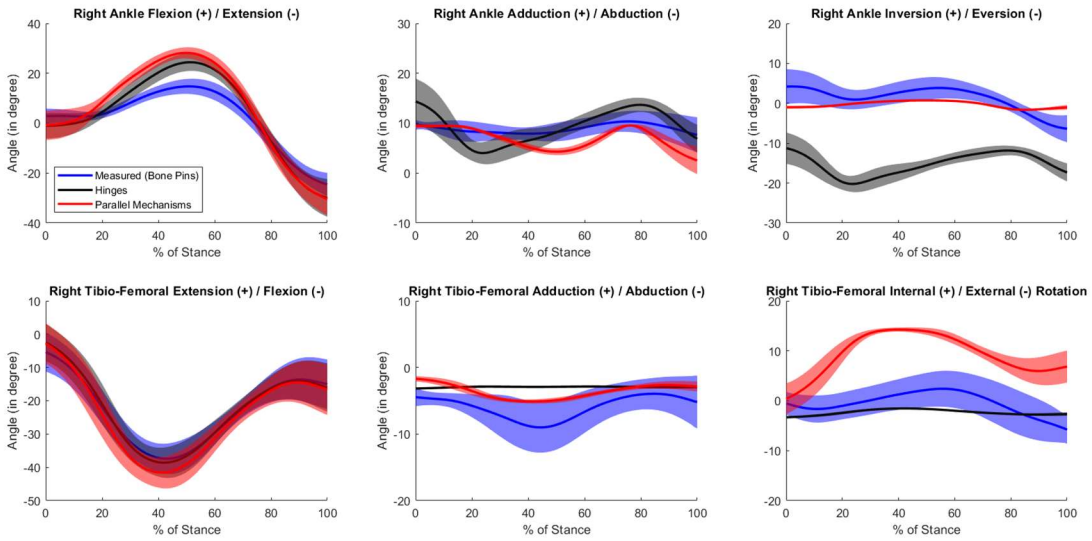


Figure: knee and ankle angles (mean and SD of all trials of the three subjects) estimated using skin markers (MKO with parallel mechanisms, in red, and with hinges, in black) and obtained from the pin markers (in blue) during the stance phase of running. ZXY and ZYX sequence of rotations are respectively used for knee and ankle.

References (Optional)

[1] Carbone et al., 2015. *J Biomech* 48: 734-741.

[2] Conconi et al., 2021. *IEEE Trans Biomed Eng* 68: 1084-1092.

[3] Reinschmidt et al., 1997. *J Biomech* 30(7): 729-732.

Acknowledgements (Optional)

This work was supported by a grant from the Franco-Italian University (Partenariat Hubert Curien) project Galileo # 48932SG.

Session Category

Musculoskeletal Biomechanics: Methods, Models and Applications

P2-180

Weakened Lumbar Multifidus Muscles Caused Altered Vertebral Mobility and Increased Lumbar Loads in Adjacent Segments Following Lumbar Interbody Fusion – Results of Muscle-Driven Simulations

Dr.-Ing. Robin Remus[1], PD Dr. med. Moritz Lodde[2], Mr. Matthias Klimek M.Sc.[2], Mr. Sascha Selkmann M.Sc.[1], Dr.-Ing. Marc Neumann[1]

[1]Biomedical Engineering Lab, Department of Mechanical Engineering, Ruhr University Bochum, Bochum, NRW, Germany. [2]Department of Trauma, Hand and Reconstructive Surgery, University Hospital Münster, Münster, NRW, Germany

Introduction

The lumbar multifidus (LMF) is a deep trunk muscle that plays a key role in spinal stability and controlling vertebral motion. Structural or functional LMF impairments are prevalent after lumbar interbody fusion (LIF) and are associated with adjacent segment disease. This study used spinal simulations to investigate how weakened LMF muscles influence spinal kinematics and loading following LIF.

Methods

Muscle-driven simulations with varying maximum isometric forces (100%–25%) of the LMF muscle were performed using a previously validated hybrid finite element (FE)–multibody (MB) spine model [1] built in ArtiSynth (www.artisynth.org). The model consisted of rigid bones (thorax–sacrum), fiber-reinforced FE intervertebral discs, facet joints, pre-tensioned ligaments, and twelve muscle groups. Following nucleotomy and facetectomy, an expandable FE intervertebral cage and bilateral posterior FE instrumentation were used to include an L4-L5 LIF (Fig.1A). To compare the effects of LMF changes on adjacent segments, forward dynamics simulations were performed for five tasks, with all other conditions held constant: T1) standing upright, T2) holding a 20kg box, T3) 45° Roman Chair back extension exercise, T4) 10° extension, and T5) 30° flexion. The intact LMF served as reference for evaluating changes in kinematics and intradiscal pressure (IDP).

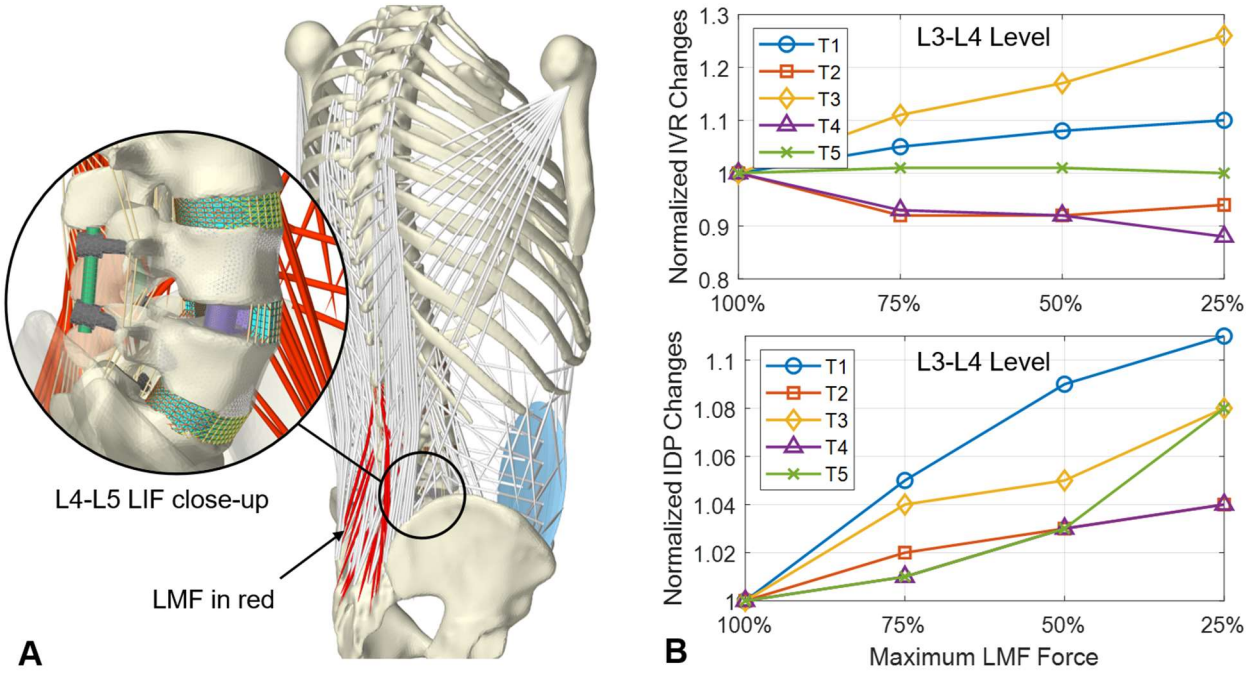
Results

Reductions in maximum LMF force resulted in altered biomechanics in adjacent segments as well as altered muscle activation patterns. Intervertebral rotations (IVR) increased cranially for T2 by up to 26% and decreased for T4 by up to -12% (Fig.1B). For all tasks, the IDP increased cranially by 1 to 11%. Caudally, IDP changes of ±2% occurred.

Discussion

This study compared the effects of reduced LMF muscle forces for different tasks using a hybrid FE-MB spine model with LIF. The results showed increased IDP and altered vertebral mobility, both of which can promote adjacent segment disease. Overall, integrating FE components into a forward-dynamics musculoskeletal model enabled simulating the interplay between muscles and passive spinal structures. This demonstrates the model's potential for investigating clinically relevant issues, such as the decision-making process for open versus minimally invasive surgical procedures, implant selection, and preoperative and postoperative physical therapy exercises for the lumbar spine.

Images (Optional)



References (Optional)

[1] Remus et al., Bioengineering 12(3):263, 2025

Session Category

Musculoskeletal Biomechanics: Methods, Models and Applications

P2-181

Validation of knee joint forces for a 3DOF ellipsoidal bi-condylar knee joint for musculoskeletal modeling

Ms Sabrina Hörmann, Dr. Nazli Tümer, Prof. Dr. Amir A. Zadpoor, Dr. Ajay Seth

Delft University of Technology, Delft, Zuid Holland, Netherlands

Introduction

The knee joint is typically defined as a one-degree-of-freedom (1DOF) cam-follower joint in musculoskeletal (MSK) models, allowing flexion–extension motion along cadaver-derived paths [1]. Thus, patient-specific bone geometry and its effect on joint kinematics are neglected. 6DOF models incorporating bone contact and ligaments can capture subject-specific motion but are computationally expensive and sensitive to uncertainties in tissue properties [2]. Therefore, we propose a 3DOF ellipsoidal bi-condylar knee model.

This study aims to validate the estimated knee joint forces against in vivo measurements and evaluate differences in knee joint force estimations compared to a 1DOF model.

Methods

We developed a 3DOF bi-condylar tibiofemoral joint in OpenSim [3], allowing motion in flexion-extension, internal-external, and adduction-abduction rotation. The model consists of two ellipsoidal joints representing the medial and lateral condyles, physiologically constraining internal-external and adduction-abduction rotations (Fig. part a). Experimental data to validate the model were obtained from the CAMS dataset [4]. The bi-condylar model was integrated into a full-body MSK model [5], scaled to the subject's anthropometry, and the ellipsoid radii were fitted to the knee implant geometry. Inverse kinematics and muscle redundancy were solved to estimate joint-reaction forces for one subject over eight gait cycles using both a 1DOF and a bi-condylar knee model.

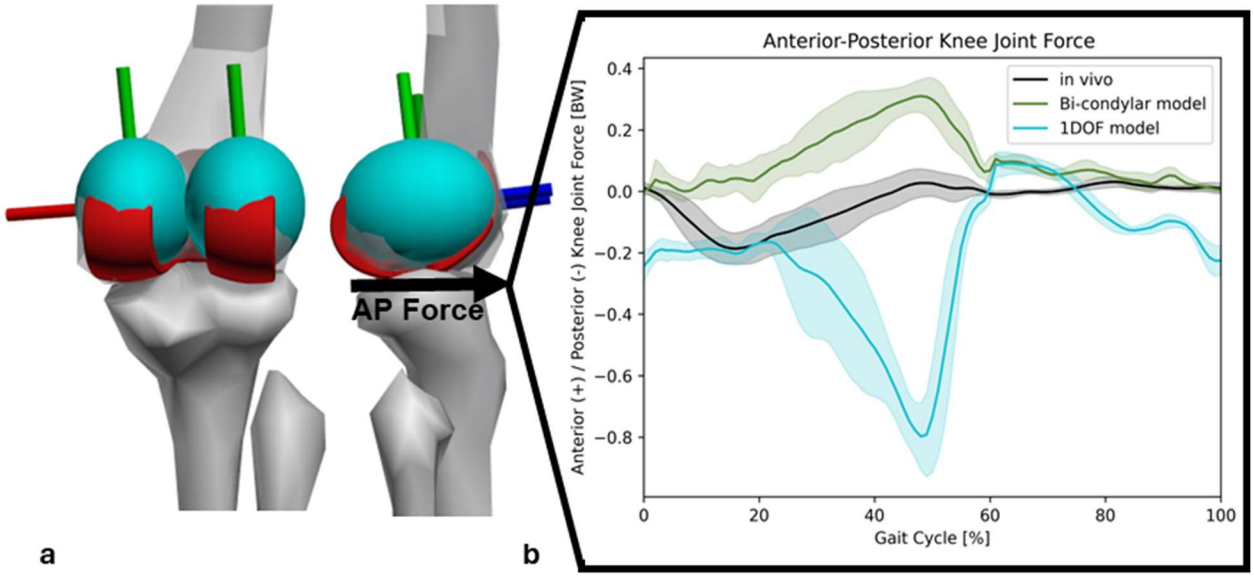
Results

Preliminary results showed reduced root-mean-square errors (RMSE), averaged over the eight gait cycles, in anterior–posterior (AP) knee joint forces from 0.29 body weight (BW) for the 1DOF joint to 0.17 BW for the bi-condylar model(Fig. part b). There were only minor differences observed in the other DOFs.

Discussion

Although knee joint compressive forces are generally well estimated with the 1DOF joint model, predictions in the anterior-posterior direction remain less accurate. The results indicate that the bi-condylar model improves the estimates of anterior-posterior knee joint forces. Further work should assess these differences across more subjects and activities in the CAMS dataset.

Images (Optional)



References (Optional)

[1] Yamaguchi GT and Zajac FE, *J Biomech*, 1989

[2] Smith CR, et al., *J Biomech Eng*, 2016

[3] Seth A, et al., PLoS ONE, 2018

[4] Taylor WR, et al., *J Biomech*, 2017

[5] Rajagopal A, et al., IEEE Trans Biomed Eng, 2016

Acknowledgements (Optional)

This conference abstract is part of the project LoaD (projectnr. NWA1389.20.009) of the NWA-ORC research programme, which is (partly) financed by the Dutch Research Council (NWO).

Session Category

Musculoskeletal Biomechanics: Methods, Models and Applications

P2-182

Estimating Spine Loading of Healthcare Workers wearing Lead Aprons using Bond Graph Modelling

Mr. Samuel Brost[1], Dr. Pushparaj Pathak[2], Dr. Qingguo Li[1]

[1]Queen's University, Kingston, Ontario, Canada. [2]Indian Institute of Technology Roorkee, Roorkee, Uttarakhand, India

Introduction

Spinal injury is common among healthcare workers who perform X-ray-based procedures that require lead aprons and static postures [1]. Using bond graph modelling, we investigated the additional loading caused by lead aprons in these maladaptive postures to understand the dominant injury mechanism. Research on healthcare workers shows large cumulative loads, but the amount that lead aprons contribute to this issue relative to the long time spent in maladaptive postures is relatively unknown [2]. Bond graph modelling was chosen as it allows for simple multidisciplinary integration, meaning it can easily incorporate interventions such as exoskeletons within the model.

Methods

The sagittal plane spinal posture of 21 Healthcare workers at Sunnybrook Health Sciences Centre (REB #5331) was recorded using a 4 IMU system. A bond graph model, adapted from [3], was used to estimate internal loading in the lumbar spine, with the trunk and the head being modelled as inertial bodies as seen in Figure 1. The recorded neutral posture was modelled with and without the weight of a lead apron, and the displacements and loads were estimated from the bond graph model.

Results

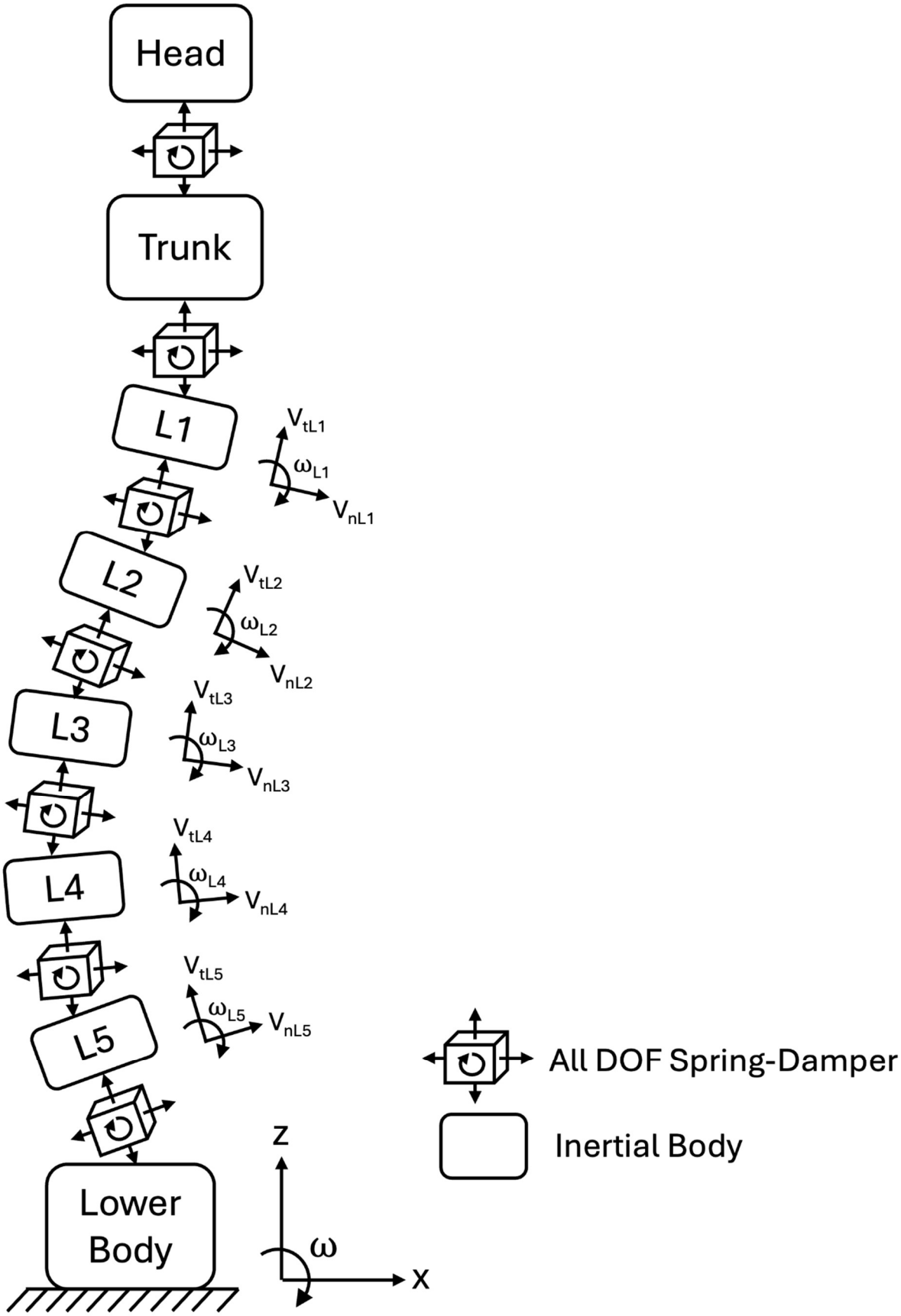
From the population measured, the average lead apron weight was 7.55 kg. This additional load resulted in an average compression of 0.45 mm and compressional force of 97 N. This loading represents a 33 % increase over the loading without a lead apron.

Discussion

The addition of the lead vest made a noticeable contribution to the loading experienced in the lumbar spine at the neutral position. This demonstrates that the lead apron weight does have a significant role in the injuries experienced, and there is a need for interventions focused on reducing its impact. This investigation of neutral posture is a preliminary application of a model that is under development. The ongoing addition of fully modelled thoracic and cervical vertebrae and associated musculature will allow for a more detailed

investigation into the reported neck injuries and high flexion postures common in the healthcare environment.

Images (Optional)


Head
Trunk
L1
L2
L3
L4
L5
Lower Body
V_{tL1}
ω_{L1}
V_{nL1}
V_{tL2}
ω_{L2}
V_{nL2}
V_{tL3}
ω_{L3}
V_{nL3}
V_{tL4}
ω_{L4}
V_{nL4}
V_{tL5}
ω_{L5}
V_{nL5}
z
ω
x
All DOF Spring-Damper
Inertial Body

References (Optional)

[1] Lloyd Klein *et al*., Catheter. Cardiovasc. Interv, 2015

[2] Samuel Brost, [MASc. Thesis, Queen's University], 2023

[3] Ali Akbari and Donald Margolis, Heliyon, 2024

Session Category

Musculoskeletal Biomechanics: Methods, Models and Applications

P2-183

Characterizing ACL Strain Using Only Knee Kinematics

Dr. Samuel Kwak PhD[1,2,3], Dr. Gregory Myer PhD, FACSM, CSCS*D[1,2,3,4], Dr. Christopher Riehm PhD[1,2,3]

[1]Emory Sports Performance And Research Center (SPARC), Flowery Branch, GA, United States. [2]Emory Sports Medicine Center, Atlanta, GA, United States. [3]Department of Orthopaedics, Emory University School of Medicine, Atlanta, GA, United States. [4]Wallace H. Coulter Department of Biomedical Engineering, Georgia Institute of Technology and Emory University, Atlanta, GA, United States

Introduction

ACL injuries are among the most studied in sports biomechanics [1]. But when considering injury risk factors, joint rotations are often used as surrogates for ACL loads [2]. However, the ACL does not deform in alignment with knee rotational axes, limiting direct inferences to ACL mechanics from measured knee kinematics. To address this limitation, we sought to develop an algebraic equation and interactive tool, derived from a knee model simulation, to quantify ACL strain in relation to 3D knee rotations.

Methods

An OpenSim knee model based on an individual's MRI-derived bone and ligament geometries [3,4], possessing an anteromedial (ACLam) and posterolateral (ACLpl) bundle with six ligament fibers each, was simulated through different knee configurations along its three rotational axes to calculate ACL strain. Using a machine learning-based symbolic regressor, PySR [5], a modeling equation was created that derives ACL strain from knee joint kinematics. We evaluated the performance of the equation using R^2 and mean absolute error (MAE). The OpenSim-based data was also used to create an interactive ACL strain tool in Render using custom Python code.

Results

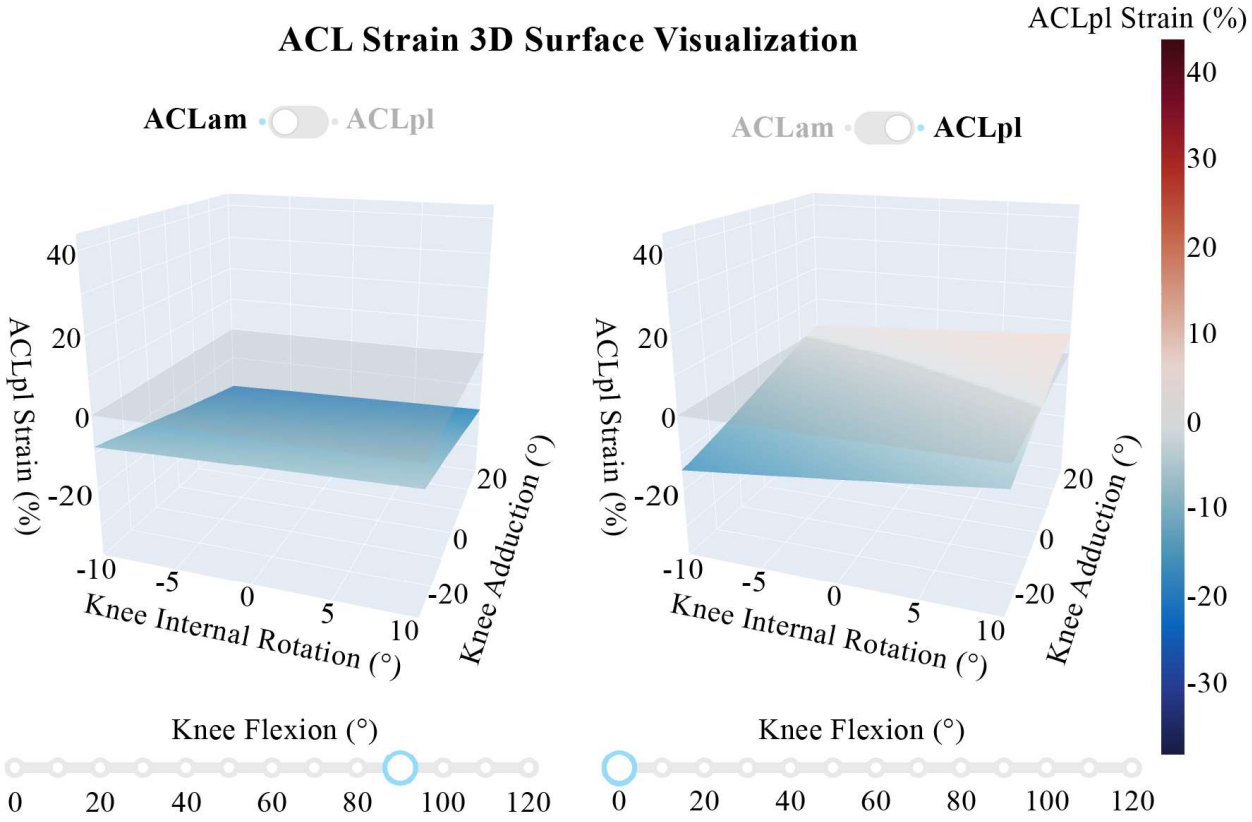
The equation estimating ACLam strain was: $\varepsilon_{ACLam} = 0.206\theta_{add} - 10.4 - (5.79*10^{-5}\theta_{flex}^2\theta_{add} + 0.135\theta_{flex} + \theta_{int} + 1.65) / (8.30*10^{-5}\theta_{flex}^2 + [245 / (\theta_{flex} - 35.1)])$. ε is percent ligament strain and θ_{flex}, θ_{add}, and θ_{int}, represent knee flexion, adduction, and internal rotation, respectively, in degrees. Relative to the simulation, this equation yielded an R^2 of 0.9986 and MAE of 0.09% strain. For ACLpl strain, the equation was: $\varepsilon_{ACLpl} = (\theta_{flex} - 0.393\theta_{flex}\theta_{int} - 2.38\theta_{add}\theta_{int} + 3.69\theta_{int}) * (1.05*10^{-5}\theta_{flex}^2 - 0.184) - 0.430\theta_{int} - 3.58$. Relative to the simulation, this equation

yielded an R^2 of 0.9943 and MAE of 0.36% strain. The interactive tool can be found here: lenhart-2015-acl-strain-plot.onrender.com.

Discussion

The proposed modeling equations and interactive tool allow for quantitative characterization of the complex interaction between knee rotation and ACL strain. Future work will include knee translation to enhance methods for kinematic derived quantification of ACL loading.

Images (Optional)



References (Optional)

[1] Belkhelladi, M. *et al.* , Orthop J Sports Med, 2025

[2] Myer, G.D. *et al.* , Br J Sports Med, 2011

[3] Lenhart, R.L. *et al.* , Ann Biomed Eng, 2015

[4] Seth, A. *et al.* , PLoS Comput Biol, 2018

[5] Cranmer, M., arXiv, 2023

Session Category

Musculoskeletal Biomechanics: Methods, Models and Applications

P2-184

Development of an Artificial Musculoskeletal Replica of the Knee Joint: Comparison of repeatability and passive joint kinematics with cadaveric data

Mr Sanjib Dutta, Mr R. Yogeshwar Rao, Dr Darshan S Shah

BiOME Lab, Department of Mechanical Engineering, Indian Institute of Technology Bombay, India, Mumbai, Maharashtra, India

Introduction

In vitro cadaveric biomechanical testing overcomes shortcomings of *in vivo* and *in silico* testing arising from invasive measurements and tissue site trueness, respectively. However, due to the limited availability, maintenance and ethical issues surrounding cadaveric specimens, artificial joint models are a more practical alternative for *in vitro* orthopaedic biomechanics research. Current artificial models typically only replicate one of the anatomical, functional or material aspects of the joint; however, all aforementioned aspects need to be replicated to accurately mimic a cadaveric joint. This study aimed to develop a biomechanically accurate and repeatable artificial musculoskeletal replica of the knee joint.

Methods

11 artificial joints were assembled using 3D-printed femur and tibia, based on synthetic bone models (Synbone, Switzerland), aligned as per standard hip-knee-ankle and lower-limb-torsional alignment. Custom artificial menisci and composite collateral and cruciate ligaments were developed to replicate the morphology, insertion sites and mechanical properties of the native tissues.[1,2] Following assembly of the aforementioned anatomical tissues, each specimen underwent three cycles of passive flexion-extension (FE), while a six-camera optical motion capture system (Qualisys, Sweden) tracked clusters of retroreflective markers rigidly affixed to the bones to provide tibiofemoral kinematics. Root mean square error (RMSE) of internal-external rotation (IErot) during FE across specimens was compared with cadaveric studies in the literature.[4,5] Bootstrap resampling confidence intervals (CI), based on root mean square (RMS) for each specimen, were calculated to assess repeatability.

Results

Mean RMSE across specimens was 5.56°, while comparisons with literature showed an RMSE of 1.54° (Fig. 1). Mean RMS across specimens was 4.08±2.93° with CI = [2.85°, 5.65°].

Discussion

The developed artificial model successfully replicated the musculoskeletal anatomy of the joint, the mechanical properties of soft tissues, and the passive coupling of knee FE and IErot.[3] Specimens exhibited moderate repeatability based on the CI, possibly owing to variable joint laxity and tissue pre-straining across specimens. Further development will focus on optimizing and standardising tissue pre-straining for a more robust and reliable artificial model.

Images (Optional)

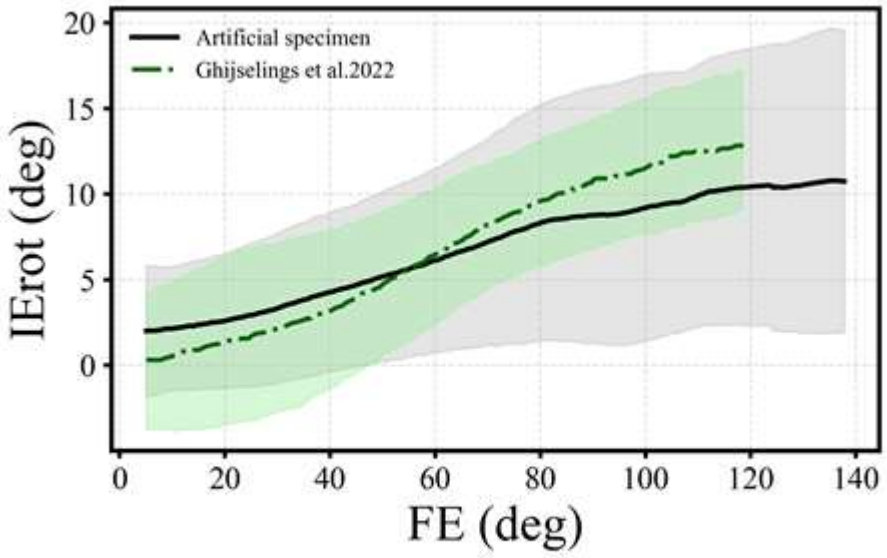


Figure 1. Coupled internal-external rotation (IErot) with knee flexion-extension (FE) (data represented as mean ± standard deviation)

References (Optional)

1. Elsner et al, J Biomechanics, 2010
2. Cho et al, J Appl. Sci, 2020
3. Ghijselings et al, Arch Orthop Trauma Surg, 2022

Acknowledgements (Optional)

The study was supported by the Wadhwani Research Centre for Bioengineering, IIT Bombay and the Developing Countries Grant Competition (DCGC) Award by the International Society of Biomechanics (ISB).

Session Category

Musculoskeletal Biomechanics: Methods, Models and Applications

P2-185

Automated Ligament Insertion Definition with Template Mapping via Geodesic-based Bayesian Coherent Point Drift

Dr. Scott Sibole[1], Ms. Maryam Nazem[2], Ms. Kate Moyle[3], Ms. Nancy Kim[3], Dr. Jason Halloran[1]

[1]Washington State University, Spokane, WA, United States. [2]University of Denver, Denver, CO, United States. [3]University of Auckland, Auckland, Auckland, New Zealand

Introduction

Identification of ligament insertion sites is a critical task in physics-based simulation of joint mechanics. Challenges arise from limitations such as poor medical image resolution and signal strength leading to intra- and inter-observer variance. Identification is also arduous and time-consuming. Automated methods for identification are thus attractive. To this end, we explored the use of a geodesic-based Bayesian coherent point drift (GBCPD) algorithm [1] to map a template femur with identified insertions to a validation set, as well as image reconstructed anatomies.

Methods

The Natural Knee Data [2] specimen DU02 femur mesh and ligament insertion points were utilized as the template femur. Ligament insertion points were projected to the closest femur mesh vertex and assigned an integer ID (Figure 1A). The template mesh was then deformed with a randomly perturbed thin-plate spline transform to create a validation set of 100 femurs (Figure 1B). GBCPD was applied to determine maps from the template mesh to each augmented mesh. Distances between the ground truth and mapped ligament insertion points were evaluated. The template mesh was also mapped to the DU03, DU04, and DU05 femora.

Results

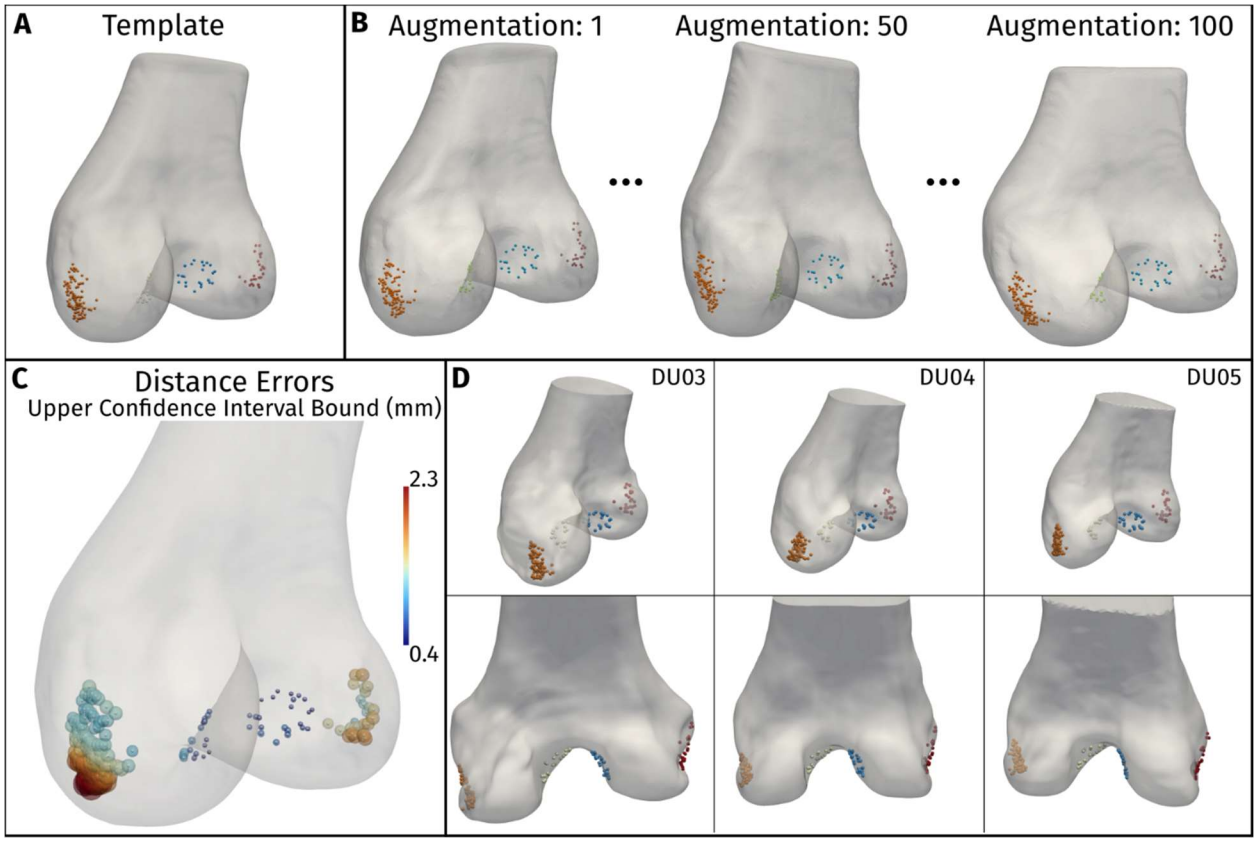
The mean and standard deviations of distance error aggregated per ligament were: ACL (0.54±0.26mm), PCL (0.59±0.38mm), MCL (1.26,0.86mm), and LCL (1.37mm,0.41mm). Pointwise errors are visualized in Figure 1C. Insertion points mapped to real anatomy are shown in Figure 1D.

Discussion

Mapping a template femur to target geometries using GBPCD for automated ligament insertion definition was demonstrated. Although the distance errors were acceptable, a future hyperparameter study to find optimal settings for the GBPCD algorithm may improve

performance. Errors of 5-8mm in ligament insertion identified in fluoroscopic images vs dissection have been reported [3], thus the observed distance errors are encouraging. Modifying the algorithm to include additional features such as mesh normals or interpolated image intensities will likely yield improved fidelity. Nevertheless, GBPCD template mapping was shown to be a viable method for the automated definition of ligament insertions.

Images (Optional)



References (Optional)

References

[1] Osamu Hirose, IEEE Trans Pattern Analy Mach Intell, 2023

[2] Michael D Harris *et al.*, J Biomech Eng, 2016

[3] Thomas J Kremen Jr *et al.*, Arthroscopy, 2020

Acknowledgements (Optional)

Funding from NIH-NIBIB R01EB024573 is greatly appreciated.

Session Category

Musculoskeletal Biomechanics: Methods, Models and Applications

P2-186

Detecting Local Differences of *In Vivo* Bone Loading Direction Using Principal Trabecular Orientation Fields

Dr. Sebastian Bachmann[1], Dr. Marine Cazenave[2], Prof. Meir M. Barak Ph.D, DVM[3], Prof. Dieter H. Pahr[1], Dr. Alexander Synek[1]

[1]Institute of Lightweight Design and Structural Biomechanics, TU Wien, Vienna, Vienna, Austria. [2]Department of Human Origins, Max Planck Institute for Evolutionary Anthropology, Leipzig, Saxony, Germany. [3]Department of Veterinary Biomedical Sciences, College of Veterinary Medicine, Long Island University, Brookville, NY, United States

Introduction

Trabecular bone is known to adapt to mechanical loading, a process known as “functional adaptation”. For example, apparent density or principal trabecular orientation (PTO) may change throughout the bone according to the loading magnitude and direction. Apparent density can be quantified, and compared holistically, i.e., on the whole bone level [1]. However, these holistic methods have yet to work for PTO analysis. To fill this gap, we developed a new method to analyze PTO fields and demonstrate its usage on experimental data.

Methods

37 micro-CT images of sheep tali (resolution 0.025 mm) were obtained from a previous study [2], in which three experimental conditions were defined:
Sedentary: the ankle-joint angle (α) was altered by approximately 7° using orthopedic shoes;
Incline: shoe-wearing except during training on a 7° inclined treadmill;
Level: control group, only trained on a level treadmill.
A statistical deformation model (SDM) was created to obtain a canonical bone, onto which all individuals were registered (Fig1A) [1]. PTO fields were measured for each individual using a mesh and background grid [1] and transformed into the canonical space using the rotational part of the deformation gradient (Fig1B) [3]. Statistical significant regions were found by removing cells with ill-defined PTO and applying permutation tests for group-wise differences in PTO [4] with $p<0.01$.

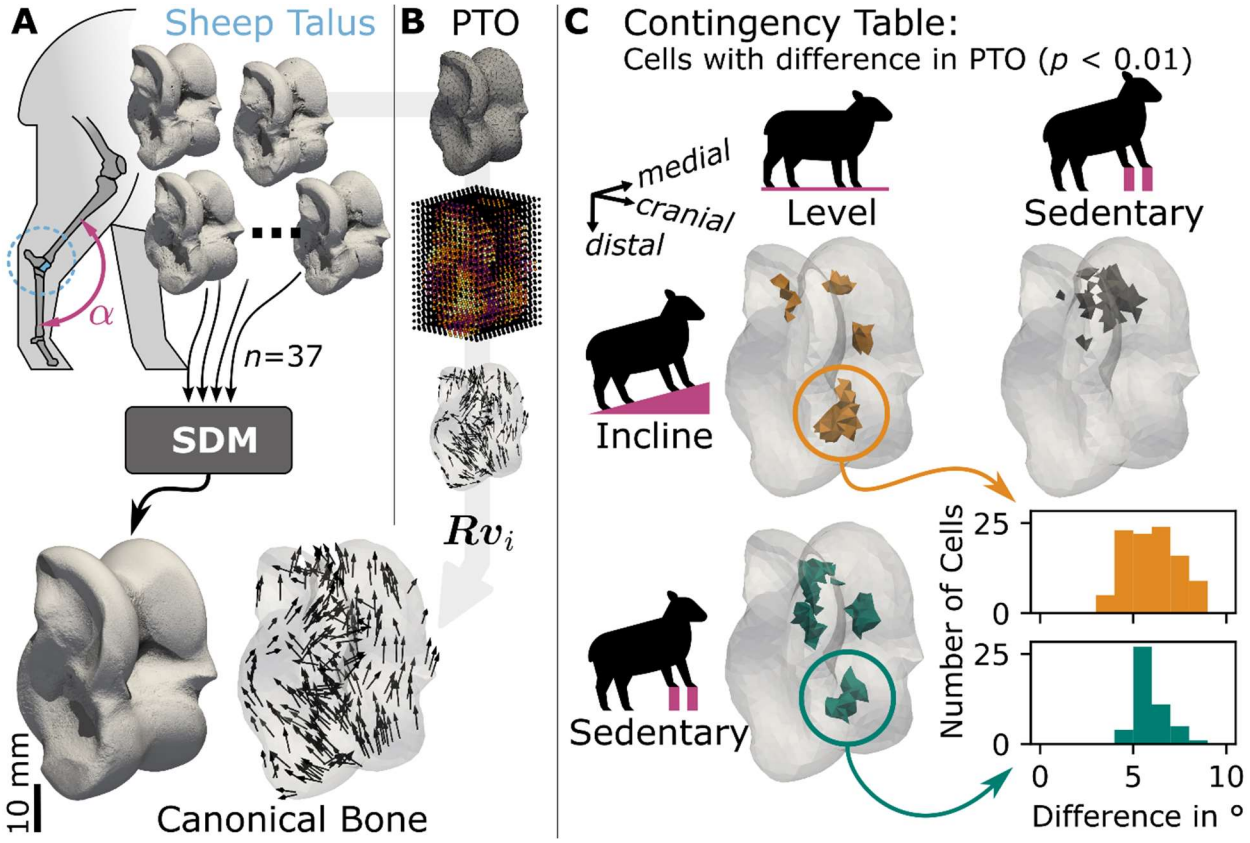
Results

Several significantly different regions were found between groups (Fig1C). In the sedentary and incline groups, cells in the distal-medial region showed a different direction than the level group, with differences between 4° and 10°. Cells in the proximal region showed a complex pattern and appeared in all group comparison, including incline versus sedentary group.

Discussion

While PTO differences in the distal-medial region can be explained by the altered joint angle of 7°, the proximal regions require further analysis. Overall, these preliminary results demonstrate the successful application of canonical PTO field analysis that is sensitive enough to detect small, localized PTO differences caused by a change of *in vivo* joint loading direction.

Images (Optional)



References (Optional)

[1] Bachmann *et al.*, *Scientific Reports*, 2022
[2] Barak *et al.*, *Bone*, 2011

[3] Panyasantisuk *et al.*, *Medical Engineering & Physics*, 2018
[4] Barak *et al.*, *Journal of Human Evolution*, 2017

Session Category

Musculoskeletal Biomechanics: Methods, Models and Applications

P2-187

Preserved Bilateral Cycling Synergies with Selective Fatigue-Driven Reweighting

Dr. Shahram Rasoulian PhD, Mr. Reza Ahmadi PhD Candidate, Professor Walter Herzog PhD, Professor Amin Komeili PhD

University of Calgary, Calgary, AB, Canada

Introduction

Neuromuscular fatigue alters muscle activation, but its effect on the modular organization of cycling remains unclear. Muscle synergies, coordinated groups of muscles activated as functional units, simplify control while preserving task performance. This study examined how fatigue during constant-power cycling affects the bilateral structure and temporal organization of muscle synergies, focusing on inter-limb symmetry and time-dependent changes in synergy weights.

Methods

Twenty recreational cyclists (8 males, 12 females; 22.6±4.5 years) performed constant-power cycling at 70% of individual maximum power until task failure. Bilateral surface EMG was recorded from seven lower-limb muscles Vastus Medialis (VM), Rectus Femoris (RF), Vastus Lateralis (VL), Biceps Femoris (BF), Tibialis Anterior (TA), Gastrocnemius Medialis (GM), Soleus (SOL) and processed into linear envelopes. Four muscle synergies per limb were extracted using non-negative matrix factorization at three normalized time points: Initial, Midpoint, and Final. Synergy composition (muscle weights) and activation profiles were compared across time points with repeated-measures ANOVA or Friedman tests (α=0.05). Effect sizes were reported as partial η^2 or Kendall's W.

Results

Four synergies explained >95% of EMG variance at all time points. Synergies 1 and 3 and synergies 2 and 4 formed mirrored inter-limb pairs with ≈180° phase-shifted activation timing (Figure 1). The overall synergy structure was preserved, but selective time-dependent changes occurred within specific muscles: significant reweighting was observed for BF (Sy2&4, p≤0.05, $p\eta^2$=0.17-0.32), RF (Sy2&4, p≤0.02, $p\eta^2$=0.23-0.32), VL (Sy1&3, p≤0.03, $p\eta^2$=0.08-0.14), SOL (Sy1&4, p≤0.04, W=0.19-0.20), VM (Sy2, p=0.02, W=0.23), and GM (Sy3, p=0.02, $p\eta^2$=0.23). Other weights showed no time-point effects. These results indicate that fatigue does not reorganize the modular framework but selectively adjusts muscle weight within paired synergies.

Discussion

The persistence of four mirrored synergies and the 180° inter-limb phase shift demonstrate stable bilateral modular control of cycling. Selective reweighting of the quadriceps, hamstrings, and plantar flexors suggests targeted adaptation to maintain force direction and power output under fatigue. The central nervous system appears to preserve overall synergy architecture while refining muscle contributions to sustain performance, reflecting compensatory rather than reorganizational plasticity.

Images (Optional)

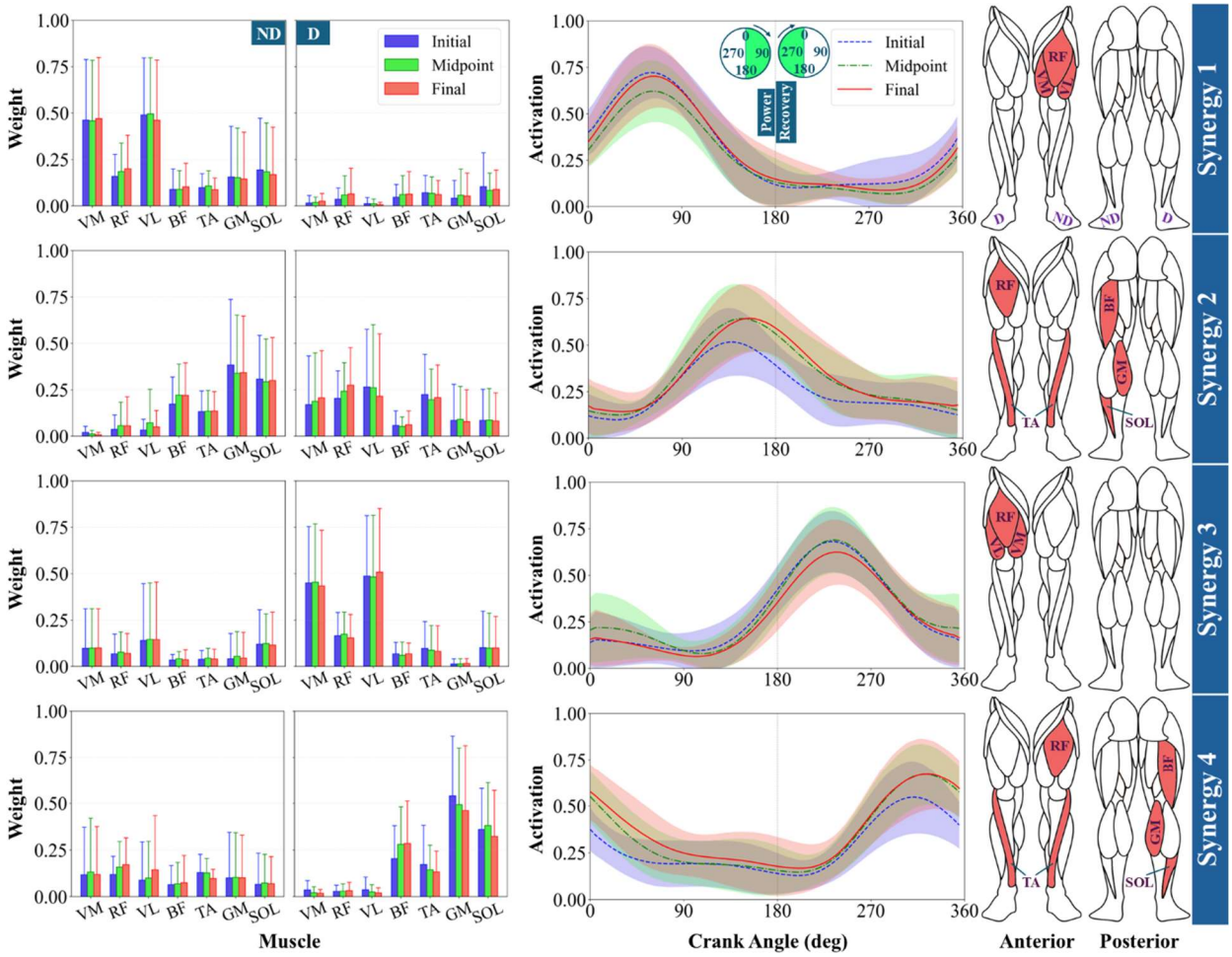


Figure 1. *Weights and activation profiles of 4 cycling muscle synergies for non-dominant (ND) and dominant (D) limbs at Initial, Midpoint, and Final time points.*

References (Optional)

1. Turpin *et al.*, J.Exp.Biol, 2011.
2. Ahmadi *et al.*, Ann.Biomed.Eng, 2025.

Acknowledgements (Optional)

The authors acknowledge financial support from the Natural Sciences and Engineering Research Council of Canada (Discovery grant 401610) and Alberta Innovates (AICE-Concept grant 222300358).

Session Category

Musculoskeletal Biomechanics: Methods, Models and Applications

P2-188

A Systematic Review of Measurement Techniques To Characterize Infant Cranial Anatomy

Ms. Shameka Kimmel[1], Mr. Tanner Pollock[2], Dr. Erin Mannen[1]

[1]Boise State University, Boise, ID, United States. [2]Idaho College of Medicine, Meridian, ID, United States

Introduction

The first 6-months of human life involve rapid skull growth driven by genetic and environmental factors. At birth, the cranium is ~25% of adult size, and by 6-months it has nearly doubled. Early identification of cranial deformities is essential for optimizing developmental outcomes, yet current assessment methods vary in accuracy, accessibility, and utility. Traditional 2D-anthropometric measures in pediatric clinics often underestimate abnormalities. Advanced imaging tools provide greater precision but remain limited by cost, feasibility, and availability. Additionally, normative data for healthy infants are scarce. This systematic review evaluates techniques used to characterize cranial morphology in infants 0–6 months and discusses the need for 3D-data to support early diagnosis and standardized assessment.

Methods

We performed systematic PubMed searches identifying studies reporting cranial measurements or shape assessments in healthy infants (<6-months). Search terms emphasized normative development, cranial shape analysis, and age. The search produced 2,617 articles, which were screened using predefined criteria. Eligible studies included healthy infant samples, objective measurement of cranial dimensions or morphology, and standardized/imaging-based methods. After screening, 28 studies met inclusion criteria.

Results

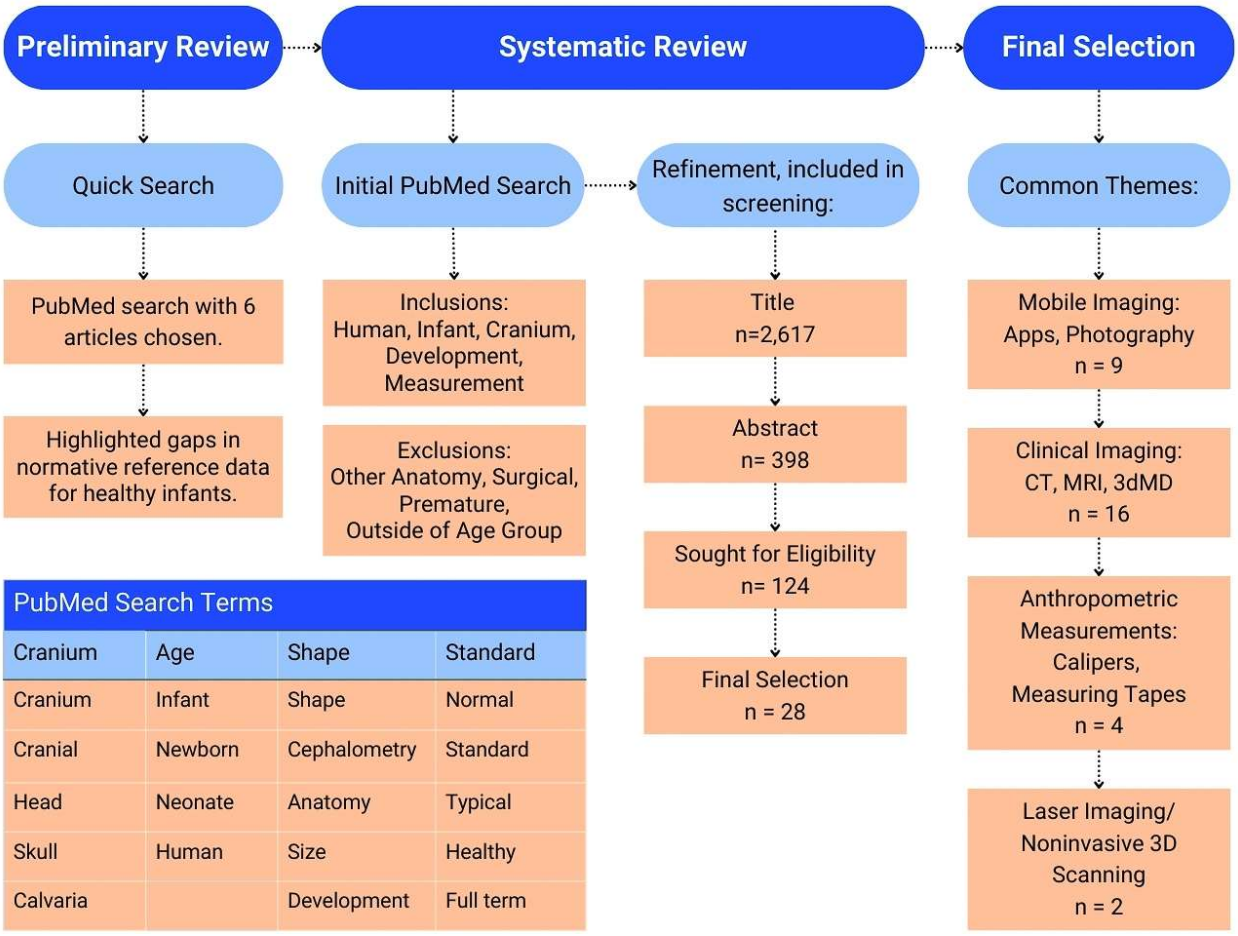
Measurement approaches varied widely, from manual anthropometric measurements (n=4) to high-resolution 3D-imaging (n=16) and noninvasive techniques capturing 3D-cranial shape (n=11). Most research targeted pathological populations or older ages, leaving limited data for ages 0–6 months. Among healthy infant studies, findings showed rapid, non-uniform cranial growth between 3–6 months [1], emphasizing needs for

repeatable measurement tools. Sample sizes were often small, geographically narrow, and methodologically inconsistent, limiting generalizability and development of reference standards.

Discussion

Existing studies provide baseline data while highlighting critical gaps. Most research on early cranial development focuses on extreme abnormalities, such as plagiocephaly and craniosynostosis, rather than natural variation [2]. 3D-imaging methods provide more precise measurements than traditional 2D-techniques. Comprehensive longitudinal studies tracking skull development in healthy infants are scarce, limiting clinicians' ability to distinguish normal variation and early deformities. Affordable 3D-modeling tools and measurement protocols are needed to support early detection, improve clinical decision-making, and advance computational modeling of infant cranial biomechanics.

Images (Optional)



PubMed Search Terms			
Cranium	Age	Shape	Standard
Cranium	Infant	Shape	Normal
Cranial	Newborn	Cephalometry	Standard
Head	Neonate	Anatomy	Typical
Skull	Human	Size	Healthy
Calvaria		Development	Full term

References (Optional)

[1] Meulstee et al., International Journal of Oral and Maxillofacial Surgery, 2020

[2] Miyabayashi et al., Neurologia medico chirurgica, 2022

Acknowledgements (Optional)

EMM owns Mannen Bio, LLC, an engineering and expert consulting company.

Session Category

Musculoskeletal Biomechanics: Methods, Models and Applications

P2-189

Validation of Knee Extensor Moment Estimates via OpenCap During a Single Leg Vertical Jump

Ms. Sophia Stemler, Ms. Alexandra Lynch M.S., Dr. Fatemeh Aflatounian PhD, Mr. Lucas Gaston, Dr. Scott Monfort PhD

Montana State University, Bozeman, MT, United States

Introduction

Assessing asymmetries in the knee extensor moment (KEM) can identify unresolved compensatory strategies following anterior cruciate ligament reconstruction (ACLR) [1]. However, data collection typically requires costly lab-based motion capture (MoCap). OpenCap is an affordable alternative that uses 2+ iOS devices for motion capture, automated cloud-based kinematic estimation, and estimation of kinetics through additional simulation [2]. OpenCap kinematics are relatively comparable to MoCap, though OpenCap kinetics remain unexplored [3]. This study addresses that knowledge gap by comparing kinetics estimated from OpenCap with simultaneously collected MoCap data during the single-leg vertical jump (SLVJ) [1]. We hypothesized that OpenCap+simulation KEM estimates would strongly correlate with MoCap.

Methods

Eight participants (4F/4M, 22.5±3.5yrs, 1.72±0.08m, 69.5±14kg) completed 3 SLVJ trials on their right leg. Trials were recorded with an 8-camera markerless system (Qualisys) and a 3-device OpenCap setup. MoCap data were processed in Theia3D and Visual3D. OpenCap kinetics were estimated with torque-driven OpenSim algorithmic differentiation simulations [4]. One trial was omitted because the simulation did not converge. Peak KEM (pKEM) values for propulsion and landing were normalized by participant height and bodyweight, and averaged for each individual. Correlations between MoCap and OpenCap pKEM values were evaluated.

Results

A significant strong correlation between MoCap and OpenCap pKEM estimates was found in the landing phase ($R=0.875, p=0.004$), while no significant correlation was found in the propulsion phase ($R=0.435, p=0.282$) of the SLVJ (Figure 1).

Discussion

OpenCap-based estimation of pKEM via torque-driven simulation characterized a similar trend as laboratory-grade kinetics. These findings may support the use of

OpenCap+simulation to identify KEM asymmetries following ACLR as an alternative to more expensive MoCap. This validation study is in progress; additional participants and comparison to marker-based MoCap is forthcoming. These findings motivate deeper investigation on OpenCap kinetic estimation due to the important clinical relevance of an accurate, affordable motion analysis system. Additional work should address dynamic tasks and kinetic measures that were not investigated in this study.

Images (Optional)

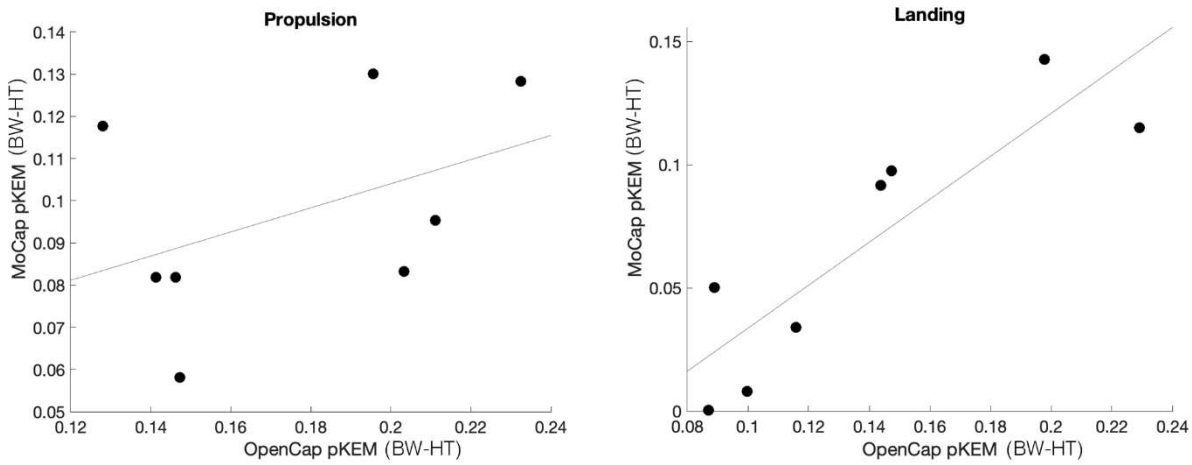


Figure 1. Scatterplots depicting pKEM estimates from OpenCap and MoCap in the propulsion (0.4s prior to takeoff until takeoff) and landing (initial takeoff until peak knee flexion) phases of the SLVJ.

References (Optional)

[1] Argyro Kostifaki et al., Br J Sports Med., 2022

[2] Scott Uhlrich et al., PLoS Comput Biol., 2023

[3] Jeffrey Turnery et al., J Biomechanics, 2024

[4] Antoine Falisse et al., PLoS One, 2019

Acknowledgements (Optional)

Supported by a MSU USP grant.

Session Category

Musculoskeletal Biomechanics: Methods, Models and Applications

P2-190

Adaptive finite element simulation to understand stress shielding from prosthetic interfaces in people with transfemoral amputation

Mrs. Isna Riski Safira, Prof Spyros Masouros, Prof Anthony MJ Bull

Imperial College London, London, England, United Kingdom

Introduction

Transfemoral amputees (TFA) have been associated with a higher risk of having low bone mineral density (BMD) in the remaining femoral bone compared with able-bodied individuals. According to Wolff's Law, mechanical loading plays an important role in bone remodelling, where aberrant loading can be due to movement compensation or the non-physiological interaction of the limb with the prosthetic interface. Computational simulations offer a cost-effective method to study internal bone mechanics under varied conditions. This study aims to (a) develop a novel TFA model and (b) to simulate bone remodelling due to different types of prosthetic interfaces.

Methods

An MRI scan of a TFA (32yo, 185cm, 86kg) was segmented to develop three FE models, representing an able-bodied scenario and 2 TFA scenarios (an end bearing socket and an osseintegration prosthesis). A series of load-cases from gait data of healthy and TFA participants [1,2], representing different phases of the gait cycle, were simulated sequentially in each model using iterative, adaptive FEA; the mechanical stimulus for a remodelling algorithm [3] is computed after each loading, which then alters accordingly the input material properties of the next FEA iteration. All models were started from the same initial density.

Results

Figure 1a shows that the stress distribution was lower in TFA compared to the healthy condition. Osseointegration resulted in lower stresses than TFA with socket prosthesis in the periprosthetic area. The longitudinal simulation resulted in lower BMD in this area for TFA with osseointegration compared to TFA with socket or the healthy condition (Figure 1b).

Discussion

This is the first study to simulate bone remodelling in TFA with a socket prosthetic interface compared to osseointegration. The lower BMD in TFA compared to the healthy scenario demonstrates a potential mechanism for the unloading osteopenia previously hypothesised in the literature [4]. The reduction in BMD with time in the osseointegration scenario suggests stress shielding of the bone through the implant stem's length.

Images (Optional)

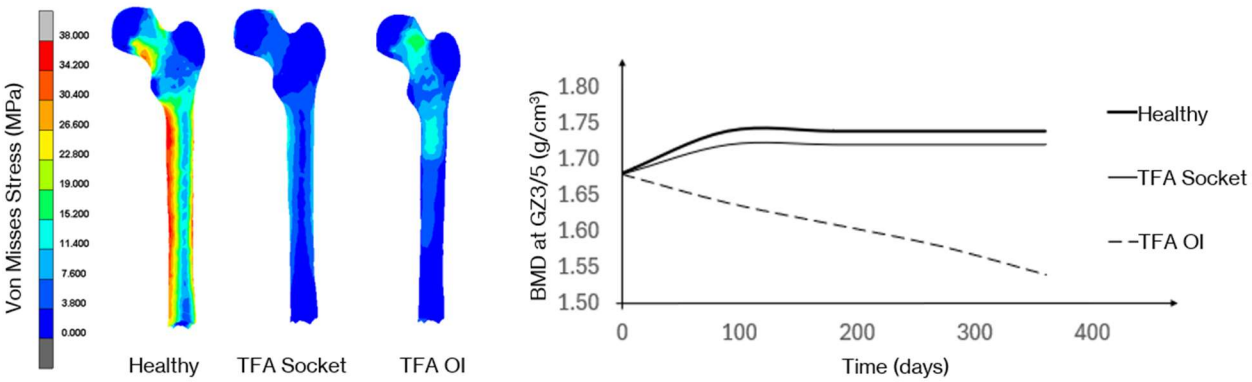


Figure 1. (A). Stress distribution at the first timepoint of recovery day and (B). Density at the periprosthetic area between healthy, TFA with socket prosthetic interface and TFA with osseointegration (OI). (1 iteration = 12 days)

References (Optional)

[1] Toderita D et al., IEEE Trans Biomed Eng, 2021

[2] Jarvis HL et al., Ann Phys Rehabil Med, 2021

[3] Mullender MG et al., J Biomechanics, 1994

[4] McMenemy L et al., J Bone & Mineral Res, 2023

Session Category

Musculoskeletal Biomechanics: Methods, Models and Applications

P2-191

Personalized Rib Cage Geometry Substantially Alters Spinal Loading Predictions in Musculoskeletal Models of Adolescent Idiopathic Scoliosis

Prof. Dr. Stefan Schmid[1,2], Ms. Kim Lieball[1,3], Mr. Philippe Bähler[1,3], Mr. Salvatore Conticello[3,1], Mr. Tim Schär[1], Prof. Dr. Moritz C. Deml[4], Prof. Dr. Carol-Claudius Hasler[5], Prof. Dr. Philippe Büchler[3]

[1]Spinal Movement Biomechanics Group, Division of Physiotherapy, School of Health Professions, Bern University of Applied Sciences, Bern, Bern, Switzerland. [2]Faculty of Medicine, University of Basel, Basel, Basel, Switzerland. [3]Computational Bioengineering Group, ARTORG Center for Biomedical Engineering Research, Faculty of Medicine, University of Bern, Bern, Bern, Switzerland. [4]Department of Orthopaedic Surgery and Traumatology, Inselspital, University Hospital Bern, University of Bern, Bern, Bern, Switzerland. [5]Orthopaedic Department and Spine Surgery, University Children's Hospital Basel, Basel, Basel, Switzerland

Introduction

Adolescent idiopathic scoliosis (AIS) is a three-dimensional deformity of the spine and rib cage of unknown etiology. Musculoskeletal models, however, typically rely on generic rib cage geometries, which may compromise the accuracy of predicted muscle forces and resulting spinal loads. This study investigated how implementing personalized rib cage geometry affects predictions of intervertebral joint forces in AIS.

Methods

An OpenSim-based musculoskeletal model of a 13-year-old girl with AIS (main curve: T6-T11, right convex, Cobb angle: 21.8°) was generated from biplanar radiographs following a previously described workflow [1], which relies on a generic rib cage geometry. A second model was then generated by integrating the patient's own rib cage geometry, obtained through semi-automated segmentation of the radiographs to define the rib centerlines (Figure 1A-B). Spinal loads during upright standing were calculated for both models (generic vs. personalized rib cage) based on muscle forces obtained from a static optimization enforcing equilibrium.

Results

The predictions indicated substantial differences between the two models (Figure 1C). In the upper part of the scoliotic curve, the personalized model showed higher anterior-

posterior shear forces (median change: +51%) and compressive forces (+14%), as well as lower medio-lateral shear forces (-15%). In the lumbar region, the personalized model predicted generally lower forces, including anterior-posterior shear (-38%), compressive (-11%), and medio-lateral shear forces (-13%).

Discussion

This study demonstrates that incorporating personalized rib cage geometry in musculoskeletal models alters predicted spinal loading patterns in AIS. While ribs could be segmented with relatively high precision on coronal radiographs, segmentation on lateral views proved challenging, primarily due to obstructed visibility in the upper thoracic region. Furthermore, it remains uncertain whether the personalized model provides more physiologically accurate predictions than the generic model, as suitable validation data are currently lacking. In conclusion, these findings underscore the influence of rib cage personalization on predicted spinal loading in AIS and highlight the need for subject-specific anatomical detail in future musculoskeletal modeling work, as well as the development of appropriate validation approaches to assess model accuracy and clinical relevance.

Images (Optional)

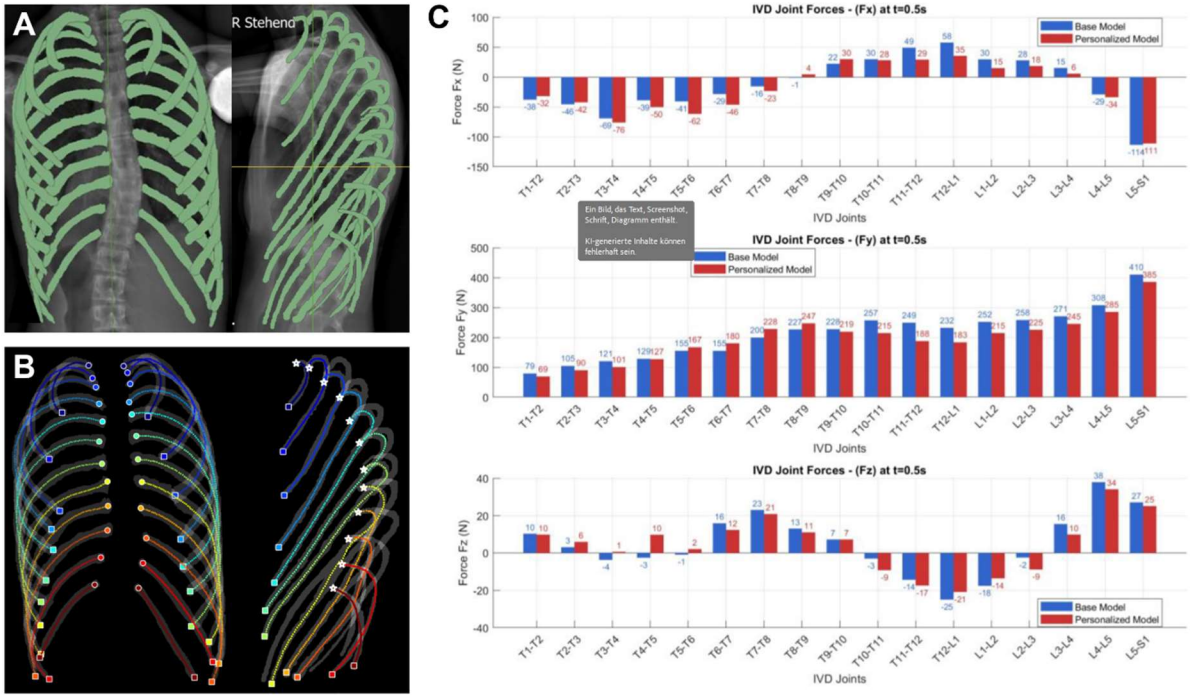


Figure 1: A-B: Segmentation and centerline estimation of the ribs on coronal and lateral radiographs. C: Intervertebral joint forces of the models with generic (blue) and personalized rib cage geometry (red). Fx and Fz represent anterior-posterior (positive values = posterior direction) and medio-lateral shear forces (positive values = right direction), respectively, while Fy represents axial compressive forces.

References (Optional)

[1] Rauber et al, J Biomech, 163:111922, 2024.

Acknowledgements (Optional)

This work was supported by the Swiss National Science Foundation (SNSF; Grant-no.: 214986).

Session Category

Musculoskeletal Biomechanics: Methods, Models and Applications

P2-192

An OpenSim-based Full-Body Musculoskeletal Model and Its Preliminary Validation

Mr. Amadeo Hoxao Undergrad Student, Mr. Gustavo Paulon Ph.D. Student, Dr. Suman Chowdhury Associate Professor

University of Florida, Gainesville, Florida, United States

Introduction

An OpenSim-based full-body musculoskeletal (MSK) model can facilitate the estimation of joint reaction forces (JRFs) and muscle activations for any given body region or the whole body, as most exertions in both occupational and daily life involve movements from multiple joints. However, developing such a full-body model requires extensive adjustments to the physiological and anatomical features of the whole-body MSK system. In this work, we will present our recently developed full-body OpenSim MSK model and demonstrate its ability to estimate muscle activations and JRFs across three work scenarios.

Methods

We started developing our model by treating the MASI model as the base structure and, using OpenSim Creator (V 0.6.2), added additional features, including 32 upper-limb muscles, 43 lower-limb muscles, 20 infra-hyoid muscles, and 377 torso muscles from previous studies. Our final model resulted in 176 bodies, 550 muscles, 131 joints, and 110 degrees of freedom. Furthermore, the scapula-clavicular joint was modeled to simulate shoulder joint kinematics by merging the acromioclavicular and the sternoclavicular joint motions with a glenoid-based reference system for the acromioclavicular joint. As of now, we have tested the Inverse Kinematics (IK) and Inverse Dynamics (ID) pipelines of our model by using data from a simple lifting task in which the subjects lifted boxes from the ground in their mid-sagittal plane and then placed them in the mid-frontal plane of their dominant side.

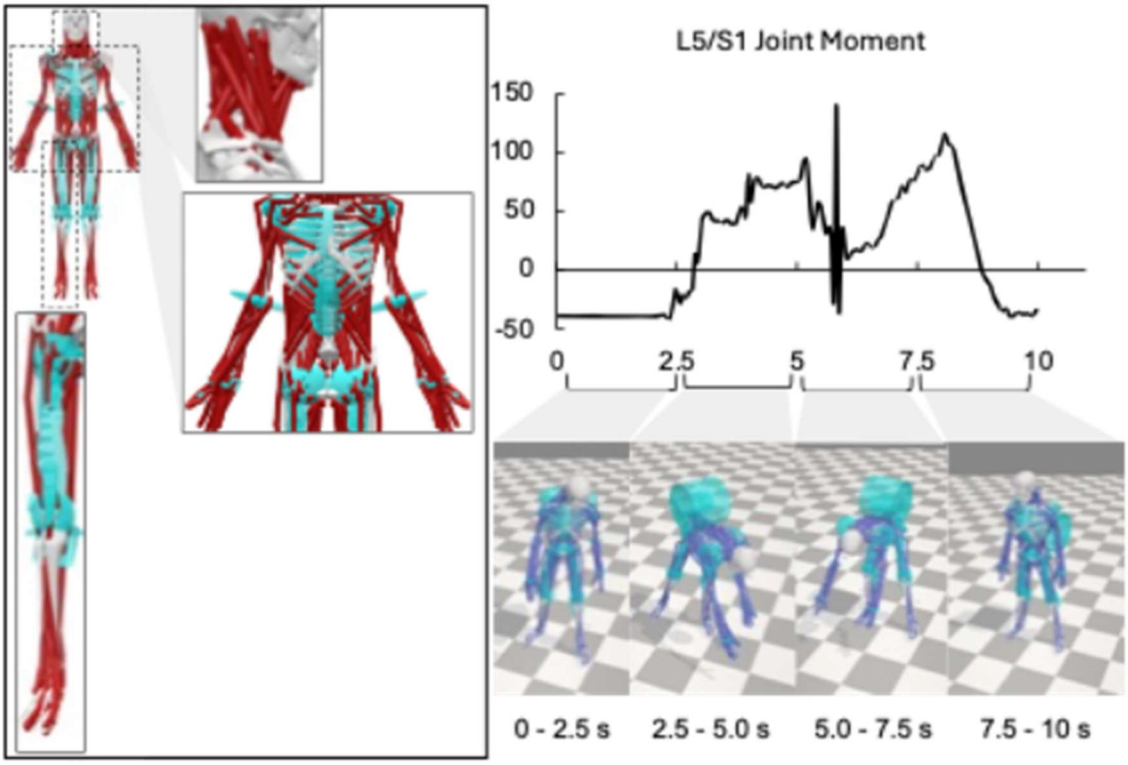
Results

Our preliminary results show that T4-T12 curvature falls under the hyperkyphosis range, with about 20 degrees of additional Cobb angle. Besides, our IK trials yielded Least Squares Errors (LSEs) between 0.02 and 0.05 m, increasing with increasing range of motion, with one trial reporting LSEs between 0.02 m and 0.03 m. Lastly, the model showed a maximum joint moment at L5/S1 of 115 N.m in the sagittal plane.

Discussion

The bending moment in the sagittal plane at the L5/S1 joint was consistent with previous studies; however, the observed hyperkyphosis of the T4-T12 curvature and the excessive Cobb angle indicated that the thoracic spine still needs adjustments. Currently, we are adjusting the model to validate its forward dynamics pipelines.

Images (Optional)



Session Category

Musculoskeletal Biomechanics: Methods, Models and Applications

P2-193

Effects of AI-Assisted Video Analysis on Interrater Reliability of Landing Movement Quality Assessment During a Vertical Hop

Dr. Teresa Szu-Hua Chen PT, PhD, Mr. Nathaniel Young SPT, Dr. Karen Lomond PhD, Dr. Katherine Spencer PT, DPT, OCS

Ithaca College, Ithaca, NY, United States

Introduction

Quality of movement assessments have become increasingly popular in rehabilitation due to their ability to detect compensatory patterns that traditional methods miss. For individuals recovering from ACL reconstruction, widely used hop tests with limb symmetry indexes often assess performance rather than movement quality, missing compensatory deficits and poorly predicting reinjury. The "Quality First" assessment offers quantitative measures to evaluate movement quality, which better predict reinjury, but interrater reliability remains uninvestigated [1]. Recent advancements in AI-assisted video analysis platforms, like Yogger, offer a potential method for reducing scoring variability between clinicians of different experience levels. This study examined whether an AI-assisted application improves interrater reliability when evaluating landing movement quality during a hop.

Methods

Twelve healthy adults participated (6 females; age: 21.8±1.4 years; height: 169.4±14.2 cm; mass: 71.1±14.5 kg). Each participant completed three vertical hop trials per leg while movements were captured from frontal and sagittal views using two iPads. KS (experienced physical therapist) and NY (first-year student physical therapist) conducted video-based scoring using "Quality First" criteria (7 items) at Time 1; NY then rescored the videos with Yogger at Time 2. Interrater reliability was calculated via intraclass correlation coefficient (ICC) and compared between conditions using bootstrap resampling with 1000 iterations. $\alpha = 0.05$.

Results

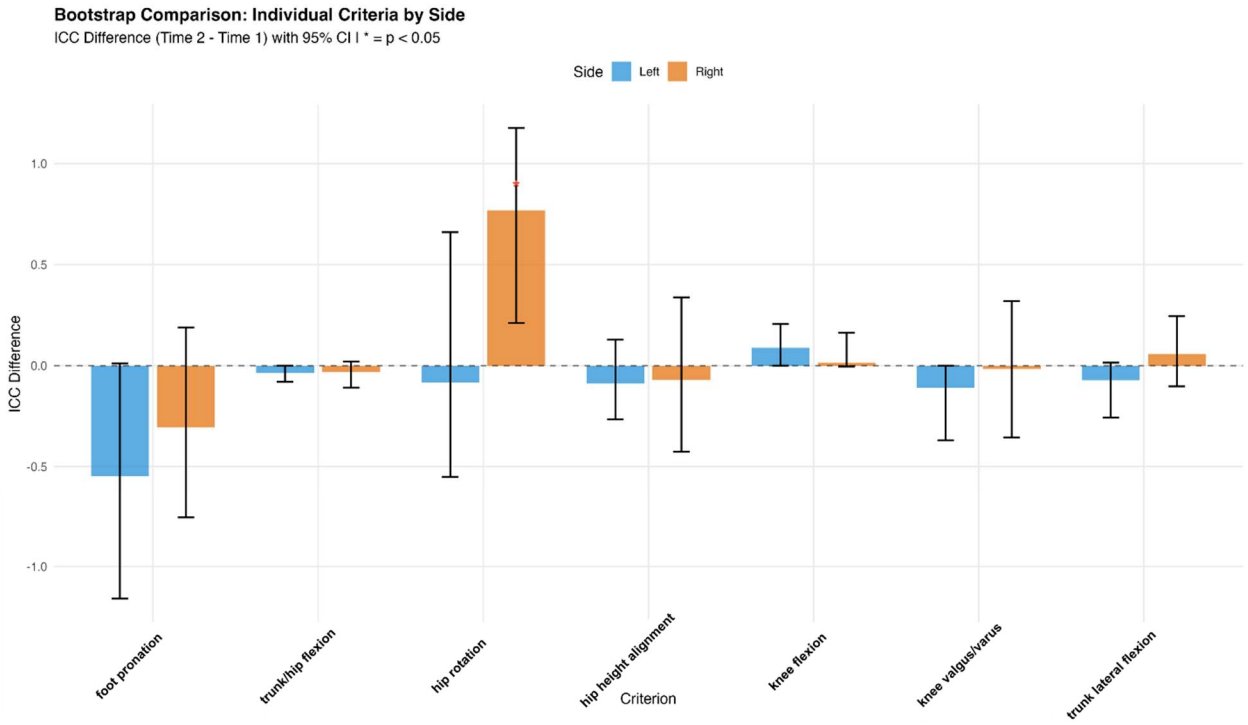
ICC revealed moderate interrater reliability at Time 1 (Left: $ICC_{(2,1)} = 0.675$, p=0.004; Right: $ICC_{(2,1)} = 0.511$, p=0.042). With Yogger, the improvement in total score was not significant for either side (Left: $\Delta = -0.073$, p=0.198; Right: $\Delta = 0.118$, p=0.354). Among individual

criteria, 1 of 7 comparisons showed significant improvement, with the largest effects in right hip rotation (Figure).

Discussion

Although overall interrater reliability did not significantly improve with Yogger, it significantly enhanced reliability for right hip rotation. This suggests AI-assisted technology might help less experienced clinicians quantify movement quality, especially for movements not easily observed, like hip rotation. In this study, the iPad captured only one frontal view, causing the right leg to be blocked by the left during landing. Future studies using two iPads for bilateral frontal views may yield greater improvements in reliability.

Images (Optional)



References (Optional)

[1] M. Mathieu-Kälin et al., Front.Sports.Act.Living, 2023

Session Category

Musculoskeletal Biomechanics: Methods, Models and Applications

P2-194

Optically Tracking Bone Interfragmentary Motion During Mechanical Testing of Circular External Fracture Fixators – Methodology Verification.

Mr Thomas Irish MEng, BEng[1], Dr Hemant Sharma FRCS (Trauma & Orth), MCh (Trauma & Orthopaedics)[2], Dr Ross Muir FRCS[2], Dr Todd Stewart PhD[1], Dr Marlène Mengoni PhD[1], Dr Peter Watson PhD[1]

[1]Institute of Medical and Biological Engineering, Leeds, West Yorkshire, United Kingdom. [2]Department of Trauma and Orthopaedics, Hull University Teaching Hospitals NHS Trust, Hull, East Yorkshire, United Kingdom

Introduction

Long bone fractures are commonly treated by circular external fixation to support the fracture and encourage healing via controlled micromotion at the fracture site. To understand the support provided, mechanical tests are often performed to determine frame stiffnesses. In recent times, a direct measure of permitted interfragmentary bone motion has become a desired measure of frame mechanics. However, 3D measurement of interfragmentary motion is difficult as the scale of motion ranges from 0.1 – 10mm within a complex construct [1]. The aim was to investigate reliability of optical tracking for measurement of axial and shear interfragmentary motion.

Methods

An Ilizarov-style Orthofix TrueLok frame was assembled with 4 pins and wires utilising 2 polycarbonate tubes as surrogate bones. A +/- 700N load was applied axially using an Instron E10000 mechanical testing machine. OptoTrak Smart Markers were placed at either side of the surrogate fracture site and tracked using an OptoTrak camera to measure interfragmentary motion. To investigate variability of the system, a series of tests were performed: Control – the frame was loaded for 10 consecutive cycles, 3 times; Frame Placement - the frame was removed and re-mounted in the E10000 machine and 10 consecutive cycles were performed, repeated 3 times; Marker Placement - a marker was altered, and 10 consecutive cycles were performed, repeated 3 times.

Results

The maximum relative error in axial interfragmentary motion was 0.10%. In comparison, maximum relative error in shear interfragmentary motion was 7.1% attributed to the lower magnitude of motion (0.1mm between 1.4 and 1.5mm). The standard deviation for each test scenario of 30 cycles was consistently minimal (0.003-0.02mm) [Figure1].

Discussion

A low (<0.03mm) standard deviation for each test and acceptable relative errors across the test scenarios shows that regardless of frame/marker physical movement and re-positioning, often required during such testing, the OptoTrak Certus tracking system could measure axial and shear motion at the fracture site with high accuracy and repeatability. Whilst the technology requires a line of sight to the imaging camera, its ability to compare fracture characteristics is very advantageous to orthopaedic surgeons wanting to understand frame mechanics.

Images (Optional)

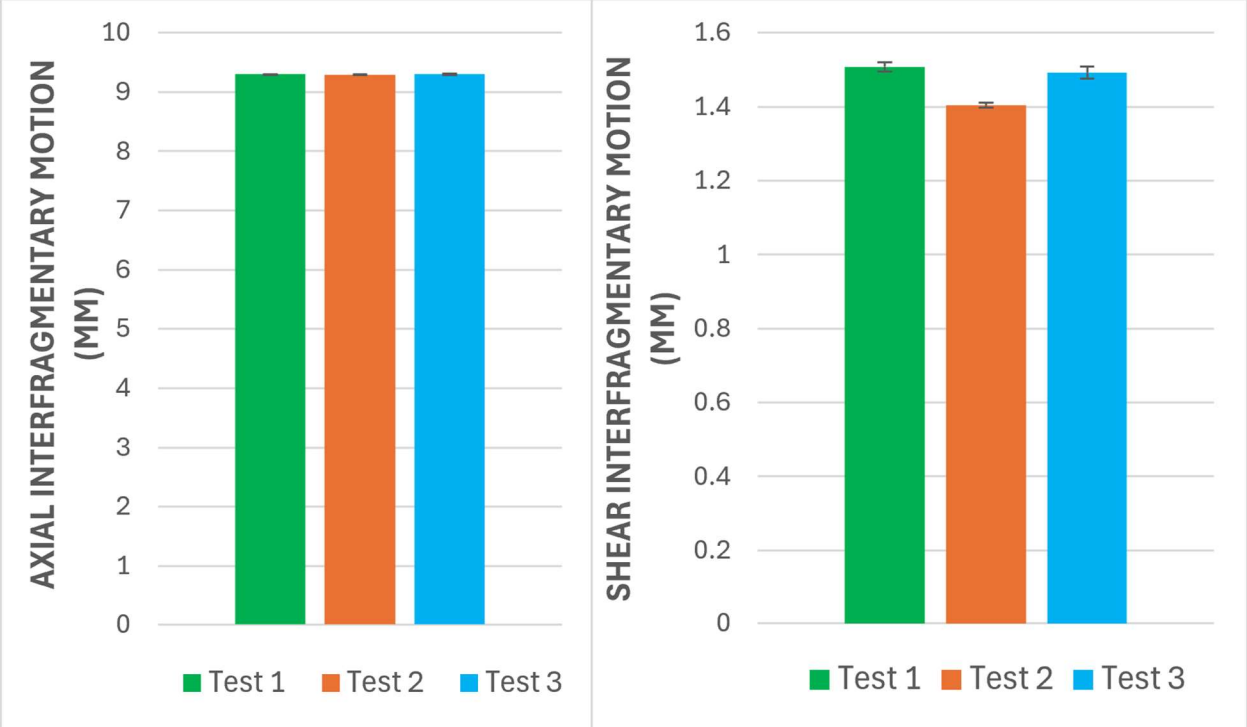


Figure 1. (left) Axial interfragmentary motion and (right) Shear interfragmentary motion during 700N compression. Error bars represent standard deviation across all 30 cycles for each test scenario.

References (Optional)

[1] Rechenmacher, A. J. et al, Eur J Orthop Surg Traumatol, 2023.

Session Category

Musculoskeletal Biomechanics: Methods, Models and Applications

P2-195

Assessing Forearm Muscle Activity During Grip Strengthening Exercises

Mr. Travis Winteler[1], Dr. Mike Sonne PhD[2], Dr. Michael Holmes PhD[1]

[1]Brock University, St. Catherines, Ontario, Canada. [2]Chicago Cubs, Chicago, Illinois, United States

Introduction

Baseball pitchers often injure the Ulnar Collateral Ligament (UCL). One mechanism of injury suggests that increased load is placed on the UCL when the forearm muscles fatigue due to repetitive high intensity throwing [1]. The flexor digitorum superficialis (FDS) supports the UCL by countering elbow torque [2]. However, it is difficult to measure the individual finger flexor compartments of FDS with surface electromyography. We aimed to assess the effect of grip strengthening devices on forearm muscle activity. A secondary aim was to explore the use of motor point detection to measure FDS.

Methods

10 university aged adults (6M/4F) completed a repeated measures protocol involving 3 grip devices: Grip Master, Handexer, and FlexPro Grip (Figure 1). Participants performed gripping tasks with both a “heavy” and “medium” intensity (defined by device). Electrodes with an 11 mm interelectrode distance (Grass Technologies, USA) were applied over flexor carpi ulnaris/radialis (FCU/FCR) and compartments of FDS. FDS compartments (index, middle, ring, little) were determined via stimulation of the motor point. Data were processed with MATLAB and included a linear envelope at 6Hz and normalized to maximal voluntary contractions (MVC).

Results

There was a significant main effect of intensity for average FCU activity ($p=.048$), as the heavy intensity generated greater muscle activity (13.5 ± 5.9 %MVC). There was no main effect of exercise for any of the muscles. Muscle activity in the FDS compartments across all conditions is listed lowest to highest: index (33.7 ± 6.7 %MVC), little (34.8 ± 5.5 %MVC), ring (45.8 ± 5.1 %MVC), and middle finger (60.2 ± 12.6 %MVC).

Discussion

Grip device did not influence muscle activity of the FDS, FCU, and FCR. Our novel motor point approach was critical to minimize crosstalk and allow isolation of FDS compartments. The FDS provides elbow stability [1] and, has lacked investigation due to measurement complexity. Many variables influence muscle development, and the notion

that higher activity directly relates to gains in strength or hypertrophy should be treated with caution [3].

Images (Optional)



Figure 1: Grip devices used from left to right: Handexer, FlexPro Grip, and Grip Master

References (Optional)

[1] Michael J. Mullaney *et al.* , *Med Sci Sports Exerc*, 2021

[2] Shota Hoshika *et al.* , *J orthop surg res*, 2020

[3] Andrew D. Vigotsky *et al.* , *Front physio, 2018*

Session Category

Musculoskeletal Biomechanics: Methods, Models and Applications

P2-196

A Coupled Mechanical-Electrophysiological Model of Muscle Contraction

Mr. Vahid Zare[1], Dr. Alessio Gizzi[2], Dr. Alfio Grillo[3], Dr. Walter Herzog[1], Dr. Salvatore Federico[1]

[1]University of Calgary, Calgary, Alberta, Canada. [2]Università Campus Biomedico di Roma, Rome, Lazio, Italy. [3]Politecnico di Torino, Turin, Piedmont, Italy

Mr. Vahid Zare

Dr. Alessio Gizzi

Introduction

The mechanism of muscle contraction started to become clear only in the 1950s. The discovery of the arrangement of the actin and myosin filaments led to the sliding filament theory and, shortly after, to the cross-bridge model of force production. Continuum mechanical models describe the bulk behaviour of muscle and use either an additive decomposition of the stress or a multiplicative decomposition of the deformation. We propose a novel approach, based on the multiplicative decomposition of the deformation and the Fenton-Karma electrophysiological model [1].

Methods

Muscle tissue is modelled as an active medium by multiplicatively decomposing its deformation into an active part, due to activation/contraction, and a passive, elastic part (this approach has historically been devised to model elastoplasticity). The active deformation, which is not measurable experimentally, is treated as an additional kinematical variable describing a rearrangement in the muscle's structure. The application of the principle of virtual work and the second principle of thermodynamics reveals a corresponding configurational force, which exerts work on the active deformation, and must be defined via a constitutive equation [2]. The configurational force, which we call activation, depends on electrophysiological (via the Fenton-Karma model), chemical (calcium concentration) and mechanical variable (muscle total and active stretch).

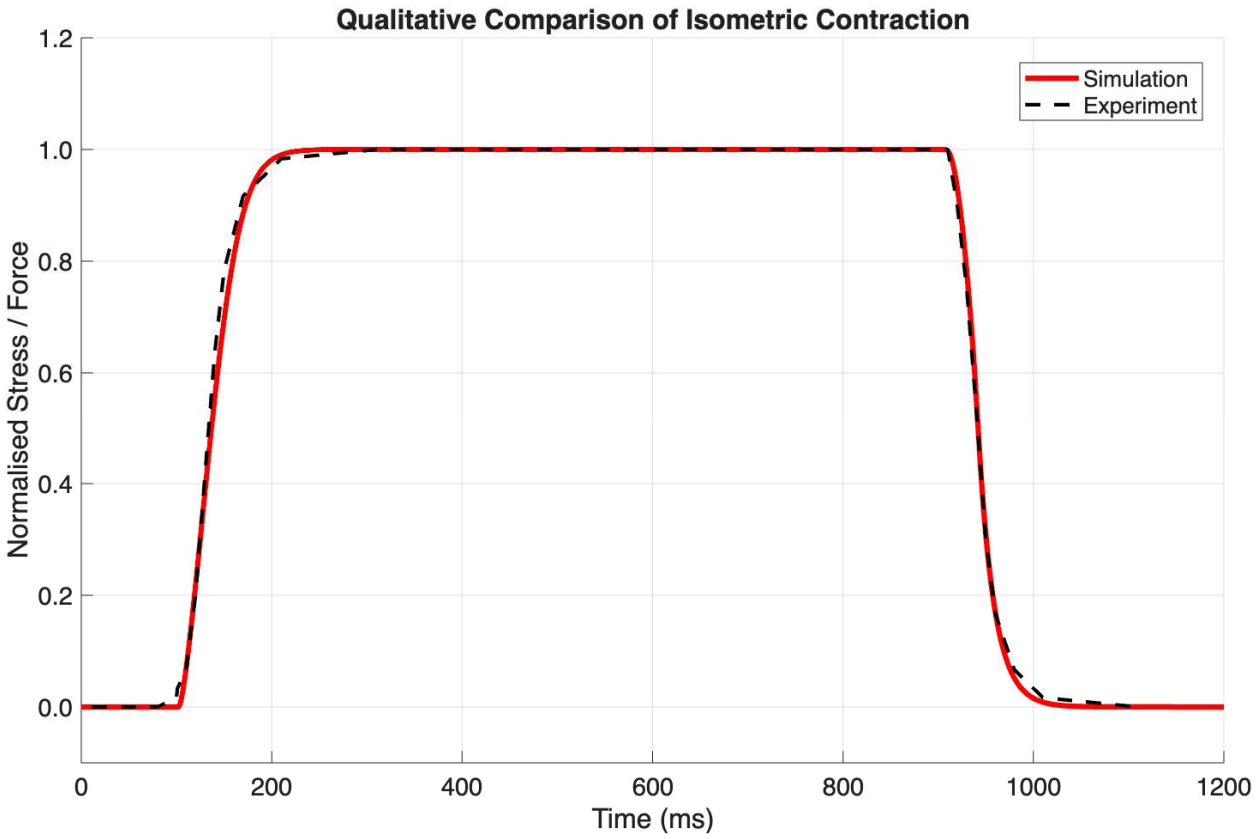
Results

The coupled mechano-electrophysiological model was solved to determine active stretch, total stretch and force generation. The model was used to reproduce the cases of isometric and isotonic contractions, as well as the classical force-length relationship. The figure shows the normalised force-time history during an isometric tetanic contraction. The solid red line represents the simulation results obtained from the proposed coupled continuum model, while the dashed black line represents the experimental data [3].

Discussion

The proposed framework robustly captures fundamental mechanical behaviours from experimental data. However, replicating complex history-dependent phenomena such as residual force enhancement requires further expanding the current kinematics. Future iterations of the model must explicitly incorporate the titin molecule to bridge this gap between standard mechanics and microstructural reality.

Images (Optional)



References (Optional)

[1] C. Cherubini et al., Phys. Rev. B, 2012

[2] A. Grillo and S. DiStefano, Math. Mech. Compl. Sys., 2023

[3] R. DeVita et al., J. Theor. Biol., 2017

Acknowledgements (Optional)

Session Category

Musculoskeletal Biomechanics: Methods, Models and Applications

P2-197

Accuracy and limitations of 3D-DXA reconstructions as surrogates for CT models of the femur: a multi-centre study

Dr Vee San Cheong[1,2], Dr Dheeraj Jha[2,3], Dr Alexander Baker[3], Dr Lorenzo Grassi[4], Dr Sang Wouk Cho[5], Dr Katelyn Greene[6], Dr Halldór Pálsson[7], Dr Ashley Weaver[6], Dr Namki Hong[8], Dr Yumie Rhee[8], Dr Sami Väänänen[9], Dr Hanna Isaksson[4], Dr Stephen Ferguson[3], Dr Benedikt Helgason[3]

[1]Insigneo Institute, University of Sheffield, Sheffield, -, United Kingdom. [2]Singapore-ETH Centre, Singapore, -, Singapore. [3]Institute for Biomechanics, ETH Zürich, Zurich, -, Switzerland. [4]Department of Biomedical Engineering, Lund University, Lund, -, Sweden. [5]Department of Internal Medicine, Yonsei University, Seoul, -, Korea, Republic of. [6]Department of Biomedical Engineering, Wake Forest University School of Medicine, Winston-Salem, North Carolina, United States. [7]Faculty of Industrial Engineering, University of Iceland, Reykjavik, -, Iceland. [8]Department of Internal Medicine, Yonsei University College of Medicine, Seoul, -, Korea, Republic of. [9]Department of Clinical Radiology, Kuopio University Hospital, Kuopio, -, Finland

Introduction

Assessments of 3D geometry, bone density distribution and bone strength currently require the use of computed tomography (CT). Estimations of 3D shape and density distribution of the proximal femur from 2D dual-energy x-ray absorptiometry (DXA) images, by using statistical shape and appearance models (SSAM), has been proposed as a low-cost and low-radiation alternative [1]. One implementation of SSAM is the commercially available 3D-Shaper software. However, there is currently no independent validation of this software on *in vivo* clinical images, across a multi-ethic dataset.

Methods

120 paired DXA and CT images from five cohorts (age: 20–85; aBMD:0.61–1.21 g/cm2; absence of disease treatment) were included in the study (Fig 1). Following semi-automatic segmentation to obtain the femoral geometry, bone mineral density (BMD) was derived from the X-ray attenuation coefficient using calibration phantom relationship. Simulated CT volumes and surfaces, termed 3D-DXA, were generated from 2D-DXA images (3D-Shaper Medical, Spain). 3D-DXA was compared to CT models to assess the geometrical and density distributional errors, using vertex-to-surface distance and voxel-based morphometry, respectively. The effect of the combined errors on predicted femoral

strength was evaluated with finite element analysis (FEA) of sideways fall in 12 orientations [2].

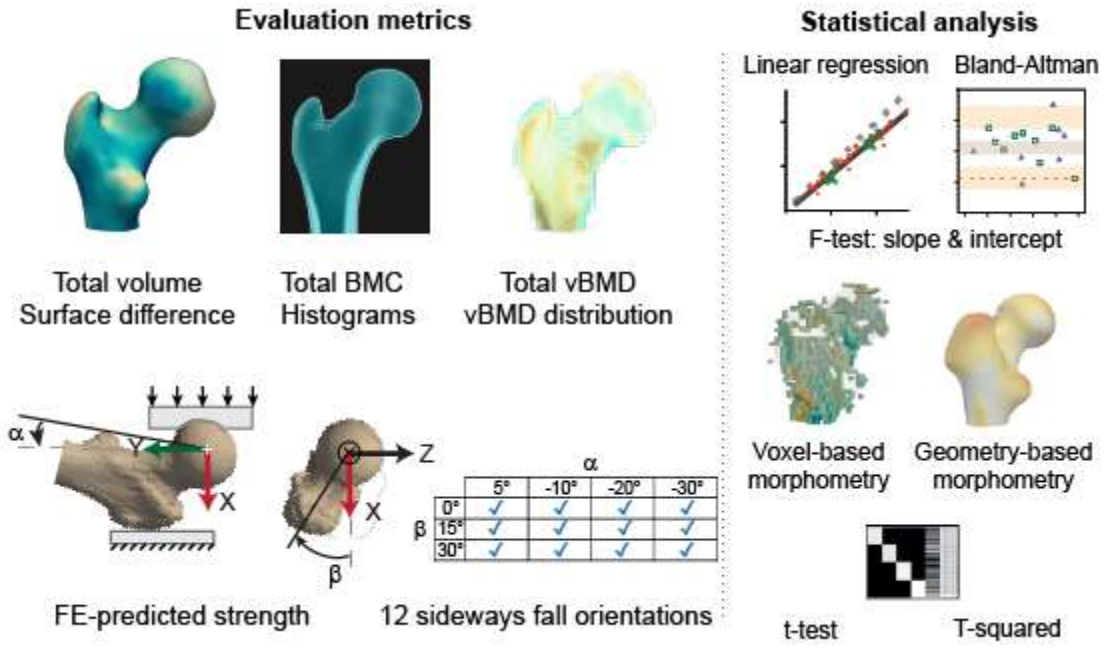
Results

Linear regression results showed that total bone mineral content were similar between 3D-DXA and CT models [AW1.1](slope=0.96, bias=1.6g), but volumetric measurements of 3D-DXA were underpredicted [AW2.1]for bone volume (slope=0.89, bias=9.73cm3) and total vBMD (slope=0.88, bias=6.27g/cm3). Cohort-specific differences in spatial distribution of vBMD were largest below the lesser trochanter and within 4 mg/cm3. However, differences in surface distance were not significantly different (Hotelling T-test). Modified Bland-Altman plots revealed positive slopes across all 12 orientations, as 3D-DXA femoral strengths were underpredicted at higher CT strengths.

Discussion

The low difference of total bone volume and error in surface distance shows that the shape of the femur is largely similar across the cohorts. However, the altered BMD distribution contributed to the underperformance of predicted bone strength. This reveals the limit of 3D-DXA as a surrogate for CT without further retraining of the statistical shape and appearance model.

Images (Optional)



References (Optional)

[1] Grassi *et al.*, Curr. Osteoporos. Rep., 2021
[2] Fleps *et al.*, Bone, 2022

Acknowledgements (Optional)

This work was supported by grants from the National Research Foundation Singapore (Future Health Technologies programme), the ETH focus area (PHRT #325, #430), the National Research Foundation of Korea (RS-2023-00231864), the Korea Health Industry Development Institute (RS-2023-00265620) and the NIH (R01AG050656, K25AG058804, F31AG069414).

Session Category

Musculoskeletal Biomechanics: Methods, Models and Applications

P2-198

Leveraging Thumb Muscle Redundancy With EMG-Based Clustering to Reduce Intramuscular Needle Insertions

Mr. Victor Akpaloo MS, Mr. Benjamin Nowak, Dr. Jennifer Nichols Ph.D.

University of Florida, Gainesville, Florida, United States

Introduction

Intramuscular electromyography (EMG) uses fine-wire needle electrodes inserted directly into muscles to record electrical activity with high spatial precision. This is especially useful for the small, overlapping muscles in the hand, where surface EMG cannot reliably separate individual muscles' activity. However, inserting electrodes into multiple muscles can cause pain and discomfort for participants and may not be necessary, as several thumb muscles are functionally redundant. As a critical first step toward designing future experiments that reduce intramuscular needle insertions without sacrificing data quality, this study aimed to identify clusters of thumb muscles with similar EMG patterns.

Methods

This analysis included 20 participants (18 females, 2 males; age: 67.5±9.5 years). Intramuscular EMG was collected from eight thumb muscles while participants performed three trials of key pinch. The EMG signals were processed using standard methods (filtering and rectification) and amplitude normalized using participant-specific maximum voluntary contractions. To identify muscle clusters, we applied and compared two k-means methods, namely a feature-based method and a method incorporating dynamic time warping (DTW) distance. Both were evaluated across k=2-7 clusters using silhouette analysis.

Results

The number of distinct muscle clusters identified were three (feature-based method) and four (DTW method). Both methods isolated EPL as a unique cluster, indicating it requires its own intramuscular insertion. The DTW method separated the remaining muscles into a flexor cluster (FPL-FPB), a radial abduction/opposition cluster (APL-EPB-OPP), and an intrinsic ulnar cluster (ADD-FDI), based on similarities in activation timing and shape (Fig. 1a). In contrast, the feature-based method separated the remaining muscles into an intrinsic cluster (FPB-ADD-FDI-OPP) and an extrinsic cluster (FPL-APL-EPB), driven by similarities in overall amplitude and variability (Fig. 1b).

Discussion

DTW identified four functionally-driven clusters, whereas feature-based clustering yielded fewer, yet intuitive, clusters at the cost of combining some temporally distinct intrinsic muscles patterns. Both approaches support the presence of thumb muscle redundancy and indicate that recording from only 3–4 representative muscles may approximate the behavior of all eight during key pinch. Ongoing work will test whether this strategy generalizes to other thumb tasks and enables accurate prediction of muscle activity from a reduced number of electrodes.

Images (Optional)

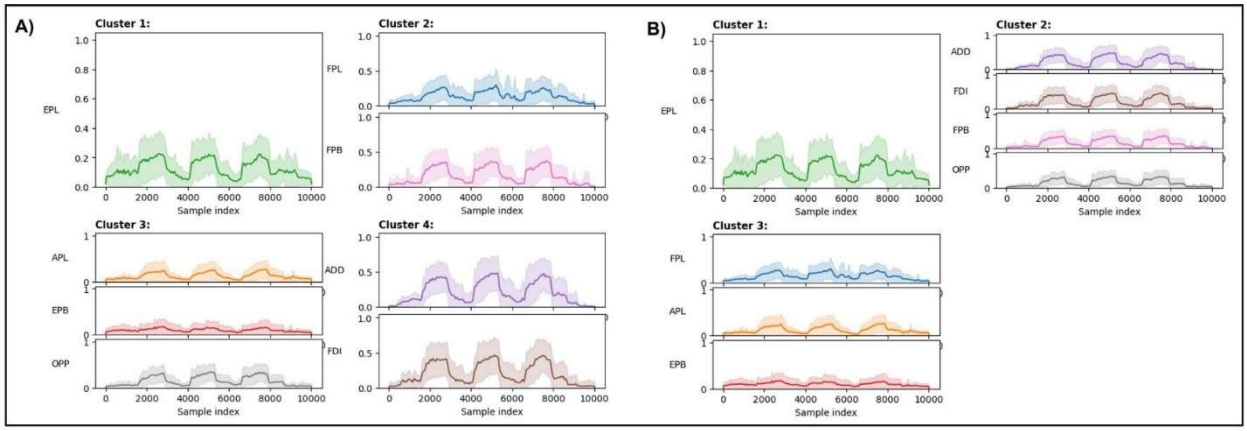


Figure 1: Average muscle activity normalized on a zero to one scale shown for (A) the four clustered identified using k-means with DTW distance metric versus (B) the three clusters identified using the feature-based k-means method. Shaded regions indicate standard deviation across subjects.

Acknowledgements (Optional)

Funding from NIH R01 AR078817.

Session Category

Musculoskeletal Biomechanics: Methods, Models and Applications

P2-199

Biomechanical Effects of Architecture in Skeletal Muscle: Fusiform vs. Unipennate Morphologies

Dr. Wei Zeng

New York Institute of Technology, Old Westbury, New York, United States

Introduction

Skeletal muscles exhibit diverse architectural patterns—including fusiform, unipennate, bipennate, and multipennate—each influencing mechanical performance. While fusiform muscles contain fibers aligned with the main axis, unipennate muscles incorporate a consistent pennation angle that alters force transmission. Capturing how these architectural differences shape active and passive behavior remains an unmet need in computational biomechanics. This study aims to develop a morphology-aware finite element (FE) framework for generating and simulating three-dimensional representative volume elements (RVEs) of fusiform and unipennate muscles using a Hill-type constitutive model with activation dynamics [1].

Methods

RVEs were constructed using Lloyd's algorithm and Centroidal Voronoi Tessellation (CVT) to generate a biofidelic distribution of fascicle-like inner cells surrounded by extracellular matrix (ECM). Two muscle morphologies were modeled: fusiform and unipennate, the latter evaluated at pennation angles of 10°, 20°, and 30°, consistent with clinical observations. Geometries were inflated to approximate physiological cross-sectional profiles. All models were meshed with 6-node C3D6 elements (element size: 0.05), with full node-to-node connectivity between fascicles and ECM. FE simulations incorporated two materials: fascicles governed by a Hill-type active model implemented through a user subroutine via Abaqus, and ECM modeled as passive connective tissue. A cohesive interaction maintained fascicle-ECM contact. Boundary conditions fixed one end of the RVE, while the opposite end underwent 10% axial elongation. Each morphology was analyzed under passive and fully activated states.

Results

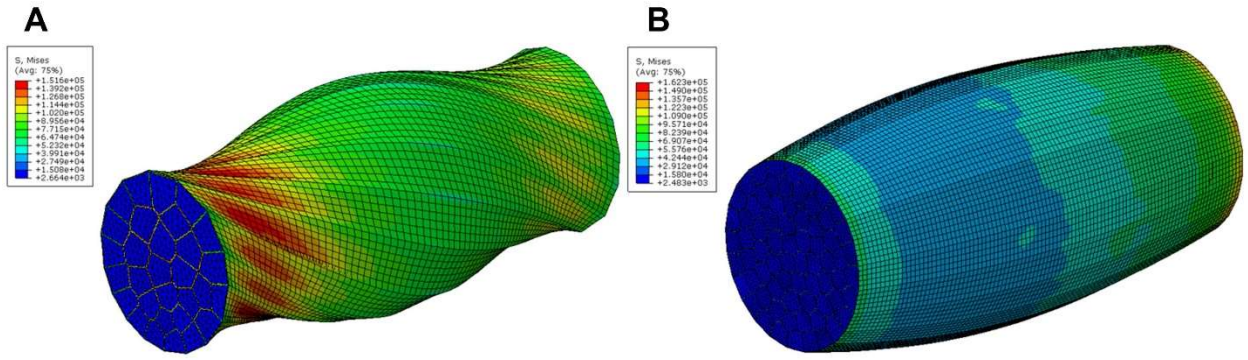
The framework successfully generated and simulated fusiform and unipennate RVEs with controlled activation. Fusiform muscles exhibited uniform stress distribution with a passive peak stress of 1.62×10^{5} Pa. In contrast, unipennate RVEs showed asymmetric stress concentrations localized near regions of reduced cross-sectional area, with patterns

varying systematically with pennation angle. Morphology-driven differences were evident across both passive and active conditions.

Discussion

This framework provides a robust approach for analyzing how muscle architecture influences mechanical response. Results highlight substantial differences between fusiform and unipennate geometries, underscoring the need for morphology-specific modeling. Future work will extend the framework to higher pennation angles, asymmetric fusiform shapes, and more complex architectures (e.g., bipennate and multipennate muscles), enabling patient-specific simulations for clinical and rehabilitation applications.

Images (Optional)



References (Optional)

[1] Zeng W, et al., Front Bioeng Biotechnol, 2023.

Acknowledgements (Optional)

This work was supported in part by the U.S. National Science Foundation (Award No. 2418992) and the 2025 Institutional Support of Research and Creativity (ISRC) program, funded by New York Institute of Technology (NYIT).

Session Category

Musculoskeletal Biomechanics: Methods, Models and Applications

P2-200

A New Load-Transfer-Based Assessment Approach for Hip Stems: Application to a Cementless Stem During Walking

Dr. Mohamed Bendjaballah, Dr. Wissal Mesfar

King Saud University, Riyadh, Central Region, Saudi Arabia

Introduction

Stress shielding remains a key concern in total hip replacement, arising when the stiff stem carries loads normally borne by the proximal femur. Existing analytical and experimental studies describe load-transfer patterns but lack a simple metric to compare stem–bone load sharing or assess how bone loading changes after implantation. This study introduces the D50/50 parameter, the stem location where implant and cortical bone carry equal internal load and physiological cortical loading begins to recover. From subject-specific FE simulations, internal loadings along the femoral shaft were used to compute D50/50, enabling comparison of cementless stem designs.

Methods

3D intact and implanted femoral models were reconstructed from CT data, refined in Geomagic Studio®, and combined with a SUMMIT-type stem in SolidWorks®. The models were meshed in ABAQUS using C3D20R elements, with orthotropic cortical bone and isotropic cancellous bone and Ti–6Al–4V stem; all interfaces were bonded. Hip joint and muscle loads from Heller et al. simulated walking [1]. Internal forces and moments were computed at 35 equidistant cross-sections and plotted along the shaft length. The D50/50 point was identified as the intersection of implant and bone curves, beyond which bone recovers its physiological load.

Results

Equal bone–stem load sharing occurred at **32% of the stem length** for axial force (Fx) and **36%** for lateral bending (My) (Figure 1), the components generating normal stress. Internal shear forces and torsional moments were minimal. The forward bending moment (Mz) increased distally under antero-posterior loading with little interplay. Thus, the **worst-case D50/50 was 36% for the studied stem under walking**.

Discussion

Model predictions showed good agreement with in-vivo and analytical reconstructions for both intact and implanted femora [2, 3], supporting the validity of the internal force calculations. The study's key contribution is the introduction of the **D50/50** parameter, a

novel, dimensionless indicator that identifies where bone and stem share equal load. By quantifying the spatial recovery of physiological loading, D50/50 offers a clear, comparative and clinically meaningful measure of stem load-transfer performance.

Images (Optional)

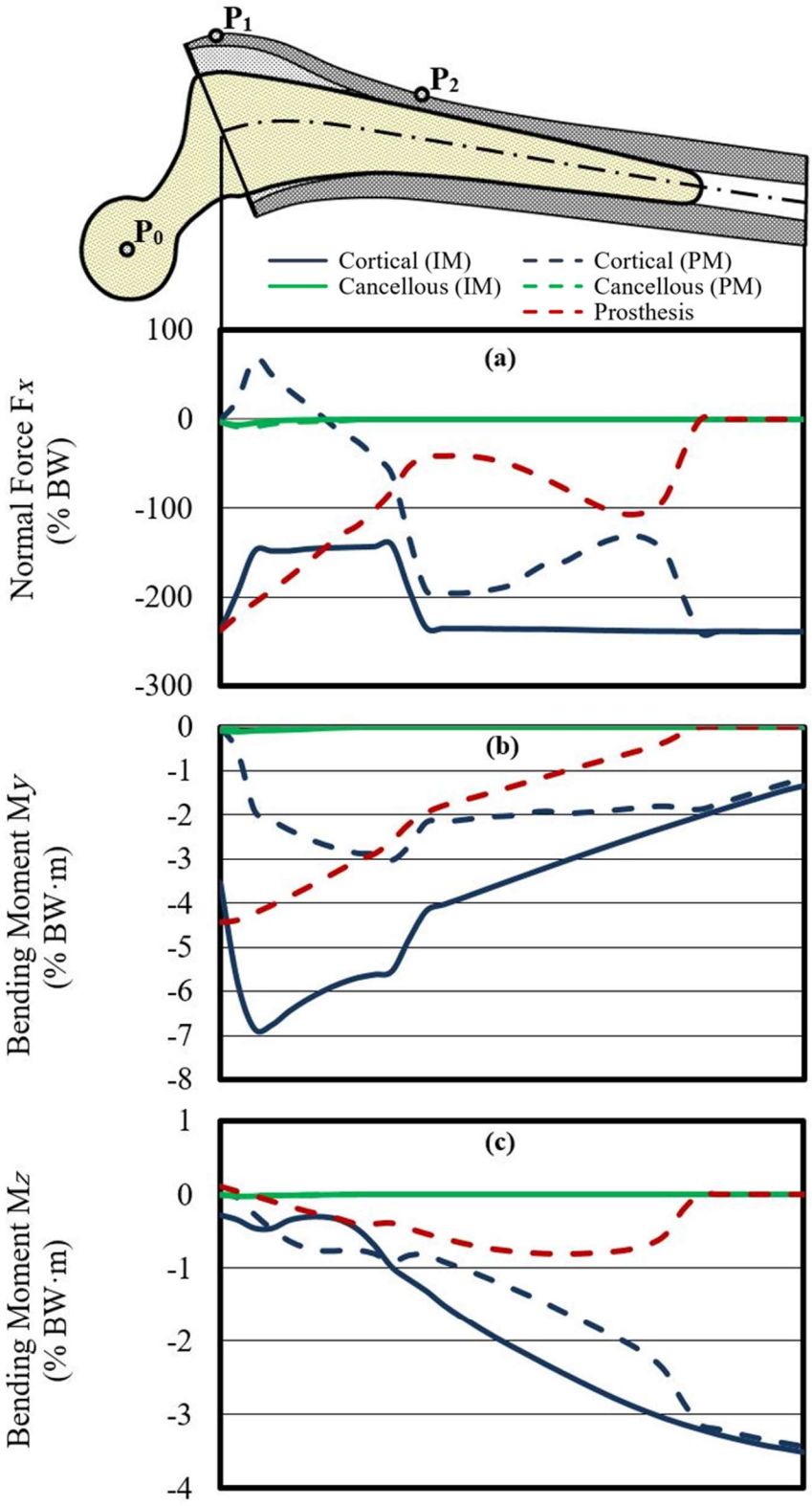


Figure 1: Internal normal force F_x (a), bending moments M_y (b) and M_z (c) expressed as a % BW and % BW·m, respectively, for the intact model (IM) and prosthetic model (PM). P_0 is the center of the femoral head/implant where the hip joint contact force acts. P_1 and P_2 are the muscles' attachment sites.

References (Optional)

[1] Markus Heller et al. , J Biomechanics, 2005

[2] Markus Heller et al. , Clin Biomechanics, 2001

[3] Georg Duda et al. , J Biomechanics, 1997

Session Category

Musculoskeletal Biomechanics: Methods, Models and Applications

P2-201

A Proposal for a Non-invasive Ligament Elongation Measurement Method

Mr. Yudai Yamamoto MA, Mr. Md Fahad Sahed BA, Dr. Katsuyuki Morishita Assistant Professor, Dr., Prof. Ikuo Mizuuchi Professor

Tokyo University of Agriculture and Technology, Koganei, Tokyo, Japan

Introduction

Measuring ligament elongation helps clarify injury mechanisms, prevent injuries, and evaluate treatment outcomes. Non-invasive methods such as fluoroscopy, CT, MRI, and motion capture exist. Although motion capture allows unrestricted, dynamic movement, it is affected by soft-tissue motion, which can introduce positional errors up to 20 mm[1]. This research aims to reduce these errors by modeling soft-tissue deformation.

Methods

We modeled knee in the frontal place by representing connections between skin and bone using ligament, flesh, and skin springs. Joint angle was estimated as the angle that minimizes total stored potential energy. We compared ligament-elongation estimation methods: (A) our proposed method, (B) estimating roll angle by minimizing error between skin-marker positions and those predicted by a rigid-link model, and (C) estimating roll angle by averaging posture defined by two selected skin markers.We also conducted an experimental comparison using a knee-joint prototype with springs representing ligament, flesh, and skin. The stiffness ratios were set to emulate human joint stiffness around the sagittal axis, and we compared method (A), (B) and (C).

Results

Using the mathematical model, we compared angle errors between the true angle and the angles estimated by each method. For all methods, error increased as the joint angle approached 30 deg. When flesh stiffness equaled skin stiffness, estimation erros tended to increase. Our proposed method outperformed the others. Evaluations using the physical prototype showed that our method achieved the highest accuracy for angles 1 to 2.5 deg. At approximately, -2.5 to 1 deg, results differed from those of the mathematical model due to measurement and modeling errors.

Discussion

Method (C) is less affected because it uses markers rigid to the shin, avoiding skin and flesh deformation. In method (B), only skin deformation is considered, causing its estimation accuracy to degrade more than that of method (A). Method (A) accounts for

both skin and flesh deformation, however contains angle estimation error due to irreversibility between forward and inverse optimization processes. Improving measurement accuracy and obtaining more precise spring coefficients, dimensions, and attachment locations would further demonstrate the superiority of the proposed method (A).

Images (Optional)

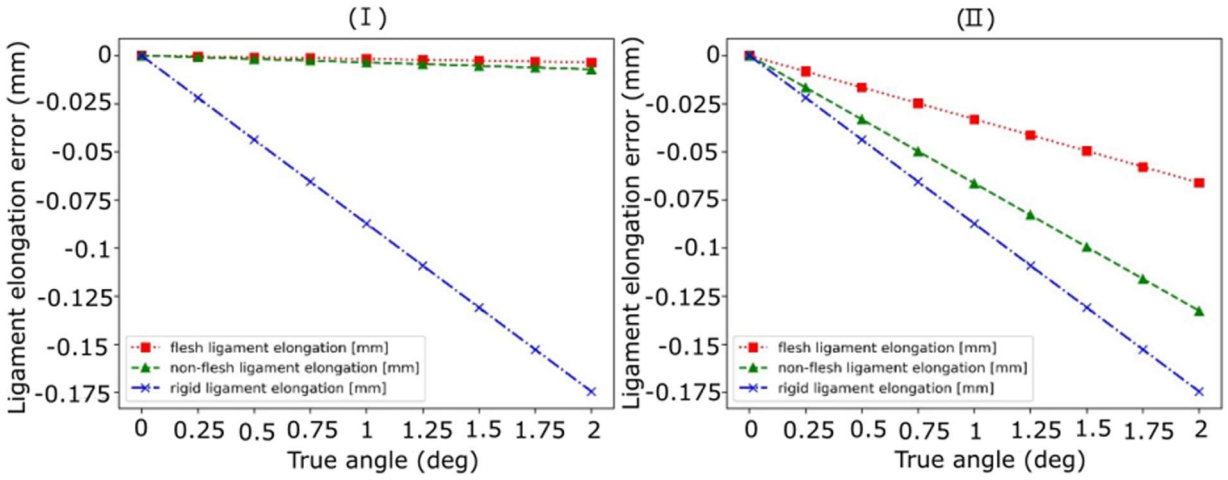


Fig.1 Ligament elongation errors (0-2 deg) obtained by three estimation methods under two parameter conditions (Ⅰ)$k_{MCL} = k_{LCL} = 1.07 \times 10, k_{flesh} = 1.5, k_{skin} = 2.5 \times 10^{-2}$ [N/mm], and(Ⅱ)$k_{MCL} = k_{LCL} = 1.07 \times 10, k_{flesh} = k_{skin} = 2.5 \times 10^{-2}$ [N/mm]. Square markers denote our proposed method (A), triangle markers indicate method (B), and cross markers indicate method (C).

References (Optional)

[1]Cappello A et al., IEEE Trans BioMed Eng., 2005.

Acknowledgements (Optional)

This work was supported by JST SPRING, Grant Number JPMJSP2116.

Session Category

Musculoskeletal Biomechanics: Methods, Models and Applications

P2-202

Influence of Transverse Work on Muscle Power Output During Cyclic Contraction

Ms. Zahra Heydari PhD Student, Biomedical Physiology & Kinesiology (BPK), Simon Fraser University[1], Mr. Harshil Pathak PhD Student, Department of Mathematics, Simon Fraser University[2], Dr. James M. Wakeling Professor, Biomedical Physiology & Kinesiology (BPK), Simon Fraser University[3], Dr. Nilima Nigam Professor, Department of Mathematics, Simon Fraser University[2]

[1]Biomedical Physiology & Kinesiology (BPK), Simon Fraser University, Burnaby, British Columbia (BC), Canada. [2]Department of Mathematics, Simon Fraser University, Burnaby, BC, Canada. [3]Biomedical Physiology & Kinesiology (BPK), Simon Fraser University, Burnaby, BC, Canada

Introduction

Muscles perform mechanical work and power in their line of action. As muscles change in length their cross-sectional area must change in an attempt to maintain their volume. Transverse bulging has can perform" lifting work", and transverse compression acts to decrease the longitudinal forces of the muscle; however, these considerations have only been for isometric contractions. This study investigated whether an oscillating transverse load could modify the power that the muscle generates in its line of action during a cyclic contraction.

Methods

A three-dimensional muscle model (Flexodeal-lite, an open-source model that represents muscle as a fibre-reinforced composite biomaterial) was used. We simulated cyclic contractions of a block of muscle that was largely active during its shortening phase. Transverse, time-varying, pressures were applied to the transverse faces of the block. The phase of these pressures relative to the longitudinal length-changes were varied. 16 conditions were tested: 2 initial pennation angles (0 and 30°), 2 compression levels (0 and 15 kPa), and 4 phases.

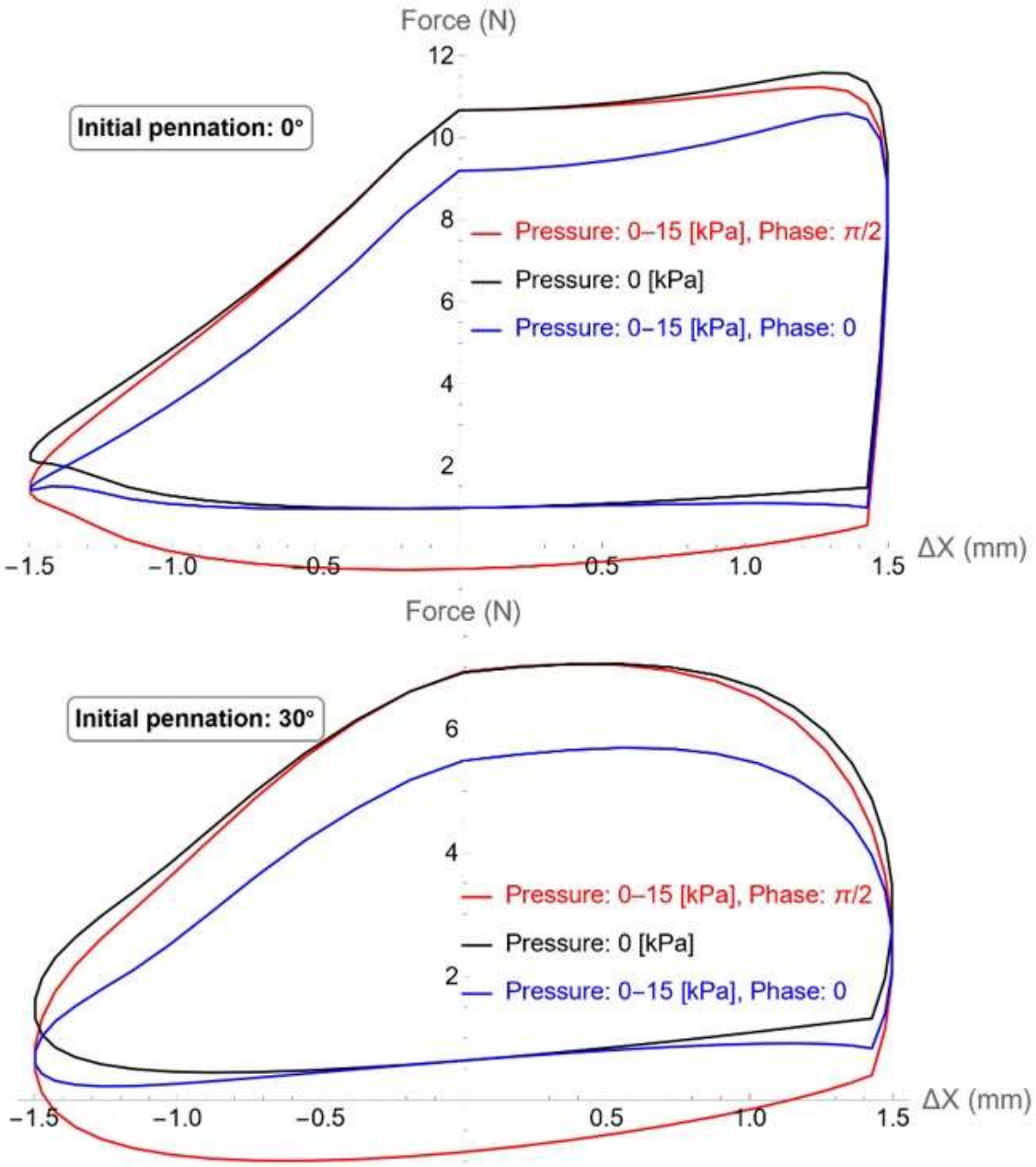
Results

The muscle block acted line a “motor” generating positive power in its line-of-action. The oscillating transverse pressure resulted in both augmentation and suppression of the power. These general effects were consistent between the parallel-fibred block (0° pennation) and the pennate (30° pennation) blocks of muscle that were simulated; however, in the 0° pennation block the deformations and transverse work were the same in the width and thickness directions, but the deformations and work differed between the width and thickness directions for the 30° pennation block.

Discussion

Doing external work on the transverse surfaces of a muscle can alter the longitudinal work done by the muscle in its line-of-action. This has implications for future design of prosthetic devices or inspire novel mechanisms for augmenting joint work and power when we move. The optimal conditions for enhancing longitudinal muscle work have not been established yet, however, even in these preliminary simulations we are observing an efficiency of about 50% that relates the transverse work applied to the enhancement of the longitudinal work

Images (Optional)



Session Category

Musculoskeletal Biomechanics: Methods, Models and Applications

P2-203

Cortical Bone Adaptive Response to Loading is Impaired in Male *Col1a1$^{Jrt/+}$* Mouse Model of Osteogenesis Imperfecta

Mr Abhimanyu Mertiya[1,2], Dr Mayumi Umebayashi[1], Mr Richard Ilianu[1], Mr Karim Elsayed[1], Dr Meet Shah[1], Dr Michael Bruccoleri[1], Dr Frank Rauch[1,3], Dr Bettina Willie[1,2]

[1]Shriners Hospital for Children, Research Center, Montreal, Quebec, Canada. [2]Faculty of Dental Medicine and Oral Health Sciences, McGill University, Montreal, Quebec, Canada. [3]Department of Pediatrics, McGill University, Montreal, Quebec, Canada

Introduction

Osteogenesis Imperfecta (OI) is a heritable bone fragility disorder, with the majority of cases caused by mutations in genes encoding type I collagen (*COL1A1* and *COL1A2*). The cross-sectional area of long bones is persistently low in people with OI, and thus may be a key factor leading to increased long bone fracture rates. We hypothesize that this reduced bone circumference is the result of reduced periosteal apposition caused by an altered response to mechanical loading. To test this hypothesis, we examined mechano-adaptation in a mouse model of OI.

Methods

Sixteen-week old male *Col1a1$^{Jrt/+}$* OI mice and their wild type (WT) littermates (n=10 mice/genotype) underwent two weeks of dynamic, compressive *in vivo* tibial loading to the left tibia (once daily, 5 days/week), while right tibia served as non-loaded control (Fig 1A). *In vivo* micro-computed tomography analysis was performed at baseline (day 0) and day 15 to quantify changes in diaphyseal cortical and metaphyseal trabecular bone mass and microstructure. ANOVA, Tukey's post-hoc, and paired t-tests were performed ($p<0.05$).

Results

Loading led to a 134% greater increase in cortical thickness of left limb compared to non-loaded right limb in WT mice (Fig 1B). We also observed a 118% greater decrease in marrow area of loaded limb compared to non-loaded limb in WT mice, although this was only trending towards significance ($p=0.06$, Fig 1C). Whereas no significant difference was measured in cortical thickness or marrow area between the loaded and non-loaded limbs in the *Col1a1$^{Jrt/+}$* mice (Fig 1B & 1C). Loading did not significantly increase metaphyseal trabecular bone in WT mice, but showed a trend of increased bone deposition in trabecular bone volume (per unit total volume) in loaded limb as compared to non-loaded limb for WT

mice, and a trend of bone loss (reduced trabecular volume per unit of total volume in loaded limb) in the *Col1a1*$^{Jrt/+}$ mice (Fig 1D).

Discussion

In line with our hypothesis, male *Col1a1*$^{Jrt/+}$ OI mice did not respond to loading. Studies in female *Col1a1*$^{Jrt/+}$ mice are ongoing. These results indicate that the male *Col1a1*$^{Jrt/+}$ OI mouse model has a reduced cortical mechano-adaptive response.

Images (Optional)

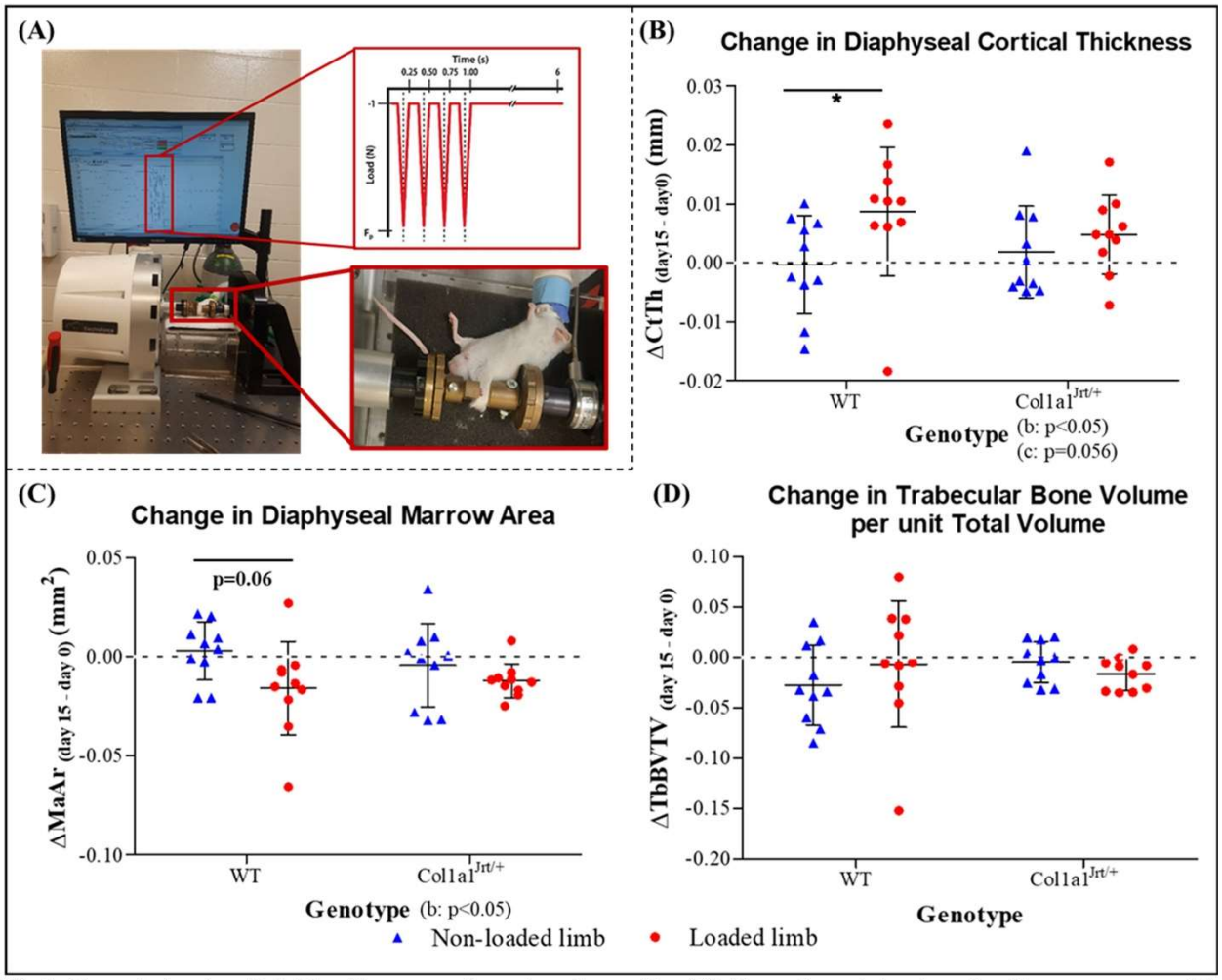


Fig.1. 2-week *in vivo* tibial loading experiment and results: (A) Experimental setup: loading apparatus with mouse position shown in bottom right and loading waveform shown in upper right; **(B) change in cortical thickness (ΔCtTh (day 15-day 0)); (C) change in marrow area (ΔMaAr (day 15-day 0)); (D) change in trabecular bone volume per unit total volume (ΔTbBVTV (day 15-day 0));** Means ± SD; ANOVA (a=genotype, b=loading, c=interaction), tukey's posthoc test; paired t-test (* p<0.05).

Session Category

P2-204

Correlating MRI-Based Paraspinal Muscle Quality and Single Fibre Contractile Function in Canines With Spinal Degeneration

Mr Adam Bui MSc[1], Dr Josh Briar PhD[1], Dr Francesca Samarani DVM[2], Dr Alex Chan DVM[1], Dr Fiona James DVM[1], Dr Stephen Everest DVM[1], Dr Stephen Brown PhD[1]

[1]University of Guelph, Guelph, Ontario, Canada. [2]Canada West Veterinary Specialists and Critical Care Hospital, Vancouver, British Columbia, Canada

Mr Adam Bui

Dr Josh Briar

Introduction

Paraspinal muscle dysfunction has been associated with low back pain in humans [1]. Magnetic resonance imaging (MRI) provides a non-invasive method for evaluating structural changes related to muscle quality. However, how this relates to contractile function is unclear. The purpose of this study was to correlate MRI-based muscle quality to single-fibre contractile function in canines being surgically treated for IVD extrusion. It was hypothesized that lower quality muscle presented on MRI would correlate to lower performance in contractile function.

Methods

Preoperative imaging of the thoracolumbar spine was performed using MRI (n=11) in canines being surgically treated for IVD extrusions. T1-weighted MRI DICOM images were taken at the level of extrusion. Regions of interests were drawn to include the bulk of the multifidus. MRIs utilized pixel intensity of the muscle normalized to a region of adjacent subcutaneous fat to create a muscle-fat index; a higher muscle-fat index indicated lower muscle quality. Muscle biopsies (n=11) were obtained during surgery, chemically permeabilized and single fibres were extracted. Single fibres were maximally activated in a calcium-rich solution, and specific force was measured.

Results

A weak positive correlation (r^2=0.17, p=0.20) was observed between T1-weighted MRI muscle-fat index and muscle fibre specific force (Figure 1).

Discussion

It was expected that lower muscle quality measured by MRI would correlate with lower performance in single-fibre contractile function. A higher muscle-fat index indicates greater fatty infiltration, or lower-quality muscle. Contrary to the hypothesis, as the muscle-fat index increased, muscle-specific force also increased, albeit in a weak, non-statistically significant manner. Previous literature has investigated the relationship between fatty infiltration and muscle force production, suggesting that an increase in fat infiltration is associated with decreased force production [2]. However, this novel study investigates force production on a single fibre level, which may offer insights into compensation mechanisms related to fatty infiltration in muscle due to lost strength in neighbouring degenerated fibres. Next steps are to increase the sample size to determine if this relationship between muscle quality and contractile function strengthens or weakens.

Images (Optional)

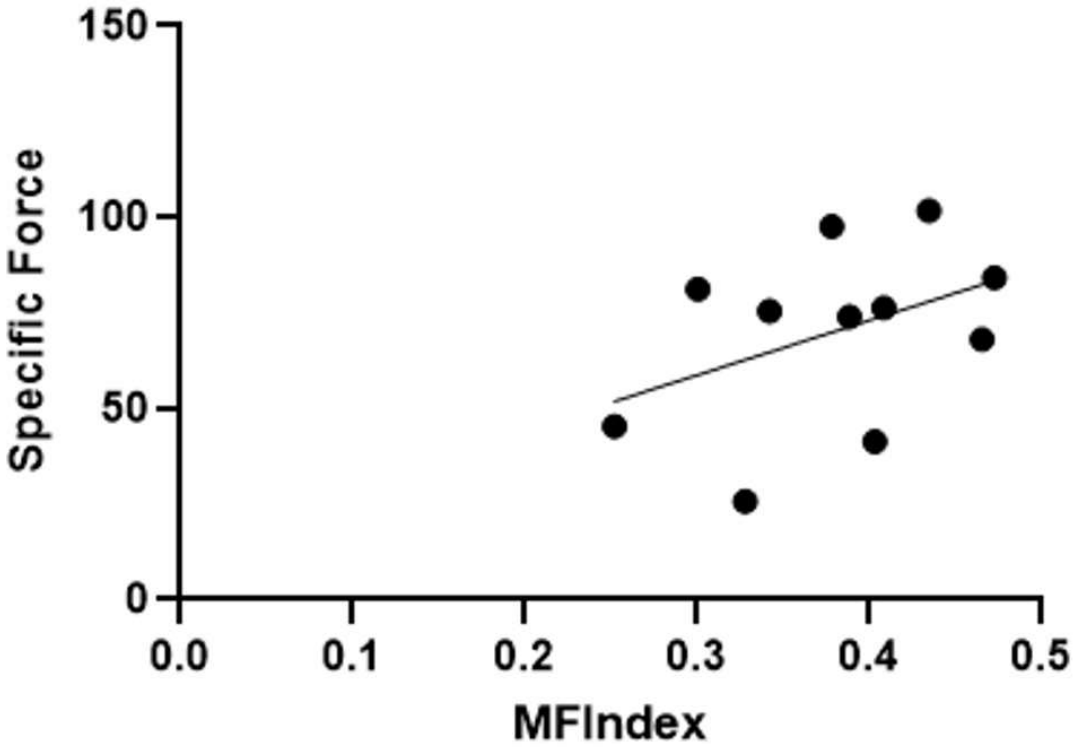


Figure 1. Relationship between MRI-based muscle-fat index and single fibre specific force. Note that a higher MFIndex indicates higher fatty infiltration.

References (Optional)

[1] Noonan AM, Brown SHM. JOR Spine 2021; doi: 10.1002/jsp2.1171

[2] Hilton TN et al. Phys Ther. 2008; doi:10.2522/ptj.20080079

Session Category

Musculoskeletal Biomechanics: Tissues

P2-205

Investigating Stretch-Shortening Cycle Performance Enhancement in Single Muscle Fibres Following Acute Hindlimb Immobilization of the Rat

Dr. Alexander Zero PhD, Dr. Geoffrey Power PhD

University of Guelph, Guelph, Ontario, Canada

Introduction

Power production of single muscle fibres is impaired following periods of immobilization. However, muscles are sensitive to their activation history and thus isolated activations may not be representative of their contractile capacity. For example, during locomotion muscles undergo stretch-shortening cycles (SSCs) in which active muscle shortening is directly preceded by active muscle lengthening. Indeed, the SSC effect can be characterized by the enhancement of power during shortening that is preceded by active lengthening compared to a pure shortening contraction. Therefore, the purpose was to assess the effect of immobilization on SSC performance of single muscle fibres.

Methods

The left hindlimb of three Wistar rats (~11 weeks) was placed in a cast and immobilized in full plantar flexion for 14 days, the right leg was an internal control. Following immobilization, fibres were dissected and chemically permeabilized from the soleus and medial gastrocnemius of both legs. Single fibres were maximally activated (pCa 4.5, 12°C) while mounted between a force transducer and length controller. For SSCs, fibres were stretched from a sarcomere length of 2.5 to 3.0μm and immediately shortened back to 2.5μm at a speed of 0.6 Lo/s for both phases.

Results

Thirty-eight fibres (11 soleus and 27 medial gastrocnemius) were tested (16 from the immobilized limb). Fibres from the immobilized limb had a ~40% smaller cross-sectional area. At a sarcomere length of 2.5μm absolute and normalized force from the immobilized limb were ~58% and ~26% lower, respectively. During active stretch (2.5 to 3.0μm) peak absolute and normalized eccentric force of the immobilized limb was ~68 and ~42% lower, respectively. During active shortening (3.0 to 2.5μm) the immobilized limb had a ~65 and ~38% lower absolute and normalized power, respectively. Following immobilization, the SSC effect occurred such that when active stretch preceded active shortening normalized power increased ~66% relative to a pure shortening contraction. However, the non-casted limb displayed a larger SSC effect of a ~84%.

Discussion

The SSC effect is still apparent at the single fibre level following acute immobilization. Therefore, despite impairments in contractile capacity, single fibres are still sensitive to activation history force enhancement albeit likely in a reduced capacity.

Acknowledgements (Optional)

Supported by NSERC.

Session Category

Musculoskeletal Biomechanics: Tissues

P2-206

Adaptations of Serial Sarcomere Number and Mechanical Function Following Unilateral Hindlimb Immobilization and Recovery in the Plantar Flexors of Female Ovariectomized and Intact Rats

Ms. Alexandra Q. Kirkup, Ms. Amelia Rilling, Dr. Alexander M. Zero, Dr. Geoffrey A. Power

University of Guelph, Guelph, Ontario, Canada

Introduction

Immobilization of muscle in a shortened position induces marked reductions in serial sarcomere number (SSN), thereby impairing contractile function. While this response is well documented in male rodents, the effects of estrogen on SSN and contractile function in female rodents following immobilization and re-ambulation remain unclear. The purpose of this study was to investigate estrogen-mediated differences in loss and subsequent recovery of SSN in the soleus and medial gastrocnemius (MG) and plantar flexor contractile function following 14 days of unilateral hindlimb immobilization and 4 weeks of voluntary ambulation.

Methods

The left hindlimb of intact (normal estrogen; n = 24; mass = 290.6g ± 25.1g) and ovariectomized (OVX; low estrogen; n = 24; mass = 317.8g ± 27.3g) adult female Sprague-Dawley rats was immobilized in maximal plantar-flexion for 14 days. In-vivo plantar-flexor mechanical testing was performed pre-cast and at 4 recovery timepoints (post-cast, 1-,2-,4- weeks following cast removal). At each recovery timepoint, n = 6 intact and n = 6 OVX rats were euthanized, both legs were fixed in formalin, the soleus and MG were harvested, and connective tissue was digested in nitric acid, then muscles were stored in glycerol. Fascicle length was measured, and laser diffraction was performed to measure sarcomere length. Serial sarcomere number was then calculated.

Results

Soleus SSN loss and plantar flexor peak torque followed similar trajectories, with comparable ~16% and ~45% decreases in both groups, respectively, immediately following casting ($P < 0.05$). By 4 weeks, intact rats demonstrated full architectural and functional recovery, with SSN returning to baseline (–1%) and torque surpassing pre-cast values (+28%; $P < 0.05$). In contrast, OVX rats showed blunted recovery across all measures, with

persistent deficits in SSN (–10%) and torque (–14%; both $P < 0.05$), indicating impaired recovery under low-estrogen conditions.

Discussion

The parallel recovery trajectories of SSN and peak torque indicate that estrogen may facilitate serial sarcomerogenesis and restoration of muscle contractile capacity following acute immobilization in female rats. Overall, these results identify estrogen as an important modulator of longitudinal muscle morphology and whole muscle contractile function in female rats.

Acknowledgements (Optional)

Supported by NSERC

Session Category

Musculoskeletal Biomechanics: Tissues

P2-207

Effects of Asymmetric Glycerol-Induced Paraspinal Muscle Degeneration on Spinal Curvature

Ms Aliza Siebenaller MSc, Dr Stephen Brown PhD

University of Guelph, Guelph, Ontario, Canada

Ms Aliza Siebenaller

Introduction

Adult degenerative scoliosis (ADS) is associated with paraspinal muscle degeneration and dysfunction; however, it remains unclear if these muscular changes drive deformity. Interestingly, this muscle degeneration presents asymmetrically in some ADS patients [1]. The purpose of this study was to evaluate the effects of induced asymmetric lumbar and thoracic paraspinal muscle degeneration on spinal deformity in mice. A resulting coronal plane imbalance and scoliotic curvature were hypothesized to occur.

Methods

23 female C57BL/6 mice were divided into three groups: control (n=6), ipsilateral (n=9), and contralateral (n=8). To induce muscle degeneration, glycerol [2] was injected into multifidus (15ul) and erector spinae (20ul) muscles of the right lumbar and thoracic regions (ipsilateral), or right lumbar and left thoracic regions (contralateral). Injections were administered two weeks apart for a total of 4 timepoints, and mice were sacrificed two weeks after the last injection. Control animals received no injections. Micro-CT imaging was used to measure spinal curvature (Cobb angle) in the coronal and sagittal planes throughout the study. Statistical significance was determined using two-way repeated measures ANOVA (a=0.05) and Tukey's multiple comparisons test.

Results

Mean coronal Cobb angles were small (<6°) at all timepoints and no significant difference was found between groups. In the sagittal plane, a significant effect of group ($p=0.0007$), time ($p=0.0002$), and interaction ($p<0.0001$) were found. Post-hoc analysis showed that only the contralateral group demonstrated a significant decrease in sagittal plane Cobb angle over time (Figure 1).

Discussion

Contrary to the hypothesis, no clinically meaningful differences were found in coronal plane Cobb angles following muscle glycerol injections. Surprisingly, significant decreases in sagittal plane Cobb angles were found in the contralateral group. The contralateral group did have higher baseline Cobb angles than the control and ipsilateral groups which could explain why a more significant decrease was observed.

Images (Optional)

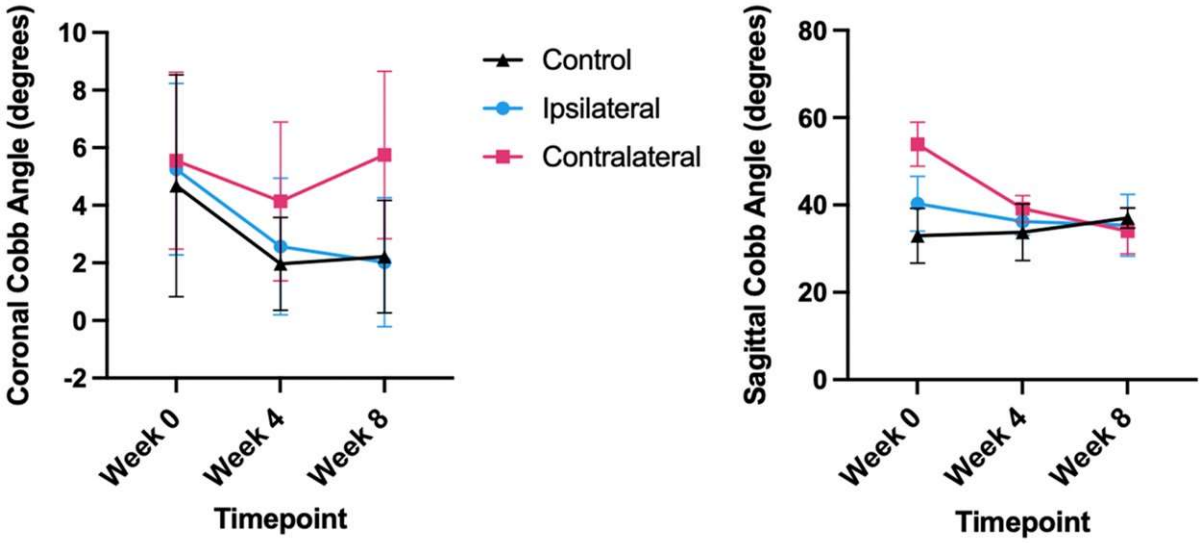


Figure 1. Mean ± SD Cobb angles in the coronal and sagittal planes for the control, ipsilateral, and contralateral groups at 0, 4, and 8 weeks

References (Optional)

[1] Najibullah Shafaq *et al.*, Spine, 2012.

[2] Alex Noonan *et al.*, Sci Rep, 2023.

Session Category

Musculoskeletal Biomechanics: Tissues

P2-208

The Impact of Eccentric Overload Training and Conventional Resistance Training on Sarcomerogenesis and Mechanical Function in Ovariectomized and Intact Rats

Ms. Amelia Rilling, Ms. Alexandra Q. Kirkup, Dr. Geoffrey A. Power

University of Guelph, Guelph, ON, Canada

Introduction

Sarcomerogenesis is the serial addition of sarcomeres in a muscle, which can impact the muscle's contractile performance. Eccentric exercise, where the muscle is stretched to long lengths, promotes sarcomerogenesis owing to the stress and strain throughout the muscle's excursion. However, during conventional (CONV) resistance training, eccentric contractions are typically performed with concentric contractions. The load-bearing capacity of eccentric contractions exceeds concentric contractions, resulting in a sub-maximal eccentric stimulus. Eccentric overload ($ECC_{OVERLOAD}$) training offers a maximal eccentric stimulus. Recently, we found a 15% greater soleus serial sarcomer number (SSN) response with $ECC_{OVERLOAD}$ training in young male and female rats. Females had the largest response. Therefore, female sex hormones may play a role in longitudinal remodeling. Estradiol, a female sex hormone, has been shown to augment muscle recovery after eccentric exercise-induced muscle damage, and thus may have a role in the muscle's response to eccentric exercise.

Methods

Using an *in-vivo* rodent model, we investigated the impact of estradiol and estradiol deficiency on the mechanical and morphological response to resistance training. Forty ovariectomized (n=20) and ovary-intact (n=20) female rats completed 4 weeks of plantar flexor $ECC_{OVERLOAD}$ (n=20) or CONV (n=20) resistance training of the left leg 3 days/week with the right leg as an internal control. Mechanical outcomes (torque at short (90°) and long (70°) muscle lengths, passive tension, and power) were assessed pre- and post-training. Following training, rats were sacrificed, the legs were fixed in formalin, and the soleus and medial gastrocnemius were harvested. Fascicles were measured, and sarcomere length was determined using laser diffraction. Fascicle length and sarcomere length were used to calculate SSN.

Results

Torque increased with training at 90° ($p<0.01$) ~17% in the $ECC_{OVERLOAD}$ and ~11% in the CONV group, similarly between groups and estradiol conditions ($p>0.05$). However, passive tension at 90° was 60% greater in OVX compared to ovary-intact rats following training

($p<0.05$). Ongoing morphological analysis currently shows soleus SSN increased ~22% in the ovary-intact and ~11% in the OVX $ECC_{OVERLOAD}$ group. Comparatively, SSN increased ~1% in the ovary intact, and ~5% in the OVX CONV group.

Discussion

Therefore, estrogen may influence longitudinal muscle remodeling in response to $ECC_{OVERLOAD}$ training.

Session Category

Musculoskeletal Biomechanics: Tissues

P2-209

Fit2Tissue: A Scalable Web Platform with Hierarchical Bayesian Data Selection

Miss Amna Aamir[1], Dr Olga Barrera[1,2], Miss Saduni Wanniarachchi[1], Dr Eleni Elia[1], Dr Hussein Rappel[3]

[1]Oxford Brookes University, Oxford, Oxfordshire, United Kingdom. [2]University of Oxford, Oxford, Oxfordshire, United Kingdom. [3]University of Exeter, Exeter, Devon, United Kingdom

Introduction

Hyperelastic constitutive models play a significant role in the modelling of soft tissue and other biological systems by capturing their non-linear mechanical response and facilitating their description through concise sets of material model coefficients. The organisation of these parameters in the literature for soft tissue remains a complex challenge due to the inherent heterogeneity of biological materials, the custom sample preparation and testing procedures and varied optimisation methods. Therefore, there is an acute need in the field for a unified collection of parameters across soft tissue with a built-in framework to link these relevant characteristics, such as sample dimensions, anatomy-specific properties and employ statistical methods such as Bayesian analysis, which leverage the accumulation of data for better informed predictions of these coefficients across datasets using a host of predictor variables.

Methods

The first phase involved developing a web-based application integrating a hyperelastic model-fitting tool and database. Platform validation used open-access data to model and store material parameters with metadata. Material models were implemented as closed-form incompressible solutions, with optimisation via non-linear least squares or minimisation using SciPy's optimise library.

To extend this architecture with a Bayesian approach, analyses are being conducted on material coefficients of a new porcine meniscus dataset, using layer depth and fibre orientation as predictors and material coefficients as targets.

Results

The robustness of the web app's model-fitting and upload functions was demonstrated using porcine aortic valve (n=12) and bovine meniscus (n=50) datasets. The influence of

independent data-related characteristics and the optimisation settings for two hyperelastic functions were reflected in the varied RMSE across the input data and their subgroups. The preliminary work on Bayesian hierarchical modelling for the porcine meniscus dataset has quantified natural variation, yielding narrower credible intervals and reduced overfitting through partial pooling

Discussion

Fit2Tissue provides a reproducible, collaborative framework for soft-tissue biomechanics by combining model-fitting tools with a growing data repository. This infrastructure enhances transparency, encourages community contribution, and supports predictive modelling. Ongoing Bayesian analyses on heterogeneous musculoskeletal data demonstrate its ability to provide probabilistic insights alongside traditional deterministic model-fitting approaches.

References (Optional)

Session Category

Musculoskeletal Biomechanics: Tissues

P2-210

Hormonal and Mechanobiological Model for Epiphyseal Bone Growth

Dr.-Ing. Andreas Lipphaus[1,2], Prof. Dr.-Ing. Ulrich Witzel[1], Prof. Dr. med. Ralf-Bodo Tröbs[3], Dr.-Ing. Marc Neumann[1], Prof. Dr. med. Jochen Hubertus[2]

[1]Biomedical Engineering Lab, Ruhr-University Bochum, Bochum, NRW, Germany. [2]Clinic of Pediatric Surgery, Marienhospital, Witten, NRW, Germany. [3]Department of Pediatric Surgery, St. Vinzenz Hospital, Paderborn, NRW, Germany

Introduction

Several mechanobiological models of bone growth at the epiphyseal plates exist in the literature. These models typically use a constant biological growth rate and a variable mechanical component based on the osteogenic index. However, during growth, the biological baseline changes due to cellular senescence and pubertal growth spurt.

Methods

The model presented here combines a mechanobiological model of epiphyseal growth [1], the narrowing of the growth plate due to cell senescence and ossification as a logarithmic function, and the increase in the biological growth rate during puberty as a Gaussian function [2]. A two 2 rotational finite element model using PLANE183 elements is established in ANSYS Mechanical 19.2. The model includes articular cartilage, cancellous and cortical bone, bone marrow, and the proliferative and hypertrophic zone of the growth plate. Growth in the proliferative zone is modeled as isotropic expansion. Growth in the hypertrophic zone is modeled as unidirectional growth in the direction of element distortion. Appophyseal growth of bone is included based on Wolff´s Law. The increase in joint load is approximated to be equal to the increase in body weight. After each iteration representing one month the model dimensions are updated and remeshed to avoid element distorsion.

Results

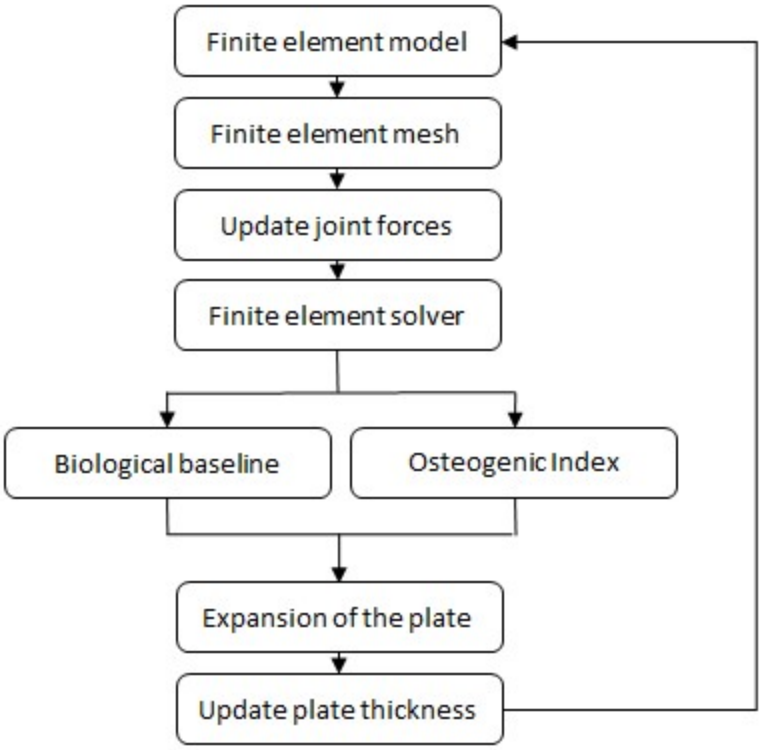
Simulating longitudinal bone growth between the age of 1 and 18 matches clinically observed growth curves by Green and Anderson [3]. The closure of the growth plates in the simplified bone is reached at the age of 16.

Discussion

To apply bone growth simulations clinically, it is necessary to take age-appropriate growth rates into account. Long-term bone growth can be modeled using remeshing to avoid element distortion. The interaction between these three factors remains unclear to date.

The combination of the presented model with a genuine bone structure and age-accurate boundary conditions is necassary for validation and clinical use.

Images (Optional)



References (Optional)

[1] Yadav *et al.*, J Biomechanics, 2016

[2] Lipphaus *et al.*, European Society of Biomechanics, 2022

[3] Anderson et al., J Bone Joint Surg, 1964

Session Category

Musculoskeletal Biomechanics: Tissues

P2-211

Investigating Asymmetrical Bone Adaptations of the Third Metacarpal in Clockwise Racing Thoroughbreds

Mr Andrew Koshyk[1], Mr Tadiwa H Waungana[1], Mr Moustafa Abbadi[1], Dr Samuel Smalley[2], Mr Martin Wong[2], Dr W Brent Edwards[1]

[1]University of Calgary, Calgary, Alberta, Canada. [2]Hong Kong Jockey Club, Hong Kong, SAR, China

Introduction

Fractures at the metacarpophalangeal (MCP) joint are among the most common and fatal injuries experienced by Thoroughbred racehorses. Thoroughbreds race at a gallop, a naturally asymmetrical gait, and consistently race and train in the same direction around a track. Consequently, their left and right forelimbs may be exposed to unequal loading, potentially leading to distinct bone adaptations and fracture risk. The objective of this work was to assess differences in bone geometry and density between the left and right forelimbs of clockwise racing Thoroughbreds.

Methods

Bilateral computed tomography scans of MCP joints were obtained from 28 clockwise racing Thoroughbreds (Canon Medical System; acquisition settings: 120 kVp, 450 mA, in-plane resolution of 0.625 × 0.625 mm, slice thickness of 0.3 mm). Third metacarpal (MC3) bones were segmented using Mimics (Materialise, Leuven, Belgium) and cropped to retain the distal most 55 mm.

Subchondral bone density was estimated at each node across the MC3 joint surface (see Figure) by averaging Hounsfield units along a 5 mm ray projected normal to the surface using the Visualization Toolkit, Simple Insight Toolkit, and PyVista libraries within Python (v3.8.5). A statistical shape model incorporating density was developed using ShapeWorks [1]. Shape and density differences between left and right forelimbs were evaluated at each particle in the model ($\alpha = 0.05$).

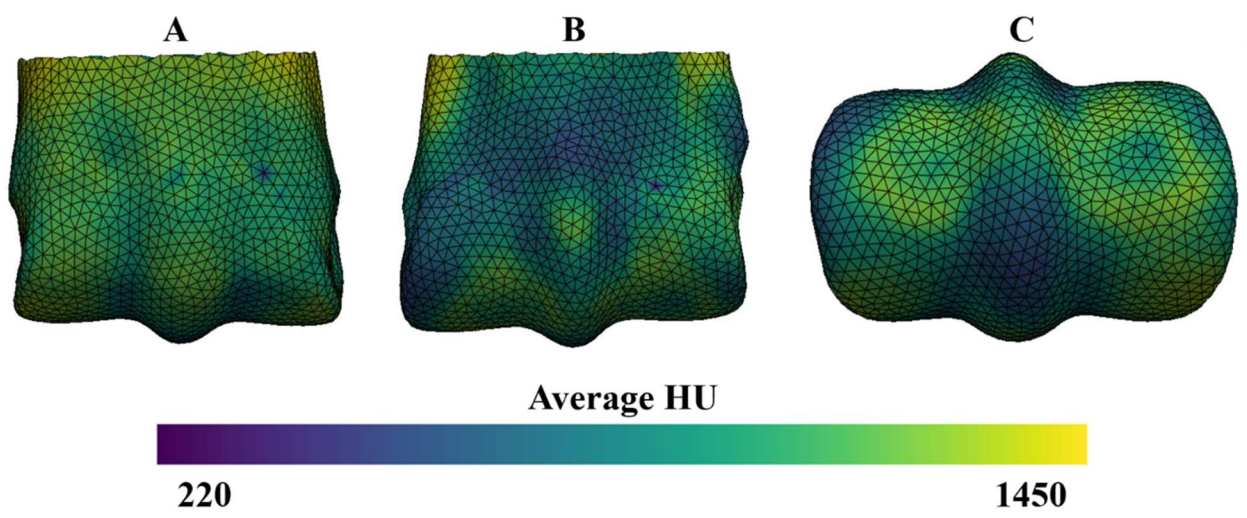
Results

The statistical shape model captured 85% of the total anatomical variation within the first 8 principal components (PCs). Including all PCs, the model achieved a generalization error of 0.36 mm and a specificity of 0.78 mm. Statistical analyses revealed no significant differences in shape or density between left and right MC3 bones.

Discussion

No significant asymmetries in MC3 bone morphology or density were observed between the left and right forelimbs of clockwise racing Thoroughbreds. These results suggest that left and right forelimbs, while potentially subjected to unequal loading, undergo similar bone adaptations.

Images (Optional)



Subchondral bone density mapped across the (A) dorsal, (B) palmar, and (C) distal aspects of the MC3 joint surface by averaging Hounsfield units (HU) along a 5 mm ray projected normal to the surface.

References (Optional)

[1] Joshua Cates, Shireen Elhabian, Ross Whitaker. "Shapeworks: particle-based shape correspondence and visualization software." Statistical Shape and Deformation Analysis. Academic Press, 2017. 257-298.

Acknowledgements (Optional)

The Hong Kong Jockey Club Equine Welfare Research Foundation Limited and the Natural Sciences and Engineering Research Council of Canada.

Session Category

Musculoskeletal Biomechanics: Tissues

P2-212

Why Does Wearing High Heels Stiffen the Achilles Tendon?

Mr. Andrew Thornton[1], Dr. Jordyn Schroeder[2], Dr. Gregory Sawicki[2,3], Dr. Owen Beck[1]

[1]University of Texas at Austin, Austin, Texas, United States. [2]Woodruff School of Mechanical Engineering, Atlanta, Georgia, United States. [3]School of Biological Sciences, Atlanta, Georgia, United States

Introduction

Modern footwear is typically designed to improve user biomechanics while worn, but not after. Habitually wearing high heels may increase user Achilles tendon stiffness [1], which has functional implications after the high heels are doffed. Interestingly, high heel use may not increase peak strain on the Achilles tendon, which is a primary factor governing tendon stiffening [2]. Here, we seek to determine the factors governing tendon stiffness changes with habitual high heel use.

Methods

Eight participants naïve to high heel use (3 female) wore shoes that set the ankle at 14° plantar flexion during standing for 13-16 weeks. Participants reported their daily steps with and without the heel lifts. We computed Achilles tendon stiffness consistent with (3) and slack length using dynamometry and ultrasonography. We calculated Achilles tendon slack length using the distance between the junction of the muscle-tendon and the insertion at the onset of passive force development during passive dynamometer trials. Further, we estimated participant Achilles tendon strain during treadmill walking at 1.3 m/s. To do so, we multiplied ground reaction forces by the ankle's gear ratio and divided by stiffness and tendon slack length.

Results

Achilles tendon stiffness increased in participants who walked in heel lifts for >1500 steps/day ($p = 0.040$), but not in those who took <1000 steps/day ($p = 0.307$). Walking in heel lifts vs. flats improved ankle effective mechanical advantage 9.1% ($p = 0.003$), contributing to the 13.7% reduced peak tendon strain per step ($p < 0.001$). Neither change in peak strain from flats to heel lifts ($p = 0.163$) nor daily steps in heel lifts ($p = 0.112$) independently related to the change in tendon stiffness due to habitually wearing heel lifts. Achilles tendon slack length did not change in heel lift users or non-users ($p \geq 0.172$).

Discussion

Habitually wearing heel-lifted footwear increased user Achilles tendon stiffness despite reducing peak strain on the tendon. The mechanism(s) underlying the Achilles tendon stiffening due to chronic high heel use remains elusive.

References (Optional)

[1] Csapo J Exp Biol 2010; [2] McMahon, J Str Cond Res 2022; [3] Beck et al., J Appl Physiol 2024

Session Category

Musculoskeletal Biomechanics: Tissues

P2-213

Upper Extremity Muscle Activation of Infants During Reaching Actions

Ms. Ipsita Sahin[1], Mr. Argishti Stepanian[2], Mr. Erik Hakopian[3], Dr. Sofia Sakellaridi[4], Ms. Michele Alaniz[5], Ms. Yovana Harris[5], Dr. Charles Liu[6], Dr. Vasileios Christopoulos[7,1,2], Dr. Elena Kokkoni[1,2]

[1]Dept. of Bioengineering, University of California, Riverside, Riverside, CA, United States. [2]Neuroscienc Graduate Program, University of California, Riverside, Riverside, CA, United States. [3]Interdisciplinary Neuroscience Program, University of California, Irvine, Irvine, CA, United States. [4]Research Institute, Casa Colina Hospital, and Centers for Healthcare, Pomona, CA, United States. [5]Department of Pediatrics, Casa Colina Hospital and Centers for Healthcare, Pomona, CA, United States. [6]Neurorestoration Center and Department of Neurological Surgery, Univ. of Southern California Keck School of Medicine, Los Angeles, CA, United States. [7]Department of Biomedical Engineering, Univ. of Southern California, Los Angeles, CA, United States

Introduction

Previous reaching studies with infants have primarily examined muscle activation in the reaching arm only. Herein, we recorded simultaneous electromyography (EMG) data from both the reaching arm and the contralateral non-reaching arm during repeated unimanual reaching actions. By looking at muscle activations in both arms, we aim to determine their coactivation and muscle synergies.

Methods

Infants (6–8 months old) participated in a single experimental session structured into alternating blocks of resting state (30s) and goal-directed reaching (60s). EMG data were collected for the following muscles on both sides of the body: anterior (AD) and posterior (PD) deltoids, biceps brachii (BB), and triceps brachii (TB). Session video recordings were used to determine the reaching onset and offsets. The raw EMG signals were filtered, full-wave rectified, and low-pass filtered to generate linear envelopes. Each EMG envelope was normalized using peak activation dynamics (i.e. maximum activation observed during reaching). To quantify how strongly muscle pairs were activated together, we computed the coactivation index (CI). The degree of coactivation CI ranges between 0 (maximal reciprocal activation) and 1 (maximal coactivation). Statistical analysis evaluated whether the level of CI for the antagonist (BB-AD and TB-PD) and agonist (BB-TB and AD-PD) muscle

pairs varied between the reaching and non-reaching arms during a reach. In addition, non-negative matrix factorization (NMF) was applied to extract the underlying muscle synergies, with the number of synergies selected based on the variance accounted for.

Results

Reaching duration was on average 0.73±0.25s. No significant differences were observed in CI levels for the antagonist and agonist muscle pairs between the reaching and non-reaching arms; however, the CI values for the antagonist and agonist muscle pairs were respectively 0.83-0.89 and 0.84-0.85, indicating a high level of coactivation. For the reaching and non-reaching arms, NMF analysis identified respectively 1–3 and 2-3 muscle synergies. Each synergy consisted of a distinct level of muscle weights.

Discussion

By characterizing the degree of coactivation and muscle synergies, this work provides insights into how infants simplify their motor control during reaching actions.

Session Category

Musculoskeletal Biomechanics: Tissues

P2-214

Failure Patterns in the Dura Mater Across Location and Loading Rates

Mr. Brandon Chelstrom[1], Mr. Will Martin[1], Dr. Corinne Henak[1,2,3]

[1]Department of Biomedical Engineering, University of Wisconsin-Madison, Madison, Wisconsin, United States. [2]Department of Mechanical Engineering, University of Wisconsin-Madison, Madison, Wisconsin, United States. [3]Department of Orthopedics and Rehabilitation, University of Wisconsin-Madison, Madison, Wisconsin, United States

Introduction

Damage to the dura mater, the dense collagenous membrane of the meninges, can lead to severe hemorrhages. While the dura mater has been shown to be nonlinear, heterogeneous, and rate-dependent, there is a lack of information on the driving factors behind how the dura mater fails. Our objective is to investigate how the underlying tissue structure and loading rate influence the failure behavior of the dura mater.

Methods

Inferior brain surface samples (Wisconsin Miniature Swine, n = 5) were collected within 2 hours post-mortem and maintained in artificial cerebral spinal fluid (aCSF) until testing. Tensile dog-bone samples (gauge: 10 mm x 1 mm) were punched from 8 anatomical locations with specific orientations (Fig.1A). Prior to mechanical testing, each sample was imaged using polarized light at 0°, 45°, and 90° to the long axis of the dog-bone to visualize the underlying collagen structure. Samples were preconditioned (1 Hz to 2 mm extension for 30 cycles), subjected to a 0.03 N preload, then loaded to failure at either 1, 10, or 100 mm/min. Gauge strain was measured via a high-speed camera using charcoal strain lines gently stamped onto the sample. Failure location was grouped into 4 bins along the sample and compared with the dominant collagen fiber orientation for that group.

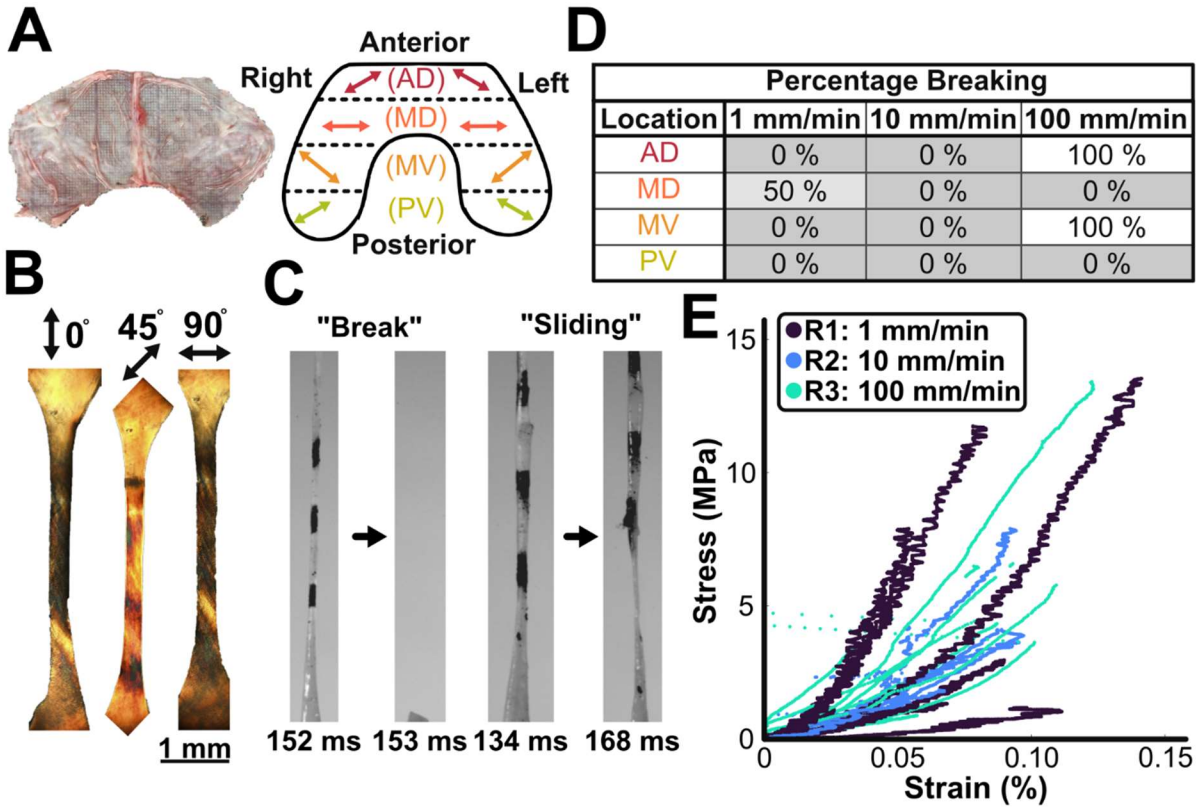
Results

Collagen fiber orientation is highly variable both within and between samples (Fig.1B). Two distinct failure patterns were observed across all samples: breaking and sliding (Fig.1C). Failure patterns vary with anatomical location and loading rate (Fig.1D). No consistent rate-dependent trend is observed in mechanical behavior (Fig.1E).

Discussion

Porcine dura mater samples were tested under uniaxial tension with varying loading rates to investigate various failure patterns. The dura mater more commonly exhibits a slower "sliding" failure but also exhibits a rapid "breaking" failure at higher rates for anterior and posterior samples (Fig.1C/D). Failure often occurred in regions with larger variation in the underlying collagen structure (Fig.1B). Rate-dependence was not observed which could be due to the relatively slow loading rate magnitudes (Fig.1D). These results give insight into the factors that influence failure of the dura mater to better predict injury outcomes.

Images (Optional)



Percentage Breaking			
Location	1 mm/min	10 mm/min	100 mm/min
AD	0 %	0 %	100 %
MD	50 %	0 %	0 %
MV	0 %	0 %	100 %
PV	0 %	0 %	0 %

Session Category

Musculoskeletal Biomechanics: Tissues

P2-215

Exploring Quantitative Magnetic Resonance Imaging Determinants of Passive Supraspinatus and Infraspinatus Shear Wave Velocity

Dr. Caleb Cordes PhD[1], Ms. Denali Hutzelmann[2], Ms. Colleen Vogel[2], Dr. Whitney Wolff PhD[1], Dr. David Lipps PhD[3], Dr. Joshua Leonardis PhD[1]

[1]The Ohio State University, Columbus, OH, United States. [2]University of Illinois at Urbana-Campaign, Urbana, IL, United States. [3]University of Michigan, Ann Arbor, MI, United States

Introduction

Shear wave elastography (SWE) estimates tissue elasticity by measuring shear wave velocity (SWV), the speed at which shear waves propagate through tissue [1]. SWV increases with increasing muscle stretch and activation [2], but the physiological mechanisms influencing passive SWV remain unclear. This study investigated whether quantitative MRI (qMRI) parameters, including fat fraction (FF), T2 relaxation time (T2*), and magnetization transfer ratio (MTR), which collectively reflect muscle fat [3], proteoglycan/water [4], and collagen content [5], predict passive SWV in two rotator cuff muscles.

Methods

Fourteen adults (9 females, 5 males; mean age 39.6 ± 16.5 years) underwent MRI of the dominant shoulder using a 3T scanner. Imaging included a multi-echo Dixon sequence to calculate FF and custom fat-suppressed ultra-short echo time (UTE) sequences to derive T2* and MTR. The supraspinatus and infraspinatus muscles were segmented in 3D Slicer, and qMRI parameters were computed using custom Python software. SWV was averaged across three images acquired from each muscle. Separate linear regression models examined the relationship between each qMRI parameter and SWV, along with a combined model with all three qMRI predictors. Interaction terms assessed whether the relationship between qMRI parameters and SWV varied across muscles (Figure 1).

Results

Individual models showed minimal predictive power for FF, MTR, and T2* (all R^2<0.042, p>0.586). In contrast, an interaction model (Figure 1) using standardized predictors and accounting for muscle type explained more than 40% of variance in passive SWV (R^2=0.437, p=0.076). Notably, T2* demonstrated a significant main effect on SWV (β=–

2.93, p=0.004) and a significant T2* × muscle type interaction (β=3.97, p=0.003), indicating muscle-specific relationships between proteoglycan-water content and SWV.

Discussion

Our findings suggest that single qMRI parameters provide limited insight into passive SWV, whereas multivariate models incorporating muscle-specific effects substantially improve explanatory power. The significant influence of T2* and its interaction with muscle type highlights the role of proteoglycan-water content, rather than fat or collagen content, in modulating passive stiffness. Collectively, these results underscore the complexity of interpreting SWE. Expanding these predictive models to include muscle architecture, sex, and age, and further histological validation will enhance the application of SWE in musculoskeletal research.

Images (Optional)

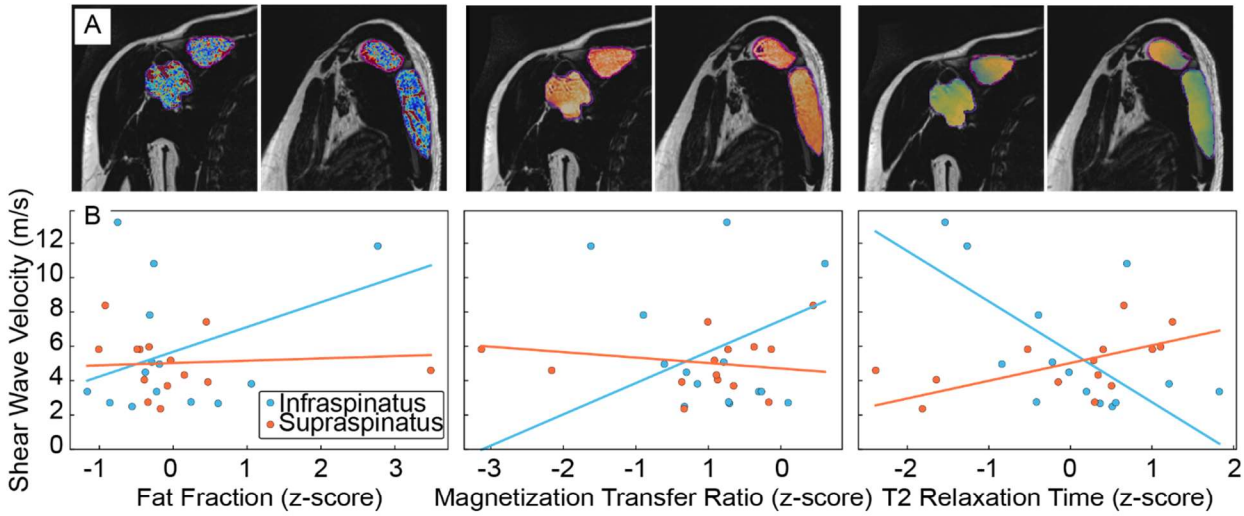


Figure 1: Quantitative MRI parameters exhibit shoulder muscle-specific relationships with shear wave velocity. (A) Fat fraction (left), magnetization transfer ratio (middle), and T2 relaxation time are depicted using heat maps for the supraspinatus and infraspinatus muscles for a representative participant, overlaid on Dixon fat images from the coronal and sagittal planes. (B) Shear wave velocity for the infraspinatus (blue) and supraspinatus (orange) muscles is shown plotted against fat fraction, magnetic transfer ratio, and T2 relaxation time. Individual participant means are shown with filled circles, and linear model results are illustrated with trend lines.

References (Optional)

Session Category

Musculoskeletal Biomechanics: Tissues

P2-216

Menopause-Related Effects on Neck-Shoulder Muscle Elasticity and Pain Sensitivity

Ms. Denali Hutzelmann[1], Dr. Whitney Wolff PhD[2], Ms. Colleen Vogel[1], Ms. Savanna Rudy[1], Dr. Caleb Cordes PhD[2], Dr. Joshua Leonardis PhD[2]

[1]University of Illinois at Urbana-Champaign, Urbana, IL, United States. [2]The Ohio State University, Columbus, OH, United States

Introduction

Menopause significantly affects musculoskeletal health through estrogen decline, which alters collagen homeostasis [1] and reduces gamma-aminobutyric acid (GABA) synthesis [2], impacting tissue elasticity and pain sensitivity. Consequently, over 50% of women experience musculoskeletal pain and dysfunction during menopause. Shear wave elastography (SWE) measures tissue elasticity via shear wave velocity (SWV), while pain pressure threshold (PPT) assesses mechanical pain sensitivity. This study investigated how menopausal status influences SWV and PPT in the upper trapezius (UT) and lateral deltoid (LD) and examined their associations with self-reported neck and shoulder pain.

Methods

Twenty-seven participants (15 postmenopausal, 12 premenopausal; 54 shoulders) underwent SWE imaging and PPT testing of the UT and LD. Menopausal status was defined by at least 12 months without menses. Neck and shoulder pain and disability were self-reported using the Shoulder Pain and Disability Index (SPADI) and Neck Disability Index (NDI). Linear models assessed the effects of menopausal status on SWV and PPT and examined the menopause-related relationships among SWV, PPT, and SPADI/NDI scores.

Results

Post-menopausal females showed higher SWV than pre-menopausal females in both the UT (12.7% greater) and LD (10.3% greater), though these differences were not statistically significant (both $p>0.12$). Menopause status significantly affected LD PPT ($p=0.04$), with post-menopausal females exhibiting 23.1% higher PPT, indicating lower pain sensitivity. UT PPT displayed a similar trend (23.8% greater) but was not significant ($p=0.12$). SWV and PPT were unrelated for either muscle ($p>0.42$) or menopausal group ($p>0.15$). LD SWV increased with increasing SPADI score regardless of menopause status ($p=0.049$) and showed a stronger association in pre-menopausal females ($\beta=8.7$, $p=0.019$). No other measure of SWV or PPT related to SPADI or NDI (all $p>0.11$).

Discussion

Post-menopausal females exhibited greater LD PPT, indicating reduced pain sensitivity. They also demonstrated generally higher SWV, though differences were not significant, suggesting limited clinical impact. This suggests reduced pain sensitivity despite increased elasticity in menopause, which possibly reflects altered pain processing. The positive association between LD SWV and SPADI, particularly in pre-menopausal females, suggests tissue elasticity may influence perceived disability. However, the lack of relationships between pain sensitivity and patient-reported outcomes indicates pain sensitivity may not drive functional limitations.

Images (Optional)

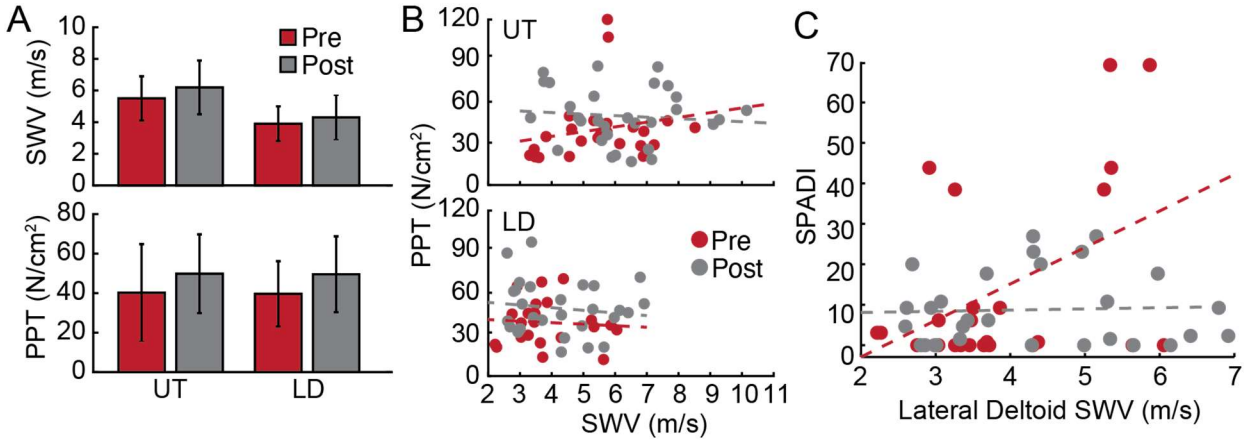


Figure 1: (A) Menopause-related differences in upper trapezius (UT) and lateral deltoid (LD) shear wave velocity and pain pressure threshold. (B) Scatterplots representing the relationship between muscle SWV and PPT for the UT (top) and LD (bottom). (C) Scatterplot representing the relationship between LD SWV and SPADI score.

Session Category

Musculoskeletal Biomechanics: Tissues

P2-217

Constitutive Parameter Inference in Full Volume Datasets of Intact and Torn Rotator Cuff Tendons

Postdoctoral Research Fellow Carla Nathaly Villacís Núñez PhD[1], Assistant Professor Siddhartha Srivastava PhD[2], Research Scientist Ulrich Scheven PhD[1], Professor Asheesh Bedi MD[1], Professor Krishna Garikipati PhD[3], Professor Ellen Arruda PhD[1]

[1]University of Michigan, Ann Arbor, MI, United States. [2]Auburn University, Auburn, AL, United States. [3]University of Southern California, Los Angeles, CA, United States

Introduction

Rotator cuff tendons are heterogeneous, anisotropic, and layered tissues prone to tearing, often causing pain and dysfunction. Modelling their complex mechanics is key to predicting tear progression and guiding clinical treatment. In this work, we combine an MRI-based experimental approach [1] with a full-volume inverse method [2] to infer constitutive behavior in an animal model of the rotator cuff. This framework offers a clinically relevant tool for identifying high-risk tears and supporting treatment planning.

Methods

Isolated infraspinatus tendons (n = 12) were cyclically loaded under quasi-uniaxial tension in an MRI-compatible chamber. A custom displacement encoding protocol [2] captured full-volume phase variations. Each tendon was tested in an intact state and after a high-grade bursal-sided tear, at physiologically relevant displacements (1 mm and 2 mm).

Unwrapped phase maps yielded displacement fields, which were smoothed and interpolated to an anatomical mesh. Fiber directions were extracted from high-resolution images. Displacements and fiber maps were input into a variational system identification (VSI) framework with a partial differential equation (PDE) refiner to infer parameters for neo-Hookean (NH), modified Holzapfel-Gasser-Ogden (m-HGO), and polynomial (Polyn) models. Forward predictions were compared to real maps using percentage errors.

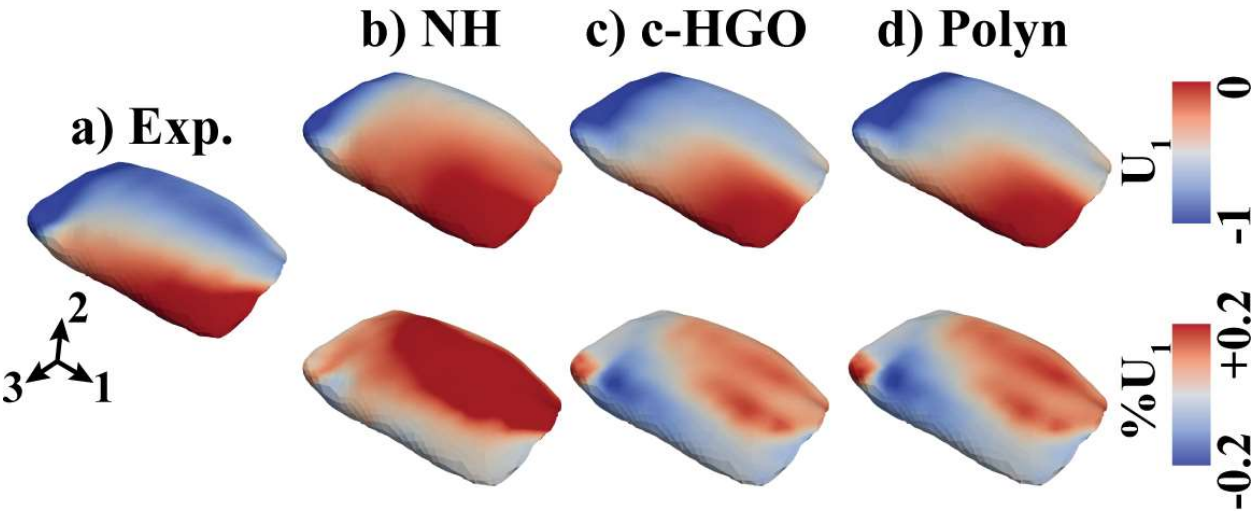
Results

The highly non-linear experimental response observed in rotator cuff tendons (Fig. 1-a) was not captured by the NH model (Fig. 1-b). The m-HGO and Polyn models displayed anisotropy, as expected, and were able to capture several experimental features (Fig. 1-c,d) of the torn tendon, such as the sliding behavior between the cut/uncut tissue. Interestingly, the polynomial model had 3 terms only. Error maps showed that the detached tissue band had the largest error magnitudes, surpassing 20% in the NH model.

Discussion

In this work, we inferred constitutive parameters from full volume displacement maps of rotator cuff tendons using a novel inverse characterization framework. Our continuum m-HGO and Polyn models captured key aspects of the torn tendon (delamination), offering potential for improved prediction of tear progression and clinical decision-making.

Images (Optional)



References (Optional)

[1] Ulrich Scheven *et al.*, J Magn Reson, 2020.

[2] Zhenlin Wang *et al.*, J Mech Phys Solids, 2021.

Acknowledgements (Optional)

This work was supported by the National Science Foundation (CMMI Grant No. 2211346).

Session Category

Musculoskeletal Biomechanics: Tissues

P2-218

Age-Related Differences in the Foot's Fat Pad Energetics During Decline, Level, and Incline Walking

Dr. Lauren Williams PhD[1], Mr. Christopher Long[1], Dr. Daniel Davis PhD[1], Dr. Jayishni Maharaj PhD[2], Dr. Jason Franz PhD[3], Dr. Kota Takahashi PhD[1]

[1]University of Utah, Salt Lake City, UT, United States. [2]Griffith University, Brisbane, QLD, Australia. [3]UNC Chapell Hill and NC State University, Chapell Hill, North Caroline, United States

Introduction

Soft tissues of the human foot change with age (e.g., fat pads have altered structure and mechanical properties [1]). When the fat pads cyclically compress, they may absorb and return energy [2] which we suspect may influence mechanical energetics in walking. We tested the effect of age on fat pad energetics using incline/decline walking to systematically alter net energetic demand. We hypothesized that older age and decline walking would increase energy absorbed by the fat pads.

Methods

Eighteen younger [9F; 24.4±3.3 years] and older [9F; 69.8±5.9 years] adults walked barefoot at 1.2 m/s on an instrumented treadmill at three slopes (decline: -5°, level: 0°, and incline: 5°).

To quantify fat pad energy [3], we first calculated total foot power using a unified deformable analysis, representing the energetics of all structures distal to the calcaneus. Next, rotational powers for the midtarsal and metatarsophalangeal joints were summed and assumed to include everything except the fat pads. Thus, we estimated fat pad mechanical power as the difference between total foot power and summed joint power. Lastly, power was integrated to calculate negative (i.e., energy absorbed) and positive (i.e., energy returned) work during two stance subphases: collision and push-off.

Results

Independent of age, decline walking increased fat pad energy absorption and return during collision ($p<0.001$) and incline walking increased fat pad energy absorption during push-off ($p<0.001$). Independent of slope, older adults absorbed more energy during push-off ($p=0.03$) but not collision ($p=0.286$) (Fig.1).

Discussion

We found that decline walking increased fat pad energy absorption during collision, which agrees with previous results examining foot power during sloped walking [4]. Furthermore, our results suggest altered fat pad energetics may partly explain findings of disproportionate foot mechanical energy losses during walking in older adults [5]. These results point to potentially modifiable factors in the human foot that could inform interventions to promote walking performance.

Images (Optional)

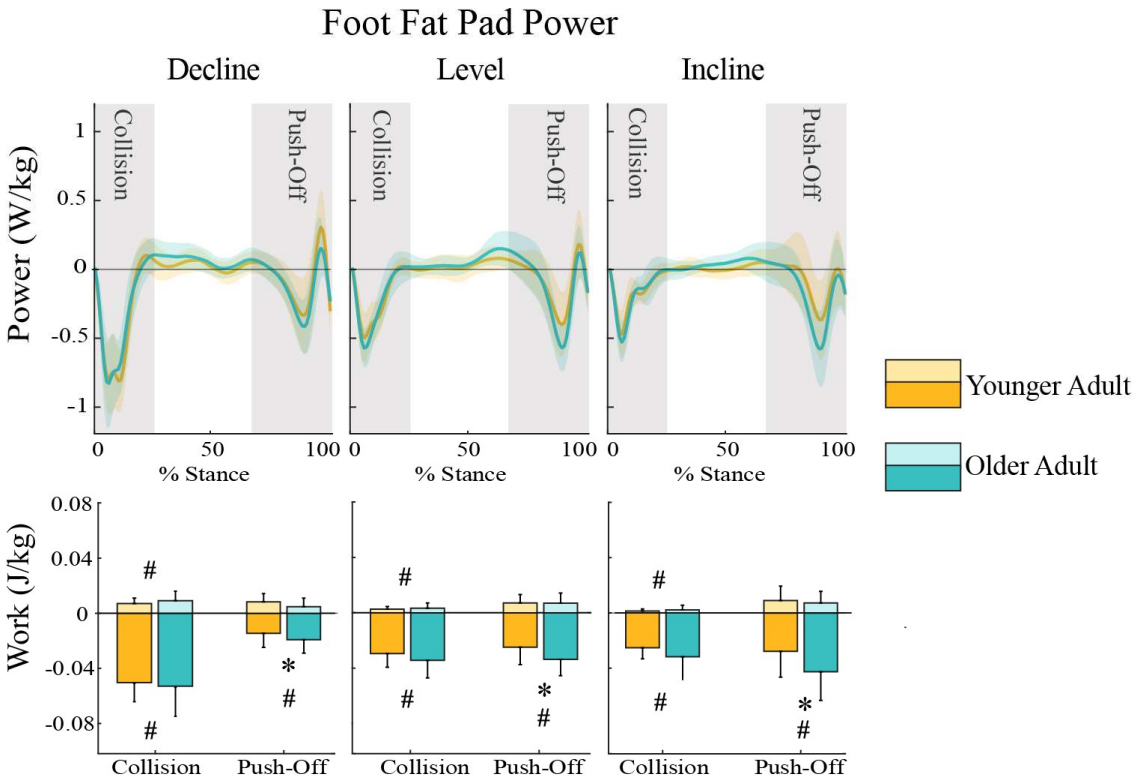


Figure 1. Foot fat pad power and work for younger and older adults during decline, level, and incline walking. # indicates a significant slope effect. * indicates a significant age effect.

References (Optional)

[1] Maemichi et al., Clin Biomechanics, 2024 [2] Ledoux et al., J Biomechanics, 2007 [3] Maharaj et al., ISB Conf, 2025 [4] Papachatzis et al., PLoS one, 2023 [5] Krupenevich et al., J Biomechanics, 2021

Acknowledgements (Optional)

NIH R01AR081287, T32TR004394

Session Category

P2-219

Load-Driven Microstructural Changes in Mouse Articular Cartilage

Ms Sarah-Maud Sombris-Picot[1], Pr Simon Le Floc'h[1], Pr Patrick Cañadas[1], Dr Emeline Perrier Groult[2], Ms Laetitia Hudecek[3], Dr Cristina Cavinato[4]

[1]LMGC, Univ. Montpellier, CNRS, Montpellier, France, France. [2]Institute for Regenerative Medicine & Biotherapy, Univ. Montpellier, INSERM, Montpellier, France, France. [3]INM, Univ. Montpellier, INSERM, Montpellier, France, France. [4]LMGC, Univ. Montpellier, CNRS, Montpellier, Montpellier, France, France

Introduction

Articular cartilage endures complex loads, yet its microstructural response to compression—especially the interaction between chondrocytes and the collagen network—remains incompletely characterized. Despite recent advances in imaging, few studies link three-dimensional microstructure to mechanical loading in intact tissue [1-2]Work supported by the French National Research Agency, ANR-22-CPJ1-0090-01 to CC and ANR-10 INBS-04, 'Investments for the future' to MRI facility. R. This work aims to assess how the murine tibial plateau responds to controlled compression by examining load-induced changes in chondrocyte orientation and collagen organization at high spatial resolution.

Methods

Tibial plateau samples from 8-week-old male C57BL/6 mice were collected immediately after sacrifice by sectioning approximately 1 mm below the articular surface. Samples were rinsed in phosphate-buffered saline and immersed in a nucleic-acid staining solution before testing.

A custom uniaxial mechanical system was developed to apply three sequential linear compression ramps of 15 µm each. An impermeable 0.2-mm-thick glass coverslip served as the compression platen. Each compression step was held for 5, 10, and 15 minutes, respectively, to allow for comparable stress-relaxation conditions.

To assess local orientation and deformation, 3D high-resolution images were acquired across the full cartilage thickness using a lateral high-resolution camera, optical coherence tomography (OCT), and multiphoton microscopy (MPM). MPM provided second-harmonic generation (collagen) and two-photon fluorescence (chondrocyte nuclei) signals

Results

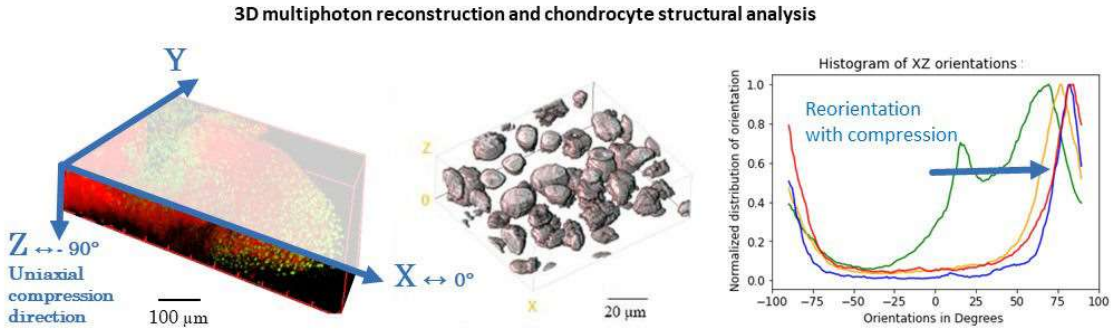
Multiphoton images revealed a slight, progressive reorientation of chondrocytes following each compression step (Fig.1). A shift toward alignment with the loading direction—

approaching 90°—was also observed. This response appeared consistent with the known heterogeneous organization of articular cartilage, where collagen architecture and cellular arrangement vary across depth. Additional image analyses are ongoing to quantify the observed changes and to compare responses across regions of the tibial plateau.

Discussion

This study demonstrates that articular cartilage exhibits measurable microstructural reorganization under mechanical stress. The observed chondrocyte reorientation suggests load-dependent adaptation mechanisms linked to the local collagen network. Comprehensive 3D analyses and quantitative mapping of local strains are further employed to accurately characterize these reorientation patterns and to elucidate the micromechanical processes that govern cartilage deformation.

Images (Optional)



References (Optional)

[1] Chang, and Tang. Cartilage, 2020

[2] Komeili, et al., Med. Eng. Phys, 2018

Acknowledgements (Optional)

Work supported by the French National Research Agency, ANR-22-CPJ1-0090-01 and ANR-10 INBS-04.

Session Category

Musculoskeletal Biomechanics: Tissues

P2-220

Myosin Activator Omecamtiv Mecarbil Dramatically Decreases Power Output in Slow Skeletal Muscle Fibers

Dr. David Lin, Mr. Austin Au, Dr. Bertrand Tanner

Washington State University, Pullman, WA, United States

Introduction

Omecamtiv mecarbil (OM) is a myosin activator that was developed to augment cardiac function after heart failure. Although OM was designed to target and activate cardiac-specific ATPase, which enhances cross-bridge formation and increases attachment time, skeletal muscle could be affected due to the similarity of cardiac and skeletal myosins. This study characterizes the effect of OM on the force-velocity (FV) properties of slow and fast skeletal muscle fibers, which has implications for the diaphragm and respiratory function.

Methods

We obtained single muscle fibers from rat medial gastrocnemius (MG; fast fibers) and soleus (SOL; slow fibers) muscles. The fibers were chemically skinned and mounted between a force transducer and motor servo. The bathing solution was exchanged from a low calcium (pCa=8) to a high calcium solution (pCa=4) to activate the fiber. An experimental trial consisted of achieving steady-state isometric force and then imposing an isotonic load within the range of 0.1 to 0.75 F_o (F_o=isometric force). One of two conditions were tested on each fiber, control (no OM) and OM (concentration=0.1 μM), for both MG and SOL fibers. Hill's equation was fit to FV data, and maximal powers were calculated from the fits.

Results

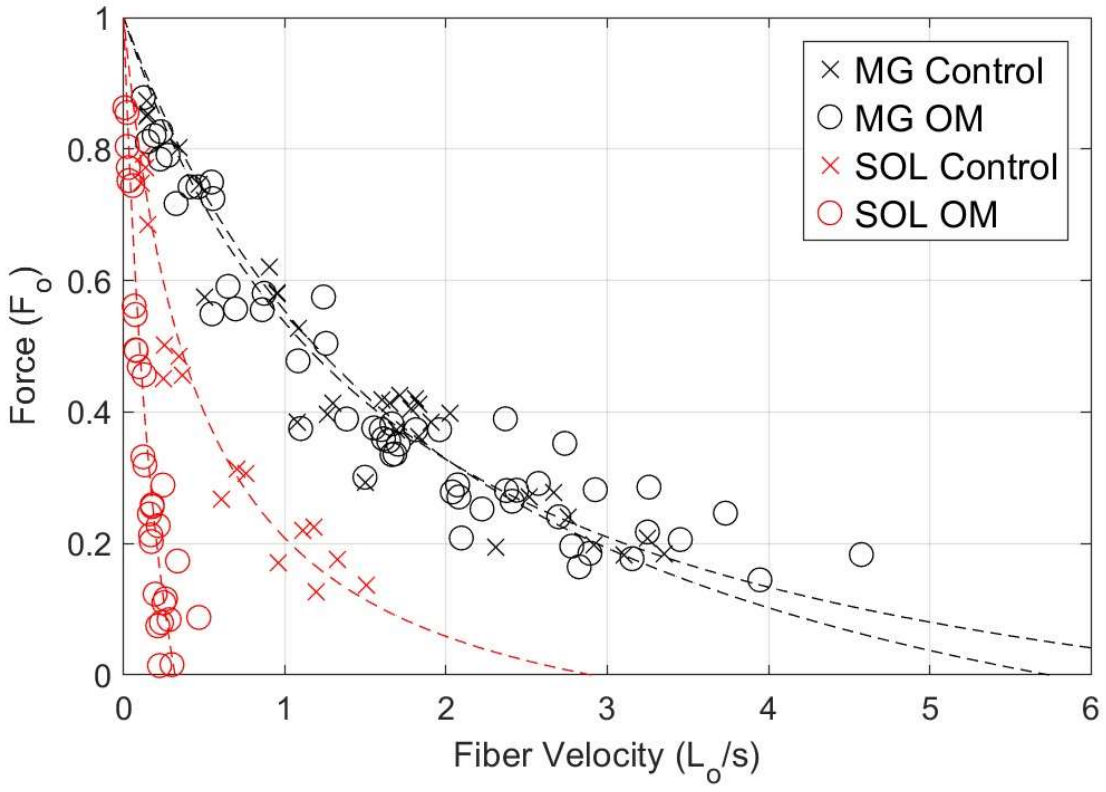
Fast fibers showed minimal difference in the FV curves between the control (n=16) and OM (n=15) fibers (see Figure), and the maximum powers were comparable (0.66 F_0-L_o/s for both; L_o=initial length). Slow fibers showed dramatic differences in the FV curves and maximum powers (0.21 vs 0.05 F_0-L_o/s for control (n=5) vs OM (n=10) fibers, respectively).

Discussion

Only slow skeletal muscle was affected by OM, consistent with cardiac and slow skeletal muscle expressing the same myosin isoforms. Fast muscle fibers did not show any effect,

likely due to OM not binding to fast skeletal myosin. The effect of OM on mechanical output on slow fibers caused a substantial decrease in power of 76%. The functional consequence of OM affecting the power output of skeletal muscles like the diaphragm, which has a high percentage of slow fibers, could contribute to the lack of improvement in exercise capacity seen in OM clinical trials.

Images (Optional)



Acknowledgements (Optional)

Funding NSF#2128545 & 2312925

Session Category

Musculoskeletal Biomechanics: Tissues

P2-221

Muscle Contractile Properties During Nonsteady-State Activation are Important for Determining the Amount of Energy that Can Be Stored in Tendons

Dr. David Lin, Mr. Austin Au, Dr. Bertrand Tanner

Washington State University, Pullman, WA, United States

Introduction

Tendon compliance is important in ballistic movements like jumping because tendon can store and return energy to augment motor performance. Our objective was to determine the optimal tendon compliance with which muscle can store energy during the initial phase of a jumping task. We also investigated whether the phenomenon of muscle force depression played a role in limiting energy transfer from the muscle to the tendon.

Methods

To test a range of tendon compliance, single muscle fibers were coupled to a servo that physically simulated a virtual tendon via force feedback. Fibers from rat medial gastrocnemius muscles were chemically skinned and mounted between a force transducer and motor servo. The bathing solution was exchanged from a low calcium to a high calcium solution to activate the fiber. During the activation, as the fiber force increased, the fiber shortened against a virtual tendon with linear elasticity such that musculotendon length was isometric. By plotting muscle work done versus tendon compliance, we determined whether there was an optimal compliance for storing energy. We plotted muscle force as functions of muscle length and work done to determine whether force depression, related to muscle work [1], was the main factors affecting muscle work capacity.

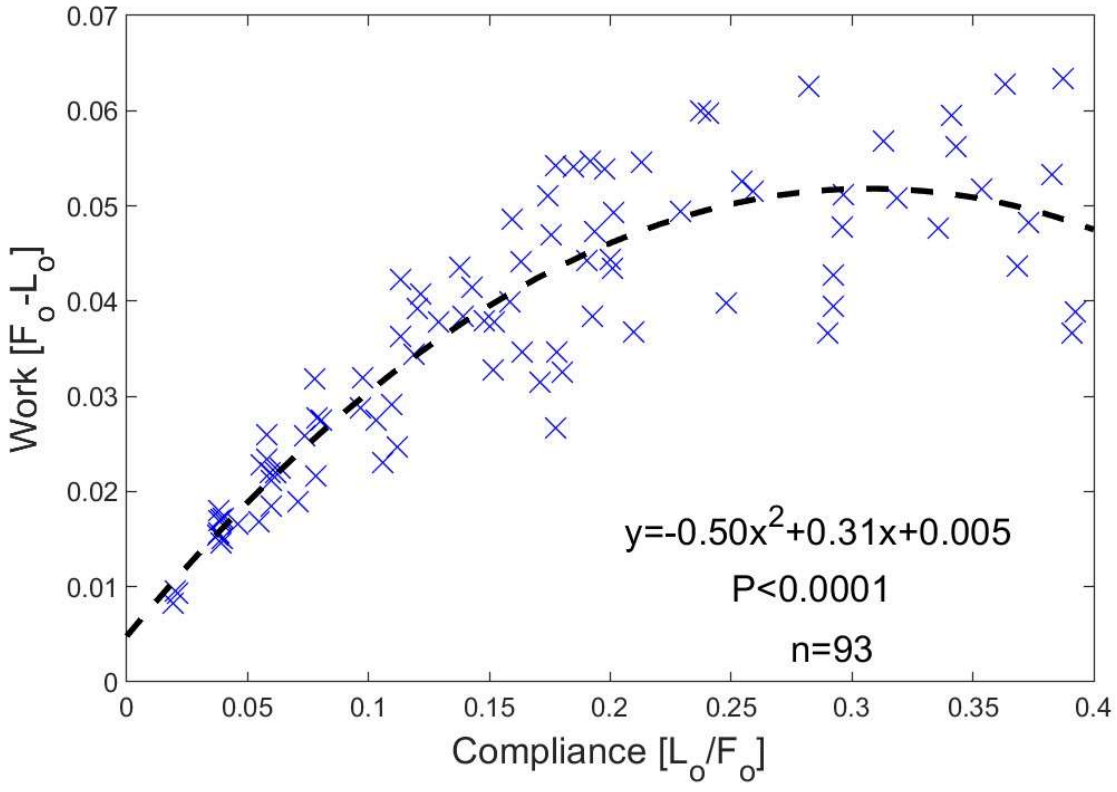
Results

The work done by muscle against a linear tendon increased as tendon compliance increased, with a clear optimal value (see Figure). Plots of muscle force versus length showed the linear decrease in force with decreasing sarcomere length, limiting the amount of energy stored in the tendon for higher compliances. The force decrease was much greater than that predicted by a sliding filament based force-length curve. A linear regression of force depression versus work done only explained 7% of the variance.

Discussion

More compliant tendons enabled muscle to store more energy in the tendon, but a limit was reached due to muscle force decreasing with increased shortening. The limitations in muscle force generating capacity were weakly explained by force depression. These results highlight that further investigation of muscle contractile properties under nonsteady activation conditions is needed.

Images (Optional)



References (Optional)

[1] Herzog et al., J Biomechanics, 2000

Acknowledgements (Optional)

Funding NSF#2128545 & 2312925

Session Category

Musculoskeletal Biomechanics: Tissues

P2-222

Towards Large-Scale, Automated FE Knee Models: Ligament Calibration and its Impact on Cartilage Mechanics

MSc. Famke Janssen[1], Dr. Ir. Thom Bitter[1], Prof. Dr. Ir. Nico Verdonschot[1,2], Dr. Ir. Dennis Janssen[1]

[1]Radboud university medical center, Nijmegen, Gelderland, Netherlands. [2]University of Twente, Twente, Overijssel, Netherlands

Introduction

Accurate representation of ligament behavior is critical for force-driven, subject-specific finite element (FE) knee models, as ligaments govern joint kinematics and influence cartilage loading. Quantifying cartilage loading in such models is crucial for understanding mechanical factors that may contribute to osteoarthritis. Simplified tibiofemoral models commonly use single-bundle ligament representations, literature-based parameters, and manually placed attachments, which limits mechanical accuracy and scalability for large cohorts. More detailed models add structures such as the patellofemoral joint, popliteus, and capsule but require extensive subject-specific input. For both approaches, manual interventions reduce reproducibility and increase dependence on modeler expertise, while using a single ligament property parameter set limits subject-specificity. This study introduces an automated ligament modeling and calibration framework and evaluates how ligament representation and parameter optimization affect cartilage contact mechanics.

Methods

A Subject-specific FE knee model was generated using a fully automated pipeline from MRI to a complete FE model (i.e., segmentation, mesh generation, and model assembly). Collateral ligaments were represented with three bundles, cruciate ligaments with two bundles. Template-based attachment sites were defined anatomically and transferred via non-rigid mesh morphing. Ligament slack lengths and stiffnesses were calibrated using normative knee laxity values for anterior–posterior and varus–valgus laxity tests at full extension and 90° of flexion. Cartilage contact pressures were evaluated during passive flexion, stance-phase gait, and squat and compared between optimized ligament properties and literature-based parameters [1,2].

Results

Preliminary results indicated that subject-specific ligament calibration substantially lowers cartilage contact pressure distributions compared to literature-based models (Figure 1). Sensitivity to ligament representation increased with flexion angle during both passive and

loaded motions, whereas stance-phase gait showed more moderate effects on cartilage contact pressures.

Discussion

Automated ligament calibration reduces excessive cartilage contact stresses during flexion in subject-specific FE knee models. The workflow enables reproducible, scalable generation of large cohorts, providing a foundation for analyzing cartilage loading and mechanical factors associated with osteoarthritis in a large cohort. Cadaveric validation of laxity response, kinematics, and contact pressures is ongoing. Performance of generalized calibration will also be compared to cadaver-specific laxity optimization.

Images (Optional)

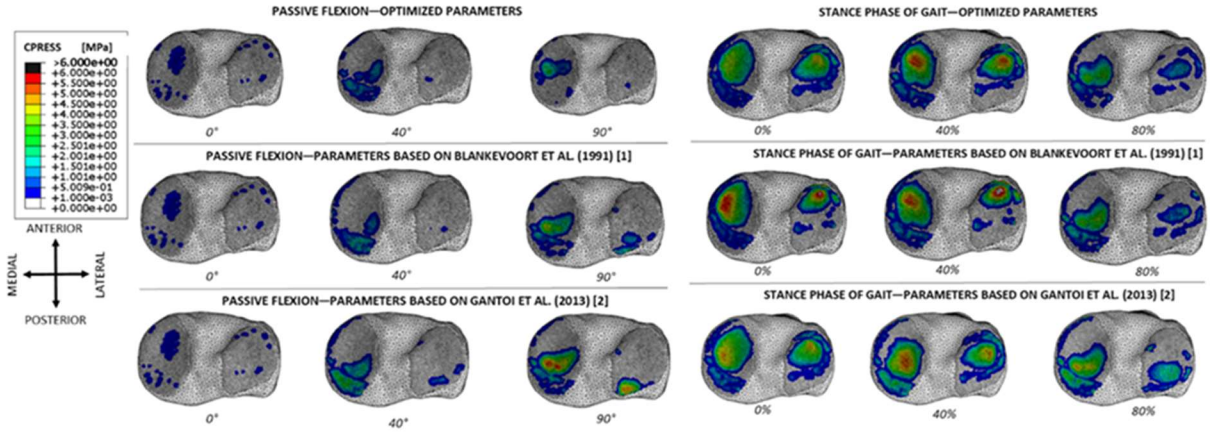


Figure 1 Contact pressures at the tibial cartilage during passive flexion and stance phase of gait using different properties for the ligaments

References (Optional)

[1] Blankevoort *et al.*, J Biomechanics, 1991

[2] Gantoi *et al.*, J Comput Nonlinear Dyn, 2013

Acknowledgements (Optional)

This study is part of the project LoaD (projectnr. NWA1389.20.009) of the NWA-ORC research programme which is (partly) financed by the Dutch Research Council (NWO).

Session Category

P2-223

Biophysical Regulation of Composite Musculoskeletal Tissue Regeneration

Miss Catherine Nguyen M.S., Dr. Cole DeForest Ph.D., Dr. Feini Qu V.M.D, Ph.D.

University of Washington, Seattle, Washington, United States

Introduction

Limb loss affects over 2 million Americans, creating a clinical need for composite musculoskeletal tissue regeneration. To this end, we study the murine digit tip, which regenerates after distal amputation via activated stem/progenitor cells (the "blastema"), but scars after more proximal amputations. While biophysical cues in the extracellular matrix (ECM) are known to modulate various cell behaviors, it remains unclear how the wound's mechanical properties may affect blastema formation and regeneration. To investigate, we quantified ECM stiffness and structure after digit amputation.

Methods

Terminal (P3) and middle (P2) phalanges of male and female 10-week-old C57BL/6 mice were resected with IACUC approval. Bone morphology was quantified via *in vivo* microcomputed tomography at various days post-amputation (DPA). Paraffinized sections of 14 DPA digits were stained with hematoxylin & eosin and picrosirius red. Cryosections of 14 and 21 DPA digits underwent force spectroscopy using an atomic force microscope with a spherical probe ($\varnothing$ = 10.8 μm, k = 0.08 N/m). ECM stiffness was determined via the Hertz model. Significance was determined by two-way ANOVA with Tukey's post-hoc test ($p \leq 0.05$).

Results

Composite musculoskeletal tissue regeneration occurred after P3, but not P2 amputation (Fig. 1). The P3 bone underwent remodeling followed by regrowth, with concomitant changes in length and volume. These changes were absent in the P2 group, which instead formed a fibrotic scar around the stump bone. The scar possessed densely aligned collagen, whereas the blastema exhibited high cell density in regions of low collagen content. The P2 scar was significantly stiffer than the P3 blastema at 14 DPA (3.6 ± 0.6 kPa vs. 1.2 ± 0.1 kPa), a difference that persisted to 21 DPA (4.4 ± 1.1 kPa vs. 1.8 ± 0.7 kPa).

Discussion

Our findings suggest that regeneration depends on the wound's emergent properties, including ECM stiffness and structure. P3 bone regrowth occurred in a compliant matrix with minimal collagen deposition, whereas the dense collagen scar may have physically

inhibited P2 bone outgrowth. A stiffer ECM may also promote a myofibroblast phenotype that perpetuates scar formation. Future work will investigate how altering matrix stiffness affects stem/progenitor cell activation and blastema formation, elucidating potential therapies for musculoskeletal regeneration.

Images (Optional)

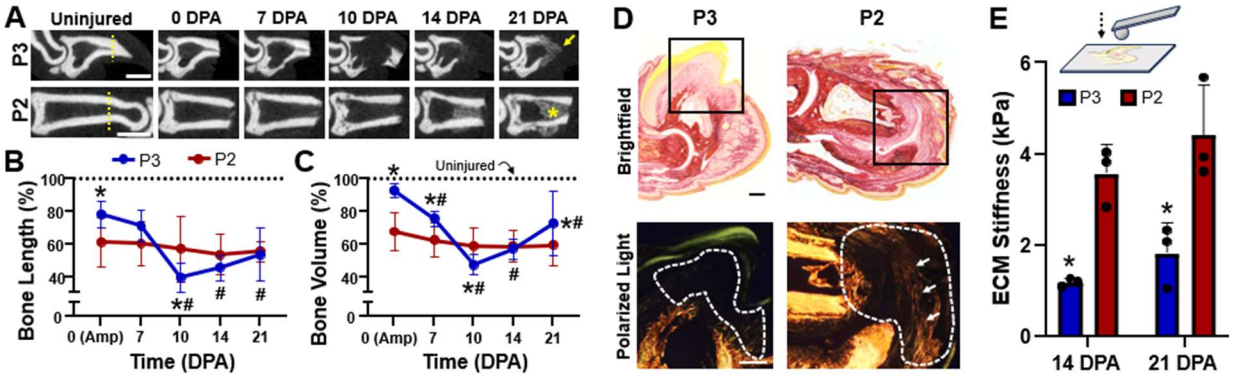


Fig. 1. (**A**) Microcomputed tomography images show bone regrowth (arrow) after P3 amputation and callus formation (asterisk) after P2 amputation. Dotted line indicates amputation plane. Scale bars = 500 μm. (**B**) Bone length and (**C**) volume over time (% of uninjured) after digit amputation (n = 6 digits/group/timepoint, mean ± SD). * = p ≤ 0.05 vs. P2, # = p ≤ 0.05 vs. 0 DPA (Amp). (**D**) Mid-sagittal digit sections at 14 DPA stained with picrosirius red, visualized with brightfield (top) and polarized light (bottom) microscopy. Box indicates magnified region in bottom image. Sections viewed under polarized light reveal collagen fibers (arrows) in the P2 scar but not the P3 blastema. Dashed line shows regions for force spectroscopy. Scale bars = 200 μm. (**E**) ECM stiffness of the P3 blastema and P2 scar, with force spectroscopy schematic (n = 3 samples/group/timepoint, mean ± SD). * = p ≤ 0.05 vs. P2.

Session Category

Musculoskeletal Biomechanics: Tissues

P2-224

Quadriceps Strength and Activation in Healthy Adults Through the Menstrual Cycle

Ms Francesca Belibi, Ms. Emma Sachs, Dr. Skylar Holmes, Dr Emily Kraus, Dr Garry Gold, Dr Carly Jones

Stanford University, Palo Alto, CA, United States

Introduction

The menstrual cycle's impact on athletic performance is a top concern for female athletes. Previous studies have found increased strength, slower muscle recovery, and higher fatiguability mid-cycle; others found no difference. Quantitative MRI (qMRI), in addition to strength testing, may be more sensitive to changes in muscle function than traditional methods. In this abstract, we focused on muscle strength and activation.

Methods

Four naturally menstruating participants completed strength testing and MRI scanning during the follicular phase and one high estrogen (mid-cycle or luteal) phase, determined via cycle tracking. The order of study visits was randomized across participants. Participants were scanned in a 3T MR scanner before and after a wall-sit exercise. The difference from peak to baseline T2/T2* signal, $\boldsymbol{\Delta}$, is related to muscle activation. Quadriceps strength was assessed using an isokinetic dynamometer at 60 degrees of flexion. Participants completed 20 maximum isometric contractions from which measurements of quadriceps peak torque ($\boldsymbol{\tau}$) and rate of torque development (RTD) were obtained. This initial cohort is too small for statistical testing.

Results

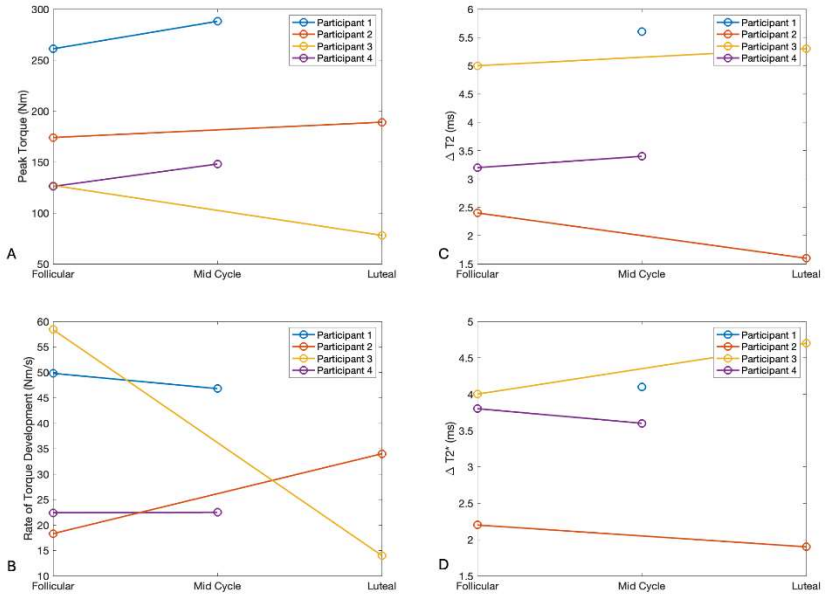
Peak torque was slightly higher, and RTD was slightly lower in the mid-cycle compared to the follicular phase. No consistent trend was observed between the follicular and luteal phases, though individual differences in RTD were larger than those observed between the follicular phase and mid-cycle (Figure 1A-B)

Participant 1 had no measure of $\boldsymbol{\Delta}$ T2/T2* for the low estrogen phase due to a hardware malfunction. No consistent trends were observed between follicular, mid-cycle, and luteal phases for $\boldsymbol{\Delta}$ T2/T2* (Figure 1C-D).

Discussion

Our preliminary observations found individual muscle strength and activation variations over the menstrual cycle; however, the conflicting group observations highlight the necessity of hormone testing to gain a better understanding of the menstrual cycle's effects. Future experiments, with a larger cohort, will use urine and saliva-based hormone tracking to confirm cycle phases.

Images (Optional)



Session Category

Musculoskeletal Biomechanics: Tissues

P2-225

The Role of Achilles Tendinopathy on the Torque-Angle Relationship During Isokinetic Plantar Flexion

Mr. Hidetaka Hayashi, Ms. Corey Whalen, Mr. Michael Hahn

University of Oregon, Eugene, OR, United States

Introduction

Achilles tendinopathy (AT) is a degenerative pathology associated with increased cross-sectional area and decreased stiffness [1]. Previous work showed that a shift in peak torque angle to a more extended position occurs with increasing joint angular velocity during isokinetic knee extension, and that this shift can be attributed to tendon compliance [2]. While it is known that AT alters tendon compliance, the effect of AT on the joint angle-peak torque relationship is unclear. Therefore, the purpose of this study was to elucidate the effect of AT on the joint angle-peak torque relationship during a concentric isokinetic plantar flexion.

Methods

. Five participants with symptoms of AT and 5 healthy age and sex matched controls participated in this study. Participants were positioned on an isokinetic dynamometer with their thigh-trunk angle at 110 degrees (180 degrees = full extension), knee fully extended, and the foot firmly fixed to the footplate. After a warm-up, participants performed 2 sets of 5 maximal concentric plantar flexion contractions at pre-set angular velocities of 30, 60, and 90 deg/sec. Isokinetic torque and angular position data were sampled at 1 kHz. The trial with the highest torque output was used for analysis and was analyzed in the range of -5 degrees (DF) to 15 degrees (PF). A mixed model ANOVA (group x angular velocity) was used to test for the effect of independent variables on the joint position at peak torque.

Results

There was a significant interaction between group and angular velocity ($p < .05$; fig. 1). Simple main effect analysis revealed a main effect of angular velocity, with significant difference between the 30 and 90 deg/sec as well as between the 60 and 90 deg/sec conditions ($p < .05$). There was no main effect of group ($p = .487$).

Discussion

While the effect of angular velocity on the peak torque angle shift towards a more plantar flexed position is consistent with previous findings for the knee extensors, the significant

interaction effect suggests altered velocity-dependent modulation of the torque-angle relationship in individuals with AT.

Images (Optional)

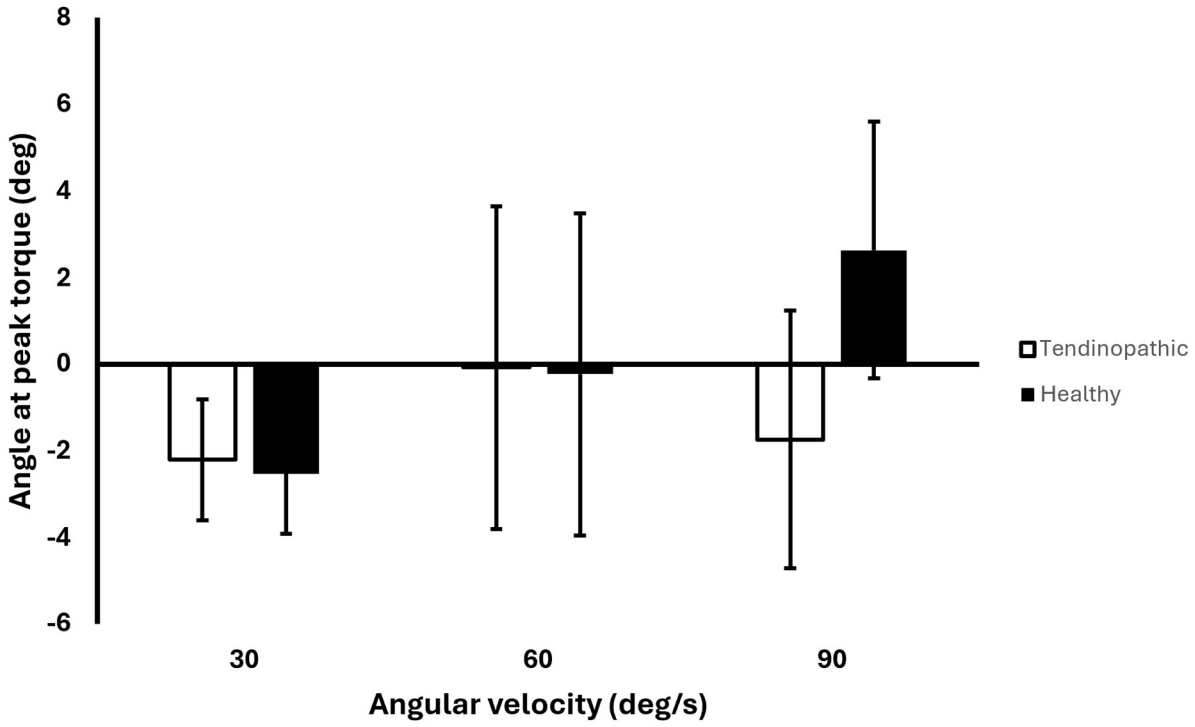


Figure 1. Ankle joint angle at peak torque as a function of joint angular velocity during isokinetic plantar flexion

References (Optional)

[1] Arya and Kulig (2010), J App Physiol

[2] Kawakami et al., (2002), Eur J App Physiol

Acknowledgements (Optional)

This work was supported by the Wu Tsai Human Performance Alliance and the Joe and Clara Tsai Foundation.

Session Category

Musculoskeletal Biomechanics: Tissues

P2-226

Region-Dependent Properties of Lamellae Constituents in the Intervertebral Disc: Possible Insights Into Herniation Mechanisms

Dr. Jackie Zehr PhD[1], Dr. Venus Joumaa PhD[2], Dr. Jack Callaghan PhD[3], Dr Walter Herzog PhD[2]

[1]University of Toronto, Toronto, Ontario, Canada. [2]University of Calgary, Calgary, Alberta, Canada. [3]University of Waterloo, Waterloo, Ontario, Canada

Introduction

Intervertebral joint bending is associated with intervertebral disc (IVD) herniations [1]. In an attempt to better understand herniation mechanisms, prior work has examined lamellar mechanics [2-4], yet the specific roles of individual constituents (collagen fibres and the intra-lamellar matrix) remain unclear. This study directly characterized the tensile properties of isolated collagen fibres and the adhesion properties of the intra-lamellar matrix in healthy IVDs.

Methods

IVDs were extracted from the C3C4 spinal level of eight porcine cervical spines. Single lamellae were dissected from the outer 1/3 of the annulus comprising the anterior and posterior regions. From each lamella, two samples were harvested: i) isolated collagen fibre and ii) two adjacent collagen fibres with the matrix that connects them, totalling 32 samples. Two types of mechanical tests were performed: i) isolated collagen fibres were exposed to uniaxial tension; and ii) the intra-lamellar matrix underwent a single lap shear test. The cross-sectional area of all samples was measured, a baseline stress was applied (5 kPa tensile tests, 0.5 kPa shear tests) to remove slack, and samples were strained at 1% per second until failure. The Young's modulus, yield and failure stresses and strains were determined. Regional differences were evaluated using paired and Wilcoxon tests.

Results

In isolated collagen fibres, the Young's modulus and ultimate stress were 45% and 51% greater in the posterior compared to the anterior region, respectively ($p<0.047$). All properties of intra-lamellar matrix adhesion were similar across regions ($p>0.151$). The isolated collagen fibers and intra-lamellar matrix experienced comparable strains at yield (32%) and failure (46%), but the ultimate tensile stress of isolated fibres was approximately five times greater than the intra-lamellar matrix adhesion.

Discussion

Regional variations within and between lamellar constituents likely reflect underlying microstructural differences (e.g., fibril density, orientation, or matrix connectivity), though this remains to be experimentally confirmed. Incorporating these findings into collagen distribution models may provide new insight into early microdamage initiation pathways that precede IVD herniation disorders.

References (Optional)

[1] Kim et al., Spine. 2009

[2] Skaggs et al., Spine,1994.

[3] Holzapfel et al., Biomech Model Mechanobiol, 2005

[4] Briar et al., Eur Spine J, 2023

Acknowledgements (Optional)

Alberta Spine Foundation

Session Category

Musculoskeletal Biomechanics: Tissues

P2-227

Characterizing Achilles Tendon Non-Uniformity using Cadaveric Simulation and Muscle-Specific Actuation

Dr. Jason Franz[1], Dr. Taija Finni[2], Dr. Raad Khair[2], Dr. William Ledoux[3]

[1]University of North Carolina at Chapel Hill, Chapel Hill, NC, United States. [2]University of Jyväskylä, Jyväskylä, Finland, Finland. [3]VA Puget Sound Health Care System, Seattle, WA, United States

Introduction

The Achilles tendon is comprised of subtendons arising from individual triceps surae muscles. Ultrasound techniques used to characterize subtendon structure-function relations are limited by anatomical and theoretical assumptions. We used cadaveric simulation and muscle-specific actuation in the robotic gait simulator (RGS) to test those assumptions.

Methods

A cadaveric specimen was transected approximately 15 cm proximal to the malleoli. The Achilles tendon was separated into gastrocnemius (medial and lateral, GAS) and soleus (SOL) compartments ("subtendons"). These two subtendons were sutured to nylon straps in series with load cells and linear tendon actuators. We tested the specimen on the RGS. With the ankle specimen in a neutral position, the RGS simulated three isometric fixed-end contractions, prescribed as symmetrical (loading/unloading) ramp tests from rest: (1) SOL 200 N + GAS 200 N; (2) SOL 400 N + GAS 0 N; and (3) SOL 0 N + GAS 400 N. We recorded cine B-mode images of the Achilles free tendon, analyzed using speckle tracking to resolve localized tendon tissue displacements and longitudinal strain, which we averaged over superficial (50%) and deep (50%) regions thought to correspond to the GAS and SOL subtendons, respectively.

Results

All three of the following discoveries were unexpected based solely on simple anatomical assumptions (Fig. 1). First, despite constant total force, peak tendon tissue displacements were largest when that force was distributed equally between the GAS and SOL. Second, tendon non-uniformity (i.e., the difference between superficial and deep tendon tissue displacements) was largest when the applied muscle forces were distributed equally between the GAS and SOL. Finally, positive strain in the superficial (or deep) tendon was largest when the SOL (or GAS) was actuated independently.

Discussion

The triceps surae muscle-subtendon units do not behave as simple linear actuators. Thus, capturing anatomical heterogeneity in the Achilles tendon—for example through recent MRI advancements [1] or combined ultrasound/electrical stimulations protocols [2]—is paramount in the design and conduct of any future study designed to understand the complex interaction between calf muscle forces and Achilles subtendon deformation.

Images (Optional)

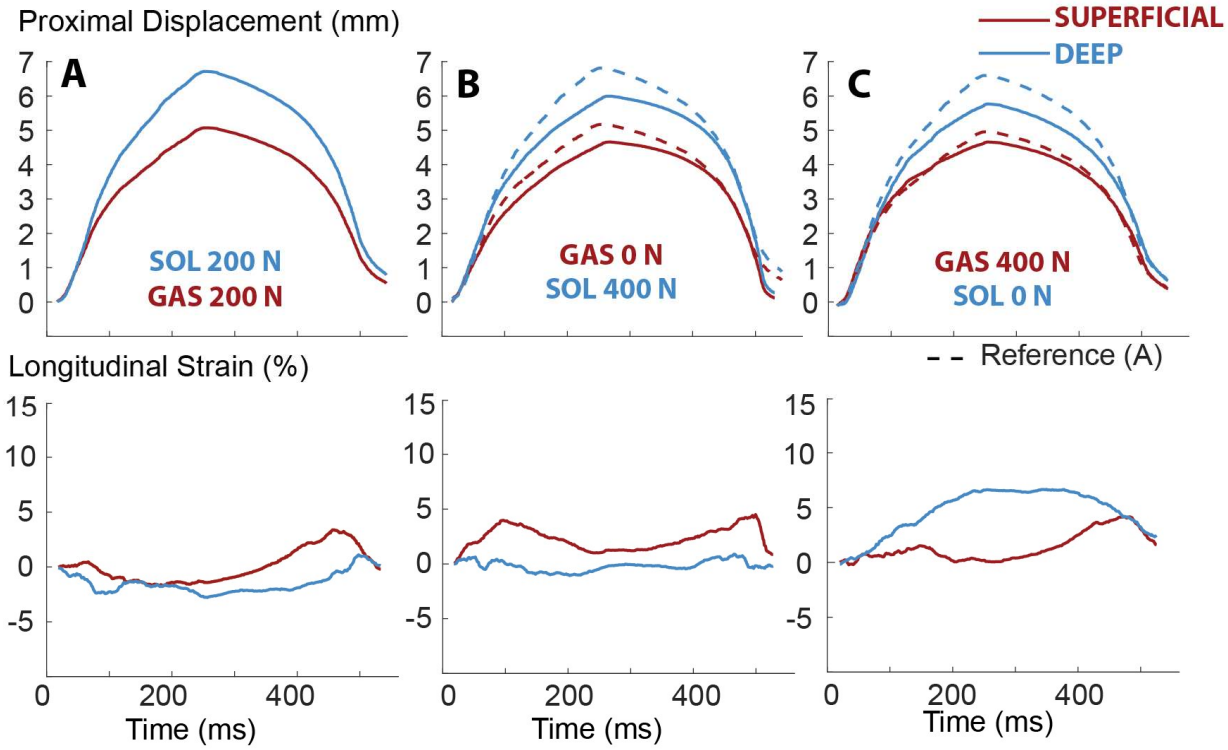


Figure 1. Superficial and deep tendon tissue responses to 3 loading conditions (A,B,C) prescribed to the cadaver Achilles specimen via a robotic gait simulator.

References (Optional)

[1] Cone SG et al., J Orthop Res. 2023.

[2] Finni T et al., Scand J Med Sci Sports. 2025.

Acknowledgements (Optional)

Session Category

Musculoskeletal Biomechanics: Tissues

P2-228

Influence of Collagen Fiber Strain on the Development of the Shear Mechanical Properties of the Superficial Region of Cartilage

Ms. Kangxin Wang, Dr. Jill Middendorf

Johns Hopkins University, Baltimore, Maryland, United States

Introduction

The superficial region of articular cartilage protects the joint from damage but remains difficult to recreate or repair, so understanding how the cartilage develops may inform future repair strategies. During maturation, unorganized collagen in the superficial region becomes aligned collagen fibers, increasing shear stiffness. Previous work has linked physiologically relevant cyclic shear loading and collagen fiber stretch to changes in fiber orientation and alterations in tissue mechanics[1,2]. However, these prior works focused on mature cartilage or hydrogels. Our study investigated how the superficial shear mechanics of immature cartilage change with collagen fiber stretch under cyclic shear loads.

Methods

Thirteen fetal bovine articular cartilage cylinders were assigned to simple shear (N = 5) or shear with 15% global compression (N = 8). These loads were chosen to induce a wide range of fiber strains (Fig. A). All samples underwent 3% global cyclic shear for 8h followed by 12h of relaxation. Horizontal and vertical photobleached lines in the superficial region tracked compressive and shear strains, while shear stress was measured. Shear stress-strain curves were obtained at 0, 4, and 8 hours and after relaxation. Collagen fiber stretch was calculated from measured tissue strains for fiber orientations between 0° and 90°.

Results

Both groups (simple shear and 15% compression) showed decreased shear modulus with loading time (Fig. B). Partial recovery was observed after relaxation in the 15% compression group, and no recovery was observed in the simple shear group. In the 15% compression group, toe and effective shear modulus decreased during loading and recovered to their 4h values after relaxation (Fig. C).

Discussion

The tensile strain in collagen fibers under simple shear and the lack of tensile fiber strain under 15% compression most likely contribute to the differences in shear mechanical recovery. This relationship between collagen fiber tensile strain and changes in shear mechanics is consistent with work in other tissues[3,4]. These findings shed light on the mechanisms of superficial region development in immature cartilage and may guide repair strategies for the cartilage.

Images (Optional)

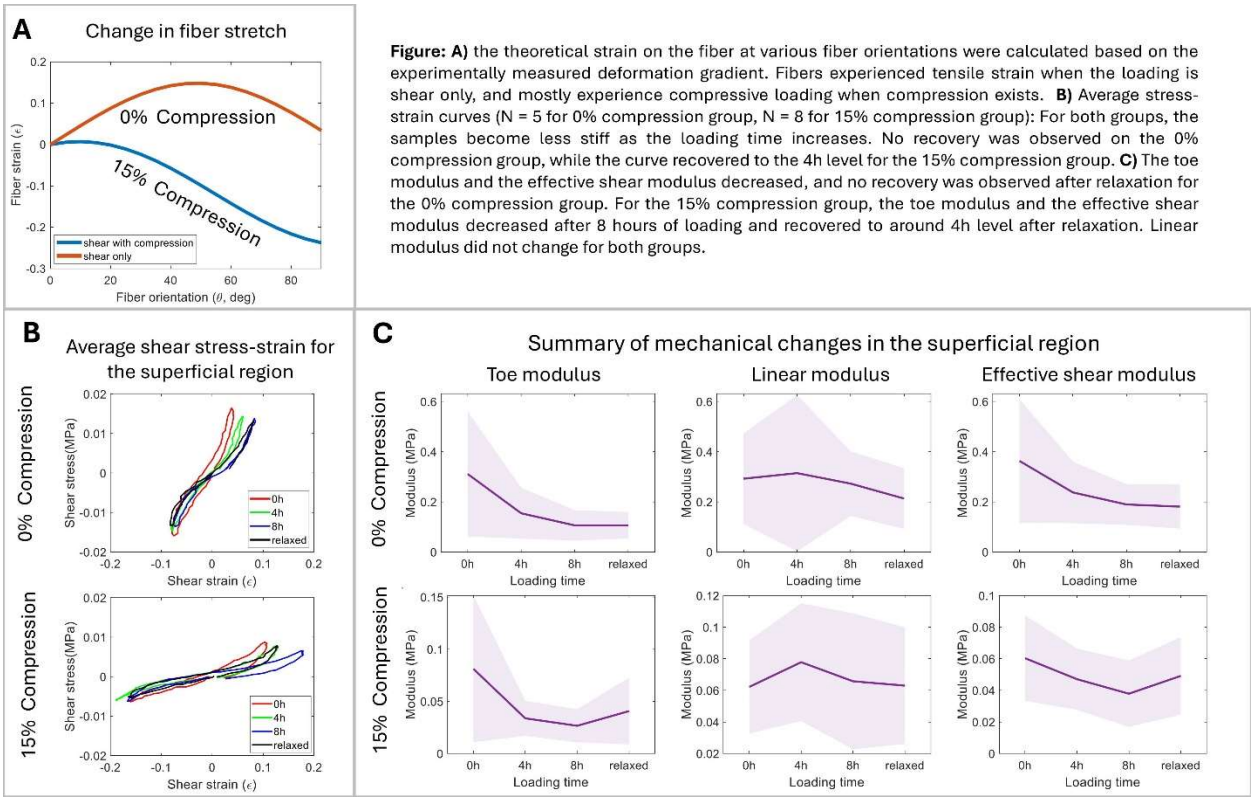


Figure: A) the theoretical strain on the fiber at various fiber orientations were calculated based on the experimentally measured deformation gradient. Fibers experienced tensile strain when the loading is shear only, and mostly experience compressive loading when compression exists. **B)** Average stress-strain curves (N = 5 for 0% compression group, N = 8 for 15% compression group): For both groups, the samples become less stiff as the loading time increases. No recovery was observed on the 0% compression group, while the curve recovered to the 4h level for the 15% compression group. **C)** The toe modulus and the effective shear modulus decreased, and no recovery was observed after relaxation for the 0% compression group. For the 15% compression group, the toe modulus and the effective shear modulus decreased after 8 hours of loading and recovered to around 4h level after relaxation. Linear modulus did not change for both groups.

References (Optional)

[1]S.R.Inamdar+ *Acta Biomater.* 2021 [2]L.M.Dedroog+ *Acta Biomater.* 2022 [3]W.Wilson+ *J. Orthop. Res.* 2006 [4]E.A.A.Neel+ *Soft Matter*.2006

Session Category

Musculoskeletal Biomechanics: Tissues

P2-229

Cartilage Redox Responds Consistently to Tensile and Compressive Loading

Postdoctoral Research Associate Jingyi Wang, Associate Professor Corinne Henak

University of Wisconsin - Madison, Madison, WI, United States

Introduction

Articular cartilage experiences complex mechanical loading *in vivo*. Although compression is the most studied loading mode, cartilage also undergoes other modes[1,2]. Tensile loading can induce various biologic responses[1,3,4]. Redox balance, the balance between the production and elimination of oxidants, is crucial for cartilage health[5-7]. Its mechanobiological response is therefore of interest. Optical redox imaging (ORI) can evaluate cartilage redox balance and is responsive to both compressive[8] and tensive loading[9]. However, it remains unclear if cartilage redox responds the same way to compression and tension, leaving a gap in understanding of mode-specific cartilage mechanobiology and making interpretation of results from tensile studies challenging. Hence, this study aims to test the hypothesis that sub-failure compression and tension cause the same response in cartilage ORI metrics.

Methods

Samples were cut from full-thickness porcine patella cartilage. Cut dimensions were ~2.5 mm x 3 mm or ~10 mm x 0.5 mm for compression and tension tests, respectively (N = 5 for each). Mechanical loading was done on a custom-built microscope-top loading device. An actuator was programmed to move at ±0.1 s^{-1} to ±0.3 strain and return to the original position. Regions of interest (ROIs) were defined in the superficial, middle and deep zones (Fig. 1A and 1B), and images were taken before and after loading in green and DAPI channels. Post-loading intensity was normalized to that of the corresponding zone from the pre-loading image. Unpaired student t-test was performed to compare the normalized intensity of compression and tension groups.

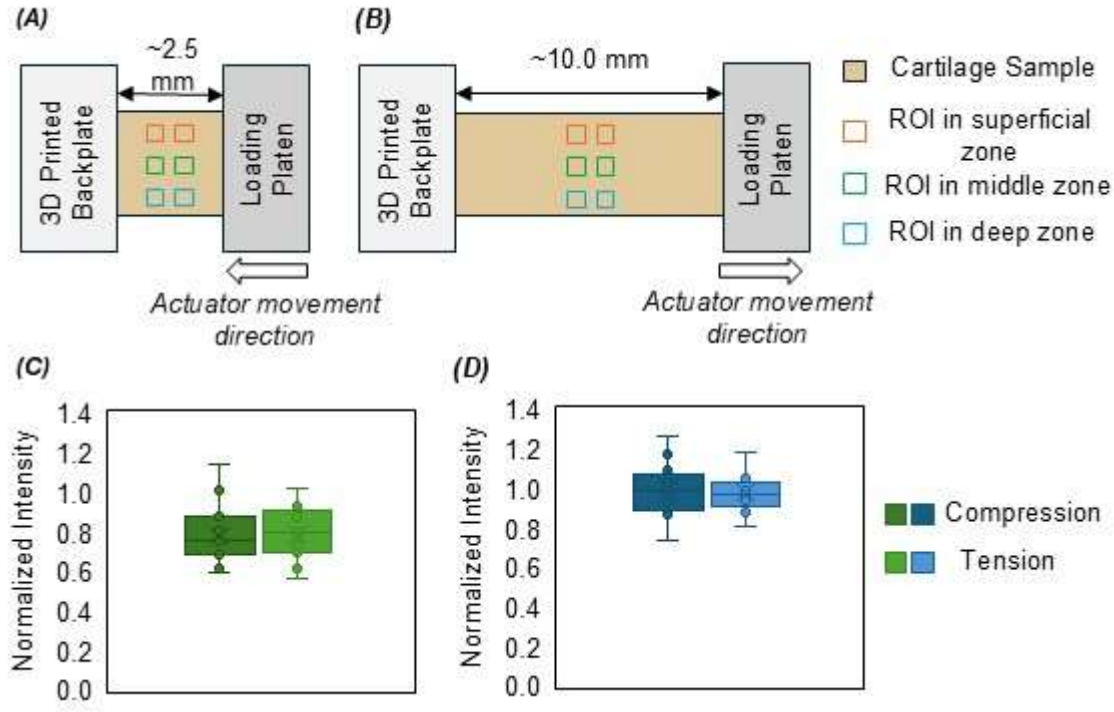
Results

No significant difference was found between compression and tension in both channels (Fig 1C and 1D).

Discussion

This study showed that acute response of cartilage redox to sub-failure compression and tension is consistent. The result advances the understanding of cartilage redox mechanobiology and highlights the potential to use various loading modes when designing *in vitro* cartilage loading models. Nevertheless, further studies are needed before making a more specific conclusion, as the achieved loading parameters could differ for each group due to backplate deformation. In addition, cultured chondrocytes demonstrate distinct responses to cyclic compression and tension[10], implying the subtle and complex nature of cartilage mechanobiology.

Images (Optional)



References (Optional)

Session Category

Musculoskeletal Biomechanics: Tissues

P2-230

Contraction-Mode Dependent Muscle Adaptations to Eccentric, Concentric, and Isometric Training in Rats

Ms Kathryn Chapman, Ms Amelia Rilling, Dr Alexander M Zero PhD, Mr Maxum A.K Stratford, Ms Alexandra Q Kirkup, Dr Geoffrey A Power PhD

Univeristy of Guelph, Guelph, Ontario, Canada

Introduction

In response to resistance training, skeletal muscle exhibits distinct mechanical and morphological adaptations depending on whether training consists of eccentric, concentric, or isometric contractions. Across separate investigations, species, and muscle groups, eccentric loading appears to increase torque production across a range of muscle lengths, while concentric training tends to preferentially improve power, and isometric training often yields joint-angle–specific strength gains. However, it remains unclear whether these contraction types differentially contribute to performance improvements when training demands are matched in the same study and population. Therefore, we examined mechanical adaptations following 6 weeks of eccentric, concentric or isometric training in young male rats.

Methods

Male Sprague-Dawley rats (n=18; 14-17 weeks; 360-565g) were randomly assigned to 6 weeks of unilateral plantar-flexor training on a dynamometer involving either eccentric, concentric, or isometric contractions (n=6/group) 3 days/week. Peak isometric torque across 3 joint angles (70°, 80°, 90°) was assessed pre- and post-training. Eccentric contractions were performed through an ankle angle range of motion of 110-70° at 40-80°/s with muscle activation (i.e., electrical stimulation) set to ~60-70% of maximal isometric torque. Meanwhile the concentric group performed contractions in the opposite range of motion (70-110° motion) at 40-80°/s, and activation/stimulation set to 100% of maximal isometric torque measures on that training day. Isometric training involved 1500ms maximal contractions at a 70° ankle angle. Across all training modes, there was progressive increases in repetitions and sets.

Results

Isometric torque increased following training for all groups ($P<0.05$). There was no joint angle, or training group × angle interaction (both $P>0.05$). However, there was an effect of group ($P<0.05$), such that the isometric group had the largest magnitude increase in torque

production (~30%) as compared with both the eccentric (~15%), and concentric (~11%) groups which increased similarly.

Discussion

All three training protocols increased isometric peak torque independent of joint angle; however, the greatest increase was observed following isometric training at a long muscle length.

Acknowledgements (Optional)

Supported by NSERC

Session Category

Musculoskeletal Biomechanics: Tissues

P2-231

Voltage-induced Demineralization Behavior of Cortical Bone in Physiological Saline

Associate Professor Kazuhiro Fujisaki, Mr. Rinto Hashiguchi, Professor Kazuhiko Sasagawa, Assistant Professor Kotaro Miura

Hirosaki University, Hirosaki, Aomori, Japan

Introduction

Bone tissue is a composite material mainly consisting of apatite and collagen. The crystalline structure of apatite provides hardness and stiffness to the tissue. It has been confirmed that the impact toughness of cortical bone can be modified through a localized demineralization treatment. Although demineralization of bone tissue is commonly performed using chelating agents such as ethylenediaminetetraacetic acid solution, precise control over the treated area is difficult with liquid supply methods. We proposed an electrical stimulation-based demineralization method for bone tissue. This study investigated the characteristics of the demineralization process and explored effective treatment conditions using a voltage application system.

Methods

Cortical bone samples were prepared from a bovine femoral bone. Plate-shaped specimens were fabricated using a low-speed wheel saw under wet conditions. The specimens were then immersed in a physiological saline, with Ti electrodes attached. Experiments were conducted using both a constant direct current (DC) voltage of 10 V and an alternating current (AC) square wave voltage of ±10 V at various frequencies (15, 50, 150, 300, and 1k Hz).

Results

Demineralization behavior was observed at the electrode contact areas under both DC (anode side) and AC conditions. Apatite deposition was also observed under both conditions. A frequency dependence was confirmed; specifically, 150 Hz showed the highest reaction rate compared to other AC conditions. The demineralization progressed from the specimen surfaces, which was recognized during microscopic observation of the cross-section of the specimens.

Discussion

The electric application method allowed for easy control of the demineralization area, suggesting its potential applicability under biological conditions. The observed frequency dependence could be induced by the gas generation behavior at the surface. Gas generation decreased under higher frequency conditions. However, higher frequency may also reduce the reaction rates of apatite dissolution and deposition. The optimal condition was likely provided by the balance of these contradictory factors. Since localized demineralization is effective in improving the mechanical characteristics of cortical bone, this electric method is expected to be used in the clinical field.

Acknowledgements (Optional)

This work was partially supported by JSPS KAKENHI 25K01114.

Session Category

Musculoskeletal Biomechanics: Tissues

P2-232

Quantification of Equine Tendon Loading During Locomotion with a Wearable Sensor

Ms. Lindsay Rehme[1], Mr. Fisher Adkisson[1], Dr. Annette McCoy[2], Dr. Alex Reiter[1]

[1]Saint Louis University, Saint Louis, Missouri, United States. [2]University of Illinois at Urbana-Champaign, Champaign, Illinois, United States

Introduction

Tendinopathies are a primary cause of lameness and decreased performance in athletic horses, particularly the superficial digital flexor tendon (SDFT).[1] Clinical evaluation relies on lameness assessment and ultrasonographic imaging; however, these methods lack sensitivity for detecting subtle biomechanical abnormalities. Recent work highlights the need for improved techniques to diagnosis and monitor injuries.[1,2] To address these challenges, novel techniques are needed to provide real-time, sensitive measurements of tendon loading. A tensiometer, previously developed for humans, can track the speed of propagating vibrations in tendon to quantify loading.3 The purpose of this study was to assess the capacity of tensiometry to capture the expected tendon loading patterns of equine during locomotion.

Methods

A healthy 8-year-old female equine (Arabian) completed treadmill locomotion under four conditions while a tensiometer recorded wave speed in the SDFT (Fig. 1A). The forelimb SDFT was assessed during level walking (1.5 m/s), incline (~4°) walking, and level trotting (4 m/s), and the hindlimb SDFT during level walking. Data were collected and processed in MATLAB to time normalize gait cycles and extract peak tendon wave speeds. Differences between conditions were analyzed using descriptive statistics.

Results

In the forelimb SDFT, incline walking induced a small increase in wave speed of ~8 m/s in the second loading peak during stance (Fig. 1A) compared to level walking. Peak wave speed increased from 103±5 m/s during level walking to 141±9 m/s during trotting (Fig. 1B). Hindlimb SDFT peak wave speed during level walking was notably lower than the forelimb by ~57 m/s (Fig. 1C).

Discussion

Tensiometry captured expected loading patterns during equine locomotion. Differences between conditions were consistent with previous studies. Forelimb ground reaction forces have been shown to increase with locomotion speed[4] similar to how wave

speed increased in this study. Furthermore, equines bear ~60% of their weight with their forelimbs compared to ~40% in the hindlimbs,[4] and wave speed magnitudes in the SDFT were similarly split between limbs. These findings demonstrate the potential of tensiometry to monitor equine tendon loading.

Images (Optional)

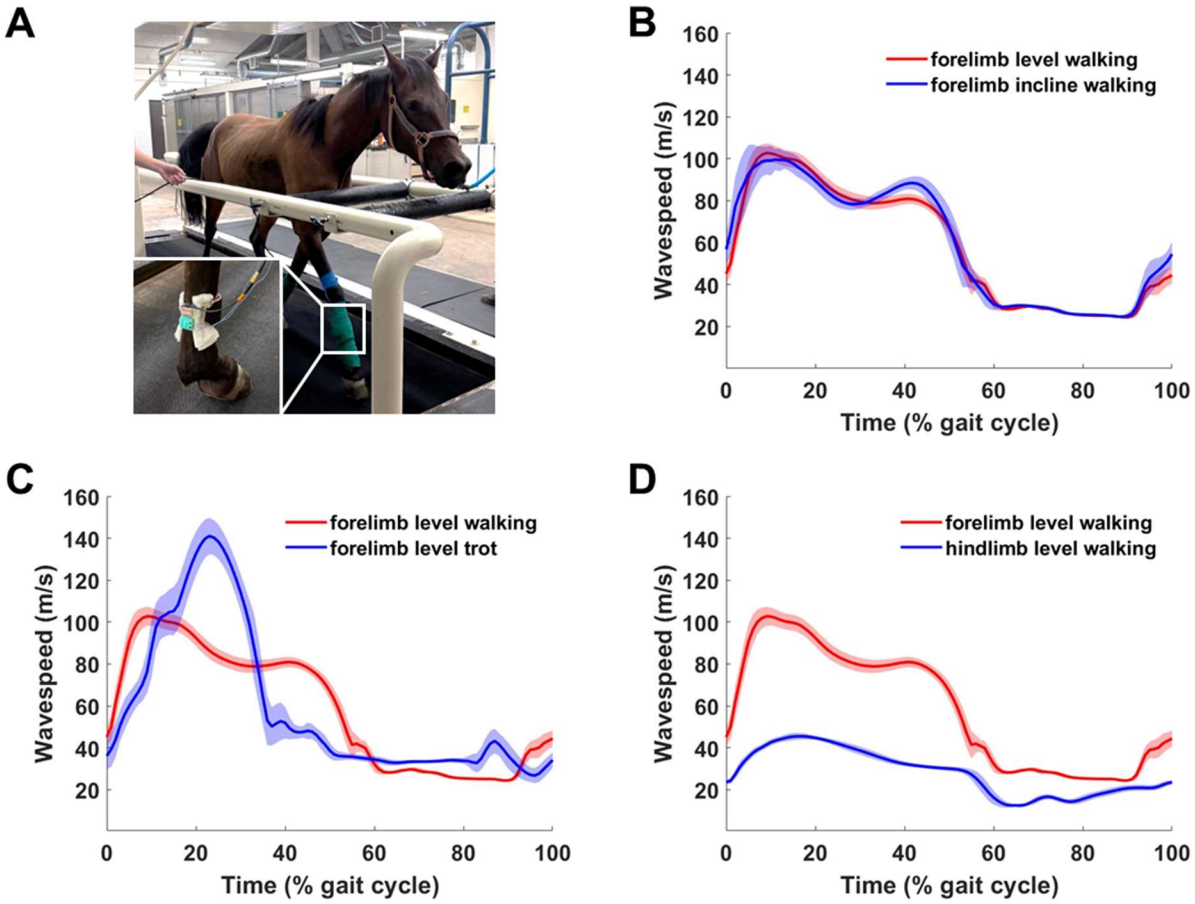


Figure 1. (A) The shear wave tensiometer recorded superficial digital flexor tendon waves speed, a surrogate for loading, during treadmill locomotion. Time series data of tendon wave speed (mean ± SD) normalized to the gait cycle comparing forelimb level walking to **(B)** forelimb incline walking, **(C)** forelimb level trot, and **(D)** hindlimb level walking.

References (Optional)

[1] Smith, EVE, 2023. [2] Madsen, FVETS, 2022. [3] Martin, NC, 2018. [4] Dutto, JEB, 2004.

Acknowledgements (Optional)

Funding from the Saint Louis University Research Institute.

Session Category

P2-233

Anterior Cruciate Ligament Size is Associated with Timing of Puberty Onset in the Skeletally Immature Porcine Knee Joint

Ms. Margaret Easson[1,2], Dr. Jacob Thompson[1,2], Dr. Sandra Shultz[3], Dr. Lauren Schnabel[1], Dr. Jeffrey Spang[4], Dr. Matthew Fisher[1,2]

[1]North Carolina State University, Raleigh, North Carolina, United States. [2]University of North Carolina- Chapel Hill, Chapel Hill, North Carolina, United States. [3]University of North Carolin at Greensboro, Greensboro, North Carolina, United States. [4]Wake Forest University School of Medicine, Winston-Salem, North Carolina, United States

Introduction

Anterior cruciate ligament (ACL) injuries are rising, with over 200,000 cases annually in the U.S. Adolescent females are 3-4 times more likely than males to sustain an ACL tear. Puberty involves hormonal and physiological changes that may influence injury risk. The relationship between puberty timing, early hormone exposure, and ACL development is not well understood. This study examines associations between puberty timing, sex hormones, and ACL morphology and function using a pig model.

Methods

Twelve female Yucatan minipigs were monitored from pre-puberty to mid-adolescence (4–10 months old). Serum was collected weekly, increasing to three times weekly before MRI and euthanasia. Body weight was recorded biweekly. Progesterone (P4) and estradiol (E2) were measured from serum. At 10 months, MRI scans were used to manually segment the ACL and its anteromedial (AM) and posterolateral (PL) bundles to determine volume and cross-sectional area. Associations between puberty onset, sex hormones, and ACL morphology were assessed using linear regression.

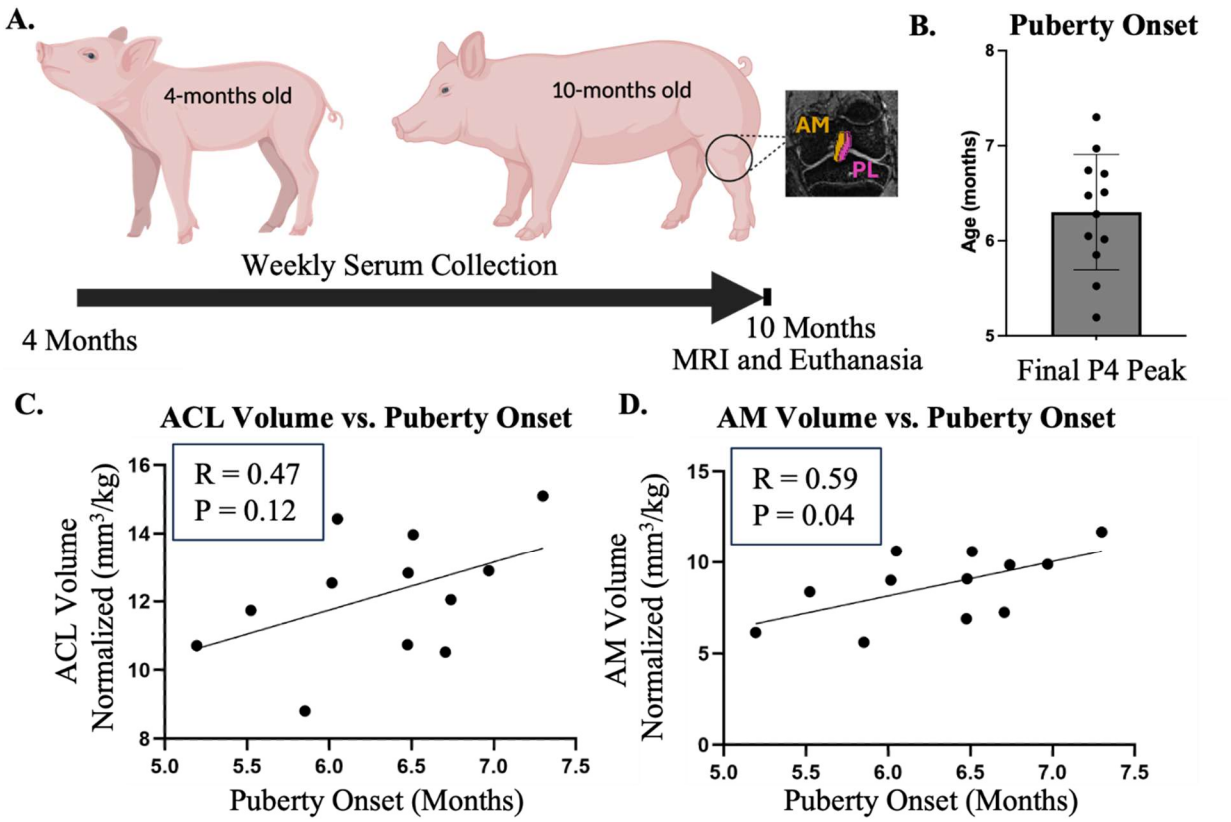
Results

Puberty onset, defined by the first progesterone peak, occurred at an average age of 6.3±0.6 months(Fig. 1B). Earlier puberty onset was moderately associated with greater final weight (R=-0.62). Later onset was moderately associated with larger ACL and bundle volumes (normalized to final weight)(Fig 1C-D). Preliminary findings also suggest associations between the final progesterone peak, body weight, and ACL size(R=0.66). Ongoing work is exploring relationships among puberty onset, hormone levels, and ACL and knee mechanics and function.

Discussion

This study shows that earlier puberty onset is linked to higher body weight and ACL size, but when normalized to weight, earlier onset corresponds to smaller ACLs. These results align with literature showing that girls who reach menarche earlier often have greater weight and BMI. Human studies have linked smaller ACL size with higher injury risk, and current data suggests that pubertal timing influences ACL size. In ongoing work, a larger set of animals as well as biomechanical and biochemical changes in the ACL will be assessed. This will allow for a comprehensive analysis on how the timing of puberty onset can impact ACL morphology and function throughout maturation.

Images (Optional)



Acknowledgements (Optional)

We would like to acknowledge the NCSU College of Veterinary Medicine and Laboratory Animal Resource as well as the Clinical Endocrinology Laboratory at UC Davis School of Veterinary Medicine for all their help.

Session Category

Musculoskeletal Biomechanics: Tissues

P2-234

A Low-Cost Biaxial Testing Set-Up to Evaluate Pregnancy-Related Changes in Birth Canal Material Properties

Dr Mariana Masteling PhD[1], Ms Xinfei Shen BS[1], Dr Noah Pearson PhD[2,3], Dr Christopher Hong MD[1], Dr Jon Estrada PhD[1], Dr John DeLancey MD[1], Dr James Ashton-Miller PhD[1]

[1]University of Michigan, Ann Arbor, MI, United States. [2]Bloom Surgical, Inc, Salt Lake City, UT, United States. [3]University of Utah, Salt Lake City, UT, United States

Introduction

Pregnancy induces remarkable changes to the birth canal tissues, whose biaxial properties are unstudied. Biaxial testing is the gold standard for soft tissue mechanical characterization, however, commercially available instruments are expensive and lack flexibility. To address these issues, we developed a low-cost, portable and customizable biaxial testing system using commercially available and custom 3D printed components.

Methods

Our biaxial testing system uses a modular, cost-effective design composed of five components: (i) four linear rods, each equipped with a stepper motor and motor driver mounted via custom 3D printed supports (~$200); (ii) two load cells attached using 3D printed supports ($120); (iii) custom grips with independent clamping units connected by a screw to accommodate varying sample thickness; (iv) a Raspberry Pi 5 to control the stepper motors and record load cell readings ($120); (v) a tripod ($15) that is perpendicular to the testing area for digital image correlation (DIC) using a smartphone camera. The system offers variable strain rate, travel range of 300 mm and load capacity up to 65 N (Figure 1A), with a total cost of ~$450.

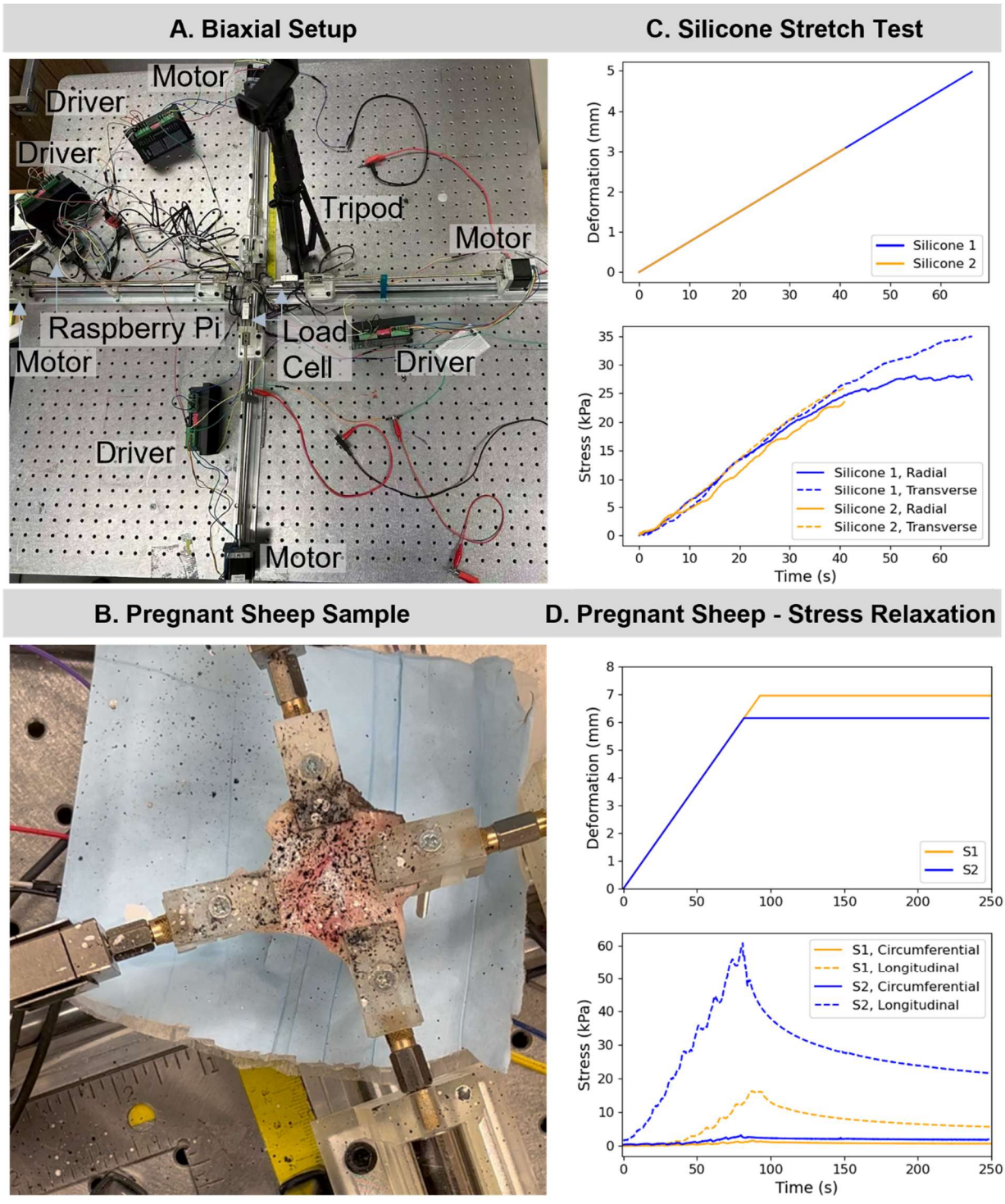
Results

Two Ecoflex 00-30 silicone samples (30x30x5 mm) were stretched biaxially at a constant rate (0.075 mm/s) to a deformation of 5 mm in both axes. The stress response shows elastic behavior in both radial and transverse directions (Figure 1C). Two birth canal samples (~20x20x6 mm), lateral to the vagina, were harvested from the same term-pregnant sheep euthanized for other studies. These tissues were tested biaxially at a constant rate (0.075 mm/s) for ~90 s followed by ~160 s relaxation period (Figure 1B, 1D). As expected, there are significant differences in the longitudinal and circumferential (up to 23x higher stress) direction in these tissues' response to stress-relaxation.

Discussion

This custom low-cost biaxial testing setup can accurately evaluate both elastic and viscoelastic materials, representing a first step for the characterization of the biaxial properties of the remarkable pregnancy-related changes in birth canal material properties. This system is portable, customizable to accommodate different motors and load cells, as well as, adjusting the angle between axis, to accurately simulate the biological stretches seen during birth.

Images (Optional)



Session Category

Musculoskeletal Biomechanics: Tissues

P2-235

Ground Reaction Forces and Biomechanical Differences Among Runners with Calf Pain Compartment Syndrome

Ms. Maryanne Anderson Lee, Dr. Ryan Nixon

University of Florida, Gainesville, Florida, United States

Introduction

Running is one of the most popular sports globally; however, running comes with a plethora of potential running-related injuries (RRI). Although there has been extensive research about the relation between ground reaction forces (GRFs), biomechanics, and injuries; there has not been comprehensive research into runners with Calf Pain Compartment Syndrome (CPCS) and how they biomechanically differ from non-injured runners. We aim to discover the biomechanical differences and differences in GRF components in runners with CPCS.

Methods

44 runners participated in the study and ran on an instrumented treadmill at self-selected speeds. Runners were categorized by injury status (CPCS or non-injured), foot strike (rearfoot or midfoot), and sex. To characterize signals obtained in more detail we developed an advanced waveform analysis that analyzes the collected GRFs and kinematic data (Nixon et al., 2025; Nixon et al., 2025). We tested whether CPCS runners would demonstrate differing or improved kinematics compared to non-injured runners.

Results

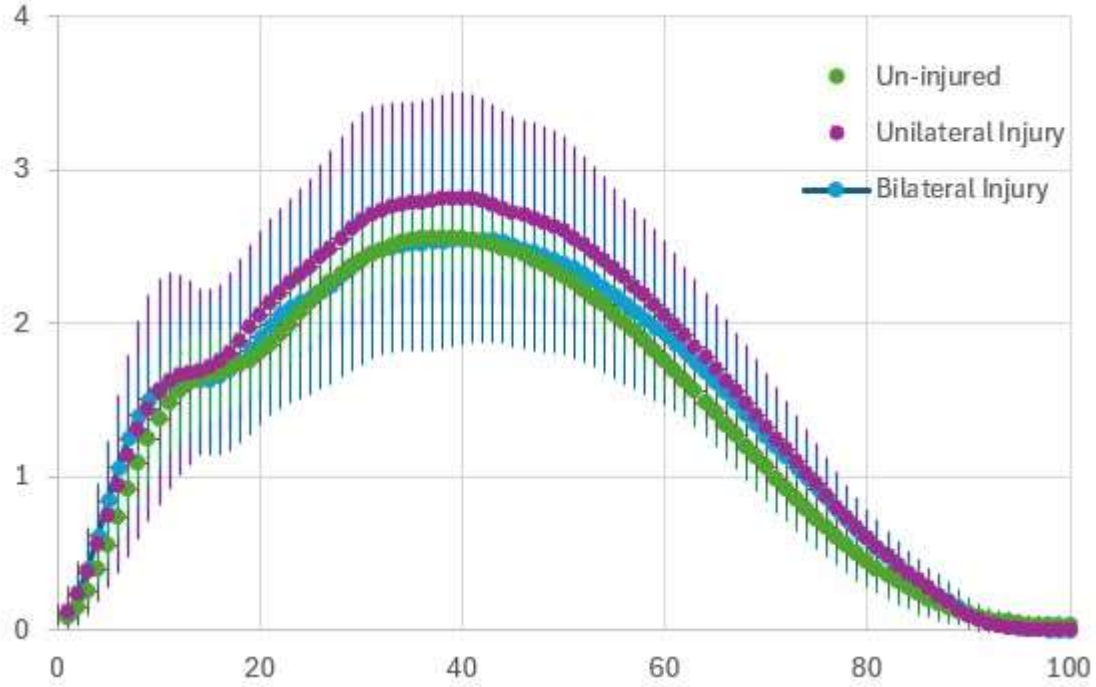
We normalized and frame-averaged unfiltered, data for RRI subsets of runners with CPCS to case-matched, non-injured runners. 59% of the non-injured runners ran at faster speeds and 77% ran more miles weekly compared to CPCS runners.

Discussion

Compared to non-injured runners, CPCS had shorter stance times and anterior-posterior GRFs (braking) for CPCS were higher on the right side (r = .38). Anterior-posterior GRFs (propulsion) were higher on the left (r = .46) and right side (r = .43) for runners with CPCS, showing moderate correlation. CPCS runners displayed higher maximum lateral force magnitude on the right side (r = .50), with there being a strong correlation, but lower maximum lateral force time on the right side (r = -.40). There was moderate correlation between CPCS and maximum load rate magnitude on the left (r = .41) and right side (r = .34), with runners with CPCS displaying higher maximum load rate magnitudes compared

with non-injured runners. On the other hand, runners with CPCS showed lower minimum load rate magnitude on the left (r = -.37) and right side (r = -.34). Runners with CPCS showed lower minimum load rate time on the left side (r = -.43) and right side (r=-.31).

Images (Optional)



References (Optional)

Session Category

Musculoskeletal Biomechanics: Tissues

P2-236

Muscle Strength, Power, and Physical Performance Associations with Volumetric Bone Mineral Density in Older Adults of the Study of Muscle, Mobility and Aging

Graduate Student Mason Shaffer[1], Dr. Nina Heilmann[1], Graduate Student Diana Madrid[1], Dr. Stephen Kritchevsky[1], Dr. Denise Houston[1], Dr. Fang-Chi Hsu[1], Dr. Shirley Bluethmann[1], Dr. Leon Lenchik[2], Dr. Jane Cauley[3], Dr. Elsa Strotmeyer[3], Dr. Peggy Cawthon[4], Dr. Ashley Weaver[1]

[1]Wake Forest University School of Medicine, Winston-Salem, North Carolina, United States. [2]Stanford University, Stanford, California, United States. [3]University of Pittsburgh, Pittsburgh, Pennsylvania, United States. [4]University of California San Francisco, San Francisco, California, United States

Introduction

Muscle and bone interactions are fundamental to movement, with forces generated by muscle contractions influencing bone remodeling. We investigated muscle strength and physical performance associations to hip/spine volumetric bone mineral density (vBMD) in older adults. We hypothesized men and women with lower muscle strength, power and physical performance would have lower vBMD.

Methods

Computed tomography (CT) scans were obtained for 320 Study of Muscle, Mobility and Aging (SOMMA) participants (86% white, BMI 27.8±4.4, ages 75.8±4.9) including a Mindways phantom for vBMD calibration. Total hip cortical and trabecular vBMD (each left/right average) and spine trabecular vBMD (L1-L4 average) were measured in mg/cm^3 using QCTPro software. A handheld dynamometer measured grip strength (kg). Leg power and strength was measured by a Keiser A420 leg press machine. Specific power ($Watts/mm^2$) was computed as leg power divided by mid-thigh muscle area from CT. Timed physical performance tests included usual-pace 4-meter walk (m/sec), usual-pace 400-meter walk (m/sec), and 5 chair sit-to-stands (sec) without utilizing arms. Sex-stratified linear regression models for men (n=140) and women (n=180) associated function/performance measures with vBMD, adjusting for age, race, BMI, education, mid-thigh subcutaneous adipose tissue area, smoking status, alcoholic drinks per week, moderate-to-vigorous physical activity, step count, fall history, multimorbidity index, arthritis, hypertension, back pain, leg pain, and osteoporosis medication.

Results

In men, faster 400-m gait speed and quicker sit-to-stand performance were associated with higher hip and spine trabecular vBMD ($p<0.03$). In women, higher leg strength was associated with higher trabecular spine vBMD ($p=0.02$), but stronger grip was associated with lower cortical hip vBMD ($p=0.04$).

Discussion

Better physical performance in men, but not leg strength or power, was associated with higher trabecular hip and spine vBMD. Higher leg strength in women, not power or physical performance, was associated with higher spine vBMD. The negative association between grip strength and cortical hip vBMD suggests upper extremity strength does not translate to higher vBMD in lower extremities in women. Muscle strength and performance associations to vBMD in older adults appear to differ by sex, body region (weight bearing vs non-weight bearing), and bone compartment (trabecular vs. cortical).

Images (Optional)

Table 1. Covariate-adjusted linear regression of muscle strength, power, and physical performance with hip and spine vBMD (mg/cm^3). Significance results bolded ($p<0.05$).	Men						Women					
	Trabecular Hip vBMD		Cortical Hip vBMD		Trabecular Spine vBMD		Trabecular Hip vBMD		Cortical Hip vBMD		Trabecular Spine vBMD	
	β	p	β	p	β	p	β	p	β	p	β	p
Grip Strength (kg)	1.3	0.62	2.9	0.51	61.7	0.99	-3.4	0.28	**-12.2**	**0.02**	-5437.4	0.28
Leg Power (Watts)	-0.5	0.84	-1.9	0.65	3695.5	0.38	-2.3	0.64	-12.3	0.13	-5591.5	0.44
Leg Specific Power (Watts/mm^2)	-1.1	0.54	-0.4	0.91	1654.4	0.59	-0.7	0.78	-6.4	0.10	-2325.7	0.51
Leg Strength (kg)	-2.6	0.25	-6.3	0.10	350.7	0.93	2.1	0.55	-5.7	0.33	**11107.6**	**0.04**
4-meter Gait Speed (m/sec)	1.7	0.45	4.0	0.29	4662.7	0.19	-1.7	0.37	1.2	0.71	-2844.1	0.33
400-meter Gait Speed (m/sec)	**6.9**	**<0.01**	0.3	0.93	**7606.9**	**0.02**	-2.1	0.31	-2.3	0.51	-4303.6	0.19
Time to Perform 5 Chair Stands (sec)	**-4.6**	**0.02**	-1.2	0.73	**-8103.6**	**0.01**	-1.2	0.48	0.7	0.79	-3382.9	0.20

References (Optional)

Acknowledgements (Optional)

We thank the participants of the SOMMA study and acknowledge the following funding sources from the National Institutes of Health: R01 AG079975 (AAW), R01 AG059416 (SBK), P30 AG021332 (SBK), T32 AG033534 (SBK, NZH). We would like to acknowledge the Translational Imaging Shared Resource and Clinical Research Unit of the Wake Forest Clinical and Translational Science Institute (WF CTSI), which is supported by the National Center for Advancing Translational Sciences (NCATS), National Institutes of Health, through Grant Award Number UM1TR004929

Session Category

P2-237

Bone Adaptation in Response to Ovariectomy and/or Hemiparetic Stroke

Graduate Student Matthew Hart BS, MS

University of Michigan, Ann Arbor, MI, United States

Introduction

Estrogen deficiency and stroke-induced motor impairment, independently, can adversely affect bone morphology and consequently reduce cortical bone strength, but their combined effects remain undefined. Ovariectomy, a model of post-menopausal estrogen loss, alters mineral composition, and weakens mechanical performance (Goulet et al. 2011 (https://doi.org/10.1007/s00223-010-9457-x). Stroke can add further cortical deterioration in affected limbs through disuse, inflammation, and elevated osteoclast activity. The current study examines how ovariectomy and stroke separately and/or together affect cortical bone morphology and mechanical properties in rat femora and tibiae.

Methods

Female Sprague Dawley rats underwent bilateral ovariectomy (Steele & Bennett, 2011 https://doi.org/10.1053/j.jepm.2011.04.008) or sham surgery at 10 wk, followed by hemiparetic stroke (McDonald et al., 2021 https://doi.org/10.1177/15459683211005019) or shamstroke surgery at 14 wk. Animals were euthanized at 30 wk, and femora and tibiae were harvested and frozen. Femora were tested in 3-point bending with a 10 N preload and 0.5 mm/s displacement to failure. Tibiae were potted with 10 mm gauge length and twisted to failure at 0.5°/s. Stiffness, maximal load, and maximal torque were calculated. Biomechanical data were analyzed using parametric Three-Way Factorial ANOVA and LME models. Due to low sample numbers, ANOVA effect sizes were adjusted for bias by calculating ω^2, which accounts for σ^2 and DOF.

Results

Models revealed a medium effect for femoral work-to-failure (ω^2=0.1149), small effects for femoral stiffness (ω^2=0.0100), and tibial work to failure (ω^2=0.0364). Cohen's d comparisons showed small effects of OVX on stiffness (d=0.246) and small stroke-related effects on stiffness (d=0.344). Figure 1A depicts bending stiffness, while figures 1B and 1C show torsional and bending work-to-failure data across groups.

Discussion

This study builds on research of Goulet et al. (2011, https://doi.org/10.1007/s00223-010-9457-x) by extending OVX-related osteoblast changes and incorporating the added complexity of hemiparetic stroke. This work demonstrates statistical approaches that provide a foundation for current methods and analyses and establishes a robust methodological and statistical foundation for future biomechanical analyses, including a-priori power.

Images (Optional)

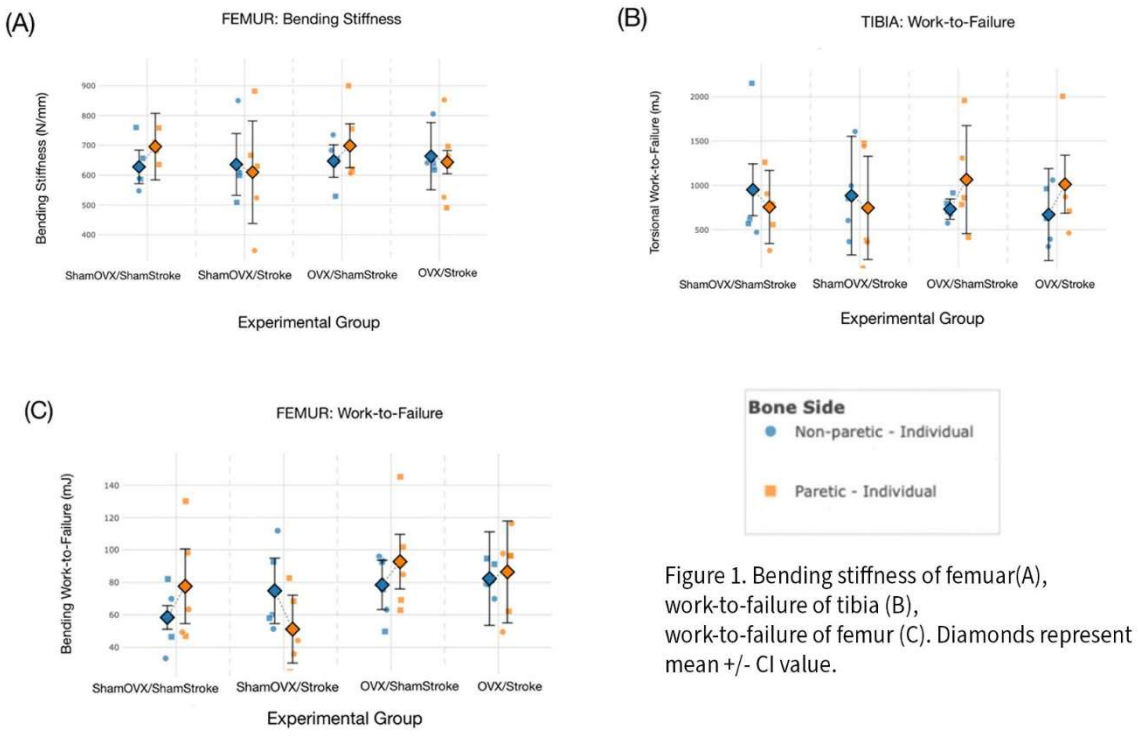


Figure 1. Bending stiffness of femuar(A), work-to-failure of tibia (B), work-to-failure of femur (C). Diamonds represent mean +/- CI value.

Acknowledgements (Optional)

The co-authors gratefully acknowledge the important contributions made by colleagues at the University of Calgary to this study: Ruth Seerattan, Aralia Leon-Coria, Andrew Swatsky, Dean Brown, Dawn Martin, and the LESARC Husbandry Staff

Session Category

Musculoskeletal Biomechanics: Tissues

P2-238

High Inherent Aerobic Capacity Mitigates Obesogenic Diet–induced Skeletal Muscle Degeneration

Mr. Mauricio Delgado[1,2,3], Mr. Darsh Tripathi[1,2], Mr. Barbod Shiri[1], Mr. Ignacio Cordero[3], Mr. Giorgio Poletto[1], Mrs. Ruth Seerattan[1], Mr. Daniel Young[2], Dr. Raylene A. Reimer[1,2], Dr. David A. Hart[1,2], Dr. Antoine Dufour[2], Dr. Lauren G. Koch[4], Dr. Walter Herzog[1,2]

[1]Human Performance Laboratory, University of Calgary, Calgary, Alberta, Canada. [2]McCaig Institute for Bone and Joint Health, Calgary, Alberta, Canada. [3]Departamento de Kinesiología, Escuela de Ciencias de la Salud, Pontificia Universidad Católica de Chile, Santiago, Región Metropolitana, Chile. [4]Department of Physiology and Pharmacology, The University of Toledo, Toledo, Ohio, United States

Introduction

Obesity and its related comorbidities often lead to reduced mobility, sedentary behavior, and musculoskeletal degeneration [1]. Obesity is also associated with altered muscle integrity, including fat infiltration, inflammation, and fibrosis [2]. We previously found that muscles composed primarily of slow-twitch, high–aerobic capacity fibers were protected, whereas fast-twitch, low–aerobic capacity muscles degenerated within days of exposure to a high fat/high sucrose (HFS) diet in Sprague Dawley rats [2]. Aerobic capacity is also crucial in regulating metabolic stress in the presence of an obesity-inducing diet [3]. Therefore, the purpose of this study was to investigate the effect of an HFS diet on skeletal muscle structural integrity in rats with inherently diverse aerobic capacity.

Methods

Thirty-five 25-week-old N:NIH male rats selectively bred for high (HCR) or low (LCR) running capacity were fed either an HFS or standard chow diet (CD) for 12 weeks, resulting in four groups (HCR-CD, n=10; HCR-HFS, n=9; LCR-CD, n=8; LCR-HFS, n=8). Vastus lateralis (VL) and soleus (Sol) muscles were collected for histology and proteomics. 10 µm mid-belly sections were used to quantify fibrosis (Picrosirius), fat infiltration (Oil-Red-O), and type 1 inflammatory macrophages (CD68 histochemistry). Shotgun mass spectrometry–based proteomics was performed to identify biomarkers and pathways related to inflammation and fibrosis.

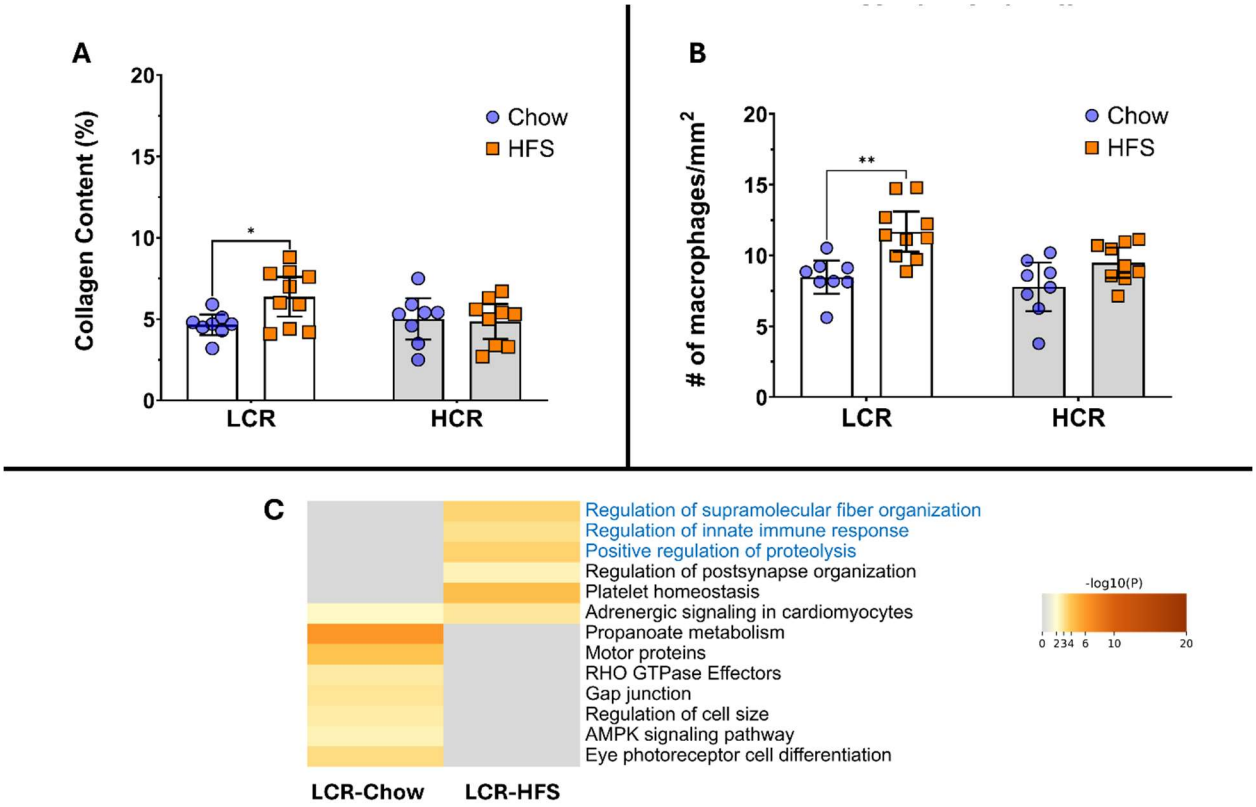
Results

In VL, collagen (p=0.03) and macrophage content (p=0.001) were increased in LCR-HFS compared to LCR-CD (Fig 1A, 1B), while fat infiltration was higher (p=0.02) in HCR-HFS versus HCR-CD. No differences in fibrosis, macrophage number, or fat infiltration were observed in Sol between diet groups. Quantitative proteomics of VL muscle in LCR-HFS revealed an upregulation of proteins associated with the innate immune response. (Fig 1C).

Discussion

Under metabolic stress, the immune response triggers myofibroblasts and fibro-adipogenic progenitors responsible for remodeling the extracellular matrix, increasing collagen crosslinking, and perimysium/ endomysium thickening, changes that may alter muscle stiffness and mechanics [4]. Our findings suggest that VL fibrosis in LCR rats may be driven by local, diet-induced inflammation, whereas high aerobic capacity in the HCR rats mitigates HFS-induced damage in fast-twitch muscle.

Images (Optional)



References (Optional)

[1] Houmard et al., JObes.2011

[2] Collins et al.,Front.Physiol.2018

[3] Koch & Britton,Physiol.Genomics.2001

[4] Theret et al.,Front. Physiol.2021

Session Category

Musculoskeletal Biomechanics: Tissues

P2-239

Force-Frequency Relationships of Pelvic Floor Muscles from Non-, Mid-, and Late-Pregnant Rats

Dr. Megan Routzong Ph.D.[1,2], Ms. Melissa Vu B.S.[2], Dr. Marianna Alperin M.D., M.S.[2,3]

[1]UT Southwestern Medical Center, Dallas, TX, United States. [2]University of California, San Diego, La Jolla, CA, United States. [3]Sanford Consortium for Regenerative Medicine, La Jolla, CA, United States

Introduction

Vaginal birth is the greatest epidemiologic risk fact factor for pelvic floor disorders due to injury sustained by pelvic soft tissues, including the pelvic floor muscles. However, not all women sustain birth injury. With the goal of elucidating drivers of injury susceptibility, we need to understand how pregnancy alters pelvic floor muscle function. In this study, we evaluated pelvic floor (pubocaudalis, PC) and tibialis anterior (TA, non-pelvic control) muscles from non-pregnant, mid-pregnant, and late-pregnant rats to determine how pregnancy alters their force-frequency relationships.

Methods

Whole PC and TA muscles were procured from 3-month-old female non-pregnant (and nulligravid), mid-pregnant (~day 12), and late-pregnant (~day 20) Sprague-Dawley rats, leaving the proximal ends attached to their respective bones. Samples were placed in a tissue bath (oxygenated Kreb's Ringer solution, pH=7.3, 37°C). Sutures were used to secure the proximal end to a clamp and the distal end to the force transducer's lever arm (Aurora Scientific, 300C). The following force-frequency data were obtained at each sample's optimal muscle length: 1Hz, 10Hz, 25Hz, 50Hz, 75Hz, 100Hz, 150Hz, and 200Hz with 2-minute rest periods and peak active force recorded for each stimulation. A sigmoidal function was fit to obtain parameters representing steepness/slope and frequency needed to reach half the maximum force (half-frequency). These parameters and forces at 1Hz and 200Hz were compared between muscles and pregnancy stages via two-way mixed MANOVA with multiple comparisons post hoc.

Results

Six non-pregnant, 3 mid-pregnant, and 3 late-pregnant animals were included in this analysis. Half-frequency and 1Hz force were significantly larger in TA muscles ($p=0.003$ and 0.046, respectively, Figure 1 top). Meanwhile, the slope factor was impacted by pregnancy ($p=0.047$, Figure 1 bottom), with curves from mid-pregnant animals being significantly steeper than those from non-pregnant animals specifically ($p=0.038$).

Discussion

This data demonstrates that pregnancy impacts skeletal muscle contractility, noted by a downward shift in mid-pregnant force-frequency curves. Though non-pregnant PC and TA curves differed, the comparable impact of pregnancy on their active mechanical behavior is indicative of global skeletal muscle remodeling during early- and mid-gestation with similarities between non- and late-pregnant data suggesting recovery of muscle function before the onset of parturition.

Images (Optional)

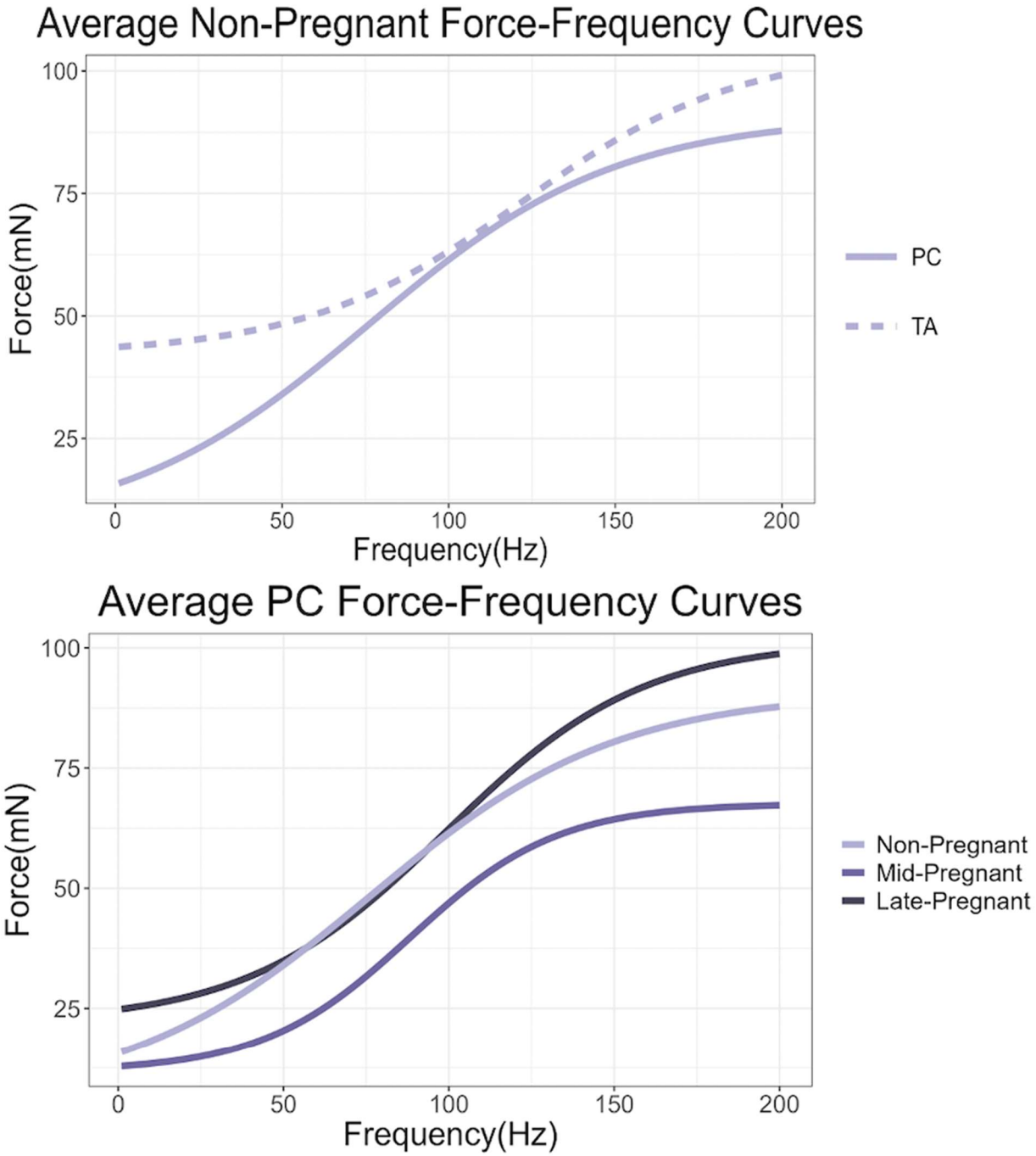


Figure 1: Top) Average force-frequency curves for PC (solid) and TA (dashed) samples from non-pregnant animals demonstrating higher TA forces at low frequencies and a rightward shift in the curve's inflection point (i.e., a higher half-frequency). Bottom) Average force-frequency curves for PC samples from non-pregnant (lighter purple), mid-pregnant (purple), and late pregnant (darker purple) animals demonstrating that the mid-pregnant data are the most distinct.

References (Optional)

Acknowledgements (Optional)

We acknowledge NIH/NICHD T32 HD007203 (MR), K99 HD115224 (MR), R01 HD102184 (MA), and R01 HD092515 (MA).

Session Category

Musculoskeletal Biomechanics: Tissues

P2-240

Absence of Integrins α1β1, α2β1 and α11β1 Affects the Structural and Mechanical Properties of Murine Bones

Dr. Miriam Weyers[1], Mr. Davin Kumpf[1,2], Ms. Maren Dreiner[1], Ms. Yvonne Sponer[1], Ms. Daniela Mählich[1], Dr. Beate Eckes[3], Prof. Dr. Anja Niehoff[1,2]

[1]Institute of Biomechanics and Orthopedics, German Sport University Cologne, Cologne, North Rhine-Westphalia, Germany. [2]Cologne Center for Musculoskeletal Biomechanics, Medical Faculty, University of Cologne, Cologne, North Rhine-Westphalia, Germany. [3]Translational Matrix Biology, Medical Faculty, University of Cologne, Cologne, North Rhine-Westphalia, Germany

Introduction

Integrins are transmembrane proteins that transmit mechanical stimuli between the extracellular matrix (ECM) and the cell. To coordinate interactions between bone cells and the ECM, the integrins α1β1, α2β1 and α11β1 bind to type I collagen (Col I). Previous studies using knockout the β1 subunit or double-knockouts of α2 and α11 subunit demonstrated that loss of these integrins impaired bone architecture and resulted in severe low bone mass and systemic dwarfism [1, 2]. In the present study, we investigated the effects of a triple knockout of the integrins α1β1, α2β1 and α11β1 on the structural and mechanical properties of femoral bone tissue in mice.

Methods

Bone properties were analyzed in femora of fifteen one-year-old female and male wildtype C57BL/6N (WT; N = 9) and triple-knockout (TKO; N = 6) mice [3] using µCT (SCANCO) and 3-point bending tests (Zwick). To assess the ECM immunohistochemical staining for Col I was performed in the femoral cortex. Group differences were evaluated using the unpaired non-parametric Mann–Whitney U-test.

Results

Femora of TKO mice were significantly shorter, and their tissue area was markedly reduced compared to WT controls. TKO mice further exhibited significantly reduced cortical thickness and cortical area, along with significantly lower marrow area. No significant differences were observed in trabecular bone structure between groups. The maximal breaking force was significantly reduced, whereas maximal strain stress was significantly increased in TKO compared to WT mice. The absence of collagen binding integrins in TKO did not affect the localization or intensity of Col I in the femoral cortical ECM.

Discussion

Consistent with findings in α1β1 and α11β1 double-knockout animals, the deficiency of integrins α1β1, α2β1 and α11β1 adversely affected the structural and mechanical properties of the femoral cortex. The absence of differences in type I collagen staining intensity may be attributable to the advanced age of the mice. Currently, we study younger animals to exclude age-related confounding effects.

References (Optional)

[1] Qin *et al.*, J Orthop Translat., 2022

[2] Blumbach *et al.*, J Biol Chem., 2012

[3] Sawant *et al.*, Ann Rheum Dis., 2023

Acknowledgements (Optional)

This study was funded by German Research Foundation (DFG project no. 384170921/FOR 2722).

Session Category

Musculoskeletal Biomechanics: Tissues

P2-241

Evaluating Rigid and Deformable Transformations for Quantifying Cranial Vault Growth in Rats

Dr. Mostafa Mohamed, Dr. Michael Baggley, Ms. Kiana Zhu, Dr. Tsolmonbaatar Khurelbaatar, Dr. Mehrdad Palizi, Dr. Samer Adeeb, Dr. Dan L. Romanyk, Dr. Lindsey Westover

University of Alberta, Edmonton, AB, Canada

Introduction

Traditional morphometrics use anatomical landmarks to study growth[1]. Alternatively, statistical shape modelling (SSM) uses 3D representations to capture anatomical variation, but requires accurate mesh alignment and underlying transformations[2]. This investigation developed a 3D morphometric pipeline to analyze rat cranial vault growth and compared two Coherent Point Drift (CPD) approaches: rigid-scaling and deformable transformation.

Methods

Four Sprague–Dawley rats (2F, 2M; age 7 weeks) underwent two in-vivo CT scans separated by two weeks (voxel size 8.9 µm, Bruker Skyscan 1176, AUP00003759 under UA ACUC). Images were segmented in Materialise MIMICS, downsampled to 17.8 µm, and the domain was trimmed in Geomagic Design X using landmark-based offsets. Longitudinal changes were quantified by registering earlier to later timepoints with CPD using rigid-scaling and deformable pipelines developed on Python. Pipeline performance was evaluated on meshes subjected to prescribed transformations and in mapping the timepoints.

Results

Under prescribed transformations, both CPD methods achieved high accuracy (average RMSE < 0.05 mm). When applied to longitudinal data, only the deformable CPD produced near-complete alignment between the moving (earlier timepoint) and reference meshes (**Figure 1A**). The RMSE using rigid and deformable workflows to map the timepoints was 0.11+/-0.02 mm and 0.05+/-0.01 mm, respectively. Vector plots showed that rigid CPD failed to capture the expected flattening and elongation behavior, whereas deformable CPD captured this behaviour (**Figure 1B**). Contour plots of the anterior–posterior displacement component demonstrated directional growth about a neutral axis near the midpoint of the sagittal suture, with movement occurring in opposite directions on either side (**Figure 1C)**.

Discussion

Cranial growth is a complex process that may not adequately represented by uniform scaling alone. These findings support the use of non-rigid CPD, which minimized error between transformed and reference meshes and produced growth vectors that are more aligned with biological expectations, including elongation/flattening, and bidirectional anterior–posterior growth. While the current pipeline shows promise in capturing global cranial growth, displacements near sutures are small and approach the error bound. Future work should focus on reducing this error, and expanding the sample size before fully implementing SSM.

Images (Optional)

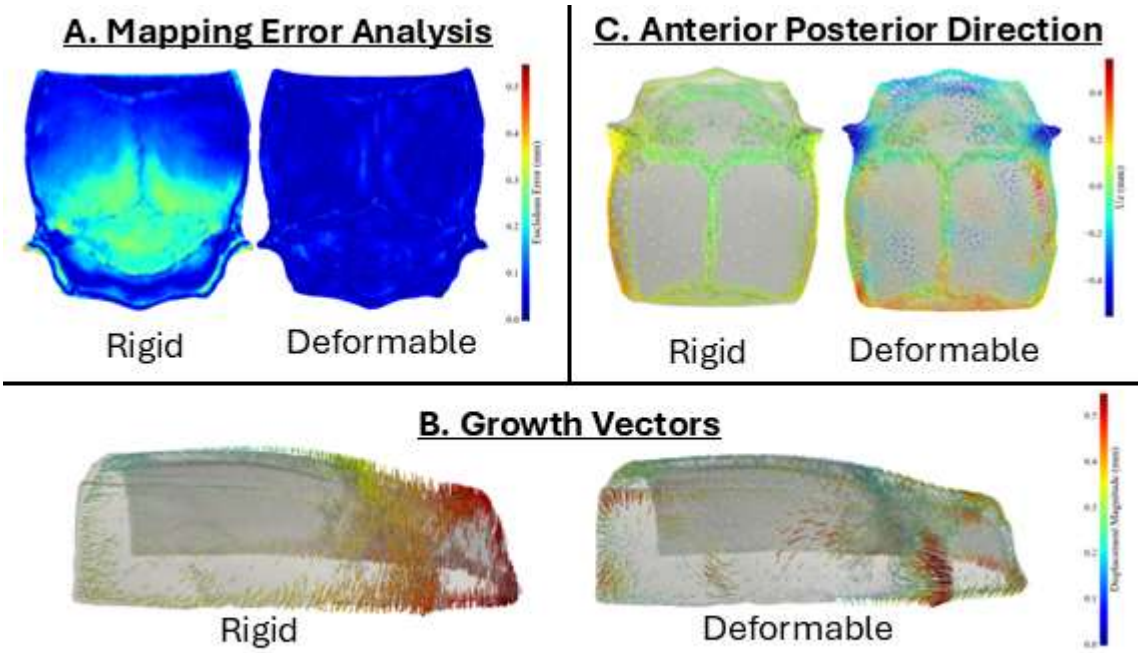


Figure 1: A. Deformable CPD achieves lower error when mapping the two time points, **B.** better represents the expected elongation and flattening behaviour, **C.** and shows more biologically relevant anterior–posterior movement.

References (Optional)

[1] Remesz *et al.*, DOI : 10.1016/j.bonr.2023.101714, 2023. [2] Palizi, DOI: 10.7939/r3-24cj-5z10, 2023.

Acknowledgements (Optional)

This work was supported by the NFRF Exploration Fund, Geoffrey and Robyn Sperber Craniofacial Research Fund, Natural Sciences and Engineering Council of Canada (NSERC).

Session Category

Musculoskeletal Biomechanics: Tissues

P2-242

Stribeck Analysis Reveals Differences in Friction Behavior of Cartilage from Femoral and Humeral Head

Mr. Nathan Briard

Cornell University, Ithaca, NY, United States

Introduction

Ball-and-socket joints provide a wide range of motion, support body weight, while sustaining varying normal loads and contact speeds that differ from other joints. These joints, located at femoral and humeral heads, are covered with cartilage that differ in thickness across regions yet maintain low friction. However, the lubrication modes of these joints and whether regional differences affect their coefficients of friction remain unclear. The Stribeck framework provides a way to characterize lubrication by relating friction to viscosity, sliding speed, thickness, and normal load. This study aims to define the lubrication modes of femoral and humeral head cartilage within the Stribeck framework and to determine whether regional variations influence frictional behavior.

Methods

A total of 16 samples per donor (20-30 years) for 3-donors with full-thickness cartilage (4mm diameter) were obtained from four regions of femoral and humeral heads. Custom cartilage on glass was used to characterize frictional behavior of 9 speeds from 0.1-10 mm/s. Samples were tested in 3 dextran solutions of viscosities (0, 9, and 23%), and friction coefficients were averaged after equilibrium.

Results

The data was well described by the Stribeck curve for both femoral head and humeral head (R^2=0.82) (**Fig.1A**). The fit coefficient showed different modes of lubrication for the two different cartilages; the femoral cartilage had lower boundary friction coefficient and greater minimum friction coefficient and transition number (**Fig.1B**). However, regional variation within femoral head cartilage revealed superior and anterior regions having similar modes of lubrication as do inferior and posterior regions (**Fig.1C**). The humeral head had similar modes of lubrication as femoral head, except superior region had higher boundary friction coefficient and transition number (**Fig.1D**).

Discussion

This study is the first to examine the tribological behavior of young, healthy human ball-and-socket cartilage using the Stribeck framework. It revealed inherent differences between the two joint cartilages; humeral head cartilage exhibited roughly twice the boundary friction coefficient of femoral cartilage but had a friction minimum an order of magnitude lower and transitioned more rapidly. These findings clarify how friction varies across femoral and humeral heads, providing essential insight for designing viscosupplements and developing strategies to protect joints from osteoarthritis.

Images (Optional)

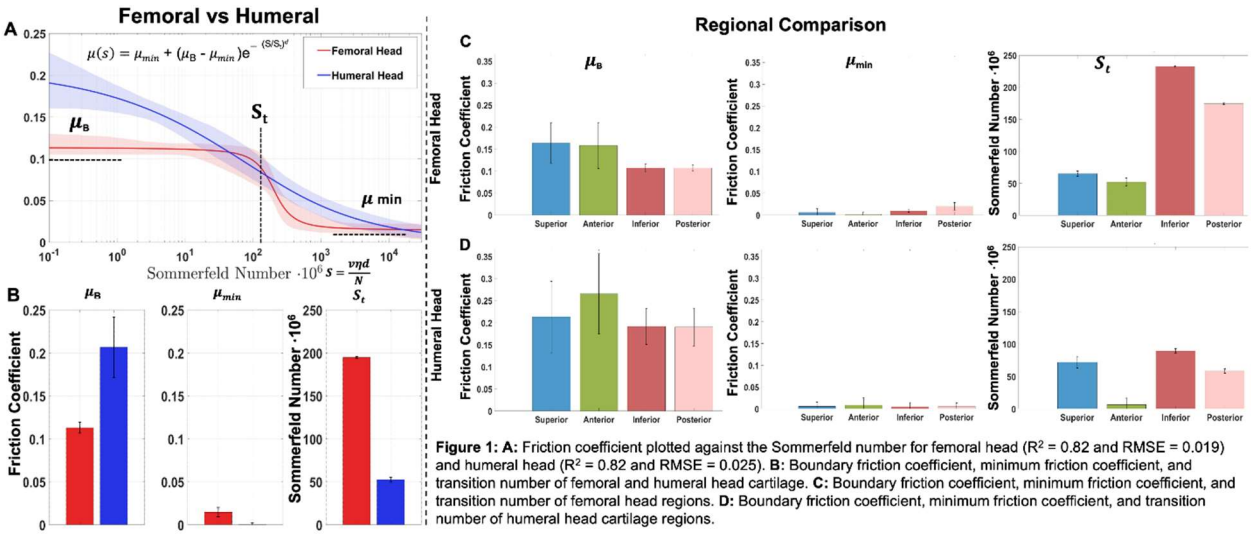


Figure 1: A: Friction coefficient plotted against the Sommerfeld number for femoral head (R^2 = 0.82 and RMSE = 0.019) and humeral head (R^2 = 0.82 and RMSE = 0.025). **B:** Boundary friction coefficient, minimum friction coefficient, and transition number of femoral and humeral head cartilage. **C:** Boundary friction coefficient, minimum friction coefficient, and transition number of femoral head regions. **D:** Boundary friction coefficient, minimum friction coefficient, and transition number of humeral head cartilage regions.

Session Category

Musculoskeletal Biomechanics: Tissues

P2-243

Determining the Combined Effects of Menopause and Stroke on Skeletal Muscle Function and Weakness

Ms. Nicole A. Conquergood, Dr. Stephanie A. Ross, Dr. Walter Herzog

University of Calgary, Calgary, Alberta, Canada

Introduction

Menopause is linked to reduced skeletal muscle strength [1], but the mechanisms are unclear. Post-menopausal women are at increased stroke risk [2], which independently reduces muscle mass and strength [3], and experience greater post-stroke mobility deficits than men [4]. However, the combined impact of menopause and stroke on skeletal muscle has not been directly examined. Therefore, this study aimed to develop a combined menopause-stroke animal model to investigate muscle mechanisms that may contribute to mobility deficits in post-menopausal stroke survivors.

Methods

Ten-week-old female Sprague-Dawley rats underwent either bilateral ovariectomy (OVX) to induce menopause or sham surgery (shamOVX). Four weeks later, photothrombotic stroke was induced in some OVX and shamOVX animals [5]. Remaining animals received a sham stroke, creating four groups: OVX/stroke (n = 13), OVX/shamstroke (n = 9), shamOVX/stroke (n = 12), shamOVX/shamstroke (n = 9). Motor function was assessed using a misstep protocol [5]. Animals were euthanized 4 months post-stroke, corresponding to the chronic phase of stroke [6].

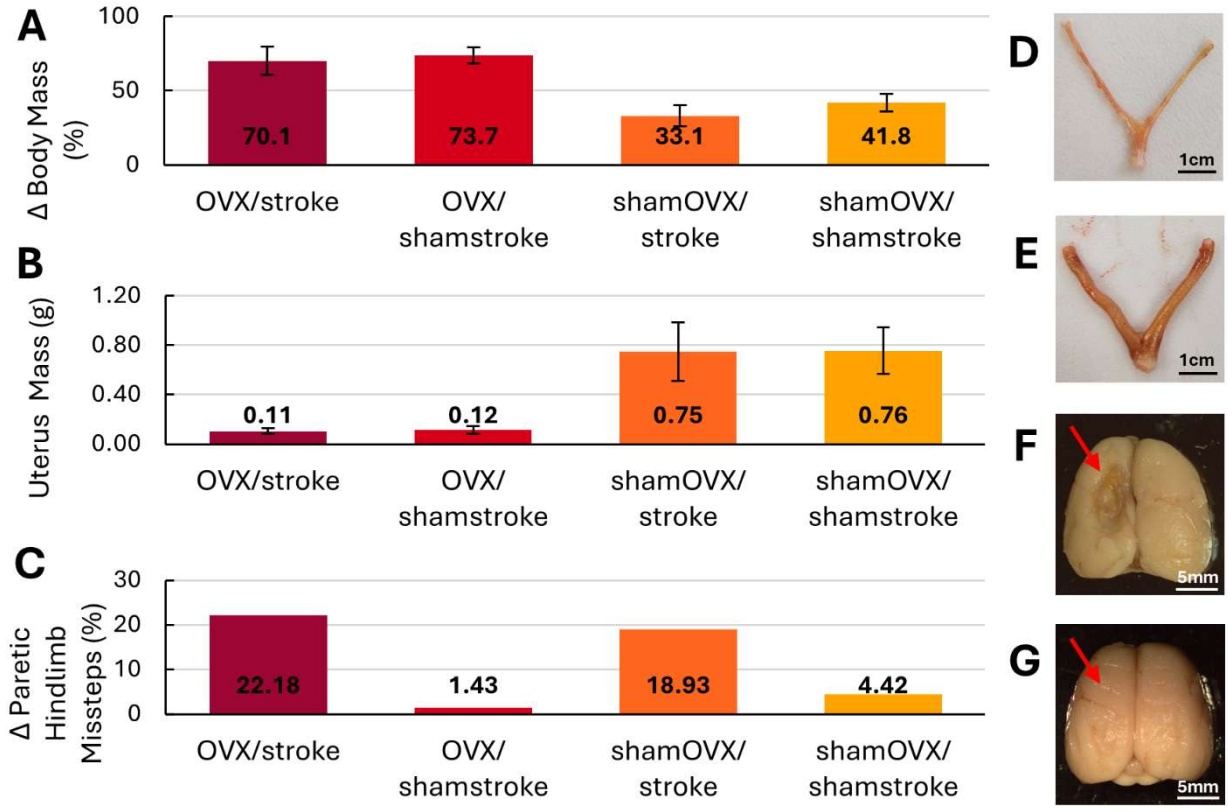
Results

Twenty weeks post-OVX, OVX animals gained 71.9±7.7% of their baseline body mass, compared to 37.2±7.9% in shamOVX animals ($p < 0.001$, Figure 1A). Uterus mass was 85% lower in the OVX animals than in sham animals (0.11±0.03 g vs. 0.75±0.21 g, $p < 0.001$, Figure 1B, example OVX/shamOVX uteri images in Figure 1D-E, respectively). Stroke animals showed an increase in paretic hindlimb missteps compared to shamstroke (20.6±14.3% vs. 2.9±8.2%, $p = 0.006$, Figure 1C, example stroke/shamstroke brain images in Figure 1F-G, respectively).

Discussion

Body and uterus mass changes confirm that the OVX was successful [1]. We also found an increase in paretic hindlimb missteps for stroke animals, consistent with previous studies [5], which suggests successful stroke induction. Therefore, the combined OVX/stroke model was successful and can be used for further analysis on post-stroke skeletal muscle adaptations following menopause.

Images (Optional)



References (Optional)

[1] Moran et al., *J Appl Physiol*, 2006.

[2] Lisabeth & Bushnell, *Lancet Neurol*, 2012.

[3] Hunnicutt & Gregory, *Top Stroke Rehabil*, 2017.

[4] Kapral et al., *Stroke*, 2005.

[5] McDonald et al., *Neurorehabil Neural Repair*, 2021.

[6] Krakauer et al., *Neurorehabil Neural Repair*, 2012.

Acknowledgements (Optional)

Ruth Seerattan and Aralia Leon-Coria for their help with harvests, Dean Brown and Dawn Martin for surgical assistance and LESARC husbandry staff for animal care.

Session Category

Musculoskeletal Biomechanics: Tissues

P2-244

Achilles Tendon Biomechanical Properties during Physiologically Representative Loads

Mr Nisal Jayaneththi, Dr Hans Gray, Prof Peter Lee

The University of Melbourne, Melbourne, Victoria, Australia

Introduction

The current study aimed to analyse the effects of different physiologically representative loads on Achilles tendon failure and how damage accumulates in different regions. We implemented a cyclic loading experiment on cadaveric specimens and used digital image correlation to measure surface strains.

Methods

Four Achilles tendons from three female donors (88.8 ± 2.89 years, 60.0 ± 9.2kg) were mounted to a tensile testing machine.

A spectrum simulating a single basketball game - where Achilles injuries are common - was constructed - 332 cycles of jogging (0.92 BW at 1.35Hz), 380 cycles of running (1.30 BW at 1.43Hz), 442 cycles of sprinting (2.24 BW at 2.33Hz) and 26 cycles of unilateral jumping and landing (1.13 BW for jumping and 1.21 BW for landing at 0.658Hz).

Activities were split equally over two blocks within the spectrum, except for jumping. Loads were scaled down from literature data based on donor age, sex, and the assumption that donors were not athletes. The spectrum was repeated until failure, where possible.

Two synchronised cameras recorded the deformation of a speckle pattern on the surface of the tendons for the duration of the experiment. Cycles were recorded intermittently: every 15th cycle for jogging, every 9th for running, every 5th for sprinting, and every 5th for jumping.

Data was processed using a digital image correlation software (VIC-3D, Correlated Solutions, SC, USA). Longitudinal strain was extracted across the tendon, and within subregions of the tendon: the insertion, midsubstance and the proximal region. Hysteresis loop areas and secant stiffnesses were calculated for each recorded cycle in each region and activity tested, and averaged across specimens.

Results

Throughout each activity, the hysteresis area and stiffness remain relatively unchanged between cycles (Figure 1). However, it appears that the insertion of the tendon has a lower stiffness on average compared to the midsubstance and proximal regions for all activities.

Discussion

This study is ongoing, and further statistical analysis is required to draw conclusions regarding the data collected. We anticipate that the results will help us understand the way tendon strains develop during cyclic loading, which will inform methods of injury prevention.

Images (Optional)

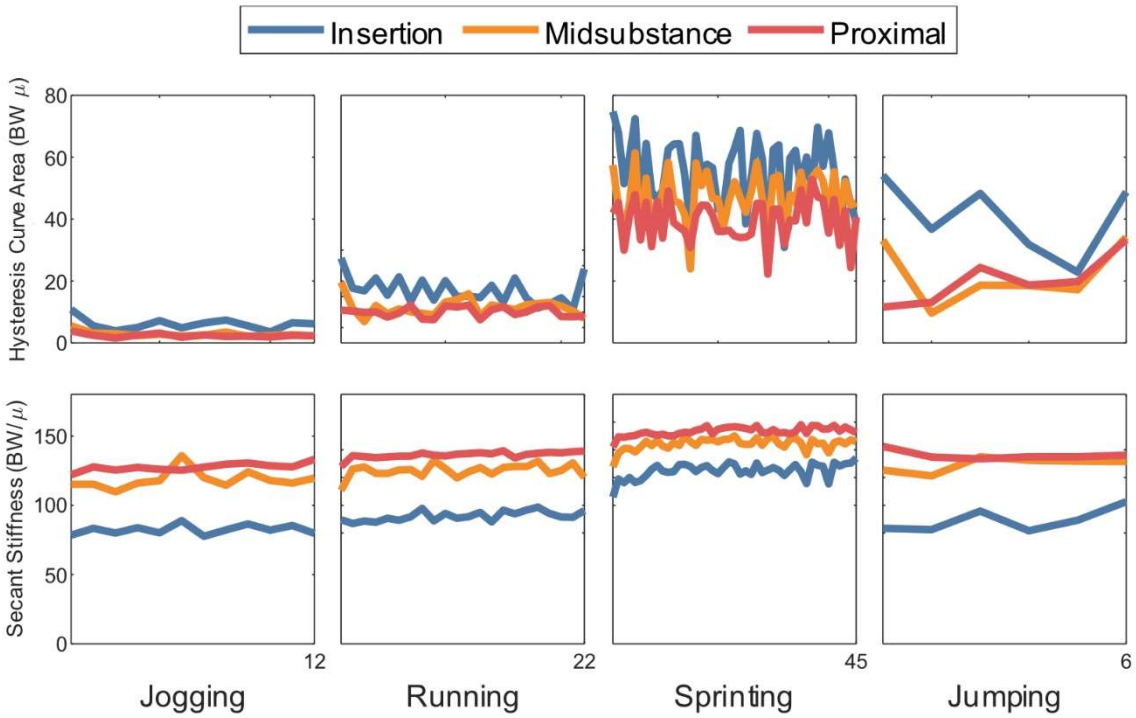


Figure 1 - Plots describing how hysteresis area and secant stiffness changes within each recorded block of each activity tested. Area and stiffness have been calculated for each region of the Achilles tendon.

Session Category

Musculoskeletal Biomechanics: Tissues

P2-245

Effects of Dynamic Load, Wrist Posture, and Venous Occlusion on Carpal Tunnel Tissue Motion in Females

Miss Noelle Donatelli H.B.Sc.Kin, Dr Peter Keir PhD

McMaster University, Hamilton, Ontario, Canada

Introduction

Carpal tunnel syndrome (CTS) has been linked to altered tendon-subsynovial connective tissue (SSCT) motion. Mechanical loading, venous congestion, wrist posture, and aging influence tendon-SSCT motion, yet their combined effects across adulthood are unclear. This study examined the effects of load, venous occlusion, wrist posture, and age on tendon and SSCT excursion during cyclic single finger motion in women.

Methods

Women aged 17-80 years completed eight randomized conditions, each repeated twice, crossing two levels of force (0 N, 2 N), wrist posture (neutral, 20° flexion), and brachial venous occlusion using a blood pressure cuff (none, 80% diastolic). In each condition, participants performed 12 isolated middle-finger flexion-extension cycles at 0.75 Hz while colour Doppler ultrasound captured tendon and SSCT motion (GE Vivid Q, 12L-RS). Tissue displacement and velocity were extracted for the middle 8 cycles to quantify tendon-SSCT gliding using two metrics. Shear strain index (SSI) reflects the percentage difference between tendon and SSCT excursion where higher values indicate greater tendon-SSCT relative motion. Maximum velocity ratio (MVR) expresses SSCT peak velocity relative to tendon peak velocity.

Results

Preliminary analyses show that younger women had similar relative tendon–SSCT motion across conditions while the older group had greater SSCT displacement, and SSI, in the no force, neutral wrist condition. Wrist flexion increased excursion in the young participants but reduced SSCT displacement in the older group. Blood flow reduction (occlusion) produced little change in younger adults but reduced SSCT velocity in the older group. Similar results were found for the loaded condition, with increased relative tendon-SSCT motion in the older group. The effect was even greater in the combined wrist flexion, finger force, and reduced blood flow condition with the highest SSI and lowest MVR.

Discussion

Younger women appeared less reactive to the experimental conditions than older women. Posture, load, and venous occlusion had mild effects in younger women but acted to reduce SSCT motion in older women. These early findings suggest aging heightens tissue sensitivity to mechanical stress and vascular compromise, increasing relative tendon-SSCT motion and shear in the carpal tunnel.

References (Optional)

Acknowledgements (Optional)

Natural Sciences and Engineering Research Council of Canada (NSERC Discovery Grant RGPIN-2023-05473)

Session Category

Musculoskeletal Biomechanics: Tissues

P2-246

Bone mechanoregulation is not altered by disease severity in adults with OI at distal tibia

Mr. Pedram Akhlaghi[1,2], Dr. Seyedmahdi Hosseinitabatabaei[1,2,3], Dr. Frank Rauch1[1,4], Dr. Bettina Willie[1,2,3,5]

[1]Shriners Hospital for Children, Research Center, Montreal, Quebec, Canada. [2]Faculty of Dental Medicine and Oral Health Sciences, McGill University, Montreal, Quebec, Canada. [3]Department of Bioengineering, McGill University, Montreal, Quebec, Canada. [4]Department of Pediatrics, McGill University, Montreal, Quebec, Canada. [5]Department of Biomedical Engineering, McGill University, Montreal, Quebec, Canada

Introduction

Osteogenesis imperfecta (OI) is an osteodysplasia which leads to bone fragility, recurrent fractures, and bone deformities. The most common types of OI, differ considerably in disease severity, with Type I being the least severe, type IV being moderate, and type III being most severe. Time-lapse high-resolution peripheral quantitative computed tomography (HR-pQCT) has emerged as a noninvasive method to assess bone formation and resorption. We combined timelapse HR-pQCT with finite element (FE) modeling to study local mechanoregulation (strain energy density [SED]) that drives bone formation and resorption, and to investigate the role of OI severity (type I vs type III or IV) on bone mechanoregulation.

Methods

Thirty-two tibial HR-pQCT scans of female adults with OI type I (N=19), and III or IV (N=13), were analyzed using timelapse and micro-FE analyses at baseline and in the absence of a placebo group, at one year after receiving a low dose of setrusumab (2 mg/kg), a sclerostin neutralizing antibody (Fig.1 A,B). First, 3D image registration was performed to register the scans at baseline and month-12 and then timelapse HR-pQCT were computed using Scanco's image processing language. The SED was calculated using micro-FE analysis at baseline. A surface-based projection method was developed to project timelapse-identified (re)modeling events onto the bone surface. The (re)modeling events were registered to the corresponding local SED fields at the bone surface. Conditional probability curves for formation, resorption, and quiescence as functions of local SED were calculated and compared across disease severity (OI type).

Results

Our results showed that after one-year of follow-up, bone had the highest conditional probability (around 90%) to be quiescent (unchanged) in both high-SED and low-SED regions, regardless of OI type (Fig.1 C). However, bone formation increased and bone resorption decreased moderately as SED magnitudes rose for both OI groups.

Discussion

Our data suggests that mechanoregulation in OI is not dependent on OI disease severity, (type I vs type III or IV) and largely quiescent. These findings correspond to prior observations that show smaller long bone circumference in people with OI, regardless of OI severity.

Images (Optional)

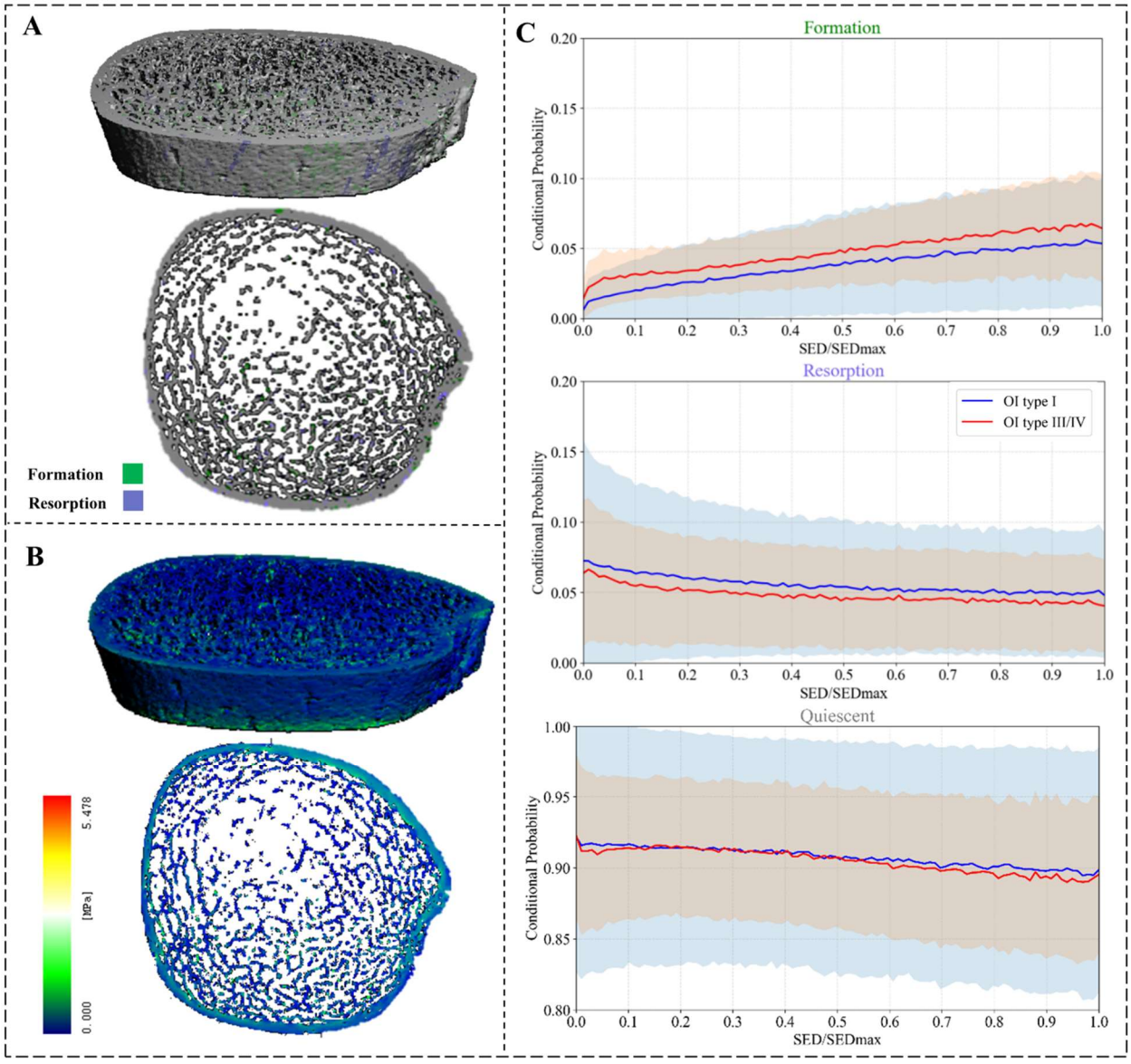


Figure 1: A one-year visualization of mechanoregulation in the human distal tibia. **A**: Regions of formed and resorbed bone obtained from timelapse analysis **B:** Corresponding micro-FE analysis shows the distribution of strain energy density (SED) within the bone. **C**: Conditional probability curves for bone formation, resorption, and quiescence over 12 months of bone remodeling at varying local SED magnitudes for individuals with OI type I (n = 19) and types

Session Category

Musculoskeletal Biomechanics: Tissues

P2-247

Activation and Force-Dependent Contributions to Short-Range Stiffness of Cat Soleus Muscles: Insights From System Identification of Viscoelasticity

Dr. Ridhi Sahani[1,2], Research Assistant Professor Daniel Ludvig[1,2], Professor Eric Perreault[1,2], Mr. Richard Casler[3], Professor Kiisa Nishikawa[4]

[1]Northwestern University, Chicago, Illinois, United States. [2]Shirley Ryan AbilityLab, Chicago, Illinois, United States. [3]Massachusetts Institute of Technology, Cambridge, Massachusetts, United States. [4]Northern Arizona University, Flagstaff, Arizona, United States

Introduction

Muscle short range stiffness (SRS) provides stability and is assumed to result from stretching bound cross-bridges. [1,2] Titin acts as a tunable viscoelastic spring in active muscles, [3] but its activation and force-dependent contributions to SRS are typically overlooked. We used system identification to compare viscoelastic properties of cat soleus muscle-tendon-units (MTUs) in response to length perturbations at matched levels of passive and active force. We hypothesized that force-dependent viscoelastic properties contribute to the short-range force response, suggesting a role for titin in SRS.

Methods

The soleus MTUs of anesthetized cats (n=4, 2M 2F) were stretched (~2% L_o at ~4 L_o/s) while passive and active forces were between 25-100% of optimal force (**Fig. 1A**). SRS was calculated with a linear fit to the initial force response (~2ms). The contribution of viscous forces after the initial SRS was determined as $\%F_{viscous}=(F_{peak}-F_{end})/F_{end}$. Single input-single output system identification was used to find the spring constants and damping coefficients using time-series data from the ramp stretch experiments, with muscle length as the input and muscle force as the output. (**Fig. 1B**).

Results

$\%F_{viscous}$ was greater in active than passive MTUs ($p=0.017$), increasing with active force ($p<0.0001$) but decreasing with passive force ($p=0.011$; **Fig. 1C**). Passive and active MTUs were fit by a Kelvin-Voigt element in series with a spring (average $R^2=0.986$). Stiffness (k1) was greater in passive than active MTUs ($p<0.048$) and increased with passive force ($p<0.017$; **Fig.1D**). Although not significantly different, damping (b1) was greater in passive (0.31-33.73 N/mm^2) than active MTUs (0.015-0.16 N/mm^2; **Fig 1E**). Series spring stiffness (k2) increased with passive ($p<0.0029$) and active ($p<0.042$) force and corresponded well with SRS ($R^2=0.69$; **Fig 1F**).

Discussion

While SRS increased with both passive and active forces, resistance to stretch was primarily elastic in passive muscles but primarily viscous in active muscles. Our results demonstrate activation and force-dependent viscoelastic contributions to SRS, suggesting a role for titin. Further research is needed to distinguish between cross-bridges and titin as potential mechanisms.

Images (Optional)

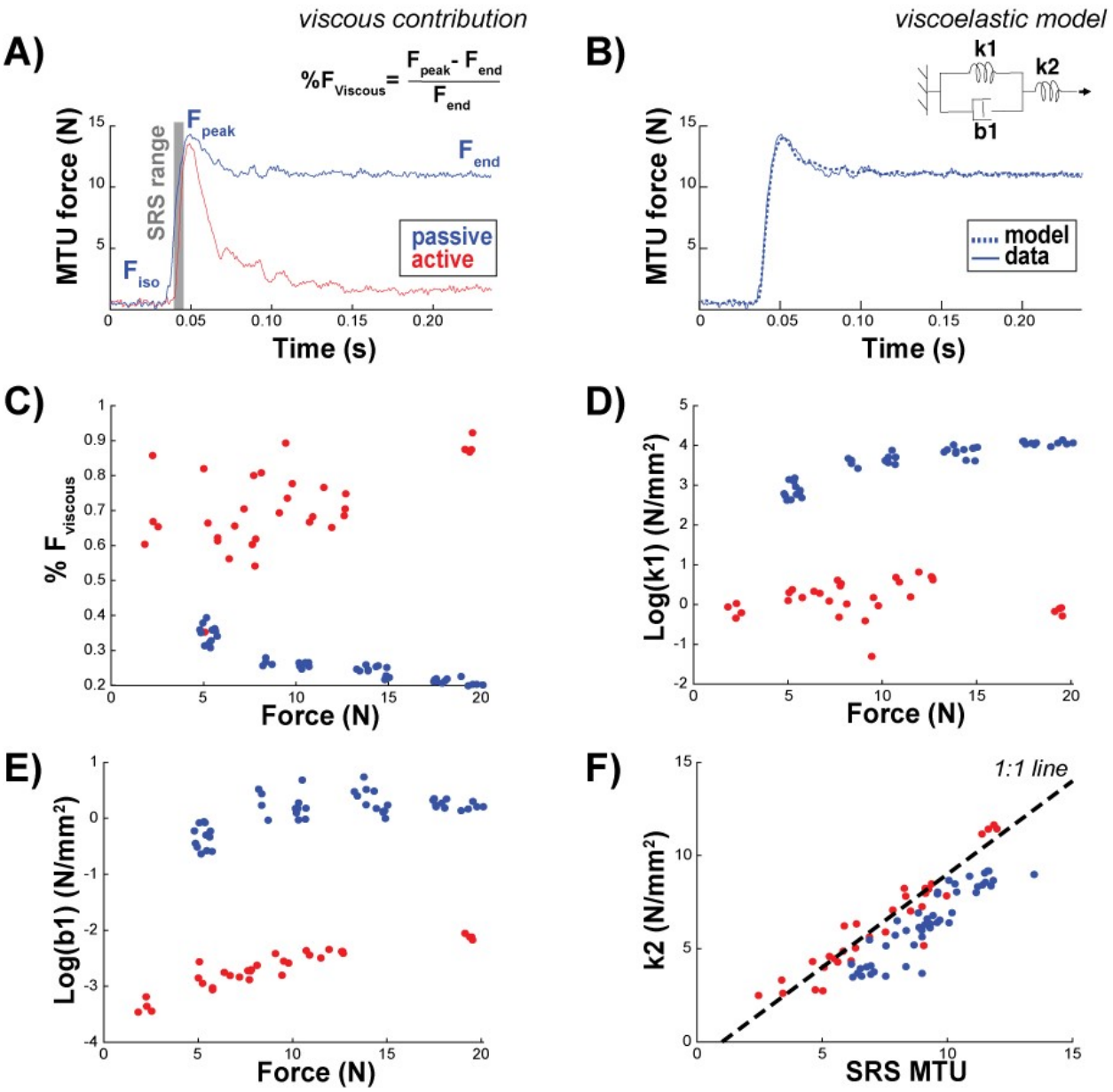


Figure 1: A) Representative force response from cat soleus to passive (blue) and active (red) ramp stretch and hold experiments, showing calculation of viscous contribution ($\%F_{viscous}$). **B)** Viscoelastic model fit to passive trial from A. **C)** Data from individual passive (blue) and active (red) trials from one cat for $\%F_{viscous}$ contribution. **D)** Log of spring stiffness (k1), **E)** log of damping constant (b1), and **F)** SRS compared with series spring stiffness (k2).

References (Optional)

[1] Rack PMH, et al. J. Physiol. 1974.

[3] Nishikawa, K. Phys. 2020.

Acknowledgements (Optional)

Thank you to our funding: NSF DBI-2319710, NIH R01AR071162 , NIH T32HD07418.

Session Category

Musculoskeletal Biomechanics: Tissues

P2-248

The Effects of Growth-Period Exercise on Adult Body and Muscle Composition

Dr. Derek J. Jurestovsky, Mr. Roberto Castro Jr., Dr. Ana Carla C. Salamunes, Dr Stephen J. Piazza, Dr. Jonas Rubenson

The Pennsylvania State University, State College, PA, United States

Introduction

Physical inactivity is linked to chronic diseases, morbidity and even mortality. However, physiological effects of childhood exercise on adult physical activity remain unclear. Previous data from our lab show, in an animal model (fowl), that uphill treadmill training throughout growth (1yr) results in a greater peak aerobic capacity after 12 months of training and that this adaptation is retained even following a 6-month non-exercise washout period [1]. Here, we explore how growth-period exercise impacts long-term body and muscle composition into adulthood and whether this may be associated with long-term adaptations to exercise capacity.

Methods

Sixty-two one-day old animals were randomly assigned to a sedentary control group (CON; N = 31) or an exercise training group (EXE; N = 31). EXE underwent uphill (6 deg) treadmill training 30 min/day, 5 days/wk from age 2 wks until 12 months (skeletally mature). CON received no training. At 12 months, subsets of animals from each group were euthanized for body composition (DXA) and muscle architecture analyses of the iliotibialis lateralis pars postacetabularis (ILPO), a key muscle used to power uphill running [2]. The remaining animals of both CON and EXE were transferred to large pens where they underwent a 6-month non-exercise washout period. After the washout period birds were euthanized for the same analyses. (The protocol used the same animals as in [1]).

Results

EXE exhibited lower body mass and a lower body fat percentage at both 12- and 18-month timepoints ($p<0.05$). Preliminary data indicate no significant differences in ILPO density (hydrostatic weighing) at 18 mo. Measurements on PCSA, optimal fiber length, pennation angle, sarcomere lengths, and tendon properties are currently underway.

Discussion

Early life exercise led to lasting differences in body composition with EXE being leaner even after a prolonged period of inactivity. Body composition may be a contributing factor to long-term effects of growth-period exercise on metabolic capacity. Preliminary data show no differences in ILPO density between groups. Additional analyses of muscle architecture are underway to further evaluate long term musculoskeletal adaptations.

References (Optional)

[1] Jurestovsky et al., ISB XXX 2025, Stockholm, Sweeden. [2] Rubenson et al. *J Exp Biol* (2006) 209 (13): 2395–2408.

Session Category

Musculoskeletal Biomechanics: Tissues

P2-249

The Articular surface is the primary site of changes in shear mechanics and composition in all stages of OA

Mr Salman Matan[1], Dr. Camila Carballo[2], MD Sabrina Strickland[2], MD Andreas Gomoll[2], MD Scott Rodeo[2], Dr. Itai Cohen[1], Dr. Lawrence Bonassar[1]

[1]Cornell University, Ithaca, NY, United States. [2]Hospital for Special Surgery, NYC, NY, United States

Introduction

: Osteoarthritis (OA) is chronic disease affecting around 500 million individuals. During OA development, ECM (collagen and aggrecan) is gradually depleted, beginning at the surface, progressing to deeper zones, and eventually exposing bone. However, little is known about how matrix depletion affects depth-dependent shear mechanics of OA human cartilage. We hypothesize that OA cartilage's mechanical and compositional changes are primarily localized at the surface. This study aims to determine how depth-dependent local compositional changes influence microscale mechanics.

Methods

A total of 13 healthy and 6 OA samples were obtained as operating room discard after IRB approval and patient consent. Healthy donors were 14-28 and 69-73 years for OA donors. Outerbridge and OARSI scoring were performed. Depth-dependent shear mechanics were measured after 15% compression and 1% peak shear strain. FT-IR and biochemical assays were utilized to study ECM composition.

Results

The shear modulus of OA was significantly lowered, and the notable difference was larger at the surface by a factor of 20, while samples remained lower throughout tissue depth compared to healthy (**Fig.1A**). The first 200μm were highlighted to demonstrate approximately 2-orders of magnitude differences in shear modulus. Healthy cartilage showed higher stiffness than OA, both in the shear-min and plateau (**Fig.1B-C**). Compositional analysis supported mechanical findings, showing collagen content decreased 4-fold within the first 200μm but remained around 3-fold throughout tissue depth compared to healthy (**Fig.1D**). Both shear min (surface) and shear plateau (deep

zone) showed strong correlation (R^2= 0.70 and R^2= 0.21, respectively) with collagen concentration (**Fig.1E**).

Discussion

This is the first study to examine depth-dependent shear mechanics on all stages of OA, showing large differences in the modulus is concentrated at the surface. The shear mechanics of OA cartilage are governed by compositional changes and are more sensitive to collagen than aggrecan, with a small decrease in collagen concentration causing an order of magnitude decrease in modulus. Future therapeutics need to stabilize the cartilage surface to stop the progression of the disease.

Images (Optional)

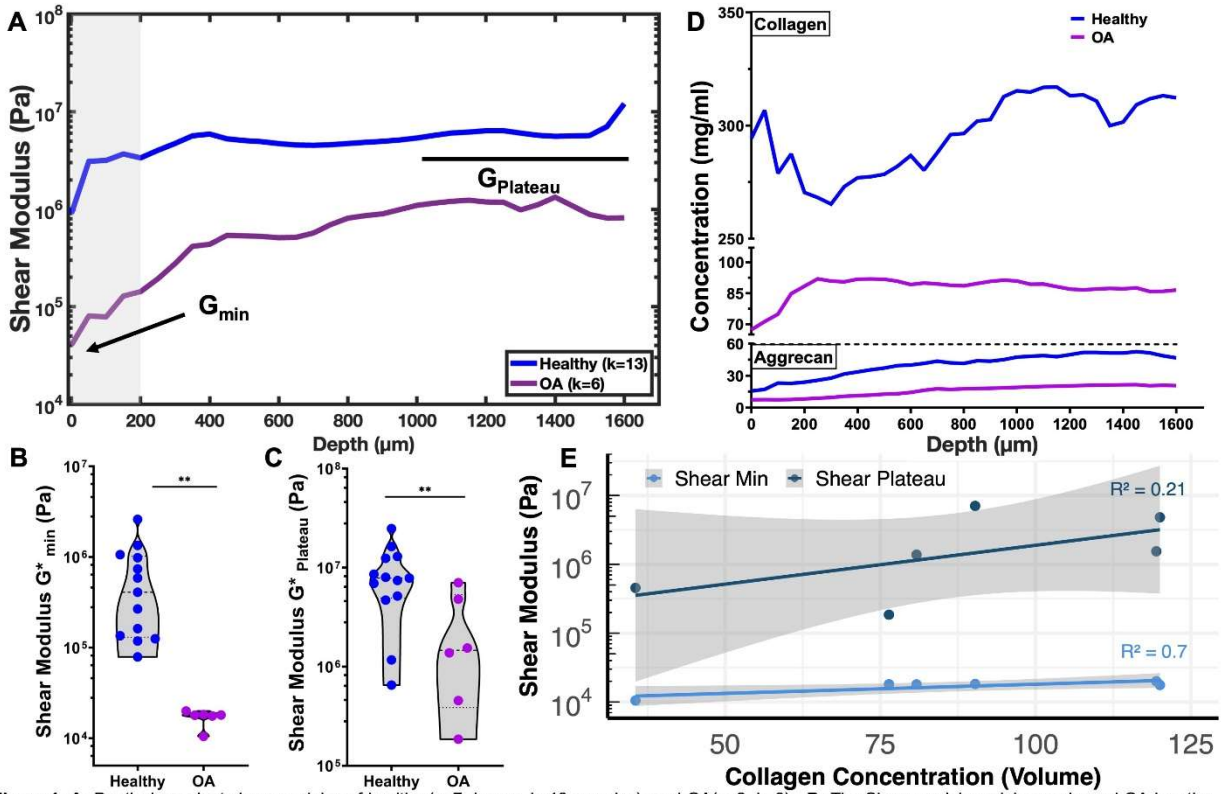


Figure 1: A: Depth-dependent shear modulus of healthy (n=7 donors, k=13 samples) and OA(n=2, k=6): **B:** The Shear modulus minimum showed OA has the lowest mechanics (p=0.0071). **C:** The shear plateau for healthy and OA (p=0.00714). **D:** Depth-dependent FT-IR composition for both collagen (top) and aggrecan (bottom) for both OA and healthy samples. **E:** Correlation plot of shear min and plateau and collagen concentration (R^2=0.70 and p=0.037) and (R^2=0.21 and p=0.364), respectively. The data shown is geometric median with quartiles. Analyzed using Welch's t-test *(α<0.05)*.

Session Category

Musculoskeletal Biomechanics: Tissues

P2-250

Collagen Fibre Volume Fraction in Healthy and Degenerated Articular Cartilage: Insights from Mixture Theory

Dr. Kotaybah Hashlamoun, Dr. Ziad Abusara, Dr. Walter Herzog, Dr. Salvatore Federico

University of Calgary, Calgary, AB, Canada

Dr. Kotaybah Hashlamoun

Introduction

Articular cartilage is a complex, multi-phasic, multi-constituent tissue, providing nearly frictionless contact and stress distribution in diarthrodial joints. Osteoarthritis (OA) is a degenerative disease that reduces the cartilage's ability to withstand physiological loading. OA-degenerated cartilage is characterised by a reduced elastic modulus (E). Thus, E can be used as an indicator of cartilage health.

Recently, Abusara et al. [1] explored the possibility of relying entirely on imaging as an alternative to mechanical testing in assessing the tissue's health. While the correlation between cell viability and E was poor, the correlation between collagen fibre volumetric fraction in the superficial zone and E was strong and nearly linear. This suggests that collagen fibre fraction may be a direct indicator of cartilage health.

The purpose of this work was to determine whether such linear relationship between E and fibre fraction can be predicted via an established microstructural model.

Methods

The solid phase of articular cartilage was modelled as an elastic composite comprised of proteoglycans (isotropic Holmes-Mow energy) and collagen fibres (isotropic Holmes-Mow energy plus an anisotropic term) [2]. A confined compression test in the direction of tissue thickness was simulated numerically. The fibre fraction was varied between 0.1 and 0.6, while the proteoglycan fraction remained fixed at 0.1.

Results

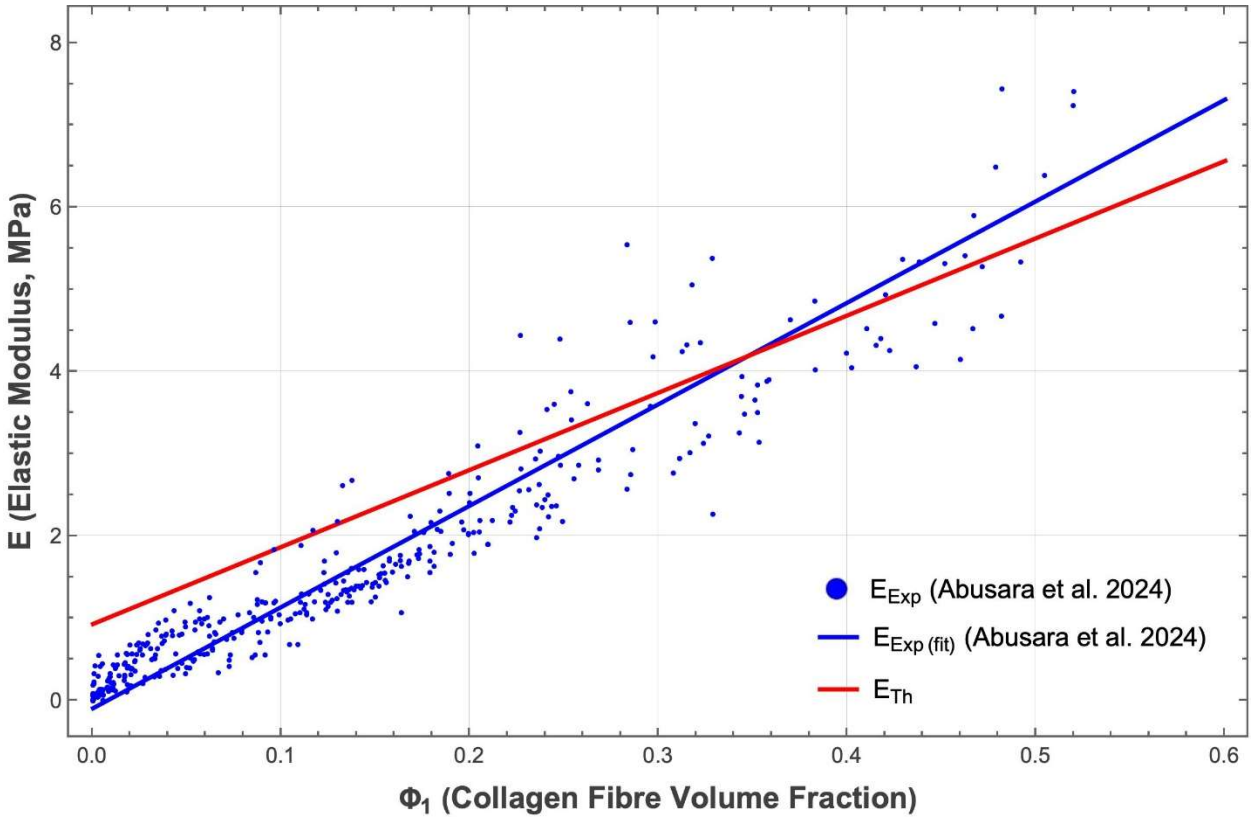
The figure shows a linear relationship between the experimental and the theoretical elastic moduli and the fibre fraction, for a value of nominal strain of 0.1, as in [1]. The ratio

between the theoretical to experimental slopes obtained for the lines describing the moduli against collagen volume fraction was about 0.76.

Discussion

The effect of fibre fraction on the elastic modulus, found experimentally, can be re-reinforced by established structural models, further supporting the reliability of using fibre fraction as an indicator of early OA. These preliminary results motivate the development of a biphasic cartilage model that can be used to investigate systematically the effect of fibre volumetric fraction on cartilage mechanical properties, and by association cartilage health, without the need for extensive experimental testing.

Images (Optional)



References (Optional)

[1] Ziad Abusara *et al*., Ann. Biomed. Eng., 2024

[2] Salvatore Federico and Alfio Grillo, Mech. Mater., 2012

Acknowledgements (Optional)

Session Category

Musculoskeletal Biomechanics: Tissues

P2-251

The Component of Synovial Fluid which Protects Cartilage from Fatigue Failure Under Cyclical Compression is Present in Fetal Bovine Serum

Mr. Justin Weiss, Mr. Haoyu Zhang, Ms. Sarah Deiters, Dr. Clark Hung, Dr. Gerard Ateshian

Columbia University, New York, NY, United States

Introduction

Synovial Fluid (SF) is conventionally thought to protect articular cartilage through lubrication. However, SF's friction-reducing effect is modest, with interstitial fluid pressurization providing the dominant effect [1]. Recent studies demonstrated that, compared to phosphate-buffered saline (PBS), SF delays cartilage fatigue failure under cyclical compression, which presents as middle-zone (MZ) delamination [2-3]. Zhang et al. showed SF protects cartilage even with no sliding, indicating a non-lubrication mechanism [2]. The SF constituents responsible for this protection remain unknown. SF consists of an ultrafiltrate of serum mixed with hyaluronan and lubricin. In [2], samples were not pre-incubated, yet protection emerged within 100 minutes, implicating low–molecular-weight constituents as the responsible factors. Because hyaluronan's large molar mass (10 MDa) and lubricin's strong surface binding prevent transport to the MZ, we hypothesize that the protective component of SF is also present in fetal bovine serum (FBS).

Methods

Cylindrical cartilage plugs (12 mm) were harvested from immature bovine femoral condyles (n=4), sectioned from the deep zone to 1.79±0.26 mm thickness, and stored in PBS. Samples were assigned to PBS (n=4), FBS (n=4), or 25% FBS in PBS (n=3). Following [2], plugs were submerged in 15 mL of fluid and subjected to a prescribed cyclical compression of 54 N at 2 Hz. Tests ended at 12,000 cycles (100 minutes) upon gross visual damage or continued to 36,000 cycles.

Results

All PBS samples showed gross damage by 12,000 cycles (Figure 1). No FBS or 25% FBS samples exhibited damage, even after 36,000 cycles, as assessed from surface roughness measurements.

Discussion

The SF component that protects cartilage against fatigue failure is also present in FBS and is independent of SF's high viscosity. SF's protection reduces in 25% dilutions [2-3], whereas 25% FBS retained full efficacy, suggesting the target component exists in FBS at

higher concentrations. These findings exclude hyaluronan and lubricin as candidates and instead point to low-molecular-weight constituents present in both fluids, and capable of diffusing from the articular surface to the MZ within 100 minutes.

Images (Optional)

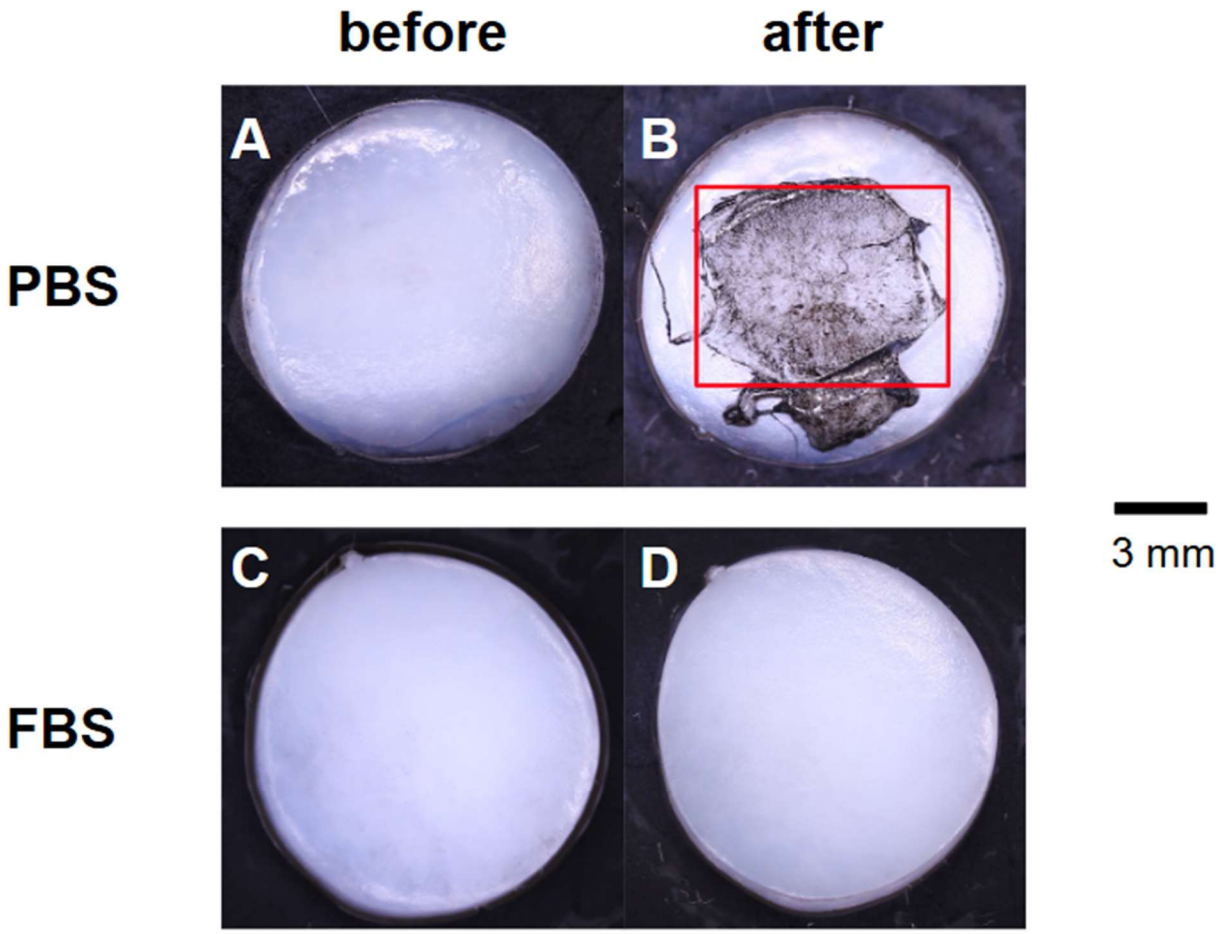


Figure 1. Representative images before (**A**, **C**) and immediately after (**B**, **D**) testing in PBS (**A, B**) and FBS (**C**, **D**). Delamination damage is outlined in red.

References (Optional)

[1] Caligaris M, Ateshian GA, Osteoarthritis Cartilage, 2008 [2] Zhang et al., Osteoarthritis Cartilage (under review, 2025) [3] Sise et al., Osteoarthritis Cartilage, 2025

Session Category

Musculoskeletal Biomechanics: Tissues

P2-252

Age-Related Decline in Impact Strength and Its Association With Collagen-Related Bone Quality in Bovine Single Trabeculae

Prof. Satoshi Yamada, Mr. Shoei Miyamoto, Ms. Mari Kasai, Ms. Miyu Kobayashi

Hokkaido University, Sapporo, Hokkaido, Japan

Introduction

Osteoporotic fragility fractures typically arise from low-energy impacts, including falls, and frequently occur in regions enriched with cancellous bone. To better understand cancellous bone behavior under impact loading, strength must be assessed at the trabecular scale. However, the impact strength of trabeculae and its underlying determinants remain unclear. This study hypothesizes that dynamic strength is associated with collagen-related bone quality and aims to compare trabecular impact strength across two bovine age groups while identifying collagen-related contributions.

Methods

Single trabeculae were harvested from mature (2 years old; n = 21) and aged (15–18 years old; n = 31) bovine femurs and shaped into cantilevered specimens. Static elastic modulus was determined using micro-cantilever bending. Impact strength was evaluated using a customized Izod-based pendulum device, calculated as fracture energy divided by the mean cross-sectional area at the fracture site. Fracture modes were classified as complete, hinge, or partial breaks. Microfocus X-ray computed tomography (micro-CT) scans were taken before and after the impact test in order to observe the specimen shape and tissue mineral density. Raman spectroscopy (785-nm laser) was performed at each fracture surface of partially broken specimens to assess crystal and molecular features.

Results

In both age groups, specimens with partial breaks displayed significantly higher impact strength than those with complete or hinge breaks. Among partially broken specimens, impact strength was significantly lower in the aged group (5.9 ± 2.2 kJ/m^2) compared with the mature trabeculae (9.6 ± 4.1 kJ/m^2) ($P < 0.05$). Neither micro-CT–derived tissue mineral density nor static elastic modulus showed significant age-related differences. The hydroxyproline-to-proline ratio, reflecting collagen molecular stability, did not differ between age groups but exhibited a significant positive correlation with impact strength ($r = 0.47$, $P < 0.05$).

Discussion

Single-trabecula impact strength varied widely, yet its upper limit declined with age. This reduction appears unrelated to bone mineral density or static elastic modulus. The observed correlation with the hydroxyproline-to-proline ratio indicates that the structural state of collagen molecules contributes to the velocity-dependent strength of trabeculae. Future studies are warranted to elucidate the complex mechanisms underlying age-related strength decline.

Acknowledgements (Optional)

This study was supported by JSPS KAKENHI (25K01114, 22K03803).

Session Category

Musculoskeletal Biomechanics: Tissues

P2-253

Greater Embryonic Movement Leads to Enhanced Postnatal Bone Mass in Chickens

Ms. Setareh Khorshidparast[1,2], Ms. Renee Garant[3], Mr. Anthony Helou[1,2], Ms. Tamara Droual[1], Mr. Karim Elsayed[1,2], Ms. Maya Arab Makansi[1], Dr. Tina Widowski[3], Dr. Bret Tobalske[4], Dr. Alexandra Harlander[3], Dr. Bettina M. Willie[1,2]

[1]Shriners Hospitals for Children-Canada, Research Centre, Montreal, Quebec, Canada. [2]Faculty of Dental Medicine and Oral Health Sciences, McGill University, Montreal, Quebec, Canada. [3]Faculty of Animal Bioscience, University of Guelph Guelph, Guelph, Ontario, Canada. [4]Division of Biological Sciences, University of Montana, Missoula, Montana, United States

Introduction

Fetal movements generate stresses necessary for normal skeletal formation. Studies in chick and mouse models show that elimination of movements by muscle paralysis disrupts joint development and weakens bone structure. However, the specific effects of more or less embryonic movement (EM) on bone structure and strength have not been examined. This study aims for the first time, to quantify embryonic movements *in ovo* and compare bone outcomes after hatch in chicks that exhibit more EM compared to those that move less. In particular, we measured tibiotarsus bone mineral density, microarchitecture, bone turnover markers, and muscles mass at hatch.

Methods

A total of 73 fertile eggs were incubated and hatched under commercial conditions at the University of Guelph. Eggs represented two genetic strains (white-feathered and brown-feathered) and both sexes. EM was measured on day 15 and 18 using a portable digital egg monitor for a duration of one minute, and the number of EM was recorded. We then performed multivariable regression analysis to assess the influence of changes in movement between 15 and 18, sex and strain on bone outcomes. One day after hatch, chicks were euthanized, and blood and bone and muscles were collected. Micro-CT was performed on the left tibiotarsus, P1NP levels were measured in the blood serum using ELISA, and leg muscle weights were recorded.

Results

Sex, genetic strain, and EM (Fig. 1A) were significant predictors of metaphyseal trabecular bone volume fraction (Tb_BV/TV) ($p < 0.05$). Higher EM, brown-feathered strain, and female

sex were each associated with increased Tb.BV/TV. Genetic strain was also a significant predictor of diaphyseal total area (Tt_Ar), with brown-feathered chicks exhibiting greater Tt_Ar (Fig. 1B). EM demonstrated a positive association with Tt_Ar as well (p = 0.095). ANOVA results did not show significant difference in P1NP levels and leg muscle in different sexes, genetic strains, or movement status.

Discussion

Our results indicate EM, sex, and genetic strain modulate trabecular and cortical bone mass. Studies are ongoing to determine how long the effect of EM persists into the juvenile period, since bone fractures in chickens, especially egg laying hens are a major animal welfare concern.

Images (Optional)

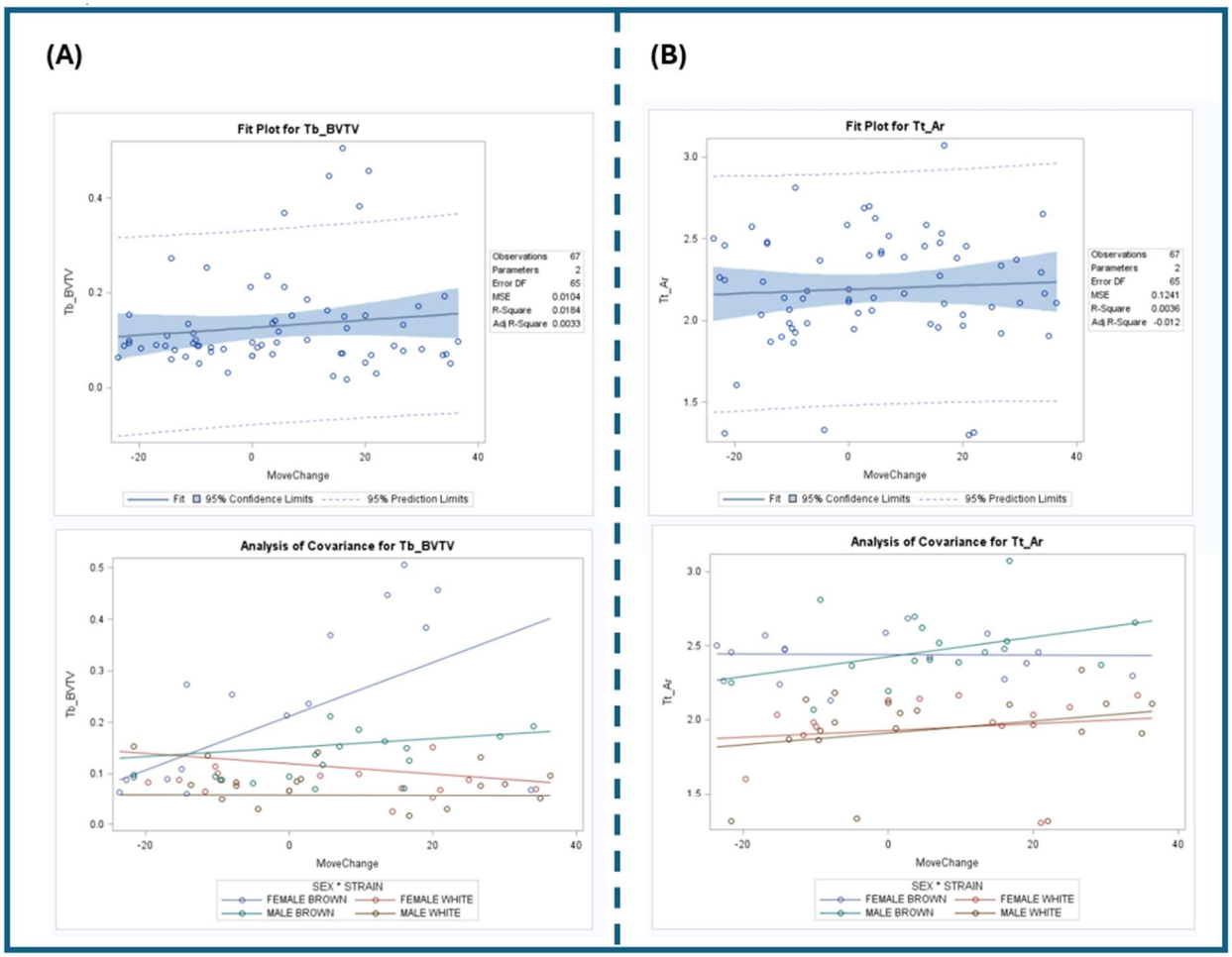


Figure 1: Univariable (top row) and ANCOVA (bottom row) regression plots for trabecular bone volume fraction (Tb_BV/TV) (A) and total area (Tt_Ar) (B); sex, strain, movement change (MoveChange = EM18 – EM 15) are significant predictors of the Tb_BV/TV. In addition, movement change is a positive indicator of Tt_Ar.

References (Optional)

Session Category

Musculoskeletal Biomechanics: Tissues

P2-254

A Longitudinal High-Resolution Peripheral Quantitative Computed Tomography Investigation of Tibial Bone Adaptation in Response to Marathon Training

Ms. Shannon Hugard, Mr. Zak Kindl MS, Dr. Michael Hahn

University of Oregon, Eugene, OR, United States

Introduction

Load-bearing bone continuously adapts to changes in mechanical demands. For this reason, weight-bearing exercise is recommended as a strategy for increasing bone strength and preventing osteoporosis. Running is one of the most popular forms of weight-bearing exercise globally. However, the efficacy of running as an exercise intervention for increasing bone strength has yet to be prospectively evaluated using high-resolution peripheral quantitative computed tomography (HR-pQCT). HR-pQCT measures of tibial density and strength are predicative of subsequent fracture risk [1]. Therefore, the objective of this study is to perform a longitudinal HR-pQCT investigation of the time course and magnitude of tibial bone adaptation in response to marathon training.

Methods

Novice marathon runners aged 19-26 (n=9, 3M/6F) performed 16 weeks of structured marathon training. This is a preliminary subset of an ongoing study with a projected sample size of 28. Marathon training increased progressively in volume and intensity through week 14, followed by a 2-week intensity reduction (taper) period. HR-pQCT scans of the tibial metaphysis were collected at baseline and every 2-4 weeks throughout training. Changes in metrics of tibial bone density, geometry, and microstructure were quantified with the manufacturer-supplied software. Changes in compressive failure load and stiffness were estimated using microfinite element analysis. Linear mixed-effects models were used to assess the effect of marathon training time on each HR-pQCT metric of bone adaptation.

Results

Preliminary results showed non-significant trends of increasing total bone volumetric mineral density (Tt.vBMD; $p=0.07$), failure load ($p=0.10$), and stiffness ($p=0.10$) with marathon training time. On average, participant Tt.vBMD increased 0.8% ± 1.16% after 16 weeks of marathon training. Notably, Tt.vBMD decreased at week 14 for most participants before increasing again at week 16 (Figure 1).

Discussion

Peak bone mineral density (BMD) is typically achieved by age 30. Every 1% increase in peak BMD is estimated to delay osteoporosis onset by more than 1 year [2]. Additional participant data are needed to investigate the preliminary trends of tibial density and strength increases with running training time.

Images (Optional)

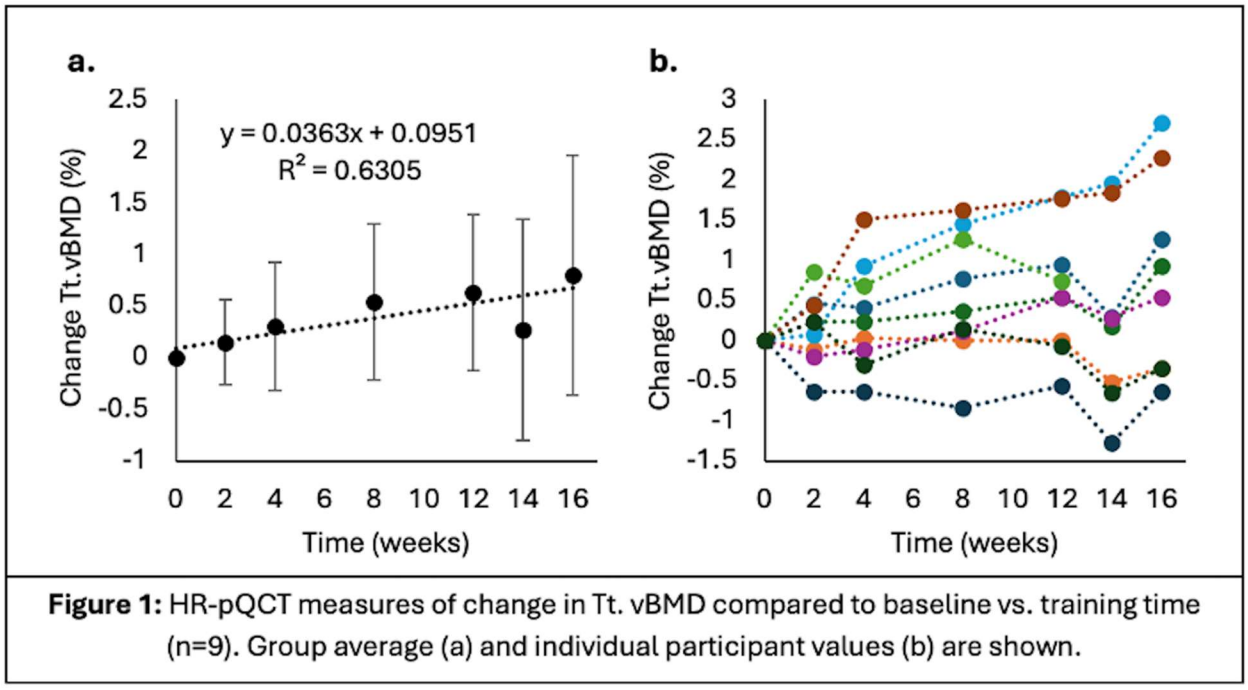


Figure 1: HR-pQCT measures of change in Tt. vBMD compared to baseline vs. training time (n=9). Group average (a) and individual participant values (b) are shown.

References (Optional)

[1] Nicholas Mikolajewicz et al. J Bone Miner Res, 2019

[2] Christopher Hernandez et al. Osteoporosis Int, 2003

Session Category

Musculoskeletal Biomechanics: Tissues

P2-255

Effect of the Degree of Achilles Tendon Twist on Three-Dimensional Force Transmission: A Finite Element Analysis

Dr. Shota Enomoto[1], Dr. Kohta Ito[2]

[1]Okayama University, Okayama, Okayama, Japan. [2]National Institute of Advanced Industrial Science and Technology (AIST), Koto-Ku, Tokyo, Japan

Introduction

The Achilles tendon (AT) is composed of three subtendons arising from the lateral (LG) and medial (MG) heads of the gastrocnemius and from the soleus muscle (SOL), and these subtendons twist around each other [1]. To date, the relationship between the twisted structure and the tendon's function of transmitting tensile forces has remained unclear. We aimed to estimate how the degree of AT twist affects three-dimensional transmitted forces at the distal end of the tendon using finite element analysis.

Methods

We created four finite element models of the AT varying the degree of twist (no-, low-, medium-, and high-twist models) (Figure A). A tensile force of 2000 N was applied to the proximal surface. We allocated the total force to each subtendon according to the relative force-generating contributions of the triceps surae reported in a previous study [2]. The forces applied to the LG-, MG-, and SOL-derived subtendons were 200 N, 500 N, and 1300 N, respectively. The interfaces between subtendons were modeled as frictionless contacts. The nodes on the distal surface were fully fixed and the nodes on the proximal surface were allowed to translate only in the proximal-distal direction. Three-dimensional forces exerted on the distal nodes were calculated, including proximal–distal, medial–lateral, and anterior–posterior components.

Results

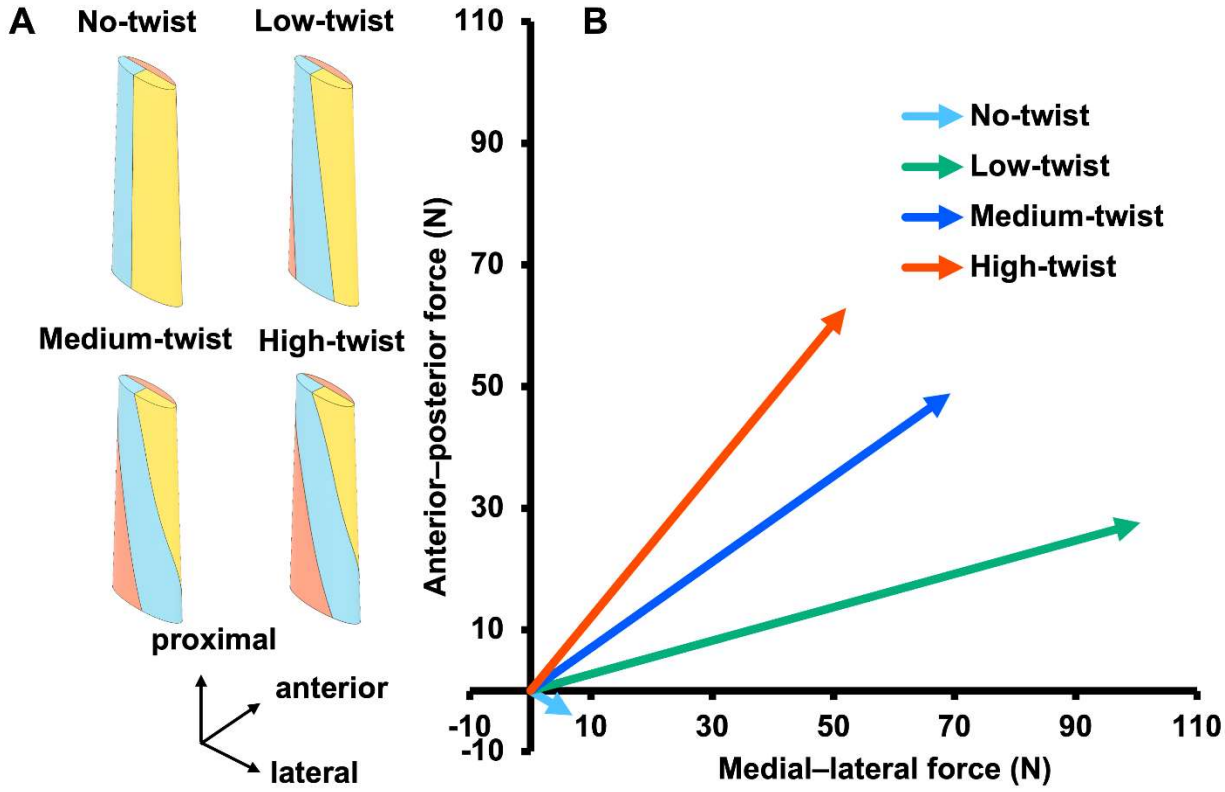
All models exhibited the same proximal-directed force of 2000 N at the distal surface. In addition, the twisted models clearly exhibited horizontal forces directed anterolaterally (Figure B). Furthermore, as the degree of twist increased, the force vectors in the horizontal plane shifted to point more anteriorly.

Discussion

Our results indicate that the uniaxial contractile force generated by the triceps surae may be transformed into triaxial tensile forces by the twisted AT structure. Although the directions of these forces vary depending on the degree of twist, they fundamentally tend

to displace the posterior calcaneus in an anterolateral direction, which might play a role in the mechanical interactions that facilitate efficient locomotion.

Images (Optional)



References (Optional)

[1] Pękala PA, et al., Scand J Med Sci Sports 27: 1705–1715, 2017.

[2] Crouzier M, et al., Med Sci Sports Exerc 52: 1076–1087, 2020.

Session Category

Musculoskeletal Biomechanics: Tissues

P2-256

Sarcomere Lengths in Paretic Muscle Affected by Chronic Stroke in Rats

Dr. Stephanie Ross, Ms. Sydney Dorscher, Dr. Timothy Leonard, Dr. Walter Herzog

University of Calgary, Calgary, Alberta, Canada

Introduction

Stroke is a leading cause of mobility impairment in adulthood, yet the mechanisms underlying these impairments at the muscle level are poorly understood. In children with cerebral palsy, which similarly results from white matter lesions and leads to muscle paresis or weakness on the affected side of the body, reduced force production is thought to be partly due to excessively long sarcomere lengths that limit cross-bridge binding [1]. Measures of sarcomere length using microendoscopy in adults with stroke have shown no difference between paretic and non-paretic sides [2]; however, microendoscopy is a newer approach with limited validation. Therefore, the purpose of this study was to measure differences in sarcomere length between paretic and non-paretic muscle more directly using laser diffraction in a rat model of stroke.

Methods

We induced hemiparetic (n=16) and sham (n=7) stroke using photothrombosis in Sprague-Dawley rats. Eighteen weeks following surgery, corresponding to the chronic phase of stroke, we euthanized the animals and harvested their tissues. We measured sarcomere length and dispersion, a measure of variability in sarcomere length, using laser diffraction [3] of fascicles isolated from the lateral gastrocnemius (LG) and extensor digitorum longus (EDL) muscles fixed at knee and ankle angles of 90 degrees. To examine differences between groups, muscles, and sides of the body, we used a linear mixed model in R, with rat included as a random effect.

Results

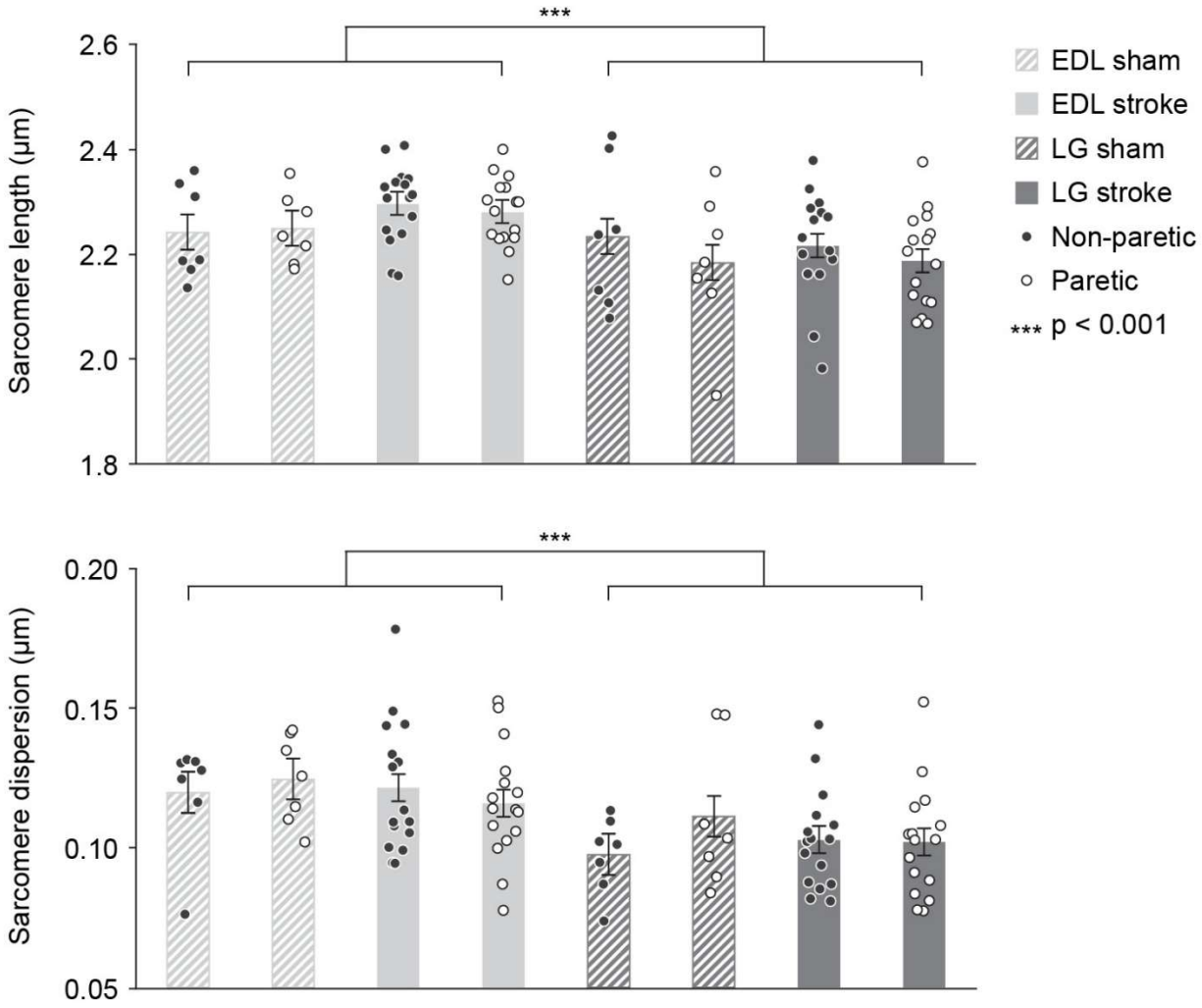
We found a statistically significant difference in least-squares mean sarcomere length and dispersion between the LG and EDL ($p<0.001$), but not between paretic and non-paretic sides or between sham and stroke groups (Figure 1).

Discussion

Our results support previous findings in humans [2] indicating that sarcomere length is unaffected by stroke. This contrasts measures of muscle affected by cerebral palsy and suggests that post-lesion growth may drive the development of elongated sarcomere lengths in paretic muscle, an effect not present in adult stroke. Although we found a

significant difference between the LG and EDL, this likely reflects differences in relative length at the selected joint angles.

Images (Optional)



References (Optional)

[1] Howard & Herzog, Front Neurol, 2021

[2] Adkins *et al.*, PNAS, 2021

[3] Ter Keurs *et al.*, J Gen Physiol, 1978

Session Category

P2-257

The Effect of Speed and Incline on Force Sharing Between the Medial Gastrocnemius and Plantaris Muscles of Sheep During Treadmill Gait

Dr. Stephanie Ross[1], Mr. Florian Schumacher[2], Mr. Esthevan Machado[1], Mr. Andrew Sawatsky[1], Dr. Timothy Leonard[1], Mr. Keiji Hopfner[1], Dr. W. Michael Scott[1], Dr. Walter Herzog[1]

[1]University of Calgary, Calgary, Alberta, Canada. [2]ETH Zurich, Zurich, Zurich, Switzerland

Introduction

Multiple muscles cross each joint, allowing numerous ways to distribute force to produce the same joint moment during gait. Previous work in cats has shown that force sharing across the plantarflexors depends on task demand, with the plantaris (PL) and medial gastrocnemius (MG) both contributing more force with increasing speed and incline, whereas the soleus contributes nearly the same force across conditions [1]. Because cats may be optimized for high-speed chases when hunting prey, it is unclear to what extent these force sharing patterns persist in other species less specialized for speed. To address this gap, we examined force sharing between the PL and MG of sheep during treadmill gait to determine whether the patterns observed in cats persist in a species with slower typical gait speeds.

Methods

We measured PL and MG forces *in vivo* in five Île-de-France sheep using buckle force transducers implanted on the isolated distal tendons. During testing, sheep walked and trotted on a treadmill at speeds and inclines ranging from 0.67 to 1.97 m/s and 0 to 6 degrees. Details of the methods can be found elsewhere [2]. Following testing, we euthanized the sheep and calibrated the force transducers. We analyzed forces from ten consecutive steady-state steps and determined the stance phase of each step from videos of the trials.

Results

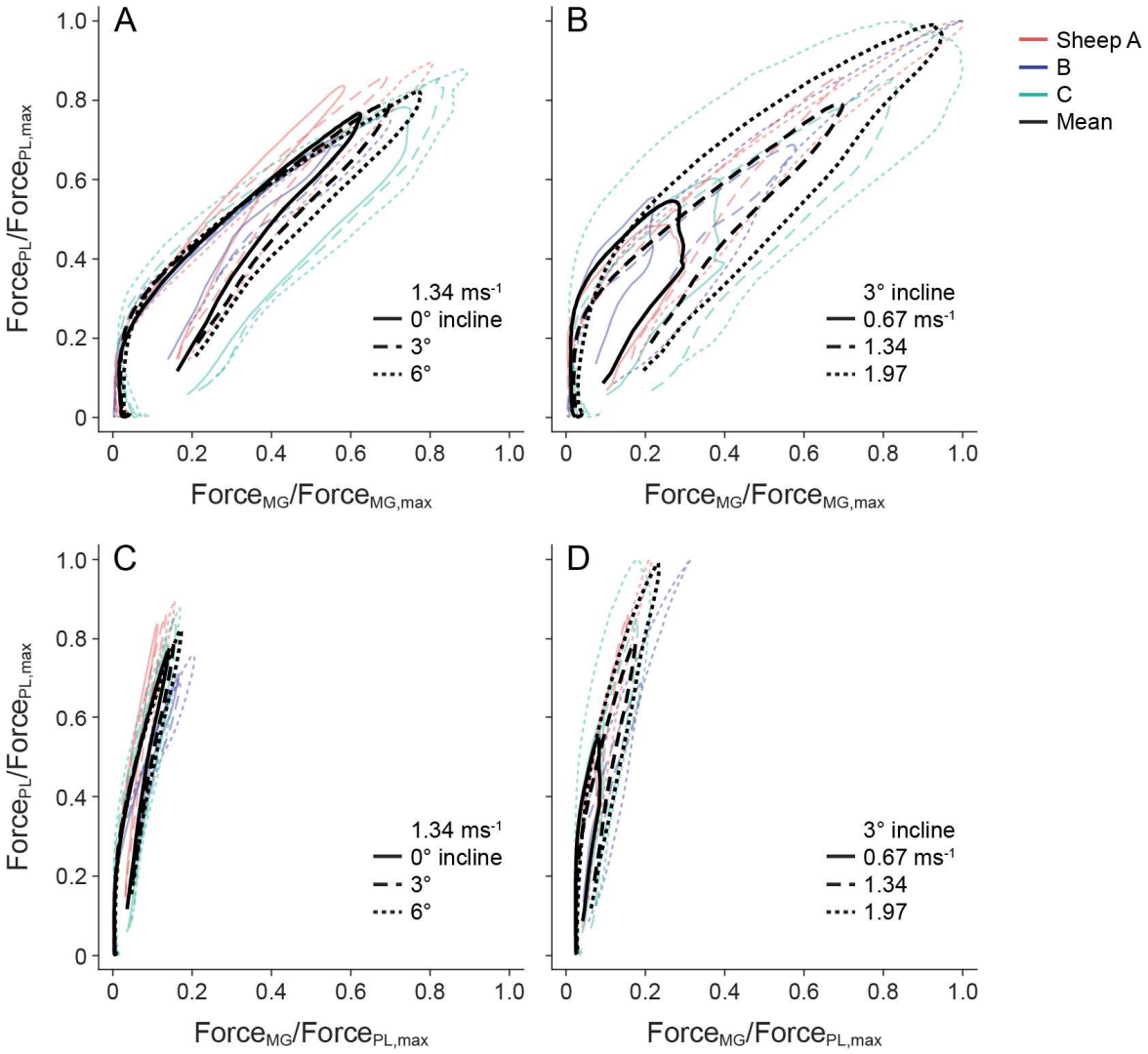
Preliminary results (n=3) indicate that PL and MG forces during stance both proportionately increased with increasing speed and incline (Figure 1A,B). PL force was substantially larger than MG force across all sheep and conditions (Figure 1C,D).

Discussion

The proportional increases in PL and MG force with increasing speed and incline are consistent with previous findings in cats [1]. Our PL forces relative to MG are much larger

than those reported in cats [1], rats [3], and wallabies [4] during gait. This may be because some studies [1,4] measured the combined force of the gastrocnemius complex, whereas we measured the isolated MG force. In other cases [3], this difference may reflect muscle design differences dictated by body morphology or locomotor specialization.

Images (Optional)



References (Optional)

[1] Herzog et al.,JBiomech,1993

[2] Bossuyt et al.,JBiomech,2023

[3] Eng et al.,JExpBiol,2019

[4] Biewener & Baudinette,JExpBiol,1995

Session Category

Musculoskeletal Biomechanics: Tissues

P2-258

Associations between Sound Limb Total Support Moment and Femoral Cartilage Thickness in those with Traumatic Lower-Limb Amputation

Dr. Steven Garcia[1], Ms Nikou Nikoumanesh[2], Ms Shraddha Suddhir[2], Dr. Lindsay Hannigan[2]

[1]Jackie and Gene Autry Orthopedic Center, Childrens Hospital of Los Angelesotion Analyi, Los Angeles, CA, United States. [2]Department of Physical Therapy, University of Illinois, Chicago, Chicago, IL, United States

Introduction

Introduction: Individuals with lower-limb amputation (LLA) develop knee osteoarthritis (OA) at high rates likely due to overreliance on the sound limb for support and mobility. Limited research has directly evaluated associations between sound limb loading and cartilage health in those with LLA. The total support moment (TSM) is linked with knee-OA progression in non-amputee groups and functionally represents lower-limb inter-joint kinetic coordination for support. Here, we evaluated associations between the TSM and ankle, knee and hip contributions to the TSM in individuals with traumatic LLA.

Methods

Methods: Ten persons with LLA (7:Transtibial, 3:Transfemoral, Age:50.3±15.8 yrs, BMI:27.1±5.9, Time Post-LLA:17.5±14.1 yrs) completed treadmill gait biomechanical assessments and femoral cartilage US. Gait biomechanics were evaluated at preferred speed and kinematic and kinetic data were filtered at 6 and 12Hz. Loading metrics included the 1st and 2nd peak TSM (TSM1, TSM2) and individual joint contributions to the TSM. Femoral cartilage US images were captured in the sound limb at the trochlea and medial femoral condyle (MFC). Cartilage thickness from three images was averaged for analysis. Pearson's *r* was used to evaluate correlations between TSM, joint contributions and cartilage thickness.

Results

Results: Greater second peak TSM2 was moderately associated with thicker MFC thickness in superior (r=0.71,p=0.03) and central regions (r=0.73,p=0.03). Moderate associations between TSM2 were observed in medial trochlear cartilage (r=0.61) and inferior MFC regions (r=0.62) but were not significant (p=0.08). Greater knee contributions to the TSM2 were associated with thinner medial femoral cartilage in superior (r=0.74,p=0.02), central (r=0.77,p=0.02) and inferior regions (r=0.74,p=0.02). No associations between TSM1 or other joint contributions were observed (p>0.05).

Discussion

Discussion: We found larger TSM2 and reduced knee contributions to TSM2 were correlated with thicker sound limb MFC. Sufficient limb extensor moments, reflected by TSM2, are important for mobility and also contribute to late stance knee compressive loads and thus may help preserve cartilage health. During late stance, limb extension is driven by ankle and hip extensor moments and thus higher knee contributions to TSM may reflect an inefficient gait pattern. Future work is needed to confirm the longitudinal link between the TSM and sound limb cartilage health after LLA.

Images (Optional)

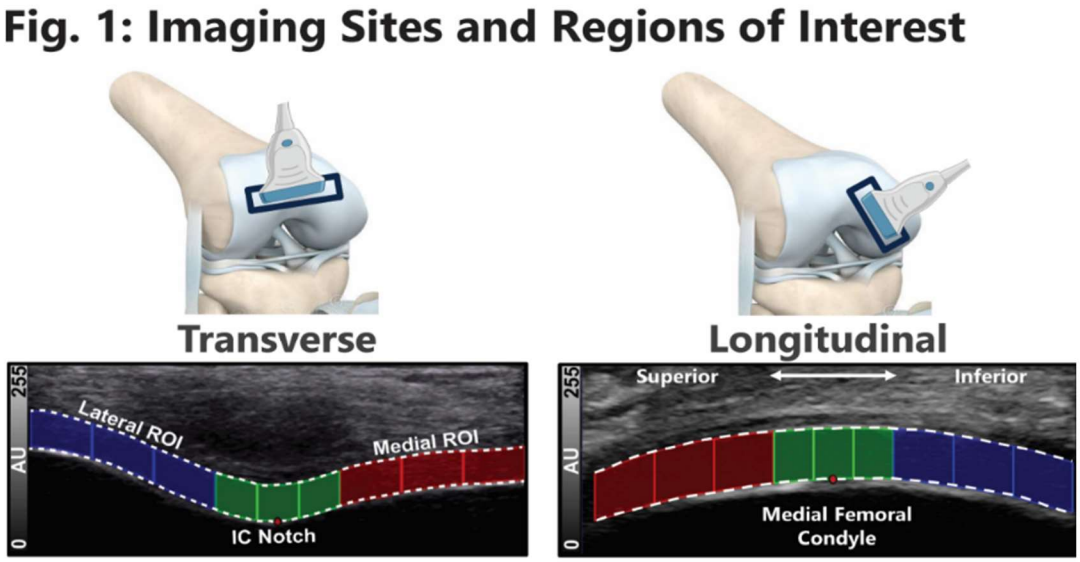


Figure 1: US Images Sites for Femoral Cartilage. Transverse View: Trochlea. Longitudinal View: Medial Femoral Cartilage (MFC). Cartilage thickness was evaluated as the minimum Euclidean distance between superficial and deep cartilage borders across all pixels in each ROI.

Session Category

Musculoskeletal Biomechanics: Tissues

P2-259

Modeling Physiological Tasks and their Impact on Cartilage Deformation and Recovery: A Robotically Controlled Joint Simulator

Mr. Tejus Surendran, Dr. Axel Moore

Carnegie Mellon University, Pittsburgh, PA, United States

Introduction

Articular cartilage functions as the joint's biological bearing, supporting load and enabling low-friction motion through poroelastic fluid pressurization. Prior work has shown that this fluid pressure limits compressive deformation; however, due to the permeable nature of cartilage there is a depressurization and a consequential increase in compressive deformation. How cartilage maintains and recovers this pressure during physiological task remains unclear. While traditional ex vivo models offer excellent experimental control and direct access to the cartilage interface, they typically use sub-physiological loads and speeds, non-native contacts, and altered boundary conditions. On the other hand, in vivo studies capture physiological relevance but experience inter-subject variability, limited control, and low measurement resolution. To bridge this gap, we apply near-physiological joint dynamics to cadaveric knees while simultaneously measuring cartilage deformation. We hypothesized that replicating native joint loading in cadaveric joints that preserve native contacts and boundary conditions would produce physiological deformations.

Methods

Five adolescent female Duroc pig stifle joints were dissected, preserving collateral and cruciate ligaments and menisci. Femoral and tibial shafts were potted in polymethyl-methacrylate and mounted in a 6-DOF robotic system (**Fig 1A**) that provided control of joint kinematics and kinetics. In each joint we simulated a series of tasks: Standing 1 (30 min), Walking (10 min, ASTM F3141), Standing 2 (30 min), and Supine (60 min). Cartilage deformation measured as a change in the position of the end effector of the robot once it achieved a target load of −245 N along the superior-inferior axis.

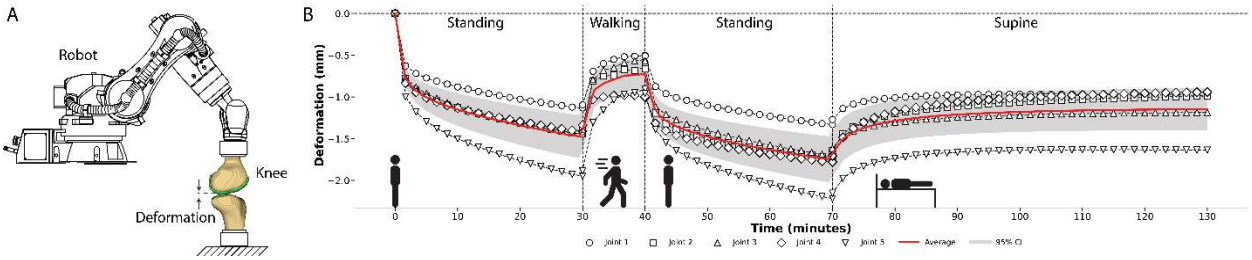
Results

Simulated standing produced compressive cartilage deformation (negative values indicate compression) with similar patterns in both Standing 1&2 (**Fig 1B**). During Standing 1, deformation increased to an average of −1.5 mm. Walking recovered 0.8 mm (51%) of deformation after 10 minutes. Following Standing 2, the compressive deformation increased to −1.8 mm. Simulating 60 min of lying supine led to a mean recovery of 0.60 mm.

Discussion

In this ex vivo cadaveric model, we observed time- and task-dependent changes in superior–inferior joint displacement consistent with cartilage deformation and recovery. The results demonstrate that simulated standing produces time-dependent compressive deformation, whereas simulated walking and lying supine promote time-dependent recovery.

Images (Optional)



Session Category

Musculoskeletal Biomechanics: Tissues

P2-260

Decorin Promotes Nascent Proteoglycan Retention in Cartilage Matrix by Strengthening Collagen II-Aggrecan Integration

Mr. Thomas Li[1], Dr. Gabriela Canziani[1], Mr. Yuchen Liu[1], Mr. Neil Patel[1], Dr. Biao Han[1], Dr. Mingyue Fan[1], Ms. Annie Porter[2], Dr. Bryan Kwok[1], Dr. Chao Wang[1], Dr. Qing Li[1], Dr. David Birk[3], Dr. Renato Iozzo[4], Dr. Irwin Chaiken[1], Dr. X. Lucas Lu[2], Dr. Robert Mauck[5], Dr. Lin Han[1]

[1]Drexel University, Philadelphia, PA, United States. [2]University of Delaware, Newark, NJ, United States. [3]University of South Florida, Tampa, FL, United States. [4]Thomas Jefferson University, Philadelphia, PA, United States. [5]University of Pennsylvania, Philadelphia, PA, United States

Introduction

Effective regeneration of cartilage is limited by our incomplete understanding of molecular activities that regulate the integrity of its extracellular matrix (ECM). Cartilage ECM, a hydrated collagen II–aggrecan composite, undergoes dynamic turnover during both normal homeostasis and disease-associated remodeling. This study aims to elucidate the role for decorin, a small proteoglycan, in mediating the retention and stability of nascent aggrecan within the ECM.

Methods

Femoral head cartilage explants from 3-week-old wild-type C57BL/6 mice were labeled with GAL to tag nascent proteoglycans via click chemistry. Explants were stimulated with IL-1β for 8 days to elicit chondrocyte catabolism, with both pre- and post-treatment of exogenous decorin (before/after IL-1β), followed by the quantification of nascent proteoglycans retained in explants versus release to media. Surface plasmon resonance (SPR) was applied to measure the effects of decorin on aggrecan and collagen II binding affinities. AFM-nanoindentation was applied to test the effects of decorin on the modulus of proteoglycan-depleted cartilage. Significance of treatment effects were assessed by one-way ANOVA followed by Tukey–Kramer post hoc multiple comparison ($\alpha = 0.05$).

Results

Pre-treatment of decorin before the onset of IL-1β attenuated the release of nascent aggrecan caused by IL-1β, but such effects were absent for post-treatment (Fig. 1a). Meanwhile, SPR showed that decorin enhanced the binding affinities among aggrecan and collagen II pairs (Fig. 1b). Furthermore, AFM-nanoindentation showed that infiltration of decorin stiffened the collagen II fibrillar network of proteoglycan-depleted murine cartilage (Fig. 1c).

Discussion

This study identifies decorin as a crucial regulator of dynamic cartilage matrix turnover, particularly in the retention of newly synthesized aggrecan. Specifically, the partial rescue of IL-β-elicited nascent proteoglycan release by decorin pre-treatment highlights the potential of decorin as a therapeutic for osteoarthritis intervention. We attribute this role to its biophysical function in stabilizing aggrecan–aggrecan, aggrecan–collagen II, collagen II–collagen II integration. In turn, such effects strengthen the collagen II fibril network, and therefore its capability of confining the entrapped aggrecan networks. Our ongoing studies are further interrogating the mechanisms and delivery of decorin-based therapeutics.

Images (Optional)

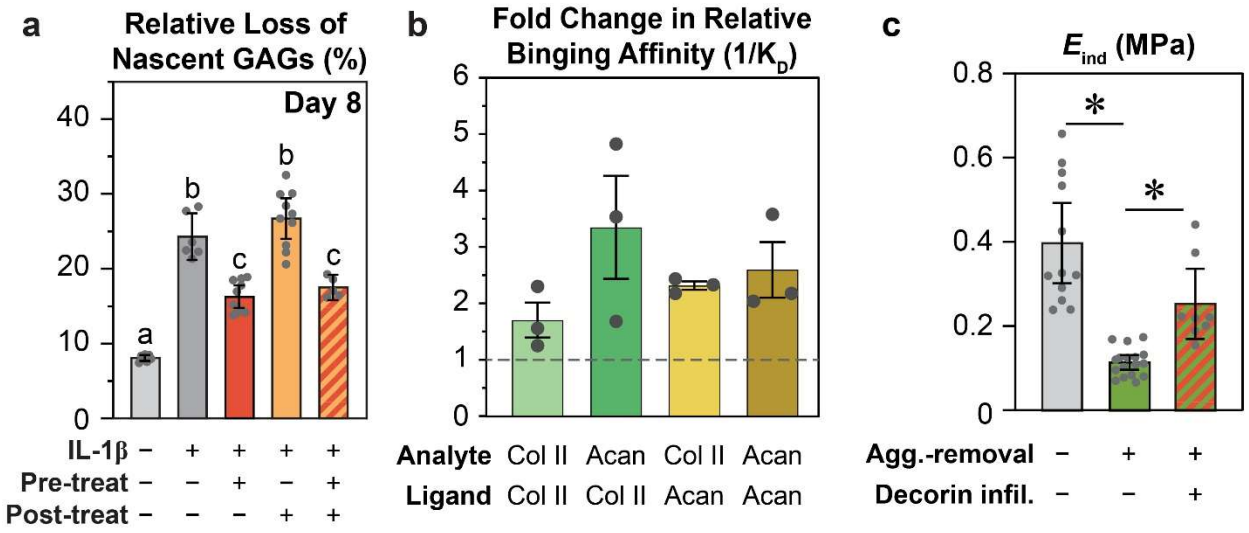


Figure 1. Decorin stabilizes the cartilage matrix via "physical linkages" during early assembly. a) Cumulative release of nascent proteoglycans from wild-type (WT) murine femoral head cartilage explants at day 8 under various decorin treatment conditions (mean ± 95% CI, n ≥ 4). **b)** Decorin-induced fold changes in the relative binding affinity, $1/K_D$, for all tested conditions (mean ± SD, n = 3). **c)** Indentation modulus, E_{ind}, of medial femoral condylar cartilage from WT mice measured via AFM-nanoindentation following the aggrecan depletion and exogenous decorin infiltration of freshly harvested tissues (mean ± 95% CI, n ≥ 6). Different letters indicate significant differences among treatments. *: $p < 0.05$ between treatment groups, n.s.: not significant.

References (Optional)

Acknowledgements (Optional)

This work was supported by NIH R01AR074490 and UPenn PCMD NIH P30AR069619.

Session Category

Musculoskeletal Biomechanics: Tissues

P2-261

Low-Dosage Temporal Effects of Botulinum Neurotoxin on Whole Skeletal Muscle's Passive Mechanical Properties

Mr. Timothy McGinley M.S., Dr. Albino Schifino Ph.D., Dr. Benjamin Binder-Markey PT, DPT, Ph.D.

Drexel University, Philadelphia, PA, United States

Introduction

Botulinum neurotoxin (BoNT) is used to reduce spasticity and resulting increased muscle resistance following neurological injuries. However, in chronic stroke patients, long-term BoNT injections are linked to increased passive muscle stresses. Yet, the temporal development of these BoNT-related increases in passive muscle mechanics remains unclear. Within this study, we aim to characterize the temporal timeline over a year of a clinically relevant low-dose injection.

Methods

Passive mechanical characteristics were collected from the lateral gastrocnemius (LG) of C57BL6 mice. Animals received an intramuscular injection of a clinically relevant low dose of 1 U/kg BoNT in their left LG. The contralateral LG was used as the control. 40 mice (20 male & 20 female) were separated into 4 groups: 1-month, 3-month, 6-month, and 12-months post-injection. Force was measured with a 5N force transducer while lengthened in 5% step increments from 0% - 30% strain. Samples were weighed and mass ratio (BoNT/Control) was compared to 1.0. Stress was calculated using the animal's PCSA. The passive stress-strain data were fit to non-linear regression models and compared using linear mixed methods.

Results

Mass ratios were significantly less than one at 1 & 3 months, but recovered by 6 months (Fig.1A). Normalized stress-strain curves indicated that BoNT-injected samples exhibited significantly higher stresses by 1-month post-injection that lasted to at least 6 months. Yet, by 12-months post-injection, muscle stresses are not significantly different between BoNT and control muscles (Fig. 1B).

Discussion

BoNT caused alterations in passive muscle mechanics, with elevated stresses persisting up to 6 months post-injection. Early atrophy is evident from muscle loss, though after muscle mass recovers and the stresses increase, indicate ECM remodeling beyond BoNT's

three-month active phase. These findings highlight that a single low dose of BoNT leads to changes that potentially resolve over time.

Understanding the temporal effects of BoNT is critical for optimizing treatment. Increased passive stresses following treatment may impair functional outcomes and rehabilitation efficacy following injections. Insights from this study provide a foundation for developing dosing protocols that minimize adverse effects.

Images (Optional)

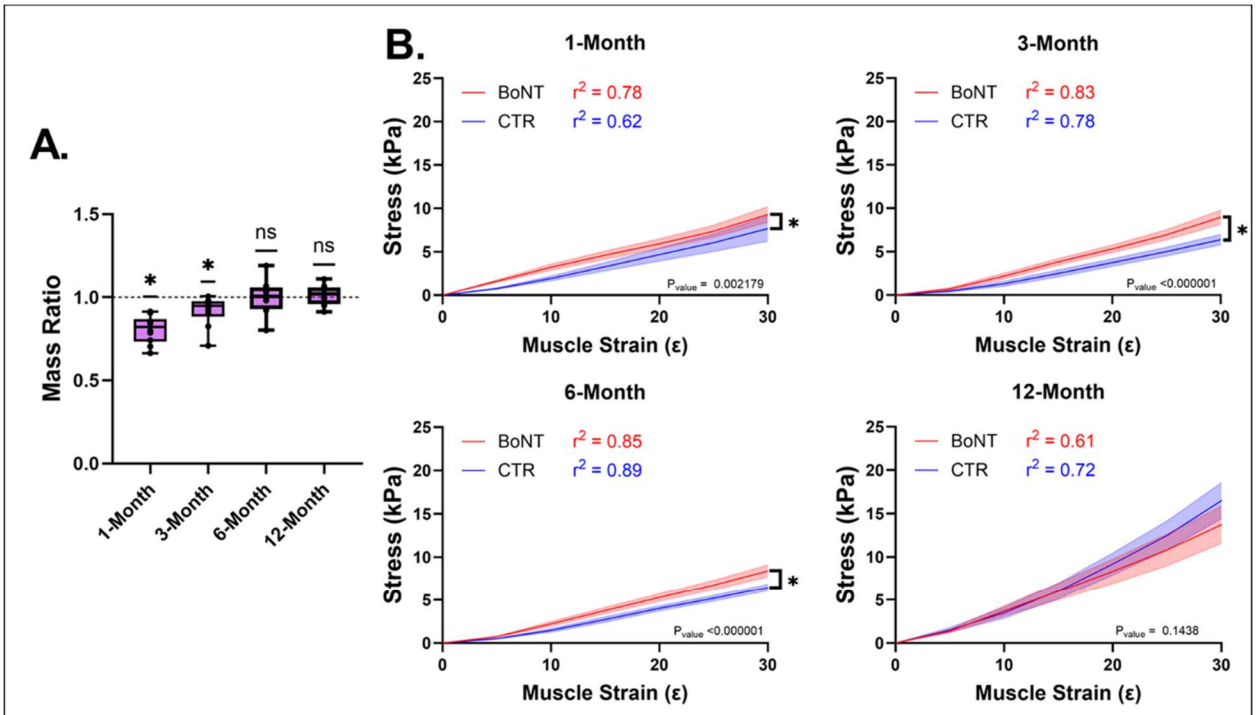


Figure 1: A. Mass ratios of BoNT to control masses compared to 1.0. B. Stress-Strain Curves for the lateral gastrocnemius of C57BL6 mice at 1, 3, 6 and 12 months comparing BoNT injected muscles (Red) and contralateral control (Blue). Data shown as averages±SD. $n_{1M, 3M, 6M, 12M} = 10$ (5M & 5F). * indicates $p<0.05$

References (Optional)

Acknowledgements (Optional)

This work was supported by The Hartwell Foundation and Foundation for PT Research.

Session Category

Musculoskeletal Biomechanics: Tissues

P2-262

Energy Consumption After Active Stretch in Single Skinned Muscle Fibres

Miss Torri Heiser BSc, Dr. Venus Joumaa PhD, Dr. Walter Herzog PhD

University of Calgary, Calgary, Alberta, Canada

Introduction

The isometric force produced at steady-state following active stretching is greater than a purely isometric contraction at the same final muscle length and level of activation. This muscle property has been observed at all structural levels and is referred to as residual force enhancement (rFE) [1]. There is increasing evidence that the passive element, titin, may contribute to rFE [1]. If so, rFE would occur with little or no increase in energy cost (ATP consumption). However, there is minimal systematic work that has measured ATP consumption simultaneously with force following active stretch in muscles [2].

The purpose of this study was to gain insight into the mechanism of rFE by measuring ATP consumption simultaneously with force at steady-state after active stretch and the corresponding isometric reference contractions in muscle fibres.

Methods

A newly developed system (1415A, Aurora Scientific) based on de Tombe and Stienen [3] allowed us to measure the rate of ATP consumption simultaneously with force in the steady-state region following purely isometric and active stretch contractions in skinned rabbit psoas muscle fibres. The purely isometric contractions were performed at an average sarcomere length (SL) of 3.2μm. In the active stretch trials, fibres were actively stretched from an average SL of 2.4μm to 3.2μm and held at this length until steady-state force was achieved.

Results

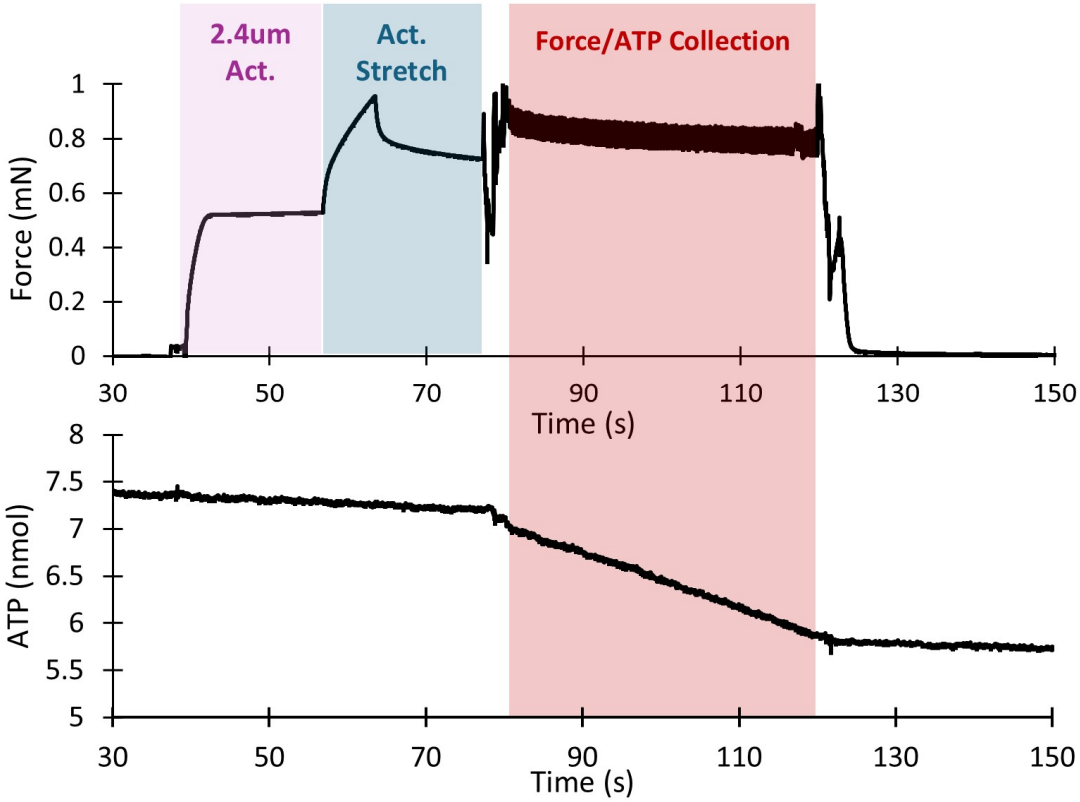
To date, our results show an average rFE of 11±0.4%. The rate of ATP consumption per unit of force was 20% lower following active stretch compared to the purely isometric reference contraction.

Discussion

From our knowledge, this is the first study to record ATP consumption simultaneously with force in rFE. The reduced ATP consumption per unit of force in rFE compared to the corresponding isometric state supports the idea that the extra force in rFE originates from a

passive element and not from increased cross-bridge activity. Titin-calcium and titin-actin interactions have been suggested to occur upon muscle activation and stretch, resulting in an increase in titin stiffness and thus, rFE without a corresponding increase in ATP consumption.

Images (Optional)



References (Optional)

[1] Herzog, J Neuroeng Rehabil, 2017

[2] Joumaa & Herzog, J Biomech, 2013

[3] de Tombe & Stienen, J Physiol, 2007

Session Category

Musculoskeletal Biomechanics: Tissues

P2-263

Why Is the Triceps Surae Muscles Pennate? A Predictive Simulation Study

Dr. Torstein Dæhlin[1], Dr. Stephanie Ross[2], Dr. Nilima Nigam[1], Dr. Friedl De Groote[3], Dr. James Wakeling[1]

[1]Simon Fraser University, Burnaby, BC, Canada. [2]University of Calgary, Calgary, AB, Canada. [3]KU Leuven, Leuven, Flemish Brabant, Belgium

Introduction

Metabolic cost of transport (COT) is one selection pressure purported to drive evolution of the human locomotor system. Mechanical work performed by the triceps surae muscles has a strong influence on COT during running [1]. These muscles are pennate, affecting their force-length-velocity characteristics [2]. Therefore, their pennation may influence how efficiently these muscles perform mechanical work. While most locomotor muscles are pennate, it remains unclear whether pennate muscles are advantageous for reducing COT. The purpose of this study was to investigate whether triceps surae pennation influences COT and joint work during the stance phase of running.

Methods

The influence of triceps surae pennation on COT and joint work during running was investigated using a predictive musculoskeletal simulation software (PredSim), and a previously validated musculoskeletal model. Soleus, medial gastrocnemius, and lateral gastrocnemius pennation angles were scaled to 0 to 200% of those of the nominal musculoskeletal model (25.0°, 17.0°, and 8.0°, respectively) in 50% increments. Simulations were generated for 2.5, 3.0, 3.5, 4.0, and 4.5 m/s running. Optimal fibre and tendon slack lengths were scaled to offset the influence of pennation on the muscles' operating length.

Results

COT was highest with the largest pennation angles and smallest when pennation angles were zero (Fig 1). Less positive and negative ankle plantar flexor work was performed when pennation angles were larger than those of the nominal model (Fig 1). The decrease in ankle plantar flexor work was accompanied by an increase in positive and negative work performed at the knee and hip (Fig 1).

Discussion

Our results predict that COT would be lower with non-pennated versus pennated triceps surae muscles. This suggests that another selection pressure may have driven the evolution of triceps surae pennation. Nonetheless, pennation angles equal to or less than those of the nominal model only minimally increase COT and have little influence on lower extremity joint work. As our model does not capture all factors influencing COT or other selection pressures, there may be further undiscovered benefits to having pennated muscles.

Images (Optional)

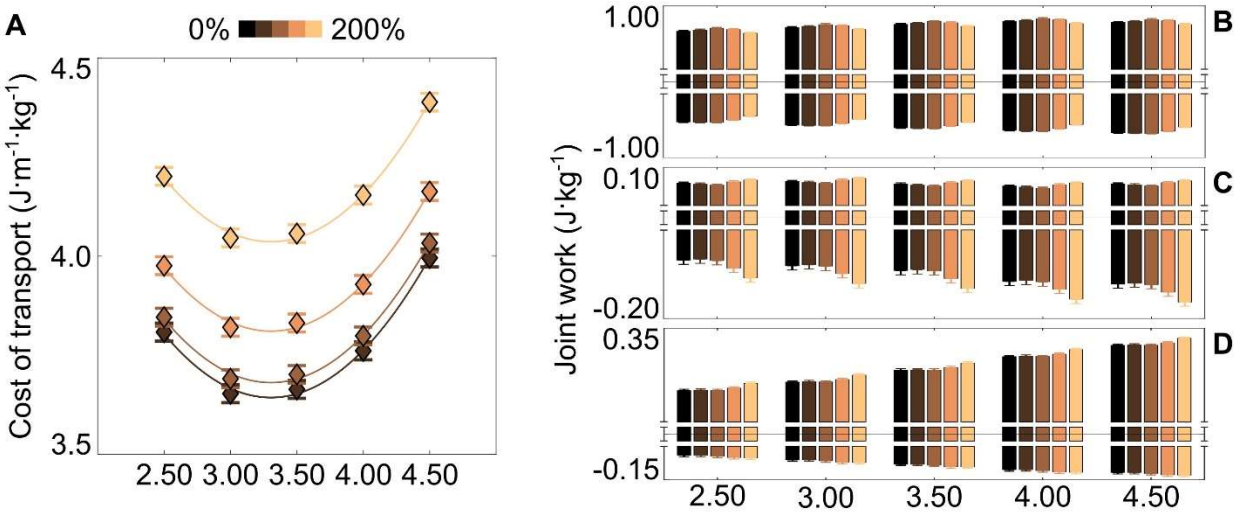


Fig 1. The cost of transport (panel A), and positive and negative ankle (panel B), knee (panel C), and hip (panel D) joint work during running. Horizontal axes are in meters per second.

References (Optional)

[1] Heise *et al.*, Eur J Appl Physiol, 2011.

[2] Van Hooren et al., Scand J Med Sci Sport, 2024.

Acknowledgements (Optional)

We acknowledge the support of the Government of Canada's New Frontiers in Research Fund (NFRF), [NFRFE-2023-00166].

Session Category

Musculoskeletal Biomechanics: Tissues

P2-264

Impact of Distinct Loading Configurations on Extracellular Matrix Structure and Function in Fibroblast-Seeded Collagen Scaffolds

Mr. Amevi Semodji[1], Ms. Dalia DeLaCruz[1], Dr. Xinzhu Pu[1], Dr. Anamaria Zavala[1], Dr. Sean Howard[1], Ms. Shaughnessy Murphy[2], Dr. Gunes Uzer[1], Dr. Julia Oxford[1], Dr. Trevor Lujan[1]

[1]Boise State University, Boise, Idaho, United States. [2]Boise High School, Boise, Idaho, United States

Introduction

Fibroblast activity in soft tissues is highly regulated by mechanical cues within their 3D extracellular matrix (ECM). However, optimal loading conditions (e.g., tension, compression, biaxial) that best promote ECM repair and remodeling by fibroblasts remain unclear due to limited direct comparisons. We developed a new experimental approach that delivers equivalent mechanical energy to 3D cell-seeded constructs under distinct loading configurations [1]. Our study objective was to evaluate how loading configuration influences ECM structure and mechanical function in 3D fibroblast-seeded collagen scaffolds.

Methods

Collagen scaffolds were seeded with mouse fibroblasts (3T3) and stimulated using our custom bioreactor at a targeted energy of 40 J/m^3 (8 h/day, 7 days) [1]. Three loading configurations were investigated (n=5/group): uniaxial tension (TO), uniaxial compression (CO), and biaxial tension-compression (TC), with an additional unstimulated control group (UC). Stiffness changes were assessed using Dynamic Mechanical Analysis, cell density was assessed using confocal microscopy, and RNA and proteins were extracted using modified TRIzol and RIPA protocols, respectively. ECM gene expression was quantified by qPCR, and protein profiles and gene ontology (GO) enrichment by mass spectrometry.

Results

Dynamic moduli significantly increased after stimulation (tensile for TO, compressive for CO, and both for TC) (**Fig. 1A**). TC displayed the highest cell density (**Fig. 1B**), while CO produced the greatest ECM expression (**Fig. 1C**) and amount of most structural proteins although the differences were not significant (**Fig. 1D**). The GO analysis revealed similar differential representation in most ECM-related terms between groups (**Fig. 1E**).

Discussion

Mechanical stimulation was applied at a target energy to fibroblast-collagen constructs in three loading configurations. TC resulted in better mechanical and cell density outcomes but showed weaker ECM gene and protein responses than CO and TO. The combined loading induced the highest distortion energy, which positively and strongly correlated with cellular and mechanical changes, suggesting that shape-changing deformations enhance cellular and mechanical outcomes. Such correlations could not be established for ECM protein expression and production, likely because fibroblasts tend to produce less during their active division phase. Future work will investigate longer stimulation periods to capture ECM responses beyond early growth phases.

Images (Optional)

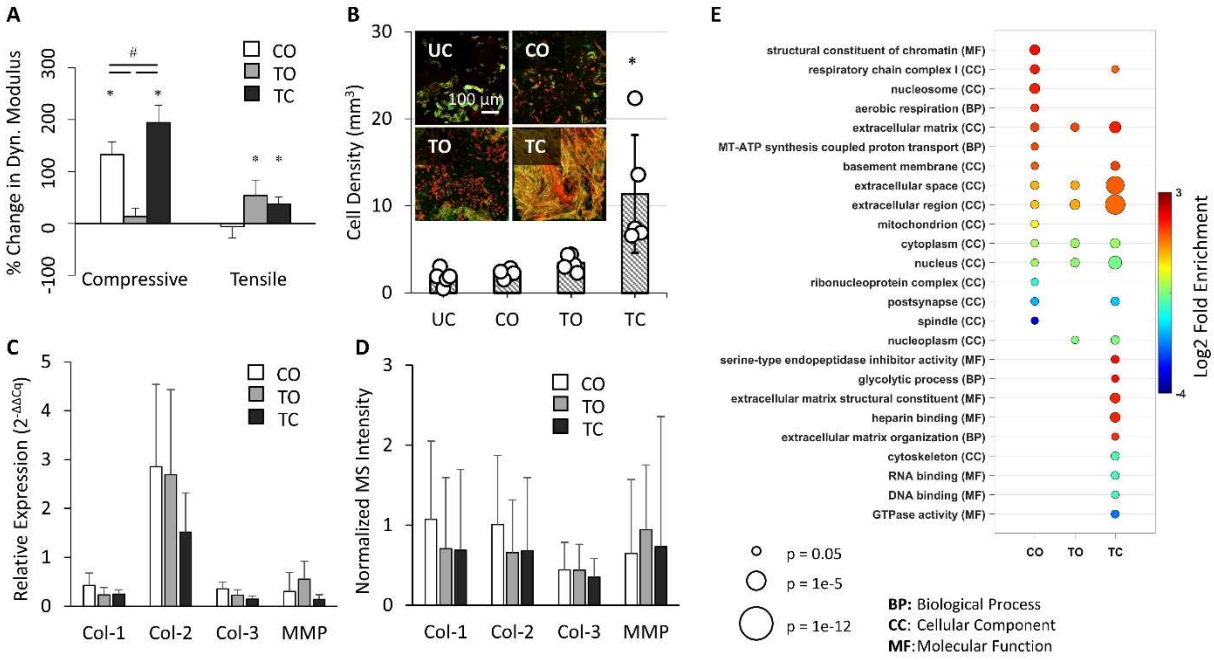


Figure 1: **A)** Percent change in dynamic modulus due to a 7-day mechanical stimulation regime in different loading configurations. **B)** Cell visualization and quantification in 3D collagen scaffolds per loading group after mechanical stimulation. Inserts represent confocal images of cell nuclei (red) and actin cytoskeleton (green). * = significantly greater than initial day. **C)** ECM gene expression from qPCR analysis per loading group. We investigated genes encoding collagen1-alpha1 (Col-1), collagen-2-alpha1 (Col-2), collagen3-alpha1 (Col-3), and matrix metalloproteinases (MMP). **D)** ECM protein intensity from Mass Spectrometry (MS) per loading group. Amounts were normalized to the controls. **E)** Gene Ontology (GO) enrichment for all loading configurations compared to the Unstimulated Control (UC) group showing log2 fold enrichment as bubble color and statistical significance strength as bubble size.
CO: Uniaxial Compression, TO: Uniaxial Tension, TC: Biaxial Tension-Compression.

References (Optional)

[1] Amevi Semodji *et al.*, JMBBM, 2025.

Session Category

Musculoskeletal Biomechanics: Tissues

P2-265

Modelling Tendons as a Fibre-Reinforced Poroelastic Material

Miss Zoe Godard, Professor Sarah Waters, Professor Derek Moulton

University of Oxford, Oxford, Oxfordshire, United Kingdom

Introduction

Tendons are connective soft tissues between muscle and bone. Tendinopathy is a common musculoskeletal disease, characterised by a range of physiological and structural changes, the underlying mechanics of which are still not well understood. Our aim is to build a mathematical model for tendons to tease out the key mechanisms that support tendon function and how they are affected by damage.

Methods

Tendons undergo large deformations and are made up of 55-70% water and a collagen-heavy solid matrix; to capture this we employ a non-linear poroelastic framework to capture the bulk mechanics of the tissue, assuming Darcy flow through the pores of the solid skeleton, and a solid constitutive law which assumes the solid is primarily formed of crimped collagen fibrils that only bear load once fully taut, embedded in a soft isotropic background matrix. The bone boundary is rigid and impermeable and the muscle boundary is permeable, where a stress is also imposed. Damage may be introduced into the model by weakening or breaking fibrils. The model is parameterised using published human tendon data.

Results

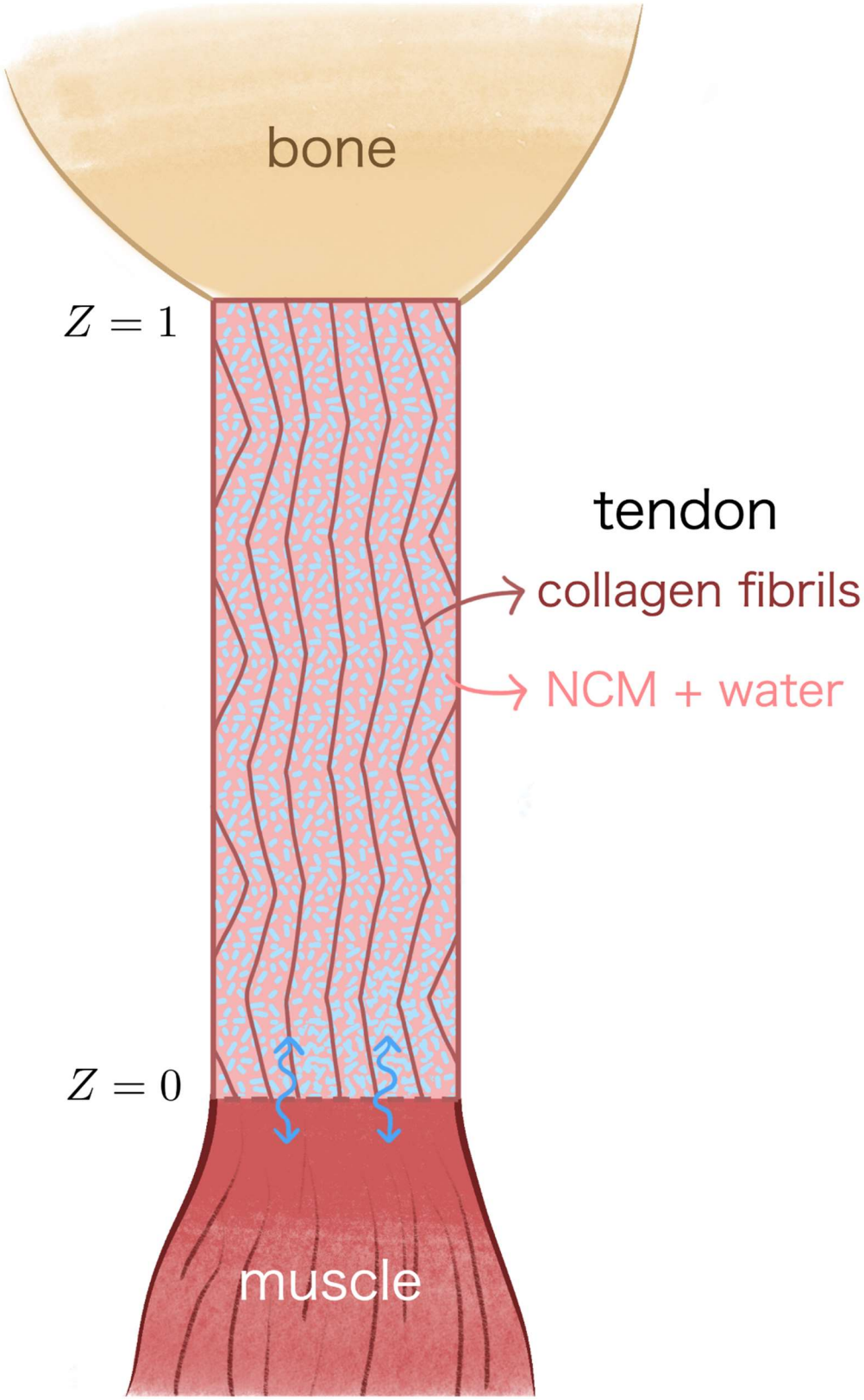
The objective of our study is to gain mechanistic insight into the interaction between constitutive components of tendon, namely the crimped collagen fibrils, the porous background matrix and fluid flow under static or dynamic loading conditions and potential damage. We reveal how the inclusion of fluid flow through the porous matrix, which introduces an inherent timescale, results in asymmetries between the dynamics of loading and unloading. We also investigate how damage to the fibrils affects the response to loading, and compare this to our previous study which neglected fibrils.

Discussion

The model provides us with access to quantitative measures of spatial and temporal stress and strain fields, as well as fluid flux, enabling us to predict where damage might occur.

Additionally, by prescribing regions of damage we can determine the impact of tendinopathies on the resulting tendon behaviour. The simplicity of this model provides us with a clear mechanistic understanding of the interplay between tendon damage and behaviour, motivating further clinical and biomechanical testing, and may serve as a guide to more complex models.

Images (Optional)



References (Optional)

Session Category

Musculoskeletal Biomechanics: Tissues

P2-266

The Effect of Firefighters' Turnout Gear on Mobility Limitations and Task Performance: Preliminary Data

Ms. Arianna Eyre, Mr. John D. Tebbetts MS, Mr. Kuanting Chen MS, CSCS, Dr. Jennifer M. Yentes PhD

Texas A&M University, College Station, Texas, United States

Introduction

Turnout gear (TG) is the personal protective equipment worn by firefighters. Due to the inherent nature of firefighting, TG is
often bulky and heavy, causing restricted movements and increased physical taxation. Understanding how TG affectsfirefighters' movements in occupational settings is imperative for improving gear design and developing training strategies to mitigate negative movement impacts. Therefore, this study aimed
to investigate how TG affected firefighters' range of
motion (ROM)and firefighting task performance.

Methods

Sixteen males (1.8±0.1m, 97.7±15.7kg, service years: 17.3±9.9 yrs) and
four females (1.7±0.1m, 97.7±9.4kg, service years: 11.8±10.9 yrs) completed two tasks with their own TG (geared) and station wear (baseline). Task 1: single-joint, active, maximal ROM movements; Task 2: firefighting circuit including ladder maneuver, victim rescue, hose manipulation, and forcible entry. Whole body kinematics were captured using Xsens inertial measurement units. Subsequent joint angles and segment angular accelerations were computed for both conditions. Changes in ROM during Task 1 were extracted. For Task 2, completion times and movement quality (i.e., root-mean-square segment angular acceleration) were computed. To assess the impact
of TG, preliminary data from 10 firefighters' geared and baseline conditions were compared using descriptive statistics.

Results

When completing Task 1, TG reduced mean shoulder flexion by 19.4±10.0°, shoulder abduction by 38.1±20.2°, elbow flexion by 8.6±8.3°, hip flexion by 16.6±8.7°, knee flexion by 4.8±3.2°, and neck extension by 11.4±11.5° compared to
baseline. During Task 2, compared to baseline, TG increased time to completion and reduced movement quality across all tasks (Table 1). Future work will include ROM during firefighting tasks.

Discussion

As reduced ROM was evident during geared single-joint, active, maximal ROM movements, these same biomechanical limitations may exist during firefighting tasks. Firefighting performance decline (i.e., increased time and decreased quality) may be partially driven by these biomechanical limitations. Due to inherent bulkiness, a degree of ROM limitation will likely be present in TG, limiting TG modifiability. Functional mobility training may help overcome these limitations. Moreover, lack of gear fit is a common complaint. Firefighters may benefit from improved processes for TG measurement, tailoring gear to their anthropometrics.

Images (Optional)

		RMS of Segment Angular Acceleration (°/s^2)				Time	
		R Upper Arm	R Upper Leg	L3	Head	Mean Time (s)	Percent Time Diff
Hose drag	Baseline	45.5 ± 21.1	78.3 ± 39.5	27.2 ± 21.9	32.1 ± 54.7	13.1	14.00%
	Gear	30.3 ± 13.0	64.3 ± 53.0	16.1 ± 9.1	15.2 ± 7.3	15.4	
Hose carry	Baseline	42.4 ± 21.7	89.2 ± 37.2	24.4 ± 13.4	38.9 ± 29.9	14.7	17.10%
	Gear	28.8 ± 6.3	61.0 ± 26.4	14.2 ± 4.6	17.6 ± 8.3	18.1	
Ladder setup	Baseline	49.0 ± 16.0	44.2 ± 12.0	19.6 ± 6.0	12.2 ± 3.5	13.3	18.30%
	Gear	37.8 ± 14.0	35.4 ± 6.8	13.0 ± 4.4	13.3 ± 3.9	17.1	
Ladder climb	Baseline	45.5 ± 11.9	34.1 ± 10.8	16.4 ± 5.0	10.0 ± 1.9	13.3	18.10%
	Gear	32.4 ± 6.1	26.8 ± 7.4	9.6 ± 1.9	11.3 ± 1.8	16.5	
Ladder remove	Baseline	33.6 ± 9.2	39.7 ± 14.4	13.4 ± 3.2	9.5 ± 2.2	10.4	8.70%
	Gear	28.4 ± 13.2	30.6 ± 10.0	9.9 ± 3.3	10.3 ± 1.8	12.3	
Forcible entry	Baseline	141.2 ± 64.6	33.1 ± 15.1	37.1 ± 17.6	17.5 ± 7.50	20.9	8.10%
	Gear	119.6 ± 71.9	29.2 ± 11.3	34.2 ± 17.70	22.1 ± 14.2	23.2	
Victim drag	Baseline	35.0 ± 22.7	55.5 ± 19.3	19.4 ± 7.0	11.8 ± 4.2	20.0	16.50%
	Gear	22.4 ± 12.5	47.8 ± 29.0	13.3 ± 4.8	13.3 ± 4.8	24.0	

Acknowledgements (Optional)

Session Category

P2-267

The Comparison of Two Virtual Reality Systems on Muscle Activity and Posture During Computer Tasks at Sit and Stand Workstations

Mr. Cameron Lang MSc[1], Dr. Michael Holmes PhD[1], Dr. Garrick Forman PhD[1], Dr. Jack Callaghan PhD[2], Ms Jessa Davidson MSc[2]

[1]Brock University, St. Catharines, Ontario, Canada. [2]University of Waterloo, Waterloo, Ontario, Canada

Introduction

Advances in technology (including design, resolution, and computing power) have allowed traditional computer work to be possible with Virtual Reality (VR) headsets. Previous research demonstrated that VR headsets are more responsive and easier to use compared to traditional computers. However, research on the physical demands of these devices on office workers is lacking, and the full potential of these technologies remains underexplored. The purpose of this study is to quantify the physical demands of immersive technologies during computer tasks.

Methods

Five individuals (3M/2F; 24.8±1.9 years) completed two 60-minute sessions using the Meta Quest 3 (MQ) or Apple Vision Pro (AVP). Muscle activity was measured using surface electromyography on 16 muscles of the upper extremity. Kinematics were measured using motion capture, with reflective markers placed bilaterally on the upper extremities, head and thorax. Trunk lateral bend and flexion/extension angles were measured using triaxial accelerometers along the spine (C7, T12, L1). To simulate office work, alternating 5-minute blocks of typing and text editing were completed for 30 minutes while sitting and standing, with both VR headsets and a physical keyboard. Muscle activity and kinematics were analyzed using APDFs (10th, 50th, 90th percentiles). Performance measures for the typing and editing tasks were also analyzed.

Results

Preliminary results show greater flexor digitorum (FD) and cervical extensor (CE) muscle activity while seated (FD: 26.8±0.8 %MVC; CE: 12.3±1.8 %MVC) compared to standing (FD: 22.1±2.1 %MVC; CE: 10.6±1.5 %MVC), with no difference between the AVP and MQ. Neck flexion angles were greater when using the MQ (15.2±1.2^0) compared to AVP (13.2±1.2^0), with no differences between sit and stand conditions. AVP demonstrated greater accuracy in typing tasks (AVP: 92.1±1.9%; MQ: 86.8±4.8%).

Discussion

Our preliminary findings are consistent with previous literature, showing a decrease in upper-limb muscle activity during typing tasks when standing vs. sitting. Increased neck flexion while using the MQ may be a result of lower visibility of external devices (i.e., keyboard), which may affect performance. A larger sample size is required before the true physical demands of VR use in office work are completely understood.

References (Optional)

Session Category

Rehabilitation Biomechanics and Human Factors: Occupational Biomechanics

P2-268

Effects of Turbans on the Biomechanical Effectiveness of Industrial Protective Headwear: Impact Attenuation and Retention Perspectives

Ms. Claudia M. Graham MHK, Dr. Andrew C. Laing PhD

University of Waterloo, Waterloo, Ontario, Canada

Introduction

Numerous religious and cultural practices incorporate head coverings. Despite their potential to influence the biomechanical effectiveness of protective headwear products, research in this domain is limited [1,2]. In some occupational settings/jurisdictions, industrial protective headwear (i.e. hardhats) is required. This study investigated the effects of turbans on industrial hardhat performance from two biomechanical perspectives: retention and impact attenuation.

Methods

Physical test methods were adapted from CSA standards [3]. Turban conditions included a magnesium headform (K1A) either bare or covered by two Dumalla-style turbans (T1=smaller, T2=larger). Tests were performed on a representative hardhat model certified by [3]. Retention: Hardhats were secured on the headform or turban. An instrumented hook/cable was secured to the hardhat's anterior brim and a vertically-oriented load was applied. Peak force to cause helmet decoupling (45° displacement) was recorded. Impact: A vertical drop tower and headform impacted the hardhats across turban conditions at crown, anterior, and lateral locations (energies of 55J, 30J, 30J, respectively). Peak resultant acceleration (g_{max}) was extracted from a triaxial accelerometer at the headform's centre of mass.

Results

Retention: Compared to the bare headform, the force required to cause hardhat retention failure was 39.7% and 32.8% lower in the large ($p=0.040$) and small turban ($p=0.057$) conditions, respectively. Impact: For lateral impacts, g_{max} was significantly greater in the bare (110.8(5.7)g, CV:9%) compared to small turban (69.5(2.3)g, CV: 7%) and large turban (62.8(11.8)g, CV:33%) conditions ($p<0.001$), and coefficient of variability was more than three-fold greater in the large turban condition.

Discussion

From a broad safety perspective, wearing a turban underneath an industrial hardhat may improve impact attenuation for some impact scenarios, but also decreases the force required to cause retention failure. Overall, adding turban materials on top of a headform created uncertainty regarding the source of impact attenuation, increased across-trial variability, and influenced hardhat positioning on the headform. Accordingly, while inclusive design for industrial hardhats is desirable, incorporating religious headwear within physical test systems is not recommended from a biomechanics perspective.

References (Optional)

[1]Rowland, JOccupAccid,1987 [2]Yu et al., AnnBiomedEng, 2024 [3]CSA Z94.1-15, 2020

Acknowledgements (Optional)

CSA Group; cultural advisor Pavitar Notey.

Session Category

Rehabilitation Biomechanics and Human Factors: Occupational Biomechanics

P2-269

Using Optical Marker Tracking for the Determination of Relative Movement Between Exoskeleton and Human

Dr. David Scherb, Prof. Robert Weidner

TU Bergakademie Freiberg, Freiberg, Saxony, Germany

Introduction

Musculoskeletal simulation is increasingly being used in the design process of support systems, like exoskeletons. Especially, the insight into resulting biomechanical effects allows a more straightlined design. However, for the performance of the designed exoskeleton, the recreation of the interface between exoskeleton and human is crucial. One major aspect of the interface is the biological soft tissue. Due to its compression during force transmission, relative movement between exoskeleton and human body occurs, influencing the support behaviour of the exoskeleton. However, this compliant behaviour of biological soft tissue is currently not sufficiently depicted in musculoskeletal simulation. Thus, a novel method for simulating the behaviour of biological soft tissue under the effect of exoskeleton support using spring-damper-elements should be developed. For this method, the parameters for stiffness and damping are elemental.

Methods

To derive these parameters, a study was conducted with participants executing over-head screwing and lifting a box over-head while wearing different shoulder exoskeletons. The participants were attached with markers at anatomical landmarkers due to the Vicon Plug-in-Gait model and additional markers at the exoskeleton to allow the derivation of the movement of exoskeletons and body segments individually and relative to each other (Figure 1a).

Results

The results show that relative movement occurs between exoskeleton and human body segment, i.e., arm. Especially, at the highest angles of the executed tasks, the highest magnitude of deviation appears (Figure 1b). Furthermore, an influence due to participant classifications (age, gender…) is identified.

Discussion

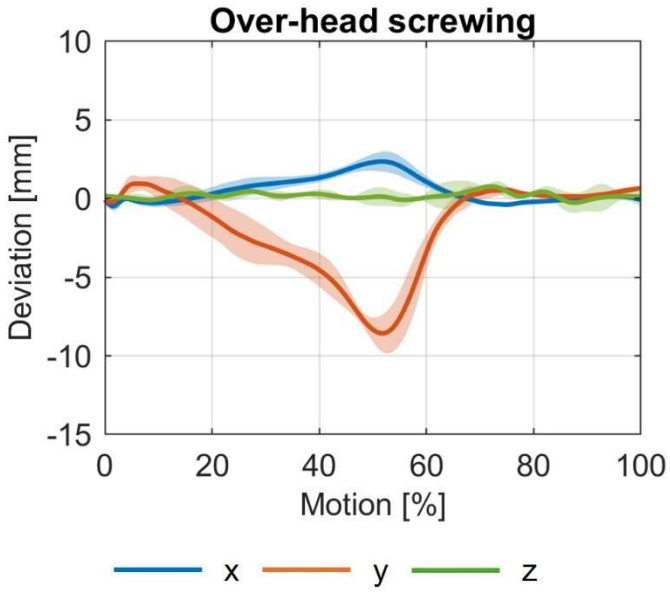
The influence of the participant classification is explained by the dependent appearance and distribution of biological soft tissue and its components (skin, muscle, adipose tissue) from these parameters. The course of the captured relative movement between human body and exoskeleton is accordingly traceable and plausible. In addition, the deviation depends on the exoskeleton and the incorporated joint kinematics. However, the magnitude can be arguable. During the calibration of the Vicon software, a discrepancy of up to 1 cm is considered as fine. Thus, some details of the occurring effects could be missed by marker tracking. In future, more accurate capturing methods (e.g. fluoroscopy) should be used to provide further insights into these promising results.

Images (Optional)

a)



b)



Session Category

Rehabilitation Biomechanics and Human Factors: Occupational Biomechanics

P2-270

Visual Cues and Physical Literacy Influence Perceived Reach Affordances in Manual Materials Handling

Mr. Dean Stewart, Dr. Olu Awosoga PhD, Dr. Hardeep Ryait PhD, Dr. Jon Doan PhD

University of Lethbridge, Lethbridge, Alberta, Canada

Introduction

Work-related musculoskeletal diseases (WR-MSDs) are common in manual materials handling (MMH) as increased musculoskeletal demands elevate injury risk. Affordance thresholds (ATs), the distances a worker feels they can safely reach, may shift when visual cues alter perceived limits. Physical literacy (PL), awareness of one's body and movement capability, may influence what is perceived as safe. This study examines whether directional visual cues (left, right, none) influence height-normalized affordances (AT/H) across reach-distance groups and whether PL moderates the likelihood of selecting conservative or higher-risk reach distances.

Methods

Sixty-three adults completed a single lateral MMH task under a randomized visual cue: Left (n=20), none (n=20), right (n=23). After a scripted briefing, participants set their safe lateral reach distance (AT), which was normalized to height (AT/H) after testing was complete and classified as: 0-0.10 (conservative), 0.11-0.2 (moderate) and >0.20 (higher risk). A subset (n=35) of participants completed a PL assessment, and we organized into high-PL and low-PL groups. Analyses included: mean AT/H by cue group, counts of individuals within AT/H categories, PL-based differences in zone classification.

Results

Mean AT/H values were similar across cue groups (Left: .238; None: .218; Right: .233), indicating limited cue effects on affordance. However, distributional patterns revealed notable differences. The higher risk zone (>0.20) contained 7 participants in the no-cue group, versus 4 in Left and 3 in Right. The conservative zone (0–0.10) contained 4 Right-cue participants and 0 from Left or None. Moderate-zone counts were more evenly distributed (Left: 5; None: 8; Right: 4). Physical literacy strongly moderated outcomes: all conservative-zone participants were high-PL (n=4), while low-PL individuals were heavily concentrated in the high-risk zone, especially under no-cue condition (6 low-PL vs. 1 high-PL).

Discussion

Although cue condition did not influence mean AT, the distributions indicate that perceptual cues meaningfully shape affordance selection. The no-cue condition produced the most participants selecting excessive reach distances, suggesting that reduced perceptual input increases judgment variability.

PL further moderated outcomes, with low-PL individuals concentrated in the high-risk zone. These findings show that affordance selection varies under uncertainty and supports physical literacy training as a potential WR-MSD risk-control measure.

Session Category

Rehabilitation Biomechanics and Human Factors: Occupational Biomechanics

P2-271

Sex differences in three-dimensional accelerometer orientation during seated whole-body vibration exposure

Ms. Eliza Cazzola B.Eng, MASc[1,2], Mr. Ian Scagnetti MSc, PhD Candidate[1], Dr. Megan Govers[1], Dr. Michele Oliver P.Eng[1]

[1]University of Guelph, Guelph, Ontario, Canada. [2]HumanSystems Inc., Guelph, Ontario, Canada

Introduction

Individuals who operate heavy mobile machinery are exposed to whole-body vibration (WBV) which is associated with back injury. Although females experience a greater incidence of back injuries compared to males, sex is generally not considered in WBV exposure analysis. ISO 2631-1 is frequently used to evaluate WBV exposure and associated health risk, where risk is assessed based on acceleration assumed to be in a basicentric coordinate system (BCS) that originates on the seat. ISO 2631-1 indicates that accelerometer orientation should not deviate more than 15° from the BCS. However, when mounted on the human body, an accelerometer's internal coordinate system becomes misaligned from the BCS which may impact accuracy of BCS acceleration measurements. The objective of this work was to investigate sex differences in triaxial accelerometer orientation relative to the BCS during seated WBV exposure.

Methods

27 females (25.4±6.0 years) and 23 males (27.4±5.8 years) were exposed to 16 vertical sinusoidal vibrations (1,3,5,7,9,11,13 and 15Hz at 0.25 and 0.50m/s^2) while sitting upright on a rigid seat with no backrest. Four orthogonal motion capture markers were attached to accelerometers at each of the sacrum (S1), lumbar spine (L3), thoracic spine (T6), and head via a bite-bar. Accelerometer orientation (roll, pitch and yaw angles) was calculated from motion capture data. Descriptive analyses were performed to determine if accelerometers deviated more than 15° from the BCS, and a mixed factorial ANOVA (p<0.05) was used to investigate sex differences in orientation.

Results

78% of participants exceeded 15° of pitch rotation in at least one spine location, and accelerometers at S1 and T6 most frequently exceeded 15°. Males and females had significantly different accelerometer orientation at S1 and T6, where females had

significantly greater anterior pitch rotation at S1 and males had significantly greater anterior pitch rotation at T6.

Discussion

The results suggest that accelerometers often deviate from the BCS despite participants adopting and maintaining an upright posture. The identified sex differences in accelerometer orientation at S1 and T6 may lead to sex differences in measurement accuracy in the BCS. The implications of accelerometer misalignment from the BCS on acceleration measurement needs to be further explored.

Session Category

Rehabilitation Biomechanics and Human Factors: Occupational Biomechanics

P2-272

Effects of a Passive Back Support Exoskeleton on Gross Lumbar Proprioception and the Flexion Relaxation Phenomenon

Ms. Emma Ratke BKin (Honours), Ms. Aurora Battis MSc, Dr. Shawn Beaudette PhD

Brock University, St. Catherines, Ontario, Canada

Ms. Emma Ratke

Introduction

The effects of a back support exoskeleton (BSE) on proprioception and the flexion relaxation phenomenon (FRP) should be assessed to understand implications of widespread BSE use in occupational settings. The purpose of this study was to: 1) assess acute BSE effects on lumbar proprioception, and 2) assess acute BSE effects on the FRP. It was hypothesized that lumbar proprioception would be reduced with BSE use. Additionally, it was hypothesized that FRP onset would occur earlier in trunk flexion with BSE use.

Methods

20 participants (10 F) were recruited. Participants' lumbar erector spinae (LES) were instrumented bilaterally with bipolar surface electrodes and IMU's bilaterally on the shoulders, upper arms and forearms, with single sensors placed on the head, sternum, and pelvis and calibrated as per manufacturer guidelines. Participants were fitted with a passive BSE (HeroWear Apex2). To assess the FRP, participants completed 5 repetitions of maximum flexion paced by a metronome. To assess proprioception, participants completed 5 midrange rematching trials. They were asked to flex forwards, told to stop at a randomized mid-range posture, return upright, and rematch the midrange posture. A one-way repeated measures ANOVA was used to compare differences in ratings of perceived exertion (RPE) across conditions and absolute lumbar angle error in the rematching trials. A two-way repeated measures ANOVA was used to compare differences between right and left LES activation and dependant variables across conditions. Pairwise post-hoc tests were used to examine any significant main effects ($a = 0.05$).

Results

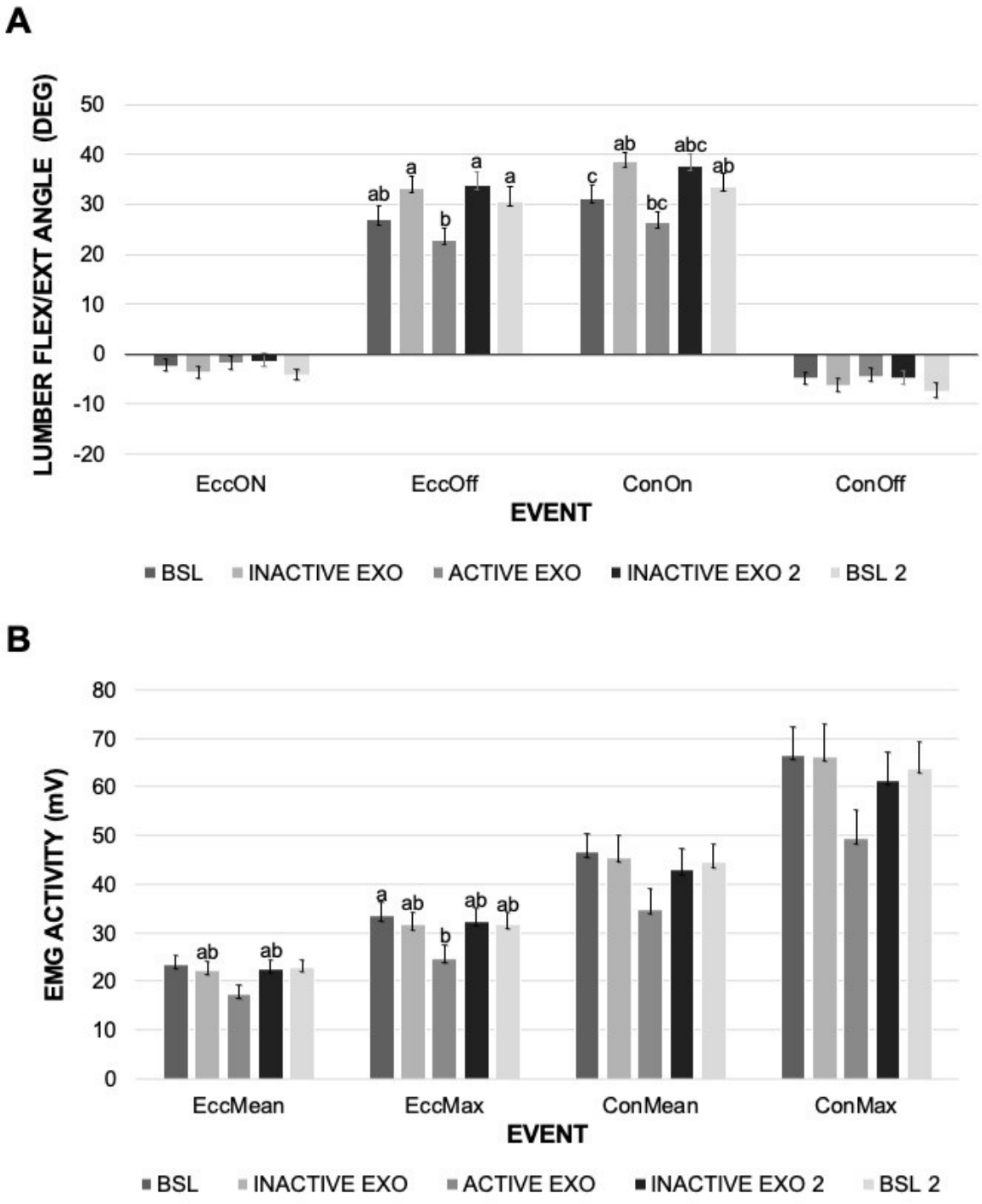
No significant differences existed in RPE ($p=0.1309$) and error in the rematching task ($p=0.6548$). Maximum flexion was significantly higher in both InactiveExo1 ($p=0.0085$) and

InactiveExo2 (p=0.0038) compared to the ActiveExo condition. Results for lumbar flexion/extension angle (Panel A) and EMG activation (Panel B) during FRP events are presented in Figure 1.

Discussion

The results suggest acute BSE use does not impact lumbar proprioception however does impact the FRP. The BSE results in a reduced capacity for trunk flexion, decreased muscle activation, and increased myoelectric silence of the paraspinals. This is likely due to the BSE offsetting gravitational torque, allowing the passive structures to support the mass of the trunk.

Images (Optional)



Session Category

Rehabilitation Biomechanics and Human Factors: Occupational Biomechanics

P2-273

Exploring Maximal Shoes as a Viable Intervention for Mitigating Low Back Pain During Prolonged Standing in Healthcare Professionals

Ms. Isabel Evans BKin[1], Dr. Jackie Zehr PhD[2], Dr. Jack Callaghan PhD[3], Dr. Kayla Fewster PhD[1]

[1]Western University, London, ON, Canada. [2]University of Toronto, Toronto, ON, Canada. [3]University of Waterloo, Waterloo, ON, Canada

Introduction

It is well established that approximately 50% of individuals are susceptible to acute low back pain (LBP) during prolonged standing [1], including healthcare workers [2]. Existing standing aids aimed at reducing standing-induced LBP, are typically immobile and thus impractical for this mobile population. Soft cushion maximal shoes were evaluated as a mobile standing intervention.

Methods

Twenty-one female healthcare workers completed a control shoe day and maximal shoe day. Non-destructive mechanical testing was completed to quantify sole mechanical properties [3]. On each day, five walking gait trials pre- and post-standing and a 75-minute prolonged standing trial were completed. EMG of bilateral trunk stabilizers, lumbar spine angle, and pain were monitored. An independent samples t-test evaluated any significant differences in shoe characteristics. A two-way repeated measures ANOVA was conducted across shoe type and time point (pre- and post-standing) to evaluate differences in gait. A hierarchical logistic regression model evaluated if any of the standing outcome variables significantly predicted the development of LBP.

Results

The maximal shoe (71.25 ± 0.33 N/mm) was significantly more compliant than the control shoe (100.72 ± 0.83 N/mm), $p<.001$. No significant differences were observed across gait trials for knee adduction moment (Maximal = 0.45 ± 0.13 Nm/kg; Control = 0.44 ± 0.13 Nm/kg; p =.49) or knee flexion angle (Maximal = 0.72 ± 6.61˚; Control = 0.10 ± 5.49˚; p=.54). In the hierarchical logistic regression, shoe type was the only significant predictor of LBP across standing variables (B = −2.38, SE = 1.14, p =.036). Maximal shoes reduced the risk developing LBP by 91%.

Discussion

In line with previous research, the more compliant material decreased LBP [4]. The mechanism for LBP reduction remains unknown as no other variables were significant pain predictors, prompting a secondary analysis into movement quality [5]. Given that LBP decreased and gait was not altered, maximal shoes could be considered an effective prolonged standing intervention for healthcare workers.

References (Optional)

[1] Nelson-Wong et al., *J E&K*, 2010.

[2] Karahan et al., *Journal of advanced nursing*, 2009.

[3] Worobets et al., *Footwear Science*, 2014.

[4] Anderson et al., *Footwear Science*, 2018.

[5] Gallagher & Callaghan, *HMS*, 2015.

Acknowledgements (Optional)

This project was funded through the Centre of Research Expertise for Prevention of Musculoskeletal Disorders (CRE-MSD).

We acknowledge the support of the Natural Sciences and Engineering Research Council of Canada (NSERC).

Session Category

Rehabilitation Biomechanics and Human Factors: Occupational Biomechanics

P2-274

Accumulation and Recovery of Prolonged Low-Frequency Force Depression and Force Stability at Different Intensities of Repetitive Isometric Contractions

Mr. Jared-Isaac Friedel MSc, BSc, Dr. Steven Fischer PhD, MSc, BSc

University of Waterloo, Waterloo, Ontario, Canada

Mr. Jared-Isaac Friedel

Introduction

Workers are still getting injured in the workplace despite peak loading being reduced, suggesting that MSDs may be impacted by lower intensity, yet frequent loading across days. Prolonged Low Frequency Force Depression (PLFFD), which is an alteration in submaximal muscle fibre firing, may be a possible explanation for this cross-day accumulation effect and may contribute to MSD risk. This research investigated whether PLFFD progressed differently between workload-matched protocols and whether PLFFD impacted task performance.

Methods

20 participants (9 males, 11 females) performed two repetitive isometric biceps flexion protocols one week apart. The protocols were four hours long and impulse-matched to expose the participants to the same total work ($N \cdot s$) at different force magnitudes and duty cycles. Participants performed the protocol in one-hour segments with a 15-minute break between each segment, followed by three hours of monitored rest. PLFFD (through transcutaneous muscle stimulation [1]), task performance metrics (through a force matching task [2]), and Maximum Voluntary Force (MVF) were measured intermittently throughout the protocol, rest hours, and on a follow-up visit and compared using ANOVAs.

Results

The protocols invoked a PLFFD effect that lasted to the next day (Table 1). The protocols invoked significant reductions in MVF that lasted for the 3 hours of rest, but not to the next day (Table 1). No significant differences between protocols were observed in PLFFD or MVF. PLFFD and MVF were both observed to be significantly correlated with reductions in task performance ($R^2 = 0.035$, $p < 0.001$ and $R^2 = 0.116$, $p < 0.001$ respectively).

Discussion

No protocol-specific effects were observed, suggesting that the progression of PLFFD within a muscle is independent of fibre type. Reductions in MVF over time more closely correlated with reductions in task performance when compared to PLFFD. Therefore, PLFFD may not have a substantial impact in the quality of occupational tasks, however muscle fatigue might. Future research investigating how muscle fatigue invoked from workload-balanced protocols impacts task performance may generate guidelines on how to facilitate optimal performance based on task requirements.

Images (Optional)

Table 1. Lo/Hi Ratio and Maximum Voluntary Force at baseline and during recovery. P-values are pairwise comparisons on the intervention arm relative to baseline.

Time Point	Lo/Hi Ratio		MVF (N)	
	Mean (SD)	P-value	Mean (SD)	P-value
Baseline	0.28 (±0.11)	-	278.3 (±90.1)	-
Post-Work	0.21 (±0.10)	0.001	251.4 (±82.5)	< 0.001
Post-Rest	0.20 (±0.09)	<0.001	263.2 (±91.4)	< 0.001
Follow-Up	0.23 (±0.10)	0.004	271.5 (±93.1)	0.081

References (Optional)

[1] Ruggiero L et al. , J of Applied Physiology, 2021
[2] Yacoubi B et al. , J of Applied Physiology, 2024

Session Category

Rehabilitation Biomechanics and Human Factors: Occupational Biomechanics

P2-275

Low and High Affordants Have Increased Risk for Musculoskeletal Disorders in a Simulated Baggage Handling Task

Dr. Jon Doan Ph.D., P.Eng., Mr. Dean Stewart, Dr. Hardeep Ryait Ph.D., P.Eng.

University of Lethbridge, Lethbridge, Alberta, Canada

Introduction

Airline baggage handling is an occupation associated with both musculoskeletal injury and affordance-rich task parameters like variable loads, alternative load couplings, some confined working spaces, and dynamic postures. The purpose of this research was to examine affordances and mechanics of handling in a simulated baggage handling task.

Methods

60 healthy adult participants (23.9 +/- 8.3 years, 36 F) were outfitted with static contrast markers on anatomical segment endpoints on their right side. Participants' feet were positioned in a defined floorspace 40 cm x 40 cm and 25 cm posterior from the centre of the suitcase target. Lateral distance to the centre of the suitcase target was set to 25% stature for each participant. Prior to mounting the suitcase, participants hoisted the load by the handle with their dominant hand to obtain a perception of mass (8 kg) and mass distribution (perimeter weighting, 57 L volume).

Participants were read the fixed script of a handling task that defined job plus task parameters. After the script, participants were instructed to chose the affordant vertical height that would "allow them to handle the bags as safely as possible without causing pain or discomfort". Each participant then completed 5 isometric handling trials at their affordant vertical height, and pulling force was recorded through the dynamometer (Lido WorkSet, Loredan Biomedical) while behaviour in the frontal plane was recorded. Video data were clipped and analyzed (DartFish TeamPro). Participants also completed a validated personality inventory.

Participants were post hoc sub-grouped by normalized affordant height into equal sized LOW, MODERATE, and HIGH affordant sub-groups. Group differences were tested with ANOVA, and significant group effects were further isolated using independent t-test.

Results

LOW, MODERATE, and HIGH sub-groups differed significantly on normalized vertical affordance for handling. These differences were manifest in significantly increased handling forces and lateral deflections amongst the LOW and HIGH groups. Simple personality typing did not explain sub-group differences.

Discussion

Perceived task performance is associated with occupational behaviours. Interventions that can modify perceptions, like physical literacy training and visual cues, may be more successful approaches to change occupational behaviours and control musculoskeletal demands.

References (Optional)

Acknowledgements (Optional)

Thanks to NSERC for funding and Montana State University for WorkSet device.

Session Category

Rehabilitation Biomechanics and Human Factors: Occupational Biomechanics

P2-276

Development and EMG Evaluation of a Spring–Actuator Module to Induce Cocontraction and Enhance Joint Stiffness in Laparoscopic Posture

Mr. Junyeol Choi MS Candidate, Prof. Ho Seon Choi Assistant Professor

Sejong University, Seoul, Seoul, Korea, Republic of

Mr. Junyeol Choi

Introduction

Laparoscopic surgeons must maintain the same posture for extended periods, and accumulated shoulder fatigue can reduce cocontraction and joint stiffness, ultimately decreasing task precision. To address this issue, we developed a spring–actuator wearable module designed to enhance shoulder joint stability even under fatigue-inducing conditions.

Methods

A spring–tube module was designed by inserting a spring inside a rubber tube to prevent lateral dispersion of elastic force during compression, and an additional elastic band was attached at the distal end to assist restoring force. This module was connected to a linear actuator that controlled spring compression and extension. Four modules were used in total—two placed over the anterior deltoid and two over the posterior deltoid. Surface EMG sensors were attached to both muscles to measure activation. The experimental task required maintaining 90° of shoulder abduction while flexing the elbow from 90° to 180° and repeatedly performing this movement for 30 seconds, a motion selected to include non-ideal ranges that may occur in laparoscopic procedures. MVC of both deltoid regions was measured individually based on the Manual Muscle Test (MMT), and muscle activation was compared across three conditions: without the device (T1), wearing the device without spring compression (T2), and wearing the device with spring compression (T3).

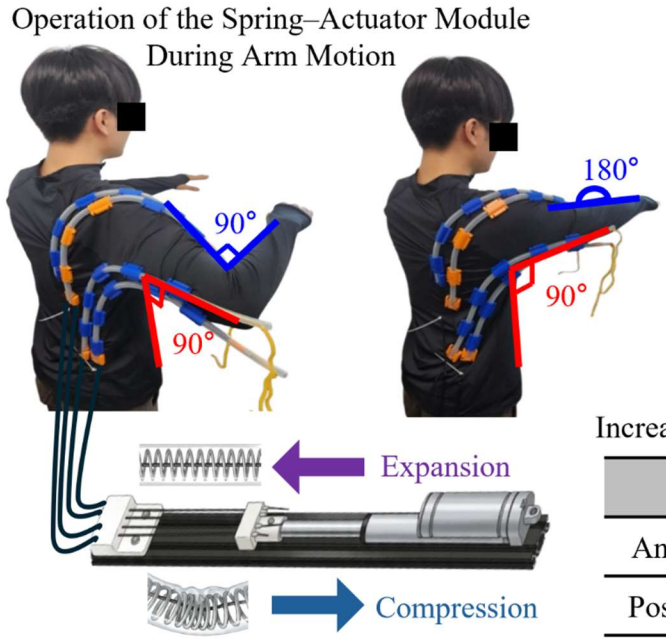
Results

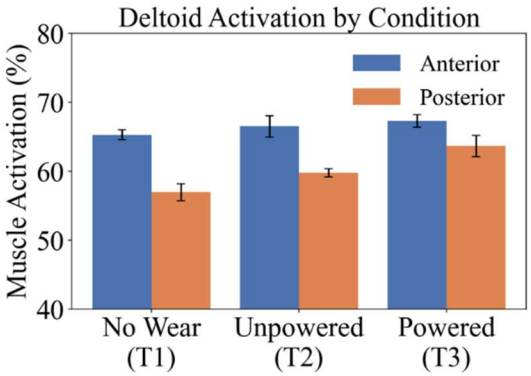
Compared with T1, muscle activation increased by 1.22% (anterior) and 2.80% (posterior) in T2, and by 1.99% (anterior) and 6.67% (posterior) in T3. These results indicate that spring compression increases mechanical resistance during movement, requiring greater muscle activation to perform the same task.

Discussion

Based on these findings, the additional mechanical resistance generated by spring compression is expected to physically reduce anterior–posterior shoulder sway. This suggests that even when fatigue reduces joint stiffness, activating the compression mechanism may artificially provide stability similar to increased cocontraction, thereby supporting posture maintenance during surgical tasks. Future work will involve determining optimal spring compression ranges through simulation-based motion analysis, integrating control algorithms into the actuator system, and conducting experiments with a larger participant group.

Images (Optional)





Increase in Muscle Activation Across Conditions

	T1 -> T2	T1 -> T3
Anterior	+1.22%	+1.99%
Posterior	+2.80%	+6.67%

Acknowledgements (Optional)

This project is currently supported by the National Research Foundation of Korea(NRF) grant funded by the Korea government (MSIT) (RS-2024-00452977). (Correspondance: choihoseon@sejong.ac.kr)

Session Category

Rehabilitation Biomechanics and Human Factors: Occupational Biomechanics

P2-277

Spine Posture and Movement in E-Sports Gamers during Computer Gaming

Ms. Kate Krivenko BSc, Ms. Jessa Davidson MSc, Dr. Jack Callaghan PhD

University of Waterloo, Waterloo, Ontario, Canada

Ms. Kate Krivenko

Ms. Jessa Davidson

Introduction

Computer gaming involves highly repetitive, fast, and precise upper-limb movements [1]. Nevertheless, the sport involves hours spent sitting which leads to neck and low back discomfort that is similar to that associated with computer work [1]. Gaming involves seemingly active behaviours in sedentary state, thus the objective of this study was to evaluate movement behaviours and metabolic demands in gamers playing computer games.

Methods

Sixteen e-sports gamers who were ranked in Valorant completed 20-minutes of osu! and Aimlabs, and one competitive game of Valorant in two gaming chairs (Embody and Titan Evo). Four tri-axial accelerometers were affixed onto spine and head to determine spine motion relative to individual standing posture (º) and range of motion (%). Lumbar spine postures (amplitude probability distribution function (APDF)) and micromovements (shifts and fidgets [2]) were evaluated. A portable metabolic system (MetaMax) was used to sample breath-by-breath gas exchange and ventilation at the mouth over steady state gaming.

Results

The spine postures showed limited variability across the APDFs, with the mean static (10%) and peak (90%) postures remaining within a 10° or 15% range. Participants performed 4 ± 4 shifts and 11 ± 3 fidgets over 20 minutes of gaming, with more fidgets in Aimlabs than osu! ($p = 0.018$). During Valorant, minute ventilation, was higher in Embody (11.3 L) than Titan (10.4 L, $p = 0.006$), likely from increases in tidal volume rather than breathing frequency.

Likewise, VO_2 and VCO_2 were also higher in Embody than Titan during Valorant ($p \leq 0.008$). The mean energy expenditure across chairs and games was 1.49 METs, indicating that computer gaming was sedentary.

Discussion

Lumbar micromovements and metabolic measures were consistent with sedentary computer work [2,3]. Increased upper limb motion in gaming did not translate to increased spine motion or metabolic demands. The current results demonstrate that e-sports gamers face similar health risks to sedentary office workers. Recommendations specific to the gaming environment such as active trunk support may mitigate those risks, while maintaining or even improving performance.

References (Optional)

[1] Antoine Dupuy *et al.*, Sports Biomechanics, 2024.

[2] Nandine M. Dunk & Jack P. Callaghan, Work, 2010.

[3] Jessa Davidson *et al.*, Work, 2025.

Session Category

Rehabilitation Biomechanics and Human Factors: Occupational Biomechanics

P2-278

Ground Reaction Forces During Locomotive Descent

Dr. Luis Nolasco PhD, Mr. Abdul Dannaoui, Dr. Natasha Vernooij PhD, Mr. Brian Weaver MS, PE

Explico Inc.,, Novi, Michigan, United States

Dr. Luis Nolasco

Mr. Abdul Dannaoui

Dr. Natasha Vernooij

Introduction

The forces associated with dismounting rail equipment are commonly claimed to cause workplace injuries in the freight rail industry. Previous research evaluated ground reaction forces (GRF) descending fire-fighting vehicles and heavy trucks [1,2], finding that facing the equipment reduced GRFs. The required height of 19” from the top of the rail for the last step of a switching locomotive results in a larger step to the ground compared to other vehicles. However, no previous research has quantified the impact forces experienced while descending locomotive steps. Therefore, the purpose of this study was to quantify these forces.

Methods

Twenty-one individuals (5F/16M; Avg. 28 years; 83.18 kg; 1.78 m) performed a ‘normal’ and ‘drop-down’ descent on replica locomotive steps with handrails (EMD SD40-2). Vertical and anterior/posterior forces were measured (1000Hz) for three trials per condition. Participants descended facing the steps, placing one foot on each step. The bottom step was 22.75” above the force plate. For the ‘normal’ descent,forces were measured on the last step and the floor. Drop-down descent: participants skipped the last step with their body-weight to carrying them from the last step to the floor.

Results

Normal descent: average GRF on the last step of the locomotive and the floor was 1 and 1.3 times body-weight, respectively (Figure 1). Drop-down descent: average GRF was 2.1 times body-weight.

Discussion

Normal locomotive descent had lower GRFs than standard stair descent [3], likely due to the support from the handrails. GRFs were lower than those from fire fighting vehicles and similar to heavy trucks, likely due to fire fighters added gear. However, the locomotive steps had a higher step compared to these other vehicles. GRFs were greatest when participants dropped to the floor by skipping the last step. However, these GRFs were similar to those of fast walking and running [4]. Thus, the impact forces while dismounting a locomotive are comparable to descending other vehicles and general, non-injurious activities.

Images (Optional)

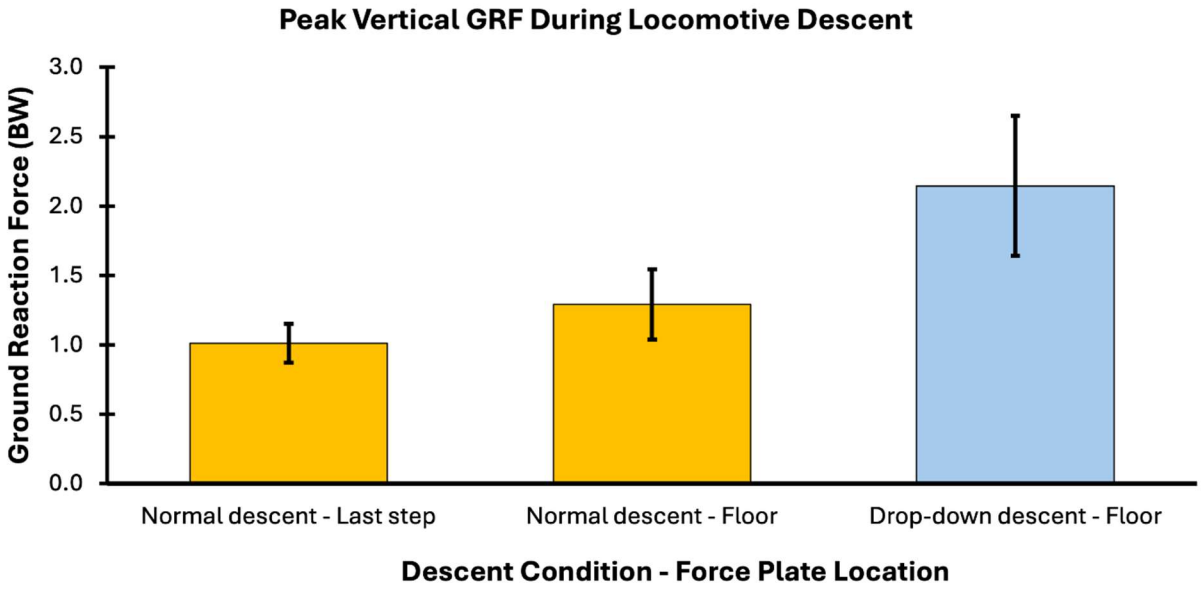


Figure 1: Peak Vertical GRF During Locomotive Descent

References (Optional)

[1]Denis Giguère, et al., *Applied Ergonomics*, 2005.

[2]Stephane Patenaude, et al., Applied Ergonomics, 2001.

[3]Alex Stacoff, et al., Gait Posture, 2005.

[4]Tony Keller, et al., Clin Biomech, 1996.

Session Category

Rehabilitation Biomechanics and Human Factors: Occupational Biomechanics

P2-279

Joint Loading in Patient Handling: Comparison With and Without Assistive Technology

Ms. Madison Holmes[1,2], Ms Michelle Léger[1,3], Ms Cynthia Dion[1,3], Dr Michelle Cardoso[3], Dr Wayne Albert[1]

[1]University of New Brunswick, Fredericton, New Brunswick, Canada. [2]Université de Moncton, Moncton, New Brusnwick, Canada. [3]Université de Moncton, Moncton, New Brunswick, Canada

Introduction

Manual patient handling [PH] is the leading risk factor for musculoskeletal injuries among healthcare workers, contributing to increased disability, lost work time, and risks to patient safety [1,2]. The Vendlet is an automated repositioning system that offers a potential solution.

The purpose of this study was to compare joint and spinal loading during patient repositioning tasks performed manually and with the Vendlet system.

Methods

Twenty-seven health science students aged 17 to 40 with no previous PH training received an in-depth expert training session on proper PH techniques. Participants performed two tasks: turning a patient onto their side and moving a patient horizontally in bed, both manually and using the Vendlet system.

A Qualisys motion capture system was used to record participants' movements, and Visual3D software was used to calculate joint angles. Following each repetition of the PH task, participants immediately replicated the hand force applied using a VALD DynaMo dynamometer. Hand forces and joint angles were used as inputs to an inverse dynamics biomechanical model to calculate joint and spinal forces. Statistical differences were assessed using Wilcoxon signed-rank tests.

Results

When turning a patient onto their side, the Vendlet system resulted in significantly lower: 1) mean and peak horizontal and vertical joint forces bilaterally at the wrist, elbow, shoulder, and trunk; 2) cumulative load at the left wrist, elbow and shoulder; and 3) mean and peak

shear and compression spinal forces. Manual techniques resulted in significantly lower cumulative loading at the right wrist, elbow, shoulder, and trunk.

When moving a patient horizontally in bed, the Vendlet system resulted in significantly lower: 1) mean and peak horizontal and vertical joint forces and cumulative load bilaterally at the wrist, elbow, shoulder, and trunk; and 2) mean and peak shear and compression spinal forces.

Discussion

Although the manual PH techniques were designed based on biomechanical principles, they still produced high joint forces and cumulative loads, exceeding recommended limits for peak shear and compression spinal forces. Compared to manual PH, the Vendlet repositioning system reduced joint and spinal forces, as well as cumulative loading.

Images (Optional)

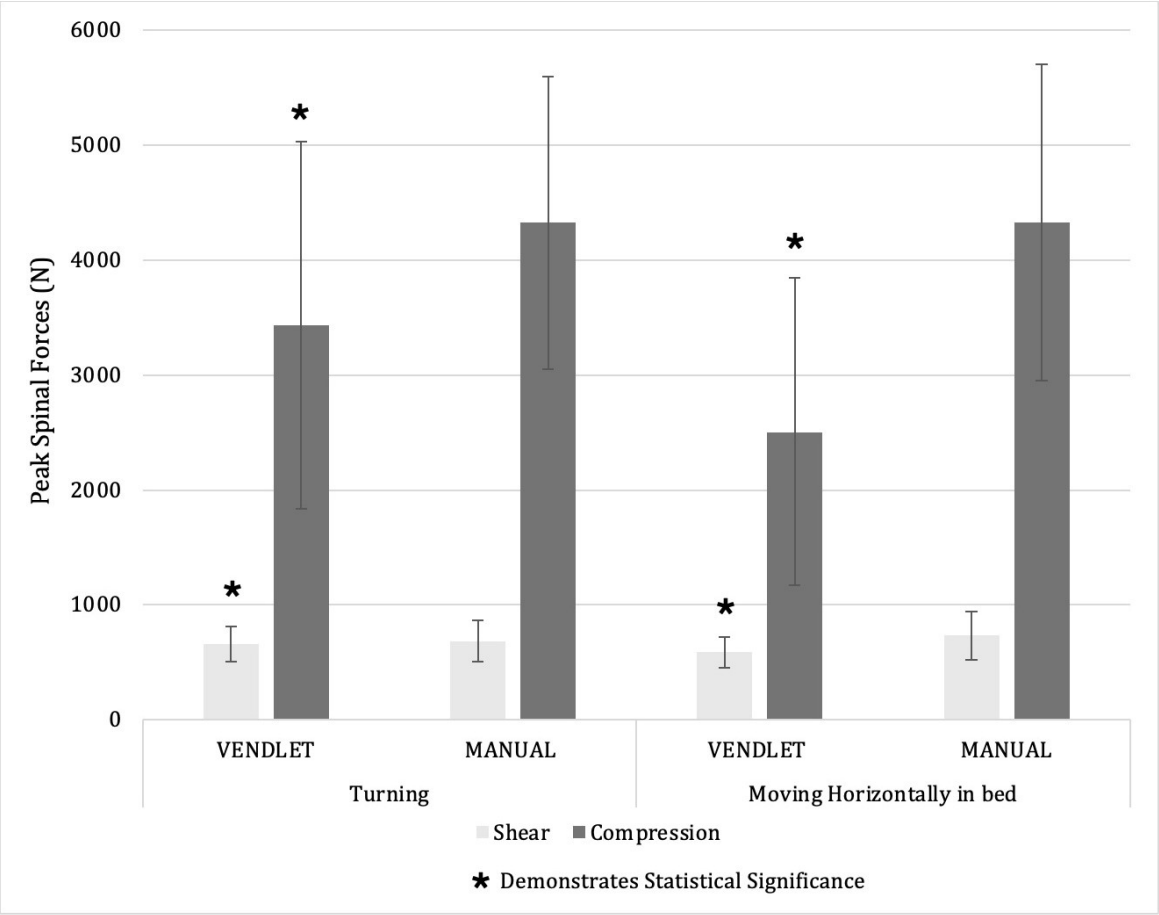


Figure 1: Peak spinal compression and shear forces while turning a patient onto their side and moving a patient horizontally in bed manually and with the Vendlet system.

References (Optional)

[1] Coggon et al., PLOS ONE, 2012

[2] Johnson et al., Physiotherapy, 2023

Session Category

Rehabilitation Biomechanics and Human Factors: Occupational Biomechanics

P2-280

Evaluating the Safety and Comfort of a Pediatric Upper Extremity Exosuit

Ms. Ipsita Sahin[1], Ms. Mehrnoosh Ayazi[2], Ms. Melanie Barahona[1], Dr. Konstantinos Karydis[2], Dr. Elena Kokkoni[1]

[1]Dept. of Bioengineering, University of California, Riverside, Riverside, CA, United States. [2]Dept. of Electrical and Computer Engineeringing, University of California, Riverside, Riverside, CA, United States

Introduction

Design considerations for assistive exosuits should consider safety and user comfort, as neglecting these factors can reduce device adoption [1]. While past studies have been conducted for exosuits developed and tested with adults, limited attention has been given to studying the safety and comfort of exosuits designed for young pediatric populations. This work assesses these parameters for a custom pediatric, upper-extremity pneumatic exosuit by evaluating exerted forces, combined with collecting user feedback.

Methods

Our approach is twofold. First, experiments were conducted on two 3D-printed test rigs to characterize the forces exerted by the soft, fabric-based, and pneumatic-powered actuators of the exosuit on parts of the rig that correspond to the forearm, upper arm, and torso segments. Each test rig incorporated two load cells to measure the normal contact forces exerted on actuator anchoring locations. Appropriateness of the generated forces was based on threshold values estimated from related literature: for an average body weight of a 12-month-old infant (10.80 kg), acceptable limits of force may vary from 43-184 N for each segment (i.e. 0.4-1.7 times the body weight) [2]. The second step includes collecting information from both infants (via assessing their facial expressions during use) and their caregivers (through questionnaires). Modified versions of the Comfort Rating Scale, System Usability Scale, and Technology Acceptance Model questionnaires were selected to measure the latter's perceptions of the fit and broader acceptance of the exosuit.

Results

Testing with the test rigs confirmed the safe operation of the exosuit's actuators, thereby supporting their functionality for pediatric exosuit design. All actuator variants generated peak forces between 4 and 32 N, which is below the estimated force comfort limits

established for the target pediatric population. This result supports safe deployment during experiments with pediatric users within this ongoing study.

Discussion

This work contributes to identifying force limits for the infant population, offers guidance on suitable actuator selection, and outlines a design framework for pediatric wearable robotic exosuits.

References (Optional)

[1] Attig et al., Comput Human Behav, 2020.

[2] Yandell et al., PLoS One, 2020.

Session Category

Rehabilitation Biomechanics and Human Factors: Occupational Biomechanics

P2-281

Identifying Overhead Work Zones: A K-Means Cluster Analysis of Maximum Acceptable Duty Cycles

Mr. Michael Watterworth PhD. Candidate, Dr. Nicholas La Delfa PhD.

Ontario Tech University, Oshawa, Ontario, Canada

Mr. Michael Watterworth

Introduction

Work-related musculoskeletal disorders are among the leading causes of global pain and disability, with the shoulder being one of the most frequently affected regions. Shoulder injury risk increases two- to threefold in jobs involving overhead work, prompting companies to restrict above-shoulder time (e.g., 33% at GM; 50% at Ford). Yet, despite widespread reliance on duty-cycle limits, existing ergonomics tools cannot directly estimate the Maximum Acceptable Duty Cycle (MADC) for a given overhead task.

Methods

The Above-Shoulder Tool was recently extended to estimate MADCs for specific force demands, directions, and hand locations. Using this new equation, an algorithmic case study examined how hand location and upward force affect MADC values in the sagittal plane. Posturing of a 50th-percentile female model throughout their viable reach envelope was performed with three constraints: neutral wrist–forearm alignment, movement restricted to the vertical plane, and an upright trunk. Z-score–normalized MADCs were clustered using K-Means (k = 7) to identify common overhead-work zones. Force demands were incrementally increased from arm weight alone until only one overhead zone remained at a 33% duty-cycle threshold.

Results

The K-Means clusters aligned with established ergonomic risk patterns, identifying zones where overhead posture and increased joint moments elevate fatigue and injury risk. Mean MADC was substantially lower at or above shoulder height (17%) compared to below the shoulder (60%). Two clusters showed particularly low MADCs (Figure 1): (1) outstretched exertions at or above shoulder height, which had the second-lowest MADC (10%) due to large moment arms (Dark Green), and (2) high overhead reaches, which had a median

MADC of 0%, indicating no acceptable duty cycle for a 5 N upward exertion (Light Blue). Conversely, an optimal overhead zone was identified where limiting work to 33% of the cycle would be acceptable (Dark Blue).

Discussion

These findings highlight the potential of posture-specific MADC estimates to improve job design, duty-cycle limits, and placement of overhead work. However, results are constrained by the model's simplified assumptions (fixed postures, standardized anthropometry and strength), limiting generalizability to all workers. Future research should perform an experimental validation of the model to refine this approach for applied ergonomics.

Images (Optional)

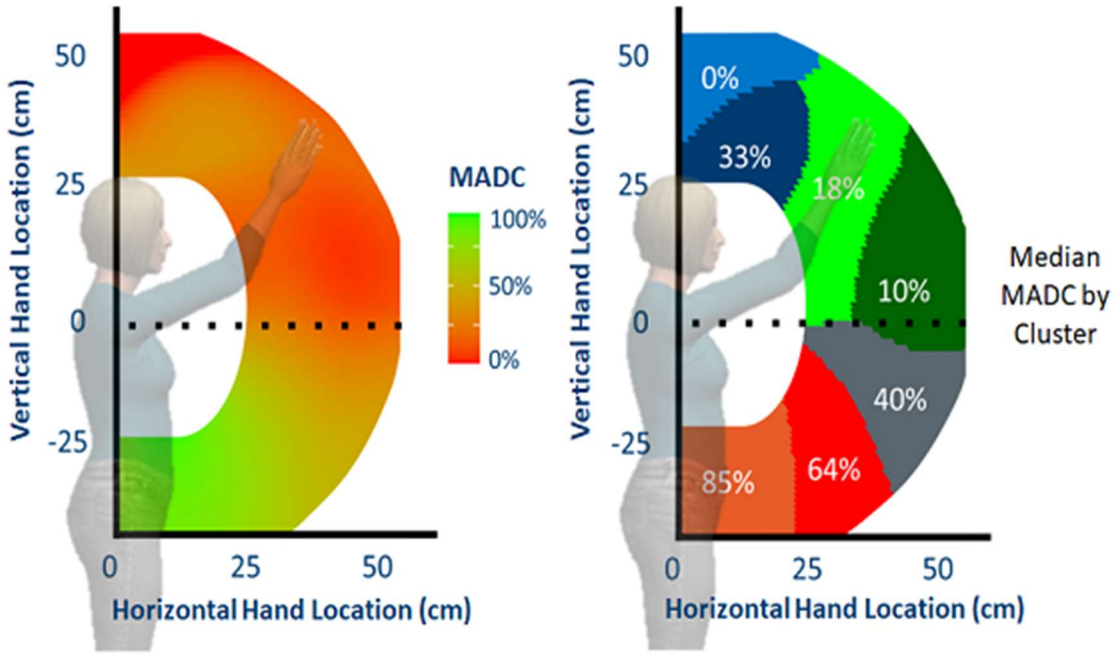


Figure 1: MADC predictions in the sagittal plane of the shoulder for a 5 N upwards exertion.

Session Category

Rehabilitation Biomechanics and Human Factors: Occupational Biomechanics

P2-282

Effects Of New Technology on Healthcare Workers' Posture During Patient Handling

Ms Michelle Léger[1], Ms Madison Holmes[1], Ms Cynthia Dion[1], Dr. Wayne J. Albert Dr.[1], Dr. Michelle R. Cardoso Dr.[2]

[1]University of New Brunswick, Fredericton, NB, Canada. [2]Université de Moncton, Moncton, NB, Canada

Introduction

Patient handling (PH) is one of the leading causes of workplace injuries among healthcare workers (HCWs) and represents a substantial proportion of their patient care activities[1]. Consistent safe PH practices are often hindered by barriers such as bariatric patients, staffing shortages, insufficient training, and work-related stress[2].

The objective of this study was to compare health care worker postures during PH techniques performed manually and with the Vendlet technology.

Methods

Sixteen HCWs aged 22-59 years were recruited for this laboratory-based study. Participants visited the laboratory both before and after their 8-hour work shift. Prior to data collection, they received training on two PH techniques: turning a patient (Technique-Turn) and moving a patient towards the bed's edge (Technique-Side),

manually and with the Vendlet technology.

Kinematic data were collected using a Qualisys motion capture system, coupled with the Theia software, to quantify the joint angles of the head, shoulders, elbows, wrists, hips, pelvis, knees, and trunk-pelvis (flexion/extension, lateral bend, and rotation). Joint angle data were normalized to 101 points. A Wilcoxon signed-rank test with a within-subject comparison was conducted on five participants to compare peak joint angles for both PH techniques, using the Vendlet versus manual techniques under pre- and post-work shift conditions. All sixteen participants will be processed and analyzed for WCB.

Results

For Turn, when using the Vendlet pre- and post-shift, participants had significantly lower peak values for the following joint angles: head, left hip, left shoulder, pelvis, right hip, right knee, and right shoulder.

For Side, when using the Vendlet pre- and post-shift, the participants had significantly lower peaks for the following joint angles: head, left shoulder, pelvis, right hip, right wrist, and trunk-pelvis.

No significant patterns were observed for lateral bend and rotation for both techniques.

Discussion

The Vendlet technology resulted in lower overall joint peak angle values, indicating that it led to more neutral postures compared to manual techniques. The Vendlet is a technology that has the potential to reduce work-related injuries and promote a safer work environment.

Images (Optional)

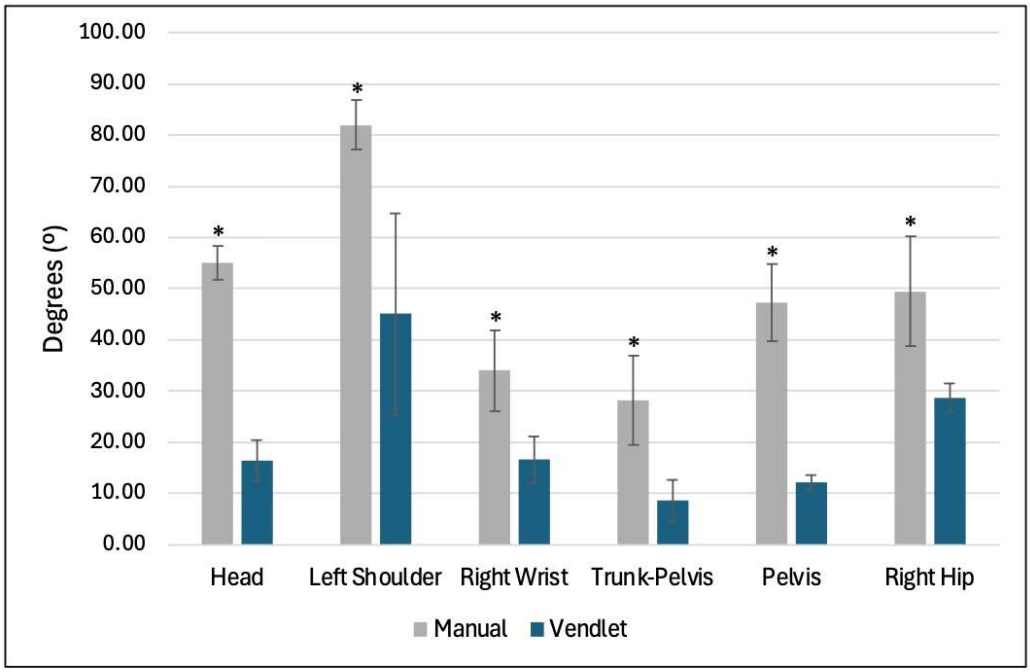


Figure 1: Significant peak joint angles for the technique: moving a patient to the edge of the bed (Side), post-shift. No statistical significance were found for the right shoulder, right elbow, left elbow, right wrist, left hip, right knee and left knee.

*Indicates Significance

References (Optional)

"[1] Menzel et al., International Journal of Nursing Studies, 2004"

"[2] Galinsky et al., Applied Ergonomics, 2021

Session Category

Rehabilitation Biomechanics and Human Factors: Occupational Biomechanics

P2-283

Single-Image Ergonomic Assessment: User-Selected vs. App-Derived Workstation Configurations

Mr. Ryan Chhiba[1], Ms. Diana Gillstrom[2], Dr. Peter J. Keir[1]

[1]McMaster University, Hamilton, ON, Canada. [2]Ellustros, The Blue Mountains, ON, Canada

Introduction

The use of ergonomic office devices and furniture is ubiquitous, yet workstation setup often falls short of recommended guidelines. Recommended setup helps prevent user discomfort and decreases the risk of developing injuries and disorders [1]. Office guidelines are important yet misunderstood by a large proportion of workers. An individual's preferred workstation setup may be deemed comfortable but may not be ergonomically appropriate. The objective of this study was to quantify differences between user-selected workstation configurations and those recommended using an AI-based ergonomic application.

Methods

Participants were asked to set up an office workstation consisting of a chair, desk and monitor. They adjusted settings such as seat and arm rest height, as well as desk and monitor heights. Using the tros.ai application (Ellustros, The Blue Mountains, Canada), an ergonomically defined setup was calculated using participant height and anatomical landmarks taken from a photo of the individual [2]. Differences between the self-selected and ergonomically appropriate workstation heights were determined.

Results

Preliminary results from 20 participants show the mean self-selected seat height (40 cm) was lower than the ergonomically defined height (43 cm). Self- selected arm rest height and desk height (68 cm, 73 cm) were higher than those determined from the app (60 cm, 61 cm). Self-selected monitor height (120 cm) was higher than the calculated height (118 cm). Figure 1 shows the mean difference between the self-selected and ergonomically (app) defined setups. Further analyses will include more participants to capture a diverse range of anthropometrics and working populations.

Discussion

Identifying discrepancies between self-selected and ergonomically determined workstation setups can identify which workstation parameters heights may be driving user discomfort. This work will inform ergonomic interventions in the office workspace and help

educate workers to decrease risk of work-related injury. Additionally, this app provides an accessible method for generating individualized ergonomic recommendations from a single image, offering a scalable tool for improving workstation setup. The results from this study suggest that individual workstation interventions may be effectively and efficiently incorporated by using a smartphone.

Images (Optional)

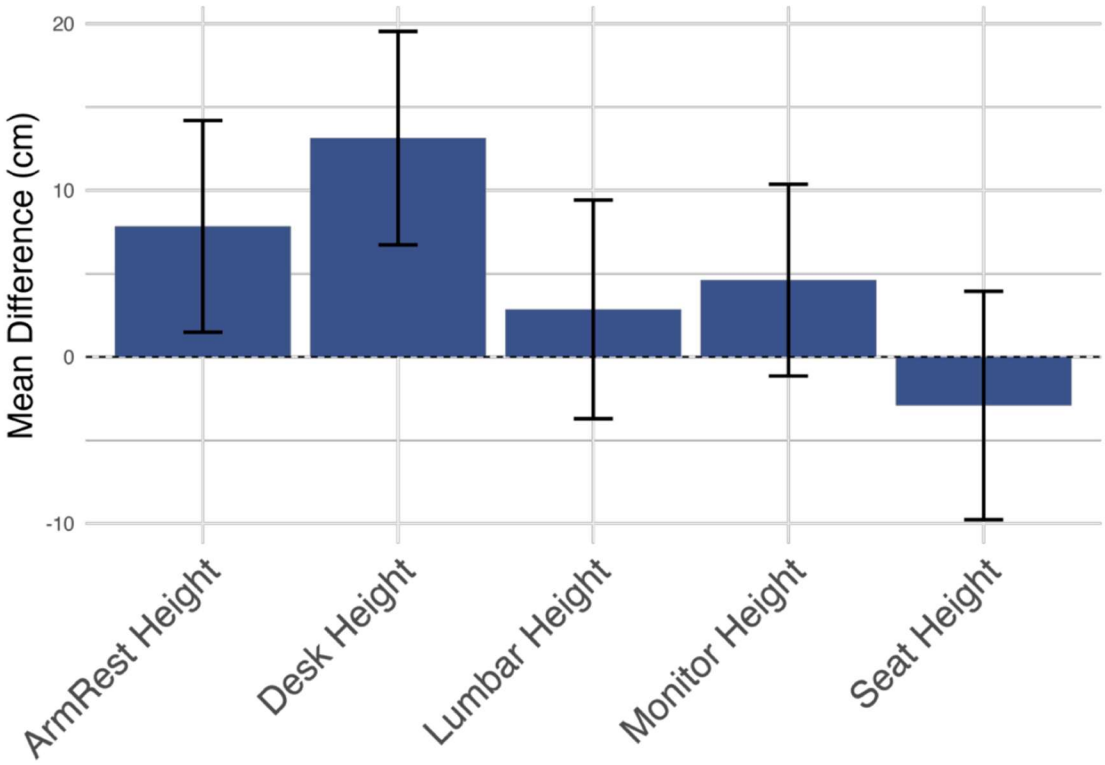


Figure 1. Mean difference (cm) between the self-selected and ergonomically defined setup. Positive mean difference indicates a higher self-selected height compared to ergonomically derived heights. Negative mean difference indicates a lower self-selected height compared to ergonomically derived heights. Error bars represent the standard deviation of mean difference (cm).

References (Optional)

[1] Robertson, M., et al., *Applied Ergonomics*, 2009. [2] Pheasant, S. *Bodyspace: Anthropometry, Ergonomics and the Design of Work*, 2018.

Acknowledgements (Optional)

This study is funded through the MITAC Business Internship Program

Session Category

Rehabilitation Biomechanics and Human Factors: Occupational Biomechanics

P2-284

Influence of Work Demands and Organization on Upper Limb Motor Variability During Repetitive Pushing

Mr. Ryan Chhiba, Ms. Joanna M. Misquitta, Dr. Peter J. Keir

McMaster University, Hamilton, ON, Canada

Introduction

Prolonged repetitive upper limb tasks are leading causes of workplace musculoskeletal disorders [1]. While true repetition repeatedly stresses the same tissues, the neuromuscular system can generate multiple movement solutions for the same task through motor redundancy, or abundance [2], which may be a protective strategy to prevent overuse injuries [3]. Little is known about the modulation of motor variability in response to task demands such as frequency and force. While most studies use a fixed cadence, many jobs are quota-driven, requiring a prescribed amount of work in a specified time. This study aims to evaluate how task demands (force, frequency, work organization) influence motor variability.

Methods

Participants completed eight randomized 5 minute upper limb pushing trials at the same workload under varied conditions. EMG, motion data, potentiometers, and rated perceived exertion captured motor variability, task accuracy and effort. Data was segmented to capture cycle-to-cycle variability. A model tested main effects of Force (2 kg/4 kg), Frequency (low/ high), Work Organization (set pace/ quota), and interactions.

Results

Preliminary analysis of ten participants are presented. The average cycle-to-cycle median absolute deviation of upper limb muscle activity during the low force, low frequency and the high force, high frequency tasks are presented in Figure 1. Higher force and frequency work conducted at a set pace had higher variability, whereas quota driven work at lower force and lower frequency demands had increased variability. Further analyses will include kinematics, performance and perceived effort to better elucidate how motor variability is modulated by word demands.

Discussion

Motor variability in relation to work demands may not depend solely on task intensity but also work structure. Larger variability in muscle activation during the high force high frequency set pace conditions suggest motor redundancy may prevent muscular fatigue

and preserve performance. Participants completed the low force low frequency condition faster than set pace, indicating self-paced movements likely elevate motor variability. By integrating neuromuscular control theories, with occupational injury mechanisms this study aims to improve our understanding of upper extremity function to provide insights into the potential risk of dysfunction.

Images (Optional)

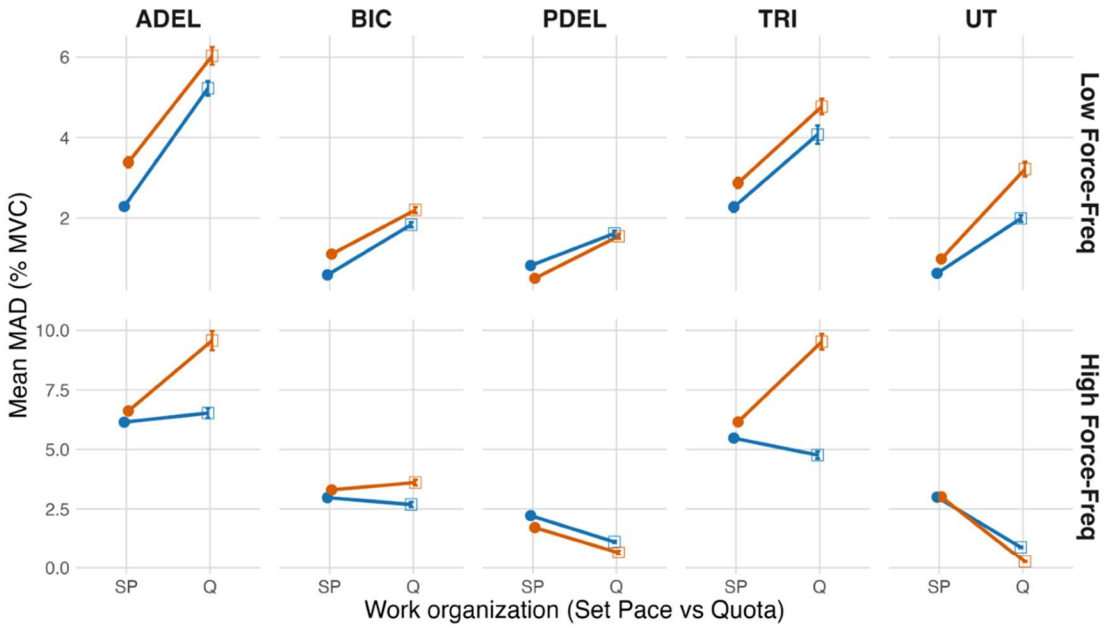


Figure 1. Mean cycle-to-cycle median absolute deviation (MAD) of muscle activity (% MVC) during Set Pace (SP - circle) and Quota (Q – square) work organizations. Muscles include, left (blue) and right (orange) anterior deltoid (ADEL), biceps (BIC), posterior deltoid (PDEL), triceps (TRI) and upper trapezius (UT). Top row = low frequency, low force condition, bottom row = high force, high frequency condition.

References (Optional)

[1] Keir, Human Factors, 2021 [2] Bernstein, 1967 [3] Srinivasan, Clinical Biomechanics, 2012

Acknowledgements (Optional)

This research was funded by the Natural Sciences and Engineering Research Council of Canada (NSERC Discovery Grant RGPIN-2023-05473) and the Centre of Research Expertise For the Prevention of Musculoskeletal Disorders Seed Grant.

Session Category

Rehabilitation Biomechanics and Human Factors: Occupational Biomechanics

P2-285

Can Acute Abdominal Bracing and Hip Motion Coaching Reduce Lumbar Spine Flexion Angles and Extensor Moments During Lifting?

Ms. Sadie Finch CAT(C), Dr. Jordan Cannon PhD

University of Waterloo, Waterloo, Ontario, Canada

Ms. Sadie Finch

Introduction

High magnitudes of lumbar spine flexion while lifting reduces the failure tolerance of the lumbar spine, alters load distribution across tissues, and compromises extensor muscles' capabilities to resist anterior shear forces; and is linked to greater low back injury risk [1]. During lifting tasks, increasing lumbar spine stiffness (via abdominal bracing) and redistributing motion and load demands to the hips may reduce low back demands. This study sought to determine if an acute abdominal bracing and hip motion coaching intervention prior to lifting could redistribute flexion motion and extensor moments from the lumbar spine to the hips.

Methods

Full-body kinematics and ground reaction forces were collected on 14 female university athletes. Bottom-up inverse dynamics calculated lumbar spine and hip moments. Floor-to-waist lifting and lowering tasks were performed pre- and post-coaching intervention with two load conditions: light (1kg) and heavy (15kg). An acute coaching intervention was implemented while participants performed quadruped rock backs, focussing on isolating the lumbar-pelvis-hip linkage to minimize lumbar spine motion and maximize hip flexion, via abdominal bracing and hip-driven cueing. Two-way repeated measures ANOVAs examined the effects of time, load, and their interaction, on peak flexion angles and extensor moments of the lumbar spine and hip.

Results

Peak lumbar spine flexion was significantly reduced post-intervention in both light and heavy conditions. Peak lumbar spine extensor moment was significantly reduced in the light but not heavy condition. Contrary to our hypothesis, peak hip flexion angles were

unchanged following the intervention while peak hip extensor moment decreased in the light but not heavy condition.

Discussion

An acute coaching intervention in a simplified, constrained task was able to reduce lumbar spine flexion motion during floor-to-waist lifting. However, lumbar spine changes were not facilitated by changes in hip motion. This suggests motion demands were distributed across other joints spanning the lower and upper extremities. Lower lumbar extensor moments only in the light condition suggest a moment distribution strategy lacking capacity for heavier demands. Small effect sizes limit practical significance but indicates potential utility in extending the coaching to a short-term intervention program to facilitate implementation of new movement solutions.

Images (Optional)

Table: Peak angle and moment differences [and percent change] from pre-to-post intervention for the lumbar spine and hips. A positive (negative) value represents an increase (decrease) in post- compared to pre-intervention.

	Light Load		Heavy Load	
	Angle (°)	**Moment (Nm)**	**Angle (°)**	**Moment (Nm)**
Lumbar Spine	-5 [-12%]	-16 [16%]	-4 [-10%]	-5 [3%]
Hip	4 [4%]	-6 [8%]	1 [1%]	-6 [5%]

References (Optional)

[1] Stuart McGill, JEK, 2004

Session Category

Rehabilitation Biomechanics and Human Factors: Occupational Biomechanics

P2-286

Effects of Lifting Task and Infant Weight on Lumbopelvic Muscle Activity, Kinematics, and Kinetics in Nulliparous Women

Dr. Safeer Siddicky Ph.D.[1], Dr. Kathryn Havens Ph.D.[2]

[1]The University of Texas at Austin, Austin, TX, United States. [2]University of Southern California, Los Angeles, CA, United States

Dr. Safeer Siddicky

Introduction

Infant caregiving involves frequent lifting, yet the biomechanics of these tasks remain understudied. Prior work in postpartum individuals shows that lift type and context influence movement patterns and loading [1,2], but baseline mechanics of nulliparous adults remain unknown. Establishing these patterns across common caregiving tasks and varying infant weights is important for identifying potential musculoskeletal risks. We therefore examined how lift type and infant weight affect trunk and lower-limb muscle activity, kinematics, and kinetics in nulliparous individuals.

Methods

Seven healthy nulliparous women (29.8 ± 3.1 years; 1.7 ± 0.1 m; 68.9 ± 12.0 kg) completed three semi-continuous lifting tasks (floor lift, car-seat lift from floor, and changing-table lift; Fig.1) using a newborn manikin (3.23 kg) and a weighted 3-month-old manikin (6.17 kg). 3D kinematics (150 Hz; Qualisys), ground reaction forces (1500 Hz; Bertec), and EMG (1500 Hz; Noraxon) were collected and processed in Visual3D and MATLAB. Descriptive statistics are reported.

Results

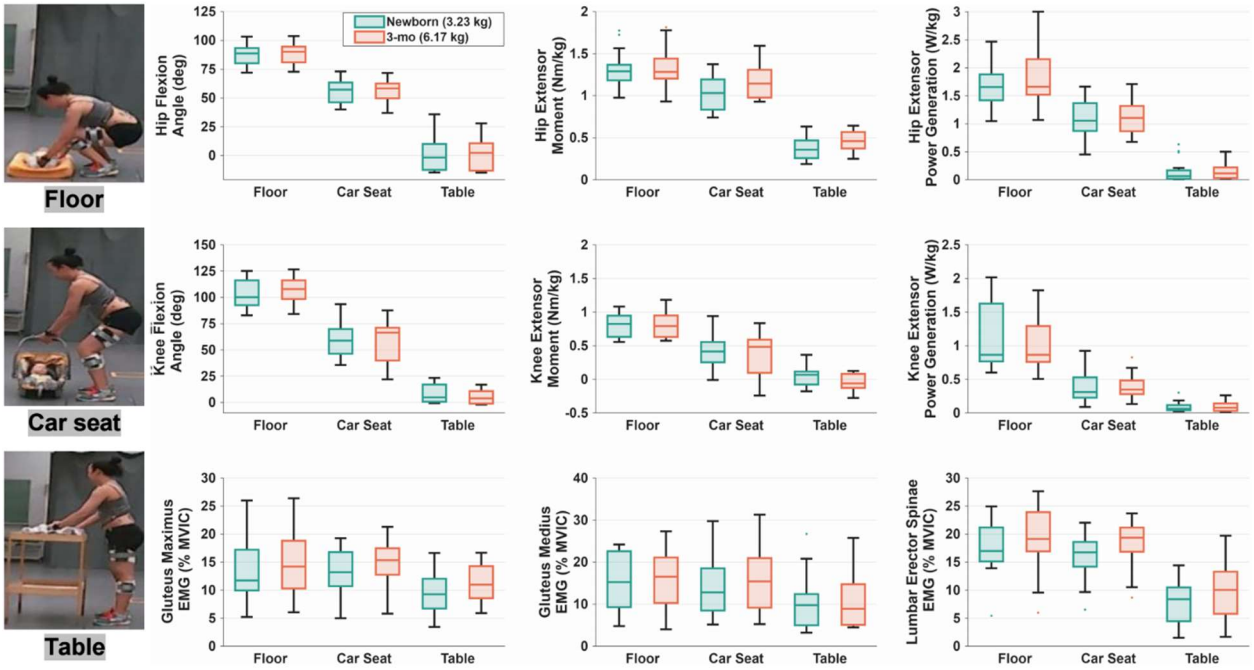
Lumbopelvic EMG and sagittal hip and knee mechanics were altered with task demand and infant weight. The floor lift required the greatest hip and knee flexion, extensor moments, and extensor power generation, along with the highest gluteus medius and lumbar erector spinae activation (Fig.1). Lifting from the changing table involved minimal hip and knee involvement and the lowest activation for all muscles. Lifting infants in a car seat introduced unique constraints due to the additional weight. The elevated handle height reduced lower-extremity flexion compared to the floor task, while producing the highest

gluteus maximus activation. Increasing infant weight increased activation across all muscles and variably affected joint moments. Hip extensor moments notably increased, while knee extensor moments remained largely unchanged [3].

Discussion

These findings highlight the demands of caregiving lifting tasks, and suggest biomechanical adaptations required as infants grow. As caregiver lifting demands continue into children's school-age years, the biomechanical differences observed with a modest ~3 kg increase are likely to become even more pronounced when lifting progressively larger loads. Future work will explore task-specific asymmetries and compare lifting mechanics with postpartum mothers.

Images (Optional)



References (Optional)

[1] Havens & Siddicky, J Biomechanics, 2025, [2] Havens *et al.*, J Applied Biomechanics, 2023, [3] Kim *et al.*, Technol Heal Care, 2022.

Session Category

Rehabilitation Biomechanics and Human Factors: Occupational Biomechanics

P2-287

The Effects of Driving and Whole-body Vibration on Upper Body Posture

Ms Sara Sagen BSc, Dr. Angelica Lang PhD

University of Saskatchewan, Saskatoon, Sk, Canada

Introduction

Farm machinery operators are frequently exposed to whole-body vibration (WBV), contributing to musculoskeletal discomfort and altered postures during prolonged work. Although WBV is commonly associated with low-back pain, it is also an important risk factor for neck and shoulder pain, possibly due to amplified vibration at the head [1]. This increased transmission highlights the need to understand upper-extremity responses to WBV, which could further contribute to neck or shoulder injury. The objective of this study was to assess if simulated WBV exposure influenced driving postures over a 60-minute exposure.

Methods

Thirty participants (9 neck/shoulder pain; 6 asymptomatic) completed two 60-minute driving simulator sessions: stationary (non-WBV) and vibration (WBV). Upper-body joint angles were recorded using inertial measurement units; the mean joint angles were analyzed in 10-minute blocks, adhering to the International Society of Biomechanics standards. A mixed repeated-measures ANOVA was conducted with condition, joint and pain group as factors.

Results

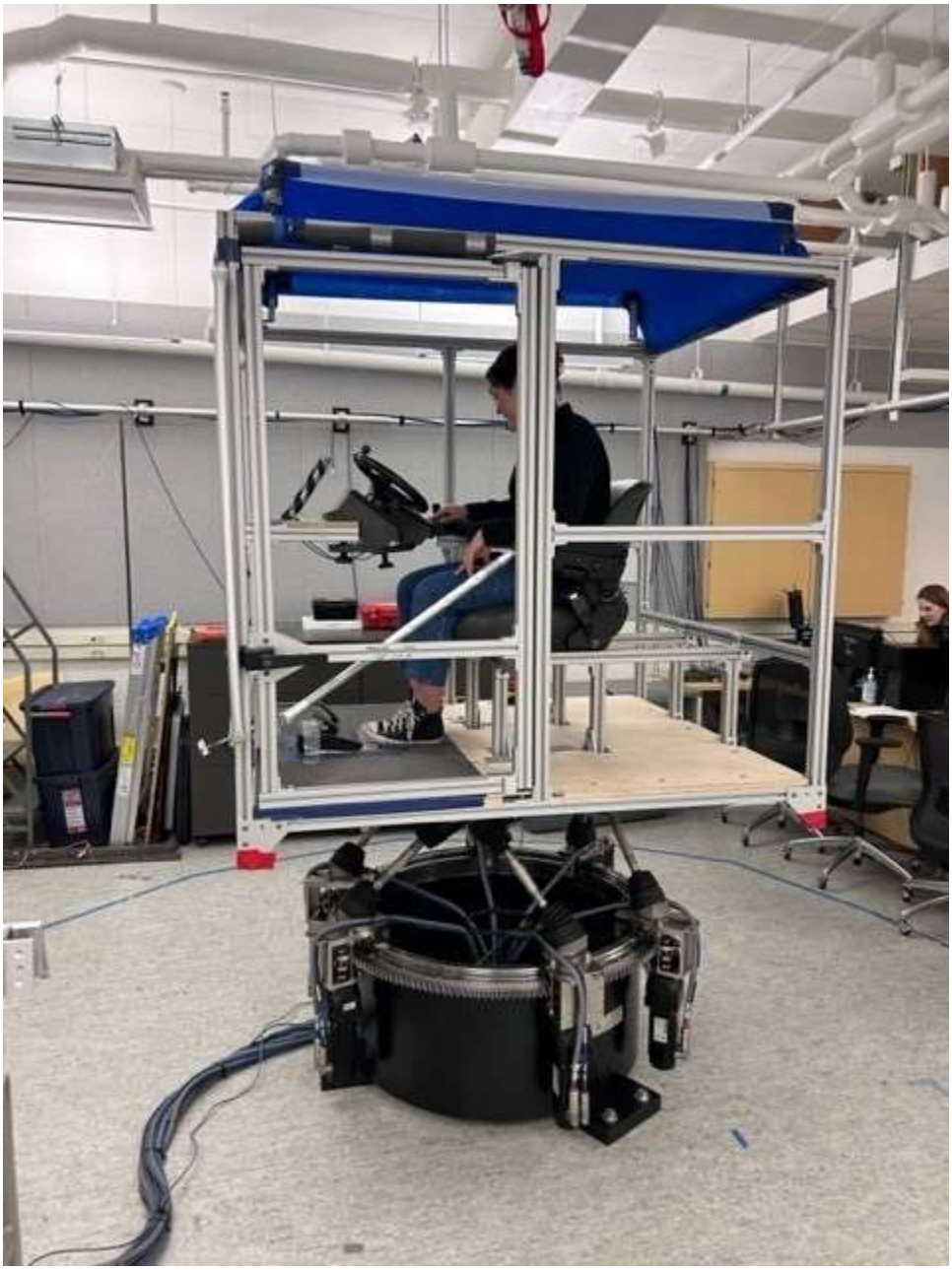
WBV significantly altered joint angles only during the first 10 minutes. Compared with non-WBV, WBV increased neck rotation (+36.2°, $p < .001$), left humeral flexion (+28.3°, $p < .001$), and right elbow pronation (+24.8°, $p = .010$), while decreasing right humeral flexion (–34.3°, $p < .001$) and right humeral rotation (–33.8°, $p < .001$). At minute 20, only the right elbow pronation increased and persisted under WBV (mean +31.7°, $p=.008$). No WBV-related differences were observed beyond 20 minutes. The pain group did not influence postural responses.

Discussion

These preliminary findings indicate that WBV produces early deviations in upper-limb posture that diminish after the first 10 minutes, likely reflecting a habituation response in which the nervous system reduces upper-body stabilizing corrections as vibration becomes predictable. This pronated elbow posture may reflect participants using a rigid

forearm position to brace the upper body and stabilize the steering wheel. Together, these results suggest that early WBV exposure elicits postural adjustments that consolidate into localized distal stabilization strategies over time. Full-sample analysis will examine in-depth how WBV and postural changes influence the development of discomfort over the driving period.

Images (Optional)



References (Optional)

[1]Kociolek, A., et al.,(2018). Exploring head and neck vibration exposure from quad bike use in agriculture

Session Category

Rehabilitation Biomechanics and Human Factors: Occupational Biomechanics

P2-288

Validation of Accuracy of an IMU-Based Machined Learning Classification Model for Detecting Injurious Patient Transfers in Healthcare Providers

Dr. Seyoung Lee PhD[1], Dr. Kitaek Lim PhD[1], Dr. Ohyun Kwon PhD[1], Dr. Chunghwi Yi PhD[1], Dr. Gwi-Ryung Son Hong PhD[2], Dr. Woochol Joseph Choi PhD[1]

[1]Yonsei University, Wonju, Kangwon, Korea, Republic of. [2]Hanyang University, Seoul, Seoul, Korea, Republic of

Introduction

Lower back injuries are common in healthcare providers, with frequent patient transfers recognized as a contributing factor [1,2]. Inertial measurement units (IMUs) are increasingly used as practical tools for analyzing movements related to injury risk [3,4], and IMU-based, injurious patient transfer detection system has recently been developed with young adults [5,6]. The objective of this study was to validate the accuracy of this system with healthcare providers.

Methods

Ten healthcare providers performed bed to wheelchair transfers while wearing five IMU sensors placed on both forearms, both upper arms, and the waist (Figure 1). Trials were acquired with different knee assist techniques, patient body masses, and manual versus mechanical lift. Transfers were classified as injurious when a compressive force at L5/S1 exceeded 3,400 N. A total of 95 trials (75 injurious and 20 non-injurious transfers) were used to test accuracy of the developed model. To address class imbalance, the training set was up-sampled. A nonlinear SVM with an RBF kernel (LIBSVM) [7] was optimized via grid search and five-fold cross-validation. Eighteen features (mean and variance of tri-axial acceleration, linear and angular velocities) were extracted from IMU signals. Model performance was evaluated across five sensor configurations and 25 combinations of lead time and window size.

Results

Depending on the sensor configuration, the accuracy for distinguishing injurious from non-injurious patient transfers ranged from 85.0% to 86.4%, while specificity ranged from 54% to 58%. Sensitivity remained consistently high at 100% across all configurations (Table 1).

Discussion

Our findings suggest that the IMU-based, injurious patient transfer detection system demonstrates potentials for practical use among healthcare providers in real-world settings. Specificity remained consistently low (54-58%) across all sensor and temporal parameter combinations, indicating that mean- and variance- based IMU features effectively detect injurious patterns but have limited ability to characterize non-injurious transfers.

Images (Optional)

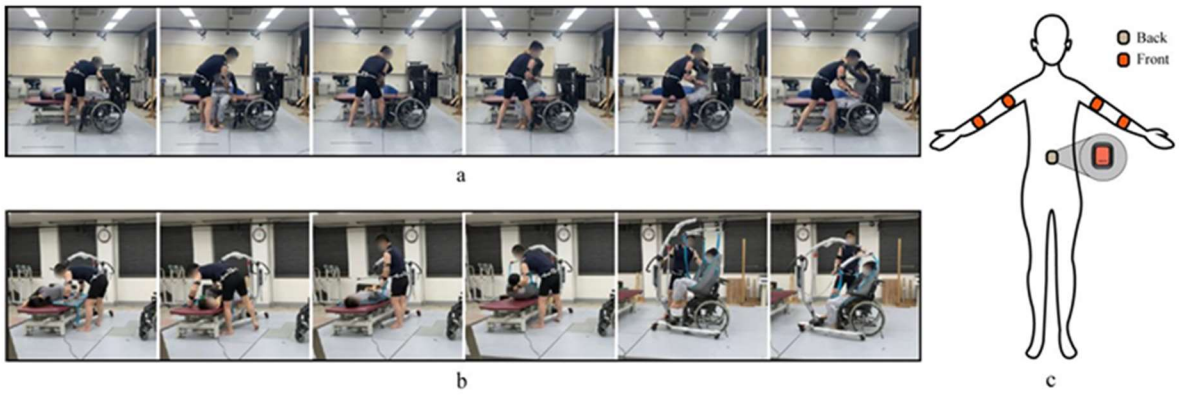


Figure 1. Patient transfer from bed to wheelchair. Participants transferred a patient (a) manually, and (b) with a mechanical lift while wearing (c) IMU sensors.

Table 1. Performance comparison of an SVM-based classification model for distinguishing injurious and non-injurious patient transfers

Location of sensors	window size/ lead time combination	Accuray (%)		Sensitivity (%)		Specificity (%)	
		Young adults	Healthcare providers	Young adults	Healthcare providers	Young adults	Healthcare providers
Waist	0.1s/ 0.1s;	100	86.4	100	100	100	58
	0.3s/ 0.3s;	100	86.4	100	100	100	58
	0.4s/ 0.3s;	100	85	100	100	100	54
	0.5s/ 0.3s	100	86.4	100	100	100	58
Both forearm	0.4s/ 0.3s	97.5	85	100	100	78.6	54
	0.5s/ 0.1s	97.5	86.4	100	100	78.6	58
Both arm	0.4s/ 0.3s	98.3	85	100	100	83.3	54
Both forearm + arm	0.3s/ 0.2s	99.2	85.7	99.1	100	100	56
	0.5s/ 0.1s	99.2	86.4	100	100	100	58
Waist + Both arm	0.2s/ 0.2s	99.2	86.4	100	100	90.9	58

References (Optional)

[1] Rezaei et al., Ann Med Surg, 2021, [2] Andersen et al., Scand J Work Environ Health, 2014, [3] Kobsar et al., J Neuroeng Rehabil, 2020, [4] Zhong et al., IEEE IoT J, 2021, [5] Lee et al., J Appl Biomech, 2024, [6] Lim et al., J Back Musculoskelet Rehabil, 2025, [7] Chang & Lin, ACM TIST, 2011

Acknowledgements (Optional)

This work was supported by the “Brain Korea 21 FOUR Project” (F21SH8303039), the National Research Foundation of Korea (NRF) grant funded by the Korea government (MSIT) (RS-2025-16071808), and by the Regional Innovation System & Education (RISE) program through the Gangwon RISE Center, funded by the Ministry of Education (MOE) and the Gangwon State (G.S.), Republic of Korea (2025-RISE-10–006).

Session Category

Rehabilitation Biomechanics and Human Factors: Occupational Biomechanics

P2-289

Evaluation of Musculoskeletal Human Models for Overhead Tasks With Shoulder Exoskeleton–a Preliminary Study.

Ms Shantha Sindhu Pudhota, Dr David Scherb, Prof Robert Weidner

Technische Universität Bergakademie Freiberg, Freiberg, Sachsen, Germany

Introduction

Overhead manual tasks elevate glenohumeral loading and rotator cuff fatigue, increasing the risk of work-related musculoskeletal disorders. Occupational exoskeletons mitigate these demands by applying external supportive torque to reduce shoulder loading. Due to the biomechanical influence of exoskeleton support, musculoskeletal human models are often used to simulate these effects, which enables the derivation of design implications and support adjustments. However, current models are not specifically designed for exoskeleton interaction, leading to high variability in simulation. Therefore, the aim is to develop a musculoskeletal human model in OpenSim specifically designed for simulations with shoulder exoskeletons; this preliminary study involves the initial evaluation of different created models using defined use cases.

Methods

Three healthy participants execute two standardized tasks (overhead drilling and bilateral overhead lifting) under unsupported and exoskeleton-supported (exoIQ S700) conditions. Data acquisition included whole-body kinematics and surface electromyography(sEMG) of the upper body musculature. Three created OpenSim musculoskeletal human models are used to simulate the biomechanical effects of the exoskeleton support for each participant. Model suitability is assessed by comparing the simulations results with captured data (e.g. muscle activation) and literature findings (e.g. joint reaction forces).

Results

The results demonstrate consistent directional effects across models: reductions in predicted deltoid and rotator cuff activity and lower glenohumeral joint reaction forces in the exoskeleton condition. Nonetheless, considerable variability is observed between models, primarily in the timing and magnitude of muscle activation and differences in the size of the simulated exoskeleton stress-reduction effect (Figure 1). One model proved most accurate and stable, consistently producing smoother muscle activity results, confirming its greater suitability for simulating human-exoskeleton interaction.

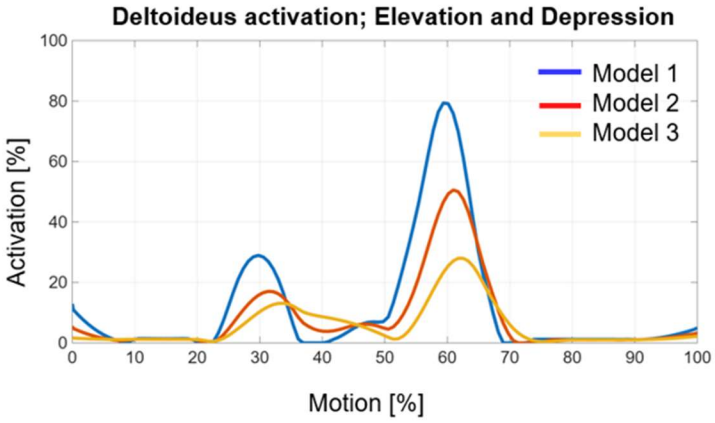
Discussion

The study indicates that while all evaluated models capture the expected unloading effect of the exoskeleton, their simulation fidelity varies substantially. This preliminary work has provided valuable insights by identifying models capable of better replicating the biomechanical behavior of human-exoskeleton support systems. This identification is essential for designing the forthcoming large-scale study, which will encompass an expanded user group, additional task types, and multiple exoskeleton configurations. The present findings provide the methodological foundation and initial selection criteria for future validation of the most suitable model for systematic exoskeleton simulation.

Images (Optional)







Session Category

Rehabilitation Biomechanics and Human Factors: Occupational Biomechanics

P2-290

Worker Perception and Lifting Behaviours in Hospital Laundry Handling

Ms. Teresa Lau[1,2], Dr. Carolyn Sparrey[1,2]

[1]Simon Fraser University, Surrey, British Columbia, Canada. [2]International Collaboration on Repair Discoveries (ICORD), Vancouver, British Columbia, Canada

Ms. Teresa Lau

Introduction

Overexertion is the leading cause of musculoskeletal injuries among hospital workers, accounting for nearly half of all injury claims in British Columbia and costing over $172 million in the last ten years [1]. While laundry handling is not traditionally classified as high-risk, hospital support staff routinely perform lifts involving awkward postures and unpredictable loads. Current ergonomic guidelines recommend a safe lifting limit of 5-6 kg for two-handed lifts [2]. However, real-world hospital demands may not always reflect these assumptions. This study characterized the biomechanical demands and perceptual biases of laundry bag handling among non-laundry healthcare staff to identify system-level contributors to overexertion risk.

Methods

27 hospital support aide workers participated in an observational task analysis and a structured load perception activity. Common lifting behaviors were noted during naturalistic observation sessions, and the weight of handled laundry bags were recorded. In the perception activity, participants estimated pre-weighed laundry bags presented in two conditions: tied bags on the floor and untied bags in standard hospital hampers. Descriptive statistics summarized weight perception trends and general lifting behaviours.

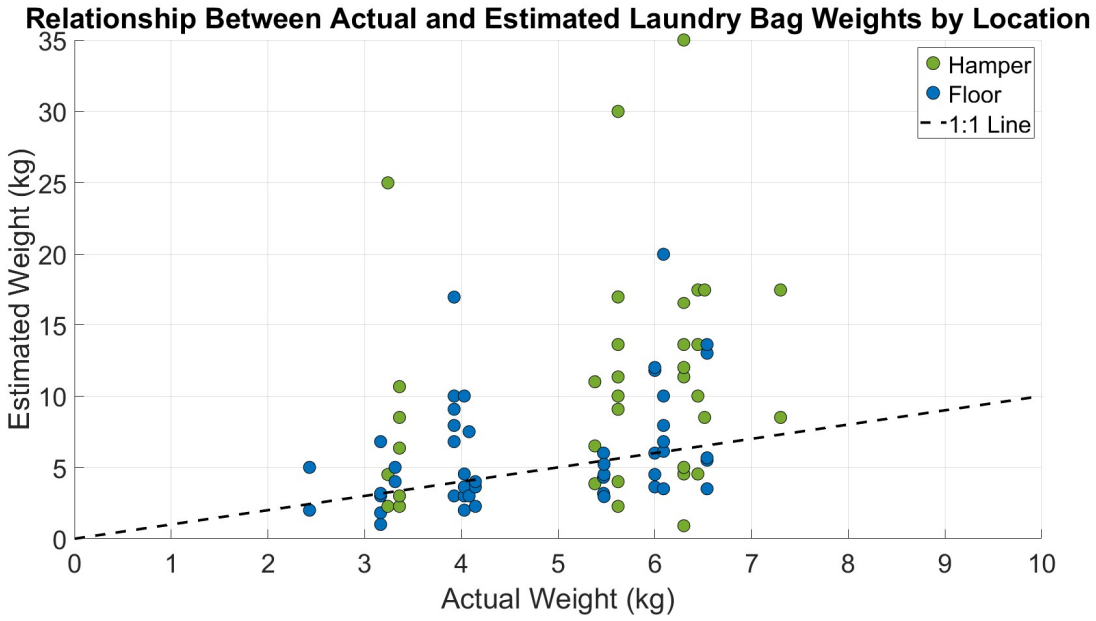
Results

Across all participants, laundry bags placed inside hampers were systematically overestimated. Bags in hampers showed an average error of approximately +100%, while bags on the floor showed smaller but consistent overestimation. Most bags handled during observation sessions weighed under 3 kg, below the safe lifting limit. Of those lifts, approximately 73% involved semi-stooping, asymmetrical, or one-handed postures, and these patterns were consistently observed across multiple sessions.

Discussion

The results show a clear mismatch between actual and perceived laundry bag weight, particularly for bags stored in hampers without clear load indicators. Participants also commented that bags “looked heavier than they actually feel,” aligning with the overestimation trends observed. These perceptual mismatches may influence how workers approach lifting tasks and help explain the frequent use of non-neutral postures, despite handling lighter loads. This behaviour contrasts assumptions in standard ergonomic guidelines for two-handed lifts, highlighting a gap between standard guidance and real-world practice. Addressing system-level factors, like improving hamper design and load transparency, could help reduce overexertion risk.

Images (Optional)



References (Optional)

[1] WorkSafeBC, 2025

[2] Erin Teeple *et al.,* New Solut., 2017

Acknowledgements (Optional)

This research was generously supported by WorkSafeBC, and the research team thanks the hospital support staff who contributed their time and insights to this study.

Session Category

Rehabilitation Biomechanics and Human Factors: Occupational Biomechanics

P2-291

Load-Displacement Behavior of Running Specific Prostheses: In-Vivo vs Machine Testing

Mr. Abed Khosrojerdi M.Sc., Dr. Isaac Kumi Ph.D., Ms. Paige Agnew M.Sc., Dr. Amit Kulkarni Ph.D., Dr. Hunter Bennett Ph.D., Dr. Stacie Ringleb Ph.D.

Old Dominion University, Norfolk, Virginia, United States

Mr. Abed Khosrojerdi

Dr. Isaac Kumi

Ms. Paige Agnew

Dr. Hunter Bennett

Introduction

The design and mechanical properties of running specific prostheses (RSPs) influence athletic performance. The only guidance given on how to select the best RSP is simply based on the user's mass. Researchers have investigated mechanical properties using laboratory testing. However, standard machine testing does not load RSPs the same way they are loaded in-vivo. The objective of this study was to compare load–displacement behavior of RSPs measured in-vivo during running with values obtained from a material testing machine.

Methods

Three individuals with lower limb amputations (two transtibial, one transfemoral) wearing RSPs rated for their mass (small, medium, and extra-large) participated in the study. Participants ran at self-selected pace over an 18m walkway. Data were acquired using a 12-camera Vicon system with three synchronized force plates. Prosthesis deformation during stance was quantified during loading and unloading phases. Peak ground reaction

force (GRF) and load-displacement curves were derived from force plate data using custom MATLAB code (R2023a, MathWorks, Inc.).

An MTS machine applied a load equivalent to twice the minimum and maximum manufacturer-specified weight the RSPs at a rate of 6 mm/s. Load-displacement curves were generated using custom MATLAB code.

Results

Hysteresis curves from in-vivo and MTS testing demonstrated similarities in loading for the transtibial amputees (Figure a and c). The in-vivo and laboratory testing were dissimilar in unloading. Specifically, unloading showed more hysteresis for all participants, possibly because the MTS machine loaded and unloaded vertically, while in-vivo data included loading through the motions of the stance phase.

Discussion

All prostheses displayed hysteresis loops indicating energy dissipation. In the transfemoral amputee, the behavior was not similar to the MTS in loading or unloading. This difference may be due to the additional influence on dynamics from the computerized knee. Thus, the energy return of RSPs is difficult to predict with the MTS machine for transtibial amputees, and material testing may not provide insight into the behavior of RSPs for transfemoral amputees. Future studies should include a larger, more diverse participant cohort with various amputation types and adjust MTS loading rates to better simulate in-vivo deformation rates during running.

Images (Optional)

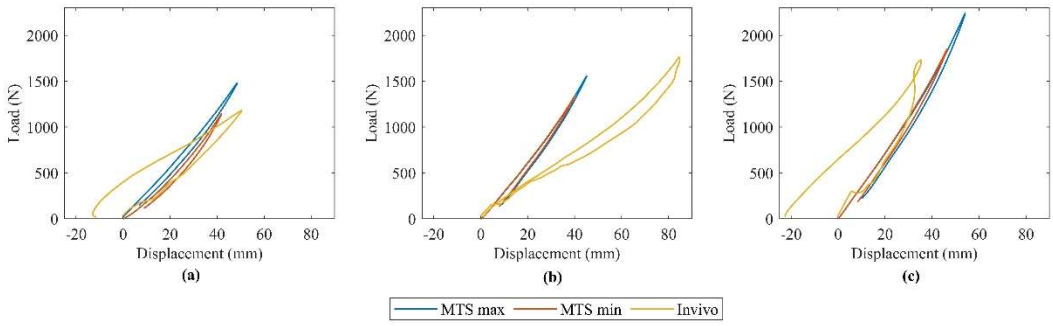


Figure. Load-displacement hysteresis curves for running-specific prostheses: (a) Small (transtibial), (b) Medium (transfemoral), and (c) Extra-large (transtibial). Blue lines represent maximum manufacturer-specified weight tolerance, red lines represent minimum weight tolerance, and yellow lines represent in-vivo measurements obtained during running.

Session Category

Rehabilitation Biomechanics and Human Factors: Rehabilitation

P2-292

Enhancing Upper Extremity Rehabilitation's Engagement & Quality in Children with Cerebral Palsy by Integrating BCI-HABIT-VR: A Feasibility Study

Ms. Mobina Masaei, Dr. Ahad Behboodi

University of Nebraska at Omaha, Omaha, Nebraska, United States

Introduction

Cerebral palsy (CP) is the most prevalent neurological disorder, permanently altering motor function, and frequently produces upper-limb deficits that constrain function. Hand and Arm Bimanual Intensive Therapy (HABIT) has demonstrated efficacy in improving manual ability in this population, but is often limited by task repetitiveness and reduced participant engagement. Brain-Computer Interface Neurofeedback Training (BCI-NFT) is another strategy coupling cortical motor signals with contingent sensory feedback (e.g., neuromuscular electrical stimulation (NMES)) to augment cortical activation and drive neuroplasticity. This study introduces BCI-HABIT-VR, a novel, gamified upper limb rehabilitation approach that integrates BCI-NFT with the HABIT-VR framework to enhance engagement and therapeutic outcomes in children with CP, using participant feedback as the primary outcome. This is the first BCI-NFT camp for children with CP.

Methods

Four children with hemiplegic or diplegic CP (ages 10-14) participated in a two-week intensive VR camp comprising 40 total training hours. During each session, participants wore a VR headset and an EEG cap while engaging in the BCI-HABIT-VR game. The primary task involved extending the more affected arm to target aliens and propel a virtual rocket, during which NMES was applied to the extensor digitorum communis to assist movement. Continuous EEG was processed to detect motor intention; detection events triggered closed-loop NMES applied to the extensor digitorum communis to assist volitional movement. Each participant completed at least 50 task repetitions per day with BCI-mediated NMES activation (BCI-NFT). Feasibility and user experience were assessed after each session using a 7-point questionnaire developed by the clinical team.

Results

Questionnaire responses indicated 'Game Fun' received the highest score (M=6.34), while 'EEG Comfort' was the lowest (M=3.61), below the midpoint of 4 (Figure 1). Other metrics scored in the moderate-to-high range.

Discussion

In this small cohort, BCI-HABIT-VR proved deliverable within an intensive camp and was well received, notably enhancing game-based engagement- an important mediator of adherence in repetitive upper-limb therapies. Suboptimal EEG comfort underscores the necessity for improved cap ergonomics and tolerability prior to broader implementation. These preliminary findings support feasibility and warrant further investigation in larger, controlled trials emphasizing both efficacy and hardware optimization.

Images (Optional)

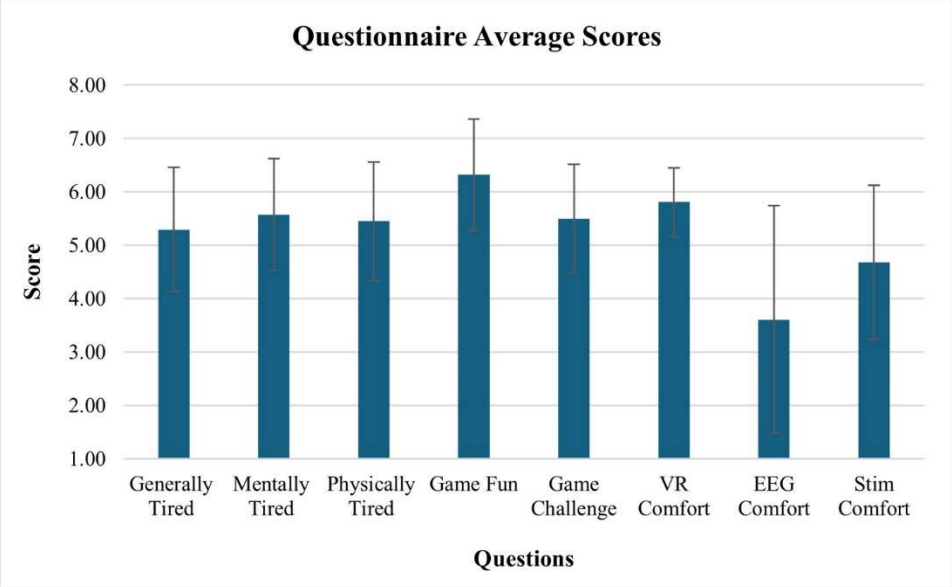


Figure 1. Items on the questionnaire assessed general, mental, and physical fatigue, as well as their enjoyment of the game, its difficulty, and their comfort with the VR headset, EEG cap, and stimulus. Mean scores and standard deviations for each item on the questionnaire across all subjects. Participants rated their experience after each day on a 7-point scale across categories related to tiredness, game experience, and comfort with the equipment. The results indicate a positive reception for game-related items and a lower comfort level with the EEG cap.

References (Optional)

Session Category

Rehabilitation Biomechanics and Human Factors: Rehabilitation

P2-293

Biomechanical Evaluation of a novel Dental Implant Design

Dr. Ahmed Fouda, Dr. Ludger Keilig, Dr. Christoph Bourauel

University Hospital Bonn, Bonn, NRW, Germany

Introduction

Recent advancements in implant technology have led to a wide range of dental implants available on the market. A crucial factor that influences the success of dental implants is the stability of the implant-abutment interface. An unstable connection can create micro-gaps at the interface, leading to microbial leakage and potential biological complications. To overcome the biological complications caused by an unstable implant-abutment interface, a new implant design featuring an external conical connection was developed. This design aims to establish a stable, gap-free junction between the implant and either titanium abutments or abutment-free restorations. The objective of this study is to evaluate the microleakage and micromovements at the Implant/Suprastrucure Junction under load.

Methods

An experimental conical connection design between the implant and suprastructure was proposed and prototypes were produced from titanium alloy. Two suprastructures were tested: Titanium Abutment (TiAbt) and Zirconia Abutment-free crown (ZrAbt-free). For the micromovement test, 20 implants were produced (n=10), patterned, and mounted to a universal testing machine (Zwick) then loaded from 0-200N with step size of 25N. A 3D Aramis scanner system was used to record micromotion under load. The angle between the implant and suprastructure was calculated using Direct Image Correlation on GOM software (Zeiss, Switzerland). A total of 12 specimens were used for the microleakage test (n=6) . The implants were drilled up to the screw level and connected to a peristaltic pump and blue dye reservoir. The test setup and procedures are explained in Figure 1.

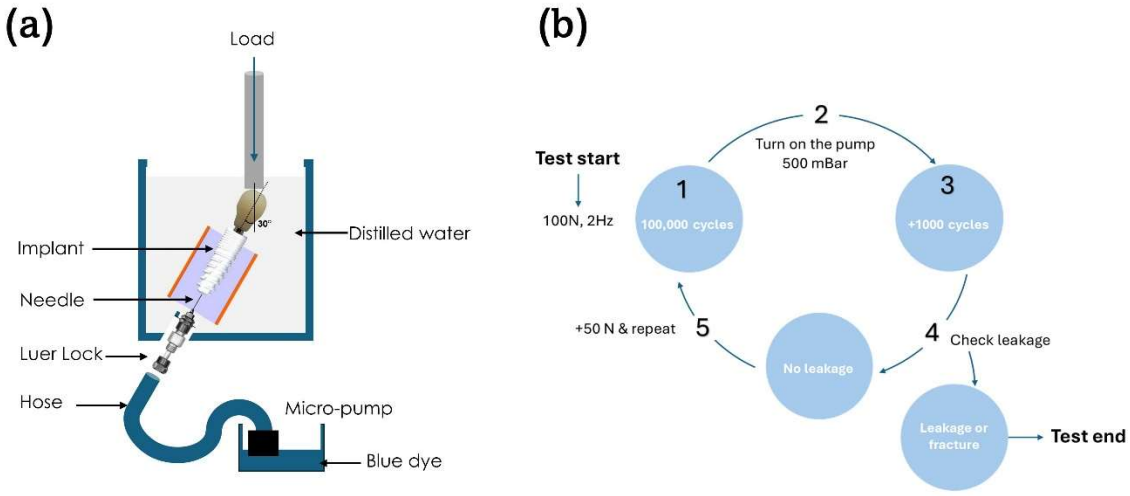
Results

The mean deviation angle between implant and ZrAbt-free crown was 0.14 ±0.06 degree at 25N and 1.97 ±0.36 degree at 200N, while for the TiAbt group, it was 0.02 ±0.01 degree at 25N and 0.58 ±0.1 degree at 200N. The microleakage results revealed that all the specimens showed no leakage under loading. The mean failure force of TiAbt group was 300N, while ZrAbt-free group had mean fracture force of 200N.

Discussion

The experimental implant design showed a stable junction between implant and suprastructure in both tested groups. The connection to Ti abutment was more stable than Abutment-free Zirconia. In the future, the design will be tested with different material combinations.

Images (Optional)



References (Optional)

Acknowledgements (Optional)

This work was supported by grant from the Zentrales Innovationsprogramm Mittelstand (ZIM). We would like to thank Mr. Evers-Dietze from Hochschule Bonn-Rhein-Sieg for providing support by the Aramis scans.

Session Category

Rehabilitation Biomechanics and Human Factors: Rehabilitation

P2-294

Mechanical Evaluation of a Novel Dynamic Shoulder Orthotic for Post-Stroke Subluxation

Miss Aliki Statiri, Dr. Angela Kedgley

Imperial College London, London, UK, United Kingdom

Introduction

Shoulder subluxation is a prevalent secondary complication for stroke survivors, affecting 17-81% of that population [1]. Treatment may include physiotherapy, FES, and external supports. Dynamic shoulder orthotics utilise elastic components to realign and support the glenohumeral joint (GHJ). This study aimed to assess the performance of a novel device featuring springs of different stiffness in 1) offloading the GHJ and 2) achieving unrestrained movement during the range of motion (RoM) typical of activities of daily living.

Methods

A custom-made orthotic was fit to a model shoulder that allowed 2 cm inferior subluxation (Figure 1a). The RoM was defined as 0-70° in both flexion and abduction [2]. A linear actuator created arm elevation. A loadcell was used to assess if the device impeded movement by measuring the force required to rotate the arm through the RoM. A second loadcell measured the vertical force on the arm across the RoM to determine the support provided by the device. Ten repetitions of four conditions were tested: three springs (k=0.416, 0.51, 1.019 N/mm) and no device (control).

Results

The device was fully weight-bearing from 0-30° flexion (Figure 1b) and 0-55° abduction (Figure 1c) for all springs. For the remaining RoM, partial weight bearing was found, except for the stiffest spring for 50-70° flexion (Figure 1b). The device did not impede the motion in any testing condition, as the horizontal elevation force matched the control throughout the RoM.

Discussion

The most compliant springs provided the best overall support. The reason was that arm rotation led to a decrease in spring deformation. This explains why softer springs can provide partial support for the whole range, whereas stiffer springs, which required smaller deformation to carry the weight of the arm, lose functionality for higher arm elevation angles. These results highlighted the effect that spring constant has on this novel device and importance of pre-clinical testing of orthoses across the full functional range.

Images (Optional)

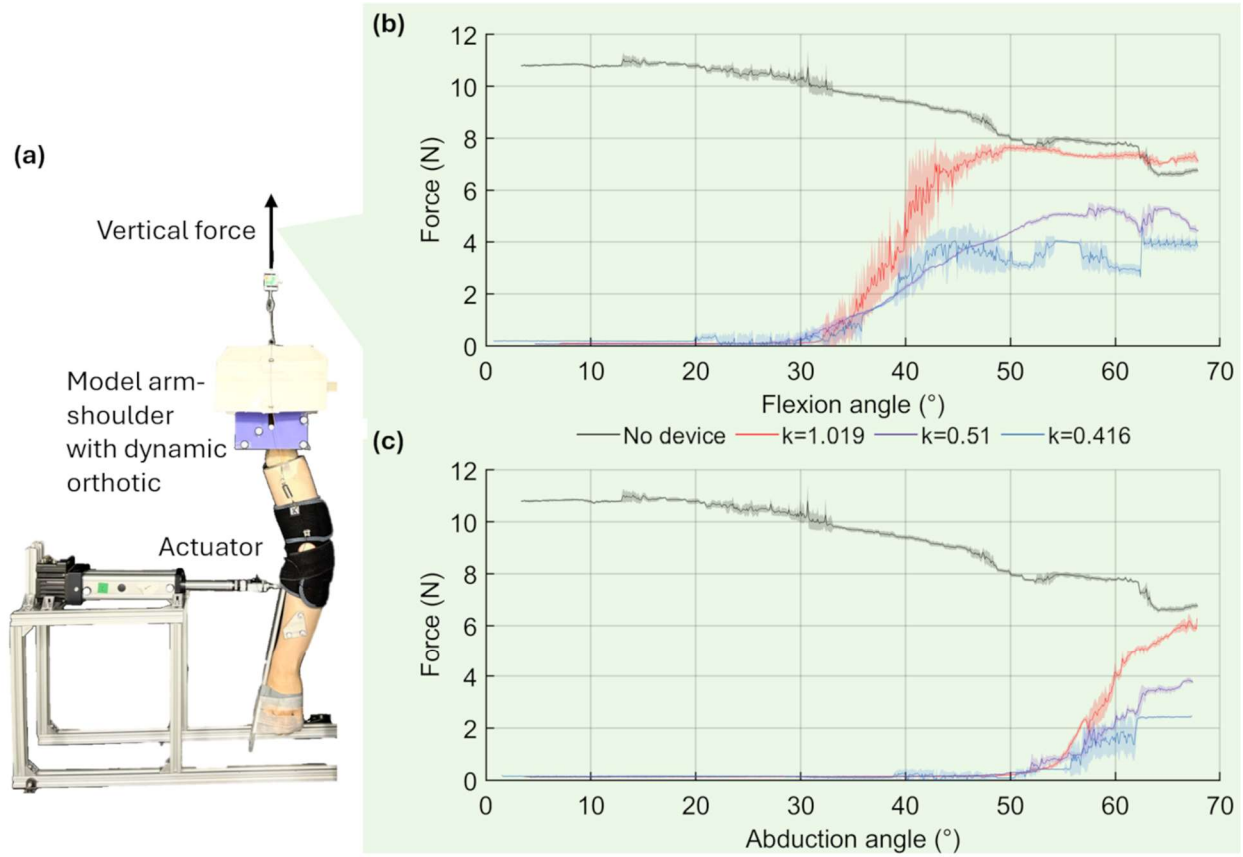


Figure 1: (a) Experimental set-up, including custom dynamic orthotic on the model arm and shoulder, linear actuator and load cells, and vertical force required by musculoskeletal structures to support the arm in (b) flexion and (c) abduction.

References (Optional)

[1] Ada et al.(2005) CDSR 1:CD003863

[2] Huang et al. (2023) *IEEE TBME* ***70*****(6):**1815–1825

Acknowledgements (Optional)

AS was supported by the UK EPSRC CDT in Prosthetics and Orthotics (EP/S02249X/1).

Session Category

Rehabilitation Biomechanics and Human Factors: Rehabilitation

P2-295

EMG and Force Biofeedback Alter Rotator Cuff Muscle Activation During Constant-Force Isometric Shoulder Abduction

Graduate Student Alireza Chalik MASc[1], Professor Arash Arami Associate Professor[1,2], Professor Clark Dickerson Professor[3]

[1]Department of Mechanical and Mechatronics Engineering, University of Waterloo, Waterloo, Ontario, Canada. [2]KITE Research Institute, Toronto Rehabilitation Institute, University Health Network, Toronto, Ontario, Canada. [3]Department of Kinesiology and Health Sciences Faculty of Health University of Waterloo, Waterloo, Ontario, Canada

Graduate Student Alireza Chalik

Professor Arash Arami

Introduction

Rotator cuff tears, especially of the supraspinatus, are common and prone to re-tear[1]. Early rehabilitation exercises may overload the healing tendon. We investigated whether an EMG- and force-guided isometric abduction task could promote alternative coordination patterns that selectively reduce supraspinatus activation while maintaining a constant abduction force [2].

Methods

Twelve healthy adults completed four sessions. Participants performed isometric shoulder abduction while gripping a 6-axis force sensor. On Day 1, each participant generated an abduction effort equal to 30% of their middle-deltoid MVC, and the resulting force was used as their personal target force for all remaining blocks and sessions. Real-time visual feedback was provided using a 2D cursor: the vertical axis represented force relative to this target, and the horizontal axis represented supraspinatus EMG (%MVC). Each daily session included 1 baseline block (no EMG feedback)(12 trials) and 4 EMG–force training blocks (12 trials each). Participants were instructed to move the cursor by applying the target force while minimizing supraspinatus activation. The RMS of filtered EMG(normalized to MVC values obtained at each session) during the force-holding period was used.

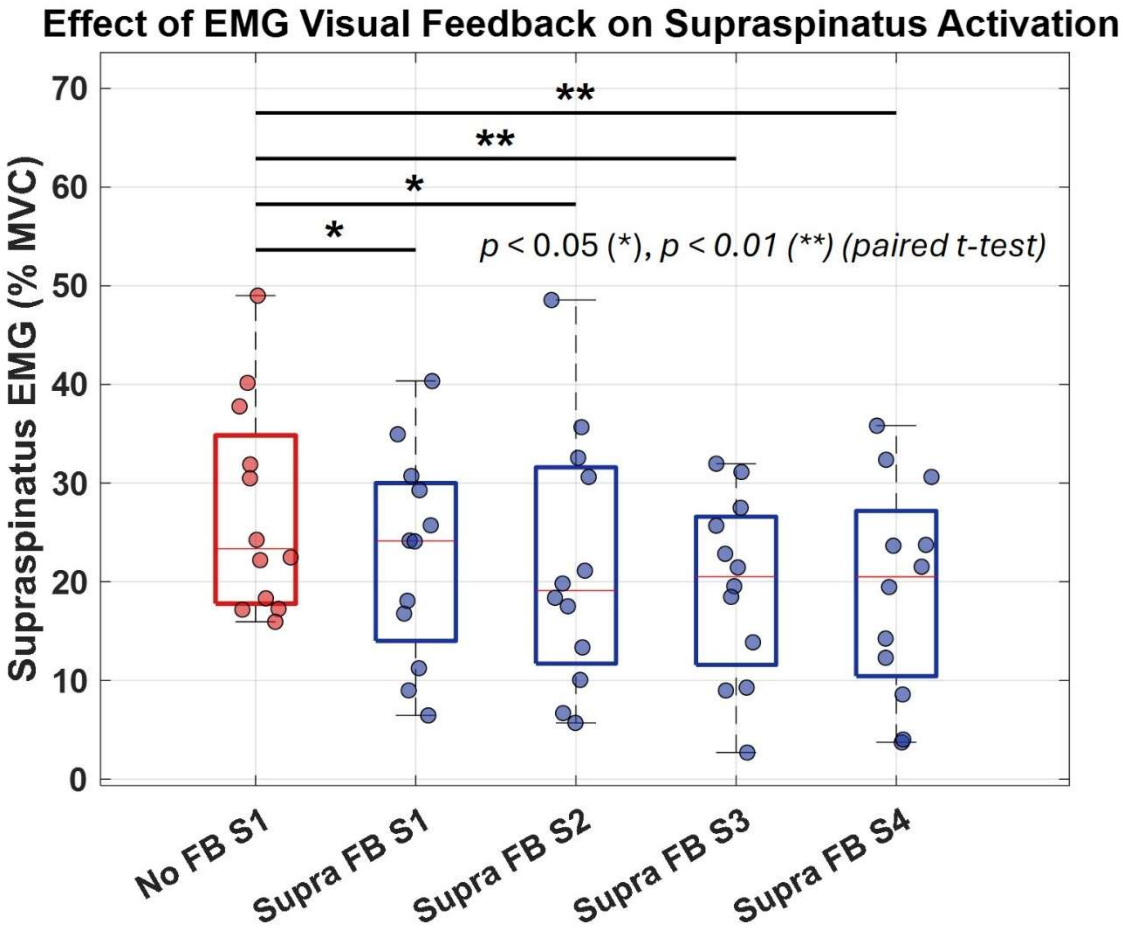
Results

Force direction and magnitude remained stable across days. Supraspinatus activation showed significant decreases with training in all sessions. The largest reduction occurred on Day 4, Block 5, where supraspinatus RMS decreased from 27.25% MVC (baseline) to 19.18% MVC ($p = 0.007$). Block-level reductions were also evident within days: on average, supraspinatus decreased by around 3.8%MVC per day, corresponding to 14% relative reductions from the first to the last block of a session. Across all participants and sessions, supraspinatus EMG variability decreased by around 20%, indicating more consistent suppression. Other muscles showed minimal change: mid-deltoid decreased by about 3%MVC across days, and anterior/posterior deltoid, infraspinatus, and upper trapezius changed by ≤2%MVC, demonstrating selective modulation rather than global reductions.

Discussion

Participants learned to reduce supraspinatus activation while maintaining a constant abduction force. These findings demonstrate that EMG-based biofeedback can reshape shoulder muscle coordination and may support tendon-protective strategies during rehabilitation.

Images (Optional)



References (Optional)

[1] S. Khoschnau et al., Eur J Orthop Surg Traumatol, 2020.

[2] G. Seo et al., J NeuroEngineering Rehabil, 2023.

Session Category

Rehabilitation Biomechanics and Human Factors: Rehabilitation

P2-296

Electromyographic and Postural Gait Characteristics Following an Independent Pole Walking Program in Parkinson Disease: A Pilot Study

Dr. Antonio Vintimilla PT, DPT, PhD[1], Dr. Tiffany Salido PT, DPT, PhD[2], Dr. Ronald Walser PT, DPT[1], Dr. Angie Meloy PT, DPT[1], Dr. Joy Cochran PT, DPT[3], Mr. Patrick Roscher MS[4], Dr. Peggy Trueblood PT, PhD[1]

[1]Pacific Northwest University, Yakima, WA, United States. [2]East Tennessee State University, Johnson City, TN, United States. [3]JOY Explorations, Watertown, WI, United States. [4]ProtoKinetics, LLC, Minneapolis, MN, United States

Dr. Antonio Vintimilla

Dr. Tiffany Salido

Dr. Ronald Walser

Dr. Angie Meloy

Dr. Joy Cochran

Mr. Patrick Roscher

Introduction

Postural dysfunction is a common debilitating feature of Parkinson Disease (PD) and associated with poor neurophysiological function across supporting postural muscles. Pole walking has emerged as an innovative approach that may enhance upright posture and address these dysfunctions. This pilot study aimed to evaluate the feasibility and effectiveness of an 8-week independent pole walking program on gait characteristics.

Methods

This was a randomized controlled single blinded pilot analysis on males and females with PD. Subjects were evaluated before and after an 8-week independent walking program with or without walking poles. Surface EMG sensors were placed on lumbar and cervical extensors. Postural gait characteristics were derived from IMUs on the thoracic spine and arms. Pre- and post-intervention data were analyzed using two-way repeated measures ANOVA with “group” and “time” as independent factors. Alpha was set to 0.05 and ηp2 was calculated for effect size (small = .01, medium = .06, large = .14).

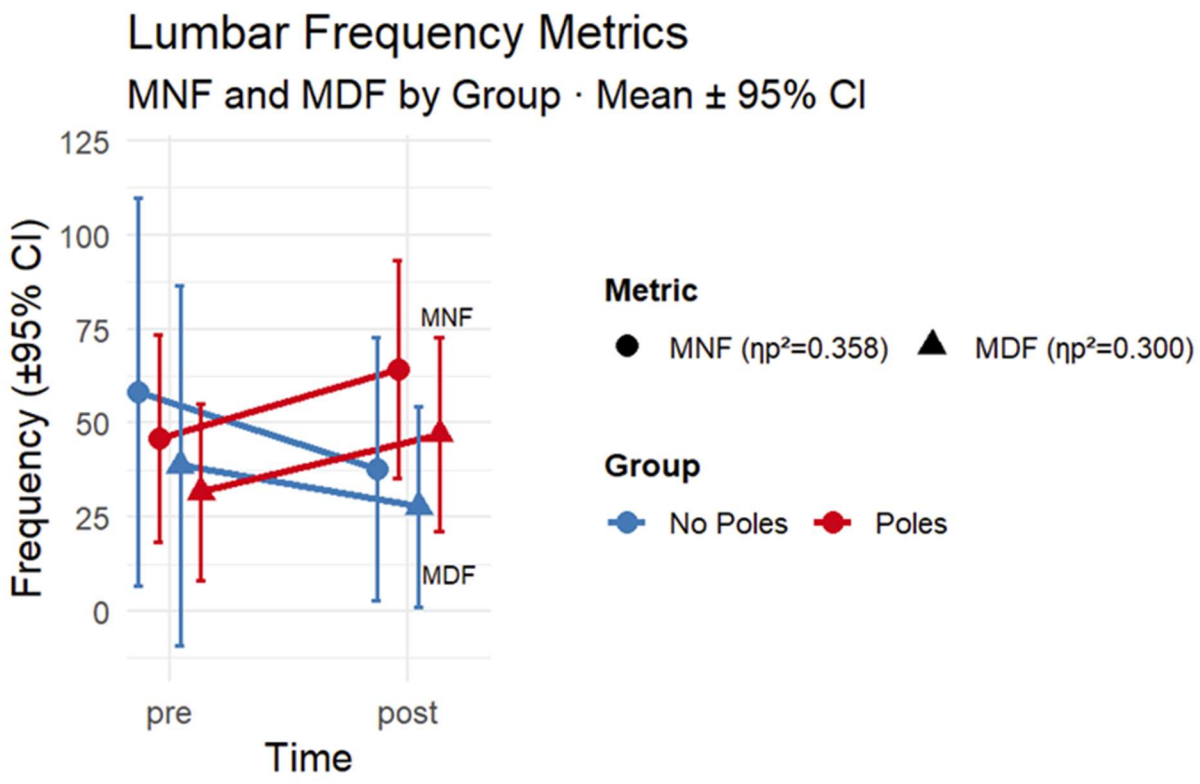
Results

11 subjects participated in the study (6 intervention, 5 controls). There were no significant differences in electromyographic or postural characteristics. Inferential analysis revealed moderate effect sizes for “time” in cervical extensor mean frequency (ηp2 = 0.092; MNF) and peak power (ηp2 = 0.105). There were large effect sizes for interactions between groups pre and post intervention in lumbar extensor MNF (ηp2 = 0.358) and median frequency (ηp2 = 0.30; MDF). Subjects in the intervention group increased across all lumbar power spectrum metrics post intervention while control subjects decreased (Figure 1). There were moderate effect sizes for “time” in thoracic forward tilt (ηp2 = 0.118) and shoulder flexion (ηp2 = 0.095) and interactions between groups pre and post intervention in thoracic rotation (ηp2 = 0.078).

Discussion

This pilot trial demonstrated that standard walking and pole walking were associated with improvements in postural alignment and muscle activity in individuals with PD, supporting the safety, feasibility and effectiveness of independent walking programs. Effect size patterns suggest that pole walking specifically may provide additional postural and neurophysiological benefits. These findings warrant further investigation in larger, fully powered studies to confirm and expand upon the potential advantages of pole walking as a rehabilitative strategy.

Images (Optional)



Session Category

Rehabilitation Biomechanics and Human Factors: Rehabilitation

P2-297

Effect of Simulator Rolling Resistance Compensation on Manual Wheelchair Propulsion Biomechanics

Ms. Ateayeh Bayat[1,2], Prof. Félix Chénier[3,2]

[1]Department of Systems Engineering, École de technologie supérieure, Montreal, QC, Canada. [2]Centre for Interdisciplinary Research in Rehabilitation of Greater Montreal (CRIR), Montreal, QC, Canada. [3]Department of physical activity science, Université du Québec à Montréal (UQAM), Montreal, QC, Canada

Introduction

Manual wheelchair simulators use dynamic models to control velocity based on user-applied force and system parameters, including rolling resistance. However, a portion of this resistance originates from the simulator's own mechanics (e.g., roller–wheel interface friction). This study investigates how two levels of simulator rolling resistance compensation—intended to neutralize this inherent friction—influence propulsion biomechanics during standardized wheelchair tasks.

Methods

Desired rolling resistance coefficients ($\mu_{desired}$) were defined for straight-line (0.01325) and ramp (0.024) surfaces. To replicate these accurately, the simulator's inherent resistance (μ_{sim}) must be deducted from the model. Coast-down tests established two compensation levels. The "one-step" configuration deducted the initially measured μ_{sim} of 0.00474. To achieve a target of zero difference between defined and simulated resistance, a second calibration yielded a total μ_{sim} of 0.0098, defining the "two-step" configuration.

Seven able-bodied participants performed straight-line and ramp propulsion tasks under both compensation settings (One-step vs. Two-step). Participants attempted to match their overground average velocity using real-time feedback. Biomechanical metrics were extracted from acceleration (ACC), constant-speed (CST), and ascending (ASC, 5.2° ramp) segments using the 10 most repeatable pushes.

Results

Despite a near two-fold difference in compensation, applied forces and moments remained similar across conditions. However, actual velocities deviated from targets. Key findings (Table 1) indicate large effect sizes in ACC and CST velocities and ACC push time. Moderate effects were noted for CST cadence and recovery time, ACC M_z, and ASC

push/recovery time. Notably, the number of collisions was lower in the one-step calibration (0.57±0.53) compared to the two-step (1.57±1.27), suggesting improved control under the higher net resistance of the one-step condition.

Discussion

Results suggest that user effort is not linearly driven by rolling resistance in virtual environments, in contrast to overground conditions. This deviation may stem from reduced physical feedback or altered effort perception not present in real-world settings. While force profiles remained stable, participants reported improved control and self-perception under the higher resistance (one-step). This underscores the role of perceptual and proprioceptive feedback (e.g., vibration, trunk involvement) in simulator realism, which should be integrated alongside mechanical optimization.

Images (Optional)

TABLE I. Mean, standard deviation (SD), and effect size comparing one-step vs. two-step rolling resistance calibration for key propulsion metrics. Effect sizes are interpreted per Cohen's convention: orange indicates moderate effects, and red indicates large effects.

	Straight			Acceleration			Ascending		
Variables	2-step calibration (μ =0.00345)	1-step calibration (μ =0.00855)	Effect Size	2-step calibration (μ =0.00345)	1-step calibration (μ =0.00855)	Effect Size	2-step calibration (μ =0.0142)	1-step calibration (μ =0.0193)	Effect Size
	Mean(±std)	Mean(±std)		Mean(±std)	Mean(±std)		Mean(±std)	Mean(±std)	
Spatiotemporal									
Cadence (push/min)	53.29 (12.75)	50.43 (10.35)	-0.52	45.86 (10.07)	41.36 (7.10)	-0.58	52.50 (11.59)	52.86 (10.29)	0.06
Contact Angle(deg)	25.18 (4.62)	24.34 (3.68)	-0.31	24.53 (5.16)	24.98 (3.59)	0.09	21.85 (4.09)	23.47 (2.53)	0.37
Push Time(s)	0.41 (0.12)	0.42 (0.10)	0.05	0.54 (0.13)	0.63 (0.11)	0.72	0.53 (0.11)	0.61 (0.15)	0.59
Recovery Time(s)	0.80 (0.26)	0.85 (0.26)	0.58	0.83 (0.29)	0.81 (0.17)	-0.13	0.51 (0.07)	0.61 (0.18)	0.6
Kinetics									
Mz (N.m)	4.32 (1.16)	4.27 (1.23)	-0.04	5.71 (1.42)	6.65 (1.90)	0.56	26.36 (4.38)	27.32 (4.22)	0.34
Total Force(N)	27.00 (7.26)	28.18 (8.94)	0.16	32.75 (5.64)	38.69 (11.58)	0.69	121.37 (21.11)	122.87 (24.36)	0.09
Total Power(W)	15.35 (3.80)	14.76 (4.88)	-0.17	16.18 (5.49)	16.89 (6.55)	0.2	62.30 (18.81)	65.62 (20.74)	0.2
Velocity(m/s)	1.15 (0.13)	1.09 (0.17)	-0.81	0.92 (0.17)	0.81 (0.13)	-1.24	0.76 (0.21)	0.74 (0.16)	-0.13
Work per Cycle(J)	15.36 (3.80)	14.76 (4.88)	-0.17	16.18 (5.49)	16.88 (6.56)	0.2	62.13 (18.84)	65.46 (20.76)	0.2
Total Work(J)	191.88 (66.96)	219.55 (108.63)	0.37	97.79 (29.41)	108.71 (28.82)	0.47	865.96 (143.32)	831.17 (184.71)	-0.35

Session Category

Rehabilitation Biomechanics and Human Factors: Rehabilitation

P2-298

Evaluation of the Advanced System for Implant Stability Testing (ASIST) for Measuring Bone Anchored Hearing System (BAHS) Implant Stability Using Polyurethane Foam

Mr. Boyu Pan[1], Dr. Mostafa Mohamed[1], Dr. Martin Johansson[2,3], Dr. Anders Palmquist[2], Mr. Thomas Eriksson[3], Dr. Dan Romanyk[1], Dr. Mustafa Gül[1], Dr. Lindsey Westover[1]

[1]University of Alberta, Edmonton, Alberta, Canada. [2]University of Gothenburg, Gothenburg, Västra Götaland County, Sweden. [3]Oticon Medical AB, Gothenburg, Västra Götaland County, Sweden

Introduction

The ASIST is a non-invasive system designed to measure implant stability by analyzing the vibration response of the implant system. Clinically, infections, bone resorption, and bone defects may occur around Bone Anchored Hearing System (BAHS) implants due to poor initial bone quality, postoperative infections, and inflammation. The objectives of this study were to evaluate ASIST in BAHS, to assess its sensitivity to variations in polyurethane foam defects surrounding the implants, and to evaluate the primary stability of several clinically used BAHS implants in polyurethane foam with different densities.

Methods

Four types of BAHS implants—Ponto BHX (3-mm and 4-mm), Acorn C4.0, and COH BI300 (4-mm)—were placed into polyurethane foam blocks with different densities following their respective surgical procedures. Primary stabilities were assessed using the maximum insertion torque (MIT), Implant Stability Quotient (ISQ), ASIST Stability Coefficient (ASC), and maximum pull-out force. Two defect configurations, unilateral and circumferential, were created in the foam blocks at depths of 0.3-, 0.6-, and 0.9-mm. For the unilateral defect, ISQ and ASC were obtained in four mutually perpendicular measurement directions, one of which aligned with the center of the unilateral defect.

Results

Figure 1 presents the ASC, ISQ, and MIT results. Pull-out tests are ongoing, and their findings will be reported at the conference. Regarding unilateral defects, no significant differences were observed in ASC or ISQ across the four directions (p>0.05).

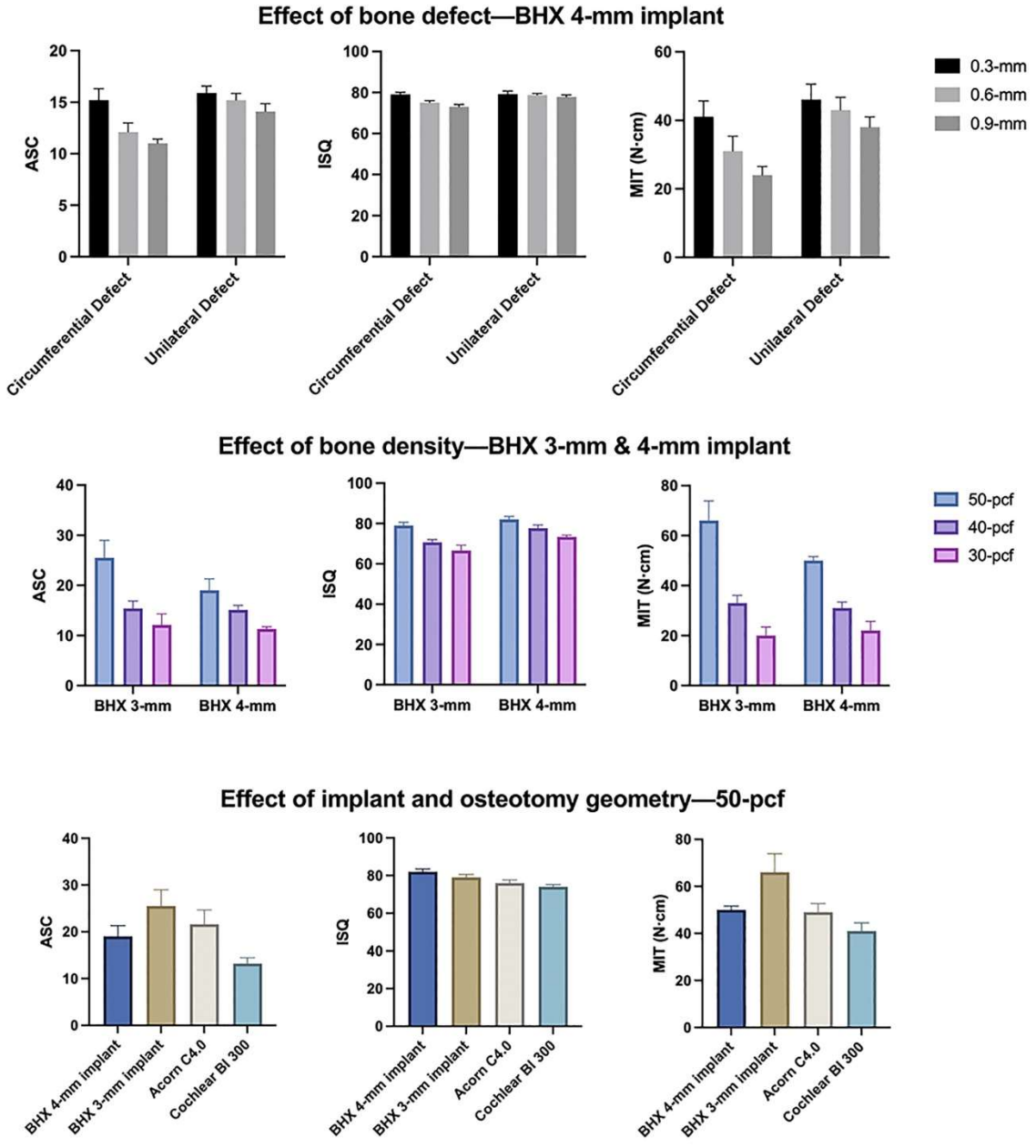
Discussion

Greater bone defect severity reduced implant stability. The BHX 4-mm exhibited the most pronounced stability change between no defect and a 0.3-mm defect, compared with other 0.3-mm defect increments, which can be attributed to compression between the flange-

neck region and the osteotomy cavity. Increased bone density enhanced stability. The BHX 3-mm demonstrated higher stability than the BHX 4-mm owing to its osteotomy diameter being 0.1 mm smaller. Although ACORN is shorter than the BHX 4-mm, the former's more aggressive geometry resulted in comparable stability. The BI300, with the largest osteotomy diameter, exhibited the lowest stability.

ASC is more sensitive to the bone defects, density and implant and osteotomy geometry compared with ISQ. Furthermore, for unilateral defects, the measurement direction has no effect on ASC and ISQ.

Images (Optional)



Acknowledgements (Optional)

The authors gratefully acknowledge the support from the Natural Sciences and Engineering Research Council of Canada (NSERC), Oticon Medical, the University of Gothenburg, the China Scholarship Council (CSC), and W&H Dentalwerk.

Session Category

Rehabilitation Biomechanics and Human Factors: Rehabilitation

P2-299

Tracking Medial Gastrocnemius-Achilles Musculotendinous Junction Excursion During Walking and Bilateral Heel Rises

Miss Camille Nguyen M.Sc., Dr. Karin Gravare Silbernagel PT, ATC, PhD, Dr. Stephanie G. Cone PhD

University of Delaware, Newark, Delaware, United States

Introduction

The Achilles tendon is connected to the muscles of the triceps surae by three individual subtendons enabling ankle plantarflexion, importantly these subtendons may be differentially affected with injury. Tracking muscle-tendon junction (MTJ) excursions during dynamic motion is needed to improve researcher and clinician understanding of Achilles tendon function in activities of daily living and in rehabilitation. This pilot study aimed to establish ultrasound methods to measure medial gastrocnemius (MG) MTJ excursion during functional rehabilitation tasks in healthy individuals.

Methods

Four participants (4 female, 28±4.4yrs, 163±5.0cm, 67.7±16.9kg) with no history of lower extremity injury in the last 6 months were evaluated. Ultrasound imaging was performed to identify the superior calcaneal notch and MG MTJ of the dominant leg [1], and free tendon length was measured. A ProbeFix holder with a VScan Air transducer was affixed while the participant was standing over the MTJ [4]. Three, 10-second ultrasound videos were captured during treadmill walking at 3 miles per hour. Participants completed 30 repetitions of bilateral heel rises on a 10 degree incline while two, 10-second ultrasound videos of the MTJ were captured. The distance between most distal and proximal MTJ locations were measured in Kinovea and reported as MTJ excursion. A paired t-test was used to compare excursions between tasks.

Results

Significant differences were found between walking and heel rise activities ($p<0.05$, Table 1). Mean excursion values were significantly higher during bilateral heel rise activity (1.45±0.16cm) compared to walking (0.77±0.04cm) across all subjects. Variable excursions emerged between subjects despite similar participant heights (Table 1).

Discussion

This study establishes a wearable ultrasound method to quantify the excursion of the Achilles-medial gastrocnemius MTJ during clinically important movements. A cordless probe afforded participant mobility, although experimental challenges with low (10Hz) sampling frequency were observed which may lead to challenges accurately quantifying higher velocity tasks. Additional challenges were experienced measuring tendon excursions in taller subjects, motivating future studies implementing probes with longer imaging footprints.

Images (Optional)

Participant Number	*Walking Average (cm)*	*Heel Rise Average (cm)*
1	0.96 ±0.07	1.02 ±0.05
2	0.74 ±0.03	1.83 ±0.11
3	0.89 ±0.18	1.71 ±0.09
4	0.49 ±0.05	1.19 ±0.07
Mean ± SD	0.77 ±0.04	1.44 ±0.16

Table 1. Individual and averaged values for MTJ excursion during walking and heel rise tasks.

References (Optional)

[1] Smitheman+, JOVE, 2023; [2] Finni+, Eur J Appl Physiol, 2022.

Acknowledgements (Optional)

Funding from NIH R01AR085639.

Session Category

Rehabilitation Biomechanics and Human Factors: Rehabilitation

P2-300

Comparing Distal-to-Shank Force, Displacement, and Work Profiles Between Prosthetic and Intact Limbs

Miss. Chelsea Haddy B.A.Sc., Dr. Jenna Burnett Ph.D, Dr. Kota Takahashi Ph.D

University of Utah, Salt Lake City, Utah, United States

Introduction

Passive prostheses act as springs to store and return energy, but they are unable to generate energy (i.e., net positive work). This inability has often been considered a limitation for replicating biological limb function during walking. However, the biological structures distal to the shank (i.e., foot and ankle) reveal notable spring-like behaviour, including ground reaction force (GRF) and center-of-pressure (COP) displacement profiles that result in nearly zero net work [1]. Whether the distal-to-shank spring-like behaviour can be replicated in passive prostheses remains unknown. Thus, we compared the distal-to-shank mechanics (COP, GRF, and work) of prosthetic and biological limbs during walking.

Methods

Nine individuals with unilateral transtibial amputation (7M/2F, 42.2±13.4 years, 82.1±13.6 kg) walked on an instrumented treadmill (1.0±0.2 m/s) while wearing a passive prosthesis. COP and GRF data were transformed into the shank's coordinate system. We used a unified-deformable segment analysis [1] to quantify power and work due to all structures distal to the shank. Paired t-tests compared prosthetic and intact distal-to-shank work. Data from healthy controls (10M/11F, 26.6±3.9 years, 69.3±9.3 kg) served as reference.

Results

There were no significant differences between prosthetic versus intact limbs in positive work (0.17±0.07 J/kg, and 0.16±0.09 J/kg; p=0.746) and negative work (-0.18±0.08 J/kg, and -0.14±0.04 J/kg; p=0.217), while healthy controls had similar or decreased magnitudes of positive and negative work (0.19±0.07 J/kg and -0.13±0.03 J/kg), respectively. The COP and GRF relative to the shank exhibited spring-like mechanics in all limbs, as evidenced by longitudinal compression and recoil (Figure 1). Notably, the prosthetic limb had GRF directed longitudinally in early stance compared to intact limbs.

Discussion

Individuals with unilateral amputation had symmetrical distal-to-shank work profiles, likely due to the utilization of spring-like properties of elastic prostheses. The prosthetic limb had

altered GRF direction in early stance, possibly as a strategy to deform the spring. Understanding the altered loading patterns in prosthesis users may inform rehabilitation strategies and improve prosthetic designs.

Images (Optional)

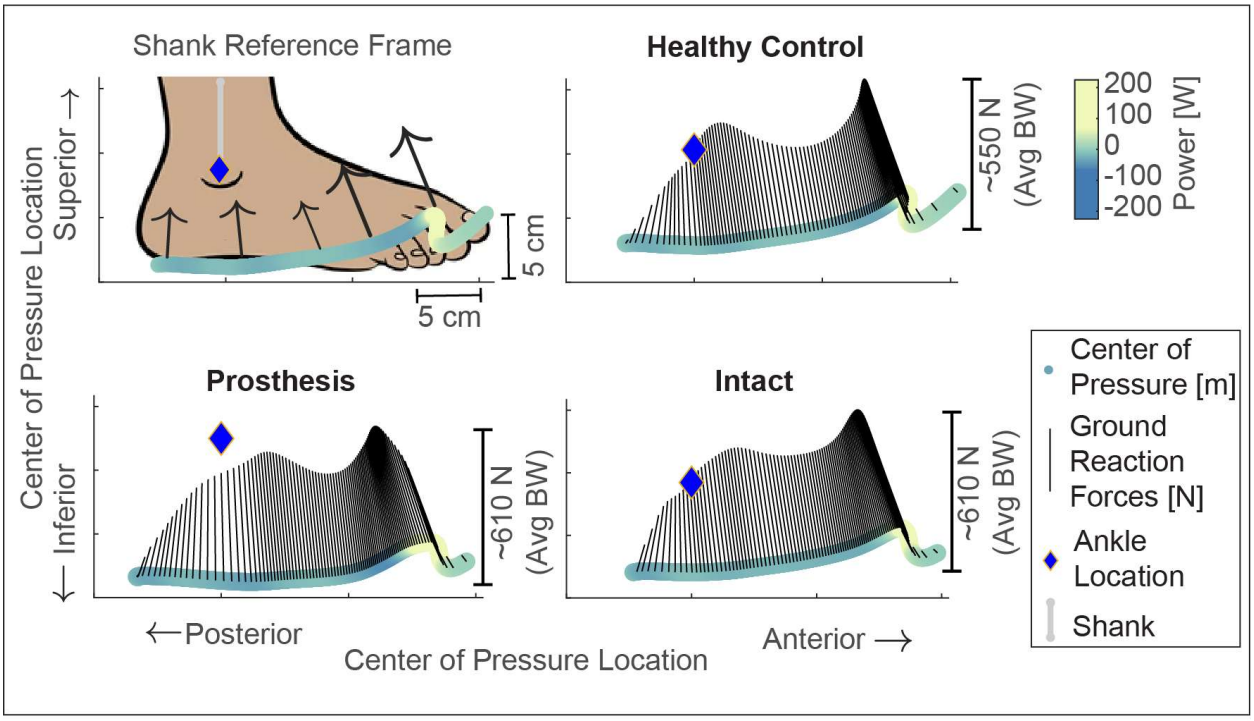


Figure 1: The top left panel shows an example of the shank's reference frame used to express the COP and GRF in all panels. The colour gradient on the COP trajectory indicates the instantaneous power (distal-to-shank).

References (Optional)

[1] Hedrick *et al.*, PLoS ONE, 2019.

Acknowledgements (Optional)

Supported by NIH R01HD106911 and NIH 1T32DK11096601 (awarded to KZT, JKB).

Session Category

Rehabilitation Biomechanics and Human Factors: Rehabilitation

P2-301

Fiber Optic Distributed Strain Sensing for Lower-limb Prosthetic Sockets

Ms. Clara Phillips, Dr. Fae Azhari

University of Toronto, Toronto, Ontario, Canada

Introduction

Mobility and function with a lower-limb prosthesis depend on the proper fit of a prosthetic socket to the residual limb. Conventional socket fabrication is advancing in several areas, including digital design and manufacturing (specifically, 3D printing), and computational models for predicting fit [1]. However, adoption of these tools is limited due to the lack of standardized bench-top testing methods that can provide evidence of their efficacy. While one standard, ISO 10328, addresses failure testing of sockets, it overlooks strain measurement. Capturing distributed strain data is essential for assessing socket structural integrity, understanding strain transfer to soft limb tissue, and validating computational models. Fiber optic sensing is a promising tool in biomechanics applications due to the fiber's small size, light weight and biocompatibility, yet its application in prosthetic sockets remains largely unexplored [2]. Here, we present a methodology for distributed strain sensing in prosthetic sockets using distributed fiber optic technology.

Methods

An optical fiber was mounted on a 3D-printed socket in longitudinal and circumferential orientations and recorded using a Luna Optical Distributed Sensing Interrogator (ODiSI). Five Fiber Bragg gratings (FBGs) were also mounted for strain comparison at discrete locations (Fig. 1). The socket was loaded according to ISO 10328 loading orientations to 200 N and 300 N, followed by 30 loading cycles from 50 N to 200 N. Strains were measured. A finite element model (FEM) of the socket was developed to simulate the loading conditions.

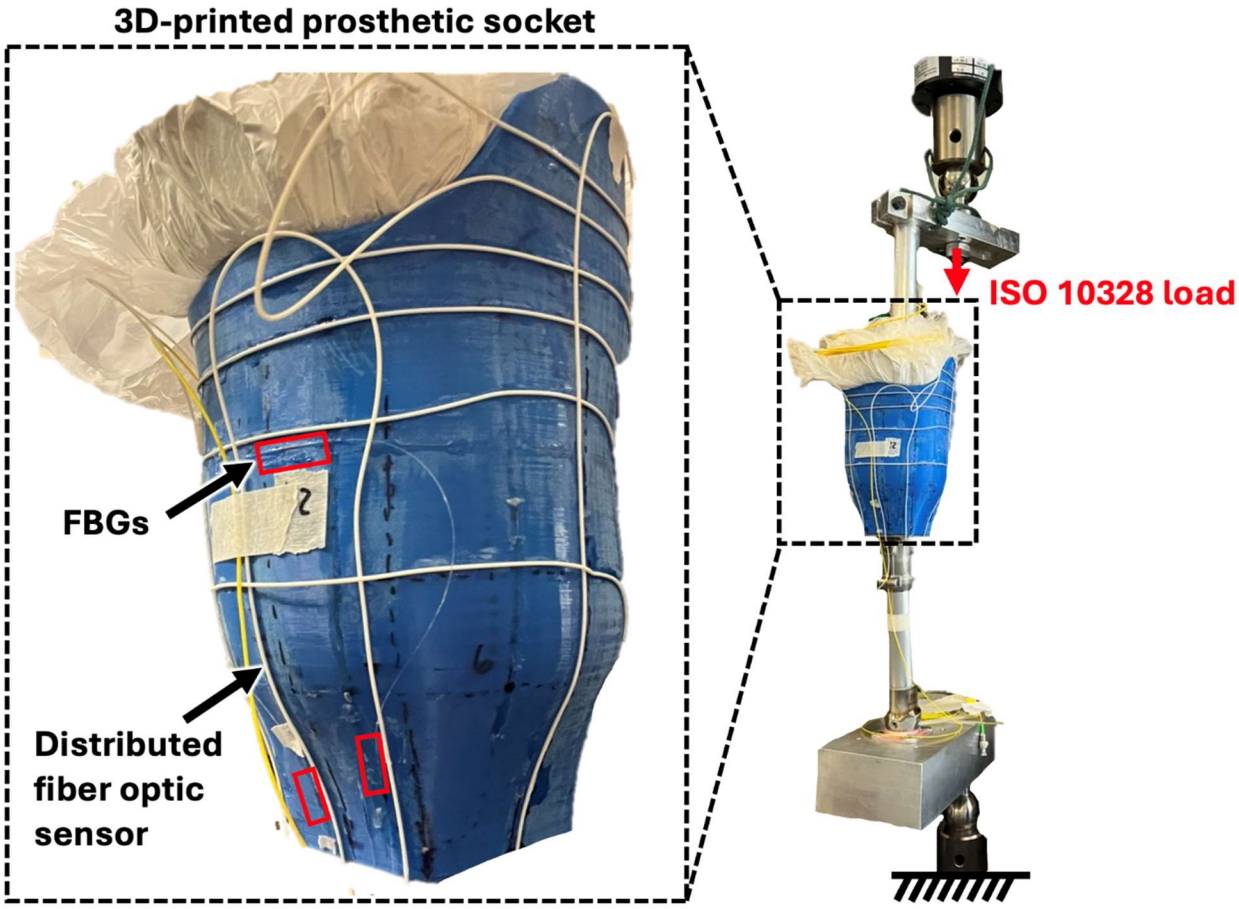
Results

Trends in strain matched between the ODiSI, the FBGs and the FEM, and the ODiSI accurately detected areas of maximum tensile and compressive strain not captured by the FBGs. Discrepancies in strain magnitudes measured by the distributed vs. discrete sensors were attributed to strain transfer efficiency.

Discussion

By visualizing socket strain distribution under clinically relevant loads, this approach identifies critical regions of deformation that are not captured by existing standards. While more work is required to improve strain magnitude measurement, this method has potential in broad biomedical contexts to inform the design of structurally-sound devices, and validate experimental and computational models of device functionality.

Images (Optional)



References (Optional)

[1] Manrique and Portilla, Biomechanics, 2025.

[2] Al-Fakih *et al.*, Sensors, 2012.

Session Category

Rehabilitation Biomechanics and Human Factors: Rehabilitation

P2-302

Adaptative Improvement in Dynamic Gait Stability to Repeated Stance-Slips in People with Mild to Moderate Parkinson's Disease

Ms. Diane Brown, Dr. Jiyun Ahn, Ms. Sara MahmoudzadehKhalili, Dr. Feng Yang

Georgia State University, Atlanta, Georgia, United States

Introduction

Falls are highly detrimental in people with Parkinson's disease (PwPD). The use of perturbation-based balance training (PBT), particularly stance-slip perturbations, to reduce falls in PwPD remains limited. As motor learning is the foundation for PBT, this study examined whether PwPD can adapt to and acquire fall-resistant skills through repeated standing-slips. Specifically, we investigated whether PwPD can adaptively improve their dynamic gait stability, as quantified by the Feasible Stability Region (FSR) theory [1], during repeated standing-slips. We hypothesized that PwPD would improve their dynamic stability across slips.

Methods

Ten PwPD (age: 69.9±5.53 years, 1 female, Hoehn & Yahr scale: 1.35±0.63 out of 5), protected by a safety harness, were exposed to five standing-slips (S1-S5) on an ActiveStep treadmill (Simbex, NH). The slip distance was 36 cm with a peak belt speed of 1.2 m/s. Their full-body kinematics were collected by a Vicon motion capture system (UK) from reflective markers attached to bony landmarks. Three time instants: slip onset (ON), recovery step liftoff (LO), and recovery touchdown (TD) were identified through foot kinematics. Center of mass (COM) kinematics were derived from filtered marker paths. COM motion state (i.e., its normalized relative position and velocity to the base of support) was compared to the FSR to compute dynamic gait stability for all three instants [2]. Repeated measures ANOVA analyzed dynamic gait stability. A significant main trial effect was followed by paired *t*-tests between consecutive slips and between S1 and S5 with appropriate corrections. SPSS 29.0 (IBM) and α=0.05 were used.

Results

No adverse events were reported. Participants showed significant improvements in proactive COM control at ON (p=0.017) and in reactive control performance at LO (p=0.009) and TD (p=0.005), with substantial early-to-late trial enhancements (Table 1).

Discussion

PwPD exhibited meaningful adaptive improvements in dynamic stability following repeated stance-slip exposure. The results support our hypothesis and suggest that stance-slip PBT training may be an effective and promising approach for reducing fall risk in this population. Our study could inform the development of effective standing-slip-based PBT fall-prevention interventions for PwPD.

Images (Optional)

Table 1. Between-slip comparisons of dynamic gait stability [in mean (standard deviation)].

Events	Stability (unitless)					*p*-value					
	S1	S2	S3	S4	S5	Overall	S1 vs. S2	S2 vs. S3	S3 vs. S4	S4 vs. S5	S1 vs. S5
ON	0.25 (0.03)	0.26 (0.02)	0.27 (0.03)	0.27 (0.02)	0.27 (0.03)	**0.017**	0.127	**0.013**	0.178	0.279	**<0.001**
LO	-0.44 (0.08)	-0.40 (0.09)	-0.37 (0.12)	-0.35 (0.10)	-0.35 (0.15)	**0.009**	0.063	0.073	0.351	0.486	**0.008**
TD	-0.13 (0.19)	-0.05 (0.20)	-0.04 (0.21)	0.04 (0.17)	0.02 (0.19)	**0.005**	**0.047**	0.444	0.104	0.339	**0.002**

References (Optional)

[1] Feng Yang *et al.*, J Biomechanics, 2014; [2] Feng Yang, Handbook of Human Motion, 2018.

Acknowledgements (Optional)

The authors thank Dr. Caroline Simpkins for assisting with the data collection.

Session Category

Rehabilitation Biomechanics and Human Factors: Rehabilitation

P2-303

A knee exoskeleton reduces peak knee contact forces during stair navigation

Dr. Emily Miller, Ms. Kai Pruyn, Dr. Lukas Gabert, Dr. Tommaso Lenzi, Dr. Scott Uhlrich

University of Utah, Salt Lake City, Utah, United States

Introduction

Osteoarthritis is a leading cause of disability, and stair navigation is difficult and painful for many individuals due to the large muscle forces and joint loads required. A knee exoskeleton may reduce potentially harmful joint contact forces [1]. This pilot study evaluated whether an exoskeleton providing knee extension torque reduces knee contact forces during stair navigation in a healthy participant, establishing feasibility for future osteoarthritis studies.

Methods

One male participant without osteoarthritis (age 31, height 1.78 m, mass 79.5 kg) wore the 5 kg unilateral Utah knee exoskeleton [1] on the right leg. He completed four trials each of stair ascent and descent at three speeds under two conditions: no exoskeleton (No Exo) and exoskeleton providing assistive torque (Exo). Motion capture, ground reaction forces, and surface electromyography from gastrocnemius medialis, vastus lateralis, and biceps femoris longus were recorded. Inverse dynamics and musculoskeletal modeling with static optimization estimated tibiofemoral contact forces, which were compared across conditions and speeds.

Results

During ascent, peak knee contact force in the Exo condition was 29% lower than No Exo, averaged across speeds and trials. Figure 1 shows representative medium-speed trials. The exoskeleton delivered 50 Nm of extension torque during early stance, reducing the biological knee extension moment by 51%. Vastus lateralis EMG amplitude decreased by 33%, consistent with a 42% reduction in model-estimated activation. During descent, peak contact forces in the Exo condition were 35% lower than No Exo across speeds, peak knee extension moment was 56% lower, and vastus lateralis EMG was 43% lower.

Discussion

This pilot study demonstrates that powered knee assistance can substantially reduce knee contact forces during stair navigation. The observed reductions of 29 to 35 percent far exceed those typically achieved through conventional interventions, which often yield only 10 to 12 percent reductions [2]. Our findings highlight the potential of powered assistance

to meaningfully decrease pain and slow cartilage degeneration in individuals with osteoarthritis [3] and support progression to patient studies where reducing knee loading may provide therapeutic benefit and improve mobility.

Images (Optional)

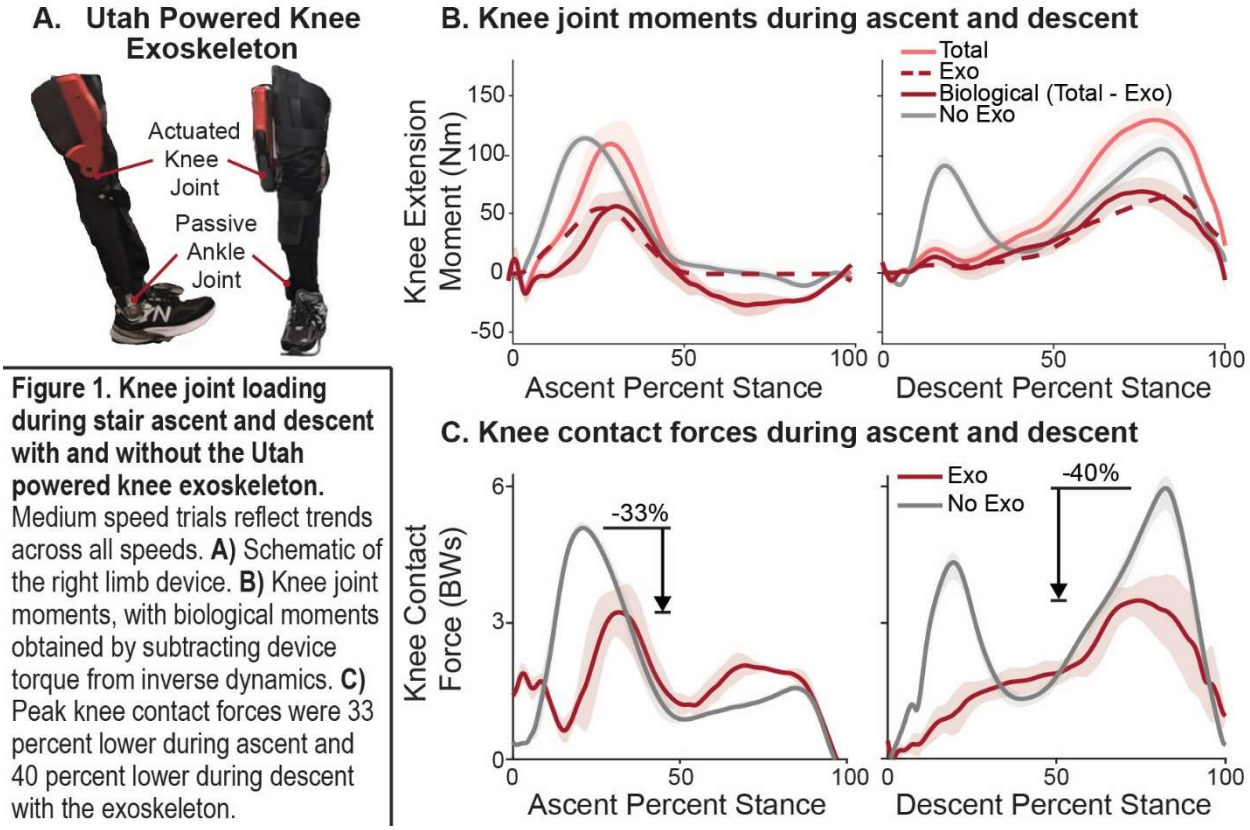


Figure 1. Knee joint loading during stair ascent and descent with and without the Utah powered knee exoskeleton. Medium speed trials reflect trends across all speeds. **A)** Schematic of the right limb device. **B)** Knee joint moments, with biological moments obtained by subtracting device torque from inverse dynamics. **C)** Peak knee contact forces were 33 percent lower during ascent and 40 percent lower during descent with the exoskeleton.

References (Optional)

[1] Boon et al., IRAL, 2025.

[2] Uhlrich et al., Lancet Rheumatol, 2025.

[3] Brisson et al., Arthritis Rheumatol, 2021.

Session Category

Rehabilitation Biomechanics and Human Factors: Rehabilitation

P2-304

Effects of Nonlinear Ankle Joint Stiffness on Metabolic Cost Using Robotic Prosthetic Emulation

Ms. Emma Caringella[1], Ms. Chelsea Haddy[1], Dr. Philippe Malcolm[2], Dr. Kota Takahashi[1]

[1]University of Utah, Salt Lake City, Utah, United States. [2]University of Nebraska at Omaha, Omaha, Nebraska, United States

Introduction

During walking, the human ankle behaves as if it were a rotational spring [1] that can store and return energy. Unlike a linear spring, where displacement is directly proportional to force, the resistance offered by the ankle changes with joint angle during stance in walking (i.e., 'nonlinear stiffening' behavior [2]). The biomechanical importance of the ankle's nonlinear stiffening behavior is evident; the ankle modulates its stiffness in response to changes in speed [2] and slope [3]. However, the influence of this nonlinear stiffness property on gait remains poorly understood. In this study, a range of ankle stiffness profiles are simulated in a wearable robotic prosthetic emulator to determine how varying degrees of nonlinearity affect the metabolic cost of walking.

Methods

1 healthy young adult (M, 25 yrs, 63.7 kg) participated in this study. The participant walked on an instrumented treadmill for 15 minutes at 1.25 m/s wearing a robotic prosthetic emulator (Humotech). The participant wore an immobilizer boot with the emulator rigidly attached at the distal end, and a lift shoe on the other foot (Figure 1). During gait, the emulator cycled through four ankle stiffness shapes while maintaining a constant overall ankle quasi-stiffness (0.0775 Nm/kg/deg). We calculated metabolic cost (W/kg) using a method for estimating instantaneous metabolic cost [4], where steady-state metabolic rate was estimated as the asymptote of an exponential curve fit to the metabolic data of each ankle stiffness profile.

Results

A nonlinear softening profile resulted in the highest net metabolic cost (6.05 W/kg) while a linear profile resulted in the lowest net metabolic cost (4.79 W/kg) (Figure 1). Data collection is ongoing.

Discussion

Preliminary results suggest the nonlinearity of the ankle during the loading phase of gait impacts metabolic cost. Findings from this study will contribute to the growing body of

knowledge on the complex ankle joint and may influence the design of prosthetic and orthotic devices to better replicate natural ankle function.

Images (Optional)

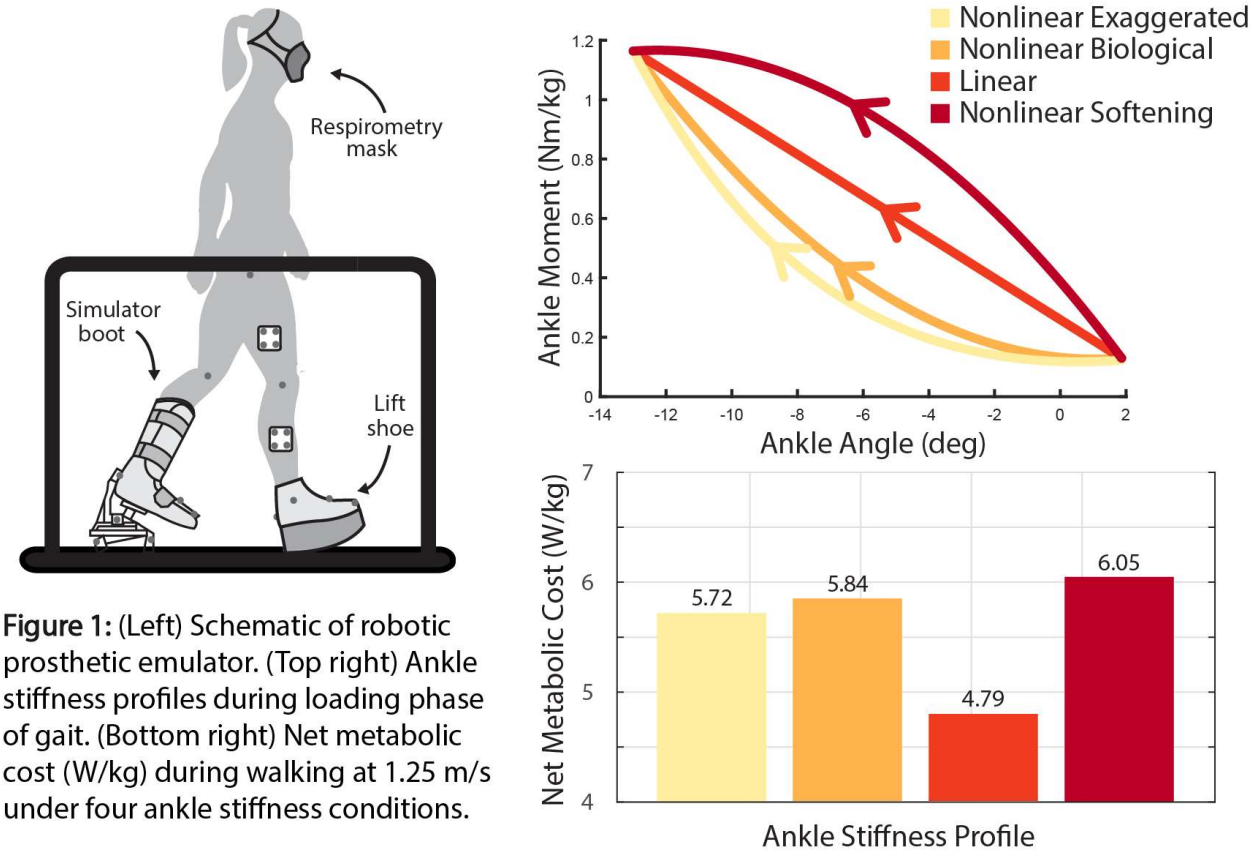


Figure 1: (Left) Schematic of robotic prosthetic emulator. (Top right) Ankle stiffness profiles during loading phase of gait. (Bottom right) Net metabolic cost (W/kg) during walking at 1.25 m/s under four ankle stiffness conditions.

References (Optional)

[1] Adamantios Arampatzis *et al.*, J. Biomech., 1999 [2] Luke Nigro *et al.*, Gait Posture, 2021 [3] Caringella et al., 2025 [4] Jessica Selinger *et al.*, J. Appl. Physiol., 2014

Session Category

Rehabilitation Biomechanics and Human Factors: Rehabilitation

P2-305

Adjustable Offloading Ankle-Foot Orthosis (AFO): Design and Evaluation during Walking

PhD Candidate Eshraq Saffuri, Assistant Professor Dana Solav Ph.D.

Technion – Institute of Technology, Haifa, North, Israel

Introduction

Numerous foot and ankle conditions may require partial or complete offloading of the affected areas using assistive devices for mobility. Crutches, though common, disrupt gait biomechanics, increase secondary injury risk, and immobilize the proximal affected leg. AFOs may offer a better alternative but can cause discomfort and abnormal gait [1]. This study proposes and evaluates a novel adjustable offloading AFO designed to improve gait dynamics and enable precise offloading levels.

Methods

Our AFO integrates several components designed to enhance functionality. A patient-specific shank brace is computationally designed from a 3D scan and fabricated using a 3D-printed polylactic acid core, externally laminated with carbon fiber, and internally fitted with a neoprene liner (Fig.1a). A height-adjustment mechanism enables precise load distribution between the shank and the foot. Medial and lateral rocker contact plates aim to compensate for the absence of ankle flexion by incorporating a roll-over-shape (ROS) derived from walking data. The ROS is computed by transforming the foot center-of-pressure trajectories to a shank-fixed coordinate system [2]. Evaluation on two healthy participants walking at self-selected speed measured plantar pressure distribution using Zebris FDM-2 walkway.

Results

Normal plantar forces during AFO walking increased progressively across five 4mm increment height adjustments (Fig. 1b), with foot impulses rising from 14%, 23%, 31%, 43% to 53%. Stance phase (SP) inter-limb symmetry index decreased from 13% at 0% load to 7% at 53% load. Contralateral SP shortened to 58% of the gait cycle, compared to 68% with

a prefabricated AFO [1]. Participants reported a comfortable, natural walking experience across all offloading levels.

Discussion

Our AFO facilitates a natural walking experience, even during complete offloading. Height adjustments resulted in a gradual reduction in offloading levels while maintaining mostly typical plantar force patterns. This advancement paves the way to enhanced rehabilitation from foot and ankle injuries. Future research will evaluate performance and long-term outcomes in clinical populations.

Images (Optional)

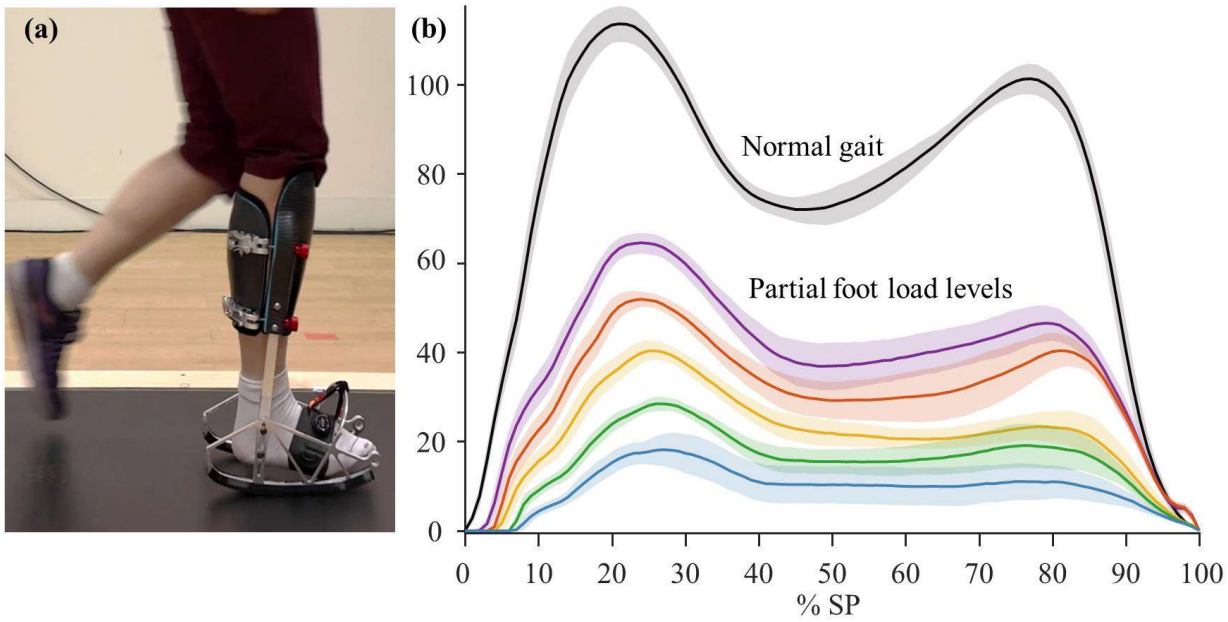


Figure 1: AFO design and evaluation. (a) AFO prototype featuring a shank brace, a height adjustment mechanism, and contact plates. It shows a participant walking with the AFO in a full offloading, where no foot-ground contact occurs during single-support. (b) Normal plantar forces (% of body weight) during the stance phase (SP) at five foot loading levels, compared to normal gait as a control condition.

References (Optional)

"[1] Saffuri et al., J NeuroEng Rehab, 2024"

"[2] Hansen et al., Clin Biomech, 2004"

Acknowledgements (Optional)

This research was supported by the Israel Ministry of Science and Technology and by the J. Tal, Gutwirth, Neubauer, and Mark S. Kahn Family Funds.

Session Category

Rehabilitation Biomechanics and Human Factors: Rehabilitation

P2-306

Characterizing Wheelchair Vibrations to Enhance Self-Motion Perception in Wheelchair Simulators

Pr Félix Chénier[1,2], Ms Julie Moison[3,4], Mr Baptiste Perrudin[3,4], Mr Mohammed El Abdoulli[3,4], M Clément Ghazouani[3,4], Pr Rachid Aissaoui[3,4]

[1]Université du Québec à Montréal (UQAM), Montreal, Quebec, Canada. [2]Centre for Interdisciplinary Research in Rehabilitation of Greater Montreal (CRIR), Montreal, Quebec, Canada. [3]École de technologie supérieure (ÉTS), Montreal, Quebec, Canada. [4]Centre de recherche du CHUM (CRCHUM), Montreal, Quebec, Canada

Introduction

Wheelchair simulators reproduce complex environment in stationary conditions, allowing users to safely train their propulsion skills. For training to be effective, users should feel as though they are moving in accordance with the simulation, even while stationary. Providing whole-body vibration during movement enhances this sense of self-motion, likely due to increased realism or by masking conflicting proprioceptive information, thus relying more on visual cues. A roller-based wheelchair simulator already generates vibrations caused by the rear tires interacting with the rollers. In this preliminary study, we measured the amplitude and frequency of these vibrations and investigated how they compare to different real-life conditions.

Methods

Four accelerometers were installed on the frame of a manual wheelchair near the axle of each wheel. The wheelchair was pulled at two constant speeds of 0.75 and 1.0 m/s over three surfaces: smooth vinyl flooring (indoor), concrete (outdoor) and grass (outdoor), while a person was seated in it. The same wheelchair was placed on a simulator with motorized rollers, and the speed of the rollers was matched to the overground conditions. The root-mean-square (RMS) and frequency spectrum centroid of the vertical acceleration were calculated separately for the front and rear wheels.

Results

The lowest vibration was observed on the vinyl surface, which most closely matched the vibration of the simulator's rear wheels. Both concrete and grass exhibited a higher vibration amplitude compared to vinyl; however, grass had a lower frequency centroid. In real-life conditions, the highest vibration was near the front wheels, whereas the opposite

was found on the simulator; this discrepancy was expected, as the front wheels were not rolling on the simulator. In every condition, higher speeds increased both the amplitude and frequency of the vibrations.

Discussion

The next step will be to generate additional vibration on the simulator using actuators, to replicate the characteristics of surfaces like concrete and grass. Both surface and speed should be considered, as they both impact vibration. The importance of reproducing or not the higher vibration at the front wheels should also be assessed, particularly for users with limited sensory perception near their feet.

Images (Optional)

Table 1. Vibration amplitude and frequency spectrum centroid for two speeds on three surfaces and on rollers.

		Rear wheels		Front wheels	
Surface	**Speed (m/s)**	**RMS (m/s^2)**	**Centroid (Hz)**	**RMS (m/s^2)**	**Centroid (Hz)**
Smooth vinyl (indoor)	0.75	0.10	23.2	0.16	13.0
	1.00	0.15	24.6	0.19	16.3
	Diff	+50%	+6%	+19%	+25%
Concrete (outdoor)	0.75	0.43	29.7	1.48	31.2
	1.00	0.69	32.4	1.84	31.3
	Diff	+60%	+9%	+24%	+0%
Grass (outdoor)	0.75	0.51	8.1	0.85	9.7
	1.00	0.64	9.4	1.05	12.2
	Diff	+25%	+16%	+24%	+26%
Rollers (simulator)	0.75	0.20	24.0	0.06	24.2
	1.00	0.29	31.9	0.09	33.1
	Diff	+45%	+33%	+50%	+37%

Session Category

Rehabilitation Biomechanics and Human Factors: Rehabilitation

P2-307

Effects of Slip Intensity on Fall Rate Reduction during Repeated Standing-Slips

Ms. Susmita Bhandari, Dr. Caroline Simpkins, Dr. Feng Yang

Georgia State University, Atlanta, Georgia, United States

Introduction

Falls are a major public safety problem. Perturbation training has been shown to be useful in preventing falls. The slip intensity is a key parameter. Our previous study reported that higher-intensity slips induce more falls than lower-intensity slips on a novel slip among young adults [1]. The goal of this study is to examine whether slip intensity affects fall rate changes across five repeated standing-slips in young adults. We hypothesized that a high slip intensity would induce a fast fall rate reduction.

Methods

Twenty-one healthy young adults (23.8±4.4 years) were assigned to two groups: lower (11) and higher (10) intensity. They experienced five repeated standing-slips (S1-S5) under the protection of a safety harness connected to a loadcell on an ActiveStep treadmill. Peak belt speeds were 1.2 and 1.8 m/s for the lower- and higher-intensity profiles, respectively. The slip distance was 0.36 m for both groups. The slip outcome was classified as a fall if the loadcell force exceeded 30% of bodyweight and was visually verified by video files. The fall rate was calculated as the number of fallers divided by the total participants in each group for each slip. Fall-rate curves were log-fitted, and slope differences were tested with a Generalized Estimating Equation model in SPSS 29 with $\alpha=0.05$

Results

Both groups showed reduced fall rates over S1 to S5: 100% to 40% in the higher-intensity group and 36.4% to 0% in the lower-intensity group. The slope of the higher-intensity group's fall rate drop is significantly higher than that of the lower-intensity group (-42.11 vs. -21.32, $p<0.001$, Fig. 1).

Discussion

Our results showed that high-intensity slips initially caused more falls, but they also produced a strong motor learning effect, leading to a faster reduction in fall rate over

repeated slips. From a fall-prevention perspective, a high slip intensity should be prescribed for perturbation training. Notably, some participants in the high-intensity group did not recover by S5. This implies that our higher slip intensity may be overly strong for some individuals to adapt to. Future studies should further examine this observation.

Images (Optional)

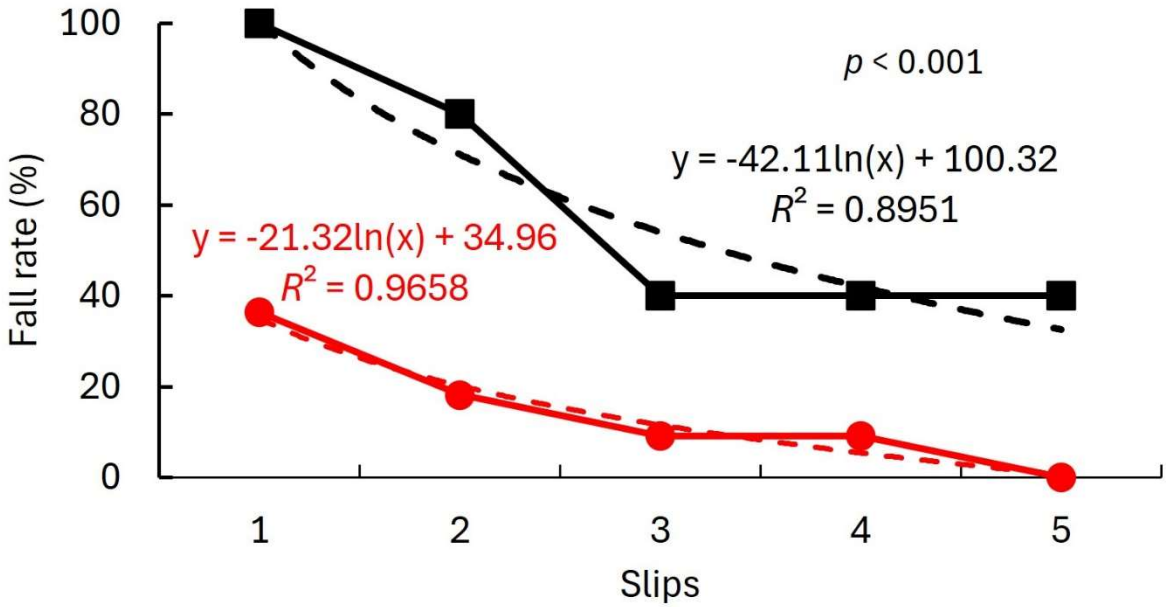


Fig. 1 Comparison of fall rate change over 5 slips between higher- and lower-intensity perturbation profiles.

References (Optional)

[1] Shin et al., J Biomechanics, 2024

Acknowledgements (Optional)

Session Category

Rehabilitation Biomechanics and Human Factors: Rehabilitation

P2-308

Enabling the Multi-Session Comparison of sEMG Features Using a Novel High-Density sEMG Electrode Shift Tracking Algorithm

Mr Fraser Douglas, Dr Calvin Kuo

University of British Columbia, Vancouver, BC, Canada

Introduction

Surface electromyography (sEMG) enables direct measurement of muscle activity during exercise with signal features holding associations to muscle fatigue, firing rate, motor unit recruitment, and force production. Thus, sEMG holds potential supporting the recovery assessment of individuals suffering neurological and musculoskeletal disorders. Despite this, sEMG is highly sensitive to changes in electrode location [1], with palpation and anatomical landmarks often insufficient to ensure consistent placement across sessions. To support longitudinal sEMG-based assessments, we developed a high-density sEMG (HDsEMG) algorithm to determine electrode shift via correlation maps [2], hypothesising that through the algorithm's application effects of electrode shift on signal features can be mitigated.

Methods

12 healthy participants (ethics H22-02423) performed isometric and dynamic exercises with HDsEMG arrays (64 electrodes, 1cm-spaced 8x8 configuration) on four leg muscles. These were repeated, reapplying arrays at shifted locations to obtain four sets of data per muscle. 3D scans taken post-exercise were used to identify the ground truth shift between recordings, with our HDsEMG algorithm estimating this shift. We extracted mean and median frequency, integrated EMG (iEMG), and max envelope amplitude from HDsEMG data. Relative feature differences between closest electrodes across recordings per ground truth and algorithm shifts were determined, as well as differences using the same electrodes across locations.

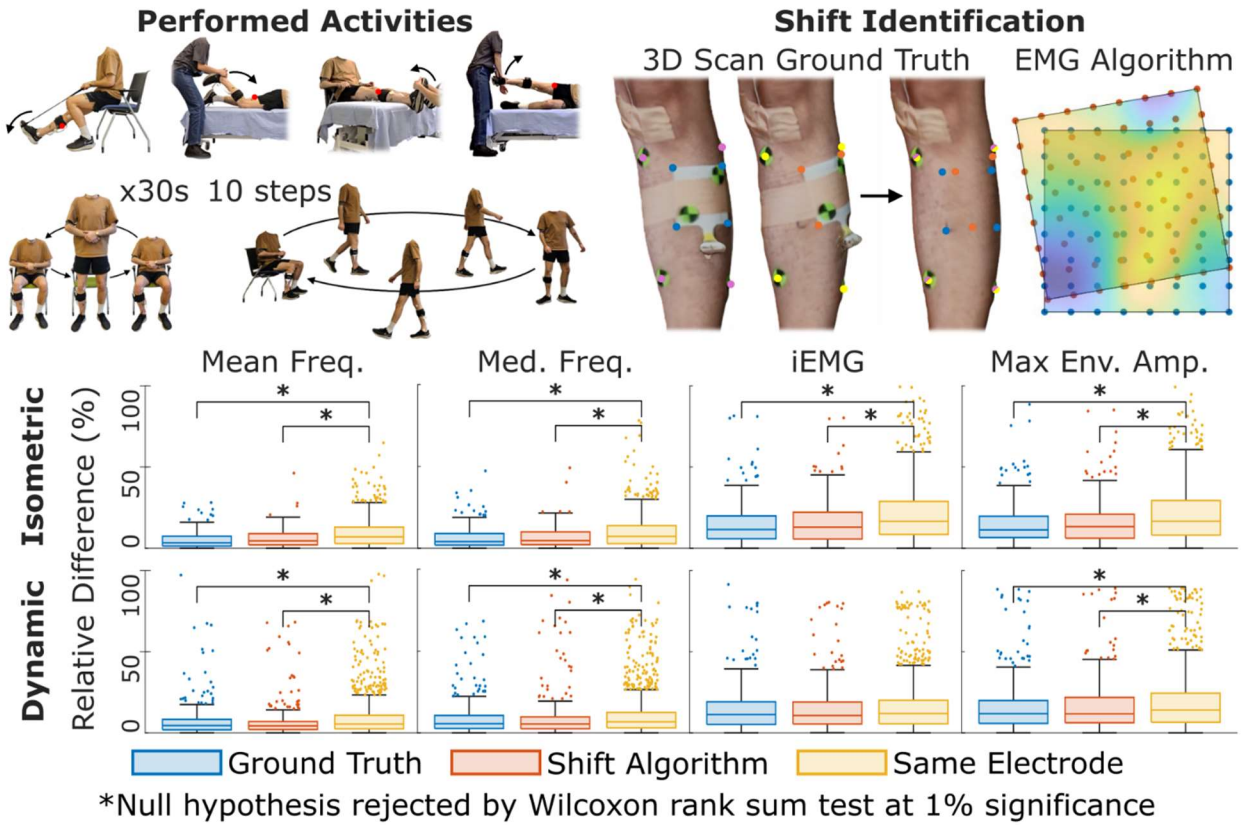
Results

Isometric results demonstrate feature differences when accounting for shift using the HDsEMG algorithm are statistically similar to when using the ground truth. Furthermore, across features the relative difference for same electrodes pre- and post-shift were significantly greater than the ground truth and algorithm. These results, excluding iEMG, were consistent with dynamic exercises.

Discussion

The similarity achieved between ground truth and algorithm results compared to same-electrode results indicate the algorithm's application effectively mitigated electrode shift effects. This approach can facilitate more direct comparisons of features across sessions while allowing for imprecise sensor placement. Remaining differences post-shift can likely be attributed to variations in skin and electrode preparation, and discrepancies in participant effort. In sum, this work represents a promising step toward robust sEMG measurement for musculoskeletal and neurological recovery tracking.

Images (Optional)



References (Optional)

[1] Fraser Douglas *et al.*, IEEE Trans. Instrum. Meas., 2025

[2] Fraser Douglas *et al.*, BMES 2024, 2024

Session Category

Rehabilitation Biomechanics and Human Factors: Rehabilitation

P2-309

Transfer Effects of Adaptive Propulsion Enhancement eXperience (APEX) Training on Gait Symmetry and Weak-Leg Joint Entropy During Overground Walking on Older Adults

Ms. Gaju Shin[1], Mr. Chihyeong Lee[1], Dr. Seoung Hoon Park[2], Dr. Beom-Chan Lee[2], Dr. Jooeun Ahn[1]

[1]Seoul National University, Seoul, N/A, Korea, Republic of. [2]University of Houston, Houston, Texas, United States

Introduction

Age-related gait asymmetry and increased stride-to-stride variability exacerbate mobility decline and falls in older adults, yet interventions targeting weak-leg propulsive deficits remain limited. The Adaptive Propulsion Enhancement eXperience (APEX) system, which incorporates an dual-belt treadmill that delivers real-time visual biofeedback (VB) of anterior ground reaction force (AGRF) with phase-specific belt-speed modulation to facilitate AGRF generation (propulsion-facilitating, PF), has been shown to enhance affected-leg propulsion after a single, short-term session (100 steps) in individuals post-stroke [1]. However, the efficacy of an intensified training protocol and the transferability of these biomechanical improvements to overgound walking remain unknown. This study investigates whether intensified APEX training elicits neuromotor adaptations in weak-leg and transfers improvements to overground gait symmetry and joint angle regularity in older adults.

Methods

Four older adults completed a single-session intensified APEX protocol, comprising baseline (30 steps), training (1000 steps), and post-training (30 steps) blocks. During training, the APEX system provided concurrent VB and PF to the participant's weaker leg. To evaluate transfer effects, a 10-meter overground walking tests were performed before and after the session. Bilateral kinematics (i.e., foot positions and knee joint angles) were recorded using a wearable motion capture system (MVN Awinda, Xsens Technologies, NL). Outcomes included the stance-time symmetry index (SI) to quantify gait symmetry and knee joint approximate entropy (ApEn) to characterize neuromotor regularity.

Results

Following the high-intensity training, participants improved tempoal gait symmetry, as demonstrated by a reduction in the stance-time symmetry index toward zero ($\Delta|SI| = 1.85 \pm 0.61$). Concurrently, knee joint angles exhibited increased requlrity and dynamic stability, quantified by a decrease in ApEn ($\Delta ApEn = -0.018 \pm 0.027$).

Discussion

The preliminary findings indicate that a single session of intensified APEX training elicits immediate transfer to overground gait in older adults. The concurrent improvements in stance-time SI and reduction in weaker-leg knee joint angle ApEn suggest that intensified training facilitated a short-term reorganization characterized by greater regularity and stability. Collectively, this proof-of-concept study demonstrates the potential of high-intensity APEX training as a viable intervention to mitigate gait asymmetry and restore gait regularity in older populations.

Images (Optional)

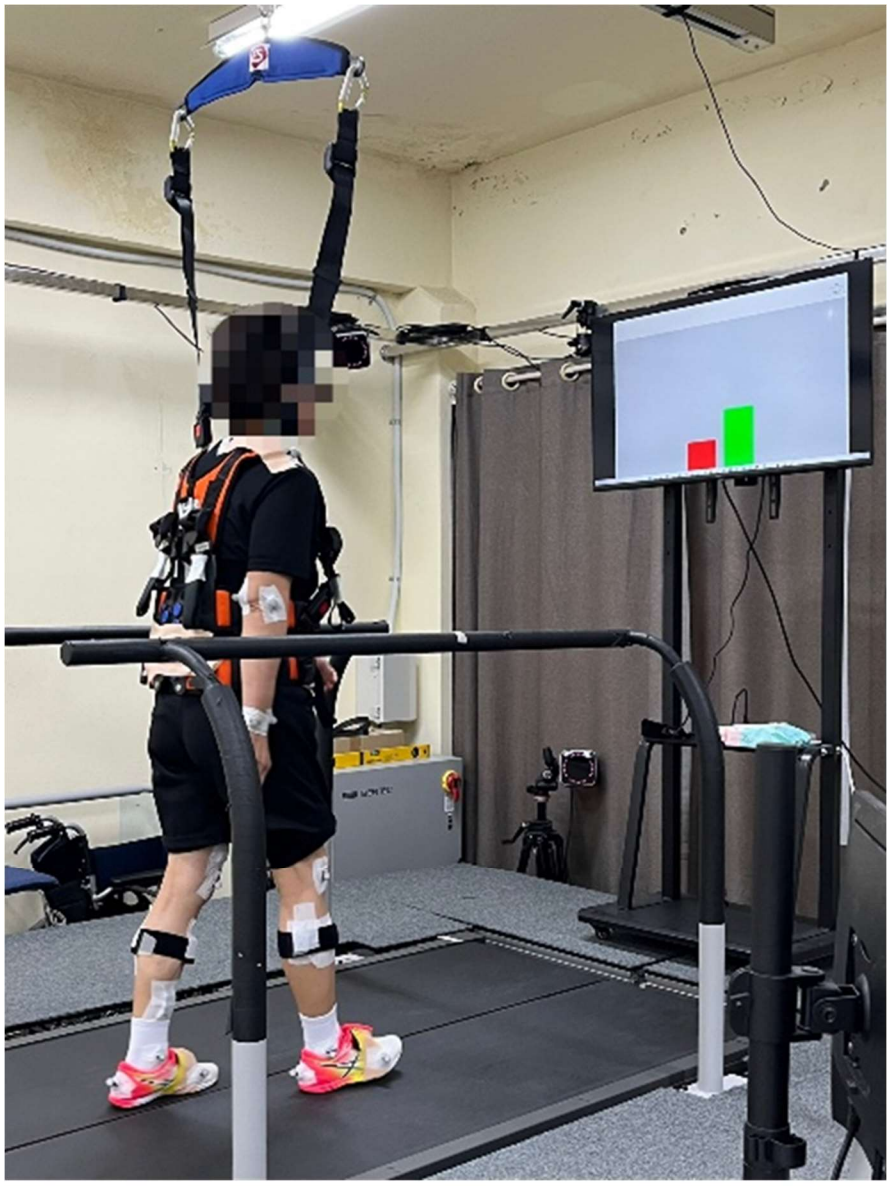


Fig. 1: Older adult participant undergoing intensified APEX propulsion training, receiving real-time visual biofeedback on anterior ground reaction force and phase-specific propulsion-facilitating belt-speed modulation.

References (Optional)

[1] Seoung Hoon Park *at al.*, IEEE Trans Neural Syst Rehabil Eng, 2025.

Acknowledgements (Optional)

This work was supported by the Brain Pool Program funded by the Ministry of Science and ICT (MSIT) through the National Research Foundation of Korea under Grant RS-2024-00446461. It was also supported in part by Korea Health Technology Research and Development Project through Korea Health Industry Development Institute (KHIDI) funded by the Ministry of Health and Welfare under Grant HK23C0071.

Session Category

Rehabilitation Biomechanics and Human Factors: Rehabilitation

P2-310

Thermal behaviour of transfemoral residual limbs in prosthetic sockets during rest, exercise, and recovery: a finite-element bioheat modelling study

Mrs Hadeel Alhamam, Prof Spyros Masouros, Prof Anthony Bull

Imperial College London, London, London, United Kingdom

Introduction

Heat buildup at the residual limb-socket interface remains a barrier to comfort and long-term prosthesis use, yet amputated limb thermoregulation within a socket is still poorly characterized. This study develops a finite-element bioheat model to quantify heat transfer and thermoregulatory responses in the transfemoral residual limb–socket system under realistic conditions.

Methods

MRI data from a unilateral transfemoral amputee were segmented into skin, fat, muscle and bone to form a multilayered geometry. This was abstracted into a 3D elliptical parametric model with preserved tissue thicknesses, including offset layers for the liner and socket. Thermal and physiological properties were assigned from literature. The Pennes equation governed heat transfer with convective, radiative, and evaporative boundary conditions. A transient three-phase protocol (rest, activity, recovery; 60 minutes each) was applied. Simulations were run under three ambient conditions: normal (24°C, 56% RH), hot–humid (32°C, 70% RH), and hot–dry (40°C, 24% RH). Prosthesis-OFF simulations allowed bare-skin heat exchange and were used to compare skin temperature against empirical data. Prosthesis-ON simulations blocked skin heat exchange and applied it to the socket exterior, testing two material configurations (silicone liner with carbon-fibre or thermoplastic sockets). A conductivity sensitivity analysis (±50%) was performed for the carbon-fibre configuration. Activity and recovery phases are still in progress.

Results

Model predictions agreed with empirical resting skin temperatures across all ambient conditions (R^2 = 0.97, RMSE = 0.36°C). Prosthesis use increased average skin temperature by ~1°C in normal conditions, with a slower temperature rise at hotter ambient due to the socket's insulating effect. Prosthesis use also altered the thermal gradient, with distal warming (~0.4°C) and greater proximal increases (~2.0°C). The proximal–distal gradient declined with increasing ambient temperature and reversed above ~37°C. For prosthesis-

ON simulations, carbon-fibre and thermoplastic material sets produced comparable temperatures. Varying conductivity by ±50%, exceeding realistic material ranges, produced minimal temperature change, demonstrating the limited thermal influence of material selection.

Discussion

This framework provides a reliable basis for residual-limb thermoregulation. Simulation findings indicate that thermoregulation-focused socket design may require active cooling rather than material changes alone, and future evaluations should include real-world ambient conditions.

Images (Optional)

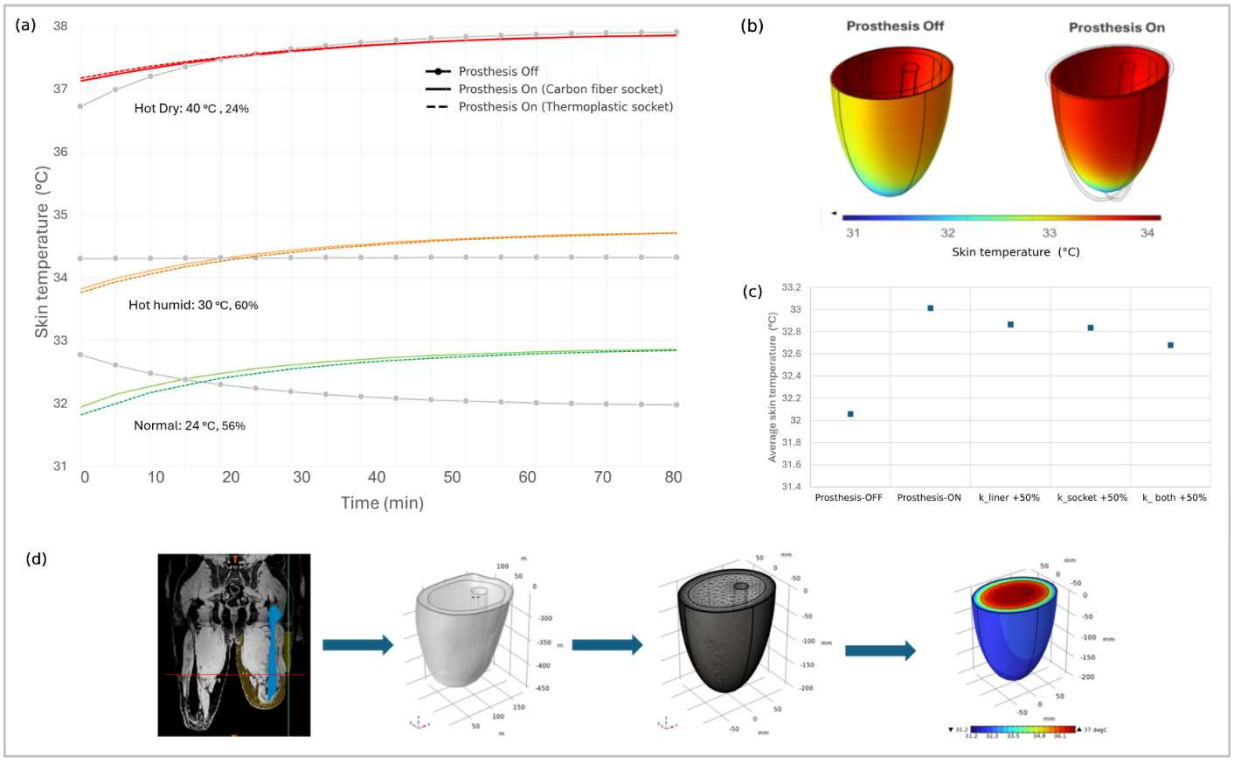


Figure1. (a) Average skin temperature under different conditions, (b) Effect of prosthesis use on skin thermal gradient (at normal ambient condition), (c) Sensitivity of average skin temperature to liner/socket conductivity (k), (d) Finite Element model development workflow

References (Optional)

Acknowledgements (Optional)

Session Category

P2-311

Compensatory Ankle Dorsiflexor Activation with a Unilateral Passive Knee Exoskeleton During Downhill Walking

Mr. Hyeonyong Lee M.S. student, Mr. Jungho Lee M.S., Mr. Hong Min M.S. student, Mr. Ji-sang Kang Ph.D.student, Professor Kyu-jin Cho Ph.D., Professor Jooeun Ahn Ph.D.

Seoul National University, Seoul, Seoul, Korea, Republic of

Mr. Hyeonyong Lee

Mr. Jungho Lee

Mr. Hong Min

Mr. Ji-sang Kang

Professor Kyu-jin Cho

Introduction

Exoskeletons are commonly designed to reduce mechanical demands on specific joints and muscles during gait [1]. Because walking emerges from coordinated interactions among multiple joints and muscles, it is important to understand how local assistance at the knee alters kinematics and muscle activation of other lower-limbs [2]. Downhill walking increases lower-limb joint loading and knee extensor demands [3], but it is still unclear how a passive knee exoskeleton affects knee kinematics or whether it induces compensatory changes. This study investigated how a passive knee exoskeleton influences knee kinematics and muscle activation of the thigh and shank during downhill walking.

Methods

Four healthy young men walked on a −6° treadmill under three 5-min conditions: no exoskeleton, adaptation with the exoskeleton, and steady-state exoskeleton walking. The

passive knee exoskeleton was worn on the right leg and provided assistance to the right knee during stance. Surface EMG was recorded bilaterally from eight lower-limb muscles, and the analysis focused on the right vastus lateralis and tibialis anterior. Ground reaction forces and three-dimensional kinematics were collected using an instrumented treadmill and a motion analysis system.

Results

Wearing the passive knee exoskeleton reduced peak right knee flexion during swing by 29.3% compared with the no-exoskeleton condition. At the muscle level, RMS EMG of the right vastus lateralis decreased by 22.8% with the exoskeleton, although this change was not statistically significant. By contrast, RMS EMG of the right tibialis anterior during pre-swing increased by 40.3% with the exoskeleton relative to the no-exoskeleton condition, representing the most pronounced and statistically significant phase-specific change in muscle activity.

Discussion

These findings suggest that a unilateral passive knee exoskeleton does not substantially unload the knee extensors but instead influences gait by mechanically limiting knee flexion. This mechanical constraint is accompanied by increased ankle dorsiflexor activation, a pattern consistent with a compensatory strategy to preserve toe clearance. Overall, unilateral knee assistive devices should be designed and evaluated with consideration for both local unloading at the assisted joint and compensatory adaptations in distal musculature and gait strategy.

Images (Optional)

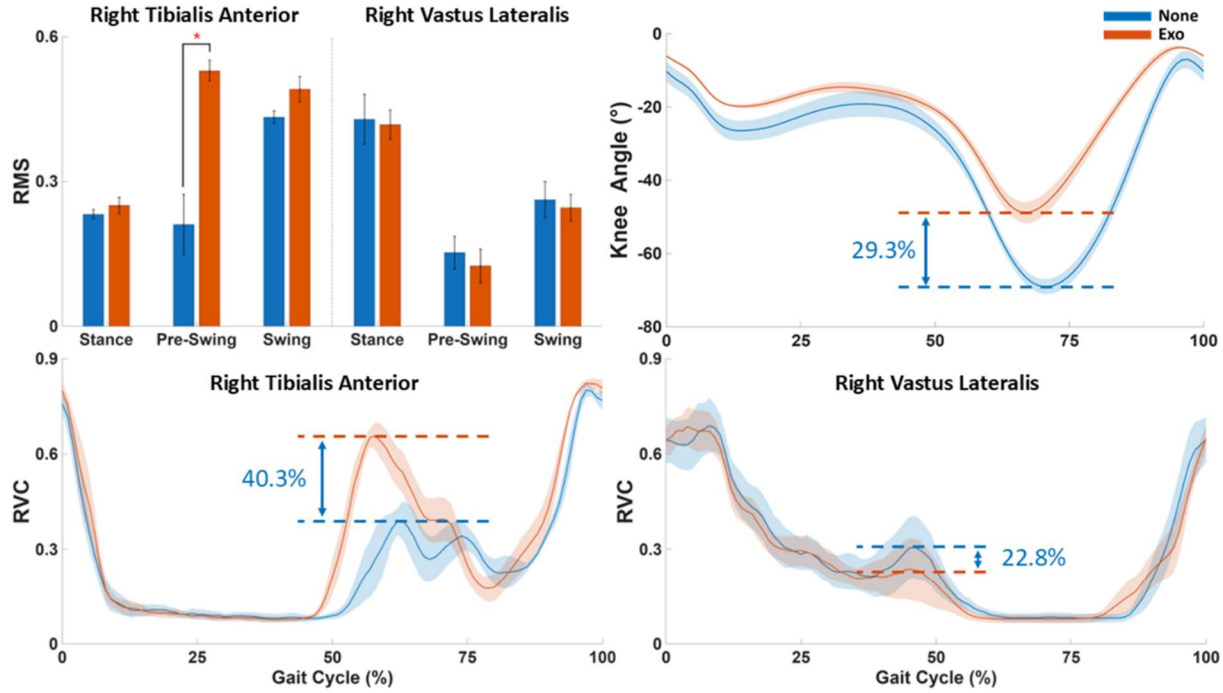


Figure 1. Group-averaged right knee flexion angle and EMG during −6° downhill walking with and without the u nilateral passive knee exoskeleton (mean ± SE). Top left: phase-specific RMS EMG of the right tibialis anterior a nd vastus lateralis in stance (0–50%), pre-swing (50–60%), and swing (60–100%) for the no-exoskeleton and exo skeleton conditions. Top right: right knee flexion angle over the gait cycle. Bottom left: normalized EMG (RVC)

References (Optional)

[1] Lin et al. (2025), Technologies,13; [2] Iranzo et al. (2023), Sensors,23; [3] Nuckols et al. (2020), PLoS One,15;

Acknowledgements (Optional)

This work was supported in part by the grant of the Korea Health Technology R&D Project through the Korea Health Industry Development Institute (KHIDI), funded by the Ministry of Health & Welfare, Republic of Korea (No. HK23C0071), Industrial Strategic Technology (No. 20018157) funded by the Ministry of Trade, Industry & Energy (MOTIE, Korea), and the National Research Foundation of Korea (NRF) grants funded by the Korean Government (MSIT) (No. RS-2023-00208052).

Session Category

Rehabilitation Biomechanics and Human Factors: Rehabilitation

P2-312

Proprioceptive Feedback from a Compliant Biomimetic Ankle Joint

Mr James Clark, Dr Peter Ellison

The University of York, York, North Yorkshire, United Kingdom

Introduction

Commercial ankle prosthetics primarily use one degree of freedom (DOF). Prior research has demonstrated that systems with two DOF improve user balance relative to one DOF devices [1]. However, pin-jointed designs lack the functional behaviour of a healthy ankle, primarily because they do not provide sufficient compliance or sensory feedback necessary for effective control. To address these limitations, we have developed an anatomically inspired ankle joint with motion constrained by soft multiplanar links analogous to ligaments.

Methods

An idealised version of the tibiotalar and subtalar joints was constructed to provide motion in the coronal and sagittal planes. Deformable waveguides were produced, representing the anterior talofibular and calcaneofibular ligaments, to provide stretch sensing. The waveguides were tested up to 10% strain, and the extension was approximated with linear regression. The joint was manipulated in dorsiflexion to 20° and plantarflexion to 35° in 5° increments. The resulting ligament stretch was recorded to establish the relationship between joint angle and ligament deformation.

Results

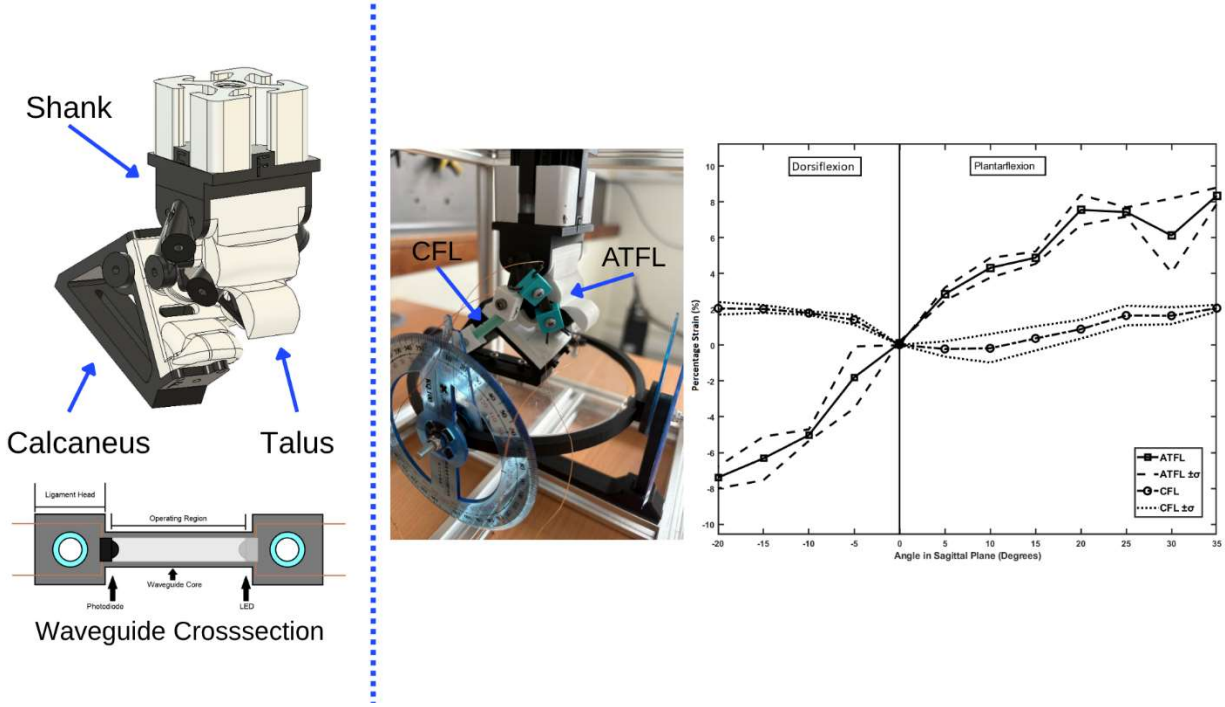
The linear regression fit produced R^2 values exceeding 0.996 between the operating range of 0-6% strain. During joint manipulation, the measured stretch of the lateral ligaments exhibited a mutually exclusive pattern across the discrete plantar direction of motion in both planes.

Discussion

The measured strain behaviour closely resembles the anatomical ligament strain profiles reported by Renström et al [2]. This indicates that the simplified joint model can replicate physiologically relevant deformation patterns, and the ligament analogues provide directional information about joint motion. In addition, the use of deformable ligament analogues inherently introduces joint compliance, offering a mechanical advantage over rigid pin-joint designs.

Because the system produces proprioceptive feedback through ligament stretch, it could be used to inform a controller for a powered prosthetic. The distinct stretch patterns of the ligaments across motion planes may allow the controller to infer joint position, serving a similar functional role to joint angle measurements in conventional control schemes. When combined with the joint's compliant behaviour, this sensing capability provides a pathway toward more adaptive, biomimetic control strategies.

Images (Optional)



References (Optional)

[1] E. Ficanha et al. , Frontiers in Bioengineering and Biotechnology, 2016

[2] P. Renstrom et al. , Foot & Ankle, 1988

Acknowledgements (Optional)

Session Category

Rehabilitation Biomechanics and Human Factors: Rehabilitation

P2-313

Quantifying Human–Exoskeleton Conformity Using Hip Joint Gait Phase Portraits

M.D. Jehyun Yoo[1,2], Mr Yoonhwan Kim[2], M.D. Juntaek Hong[2], M.D. Junmin Cha[2], Mrs Yebin Cho[2], M.D. Ph.D. Dong-wook Rha[2]

[1]Department of Rehabilitation Medicine, Gachon University Gil medical center, Incheon, Incheon, Korea, Republic of. [2]Department and Research Institute of Rehabilitation Medicine, Yonsei University College of Medicine, Seoul, Seoul, Korea, Republic of

Introduction

Wearable exoskeletons are increasingly used in industrial applications and rehabilitation. Despite their growing use, robot-assisted rehabilitation entails potential risks, due to the mismatch between standardized device designs and highly variable patient anthropometry. Such mismatch can result in improper fitting, malalignment, and inadequate timing and amount of torque assistance, reducing therapeutic effectiveness. Although interest in wearable exoskeletons is expanding, quantitative assessments of human–exoskeleton conformity remain limited. A major challenge is the difficulty in independently capturing human and device kinematics, as exoskeleton hardware often obscures anatomical landmarks required for marker-based motion capture.

In this study, we propose a novel approach for quantifying human–exoskeleton conformity by employing a hybrid motion capture setup that integrates IMU-based and marker-based systems. This dual-measurement strategy enables the independent acquisition of human and exoskeleton kinematics, allowing for a direct comparison. We also introduce new quantitative parameters specifically designed to evaluate the kinematic conformity between the user and the device.

Methods

Seven-healthy adults walked on a treadmill wearing a commercial exoskeleton(Angel Suit H10, Angel Robotics) at a self-selected speed for 3minutes. Human kinematics were measured using three IMUs placed on the pelvis and bilateral femurs, while exoskeleton kinematics were simultaneously recorded with a VICON system using three reflective markers per joint. Phase portraits of hip angle versus angular velocity were independently constructed, and similarity was computed using an area-overlap method:Similarity=$(A \cap B)/(A \cup B)$. The 3-minute trial was divided into three 1-minute intervals, from which the middle ten gait-cycles were analyzed. Additional metrics included point-wise Euclidean distance and centroid-drift of the phase portraits. Four torque levels(0%,30%,50%,70%)

were tested, and changes in similarity across torque and time were analyzed using linear mixed-effects models.

Results

Similarity significantly decreased as torque increased (slope = −0.02, $p < 0.05$), whereas no significant change was observed across early, middle, and late phases of walking.

Discussion

This study presents a novel quantitative framework for assessing human–exoskeleton conformity using independent kinematic measurements. Phase portrait similarity decreased with higher assistive torque, suggesting increased kinematic discrepancy. These conformity metrics may support individualized tuning of exoskeleton assistance and guide the development of patient-specific control strategies.

Images (Optional)

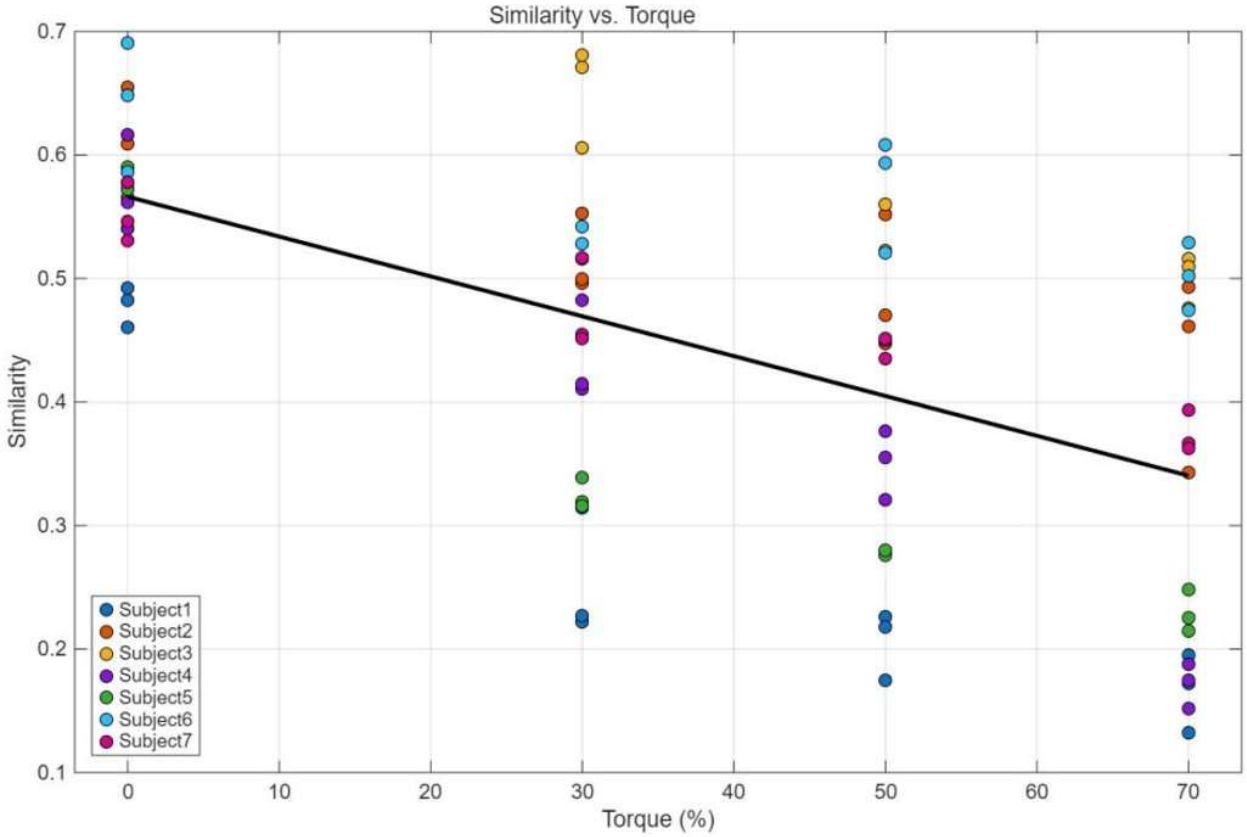


Figure Similarity changes across different torque conditions (0%, 30%, 50%, 70%)

Session Category

Rehabilitation Biomechanics and Human Factors: Rehabilitation

P2-314

Uneven Terrain Training for Prosthesis Users: Interim Analysis of the First Cohort in a Phase I Clinical Trial

Dr. Jenny Kent PhD, CSci[1], Ms Katie Bricarell MS[1], Dr. Stefania Fatone PhD, BPO(Hons.)[2], Dr. Szu-Ping Lee PT, PhD[1]

[1]University of Nevada Las Vegas, Las Vegas, Nevada, United States. [2]University of Washington, Seattle, Washington, United States

Introduction

Persistent mobility deficits impact participation and quality of life of many lower limb prosthesis users (LLPUs). However, empirically-tested interventions to address these deficits are scarce. Exposure to uneven terrain (UT) may encourage exploration of new movement strategies, facilitate learning to respond to perturbations, and attenuate fears of the unknown. We aim to determine whether UT training can improve prosthetic skill and confidence. Here, we present findings from the first cohort of a Phase I clinical trial exploring UT training feasibility in LLPUs, following an established framework [1].

Methods

Training consisted of 12 sessions, during which LLPUs walked on a UT treadmill (UTT) or a flat terrain treadmill (FTT; to assess feasibility of control group only) for 12 two-minute bouts, wearing a safety harness. Handrail use, treadmill speed, and UT contour height were progressed to maintain level of challenge. Whole-body kinematics were collected via motion capture. Pre-post assessments included: Activities-specific Balance Confidence scale, Prosthetic Limb Users Survey of Mobility, L-test, Two-Minute Walk Test, Four Square Step Test, Single Leg Stand tests, and 7-day activity monitoring. Participant feedback was recorded throughout all sessions, and via an acceptability questionnaire.

Results

Eight individuals with unilateral amputation attended an average of 11.5 training sessions (Table 1). All could walk on their assigned treadmill. Session termination reasons included pain, fatigue, and time constraints. The handrail and harness system obscured biomechanical markers; remedied by careful camera placement. Several participants indicated that faster speeds made walking on the UTT easier. Activity monitoring periods did not reflect all participants' normal day-to-day activity.

Participants reported a positive experience. Of the seven who trained on the UTT, five agreed/strongly agreed that the training improved their balance, and six, their balance

confidence. While anecdotal reports of increased confidence and improved stumble recovery during daily life were provided, there were no changes in outcome measures.

Discussion

Individuals of all amputation levels demonstrated ability to participate in UT training, and described positive impacts. However, alternative outcome measures capable of detecting the impact of training described by participants must be identified before a Phase II clinical trial is conducted.

Images (Optional)

	Group	Age (yrs)	Sex	Mass (kg)	Ht. (m)	Amp. level	Amp. Et.	Time since amp. (yrs)	Session outcomes		
									N sessions (max 12)	Mean N walking bouts/ session	Mean bout duration (s)
1	UTT	38	M	88.8	1.75	TF	Tr	13.1	12	11.2	120.0
2	UTT	38	M	106.7	1.60	HD	Sa	8.2	12	4.3	119.5
3	UTT	50	M	92.0	1.69	TT	Tr	1.1	12	11.6	120.0
4	UTT	48	M	93.9	1.81	TT	Tr	3.8	12	12.0	120.0
5	UTT	32	M	76.6	1.83	TT	Tr	11.4	11	12.0	120.0
6	UTT	53	M	102.8	1.81	TF	Tr	4.9	9	12.0	120.0
7	UTT	64	F	68.1	1.68	KD	Tr	1.7	12	12.0	120.0
8	FTT[a]	75	F	56.0	1.58	TF	Va	9.2	12	9.8	95.1
Mean (SD)		49.8 (14.4)		85.6 (17.42)	1.72 (0.10)			6.7 (4.47)	11.5 (1.13)	10.6 (2.67)	116.8 (8.67)

Table 1. Characteristics and session outcomes by participant.

UTT – uneven terrain treadmill, FTT – flat terrain treadmill[a]; Ht. – height; Amp. – amputation; TT – transtibial, KD – knee disarticulation, TF – transfemoral, HD – hip disarticulation; Et. – etiology; Tr – traumatic, Sa – sarcoma, Va – vascular.

[a]Flat terrain treadmill group included to assess feasibility of the control arm only.

References (Optional)

[1] Orsmond *et al.*, OTJR, 2015.

Acknowledgements (Optional)

We would like to thank Ashton Pearson for his assistance with designing and building the uneven terrain treadmill. This work was supported by the Department of Defense CDMRP [HT9425-24-1-0444], Nevada INBRE [GM103440], and a Top Tier Doctoral Graduate Research Award from the University of Nevada, Las Vegas.

Session Category

P2-315

Smoother Ground Reaction Force Profiles while Ambulating with a Tensegrity Crutch: A Biologically Inspired Design for Compliant Mobility Assistive Devices

MS. Jingxian Gu, Dr. Dobromir Dotov

University of Nebraska Omaha, Omaha, NE, United States

MS. Jingxian Gu

Introduction

Six million people use crutches as mobile aids in the US. Crutches need to enable dynamic balance and efficient walking. They can be the only support of the body during the swing phase. Rigid designs with no axial mobility limit sensory feedback from the ground and lead to secondary injury on the upper joints. Spring-loaded designs offer compliance at the expense of dynamic stability.

We designed a crutch with compliance in multiple axes by using a structural principle studied in biology and robotics. Its tensegrity module consists of a closed network of pre-stressed compressive and tensile elements. Musculoskeletal systems exploit this principle for stability and proprioception. We compared commercial rigid, spring-loaded, and our compliant design in overground walking trials.

Methods

Young healthy adults (N=17) with no recent lower-body injury performed straight walking and turning trials (reported separately) at a comfortable self-selected pace. This was a within-subject design with random order of blocks of crutch type. A knee blocker simulated unilateral injury of the dominant leg. Integrated force plates and a 12-camera motion capture system collected ground reaction force (GRF) and kinematic data. Participants completed questionnaires of perceived effort, comfort, and tool usability.

Results

In straight walking, the compliant crutches with a tensegrity terminal module produced a smoother vertical GRF profile, expressed as a lower peak loading rate after initial contact with the ground (p<.05), see Figure 1. Axial stiffness was 10 kN/m in the spring-loaded crutch and 22 kN/m in our design which agrees with some participants' observation that

the spring-loaded type felt too soft and could bottom out. Upper body stability and kinematic gait parameters are being analyzed.

Discussion

Our innovative approach promises to improve crutch features that are associated with secondary injury and non-use which are linked to repeated falls in chronic users. The modular biomechanical design principle is generic and promises exciting possibilities for improving a range of other types of assistive devices.

Images (Optional)

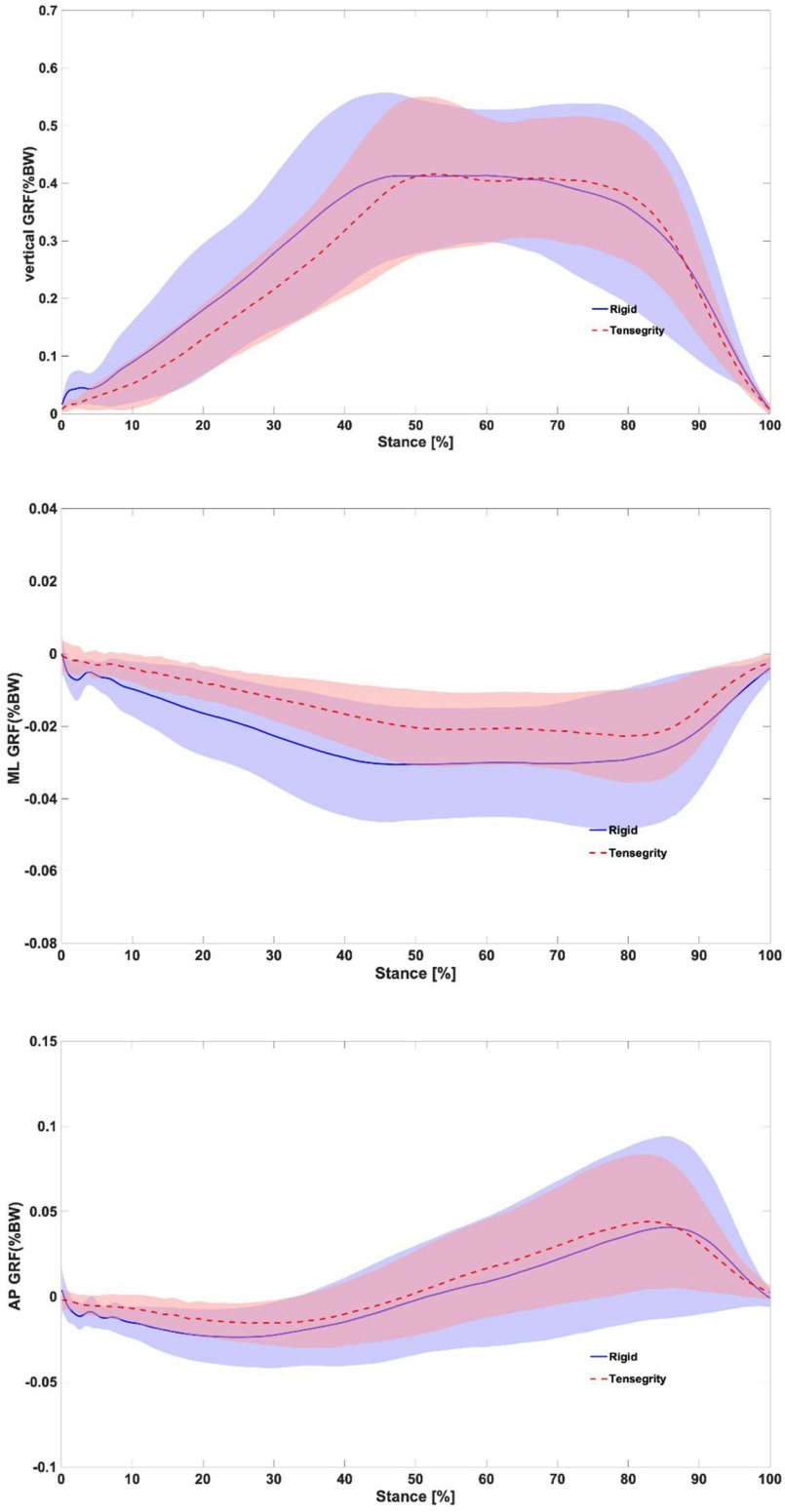


Figure 1. Representative vertical GRF profiles (Mean±95% CI across steps of one participant) with smoother loading rate in the compliant compared to the rigid condition.

Acknowledgements (Optional)

J.G. was supported by NIHP20GM109090 and NIH5P20GM152301-02.

Session Category

Rehabilitation Biomechanics and Human Factors: Rehabilitation

P2-316

Evaluation of Multiple Motion-Detection Algorithms and Thresholding Methods for In-Bed Exercise Tracking Across Individuals with Diverse Movement Capacities, Including Bedridden Patients

Ms. Jiwon Ryu[1], Mr. Cheoljae Lee[1], Ms. Gahyun Lee[1], Prof. Gwanseob Shin[1], Prof. Won Kim[2]

[1]Ulsan National Institute of Science and Technology (UNIST), Ulju-gun, Ulsan, Korea, Republic of. [2]Asan Medical Center, University of Ulsan College of Medicine, Songpa-gu, Seoul, Korea, Republic of

Introduction

The majority of bedridden patients become inactive, so a systematic and motivating exercise program is necessary. Motion-tracking exergames may offer a solution, however, most of the existing exergames require standing and highly active movements, which might be unsuitable for the inpatients. Furthermore, the movement patterns of the inpatients and movement capacity might be different from those observed in healthy individuals. As the first step of developing a suitable exergame for rehabilitating the bedridden patients, this study aimed to create a motion-detection algorithm which can track in-bed exercise motions across individuals with diverse movement abilities, including the bedridden inpatients.

Methods

Eight asymptomatic participants (4 females, 4 males) and four inpatients (1 female, 3 males) conducted three in-bed exercises: 1) shoulder flexion, 2) single leg raise (SLR), and 3) hip-knee flexion. The participants performed each exercise while lying on a hospital bed, with four inertial measurement units (IMUs) attached to both sides of wrists and ankles. The exercise motions were quantified at 100Hz. For the bedridden inpatients, the motion data were collected during regular rehabilitation sessions with clinical experts.

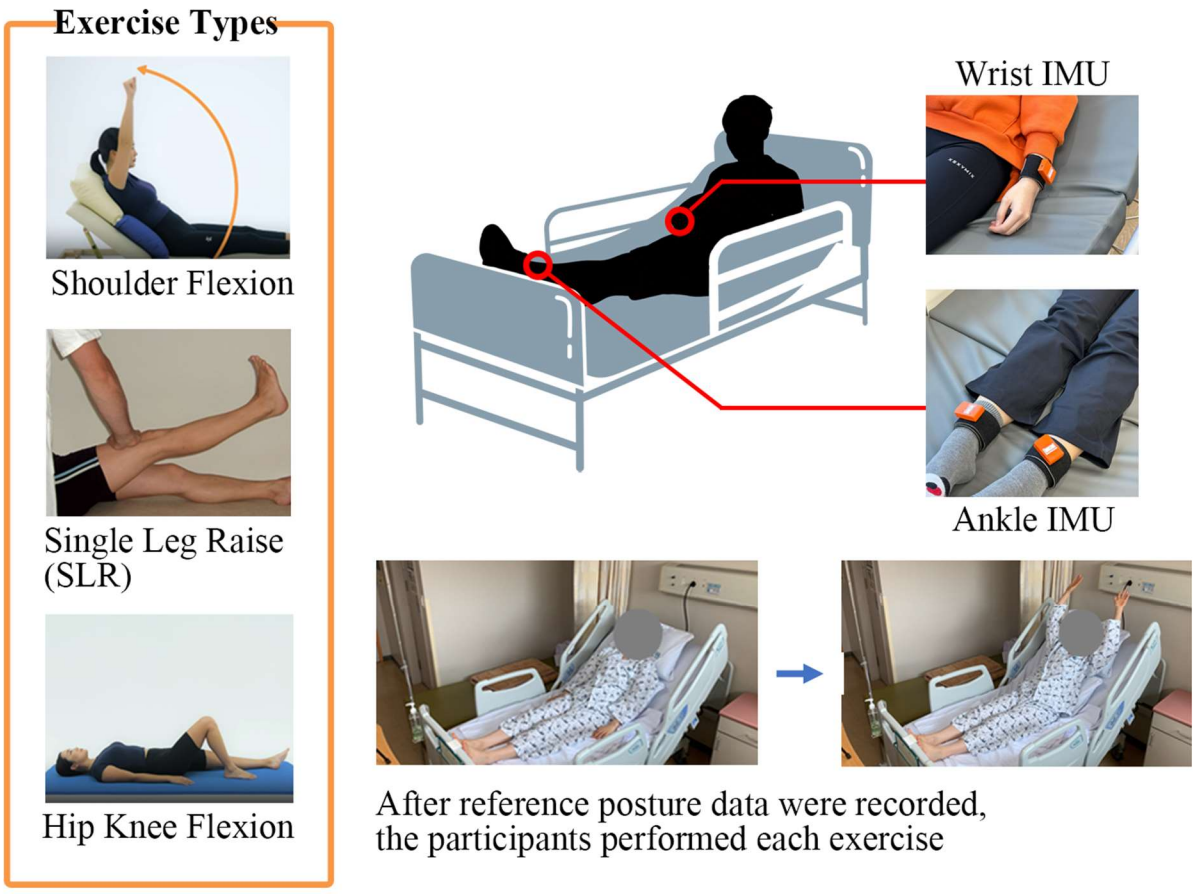
Results

The proposed algorithm utilized moving mean and moving variance of a vector magnitude of tri-axial linear acceleration for measuring movement intensity [1], combined with one principal Euler orientation angle. The algorithm first automatically determined thresholds of main parameters using the first few cycles of each exercise, then detected exercise and non-exercise segments in the remaining cycles. The algorithm achieved over 90% accuracy in identifying the exercise and non-exercise segments for both shoulder flexion and SLR motions across all participants. For the inpatients, the average accuracy was approximately 94% in shoulder flexion and 91% in SLR.

Discussion

The current study showed that the designed algorithm effectively detects the initiation and termination of major in-bed exercise movements from the people with various movement capacities, including the bedridden inpatients. Main findings of the study can be utilized as a core component for an in-bed exergame system. Future studies need to evaluate its performance with larger populations and additional exercises.

Images (Optional)



References (Optional)

[1] Komaris et al. , BMC Sports Sci Med Rehabil, 2022

Acknowledgements (Optional)

This research was supported by National Research Foundation of Korea (NRF) grant funded by the Korea government (MSIT) (No.RS-2024-00346048) and Asan Institute for Life Science (2024IP0097).

Session Category

Rehabilitation Biomechanics and Human Factors: Rehabilitation

P2-317

A Taxonomy for Ankle-Foot Orthosis Testing Methods

Ms Katherine Vaiciulis, Mr Zachary Williston, Dr Deema Totah PhD

University of Iowa, Iowa City, IA, United States

Introduction

Ankle-foot orthoses (AFOs) are used by individuals with impaired gait. The amount of support AFOs provide largely depends on their mechanical properties, like stiffness. AFO stiffness is calculated from the slope of ankle flexion torque vs angle curve. Although individually optimizing AFO stiffness can improve gait [1], it is not quantified in clinical practice. Measurement techniques for AFO mechanical properties are not standardized, causing a significant lack of inter-method repeatability [2]. To address these challenges, this work performs a scoping review and introduces the first classification taxonomy for AFO mechanical testing to facilitate inter-study comparisons and guide future development.

Methods

A database search was conducted in PubMed, Engineering Village/Compendex, and Web of Science following the PRISMA guideline extension for scoping reviews. A snowballing search was conducted beginning from two published literature reviews. Articles that experimentally measure the mechanical properties of AFOs were eligible for inclusion. Exclusion criteria included insufficient details, using previously published testing methods, or measuring AFO properties using onboard sensors.

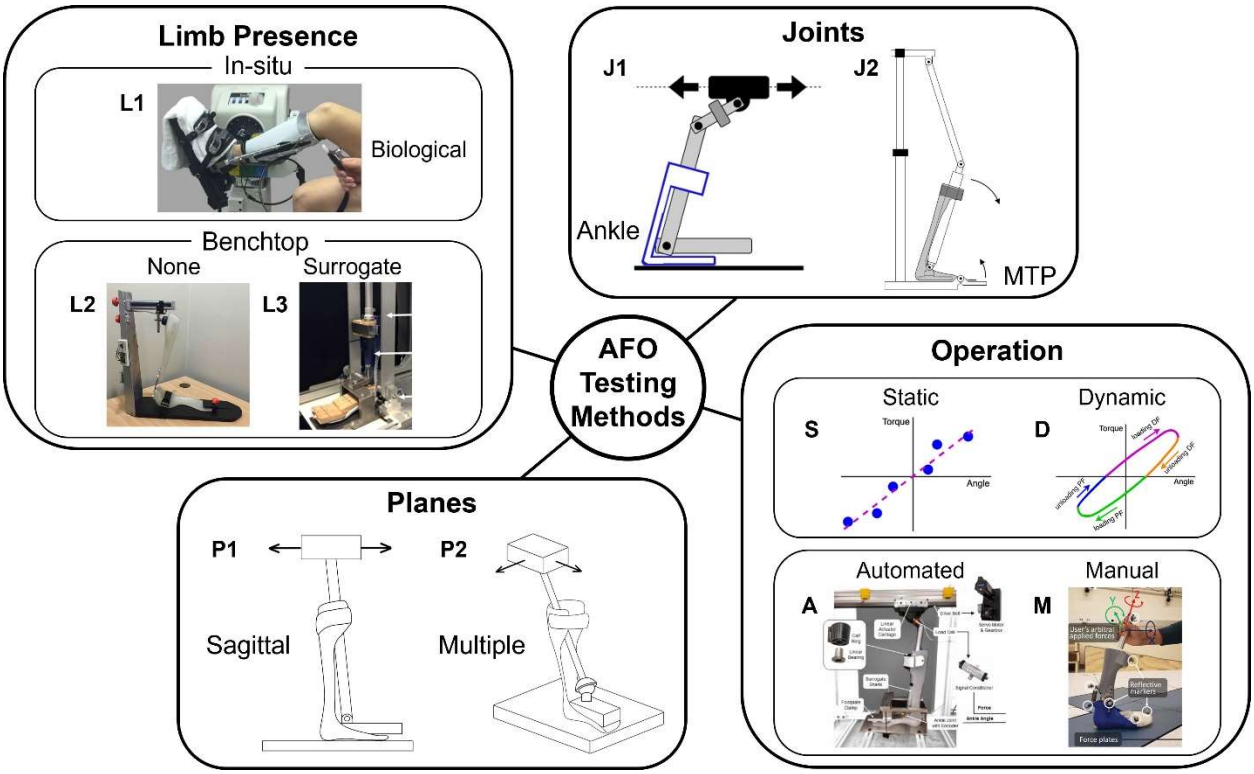
Results

Forty-six of 492 potential papers were identified for inclusion and analyzed to develop a taxonomy (categories in parentheses) for classifying AFO testing methods according to design and operation properties. Most methods use benchtop testing (L2,3), while a few in-situ (L1) methods involve a biological limb. Most methods deflect AFOs in the sagittal plane only (P1), while some deflect AFOs in multiple planes (P2). Most methods model the ankle joint only (J1), while a few also model the metatarsophalangeal (MTP) joint (J2). Methods also vary in operation, collecting static (S) or dynamic (D) data, through automated (A) or manual (M) operation.

Discussion

The proposed taxonomy provides the first framework for efficient categorization and comparison of specifications across AFO testing methods. Key elements that may affect measurements and would benefit from standardization include the ankle location, planes of motion, and testing speed. This work guides future standardization of methods and protocols for implementing AFO testing into clinical practice and quality control in manufacturing. This would support data-driven, individualized AFO prescription, design, and production towards optimized user outcomes.

Images (Optional)



References (Optional)

[1] Jacob Skigen et al., JNER, 2024

[2] Benjamin Shuman et al., JNER, 2024

Session Category

Rehabilitation Biomechanics and Human Factors: Rehabilitation

P2-318

Quantifiable Metrics of Saccadic Eye-Movement Improve With Time in Concussed Subjects

Miss Katherine Wiebe BSc., PhD candidate

Carleton University, Ottawa, ON, Canada

Introduction

Current concussion assessment tools rely on qualitative and subjective methods. Our objective is to determine if saccadic eye-movements are correlated with the Vestibular Ocular Motor Screening (VOMS) test. A second objective is to compare commercial eye-trackers with open-source tools for this task.

Methods

Twenty concussed subjects performed the VOMS test and subsequently a saccadic eye-movement task, while being concurrently recorded using a webcam and a commercial eye-tracking tool. We developed analysis software for quantifying and comparing the eye tracking movements. Metrics of interest included the time constant (τ [ms]) of a transition event, and the concurrence of eye position before, during, and after each transition.

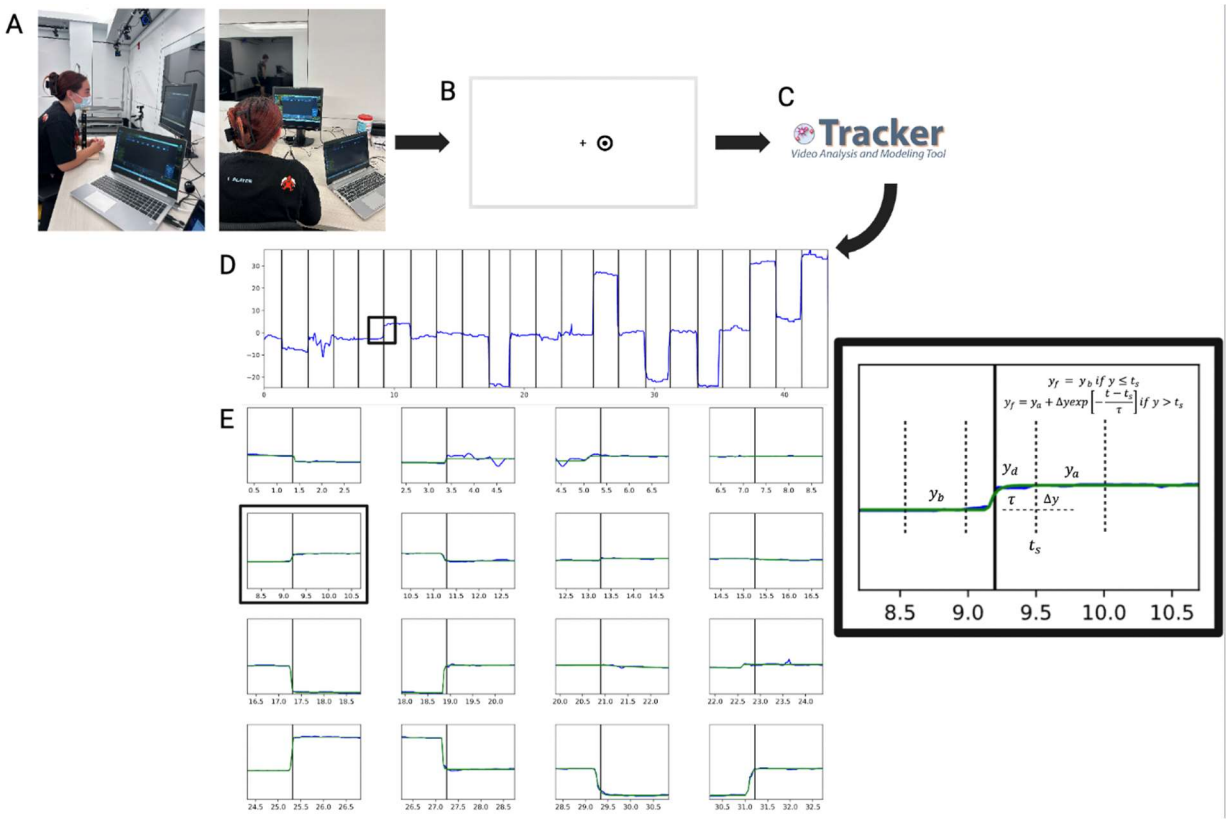
Results

A significant difference in all parameters between the control and concussed subjects, indicated that concussed subjects had slower transition time and difficulty fixating on a target. We discuss how the VOMS results may be correlated with eye-tracking. No significant differences were found between the calculated metrics from the webcam and the commercial eye-trackers.

Discussion

Correlations between eye-tracking metrics and VOMS test scores may call to question the specificity of the VOMS test in assessing concussions. This study supports the use of accessible eye tracking and open-source tools.

Images (Optional)



Session Category

Rehabilitation Biomechanics and Human Factors: Rehabilitation

P2-319

Model-based Reinforcement Learning for Personalized Hip Exoskeleton Assistance to Enhance Walking Mobility in Older Adults

PhD Candidate Ke Feng, Dr. Thomas Yang, Dr. Shuzhen Luo

Embry-Riddle Aeronautical University, Daytona Beach, Florida, United States

Introduction

Powered hip exoskeletons offer a promising solution for age-related mobility decline, as the hip joint contributes substantially to forward propulsion. User studies [1] show strong acceptance of lower-limb exoskeletons among older adults, with walking efficiency rated as the top factor influencing their acceptance. However, current hip exoskeleton controllers are designed mainly for healthy adults and require hours of human testing and parameter tuning to identify optimal torque profiles [2]. Phase-based controllers may also produce discontinuous assistance [3]. No prior work has developed personalized assistance specifically for older adults. Achieving truly "wear-and-go" assistance that adapts automatically without human-involved tuning remains a major challenge and is essential for community deployment.

Methods

Building on our Nature publication [4], this work presents a model-based reinforcement learning framework for personalized hip exoskeleton assistance. We incoporate a Hill-type muscle–tendon model with reduced maximum isometric force, increased passive stiffness, and slower activation dynamics, enabling the neuromusculoskeletal model to reproduce gait characteristics of older adults. A neural network controller is jointly trained with this personalized human model to optimize hip torque assistance and improve walking mobility. Through co-adaptation, the controller learns autonomous assistance aligned with user-specific neuromuscular coordination. Trained entirely in simulation, it autonomously delivers personalized torque assistance during real-world walking with no parameter tuning.

Results

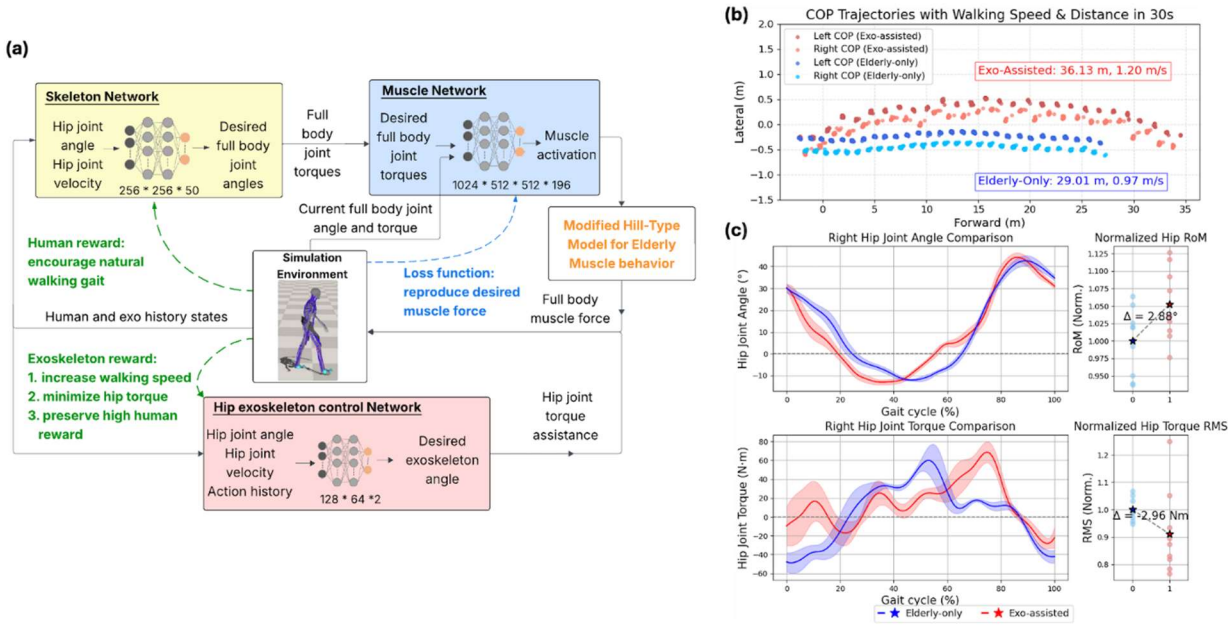
Simulation results (Fig. 1c,d) showed that exoskeleton assistance increased gait speed from 0.97 to 1.20 m/s, improved hip range of motion by 7.2%, and reduced biological hip torque by 8.7%. In a pilot human subject test, the personalized controller increased hip

range of motion by 12.7% compared with the no-exoskeleton condition. Additional subject data are currently being collected for broader validation.

Discussion

This study shows that a simulation-trained, aging-informed controller can provide personalized hip assistance and improve mobility without human-involved tuning. By overcoming the simulation-to-reality gap and generalizing across exoskeletons and musculoskeletal conditions, it offers strong potential for rehabilitation and community mobility.

Images (Optional)



References (Optional)

[1] Raitor, M. et al., IEEE Trans. Neural Syst. Rehabil. Eng., 2024.

[2] Ding, Y., Kim, M., Kuindersma, S. and Walsh, C.J., Sci. Robot., 2018.

[3] Lim, B. et al., IEEE Trans. Robot., 2019.

[4] Luo, S. et al., Nature, 2024.

Acknowledgements (Optional)

Session Category

Rehabilitation Biomechanics and Human Factors: Rehabilitation

P2-320

Effects of Agonist-Antagonist Myoneural Interface on Trunk Kinematics During Walking Among Individuals With Unilateral Transtibial Limb Loss

Mr. Kiichi Ash MS[1,2], Dr. Pawel Golyski PhD[2,3], Dr. Brad Hendershot PhD[2,3,4], Dr. Courtney Butowicz PhD[2,3,4]

[1]Henry M. Jackson Foundation for the Advancement of Military Medicine, Inc., Bethesda, MD, United States. [2]Walter Reed National Military Medical Center, Bethesda, MD, United States. [3]Extremity Trauma & Amputation Center of Excellence, Falls Church, VA, United States. [4]Uniformed Services University of the Health Sciences, Bethesda, MD, United States

Introduction

Traditional lower-limb amputation transects native agonist–antagonist muscle connections, reducing proprioceptive feedback and forcing greater reliance on vision during walking. The agonist–antagonist myoneural interface (AMI) procedure restores these muscle pairs, potentially improving proprioception and motor control. However, since this construct was designed for use with myoelectric prostheses that are not commercially available, it is unclear if AMI improves walking mechanics when using a conventional prosthesis. The purpose of this work was to evaluate postural control during walking with a conventional prosthesis, as quantified by trunk kinematics, during level treadmill walking in persons with unilateral transtibial limb loss (UTTLL), with and without AMI. We hypothesized that persons with AMI would exhibit reduced trunk–pelvis range of motion (ROM) compared to traditional amputation, indicating better postural control due to increased residual limb proprioception.

Methods

Seven service members with UTTLL donning passive-energy storing and returned ankle-foot prostheses, two with AMI (37.0 ± 2.8 y) and five without (38.0 ± 11.1 y), completed a one-minute, full-body gait assessment on a treadmill at controlled velocity of 1.0 m/s. Prosthetic-side strides were parsed and analyzed to compute trunk range of motion (ROM) using OpenSim (v4.4) and custom MATLAB (2024b) scripts. Group differences were assessed with independent-samples *t*-tests (α=0.05).

Results

Participants with AMI exhibited 48.93% and 29.27% smaller trunk–pelvis ROM in the sagittal ($p = 0.249$) and frontal plane ($p=0.219$), but 5.72% larger trunk–pelvis ROM in the transverse plane ($p= 0.838$).

Discussion

Individuals with AMI did not exhibit differences in trunk–pelvis ROM compared to traditional UTTLL. Individuals with AMI exhibited trunk–pelvis ROM comparable to uninjured individuals (4.4°±2.4° sagittal, 11.6°±4.0° frontal, 13.9°±5.2° transverse), versus individuals with traditional amputation techniques. This comparison may suggest that the benefits of AMI, particularly enhanced proprioception and improved prosthesis embodiment, may extend to users of conventional prostheses, improving stability by reducing compensatory movement. This may indicate a myoelectric prosthesis may not be required to obtain postural control benefits from AMI and the use of a conventional prosthesis with AMI should be further explored. However, given the small sample size, these results must be taken cautiously.

Images (Optional)

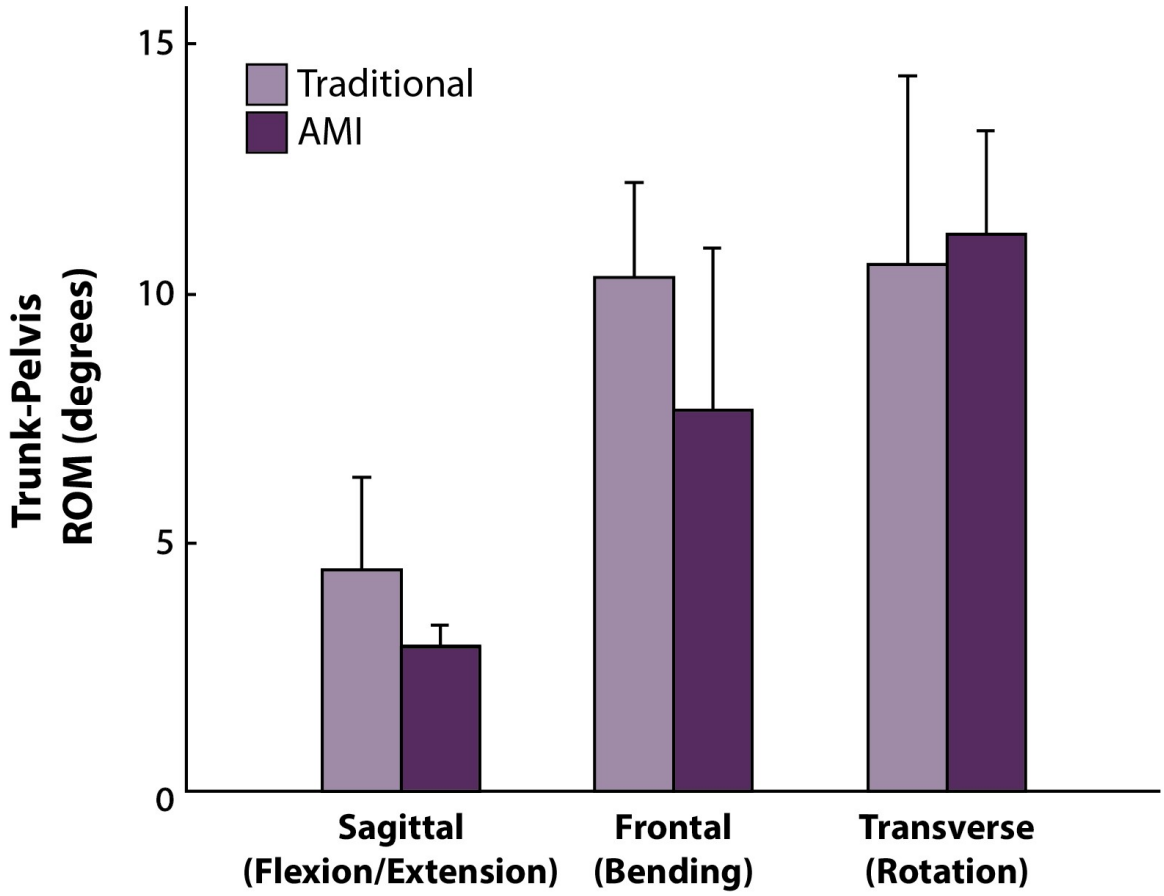


Figure 1: Maximum trunk-pelvis range of motion (ROM) during a 1-minute treadmill walk at a controlled velocity (1.0 m/s). Ranges were calculated during prosthetic-side strides.

References (Optional)

Acknowledgements (Optional)

This work was supported by NIH award 1R03HD114176-01. The views expressed herein are those of the authors and do not reflect the views of Henry M. Jackson Foundation for the Advancement of Military Medicine, Inc., USUHS, DHA, DoW, VA, nor the U.S. Government.

Session Category

Rehabilitation Biomechanics and Human Factors: Rehabilitation

P2-321

Evaluating Cortical Activation Patterns Associated With Auditory Biofeedback for Gait Retraining

MS, PT Luisa Cedin[1], MS Camilla Antognini[1], BS Emily Timm[1], . Emma Struck[1,2], PhD Christopher Knowlton[1], PT, PhD Joan O'Keefe[1], PhD Markus Wimmer[1]

[1]Rush University Medical Center, Chicago, IL, United States. [2]Case Western Reserve University, Cleveland, OH, United States

Introduction

Engaging the patient during gait retraining is an emerging strategy in rehabilitation. Auditory feedback is a promising approach as it enables rapid motor responses without constraining movements. We developed a musical feedback system to shift the center of pressure (CoP) through an intuitive, engaging auditory cueing approach [1]. A key concern of this technology is the involved cortical load. Therefore, this pilot study aimed to detect changes in motor planning and auditory cortical activation patterns of musical feedback while patients were cued to modify their gait line.

Methods

Ten healthy adults were asked to walk at a self-selected speed under four auditory conditions: silence (S), self-selected music (M), musical feedback (MF) and verbal feedback (VF). MF and VF were randomized and cued the subjects to either medialize or lateralize CoP. Musical feedback was provided by measuring real-time plantar pressure (Moticon ReGo insoles) to modulate a low-pass filter that muffled the music whenever lateral CoP exceeded 25% of baseline. Simultaneous functional near-infrared spectroscopy (fNIRS) data was recorded bilaterally from the superior and middle temporal gyri of the temporal lobe (TL), and the combined premotor cortex (PMC) and supplementary motor area (SMA) during all assessments.

Results

Compared to the silent condition (S), participants walked faster with longer step length when listening to music. VF led to slower gait and shorter stride. MF did not alter spatiotemporal parameters compared with S. Only VF increased PMC/SMA activation relative to S ($p = 0.044$, Table 1). A trend of higher TL activation ($p = 0.065$) was observed in M, while MF and VF seemed to elicit similar activations.

Discussion

This is first study that investigates the cortical load associated with auditory biofeedback for gait retraining. Music seemed to be motivating, increasing walking speed and attenuating the expected slowdown with learning a new walking pattern observed during VB. Motor planning area was more active with VF, while no significant increase in auditory processing activity was observed. Overall, MF imposed minimal additional recruitment of motor planning and auditory processing regions of the cortex relative to silent walking, supporting its suitability for gait-retraining applications.

Images (Optional)

Table 1. Spatiotemporal parameters and Δ HbO_2 concentration

	Silence (S)	**Music only (M)**	**Musical Feedback (MF)**	**Verbal Feedback (VF)**
Speed (m/s)	1.10 ± 0.15	1.18 ± 0.14*	1.10 ± 0.14	1.03 ± 0.12*
Step Length (m)	1.33 ± 0.13	1.39 ± 0.12*	1.33 ± 0.14	1.29 ± 0.12*
Δ HbO_2 PMC/SMA (mmol/L)	-0.13 ± 0.46	0.05 ± 0.67	0.01 ± 0.61	0.12 ± 0.48*
Δ HbO_2 TL (mmol/L)	0.95 ± 1.03	1.55 ± 1.50	1.71 ± 1.10	1.19 ± 1.40

Δ HbO_2 = average concentration of oxyhemoglobin change; PMC/SMA: premotor cortex and supplementary motor area; TL: temporal lobe. *p > 0.05 compared to Silence condition.

References (Optional)

[1] L CEDIN, et.al, Healthcare, 2025

Session Category

Rehabilitation Biomechanics and Human Factors: Rehabilitation

P2-322

Effects of transcutaneous spinal cord stimulation amplitude on gait in children with cerebral palsy

Ms. Madeleine McCreary BS, Mrs. Katie Landwehr-Prakel BS, MS, Dr. Anna Fragomeni PT, DPT, PCS, Dr. Heather Feldner PT, PhD, PCS, Dr. Katherine Steele PhD

University of Washington, Seattle, Washington, United States

Ms. Madeleine McCreary

Mrs. Katie Landwehr-Prakel

Dr. Anna Fragomeni

Dr. Heather Feldner

Introduction

Transcutaneous spinal cord stimulation (tSCS) is a noninvasive neuromodulation technique that, when combined with locomotor training, may improve gait function in children with cerebral palsy (CP). For a given session, stimulation is delivered to two vertebral locations at preset amplitudes. These preset amplitudes are typically determined by visual observation and trial-and-error, which is highly subjective and time-intensive. Thus, this study aimed to quantify the effect of tSCS amplitude on gait parameters in children with CP.

Methods

Three children with CP walked on a treadmill with tSCS for 24 one-minute stimulation conditions. The amplitudes at T11 and L1 vertebrae for each stimulation condition were determined via Latin hypercube sampling, and their order was randomized. For each gait cycle, step length, step width, peak hip extension, peak knee flexion, and quadriceps-hamstrings co-contraction were quantified. To quantify the effects of stimulation amplitude, we trained individual Bayesian additive regression tree models. Time into visit

was included as a covariate in the models to account for fatigue. Model fit was evaluated by R^2 values and accumulated local effect (ALE) plots were used to quantify individual parameter effects.

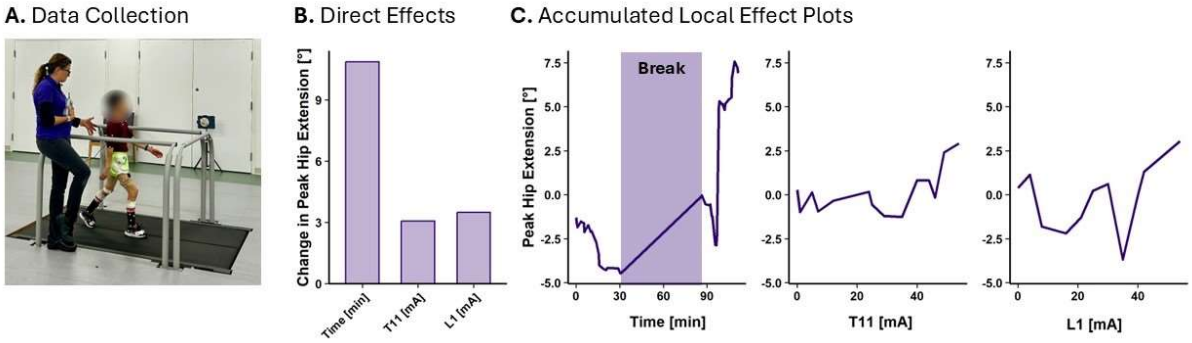
Results

Stimulation amplitude had the greatest influence on peak hip extension. For one participant, model fit was the highest for peak hip extension (R^2=0.34) and the lowest for step width (R^2=0.11). For all outcome measures, the direct effect of time was greater than the direct effect of T11 or L1 amplitude. The ALE plots indicate that peak hip extension increased as T11 amplitude increased above 40 mA and there were variable effects with L1 amplitude.

Discussion

Preliminary results indicate that minor changes in stimulation amplitude can alter gait outcome measures, such as peak hip extension. We expect results from additional participants will indicate that these effects vary across individuals due to the heterogeneity of CP. Determining whether there is an "optimal" stimulation condition to improve gait for a given individual remains an open question that needs to be addressed to maximize intervention effectiveness. These findings may be used to develop an evidence-based methodology to identify the appropriate stimulation parameters for future tSCS research, enabling consistency across sessions and institutions.

Images (Optional)



Acknowledgements (Optional)

This material is based upon work supported by the National Institutes of Heath [Grant Number R01NS091056] and the National Science Foundation Graduate Research Fellowship Program [Grant Number DGE-2140004]. Any opinions, findings, and conclusions or recommendations expressed in this material are those of the author(s) and

do not necessarily reflect the views of the National Institutes of Heath or National Science Foundation.

Session Category

Rehabilitation Biomechanics and Human Factors: Rehabilitation

P2-323

Is Exoskeleton-Assisted Walking Active? Evaluating Metabolic Cost and Weight-Bearing in Children with Cerebral Palsy

Miss Marita Cafazzo BASc[1,2], Dr. Tom Chau PhD, PEng[1,2], Dr. Virginia Wright PhD[1,2]

[1]University of Toronto, Toronto, Ontario, Canada. [2]Holland Bloorview Kids Rehabilitation Hospital, Toronto, Ontario, Canada

Introduction

Cerebral palsy (CP) affects 2–2.5 per 1000 children annually in Canada and is the leading cause of childhood physical disability. Children at Gross Motor Function Classification System (GMFCS) Levels III–IV have limited walking ability, often rely on wheelchairs for mobility, and consequently have few opportunities for physical activity, increasing their risk of cardiovascular disease. Motorized lower-limb exoskeletons, such as the pediatric Trexo Plus, offer a promising rehabilitation tool; however, the physical demands of robot-assisted gait training (RAGT) - particularly its potential as an exercise modality - remain insufficiently understood in this population.

This study aims to quantify the metabolic cost (MC) of Trexo-assisted walking in children with CP (GMFCS III–IV), assess their level of active engagement, evaluate weight-bearing during, and develop a predictive model of MC using accessible biomechanical markers to guide clinical decision-making.

Methods

This study involves 15 children with cerebral palsy (GMFCS III–IV) completing two visits involving anthropometric measurements, equipment familiarization, and metabolic testing during Trexo-assisted walking. Participants complete a seated 8-minute baseline followed by three 6-minute walking trials at increasing step rates while breath-by-breath oxygen consumption and carbon dioxide production are recorded, alongside weight bearing, external oblique engagement, head movement, heart rate, and perceived exertion. MC is calculated through Weir's equation, applied to a minute-long steady-state portion of each trial. Analyses include ANOVA, correlation testing, and predictive modeling using a hidden Markov model.

Results

Building on a pilot study (PRISM Lab, 2022–2024) that observed visual signs of fatigue during exoskeleton-assisted walking, this study will provide objective physiological measures of exertion and metabolic demand [1]. No results are available at this stage.

Discussion

Understanding the MC of Trexo-assisted walking will clarify the extent to which exoskeleton use facilitates meaningful physical activity for children with CP. Findings may support more effective therapy planning, expand opportunities for exercise participation, and ultimately enhance mobility and quality of life.

References (Optional)

[1] S. Bradley *et al*, "Physiotherapy-assisted overground exoskeleton use: mixed methods feasibility study protocol quantifying the user experience, as well as functional, neural, and muscular outcomes in children with mobility impairments," *Front. Neurosci.,* vol. 18, pp. 1-17, 2024.

Session Category

Rehabilitation Biomechanics and Human Factors: Rehabilitation

P2-324

Prosthetic Proprioception: Complaint Ligaments for Joint Angle Estimation in a Robotic Bicondylar Knee

Mr Mark Wolstenholme, Dr Peter Ellison

University of York, York, North Yorkshire, United Kingdom

Introduction

Current designs of bionic knee are usually pin joined and rely on predefined control architectures to generate motion. Bicondylar designs modelled on anatomy have the potential to allow more natural motion for the user, however due to their compliant nature joint angle cannot be directly measured by encoders. Here we investigate the use of cruciate ligaments as a mechanism of estimating joint angle in a bicondylar knee design.

Methods

A robotic knee rig was used to simulate knee motion. A pair of LVDTs were used to measure the relative displacement of elastic mechanical ligaments while the joint was driven through a sinusoidal profile. The joint was driven between 30° and 110° flexion-extension at periods between 2 and 6 seconds. Results were averaged across 10 cycles for each dataset. The driving force was delivered by 2 servo motors attached to pulleys acting as quadriceps and hamstrings. The level of antagonistic co-contraction was varied from 22N to 154N.

Results

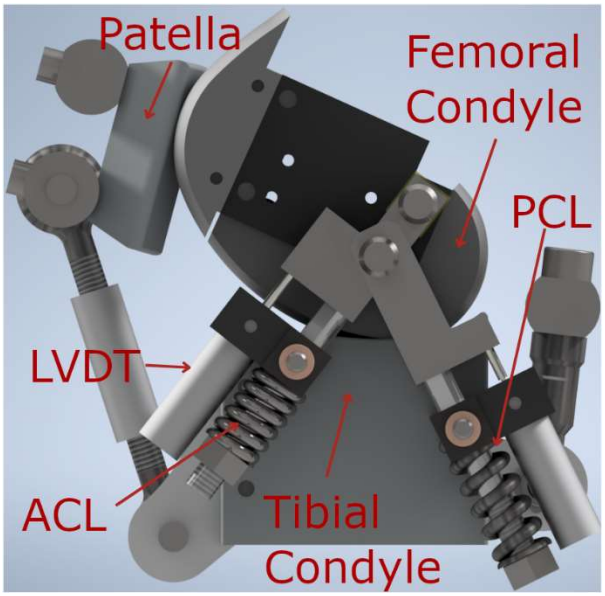
Ligament displacement was independent of joint speed, with no significant variation observed between datasets for the majority of the cycle. The most variation was shown by the PCL with 0.05mm difference at 56% cycle. ACL and PCL are affected by co-contraction level and ligament length. The ACL saw at maximum 0.094mm divergence between lowest and highest co-contraction level, and 0.143mm when varying ligament length . For the PCL, these values were 0.138mm and 0.252mm, respectively.

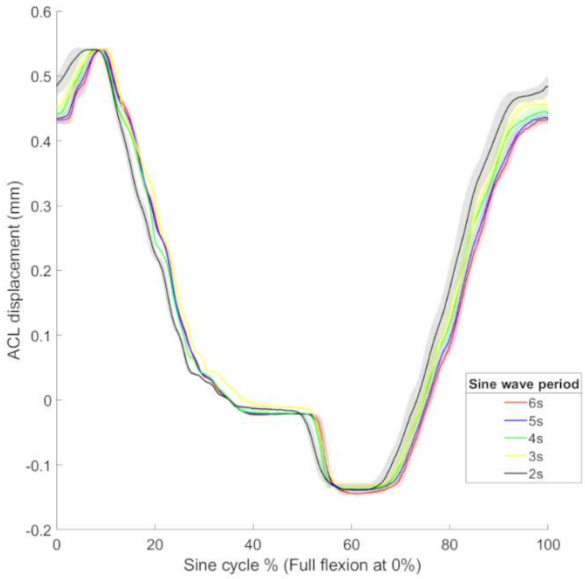
A predictor was constructed based on a Gaussian mixture model with means given by the two possible angles from each LVDT. The predictor achieved a mean square error of 250 deg^2 on test data.

Discussion

Cruciate ligament stretch provides a viable mechanism for estimating joint angle in a bicondylar knee design. A single ligament measurement provides two possible joint configurations, the combined stretch/displacement of the ACL and PCL enabled accurate estimation of joint position. Incorporating additional state variables such as speed or actuator force may further improve estimation accuracy. Overall, this study demonstrates a practical control strategy for compliant bicondylar joints and offers promising foundation for advancing prosthetic knee technologies.

Images (Optional)





References (Optional)

[1] F.Russel at al. *2017 International Conference on Rehabilitation Robotics 2017*

Acknowledgements (Optional)

Session Category

Rehabilitation Biomechanics and Human Factors: Rehabilitation

P2-325

Acute Effects of Whole-Body Transcutaneous Electrical Nerve Stimulation on Gait and Functional Mobility: A Mini-Longitudinal Case Study in Hereditary Spastic Paraplegia

Prof. Massimiliano Pau[1], Ms. Francesca Taccori[1], Dr. Micaela Porta[2]

[1]University of Cagliari, Cagliari, Sardinia, Italy. [2]Unibversity of Cagliari, Cagliari, Sardinia, Italy

Introduction

Individuals with Hereditary Spastic Paraplegia (HSP) typically present with a stiff, spastic gait featuring reduced knee flexion, limited ankle dorsiflexion, a generalized decrease in dynamic range of motion of all lower limb joints. Recently, transcutaneous electrical nerve stimulation (TENS) has been demonstrated beneficial in terms of lower-limb strength, joint range of motion, pain, and spasticity in neurological populations. Nonetheless, quantitative evidence supporting its effectiveness in HSP remains limited, underscoring the need for dedicated studies in this population.

Methods

A 60-year-old man with HSP presented with bilateral drop foot, right-accentuated forefoot drag, increased hip adductor and knee extensor tone. He routinely used the Exopulse Mollii Suit, delivering individualized low-intensity TENS for 60 minutes every two days. Over 100 hours, he completed two TENS sessions, with gait and functional mobility instrumentally assessed seven times to capture acute effects and washout. Gait was analyzed using an 8-camera motion-capture system, and functional mobility via an instrumented Timed Up and Go test.

Results

Main results are reported in Table 1. After the first TENS session, marked improvements in gait were observed: speed increased to 0.9 m/s and, similarly, increases in stride length and cadence were observed, together with a 16% reduction in double support. Dynamic ROM in the ankle joint of the more affected limb increased by 42%. These effects diminished after 48 hours (T74), returning to near pre-treatment values. In the iTUG test, performance improved in both sessions, with total time reductions of ~4 s and ~9 s, primarily driven by faster 180° turns. These benefits dissipated within two days, although second-session effects were more pronounced.

Discussion

This case study provides preliminary evidence that short-term full-body TENS via the Exopulse Mollii Suit can induce acute, clinically meaningful improvements in gait and functional mobility in HSP. A single 60-minute session led to increased gait speed, stride length, cadence, reduced double-support duration, and improved ankle ROM, with similar, reproducible effects after a second session. iTUG performance also improved, particularly during turning. These benefits were transient, returning to baseline within 48 hours, underscoring the need for repeated or sustained intervention and larger controlled studies.

Images (Optional)

Spatio-temporal Parameters

	T0	T24	T26	T50	T74	T98	T100
Gait speed (m/s)	0.40	0.60	**0.90**	0.70	0.60	0.50	**0.90**
Cadence (steps/min)	72.68	88.13	**108.53**	92.80	84.82	79.97	**106.29**
Stride Length (m)	0.74	0.83	**1.00**	0.86	0.81	0.77	**0.97**
Step width (m)	0.22	0.20	**0.20**	0.19	0.21	0.21	**0.23**
Stance phase duration	71.29	66.61	**63.99**	66.35	67.16	68.38	**64.41**
Swing Phase Duration	28.71	33.39	**36.02**	33.66	32.85	31.62	**35.59**
Double support phase duration	21.25	17.10	**14.36**	16.93	16.88	18.32	**14.41**

Dynamic Range of Motion

		T0	T24	T26	T50	T74	T98	T100
Hip	Right	38.0	39.0	**41.0**	37.4	38.0	35.9	**38.1**
	Left	42.9	42.3	**40.6**	39.9	41.2	41.7	**42.2**
Knee	Right	46.2	46.2	**47.1**	46.2	45.1	44.9	**43.7**
	Left	47.4	46.9	**41.5**	44.7	47.1	45.6	**41.6**
Ankle	Right	15.3	17.5	**24.8**	23.4	16.6	13.3	**17.7**
	Left	21.7	24.2	**26.1**	22.2	21.3	21.4	**23.8**

References (Optional)

Session Category

Rehabilitation Biomechanics and Human Factors: Rehabilitation

P2-326

Informing Exosuit Design: Analyzing Infant Reaching Duration and Coordination Strategies to Determine Actuator Operational Parameters

Miss Melanie Barahona Masters of Science Student, Bioengineering Dept, Miss Ipsita Sahin Ph.D Student, Bioengineering Dept, Miss Mehrnoosh Ayazi Ph.D Student, Electrical & Computer Eng Dept, Dr. Konstantinos Karydis Associate Professor, Electrical & Computer Eng Dept, Dr. Elena Kokkoni Assistant Professor, Bioengineering Dept & Electrical & Computer Eng Dept

University of California, Riverside, Riverside, CA, United States

Introduction

Reaching is a critical motor milestone fundamental to early environmental exploration [1]. Infants with or at risk of upper extremity impairments may face significant challenges in achieving this milestone. Wearable assistive technology, such as exosuits, offers a promising solution, as demonstrated in adult populations [2]. A key design element involves integrating fabric-based pneumatic actuators into the wearable exosuit. To optimize actuator performance, crucial information regarding reaching behavior is required. Specifically, we investigate the required actuator operating speeds (informed by reach duration) and coordination strategies (unimanual versus bimanual reaching based on targeted object size).

Methods

The KIRA dataset was used to extract this information. This dataset includes videos of infants up to 12 months of age reaching for objects in a sitting position in natural environments. The size and location of the presented objects varied. The final sample included eight infants exhibiting both unimanual and bimanual reaching actions, contributing 86 total reaches (24 being bimanual). Reaching duration was computed based on the annotated onset and offset frames. Object size categories were defined relative to the infant's hand size: small (equal to or smaller than one hand), medium (larger than one hand but smaller than two hands), and large (equal to or larger than two hands). Potential variations in reaching durations and coordination strategies were examined.

Results

Overall, reaching duration ranged from 0.2-1.8s, with the location of the object and the initial position of the hand contributing to variations. Unimanual and bimanual reaching duration was similar at 0.7s, while preliminary examination of object size did not seem to affect reaching duration or coordination strategy, in contrast to previous studies.

Discussion

Information on infant motor control is limited, yet critical for developing effective wearable actuator control systems. This work provides baseline data, essential for defining the operational parameters (speed and co-activation timing) of the exosuit's actuators.

References (Optional)

[1] Fagard et al., Infant Behav Dev, 2005

[2] Sahin et al., Front Robot AI, 2024

Session Category

Rehabilitation Biomechanics and Human Factors: Rehabilitation

P2-327

Masters-Aged Runners With Knee Osteoarthritis Manage Symptoms With Load-Modifying Strategies to Continue Running: A Qualitative Inquiry

Ms Michaela Khan, Dr W. Ben Mortenson, Dr Jackie Whittaker, Dr Michael Hunt

University of British Columbia, Vancouver, BC, Canada

Introduction

Runners with knee osteoarthritis (OA) are a distinct subgroup of the knee OA population who remain highly functional. In our clinical experience, this group reports using various strategies to manage their knee symptoms, many of which appear to address the load experienced by the body. Given this has never been formally investigated, we aimed to qualitatively summarize load-modifying strategies that runners with knee OA use to manage their knee symptoms and continue running.

Methods

We used an interpretive description methodology [1] to identify patterns in strategies used by masters-aged recreational runners with a clinical diagnosis of knee OA. Participants were recruited - using intensity sampling - from a previous study examining responses of osteoarthritic cartilage to running. We collected data through one-on-one, semi-structured, videoconference interviews and analyzed using reflexive content analysis [2].

Results

We interviewed twelve runners who had either mild (n=10) or moderate (n=2) disease severity, and varied in age (50-76 years), gender (n=7 women), running experience (3-55 years), duration of knee symptoms (1-15 years), and current weekly running distance (0-50 km/week). Participants preferred running uphill and on soft surfaces, and modified their gait by reducing step length, increasing cadence, or running “softly”. They emphasized the importance of weight management but expressed mixed opinions about shoe selection and wearing a knee brace. Participants also balanced consistent running training with caution by incorporating rest days, shortening long runs, and slowing their pace.

Discussion

With a paucity of evidence to guide the education of runners with knee OA, our findings provide a foundation for quantitative research into load-modifying strategies for runners with knee OA. Some strategies (e.g., increasing cadence, running “soft”) align with evidence that they reduce load and improve pain, whereas others have not been linked to symptom management (e.g., running uphill). As masters-aged runners constitute the most

rapidly expanding group within the running community, and the incidence of knee OA is rising, clinicians, coaches, and runners should be aware of these experiential strategies. Future investigations should involve novice runners or those with more advanced knee OA disease.

References (Optional)

[1] Thorne *et al.*, *Med Educ*, 2021

[2] Nicmanis., *Int J Qual Methods*, 2024

Session Category

Rehabilitation Biomechanics and Human Factors: Rehabilitation

P2-328

Active Prosthetic Wrist and Multi-grip Control on Trunk Movement Compensations and Smoothness

Ms. Mira Mutnick M.S.E., Mr. Dylan Wallace, Dr. Paul Cederna M.D., Dr. Cynthia Chestek Ph.D., Dr. Deanna Gates Ph.D.

University of Michigan, Ann Arbor, MI, United States

Introduction

Commercial muscle-activated upper limb prostheses enable active grip selection but lack active wrist motion due to the lack of available musculature for control. Intramuscular electrodes coupled with a surgical construct, the regenerative peripheral nerve interface (RPNIs), provide additional control signals for more natural prosthetic hand movement. The ability to actively control the wrist unit might reduce the compensatory movement upper limb prosthesis users make to properly orient their hand to interact with objects. The purpose of this study was to assess the role of active wrist control with multiple grips during functional tasks on trunk movement compensations and smoothness.

Methods

One female with unilateral transradial amputation used a multi-grip myoelectric prosthetic hand with and without active wrist rotation to perform two functional assessments, the Coffee Task and the Clothespin Relocation Test, over eight sessions. Sequential pattern recognition classifiers were trained to decode either surface electromyography (EMG) or intramuscular EMG from residual muscles and RPNIs into multi-grip only or multi-grip and wrist rotation. Primary outcome measures were peak segmental trunk angles and range of motion (ROM), the number of submovements, the Speed Metric, and spectral arc length (SPARC). We compared the movement compensations and smoothness between wrist conditions using a Wilcoxon rank sum exact test (alpha = 0.05).

Results

For the pouring motion in the Coffee Task, including active wrist rotation had minimal effect on peak trunk angles and ROM. While the number of submovements was unchanged ($p=0.09$), the addition of wrist rotation decreased both the Speed Metric and SPARC ($p=0.04$). For the Clothespin Relocation Test, including active wrist rotation decreased trunk lateral lean and flexion/extension ROM ($p<0.02$) (Figure 1).

Discussion

While active wrist motion was available, it was hard to achieve consistent and precise hand position using these control approaches during object manipulation. This difficulty may have discouraged use of this feature, resulting in similar compensatory patterns. Future studies should iterate on the control approach used to activate the wrist to better improve compensatory movements.

Images (Optional)

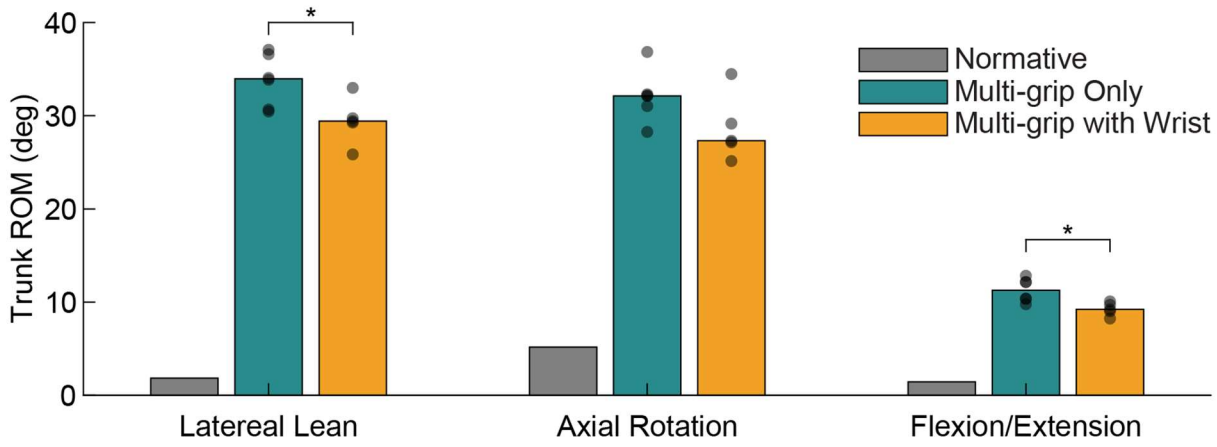


Figure 1. Three-dimensional trunk range of motion (ROM) when transferring a clothespin from a horizontal bar up to a vertical bar during the Clothespin Relocation Test with (gold) and without (teal) active wrist control. Normative angles (gray) from an individual without limb loss are provided for visual comparison. Dots represent the average ROM of all full attempted clothespin transfers using the controller during the session. Bars represent the median across controllers and sessions for each wrist condition. *p<0.05.

Acknowledgements (Optional)

This work was supported by the National Institutes of Health under Award R01NS105132 and RNS134834A. M.E.M. was supported by T32 TR004371.

Session Category

Rehabilitation Biomechanics and Human Factors: Rehabilitation

P2-329

Comparison of Components of the Timed Up and Go and the Three Times Figure-of-Eight tests for People with Lower Limb Amputation

Dr. Molly Gries PT, DPT, PhC[1], Mr. Saifullah Farrag M.S.[2], Ms. Katheryn Allyn LCPO, FAAOP[3], Mr. James Colvin M.S.[4], Dr. Matthew Wernke Ph.D.[4], Dr. Andrew Humbert Ph.D.[1], Dr. M. Jason Highsmith PhD, PT, DPT, CP, FAAOP(D)[2,5], Dr. Stephanie Carey Ph.D.[2], Dr. Murray Maitland PT, PhD, FAPTA[1]

[1]University of Washington, Seattle, WA, United States. [2]University of South Florida, Tampa, FL, United States. [3]Kate Allyn Prosthetics Research LLC, Seattle, WA, United States. [4]Willowwood Global, Mt. Sterling, OH, United States. [5]US Department of Veterans Affairs, Washington, DC, United States

Introduction

People with lower extremity amputation (LEA) struggle with daily mobility, especially turning. Previous studies reported test time and forward walking spatiotemporal variables, but often omit other components of gait, such as turning, that are assessed in functional tests. The purpose of this study was to analyze spatiotemporal components of the Timed Up and Go (TUG) and the Three Times Figure Eight Test (3XF8T) for people with LEA.

Methods

Data were analyzed from a single visit. Participants completed clinical tests (10-m walk, TUG, 3XF8T) on a pressure-sensitive mat (Protokinetics Zeno Walkway, Havertown, PA) using their usual prosthetic foot. The total TUG and total 3XF8T were divided into components geometrically in MATLAB using exported footfall data. The TUG was split into (1) rising and sitting (excluded), (2) straight walking (footfalls away/toward the chair were averaged), and (3) turning. The 3XF8T was divided into right and left turns. Analysis compared the TUG and 3XF8T to each other and to the total test. Statistical analysis was conducted in RStudio using multiple linear regression methods, with interaction tests for amputation level and gait speed, and significance at $p < 0.05$.

Results

Sixty-one participants (bilateral (BA) = 13, K2 below knee (BKA) = 15, above knee (AKA) =33) were included. Spatiotemporal and regression results are in Table 1. Significant differences were found between the total, straight, and turning portions of the TUG. Except for stride width, there were no differences between the total, right, and left turns in the 3XF8T. Compared to AKA, BA was associated with slower stride velocity and longer stride and swing time for BA and BKA during TUG and 3XF8T. Generally, an increase in gait speed was

associated with increases in stride velocity and stride length and decreases in stride time and width.

Discussion

Gait varies across TUG components, and to a lesser extent, the 3XF8T, highlighting the importance of examining components of gait, such as turning, that mimic daily activities in LEA. Amputation level affects gait performance, and gait speed modifies spatiotemporal measures. Understanding both the forward and components of gait will help characterize gait patterns and improve knowledge of LEA's mobility.

Images (Optional)

Table 1. Mean and significance of Spatiotemporal Variables for total and geometrically divided components of the Timed Up and Go (TUG) and Three Times Figure-of-Eight Test (3XF8T) Right and Left Turns

Test	Variable	Condition	Mean (s.d.)	p-value		
				total vs straight	total vs turn	straight vs turn
TUG-RIGHT	Stride velocity (cm/s)	Total	71.5 (18.6)	-	-	-
		Straight	79.3 (21.8)	**0.05**	-	-
		Turn	69.4 (20.1)	-	0.99	**<0.05**
	Stride Time (s)	Total	1.4 (0.3)	-	-	-
		Straight	1.2 (0.2)	**<0.05**	-	-
		Turn	1.3 (0.2)	-	**<0.05**	0.08
	Swing Time (s)	Total	0.4 (0.1)	-	-	-
		Straight	0.4 (0.1)	0.95	-	-
		Turn	0.4 (0.1)	-	0.07	0.14
	Stride Length (cm)	Total	89.6 (18.4)	-	-	-
		Straight	93.4 (18.9)	**<0.05**	-	-
		Turn	85.5(18.8)	-	0.8	**<0.05**
	Stride Width (cm)	Total	18.9 (4.3)	-	-	-
		Straight	23.9 (4.1)	**<0.05**	-	-
		Turn	20.5 (6.7)	-	**<0.06**	0.47
TUG-LEFT	Stride velocity (cm/s)	Total	71.3 (18.2)	-	-	-
		Straight	89.6 (22.4)	**<0.05**	-	-
		Turn	72.1 (9.8)	-	0.97	**<0.05**
	Stride Time (s)	Total	1.5 (0.3)	-	-	-
		Straight	1.2 (0.2)	**<0.05**	-	-
		Turn	1.2 (0.2)	-	**<0.05**	0.29
	Swing Time (s)	Total	0.4 (0.1)	-	-	-
		Straight	0.4 (0.1)	0.85	-	-
		Turn	0.4 (0.1)	-	0.23	0.51
	Stride Length (cm)	Total	89.3 (18.0)	-	-	-
		Straight	103.5 (19.5)	**<0.05**	-	-
		Turn	88.1 (16.9)	-	0.93	**<0.05**
	Stride Width (cm)	Total	18.6 (4.5)	-	-	-
		Straight	23.7 (5.1)	**<0.05**	-	-
		Turn	23.2 (3.8)	-	**<0.05**	0.83
				total vs. right	total vs left	right vs left
3XF8T	Stride velocity (cm/s)	Total	64.9 (15.8)	-	-	-
		Right	62.4 (15.6)	0.69	-	-
		Left	62.4 (17.5)	-	0.69	1.0
	Stride Time (s)	Total	1.3 (0.2)	-	-	-
		Right	1.3 (0.18)	0.95	-	-
		Left	1.3 (0.2)	-	0.96	1.0
	Swing Time (s)	Total	0.4 (0.1)	-	-	-
		Right	0.5 (0.1)	0.89	-	-
		Left	0.4 (0.1)	-	0.90	1.0
	Stride Length (cm)	Total	68.0 (4.3)	-	-	-
		Right	76.2 (15.1)	0.44	-	-
		Left	77.9 (16.4)	-	0.81	0.81
	Stride Width (cm)	Total	20.4 (4.1)	-	-	-
		Right	23.5 (4.3)	**<0.05**	-	-
		Left	22.3 (3.9)	-	**0.03**	0.28

Key: Total = spatiotemporal measures as generated by Protokinetics software. P-value is based on multiple linear regression models, significance <0.05, in bold.

References (Optional)

Acknowledgements (Optional)

Session Category

Rehabilitation Biomechanics and Human Factors: Rehabilitation

P2-330

Spatiotemporal Digital Biomarkers of Gait Impairment During Turning Phase of the Timed Up and Go Test

Mr. Muhammad Taimoor Adil PhD Student[1], Dr Parthasarathi Mandal Reader[2]

[1]University of Manchester, Manchester, Manchester, United Kingdom. [2]University of Manchester, Manchester, Mancehster, United Kingdom

Introduction

Turning strategy is an important predictor of fall risk in individuals with balance deficits [1]. It is a biomechanically demanding task that requires coordinated modulation of step placement, timing, and centripetal acceleration, yet remains far less studied than straight-line walking. The present study examined step-level spatiotemporal features during the turning phase of a Timed Up-and-Go (TUG) test to identify markers that differentiate normal from pathological gait with high fall risk.

Methods

Pose estimation was applied to video recordings from publicly available dataset [2] to reconstruct full-body kinematics. The turning phase and step events were identified using foot and pelvis trajectories. For each participant, mean and standard deviation of spatiotemporal parameters, together with centripetal acceleration, were computed. Participants were classified as normal (n = 10) or pathological (n = 7). Group differences were tested using t-tests or Mann–Whitney U tests, with Cohen's d quantifying effect sizes. An L1-regularised logistic regression model was then implemented to identify the subset of features most discriminative of gait pathology.

Results

Statistically significant differences ($p < 0.05$) were found for several parameters (Table 1). Participants with pathological gait took shorter, slower, and less variable steps, required more steps to complete the turn, and spent longer turning, thus, indicating reduced efficiency and impaired balance control. Multivariate analysis further showed that lower step-width variability, shorter step length, and reduced swing time, together with increased total turning duration, were the strongest predictors of pathological gait.

Discussion

The findings suggest that individuals with pathological gait adopt a conservative turning strategy that prioritises stability over efficiency. Reduced centripetal acceleration indicates limited capacity to generate lateral forces required for controlled redirection of the body during turning. Lower step-width variability further suggests a stiffer mediolateral control strategy that restricts foot placement to minimise balance threats. Detailed turning analysis within the TUG framework offers a practical means of extracting clinically relevant digital biomarkers of gait and may support early identification of mobility deficits. The small sample size remains a key limitation, warranting validation in larger cohorts.

Images (Optional)

Table 1: Spatiotemporal parameters extracted from steps in Turning Phase of TUG
MH: Mean Healthy, MP: Mean Pathological, LRC: Logistic Regression Coefficient

Parameters	p	d	MH	MP	LRC	OR
step_width_std*	0.005	1.50	0.18	0.11	-0.61	0.62
step_length_mean*	0.033	1.08	0.18	0.11	-0.48	0.54
swing_time_mean	0.479	0.33	0.45	0.43	-0.46	0.63
total_time*	0.028	-1.50	2.03	3.22	0.30	1.35
step_length_std	0.182	0.65	0.16	0.13	0.00	1.00
step_time_std	0.526	-0.21	0.09	0.11	0.00	1.00
step_time_mean	0.818	-0.12	0.64	0.65	0.00	1.00
step_velocity_std*	0.029	1.09	0.28	0.18	0.00	1.00
step_velocity_mean*	0.027	1.11	0.51	0.30	0.00	1.00
step_width_mean*	0.044	0.99	0.23	0.17	0.00	1.00
swing_time_std	0.417	-0.07	0.07	0.07	0.00	1.00
stance_time_std	0.133	-0.51	0.08	0.13	0.00	1.00
stance_time_mean	0.530	-0.33	0.78	0.82	0.00	1.00
dst_std*	0.045	-0.87	0.02	0.05	0.00	1.00
dst_mean	0.174	-0.84	0.17	0.20	0.00	1.00
ac_std*	0.023	1.11	3.79	2.24	0.00	1.00
ac_mean*	0.014	1.23	4.18	2.37	0.00	1.00
number of steps*	0.044	-1.32	0.00	0.00	0.00	1.00

References (Optional)

[1] Rania Almajid et al., Gait & Posture, 2020

[2] Yanhong Wang et al. IEEE Trans., 2021

Session Category

Rehabilitation Biomechanics and Human Factors: Rehabilitation

P2-331

Mobility Device Misuse and Fall Circumstances Among Older Adults in Long-Term Care

Ms. Brianna Reilly[1], Dr. Katherine Mayes MD, PhD[2,3], Dr. Damon Kuehl MD[2,3], Dr. Steve Rowson PhD[1], Dr. Nicole Stark PhD[1]

[1]Virginia Tech, Blacksburg, VA, United States. [2]Virginia Tech Carilion School of Medicine, Roanoke, VA, United States. [3]Carilion Clinic, Roanoke, VA, United States

Introduction

The number of U.S. adults aged 65 and older is expected to nearly double, reaching 98 million by 2060. As the older adult population grows, understanding fall risk factors becomes increasingly critical [1]. Although mobility devices aim to improve safety, they can also pose new risks. This study uses video analysis to characterize how mobility devices contribute to falls among older adults living in long-term care (LTC) facilities.

Methods

A trained reviewer analyzed 300 open-access LTC fall videos, documenting fall characteristics, injury types, demographics, and clinical information [3]. Mobility devices were categorized by: cane, wheelchair, two-wheeled walker, and rollator. We examined the characteristics of falls, injury patterns, and instances of device misuse across these groups and compared them with falls that occurred without device use.

Results

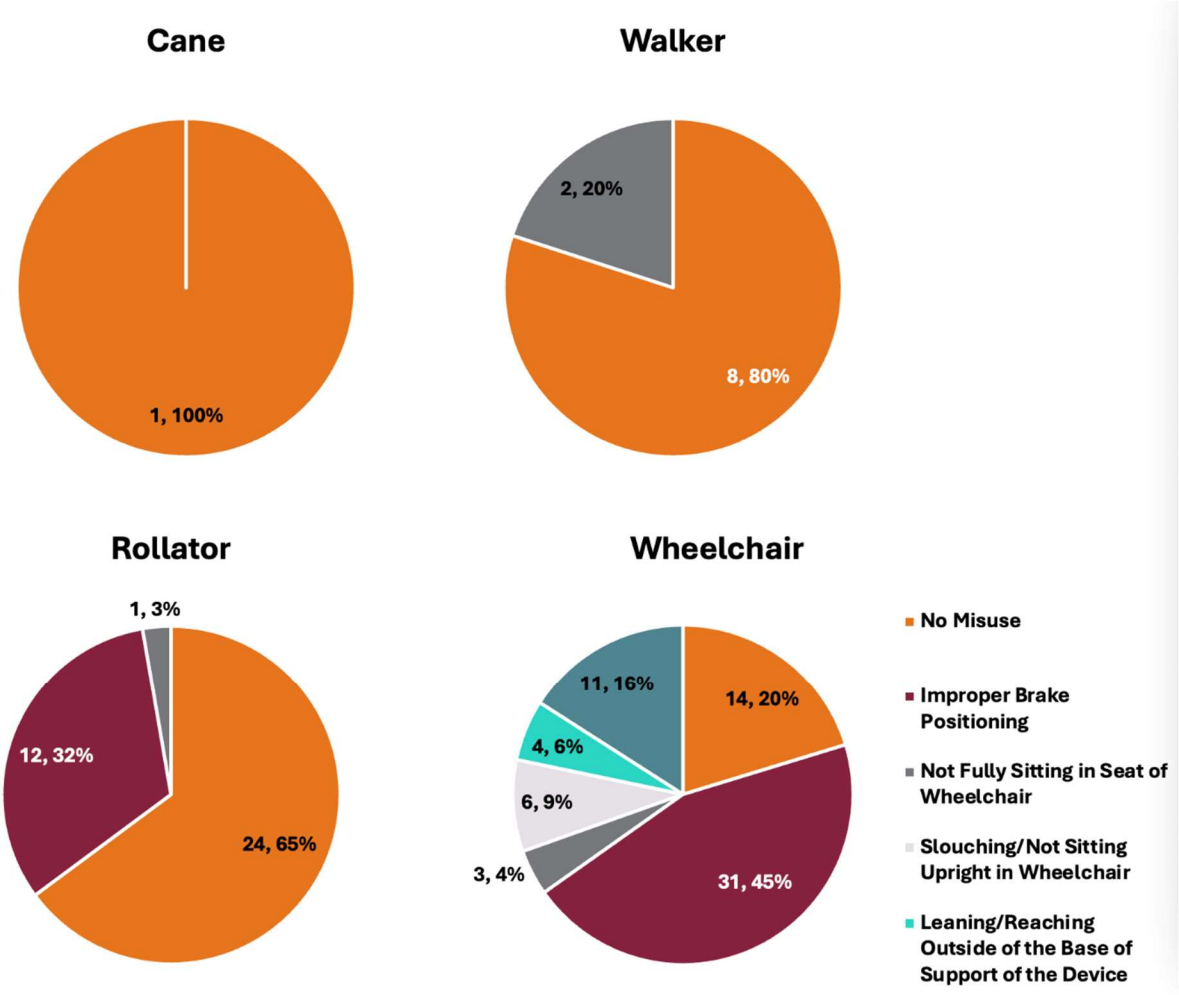
Most falls occurred without the use of a mobility device, accounting for 60.7% (182 out of 300) of the incidents. Among device-related falls, 23.3% involved wheelchairs, 12.3% rollators, 3.3% walkers, and 0.3% canes. Nearly half of device-free falls occurred while walking (46.7%). Falls related to wheelchairs commonly occurred while the individual was seated/wheeling (38.65%) or during transfers (37.1%). Across all types of mobility devices, the most frequent causes of falls were improper transfers and incorrect weight shifting. Misuse of mobility devices was often observed, particularly among four-wheeled devices (Figure 1).

Among falls without mobility devices, 42.9% resulted in injury. Injury rates were similar for rollator users (45.9%) and walker users (40%), while wheelchair users had the lowest injury rate (24.3%).

Discussion

The main cause of falls involving wheeled mobility aids was improper braking, highlighting a design and usability issue. Wheelchair users often fell due to losing external support, indicating instability in the environment or difficulties during transfers. Rollator and walker users, like those who fell without devices, most frequently fall due to improper transfer or weight-shifting. These differences emphasize the need for targeted fall prevention strategies tailored to each type of mobility device, as falls among LTC residents vary greatly by device, with different mechanisms and misuse patterns.

Images (Optional)



References (Optional)

[1] T. Roman-de-Mettelinge, D. Cambier, *Journal of Geriatric Physical Therapy*, 2015.

[2] S. Robinovitch, *Databrary, 2018*.

Session Category

Rehabilitation Biomechanics and Human Factors: Rehabilitation

P2-332

Virtual Reality Training for Prosthetic Arm Control: Test Setup and Performance Analysis

Dr. Peter Bishay[1], Mr. Gerbert Funes Alfaro[1], Mr. Marek Kwasek[2], Ms. Jacqueline Hunt[3], Mr. Kenneth Mazariegos[2], Dr. Stefanie Drew[3], Dr. Thomas Chan[3], Dr. Jacob Hinkel-Lipsker[2]

[1]Department of Mechanical Engineering, California State University, Northridge, Northridge, California, United States. [2]Department of Kinesiology, California State University, Northridge, Northridge, California, United States. [3]Department of Psychology, California State University, Northridge, Northridge, California, United States

Dr. Peter Bishay

Mr. Gerbert Funes Alfaro

Mr. Marek Kwasek

Ms. Jacqueline Hunt

Mr. Kenneth Mazariegos

Dr. Stefanie Drew

Dr. Thomas Chan

Introduction

Virtual reality (VR) has gained popularity as a tool for motor learning and rehabilitation. This technology has advanced to the point that prosthetic controllers can be connected to virtual prosthetic arms, allowing users to train with them before owning a prosthesis. This

presentation details the development of a foot-based prosthetic controller, a VR environment for the controller, and the results obtained so far in using VR to train participants.

Methods

Ongoing participant recruitment is focused on users with (*n=10)* and without (*n=40)* a transradial amputation. These participants undergo a seven-week training program that consists of five weeks of VR sessions between two weeks of real-world baseline (week 1) and retention (week 7) sessions. Each session includes 3 trials with strict 10-minute rest. The participants are divided into 8 different training configurations defined by visual fidelity (*high (HV) or low (LV)),* cognitive demand (*high (HC) or low (HC)),* and adaptivity (s*tatic or adaptive*). Using a real-world foot-based prosthesis controller, participants sort an assortment of randomized blocks labeled with vocabulary terms under a given time limit.

The controller includes two components: an IMU-based controller unit and an insole inserted into a shoe for the participant to wear. Participants in adaptive VR conditions train across ten difficulty levels, where progressing to higher levels reduces available time and introduces blocks of varying sizes. Depending on condition and level, task time limits range from 5 to 15 minutes.

Results

Initial findings (*n = 11, all amputation-free*) suggest that VR training improves user performance, with participants showing rapid improvement over the course of five weeks. Faster completion speeds without sacrificing sorting accuracy demonstrated participants' increasingly reliable prosthesis control. Performance patterns also revealed clear condition-based effect: LC participants generally achieved higher speeds than HC participants, and HV participants outperformed LV, supporting our hypothesis about visual fidelity and cognitive demand.

Discussion

The outcomes of the participants' real-world retention sessions were comparable, demonstrating how VR training facilitates effective transfer to real-world applications. These findings highlight the potential VR can have as a scalable training platform and provides insight into condition-specific factors that shape learning trajectories for prosthesis control.

Images (Optional)

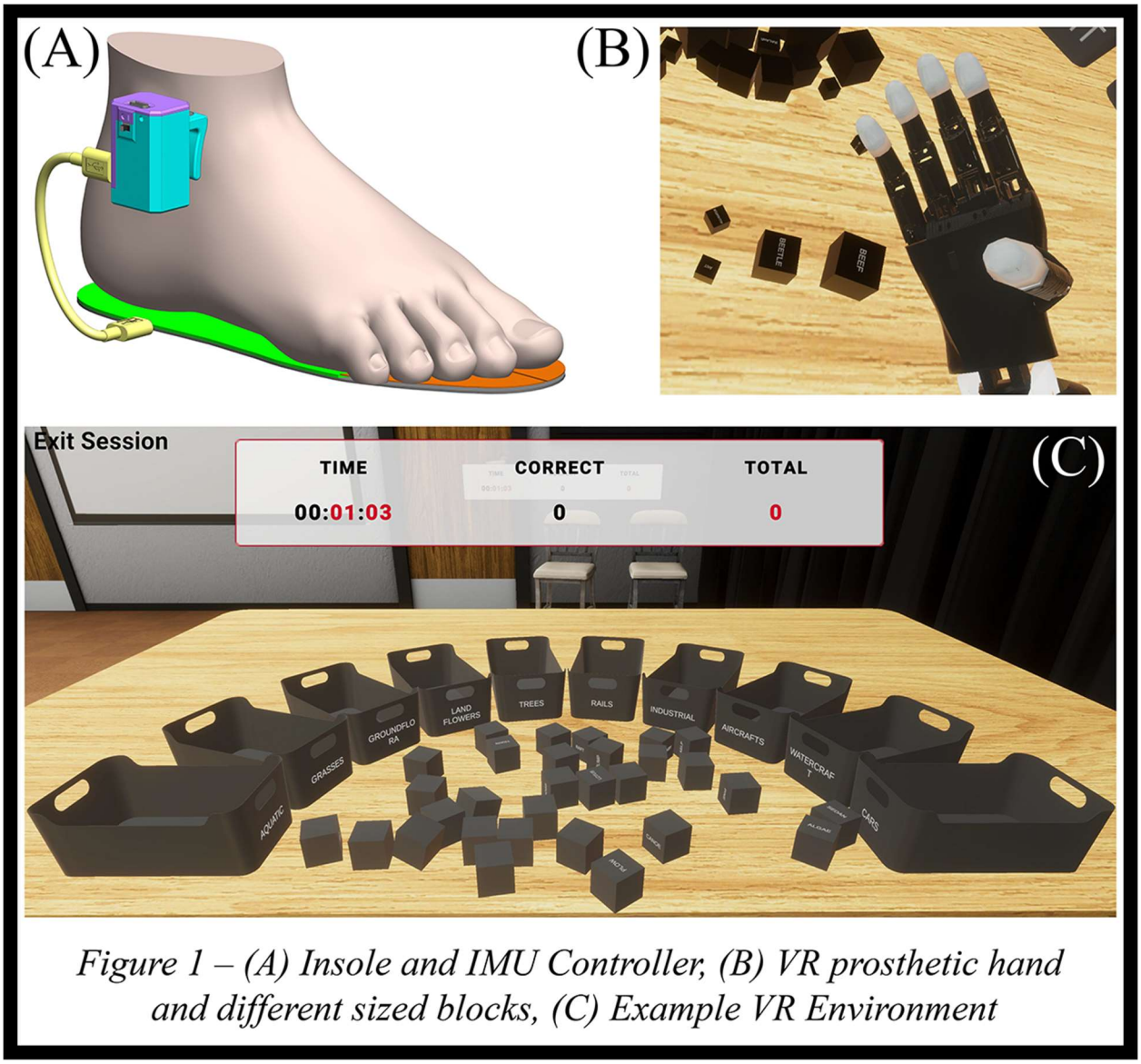


Figure 1 – (A) Insole and IMU Controller, (B) VR prosthetic hand and different sized blocks, (C) Example VR Environment

References (Optional)

Acknowledgements (Optional)

The work is funded by the National Science Foundation's Mind, Machine, and Motor Nexus (M3X) program (NSF Award Number 2225135).

Session Category

Rehabilitation Biomechanics and Human Factors: Rehabilitation

P2-333

Development of Multidirectional Perturbations for Fall-Prevention Training Using the FLOAT Body Weight Support System

Ms. Nooshin Seddighi, Mr. Merrick Mar, Dr. Cecilia Monoli, Dr. Anna Render, Dr. Peter Fino

University of Utah, Salt Lake City, Utah, United States

Introduction

Improving reactive balance is critical for reducing falls in older adults [1]. However, few methods can safely and consistently deliver perturbations during standing and overground walking [1]. This study aimed to develop and evaluate the feasibility of controlled multidirectional perturbations using FLOAT, a 3D cable-driven robotic body weight support (BWS) system [2]. We evaluated the feasibility of using FLOAT's open-control mode by delivering perturbations of varying direction and magnitude during standing and overground walking.

Methods

Two healthy adults (female:30 years, 175.3cm, 83.9 kg; male:19 years, 177.8cm, 72.6kg) completed a validation protocol including standing and walking tasks. Thirty-Two perturbations were delivered at two magnitudes (standing:10% vs 15% BW; walking:7.5% vs 12.5% BW), two impulse durations (0.3 vs 0.5s), and eight directions in the transverse plane spanning 0-360° in 45° increments to assess directional stepping sensitivity. Baseline BWS was maintained throughout (standing:15%; walking:10% BW). Perturbations were randomized, and during walking, they were delivered at randomized intervals of 3-5m, ensuring variability in timing and direction. Perturbation-induced acceleration vectors, defined as the first peak magnitude of acceleration following each perturbation, were collected from inertial sensors mounted on the FLOAT bar, the participant's sternum, and lumbar. For each sensor, linear mixed-effects models assessed whether perturbation-induced accelerations differed by perturbation type (magnitude and intended direction).

Results

Preliminary data indicate that FLOAT successfully delivered perturbations at different magnitudes and directions during both standing and walking (Figure 1). During standing, acceleration of the bar, sternum, and lumbar sensors confirmed transmission of perturbations from the FLOAT to upper and lower trunk segments, but the acceleration

angle deviated slightly from the desired oblique directions. Perturbation-induced acceleration varied by magnitude at the bar (standing and walking: $p<0.001$), sternum ($p=0.01$), and lumbar ($p<0.001$) locations. The direction of perturbation-induced acceleration also differed by directional condition ($p<0.001$), confirming that the system can deliver perturbations in repeatable, different magnitudes and directions during standing and walking.

Discussion

This technical validation demonstrates that FLOAT with open-control mode can deliver controlled, multidirectional perturbations with adjustable parameters suitable for future perturbation-based training studies in older adults.

Images (Optional)

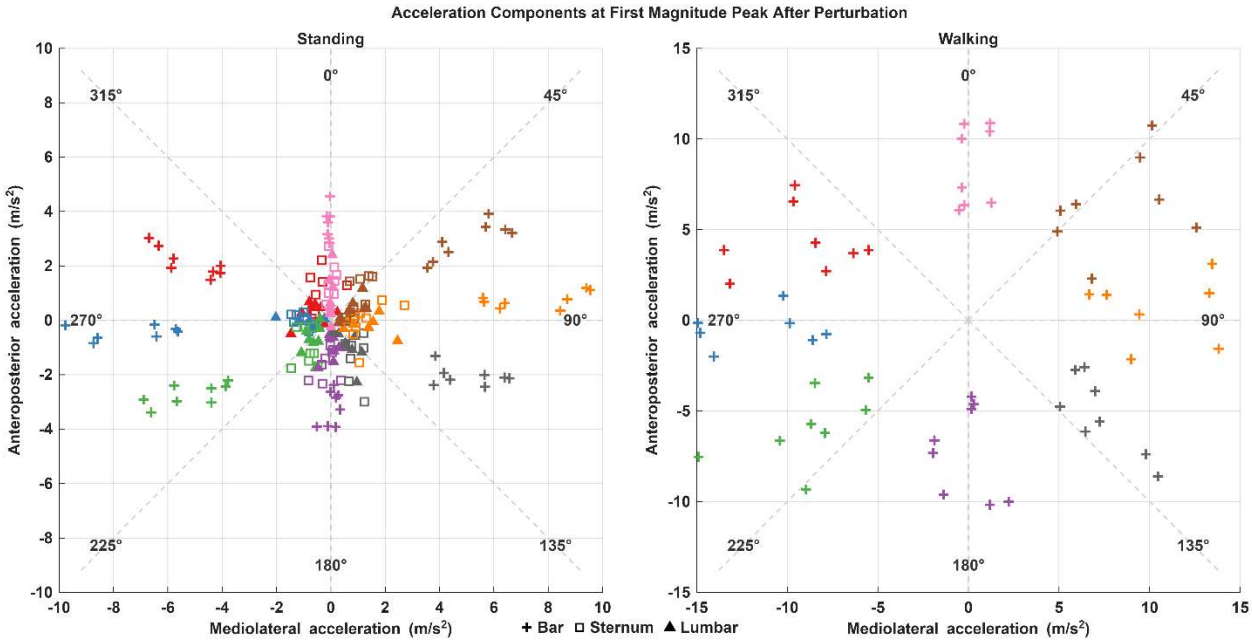


Figure 1. Perturbation-induced accelerations of the FLOAT support bar (−), participants' sternum (□), and participants' lumbar spine (▲) during standing (Left). The right panel shows walking responses, where (+) denotes the bar sensor. Colors indicate the acceleration direction relative to the participant. The main directions are anterior (0°), posterior (180°), right (90°), and left (270°). Diagonal angles correspond to combined directions: antero right (45°), antero-left (315°), postero right (135°), postero left (225°).

References (Optional)

[1] McCrum, C., Front. Sports Act. Living, 2022

[2] Vallery, H., IEEE ICORR, 2013

Acknowledgements (Optional)

Funding provided by Reha-Stim MedTec.

Session Category

Rehabilitation Biomechanics and Human Factors: Rehabilitation

P2-334

Effectiveness of a Contralateral Shoe Balancer on Reducing Gait Alterations in Achilles Tendon Rupture Rehabilitation Boots

Ms. Phoebe Cheung[1], Dr. Julie A. Stebbins[2,3], Prof. David J. Keene[2], Prof. Amy B. Zavatsky[1]

[1]Department of Engineering Science, University of Oxford, Oxford, Oxfordshire, United Kingdom. [2]NDORMS, University of Oxford, Oxford, Oxfordshire, United Kingdom. [3]Oxford Gait Laboratory, Oxford University Hospitals NHS Foundation Trust, Oxford, Oxfordshire, United Kingdom

Introduction

Achilles tendon rupture (ATR) patients wear an immobilization boot for about two months to facilitate healing, with the ankle transitioning from 30° plantarflexion (PF) to 0° over several weeks. To compensate for leg length asymmetry caused by the boot, a shoe balancer is occasionally worn on the uninjured (contralateral) side. Previous literature on balancer effectiveness only focused on boots with a neutral ankle position [1]. This study aims to determine the effectiveness of a balancer in reducing gait alterations when the immobilized ankle is at 30° PF.

Methods

Three healthy adult participants (ongoing study, target n=12) completed walking trials in two common ATR boots (VACOped and AirSelect) set at 30° PF and 0°, with and without a balancer (EVENup). Baseline walking data in shoes was also captured. Kinematic data was collected with marker-based motion capture (Vicon) using conventional model lower limb markers and processed with clinical protocols for calculating joint kinematics.

Results

Hip flexion-extension was selected for initial data analysis, as lower back and hip pain are most common in patients wearing rehabilitation boots [2]. Visual inspection of the preliminary data suggest that wearing a balancer partially reduces gait alterations at the hip (Figure 1). Greatest improvement is seen in the ipsilateral hip in the 30° PF configuration for both boots, with improved peak hip extension during stance. The balancer has little effect on contralateral hip motion.

Discussion

A study on the AirSelect at 0° reported that balancers partially restored kinematics towards the shoe baseline [1], while this study's initial findings show minimal visual change in this configuration. Upon completion of the study, the balancer's ability to reduce gait alterations at other joints and in other planes of motion will also be quantified, allowing the effectiveness of the balancer to be assessed fully. While the study is only observing the effects on healthy participants and does not consider pathological gait of ATR patients, its early results already reinforce the importance of wearing a balancer during the early stages of rehabilitation when the booted ankle is most plantarflexed.

Images (Optional)

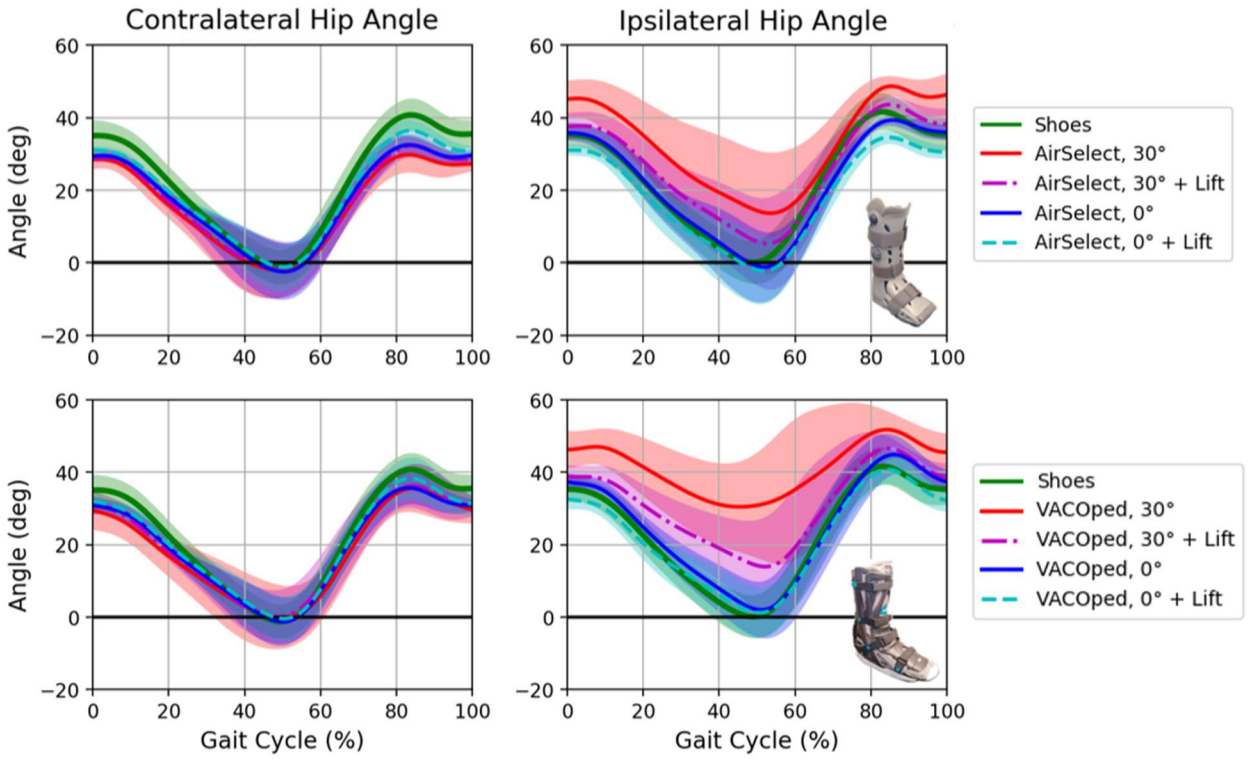


Figure 1. Contralateral and ipsilateral hip flexion (+) and extension (-) angle normalized to the full stance-swing gait cycle (0-100%) for AirSelect (top) and VACOped (bottom) boots.

References (Optional)

[1] Cecilia Severin *et al.*, Gait Posture, 2019

[2] Lauren Ready *et al.*, JAAOS Global, 2018

Session Category

Rehabilitation Biomechanics and Human Factors: Rehabilitation

P2-335

Haptic Wheelchair Propulsion Training Using Real-Time 3D Inverse Dynamics and Reinforcement Learning Approach

professor Rachid Aissaoui RA[1,2], MSc Clément Ghazouani CG[1], MSc Manon Perez MP[1], PhD Philippe Nadeau PN[3]

[1]École de technologie supérieure, Montréal, Québec, Canada. [2]CRCHUM, Montréal, Québec, Canada. [3]University of Toronto, Toronto, Ontario, Canada

Introduction

Manual wheelchair propulsion (MWP) is an important form of mobility [1]. High prevalence of shoulder pain and injury are reported during MWP, but the exact cause-effect relation remains unclear [2]. Current wheelchair provision guidelines provide little insight into the biomechanical context about MWP efficiency while preserving from shoulder joint injury [3]. Recently, we developed a haptic wheelchair simulator [4,5] which has the capacity to estimate the bilateral 3D real-time inverse dynamics at shoulder, elbow and wrist joints as well as the physiological cost (PC) during MWP. The purpose of the present work is to train wheelchair user to modify their pattern of propulsion while enhancing their mechanical efficiency (MEF) and reducing their PC using real-time reinforcement learning approach.

Methods

Eighteen able-bodied subjects participated in this study. They were asked to propel the wheelchair at 1m/s onto the haptic simulator during 3 mn whereas the RL algorithm learn the pattern of their propulsion. Six conditions of training were applied randomly. 3D inverse dynamics of upper limb was assessed in a real-time using Simulink in Speedgoat computer. The dependent variables are the average and maximal value of MEF and PC during the push cycle of MWP for each condition at a controlled speed of 1m/s.

Results

Table 1 shows the 6 conditions with respect to the baseline. The results indicate that MEF was enhanced for all conditions of propulsion. RL training help reducing the joint moment at the shoulder level when using assistive/resistive condition.

Discussion

This work demonstrate that it is possible to enhance MEF while reducing shoulder joint moment. Any reduction of the shoulder joint moment is beneficial for the integrity of the shoulder complex as well as for the reduction of risk of glenohumeral joint injury.

Images (Optional)

Left side	Av. Shoulder joint flexion Moment (N.m)	Peak Shoulder joint flexion Moment (N.m)	Av. Shoulder joint extension Moment (N.m)	Peak Shoulder joint flexion Moment (N.m)	Av. MEF	Peak MEF
Baseline	7,77	14,46	2,2	4,49	0,532	0,855
MEF (Res)	**10,4***	**19,11***	**2,72***	**5,27***	0,566	0,871
MEF (Assist/Res)	7,78	14,7	2,16	4,35	0,529	0,864
PC (Res)	**10,49***	**19,97***	2,58	4,96	0,539	0,872
PC (Assist/Res)	7,69	14,92	2,23	4,52	0,515	0,85
MEF + PC (Res)	**10,01***	18,62	2,28	4,51	0,546	**0,892***
MEF + PC (Assist/Res)	7,98	15,59	2,24	4,53	0,504	0,842

Right side	Moment flex moy (N.m)	Moment flex max (N.m)	Moment ext moy (N.m)	Moment ext max (N.m)	MEF mean	MEF max
Baseline	8,53	15,6	2,13	4,13	0,553	0,893
MEF (Res)	**10,58***	**19,84***	2,46	4,57	0,589	0,91
MEF (Assist/Res)	8,17	15,21	2,15	4,16	0,567	0,9
PC (Res)	**11,23***	**21,08***	**2,88***	**5,08***	0,57	0,902
PC (Assist/Res)	8,76	16,39	2,06	3,95	0,55	0,886
MEF + PC Res	**10,14***	**18,94***	2,31	4,47	0,578	0,917
MEF + PC (Assist/Res)	8,76	16,62	2,26	4,2	0,539	0,889

*: p<0.0083 with respect to the Baseline
Green color: diminution of joint moment and augmentation of MEF with respect to the Baseline

References (Optional)

[1] Cooper Rory et al., Am. J. Phys. Med. & Rehab, 1999.

[2] Salzmann Inge P. et al., J. Biomechanics, 2025.

[3] Kimberly Charlton et al., Australian Occupational Therapy Journal, 2023.

[4] Martine Blouin et al., IEEE Trans. on Neural Sys & Rehabil Eng, 2015.

[5] Aissaoui Rachid et al., Frontiers in Rehabilitation Sciences, 2022.

[6]. Rusta Mohammed Mahdi. Computers in Biology and Medicine, 2025.

Acknowledgements (Optional)

Financial support from NSERC and INTER (FRQNT)

Session Category

P2-336

The Influence of Virtual Reality Design Factors on Obstacle Negotiation and Spatiotemporal Gait Mechanics

Mr. Ryan Dang B.S., Ms. Mrital Patel, Ms. Anais Unanyan B.A., Mr. Kenneth M Mazariegos B.A., Dr. Stefanie A Drew Ph.D., Dr. Thomas Chan Ph.D., Dr. Peter L Bishay Ph.D., Dr. Jacob W Hinkel-Lipsker Ph.D.

California State University, Northridge, Northridge, CA, United States

Mr. Ryan Dang

Ms. Mrital Patel

Mr. Kenneth M Mazariegos

Dr. Stefanie A Drew

Dr. Thomas Chan

Dr. Peter L Bishay

Introduction

Research has described mixed outcomes for gait rehabilitation in virtual reality (VR), which may be related to the design of the VR experience itself [1]. Some design factors that might influence gait rehabilitation in VR include visual fidelity (i.e., visual realism) and cognitive demand (i.e., psychological realism). It is not known how the combination of these factors drives learning and/or enhancement of gait. Therefore, this study seeks to understand how systematically manipulating VR design factors affects gait biomechanics during a novel obstacle negotiation task.

Methods

Participants with and without stroke (anticipated n = 40 without and n = 10 with stroke) are being recruited for this ongoing study. Each participant performs an obstacle negotiation task while simultaneously completing a secondary cognitive task (simulating texting and walking). After a real-world baseline assessment, participants practice this task on an omnidirectional treadmill twice per week for five weeks in a virtual environment that differs in terms of visual fidelity (high (HV) or low (LV)) and cognitive demand (high (HC) or low (HC)). All participants then perform real-world retention and transfer tests. Inertial measurement units (IMUs) placed on the pelvis, legs, and feet are used to calculate spatiotemporal gait outcomes as well as obstacle negotiation mechanics.

Results

Preliminary results (n = 5, all without stroke) indicate that training in LV VR resulted in large increases in leading limb angles at the moment of obstacle negotiation, while training in HV VR resulted in large decreases in the same angle (Figure 1). There were no evident differences between training in HC and LC on obstacle negotiation mechanics. Very few differences in spatiotemporal outcomes were evident across all comparisons.

Discussion

Results indicate that VR realism can impact obstacle negotiation mechanics, highlighting the need for VR-based interventions to consider this factor when designing a training experience. Moreover, how an environment in VR is perceived has downstream effects on motor output. In total, this work describes how not all VR experiences are equal for skill learning, and thus better informs why the literature to date is mixed with regards outcomes in VR-based interventions.

Images (Optional)

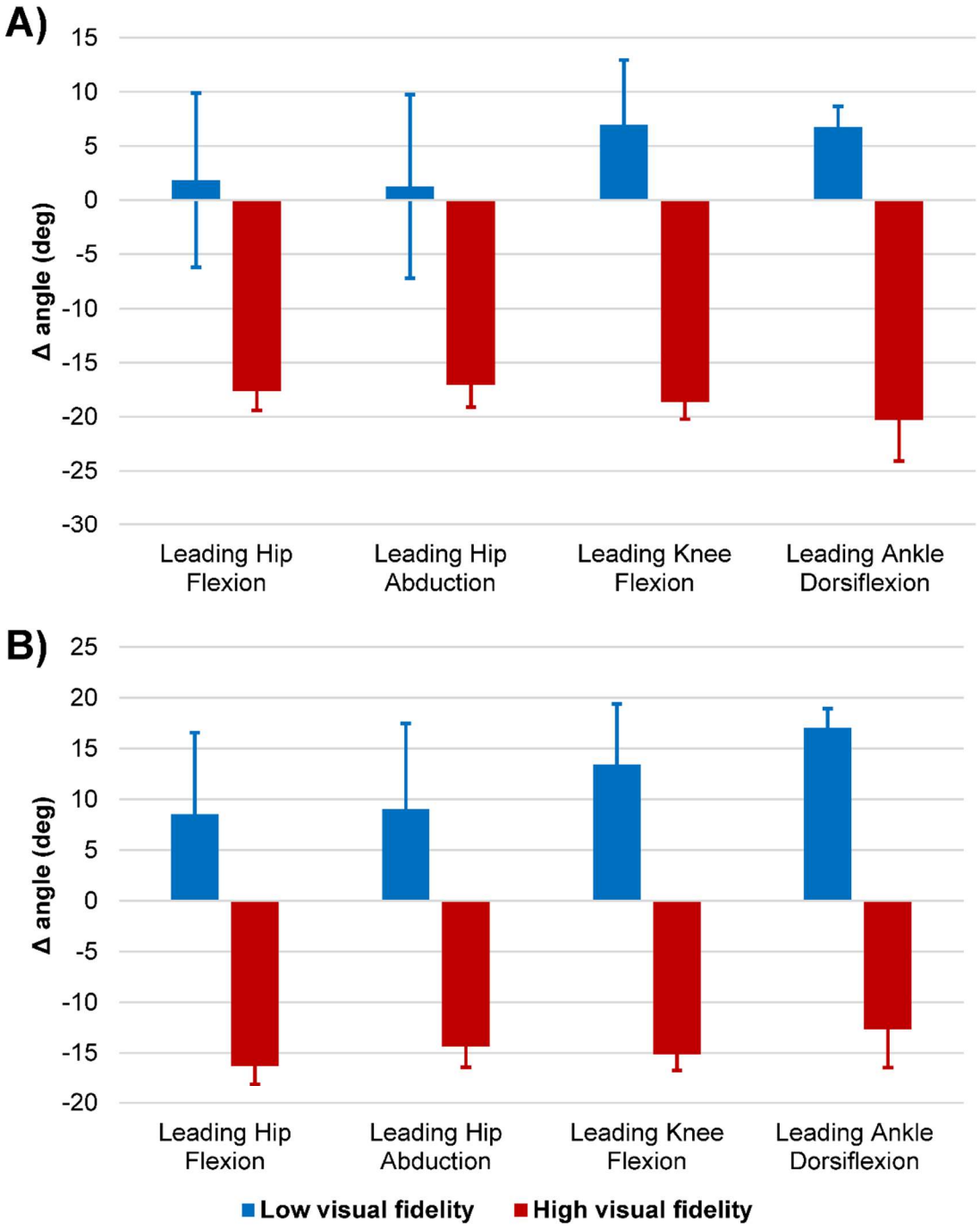


Figure 1. Differences between low and high visual fidelity VR training experiences. Values reflect changes in leg joint angle during obstacle clearance between A) Baseline and retention; B) Baseline and transfer.

References (Optional)

[1] Howard, M. C., Comp Hum Behav, 2017

Acknowledgements (Optional)

This project is funded by the National Science Foundation's Mind, Machine, and Motor Nexus (M3X) program (NSF Award Number 2225135).

Thank you to all other members of the Gait, Oculomotor, and Lower-extremity Dynamics (GOLD) Lab, Design of Smart Mechanical And Reconfigurable Technologies (SMART) Lab, Visual Information Science and Neuroscience (VISN) Lab, Positive Aging Research and Development (PAR-D) Lab for data collection and analysis.

Session Category

Rehabilitation Biomechanics and Human Factors: Rehabilitation

P2-337

Exercising With a Resistive Hip Exosuit Induces Stroke-Relevant Gait Aftereffects in Healthy Adults

Doctoral Student Sangwon Shin, Ph.D. Pieter Van den Berghe, Associate Professor Mukul Mukherjee, Associate Professor Philippe Malcolm

University of Nebraska at Omaha, Omaha, NE, United States

Introduction

Post-stroke walking leads to biomechanical deficits [1] such as asymmetric step length and propulsion, drop foot, insufficient toe clearance, hip hiking, and circumduction [2, 3]. Other groups have developed motorized devices to target stroke-relevant variables on each joint: e.g., split-treadmills to retrain propulsion [4], ankle exosuits to help with push-off and toe clearance [5], hip exosuits to help with circumduction and hip hiking [6]. We have developed a soft passive hip exosuit with quasi-force retractors asymmetrically spanning the hip joints. Our device made the aftereffect on step-length symmetry in healthy adults [7]. To expand this finding, this study aimed to evaluate whether an unpowered resistive device could alter stroke-relevant variables, such as trailing limb angle, propulsive/braking impulse, minimum toe clearance, hip hiking, and drop-foot angle, in healthy adults. We hypothesized that a passive hip resistive exosuit would affect sagittal hip kinematics but not other variables.

Methods

Eight healthy adults walked overground for 15 minutes while wearing an exosuit that applied 15% and 10% of body weight on the anterior right thigh and the posterior left thigh. Before and after this 15-minute bout, participants also walked overground for 15 minutes with the retractors disconnected. We measured stroke-relevant biomechanical variables using motion capture and ground reaction force measurement. We quantified the symmetry of these variables using the symmetry index [8], calculated as: We exponentially fitted phase evolutions and performed repeated measures ANOVA (*Baseline*, *Initial Adaptation*, and *Initial After*) and post-hoc tests using the Holm correction.

Results

The aftereffect on the trailing limb angle aligned with our hypothesis; however, immediately *after* disconnecting the exosuit, healthy adults increased trailing limb angle and braking impulse on the right side, coinciding with greater minimum toe clearance and drop-foot angle on the left side (Fig. 1). These aftereffects were not expected.

Discussion

A soft, passive hip exosuit produced significant aftereffects in four of six stroke-relevant gait parameters, challenging the joint-specific paradigm and indicating that a single-joint device can drive multi-joint adaptations. Future stroke trials are needed to determine how passive-resistance exosuits shape the rehabilitation of chronic stroke survivors.

Images (Optional)

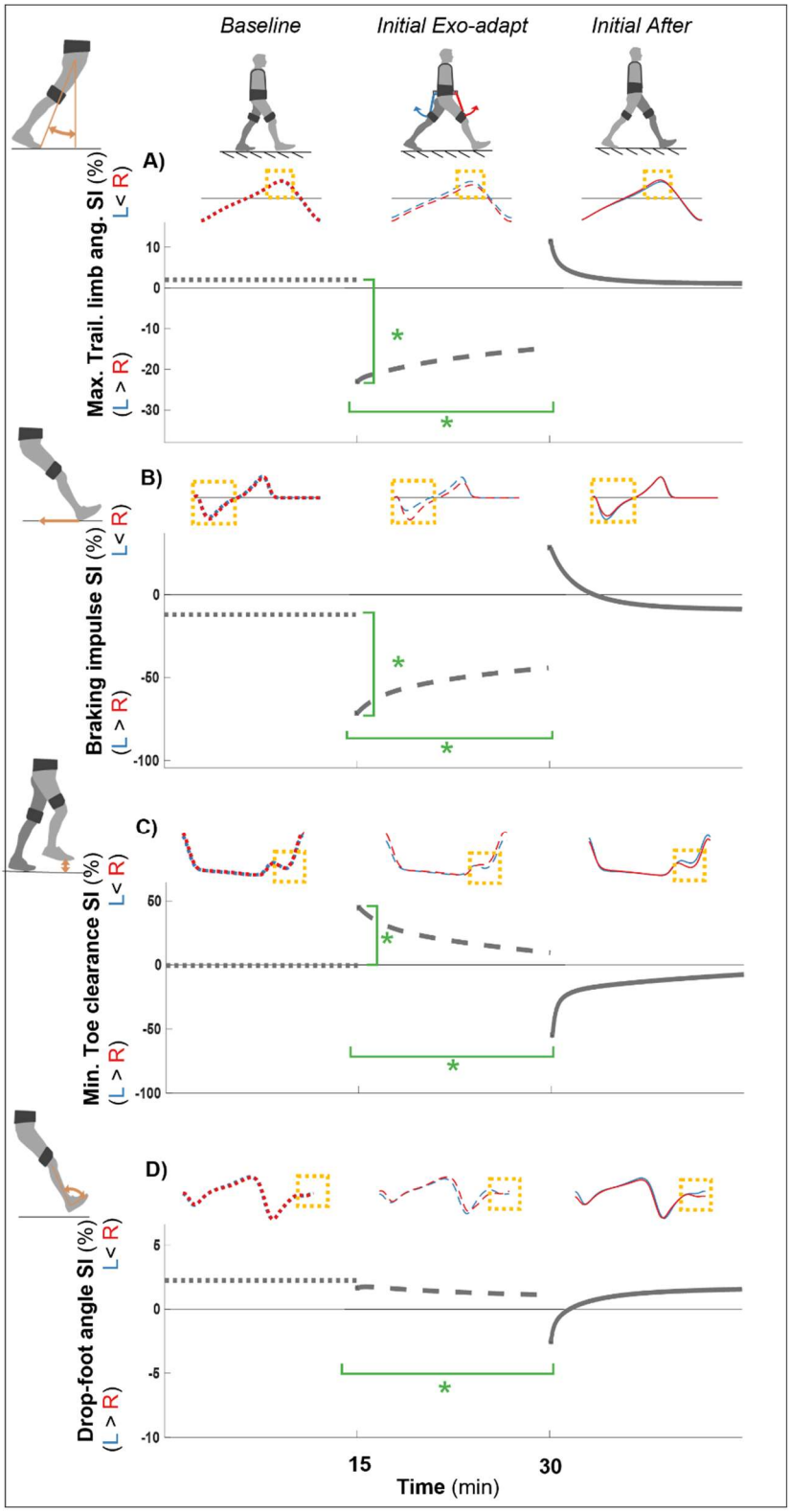


Fig. 1: Symmetry indices of stroke-relevant variables. Trends for stroke-relevant parameters SI across Baseline (dotted), Exosuit Adaptation (dashed), and After (solid lines) phases. Red and blue dotted lines represent the underlying right- and left-stride normalized timeseries used to calculate SI. The yellow box marks the instant in the gait cycle where SI was calculated. (SI: Symmetry Index, *: $p<0.05$)

References (Optional)

Acknowledgements (Optional)

NU GRACA; AHA 25PRE1378622; NIH P20GM109090 and P20GM152301; NSF 2203143. Authors are inventors of WO2023192982A2 and 63/900 105 25064P).

Session Category

Rehabilitation Biomechanics and Human Factors: Rehabilitation

P2-338

Enhancing Passive Gravity Compensation in a Lower-Limb Exoskeleton with a CAM Mechanism

Ms. SeHee Jung MS Candidate, Prof. Ho Seon Choi Assistant Professor

Sejong University, Seoul, Seoul, Korea, Republic of

Ms. SeHee Jung

Introduction

As the weight of the exoskeleton may limit the performance of the walking assistance algorithm, we investigated a non-powered gravity compensation(GC) mechanism to mitigate this effect. However, the previous structure provided insufficient Z-axis compensation due to geometric constraints of the moment arm. Therefore, this study aims to enhance GC across all three axes by integrating a CAM-based additional compensation mechanism into Joint1 to directly address the residual Z-axis moment.

Methods

The compensation torque was calculated from the spring deformation and moment arm generated by each joint rotation in a 3-DOF passive exoskeleton with the GC mechanism located at the hip joint. The joint design parameters and spring constants were defined as optimization variables, and an optimization was performed to minimize the squared error between the gravity moment and the GC moment over the gait cycle. To address the insufficient Z-axis compensation, a CAM mechanism was additionally integrated into Joint1, and the CAM radius profile was obtained by inversely calculating the design variable x that satisfies the target torque at each angle. The target torque was generated through an optimization process incorporating slope and curvature limits, static torque minimization around 0°, and constraints to prevent overcompensation.

Results

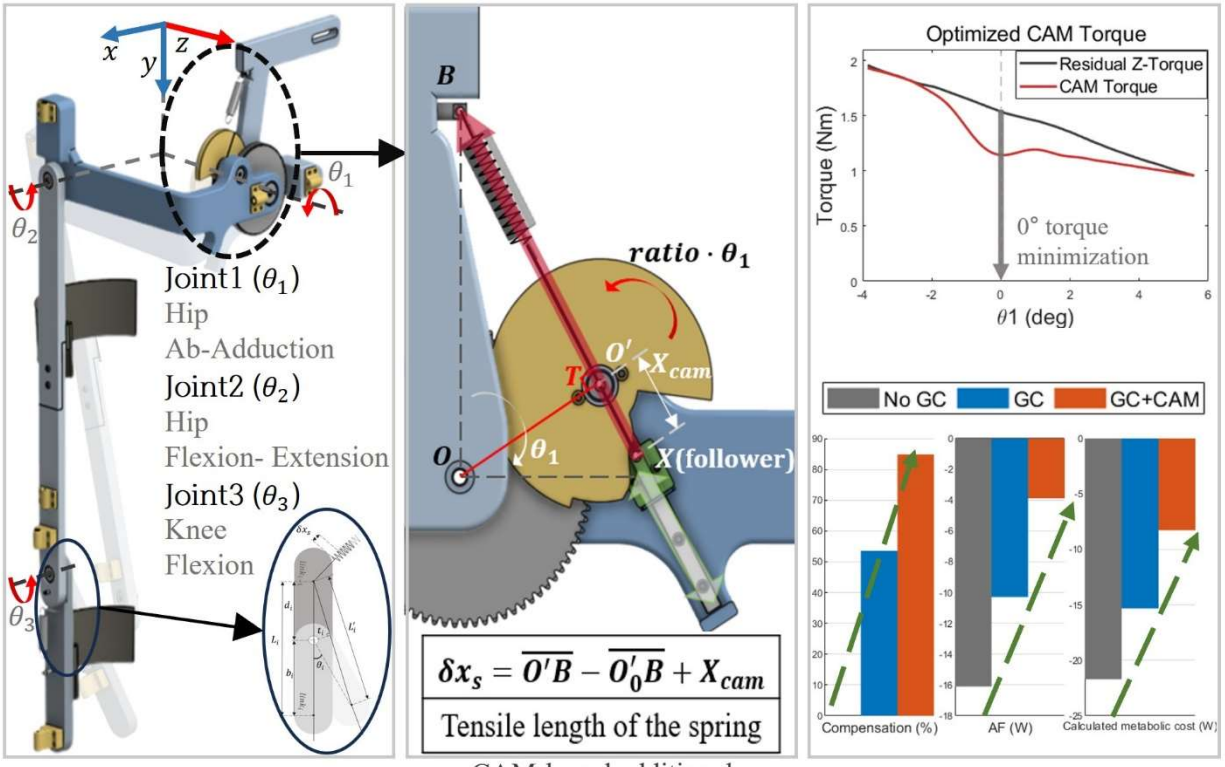
A CAM profile capable of being tracked by a 3-mm follower was designed using curvature-constrained optimization, and the resulting CAM torque reliably followed the target torque while reducing overcompensation near 0°. Under a 2.9-kg exoskeleton load during walking for a 170-cm-tall adult, the moment compensation rate increased from 53.67% to 85.62% with the CAM mechanism. Furthermore, applying the AF–metabolic cost correlation

proposed by Mooney et al.[1] showed that the estimated metabolic cost loss decreased by 32.55%, from 15.34 W to 8.28 W.

Discussion

The proposed CAM-based additional compensation mechanism enhances the previously limited Z-axis compensation caused by the geometric constraints of the spring arrangement, achieving this improvement in a fully passive system. However, as the current findings rely on model-based optimization, further validation through prototype testing, including in-gait torque measurement and metabolic cost evaluation, is required.

Images (Optional)



Entire exoskeleton

CAM-based additional compensation mechanism

Calculated results

References (Optional)

[1] Mooney LM et *al.* , J Neuroeng Rehabil, 2014

Acknowledgements (Optional)

This project is currently supported by the National Research Foundation of Korea(NRF) grant funded by the Korea government (MSIT) (RS-2024-00452977). (Correspondance: choihoseon@sejong.ac.kr)

Session Category

Rehabilitation Biomechanics and Human Factors: Rehabilitation

P2-339

Effects of Pain and Exercise Intensity on Lower Limb Asymmetry During Cycling

Ms. Sierra Sweeney BSc, Mr. Amirreza Hosseini, Dr. Shahram Rasoulian, Dr. Amin Komeili, Dr. Saied Jalal Aboodarda

University of Calgary, Calgary, Alberta, Canada

Introduction

Lower-limb pain is a clinical problem that disrupts movement, leading to compensatory motor strategies that increase biomechanical asymmetry and limit rehabilitation effectiveness [1]. Cycling is frequently prescribed in rehabilitation for individuals with lower limb asymmetry. Studying the effect of joint pain on physical performance using patients is challenging. This study aimed to develop an adaptive joint-pain induction protocol for varying exercise intensities and to quantify how unilateral lower-limb pain affects cycling performance in healthy adults. We hypothesized that pain would increase asymmetry and would be amplified at higher workloads.

Methods

Six healthy adults (2 female, 4 male) completed four randomized 2-min cycling trials: no pain at low-intensity (NPLI), with pain at low-intensity (PLI), no pain at high-intensity (NPHI), and with pain at high-intensity (PHI). Electrical stimulation over the right patella induced individualized pain levels applied during the downstroke, scaled to pedal force. Pedal kinetics were recorded using Sensix 3D force–torque pedals on a modified Echelon EX-5 ergometer. The Normalized Symmetry Index (NSI) was calculated to determine limb distribution. NSI from the first 25% and last 25% of each trial were averaged to assess early and late behavior. A three-way repeated-measures ANOVA (Pain × Intensity × Time) tested effects on NSI.

Results

Descriptive statistics showed greater asymmetry during trials with induced pain compared to those without pain. Additionally, NSI increased from **18.61 ± 10.38%** in PLI to **21.73 ± 8.26%** in PHI. The ANOVA revealed a **significant main effect of pain** (p=.027, partial η^2=.655). Intensity (p=.831) and time (p=.849) were not significant. A **Pain × Intensity interaction** was significant (p=.042, partial η^2=.595), indicating amplified asymmetry at higher workloads. No other interactions were significant (p>.33).

Discussion

Pain increased NSI values, and was amplified at higher workloads, consistent with evidence that nociception alters motor control [2]. This suggests that the proposed system can generate intensity-adaptive pain responses and capture compensatory loading strategies relevant to rehabilitation in individuals with lower-limb asymmetry. However, the small sample size limits generalizability, and ongoing studies in larger clinical populations are needed to validate these results.

Images (Optional)

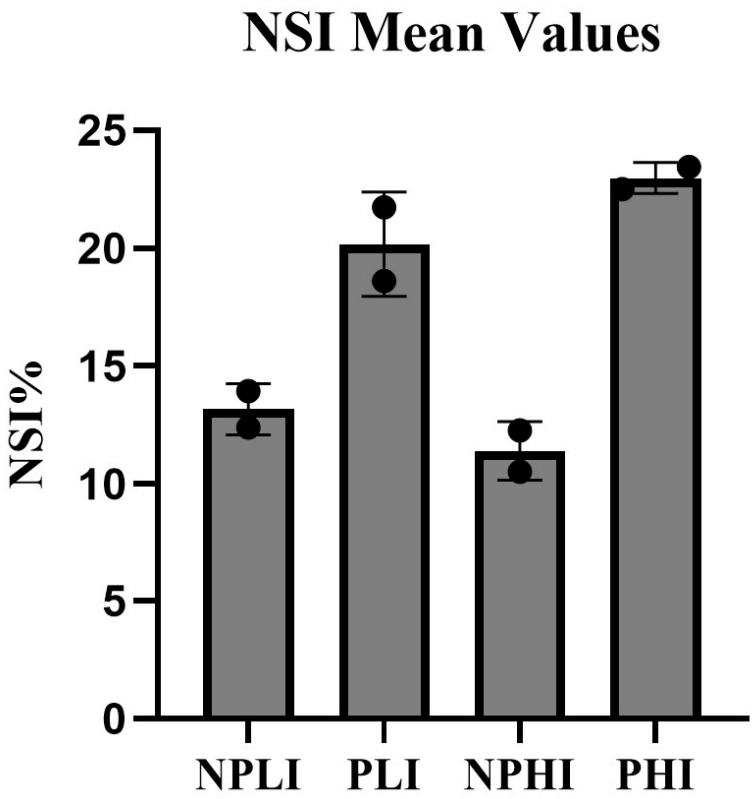


Figure 1: NSI mean and standard deviation values. No pain low intensity (NPLI), pain low intensity (PLI), no pain high intensity (NPHI), pain high intensity (PHI).

References (Optional)

[1] Sara Muller *et al.* , Pain, 2012

[2] Shailesh Kattak *et al.* , Physical Therapy, 2022

Session Category

Rehabilitation Biomechanics and Human Factors: Rehabilitation

P2-340

Modulation of the Brain–Movement Connection via Combined Transcranial Direct Current Stimulation (tDCS) and Mirror Therapy in Chronic Stroke: Insights From Baseline and Post-Training Comparisons

Dr. Thi Bang Giao Nguyen MD[1], Dr. Chia-Lun Liu PhD[2], Dr. Tsai-Yu Shih PhD[2], Prof. Ching-Yi Wu ScD[2,3,4]

[1]Graduate Institute of Rehabilitation Science, School of Physical Therapy, College of Medicine, Chang Gung University, Taoyuan, None, Taiwan. [2]Department of Occupational Therapy and Graduate Institute of Behavioral Sciences, College of Medicine, Chang Gung University, Taoyuan, None, Taiwan. [3]Healthy Aging Research Center, Chang Gung University, Taoyuan, None, Taiwan. [4]Department of Physical Medicine and Rehabilitation, Chang Gung Memorial Hospital, Linkou 333, Taoyuan, None, Taiwan

Dr. Thi Bang Giao Nguyen

Dr. Chia-Lun Liu

Dr. Tsai-Yu Shih

Introduction

The recent motor training following stroke, such as transcranial Direct Current Stimulation (tDCS) hybridized with mirror therapy, requires coordination between motor preparation and execution stages, involving multiple cortical regions. Electroencephalogram (EEG) measures cortical activity, while kinematics assesses the two motor stages of preparation and execution. Identifying the coupling of cortical activity and kinematics can enhance our understanding of movement inefficiency and compensation during preparation and execution, which remains limited. This research examines how different brain cortical regions contribute to the motor control of these two stages before and after training.

Methods

Data for this project were obtained from a randomized, double-blind, placebo-controlled parent RCT involving 36 individuals with chronic stroke (FMA-UE score of 18–56). In that

trial, participants were allocated to the primary motor cortex, premotor cortex, or sham group and received 90 minutes of tDCS, mirror therapy, and functional task practice per day, five days a week, for four weeks. Outcome measures included EEG, specifically, beta-band event-related synchronization (ERS), dividing into low-beta (13-16 Hz), medium-beta (17-20 Hz), and high-beta (21-30 Hz) in central, frontal, and parietal regions; and kinematics involving reaction time (RT) and arm-trunk contribution slope (A-TCS) were extracted. Pearson and Spearman correlation analyses were conducted to examine the relationships between EEG measures and kinematic indices at baseline, and between post-pre change (Δ) in EEG measures and Δkinematic indices following training.

Results

At baseline, high-beta ERS in frontal and parietal regions correlated with RT; medium- and high-beta ERS in central, frontal, and parietal regions correlated with mid-phase A-TCS. After training, there was no significant correlation between Δhigh-beta ERS and ΔRT; Δlow-beta ERS in central and frontal regions was associated with Δmid-phase A-TCS, while Δmedium- and Δhigh-beta ERS in central, frontal, and parietal regions correlated with Δearly phase A-TCS.

Discussion

At baseline, arm and hand functions rely heavily on top-down control, extended motor preparation, and limited mechanical support from trunk compensation. After training, the shift from cognitive, time-based strategies to more automatic and spatially optimized strategies.

Images (Optional)

Table. Correlations between EEG and kinematic indices at baseline (A) and between change (Δ) in EEG and ΔKinematic indices following combined tDCS and mirror therapy training (B).

A. BASELINE				
Task	EEG Measure (ERS)	Kinematic Index	r	p
Unilateral	parietal high-beta	Trunk RT	0.406	0.032
Bilateral	frontal high-beta	Trunk RT	0.420	0.026
	parietal high-beta	Index RT	0.419	0.027
	central medium-beta	A-TCS_mid	-0.408	0.031
	frontal medium beta		-0.385	0.043
	central high-beta		-0.429	0.023
	parietal high-beta		-0.385	0.043
B. POST-PRE CHANGE (Δ)				
Task	ΔEEG Measure (ERS)	ΔKinematic Index	r	p
Unilateral	central low-beta	A-TCS_mid	0.448	0.019
	frontal low-beta		0.404	0.037
Bilateral	central medium-beta	A-TCS_start	-0.393	0.042
	frontal medium-beta		-0.539	0.004
	parietal medium-beta		-0.482	0.011
	central high-beta		-0.513	0.006
	frontal high-beta		-0.622	0.001
	parietal high-beta		-0.397	0.040

tDCS transcranial direct current stimulation, *EEG* electroencephalogram, *ERS* event-related synchronization, *RT* reaction time, *A-TCS_start* arm-trunk contribution slope in the early phase of movement, *A-TCS_mid* arm-trunk contribution slope in the middle phase of movement.

References (Optional)

"[1] C. L. Liu *et al.* , IEEE Trans Neural Syst Rehabil Eng, 2024"

"[2] C. Y. Wu *et al.* , J Neuroeng Rehabil, 2013"

Acknowledgements (Optional)

This study was supported in part by the Chang Gung Memorial Hospital under Grant BMRP553 and Grant CMRPD1P0022; in part by the National Science and Technology Council (NSTC), Taiwan, under Grant NSTC 113-2314-B-182-049 MT3; in part by the National Health Research Institutes under Grant NHRI-EX114-11105PI; and in part by the Healthy Aging Research Center, Taiwan, under Grant URRPD1Q0181.

Session Category

Rehabilitation Biomechanics and Human Factors: Rehabilitation

P2-341

Differences in quadricep activation patterns through the knee range of motion between open- and closed-kinetic chain exercises

Ms. Tiffany Tiu PT, MScPT, BKin, CSCS

University of Toronto, Toronto, ON, Canada. The Pain and Wellness Centre, Vaughn, ON, Canada

Introduction

Rehabilitation following anterior cruciate ligament reconstruction (ACLR) includes regaining strength in the quadriceps. Existing research comparing open kinetic chain (OKC) and closed kinetic chain (CKC) exercises has used a single maximal electromyographic (EMG) signal in the movement to compare quadriceps activation between the exercises, without accounting for how muscle activation changes as the knee moves through its range of motion (ROM). During ACLR rehabilitation, 6-12 weeks are often needed to regain full knee ROM. Current research has not examined the interaction between muscle activation at different knee ROM during OKC and CKC exercises.

The purpose of this study is to compare quadriceps activation by knee angle between submaximal isokinetic OKC and CKC exercises and their different loading conditions.

Methods

Twenty-three healthy adults (18-40 years) performed OKC (unilateral knee extension (KE)) and CKC exercises (bilateral squat (SQ) and unilateral step-up (SU)) at body weight (BW/no added weight), with an added 10% BW load, and 25% BW load. Participants performed three trials of each condition in a randomized order. Surface EMG were collected from rectus femoris (RF), vastus medialis (VM), and vastus lateralis (VL), and reported as a percentage of maximum voluntary isometric contraction (%MVIC). Knee kinematics were quantified using an eight-camera markerless motion capture.

For each muscle (RF, VM, and VL) and each dependent variable (peak %MVIC and knee angle), two-way repeated-measures ANOVAs were performed: within-subject factors were exercise (KE, SQ, SU) and load (BW, 10%BW, and 25%BW). Post-hoc Bonferroni-adjusted pairwise comparisons were performed.

Results

KE provided the highest activations at more extended knee ranges (24-48°), while SQ and SU at more flexed ranges (99-123°) (p<.001). There was no difference between SQ and SU at the knee angles at which peak activation was achieved. SU elicited the most activation for all three muscles (72-121 %MVIC, p<.001).

Discussion

From an activation-by-knee-angle perspective, OKC and CKC exercises serve complementary roles in quadriceps strengthening. Within the ACLR patients' available knee ROM, both types of exercises are warranted to provide quadriceps strengthening through the knee's ROM. As a unilateral weight-bearing exercise, SU can be used early in rehabilitation to elicit high quadriceps activation, even at body weight.

Session Category

Rehabilitation Biomechanics and Human Factors: Rehabilitation

P2-342

Feasibility Study of a Custom Mixed-Reality Game Suite for Pediatric Motor Training

Mr. Tristan McCarty[1], Ms. Suhani Chaudhary[1], Mr. Weijia Zhang[2], Dr. Jiasi Chen[2], Dr. Elena Kokkoni[1]

[1]University of California, Riverside, Riverside, CA, United States. [2]University of Michigan, Ann Arbor, MI, United States

Introduction

Existing motor training interventions often rely on repetitive training tasks, which may lead to reduced motivation and adherence to motor training [1]. Mixed reality (MR) has emerged as a potential tool to enhance training by embedding motor tasks into immersive gamified environments. In contrast to screen-based systems, MR training environments allow users to move in a more naturalistic manner. By turning training into play, motor training paradigms for pediatric populations can become more engaging [2]. The efficacy of gamified training, however, also relies on how task difficulty is perceived and adapted over time [3]. Here, we report on a suite of four custom-designed MR games for use by children to train clinically relevant motor skills.

Methods

Our study design involves a single experimental session consisting of two blocks, with each block containing three minutes of exposure to each of the four MR games. One block retains a static pre-defined difficulty based on the participant's overall activity level, whereas the other uses a dynamic difficulty adjustment (DDA) algorithm to adjust task difficulty in real-time throughout exposure. The target population (children 5-9 years old) is exposed to the games via an MR head-mounted display, while multi-view video recordings are collected for annotation of events of interest. Electromyography (EMG) and inertial sensors are used to record muscle activity and limb acceleration, respectively.

Results

Literature-derived baseline metrics (gait speed and EMG root mean square) defined the initial in-game difficulty levels, with an average gait speed (~1.28 m/s) assigned to users and then adjusted towards the maximal and minimal difficulty values (two standard deviations) based on task performance. Ongoing efforts, including further data analysis

and collection of user and caregiver feedback, aim to identify potential areas of improvement in the system.

Discussion

This pilot study marks a significant step towards the development of an integrated MR-based DDA motor training system for children. It shows preliminary feasibility for use with pathological populations and provides feedback which can be used by clinicians to enhance training outcomes.

References (Optional)

[1] Levac, *Dev Med Child Neurol.*, 2024.

[2] Bonnechère, Serious Games Rehabil, 2018

[3] Houzangbe et al., *JMIR Res. Protoc.*, 2024.

Session Category

Rehabilitation Biomechanics and Human Factors: Rehabilitation

P2-343

Effects of Hopping Directions on Knee Mechanics and Knee Extensors and Flexors Muscle Activation

PhD student Yu Gu, PhD student Wanyan Su, Dr. Yu Song

University of Kansas, Lawrence, Kansas, United States

Introduction

Single-leg forward and vertical hopping are widely used in clinics to evaluate knee function after anterior cruciate ligament reconstruction (ACLR). However, previous studies have shown that performance on these tasks demonstrates limited agreement with underlying knee mechanics and control. Therefore, a knee-specific clinical assessment is warranted. Recently, single-leg backward hopping has been proposed as a more knee-demanding task, given its greater knee power and work. Nevertheless, muscle activation across the knee joint aligned with the knee mechanics compared to forward and vertical hopping remains unclear.

Methods

Forty-eight injury-free participants (30 females and 18 males; 20.9 ± 0.7 yrs; 1.7 ± 0.1 m; 68.1 ± 12.0 kg) performed single-leg forward/vertical/backward hopping with motion, force, and surface electromyography (quadriceps, hamstrings, and triceps surae) data collected. Maximum voluntary contraction (MVC) was recorded for each muscle group. Peak knee flexion angles and moments during jumping were calculated. Peak and mean muscle activation during jumping were also calculated and normalized to MVC. One-by-three repeated-measures ANOVA was conducted to quantify the effects of hopping directions (p-value = 0.05).

Results

Forward hopping demonstrated significantly greater hamstring activation, but smaller knee angle/moment and quadriceps activation compared to vertical and backward hopping (Table 1). Vertical hopping showed the greatest knee flexion angle among hopping directions. Backward hopping showed the smallest muscle activation of biceps femoris/gastrocnemius medialis/soleus with the greatest knee moment compared to forward and vertical hopping.

Discussion

Single-leg forward hopping requires less quadriceps activation and knee engagement compared to vertical and backward hopping, indicating forward hopping alone may be insufficient to directly evaluate knee function. Vertical hopping, characterized by greater quadriceps activation and knee flexion angle, may be more appropriate for assessing quadriceps function and knee control. Backward hopping imposes the greatest knee moment while minimizing the involvement of hamstring and triceps surae, indicating its potential as an additional task to isolate knee extensors and identify knee deficits after ACLR. Further evidence from ACLR populations is necessary to support single-leg backward hopping as an additional rehabilitation assessment tool.

Session Category

Rehabilitation Biomechanics and Human Factors: Rehabilitation

P2-344

The Effects of Augmented Visual Feedback during VR-Based Motor Training of the Upper-Limb with Increasing Levels of Difficulty

Mr. Yu Shi, Ms. Sophie Dewil, Mr. Zachary Marvin, Dr. Raviraj Nataraj

Stevens Institude of Technology, Hoboken, NJ, United States

Introduction

Virtual reality (VR) can reduce the loss of training gains that accompanies repetitive rehabilitation after neuro-injury by making physical therapy more engaging. This study examines how VR-rehabilitation may be optimized through manipulation of two controllable training elements: augmented sensory feedback (ASF) and task difficulty. Visual ASF provides real-time, intuitive performance information and can yield substantial post-training gains [1], [2]. Task difficulty is tuned to match task complexity to the learner's capability, thereby supporting more effective rehabilitation gains [3]. This pilot study examined how post-training error reduction varies with difficulty in the presence of ASF with training.

Methods

Eight right-handed neurotypical participants controlled a spherical cursor in VR to trace trajectories by exerting forces with their dominant arm on a brace instrumented with a multi-axis load cell. The trajectories were either sinusoids (training trials) or semi-elliptical (testing trials, before or after training) to require persistent challenge in tracking curved paths. During training, difficulty levels were modulated by varying the amplitude of the sinusoidal trajectory. Training was repeated for two conditions (no ASF, visual ASF). Testing trials were conducted without ASF to evaluate training effects based on pre–post reductions in trajectory-tracking error.

Results

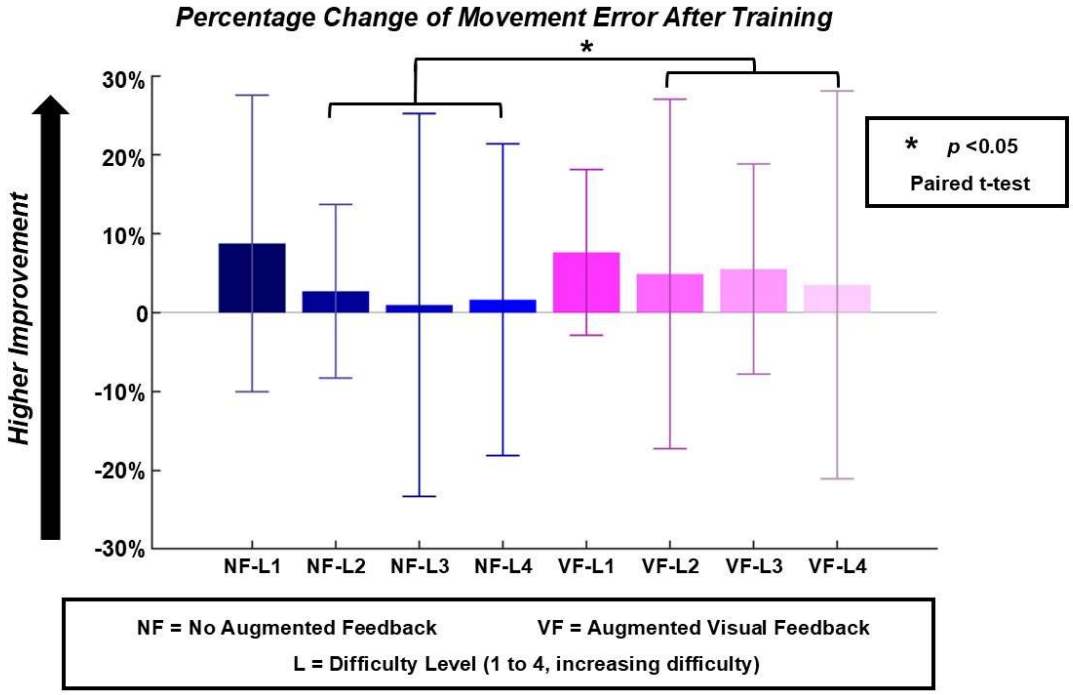
Motor performance was quantified as a percentage change in trajectory-tracking error, as shown in Figure 1. Performance gains generally declined with increasing difficulty for both training conditions; however, when comparing the three most difficult levels (paired t-test), visual ASF significantly preserved higher performance ($p = 0.0211$).

Discussion

The findings indicate that ASF and task difficulty jointly influence performance in this VR-based rehabilitation task. Although performance gains decreased as difficulty increased, a clear divergence emerged at higher difficulty: visual ASF reliably preserved training

benefits, whereas performance under no ASF declined more sharply. This suggests that visual ASF provides stabilizing guidance when error signals intensify, making it especially valuable for difficult tasks and an important component to prioritize in personalized rehabilitation protocols.

Images (Optional)



References (Optional)

[1] Shi Y, et al., IEEE CBMS, 2024.

[2] Sanford S., et al., Frontiers Virtual Reality, 2022.

[3] Prasad S., et al., Asian Spine, 2018.

Acknowledgements (Optional)

This project was supported by the National Science Foundation (CAREER award#2238880) and the Charles V. Schaefer School of Engineering and Science at Stevens Institute of Technology.

Session Category

P2-345

Nanoindentation and Correlative Microscopy to Evaluate Scaffold Degradation and Bone Micromechanics in Additively Manufactured 13-93 Bioactive Glass and Titanium Scaffolds in Ovine Critical Size Defects

Mr Benjamin Morrison[1], Dr Sarah Davis[1], Prof Gordon Blunn[2], Dr Roxane Bonithon[1], Dr Agathe Heyraud[3], Dr Francesca Tallia[3], Prof Julian R Jones[3], Dr Aikaterina Karali[1]

[1]School of Electronic and Mechanical Engineering, University of Portsmouth, Portsmouth, Hampshire, United Kingdom. [2]School of Medicine, Pharmacy and Biomedical Sciences, University of Portsmouth, Portsmouth, Hampshire, United Kingdom. [3]Department of Materials, Imperial College London, South Kensington, London, United Kingdom

Introduction

Additively manufactured biodegradable scaffolds can enhance bone formation in critical-size defects compared with metallic implants, as they can be replaced by new bone and have tuneable mechanical properties for better synergy with native tissue. Previously, 13-93 bioactive glass scaffolds have demonstrated substantial bone formation in a rabbit model, assessed using X-ray computed tomography[1]; however, the mechanical impact was not investigated. Here we compare micromechanics and mineralisation of newly formed bone and assess degradation of 13-93 scaffolds.

Methods

Defects (D=8 mm, H=12 mm) were created in the frontal plane of ovine femoral condyles and implanted with either Titanium (Ti) or 13-93 scaffolds, additively manufactured with log-pile geometry and 400-450um pores. Specimens with surrounding bone were harvested at 6 and 12 weeks (n=6/scaffold/time point). Samples were resin-embedded, sectioned transversely, and polished. Histomorphometry quantified osseointegration and local bone/soft tissue formation. Depth-control nanoindentation (Hysitron, Bruker) assessed bone maturation (10 nm/s, 500nm depth, 30s hold, 10×10 matrices, 10μm spacing), while load-control nanoindentation was performed on scaffolds (10,000μN, 30s loading/hold/unloading, 4×4 matrices, 10μm spacing). Sections were carbon-coated (10nm) and imaged using BSE microscopy (Mira 3, Tescan), with EDS (AZtec, Oxford Instruments, 20 kV, ~15 mm working distance). Corresponding histological sections were stained with modified Paragon (toluidine blue/fuchsin), imaged (AX10, Zeiss), and correlated to BSE microscopy (Fig.1).

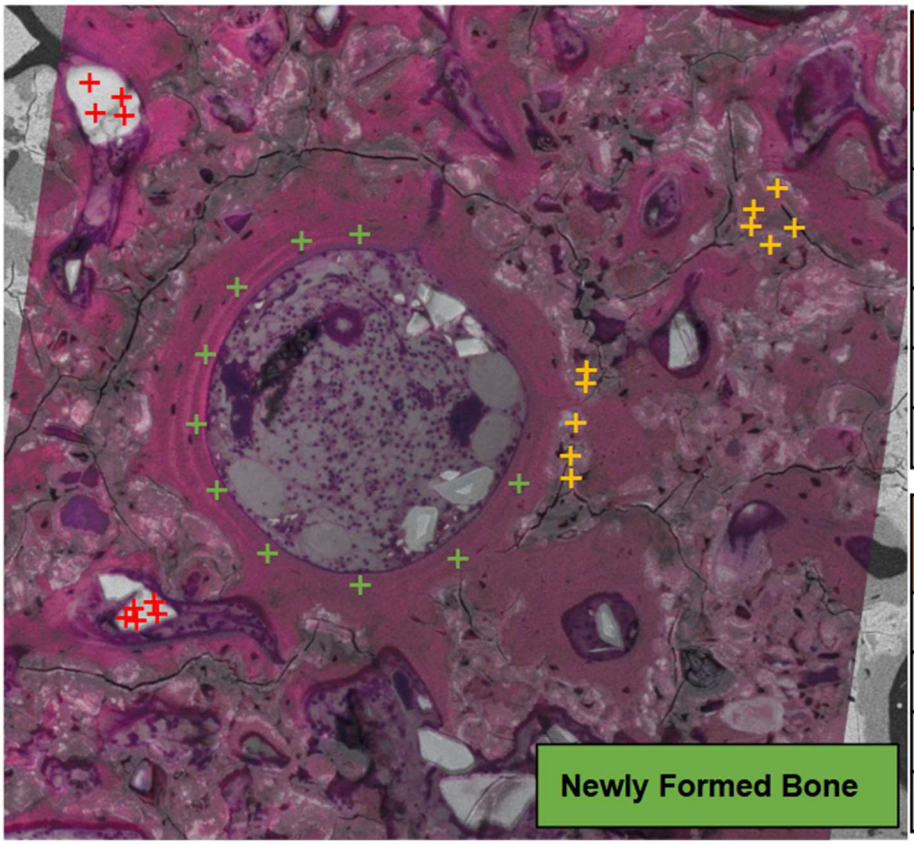
Results

Bone formation was observed throughout 13-93 scaffolds, with 71% osseointegration at 12 weeks, whereas Ti scaffolds showed 15% bone integration , limited to the periphery. At T=12, newly formed bone stiffness was 28.8±16.7 and 38.2±3.1uN/nm for 13-93 and Ti, respectively. 13-93 scaffold stiffness and reduced modulus decreased from 104.5±6.9uN/nm and 80.3±6.8GPa at T=0 to 51.8±9.7uN/nm and 24.7±4.2GPa at T=12w. EDS of 13-93 revealed loss of Si, K, Na, Mg and increased Ca and P over time.

Discussion

13-93 scaffolds support extensive bone formation and osseointegration, while titanium scaffolds show limited peripheral growth. Declining 13-93 stiffness and modulus, together with elemental changes, reflect scaffold degradation and mineralised matrix formation. Work in progress includes quantitative BSE analysis to assess mineralisation of newly formed bone.

Images (Optional)



Intact 13-93 by Wt %	
Si	26.29 ±0.63
Ca	14.48 ±0.33
K	7.89 ±0.29
Na	4.17 ±0.17
P	3.55 ±0.15
Mg	2.90 ±0.12

Resorbed 13-93 by Wt %	
Ca	35.55 ±0.81
P	18.05 ±0.59
Na	1.59 ±0.23
Mg	0.67 ±0.44

References (Optional)

[1] Nommeots-Nomm et al, Acta Biomaterialia, 2017

Session Category

Tissue Engineering: Mechanobiology

P2-346

A Microstructure and Grain Orientation Based Framework for Predicting Corrosion in Magnesium WE43: A Phenomenological Approach

Mrs Fatemeh Karamifard

University of Galway, Galway, Ireland, Ireland

Introduction

Bioresorbable materials such as magnesium (Mg) alloys allow medical implants to safely degrade after completing their temporary function. However, Mg corrodes rapidly in physiological conditions, risking early loss of mechanical support before tissues have fully healed. Crystallographic orientation strongly influences corrosion, with basal-oriented grains showing higher susceptibility. In this work, we model a polycrystalline microstructure in which each grain has a defined lattice orientation, allowing corrosion behaviour to vary based on local crystallography. A phenomenological, statistically based finite element framework is used to examine how grain orientation affects corrosion initiation and propagation in Mg WE43.

Methods

A phenomenological corrosion model is employed, using a scalar damage field to represent degradation, implemented through a user-defined USDFLD subroutine in Abaqus. As shown in (Fig. 1(a–b)), the microstructure consists of 24 hexagonal HCP grains, each assigned a random crystallographic (basal plane) orientation. Orientation effects on corrosion are incorporated by weighting the local damage rate term, resulting in higher rates in the basal plane direction. Corrosion is initiated from a small surface pit representing local breakdown of the protective layer. Grain-specific corrosion then progresses preferentially on the basal planes, as guided by experimental observations.

Results

A sample of the modelling results are shown in (Fig.1(c)); corrosion initiates at a surface pit in a grain with horizontally oriented basal planes, and progresses layer by layer through the grain, and then spreads into neighbouring grains with orientations of approximately 45° and

90° (Fig.1(d)). Progression over time ultimately produces the non-uniform, multi-directional corrosion profile shown in (Fig. 1(e)).

Discussion

This study introduces a novel framework in which crystallographic orientation effects are incorporated into corrosion modelling, enhancing pitting corrosion prediction capability for Mg WE43. The model affords the assessment of how microstructure (grain size and orientation) influences corrosion progression, allowing for microstructural design recommendations to be made. Future work will implement a full 3D model informed by diffraction contrast tomography (DCT) to provide more detailed microstructural representation.

Images (Optional)

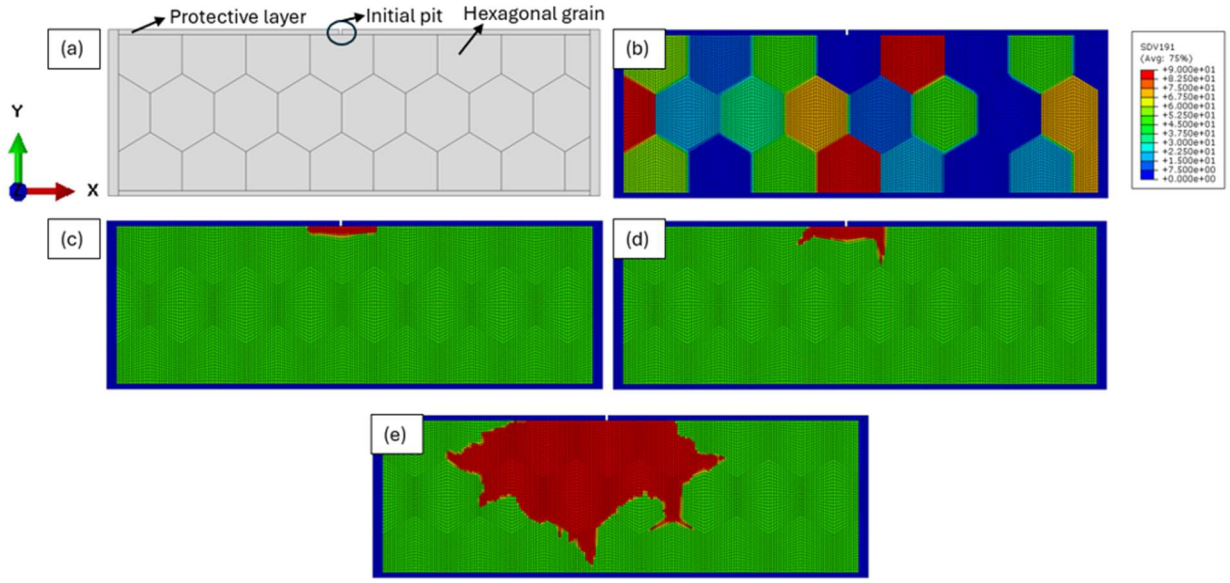


Fig.1. a) Model geometry (b) Grain orientations. (c) Corrosion initiating in the basal oriented grain. (d) Propagation into neighbouring grains. (e) Corrosion profile at an arbitrary time

Session Category

Tissue Engineering: Mechanobiology

P2-347

Host Response to Compliance Matching of Tissue Engineered Vascular Grafts is Sex Specific

Ms. Katarina Martinet, Dr. David Maestas, Dr. Keishi Kohyama, Ms. Jacqueline Avila, Mr. Leon Min, Ms. Reyhaneh Gholami, Dr. Kang Kim, Dr. William Wagner, Dr. Jonathan Vande Geest

University of Pittsburgh, Pittsburgh, PA, United States

Introduction

Tissue engineered vascular grafts (TEVGs) are a promising solution to the challenges faced in small diameter vascular grafting procedures. Compliance matched TEVGs (CM TEVGs) have shown increased vascular smooth muscle cell (VSMC) presence in acute remodeling. There are known sex specific differences in VSMC behavior in vascular injury which are understudied in TEVGs. This study aims to understand if biological sex influences responses to compliance matching in CM TEVGs.

Methods

CM TEVGs and hypocompliant TEVGs (Hypo TEVGs) were fabricated via electrospinning polyester urethane urea:gelatin solutions with a non-thrombogenic inner layer of polyester sulfobetaine urethane urea – 50. TEVGs were confirmed to be compliant using a custom tubular biaxial device. Grafts were implanted as interposition grafts into the abdominal aortas of Sprague Dawley Rats. In short term studies, CM TEVGs and shams were implanted in n = 4 rats of each sex for 28 days. For long term studies, CM TEVGs, Hypo TEVGs, and shams were implanted for six months in n = 4 rats of each sex. Explants were analyzed with IHC, IF, 2P imaging, and qRT – PCR.

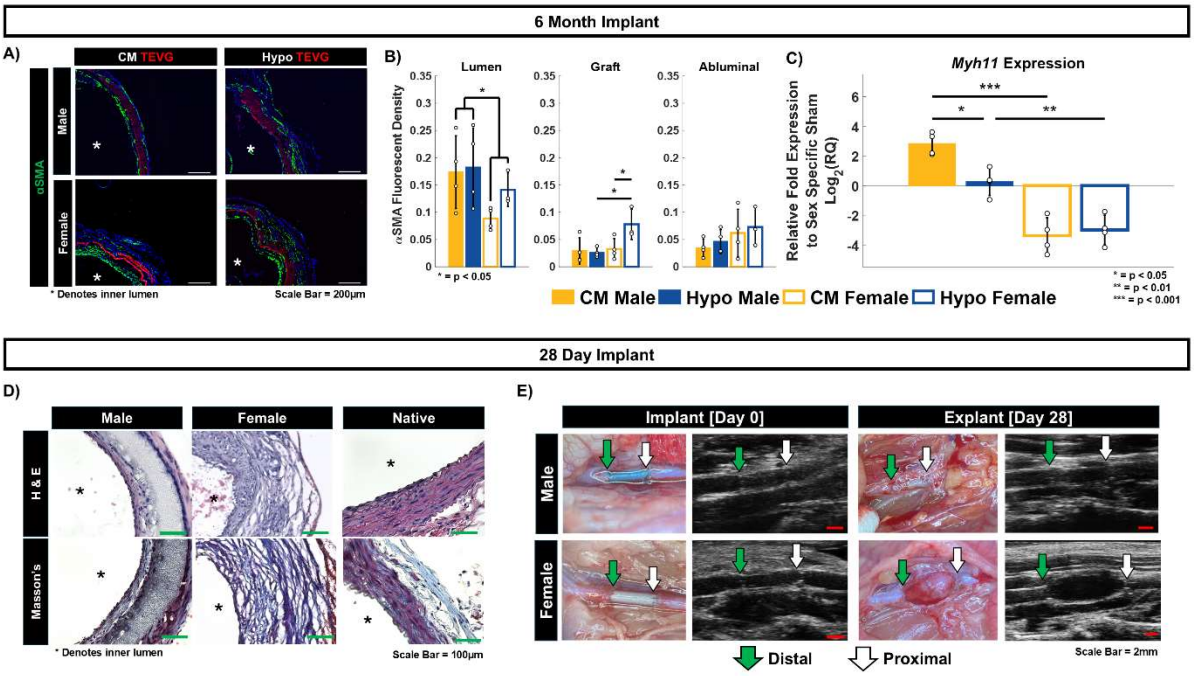
Results

TEVGs fell within their targeted compliance ranges. In acute studies, we saw increased degradation and increased collagen deposition in females over 28 days (A). This included one female sample that formed a pseudoaneurysm (B). After 6 months, there was increased degradation of the graft material in CM TEVGs (C). Female rats had significantly increased thickness over both graft types (Female: 58.22 ± 36.22 μm, Male: 16.41 ± 6.57 μm). A significant decrease in VSMC density (αSMA) was seen in female implants (D). Compliance increased contractile VSMC genetic marker expression in male rats (E).

Discussion

While compliance matching improves TEVG remodeling outcomes (increased remodeling of graft material), the degree of these effects is influenced by sex. Sex influences VSMC behavior, which is a major cell type involved in TEVG remodeling and formation of intimal hyperplasia. These responses to compliance matching can be captured acutely as well, allowing us to begin higher throughput studies looking at the role of how sex influences responses to changes in compliance.

Images (Optional)



Acknowledgements (Optional)

NIH R01HL157017 & F31 HL176056 & T32HL076124

Session Category

Tissue Engineering: Mechanobiology

P2-348

Effects of Hydrogel-Based Mechanical Confinement on Morphological and Biochemical Characteristics of Cervical Cancer Spheroids

Mr. Kazuki Haneda M.S. Student, Mr Riku Akiyama B.S. Student, Dr. Shogo Miyata Ph.D.

Keio University, Yokohama, Kanagawa, Japan

Introduction

Cervical cancer is the fourth most common cancer among women worldwide, with about 10,000 new cases and 2,900 deaths each year in Japan. Because diagnosis often occurs during pregnancy, understanding how the tumor grows in a controlled mechanical environment is important for protecting both mother and fetus. Mechanical microenvironments such as compressive stress have risks to cause phenotypical transition, which may increase tumor aggressiveness. Although earlier studies suggest that the mechanical environment affects tumor behavior, how confinement influences the earliest steps of cervical cancer invasion remains poorly understood. This study aimed to clarify how different stiffness levels affect the invasion dynamics and biochemical characteristics of cervical cancer spheroids.

Methods

HeLa cell spheroids were generated in U-bottom 96-well plates and embedded in 0.5% or 2.0% agarose gels to establish mechanically confined tumor models. Spheroid morphological changes were monitored by phase-contrast microscopy, and three-dimensional structures were visualized using confocal microscopy. Cytoskeletal organization and cell-cycle dynamics were further assessed by fluorescence microscopy.

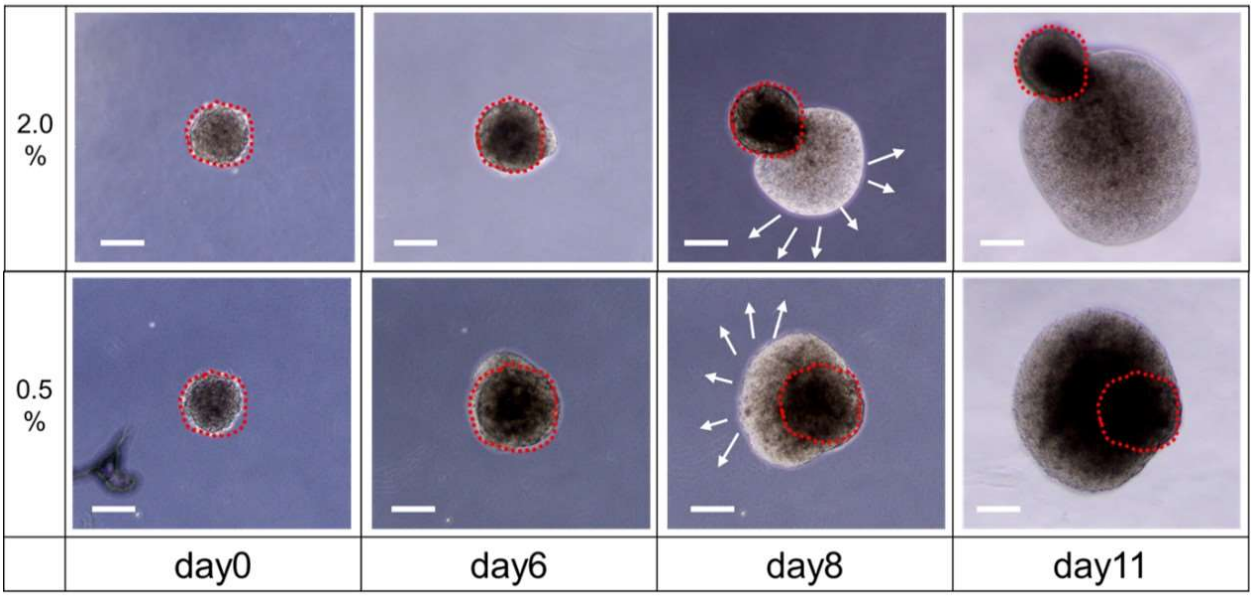
Results

In both gel conditions, spheroids expanded isotropically until day 7. Thereafter, protrusive growth regions extended into the agarose, with more pronounced directional growth observed in the 2.0% gel. The protrusive regions were thicker and more widely spread in the 0.5% gel, whereas spheroids in the 2.0% gel exhibited larger centroid displacement. Actin staining showed more developed cytoskeletal structures at the invasive edges, particularly in the stiffer gel. Cell-cycle staining further indicated rapid cell-cycle progression within the spheroid interior, while cells at the periphery and in the protrusive regions predominantly remained in the G1/G0 phase.

Discussion

These results indicate that gel stiffness modulates both the growth patterns and cellular responses of cervical cancer spheroids. Softer matrices permitted greater vertical expansion, whereas stiffer gels facilitated more pronounced directional extension. At the invasive edges, cytoskeletal structures were more developed, which is consistent with an enhanced migratory and invasive potential. In addition, cells remaining in the G1/G0 phase at these regions suggest a transition toward a motility-associated phenotype. In summary, these findings demonstrate the importance of the mechanical microenvironment in regulating early invasive behavior in cervical cancer.

Images (Optional)



Session Category

Tissue Engineering: Mechanobiology

P2-349

Improving Reconstructed Dermal Skin Through Shear Wave Mechanical Stimulation

Ms Koloina Randrianavony[1,2], Mrs Coralie Privet-Thieulin[1,2], Mrs Lara Jobeili[3], Mrs Dominique Sigaudo-Roussel[3], Mr Hassan Zahouani[1]

[1]Ecole centrale de Lyon, Ecully, Auvergne Rhône Alpes, France. [2]LyRIDS, Paris, Ile de France, France. [3]LBTI, Lyon, Auvergne Rhône Alpes, France

Introduction

Reconstructed skin is an in vitro model widely used to study skin's biological behavior and tissue maturation. Contrary to human skin, it allows invasive measurements. It also enables to have a neutral baseline without interindividual variability. The dermal layer, mainly composed of extracellular matrix (ECM) and fibroblasts, provides the skin's load bearing capacity. The fibroblasts produce collagen and elastin fibers responsible for the skin's rigidity and elasticity. In this study, we propose to stimulate the reconstructed dermal skin with a Shear Wave Stimulation device (SWS) [1], a non-contact device using air pressure to mechanically stimulate it with shear and compression waves. The impact of different air pressures on collagen production is studied.

Methods

The study was performed on reconstructed dermal skin cultured for 14 days. Primal dermal fibroblasts of a 29-year-old woman was used. The samples were stimulated for 2 min twice a day separated by 6 hours, for 2 days. An opening time of 10ms (closing time 490ms) was chosen and the SWS was done with two different air pressures: 0.5 and 0.7 bar. 24 hours after the last stimulation, the samples were fixed and then undergone immunofluorescence (IF) collagen type I staining. A mechanical model was developed to characterize the effect of internal tissue forces on image pixel morphology, expressed for each pixel by an intensity, a spatial frequency, and a wavelength in Fourier space. Three tension indices are quantified before and after stimulation.

Results

The deformation induced by the stimulation along the X and Y axis has been computed with DX=0.17 and DY=0.3, which indicates that the stimulation caused an extension along the two axis. The stimulation improved the mechanical tension of the reconstructed skin by 5 times compared to the control group (IT index). The stimulation also impacted the number of fibroblasts cells (-15%) and collagen production (+13%) with the apparition of hyperdense collagen fibers on the surface.

Discussion

These results are certainly the response of fibroblasts from mechanical stimulation leading to mechanotransduction and a mechanical effect on the ECM.

Images (Optional)

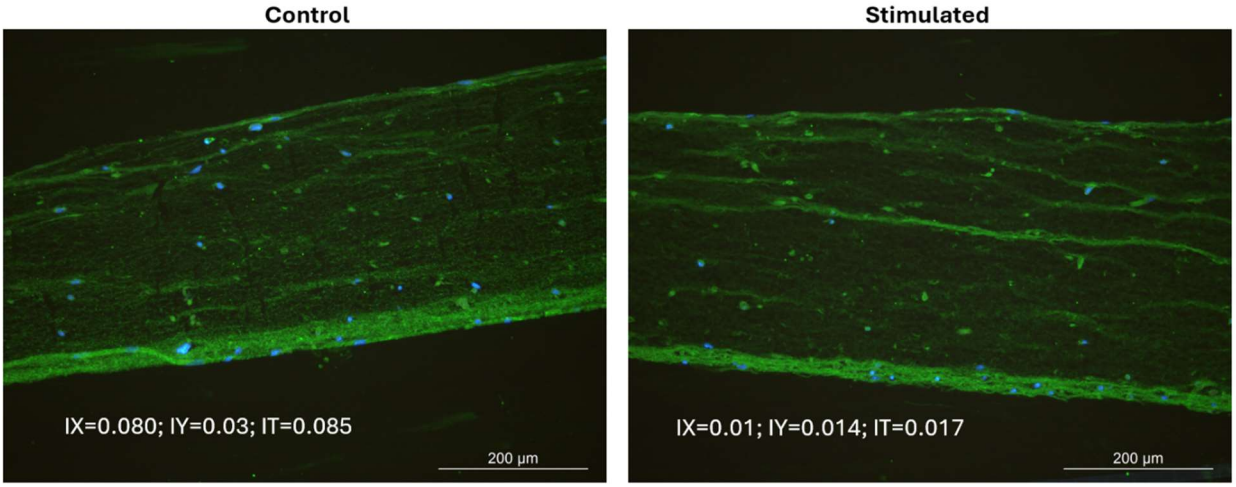


Figure 1. IF staining collagen type I of reconstructed skin for the control group and the stimulated one (in green collagen fibers and in blue cell nuclei) with the corresponding tension index (in X and Y direction and in the plane XY: IT).

References (Optional)

[1] N. Qiao *et al.*, *Journal of the Mechanical Behavior of Biomedical Materials*, 2024.

Session Category

Tissue Engineering: Mechanobiology

P2-350

Mechanobiology-Driven Reinforcement of Bioactive Cement for Enhanced Hard-Tissue Function and Antibacterial Performance

Frau Lilly Völkel[1], Dr Sabina Karacic[2], Prof. Dr.rer.nat Christoph Bourauel[1], Priv.-Doz. Dr. Lamia Singer[1]

[1]Oral medicine Technology, University Hospital Bonn, Bonn, North Rhine–Westphalia, Germany. [2]Institut für Medizinische Mikrobiologie, Immunologie und Parasitologie, University Hospital Bonn, Bonn, North Rhine–Westphalia, Germany

Introduction

Glass-ionomer cement (GIC) is a clinically used bioactive cement capable of chemically bonding to mineralised tissues and releasing ions that support hard-tissue integration. However, brittleness, moisture sensitivity, and insufficient antibacterial protection limit long-term performance in load-bearing or infection-prone environments. Reinforcing GIC with biologically relevant fillers has emerged as a promising strategy to enhance its suitability for hard-tissue repair. Hydroxyapatite (HA), the main mineral component of bone and dentine, may improve biological interaction, while nanodiamonds (ND) and hexagonal boron nitride (BN) offer enhanced mechanical integrity and microbial resistance. This study aimed to evaluate the mechanical, physical, antibacterial, and bioactivity characteristics of GIC modified with HA alone and combined with either ND or BN to support improved performance in tissue engineering applications.

Methods

Four formulations were prepared: Control (unmodified GIC), GIC+HA, GIC+HA+BN, and GIC+HA+ND. Powders were homogenised with additives before mixing with liquid. Compressive strength was measured following ISO 9917-1; flexural strength via three-point bending; and Vickers microhardness by indentation. Water sorption and colour stability (ΔE) were assessed after 7-day storage at 37 °C in aqueous media. Bioactivity was examined by immersion in simulated body fluid (SBF) for 14 days to assess surface apatite formation. Antibacterial activity against *Streptococcus mutans* was evaluated using agar

diffusion. Mechanical tests used 10–15 specimens per group; micro-scale tests in triplicate. One-way ANOVA identified significance ($p < 0.05$).

Results

Both nanoreinforced groups demonstrated significantly improved performance compared to the Control and HA-only groups ($p < 0.05$). HA+ND achieved the highest flexural strength (21.8 ± 2.7 MPa), compressive strength (130 ± 6.3 MPa), microhardness (74.8 ± 3.1 VHN), and antibacterial inhibition zone (12.4 ± 0.9 mm). HA+BN exhibited the lowest water sorption (21.6 ± 1.8 μg/mm^3) and greatest colour stability. Both dual-reinforced groups showed increased apatite formation after SBF immersion, confirming enhanced remineralisation potential.

Discussion

Reinforcement of bioactive cement with HA combined with ND or BN significantly improved its mechanical resilience, antibacterial activity, and biological response. ND offered the strongest strengthening and antimicrobial benefits, whereas BN improved environmental stability. These modified cement systems show promise for durable restorative and craniofacial hard-tissue repair within tissue engineering applications.

Acknowledgements (Optional)

The authors would like to acknowledge Dentsply for kindly providing the glass ionomer cement materials used in this study.

Session Category

Tissue Engineering: Mechanobiology

P2-351

Comparison of Micro- and Macro-Mechanical Responses of α- and β-Phase 3D-Printed Titanium Alloys for Biomedical Applications

Ing. Petr Bočan, Ing. Jiří Němeček, prof. Jan Vorel, doc. Aleš Jíra

Czech technical university, Prague, Czech republic, Czechia

Introduction

The increasing use of porous architectures on implant surfaces enhances osseointegration by enabling bone ingrowth and improving mechanical compatibility at the bone–implant interface. Additive manufacturing, particularly Selective Laser Melting, enables precise control of pore size, geometry, and mechanical behavior, though clinical adoption is still limited by material certification. The widely used α-phase alloy Ti-6Al-4V offers high strength but has drawbacks such as high stiffness and concerns regarding aluminum and vanadium cytotoxicity. The β-phase alloy Ti-25Nb-4Ta-8Sn provides improved biocompatibility and a lower elastic modulus closer to bone, making it a promising alternative for next-generation implants.

Methods

This study evaluates the macro- and micro-mechanical behavior of these two alloys. Three-point bending tests were performed on thin notched beam specimens of three geometries (Figure (c)), using a 3D micro-DIC system to measure strain fields. Flexural strength and apparent fracture toughness were determined, supported by numerical simulations mirroring the tests. Micro-mechanical analysis focused on Ti-6Al-4V, using nanoindentation on three 3D-printed gyroid lattices (Figure (a), (b)) to assess hardness and reduced modulus in both surface and internal regions.

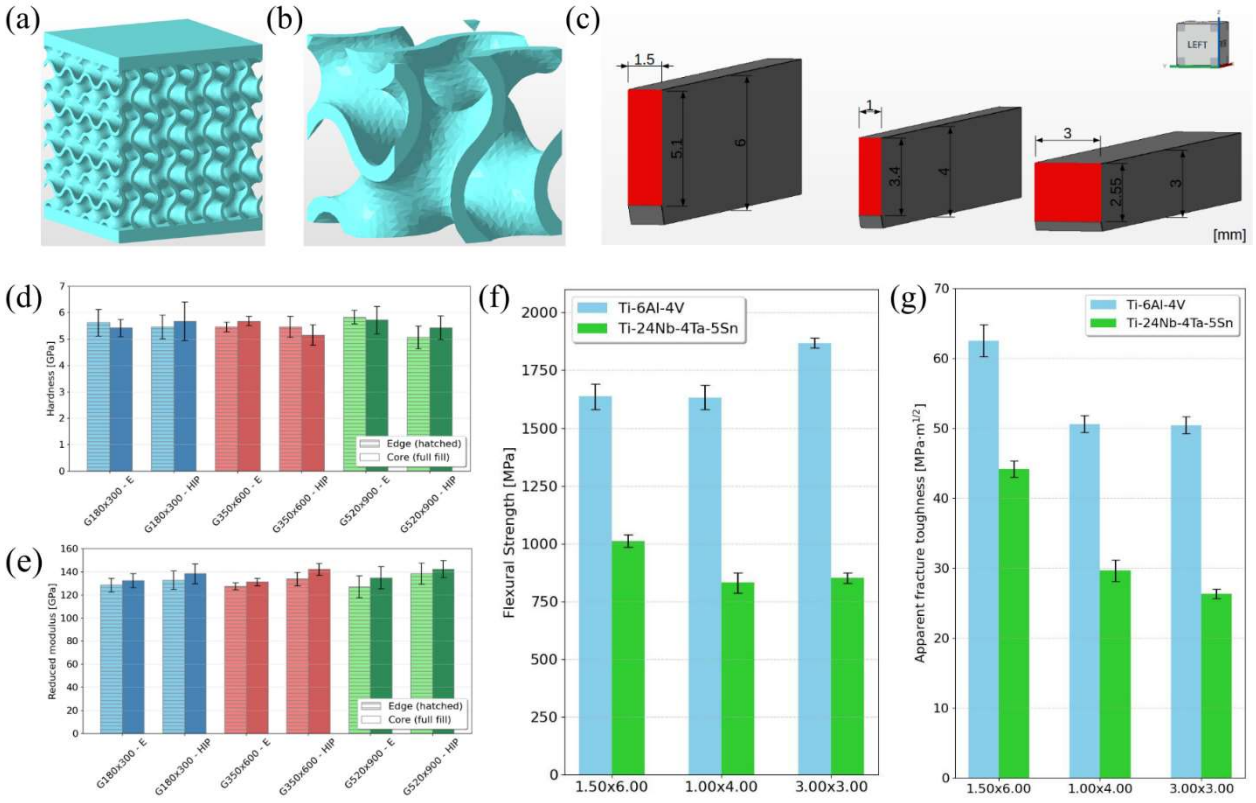
Results

Ti-6Al-4V showed higher flexural strength (1630–1870 MPa) than Ti-25Nb-4Ta-8Sn (830–1010 MPa) (Figure (f)). Apparent fracture toughness was also higher for the α alloy (50.5–62.5 MPa$\sqrt{m}$) compared with the β alloy (26.3–44.2 MPa$\sqrt{m}$) (Figure (g)). Numerical simulations agreed closely with experimental load–deflection results. Nanoindentation of Ti-6Al-4V gyroids revealed hardness values of 5.06–5.83 GPa and reduced modulus values of 125.8–142.3 GPa, with only minor variation between edge and core regions (Figure (d), (e)).

Discussion

These findings confirm the superior mechanical performance of Ti-6Al-4V for load-bearing applications but highlight the improved biocompatibility of Ti-25Nb-4Ta-8Sn, suggesting its potential where lower stiffness is advantageous. The consistent microscale behavior of Ti-6Al-4V gyroid lattices supports their use in surface architectures designed to promote bone ingrowth. Future work will include microscale testing of β-phase structures and expanded evaluation of lattice-based surfaces to optimize material–architecture combinations for implants requiring reliable mechanical performance and enhanced biological integration.

Images (Optional)



Session Category

Tissue Engineering: Mechanobiology

P2-352

Degradation-Induced Changes in Mechanical Properties of Resorbable Implant Materials.

Dr. Steffen Braun, B.Sc. Leonie Thiele, B.Pro. Jonas Dresen, B.Sc. Jan Marc Schehl, B.Eng. Lisa Veeser, Dr. Tobias Wolfram

KLS Martin SE & Co. KG, 78570-Mühlheim, Baden-Württemberg, Germany

Introduction

Resorbable biomaterials are subject to high requirements in terms of biocompatibility and controlled biodegradability with sufficiently long-lasting mechanical stability. The aim was to investigate the degradation behavior of resorbable implant materials while evaluating their mechanical strength.

Methods

In this study, bioresorbable implant materials PDLLA, PDLLA+$CaCO_3$, PLLA+PGA, WE43 as a magnesium alloy, and PEEK were investigated. After sterilization, samples were incubated in DMEM (pH7.4; 37°C) for zero (T0), four (T1), six (T2), and eight (T3) weeks to simulate degradation [ISO-13781]. Mechanical characterization was performed at defined time points using standardized tensile tests [EN-ISO-527], with polymers being loaded in medium at 37°C.

Results

The stiffness of resorbable polymers ranged from 3927 MPa (PDLLA) to 5234 MPa (PDLLA+$CaCO_3$) and decreased by up to 82% (PDLLA+$CaCO_3$) after four weeks. PDLLA showed an linear 35% reduction from T0 to T2. PDLLA+$CaCO_3$ (−82%) and PLLA+PGA (−40 %) exhibited the greatest decline after four weeks, with PDLLA+$CaCO_3$ reaching −90% over the entire period. WE43 and PEEK showed a 17% decrease in tensile modulus after eight weeks (WE43: 103,635 MPa; PEEK: 6045 MPa).

Tensile strength decreased particularly sharply after eight weeks in PLLA+PGA (−90%) and PDLLA+$CaCO_3$ (−84%) (PDLLA: −58%). After four weeks, PDLLA and PLLA+PGA decreased by 23–37%, while PDLLA+$CaCO_3$ had already reached −72%. WE43 started at 296 MPa (8.3× higher than polymers) but fell 28 % after four weeks. PEEK showed a 5.4% loss over eight weeks, with 4 % after four weeks.

PDLLA showed a significant increase in elongation at break from 5.35% (T0) to 372.70% (T1). PDLLA+$CaCO_3$ increase slightly from 4.48% (T0) to 9.83% (T3), while PLLA+PGA

dropped from 10.74% to 0.28%. WE43 decreased from 9% to 2.03%, and PEEK from 36.60% to 20.50%.

Discussion

All materials showed changes in mechanical properties due to simulated degradation. In polymers, this results from hydrolytic chain decomposition and loss of structural integrity. Salts in DMEM and additive manufacturing may influence degradation of PEEK. In vitro results are only partly transferable to in vivo conditions but provide key insights for material modification in the develop ment of implant materials.

References (Optional)

Session Category

Tissue Engineering: Mechanobiology

P2-353

Effect of Manufacturing Process on the Mechanical Performance of Resorbable Implant Materials in Simulated Biological Environments

Dr. Steffen Braun, B.Sc. Sofie-Josephine Scheuch, B.Eng. Lisa Veeser, B.Sc. Jan Marc Schehl, B.Pro. Jonas Dresen, Dr. Tobias Wolfram

KLS Martin SE & Co. KG, 78570-Mühlheim, Baden-Württemberg, Germany

Introduction

Resorbable materials offer new therapeutic options in craniomaxillofacial surgery. Complex physiological conditions demand high biocompatibility, controlled biodegradability, and mechanical stability. The aim was to investigate the influence of different manufacturing processes on the mechanical properties of resorbable materials.

Methods

This study examined bioresorbable implant materials poly(-ε-caprolactone) (PCL) and poly(D,L-lactide) (PDLLA), with Polyetheretherketon (PEEK) as a non-degradable control material. Samples were produced by milling, injection molding, and 3D printing. Degradation studies (PBS solution: pH7.4; 37 °C) were conducted in a biologically relevant environment [1,2] at three time points (T0: 0 weeks; T1: 1 week; T2: 4 weeks). Characterization included microscopy (LM, SEM), thermal analysis (DSC) [3], and mechanical analysis with standardized tensile [4] and bending tests [5].

Results

Standardized tests [4,5] on PEEK confirmed method validity through comparability with material data sheets. Injection-molded PDLLA samples showed significantly higher tensile strength than milled samples (58.1 vs. 54.0 MPa), while bending properties were similar. After one-week, tensile modulus (injection molding: -30%; milled: -23.5%) and tensile strength (injection molding: -28%; milled: -12.0%) decreased significantly, accompanied by a significant increase in elongation (injection molding: +26%; milled: +19%). Bending properties of injection-molded PDLLA samples declined after one week, whereas milled samples showed this effect only after four weeks.

Additively manufactured PCL samples showed significantly lower tensile strength (19.0 MPa vs. 23.9 MPa) and bending strength (18.9 MPa vs. 32.6 MPa) than milled samples. Degradation reduced tensile modulus (−8%) and strength (−2.5%) in milled PCL samples, while additively manufactured samples remained more stable in tensile strength. Bending properties remained almost unchanged in both groups.

DSC analysis revealed higher crystallization and melting peaks in additively manufactured samples, suggesting a strong influence of manufacturing process on thermal properties.

Discussion

Results indicate a significant impact of manufacturing processes on material properties, degradation behavior, and kinetics. Injection molding and 3D printing showed the most pronounced changes in mechanical parameters during degradation. These findings provide an important basis for assessing biomaterial performance under biologically relevant conditions and guide the selection of suitable manufacturing processes for medical implants.

References (Optional)

[1] ISO-13781;
[2] ASTM-F3268;
[3] DIN EN ISO-11357;
[4] EN ISO-527;
[5] EN ISO-178

Session Category

Tissue Engineering: Mechanobiology

P2-354

Guidance of Cell and Matrix Morphology in Fiber/Hydrogel Composite Scaffold

Mr. Takumi Asakawa, Dr. Pen-hsiu Grace Chao

National Taiwan University, Taipei, Taiwan, Taiwan

Introduction

Electrospun fiber scaffolds are widely used in tissue engineering as they can recapitulate the structural and mechanical performance of native tissues. However, their lack of bioactivity limits matrix remodeling and graft integration [1]. Conversely, fibrin hydrogel can offer bioactive signals that drive cell-mediated remodeling but lack the mechanical integrity and structural cues of fibrous materials [2]. Here, we fabricated a composite construct by incorporating fibrin into electrospun fibrous scaffolds and investigated the influence on cell morphology.

Methods

Type I collagen-coated poly-L-lactide (PLA) scaffolds were fabricated as described previously [3]. Adipose-derived mesenchymal stem cells were suspended in fluorescently labeled fibrinogen solution. This suspension and thrombin solution were absorbed into the scaffolds from both sides and incubated for gelation and culture.

Results

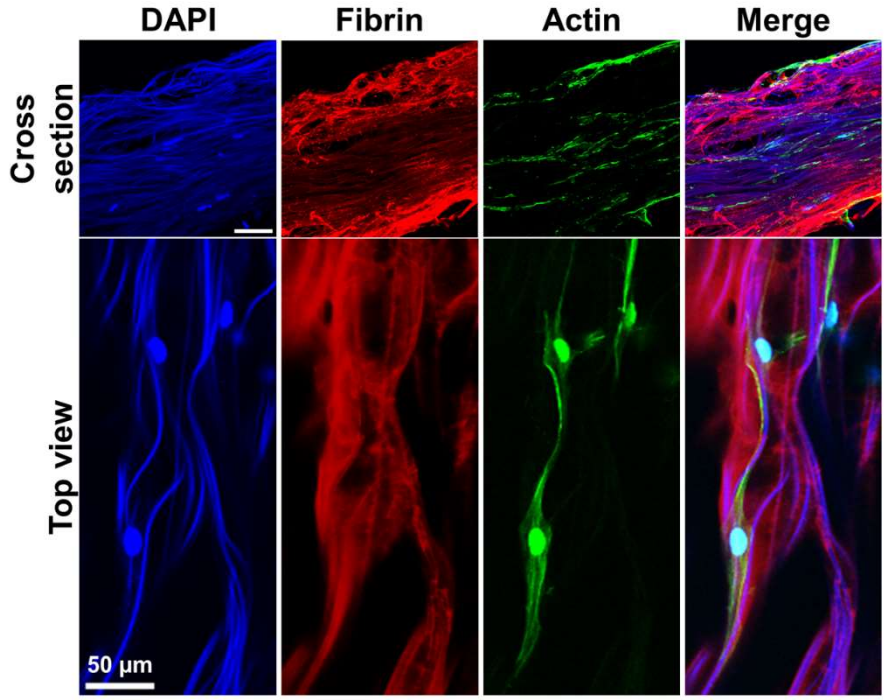
Cross-sectional images confirmed infiltration of the fibrin throughout the scaffold. The fibrin network organized along the polymeric fiber structure (Figure). Cells were localized on the construct surface on day 1 (data not shown), migrated to the center of the composites by day 7, and followed the fiber/fibrin structure with an elongated morphology.

Discussion

We have previously found laminating electrospun fibrous scaffolds with fibrin gels not only increased construct size, but improved matrix deposition and mechanical properties of engineered ligament tissue, demonstrating the interactive role of fibrin with fibrous scaffolds [3]. We also reported synergistic effects of fibrin and growth factor supplementation, confirming the role of fibrin for growth factor binding and stabilization [2, 3]. In the previous study, however, fibrin was added after one week of culture and limited to the scaffold surface. Here, we fully incorporated the fibrin within the fibrous scaffold. Notably, the fibrin gel formed networks that closely followed the collagen-coated fiber structure, consistent with previous findings that collagen fibrils guide fibrin network formation [4]. Thus, the composite provides contact guidance from both fiber and fibrin

while supporting a bioactive environment. Current studies are investigating the long-term effects on matrix deposition and tissue development.

Images (Optional)



Representative maximum projection confocal micrograph of the composite scaffold in cross section and top views. PLA fibers can be seen in the DAPI channel due to autofluorescence.

References (Optional)

[1] Ratcliffe, A+, Ann. Biomed. Eng, 2015.

[2] Martino, M.M+, PNAS, 2013.

[3] Chang C-W+, Tissue Eng A, 2020.

[4] Reyhani, V+, Biochem J, 2014.

Acknowledgements (Optional)

This study was supported by the Taiwanese National Science and Technology Council (NSTC 114-2221-E-002-091-MY3, 114-2923-E-002-017-MY3, and 114-2122-M-001-002).

Session Category

P2-355

Evaluating Decellularisation-Induced Microstructural Changes in Porcine Tendon via Raman Spectroscopy, Second Harmonic Generation and Scanning Electron Microscopy

Mrs Victoria Haines MEng, MSc[1], Dr Benjamin Johnson BSc (hons) Biochemistry with Medical Biochemistry, MSc Analytical Chemistry, PhD Biomimetic Scaffolds for Phospholipid Bilayers, Experimental Officer[2], Dr Julia Gala de Pablo BSc Biochemistry, BSc Physics, PhD, Lecturer in Biomedical Approaches for Healthcare[2,3], Dr Hazel Fermor BSc Biology, PhD Tissue Engineering, Lecturer in Musculoskeletal Regenerative Medicine[1], Dr Anthony Herbert CEng, CSci, MIMechE, MIPEM, Royal Academy of Engineering/Leverhulme Trust Fellow, Medical Engineering Programme Manager[1]

[1]Institute of Medical and Biological Engineering, University of Leeds, Leeds, West Yorkshire, United Kingdom. [2]Molecular and Nanoscale Physics Group, School of Physics and Astronomy, University of Leeds, Leeds, West Yorkshire, United Kingdom. [3]Leeds Institute of Medical Research, School of Medicine, University of Leeds, Leeds, West Yorkshire, United Kingdom

Introduction

Anterior cruciate ligament ruptures occur at an estimated annual rate of ~80 cases per 100,000 individuals in the general population [1], typically requiring surgical reconstruction using autografts or allografts. Decellularised porcine tendon offers a promising graft alternative, creating an immunologically compatible scaffold through removal of native cellular components [1]. Recent research in our group compared a novel 4-day decellularisation protocol with an established 26-day process, demonstrating that the shortened protocol better preserved the tissue's tensile and viscoelastic properties. Further, Picro-Sirius Red staining demonstrated altered collagen organisation and birefringence following decellularisation. Similar variations have been reported previously in the literature, although their underlying causes have been interpreted differently. This study employed Raman spectroscopy, second harmonic generation (SHG), and scanning electron microscopy (SEM) to characterise microstructural changes in the tissue following decellularisation. We hypothesised that this multimodal imaging approach would provide enhanced sensitivity to alterations in collagen and other extracellular matrix components.

Methods

Three tendon groups (native, 4-day, and 26-day processed; n = 3 each) were imaged using a Stellaris 8 microscope with multimodal chemical imaging capabilities including coherent anti-Stokes Raman spectroscopy (CARS), stimulated Raman spectroscopy (SRS), 2-photon fluorescence and SHG. Samples were imaged hydrated in phosphate-buffered saline. One sample from each group was examined using a Tescan AmberX Plasma FIBSEM following cryofracture, freeze-drying, and carbon coating.

Results

SRS symmetric stretching at ~2935 cm^{-1} imaged proteins, ~2850 cm^{-1} imaged lipids and SHG imaged collagen organisation (fig.1.A-C). Results from all imaging techniques demonstrated that the 26-day group exhibited pronounced microstructural changes, including lack of definition and consistency of fibrils, smoothing of crimping, and reduced organisation (fig.1.B,E). In contrast, the 4-day group more closely resembled the native tendon (fig.1.C,F). Stronger signals of lipids were visible in the native group when compared to the decellularised groups.

Discussion

In conclusion, Raman spectroscopy and SHG provide non-destructive imaging of hydrated biological tissue without fixation, offering detailed insights into tendon microstructural changes following decellularisation. SEM findings corroborated these observations. This study confirms the new 4-day decellularisation process better preserves the native tendon microstructure than the 26-day process.

Images (Optional)

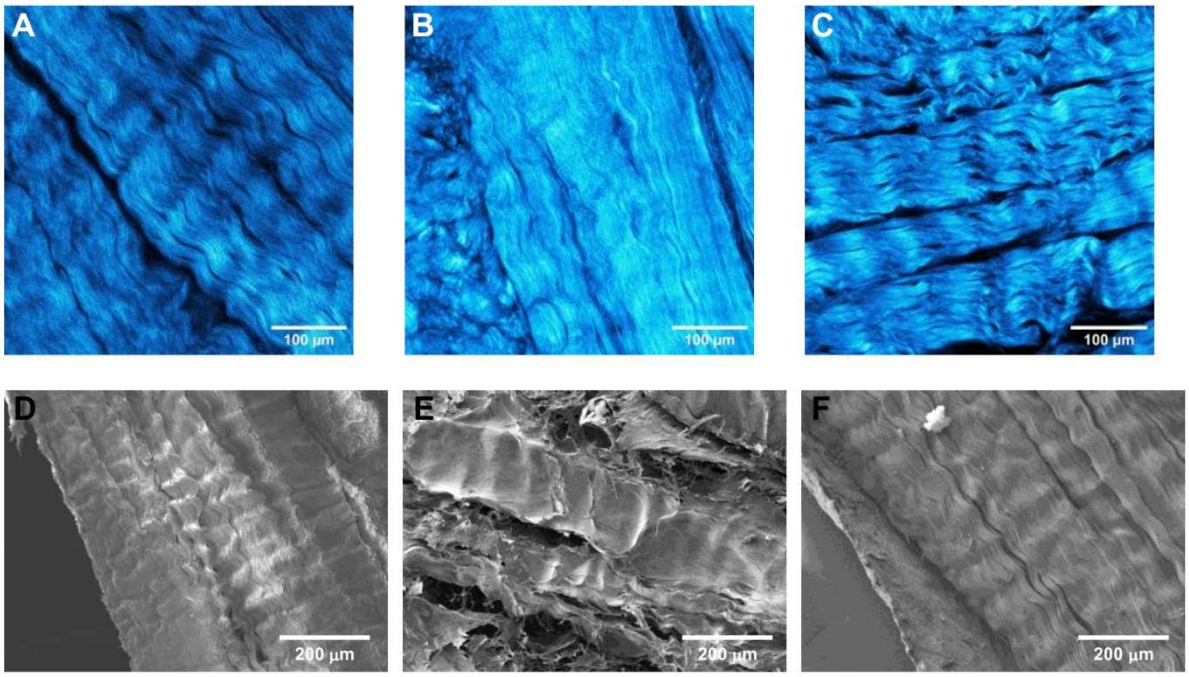


Fig. 1. Images of porcine super flexor tendons: native (**A, D**), 26-day decellularisation group (**B, E**), and 4-day decellularisation group (**C, F**). Tissue imaged using SHG showing collagen (**A–C**) and SEM **(D-F)**.

References (Optional)

[1] Solis-Cordova, J. et al. *J Mech Behav Biomed Mater.* 2023, 139(105671)

Session Category

Tissue Engineering: Mechanobiology

P2-356

Image-guided Microstructural Mechanical Evaluation and Quantification of Cartilage Under *In Situ* Compression

Ms. Xi Chen PhD Candidate[1], Dr. Catherine Disney PhD[2], Dr. Brian Bay Associate Professor[3], Dr. Kathryn Stok Professor[1]

[1]The University of Melbourne, Melbourne, Victoria, Australia. [2]University of Manchester, Manchester, North West England, United Kingdom. [3]Oregon State University, Corvallis, Oregon, United States

Introduction

A novel validated device, FELIX, enables image-guided micromechanical evaluation of complex soft tissues [1]. This opens up opportunities to explore heterogenous, depth-dependent fibre architecture in loaded (compressed, fluid pressurised) environments that bulk measurement and isotropic models fail to capture [2]. Characterising fibre mechanics under load helps explain how microstructure give rise to the macroscopic response. In this proof-of-concept study we combine data from FELIX with a point-cloud digital volume correlation (DVC) approach to directly visualise and quantify collagen deformation under compression *in situ*.

Methods

Stepwise, unconfined stress relaxation with 5% and 15% strain was carried out on 6 bovine auricular discs of 3 mm diameter, using FELIX. Volumetric images (512 x 512 x 65, 0.9943µm x 0.9943µm x 1µm) were captured using second harmonic generation (SHG) on a two-photon microscope (Olympus FV-MPERS), Figure 1A. Fibres were segmented using custom code (MATLAB, R2024b), and a point cloud was populated among the fibres for analysis using DVC (ver25.00) [3]. Displacement fields were computed and converted to Green-Lagrange strain tensors to quantify maximum, minimum and shear strain within the collagen network (Figure 1B, C).

Results

Preliminary results demonstrate fibre-scale displacement fields can be quantified from SHG volumes, showing a clear heterogenous response. Localised clusters of higher strain coincided with regions of higher fibre density, and regions with more chondrocytes exhibited lower strains. Shear strain had the highest average, compared to maximum and

minimum strain. This suggests that fibre re-alignment occurred and is consistent with reported collagen deformation mechanisms [4].

Discussion

This study demonstrates feasibility of combining SHG imaging, *in situ* compression and DVC to directly visualise and quantify cartilage microstructural mechanics. Sample preparation was kept to a minimum using non-destructive loading and non-labelling. Future work includes implementing confined compression to capture deformation with fluid pressurisation, enabling a thorough evaluation of this biphasic material. This will provide insight into substructural micromechanics for improving engineered cartilage constructs.

Images (Optional)

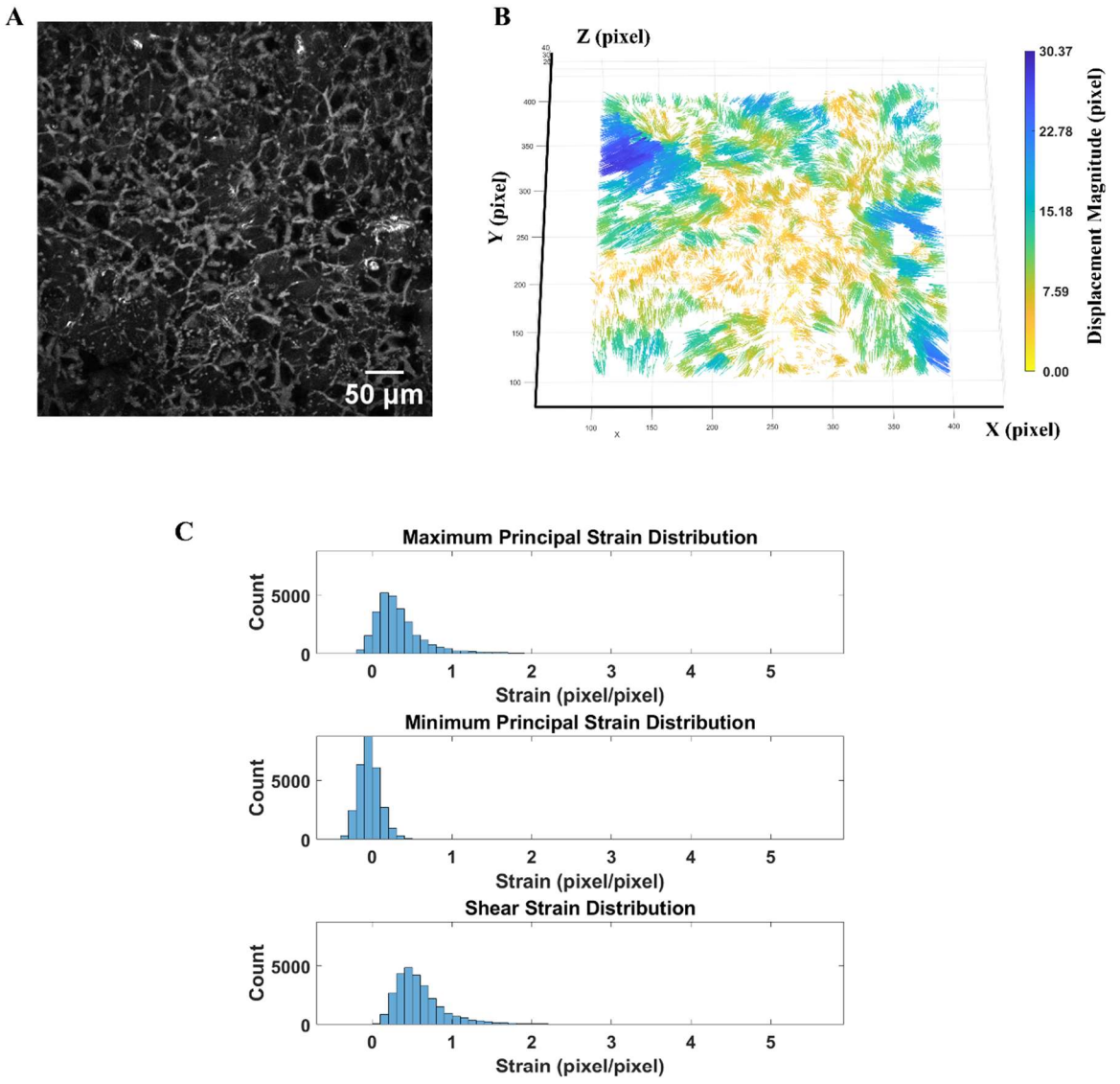


Figure 1: A) Example of raw auricular cartilage image, taken using second harmonic generation. B) 3D displacement map generated from raw DVC results, with arrows pointing in the direction of cartilage fibre movement and color indicating magnitude. C) Histogram of strain component distribution against magnitude.

References (Optional)

[1] Boos MA *et al.*, J Mech. Behav. Biomed. Mater., 2023

[2] Buckwalter JA *et al.*, Instr Course Lect., 1998

[3] B. K. Bay TSS *et al.*, Experimental Mechanics, 1999

[4] C. M. Disney *et al*., Acta Biomater., 2019

Acknowledgements (Optional)

We acknowledge the use of imaging data provided by Dr Manula S. B. Rathnayake. We thank the Collaborative Computational Project in Tomographic Imaging for sharing the DVC code.

Session Category

Tissue Engineering: Mechanobiology

P2-357

In Vitro Culture Model Mimicking Mechanical Environment of Spontaneous Pneumothorax to Elucidate Frictional Force-Induced Cellular Response

Mr. Yu Akiyama Master's Student, Prof. Shogo Miyata Ph.D.

Keio University, Yokohama, Kanagawa, Japan

Mr. Yu Akiyama

Introduction

Primary spontaneous pneumothorax (PSP) occurs suddenly in individuals without underlying lung disease, caused by air leakage from the visceral pleura leading to lung collapse and dyspnea. PSP is associated with the formation and rupture of blebs and bullae, predominantly in the apex of the lung, although the mechanical triggers remain unclear. PSP mainly affects tall, thin young males and shows a high recurrence rate, reducing quality of life. Previous studies reported that patients exhibit an elongated, laterally expanded, and anteroposteriorly flattened thoracic shape, resulting in up to 20 times higher tensile stress in the apex of the lung than in other regions. This study hypothesized that strong frictional force in the narrow apex of lung induces the degeneration of lung tissues resulting in rupture of blebs and bullae. To elucidate the pathogenesis of PSP, we developed an in vitro cell culture model mimicking the mechanical environment and evaluated effects of frictional forces on lung-derived cells.

Methods

Human fetal lung–derived fibroblasts were embedded in type I collagen gel at a density of 4.0×10^5 cells/mL and incubated for 24 h before stimulation. A custom-made culture device with motorized linear stage was developed to impose frictional stimulation on the cell-containing collagen gel. Frictional displacement for 5 mm was applied at 0.262 Hz for 24 h. Cell viability and morphology were evaluated by fluorescence microscopy with Calcein-AM and PI staining. Cell responses in regions with and without frictional stimuli were evaluated.

Results

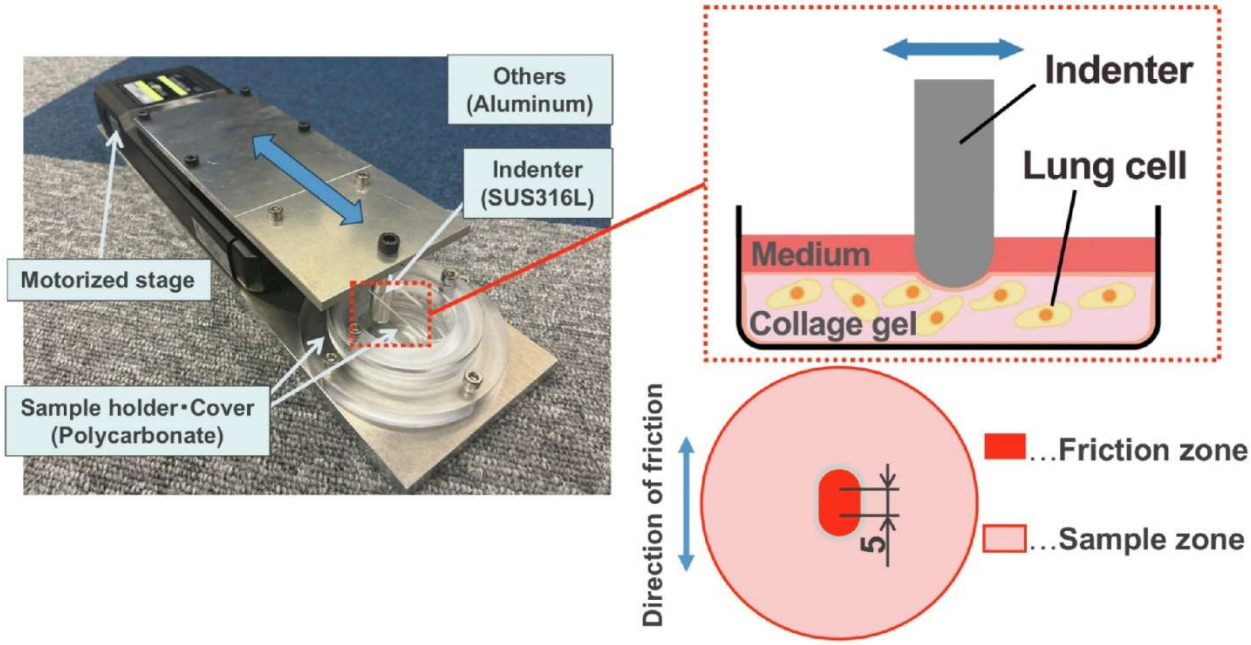
Cell viability was maintained in both regions with and without frictional stimuli throughout the culture period. However, cell aggregation was observed exclusively in regions subjected

to frictional stimulation, and a higher number of dead cells was detected around the aggregation sites compared with other regions.

Discussion

From results of this study, frictional stimuli could be imposed on the cell-laden collagen gel without direct cellular damage. Moreover, the cell aggregations under frictional stimuli was considered to indicate the cellular degeneration mimicking those in spontaneous pneumothorax.

Images (Optional)



Session Category

Tissue Engineering: Mechanobiology

P2-358

Modeling Solute Transport and Clearance in Synovial Joints: Implications for Predicting Cartilage Penetration of Injectable Therapeutics in Preclinical and Clinical Models

Ms. Aiyana Fortin M.S., B.S., Ms. Zongyin Dong B.S., Dr. Ulrich Wiesner Ph.D., Dr. Lawrence Bonassar Ph.D.

Cornell University, Ithaca, NY, United States

Introduction

The effectiveness of intra-articular (IA) drug delivery approaches for osteoarthritis is hindered by rapid synovial clearance and the dense, avascular cartilage matrix that limit therapeutic penetration. Particle-based delivery vehicles yield modest improvements in drug residence time, but joint retention in large animals and humans has not been optimized (**Fig.1A**). Recently, solute transport properties in cartilage were found to correlate with molecular weight (MW). However, there is no unifying framework that combines synovial kinetics and cartilage transport. Our objective was to examine the relationship between clearance kinetics, diffusivity and cartilage penetration following IA injection.

Methods

PubMed was searched (terms: injection, intra-articular, knee) to find studies with longitudinal clearance data following an IA injection. Models of exponential decay ($y=Ae^{(-t/\tau)}+c$ or $y=A_1e^{(-t/\tau)}+A_2e^{(-t/\tau_2)}+c$) and linear regressions ($\log(y)=b*\log(x)+a$) were fit in Origin Pro. Half-lives were calculated: $t_{1/2}=\ln(2)*\tau$. Diffusivities (D) were estimated using a power-law relationship. Penetration depths were calculated: $Z_{penetration}=\sqrt{(2D\tau)}$. General linear F tests, ANCOVA, and Tukey's post-hoc tests were performed in RStudio ($\alpha=0.05$).

Results

IA half-lives of solutes and vehicles were predicted by MW and hydrodynamic radius (r_h) via a power-law relationship (solutes: $y=0.52x^{0.269}$, $R^2=0.29$, $p=0.00013$; vehicles: $y=9.9x^{0.321}$, $R^2=0.20$, $p=0.0016$). Half-lives in rats were 10-fold greater than in rabbits (**Fig.1B**, $p<0.001$). Clearance kinetics in mice were poorly correlated with MW (**Fig.1B**, $p=0.79$). Clearance kinetics of untargeted vehicles correlated with r_h (**Fig.1C**, $p=0.002$), but targeted vehicles did not ($p>0.6$). Large vehicles ($r_h>30$nm) penetrated <500μm in cartilage while small vehicles ($r_h<30$ nm) diffused >500μm (**Fig.1D**).

Discussion

Vehicles exhibited 10-fold greater half-lives than solutes. Given that clearance and diffusion kinetics are both linked to r_h, further investigation of smaller vehicles (r_h<30nm) may enhance cartilage targeting and joint retention (**Fig.1D**). Nearly all vehicles penetrated the full thickness of mouse cartilage (~50μm) but few would penetrate human cartilage (~1.5mm) before being cleared (**Fig.1D**). These data partially explain why many IA therapies are successful in rodents but translation to larger animals and humans is lacking. This model of IA transport highlights the value of large animal models to predict therapeutic efficacy in humans.

Images (Optional)

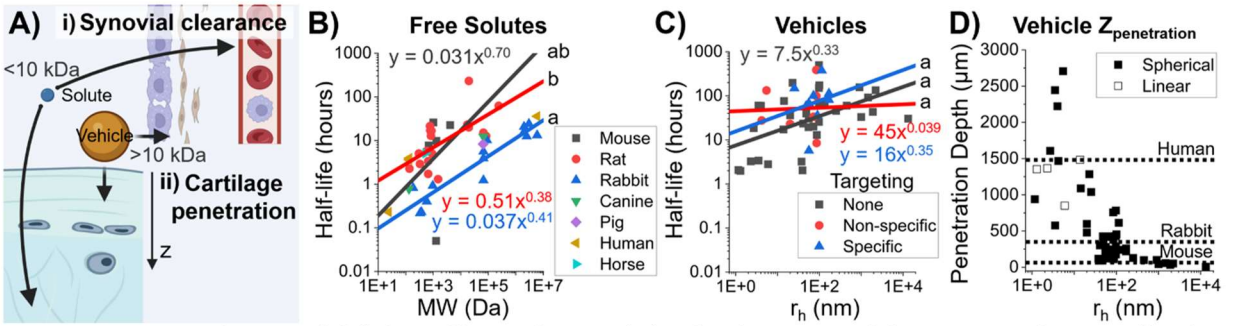


Figure 1: (A) (i) The synovial lining offers a size-restrictive barrier to material transport, where small solutes (<10kDa) clear rapidly (long arrow) and large solutes (>10kDa) clear slowly (short arrow). **(ii)** Similarly, diffusive transport in cartilage is also size-dependent: small solutes (<10kDa) diffuse rapidly (long arrow) and large solutes (>10kDa) diffuse slowly (short arrow). **(B)** Solute half-lives exhibited a 10-fold increase over 4 orders of magnitude in MW. Half-lives were 10-fold greater in rats than in rabbits. **(C)** Vehicle half-lives exhibited a 10-fold increase over 4 orders of magnitude in size. Surface functional groups (i.e., 'non-specific' indicates cationic surface charge; 'specific' indicates reversible binding with cartilage is possible) obscured the relationship between vehicle size and clearance kinetics. **(D)** Cartilage penetration of vehicles decreased with r_h in this model. Smaller vehicles (r_h<30nm) can diffuse farther into tissue than larger vehicles, exceeding full-thickness penetration in human cartilage (i.e., 1.5-2mm). Shared letters between groups denote no significant difference (α=0.05).

Session Category

Tissue Engineering: Methods, Models and Applications

P2-359

Laser-Templated Microvascular Construction With Predefined Geometries via Flow Stimulation and Initial Cell Introduction Control

Mr. Akira Ono[1], Mr. Ryo Aoyama[1], Mr. Masahiko Suda[1], Mr. Keisuke Shibata[1], Dr. Tadahiro Yamashita[1,2], Dr. Yoshihiro Taguchi[1,2], Dr. Ryo Sudo[1,2]

[1]School of Integrated Design Engineering, Graduate School of Science and Technology, Keio University, Yokohama, Kanagawa, Japan. [2]Department of System Design Engineering, Keio University, Yokohama, Kanagawa, Japan

Introduction

In tissue engineering, capillary networks play a crucial role in delivering oxygen and nutrients into 3D parenchymal constructs, and each organ has a distinct capillary architecture. For example, the hepatic lobule contains a radial vascular network called sinusoids, whereas the kidney contains densely packed spherical capillary structures in the glomerulus. Therefore, constructing capillary networks with organ-specific geometries is essential for recapitulating organ-specific metabolism.

In this study, we established a method to construct capillary-scale vasculature with pre-defined geometries. We demonstrated that flow stimulation and the manner of initial cell introduction into the template channels immediately after seeding are critical for successful vascular formation. These findings offer a promising approach for engineering organ-specific microvasculature for tissue regeneration.

Methods

For hydrogel preparation, a type I collagen prepolymer solution was injected into the hydrogel port. Cylindrical hollow channels with straight, linear geometries, serving as templates, were fabricated inside the hydrogels using a femtosecond laser. For template-guided microvessel construction, human umbilical vein endothelial cells (HUVECs) were seeded onto the hydrogel surface by injecting a cell suspension into the medium port.

Results

With a 20-μm-diameter template, which falls within the size range of native capillaries, HUVECs failed to form vascular structures under static conditions. In contrast, under

interstitial flow, the cells covered the entire luminal surface, leading to the formation of straight vascular structures along the channels.

To further regulate early cell introduction, narrowed constriction structures were created within the hydrogel channels. The position of these stenotic structures influenced the rate and extent of vascular formation.

Discussion

Overall, we demonstrate that the application of interstitial flow, together with controlled initial cell introduction, is essential for robust vascular formation. We hypothesized that successful formation along the template requires sequential processes: initial cell adhesion, establishment of cell–cell junctions, and subsequent collective migration.

The primary advantage of this methodology is its ability to reproducibly generate capillaries with predefined geometries. Such reproducibility is crucial for investigating vascular remodeling in vitro and holds significant potential for tissue engineering applications aimed at regenerating organ-specific vascular networks, such as those in the liver and kidney.

References (Optional)

Session Category

Tissue Engineering: Methods, Models and Applications

P2-360

A Confined Dynamic Compression Framework for Characterizing Melt Electrowritten-PVA Composite Scaffolds for Articular Cartilage Repair

MSc Alessio Amicone[1], Dr. Remco Doodkorte[2], Prof. MD ScD Keita Ito[2], Prof. Dr. Stephen J. Ferguson[1]

[1]ETH Zurich - Institute for Biomechanics, Zurich, Zurich, Switzerland. [2]Eindhoven University of Technology - Orthopaedic Biomechanics, Eindhoven, Noord-Brabant, Netherlands

Introduction

Articular cartilage withstands intense cyclic loading through a collagen-rich network and poroviscoelastic fluid pressurization. Mimicking this dual mechanism in engineered constructs remains challenging: hydrogels lack reinforcement, while scaffolds must ensure mechanical stability and load distribution. Prior studies show that porous polymer scaffolds filled with PVA hydrogels improve performance under compression [1], and melt electrowritten (MEW) architectures offers tunable structural reinforcement by limiting lateral expansion [2]. Despite the relevance of confined compression in cartilage biomechanics [3], MEW-hydrogel composites remain underexplored in such settings. This study quantifies the viscoelastic response of tri-layer MEW scaffolds, with and without PVA, under confined dynamic compression.

Methods

Tri-layer scaffolds were fabricated via MEW using medical-grade poly(ε-caprolactone), mimicking cartilage zonal architecture. Constructs (8 mm ø) were prepared as PVA-only (S2), MEW-only (S3), or MEW-PVA composites (S1) via gel infiltration and freeze-thaw cycling. Confined compression testing followed Patel's cartilage protocol [3], adapted to scaffold mechanics (Fig.A). After applying a 2N tare load, samples were compressed 10% at 2 mm/s and held for 1200s (stress-relaxation), then cycled at ± 5% strain, 1Hz for 500 cycles (Fig.B). Viscoelastic parameters were extracted through Matlab analysis.

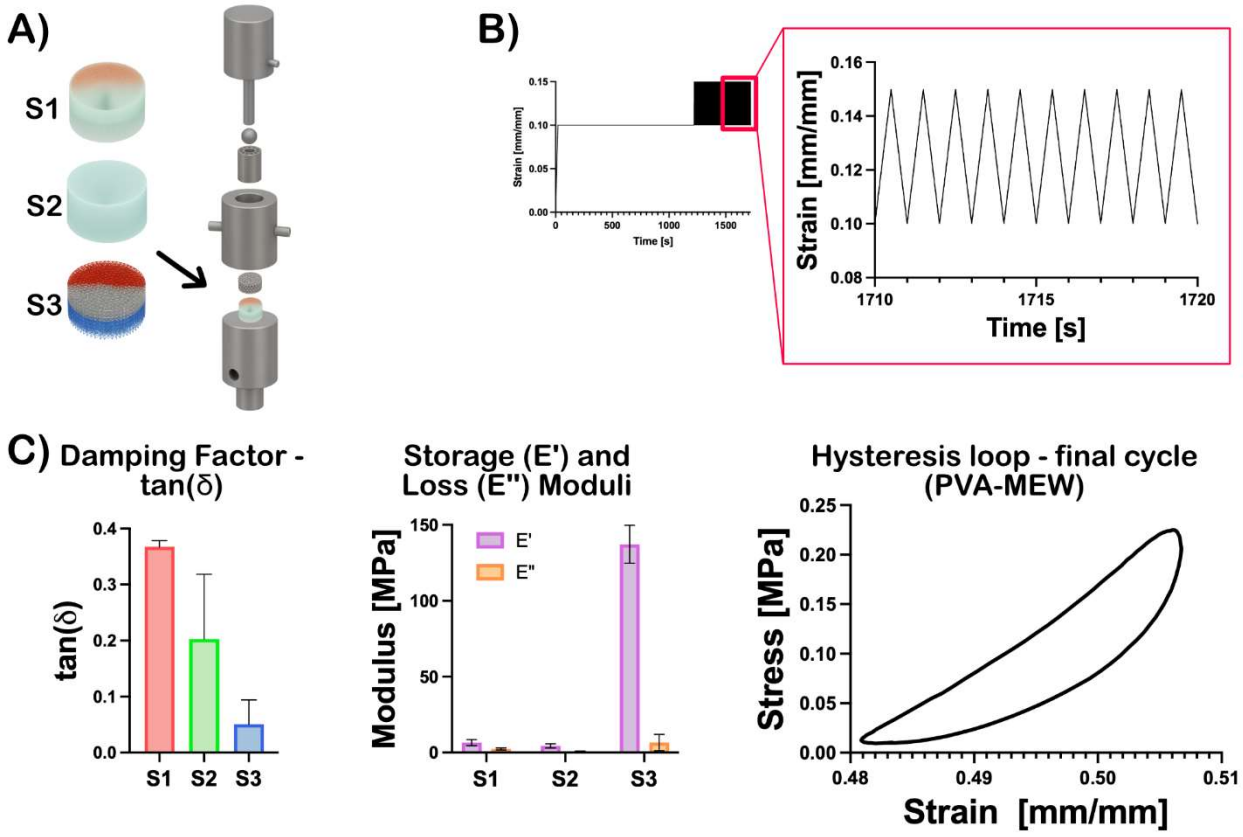
Results

Relaxation curves were fit to a bi-exponential model (mean R^2=0.91), with $\tau_1 \approx$ 1-24s and $\tau_2 \approx$ 100-590s. MEW-only (S3) had high stiffness (E' = 128-146 MPa) and low damping ($\tan\delta \approx$ 0.02-0.08). PVA-only (S2) was softer (E' ≈ 3.4-5.4 MPa), while MEW-PVA (S1) showed intermediate stiffness (E' ≈ 3.5-8.0MPa) and greater damping (E'' ≈ 1.4-2.9MPa, $\tan\delta \leq 0.4$). Hysteresis in a representative S1 sample confirmed energy dissipation (Fig.C).

Discussion

Mechanical trends reflect construct structure. The excessively high modulus in S3 (Fig.C) likely reflects fluid incompressibility in the open MEW structure, rather than an intrinsic stiffness. S1 composites combined elastic reinforcement with damping, evident in modulus values and hysteresis. Compared to native cartilage (7-40 MPa, tanδ ≈ 0.1-0.2 at 1Hz [4]), S1 approaches physiological damping. These preliminary findings support the value of MEW-PVA systems for cartilage scaffolds and confined compression for evaluating cartilage-mimetic mechanics.

Images (Optional)



References (Optional)

[1] Vikingsson Line et al. , J Biomechanics, 2015

[2] Castilho Miguel et al. , Scientific Reports, 2018

[3] Patel Jay et al. , Tissue Engineering, 2019

[4] Kabir Wassif et al. , Cartilage, 2020

Acknowledgements (Optional)

Supported by the doc.Mobility ETH Program

Session Category

Tissue Engineering: Methods, Models and Applications

P2-361

A Multi-Modal Bioreactor System Designed for Characterising Chondrogenic Effects of Dynamic Mechanical Stimulation in Cartilage Tissue Engineering

Mr. Jiaqi K. Shen, Ms. Cecily X. Chen, Prof. Kathryn S. Stok PhD

Department of Biomedical Engineering, The University of Melbourne, Parkville, Victoria, Australia

Introduction

Dynamic mechanical stimulation is a central pillar in cartilage tissue engineering, yet progress in the field is hindered by the lack of standardised platforms for delivering and tuning mechanical cues essential for cartilage matrix development [1]. A recent systematic review by the authors revealed that current studies report chondrogenic outcomes without characterising the applied mechanical stimulus at sub-tissue scales, and the substantial heterogeneity of custom-built bioreactors further limits cross-study comparison [2]. This work aims to develop a multi-modal bioreactor system capable of delivering controlled mechanical stimulation under standardised *in vitro* conditions to enable comprehensive mapping and comparison of chondrogenic responses across conventional loading modalities.

Methods

A traceable, evidence-based engineering design process was implemented to ensure mechanical feasibility, biocompatibility, and operational robustness. The platform integrates configurable stimulation modules that support compression, shear, tension, hydrostatic pressure, fluid-induced shear, and combined loading. Standardised protocols were defined for tuning mechanical inputs and quantifying biological outputs, forming the basis of a parametric analysis workflow for mechanically stimulated chondrogenesis.

Results

The resulting multi-modal bioreactor system (Figure 1) consists of: (a) mechanical actuation for direct-contact stimuli, (b) fluid actuation for fluid-mediated stimuli, (c) a circulation subsystem to maintain nutrient transport, and (d) gas exchange to regulate incubation environments. Together, these subsystems provide a modular infrastructure for delivering reproducible mechanical inputs under consistent conditions. A culture chamber has been prototyped and assembled (Figure 1) to initiate functionality tests using a dual-

piston pump, which allows for dynamic modulation of 0-10 MPa fluid pressure as well as a tuneable range of 0-400 ml/min continuous flow to induce fluid shear stimulation.

Discussion

While further validation and refinement are ongoing, this multi-modal bioreactor presents a viable framework for cross-comparison under a unified experimental workflow. The successfully prototyped culture chamber confirms the technical feasibility of the bioreactor design. Overall, this device serves as a foundation for standardising mechanically stimulated cartilage tissue engineering, generating reliable mechanobiological datasets, and supporting optimisation of stimulation strategies toward future regulatory acceptance of engineered cartilage constructs for regenerative medicine.

Images (Optional)

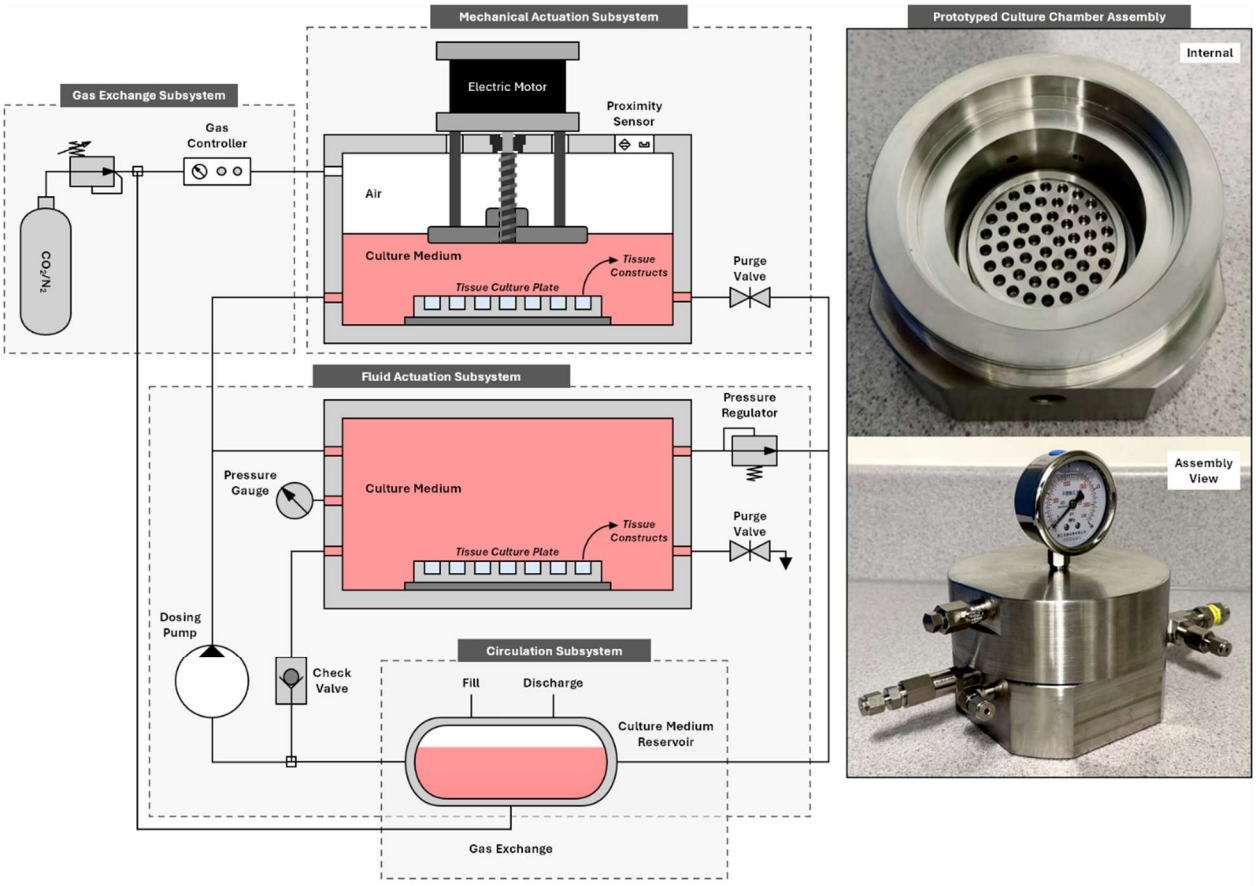


Figure 1: (Left) Overview of the multi-modal bioreactor system diagram comprised of four major subsystems of mechanical actuation, fluid actuation, circulation and gas exchange, and (Right) the prototyped culture chamber assembly.

References (Optional)

[1] Devon E. Anderson & Brian Johnstone, *Front. Bioeng. Biotechnol.*, 2017.

[2] Jiaqi K. Shen et al., *OSF*, 2024. doi:10.17605/OSF.IO/NHEUF

Acknowledgements (Optional)

We thank Dr Elias Salzer (Department of Orthopaedics and Sports Medicine, Erasmus MC, University Medical Center Rotterdam, Rotterdam, The Netherlands) for his valuable engineering advice and guidance during the design phase of the bioreactor. This project is supported by the Australian Research Council Discovery Project funding scheme (DP240102160), and Jiaqi K. Shen is a recipient of Melbourne Research Scholarship from the University of Melbourne.

Session Category

Tissue Engineering: Methods, Models and Applications

P2-362

Advancing Articular Cartilage Regeneration: A Multiscale Scaffold Approach And Physical Characterisation

MSc Elisa Bissacco[1], MPhil Neeraj Sakhrani[2], Dr. Jack Rogot[2], MS Haoyu Zhang[2], Prof. Dr. Clark T. Hung[2], Prof. Dr. Gerard A. Ateshian[2], Prof. Dr. Stephen J. Ferguson[1]

[1]ETHZ, Zürich, Switzerland, Switzerland. [2]Columbia University, New York City, New York, United States

Introduction

Articular cartilage (AC) degeneration remains a major clinical challenge. Tissue engineering integrates cells, growth factors, and biodegradable scaffolds to support its repair. Here, we developed bilayered PCL scaffolds via Solution Electrospinning (SES) and Melt Electrowriting (MEW), embedded in porous SBMA-GelMA-quaternized chitosan hydrogels, and evaluated gel morphology and the influence of fiber geometry on mechanical properties, solute diffusivity and tribological response.

Methods

SBMA-GelMA-qChitosan (Gel) hydrogels were formulated at 4%, 6%, and 2.4% (w/v), respectively. Bilayered PCL scaffolds were produced via SES and MEW in three architectures differing in wall spacing (WS) and fiber orientation: O-WS500, O-WS150/350, and X-WS500 (Figure1A). Preliminary characterization of Gel and Gel+O-WS500 included compression testing under 60% strain and SEM analysis of pore size and fiber-gel integration. Tribological performance was assessed by measuring the coefficient of friction (μ) under reciprocating sliding (contact stress of 130 kPa) against bovine tibial cartilage in synovial fluid for 120 min at 1mm/s [1]. Diffusion was quantified by Fluerescence-Recovery-after-Photobleaching (FRAP) using 70kDa FITC-dextran.

Results

Compression testing showed an elastic modulus of 41.6±20.4kPa for Gel and 432.8±76.5kPa for Gel+O-WS500. Gel and Gel+O-WS500 exhibited average pore sizes of 91.4±22.8μm and 82.0±18.3μm, respectively. μ_{avg} values were 0.032±0.009, 0.040±0.012, and 0.089±0.036 for Gel+O-WS500, Gel+O-WS150/350, and Gel+X-WS500, respectively (Figure1C). Gel displayed significantly higher solute diffusivity (113.7±15.4$\mu m^2/s$) compared to Gel+O-WS500, Gel+O-WS150/350, and Gel+X-WS500 (58.6±15.9, 49.1±19.8, and 58.2±13.6$\mu m^2/s$, Figure1D).

Discussion

As expected, incorporation of PCL fibers substantially increased the mechanical stiffness of the hydrogel, reaching the lower range of physiological compressive modulus for AC. SEM analysis revealed good gel-fiber integration and homogeneous pore size distribution, suitable for chondrocyte infiltration. Tribological testing showed relatively stable coefficients of friction across all scaffold geometries, with μ_{avg} approaching the upper range of AC values. FRAP analysis indicated that solute diffusivity was higher in Gel, suggesting that increased volume fraction due to fibers reduces molecular transport. Overall, all constructs exhibited diffusivity values comparable to AC [2], supporting their suitability for cell and growth factor delivery.

Images (Optional)

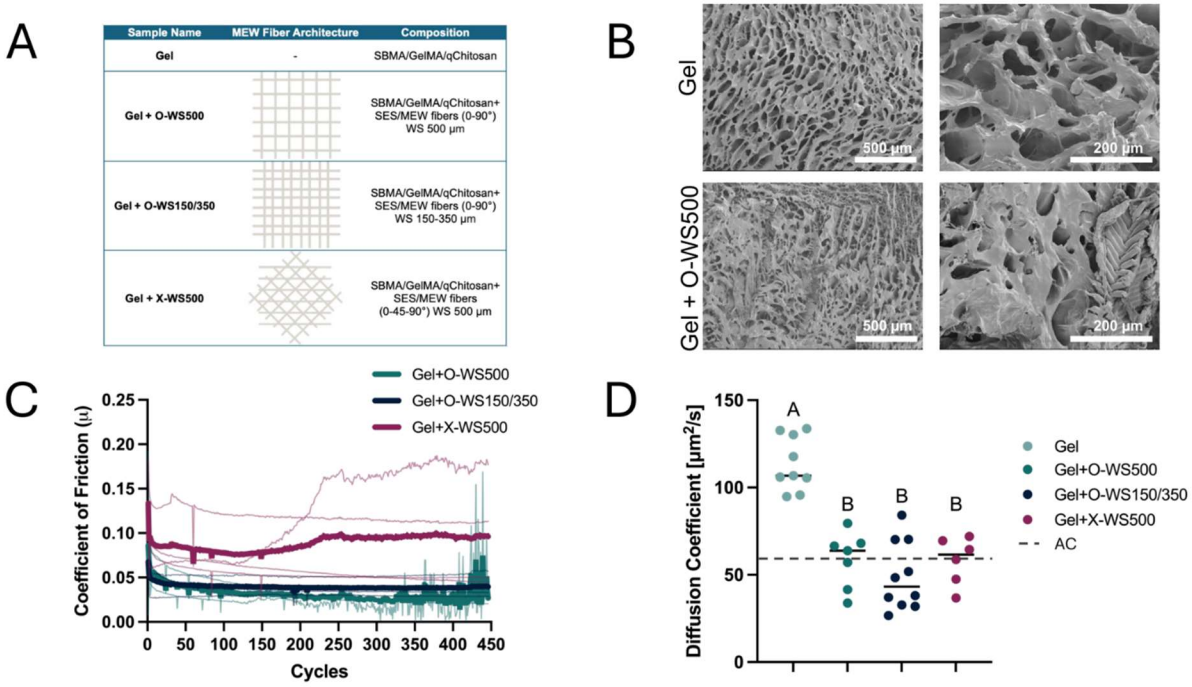


Figure1: A. Sample types. B. SEM cross-sections of Gel and Gel+O-WS500. C. Coefficient of friction over sliding cycles. Individual lines correspond to separate runs for each sample type, darker lines represent the average. D. Solute diffusion coefficients. Group with the same letter are not significantly different. (AC value from Leddy H. et al.).

References (Optional)

[1] Lianna Gangi *et al.*, J. Vis. Exp., 2022.

[2] Holly Leddy *et al.*, Ann. Biomed. Eng., 2003.

Acknowledgements (Optional)

This study was supported by the ETH Zurich Doc.Mobility Fellowship. Funded by European Union's Horizon 2020 Research and innovation programme under grant agreement No. 956004 (BioTrib).

Session Category

Tissue Engineering: Methods, Models and Applications

P2-363

Investigating the Mechanical Efficiency of Genipin Crosslinking on Demineralized Cancellous Bone Scaffolds for Articular Cartilage Repair

Mr. Shengming Hu B.M.E.[1], Dr. Andreja Zupan Ph.D.[1], Dr. Darryl Dickerson Ph.D.[2], Dr. Eric Nauman Ph.D.[1]

[1]University of Cincinnati, Cincinnati, Ohio, United States. [2]University of New Mexico, Albuquerque, New Mexico, United States

Introduction

Articular cartilage injuries in the knees affect approximately 900,000 Americans annually. Due to its avascular nature, cartilage has limited healing potential and current repair strategies have long recovery times largely because they don't adequately support the damaged area while facilitating nutrient transport. We evaluated the mechanical properties of a Genipin-crosslinked, regionally-demineralized cancellous bone scaffold to enhance stiffness, provide structural support, and facilitate nutrient delivery.

Methods

Crosslinking was performed after osteoinductivity removal and before sterilization. Genipin powder was diluted in 99.5% ethanol. Scaffolds were then submerged in the Genipin solution for 24 hours at 37 ºC, and rinsed in deionized water.

A Biomomentum MACH-1 was used to record compressive forces up to 30% strain at rates of 0.05, 0.5, 5, and 50%/s. The 30% strain level was chosen based on MRI scans of knee cartilage deformation under load and the highest strain rate approximated the knee cartilage deformation rate during moderate-intensity walking. Six unconfined cyclic compression loads were applied to each 7 mm diameter, 2.5 mm thick sample (12 each of control, 0.5% Genipin, and 2% Genipin) for each strain rate.

Results

Estimated peak knee joint force was 385% of body weight and the mean unloaded contact area was approximately 210 mm^2. Under loading, contact areas increased by 24%. The estimated stress values were 5.65 MPa for females and 6.54 MPa for males under a double-leg stance. For comparison, the peak stresses measured in the Genipin crosslinked samples ranged from 12.7 – 164 kPa (Table 1). As expected, 2% Genipin crosslinking significantly increased the peak stress more than 10-fold greater that of controls, though still less than the stresses experienced during normal activities.

Discussion

With 2% Genipin, the peak stress increased more than 10-fold, but the peak stress remained lower than the estimated stresses in the knee condyle. In vivo testing will be required to determine whether this is sufficient to promote the restoration of the cartilage-bone interface.

Images (Optional)

Table 1: Holm-Sidak Post Hoc Comparison Test Results

Group	N	Mean (kPa)	Grouping		
2%Genipin24hr	48	164	A		
0.5%Genipin24hr	48	94.9		B	
Control	48	12.7			C

References (Optional)

Session Category

Tissue Engineering: Methods, Models and Applications

P2-364

Development of Articular Cartilage Model Considering Fiber Orientation Using Particle Method

Ms. Fuyu Mima B.S.[1], Prof. Yoshimori Kiriyama Ph.D[1], Prof. Katsumasa Tanaka Ph.D[1], Prof. Salvatore Federico Ph.D[2]

[1]Kogakuin University, Shinjuku, Tokyo, Japan. [2]The university of Calgary, Calgary, Alberta, Canada

Introduction

Collagen fibers in the articular cartilage exhibit a depth-dependent architecture, transitioning from a horizontal orientation in the superficial zone to a vertical orientation in the deep zone. The mechanical behavior of cartilage arises from the interaction between the collagen network and interstitial fluid. In osteoarthritis, fiber rupture and fibrosis are frequently observed, highlighting the need for models that represent fiber behavior and failure. In this study, we developed an articular cartilage model based on a particle method in which collagen fibers and interstitial fluid are expressed as particle assemblies, enabling mechanical response failure.

Methods

This study employed the Moving Particle Semi-implicit (MPS) method. Collagen fibers were modeled as linearly elastic solids, whereas the interstitial fluid was treated as incompressible. The fibers were represented by particles connected in straight chains, with the spacing set to the mean collagen fiber diameter (20 μm). Tentative positions are first calculated explicitly and then corrected using the pressure among the particles obtained implicitly. Fiber deformation was evaluated from the corrected positions to assess the behavior and rupture. A uniaxial compression test was simulated by prescribing a vertical displacement at the top surface.

Results

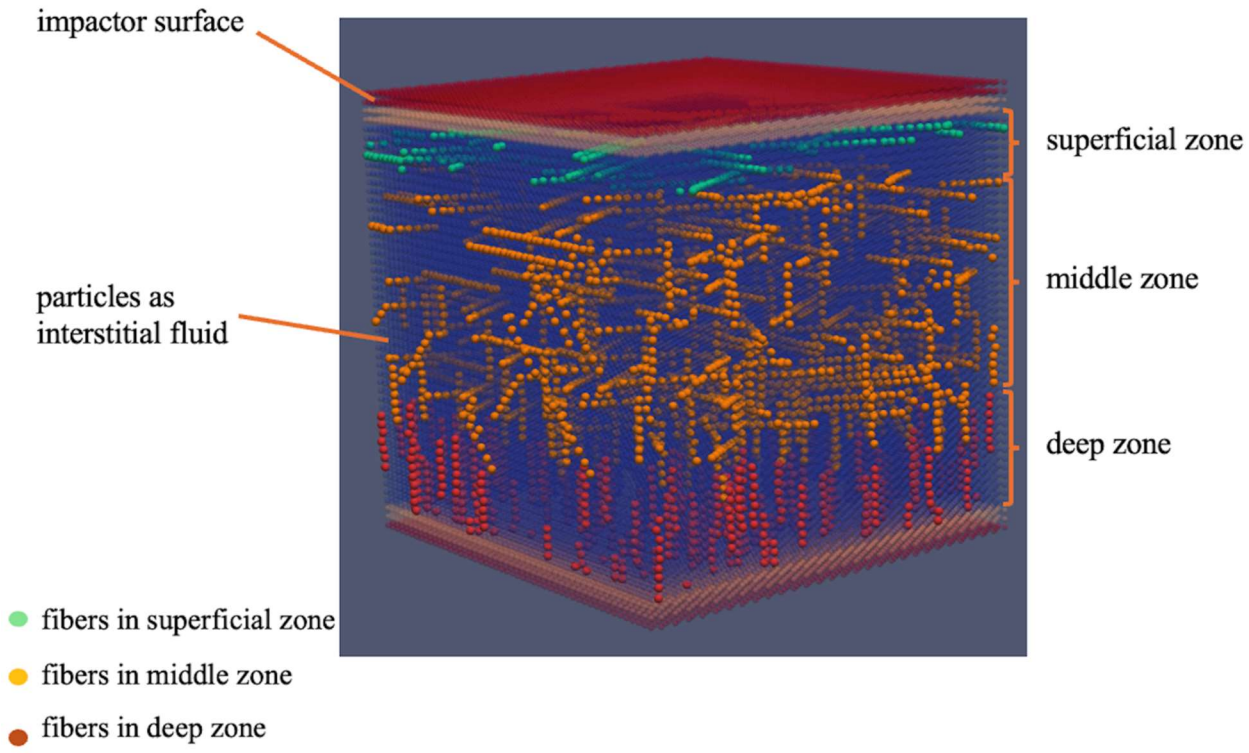
A three-dimensional articular cartilage model was constructed. The fiber particles were statistically distributed to reproduce the histological depth-dependent collagen architecture: in the superficial zone, fibers ran parallel to the articular surface; in the middle zone, they ran obliquely and intersected; and in the deep zone, they ran vertically toward the subchondral bone plate. Under vertical compression, fluid particles moved

laterally while continuing to transmit vertical stress, indicating that the characteristic compressive response of the cartilage was reproduced.

Discussion

The proposed model reproduces the native tissue structure and depth-dependent fiber orientation, enabling individual fibers to deform under compression. This allows a detailed analysis of the depth-wise differences in fiber behavior and rupture. Incorporating a mechanism by which multiple fibers aggregate and form fibrosis into the particle framework enables the reproduction of stepwise tissue-level failure. Therefore, this model could be useful for elucidating the histopathological progression of osteoarthritis.

Images (Optional)



Session Category

Tissue Engineering: Methods, Models and Applications

P2-365

A Thermodynamic Framework for Coupled Electromechanical Bone Remodeling, Damage, and Healing

Dr Ibrahim Goda

University of Lorraine, Metz, 57073, France

Introduction

Bone is a complex hierarchical material whose structural evolution is governed by the interaction of mechanical loading, electrical fields, and biological regulatory mechanisms. This interdependence motivates the need for predictive mathematical models capable of capturing these coupled effects.

Methods

In this work, a unified thermodynamically consistent formulation is developed within the theory of irreversible processes in order to model coupled internal and external bone remodeling, damage progression, and healing in brittle bone tissue under simultaneous mechanical and electrical stimulation. The approach relies on irreversible thermodynamics and Eshelby-type configurational forces, with internal remodeling described by density evolution driven by the trace of the Eshelby stress and external remodeling represented through a surface growth law derived from a surface potential that depends on elastic surface strain and the local normal vector [1], while healing is incorporated through a scalar or tensorial variable interpreted as a negative counterpart to damage. Numerical simulations are performed on multiple geometric configurations including individual hexagonal trabeculae, clusters of trabeculae within a representative region of analysis, and macroscale bone samples, and electromechanical coupling is included to account for the piezoelectric behavior of bone and the associated conversion of mechanical stress into electrical potential.

Results

The simulations reveal that mechanical and electrical stimuli, whether applied separately or simultaneously, enhance bone formation, facilitate healing, and generate bone density distributions that are consistent with radiographic observations and experimental evidence.

Discussion

The findings suggest that the proposed unified framework is able to reproduce key mechanobiological mechanisms driving bone adaptation and recovery and thus provides a

robust platform for assessing the influence of natural and therapeutic electromechanical environments on bone remodeling, damage repair, and long-term structural evolution.

References (Optional)

[1] I. Goda, J.-F. Ganghoffer, G. Maurice, Combined bone internal and external remodeling based on Eshelby stress, International Journal of Solids and Structures, 94-95, 2016, 138-157.

Session Category

Tissue Engineering: Methods, Models and Applications

P2-366

Development of Two-Photon Biofabricated Tissue-Engineered Vascular Graft

Ms. Jacqueline L. Avila[1], Dr. Jonathan P. Vande Geest, Ph.D.[1,2,3]

[1]Department of Bioengineering, University of Pittsburgh, Pittsburgh, PA, United States. [2]McGowan Institute for Regenerative Medicine, University of Pittsburgh, Pittsburgh, PA, United States. [3]Department of Mechanical Engineering and Material Science, University of Pittsburgh, Pittsburgh, PA, United States

Ms. Jacqueline L. Avila

Introduction

Coronary artery disease (CAD) is characterized by plaque buildup in the coronary arteries, leading to vessel narrowing and reduced blood flow to the heart. CAD results in about 610,000 annual deaths in the United States and in advanced cases, it is treated surgically with coronary artery bypass grafting (CABG). Although autologous vessel grafts such as the saphenous vein are the current gold standard, they have limited availability and have high failure rates of about 50% at 10 years. Tissue-engineered vascular grafts (TEVGs) offer a promising alternative. However, conventional fabrication methods such as electrospinning have limitations, including reduction of pore size due to compacted fibers, which hinder cell infiltration. Two-photon polymerization (2PP) supports high-resolution, three-dimensional fabrication with feature sizes ranging from hundreds of nanometers to centimeters. The objective of this study was to utilize 2PP to fabricate a small-diameter TEVG that mimics key geometrical features of the extracellular matrix (ECM), including fiber orientation, porosity, and topology.

Methods

A cross-section of a Sprague-Dawley rat abdominal aorta was imaged using an Olympus BX51 upright laser-scanning microscope. The resulting two-photon image was processed in MATLAB to generate a binary input image that guided TEVG fabrication (**Figure 1A**). The photoresin IP-S was used to fabricate a tubular construct by 2PP using the 4X objective on the same microscope. After fabrication, a grayscale image of the TEVG was acquired, binarized, and compared to the original input image using the Dice similarity coefficient (DSC) to evaluate spatial overlap (**Figure 1B**).

Results

The TEVG was successfully biofabricated in 2h 1m 52s, with an inner diameter of 0.694 mm, an outer diameter of 1.214 mm, and a length of 12.67 mm (**Figure 1C**). A DSC of 0.6027 was obtained between the input and output binary masks, indicating substantial geometric similarity between the designed and fabricated structures.

Discussion

Future work will include fabricating grafts using a biodegradable gelatin-based photoresin (Hydrobio INX N400) to improve biocompatibility and promote tissue remodeling. Mechanical testing will assess compliance matching to native vessels, a critical factor in preventing graft failure. Subsequently, TEVGs will be interpositionally implanted in Sprague-Dawley rats to evaluate *in-vivo* remodeling, patency, and long-term functionality.

Images (Optional)

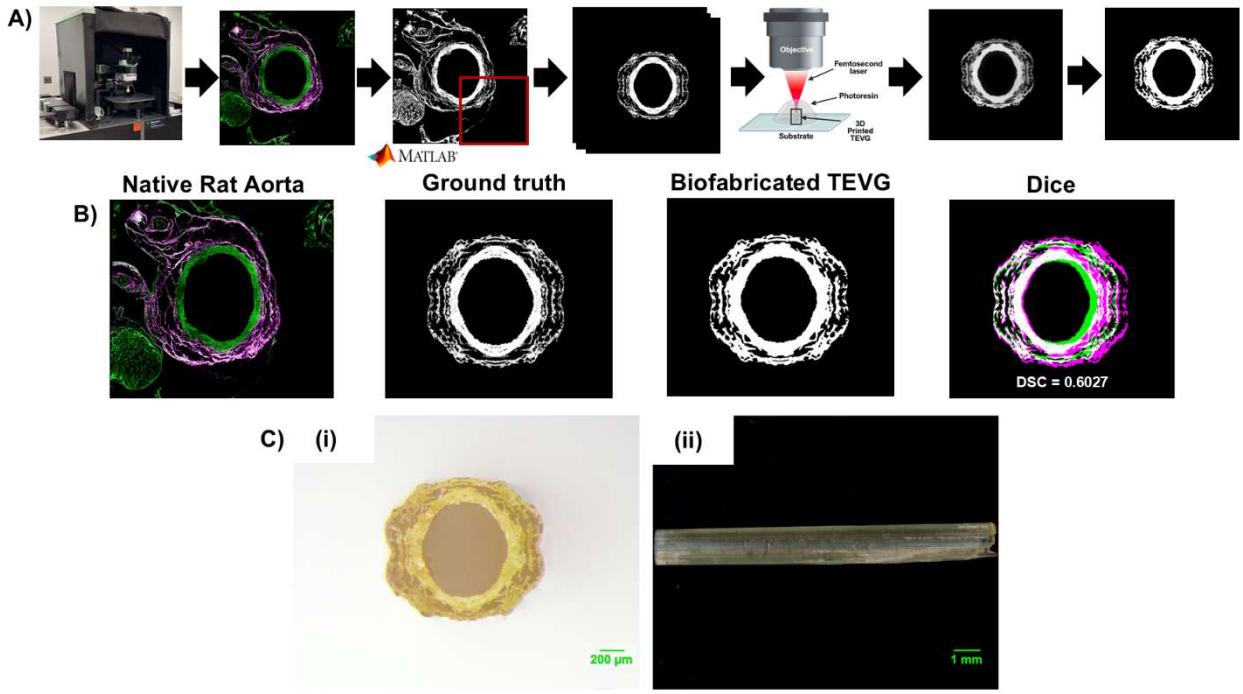


Figure 1. Biofabrication of a tissue-engineered vascular graft (TEVG).
(A) Step-by-step schematic of the two-photon polymerization (2PP) fabrication process. **(B)** Dice similarity coefficient (DSC)-based comparison between the designed input mask (ground truth) and the fabricated TEVG mask (output) **(C)** Final biofabricated TEVG printed using IP-S: **(i)** cross-sectional geometry with an inner diameter of 0.694 and an outer diameter 1.214 mm, and **(ii)** a total graft length of 12.67 mm.

References (Optional)

Session Category

P2-367

Optimization of a Custom-Designed Perfusion Bioreactor for Human Bone Tissue Culture

PhD Mahsa Zojaji[1], BSc Annelise Grace Pageau[1], BSc Teodora Maluckov[1], MSc. Eng. Johannes Eichwalder[1], PhD Corey Daniel Smith[2], MD, FRCSC George Athwal[2], PhD, PEng Louis Miguel Ferreira[3,2], PhD Nikolas Knowles[1]

[1]Department of Kinesiology and Health Sciences, University of Waterloo, Waterloo, Ontario, Canada. [2]Roth McFarlane Hand and Upper Limb Centre, London, Ontario, Canada. [3]Department of Mechanical and Materials Engineering, Western University, London, Ontario, Canada

Introduction

Perfusion bioreactors maintain trabecular bone culture by preserving marrow and the native extracellular matrix by providing continuous fluid flow under osteogenic conditions [1]. Previous studies using this system have reported increases in apparent bone stiffness [2-3]. A recent modification enabled larger bone cores though perfusion was not optimized for these samples [3]. This study developed a redesigned, 3D-printed ZETOS bioreactor with three internal inlet channels to improve multidirectional perfusion. Computational simulations optimized the design and flow rate, and experiments evaluated cell viability, metabolic activity, and osteogenic function in human osteoarthritic bone samples.

Methods

Human trabecular bone cores (Ø9.15±0.14×9.5±2.0mm, n=22) obtained from four arthroplasty patients (Fig.1) were cultured for 21 days under static or dynamic (two perfusion rates;252 and 752µL/min) conditions. Metabolic activity, cytotoxicity, and osteogenic markers were measured throughout culture, with live/dead cell distribution visualized via confocal microscopy and genomic content (dsDNA) quantified on Day 21. Micro-computed tomography characterized bone microstructure, and computational simulations evaluated fluid flow through the porous tissue at both perfusion rates.

Results

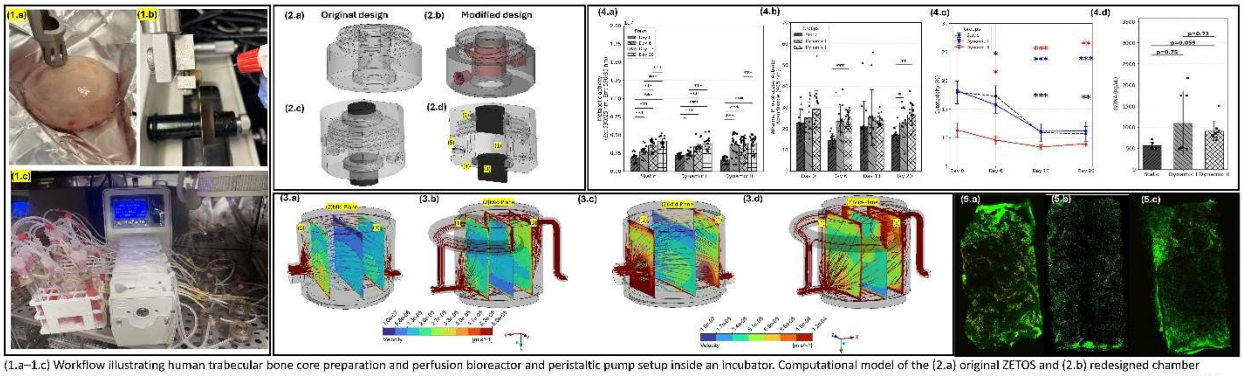
Computational analysis demonstrated that the modified bioreactor increased mid-plane velocity and wall shear stress relative to the original ZETOS design, reducing the surface-to-center velocity drop by 50% and nearly doubling intrachamber pressure (Fig.2&3), thereby

improving fluid infiltration into trabecular regions [4]. Experimentally, metabolic activity rose in all groups, with the highest increase in the faster perfusion group (Fig.4a). Cytotoxicity decreased earliest under perfusion, and pH remained within physiological ranges (Fig.4b/c). Osteogenic activity was elevated in perfused groups at Days 6 and 20, and dsDNA trended higher with flow (Fig.4d). Live/dead imaging confirmed widespread cell viability throughout the explants (Fig.5).

Discussion

The findings demonstrate the redesigned 3D-printed bioreactor enhances fluid distribution, sustaining cell viability and osteogenic activity in human trabecular bone explants. This platform provides a physiologically relevant model for mechanobiology studies and lays the groundwork for future investigations incorporating cyclic mechanical loading and long-term bone adaptation.

Images (Optional)



(1.a–1.c) Workflow illustrating human trabecular bone core preparation and perfusion bioreactor and peristaltic pump setup inside an incubator. Computational model of the (2.a) original ZETOS and (2.b) redesigned chamber featuring three internal inlet channels to enhance multidirectional perfusion. (2.c) Bioreactor assembly and (2.d) cross-section showing: (1) bone chamber within the body component, (2) bioreactor cap, (3) load applicators at the top and bottom, (4) X-ring/O-rings preventing fluid leakage at both ends, and (5) integrated luer fitting for external connection to tubing. Computational fluid dynamic simulations comparing (3.a , 3.c) the original and (3.b , 3.d) redesigned bioreactors under Dynamic I (252 µL/min, a,b) and Dynamic II (752 µL/min, c,d) perfusion; mid-plane velocity fields and streamlines demonstrate improved flow uniformity, increased mid-plane velocity, and enhanced fluid penetration into central trabecular regions in the new design. (4.a–4.d) Biological responses of bone cores cultured under Static, Dynamic I (252 µL/min), and Dynamic II (752 µL/min) perfusion for 21 days: (3.a) metabolic activity, (3.b) alkaline phosphatase activity (ALP), (3.c) cytotoxicity, and (3.d) genomic content (dsDNA) on Day 21. Metabolic activity increased significantly over time in all groups, with Dynamic II showing the earliest and largest rise by Day 6. ALP as indicator of osteogenic differentiation varied with perfusion, with Static significantly lower than Dynamic I and II at Days 6 and 20. Cytotoxicity significantly under dynamic culture by day 6, whereas in static culture, no significant change was observed until day 13. Total dsDNA content trended higher in Dynamic II versus Static ($p = 0.059$) while no significant difference was found among groups. Representative live/dead confocal images (2x) showed cell viability throughout trabecular cores under (5.a) Static, (5.b) Dynamic I, and (5.c) Dynamic II confirming that bone cutting and coring did not compromise cell survival at the bone surfaces. All data were tested for normality using the Shapiro-Wilk test; within-group changes over time were analyzed using the Wilcoxon signed-rank test, and between-group comparisons were analyzed using Kruskal-Wallis tests.*$p < 0.05$, **$p < 0.01$, ***$p < 0.001$.

References (Optional)

[1] Endres et al.. J Musculoskelet Neuronal Interact. (2009)

[2] Meyer et al. ASME. *J Biomech Eng*. (2026)

[3] Kunath et al. J Mech Behav Biomed Mater (2024).

[4] Gabetti et al., *Sci Rep*(2022).

Session Category

P2-368

EFFECT OF Porosity Gradients on the Mechanical Performance of SLA 3D-Printed TPMS Scaffolds

Ms Catalina Araya Student[1], Mr Benjamín Rodríguez Student[2], PhD Luis Pérez Assistant Professor[3], Mr José Contreras PhD (c)[2], PhD Ameet Aiyangar Senior Researcher[4], Mr Bernhard Weisse Deputy Head of Laboratory[4], PhD Juan Vivanco Associate Professor[2]

[1]Federico Santa María Technical University, Valparaíso, Valparaíso, Chile. [2]Adolfo Ibañez University, Viña del Mar, Valparaíso, Chile. [3]Adolfo Ibañez University, Valparaíso, Valparaíso, Chile. [4]Swiss Federal Laboratories for Materials Science and Technology, Zurich, Zurich, Switzerland

Introduction

Triply periodic minimal surfaces (TPMS) have gained significant interest in the biomedical field due to their potential in bone tissue engineering. Prior studies have shown the promise of TPMS structures, demonstrating strong mechanical performance and biocompatibility [1,2]. Three-dimensional porous scaffolds with graded porosity can better mimic the natural bone architecture [3]. However, the influence of radial porosity gradients on SLA 3D-printed TPMS structures remains insufficiently explored. This study evaluates the mechanical performance of Diamond and Gyroid TPMS designs with functional porosity gradients, focusing on their elastic modulus, yield strength, and toughness.

Methods

Diamond and Gyroid TPMS structures with four radial porosity gradients (ranging from 40% to 60%), including increasing and decreasing configurations, and a uniform-porosity control group, were fabricated using stereolithography (SLA) printing with Creality's high-precision 8K UV resin. Outer dimensions and porosity were measured experimentally. Compression testing was performed in accordance with ASTM D695-15, reporting elastic modulus, yield strength, and toughness. Micro-computed tomography (MicroCT) imaging was used to validate internal architecture and assess geometric accuracy through surface distance analysis.

Results

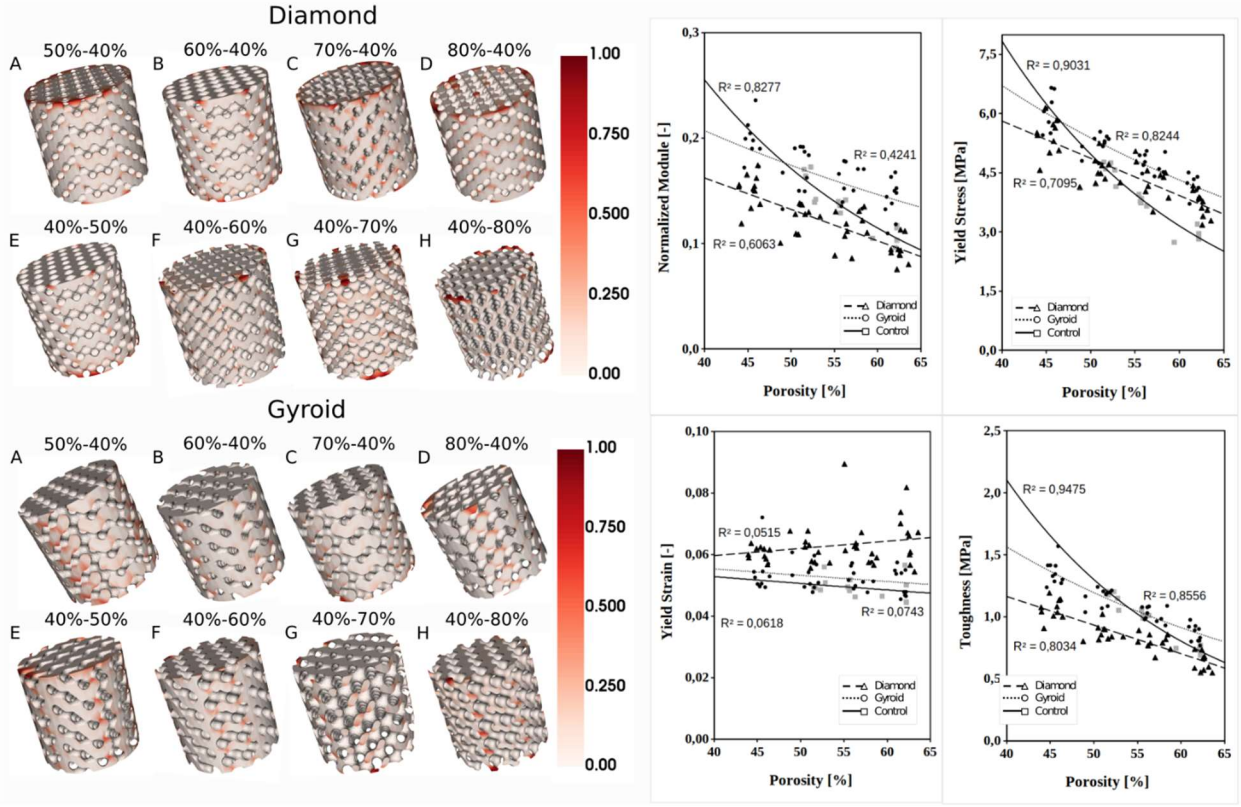
Fabricated samples showed high printing fidelity, with porosity within 5% of theoretical values. Micro-CT analysis and surface distance measurements confirmed high geometric accuracy (95%HD: 0.17 ± 0.04 mm). Diamond scaffolds exhibited lower error (0.15 ± 0.02

mm) than Gyroid scaffolds (0.20 ± 0.04 mm). Radial gradients remained below 0.25 mm, indicating minimal impact on geometric accuracy. Gyroid structures demonstrated higher mechanical properties than Diamond. Radial porosity gradients had little influence on TPMS scaffold mechanical performance, producing limited changes in the elastic modulus.

Discussion

Distinct responses between structures show that geometry primarily drives mechanical behavior. Micro-CT confirms that differences arise from intrinsic design features rather than printing errors, validating the reliability of SLA-printed TPMS scaffolds. The minimal impact of radial porosity gradients suggests that stronger or multi-axis gradients may be needed to generate measurable effects. Overall, the results support TPMS scaffolds for bone engineering and encourage exploring gradients along additional axes.

Images (Optional)



References (Optional)

[1] Castro et al, CMBBE, 2019.

[2]Liu et al, Materials, 2020.

[3] Montazerian et al, Acta Biomaterialia, 2019.

Acknowledgements (Optional)

Research funding for this project was provided by FONDECYT (Award No. 1231708).

Session Category

Tissue Engineering: Methods, Models and Applications

P2-369

Investigation of the Protective Effect by Pressurized Dissolution of Argon Gas Under Cold Storage of Monolayer Cells

Mr Kenshi Mimura[1], PhD Kazuhiro Yoshida[2,1], PhD Rina Sakai[3,1], PhD Masanobu Ujihira[3,1]

[1]Kitasato University Graduate school of Medical Science, Sagamihara, Kanagawa, Japan. [2]Kitasato University Shcool of Allied Health Sciences, Sagamihara, Sagamihara, Japan. [3]Kitasato University Shcool of Allied Health Sciences, Sagamihara, Kanagawa, Japan

Introduction

Currently, all organs, as well as many tissues and some cells are typically maintained under cold storage at 0 to 4°C due to occurrence of cellular damage below 5°C. The purpose of this study was to investigate cellular protective effect by pressurized dissolution of argon gas under cold storage in rat cardiomyocytes monolayer.

Methods

The cell monolayers in a culture dish incubated for 24 h were prepared as test samples and control. Dulbecco's Modified Eagle Medium which has poor effect on cold protection, was used as the cold storage solution. First, the samples were pressurized in 0 to 1.0 MPa in argon gas, then preserved at 2 to 6°C for 24 h. Secondly, the samples were similarly, they were pressurized in 0 and 0.8 MPa in argon gas, then preserved at 6°C for 0 to 72 h.

Results

The first results showed that there was low, regardless of applied pressure at 2°C. It increased with increasing the pressure at 4 to 6°C, but plateau or decreased at pressure of higher than 0.8 MPa. Furthermore, the highest value was observed under 6°C and 0.8 MPa. The second results showed that there decreased significantly within 24 h when no pressure was applied. Although the value remained high for up to 24 h, decreased thereafter at 0.8 MPa. Pressurized storage at any time points between 24 and 72 h showed significantly higher than the case of 0 MPa.

Discussion

The relative cell viability at 4 to 6°C showed a plateau at pressures higher than 0.8 MPa, suggested that 0.8 MPa is the optimal pressure for maximum cell protection. In our previous studies using xenon gas, it was considered that argon gas has optimal dissolution

amount like xenon gas. The relative cell viability at 6 °C was higher than that observed at other temperatures, 6°C is considered to be the optimal storage temperature in this study.

Session Category

Tissue Engineering: Methods, Models and Applications

P2-370

Novel Nested Transwell for Developing Lung Immuno-Organoids

Ms Lara Herlah, Dr. Luc Mongeau

McGill University, Montreal, Quebec, Canada

Introduction

Organoids often lack immune cells; a key component when studying disease. Monocytes and macrophages are the most common immune cells found in the lung and play a significant role in homeostasis and pathological conditions. Including these cells is essential to accurately mimic respiratory infections. This study employs an heterogenous lung organoid that shows markers of the proximal and distal lung. We aimed to establish a lung organoid and monocyte co-culture to investigate the role of monocyte migration and activation in infected organoids. The infiltration of monocytes was performed using a nested transwell, which was designed and validated. The organoid sits in one transwell and THP-1 monocytes are added to a second transwell. Upon infection, the organoid releases chemokines, attracting monocytes toward the organoid. Monocytes extravasate through the transwell membrane making the model more representative than direct co-cultures.

Methods

A 3D-printed nested transwell system was designed and validated through cell compatibility and extravasation assays. An indirect co-culture of monocytes and the lung organoid was established and optimized. The organoid and THP-1 co-culture was infected with H1N1 to compare the response of organoids to H1N1 with and without monocytes. Monocyte extravasation and differentiation into macrophages were assessed using qPCR, flow cytometry and fluorescence imaging.

Results

3D-printed transwells were found to be biocompatible (1% dead cells in Live/Dead assay), functional (75% of monocytes extravasated within 3 hours when exposed to CCL-2) and allowed for a physical separation between organoids and monocytes. Studies related to immuno-organoid infection are still in progress.

Discussion

This approach establishes a framework for immune-integrated lung organoids that better recapitulate the lung. The nested transwell can be useful in a variety of other organoid or cell studies, e.g when studying inter-organ communication or immune-organoid crosstalk. Additionally, by adding macrophages, the organoid may be used for tuberculosis

infections as tuberculosis primarily infects macrophages; a future study will include TB infections. While there is a diverse set of immune cells active in the lung, monocytes were the only immune cells added to the organoid; future studies should look at incorporating other immune cells, like T- and B-cells to further improve the lung model.

Acknowledgements (Optional)

NIH NIDOCD R01 DC 018577 (PI: Luc Mongeau)

Session Category

Tissue Engineering: Methods, Models and Applications

P2-371

Biocompatibility Assessment of 3D Printed Hydroxyapatite/Polycaprolactone Composites for Intra-oral Bone Regeneration

Ph.D. Candidate Margaryta Ivanets[1], Postdoctoral Researcher Sandy Anania[1], Senior Scientist Christine Kermel[2], Program Manager Stéphane Hocquet[2], Postdoctoral Researcher Bernard Staumont[1], Associate Professor Dorien Van hede[1], Professor France Lambert[1], Full Professor Liesbet Geris[1]

[1]University of Liège, Liège, Liège, Belgium. [2]Belgian Ceramic Research Centre, Mons, Hainaut, Belgium

Introduction

The loss of one or more teeth is frequently associated with alveolar bone resorption, which can compromise the placement of dental implants. To address this issue, a procedure known as guided bone regeneration (GBR) was developed several decades ago. This technique promotes bone regeneration through the combined use of a barrier membrane and a bone graft material, supporting bone cell attachment and bone neoformation (osteoconduction). While deproteinized hydroxyapatite (HA) xenogeneic particles are clinically used as bone grafts for GBR, they lack structural integrity and show limited performance to repair large and complex defects. Therefore, in line with regenerative and personalized medicine, research increasingly focuses on synthetic biomaterials for bone regeneration with self-supporting, patient-specific, and three-dimensional shapes. Building on this progress, our objective is to develop bioactive 3D-printed synthetic composite biomaterials with enhanced efficacy for intra-oral bone regeneration.

Methods

In this study, pellet additive manufacturing (PAM) 3D printing was used to print composite HA/polycaprolactone (PCL) disks. Contact angle measurement and scanning electron microscopy (SEM) were performed to evaluate surface wettability and microstructural features of the disks. Human mesenchymal stem cells and L929 fibroblasts were seeded onto disks composed of pure PCL, HA (20% v.v)/PCL, HA (41% v.v)/PCL, pure HA, and cultured up to 21 days. Cell-seeded disks were subsequently assessed for viability (Live/Dead staining, LDH assay), proliferation (DNA quantification), and morphology (SEM).

Results

Correlations were identified between HA content and contact angle measurements. SEM imaging showed that cells displayed a spread morphology in all compositions, including pure PCL (Figure). All groups demonstrated viability levels exceeding 80%, and DNA quantification indicated an increase in DNA content over time for each composition.

Discussion

To evaluate the suitability of the PAM printing method and HA/PCL compositions, in vitro studies were performed on 2D disks. The initial results confirmed the biocompatibility of the PAM-printed HA/PCL composites. The next step will be to assess whether the different formulations can induce osteogenic differentiation. Compositions demonstrating the most favorable outcomes in terms of viability, proliferation, and differentiation will subsequently be implemented in 3D gyroid scaffolds to investigate extracellular matrix deposition and early bone tissue formation.

Images (Optional)

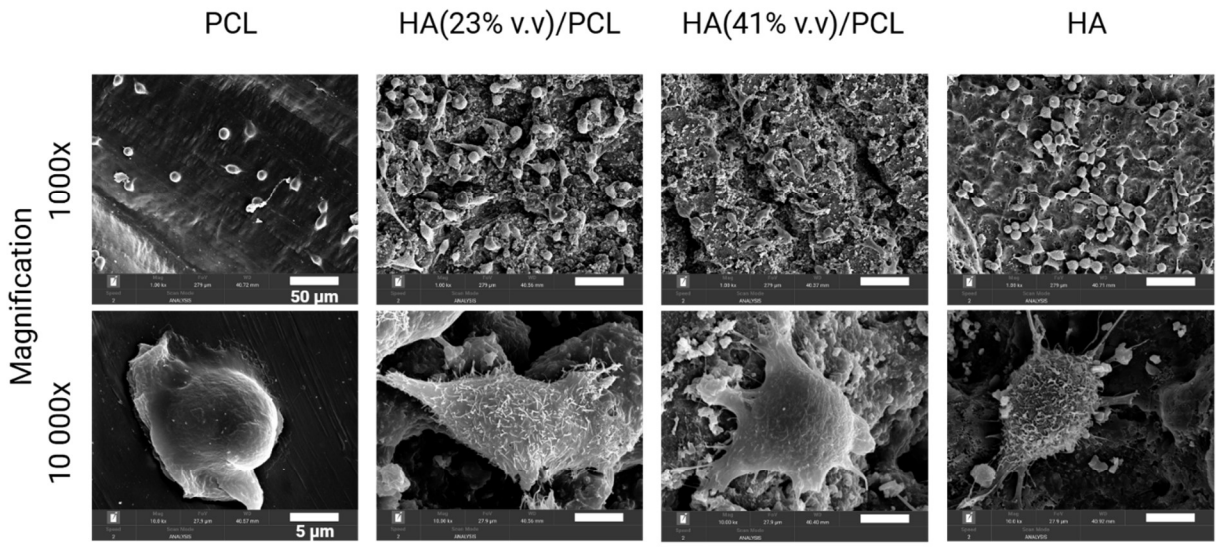


Figure Scanning electron microscopy images of L929 fibroblasts seeded on disks with different compositions after 1 day of culture. Upper row: scale bar = 50 µm. Lower row: scale bar = 5 µm.

Acknowledgements (Optional)

We would like to express our sincere gratitude to Professor Christine Jérôme's laboratory at the Center for Studies and Research on Macromolecules (CERM) at the University of Liège

for providing the equipment necessary for measuring the contact angle. We also gratefully acknowledge the GreenMAT laboratory of the University of Liège for providing access to their SEM facilities.

Session Category

Tissue Engineering: Methods, Models and Applications

P2-372

Engineering Reproducible Vessel-Like Constructs: Optimizing FRESH Bioprinting and Mechanical Characterization of Alginate–Gelatin Hydrogels

Prof Michele Conti[1], Dr. Franca Scocozza[2], Dr. Delgrosso Elena[2]

[1]University of Pavia, Pavia, Italy, Italy. [2]University of Pavia, Pavia, IT, Italy

Introduction

The fabrication of mechanically stable, anatomically relevant vascular constructs remains challenging due to the complex geometry and anisotropic properties of blood vessels, which soft hydrogels struggle to replicate. The FRESH technique improves structural fidelity by supporting low-viscosity inks during deposition, yet standardized quantitative workflows are limited. Using alginate–gelatin blends as reproducible model inks, we established an engineering-focused pipeline combining optimized printing and mechanical testing to assess robustness and batch-to-batch consistency.

Methods

A sodium alginate–gelatin hydrogel was prepared as a reproducible model ink and printed using an optimized FRESH workflow, including a gelatin microparticle support bath and controlled extrusion through 0.4–0.6 mm nozzles. Post-printing stabilization combined thermal bath melting and Ca^{2+}-mediated reinforcement. Mechanical performance was quantified through confined compression and ring tensile tests across multiple batches, enabling evaluation of stiffness, failure behavior, and variability in printing, coating, and crosslinking.

Results

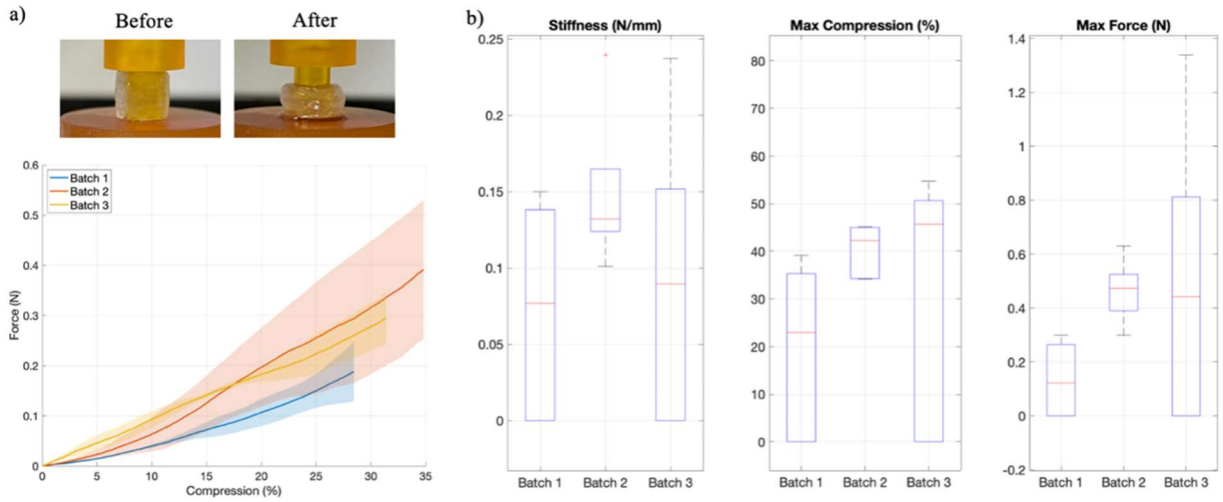
Optimizing the FRESH workflow yielded reproducible SA–GEL tubular constructs. For 6% SA, a 0.41 mm nozzle required ~50 kPa for stable extrusion, while 30 kPa caused collapse; 3% SA was unsuitable. Confined compression showed stiffness of 0.07–0.15 N/mm, maximum force 0.13–0.48 N, and compression 19–40% across four batches. Ring tensile tests gave 0.06–0.13 N/mm stiffness, failure strains of 60–130%, and forces of 0.4–1.2 N, confirming consistent axial and circumferential behavior.

Discussion

FRESH bioprinting overcomes filament spreading typical of soft hydrogels, enabling accurate lumenized geometries and supporting micro-CT–based evaluation. Integrating optimized printing with mechanical testing provided a quantitative, reproducible workflow. Constructs showed controlled axial and circumferential behavior (compression stiffness

0.07–0.15 N/mm; tensile stiffness 0.06–0.13 N/mm). Low inter-batch variability confirmed process robustness. Overall, this integrated strategy offers a reliable platform to guide parameter optimization and support future developments with advanced biomaterials and cellularized vascular models.

Images (Optional)



Fugure. Mechanical response of hydrogel ring specimens under uniaxial compression. (a) Mean force–elongation curves with standard deviation for three batches. (b) Boxplots showing stiffness, maximum elongation, and maximum force, highlighting low inter-batch and moderate intra-batch variability.

References (Optional)

Session Category

Tissue Engineering: Methods, Models and Applications

P2-373

Impedance as a Novel Diagnostic Measure of Vascular Health and Disease

Mr Ali Farshad, Mr Md. Ashadujjaman, Prof. Abhay Ramachnadra Ph. D., Prof. Pranav Shrotriya Ph. D.

Iowa State University, Ames, Iowa, United States

Introduction

Vascular microstructure is important for its function and is known to change in disease (e.g. aortic aneurysm or aging) or during preservation. The influence of microstructure on intramural transport is not well understood. We use electrochemical impedance spectroscopy (EIS) as a non-destructive method to quantify transport within the wall, with electrical impedance serving as a surrogate measure of transport. The impedance characteristics of porcine vascular tissues are presented under three different conditions: 1) enhanced collagen cross-linking (using glutaraldehyde, representative of aging), 2) elastin damage (using elastase, representative of aortopathy), and 3) freezing. To demonstrate the versatility of the approach, results are presented for two vascular tissues of different sizes (aorta and innominate artery).

Methods

Fresh porcine aorta (AO) and innominate artery (IN) tissues were harvested from humanely euthanized animals used for meat; euthanization used approved methods. Tissues were examined under fresh conditions and then subjected to the three treatments (n = 5 treatments per tissue type). EIS measurements were performed in Hank's balanced salt solution using a four-electrode setup with Pt counter/working and Ag/AgCl reference/sense electrodes. Each sample was repeatably scanned three times to confirm the stability and reproducibility of the signals. Resistance was evaluated across four frequency ranges, and the distribution of relaxation times (DRT) analysis was used to interpret frequency-dependent features of the impedance.

Results

Multiple treatments showed changes in impedances across the frequency range. At 10,000 Hz, the average resistance of AO samples decreased by 33%±6.3% after glutaraldehyde treatment, 29%±16.5% after elastase treatment, and 13%±5.4% after freezing. These changes were statistically significant ($p<0.05$). Consistent reductions in impedance following treatments aligned with increased ionic accessibility caused by softening or

structural disruption. The distinct baseline differences between AO and IN tissues were maintained, and the DRT analysis revealed definitive treatment-dependent characteristics, suggesting that each treatment induced distinct alterations in the tissue matrix.

Discussion

The results demonstrate that EIS is sensitive to changes in structure and mechanics induced by various treatments. The stable and repeatable electrical signatures across treatments suggest that EIS could serve as a promising diagnostic measure of vascular health or disease.

Session Category

Tissue Engineering: Methods, Models and Applications

P2-374

Construction of Vascularized Three-Dimensional Hepatocyte Tissues Using Microfluidic Devices

Mr. Yen-Hsiang Huang, Dr. Tadahiro Yamashita, Prof. Ryo Sudo

Keio University, Yokohama, Kanagawa, Japan

Introduction

Advances in tissue engineering have enabled the construction of various tissues; however, generating complex three-dimensional (3D) tissues containing microvascular networks remains a major challenge. This study focuses on liver tissue engineering because the liver is one of the most important organs, owing to its vital functions such as detoxification. In the native liver, hepatocytes form parenchymal structures known as hepatic cords, while endothelial cells (ECs) form liver-specific microvessels, or sinusoids, between these cords. This highly organized architecture enables intimate interaction between hepatocytes and microvessels, which is indispensable for maintaining hepatic metabolic function. Therefore, constructing 3D hepatocyte tissues that incorporate microvascular networks—so-called vascularized hepatocyte tissues—is crucial for recapitulating native hepatic physiology in vitro.

Methods

We investigated two approaches for constructing vascularized hepatocyte tissues using microfluidic devices made of polydimethylsiloxane. In the first approach, hepatocyte spheroids containing fibroblasts, which serve as a source of pro-angiogenic factors, were formed and embedded within a hydrogel region of the microfluidic device. These spheroids were cocultured with ECs seeded in adjacent microchannels [1]. In the second approach, a cryogel scaffold containing fibroblasts was incorporated into a microfluidic device to generate a local paracrine-factor gradient [2]. Under these conditions, ECs successfully formed microvascular networks. Hepatocytes were subsequently introduced into the microchannels to construct 3D hepatocyte tissues interfacing with the microvascular networks.

Results

In the first approach, hepatocyte spheroids containing fibroblasts induced angiogenesis. ECs formed microvascular networks that extended toward and penetrated the spheroids. The resulting vascularized hepatic spheroids closely resembled hepatic sinusoids, with hepatocytes in intimate contact with the microvessels. These vascularized

spheroids exhibited significantly enhanced hepatic functions, including increased albumin secretion and urea synthesis.

In the second approach, microvascular networks formed under a local paracrine-factor gradient successfully integrated with 3D hepatocyte tissues. Functional perfusion through microvessels penetrating the 3D hepatocyte constructs was confirmed. Furthermore, hepatocyte proliferation was observed under this perfusion culture condition.

Discussion

These approaches demonstrate effective strategies for constructing perfusable 3D hepatocyte tissues and lay the groundwork for the future development of transplantable liver tissue in vitro.

References (Optional)

[1] Yen-Hsiang Huang *et al.* , Biofabrication, 2025

[2] Yen-Hsiang Huang *et al.* , BioRxiv, 2025

Session Category

Tissue Engineering: Methods, Models and Applications

P2-375

Cellular Particles as Modular Building Blocks for Vascular Network Formation

Dr. Seiji Omata Assistant Professor, Mr. Akihiro Ueda, Mr. Kaito Tanaka, Dr. Yasuyuki Morita Professor

Kumamoto University, Kumamot, Kumamoto, Japan

Introduction

A major challenge in the development of regenerative tissues is the rational design of vascular networks within engineered constructs. In most current approaches, vascular cells are merely mixed into the tissue, resulting in random microvascular structures that reproduce only capillary-level networks. Conversely, when microfabrication techniques are used to recreate vascular architectures, it becomes difficult to adapt these predefined structures to injuries of varying shapes and scales. For these reasons, a method capable of simultaneously designing both capillaries and larger vessels is urgently needed. The present study aims to propose a highly transplantable design strategy based on a new concept termed "cellular particles".

Methods

In this approach, biodegradable particles are dispersed throughout a target regenerative tissue and gradually dissolve over time, thereby creating voids. We hypothesized that these voids would serve as initiation sites for angiogenic sprouting by vascular cells, ultimately leading to the formation of an integrated vascular network. To realize this concept, we fabricated “cellular particles” by attaching vascular-related cells to biodegradable polymer particles. The biodegradable particles, composed of polylactic-acid–based polymers, were generated with controlled diameters by dripping into microfluidic channels. Furthermore, to enhance cell adhesion while accelerating particle dissolution, the particles were engineered to be porous. Endothelial cells were used as the model vascular cell type and were successfully adhered to the particle carriers. These cellular particles were then embedded and cultured within collagen gels.

Results

To evaluate the behavior of endothelial-cell-laden particles within the collagen matrix, confocal laser microscopy was performed using CD31, an endothelial surface marker. The imaging confirmed the presence of numerous endothelial cells on the surface of the cellular particles, demonstrating successful seeding and retention within the gel. However,

after seven days of culture, no observable cellular infiltration into the surrounding matrix or formation of nascent vascular structures was detected.

Discussion

This study successfully established the foundational techniques required for fabricating and culturing cellular particles. We confirmed that the particles can be embedded directly into collagen gels and maintained for a seven-day culture period. To induce robust neovascularization, future work must incorporate macrophage-mediated extracellular-matrix remodeling to facilitate endothelial cell invasion and subsequent capillary formation.

Acknowledgements (Optional)

This work was supported by JSPS KAKENHI Grant Number 25K15871.

Session Category

Tissue Engineering: Methods, Models and Applications

P2-376

Multilevel Characterization of Osteocyte Lacunar Microarchitecture in Healthy, Osteoporotic, and Post–COVID-19 Human Trabecular Bone

Dr. Seyedeh Fahimeh Hosseini[1], Dr. Isabella Poles[1], Dr. Eleonora D'Arnese[2], Prof. Laura Vergani[1], Dr. Federica Buccino[1]

[1]Politecnico di Milano University, Milan, Lombardy, Italy. [2]University of Edinburgh, Edinburgh, Scotland, United Kingdom

Introduction

Osteocyte lacunae form the mechanosensory network of bone, regulating bone remodeling. Despite their central role, human evidence on pathology-driven lacunar alterations remains limited. This study investigates how pathological conditions reshape lacunar microarchitecture using synchrotron micro-CT, AI-based segmentation, and multilevel statistical modeling.

Methods

This cross-sectional study analyzed trabecular bone from ex vivo human femoral heads (FH) of healthy, osteoporotic, and COVID-19 patients undergoing total hip arthroplasty. Human FHs were collected at Galeazzi-Sant'Ambrogio Hospital (Milan, Italy) during 2021-2025. High-resolution synchrotron phase-contrast micro-CT images were preprocessed for 3D evaluation and segmented using a validated CNN based on the Keras VGG16 architecture [1]. This automated framework enabled the large-scale extraction of lacunar shape-orientation descriptors, including volume, surface area, sphericity, principal axes and their orientations, stretch, and oblateness. Given the hierarchical structure of the dataset, linear mixed-effects models (LMMs) were applied at the lacuna level, with age as a covariate and patient as a random effect. At the patient level, aggregated features were subsequently analyzed using covariate-adjusted MANOVA.

Results

In this study, bone samples from 48 female-only patients, divided into Healthy, Osteoporosis, and COVID-19 groups (n = 16 each, mean age = 72.0 ± 7.4, 77.8 ± 8.9, 68.1 ± 14.0 years, respectively), were analyzed. Bone volume fraction differed significantly across groups, with lower values in osteoporosis than in the healthy group ($p < 0.05$). LMMs of 8.96 million lacunae uncovered that lacunar volume, surface area, and semi-minor axis length were significantly larger in osteoporotic bone than in COVID-19 samples (all $p < 0.05$).

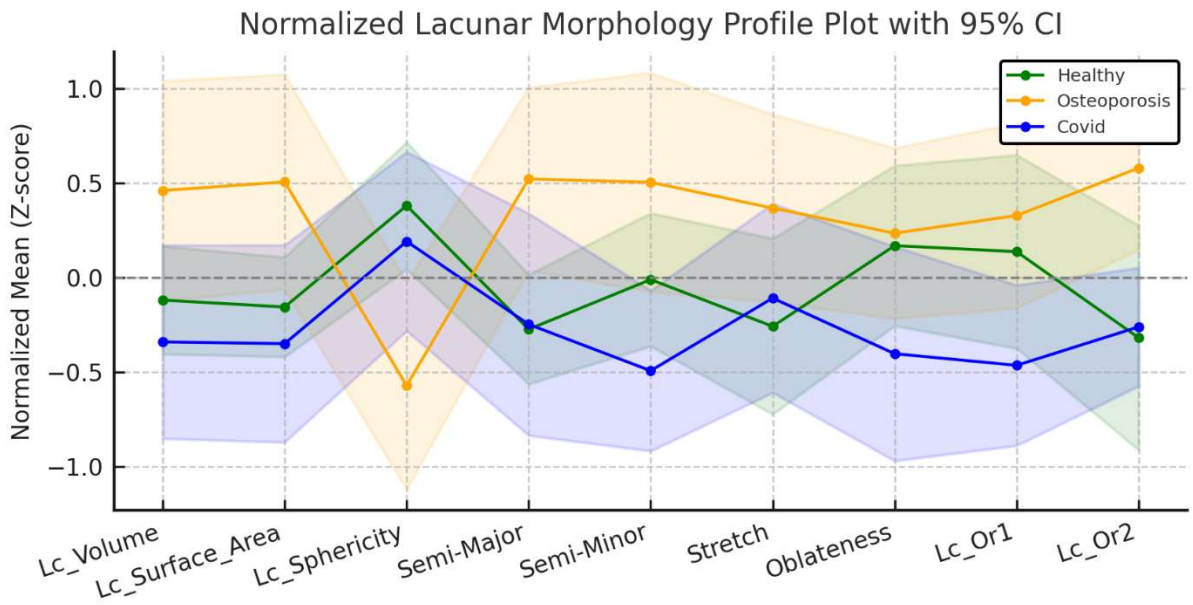
Minor-axis orientation (Lc_Or2) differed between osteoporosis and healthy ($p < 0.05$) and approached significance between osteoporosis and COVID-19 ($p < 0.1$), suggesting disease-specific alignment shifts.

At the patient level, MANOVA confirmed a significant overall group effect ($p < 0.05$), mainly driven by semi-minor axis length and near-significant sphericity, with the lowest sphericity in osteoporosis. The observed power (0.965) indicated high sensitivity to detect multivariate differences.

Discussion

This is a large-scale human study providing evidence that osteoporosis and COVID-19 leave quantifiable, disease-specific fingerprints on lacunar microarchitecture (figure). These morphological signatures probably reflect distinct remodeling microenvironments that will be investigated in further studies.

Images (Optional)



References (Optional)

"[1] Federica Buccino et al. , J Materials & Design, 2023"

Acknowledgements (Optional)

I gratefully acknowledge Barbara Canciani and Laura Mangiavini from the Tissue Engineering and Biomaterials Laboratory at IRCCS Ospedale Galeazzi-Sant'Ambrogio (Milan, Italy) for providing the femoral heads and for their essential support in the preparation of the bone samples. Their contribution was fundamental to the completion of this study.

Also, this project has received funding from the Marie Skłodowska-Curie Actions (MSCA) program under the European Union's Horizon 2020 research and innovation framework, within the GAP Project—Image-Guided Computational and Experimental Analysis of Fractured Patients (Grant Agreement No. 101120290). The MSCA GAP Project is coordinated as a doctoral network for advanced interdisciplinary training in biomechanical and biomedical research.

Session Category

Tissue Engineering: Methods, Models and Applications

P2-377

Characterizing ZIF-8 Degradation and Surface Topographies in Fibrous Scaffolds

Ms. Shu-Hsuan Chang, Dr. Pen-Hsiu Grace Chao

National Taiwan University, Taipei, Taiwan, Taiwan

Introduction

Nano- to micro-scale topographies enhance osteogenic differentiation [1]. By coating electrospun fibrous scaffolds with zeolite imidazolate framework-8 nanoparticle (ZIF-8 NP), we found the composite nanotopography promoted osteogenesis in mesenchymal stem cells (MSC) [2]. However ZIF-8 is unstable in cell culture medium such as DMEM [3]. It is unclear how the changing topography, as well as the released zinc ions, impact osteogenesis. In this study, we characterized ZIF-8 degradation in cell culture medium to delineate the chemical and topographical mechanisms.

Methods

Electrospun poly-L-lactide (PLA) fibrous scaffolds were fabricated as previously described [4]. To facilitate uniform coating, the scaffolds were wetted by brief ethanol (EtOH) treatment or sonication in ddH2O before in situ ZIF-8 synthesis [2]. Human bone marrow-derived MSCs were cultured in osteogenic medium on the scaffolds coated with collagen for 21 days and mineralization was assessed by Alizarin Red [5]. ZIF-8 degradation was monitored by measuring zinc ionic concentration with zincon [6].

Results

Pretreatment significantly impacted ZIF-8 NP size, where EtOH and sonication resulted in NP diameters of ~300 and ~90 nm, respectively (Fig A). The EtOH-treated scaffolds enhanced osteogenesis (Fig B). Release profile revealed that zinc concentration reached equilibrium within 20 hours of incubation (Fig C). Interestingly, scanning electron micrographs found persistent nanotopographies even after 5 days of incubation (Fig D).

Discussion

ZIF-8 NPs are widely studied for drug delivery applications for its biocompatibility and anti-bacterial properties. Zinc ions have also been shown to be osteogenic [7]. In this study, we found that zinc release from ZIF-8 NPs reaches equilibrium within one day. Since medium was refreshed every three days, cells might be exposed to zinc ions only at the initial stage of osteogenic induction. Current studies are ongoing to examine the effects of initial zinc

exposure, zinc ion dosage, and delineate the role of chemical and topographical cues on osteogenesis.

Images (Optional)

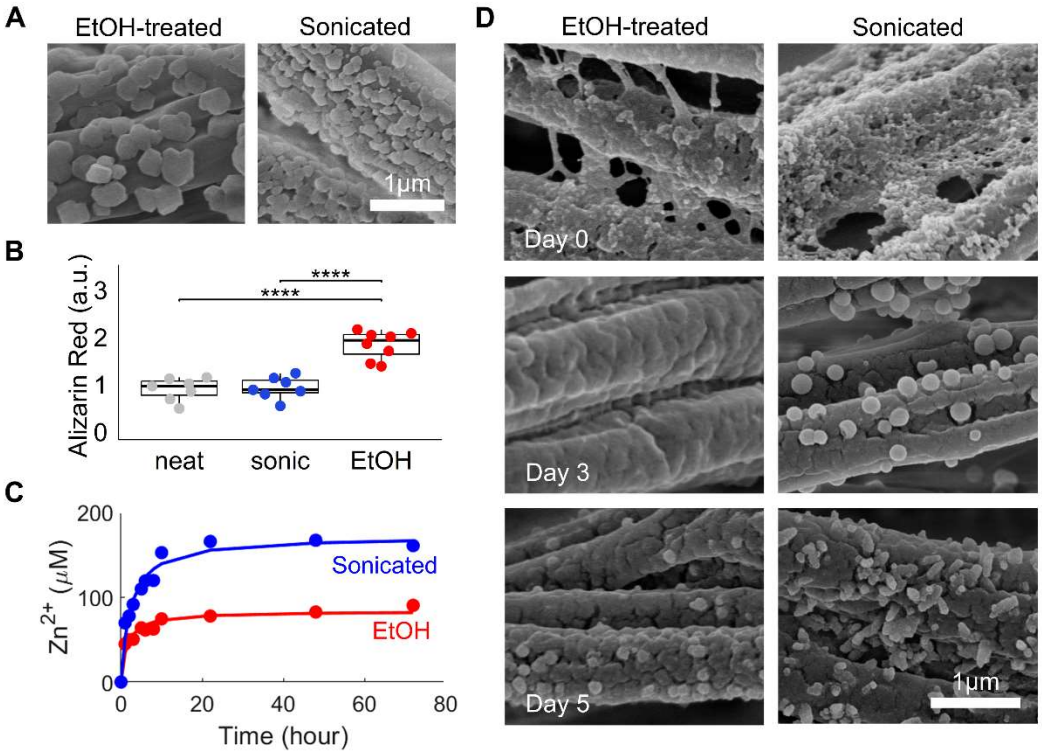


Figure 1. (A) ZIF-8 NP on PLA fibers. (B) ZIF-8 coating on EtOH-treated fibers enhanced MSC osteogenesis. (C) Zinc release in DMEM. (D) Collagen-coated scaffolds in DMEM.

References (Optional)

[1] Zhu L+, International Journal of Oral Science, 2020.

[2] Ting S+. in *ORS*. 2024.

[3] Spitsyna AS+ Molecules, 2022.

[4] Chao PG+, Biofabrication, 2014.

[5] Liao Y-H+, Biomaterials, 2014.

[6] Kocyla A+, J Inorg Biochem, 2017.

[7] Liu Y+, ACS Omega, 2024.

Acknowledgements (Optional)

This study was supported by the Taiwanese National Science and Technology Council (NSTC 114-2221-E-002-091-MY3, 114-2923-E-002-017-MY3, and 114-2122-M-001-002).

Session Category

Tissue Engineering: Methods, Models and Applications

P2-378

Biocompatibility of a Technical-Grade SLA Resin: Mechanical and Biological Evaluation of 3D print samples for Tissue Engineering

Mr. Vincenzo Marchese[1,2], Mr. Jose Ignacio Contreras[1], Dr. Carola Millan[1], Dr. Heidi Lynn Ploeg[2], Dr. Juan Francisco Vivanco[1]

[1]Universidad Adolfo Ibañez, Viña del Mar, Valparaiso, Chile. [2]Queens University, Kingston, Ontario, Canada

Introduction

Osteoporosis increases fracture risk and highlights the need for improved scaffolds in bone tissue engineering. Current designs face limitations in geometry and material selection [1]. SLA printing offers precision and low-cost fabrication [2], but most resins are cytotoxic [3]. This study evaluated a resin in terms of mechanical performance and biological compatibility.

Methods

Specimens were printed using FormLabs 4B and Fast Model V1. Mechanical properties were assessed through compression testing of 10×10×10mm cubes for anisotropy (n=5) and porous scaffolds of 45%, 55%, and 65% (n=5). Biological assays used well-shaped specimens (5 mm diameter, 1.6 mm height, n=4). Human gingival stem cells were cultured in DMEM with SBF at 37 °C and 5% CO_2. Biocompatibility was evaluated through cell adhesion (fluorescence imaging) and viability using MTS assays on Days 1, 3, and 7.

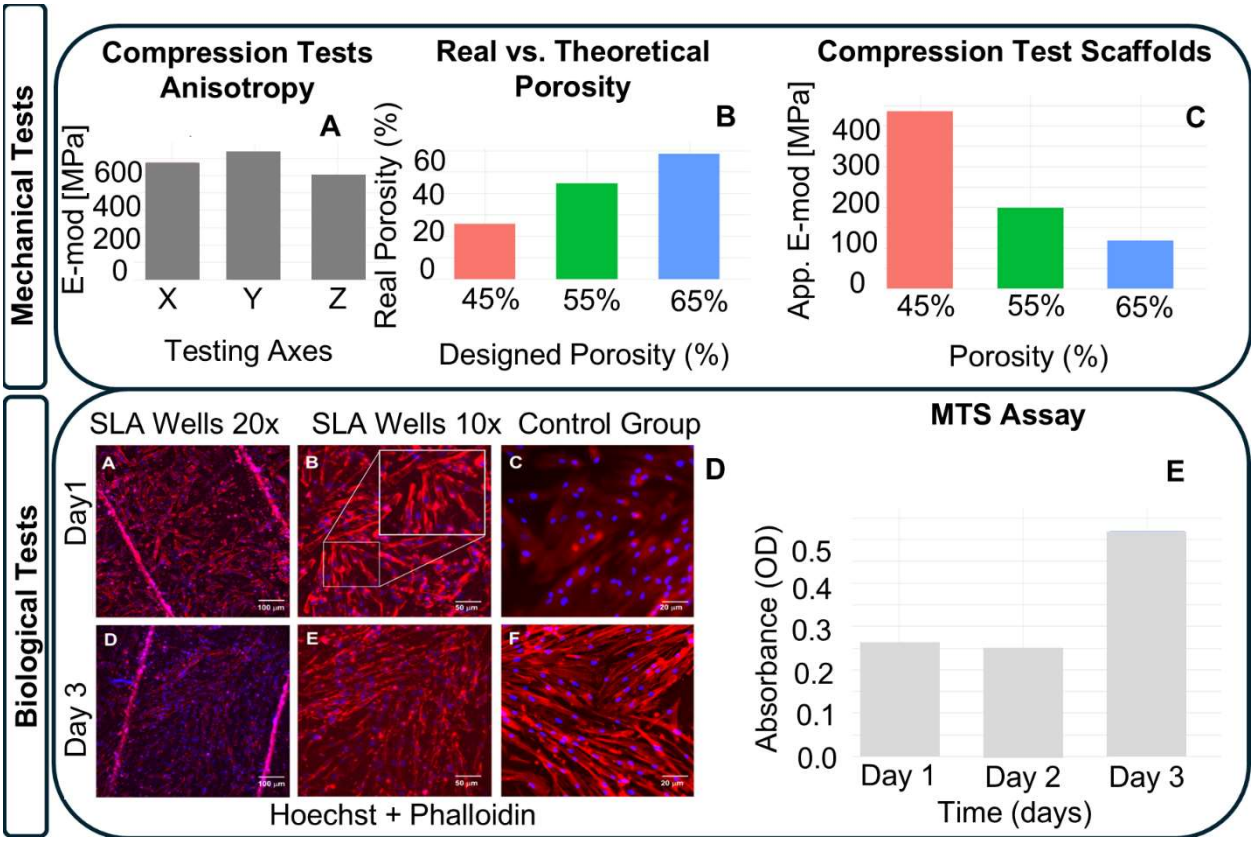
Results

Compression testing revealed transversely isotropic behavior, with elastic modulus of 676±30.0MPa, 719±18.9MPa, and 605±26.8MPa for X, Y, and Z axes, with statistical significance in Z ($p<0.00001$). Porosity was 26%, 45% and 58% for the 45%, 55% and 65% groups respectively and apparent elastic modulus decreased with increasing porosity: 435±14.0MPa (45%), 199±12.5MPa (55%), and 118±17.3MPa (65%). Fluorescence imaging confirmed adhesion and proliferation, with nuclei increasing from ~1200 at Day 1 to 1700–2000 at Day 3. MTS activity rose from 0.26±0.13 at Day 1 to 0.52±0.174 at Day 7, supporting short-term adhesion and biocompatibility.

Discussion

Mechanical results confirmed anisotropy and an inverse relation between porosity and elastic modulus. The higher modulus at 45% porosity is explained by trapped resin, highlighting limitations of post-processing methods. Biological assays showed that MSC adhered and proliferated, suggesting non cytotoxicity. These results position the resin as an accessible model for in *vitro* evaluation. Limitations include short culture duration, single cell type, and assays restricted to wells rather than scaffolds. Future work will extend culture time, dead-live cytotoxicity and scaffolds tests, considering studies on effects of trapped uncured resin.

Images (Optional)



References (Optional)

[1] Vallejos Baier R et al., Mater Sci Eng C, 2021

[2] Gabrieli R et al., Materials, 2024

[3] Liao AS et al., bioRxiv, 2024

Session Category

P2-379

Mechanical and biological evaluation of functionally graded TPMS porous structures fabricated via SLA 3D printing

Mr. Vincenzo Marchese[1,2], Dr. Carola Millan[1], Dr. Juan Francisco Vivanco[1], Dr. Heidi Lynn Ploeg[2]

[1]Universidad Adolfo Ibañez, Viña del Mar, Valparaiso, Chile. [2]Queens University, Kingston, Ontario, Canada

Introduction

Osteoporosis increases fracture risk and underscores the need for improved scaffolds in bone tissue engineering [1]. Current scaffold designs face limitations such as poor cell distribution, low growth efficiency, and inefficient cell loading [2]. Triply Periodic Minimal Surface (TPMS) structures show promise with interconnected geometry [3]. Gradients enhance scaffold performance with porosity distribution [2]. This study evaluated the impact of a structural gradient in TPMS scaffolds mechanical and biological response.

Methods

Uniform and graded Gyroid, Diamond, and Schwarz-P scaffolds were fabricated with Biomed White Resin FormLabs. For compression tests, 10×10×10mm cubes (n=5) were used to analyze anisotropy, and porous TPMS scaffolds with 50–60% porosity (n=5). For biological assays, Gyroid scaffolds were tested. Human gingival stem cells were cultured in DMEM with SBF at 37 °C and 5% CO_2. Proliferation was assessed via MTS assays (Days 1, 3), and adhesion by fluorescent microscopy with phalloidin.

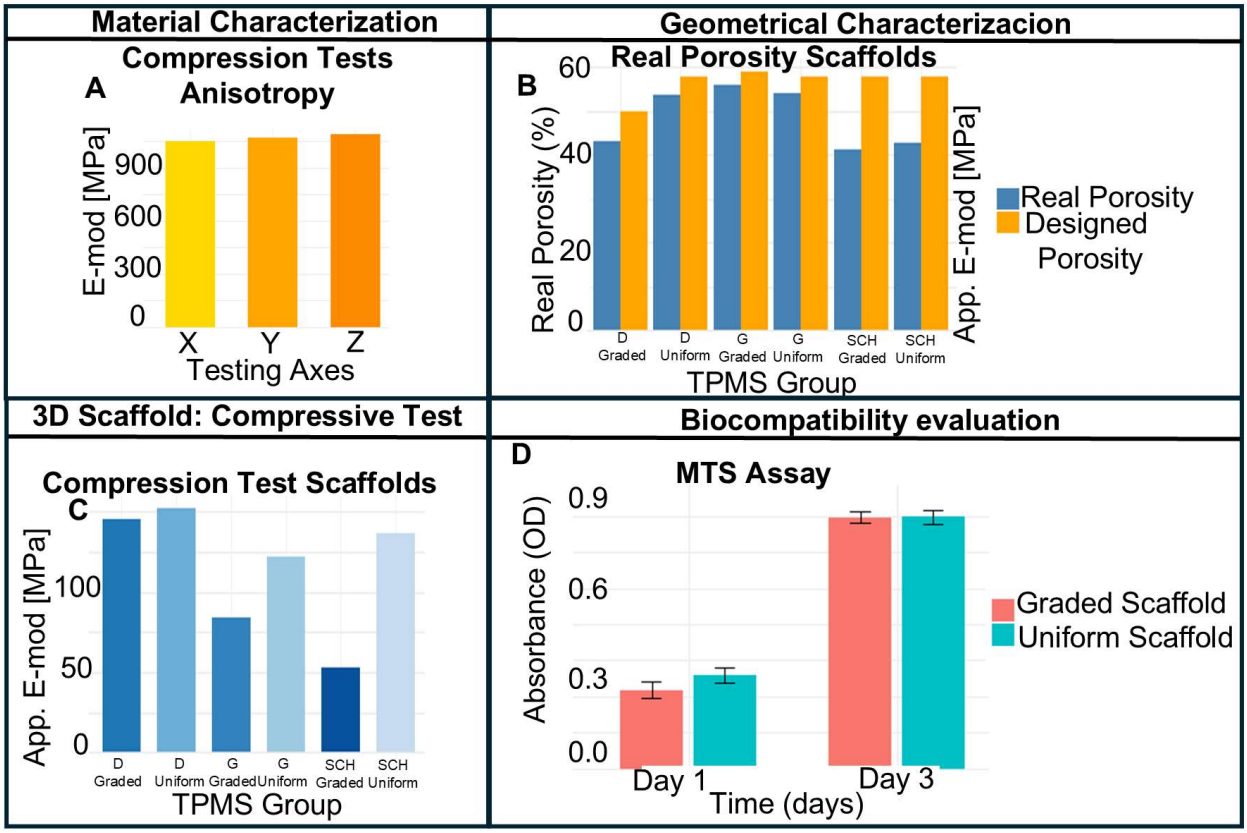
Results

Compression testing revealed isotropic mechanical behavior, with elastic modulus values of 1053±45.23, 1073±28.53, and 1089±40.61 MPa for the X, Y, and Z axes. Porosity was 54%/56% for Gyroid, 54%/43% for Diamond, and 43%/41% for Schwarz-P, uniform and graded respectively. Uniform scaffolds showed apparent elastic modulus of 122±22.4, 152±9.3, and 136±20.4 MPa for Gyroid, Diamond, and Schwarz-P, while gradients exhibited lower values: 84.5±7.18, 146±13.9, and 52.5±8.79 MPa. Biological assays improved initial cell distribution in gradients, but MTS assays showed no statistically significant differences, with OD rising from 0.39±0.029 and 0.32±0.032 on day 1 to 0.79±0.025 for both at day 3, indicating similar adhesion and early proliferation.

Discussion

Mechanical results show gradients reduce apparent elastic modulus. Schwarz-P proved most sensitive to structural changes, followed by Gyroid, while Diamond showed no variation compared to its uniform form, suggesting it is the best for modifications. Biologically, gradients may facilitate efficient initial cell loading, but quantitative assays showed no advantage in adhesion or proliferation during short-term. Future work will consider longer assays and cytotoxicity tests.

Images (Optional)



References (Optional)

[1] Vallejos R et al., MSCE, 2021

[2] Sobral JM et al., Acta Biomater, 2011

[3] Ma S et al., Acta Biomater, 2020

Session Category

Tissue Engineering: Methods, Models and Applications

P2-380

Regional Control for Monolithic Enthesis Engineering

MS Wen-Xuan Chen, Dr. Pen-hsiu Grace Chao

National Taiwan University, Taipei, Taiwan, Taiwan

Introduction

With distinctive zones of cell and matrix composition, the enthesis plays a crucial role in transferring mechanical loads from soft ligament/tendon to stiff bones while preventing stress concentration [1]. Restoration the structure and function of this interface is a major challenge. We previous optimized ligament tissue engineering with a growth factor supplementation regime using ligament fibroblasts (LF) [2]. In this study, we developed a monolithic construct composed of bone and ligament zones with mesenchymal stem cell (MSC) and LF. Using a physical barrier to confine cell seeding to defined scaffold regions, we created a co-culture system with spatially controlled bone and ligament development.

Methods

Human MSCs and porcine LFs were seeded on either sides of electrospun fibrous scaffolds with a temporary PDMS barrier to minimize mixing. In some studies, MSCs expressing Lifeact-mScarlet3 were used to track the initial seeding location and the subsequent cell migration. To optimize the chemical signals, osteogenic medium (OSM, supplemented with dexamethasone and β-glycerol phosphate) and ligamentogenic medium (LM, supplemented with bFGF and TGFβ), or mixed medium (MM) were investigated.

Results

The PDMS barrier successfully minimized cell mixing during seeding, as evidenced by the red MSCs only on one side of the scaffold (Figure A). After 2 weeks of culture, the MSCs were still restricted to one side, indicating successful regional control. This finding was supported by the restricted alizarin red positive region with osteogenic induction (Figure B). Looking into the effects of mixed chemical signal, we cultured MSCs and LF in MM and found significant, albeit slightly reduced, mineralization in the MSCs and no calcium deposition from the LF (Figure C).

Discussion

Spatial control of tissue organization has been a major challenge in organ engineering. While other fabrication approaches can generate complex structures, long term chemical signaling and specification remains an issue. We demonstrate regional control of undifferentiated and differentiated cell types allow long-term phenotypic specification

even in the mixed induction medium. Current studies are investigating ligament tissue development in the mixed medium and potential interactions between two cell types.

Images (Optional)

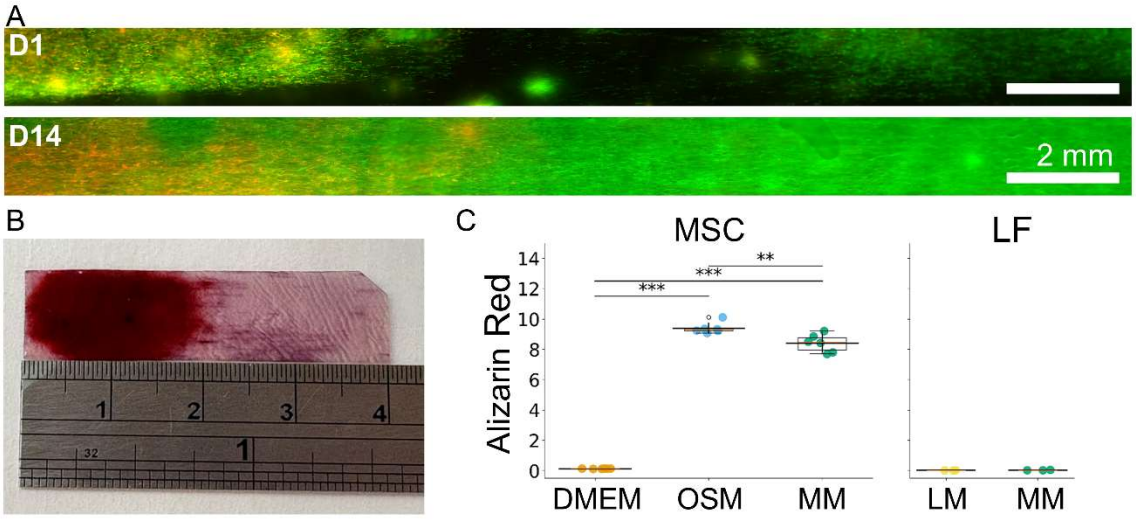


Figure (A) Regional control of cell distribution after cell seeding (D1) and after 2 weeks (D14). MSCs expressing mScarlet3 (red) were found only on the left side of the scaffold, while green indicate f-actin for all cells. **(B)** Alizarin red staining of MSC (left) and ligament fibroblast (right) coculture in OSM. **(C)** Effects of mixed osteogenic and ligamentogenic factors on MSC and LF calcium deposition.

References (Optional)

[1] Calejo I+, Tissue Engineering Part B: Reviews, 2019

[2] Chang C-W+, Tissue Engineering Part A, 2019

Acknowledgements (Optional)

This study was supported by the Taiwanese National Science and Technology Council (NSTC 114-2221-E-002-091-MY3, 114-2923-E-002-017-MY3, and 114-2122-M-001-002).

Session Category

Tissue Engineering: Methods, Models and Applications

P2-381

Small Molecule Therapies to Rescue Gap Junctional Intercellular Communication to Overcome Stiffness-Induced Chemoresistance

Ms Charlotte Turner, Dr Raja Vadivelu, Dr Eoin McEvoy

University of Galway, Galway, Galway, Ireland

Introduction

Breast cancer (BC) is the leading cause of cancer death in women globally. Matrix stiffening, reduced cell proliferation, and a loss of functional gap junction (GJ) expression are associated with BC progression. In this study, we investigate how these factors could influence sensitivity to chemotherapy in BC and identify potential pathways to mitigate such chemoresistance.

Methods

T47D cells were cultured in supplemented RPMI and passaged once reaching 80% confluency. Low passage (LP) and high passage (HP) cells fall between P1-10 and P11-20 respectively. For spheroid culture, cells were seeded into gelatin-mTG hydrogels. Samples received 24-hour treatment with all-trans retinoic acid (ATRA), dipyridamole (DIP), or resveratrol (RES) in DMSO prior to doxorubicin (DOX). The parachute assay tracked calcein diffusion between connected cells to characterise GJ functionality. For immunofluorescence (IF), samples were stained with Cx43, E-cadherin, or N-cadherin primary antibodies and counterstained with DAPI and Phalloidin-FITC.

Results

Spheroids exhibited stiffness-dependent growth, with those encapsulated in stiff hydrogels (sfH) significantly smaller and more compact than spheroids in soft hydrogels (stH) (**Figure1.A**). Interestingly, stH spheroids reduced in size following treatment with DOX, while no significant differences were observed for sfH-spheroids (**Figure1.B**).

Cx43 expression and function which was significantly higher in LP compared to HP T47D cells. For all passages, Cx43 localization was highly concentrated to the cytoplasm and nuclear envelope. Following treatment with ATRA, DIP, and RES, Cx43 was significantly increased in later passages. ATRA (20μM) and DIP (60μM) pushed Cx43 expression to the membrane, specifically at the cell-cell interfaces (**Figure1.C-E**).

DOX treated sfH-spheroids decreased in size when treated in combination with ATRA, DIP, or RES compared to without (**Figure1.F**), potentially overcoming stiffness-induced chemoresistance.

Discussion

T47D cells cultured under higher mechanical stress developed into smaller, more compact spheroids, regulated via mechanosensitive pathways. Increased cell density and lower proliferation interfere with chemotherapy diffusion and sensitivity. As T47D cells mature through passages, they appear to lose GJ expression which may compound chemoresistance, but GJ assembly was overcome through treatment with small molecule drugs, particularly ATRA and DIP. Overall, we identified that combinational therapy to enhance gap junctional intercellular communication promoted chemotherapy diffusion and sensitivity in BC spheroids.

Images (Optional)

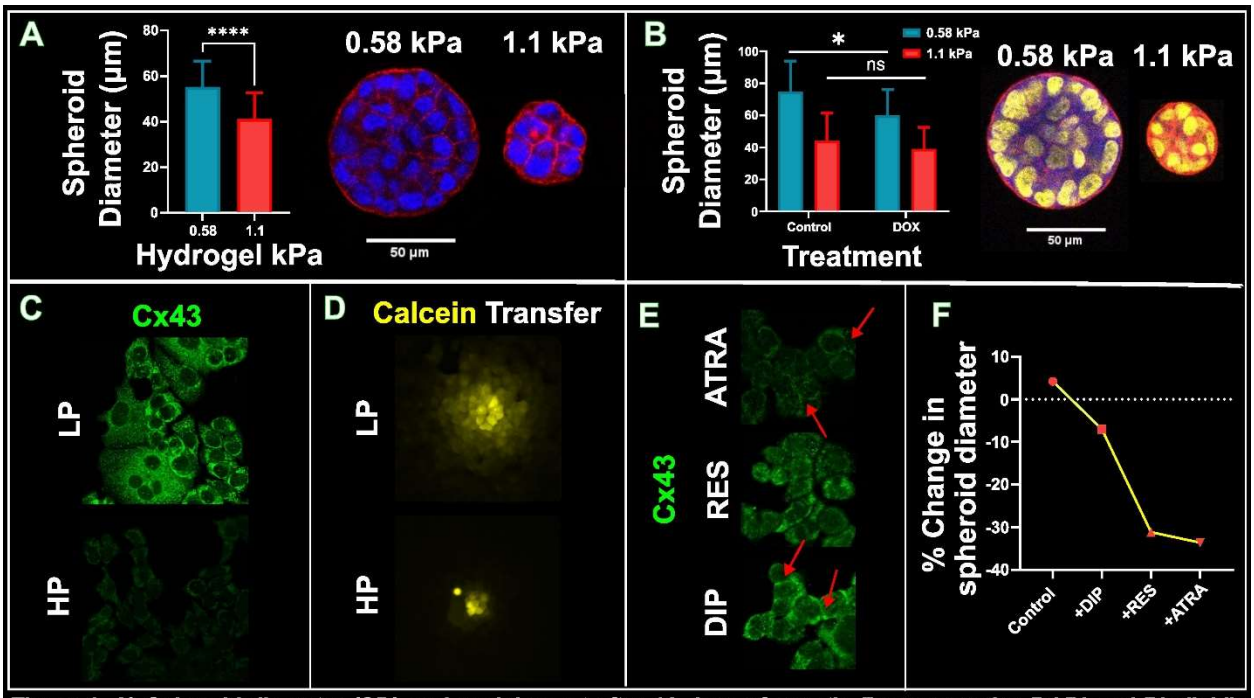


Figure 1. A) Spheroid diameter (SD) and nuclei count after 10 days of growth. Representative DAPI and Phalloidin images. B) Change in SD following 10µM DOX treatment. Representative DAPI, Phalloidin, and DOX (yellow) images.C) Cx43 IF. D) Parachute Assay. E) Cx43 IF of HP 24hr treatment with ATRA (20µM), RES (20µM), or DIP (60µM). F) % Change in SD following 10µM DOX treatment in combination with ATRA, RES, or DIP.

Acknowledgements (Optional)

This work was supported by the European Research Council (Grant number 101116234).

Session Category

P3-001

Use of Kinematic Variables for Missing Value Imputation of Athlete Rating of Perceived Exertion With Machine Learning Strategies

Dr Amarah Epp-Stobbe[1], Dr Ming-Chang Tsai[1], Dr Marc Klimstra[2,1]

[1]Canadian Sport Institute Pacific, Victoria, BC, Canada. [2]University of Victoria, Victoria, BC, Canada

Introduction

Managing athlete workloads, through rating of perceived exertion(RPE) or mechanical work calculated by GNSS, ensures safe, successful sport participation[1]. While GNSS is the ideal technology, its cost and limitations make RPE popular[1,2]. However, RPE utility relies on consistent reporting. Where missing, imputation strategies may mitigate RPE loss[1,3]. Daily-team-mean-substitution(DTMS), an easy-to-use strategy, is outperformed by methods like random forest(RF)[3-5]. Bayesian approaches are also promising, with unique advantages due to the inclusion of posterior distributions and prior beliefs[4]. However, Bayesian approaches including multivariate imputation by chained equations(MICE), have been limited in application on team sport workloads[2,4]. This investigation assesses RPE imputation using mechanical work, augmented by DTMS, RF, and MICE.

Methods

1002 datasets from 103 rugby sevens matches were analyzed. Athlete-worn GNSS collected playing-time, distance, and speed, with acceleration derived, from 22 female athletes. Mass, match-number, and opponent were collected pre-match; RPE post-match. Work was the cumulative sum of instantaneous absolute power multiplied by 0.1s-intervals. Data were imputed 100-times, predicting RPE using work, match-number, opponent, and player. RMSE, R^2, and accuracy were calculated. All model accuracies were tested across 5–30%missingness via ANOVA by model, missingness, and interaction, with a planned comparison evaluating differences. $RPE_{predicted}$ and RPE_{true} were compared using paired-sample equivalence tests.

Results

ANOVA found significant differences by model ($F(2,1782)=1457, p<0.05$), by missingness ($F(5,1782)=14205, p<0.05$), and interaction ($F(10,1782)=2323, p<0.05$). Planned comparison found all accuracies differed significantly($p<0.05$). Paired-samples equivalence tests found DTMS- and RF-$RPE_{predicted}$ equivalent to RPE_{true}($p<0.05$) but MICE-$RPE_{predicted}$ differed($p>0.05$).

Discussion

This investigation found MICE more accurate than RF and DTMS. RF demonstrated better R^2 and RMSE than MICE and DTMS[2-5]. Poor R^2 and accuracy affirm challenges in imputing RPE[2]. Equivalence testing suggested similarities between RPE_{true} and RF- and DTMS-RPEpredicted but not MICE-$RPE_{predicted}$, due to limited variability in predictors causing oversmoothing. The ANOVA and planned comparison indicated differences by model, inferring model selection remains an important consideration for practitioners.

Images (Optional)

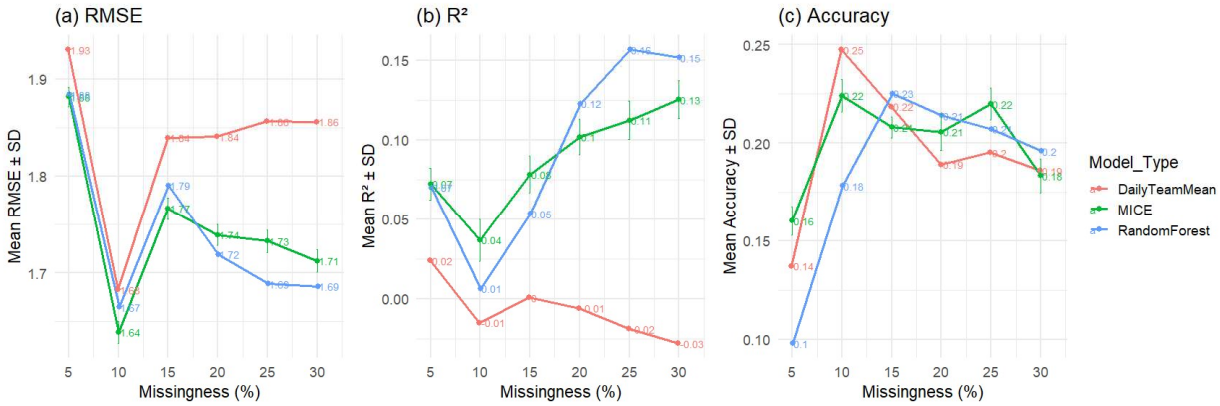


Figure 1: Model (a) RMSE, (b) R2, and (c) accuracy, by missingness from 5–30% data missingness.

References (Optional)

[1]Griffin et al.,J Sports Sci,2021.

[2]Epp-Stobbe et al.,Appl Sci,2025.

[3]El-Masri & Fox-Wasylyshyn,Can J Nurs Res,2005.

[4]Carey et al.,Int J Comput Sci Sport,2016.

[5]Epp-Stobbe et al.,Mach Learn Knowl Extr,2022.

Acknowledgements (Optional)

The authors thank Rugby Canada and Mitacs.

Session Category

Emerging Areas: N/A

P3-002

Multimodal Prediction of Treatment Success in Degenerative Spondylolisthesis: Integrating Deep Learning–Derived Imaging Features and Clinical Data

Dr Andrea Cina[1,2], Dr Fabio Galbusera[1]

[1]Schulthess Klinik, Zurich, Zurich, Switzerland. [2]ETH Zurich, Zurich, Zurich, Switzerland

Introduction

Accurately predicting postoperative improvement in patients undergoing surgery for degenerative spondylolisthesis remains challenging. In low back pain research, achieving a ≥2.2-point reduction in the Core Outcome Measures Index (COMI)—the minimal clinically important change (MCIC)—defines treatment success. Existing predictive models rely mainly on demographic and questionnaire data [1]. We hypothesised that quantitative imaging biomarkers automatically extracted from preoperative radiographs and MRI could enhance the prediction of MCIC achievement at 1 year.

Methods

We retrospectively analysed 333 surgically treated patients. Baseline variables included age, sex, BMI, comorbidities, preoperative COMI, and imaging features. Two previously developed deep learning models were used to extract radiological findings from MRI and spinopelvic alignment parameters from standing radiographs. The outcome was the achievement of MCIC at 1-year follow-up. Three variable sets were compared: (1) demographics + radiological features; (2) demographics + questionnaire data; (3) all variables combined. An LGBM classifier was trained using 10-fold cross-validation, and performance was evaluated on an independent 20% test set. Balanced accuracy and AUC were estimated using 100 bootstrap resamplings. SHAP values were used for model interpretation.

Results

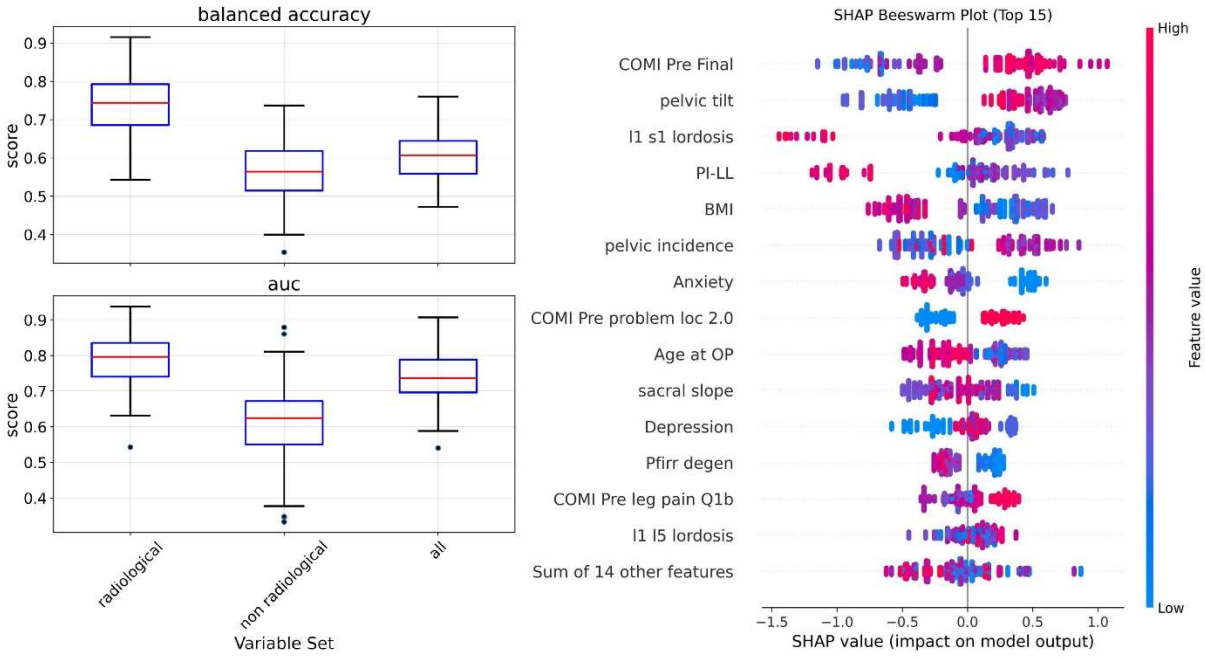
Models using radiological features achieved the highest performance, with a mean balanced accuracy of 0.738 ± 0.076 and an AUC of 0.787 ± 0.069. Questionnaire-based models performed substantially worse (balanced accuracy 0.564 ± 0.077, AUC 0.608 ± 0.110). Combining all variables improved performance relative to the questionnaire-only model but did not exceed the radiological model (balanced accuracy 0.603 ± 0.059, AUC 0.739 ± 0.074). SHAP analysis identified preoperative COMI, pelvic tilt, L1–S1 lordosis, PI–

LL mismatch, BMI, pelvic incidence, and psychological factors (anxiety and depression) as the strongest predictors of MCIC (Figure 1).

Discussion

Spinopelvic alignment parameters were more informative for predicting postoperative improvement than demographic or questionnaire-based variables. The absence of performance gains when combining all features likely reflects noise and redundancy introduced by weakly predictive clinical variables, which can lead to overfitting. The strong performance and balanced discrimination of the radiological model highlight the relevance of automated imaging-derived features for characterising surgical outcomes. These findings support incorporating multimodal imaging biomarkers into preoperative decision-support tools for degenerative spondylolisthesis. Future studies should explore larger cohorts.

Images (Optional)



References (Optional)

[1] Staartjes Victor et al. Fuse-ML, ESJ

Session Category

Emerging Areas: N/A

P3-003

Offset vision in virtual reality alters limb symmetry during a bilateral task

Mr. Taylor Wilson, Dr. Andy Karduna

University of Oregon, Eugene, Oregon, United States

Introduction

Virtual reality (VR) is increasingly used in research due to its ability to manipulate environments and sensory feedback. Our lab previously demonstrated that during a joint position sense task, participants primarily relied on incorrect visual information, undershooting a 90° shoulder-flexion target when given +8° offset vision (OV). It remains unclear whether individuals similarly rely on OV during a bilateral, moving limb-symmetry task. The present study examined the effects of right-hand OV while the left hand received accurate vision (AV) during a bilateral out-and-back reaching task. We hypothesized that right-hand OV would increase limb asymmetry (LA) compared with AV of the right hand.

Methods

Twenty healthy adults (13F/7M; 25.3 ± 6.6 yrs) were recruited. Exclusion criteria included recent upper-body pain or injury. Participants wore an HTC VIVE VR headset and arm-mounted trackers. A minimalist virtual environment displayed each hand as a black glove.

Participants performed ten repetitions of a bilateral reaching task, maintaining symmetry through the middle 80% of the movement (from ~90° elbow flexion to full extension). Four blocks were completed: AV for both hands, and three OV blocks where the right hand was visually shifted forward by 5, 7.5, or 10 cm with AV in the left-hand.

LA was calculated at the end point (80% elbow extension) of the 10th trial. A 1-RM ANOVA compared LA in the AV block against the three OV blocks, followed by Holm-corrected post-hoc tests.

Results

Block significantly affected LA ($p < .001$, $\eta^2 = 0.28$). Post-hoc tests indicated increases in LA as OV increased ($p < .01$; Cohen's $d = 0.69–1.61$). Means and standard deviations in LA per block are presented in Table 1. Interestingly, a 10-cm offset produced only a 3.7-cm increase in LA compared to the AV block.

Discussion

As hypothesized, OV of the right-hand increased LA, indicating a strong visual influence during a bilateral task. However, LA did not translate linearly to OV changes, suggesting proprioception from both limbs mitigates visual distortion. These findings contribute to a larger project examining how sensory availability of the opposite limb modulates reliance on OV, with future applications toward understanding age-related sensory integration in VR.

Images (Optional)

Block	Mean LA (cm)	SD LA (cm)
VPAV_000	0.38	1.84
VPOV_050	1.51	2.13
VPOV_075	2.39	2.23
VPOV_100	4.10	2.66

References (Optional)

Session Category

Emerging Areas: N/A

P3-004

Does a High Fat Sucrose Diet Affect the Forelimb Muscle Integrity in Rats with Diverse Inherent Aerobic Capacity?

Mr. Barbod Shiri[1], Mr. Mauricio Delgado[1,2,3], Mr. Darsh Tripathi[1,2], Mr. Giorgio Giorgio[1], Ms. Ruth Seerattan[1], Dr. Raylene Reimer[1,2], Dr. David Hart[1,2], Dr. Lauren G Koch[4], Dr. Walter Herzog[1,2]

[1]Human Performance Laboratory, University of Calgary, Calgary, Alberta, Canada. [2]McCaig Institute for Bone and Joint Health, University of Calgary, Calgary, Alberta, Canada. [3]Departamento Ciencias de la Salud, Pontificia Universidad Católica de Chile, Santiago, Santiago, Chile. [4]Department of Physiology and Pharmacology, The University of Toledo, Toledo, Ohio, United States

Introduction

A high-fat and high-sucrose diet (HFS) is one of the leading causes of obesity. Obesity often leads to reduced mobility, sedentary lifestyle, and musculoskeletal degeneration, such as fibrosis which has been linked to muscle inflammation [1]. Furthermore, in previous studies, we showed that muscles with primarily slow twitch fibers with a high aerobic capacity, were protected from degeneration in the presence of an HFS diet [2]. Based on these findings, we hypothesized that high aerobic capacity may offer protection to forelimb muscles composed of mixed fiber types in rats subjected to an HFS diet. We tested this hypothesis by quantifying muscle inflammation and fibrosis in rats with high aerobic capacity (HCR) and low aerobic capacity (LCR) following exposure to an HFS diet.

Methods

Results

In the Biceps Brachii, fibrosis significantly increased in both the LCR, and HCR rats fed the HFS diet, and the LCR rats had greater fibrosis than HCR rats [Figure 1]. The differences in fibrosis in the HCR and LCR rats, and the HFS and Chow diet were not associated with corresponding differences in the in macrophage content

Discussion

Greater fibrosis in LCR compared with HCR rats suggests a potential protective effect of high Greater fibrosis in the Biceps Brachii in LCR compared with HCR rats suggests a potential protective effect of high aerobic capacity against obesity-induced muscular maladaptation. These differences in fibrosis across groups was not associated with corresponding differences in macrophage content, thus excluding local inflammation at the end of the diet intervention as a cause for the differential fibrosis results. In future work, we will analyze mitochondrial function to determine how mitochondrial dysfunction and altered biogenesis may contribute to the differences in fibrosis across the experimental groups observed here.

Images (Optional)

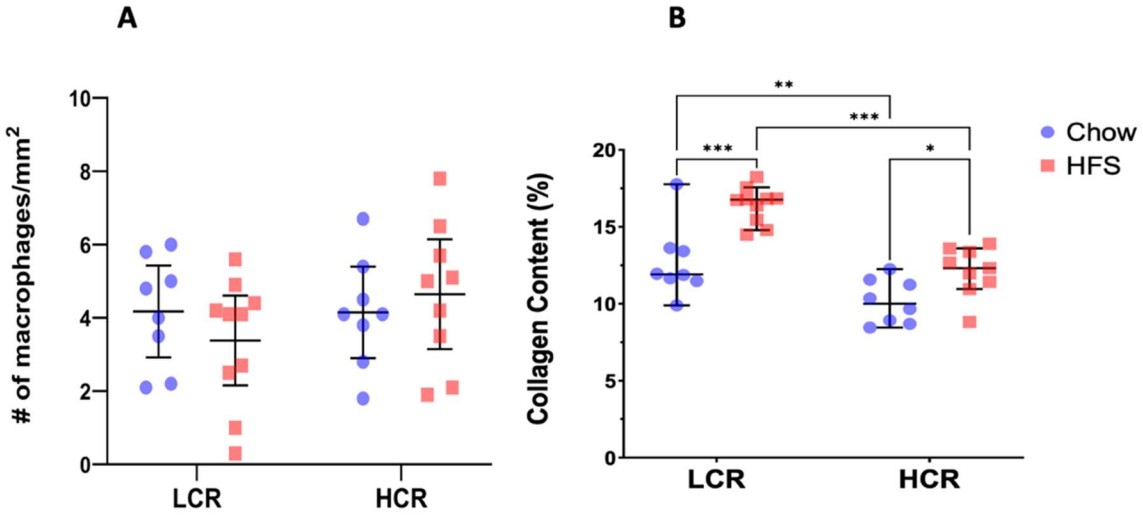


Figure 1: Macrophage (A) and Collagen (B) content in Biceps Brachii cross sections across four groups (HCR+chow; HCR+HFS; LCR+chow; LCR+HFS) (*p = 0.041, **p =0.009, ***p <0.001).

References (Optional)

Acknowledgements (Optional)

Barbod Shiri[1], Mauricio Delgado[1,2,3], Darsh Tripathi[1,2], Giorgio Poletto[1], Ruth Seerattan[1], Raylene Reimer[1,2], David Hart[1,2], Lauren G. Koch[4], and Walter Herzog[1,2]

[1]Human Performance Laboratory, University of Calgary, AB, Calgary, Canada.

[2]McCaig Institute for Bone and Joint Health, University of Calgary, AB, Calgary, Canada.

[3]Departamento Ciencias de la Salud, Pontificia Universidad Católica de Chile, Santiago, Chile.

[4]Department of Physiology and Pharmacology, The University of Toledo, Toledo, Ohio, USA.

Session Category

Emerging Areas: N/A

P3-005

Toward Human-Like Motion in Musculoskeletal Simulation: Generative Adversarial Imitation from Observation (GAIfO)

Mr. Chihyeong Lee[1], Dr. Beom Chan Lee[2], Dr. Jooeun Ahn[1]

[1]Seoul National University, Seoul, Seoul, Korea, Republic of. [2]University of Houston, Houston, Texas, United States

Introduction

Reinforcement learning (RL) enables musculoskeletal simulation without extensive experimentation. However, it often produces unnatural movements that exploit simulation physics rather than replicating human motion. Imitation learning can improve realism, yet these methods require action spaces such as joint torques, which cannot be collected in typical biomechanical studies [1]. GAIfO addresses this limitation by learning solely from observable state transitions, allowing the use of experimentally measurable data [2]. Therefore, this study explored whether incorporating GAIfO into an RL framework could guide a musculoskeletal agent toward more human-like gait.

Methods

Twenty-four healthy adults walked on a treadmill at their preferred speed (1.0 ± 0.1m/s). Hip, knee, and ankle angular velocities were extracted to train a GAIfO discriminator. A musculoskeletal model in SCONE with the Hyfydy physics engine walked on a treadmill moving at 1.0 m/s. One agent was trained using Proximal Policy Optimization (PPO) alone, and another was trained using PPO combined with GAIfO. Their gait patterns were compared against experimental data using joint kinematics and symmetry differences.

Results

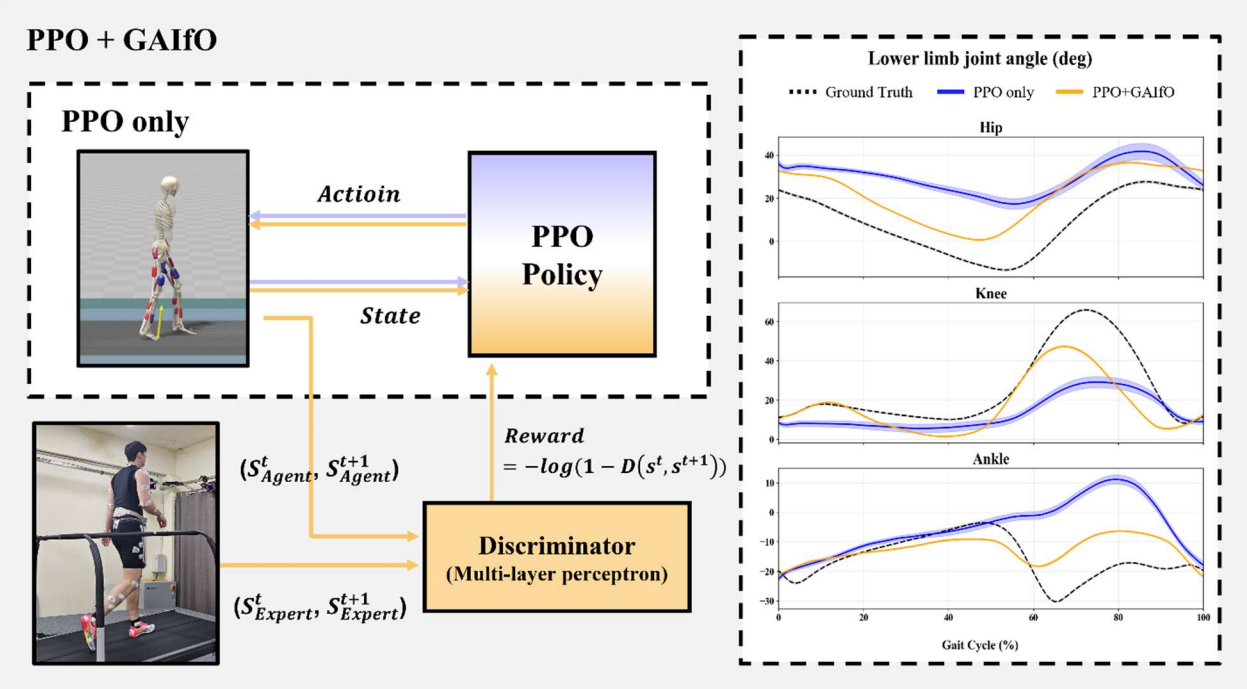
Across fifty 20-second rollouts, PPO+GAIfO achieved higher mean reward, longer episode duration, and a substantially lower fall rate (90% vs 16%) compared to PPO only. PPO+GAIfO also exhibited lower root-mean-square error with experimental joint angles (Hip: 22.2° vs 13.5°, Knee: 17.1° vs 12.7°, Ankle: 16.1° vs 7.4°) and produced more symmetric lower-limb movement (Hip: 26% vs 83%, Knee: 9% vs 99%, Ankle: 56% vs 72%).

Range-of-motion analysis showed significant deviations across all joints for PPO, whereas PPO+GAIfO matched knee and ankle ROM without significant differences.

Discussion

Overall, the results highlight that GAIfO effectively leverages experiment-derived information to improve motion realism, guiding simulation agents toward more natural and symmetric movement patterns. GAIfO does not simply mimic recorded movements but instead shapes the agent's behavior toward human-like strategies while maintaining task objectives. These findings indicate that the PPO+GAIfO framework captures coordination characteristics that PPO alone fails to reproduce. The framework therefore provides evidence that it can be effectively applied to musculoskeletal models to generate realistic movement using only experiment-derived data.

Images (Optional)



References (Optional)

[1] Chiu YH et al. ICORR, 2025.

[2] Torabi F et al. arXiv, 2018.

Acknowledgements (Optional)

- The study was supported in part by the grant of the Korea Health Technology R&D Project through the Korea Health Industry Development Institute (KHIDI), funded by the Ministry of Health & Welfare (no. HK23C0071), and the National Research Foundation of Korea (NRF) grants funded by the Korean Government (MSIT) (No. RS-2023-00208052).

Session Category

Emerging Areas: N/A

P3-006

Machine Learning–based Assessment of Triceps Muscle Fatigue Using Mechanomyographic Signals

Ms Raneda Kerfi[1], Dr Coralie Privet-Thieulin[1,2], Dr Hassan Soubra[1]

[1]LyRIDS, ECE research center, Lyon, Rhône-Alpes, France. [2]Laboratory of Tribology and Dynamic Systems, Lyon, Rhône-Alpes, France

Dr Coralie Privet-Thieulin

Introduction

Muscle fatigue assessment is crucial in sports, rehabilitation, and injury prevention. Conventional methods are accurate but often costly, invasive, and impractical for daily use. Inertial Measurement Units (IMUs), which record mechanomyographic (MMG) signals via acceleration and angular velocity, provide a portable and low-cost alternative. Yet, triceps brachii fatigue remains largely unexplored. This study proposes a quantitative approach to detect triceps fatigue using inertial signals during controlled upper-limb exercises.

Methods

Fifty participants were recruited in two groups:
(1) Thirty-four subjects performed two 1-minute exercise phases separated by 30 seconds of rest.
(2) Sixteen subjects repeated the exercise until muscular failure.
A triaxial IMU (MPU6050), placed over the triceps, recorded accelerometer (AX, AY, AZ) and gyroscope signals. Data processing included timestamp harmonization, segmentation into labeled phases, and extraction of amplitude, movement frequency, and signal averages, along with computation of the acceleration norm.
Two classification models were developed—Random Forest and Long Short-Term Memory (LSTM) neural networks—to distinguish Exercise vs. Rest and to attempt differentiation between Phase 1 and Phase 2 (pre- vs. post-fatigue).

Results

Descriptive analyses showed a consistent decrease in movement frequency and number of repetitions from Phase 1 to Phase 2, particularly on the vertical axis (AZ), along with a

general reduction in amplitude across subjects. A decrease in mean acceleration values was also observed during late-fatigue stages, most notably on AZ.

The Random Forest model achieved 81% accuracy (recall 92% for Exercise) for Exercise vs. Rest classification. The LSTM achieved 84% validation accuracy, demonstrating improved sensitivity to temporal variations. Both models showed limited ability to distinguish Phase 1 from Phase 2 (≈ 50% accuracy), reflecting the subtlety of early fatigue patterns.

Discussion

IMU-derived MMG signals show strong potential for non-invasive fatigue monitoring. While the identification of active vs. resting periods is robust, detecting early fatigue requires additional features, improved stabilization methods, or enhanced temporal modeling. Future work should refine acquisition protocols and explore more advanced neural architectures.

References (Optional)

[1] Biró Attila *et al.*, *Sensors,* 2024

[2] Hwang Soree *et al.*, *Sensor, 2025*

[3] Daud Muhamad Aliff Imran *et al., Mekatronika: Journal of Intelligent Manufacturing and Mechatronics,* 2024

Acknowledgements (Optional)

The authors thank all ECE students and staff who contributed to the data acquisition and experimental procedure.

Session Category

Emerging Areas: N/A

P3-007

Prediction of Human Cortical Bone Work-of-Fracture Based on Bone Collagen Denaturation and Machine Learning

Mr. Corin Seelemann, Dr. Daniel Dapaah, Prof Charbel Azzi, Prof Thomas Willett

University of Waterloo, Waterloo, Ontario, Canada

Introduction

The determinants of bone fracture resistance and the mechanisms of its loss are not fully understood. Factors such as oxidative damage or porosity partially degrade fracture resistance. A challenge is bone's hierarchical structure which provides multiscale toughening mechanisms, notably the denaturation of bone collagen as an energy sink during fracture. Our prior work correlating fluorescently labelled collagen hybridizing peptides (F-CHP) staining intensity to work-of-fracture (WFx) showed weak correlation (R^2=0.13). Recent research has fractographically predicted mechanical behavior of engineering materials using machine learning (ML) [1,2]. Here we apply these methods to determine WFx from F-CHP stained bone fracture surfaces. To our knowledge, quantitative fractography has not been used to predict WFx of human cortical bone.

Methods

Notched cortical bone beams were machined from 60 femora from a diverse set of human donors. These were fractured at quasi-static rates and WFx was calculated [3]. Fracture surfaces were imaged as per our prior work [4].

We developed a novel, fracture-surface–specific preprocessing and learning pipeline for confocal F-CHP images, combining per patch intensity normalization to remove background bias, patch-based texture sampling, and a ResNet18 model trained with donor-separated validation to quantitatively predict WFx from a single post-fracture image.

Results

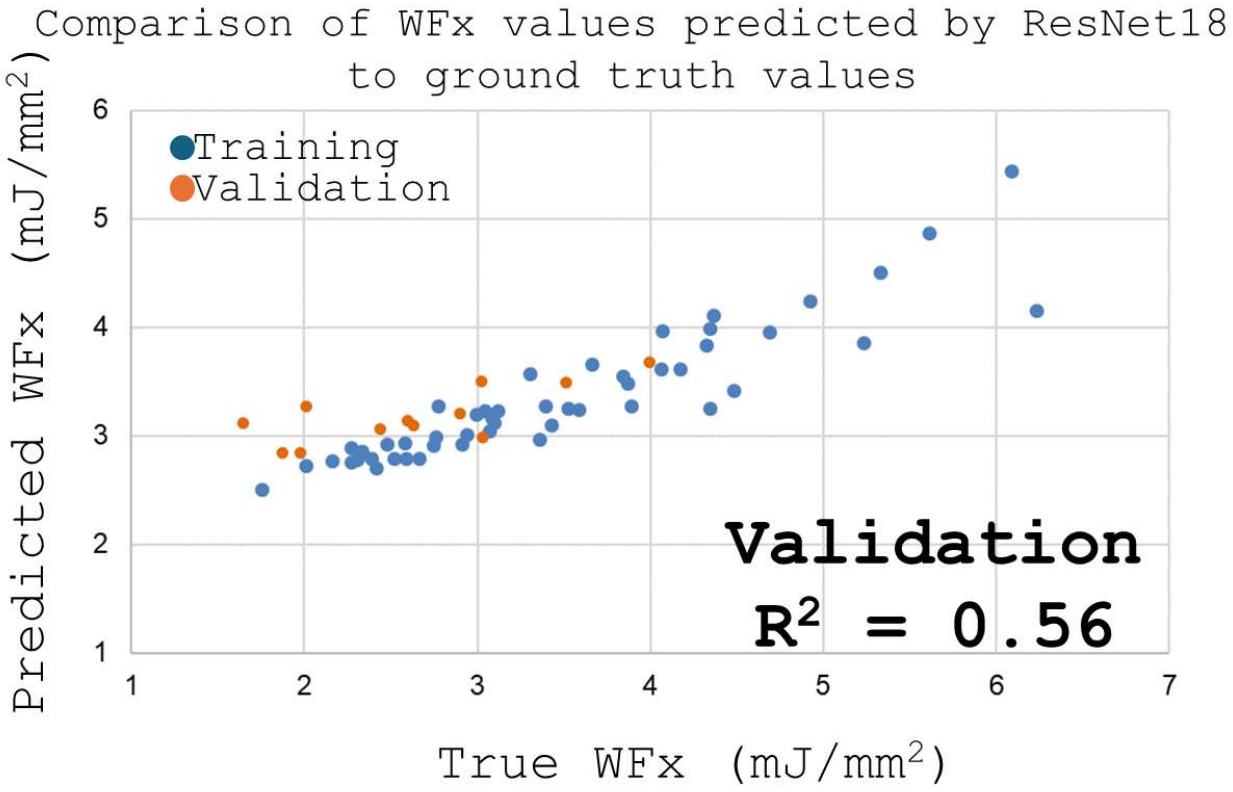
The best training conditions resulted in an R^2 value of 0.56 for the validation data set. Comparatively linear regression using F-CHP staining only achieved an R^2 of 0.13.

Discussion

The complexity of bone tissue makes understanding the mechanisms of bone tissue quality and its loss difficult. Here, the morphology and collagen denaturation signal of a fracture surface predicted the work-of-fracture required for fracture. The R^2 of 0.56 shows greater correlation with fracture resistance than a single Raman biomarker (R^2 of 0.47)[5].

This suggests that microstructure and collagen denaturation patterns encoded on the fracture surface capture micro-scale toughening mechanisms that determine WFx. This motivates the development of new models to elucidate the determinants of bone tissue quality.

Images (Optional)



References (Optional)

[1] Motoaki, Y. et al. (2022).

[2] Zhang, N. et al. (2023).

[3] Dapaah, D., & Willett, T. (2022).

[4] Seelemann, C. A., & Willett, T. L. (2022).

[5] Unal, M. et al. (2019).

Session Category

Emerging Areas: N/A

P3-008

Uncertainty-Aware Cardiovascular Flow Reconstruction Using a Latent Diffusion Model

Dr. Dana Lynn Lavacot, Dr. Fanwei Kong

Washington University in St. Louis, St. Louis, MO, United States

Introduction

Echocardiography (echo) is a medical imaging technique that is widely used in clinical settings due to its accessibility, non-invasiveness, and ability to provide real-time visualization of cardiovascular structure and flow at the bedside. However, echo data is often noisy and limited, making it challenging to interpret and use for diagnosis. Thus, inherent to echo measurements are uncertainties in flow quantities and geometry characterization. Advances in machine learning, such as diffusion models, show potential in enhancing echo data within uncertainty-aware frameworks.

Methods

We utilize a framework based on the latent diffusion model of [1], which leverages a conditional neural field autodecoder so that the model learns and generates in the latent space. We guide generation to reconstruct flow fields that are consistent with echo measurements and physics. As a proof of concept, we demonstrate the framework for the simplified problem of idealized blood vessels with varying degrees of stenosis and aneurysm.

Results

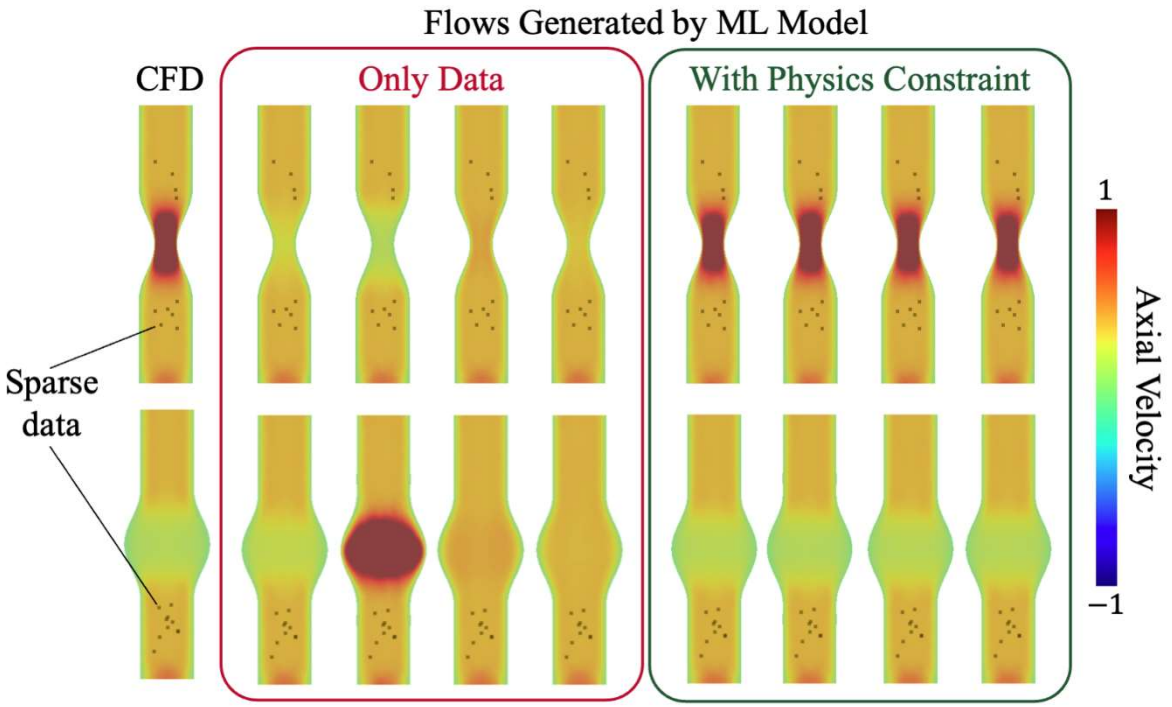
We find that the diffusion model can conditionally generate physically-reasonable flow fields given limited measurements from the original simulations. We find that when the measurements are plausibly from multiple blood vessel shapes, the model generates a wide distribution of flows, most of which are not physically consistent with the geometry. By enforcing physics constraints, we can collapse the generated distribution to the original flow.

Discussion

From this proof of concept, we find that diffusion models are a promising framework for cardiovascular flow reconstruction from clinical data. When we apply this framework to the full cardiac problem, we expect to be able to quantify uncertainties through analysis of the

generated distributions. In our ongoing work, we are investigating the performance of the diffusion model for more complex and more realistic geometries. Ultimately, we will use a generative model [2] to create various realistic cardiac geometries for training a diffusion model that can be applied in clinical settings.

Images (Optional)



Different realizations of flow fields reconstructed using sparse measurements from CFD simulations, represented by small black squares. Red box (left): uncertainty due to limited data results in a wide distribution of flows. Green box (right): information is complete and leads to distribution collapse.

References (Optional)

[1] Pan Du *et al.*, Nature, 2024

[2] Fanwei Kong *et al.*, Medical Image Analysis, 2024

Session Category

Emerging Areas: N/A

P3-009

Mapping the Age-Related Constriction of Gait Strategies via Semi-Supervised Deep Learning

Ms Diana C. Martinez[1], PhD Diego F. Villegas[1], PhD Aaron D. Likens[2]

[1]1School of Mechanical Engineering, Universidad Industrial de Santander, Bucaramanga, Santander, Colombia. [2]Division of Biomechanics and Research Development, Department of Biomechanics and Center for Research in Human Movement Variability, University of Nebraska at Omaha, Omaha, Nebraska, United States

Introduction

Recent advances in gait rehabilitation and prosthetic control suggest that restoring functional mobility depends not only on targeting discrete kinematic metrics, but also on the inherent robustness of human locomotion [1]. According to the "loss of physiological complexity" hypothesis [2], aging reduces the adaptive capacity of physiological systems. Based on this finding, we hypothesize that mapping the intrinsic organization of gait strategies using semi-supervised deep learning could reveal distinct gait subphenotypes and quantify the motor diversity that underpins healthy gait adaptability.

Methods

~460,000 gait cycles from the open-access NONAN GaitPrint database [3-5], containing full-body IMU kinematics (321 variables) from young (19–35 years), middle-aged (36–55 years), and older adults (≥56 years) were analyzed. A semi-supervised bidirectional long short-term memory (BiLSTM) autoencoder (AE) was trained to learn compact gait representations. Subsequently, Hierarchical Density-Based Spatial Clustering of Applications with Noise (HDBSCAN) was applied to identify distinct data-driven subclusters, with separability assessed via cluster purity. Explainability followed a two-stage approach: (1) a gradient-boosting proxy classifier identified the primary kinematic discriminators (validated by SHAP scores), and (2) macro-profiles were computed to characterize the coordination strategies underlying each subphenotype by quantifying relative changes in dynamic range.

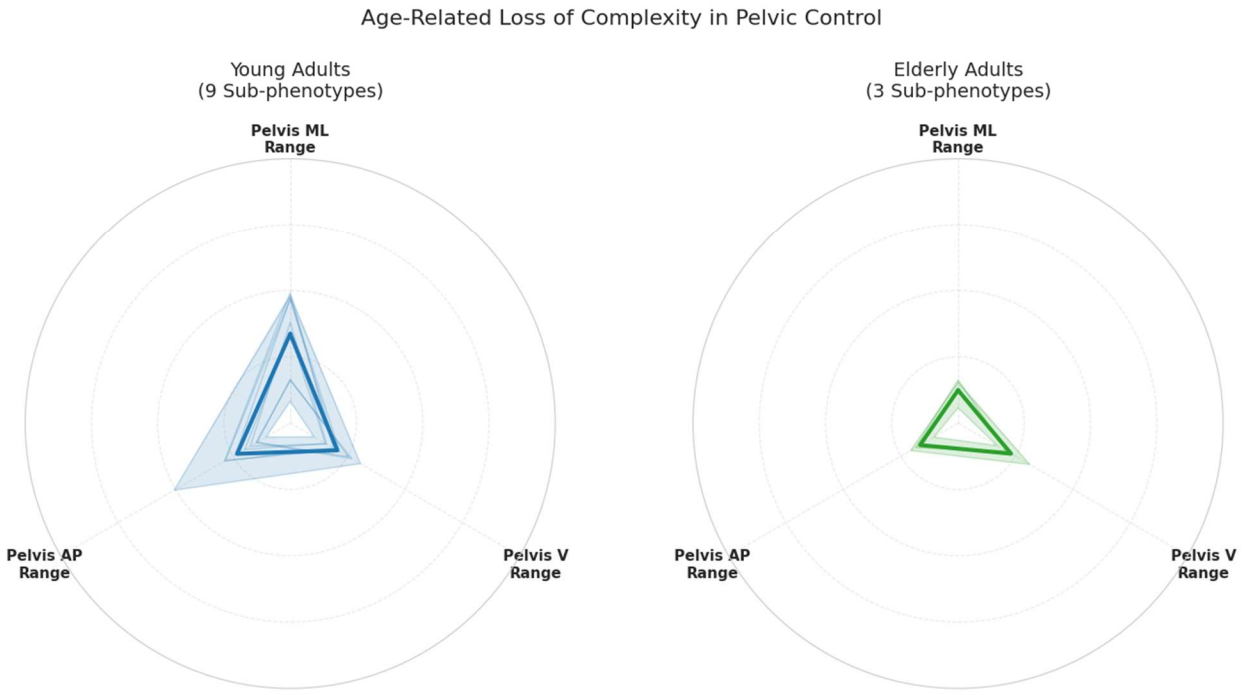
Results

The explainability framework identified tri-axial pelvis accelerations as the key discriminators with high fidelity (Proxy Accuracy: 81.7%; SHAP scores > 0.38). HDBSCAN identified 20 subclusters with 100% age-group purity. An inverse relationship between age and phenotype diversity was observed: young adults expressed nine distinct subphenotypes, revealing a rich repertoire of pelvic and hip strategies. Middle-aged adults formed eight transitional subclusters, while older adults consolidated into only three stereotyped subclusters [Figure 1]. Quantitative profiling of these older adult phenotypes revealed a systemic "stiffening" strategy: macro-profiles showed a 24.0% reduction in tri-axial pelvic acceleration amplitude compared to young adults.

Discussion

These findings reveal distinct gait substructures that closely aligned with physiological aging. The age-related reduction in subphenotypes validates the loss-of-complexity hypothesis, reflecting a shift toward fewer, more constrained coordination strategies for controlling the center of mass. Quantifying this constriction of the locomotor solution space provides a data-driven foundation for tools with the potential to assess gait adaptability through changes in the motor repertoire.

Images (Optional)



References (Optional)

Acknowledgements (Optional)

This research was supported by a Fulbright Colombia scholarship.

Session Category

Emerging Areas: N/A

P3-010

Deep Learning Enables Prediction of Bilateral Joint Kinetics of Walking in Young and Older Adults Before, During, and After Functional Electrical Stimulation of Plantar Flexors

Mr. Dylan M. Page MS[1], Ms. Ningzhen Zhao MS[1], Ms. Arianna S. Monteiro[1], Mr. Changseob Song MS[2], Dr. Inseung Kang PhD[2], Dr. Owen N. Beck PhD[1], Dr. Nicholas P. Fey PhD[1]

[1]The University of Texas at Austin, Austin, TX, United States. [2]Carnegie Mellon University, Pittsburgh, PA, United States

Introduction

Biological joint moment estimators have been used to inform assistive technologies [1]. However, data-driven technique performance can suffer outside of the training dataset, including untrained walking patterns from older adults using neuromodulation interventions. We developed temporal convolutional networks (TCNs) that predict walking lower-limb joint kinetics across age groups and functional electrical stimulation (FES) conditions.

Methods

10 young (21.6±2.2 yrs) and 8 older (77.8±5.7 yrs) adults performed treadmill walking trials before, during, and after FES applied bilaterally over soleus muscles during late-stance [2]. Moments and power of hip, knee, and ankle joints and inertial measurement unit (IMU) signals of the pelvis, thigh, shank, and foot were computed bilaterally. Two TCNs with temporal dilations used IMU signal inputs to predict sagittal plane joint kinetics. The networks were evaluated using leave-one-subject-out cross-validation. Additional within-participant networks were trained and tested. Linear mixed effects models were used to fit Root Mean Square Error (RMSE) and included age group, FES condition, and joint, $\alpha=0.05$.

Results

The cross-validated networks resulted in average RMSE of 0.231±0.130 Nm/kg and 0.363±0.189 W/kg. The cross-validated network predicted joint kinetics worse than within-participants networks (RMSE=0.061±0.054 Nm/kg, $p<0.001$; RMSE=0.139±0.154 W/kg, $p<0.001$). Moment RMSE increased during FES ($\beta=0.020$, $p=0.027$). Young adults had greater power RMSE ($\beta=0.123$, $p=0.032$), and hip power RMSE was lower than ankle ($\beta=-0.068$, $p=0.014$). All other covariates showed no difference.

Discussion

The networks demonstrated robustness across age groups for moments and FES conditions for power. Moment error was higher during FES as expected as FES alters joint work distribution. Power error was unexpectedly lower for older adults. Our user- and neuromodulation-agnostic networks, when tested on *older* adults, performed similarly (0.15 Nm/kg RMSE) as prior studies [1] that predict hip and knee moments during 22 ambulation tasks in control subjects, with considerably less training data. Our networks predictions of lower-limb joint kinetics across FES conditions offer an opportunity to use this approach to better identify neuromotor adaptation. Next, we will optimize hyperparameters and expand the dataset to improve prediction performance.

Images (Optional)

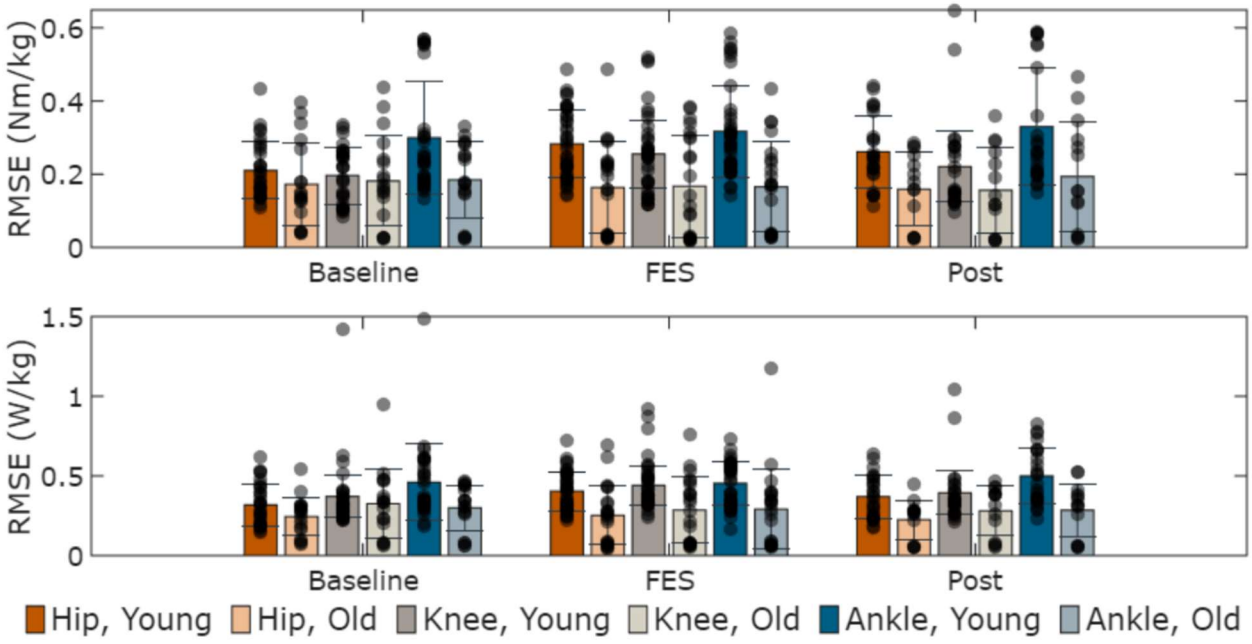


Figure 1. The networks show robust predictions across age groups in joint moments and FES condition in joint power. Panel A shows moment RMSE and panel B shows power RMSE. Bars indicate means, error bars represent standard deviations, and black points show individual values.

References (Optional)

[1] Molinaro et al. Nature 2025, [2] Zhao et al. J Appl Physiol 2025

Session Category

Emerging Areas: N/A

P3-011

AutoSSM: Nonlinear Statistical Shape Modelling via a Variational Autoencoding Framework

Ir. Edwin Tay, Dr. ir. Nazli Tümer, Prof.dr. Amir Zadpoor

Delft University of Technology (TU Delft), Delft, Zuid-Holland, Netherlands

Ir. Edwin Tay

Dr. ir. Nazli Tümer

Introduction

Dynamic growth and adaptation processes, from the cellular to the organ-scale, result in an expansive envelope of possible shape variation. These inherently nonlinear processes culminate in similarly nonlinear shape variations, resulting in a complex underlying shape space. Nevertheless, characterizing this time-varying shape space and deepening our understanding of physiological and pathological shape development can support many clinical applications, such as diagnosis and prognosis.

Existing methods often rely on processes that linearize inherently nonlinear data and use rule-based heuristic pipelines for discretization, which can lead to information loss. We propose that deep learning-based frameworks offer a more viable path towards nonlinear shape models that account for biological growth and development.

Methods

We developed an AutoSSM framework that amalgamates advances in variational autoencoders (VAEs), multi-scale modules, latent space disentanglement, and contrastive learning. Together, these components enable unsupervised learning and the structuring of shape spaces via latent variables. Wherein, each variable represents a unique and rich dimension of spatial variability. We demonstrate the efficacy of our framework via synthetic (generated shapes) and biological data (medial phalanges).

Results

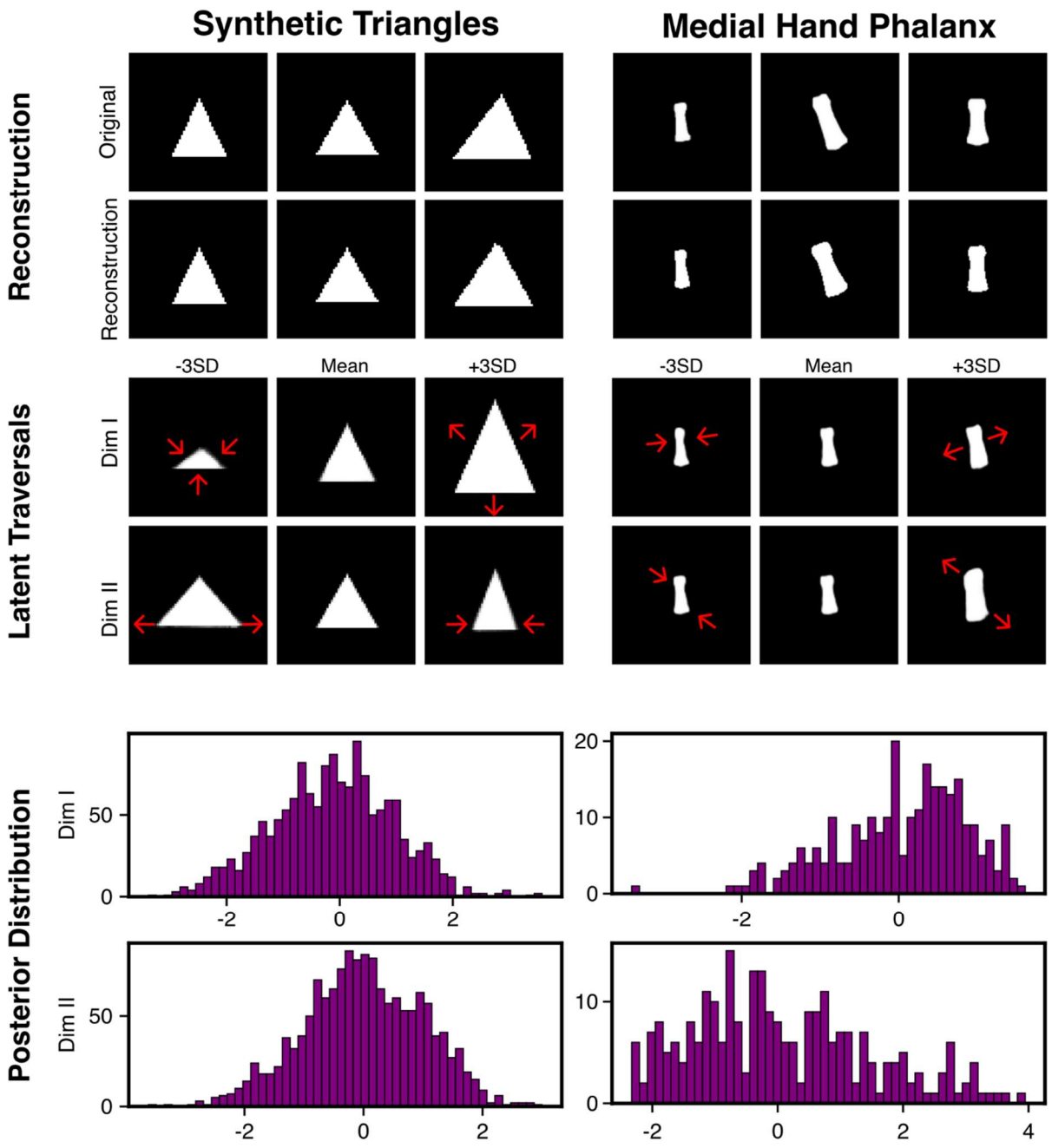
Our Inception-based VAE generates high fidelity reconstructions (Jaccard = 0.949±0.042, Dice = 0.9733±0.023). Through disentanglement and self-supervision, the resulting

encoded latent variables capture distinct dimensions of spatial variation, closely aligning with those identified by traditional PCA-based SSMs. Each dimension can then be considered a probabilistic prior which, taken together, constitutes the overall shape space. Consequently, traversing and randomly sampling from the learned posteriors of each dimension provides physiologically valid shapes constrained within our learned shape space.

Discussion

Initial results demonstrate the feasibility of our AutoSSM framework for unsupervised learning of the underlying shape space. This is done without linearizing inherently nonlinear data (*i.e.,* biological growth and variation). Our framework further avoids heuristic, rule-based preprocessing pipelines, and each learned latent dimension captures richer, more expressive aspects of shape variation. Nevertheless, further work is necessary to develop a comprehensive evaluation of the underlying shape space identified via our framework. Regardless, our framework can also be further extended to explore the encoding of textural information for holistic shape and appearance modelling, and for applications to alternative shape representation media.

Images (Optional)



Session Category

Emerging Areas: N/A

P3-012

Performance Assessment of Machine Learning Algorithms for Hop Classification and Functional Profiling of 1,878 Hop Tests

Miss Eleonora Cabai MS[1,2], Dr. Jorge Chahla MD, PhD[3], Dr. Leonardo Metsavaht MD, PhD[4], Dr. Gustavo Leporace PhD, MSc[4], Dr. Jonathan Gustafson PhD[2]

[1]Politecnico di Milano, Milan, Milan, Italy. [2]Rush University Medical Center, Chicago, Illinois, United States. [3]Midwest Orthopaedics at Rush, Chicago, Illinois, United States. [4]Instituto Brasil de Tecnologias da Saúde (IBTS), Rio de Janeiro, Rio de Janeiro, Brazil

Introduction

Machine learning (ML) has shown significant potential for biomechanical subgroup classification [1], providing a valuable tool to personalize clinical decision-making [2]. However, no consensus exists regarding the optimal ML approach. This study investigates the performance of multiple algorithms to identify the optimal configuration for accurate subgroup classification given biomechanical data from 1,878 horizontal hop landing tests.

Methods

The dataset consisted of 24 biomechanical features (trunk/pelvis/hip/knee/ankle kinematics) extracted from the horizontal hop test of 1,878 subjects, collected at a private motion analysis institute, and grouped into 6 functional profiles. We used these data to evaluate the classification accuracy (80-20 train-test split) of five algorithms: Gaussian Naive Bayes (GNB), Multi-Layer Perceptron (MLP), Random Forest (RF), Support Vector Machines (SVM), and Deep Learning Neural Networks (DL). Our approach involved: (1) random state optimization to identify the best configuration, (2) performance evaluation with the best random state, and (3) recursive feature elimination to determine the optimal feature subset. Model performance was assessed using weighted average metrics, including accuracy, precision, recall, and F1-score to account for potential class imbalances.

Results

SVM and GNB exhibited the lowest performance across all configurations, with average accuracies of 80.6% ± 2.5% (Table 1). RF and DL demonstrated robust performance with average accuracy scores of 83.1% ± 1.4% and 86.2% ± 1.5% respectively. MLP showed the best performance, achieving an average accuracy of 87.7% ± 1.7%. The confusion matrices revealed that some subgroups with unique movement strategies at the knee and ankle

were more challenging to classify than others. The recursive feature elimination process identified minimal redundancy in the feature set.

Discussion

We successfully identified an optimal configuration for subgroup classification of horizontal hop landing tests using ML. The variation in performance across different models and random states highlights the importance of model selection and parameter optimization, particularly with the high variance in human-related data. The recursive feature elimination identified the importance of all the 24 features for hop classification. This ML-based approach can serve as a foundation for future studies aiming to establish functional classifications to support clinical decision-making in orthopedics.

Images (Optional)

Algorithm	Accuracy	Precision	Recall	F1
Gaussian Naive Bayes (GNB)	0.805 ± 0.028	0.812 ± 0.028	0.805 ± 0.028	0.806 ± 0.028
Multi-Layer Perceptron (MLP)	0.877 ± 0.017	0.879 ± 0.018	0.877 ± 0.017	0.876 ± 0.017
Random Forest (RF)	0.831 ± 0.014	0.836 ± 0.013	0.831 ± 0.014	0.828 ± 0.013
Support Vector Machines (SVM)	0.808 ± 0.022	0.809 ± 0.022	0.808 ± 0.022	0.806 ± 0.021
Deep Learning Neural Networks (DL)	0.862 ± 0.015	0.865 ± 0.015	0.862 ± 0.015	0.861 ± 0.015

References (Optional)

[1] Halilaj, J Biomech, 2018; [2]: Leporace, Clin Biomech, 2021.

Acknowledgements (Optional)

The authors would like to thank Felipe Fernandes Gonzalez for reviewing this work and the Rush-IBTS Research Fellowship Program for funding.

Session Category

Emerging Areas: N/A

P3-013

Building the Foundations for AI-Based Diagnostic Models of Human Movement Using Real-World Video

Ms. Ellie Thompson, Mr. Shanren Yang, Mr. Mahan Bagheri, Dr. Max Donelan

Simon Fraser University, Burnaby, BC, Canada

Introduction

Differences in how people move can make a task efficient, unstable, or painful, yet identifying these issues remain challenging. Movement analysis often relies on subjective observation, introducing variability across coaches, clinicians, and therapists. Most individuals receive feedback from a single expert, limiting opportunities to compare and validate assessments. While artificial intelligence (AI) now matches expert performance in static diagnostic tasks, human movement is dynamic, multi-joint, and difficult to describe consistently. We developed a camera-agonistic system that integrates an AI-based video analysis tool with a real-world video collection and coach review platform. This system provides the foundational components for future high-throughput, AI-driven movement diagnostics.

Methods

We developed a web platform that enables athletes to upload videos from mobile devices and certified coaches to review them. The platform supports structured feedback through time-stamped comments, voice-to-text transcription, and tagging tools. Separately, we built a custom AI-based tool using Python infrastructure that analyzes uploaded videos to identify movement type and extract key frames representing major movement phases. Building on existing multimodal embeddings, we map video content and coach feedback into a shared semantic space, bringing aligned pairs closer together and pushing mismatched pairs apart. During the pilot period, 16 athletes submitted 144 videos, contributing to our goal of 300 videos for initial model training.

Results

Athletes successfully uploaded videos through the platform, confirming its reliability for real-world data collection. We selected the bar muscle-up—a movement requiring coordination and control—as the model task. The automated analysis software accurately detected attempts and extracted clean, representative frames from each video. Coaches

provided high-quality feedback using the review platform, with voice-to-text tools improving efficiency. Using these annotations, we generated early prompts that enabled the system to produce draft feedback from video input. Initial qualitative review showed alignment between the system-generated feedback and coach-identified movement issues.

Discussion

These pilot findings demonstrate the feasibility of integrating real-world video collection, automated movement analysis, semantic evaluation, and expert coaching into an AI-driven diagnostic system. The tools we established provide a foundation for high-throughput, consistent movement assessment applicable to athletic performance, rehabilitation, and injury-prevention.

Session Category

Emerging Areas: N/A

P3-014

A Principled Validation Framework for Explainable AI in Gait Analysis: Sensitivity, Faithfulness, and Cross-Method Coherence

Mr Ching Hang Chiu[1], Ms Elodie Drew[2], Mr Alpesh Kothari[1,3], Dr Julie A. Stebbins[1,3], Prof Amy B. Zavatsky[4], Dr Philippe C. Dixon[2]

[1]NDORMS, University of Oxford, Oxford, Oxfordshire, United Kingdom. [2]Department of Kinesiology and Physical Education, McGill University, Montreal, Quebec, Canada. [3]Oxford Gait Laboratory, Oxford University Hospitals NHS Foundation Trust, Oxford, Oxfordshire, United Kingdom. [4]Department of Engineering Science, University of Oxford, Oxford, Oxfordshire, United Kingdom

Introduction

Machine learning provides powerful tools for analysing complex gait patterns, yet its opaque decision-making mechanisms hinder clinical trust. While post-hoc explainable artificial intelligence (XAI) can identify features driving model decisions, its fragility to noise raises concerns about biomechanical validity. We propose here a validation framework to evaluate XAI across three dimensions: sensitivity (whether highlighted features influence model output), faithfulness (whether explanations reflect learned representations), and coherence (cross-method consistency) [1,2]. The framework is demonstrated on a task with a known discriminative feature to establish its reliability and support its extension to more subtle applications.

Methods

Kinematic data from 18 idiopathic toe walking (ITW) and 18 typically developing (TD) children (20 cycles per subject; pelvis/hip all planes, knee/ankle sagittal; normalised to 101 timepoints) were analysed. A 1D Convolutional Neural Network (CNN) was trained with five-fold subject-stratified cross-validation to classify ITW vs TD gait. Attribution maps, showing which parts of the input contributed to the model's decision, were derived from 6 XAI techniques: Saliency, Input×Gradient, Integrated Gradients, Guided Backprop, DeepLIFT, and GradientSHAP. Sensitivity was assessed via relevance-guided masking (removing the top 5–50% attributed features) and measuring associated AUROC decline. Faithfulness was assessed through progressive weight- and label-randomisation, with attribution similarity drop quantified using Pearson correlation. Coherence was examined by changes in global attribution similarity after removing each method. Validated attributions were then ensemble-averaged and qualitatively compared with 1D Statistical Parametric Mapping (1d-SPM) effect-size heatmaps representing ITW–TD group differences.

Results

The CNN model achieved high performance (AUROC: 0.99 ± 0.02). Sensitivity testing confirmed that all methods identified functionally relevant features. Faithfulness tests showed that Guided Backprop failed to degrade under weight-randomisation and that Saliency was unstable across retraining with no label-randomisation, indicating unfaithful attributions. Coherence analysis likewise showed that both methods weakened global similarity, leading to their exclusion. XAI validation was further supported by XAI–SPM agreement (Fig 1), with both marking the ankle sagittal plane as highest-importance.

Discussion

This framework distinguished plausible from artefactual explanations. Methods that passed sensitivity but failed faithfulness produced relevant yet non-discriminative attributions driven by generic input sensitivity.

Images (Optional)

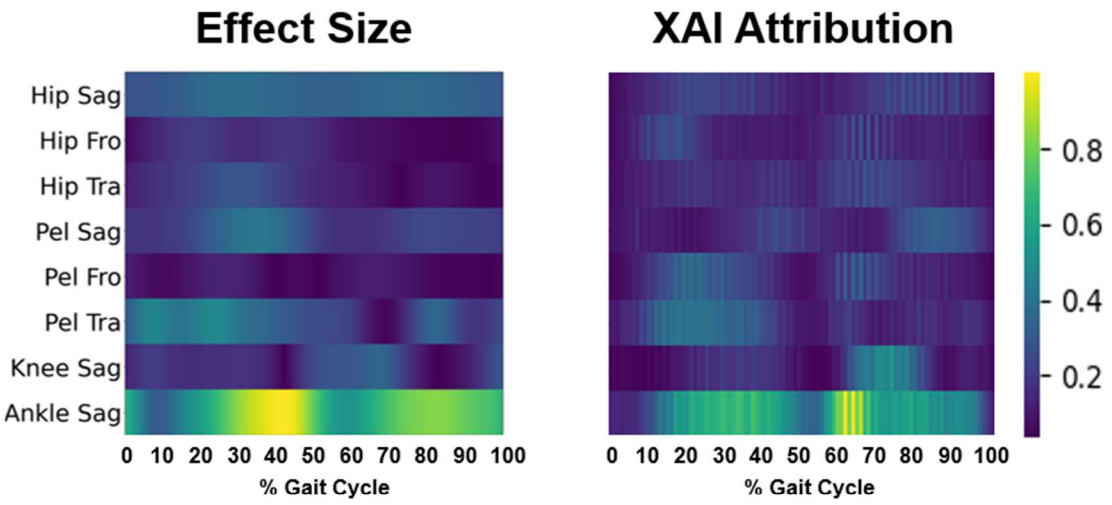


Figure 1. Heatmaps showing (left) 1D-SPM effect sizes for ITW–TD group differences and (right) ensemble-averaged XAI attributions from validated explainability methods. *Both analyses highlight ankle sagittal kinematics as the dominant region of discriminative information, supporting the biomechanical validity of the XAI explanations.*

References (Optional)

[1] Adebayo et al. (2018)

[2] Ribeiro et al. (2024)

Session Category

Emerging Areas: N/A

P3-015

Advancing Real-Time and Automated Inertial Sensor Analysis Across Biomechanics Applications with Time-Series Transformers

Mr. Gerard Aristizábal Pla[1], Prof. Michael Potter[2], Prof. Wouter Hoogkamer[3], Prof. Kurt Beschorner[1]

[1]University of Pittsburgh, Pittsburgh, Pennsylvania, United States. [2]Francis Marion University, Florence, South Carolina, United States. [3]University of Massachusetts Amherst, Amherst, Massachusetts, United States

Introduction

Real-time and automated inertial measurement unit (IMU) analysis is critical because many biomechanics applications require immediate feedback, minimal manual intervention, and continuous monitoring outside laboratory settings. Transformers meet these requirements and are versatile across context, but have not been applied extensively to IMU data. We evaluated a time-series transformer (TST) model across five methodologically and application-diverse tasks: gait event detection, stride length estimation, human activity recognition, and freezing of gait detection.

Methods

Five TST models (4 attention heads, 3 layers) were trained and cross-validated across distinct IMU datasets. For gait event detection, 17 subjects performed walking, jogging, running, and sprinting trials with shoe-mounted IMUs. For contact time validation, 20 participants ascended and descended three outdoor staircases at varying speeds with shoe-mounted IMUs [1]. Stride-length estimation used sprint trials from 17 subjects [2]. Human activity recognition involved 30 participants performing six activities with a pelvis-mounted IMU [3]. Freezing-of-gait detection used data from 35 individuals with Parkinson's disease completing 2-minute walking tests with shank-mounted IMUs [4]. Each model processed sliding windows of IMU data, producing either frame-wise probabilities, window-level probabilities, or stride-length estimates. Training used Adam optimization, gradient clipping, task-specific loss functions, and strict leave-one-subject-out validation. Performance was evaluated using F1-score, mean absolute error, mean bias or area under the receiver operating characteristic curve, averaged across folds, as appropriate.

Results

TST models achieved strong performance that matched or exceeded heuristic approaches (Table 1, where bold indicates best performance).

Discussion

TST models offer an efficient and fully automated way to process IMU signals. Unlike heuristic methods, TST models learn temporal patterns directly from raw data without assumptions. Their probabilistic, window-based design supports real-time inference, making TST models a scalable solution for automated gait analysis in biomechanics applications. Future work will explore developing a single unified Transformer capable of handling all tasks within one model.

Images (Optional)

Application	Outcome	Performance, method (study)	Performance (ours)
Gait event detection	F1-score		**0.95**
Stair contact time validation	Contact time (mean absolute error in ms)	22.37ms, Peak Detection [1]	**16.31ms**
Stride length estimation	Bias (%)	**-0.27%, Zero-Velocity Update Method [2]**	-0.40%
Human activity recognition	F1-score	**0.96, Support Vector Machine [3]**	0.88
Freezing of gait detection	Area under the operating receiver curve	0.80, Custom Convolutional Neural Network [5]	**0.83**

References (Optional)

[1] Roth *et al.* , Sensors, 2021; [2] Aristizabal Pla *et al.* , PLOS ONE, 2024 [3]; Anguita *et al.* , ESANN, 2013; [4] Ribeiro de Souza *et al.* , Front Neurosci, 2022. [5] O'Day *et al.* , J Neuroeng Rehabil, 2021.

Acknowledgements (Optional)

We thank Jun-Yan Zhu and Felipe San Martin for sharing their insights.

Session Category

Emerging Areas: N/A

P3-016

Reliability assessment of a neural network-based ecological framework for remote gait analysis in Parkinson's Disease

Mr. Giulio Rigoni[1], Mr. Oier Zazpe[1,2], Ms. Fabiola Spolaor[1], Prof. Damiano Varagnolo[1], Prof. Daniele Volpe[3], Prof. Zimi Sawacha[1]

[1]University of Padova, Padova, Veneto, Italy. [2]Mondragon Unibertsitatea, Mondragòn, Basque country, Spain. [3]Fresco Parkinson Foundation Villa Margherita, Vicenza, Veneto, Italy

Introduction

Global physiotherapy demand is rising, driven by aging populations and the increasing prevalence of neurodegenerative conditions like Parkinson's disease (PD). With growing complexity in treating neurological patients in traditional facilities, remote rehabilitation services are emerging as promising options, alongside methodologies for remote assessment of treatment effects. This study proposes a neural network (NN)-based framework to assess gait alterations in PD individuals through both kinematics (i.e., spatio-temporal and joint kinematics) and kinetics (ground reaction forces, GRF) relying only on video data.

Methods

We developed a NN-based approach that, from markerless-based (i.e., Pose2Sim [1]) anatomical landmarks (ALs) trajectories, identifies the stance phase and estimates three-dimensional GRFs through two NNs: 1. a Spatio-Temporal Graph Convolutional Network (ST-GCN); 2. a modified image-based NN [2]. A proprietary training dataset of 401 gait cycles from 39 healthy adults (45.40 ± 20.47 Years, 24.58 ± 3.57 kg/m^2) and 26 PD subjects (70.74 ± 7.56 Years, 25.78 ± 3.39 kg/m^2) was applied. For validation, gait data of 10 PD individuals (73.50 ± 6.64 years; BMI 25.39 ± 1.73 kg/m^2) not included in training were used. An 8-camera Vicon system, two Bertec force plates and two GoPro Hero7 cameras (sagittal and frontal) were used. Inverse kinematics was performed in OpenSim from AL trajectories obtained via Pose2Sim and marker-based data. GRFs were estimated through the two NNs using markerless AL trajectories and compared with force plate data through RMS, coefficient of multiple correlation and 1D-SPM [3].

Results

While large differences emerged between markerless and marker-based inverse kinematics (RMS>6.78°, **Figure 1.1**), both GRF predictors showed good agreement with the

experimental measures, particularly for the vertical and mediolateral components (**Figure 1.3**).

Noticeably, stance phase identification showed good accuracy (97.29%, **Figure.1.2**).

Discussion

The two ecological approaches show potential for remotely monitoring PD individuals, paving the way for gait analysis on individuals with pathological conditions using only common, off-the-shelf cameras.

Images (Optional)

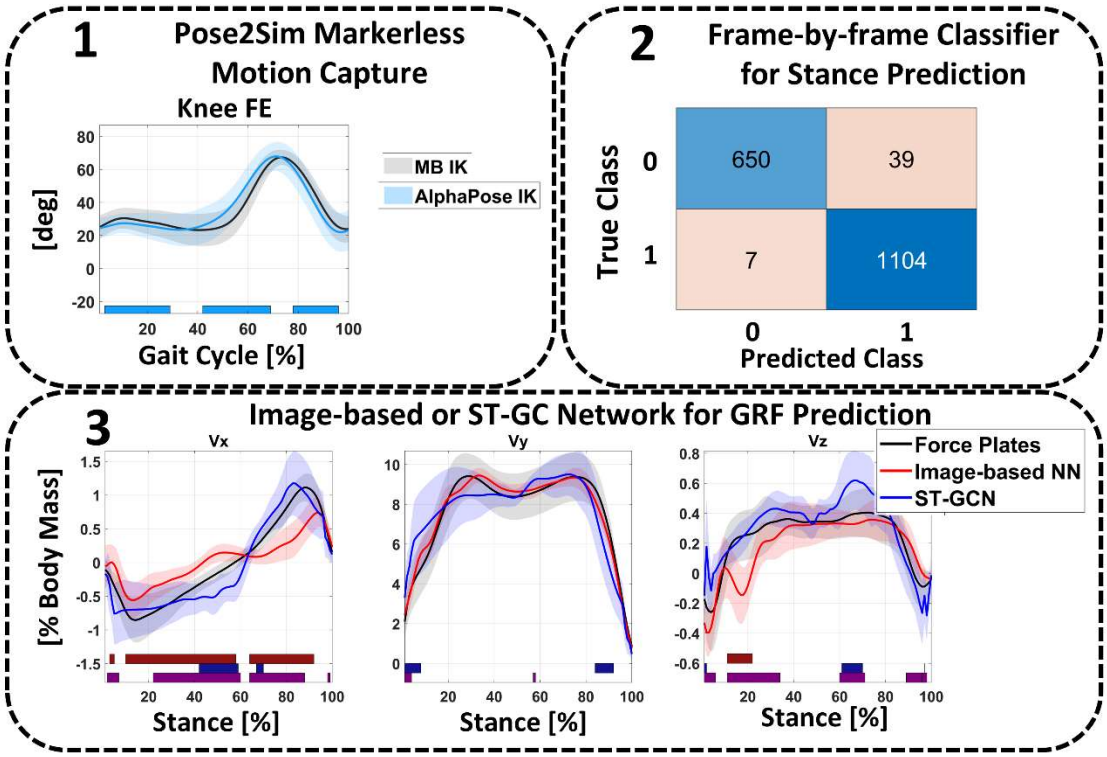


Figure 1. Workflow of the Proposed NN-based data processing

References (Optional)

[1] Pagnon D, et al., Sensors 2022.

[2] Johnson WR, et al. TBME. 2019.

[3] Pataky TC, et al. CMBBE. 2012.

Session Category

Emerging Areas: N/A

P3-017

Neural Network With Cross-Domain Knowledge Transfer From Force Plates to Wearable Insoles for the Estimation of 3D Ground Reaction Force components.

MSc Gloria Scanagatta[1,2], Dr Miel Willem[1], Dr Bryce A Killen[1], Prof Ilse Jonkers[1]

[1]KU Leuven, Leuven, Vlaams-Brabant, Belgium. [2]Università degli studi di Padova, Padova, Padova, Italy

Introduction

Accurately measuring ground reaction forces (GRFs) remains a major challenge in out-of-lab human movement analysis. This study proposes a deep learning framework capable of estimating three-dimensional GRFs from pressure insole data with high accuracy, enabling reliable force measurement in real-world settings.

Methods

Force platform (FP) data were recorded in a total of 36 participants (healthy and osteoarthritic) while walking on an instrumented treadmill at self-selected pace, afterwards 2 heathy subjects were acquired with sychronized data from FP and insoles. Data was preprocessed in MATLAB to segment stance phases, filter signals (Butterworth filter), and compute resultant force vectors for model training. A multilayer BiLSTM neural network with concatenate attention layer, global features, was developed and trained using supervised learning on gold standard FP measurements. The model was trained with a weighted Huber loss, given the high variability and limited amplitude of the Medio-Lateral(ML) and Antero-Posterior(AP) components of the GRFs during stance. Recurrent layers were selected to preserve temporal dependencies and reconstruct GRF waveforms. A patient-aware split was applied to create training, validation, and independent test sets. Final trained weights were deployed in an inference-only network on pressure insoles data and evaluated against the ground truth FP data.

Results

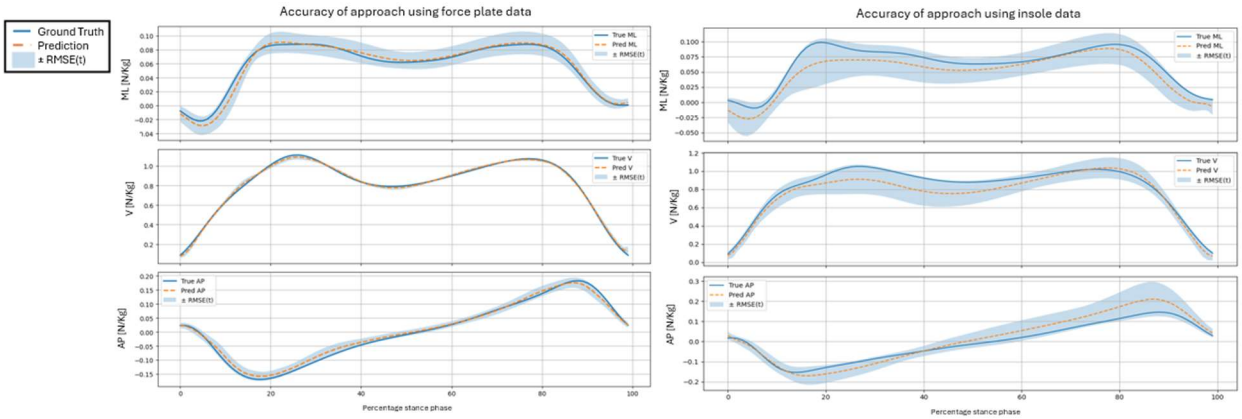
The network achieved excellent performance for FP data, achieveing for the vertical component, RMSE = 1.56 ± 0.35 %BW, NRMSE = 1.53 ± 0.31%, and correlation = 0.9983 ± 0.0007. When applied to insole data, errors slightly increased but remained robust, with NRMSE values below 19% and correlations above 0.90 for all three components. The vertical component showed the best generalization (NRMSE = 11.47 ± 1.66% and

correlation = 0.9542 ± 0.0093). Qualitative analysis (Figure 1), demonstrates that the network accurately learns the GRF pattern and maintains strong cross-domain generalizability.

Discussion

These results indicate the proposed deep learning approach generalizes effectively to unseen subjects and to data acquired from different modalities. It reaches accuracy levels consistent with in-domain validation studies found in the literature, despite no adaptation to the insoles domain. This work provides strong evidence that pressure insoles, combined with advanced neural network models, can serve as a reliable tool for estimating GRFs outside laboratory environments.

Images (Optional)



Session Category

Emerging Areas: N/A

P3-018

MoveDB: Toward a Scalable Biomechanics Database Platform for Reproducible Research

Mr. Hudson Burke

University of Virginia, Charlottesville, Virginia, United States

Introduction

One of the major challenges facing modern biomechanics research is a cohesive strategy to handle "Big Data". At the American Society for Biomechanics 2025 meeting, a majority voted that biomechanics was not prepared or capable of properly utilizing datasets at scale. Studies generate large volumes of complex data from motion capture, force plates, electromyography, and wearable sensors. However, the lack of standardized platforms hinders reproducibility and collaboration. MoveDB is an open source software platform addressing these challenges by providing scalable tools for data management, analysis, and sharing

Methods

Predominantly, the biomechanics community uses MATLAB for data analysis. While familiar and capable, MATLAB requires a license, which can be a barrier for collaboration, and as a closed-source platform with limited package management, it can lead to issues with reproducibility. Biomechanics datasets are also predominantly file-based, with C3D files being the most common format for motion capture data and OpenSim analyses relying on a wide variety of specific file types. Thus, MoveDB was developed using Python to leverage its strengths in data science, free and open source ecosystem, and portability. The core components of MoveDB include SQL for efficient querying of metadata, HDF5 for scalable management of time series data, EZC3D for reading C3D files, and OpenSim's Python API for biomechanical modeling and simulation.

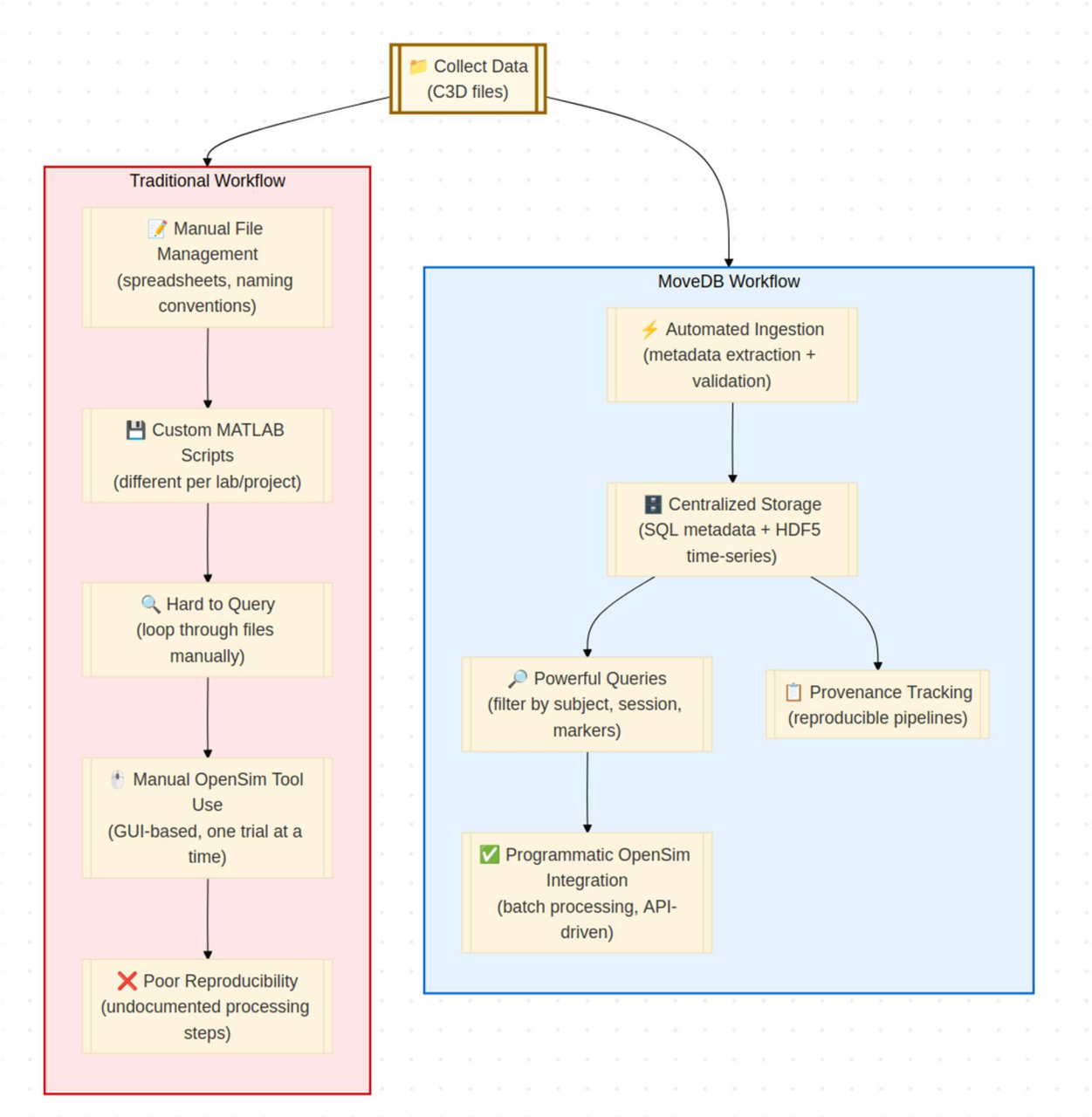
Results

The platform supports efficient data ingestion, allowing users to upload C3D files and automatically extract relevant metadata. Once ingested, users can perform complex queries to filter datasets based on various criteria, such as subject demographics, experimental conditions, or specific markers, and then utilize OpenSim's Python API to run batch simulations and analyses programmatically. MoveDB also enables flexible deployment options, from local installations for individual researchers to cloud-based solutions for larger collaborations.

Discussion

MoveDB is currently in active development, and community involvement is essential for its success. The project is open source, and we invite biomechanics researchers to contribute to the development of MoveDB by providing feedback, suggesting features, and participating in testing. By working together, we can create a robust and scalable platform that meets the needs of the biomechanics community and advances the field as a whole.

Images (Optional)



Session Category

Emerging Areas: N/A

P3-019

Improving Energy Expenditure Estimation From a Single Wrist IMU by Learning Musculoskeletal Joint Kinematics

M. Sc. Ilias Masmoudi[1], Dr. med. Elisabetta Gazzerro[2], Prof. Dr. Anne Koelewijn[1]

[1]Chair of Autonomous Systems and Mechatronics, Department of Electrical Engineering, Friedrich-Alexander-Universität Erlangen-Nürnberg (FAU), Erlangen, Bavaria, Germany. [2]Unit of Muscle Research, Experimental and Clinical Research Center Charité Universitätsmedizin and Max Delbrück Research Center, Berlin, Berlin, Germany

Introduction

Accurately estimating energy expenditure from wearable sensors is important for biomechanics, rehabilitation, and ambulatory monitoring. However, upper-limb energy expenditure estimation using a single wearable remains underexplored. We ask whether inferring internal joint kinematics from a single wrist inertial measurement unit (IMU) can improve estimates of upper-limb metabolic energy expenditure, by providing an intermediate, physiologically informed representation linking sparse external signals to muscle energetics.

Methods

Using the OpenSim MoBL-ARMS model (7 DOF, 50 musculotendon actuators) [1,2], we generated 5-s joint-angle trajectories by sampling sums of sinusoids with added Gaussian noise and randomized biases to produce diverse, plausible motions. A virtual wrist IMU with realistic noise produced accelerometer and gyroscope signals. Computed muscle control produced time-varying muscle excitations, and total metabolic energy expenditure was computed with the Umberger model [3]. Signals were resampled to 50 Hz and segmented into overlapping 1.0 s windows (10% overlap); each window was labeled by mean metabolic energy expenditure. Shoulder and elbow angles and angular velocities served as ground-truth kinematics. We trained four time-series neural networks: IMU-only → energy-expenditure, measured-kinematics-only → energy-expenditure, IMU + measured kinematics → energy-expenditure, and a two-stage pipeline: (1) IMU → predicted kinematics, (2) IMU + predicted kinematics → energy-expenditure. Performance was evaluated by test mean absolute percentage error (MAPE) on held-out runs.

Results

Test MAPE on held-out runs was: IMU-only 32.6%, Kinematics-only 26.6%, IMU+Kinematics 18.1%, and Two-Stage 19.3%. Incorporating measured joint kinematics reduced error by 44.5% relative to IMU alone, and the two-stage approach achieved comparable accuracy.

Discussion

Augmenting minimal wearable data with musculoskeletal joint kinematics substantially improves simulated upper-limb energy expenditure estimation. A learned kinematics estimator from a single wrist IMU can bridge sparse wearable signals and internal muscle energetics, enabling more accurate, low-burden monitoring. The study is limited to simulations and depends on model assumptions. Next steps include experimental validation with human participants, investigation of inter-individual variability and personalization, and assessment of real-time deployment.

References (Optional)

[1] Delp SL et al., IEEE Trans Biomed Eng, 2007
[2] Saul KR et al., Comput Methods Biomech Biomed Engin, 2015
[3] Umberger BR et al., J R Soc Interface, 2010

Session Category

Emerging Areas: N/A

P3-020

Assessing the Performance of Deep Learning 3D Reconstruction Models of the Pelvis from Bi-Planar X-Rays using Spinopelvic Parameters

Ms. Isabella Tierney, Ms. Marie De Mey, Mr. Jeffrey Lee, Dr. Stewart McLachlin, Dr. John McPhee

University of Waterloo, Waterloo, Ontario, Canada

Introduction

Preoperative planning using 3D pelvis reconstructions from computed tomography (CT) scans currently outperforms 2D X-ray preoperative planning in prosthetic matching and implant positioning. With advances in deep learning (DL), recent work aims to generate 3D pelvis reconstructions from bi-planar X-rays. However, due to the absence of publicly available paired X-ray and ground truth CT datasets, most studies generate synthetic X-rays using digitally reconstructed radiograph (DRR) techniques. However, 3D reconstruction models solely trained on DRRs may limit clinical translation, due to differences in appearance compared to real X-rays. To demonstrate, we created a paired bi-planar DRR/CT dataset using CTPelvic1k and TIGRE and our Attention U-Net model (PelvisNet) achieved a Dice score of 75.2%; however, when real X-rays were tested on the model the results were poor (Figure 1).

Methods

This study investigates the methods needed to generate accurate 3D reconstructions from X-rays. Since these X-rays do not have a corresponding ground truth CT scan, DL evaluation metrics cannot be used to assess the performance. Instead, the 3D reconstructions from both the X-rays and DRRs will be evaluated based on measurements of spinopelvic parameters such as pelvic incidence (PI), sacral slope (SS), and pelvic tilt (PT) using automatic 3D landmark detection methods [1-2].

To gauge the results from both DRR and X-ray reconstructions, an automated spinopelvic detection method for lateral X-rays, LanDet, with an accuracy of 98% for PT, will be used as the standard [3]. Methods for the translation of X-rays to be used on DRR trained models include style transfer using Cycle-CAN [4] and cropping/sampling methods.

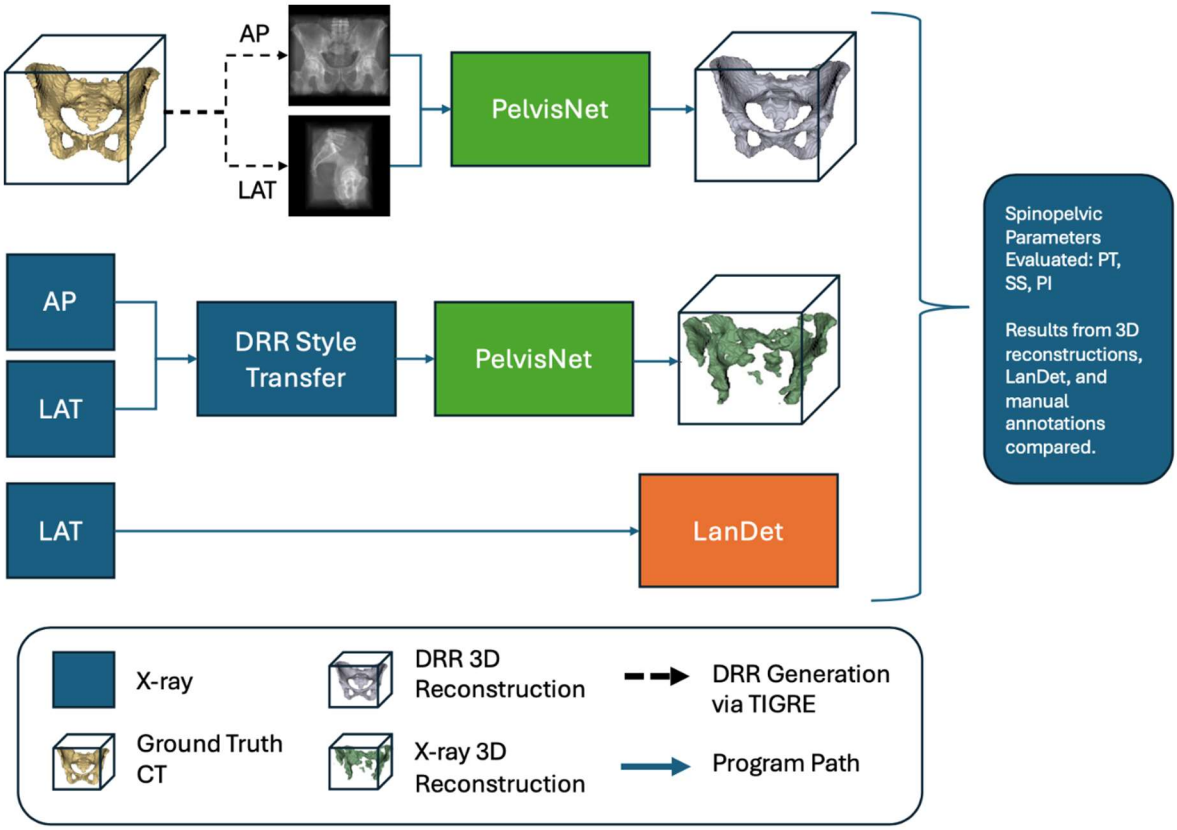
Results

Preliminary results are encouraging; final results will be included in the WCB presentation.

Discussion

To our knowledge, this will be the first study to evaluate 3D pelvic reconstruction models on X-rays using spinopelvic parameters, offering significant potential to improve and increase accessibility for pre-operative surgical planning.

Images (Optional)



References (Optional)

[1] M. Fisher et al., *Nature*, 2019.

[2] H. Chen et al., *J. Orthop. Surg. Res.*, 2019.

[3] A. Mohammadi Nasrabadi et al., *J. Orthop. Surg. Res.*, 2024.

[4] Kasten et al., *MLMIR*, 2020.

Session Category

Emerging Areas: N/A

P3-021

Kinematics-Based Technique Clustering of Freestyle Swimmers

PhD student Itay Coifman, MsC. May Hakim, Prof. Gera Weiss, Prof. Raziel Riemer

Ben-Gurion University of the Negev, Beer-Sheva, Israel, Israel

Introduction

Swimmers adapt their stroke mechanics based on race distance, individual strength, and physiological capacities. These adaptations may involve variations in limb motion(i.e, tchequnie), stroke rate, and stroke length, allowing athletes to optimize performance across different event demands[1,2]. The wrist trajectory is affected by the movement of the entire body and limbs. Therefore was used for the classification of swimming techniques by applying unsupervised clustering using wrist motion.

Methods

Motion of skeletal joints and keypoints (17) data were extracted from side-view videos of 155 swimmers (55 female) freestyle trials (n=254) using a custom human pose estimation pipeline [3]. The analysis focused on standardized wrist trajectories (see figure 1) to isolate the technique from differences in anthropometry, stroke rate. The distance between two trajectories was defined by using Dynamic Time Warping (DTW) combined with a term that accounts for the time displacements between two wrapped trajectories to measure the spatial and temporal distances. The K-Medoids algorithm was applied to this matrix to identify the movement archetypes. The number of clusters was determined using K that maximizes the silhouette score.

Results

The algorithm identified two distinct clusters, with statistically significant differences. Group-A(54%) was characterized by a Deep Push trajectory (depth μ=67.0), an early push phase (starting at μ=41.1%), faster trial times (μ=14.5s/ 25m), less time underwater (71.7%), and a higher stroke rate (μ=55.5 cycles/min). Group-B exhibited a Shallow Push trajectory (depth μ=56.93), a late push phase(starting at μ=49.8%), slower trial times (μ=15.4s/25m), more time underwater(75.0%), and a lower stroke rate (μ=45.3 cycles/min).

Discussion

Applying trajectory clustering to joint kinematics successfully distinguished swimmers by performance level. The distinct separation between profiles confirms that wrist displacement is a sufficient proxy for technical efficiency. The "Deep Push" group engaged

propulsion earlier and deeper (indicated by the higher normalized L value), correlating with higher velocity. These findings suggest that wrist trajectories are highly correlated with other key indicators of technique assessment. This enables coaches to use simplified guidelines for explaining different techniques.

Images (Optional)

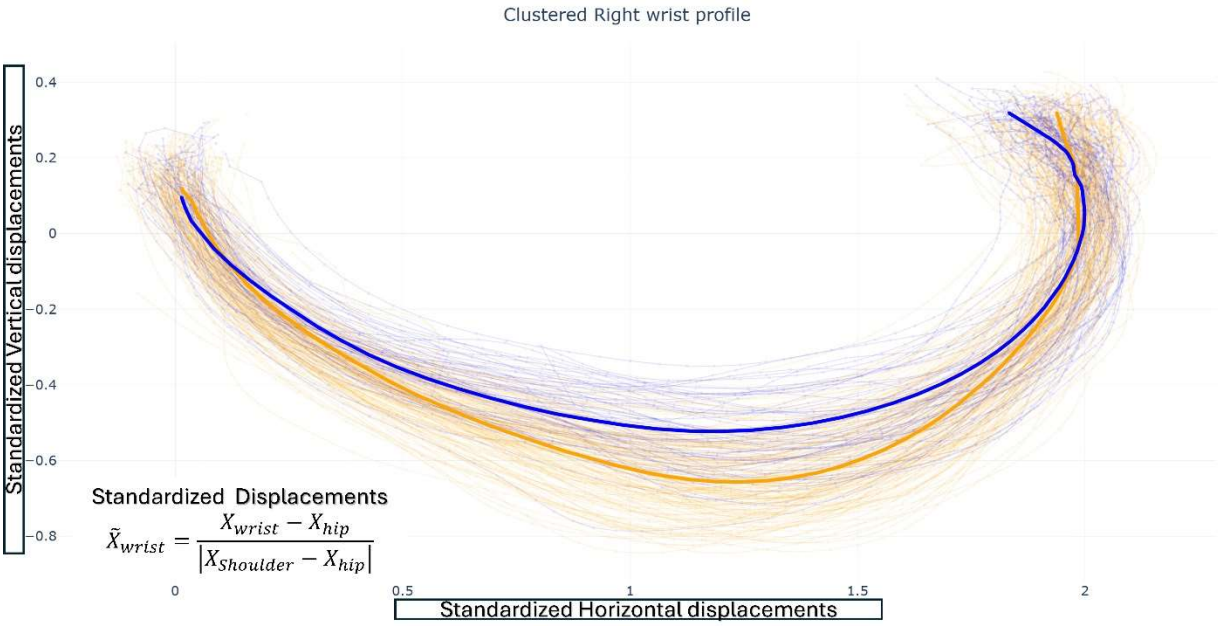


Figure 1: Standardized horizontal and vertical wrist displacement for Deep Push Cluster (Blue) and Shallow Push Cluster (Orange). Bold trajectory represents Cluster Average. Transparent trajectories represents individual samples.

References (Optional)

[1] Morais et al., Front Physiol, 2022 [2] McCabe et al., J Sports Sci, 2011 [3] Coifman et al., ISB, 2024

Acknowledgements (Optional)

This work was supported by Ben-Gurion University of the Negev through the Agricultural, Biological and Cognitive Robotics Initiative (funded by the Marcus Endowment Fund and the Helmsley Charitable Trust), the Sylvan Adams Fund, and partially supported by the Israel Innovation Authority.

Session Category

Emerging Areas: N/A

P3-022

Development of a Data Warehouse System for Storage, Analysis, and Downstream Applied Research with Multimodal Biomechanics and Injury Assessment Datasets Using Open Source Tools – Architecture and Proof of Concept

Dr. Mitchell Abrams PhD, Dr. Jason Luck PhD

Duke University, Durham, North Carolina, United States

Introduction

Biomechanics research groups rely on increasingly multimodal data in their projects. For example, one study could incorporate wearable data sources, survey data, laboratory testing, and video footage. While linking data sources by subject or collection session is feasible in small-scale studies, when scaling data collection efforts to hundreds or thousands of participants across multiple years and research sites, data aggregation and cross-referencing can become cumbersome, time consuming and computationally expensive. We develop here a framework for a robust, extensible technology stack using open source tools, facilitating data intake, processing, and analysis by researchers of multiple skill levels.

Methods

A technical stack consisting of Apache Iceberg (data lakehouse), MinIO (S3 object storage), Apache Spark + Hive (querying and metadata storage), Prefect (data processing workflows), Jupyter, Nimtable and Metabase (data analysis) was developed (see Figure). Docker containers running these services were deployed on a secure university server. For proof-of-concept analysis, a subset of data from an ongoing study was used. Wearable in-ear sensor data from youth football players (n=4; triaxial accelerometer and angular rate; Duke DASHR) was compared with weekly self-reported athletic activity contact exposure questionnaires (AACEQ) across 20 data collection sessions. Raw data were uploaded to the MinIO object store for staging, and preprocessed with Prefect (DASHR) and Jupyter notebooks (AACEQ). Jupyter and Metabase were used for analysis. Coarse event detection identified potential head acceleration events [HAE] (>10g). Events were considered on days where the athlete reported they participated in football-related activities, and had body-to-body contact, with or without head contact of another player or the ground.

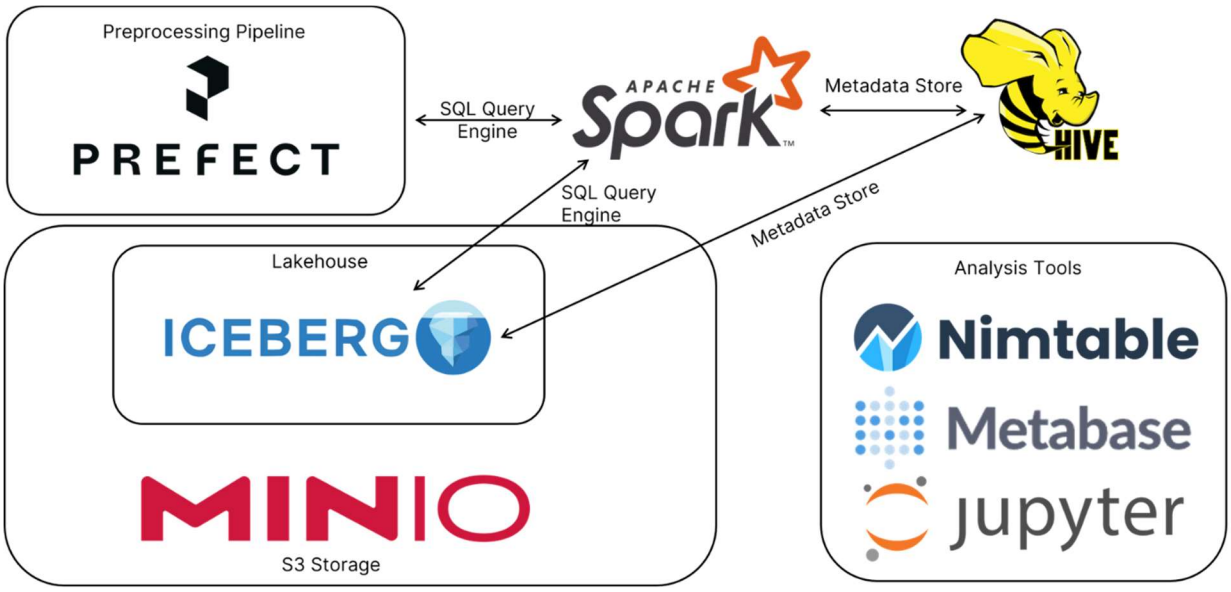
Results

On days with reported contact exposure, athletes sustained 353 potential HAE, averaging 17.7 events per athlete per day. On six days with reported contact, no HAE were detected in the wearable data.

Discussion

Deploying a robust technical stack enables and streamlines the application of data science methods to multimodal data sources. This sample analysis is easily completed in under an hour following data intake, and is readily extended with machine learning, AI, or other complex techniques. Using this system in a multi-site study would facilitate exploration of injury mechanisms and broader research questions.

Images (Optional)



Acknowledgements (Optional)

The authors acknowledge the support of Bass Connections at Duke University and the Duke University Center for Computational and Digital Health Innovation.

Session Category

Emerging Areas: N/A

P3-023

Determinants of thoracic aorta shape: a statistical analysis on a healthy subset of the UK Biobank

MSc Jellis Bollens[1,2,3], MSc Beatrice Moscoloni[1,4,5], BS Cameron Beeche[6,5], Prof. Nele Famaey[2], Prof. MD Julio A. Chirinos[5], Prof. Patrick Segers[1]

[1]Institute for Biomedical Engineering and Technology, Ghent University, Ghent, Flanders, Belgium. [2]Soft Tissue Biomechanics Group, Department of Mechanical Engineering, KU Leuven, Leuven, Flanders, Belgium. [3]Center for Global Health, University of Pennsylvania, Philadelphia, PA, United States. [4]Department of Biomechanical Engineering, Delft University of Technology, Delft, South-Holland, Netherlands. [5]Division of Cardiovascular Medicine, Hospital of the University of Pennsylvania, Philadelphia, PA, United States. [6]Department of Bioengineering, University of Pennsylvania, Philadelphia, PA, United States

Introduction

Understanding the natural variability and aging of aortic anatomy is essential for improving diagnosis, treatment planning, and computational modelling of thoracic aorta disease. Statistical shape modelling (SSM) provides a framework to quantify population-level geometric variation and identify factors driving aortic morphology differences. In this work, we developed a SSM of the healthy thoracic aorta to characterise its main modes of variation and assess how subject characteristics influence aortic geometry.

Methods

A subset of 1484 healthy individuals (aged 47-82 years; 50% male) was selected from the UK Biobank, and their aortas were segmented with a convolutional neural network [1]. After mesh extraction, spatial alignment and establishing point-to-point correspondence, principal component analysis (PCA) was applied to extract the dominant modes of anatomical variation in the population.

A multivariate analysis of covariance (MANCOVA) evaluated the combined effect of age, systolic & diastolic blood pressure, height, weight, and sex on the shape modes. Additionally, linear regression related PCA shape coefficients to these characteristics, enabling interpretation of how each factor influences aspects of aortic shape variation.

Results

The MANCOVA results demonstrated that all considered covariates significantly influenced aortic shape. Based on Pillai's trace, which quantifies the effect of each variable while adjusting for all others, age showed the strongest overall effect on aortic shape (0.31), followed by sex (0.13) and height (0.12).

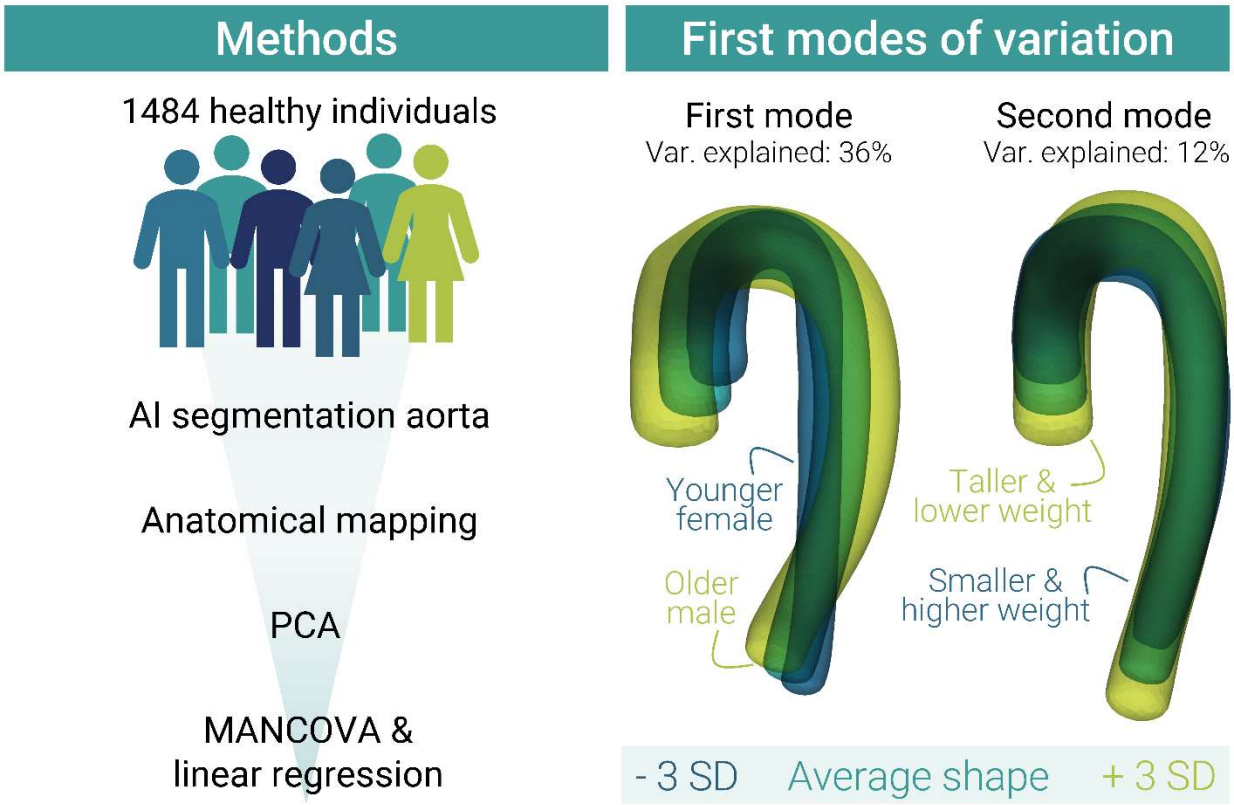
Age showed the largest effect on the first principal mode (see figure), explaining 36% of population variance and representing changes in aortic diameter and arch curvature; sex also mostly influenced this mode. Height and weight had the strongest impact on the second mode, explaining 12% of the variance, accounting for changes in length and in-plane curvature.

Discussion

The findings show that individual characteristics significantly shape aortic geometry, with age as the dominant factor, reflecting known age-related remodeling such as dilatation and increased curvature. Sex influences aortic geometry not only through scaling and dilatation but also through curvature, meaning male and female aortas are not simply scaled versions of one another.

Ongoing work will refine shape interpretation and enable generation of virtual aortic populations for *in silico* trials.

Images (Optional)



References (Optional)

[1] Beeche Cameron *et al.* , Eur Heart J, 2024

Acknowledgements (Optional)

This works was supported by the Research Foundation - Flanders (FWO) grant no: 11A3Q25N.

Session Category

Emerging Areas: N/A

P3-024

Towards a Single-Camera Markerless Approach to Quantify Upper-Limb Kinematics in Children with Cerebral Palsy

Ms. Jingwen Hu[1], Dr. Michelle Spirtos[1], Dr. Damien Kiernan[2], Prof. Ciaran Simms[1]

[1]Trinity College Dublin, Dublin, Dublin, Ireland. [2]Central Remedial Clinic, Dublin, Dublin, Ireland

Introduction

Upper-limb evaluation is essential for understanding movement difficulties and guiding treatment in children with cerebral palsy (CP). Conventional functional assessments rely largely on visual observation and are therefore qualitative and subjective. Marker-based multi-camera motion capture systems enable quantitative analysis but are costly, require dedicated laboratory environments, and do not reflect children's natural daily movements. A low-cost, single-camera markerless system (e.g., a mobile phone) that operates in everyday settings would greatly improve the accessibility of upper-limb kinematic assessment. This study investigates whether a transformer-based model can accurately and stably quantify upper-limb motion assessment in children with CP from single-camera recordings.

Methods

The transformer-based model predicts 3D upper-limb kinematics from single-camera 2D video. During training, to improve clinical applicability, the loss function was redesigned to incorporate not only keypoint position errors but also anatomically meaningful constraints, including skeleton segment-length consistency and joint-angle errors. Training data consisted of 3D motion-capture recordings collected with a marker-based multi-camera system. Model training and evaluation are planned to be conducted using upper-limb assessment data from children with CP.

Results

Preliminary training was performed using a small dataset of upper-limb assessment trials from six healthy adults. For the clinically relevant movement of shoulder abduction angle in upper-limb assessment, the model achieved a mean error of 3.1° with a standard deviation of 6.3°. Compared with an open-source baseline trained using a conventional loss function, the error of maximum shoulder adduction angle decreased from 6.7° to 4.1°. Continued training using the dataset of children with CP is expected to further reduce joint-angle errors and enable quantitative estimation across additional clinically relevant upper-limb assessments. These results will be presented.

Discussion

This transformer-based single-camera method may offer promising prospects as a low-cost and accessible tool for quantitative upper-limb assessment in children with CP. The current preliminary findings are limited to shoulder adduction, and further investigation is needed to determine whether the approach can provide reliable joint-angle measurements across other upper-limb functional tasks. Future work will include full training and testing on CP datasets, evaluation of repeatability, and assessment of agreement with clinical standards.

Images (Optional)

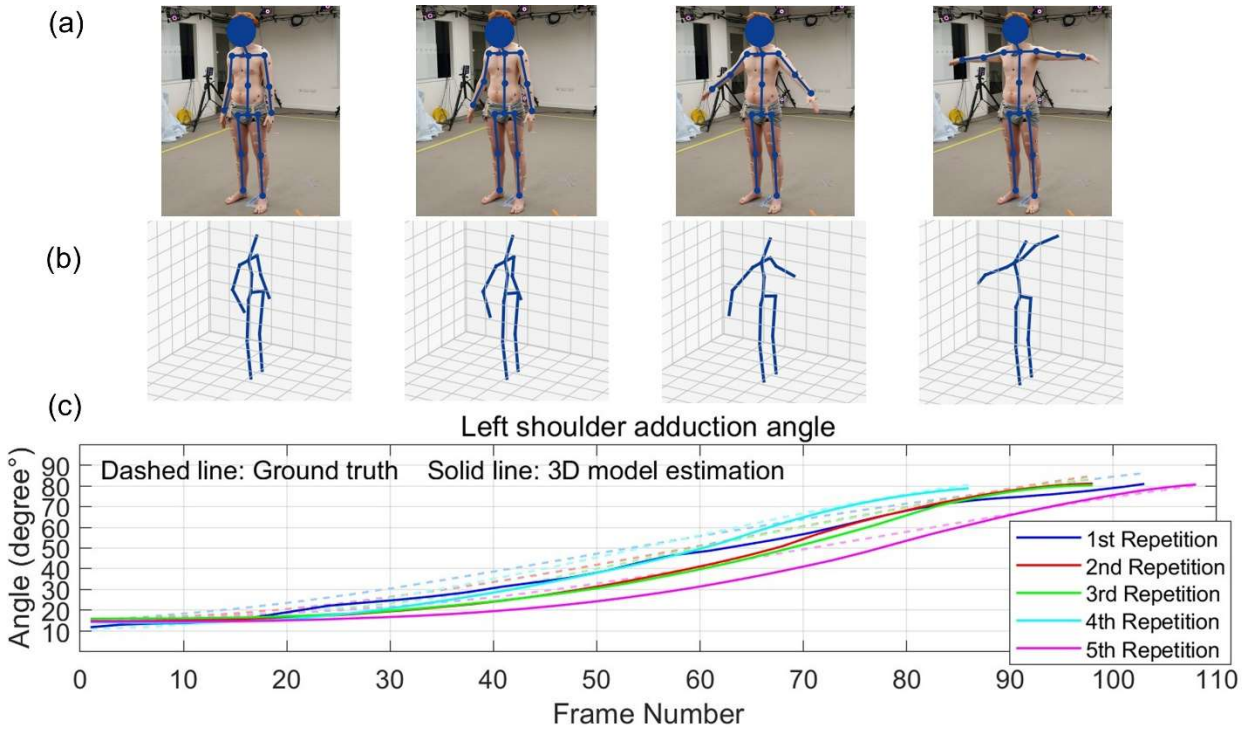


Figure 1. Quantification of shoulder adduction angle in the upper-limb assessment. (a) Input 2D video & 2D keypoints detected by the model. (b) Estimated 3D human pose. (c) Comparison between predicted Left shoulder adduction angle and ground-truth data.

Session Category

Emerging Areas: N/A

P3-025

Prediction of Skin Growth and Deformation in Tissue Expansion using Neural Ordinary Differential Equations

Mr Joel Laudo, Dr Adrian Buganza Tepole

Columbia University, New York, NY, United States

Introduction

Tissue expansion (TE) is widely used in reconstructive surgery, where the gradual inflation of a subcutaneous expander induces skin growth through stretching. High-fidelity finite element (FE) models can accurately predict deformation and growth outcomes, including in patient-specific applications [1], but their computational cost limits clinical deployment. In this work, using an idealized skin patch geometry, we develop a Neural Ordinary Differential Equation (NODE) framework that learns the dynamics of an FE-based TE model as an essential step toward real-time predictive tools for clinical use.

Methods

We performed a 1000-simulation design of experiments using a 150 mm diameter expander inflating a 300 × 300 mm square patch of skin. Material properties, growth parameters, and final inflation volume were varied in a Latin Hypercube Sample. Displacement snapshots across the dataset were projected to a reduced basis ($r = 9$) via Principal Component Analysis. An NODE designed to match the dependencies of the underlying FE model was trained to predict latent displacement and volume trajectories using an 80/20 train–test split. The NODE input included features from the PI-based FE volume controller (setpoint, error, integrated error). From the predicted displacement fields (following projection from latent to physical space), we solved the growth ODEs to predict principal growth stretch trajectories.

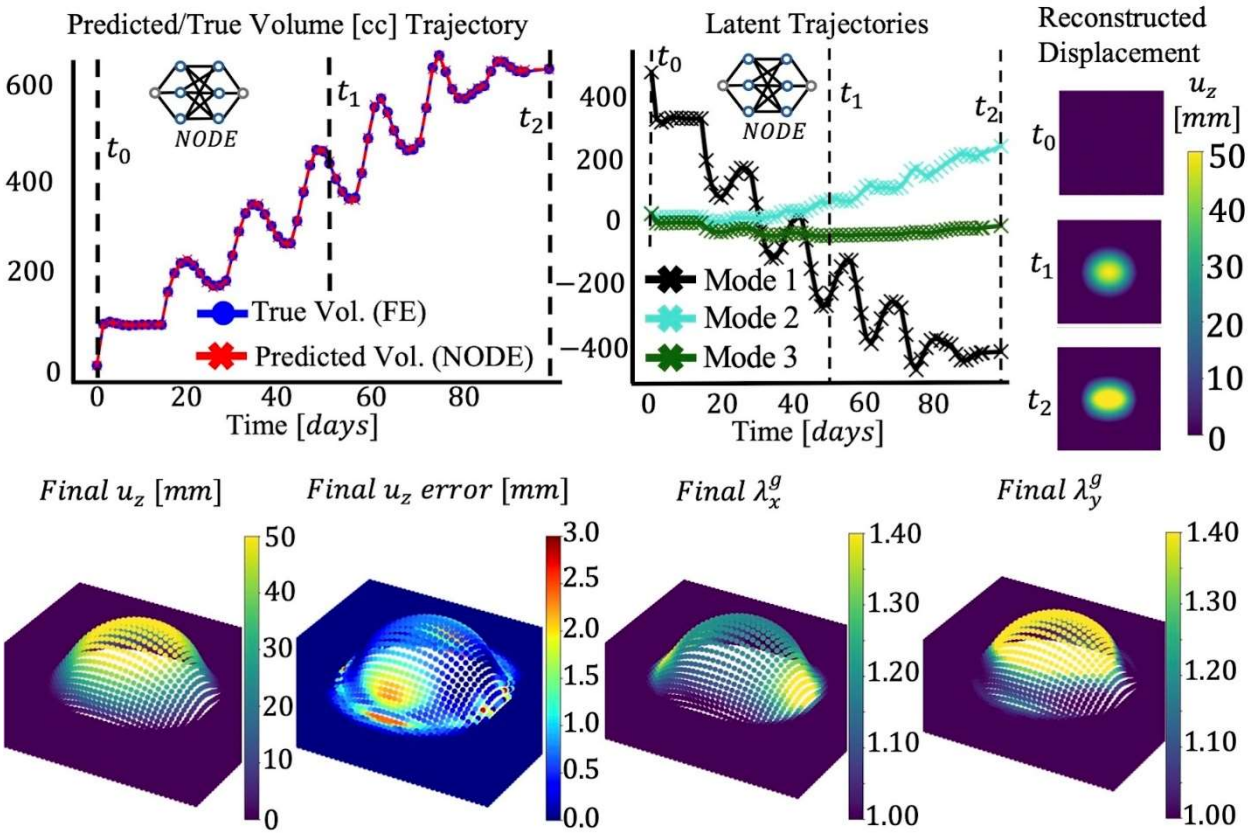
Results

We tested the NODE approach on 185 unseen validation simulations. At the final predicted timepoints, the relative displacement error was 3.2 ± 2.1%, the relative volume error was 0.78 ± 0.23%, and the relative growth principal stretch error was 1.9 ± 2.2%. The total mean prediction time was 24.5 ± 9.2 seconds, with latent trajectory prediction taking 0.073 ± 0.012 seconds, full displacement field reconstruction taking 0.35 ± 0.035 seconds and growth integration taking 24.0 ± 9.2 seconds.

Discussion

Even on an idealized geometry, the NODE framework achieves >200× speedup over FE simulations while preserving excellent accuracy. Additional optimizations (i.e. code parallelization) can increase speedup even more. This approach provides a foundation for future patient-specific surrogate models capable of real-time prediction of skin growth and deformation. Ongoing work will investigate model enhancements, alternative time-series architectures and projection-based reduced order models to achieve rapid, trustworthy predictions.

Images (Optional)



References (Optional)

[1] Joel Laudo *et al.*, Acta Biomaterialia, 2025

Session Category

Emerging Areas: N/A

P3-026

Unsupervised Clustering of Temporal-Spatial Biomechanics Identifying Functional Phenotypes Independent of Anthropometric Constraints

M.Eng. Julia Wilk, D.Sc., Ph.D., M.Eng. Cezary Rzymkowski

Warsaw University of Technology, Warsaw, Mazovian, Poland

M.Eng. Julia Wilk

Introduction

Kinematic, dynamic, and EMG data were merged from heterogeneous sources, including Moreira [1], Baček [2], Van Criekinge [3], Lencioni [4], Scherpereel [5], and Wei [6]. The primary objective was to replace anthropometric clustering with direct unsupervised biomechanical clustering. It was hypothesized that functional phenotypes depend on the feature set; therefore, magnitude-focused features were compared against temporal-spatial controls to determine how feature granularity alters gait strategy identification. This approach facilitates development of generalized biomechanical models applicable across populations.

Methods

From a consolidated dataset of 289 subjects, a standardized gait subset (N=171) was isolated. Preliminary anthropometric labels were projected onto the biomechanical space for evaluation. Subsequently, two feature extraction pipelines were implemented: a magnitude-focused set prioritising peak exertion (e.g., peak force) and a temporal-spatial set prioritising motor control (e.g., impact loading rate). Features were averaged across limbs, then Z-score normalised and clustered using k-means.

Results

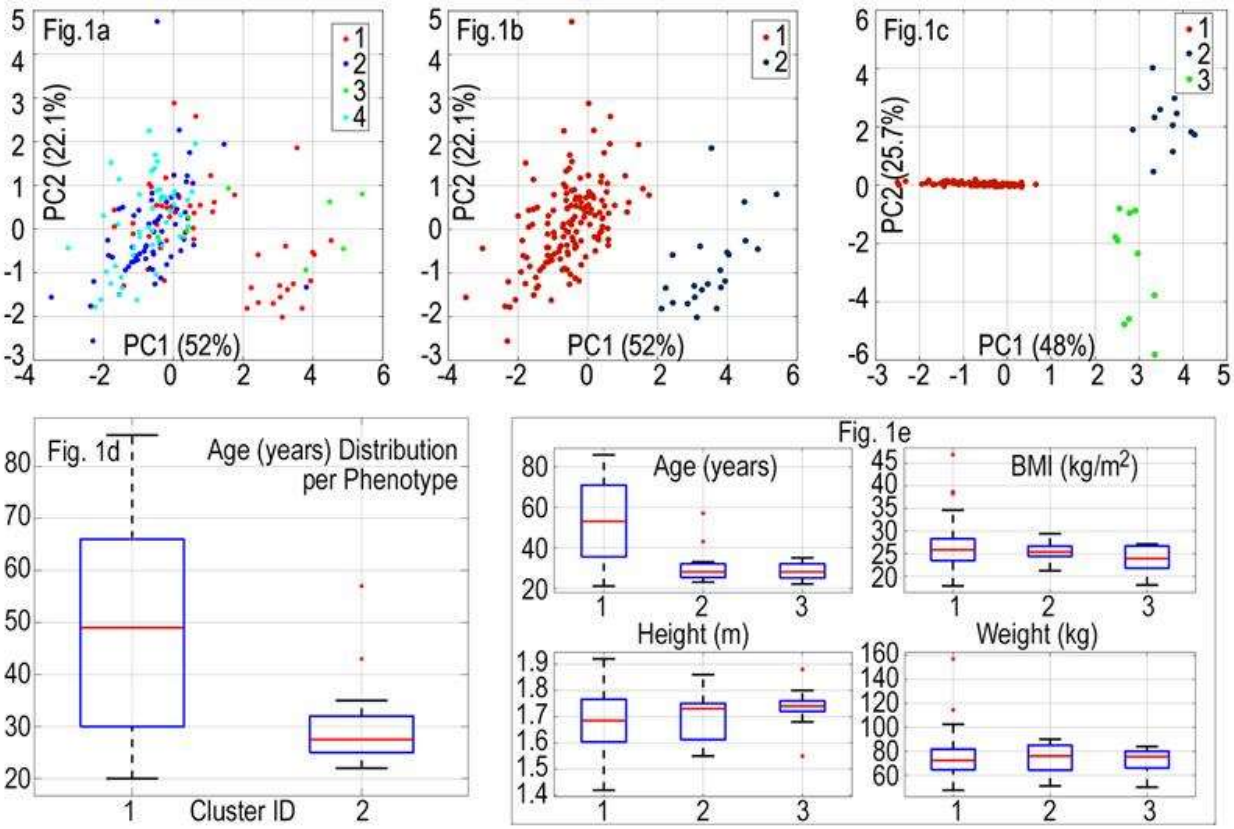
Anthropometric labels failed to predict movement strategy, evidenced by negative cohesion (Silhouette -0.109) where body-type clusters were dispersed randomly (Figure 1a). The magnitude-focused pipeline identified two age-correlated phenotypes (Silhouette 0.746), distinguishing between restricted-ROM/high-activation walkers and high-velocity/low-activation walkers (Figures 1b, 1c). Conversely, the temporal-spatial set revealed three clusters (Silhouette 0.858) (Figure 1d), distinctively isolating a "high-impact"

strategy characterized by a high loading rate. Demographic analysis (Figure 1e) confirmed these functional choices exist independently of anthropometric characteristic.

Discussion

The limitations of using anthropometry as a gait proxy are illustrated, as somatic labels failed to translate into distinct functional behaviours. While magnitude-based clustering recapitulated biological ageing, deeper insight was provided by temporal metrics, which isolated impact loading as a key discriminator. Distinct strategies were identified independent of body type, with the high-effort group demonstrating neuromuscular inefficiency via significantly higher muscle activation for standard stance times. Anthropometric clustering is rejected in favour of feature extraction to detect phenotypes missed by somatic data.

Images (Optional)



References (Optional)

[1] Luís Moreira et al., Scientific Data, 2021

[2] Tomislav Baček et al., Scientific Data, 2024

[3] Tamaya Van Criekinge et al., Scientific Data, 2023

[4] Tiziana Lencioni et al., Scientific Data, 2019

[5] Keaton Scherpereel et al., Scientific Data, 2023

[6] Wenhao Wei et al., Scientific Data, 2023

Session Category

Emerging Areas: N/A

P3-027

AI-Assisted Preoperative Osteosynthesis Planning for Complex Fractures

M.Sc. Julian N. Zierke[1], Dr.-Ing. Mark Heyland[1], PhD Tom Meyer[2], M.Sc. Alaa Bejaoui[3], Prof. Heiko Tzschätzsch[3], Dr. Niklas Tuttle[4], Dr. Sebastian Hölzl[4], Dr. Annika Steinmeier[4], M.Sc. Hongyou Zhou[5], PD Dr.-Ing. Philipp Damm[1], PD Dr. Timo A. Auer[2], Prof. Georg N. Duda[1], Prof. David A. Back[4]

[1]Julius Wolff Institute, Berlin Institute of Health, Charité – Universitätsmedizin, Berlin, Berlin, Germany. [2]Department of Radiology, Charité – Universitätsmedizin, Berlin, Berlin, Germany. [3]Institute of Medical Informatics, Charité – Universitätsmedizin, Berlin, Berlin, Germany. [4]Center for Musculoskeletal Surgery, Charité – Universitätsmedizin, Berlin, Berlin, Germany. [5]Technische Universität Berlin, Learning and Intelligent Systems, Berlin, Berlin, Germany

Introduction

Complex fractures, such as those of the proximal tibia, often pose a challenge in trauma surgery. The success of the operation depends, among other factors, on the experience of the surgeon [1]. Pre- and intraoperative support in the planning of the operation can help to provide more effective care for complex cases of repositioning and fracture stabilization. For this purpose, an AI-based algorithm was developed that provides evidence-based recommendations for anatomical repositioning and biomechanically optimal fracture fixation.

Methods

Starting from preoperative CT data, the workflow comprises several sub-algorithms, such as CT fracture segmentation using neural networks and virtual fracture reduction using spatial transformer networks, autoencoder architectures [2], and blackbox optimization for registration and prediction of the correct fragment repositioning. Subsequent fracture classification and landmark detection then enable recommendations for the selection and placement of the osteosynthesis using a decision algorithm based on surgical evidence from scoping reviews and retrospectively analyzed fracture cases with optional subsequent biomechanical evaluations (finite-element analysis). The main goal is to implement the planning algorithm on an internal server structure and make it accessible via a web-based application, supported by the Charité High-Performance Computing (HPC) cluster.

Results

After uploading a test case CT of a lateral tibial split depression fracture, the prototype of the web-based application executes the planning algorithm on an HPC cluster and provides recommendations for fracture reduction as well as implant type and placement. The results are displayed in several panels (Fig. 1), including a CT viewer (axial, coronal, sagittal) with segmentation, a text-based analysis section, and a 3D viewer for bones and implants.

Discussion

The initial website prototype was successfully implemented, and the first planning test case demonstrated correct plate selection and plausible positioning. However, several intermediate steps still required manual post-correction to ensure overall system functionality. Future work will focus on improving individual sub-methods, generating new training datasets for machine-learning-based CT segmentation, and adding automated biomechanical finite element analysis. At later stage, the application will be prospectively evaluated by surgeons in clinical practice.

Images (Optional)

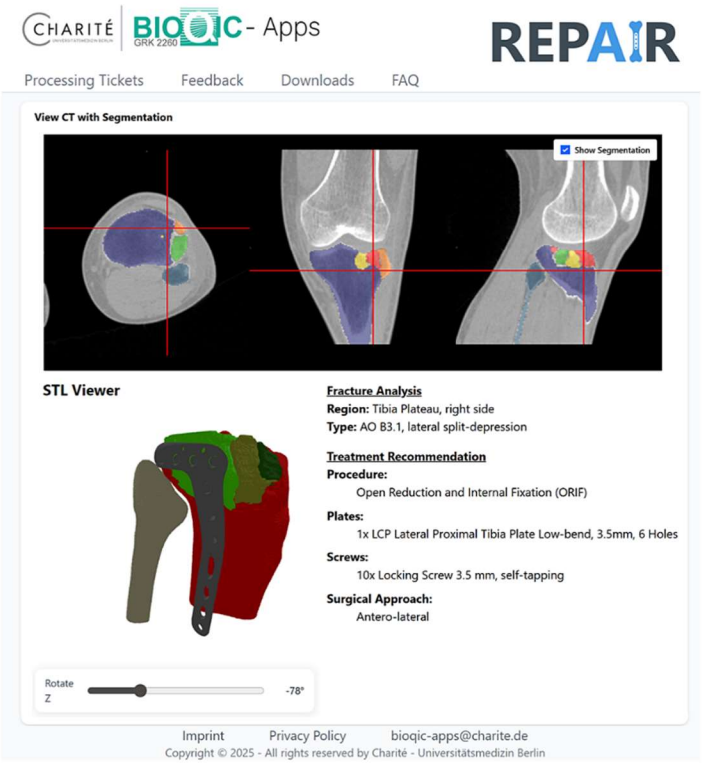


Fig. 1: Prototype of the web application displaying the results of osteosynthesis planning.

References (Optional)

[1] Maruthappu et al., Annals of Surgery 26:642-647, 2015

[2] Hongyou Zhou et al., Deep Generative Models. DGM4MICCAI, 2025

Acknowledgements (Optional)

REPAIR Project (https://repair.charite.de , G-BA, No. 01VSF22039), German Research Foundation (SFB1340 Matrix in Vision, GRK2260 BIOQIC, FOR5628), OrthoLoad Club

Session Category

Emerging Areas: N/A

P3-028

Promoting Efficient and Robust Exploration in Predictive Musculoskeletal Simulation by Decoupling Control and Exploration Spaces

Mr. Jun Hyuk Lee Master's Student, Prof. Jooeun Ahn Ph.D.

Seoul National University, Seoul, Seoul, Korea, Republic of

Introduction

Predictive musculoskeletal simulation is crucial in biomechanics for surgical support, rehabilitation, athletic performance optimization, and exoskeleton controller design. It also augments data when human experiments are limited or risky. Optimization in musculoskeletal simulation is harder than torque level robotics because the control space (muscle activations) and the exploration space (joint angles) are misaligned [1]. The activation–configuration mapping is highly nonlinear, making approximation difficult. Nevertheless, methods such as Proximal Policy Optimization (PPO) typically encourage exploration by maximizing entropy in the muscle activation space. This often yields inefficient exploration of the joint configurations that matter for task performance. We propose rewarding novelty directly in joint space to reduce this mismatch.

Methods

We used SCONE (Hyfydy) and Sconegym. We augmented the PPO reward with a Random Network Distillation (RND) [2] term. We applied RND to joint angle vectors and used the prediction error as a novelty score. The novelty score, scaled by an exploration coefficient, was added to the task reward. The policy acts in activation space, but the bonus is computed from joint space visitation. On a locomotion task, we evaluated whether broad early visits to diverse joint configurations improve early convergence and robustness.

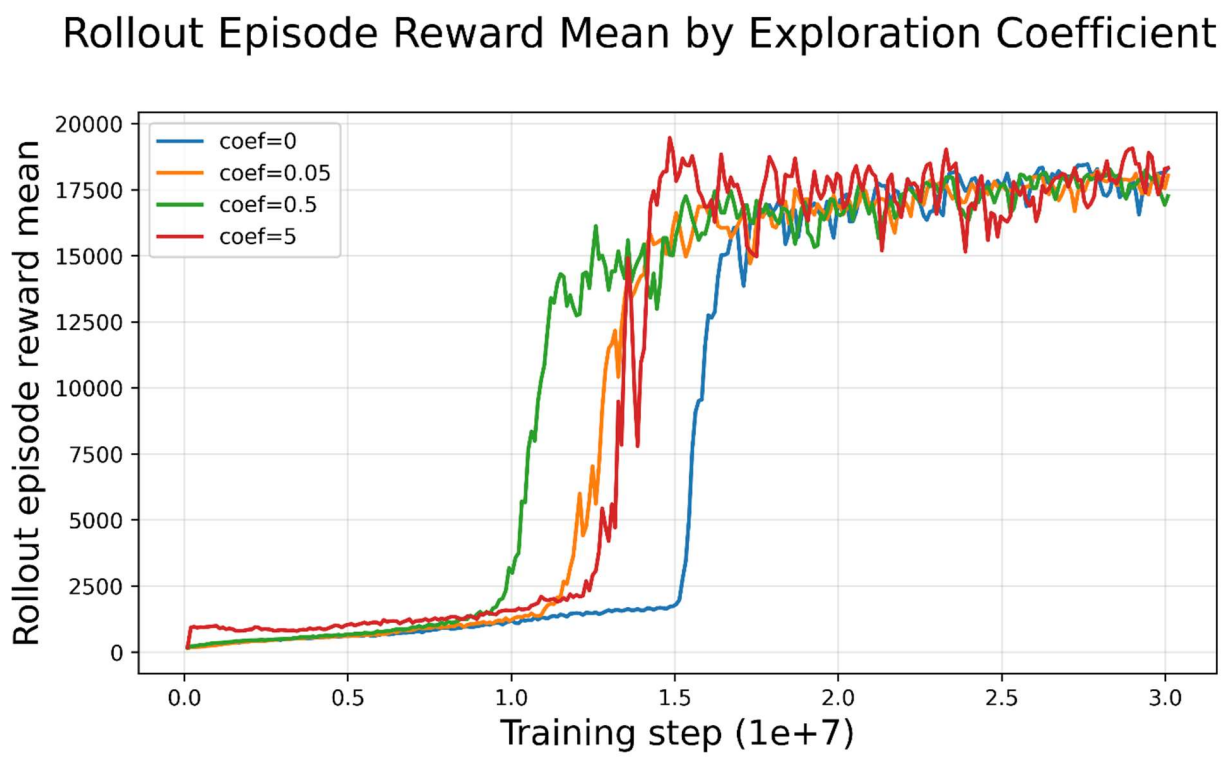
Results

Increasing the exploration coefficient noticeably improved early convergence, indicating more efficient exploration. However, excessively large coefficients delayed early convergence due to over-exploration. At very large coefficients, joint trajectories became unpredictable across gait cycles during plateaus, yet the agent remained robust and did not fall.

Discussion

A joint space visitation bonus mitigates the control-exploration gap and enables more sample-efficient exploration. Excessive novelty weighting can undermine training stability, motivating coefficient scheduling or adaptive tuning across training phases. We will test whether this approach achieves better optima than conventional exploration and greater robustness to perturbations.

Images (Optional)



References (Optional)

[1] D. Driess et al., 2018 IEEE International Conference on Robotics and Automation (ICRA), 2018.

[2] Y. Burda et al., arXiv preprint arXiv:1810.12894, 2018.

Session Category

Emerging Areas: N/A

P3-029

A Pilot Study on Utilization of a Conditional Generative Adversarial Network to Predict Wall Stress in Abdominal Aortic Aneurysm

Ms. Katherine Kerr[1], Dr. Indrani Sen MBBS[2], Dr. Joseph Wildenberg MD PhD[2], Dr. David Vorp PhD[1], Dr. Timothy Chung PhD[3]

[1]University Of Pittsburgh, Pittsburgh, Pennsylvania, United States. [2]Mayo Clinic Health Systems, Eau Claire, Wisconsin, United States. [3]University of Texas at San Antonio, San Antonio, Texas, United States

Introduction

Abdominal aortic aneurysm (AAA) is a localized dilation of the infrarenal aorta. AAA rupture, a biomechanical failure of the aortic wall, carries up to a 90% mortality rate. Biomechanics plays an important role in AAA stability, but finite element analysis (FEA), the gold standard for stress analysis, is time and expertise intensive. Prediction of stress maps from medical images directly could expedite clinical adoption. In this preliminary work, we train a conditional generative adversarial network (cGAN), Pix2Pix, to output stress maps based on input sections of AAA.

Methods

Computed tomography scans were acquired from Mayo Clinic Health Systems through DUA00004445. Five AAA cases were randomly selected. Each AAA was segmented using 3D Slicer, and FEA was performed in Abaqus using a validated in-house pipeline. A minimum of 600 axial slices per AAA were acquired orthogonal to the centerline. For model training, these slices were labelled based on the Euclidean distance of the wall to the centerline (i.e., radius) and used for input while the von Mises stress was used for the target. Pix2Pix[1] was trained for 10,000 epochs using a NVIDIA GPU workstation. The model consisted of eleven upsampling layers, thirteen downsampling layers, and six discriminator layers. The model was tested using 20% holdout testing, and the predicted stresses were compared to the ground truth by root mean square deviation (RMSE).

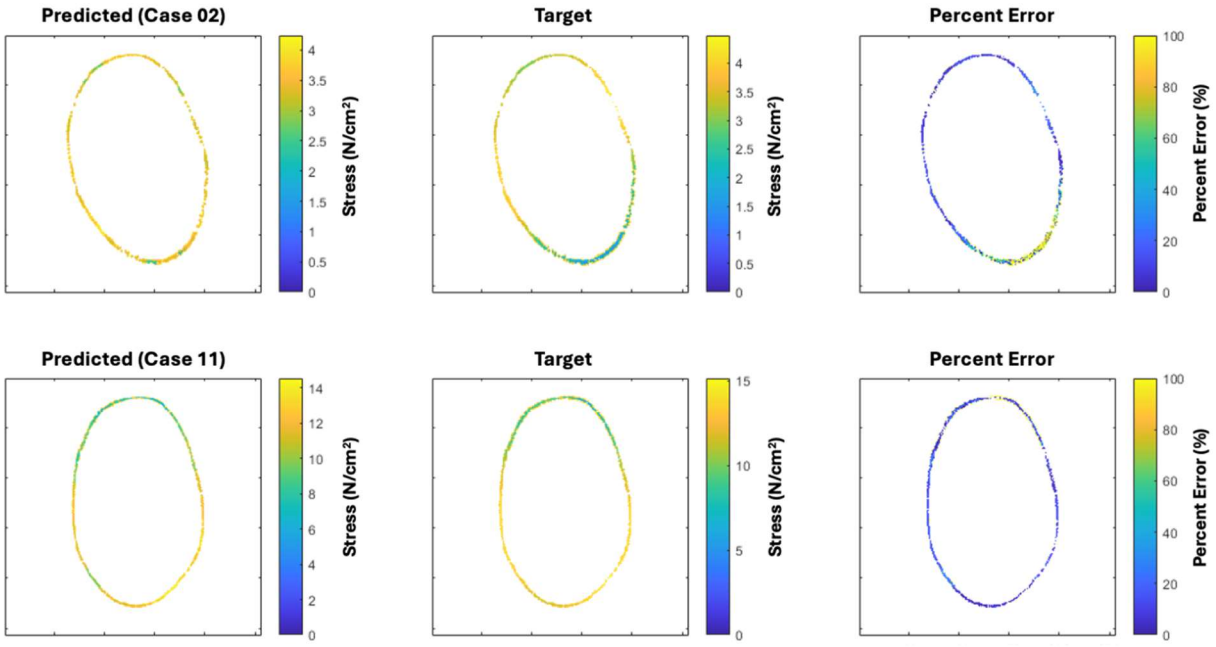
Results

The RMSE for von Mises stress for each case was 1.11 N/cm^2, 3.67 N/cm^2, 2.20 N/cm^2, 2.43 N/cm^2, and 2.01 N/cm^2 (average: 1.45 N/cm^2) and the mean percent error was 21.76%, 47.35%, 37.61%, 32.83%, and 13.58% (average: 31.33%). Figure 1 shows example slices.

Discussion

Stress analysis provides insight into the stability of AAA, but FEA limits clinical adoption. The cGAN trained in this preliminary work was able to predict stress with an average percent error of 31.33%. Limitations of this study include only five cases from a single institution being included. In the future, we will include more cases in our model training and testing, train a model directly from DICOM images, and further train the model using a GPU cluster.

Images (Optional)



References (Optional)

[1] P Isola et al., IEEE CVPR, 2017

Session Category

Emerging Areas: N/A

P3-030

Dynamic Finite Element Analysis of Breast Motion under Bra Support: Effects of Internal Structure and Bra Type

Prof. Kohei Murase Ph.D.[1], Prof. Mariko Inui Ph.D.[2]

[1]University of Osaka, Toyonaka, Osaka, Japan. [2]Kurashiki City College, Kurashiki, Okayama, Japan

Introduction

Brassieres (bras) support breast weight, but breast shape and glandular tissue distribution vary widely among individuals, so cup size alone may be insufficient for bra selection. This study used finite element analysis of MRI-derived breast geometries to examine deformation under two bras and clarify how internal structure affects reshaping and vibration.

Methods

Breast MRI was obtained in two C-cup women, and finite element models were generated by segmenting skin, adipose, and glandular tissues, each modeled as Neo-Hookean hyperelastic material. A “three-quarter-cup” bra with resin underwire along the breast base line and a wire-free “full-cup” bra were laser-scanned. Bra fit was reproduced by prescribing displacements at the straps, center front, and side panels. After applying gravity, a 1 Hz vertical harmonic base excitation simulating trunk motion during walking was applied, and breast displacement and skin strain were evaluated.

Results

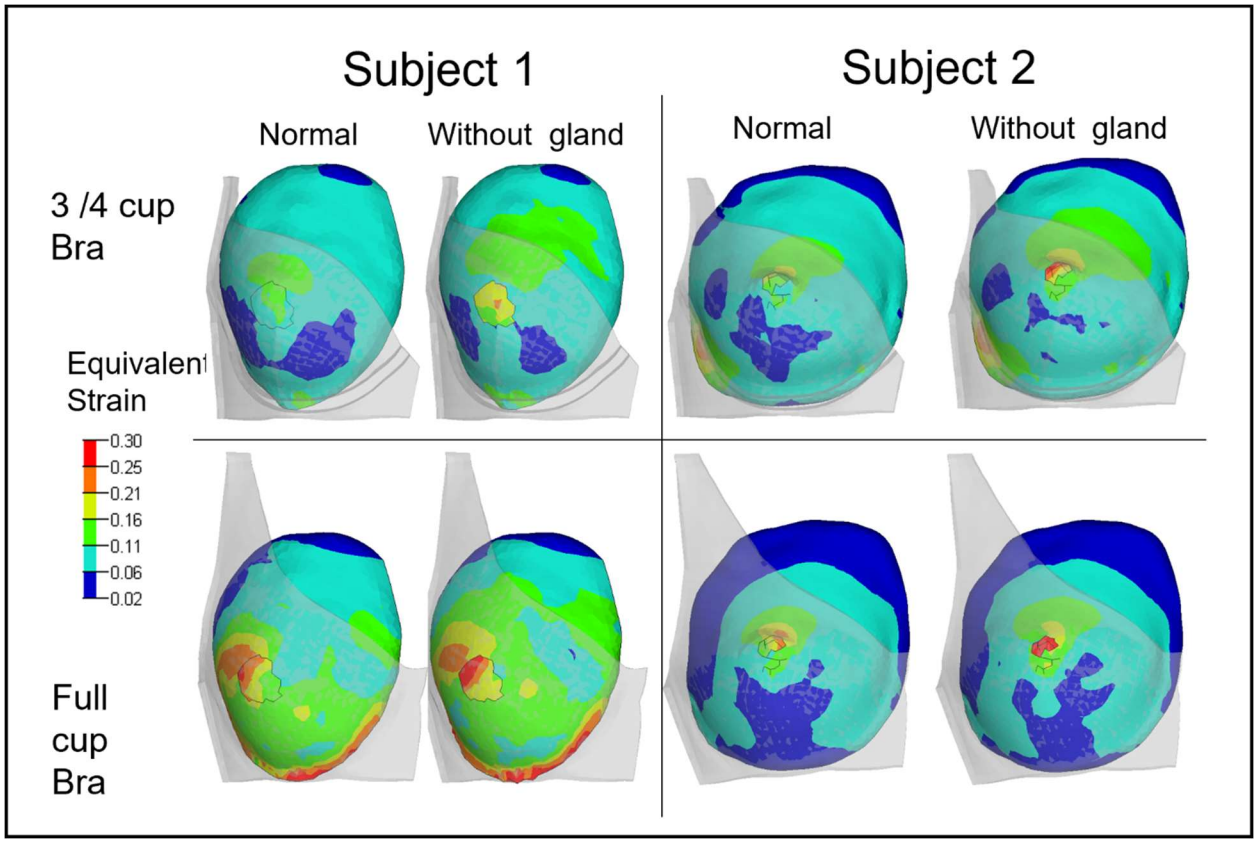
Simulated breast geometries under bra-wearing conditions closely matched those observed on upright MRI[1]. The three-quarter-cup bra produced greater cranial displacement and a more lifted contour, whereas the full-cup bra yielded a more compressed shape with limited upward movement. Despite the same cup size, the two subjects showed distinct skin strain patterns: in one, strain concentrated at the upper pole and medial region; in the other, it localized in the lower-lateral region. Under 1 Hz excitation, displacement amplitudes differed markedly between skin over glandular tissue and regions without glands, and larger, stiffer glandular regions were associated with higher skin strain around the gland boundary and nipple.

Discussion

These findings indicate that cosmetic and stabilizing effects of bras depend on breast morphology, particularly glandular volume and distribution, which decrease with age from

young adulthood to middle age [2], as well as on bra type and cup size. Dynamic vertical excitation made subject-specific differences in breast motion more evident. This simulation approach may support discussion of appropriate wearing conditions, such as strap adjustment and bra type selection according to individual morphology and age-related glandular changes, and provide a biomechanical basis for considering comfort and skin loading.

Images (Optional)



References (Optional)

[1] Mariko Inui et al. , Int. Clothing Sci. and Tech., 2012.

[2] Checka CM et al., AJR, 2012.

Session Category

Emerging Areas: N/A

P3-031

Temperature-Controlled Centrifuge Force Microscope for Exploring DNA-Protein Interactions

- Koushik Bar

Simon Fraser University, Burnaby, BC, Canada

Introduction

The development of technologies for precise single-molecule force measurements has substantially advanced research in single-molecule mechanics. This major successes has been aided by the development of instruments such as the AFM (Atomic Force Microscopy) and optical tweezers. Despite huge success, they come with a complex setup, high cost ($100,000+), difficulty in creating a large uniform force field, and can usually probe only one molecule at a time, making statistical analysis of single-molecule biophysics experiments notoriously tedious. Multiplexed magnetic-tweezer & early models of Centrifuge Force Microscopy (CFM) [1] are potential cost-effective alternatives, which can provide significantly higher-throughput measurements. Further development of CFM to increase throughput and features like temperature control can lead to significant improvement in fundamental molecular understanding of force-dependent biological interactions.

Methods

We have developed a temperature-controlled, cost-effective (~$200) CFM for single-molecule force spectroscopy with higher throughput, capable of measuring temperature-influenced force response of thousands of single molecules in parallel. This next-generation CFM is a further development of the work of Kirkness and Forde [2], where a commercial benchtop centrifuge was used for applying piconewtons forces to single molecules. In this new CFM, we incorporate remote temperature control with an accuracy of ±0.1 °C. We have massively increased the throughput (> 1000 molecules per run) compared to earlier models [1,2].

Results

To showcase the capabilities of our newly developed CFM, we are investigating the interaction between LacI proteins and DNA. This study focuses specifically on sequence-dependent dissociation rates and temperature-dependent kinetics measured at different forces. Our initial observations have revealed sequence-dependent off-rates. The next phase of this study focuses on quantifying the kinetics of these interactions at physiological temperatures.

Discussion

Although prior studies have explored LacI binding with force-dependent assays [3], they have been limited to room temperature and capture a significantly lower number of binding events than enabled by CFM. Our study leverages a much larger ensemble of single-molecule LacI-DNA interactions, which will help elucidate a more robust understanding of the binding mechanism of LacI to DNA. Furthermore, it serves as a powerful-demonstration of our newly-developed tool's capabilities.

References (Optional)

[1]-Halvorsen et.al. Biophysical-Journal, 2010

[2]-Krikness et.al. Biophysical-Journal, 2018
[3]-Tempestini et.al, Nucleic-Acids-Res. 2018

Acknowledgements (Optional)

Authors: K Bar[a], T Kekic[b], A Zink[c], B Höcker[c], H Linke[b], NR Forde[a]

[a]Department of Physics, Simon Fraser University, Burnaby, BC V5A 1S6, Canada
[b]NanoLund and Solid State Physics, Lund University, Box 118, 221 00 Lund, Sweden
[c]Department of Biochemistry, University of Bayreuth, 95447 Bayreuth, Germany

Funding:
NSERC - Natural Sciences and Engineering Research Council of Canada
CFI - Canada Foundation for Innovation

Session Category

Emerging Areas: N/A

P3-032

Accurate Estimation of Articular Hip Loading in Hip Osteoarthritis From a Physics-Informed Smart Garment

Mr Bradley Cornish BExSc, A/Prof Claudio Pizzolato PhD, A/Prof David Saxby PhD, Dr Nathan Lyons PhD, Dr Yana Salchak PhD, Dr Matthew Worsey PhD, Prof Laura Diamond PhD

Australian Centre for Precision Health and Technology, Gold Coast, Queensland, Australia

Introduction

Articular loading is necessary for cartilage remodelling, though abnormal loading (insufficient, excessive, or concentrated) drives cartilage degeneration. Hip articular loading is modifiable with gait retraining, which may promote cartilage health and slow osteoarthritis (OA) processes, but cannot currently be measured in natural environments. This study assessed the validity of a smart garment that used a physics-informed neural network (PINN) to estimate hip angles, moments, muscle forces, and contact forces in a person with hip OA during walking.

Methods

One female participant with moderate hip OA completed two gait retraining sessions 1-week apart on an instrumented treadmill whilst equipped with optical motion capture, electromyography (EMG), and custom smart-shorts which included 3 inertial measurement units and recorded EMG from 4 muscles. The participant walked using nine gait modifications, aided by visual biofeedback.

Hip angles, moments, muscle and contact forces for each gait modification were calculated using OpenSim and an EMG-assisted NMS model. A previously developed PINN was finetuned using smart-short data recorded from the first session. The PINN was then used to estimate hip angles, moments, muscle and contact forces for smart-short data recorded during the second session and compared to NMS outputs.

Results

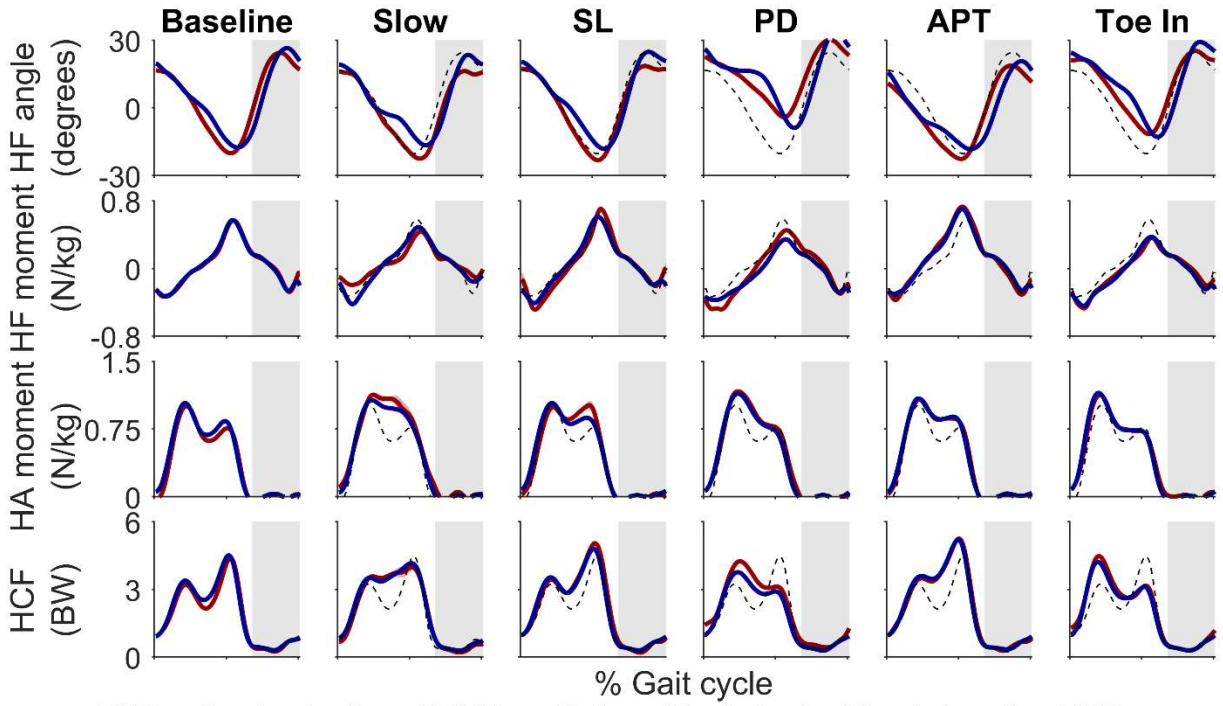
The PINN estimated hip angles, moments, muscle and contact forces with low error compared to NMS (RMSE: 5.71±1.05 degrees, 0.07±0.02 N.m/kg, 0.41±0.42 N/kg, and 0.24±0.06 BW, respectively) (Figure 1). Peak hip contact force showed excellent agreement between NMS and PINN (r^2: 0.82, slope: 0.91) with limits of agreement between -0.48 and 0.34 BW (-10.7 to 6.8% of peak). Gait modifications had distinct responses (i.e., increases

or decreases to peak contact force) for which the PINN correctly accounted. The minimum detectable difference at 90% confidence was 0.33 BW (~7.4% change from baseline peak).

Discussion

The smart garment detected small changes in hip motion and loading that occurred during gait retraining interventions, which are highly relevant to cartilage health and adaptation. Future work will retrain the PINN using a large sample of people with hip OA to provide a generalisable, affordable, and scalable gait retraining system capable of measuring person-specific hip biomechanics out of the laboratory.

Images (Optional)



NMS estimates (red) and PINN predictions (blue). Dashed line is baseline NMS.
SL = Increased step length, PD = decreased contralateral pelvic drop, APT = Anterior pelvis tilt, HF = hip flexion, HA = hip adduction, HCF = hip contact force

Session Category

Emerging Areas: N/A

P3-033

Generative Ai and Synchrotron Imaging Uncover a Connectivity-Controlled Mechanical Regime in Bone

Prof. Laura Vergani[1], Dr. Federica Buccino[1], Dr. Milad Masrouri[2], Prof. Zhao Qin[2]

[1]Politecnico di Milano, Milano, Lombardy, Italy. [2]University of Syracuse, Syracuse, New York, United States

Introduction

Bone's mechanical competence emerges from its hierarchical architecture, yet how mechanical laws transition across scales—and how osteocyte lacunar morphology governs local stiffness—remains unresolved [1]. Traditional metrics such as bone mineral density poorly predict fragility, highlighting the need for mechanistic, architecture-informed descriptors.
This study integrates synchrotron imaging, physics-based micromechanics, and generative AI to reveal previously inaccessible structure–function relationships and to determine whether lacunar-scale mechanics follow a distinct scaling law beyond classical trabecular behavior.

Methods

In-situ synchrotron micro-tomography (voxel: 1.6 μm) was performed on human femoral trabeculae from healthy, osteoporotic, and Covid-19–affected donors. These scans provided both macroscopic deformation and lacunar-scale detail. To overcome the limited statistical sampling inherent to synchrotron imaging, we trained a class-conditional denoising diffusion probabilistic model on 1,500 slices, generating realistic synthetic microstructures with disease-specific morphological signatures.
Thousands of real and AI-generated tiles (160×160 μm^2) were used in tensile simulations using a bead–spring elastic network governed by a Morse potential calibrated to trabecular tissue. Morphology–mechanics surrogate models were trained to map lacunar descriptors and image embeddings to local stiffness, strength, and toughness.

Results

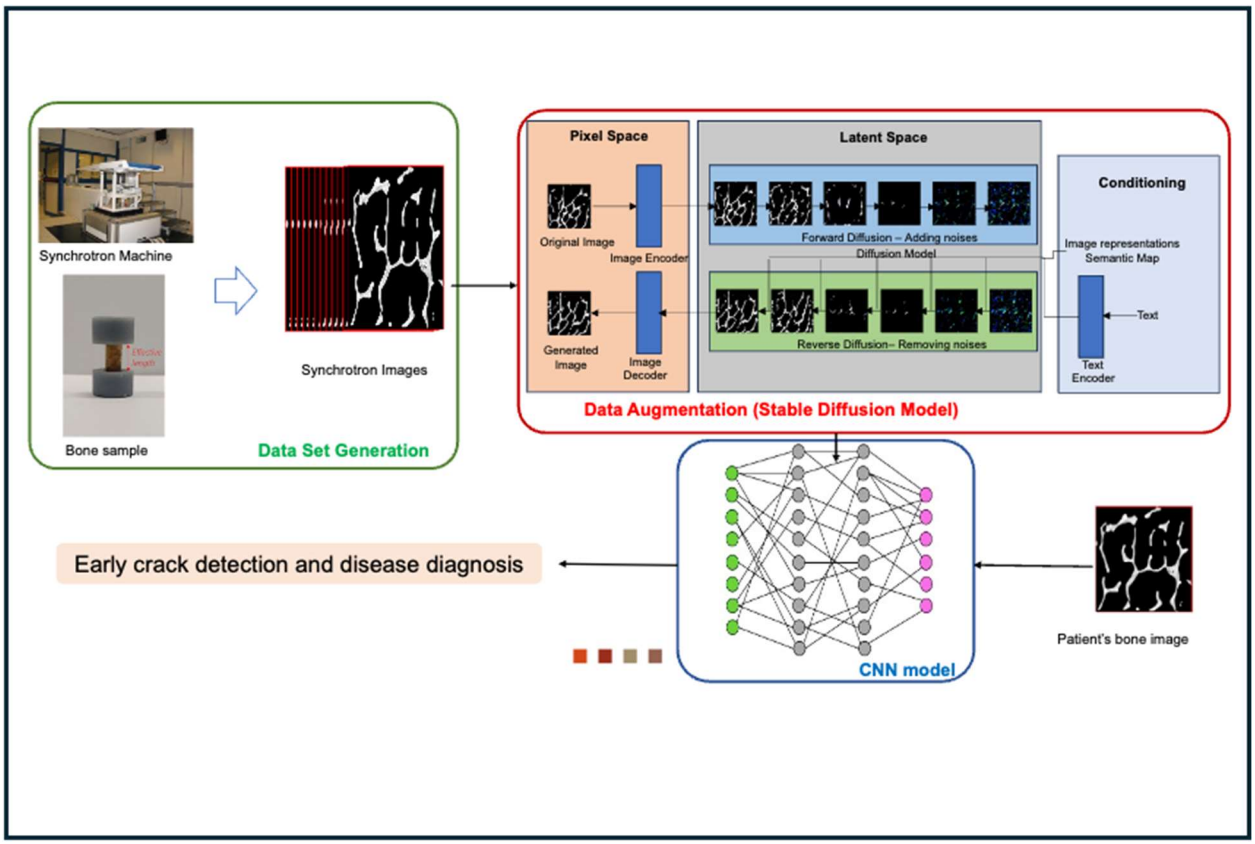
Macroscopic tests reproduced the classical Gibson–Ashby scaling ($E \propto (BV/TV)^2$). In contrast, lacunar-scale simulations revealed a hypersensitive stiffness law, E ∝ (BV/TV)^m, where $m \approx 6$, indicating a transition to a rigidity-percolation regime. A 5% decrease in local tissue fraction resulted in ≈25% loss of stiffness, consistent with stress-field coalescence around interacting lacunae. AI-generated microstructures reproduced pathological increases in lacunar density and oblateness, enabling robust statistical inference.

Surrogate models yielded high accuracy (R^2: stiffness 0.95), visualizing heterogeneity as compliant pockets embedded within stiff zones.

Discussion

AI-augmented multiscale mechanics revealed a scale-dependent transition in bone's mechanical law: from bending-dominated trabecular mechanics to topology-controlled lacunar percolation. This provides a mechanistic explanation for the fragility observed in osteoporosis and Covid-19–affected bone, where small morphological changes drive large stiffness losses. The work demonstrates how diffusion models, in silico testing, and surrogate mechanics overcome data scarcity, enabling patient-specific mechanical risk estimation.

Images (Optional)



References (Optional)

[1] Rowe, J. *et al. Prog. Mater. Sci.* 2025

Acknowledgements (Optional)

The authors acknowledge that the presented work was realized using the infrastructure provided by the Euro-BioImaging initiative https://www.eurobioimaging.eu/

F.B and L.M.V. acknowledge the financial support from the European Union Horizon Europe research and innovation programme under the Marie Skłodowska-Curie (MSCA) grant agreement No 101120290 (GAP).

F.B. and L.M.V. acknowledge financial support under the National Recovery and Resilience Plan (NRRP), Mission 4, Component 2, Investment 1.1, Call for tender No. 104 published on 2.2.2022 by the Italian Ministry of University and Research (MUR), funded by the European Union – NextGenerationEU– Project ARCHIMEDES – CUP D53D23003940006 - Grant Assignment Decree No. 2022R4KA9X adopted on 02/02/2022 by the Italian Ministry of Ministry of University and Research (MUR).

Session Category

Emerging Areas: N/A

P3-034

Feasibility of Extracting Spatio-Temporal Gait Parameters from Foot-Mounted Inertial Sensors in Hereditary Spastic Paraplegia

Mr. Connor LaBo, Ms. Alondra Rodriguez, Mr. Peter Nguyen, Ms. Isha Verma, Ms. Jodi Mullet, Mr. Lauro Ojeda, Dr. John Fink, Dr. Hugo Gonzalez Villasanti

University of Michigan, Ann Arbor, MI, United States

Introduction

Hereditary spastic paraplegia (HSP) causes progressive gait disturbance [1]. Traditional assessments are resource-intensive, limiting routine use. Wearable inertial measurement units (IMUs) provide a compact, continuous alternative, though their utility in HSP is underexplored. This study evaluates whether foot-mounted IMUs can reliably extract spatio-temporal gait parameters in HSP patients. Demonstrating feasibility could support the wider use of wearable sensors for objective gait assessment in clinical care.

Methods

This study assessed the feasibility of extracting spatio-temporal gait parameters from foot-mounted IMUs in HSP patients. Forty-four participants (38 uncomplicated UHSP, 6 complicated CHSP [2]) who walked independently were recruited; those using assistive devices or with incomplete data were excluded. After consent, subjects performed a 2-minute walking test with Xsens DOT IMUs on both feet and trunk. Data were collected at 100 Hz (accelerometers ±16g, gyroscopes ±2000°/s) [3]. Signals were processed and stance/swing phases segmented [4]. Descriptive statistics compared parameters by diagnostic group.

Results

IMUs reliably extracted spatio-temporal gait parameters in HSP. Median stance time ranged from 0.421–0.582 s (UHSP) and 0.461–0.813 s (CHSP). Swing times were 0.649–0.729 s (UHSP) and 0.665–0.887 s (CHSP). Swing speed ranged from 1.32–1.86 (UHSP) and 0.728–1.61 (CHSP), showing longer swing phases and slower speeds in CHSP. The workflow was consistent and confirmed the feasibility of wearable IMUs for objective gait quantification in HSP.

Discussion

This study shows foot-mounted IMUs reliably capture spatio-temporal gait metrics in individuals with HSP. IMU-derived parameters, such as stance time, swing time, and swing speed, aligned with expected clinical patterns and were consistently obtained across the

cohort. IMUs offer a practical, portable alternative to traditional lab-based systems, supporting objective gait assessment and frequent, longitudinal monitoring. These findings highlight the promise of wearable IMUs for improving clinical care and research in neurologic gait disorders.

References (Optional)

[1] J. K. Fink, Acta Neuropathol, 126(3), 307–328, 2013.
[2] J. K. Fink, CONTINUUM, 27(1), 185–204, 2021.
[3] L. Ojeda, J. Borenstein, J Navig, 60(3), 391–407, 2007.
[4] J. R. Rebula et al., Gait Posture, 38(4), 974–980, 2013.

Session Category

Emerging Areas: N/A

P3-035

Roadmap for building the Virtual Human Twin

Prof. Dr. Liesbet Geris

University of Liège, Liège, Wallonia, Belgium. KU Leuven, Leuven, Flanders, Belgium. VPH Society, Leuven, Flanders, Belgium

Introduction

Research into the use of computer modeling and simulation in all areas of health and care has significantly increased over the past decades. It is known under many names, including in silico medicine, digital twins or virtual human twins. The common element they all share is the use of digital technologies, ranging from AI to mechanistic models, to answer specific problems related to prevention, diagnosis, treatment prediction and follow-up of the patient, or to design, optimize, de-risk and personalize medical therapies. While big strides have been taken in terms of technology development and regulatory science, many challenges remain that are holding back acceleration and uptake of the technologies in clinical practice.

Methods

From 2023 to 2025, the European Commission's EDITH project worked on proposing a strategy to address these challenges by bringing together the entire ecosystem and jointly developing a roadmap for the implementation of the Virtual Human Twin [1]. A wide range of online and onsite meetings was held with all stakeholders, including academia, industry, patients, healthcare providers, regulators, health technology assessment agencies and policy makers. Through these meetings, over 800 individuals from all across the world contributed to the initiative.

Results

The roadmap provides a comprehensive overview, starting with the current context, the identified challenges and the stakeholders' needs. It continues with a description of the available and required technologies, and possible infrastructural solutions that could facilitate the implementation and credibility assessment of digital twin solutions. Next, the regulatory, health technology assessment, standardization, legal, ethical and social dimensions are analysed. Subsequently, the market and business elements are discussed, along with possible incentives for stimulating the uptake of VHTs for different stakeholder

groups. Finally, 30 recommendations are formulated to facilitate and accelerate the development and adoption of VHTs in clinical practice.

Discussion

The roadmap provides a high level vision for realizing the potential of Virtual Human Twins, while also providing tangible tools for addressing challenges such as interoperability, access and hardware needs. As such, this roadmap can provide a tangible guide for the many digital twin initiatives and consortia, facilitating synergies through an interoperability-by-design strategy.

References (Optional)

[1] https://zenodo.org/records/14769224

Acknowledgements (Optional)

EDITH-CSA-DigitalEurope-101083771

Session Category

Emerging Areas: N/A

P3-036

Towards Individualized Bone Conduction Hearing Models: A Benchmark Comarison With the State-of-the-Art Model

Mr. Linus Taenzer[1], Mr. Johannes Niermann[2], Dr. Ivo Dobrev[2], Dr. Paolo Tiso[3], Dr. Bart Van Damme[1]

[1]Empa, Dübendorf, Zürich, Switzerland. [2]Universitätsspital Zürich, Zürich, Zürich, Switzerland. [3]ETH Zürich, Zürich, Zürich, Switzerland

Introduction

Despite its importance in hearing and device design, the role of the bone conduction transfer path is still not fully understood. The LiU head finite element (FE) model, widely used in research, represents one specific individual reconstructed from cryosectional images. While it has been compared to numerous experimental datasets from different subjects, the associated specim has not been measured [1,2]. Therefore, this study introduces a model from another individual to compare their differences. This model is the first of its kind to be eventually compared against experimental data from the same head.

Methods

Subject-specific head models were generated using photon-counting CT scans, enabling high-resolution imaging of anatomical structures [3]. Segmentation was performed to define distinct domains with varying levels of geometric detail and accuracy using Simpleware (Synopsis, USA), Fig. 1. Regions critical to energy transmission of the bone conduction transfer path, such as the ear canal and cochlea, were modeled with fine resolution, while less sensitive areas were represented with coarser meshes. The model includes cortical bone, homogenized diploë, cerebrospinal fluid (CSF), brain tissue, and skin.

Finite element simulations were conducted to analyze wave propagation caused by an idealized bone anchored hearing aid. Comparative simulations were performed between personalized models and the LiU head to assess differences in vibration patterns and transfer paths.

Results

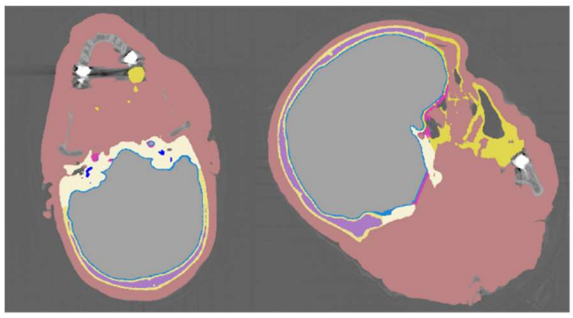
Thw results illustrate the frequency response functions between different excitation positions (BAHA, mastoid position) and the lateral and contralateral promontory position. The model is compared with transfer functions of the LiU head model, highlighting the

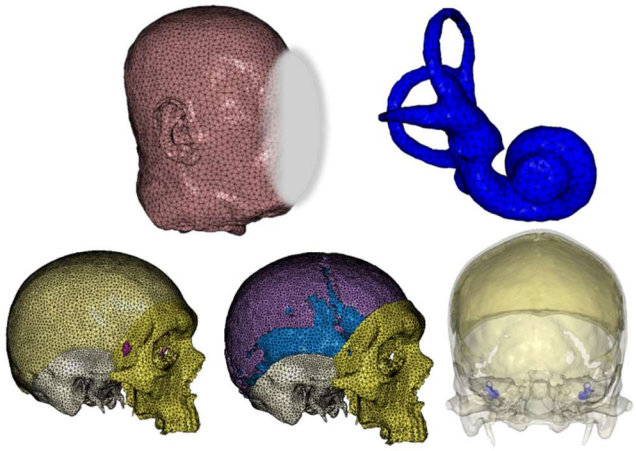
differences in magnitude between two different geometries. Additionally, the sensitivity of mask homogenization of the area in the ear canal is investigated, demonstrating the impact of local changes.

Discussion

The comparison between two FE models highlights the importance of accounting for individual anatomical variability in bone conduction simulations. The integration of tailored models could enable a more accurate prediction of bone-anchored devices and support individualized treatment strategies. Future work should focus on experimental validation across diverse anatomical datasets.

Images (Optional)





References (Optional)

1. Chang et al., J Acoust Soc Am, 2016
2. Dobrev et al., J Acoust Soc Am, 2025
3. Niermann et al., Biomimetics, 2025

Acknowledgements (Optional)

This work was supported by grant 213127 from the Swiss National Science Foundation.

Session Category

Emerging Areas: N/A

P3-037

Remote Running Gait Analysis Using Smartphone Video and Monocular Pose Estimation: A Feasibility Study

Mr Luke VanKeersbilck, Dr Dustin Bruening PhD, Dr Iain Hunter PhD

Brigham Young University, Provo, UT, United States

Introduction

Running is a common form of exercise that comes with many health benefits; however, many people stop running because of the high injury risk. Running injury relates to biomechanical risk factors. Yet, these risk factors often show inconsistent and conflicting results across studies, partially due to small sample sizes. Low subject numbers may be related to the limitations of traditional motion capture. Monocular pose estimation offers a promising alternative by using machine learning to track body landmarks from a single camera, allowing data to be collected remotely. This study evaluated the feasibility of remotely collecting running biomechanics data using monocular pose estimation while exploring associations between running mechanics with running injury.

Methods

Participants were recruited via social media and flyers at running stores. They completed a survey on injury history and performance, then ran on their own treadmill at 3.35 m/s while recording themselves at 240Hz for 30 seconds. Mediapipe Pose was used to track body landmarks three-dimensionally. Logistic regressions were run between four injury categories (lower leg injuries, knee injuries, upper leg injuries, and bone injury) and running mechanics.

Results

A total of 310 people participated. Of those, just 69 videos were successfully uploaded but needed to exclude 24 people for poor camera quality or positioning. Significant predictors of prior injury were found in all but one of the injury categories.

Discussion

Monocular pose estimation can be used for the remote collection of running mechanics data but presents several key concerns. The number of subjects in the final analysis was low due to upload failures and video quality issues. Despite these issues, this study found significant predictors of injury consistent with previous literature but also several that have received little attention previously. These possible new predictors could be due to our larger sample size and inclusion of additional predictor variables. Even with this, a

significantly larger sample size is likely needed to improve confidence in the biomechanical risk factors. Future work will focus on more reliable methods for the submission of quality videos and work to further increase sample size.

Images (Optional)

Table 1. Regression Results by Injury site

Injury site	Predictor variable	Estimate	SE	p-value
Lower Leg	Knee angle at IC	-0.121	0.059	**0.037**
	Ankle angle at IC	-0.172	0.087	**0.048**
	Vertical oscillation	102.37	36.13	**0.005**
	Knee angle at MS	0.176	0.102	0.083
	Hip angle at MS	-0.143	0.087	0.1
Knee	Ankle angle at IC	-0.335	0.116	**0.004**
	Hip angle at IC	-0.163	0.064	**0.011**
	Knee angle at MS	0.189	0.085	**0.027**
	Footstrike Type	-2.036	1.123	0.07
	Footstrike Type	-2.036	1.123	0.07
Upper Leg	Vertical oscillation	63.00	24.60	**0.011**
	Ankle angle at MS	0.130	0.060	**0.044**
	Ankle angle at IC	-0.100	0.050	0.056
	Hip angle at IC	-0.070	0.040	0.06
	Stride rate	8.26	4.43	0.062
Bone	Knee angle at MS	-0.222	0.126	0.078

Note: All angles measured in degrees. Vertical oscillation measured in leg lengths. Stride rate in steps per second. IC = Initial contact; MS = Midstance.

References (Optional)

Session Category

Emerging Areas: N/A

P3-038

Transtibial Limb Loss Reduces Metabolic Cost of Walking When Loosely Constrained to Track Able-Bodied Gait: A Simulation Study

Ms. Maliheh Fakhar, Dr. Jae Kun Shim PhD, Dr. Ross Miller PhD

University of Maryland, College Park, MD, United States

Introduction

Prior studies simulating walking with optimal control methods, that minimize a combination of metabolic cost and deviations from able-bodied gait mechanics, suggest that metabolic cost can remain unchanged after transtibial limb loss, especially if muscle strength is fully preserved [1,2]. Examining if limb loss and prosthesis use change the minimum possible metabolic cost of walking, regardless of gait deviations, could speak to whether limb loss *per se* increases metabolic cost. This study, therefore, tested the effect of transtibial limb loss on the minimum metabolic cost of walking. Identifying this absolute minimum metabolic cost is well suited to optimal control simulations, vs. studies of human participants where it is difficult to determine if metabolic cost was minimized absolutely.

Methods

Simulations of walking were performed using a full-body OpenSim model with 31 degrees of freedom and 120 muscles (Fig.1A; [3]). A transtibial limb loss model was created by removing the right ankle muscles and altering the joint and inertial properties of the right foot and shank (Fig.1B; [1]). For both models, OpenSim Moco computed muscle excitations that minimized a cost function defined as the weighted sum of metabolic cost and deviations from able-bodied gait mechanics, with constraints of periodicity and walking speed of 1.45 m/s [1,3]. Simulations were repeated with progressively reduced weight on the gait-deviation term, until further reductions no longer changed the metabolic cost.

Results

For both models, metabolic cost stabilized at a gait-deviation weight of ~10^{-3} (Fig.1C), indicating convergence toward the absolute minimum metabolic cost under minimally constrained tracking. At this minimum, the metabolic cost was 9% lower for the transtibial model vs. the able-bodied model (2.12 vs. 2.34 J/m/kg).

Discussion

Results support previous findings that transtibial limb loss does not necessarily increase metabolic cost of walking [1,2,4] and suggest transtibial limb loss in fact reduces metabolic cost. We speculate this result is due to low prosthesis mass, reducing energy requirements of leg swing, combined with prosthesis stiffness optimized for energy return during stance phase.

Images (Optional)

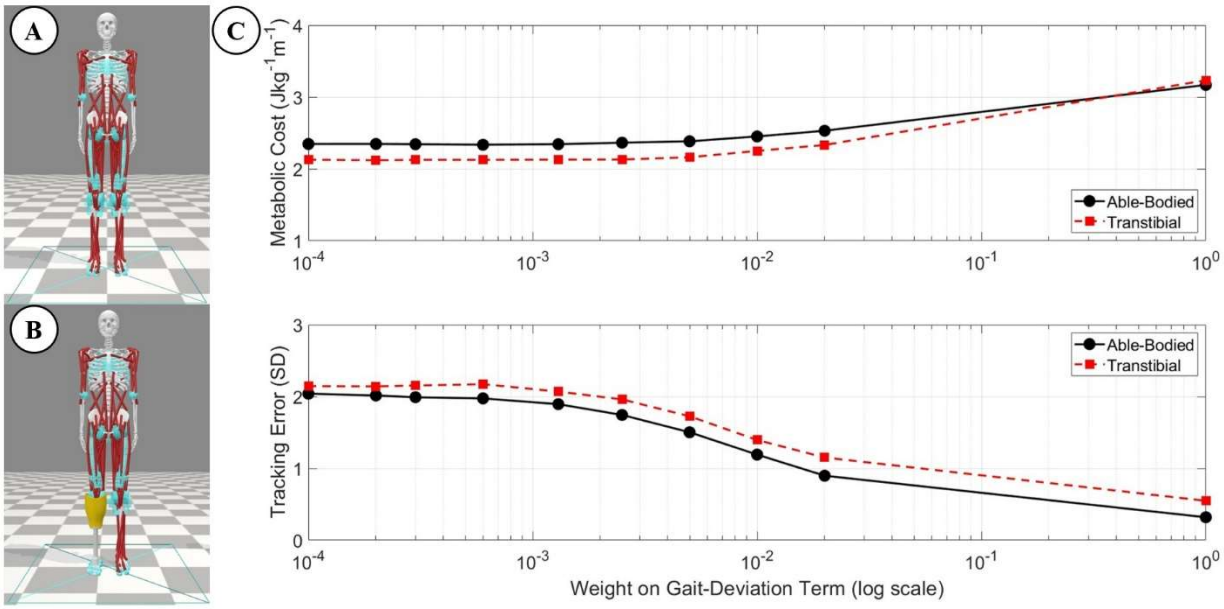


Fig.1: (A) full body model (B) transtibial limb-loss model (C) Metabolic cost and tracking error across different gait-deviation weight values. Solid and dashed lines represent able-bodied and transtibial simulation results, respectively.

References (Optional)

[1] Miller and Russell Esposito, PeerJ,2021. [2] Russell Esposito and Miller, PloS One,2018.

[3] Miller et al., PeerJ,2024. [4] Russell Esposito et al., JRRD,2014.

Acknowledgements (Optional)

Funded by CDMRP award HT9425-23-1-0103.

Session Category

Emerging Areas: N/A

P3-039

CNN-Based Deep Learning for Multi-Region Classification and Prediction of Cobb Angles from Markerless 3D Surface Topography in Adolescent Idiopathic Scoliosis

Graduate Research Assistant Mariam Ezzat, Graduate Research Assistant Mahmoud Hashim, Postdoctoral Scholar Bruna da Rosa, Assistant Lecturer Behzad Vafaeian, Assistant Professor Qipei Mei, Professor Samer Adeeb, Associate Professor Lindsey Westover

University of Alberta, Edmonton, Alberta, Canada

Introduction

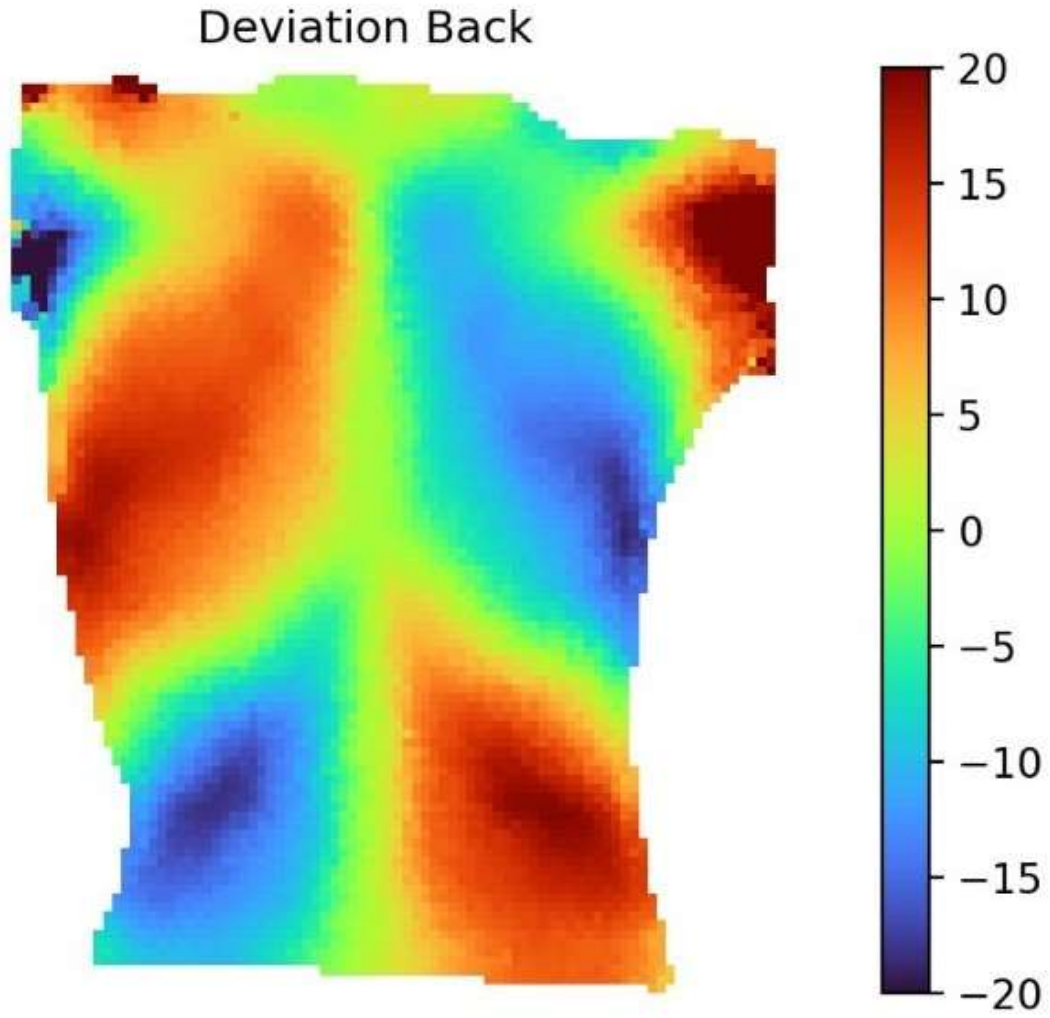
Methods

Results

Discussion

This framework validates ST as a primary monitoring tool. The classification model shows strong performance in distinguishing Single versus Double curves, proving the system's reliability for initial curve typing. However, the model has slight difficulty distinguishing single curves as thoracic or lumbar, suggesting a refinement opportunity. The regression model meets the accepted clinical error for X-ray readings for lumbar CAs with a 3.29° MAE. Future efforts will focus on minimizing the thoracic MAE of 4.71°.

Images (Optional)



References (Optional)

[1] F. Altaf, A. Gibson, Z. Dannawi, and H. Noordeen, *BMJ*, 2013.
[2] N. Mohamed et al., *Sci. Rep.*, 2025.
[3] M. Hassan et al., *Med. Eng. Phys.*, 2025.

Acknowledgements (Optional)

Session Category

Emerging Areas: N/A

P3-040

Three-dimensional Reconstruction of the Pelvis from Simulated Bi-Planar X-Rays using Deep Learning

Ms. Marie De Mey, Ms. Isabella Tierney, Mr. Jeffrey Lee, Dr. John McPhee, Dr. Stewart McLachlin

University of Waterloo, Waterloo, Ontario, Canada

Introduction

Patient-specific 3D models of the pelvis are essential to pre-operative surgical planning for joint arthroplasty. Although models are conventionally derived from segmented computed tomography (CT) scans, there is increasing motivation to generate 3D pelvic models from X-rays due to lower radiation exposure, lower cost, and improved accessibility. As a starting point towards this goal, we developed a deep learning (DL) pipeline that converts a CT scan to synthetic bi-planar digitally reconstructed radiographs (DRR) and reconstructs the corresponding 3D pelvis from the DRR using an Attention U-Net architecture [1].

Methods

Since paired datasets of X-rays and associated 3D CT scans are not publicly available, the model was trained on synthetic anterior-posterior and lateral DRRs developed from the CT pelvic scan dataset CTPelvic1k. The synthetic DRRs were generated using the TIGRE toolbox, a physics-based digital radiograph simulation framework. Additionally, to reduce the domain gap, we investigated the application of a bone-enhancement filtering algorithm to more closely resemble the appearance of a pelvis X-ray [2]. The model performance was evaluated using standard reconstruction metrics such as the Dice similarity coefficient (DSC), 95th percentile Hausdorff distance (95HD), and the average surface distance (ASD). To assess the performance of the model in a clinical context, an automatic detection algorithm was used to evaluate the Euclidian distance between eight pelvis landmarks on the ground truth and predicted output [3].

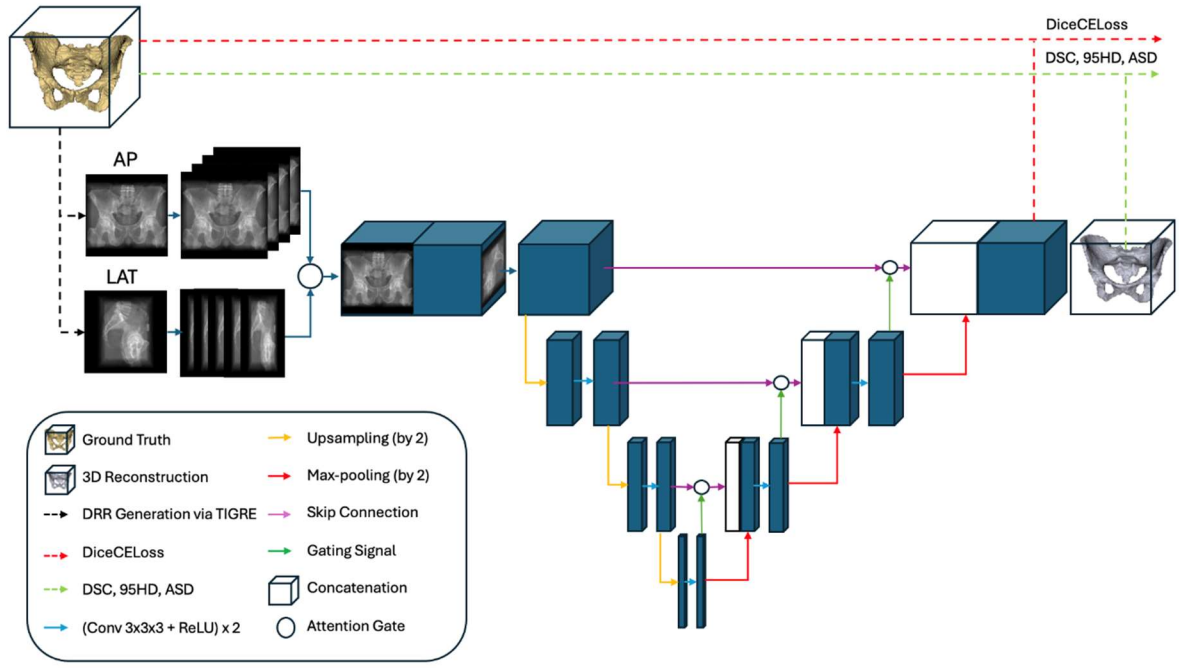
Results

Experiments on the test data determined that the model achieved an average DSC of 75.2%, an average 95HD of 9.3 mm, and an ASD of 3.1 mm. The model achieved average localization errors of 16.1 mm for the anterior superior iliac spines, 17.4 mm for pubic tubercles, 23.8 mm for the ischial spines, and 22.0 mm for the posterior superior iliac spines.

Discussion

Our 3D pelvis reconstructions show that this DL pipeline has the potential to enhance clinical end-use applications. Additional experiments and training data are planned to further evaluate the impact of the bone-enhancement filtering mechanism on model performance.

Images (Optional)



References (Optional)

[1] M. Shakya and B. Khanal, *arXiv*, 2023.
[2] C. Yang et al., *Diagnostics*, 2022.
[3] M. Fisher et al., *Nature*, 2019.

Session Category

Emerging Areas: N/A

P3-041

Auto-Classification of Manual Wheelchair Propulsion Stroke Patterns in Children with Spinal Cord Injury Using Machine Learning

Mr. Marko Vucelic BS, Dr. Alyssa Schnorenberg MS, PhD, Dr. Brooke Slavens MS, Phd

University of Wisconsin-Milwaukee, Milwaukee, Wisconsin, United States

Introduction

Manual wheelchair propulsion is a crucial activity of daily living for individuals with spinal cord injury (SCI), which affects an estimated 296,000 Americans. Hand motions during propulsion are classified into different types of stroke patterns, which vary significantly and impact musculoskeletal health and injuries. Currently, stroke patterns are visually, manually classified, which is time consuming and subjective. This project aims to develop and evaluate a machine learning (ML) framework for automated, objective classification of wheelchair stroke patterns using kinematic time-series data.

Methods

We developed and evaluated a ML-based classification pipeline using kinematic data (Vicon) of 508 stroke patterns from 36 children with SCI (aged 6-21 years). Datasets were trained with multiple supervised ML models, including k-nearest neighbors (KNN), decision tree (DT), random forest (RF), support vector machines (SVM), multi-layer perceptron (MLP), and recurrent neural networks (RNN). To expand training data, a variational autoencoder generated 600 synthetic cycles. Model performance was evaluated using standard ML metrics: accuracy, F1-Score, confusion matrices, and AUC-ROC curves. The classifications include four adult patterns and two novel pediatric patterns: arc, double over-looping (DL), single over-looping (SL), and semicircular (SC), bean (BEAN), and tiny loop (TL).

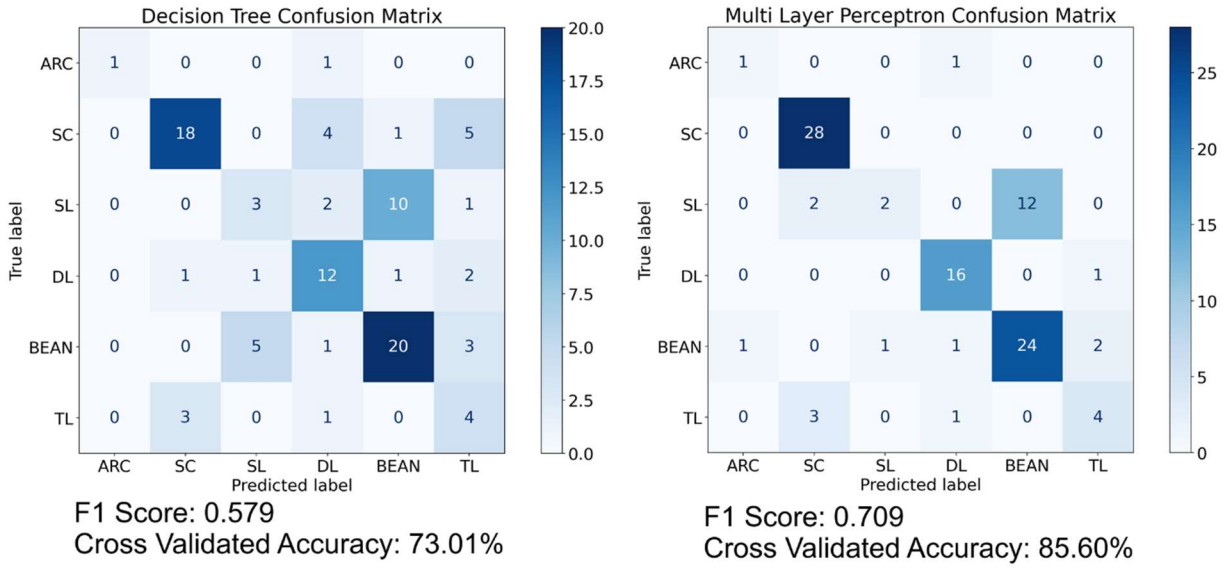
Results

Classification accuracies ranged from 73% to 85% across models (Figure 1). The MLP model achieved the highest performance, classifying DL most accurately and SL least accurately. SVM had the highest rate of incorrect classification instances. The introduction of synthetic data increased the accuracy by 15-25%.

Discussion

A machine learning approach for classifying six wheelchair stroke patterns proved feasible. MLP was the most accurate, however the training time was greater in comparison to the other models. The enhanced accuracy with synthetic data highlights its ability to enhance classification models in biomechanical applications where data may be sparse. Future directions will involve utilizing this classification model to assess pattern use and pathology in a larger dataset of manual wheelchair users across the lifespan. This approach will enable efficient and objective assessment of propulsion biomechanics for investigating musculoskeletal injury prevention.

Images (Optional)



Session Category

Emerging Areas: N/A

P3-042

Performance of OpenCap from Non-Recommended Viewpoints

Ms. Maya Ansu-Kyeremeh, Ms. Ishi Arora, Dr. Calvin Kuo PhD,P.Eng

University of British Columbia, Vancouver, British Columbia, Canada

Introduction

Markerless motion capture technologies are becoming more popular to easily collect high-quality motion data in different out-of-lab environments. OpenCap is a markerless motion capture technology that uses two or more synchronized cameras to reconstruct 3D kinematics. OpenCap recommends a two-camera setup at a 30-45° angle off the participant's frontal line [1]. However, following these recommendations might not always be possible in constrained motion capture environments. The purpose of this study is to assess whether changes in the camera angles affect OpenCap knee joint angle estimates.

Methods

29 participants (24±4yo, 15F) performed dynamic movements related to return to sport assessment. The movement was captured by 8 Sony RX0II cameras (60Hz) spaced at 45-degree intervals around the participant. A localized version of OpenCap was used to compute knee joint angles using different combinations of cameras with spacings of 45°, 90°, 135°, and 180 ° from the front. We also used a camera pair spaced 90° from the back view. We computed normalized Root Mean Square Error (nRMSE) between OpenCap knee joint angle estimates against a marker-based motion capture (8-camera 960Hz PhaseSpace with 50 markers) estimate for each condition.

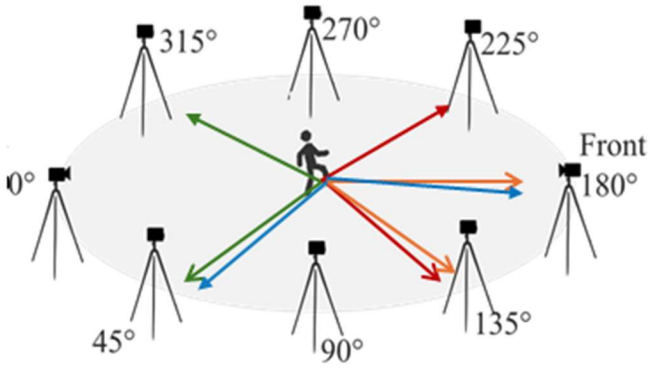
Results

For a single participant completing a single-leg triple crossover jump, we computed nRMSE with increasing camera spacing. The 45-degree spacing had the lowest nRMSE, and the 135-degree spacing had the highest. The 180-degree spacing did not time synchronize in OpenCap, so it was not included in the analysis. The 90-degree spacing from front and back had the same nRSME score of 0.3456.

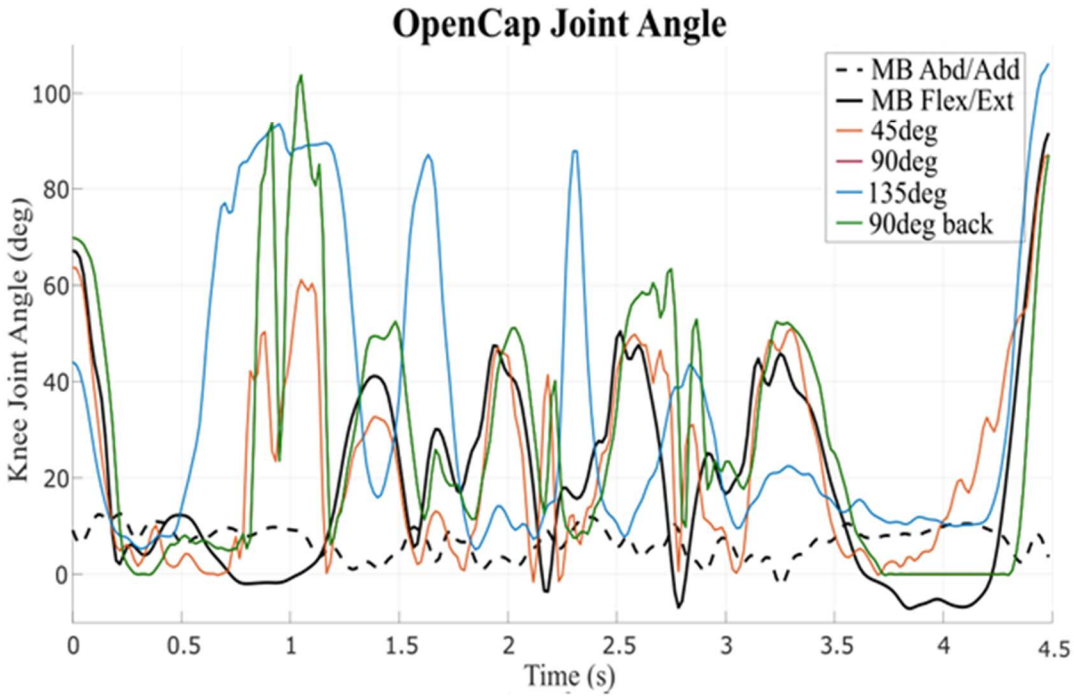
Discussion

OpenCap is an established technology to estimate knee joint angles from a 2-camera markerless setup. These results suggest that OpenCap recommendations for camera spacing should be followed, but that they do not necessarily need to be from the front. The next steps for this project will assess other camera combinations from the 8-camera setup across more participants and movements to generalize findings.

Images (Optional)



Condition	RMSE
45°	0.2427
90° (front)	0.3456
90° (back)	0.3456
135°	0.5232



References (Optional)

[1] Uhlrich S. (2023). PloS Comput Biol

Session Category

Emerging Areas: N/A

P3-043

Effects of Altered Depth Perception on Gait in Virtual Reality Walking Tasks

Student Researcher Michael Thorne

UC Irvine, Irvine, California, United States

Introduction

Virtual Reality (VR) Environments are increasingly being used as tools for studying human locomotion adaptations during overground walking tasks. In particular, this work aims to examine how visual depth perception manipulation influences locomotor behavior, particularly during gait adaptation tasks. Differing levels of depth visibility allow for dynamic control of visual perception to learn how users perceive virtual environments of differing levels of vision and how this manipulation of vision can be used for training in rehabilitation, balance control, and spatial navigation.

Methods

Fourteen adults walked in Virtual Reality on a split belt treadmill in 3 different walking tasks each with 3 differing visual depth perception settings defined by a unity fog shader to change contrast, sharpness, and visibility of their surrounding environment. This allows for changing the amount of visual information the user is able to work with for each task and evaluate how different sensorimotor adaptations and compensations are utilized during each trial. Each test involved normal overground treadmill walking in each scene walking Vicon markers were utilized to analyze step lengths (SL), step widths (SW), torso sway, and each of their respective variabilities during the last 2 minutes of each 5 minute trial. Motion sickness questionnaires, particularly the Motion Sickness Susceptibility Questionnaire and Simulator Sickness Questionnaire were conducted to ensure participants were comfortable walking in Virtual Reality settings.

Results

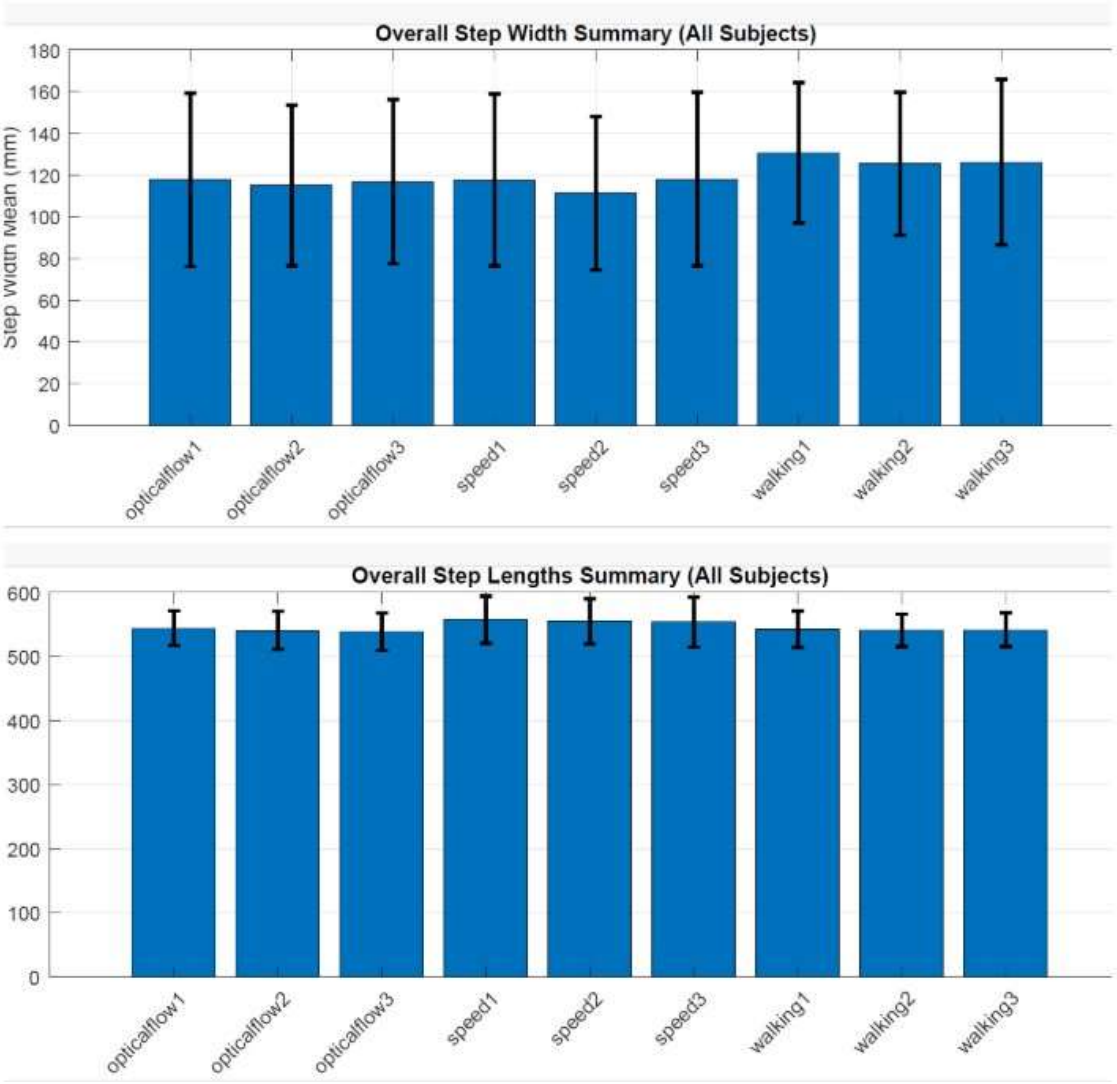
Preliminary results show that participants tend to gravitate towards more cautious walking gaits which is illustrated in significantly smaller step widths and generally smaller step lengths on average for all participants.

Discussion

This experiment provides evidence that walking in virtual reality is an effective tool for introducing virtual perturbations in overground walking that can simulate real world

environments and be effective in assessing and training participants in their gait for specific tasks. Future work would include working with subjects with impaired levels of depth perception to test the usability of this work for training in Virtual Reality.

Images (Optional)



Session Category

Emerging Areas: N/A

P3-044

Shunt Hemodynamics Abnormalities In sublingual Microcirculation as Indication for Sepsis

Mr Kavin Vishnu[1], MD Matthias P Hilty[2], MD Alessandro Candreva[3], Dr Monika Colombo[1]

[1]Department of Mechanical and Production Engineering, Aarhus, Jutland, Denmark. [2]Institute of Intensive Care, Zurich University Hospital, Zurich, ZH, Switzerland. [3]Department of Cardiology, Zurich University Hospital, Zurich, ZH, Switzerland

Introduction

The shunting theory of sepsis [1] states that venules shunting leads to impaired oxygenation in certain microvasculature regions. Impaired recruitment of the sublingual vessels caused by shunting can provide insight into the clinical state of sepsis [1]. Here we show, through a machine learning (ML) approach, that hemodynamic abnormalities detected in the sublingual microcirculation (SM), in terms of red blood cells (RBCs) velocity and concentration, contribute to detecting and classifying shunt within capillary network.

Methods

Handheld vital microscopy SM images (Fig. 1-A) and related hemodynamic data are derived from previous works of the group [2,3] and prospective data collection of coronary microvascular disease patients, considering both controls and altered hemodynamic conditions through the application of two vasodilators (nitroglycerin and acetylcholine) to increase capillary recruitment and total vessel density (TVD). The capillary network is visualized through electronic analogue in Fig. 1-B. Hemodynamic data and RBC properties are extracted for each detected vessel. We employed labelled data to calculate hemodynamics correlations (e.g. Fig. 1-C) associated with shunts. K-means clustering is applied using unlabeled data based on features representing these known hemodynamics correlations, aiming at sorting shunts in both controls and when vasodilators were applied.

Results

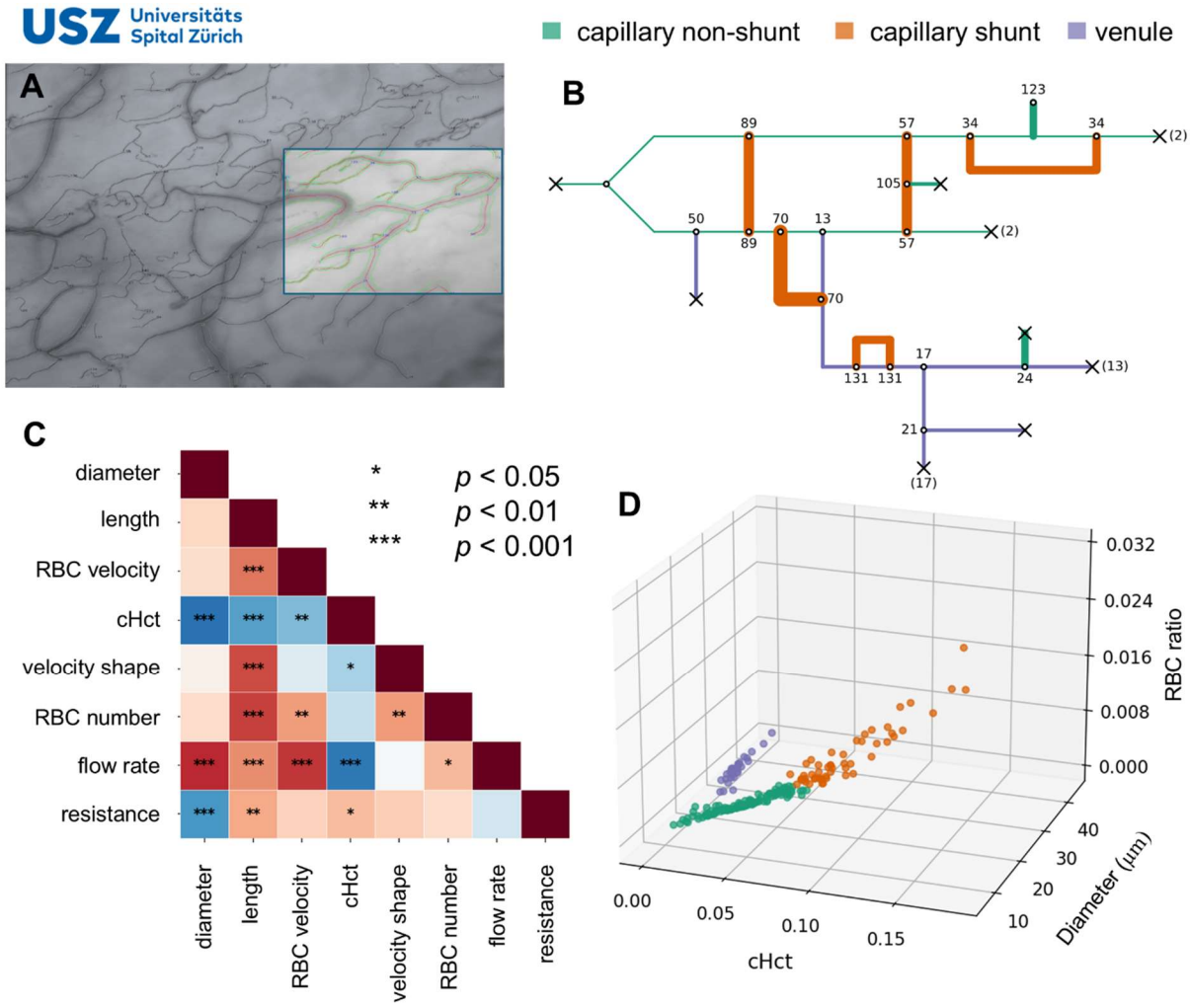
A grading scale for identifying shunts in the three cases (Fig. 1-B) was created based on ranges of hemodynamic properties, flow properties, and clustering, with the parameters of this grading scale optimized by further application of ML algorithms. Preliminary results demonstrate notable differences in the trends and strongly significant correlations between shunts and non-shunt SM allowing for identification. Further, cases with higher

TVD (following vasodilators application) additionally showed unique trends and clustering behavior (Fig. 1-D).

Discussion

The shunting grading scheme shows promising results in its ability to identify patients with sepsis. More data is expected to lead to a robust detection method for shunts in patients with different SM conditions, leading to the identification of underlying diseases such as sepsis, defining a paradigm shift in critical care management of patients.

Images (Optional)



References (Optional)

[1] Gruartmoner G et *al., Medicina Intensiva,* 2017

[2] Hilty MP et *al.*, *Critical Care Medicine*, 2020

[3] Hilty MP et *al., Communication Biology, 2019*

Session Category

Emerging Areas: N/A

P3-045

Automatic CT Image Quality Analysis for Selection of Optimal Phase in Large Machine Learning Datasets

Mr Jesper O Kragballe[1], Mr Henrik P Lind[1], Dr Vibha Gupta[2], Dr Fredrik E Fossan[3], MD, Dr Jonathan N Dahl[4], MD, Dr Laust D Rasmussen[4,5], MD Gitte S Brix[4], MD Ida M Bøhme[4], MD, Dr Araz Rawshami[2], Prof Samuel E Schmidt[1], MD, Prof. Simon Winther[4,6], Dr. Monika Colombo[7]

[1]Department of Health Science & Technology, Aalborg University, Aalborg, NA, Denmark. [2]Department of Molecular and Clinical Medicine, University of Gothenburg, Gothenburg, NA, Sweden. [3]Center for innovation, medical devices and technology, St. Olavs hospital, Trondheim, NA, Norway. [4]Department of Cardiology, Gødstrup Hospital, Herning, NA, Denmark. [5]Department of Cardiology, Aalborg University Hospital, Aalborg, NA, Denmark. [6]Department of Clinical Medicine, Aarhus University Hospital, Aarhus, NA, Denmark. [7]Department of Mechanical and Production Engineering, Aarhus University, Aarhus, NA, Denmark

Introduction

High-quality cardiac CT imaging is essential for accurate coronary assessment and downstream machine learning (ML) applications [1]. Large-scale datasets often contain heterogeneous image quality due to variations in acquisition protocols, scanner models, and patient factors. Furthermore, a single CT-acquisition often contains several series, representing different phases and/or reconstructions. Manual quality assessment is time-consuming and subjective, motivating the need for automated solutions.

We propose a convolutional neural network (CNN)-based framework for direct comparison between clinical annotated and automatic overall diagnostic quality (ODQ). The model is trained on manually-extracted image quality scores to facilitate optimal series/phase selection in large cardiac CT datasets.

Methods

A cohort of 300 patients was selected from the Western Danish Cardiac CT Registry, with 1-10 different phases per patients yielding 2,203 axial, contrast-enhanced series. Patients were stratified by scan year and scanner model. Clinical annotation included Likert-scale categorical scoring of five quality classes at epicardial coronary segments, and attenuation values in right ventricle (RV), left ventricle (LV), left atrial appendage (LAA), and ascending

aorta (AA). These annotations served as ground-truth for supervised training and cross-validation (80%), and testing (20%).

The 3D CNN model [2], takes full image volumes as inputs, resampled to isotropic image dimensions. It outputs an ODQ score and evaluates: (1) general noise, (2) motion/sharpness, (3) contrast quality, (4) step artifact in LV and in (5) coronaries.

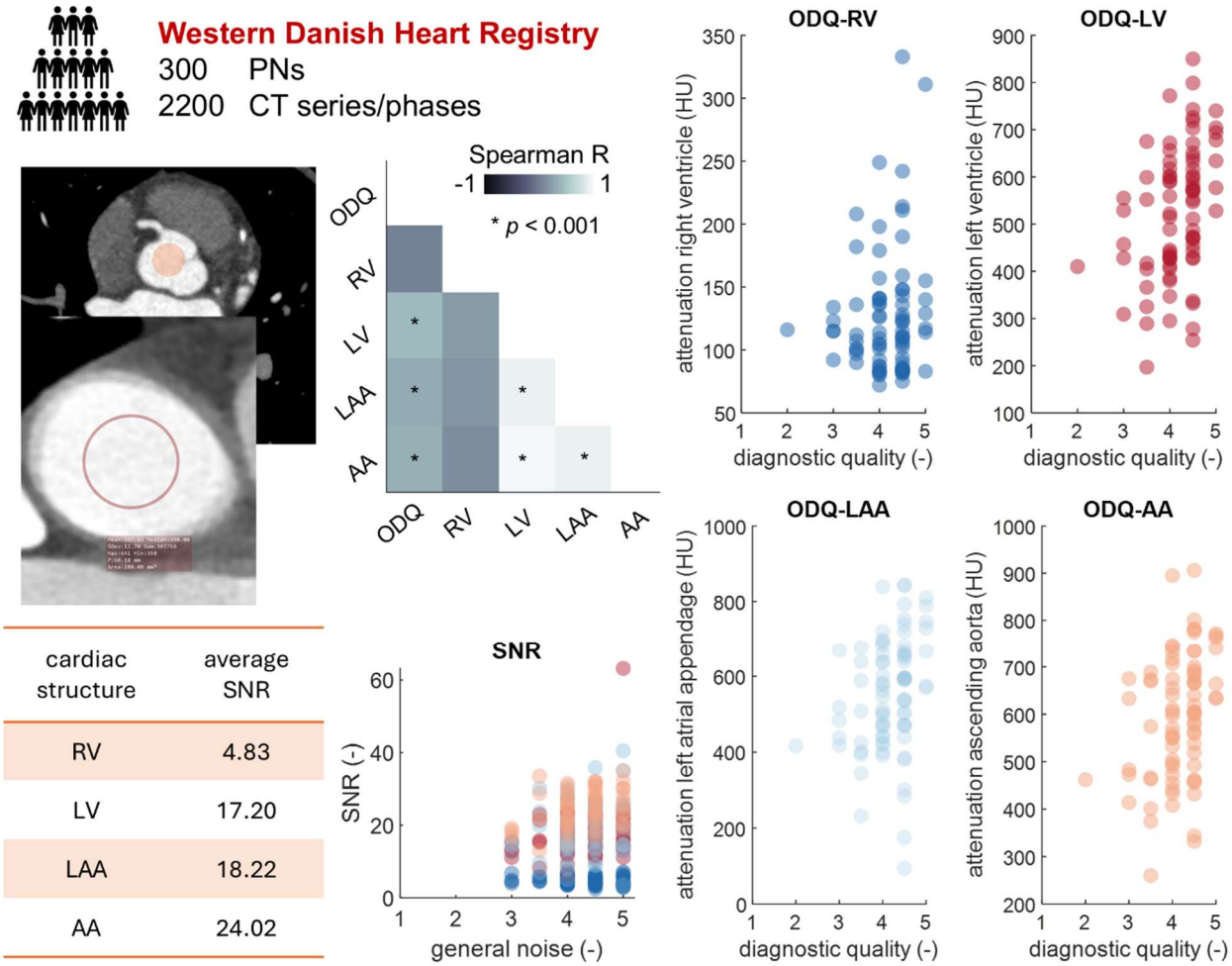
Results

Fig-1 shows the preliminary results on 100 series, highlighting strongly significant positive Spearman correlation between ODQ and contrast (HU) value in all cardiac structures but RV. Similarly, signal-to-noise ratio shows a linear positive association with the general noise (in Likert-scale).

Discussion

Our preliminary analyses demonstrate that the CNN effectively predicts overall quality and individual artifact classes, enabling automated filtering of suboptimal series. Automated CT IQA using deep learning can standardize phase selection and improve data integrity for ML applications in cardiac imaging. Future work will focus on including the CT IQA algorithm in a larger ML pipeline for fully automatic optimal selection and segmentation of our ~100’000 patients dataset.

Images (Optional)



cardiac structure	average SNR
RV	4.83
LV	17.20
LAA	18.22
AA	24.02

References (Optional)

1] Nieman K *et al*, *JCCT*, 2024

[2] Piccini D *et al*, *Radiology Artificial Intelligence*, 2020

Acknowledgements (Optional)

We acknowledge support from Novo Nordisk Foundation, Exploratory Grant for the Nordic collaboration on AI and cardiac imaging (Grant ID: NNF25SA0109978).

Session Category

Emerging Areas: N/A

P3-046

Comparing Feature Sets for Motion Prediction Model Training

Mr. Cylus Robinson, Mr. Brandon Nunley MSBE, Mr. Praneel Seth, Dr. Justin Hart PhD, Dr. Nick Fey PhD

University of Texas at Austin, Austin, Texas, United States

Introduction

Motion prediction is an emerging technology in biomechanics and is becoming more utilized as data and greater computational power become more accessible to researchers. Fields such as engineering, biomechanics, prosthetics control, computer graphics, and more employ motion prediction to fill the gaps in trajectories and joint positions in many respective applications. In this study, we included segmental angular momentum as a training feature alongside joint positions, which we tested against the performance of a model trained exclusively on joint positions for predicting future joint positions.

Methods

The Theia3D markerless motion capture system employing fourteen Sony cameras was used to collect kinematic data of participants performing three diverse walking tasks. We collected over 1.25 million frames of data over approximately 150 trials, and computed segmental angular momentum locally using the kinematic data before training the model. Two non-autoregressive encoder-decoder transformer models with 128 dimensional embeddings were trained over 100 epochs: one with joint positions as input features, and the other using joint positions and segmental angular momentum. The model implemented two heads per transformer layer and two encoder and decoder layers.

Results

Model performance was evaluated using Mean Per Joint Position Error (MPJPE). Incorporating segmental angular momentum reduced prediction error by 66.7% at a 250 milliseconds horizon and by roughly 50% at 500–1000 milliseconds compared to joint positions alone.

Discussion

The superior performance of the model incorporating segmental angular momentum highlights the importance of selecting appropriate input features to improve motion prediction accuracy. Our results suggest that including segmental angular momentum can

significantly enhance predictive performance, and other features may further refine model predictions. Accurate motion prediction has important applications even now. For example, human–robot interaction relies on predicting human movements to optimize trajectory planning, and lower-limb prosthetics are tailored to enable more natural gait by using model predictions based on an individual's physical dimensions. Recognizing the importance of feature richness can improve predictions and drive innovations in modeling, advancing motion prediction across a range of applications.

Images (Optional)

Input Features	Time Horizon (milliseconds)	Global MPJPE (meters)
Local Joint Positions	250	0.09
	500	0.08
	1000	0.09
Local Joint Positions & Segmental Angular Momentum	250	0.03
	500	0.04
	1000	0.04

Session Category

Emerging Areas: N/A

P3-047

3D Human Pose Estimation of Golf Swings using Multimodal Deep Learning Models

Mr Nishad Rajmalwar, Professor John McPhee

University of Waterloo, Waterloo, Ontario, Canada

Mr Nishad Rajmalwar

Introduction

Human pose estimation (HPE) in sports can improve performance analysis and injury prevention, but models trained on existing datasets generalize poorly to rapid 3D motions like golf swings. Vision-based methods often produce physically implausible poses due to occlusions of body parts and unconstrained limb lengths. Multimodal input data such as video, IMU, and depth information can improve accuracy by providing complementary information and enabling enforcement of segment length constraints. This study evaluates an existing model on golf data and develops a multimodal deep learning (DL) model using the TotalCapture dataset.

Methods

Golf swing data was collected from a male recreational golfer using a Vicon motion capture system (240 Hz) with synchronized Vue video camera (120 fps, frontal view) and Bertec force plates (960 Hz) under each foot. Full-body markers were used and 14 shots were captured using 3 clubs (Driver, 6 Iron, 9 Iron) to create variance in swing movement. 11 shots were used for training and 3 for testing to evaluate and train VideoPose3D, a DL HPE model pre-trained on the Human3.6M dataset.

Using a multimodal approach, a Vision Transformer (ViT) model was trained on the TotalCapture dataset using single-view video, IMU data from left forearm and forehead, and bone lengths. Data was fed to Spatial and Temporal Transformer Blocks to model spatial and temporal dependencies. The loss function included mean per-joint position error (MPJPE) weighted by joint distance from pelvis and segment length loss enforcing body segment length consistency.

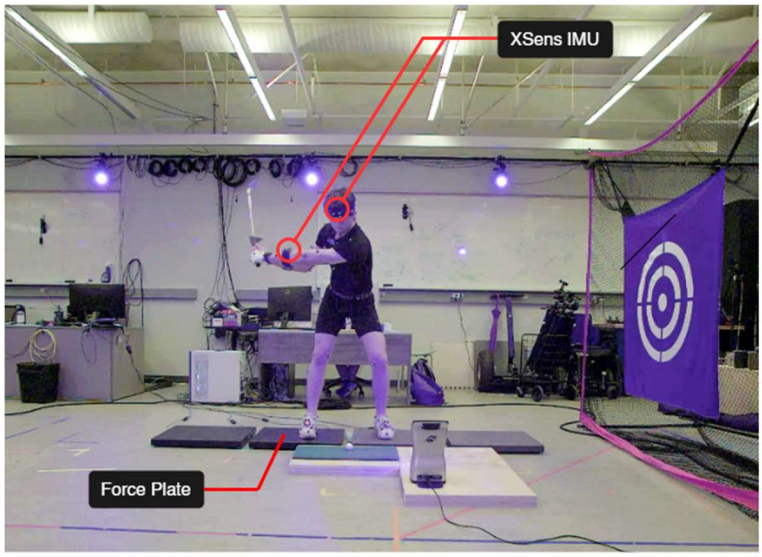
Results

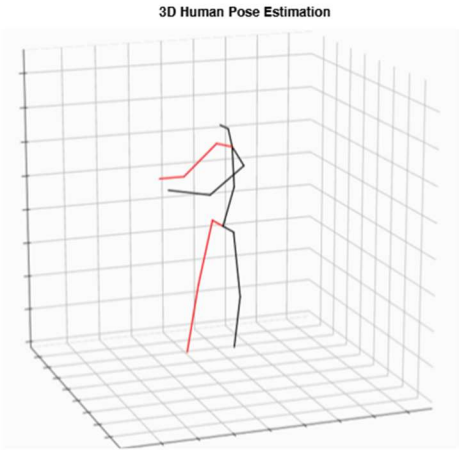
The pre-trained VideoPose3D model, despite performing well on Human3.6M benchmarks (MPJPE of 46.8mm), had an MPJPE of 138.8mm on our golf dataset. When trained from scratch on golf-specific data, the error reduced to 9.4mm. The ViT-based model achieved 62.4mm MPJPE on the TotalCapture test set.

Discussion

The poor performance of an existing model on our golf data demonstrates the need for domain-specific training. Qualitative analysis revealed unreasonable limb lengths and unrealistic joint angles. The ViT model showed encouraging results from multimodal input data for TotalCapture, so we will develop a ViT model using multimodal data from a larger golf data collection.

Images (Optional)





Session Category

Emerging Areas: N/A

P3-048

Deep Learning Ensemble Architectures for OCT-Based Diabetic Retinal Health Monitoring

MsC Pedro Rebolo[1], MsC Guilherme Barbosa[1], MsC Eduardo Carvalho[1], PhD Bruno Areias[1], PhD Ana Guerra[1], MsC Sónia Torres-Costa[2], PhD Nilza Ramião[1], PhD Manuel Falcão[2,3], PhD Marco Parente[1,4]

[1]INEGI—Institute of Science and Innovation in Mechanical and Industrial Engineering, Porto, Porto, Portugal. [2]Department of Ophthalmology, Centro Hospitalar e Universitário São João, Porto, Porto, Portugal. [3]Department of Surgery and Physiology, Faculty of Medicine, University of Porto, Porto, Porto, Portugal. [4]DEMec, Faculty of Engineering, University of Porto, Porto, Porto, Portugal

Introduction

Retinal vein occlusion (RVO) is the second most common retinal vascular disease after diabetic retinopathy, affecting approximately 16 million individuals worldwide and representing a major cause of vision loss [1]. Differentiating RVO-related macular edema from diabetic macular edema (DME) on OCT is challenging, as both conditions exhibit increased retinal thickness, which can lead to misclassification by non-specialists. Deep learning (DL) has shown promise in retinal imaging [2], but few studies have targeted OCT-based RVO detection [3]. This study evaluates stacked convolutional neural networks (SNNs) to enhance OCT-based classification, with a focus on differentiating RVO from DME.

Methods

This study used a private dataset from ULS São João (5360 OCT images; Normal, DME, RVO, Other). VGG16 and YOLOv8 architectures were fine-tuned with transfer learning and combined into an SNN configuration. Training employed weighted sampling, patient-wise data separation, augmentation, five-fold cross-validation, L_2 regularisation, and early stopping. Model performance was assessed with accuracy, precision, recall, F_2-score, and AUROC.

Results

Preliminary results show that the VGG16 and YOLOv8 networks achieved accuracies of around 84.6% and 85.8%, respectively. The stacked network of the two used models attained an accuracy of 92%. The F2-score of the single models reached around 87%, and the stacked network achieved an F_2-score of 93%.

Discussion

This study demonstrates that stacking CNNs enhances OCT-based classification of retinal diseases, particularly in distinguishing RVO-associated edema from DME. Performance improvements were linked to the number of features extracted:

- VGG16: 25,088 features
- YOLOv8:12,544 features.

Compared to fundus-based DL approaches, this SNN achieved superior diagnostic accuracy, aligning with or surpassing recent ensemble methods [3]. Limitations include a lack of external validation and a heterogeneous “other” pathology class. Future studies include multimodal integration and multi-device training for broader generalizability.

References (Optional)

[1] Rogers et al., J Ophthalmology, 2010

[2] Lee et al., J Ophthalmology Retina, 2017

[3] Kulyabin et al., Scientific Data, 2024

Acknowledgements (Optional)

The authors acknowledge Fundação para a Ciência e a Tecnologia (FCT) for its financial support to LAETA via the project UID/50022/2025
(DOI: https://doi.org/10.54499/UID/50022/2025).

Session Category

Emerging Areas: N/A

P3-049

Integrating Near-Infrared Spectroscopy, Support Vector Machines, and Fibril-Reinforced Poroelastic Finite Element Modeling for Constituent-Specific Human Cartilage Characterization

Mr. Janne J. Kankkunen[1], Dr. Mithilesh Prakash[1], Dr. Jaakko Sarin[1,2], Prof. Juha Töyräs[1,3,4], Assoc. Prof. Isaac O. Afara[1,3], Adj. Prof. Petri Tanska[1,4]

[1]University of Eastern Finland, Kuopio, North Savo, Finland. [2]Tampere University Hospital, Wellbeing Services County of Pirkanmaa, Tampere, Pirkanmaa, Finland. [3]The University of Queensland, Brisbane, Queensland, Australia. [4]Kuopio University Hospital, Wellbeing Services County of North Savo, Kuopio, North Savo, Finland

Introduction

Fibril-reinforced poroelastic (FRPE) material properties of cartilage, particularly hydraulic permeability, are altered in osteoarthritis, and may serve as early OA biomarkers. We investigated whether near-infrared spectroscopy (NIRS) combined with finite element (FE) modeling and machine learning can estimate FRPE properties of human cartilage, with emphasis on permeability.

Methods

Human osteochondral samples (n=171, diameter 8 mm) were harvested from femur, tibia, and patella of seven cadavers (68-79 years; approval #150/2016) stored in phosphate buffered saline in -20°C. Before testing, samples were thawed and measured with a NIRS system (average of three spectra per sample [1], Fig 1A). Mechanical properties were assessed using indentation (12.5 kPa pre-stress and three indentation steps at 5% strain with 15 min relaxation; indenter diameter: 667 or 728 µm). Sample-specific FE models with FRPE cartilage were fitted to experimental force–time responses, yielding constituent-specific parameters: initial (E_0) and strain-dependent (E_ε) fibril network moduli, non-fibrillar matrix modulus (E_m), initial permeability (k_0), and permeability strain dependency (M) [2]. We compared several spectral dimensionality-reduction approaches (random forest, principal component analysis, partial least squares, support vector machine [SVM]) and selected SVM with the best preliminary predictive capability. SVM-derived spectral features were then used as fixed effects in a linear mixed effects (LME) model, cadaver, cartilage surface, and location on surface considered as random effects to account for within-subject dependencies. A leave-one-cadaver-out design with 10-fold cross-validation in training was used. Performance was quantified using Spearman's ρ, and spectral importance was inferred from SVM.

Results

FRPE fits showed excellent agreement with experiments (median R^2: 0.94; 25th-75th percentiles: 0.87-0.97). In training and testing, the SVM-LME model achieved ρ=0.68 and ρ=0.34 (Fig. 1B). E_0 and E_ε were associated with collagen bands, E_m with proteoglycan bands, and k_0 and M with water bands (Fig. 1C).

Discussion

NIRS with SVM-based dimensionality reduction, combined with physics-based FRPE modeling enables spectroscopy-based estimation of constituent-specific human cartilage properties, including permeability. Together with physically interpretable spectral features, this framework is a promising tool for evaluation of cartilage and engineered tissue mechanical properties with further validation.

Images (Optional)

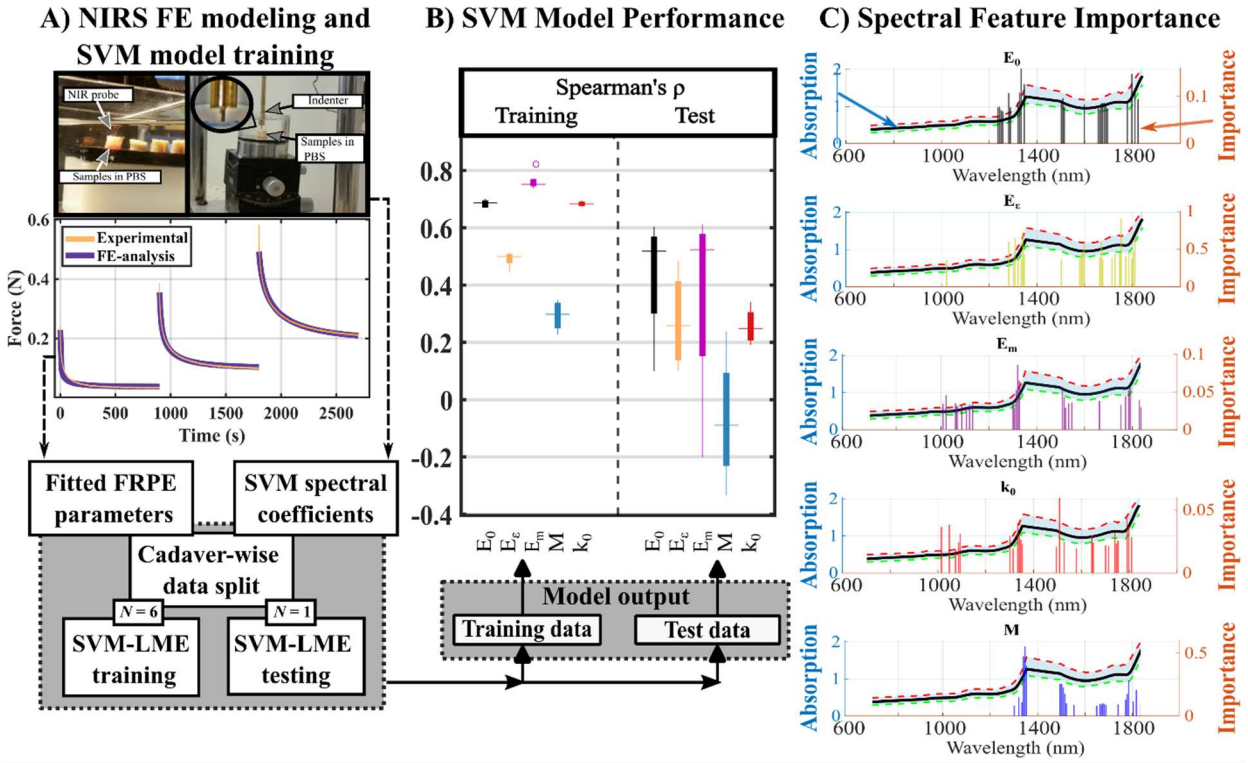


Figure 1: (A&B) Near-infrared spectroscopy measurement, fitting FRPE material model to mechanical test, SVM-LME model training, and SVM model performance. (C) Spectral feature importance analysis for each FRPE material parameter.

References (Optional)

[1] M Prakash *et al.* , Osteoarthritis and Cartilage, 2019.

[2] M Ebrahimi *et al.* , Ann. Biomed. Eng., 2021.

Acknowledgements (Optional)

Research Council of Finland (grants 315820, 339130, 354916), Päivikki and Sakari Sohlberg Foundation (grants 240074, 250070), Sigrid Jusélius Foundation, Maire Lisko Foundation.

Session Category

Emerging Areas: N/A

P3-050

Direct Regression of Kinematics, Keypoints, and Identity for Monocular and Multiview Video

Dr. R. James Cotton MD / PhD

Shirley Ryan AbilityLab / Northwestern University, Chicago, IL, United States

Introduction

While markerless motion capture for biomechanics is advancing rapidly, it often relies on vision algorithms not designed for this purpose. This necessitates complex multistage pipelines including associating people across views and time, keypoint detection, and inverse kinematics. Additionally, the constituent models are trained on able-bodied individuals rather than clinical populations. Here, we developed a unified algorithm to simplify both monocular and multiview biomechanics and trained it on a dataset of clinical motion analysis.

Methods

Our model architecture is most similar to the recent Multi-HMR algorithm, but ours is adapted to regress kinematic parameters for a biomechanical model along with model scale and marker offsets. To support multi-view geometry, we extended it to output keypoint for the 87 keypoints in the BML-MOVI dataset. This enables us within-view and cross-view consistency between the predicted 3D marker locations on the biomechanical model and the heatmaps. Finally, we incorporated a re-identification head trained to learn a stable signal for identity and tracking, which was learned contrastively across views and time. This was trained on an extensive dataset of diverse clinical movements.

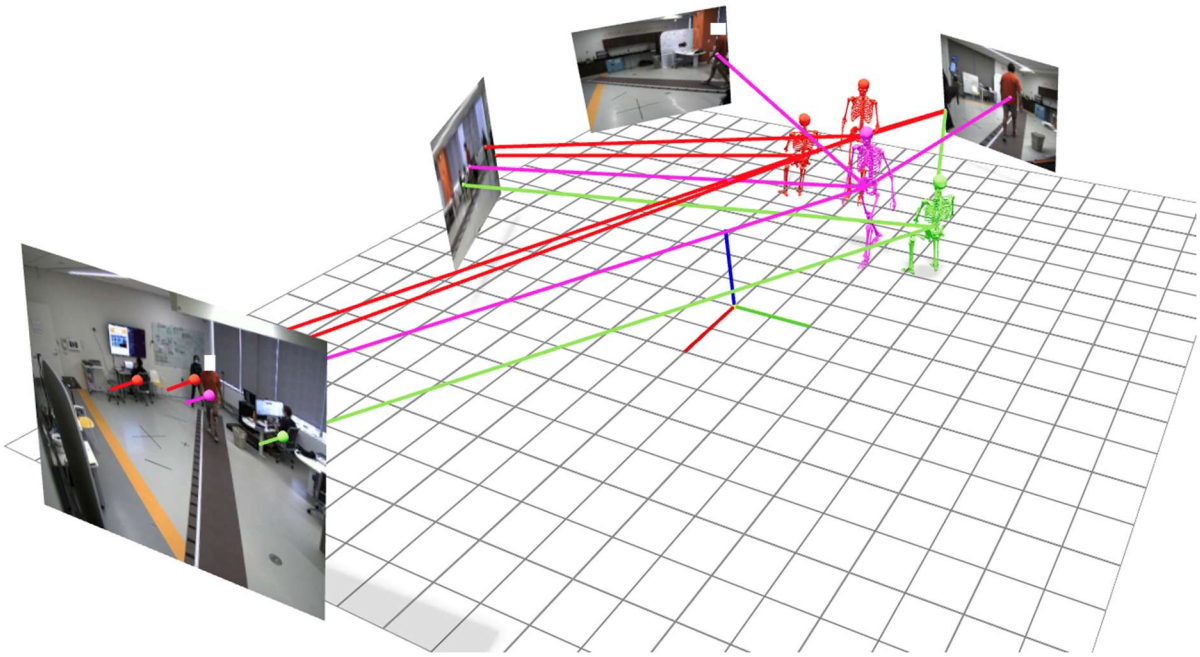
Results

In monocular mode, this algorithm achieves a mean absolute joint angle error of less than 5 degrees. While this underperforms our end-to-end optimization-based monocular approaches, it can perform in real time, and the results can be refined through additional optimization. The ReID head also achieves excellent separation between participants. This allows us to link detected people across views and refine the kinematics using multi-view geometry. Because this ReID association can be solved efficiently, it can be incorporated into training to enable additional biomechanically-constrained self-supervised learning. It can also be used during inference for multiview markerless motion capture.

Discussion

This model is an import step to wider use of markerless motion capture, as this architecture is expressly designed for the purpose of biomechanics with both direct regression of body scale and kinematics, which can be further refined by the set of biomechanically sufficient keypoints. In addition to achieving realtime performance and being trained on clinical data, this opens up important avenues for further improvement through biomechanically constrained self-supervised learning.

Images (Optional)



Session Category

Emerging Areas: N/A

P3-051

AI-Powered Real-Time Pose Estimation Linked with Biomechanical Simulation for Personalized Squat Injury Prevention

Dr. habil. Sabine Bauer[1], MA Ivanna Kramer[2], BA Lara Blomenkamp[2]

[1]University Sports, University of Koblenz, Koblenz, Rheinland-Pfalz, Germany. [2]Institute for Computational Visualistics, University of Koblenz, Koblenz, Rheinland-Pfalz, Germany

Introduction

Sports-related knee injuries such as ACL tears are common and increase the risk of long-term osteoarthritis, emphasizing the need for preventive strategies. Vision-based systems can classify major squat errors but cannot estimate internal loads. In contrast, biomechanical simulations can, yet they require markers or complex setups. We present a real-time, markerless, multi-view pipeline combining AI-based pose estimation with biomechanical modeling to provide kinematic feedback and subject-specific load insights for injury prevention.

Methods

Twelve healthy volunteers (six female, six male) performed three squats each, recorded from frontal and lateral perspectives using Intel RealSense cameras (30 fps). RTMPose extracted 2D keypoints, which were triangulated into 3D coordinates after calibration. Real-time rule-based feedback targeted three lateral criteria (heels flat, hip above knee, knee not beyond toes) and one frontal knee angle criterion [1]. For kinetic estimates, keypoints were scaled in an OpenSim musculoskeletal model (Pose2Sim), applying inverse kinematics and dynamics to derive joint moments and muscle forces. The system generated two types of outputs: frame-by-frame compliance indicators showing whether movement criteria were met at each instant, and trial-level summaries of muscle force distributions characterizing how loads were shared across muscles throughout the squat.

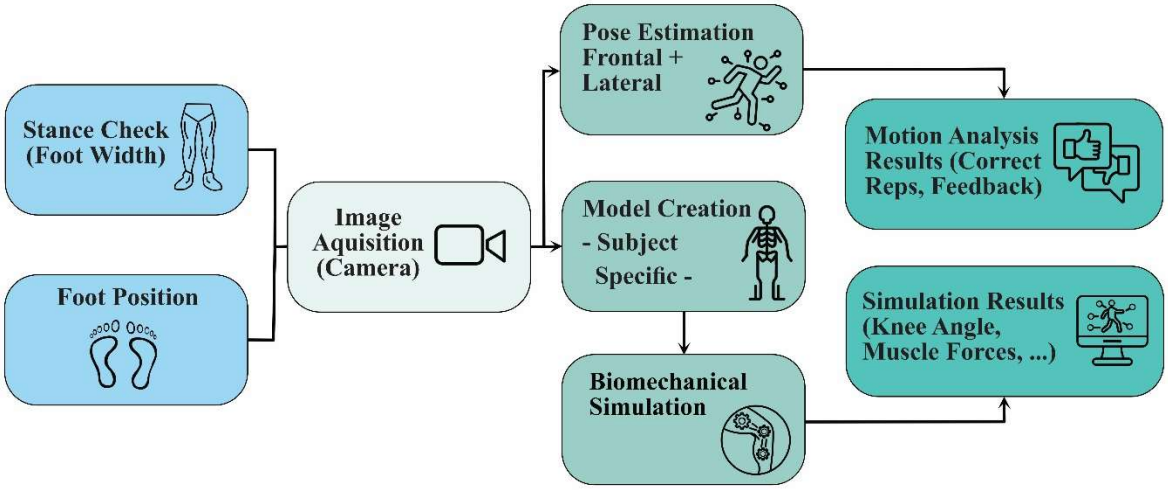
Results

Pose estimation achieved mean absolute errors of 3.5-4.2° for knee angles, consistent with marker-based systems, though larger maximum errors occurred due to occlusion and clothing. Simulation results showed ~6° deviation from ground truth producing physiologically plausible muscle force patterns. At maximal knee flexion, quadriceps dominated load distribution, with the vastus lateralis contributing >50%, consistent with published data. Hamstring contributions also matched literature ranges. The system thus delivered actionable kinematic feedback while producing load estimates aligned with established biomechanical findings.

Discussion

This pipeline links real-time AI-based pose estimation with subject-specific biomechanical simulation, enabling accessible, low-cost, and physiologically valid squat analysis. Although higher maximum errors indicate sensitivity to occlusion and visual conditions, overall accuracy supports markerless feedback for applied contexts. Real-time detection of dynamic knee valgus enhances clinical relevance for ACL injury prevention. Key strengths include real-time analysis, open datasets, and reproducibility, while limitations involve small sample size and a restricted population.

Images (Optional)



References (Optional)

[1] Sabine Bauer et al., International Conference on AMLDS, 2025

Session Category

Emerging Areas: N/A

P3-052

Evaluating the Impact of Camera Motion on Knee Angle Accuracy using World-Grounded Human Motion Recovery (GVHMR)

Ms. Sarah Dumont, Dr. Calvin Kuo

University of British Columbia, Vancouver, BC, Canada

Introduction

Advancements in computer vision have led to the development of pose estimation technologies, such as GVHMR. The markerless tracking system utilizes a single camera to generate 3D position data, presenting a potential solution for remote assessment to address the limitations of the marker-based gold standard [1]. However, before implementing this technology, it is critical to determine the practical constraints and recording conditions required to ensure accurate, meaningful data outputs. Specifically, this study aims to determine if a stationary camera is an important constraint to enforce during out-of-lab data collection.

Methods

We recruited three participants (22±1.7yo; 1F) to complete movements relevant to return-to-sport assessment, such as triple crossover hop and 45° cut. Participants were recorded simultaneously with two Motorola 5G (30Hz) cameras. One camera was affixed stationary to a tripod positioned approximately 45° relative to the participant. The second camera was handheld by the researcher and moved laterally following the participant. Camera movement was classified as low, medium, or high speed, with each condition repeated three times. All videos were processed using GVHMR to extract 3D joint position. Data was filtered and interpolated to compute knee joint angles (cosine law).

Results

The root mean square error (RMSE) of the knee angles was calculated relative to its corresponding stationary camera recording. A Kruskal-Wallis test indicated significant differences in RMSE across movement levels ($p = 0.00011$). Post-hoc Stepdown Dunn's tests showed:

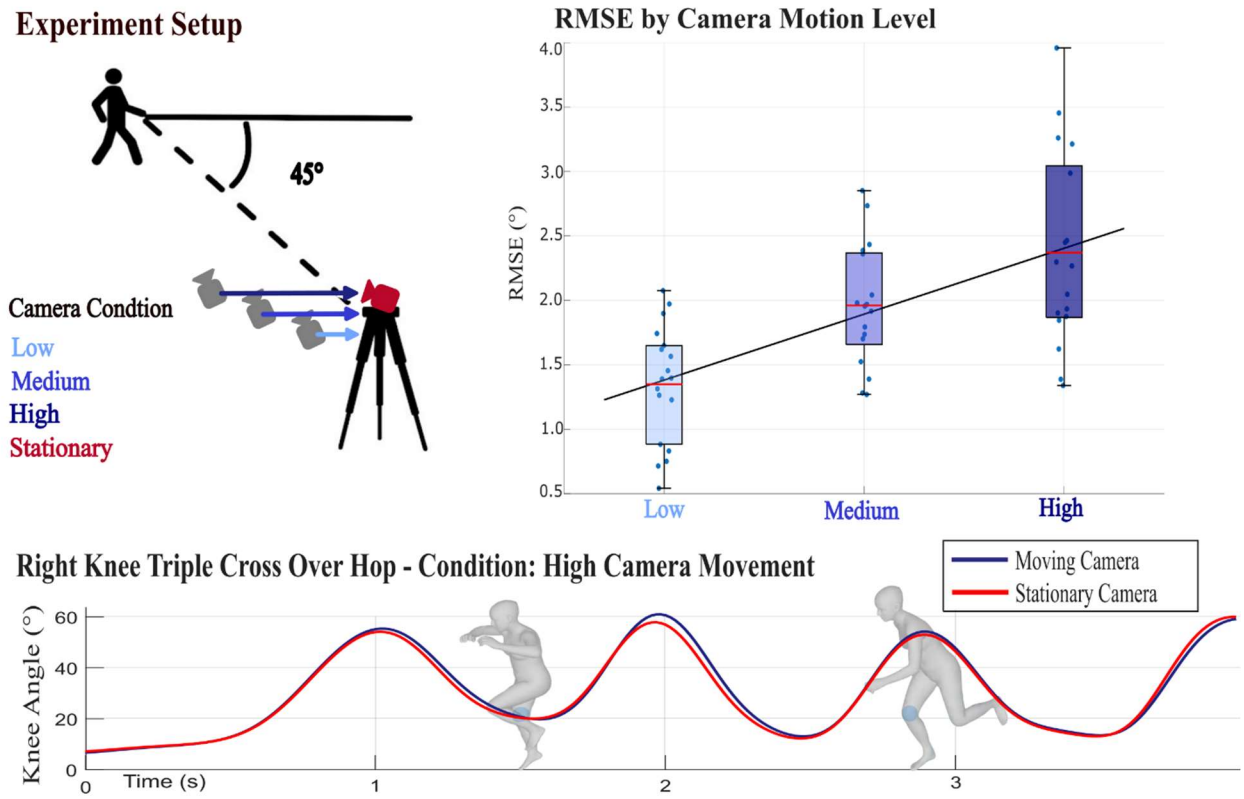
- **Low vs. Medium:** $p = 0.0039$
- **Low vs. High:** $p = 0.000035$
- **Medium vs. High:** $p = 0.22$

Only comparisons involving the low movement condition reached statistical significance, showing that introducing movement increases error significantly, while increased movement has less effect. Despite this, the overall average RMSE across all trials and conditions was 2.1°, indicating good accuracy of GVHMR.

Discussion

Results show promise for out-of-lab data collection, as the reduced constraints make this technology more accessible and easier to use for nontechnical users. The next steps for this project will be to validate GVMHR joint angle estimates against marker-based data, as well as to look into other metrics used in return-to-sport evaluations.

Images (Optional)



References (Optional)

[1] Shen Z. (2024). SIGGRAPH.

Session Category

Emerging Areas: N/A

P3-053

Development of Automated Coronal Plane Alignment of the Knee Classifier Using Machine Learning With Digitally Reconstructed Radiograph

Dr. Satoru Ikebe[1], Dr. Takahiro Inoue[2], Dr. Takeshi Shimoto[3], Dr. Satoshi Hamai[2], Prof. Shingo Mabu[1], Prof. Yasuharu Nakashima[4], Prof. Hidehiko Higaki[5]

[1]Yamaguchi University, Ube, Yamaguchi, Japan. [2]Kyushu University, Fukuoka, Fukuoka, Japan. [3]Fukuoka Institute of Technology, Fukuoka, Fukuoka, Japan. [4]Kyushu University, Fukuoka, Fukuoka, Jordan. [5]Kyushu Sangyo University, Fukuoka, Fukuoka, Japan

Introduction

The coronal plane alignment of the knee (CPAK) classification is one method for evaluating lower leg alignment, and automated CPAK classifier have been developed. However, preparing sufficient training data for machine learning algorithms in the medical field is difficult because annotation requires specialized knowledge. Applying CT-based digitally reconstructed radiograph (DRR) as training data can reduce annotation costs. Therefore, this study aimed to develop an automated CPAK classifier using machine learning with DRR.

Methods

Pixels of target object in CT images were annotated to create annotated DRR. Annotated DRRs were created using seven lower limb CT images before total knee arthroplasty. The automated CPAK classifier was developed using object detection and segmentation algorithm. The femoral head, distal femur, proximal tibia, and ankle joint were detected using FCOS, and segmentation images were generated by HRNet, and landmarks were detected. Measurements of the lateral distal femoral angle (LDFA), the medial proximal tibial angle (MPTA), arithmetic hip-knee-ankle angle (aHKA), and joint line obliquity (JOL) were performed and CPAK was classified based on references by S. J. MacDessi et al. The automated CPAK classifier was evaluated using measurements from full-leg radiographs of 15 patients by clinicians.

Results

The feature objects were detected by FCOS and the detected images were segmented by HRNet. The landmarks for CPAK classification were detected from segmented images. The root mean square error (RMSE) result for LDFA was 1.6 degrees and MPTA was 1.9 degrees. The RMSE results for aHKA and JLO were 2.5 and 2.6 degrees, respectively. Classification accuracy of CPAK was 80%.

Discussion

FCOS and HRNet were trained using a total of 80,000 annotated DRR images created from seven lower limb CT images. Annotated DRR reduced annotation costs and allowed for object detection and segmentation using machine learning. The landmarks for CPAK classification were able to be detected from full-leg radiographs for evaluation. The accuracy of LDFA, MPTA, aHKA and JLO were within 3.0 degrees and classification accuracy of CPAK was 80%. High-accuracy landmark detection is required for automated CPAK classifiers, necessitating the addition of annotated DRRs from healthy subjects to the training data.

Session Category

Emerging Areas: N/A

P3-054

Observer Network: Validating Human Motor Control Policies via Q-network Knowledge Distillation

Mr. Seungju Mok MS Candidate, Prof. Ho Seon Choi Assistant Professor

Sejong University, Seoul, Seoul, Korea, Republic of

Mr. Seungju Mok

Introduction

Neuromusculoskeletal simulations are widely used in rehabilitation and neuroscience, and reinforcement learning (RL) is increasingly applied to train motor control policies. In Actor–Critic algorithms, a Q-network critic guides the actor toward actions with higher expected returns. Policy validation typically relies on comparing simulated joint kinematics/kinetics, or muscle activations with clinical measurements, but variability of biological systems limits the interpretability of such direct comparisons. To address this, we propose a novel validation framework that combines Q-network with knowledge distillation. Specifically, we introduce an observer network designed to quantify the similarity between learned policies and human motor control strategies.

Methods

RL state–action pairs include variables observable only in simulation and those measurable clinically. We designed an observer network that receives only clinically observable data but is trained to imitate the full Q-network through knowledge distillation. In the MyoSuite myoLeg environment, the musculoskeletal model features a 403-dimensional state space and an 80-dimensional action space. For the observer, we used sagittal-plane hip, knee, and ankle angles as state inputs and five lower-limb muscle activations as action inputs. The observer was trained using MSE against the corresponding Q-network output. Pre-trained locomotion policies, SAR and OptSyn, provided training data, and human gait data[1] were later used for evaluation. An overview of the framework is shown in the figure.

Results

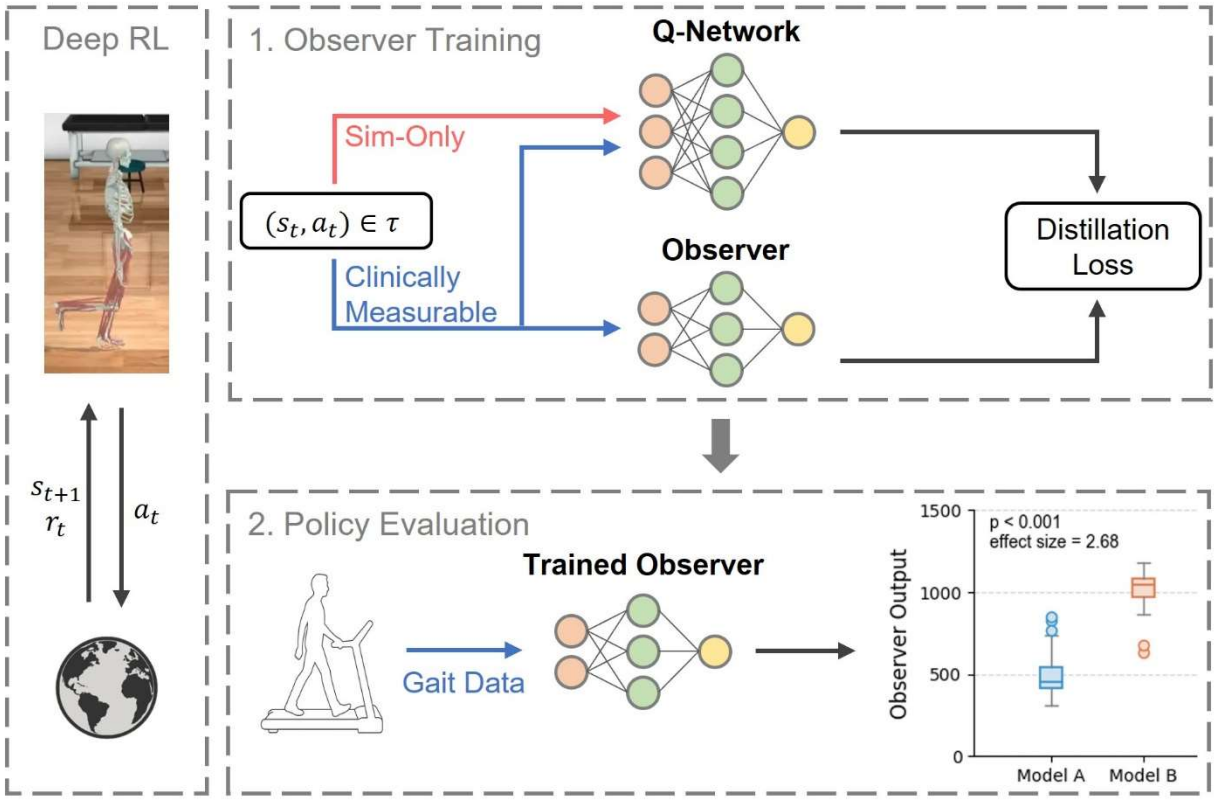
Observers trained on SAR and OptSyn achieved rRMSE values of 0.11 and 0.08, and R^2 values of 0.92 and 0.83. For gait data from 20 subjects, observer outputs differed

significantly between the two policies (487.52 ± 47.44, $p < 0.001$, effect size = 2.68). Notably, OptSyn—also the policy with higher training return—yielded higher observer outputs. Corresponding box plots are provided in the figure.

Discussion

The observer's rRMSE and R^2 demonstrate successful knowledge distillation and accurate imitation of Q-network behavior. The higher observer outputs for OptSyn suggest that it not only generates more seemingly natural gait patterns but learns motor control strategies more consistent with human behavior. Beyond policy validation, the observer could potentially estimate impairment severity in neurological patients by quantifying deviations from healthy motor control strategies.

Images (Optional)



References (Optional)

[1] Van Criekinge et al., Scientific data, 2023

Acknowledgements (Optional)

This project is currently supported by the National Research Foundation of Korea(NRF) grant funded by the Korea government (MSIT) (RS-2024-00452977).
(Correspondance: choihoseon@sejong.ac.kr)

Session Category

Emerging Areas: N/A

P3-055

Sex-Hormone and Adipose Tissue Amounts Impact Magnitude of Breast Tissue Acceleration

Dr. Stacey Gorniak PhD, Ms. Saba Yazdekhasti MPO, Dr. Rebekah Maddox PhD, Dr. Emily LaVoy PhD

University of Houston, Houston, TX, United States

Introduction

Breast biomechanics studies have traditionally used 3D motion capture systems extensively to measure breast tissue acceleration based on passive marker displacement values without consideration of how health state covariates—including sex-hormone levels—may influence breast tissue kinematics. To address this issue, our study aimed to investigate potential physiological and anthropometric covariates of breast tissue acceleration magnitude in women with larger breasts.

Methods

In this study, 20 healthy female volunteers (33 ± 12 years of age, BMI = 30.2 ± 6.5 kg/m^2), spanning a range of D to G bra cup sizes, participated in a comprehensive breast motion analysis involving both a 3D motion capture system and Delsys Trigno sensors (built-in triaxial accelerometers) to assess breast acceleration during exercise. Potential covariates were collected via body composition via dual-energy X-ray absorptiometry (DXA) and a venous blood draw to assess the influence of sex-hormone levels and common cardiometabolic health markers on breast tissue kinematics.

Results

While differences emerged between breast acceleration values measured via triaxial accelerometry and traditional 3D motion capture, influences of sex-hormones such as sex hormone binding globulin (SHBG), progesterone, and cardiometabolic health via glycated hemoglobin all significantly influence the magnitude of breast tissue acceleration ($p < 0.01$). Additional anthropometric covariates related to trunk size (e.g., total body fat percentage and bra band size) also emerged ($p < 0.01$).

Discussion

This data supports our prior reports of differences in the magnitude of breast tissue acceleration values depending on measurement modality [1]. Additionally, these data point to important physiological and anatomical contributions to breast tissue acceleration magnitudes. Specifically, influences of the endocrine system through sex-hormone

secretion and glycated hemoglobin control were notable in the covariates found in this study. Contributions of increased trunk size and increased adipose tissue distribution within the trunk region also influenced the magnitude of breast tissue acceleration. These data enhance our understanding of how breast dynamics are influenced by physiological influences which are not typically considered in biomechanical studies.

References (Optional)

[1] Yazdekhasti S, LaVoy EC, Gorniak SL. Assessing breast acceleration while using sports bras and conventional bras: A comparative analysis of measurement techniques. *Journal of Biomechanics*. 2025;183:112640. doi:10.1016/j.jbiomech.2025.112640

Session Category

Emerging Areas: N/A

P3-056

A Data-Driven Approach to Optical Motion Capture Gap-Filling

Ms. Sarah Hynes, Mr. Jonathan Chu, Mr. Daniel Fournier, Dr. Clark Dickerson, Dr. Stewart McLachlin

University of Waterloo, Waterloo, Ontario, Canada

Introduction

Marker-based optical motion capture (MOCAP) is widely used for movement analysis, but marker occlusion creates gaps that require post-processing [1]. Traditionally, these gaps are filled manually using interpolation methods, a process that is time-consuming and prone to variability, particularly for longer gaps [2]. This study investigated the use of a machine learning (ML) approach to automate marker gap-filling by incorporating inertial measurement unit (IMU) data as a reference during marker dropout.

Methods

A dataset of 84 participants performing nine physiotherapy exercises while wearing seven markers on the right arm and upper torso was analyzed. Movements were captured using a 13-camera VICON MX20 motion capture system (VICON Motion Systems Ltd, Oxford, UK), while an IMU (Mobvoi TicE Smartwatch, Beijing, CN) was worn on the right wrist. The original MOCAP data was manually gap-filled to establish ground truth values. Artificial gaps ranging from 0.5 to 2 seconds were then introduced randomly across all markers. The incomplete MOCAP data and corresponding IMU signals were used as inputs for a long short-term memory (LSTM) recurrent neural network, designed to predict and reconstruct missing marker trajectories. The dataset was split into training (70%), validation (15%), and testing (15%) sets.

Results

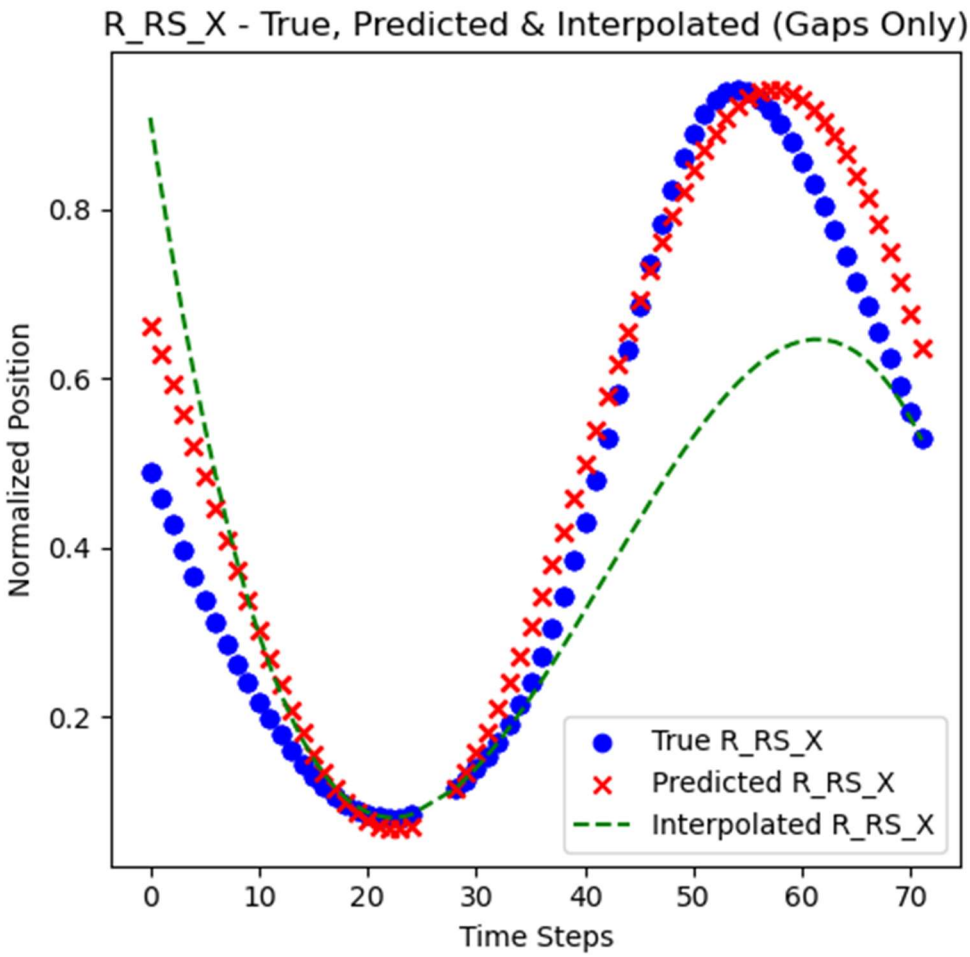
The model converged after 54 epochs, achieving a mean squared error (MSE) of 0.0213 for training and 0.0212 for testing. Compared to traditional interpolation techniques, the model demonstrated superior performance during non-linear and complex movements, reducing error by up to 50% in certain cases.

Discussion

By combining IMU and MOCAP data, this ML-based approach effectively automated the marker gap-filling process and produced smooth, physiologically plausible trajectories during short-term marker loss. This method offers a consistent and less labor-intensive alternative to traditional gap-filling techniques. Future work will focus on model

optimization, comparative analysis with additional time-series architectures, and exploring potential real-time implementation.

Images (Optional)



References (Optional)

[1] Jonathan Camargo *et al.* , Comput Methods Biomech Biomed Engin, 2020

[2] Przemyslaw Skurowski *et al.* , Sensors, 2021

Session Category

Emerging Areas: N/A

P3-057

Accuracy of AI-Based Multimodal Models in Automatically Detecting Falls in Older Adult from Video Footage

Ms. Teah Cribbie, Dr. Max Donelan, Dr. Stephen Robinovitch

Simon Fraser University, Burnaby, British Columbia, Canada

Introduction

Falls are the leading cause of injury in older adults (aged 65+). Often, older adults are unable to rise independently after falling, and the "long lie" increases the clinical consequences of the fall. Video cameras are increasingly accessible, and advancements in AI models are creating the potential for "smart" cameras that can automatically detect falls and alert care providers.

To date, research on the accuracy of video-based automatic fall detection has involved small numbers of simulated falls by young adults in artificial environments. Furthermore, no study to our knowledge has evaluated the video-based fall-detection performance of multimodal models (e.g., GPT or Gemini). We addressed this knowledge gap by evaluating the zero-shot performance of GPT 4.1 and Gemini 2.5 Pro in automatically detecting real-life falls by older adults in long-term care using video footage. We also assessed how model performance depends on video characteristics (resolution, lighting, distance from camera, occlusions, number of background individuals) and movement characteristics (non-fall activity, activity at time of fall, cause of imbalance leading to fall).

Methods

Videos of 20 falls and 24 non-falls (activities of daily living) were included in the analysis. Images were extracted from each video at 5 frames per second. A hierarchical prompt was used, specifying identity, instructions, fall definition, and context. The images and the prompt were sent to GPT 4.1 and Gemini 2.5 Pro for fall versus no-fall classification.

Results

The classification accuracy was 86% for Gemini 2.5 Pro and 80% for GPT 4.1. Both models were more likely to yield false negatives (i.e., classify falls as non-falls) than false positives (classify non-falls as falls). The sensitivity was 70% for Gemini and 65% for GPT, and the specificity was 100% for Gemini and 92% for GPT. Classification accuracy depended on both video and movement characteristics (Table 1).

Discussion

In this preliminary study, we found promising results of 80-86% accuracy for AI-based multimodal models in automatically detecting older adult falls from video footage. Ongoing work with a larger sample is examining how classification accuracy depends on the independent and interacting effects of movement and video characteristics, as well as the prompt design.

Images (Optional)

Table 1. Effect of video and fall characteristics on classification accuracy

		N	Gemini accuracy	GPT accuracy
Distance from camera	Close	7	1.00	0.86
	Medium	6	0.83	0.67
	Far	7	0.29	0.43
Background individuals	None	8	0.75	0.88
	Few	5	1.00	0.80
	Many	7	0.43	0.29
Occlusions	None	13	0.77	0.77
	Partial	3	0.67	0.67
	Almost full	4	0.50	0.25
Lighting	Bright	8	0.63	0.75
	Dim	9	0.78	0.67
	Dark	3	0.67	0.33
Resolution	720*480	1	0.00	1.00
	640*480	12	0.75	0.67
	352*240	7	0.71	0.57
Cause of the fall	Hit/bump	1	1.00	1.00
	Trip/stumble	4	1.00	1.00
	Lost support w/ external object	5	0.60	0.40
	Slip	1	0.00	1.00
	Incorrect shifting bodyweight	9	0.67	0.56
Activity at the time of the fall	Sitting	2	1.00	0.00
	Standing	2	1.00	1.00
	Walking	8	0.50	0.63
	Transfer - sitting to standing	4	0.50	0.50
	Transfer - standing to sitting	4	1.00	1.00

Session Category

Emerging Areas: N/A

P3-058

GO Viz: An Open-Source Application for the Visualization of Gene Ontology Enrichment Analysis Across Multiple Comparisons

Mr. Amevi Semodji, Dr. Trevor Lujan

Boise State University, Boise, Idaho, United States

Introduction

Gene ontology (GO) enrichment analyses have been instrumental in transcriptomics and proteomics to identify biological events associated with differential expression patterns. Although multiple online tools and statistical packages provide visualization capabilities, none support user-friendly comparisons across multiple experimental conditions. To address this limitation, we developed GO Viz, an open-source MATLAB-based standalone application that streamlines GO enrichment visualization through the handling of multiple comparisons and diverse input file types.

Methods

GO Viz offers a user-friendly graphical interface (**Fig. 1A**) that allows users to select multiple experimental comparisons as text- or spreadsheet-based files, which are common outputs from GO enrichment platforms. The application imports log2 fold enrichment and Benjamini-Hochberg (FDR) data, and after an optional filtering by statistical significance, creates a two-dimensional color-scale bubble plot with bubble size representing significance and color representing log2 fold. The resulting layout enables clear and direct comparison of GO terms across different conditions. Users can export visualization results as high-resolution images and editable MATLAB figures, facilitating tuning for publications. We tested the performance of GO Viz by visualizing generated GO data from 1, 5, 10, and 20 comparisons with up to 10,000 GO terms and in '.xlsx', '.tsv', and '.csv' formats.

Results

GO Viz successfully loaded and plotted data from all sets of comparisons and GO terms in less than 20 seconds (**Fig. 1B**). It also successfully loaded all three file formats with an average of 0.5 second and no significant difference in loading time between formats (**Fig. 1C**).

Discussion

GO Viz's objective is to visualize GO enrichment data across multiple experimental comparisons in an intuitive and user-friendly bubble format and thereby address limitations with current platforms. For example, REVIGO and GO Figure! only provide bubble-format visualization for single comparisons, while GO Term Viewer can handle multiple comparisons, but in a hierarchical manner that is difficult to visualize. Here we demonstrated that GO Viz can handle multiple comparisons and multiple file formats with significant amounts of GO terms. Future work will include reduced-redundancy implementation and GO term search.

Images (Optional)

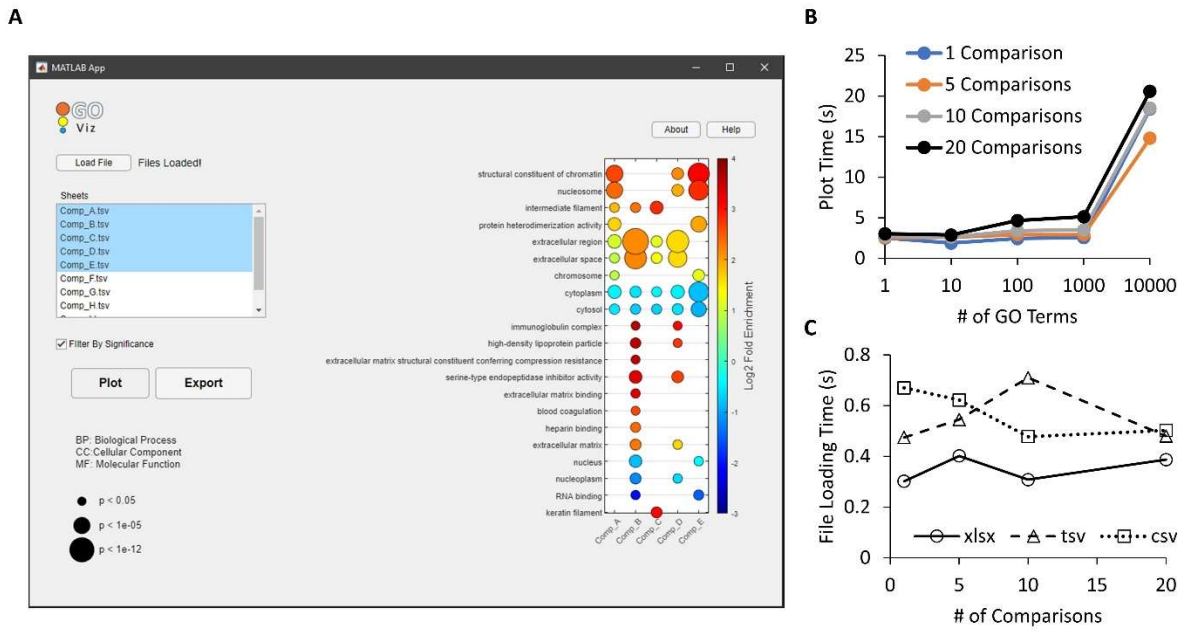


Figure 1: A) Graphical interface of GO Viz showing an example of plot across multiple comparisons. B) GO Viz successfully loaded and plotted data from 1, 5, 10, and 20 comparisons that each had 1, 10, 100, 1000, and 10000 GO terms. C) GO Viz successfully loaded different file formats for analysis with no minor differences in loading time between formats

Session Category

Emerging Areas: N/A

P3-059

Cognitive Load and Knee Motion While Driving in Teens After Anterior Cruciate Ligament Reconstruction Surgery

Dr. Valentina Graci[1,2], Ms Maitland Witmer MSE[1,2], Ms Chelsea Ward-McIntosh BS[1], Dr. Hasan Ayaz PhD[2], Dr. Divya Jain PhD[1], Dr. Catherine McDonald PhD[1,3], Ms. Kevin Landrum BS[4], Dr. J. Todd Lawrence MD, PhD[4], Dr. Theodore Ganley MD[4], Dr. Elliot Greenberg PT, DPT, PhD[4]

[1]Center for Injury Research and Prevention,Children's Hospital of Phialdelphia, Philadelphia, PA, United States. [2]School of Biomedical Engineering, Science and Health Systems, Drexel University, Philadelphia, PA, United States. [3]School of Nursing, Philadelphia, PA, United States. [4]Department of Orthopedic Surgery, Philadelphia, PA, United States

Introduction

Evidence-based guidelines to determine capacity to safely return-to-drive after Anterior Cruciate Ligament Reconstruction (ACLR) in teens are lacking. Although divided attention and cognitive tasks can influence knee biomechanics, the interplay between driving cognitive demands and lower limb motion remains unknown in teens post-ACLR. Our objective was to examine cognitive load, knee motion, and brake force in teens after ACLR versus healthy controls.

Methods

Six healthy teens (4 males, 2 females; age 16.7-18.9 years old) and four teens post-right ACLR (1 male, 3 female; age 16.9-19.6 years old; 30-64 days post-op) completed three 7–9 minute drives in a driving simulator, each including scenarios with a lead vehicle abruptly stopping. Inertial Sensor Unit system (IMU) recorded right knee movement. A portable functional near-infrared spectroscopy (fNIRS) measured prefrontal cortex oxygenation changes (HbO). Brake force (N) and knee angle (°) were averaged across drives and compared between groups with Mann-Whitney U tests. HbO was averaged during the brake event and during a ‘straightaway’ drive, and compared between events and groups with a linear mixed model ($p<=0.05$).

Results

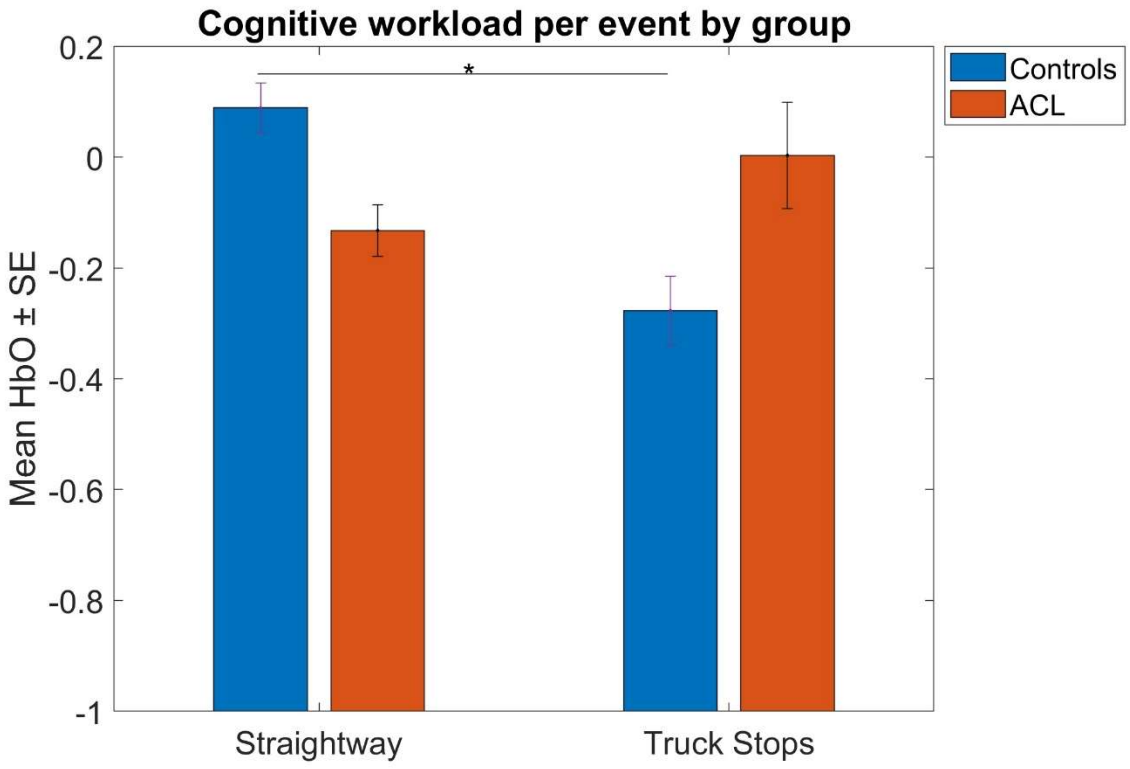
Teens 4-6 weeks post-ACLR showed significantly decreased braking force (Control 11.2 ± 30.2 N vs post-ACLR 7.7± 21.0 N, $p=0.01$) but similar knee angle compared to the controls

(p=0.08). HbO showed a significant interaction effect in group*event ($p<0.05$). Post-hoc comparisons showed that the post-ACLR group had similar cognitive workload between events (p=0.5) while the controls demonstrated decreased cognitive workload in the braking event compared to the straightaway drive ($p<0.03$, Figure 1).

Discussion

In healthy teens, quick brake reactive actions may require less brain activity in the areas dedicated to executive functions, with non-primary motor areas and subcortical structures potentially being more active to rapidly produce the correct crash avoidance motor response. Post-ACLR teens may require higher cognitive workload to brake, which may delay motor output. This may help explain the reduced brake force in the ACLR group while maintaining a similar knee position as the controls. Cognitive workload may be an important metric to assess return-to-drive readiness in teens post-ACLR.

Images (Optional)



Session Category

Emerging Areas: N/A

P3-060

Sensitivity of Markerless 3D Reconstruction to Different Simulated Video Acquisition Scenarios

BSc. Vanessa Yelós Tellagorry[1,2], MSc. Ariel E. Stassi[1], AD. Martín Arévalo[1], PhD. Germán Pequera[1,2], PhD. Carlo M. Biancardi[2]

[1]Departamento de Ingeniería Biológica, CENUR Litoral Norte, Universidad de la República, Paysandú, Paysandú, Uruguay. [2]LIBiAM Biomechanics Lab, Dep. of Biological Sciences, CENUR Litoral Norte, Universidad de la República, Paysandú, Paysandú, Uruguay

Introduction

Markerless technique has been positioned as a valuable tool comparable to gait labs [1]. However, its ability to achieve reliable results in different video acquisition scenarios has been poorly explored. The objective of this ongoing work is to investigate the impact of changes in video features on 3D markerless reconstruction performance.

Methods

One subject (Male, 38 yr, height 174cm, weight 69.4 Kg), equipped with 18 markers [2], walked on a treadmill at 5 km/h. The study was approved by the university ethics committee.

Data acquisition: Kinematic data were acquired using a motion capture system (Vicon Motion Systems) with 8 cameras at 120 Hz, and a markerless system simultaneously, which was composed by 4 iPhone SE (Apple) to register videos at 60 Hz.

RGB video data augmentation: Videos were generated synthetically combining the modification of 3 parameters of the RGB videos: “Add” (impact on brightness), “Mul” (impact on contrast), and “Sigma” (impact on sharpness) using vidaug Github Library (https://github.com/okankop/vidaug). 63 combinations were generated from ordered sequences of video augmentations.

Markerless video processing: MMPose and Pose2Sim [2] were used to reconstruct the position of 18 keypoints. Two classic error metrics, MPJPE and threshold τ^* for MPJLE≥90% [3], were used to evaluate performance changes.

Results

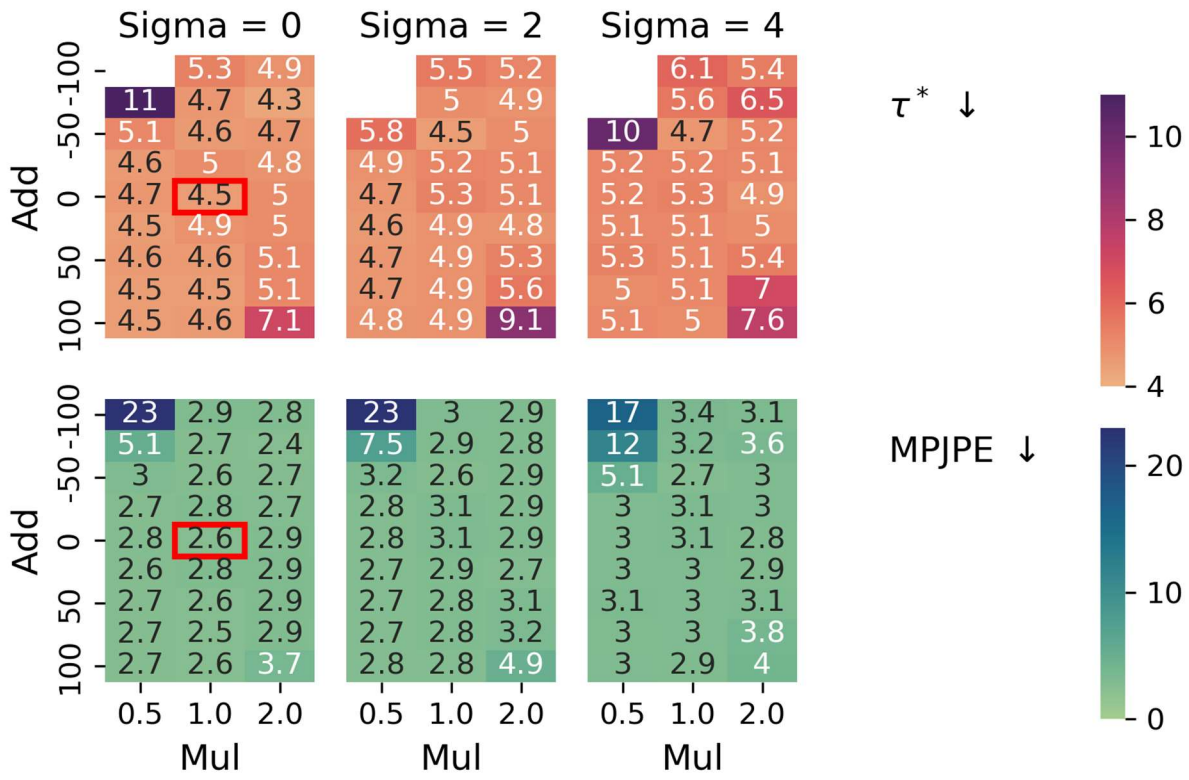
Preliminary results showed that modifying the brightness with respect to the original scene (red box), didn't have a great impact. The same behavior could be seen when contrast was modified. When brightness and contrast perturbations were combined, the system

performance showed the worst results, mainly when brightness and contrast were decreased. However, extreme perturbations on brightness while contrast was increased, didn't worsen the performance. Blur the scene seems to have minimal impact on the markerless performance.

Discussion

Markerless system revealed robust behavior when different scenarios were simulated. Isolated brightness, contrast or sharpness modifications had little impact on performance. However, when the perturbations were combined in a certain way, the performance could decrease significantly.

Images (Optional)



References (Optional)

[1] Pagnon et al. (2022). Sensors, 22(7), 2712.

[2] Pavei et al. (2017). Frontiers Physiol, 8, 129.

[3] Ionescu et al. (2013). IEEE transactions on pattern analysis and machine intelligence, 36(7), 1325-1339.

Acknowledgements (Optional)

Agencia Nacional de Investigación e Innovación for economical support.

Session Category

Emerging Areas: N/A

P3-061

Heel Strike Detection using IMU-Based Multi-Scale Temporal Convolutional Network

Mr. Jainil Patel[1], Ms. Celeste Thai[2], Mr. Chengkang Zhou[1], Dr. Tianxiang Gao[1], Dr. Ying Fang[2]

[1]DePaul University, Chicago, IL, United States. [2]Rosalind Franklin University, North Chicago, IL, United States

Introduction

Detecting heel strikes of gait cycles is critical in gait analysis that is relevant to rehabilitation. Standard techniques rely on ground reaction force (GRF), which can be measured by force plates that are often not available outside the lab. In our study, we trained a deep learning model using only inertia measurement unit (IMU) data to detect heel strikes to support real-world gait analysis.

Methods

GRF and IMU data (42 1-minute walking trials) from four young adults (walked at 8 speeds between 0.6-1.3 m/s) and 12 older adults (walked at self-selected speeds between 0.2-1.1m/s) was used for model training and evaluation. GRF data was used to determine ground truth heel strike labels. A Multi-Scale Temporal Convolutional Network (MSTCN) was trained using shank and thigh IMU data (MetaBase) as the input. The model outputs probability of stance phase at each frame, and a threshold of 0.6 was used to determine heel strike times (Figure 1). We used focal loss to account for the unequal swing and stance phase frames. We evaluated the model on a held-out test set of 10 walking trials from 4 young and 2 older adults.

Results

The model achieved an F1 score of 0.85±0.12, precision of 0.85±0.11, and recall of 0.86±0.11. The mean absolute error for the predicted heel strike time was 45±16ms.

Discussion

The current model achieved good performance (criteria: F1 score between 0.7-0.9) in distinguishing the stance and swing phase. Additionally, the error of predicted heel strike timing was within 3 frames (IMU data collected at 50 Hz), demonstrating the potential of using IMU-based TCN to distinguish gait cycles. The current model was evaluated on one held-out test set. When including different trials in the test set, we observed varied model performance that was influenced by walking speed and age group. Future work will include a larger training set with a wider range of walking speed and age, and use cross-validation for model evaluation. While prior studies have explored step detection using AI, few have

focused specifically on identifying the precise heel strike time, highlighting the novelty of our approach.

Images (Optional)

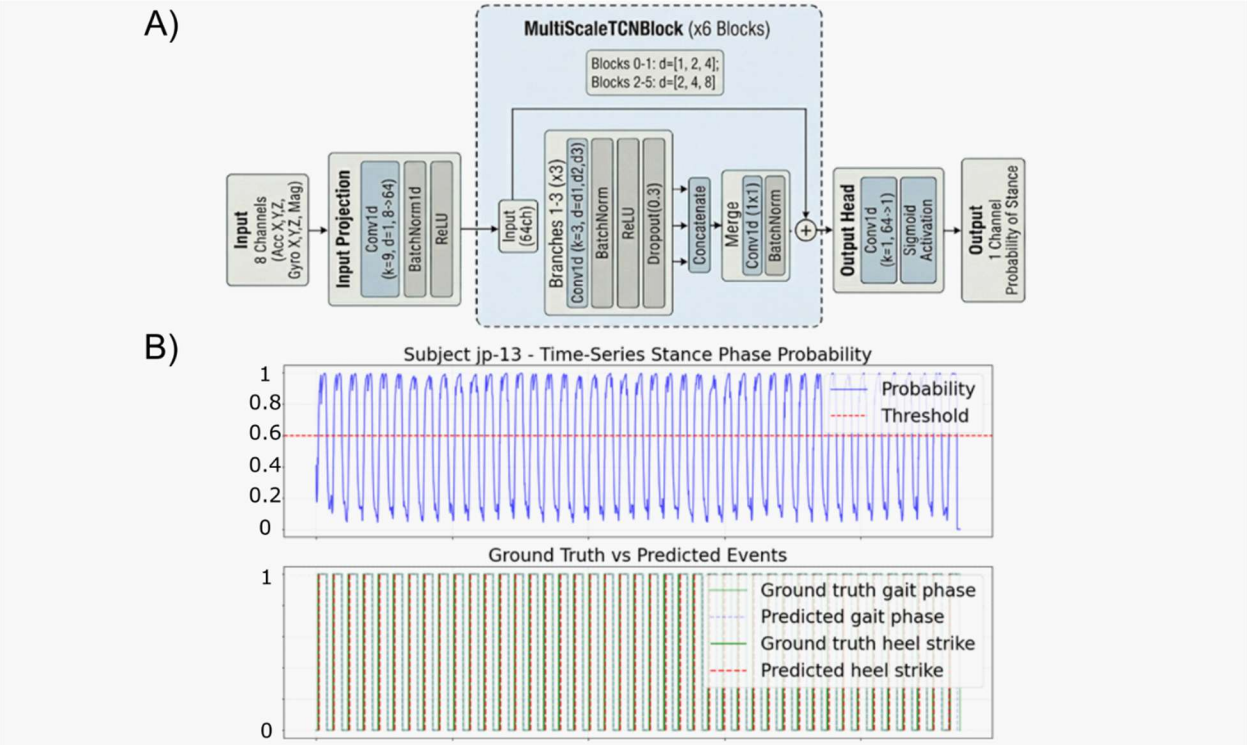


Figure 1: A) Overview of the Multi-Scale Temporal Convolutional Network architecture, including six residual blocks with parallel dilation paths to capture temporal gait patterns at different scales, with the output being probability of stance phase (0: swing, 1: stance) for each time frame. **B)** Data from one participant showing the model's predicted stance probability, and predicted and ground truth heel strike times.

Session Category

Emerging Areas: N/A

P3-062

Quantitative-Feature Analyses of Fear of Falling Through Artificial Intelligence Methods

Dr. Zhanxin Sha[1], Dr Benjamin Meador[2], Mr. Yicai Yao[3], Dr Kesheng Wang[4], Dr Juefei Yuan[3]

[1]Geogia Southwestern State University, Americus, Georgia, United States. [2]Georgia Southwestern State University, Americus, Georgia, United States. [3]Southeast Missouri State University, Cape Girardeau, Missouri, United States. [4]University of South Carolina, Columbia, South Carolina, United States

Introduction

Fear of falling increases the risk of future falls and contributes to disability and declining health-related quality of life. Its assessment is challenging because it is influenced by multiple psychological, social, and balance-related factors. Artificial intelligence methods offer an alternative approach because they can work directly with different forms of input data, including manually selected features, automatically extracted features, or raw time-series signals. These methods may help researchers identify factors associated with fear of falling. However, there is a paucity of research examining features based on anthropometric characteristics, physical activity level, and static balance assessments in relation to fear of falling. The purpose of this study was to classify fear of falling using quantitative features through artificial intelligence methods.

Methods

The present study used a public dataset that included 147 healthy participants (aged 18–85 years). Each participant completed the Falls Efficacy Scale–International (FES-S, total score) and the International Physical Activity Questionnaire–Short Form (IPAQ). The dataset also included ground reaction forces (Fx, Fy, and Fz), ground reaction moments (Mx, My, and Mz), and center of pressure (COPx and COPy) collected under four conditions (eyes open vs. closed & firm vs. foam surface). 98 features were used as inputs, including anthropometric data, physical activity status, and time- and frequency-domain features calculated from kinetic signals. FES-S (classified as low, moderate, and high) served as the classification and prediction outcomes.

Three artificial intelligence methods were used to classify outcomes based on selected features: 1. Random Forest, 2. Fully Connected Neural Network (FCNN), 3. One-dimensional Convolutional Neural Network (1D-CNN).

Results

The 1D-CNN achieved the highest accuracy for classifying FES-S, with performance of 90.25%. FCNN and Random Forest models demonstrated moderate accuracy (85.94% and 85.49%, respectively). Feature importance analyses consistently identified physical activity level, age, foot length, and BMI as the most influential predictors of FES-S.

Discussion

The present study integrates quantitative features to predict and classify fear of falling in a healthy population. Future research is needed to validate these findings in clinical populations and to examine whether additional biomechanical or sensor-based features can further enhance predictive performance.

References (Optional)

Acknowledgements (Optional)

None

Session Category

Emerging Areas: N/A

P3-063

Delineating the Role of Right Ventricular Viscosity and Elasticity in Organ Performance Using a Lumped Parameter Multiscale Computational Model

Dr. Kristen LeBar[1], Dr. Lik Chuan Lee[2], Dr. Zhijie Wang[1]

[1]San Diego State University, San Diego, California, United States. [2]Michigan State University, East Lansing, Michigan, United States

Introduction

Myocardium is viscoelastic: both viscous and elastic resistances exist during deformation. We have shown marked increases in right ventricular (RV) viscosity and elasticity with disease, and *in vivo* reduction of RV viscoelasticity improves function. However, altering viscoelasticity experimentally induces multifactorial changes and prevents isolating the independent effects of viscoelasticity.

Multiscale computational models separate these factors, though myocardial viscosity is typically neglected. **Therefore, our goal was to develop a lumped-parameter model that incorporates RV elasticity and viscosity to predict RV pressure–volume (PV) behavior**. We hypothesized that viscosity and elasticity distinctly impact RV performance.

Methods

We modeled the cardiopulmonary circulation using a previously developed closed-loop lumped-parameter framework. RV viscoelastic stress was incorporated using a modified Kelvin–Voigt formulation. Passive stress ($\sigma_{passive}$) is given by

$$\sigma_{passive}=\sigma_{elastic}+\sigma_{viscous}$$

where

$$\sigma_{elastic}=2Cb_{ff}E_f\lambda_f^2e^Q,\ \sigma_{viscous}=-1.0*sign(Vdot)*1000*\eta(1/3)*((1/v)^{2/3}V_{RV}^{-2/3})*abs(Vdot)$$

Vdot: volume rate of change; C: passive stiffness; η: viscosity. We modulated C and η to mimic healthy and diseased RV mechanics, while keeping active stress (Hill model) unchanged under four conditions: 1) healthy viscoelasticity; 2) increased stiffness; 3) increased viscosity; 4) diseased viscoelasticity. We derived hemodynamic parameters to assess independent and combined effects of viscosity and elasticity.

Results

Changes in elasticity impacted RV pressures, volumes, and systolic function (green). RV contractility parameters (blue) consistently decreased with higher elasticity, whereas increased viscosity produced no change in dP/dt_{min} or ESPVR, but increased dP/dt_{max}. When elasticity and viscosity were increased together (disease) the contractile response resembled that of increased elasticity alone, indicating that stiffness dominates contractility. Increasing passive stiffness alone only slightly increased EDPVR, whereas viscosity markedly increased EDPVR, driving the larger diastolic stiffening seen in the diseased state.

Discussion

Our results reveal distinct effects of passive viscosity and elasticity on RV function. The findings suggest that stiffness dominates RV performance, but increased viscosity (as observed in disease) may be adaptive and preserve function. One limitation is that active stress was unchanged; future work should integrate viscoelastic effects on muscle contraction to fully capture organ physiology. Delineating the roles of viscosity and elasticity enhances our understanding of RV pathophysiology and points to potential therapeutic targets.

Images (Optional)

	Healthy RV		Diseased RV	
	Low C and η	**High C Low η**	**Low C High η**	**High C and η**
ESV (mL)	77.3	73.5	77.2	73.5
EDV (mL)	159.5	130.9	159.5	130.9
ESP (mmHg)	30.2	21.5	30.2	21.5
EDP (mmHg)	4.3	4.5	4.3	4.5
SV (mL)	82.3	57.5	82.3	57.5
SW (mmHg*mL)	2486	1237	2486	1237
EF (%)	51.6	43.9	51.6	43.9
CO (L/min)	4.9	3.4	4.9	3.4
dP/dt max (mmHg/min)	0.42	0.29	0.55	0.35
dP/dt min (mmHg/min)	-0.89	-0.69	-0.89	-0.69
ESPVR (mmHg/mL)	0.39	0.29	0.39	0.29
EDPVR (mmHg/mL)	0.16	0.165	0.22	0.18

References (Optional)

Session Category

Emerging Areas: N/A

P3-064

Identifying Fragile X Syndrome Biomarkers: a Supervised Machine Learning approach based on Gait Analysis data

Phd student Federica Beghetti[1], PhD Fabiola Spolaor[1,2,3], PhD Roberta Polli[3,2], Phd Elisa Bettella[3,2], MD Valentina Liani[2], Mr. Francesco Campulla[4], Prof. Stefano Sartori[5], Prof. Giorgio Perilongo[2,3], PhD, Prof. Damiano Varagnolo[6,1], PhD, Prof. Zimi Sawacha[1]

[1]Department of Information Engineering, University of Padova, Padova, Veneto, Italy. [2]Department of Women's and Children's Health, University of Padova, Padova, Veneto, Italy. [3]Pediatric Research Institute Città della Speranza, Padova, Veneto, Italy. [4]University of Padova, Padova, Veneto, Italy. [5]Child Neurology and Clinical Neurophysiology Unit, Padova University Hospital, Padova, Veneto, Italy. [6]Department of Engineering Cybernetics, Norwegian University of Science and Technology, Trondheim, Trøndelag, Norway

Introduction

Fragile X Syndrome (FXS), the most common inherited cause of intellectual disability and ASD [1], is often underdiagnosed due to inconsistent genetic testing. Because children with FXS frequently show gait alterations, such as flat feet, ligamentous laxity, and hypotonia, gait analysis (GA) offers an objective assessment method. Prior work has shown distinct kinematic and sEMG patterns in children with FXS compared to typically developing peers[2]. Therefore, this study investigates gait-based biomarkers for FXS by evaluating multiple supervised ML models using EMG-derived and kinematic features to discriminate among controls subjects (CS), full-mutation FXS (FXSFull), and mosaic FXS (FXSMos).

Methods

As FXS affects males more frequently due to their single X chromosome, the study analyzed 35 male children with FXSFull (BMI 19.12 ± 6.3 kg/m^2; age 10.4 ± 3.7 years), 20 with FXSMos (BMI 17.19 ± 7.8 kg/m^2; age 10.3 ± 2.5 years), and 14 age- and BMI-matched controls. GA was conducted at self-selected speed using four synchronized GoPro Hero7 cameras (60 fps) and an 8-channel Cometa sEMG system (2000 Hz) recording bilateral lower-limb muscle activity. Six trials per participant were processed to extract spatiotemporal parameters and muscle envelopes, from which DTW-based [3] and sEMG-derived features were computed [2,4]. Supervised ML models were trained with 5-fold cross-validation and evaluated on independent training and test set. Model performance, accuracy, precision, and recall, was assessed for three classification tasks: CS vs. FXS; CS vs. FXSFull vs. FXSMos; FXSFull vs. FXSMos.

Results

Classification performance reliably distinguished CS from FXS. Excluding CS from training improved discrimination between FXSFull and FXSMos.

Discussion

Classification between FXS phenotypes remained challenging, with lower accuracy irrespective of model or feature set. These findings suggest that although sEMG-derived gait features contain discriminative information about the presence of FXS, identifying a robust biomarker for distinguishing FXS subtypes may require additional data modalities or more advanced modeling techniques. Future research will integrate advanced learning methods to improve phenotype-level discrimination and move closer to a clinically actionable biomarker for FXS.

Images (Optional)

Mean value of accuracy of the cross validation of the Test Set		Space-time	Durations of muscle activations	DTW-derived features	EMG fiber derived features	Peak and Position of the Peak of the envelope
CS vs FXS	Gradient Boosting	0,792	0,856	0,8	0,81	0,79
	K-Nearest Neighbors	0,822	0,866	0,76	0,802	0,74
	Multi-layer Perceptron	0,812	**0,874**	0,78	0,828	0,75
	Random Forest	0,81	**0,874**	0,79	0,794	0,78
	Support Vector Machine	0,792	0,848	0,79	0,852	0,8
CS vs FXSFull vs FXSMos	Gradient Boosting	0,452	0,486	0,45	**0,51**	0,39
	K-Nearest Neighbors	0,464	0,462	0,43	0,498	0,36
	Multi-layer Perceptron	0,5	0,478	0,45	0,508	0,36
	Random Forest	0,452	0,47	0,44	0,502	0,42
	Support Vector Machine	0,454	0,438	0,41	0,426	0,41
FXSFull vs FXSMos	Gradient Boosting	0,5	0,554	0,57	0,578	0,55
	K-Nearest Neighbors	0,53	0,512	0,57	0,59	0,52
	Multi-layer Perceptron	0,5	0,536	0,58	0,546	0,51
	Random Forest	0,59	0,556	0,55	**0,622**	0,49
	Support Vector Machine	0,568	0,544	0,59	0,522	0,56

Table 1: Accuracy values are reported for each feature subset and for each comparison (CS vs. FXS in orange, CS vs. FXSFull vs. FXSMos in green, and FXSFull vs. FXSMos in blue). The highest accuracy achieved across all ML models and feature subsets is shown in bold, while the best accuracy within each feature subset and comparison is underlined.

References (Optional)

[1]Hagerman RJ, et al. Front Psychiatry. 2018

[2]Sawacha Z, et al. Sensors. 2021

[3]Steinmetzer T, et al. IWOBI-IEEEconference. 2018

[4]Spolaor F, et al. JIDR. 2025

Session Category

Emerging Areas: N/A

P3-065

Stress Wave Induced High Shear Strain and Shear Strain Rates as a Potential Mechanism to Explain Blast Traumatic Brain Injury.

Mr. Aashutosh Kulakarni Prachet, Dr. Haneesh Kesari

Brown University, Providence, RI, United States

Introduction

Blast traumatic brain injury is a prevalent injury among modern military personnel, with adverse cognitive and behavioral effects. However, the mechanism of the injury in the brain is still unclear. In recent years, cavitation in the cerebrospinal fluid (CSF) has been pursued as a potential mechanism of injury. The short time scales of a potential cavitation event (~2 ms) has led to investigations of the blast event for durations around 10 ms [1, 2]. In this work, we perform numerical simulations to investigate the dynamics of simplified 2D and 3D models of the head for durations greater than 200ms when subject to blast overpressures close to 300 kPa.

Methods

The brain matter and CSF are modeled as nearly incompressible materials, and we use a mixed finite element formulation to address numerical challenges associated with simulating incompressible materials.

Results

We observe in our simulations that the shear strain peak reached at short time scales (< 5 ms) is only a local peak, and that the true shear strain peak occurs at longer time scales (> 50 ms) and are in the range to cause brain injury.

Discussion

The large strains are caused by flexural waves of the skull which propagate slower than the pressure waves and therefore cause large strains at later time durations. This indicates that the vibrational dynamics of the head may be a key mechanism causing brain trauma from blast events and presents immediate insights to manufacture better helmets.

References (Optional)

[1] Jacques Goeller *et al.*, J Neurotrauma, 2012.

[2] Scott T. Miller *et al.,* Frontiers in Neurology, 2021.

Acknowledgements (Optional)

We gratefully acknowledge support from the PANTHER program, TIGER program, and the office of Naval research (Dr. Timothy Bentley).

Session Category

Injury Biomechanics: N/A

P3-066

A MRI-Safe, Pneumatic Rotation Device to Measure Large Brain Deformations using Tagged MRI

Mr. Peace Aina[1], Dr. Yuan-Chiao Lu[2,3], Dr. Joy Mojumder[2,3], Dr. Dzung L. Pham[2,3], Dr. Ahmed Alshareef[1]

[1]University of South Carolina, Columbia, SC, United States. [2]Uniformed Services University, Bethesda, MD, United States. [3]Henry M. Jackson Foundation, Bethesda, MD, United States

Introduction

Tagged Magnetic Resonance Imaging (tMRI) is currently used to measure in vivo brain deformation to understand tissue vulnerability to injury and calibrate computational models. In current experiments, a rotation device is used to impart low head accelerations, with peaks of 250-300 rad/ s^2. The primary aim of this study is to design a MRI-safe axial rotation device that induces higher accelerations with high repeatability to measure large brain deformations.

Methods

A head-rotation cradle and axle were 3D printed from carbon-fiber nylon and anchored within a Delrin bearing block. A MRI-safe optical position encoder was linked to the rotating axle to measure kinematics. A pin mechanism held the cradle level; once released, a counterweight rotated downward with gravity, driving the cradle 35° until it contacted a sorbothane pad. To allow for increased accelerations, a MRI-safe pressure chamber was mounted below the lever arm and was triggered after 2° of travel to boost angular velocity. The input pressure was calibrated based on an analytical solution of the system and desired angular kinematics (3-12 rad/s and 200-1400 rad/s^2). Initial tests were run to confirm peak kinematics and repeatability. Trials were conducted with and without piston assistance. 2D tagged MRI acquisitions were acquired on a Sylgard 527 clyndrical phantom and headform phantom on a Siemens 3T scanner.

Results

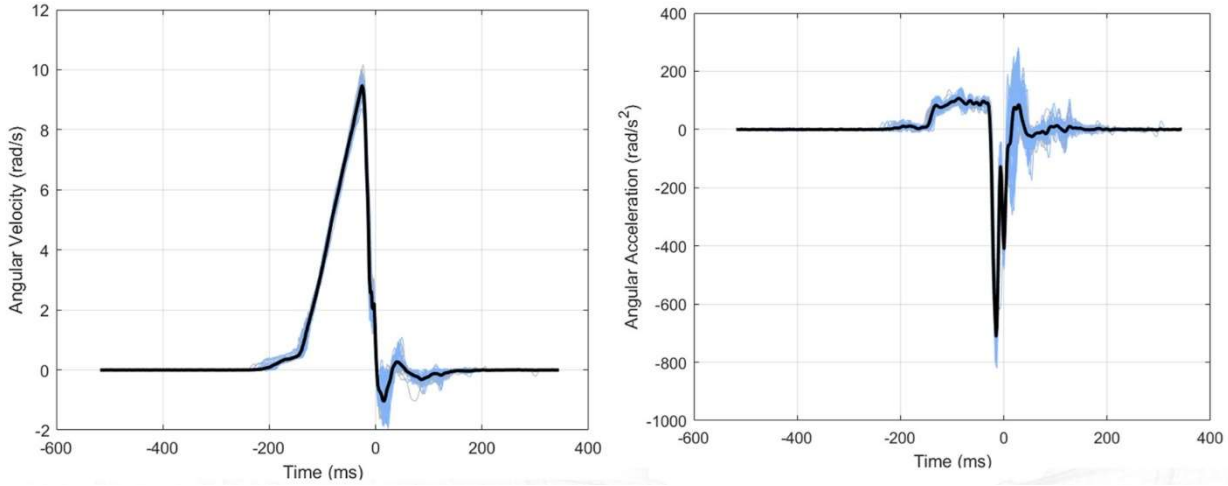
The new device yielded higher peak velocity, greater angular acceleration, and lower peak-value variability than those reported in previous tagged-MRI experiments. The piston-assisted device had accelerations of 1425 ± 18 rad/ s^2 at impact with excellent repeatability across 70 rotations (Figure 1). Single slice tagged MRI acquisitions in two phantom were successful at the low-severity (300 rad/s^2) and high-severity (1400 rad/s^2) conditions, with the piston (at 30 PSI) performing as expected with no safety concerns. Tag

tracking and strain calculations are ongoing to validate the strain fields against previous experiments and computational models.

Discussion

This MR-compatible head-rotation device delivers repeatable, axial rotations with higher accelerations. The design paves the way for high-acceleration tMRI experiments on head surrogates and cadaveric specimen that reproduce real-world traumatic loading and can refine next-generation computational brain-injury models.

Images (Optional)



Acknowledgements (Optional)

NIH NINDS R01NS112120 (Alshareef)

Session Category

Injury Biomechanics: N/A

P3-067

Periodic Activation Functions for Identifying Injured Movement

Dr. Alex Dzewaltowski PhD, Dr. Christopher Connaboy PhD

Rosalind Franklin University of Medicine and Science, North Chicago, Illinois, United States

Introduction

Movement presents indicators of musculoskeletal injury but these indicators can be subtle. Machine learning methods may aid injury identification and early detection thereby, limiting injury progression and symptom severity. The purpose of this study was to assess changes in classification accuracy of injured or uninjured walking and running from exchanging activation functions.

Methods

Data analyzed were from a freely available dataset[1] composed of 1798 unique participants with and without a variety of musculoskeletal injuries. Retroreflective marker position collected via motion capture were tracked and filtered using a low-pass Butterworth filter with a cutoff of 10Hz. Sacrum, thigh, shank, and foot tracking marker positions and their derivatives for velocity and acceleration as well as the relative phase between leg segments relative to the sacrum were provided as inputs (90 features in total) to a multilayer perceptron with three linear layers each followed by a varying activation function, one linear layer with a Rectified Linear Unit (ReLU) activation function, and a final linear layer which outputs four likelihoods for the classification of uninjured walking, uninjured running, injured walking, and injured running. Three different models were trained, exchanging the varying activation function for either a sine function (SIREN), ReLU, or Exponential Linear Unit (ELU) using a train to test data split of 75% to 25%.

Results

Every model, regardless of activation function, perfectly classified walking versus running of test data. The model with SIREN had the most accurate test classification of uninjured vs injured movement (80%, F1-score = 0.84). The model with only ReLU had similar but slightly weaker performance to SIREN (77%, F1-score = 0.83). Model performance using ELU had a test accuracy of 71% and F1-score of 0.79.

Discussion

Inclusion of periodic nonlinearities in a simple machine learning model may have slightly improve classification of musculoskeletal injury. Despite ELU being similar to ReLU but including negative values, this resulted in a drop in classification accuracy. This work

supports future collection of a dataset which has the intent to support a machine learning model that monitors movement to minimize injury progression.

References (Optional)

[1] Reed Ferber *et al*., Scientific Data, 2024

Session Category

Injury Biomechanics: N/A

P3-068

Development of Posture-Validated HBMs for Reclined Seating Use Cases

Mr. Alex Kalmar-Gonzalo B.S., Mr. Bharath Koya, Dr. F. Scott Gayzik PhD, M.S., B.S.

Wake Forest University School of Medicine, Winston-Salem, NC, United States

Introduction

The use of Human Body Models (HBMs) in the injury biomechanics and automotive regulatory space has gained significant momentum in recent years. Concurrently, alternative seating modes in vehicles are rapidly appearing in market, particularly with respect to reclined seating. While HBMs are typically validated using standard seated and pedestrian postures, there is no study validating initial posture in reclined seated environments. The goal of this study is to leverage published human volunteer data to generate posture-validated node sets for eight HBMs in 45° reclined seating configurations (F05, F50, M50, and M95 in simplified and detailed configurations).

Methods

This study employs the Global Human Body Models Consortium (GHBMC) series. We used regression algorithms published by Reed et al. 2019 [1]. HBM and environmental features such as stature, body weight, erect seating height, seatback angle, and head rest presence were used to calculate postural targets. Anthropometric data from the volunteers who were used to generate GHBMC models were used as inputs. The HBMs were then positioned according to predicted pelvis, lumbar, thorax, neck, head, and hip-eye angles using positioning tools in Oasys Primer (Arup, London UK). A fine-tuning step using Boundary Prescribed Final Geometry cards in LS-Dyna was used as needed to match postural targets within a 5% tolerance. Simulations were conducted using LS-Dyna R.12.2.1 (ANSYS, Cannonsburg, PA).

Results

The eight models were positioned in the 45° reclined posture based on predicted outcomes calculated through regression equations. All angle measurements were within 5% of their predicted measurements.

Discussion

HBMs are customarily delivered in a posture commensurate with a driver seatback angle of 23 degrees from vertical. These models, which are simply node sets describing the posture

change, provide a platform which will ease comparisons across reclined HBM studies using GHBMC models and will obviate the time consuming repositioning step typically required before injury risk analysis can begin. To date, pre-set and validated reclined postures of widely used HBMs have not been available. The presented models can be integrated with publicly available or OEM seats, and require gravity settling and belting for use in crash simulation.

References (Optional)

[1] Reed, M.P. et al. , Traffic Injury Prevention, 2019

Acknowledgements (Optional)

This study was funded by the Global Human Body Models Consortium (WFU-006) and supported by the National Highway Traffic Safety Administration.

Session Category

Injury Biomechanics: N/A

P3-069

Investigating the Relationship Between Kinematic Brain Injury Metrics and Brain Tissue Strain for a Football Helmet Test Standard

Mr. Alex Sanchez, Dr. Clara Karton, Dr. Thomas Blaine Hoshizaki

University of Ottawa, Ottawa, ON, Canada

Introduction

Since the institution of helmet performance standards by the National Operating Committee on Standards for Athletic Equipment (NOCSAE), the incidence of traumatic brain injuries has significantly reduced in American football; however, concussions continue to be a common concern. This may in part be due to the limitations of the current helmet performance test metric, the Gadd Severity Index (GSI), to effectively measure concussive injury risk. Maximum principal brain tissue strain (MPS) has been demonstrated as an effective predictor for the risk of concussion; however, the computational time required to calculate MPS makes it unrealistic for helmet standards to incorporate as a performance measure. This research was designed to compare kinematic brain injury metrics obtained from NOCSAE football helmet testing to MPS values. Findings will inform the development of helmet performance criteria for evaluating risk of concussive injury.

Methods

NOCSAE-standard impact testing was conducted on three NOCSAE certified adult football helmet models, totalling 96 impacts. Resultant linear and rotational acceleration time histories of each impact were used to obtain peak kinematic values to calculate six kinematic brain injury metrics. MPS was calculated for each trial using the University College Dublin Brain Trauma Model 2.0. Each peak kinematic variable and injury metric was linearly regressed against MPS, and correlations were determined by each regression model's R^2 value.

Results

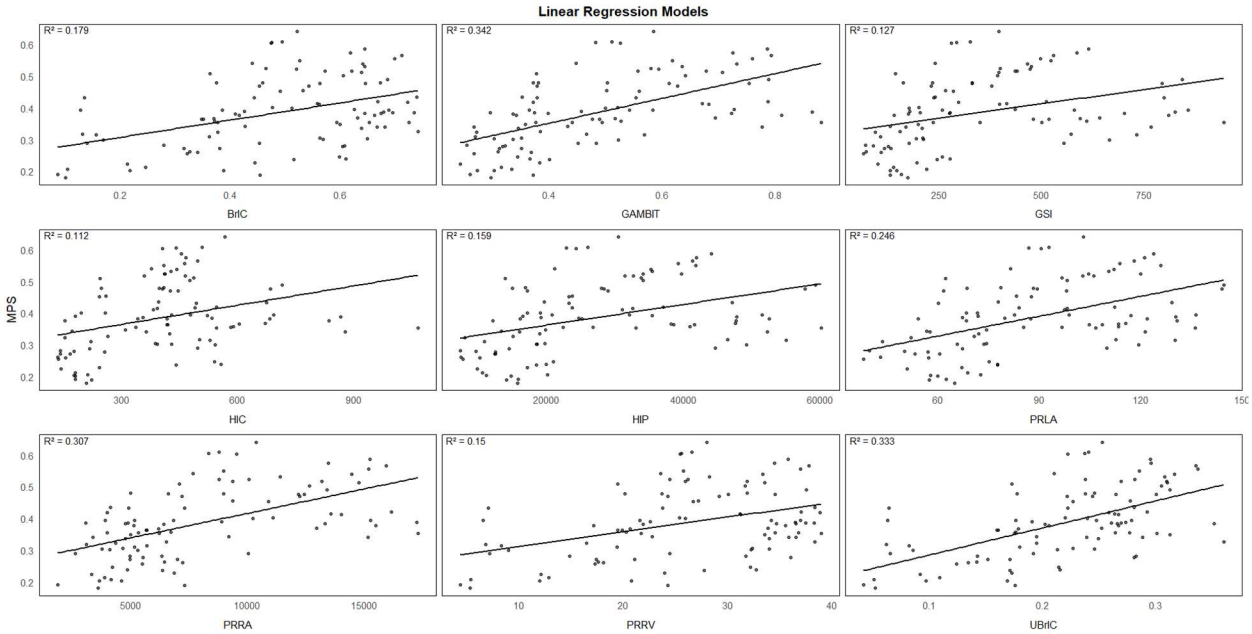
GAMBIT revealed the highest correlation with MPS ($R^2 = 0.342$), followed by UBrIC ($R^2 = 0.333$). Peak Resultant Rotational Acceleration (PRRA) demonstrated the highest correlation of all peak kinematic variables ($R^2 = 0.307$). The GSI had the second-lowest correlation ($R^2 = 0.127$), outperforming only HIC ($R^2 = 0.112$).

Discussion

Kinematic brain injury metrics were found to correlate poorly with MPS under NOCSAE-standard impact conditions, suggesting that alternative measurement criteria may be

helpful when evaluating the capacity of football helmets to mitigate the risk of concussive injury. This research contributes to a better understanding of football helmet performance in mitigating the risk for concussive injuries in football.

Images (Optional)



Session Category

Injury Biomechanics: N/A

P3-070

The Effect of Trochanteric Soft Tissue Thickness on Hip Protector Efficacy during Simulated Lateral Falls: Assessing Impact Force Attenuation using a Hybrid Cadaveric Soft Tissue-Surrogate Pelvis Testing System

Mr Steven Pretty, Ms. Alyssa Tondat, Dr. Andrew Laing

University of Waterloo, Waterloo, ON, Canada

Introduction

Hip protectors are designed to reduce the risk of hip fracture through impact attenuation during a fall; however, their biomechanical efficacy varies widely across products and testing systems/paradigms. A potential limitation of previous test systems is the use of surrogate materials (e.g., foams) of relatively thin thickness to represent the trochanteric soft tissues. Improved biofidelity and inclusion of biological variability in testing systems could enhance clinical guidelines for currently available protectors and inform the development of more effective designs. This study aimed to evaluate the influence of human cadaveric trochanteric soft tissue thickness (TSTT) on the force attenuation provided by hip protectors during simulated lateral-fall impacts.

Methods

Fresh (never frozen or fixed) trochanteric soft tissue samples (15x15 cm; TSTT = 1.0-4.7 cm) were extracted from 12 post-mortem human donors. They were affixed over a surrogate pelvis system, including a composite femur instrumented with a femoral neck load cell. Impact trials (velocity = 2 m/s) were completed with and without a commercial hip protector (HipSaver). Peak force at the femoral neck (F_{Neck}) and force platform ($F_{Surface}$) were extracted. Bivariate Pearson correlations were utilized to assess the influence of TSTT on hip protector effectiveness.

Results

The mean (SD) force attenuation provided by the hip protector was 7.0 (10.3) and 19.4 (14.3)% for $F_{Surface}$ and F_{Neck}, respectively. However, strong negative correlations were observed between force attenuation and TSTT ($r^2 > 0.79$). A 1 cm increase in TSTT was associated with a decrease in $F_{Surface}$ and F_{Neck} attenuation of 9.5 and 13.1%, respectively. Notably, for samples above 4 cm of TSTT, the hip protector provided negligible force attenuation (< 1%).

Discussion

This is the first study to evaluate hip protector efficacy using cadaveric tissues and provides novel insights for test system validations. Mean force attenuation from the tested hip protector is similar to previous research utilizing soft tissue surrogates [1], which supports their use as an alternative to cadaveric testing. However, low-TSTT testing/systems likely overestimate hip protector effectiveness across the target population. The current results highlight the importance of considering TSTT in hip protector interventions and future designs.

References (Optional)

[1] Laing and Robinovitch, J Biomech Eng, 2008

Session Category

Injury Biomechanics: N/A

P3-071

Mapping External Garment Pressure to Internal Vascular Loads: A Modular Rig Coupled with 3D–1D Hemodynamic Modelling

Dr Angelo Karunaratne PhD, MEng, CEng, Prof Hari Arora PhD, MEng

Department of Biomedical Engineering, Swansea University, Swansea, Wales, United Kingdom

Introduction

Compression garments are widely used across sport and medicine, yet how skin-level pressure translates to internal vascular loads and hemodynamic impact on realistic limb anatomy remains poorly quantified. We aimed to map measured external pressure to vessel transmural pressure, shape change, and flow effects, providing an evidence path for safe, effective use.

Methods

We combined (i) a sensorized anthropometric limb rig to set/read circumferential pressure with PicoPress and estimate outer→internal transfer after a seating/rest protocol; (ii) bench wraps using 30-mm bands taken from commercial garments to confirm repeatability along the limb; and (iii) a modelling pipeline: rig pressures drove a 3D FE limb model (skin/muscle/bone with embedded vessels) to predict transmural pressure and cross-sectional change, which parameterized a 1D cardiovascular model to estimate local resistance and flow under controlled assumptions.

Results

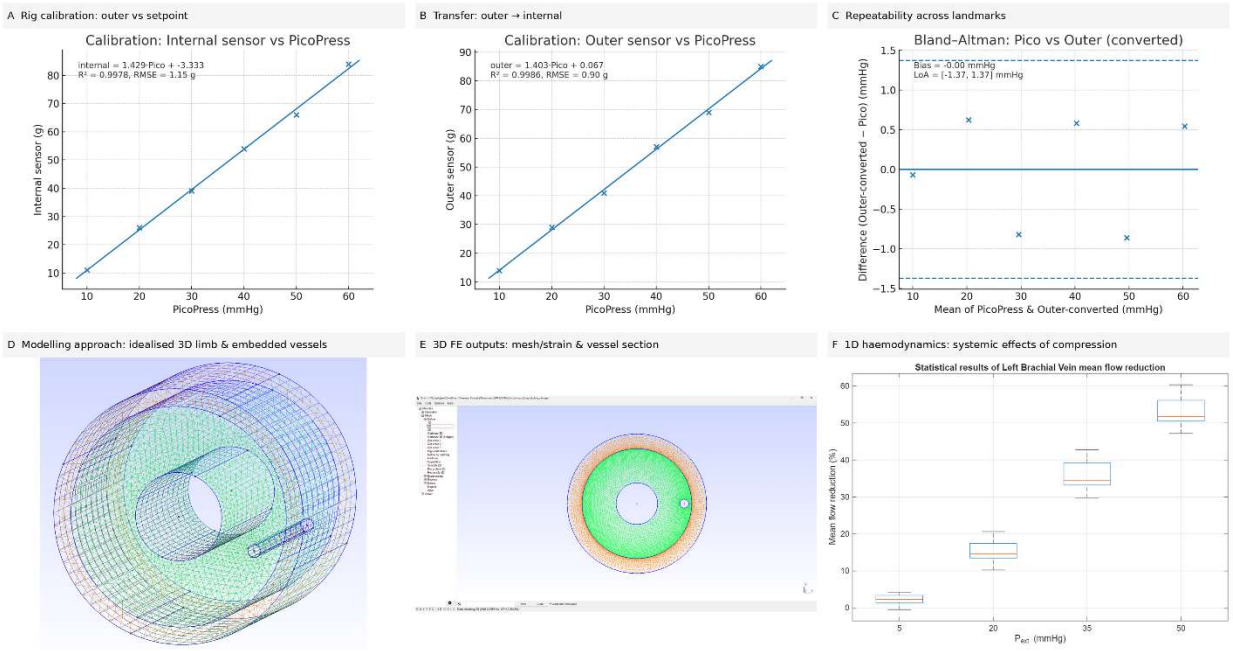
Rig commissioning showed outer pressure closely matched setpoint (±1–2 mmHg) with a predictable internal shortfall (~10–15%), yielding stable boundary conditions. On representative 3D simulations, external compression produced depth- and location-dependent vessel responses: near-surface vessels experienced tens of mmHg transmural loads and ~30–37% area reduction; mid-depth vessels showed smaller shape change. Coupling to 1D flow indicated that such deformations can increase segmental resistance and reduce local flow, with sensitivity to vessel stiffness and surrounding tissue compliance. Together, the measurements and models form a pressure-to-outcome chain linking achievable garment pressures to likely vascular loading and flow consequences.

Discussion

This integrated rig-plus-modelling approach provides traceable, anthropometry-aware guidance for compression use in sport and medical settings. Rather than relying on labeled

“class,” internal loads depend on geometry, tissue properties, and donning, highlighting the need for standardized tests and pressure×time safety envelopes. The framework supports actionable specifications (target mmHg bands and tolerances) and prioritizes user-centered validation. Next steps include parameter sweeps for pattern/material choices, comparison with cuff literature and non-invasive in-vivo surrogates, and extension to dynamic tasks to understand time-varying effects.

Images (Optional)



References (Optional)

[1] Partsch H, *Ann Vasc Dis*, 2012.

[2] Macintyre L, Baird M, *J Wound Care*, 2006.

[3] Alastruey J et al., *Med Eng Phys*, 2012.

[4] Holzapfel GA, Ogden RW, *Biomech Model Mechanobiol*, 2010.

Acknowledgements (Optional)

Funded by the Dstl Advanced Materials Programme through DMEx. We thank Dr Dean Fletcher (Dstl/DMEx) and collaborators for programme support. Classification: UK OFFICIAL.

Session Category

Injury Biomechanics: N/A

P3-072

Evaluation of a Device for Mitigation of Neck Muscle Fatigue in Fighter Pilots

Dr. Ritwik Rakshit Ph.D.[1], Ms. Kaylie McGuckin[2], Dr. Lucy Fitzgerald Ph.D.[3], Mr. Brandon Sheely B.S.[3], Dr. Kelley Virgilio Ph.D.[3], Dr. Anita Vasavada Ph.D.[1]

[1]Washington State University, Pullman, WA, United States. [2]University of Rochester, Rochester, NY, United States. [3]Luna Labs, Charlottesville, VA, United States

Introduction

Neck pain is a significant problem in military pilots. Luna Labs has developed a cervical spine protection device to decrease fatigue in neck muscles. We hypothesized that with the device, participants will experience less neck muscle fatigue during an endurance task.

Methods

15 participants (8 F, 7 M; age 18-35) visited the lab twice, 7-11 days apart. Subjective ratings of fatigue and neck extension strength were collected before and after an endurance test which consisted of supporting an extension load of 30% of maximum until exhaustion (Figure 1a). Muscle activity (EMG) was measured with surface electrodes in eight neck muscles. At one visit (randomized), the device applied a tensile force between a helmet and a harness on the torso (assistance condition). Paired t-tests or Wilcoxon signed rank tests were used to compare outcome measures (subjective ratings, endurance time, decrease in extension strength and changes in EMG amplitude and median frequency) with and without assistance.

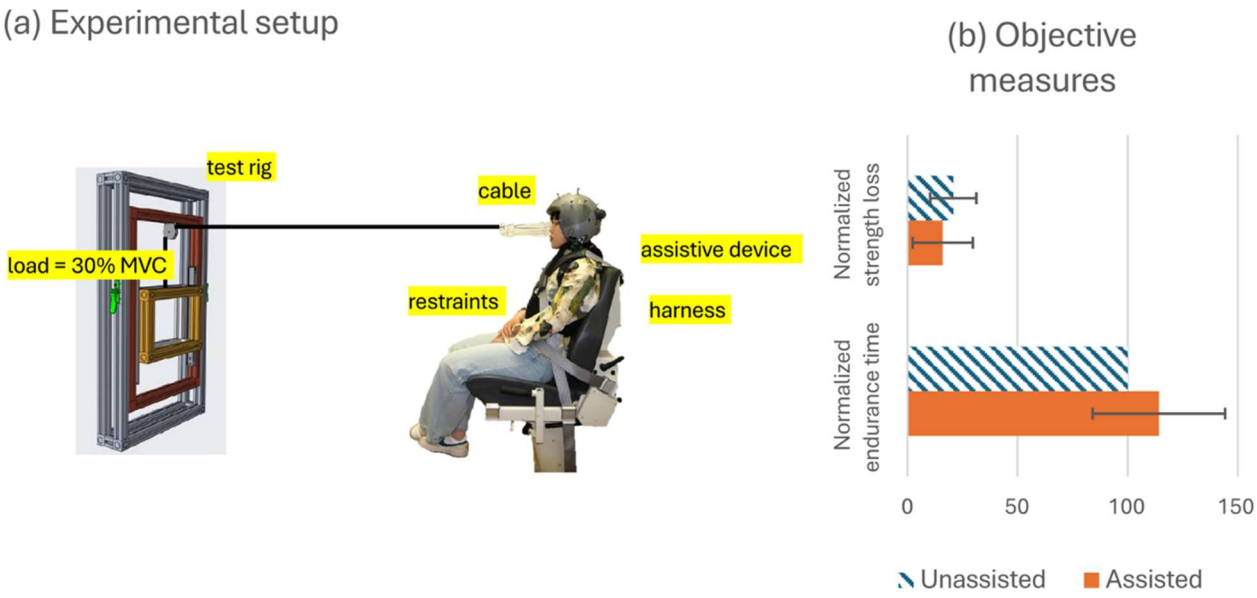
Results

Participants exhibited fatigue during both assisted and unassisted conditions as evidenced by a decrease in maximum neck extension strength, increase in EMG amplitude and decrease in EMG median frequency. Normalized endurance time was 14% longer in the assisted condition ($p=0.045$; Figure 1b). With assistance, participants' maximum neck extension strength decreased less than without assistance (16% vs. 21%; $p=0.046$). However, subjective ratings of fatigue and the rate of EMG amplitude increase were not significantly different between conditions. The rate of EMG median frequency decrease between conditions was only significant for one muscle (left splenius capitis; $p=0.035$).

Discussion

The cervical spine protection device acts as an exotendon between a pilot helmet and harness on the torso, and it is expected that participants should require less neck muscle force to hold up the same load. With the device, participants exhibited objective differences in endurance time and loss of strength, but no significant differences in subjective measures of fatigue. EMG measures demonstrated evidence of muscle fatigue, but there was no significant effect of assistance. Helmet fit and participant motivation likely also played a role in device performance and endurance time.

Images (Optional)



Acknowledgements (Optional)

Department of Defense SBIR Program, Contract No. HT942523C0026.

Session Category

Injury Biomechanics: N/A

P3-073

Timing and Dominant Components of Peak Linear and Angular Head Accelerations in Low-Speed Rear End Collisions: A Study of Human Responses

Author Avery Scurlock[1,2], Co-Author Patrick Fischer[1], Co-Author John Abercrombie[1], Co-Author Richard Watson[1]

[1]Biodynamic Research Corporation (BRC), San Antonio, TX, United States. [2]University of Texas at San Antonio (UTSA), San Antonio, TX, United States

Introduction

The Biofidelic Rear Impact Dummy (BioRID) is designed to replicate the human response during low-speed rear end collisions (LSRC). However, its design limits frontal and transverse head motion. Additionally, the BioRID may not appropriately capture energy dissipation achieved through selective neck muscle activation when the occupant rebounds into the seatbelt. This study addresses these limitations by analyzing LSRC with human test subjects to better assess the timing and predominant components of head acceleration as they relate to mild traumatic brain injury (mTBI).

Methods

Eleven instrumented LSRC were conducted. During a crash test, a human subject using a lap-and-shoulder belt was seated in a vehicle which was impacted from the rear, causing a back-to-front acceleration. Angular head accelerations were derived from angular velocity measures (**Figure 1**). Linear head accelerations were measured directly.

Results

For peak vehicle acceleration of 3.8±1.0g, peak linear head accelerations were 6.0±2.2g (range: 2.4-10.1). Linear accelerations peaked during the head contact phase with the headrest. Sagittal accelerations were predominant (96.3±4.2% of resultant). Compared to published tolerances, linear head accelerations in rear-end crash tests represented mTBI risk between 0.005%-0.006%.

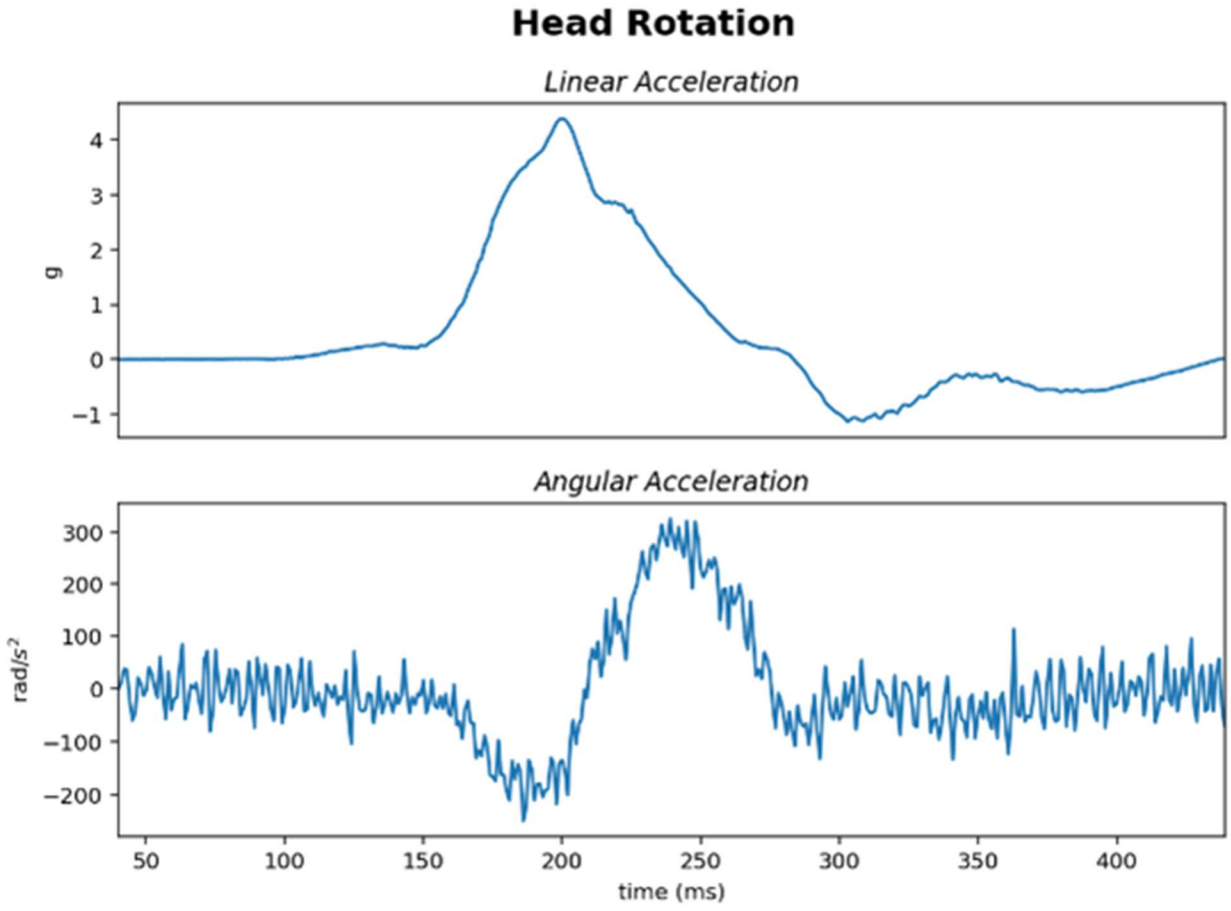
Peak angular head accelerations were 249.1±124.7rad/s^2 (range: 90.0-407.2). Angular acceleration peaked ~50ms after peak linear head acceleration. Sagittal angular head accelerations were predominant (98.4±1.0% of resultant). Compared to published tolerances, angular head accelerations in rear-end crash tests represented mTBI risk between 0.004%-0.005%.

Combined effects of linear and angular acceleration represented mTBI risk between 0.004%-0.008%.

Discussion

This study suggests angular and linear accelerations are coupled in LSRC. Linear acceleration peaked during headrest contact, and angular acceleration peaked ~50ms after. As expected, back-to-front and sagittal components predominated the linear and rotational head accelerations, respectively, indicating a primarily sagittal response pattern. The belt-loading phase did not result in a second peak in head acceleration. The human response to LSRC involves gradual deceleration of head motion through selective muscle activation, minimizing inertial loading. Capturing the full sagittal response, including the rebound phase, provided a complete characterization of timing and signal behavior, thereby addressing prior uncertainties in BioRID analysis and confirming the LSRC rebound phase does not represent appreciable inertial loading in humans.

Images (Optional)



Session Category

Injury Biomechanics: N/A

P3-074

Mesh Convergence Depends on Element Formulation for Finite Element Brain Models

Ms. Azilis Even, Dr. Zhou Zhou, Prof. Svein Kleiven

Division of Neuronic Engineering, KTH Royal Institute of Technology, Stockholm, Stockholms län, Sweden

Ms. Azilis Even

Dr. Zhou Zhou

Introduction

Finite element head models are virtual tools to study brain biomechanics, but one prerequisite before usage is for these numerical surrogates to have a convergent behavior. Previous convergence studies focused on the influence of mesh size, but the potential compounding effect of element formulation was often ignored with the exception of a few studies [1]. This study aimed to evaluate the influence of element formulation on the mesh convergence responses of a finite element head model.

Methods

The base model for this study was the KTH Head model, with brain mesh size as 6.4 ± 1.9 mm [2]. We modified the mesh in the original model to generate three derivatives, all of which have the same mesh topology but different element sizes (Fig 1a), i.e., a coarse model (mesh size: 12 ± 4.0 mm), a medium model (mesh size: 3.2 ± 0.97 mm), and a fine model (mesh size: 1.6 ± 0.48 mm). Three commonly used element formulations (i.e., constant stress solid, selectively reduced (S/R) integration and fully integrated elements) were implemented to the brain elements in these four models. An experimental rotational loading profile (angular velocity peak: 40 rad/s, duration: 30 ms) along three anatomical directions was imposed to all models [3]. The 95^{th} percentile maximum principal stress (MPS) over the entire brain was analyzed and compared across the different cases.

Results

Regardless of rotational direction, selectively reduced integration yielded the best convergence results (Fig 1b), with less than a 25% difference at each refinement step, and less than a 5% difference between the original and medium meshes. In contrast, the constant stress solid and fully integrated element meshes did not converge when applying a mesh convergence criterion of less than a 5% difference in output between the medium and fine meshes.

Discussion

This study shows that the mesh convergence behavior of finite element brain models is affected by the choice of element formulation. Selectively reduced integration contributes to a faster mesh convergence behavior.

Images (Optional)

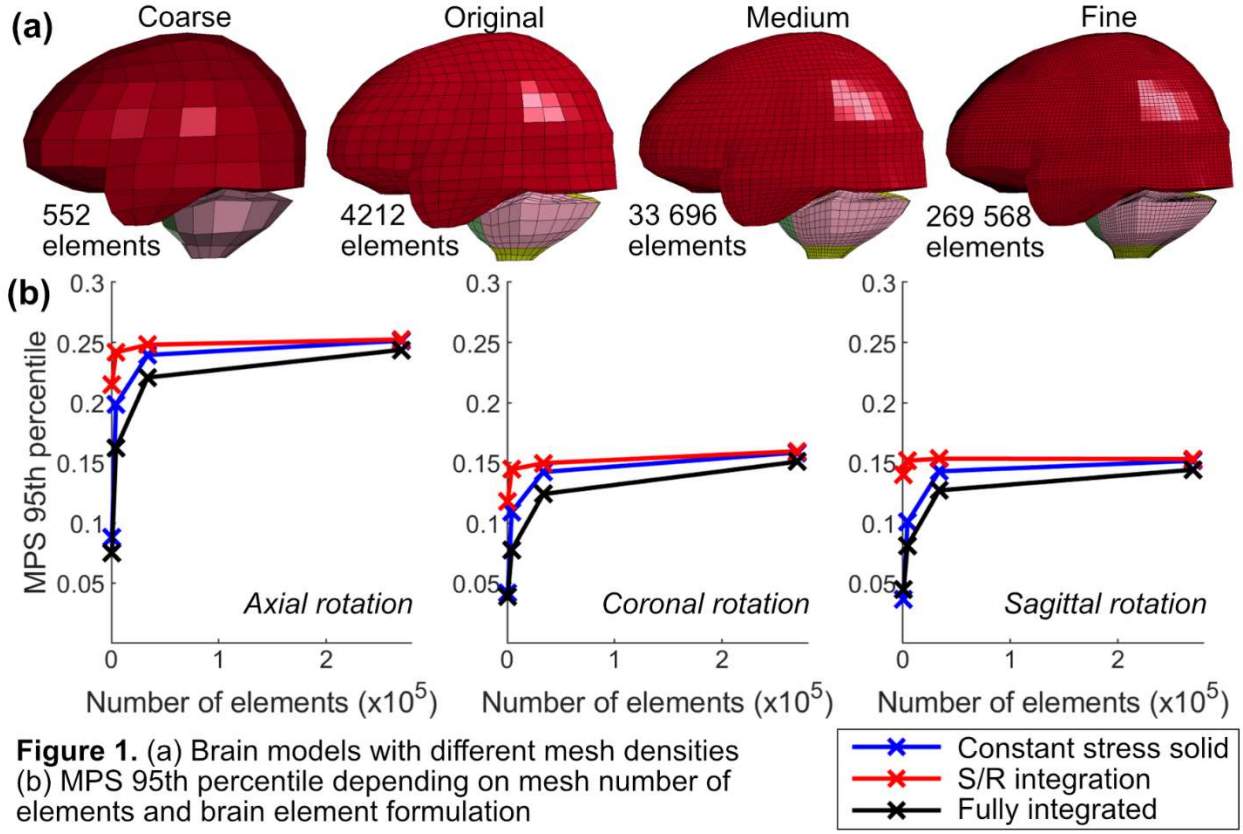


Figure 1. (a) Brain models with different mesh densities (b) MPS 95th percentile depending on mesh number of elements and brain element formulation

References (Optional)

[1] J. Sebastian Giudice *et al*, Ann. Biomed. Eng., 2019

[2] Svein Kleiven, Stapp Car Crash J., 2007

[3] Ahmed Alshareef *et al.*, J. Neurotrauma, 2020

Acknowledgements (Optional)

This research has received funding from KTH Royal Institute of Technology (Stockholm, Sweden), the Swedish Governmental Agency for Innovation Systems (VINNOVA) (no. 2023-00753 and no. 2024-03635), Swedish Research Council (VR-2024-05848 and VR-2024-02782), Skyltfonden from the trafiksäkerhet (TRV 2024/23811 and TRV 2024/50301). The content of this article is solely the responsibility of the authors and does not necessarily represent the official views of funding agencies. The computational simulations were enabled by resources provided by the National Academic Infrastructure for Supercomputing in Sweden (NAISS) at the centre for High Performance Computing (PDC) partially funded by the Swedish Research Council through grant agreement no. 2022-06725. The authors declare that they have no known competing financial interests or personal relationships that could have appeared to influence the work reported in this paper.

Session Category

Injury Biomechanics: N/A

P3-075

Effects of Cues to Walk Softly and Quietly on Gait Mechanics During Load Carriage

Dr. Caleb Johnson FACSM, Mr. David Zeppetelli, Mr. Cole Dempsey, Mr. Lucas Sarantos

U.S. Army Research Institute of Environmental Medicine, Natick, MA, United States

Introduction

Walking with load carriage is a common military activity, that also leads to high rates of musculoskeletal injury. Gait alteration cues to run softly/quietly have been shown to reduce external forces related to injury in runners. However, the effects of these cues have yet to be explored for walking with load carriage.

Methods

38 participants completed testing on an instrumented treadmill, while kinematics were tracked via optical motion capture. Participants first completed a habitual load carriage trial (HAB), at a self-selected pace (1.21 ± 0.11 m/s) and while carrying an 18kg weighted vest. They were given a 5-min warm-up followed by data collection. Participants were then cued to modify their gait by walking "quietly and softly" (SOF). They were given one minute for accommodation, followed by data collection. Outcome variables were averaged over 20 strides for the right leg, including: double-stance time, stride length, peaks and loading rates for vertical/posterior forces, peaks/excursion for sagittal/frontal plane hip/knee angles and moments (peaks only). Variables were selected based on their relevance for changes in gait or potential increases in injury risk with load carriage. Paired t-tests or Wilcoxon signed-rank tests were used to compare gait conditions.

Results

Full results are reported in the Table. The largest changes ($d > 0.8$) in gait in SOF were decreased 2nd peak vertical forces and increased peak hip and knee flexion angles and knee extension moments. Peak frontal plane moments were also consistently lower in SOF, for the hip and knee, although the effect sizes ranged from small to moderate.

Discussion

These results show significant changes in load carriage gait mechanics with cues to walk softly/quietly. While decreases in peak vertical forces and frontal plane moments may be associated with reduced injury risk, we also found an increase in peak sagittal plane angles corresponding to increased sagittal peak moments. Future research should focus on the implications of this trade-off in external forces, e.g. translation to tissue strain/stress, to better understand the real implications for injury risk.

Images (Optional)

Table. Descriptive statistics and results of tests for mean differences between gait conditions

Variable	HAB (Mean ± SD)		SOF (Mean ± SD)		Cohen's d Effect Size	p
Spatio-temporal & GRFs						
Double-stance Time (s)	0.167±	0.016	0.163±	0.018	-0.24	0.14
Double-stance Time (% of stance)	23.39±	1.38	23.01±	1.76	-0.27	0.11
Stride Length (m)	1.34±	0.11	1.34±	0.16	0.05	0.76
Vertical Loading Rate (BW/s)	16.49±	3.80	16.98±	4.11	0.13	0.99
1st Vertical Peak Force (BW)	1.30±	0.09	1.35±	0.12	0.56	<0.01
2nd Vertical Peak Force (BW)	1.22±	0.08	1.16±	0.11	-0.84	<0.01
Posterior Peak Force (BW)	-0.239±	0.039	-0.229±	0.042	-0.35	<0.01
Hip						
FLX Angle Peak (°)	23.44±	7.15	25.86±	6.80	0.85	<0.01
FLX/EXT Angle Excursion (°)	39.20±	4.05	39.27±	5.68	0.02	0.62
ADD Angle Peak (°)	9.51±	3.32	9.51±	3.53	0.01	0.96
EXT Moment Peak (Nm/kg)	0.698±	0.148	0.716±	0.177	0.23	0.18
1st ABD Moment Peak (Nm/kg)	1.07±	0.19	1.10±	0.21	-0.28	0.09
2nd ABD Moment Peak (Nm/kg)	0.843±	0.185	0.785±	0.193	-0.47	<0.01
Knee						
FLX Angle Peak (°)	19.86±	5.00	24.55±	6.69	1.00	<0.01
FLX/EXT Angle Excursion (°)	17.64±	3.20	18.64±	4.02	0.38	<0.01
ABD Angle Peak (°)	-5.58±	3.38	-5.49±	3.54	0.12	0.48
EXT Moment Peak (Nm/kg)	0.652±	0.227	0.840±	0.284	0.88	<0.01
1st ABD Moment Peak (Nm/kg)	0.408±	0.121	0.392±	0.135	-0.24	0.15
2nd ABD Moment Peak (Nm/kg)	0.272±	0.100	0.249±	0.111	-0.34	0.04

- GRF, ground reaction force; FLX, flexion; EXT, extension; ADD, adduction; ABD, abduction; E weights; HAB/SOF, habitual, forefoot strike, soft/quiet running conditions; SD, standard deviation
- All joint kinetics expressed as internal moments

Acknowledgements (Optional)

Opinions in this manuscript are not official policy or views of the US Army.

Session Category

Injury Biomechanics: N/A

P3-076

Recovery of the lumbar intervertebral disc revealed by coupled mechanical testing and high-contrast soft tissue cryogenic microCT

Dr. Elizabeth Dimbath PhD[1], Mr. Blake Robertson BS[1], Ms Nicole Turpin BS[1], Mr Jason Kait MS[1], Ms Angela Abraham MS[2], Ms Anna Grunkemeyer BS[2], Dr. Laura Dalton PhD[1], Dr. Jason Luck PhD[1], Dr. Cameron Bass PhD[2]

[1]Duke University, Durham, NC, United States. [2]Wayne State University, Detroit, MI, United States

Introduction

Low back pain (LBP) is associated with intervertebral disc (IVD) hydration through avascular diffusion, remaining a leading cause of disability worldwide. Common occupational/military tasks involve poorly characterized repetitive combined spinal loading. Understanding how loading influences IVD recovery is crucial in identifying factors that influence fluid-flow/spinal pathophysiology. This study combines mechanical and imaging approaches to link IVD recovery after loading with three-dimensional structural changes, elucidating early contributors to LBP.

Methods

Occupationally relevant cyclic flexion-compression was applied to porcine FSUs at peak compressive stresses of 1-3 MPa and durations of 0.5-9 hours, followed by an unloaded recovery phase (load-controlled). Specimens were imaged with high-contrast cryogenic X-ray microCT. Six baseline specimens were tested at 1 MPa peak compressive stress for 1 hour to assess recovery at low loads. Three specimens not frozen and were used to assess freezing effects. Disc height recovery was measured using displacement-time data, and nucleus pulposus (NP) volume change was measured from semi-automated segmentation of scans obtained before loading, post-loading, and post-recovery. Peak compressive stress and loading duration were evaluated as statistical factors in IVD recovery.

Results

Mean disc height recovered to 100±30% in the imaged baseline specimens compared with 89±14% for the baseline specimens not exposed to cryogenic imaging (not significantly different). Recovery from displacement measurements (0.59±0.12 mm) matched changes in height measured from the microCT (0.54±0.19 mm). Regression analyses revealed that stress magnitude, but not duration, significantly influenced both NP volume change and overall height recovery. NP volume exhibited a nonlinear dependence on stress magnitude, indicating permeability-limited fluid transport, while height recovery followed a more linear

decline with increasing stress. MicroCT imaging also revealed previously unreported localized endplate compaction at higher loads, suggesting low-level microstructural changes that may restrict rehydration.

Discussion

This study demonstrated high rates of recovery *in vitro* following cyclic combined loading. Findings demonstrate that IVD recovery under cyclic combined loading is primarily governed by stress magnitude rather than duration, with higher stresses reducing both recovery fluid reabsorption and mechanical recovery. From a translational standpoint, understanding recovery is critical to identifying early mechanical dysfunction that may precede structural degeneration.

Session Category

Injury Biomechanics: N/A

P3-077

Validation of a Sex-Specific Finite Element Head Model, Automotive Reconstructions and Female Soccer Head Impact Data

Mr. Carlos Cardoso[1], Mr. Afonso Silva[1], Dr. Andre Egger[2], Dr. Marcus Wisch[2], Dr. Thomas Kaminski[3], Dr. Nina Costa[4], Dr. Fábio Fernades[1], Dr. Ricardo de Sousa[1]

[1]TEMA - Centre for Mechanical Engineering Technology and Automation, University of Aveiro, Aveiro, Aveiro, Portugal. [2]Federal Highway and Transport Research Institute, Bergisch Gladbach, Bergisch Gladbach, Germany. [3]Department of Kinesiology and Applied Physiology, Athletic Training Research Lab, University of Delaware, Delaware, Newark, United States. [4]ID+ - Research Institute for Design, Media and Culture, University of Aveiro, Aveiro, Aveiro, Portugal

Introduction

Epidemiological studies have reported a higher incidence of concussion in female athletes compared with males in sports where the two sexes compete against each other [1,2], and sex-dependent differences in both acute and long-term recovery have been observed [3]. This underscores the necessity for anatomically accurate, validated finite element head models (FEHMs) to comprehend brain biomechanics in real-world impacts. The present study proposes the validation and application of a detailed female FEHM (FeFEHM) [4] using cadaveric impact data and kinematic inputs from automotive crash reconstructions and female youth soccer players.

Methods

The improved FeFEHM includes a cortical–trabecular skull, dura mater, falx cerebri, tentorium cerebelli and ventricles. Brain tissues were assigned viscohyperelastic properties from experimental data. Validation used intracranial pressure measurements from the Nahum et al. cadaver impacts [5], comparing pressure–time histories at frontal, parietal, occipital and posterior fossa sites. Real-world loadings consisted of THUMS-based BASt automotive reconstructions and triaxial head accelerations recorded from youth female soccer players using Triax sensors. All loadings were applied at the head centre of gravity. Output measures included maximum principal strain (MPS), intracranial pressure and cumulative strain damage measure (CSDM).

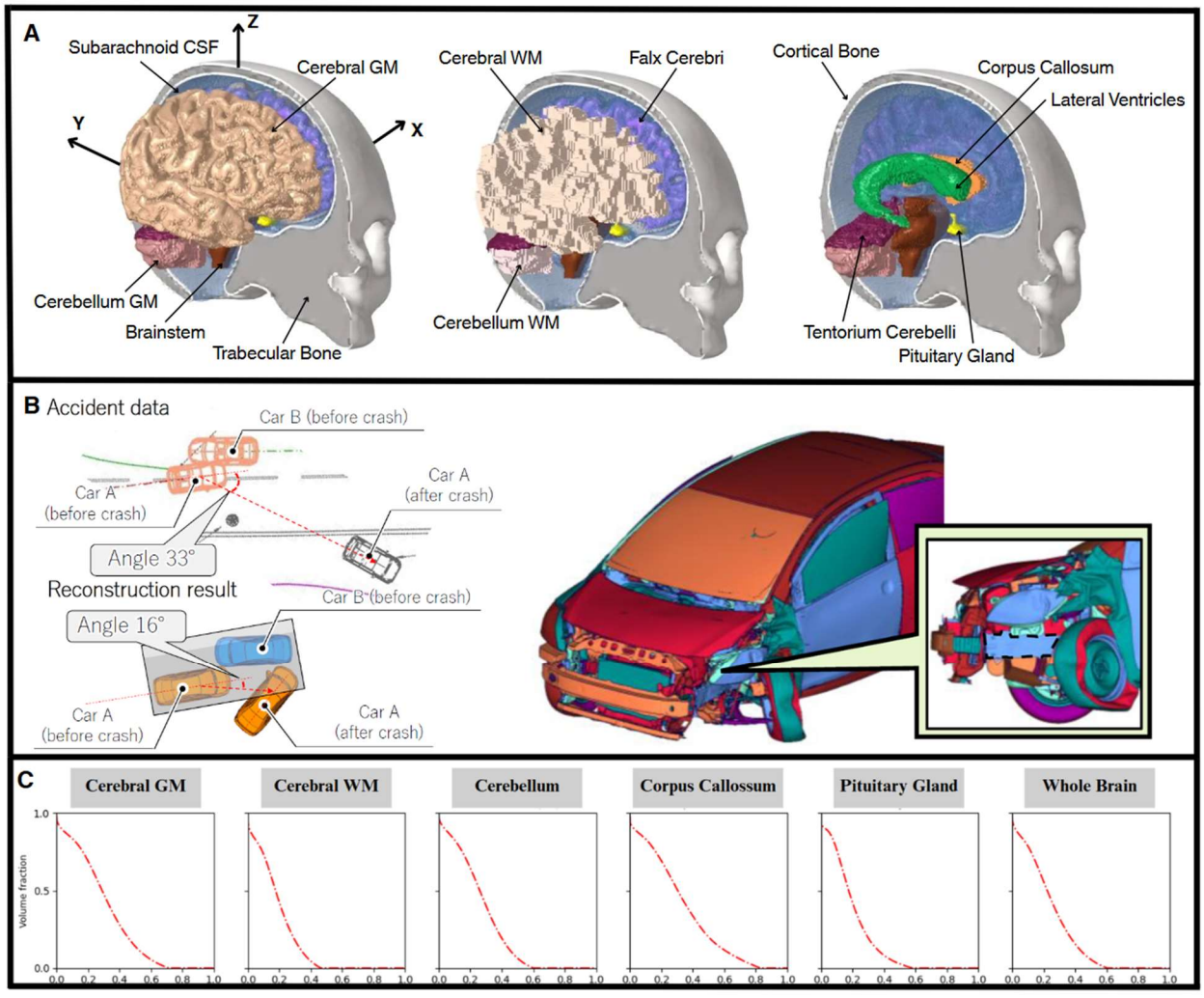
Results

The FeFEHM reproduced the principal features of the Nahum curves, with CORA scores ranging from 0.452 to 0.889. BASt loadings produced the greatest deformation (whole-brain strain 0.37–0.53). Soccer headings generated lower responses but consistent regional patterns: cerebral GM and WM dominated volume fractions, whereas the corpus callosum and pituitary gland showed localized peaks. Peak MPS (95th percentile) ranged from 0.25 to 0.35.

Discussion

Automotive impacts produced the largest global deformation, aligning with expected crash biomechanics. Soccer impacts, although lower in magnitude, revealed regional strain distributions and sensivity. These findings demonstrate that the FeFEHM captures both severe and sub-concussive loading patterns, supporting its use in evaluating female-specific brain injury mechanisms across diverse real-world scenarios.

Images (Optional)



References (Optional)

[1] Udit Dave et al., The Physician and sportsmedicine, 2022

[2] Jennifer Cheng et al., Sports health, 2022

[3] Nathan Churchill et al., Human Brain Mapping, 2021

[4] Gustavo Carmo et al., Computer Methods and Programs in Biomedicine, 2023

[5] Alan Nahum et al., SAE Technical Paper 770922, 1977

Acknowledgements (Optional)

The authors acknowledge the support given by Fundação para a Ciência e a Tecnologia (FCT) through the project PTDC/EME-EME/1239/2021 (BAFHTA).

Session Category

Injury Biomechanics: N/A

P3-078

Experimental Reconstruction of Head Impact Loading in Real-World Forensic Injury Scenarios

Dr. Julia de Lange Ph.D., P.Eng.[1,2,3], Ms. Brittany Sinclair B.Eng., P.Eng.[1], Dr. Chad Gooyers Ph.D., M.B.A., P.L.Eng.[4,5], Dr. Rob Parkinson Ph.D.[1,5]

[1]30 Forensic Engineering, Toronto, Ontario, Canada. [2]McMaster University, Hamilton, Ontario, Canada. [3]University of Guelph, Guelph, Ontario, Canada. [4]30 Forensic Engineering, Vancouver, British Columbia, Canada. [5]University of Waterloo, Waterloo, Ontario, Canada

Introduction

Acceleration-based head injury metrics derived from anthropomorphic test devices (ATDs), human volunteers, and cadavers in a variety of loading events constitute a valuable source of data for understanding the biomechanical responses of the head during impact events and the associated risk of injury. This study expands the empirical literature (containing primarily controlled motor-vehicle or sports-related loading scenarios) by characterizing head-impact loading documented in forensic investigations of real-world injury claims, thereby widening the context in which head-injury biomechanics are evaluated.

Methods

In this study, the Hybrid III headform (the most widely used ATD worldwide) was instrumented with a triaxial accelerometer positioned near the estimated head center of gravity to quantify linear head acceleration. Nine head-impact scenarios derived from real-world forensic injury claims involving reported concussions were reconstructed experimentally. Acceleration data were sampled 1,250 Hz and retained in their unfiltered form for analysis.

Results

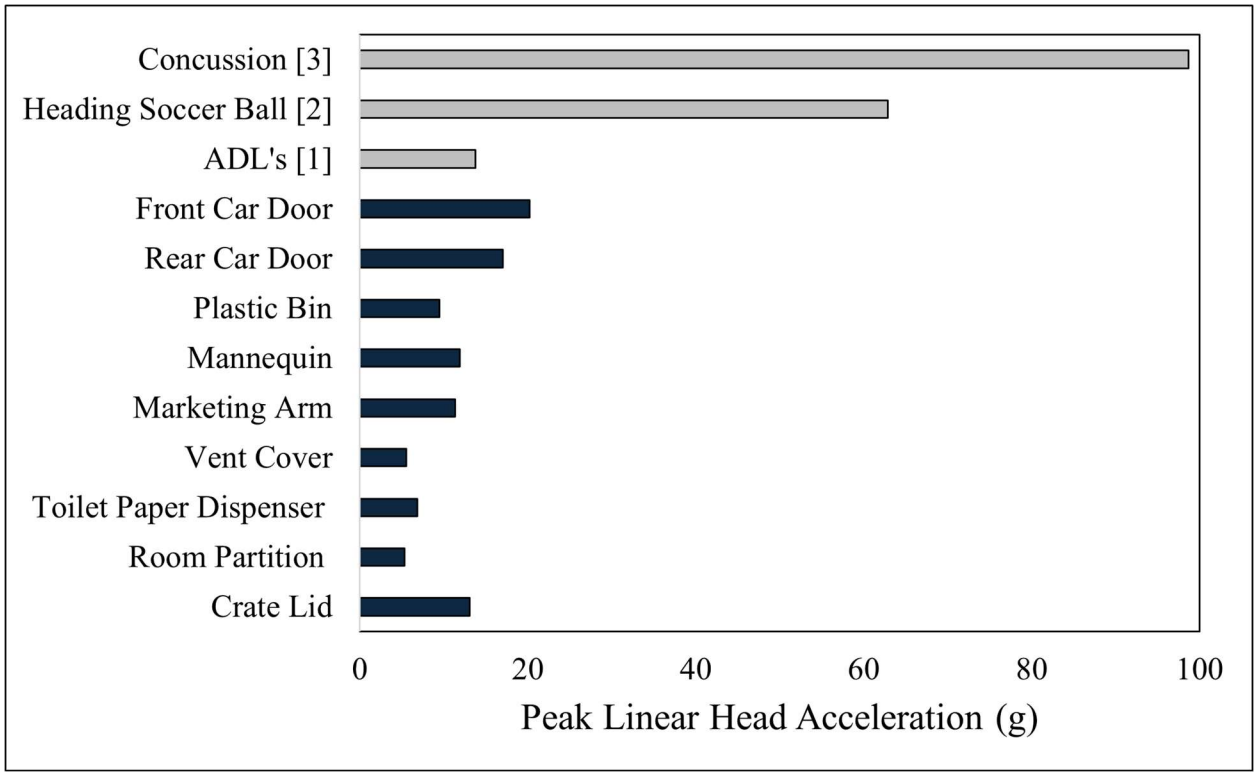
A total of 116 trials were performed across the nine reconstructed scenarios. Impacts involved a diverse set of objects striking the head, including a crate lid, a movable room partition, a toilet paper dispenser lid, a vent cover, a marketing arm (sign), a mannequin torso, an empty plastic bin, as well as a rear and front car closing door. Object drop heights or impact distances varied by scenario, ranging from 0.05 to 0.96 m, producing peak resultant head accelerations between 1.9 and 21.3 g.

Discussion

The accelerations observed in the reconstructed scenarios align closely with peak head accelerations experienced in activities of daily living (ADLs [1]) or associated with impacts from heading a soccer ball in girls youth soccer ([2]) and fall well below the linear head acceleration associated with concussion ([3]). The average peak resultant acceleration from each scenario is presented (Figure 1).

By synthesizing this data, this study provides a practical biomechanical reference for forensic investigations of reported head injuries. These findings underscore the importance of quantifying head impact magnitude when assessing the biomechanical plausibility of concussion within a forensic engineering context.

Images (Optional)



References (Optional)

[1] Logan Miller et al., *Biomech Model Mechanobiol*, 2020

[2] Erin Hanlon et al., *Med Sci Sports Exerc,* 2012

[3] James Brennan et al., *Sports Med*, 2017

Session Category

Injury Biomechanics: N/A

P3-079

Head Kinematics and Pathology in a Large Animal Model of Non-Penetrating Head Impact

Mr. Charlie Magarey[1], A/Prof. John Finnie[1], Mr. Jim Manavis[1], Prof. Peter Blumbergs[1], Prof. Peter Cripton[2], A/Prof. Claire Jones[1]

[1]Adelaide University, Adelaide, South Australia, Australia. [2]The University of British Columbia, Vancouver, British Columbia, Canada

Introduction

Large animal models with well characterised head kinematics and pathology can help elucidate relationships between traumatic brain injury (TBI) mechanics and pathophysiology. Clinically, most TBIs result from head impact without skull penetration, but there is a lack of large animal models that simulate this injury mechanism. The aim of this study was to characterise pathology and head kinematics in a sheep model of closed head impact-induced head rotation, across several impact energies.

Methods

Fourteen anaesthetised sheep were instrumented with a skull mounted kinematics sensor array, and their head fixed to a planar constraint apparatus via a bite plate, limiting head motion to the sagittal plane (Fig. 1A). The frontal bone region was impacted, via an interface plate, at one of three energy levels (180 J n=6; 280 J n=2; 350 J n=6) resulting in approximately 110° of flexion rotation about the second cervical vertebra (Fig. 1B). Three animals were controls. Gross neuropathology was assessed via haematoxylin and eosin histology, and axonal and neuronal pathology were assessed via amyloid precursor protein (APP) immunohistochemistry, at 6h post injury. Linear mixed effects models were developed to assess associations between axonal/neuronal pathology scores and either experimental group or peak kinematics measures.

Results

In 2/6 animals, 350 J head impact caused penetrating skull fracture with contusion, laceration, haemorrhage, neuronal injury and diffuse axonal injury (DAI). Contusion, subarachnoid haemorrhage, and focal axonal injury were observed in the 350 J non-penetrating group, but not for lower energy impacts. Neuronal APP expression was elevated in all groups, compared to Control, and was positively associated with head peak angular

velocity (Fig 1D, E). Axonal APP expression was not higher than Control for any non-penetrating injury groups (Fig 1C) and was not associated with peak head kinematics.

Discussion

Widespread neuronal reaction, but not DAI, was observed for non-penetrating head impacts at three energy levels. In some animals, a 350 J impact resulted in penetrating skull fracture and severe TBI. Future studies with this model may explore additional markers of pathology, and the effects of increased post-injury survival time and repeated impacts on the pathological outcomes.

Images (Optional)

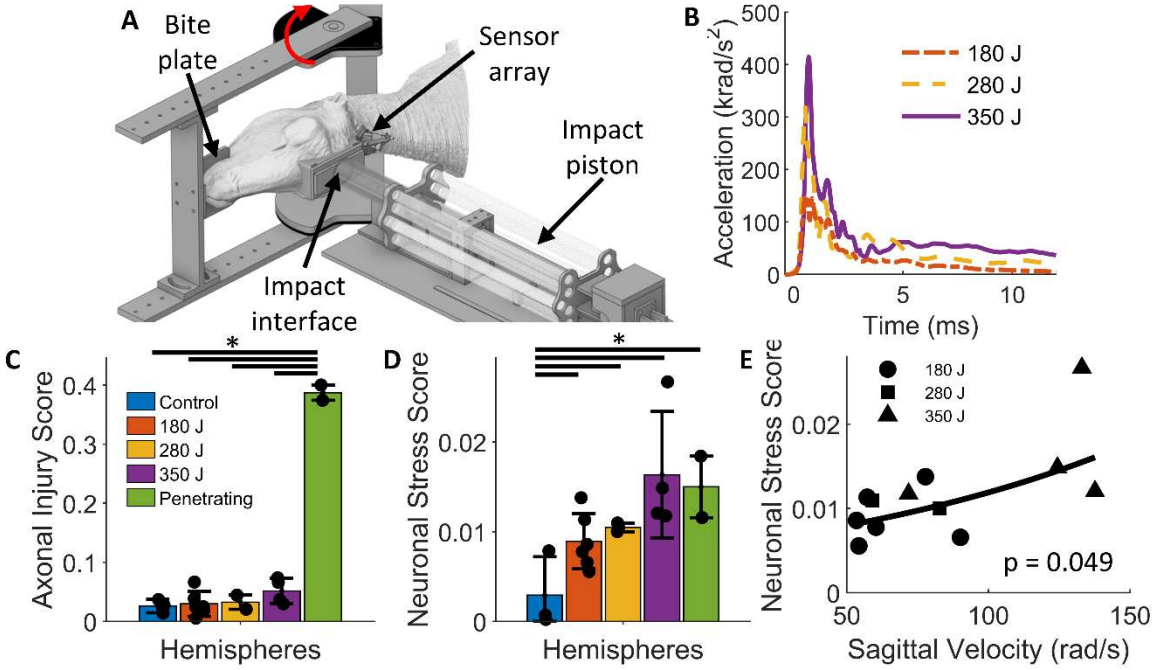


Figure 1A: Sheep head impact induced rotation apparatus. **B**: Mean resultant head angular acceleration versus time. **C-D**: Mean ± 1 standard deviation axonal injury and neuronal stress scores for all groups. Black bars with asterisk represent significant group differences ($p<0.05$). **E**: Scatter plot with regression line showing relationship between peak sagittal velocity of the head and neuronal stress score.

Session Category

Injury Biomechanics: N/A

P3-080

The effect of size on the male hand and forearm injury tolerance when subjected to loading representative of behind-shield blunt trauma

Dr. Julia de Lange Ph.D., P.Eng.[1,2,3], Mr. Liam Burrows M.A.Sc.[2], Dr. Cheryl Quenneville Ph.D., P.Eng.[2]

[1]30 Forensic Engineering, Toronto, Ontario, Canada. [2]McMaster University, Hamilton, Ontario, Canada. [3]University of Guelph, Guelph, Ontario, Canada

Introduction

Behind-shield blunt trauma (BSBT) is an injury mechanism associated with the deformation of a ballistic shield's back face into the user from a ballistic impact. The proximity of the arm to the back of the shield can lead to localized blunt trauma, resulting in different injury mechanisms and thresholds than automotive loading conditions, as demonstrated on 50th percentile male post-mortem human subjects (PMHS) [1]. While the military population has been primarily male dominated, there has been increasing participation of a wider range of demographics, as well as an overall growth in anthropometric measures within the population. This means injury metrics developed for traditional 50th percentile male size (78 kg, 1.75 m) may not protect all users of ballistic shields.

Methods

High-rate (14 m/s), short-duration (< 5 ms) impacts associated with BSBT were applied to two locations on both small (< 15th percentile by height and weight) and large (> 75th percentile by height and weight) PMHS cohorts (N = 8 each) to assess injury tolerance. The hand and forearm were selected as vulnerable locations based on their proximity to the shield and their independence of joint orientation. Specimens were impacted at increasing energy levels until fracture occurred, confirmed by x-ray imaging, and efforts to minimize the number of impacts on each specimen were taken.

Results

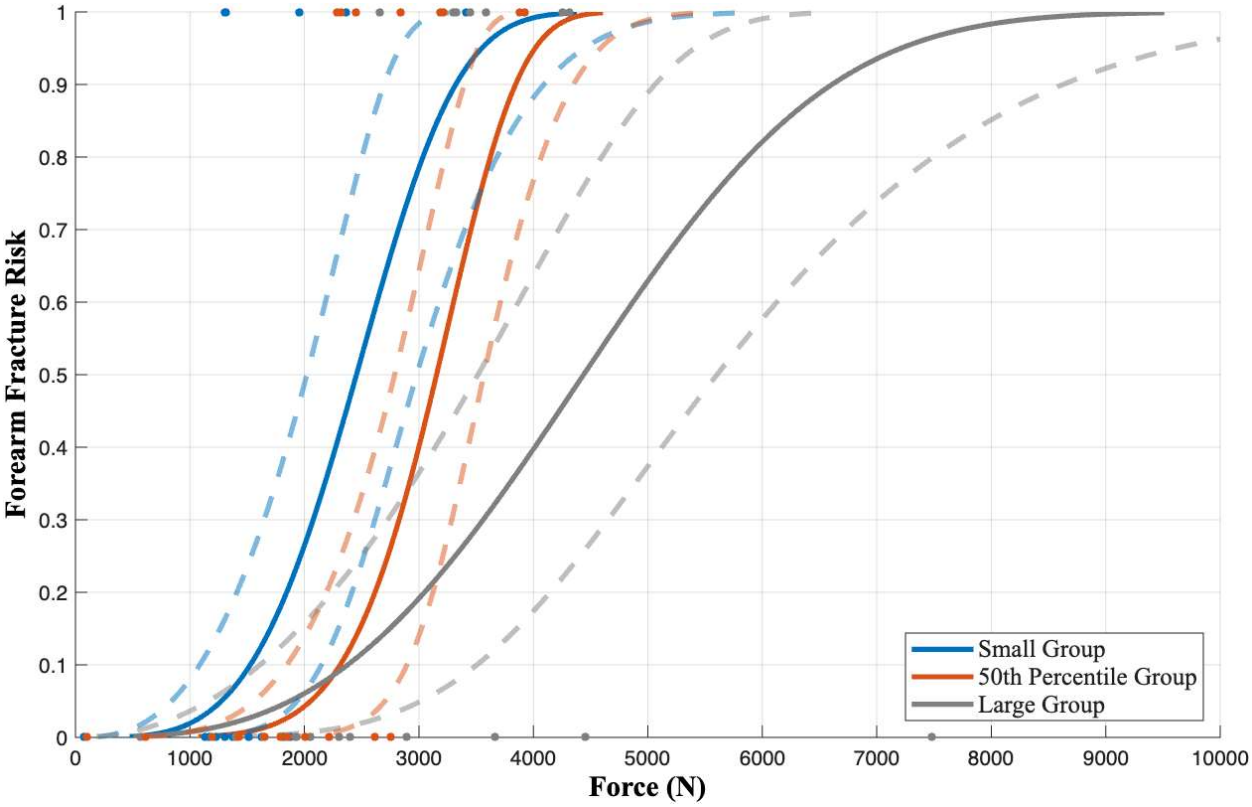
Upon inspection of collected specimen vBMD, one specimen in the small cohort was found to be osteoporotic; as such, was excluded from further analysis. At the hand, fractures were generated at forces of 3,072 ± 1,384 N in the small cohort, and 3,637 ± 774 N in the large cohort. Comparatively, forces of 2,267 ± 827 N and 3,647 ± 445 N were required to cause forearm fractures in the small and large cohorts, respectively. The

fracture threshold was significantly lower for the small group as compared to the large for the forearm ($p < 0.01$) but not the hand.

Discussion

The injury risk curves generated from these data varied among size groups (Figure 1), underscoring the importance of considering anthropometric size when developing and testing protective equipment for all.

Images (Optional)



References (Optional)

[1] de Lange et al., J. Biomech Eng, 2024

Session Category

Injury Biomechanics: N/A

P3-081

Increased Age, Head on Collisions and Facial Impact Location Influence Head Injury in 353 RAIDS Motorcyclists in 2013-2025 Road Accident In-Depth Studies Data

Dr Claire Baker, Dr Mazdak Ghajari, Professor David Sharp

Imperial College London, London, Greater London, United Kingdom

Introduction

Motorcyclists and other powered two-and three-wheeler (PTW) riders make up over 30% of the 1.19 million annual road traffic deaths globally [1]. Despite being among the most vulnerable road users (VRUs), the popularity of PTWs is rising, with the number nearly tripling in the decade to 2021. Helmet use has shown reducing serious head and neck injury as well as fatality [1]. Despite this, brain injury remains a prevalent challenge, with a high association between traumatic brain injury (TBI) and the severest outcomes.

Methods

We analysed 353 motorcycle collisions over 12 years from Great Britain's Road Accident In-Depth Studies (RAIDS) collision database (April 2013 – March 2025). Injuries were classified using the abbreviated injury scale and free-text as previously summarized [2]. Interactions between speeds, collision configurations and ages (under 55yrs and 55+yrs) were analysed with Chi-squared (X^2) and Mann-Whitney (U_{MW}) statistics.

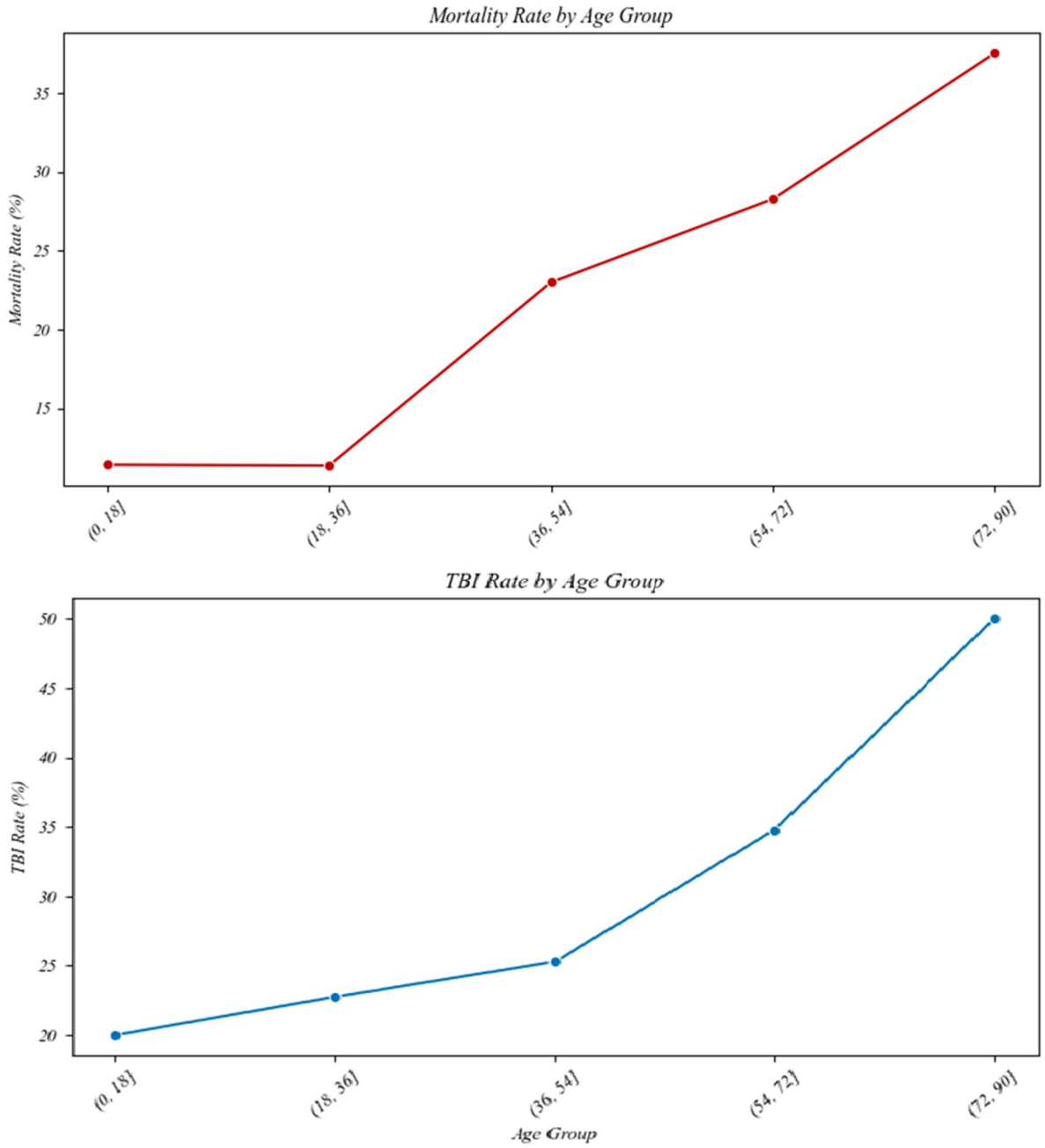
Results

Most (93.5%) of riders were injured (17% fatally injured) and a third (32.6%) sustained a head injury. Only 2% of riders did not wear a helmet. Half (50.4%) of damage-confirmed head impacts were to the facial region, with more impacts to the upper face and chinbar compared to the visor. One third of motorcyclists sustained one or more types of head injuries, 23.6% sustained a Mayo-classified TBI (16.9% moderate-severe). Age (Figure 1) significantly influenced both mortality (<55yrs versus 55+yrs: $p=0.008$, $X^2=6.95$) and TBI outcomes (<55yrs versus 55+yrs: $p=0.003$, $X^2=4.61$). Mortality ($U_{MW}=9364.0$, $p<0.000001$) and TBI ($U_{MW}=11587.0$, $p<0.000001$) occurred at higher travel speeds. Head on collisions were responsible for a significantly higher prevalence of TBI ($p=0.005$, $X^2=7.88$) and moderate-severe TBI ($p=0.006$, $X^2=7.53$), while loss of control on straight roads had reduced TBI prevalence ($p=0.023$, $X^2=5.14$).

Discussion

We present a large, contemporary study detailing motorcycle collision configurations, speeds and head impact locations and their associated TBI outcomes. Our results highlight that despite improvements in head injury rates since COST327, collision configuration and facial impact location influence outcomes. Our results identify outcome inequality in age and support ongoing data analysis to support better infrastructure and protective equipment design and testing.

Images (Optional)



References (Optional)

1. World Health Organization, Global Road Safety Report 2023.

2. Baker et al. (2022), Brain Communications.

Session Category

Injury Biomechanics: N/A

P3-082

Pathology and Head Kinematics in a Large Animal Model of Closed Head Trauma With and Without Head Impact

Mr. Charlie Magarey[1], A/Prof. John Finnie[1], Mr. Jim Manavis[1], Prof. Peter Blumbergs[1], Prof. Peter Cripton[2], A/Prof. Claire Jones[1]

[1]Adelaide University, Adelaide, South Australia, Australia. [2]The University of British Columbia, Vancouver, British Columbia, Canada

Introduction

Understanding relationships between traumatic brain injury (TBI) mechanics and pathology can drive design and evaluation of protective equipment and safety features, and help identify opportunities for clinical intervention. Head impact is known to cause focal pathologies in closed head TBI; however, the contribution of cranial impact to diffuse pathologies caused by rapid rotation of the head and brain, is not understood. The aim of this study was to compare head kinematics and pathology outcomes in a sheep model that induces rapid head rotation with and without head impact, with the same energy input.

Methods

Ten anaesthetised sheep were attached to a planar constraint via a bite plate. Rapid sagittal head rotation (~110°) was induced via impact to the frontal skull via an interface plate (head-impact, HI; n=4; Fig. 1A), or impact of the planar constraint apparatus (offset-impact, OI; n=6; Fig. 1B); three animals were controls. Impact energy in both configurations was nominally 350J. Head kinematics were measured with a skull mounted sensor array. Gross neuropathology was assessed via haematoxylin and eosin histology, and axonal and neuronal pathology were assessed via amyloid precursor protein immunohistochemistry, at 6h post injury. Associations between experimental group and axonal/neuronal pathology were assessed with linear mixed effects models.

Results

HI, but not OI, animals experienced an initial high magnitude, ~2ms duration, angular acceleration peak due to skull deformation; following this, resultant angular velocity traces were similar for both groups (Fig. 1C-D). Contusion and subarachnoid haemorrhage were observed in HI animals; no focal pathology was observed in OI animals. Axonal injury in the brain hemispheres was higher in HI animals than OI animals (Fig. 1E), due to focal axonal

injury adjacent to contusion sites. Neuronal pathology was increased compared to Control in both injury groups and qualitatively was higher for HI animals (Fig. 1F).

Discussion

Focal pathologies observed in HI animals were likely caused by local skull deformation. Diffuse neuronal pathology was apparently higher in HI animals, suggesting skull impact effects may have contributed. The neuronal APP expression likely represented a transient stress response. Further investigation of additional injury markers may elucidate relationships between diffuse pathologies and impact effects.

Images (Optional)

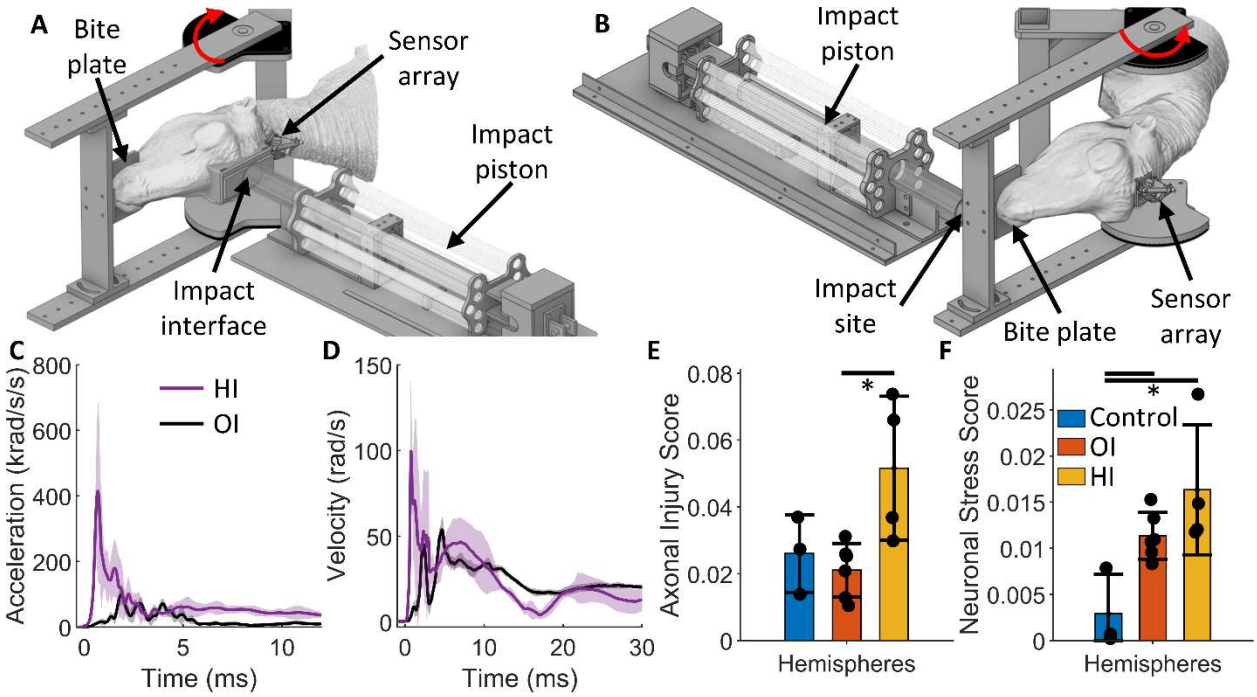


Figure 1: **(A)** Sheep head impact (HI) and **(B)** offset impact (OI) rotation setups, red arrows show direction of rotation about planar constraint pivot point. **C-D**: Mean ± 1 standard deviation resultant head angular kinematics versus time. **E-F**: Mean ± 1 standard deviation axonal injury and neuronal stress scores for all groups. Black bars with asterisk represent significant group differences ($p<0.05$).

Session Category

Injury Biomechanics: N/A

P3-083

Characterizing Head Acceleration Events in Stock Car Auto Racing by Kinematic-Derived Principal Direction of Force (PDOF)

Mr. Cole Smith MS[1,2], Ms. Zoie Mink[1,2], Dr. Nicholas Pritchard PhD[1,2], Dr. Garrett Bullock PhD[1], Mr. Matthew Harper PE[3,1,2], Dr. Jillian Urban MPH, PhD[1,2], Dr. John Patalak PhD, PE[3], Dr. Joel Stitzel PhD[1,2]

[1]Wake Forest University School of Medicine, Winston Salem, NC, United States. [2]Virginia Tech - Wake Forest University School of Biomedical Engineering and Sciences, Winston Salem, NC, United States. [3]National Association for Stock Car Auto Racing, LLC, Daytona Beach, FL, United States

Introduction

Stock car auto drivers are exposed to non-concussive head acceleration events (HAEs) during active racing maneuvers or crashes, which may present a risk to brain health and function [1]. Research using principal direction of force (PDOF) derived from chassis data has found that right lateral vehicle impacts yielded lower driver injury risks [2]. This approach has not been applied to head acceleration data. The objective of this study was to characterize HAEs by PDOF using head kinematics measured with an instrumented mouthpiece system.

Methods

Head kinematic data was collected from 20 NASCAR Cup Series drivers during 41 races in the 2024 season using instrumented mouthpiece sensors (1600Hz, 4g threshold). Events were classified as race or crash events (i.e. a driver's vehicle interacted with an external object, resulting in a caution) and visually verified. Events with multiple impacts were separated into individual HAEs. Resultant linear acceleration was calculated in the transverse plane and HAE start/end times were approximated using thresholds of 5g (if peak >10g) or 2.5g (if peak ≤10g). Linear velocity was calculated by integrating acceleration data and the angle of velocity change assigned each HAE to a PDOF (Figure 1). Peak linear/rotational accelerations and velocities, ΔLV, and DAMAGE were calculated per HAE.

Results

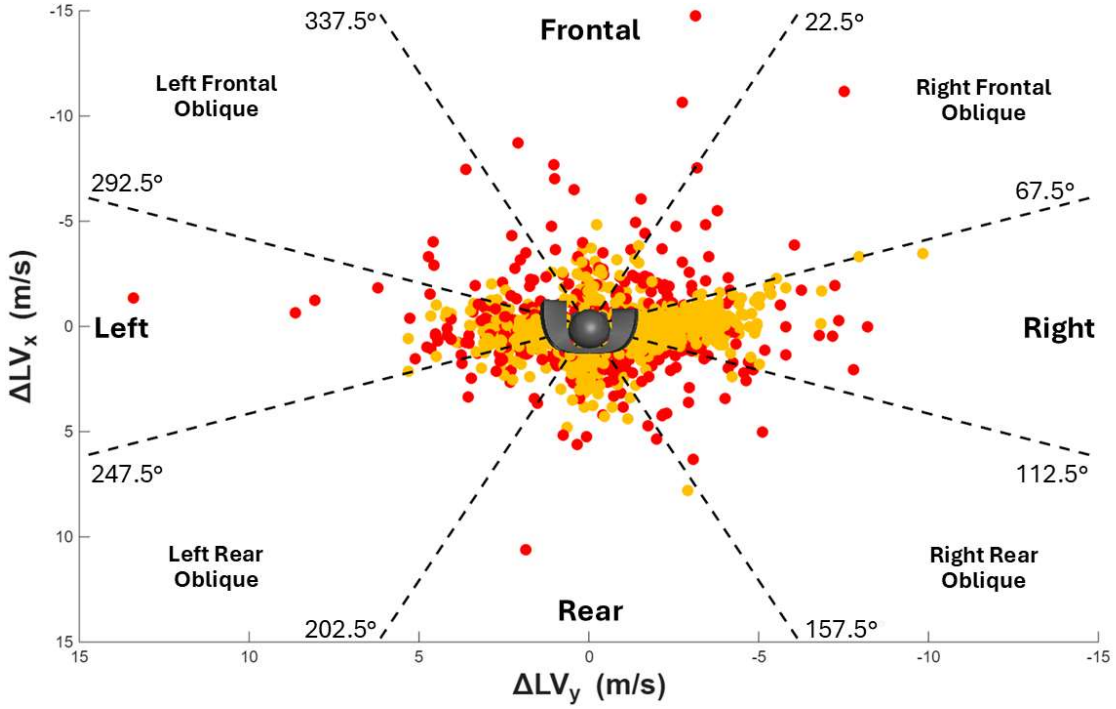
3,156 events resulted in 5,198 HAEs. Events not exceeding 4g in the transverse plane (n = 720) were excluded yielding 4,478 HAEs (3,818 race; 85%, 660 crash; 15%) for analysis. Drivers experienced 2,476 right-side impacts, accounting for 55.3% of all HAEs. Median

ΔLV was greatest in right frontal oblique impacts for crashes (2.7 m/s) and frontal impacts for race events (1.5 m/s).

Discussion

This study characterized HAEs by PDOF during NASCAR Cup Series races. The PDOFs with maximum head loading differed between event types, with frontal and left-side events producing the largest ΔLVs for crashes and right-side events for races. Results can inform driver safety research and regulations in stock car racing. Future work should compare head kinematics-derived PDOF with vehicle chassis PDOF during crashes.

Images (Optional)



References (Optional)

[1] Mainwaring, L. *et al.,* Int. J. Psychophysiol., 2018

[2] Patalak, J.P. *et al.*, Accid. Anal. Prev., 2020

Acknowledgements (Optional)

The authors thank the drivers for participating in this study as well as Sophia Zoch, Logan Miller, and Lindsay Bonsall for their assistance in data collection for this study. This work was supported by the National Association of Stock Car Auto Racing (NASCAR). Authors Joel Stitzel and Jillian Urban have a patent pending for the mouthpiece instrumentation used in the study.

Session Category

Injury Biomechanics: N/A

P3-084

Comparison of Positive and Negative Mold Scanning Techniques for the Assessment of Back Face Deformation in Armor

Mr. Cristian Pampu[1], Ms. Katarzyna Ochocki B.S.[1], Mr. Donald Sherman M.S.[1], Mr. Andrew Davis MPH[1], Dr. Karin Rafaels Ph.D[2], Dr. Cynthia Bir Ph.D[1]

[1]Biomedical Engineering, Wayne State University, Detroit, MI, United States. [2]US DEVCOM Army Research Laboratory, Adelphi, MD, United States

Introduction

The measurement of back face deformations (BFDs) is a critical part of certification testing for soft and hard armor. Historically, these measurements were done with simple techniques such as depth calipers and include only peak deformation. Previous research suggests that the shape (volume, curvature) of the BFDs is also important to consider. As such, a 3-dimentional scanner was used to capture additional parameters; however, two varying techniques were assessed. The aim of this research is to compare these methods to provide guidance for future testing.

Methods

A total of sixteen ballistic impacts were conducted using 9 mm FMJ RN fired at 448 m/s against handgun 2 (HG2) armor panels placed in front of a witness material as previously described [1]. After each impact, the BFD was measured using depth calipers. In addition, the resulting deformation (negative) was scanned using the Revopoint Miraco Plus 3-D scanner (Revopoint, Los Angeles Ca). A positive mold of the deformation was also created using Polytek EasyFlo 60 (Polytek Development Corporation). After the mold cured, it was also scanned. The BFDs from calipers were compared to the positive and negative scans measured with CloudCompare.

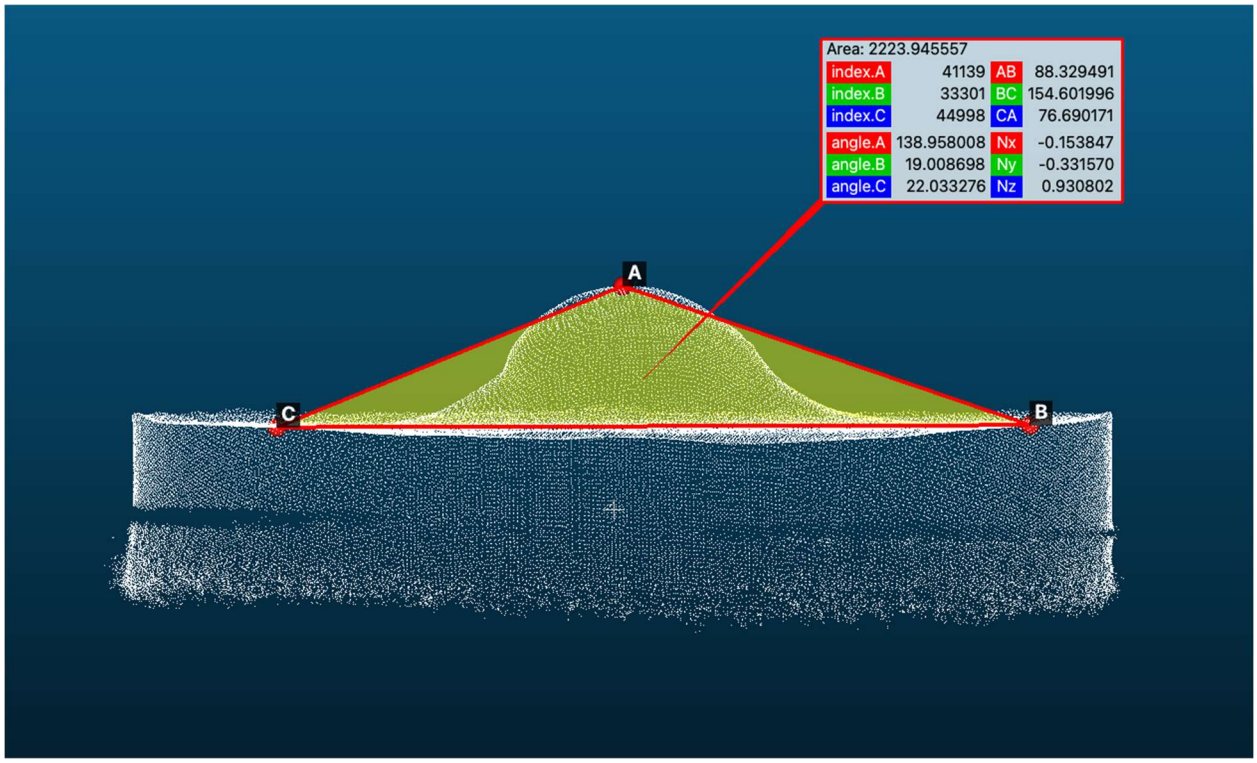
Results

The average maximum BFD measured with calipers was 28.54 ± 0.01mm for a silicone composite clay and 27.54 ± 0.01mm for Roma Plastalina No. 1 (RP1). For the negative scans, the average maximum BFD was 29.23 ± 0.02mm for the silicone composite and 29.12 ± 0.02mm for RP1. For the positive scans, the average maximum BFD was 29.12 ± 0.02mm for the silicone composite and 27.6 ± 0.02mm for RP1. There was no significant difference ($p<0.05$) between any techniques for either witness material.

Discussion

The use of ballistic clay and a single maximum deformation point for the evaluation of BFD has long been the standard for armor certification. The use of scanning technology can provide more details about the BFD; however, accurate methodologies must be established before they can be widely used.

Images (Optional)



References (Optional)

"[1] Ochocki *et al*. ,International Ballistics Society, 2025"

Session Category

Injury Biomechanics: N/A

P3-085

Quantifying Seated Pregnant Occupant Anthropometry Using a 3D LiDAR Scanner

Ms. Danielle Rowlands BASc.[1], Ms. Vivian Chung MASc., P.Eng.[1], Mr. Dean Harris[1], Ms. Jade Levine MASc.[1], Dr. Jason Burrows MD, FRCSC[1], Dr. Desiree Reichhardt DNP, NP(F), RDMS[1], Dr. Jason Forman Ph.D.[2], Dr. Jason Hallman Ph.D.[3], Dr. Ananna Ahmed Ph.D.[3], Dr. Peter Cripton Ph.D.[1]

[1]The University of British Columbia, Vancouver, British Columbia, Canada. [2]University of Virginia, Charlottesville, Virginia, United States. [3]Toyota Motor North America R&D, Ann Arbor, Michigan, United States

Introduction

Motor vehicle collisions are a leading cause of trauma death for pregnant women [1]. Anatomical changes occur throughout the pregnancy. Interactions between the seatbelt and external pregnant anatomy are neither well documented nor well understood. This study aims to explore how anthropometry may influence the seatbelt path during pregnancy through the use of 3D imaging.

Methods

Pregnant participants were provided NHTSA's guidelines demonstrating correct seatbelt placement during pregnancy. 3D images are then captured in two environments:

1. A hand-held LiDAR scanner captures a 3D image of participants wearing their seatbelt while seated in a simulated vehicle seat.
2. A GoPro camera captures a video of participants wearing their seatbelt in their own vehicle. A 3D image is then reconstructed using photogrammetry.

Data collection is currently ongoing, with 259 of the targeted 500 participants scanned thus far.

Results

Initial analyses of 101 scans examine shoulder belt placement and offset from the jugular notch (JN). Preliminary results suggest that the horizontal distance from the JN to the shoulder belt varies, with values ranging from 13.42-97.06mm. However, trends can be noted:

The horizontal distance from the JN to the shoulder belt tends to increase with an increase in sitting height (regression coefficient=2.89; R^2=0.253; p-value=3.75E-07) and standing height (regression coefficient=1.18; R^2=0.173; p-value=4.09E-05). The horizontal JN to

shoulder belt distance tends to decrease as gestational age increases (regression coefficient=-0.85; R^2=0.095; p-value=0.00293).

Discussion

This study provides a large dataset demonstrating seatbelt placement for pregnant occupants. In examining the horizontal JN to shoulder belt distance, a decrease in this distance suggests that the shoulder belt is resting closer to the neck. This may result in the shoulder belt crossing over the breasts, impacting one's ability to accurately follow seatbelt placement guidelines [2].

The relatively weak correlations observed in preliminary results highlight the complexity of predicting the seatbelt path when high inter-subject variability is present. This further illuminates the effect that pregnant anthropometry may have over non-pregnant participants that have been previously evaluated [3].

Images (Optional)



References (Optional)

[1] Natthida Owattanapanich et al., J Trauma Acute Care Surg, 2021

[2] Serpil Acar et al., Safety, 2017

[3] Olivia Mergler et al., J. Biomech, 2025

Session Category

Injury Biomechanics: N/A

P3-086

Unexpected Source of Behind Armor Blunt Trauma (BABT) Lung Injury

Dr. Joost Op't Eynde PhD[1], Mr. Jason Kait MS[1], Mr. Derek Pang MS[2], Dr. Robert Salzar PhD[3], Mr. B. Joseph McEntire MS[4], Dr. Cameron R. 'Dale' Bass PhD[2]

[1]Duke University, Durham, North Carolina, United States. [2]Wayne State University, Detroit, Michigan, United States. [3]University of Virginia, Charlottesville, Virginia, United States. [4]US Army Aeromedical Research Laboratory, Fort Rucker, Alabama, United States

Introduction

The typical behind armor blunt trauma (BABT) injury paradigm in the lung is based on the hypothesis that a large displacement into the lung causes lung contusions. The speed of sound in the lung is approximately (~) 20 m/s. Since armor backface/chest wall velocity often exceeds 20 m/s, there is a potential for compressive shock wave development in the lung. This study elucidates the theoretical basis for shock development, experimental shock pressure measurements, and characteristic injuries for this new principal injury mechanism of BABT.

Methods

An ideal theoretical framework was developed to assess shock wave development in the live adult porcine lung. Experimentally, a BABT indenter representing a realistic rifle threat (7.62x51 NATO) impacted the torso at representative velocities between ~20 and 80 m/s. Indenter motion was tracked using high speed video and acceleration was measured with a triaxial accelerometer. Pressure was measured in the lungs bilaterally. Post-test necropsy assessed local lung injury.

Results

Theoretical shock formation distance was calculated in the lung ~10 mm from the pleural interface inside the lung, and formation time was less than 0.5 ms. Shock formation distance and time increased with decreasing velocity. This is consistent with shocks occurring in the lung from backface velocity. Researchers saw strong evidence of fast rising pressure and shock formation from the lung pressure data taken in the trachea. Histology showed lung damage distant from the impact site with less damaged tissue closer to the site (Figure 1). For the higher velocity tests, this damage often progressed into the contralateral lung.

Discussion

This is the first study to show a theoretical and experimental basis for lung shock injuries in BABT. Given the typical BABT chest wall velocity ranges (between ~20 and 100 m/s), this is likely a principal wounding mechanism that competes with wounds caused by rib displacement, depending on the armor characteristics. This result, especially the deep injuries in the unimpacted lung, is difficult to explain based on previous strain-based lung injury concepts.

Images (Optional)

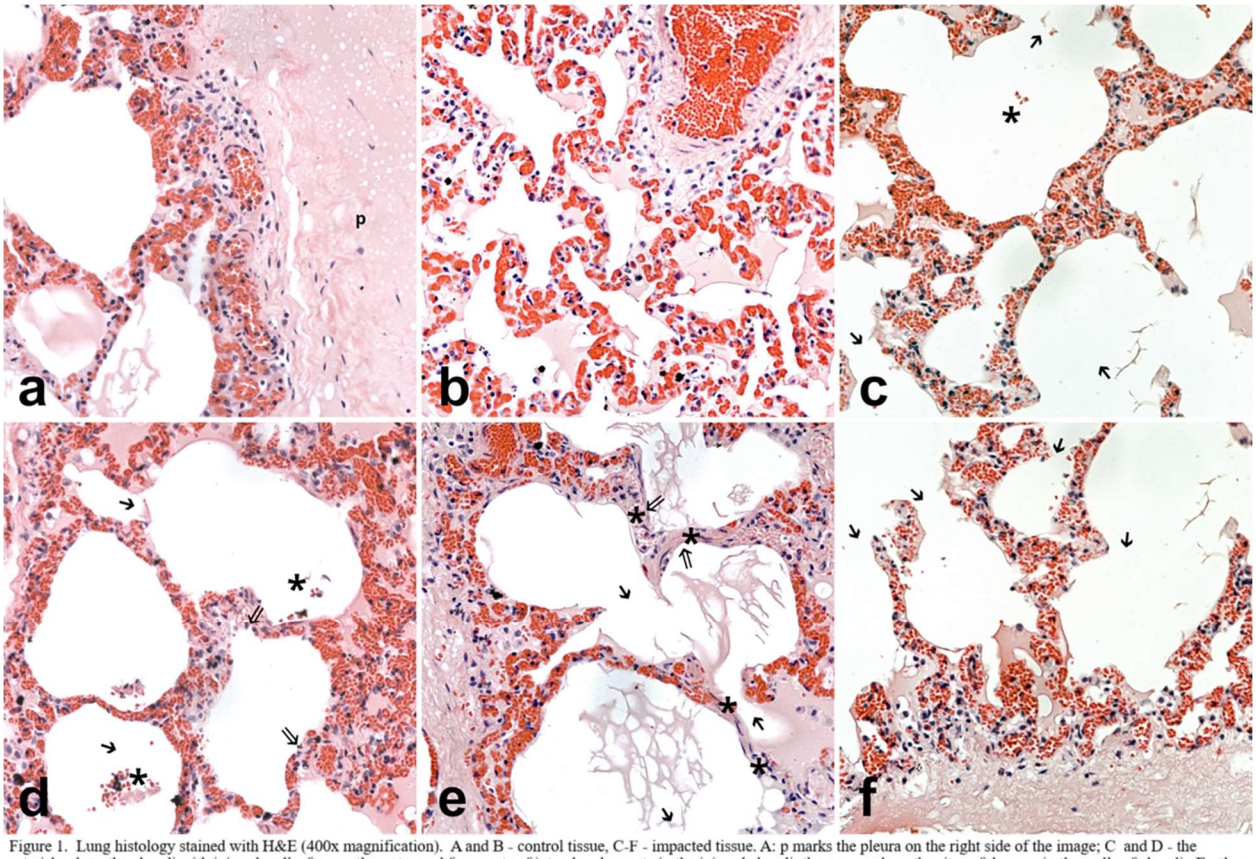


Figure 1. Lung histology stained with H&E (400x magnification). A and B - control tissue, C-F - impacted tissue. A: p marks the pleura on the right side of the image; C and D - the asterisks show the alveoli with injured walls, free erythrocytes and fragments of interalveolar septa in the injured alveoli; the arrows show the sites of damage in the walls of alveoli. E - the asterisks with thick arrows mark the areas of interalveolar walls free of capillaries; thin arrows show the rupture of alveolar walls. F subpleural region of the impacted lung. Small arrows show the rupture of alveolar walls. C-F - note considerably diminished number of alveolar capillaries typical of the impacted tissue compared to the control tissue resulting from damage of capillaries.

Session Category

Injury Biomechanics: N/A

P3-087

Acoustic Source Localization of Fractures in Heterogenous Biological Tissue

Ms. Diana D. Tarakhovsky[1], Dr. Karin A. Rafaels[2], Dr. Cameron R. 'Dale' Bass[1]

[1]Wayne State University, Detroit, MI, United States. [2]US DEVCOM Army Research Laboratory, Adelphi, Maryland, United States

Introduction

Acoustic emission (AE) is a powerful, noninvasive tool for detecting and localizing fractures. To avoid disrupting tissue and remain truly noninvasive, acoustic sensors must be mounted on the skin and not directly on bone. However, because hard tissues and soft tissues exhibit different mechanical behaviors and wave propagation characteristics, accurate source localization using conventional approaches that assume homogeneity with a constant propagation speed is inadequate. This study applies an effective speed-of-sound method to improve predictive diagnostics in biomechanical applications compared to using a speed-of-sound based only on soft-tissue propagation.

Methods

To expand on the previous analysis that assumed a constant propagation speed, post-test CT-scans of the porcine specimens were analyzed to obtain soft tissue, bone, and fracture geometries. CT-based segmentations defined anatomical boundaries and impedance changes used to ray-trace propagation and estimate an effective speed-of-sound. The fracture localization obtained using the original method and the effective speed-of-sound in this study were compared with each and other and to the actual fracture locations.

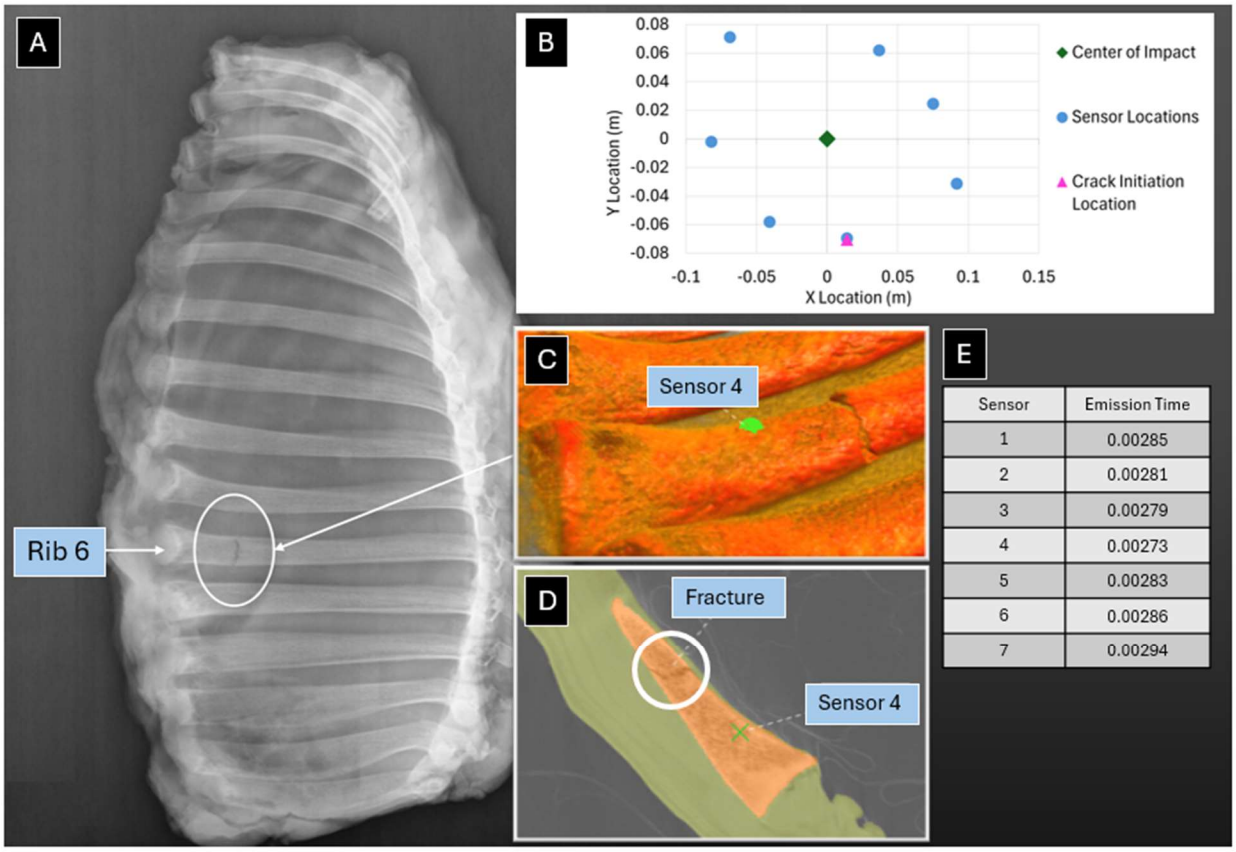
Results

Post-test CT-scans were segmented into soft tissue, bone, and fracture regions, providing the anatomical basis for analyzing waveform propagation. Through numerical optimization, the multilateration algorithm identified the most probable fracture location and emission onset-time relative to the eight-sensor array. Localization results aligned with anatomical inspection, rib projections, and post-impact X-rays. The method utilizes an effective speed-of-sound accounting for the acoustic signal propagating through multiple tissue types, improving the localization of fractures.

Discussion

This study provides a noninvasive method of localizing initial fractures, demonstrating potential as a real-time tool for advancing understanding of skeletal fracture-mechanics. A limitation is the use of an effective speed-of-sound, which simplifies the complex wave behavior across material interfaces. Acoustic emissions propagate as compressional, shear, surface, and plate waves, each influenced by sensor position. This paper presents experimental methods, algorithmic strategies, and validation for noninvasive AE-based fracture localization using an effective sound speed in multi-tissue systems. These findings support the feasibility of fracture-source localization and the integration of AE techniques in biomedical-engineering and tissue-mechanics research.

Images (Optional)



Sensor	Emission Time
1	0.00285
2	0.00281
3	0.00279
4	0.00273
5	0.00283
6	0.00286
7	0.00294

Fig. 2. A: X-ray of the ribcage specimen showing the location of the fracture on Rib 6. B: Example multilateration output demonstrating the calculated initial fracture location relative to sensor positions and impact center. C: MicroCT image showing the fracture morphology and the position of Sensor 4 relative to the fractured rib. D. 2D segmentation showing soft tissue, bone, fracture region, and sensor placement. E: Acoustic emission arrival times for each sensor used in fracture localization.

References (Optional)

Session Category

Injury Biomechanics: N/A

P3-088

Head Impact Kinematics in Reconstructed Youth Body-First Rear Falls

Ms. Emilie Ethier, Mr. Thomas Hoshizaki MSc, Ms. Taylor Sims BSc, Dr. Thomas Blaine Hoshizaki PhD

University of Ottawa (Neurotrauma Impact Science Lab), Ottawa, Ontario, Canada

Introduction

Body-first falls are a common event in youth sport, with observational data reporting 90% of impacts involve the body contacting the surface before the head. Youth have lower neck strength and neuromuscular control than adults, which influence head kinematics and injury risk (1). Adult surrogate studies show neck stiffness affects linear and rotational head impact accelerations; however, few studies have investigated body-first head impacts in youth. This study compared peak linear (PLA) and rotational acceleration (PRA) for body-first head impacts at 2 and 4 m/s using a youth specific neck spring apparatus (2).

Methods

Impacts were conducted using a drop-rig system and the University of Ottawa Neck Spring Apparatus (UONSA). Youth neck stiffness was, set to 70 % of adult neck stiffness (60% MVC) Video body-first youth football falls footage was used to guide impact reconstruction. The Hybrid III 5th percentile head form was dropped onto a MEP anvil in two conditions: (1) body-first falls onto compliant vinyl nitrile foam pad and (2) direct head impacts. Two velocities (2 and 4 m/s) were tested 3 times per condition. PLA and PRA were recorded using a slice accelerometer.

Results

The body-first impacts at 2 m/s resulted in a mean PLA of 17.47 g (SD 1.30) and mean PRA of 2783.5 rad/s^2 (SD 166.7). At 4 m/s, body-first PLA increased to 91.73 g (SD 4.04) and PRA to 10335.1 rad/s^2 (SD 343.8). Direct 2 m/s impacts produced far higher PLA 90.87 g (SD 0.70) and a lower PRA 4206.1 rad/s^2 (SD 260.0). At 4 m/s, direct impacts recorded the highest PLA values 207.37 g (SD 4.24) and PRA values of 10930.4 rad/s^2 (SD 2791.1).

Discussion

These findings revealed direct impacts produced 4–6x higher linear accelerations, while body-first falls generated rotational accelerations approaching direct impacts at 4 m/s. Since rotational acceleration is linked to head injury risk, these results highlight the need to

evaluate both linear and rotational loading when assessing youth fall-related head injury risk.

Images (Optional)

Table 1: Mean linear and rotational acceleration values.

		Body First Impacts	Direct Impacts
2m/s	Linear acc. (g)	17.5g (SD 1.4)	90.9 g (SD 0.7)
	Rotational acc. (rad/s^2)	2783.5 rad/s^2 (SD 166.7)	4206.1 rad/s^2 (SD 260.0)
4m/s	Linear acc. (g)	91.7 g (SD 4.0)	207.4 g (SD 4.2)
	Rotational acc. (rad/s^2)	10335.1 rad/s^2 (SD 343.8)	10930.4 rad/s^2 (SD 2791.1)

References (Optional)

(1) Jadischke R et al., BMJ Open Sport Exerc Med, 2020

(2) Cournoyer J et al., J Biomechanics, 2021

Session Category

Injury Biomechanics: N/A

P3-089

Evaluation of Female Head X-Acceleration Responses Between Volunteers and Anthropomorphic Test Devices in Frontal and Frontal-Oblique Sled Tests

Ms. Emily Arana Barcala, Ms. Keya Zambare, Dr. Kevin Adanty, Dr. Sean Shimada

Aperture LLC, Davis, CA, United States

Introduction

Female occupants face higher injury risks in frontal crashes [1]. Currently, female head responses are characterized by female anthropomorphic test devices (ATDs) including the 5th-percentile THOR-05F and the Hybrid III (HIII-5F), a scaled-down male ATD [1]. To our knowledge, no comparative analysis has evaluated whether both existing female ATDs accurately capture head kinematics of human female occupants. While studies have evaluated female ATD biofidelity at low speeds [2], it remains unclear whether these findings extend across varying crash severities. Therefore, this study aims to compare 5th-percentile female volunteers with THOR-05F and HIII-5F ATDs in frontal and frontal-oblique impacts to assess female ATD head x-acceleration biofidelity.

Methods

Anteroposterior head x-accelerations were collected from (1) low-speed frontal-oblique (impact angle: 330°) sled tests with unbraced 5th-percentile female volunteers and (2) low-to-high-speed frontal (0°) and frontal-oblique (0±30°) sled tests with THOR-05F and HIII-5F ATDs. Data was sourced from literature [2] and the National Highway Traffic Safety Administration Biomechanics Database, respectively. Head x-acceleration plots were normalized by peak sled acceleration and crash duration (%CD).

Results

Frontal-oblique volunteer and frontal ATD acceleration responses peaked at similar times (31.0%CD and 31.8–33.3%CD). Further, frontal-oblique HIII-5F (345° and 15°) peaked at comparable times to volunteer tests (29.3-29.9%CD), whereas THOR-05F (330°) peaked later (60.6%CD) (Figure 1). Statistical analysis demonstrates that frontal THOR-05F and HIII-5F closely matched volunteer curves (r=0.959-0.967; RMSE=0.137-0.152). Frontal-oblique HIII-5F pulse alignment to volunteers was moderate (r=0.644-0.687, RMSE=0.196-0.221), however THOR-05F alignment was weak (r=0.118, RMSE=0.441).

Discussion

Frontal-oblique female volunteer acceleration pulses aligned more closely with ATD pulses in frontal than frontal-oblique impacts. Although limited by sample size, these results

suggest weaker frontal-oblique head x-acceleration biofidelity for current female ATDs, particularly THOR-05F. Normalized ATD head-to-sled acceleration magnitudes increased with crash severity, suggesting that female ATD head response may not scale proportionally with greater sled accelerations. Consequently, these findings are consistent with previous reports of greater volunteer–ATD differences at greater sled accelerations [2]. This underscores the need for expanded female datasets to refine frontal-oblique ATD head responses, improve injury prediction, and strengthen female-specific safety standards.

Images (Optional)

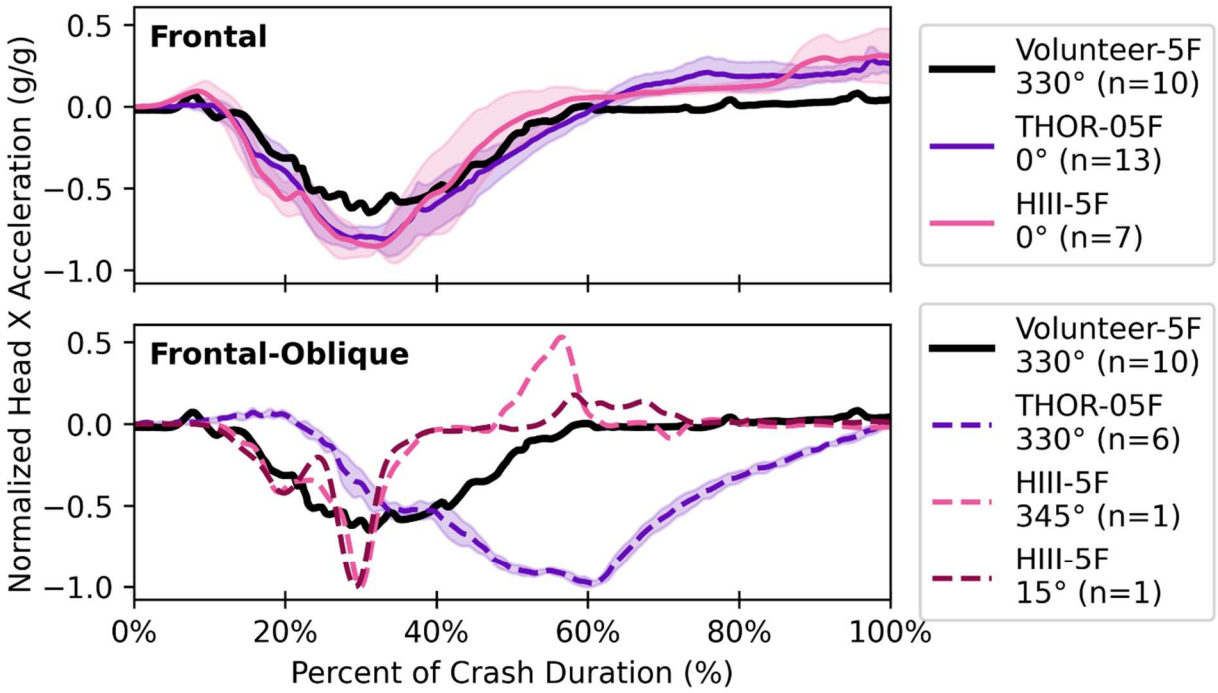


Figure 1. Normalized average head x-accelerations with 95% confidence intervals for female volunteers (frontal-oblique only) versus THOR-05F and HIII-5F ATDs in frontal and frontal-oblique impacts. Volunteer tests: 2.5g, ATD tests: 4-25g.

References (Optional)

[1] Linder and Svensson, Interdisciplinary Science Reviews, 2019.

[2] Albert et al., IRCOBI Conference, 2024.

Session Category

Injury Biomechanics: N/A

P3-090

Electromyographic Activity in Frontal and Rear End Sled Tests and Activities of Daily Living

Ms. Emily Arana Barcala, Mr. John Caraan, Dr. Kevin Adanty, Dr. Sean Shimada

Aperture LLC, Davis, CA, United States

Introduction

The forces acting on the cervical spine in a motor vehicle accident (MVA) are often compared to those generated in non-injurious activities of daily living (ADLs) to evaluate potential injury risks in MVAs. However, when compared to ADLs, there may be distinctions in the underlying muscle activity of critical neck stabilizers during whiplash-type responses in MVAs [1]. These differences in neuromuscular activation may explain the greater injury potential associated with MVAs. This study compares neck muscle activity reported in previous literature between low-speed simulated sled tests (front and rear-end impacts) and common ADLs to quantify the differences in muscle activity for each respective scenario and identify potential injury risk.

Methods

Electromyographic (EMG) activity, represented as percent maximum voluntary contraction (%MVC), was collated from peer-reviewed literature. An analysis of sternocleidomastoid (SCM) and trapezius EMG activity was performed to identify differences between ADLs and unexpecting occupants in low-speed frontal-oblique and rear sled tests. ADLs included sitting, overhead work (OW) described as pushing a load up a vertical distance, holding a 1kg camera at eye level, and shrugging both shoulders towards the ears.

Results

SCM and trapezii EMG activity for frontal-oblique and rear sled tests and ADLs were plotted (Fig. 1) [1-3]. Sled test EMG values were consistently greater in the primary activated muscle than those measured during ADLs. The SCM and trapezius EMG activity during rear and frontal-oblique impacts, respectively, exceeded those reported during ADLs. Trapezius EMG activity was greatest for ADLs during shrugging and was most comparable to frontal-oblique sled tests at 0.5g accelerations.

Discussion

Overall, findings suggest that EMG activity during MVAs exceeds that measured during ADLs. These differences may be attributed to ADLs producing low-intensity muscle activation patterns, whereas MVAs generate rapid, high-amplitude muscle activation

responses of the neck muscles driven by sudden acceleration [1]. Elevated neck muscle activation during sled tests indicates a stabilizing role during unexpected loading and should be considered by forensic engineers as it may contribute to increased neck injury risk relative to ADL tasks.

Images (Optional)

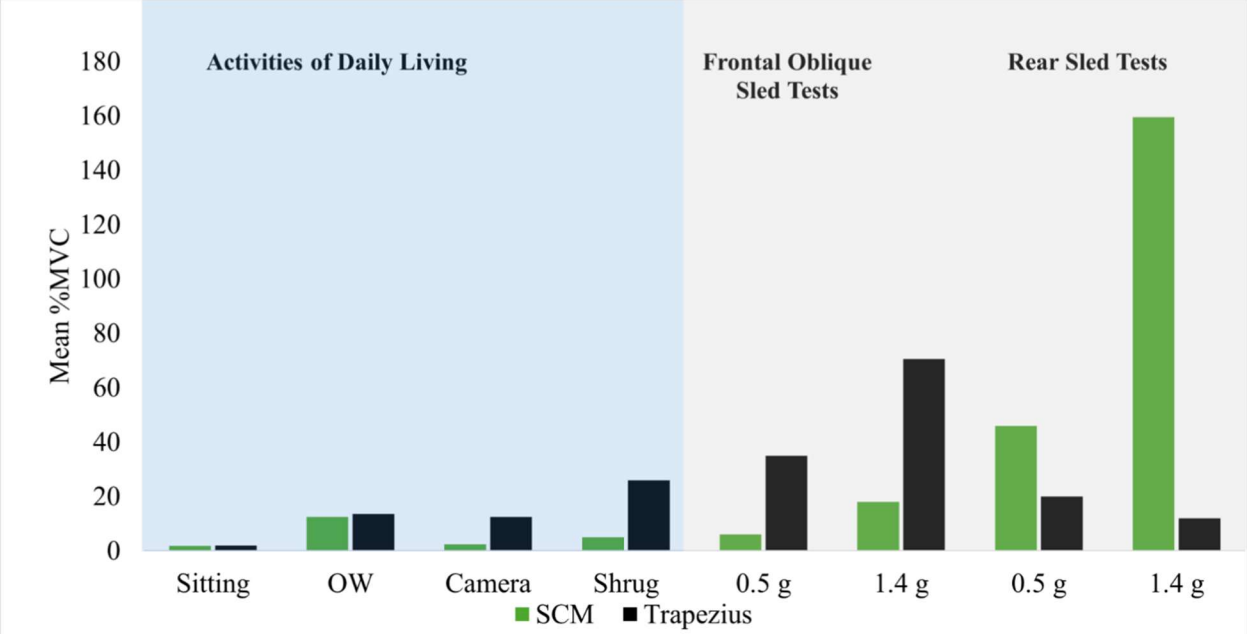


Figure 1. Mean EMG activity of ADLs and sled tests for SCM and trapezii. Peak sled accelerations reported.

References (Optional)

[1] Kumar et al., Clinical Biomechanics, 2003

[2] Shin and Yoo, Work, 2015

[3] Ng et al., Applied Ergonomics, 2014

Session Category

Injury Biomechanics: N/A

P3-091

Slopes, Spirals, and Splashes: Rider Biomechanics on Three Common Recreational Water Slides and Rides

Dr. Emily Bliven PhD, Mr. Noah Schneider BS, Dr. Elaine Serina PhD

Talas Engineering, Inc., Hayward, CA, United States

Dr. Emily Bliven

Introduction

Water slides and rides are popular forms of recreation found at resorts and amusement parks. Like roller coasters, water rides carry riders through prescribed courses while imparting forces and accelerations on their bodies. Biomechanics research on water slides and rides is nascent; however, such data is essential for understanding ride dynamics and "thrill" aspects. Our objective was to characterize rider accelerations on water rides with consideration of ride features (e.g., curves and descents).

Methods

Testing was conducted on a funnel slide, bowl slide, and log flume. The slides each had two riders seated in a two-person tube, with rider weights representative of a 25th percentile male and female. The log flume had two riders seated in the log vehicle: a 144-lb female and 343-lb male. A triaxial accelerometer was mounted near the center of mass of each tube rider and of the log vehicle. Data was collected for the entirety of each ride at a minimum rate of 100 Hz and filtered per SAE J211 with cut-offs of 5 Hz. Subsections were isolated to analyze features of interest identified via video review. The data presented includes gravity.

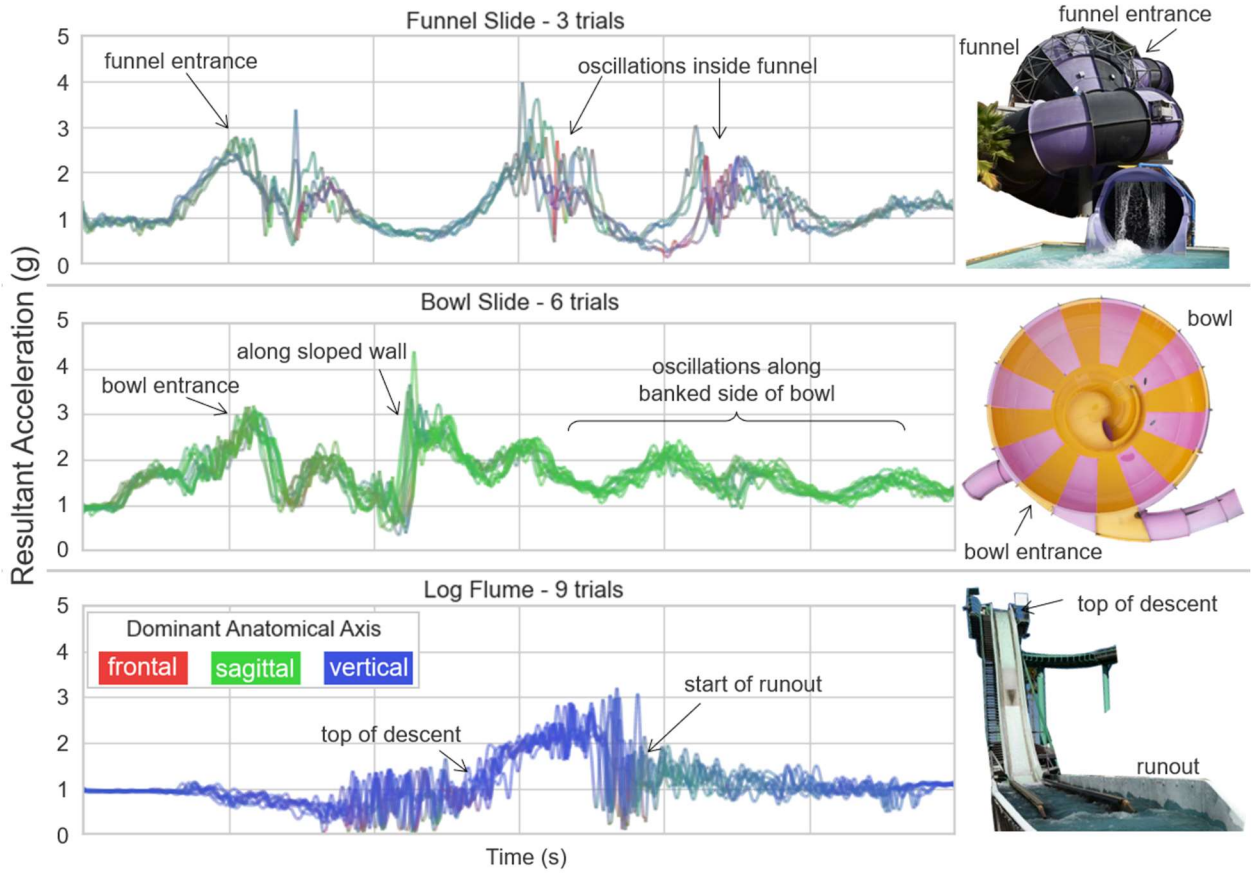
Results

Average peak resultant accelerations for the funnel slide, bowl slide, and log flume were 3.2 g, 3.3 g, and 2.9 g, respectively. Resultant accelerations during any ride did not exceed 4.4 g. Higher acceleration values were associated with features like travel into or along sloped bowl and funnel walls. With respect to rider anatomical axes, accelerations were predominately sagittal for the bowl slide, and vertical for the log flume.

Discussion

This study is one of the first to characterize rider biomechanics on water slides and rides, expanding on previously published data of water slide rider exit velocity [1]. The accelerations presented are comparable to those of activities of daily living like running and jumping. This suggests that rides provide "thrill" aspects through experiences like splashing or darkness, rather than excessive ride dynamics. Future work would include larger rider populations and other types of water rides.

Images (Optional)



References (Optional)

[1] Blitvich and McElroy, *Int J Inj Contr Saf Promot*, 2007

Session Category

Injury Biomechanics: N/A

P3-092

Plantar Pressure while Running in Advanced Footwear Technology: Implications for Navicular Stress Fracture Risk

Ms. Gayatheri Mahesh Hema Iyer[1], Dr. J.J. Hannigan[2]

[1]Oregon State University, Corvallis, OR, United States. [2]Oregon State University - Cascades, Bend, OR, United States

Introduction

Advanced Footwear Technology (AFT), characterized by a carbon fiber plate embedded within compliant midsole foam, has recently improved long-distance running performances. However, a case series [1] reported multiple navicular stress fractures (NSF) in runners using AFT, suggesting a potential link between AFT shoe design and NSF risk. Elevated plantar loading has been observed in athletes with NSFs [2]. However, in-shoe plantar pressure has not been directly compared between AFT and non-AFT footwear, and it remains unclear whether increasing foot–plate distance can reduce potentially harmful loading. Therefore, the purpose of this study was to compare plantar pressure across three conditions: a standard AFT shoe (AFT), a modified AFT shoe with an additional 3-mm insole (AFT+), and a non-AFT control shoe (CON). We hypothesized that medial midfoot pressure would be significantly higher in AFT compared to CON and AFT+.

Methods

After warming up, ten competitive runners completed 5-minute treadmill trials at their marathon pace in each footwear condition in randomized order. Plantar pressure was collected at 150 Hz using the XSENSOR in-shoe pressure system during the final minute of each run. Primary variables were peak and average whole-foot and regional (medial midfoot and 1st metatarsal) plantar pressure (Fig 1). Repeated-measures ANOVAs ($\alpha = .05$) tested for differences across conditions with follow-up Bonferroni-corrected pairwise comparisons.

Results

Medial midfoot peak pressure was significantly higher in the AFT condition (10.7±3.2 N/cm^2) compared to the AFT+ condition (9.5±2.9 N/cm^2), p=.032. Whole-foot peak pressure was significantly higher in the CON condition (37.9±5.1 N/cm^2) compared to the AFT+ condition (34.6±6.7 N/cm^2), p=.006. No other significant differences were identified (p>.05).

Discussion

Increasing foot-plate distance through additional insole cushioning effectively reduced medial midfoot plantar loading in AFT shoes, suggesting a modifiable design feature that may lower NSF-related loading. However, no differences were noted between AFT and CON footwear, suggesting that the NSF injuries in AFT may result from additional factors beyond elevated plantar pressure. Future work should incorporate kinetic and kinematic analyses at the foot to better understand navicular loading mechanisms.

Images (Optional)

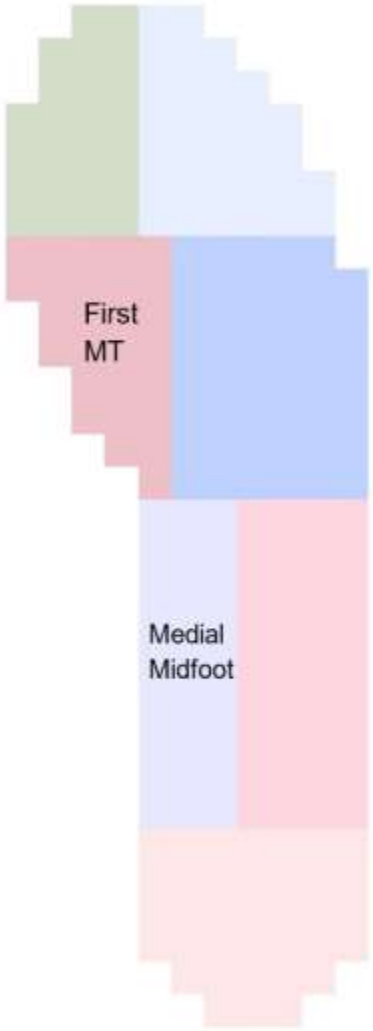


Fig 1. Plantar regions of interest

References (Optional)

[1] Tenforde et al., *Sports Med*, 2023.

[2] North & Foley, *J Foot Ank Res*, 2013.

Acknowledgements (Optional)

The authors would like to thank Kathy Reyes, Jesse May, Bethany Burr, and Colton Sachs for their assistance with data collection.

Session Category

Injury Biomechanics: N/A

P3-093

Can Wearable-Sensor Errors Confound the Mechanics Responsible for Concussion Injury?

Dr. Gunter Siegmund PhD[1,2], Dr. Benjamin Elkin PhD[3], Dr. Stephanie Bonin PhD[1]

[1]MEA Forensic Engineers & Scientists, Laguna Hills, CA, United States. [2]University of British Columbia, Vancouver, BC, Canada. [3]MEA Forensic Engineers & Scientists, Toronto, ON, Canada

Introduction

Field data sometimes show that concussion injury risk correlates best with peak linear head acceleration [1,2]. Animal and computer models, however, suggest that diffuse brain injuries like concussion are caused by angular kinematics [3,4]. Our goal was to evaluate if on-field measurement errors might explain these contradictory findings.

Methods

We used Monte-Carlo methods to assess how concussion-injury risk functions are affected by sensor errors in linear and angular kinematics. We simulated a cohort of 58 players who experienced head impacts with combinations of peak linear acceleration (a=20−140g) and peak angular acceleration (α=1.2−10krad/s^2) based on reconstructed data [1]. Angular velocity (ω) was integrated from the sinusoidal angular acceleration (random pulse duration 7.5−12.5ms). We then assumed a hypothetical injury risk function based solely on angular velocity (50% risk at 34.5rad/s; risk=1/[1+exp[-18.13+0.525ω]]) and used it to probabilistically determine if a concussion occurred. To address our goal, we introduced field errors into the linear (±10%, ±20%…±100%) and angular (±10%, ±20%…±200%) accelerations [5], and re-calculated injury risk functions using the field data with simulated errors. For each combination of linear- and angular acceleration errors, we ran 500 iterations of the cohort to generate 500 sets of injury risk functions and calculated the percentage of risk functions where concussion correlated better with linear acceleration than with angular velocity.

Results

Higher angular acceleration errors yielded a higher likelihood that concussion correlated better with linear acceleration than with angular velocity (Fig. 1). Concussion was likely to correlate better with peak linear head kinematics at angular acceleration errors above ±70%.

Discussion

Wearable sensors can yield large errors, particularly for angular kinematics [5]. Even if concussions are solely caused by angular head kinematics, large errors in the angular data can make it appear as though concussion injury correlates better with linear kinematics. These findings highlight the importance of understanding on-field sensor errors and the need for better angular sensors to avoid confounding the head kinematics responsible for concussion injuries.

Images (Optional)

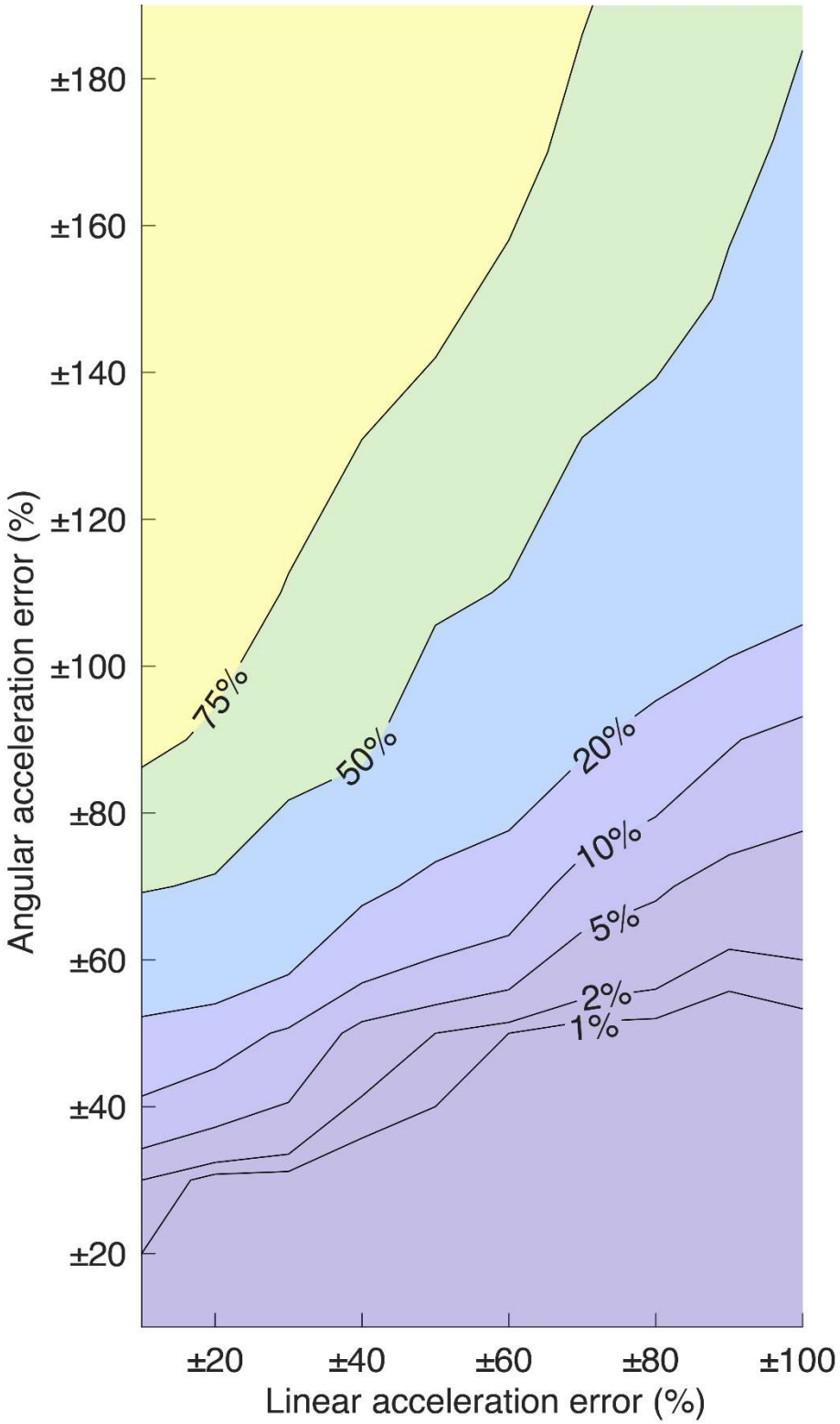


Figure 1. Proportion of iterations where concussion correlated more strongly with linear acceleration than with angular acceleration.

References (Optional)

[1] Pellman, Neurosurgery, 2003; [2] Towns, arXiv:2507.09098, 2025; [3] Ommaya, Brain, 1974; [4] Elkin, J Orthop Sports Phys Ther, 2016; [5] Siegmund, Ann Biomed Eng, 2016.

Session Category

Injury Biomechanics: N/A

P3-094

Head Injury Risk in Low-Height Falls: Comparative Analysis Using THUMS Human FE Model and Hybrid III Dummy Experiments

Dr. HAEYOUNG KIM Researcher[1], Dr. HIROKI TAKAHASHI Researcher[1], Mr. YASUMICHI HINO Researcher[1], Dr. KATSUTOSHI OHDO Researcher[1], Dr. HIDEKI OYAMA Researcher[1], Dr. MASAHIRO OKAMURA Researcher[2]

[1]National Institute of Occupational Safety and Health, Japan, Kiyose, Tokyo, Japan. [2]JSOL Co., Tokyo, Tokyo, Japan

Introduction

Falls from heights of 2 meters or less remain a leading cause of serious occupational injuries, particularly in the construction industry where head trauma is common even at low elevations. However, the injury mechanisms associated with low-height falls are not well understood, and the protective effectiveness of industrial helmets under such conditions has not been fully quantified. This study aims to clarify head injury risk by combining finite element (FE) simulations and full-scale experiments, evaluating how fall angle, initial head height, and helmet use influence resultant head acceleration and injury severity.

Methods

A 50th percentile adult male model from THUMS Version 4 was used to conduct FE simulations in LS-DYNA. Fall scenarios were modeled with four impact angles (10°, 20°, 30°, 40°) and head heights ranging from 41 to 107 cm. Helmet and non-helmet cases were included.
In parallel, fall experiments were performed using a Hybrid III 50th percentile pedestrian dummy equipped with tri-axial head accelerometers. A release mechanism ensured a consistent initiation of the fall. Experimental configurations replicated the numerical cases. Data collection included time histories of resultant head acceleration and calculation of HIC15.

Results

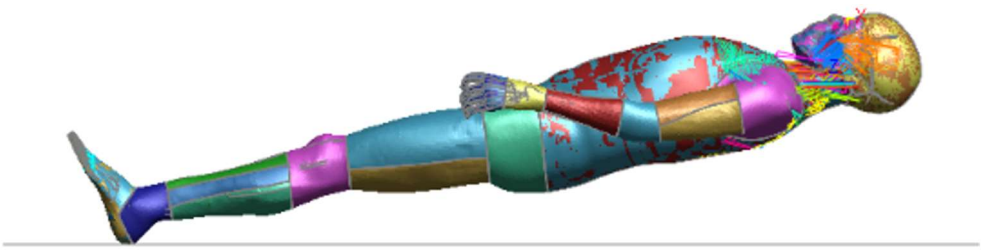
Both simulations and experiments demonstrated that head acceleration increased with fall height and impact angle. Experimental peak accelerations ranged from 117 G to over 700 G, and HIC15 frequently exceeded 3000 for head heights above 88 cm, indicating a high probability of AIS 6 injury. Analytical results showed similar trends. Helmet use reduced

peak acceleration by about one-third and lowered HIC15 from 5189 to 1288, demonstrating substantial protective effects.

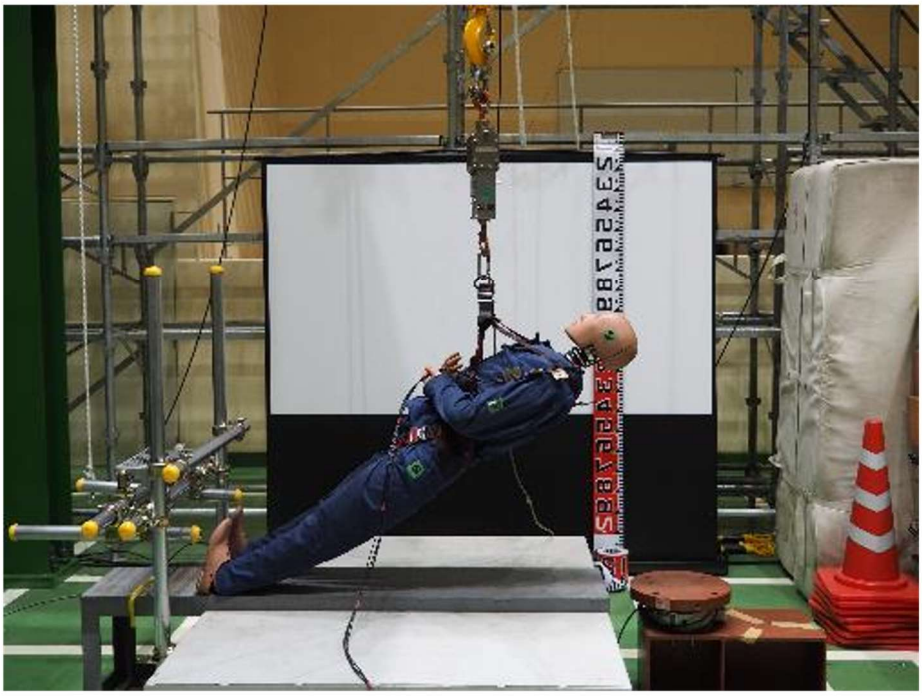
Discussion

The results confirm that severe head injuries may occur even from falls below 1 m. Differences between simulations and experiments largely reflect challenges in reproducing human defensive actions in both models. Helmet use consistently decreased acceleration magnitude and injury metrics, demonstrating its critical effectiveness for preventing head trauma in low-height falls.

Images (Optional)



(a) Analysis with human model, Thums



(b) Experiments with Hybrid III dummy

Figure 1. Example of a fall simulation

Session Category

Injury Biomechanics: N/A

P3-095

Design and Additive Manufacturing of Tunable Triply Periodic Minimal Surface (TPMS) Lattices to Enhance the Biomechanical Impact Protection of Hip Protectors

Mr. Haoming MO PhD Candidate, Prof. Yi-jian YANG Professor, Prof. Xu SONG Professor

The Chinese University of Hong Kong, Shatin, N.T., Hong Kong

Introduction

Hip fracture is a leading cause of injury-related hospitalization in older adults. Although hip protectors have been promoted to prevent fractures, existing models often underperform due to poor mechanical stability and low breathability, resulting in low adherence. Additive manufacturing (3D printing) has emerged as a transformative approach for mass customization and fabrication, enabling complex lattice structures with tailored mechanical properties for effective impact protection. Hence, we exploited this capability to (i) create tunable TPMS lattices with enhanced energy absorption and (ii) integrate them into lightweight, mass-customized hip protectors to improve comfort and long-term adherence.

Methods

P-type TPMS shell–lattice units were "trimmed" by introducing controlled holes to tune layer-by-layer crushing and stabilize stress fluctuations. A hyper-elastic Marlow model calibrated from tensile data was used in ABAQUS/Explicit; 4×4×4 unit-cell meshes with sensitivity checks captured non-periodic post-yield behavior. Pelvis geometries of 32 older adults were captured via 3D scanning and reconstructed for iso-parametric mapping of TPMS lattices onto patient-specific contours. Lattice hip protectors were printed using elasticity photopolymer 3D printing. Impact performance followed CSA Z325:20, while air permeability was tested per ISO 9237:1995 (100 Pa). A pilot trial evaluated adherence and comfort across three one-month rounds.

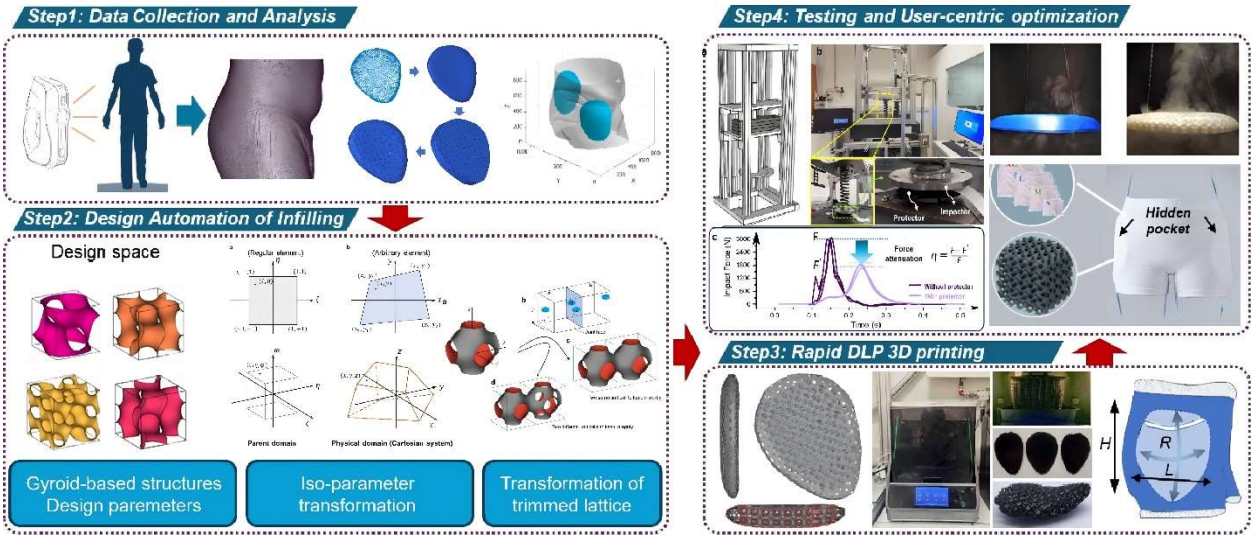
Results

Trimming systematically reduced stress fluctuation and mitigated buckling, leading to stable post-yield responses and tunable energy absorption through varying hole size and location. The 3D-printed hip-protector prototype achieved force attenuation of 40–43% with >96% retention after 150 impacts and a one-year follow-up. Air permeability reached 6501 $L/m^2/s$, supporting thermal comfort. Simulation stress–strain curves exhibited concordance with compression tests across trimming designs. Participants reported high adherence score and comfort score , indicating improved user compliance and consistent wearing behavior comparing to conventional protectors.

Discussion

Trim-based modification of TPMS lattice design offers a robust method to stabilize nonlinear mechanical responses while preserving geometry-induced mechanical property tunability and air permeability, addressing the longstanding trade-off between protection and wearing comfort. The integration of inverse design, iso-parametric lattice mapping, and polymer additive manufacturing enables scalable mass customization based on anatomical variation. Both finite element simulation and experimental evidence support the fact of performance gain in biomechanics.

Images (Optional)



Session Category

Injury Biomechanics: N/A

P3-096

Effect of a Rapid Transition From Concentric to Eccentric Contraction on Fiber Strain in the Rectus Femoris

Mr. Hayata Egawa B.S, Prof. Yoshimori Kiriyama Ph.D, Prof. Katsumasa Tanaka Ph.D

Kogakuin University, Shinjuku, ToKyo, Japan

Introduction

Rectus femoris injuries during change-of-direction tasks can occur even when the muscle–tendon unit (MTU) is not maximally lengthened. Before foot contact the muscle contracts concentrically to increase joint stiffness, and immediately after landing it is stretched and loaded eccentrically. Because concentric contraction generates relatively low force, this rapid transition may permit over-lengthening and muscle damage. How such abrupt changes in contraction mode affect fiber strain remains unclear; this study used finite-element (FE) analysis to examine how the pre-eccentric contraction pattern influences rectus femoris fiber strain.

Methods

An FE model of the rectus femoris and tendons was generated from MRI of one female. The proximal tendon was fixed and a prescribed displacement was applied to the distal tendon to reproduce MTU length changes. Muscle was modelled as a transversely isotropic hyperelastic material with passive and active components; the active part incorporated Hill-type force–length and force–velocity properties. Two loading histories were simulated: ConEcc, where MTU strain decreased from 0.05 to 0.00 at $-1.0\ s^{-1}$ and then increased to 0.10 at $1.0\ s^{-1}$; and PureEcc, where MTU strain increased from −0.05 to 0.10 at $1.0\ s^{-1}$. Muscle activation was fixed at 0.4. Dynamic Implicit FE analyses were performed and fiber-direction strain was evaluated.

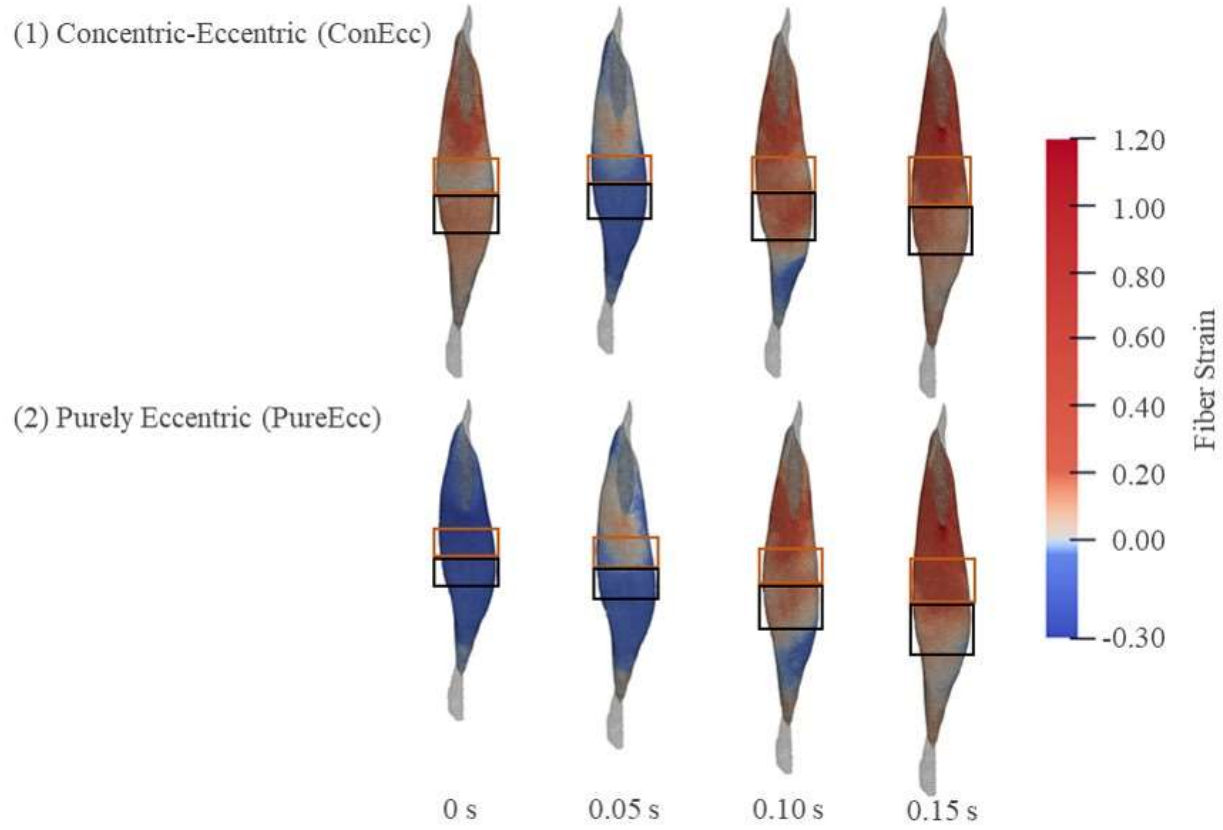
Results

At 0.10 and 0.15 s both conditions showed strain concentrations near the proximal myotendinous junction. The orange and black boxes indicate regions near the largest cross-sectional area along the direction of stretch. At 0.05 s fiber strain in the orange box was smaller in ConEcc than in PureEcc, whereas at 0.10 and 0.15 s strain in the black box was more broadly distributed in ConEcc.

Discussion

Regardless of condition, eccentric loading concentrated fiber strain near the myotendinous junctions, consistent with discontinuity between muscle and tendon and typical injury locations. In ConEcc, mid-belly shortening between 0 and 0.05 s, when fibers were near optimal length and generated little force, appears to have reduced resistance to subsequent stretch and broadened tensile strain after 0.10 s. Thus, a rapid transition from concentric to eccentric contraction may spread tensile fiber strain widely at the onset of eccentric loading.

Images (Optional)



Session Category

Injury Biomechanics: N/A

P3-097

Multi-Dimensional Joint Angle Analysis for Pitching Fatigue Detection: A Skeleton Detection and Deep Learning Approach

Ms. Hung-Chun Huang[1], Mr. Jing-Min Liang[1], Mr. Hsuan-Wei Chu[1], Mr. Sheng-Jie Kao[2], Prof. Tsì-Uí Ík[2], Prof. Wel-Lan Wu[1]

[1]Kaohsiung Medical University, Kaohsiung, Kaohsiung, Taiwan. [2]National Yang Ming Chiao Tung University, Hsinchu, Hsinchu, Taiwan

Introduction

Baseball pitching practice is characterized by high repetition and high physical loads, potentially leading to fatigue accumulation and musculoskeletal injuries. AI-based deep learning pose estimation methods are increasingly mature and can be used as auxiliary tools for sports training through real-time motion recognition. This study aimed to analyze kinematic features under continuous pitching and develop a fatigue detection model using Long Short-Term Memory (LSTM) networks.

Methods

Seven college baseball players with recent competition records in University Baseball League were recruited into this study. The camera lens was positioned on the throwing-arm side, at a height of 125 cm above the ground and a linear distance of 450 cm from the pitcher's plate. The simulated game protocol: 20 pitches/inning, 6-min rest between innings until stopping criteria were met (velocity drops ≥8 km/hr from max for 3 consecutive pitches or rating of perceived exertion (RPE) ≥18). The fatigue onset was labeled at the inflection point of the smoothed velocity trajectory (moving average, window=5) followed by a sustained decrease below the average speed. A total of 428 pitches were collected, consisting of 326 non-fatigue and 102 fatigue trials. Python (3.12.7) and MediaPip were employed for 33 skeleton keypoints with hip-centered coordinates. Six pose parameters were calculated (elbow flexion, shoulder horizontal abduction, shoulder abduction, shoulder external rotation, pelvic rotation, trunk rotation) as the input data. The LSTM architecture featured two hidden layers (64/32 units) with dropout. To address class imbalance, Focal Loss and SMOTE were applied. The dataset was divided using an 80/20 stratified train-test split. Training incorporated early stopping to prevent overfitting, with model validity assessed via the F1-score.

Results

Experimental results demonstrated that the model effectively distinguishes fatigue states with an overall Accuracy of 71.3%. For injury prevention, the model had a high recall of 83.6% for the fatigue class, ensuring that the majority of at-risk instances were identified.

Discussion

In conclusion, this study provides a viable deep learning approach for monitoring pitching fatigue. The high recall rate suggests its potential as a robust screening tool to minimize injury risks, offering valuable insights for players and coaches to manage training loads.

Acknowledgements (Optional)

The study was supported by a grant from the National Science and Technology Council (NSTC) (#NSTC 114-2410-H-037 -020 -MY2)

Session Category

Injury Biomechanics: N/A

P3-098

Punch-Type-Dependent Effect of Neck Muscle Strength on Brain Injury Risk in Boxing

MSc Carola Birk[1], MSc Talha Üzümcü[1], Prof. Wolfgang Potthast[1], Dr. Igor Komnik[1,2]

[1]Insitute of Biomechanics and Orthopaedics, German Sport University Cologne, Cologne, North Rhine-Westphalia, Germany. [2]Institute of Movement and Sport Gerontology, German Sport University Cologne, Cologne, North Rhine-Westphalia, Germany

Introduction

Repetitive head impacts in boxing are linked to acute concussion and long-term neurodegeneration, yet the mechanical determinants of brain loading remain poorly understood. Neck muscle strength is a proposed modifiable factor to mitigate head motion, but experimental evidence is inconsistent and may depend on impact direction. The aim of this study was to quantify how the protective effect of neck muscle strength on brain injury criterion (BRIC) depends on punch type during simulated boxing impacts.

Methods

A musculoskeletal head–neck model was used in OpenSim for forward dynamic simulations of boxing impacts. Force–time histories for four punch types (cross chin, cross nose, hook chin, hook temple) were experimentally derived from impacts to a crash-test dummy head (THOR-50M) and scaled to peak forces between 500 and 3000N (15 steps). Neck muscle strength was scaled from 0.5 to 2.0 times average male capacity (15 steps). Head kinematics were exported to compute BRIC. A General Linear Model (GLM) was fitted to BRIC with punch type, punch force and muscle strength as predictors, along with two-way interaction terms (punch type×strength, punch type×force and punch type×force^2).

Results

Across 900 simulations, the GLM explained 99.9% of variance in BRIC (R^2 = 0.999). At average strength and force, cross-chin produced the highest BRIC (1.52); compared with cross-chin, cross-nose, hook-chin and hook-temple had lower BRIC with β = –0.391, –0.433 and –0.656, respectively (all $p < 0.001$). Neck strength reduced BRIC most in cross-chin (β = –0.21) moderately in cross-nose (β = –0.14), and minimally in hook impacts (β = –0.02 and –0.03).

Discussion

This simulation shows that the protective effect of neck muscle strength is strongly punch-type dependent. Cross punches to the chin produced the highest BRIC values, but also the largest strength-related reductions (12.3% with doubled neck strength; Fig.1). In contrast, hook punches generated lower BRIC overall and gained little additional protection (hook-chin: 1.8% and hook-template: 3.7%). This might be since cross punches load the head primarily in the sagittal plane, where strengthened flexors can effectively oppose motion, while hook punches involve complex frontal/transverse plane rotations that are less amenable to simple co-contraction.

Images (Optional)

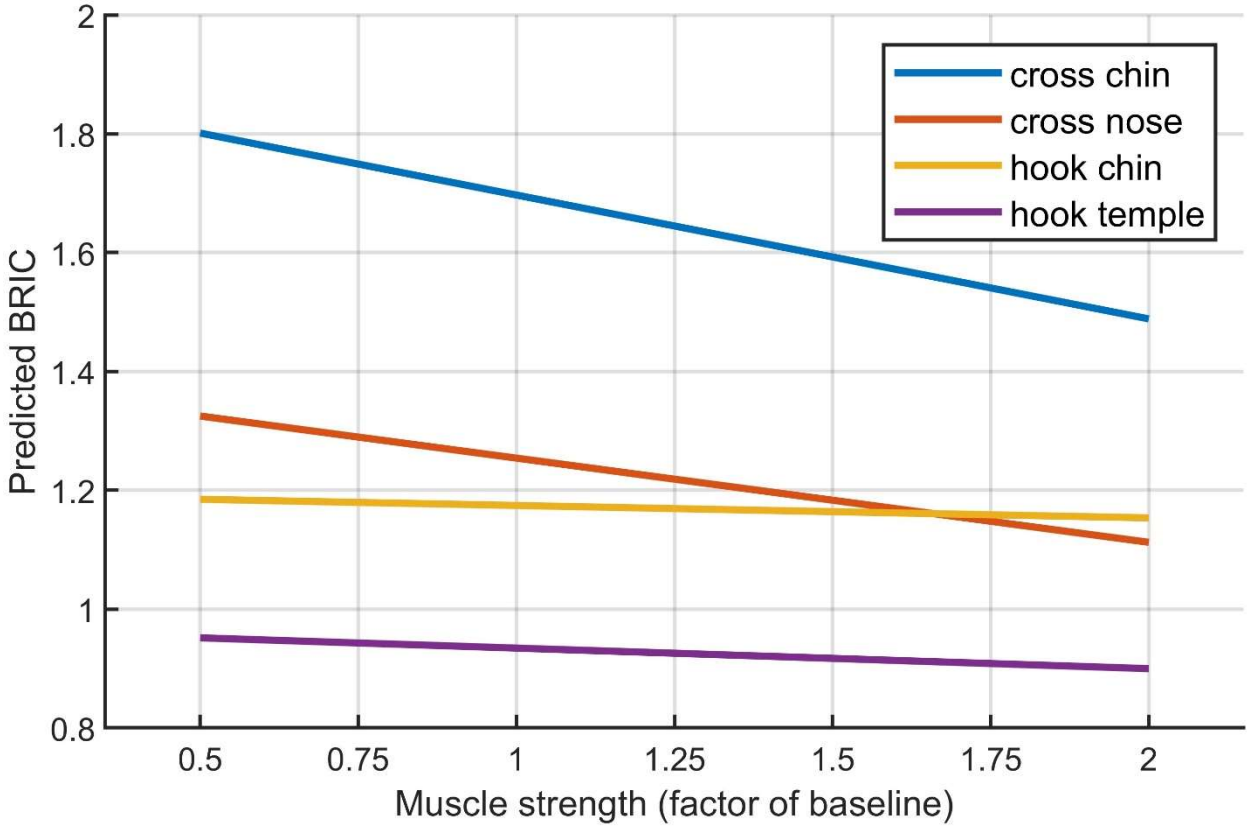


Figure 1: Predicted BRIC across neck muscle strength (0.5–2.0× baseline) at 2000 N.

Session Category

Injury Biomechanics: N/A

P3-099

ACL Injury Resilience Score Differs Between Preadolescent and Adolescent Female Athletes

Dr. Jack Williams PhD, Dr. Julie Kolesar PhD, Dr. Kirsten Seagers PhD, Dr. Krithika Swaminathan PhD, Dr. Sam Hamner PhD, Ms. Julie Muccini MS, OTR/L, Dr. Jennifer Hicks PhD, Dr. Scott Delp PhD

Stanford University, Stanford, CA, United States

Introduction

ACL injuries are common among young athletes and disproportionately affect females. Biomechanical risk factors are well-documented and considered modifiable targets for injury prevention. We have developed the ACL Injury Resilience (AIR) Score to compare biomechanics during athletic maneuvers to population data adjusted for known injury thresholds, represented as z-scores. Subscores are calculated for the trunk, hip, knee, and foot, and then averaged to compute a total score. While prior work suggests preadolescent and adolescent biomechanics differ[1] and that both may display more biomechanical risk factors for ACL injury than adults[2], it is unknown if the AIR Score can identify differences across pubertal stages. Thus, we aimed to compare AIR Scores between preadolescents and adolescents, hypothesizing that we would see differences between groups.

Methods

This secondary analysis used baseline data from a cohort of female soccer players ($N_{Preadolescent}$ = 43; $N_{Adolescent}$ = 37) performing single-leg drop jumps and run-cuts[3]. The AIR Score and subscores were calculated for each participant using metrics from both activities. We used a two-tailed t-test to compare the total AIR Score between groups, and a MANOVA to assess differences among subscores. Post-hoc subscore analyses included two-tailed t-tests with Bonferroni corrections and effect size (ES) characterization using Cohen's d.

Results

On average, adolescent athletes displayed higher total AIR Scores compared to preadolescents ($p < 0.001$; ES: 0.62); however, only the foot subscore, which incorporates ankle flexion at initial contact and peak vertical ground reaction force, was significantly different ($p_{MANOVA} < 0.001$; $p_{Foot} < 0.001$; ES_{Foot}: 1.30; Figure 1).

Discussion

The higher average AIR Score observed in adolescents supports our hypothesis, demonstrating sensitivity to differences between groups. While this average provides valuable insight into sample-wide trends, most participants will not sustain an ACL injury. This is reflected in our data, where all metrics were positive, indicating that, on average, both groups were more aligned with uninjured populations. Future work focused on those who deviate most from the uninjured population may provide a more nuanced and clinically valuable understanding of injury risk in these age-groups.

Images (Optional)

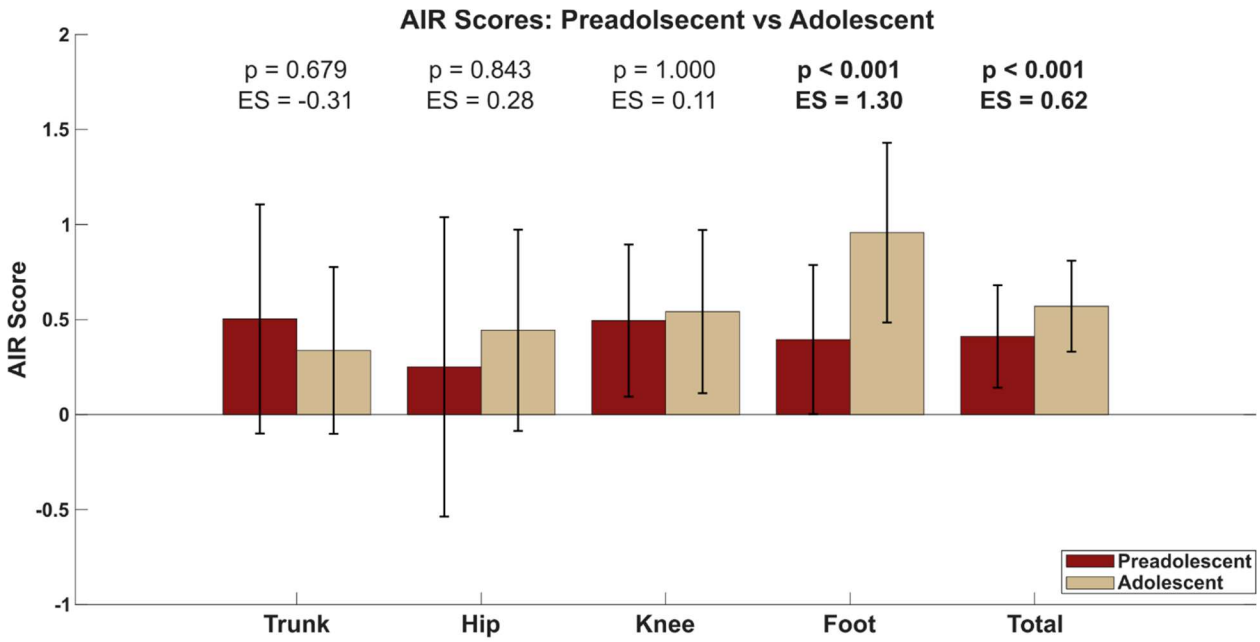


Figure 1. Average ACL Injury Resilience (AIR) Scores in preadolescent (red) and adolescent (tan) athletes.

References (Optional)

[1] Ramachandran AK, (2024) *Sports Medicine*. [2] Swartz EE (2005), *J. Athl. Train*. [3] Kolesar JA (2018), *AJSM*.

Session Category

Injury Biomechanics: N/A

P3-100

Predicting Cumulative Head Acceleration Exposure Using Video-Derived Metrics in Professional Rugby League

Dr James Tooby[1], Dr Cameron Owen[1], Dr Thomas Sawczuk[1], Dr Gregory Roe[1], Dr Dane Vishnubala[2], Professor Kevin Till[1], Professor Ben Jones[1]

[1]Leeds Beckett University, Leeds, West Yorkshire, United Kingdom. [2]University of Leeds, Leeds, West Yorkshire, United Kingdom

Introduction

Cumulative exposure to head acceleration events (HAEs) in sport is linked to chronic neurological conditions, including chronic traumatic encephalopathy and neurodegenerative diseases. Accurate quantification of cumulative HAE exposure is essential to investigate these risks. Instrumented mouthguards (iMGs) provide objective measurements but often produce incomplete datasets due to player non-compliance or device failures. This study developed a predictive model using video-derived metrics to estimate total HAE exposure among male professional rugby league players when iMG data are missing.

Methods

A prospective study collected data across the Men's Super League 2024–2025 seasons from 347 iMG-wearing players, recording 49.1% (n=4,645) of their player-matches. HAEs were classified into low, moderate, and high magnitude bands using combined peak linear and angular acceleration thresholds with an elliptical boundary: 10*g*/1000 rad/s^2, 25*g*/2000 rad/s^2, and 40*g*/3000 rad/s^2, respectively. A generalised linear mixed model (GLMM) predicted HAE counts using a range of predictors derived from commercial video analysis data, such as minutes played and number of tackles and carries made. Predictive performance was evaluated via mean absolute error (MAE) and root mean squared error (RMSE). Cumulative HAE exposure over two seasons was estimated for players with at least five iMG-recorded matches in each season (n=104).

Results

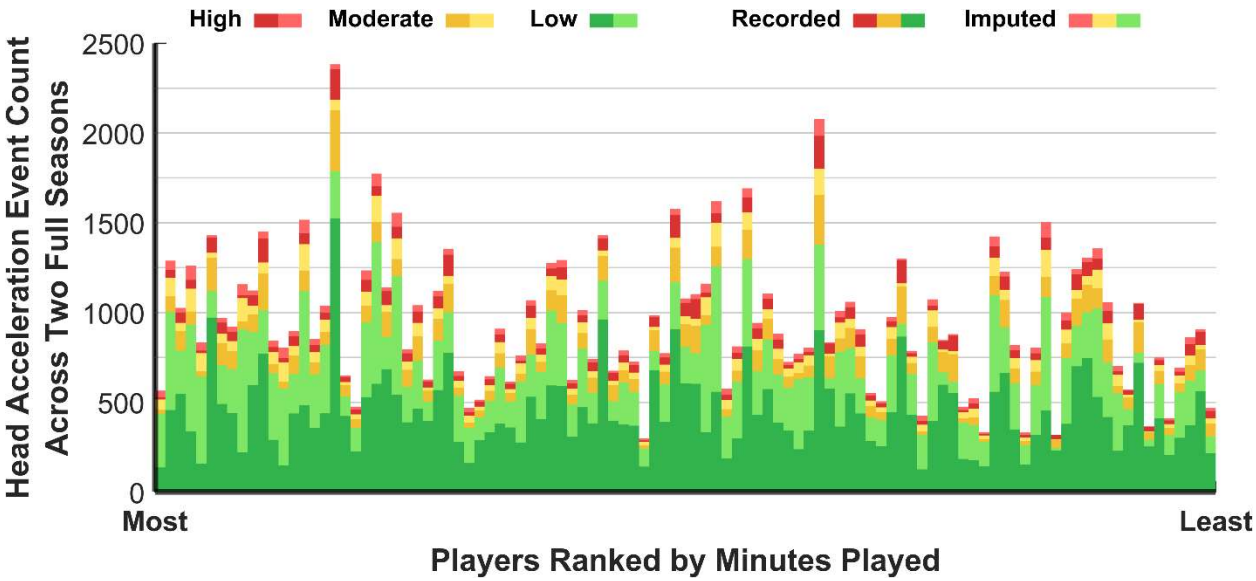
The MAE (normalised to HAE count) of prediction was 1.9 (13.2%), 1.3 (39.0%), and 0.9 (53.9%) for low-, moderate-, and high-magnitude HAEs, while RMSE (normalised to HAE count) was 2.4 (16.8%), 1.6 (49.5%), and 1.3 (74.3%). The median (interquartile range [IQR]) estimated HAE count across two seasons was 667 (551-904), 142 (96-188), and 73 (50-99), for low-, moderate- and high-magnitude HAEs. Exposures were right-skewed with outliers

(Figure 1), including 18 players exceeding 1,000 low-magnitude HAEs and one with 250 high-magnitude HAEs.

Discussion

These findings demonstrate the feasibility of using video-derived variables to impute missing iMG HAE data, improving estimates of cumulative head impact exposure. Such comprehensive exposure assessment is critical for understanding potential neurological risks and monitoring pre- and post-season variations linked to HAE load. Notably, exposure variability suggests subsets of players may face elevated risk from high cumulative HAEs, warranting targeted surveillance and intervention. Future model refinement may improve accuracy.

Images (Optional)



Session Category

Injury Biomechanics: N/A

P3-101

Adaptive Flyband® ExoBoot Improves Proximal Joint Mechanics Without Restricting Ankle Function

Miss Gabrielle Moser[1,2], Miss Jania Williams[1,2], Dr. Corbin Rasmussen[1,3], Dr. Farah Fallahtafti[1,2], Dr. Arash Mohammadzadeh Gonabadi[1,4], Mr. Keith Eriks[5], Mr. Thomas Cotton[5], Mr. Mark Roser[5], Dr. Sara Myers[1,2]

[1]Dept. of Biomechanics, University of Nebraska-Omaha, Omaha, Nebraska, United States. [2]Research Service, Omaha Veterans' Affairs Medical Center, Omaha, NE, United States. [3]Dept. of Exercise Science & Pre-Health Professions, Creighton University, Omaha, Nebraska, United States. [4]Institute for Rehabilitation, Madonna Rehabilitation Hospitals, Omaha, Nebraska, United States. [5]Results Group LLC dba Motive Labs, Glastonbury, Connecticut, United States

Introduction

Musculoskeletal overuse injuries are the leading cause of lost duty time in U.S. service members, with lateral ankle sprains being the most common. Conventional military boots and braces stabilize the ankle, but they limit natural ankle motion and increase compensatory knee and hip loads. The Flyband® ExoBoot, with an exoskeleton and interchangeable carbon-fiber cartridges, aims to preserve ankle mobility while enhancing lateral stability. This study evaluated knee and hip joint mechanics in Flyband compared to conventional configurations.

Methods

Healthy adults (19–45 yrs) completed walking trials under six randomized conditions: conventional boot/bracing conditions including low, medium, high brace stiffness, and Flyband configurations with matching low, medium, and high cartridge stiffness in the lateral sides. Three-dimensional motion capture (17 cameras, 100 Hz) and force plates (1000 Hz) recorded knee and hip joint angle, moments, and powers across the gait cycle. Discrete peak variables were analyzed using repeated-measures ANOVA ($p < 0.05$). Statistical Parametric Mapping (SPM) identified time-varying differences across the gait cycle (Sidak-Holm corrected).

Results

Flyband conditions produced meaningful improvements in knee and hip kinetics compared with conventional boots. Conventional configurations generated higher knee flexion torques in early and late stance (Figure 1; $p < 0.05$), while Flyband use increased early- and mid-stance knee power absorption and reduced frontal-plane knee abduction torque

during initial loading ($p < 0.05$). At the hip, Flyband conditions increased energy absorption during early stance and reduced swing-phase power demands.

Discussion

The proximal kinetic changes observed with the Flyband configuration suggest a more efficient and coordinated transfer of frontal-plane loads through the lower limb, reducing the compensatory torque patterns commonly associated with stiff military boot designs. These changes, along with the redistributed energy absorption during stance, indicate that the Flyband system may create a mechanical environment that better supports the ankle's ability to manage inversion–eversion demands. Importantly, this improved proximal control may help stabilize the ankle without restricting its natural motion. Taken together, these findings highlight the potential for optimizing knee and hip mechanics to indirectly reduce distal inversion loading, offering a promising strategy for mitigating lateral ankle sprain risk in operational settings.

Images (Optional)

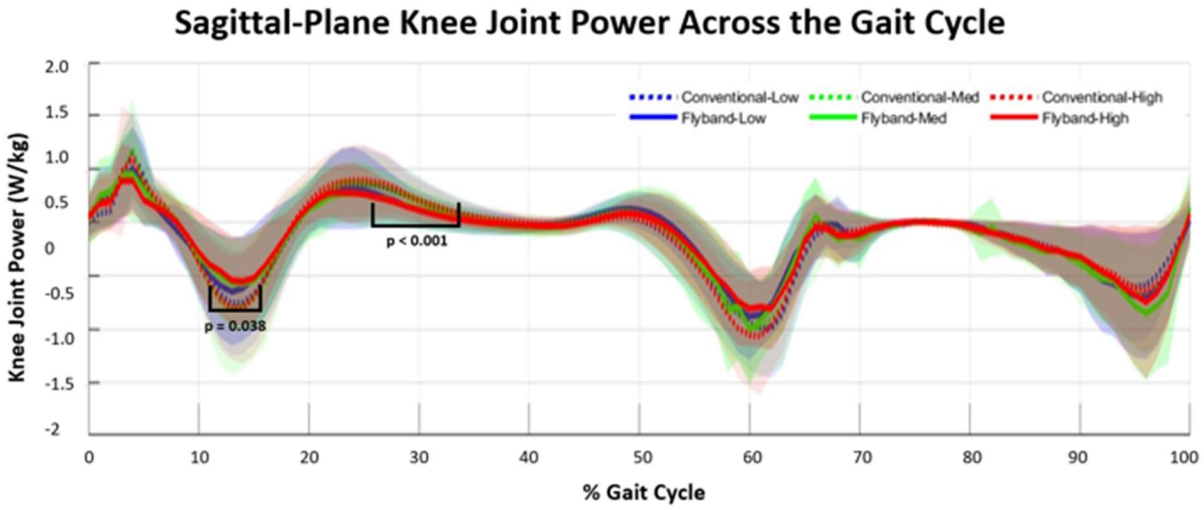


Figure 1. A significant main effect of boot condition on knee joint power was observed at 10–15% ($p = 0.038$) and 25–35% ($p < 0.001$) of the gait cycle.

Session Category

Injury Biomechanics: N/A

P3-102

Head Impact Exposure Device Validation Through Variation in System Coupling

Mr. Blake Robertson MS, Dr. Mitchell Abrams PhD, Dr. Jason Luck PhD

Duke University, Durham, North Carolina, United States

Mr. Blake Robertson

Introduction

Traumatic brain injury research focusing on characterizing head impact exposure (HIE) in sports has spawned a variety of measurement systems. Historically, these systems have varied attachment methods resulting in wide variations in coupling. With coupling being a core consideration in how a system accurately measures head kinematics, it is important to assess the effects of coupling variations on data quality, especially when this data is used to progress scientific understanding of head injury.

Methods

A modified anthropomorphic test device (ATD) head incorporating an "ear" attachment, that accommodates individualized ear canal inserts was used to assess the effects of variation in sensor coupling. A wearable HIE sensor (Duke DASHR) was placed in the ATD "ear" and dropped at three heights (10, 30, 60 cm), yielding impacts ranging from ~25g to ~110g . A Riddell Speed helmet was placed on this modified Hybrid III 50^{th} male headform. Two conditions were tested (coupled, "less" coupled) and drops were conducted at the vertex of the helmeted ATD, with three replicates of each condition. A six-degree-of-freedom reference block (Endevco 7264C-2000; DTS ARS PRO-8K) was placed at the ATD center of mass (CoM). Data was sampled at 100kHz for 1300 ms (650 ms of pre-trigger). Raw signals were filtered with an eighth-order Butterworth low-pass filter with a 300Hz cutoff frequency. DASHR data was transformed from the location of the ear to the headform CoM. Peak resultant linear accelerations between the DASHR and reference were compared for the two conditions.

Results

Initial findings indicate good agreement between the DASHR and reference in impacts under both conditions (Figure 1a/1b). Regression slopes for linear acceleration were similar between the coupled (m=0.93; R^2=0.998) and "less" coupled condition, (m=0.92;

R^2=0.996). On-going testing will evaluate the two conditions in frontal, facemask, oblique, parietal and occipital impacts.

Discussion

These findings demonstrate proof-of-concept for a novel wearable testing platform and methodology, incorporating subject-specific anatomic features and variable degrees of coupling. This enables testing and validation of wearables for use in exposure conditions, and provides the potential to evaluate best and worst case coupling states for instrumentation prior to field deployment, better contextualizing system error and field collection results.

Images (Optional)

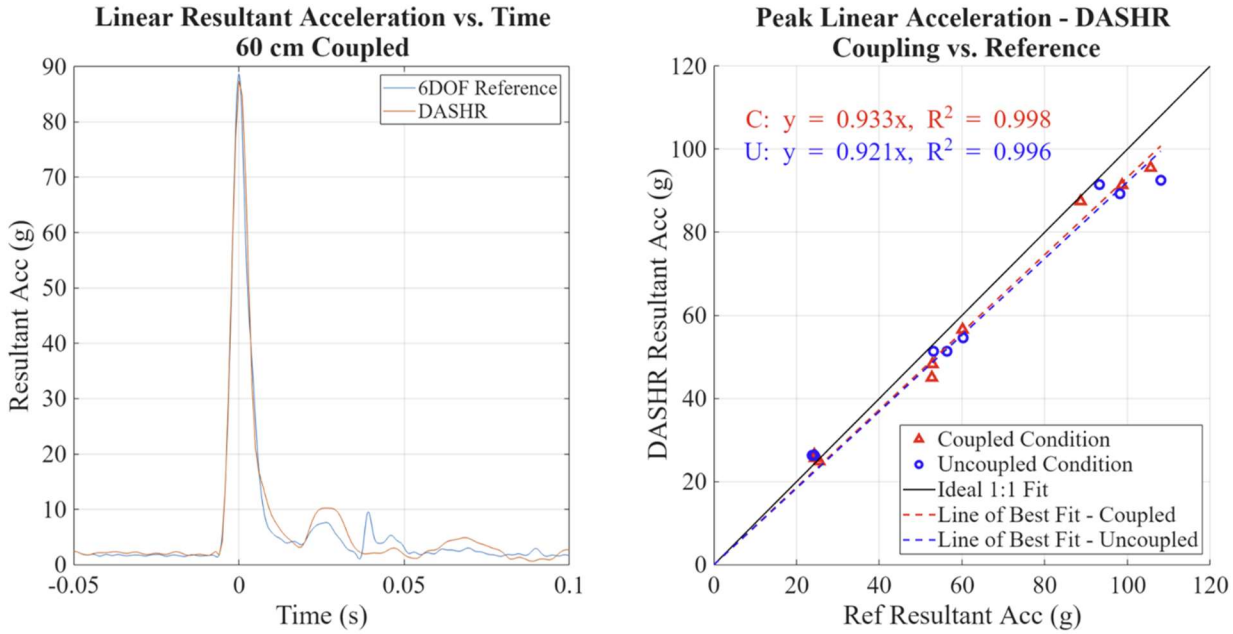


Figure 1: (a) DASHR and 6DOF resultant linear acceleration from a 60 cm helmeted vertex impact and (b) DASHR accelerations in both coupled conditions are similar to 6DOF reference

Acknowledgements (Optional)

This work was made possible through support from the Duke University Department of Biomedical Engineering with the MS Research Fellowship Award.

Session Category

Injury Biomechanics: N/A

P3-103

A Regularized Framework for Accelerometer-Only Determination of Rigid-Body Motion, With Applications in Mild Traumatic Brain Injury

Ms Jeetika Patangia, Dr Haneesh Kesari

Brown University, Providence, Rhode Island, United States

Introduction

Rapid accelerations and decelerations can cause mild Traumatic Brain Injury (mTBI). Continued exposure to mTBIs can lead to the onset of neurodegenerative diseases, such as Chronic Traumatic Encephalopathy (CTE). Because mTBIs often lack clear and immediate symptoms, quantities related to head kinematics, such as those used in the Head Injury Criterion (HIC) and the Brain Injury Criterion (BrIC), are commonly used as measures of the risk of injury (RoI) during falls and blunt impacts. The availability of comprehensive and high-quality kinematic data enables the development and application of improved RoI measures.

Methods

Recent work has introduced algorithms that provide comprehensive information about the head's kinematics from four surface-mounted tri-axial accelerometers. These algorithms are referred to as the Accelerometer-Only (AO) algorithm [1, 2]. In these algorithms the head's motion is approximated as that of a rigid body. Among other quantities they yield an estimate the head's angular acceleration. This is quite a valuable quantify since it is significantly involved in creating brain strains, and strain rates and hence mTBI; and the only other way of obtaining it is through the numerical differentiation of angular velocity, which that method is known to greatly amplify the experimental noise.

Results

However, the AO algorithms are constrained by the fact that the sensors cannot be placed arbitrarily. When the four sensors get close to a planar configuration, a matrix involved in its application becomes ill-conditioned. In the present work, we address this limitation by using Tikhonov regularization to invert the ill-conditioned matrices. We show that using Tikhonov regularization it is now possible to apply the AO algorithm to cases on which it previously failed. We demonstrate this using both synthetic and experimental data.

Discussion

For head-worn applications, sensors are commonly positioned along accessible regions like the forehead, where stable contact can be ensured. This inevitably creates a nearly coplanar layout, making the regularized AO approach especially useful for preserving reconstruction accuracy.

References (Optional)

[1] Rahaman, M. M. et al., *Journal of the Mechanics and Physics of Solids,* 2020

[2] Wan, Y. et al., *Computer Methods in Applied Mechanics and Engineering,* 2022.

Session Category

Injury Biomechanics: N/A

P3-104

Relationships Between Applied Force and Selected Anthropometric Measures on Hand-Arm Vibration Transmissibility During Hand-Held Power Tool Use

Mr. Jeffrey Lim B.Eng., Dr. Karen Gordon Ph.D., P.Eng., Dr. Michele Oliver Ph.D., P.Eng.

University of Guelph, Guelph, Ontario, Canada

Introduction

Hand-arm vibration (HAV) syndrome can occur from the use of handheld power tools. ISO 5349-1 provides guidance on hand-arm vibration exposure limits; however, anthropometric and force application factors are not incorporated into the standard. The purpose of this research was to determine if selected anthropometric and force factors are correlated to unweighted and ISO 5349-1 weighted HAV transmissibility.

Methods

7 males (22.6±2.5 yrs.; 176.0±9.4 cm.; 77.2±12.3 kg.) and 5 females (22.4±1.1 yrs.; 162.4±7.4 cm.; 60.8±4.7 kg.) took part in the study. Refer to Table 1 for additional anthropometric measures used. Using 2 triaxial ICP accelerometers, one attached to the tool and one to the wrist as per ISO 5349-2, data was collected while participants completed 2 tasks using a drill (drilling a hole or inserting a screw) and 2 tasks using a sander (sanding using 60 or 220 grit sandpaper). Each task took approximately 5 seconds and 3 trials of each task were completed in random order. Unweighted and weighted (as per ISO 5349-1) transmissibility was calculated for each task and trial using a vector sum of the tool and the wrist accelerations. A force plate placed below the work surface collected triaxial force data and participants stood on a variable height platform, which was adjusted such that their elbow angles were approximately 90º. Correlations between weighted and unweighted transmissibility, applied force (X,Y,Z, vector sum), and anthropometric measures were quantified using Spearman's Rank correlation coefficients. All statistics were performed using IBM SPSS ($p \leq 0.05$).

Results

Significant correlations ($p<0.05$) are presented in Table 1.

Discussion

Unweighted transmissibility showed increased correlation with higher significance than weighted transmissibility. Unweighted correlations showed drilling a hole correlated positively with vector sum force and negatively with height. Both sanding tasks correlated positively for the vector sum and Z-axis applied force and negatively for height, hand length, and arm length. The reduced correlation for the weighted transmissibility may be due to the non-linear weighting from ISO 5349-1's effect on the monotonic Spearman test. This research suggests that ISO 5349-1 should consider applied force and anthropometric variables due to their correlations with transmissibility.

Images (Optional)

Table 1: **Spearman's Rank Correlation for ISO-5349 weighted and unweighted transmissibility.** Results from Spearman Rank Correlation tests correlating weighted and unweighted transmissibility in each task using anthropometric and force factors. Variables were included if $p<0.05$ and $|\rho|\geq 0.4$.

	Task	*Variable*	*Spearman Rank Correlation (ρ)*	*p-value*
ISO 5349-1 Weighted Transmissibility	Sander (60 grit)	Y-Axis Force	0.425	0.022
		Sex	0.522	0.004
		Height	-0.544	0.002
		Grip Strength	-0.503	0.005
		Hand Length	-0.491	0.007
		Arm Length	-0.515	0.004
	Sander (220 grit)	Z-Axis Force	0.402	0.034
Unweighted Transmissibility	Drilling Hole	Vector Sum Force	0.417	0.024
		Y-Axis Force	0.405	0.029
		Height	-0.410	0.027
	Inserting Screw	Y-Axis Force	0.370	0.048
	Sander (60 grit)	Mean Force	0.510	0.005
		Y-Axis Force	0.403	0.030
		Z-Axis Force	0.486	0.007
		Sex	0.622	<0.001
		Height	-0.546	0.002
		Grip Strength	-0.521	0.004
		Hand Length	-0.689	<0.001
		Arm Length	-0.549	0.002
	Sander (220 grit)	Vector Sum Force	0.72	<0.001
		Z-Axis Force	0.673	<0.001
		Height	-0.445	0.015
		Hand Length	0.400	0.032
		Arm Length	-0.425	0.022

References (Optional)

Acknowledgements (Optional)

Session Category

Injury Biomechanics: N/A

P3-105

Modeling How the Neck Constrains Head Motion in Contact Sport Impacts: Sex and Directional Differences

Miss Jessica Toone, Mr. Zaryan Masood, Dr. Lyndia Wu PhD

University of British Columbia, Vancouver, British Columbia, Canada

Introduction

Contact sports athletes experience hundreds of head impacts per season [1]. During these impacts, linear and angular kinematics are coupled through the head-neck musculoskeletal system, which can be modeled as an inverted pendulum [2]. The pendulum's effective length, represented by the distance between the head's center of gravity (CoG) and a pivot point along the spine, may reflect neck and torso engagement during impacts. This study examined the effects of plane and sex on pendulum length during impacts.

Methods

Head impact kinematics were collected using Prevent Biometrics instrumented mouthguards (iMGs) for women's rugby and men's hockey. Only video-verified direct head impacts were included. Raw iMG data was processed using a standardized pipeline and transformed to the head's CoG. Pendulum length was calculated as the ratio between linear and angular accelerations in the sagittal and coronal planes. Values were normalized by athlete height. Only impacts consistent with the inverted pendulum assumption (with positive lengths) were included. A linear mixed effect model tested the effects of plane and sex on mean pendulum length, with player ID as a random effect.

Results

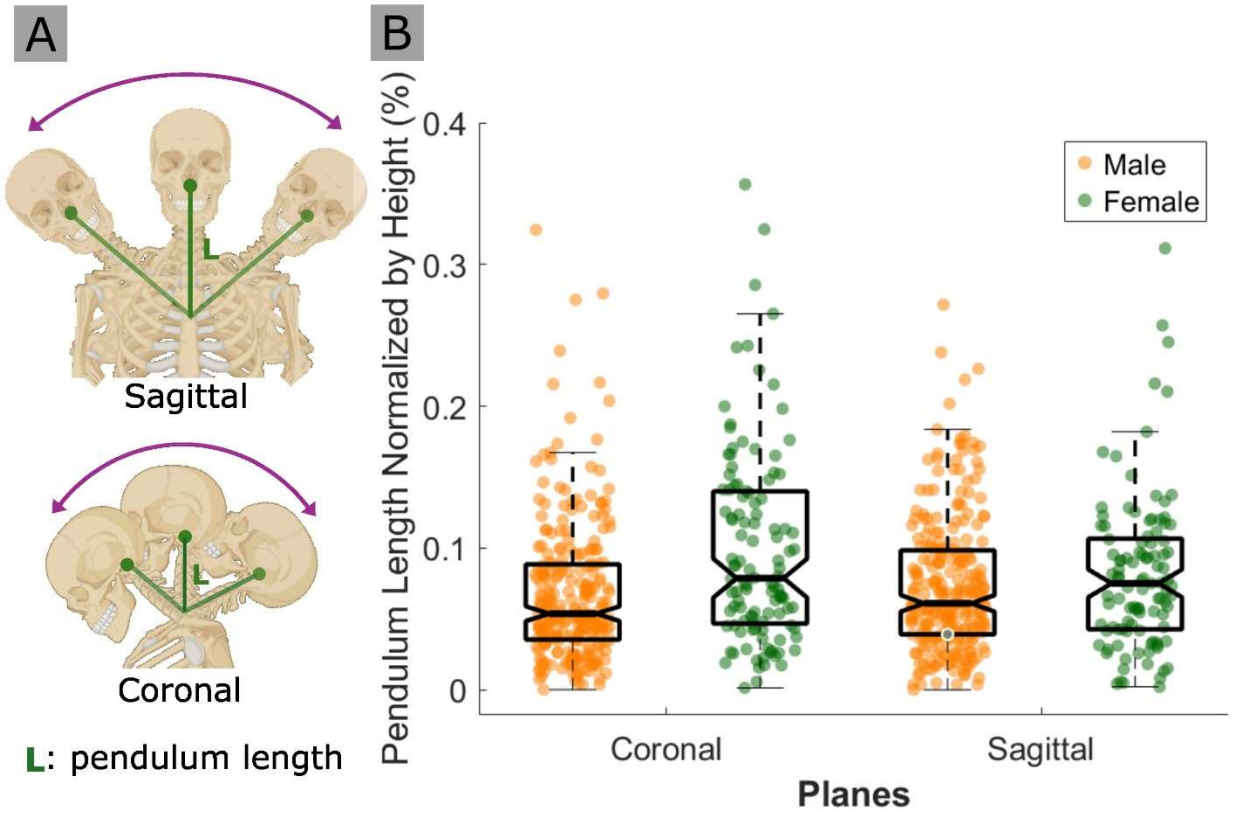
Of 608 men's hockey and 411 women's rugby impacts, 291 and 162, respectively, had positive pendulum lengths in either plane. Mean lengths were 13.7 cm in the sagittal plane and 14.0 cm in the coronal plane. Males exhibited shorter pendulum lengths than females. Sagittal lengths were on average 1.7 cm lower than coronal values. A significant plane-by-sex interaction indicated plane differences varied by sex.

Discussion

This study provided insights into how the spine constrains head motion during impact. Longer coronal pendulum lengths align with prior findings [2]. The finding that males have shorter pendulum lengths is unexpected given that males have longer necks than females [3]. These results may reflect sport-specific impact scenarios rather than purely

anatomical differences A key limitation is sex comparisons were drawn from different sports. Future studies should investigate sex-based differences within the same sport to better isolate biomechanical contributions to head–neck kinematics.

Images (Optional)



References (Optional)

[1] J.J. Crisco *et al.* , J Athl Train, 2010

[2] T. Wang *et al.* , Ann Biomed, 2021

[3] C.C Gordon *et al.*, Ansur II, 2015

Session Category

Injury Biomechanics: N/A

P3-106

Multi-directional volunteer fall experiments during bus braking maneuvers

Mr Jia-Cheng Xu MSc[1,2], Mr Zhou Zhou PhD[1], Mr Christer Ahlström PhD[2], Professor Svein Kleiven PhD[1]

[1]KTH Royal Institute of Technology, Huddinge, Stockholm, Sweden. [2]VTI, Swedish National Road and Transport Research Institute, Linköping, Östergötland, Sweden

Introduction

Bus transport is central to sustainable urban mobility, yet non-collision accidents such as harsh braking often lead to fall-related injuries, including traumatic brain injuries and hip fractures. Preventing such falls is essential to promote safe public transport use. However, bus-related falls remain understudied. Understanding fall kinematics and impact configurations can inform both active safety (driver maneuvers) and passive safety (impact-friendly floors and handrails).

This study presents the first volunteer fall experiments in three fundamental directions (forward, sideways, backwards) during realistic braking maneuvers. The objective is to evaluate impact sequences and kinematics during falls from standing height inside a moving vehicle.

Methods

Nineteen healthy adults (20–43 years, 7 females and 12 males) participated. To avoid impacts with bus handrails, the experiments were conducted on a truck bed, equipped with 30 cm gymnastic mattresses. Participants wore helmets and wrist guards for safety. They initially held a vertical handrail during acceleration but released it well before the braking phase to ensure natural falls. Participants were instructed to remain upright and avoid compensatory stepping. The truck accelerated to a constant velocity of 20 and 25 km/h, then braked to produce average peak decelerations of 2.5 and 3.5 m/s^2.

Results

Preliminary observations indicate distinct impact patterns for each fall direction. Forward falls generally resulted in initial hand and wrist impacts, reducing direct head contact. Sideways falls typically began with the ipsilateral leg or knee, followed by hip impact and

occasional rotational head contact in the frontal plane. Backward falls started with the buttocks and outstretched hands absorbing the initial impact, but were consistently followed by a clear head impact in the sagittal plane.

Discussion

Compared to laboratory fall experiments, the longer duration of braking maneuvers (several seconds) may increase head injury risk. Our findings will inform bus safety simulations using finite element human body models to predict common injuries to the head, hip, and wrist.

Session Category

Injury Biomechanics: N/A

P3-107

Comparison of Cervical Spine Compression, Tension, and Shear Forces in Low Speed Rear-End Collisions

Mr. Jordan Ogbu Felix, Ms. Keya Zambare, Dr. Kevin Adanty, Dr. Sean Shimada

Aperture LLC, Davis, CA, United States

Introduction

Studies often cite compression as a potential mechanism for neck injury during motor vehicle collisions. However, rear-end impact studies show that the greatest occupant neck force magnitudes are in the transverse plane, generating shear and tensile forces on the spine [1]. This study compares anteroposterior shear, tensile, and compressive forces in the cervical spine during rear-end impacts. Quantifying relative magnitudes of these forces may clarify which loading mechanism most warrants mitigation efforts to reduce neck injury risk in rear-end collisions.

Methods

Peak upper (C1-occipital condyles) and lower-neck (T1) tension, compression, and anterior/posterior shear forces were obtained during head-restraint contact from rear-end sled tests from the Insurance Institute for Highway Safety database (n=322). All tests used belted BioRID-II ATDs, simulating 16 kph delta-v impacts. Peak neck force magnitudes and corresponding peak force times were compared using a one-way repeated-measures ANOVA.

Results

Upper Neck

Tension loads (603±43N) were significantly greater than shear and compression ($p<0.001$) (Table 1). There were no significant differences between posterior and anterior shear loads ($p=0.20$) and between anterior shear and compression ($p=0.19$). Time-to-peak differed significantly between all loading mechanisms ($p<0.001$) except between posterior shear and compression ($p=0.58$).

Lower Neck

Anterior shear loads (352±85N) and tension (252±163N) were significantly greater than posterior shear and compression ($p<0.001$). Differences in time-to-peak were not significant between tension and compression ($p=0.27$) and between anterior shear and

compression ($p=0.17$) but were significant between all other loading mechanisms ($p<0.05$).

Discussion

In the upper neck, tension loads were the greatest, while shear forces were the lowest. Conversely, in the lower neck, anterior shear and tension loads were the greatest, with posterior shear being the lowest. These patterns align with studies indicating tension has the greatest magnitude in upper cervical loading [2] and that lower cervical segments experience elevated shear and tension loads [3]. Our results suggest that tensile and shear forces generally exceeded compressive forces in rear-end crashes, therefore, future research should prioritize strategies that mitigate these dominant loading mechanisms to help reduce neck injury risk.

Images (Optional)

Table 1: Cervical spine average peak forces and time to peak force

Neck Region	Load Type	Average Peak Force (N)	Average Time to Peak force (ms)
Upper Neck	Anterior Shear (n=318)	91.3 ± 91.9	130 ± 14.4
	Posterior Shear (n=97)	91.8 ± 38.6	91.3 ± 14.7
	Tension (n=310)	603 ± 282	93.4 ± 40
	Compression (n=216)	105 ± 43.3	110 ± 13.6
Lower Neck	Anterior Shear (n=127)	352 ± 188	115 ± 14.1
	Posterior Shear (n= 243)	33 ± 14.2	93.4 ± 49.2
	Tension (n=319)	242 ± 163	111 ± 15.8
	Compression (n= 146)	175 ± 90.4	113 ± 36

References (Optional)

[1] Erbulut, Turkish Neurosurgery, 2014.

[2] Tencer et al., Spine, 2002.

[3] Kazmierczak et al., SAE Technical Paper, 2025.

Session Category

Injury Biomechanics: N/A

P3-108

THUMS AM50 Upper Extremity Response to Ballistic Shield Loading in Comparison to Experimental Data

Dr. Julia de Lange Ph.D., P.Eng.[1,2,3], Dr. Cheryl Quenneville Ph.D., P.Eng.[2]

[1]30 Forensic Engineering, Toronto, Ontario, Canada. [2]McMaster University, Hamilton, Ontario, Canada. [3]University of Guelph, Guelph, Ontario, Canada

Introduction

Innovative finite element models are important for the design and advancement of safety systems due to the complexities surrounding post-mortem human surrogate (PMHS) and physical surrogate testing. To ensure biofidelity, these models must be verified against experimental data. Behind shield blunt trauma (BSBT) is an injury mechanism that describes blunt trauma resulting from rapidly deforming ballistic shields. This unique loading condition to the upper extremity has resulted in vastly different injury mechanisms and thresholds than automotive loading conditions [1]. Models like the Total Human Model for Safety (THUMS) can help with developing protective devices but must have an appropriate response under this unique injurious scenario. The THUMS upper extremity has been previously shown to agree with experimental fracture data at airbag-level loading rates (3 m/s and 7.6 m/s) [2]. The purpose of this study was to assess the fracture response of the THUMS forearm to BSBT impacts through comparison with previous experimental work.

Methods

Experimentally, eight mid-sized male PMHS were impacted at the forearm at loading rates representative of a deforming ballistic shield (velocity of 16.9 m/s) [1]. One specimen was instrumented with triaxial strain gauges at the mid-radius and mid-ulna to collect bone strain. The THUMS 50M upper limb was used, with fracture implemented using an element erosion technique. Critical plastic strain was informed by the radial strain (1.26%) measured during the experimental impact. The impact conditions that resulted in fracture were recreated against the THUMS model.

Results

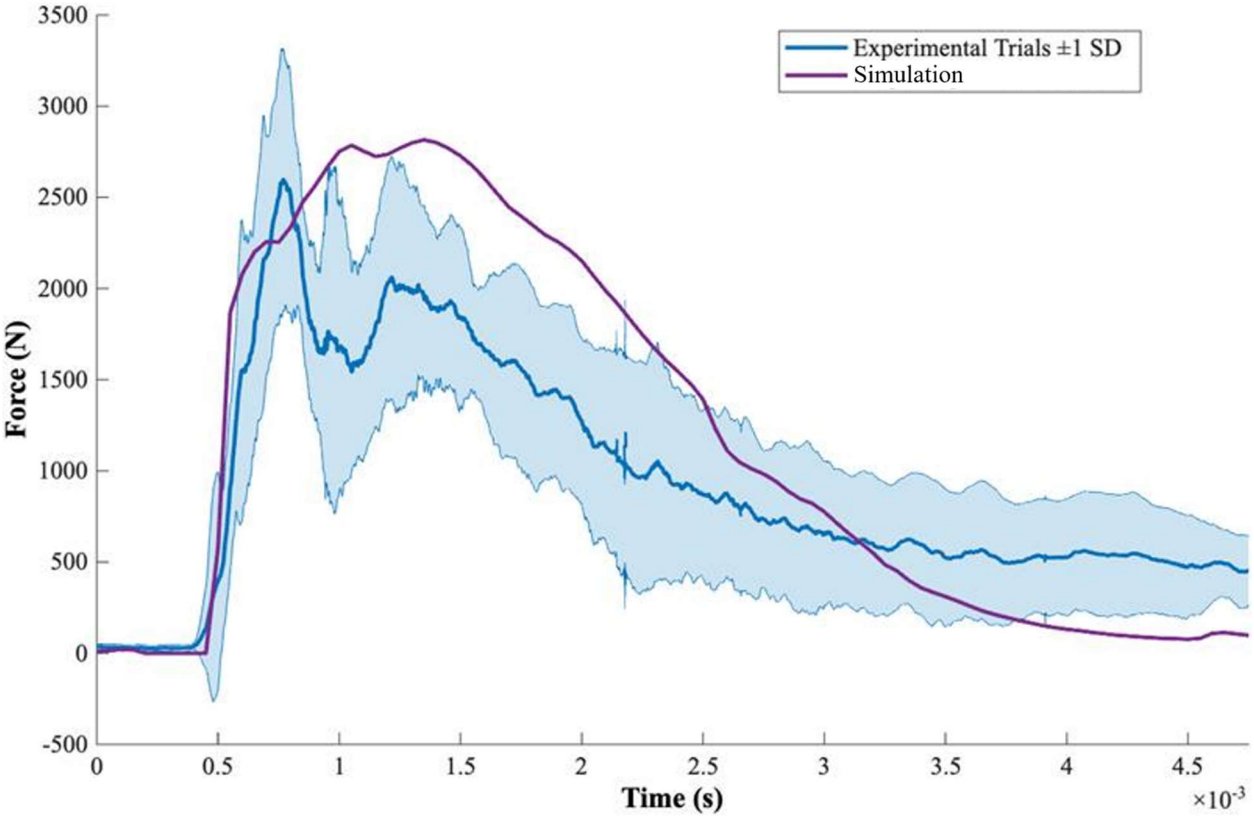
The peak applied force during the THUMS simulation was 2,815 N (<1% lower than the experimental test of the gauged specimen). Both the ulna and radius fractured in the simulation, in agreement with the experimental impact; however, unlike the experimental

results, the radius only fractured at one location. Additionally, the force-time curve did not display a drop after the initial peak, as occurred experimentally.

Discussion

Additional computational modelling is ongoing to improve the model response. Once validated, these models may be useful for early shield design and corresponding injury risk assessment.

Images (Optional)



References (Optional)

[1] Julia de Lange *et al.*, J. Biomech Eng, 2024

[2] Carson Brewer *et al.*, J. Biomech Eng, 2024

Session Category

Injury Biomechanics: N/A

P3-109

Effectiveness of Restraint Use in Reducing Lower-Extremity Injury Severity During High-Speed Frontal Collisions: A Case Study Utilizing MADYMO

Dr. Kari Verner Ph.D., P.E.[1], Dr. Delanie Lynch Ph.D.[2], Mr. Dominic Demma M.S.[3], Dr. Steve Rundell Ph.D., P.E.[3]

[1]Explico, Englewood, Colorado, United States. [2]Explico, Englewood, colorado, United States. [3]Explico, Novi, Michigan, United States

Introduction

High-severity frontal impacts can cause AIS 2+ lower-extremity injuries, even for restrained occupants[1], and intrusion further increases incidence and severity of these injuries[2].

The objective of the present study was to quantify the influence of restraint use (seatbelt and frontal airbag) on tibial axial loading during a high-severity frontal impact with measurable occupant compartment intrusion. We hypothesized that seatbelt use would decrease the effective mass transmitted to the lower extremities and, consequently, reduce the likelihood of tibial fracture even under intrusion conditions representative of a real-world crash.

Methods

A MADYMO simulation was developed to replicate a real-world frontal collision scenario using the EDR-recorded crash pulse (delta-V = 41mph), 3D geometry of the damaged occupant compartment, and a virtual Hybrid III 50th percentile ATD scaled to the actual driver's height and weight (72in, 265lb). Airbag deployment and seatbelt pretensioner firing were modeled according to the EDR-recorded data. Four scenarios were simulated: Unbelted+No Airbag, Unbelted+Airbag, Belted+No Airbag, and Belted+Airbag. Tibial axial loading was determined in both legs for each scenario.

Results

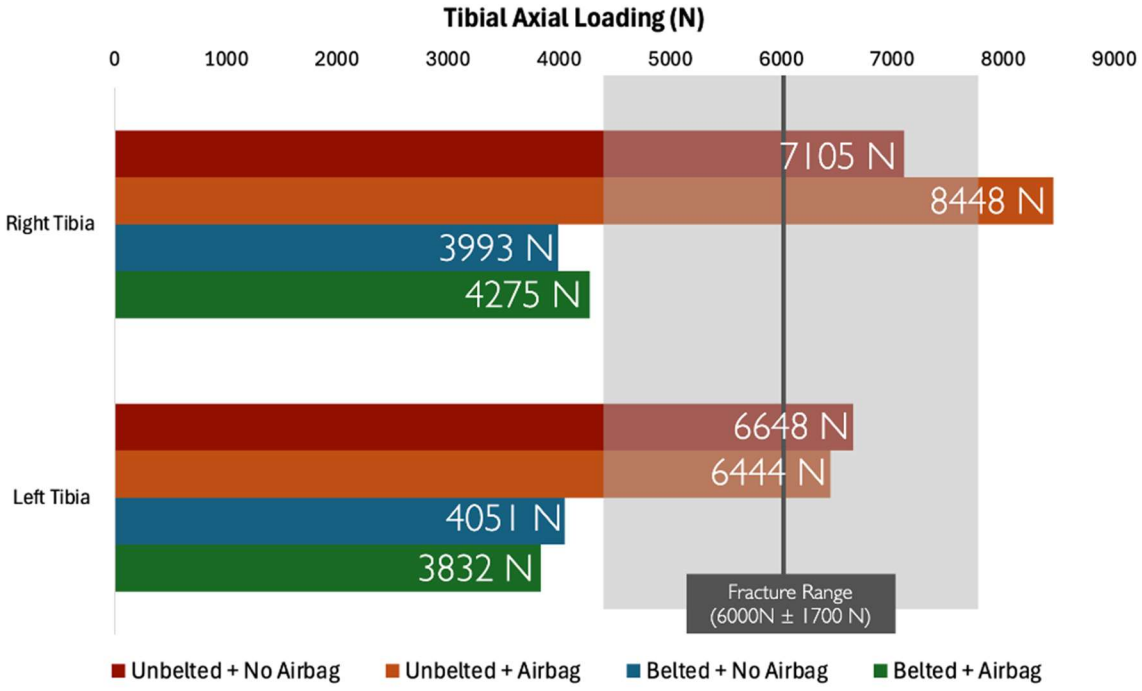
In belted conditions, tibial loads were similar between sides and remained below the experimental fracture range (4.8kN-7.6kN)[3] regardless of airbag deployment. In contrast, unbelted scenarios were all within or greater than the fracture range, with higher forces on the right. The absence of a seatbelt increased tibial axial force by 64-98% (Figure 1).

Discussion

Seatbelt use reduces tibial plateau fracture risk in high-speed frontal collisions with occupant compartment intrusion, while airbag deployment alone had minimal effect. Higher forces on the right tibia were observed in unbelted scenarios, likely due to leg entrapment between the brake pedal and dash. This finding, and the findings in general, align with the actual subject injuries: the unrestrained driver sustained bilateral tibial plateau fractures, with the right side more severe.

Consistent with prior research, our findings show that seatbelts mitigate lower-extremity injuries in high-energy frontal collisions, while airbags alone may actually increase injury severity[1].

Images (Optional)



References (Optional)

[1]Estrada et al., *J Trauma* 57(2):323–328,2004

[2]Loo et al., *J Trauma* 41(6):935–951,1996

[3]Funk et al., *IRCOBI Proc.*:95–108,2000

Session Category

Injury Biomechanics: N/A

P3-110

Development of a Subject-Specific MADYMO Model Predictive of Tibial Plateau Fractures in a High-Speed Frontal Collision Case Study

Dr. Kari Verner Ph.D., PE[1], Dr. Delanie Lynch Ph.D.[1], Mr. Dominic Demma MS[2,3], Dr. Steve Rundell Ph.D., PE[2]

[1]Explico, Englewood, CO, United States. [2]Explico, Novi, MI, United States. [3]Wayne State University, Detroit, MI, United States

Introduction

Despite the low incidence of tibial plateau fracture (~10% of lower extremity injury [1]) in motor vehicle crashes, these high-energy fractures carry poor long-term outcomes.

We encountered a case study of a high-energy frontal crash (EDR recorded longitudinal delta-v: -41 mph) with significant underride and an unbelted driver who sustained bilateral tibial plateau fractures, with greater severity on the right. The objective of the present study was to develop a computational model capable of simulating a this high-energy frontal collision with substantial occupant compartment intrusion and an unrestrained occupant. We hypothesized that modeling of the occupant compartment intrusion would result in forces on the lower extremities consistent with the real-world injuries.

Methods

The vehicle interior was modeled in MADYMO based on a 3D point cloud of an undamaged exemplar vehicle. A virtual Hybrid III 50th-percentile ATD ellipsoid model was scaled to the subject driver's height and weight (72 in, 265 lb) and positioned using the driver's testimony and post-incident seat photos. The steering wheel airbag was deployed but a seatbelt was not utilized.

The knee bolster initial position was modeled based on the undamaged exemplar, and then iteratively translated and rotated to simulate increasing amounts of intrusion. The amount of intrusion was assumed to be completed by the time the occupant interacted with the knee bolster.

Results

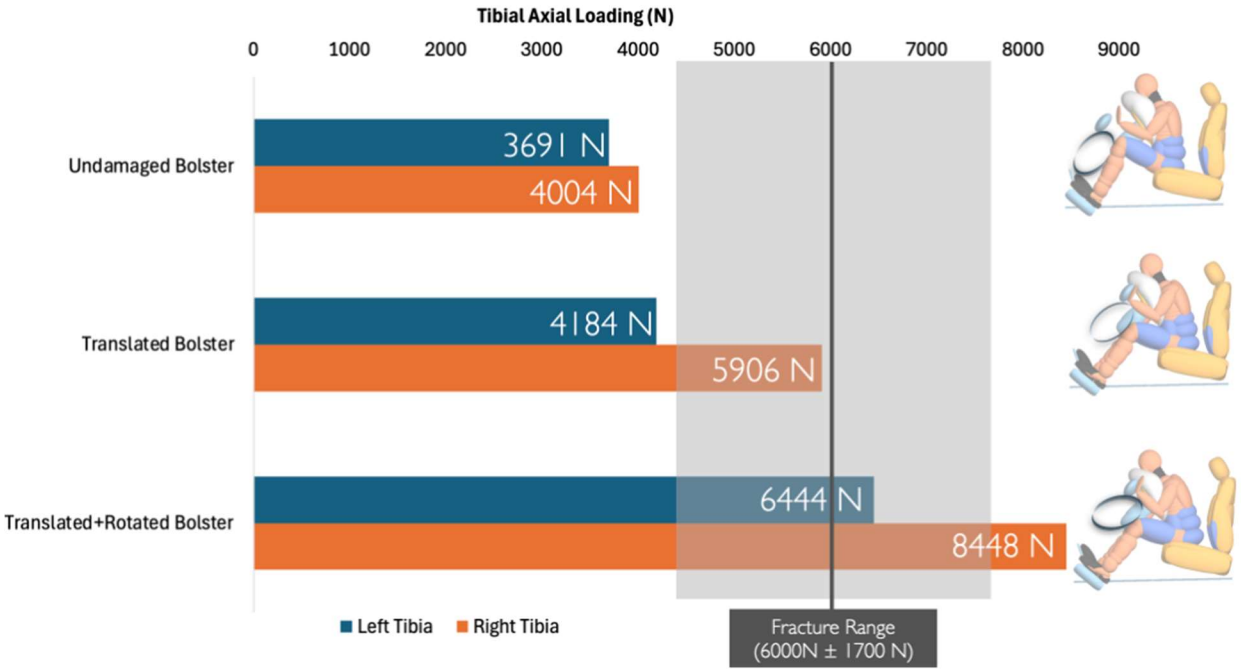
Increasing rearward and upward translation with clockwise rotation of the knee bolster led to higher axial tibial loads bilaterally, with forces about twice as high as those predicted by

the undamaged exemplar configuration [**Figure 1**]. Additionally, in all configurations, loads in the right tibia were greater than the left.

Discussion

In the fully translated and rotated condition (representative of intrusion), the tibial loading predicted by the model was consistent with both the real-world resulting injuries (bilateral tibial plateau fractures) and published fracture tolerances. The predicted axial loads in the tibia were within experimental ranges for tibial plateau fractures (4.8kN-7.6kN) [1]. Notably, the model also predicted higher forces in the right tibia relative to the left, which was consistent with fracture severities documented in the real-world scenario.

Images (Optional)



References (Optional)

[1] Funk *et al.* IRCOBI Proc.:95–108, 2000

Session Category

Injury Biomechanics: N/A

P3-111

Calculating Low Back Moments of Personal Support Workers using Bottom-up Models Driven by Smart Insoles Versus Top-down Models Driven by Estimated Hand Forces

Ms Kate M. Posluszny MSc, Mr. Justin B. Davidson MSc, CSCS, Dr. Steven L. Fischer PhD, RKin, CCPE

University of Waterloo, Waterloo, ON, Canada

Introduction

Community-based personal support workers (PSWs) need effective interventions to reduce the high prevalence of low-back musculoskeletal disorders. However, effective interventions require insight on exposure where knowledge of PSWs' low back loads is sparse. Few methods are available to measure low back exposure data in-field with sufficient rigor necessary to inform intervention. Therefore, this study aimed to test how peak lumbar (L4/L5) extensor moments calculated using top-down quasi-dynamic model differed from those calculated using a bottom-up model with ground reaction forces estimated using a field-ready insole sensor.

Methods

Kinematic and kinetic data were collected from 20 PSWs (17F, 3M) simulating 12 PSW tasks [1], where this abstract focused on a patient repositioning task. Top-down quasi-dynamic and bottom-up inverse dynamic rigid link models were developed in Visual3D x64 Professional™ (HAS-Motion Inc., Boyds, MD, USA) to calculate PSWs' lumbar extensor moments. Model inputs included whole-body 3D kinematics collected using a 12-camera Vicon© motion capture system (Centennial, CO, USA), and peak hand forces collected with a Mark-10© force gauge (Copiague, NY, USA) (top-down analysis) or dynamic ground reaction forces collected using Loadsol® pro-mlp (Novel Electronics Inc., St. Paul, MN, USA) (bottom-up analysis). Wilcoxon Signed Rank tests were conducted with JASP© (Amsterdam, Netherlands) to compare differences between the top-down and bottom-up estimated peak extensor moments.

Results

Statistically significant (p=.01) differences in PSWs' extensor moments emerged. Specifically, bottom-up model outputs estimated an average peak extensor moment of 72.6(±60.2)Nm, while the top-down models estimated an average peak extensor moment of 104.6(±38.6)Nm.

Discussion

Due to the use of a hand force matching to estimate peak hand forces, the top-down model estimates may be influenced by subjective errors, while the bottom-up models may provide more reasonable extensor moment estimates. However, further analysis is required to confirm whether the models are primarily influenced by the model's force inputs. It is further important to highlight that criterion kinematics were used to develop these models, which may not be suitable for in-field use. Consequently, future research will also examine the use of wearables to obtain PSWs' position data when in-field.

References (Optional)

[1] Daphne C. Ho *et al.,* Appl Ergon, Submitted

Session Category

Injury Biomechanics: N/A

P3-112

Investigation of Cushion Type for Mitigating Lumbar Spine Loads caused by Under Body Blasts

Ms. Katerena Sirhan MS[1], Mr. Mark Shafer MS[2], Mr. David Weyland MS[2], Dr. Cameron 'Dale' Bass PhD[1]

[1]Wayne State University, Detroit, MI, United States. [2]GVSP, Warren, MI, United States

Introduction

Seated personnel exposed to underbody blast (UBB) in military vehicles have an increased risk for lumbar spine injuries owing to direct inferior to superior compression caused by the blast. The purpose of this study is to determine seat pan material that could improve force mitigation to the lumbar spine during an UBB event. A range of simulated UBB events were conducted using a Sub System Drop Tower (SSDT).

Methods

The instrumented 50th Hybrid III ATD was placed on a rigid seat mounted to the SSDT platform with three different energy absorbing (EA) material configurations: (1) polyurethane (PU) foam, (2) PU foam layered over EA insert A and (3) PU foam layered over EA insert B. Two analysis methods were used to assess injury risk of the lumbar spine. The first method utilized Injury Assessment Reference Value (IARV) percentages, created by Occupant Centric Platform Technology Enabled Capability Demonstration (OCP TECD). Trendlines were created for each foam thickness comparing IARV% and peak platform acceleration. Acceptable (75%) and Not Acceptable (100%) threshold values were calculated to compare foam thickness to peak platform acceleration.

The second method is the compression/flexion cadaveric lumbar injury criterion proposed by Ortiz-Paparoni et. al. (2020). The lumbar injury criterion (L_{ic}) risk is calculated: (Image)

F_r is the lumbar resultant force, My is the y-axis lumbar moment. L_{ic} is the risk of sustaining a vertebral body injury. MATLAB (MathWorks, Inc) was utilized to calculate constant k created from the resultant force and My.

Results

The relationship between peak platform acceleration and thickness of foam correlating to 75% and 100% IARV were further explored to determine the optimal EA cushioning combination appropriate for any given threat within the tested range.

Increasing L_{ic} values are generally associated with increasing seat acceleration. There is a clear asymptotic effect in the data for sufficiently large accelerations. The 76 mm thickness PU foam results were statistically different from the other test conditions ($p>0.01$).

Discussion

The results show a nonlinear relationship between Lic injury assessment criterion and OCP TECD IARV Percentages. Future work will investigate cushion characteristics to identify viable EA solutions up to the desired acceleration range

Images (Optional)

$$k = \frac{F_r}{5824} + \frac{M_y}{1155}$$

$$L_{ic} = \frac{1}{2} + \frac{1}{2} * \mathrm{erf}\left(\frac{\ln(k) - 0.0578}{0.32148\sqrt{2}}\right)$$

Acknowledgements (Optional)

DISTRIBUTION STATEMENT A. Approved for public release; distribution is unlimited. OPSEC10192

Session Category

Injury Biomechanics: N/A

P3-113

Voxel-Wise 3D Multiparameter Hyperelastic Tissue Characterization Through Combining Physics-Informed UNet and Optimal Input Loading Dataset Design

PhD Student Amir Asadi AA, Associate Professor Kaveh Laksari KL

UCR, Riverside, California, United States

PhD Student Amir Asadi

Introduction

Brain tissue is heterogeneous, exhibiting different mechanical characteristics depending on anatomical function and location. These characteristics change in inured tissue or tumors, which renders them as important disease biomarkers. However, mechanical characteristics maps are usually limited to simple linear materials or homogenous approximations for deformation and stress fields, which leads to dismissal of valuable information and inaccurate identification of pathologies [1, 2]. Moreover, it has been demonstrated that material parameter identification is highly sensitive to loading modes and magnitudes as well as measurement noise [3]. Here, we present an optimal experimental design framework to improve robustness of inverse material characterization, and subsequently develop a physics-informed UNet (PI-UNet) framework to determine voxel-wise material parameters for a hyperelastic Mooney-Rivlin model.

Methods

Our novel optimal experimental design framework quantifies conditioning of a given loading scenario by its stress-material Jacobian matrix, motivated by Fisher Information of the inverse problem.

Once optimal loading scenarios are determined, we set out to determine the heterogeneous material parameters of several simulated examples of a cubic sample with various internal structures, including homogeneous matrix with a stiff spherical inclusion, and matrix embedded with tumorous brain tissue. Without a priori knowledge of the distribution of material properties within the cube, and having access only to boundary stress values and 3D displacements, PI-UNet can determine the hyperelasticity and recover the internal structure accurately.

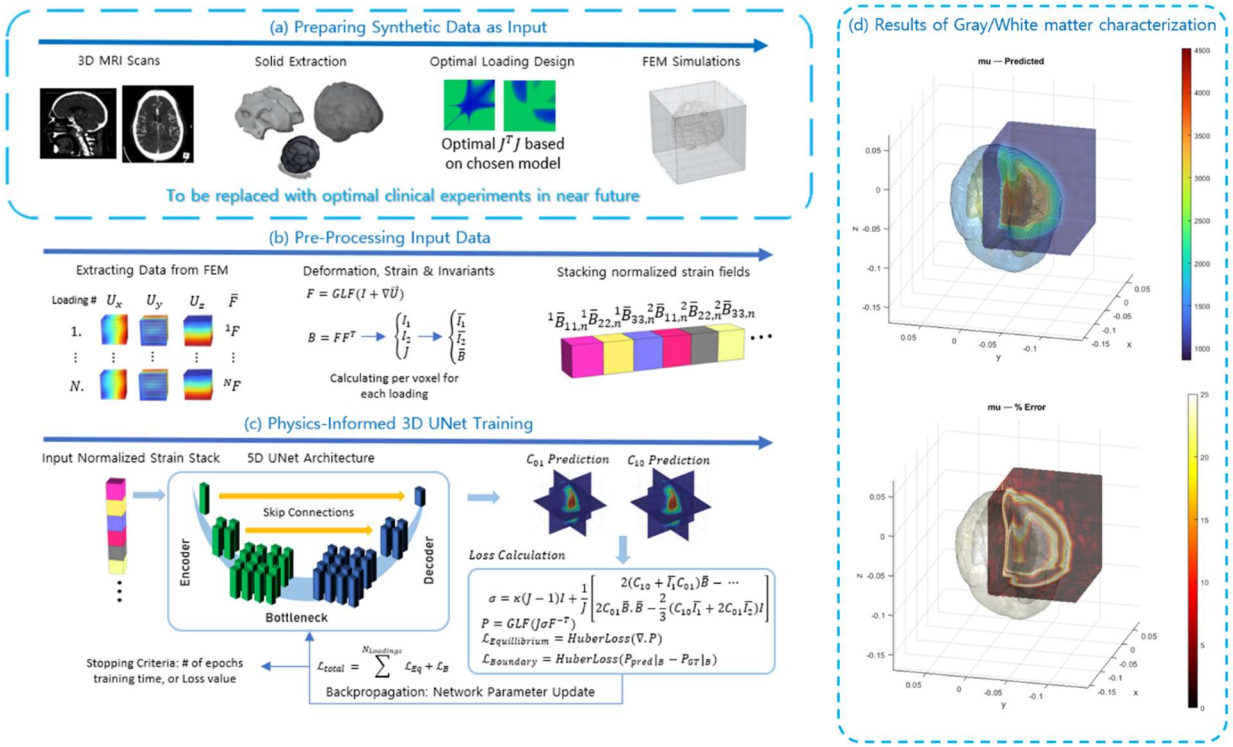
Results

The optimal loading conditions roughly reduce number of required measurements to third to achieve the similar conditioning as random loadings. Using these optimal loads, the PI-UNet framework successfully approximated the material parameters and reconstructed each tissue region by less than 5% error. Moreover, the use of unsupervised clustering within the tumor in brain example led to localization of the lesion based on shear modulus values with Dice similarity of 96%, significantly improving the solely displacement-based approach that assumes a uniform stress distribution leading to Dice similarities of 20-30%.

Discussion

We introduce two novel methodology and validate them on synthetic noisy FE data, demonstrating the feasibility for potential clinical use to achieve more reliable/sophisticated biomarkers in detecting/treating pathologies, surgical planning, and twin modeling.

Images (Optional)



References (Optional)

1. https://doi.org/10.1016/j.jmbbm.2023.106228
2. https://doi.org/10.1016/j.actbio.2024.06.038
3. https://doi.org/10.1016/j.jmbbm.2025.107104

Session Category

Injury Biomechanics: N/A

P3-114

Raman Microscopy Identification of Overstretch-Induced Collagen Damage in Cerebral Arteries

Mr. William Anderl[1], Ms. Yawen Xue[2], Ms. Nathalie Munoz[2], Dr. Jiaqi Jin PhD[2], Dr. Kenneth Monson PhD[1]

[1]University of Utah, Department of Mechanical Engineering, Salt Lake City, UT, United States. [2]University of Utah, Metallurgical Engineering, Salt Lake City, UT, United States

Introduction

Aside from acute effects, TBI is associated with a variety of long-term sequelae including stroke [1] and neurodegenerative illness [2]. The underlying causes of these prolonged risks are unknown but may be influenced by subtle damage to embedded blood vessels. Detection of sub-failure damage in cerebral vasculature has given mixed results, particularly when examining vessels stretched below yield [3]. Raman microscopy may allow for more precise measurement of subtle vessel damage.

Methods

An ovine middle cerebral artery (MCA) was cut into control, heat denatured, and mechanically damaged sections. The heat denatured vessel was heated at 68˚C for 10 minutes. The mechanically damaged vessel was secured on canulae and pulled axially until failure. Each vessel was fixed and wet mounted on glass slides. Raman spectra were captured using an Invia Qontor microscope (514 nm, 2400 g/mm). For each vessel, two randomly selected areas within the adventitial layer were imaged resulting in 200 sampled points. After preprocessing, intensity ratios were calculated at 1670/1640 cm^{-1}.

Results

Both the mechanical ($p = 0.003$) and heat-denatured ($p<0.001$) vessels showed an increase in the ratio relative to the paired control. Additionally, the mechanically damaged vessel had a lower ratio than the heat denatured sample ($p=0.002$).

Discussion

Unal et al. demonstrated that an increasing 1670/1640 ratio is indicative of collagen triple-helix damage[4]. This is consistent with our findings, in which both mechanically and thermally damaged collagen resulted in an increase in mean ratio (control = 1.24, mechanical = 1.39, heat = 1.476). The ratios are consistent with expected damage levels,

with heat denaturing causing widespread damage. Our findings suggest that Raman microscopy is an appropriate tool to measure focal collagen damage in cerebral arteries, and its implementation may improve future understanding of vessel collagen damage.

Images (Optional)

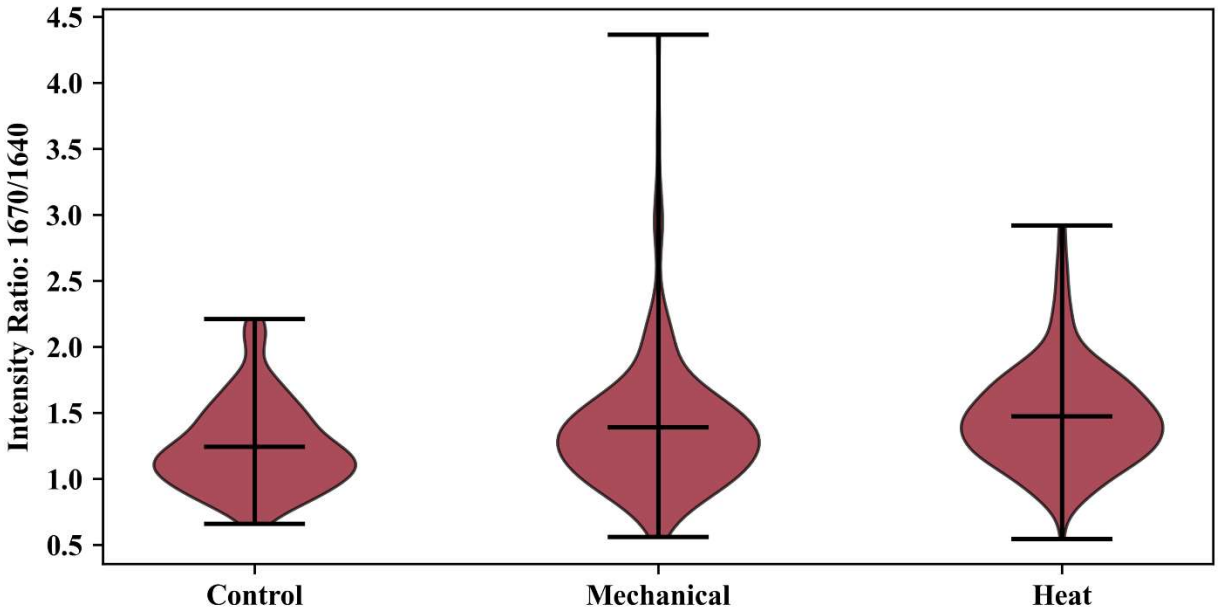


Figure 1. Violin plots of the 1670/1640 intensity ratio for control, mechanical, and heat groups. Central horizontal bars indicate mean, while upper and lower horizontal bars show the full data range. The red violins show the distribution of ratios within each group, where wider portions mark more frequent values. All groups differ significantly from one another, with higher mean ratios in the heat group consistent with more severe global damage compared to mechanical damage.

References (Optional)

[1] Burke JF et al. *Neurology*. 2013
[2] Sandsmark DK et al. *Neuron*. 2019
[3] Pearson N et al. *J Mech Behav Biomed Mater*. 2025
[4] Unal M, Jung H, Akkus O. *J Bone Miner Res*. 2016

Acknowledgements (Optional)

We would like to acknowledge Dr. Ozan Akkus for his guidance, as well as the Jin group for assistance with data acquisition and analysis.

Session Category

Injury Biomechanics: N/A

P3-115

Can Machine Learning Discriminate Between Injured and Uninjured Service Members Using Single Leg Squats?

Dr. Krista G. Clark[1,2], Dr. Pawel R. Golyski[2,3], Dr. Matthew B. Bird[3,4,5,6], Dr. Megan H. Roach[3,6,7], Dr. Courtney M. Butowicz[2,3,7]

[1]Henry M. Jackson Foundation for the Advancement of Military Medicine, Inc., Bethesda, MD, United States. [2]Department of Rehabilitation, Walter Reed National Military Medical Center, Bethesda, MD, United States. [3]Extremity Trauma and Amputation Center of Excellence, Defense Health Agency, Falls Church, VA, United States. [4]Human Performance and Nutrition Research Institute, Oklahoma State University, Stillwater, OK, United States. [5]Oak Ridge Institute of Science and Engineering, Fort Bragg, NC, United States. [6]Womack Army Medical Center, Fort Bragg, NC, United States. [7]Uniformed Services University of the Health Sciences, Bethesda, MD, United States

Introduction

Lower extremity musculoskeletal injuries (MSKI) are a leading problem in military personnel. Thus, rapid and accurate injury screening is crucial for maximizing readiness. A single leg squat (SLS) is a promising screening tool as it is functionally demanding and identifies movement quality impairments associated with injury risk. Machine learning can facilitate automated assessment of motion quality to identify or classify injury status, a precursor to risk prediction. This study determined if machine learning can differentiate between injured and uninjured service members performing SLS

Methods

153 service members with (n=72) and without (n=81) low back or lower extremity MSKI participated in this study (22 F/129 M, mean±SD age:23.8±5.2yr, BMI: 26.7±4.0kg/m^2). Participants performed three SLS per leg while full body motion was collected using markerless motion capture (100Hz, HumanTrak, VALD). We estimated 3D center of mass (COM) peak velocities, accelerations, forces, and power along each axis using a custom Python script. Recursive feature elimination (RFE) identified 7 of 26 top variables for classification, which were used in a linear discriminant analysis (LDA) to classify injured and uninjured participants with an 80-20 train-test split.

Results

Top RFE variables included peak velocity, acceleration, and force in the mediolateral and vertical directions. The LDA model correctly identified 12/15 injured and 12/16 uninjured

participants from the test dataset and accurately classified 77% of injured from uninjured participants with an F1 score of 0.774 and ROC-AUC of 0.804 (Fig. 1).

Discussion

COM control during SLS is linked to lower limb joint alignment, an injury risk factor. Using COM outcomes, model performance was moderate at injury status classification. Influence of the variables varied with inputs into the RFE, model split and sample size. Model refinement, including lower limb kinematics, will likely improve classification. SLS can be especially challenging while injured, thus future research should examine whether other assessments (e.g., double-limb squat, hip strength) could improve modifiable risk factor identification and facilitate earlier treatment.

Images (Optional)

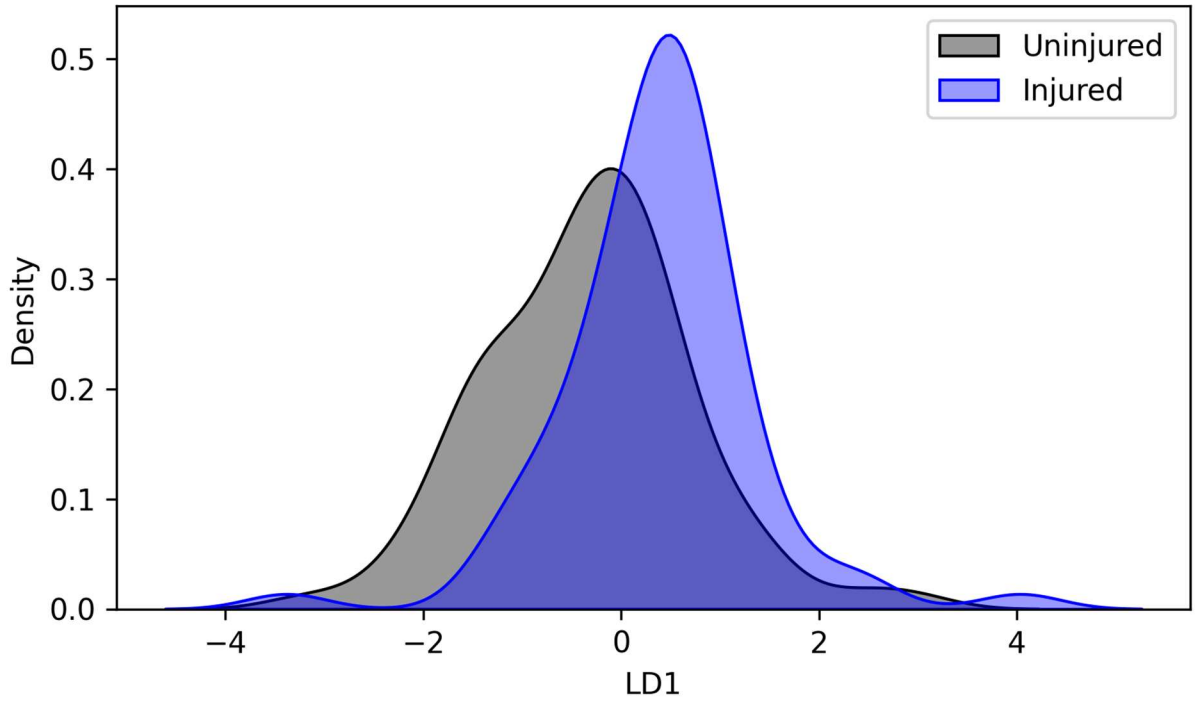


Figure 1: Density plot of the injured (blue) and uninjured (gray) groups projected onto the first linear discriminant axis (LD1). The visual separation aligns with our model performance of moderate discrimination.

References (Optional)

Acknowledgements (Optional)

This work was supported by funding from MOMRP-JPC5-HU00012220033. The contents of this presentation are the sole responsibility of the author(s) and do not necessarily reflect

the views, opinions or policies of Uniformed Services University of the Health Sciences (USUHS), The Henry M. Jackson Foundation for the Advancement of Military Medicine, Inc. (HJF), or the U.S. Government.

Session Category

Injury Biomechanics: N/A

P3-116

Pure Shear Loading in the Cervical Spine: Replicating Injurious Boundary Conditions

Mr Luis Dias P. Eng[1], Dr Shun Yamamoto[2], Dr Thomas Oxland P. Eng[1], Dr Peter Cripton P. Eng[1]

[1]UBC, Vancouver, BC, Canada. [2]Jikei University School of Medicine, Minato, Tokyo Prefecture, Japan

Introduction

Shear is an understudied loading mode in the cervical spine, especially considering its significant role in the formation of fracture-dislocation (FD) injuries [1]. There is a particular paucity of data on pure shear loading under high rates and in combination with a compressive axial preload, which are boundary conditions present in the impact scenarios that result in FD injuries. The objective of this study was to determine the effect of realistic shearing rates and compressive preloads on the sagittal stiffness of the lower cervical spine under pure shear loads.

Methods

Thirty-nine *ex vivo* human Functional Spinal Units (FSUs) were potted in bone cement and attached to a shear loading fixture on a high-rate tensile testing machine. Each FSU was loaded to failure at one of three rates (1, 500, 2000 mm/s) and under one of two compressive preloads (0, 1500 N). Sagittal stiffness was measured from the slope of the pre-failure load-displacement response, and the effects of the displacement rate and compressive preload were evaluated using multivariate linear regression, controlling for demographic (donor age and sex) and anthropometric (disc and facet joint degeneration, bone volume fraction (BV/TV), Anteroposterior width) factors.

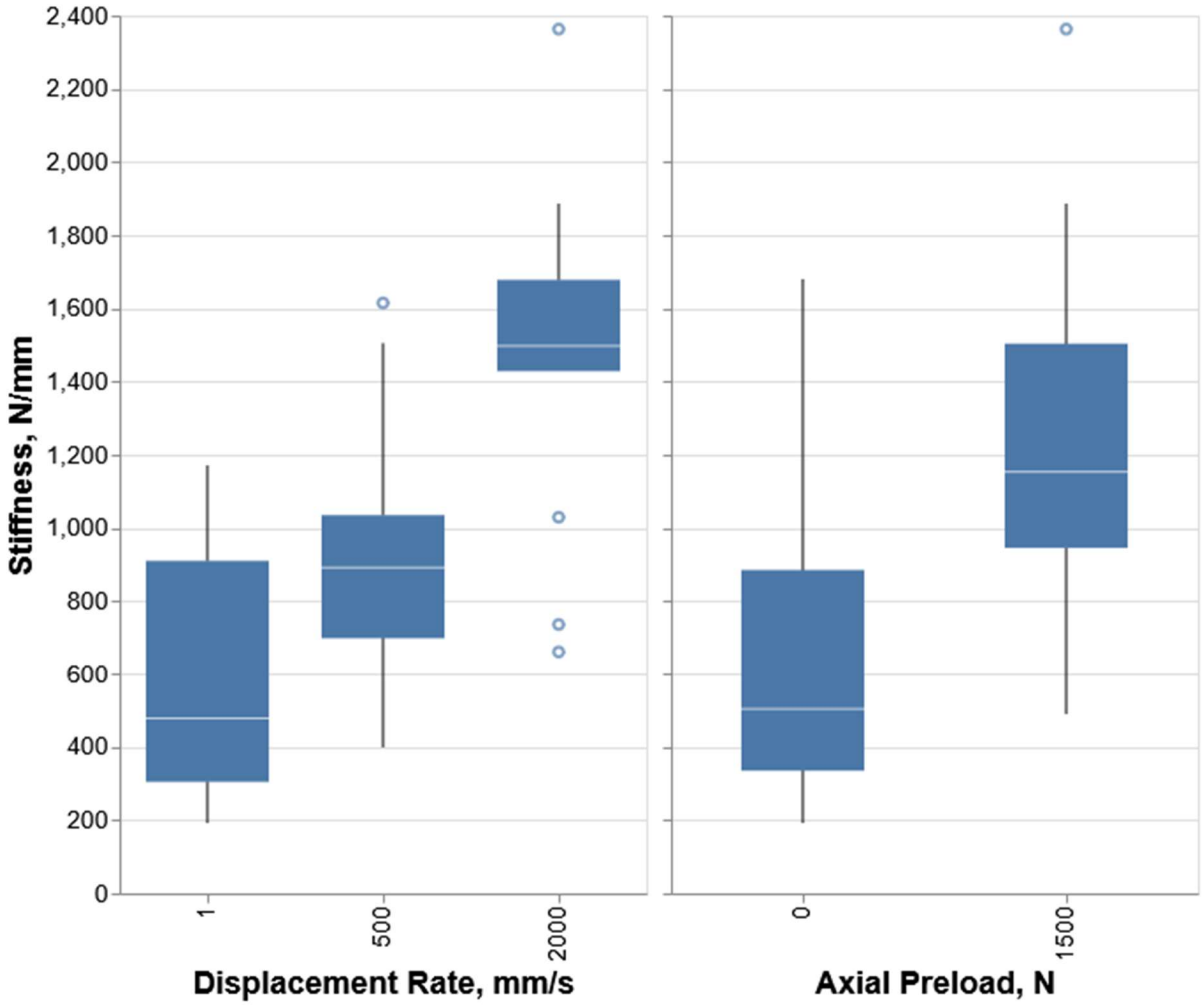
Results

Shearing rates of 1, 500, and 2000 mm/s resulted in mean stiffnesses of 588 (SD=332), 915 (SD=367), and 1482 (SD = 463) N/mm, respectively. In the presence of a combined axial preload, specimens had a mean stiffness of 1249 (SD=456) N/mm, compared to specimens with no preload, with a mean stiffness of 693 (SD=465) N/mm. Shearing rate and combined axial preload were both strongly correlated with sagittal stiffness ($p<0.001$ for both), as illustrated in Figure 1. Anteroposterior width and BV/TV were also positively correlated with sagittal stiffness, with $p=0.005$ and $p=0.011$, respectively.

Discussion

Our findings suggest that, under boundary conditions representative of real-world injuries, the cervical spine is much stiffer in shear. As the overwhelming majority of existing *ex vivo* data for the human spine is quasi-static, these findings are particularly salient for computer model validation, especially when such models are to be used for injury simulation.

Images (Optional)



References (Optional)

[1] Nightingale *et al.* , Clin Biomech, 2019

Session Category

Injury Biomechanics: N/A

P3-117

Sensitivity of Disc Herniation Risk to Variations in Occupant Posture and Seat Positioning During Rear End Collisions

Ms. Yun Cai[1], Dr. Stephanie Rossman[2], Dr. Steven Rundell[1], Dr. Luis Nolasco Ph.D.[1]

[1]Explico, Novi, MI, United States. [2]Explico, St. Petersburg, FL, United States

Introduction

The potential effect of an occupant's posture on spinal loading and disc herniation risk during a rear-end collision has not been previously evaluated. The objective of this study was to use validated computational simulations of rear-end collisions to evaluate how spinal compressive loading responds to variations in occupant posture and seat position. We hypothesized that realistic changes in posture and seat positioning would have minimal influence on spinal compression and, consequently, would not meaningfully affect the risk of intervertebral disc herniation.

Methods

Computational models of the seats of a 2019 Nissan Altima and 2013 Buick Encore were validated using publicly available physical test data of a 10-mph delta-V rear-end collision. Multiple positions and postures were modeled for a 50th percentile male seated in the aforementioned seats. These positions and postures included seatback angle, head facing to the side, torso leaned to the side, and torso twisted. All positions and postures were exposed to a rear-end impact with a change in velocity of 5 mph and an impulse of 100 msec.

Results

The seatback deformation predicted by the computational simulation matched closely with that occurring during the physical crash test (Figure 1). In general, the compressive force experienced at the cervical and lumbar spine was not influenced meaningfully by the variations in occupant posture and seat position. The average peak compression in the cervical and lumbar spine for the Altima seat was 23±1.5 lbs., and 151±10 lbs., respectively. The average peak compression in the cervical and lumbar spine for the Buick seat was 28.5±9 lbs., and 231±18 lbs., respectively.

Discussion

Intervertebral disc herniation is generally associated with compressive loading of the spine, whether arising from a single high-load event or from repetitive loading cycles. In the present study, spinal compressive forces generated during moderately severe rear-end collisions were found to be low relative to both injurious and commonly non-injurious loading thresholds reported in the literature. These findings support the hypothesis that realistic variations in occupant posture and seat positioning do not meaningfully increase spinal compression and, as a result, do not introduce a biomechanical risk of disc herniation.

Images (Optional)



Figure 1: Results of the computer simulation overlayed on physical test data for a 2013 Buick Encore.

References (Optional)

Session Category

Injury Biomechanics: N/A

P3-118

Comparison of Gelatins as Surrogates for Backface Deformation Analysis of Soft Armor

Ms. Madeleine Tarter, Mr. Andrew Davis, Mr Donald Sherman, Dr. Cynthia Bir

Wayne State University, Detroit, MI, United States

Introduction

Ballistic gelatins are widely used as soft tissue simulants to assess dynamic backface deformation (BFD) of soft body armor to provide insight into armor performance and potential injury risk. Although synthetic gelatins offer shelf stability and reusability compared to the historical gold standard, ordnance gelatin, the comparability of BFD responses between various gelatin formulations remains unknown. This study aims to compare the BFD responses of different gelatin formulations as backing materials using Level II (HG1) soft body armor panels.

Methods

High speed video (20,000 fps) was used to evaluate a total of six different simulants including ordnance gelatine in 10% and 20% concentrations, Clear Ballistics 10% and 20% products, a Perma-Gel 10% product, and a Styrene-Ethylene-Butylene-Styrene (SEBS)-based gel. Ballistic tests were performed using 9 mm FMJ Luger 124-grain projectiles at a velocity of 1140 ± 20 ft/s. Each gelatin type was shot three times from a standoff distance of 5 feet. Post-impact, video analysis was performed using MATLAB scripts[1] to quantify the maximum deformation depth (D_{max}), maximum deformation velocity (DV_{max}), maximum volume (VOL_{max}), and volume growth rate (VGR).

Results

Independent samples t-tests (Table 1) show that 10% ordnance gelatin, 10% Clear Ballistics, and 10% Perma Gel showed no key differences in BFD characteristics. 20% ordnance gelatin and 20% Clear Ballistics gelatin differed in VOL_{max} and VGR with the ordnance gelatin being statistically significantly larger ($p<0.05$). SEBS gel exhibited a smaller VGR than 10% ordnance gelatin and showed significant differences from 20% ordnance gelatin across all metrics ($p<0.05$).

Discussion

Given the variety of gelatins currently being used by the ballistics community, it is important to understand if and how they differ. The SEBS used in the current study was a 30/70% powder/mineral oil composition which was significantly different from the 20%

ordnance gelatin but compared well with the 10% ordnance gelatin. Characterizing the differences in performance will improve interpretation of BFD outcomes and aid in simulant selection for ballistic testing.

Images (Optional)

	t-test Results (p-value)					
	10% Concentration			20% Concentration	SEBS vs Ordnance	
BFD Characteristics	Ord10 vs CB10	Ord10 vs Perma	CB10 vs Perma	Ord20 vs CB20	Ord10 vs SEBS	Ord20 vs SEBS
D_{max} (mm)	0.673	0.624	1.000	0.752	0.098	0.031
DV_{max} (m/s)	0.163	0.144	0.909	0.492	0.513	0.004
VOL_{max} (cm^3)	0.406	0.096	0.393	0.036	0.178	0.004
VGR (m^3/s)	0.715	0.346	0.445	0.009	0.045	0.001

References (Optional)

[1] Bracq, A. *et al.*, Int. J. Impact Eng., 2021

Session Category

Injury Biomechanics: N/A

P3-119

Concussion Detection in Multiple Men's and Women's Contact Sports Using Instrumented Mouthguards

Mr Mathias LE MAIGAT[1], Mr David LUKE[2], Mr Zaryan MASOOD[2], Mr Daniel BONDI[2], Dr Rebecca BECKENNY[2], Dr Adam CLANSEY[3], Mr Antonin MINVIELLE[4], Mr Olivier CHAPLAIN[4], Dr Lyndia WU[2]

[1]École Normale Supérieure Paris-Saclay, Gif sur Yvette, Ile de France, France. [2]The University of British Columbia, Vancouver, British Columbia, Canada. [3]The University of British Columbia, VANCOUVER, British Columbia, Canada. [4]Fédération Française de Rugby, Marcoussis, Ile de France, France

Introduction

Brain injuries remain a major concern in contact sports, and no practical, reliable on-field method currently exists to detect concussions in real time. Medical staff must rely on observable symptoms, which are often subtle or delayed. This study aims to improve concussion detection under real-game conditions using data from instrumented mouthguards that recorded both concussive and non-injury head impacts across multiple men's and women's contact sports.

Methods

A total of 4,846 verified head impacts, including 20 concussions, were collected from male and female athletes of the French National Rugby Teams and varsity rugby and ice hockey players at the University of British Columbia. Each impact included a 50 ms window of linear acceleration, angular acceleration, and angular velocity sampled at 3200 Hz using Prevent Biometrics mouthguards. Signals were processed using two filtering pipelines: the manufacturer's proprietary filter and a 4th-order Butterworth low-pass filter at 300 Hz.

From these signals, several biomechanical criteria—such as BrIC, HIP, and DAMAGE—were computed to discriminate concussive from non-injury events. Model performance was evaluated using three complementary approaches: global detection ability using the area under the ROC curve (AUC), game-oriented evaluation prioritizing specificity followed by sensitivity, and constrained evaluations fixing true positive or false positive rates to allow direct comparison with World Rugby thresholds (75 g and 4500 rad/s^2 for men; 65 g and 4500 rad/s^2 for women).

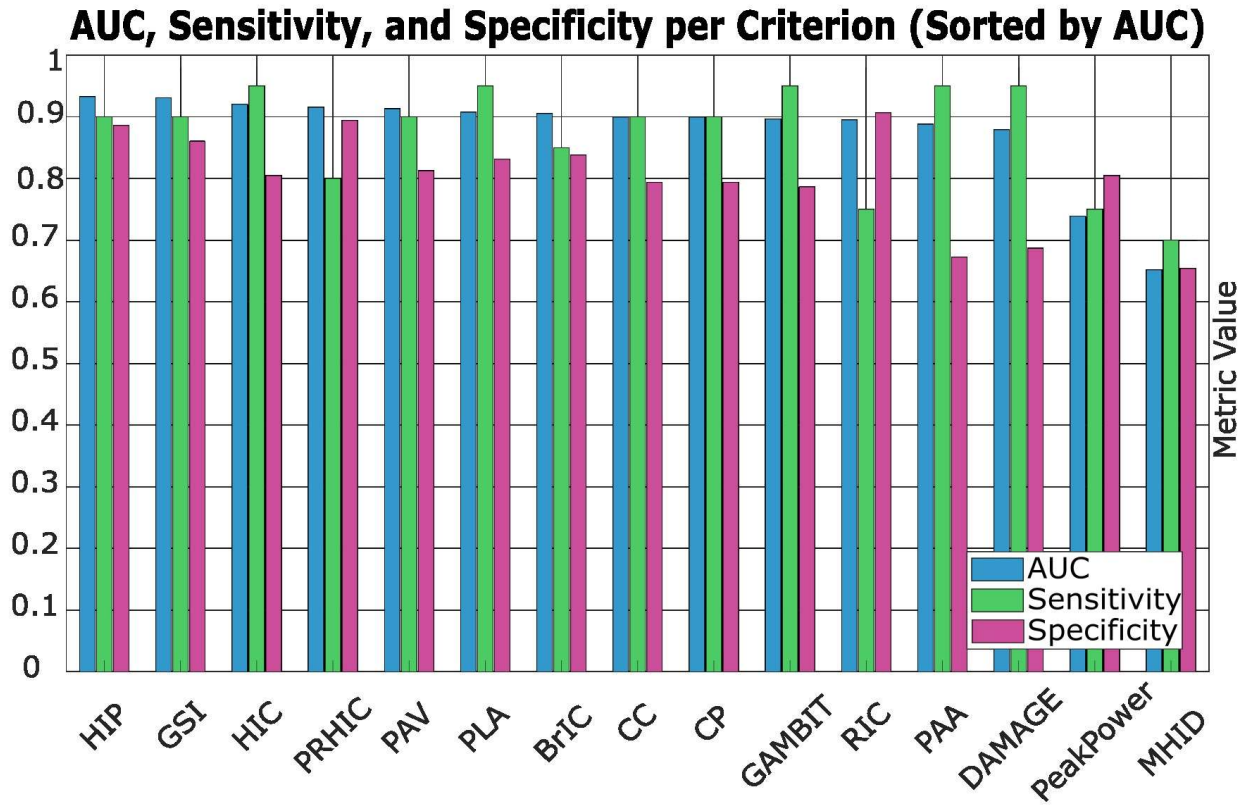
Results

The best global detection model used the HIP criterion and achieved an AUC corresponding to 93% accuracy. HIP also produced the best specificity-prioritized model, reaching 0.992 specificity. Under fixed TP and FP constraints, the GSI and HIC criteria outperformed others, matching the number of concussions detected by current World Rugby thresholds while reducing false positives by one.

Discussion

Instrumented mouthguards combined with optimized biomechanical criteria show strong potential for improving on-field concussion detection. This approach could support medical decision-making by identifying players who require sideline assessment, improving player safety, limiting unnecessary removals, and helping reduce long-term neurological risks associated with repetitive head impacts.

Images (Optional)



Session Category

Injury Biomechanics: N/A

P3-120

Differences in Lower Extremity Posture between Male and Female Drivers

Dr Matthew Reed PhD

University of Michigan, Ann Arbor, MI, United States

Introduction

Analyses of crash injury data have shown that female drivers are at increased risk of lower-extremity injury in frontal crashes [1]. Some of the difference in risk persists after accounting for vehicle differences that are not fully addressed by adjusting for delta-V [2]. On average, female drivers have shorter stature and sit further forward in the vehicle [3]. Few studies have addressed sex differences in lower-extremity posture for drivers.

Methods

As part of a laboratory study of driver and passenger body shape, posture, and belt fit [4], driving postures were recorded for 97 male and female drivers as they sat in a laboratory mockup in up to 9 different package conditions characterized by different seat heights and steering wheel positions.

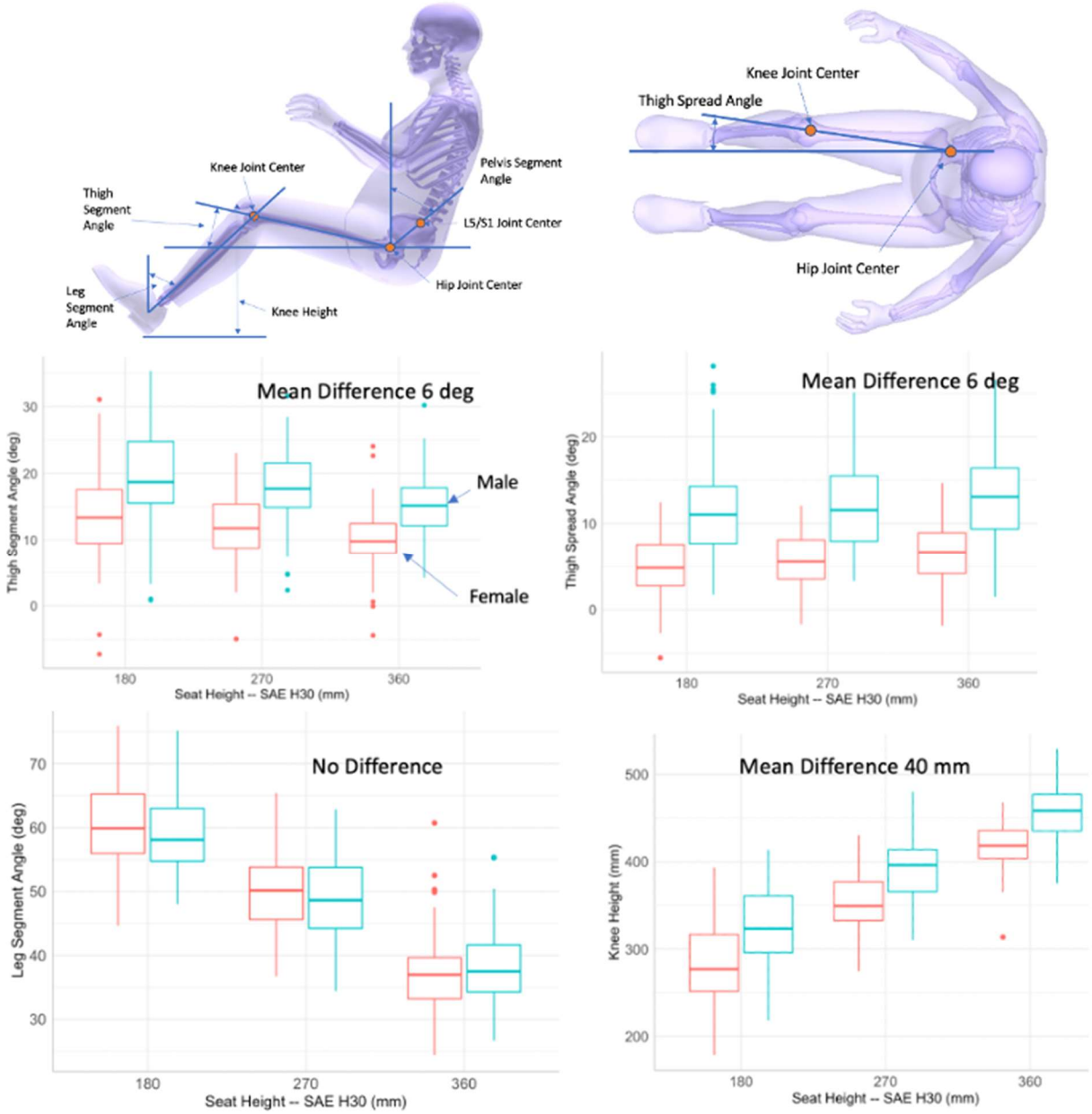
Results

Female drivers sat with their thighs closer to horizontal in side view (12±5˚ for female, 17±6˚ for male) and closer to fore-aft in top view (6±3˚ for female, 12±5˚ for male). Across package conditions, about 75% of the driver postures with a side-view thigh angle within 10 degrees of horizontal were female. Leg segment angles with respect to vertical in side view were not significantly different between male and female drivers (49±3˚ for female, 49±5˚ for male). Although the mean values of the thigh side-view angle and leg segment angle varied with seat height and steering wheel position, the sex differences were not significantly different across conditions. Due to shorter leg lengths for female drivers and similar leg angles, the knee was lower and more forward for female drivers.

Discussion

Driver posture may affect lower extremity injury risk in frontal crashes by changing the loading patterns. Simulation studies suggest that a flatter initial thigh angle may result in the knee being driven down the bolster, increasing the axial load on the leg and increasing the risk of ankle injury. This study is limited by the static laboratory setting with a single vehicle seat and short duration.

Images (Optional)



References (Optional)

[1] Forman et al. *Traffic Injury Prevention* 2019

[2] Brumbelow et al. *IRCOBI*. 2023

[3] Reed et al. *Human Factors, 2000*

[4] Reed & Ebert. UMTRI-2013-26.

Session Category

Injury Biomechanics: N/A

P3-121

Towards a Biofidelic Test for Evaluating Equestrian Helmet Performance During Crush Scenarios

Miss Jasmin Stoff[1], Prof Michael Gilchrist[2], Prof Aisling Ni Annaidh[2], Miss Megan Barnes-Wood[1], Dr Peter Theobald[1]

[1]Cardiff University, Cardiff, Wales, United Kingdom. [2]University College Dublin, Dublin, Ireland, Ireland

Introduction

Horse-related crush injuries pose a significant risk to riders. Currently, equestrian helmet standards assess lateral crush resistance using quasi-static loading between two metal plates, typically only up to about 0.8 kN [1]. This method does not accurately simulate real accident conditions and is further compromised by the absence of a headform during the tests. This study investigates whether existing crush certification tests, and the pass/fail criteria associated with lateral helmet deformation, represent a meaningful measure of head injury risk during horse crush scenarios.

Methods

Finite element (FE) models of multiple horse regions (sacral, lumbar, side) and a PAS015-certified equestrian helmet were developed and validated against equine cadaveric impact data [2]. Impacts were then simulated onto both a rigid standard headform and a biofidelic finite element head model (FEHM) [3] across a range of surfaces, including deformable turf, synthetic and dirt tracks, and a rigid flat steel anvil.

Results

The FE horse impactors were validated against cadaveric data, with 8–24% mean error. The biofidelic FEHM consistently reported higher peak forces than the rigid headform, typically 22% or more. Deformable surfaces reduced peak forces and increased impact duration relative to the rigid flat, steel anvil (Figure 1). However, even the most favourable surface conditions produced forces well above established skull fracture criteria in both the FEHM and headform simulations.

Discussion

The results indicate that modifying the current test method by integrating a FEHM or physical headform creates opportunity to better understand ‘real life’

interactions. Replicating such tests, the FEHM far exceeded the skull fracture thresholds [4]. Such risk is not captured by the current lateral crush test, which omits a headform and therefore cannot quantify skull deformation or loading levels associated with severe injury. These findings highlight the need to revise certification protocols to include headform, or preferably biofidelic FE simulations, to ensure helmet designs are evaluated against metrics that reflect the true injury mechanisms present in equestrian crush incidents.

Images (Optional)

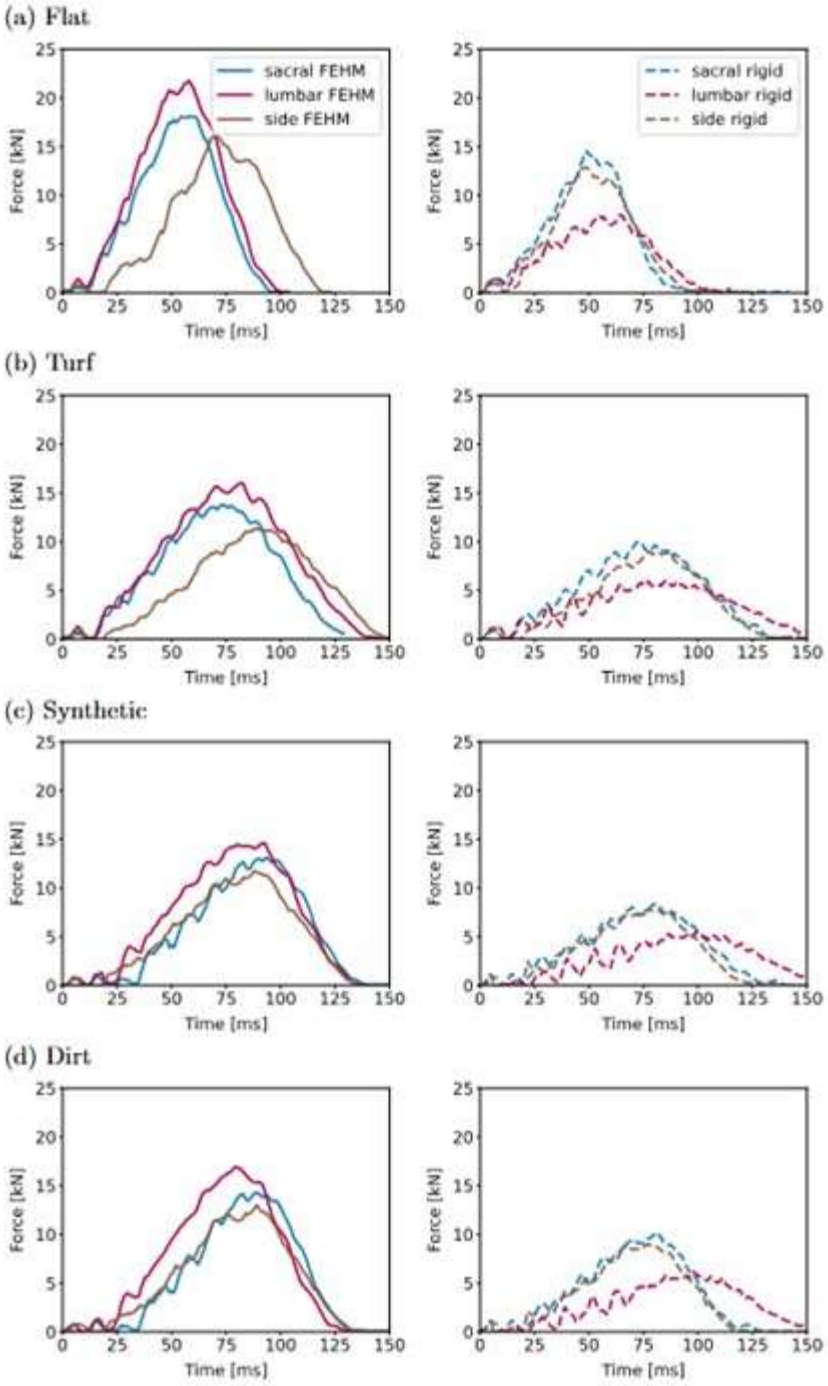


Figure 1: Peak force recorded on the finite element head model (FEHM) and the rigid headform when wearing an equestrian helmet and crushed with 3 horse impactors (sacral, lumbar, side) upon a flat steel anvil (a), turf (b), synthetic (c) and dirt surfaces (d).

References (Optional)

[1] PAS015:2011. British Standards Institution, 2011.

[2] TA Connor *et al.* App Eng Sci, 2021.

[3] A Trotta *et al.* Int J Mech Sci, 2020.

[4] N Yoganandan *et al.* J Neurotrauma, 1995.

Session Category

Injury Biomechanics: N/A

P3-122

Head Acceleration Exposure Incidence and Severity in University-Level Female Rugby Players

Miss Megan Barnes-Wood, Mr Edward Williams, Dr Peter Theobald

Cardiff University, Cardiff, Wales, United Kingdom

Introduction

Acute, severe head acceleration exposures (HAE) can cause concussion, whilst a high incidence of sub-concussive HAEs are strongly associated with long-term neurological risk, especially chronic traumatic encephalopathy. Rugby union manages player welfare using head injury assessment (HIA) thresholds and return-to-play protocols; however, these are primarily developed from male data [1], [2]. Women now represent over a quarter of global rugby participants [3], though their head impact biomechanics remain poorly understood. Safety protocols have adopted a peak linear acceleration (PLA) threshold (65g) 12% lower than male data; however, the peak angular acceleration (PAA) threshold, with a stronger association to brain trauma, remains 4500 rad/s^2. This study provides the first insight into the relative risks faced by amateur female athletes in top-tier, university-level rugby.

Methods

Twenty-six female university-level rugby players wore instrumented mouthguards (iMGs) for a longitudinal head impact monitoring study. For this analysis, data were extracted from four competitive fixtures, with each game involving 11-15 players wearing iMGs. The iMGs captured kinematic data for all impacts exceeding an 8 g threshold. Internal quality auditing verified true head contacts.

Results

HAE incidence-severity curves are presented in Fig 1 (a, b). A high incidence of low severity kinematic data was recorded (19.1 impacts per player hour at > 8 g; PAA: 17.9 impacts per player hour at > 500 rad/s^2), declining when considering higher severity HAEs. An average 4 impacts occurred above the 65g HIA PLA, and PAA, thresholds across 4 games.

Discussion

University-level female rugby players are exposed to significant HAEs. Incidence and severity exceeded elite data (Fig 1 c, d), meaning the player pool at greatest risk of short-

and long-term brain injuries should be expanded beyond just professional athletes. Further work will use iMG-derived kinematics in finite element analysis to relate measured impacts to internal brain loading and injury risk, whilst also aspiring to determine how thresholds should be adjusted to reflect female physiology.

Images (Optional)

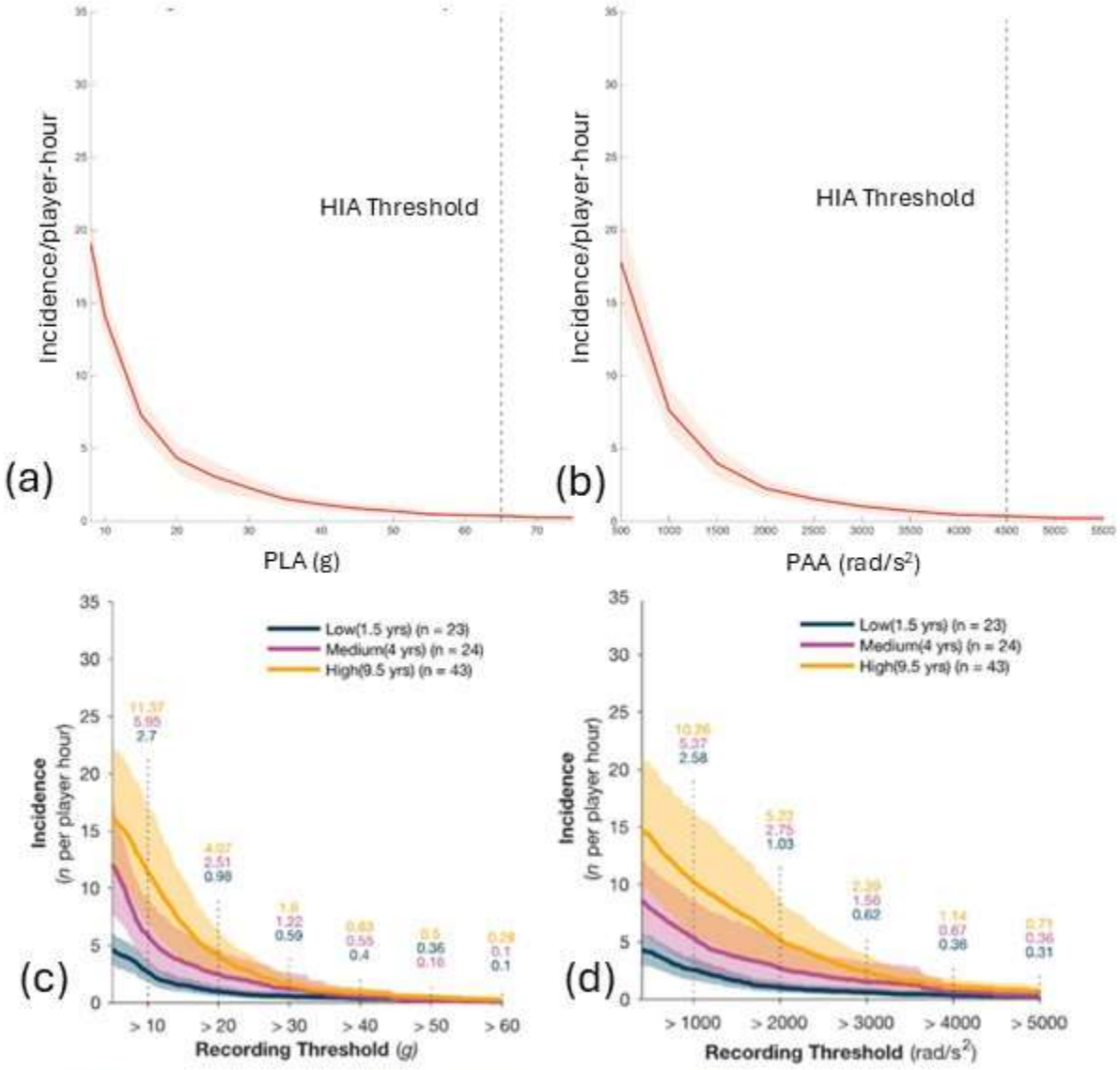


Figure 1. HAE incidence-severity curves describing iMG data from female rugby players. (a) Mean curves for PLA across the 4 analysed games of the university-level rugby team. (b) Mean curve for PAA across the 4 analysed games of the university-level rugby team. (c) PLA, and (d) PAA data, adopted from [4] that describes comparative HAE data drawn from elite women's rugby team, classified based on experience.

References (Optional)

[1] L. Mainwaring *et al.,* Int. J. Psychophysiol, 2018.

[2] A.J. Gardner *et al.* Sports Med. Auckl. NZ, 2014.

[3] 'World Rugby Year In Review 2017'.
Available: https://publications.worldrugby.org/yearinreview2017/en/4-1/, 2025.

[4] M.D. Bussey *et al*. Sports Med, 2025.

Acknowledgements (Optional)

HITIQ Ltd generously provided the iMGs used in this study, whilst also providing technical support during system deployment and data collection. The enthusiastic engagement of CULRFC players is also gratefully acknowledged.

Session Category

Injury Biomechanics: N/A

P3-123

Examining Plantar Pressure and Tibial Acceleration Patterns to Identify Biomechanical Variations Associated With Patellofemoral Pain – a Pilot Study

Miss Megan Gordon M.S.[1], Dr. Eddie Austin Ph.D., DPT[2], Dr. Luke Bunch DPT[2], Dr. Hyun K Kim Ph.D.[1], Mr. Derek D Calvert AT[3]

[1]Louisiana State University, Baton Rouge, Louisiana, United States. [2]Ochsner Physical Therapy, Baton Rouge, Louisiana, United States. [3]Louisiana State University Athletics, Baton Rouge, Louisiana, United States

Introduction

Patellofemoral pain (PFP) is a common overuse injury [1]. Identifying biomechanical variations in individuals with PFP may improve understanding of its underlying mechanisms. This study aimed to determine key regional plantar pressure and tibial acceleration features associated with PFP during functional tasks.

Methods

Five participants with unilateral PFP (4F, 1M; 23.4±3.8yrs) and five healthy controls (3F, 2M; 23.6±3.6 yrs) performed walking, running, and single-leg squat (SS) tasks. Plantar pressure distribution was recorded using XSENSOR insoles (Calgary, Canada). Tibial acceleration was measured using inertial measurement units (IMUs; Xsens) placed on the anterior-medial aspects of the distal tibia. For gait tasks, peak tibial acceleration (g), resultant tibial acceleration (RTA=square root of $ax^2+ay^2+az^2-1$) and peak plantar pressure (kPa) were averaged across strides. For the SS task, ascent and descent phases were determined, and the same variables were obtained. The symmetry index (SI%; $X_r-X_l)/0.5(X_r+X_l)\times100$) was calculated to quantify side-to-side differences. Two-way mixed ANOVAs (group × condition) assessed main and interaction effects on peak pressure, SI%, and tibial acceleration variables. Paired and independent t-tests examined within- and between-group peak values.

Results

A significant interaction for peak RTA (p=.026) was found. Also, a significant group effect was identified for RTA (p=.008). Furthermore, significant condition effects were found for symmetry index of RTA (p=.003) and for peak tibial acceleration (p<.001) and peak RTA (p<.001), with running producing the highest values. Finally, independent t-tests showed between-patient asymmetry (injured limb vs dominant limb), with higher lateral heel loading on the injured side (p=.04) during walking. No overall group effects were found for plantar regions.

Discussion

Across all tasks, participants with PFP exhibited higher RTA. Specifically, the interaction effect shows as functional load increased from walking to running, PFP participants demonstrated disproportionately greater increases in RTA, suggesting increased tibial loading and reduced shock absorption. These findings are consistent with previous research suggesting elevated RTA is linked to increased knee joint loads and higher patellofemoral stress which is accentuated via pain in the knee [2].

References (Optional)

[1] Boling MC et al., *Am J Sports Med*, 2009

[2] Doyle E et al. *ABC12:Conf. Program,* 2021

Session Category

Injury Biomechanics: N/A

P3-124

Musculoskeletal Injuries in American Ballroom Dancers—A Survey-based Study

Mr Mohammad Salsali[1], Dr Meredith Wells[2], Dr Feng Yang[1]

[1]Department of Kinesiology and Health, Georgia State University, Atlanta, Georgia, United States. [2]Exponent, Inc. Biomechanics Practice, Farmington Hills, Michigan, United States

Introduction

Ballroom dance demands high physical control, flexibility, and endurance [1], which increase the risk for musculoskeletal injuries, particularly in the lower limbs [2]. Despite growing evidence on ballroom-related injuries [3], no study has been dedicated specifically to investigating ballroom dancers in the U.S., nor has it recorded the impact of injuries. Therefore, this study aimed to determine the prevalence, anatomical location, and impact of musculoskeletal injuries among ballroom dancers in the U.S.

Methods

A total of 138 American ballroom dancers completed an online survey, which focused on their dance experience, injury history, and the impact of injuries. Descriptive statistics were conducted in SPSS v29 (IBM) to quantify injury incidence, anatomical injury location, and injury impact.

Results

Among the surveyed dancers, 80 were female, and 56 were male. The sex of two participants was unspecified. Their ages ranged from 18 to 85 years, and their ballroom dance experience ranged from 1 month to 62 years. 71 (51.4%) and 50 (36.2%) reported at least one injury and multiple injuries, respectively. Among reported injuries, the most commonly injured locations were the feet/toes (18.9%), knees (13.4%), ankles (12.2%), back (11.8%), and shoulders (10.5%, Fig. 1). Injured dancers reported negative impact on performance (41%), quality of life (44%), financial situation (20%), and love of dance (6%).

Discussion

The current study provides insights into the prevalence and impact of musculoskeletal injuries among ballroom dancers in the U.S. Our finding that the lower leg is most prone to injuries confirms previous research [3]. Although lower limb injuries are the most common, especially in the feet, knees, and ankles, some injuries affect the upper body. Many dancers also reported significant impacts of injuries on performance, finance, and quality of life. These findings suggest that ballroom dancers in the U.S. need improved education on rehabilitation services to prevent injuries. Future studies involving large, diverse sample populations are needed to expand our understanding of how ballroom dancing causes injuries.

Images (Optional)

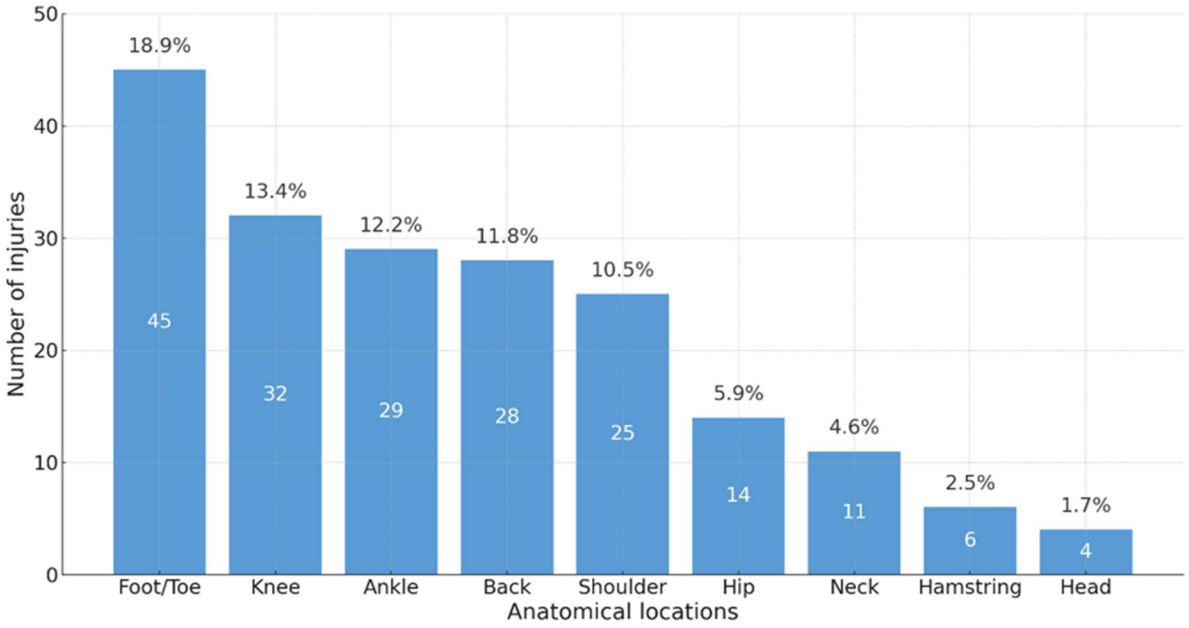


Fig. 1: Total number of injuries across anatomical regions.

References (Optional)

1. Liu, X., et al., Front Psychol, 2023.
2. Cardoso, A.A., et al., Motriz: Revista de Educação Física, 2020.
3. Keijsers, P.J.H., et al., Journal of Dance Medicine & Science, 2023.

Acknowledgements (Optional)

The author thanks all participants for their time and contributions to this study.

Session Category

Injury Biomechanics: N/A

P3-125

Airbags for Neck Protection: A Computational Analysis of Head-First Motorcycle Crash Dynamics

Dr. Mohammad Nasim[1,2], Mr. Muhammad Asif Zawad[1], Ms. Tahia Ilham[1], Prof. Ugo Galvanetto[2]

[1]Islamic University of Technology, Dhaka, Dhaka, Bangladesh. [2]University of Padova, Padova, Padova, Italy

Introduction

Motorcyclists are among the most vulnerable road users. Cervical spine injuries due to direct or transmitted impact forces remain at significant injury risk during a motorcycle accident. While traditional neck braces aim to restrict head movement to protect the neck, their bulky design often compromises comfort and rider dynamics. This study investigates the potential of airbag technology as an adaptive solution for mitigating neck injuries during motorcycle crashes.

Methods

Using the validated D-Neck finite element (FE) model, two airbag jacket configurations (one-layer and two-layer) were evaluated alongside helmet-only scenarios to assess their protective performance during head-first compressive impacts. Simulations were conducted across impact velocities of 3.2 m/s, 5.2 m/s, and 7.2 m/s, and at impact angles of +15°, 0°, and –15°. The effectiveness of each design was quantified based on predicted AIS2+ and AIS3+ neck injury risks using the neck injury criterion (Nij).

Results

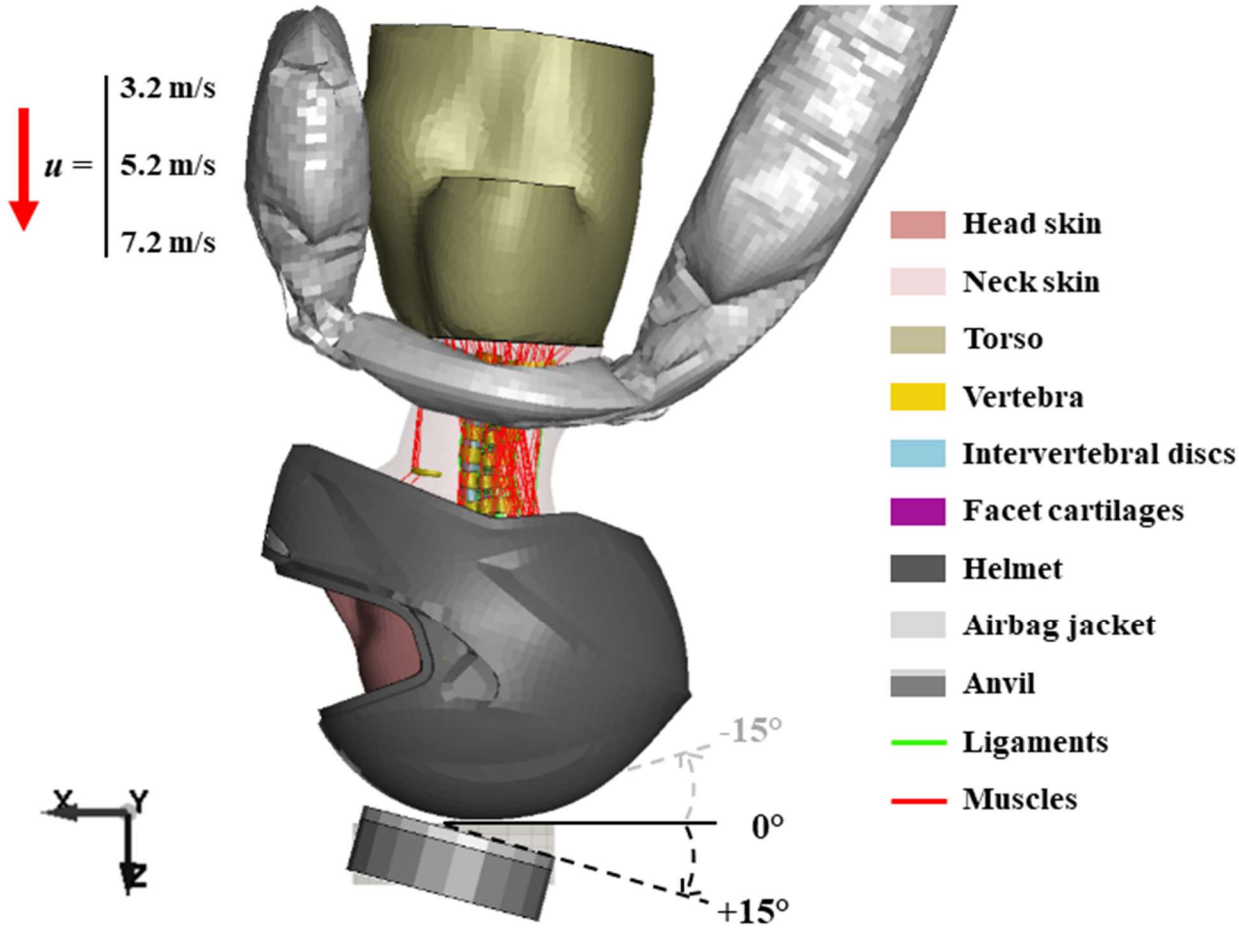
Both airbag jacket configurations substantially reduced neck loading compared to the helmet-only condition, particularly at low impact velocity. At 3.2 m/s, the one-layer and two-layer airbags consistently decreased peak upper-neck forces and resulted in noticeably lower predicted AIS2+ and AIS3+ injury risks. At higher velocities (5.2 m/s and 7.2 m/s), however, the protective benefits were not fully sustained; in several cases, the airbags produced greater neck forces than the helmet-only condition, indicating potential performance limitations under more severe impacts.

Discussion

The one-layer airbag consistently outperformed the two-layer configuration across most conditions, underscoring the importance of achieving an optimal balance between support and mobility; excessive stiffness or bulk can inadvertently restrict natural neck motion and

elevate injury risk. Airbag performance was also strongly dependent on impact angle: the most substantial risk reductions occurred at +15°, while responses at 0° and –15° were more variable, indicating sensitivity to impact direction and load path. To enhance robustness, future airbag systems should incorporate optimized or adaptive design features that adjust stiffness, inflation behavior, or geometry to impact direction and severity, maximizing protection without introducing secondary risks.

Images (Optional)



Acknowledgements (Optional)

The research leading to these results initially received funding from the People Programme (Marie Curie Actions) of the European Union's Seventh Framework Programme FP7/2007-2013/ under REA grant agreement n° 608092. The research received further support by the ECCELLENZA programme of the CARIPARO Foundation under the REDIPhE project. The authors would like to thank Mr. Franco Gatto from Dainese S.p.A. for providing the CAD file of the single-layer airbag jacket.

Session Category

Injury Biomechanics: N/A

P3-126

Head Impact Kinematics in Male U17A Box Lacrosse and U16AA Ice Hockey: A Comparative Pilot Study Using Instrumented Mouthguards

Mr. Nicholas Deaver BSc[1], Dr. Ash Kolstad PhD[1,2,3,4], Mr. Daniel Bondi MSc[5], Dr. Adam Clansey PhD[5], Ms. Haley Truscott BSc[1], Mr. Eric Gibson MSc[1,2,6], Dr. Nick Reed PhD, MScOT[7], Dr. Brent Hagel PhD[1,2,8,9,10], Dr. Lyndia Wu PhD[5,11], Dr. Stephen West PhD[1,2,3,4,8,12,13], Dr. Carolyn Emery PT, PhD[1,2,3,4,6,8,9,10]

[1]Sport Injury Prevention Research Centre, Calgary, Alberta, Canada. [2]Alberta Children's Hospital Research Institute, Calgary, Alberta, Canada. [3]Integrated Concussion Research Program, Calgary, Alberta, Canada. [4]Hotchkiss Brain Institute, Calgary, Alberta, Canada. [5]Department of Mechanical Engineering, Vancouver, British Columbia, Canada. [6]McCaig Institute for Bone and Joint Health, Calgary, Alberta, Canada. [7]Department of Occupational Science & Occupational Therapy, Toronto, Ontario, Canada. [8]O'Brien Institute for Public Health, Calgary, Alberta, Canada. [9]Department of Pediatrics, Calgary, Alberta, Canada. [10]Department of Community Health Sciences, Calgary, Alberta, Canada. [11]School of Biomedical Engineering, Vancouver, British Columbia, Canada. [12]UK Collaborating Centre on Injury and Illness Prevention in Sport, Bath, Somerset, United Kingdom. [13]Centre for Health, and Injury and Illness Prevention in Sport, Bath, Somerset, United Kingdom

Introduction

Ice hockey and box lacrosse are collision sports with elevated concussion rates. Head acceleration events (HAEs) quantify biomechanical loading and impact exposure. Limited data exist for head kinematics in adolescent athletes. Instrumented mouthguards (iMGs) offer accurate HAE measurement. To compare HAE incidence rates and head kinematics using iMGs and player-to-player contact metrics via video analysis between adolescent male hockey and lacrosse players.

Methods

A prospective cohort study was conducted during the 2024 lacrosse and 2024–2025 hockey seasons involving one male U17A lacrosse team (ages 15-16;n=19;iMG=9) and one male U16AA ice hockey team (ages 14-15;n=20;iMG=11). HAEs were video-verified using synchronized iMG data following standard protocol. Median kinematic values were compared using the Wilcoxon rank sum test. Player-to-player contacts were analyzed by video analysis. Statistical analysis included Poisson regression to estimate incidence rates and rate ratios with 95% confidence intervals.

Results

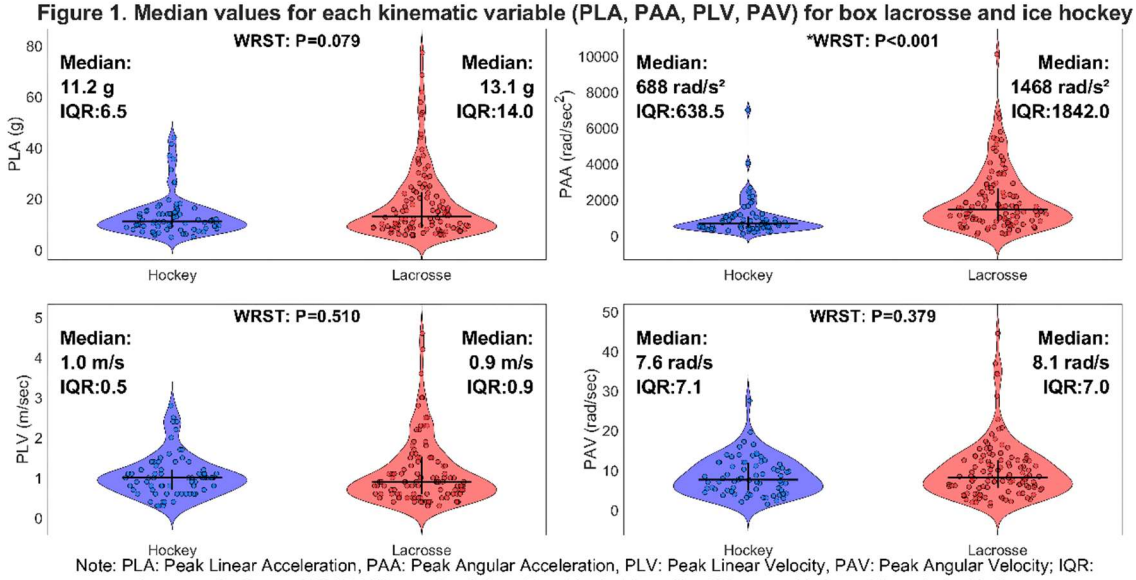
Across six games/sport, iMG athletes recorded 110 HAEs in lacrosse (22.2 HAEs/game; 95% CI:18.6–27.0) versus 71 in hockey (12.0 HAEs/game; 95% CI:9.6–15.0) (IRR=1.55; 95% CI:1.15–2.09). Peak angular acceleration was significantly higher in lacrosse (median:1,467.5rad/sec^2; 25th-75th%:803.0-2,645.0) compared with hockey (median:688rad/sec^2; 25th-75th%:425.0-1,063.5), while peak linear acceleration, linear velocity, and angular velocity did not differ (Figure 1). Video analyzed head contact rates were 1.67-fold higher in lacrosse (IR=18.0/game; 95% CI:15.6–20.4) than hockey (IR=10.8/game; 95% CI:7.8–13.8) (IRR=1.67; 95% CI:1.25–2.22). Direct head contact rates were 2.66-fold higher in lacrosse (IR=16.8/game; 95% CI:14.4–19.2) than hockey (IR=6.0/game; 95% CI:3.0–11.4) (IRR=2.66; 95% CI:1.49–4.73), primarily due to cross-checking (71% of total contacts) in lacrosse and body-checking (79%) in hockey. The cross-checking rate was 9.44-fold higher in lacrosse (IR=433.8/game; 95% CI:410.4–458.4) than hockey (IR=45.6/game; 95% CI:34.8–60.0) (IRR=9.44; 95% CI:7.24–12.30) and body-checking rates were 2.80-fold higher in hockey (IR=154.8/game; 95% CI:127.2–187.8) (LacrosseIR=55.2/game; 95% CI:45.6–67.2) (IRR=0.35; 95% CI:0.27-0.46).

Discussion

Lacrosse demonstrated higher rates of HAEs, angular accelerations, direct head contacts, and head-contact mechanisms compared with hockey (which revealed higher body-checking rates). These findings highlight sport-specific biomechanical profiles, with lacrosse characterized by higher rotational loading. Results can inform tailored prevention strategies including rule changes, equipment design, and education.

Images (Optional)

Figure 1. Median values for each kinematic variable (PLA, PAA, PLV, PAV) for box lacrosse and ice hockey



Note: PLA: Peak Linear Acceleration, PAA: Peak Angular Acceleration, PLV: Peak Linear Velocity, PAV: Peak Angular Velocity; IQR: Inter-quartile Range; WRST: Wilcoxon Rank Sum Test. Vertical lines (|) = IQR range; Horizontal lines (—) = Median.

References (Optional)

Session Category

Injury Biomechanics: N/A

P3-127

Detecting Functional Spinal Stenosis Using Cerebrospinal Fluid Dynamics: A Pre-Clinical Study in the Pig

Ms. Nikoo Soltan[1], Dr. Madeleine Bessen[1,2], Dr. Najmeh Kheram[2,3], Dr. Vartan Kurtcuoglu[2], Dr. Carl Zipser[3,2], Dr. Claire Jones[1]

[1]Adelaide University, Adelaide, SA, Australia. [2]University of Zurich, Zurich, Zurich, Switzerland. [3]Balgrist University Hospital, Zurich, Zurich, Switzerland

Introduction

Traumatic spinal cord injury can result in swelling-induced compression of the neural tissues and stenosis of the cerebrospinal fluid (CSF) space. Timely and sufficient decompression of the spinal cord is recommended to improve injury outcomes. However, routine structural imaging has constraints in quantifying functional stenosis and postoperative restoration of spatial conditions. Given the close coupling of the spinal cord and CSF system, CSF pressure/flow dynamics could be functional biomarkers of spinal stenosis and aid clinical management. CSF dynamics are affected by many interacting physiological factors including arterial carbon dioxide partial pressure ($PaCO_2$). Using a pre-clinical pig model, the aim of this study was to determine if $PaCO_2$ modulation of CSF pressure is differentially altered superior and inferior to spinal stenosis.

Methods

Eight anaesthetized pigs (27±3 kg, Ethics: SAM-24-011) underwent surgical placement of fiber-optic pressure transducers in the brain lateral ventricle (LV) and spinal CSF space cranial (SCr) and caudal (SCa) to the planned level of stenosis (Fig.1A). Spinal stenosis was modelled via surgical extradural ligation of the intrathecal space at the T12 spinal level, and $PaCO_2$ was modulated by delivering CO_2 in the ventilatory circuit to increase end-tidal CO_2 from 38±4 (normocapnia) to 69±2 mmHg (clinically permissive hypercapnia). Mean CSF pressures ($CSFP_m$) at each site were measured in normocapnia and hypercapnia, pre- and post-ligation. The effect of $PaCO_2$ modulation on $CSFP_m$ was assessed using a linear mixed-effects model with random effect of animal (α=0.05).

Results

Pre-ligation, $CSFP_m$ increased during hypercapnia, compared to normocapnia, at all three sites (LV: +18%, p=0.045; SCr: +19%, p=0.037; SCa: +35%, p=0.003). Post-ligation,

$CSFP_m$ increased during hypercapnia at the supra-stenotic sites (LV: +25%, p<0.001; SCr: +26%, p=0.001) but not at the infra-stenotic site (SCa: +10%, p=0.418) (Fig.1B).

Discussion

$CSFP_m$ response to hypercapnia was limited to the supra-stenotic compartment in the presence of complete extradural ligation. These data suggest that the absence of an infra-stenotic $CSFP_m$ response to $PaCO_2$ modulation could be a functional indicator of upstream spinal stenosis. Although infra-stenotic $CSFP_m$ measurement is clinically feasible via lumbar puncture, ongoing pre-clinical work will investigate if non-invasive CSF flow measurements can detect a similar compartment-dependent response.

Images (Optional)

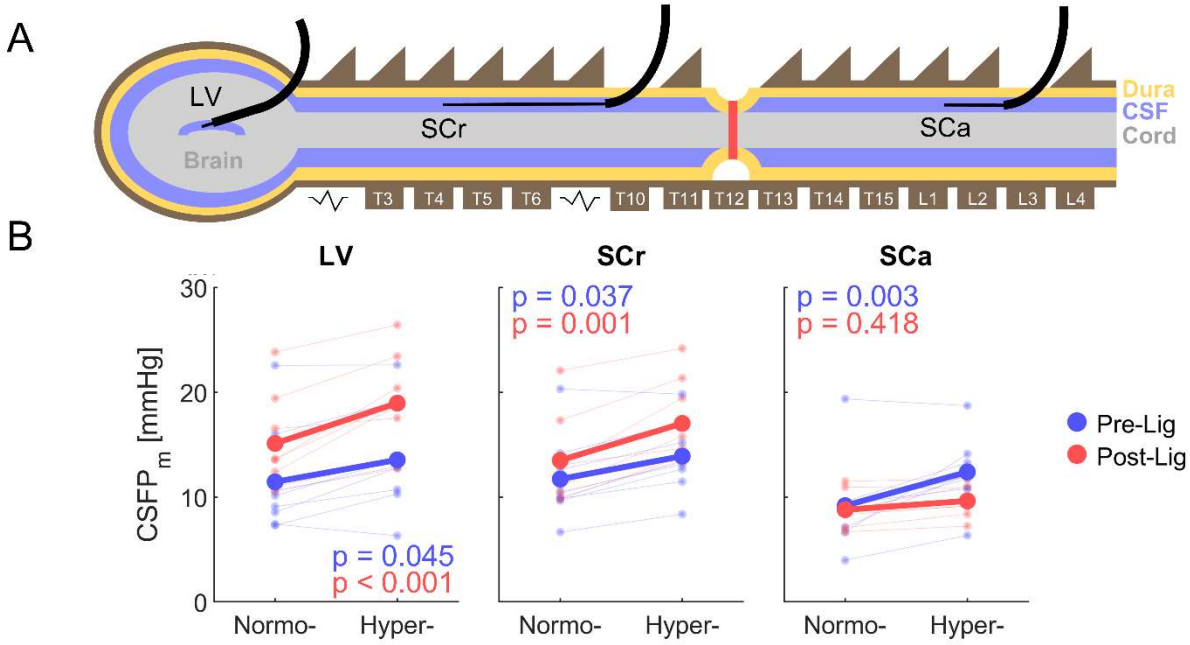


Figure 1: (A) Anatomical schematic with locations of intrathecal catheters (thick black lines), pressure transducers (thin black lines) and extradural ligation (red line). (B) Mean cerebrospinal fluid pressure ($CSFP_m$, small markers: individual animal, large markers: mean of all animals) along the neural axis in normo- and hypercapnia pre- (blue) and post- (red) extradural ligation. p-values from planned pairwise comparisons.

Session Category

Injury Biomechanics: N/A

P3-128

Contextualizing Head Accelerations During Rear-End Collisions: A Pilot Study

Dr. Patrick Fischer[1], Ms. Avery Scurlock[1,2], Dr. John Abercrombie[1], Dr. Richard Watson[1]

[1]Biodynamic Research Corporation, San Antonio, Texas, United States. [2]University of Texas, San Antonio, San Antonio, Texas, United States

Introduction

Mild traumatic brain injuries (mTBI) pose a diagnostic challenge following automotive collisions; biomechanical analysis of post-mTBI neuromuscular adaptations are not standard practice. The purpose of this study was to quantify linear and angular head accelerations during simulated rear-end collisions, and to contextualize the results with respect to mTBI risk.

Methods

Twenty simulated collisions from the Insurance Institute for Highway Safety (IIHS) were analyzed. During an IIHS test, an ATD is positioned in a production car seat, restrained with a seatbelt, and subjected to a 10-g forward acceleration while kinematic and high-speed video data are recorded. Head linear accelerations were collected in accordance with SAE J211. Head angular acceleration data were derived from sagittal video recorded during each test: markers at the head center-of-gravity and chin were tracked to determine sagittal head rotation (**Figure 1**). Angular accelerations were determined using numerical differentiation.

Results

Peak linear head accelerations were 20.9±2.0g (range: 17.8-25.7). Front-to-back linear accelerations were predominant for all tests (20.7±2.0g). For all tests, linear head acceleration peaked during the head contact period with the headrest. Peak linear head accelerations during IIHS tests represented mTBI risk between 0.008%-0.011%.

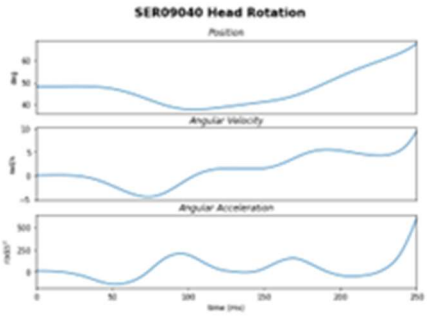
Peak angular head accelerations were 324.6±94.4rad/s2 (range: 167.7-606.4). Angular head acceleration did not peak at consistent phases across trials. Peak angular head accelerations during IIHS tests represented mTBI risk between 0.004%-0.006%.

Combined effects of linear and angular acceleration represented mTBI risk between 0.009%-0.019%.

Discussion

Preliminary results suggest linear and angular head accelerations experienced by a belted occupant do not represent an appreciable risk of mTBI during rear-end collisions up to 10-g. We noted that linear and angular accelerations may peak at different phases of the crash sequence. Combined effects of linear and angular head accelerations on mTBI risk in a rear-end collision is best determined as a time-history analysis of the crash sequence. We expect that frontal and transverse head angular accelerations were negligible compared to sagittal accelerations during IIHS tests, given that linear front-to-back head accelerations predominated the resulting head motion and translate to sagittal head rotation. However, further work is needed to confirm at the cohort level.

Images (Optional)



Session Category

Injury Biomechanics: N/A

P3-129

Application of Machine Learning Methods to Investigate Joint Load in Agility on the Soccer Field

Dr. Stefano Di Paolo[1], Dr. Margherita Mendicino[1], Dr. Eline Nijmeijer[2], Dr. Pietro Margheriti[1], Prof. Stefano Zaffagnini[1,3], Prof. Alli Gokeler[4,5], Prof. Anne Benjaminse[2]

[1]2nd Orthopaedic and Traumatologic Clinic, IRCCS Rizzoli Orthopaedic Institute, Bologna, Emilia Romagna, Italy. [2]Department of Human Movement Sciences, University Medical Center Groningen, University of Groningen, Groningen, Groningen, Netherlands. [3]Department of Biomedical and Neuromotor Sciences, University of Bologna, Bologna, Emilia Romagna, Italy. [4]Exercise Science and Neuroscience Unit, Department of Exercise and Health, Paderborn University, Paderborn, Paderborn, Germany. [5]Faculty of Health, Master Performance Sport and Health, Amsterdam University of Applied Sciences, Amsterdam, Amsterdam, Netherlands

Introduction

ACL injuries in female youth soccer are strongly influenced by the interaction between athlete, task, and environment, making on-field assessment essential for ecological validity. Building on a previously trained lab-based machine learning model[1], this study uses wearable sensors to estimate knee abduction moments (KAMs) during real-game contexts. Specifically, it investigates how kinematics, performance, and task complexity influence joint loading in real game conditions.

Methods

On-field data were collected on fifty-two healthy elite female soccer players (14.8±0.9 years), using a validated 17-IMU full-body system (240Hz; Xsens Technologies). A 75-min training including soccer-specific exercises (F-EX) and a training match (F-GAME) was recorded for each player[1]. Dominant-limb cutting movements were manually identified. Lower-limb and pelvis kinematics was extracted in three anatomical planes, and calculation of performance metrics (cut angle, center-of-mass velocity, acceleration during entry and exit phases of the cut stance phase). A previously developed Fine Gaussian SVM model[1] classified each trial as high or low KAM. The two groups were compared using Student's t-tests, separately for F-EX and F-GAME conditions. Effect sizes were quantified using Cohen's d.

Results

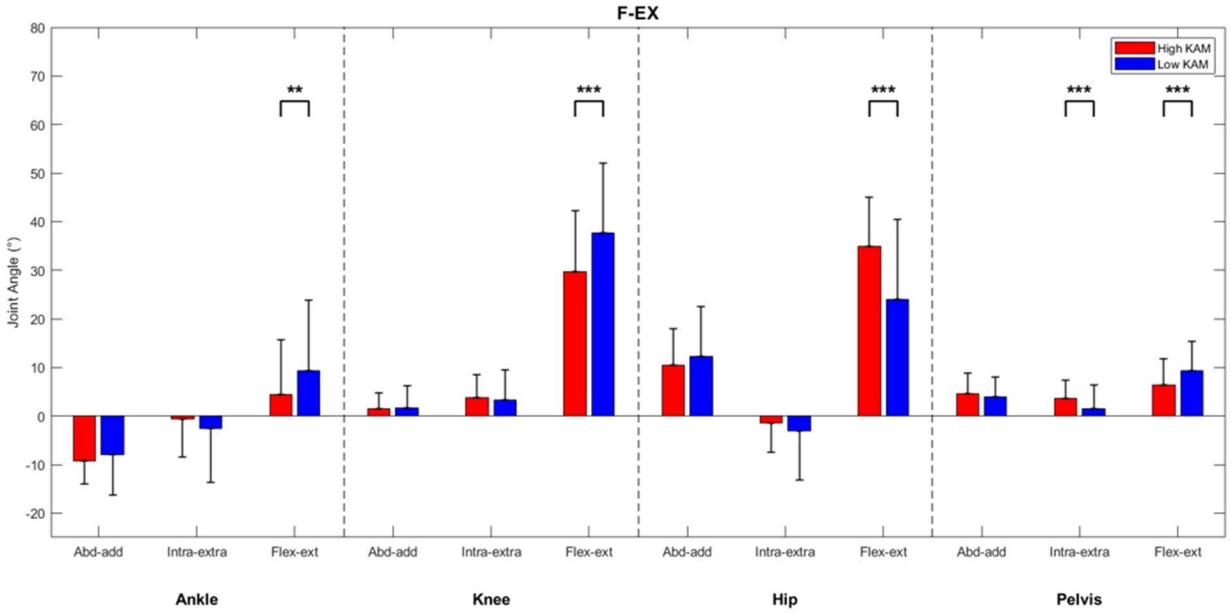
Analysis included 662 cutting trials (442 F-EX, 220 F-GAME). Trials classified as high KAM were 54 (12.2%) for F-EX and 20 (9.1%) for F-GAME. In high KAM trials, players exhibited

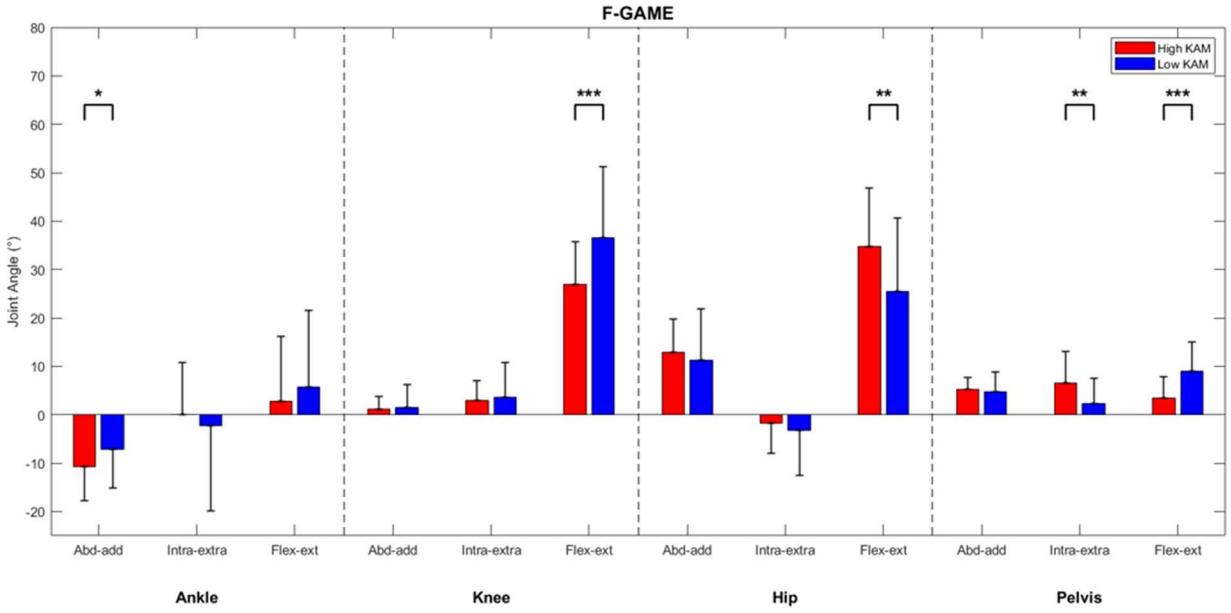
lower knee flexion ($p<0.001$), reduced pelvis anteversion ($p<0.001$), higher hip flexion ($p<0.004$), and greater pelvis ipsilateral rotation ($p<0.008$) in both F-EX and F-GAME. Lower ankle dorsiflexion was observed in F-EX ($p=0.005$), and greater ankle inversion ($p=0.042$) in F-GAME. The high KAM group showed smaller cut angles in F-EX (41°vs.55°,$p=0.013$) and higher entry peak acceleration in F-GAME ($p=0.040$). No differences were observed for peak velocity ($p>0.05$).

Discussion

On-field cutting tasks were classified as high KAM in 9–12% of trials. Lower knee and ankle flexion angles and higher accelerations were noted in the high compared to low KAM trials. Findings suggest considerable exposure to knee joint loading during sport-specific cutting tasks and primary ACL injury prevention strategies targeting biomechanical and neuromuscular control. Future work should validate interventions on-field and explore longitudinal injury risk outcomes.

Images (Optional)





References (Optional)

[1] Anne Benjaminse *et al*., Sensors, 2024

Session Category

Injury Biomechanics: N/A

P3-130

Helmet Protective Performance in High Velocity Oblique Impacts for Electric Bicycle Riders

Dr. Qi Huang, Dr. Chengbin Li, Dr. Zhou Zhou, Prof. Svein Kleiven

KTH Royal Institute of Technology, Stockholm, Stockholm, Sweden

Introduction

Electric bicycle (e-bike) riders generally travel at higher speeds than conventional cyclists [1], yet limited research has evaluated how effectively helmets protect e-bike users from traumatic brain injury. With the introduction of a new standard that requires helmet evaluation at higher impact velocities, there remains a need to understand helmet protective performance under higher-velocity oblique impacts. This study aimed to assess the protective performance of helmets associated with traditional and electric bicycles.

Methods

Three helmet models, all equipped with one rotational mitigation system, were evaluated following a previously established test protocol [1]. A newly developed headform according to EN17950 standard was used to provide a better representation of the moments of inertia and the coefficient of friction of the human head. Each helmet was subjected to four oblique impact configurations (side:pXR, front:pYR, rear:nYR, and front-side:pZR, see Figure 1) at two velocities (6 m/s and 7.5 m/s) against a 45° anvil, resulting in a total of 24 tests. These two velocities represent the head-impact speeds of conventional and e-bike cyclists.

Linear and rotational kinematics were recorded using a wireless data acquisition system and were filtered to compute injury metrics, such as peak linear acceleration (PLA), peak angular velocity (PAV), Head Injury Criterion (HIC), and Brain Injury Criterion (BrIC).

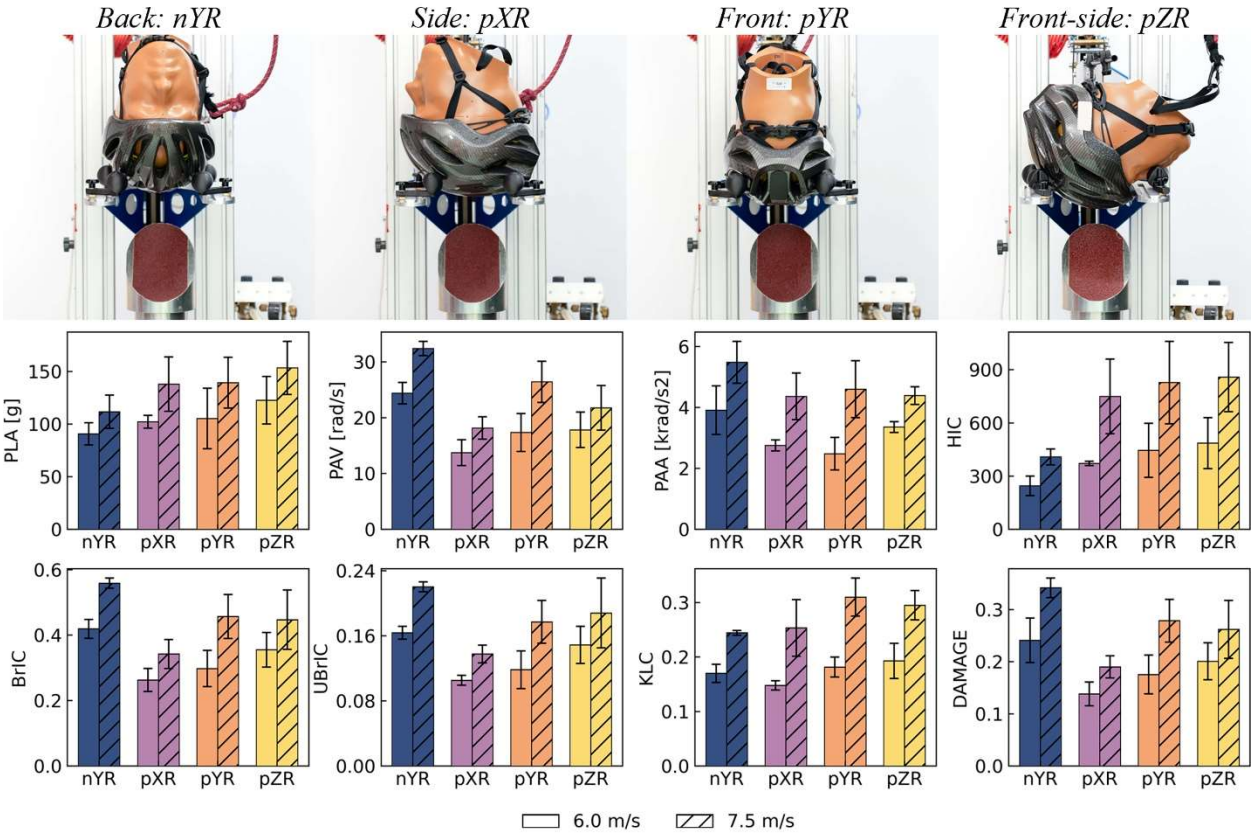
Results

Among the four impact locations, nYR impact generated the lowest linear-based injury metrics (e.g., PLA, HIC) but produced the highest rotational-based metrics (e.g., PAV, BrIC). Increasing the impact velocity from 6 m/s to 7.5 m/s elevated all injury metrics, e.g. average PLA increased by 29% and average PAV by 35% at the higher velocity (see Figure 1).

Discussion

The substantial increases in injury metrics with higher velocity highlight the importance of evaluating helmets for e-bike riders. Our preliminary investigation only includes three helmet models and one rotational mitigation system, which limits the generalizability of the findings. We are expanding the test to a broader range of helmet designs and protective technologies, and including repeatability assessments and finite element simulations to better characterize helmet performance under high-velocity impacts.

Images (Optional)



References (Optional)

[1] Baker, C. *et al*. , Ann. Biomed. Eng., 2024

Acknowledgements (Optional)

This work was supported by the Skyltfonden [no. 2024-107146, 2024-106547, and 2025-27050].

Session Category

Injury Biomechanics: N/A

P3-131

A Multimodal Measurement Approach for Analyzing and Characterizing Shaking Dynamics in Shaken Baby Syndrome Using Optical Motion Tracking, Accelerometers, and Force-Sensing Films with Offender-Profile-Aligned Participant Sampling

M.Ed. Raphael Grau[1], M.Sc. Florian Stöckl[2], B.Sc. Julian Schneider[1], PD Dr. Med. Katharina Feld[3], Dipl.-Ing. Katharina Bause[1], Univ.-Prof. Dr.-Ing. Tobias Düser[1]

[1]IPEK – Institute of Product Engineering, Karlsruhe Institute of Technology (KIT), Karlsruhe, Baden-Württemberg, Germany. [2]Robot and Human Motion Lab, DHBW Karlsruhe, Karlsruhe, Baden-Württemberg, Germany. [3]Institute of Forensic and Traffic Medicine, Heidelberg University, Heidelberg, Baden-Württemberg, Germany

Introduction

Shaken Baby Syndrome is the leading non-natural cause of death in infancy, yet its biomechanical mechanisms remain insufficiently understood. The scarcity of clearly identifiable cases and limited reliable validation data hinder a differentiation between abusive and non-abusive injury patterns. Existing shaking studies have primarily examined the motion response of non-biofidelic infant dummies, leaving the underlying initial excitation unexplored and failing to reflect offender-related demographic profiles or the applied contact forces that contribute to associated injuries. This work addresses this gap by experimentally characterizing the initial excitation and realistic load cases of shaking events.

Methods

The study employed complementary, time-synchronized sensor systems to obtain robust coherent multimodal measurements. After ethics and data protection approval, 25 participants (aged 21-35) completed pre-study questionnaires to record anthropometrics and screen for exclusion criteria (e.g. musculoskeletal injuries, psychological disorders). The setup combined two marker-based motion-tracking systems (Aruco/Vicon), an accelerometer, and a force-sensing film placed on the palmar surfaces. Grip selection was left unconstrained to reflect natural handling. Participants were instructed to shake the 7lb, 21-inch dummy fast and forcefully in three trials. Trained observers documented all sessions to clarify potential measurement deviations retrospectively. Sensor data are recorded in CSV-format and processed and analyzed using Python scripts.

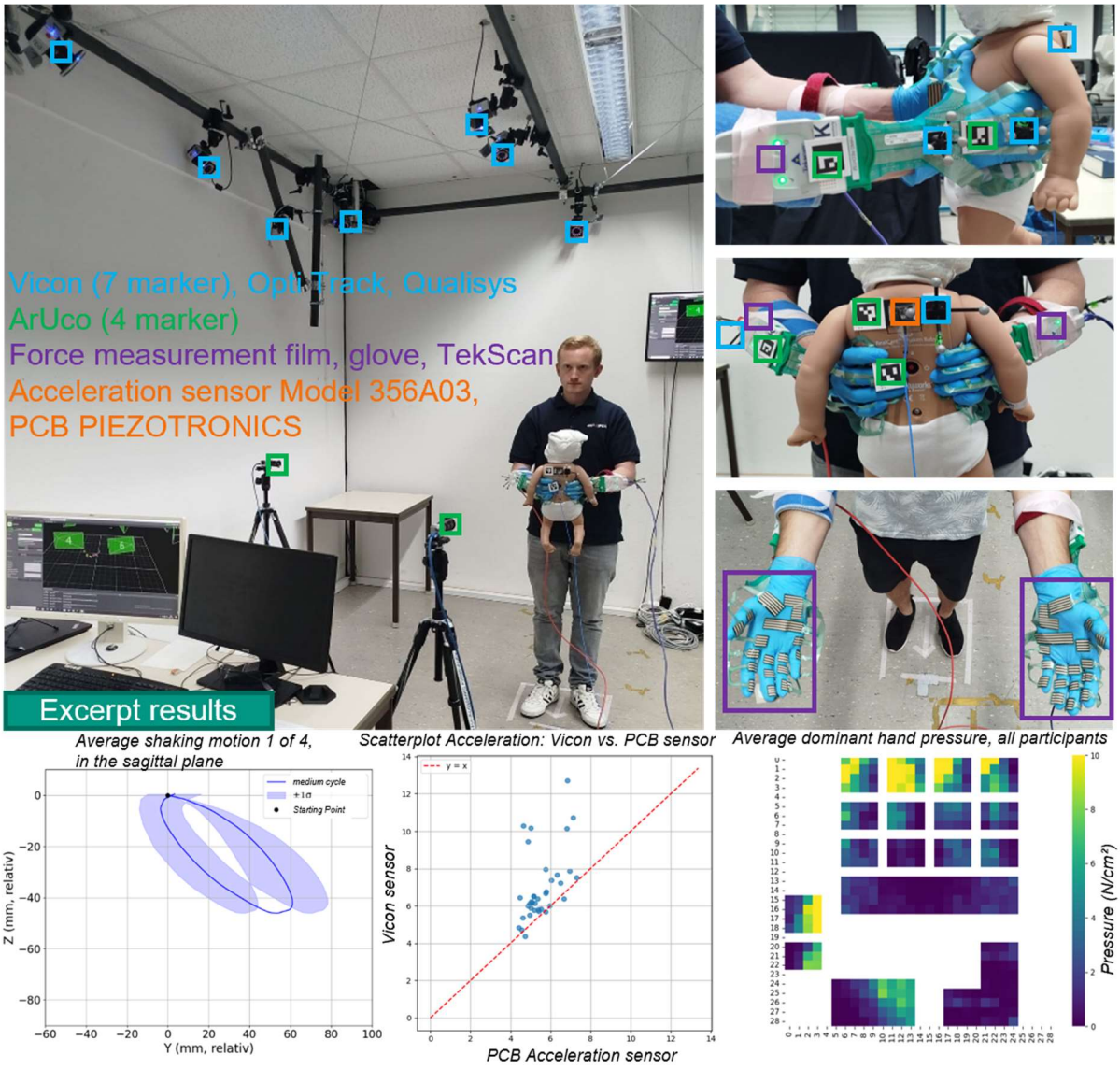
Results

All participants consistently selected a grip position at the dummy´s thorax. The primary motion occurred in the sagittal plane with peak-to-peak displacements ranging from 20-100mm. Four foundational movement patterns were identified. The motion-tracking systems showed consistent agreement in measured motion patterns. Mean shaking frequencies were 5.5Hz (accelerometer) and 6.3Hz (Vicon). Measured pressure values ranged 50-194N/cm^2, showing substantial inter-individual variability while still revealing clear overall trends. The highest loads were concentrated at the middle finger tip. No clear sex differences have been observed.

Discussion

The observed movement patterns and shaking frequencies indicate an expanded range compared to previously limited data. Participants of offender age shake at higher frequencies than reported in literature. The simultaneous measurement of forces applied to the dummy is conducted here for the first time, highlighting a further research gap. Future work will include additional participants and incorporate a preliminary stress induction to better simulate realistic shaking motions.

Images (Optional)



Session Category

Injury Biomechanics: N/A

P3-132

Estimated Ankle Ligament Strains During Roundhouse Kicks at Different Heights

Miss Renee Alexander, Dr Timothy Derrick

Iowa State University, Ames, Iowa, United States

Introduction

Over half of injuries during taekwondo sparring and demonstrations are ankle injuries [1]. However, there is limited research on the supporting leg during martial arts kick to varying heights and less on the supporting ankle or ankle injury risk related to kicking height. It was hypothesized that higher kicks would change estimated medial and lateral ankle ligament strains.

Methods

Twenty-six black belts were recruited. Marker clusters were placed on both legs and on the left ankle and foot. 3D kinematics were collected during five trials of roundhouse kicks to a paddle held at hip height and then at neck height. Trials were trimmed based on the kicking foot leaving and returning to the ground. Ankle angles were derived based on the relative motion of their segment markers using helical angles. Kinematic data were used to animate the talus, leg, and calcaneus of a musculoskeletal model of the foot. SPM with an alpha of 0.05 was used to compare strains based on kick height.

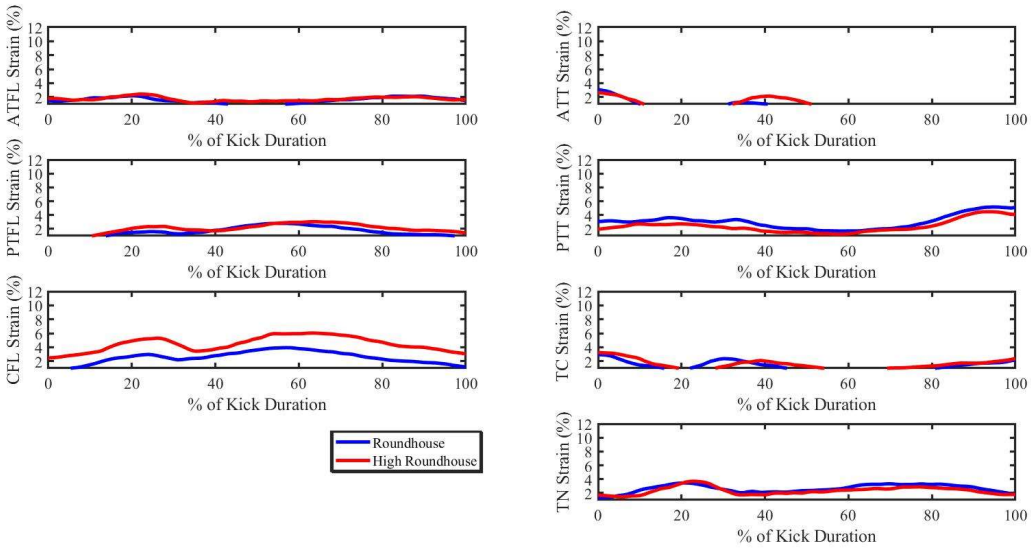
Results

Estimated anterior talofibular ligament (ATFL) strains for higher kicks were close to those estimated for kicks to the waist (Figure 1). Posterior talofibular ligament (PTFL) strains were higher until 40 to 55% of the kick with increased height. Height increased strains in the calcaneofibular (CFL) ligament throughout the entire kick. Anterior tibiotalar (ATT) ligament strains increased between 34 and 50% of the kick, while posterior tibiotalar ligament (PTT) strains were decreased throughout with an increase in kick height. Strains were increased in the tibiocalcaneal (TC) ligament until 20% and after 36% of the kick. Tibionavicular (TN) strains were decreased except before 4% and 20 to 30% of the kick. No statistically significant differences were found.

Discussion

Estimated ligament strains in the lateral ligaments generally increased with an increase in kicking height, while strains in the medial ligaments decreased. There may be a lateral shift in the ankle as height increases. Further testing and analysis is needed to determine any increased injury risk at the supporting ankle due to increasing kick height.

Images (Optional)



References (Optional)

[1] Hee Seong Jeong *et al.*, J Athl Train, 2022

Session Category

Injury Biomechanics: N/A

P3-133

Biomechanical Effects of a NiTiNOL Staple and Buttress Plating in Pauwels III Femoral Neck Fractures: A Cadaveric Comparison with Cannulated Screws

Dr. Rita Aoun Ph.D.

Arthrex, Naples, Florida, United States

Introduction

Vertical Pauwels III fractures, commonly due to high-energy trauma, are associated with complications like nonunions, necrosis, and implant failure and the reconstruction approach is controversial.[1,2] Standard three screws colinearly to the neck help reduce but may not prevent shear motion.[3] An inferomedial buttress plate can resist shear motion but may result in asymmetric stabilization, with probable superior gapping.[4,5] A NiTiNOL staple superio-anteriorly provides compression and stabilization. The purpose was to evaluate the fracture gap and biomechanically compare strengths of constructs with or without buttress plate and NiTiNOL staple.

Methods

Twenty-one matched pairs of fresh-frozen cadaveric femurs were contralaterally assigned to three screws (3S) versus 3S + buttress plate (3S+P), 3S + a NiTiNOL (DynaNite, Arthrex), staple (3S+St), or 3S + buttress plate + NiTiNOL staple (3S+P+St). Fracture creation and fixation were surgically applied under fluoroscopic guidance.[5] Specimens, dissected with the acetabulum intact, were CT-scanned and potted in 3D customized fixtures to keep alignment of the mechanical axis. Ramped compression to 500N (15N/s) followed by cyclic loading at 2Hz were applied, increasing the peak by 100N every 100 cycles until failure. Motion tracking was conducted to detect failure.

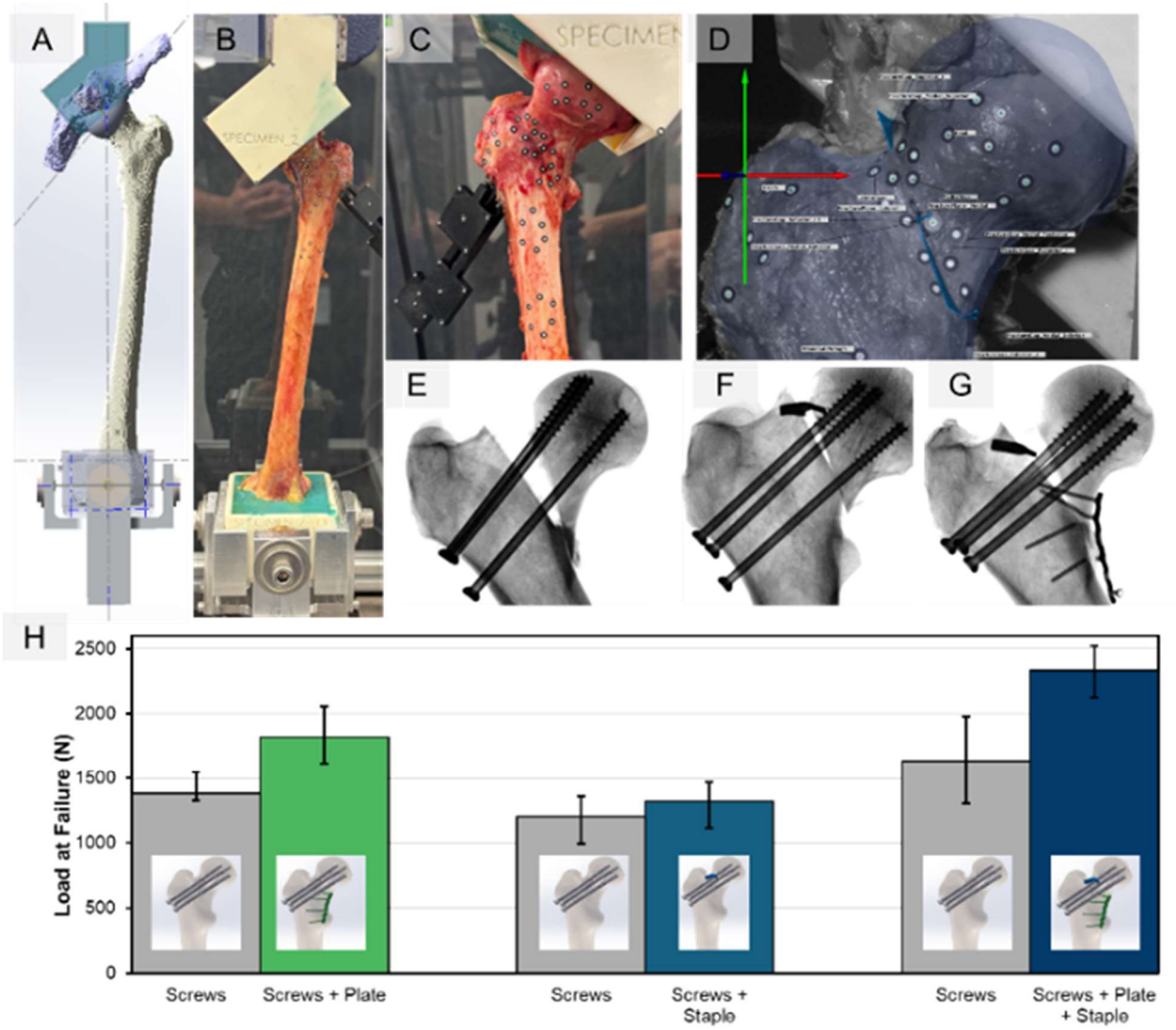
Results

Mean load to failure was highest in 3S+P+St group, occurring at loads 43% higher than its respective 3S control. Second highest failure loads were in 3S+P group, 32% higher than its respective 3S group and failure was observed superiorly. 3S+St group had larger failure loads than its respective control, and 60% failed simultaneously at all point pairs. Across all control (3S) specimens, 48% failed simultaneously at all point pairs.

Discussion

Shear failure was most apparent in constructs without plates. Plates provided increased load to failure, resulting in screw breakage. Superior gapping may be mitigated by adding a staple, resulting in the highest failure loads.

Images (Optional)



References (Optional)

[1] Sekeitto AR. et al., EFORT Open Rev. 2021;6:139–144.

[2] Sciacca S. et al., Injury. 2015;46:S57–S60.

[3] Stoffel K. et al. J Orthop Trauma. 2017;31:131–137.

[4] Liu J. et al. BMC Musculoskelet Disord. 2022;23:1–7

[5] Li J. et al. Injury. 2019;50:1895–1900.

[6] Bergmann G. et al. J Biomech. 1984;17.

[7] Speirs AD. et al. J Biomech. 2007;40:2318–2323.

Acknowledgements (Optional)

Rita Aoun[1], Zachary Koroneos[1,2], Andrea Attenasio[3], Oliver Hauck[1], Erik Kubiak[3]

Session Category

Injury Biomechanics: N/A

P3-134

BIPED mk2 Finite Element Model Pressure Sensitivity in a Helmeted Impact Protocol

Mr. Robert Chauvet[1], Mr. Aaron Brice[2], Mr. Simon Ouellet[3], Dr. Lindsey Westover[1,4], Dr. Christopher Dennison[2]

[1]Department of Mechanical Engineering, University of Alberta, Edmonton, Alberta, Canada. [2]Department of Biomedical Engineering, University of Victoria, Victoria, British Columbia, Canada. [3]Defense Research and Development Canada, Valcartier Research Center, Quebec, Quebec, Canada. [4]Department of Biomedical Engineering, University of Alberta, Edmonton, Alberta, Canada

Introduction

Accurate prediction of intracranial pressure during head impacts is critical for evaluating traumatic brain injury (TBI) risk and helmet performance [1]. The Brain Injury Protection Evaluation Device (BIPED mk2) is a physical surrogate, that can be used in impact experiments and has a finite element (FE) twin [2]. There is evidence that the FE pressure outputs are sensitive to nodal keypoint location [3], an undesirable trait. It is unproven whether the twin can detect coup/contra mechanics. This study tests the hypothesis that keypoint node mismatch relative to physical sensor location can lead to pressure errors; and, that the model can detect coup/contra mechanics.

Methods

We performed tests using The Advanced Combat Helmet test protocol [4]. Measured kinematics from the collected experimental data were applied as boundary conditions in FE simulations. Pressure outputs were calculated from elements at the nominal sensor location and adjacent nodes (≈5mm offset) in three directions. Percent differences were computed to assess positional sensitivity. Additionally, pressure gradients along the impact line were analyzed to determine if the sensor nodes captured both positive and negative pressures (coup/contra mechanics).

Results

Results indicate an overall sensitivity of 6.4% to sensor location, with a directional bias parallel to the impact (up to 15.1% for far sensors). Perpendicular offsets produced minimal variation (<4%). Gradient analysis confirmed that coup/contrecoup pressures follow a near-linear distribution across the brain slice. While the two-sensor nodes characterized frontal and rear impacts, it did not capture the coup/contrecoup pressures for crown and lateral impacts, where sensor nodes were not aligned with the impact direction.

Discussion

These findings show that mismatch between physical sensor location, and location in an in-silico model, can drive discrepancies in physical and in-silico pressure results. Further, that pressure sensors should be placed to capture coup/contra mechanics. This study shows the importance of sensor location and fidelity between in-silico and physical models and the extent to which lack of fidelity can pose limitations on the validity of results.

Images (Optional)

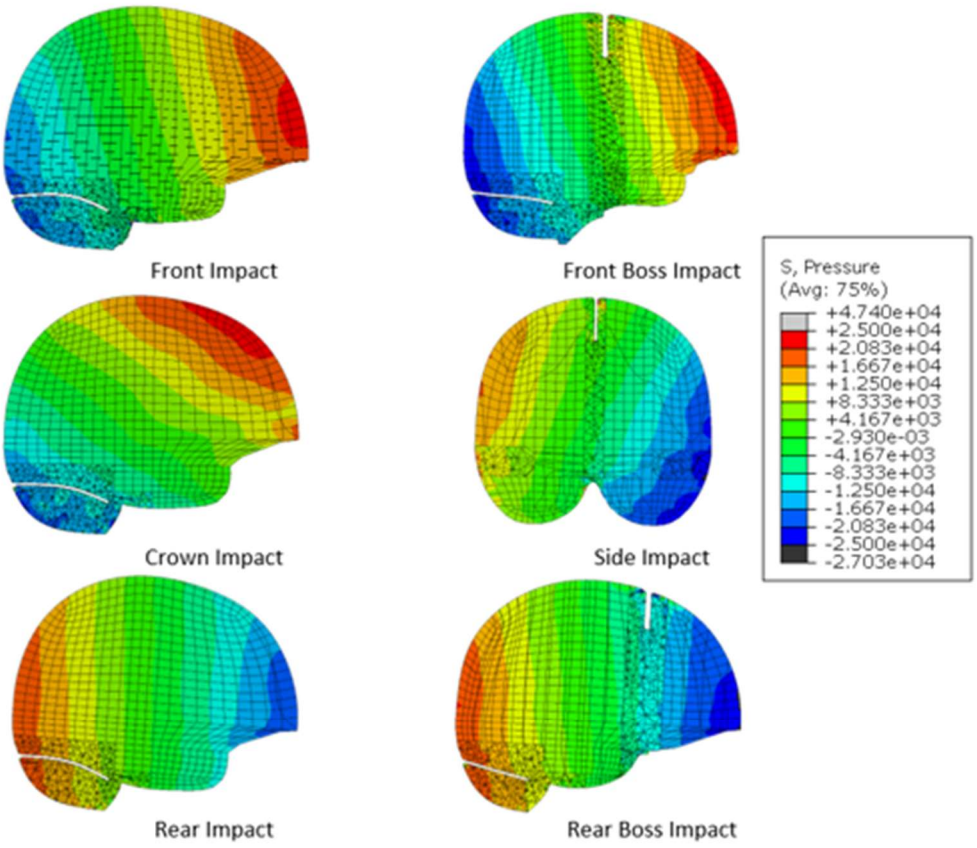


Figure 1: Linear pressure gradients due to low-speed helmeted impacts for each impact orientation: front, front boss, crown, side, rear, and rear boss.

References (Optional)

[1] Li et al. 2021 *J.Biomech.Eng.*

[2] Chauvet et al. 2025 *Ann.Biomed.Eng*.

[3] Chauvet et al. 2022 *IRCOBI*

[4] McEntire et al. 2005 *USArmy*

Acknowledgements (Optional)

We gratefully acknowledge funding from an NSERC Alliance Grant.

Session Category

Injury Biomechanics: N/A

P3-135

Design of 3D-Printed Biomimetic Porous Architectures for Head-Protective Materials

Prof. Satoshi Yamada[1], Prof. Yuelin Zhang[2], Mr. Keita Kawashima[3], Dr. Saori Miyajima[3], Mr. Yugo Motoi[1], Mr. Ryuki Sunada[1]

[1]Hokkaido University, Sapporo, Hokkaido, Japan. [2]Sophia University, Chiyoda-ku, Tokyo, Japan. [3]Hokkaido Research Organization, Sapporo, Hokkaido, Japan

Introduction

We developed a three-dimensional (3D)-printed biomimetic porous architecture [1] inspired by cancellous bone biomechanics [2], providing high design freedom, 3D isotropy, and excellent energy absorption for advanced shock-absorbing applications. Expanded polystyrene (EPS), a conventional helmet-liner material, provides good impact absorption and is light in weight. However, it poses several limitations such as poor durability under repeated impacts, limited personalization, and low breathability. This study aimed to investigate the use of the proposed architecture—synthesized from thermoplastic polyurethane (TPU) via 3D printing—as a next-generation head-protective material. Initially, its shock-absorbing performance was evaluated and compared with EPS.

Methods

Architectures were generated stochastically by iterating the creation and branching of struts according to probability distributions for strut length and bifurcation. Nine isotropic models (50-mm diameter and 25-mm height) with volume fractions from 15% to 50% were designed by adjusting the strut parameters including diameter, length, and bifurcation. An additional anisotropic model was developed by distributing the length along the orientation. All specimens were additively manufactured through material extrusion using six commercial TPU filaments of different stiffness. Drop-tower impact tests at 50 J were conducted, with each specimen subjected to up to three consecutive impacts. Further, maximum force and deformation were assessed. EPS specimens of three helmet-grade densities were tested under similar conditions.

Results

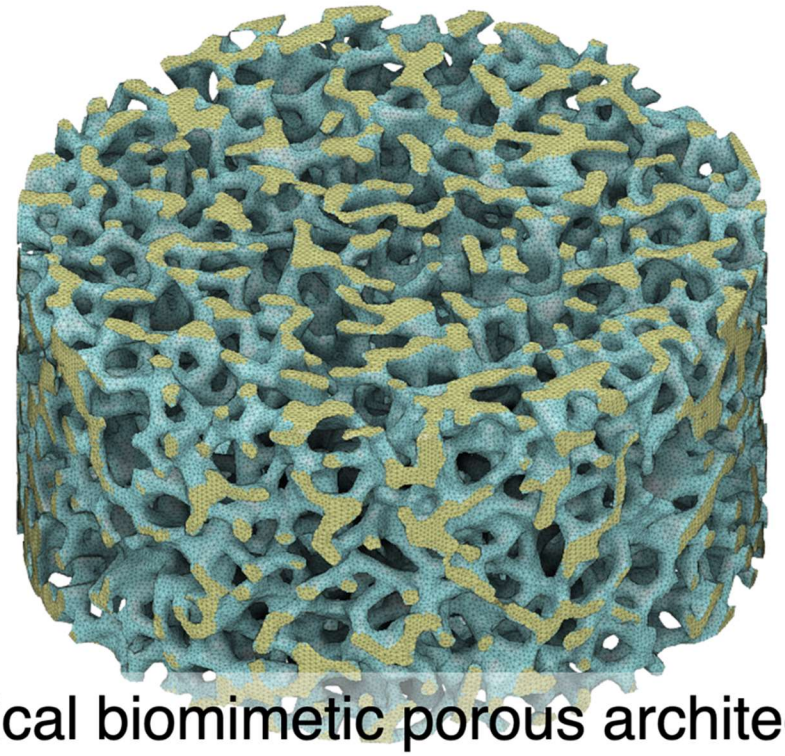
TPU-based biomimetic specimens withstood all three impacts and altogether exhibited lower maximum forces and deformations than the lowest-density EPS specimens, which collapsed after the first impact. Exceptions occurred for low-volume-fraction specimens fabricated with soft filaments. Isotropic models showed parabolic relationships between maximum forces and deformations, based on volume fraction and material stiffness,

whereas structural variations had minimal influence. The anisotropic model demonstrated higher stiffness, and the maximum force value changed accordingly.

Discussion

These results indicate that 3D-printed biomimetic architectures exhibit EPS-comparable impact absorption while providing improved multi-impact resistance and tunable performance. Further studies are warranted to clarify their head-protection performance.

Images (Optional)



A typical biomimetic porous architecture with a 30% volume fraction

References (Optional)

[1] Satoshi Yamada *et al.*, Mater Des, 2025.

[2] Satoshi Yamada *et al.*, Med Eng Phys, 2022.

Acknowledgements (Optional)

This study is supported by Adaptable and Seamless Technology transfer Program through Target-driven R&D (A-STEP) from Japan Science and Technology Agency (JPMJTR24R5).

Session Category

Injury Biomechanics: N/A

P3-136

Comparison of football helmet performance with and without Guardian Cap

Mr. Sean Bucherl MS, Dr. Eric Nauman PhD

University of Cincinnati, Cincinnati, Ohio, United States

Introduction

With the NFL approving Guardian Cap usage for practice and games, Guardian caps, or similar after-market additions, will inevitably find their way into lower levels of play. It is important therefore, to determine their effect on impact severity.

Methods

Two models of helmets (Riddell SpeedFlex and Vicis Zero2 Elite) were tested with and without the Guardian Cap, resulting in four test cases compared to a baseline bare Hybrid 3 50th percentile male head. Three helmets within each model were tested. Helmets and Guardian Caps were fitted to an instrumented Hybrid 3 head and neck mounted to a steel base. Each helmet - Guardian Cap combination was tested by delivering 20 impacts each, to 14 different locations (4 each within 5 different impact ranges). The recorded impact impulses, and peak linear and angular accelerations at the head form center of mass were used to calculate dimensionless parameters and corresponding functions for linear and angular acceleration. Comparing the effect size between the helmeted head and the bare head made it possible to determine the effect that the helmet – Guardian Cap combination has on the resultant linear and angular accelerations.

Results

Both helmets demonstrated improvement in protection with the Guardian Cap, but this improvement was not uniform. The SpeedFlex helmet exhibited the most overall improvement. However, normalizing the effect sizes for the mass of the helmet, or helmet with Guardian Cap, nearly erases the observed improvements. However, even after mass-normalizing, the SpeedFlex does show some improvement in mitigating angular accelerations with the Guardian Cap.

Discussion

With the Guardian Cap increasing the mass of each helmet ~9%, it is possible that the observed improvements seen were primarily due to the additional mass of the system, but further testing is needed to test this theory. The improvement observed in the SpeedFlex after mass-normalizing could be due to the fact the Guardian Cap is providing a slip layer that moves during impact but this also needs to be investigated further.

Session Category

Injury Biomechanics: N/A

P3-137

Injury Reponses of an Undulated Male Axon in Dynamic Stretch Loading

RA Chaokai Zhang, Professor Songbai Ji

Worcester Polytechnic Institute, Worcester, MA, United States

Introduction

Understanding how axons respond mechanically to stretch is crucial for deciphering mechanisms of traumatic axonal injury. Most axonal injury models assume a straight axon. However, axon undulation is common in a living brain, which may influence substructural injury risk. This study investigates the significance of axonal undulation on cytoskeletal responses in stretch.

Methods

A male axon injury model [1] was modified to incorporate a sinusoidal undulation (wavelength: 28 μm, amplitude: 3 μm) based on morphological measurements [2]. The undulated axon's centerline (~15.5 μm) was ~10% longer than a straight 14 μm axon of equal end-to-end length. A rotational anti-symmetric periodic boundary condition was developed to halve the model for simulation. Straight and undulated axons were subjected to an identical stretch (peak strain of 10% and strain rate ~10 s^{-1}).

Results

While the straight axon became undulated after stretch and recovery, the initially undulated axon retained its wavy geometry, as the applied stretch magnitude was not enough to straighten it. This led to substantially lower peak strain in microtubules (MTs; 7% vs. 13%) and tau failure (0% vs. 2.2%) than the straight axon. However, the initially undulated axon also resulted in higher axolemma peak strain (19.2% vs. 17.3%) and a much higher neurofilament failure (13.1% vs. 2.8%) due to increased local contact between MTs and axolemma during the flattening of its morphology. **Figure 1** compares their responses in a local Ranvier node region.

Discussion

The initial axonal morphology is a significant biomechanical mediator to alter strain and damage distribution within the cellular substructure. An initially undulation axon protects microtubules and tau proteins during rapid stretch at the expense of higher neurofilament failure and peak strain in axolemma. Therefore, it is important to incorporate undulation into the axonal injury model, where appropriate, to study injury mechanisms. The anti-symmetric periodic boundary condition is shown effective in substantially reducing

simulation runtime. Future work will extend to different levels of peak strain and strain rate, as well as to the female axonal injury model.

Images (Optional)

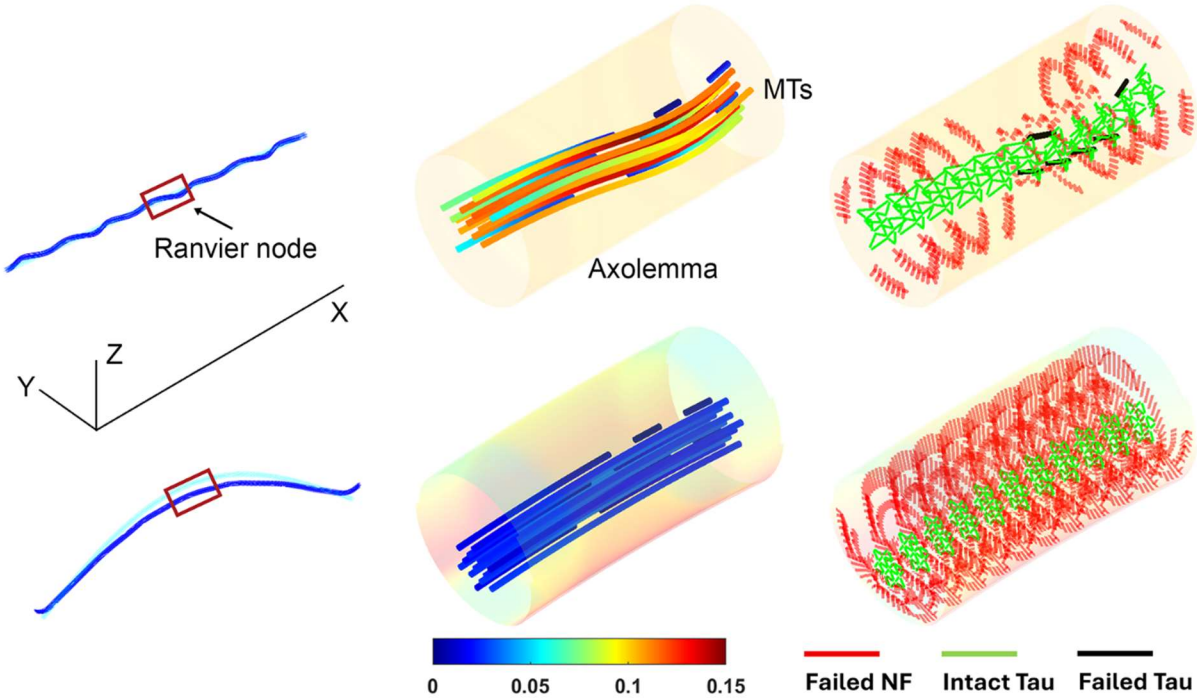


Figure 1. Comparison of axonal substructural responses in a Ranvior node region for a straight versus an undulated axon under a 10% peak stretch

References (Optional)

[1] C. Zhang and S. Ji, *J Neurotrauma*, 2023

[2] H. H. Lee et al., *NMR in Biomedicine*, 2024

Acknowledgements (Optional)

Funding is provided by the US National Science Foundation (NSF) Division of Civil, Mechanical and Manufacturing Innovation (CMMI) award #2114697 and the National Institutes of Health (NIH) R21NS136884 award.

Session Category

Injury Biomechanics: N/A

P3-138

Effect of Center of Mass Height on Hip Impact Forces During Simulated Sideways Falls from Standing Height

Ms. Soyeon Yoon PT, Dr. Kitaek Lim PT, PhD, Mr. Junwoo Park PT, MSc, Dr. Seyoung Lee PT, PhD, Mr. Sungmin Chun PT, Mr. Donggeon Kim PT, Prof. Woochol Joseph Choi PT, PhD

Injury Prevention and Biomechanics Laboratory, Yonsei University, Wonju, Gangwon-do, Korea, Republic of

Introduction

Falls are a major cause of hip fractures in older adults. Although fall risk increases by 37% for every 1% rise in center of mass (COM) height [1], few studies have investigated how COM height influences impact severity during a fall. In this study, we examined how fall kinetics were affected by variations in COM height.

Methods

Ten young adults self-initiated sideways falls on a mat (Figure 1). Trials were acquired with three knee positions at landing (knees together, knee on the mat, and knee free), and with three COM heights (1% increased, 1% decreased, and unchanged) (Figure 2). Fall kinetics and kinematics were collected using a force plate positioned beneath the mat and a motion capture system, respectively. Body contact area was measured to determine the mat stiffness at impact, which was then used to estimate the actual (unattenuated) hip impact force using a mass–spring model consisting of two springs in series. Outcome variables included body stiffness (k) and unattenuated hip impact force ($F_{unattenuated}$) that normalized to body weight (BW). A two-way repeated measures ANOVA was performed to assess whether these outcomes were influenced by COM height and knee position.

Results

$F_{unattenuated}$ was associated with knee position ($F=6.86$, $p=0.006$), but not with COM height ($F=1.66$, $p=0.218$) (Table 1). $F_{unattenuated}$ was the smallest with the knee on mat. Similarly, k was associated with knee position ($F=3.67$, $p=0.046$), but not with COM height ($F=1.50$, $p=0.247$).

Discussion

Our results indicate that hip impact severity is strongly influenced by lower-extremity kinematics at landing, consistent with previous findings [2]. Although a higher center of mass (COM) is theoretically associated with increased impact energy, we did not observe a corresponding increase in impact severity when COM height was adjusted by ±1%

(approximately a 1 cm difference for a 170 cm individual). These findings suggest that such a small change in COM height does not meaningfully affect impact severity or hip fracture risk.

Images (Optional)

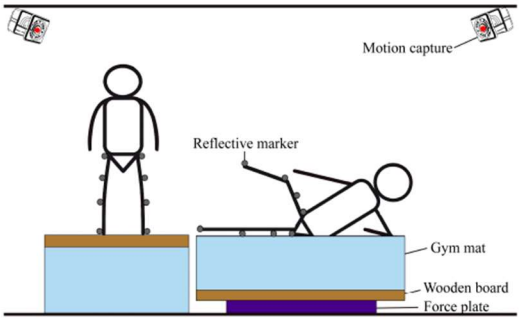


Figure 1. Experimental setup

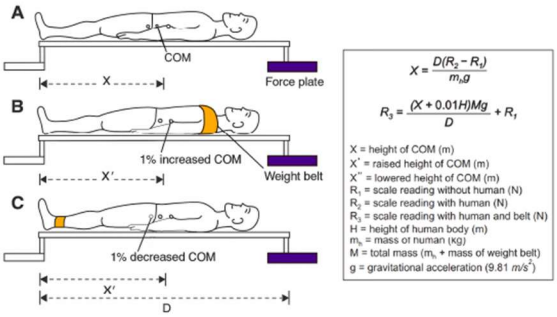


Figure 2. Reaction board method to change COM height

Table 1. Average values of outcome variables (with SD shown in parentheses)

	COM 1% increased			COM not changed			COM 1% decreased			p-value		
	KF[a]	KT[b]	KOM[c]	KF	KT	KOM	KF	KT	KOM	COM height	knee position	COM height * knee position
Body stiffness (kN/m)	121.2 (245.4)	116.8 (143.7)	25.4 (13.4)	51.2 (40.3)	48.8 (44.0)	21.6 (13.2)	54.4 (39.8)	80.2 (87.4)	22.4 (12.0)	0.247	0.046*	0.443
Hip impact force (N/BW)	9.56 (6.5)	10.03 (6.0)	5.39 (1.4)	7.91 (3.4)	7.50 (2.8)	4.97 (1.61)	8.34 (2.9)	10.06 (7.5)	5.10 (1.6)	0.218	0.006*	0.521

[a] *KF* knee free, [b] *KT* knee together, [c] *KOM* knee on mat

References (Optional)

[1] Almeida et al., Gait & Posture, 2011; [2] Lim and Choi, Osteoporos Int, 2020

Acknowledgements (Optional)

This work was supported by the “Brain Korea 21 FOUR Project” (F21SH8303039), the National Research Foundation of Korea (NRF) grant funded by the Korea government (MSIT) (RS-2025-16071808), and by the Regional Innovation System & Education (RISE) program through the Gangwon RISE Center, funded by the Ministry of Education (MOE) and the Gangwon State (G.S.), Republic of Korea (2025-RISE-10–006).

Session Category

Injury Biomechanics: N/A

P3-139

Sex Impacts Resultant and Cumulative Tibial Bending during a Walk, Jog, and Run

Mr Thomas Wenzel[1,2], Ms Iona Halliday[1], Dr Tyler Brown[1]

[1]Boise State University, Boise, ID, United States. [2]lululemon, Portland, Oregon, United States

Introduction

Women are twice as likely to suffer tibial stress fractures as men [1]. During locomotion, tibial bending reportedly produces damaging bone stresses that lead to tibia stress fracture [2]. Yet, it is unknown whether discrete (peak and mean) or cumulative resultant tibial bending of locomotion differ between sexes or are impacted by common locomotion factors, like speed and surface.

Methods

Twenty-four recreational runners (12 M, 12 F) had tibial bending quantified as they walked (1.3 m/s), jogged (3.0 m/s), and ran (4.5 m/s) over a flat, uneven, and medial and lateral banked surfaces. Peak and mean resultant tibial bending moment and cumulative-weighted tibial bending impulse (CWTI) were submitted to a 3-way mixed model ANOVA.

Results

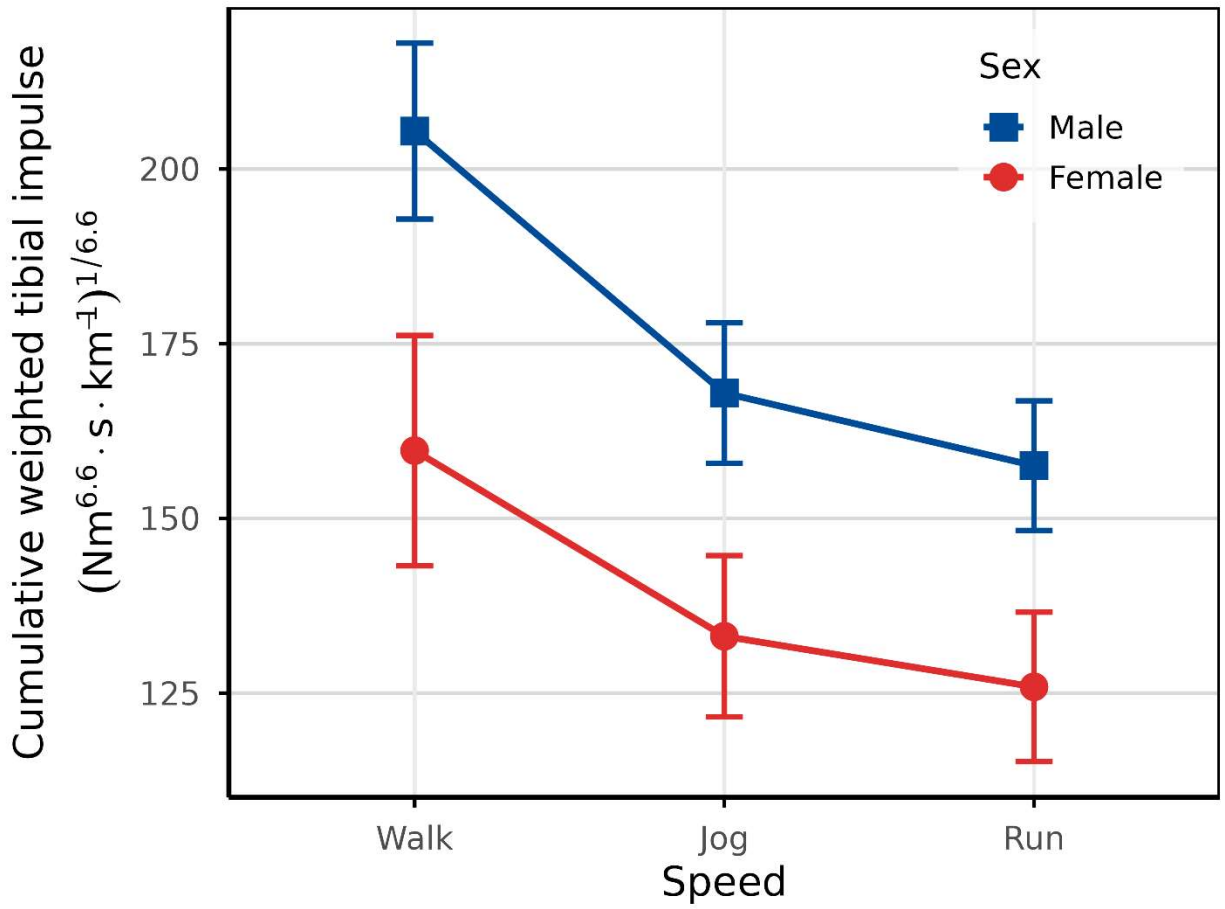
Significant sex by speed interactions were observed for mean and peak resultant tibial bending and CWTI (all: $P<0.001$), as men exhibited greater resultant bending and CWTI (all: $P<0.001$), and larger increases in resultant bending and CWTI due to speed than women (all: $P<0.001$). Significant speed by surface interactions (all: $P<0.025$) were observed for mean and peak resultant tibial bending. Resultant bending was smaller on uneven and banked surfaces compared to flat surface (all: $P<0.041$) but only differed between surfaces during jog and run (all: $P<0.001$). Speed increased mean and peak tibial bending (all: $P<0.001$), but decreased CWTI (all: $P<0.001$).

Discussion

Despite having lower tibial stress-fracture rates, men may be more susceptible to hazardous bone microdamage during each step. They demonstrated greater discrete and cumulative resultant bending and larger speed related increases in tibial bending than women. Faster locomotor speed may increase bone microdamage likelihood as discrete resultant tibial bending was larger with each addition of speed. But unexpectedly, cumulative tibial bending decreased with 1 km of jogging and running. Challenging surfaces may decrease injury risk or potential bone damage, as discrete resultant tibial

bending was smaller on the uneven and banked surfaces. Yet, further study on the impact of injury risk is needed as surfaces did not lead to a similar reduction in cumulative tibial bending.

Images (Optional)



References (Optional)

[1] Callahan *et al.,* Clinics in Sports Med. 2000, [2] Derrick *et al*, J Biomech, 2022

Acknowledgements (Optional)

NIH NIGMS (2U54GM104944, P20GM109095, P20GM148321) supported this work.

Session Category

Injury Biomechanics: N/A

P3-140

Finite Element Analysis of Force Transmission in Behind Armor Blunt Trauma Across Different Backing Materials

Dr. Alan Goertz Ph.D.[1], Mr. Tony Hatzigeorgiou[2], Mr. Donald Sherman MS[2], Dr. Cynthia Bir Ph.D.[2], Dr. Karin Rafaels Ph.D.[3]

[1]SURVICE Engineering, Detroit, MI, United States. [2]Wayne State University, Detroit, MI, United States. [3]US DEVCOM Army Research Laboratory, Aberdeen, MD, United States

Introduction

Behind armor blunt trauma (BABT) arises when the kinetic energy of a non-penetrating projectile is transferred through body armor, resulting in trauma to the underlying tissue. Traditional certification methods rely on backface deformation (BFD) measurements in surrogate materials such as ballistic clay or gelatin, yet the metrics from these surrogate materials inadequately capture tissue-level stress and injury risk. To help relate the responses witnessed in these backing materials to the human body, a quantification of the force responses of ballistic clay, gelatin, and the human body could be used to develop improved injury evaluation methods.

Methods

In this study, we employed detailed finite element (FE) simulations to quantify the forces induced on backing materials of differing mechanical properties. Backing materials modeled included ballistic clay (Roma Plastilina No. 1), ballistic ordnance gelatin, and a validated human torso FE model representing the 50th percentile male. The behind-armor blunt impact model in the simulations was derived from high-velocity ballistic experiments on hard armor. Force transmission to each backing material was extracted and analyzed over time to produce contact force profiles for comparison.

Results

Results indicate that stiffer backing materials, such as ballistic clay, produced higher peak impact forces, whereas more compliant gelatin reduced peak forces but altered the duration of applied loads, potentially affecting predicted injury patterns. The shape of the loading profile of the homogenous surrogates differed from the structurally complex human body.

Discussion

The simulations highlight the sensitivity of backing material characteristics on the measured response from BABT impacts and emphasize the necessity of understanding the

relationship between test materials and the human body for properly predicting the potential for injury. These findings advance the understanding of energy transfer in non-penetrating ballistic events and provide a framework for optimizing armor design and evaluation criteria to mitigate behind armor blunt trauma. The study further demonstrates the efficacy of FE modeling as a tool to systematically investigate BABT mechanisms across a range of backing configurations.

Session Category

Injury Biomechanics: N/A

P3-141

The Passenger Inside: How Posture Influences Uterine Geometry and Lumbar Curvature During Pregnancy

Ms. Vivian Chung MASc., P.Eng.[1], Ms. Jade Levine MASc.[1], Ms. Danielle Rowlands BASc.[1], Dr. Jason Forman Ph.D.[2], Dr. Michelle Oyen Ph.D.[3], Ms. Desirée Reichhardt DNP, NP(F), RDMS[1], Dr. Jason Hallman Ph.D.[4], Dr. Ananna Ahmed Ph.D.[4], Dr. Jason Burrows MD, FRCSC[1], Dr. Peter Cripton Ph.D.[1]

[1]The University of British Columbia, Vancouver, British Columbia, Canada. [2]University of Virginia, Charlottesville, Virginia, United States. [3]Wayne State University, Detroit, Michigan, United States. [4]Toyota Motor North America R&D, Ann Arbor, Michigan, United States

Ms. Vivian Chung

Ms. Jade Levine

Ms. Danielle Rowlands

Dr. Jason Forman

Dr. Michelle Oyen

Ms. Desirée Reichhardt

Dr. Jason Hallman

Dr. Ananna Ahmed

Dr. Jason Burrows

Introduction

For pregnant women, motor vehicle collisions (MVCs) are a leading cause of injury and traumatic fetal loss [1]. To understand these injury mechanisms, anatomical data acquired in realistic automotive postures is needed to advance the development of pregnant human body models (HBMs) [2]. In this study, we present anatomical data captured using Upright Open MRI to explore how posture influences uterine geometry and lumbar curvature.

Methods

Pregnant volunteers were scanned in three postures: upright driving (seated), reclined (seated), and supine. Volunteer 'A' was scanned during her 24-week gestation, and volunteer 'B' was scanned in her 30th and 36th weeks of gestation. All measurements were acquired using the mid-sagittal image.

Given the available field of view, lumbar curvature was approximated by measuring the sagittal Cobb angle from the L4 to S1 vertebrae. Uterine length and width measurements were acquired along the uterine long and short axes – identified using principal component analysis (PCA) of 30 digitized points along the uterine outline.

Results

The uterine width in supine was on average 38 mm less than that of the upright posture. In the 30th and 36th week scans, this difference was particularly pronounced at 56 and 53mm, respectively. As backrests were lowered from upright to reclined - we saw a 5% average increase in the uterine length-to-width ratio, which was further increased by 52% in supine, indicating an elongation of the uterine shape as the backrest approached horizontal.

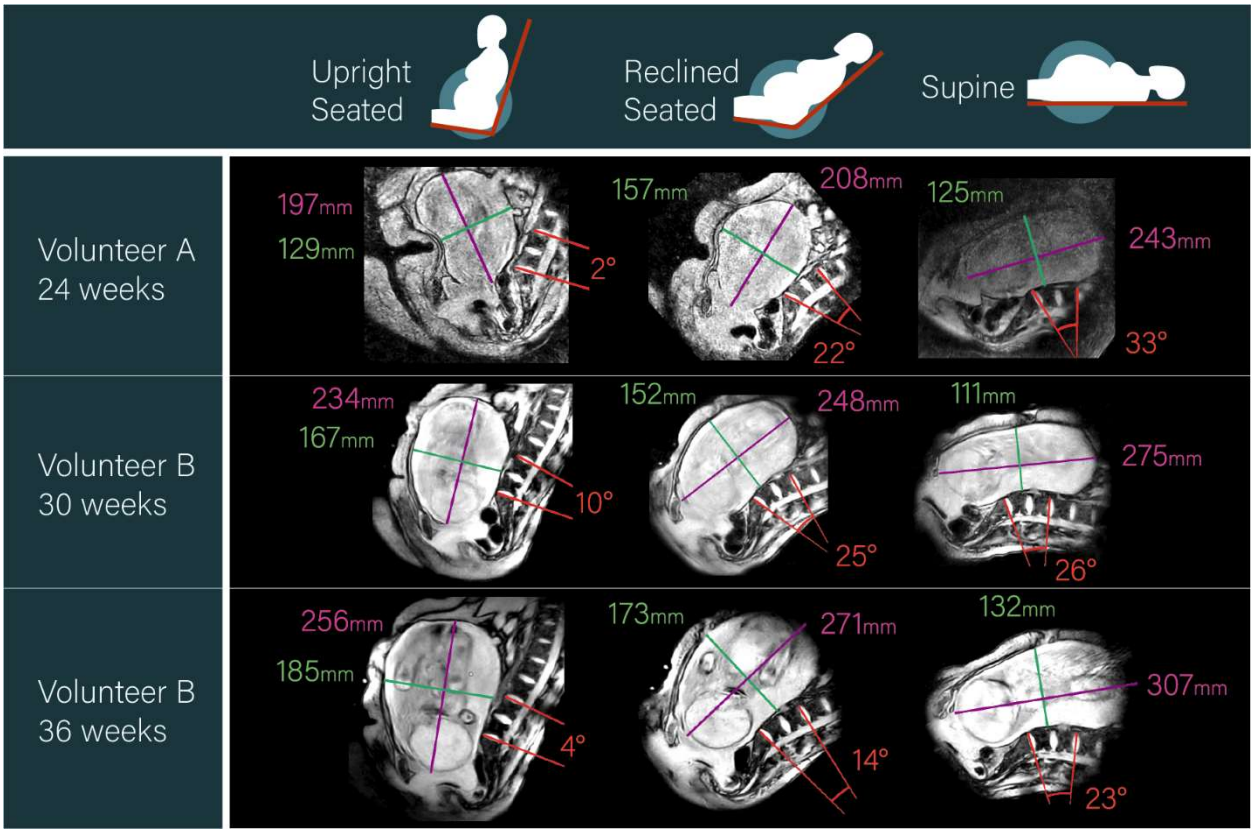
From upright to supine, the lumbar curvature increased by 22° on average.

Discussion

This study offers a first look into the internal anatomy of pregnant women across three postures relevant to automotive travel. The results demonstrate that the uterus is a highly pliable structure that changes shape with posture, highlighting the importance of developing HBMs using geometries acquired in the posture that the HBM intends to model.

As lumbar curvature also plays a role in MVC injury risks [3], the interplay between lumbar curvature and uterine shape at various stages of pregnancy should be further investigated.

Images (Optional)



References (Optional)

[1] Harold Weiss, Accid Anal Prev, 2001
[2] Florent Auriault et al., J Biomechanics, 2014
[3] Rachel Richardson et al., Traffic Inj Prev, 2020

Session Category

Injury Biomechanics: N/A

P3-142

Investigating Soft Tissue Contributions to Thoracic Responses with a Whole Human Body Model

Dr. Wei Zeng

New York Institute of Technology, Old Westbury, New York, United States

Introduction

The human thorax is a mechanically complex structure in which the rigid ribcage and surrounding soft tissues jointly determine global and local responses. While the bony skeleton provides the primary load-bearing framework, the musculature, adipose layers, skin, and intrathoracic organs also contribute to energy absorption and deformation patterns during impact. These tissues exhibit viscoelastic behavior that can modulate thoracic stiffness, yet their contributions remain insufficiently quantified in human body models (HBMs). This study evaluates how variations in soft tissue properties, geometry, and organ–organ interaction modeling affect thoracic responses under frontal impact.

Methods

Dynamic frontal pendulum impact simulations were performed using a detailed mid-sized male HBMs (GHBMC M50-O). Soft tissue characteristics were varied independently, including material properties of chest muscles, adipose tissue, skin, and lungs; geometric features such as intercostal muscle volume and anterior chest flesh thickness; and intrathoracic interaction modeling using sliding tiebreak contact (STBC). Thoracic responses—sternum deflection, impact force, and force–deflection behavior—were compared with established PMHS corridors.

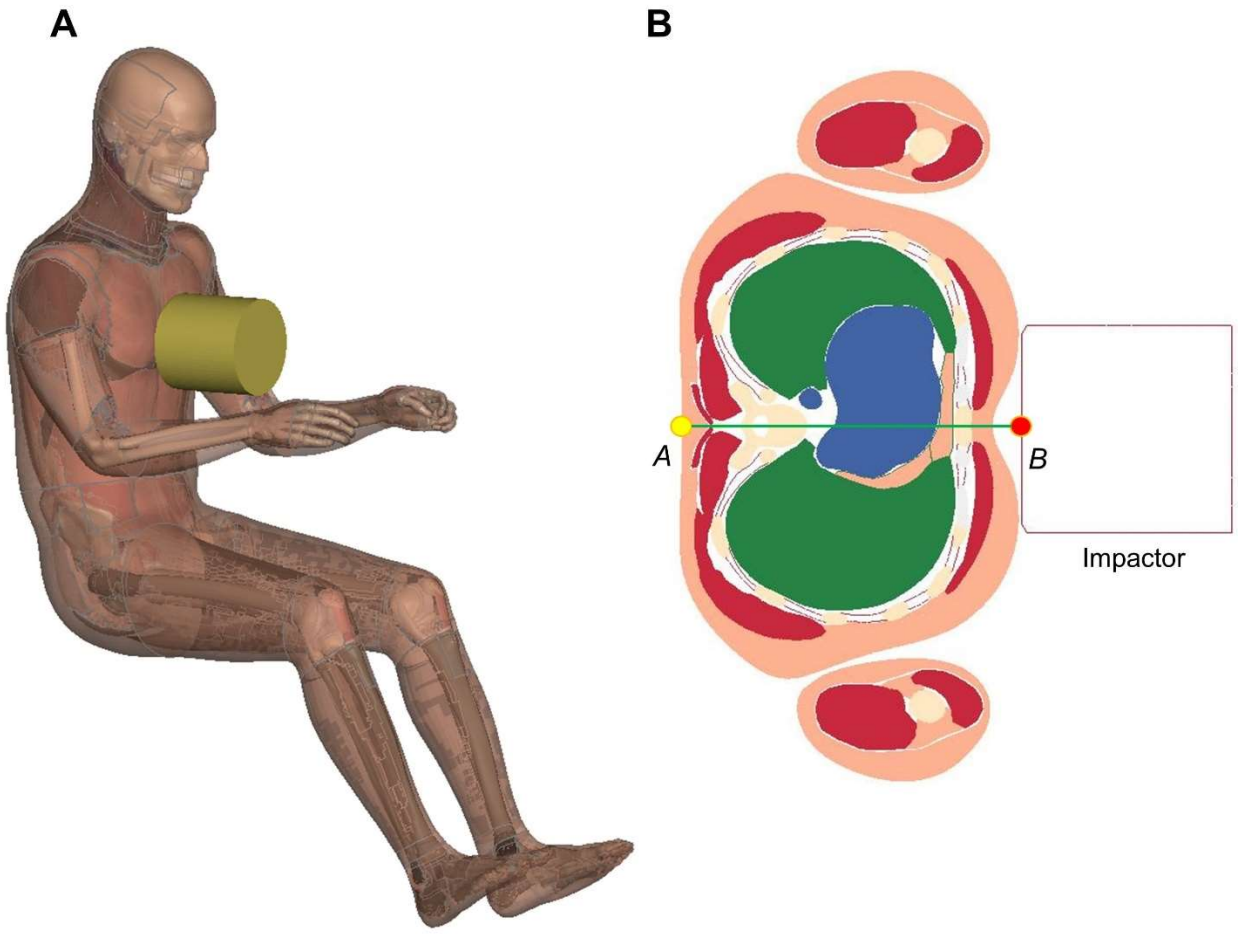
Results

Soft tissue representation produced distinct changes in response. STBC slightly increased peak deflection and reduced peak force (<5%). Lung material properties had the greatest influence: simplified rubber and Hill-foam materials increased deflection by 7% and 20% and reduced force by 8% and 13%, respectively, with delayed timing. Increasing anterior chest flesh thickness reduced deflection by 12.8% with minimal effect on force (<1.2%). Modifying intercostal muscle geometry (greater thickness or 2D-to-3D elements) produced negligible changes (<3.6% in force, ~1% in deflection). Stiffer passive muscle, adipose, and skin properties stiffened the response, with skin affecting force more than deflection. Overall, lung material updates and STBC softened the response, whereas increased chest flesh and stiffer tissues increased thoracic stiffness.

Discussion

Soft tissues—particularly the lungs, passive muscles, and adipose layers—substantially shape the magnitude and timing of chest deformation. Lung influence reflects its large volume and material sensitivity. Intercostal geometry changes were minimal, highlighting the importance of tissue volume and placement. Anterior chest flesh primarily altered compressibility, while organ contact mechanics had modest effects. These findings highlight the need for accurate soft tissue modeling to improve HBM thoracic injury prediction.

Images (Optional)



Session Category

Injury Biomechanics: N/A

P3-143

Preliminary Analysis of Spatial Position and Observed Airway Risks in a Bedsharing Environment

Ms Yafa Benavidez Graduate Research Assistant[1], Ms Megan McCartney Undergraduate Research Assistant[1], Ms Laina Beasley Undergraduate Research Assistant[1], Mr Christopher Wilson[1], Dr Kyran Quinlan MD[2], Dr Gina Lowell MD[2], Dr Erin Mannen PhD[1]

[1]Boise State University, Boise, Idaho, United States. [2]Rush University Children's Hospital, Chicago, Illinois, United States

Introduction

Sharing a sleep surface (i.e. co-sleeping or bedsharing) nearly triples the risk of sleep-related Sudden Unexpected Infant Death [1]. Airway-obstruction or chest compression from soft bedding, wedging, overlay, or a combination of these can lead to suffocation in a bedsharing environment [2]. However, there is little biomechanical understanding of bedsharing and the associated risks. The purpose of this study is a preliminary analysis of pilot data collected for a larger longitudinal study on the biomechanics of bedsharing.

Methods

Three mother-infant dyads were recorded using a single night-vision camera (Phasm Cam) during bedsharing at home. Infants were aged 1.0-2.9 months. A calibration grid (checkerboard-pattern) was used to calibrate a 2D-plane on the sleep surface. Videos were reviewed to mark movement-events, mother-infant contact, and instances of observed airway-obstruction risks. A method for mapping mother-infant positions throughout the night was developed using Python and OpenCV. Frames between movement-events were extracted, and mother-infant positions were identified to create visual maps representing spatial body positions over time. These were used to calculate bedspace occupied by mother and infant, overall bedspace used, and mother-infant overlap.

Results

Each mother-infant dyad presented unique posture and movement data (Figure-1). Mothers occupied 59% and infants 9% of the total bedspace, and combined occupied 60%. Of the bedspace occupied, mother and infant overlap ranged from 0-19%. Dyads 1, 2, and 3 were in contact 100%, 79%, and 0% of the time spent bedsharing. Duration of possible airway-obstruction instances relative to time spent bedsharing was 20.4%, 2.9%, and 0.1% for dyads 1, 2, and 3, respectively.

Discussion

We developed and piloted a novel method of evaluating mother-infant biomechanics during bedsharing in an at-home environment. Each dyad in this study presented unique bedsharing habits. Mothers 1 and 2 slept with their infants in close proximity. Mother 3 placed their infant in an in-bed sleeper. The position map results indicate overlapping bedspace for 2 of the dyads, which may enable suffocation risks. Future work will increase sample size and infant ages to more fully capture the biomechanics of bedsharing.

Images (Optional)

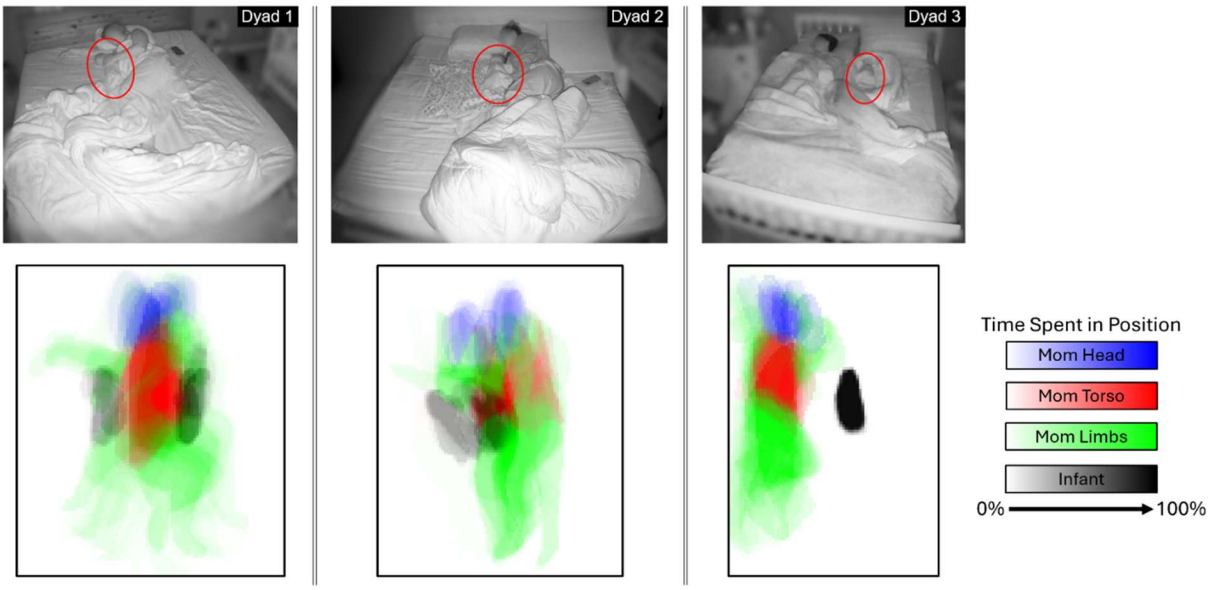


Figure 1: Images from collected videos and maps showing mother-infant spacial positions throughout night of bedsharing. Darker colors represent longer time spent in a given space.

References (Optional)

[1] Moon et al. , Pediatrics B150, 2022.
[2] CDC, SUIDS and SIDS Data and Statistics, 2022.

Acknowledgements (Optional)

Supported by the American SIDS Institute. EMM owns Mannen Bio, LLC, an engineering and expert consulting company.

Session Category

Injury Biomechanics: N/A

P3-144

Head Protection Performance of 3D-Printed Biomimetic Porous Architecture Using Child Head Impactor Drop Analysis

Prof. YUELIN ZHANG[1], Prof. SATOSHI YAMADA[2]

[1]Sophia University, Tokyo, okyo, Japan. [2]Hokkaido University, Sapporo, Hokkaido, Japan

Introduction

The development of head-protection materials capable of effectively mitigating impact forces remains an important challenge in injury-prevention research. We have been experimentally and numerically developing protective materials that provide reliable head protection while maintaining the ability to be used repeatedly and ensuring adequate breathability. These materials incorporate a biomimetic porous architecture [1] and can be fabricated through 3D printing, enabling customization for individual users. In this study, we evaluated the head-protection performance of the developed material using drop analyses with a child head impactor to clarify the relationship between its structural characteristics and impact-mitigation behavior.

Methods

Drop analyses were conducted from a height of 1.5 m onto disk-shaped samples of the protective material with a diameter of 200 mm and a thickness of 25 mm. The acceleration at the center of gravity of the impactor was measured during impact. Thermoplastic polyurethane (TPU) was used for the porous structures, and samples were prepared with volume fractions of 20%, 30%, and 40%. For each configuration, the peak acceleration and the Head Injury Criterion (HIC) were calculated from the measured acceleration time histories. The compressive properties of the porous structures were characterized through drop-tower tests, while tensile properties were obtained from uniaxial tensile testing.

Results

The results showed that samples with higher solid volume fractions (lower porosity) tended to produce lower peak accelerations. Regarding the HIC, the 30% volume-fraction sample produced the smallest value, indicating the most effective impact mitigation under the tested conditions.

Discussion

The 20% volume-fraction sample, having the lowest bending stiffness and the softest structure, was almost completely crushed upon impact, causing the ground effect to dominate the response; consequently, both the peak acceleration and HIC were the

highest for this configuration. Although the 40% volume-fraction sample exhibited a lower peak acceleration than the 30% sample, its shorter impact duration resulted in a higher HIC value. These findings suggest that an optimal balance between stiffness and deformation capacity exists within the biomimetic porous architecture.

References (Optional)

[1] Satoshi Yamada et al., Mater Des, 2025.

Acknowledgements (Optional)

This study is supported by Adaptable and Seamless Technology transfer Program through Target-driven R&D (A-STEP) from Japan Science and Technology Agency (JPMJTR24R5).

Session Category

Injury Biomechanics: N/A

P3-145

Directional Dependence of Multiscale White Matter and Axonal Injury Metrics from Real-World Head Impacts

Mr. Zaryan Masood[1], Mr. Chaokai Zhang[2], Mr. Daniel Bondi[1], Mr. Alexander Jaffray[1], Mr. David Luke[1], Dr. Rebecca Kenny[1], Dr. Adam Clansey[1], Dr. Paul van Donkelaar[1], Dr. Alexander Rauscher[1], Dr. Songbai Ji[2], Dr. Lyndia Wu[1]

[1]University of British Columbia, Vancouver, British Columbia, Canada. [2]Worcester Polytechnic Institute, Worcester, Massachusetts, United States

Introduction

Traumatic axonal injury (TAI) has shown directional vulnerability in animal studies[1], but this remains less understood in humans, particularly at microstructural scales. Advances in wearable sensors, neuroimaging, and computational modeling now allow large-scale subject-specific simulations of real-world head impacts to estimate deformation from whole-brain to axonal structures. This study examined the directional dependence of white matter fiber strain and axonal substructural damage.

Methods

University men's ice hockey athletes (n = 18; UBC ethics: H21-00400) wore custom instrumented mouthguards (iMGs) over one season, and completed a structural brain MRI scan for subject-specific modeling. We simulated voxel-wise white matter fiber strains and axonal substructural deformations using a deep-learning model[2]. An impact was classified coronal-, sagittal-, or horizontal-dominant when the peak angular velocity in that plane exceeded 90% of the resultant magnitude. We used linear mixed-effects models to determine how rotational plane and peak angular velocity influence 95th percentile fiber strains and axonal substructural injury metrics, with subject ID as a random effect.

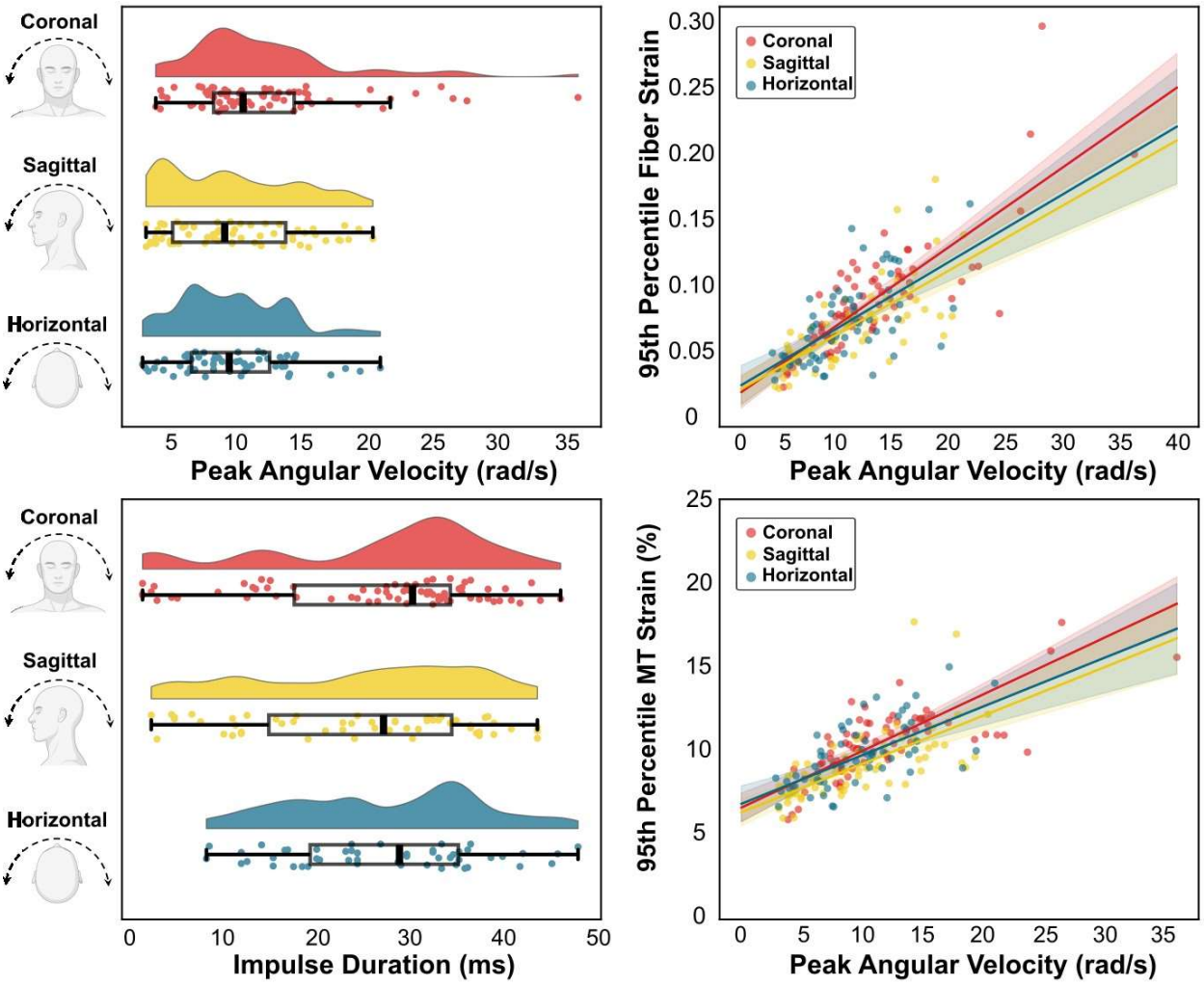
Results

We analyzed 608 impacts: 88 coronal-dominant, 86 sagittal-dominant, and 61 horizontal-dominant. Coronal-dominant impacts showed the highest median peak angular velocity (10.5 rad/s) and longest impulse durations (30.3 ms) compared with sagittal (8.4 rad/s, 26.1 ms) and horizontal (8.7 rad/s, 29.7 ms). Coronal- and horizontal-dominant impacts produced significantly higher fiber strains (coronal: $\beta = 0.0087$, $p = 0.028$; horizontal: $\beta = 0.0043$, $p = 0.313$) and microtubule strains (coronal: $\beta = 0.801$, $p = 0.004$; horizontal: $\beta = 0.290$, $p = 0.312$) compared with sagittal-dominant impacts. Neurofilament and tau failure did not differ by rotational plane. Between-subject variance was low, indicating consistent directional effects.

Discussion

Our study uniquely examined the directional dependence of microstructural injury risk using real-world head impact data and neuroimaging-enabled subject-specific multiscale modeling. Coronal- and horizontal-dominant impacts may pose a higher risk for axonal damage relative to sagittal-dominant impacts. The directional vulnerability is further compounded by higher severity coronal impacts sustained on-field, warranting protective equipment improvements and potential rule changes to mitigate high-risk impact directions.

Images (Optional)



References (Optional)

[1] Hill et al., Trends in Neurosciences, 2021

[2] Zhang et al., Biomechanics & Modeling, 2025.

Session Category

Injury Biomechanics: N/A

P3-146

Comparison of Impact Loads during Simulated Falls of 3D-Printed versus Plaster Wrist Casts

Mr. Zhenhao Yang, Mr. Christopher Coluni, Mr. Carl Iven, Ms. Longyu Li, Mr. Yunseo Min, Ms. Iris Zhao, Dr. Peter Cripton, Dr. Agnes d'Entremont

The University of British Columbia, Vancouver, British Columbia, Canada

Introduction

Wrist fractures are common skeletal injuries, inducing great societal and personal costs. Secondary wrist fractures were observed in many patients after treatment, which traditionally involves the use of a circumferential wrist plaster cast. Although effective in stabilising the primary injury, the protection offered in a fall after treatment, leading to a secondary impact, is unknown. A study of the impact loads of novel 3D-printed and plaster casts is needed to assess their comparative performance under secondary impacts.

Methods

The impacts were replicated using a drop tower with a vertical translating carriage at 40 cm high, weighing 14.2 kg to simulate the effective mass of the arm, shoulder, and torso. The impact anvil was tilted at 50 degrees, mimicking oblique hand-to-ground impacts (Fig.1). A six-axis load cell on the carriage recorded reaction loads at 10,000 samples per second. The proximal ends of the custom-made thermoplastic polyurethane distal forearm models were attached to the load cell (Fig.1). The two forearm models were housed in the plaster and 3D-printed (polylactic acid) casts, whose Voronoi cell structure was generated using Blender. A high-speed camera (Phantom v1212) (Fig.1) evaluated qualitative motion and failure evaluation at 19,000 frames per second.

Results

The 3D-printed cast exhibited more proximal deflection and slightly deformed shells, whereas the plaster cast deflected less proximally and showed thin surface cracks. The peak axial impact forces of 706 N and 1049 N were recorded for the 3D-printed and plaster casts, respectively. Due to the larger deflection angle, the 3D-printed cast generated a greater peak proximal moment (My) of 17 Nm versus 8.6 Nm of the plaster cast.

Discussion

The experiment represented the secondary impacts on immobilised broken wrists. Given the larger deflection and moment of the 3D-printed cast, the novel design is stiffer around the wrist, thus offering better structural integrity to maintain the wrist fracture stabilisation.

The higher force and fracture surfaces on the plaster cast suggest less deformation versus the 3D-printed cast, showing no damage and lower force due to its cellular structure. These findings prove that both casts prevented excessive wrist motion, and better compliance and protection were associated with the 3D-printed cast.

Images (Optional)

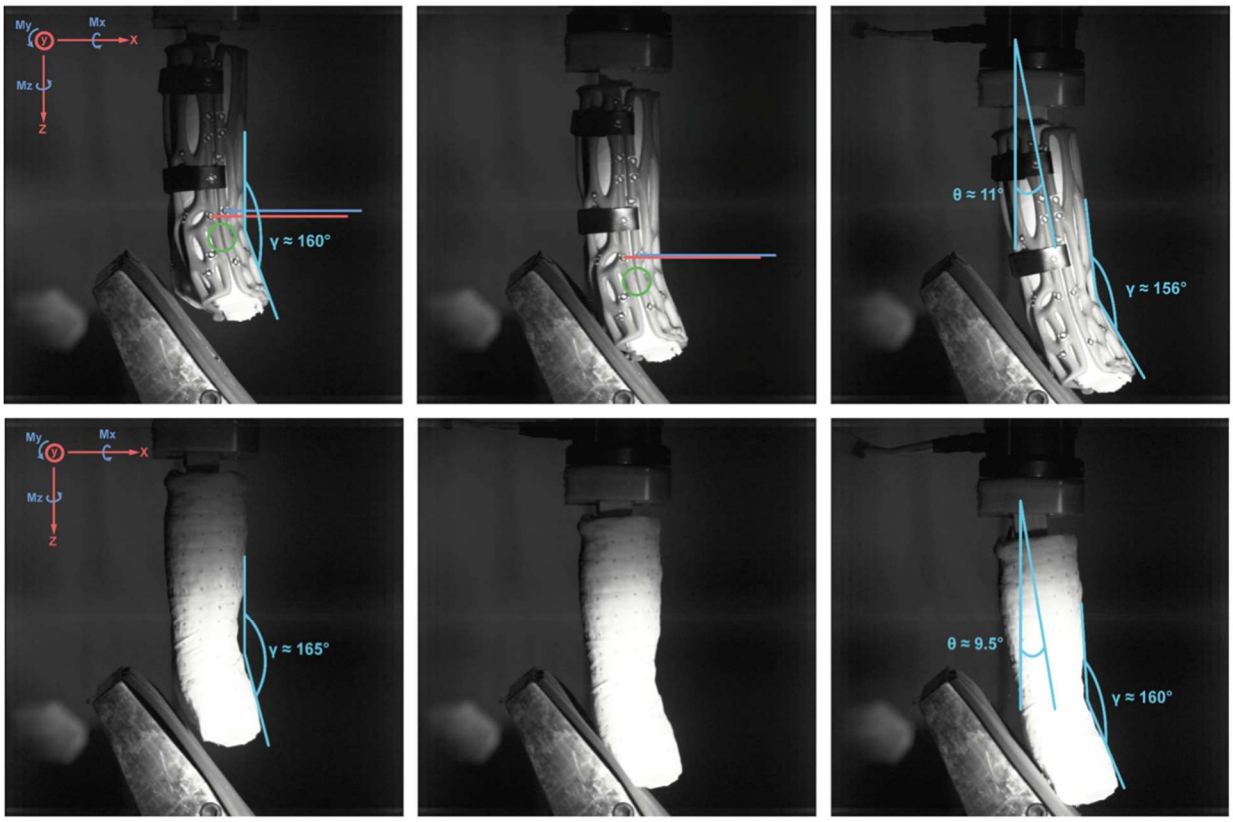


Figure 1: High-speed video images of the 3D-printed (top) and plaster (bottom) wrist casts before (left), during (middle), and after (right) the impact.

Session Category

Injury Biomechanics: N/A

P3-147

Constructing Characteristic Signals of Head Acceleration Events in Stock Car Racing

Miss Zoie Mink[1,2], Mr. Cole Smith[1,2], Dr. Nicholas Pritchard[1,2], Dr. Garrett Bullock[1], Mr. Matthew Harper P.E.[3,1,2], Dr. Jillian Urban[1,2], Dr. John Patalak[3], Dr. Joel Stitzel[1,2]

[1]Wake Forest University School of Medicine, Winston-Salem, NC, United States. [2]Virginia Tech – Wake Forest University School of Biomedical Engineering and Sciences, Winston-Salem, NC, United States. [3]National Association for Stock Car Auto Racing, LLC, Daytona Beach, FL, United States

Introduction

Drivers in stock car racing are exposed to head acceleration events (HAEs) during racing. While methods exist to create representative corridors in sports, such as soccer headers, no such corridors have been developed in a motorsports setting [1]. The variability of loading in motorsport HAEs may not be adequately accounted for using these approaches. Therefore, ARCGen was employed which uses arc-length reparameterization and signal registration to develop representative corridors in a wide range of settings [2]. The objective of this study was to characterize HAEs in a motorsport setting using ARCGen-generated representative corridors.

Methods

Head kinematics were collected from 20 NASCAR Cup Series drivers over 41 races during the 2024 season using instrumented mouthpiece sensors configured to collect linear and rotational head kinematics (1600 Hz, 4g threshold). HAEs containing multiple impacts exceeding the trigger threshold were separated into individual impacts. For each impact, peak kinematics including peak linear velocity/acceleration (PLV/PLA) and peak angular velocity/acceleration (PRV/PRA) were calculated. Impacts were grouped into bins by principal direction of force (PDOF), kinematic percentile, and event type (race, crash, combined). ARCGen was used to generate representative kinematic corridors for each bin (x, y, z, x-y resultant, and x-y-z resultant) [2]. Signals were time-aligned using the optimal alignment of PLA.

Results

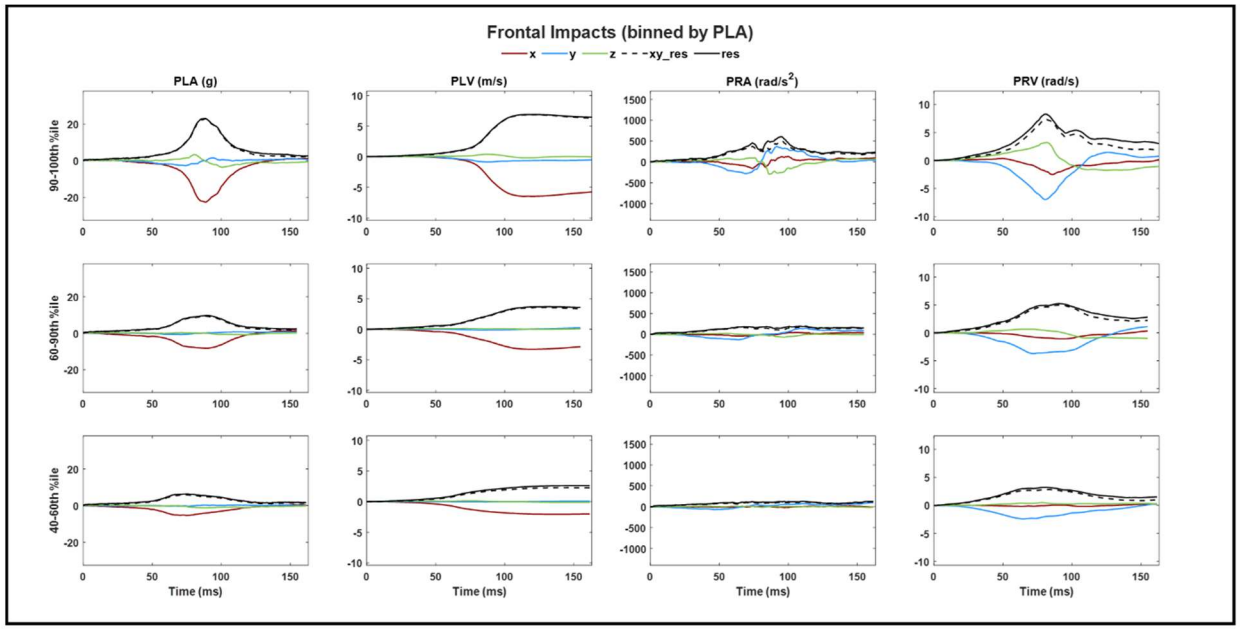
3,156 HAEs, separated into 4,478 impacts (n=3,818 race, n=660 crash), were recorded during the 2024 season. Corridors, or characteristic signals, were generated for 2,880 distinct bins (Figure 1). When binning the combined dataset by PLA, 40-60th percentile x-y-z

resultant PLA peaks ranged from 3.89 to 6.83 g's while 90-100th ranged from 11.6 to 27.5 g's. Right side impacts had the lowest PLA peaks across percentile bins when binning by PLA and PRA, while rear impacts had the highest when binning only by PLA.

Discussion

Characteristic signals reflecting stock car racing HAEs were created. These may inform driver safety including helmet testing standards, finite element analysis and model validation, and safety system enhancements. This work facilitates cross-sport comparisons to contextualize motorsport racing HAEs relative to other environments.

Images (Optional)



References (Optional)

[1] Filben *et al.*, J Biomechanics, 2021

[2] Hartlen *et al.* Front. Bioeng. Biotechnol, 2022

Acknowledgements (Optional)

The authors thank the drivers for participating in this study and all members of the research team who assisted with this study. This work was supported by the National Association of Stock Car Auto Racing (NASCAR).

Session Category

Injury Biomechanics: N/A

P3-148

Fluid Dynamics and Diffusion Study of an Open-Source 3D-Printable Bioreactor and Mechanical Loading System for E*x Vivo* Bone Culture

Ms. Alejandra Correa-Belloso Ph.D. (c)[1], Dr. Mahsa Zojaji[2], Dr. Roshni Rainbow[1], Dr. Heidi Ploeg[1]

[1]Dept. of Mechanical and Materials Engineering, Queen's University, Kingston, Ontario, Canada. [2]Dept. of Kinesiology and Health Sciences, University of Waterloo, Waterloo, Ontario, Canada

Introduction

Bioreactors are used to study the response of *ex vivo* bone tissue to mechanical stimulation. An open-source 3D-printable chamber was designed [1] to be more cost-effective/adaptable than the original Zetos system. However, the culture media dynamics within the 3D-printable bioreactor chamber (BC), and whether it allows media diffusion to the bone core to maintain tissue viability, remain unknown. This study aimed to **(1)** evaluate the culture media dynamics in the 3D-printable BC, and **(2)** assess culture media diffusion using *ex vivo* bone cores in bioreactors.

Methods

(1) Computational-Fluid-Dynamics (CFD) analyses were performed within the BC (flowrate=6.6mL/hr). Culture medium was modelled as water and bone core as 10×10mm (height×diameter) solid cylinder. **(2)** 10×10mm *ex vivo* bovine-bone cores were used to evaluate the diffusion time of culture medium to the core in static and dynamic (6.6mL/hr) culture. Phosphate-buffered-saline+10% disulphine-blue stain mimicked culture medium. Each bone core was cut in half to measure radial stain infiltration at 3, 6, 9, and 12hr (n=5/group). An Aligned-Rank-Transform, followed by post-hoc tests, were used to assess statistical significance (α=0.05).

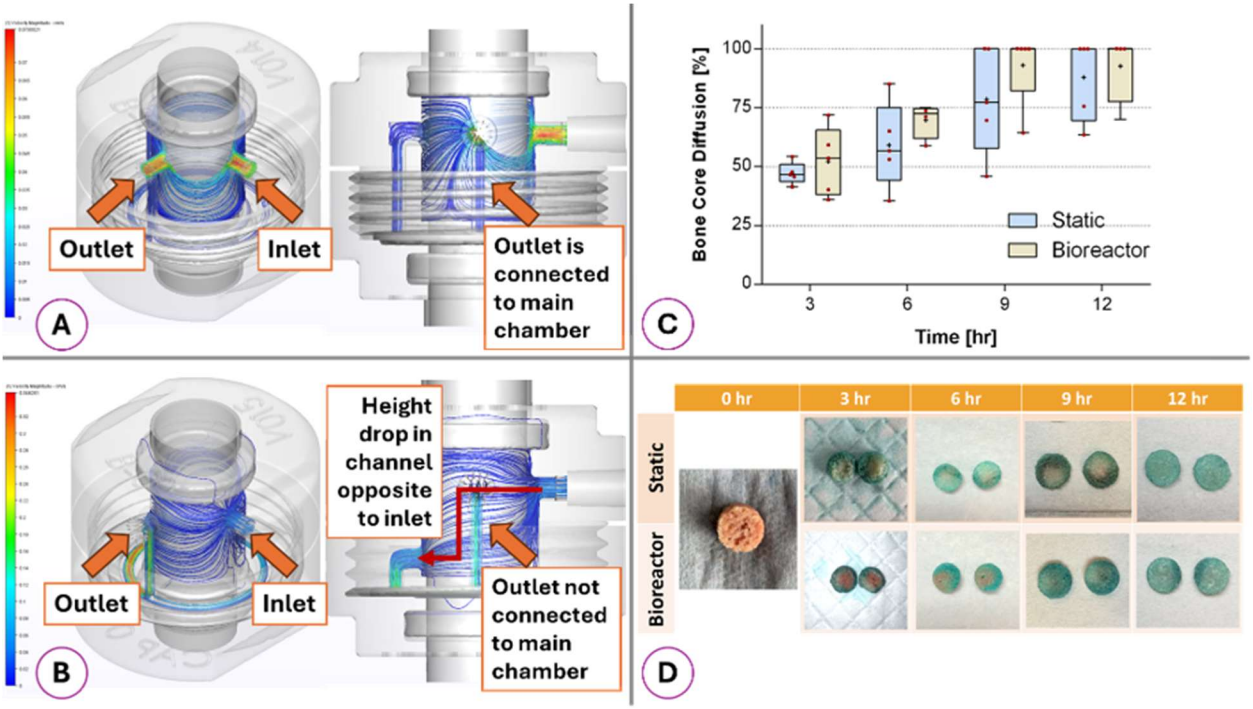
Results

(1) Most of the fluid left the BC without diffusing through the bone core due to the closeness between inlet-outlet channels (Figure-A). The BC design was modified and consecutive CFD validation is shown (Figure-B), where zero-velocities are observed surrounding the core. **(2)** Time showed a significant effect in media diffusion ($p<0.001$) (Figure-C). Complete diffusion was observed between 6-9h (Figure-D). After 9h, 80% of the bioreactor samples were completely stained, but only 40% in static-control.

Discussion

Our main findings suggest that 10×10mm bone cores are fully immersed in culture media within the first 6-9h in the 3D-printable BC. The advantageous zero-velocities surrounding the core allow for isolation of mechanical loading as the only source of external stimulation in *ex vivo* bone studies. The validated design is shared with the scientific community to promote *ex vivo* bone research. Future work will improve the accuracy of CFD analyses using bone core models for a better understanding of culture media dynamics and potential shear stresses in bone cells.

Images (Optional)



References (Optional)

[1] Kunath *et al.*, J. Mech. Behav. Biomed. Mater., 2024

Session Category

Organ and Tissue Biomechanics: N/A

P3-149

Fiber Rearrangement Redistributes Energy and Modulates Intrinsic Cutting Energy in Bovine Glisson's Capsule

Mr Shaobo Zhan[1], Dr Shelby Hutchens[1], Dr Amy WagonerJohnson[1,2]

[1]University of Illinois, Urbana Champaign, Urbana, IL, United States. [2]Chan Zuckerberg Biohub Chicago, Chicago, IL, United States

Mr Shaobo Zhan

Dr Shelby Hutchens

Introduction

In collagenous membranes like bovine Glisson's capsule (bGC), fiber networks redistribute energy during deformation, but how this fiber rearrangement contributes to fracture energy remains unclear. Y-shaped cutting [1] localizes crack-tip stress field and separates intrinsic cutting energy, Gcut*, from boundary effects that confound standard tearing tests. Coupling cutting with in-situ SHG imaging, our objective is to measure how blade radius and fiber rearrangement influence cutting-based fracture descriptors, aiming to guide design of collagen-based biomaterials and tissue surrogates.

Methods

We use Y-shaped cutting on fresh-frozen bGC, with different blade radii and applied far-field tearing according to [1]. We measure cutting and tearing energies to establish Gcut* and the corresponding critical blade radius, r^*, while imaging with SHG to capture fiber rearrangement.

Results

With sharp blades and small tearing, apparent cutting energy converges to an intrinsic cutting energy, Gcut*. At $r \geq r^*$, the slope of cutting energy vs blade radius describes sensitivity to cutting tools [1]. Gcut* is larger and r^* is smaller for bGC [2], but its Gcut*

from cutting is ~2x lower than expected from tearing-based fracture tests [3]. bGC's apparent cutting energy increases with blade radius at a rate ~17x that of silicone, suggesting that local energy redistribution contributes to far-field fracture resistance. The applied-vs-cutting energy slope shows that bGC is less efficient in transmitting far-field energy to crack tip. Together, these energetic signatures are consistent with crack-tip fiber rearrangement, energy redistribution, and higher fracture resistance.

Discussion

Classic fracture tests entangle intrinsic fracture energy and boundary condition effects. Y-shaped cutting allows for Gcut* measurement, along with multiple other size-independent failure descriptors. Results here show that bGC isolates crack tip, likely due to fiber rearrangement, and increases fracture resistance compared to silicone. We will examine fiber rearrangement in depth using glutaraldehyde (GA) treatment, which increases crosslinking without altering fiber network. We expect that increased crosslinking will raise Gcut* by increasing fiber failure cost, whereas GA-stiffened fibers will resist rearrangement and thus lower sensitivity to blade radius and far-field tearing.

Images (Optional)

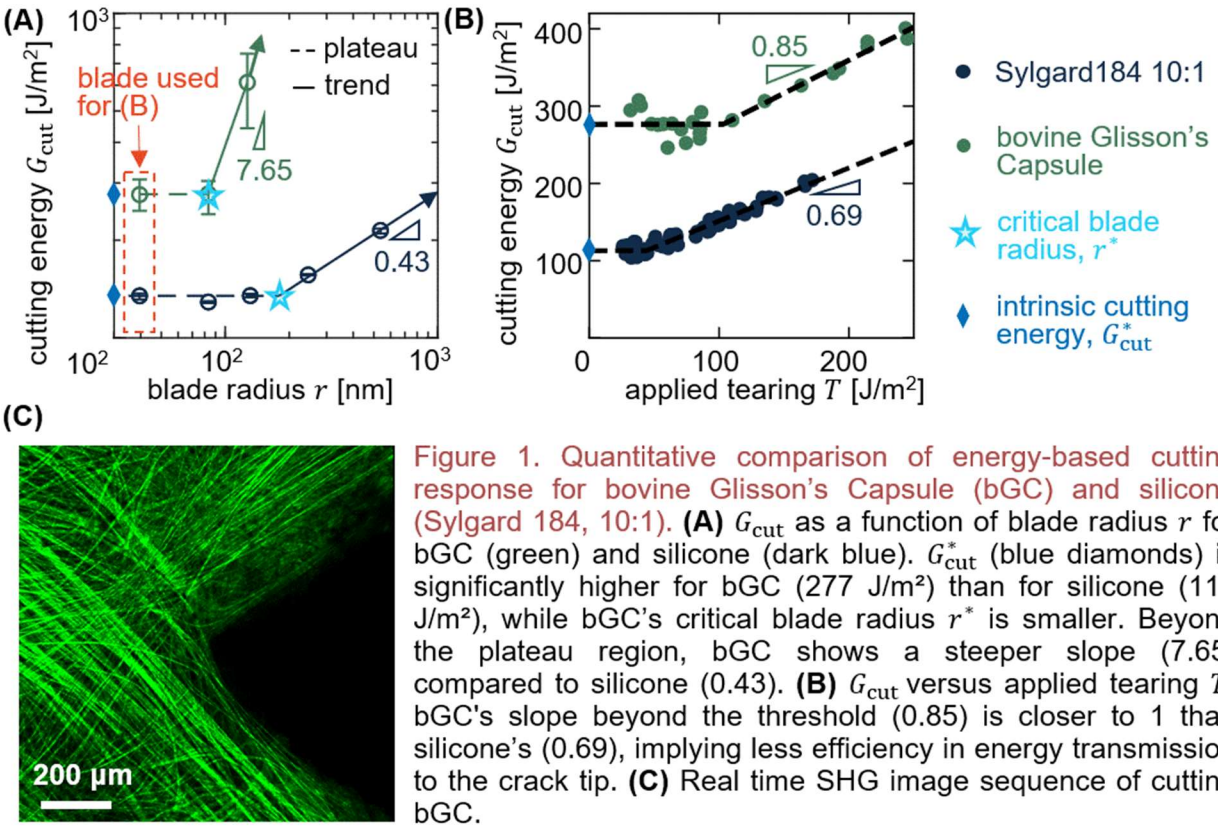


Figure 1. Quantitative comparison of energy-based cutting response for bovine Glisson's Capsule (bGC) and silicone (Sylgard 184, 10:1). **(A)** G_{cut} as a function of blade radius r for bGC (green) and silicone (dark blue). G^*_{cut} (blue diamonds) is significantly higher for bGC (277 J/m²) than for silicone (113 J/m²), while bGC's critical blade radius r^* is smaller. Beyond the plateau region, bGC shows a steeper slope (7.65) compared to silicone (0.43). **(B)** G_{cut} versus applied tearing T. bGC's slope beyond the threshold (0.85) is closer to 1 than silicone's (0.69), implying less efficiency in energy transmission to the crack tip. **(C)** Real time SHG image sequence of cutting bGC.

References (Optional)

[1] Shaobo Zhan et al., Exp Mech, 2024

[2] Shaobo Zhan et al., submitted to Matter

[3] Kevin Bircher et al., Nat Commun, 2019

Session Category

Organ and Tissue Biomechanics: N/A

P3-150

Improving Tissue Deformation Tracking in Blood Vessel Burst Pressure Tests

Ms. Kaitlyn Murphy[1], Mr. Michael Queenan[1], Ms. Erin Gibbons[1], Mr. Joseph Maucieri[1], Mr. Joe Orban[2], Mr. Don Wilson[2], Dr. Isaac Macwan[1], Dr. Ana Estrada[1]

[1]Fairfield University, Fairfield, Connecticut, United States. [2]Intuitive Surgical, Orange, Connecticut, United States

Introduction

Burst pressure mechanical tests are a key assessment of the effectiveness of blood vessel ligation techniques, and they also serve as an important tool for comparing the material properties and failure modes between natural tissue and synthetic graft alternatives. The project presented here is focused on improving previous burst pressure protocols by incorporating tissue deformation tracking in order to better measure and compare the material properties of porcine renal and carotid arteries to synthetic alternatives.

Methods

We developed a low-cost burst pressure testing accessory table that allows us to record full tests and track tissue deformation. The testing table is a custom-designed 3D printed structure with a camera holder allowing full recordings of sample inflation and pressure sensor readings, as well as a lower platform with 1mm notches to serve as a reference of total sample deformation. The samples, both porcine renal and carotid arteries or synthetic alternatives, are ligated at the free end and connected by a mechanical iris to a needle that pressurizes them with water at a flow rate of 200ml/hr. After the test, the open-source application Tracker is used to calculate the deformation based on markers on the surface of the sample.

Results

We performed preliminary tests on fresh porcine renal arteries (n = 5), with an average time to failure of 93 ± 3 seconds (mean ± 1SD) and a pressure of 2072 ± 366 mmHg. Two initial successful tests yielded an axial strain of 0.40 ± 0.21 and circumferential strain of 0.93 ± 0.32.

Discussion

Preliminary tests demonstrate that the custom-built testing accessory table allows us to properly capture full burst pressure tests and measure tissue deformation. Additional refinement of the testing protocol will allow us to collect more data on porcine and synthetic vessels. This new testing protocol will also be broadly applicable to other

vasculatures. A finite element model of the burst pressure test is being developed in conjunction with the mechanical tests, in order to help characterize and fit material properties of native porcine tissue and synthetic alternatives. This characterization will help us optimize new synthetic graft materials for testing of blood vessel ligation techniques.

Acknowledgements (Optional)

This study has been supported by Intuitive Surgical as part of a sponsored undergraduate senior design project at Fairfield University.

Session Category

Organ and Tissue Biomechanics: N/A

P3-151

Subject-Specific Characterization of the Trochanteric Soft Tissues Improves Impact Force Predictions during Lateral Falls on the Hip: A Comparison of Non-Destructive Inverse Finite Element Modelling and Shear Wave Elastography Approaches

Mr. Steven Pretty, Ms. Alyssa Tondat, Dr. Andrew Laing

University of Waterloo, Waterloo, ON, Canada

Introduction

Increased trochanteric soft tissue thickness (TSTT) is associated with reduced hip fracture risk through impact attenuation during a fall. Beyond thickness, subject-specific variations in the stress-strain behavior of these tissues likely influence impact-loading; however, conventional material characterization approaches are not applicable for clinical screening. The study objectives were to: 1) validate and compare non-destructive trochanteric soft tissue characterization approaches; and 2) evaluate the influence of material behavior on impact attenuation during a fall.

Methods

Fresh soft tissue-femur complexes were extracted from 12 post-mortem human donors. Each side was randomly assigned to one of two tissue characterization approaches.

1. Inverse-Finite Element Modelling (iFEM): Visco-hyperelastic models were defined through iterative-optimization. The objective function was to minimize RMSE between experimental and simulated force-time histories during indentation and stress-relaxation trials. Force-time histories during dynamic loading trials were utilized for validation.

2. Shear Wave Elastography (SWE): Acoustoelastic models were defined through linear fitting of instantaneous shear modulus data across indentation depths applied with an ultrasound transducer. Material parameters and predicted stress-strain responses were compared to contralateral iFEM models to assess agreement.

Following characterization, soft tissues were isolated and mounted to a surrogate pelvis system. Fall simulations were performed at 2 m/s, and peak femoral neck impact force (F_{Neck}) was extracted from an in-line load cell. Pearson correlations and linear regressions were utilized to assess the influence of iFEM and SWE-derived material parameters on F_{Neck}.

Results

Mean (SD) normalized RMSE for iFEM-predicted dynamic loading forces was 5.6 (2.5)%. Absolute agreement between iFEM and SWE models was poor; however, hyperelastic material parameters were moderately to highly correlated (r^2 = 0.54-0.82). For both iFEM and SWE model parameters, non-linear shear modulus was the only predictor of F_{Neck} independent of TSTT (r^2 = 0.36-0.43). iFEM and SWE-predicted strain energy densities improved the explained variance in F_{Neck} by 5.2-7.0%, compared to TSTT alone.

Discussion

Our results suggest both iFEM and SWE characterization methods can improve impact force predictions compared to TSTT alone, driven primarily by subject-specific variation in tissue non-linearity. The more clinically-applicable SWE method exhibited similar performance in assessing material parameter differences between tissues; however, absolute values should be cautiously interpreted.

Session Category

Organ and Tissue Biomechanics: N/A

P3-152

Parameters Affecting Shear Modulus and Shear Wave Speed in Pressurized Biological Tissues

Ir. Ariana Cihan[1], Prof. Dr. Patrick Segers[1], Dr. Annette Caenen[1,2]

[1]Ghent University, Ghent, Oost-Vlaanderen, Belgium. [2]KU Leuven, Leuven, Vlaams-Brabant, Belgium

Introduction

Shear wave elastography (SWE) estimates stiffness by tracking induced shear waves. As shear wave speed (SWS) reflects interstitial fluid pressure (IFP) in biological tissue[1], SWE may enable non-invasive IFP evaluation, advancing non-invasive diagnosis of a.o. cerebral, hepatic, or renal disorders. To study how pressure affects shear modulus and SWS, we consider poroelastic materials with altered fluid pressure subjected to shear deformation and conduct a parameter study.

Methods

We study the strain energy density of pressurized porohyperelastic materials subjected to simple shear: coupled Neo-Hookean (NH), uncoupled Ogden (OG), and coupled St. Venant-Kirchhoff (SVK). We derive shear stress, tangent shear modulus, and average density analytically. Pressure-dependent SWS is calculated from density and shear modulus at infinitesimal shear strain. This method deviates from the approach of incremental waves in prestressed media[2]. We verify the method using finite element models of acoustically induced shear waves[3]. An initial shear modulus of 4kPa and a pressure range of –4-4kPa were considered.

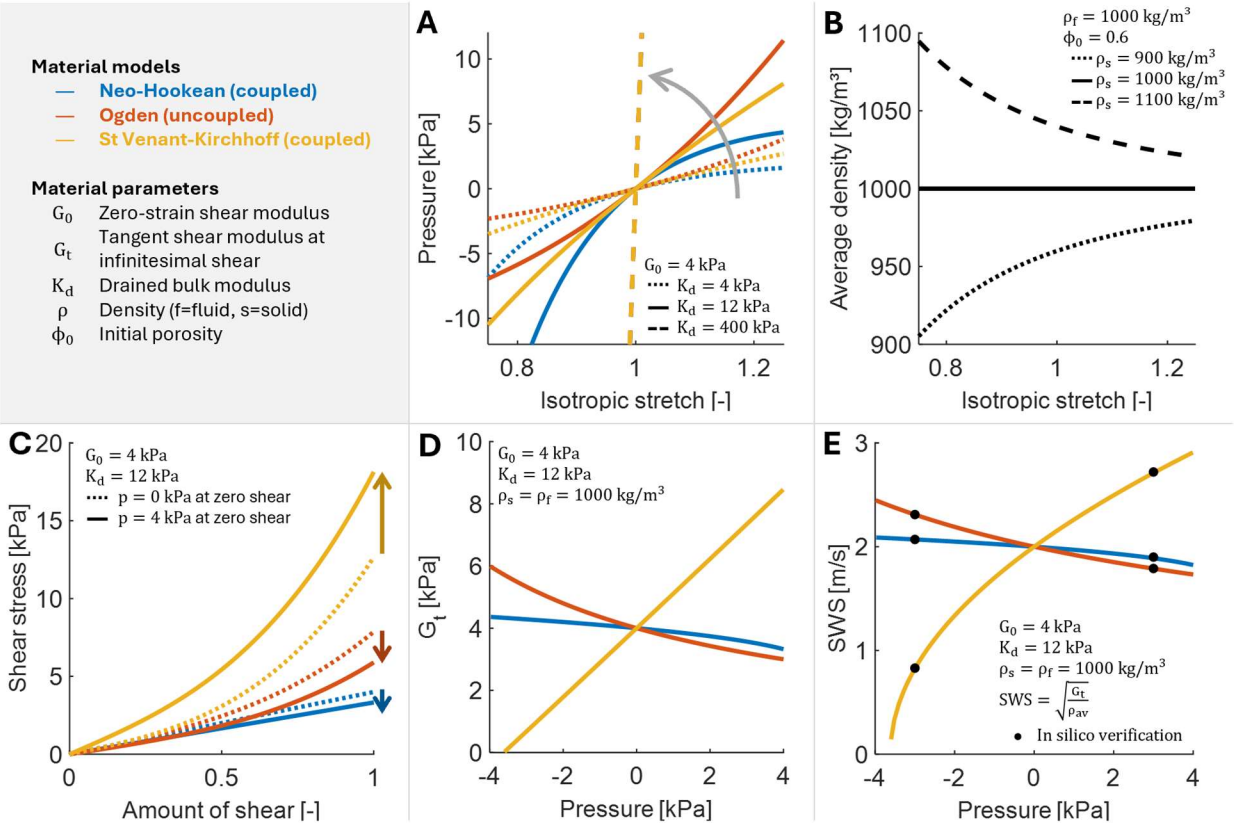
Results

The strength of pressure-stretch coupling is governed by the drained bulk modulus (Fig. A). The average density is affected by the resulting dilatation (Fig. B) and initial porosity (not shown); it decreases with pressure for a denser solid and vice-versa. Fig. C demonstrates how shear stress-strain curves shift downwards for NH and OG and upwards for SVK at 4kPa. Fig. D quantifies the change in tangent shear modulus with pressure at infinitesimal shear. Fig. E shows the pressure-dependent SWS. Simulation results are added for verification. Over –4-4kPa, SWS decreases by 0.27 and 1.72m/s for NH and OG, and increases by 2.9m/s for SVK.

Discussion

This study introduces a novel analytical framework to estimate SWS in pressurized porohyperelastic materials. Results demonstrate that SWS sensitivity to pressure strongly depends on selected material models and parameters. Of the models examined, only SVK follows the experimentally-observed SWS increase with pressure in ex vivo livers and breasts[1,3]. This highlights the need for future work on experimental calibration and validation. The framework can also be inverted for pressure estimation through SWE.

Images (Optional)



References (Optional)

[1] Rotemberg et al., PMB, 2012

[2] Nazari et al., JMPS, 2018

[3] Cihan et al., PMB, 2024

Acknowledgements (Optional)

This work is supported by the Research Foundation Flanders (FWO, Belgium) under grants 1173625N to Ariana Cihan and 12B3124N to Annette Caenen.

Session Category

Organ and Tissue Biomechanics: N/A

P3-153

Evaluating Stiffness and Volume Changes in Pressurized Ex Vivo Kidneys With Ultrasound and Magnetic Resonance Imaging

Ir. Ariana Cihan[1], MSc Yanglei Wu[2], MSc Jennifer Heyl[2], Mr. Pedro Dantas de Moraes[2], MD Paul Spiesecke[2], Prof. Dr. Jing Guo[2], Prof. Dr. Ingolf Sack[2], Prof. Dr. Patrick Segers[1], Dr. Annette Caenen[1,3], Dr. Tom Meyer[2]

[1]Ghent University, Ghent, Oost-Vlaanderen, Belgium. [2]Charité – Universitätsmedizin Berlin, Berlin, Berlin, Germany. [3]KU Leuven, Leuven, Vlaams-Brabant, Belgium

Introduction

Renal elastography is influenced by both intrinsic tissue stiffness and intrarenal pressure, hindering accurate differentiation of fibrosis and pressure. Evaluation of pressure-induced changes in both volume and stiffness may help towards uncoupling these effects, as proposed for the liver [1] using magnetic resonance imaging/elastography (MRI/MRE). To assess the applicability of this strategy to the kidney, we applied MRI and ultrasound modalities to pressurized ex vivo pig kidneys.

Methods

Six ex vivo pig kidneys were pressurized through the renal artery (0-60mmHg) with ligated renal vein and ureter. Cross-sectional areas were measured from anatomical views in 3D (MRI) and 2D (US) as a proxy for volume. Elastography measurements were performed first on ultrasound-based time harmonic elastography (THE; GAMPTmbH), and clinical shear wave elastography (SWE; Canon Aplio i800) and MRE (3T Siemens Lumina) at another timepoint. Stiffness was estimated based on the propagation speed of shear waves (SWS) induced acoustically (SWE) or external vibration (THE & MRE, 60-80Hz). Fig. A shows the measurement setup with transducer fixations. Regression slopes for volume and parenchymal stiffness over pressure were calculated per kidney and are reported as median [min.,max].

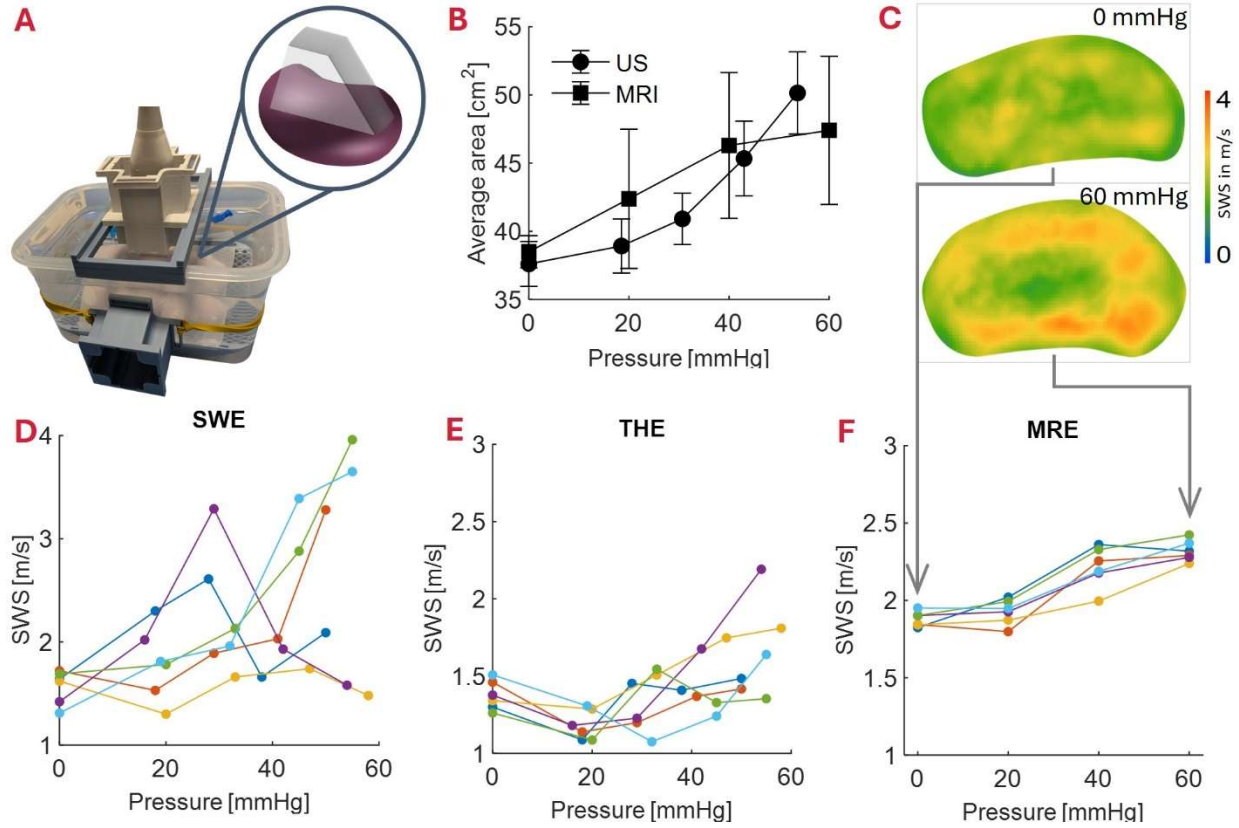
Results

Volumes estimated with MR and ultrasound were sensitive to pressure (Fig. B), with slopes of 0.23[0.20,0.26]cm^2/mmHg. Changes of SWS with pressure are shown in Fig. D-F. The median slopes are 0.0154[0.0009,0.0450]m/s/mmHg for SWE, 0.0041 [0.0003,0.0152]m/s/mmHg for THE, and 0.0082[0.0066,0.0095]cm^2/mmHg. Fig. C displays representative MRE elastograms at baseline and maximum pressure with visible increases in parenchymal stiffness and volume.

Discussion

We present the first combined assessment of renal volume and stiffness changes across controlled pressure levels. Preliminary findings indicate that imaging-based assessment of volume as proxy for pressure combined with stiffness may support uncoupling of fibrosis and pressure. Consistent trends across ultrasound and MRE modalities underscore the potential of this approach, despite differing sensitivities potentially caused by different wave frequencies and transducer locations. Ongoing analysis of the full dataset (including fiber tracking, dispersion, and 3D-ultrasound volume) and biomechanical model calibration will provide further insights into the pressure-volume-stiffness relationship.

Images (Optional)



References (Optional)

[1] Jaitner et al., Acta Biomaterialia, 2025.

Acknowledgements (Optional)

This work is supported by the Research Foundation Flanders (FWO, Belgium) under grants 1173625N to Ariana Cihan and 12B3124N to Annette Caenen as well as by the German Research Foundation (GRK 2260, SFB 1340, FOR 5628).

Session Category

Organ and Tissue Biomechanics: N/A

P3-154

Averaging Material Parameters in Hyperelastic Models: Impact of Polynomial vs Exponential Forms

Vanier Scholar Arya Amiri[1], Associate Professor Thomas Willett[1], Assistant Professor Taisiya Sigaeva[2]

[1]University of Waterloo, Waterloo, Ontario, Canada. [2]University of Calgary, Calgary, Alberta, Canada

Introduction

Hyperelastic constitutive models are mathematical expressions that relate deformation to stress in soft biological tissues. Each model has one or more parameters that are identified by fitting the model to experimental stress-deformation data. For a group of specimens, a single set of parameters is often reported to represent the average behavior. While linear algebra properties like “additivity” and “homogeneity” can predict when averaged parameters yield an average response, it is generally thought that nonlinearity of these models prevents this [1]. The objective is to investigate whether average parameters can reproduce the population’s average responses for several commonly used models and to assess any discrepancies.

Methods

Three polynomial (Mooney-Rivlin, Yeoh, and Polynomial) and three exponential models (Fung, Holzapfel-Gasser-Ogden, and Four-Fiber-Family) were investigated. Uniaxial data was used for the first four models, and equibiaxial data for the last two. Two approaches, algebraic and statistical, were employed for the analysis. The normalized root-mean-square error (NRMSE) was used to quantify the discrepancy between the predicted responses from averaged parameters and the actual averaged responses.

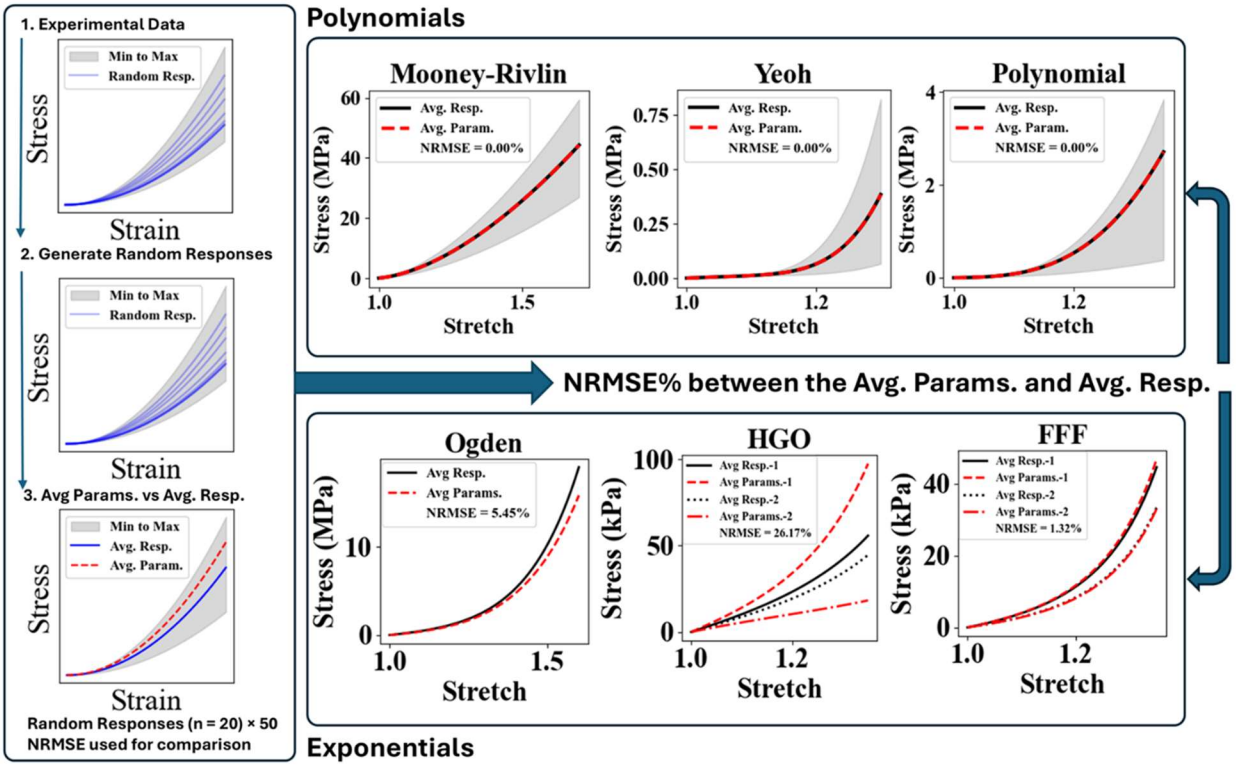
Results

Both algebraic and statistical results show that constitutive models can be classified into two categories: polynomial and exponential. For polynomial models, average parameters reproduce the average response, despite their nonlinear behavior. In contrast, for exponential models, the deformation level affects how well average parameters predict the average response.

Discussion

A new finding that has not been previously reported is that for polynomial models, average parameters reproduce the mean mechanical response without any discrepancy, suggesting that model type, not nonlinearity alone, is the key factor. Even for exponential models, average parameters can predict the mean response of the population with an NRMSE as low as 2.5% at typical experimental stretches, although the discrepancy increases at higher stretches. These results clarify the behavior of various constitutive models and support using average parameters to represent a population when appropriate. As a limitation of this study, it should be noted that although the algebraic approach allows generalization to all constitutive models, only six models under uniaxial and equibiaxial testing protocols were investigated.

Images (Optional)



References (Optional)

[1] Douglas Cook and Daniel Robertson, J Biomechanics, 2016

Acknowledgements (Optional)

This work was supported by the Vanier Canada Graduate Scholarship program, administered by the Natural Sciences and Engineering Research Council of Canada (NSERC), and by the NSERC CREATE Training Program in Global Biomedical Technology Research and Innovation.

Session Category

Organ and Tissue Biomechanics: N/A

P3-155

Musculoskeletal–finite element modeling of knee joint mechanoinflammation and cartilage adaptation

Dr. Atte Eskelinen Ph.D.[1], Dr. Joonas Kosonen Ph.D.[1], Mr. Joose Peitola M.Sc.[1], Prof. Rami Korhonen Ph.D.[1], Adj. Prof. Petri Tanska Ph.D.[1,2], Dr. Amir Esrafilian Ph.D.[1]

[1]Department of Technical Physics, University of Eastern Finland, Kuopio, North Savo, Finland. [2]Cancer Center, Kuopio University Hospital, Wellbeing Services County of North Savo, Kuopio, North Savo, Finland

Introduction

Abnormal biomechanics and joint inflammation are key factors for knee osteoarthritis progression. Previous joint-level computational models have typically considered cartilage stresses and strains [1] and inflammation as separate candidate mechanisms for disease progressors, thereby overlooking their combined effects. Specifically, mechanical activation of mechanosensitive cell receptors resulting in cellular release of cartilage-degrading enzymes, termed mechanoinflammation, has not been implemented in joint-level models. The objective of this proof-of-concept study was to establish the first computational knee joint model that integrates cartilage mechanical responses from musculoskeletal–finite element (MS–FE) analysis, subsequent chondrocyte responses with downstream mechanoinflammation, exogenous pro-inflammatory cytokine diffusion, and adaptation of tissue composition and mechanical properties.

Methods

Knee magnetic resonance imaging- and motion capture-based personalized MS–FE model [2,3] was created for a single subject (Fig. 1A). MS model provided inputs (knee flexion angle, medial vertical joint contact force) to FE model of medial tibiofemoral joint with fibril-reinforced poroviscoelastic cartilage (Abaqus). FE simulation estimated cartilage maximum shear strain distributions, used as input to mechanoinflammatory model (COMSOL Multiphysics), with strains >15% [1] triggering phenotypic transition of chondrocytes from “healthy” to “damaged” state. Damaged cells and cells interacting with diffusing pro-inflammatory cytokines (94 pg/ml at synovial fluid–cartilage-interface [4]) released aggrecan-degrading enzymes. Resulting aggrecan loss was linked to increased permeability, and tensile stresses >7 MPa to collagen loss in iteratively updated material [1]. Three consecutive iterations estimated 3-year cartilage adaptation.

Results

The 3-year simulation transitioned 30% of total cells into “damaged” state in cartilage contact region with excessive shear strains (Fig. 1B). Aggrecan content decreased by 53% in this region and 31% in regions experiencing only exogenous inflammation at 3-year timepoint.

Discussion

Mechanoinflammation was localized as opposed to cytokine diffusion, with cell state distribution and aggrecan loss similar to experimental *ex vivo* estimates although needing rigorous *in vivo* calibration [4]. MS–FE-mechanoinflammation modeling helps designing interventions such as gait retraining and anti-inflammatory drugs.

Images (Optional)

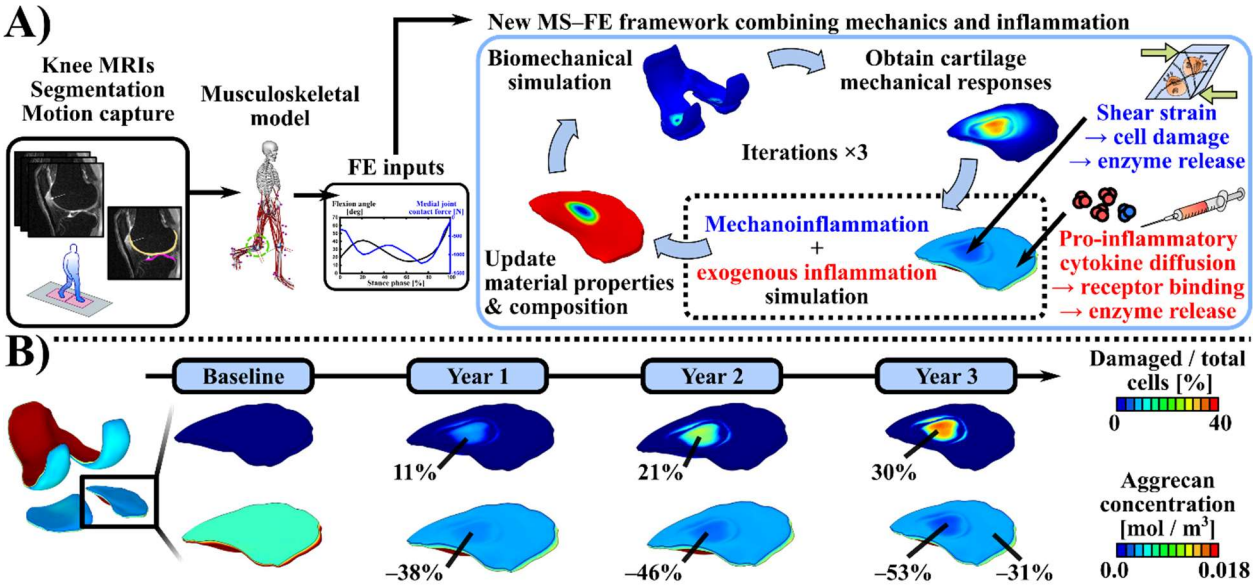


Figure 1. (A) Knee MRIs were used to create a personalized musculoskeletal (MS) and a finite element (FE) model. The MS model and motion data were used to obtain FE model inputs. The FE model estimated cartilage mechanical responses, out of which the shear strain response (→ cell damage → mechanoinflammatory ADAMTS enzyme release) was simulated together with exogenous pro-inflammatory cytokine diffusion. The framework within the blue box was looped over three iterations, with updated material properties and composition. **(B)** In the mechanoinflammatory simulation, the cell damage decreased locally in highly sheared regions, resulting in ~50% local aggrecan loss between baseline and 3-year timepoint. Exogenous inflammation led to ~30% aggrecan loss.

References (Optional)

[1] ME Mononen *et al.*, J Orthop Res, 2018; [2] A Esrafilian *et al.*, IEEE Trans Biomed Eng, 2025; [3] A Esrafilian *et al.*, IEEE Trans Neural Syst Rehabil Eng, 2021; [4] K Amano *et al.*, Am J Sports Med, 2018.

Acknowledgements (Optional)

Novo Nordisk Foundation (NNF21OC0065373), Research Council of Finland (354916, 363459), Finnish Cultural Foundation (00230091), Sigrid Jusélius Foundation,

Väisälä Foundation, Päivikki and Sakari Sohlberg Foundation (240074). This project has received funding from the European Union's Horizon 2020 research and innovation programme under the Marie Skłodowska-Curie grant agreement (No. 101108335). This work was supported by the Finnish Ministry of Education and Culture's Pilot for Doctoral Programmes (Pilot project Mathematics of Sensing, Imaging and Modelling).

Session Category

Organ and Tissue Biomechanics: N/A

P3-156

Biomechanical and Structural Characterisation of Perineal Tissues Across Multiple Scales

PhD Beatrice Bisighini[1], PhD Cristina Cavinato[2], PhD Sarah Iaquinta[3], Prof Anne-Sophie Caro[3], PhD Baptiste Pierrat[1]

[1]Sainbiose, Mines Saint-Étienne, Saint-Étienne, Auvergne-Rhône-Alpes, France. [2]LMGC, Université de Montpellier, Montpellier, Occitanie, France. [3]LMGC, Mines Alès, Alès, Occitanie, France

Introduction

Perineal tears affect more than 85% of primiparous women undergoing vaginal delivery and can involve multiple tissue layers, leading to long-term consequences. Yet, the mechanical behaviour of the perineal tissues remains poorly characterised, limiting the accuracy of existing biomechanical models [1]. To address this gap, this study provides a comprehensive, multi-scale assessment of the mechanical behaviour and structural organisation of five porcine perineal tissues: the skin, vaginal and anal mucosae, and internal and external anal sphincters.

Methods

Ex-vivo tissue samples cut into dog-bone specimens along two perpendicular directions–except for the external anal sphincter, tested only along its main axis. Mechanical experiments were designed to reproduce the in-vivo loading conditions of labour, performing uniaxial tensile tests under cyclic loading at different strain levels up to specimen rupture. Digital image correlation ensured accurate strain measurements. The mechanical response of each tissue was characterised through inverse analysis using a Veronda–Westmann hyperelastic model. Structural characterisation complemented mechanical testing: two-photon excitation microscopy quantified 3D microscale collagen organisation of each layer, while micro-CT imaging provided 3D information on the fibrous architecture of whole perineum.

Results

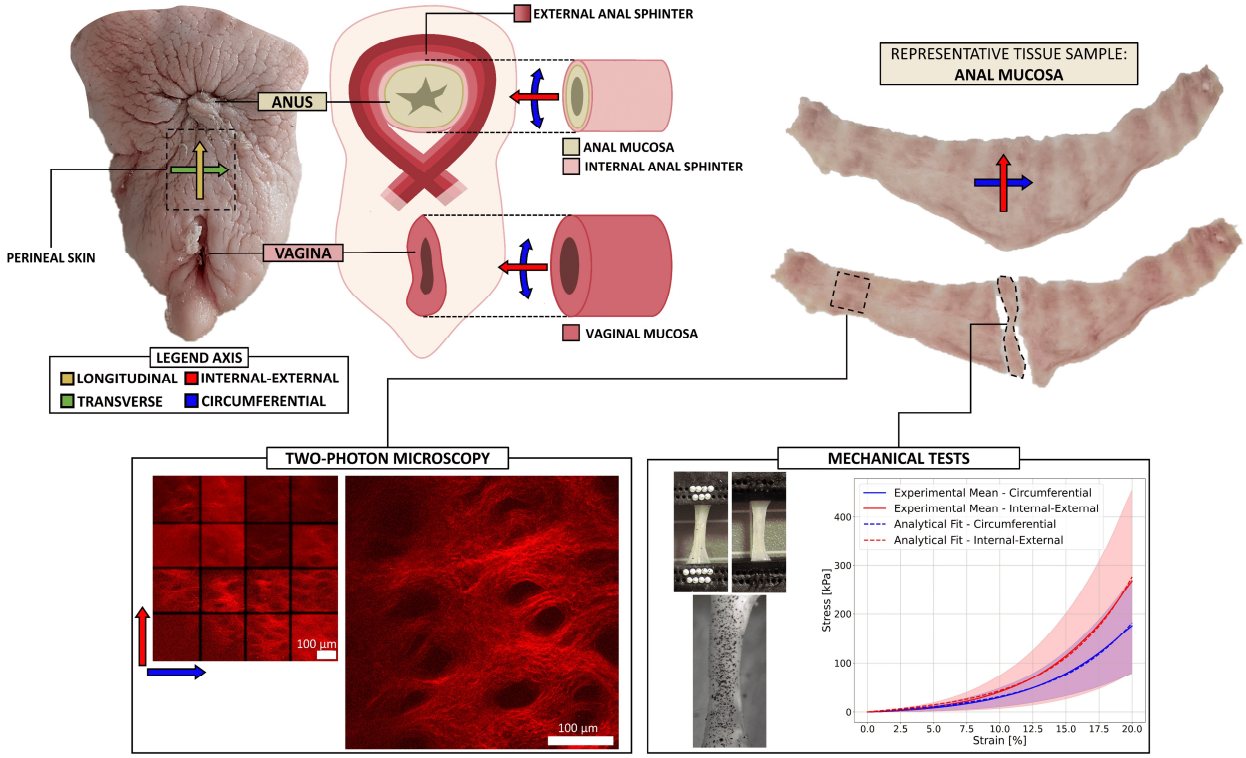
The five perineal tissues exhibited distinct mechanical responses. During the cyclic loading, the anal and vaginal mucosae demonstrated the highest stiffness, the skin showed an intermediate response, and the sphincters presented the lowest stiffness, consistently with literature [2]. Direction-dependent behaviour was observed, especially for the internal anal sphincter. Structural imaging revealed distinct collagen architectures aligning with mechanical behaviour. The skin contained thin, transversely oriented fibres,

whereas the anal mucosa exhibited a laminar structure with pores slightly elongated circumferentially. The vaginal mucosa showed a more compliant, loosely arranged collagen network. Both sphincters contained thick, wavy collagen fibres. Micro-CT confirmed the anisotropic architecture of the sphincters and highlighted the folded morphology of the anal mucosa and skin in their physiological configuration.

Discussion

The study established essential baseline mechanical and structural markers for perineal tissues, emphasising their anisotropy and layered heterogeneity. Future developments will include in-situ-imaging under controlled loading to better reflect in-vivo fibre orientation, high-rate tests, and detailed viscoelastic characterisation.

Images (Optional)



References (Optional)

[1] Parente et al., *J. Biomech.*, 2009.
[2] Kadiaké et al., *J. Biomech.*, 2024.

Session Category

Organ and Tissue Biomechanics: N/A

P3-157

Variations in the Contribution of Fluid Pressurization to Compressive Muscle Stiffness from Local to Global Indentation

Dr. Benjamin Wheatley[1], Mr. Gianni Valentine[1], Dr. Pierre-Yves Rohan[2]

[1]Bucknell University, Lewisburg, Pennsylvania, United States. [2]ENSAM, Paris, Ile-de-France, France

Introduction

Fluid pressurization has been proposed as a contributor to passive skeletal muscle stiffness under compression. However, it remains unclear whether this behavior depends primarily on global fluid drainage conditions or on local fluid–solid interactions arising near the contact region. Our working hypothesis is that global stiffness is relatively insensitive to changes in global drainage, while local deformation scale and permeability would modulate the extent of fluid pressurization, with smaller indenters generating proportionally greater fluid-supported loads.

Methods

Micro-indentation tests were performed on passive skeletal muscle under two drainage configurations: intact (whole) and sectioned (to increase global fluid escape) on three different muscles (n=20 each, lateral gastrocnemius, medial gastrocnemius, and vastus intermedius). Each test involved a pre-load via an outer sheath followed by 0.4 mm indentation with an inner indenter. Statistical comparisons across muscle groups were performed using one-way ANOVA with post-hoc tests, with significance set at $p < 0.05$. An axisymmetric finite element model (Figure 1A-B) was developed using (i) a biphasic formulation with Holmes–Mow hyperelasticity (E = 0.01 MPa, nu = 0.1, beta = 4, Phi0 = 0.01) with isotropic permeability (k = 0.075), and (ii) an equivalent solid-only formulation. Indenter radius was varied from 0.5–5 mm to evaluate scaling effects on pressurization and load sharing.

Results

Any effects of whole versus sectioned or muscle group on peak indentation force (515 mN, p=0.20) and relaxation rate (-17 mN/sec, p=0.14) were not statistically significant. In contrast, simulation results showed a clear scale effect, specifically the fraction of

indenter reaction force due to fluid pressurization increased with increasing indenter radius (Figure 1C-D).

Discussion

Results indicate that skeletal muscle stiffness under compression - specifically the contribution of fluid pressurization to tissue stiffness - depends on deformation scale. Our experimental results show that global fluid drainage does not affect local tissue stiffness. The rapid increase in fluid-supported load with increasing indenter radius observed in our finite element simulations suggests that fluid pressurization dictates compression stiffness under volumetric compression. These findings can help understand specific mechanisms of clinically relevant compressive muscle behavior *in vivo*, such as the interaction with a prosthetic socket.

Images (Optional)

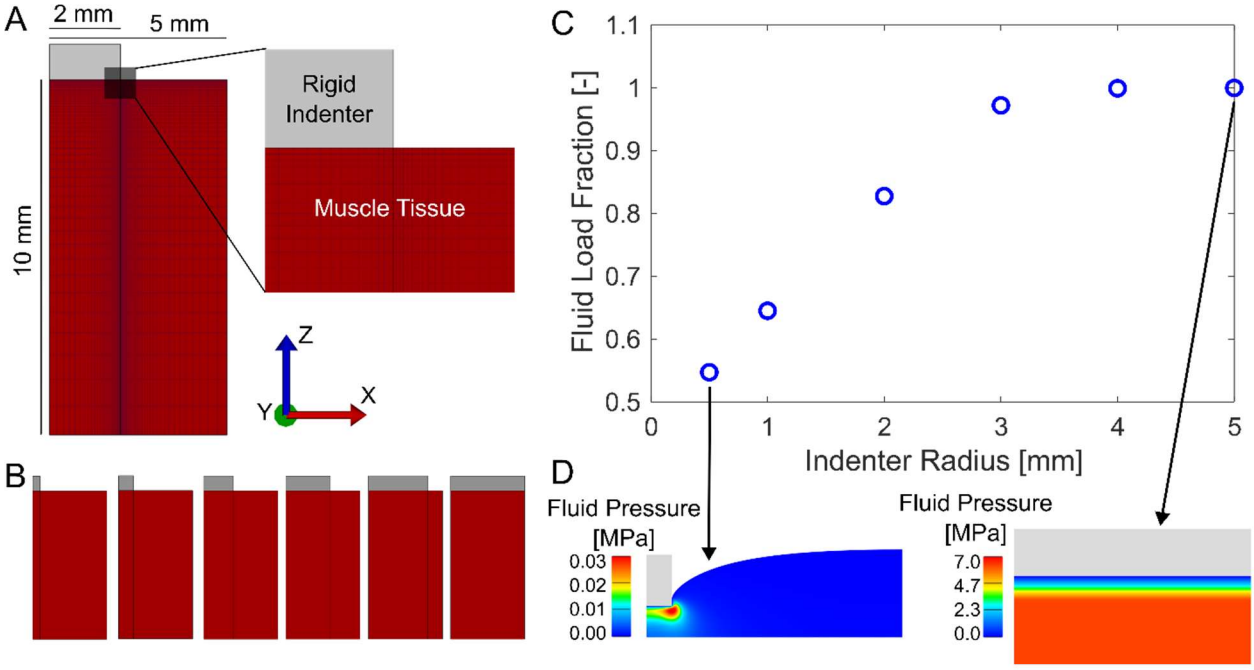


Figure 1. A) Indentation finite element model geometry with enlarged region showing finer mesh density. Top surface of the muscle was defined as free draining with all other surfaces as no fluid flow. Indenter was prescribed a 1 mm (10% nominal strain) displacement in the -Z direction over 1 second. Displacement boundary conditions on lateral sides of the muscle created an axisymmetric, confined condition. B) Six model geometries used for the six different indenter sizes. C) Fluid load fraction (defined as 1 - the ratio between solid-only model and biphasic model indenter reaction forces) as a function of indenter radius. This describes the evolution the fluid-pressurisation to the global compressive stiffness. D) Fluid pressure [MPa] distribution in muscle tissue for indenter radius of 0.5 mm (left) and 5 mm (right) respectively.

Session Category

Organ and Tissue Biomechanics: N/A

P3-158

Characterizing the Cyclic Viscoelastic Response of Human Penile Tissues for Improved Inflatable Penile Prosthesis Applications

Dr. Jhaleh Amirian[1,2,3], Dr Majid Akbarzadeh Khorshidi[1,2,3], Mr. Brian Watschke[4], Mr. Thomas Sinnott[5], Prof. Caitríona (Tríona) Lally[1]

[1]Department of Mechanical, Manufacturing & Biomedical Engineering, School of Engineering, Trinity College Dublin, Dublin, Dublin, Ireland. [2]Trinity Centre for Biomedical Engineering, Trinity Biomedical Sciences Institute, Trinity College Dublin, Dublin, Dublin, Ireland. [3]Advanced Materials and Bioengineering Research Centre (AMBER), Royal College of Surgeons in Ireland and Trinity College Dublin, Dublin, Dublin, Ireland. [4]Urology, Boston Scientific Corp, Inc, Minnetonka, MN, United States. [5]Urology, Boston Scientific Corp, Inc, Clonmel Co, Tipperary, Ireland

Dr. Jhaleh Amirian

Introduction

More than half of men aged 40–70 experience erectile dysfunction (ED) [1,2]. Inflatable penile prostheses (IPPs) are the gold-standard treatment for patients who do not respond to medical therapy [3]. Their long-term performance is, however, often limited by damage or erosion to surrounding penile tissues, whose complex composition and viscoelastic behavior have remained poorly characterized [3]. Understanding penile tissue biomechanics is crucial to evaluating IPP-tissue interactions [1]. Among these tissues, the corpus cavernosum (CC) and tunica albuginea (TA) play the most influential roles during implantation [2]. Considering that successful implantation and long-term function of IPPs are dependent upon the biomechanical properties of the TA and CC, this study explores the effects of strain rate and loading history on these tissues.

Methods

Three human penises (75–89 years, post-mortem interval 1–5 days) were obtained from Science Care. Segments were prepared from TA (5:1 length-to-width ratio) and CC (6 mm length, 4.6 mm diameter) (Figure 1a–b). TA samples underwent tension to 10% strain and CC samples compression to 50%, with three loading cycles applied, each followed by 10 minutes of holding at maximum strain and 10 minutes relaxation.

Results

Both CC and TA displayed nonlinear stress-strain behaviour and clear viscoelasticity (Figures 1c–d). Both tissues displayed increased stiffness with strain rate (CC: 4.7 → 12.4 MPa; TA: 4.5 → 9.3 MPa) (Figure 1e–f). Following a 30-minute relaxation period, CC demonstrated a noticeable return to its original shape, confirming a time-dependent behaviour. CC and TA exhibit viscoelasticity, strain-rate dependence, and time dependence, which is crucial to understanding the interaction between IPPs and tissue.

Discussion

Both CC and TA showed viscoelastic and strain-rate–dependent behavior. Strain rate strongly increased tissue stiffening in both CC and TA, linking tissue response directly to IPP inflation rate. These findings show that the IPP inflation rate significantly affects tissue stresses and should be considered in device design and in user inflation guidelines to reduce the risk of tissue damage.

Images (Optional)

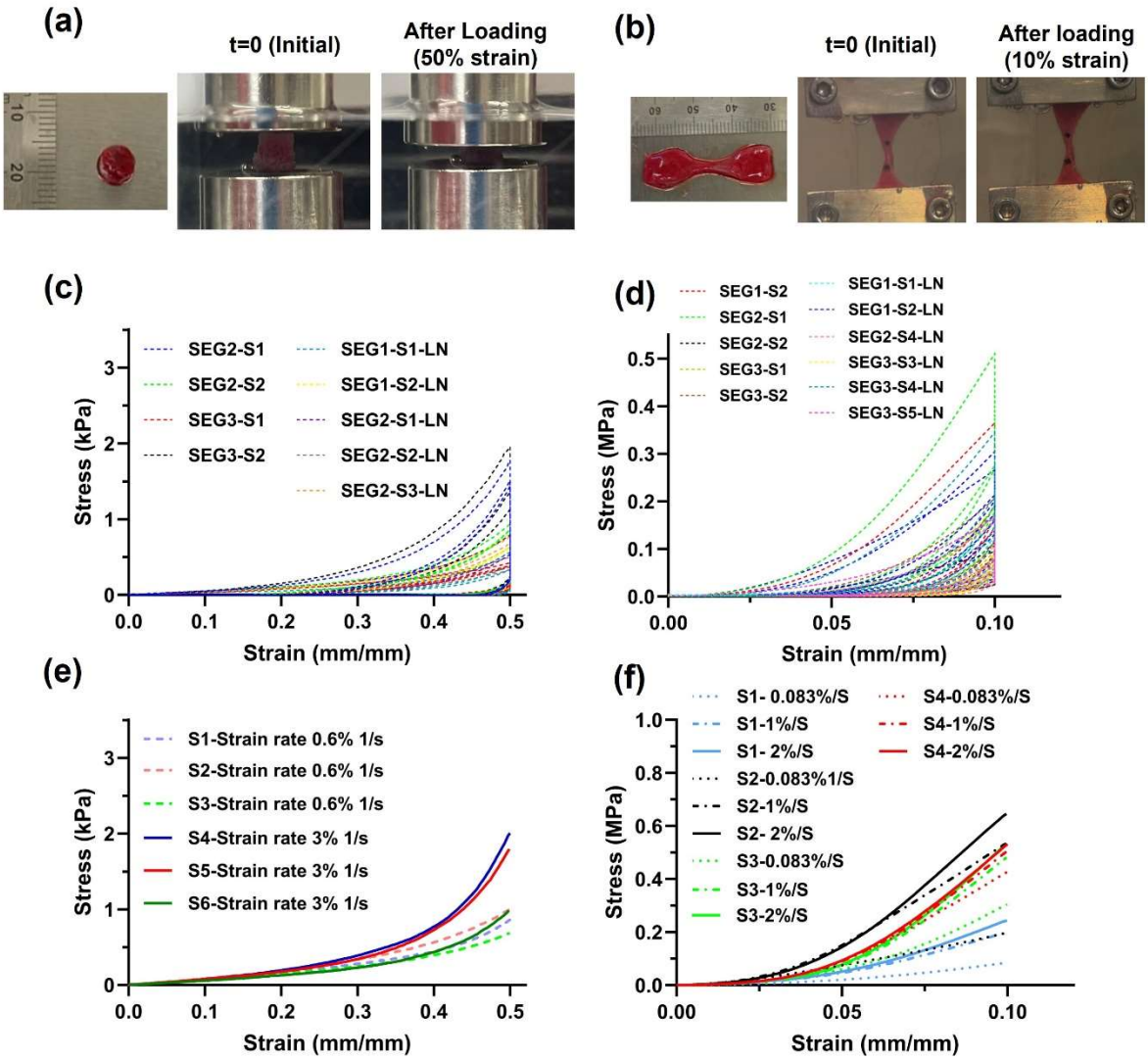


Figure 1 (a) CC before and after 50% compression; (b) TA before and after 10% tension; (c–d) three loading cycles with 10-min hold and 10-min relaxation for CC and TA, respectively (n≥4); (e–f) strain-rate dependency of CC and TA, respectively (n=3).

References (Optional)

[1] Joseph MH Lemmens *et al.* Med. Devices. 2019

[2] Majid Akbarzadeh Khorshidi *et al.* Acta Biomater. 2024

[3] Jacob Good *et al.* Transl Androl Urol. 2024.

Acknowledgements (Optional)

Session Category

Organ and Tissue Biomechanics: N/A

P3-159

A Virtual-Fields-Based Metric to Assess Elastography Data Quality for Anisotropic Inversion

Mr. Adam Quin, Prof. Callan Luetkemeyer Ph.D.

University of Illinois Urbana-Champaign, Urbana, IL, United States

Mr. Adam Quin

Introduction

Magnetic resonance elastography (MRE) estimates tissue mechanical properties from displacement fields, but traditional inversion methods assume isotropy, limiting diagnostic specificity for anisotropic tissues like brain white matter. The optimized virtual fields method (OVFM) is a robust, computationally efficient approach to the inverse problem, enabling implementation of microstructure-informed constitutive models. However, its performance hinges on whether experimental data contain adequate information to reliably calibrate parameters, which likely depends on directions of wave propagation and relative to fibers. To guide experimental design and interpretation, we propose a robust metric for assessing data quality prior to inversion.

Methods

Steady-state harmonic finite element simulations were performed in Abaqus to mimic elastography experiments on a cube of transversely isotropic material, with single or dual harmonic actuations. Simulated displacement fields were processed through the OVFM pipeline to estimate homogeneous material properties. To test noise robustness, 20 Gaussian noise copies ($\sigma = 5\%$) were added to each displacement field prior to inversion. Performance was evaluated across datasets varying fiber orientation, actuation phase offset, and number of actuation directions. The proposed metric was defined as the ratio of the L2 norm of the OVFM constraint vector for each parameter to the same value computed on a noise-only field, providing a signal-to-noise-like measure for each constitutive parameter.

Results

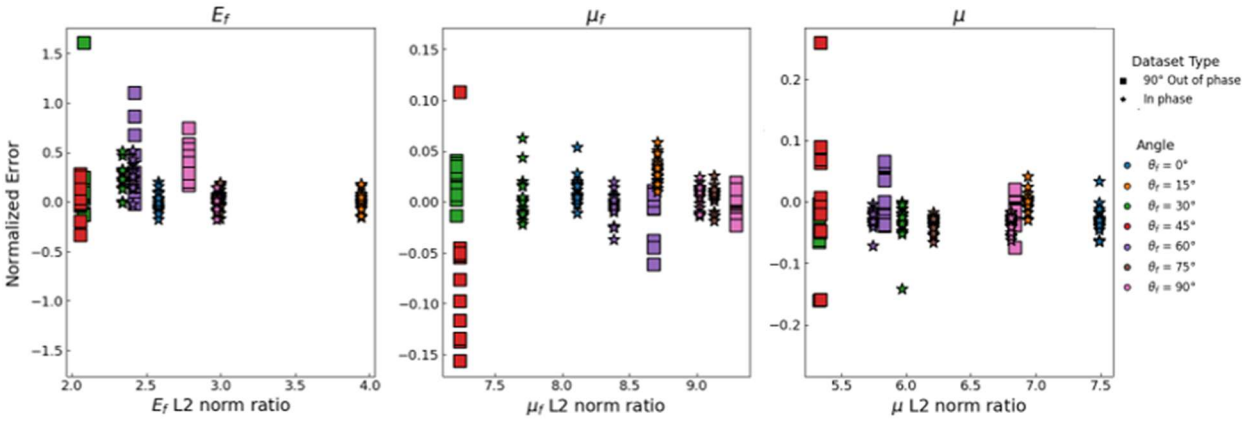
Higher L2 norm ratios consistently predicted improved inversion performance, reflected by reduced error variability and increased convergence. Data quality was strongly influenced

by fiber orientation (performance degraded near 45°), number of wave propagation directions (dual actuation outperformed single), and relative phase of dual waves (out-of-phase was superior to in-phase).

Discussion

These findings demonstrate that the proposed metric effectively captures data richness and predicts inversion reliability for anisotropic OVFM. Results highlight the sensitivity of elastography inversion to experimental factors and underscore the importance of thoughtful experimental strategies. Future work will apply this metric to experimental datasets to guide elastography protocol design and provide confidence measures for estimated parameters.

Images (Optional)



Session Category

Organ and Tissue Biomechanics: N/A

P3-160

Biophysics-informed Computational Platform of Shear Wave Elastography for Assessing Cervical Remodeling

Postdoctoral Researcher Camilo Duarte-Cordon Ph.D.[1], Undergraduate Researcher Eden Katz[1], Assistant Professor Ivan Rosado-Mendez Ph.D.[2], Professor Kristin Myers Ph.D.[1]

[1]Columbia University, New York, New York, United States. [2]University of Wisconsin Madison, Madison, Wisconsin, United States

Introduction

Spontaneous preterm birth (sPTB) is the leading cause of neonatal death, affecting 1 in 10 pregnancies worldwide. Unfortunately, sPTB rates have remained stagnant, partly due to the lack of effective diagnostic methods. Shear Wave Elastography (SWE) is a promising ultrasound technology for evaluating sPTB risk. Shear wave speed (SWS), a SWE parameter, can be used to estimate tissue stiffness as shear waves travel faster in stiffer tissues. Given that some pathways leading to sPTB induce premature cervical softening, SWS may serve as a biomarker for sPTB. However, SWS measurements are highly variable due to the cervix's complex mechanical behavior and microstructure, which limit SWE application in obstetrics.

Methods

To better understand the effects of cervical mechanics and microstructure on SWS, we implemented a SWE finite element (FE) platform in the software FEBio. Shear waves are generated by applying a transient Gaussian body force at a focal point within the geometry. This simulates the application of an acoustic radiation force (ARF) field by an ultrasound transducer. FE simulations of shear wave propagation in the cervix are run using two 3D geometries (see Fig. 1): a representative volume element (RVE) of the cervical stroma and a cylindrical model that accounts for the cervix's layered collagenous structure. A constitutive material model was assigned to each geometry, which captures the cervix's microstructural anisotropy, nonlinear elasticity, and viscoelasticity at non-pregnancy and late pregnancy. SWS was estimated as the shear-wave group velocity using the time-to-peak displacement algorithm, which employs the FE node-displacement field.

Results

Our results indicate that SWS is sensitive to material properties, including the initial fiber stiffness of collagen fibers, fiber dispersion, anisotropy, and the degree of nonlinear elasticity within the tissue. Consequently, as gestation progresses, SWS decreases as fiber

dispersion increases and stiffness decreases. Additionally, SWS is sensitive to the anatomical location at which it is measured.

Discussion

This work emphasizes the importance of accounting for tissue anisotropy, nonlinear stiffness, and viscoelasticity when estimating tissue stiffness from SWS. Future efforts should focus on developing SWE protocols that account for biological sources of variability and maximize sensitivity to cervical remodeling pathways that are early predictors of sPTB.

Images (Optional)

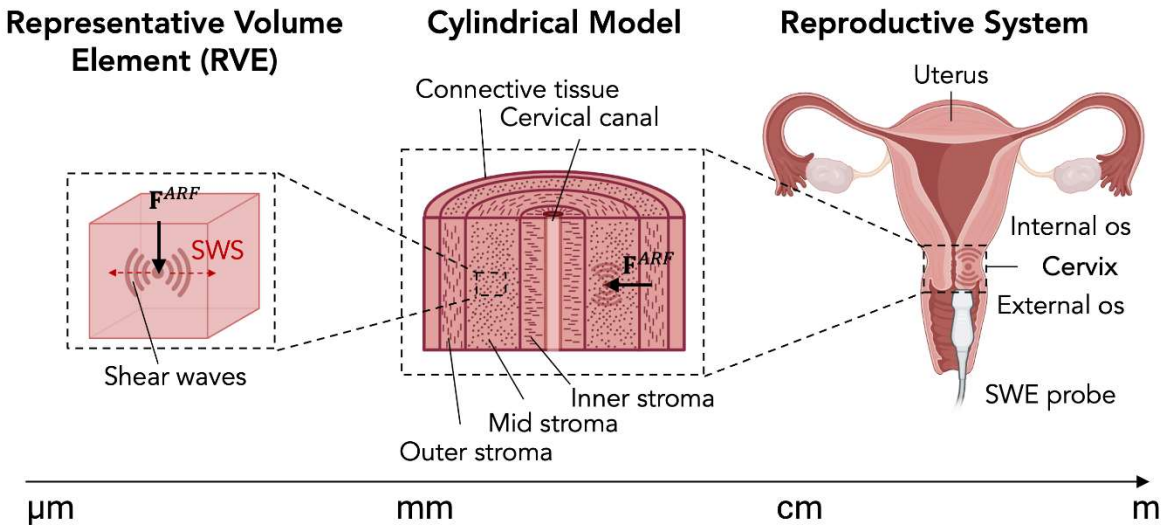


Fig. 1. 3D geometries used for finite element simulations of shear wave propagation, including a representative volume element (RVE) of cervical tissue from the mid stroma and a cylindrical model depicting the cervical canal, the inner stroma with radially oriented collagen fibers, the mid stroma with circumferentially oriented fibers, the outer stroma with longitudinally oriented fibers, and an outer layer of connective tissue.

Session Category

Organ and Tissue Biomechanics: N/A

P3-161

Vascularisation Dynamics in Endometriotic Lesions: A Mathematical Model of Angiogenic Factors and Blood Flow

Ms Cécilia Olivesi, Prof Alys Clark, Dr Claire Miller

Auckland Bioengineering Institute, the University of Auckland, Auckland, Auckland, New Zealand

Introduction

Endometriosis, a condition where endometrial-like tissue grows outside the uterus, impacts 1 in 10 women of reproductive age. For endometriotic lesions to implant and grow they require a blood supply, which is established via angiogenesis. Lesions are categorised based on characteristics related to vascularisation: red lesions are highly vascularised and active (presence of inflammation with ongoing cell proliferation); black lesions are less vascularised with old blood deposits; and white lesions are mostly inactive. VEGF, an angiogenic factor, has been found in higher concentration near red lesions in comparison to other lesion types. This study aims to test if the primary source of VEGF influences the lesion's level of vascularisation and how it affects the structural and hemodynamic characteristics of the blood network.

Methods

We apply an agent-based model of angiogenesis to the microenvironment of an endometriotic lesion, using an overlapping spheres method for describing vessel dynamics and a continuum model of VEGF concentration. Blood flow through the emergent vascular network is described using Poiseuille's law, assuming low Reynolds number flows. System behaviour is assessed under two VEGF scenarios: 1) an increased extracellular matrix (ECM) VEGF concentration in the lesion microenvironment (ECM hypothesis); 2) a high production of VEGF inside the lesion diffusing into the ECM (lesion hypothesis).

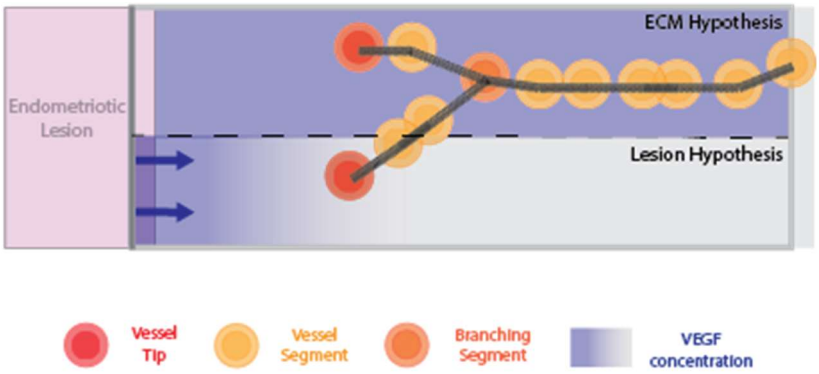
Results

The model predicts a higher number of branches under the ECM hypothesis compared to the lesion hypothesis; therefore, the total vascular supply inside the lesion is increased. However, under the lesion hypothesis, the vascular network reaches the lesion faster, which could increase the lesion's survival prospects. In the lesion hypothesis, the vascular network grows predominantly in the direction of the lesion compared to the ECM hypothesis, in which the network supplies both the lesion and its surrounding tissue.

Discussion

Our study shows that different VEGF profiles could explain the heterogeneity in endometriotic lesion vascular networks. In the future, we aim to explore if the ECM and lesion hypotheses could describe the different vascular networks observed in red and black lesions by comparing our computational results to imaging.

Images (Optional)



Session Category

Organ and Tissue Biomechanics: N/A

P3-162

Regionally Varying Biomechanical and Structural Remodeling of the Murine Colon in an Acute Model of Inflammatory Bowel Disease

Ms. Chastity Chavez[1], Mr. Soto Kubo[1], Ms. Piper Welsh[1], Ph.D. Christy Gliniak[2], Ph.D. Philipp Scherer[2], Ph.D. Jacopo Ferruzzi[1]

[1]The University of Texas at Dallas, Richardson, TX, United States. [2]University of Texas at Southwestern, Dallas, TX, United States

Introduction

Inflammatory bowel disease (IBD) is characterized by excessive immune responses within the gastrointestinal tract which trigger extracellular matrix (ECM) remodeling. This process involves structural modifications in fibrillar collagen that disrupt colonic function and create a risk for IBD-induced colon cancer. Prior literature used microindentation testing to demonstrate an increased stiffness in human IBD samples but failed to capture the physiologically relevant multi-axial loading state. Here, we hypothesized that acute inflammation impacts the biomechanical function of the colon in a regionally heterogenous manner, reflecting structural differences along the length of the colon.

Methods

Adult mice (C57BL/6J, 12-week-old) of both sexes (18 females and 18 males) were randomly assigned into treatments groups of 0%, 2.5%, or 5% dextran sodium sulfate (DSS) in drinking water to trigger acute IBD. After five days of DSS exposure, the colon was harvested and divided into four cylindrical sections: two proximal (P1 and P2) and two distal (D1 and D2) regions. Each region underwent biaxial inflation-extension mechanical testing to obtain circumferential and axial properties. Fixed sections were stained with Hematoxylin and Eosin (H&E) and Picro–Sirius Red (PSR) for microstructural analysis.

Results

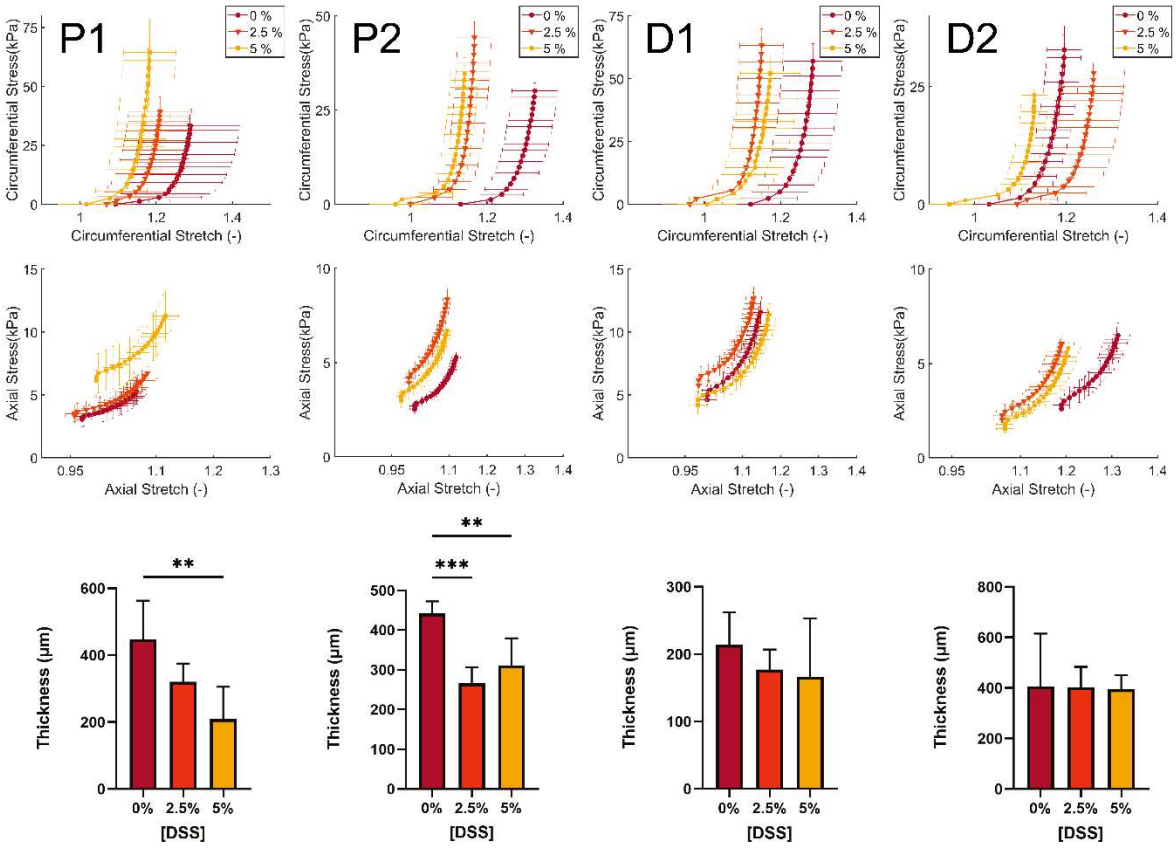
Fig. 1 shows the regional stress-stretch and unloaded thickness plots in response to different DSS concentrations for the male cohort. We found that proximal regions displayed circumferential stiffening and decreasing wall thickness with increasing DSS exposure. Instead, the distal regions were structurally unaffected. Remarkably, the most distal section of the colon (D2) displayed axial stiffening. This axial stiffening correlated with an

increased content of fibrillar collagen in the submucosal layer, as observed from the analysis of PSR-stained colonic cross sections.

Discussion

Despite recent advances in treating gastrointestinal diseases, there is limited knowledge on structure-function relationships for the normal and diseased colon, particularly in IBD which continues to affect millions worldwide. In this study, we demonstrated that colonic remodeling in response to an acute form of IBD exhibits regional heterogeneity with circumferential stiffening proximally and axial stiffening distally. These findings suggest that IBD-induced alterations in mechanical function are regionally specific and may require targeted therapies. Future work will investigate whether these patterns persist in chronic IBD.

Images (Optional)



Session Category

Organ and Tissue Biomechanics: N/A

P3-163

Canine Cadaveric Validation of Epidural needle Insertion Force Versus Displacement in Novel Physical Simulator

Ms. Claudia Smith M.A.Sc., B.Eng., Dr. Carolyn Kerr DVM, DVSc, PhD, Diplomate A.C.V.A., Dr. Scott Brandon PhD, P.Eng.

University of Guelph, Guelph, Ontario, Canada

Introduction

In medical education, simulators allow clinicians to practice skills in a safe, repeatable environment before attempting procedures on living patients. Simulator materials are often chosen based on subjective feedback from expert clinicians. However, there is a lack of objective validation of the force-insertion relationship as a needle passes through skin, muscle, and ligament, particularly in canine-specific simulators. Therefore, the objective was to develop a novel, multi-layer composite material "sandwich" simulator that replicated the peak forces of relevant tissues during epidural needle insertion in canines.

Methods

Potential synthetic materials (textiles, hydrogels, and polymers) were puncture-tested at 2mm/s using a Mechanical Testing Machine (Instron) loaded with a 2.5", 20 gauge, Quincke spinal needle. Samples were cut to approximately 50 x 50mm and clamped in place. Materials were iteratively tested to identify layers, and layer thicknesses, that replicated peak tissue puncture forces from prior fresh, ethically-sourced cadaveric data. A final three-layer "sandwich" simulator was assembled and tested. Local force maxima and minima were identified and compared.

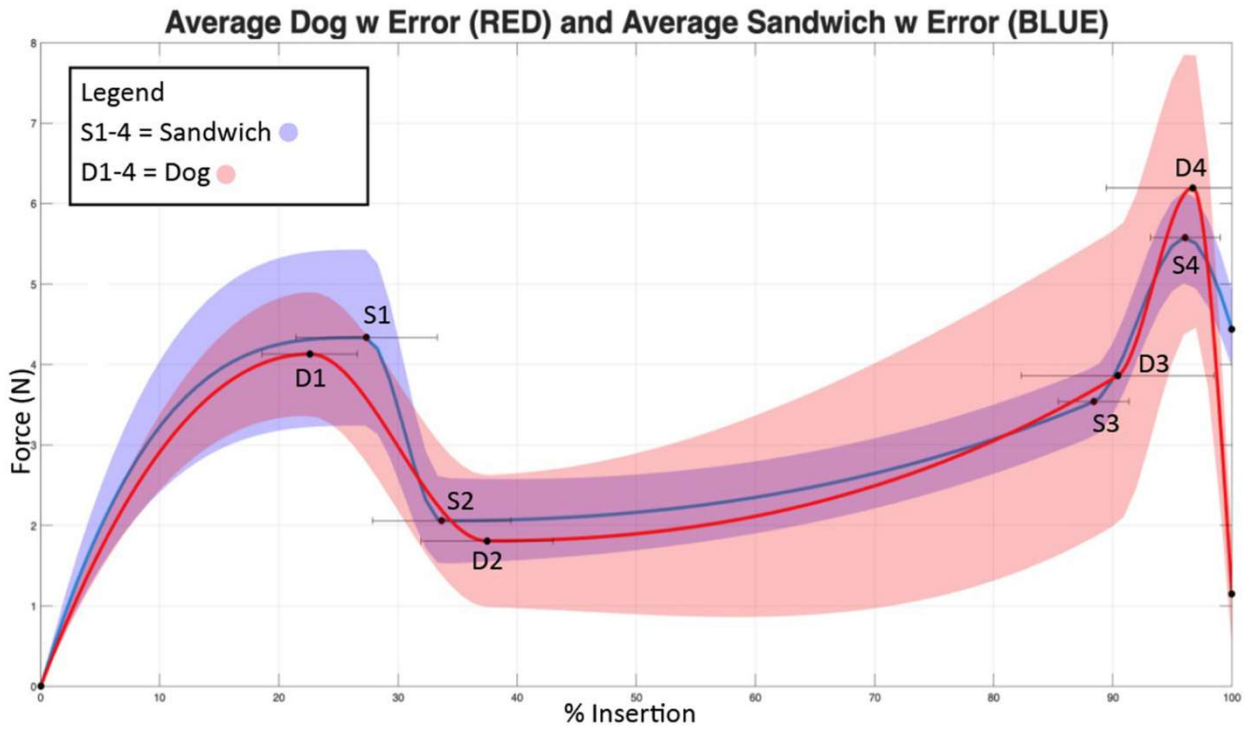
Results

Iterative testing resulted in a final simulator design consisting of 2mm of vinyl leather (skin), 24mm of upholstery foam (muscle), and 1 mm of 100% polyurethane (ligament). All force peaks and drops in the artificial material data were within the variance found for the corresponding points in the cadaver data. Peak forces for the simulator (cadaver) were: a) skin = 4.3N (4.1N), b) muscle = 3.5N (3.9N), and c) ligament = 5.6N (6.2N).

Discussion

Tissue mechanics are crucial for an accurate epidural training simulator so the force required to puncture each tissue feels correct. The local maxima (S1, S3, S4) and minima (S2) in the artificial materials were within the variability of the cadavers, however, artificial skin had larger variance than cadaver skin (0-33% Insertion in Fig 1). This was the most challenging material to replicate, as despite the many skin simulators available on the market, these samples did not accurately replicate the needle/skin mechanics during insertion. This novel simulator has the potential to reduce costly clinical errors by enabling more training and therefore reducing the use of live animals in medical education.

Images (Optional)



Session Category

Organ and Tissue Biomechanics: N/A

P3-164

Print-A-Punch: A Customizable 3D-Printed Cutting System for Tensile Testing of Soft Biomaterials

Mr. Cody Willson, Mr. Steven Szymeczek, Dr. Trevor Lujan

Boise State University, Boise, Idaho, United States

Introduction

Tensile tests are an essential experiment for characterizing fundamental mechanical properties of biological tissues and biomaterials. To ensure validity and reproducibility, these tensile tests should be performed using sectioned test specimens, called coupons, that are dumbbell-shaped [1]. Our group previously developed the Print-A-Punch cutting system to provide researchers with a reliable and economical tool to punch dumbbell-shaped specimens from layers of soft materials (Fig. 1A) [2]. This build-your-own device, composed of 3D-printed parts and flexible razors, has been an asset to the biomechanics community, yet limitations exist. In particular, the narrow gauge section was not uniform due to razor "spring back", which can cause undesirable failures outside of the coupon mid-section. Also, the coupon dimensions were not customizable, and users had difficulty printing the device. Our objective was to enhance the dimensional accuracy of the Print-A-Punch for a broad range of coupon dimensions, and to make this device more accessible to the biomechanics community.

Methods

To reduce spring back, we developed a custom device to rapidly and repeatedly plastically deform the flexible razors prior to inserting into the punch (Fig. 1B). The dimensional accuracy of these pre-bent blades was compared to standard straight blades for variable gauge sections (4-14mm) using an automated image processing program. Ten elastomer coupons were cut from each gauge length and were pulled to failure. A Prusa MK4S 3D-printer with polylactic acid filament was used for printing.

Results

Pre-bent razors had gauge width variability of 0.019 ± 0.003 mm, an improvement of 59% relative to straight razors (Fig. 1C). On average, 90% of the specimens punched with the pre-bent blades failed in the mid-section, compared to only 65% of the specimens punched with straight razors.

Discussion

The Print-A-Punch offers researchers an accurate and customizable solution to conducting tensile tests on soft biomaterials. This technology can facilitate the broad adoption of standard test methods that improve the quality and reproducibility of tensile tests in biomechanics. To improve accessibility, we are launching a website where users can order a Print-A-Punch with customizable dimensions.

Images (Optional)

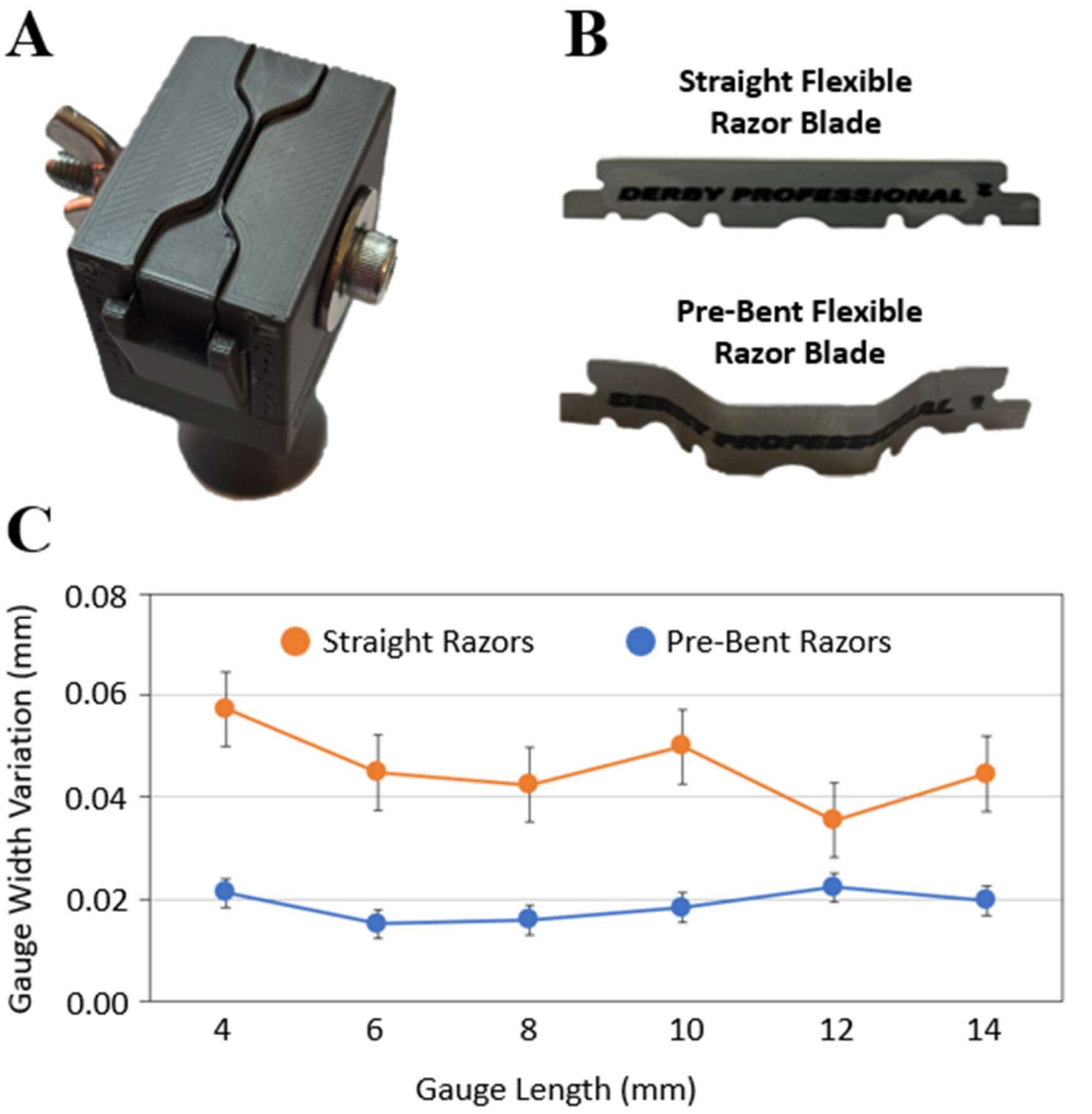


Figure 1. A) The Print-A-Punch device. B) Straight flexible razor blade vs. pre-bent flexible razor blade. C) Comparison of width variation in the gauge section of coupons punched with straight razors vs. pre-bent razors.

References (Optional)

[1] Wale, Madison E *et al.* , J Biomech Eng, 2021

[2] Nelson, Sean J *et al.* , J Biomech, 2020

Session Category

Organ and Tissue Biomechanics: N/A

P3-165

Extracellular Matrix Mechanics and Collagen Architecture Remodeling in Tissue Regeneration: A Microstructural Analysis

M.Sc Florian Pouzet[1], PhD Sarah-Maud Sombris-Picot[2], Dr Corinne Lorenzo[1], Dr Marielle Ousset[1], Dr Cristina Cavinato[2], Dr Jenny Paupert[1]

[1]University of Toulouse, CNRS UMR 5070, INSERM U1301, EFS, ENVT, Institut RESTORE, Toulouse, Occitanie, France. [2]LMGC, University of Montpellier, CNRS, Montpellier, Occitanie, France

Introduction

After injury, adult mammals typically heal by scar formations, resulting in structural and functional loss, whereas newborn can regenerate completely [1]. Tissue function is closely linked to tissue architecture, with fibrillar collagen–a major extracellular matrix (ECM) component–governing passive mechanical response through its abundance, configuration, and degree of cross-linking. Our previous work showed that transient inhibition of collagen cross-linking after adipose tissue resection in adult mice can shift repair from scarring to regeneration, suggesting that ECM organization may influence repair outcomes [2]. A better understanding of the microstructural and micromechanical properties of the ECM under physiologic loading conditions, could help prevent functional decline associated with architectural alterations occurring during repair, chronic inflammation, or ageing. Here, we investigate how ECM mechanical properties relate to regenerative potential by analyzing fibrillar collagen organization using an induced regeneration model in mouse adipose tissue over time.

Methods

Uninjured, scarred and regenerated subcutaneous adipose tissues were mechanically tested performing *ex vivo* uniaxial tensile tests coupled with *in-situ* synchronized multiphoton scanning microscopy at multiple strain levels allowed quantify micromechanical and microstructural metrics. Microstructural analysis was assessed by computing structure tensors, volume fractions and fiber geometrical distributions, enabling quantification of fiber density, alignment and anisotropy as a function of uniaxial mechanical conditions. Mean axial stress was calculated from axial force normalized by local cross-sectional area measured with Optical Coherence Tomography.

Results

Based on our current data, quantitative microstructural analysis revealed that scarring tissues have lower initial fiber anisotropy in the unloaded configuration, which increased

rapidly with strain, suggesting a higher deformability. In contrast, healthy tissues displayed higher mean axial stress and maintained a more stable reorientation scheme throughout loading with a delayed fiber alignment, reflecting greater mechanical resistance and a more robust load-bearing structure.

Discussion

Together, these findings indicate that scar tissue is mechanically more compliant, and structurally more labile, while healthy tissue exhibits higher stiffness and a more organized collagen framework, providing insight into how ECM mechanics may regulate tissue repair and regenerative potential.

Images (Optional)

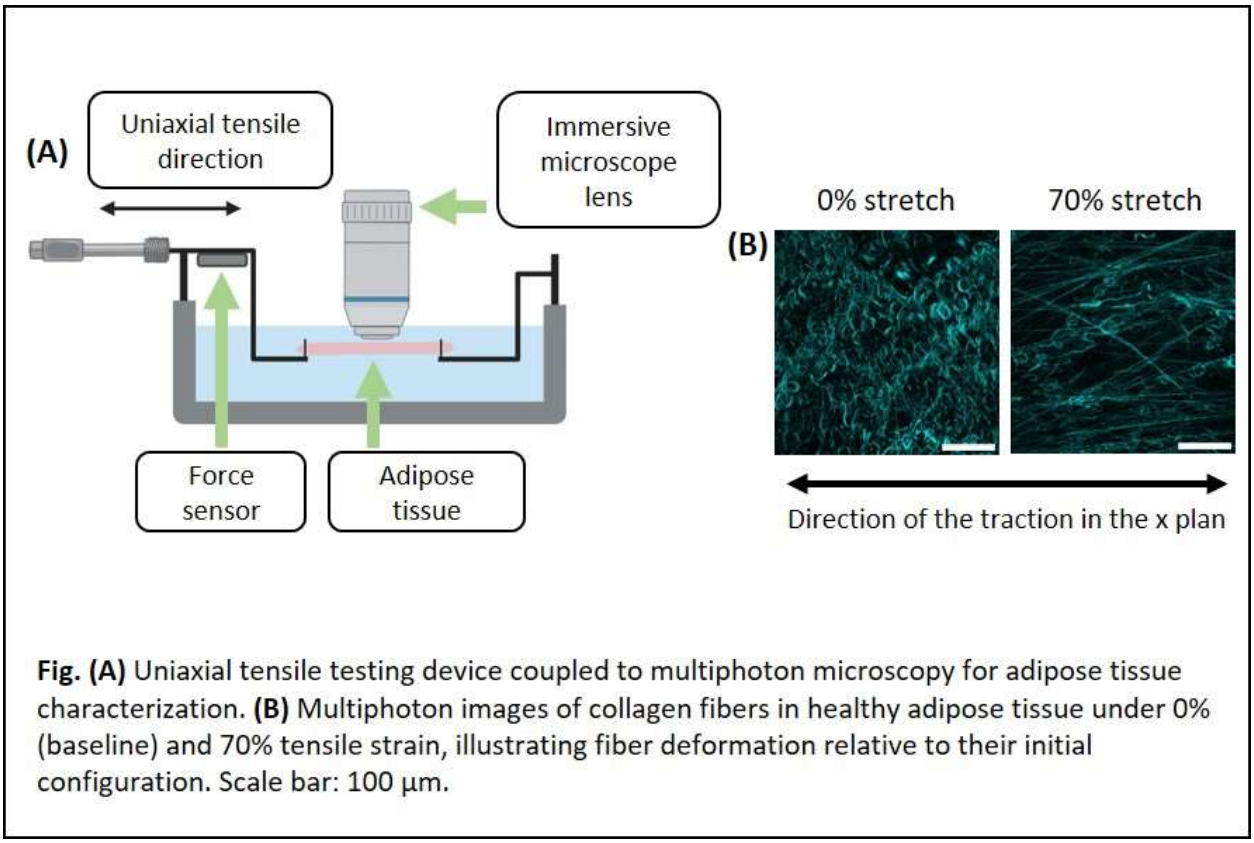


Fig. (A) Uniaxial tensile testing device coupled to multiphoton microscopy for adipose tissue characterization. **(B)** Multiphoton images of collagen fibers in healthy adipose tissue under 0% (baseline) and 70% tensile strain, illustrating fiber deformation relative to their initial configuration. Scale bar: 100 µm.

References (Optional)

[1] Enzo E. Porrello et *al.*, Science, 2011

[2] Anastasia Pacary et *al.*, npj Regenerative Medicine, 2024

Session Category

Organ and Tissue Biomechanics: N/A

P3-166

Site-Dependence of Frictional Properties in the Anterior Cruciate Ligament

Mr. Hayato Inoue B.S.[1], Mr. Daichi Ishii Ph.D[1], Prof. Hiromichi Fujie Ph.D.[1,2]

[1]Graduate School of Systems Design, Tokyo Metropolitan University, Hachioji, Tokyo, Japan. [2]Research Center for Medicine-Engineering Collaboration, Hachioji, Tokyo, Japan

Introduction

For efficient joint motion, low friction is required in all tissue-to-tissue contacts. Ligaments are not immune to contact with surrounding tissues during tensile loading due to the presence of surrounding tissues. The present study focuses on the anterior cruciate ligament (ACL). The ACL encounters the posterior cruciate ligament (PCL), medial meniscus, and the femoral articular cartilage during joint motion [1] (Fig). Although Qu et al. have determined the overall average frictional property of the ACL [2], the local frictional property of the ACL has not been quantified. The authors found the frictional property of the ACL portion that encounters the PCL is significantly lower than that of other portions [3][4]. Therefore, the objective of the present study is to determine the distribution of frictional properties throughout the entire ACL.

Methods

Porcine ACLs were divided into four regions: 3 regions that encounter the PCL, lateral femoral condylar cartilage, and medial meniscus, and a contact-free region near the femoral insertion. For comparison, the central medial portion of the patellar tendon (PT) was chosen. Reciprocating friction tests were performed for each portion at a load of 0.5 N against an alumina ceramic ball of 6 mm in diameter. Compression DMA were performed to investigate the effect of ploughing friction.

Results

Results revealed that the coefficient of dynamic friction was significantly lower in the PCL-contact and medial meniscus-contact regions than in the lateral condyle cartilage-contact and the PT. The storage modulus Was significantly higher in the meniscus-contact region than in other contact regions.

Discussion

Plowing friction may be more severe in the PCL-contact region, because more deformation occurs due to lower modulus than in the meniscus-contact region. It is suggested that the sliding frictional property is superior in the PCL-contact region compared to those in other contact regions.

Images (Optional)

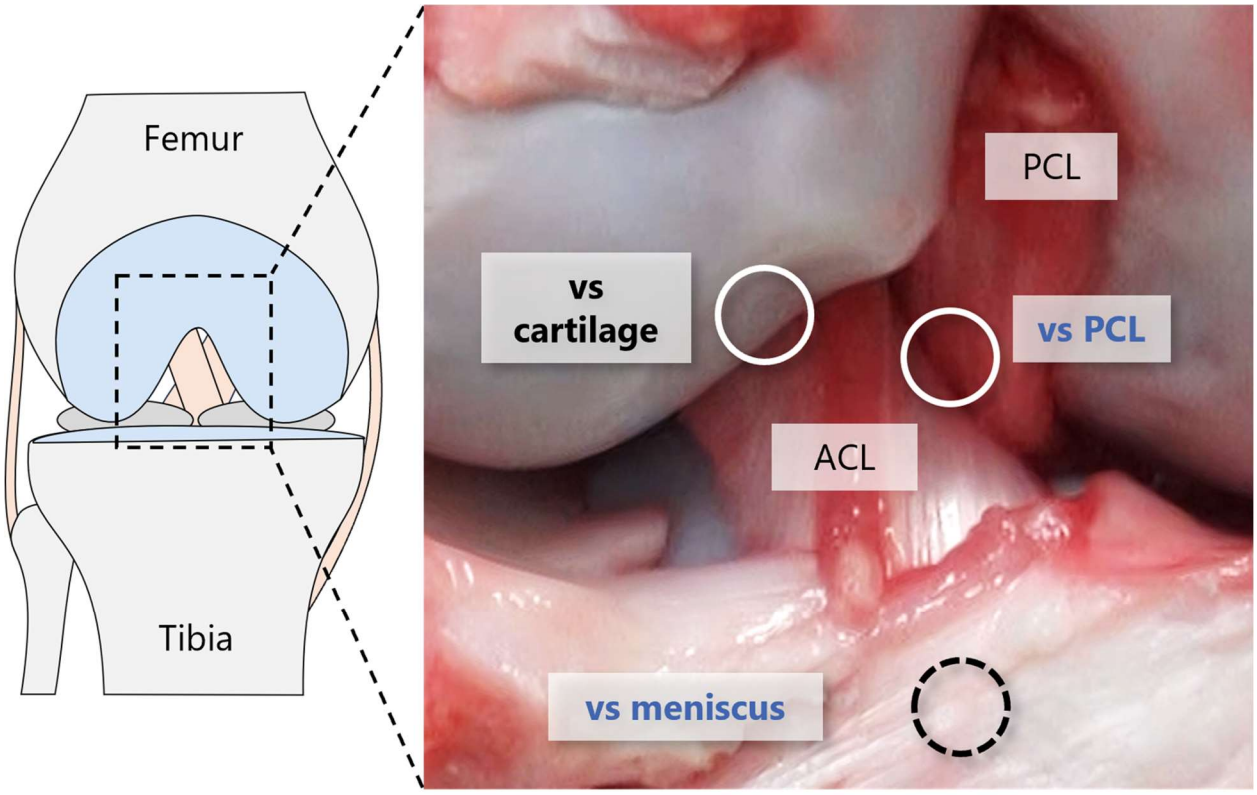


Fig. Contact of the ACL with the PCL, medial meniscus, and femoral lateral cartilage at 90 degrees of flexion in a porcine knee.

References (Optional)

[1] Kropf EJ *et al*, Knee Surg Sports Traumatol Arthrosc, 2013.

[2] Qu J *et al*, J Biomech, 2015.

[3] Fujie H *et al*, ICoBB, 2024.

[4] Inoue H *et al*, APBiomech, 2025.

Acknowledgements (Optional)

This research was supported by TERUMO life Science foundation 2025-2029.

Session Category

Organ and Tissue Biomechanics: N/A

P3-167

Testing the Hypothesis That Axons Passing Through Large Lamina Cribrosa Pores Suffer Larger Deformations Than Those Passing Through Small Pores

Dr Ian Sigal, Dr. Susannah Waxman, Ms Sofia Lusvardi, Dr. Yuankai Lu, Ms Yingzhe Han, Ms. Ashley Linton, Mr. Qi Tian, Dr. Miriam Bohlmann Kunz, Dr. Bingrui Wang

University of Pittsburgh, Pittsburgh, PA, United States

Introduction

The collagen beams of the lamina cribrosa (LC) provide mechanical support to the frail axons passing through the LC pores. A long-standing theory states that larger LC pores cannot provide as good mechanical support to the axons as smaller pores, rendering the axons at increased risk of damage. Our goal was to test the hypothesis that large LC pores provide worse protection to the axons from increased IOP than small pores.

Methods

We used a combination of experiments and computational modeling to test the hypothesis. The LC of 6 fresh sheep eyes was exposed by sectioning the optic nerve transversely, and imaged by second harmonic generation microscopy at low (5 mmHg) and high (40 mmHg) intraocular pressures. Digital image correlation was used to measure the deformations of the collagenous beams. We manually segmented and reconstructed pore-specific finite element models of the visible pores and assigned boundary conditions from the beam deformations. Pore interior was assumed to be formed of retinal ganglion cell axon bundles embedded surrounded by astrocytes. Axons and astrocytes were assumed to have the same mechanical properties. To account for variations in axon size we repeated the study using axon diameters varying from 0.5μm to 2μm. We measured the axonal distortion using the FE-produced changes in local tissue aspect ratio

Results

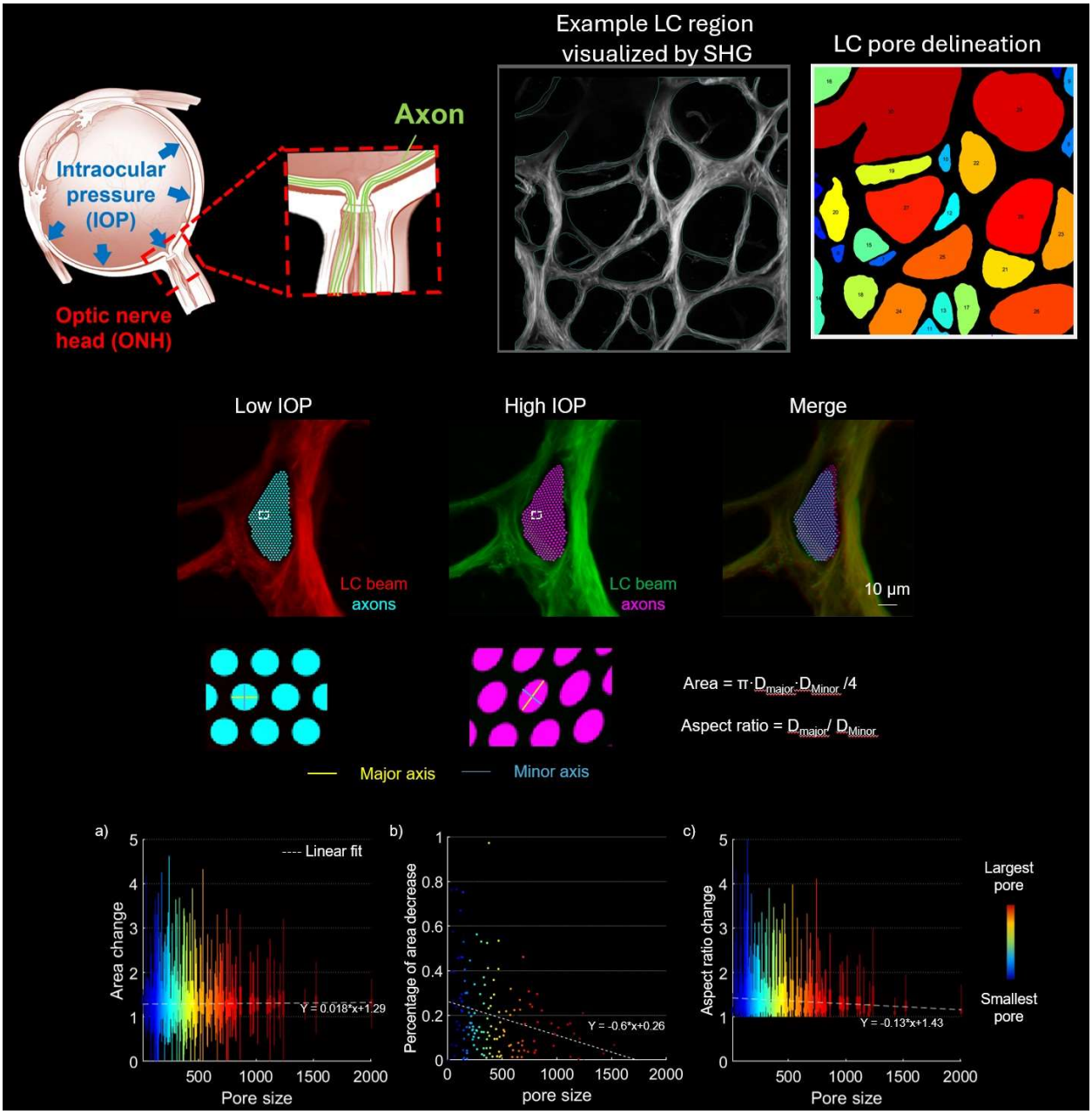
A total 148 pores were analyzed. With 1 um-wide axons this led to 46 to 10,102 axons per pore, depending on pore size. The aspect ratio change of the axons was 1.33 ± 0.45 (mean ± SEM), with the lowest value of 1 (no change) and the 95th percentile of 1.98. The aspect ratio change was significantly negatively correlated with the initial pore size ($p<1e-5$, Fig), indicating that larger pores had smaller deformations.

Discussion

The results show that overall axons in smaller pores actually suffer larger deformations than axons in larger pores, contrary to our hypothesis. The axons suffered anisotropic

distortions that are known to be particularly detrimental to axons. There were, however, wide variations in pore and axonal distortions, with many axons in small pores suffering only small deformations.

Images (Optional)



Acknowledgements (Optional)

NIH R01-EY023966, R01-EY031708, P30-EY008098 and T32-EY017271 (Bethesda, MD), Research to Prevent Blindness (unrestricted grant to UPMC ophthalmology, and Stein innovation award to Sigal IA), BrightFocus Foundation

Session Category

Organ and Tissue Biomechanics: N/A

P3-168

Using High-Resolution MRI in Quantification of Passive Elastic Modulus of Muscle in Stepwise Tensile Testing

Mr. Iraj Dehghan Hamani[1], Dr. Stephen H. M. Brown[2], Dr. Thomas R. Oxland[1]

[1]University of British Columbia, Vancouver, BC, Canada. [2]University of Guelph, Guelph, ON, Canada

Introduction

Passive mechanical properties of skeletal muscles, particularly elastic modulus, are important in joint mechanics and muscle pathology. Therefore, their precise quantification is valuable. Although elastic modulus is typically derived from static tensile tests, these experiments often lack rigorous verification. Specifically, potential slippage at gripping interfaces is rarely examined, which affects strain accuracy. Additionally, physiological cross-sectional area (PCSA) calculations often rely on literature values for muscle density rather than direct measurement [1]. Notably, prior studies have not directly measured muscle volume during stretching. In this study, we aim to improve stress–strain calculation and elastic modulus assessment, using a high-field MRI to record muscle length and PCSA during stepwise tensile testing.

Methods

Ten tibialis anterior muscles from five male Sprague-Dawley rats underwent stepwise tensile testing (6% strain/step) immersed in Tyrode's solution in a 9.4 T Bruker BioSpec MRI scanner. T2-weighted RARE MRI scans (0.2 mm isotropic voxels) were acquired at each 4-minute interval. Muscle volume (length and PCSA) was measured using 3D Slicer. Muscle elongation was utilized to calculate strain, and muscle volume at slack length determined PCSA. Stress was calculated by dividing the measured force at each step by the PCSA. Fitting a quadratic curve to stress–strain data enabled elastic modulus calculation.

Results

Average stress-strain data revealed a robust quadratic relationship ($R^2 = 0.99$) (Fig. 1). The specimens also showed an average volume increase of ~13% when stretched from their slack state to nearly 35% muscle strain. Average elastic moduli are shown in Fig. 1 for different strains.

Discussion

MRI scans provided 3D geometry of each specimen at every stretch, enabling consistent quantification of strain and PCSA. High-resolution imaging allowed for repeated assessments and result verification. Notably, this novel method enabled precise measurement of actual muscle length rather than grip-to-grip distance, thereby accounting for potential slippage or tendon effect in muscle-tendon unit elongation. Also, the observed volume increase during stretching likely results from fluid absorption by the muscle [2]. This method holds significant value for 3D muscle modeling and tensile testing simulations.

Images (Optional)

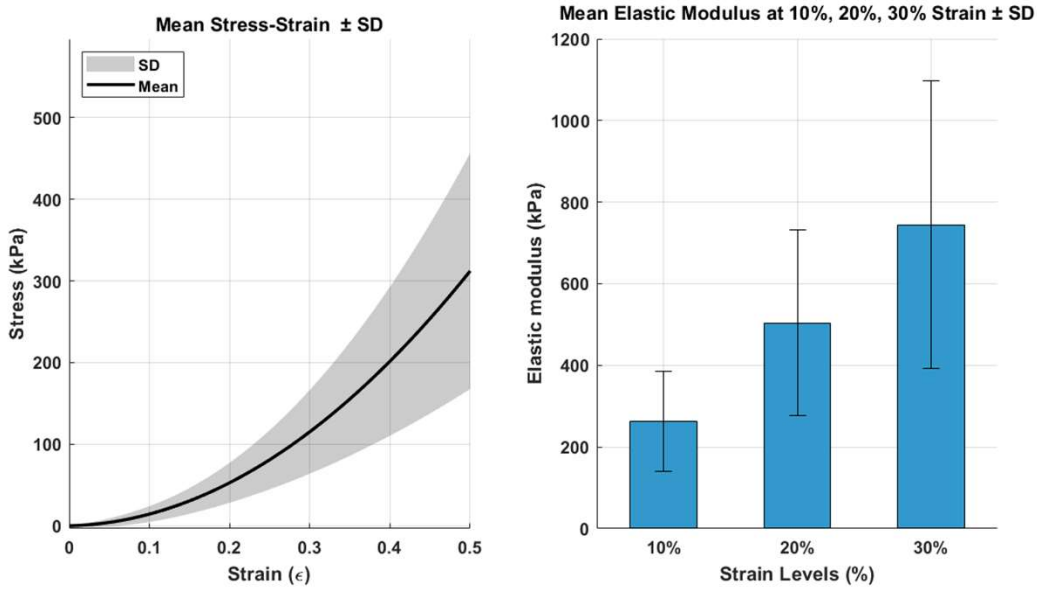


Fig.1 – Mean stress-strain curve ± standard deviation (SD) (left), and the mean elastic modulus ± SD at different strain levels (right)

References (Optional)

[1] Dehghan-Hamani et al., J Mechanical Behavior of Biomedical Materials, 2025
[2] Sleboda et al., J Experimental Biology, 2019

Session Category

Organ and Tissue Biomechanics: N/A

P3-169

Placental Tissue-Mimicking Materials for Ultrasound Elastography: A Preliminary Study of Polyvinyl Alcohol Cryogels and Silk Hydrogels

Ms Jennifer Chimwaza PhD student[1,2], Dr Andrew N Cookson Senior Lecturer[1,2], Dr Katharine Fraser Senior Lecturer[1,2]

[1]University of Bath, Bath, South West, United Kingdom. [2]Centre for Bioengineering and Biomedical Technologies, Bath, South West, United Kingdom

Introduction

Preeclampsia (PE) causes 2–8% of maternal morbidity worldwide. Literature suggests elevated placenta stiffness may be an early indicator of PE as it is linked to altered angiogenesis during placenta development. Ultrasound shear wave elastography (US-SWE) is a non-invasive technique that may be used to measure stiffness of the placenta, but the changes in stiffness with gestational age need to be better characterised to make this a reliable clinical biomarker.

Tissue mimicking materials (TMMs) provide a cost-effective means of understanding soft tissue non-invasively by considering easily accessible materials with varying stiffness to ascertain placenta biomechanics in PE.

The aim of this research was to characterise Polyvinyl alcohol cryogel (PVA-c) and self-gelled silk fibroin (SG-SF) phantoms as placenta TMMs by comparing their stiffness and acoustic properties with clinical values.

Methods

Homogenous PVA-c and SG-SF phantoms were fabricated. US-SWE speeds were taken at five locations per phantom using a Verasonics Vantage 256 system with multiple tracking, coupled with a 5 MHz, 192-element linear transducer. Compression stress relaxation tests were done on the phantoms using an Instron 5965 system to validate the SWE measurements. Elastic (storage modulus) and viscous (loss modulus) parameters were estimated from both ultrasound and mechanical data using a least-squares fitting of the Kelvin-Voigt Fractional Derivative (KVFD) model. Plane wave b-mode image data was used to compute speed of sound within each phantom.

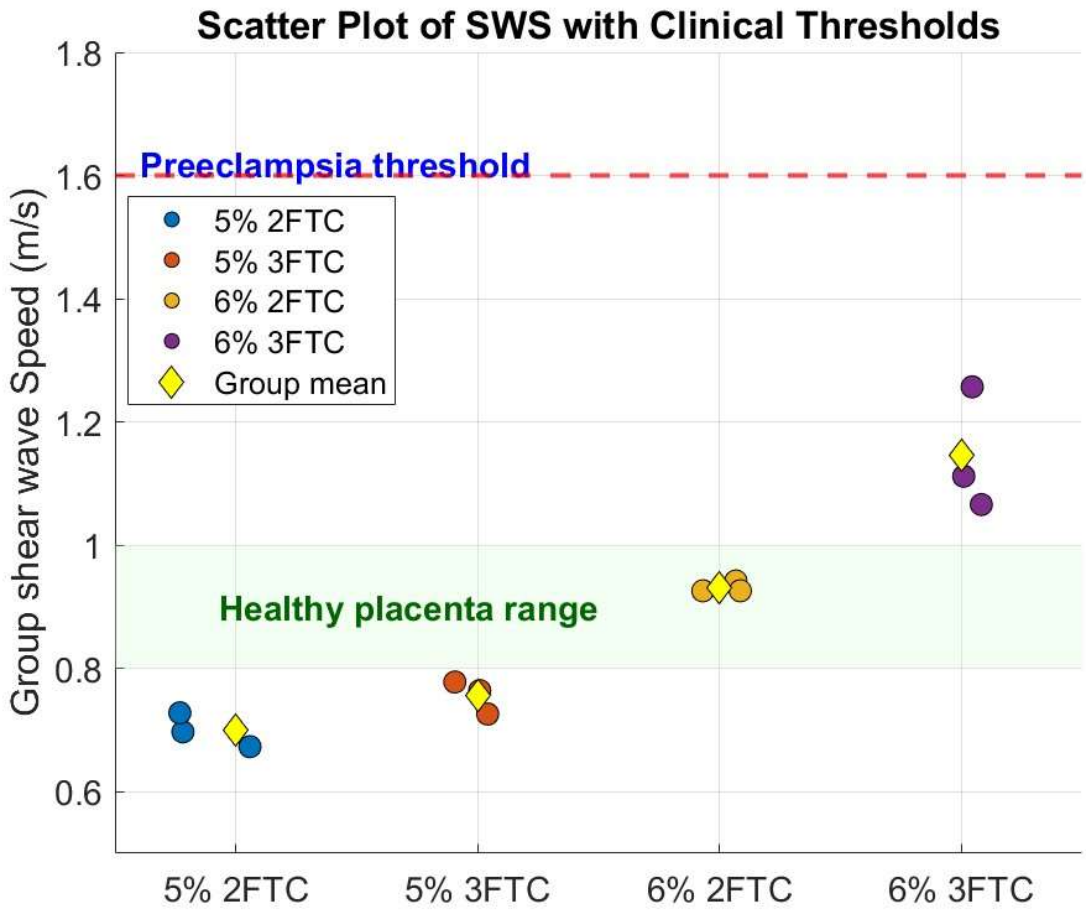
Results

5-6% PVA-c phantoms (Figure 1) could mimic different placenta stiffnesses by varying the PVA concentration and freeze-thaw cycle (FTC) processes more easily and reliably than the SG-SF phantoms. The storage (1-2 kPa) and loss (0.15-1.5 kPa) moduli observed in PVA-c phantoms reflect the elastic behaviour of placental tissue better than SG-SF (>10*PVA-c) phantoms. The ultrasound acoustic speed was 1546±33 m/s (clinical reference=1540 m/s), and independent of PVA or SF concentration.

Discussion

PVA-c TMMs are a promising standardised tool for US-SWE in placental biomechanics, an under researched but important area. Increasing the PVA-c FTC processes could provide stiffer TMMs for investigating preeclamptic placenta. Combining mechanical test methods with US-SWE could provide an effective way of standardising results. Future work will explore embedding disease specific features in TMMs.

Images (Optional)



Session Category

Organ and Tissue Biomechanics: N/A

P3-170

Estimating Large-Deformation Strain Fields in Soft Phantoms Using Ultrasound Digital Image Correlation: A Triangle-Based Approach for Full-Field Strain Determination and A Reference Subset Updating Strategy

Prof. Jin-Jia Hu[1], Mr. Chih-Chia Liu[2]

[1]Department of Mechanical Engineering, National Yang Ming Chiao Tung University, Hsinchu, Taiwan, Taiwan. [2]Department of Biomedical Engineering, National Cheng Kung University, Tainan, Taiwan, Taiwan

Introduction

Understanding internal strain distributions in soft tissues is essential for characterizing their mechanical behavior, yet optical methods are limited to surface measurements. This study developed an ultrasound-based digital image correlation (DIC) approach to quantify full-field internal strains in soft hydrogels during tensile loading. By combining high-frequency ultrasound imaging with a triangle-based strain formulation and an adaptive subpixel-wise reference-update strategy, we aimed to achieve robust, noninvasive strain estimation under large deformation while validating the method against commercial VIC-2D and optical tracking.

Methods

A 35-MHz ultrasound system acquired 301 B-mode frames during 300 tensile steps of 0.04 mm. RF data were envelope-detected and converted to grayscale images. Digital image correlation was performed on a structured node grid, with subpixel displacements obtained via nine-point Gaussian interpolation. An adaptive subpixel-wise reference-update strategy synthesized updated subsets using linear interpolation to reduce decorrelation. Full-field strain was computed using triangle-based deformation gradients. Three types of PVA hydrogels (uniform, stiffness-contrast, asymmetric) were tested and compared with VIC-2D and optical tracking.

Results

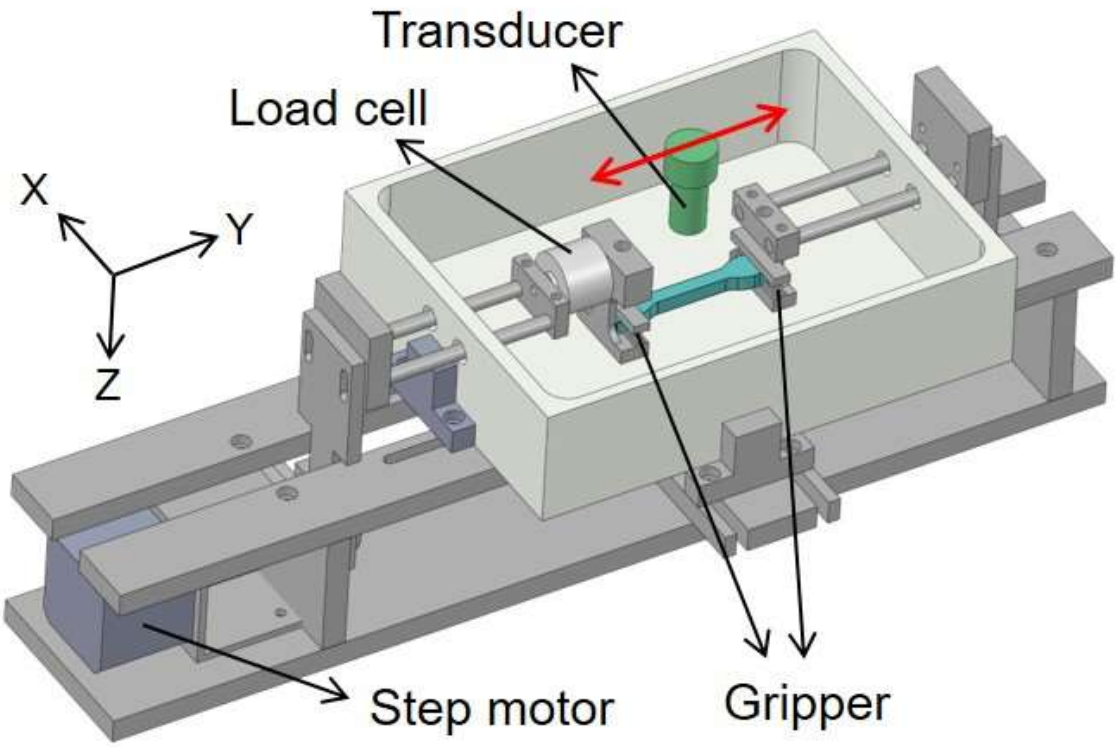
Subpixel-wise updating produced smoother and more stable strain fields than pixel-wise or no-update strategies, particularly along the ultrasound propagation direction. Tracking remained reliable across large deformations, whereas the no-update strategy failed by frame 109. Strain evolution showed strong agreement with VIC-2D, and localized strain reductions in stiffness-contrast and asymmetric samples were consistently identified. Adding 1% cellulose improved ultrasound scattering without altering tensile stiffness.

Stress–strain curves derived from ultrasound-based strain matched those from optical tracking, demonstrating accurate mechanical characterization.

Discussion

The proposed ultrasound-based DIC framework successfully quantified internal strain fields in soft hydrogels, overcoming surface-only limitations of optical imaging. Subpixel-wise reference updating proved critical for preserving speckle coherence during large deformation, enabling robust long-range tracking. Agreement with VIC-2D and optical data confirms the method's accuracy for heterogeneous and geometry-dependent strain patterns. While axial resolution and focal depth limit the usable imaging region, the results highlight ultrasound-based DIC as a promising tool for internal deformation analysis in soft biomaterials and tissue-mimicking phantoms.

Images (Optional)



Acknowledgements (Optional)

Technical support for the ultrasound imaging system from Prof. Shyh-Hau Wang is gratefully acknowledged.

Session Category

Organ and Tissue Biomechanics: N/A

P3-171

Tuning Injection Flow Rate to Minimize Drug Leakage During Intratumoral Injection

Ms. Julia Ding[1,2], Mr. Jihoon Park[1], Ms. Claire Kelley[1], Ms. Lila Cheek[1], Dr. Alex Abramson[1]

[1]Georgia Institute of Technology, Atlanta, GA, United States. [2]Emory University, Atlanta, GA, United States

Introduction

Compared to systemic delivery, intratumoral injection can increase local drug concentration while reducing systemic side effects. However, clinicians frequently report suboptimal drug accumulation in the tumor due to crack-like leakage pathways through tumor tissue [1]. The mechanical response of tumors to injection-induced fluid pressure is poorly understood. Here, we characterize pressure-driven fluid flow during intratumoral injection and identify injection flow rate as a simple, tunable parameter to improve delivery accuracy and reduce drug escape.

Methods

We characterized injection-induced leakage in ex vivo 4T1 murine breast tumors (100-200 mm^3). Fluid transport and fracture-like pathways were visualized using post-injection micro-CT and histological sectioning (n=3 per group). To quantify fluid leakage, tumors were submerged in phosphate-buffered saline, injected with a model drug fluorescein (FITC), and FITC concentration in the bath was measured over time. Tumors (n=3) were injected with fixed injection volume and rate (50 µL, 6 µL/min) and monitored for time course of leakage. To characterize the effect of flow rate on leakage, we then injected at high (60 µL/min) versus low flow rates (≤12 µL/min) and quantified leakage (n=5 per group).

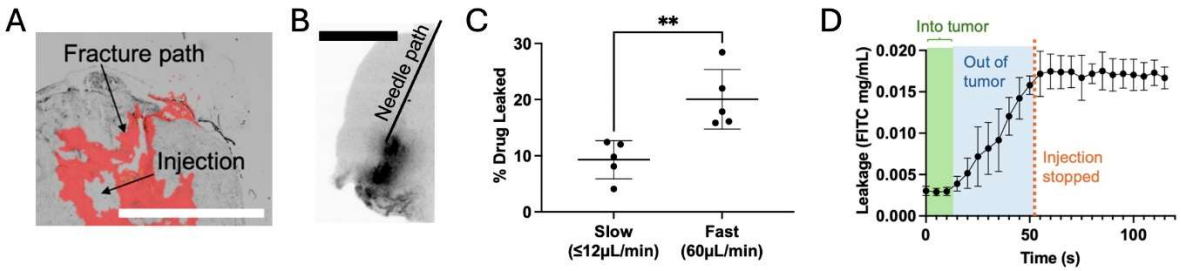
Results

Histology and 3D reconstructions revealed fluid-driven fracture pathways, even at a very low flow rate of 6 µl/min (Fig. A, B, scale bar = 5mm). Injection flow rate strongly affects drug localization (Fig. C). High flow (60 µL/min) more than doubled leakage relative to low rates (≤12 µL/min; 20.1% leaked versus 9.3% injected dose leaked, $p<0.01$). Further, leakage occurred only during the active injection period (Fig. D). After injection onset, drug was initially localized to the tumor. When injection volume reached 7.29 ± 1.17% of total tumor volume, leaked drug suddenly increased, consistent with a yielding event. Stopping injection also stopped leakage, indicating that leakage is mechanically driven by injection pressure.

Discussion

These findings enhance our understanding of how injected drugs distribute in soft tissue, thereby facilitating mechanical approaches for optimizing drug delivery. We demonstrate that lowering flow rate reduces mechanically-driven drug escape, identifying injection rate as a simple yet powerful parameter to improve intratumoral therapy.

Images (Optional)



References (Optional)

[1] R. A. Sheth *et al.*, *Radiology*, 2024.

Session Category

Organ and Tissue Biomechanics: N/A

P3-172

Indentation Modeling of a Saturated Poroelastic Multi-Layered Medium for Mechanical Characterization of Articular Cartilage

Assistant Professor Kotaro Miura[1], Professor Makoto Sakamoto[2], Professor Kazuhiko Sasagawa[1], Associate Professor Kazuhiro Fujisaki[1]

[1]Hirosaki University, Hiorsaki, Aomori, Japan. [2]Niigata Universirty, Niigata, Niigata, Japan

Introduction

Articular cartilage exhibits a depth-dependent layered structure and shows pronounced time-dependent deformation under indentation. However, the respective roles of layering and poroelastic fluid–solid interactions in governing stress relaxation remain insufficiently understood.

Methods

This study develops a semi-analytical solution for the axisymmetric indentation of a poroelastic multi-layer coating bonded to a poroelastic substrate. The layered system is modeled under a rigid, flat-ended cylindrical indenter, and the time-dependent consolidation response is evaluated. The governing formulations are based on the classical poroelasticity framework.

Results

Discussion

These findings demonstrate that the analytical formulation accurately captures time-dependent poroelastic behavior and is applicable to both single- and multi-layer configurations. The convergence with previously published results validates the numerical implementation and confirms the reliability of the solution framework under different permeability boundary conditions.

The findings of this work provide theoretical insight into the mechanisms governing stress relaxation in cartilage and establish a basis for interpreting indentation tests in terms of intrinsic material parameters.

Images (Optional)

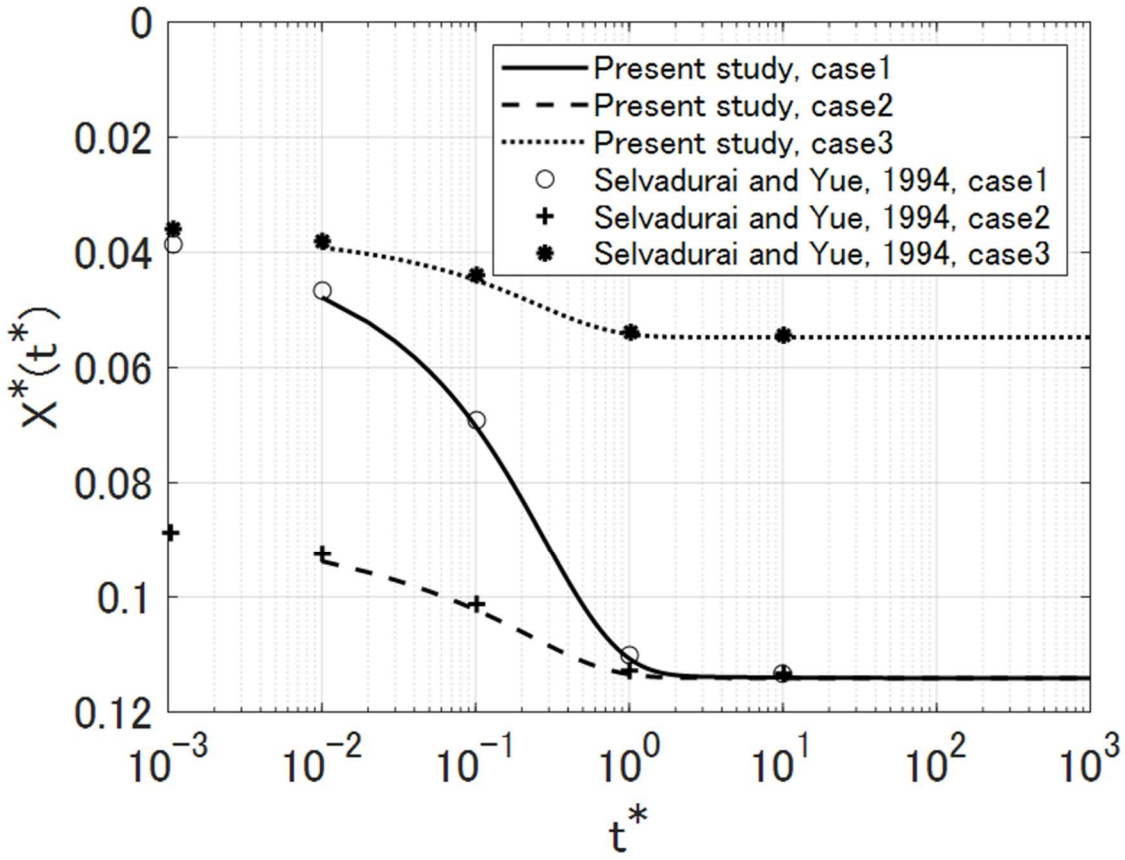


Fig. 1 Comparison of consolidation results under pervious surface condition with Selvadurai and Yue [1]. (Vertical axis: normalized axial displacement; horizontal axis: normalized time.)

References (Optional)

[1] Miura, K., et al., ZAMM, 2025

[2] Selvadurai, A.P.S. and Yue, Z., Int. J. Numer. Anal. Methods Geomech., 1994

Acknowledgements (Optional)

This work was supported by JSPS KAKENHI Grant Numbers 20K14612, 23K13212.

Session Category

Organ and Tissue Biomechanics: N/A

P3-173

Methodological Variability in Artificial White Spot Lesion Formation: Insights from A Meta-Analysis of Microhardness Outcomes

Mr. Lev Sushanek, Dr. Svetlana Komarova

University of Alberta, Edmonton, Alberta, Canada

Introduction

White spot lesions (WSLs) affect 25–50% of patients undergoing orthodontic treatment, due to the altered mechanical environment that disrupts enamel loading and promotes plaque retention. Developing a controlled protocol for creating artificial WSLs is essential for evaluating new strategies to prevent or treat these lesions. Our objective was to analyze existing in-vitro protocols for inducing WSLs in human enamel to assess their reproducibility.

Methods

The systematic search in Medline, Embase and Web of Science retrieved 4835 unique articles, of which 556 were included after title/abstract screening. Following full text screening, 118 studies describing de- and remineralization protocols using extracted human teeth were included.

Results

The protocols used molars 57/118, premolars 37/118 and incisors 6/118, and reported to create lesions within 2 weeks. Reported solution concentrations of Ca and PO4 were consistently around 2 mM, while Na, K and Cl had wider ranges. For meta-analysis, we identified 27/118 articles that reported tooth microhardness at multiple timepoints. The microhardness of intact teeth ranged from 259 to 569 N/mm^2 with the mean of 357 ± 67 N/mm^2, with no associations between microhardness values and method used (Knoop vs Vickers), load or dwell time. The single study effect size was percentage normalized mean difference, random effects model with restricted ML tau estimator was used for meta-analysis. Demineralization protocols led to an overall -49.8% reduction in microhardness with the 95% confidence interval of [-66.0, -33.6] and high heterogeneity, I^2 = 99.7%. Remineralization protocols of initially demineralized teeth resulted in overall increase in microhardness by 9.8% [1.5, 18.1], I^2 = 98.9%. Importantly, the overall effect of remineralization procedure compared to naïve teeth was similar to the demineralization protocols alone -53.6% [-71.0,-36.2], I^2 = 99.8%, and none of the studies reported complete tooth remineralization. Duration of demineralization and remineralization protocols was not associated with the outcome. Solution pH minimally affected the

outcome of demineralization, but was positively associated with the outcome of remineralization.

Discussion

We demonstrate substantial variability and limited reproducibility across in-vitro protocols for creating artificial WSLs, despite similar protocols. Establishing standardized lesion model is needed to support biomechanical investigations into how orthodontic appliances contribute to enamel demineralization.

Session Category

Organ and Tissue Biomechanics: N/A

P3-174

A Virtual Fields Method for Estimating Optic Nerve Head Tissue Elastic Properties from Deformation Field

Dr Manuel Lucas Sampaio de Oliveira[1], Prof. Stephane Avril[2], Prof. Thao Nguyen[1]

[1]Johns Hopkins University, Baltimore, MD, United States. [2]Mines Saint-Étienne, Saint-Étienne, Auvergne-Rhône-Alpes, France

Introduction

Glaucoma is characterized by progressive damage to the axons of retinal ganglion cells (RGCs) at the level of the optic nerve head (ONH). The extent of mechanical injury to the RGCs depends on the elastic properties of the ONH tissues. Previously, we developed a method to map the deformation response of ONH tissues to changes in the intraocular pressure (IOP) using digital volume correlation of optical coherence tomography images. We aim to develop a robust virtual field method (VFM) to determine the elastic properties of the ONH tissues from the DVC deformation map.

Methods

Applying VFM to analyze the in vivo deformation response of the ONH requires addressing three challenges: 1) the unknown pre-stress state in ONH tissues arising from the baseline IOP; 2) the complex deformation state of the ONH; and 3) limitations in the experimental methods to capture all ONH regions. We developed a VFM framework with the objective selection of virtual fields from perturbations in material properties and an optimization algorithm that estimates the prestress state of material properties. We demonstrated that the VFM framework can determine the material properties from FEA-generated synthetic data, first, for a simple structure of a soft inclusion in a stiff plate (Fig. 1a), and for the ONH structure in the posterior scleral shell (Fig. 1b). We examined the effect of uncertainties in the geometry and material properties of the tissues at the posterior ONH.

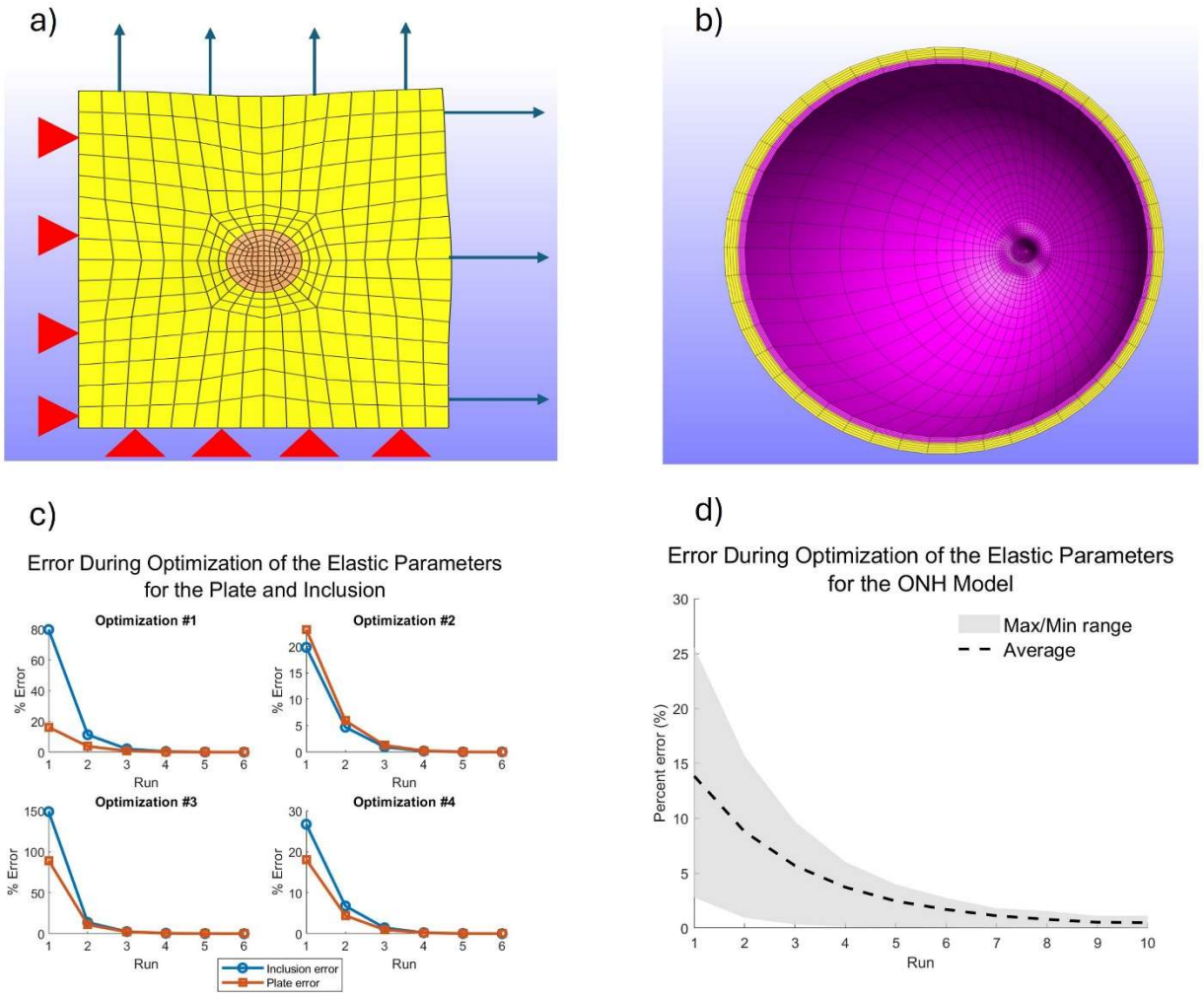
Results

We considered 4 random starting guesses for the material properties to determine the global optimum. The VFM framework was able to determine the elastic properties for the inclusion and plate with 99.9% precision. For each initial guess, the algorithm converged to the same values within 5 runs. Initial results for the ONH model show that the method recovered elastic parameters with 98.8% precision within 10 runs.

Discussion

We have developed a robust VFM framework to determine the material properties of ONH tissues from in vivo measurements of the ONH deformations. Current work involves adding contact to the problem, speeding up calculation of the internal virtual work, studying the sensitivity of the parameters that we don't have data.

Images (Optional)



References (Optional)

Session Category

Organ and Tissue Biomechanics: N/A

P3-175

Assessing synthetic bone surrogates: four-point bending and strain mapping of cortical bone vs Sawbones

Ms Marta Spataro[1], Mr Davide D'Andrea[1], Dr. Piyush Uniyal[2], Prof. G.Harry van Lenthe[2], Prof. Dario Francesco Santonocito[1], Prof. Dario Milone[1]

[1]Dept. of Engineering,University of Messina, Messina, Italy, Italy. [2]Dept. Mechanical Engineering, KU Leuven, Leuven, Belgium, Belgium

Introduction

Synthetic surrogates have been adopted for repeatable and cost-effective mechanical testing [1]. Questions remain regarding how closely they reproduce real cortical bone behaviour under mechanical loading. This study compares bovine cortical bone and Sawbones® under four-point bending using digital image correlation (DIC), evaluating displacement and strain evolution over time to assess how closely the synthetic material mimics the real bone

Methods

Prismatic specimens (N = 5, 7.68±0.42 × 8± × 60± mm^3) were prepared from mid-diaphysis bovine tibiae (14–15 months) and Sawbone®, ensuring comparable geometry [2]. Samples were speckled for digital image correlation (DIC) and tested in four-point bending. Displacement was applied at 0.01 mm/s on a uniaxial machine with a 25 kN load cell. A high-resolution camera enabled full-field deformation measurement Euler–Bernoulli beam theory was used to obtain stress–strain curves from load–displacement data and to evaluate flexural rigidity EI, which was further adjusted using DIC measurements (2). Python routines extracted DIC strain maps and time-dependent ε_{xx} in the constant-moment region.

Results

DIC maps showed localized deformation in Sawbone, enabling clear identification of the fracture site, whereas cortical bone displayed a more homogeneous strain field. Bone exhibited higher stiffness and a more brittle response. Failure strength was comparable (bone 142 ± 41 MPa; Sawbone 104.0 ± 23.3 MPa), but Sawbone showed much higher failure strain (2.24 ± 1.04 vs 0.59 ± 0.19). Flexural rigidity (EI) differed markedly (bone 7.09×10^6 ± 2.84×10^6 $N\cdot mm^2$; Sawbone 4.55×10^6 ± 5.63×10^5 $N\cdot mm^2$).

Discussion

The mechanical response of cortical bone and Sawbone composite showed marked differences in deformation behaviour. We found that Sawbone can reproduce load-to-failure response within the same order of magnitude but does not replicate the elastic behaviour nor the brittle failure mode of cortical bone. Caution should be taken when stiffness-driven mechanics are of interest. Preliminary observations indicate that certain regions, such as the posterior area, might be better approximated by the surrogate but further investigation is needed to verify this hypothesis.

Images (Optional)

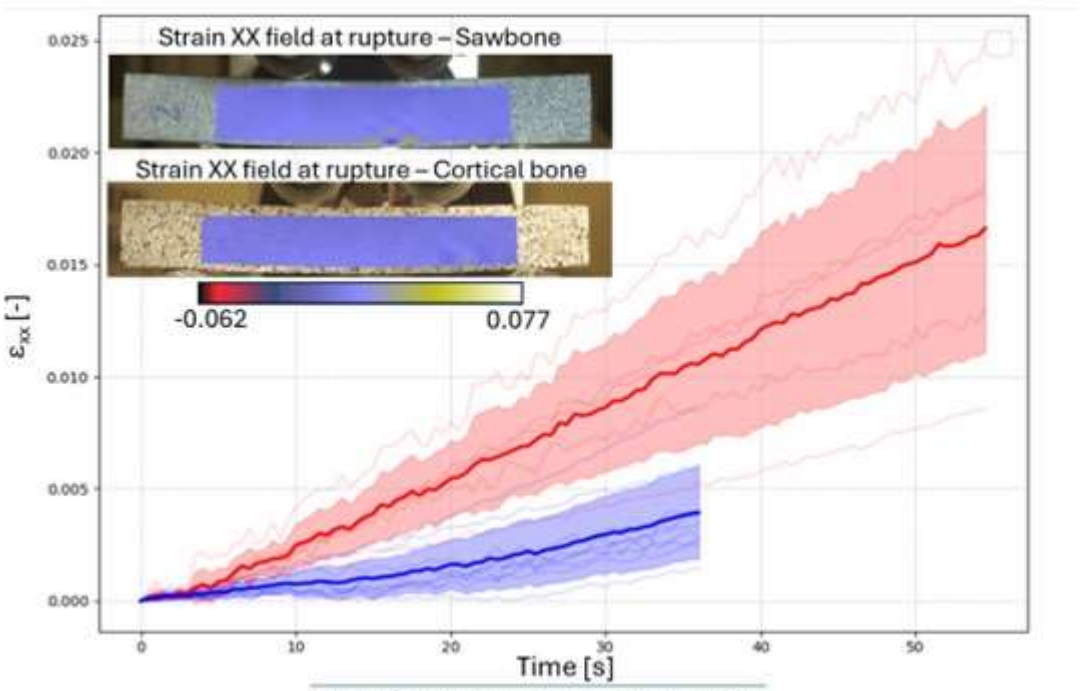


***Fig.1** DIC contour maps (upper-left side); strain as a function of time of tensile fibers: red = Sawbone, blue = Bone (background)*

References (Optional)

[1] Cristofolini et al., J Biomechanics, 2000

[2] Meng et al., J Mech Behav Biomed Mater, 123:104774, 2021.

[3] Collins et al., J. Mechanical Behaviour of Biomedical Material

Acknowledgements (Optional)

Session Category

Organ and Tissue Biomechanics: N/A

P3-176

Biomechanical Regulation of Liver Injury and Regeneration

Prof. Mian Long

Institute of Mechanics, Chinese Academy of Sciences, Beijing, Beijing, China. University of Chinese Academy of Sciences, Beijing, Beijing, China

Introduction

Mechanical niche of hepatic sinusoids is crucial for maintaining liver homeostasis and regulating injury and regeneration, but the underlying regulatory mechanisms remain largely unknown. This work focuses on elucidating the physiological and pathological alterations of hepatic mechanical microenvironment and their effects on the phenotype and function of hepatic cells.

Methods

This work combines in vivo experimental methods such as murine liver perfusion, partial liver resection, and liver fibrosis models, as well as in vitro biomechanical techniques such as microfluidic chips, biaxial stretch, stiffness-adjustable hydrogels, and osmotic pressure modulation, to analyze the mechanotransduction mechanisms in liver injury and regeneration.

Results

After partial liver resection, the blood flow per unit volume of residual liver is promptly augmented. On one hand, this alteration can increase the interstitial flow shear stress sensed by hepatocytes, promoting the nuclear translocation of Yes-associated protein (YAP) and facilitating hepatocytes re-entering the cell cycle [1]. On the other hand, it can enhance the mechanical stretch of blood vessels, activating the mechanocrine of liver sinusoidal endothelial cells (LSEC) through YAP pathway, releasing heparin-binding epidermal growth factor-like growth factor (HB-EGF), and promoting the proliferation of hepatocytes [2]. In the progress of liver fibrosis, LSECs can sense the increase in matrix stiffness through focal adhesion kinase, induce the activation of p38 and its downstream signaling pathways, and promote the LSEC defenestration in a cytoskeleton reorganization-dependent manner [3]. Meanwhile, the fenestrae of LESCs are found to be negatively regulated by cell membrane tension, implying mechanically-specific regulation in LESC capillarization.

Discussion

These findings further understand the roles of mechanical cues in liver injury and repair, offering new strategies to prevent and treat liver fibrosis and other diseases.

References (Optional)

[1] Li et al., JHEP Reports. 2023; 5: 100905.

[2] Wu et al., Hepatology. 2024; 82:370-387.

[3] Zhang et al., Biomaterials. 2024; 305:122462.

Session Category

Organ and Tissue Biomechanics: N/A

P3-177

Deep learning surrogate of patient-specific finite element surgery simulations for fast optimization of refractive interventions

Dr Miguel Angel Ariza-Gracia[1], Yannic Eltschinger[1], Dr Theo Seiler MD[2,3], Dr Philippe Büchler[1]

[1]ARTORG / University of Bern, Bern, Bern, Switzerland. [2]Department of Ophthalmology/Inselspital Bern, Bern, Bern, Switzerland. [3]Institut für Refraktive und Ophthalmo-Chirurgie (IROC), Zürich, Zürich, Switzerland

Introduction

Patient-specific finite element (FE) models can simulate refractive interventions and predict postoperative refractive outcome, but runtimes prevent surgical optimization and real-time planning. We present a hybrid pipeline where FE generates a simulation database, a deep learning (DL) surrogate replaces the FE solver, and the surrogate is used to optimize patient-specific surgical parameters.

Methods

Personalized corneal geometries from tomography were used to run FE simulations of PRK, LASIK, and keratorefractive lenticule extraction (KLEx) with structured hexahedral meshes (~80k elements), physiological intraocular pressure (IOP; 15 mmHg), depth-dependent anisotropic stromal behavior, and nonlinear contact for flap/cap interfaces. Postoperative optical metrics were computed from the deformed curvature [1]. To enable optimization, large-scale FE sampling on HPC generated thousands of simulations spanning patient geometries and intervention parameters (optical zone, ablation/lenticule profile, flap/cap settings, and refractive targets). These simulations defined supervised targets for a surrogate model: (i) scalars (sphere/cylinder prediction error) and (ii) spatial outputs (curvature-change maps). The surrogate leveraged a deep-learning autoencoder-style latent embedding of geometry, combined with a late-fusion fully connected network to integrate clinical biomarkers and produce the final predictions. [2]. Training minimizes a weighted loss combining refractive-output error and structured regularization for surgical consistency. Surgical planning is posed as constrained Bayesian optimization over intervention parameters using the surrogate as a fast forward model.

Results

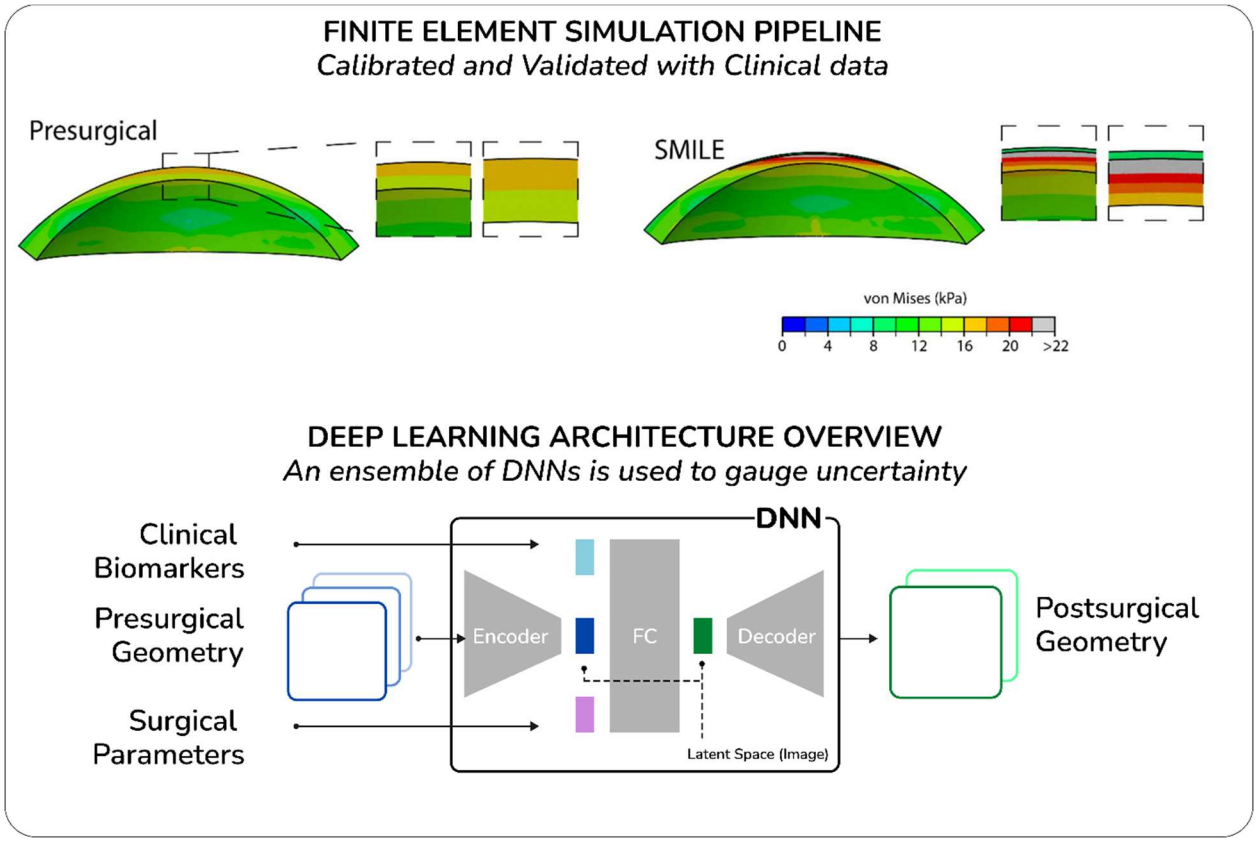
The stromal constitutive model was calibrated and validated against three human ex-vivo tests. All FE procedures showed systematic undercorrection increasing approximately linearly with intended correction; for ~7 D spherical targets, undercorrection exceeded ~2

D in LASIK and KLEx, requiring planning adjustments up to ~50 µm depth. Preliminary deep-learning surrogate results indicated a 100–500× reduction in compute time versus the full FE pipeline, while maintaining prediction errors within an ophthalmically acceptable tolerance (±0.25 D).

Discussion

Clinical validation of the FE workflow supports its use as a reliable patient-specific reference model for refractive intervention simulation. DL surrogate permits near real-time, constrained Bayesian optimization of surgical parameters, while retaining FE-consistent predictions and enabling integration of imaging and clinical biomarkers.

Images (Optional)



References (Optional)

[1] Balu A et al., *Sci Rep*, 2019. doi:10.1038/s41598-019-54707-9
[2] Ariza-Gracia MA et al., *Curr Dir Biomed Eng*, 2025. doi:10.1515/cdbme-2025-0130

Acknowledgements (Optional)

This work was supported by the Swiss National Science Foundation (SNSF; IZLIZ3_182975) and Innosuisse (116.255 IP-LS). MA Ariza-Gracia is recipient for a Fellowship from the Center for Artificial Intelligence in Medicine (2024), University of Bern.

Session Category

Organ and Tissue Biomechanics: N/A

P3-178

Poromechanical Properties of Human Articular Cartilage Estimated from Creep Experiments Using Neural Network Models

Mr. Nurkeldi Iznat[1], Dr. Elizabeth Clarke[2], Dr. Ashvin Thambyah[3], Dr. LePing Li[1]

[1]The University of Calgary, Calgary, Alberta, Canada. [2]The University of Sydney, Sydney, New South Wales, Australia. [3]The University of Auckland, Auckland, Auckland, New Zealand

Introduction

Articular cartilage properties are needed to quantify tissue health and joint functions. They are conventionally determined from non-invasive indentation creep/relaxation experiments by iteratively fitting the data using finite element (FE) methods, which may not converge to the true material properties, e.g., a random initial guess can lead to an incorrect estimate. The objective of the present study was to develop a neural network (NN) surrogate model that adequately extracts cartilage properties from indentation creep data. Our ultimate goal is to establish such models that may be used by end-users without requiring FE analysis once trained on sufficient datasets.

Methods

Indentation creep experiments were performed on 146 human cartilage-bone samples from finger, elbow, shoulder, hip, knee and ankle joints of 8 donors (ethics approved). The loading included a 10-second ramp compression followed by one hour of creep, corresponding to an average pressure of 4.5 MPa on the cylindrical indenter. Experimental data included cartilage thickness and creep displacement–time curves from all specimens.

After initial evaluations, long short-term memory (LSTM) and transformer-based NN models were selected to independently estimate cartilage properties from indentation tests, given their ability to model sequential patterns and nonlinear load responses exhibited in creep. Each model was trained on ~3000 FE simulations spanning varied tissue properties, indenter sizes, and cartilage thicknesses.

Results

Despite variations in cartilage thickness among joints—and the corresponding need for multiple indenter sizes—both FE-trained NN models successfully estimated cartilage properties for all samples with similar results (Fig. 1). Statistical analysis of tissue

properties showed that knee cartilage differed significantly from elbow cartilage, whereas thumb cartilage did not differ significantly from elbow cartilage.

Discussion

Transformers are widely used in language, signal processing and computer vision applications. In our study, the transformer model was slightly more effective than the LSTM model in capturing the cartilage creep response. Nevertheless, both NN models streamline the extraction of cartilage properties from large experimental datasets by replacing traditional iterative curve-fitting and mitigating uncertainties caused by initial guess selection. We are further testing the model's robustness in producing unique results by using different training parameter configurations and architectures.

Images (Optional)

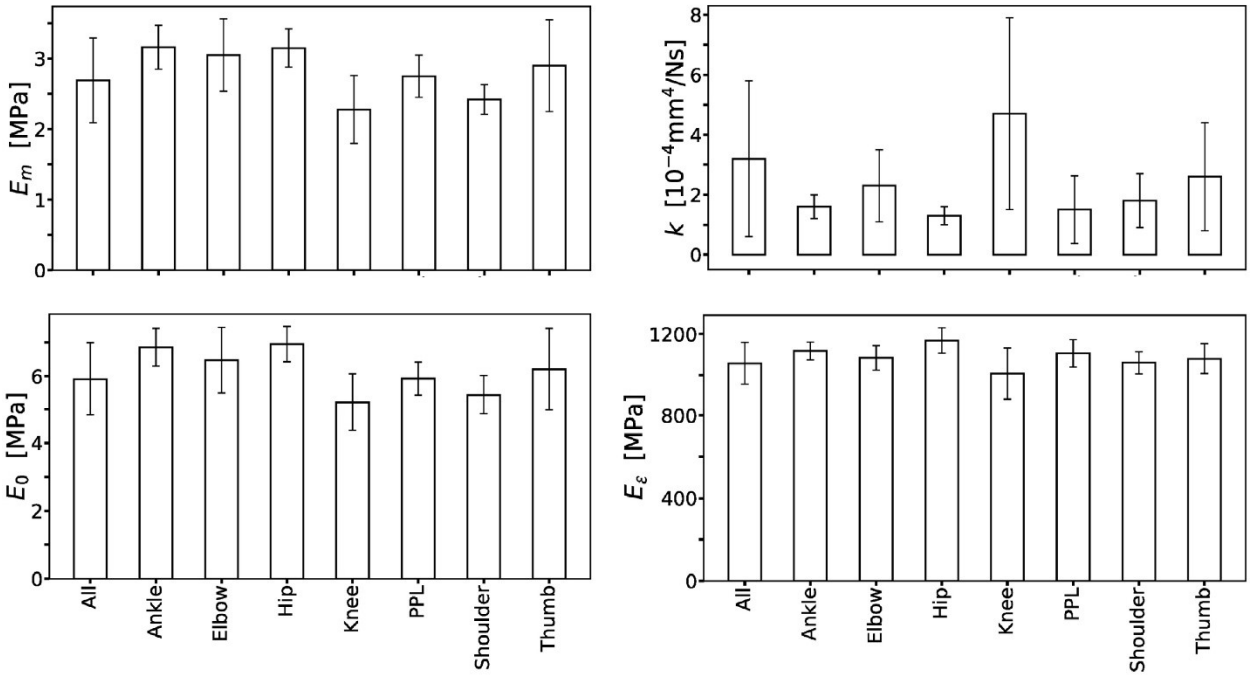


Figure 1. Mean and standard deviation of joint-specific cartilage properties. A fibril reinforced model was used: E_m – modulus of nonfibrillar matrix; $E_f = E_0 + E_\varepsilon \varepsilon$ – modulus of fibrillar matrix if $\varepsilon > 0$; $E_f = 0$ if $\varepsilon \leq 0$; k: permeability. PPL: Little finger metacarpophalangeal joint.

Session Category

Organ and Tissue Biomechanics: N/A

P3-179

Correlative Microscale Mapping of Human Meniscus Biomechanics and Biochemistry by AFM Micro-Indentation and MALDI-FTICR Mass Spectrometry Imaging

MSc. Aleksandra Lebedeva[1], BSc. Matis Mühlpointner[1], Dr. Orestis Andriotis[1], Dr. Stefan Tögel[2], Dr. Lena Hirtler[2], Dr. Martina Marchetti-Deschmann[1], Dr. Philipp Thurner[1]

[1]TU Wien, Vienna, Vienna, Austria. [2]Medical University of Vienna, Vienna, Vienna, Austria

Introduction

Meniscus degeneration is a major contributor to chronic knee pain and osteoarthritis (OA) [1], while its biochemical–mechanical relationships remain unclear. The objective of this study was to establish a correlative workflow integrating atomic force microscopy (AFM) micro-indentation with matrix-assisted laser desorption/ionization Fourier-transform ion cyclotron resonance mass spectrometry imaging (MALDI-FTICR MSI) to determine how biochemical alterations correspond to local mechanical changes in healthy and osteoarthritic menisci.

Methods

Two human menisci were analyzed: one osteoarthritic sample from a patient >60 years undergoing knee replacement and one healthy cadaveric sample from a donor aged 72–99 years. For each specimen, three consecutive cryosections were examined. AFM micro-indentation was performed in the red-red (RR), red-white (RW), and white-white (WW) zones. In each zone, three 100 × 100 µm regions (50 µm step) were mapped with a 15 µm spherical probe under near-physiological conditions. Each map (20 × 20 µm, 4 × 4 pixels) produced 432 force–indentation curves, fitted with the Hertz model ($R^2 > 0.95$) [2]. Matched sections were analyzed by MALDI-FTICR MSI at 50 µm spatial resolution to quantify peptide distributions, particularly collagen-derived peptides. Stiffness differences across zones were assessed using the Kruskal–Wallis test ($p < 0.001$).

Results

Healthy menisci exhibited a strong zonal stiffness gradient (RR > RW > WW; $p < 0.001$) (Fig.1c). In OA samples, this gradient was markedly reduced, with RR stiffness substantially decreased and no significant difference remaining between RR and WW (Fig.1d). MSI showed corresponding biochemical changes: healthy tissue contained continuous collagen I/II/III gradients, whereas OA tissue displayed fragmented, irregular collagen patterns and loss of peripheral-to-central organization (Fig.1a,b) [3].

Discussion

The integrated AFM–MSI workflow demonstrates that healthy menisci maintain coordinated mechanical and molecular organization, while OA tissue exhibits mechanical softening and disrupted collagen distribution. This combined approach enables the detection of early degenerative alterations and supports identification of spatial biochemical markers relevant to OA progression.

Images (Optional)

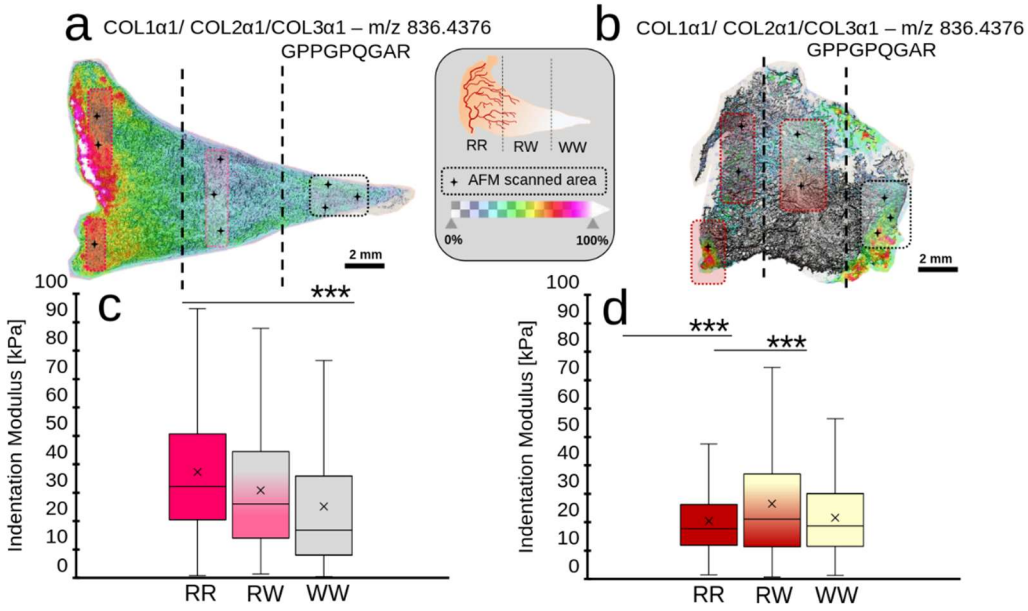


Fig.1.Spatial distribution of collagen I/II/III–derived peptides (m/z 836.438, TIC-normalized) in a) healthy and b) osteoarthritic meniscus, and corresponding zonal indentation moduli in c) healthy and d) osteoarthritic meniscus.

References (Optional)

[1] Alice Fox et al., *Sports Health*, 2012

[2] Kontomaris SV et al., *Micron*, 2022

[3] Derek Q. Nesbitt et al., *J. Orthop. Res.,* 2024

Session Category

Organ and Tissue Biomechanics: N/A

P3-180

Auxetic Lamina Cribrosa Beams Protect Axons and Capillaries Under IOP Elevation

Mr. Qi Tian BS[1,2], Ms. Yingzhe Han MS[1,2], Dr. Xuehuan He PhD[1], Dr. Po-Yi Lee PhD[3], Dr. Miriam Bohlmann Kunz PhD[1], Dr. Ian A. Sigal PhD[1,2]

[1]Department of Ophthalmology, University of Pittsburgh, Pittsburgh, PA, United States. [2]Department of Bioengineering, University of Pittsburgh, Pittsburgh, PA, United States. [3]Wellman Center for Photomedicine, Massachusetts General Hospital, Boston, MA, United States

Introduction

The lamina cribrosa (LC) collagen beams provide mechanical support to both axons and capillaries within the optic nerve head. Because inadequate support from the beams is thought to lead to axon damage and vision loss, understanding how beams deform under load is of great interest. LC biomechanics studies have frequently assumed that the LC beams are incompressible. To the best of our knowledge, the incompressibility assumption has never been experimentally verified. Our goal was to characterize LC beam behavior under load experimentally and determine whether they are incompressible.

Methods

Twelve 45-μm-thick coronal LC sections from three sheep eyes were stretched biaxially while imaged with instant polarized light microscopy (IPOL) [1, 2]. For 20 well-visible and fully-contained beams we measured width and length during loading and calculated stepwise Poisson's ratios. IPOL's high spatial resolution enabled precise 2D tracking of beam deformation. Because ratio calculations are sensitive to noise, we fitted quadratic functions to the width and length curves and computed Poisson's ratios from the fitted values. To verify that 2D measurements reflected true volumetric behavior, we repeated the study for four beams but using second-harmonic generation (SHG) microscopy and measured their thickness changes.

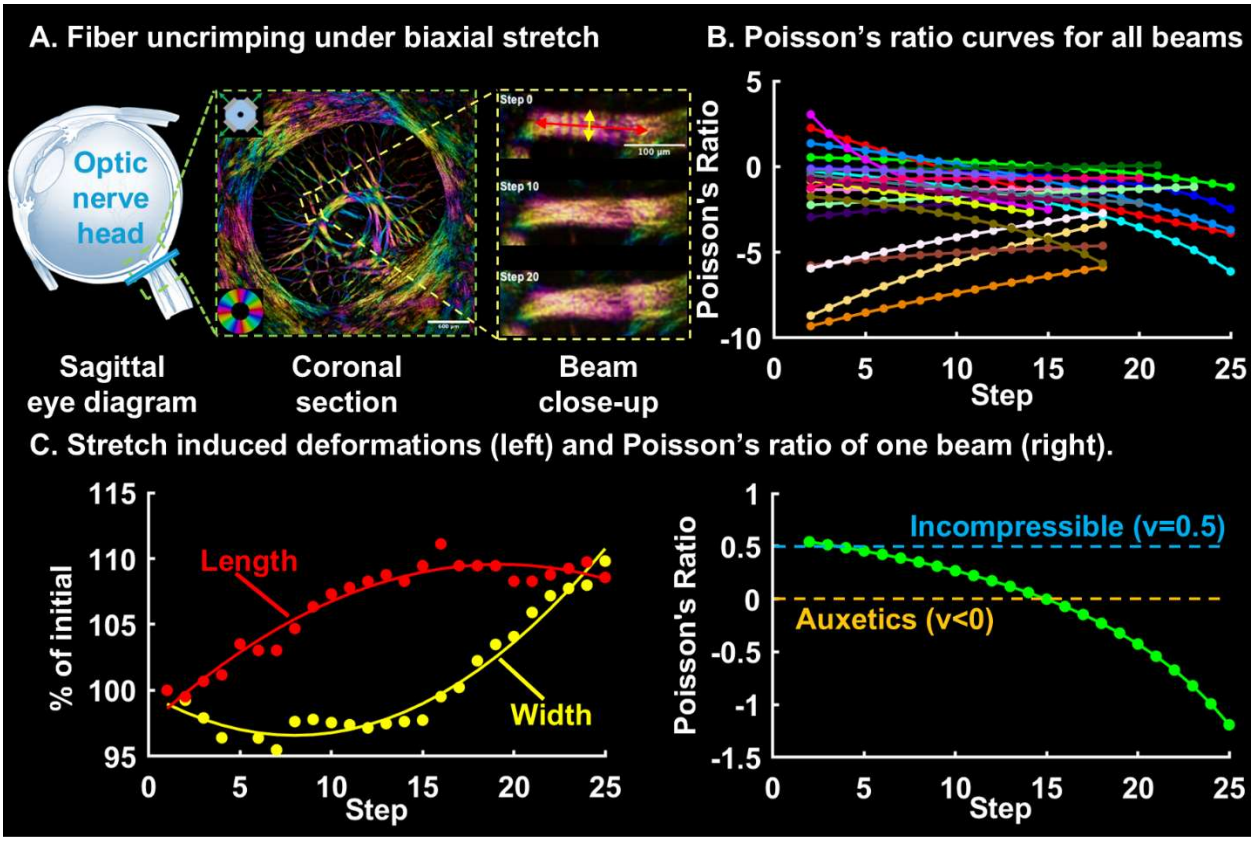
Results

All 20 beams widened laterally during stretch, with Poisson's ratios shifted from −1.7 ± 3.3 (range −9.3 to 3.1) at the initial step to −2.7 ± 1.8 (range −6.1 to 0.1) at the last step, indicating strong auxetic behavior. Three of four beams imaged by SHG thickened under stretch, whereas the fourth one showed no significant change.

Discussion

Our findings directly contradict the long-standing assumption that LC beams are incompressible [3]. Instead, 96% of the LC beams widened under load, revealing a robust auxetic response. We suspect that this behavior helps avoid compressing capillaries within the beams, affecting hemodynamics, or stretching axons adjacent to the beams.

Images (Optional)



References (Optional)

[1] Lee PY *et al.*, Acta Biomater, 2024.

[2] Lee PY *et al.*, Exp Eye Res, 2022.

[3] Voorhees AP *et al.*, Acta Biomater, 2017.

Acknowledgements (Optional)

NIH R01-EY023966, P30-EY008098 and T32-EY017271 (Bethesda, MD), Research to Prevent Blindness (unrestricted grant to UPMC ophthalmology, and Stein innovation award to Sigal IA) and BrightFocus Foundation.

Session Category

Organ and Tissue Biomechanics: N/A

P3-181

Thermal Lag in Perfused Kidneys and Its Implications for Bioheat Transfer Modeling

Ms. Maria Londono MS[1], Dr. Joseph R. Kangas PhD[2], Ms. Dominika Wilczok[3,4], Mr. Ryan Nadybal[2], Dr. Bat-Erdene Namsrai MD[2], Dr. Anudari Chimedtseren MD[2], Dr. Erik Finger MD, PhD[2], Dr. Paul A. Iaizzo PhD[2], Dr. R. Lyle Hood PhD[1], Dr. Robert A. De Lorenzo MD[5], Dr. John C. Bischof PhD[2]

[1]The University of Texas at San Antonio, San Antonio, Texas, United States. [2]University of Minnesota, Minneapolis, Minnesota, United States. [3]Duke University, Durham, North Carolina, United States. [4]Duke Kunshan University, Kunshan, Jiangsu, China. [5]University of Texas at San Antonio, San Antonio, Texas, United States

Introduction

Temperature control in perfused tissues is central to hyperthermia, cryotherapy, and organ preservation, yet predicting how heat propagates through tissue remains challenging. Current bioheat models, such as the Pennes equation (PE), assume instantaneous thermal equilibrium between blood and tissue [1, 2], an assumption that breaks down when perfusate and tissue temperatures differ substantially. To investigate this limitation, we performed continuous temperature measurements during alternating *ex vivo* perfusion of porcine kidneys to quantify transient gradients in temperature during perfusion and evaluate the extent to which Penne's equilibrium assumption fails, informing improved thermal control strategies for treatment and preservation.

Methods

Fresh porcine kidneys were perfused with an isotonic solution at 15 mL/min. Temperatures were continuously recorded at the inlet and four intrarenal locations using a multilevel thermocouple probe, with sensors located 10, 18, 22, and 30 mm from the renal artery. The kidneys were subjected to six thermal perfusion phases, alternating between normothermic (37 °C) and cold (5 °C) PBS, each lasting 20 minutes. We quantified the time lag (t_{lag}) in the onset of temperature change between the inlet and the kidney in response to a change in perfusate temperature. This was reported as the mean ± SD across all cycles. Data shown are from one kidney (six thermal phases); data for six additional kidneys are being collected.

Results

Mean t_{lag} increased with distance from the inlet: 22.4 ± 5.1 s at 10 mm, 34.9 ± 8.0 s at 18 mm, 79.2 ± 15.3 s at 22 mm, and 360.1 ± 2.5 s at 30 mm, indicating a velocity of thermal propagation through the kidney rather than instantaneous equilibration perfusate/tissue.

Discussion

These findings quantify the extent of thermal gradients during perfusion and demonstrate that the PE is insufficient to capture this behavior. Incorporating a perfusion-tissue coupling term or a two-parameter model could improve model fidelity in predicting temperature distribution in perfused organs. Such modification could improve predictive accuracy in thermal therapy, cryopreservation, and organ perfusion, where transient temperature gradients critically affect tissue function and viability.

References (Optional)

[1] Pennes, H.H., Journal of Applied Physiology, 1948

[2] Crezee, J. and J. Lagendijk, Physics in Medicine & Biology, 1990

Acknowledgements (Optional)

This work is supported by the National Science Foundation (NSF) Engineering Research Center (ERC) for Advanced Technologies for the Preservation of Biological Systems (NSF ATP-Bio) under Grant No. EEC 1941543 and the National Institute of Health (NIH) R01 on kidney cryopreservation under Grant No. DK117425.

Session Category

Organ and Tissue Biomechanics: N/A

P3-182

Tactile Visualization of "Mochi Skin" Texture Using a Thin Triaxial-Stress Sensor

Graduate Student Rin Nagane, Professor Kazuhiko Sasagawa, Associate Professor Kazuhiro Fujisaki, Assistant Professor Kotaro Miura

Hirosaki University, Hirosaki, Aomori, Japan

Introduction

One of the ideal facial skin conditions is known as “mochi skin” in Japanese, characterized by a soft, elastic, and smooth texture. In daily life, the mochi-mochi feeling of the cheeks is detected by hand touching. Although various devices have been developed to measure skin surface conditions such as water and oil content, no quantitative indicator exists for evaluating "mochi skin". This study aimed to establish a quantitative evaluation method by visualizing tactile sensation.

Methods

Ten subjects (five males and five females, average age 22) participated. First, the water and oil content of the left cheeks were measured three times using a commercial device. Next, sensory evaluation experiments were conducted in which participants touched one another’s cheeks and rated the mochi-mochi feeling on a five-point scale (5: very mochi-mochi feeling, 4: rather mochi-mochi feeling, 3: undecided, 2: rather un-mochi-mochi feeling, 1: no mochi-mochi feeling sensation). Finally, the triaxial stress sensor was attached to the index fingertip, and subjects performed sliding motions three times so as lifting their own cheeks. Contact stresses during sliding were recorded.

Results

The instantaneous friction coefficient of the skin was calculated from the measured triaxial stresses. Results indicated that the maximum static friction coefficient showed the strongest correlation with the degree of mochi-mochi feeling, whereas the dynamic friction coefficient had little effect. The friction coefficient was calculated by dividing shear stress friction force by contact pressure vertical force. The maximum static friction coefficient was obtained just before the fingertip began sliding, while the dynamic friction coefficient was defined as the average of the plateau region during sliding. Using data of water and oil content, maximum static friction, dynamic friction, and sensory ratings, multiple regression analysis was performed to derive a predictive model for mochi skin evaluation.

Discussion

The derived model equation demonstrates potential as a novel quantitative indicator for evaluating "mochi skin", and further analysis is required to improve the reliability of the prediction equation.

Images (Optional)



References (Optional)

[1] Y. Kudo et al., Mechanical Engineering Letters, 2023

Session Category

Organ and Tissue Biomechanics: N/A

P3-183

Ex Vivo Culture of Porcine Corneas in a Silicone Flow Bioreactor Improves Epithelial Preservation and Recovery After Injury

Ms. Sabina Eibichova[1], Mr. Thomas Schwarz[2], Ms. Fabiola Walz[1], Dr. Constantin Berger[2], Ms. Annika Goy[3], Dr. Annika Bohne[3], Dr. Malik Salman Haider[3], Dr. Daniel Kampik[3], Prof. Jost Hillenkamp[3], Prof. Jan Hansmann[4,2], Dr. Christian Lotz[2,1,5]

[1]University Hospital Würzburg, Department for Functional Materials in Medicine and Dentistry, Würzburg, Bavaria, Germany. [2]Translational Center for Regenerative Therapies, Fraunhofer Institute for Silicate Research, Würzburg, Bavaria, Germany. [3]University Hospital Würzburg, Department of Ophthalmology, Würzburg, Bavaria, Germany. [4]Faculty of electrical engineering, University of Applied Science Würzburg-Schweinfurt, Schweinfurt, Bavaria, Germany. [5]Esslingen University of Applied Sciences, Institute for Sustainable Energy Technology and Mobility (INEM), Esslingen, Baden-Wuerttemberg, Germany

Introduction

Porcine corneas are widely used as ex vivo models because their similarity to human tissue enables studies of epithelial wound healing, drug permeation and tissue preservation. However, ex vivo cultivation is mostly performed under static conditions, which lack physiological mechanical cues such as shear stress and do not recreate the continuous nutrient supply present in vivo. Available dynamic systems can reproduce some of these factors but are costly, technically demanding and difficult to adapt. To address this, we developed a customizable and accessible silicone-based flow bioreactor that applies intermittent medium flow within physiological shear levels to more closely mimic the physiological corneal microenvironment.

Methods

The bioreactor consisted of two PDMS components fabricated by SLA 3D printing and silicone casting. Corneas were mounted using a 3D printed clamping ring separating apical and basolateral circuits. Flow simulations estimated shear stress in the bioreactor based on pump-controlled flow rates. Corneas were cultured statically or under intermittent medium flow for up to seven days. To study the effect of dynamic culture on corneal healing, standardized 6 mm epithelial wounds were created by excimer laser ablation. Tissue morphology was analyzed by hematoxylin and eosin staining and

immunofluorescence. Wound healing was monitored by OCT, segmenting wound-margin distance (closure phase) and epithelial thickness over the wound bed (regenerative phase).

Results

Dynamic cultivation preserved the multilayered epithelium and maintained epithelial and limbal marker expression, including E-cadherin, CK12, CK14 and p63α, whereas static culture led to epithelial thinning and loss of marker expression. Flow simulations yielded shear stresses within the physiological tear-film range. Wound-margin progression during the closure phase did not differ between groups. During the regenerative phase, epithelial thickness diverged from day 5 onward, with significantly greater thickness under dynamic flow at day 7 ($p = 0.002$), approaching pre-wounding values, while static culture showed incomplete recovery.

Discussion

The silicone-based flow bioreactor provides an accessible platform for dynamic cultivation of ex vivo corneas. Intermittent medium flow supported epithelial regeneration and maintained a multilayered architecture. Further development, including integration of non-invasive monitoring tools, may extend its applicability beyond porcine models and offer an improved system for the storage of human donor corneas.

Session Category

Organ and Tissue Biomechanics: N/A

P3-184

Whole Organ Multiscale Placental Perfusion Models to Assess the Effect of Fetal Sex on Vascular Structure and Function in Growth Restricted Pregnancies

Dr Sahan Jayatissa[1], Ms Mary Spring[2], Prof Joanna James[2], Prof Alys Clark[1]

[1]Auckland Bioengineering Institute, University of Auckland, Grafton, Auckland, New Zealand. [2]Department of Obstetrics, Gynaecology and Reproductive Sciences, Faculty of Medical and Health Sciences, University of Auckland, Grafton, Auckland, New Zealand

Introduction

Pregnancy disorders including fetal growth restriction (FGR) are associated with insufficiencies in placental function. Male fetuses are more likely to be growth restricted or stillborn, theorized to be related to a reduced placental reserve [1]. We aim to assess sex-specific features of the FGR placenta via a data-driven computational model of the placental vasculature.

Methods

Chorionic arteries (large arteries covering the fetal aspect of the placenta) were manually segmented from photographs of normal (female n= 20, male n=22) and FGR (female n =3, male n=6) human term placentae. Myography was conducted in isolated arteries. Vascular branch length and diameter were categorized by Strahler order and mapped onto an in silico placental volume with the distal vasculature generated using previously published algorithms [2]. Efficient algorithms for simulating Poiseuille flow in these networks were implemented in Python using graph theory [3]. The impacts of incorporating non-linear rheology, flow disruptions at bifurcations (due to asymmetry), and compliance were assessed in the computational model. Compliance differences between FGR and normal arteries were defined based on literature and myography data.

Results

Chorionic vessels were longer in with reduced diameter in male FGR placentae than normal male/female, or female FGR. Simulations of haemodynamics in population models predicted a 2.6 fold increase in vascular resistance in male FGR models compared to all other cohorts (normal male and female, female FGR). Simulating non-linear rheology had a small impact on vascular resistance, however, a larger increase in resistance is seen when incorporating effects of flow disruptions at bifurcations. Lower compliance was seen in FGR blood vessels, which further exacerbates predicted increases in resistance.

Discussion

Male FGR placentae have longer, smaller diameter blood vessels than normal male placentae, but this anatomical perturbation is not seen in female FGR. These structural differences combined with reduced vascular compliance in a haemodynamic population-based model suggests at least a 2.6 fold increase in vascular resistance, potentially contributing to increased vulnerability during pregnancy in male fetuses.

References (Optional)

[1] Erikkson et al., Am J Hum Biol, 2010

[2] Byrne et al., J Theoret Biol, 2021

[3] Wijnakker et al., Electr Power Syst Res, 2025

Session Category

Organ and Tissue Biomechanics: N/A

P3-185

Differentiable Inverse Finite Element Solver for Multiaxial Characterization of Brain Tissue

Mr Saikat Pal, Mr. Umesh Gautam, Mr. Sitikantha Roy

IIT DELHI, New Delhi, New Delhi, India

Introduction

Differentiable simulation has emerged as a promising approach for automating the entire process of solving inverse problems involving material nonlinearity. This approach allows the numerical solution procedure to be represented as a computational graph, which can be differentiated using Automatic Differentiation (AD) and adjoint methods. The present study demonstrates the application of a differentiable inverse (FE) framework for solving inverse problems of quasi-static hyperelasticity modelling in brain tissue. The framework employs a differentiable FE solver to solve PDEs and efficiently compute gradients using AD-based adjoint methods.

Methods

In the computational pipeline, forward simulations were preserved as computational graphs using the JAX framework. The calculations for each element in the finite element method were vectorized so that they could be computed in parallel. This computational graph of the forward simulation helps automate the gradient computation process throughout the entire simulation. The adjoint method helps compute gradients through the iterative loop of the solver inside the simulation. We used the 2-term Ogden model to characterize the hyperelasticity of each region of the human brain. A normalized loss function was used as the objective function for the multi-objective minimization problem.

Results

All data from the different loading modes were considered for the hyperelastic parameter estimation for different regions of the brain. The average elastic response in each direction was optimized to obtain a parameter set that can be used to model multimodal and complex loading conditions. The parameters obtained indicated differences between the white and gray matter. Interestingly, white or gray matter properties also vary with respect to the anatomical region of the brain. We also observed that the gradients are in good agreement with the finite difference-based gradients in the Adjoint Sensitivity analysis.

Discussion

In this study, we performed multimodal multiaxial complex mechanical testing of human cadaveric brain tissues. In addition, we developed a differentiable inverse Finite Element solver scheme for parameter estimation using Automatic Differentiation and Adjoint Sensitivity methods. Our aim was to provide hyperelastic parameters for different anatomical regions of the brain that can be used in full-scale brain simulations.

Session Category

Organ and Tissue Biomechanics: N/A

P3-186

Investigating the link between advanced diffusion imaging parameters and brain tissue mechanics using finite element models of the brain

Dr. Sarah Vandenbulcke[1], Dr. Christoffer Olsson[1], Prof. Thomas Christian Gasser[2], Prof. Lisa Prahl Wittberg[2], Prof. Rodrigo Moreno[1]

[1]Department of Biomedical Engineering and Healthy systems, KTH Royal Institute of Technology, Huddinge, Stockholm, Sweden. [2]Department of Engineering Mechanics, KTH Royal Institute of Technology, Stockholm, Stockholm, Sweden

Introduction

Magnetic resonance elastography (MRE) studies have shown that brain stiffness decreases with aging and in neurodegenerative disorders such as Alzheimer's disease [1]. Therefore, brain stiffness has been identified as a potential biomarker for neurodegeneration. Multidimensional diffusion magnetic resonance imaging (MD-dMRI) provides parameters describing the variation in the brain's microstructure at sub-voxel level [2]. By using these parameters as measures of structural heterogeneity, we could reveal the microstructural changes underlying this stiffness reduction, a link that is not yet fully understood. In this study, we investigate how microstructural variations measured with MD-dMRI can impact the brain's mechanical behavior.

Methods

MD-dMRI was connected to brain tissue mechanics by generating tensor distributions and incorporating them into a block-shaped finite element model of brain tissue as material parameter distributions. Each distribution consisted of tensors of varying sizes and shapes, characterized by a set of four MD-dMRI based parameters describing the mean and variance for each distribution [2]. Brain tissue was modeled as a linear poroelastic material in COMSOL Multiphysics. The mechanical response was evaluated under boundary conditions simulating MRE acquisition, with a 50 Hz horizontal displacement inducing shear wave propagation (Figure Panel **A**).

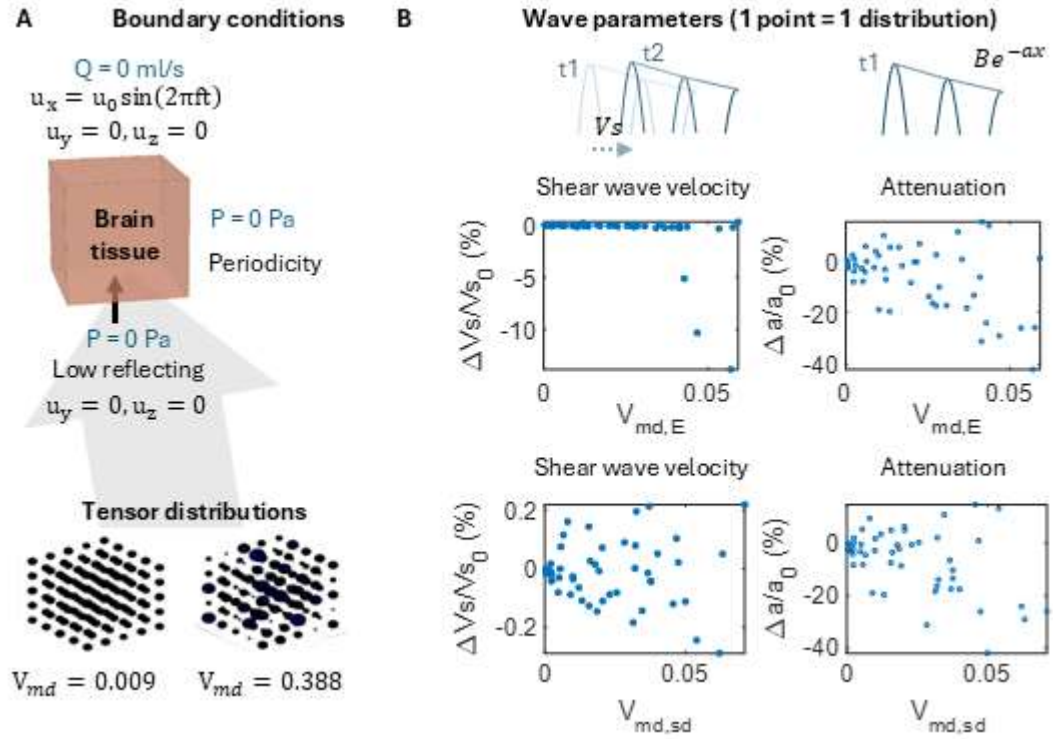
Results

Figure (Panel **B**) shows the relation between the variance in tensor size calculated across different distributions (with constant mean size) of the Young's modulus ($V_{md,E}$) and solid density ($V_{md,sd}$), and the wave characteristics shear wave velocity (Vs) and attenuation (a). The results show that changing $V_{md,E}$ or $V_{md,sd}$ can alter the attenuation coefficient by up to 50 %. Meanwhile, the shear wave velocity shows minor variations, except for a few outliers at higher $V_{md,E}$.

Discussion

Our results indicate that shear wave attenuation can differ significantly between voxels with the same mean Young's modulus and solid density, depending on the sub-voxel material parameter distribution. We hypothesize that this variation in sub-voxel distributions reflects the underlying variation in microstructure, which might be overlooked when assessing properties in MRE at voxel scale only. This motivates including measures that describe sub-voxel microstructure, such as MD-dMRI parameters.

Images (Optional)



References (Optional)

[1] Murphy et al., NeuroImage: Clinical, 2016.

[2] Westin et al., NeuroImage, 2016.

Acknowledgements (Optional)

We thank Digital Futures and MedTechLabs for providing financial support to this project.

Session Category

Organ and Tissue Biomechanics: N/A

P3-187

A Testing Platform to Study the Deformation Mechanism of Epithelia

Miss Sristi Gurung, Professor Yuan Lin

The University of Hong Kong, Hong Kong, N/A, Hong Kong

Introduction

Epithelia are sheets of cells lining the surface of many organs. They act as protective barriers and carry out numerous physiological functions such as absorption, secretion, transport and more. Studies have shown that disruptions in epithelia mechanics are often linked to diseases such as cancer. However, understanding of epithelia mechanics remain limited due to lack of proper equipment at tissue level. To combat this, we have developed a testing platform to measure the mechanical properties of epithelia through the deformation of epithelial cell monolayer which are the simplest form of tissue.

Methods

Polydimethylsiloxane (PDMS) microfluidic chip was fabricated with a designated inlet and outlet. A thin collagen scaffold was prepared at the outlet, on top of which Madin-Darby Canine Kidney (MDCK) cells were cultured until confluency. Collagenase was then used to digest the collagen scaffold such that the epithelial cell monolayer was freely suspended in air. The monolayer was then stained with Calcein AM for fluorescent and confocal microscope imaging. Desired pressure was input into the chip through the inlet and time-lapse images and videos were recorded during monolayer deformation. The data were then analyzed to get mechanical quantifications of the monolayer deformation against time.

Results

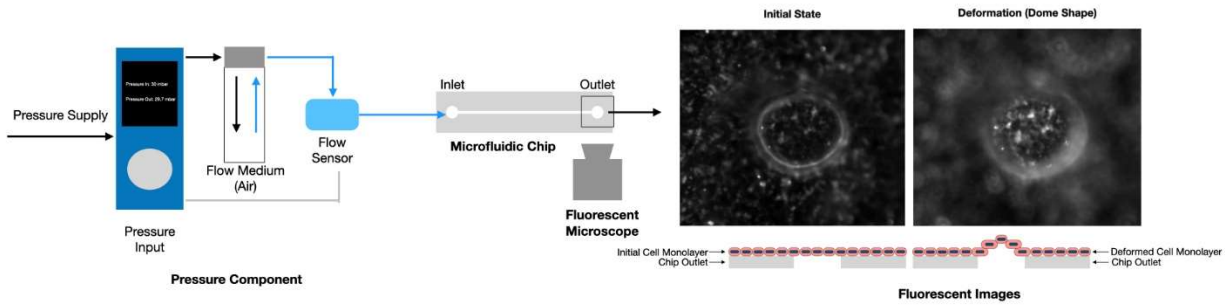
A blister test was conducted on the freely suspended epithelial monolayer using the testing platform. During deformation, fracture occurred either through delamination or by rupture in the monolayer. Delamination occurred when cell-substrate adhesion was weak and air escaped through the cell-substrate interface. On the other hand, rupture occurred when cell-cell adhesion was weaker than the cell-substrate adhesion. It was also recorded that an average of 53.8 mbar was needed to delaminate the cell monolayer from its substrate.

Discussion

It was observed that deformation of cell monolayers resulted in different types of fracture. This proved that monolayer response was directed by the adhesion energy difference at

cell-substrate and cell-cell level. Our testing platform allowed direct measurements of epithelial cell monolayer to study the deformation mechanisms of epithelia in a precisely controlled manner. By studying the mechanics of epithelial cell monolayer, we hope to bridge the gap between epithelia mechanics and disease mechanisms for better therapies in the future.

Images (Optional)



Session Category

Organ and Tissue Biomechanics: N/A

P3-188

The Biomechanical Role of the Meniscus in Distributing Load and Providing Stability

Mr Sufyan Dalal, Dr Roberto L Diaz, Dr Marlène Mengoni, Dr Alison Jones, Professor Ruth Wilcox

University of Leeds, Leeds, West Yorkshire, United Kingdom

Introduction

The menisci play an important role in knee biomechanics, with both meniscus extrusion and meniscectomy linked to the accelerated progression of osteoarthritis. There are emerging techniques to repair or replace menisci, but limited methods are available to compare their performance. The aim of this study was to develop an *in-vitro* testing method to evaluate the biomechanical role of the menisci in distributing load and providing stability across a range of flexion angles.

Methods

Testing was conducted using porcine knee specimens (N = 3). The natural knee position was secured using a brace before the removal of all surrounding tissue and ligaments. The specimens were then potted using a custom rig which was also used to align the centre of rotation.

A series of static tests were conducted with the meniscus intact and then removed using a six degree-of-freedom knee simulator. Loads of up to 1000 N were applied at different flexion angles (0°, 15°, 30°, 45°, 60° and 90°). The AP displacement was held and the reaction force measured whilst pressure sensors were placed below the menisci to map the contact pressure distribution.

Results

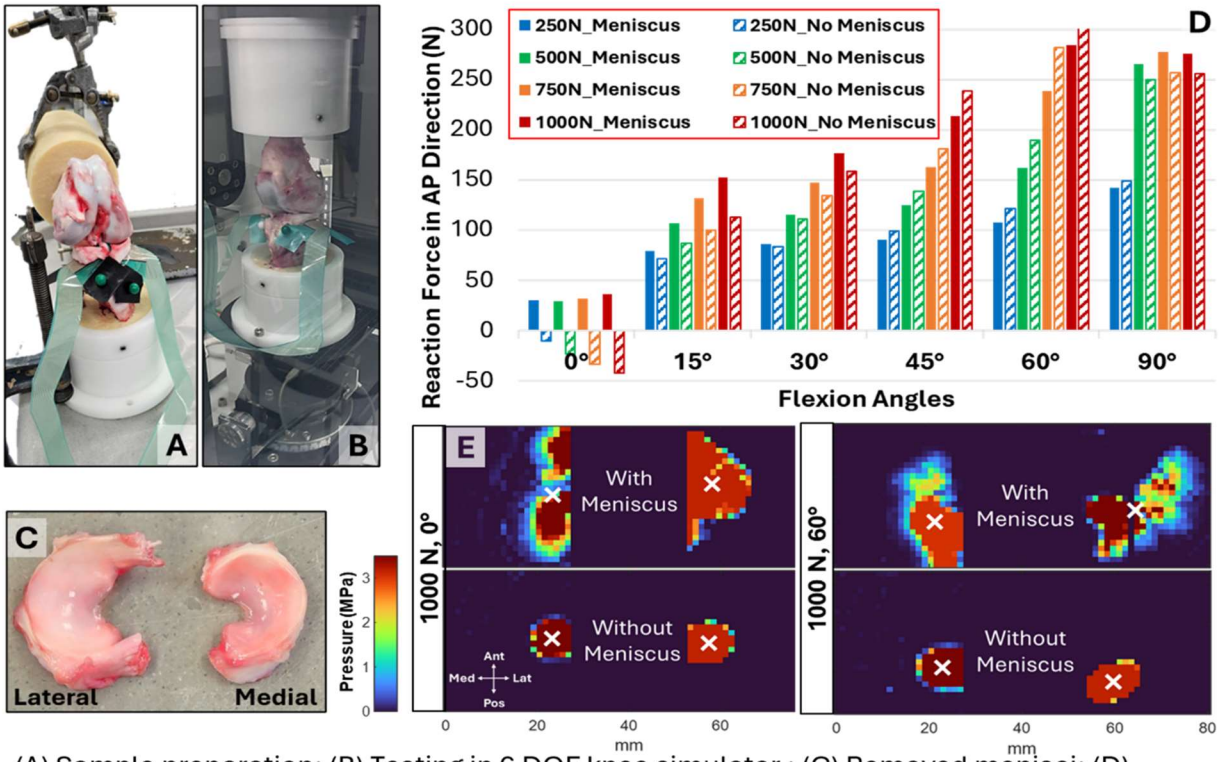
A reduction in contact area of up to 70% was identified after the removal of the meniscus. Pressure in the medial compartment of the knee increased after meniscus removal while there was little change in the lateral compartment. There were also differences in the AP reaction force between the intact and removed meniscus cases that were more marked at lower flexion angles.

Discussion

The results demonstrate the menisci's role in load distribution by increasing contact area and decreasing pressure, as well as a smaller role in providing stability particularly at

smaller flexion angles. The methods developed can be extended to assess other loading scenarios and evaluate different meniscus repair strategies

Images (Optional)



(A) Sample preparation; (B) Testing in 6 DOF knee simulator ; (C) Removed menisci; (D) Anterior posterior reaction forces; (E) Knee contact pressure maps

Session Category

Organ and Tissue Biomechanics: N/A

P3-189

Classification of Healthy Placenta, Placenta Previa and Placenta Accreta Spectrum Using Machine Learning and Texture and Shape Features Extracted From Placental MRI.

Miss Suzie Coldman MSc[1,2], Mr Guanglong Zhou MSc[1,2], Mr Dengjiang Wu MSc[1,2], Dr Lingzhong Guo PhD[1,2], Dr Elspeth Whitby MBChB(hons) PhD[3], Dr Xinshan Li PhD[1,2]

[1]University of Sheffield, Sheffield, South Yorkshire, United Kingdom. [2]Insigneo Institute, Sheffield, South Yorkshire, United Kingdom. [3]Sheffield Teaching Hospitals NHS Foundation Trust, Sheffield, South Yorkshire, United Kingdom

Introduction

Abnormalities such as placenta accreta spectrum (PAS) and placenta previa (PP) are diagnosed using MRI. However, clinically only 30-66% of PAS pregnancies are identified before birth [1-3], due to limited resources and expert radiologists. The aim of this study was to determine if texture and shape features derived from placental MRIs could be used to classify healthy placenta, PAS and PP using machine learning.

Methods

48 healthy (33 pregnancies), 41 PAS (40 pregnancies) and 35 PP (35 pregnancies) MRIs were obtained by Sheffield Teaching Hospital (Siemens 1.5T, sagittal T2 HASTE). Using PyRadiomics 2525 texture and shape features were extracted from each MRI.

Training-test split was 80-20. The training set was used for feature selection, which involved intraclass correlation coefficient, zero-variance and variance inflation factor filters and lasso logistic regression (10-fold cross-validation and 750 bootstraps).

Four algorithms were trained on the selected features with 15-fold cross-validation: Logistic Regression (LR), Support Vector Machine (SVM), Random Forest (RF), Gradient Boosting (GB). Binomial (healthy and PP vs PAS) and multinomial (healthy vs PP vs PAS) classification were investigated with 3 repeats.

Results

LR and RF achieved the highest accuracy for multinomial and binomial classifications respectively (Table 1). Computational time was lowest for LR and SVM (minutes) and highest for RF and GB (hours/days). Across all four algorithms, multinomial classification

exhibited lower accuracy than binomial classification. In multinomial classification, the PP group displayed the lowest precision and sensitivity.

Discussion

MRI texture and shape features can be successfully used to classify healthy versus abnormal placenta, achieving an accuracy of 0.85 for binomial classification using LR, which required less than 5 minutes to run. In the multinomial case, PP was the most challenging group to classify. Clinically, PP is diagnosed by measuring the distance of the placenta to the os on MRI; this metric could be added to improve classification outcome. Future work will also involve comparing the classification ability of MRI indications and clinical factors such as maternal age and the number of previous c-sections, to texture and shape features.

Images (Optional)

Table 1: Evaluation Metrics for the four machine learning classification algorithms, including the mean (± standard deviation) accuracy, precision and sensitivity for binomial (healthy and PP vs PAS) and multinomial (healthy vs PAS vs PP) classification. LR = Logistic Regression, SVM = Support Vector Machine, RF = Random Forest, GB = Gradient Boosting.

	Accuracy		Precision		Sensitivity	
	Binomial	Multinomial	Binomial	Multinomial	Binomial	Multinomial
LR	0.81±0.02	**0.75±0.02**	0.83±0.03	0.74±0.05	0.81±0.02	**0.75±0.02**
SVM	0.84±0.06	0.71±0.02	0.82±0.05	0.70±0.02	0.81±0.05	0.71±0.02
RF	**0.85±0.04**	0.67±0.05	**0.86±0.04**	0.63±0.12	**0.85±0.04**	0.64±0.08
GB	0.85±0.05	0.75±0.08	0.86±0.05	**0.78±0.11**	0.85±0.05	0.75±0.08

References (Optional)

1. McCall et al., BJOG, 2022.
2. Fitzpatrick et al., BJOG, 2014.
3. Thurn et al., BJOG, 2016.

Session Category

Organ and Tissue Biomechanics: N/A

P3-190

Crystal Interface Mechanics Control the Strength and Resilience of Cold-Water Coral Skeletons

Dr Nikolai Kvashin[1], Dr Ali Ozel[2], Dr Marta Peña Fernández[2], Dr Senthil Thangadurai[1], Prof. Dr. Uwe Wolfram[1]

[1]Clausthal University of Technology, Clausthal-Zellerfeld, Lower-Saxony, Germany. [2]Heriot-Watt University, Edinburgh, Scotland, United Kingdom

Introduction

Biomineralized tissues exhibit exceptional mechanical properties due to complex material architectures [1,2]. For example, cold-water corals utilise strong aragonite crystals (4-6 GPa) to build their skeleton. Micromechanical experiments, however, show that the bulk skeletal tissue fails at ~462 MPa [1,3]. Understanding this mechanical scale transition is important for developing advanced bio-inspired materials and for predicting how these organisms will fare in climate change-affected oceans [1,4]. We aimed at investigating this scale transition and we hypothesised that it is controlled by the interface mechanics.

Methods

We performed molecular dynamics simulations to explore the mechanical response of crystal interfaces [3], contrasted by experimental results [1]. We performed tensile and shear tests on three limiting interface types: (i) dry aragonite twin boundaries, (ii) hydrated interfaces containing biomineralisation proteins which we confirmed through Raman spectroscopy, and (iii) interfaces separated by water layers of varying thickness. We analyse stiffness, strength, and failure mechanisms of each interface type.

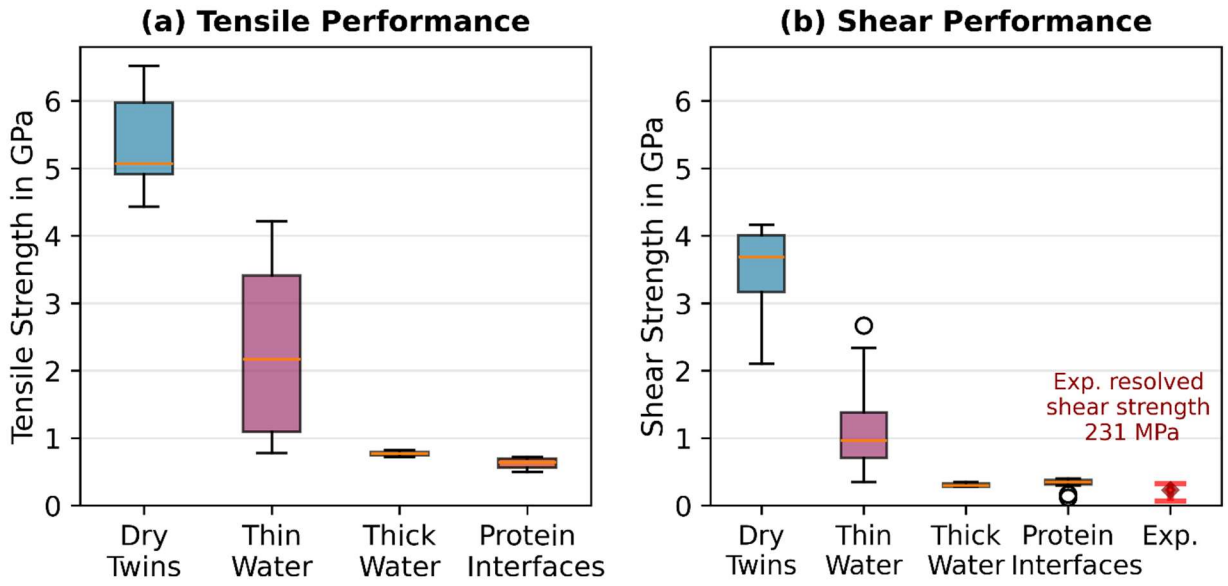
Results

Simulations revealed an interface strength hierarchy (Fig. 1). Dry twin boundaries are strong (~6.5 GPa). Hydrated protein-mediated interfaces are significantly weaker (0.3-0.8 GPa), but exhibit damage tolerance through progressive reorganisation of water-mediated hydrogen bonds. Strength of pure water interfaces is thickness-dependent (>3 GPa for thin (<5 Å) and ~0.8 GPa for thick (>10 Å) layers). Experimental strength (~462 MPa [1]) is consistent with simulated shear strength of protein interfaces (~300 MPa). Resolved shear stress analyses links interface shear strength to ~600 MPa predicted compressive strength, confirming that failure is governed by interface decohesion.

Discussion

Cold-water coral skeletal tissue strength is controlled by decohesion of hydrated organic interfaces. These interfaces define bulk strength and may provide mechanisms for toughness and damage tolerance. We provide the first quantitative data on the mechanics of these interfaces, offering an explanation for the remarkable strength of the bulk tissue (10x that of concrete) [1]. Our findings may inform prediction of coral viability in climate change-affected oceans and development of advanced bio-inspired materials.

Images (Optional)



References (Optional)

[1] Wolfram et al., Sci Rep, https://doi.org/10.1038/s41598-022-11266-w, 2022.

[2] Cohen et al., Geoch Geoph Geos, https://doi.org/10.1029/2009GC002411, 2009.

[3] Kvashin et al., bioRxiv, https://doi.org/10.1101/2025.10.29.685320, 2025.

[4] Barnhill et al., Nat. Clim. Chang., https://doi.org/10.1038/s41558-022-01565-5, 2023.

Acknowledgements (Optional)

The project was supported by Leverhulme Trust (RPG-2020-215) and Deutsche Forschungsgemeinschaft (DFG WO 1543/2-1)

Session Category

Organ and Tissue Biomechanics: N/A

P3-191

A Personalized In Silico Model of Brain Metastasis Development and Response to Radiation Treatment

Dr Eleftherios Ioannou[1], Mr Christos Panagiotis Papanikas[1], Dr Dimitra Flouri[1], Dr Loizos Siakallis[1,2], Dr Elisavet Papageorgiou[3], Dr Marilena Theodorou[3], Dr Vasileios Vavourakis[1,2]

[1]University of Cyprus, Nicosia, Nicosia, Cyprus. [2]University College London, London, London, United Kingdom. [3]Bank of Cyprus Oncology Centre, Nicosia, Nicosia, Cyprus

Introduction

Brain metastases (BMs), secondary brain tumours, affect an estimated 20% of cancer patients [1]. Current treatment typically involves surgery, radiation therapy or/and combined with systemic therapy. They can offer improved survival and reduced patient morbidity, while avoiding whole-brain radiotherapy, which causes cognitive impairment [2]. However, predicting patient response to treatment on an individual basis remains elusive, due to the lack of reliable digital tools for clinical decision-making for patients diagnosed with BMs.

Methods

We present an organ-scale *in silico* model that simulates the dynamics of BM in response to stereotactic radiotherapy (SRT) by incorporating key biological processes: the dynamics of the tumour enhancing region, necrosis and oedema. The model is formulated as a system of partial differential equations, discretised using finite elements, representing the spatiotemporal dynamics of each component and their interactions. It also integrates patient-specific data, i.e., the brain geometry (from MRIs), SRT dose distribution and tumour/necrosis/oedema region, to provide a personalised framework for predicting BM progression and treatment efficacy.

Results

The *in silico* model is applied to a recently published set of 40 BM patients [3]. It is calibrated based on the actual regions of tumour/necrosis/oedema derived from two to five time points per patient. Results demonstrate the model's capability to replicate the spatiotemporal evolution of metastatic brain tumours, including tumour growth, necrosis and oedema development. Further, a data assimilation technique was applied to predict tumour evolution using input from only one or two initial follow-ups and was able to predict tumour evolution in the remaining follow-ups for most cases.

Discussion

We demonstrate the ability of the proposed *in silico* model to predict BM progression and SRT outcome. By incorporating patient data, the model provides a personalised *in silico* framework that encompasses tumour heterogeneity and individual anatomical differences. The capability of data assimilation technique shows great potential for clinical application. Generating accurate predictions of BM evolution utilizing follow-up evidence after treatment can inform clinical decision-making, providing an early indication of SRT outcome trajectory.

Images (Optional)

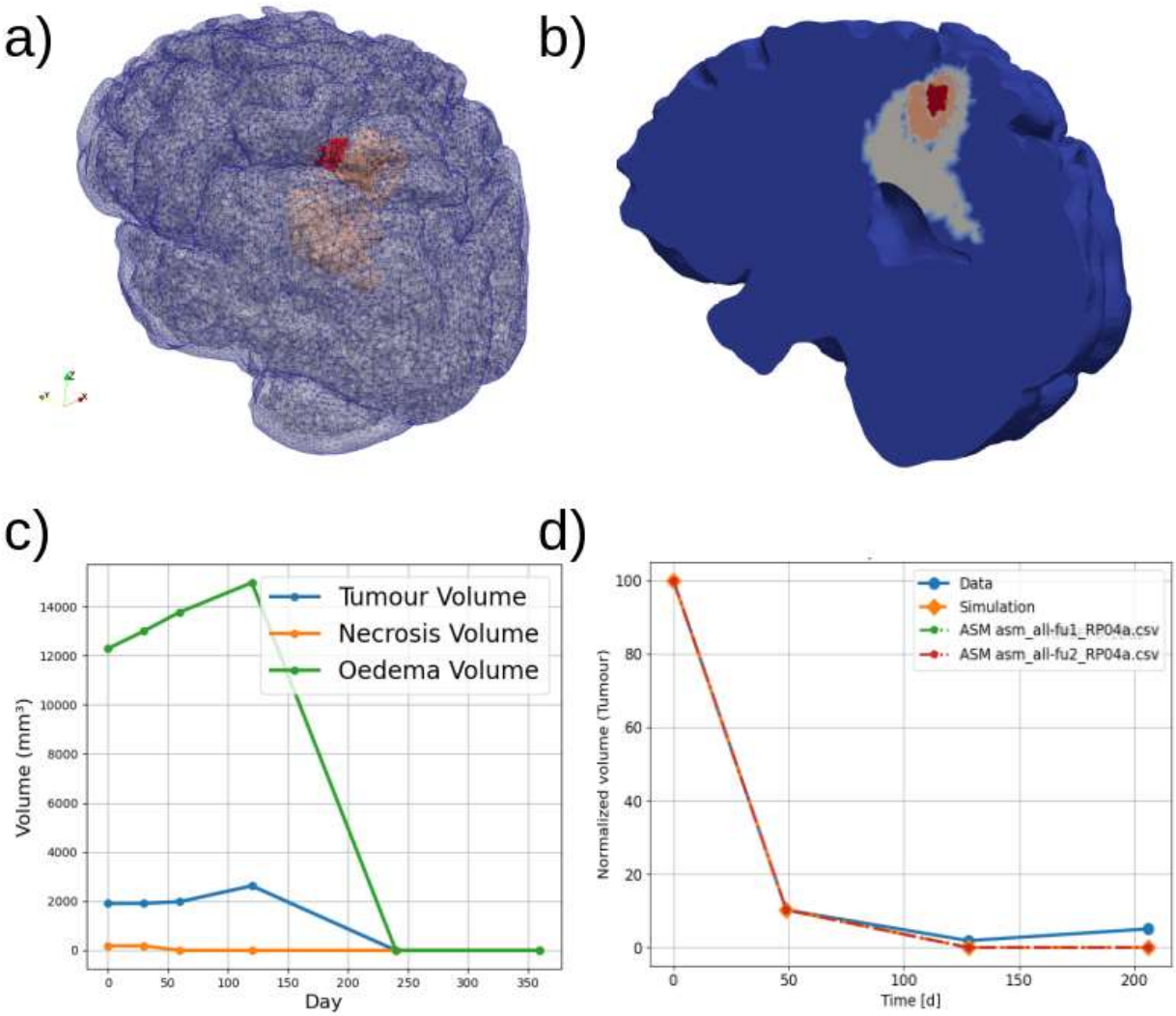


Figure 1: a) The mesh of the extracted brain geometry, highlighting the tumour region (red) and oedema (orange) b) Slice through the tumour region illustrating the initial necrosis (red), tumour (orange) and oedema regions. c) The evolution of the three regions of interest overtime which show regression due to the RT treatment. d) The evolution of tumour predicted by the model using the assimilation technique which considers only one or two of the initial follow-ups.

References (Optional)

[1] Achrol et al., Nat Rev Dis Primers, 2019

[2] Kuntz et al., Radiation Oncol, 2023

[3] Flouri et al., Sci Data, 2025

Acknowledgements (Optional)

The authors thank Dr Haralampos Hatzikirou for his guidance in the development of the *in silico* model. This work was financially supported by the Cyprus Cancer Research Institute (Project acronym: PROTEAS; Grant ID: CCRI_2021_FA_LE_105).

Session Category

Organ and Tissue Biomechanics: N/A

P3-192

Biomechanical Fatigue Analysis of Vertebral Endplates Under Four-Point Bending

Mrs Verushca Gasiorowski[1,2], Dr William Curry[2,3], Dr Brian Stemper[1,2,3]

[1]Department of Biomedical Engineering - Medical College of Wisconsin, Milwaukee, WI, United States. [2]Neuroscience and Biomechanics Research Laboratories - Zablocki VA Medical Center, Milwaukee, WI, United States. [3]Department of Neurosurgery - Medical College of Wisconsin, Milwaukee, WI, United States

Introduction

Occupations like truck drivers [1], tractor drivers [2] and helicopter pilots [3] subject individuals to whole-body vibration (WBV) due to long-duration, repetitive loading at higher-than-normal frequencies [4] (5 Hz or higher). The spine provides structural support to the body during WBV. While the fatigue response of the intervertebral disc has been well-studied [5, 6] , vertebral endplate has received less attention despite its integral role in resisting compressive loads[7, 8]. This study explored endplate fatigue-life behavior to better understand chronic injury mechanisms and determine occupational exposure limits.

Methods

Porcine cervical endplate specimens (approximately 30 mm × 10 mm × 1.5 mm) were tested in 4-point bending at 5 Hz until failure. Fatigue curves and stiffness were analyzed in MATLAB, using the force-displacement data, and RStudio for statistical analysis.

Results

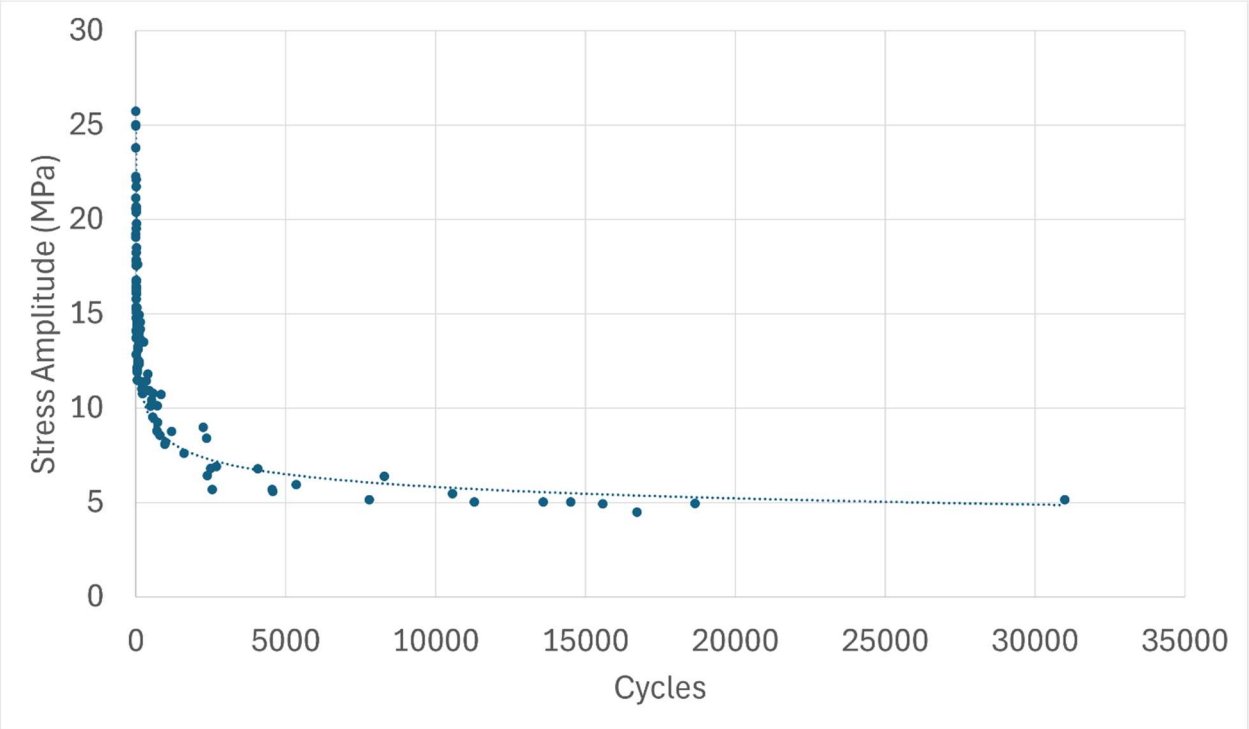
The figure shows the fatigue life curve of 115 tests (R^2= 0.90), identifying high-cycle (HCF) (n = 33, R^2 = 0.86) and low-cycle (LCF) (n = 82, R^2 = 0.77), which are separated when loading typically exceeds the yield point (41.02MPa), which was determined from previous failure testing we conducted. HCF stiffness showed an average drop of 23.97% (SD = 12.69%) from baseline to terminal stiffness. In the infinite-life region, the specimen did not break at a stress amplitude of 4.89 MPa or less, and the average stiffness drop between baseline and end-of-test stiffness was -0.49% (SD = 3.43%), which was significantly ($p<0.05$) different from HCF.

Discussion

A first-of-its-kind fatigue-life curve for endplates has been established. The stiffness of infinite-life showed minimal change across loading cycles and did not fail under >30,000 loading cycles. These findings can inform seat design criteria to limit stress, ensuring the

subject is in the HCF or infinite-life region, thereby preventing endplate fractures and the likelihood of disk degeneration and severe back pain.

Images (Optional)



References (Optional)

[1] M. Miyamoto et al.,JNMS, 2000

[2] M. Bovenzi et al., *Appl Ergon,* 1994

[3] P. M. Bongers et al., Ergonomics,1990

[4] C. G. De Oliveira et al., *ASEM*, 2005

[5] N. Yoganandan et al., JMBBM, 2017

[6] S. Umale et al., *ASJ*, 2018

[7] J. P. Grant et al.,*Spine*, 2001

[8] U. Zehra et al.,*Spine,1976*

Acknowledgements (Optional)

This research was supported through Office of Naval Research contract MTEC 18-04-I-PREDICT (W81XWH1590001): Incapacitation Prediction for Readiness in Expeditionary

Domains: an Integrated Computational Tool (I-PREDICT). Support was also provided by the Department of Veterans Affairs Medical Research.

Session Category

Organ and Tissue Biomechanics: N/A

P3-193

In Vivo Assessment of Corneal Mechanical Properties After Corneal Collagen Cross-linking Surgery Based on Optical Coherence Elastography

Dr. Yuqi Liu[1], Prof. Haixia Zhang[1], Prof. Xiuqing Qian[1], Prof. Guoyang Li[2]

[1]Capital Medical University, Beijing, Beijing, China. [2]Peking University, Beijing, Beijing, China

Introduction

Corneal cross-linking (CXL) enhances corneal biomechanical properties, but quantitative and spatially resolved assessment methods remain limited. Optical coherence elastography (OCE) enables non-invasive measurement of localized corneal elasticity, providing an assessment tool for evaluating biomechanical changes following corneal cross-linking. This study aims to validate the feasibility of OCE technology in assessing corneal mechanical properties following corneal cross-linking surgery and to explore its capability in resolving localized mechanical inhomogeneities.

Methods

A homogeneous silicone corneal model was fabricated to verify the accuracy and repeatability of the OCE system, and a centrally softened heterogeneous silicone corneal model was fabricated to evaluate the system's ability to distinguish localized elasticity variations. Six rabbit corneas underwent half-CXL to establish a model of region-specific biomechanical enhancement, followed by in vivo OCE measurements two weeks postoperatively. Elastic wave propagation velocities were reconstructed using the phase-gradient method to generate spatial maps of corneal elastic modulus. After completion of the in vivo experiments, corneal tissues were immediately harvested, embedded, and processed into cryosections, followed by indentation testing to validate the results obtained from OCE.

Results

In the homogeneous silicone corneal model, the OCE-fitted modulus showed a highly linear correlation with the tensile modulus ($r = 0.998$, $P = 0.002$), described by the relationship $E_{OCE} = 2.11E_{tensile} - 0.07$, confirming the reliability of OCE in characterizing material mechanical properties. In the centrally softened heterogeneous silicone model, the wave speed in the softened region was markedly lower than in the surrounding area, and the modulus ratio matched the tensile testing results, demonstrating that OCE can

accurately resolve localized mechanical heterogeneity. In the half-CXL animal model, OCE clearly delineated the boundary between the half-CXL and non-CXL regions, and the reconstructed modulus maps visually revealed localized biomechanical enhancement. Indentation testing performed on corneal cryosections exhibited strong agreement with OCE measurements, further validating the reliability of OCE for assessing localized corneal elasticity changes in vivo.

Discussion

This study demonstrates that OCE technology reliably reveals variations in local elastic modulus, providing technical support for personalized CXL assessment. Given differences between rabbit and human corneas, subsequent research will further validate the stability and clinical applicability of OCE technology in human subjects.

Session Category

Organ and Tissue Biomechanics: N/A

P3-194

Relationship Between the Structural and Mechanical Properties of the Semitendinosus Intermediate Aponeurosis: Implications for Hamstring Strain Injuries

Dr. Xiyao Shan[1,2], Mr. Masato Saito[2], Dr. Kanae Umemoto[2], Mr. Hiroki Kajiura[2], Dr. Shun Otsuka[2], Prof. Xiang Fan[1], Prof. Munekazu Naito[2]

[1]Department of Physical Education, Shanghai Jiao Tong University, Shanghai, Shanghai, China. [2]Department of Anatomy, School of Medicine, Aichi Medical University, Nagakute, Aichi, Japan

Introduction

The semitendinosus muscle (ST) in the hamstrings is the most frequently injured muscle in jumping sports. Within the ST, the intermediate aponeurosis located slightly proximal to the muscle belly has been identified as a potential risk factor for strain injuries. However, how its structure relates to the mechanical properties remains unclear. In this study, we conducted tensile tests on the ST specimens containing the intermediate aponeurosis to investigate the relationship between its morphological and mechanical properties.

Methods

ST specimens were obtained from twenty legs of ten human cadavers (5 males and 5 females, age: 86.6±8.4 years) donated to Aichi Medical University. First, the ratio of ST aponeurosis area (aponeurosis area/total muscle and aponeurosis area) and running angle were measured. Then, tensile tests until rupture were performed, and yield strength (YS), ultimate tensile strength (UTS), and necking point (NP) were determined from the strain-stress curves. Lastly, Pearson's correlation was used to analyze the correlations between the structural and mechanical properties of the ST intermediate aponeurosis.

Results

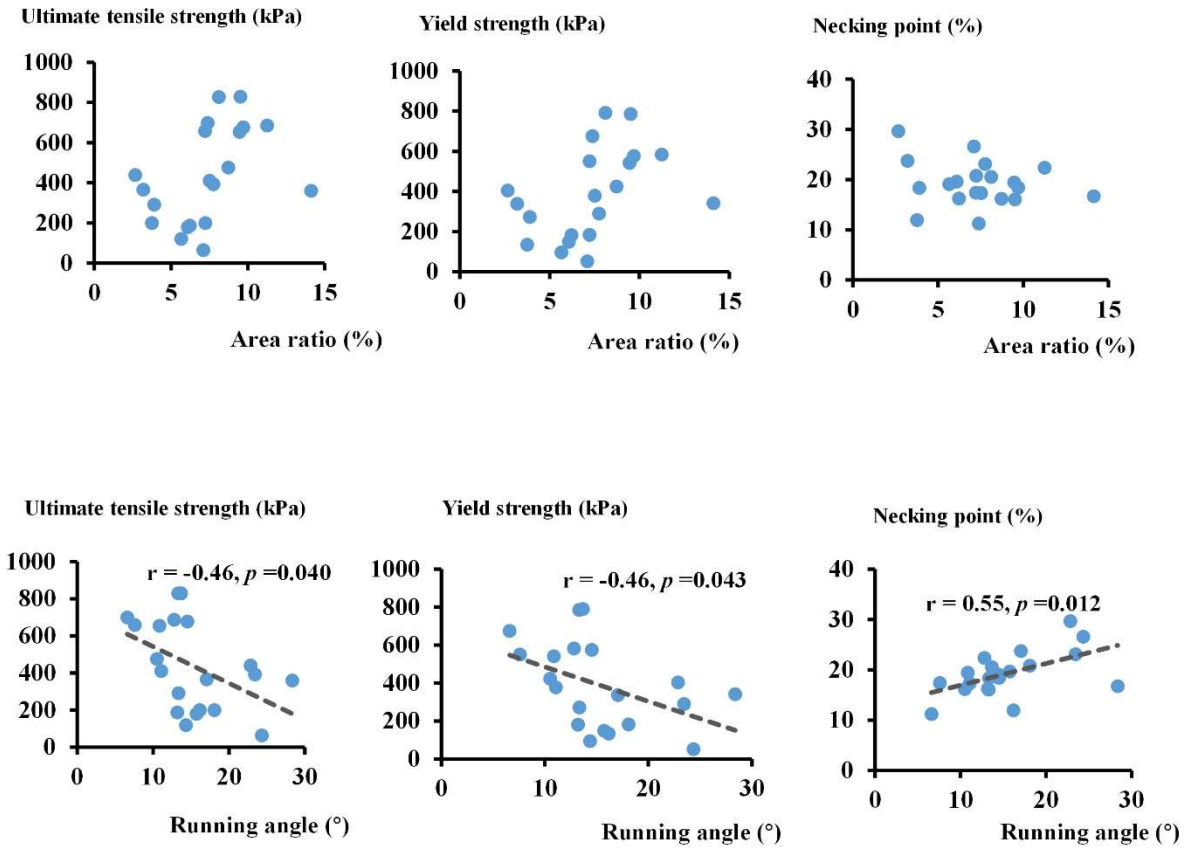
No significant correlations were found between the ratio of ST aponeurosis area and YS, UTS, or NP. There was a negative correlation between the running angle and YS and UTS, respectively (YS, $r = -0.46$, $p<0.05$; UTS, $r = -0.46$, $p<0.05$), whereas a positive correlation was found between the running angle and NP (NP, $r = 0.55$, $p<0.05$).

Discussion

A positive correlation was found between the running angle and NP, while a negative correlation was found between the running angle and YS and UTS. The mechanical

behavior of the ST would be influenced by the running angle of its intermediate aponeurosis. A larger running angle of the aponeurosis may contribute greater tissue extensibility prior to failure at the expense of reduced strength. Consequently, the running angle may be an important morphological factor influencing athletic susceptibility to ST strain injuries.

Images (Optional)



Session Category

Organ and Tissue Biomechanics: N/A

P3-195

Direct Fiber Modeling of Lamina Cribrosa Beams Predicts Experimentally-Observed Behavior Better Than Continuum Models

Ms. Yingzhe Han, Dr. Xuehuan He, Mr. Qi Tian, Dr. Ian A. Sigal

University of Pittsburgh, Pittsburgh, PA, United States

Introduction

Collagen fibers are the primary load-bearing component of the lamina cribrosa (LC) beams in the back of the eye [1]. Nevertheless, most modeling efforts use continuum (CC) descriptions that do not account for potentially crucial fiber-level interactions or long-range load transmission, and often assume incompressibility. Direct fiber (DF) models have reproduced the mechanics of other eye fibrous tissues, including sclera [2]. We hypothesize that LC beam mechanics will be better predicted when their fiber architecture is explicitly represented. We test this hypothesis by comparing how DF and CC models of LC regions replicate experimental observations.

Methods

Sheep LC specimens were stretched biaxially while imaged with instant polarized light (IPOL) microscopy, and image registration provided in-plane displacements. Two LC regions of interest were selected, and about 10 beams were segmented in each. For each region we built (i) DF models in which discrete fibers followed local orientations and were interconnected by uniformly distributed crosslinks with prescribed densities, and (ii) a CC model using a Holzapfel-Gasser-Ogden (HGO) formulation with fiber orientation and dispersion mapped from the same data [3]. IPOL-measured displacements were applied as boundary conditions. Beam width, length, Poisson's ratio, tortuosity, and waviness were quantified across loading steps, and representative results from one region are shown.

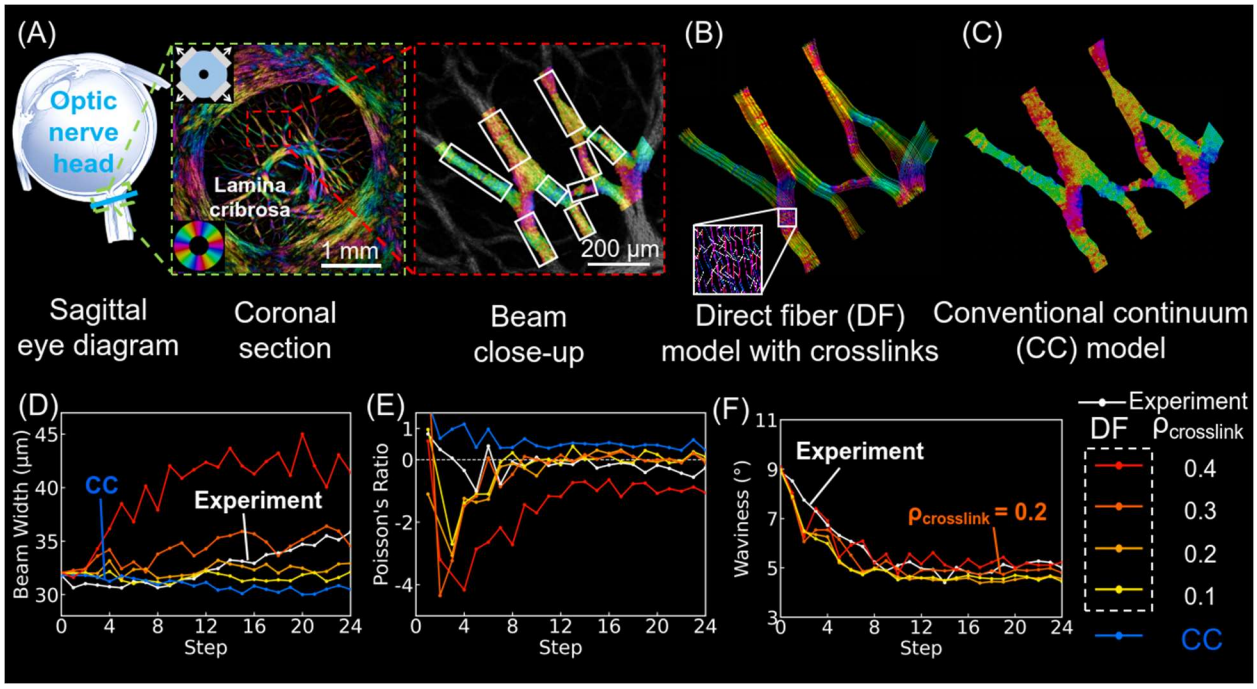
Results

The CC model predicted narrowing of LC beams and consistently positive Poisson's ratios. DF models predicted widening and negative or near-zero Poisson's ratios, matching experimental trends more closely. Crosslink density altered DF behavior: lower densities produced greater waviness and larger beam widths, and across all metrics, increasing crosslink density moved DF predictions progressively closer to the continuum-like behavior observed in the CC model.

Discussion

Our results suggest that LC beam-level behaviors are better captured when fiber architecture is explicitly represented. The CC model's beam narrowing and positive Poisson's ratios highlight limitations of a continuum description, whereas DF models reproduced observed trends. Crosslink density influenced inter-fiber coupling: low densities allowed larger width and waviness changes, whereas higher densities yielded a stiffer, less widening response.

Images (Optional)



References (Optional)

[1] Lee PY et al., Acta Biomater, 2024

[2] He XH et al., Acta Biomater, 2024

[3] Voorhees AP et al., Acta Biomater, 2017

Acknowledgements (Optional)

NIH R01-EY023966, R01-EY031708, P30-EY008098 and T32-EY017271 (Bethesda, MD), Research to Prevent Blindness (unrestricted grant to UPMC ophthalmology, and Stein innovation award to Sigal IA), BrightFocus Foundation

Session Category

Organ and Tissue Biomechanics: N/A

P3-196

A Framework for Predicting Lamina Cribrosa Blood Flow and Oxygenation From Localized Vasculature Imaging

Dr Yuankai Lu, Ms Ashley Linton, Dr Ian Sigal

University of Pittsburgh, Pittsburgh, PA, United States

Introduction

Despite its importance in the physiology and pathology of the eye, direct measurement of blood flow and oxygenation in the lamina cribrosa (LC) remains extremely challenging. Recent advances, such as adaptive-optics OCT angiography, enable some visualization but remain limited to small fields of view, resulting in patchy, incomplete vasculature. Methods that can infer physiology from such small, incomplete data are needed. We present a framework for predicting hemodynamics and oxygenation in a small, incomplete LC region. The framework is based on embedding the experimental data into a standardized whole-LC vascular model developed from detailed reconstructions of the complete LC vasculature, blood flow, and oxygenation.

Methods

Detailed 3D LC vascular networks from monkey eyes were reconstructed using histological imaging [1], and then combined to create a standardized vascular template representing typical LC geometry and boundary conditions. To predict flow and oxygenation in a localized region, its vessel network was aligned and embedded at the corresponding anatomical location within the template. Free ends were connected to nearby template network branches to provide physiological inlet and outlet conditions. Hemodynamic and oxygenation simulations were then performed [2], yielding predicted flow and oxygenation for the original localized region. For validation, small vascular patches were extracted from a fully reconstructed LC with existing ground-truth hemodynamics and oxygenation. Each patch was embedded and simulated using the same procedure, and the predictions were compared with ground truth to quantify accuracy.

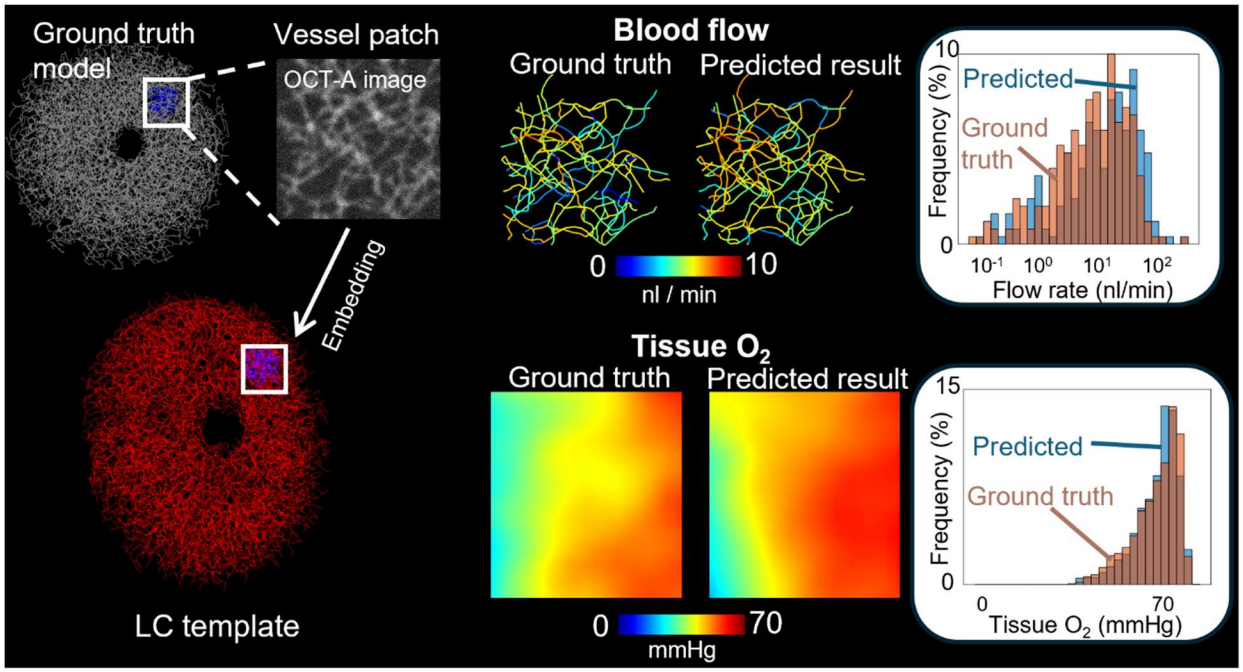
Results

Across four test cases, the predicted oxygenation and hemodynamic fields showed strong agreement with ground truth. In the illustrated figure, both spatial patterns and histogram distributions matched the reference data. The mean oxygenation difference was 2.11 mmHg, and the mean flow difference was 0.47 nl/min.

Discussion

We present an embedding-based modeling approach that predicts blood flow and oxygenation from localized LC vasculature. The prediction matched the ground truth in validation tests. Future work will incorporate additional information, such as OCTA-derived flow metrics, to improve accuracy. This framework enables the physiological interpretation of small-field in-vivo data and extends localized measurements to whole-LC hemodynamic insights.

Images (Optional)



References (Optional)

[1] Po-Yi Lee *et al.*, J Biomechanics, 2022

[2] Yuankai Lu *et al.*, IOVS, 2024

Acknowledgements (Optional)

NIH R01-EY023966, R01-EY031708, P30-EY008098 and T32-EY017271 (Bethesda, MD), Research to Prevent Blindness (unrestricted grant to UPMC ophthalmology, and Stein innovation award to Sigal IA), BrightFocus Foundation

Session Category

Organ and Tissue Biomechanics: N/A

P3-197

3D Matrix Confinement Induces Partial Epithelial-Mesenchymal Transition and Increases Chemoresistance

Mr. Yuta Iijima[1], Ph.D. Gen Hayase[2], Prof. Daisuke Yoshino[1]

[1]Tokyo University of Agriculture and Technology, Koganei, Tokyo, Japan. [2]National Institute for Materials Science, Tsukuba, Ibaraki, Japan

Introduction

Metastasis is a leading cause of cancer-related death, yet the process by which tumor cells leave their original environment is not fully understood. Cancer cells must adapt to various microenvironmental changes to survive. Epithelial-mesenchymal transition(EMT) plays a crucial role in breast cancer development by enabling cells to acquire migratory and invasive traits. EMT has also been strongly associated with the development of chemoresistance. In this study, we used a 3D spheroid model developed in our previous research [1, 2] to track changes in the morphology and protein expression of breast cancer cells as they escaped from the spheroid. We also analyzed whether escaped cells acquired resistance to anticancer drugs.

Methods

MDA-MB-231 spheroids were generated on a superhydrophobic substrate and cultured for five days. The cells that migrated outward were harvested, reseeded, and compared with conventional 2D controls. We analyzed their morphology and pseudopodia dynamics using phase-contrast and F-actin imaging. Immunoblotting was used to quantify EMT-associated markers and invasion-related enzymes. Doxorubicin-induced cytotoxicity assays were performed to evaluate chemoresistance.

Results

Escape from the spheroids led to significant cellular miniaturization and robust formation of lamellipodia- and filopodia-like protrusions. These changes were accompanied by strong upregulation of α-SMA, Snail, and N-cadherin, though ZO-1 remained essentially unchanged, indicating a transition toward partial EMT. Escaped and reseeded cells exhibited significantly elevated MMP-3 expression, whereas MMP-9 expression showed only modest variation. Both escaped and reseeded populations displayed pronounced resistance to doxorubicin, and this phenotype persisted even after cells were replated in 2D (Fig.1). This implies that confinement has a lasting effect.

Discussion

Physical confinement within a 3D matrix and subsequent release induced a cohesive set of changes involving partial EMT, cytoskeletal reorganization, and metabolic reprogramming. The sustained expression of mesenchymal markers and continued chemoresistance after reseeding highlight that even short-term confinement can exert durable influence on malignant potential. This spheroid-based platform rapidly generates invasive, drug-resistant populations and provides a practical tool for probing early metastatic events and for screening therapeutics aimed at preventing escape-driven disease progression.

Images (Optional)

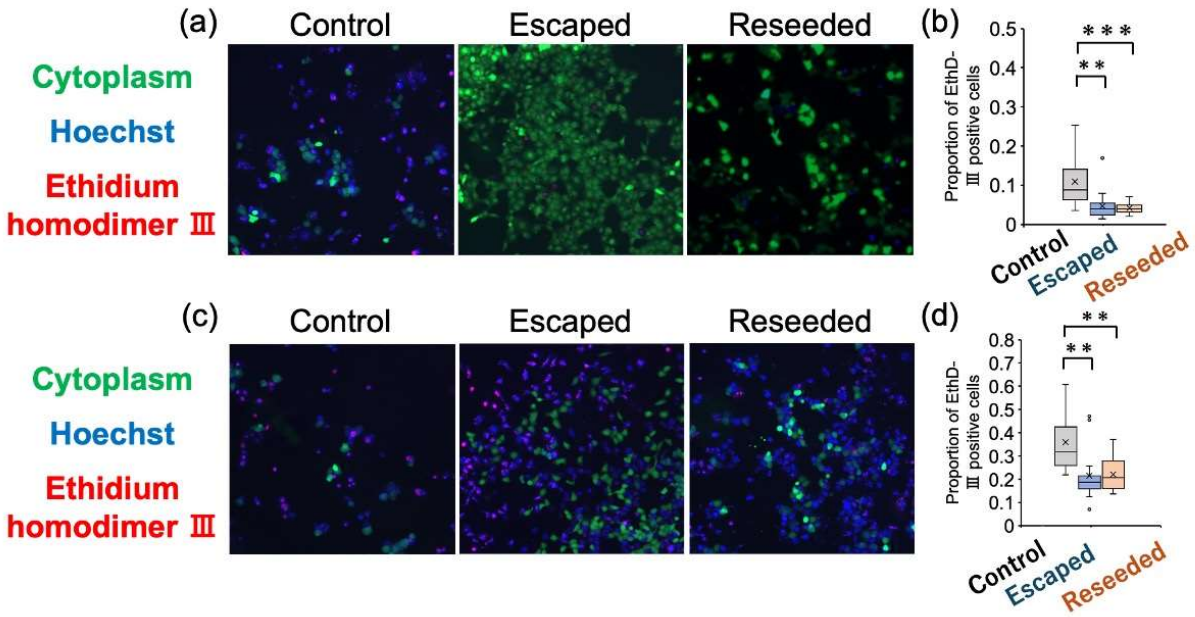


Fig. 1. Escape from spheroids leads to increased chemoresistance. (a) Cell viability assessment and (b) quantified proportion of Ethidium homodimer-III (EthD-III) positive cells out of the total number of cells after 24 hours of culture with the addition of 5 μM of doxorubicin hydrochloride. (c) Cell viability assessment and (d) quantified proportion of EthD-III positive cells out of the total number of cells after 24 hours of culture with the addition of 10 μM of doxorubicin hydrochloride. n = 15 images. ** $p < 0.01$; *** $p < 0.001$ (Tukey–Kramer test).

References (Optional)

[1]Gen Hayase and Daisuke Yoshino. ACS Appl. Bio Mater, 2020. https://doi.org/10.1021/acsabm.0c00719.
[2]Yuta Iijima et al. In Vitro Models, 2024. https://doi.org/10.1007/s44164-024-00066-3.

Session Category

Organ and Tissue Biomechanics: N/A

P3-198

Effects of Repeated Squat Movements on the Results of Craig's Test to Determine Hip Anteversion/Retroversion

Dr Scott Lynn PhD[1,2], Mr Logan Kaptis DPT[2], Mr Dylan Darling DPT[2], Ms Abigail Brittain MS[2], Dr Abigail Schmitt PhD[3,2]

[1]California State University, Fullerton. Center for Sport Performance., Fullerton, California, United States. [2]University of Arkansas Medical School (UAMS), Little Rock, Arkansas, United States. [3]University of Arkansas. Health, Human Performance and Recreation, Fayetteville, Arkansas, United States

Introduction

Malalignments in hip rotational version is associated with various pathologies[1-2] but determining the alignment of the hip non-invasively is difficult. The Craig's Test, designed to measure the alignment of the bony anatomy, has been used to measure femoral version[3] but it is possible that the mobility of the soft tissues around the hip joint could influence the results. Therefore, we examined the results of Craig's Test before and after squatting exercises requiring large ranges of motion at the hip joint. We hypothesized that the results would differ before and after the squatting protocol.

Methods

38 participants free of any musculoskeletal pathology volunteered for this study (20 males). Two sets of three repetitions of Craig's Test were done on each leg by a single experienced clinician, one set before doing the squat exercises, and one set immediately after. Craig's Test procedures are shown in Figure 1. Following the initial set of Craig's Tests, participants performed 22 total squats: 10 bilateral squats and 12 unilateral squats (6 per leg). For each squat, they were instructed to squat as low as they could comfortably control. The Craig's Test trials on each leg were averaged together to give one alignment score for each leg before and after the squatting trials. Paired sample *t*-tests were run separately on each leg to compare before and after squatting.

Results

All results showed Craig's Test scores increased following squatting. Right Leg Pre = 23.1 ± 9.3 deg, Right Leg Post = 25.3 ± 9.9 deg ($p<.05$). Left Leg Pre = 21.9 ± 8.2 deg, Left Leg Post = 24.3 ± 9.2 deg ($p<.05$).

Discussion

The primary finding of this research study is that any tightness in soft tissues around the hip joint can potentially alter the results of Craig's Test. Therefore, we recommend some form of warm-up involving movements requiring large ranges of motion at the hip joint before performing Craig's Test.

Images (Optional)

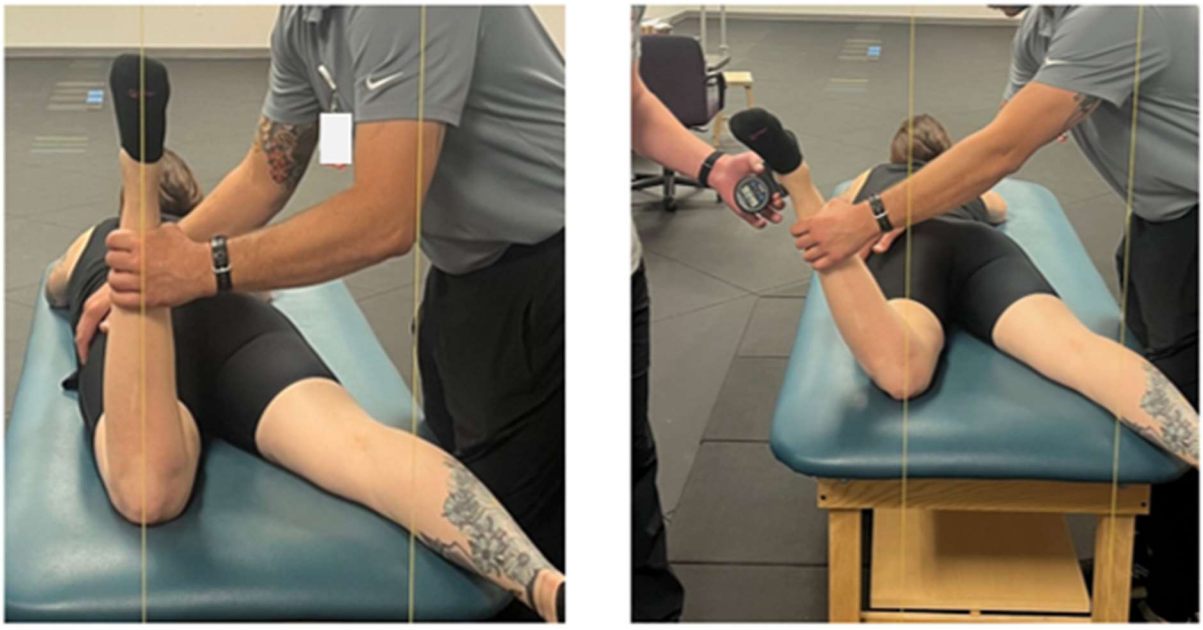


Figure 1 – Craig's Test experimental procedures modified from Choi & Kang [4]. (A) Shows the set-up position with the subject's tibia aligned with a plumb line hung from the ceiling. (B) Shows measurement of the difference between starting position using digital inclinometer.

References (Optional)

[1] Lerch *et al.,* Orthop J Sports Med, 2021. [2] Eckhoff *et al.,* J Pediatr Orthop, 1994. [3] Ruwe *et al.*, J Bone Joint Surg, 1992. [4] Choi & Kang, J Phys Ther Sci, 2015.

Session Category

Orthopaedic Biomechanics: Lower Extremities

P3-199

The Effect of Task on Cartilage T2 Relaxation Time in Osteoarthritic Knees

Mr Advait S. Madhekar[1], Mr Tejus Surendran[1], Ms Kyndall Tatum[1], Dr Dawn M. Elliot[2], Dr Daniel K. White[2], Dr Sophie Darwiche[3], Dr Ting Cong[3], Dr Axel C. Moore[1]

[1]Carnegie Mellon University, Pittsburgh, PA, United States. [2]University of Delaware, Newark, DE, United States. [3]University of Pittsburgh, Pittsburgh, PA, United States

Introduction

Understanding how articular cartilage responds to activities of daily living is essential for identifying early signs of joint dysfunction and chondro-preserving activities. Previous work has demonstrated that tibiofemoral cartilage undergoes measurable thickness changes (deformation) in response to physiologic tasks, such as walking and lying supine. The present study examines whether T2 relaxation time, a quantitative MR metric that is correlated with water and proteoglycan content, is responsive to physiological tasks from daily activities in knees with osteoarthritis (OA).

Methods

We recruited eight participants with symptomatic knee OA. Each participant completed a fixed task series consisting of 30 minutes of standing (Standing_1), 10 minutes of walking (Walking), a second period of standing for 30 minutes (Standing_2), and finally lying supine for 50 minutes (Supine). After each task, a multi-slice, multi-echo T2-weighted scan was acquired on a 3T MR scanner using a 15-channel Tx/Rx knee coil.

Femoral and tibial cartilage were manually segmented. Each segmentation was registered to the baseline scan, which was acquired just before the task sequence. T2 relaxation times were computed on a voxel-by-voxel basis by fitting a mono-exponential decay function. The mean femoral and tibial T2 relaxation times were computed within the region of cartilage-cartilage contact. Non-parametric testing was used to detect significant effects (Friedman and Wilcoxon signed-rank tests).

Results

Relative to baseline, all tasks led to a decrease in T2 relaxation time; however, only the tibia was significantly affected by the task ($p=0.017$). Pairwise comparisons to baseline revealed significant reductions in T2 relaxation time following Standing_2 (-14%, $p=0.031$) and Supine (-13%, $p=0.031$).

Discussion

While this is a small cohort study in a highly diverse and variable musculoskeletal disorder, these findings provide evidence that the T2 relaxation time of OA cartilage is responsive to physiological tasks. Furthermore, these findings are consistent with our prior work investigating the effect of task on cartilage deformation. Taken together, this work begins to establish a framework for evaluating the effect of task on cartilage composition and mechanics in vivo. Elucidating the effect of task, intensity, and duration may inform safe and chondro-preserving activities.

Images (Optional)

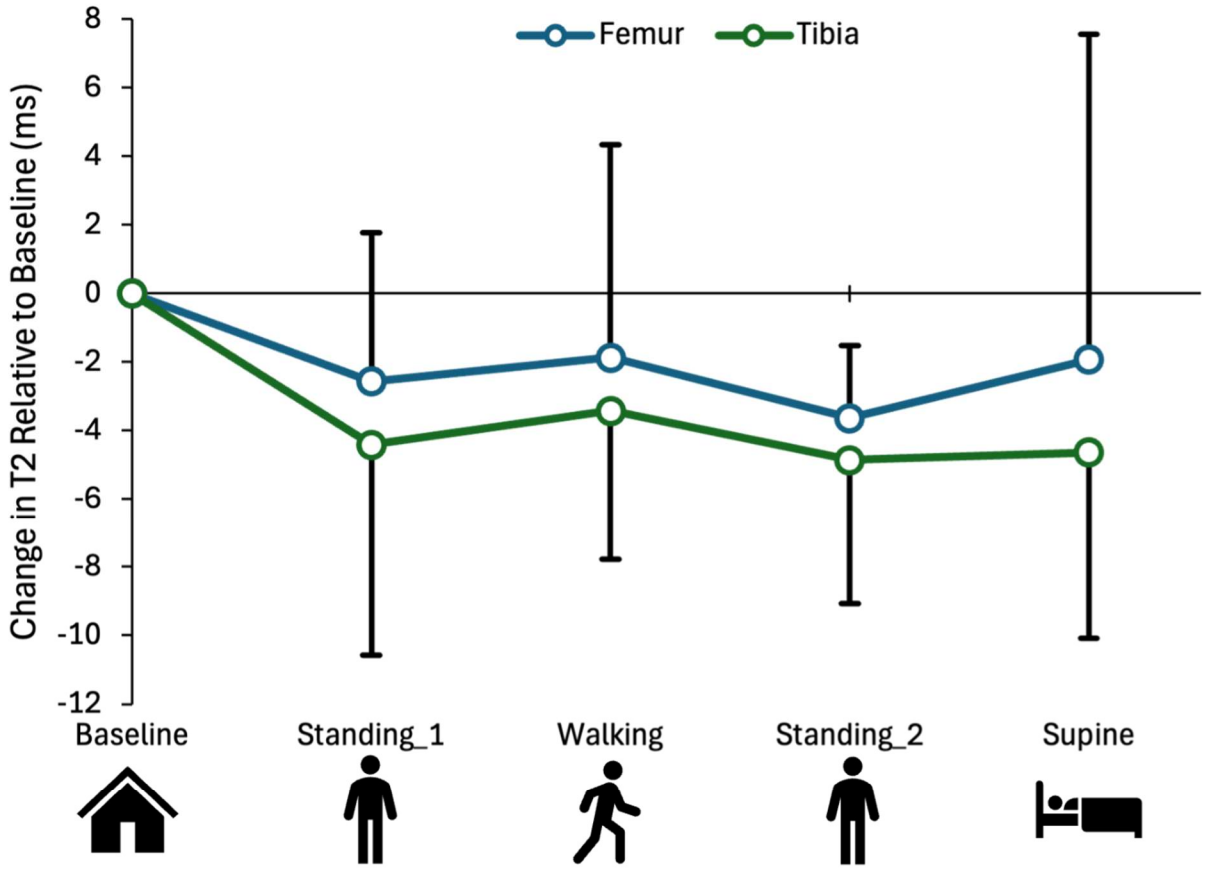


Figure 1. The effect of task on T2 relaxation time in the region of cartilage-cartilage contact for the femur (p=0.223) and tibia (p=0.017). The mean and standard deviation are shown (+/- error bars are shown for figure clarity).

Session Category

Orthopaedic Biomechanics: Lower Extremities

P3-200

Using a Biomechanics-Informed Neural Network for Fast Predictions of Activity-Specific Metastatic Femur Fracture Risk From 2D Radiographs

Dr. Alexander Synek[1], Ms. Luisa Scheuring[1], Dr. Willi Koller[2,3], Ms. Clara Egner[2,3], Mr. Kevin Kitir[2,3], Assoc. Prof. Hans Kainz[2,3], Prof. Dieter Pahr[1]

[1]Institute of Lightweight Design and Structural Biomechanics, TU Wien, Vienna, Austria, Austria. [2]Neuromechanics Research Group, University of Vienna, Vienna, Austria, Austria. [3]Centre for Sport Science and University Sports, University of Vienna, Vienna, Austria, Austria

Introduction

Pathological femur fractures are a significant complication of metastatic bone disease, yet existing clinical tools demonstrate insufficient diagnostic accuracy [1]. Biomechanical models could enhance accuracy and even provide fracture risk estimations for specific activities. However, their requirements of 3D imaging, computational resources, and processing time limit clinical translation. Here, we present the proof-of-concept of a biomechanics-informed neural network to predict activity-specific femur fracture risk directly from 2D radiographs in a fast and highly automated way.

Methods

A virtual cohort representing a single patient with various cases of metastatic bone disease (n=1000) was created by randomly inserting lytic lesions into the CT scan of a healthy subject [2]. Physiological peak hip joint loads (F_{phys}) of a size- and weight-matched subject during eight activities (e.g. walking, side-lunge, jumping) were computed using a musculoskeletal model [3] (Fig1.A). Femoral failure loads (F_{max}) were assessed using validated, CT-based finite element (FE) models [4] accounting for the activity-specific hip joint load direction (Fig1.B). The safety factor $S=F_{max}/F_{phys}$ was calculated as the fracture risk metric for each activity. A convolutional neural network was then trained on 900 cases to predict the activity-specific failure loads directly from simulated 2D radiographs and the safety factors were computed (Fig1.C). Neural network and FE model predictions were compared on the remaining 100 cases.

Results

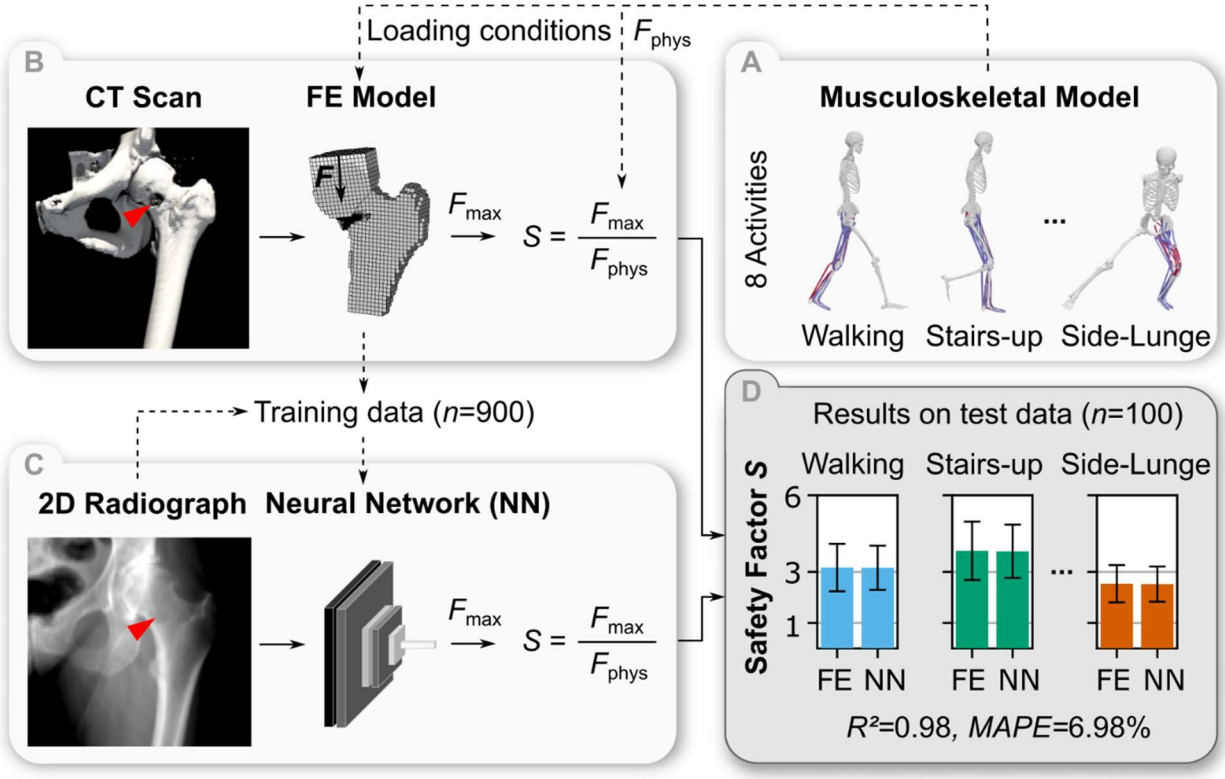
FE-predicted safety factors showed a wide range across all 1000 cases and activities (S=0.2–4.8). The neural network-predicted safety factors demonstrated excellent

agreement with FE results on the test cases (n=100, R^2=0.98, mean absolute percentage error=6.98%, Fig1.D), at an average prediction time of 77ms.

Discussion

The neural network predicted activity-specific metastatic femur fracture risk for a single subject in good agreement with CT-based FE modelling, while requiring only 2D radiographs and minimal processing time. With further development and validation on a larger cohort, this approach could offer a clinically viable tool for personalized activity guidance in patients with metastatic bone disease.

Images (Optional)



References (Optional)

[1] Benca et al., Bone Reports, 2016

[2] Aldieri et al., HFValid collection, 2023

[3] Rajagopal et al., IEEE Trans Biomed Eng, 2016

[4] Synek et al., CMPB, 2025

Acknowledgements (Optional)

Session Category

Orthopaedic Biomechanics: Lower Extremities

P3-201

Establishing Standardized Coordinate Systems for 3D Foot and Ankle Analysis Across Clinical Pathologies

Dr Amy Lenz PhD[1], Mr Andrew Peterson MS[1], Dr Michele Conconi PhD[2], Dr Sorin Siegler PhD[3], Dr William Ledoux PhD[4,5], Dr Eric Thorhauer PhD[5], Dr David Williams PhD[6], Dr Kevin Dibbern PhD[7], Dr Cesar de Cesar Netto MD, PhD[8], Dr Arne Burssens MD[9], Dr Michael Rainbow PhD[10], Dr Lauren Welte PhD[11], Dr Tom Turmezei MD[12], Dr Phillip Hansen MD[13], Dr François Lintz MD, PhD[14], Dr Alberto Leardini PhD[15], Dr Karen Kruger PhD[16,17]

[1]University of Utah, Salt Lake City, UT, United States. [2]Alma Mater Studiorum Università di Bologna, Bologna, Italy, Italy. [3]Drexel University, Philadelphia, PA, United States. [4]VA Puget Sound Health Care System, Seattle, WA, United States. [5]University of Washington, Seattle, WA, United States. [6]Cardiff University, Cardiff, Wales, United Kingdom. [7]University of Nebraska Medical Center, Omaha, NE, United States. [8]Duke University, Durham, NC, United States. [9]Ghent University Hospital, Ghent, Ghent, Belgium. [10]Queens University, Kingston, ON, Canada. [11]University of Alberta, Edmonton, Alberta, Canada. [12]Norwich University Hospitals NHS Foundation Trust, Norwich, UK, United Kingdom. [13]Bispebjerg-Frederiksberg University Hospital, Copenhagen, Denmark, Denmark. [14]Centre de Chirurgie de la Cheville et du Pied, Saint Jean, France, France. [15]IRCCS Istituto Ortopedico Rizzoli, Bologna, Italy, Italy. [16]Marquette University, Milwaukee, WI, United States. [17]Shriners Children's Chicago, Chicago, IL, United States

Introduction

Biomechanical 3D analyses are crucial to understanding the complex nature of the foot and ankle. A key component of 3D analyses is defining reliable and consistent anatomic coordinate systems (ACS) that are accessible to the biomechanics community. While several potentially viable automatic coordinate systems exist, their reliability is unclear. Unreliable coordinate systems may introduce nuisance variability and limit the ability to compare data across sites. This study aims to evaluate the reliability and accuracy of four ACSs to help determine standardized definitions for the foot and ankle.

Methods

Weightbearing CT scans from individuals representing four pathologies (rectus, cavus, flatfoot, and tibiotalar osteoarthritis) were used to generate 3D models of 14 bones. We generated statistical shape models (SSMs) to represent mean shapes and ±2 SD. ACS definitions [1-4] were applied to each bone.

Angular differences were calculated by comparing ACSs using rotation matrices to derive principal angles based on an XYZ convention. Intra- and inter-rater reliability was assessed on the Conconi and Siegler ACSs using ICC, while the Peterson and Thorhauer definitions are fully automatic. SSM particle locations were used to access reliability of each definition across pathologies.

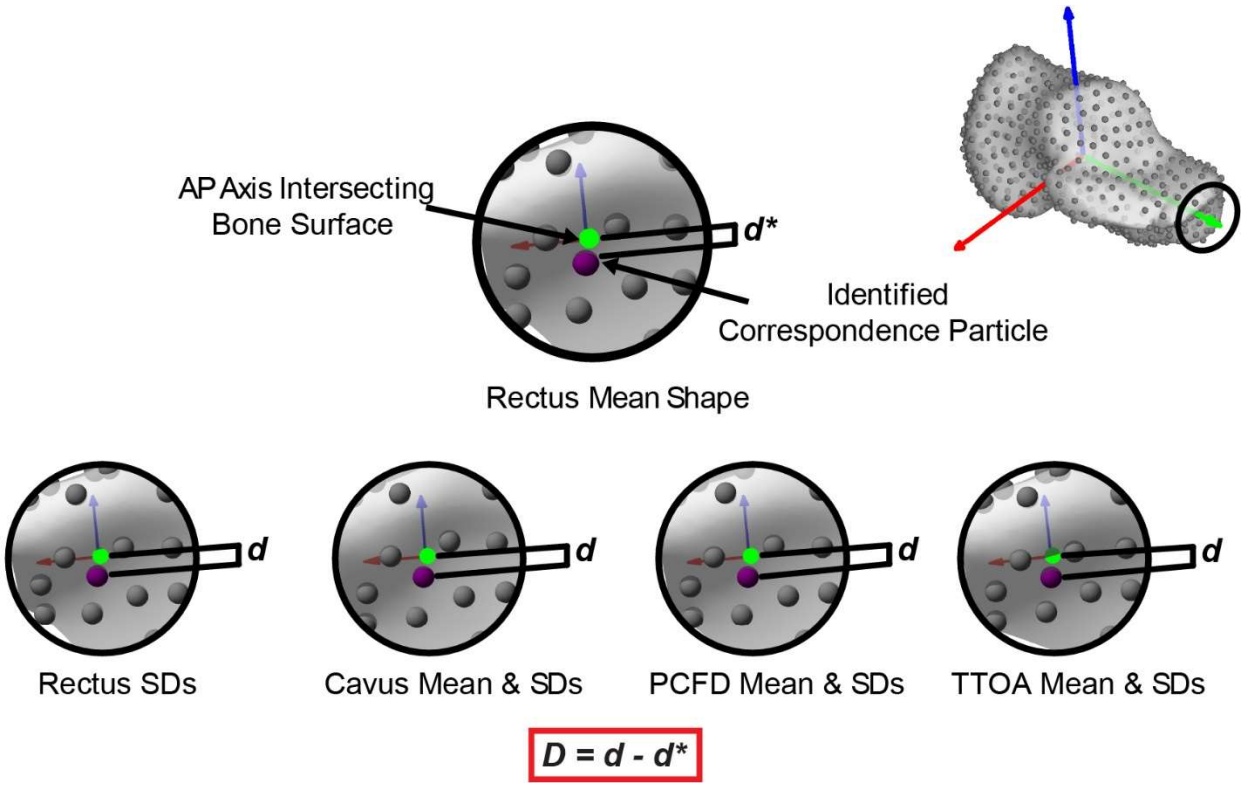
Results

Comparison of ACS definition accuracy revealed sub-millimeter differences among definitions and across pathologies. The ICC analysis reported the Conconi method showed excellent agreement for the talus and good to excellent agreement for the calcaneus.

Discussion

This study highlights the status of standardized foot and ankle ACSs as part of an international task force [5]. Analyzing ACS methodologies across pathologies has implications for research and clinical practice. Our reliability analysis showed promising results with both automated and manual methods are highly reliable across pathologies. The results are encouraging because automated methods eliminate the requirement of time-consuming user input, specialized training, and repeated reliability assessments. This work ultimately aims to provide fully automated ACS definition that can be used as a standard for 3D biomechanical foot and ankle analyses.

Images (Optional)



References (Optional)

1. Conconi et al. JFAR, 2021
2. Peterson et al. Front Bioeng Biotechnol, 2023.
3. Siegler et al. FAC, 2023.
4. Thorhauer et al. J Biomech Eng, 2023
5. Kruger er al. Foot Ank Clin N Am, 2025

Session Category

Orthopaedic Biomechanics: Lower Extremities

P3-202

Effect of Insoles on Joint Contact Forces During Walking and Running in Overpronated Foot Type

M.Sc. Andrea Arensmann[1], M.Sc. Thomas Stief[2], PD Dr. Marc de Lussanet[1,3], Dr. Kim Joris Boström[1], Prof. Dr. Heiko Wagner[1,3,4]

[1]University of Münster, Münster, North Rhine-Westphalia, Germany. [2](ts)^2, Osnabrück, Lower Saxony, Germany. [3]Otto Creuzfeldt Center for Cognitive and Behavioral Neuroscience, Münster, North Rhine-Westphalia, Germany. [4]Center for Data Science and Complexity (CDSC), Münster, North Rhine-Westphalia, Germany

Introduction

Excessive pronation is a common misalignment, that appears to increase the risk of various lower-extremity injuries. To prevent these injuries, insoles are often used to compensate for misalignments. Various studies have investigated the effect of insoles on the kinematics and kinetics of the lower extremities. However, their influence on joint contact forces (JCFs) received little research attention, even though high forces could lead to joint injuries and disorders. The aim of this study was therefore to investigate the effect of a pronation insole (ps), a bionic insole (bs) and no insole (ws) on JCFs in the hip, knee and ankle during walking and running

Methods

Data were recorded using the Gait Real-Time Analysis Interactive Lab (GRAIL, Motek Medical; Utrecht, Netherlands), a treadmill with two integrated force plates synchronised with 10 cameras (VICON Motion Systems Ltd.; Oxford, UK). 12 participants with an overpronated foot type walked (1.3m/s) and ran (2.5m/s) in each of the three conditions. JCFs were calculated using Computermyography (Predimo GmbH, Münster, Germany). All forces were normalized to subject's bodyweight and statistically analysed using a generalised linear mixed model.

Results

Overall, hardly any significant differences could be found between the conditions for walking or running. The JCFs in the ankle decreased in bs compared to the other conditions, but only during running. In the knee, only ps showed higher JCFs compared to bs. When walking, however, the JCF of bs is higher than that of ps. No differences in the JCFs were found in the hip. However, comparing the individual percentage changes reveals large differences in the direction and magnitude of the values (Fig.1).

Discussion

Our results show that bs insoles can reduce JCFs in the ankle and knee during running, although the effect sizes are very small. The hip is unaffected by the insoles. In walking only minor differences could be found. Overall, however, there are strong individual differences between participants, which may explain the small effect sizes and have also been observed in studies comparing different types of footwear. The results presented here are preliminary results, as not all participants have been evaluated yet.

Images (Optional)

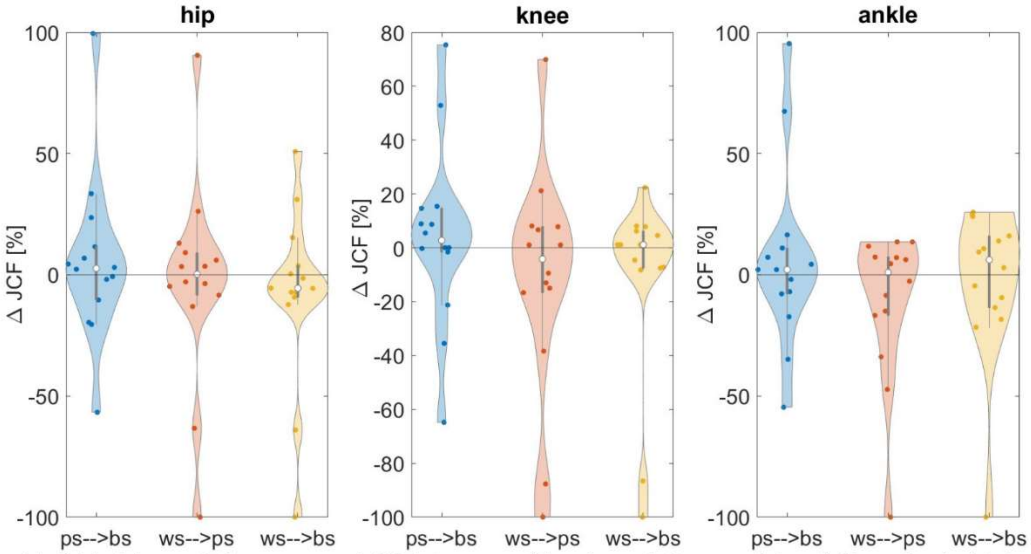


Figure 1: Individual changes in the average peak JCFs between conditions (every dot is one participant). Change is calculated relative to the first condition (e.g. (bs-ps)/ps). White dot=median. Grey bar=interquartile ranges.

Acknowledgements (Optional)

We thank (ts)^2 analytiX motion lab for providing the insoles and Predimo GmbH for providing the Myonardo software.

Session Category

Orthopaedic Biomechanics: Lower Extremities

P3-203

Shape-Based Alterations in Cartilage Contact Mechanics Precede Radiographic Knee Osteoarthritis

Dr. Anthony Gatti[1], Ms Kathryn R. Marusich[1], Dr. Allison Clouthier[2], Dr. Carmichael Ong[1], Dr. McKenzie S. White[1], Dr. Amir Esrafilian[1,3], Dr. Constance Chu[1], Dr. Seth Sherman[1], Dr. Garry E. Gold[1], Dr. Scott L Delp[1], Dr. Feliks Kogan[1], Dr. Akshay S Chaudhari[1]

[1]Stanford University, Stanford, CA, United States. [2]University of Ottawa, Ottawa, ON, Canada. [3]University of Eastern Finland, Kuipio, Northo Savo, Finland

Introduction

Mechanics have long been linked to knee osteoarthritis (OA) initiation and progression.

While many studies investigate external mechanics, studies on tissue-level mechanics are limited due to challenges in estimating these at scale. Recent large-scale datasets and simulation methods could help elucidate mechanics at scale. **Purpose**: To test whether shape specific cartilage contact mechanics during gait are predictive of knee OA progression in participants from the Osteoarthritis Initiative (OAI).

Methods

We extracted data for three groups based on Kellgren–Lawrence (KL) grade: Healthy (KL < 2 at baseline and 4-years), Progressor (KL < 2 at baseline, KL ≥ 2 at 4 years), and Mild OA (KL = 2 at baseline).

We developed an automated pipeline to create personalized 24 degree-of-freedom knee models from baseline knee MRIs and simulated cartilage contact during gait. We autosegmented bones, cartilage, and menisci, and fit a Neural Shape Model to segmentations yielding smooth surfaces for simulations and implicitly matched points to update ligament attachments and wrap surfaces. All knee models were isotropically scaled to match the size of a reference knee. We used the Concurrent Optimization of Muscle Activations and Kinematics (COMAK) algorithm to simulate cartilage-cartilage and cartilage-menisci contact during gait[1]. Simulations tracked a single reference person's kinematics and ground reaction forces, isolating differences due to shape. We used SPM 1D ANOVA to test group differences in cartilage pressure and contact area.

Results

Simulations for 658 participants were included (222 Healthy, 226 Progressor, 210 Mild OA). Medial tibial cartilage pressure and contact area were different throughout stance (Figure 1). Healthy knees had higher medial pressure than OA knees throughout stance, and than Progressor knees in early stance. Mild OA had greater contact area than Healthy and Progressor groups.

Discussion

Higher contact area in OA knees is consistent with OA pathophysiology, where weight-bearing areas enlarge with disease. Lower pressure in Mild OA is likely due to distribution of similar loads over greater area. Graded medial pressure (Healthy > Progressor > Mild OA) suggests Progressors exhibit remodeling prior to radiographic OA, positioning shape-based mechanics as sensitive indicators of early disease susceptibility.

Images (Optional)

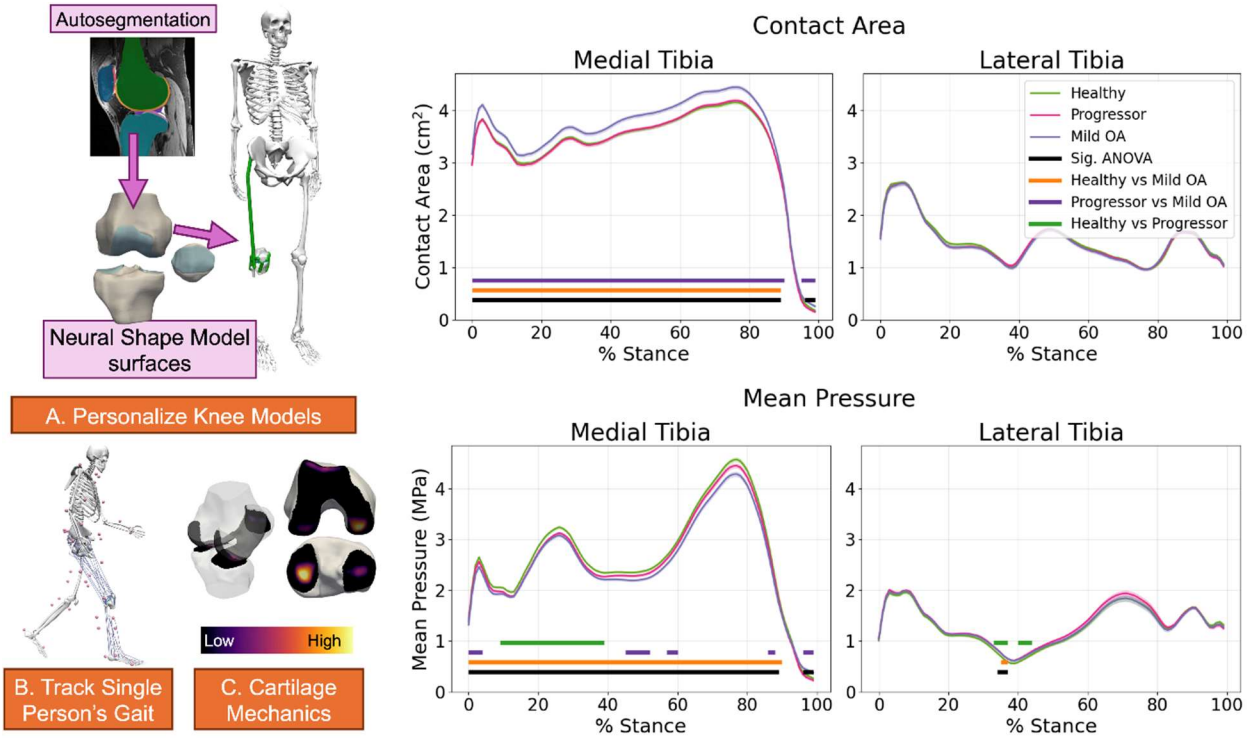


Figure 1. (Left) Automated pipeline: **A.** Neural Shape Model-based generation from MRI. **B.** Gait simulation using the COMAK algorithm with standardized kinematics and kinetics to isolate shape effects. **C.** Calculation of cartilage contact mechanics. **(Right)** Tibial cartilage mechanics during stance (mean ± SE). Horizontal bars at the bottom indicate significant differences ($p<0.05$, SPM 1D).

References (Optional)

[1] Smith C. et al., JOB, 2019

Session Category

P3-204

Representing Clinically Relevant Kinetic Gait Outcomes with a Wearable Inertial Sensor System in Patients Before and After Knee Arthroplasty

Mr. Ben MacDonald[1], Mr. Adam Dorrance[1], Dr. Michael Dunbar[1,2], Dr. Glen Richardson[1,2], Dr. Jennifer Leighton[1,2], Dr. Janie Astephen Wilson[1,2]

[1]Dalhousie University, Halifax, NS, Canada. [2]Nova Scotia Health, Halifax, NS, Canada

Introduction

The temporal patterns of frontal and sagittal plane knee joint moments are clinically relevant outcomes of knee arthroplasty (KA) surgery, having been associated with implant stability, and not meaningfully improving for many patients one year after surgery [1,2]. Specific temporal patterns of the knee flexion/extension (KFM) and knee adduction moments (KAM) are characterized by a lack of midstance unloading, or kinetic stiffening in both planes [3]. Traditionally, these outcomes have required optoelectronic motion capture and in-ground force plates in laboratory environments. Inertial measurement units (IMUs) offer a lower-cost alternative for out-of-lab assessments. The purpose of this study was to represent clinically relevant kinetic outcomes using an IMU system in patients before and after KA.

Methods

Twenty-one perioperative KA patients (100 trials) provided consent for gait analysis. IMUs (Opal, APDM) were placed on the shank, thigh, and foot of the affected leg. Data from the sensors were aligned to each segment using functional calibration [4], and strides were segmented [5]. Simultaneous data from a motion capture system (Motion Analysis) and in-ground force platforms (AMTI) were used to calculate knee joint moments. Principal component analysis was applied to KAM and KFM waveforms, with PC2 extracted to specifically represent the midstance knee stiffening pattern. Acceleration and angular velocity features were selected from IMU axes, informed by literature and univariate correlations with KAM and KFM PC2. Multivariate linear regression analysis was used to examine the association of KAM and KFM PC2 with independent IMU features.

Results

Optimal regression models were based on features of accelerations and angular velocities from shank and foot sensors (R^2=0.67 KFM PC2 model, R^2=0.69 KAM PC2 model; $p<0.05$; Table 1).

Discussion

These findings support the feasibility of predicting clinically relevant kinetic outcomes using IMU data in patients with end-stage knee OA. The models enable potential monitoring of knee joint loading profiles in natural environments to remotely monitor clinically relevant gait changes to support personalized clinical decisions.

Images (Optional)

Model	Predictors	Model Outcomes
Midstance Pattern of KFM (PC2)	**Shank IMU Features:** AP Acc Range Early Mid Stance; Vert Acc Width @ Half Max Late Stance Peak; Acc AP Early Stance Negative Impulse x AP Acc Impulse Early Mid Stance Positive; Gyr ML Timing Late Stance Peak; Vert Acc Impulse Stance **Foot IMU Features:** Vert Acc Impulse During Stance; Gyr ML Mean Stance; AP Acc Ratio Braking vs Propulsion	Adj R^2: 0.67, $p < 0.0005$ LOO CV R^2: 0.65
Midstance Pattern of KAM (PC2)	**Shank IMU Features:** AP Acc Range Early; AP Acc Positive Impulse Stance; AP Gyr Early Peak; ML Gyr Δt Early – Late Peak Stance; Vert Acc Width @ Half Max Late Stance Peak. **Foot IMU Featutres:** ML Gyr Mean Stance; Vert Acc Positive Impulse Early Stance; AP Acc RMS Stance	Adj R^2: 0.69, $p < 0.0005$ LOO CV R^2: 0.67

KFM: Knee Flexion Moment; KAM: Knee Adduction Moment; AP: Anterior-Posterior Direction; ML: Medial-Lateral Direction; Vert: Vertical direction; Acc: acceleration; Gyr: gyroscope; RMS: Root Mean Square; LOO CV: Leave one out Cross Validation

References (Optional)

[1] Young-Shand et al., *J Orthop Res,* 2023.

[2] Astephen-Wilson et al., *J Orthop Res,* 2019.

[3] Hatfield et al., *J Arthroplasty,* 2011.

[4] Kong et al., *Sensors*, 2016.

[5] Mariani et al., *Gait Posture*, 2013.

Session Category

Orthopaedic Biomechanics: Lower Extremities

P3-205

An IMU Sensor System for Representing Sagittal and Frontal Knee Angles During Gait in Patients with Knee Osteoarthritis Before and After Arthroplasty

Mr. Ben MacDonald[1], Mr. Adam Dorrance[1], Dr. Michael Dunbar[1,2], Dr. Glen Richardson[1,2], Dr. Jennifer Leighton[1,2], Dr. Janie Astephen Wilson[1,2]

[1]Dalhousie University, Halifax, NS, Canada. [2]Nova Scotia Health, Halifax, NS, Canada

Introduction

Individuals with advanced knee osteoarthritis (OA) walk with significant differences in knee joint angles compared to healthy controls. Common patterns include a stiff-knee gait, defined by reduced magnitude and range of knee flexion/extension angles, and elevated knee adduction angles during stance [1]. Knee flexion and adduction angles during walking are key outcomes of knee arthroplasty (KA), yet stiff-knee gait patterns often persist after surgery [1]. These outcomes are typically measured with laboratory motion capture, limiting accessibility and clinical uptake. Inertial measurement units (IMUs) offer an affordable alternative and enable free-living data collection. The purpose of this study was to examine agreement between clinically relevant knee angle outcomes captured through optoelectronic motion capture and IMUs in knee OA.

Methods

Twenty-one perioperative KA patients completed overground gait trials with simultaneous optoelectronic (Motion Analysis) and IMU (Opal, APDM) motion capture. IMUs were placed on bilateral shank and thighs, with sensor-to-segment alignment performed using functional calibration, strides segmented and knee joint angles calculated using a quaternion-based filter [2,3,4]. Clinically relevant features of sagittal and frontal plane knee angles [1] were extracted and compared using Bland-Altman analysis.

Results

Across 21 patients, 100 gait cycles, IMU-derived outcomes demonstrated good agreement with motion capture for all knee angle measures ($p > 0.05$; Table 1). Mean bias for the flexion/extension range of motion (ROM) and adduction mean fell within previously reported minimal clinically important differences for this population [5]. Mean bias for flexion/extension ROM in stance, adduction ROM in stance, and ROM in early stance were smaller than inter-session variability [6].

Discussion

These findings indicate that IMU data from shank and thighs can be processed to capture clinically relevant sagittal *and* frontal plane knee kinematics in patients with end-stage knee OA. Sagittal plane knee angles have been represented with IMUs in past research, feasibility of capturing clinically relevant frontal plane knee angles during gait has been less studied.

Images (Optional)

Gait Variable	Mean Bias (°) (SD)	95% CI (°)	LoA Lower (°)	LoA Upper (°)
Knee Flexion Angle Range	1.02 (10.9)	-3.95, 6.00	-20.4	22.5
Knee Flexion Angle Range During Stance	-2.16 (6.06)	-4.93, 0.59	-14.1	9.71
Knee Adduction Angle Mean During Stance	-0.07 (7.11)	-3.31, 3.16	-14.0	13.9
Knee Adduction Angle Range During Stance	0.39 (4.59)	-1.69, 2.49	-8.59	9.39
Knee Adduction Angle Range During Early Stance	0.12 (2.71)	-1.11, 1.39	-5.19	5.44

References (Optional)

[1] Outerleys et al., *Appl Biomech,* 2021

[2] Kong et al., *Sensors*, 2016

[3] Mariani et al., *Gait Posture*, 2013

[4] Laidig et al., *Inf Fusion,* 2023

[5] Laudanski et al., *Appl Biomech,* 2025

[6] McGinley et al., *Gait Posture,* 2009

Session Category

Orthopaedic Biomechanics: Lower Extremities

P3-206

Finite Element Analysis for the Design of Patient-Specific Offloading Ankle-Foot Orthosis

Mr. Benjamin Sarfati, Dr. Dana Solav, Mr. Lee Jordan, Ms. Eshraq Saffuri

Technion, Haifa, Haifa, Israel

Introduction

Complete offloading of an injured foot or ankle via an Ankle-Foot Orthosis (AFO) has been shown to provide potential improvements in gait biomechanics and recovery outcomes in comparison to more common assistive devices [1]. However, the AFO's brace shells (Figure 1a), which transfer ground reaction forces (GRFs) to the shank, must distribute stresses across soft tissues properly to minimize tissue damage or discomfort. Finite Element Analysis (FEA) can provide quantitative, evidence-based metrics to this end. This study constructs and validates a FEA framework for simulating the mechanical response of tissues subject to AFO loading to facilitate data-driven design.

Methods

MRI scans of a healthy participant's lower leg are obtained, followed by segmentation and 3D reconstruction. Skin geometry is used to model the AFO's brace shells (Figure 1b). Bones and brace shells are modelled as rigid bodies, whereas muscle tissue, patellar tendon, and neoprene liner are meshed with quadratic tetrahedral elements and each assigned hyper-elastic material parameters informed by experimental measurements. A dual-step FEA is implemented; the first step replicates AFO donning by tightening the brace around the shank. Then, GRF is applied to the brace to simulate standing. For validation, predicted reaction forces between brace shells are compared to measurements from load cells mounted on the AFO's fastening buckles.

Results

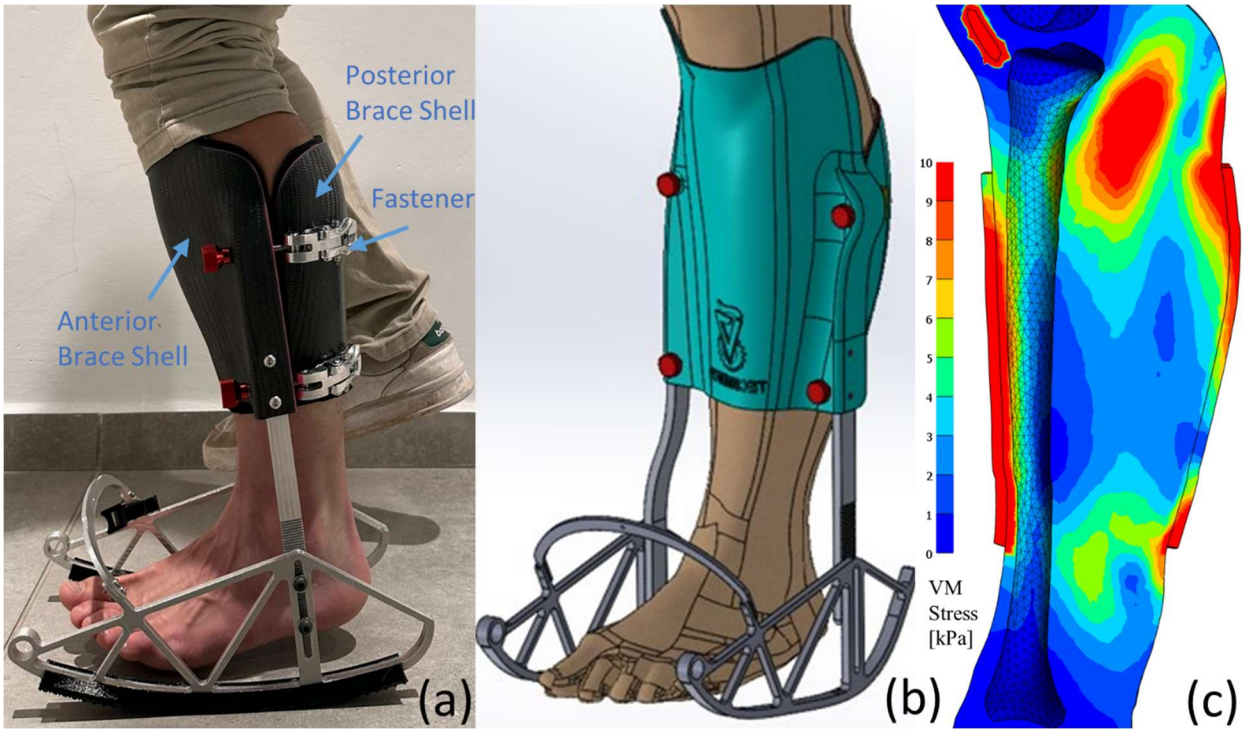
Figure 1c shows the results of Von-Mises stress values from standing with the donned AFO on a sagittal section at minimal anterior soft tissue thickness. Lower thickness soft tissue regions exhibit larger stresses. Significant shearing of the neoprene outer layer is evident, matching experimental observations.

Discussion

Current work further compares FEA predictions to experimental measurements. In the future, multiple simulated instances of the walking gait cycle will provide more comprehensive results. This work highlights the value of FEA in optimizing the tissue-

device biomechanical interface and advancing patient-specific orthotic and prosthetic design automation.

Images (Optional)



References (Optional)

[1] Saffuri et al, J Neur Eng Rehab 21.1:67, 2024

Acknowledgements (Optional)

This research was supported by the J. Tal Equipment and Research Fund, the Mark S. Kahn Family Fund, the Gutwirth Fund, and the Ministry of Science and Technology of Israel.

Session Category

Orthopaedic Biomechanics: Lower Extremities

P3-207

Do All Ultra-Congruent Knees Behave the Same? A Biomechanical Insight into Stability and Motion

Prof Bernardo Innocenti PhD

ULB, Bruxelles, Belgium, Belgium

Introduction

This study investigated whether different ultra-congruent (UC) total knee arthroplasty (TKA) designs display comparable biomechanical performance. Specifically, the Link SymphoKnee (LSK) UC was compared with the Zimmer-Biomet Persona (PRSN) UC to check similarities and differences in joint stability and tibio-femoral kinematics under different loading and motion conditions.

Methods

Both UC implants were analyzed, using validated finite element models, under standardized testing conditions, comparing:

1. antero-posterior (AP) stability under AP forces at different flexion angles from 0° to 120°;
2. internal-external (IE) stability under IE torques across the same flexion range;
3. tibio-femoral biomechanics during a gait cycle, using forces, torque and boundary conditions defined in accordance with ISO 14243-1 ;
4. tibio-femoral biomechanics during a squat up to 120° of flexion; the boundary conditions of this movement, in terms of flexion-extension angle, axial and anterior-posterior force, were taken accordingly to previously experimental activities

For the stability tests, femoral displacement relative to the fixed tibia was evaluated at each flexion angle and compared between the two implants.

For the dynamic activities, the following information was extracted analyzed and compared:

- Tibio-Femoral kinematics (in terms of internal/external rotation and antero-posterior translation);
- Medial and lateral contact area and antero-posterior displacement.

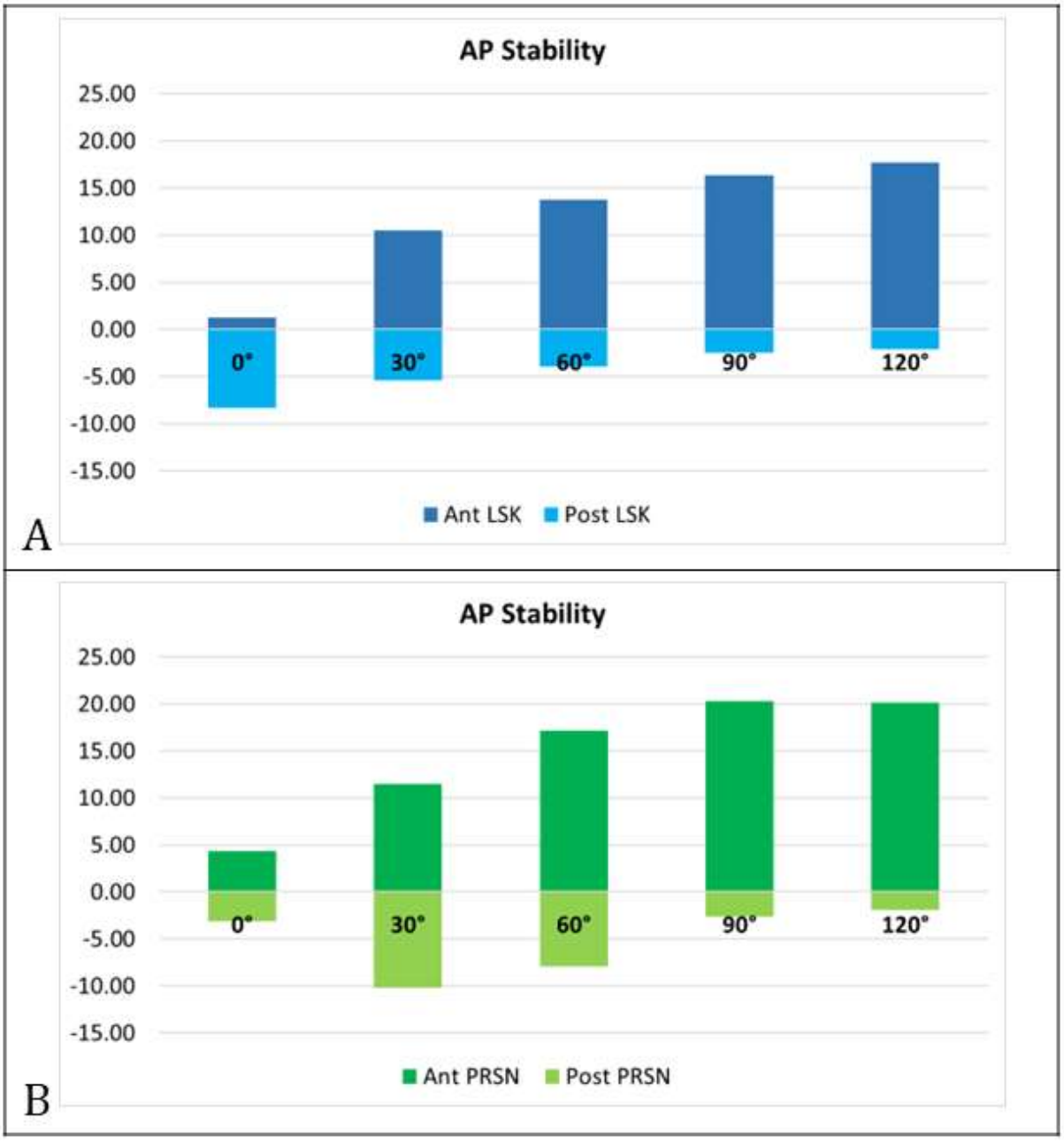
Results

Both UC implants demonstrated similar overall biomechanical trends. The LSK showed reduced displacements and rotations, indicating greater stability at all flexion angles except at 0° posterior, where PRSN was slightly superior (Figure 1). During walking, both implants exhibited almost identical tibio-femoral kinematics in AP translation and IE rotation, with comparable medial and lateral contact areas and contact point displacements. During squat, both designs showed analogous kinematics and contact mechanics across the full flexion range, with the LSK demonstrating more symmetrical medial-lateral contact behavior than the PRSN in deep flexion.

Discussion

Although both UC implants exhibited comparable biomechanical behavior in terms of stability, gait, and squat kinematics, subtle differences emerged. The LSK provided slightly enhanced stability and more symmetric kinematics, suggesting that not all UC implants behave identically. These findings underscore the importance of implant-specific design considerations in UC TKA selection.

Images (Optional)



Session Category

Orthopaedic Biomechanics: Lower Extremities

P3-208

Biomechanical Analysis of Surgical Technique on Distal Femoral Replacement Implant Performance

Prof bernardo innocenti PhD

Beams Department ULB, Bruxelles, Belgium, Belgium

Introduction

When distal femoral resection is required due to bone tumors, a Distal Femur Replacement (DFR) can restore joint function [1]. Implant stability depends on the integrity of the remaining femur and on the efficiency of the bone–implant interface in transmitting loads. Both cemented and press-fit fixation techniques are clinically used, and choices regarding resection height and stem length strongly influence lower-limb biomechanics. This study aims to provide surgical guidelines by evaluating the biomechanical effects of different DFR solutions through comparative stress analysis in multiple femoral configurations.

Methods

A validated finite element model was developed using the cortical bone geometry of a standard femur [2,3]. DFR components (stem, collar, shaft) were modeled based on Adler Ortho geometries (Cormano, Italy).

The following surgical parameters were investigated:

• press-fit vs. cemented stems;

• short vs. long stems (85 mm and 115 mm);

• short, medium, and large resections (97 mm, 147 mm, 207 mm);

• healthy vs. osteoporotic bone;

• axial (0°) vs. anteroposterior (AP, 90°) loading.

A total of 48 models were generated. Cortical bone was defined as transversely isotropic [2–5], whereas implant components were modeled as isotropic using manufacturer-provided properties [5,6]. Loads of 1000 N were applied either along the mechanical axis (0°) or anteriorly (90°), with the femoral head fixed. Stress distribution was evaluated qualitatively and quantitatively in selected bone and implant regions.

Results

Axial loading produced minimal variation in bone stress distribution across configurations. In contrast, AP loading generated substantially higher stresses, with resection height emerging as a major determinant. Larger resections led to increased stress concentration, especially in press-fit stems with incomplete bone–implant contact. Across all scenarios, cemented fixation consistently reduced cortical stress peaks and produced a more uniform stress distribution.

Discussion

While axial loading showed limited influence on bone stress, AP loading highlighted the critical importance of resection height and fixation technique. Cemented fixation demonstrated superior ability to mitigate stress concentration and stabilize the mechanical environment, particularly in large-resection cases where press-fit contact may be suboptimal.

References (Optional)

1. Song et.al,J.Surg.Oncol,2011.
2. Innocenti et.al, J.Arthrop,2014.
3. Innocenti et.al, J.Arthrop,2016.
4. Innocenti and Bori, J Orthop,2020.
5. Piovan et.al, JOSR,2024.
6. Burastero et.al, AOTS,2020.

Acknowledgements (Optional)

This work was financially supported by the Fonds De La Recherche Scientifique - FNRS, CDR grant # 40008102.

Session Category

Orthopaedic Biomechanics: Lower Extremities

P3-209

A Multivariable Analysis of Mechanical Tibiofemoral Alignment on Patellofemoral Force using a Novel In-vitro Knee Simulator

Mr Bulut Freear BA (Hons)[1], Dr Raelene M Cowie MEng, PhD[1], Dr Louise M Jennings MEng, PhD[1], Mr John Naybour BSc[2], Mr Hemant Pandit FRCS, DPhil[3,4], Dr Todd Stewart BSc, PhD[1]

[1]Institute of Medical and Biological Engineering, Leeds, Yorkshire, United Kingdom. [2]Eventum Orthopaedics, Leeds, Yorkshire, United Kingdom. [3]NIHR Leeds Biomedical Research Centre, Leeds, Yorkshire, United Kingdom. [4]institute of Rheumatic and Musculoskeletal Medicine, Leeds, Yorkshire, United Kingdom

Introduction

Following total knee replacement there is a high occurrence of anterior knee pain linked to increased patellofemoral loads, namely overstuffing [1]. Anterior knee pain occurs irrespective of patella resurfacing [2]. The multitude of interrelating knee alignment variables makes their individual influence on the patellofemoral force vector difficult to consider. This study aimed to determine the sensitivity of tibiofemoral knee prosthesis alignment on the patellofemoral joint load using a multivariate analysis.

Methods

A novel in-vitro simulator was designed to allow for the simultaneous variation in mechanical alignment of a knee joint focussing on the relative patella height and position of the trochlear contact and its influence on intraoperative patellofemoral joint forces (Figure 1). A multivariable analysis was carried out varying the tibial posterior slope, femoral prosthesis flexion, femoral prosthesis valgus rotation and femoral prosthesis internal/external rotation. Loads were measured using Quadsense (Eventum Orthopaedics, UK), this records the distribution of the patellofemoral load across four pads. For each alignment combination, the knee was flexed from 0-90°. The distribution and magnitude of the patellofemoral load was recorded at peak flexion and compared between cases.

Results

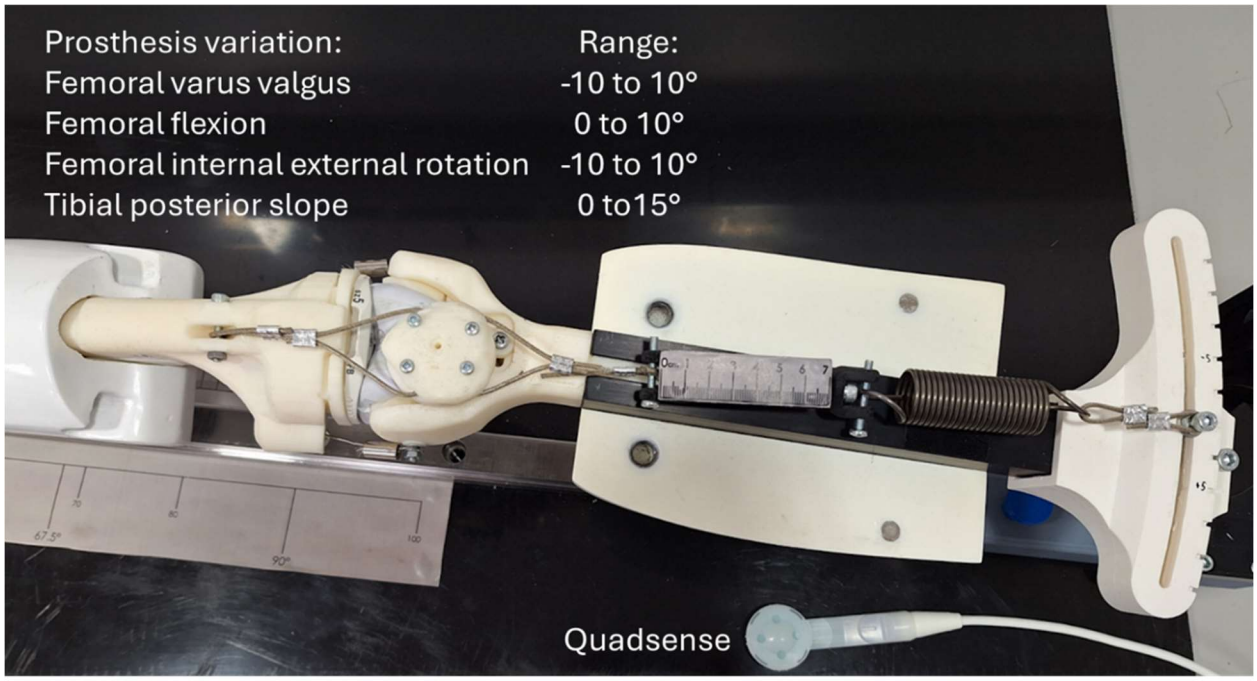
Observed trends showed that increasing femoral valgus rotation generally caused average patellofemoral loads to increase by 4.3% above the mean. A high varus or valgus femoral position was the main indicator for patella dislocation. High tibial slope caused loads to drop 6.5% on average, whilst increasing femoral flexion and internal/external femoral rotation produced similar decreases. Despite these trends, specific alignment cases also

caused a deviation in this trend; this suggests there are secondary and higher order interactions between variables.

Discussion

Altering tibiofemoral alignment had a measurable effect on the magnitude and distribution of the patellofemoral force; this supports clinical observations of patellofemoral pain. The results highlight the complexity of knee biomechanics, while most variables followed trends, there were many specific alignment interactions between variables that caused the load to alter in unpredictable ways. Altering the varus/valgus femoral prosthesis rotation had the largest and least predictable effect on patellofemoral loads and patella tracking. Further experimentation is planned to vary the alignment of the patella.

Images (Optional)



References (Optional)

[1] Kandhari,V.K,JournalofClinicalandDiagnosticResearch,2017

[2] Petersen,W,InternationalOrthopaedics,2013

Session Category

Orthopaedic Biomechanics: Lower Extremities

P3-210

Quantifying the effect of Quadriceps Alignment on Patellofemoral Force and Patella Tracking using a Novel in-vitro Experiment.

Mr Bulut Freear BA (Hons)[1], Dr Raelene M Cowie MEng, PhD[1], Dr Louise M Jennings MEng, PhD[1], Mr John Naybour BSc[2], Mr Hemant Pandit FRCS, DPhil[3,4], Dr Simon Talbot MBChB, FRACS[5], Dr Todd Stewart BSc, PhD[1]

[1]Institute of Medical and Biological Engineering, Leeds, Yorkshire, United Kingdom. [2]Eventum Orthopaedics, Leeds, Yorkshire, United Kingdom. [3]Leeds institute of Rheumatic and Musculoskeletal Medicine, Leeds, Yorkshire, United Kingdom. [4]NIHR Leeds Biomedical Research Centre, Leeds, Yorkshire, United Kingdom. [5]Department of Orthopaedic Surgery, Melbourne, Victoria, Australia

Introduction

Quadriceps Muscle weakness and imbalance have been linked to anterior knee pain post-TKA [1]. This suggests that an altered Quadriceps angle may change the load and contact conditions on the patella as it tracks the trochlea groove. The study aimed to vary the coronal angle of the quadriceps muscle and measure the effect on the magnitude and distribution of the patellofemoral load for a neutral, valgus and varus knee.

Methods

An in-vitro simulator was designed to replicate the clinical positioning of a knee joint allowing investigations into mechanical alignment focussing on the relative patella height and position of the trochlear contact. Quadriceps alignment was measured using the Quadriceps tendon coronal alignment (QTCA) [1]. Loads were measured using Quadsense (Eventum Orthopaedics, UK), this measures the distribution of the patellofemoral load across four pads. The QTCA angle was varied up to 7.5° medial and lateral from a neutral position. This was repeated with a neutral, 5° varus and 5° valgus femoral prosthesis. For each experiment the knee was flexed from 0° to 90° and the highest cumulative load reading was recorded along with the individual pad readings at this peak.

Results

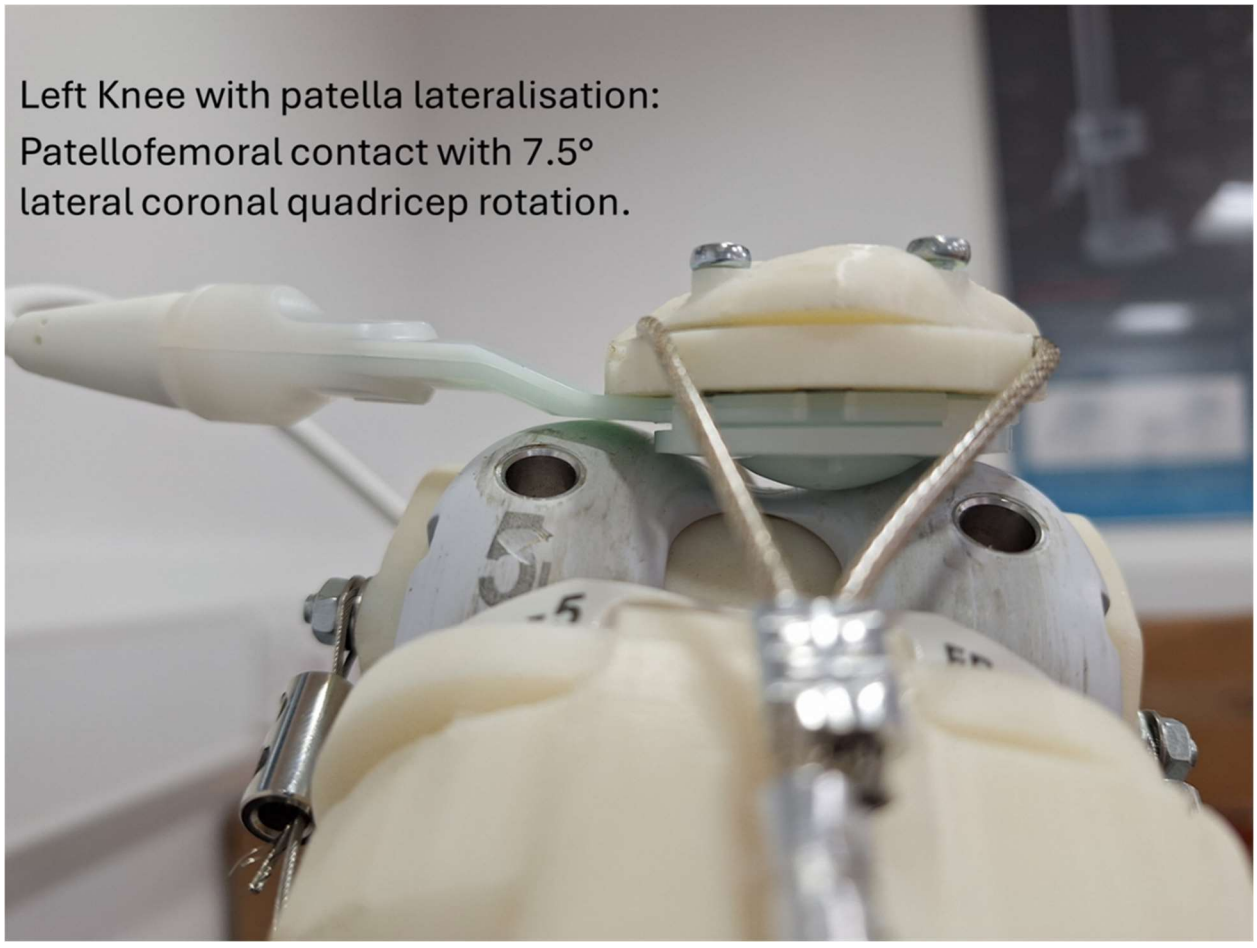
During testing, the mediolateral patella position was observed to move with quadriceps angle (Figure 1). Increasing QTCA to 7.5 from -7.5 decreased cumulative load by 38%. Pairing a -7.5° QTCA rotation, with a valgus joint, resulted in high medial loads, with the patella riding against the medial side of the trochlea groove. In contrast, pairing the same -

7.5° QTCA rotation with a varus joint caused lateral loads to increase with visible patella lateralisation. The valgus joint had mean loads 9.5% higher compared to the neutral joint and the varus had loads 5.6% lower.

Discussion

The results suggest that the quadriceps angle can affect the relative patella height of the trochlear contact point, and thus the patellofemoral load vector, more than a varus/valgus deformity. This highlights the importance of considering the detailed quadriceps mechanism and any congenital deformities as these have a significant role in the magnitude and distribution of the patellofemoral force.

Images (Optional)



References (Optional)

[1] Petersen,W,InternationalOrthopaedics,2013

[2] Talbot,S,*KneeSurgery,SportsTraumatology,Arthroscopy,2023*

Session Category

Orthopaedic Biomechanics: Lower Extremities

P3-211

The Influence of the Rate of Knee Extensor Moment on Bone Mineral Density After an ACL Reconstruction

Dr. Camille Johnson PhD, Mr. Charles Eisner, Dr. Meredith Owen PhD, Mr. Douglas Long MS, Dr. Michael Samaan PhD, Dr. Darren Johnson MD, Dr. Christopher Fry PhD, Dr. Brian Noehren PT, PhD

University of Kentucky, Lexington, KY, United States

Introduction

Bone mineral density (BMD) deficits persist following ACL reconstruction (ACLR) and may be related to aberrant loading rates. Prior work has shown that the rate of knee extensor moment (RKEM) during walking and quadriceps rate of torque development (RTD) are reduced in the post-ACLR limb and may influence BMD recovery. The study purpose was to determine if changes in RKEM and RTD from baseline to six months post-ACLR influence BMD recovery. We hypothesized improved RKEM and RTD would correlate to improved involved limb BMD.

Methods

16 individuals (9F, 18.4±3.9yrs, height: 1.7±0.1m, BMI: 26.3±3.9kg/m2) participated in this study. Data were collected at baseline and six months post-ACLR. Dual-energy x-ray absorptiometry (DXA) scans of the involved distal femur and proximal tibia were acquired. Participants then performed an instrumented gait analysis walking at a self-selected speed while kinematic data and ground reaction forces were collected (200Hz, 2000Hz). Quadriceps RTD was assessed via four maximum voluntary isometric contractions.

Femoral and tibial BMD was quantified from segmented DXA scans. Knee extensor moments (KEM) were computed and RKEM was calculated ([KEM_max-KEM_min]/[delta time]). Paired t-tests or Wilcoxon tests assessed differences in RKEM, RTD, and BMD between timepoints. Spearman's correlations assessed relationships between changes in BMD, RKEM, and RTD between timepoints (significance: $p<0.05$).

Results

Average walking speed was 0.8±0.3m/s at baseline and 1.1±0.3m/s at follow-up. Involved limb BMD decreased 0.2±0.1g/cm^2 and 0.1±0.1g/cm^2 in the femur and tibia ($p<0.001$) (Figure 1-A). RKEM improved by 1.6±2.4([N*m]/[kg*m*s]) ($p=0.007$) (Figure 1-B) and RTD decreased by 1.0±2.5([N*m]/[kg*s]) ($p=0.230$) (Figure 1-C). Neither correlated to improved

BMD (RKEM: ρ_{Femur}=-0.083 [p=0.76], ρ_{Tibia}=0.119 [p=0.66]; RTD: ρ_{Femur}=0.240 [p=0.37], ρ_{Tibia}=-0.007 [p=0.98]).

Discussion

Despite improvements to RKEM during walking, RTD did not change, suggesting greater attention needs to be devoted to interventions that promote quick force development. The lack of correlation suggests that knee loading rate from walking may not be sufficient stimulus to promote BMD recovery. Evaluating recovery of BMD during higher impact activities at later stages of recovery may provide additional insights into factors that promote recovery of BMD after an ACLR.

Images (Optional)

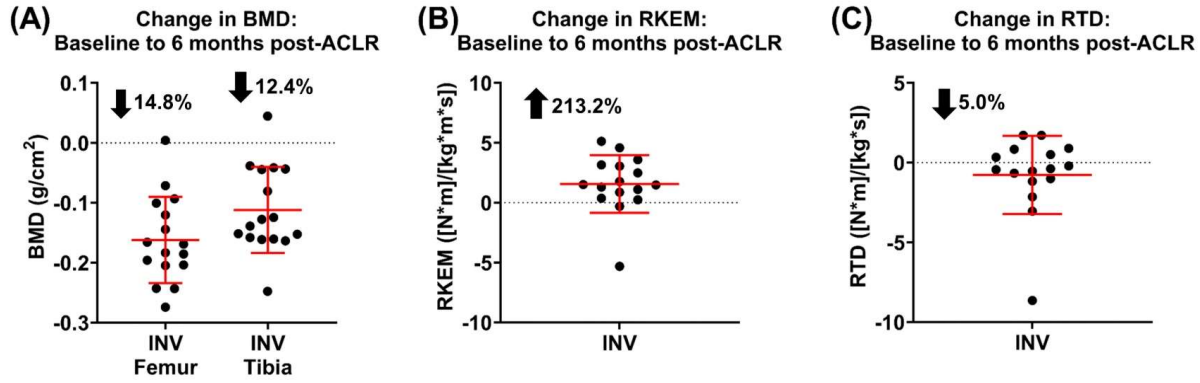


Figure 1: Change in involved (INV) limb (A) femoral and tibial BMD, (B) RKEM, and (C) RTD from baseline to six months post-ACLR. Average percent change from baseline to follow-up is indicated on each panel.

Session Category

Orthopaedic Biomechanics: Lower Extremities

P3-212

KneeHub: A Standardised Method for Determining Ligament Attachment Sites for Tibiofemoral Joint Modeling

Ms Kate Moyle PhD Student[1], Ms Nancy Kim PhD Student[1], Ms Maryam Nazem Masters Student[2], Dr Jason Halloran[3], Dr Thor Besier[1], Dr Peter Laz[2], Dr Snehal Chokhandre[4], Dr Carl Imhauser[5], Dr Ahmet Erdemir[4]

[1]Auckland Bioengineering Institute and Department of Engineering Science, University of Auckland,, Auckland, Auckland, New Zealand. [2]Center for Orthopaedic Biomechanics, Department of Mechanical and Materials Engineering, University of Denver, Denver, Colorado, United States. [3]Applied Sciences Laboratory, Institute for Shock Physics, Washington State University, Spokane, Washington, United States. [4]Computational Biomodeling (CoBi) Core, Lerner Research Institute, Cleveland Clinic, Cleveland, Ohio, United States. [5]Department of Biomechanics, Hospital for Special Surgery, New York, New York, United States

Introduction

Accurate representation of ligaments in finite element modeling is essential for reproducing physiologically relevant kinematics. Modeling outcomes are highly sensitive to variations in ligament attachment locations [1]. However, ambiguity remains, with studies reporting femoral ACL attachment variances up to 25.67mm^2 between researchers segmenting the same data [2]. Such variations can compromise the accuracy of models, especially in clinical settings. The 'KneeHub' project aims to unify knee modelling approaches through developing a consensus-based workflow. This study uses the workflow to determine ligament attachments in a systematic and reproducible manner.

Methods

A knee modeling workflow was developed by experienced modelers and followed by three novice modellers. Modelers manually segmented MR images of the same knee. ACL and PCL attachments were defined based on published anatomical descriptions. Ellipses were fit to attachment point clouds and divided into quadrants representing bundles. For the ACL, the proximal half of the femoral ellipse and the anterior half of the tibial ellipse define the anteromedial bundle, while remaining halves define the posterolateral bundle. Attachments were represented by springs positioned at quadrant centres and projected onto the bone surface. Modelers repeated segmentations twice, with inter- and intra-observer centroid variance evaluated.

Results

For three attachments, the centroid variance (σ^2) relative to the group mean decreased after the ellipse fit compared with the raw segmentation. The tibial ACL attachment showed the largest reduction in centroid variance, from 4.12mm^2 in the raw segmentation to 3.34mm^2 after ellipse fitting. Centroid intra-observer error did not consistently fall within twice the image resolution.

Discussion

Fitting the ellipse to the raw segmentation of the attachment site decreased the centroid variance between modellers. Variance in the tibial ACL attachment dropped to 3.34mm^2, nearly half the 6.33mm^2 reported in a prior study lacking a consensus workflow [2]. This method helps standardise and simplify modelling approaches across different modelers, making work reproducible and thus clinically relevant. Although intra-observer error values weren't consistently within the target range, additional segmentation rounds could improve consistency. In future, these techniques will be applied to all modeled ligaments.

Images (Optional)

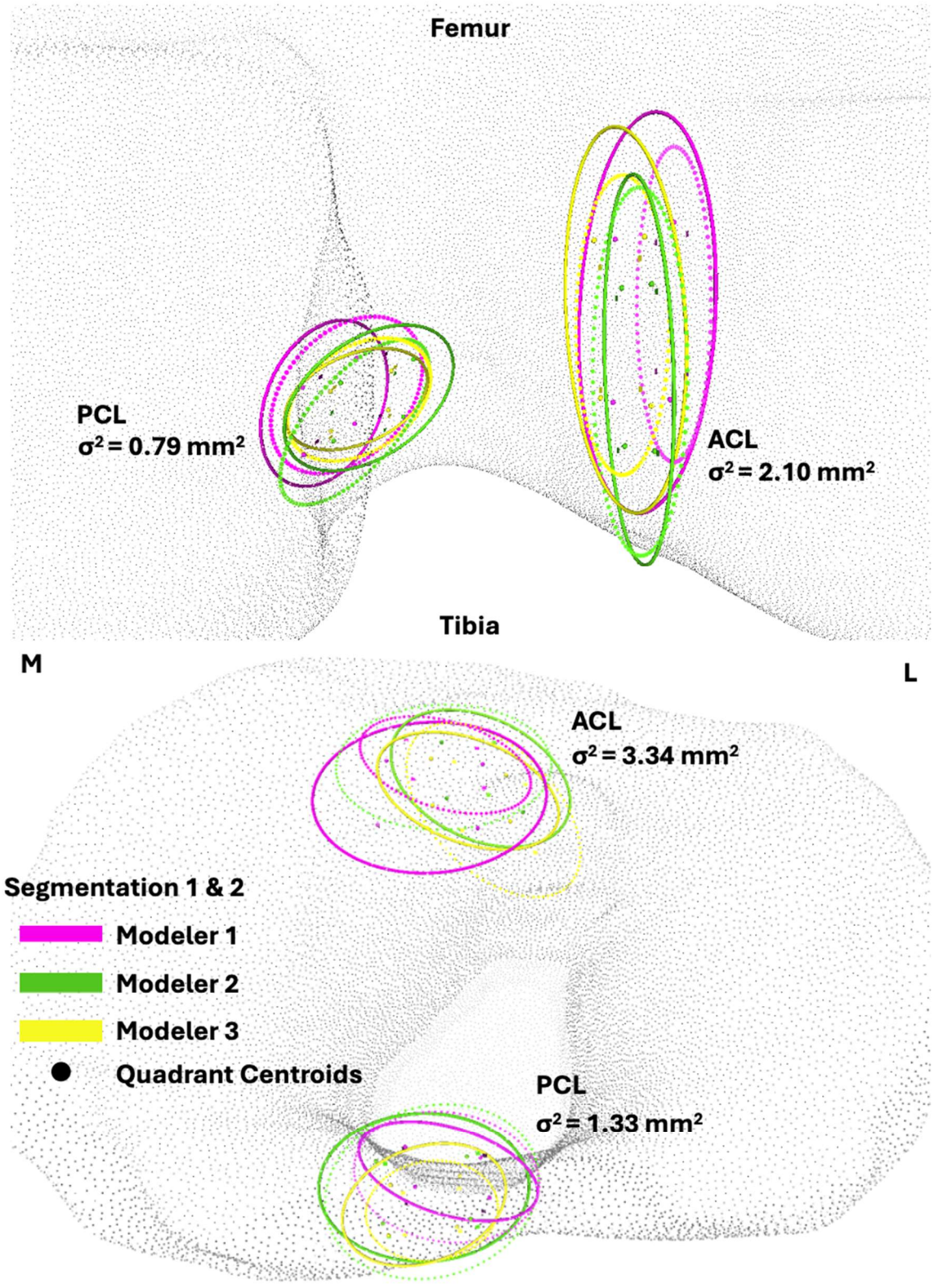


Figure 1. Femoral and tibial attachment sites of the ACL and PCL: segmented twice and fitted with ellipses by three modelers. The variance (σ^2) represents the distance between each modeler's centroid and the overall mean centroid for each site. The medial and lateral sides are labelled by M and L, respectively.

References (Optional)

[1] W. Zaylor and J. Halloran, *Cleveland State University*, 2021

[2] N.B. Rooks et al. , *J Biomechanics*, 2021

Acknowledgements (Optional)

NIH-NIBIB R01EB024573

Session Category

Orthopaedic Biomechanics: Lower Extremities

P3-213

Influence of Stem Neck Design and Polyethylene Liner Configuration on the Range of Motion and Mechanical State of the Liner During Neck-Liner Impingement in Hip Prosthesis

Professor Changhee Cho

The University of Kitakyushu, Kitakyushu, Fukuoka, Japan

Introduction

Wear and damage of ultra-high-molecular-weight polyethylene (UHMWPE) liners after total hip arthroplasty cause serious clinical and biomechanical complications, thereby restricting the longevity of hip prostheses. In retrieved hip prostheses, wear and damage of the UHMWPE liner due to neck-liner impingement are frequently observed. It is well established that the neck-liner impingement significantly contributes to increases in wear and damage of the liner. This study aimed to investigate the influence of stem neck design and liner configuration on the range of motion (ROM) and mechanical state of the liner during neck-liner impingement.

Methods

Finite element simulations of neck-liner impingement were performed. The stem neck, femoral head, and acetabular cup were modeled using Ti-6Al-4V alloy, while the UHMWPE liner was defined as an elastic-plastic material with a Poisson's ratio of 0.45. Two types of neck geometries, a tapered neck and a cylindrical neck, were designed with an equivalent safety factor. Two liner configurations, a standard liner and an elevated rim liner, were also modeled, resulting in a total of four different neck-liner combinations. A coefficient of friction of 0.1 was assigned to all contact interfaces.

Results

Among the four combinations analyzed, the tapered neck with the standard liner showed the greatest ROM, whereas the cylindrical neck with the elevated rim liner showed the smallest ROM. Regarding the mechanical state of the liner during impingement, the cylindrical neck with the standard liner produced the lowest contact stress and plastic strain at the liner, whereas the cylindrical neck with the elevated rim liner resulted in the highest values. These results indicate that both stem neck design and its combination with the liner configuration markedly influence ROM and mechanical state during impingement.

Discussion

Accurate evaluation of the influence of stem neck design on neck-liner impingement in hip prosthesis requires comparisons to be performed using stem necks designed with equivalent safety factors. To minimize the wear and damage of the UHMWPE liner due to neck-liner impingement, the stem neck design should be optimized by balancing the safety factor, range of motion, and the mechanical state of the UHMWPE liner.

Acknowledgements (Optional)

This work was supported by JSPS KAKENHI Grant Number JP24K15751.

Session Category

Orthopaedic Biomechanics: Lower Extremities

P3-214

Lateral Wedge Insoles Modulate Lower-Limb Biomechanical Strategy During Level Walking in Patient with Anterior Cruciate Ligament Deficiency

Mr. Chia-Han Hu[1], Dr. Jr-Yi Wang[1,2], Dr. Shiuan-Huei Lu[1], Dr. Kuan-Wen Wu[3,4,5], Dr. Ting-Ming Wang[3,4,5], Prof. Tung-Wu Lu[1,4,5]

[1]Department of Biomedical Engineering, National Taiwan University, Taipei, Taipei, Taiwan. [2]Department of Orthopaedics, Shuang Ho Hospital, Taipei Medical University, Taipei, Taipei, Taiwan. [3]Department of Orthopaedic Surgery, School of Medicine, National Taiwan University, Taipei, Taipei, Taiwan. [4]Department of Orthopaedic Surgery, National Taiwan University Hospital, Taipei, Taipei, Taiwan. [5]Health Science and Wellness Research Centre, National Taiwan University, Taipei, Taipei, Taiwan

Introduction

Anterior cruciate ligament deficiency (ACLD) alters gait patterns and knee joint loading, potentially increasing the risk of secondary joint degeneration. Lateral wedge (LW) insoles have been proposed as a conservative intervention to redistribute joint loading [1], yet their effects on spatiotemporal behaviour and lower-limb kinetics—including joint moments and forces—during level walking in individuals with ACLD remain insufficiently understood.

Methods

Thirteen ACLD patients and twelve healthy controls performed level walking under three footwear conditions: control shoes, 3° lateral wedge, and 6° lateral wedge insoles. Spatiotemporal parameters and three-dimensional knee joint moments and forces were calculated using inverse dynamics [2]. Analyses were conducted at gait events—heel strike (HS), contralateral toe-off (CTO), contralateral heel strike (CHS)—and gait phases—initial double-limb support (IDLS), single-limb support (SLS), and terminal double-limb support (TDLS). Statistical significance was set at $p < 0.05$.

Results

Lateral wedges produced mechanics alterations across the hip, knee, and ankle during ACLD gait. Hip anterior force decreased at HS but increased during SLS and CTO, whereas proximal force decreased only in SLS and lateral force rose throughout IDLS–TDLS except at HS and TO. Knee mechanics showed reduced adduction moment at HS, increased early-stance flexion moment, and elevated anterior joint force across IDLS and SLS. Ankle mechanics demonstrated increased abduction moment at HS and CTO but decreased values during SLS and TDLS, with flexion moment elevated at HS and IDLS. Corresponding

joint forces increased anteriorly at IDLS, proximally at HS, and laterally at CTO, indicating phase-dependent redistribution of distal loading.

Discussion

Lateral wedges altered lower-limb kinetics through phase-dependent redistributions rather than uniform unloading. Increased hip and ankle loading during SLS and CTO suggests compensatory adjustments to maintain frontal-plane stability in ACLD gait, while reduced knee adduction moment at HS indicates partial medial-knee unloading. The selective increases in distal joint forces at IDLS and CTO further reflect shifts in foot–ground interaction that propagate proximally. Collectively, these findings highlight wedge-induced changes that modify—but do not normalize—the ACLD kinetic strategy.

Images (Optional)

Table 1. Effects of lateral wedge angles on knee joint moments and joint forces during level walking.

LW (deg)	0°	3°	6		0°	3°	6°
Abduction Moment				**Anterior Force**			
HS	0.17 ± 0.23	0.17 ± 0.33	0.08 ± 0.25	CTO	15.48 ± 6.68	15.62 ± 5.95	15.69 ± 7.23
CTO	3.79 ± 1.18	3.86 ± 1.15	3.42 ± 0.69	IDLS	10.42 ± 2.99	10.58 ± 2.99	10.53 ± 3.46
CHS	3.56 ± 0.93	3.31 ± 1.02	3.04 ± 0.99	SLS	4.12 ± 5.92	3.86 ± 5.24	4.87 ± 6.24
SLS	3.87 ± 0.83	3.55 ± 0.91	3.44 ± 0.77	**Proximal (Axial) Force**			
TDLS	−0.30 ± 1.92	−0.32 ± 1.83	0.06 ± 2.25	HS	4.13 ± 0.95	3.58 ± 1.19	3.83 ± 1.08
Flexion Moment				**Lateral Force**			
SLS	−0.30 ± 1.92	−0.32 ± 1.83	0.06 ± 2.25	HS	−1.52 ± 0.74	−1.30 ± 0.66	−1.14 ± 0.59
Rotation Moment				IDLS	6.45 ± 3.07	6.38 ± 3.21	6.03 ± 3.27
CTO	−0.40 ± 0.44	−0.43 ± 0.49	−0.30 ± 0.45	SLS	10.59 ± 6.26	10.36 ± 6.15	10.14 ± 6.18
LW (deg): 0° = shoe-only condition; 3° and 6° = lateral wedges				TDLS	6.92 ± 3.84	6.67 ± 3.81	6.60 ± 3.91

References (Optional)

[1] Calvin, T. F., et al. J. Appl. Biomech 40(4), 270-277, 2024.

[2] TW Lu and J.J.O'Connor. J. Biomech 90: 129-134, 1999.

Acknowledgements (Optional)

This work was supported by a grant from Taipei Medical University–Shuang Ho Hospital (110TMUSHH-09). We thank all co-authors for their contributions to this study.

Session Category

Orthopaedic Biomechanics: Lower Extremities

P3-215

Reliability of a Single Mobile Device Platform for Measuring Lower Extremity Joint Angles

Ms Rebecca Ward BSc physio[1], Prof Ciaran Knut Simms BA BAI PhD[1,2], Ms Alice Hussey BSc[1], Ms Thea Flanagan BSc[1], Ms Aileen Stenson BSc[1], Dr Fearghal Behan PhD[1]

[1]Trinity College Dublin, Dublin, Leinster, Ireland. [2]KineMo, Dublin, Leinster, Ireland

Introduction

There is a clinical need for a quick and accessible method to evaluate an athlete's movement quality to aid the prevention and treatment of injuries. However, visual observation is often the only method used to assess kinematics, due to challenges with using goniometers in non-static poses and the high cost and time-consuming process required with wearable sensors and multi-camera motion capture systems. A newly developed platform (KineMo), using a single mobile device camera, measures three-dimensional whole-body joint angles and aims to address this clinical need. Although the accuracy has been previously reported [1] and the platform is in use, the reliability and its suitability for clinical practice have not been previously assessed. Knee flexion angles during squatting movements have been found to decrease following ACL injury [2]. Therefore, tracking the return of knee flexion towards baseline is an important marker of injury recovery [2].

Methods

Following ethical approval, twenty-six healthy participants completed three commonly used clinical movements; back squat, sit to stand (STS) and single leg squat (SLS). Maximum and minimum knee flexion angles were extracted. Intra-rater reliability was assessed using the Intraclass correlation coefficient (ICC), minimal detectable change (MDC) and standard error of measure (SEM). Reliability was assessed by comparing two trials each consisting of three repetitions. Concurrent validity was also assessed using side view cameras.

Results

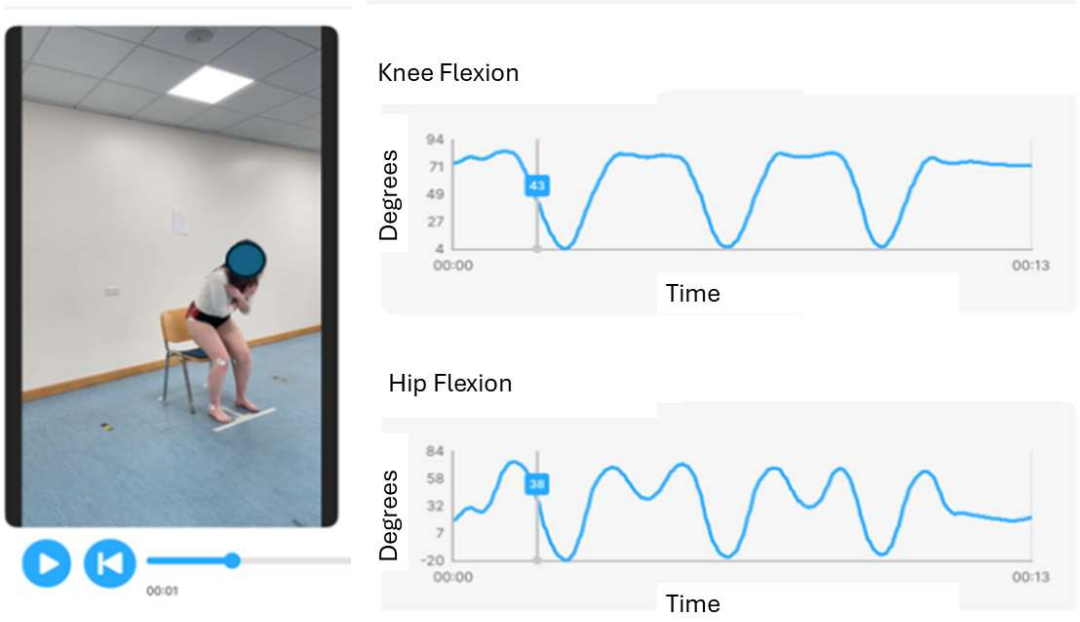
The platform demonstrated excellent intra-rater reliability (ICC values >.9). SEM ranged from 0.6-2.7 degrees and MDC 1.7-7.6 degrees. STS showed the lowest measurement error while SLS demonstrated higher SEM and MDC values, indicating reduced reliability with more complex tasks. Comparing knee angle range of movement measurements from

KineMo and side view cameras, the mean differences for back squat, SLS and STS were respectively 1, 3 and 5 degrees.

Discussion

The platform was found to be highly reliable for measuring knee flexion angles in squats, single leg squats and sit to stand movements in healthy adults. These findings suggest it may be suitable for reliably measuring lower limb kinematics in clinical practice.

Images (Optional)



References (Optional)

1]. Mercadal-Baudart et al., Cell Heliyon 2024.

[2] Chiu et al., J Ortho Surg., 2002.

[3] Yokoyama et al., J Phys Ther Sci. 2021

Session Category

Orthopaedic Biomechanics: Lower Extremities

P3-216

Limb Asymmetry of Gastrocnemii Cross-Sectional Area in Individuals with Unilateral Achilles Tendinopathy

Dr. Claudia Kacmarcik PT, DPT, Dr. Stephanie Cone PhD, Dr. Karin Silbernagel PT, ATC, PhD, FAPTA

University of Delaware, Newark, Delaware, United States

Introduction

Achilles Tendinopathy is a chronic condition characterized by altered tendon structure, pain with activity, and functional deficits. The degree of impairment varies widely; however, it is unknown if this is related to pain, muscle atrophy, or both. Therefore, the purpose of this study was to assess gastrocnemius muscle size symmetry and changes over a 16-week exercise intervention in individuals with unilateral Achilles tendinopathy.

Methods

108 participants (59 female) aged 47.3±12.7, with unilateral Achilles tendinopathy participating in an IRB-approved, prospective, 16-week standard exercise program were evaluated at baseline, 8, and 16 weeks. Symptom questionnaires, pain with palpation and hopping, and ultrasound imaging were assessed.

Extended-field-of-view B-mode ultrasound (10MHz) was used to obtain cross-sectional area (CSA, cm^2) of the gastrocnemii at 1/3 tibial length. Gastrocnemii CSA limb symmetry (LSI, [(most symptomatic limb/least symptomatic limb)*100], %) was determined. Participants were grouped by baseline muscle size LSI: <90%, 90-110%, and >110%. One-way ANOVA assessed group differences in demographics, symptoms, and function, and a 3x3 Mixed Model assessed differences in gastrocnemii CSA LSI across groups over time, with post-hoc comparisons as needed.

Results

At baseline, there were no differences between groups in age, sex, BMI, Achilles tendon CSA, VISA-A score, pain with hopping, or pain with palpation (Table 1). The <90% muscle size LSI group had worse function, with lower heel-rise work LSI compared to other groups($F[2,102]=5.47$, $p=0.006$).

For gastrocnemii CSA LSI, there was a significant main effect of group ($F[2,88.93]=49.82$, $p<0.001$), but not timepoint ($F[2,84.11]=0.30$, $p=0.741$) and a significant interaction of

group and timepoint (F[2,84.37]=9.15, p<0.001). At each timepoint, limb symmetry was lowest in <90% and highest in >110%, except at 16 weeks when <90% was not significantly different from 90-110%. Compared to baseline, <90% LSI and >110% LSI were more symmetrical at 8 and 16 weeks.

Discussion

There were no differences in pain between groups, while gastrocnemii CSA LSI converged towards symmetry during a standard 16-week treatment. These findings suggest functional ties to muscle atrophy and indicate that exercise treatment for unilateral Achilles tendinopathy is effective in normalising muscular symmetry.

Images (Optional)

Gastrocnemius LSI grouping		**<90%** Mean ± SD	**90-110%** Mean ± SD	**>110%** Mean ± SD	**Sig** (p)
Age (years)		52 ± 10	48 ± 13	49 ± 13	0.190
BMI (kg/m2)		32 ± 6	29 ± 6	29 ± 5	0.478
Achilles Tendon CSA LSI (%)		155.7 ± 75.2	134.4 ± 43.7	163.5 ± 70.0	0.063
Pain with Hopping		3.7 ± 3.1	3.3 ± 2.2	4.1 ±2.6	0.357
Heel Rise Work (J)		58.7 ± 47.6	89.0 ± 33.9	100.7 ± 30.9	<0.001
Gastrocnemius CSA LSI (%)	Baseline (*group designation)	82 ± 6	100 ± 5	121 ± 8	
	8 Weeks	92 ± 9	101 ± 11	111 ± 12	
	16 Weeks	95 ± 11	100 ± 9	111 ± 15	

Table 1: Demographic and baseline characteristics across groups *determined by baseline gastrocnemius CSA LSI, as well as gastrocnemius CSA LSI across timepoints.

Acknowledgements (Optional)

Funding from R01AR072034

Session Category

Orthopaedic Biomechanics: Lower Extremities

P3-217

From Nanosheets to Joint Longevity: MXene-Enhanced CoCrMo for Orthopaedic Implants

Dr David Necas[1], Mr Daniel Nemecek[1], Dr Max Marian[2,3], Prof Martin Vrbka[1]

[1]Brno University of Technology, Brno, South Moravian Region, Czechia. [2]Universidad Católica de Chile, Santiago, Santiago, Chile. [3]Leibniz University Hannover, Garbsen, Garbsen, Germany

Dr David Necas

Mr Daniel Nemecek

Dr Max Marian

Introduction

Orthopedic implants face persistent challenges of wear and debris generation, limiting their longevity. Conventional alloys such as CoCrMo are strong and biocompatible but suffer from insufficient tribological stability. Two-dimensional (2D) nanomaterials, especially MXenes, have emerged as promising reinforcements, coatings, or lubricant additives due to their layered structure and self-lubricating potential. Recent studies suggest that MXenes embedded in metallic matrices or fluids may form tribo-films that reduce friction and wear. This study explores MXene-reinforced CoCrMo composites tested in simulated physiological environments, providing preliminary experimental validation of their tribological benefits.

Methods

MXene-reinforced CoCrMo pins were fabricated and tested using a pin-on-plate setup against UHMWPE plates. Two lubricants were applied: phosphate-buffered saline (PBS,) and simulated synovial fluid (SK). During sliding, the coefficient of friction (CoF) was continuously recorded. Before and after testing, worn surfaces were inspected to evaluate wear scars and detect possible nanoparticle embedding. Reference pins from stainless

steel were included for comparison. Surface preparation prior to testing ensured consistent contact conditions and reduced variability.

Results

The integration of MXenes into CoCrMo composites consistently improved tribological and mechanical performance. Reinforced samples demonstrated higher surface hardness, leading to better resistance against plastic deformation. Friction measurements revealed a more stable coefficient of friction compared to reference pins, with lower overall values in both lubricating environments. Wear analysis confirmed reduced surface damage on MXene-containing samples, where smoother wear tracks and fewer scratches were observed. Additionally, nanoparticles appeared embedded in the contact zone, suggesting the formation of protective tribo-layers. Biocompatibility assessments showed no adverse effects, supporting the potential for biomedical applications.

Discussion

Although preliminary, the findings indicate that MXenes enhance tribological stability of CoCrMo/UHMWPE pairs under physiological conditions. Differences between PBS and SK highlight the importance of lubricant chemistry, while nanoparticle embedding suggests a potential self-lubricating mechanism. Compared to stainless steel, MXene-reinforced CoCrMo demonstrated both lower CoF and reduced wear, supporting its promise for next-generation implants. Future studies should quantify wear volumes, extend testing durations, and optimize MXene concentration. Together, these early results contribute to the broader vision of integrating 2D nanomaterials into biomedical implants for improved durability and patient outcomes.

References (Optional)

Acknowledgements (Optional)

Czech Science Foundation 25-15390S

Session Category

Orthopaedic Biomechanics: Lower Extremities

P3-218

A Navigation-Guided A-mode Ultrasound System for Improving Non-Invasive Tibiofemoral Joint Kinematic Estimation

Mr. Dennis Christie[1], Dr. René Fluit[2], Dr. Guillaume Durandau[3], Prof. Massimo Sartori[1], Prof. Nico Verdonschot[1,4]

[1]University of Twente, Enschede, Overijssel, Netherlands. [2]University of Groningen, Groningen, Groningen, Netherlands. [3]McGill University, Montreal, Quebec, Canada. [4]Radboudumc, Nijmegen, Gelderland, Netherlands

Introduction

Accurate measurement of knee joint kinematics is essential for studying musculoskeletal function, yet current imaging techniques are limited by radiation exposure or restrictive setups. A-mode ultrasound with optical trackers offers a safer alternative, but its dynamic reliability remains underexplored. Earlier proof-of-concept showed the method is technically feasible but failed to reproduce the ground-truth kinematic pattern. We argued that it originated from bone-peak misidentification in the one-dimensional A-mode signal. We addressed this by developing an intuitive guidance for A-mode placement. It used B-mode ultrasound to reconstruct bone surface to guide A-mode placement and peak selection, aiming to improve femoral and tibial pose and tibiofemoral kinematics.

Methods

A cadaveric leg was CT-scanned and instrumented with optically tracked bone pins as ground truth. During initialization phase, a tracked B-mode probe reconstructed local bone surfaces. A-mode beams were visualized relative to the surface to optimize placement and bone-peak selection. A-mode depths were converted into 3D bone points and rigidly registered to CT-derived tibial and femoral bone models. Tibiofemoral kinematics were computed using a joint coordinate system and filtered using Unscented Kalman Filter framework. Navigation-guided measurements were compared with non-navigated as the baseline.

Results

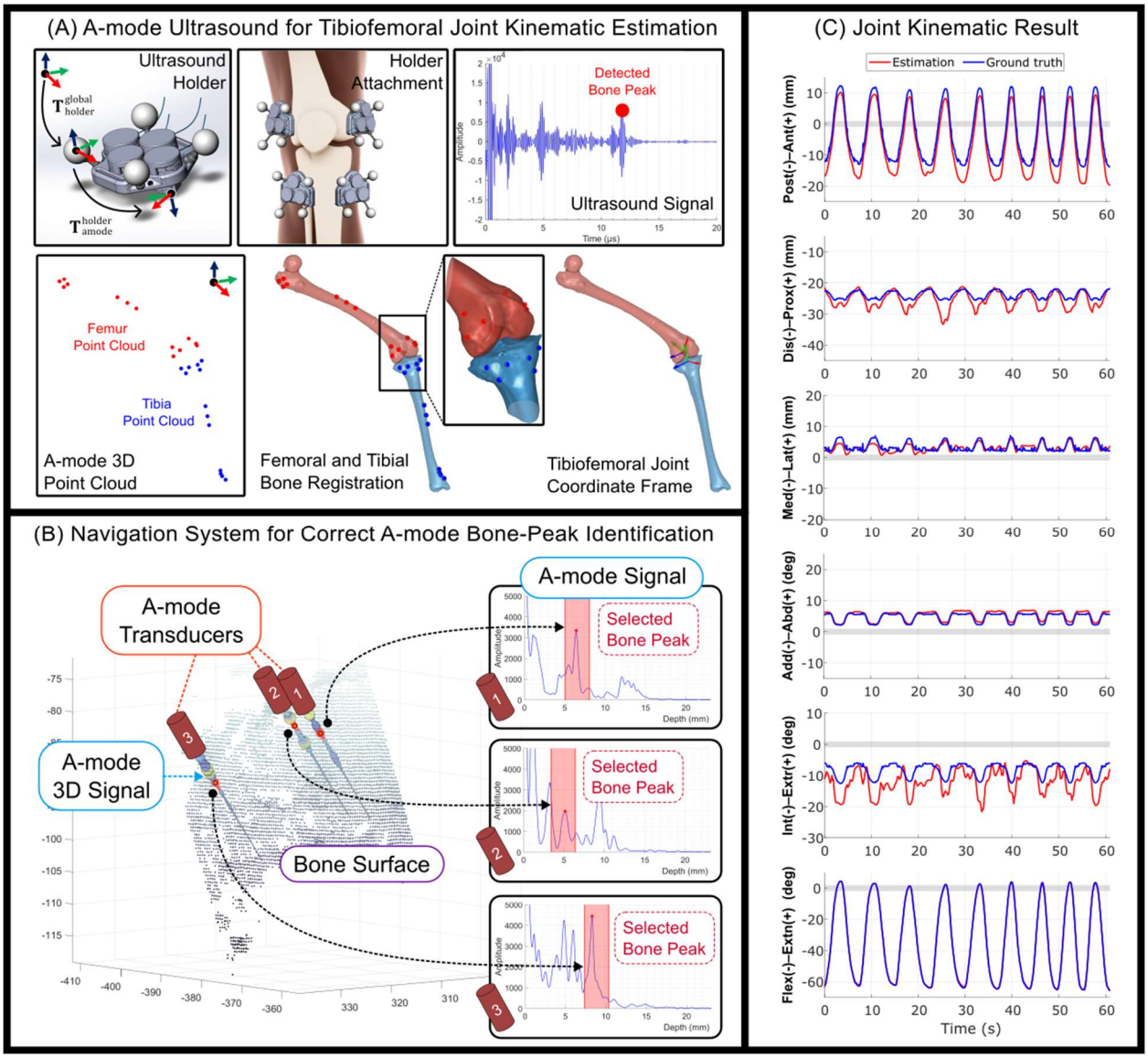
During cyclic flexion–extension task, the navigation-guided approach achieved joint kinematic RMSE 0.51±0.49° and 0.72±0.97° for adduction–abduction and flexion–extension, 1.00±0.97 mm for medial–lateral translation; distal–proximal and anterior–posterior translations were higher at 2.30±1.60 and 3.70±1.06 mm. Internal–external

rotation had the largest error at 4.56±2.52° yet still outperformed non-navigated baselines. Cycle-wise translation and rotation errors remained stable; linear fits showed no significant trends, with navigation-guided estimates consistently yielding the lowest errors per cycle. Throughout cycle, bone registration with navigation-guided yielded the lowest RMSE as well.

Discussion

Across experiments, the navigation-guided approach consistently outperformed the non-navigated baseline. By visualizing A-mode beams directly against B-mode–derived bone surfaces, bone-peak selection becomes a geometrically constrained task rather than a purely signal-driven guess. This stabilizes the full processing chain, from point-cloud generation to pose and joint kinematic estimation. Overall, the findings demonstrate a clear message: accurate initialization at the signal level is essential for reliable ultrasound-based tibiofemoral kinematics.

Images (Optional)



Session Category

Orthopaedic Biomechanics: Lower Extremities

P3-219

Effect of Custom In-Shoe Orthotics on the Talus-First Metatarsal Angle in Adult Flatfoot: A Pilot Study

Ms. Devin Wong BS, Dr. Bopha Chrea MD, Dr. Donald Anderson PhD, Dr. Jason Wilken PT, PhD

University of Iowa, Iowa City, IA, United States

Introduction

Progressive collapsing foot deformity, commonly known as flatfoot, affects as many as five million individuals in the US, causing foot pain and instability [1]. In-shoe orthotics are a primary non-invasive treatment to provide mechanical support, correct foot posture, and mitigate pain with flatfoot–however, efficacy data are inconsistent [2]. This study utilizes cone-beam weight bearing CT (WBCT) to explore changes in the physiologically loaded talus-first metatarsal angle (TFMA), a measure of foot collapse, in response to custom in-shoe orthotics in adults with flatfoot.

Methods

Individuals aged 18-65yrs with flatfoot who wear prescribed, custom, full-length, stiff, in-shoe orthotics were recruited. Standing bilateral foot and ankle WBCT scans (HiRise; CurveBeam AI) were obtained while shod: one with and without in-shoe orthotics. Scans were automatically segmented using a commercial service (BoneLogic; Disior) to obtain bone models. Bone local coordinate reference frames were obtained using the AAFACT toolbox [3]. The 3D TFMA was measured relative to the anterior-posterior axis using Euler rotation methodology and projected onto anatomical planes [4]. The 2D TFMA was manually measured from CT slices including the talus and first metatarsal using custom-written code (MATLAB; MathWorks) [5].

Results

Three participants (i.e., six feet) are included in this ongoing study (2F/1M, 43±4.4yrs, 1.71±0.10m, 66±4kg). The 2D TFMA was 15.0±6.6° without and 12.0±7.4° with an orthotic. The mean change between conditions was -4.1±4.9°. The 3D TFMA projections are displayed in Figure 1.

Discussion

These preliminary data show how custom in-shoe orthotics alter bony alignment in adults with flatfoot. The average 4.1° decrease in the 2D TFMA indicates that orthotics elevate the otherwise-collapsed medial arch. An improved understanding of how custom in-shoe

orthotics change bony alignment can inform orthotic design to mitigate pain and provide support.

Images (Optional)

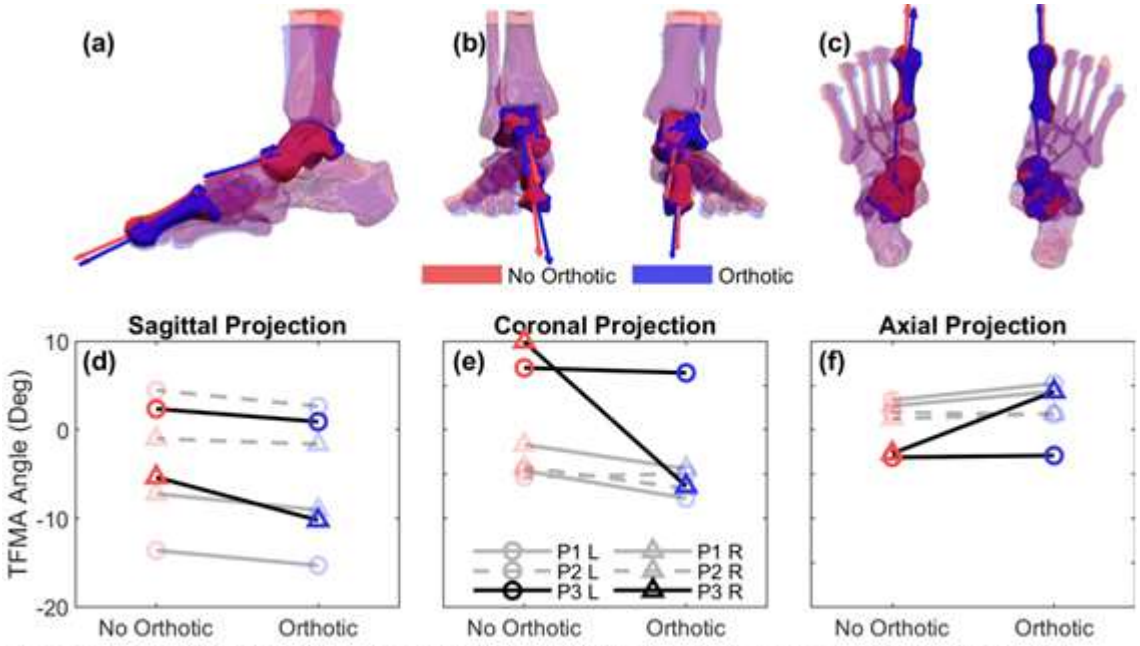


Figure 1. The TFMA projected onto anatomical planes. (a-c) 3D foot and ankle models of P3 with the anterior-posterior axes of the talus and first metatarsal. (a) The sagittal plane shows the right foot only. The models are registered with respect to the calcaneus center origin. (d-f) The TFMA projections by orthotic condition and participant. L is the left foot; R is the right foot. Dorsiflexion and abduction are represented by positive angles.

References (Optional)

[1] Yurt Y et al., Eur J Phys Rehabil Med, 2019. [2] Herchenröder M et al., J Foot Ankle Res, 2021. [3] Peterson AC et al., Front Bioeng Biotechnol. 2023. [4] Cai Y et al., BMC Med Imaging, 2024. [5] Fayed AM et al., Foot & Ankle Orthop, 2025.

Acknowledgements (Optional)

Tyce Marquez produced the bone models while visiting the Lenz Lab at the University of Utah.

Session Category

Orthopaedic Biomechanics: Lower Extremities

P3-220

Long Bone Pediatric Morphological Analysis of Charcot Marie Tooth Disease

Ms. Eliana Moreno, Ms. Melissa Requist, Mr. Andrew Peterson, Dr. Amy Lenz

University of Utah, Salt Lake City, UT, United States

Introduction

Charcot-Marie-Tooth disease (CMT) is a sensory and motor neuropathy associated with cavovarus foot deformity, consisting of differences in foot alignment and bone structure. Cortical thickness and bone mineral density are correlated with muscle strength, which decreases in CMT. Health of long bones, specifically tibia, fibula, and metatarsals, can be measured by analyzing cortical thickness in the diaphysis. Decreased cortical thickness is associated with increased fracture risk. Increased fracture risk has been seen in children with CMT, as has variation in bone shape in the foot and ankle, but the impact of CMT on bone structure and health is not well characterized. This study investigates differences in cortical thickness between pediatric patients with CMT and controls to better understand fracture risk and bone health in this disease.

Methods

Weight-bearing computed tomography (WBCT) images were prospectively collected from pediatric patients, 5 with CMT and 5 controls, with no difference in age between groups. Segmentations were created semi-automatically, manually cleaned, verified, and thresholded to only include cortical bone. Three-dimensional parts were generated, aligned to an anatomic coordinate system, and consistently cut to isolate diaphyseal bone. Automatic cortical thickness analysis was applied and averaged across each bone. Differences in cortical thickness between CMT and control groups were tested using a two-tailed t-test (α=0.05).

Results

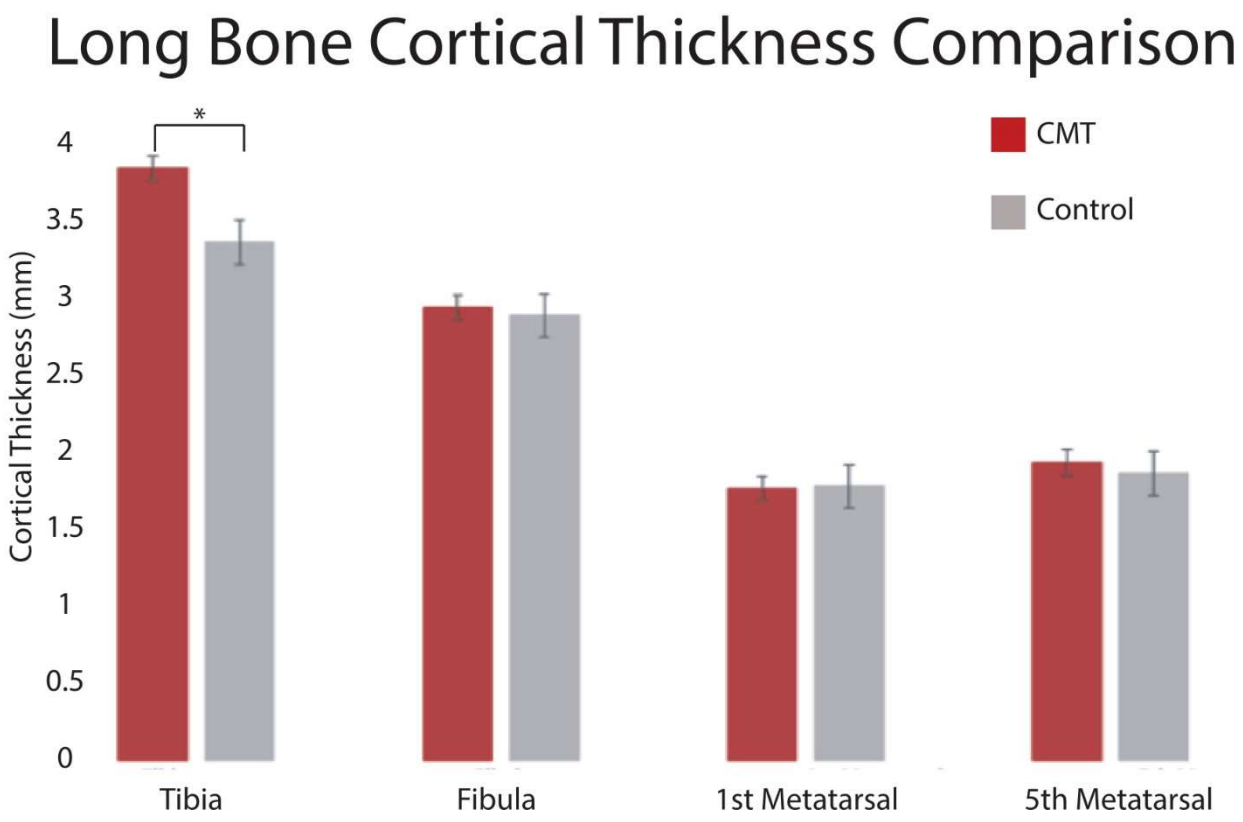
A significantly greater cortical thickness was seen in the CMT versus control groups in the tibia (p=0.02) (Fig. 1). However, there were no significant differences in cortical thickness between groups in the other bones, but the CMT group showed trends of higher cortical thickness.

Discussion

This data shows a significantly greater cortical thickness in pediatric CMT than in pediatric controls for the tibia. Factors contributing to differences may include differences in bone geometry, bone loading, or neurologic input between CMT and control during the

development of the foot and ankle bones. A higher fracture risk has been seen among children with CMT, but these data suggest this may not be due to cortical thickness. Inclusion of additional data may allow for better analysis of regional differences in cortical thickness in CMT. Further, analysis of bone density may better characterize bone structure within CMT.

Images (Optional)



Session Category

Orthopaedic Biomechanics: Lower Extremities

P3-221

Primary Stability of Percutaneous Implants for Transfemoral Amputees: A Biomechanical Ex Vivo Study

Mr Emir Benca[1], Ms Elise Joulain[2,1], Mr Pablo Vazquez Conde[1], Mr Andreas Strassl[1], Ms Lena Hirtler[1], Prof Reinhard Windhager[1], Prof Dieter Pahr[3], Prof Rickard Brånemark[4,5], Mr Gerhard Hobusch[1], Mr Alexander Synek[3]

[1]Medical University of Vienna, Vienna, Vienna, Austria. [2]École Polytechnique Fédérale de Lausanne (EPFL), Lausanne, Waadt, Switzerland. [3]TU Wien, Vienna, Vienna, Austria. [4]Gothenburg University, Gothenburg, Västra Götalands län, Sweden. [5]Massachusetts Institute of Technology, Cambridge, Massachusetts, United States

Introduction

The prevalence of lower extremity amputation is substantial. An alternative rehabilitation option is the direct attachment of the prosthesis to the bone following amputation via percutaneous osseointegration [1]. The treatment of transfemoral amputees with osseointegrated implants for prosthetic anchorage requires long rehabilitation periods to minimize relative motion between bone and implant, which could impair osseointegration and implant stability. This study aimed to assess the primary stability of the Osseointegrated Prostheses for the Rehabilitation of Amputees (OPRA) Implant System under uniaxial loading, with the goal of supporting earlier load bearing and patient mobilization.

Methods

Fifteen human femoral specimens were prepared and instrumented with the OPRA implant system. Each specimen was subjected to 4,750 loading cycles with amplitudes increasing from 200 to 2,000 N at 10° hip flexion and 10° hip adduction mimicking the heel strike position (Figure 1). Relative displacement between the implant system and the proximal, middle, and distal femoral shaft was measured using a motion tracking system, and stiffness was calculated at the corresponding positions.

Results

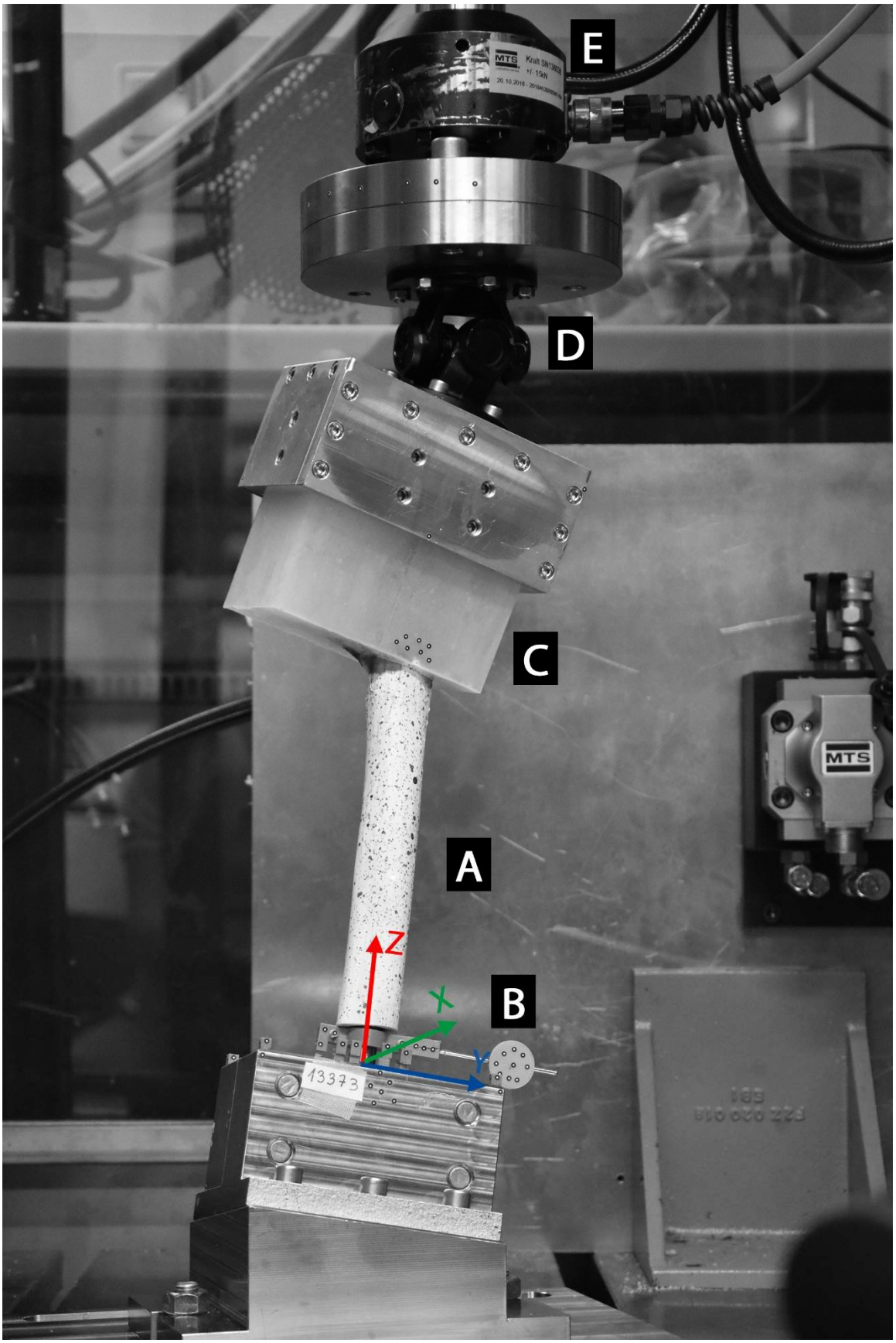
No implant failure or loosening was observed in any of the specimens. Maximum relative displacement of the proximal, middle, and distal femur remained below 80 µm, 60 µm, and 10 µm, respectively. Existing literature reports a mean micromotion of approximately 112

μm for implants that successfully osseointegrate, compared with about 349 μm for implants that fail to do so [2]. Stiffness did not change with increasing applied loads ($0.332 \leq p \leq 0.736$).

Discussion

The absence of stiffness changes and the low displacement values, particularly in the distal femur, indicate no loosening or failure at the bone–implant interface. These results suggest that the OPRA implant system provides sufficient primary stability under predominantly axial loading in more aggressive rehabilitation. Further research should investigate primary stability under bending and torsional conditions.

Images (Optional)


E
D
C
A
B
Z
X
Y
13373
MTS

References (Optional)

[1] Rickard Brånemark *et al.*, J Rehabil Res Dev, 2001
[2] Nupur Kohli *et al.*, Sci Rep, 2021

Acknowledgements (Optional)

This study was partially funded by the Austrian Society for Orthopedics (Österreichische Gesellschaft für Orthopädie). Implants and instruments were provided by Integrum AB.

Session Category

Orthopaedic Biomechanics: Lower Extremities

P3-222

Injury-Specific Asymmetry in Achilles Tendon and Triceps Surae Morphology in Individuals With Achilles Tendinopathy and Achilles Tendon Rupture

Dr. Erica Bell PhD, Miss Meghna Annasagaram, Dr. Karin Gravare Silbernagel PT, ATC, PhD, FAPTA, Dr. Stephanie Cone PhD

University of Delaware, Newark, Delaware, United States

Introduction

The Achilles tendon is composed of three subtendons that insert at the medial gastrocnemius, lateral gastrocnemius, and soleus. Common injuries to the Achilles tendon include Achilles tendinopathy (repetitive overuse) and Achilles tendon rupture (acute overload). Although both pathologies involve the Achilles tendon, they have distinct etiologies, injury progressions, clinical indications, and treatments [1]. Thus, injury-specific research and clinical management is pivotal. The objective of this study was to identify specific morphological changes in the Achilles tendon and triceps surae muscles in individuals with Achilles tendinopathy and Achilles tendon rupture.

Methods

Fifteen subjects were recruited, with five subjects each in the healthy control (3F/2M, Age: 40.0 ± 19.4), Achilles tendinopathy (3F/2M, Age: 53.8 ± 9.9), and Achilles rupture groups (2F/3M, Age: 33.4 ± 12.5). Each subject completed a 3TMRI scan using published sequences [2]. Subtendon length was measured across injuries, and MRIs were segmented to measure muscle and tendon cross-sectional areas (CSAs) bilaterally. Two-way repeated-measures ANOVA (tissue x side) were conducted to determine effects of injury type on Achilles subtendon length and triceps surae muscles CSA.

Results

Gastrocnemius and soleus subtendons were significantly longer than the intact side in the previously ruptured group ($p<0.05$). Previously ruptured tendons had significantly larger CSA than both contralateral tendons and average tendinopathic and healthy groups ($p<0.05$). Soleus CSA was lower in limbs with prior Achilles rupture compared to the intact side ($p<0.05$). Along the length of each tissue, healthy subjects showed symmetrical, tissue-specific morphology, whereas previously ruptured subjects had the most severe between-limb asymmetry (Figure 1).

Discussion

Injury-specific morphometric changes indicate that tendon elongation and CSA vary between Achilles tendinopathy and rupture. Individuals with Achilles tendon rupture have the largest morphometric changes in the injured side compared to individuals with Achilles tendinopathy and healthy individuals. Ongoing work assessing functional outcomes will enhance understanding of the biomechanical impacts of these changes.

Images (Optional)

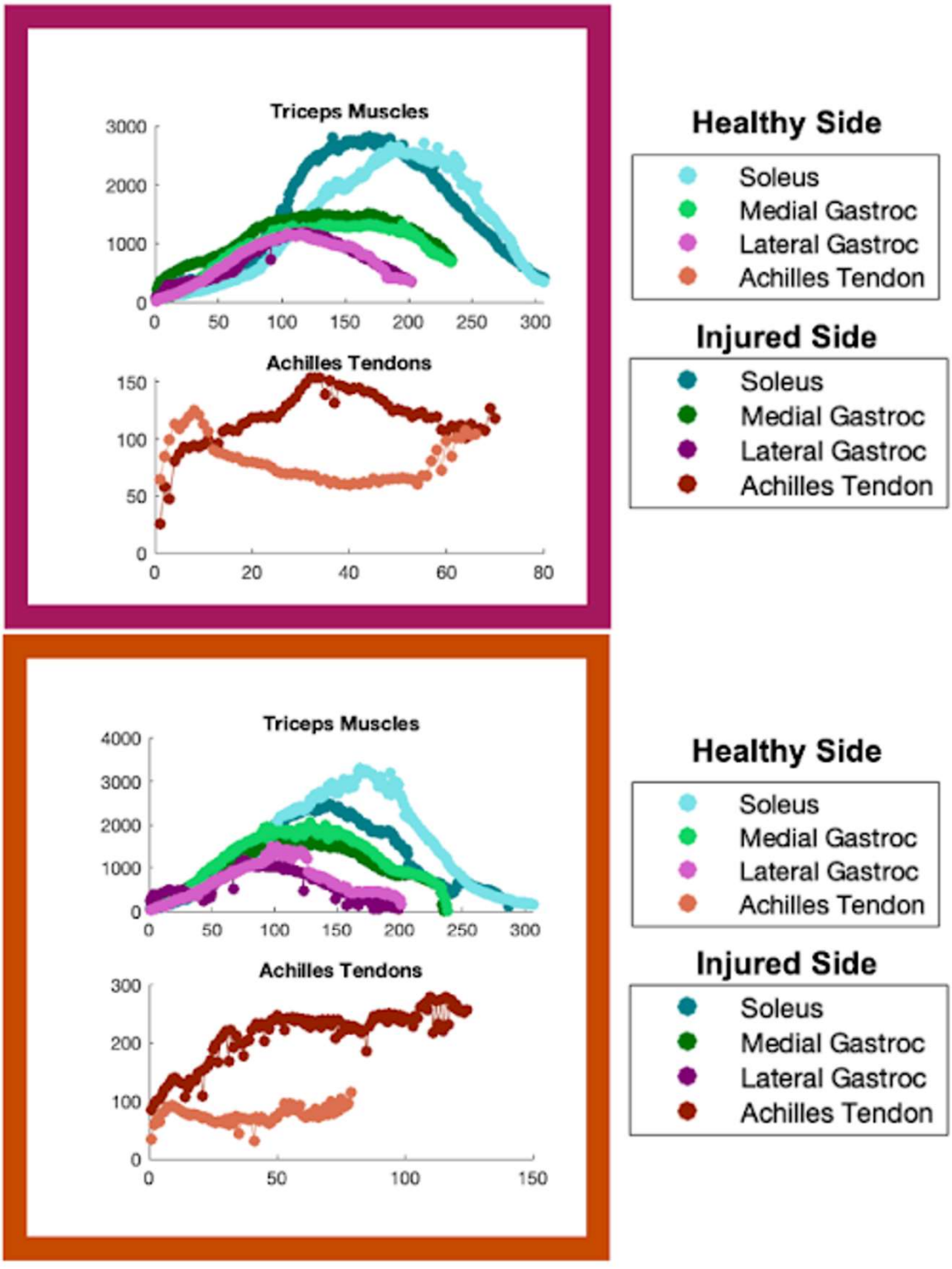


Figure 1 Morphometric changes along tissue length for representative subject of each Achilles tendon pathology, tendinopathy (pink box) and rupture (orange box).

References (Optional)

[1] Maffulli *et al.* , Clinics in Sports Medicine, 2015; [2] Pinel *et al.* , Experimental Gerontology, 2021.

Acknowledgements (Optional)

Funding from NIH R01AR085639.

Session Category

Orthopaedic Biomechanics: Lower Extremities

P3-223

Quantifying the Effect of Orthopedic Foot Surgery in Cerebral Palsy Using Weight-Bearing CT Scans

MSc. Gaia van den Heuvel[1,2], BSc. Lynn Dijkshoorn[1,3], Dr. Ruud Wellenberg[4,2], Dr. Iwan Dobbe[5,2], Dr. Melinda Witbreuk[6], Dr. Geert Streekstra[5,2], Prof. Dr. Mario Maas[4,2], Dr. Wouter Schallig[7,1], Dr. Marian van Beers[1], Prof. Dr. Annemieke Buizer[1,2,8], Dr. Marjolein van der Krogt[1,2]

[1]Amsterdam UMC location Vrije Universiteit Amsterdam, Rehabilitation Medicine, Amsterdam, Noord-Holland, Netherlands. [2]Amsterdam Movement Sciences, Rehabilitation & Development, Amsterdam, Noord-Holland, Netherlands. [3]Delft University of Technology, Department of Biomechanical Engineering, Delft, Zuid-Holland, Netherlands. [4]Amsterdam UMC location University of Amsterdam, Radiology and Nuclear Medicine, Amsterdam, Noord-Holland, Netherlands. [5]Amsterdam UMC location University of Amsterdam, Biomedical Engineering and Physics, Amsterdam, Noord-Holland, Netherlands. [6]Amsterdam UMC location University of Amsterdam, Orthopedic Surgery and Sports Medicine, Amsterdam, Noord-Holland, Netherlands. [7]Erasmus Medical Center, Radiology and Nuclear Medicine, Rotterdam, Zuid-Holland, Netherlands. [8]Emma Children's Hospital, Amsterdam UMC, Amsterdam, Noord-Holland, Netherlands

Introduction

In children with cerebral palsy (CP), foot deformities commonly develop due to altered motor control and loading. If these deformities become severe, orthopedic surgery is necessary to correct the alignment of the foot. However, due to the complex anatomy of the foot, accurate assessment of foot posture from 2D imaging is challenging. Weight-bearing CT (WBCT) enables evaluation of foot posture in three dimensions under natural loading and positioning [1]. However, this has not previously been used to evaluate treatment in children with CP. Therefore, our aim was to quantify the effects of surgery on foot posture using WBCT scans.

Methods

WBCT scans have been acquired before and one year after orthopedic foot surgery, according to clinical practice. From this dataset, we present one representative case. The child with bilateral spastic CP (age 16 years) underwent gastrocsoleus lengthening and plantar fascia release surgery to correct a plantarflexion contracture and cavovarus foot deformity. Local coordinate systems for each foot bone were automatically computed based on the inertial axes of the bones using custom software [2]. Bone translations and

rotations relative to the talus, and the differences between these values pre- and postoperatively, were calculated.

Results

The calcaneus, navicular and first metatarsal all translated more lateral relative to the talus post-operatively (Δ=-3.8, -5.0, -20.2 mm, respectively), and more superior (Δ=0.5, 1.2, 9.5 mm, respectively); see Figure 1. All three bones rotated around the x-axis (mediolateral) more towards dorsiflexion (Δ=-4.5, -4.8, -9.3°, respectively), and around the y-axis (longitudinal) more towards valgus (Δ=10.2, 15.3, 8.4°, respectively). Around the z-axis (transversal), the navicular and first metatarsal rotated more towards abduction (Δ=-17.7, -16.5°, respectively), while the calcaneus relative to the talus rotated slightly more towards adduction (Δ=1.3°).

Discussion

We quantified the effect of orthopedic surgery on a cavovarus foot, indicating the bones translate and rotate such that varus and adduction decrease, realigning the foot to a more neutral position. Based on the full dataset, it will be further investigated which foot posture parameters have most clinical relevance for describing foot deformity correction in CP.

Images (Optional)

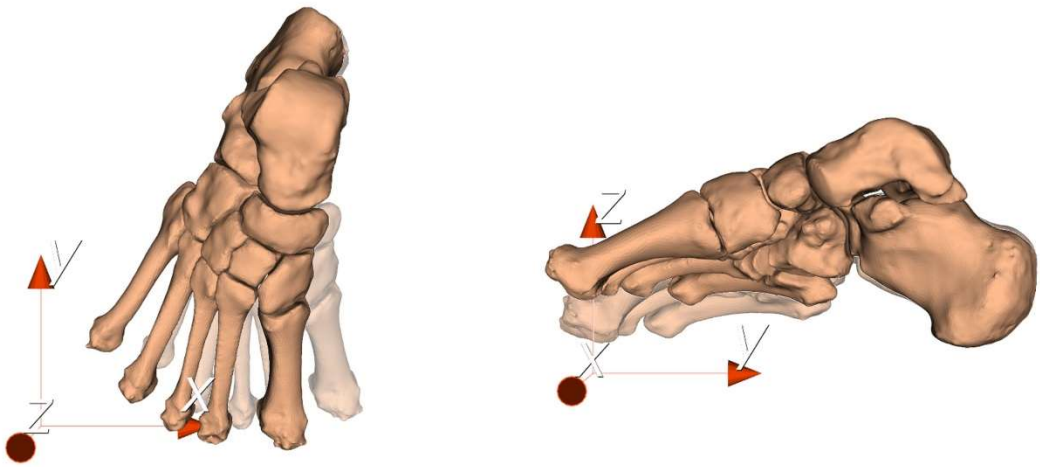


Figure 1. Pre-surgical (semi-transparent) versus post-surgical foot posture (front).

References (Optional)

[1] Wellenberg *et al.*, Skeletal Radiol, 2023

[2] Dobbe *et al.*, IEEE Trans Med Imaging, 2019

Session Category

Orthopaedic Biomechanics: Lower Extremities

P3-224

Subtendon-Specific Load Sharing Modulates Achilles Tendon Stress Concentration: A Finite Element Analysis During Midstance

Mrs. Gisell Natalia Romero Delgado[1], Mr. Santiago Torres Serrato[1], Mr. Chandra Pasapula[2], Dr. Christian Cifuentes - De La Portilla[1]

[1]Universidad de Los Andes, Bogotá, Bogotá D.C, Colombia. [2]Queen Elizabeth Hospital Kings Lynn, King's Lynn, Norfolk, United Kingdom

Mrs. Gisell Natalia Romero Delgado

Introduction

The Achilles tendon (AT) is composed of three subtendons arising from the soleus, medial gastrocnemius (MG), and lateral gastrocnemius (LG). Biomechanical studies suggest that variations in subtendon loading and the twist of the tendon may shape local stress patterns and contribute to the characteristic localization of mid-portion tendinopathy. However, the mechanical relationship between subtendon-specific force distribution and internal stress development remains poorly quantified. We designed a computational foot model that includes a detailed AT anatomy and evaluated its behavior during the midstance. Results suggests that physiologically relevant load patterns influence stress concentration within the tendon.

Methods

A three-dimensional finite element (FE) model of the foot and AT was developed, segmenting the three subtendons and incorporating physiologic fibre twist. The second rocker of gait was simulated, corresponding to maximal tendon elongation. Tendon tissue was modelled as transversely isotropic hyperelastic, and quadratic tetrahedral elements ensured spatial stress resolution. Different loading distribution scenarios for the soleus, MG, LG were applied based on triceps surae activation patterns. Von Mises stress, and deformation patterns were quantified and compared with baseline behavior and with estimates from a previously available simplified AT model.

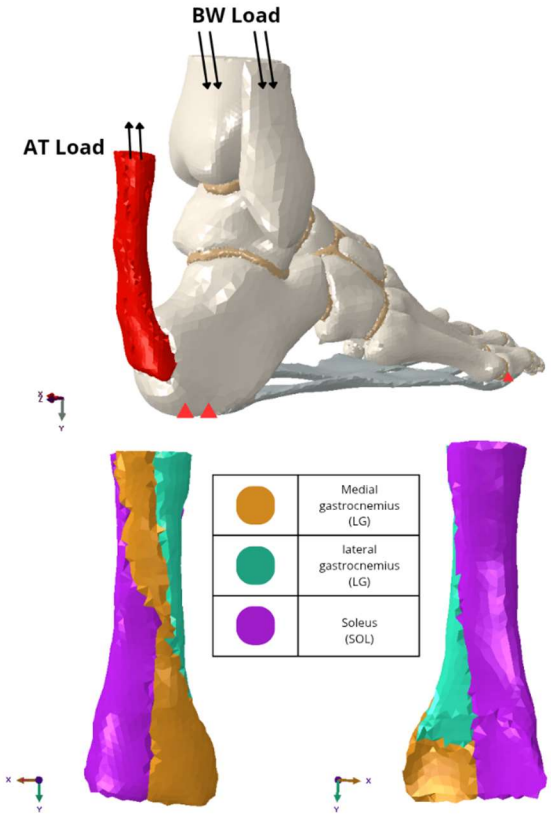
Results

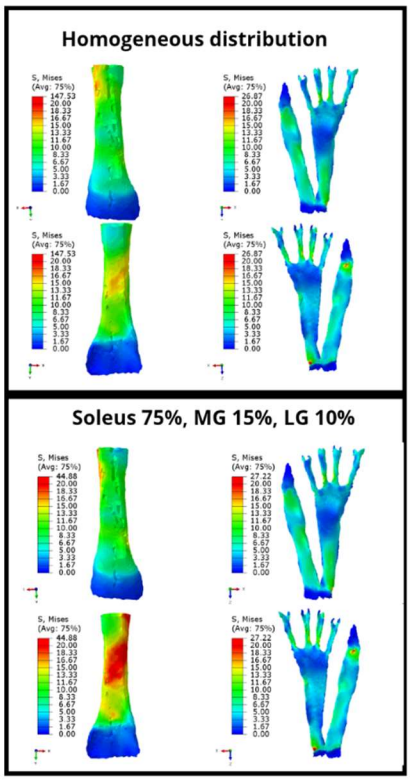
Increasing soleus loading produced the highest internal stresses, with focal concentrations in the medial–anterior mid-portion of the watershed zone. The loading distribution of Soleous (75%), MG (25%) and LG (10%) generated the greatest magnitudes and a superior migration of the hotspot, while the distribution of 40-40-20 reproduced this shift. Although the distribution 50-20-30 lowered overall stress, medial asymmetry persisted. A constricted narrowing further amplified these concentrations. In contrast, increased MG or LG loading did not redistribute or reduce stresses induced by soleus dominance. Only the subtendon model captured the resulting internal shear pathways and migrating stress clusters.

Discussion

Differential subtendon loading has a substantial mechanical effect on AT stress distribution, with soleus force emerging as a primary driver of focal stress in the watershed region. These findings provide a biomechanical explanation for the predictable anatomical location of Achilles tendinopathy and underscore the importance of subtendon representation in computational gait models. Understanding these mechanisms may inform both preventive strategies and targeted rehabilitation approaches for Achilles pathology.

Images (Optional)





Session Category

Orthopaedic Biomechanics: Lower Extremities

P3-225

Volumetric Wear Assessment and Wear Scar Analysis of Retrieved Tibial Liners in Unicompartmental Knee Arthroplasty: A Comparative Study of Polyethylene Types and Patient Characteristics

Ms. Carolina S. Haboba Nebel MS, Mr. Ajay S. Potluri BS, Ms. Aditya S. Yadav MS, Dr. Anne Debenedetti MS, Ms. Jennifer L. Wright, Ms. Deborah J. Hall, Dr. Robin Pourzal PhD, Dr. E. Bailey Terhune MD, Dr. Craig J. Della Valle MD, Dr. Hannah J. Lundberg PhD

Rush University Medical Center, Chicago, IL, United States

Introduction

Unicompartmental knee arthroplasty (UKA) is an established treatment for knee osteoarthritis in patients with intact cruciate ligaments. Despite favorable functional outcomes, long-term implant survival remains limited in part by polyethylene (PE) wear and osteolysis. This study evaluated retrieved tibial inserts made from conventional PE (CPE) and highly cross-linked PE (HXLPE) to characterize volumetric wear, wear scar morphology, and patient-related factors associated with wear patterns.

Methods

Forty-five liners collected between 2006 and 2024 were analyzed: 23 CPE (*ZUK, Zimmer Biomet*), and 22 HXLPE (*Sigma, DePuy*). Wear scar area, articulating surface area and centroidal shift between the articulating and worn regions were quantified using ImageJ. Volumetric wear was measured with an optical coordinate system (*OrthoLux, RedLux, UK*). The influence of implant type, sex, knee and compartment side, BMI, and time in situ was assessed using Kruskal Wallis, Mann Whitney U, and Spearman correlation tests. Analyses were performed on the full dataset, after excluding implants with <1 year in situ to avoid confounding due to early failure or infection, and comparing two subgroups: 1-5 years, and >5 years.

Results

Mean articulating surface area was 944.6 ± 445.5 mm^2, with wear scars averaging 34.2% of the surface. No significant differences were observed across PE types in wear scar area per year or centroidal shift ($p > 0.1$). Mean volumetric wear rate was 29.12 mm^3/year (CPE, >5 years) and 15.74 mm^3/year (HXLPE, >5 years), showing a trend toward higher values in CPE versus HXLPE for implants >5 years in situ ($p = 0.068$). No significant differences were identified in the 1-5 years group. Wear parameters demonstrated no significant correlation with time in situ, BMI, or sex; however, multivariable modeling identified male sex as an independent predictor of higher volumetric wear.

Discussion

We found a consistent trend toward higher long-term volumetric wear in CPE liners, confirming that HXLPE is more durable. The absence of correlations with BMI, side, or compartment indicates that patient-related mechanical factors may play a smaller role than implant design. Larger datasets are warranted to further evaluate long-term performance differences between PE types in UKA and corresponding tissue responses.

Images (Optional)

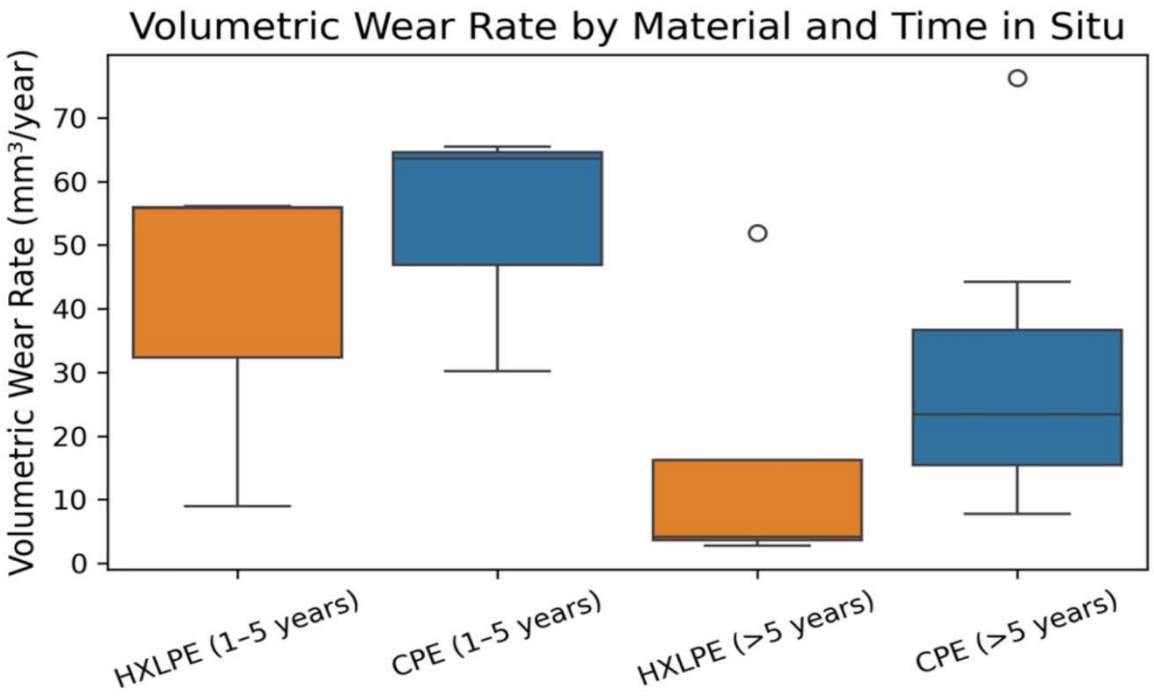


Figure 1 - Volumetric Wear Rate (mm³/year) by PE type (HXLPE, CPE) in two groups (1-5 years in situ, > 5 years in situ)

Session Category

Orthopaedic Biomechanics: Lower Extremities

P3-226

A Custom Musculoskeletal Model for Ankle Contact Loads at the Medial and Lateral Components

Dr. Hoon Kim[1,2], Mr. Taewoong Kong[2], Dr. Danilo Catelli[3,4]

[1]Department of Sports Medicine, Soonchunhyang University, Asan, Chungcheongnam-do, Korea, Republic of. [2]Department of Software Convergence, Soonchunhyang University, Asan, Chungcheongnam-do, Korea, Republic of. [3]School of Human Kinetics, University of Ottawa, Ottawa, Ontario, Canada. [4]Department of Physical Activity Science, Université du Québec à Montréal, Montreal, Quebec, Canada

Introduction

Uneven distribution of load between the medial and lateral compartments of the ankle has been implicated in the development of post-traumatic osteoarthritis and chronic instability. However, most musculoskeletal models estimate ankle joint contact forces at a single point and cannot resolve compartment-specific contact loading. Experimental estimations of talar-dome force distribution typically require high-cost CT- or MRI-based modeling, limiting their feasibility in many applications. Extending compartment-based approaches previously applied to the knee, we developed a custom model to estimate medial and lateral ankle contact forces during dynamic tasks.

Methods

Five participants performed three trials of level walking and squats with a bar of 50% of their body weight (BW). Using a generic model designed for large hip and knee flexion, two massless bodies, “med_comp” and “lat_comp”, were attached to the “talocrural_articulation_frame” via CustomJoints at offsets (mediolaterally ±0.01 m). The “talar_dome” was welded to “lat_comp” and constrained to “med_comp”, defining medial and lateral ankle contact frames for compartmental load decomposition. Data were validated by confirming that mediolateral ankle contact forces and impulses matched the original single-point values.

Results

Across level walking and squat trials with a 50%BW weighted barbell, the summed medial and lateral ankle contact forces closely matched the original single-point ankle joint contact force. The lateral compartment carried 65% (squat) and 53% (walking) of total impulse, with the medial compartment carrying 35% and 47%. Normalized-root-mean-

squared-error in joint contact force and impulse were 0-1% across all trials and participants. The findings support the internal consistency and numerical validity of the compartmental ankle model.

Discussion

Compartmentalizing the ankle joint into medial and lateral contact frames allowed us to resolve side-specific loading patterns while preserving overall joint reaction force estimates and the integrity of the original model scheme. The close agreement between the summed compartmental forces/impulses and the original single-point ankle force/impulse indicates that the remodeling did not introduce substantial numerical artifacts. These findings supported the use of the proposed model to study medial and lateral load distribution during walking and squatting, providing a foundation for future analyses of ankle osteoarthritis mechanisms, surgical strategies, or footwear-induced shifts in compartment loading, and targeted rehabilitation.

Images (Optional)

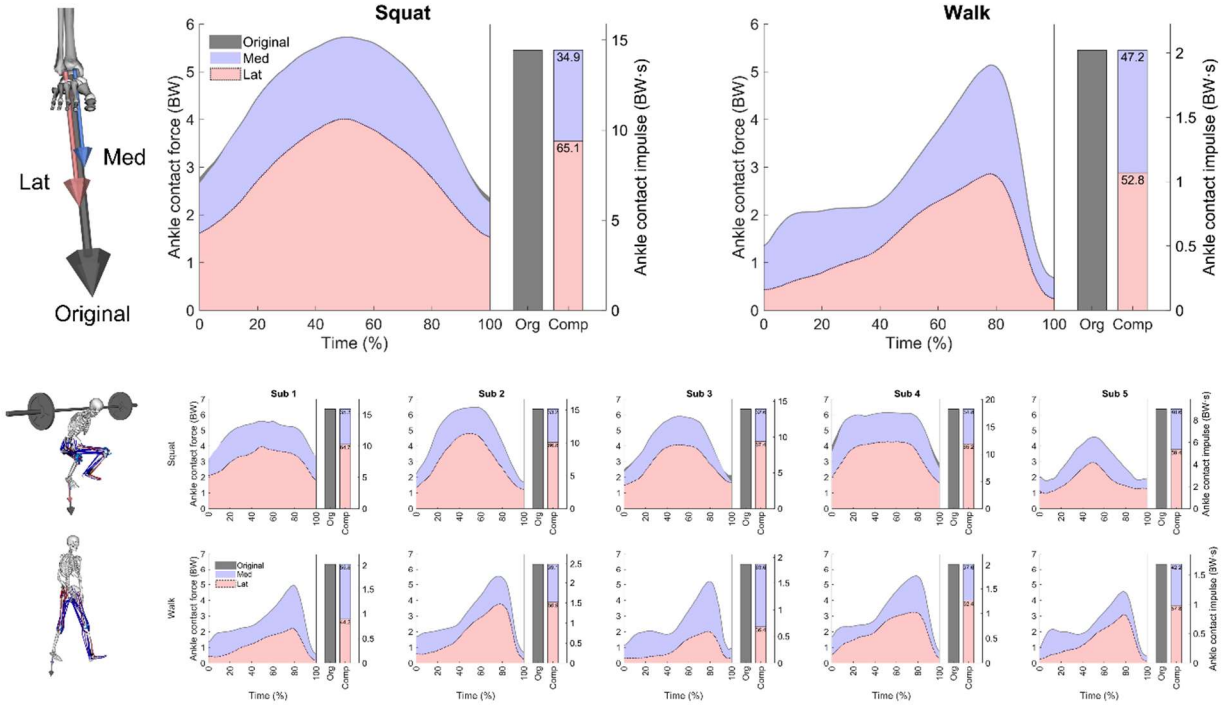


Figure 1. Consistency of ankle joint loading between the original single-point ankle joint and the medial and lateral ankle compartments. The top row shows mean ankle joint contact force-time curves and corresponding impulses for the original single-point, medial, and lateral components during squats with a 50% body-weight barbell (left) and level walking (right). The ten panels in the lower rows present the same measures for both tasks in all five subjects, illustrating the reproducibility of the compartment-based decomposition at the individual level.

Acknowledgements (Optional)

This work was supported by the Soonchunhyang University Research Fund and BK21 FOUR (Fostering Outstanding Universities for Research) (No. 5199990914048).

Session Category

Orthopaedic Biomechanics: Lower Extremities

P3-227

Stiffness-Graded Octet-Truss Lattices: Mitigating Stress Shielding in Orthopaedic Implants

Mr Arandeep Prehar, Mr Jack Clarke, Mr James D. Clark, Dr Peter Ellison

University of York, York, Yorkshire, United Kingdom

Introduction

The stiffness mismatch between traditional orthopaedic implants and natural bone often leads to stress shielding, resulting in bone loss and eventual implant loosening. 3D printing can manufacture structures of varying porosity offering a path to mitigate stress shielding, match implant stiffness to bone, and significantly enhance implant longevity. This work investigated functionally graded porous lattice structures, focusing on the octet-truss geometry. The aim was to develop a relationship between unit cell geometry and the resulting stiffness, enabling the implants to be tailored to individual's bone properties.

Methods

Lattices with four porosity levels (ϕ = 20%, 40%, 60%, 80%) and a solid control were manufactured (n = 6 per group) in polylactic acid (PLA) using fused filament fabrication (FFF) to evaluate how porosity influences compressive and tensile mechanical performance. Specimens were based on modified versions of ASTM standards, with gauge regions consisting of 6mm^3 OT unit cells to ensure consistent lattice geometry across density groups. To account for the relative density, stress-strain was calculated using the effective cross-sectional area of the lattice.

Results

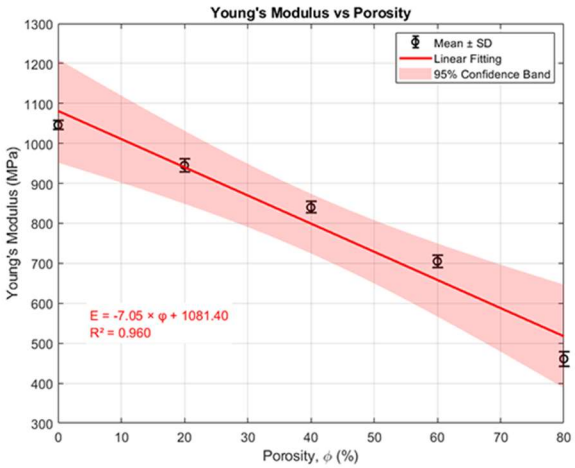
The Elastic modulus (E) was calculated from the linear region of stress-strain curves. Experimental data showed a linear relationship between porosity (ϕ) and both the tensile (E_t) and compression (E_c) moduli.

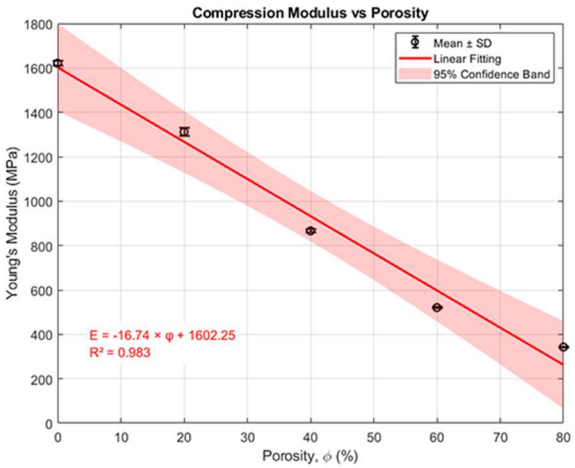
Discussion

Fundamentally, this study was successful in showing that the relative mechanical properties of an PLA FFF 3D printed octet lattice can be varied as a function of its porosity. A negative correlation was demonstrated between the porosity and the elastic modulus. The linear model between the elastic modulus would allow for the non-discrete selection of any desired modulus within the measured range. By implementing functionally graded

volume fractions across cell arrays, mechanical properties can be patient-specifically tailored to closely replicate native bone stiffness. This approach promises to significantly improve load distribution, mitigate the stress shielding effect, and ultimately enhance long-term patient recovery and implant outcomes.

Images (Optional)





Session Category

Orthopaedic Biomechanics: Lower Extremities

P3-228

Assessment of Lower Extremity Kinematics, Kinetics, and Patellar Tendon Loading Pre- and Post-Fatigue

Mr. Jack Felipe, Mr. Kingsley Royal, Dr. Stephanie Cone

University of Delaware, Newark, DE, United States

Introduction

In the United States, 200,000 people receive anterior cruciate ligament (ACL) reconstruction (ACLR) surgery each year [1]. Unfortunately, individuals with a history of ACLR are up to 6 times more likely to tear an ACL compared to previously uninjured individuals. Current return to play criteria lacks a focus on fatigue effects, highlighting a need for improved understanding of the effect of fatigue on knee function following ACLR. To establish fatigue effects on knee function, the purpose of this study was to evaluate the effect of fatigue on interlimb symmetry in gait biomechanics in a healthy population.

Methods

19 healthy adults (11 M, 8F, 25.8±5.1 years) were recruited. Participants were fitted with shear wave tensiometers [2] bilaterally over the patellar tendons to measure dynamic tendon load and 39 retroreflective markers to track skeletal movement. Participants walked on an instrumented treadmill at a self-selected speed for 30 seconds to measure joint kinematics, kinetics, and patellar tendon loading patterns. Participants completed bodyweight squats to failure at a set tempo (160-1600 total repetitions). Immediately following fatigue, participants walked at the same speed as pre-fatigue. A mixed model with a post hoc paired t-test in 1D statistical parametric mapping was used to identify differences in joint kinematics, kinetics and patellar tendon loading patterns between limb and fatigue state.

Results

There was a significant main effect of fatigue across several metrics (Figure 1). On average, tendon shear wave speed increased by approximately 28% in a fatigued state ($p<0.05$). There were significant decreases in knee ($p=0.006$) and hip flexion angle ($p=0.005$) of approximately 8% and 10%, respectively. In addition, there was a significant decrease in knee moment ($p<0.001$) of roughly 17%.

Discussion

Knee function varied significantly from pre- to post-fatigue with changes in the magnitude of shear wave speed and sagittal hip angle, knee angle, and knee moment at both heel

strike and toe off. These effects of fatigue in healthy gait biomechanics motivate future work assessing these effects on movement quality and performance in athletes with a history of ACL injury.

Images (Optional)

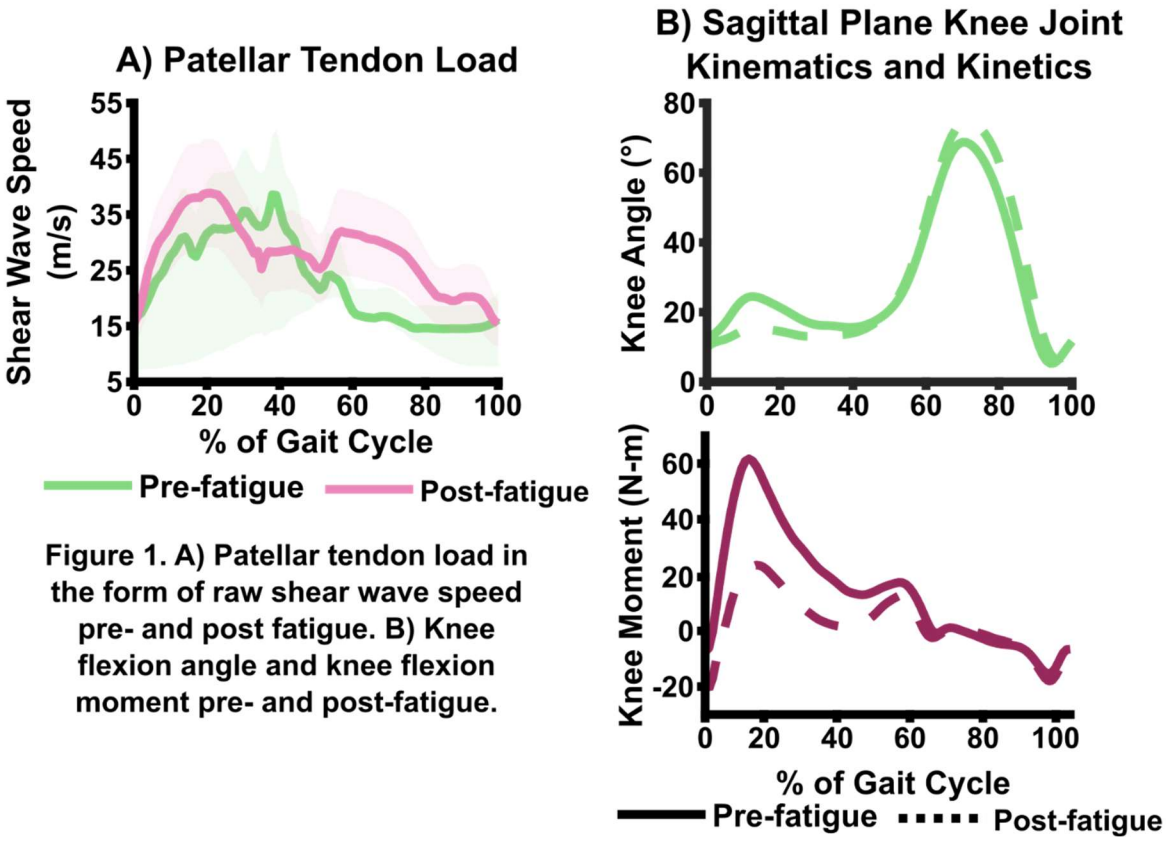


Figure 1. A) Patellar tendon load in the form of raw shear wave speed pre- and post fatigue. B) Knee flexion angle and knee flexion moment pre- and post-fatigue.

References (Optional)

[1] Evans+, StatPearls, 2024. [2] Martin+, Nat Commun, 2018.

Acknowledgements (Optional)

Funding from NIH P20GM139760.

Session Category

Orthopaedic Biomechanics: Lower Extremities

P3-229

Investigating the Effects of Eccentric Calf Exercise on Achilles Tendon Fluid Content Using Magnetic Resonance Imaging

Mr. Jarod Forer, Dr. Jolinda Smith, Dr. Nick Willett, Dr. Michael Hahn

University of Oregon, Eugene, Oregon, United States

Introduction

Achilles tendinopathy is a common diagnosis without a universally effective solution. Rehabilitative eccentric exercise can be successful as a treatment, but the mechanisms by which it improves tendon health are not well understood. Through repetitive loading and straining of the tendon, rehabilitative exercise is hypothesized to drive fluid movement in human Achilles tendons. However, while Achilles tendon fluid content has been modeled with Magnetic Resonance Imaging (MRI), it has not been studied in the context of the temporal response to exercise. We hypothesized that fluid content in healthy Achilles tendons would decrease immediately after exercise as shown with T2* values captured from ultrashort-time-to-echo (UTE) MRI.

Methods

3 healthy participants (1F, 26±3.56 years old) completed an eccentric exercise protocol between three separate MRI scans. The exercise consisted of 100 continuous unilateral heel drops on a raised platform, 50 with an extended knee and 50 with a slightly flexed (20°) knee. The scans took place immediately before (Pre), immediately after (Post), and 2 hours after exercise (2Hr Post). MRI scans were acquired on a 3T Skyra (Siemens) and included 2 acquisitions of a UTE 3D Radial sequence with 4 echo times each. The tendon midsection was segmented using a semi-automatic method in ITK-SNAP. T2* values were calculated by fitting voxel-wise normalized intensity data with a biexponential decay curve. Statistical analysis was conducted using a one-way repeated measures ANOVA in Prism (GraphPad) with an alpha of 0.05.

Results

No significant differences were found in tendon midsection volume, the short component of $T2^*$, the long component of $T2^*$, or the short fraction of the biexponential fit (Figure 1, all $p>0.05$).

Discussion

No conclusions can be made as to the effects of eccentric exercise on Achilles tendon fluid content based on a preliminary cohort of participants (expected sample size of ten).

Further analyses should also investigate the insertional and myotendinous regions of the Achilles tendon. Through the calculation of T2* relaxation times, this work provides the first data modeling fluid content of the human Achilles tendon in response to exercise.

Images (Optional)

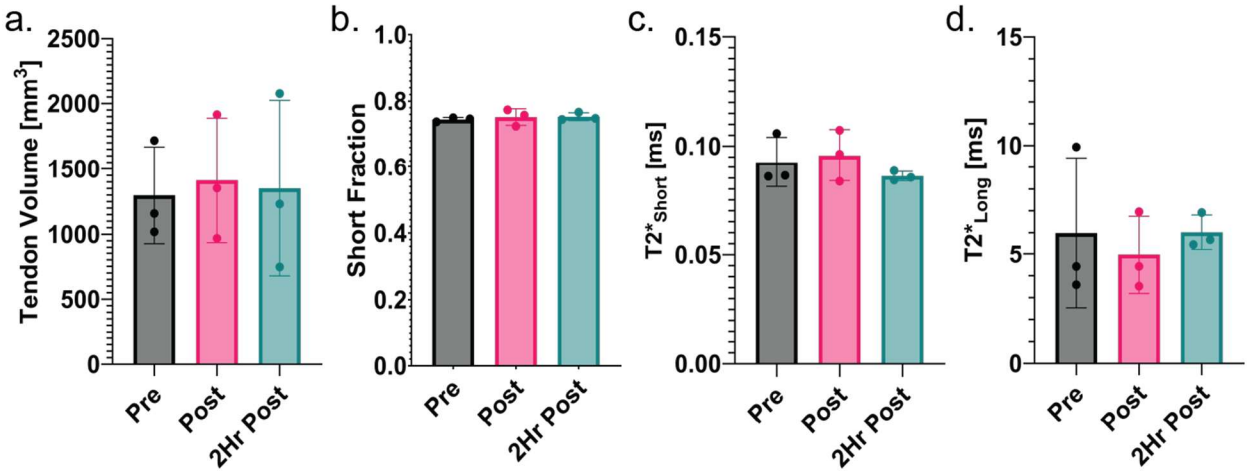


Figure 1: Tendon midsection MRI derived parameters for (a) volume, (b) the fraction of the biexponential decay attributed to bound water, (c) the short decay relaxation time describing bound water, and (d) the long decay relaxation time describing unbound water.

Acknowledgements (Optional)

Support for this work was provided by the Wu Tsai Human Performance Alliance and the Joe and Clara Tsai Foundation. Siemens supplied the sequences for MRI scanning. The Lewis Center for Neuroimaging and Vince Quesada provided MRI support.

Session Category

Orthopaedic Biomechanics: Lower Extremities

P3-230

KneeHub: A Consensus Context of Use for Simulation-Based Prediction of Movement After ACL Reconstruction and Risk Assessment of Post-Traumatic OA

Mr Jason Halloran[1], Mrs Snehal Chokhandre[2], Ms Kate Moyle[3], Ms Nancy Kim[3], Ms Maryam Nazem[4], Mr Scott Sibole[1], Mr Peter Laz[4], Mr Thor Besier[3], Mr Carl Imhauser[5], Mr Ahmet Erdemir[2]

[1]Washington State University, Spokane, WA, United States. [2]Cleveland Clinic, Cleveland, OH, United States. [3]University of Auckland, Auckland, Auckland, New Zealand. [4]University of Denver, Denver, CO, United States. [5]Hospital for Special Surgery, New York, NY, United States

Introduction

Modeling and simulation requires a clear context of use (CoU), which promotes informed decisions on the construction, orchestration, credibility, and communication of simulation studies. The NIH-sponsored “KneeHub” project has disseminated how modelers’ preferred workflows affect simulation outcomes [1]. The project now aims to establish consensus-based workflows to serve as community standards, to augment reproducibility, and to streamline multi-center studies. The goal of this abstract is to present the CoU for an internal consensus among the five teams that participate in the KneeHub project. This internal effort complements an ongoing external community-based Delphi study to define a second CoU and corresponding workflow.

Methods

The participants conducted a literature search in knee modeling and met weekly to discuss CoUs with pragmatic consideration of available data, contemporary modeling approaches, and potential clinical implications. Ultimately, the group focused on pinpointing the limits of simulation capabilities in a data-rich setting, i.e., research that may transform into clinically meaningful simulation workflows. While anatomy can be acquired in the clinic (e.g., MRI), joint- or tissue-level mechanics may be missing. Our framing helped define a clinically relevant CoU, and later a CoU-specific workflow, with the intent to establish the bounds of model fidelity and predictive quality.

Results

CoU summary - For an active female with an anterior cruciate ligament (ACL) injury, a physician would like to understand the biomechanics before injury, joint- and tissue-level consequences of the injury, performance of a reconstruction, and changes after surgery as potential indicators of reinjury or post-traumatic OA. The injury presents as complete tears

of the ACL and posterior root of the lateral meniscus. The surgery aims for ideal graft placement and tension using the patellar tendon with preservation of the meniscus using sutures at the horn insertion.

Discussion

We summarize our internal consensus CoU to inspire discussion and complement related progress toward a community-wide Delphi-based second CoU and workflow. We hope to present this alongside our work defining and testing a corresponding modeling workflow. In the future, the CoU and its workflow will serve as the basis for customization, with potential losses evaluated to accommodate the data constraints of a clinical setting.

References (Optional)

[1] https://simtk.org/projects/kneehub

Acknowledgements (Optional)

NIH-NIBIB R01EB024573

Session Category

Orthopaedic Biomechanics: Lower Extremities

P3-231

KneeHub – A Consensus Workflow for Simulation-Based Prediction of Movement After ACL Reconstruction and Risk Assessment of Post-Traumatic OA

Mr Jason Halloran[1], Mrs Snehal Chokhandre[2], Ms Nancy Kim[3], Ms Kate Moyle[3], Ms Maryam Nazem[4], Mr Scott Sibole[1], Mr Peter Laz[4], Mr Thor Besier[3], Mr Carl Imhauser[5], Mr Ahmet Erdemir[2]

[1]Washington State University, Spokane, WA, United States. [2]Cleveland Clinic, Cleveland, OH, United States. [3]University of Auckland, Auckland, Auckland, New Zealand. [4]University of Denver, Denver, CO, United States. [5]Hospital for Special Surgery, New York, NY, United States

Introduction

Modeling and simulation requires a clear context of use (CoU) and workflow, which promotes informed decisions on the construction, orchestration, credibility, and communication of simulation studies. The NIH-sponsored "KneeHub" project has disseminated how modelers' preferred workflows affect simulation outcomes [1]. The project now aims to establish consensus-based workflows to serve as community standards, to augment reproducibility, and to streamline multi-center studies. The goal of this abstract is to present a CoU-specific categorically-defined workflow that was determined by an internal consensus among the five teams in the KneeHub project. This internal effort complements an ongoing external community-based Delphi study to define a second CoU and corresponding modeling workflow.

Methods

The seeding CoU: A physician would like to understand the joint- and tissue-level biomechanics of a female patient with anterior cruciate ligament and lateral meniscus posterior root tears before the injury, after the injury, and any post-surgery (patellar graft) changes as potential indicators of reinjury or post-traumatic OA. The CoU focused on adoption of an extensive experimental data set as foundational work towards clinical translation.

Over a six-month period, the team met weekly to discuss and document the CoU-specific workflow with pragmatic consideration of data, contemporary modeling approaches, and potential clinical implications. We broke down the modeling process from high level objectives to task-specific activities, including credibility and outreach. For some tasks, consensus focused on target outcome measures versus prescription of specific methods,

particularly when an objective strategy was not identifiable. Consensus was achieved when all teams agreed to specific workflow details.

Results

Workflow summary: “Broad design of the simulation study” encompasses the why (not “how”), which we delineated into context relevant categories (Fig. 1). The specifics (the “how”) include: development and calibration, benchmarking, use and outreach, and credibility. Documentation is largely complete with two KneeHub groups implementing the workflow (Fig. 1).

Discussion

Internal implementation of the CoU-specific modeling workflow has informed deployment of the complementary community wide Delphi process (expert-informed consensus). Further, the CoU and its workflow were designed to serve as the basis for customization, with potential losses evaluated to accommodate the data constraints of a clinical setting.

Images (Optional)

Workflow Documentation Tree

Broad Design of Simulation Study (*the "why"*)
Context relevant:
- Specificity
- Simulation Conditions
- VVUQ Requirements & Strategy
- Data Requirements & Availability
- Simulation Strategy
- Outputs to Post-Process
- Credibility & Outreach Strategy

Modeling and Simulation Specifics (*the "how"*)
- Development and Calibration
  - Tissues/components/interactions
  - Loading & BCs
  - What/how to calibrate
  - etc....
- Benchmarking
- Use and Outreach
- Overall Credibility



Figure 1. (left) Summary of the workflow documentation that highlights the categories used to describe the high level modeling goals (the "why") versus the modeling specifics (the "how"). (right) Two views of an example model developed at the University of Denver using the documentation. The model is currently at the development stage (i.e., a running model before calibration).

References (Optional)

[1] https://simtk.org/projects/kneehub

Acknowledgements (Optional)

NIH-NIBIB R01EB024573

Session Category

Orthopaedic Biomechanics: Lower Extremities

P3-232

Principal Component–Based Analysis of Bilateral Knee Morphology in ACL-Injured Patients

Dr. Jeongseok Oh[1], Prof. Joonho Wang[2], Prof. Seungbum Koo[1]

[1]KAIST, Daejeon, Daejeon, Korea, Republic of. [2]Samsung Medical Center, Seoul, Seoul, Korea, Republic of

Introduction

Anterior cruciate ligament (ACL) rupture has long been linked to underlying anatomical factors, yet prior work has largely focused on population-level associations without fully clarifying which specific morphological features drive injury risk [1,2]. Recent statistical shape modeling studies have demonstrated that variations in bony morphology can meaningfully influence joint loading and ACL vulnerability, but the extent to which subtle bilateral differences within the same individual contribute to rupture remains insufficiently understood [2]. Examining side-to-side morphological asymmetries may offer new insight into shape features associated with ACL injury.

Methods

Thirty patients with unilateral ACL rupture were included, providing a total of 60 knee shape datasets, of which 20 patients had previously undergone single-bundle or double-bundle ACL reconstruction. Three-dimensional knee models were reconstructed using biplanar fluoroscopy and fitted into a pre-established statistical shape and intensity model (SSIM) to extract shape weights. Registration was done with 20 principal component (PC) weights for each model. Independent t-tests were conducted to compare SSIM weights between the injured and uninjured sides, with significance defined at $p < 0.05$.

Results

Four PCs of the femur showed statistically significant differences between sides, and the morphological changes associated with each PC are illustrated in Figure 1. The first PC indicated a sharper femoral shaft with mediolateral narrowing of the medial condyle. The second PC similarly reflected shaft sharpening accompanied by anteroposterior hypertrophy of the medial condyle. The third PC represented a relatively narrower intercondylar notch. The fourth PC demonstrated mediolateral enlargement toward the condylar region. No statistically significant components were identified in the tibia.

Discussion

Bilateral comparison of skeletal morphology revealed femoral shape characteristics associated with ACL rupture. A relatively narrower intercondylar notch may increase the likelihood of ACL impingement against the medial wall of the femur. The mediolateral enlargement of the condyle may alter the joint's rotational axis and increase the stabilizing demand placed on the ACL during tibial rotation. These findings provide insight into anatomical risk factors and may contribute to improved strategies for ACL injury prevention.

Images (Optional)

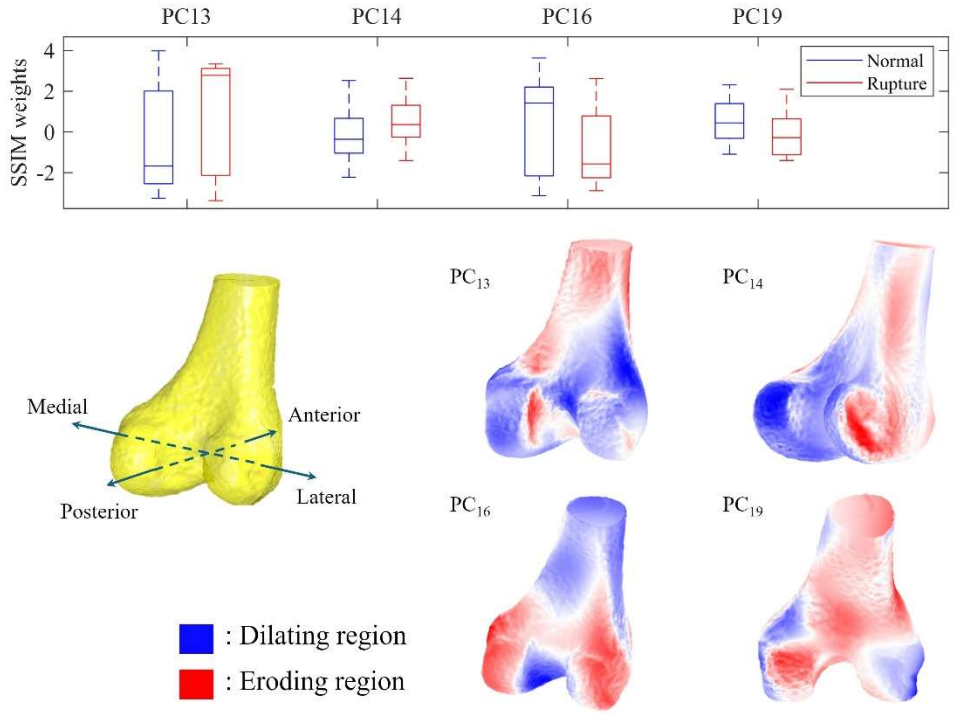


Figure 1. SSIM weights of PCs that showed significant differences between normal and ruptured knees (top), and deformation patterns indicating the morphological trend associated with ACL rupture (bottom).

References (Optional)

[1]Pedoia, Valentina, et al. Osteoarthritis and cartilage, 2015

[2]Polamalu, Sene K., et al. Journal of Orthopaedic Research, 2022

Acknowledgements (Optional)

This research was supported by the National Research Foundation of Korea (NRF) grant funded by the Korea government (MSIP) (No. RS-2023-00277425), and by the Pioneer Research Center Program through the NRF funded by the Ministry of Science and ICT (Project No. 2022M3C1A3080598).

Session Category

Orthopaedic Biomechanics: Lower Extremities

P3-233

A Novel Quasi-Static Loading Profile for Tearing the ACL in Cadaveric Studies

Jeremy Loss MS, Miss Elizabeth Pace, Dr. Robb Colbrunn PhD, Dr. Tara Nagle PhD

BioRobotics Core, Cleveland Clinic Research, Cleveland, OH, United States

Introduction

The anterior cruciate ligament (ACL) is one of the most commonly injured knee ligaments. Many researchers study the biomechanics of ACL reconstruction (ACLR) on cadavers. However, the methodology for creating the rupture oftentimes requires a surgeon to arthroscopically incise the ACL. This method does not provide any insights into the biomechanics of the knee during the ACL rupture. Previous studies found that high tibiofemoral compression force, valgus moment, and internal rotation (IR) torque produce the highest force on the ACL at 30° flexion [1]. However, these studies did not examine damage to other structures. We aimed to build upon these target loads to develop a novel loading profile for tearing the ACL that mimics non-contact injury to the ACL without damaging other structures.

Methods

Two knees were tested using a simVITRO 6 degree-of-freedom robotic testing system. We chose not to include a valgus moment to preserve the meniscus. First, the knee was flexed to 30° and the IR position at 5 Nm IR torque with 20 N compression was recorded. The ACL tear trajectory consisted of: 1500 N compression, the aforementioned IR position at 5 Nm, and anterior tibial displacement ramped at 1 mm/sec until failure. All other loads were minimized. Lachman tests consisting of 134 N anterior drawer and 20 N compression at 30° flexion were run pre- and post- failure to measure anterior displacement (Table 1). After failure, each knee was dissected and inspected for both intentional and unintentional damage.

Results

Post-testing dissection on both knees revealed ruptured ACLs with no discernible damage to other internal structures. Failure metrics can be seen in Table 1. The Lachman test showed a substantial increase in anterior translation after failure, indicating a damaged ACL.

Discussion

Additional specimens are required to validate the efficacy of this profile. However, this is a promising method for reliably tearing the ACL robotically, removing the need for a surgical

resection. Additionally, the ability to measure kinetics and kinematics throughout the failure trajectory may be especially valuable for researchers interested in ACL and ACLR failure mechanisms.

Images (Optional)

Table 1: Failure forces/torques and displacements/rotations for position-controlled degrees of freedom (Anterior, IR, Flexion), and pre-tear and post-tear Lachman test displacements.

	Sample 1	Sample 2
Anterior Force at Failure (N)	342	512
Anterior Displacement at Failure (mm)	18.6	25.8
Internal Rotation Torque at Failure (Nm)	2.72	3.25
Internal Rotation Angle (at 5 Nm)	24.4°	18.7°
Extension Torque at Failure (Nm)	5.96	7.93
Pre-tear Lachman Anterior Displacement (mm)	6.91	7.03
Post-tear Lachman Anterior Displacement (mm)	25.9	20.4

References (Optional)

[1] Markolf et al., J Orthop Research, 2019

Session Category

Orthopaedic Biomechanics: Lower Extremities

P3-234

The Effect of Changes in Bone Density on the Mechanical Response of THA Femurs

Dr. Jonas Pramudita, Mr. Kei Matsushita, Mr. Yosei Ooba

Nihon University, Koriyama, Fukushima, Japan

Introduction

Bone mineral density (BMD) of the femur is known to change after total hip arthroplasty (THA). However, the influence of long-term postoperative changes in BMD on the mechanical response of the femur has not yet been sufficiently investigated, and the change in fracture risk associated with the change of BMD remains unclear. Therefore, we incorporated postoperative temporal changes in BMD and Young's modulus into a previously developed femoral finite element (FE) model to evaluate their effect on the mechanical response of the femur and to assess fracture risk based on the implementation of a fracture criterion.

Methods

Femoral FE models developed in a previous study [1] were used. Bone density and Young's modulus were estimated from the Hounsfield units of patient CT images. Postoperative changes in bone density were assumed to follow the trend reported in the literature [2]. FE models reflecting the bone density distribution at 1 year (1Y) and 5 years (5Y) after surgery were generated by applying the ratio of BMD change in each Gruen zone. FE analysis was then conducted under the same boundary and loading conditions as in the previous study. A fracture criterion was additionally incorporated to evaluate the postoperative risk of fracture.

Results

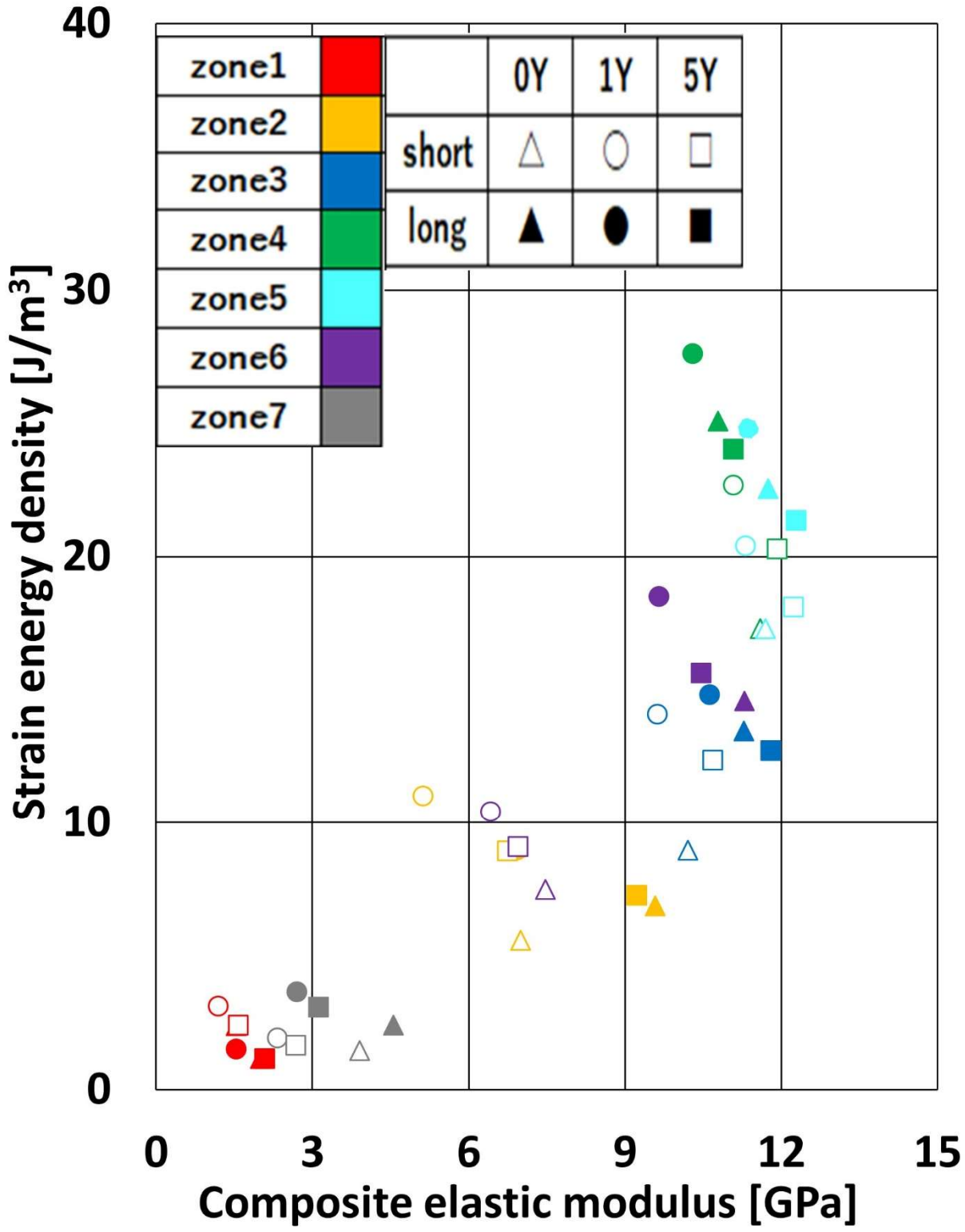
The figure showed the relationship between strain energy density and composite elastic modulus for short- and long-stem models at 0Y, 1Y, and 5Y. The strain energy density at 0Y tended to be lower than at 1Y and higher than at 5Y. From the fracture evaluation, the maximum proportion and volume fraction of failed elements were 0.17% and 0.41%, respectively.

Discussion

At 1Y, reduced BMD due to stress shielding increased femoral deformation, leading to higher strain energy density. At 5Y, increased BMD caused by bone–stem adhesion and recovery of physical activity resulted in reduced strain energy density. The postoperative fracture risk was considered extremely low. Although the long-stem model and the 1Y

model showed a slightly higher proportion of failed elements than the short-stem model and the 5Y model, the difference remained small.

Images (Optional)



References (Optional)

[1] Nobuhiro Kaku et al., J Orthop Surg Res, 2022

[2] Kunitomo Minakawa, J Kyorin Med Soc, 2003

Acknowledgements (Optional)

This work was supported by the JSPS KAKENHI Grant Number 25K07506 and Nihon University Research Grant-in-aid for Early-Career Scientists.

Session Category

Orthopaedic Biomechanics: Lower Extremities

P3-235

Subject and Activity Variations on FE-simulated Knee Prosthesis Wear using the CAMS-Knee Datasets

Mr. Bernhard Weisse Group Leader Biomed. Eng.[1], Mr. Andrea Mäusli MSc Mech Eng student[2], Mr. José I. Contreras Raggio PhD student[1,3], Mr. Silvain A. Michel MSc Mech Eng[1], Dr. Michael J. Dreyer MSc Mech Eng[4], Dr. Seyyed H. Hosseini Nasab Group Leader Computational Biomechanics[2], Prof. Dr. William R. Taylor Head of Department[2]

[1]Empa - Material Science and Technology, Dübendorf, Zurich, Switzerland. [2]ETH Zurich, Zurich, Zurich, Switzerland. [3]Universidad Adolfo Ibanez, Vina del Mar, Valparaiso, Chile. [4]Carbo-Link AG, Fehraltorf, Zurich, Switzerland

Mr. Bernhard Weisse

Introduction

Polyethylene wear remains a major cause of long-term failure in knee arthroplasty. Understanding how patient-specific tibio-femoral loading&kinematics drive abrasive wear is therefore essential. In this study, we investigated subject, activity, and repetition variability on knee prosthesis wear. We hypothesized that the most dominant influence on wear is the activity, followed by subject and repetition.

Methods

In vivo tibio-femoral loads&kinematics from six CAMS-Knee subjects [1] performing several repetitions of five activities were used as inputs to an FE-based framework [2] to compute wear volume over one million cycles (mc), yielding more than 150 simulations for the INNEX FIXUC prosthesis (ZimmerBiomet, Switzerland). A statistical analysis was carried out to determine the influence of subject, activity (walking, downhill walking, stair descent, sit-to-stand-to-sit, and squat), and repetition on wear. Furthermore, a machine-learning (ML) analysis using a linear mixed-effects model was trained to identify which of the surface contact variables most influenced the resulting wear.

Results

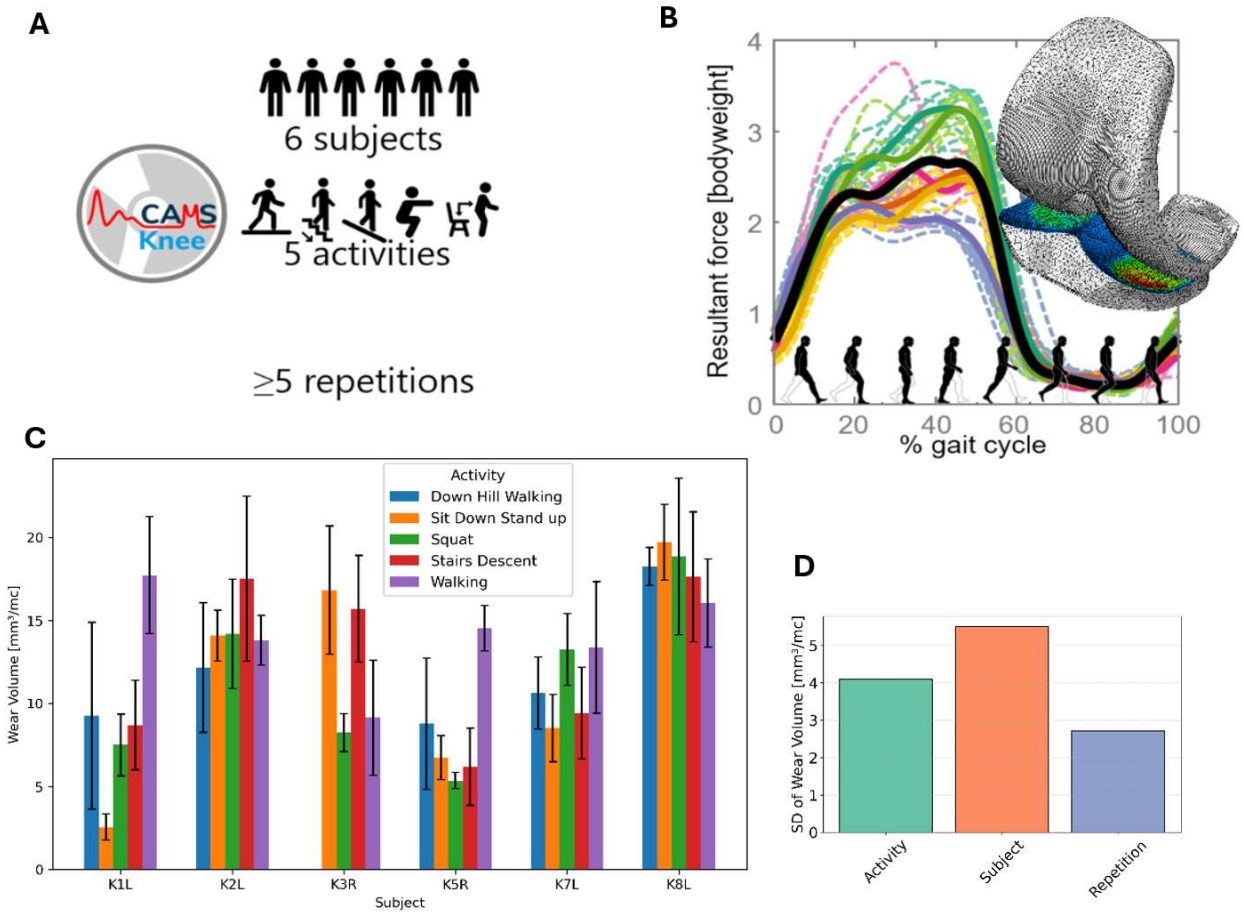
The wear volume varied substantially across subjects and activities, not allowing any clear ranking. The statistical analysis contradicted the hypothesis, showing that variation of subject (5.51 mm^3/mc) was the largest contributor to the wear variability, followed by

activity (4.10 mm^3/mc), and then repetition (2.71 mm^3/mc), see Figure. No significant difference in wear could be found between most activities, except for level-walking, which shows slightly a higher impact on wear. The findings of the ML analysis highlight that beside contact pressure and sliding distance, cross-shear and implant alignment are also important wear influencing factors.

Discussion

The relatively low variability of wear between repetitions demonstrates the repeatability of wear patterns. Therefore, the observed differences in wear related to activity and subject are not due to any inaccuracies in the in-vivo loading and kinematic measurements, but most likely because of the individual movement and loading patterns occurring as a result of anatomical and muscle recruitment differences, as well as implantation. Future work will focus on refining predictive models to better identify the key subject-specific biomechanical factors influencing implant wear.

Images (Optional)



References (Optional)

[1] Taylor et al., J Biomechanics, 2017

[2] Dreyer et al., BioMedical Eng. 2024

Session Category

Orthopaedic Biomechanics: Lower Extremities

P3-236

Friction in Artificial Hip Joints: In Vivo Insights into Tribologically Relevant Parameters

M.Sc. Julian N. Zierke[1], Dr. Alwina Bender[1], M.Sc. Maurice Weiß[2], Dr. Stefan Schröder[2], Prof. Jan Philippe Kretzer[2], Prof. Georg N. Duda[1], PD Dr.-Ing. Philipp Damm[1]

[1]Julius Wolff Institute, Berlin Institute of Health at Charité – Universitätsmedizin, Berlin, Berlin, Germany. [2]Research Center of Biomechanics and Implant Technology, Department of Orthopaedics, Heidelberg University Hospital, Heidelberg, Baden-Württemberg, Germany

Introduction

Aseptic loosening remains a major cause of implant revision [1], with friction and wear being key contributing factors [2] investigated through in-vitro simulators [3]. While they allow systematic parameter variation, their underlying model assumptions often fail to capture realistic loading conditions, kinematics, and lubrication, leading to discrepancies compared to in-vivo observations. It was shown that friction in-vivo is highly dynamic and patient-specific, influenced by loading and kinematics as well as implant position and joint coverage [4]. To bridge the gap, the project aims to integrate both approaches and systematically analyze friction in-vivo to achieve a deeper understanding of its influencing factors.

Methods

A combinatorial approach is applied, integrating in-vivo measurements, in-vitro simulators, and in-silico models to investigate hip joint friction. Rheological analyses of patient synovia are conducted to characterize lubrication properties. Numerical and experimental studies will assess the influence of fluid characteristics, implant orientation, and activity-dependent loading on joint friction.

Results

The joint force (F_res) showed typical double-peak pattern with non-linear offset induced by additional body weight. While F_res increased linearly with the added load, the friction (M_res) demonstrated phase-dependent and non-linear behavior (Figure-1A). M_res rose during stance phase, peaked shortly after contralateral heel strike, dropped during transition into flexion, and increased again toward terminal stance. With an additional load, M_res elevated throughout, however, a further increase of weight produced only phase-specific increases, and at the time of peak force, M_res was even lower than during unloaded walking. Complementary rheological analyses of the patient's synovia revealed

non-Newtonian behavior (Figure-1B), differing from synthetic synovia (ISO-14242) commonly used in simulators.

Discussion

The findings indicate a complex interaction between joint forces and friction in-vivo. Contrary to in-vitro studies, in-vivo data reveal distinctly phase-dependent friction behavior, consistent with dynamic lubrication influenced by joint kinematics and loading. The properties of the synovia and its deviation from synthetic lubricants further underline the importance of individual lubrication environments. Future work will integrate these fluid characteristics, implant orientation effects, and kinematics into in-vitro and in-silico models. This enables systematic parameter-variation with aim to develop tribologically optimized Safe Zones for implantation and activity recommendations.

Images (Optional)

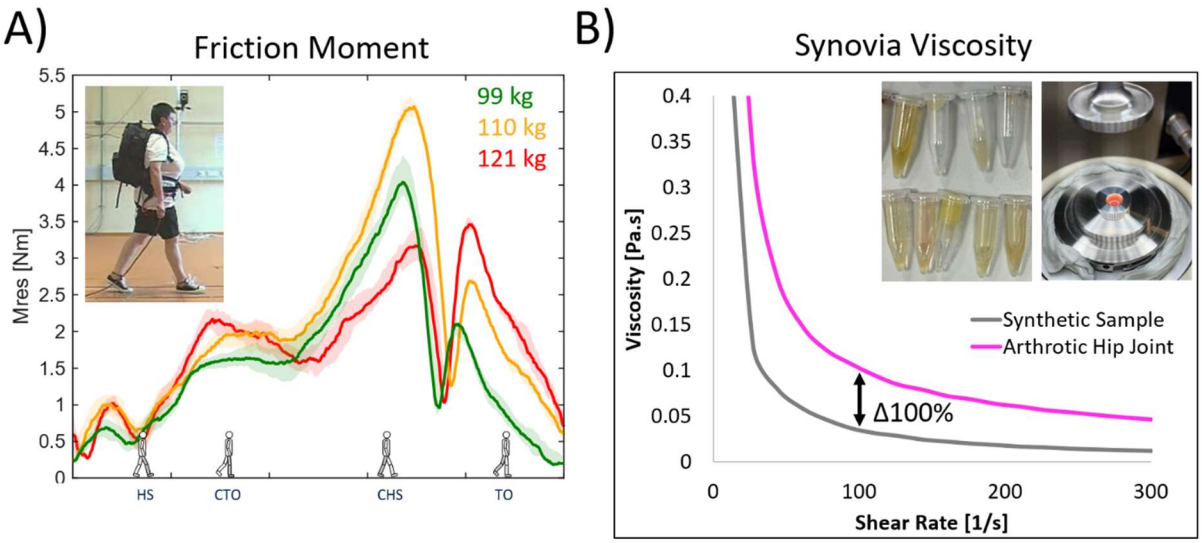


Figure 1: A) Variation of the friction moment at 3 weight levels during gait cycle and B) Variation of the viscosity of a synthetic synovial fluid according to ISO 14242 and a real arthrotic synovial fluid

References (Optional)

[1] Lewis2024

[2] Kaddick2009

[3] Sonntag2021

[4] Damm2021

Acknowledgements (Optional)

DFG (DA 1786/5–2, KR 3755/13–2) and the OrthoLoadClub

Session Category

Orthopaedic Biomechanics: Lower Extremities

P3-237

Changes in Midflexion Knee Laxity in Multiple Planes Between 3-Months and 1-Year After Cruciate-Retaining Total Knee Arthroplasty

Ms. Julianna Villella, Mr. David Z. Shamritsky, Mr. Swaneet Jha, Mr. Claude Regis, Dr. Timothy M. Wright PhD, Dr. Stephen Lyman PhD, Dr. Cynthia A. Kahlenberg MD, Dr. Eytan M. Debbi MD, Dr. William J. Long MD, Dr. Geoffrey H. Westrich MD, Dr. David J. Mayman MD, Dr. Peter K. Sculco MD, Dr. Brian P. Chalmers MD, Dr. Carl W. Imhauser PhD

Hospital for Special Surgery, New York, New York, United States

Introduction

Instability after total knee arthroplasty (TKA) can arise from excessive ligamentous laxity in several anatomic planes. Surgeons often perceive that knee laxity increases between early and later post-operative time-points. However, the amount by which laxity changes over time after TKA remains poorly understood. We are conducting a prospective study in patients undergoing cruciate-retaining (CR) TKA with the objective of measuring the mean and variance of laxity changes between 3-months and 1-year.

Methods

With IRB approval, 46 subjects (48% female; mean age: 64±6 years; mean BMI: 29±3) were prospectively enrolled and underwent robotic-assisted TKA with a single design of PCL-retaining implant. Laxity testing occurred 3 months (mean follow-up: 96±15 days) and 1 year after surgery (mean follow-up: 383±28 days). Knee laxity was measured at 30° of flexion in response to varus-valgus (VV) moments (±6 Nm) and anterior-posterior (AP) forces (30 N posterior and 50 N anterior) using a custom-designed multiplanar arthrometer. Four cycles of loads were manually applied, and laxity was defined as translation or rotation from the position at no applied load to the load target in each direction. Mean changes in laxity between 3 months and 1 year after TKA were assessed using paired t-tests ($\alpha = 0.05$). In addition, the standard deviation (SD) of laxity changes between the two time-points were reported to describe the inter-subject variance.

Results

No mean increases in anterior, posterior, varus, or valgus laxities were detected between 3 months and 1 year. The SD of laxity changes were 3.2 mm and 2.0 mm in the anterior and posterior directions, respectively, and 1.4° and 1.3° in the varus and valgus directions, respectively (Figure 1).

Discussion

Our findings suggest that while laxity, on average, does not change for all patients, individual patients may have increases or decreases in laxity over time. This analysis is part of a larger prospective study to relate patients' laxity measures to any perceptions of instability or other complications after CR-TKA. This will establish thresholds for clinically meaningful changes in laxity which can lead to improved intra-operative decision-making.

Images (Optional)

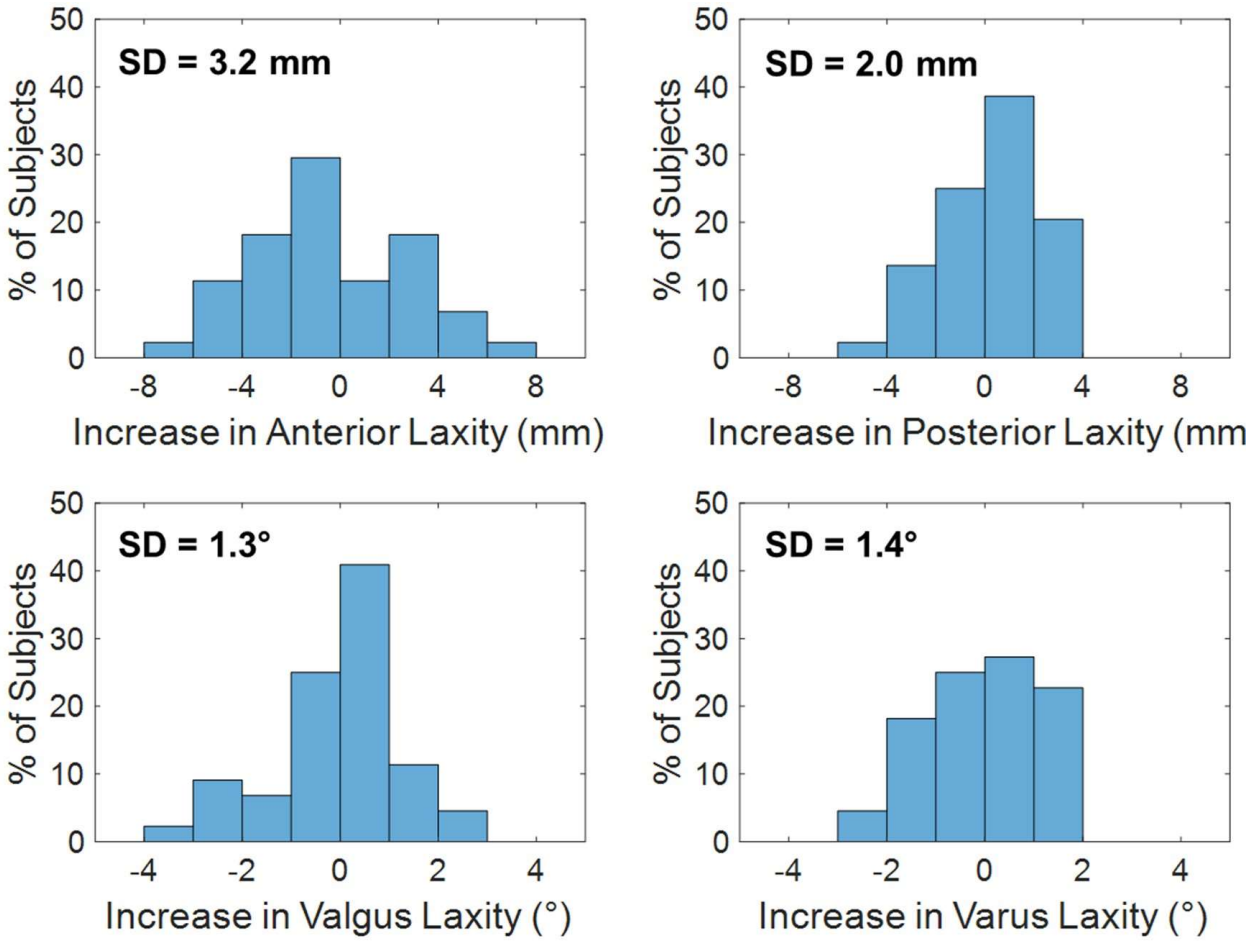


Figure 1. Histograms of changes in laxity between the 3-months and 1-year timepoints after total knee arthroplasty in the A) Anterior, B) Posterior, C) Valgus, and D) Varus directions. SD = Standard deviation

Acknowledgements (Optional)

Orthopedic Research and Education Foundation, Marina Kellen French Scholar Award, Clark and Kirby Foundations

Session Category

Orthopaedic Biomechanics: Lower Extremities

P3-238

Personalized Finite Element Analysis of Knee Contact Loading During Level Walking and Sit-to-Stand Movement Before and After High Tibial Osteotomy

Dr. Kao-Shang Shih[1], Mr. Yu-Ting Chen[2], Mr. Jing-Huei Siao[2], Mr. Kuan-Hsien Wu[2], Prof. Tung-Wu Lu[2,3,4]

[1]Department of Orthopedic Surgery, Shin Kong Wu Ho Su Memorial Hospital, Taipei, Taiwan, Taiwan. [2]Department of Biomedical Engineering, National Taiwan University, Taipei, Taiwan, Taiwan. [3]Department of Orthopaedic Surgery, School of Medicine, National Taiwan University, Taipei, Taiwan, Taiwan. [4]Health Science and Wellness Research Centre, National Taiwan University, Taipei, Taiwan, Taiwan

Introduction

High tibial osteotomy (HTO) corrects varus malalignment and reduces medial tibiofemoral loading in medial knee osteoarthritis. However, whether load redistribution after HTO is consistent across common daily activities remains unclear. This study quantified postoperative changes in contact force distribution during level walking and sit-to-stand (STS) using subject-specific finite element (FE) analysis driven by in vivo fluoroscopic kinematics.

Methods

Eight patients with medial osteoarthritis (62.5 ± 6.0 yrs) were evaluated before and six months after open-wedge HTO. Subject-specific bone and cartilage geometries were reconstructed from computed tomography and magnetic resonance imaging. Dynamic biplane fluoroscopy recorded knee motion during level walking and STS. Tibiofemoral kinematics were obtained using validated 3D/2D registration and served as boundary conditions for FE simulation. Compartmental contact forces normalized to body weight (BW) were compared between time points using paired t-tests ($\alpha = 0.05$). Walking analyses focused on stance phase peak loading, while STS forces were extracted across representative flexion angles to characterize task-dependent loading responses.

Results

After HTO, lateral loading increased and medial loading decreased during both activities (Table 1). In walking, lateral peak force increased (75.32% BW to 89.74% BW), while medial peak force decreased (134.87% BW to 110.28% BW), reflecting a shift toward more balanced load sharing during stance. STS demonstrated a similar but more pronounced redistribution throughout the movement cycle, especially at deeper flexion associated with higher joint demand. The timing of loading also changed postoperatively, with reduced

medial dominance during the transition from sit to full extension. Peak total loading showed consistent improvements in load distribution but was not statistically significant due to variability in individual responses.

Discussion

HTO successfully improved tibiofemoral load sharing during both gait and functional movement. The larger effect observed in STS indicates that task demand influences how realignment translates into joint-level mechanics. Fluoroscopy-driven personalized FE analysis provides a sensitive framework to evaluate functional outcomes of HTO beyond radiographic alignment, offering clinically relevant insight for rehabilitation strategies focused on restoring knee loading during everyday activities.

Images (Optional)

Table 1. Tibiofemoral contact force during level walking and sit-to-stand movement pre- and post-high tibial osteotomy (Mean ± SD; Unit: % Body Weight)

Contact Force - Level Walking				
	Compartment	Pre-op	Post-op	p-value
Stance Phase Peak Force	Lateral	75.32 ± 21.57	89.74 ± 19.86	0.03*
	Medial	134.87 ± 29.66	110.28 ± 25.41	0.04*

Contact Force - Sit-to-Stand				
Flexion Angle (°)	Compartment	Pre-op	Post-op	p-value
20	Lateral	24.45 ± 4.67	43.15 ± 7.50	0.03*
	Medial	42.65 ± 6.32	31.22 ± 4.65	0.03*
30	Lateral	22.12 ± 4.46	39.00 ± 7.50	0.03*
	Medial	38.80 ± 5.83	28.13 ± 4.54	0.03*
40	Lateral	20.28 ± 4.10	35.15 ± 7.04	0.03*
	Medial	35.43 ± 5.19	25.17 ± 4.51	0.03*
50	Lateral	17.85 ± 3.52	29.55 ± 6.99	0.03*
	Medial	31.55 ± 5.32	20.37 ± 4.44	0.03*
60	Lateral	16.22 ± 3.62	23.73 ± 6.97	0.03*
	Medial	29.02 ± 6.25	15.95 ± 4.14	0.03*
70	Lateral	14.18 ± 3.38	20.13 ± 7.32	0.03*
	Medial	25.72 ± 6.02	13.37 ± 4.25	0.03*
80	Lateral	11.87 ± 2.83	16.88 ± 6.67	0.03*
	Medial	21.97 ± 5.19	11.13 ± 4.31	0.03*
Maximum	Lateral	9.03 ± 2.53	14.73 ± 6.43	0.08
	Medial	17.07 ± 4.03	9.65 ± 4.33	0.07

Acknowledgements (Optional)

This study was funded by the National Science and Technology Council of Taiwan (111-2221-E-341-003- and 112-2221-E-341-001-).

Session Category

Orthopaedic Biomechanics: Lower Extremities

P3-239

Lateral Pivoting Prevalence Across Coronal Plane Alignment of the Knee (CPAK) Phenotypes Increases Progressively From Type I to Type III During Squatting

Mr. Orçun Taylan MSc[1], Mr. Gérard Peersman[1], Dr. Junya Itou MD, PhD[2], Dr. Geert Peersman MD[3], Prof. Dr. Johan Bellemans MD, PhD[4], Prof. Lennart Scheys PhD[1]

[1]IORT, KU Leuven, Leuven, Vlaams Brabant, Belgium. [2]Tokyo Women's Medical University, Tokyo, Honshu, Japan. [3]ZAS, Antwerp, Antwerp, Belgium. [4]AZ Vezalius, Limburg, Vlaams Brabant, Belgium

Introduction

Medial pivoting has long been considered the dominant kinematic pattern of the native knee during flexion. Nevertheless, recent evidence shows that lateral pivoting frequently occurs during functional tasks. Prior studies have demonstrated distinct kinematic patterns in varus and valgus knees. The recently introduced Coronal Plane Alignment of the Knee (CPAK) classification expands traditional varus, neutral, and valgus categories into nine phenotypes by combining the arithmetic hip–knee–ankle angle (aHKA) with joint line obliquity (JLO). However, the relationship between CPAK phenotype and pivoting motion remains unexplored. This study evaluated pivoting across all CPAK phenotypes during *ex vivo* simulated squatting.

Methods

Tibiofemoral kinematics from 69 fresh-frozen cadaveric knees were analyzed. Specimens with bone-pin–mounted markers were subjected to dynamic squatting (35°–100°) on a knee simulator while 3D trajectories were recorded (Vicon, UK). CPAK phenotype was determined from full-leg CT scans. Pivoting was assessed using the Instantaneous Center of Rotation (ICOR). The femoral medial–lateral flexion axis was projected onto the tibial transverse plane, and intersection points of this projected axis were computed for each flexion interval, producing ICOR positions as a function of flexion. ICOR medial or lateral to the tibial knee center indicated medial or lateral pivoting. Specimens were classified as lateral-pivot dominant if >50% of flexion angles exhibited lateral ICORs. A generalized linear mixed-effects model assessed the influence of aHKA, JLO, and flexion angle.

Results

Lateral pivoting occurred in CPAK types I–III. The probability of lateral pivoting was 28% in CPAK I (1/8 dominant), 39% in CPAK II (10/28 dominant), and 48% in CPAK III (8/17 dominant). In Type III, all knees demonstrated lateral ICORs, predominantly at flexion angles ≥58.5°. Across groups, the likelihood of lateral pivoting increased with flexion.

Flexion angle was a significant predictor of pivoting behavior, whereas aHKA and JLO showed no significant effects.

Discussion

All analyzed CPAK types exhibited lateral pivoting during squatting, with increasing prevalence from varus- to valgus-aligned phenotypes, reflecting a lateral shift in the load-bearing axis. These findings suggest that phenotype-specific assessment of knee kinematics may play an important role in surgical planning. Further work integrating patella contributions and three-dimensional morphology is warranted.

Images (Optional)

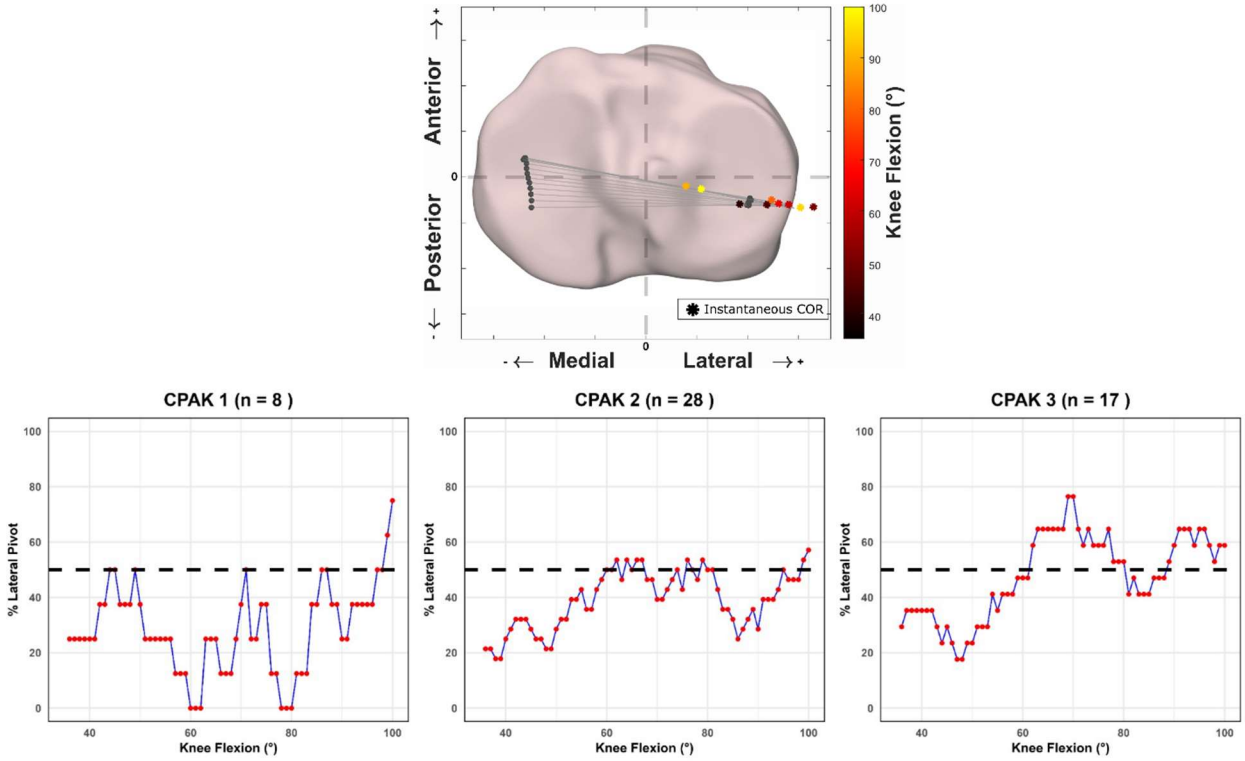


Figure 1: Instantaneous center of rotation (ICOR) as a function of knee flexion angle (top row), and the proportion of lateral pivot motion across CPAK Type I–III specimens (bottom row). Only these three CPAK types were present in the dataset.

Session Category

Orthopaedic Biomechanics: Lower Extremities

P3-240

Benefits in Terms of Fit-and-Fill and Implant Primary Stability of a OsteoCustom Stem for Transfemoral Amputees

Ph.D Giulia Galteri[1], Ms. Silvia Casadei[1], Mr. Edoardo Hirschberg[1], Dr. Domenico Alesi[2], Prof. Stefano Zaffagnini[2], Mr. Kavin Morellato[3], PhD. Emanuele Gruppioni[3], Prof. Luca Cristofolini[1]

[1]UNIVERSITY OF BOLOGNA, BOLOGNA, EMILIA ROMAGNA, Italy. [2]ISTITUTO ORTOPEDICO RIZZOLI, BOLOGNA, EMILIA-ROMAGNA, Italy. [3]Centro Protesi INAIL, VIGORSO DI BUDRIO, EMILIA-ROMAGNA, Italy

Introduction

Commercial transfemoral osseointegrated prostheses often do not match the patient's femoral canal, leading to mechanical instability or patient ineligibility. OsteoCustom is defined by discrete parameters' combination that should better match anatomical variability. Its actual benefits remain unclear, and a quantitative assessment is still missing. The aim of this study is to quantify the fit-and-fill and cortical bone removal to evaluate potential advantages of OsteoCustom, and to investigate whether these metrics correlate with implant primary stability.

Methods

Twelve paired human cadaveric femurs were used. Pre-implant CT scans were acquired (slice-thickness=0.625mm; in-plane-resolution=0.512mm). Surgical planning and implantations were performed by orthopedic surgeons, followed by post-implant CT acquisition. Each pair was implanted with a commercial OFI-C on one femur and the OsteoCustom stem on the contralateral femur. Compression-flexion and torsion tests were performed. A 3D-DIC system was used to measure the primary stability in terms of elastic micromotions and permanent migration. CT-images were upscaled fourfold (SRCNN,final in-plane-resolution=0.128) and segmented. Stem-bone contact area was computed along the stem (Matlab). Cortical bone removal was quantified subtracting the co-registered pre- and post-implant CTs, using the Goldman eight-sector method to evaluate bone loss locally and globally. A Wilcoxon paired-test was used (Prism9.5.1, $p<0.05$). Moreover,_a preliminary anatomical analysis explored the correlation between the primary stability and the contact area and the bone removal.

Results

For both loading scenarios, the OsteoCustom stem showed inducible micromotions more than threefold lower than those of the OFI-C stem($p<0.05$), and permanent migration more

than 1.5-fold lower($p<0.05$). The OsteoCustom showed benefit compared to the commercial one, with a significant increase in stem-bone contact area($p=0.041$) and a reduction in cortical bone removal ($p=0.026$) across all twelve paired femora. Contact area was linked to primary stability: specimens with >75% contact, whether implanted with the commercial or the OsteoCustom stem, consistently exhibited good primary stability. Conversely, bone removal did not show a direct correlation with primary stability.

Discussion

Nevertheless, preserving bone stock remains clinically crucial, as it reduces fracture risk and facilitates potential revision surgery. Although larger cohorts are needed, these preliminary findings highlight the potential advantages of OsteoCustom in terms of fit-and-fill and primary stability.

Images (Optional)

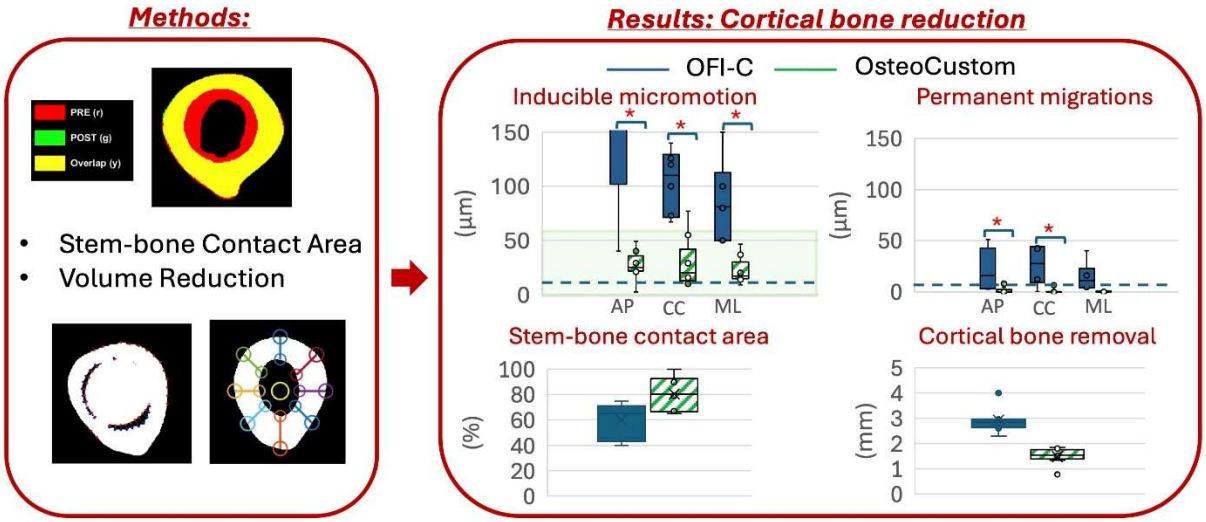


Figure 1: ***Left, Methods:*** *Overlay of pre- and post-implant CT images used to compute stem–bone contact area and cortical bone removal.* **Right, Results**: on the top the primary stability of both commercial (OFI-C) and OsteoCustom stem in terms of inducible micromotion and permanent migrations, while on the bottom the stem-bone contact area and cortical bone removal

Acknowledgements (Optional)

Work funded by INAIL (PR23-CR-P5-OsteoAMI).

Session Category

Orthopaedic Biomechanics: Lower Extremities

P3-241

Predicting Tibial Contact Mechanics Following Osteotomy: A Systematic Review and Meta-Analysis

Mr. Mahziyar Darvishi PhD candidate[1], Dr. Stavan Amin Clinical Fellow[2], Mr. Christopher fenelon MD[1], Mr. Michael Catapano Assistant Professor[1], Dr. David Wasserstein Assistant Professor[1], Dr. Timothy Burkhart Assistant Professor[1]

[1]University of Toronto, Toronto, Ontario, Canada. [2]Sunnybrook Holland Centre, Toronto, Ontario, Canada

Introduction

Lower limb malalignment, including varus and valgus deformities, alters knee joint loading and accelerates unicompartmental osteoarthritis [1]. Tibial osteotomy aims to restore alignment and redistribute contact forces across the tibial plateau [1]. Although postoperative changes in contact pressure and contact area are widely reported, the relationship between correction magnitude and resulting contact mechanics remains inconsistent. This lack of a predictive framework limits preoperative planning. The objective of this study was to quantify the relationship between tibial osteotomy correction magnitude and postoperative tibial contact mechanics using a systematic review and meta-analysis.

Methods

A systematic literature search identified experimental in vitro studies of tibial alignment manipulation in cadaveric knees across neutral, varus, and valgus configurations. Studies using tibial osteotomy or controlled mechanical realignment and reporting mean contact pressure, peak contact pressure, and/or contact area under controlled loading were included. Contact pressures were normalized to the applied axial load reported in each study. Outcomes were analyzed separately for medial and lateral compartments. Correction magnitude was quantified using mechanical tibiofemoral angle (TFA) and tibial plateau width percentage (TPW%), yielding regression models to predict post-osteotomy tibial contact mechanics.

Results

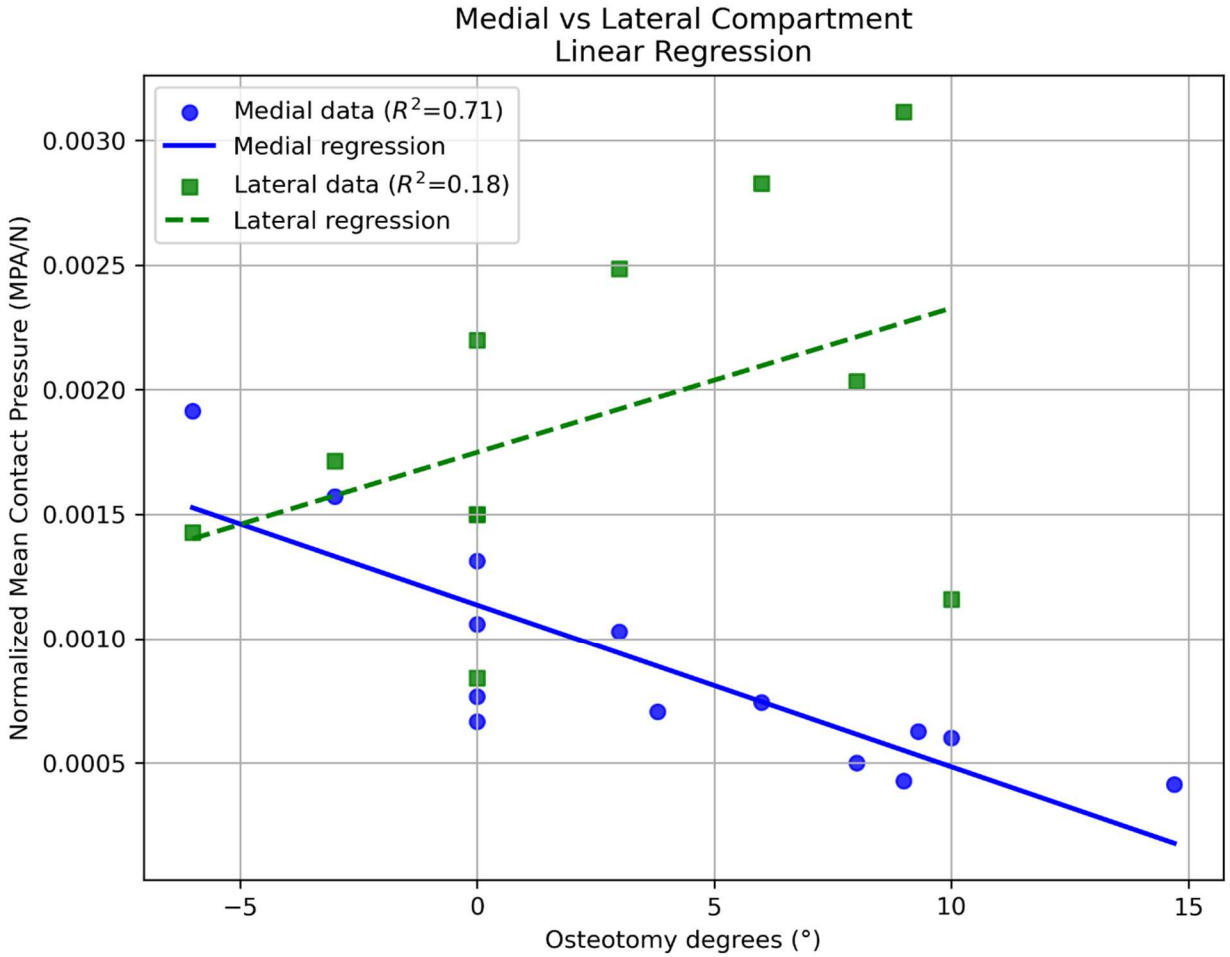
Nine studies met the inclusion criteria. Across all outcome metrics, consistent compartment-specific trends were observed (Figure 1). Increasing correction toward valgus alignment reduced medial mean and peak contact pressures with corresponding increases in lateral compartment loading. Meta-regression revealed predominantly linear relationships between correction magnitude and normalized contact mechanics in both

compartments. Contact area demonstrated complementary redistribution with increasing correction. Similar linear associations were observed using TFA or TPW%, indicating that both descriptors captured postoperative changes in tibial contact mechanics.

Discussion

These findings align with biomechanical theory that valgus-directed correction redistributes loads from the medial to the lateral compartment. Quantifying the relationship between correction magnitude and contact mechanics advances prior experimental work toward a predictive framework. Using both angular and geometric descriptors improves generalizability across experimental protocols. One limitation is that the included studies relied on cadaveric models and simplified loading. Future work will validate these relationships using subject-specific data and incorporate them into osteotomy planning tools.

Images (Optional)



References (Optional)

[1] Giordano Valente *et al.*, J exp Orthop, 2025

Session Category

Orthopaedic Biomechanics: Lower Extremities

P3-242

Biomechanical Analysis of Cotton Osteotomy in Flat Feet Using Finite Element Simulations

BSc Student Laura Valentina Muñoz Estevez BSc (Biomedical Engineering) in progress[1], BSc Student María Alejandra Bustos Bautista BSc (Biomedical Engineering) in progress[1], PhD Javier Bayod[2], PhD Christian Javier Cifuentes de la Portilla PhD[1]

[1]Universidad de Los Andes, Bogotá, Cundinamarca, Colombia. [2]Universidad de Zaragoza, Zaragoza, Aragón, Spain

Introduction

Flatfoot is a common deformity characterized by collapse of the medial arch and hindfoot valgus, which can lead to pain, functional limitation, altered load distribution, and progressive joint degeneration. In severe cases, one surgical option is the Cotton osteotomy, which involves making an opening in the medial cuneiform and inserting a wedge-shaped graft to restore the longitudinal arch and improve alignment, thereby promoting more adequate load distribution and reducing pain. However, its effectiveness depends on factors such as the opening angle, the location of the cut, and the type of graft used, decisions that are often based on the surgeon's experience. Therefore, this project proposes the use of computer simulations to evaluate different surgical configurations and support clinical decision-making.

Methods

To develop this project, three wedges measuring 4, 6, and 8 mm were modeled in Fusion 360. Each was positioned in the medial cuneiform using ICEM, simulating the procedure and allowing for the geometric reconstruction of the medial arch. Subsequently, a mesh with tetrahedral elements between 1 and 2 mm was generated, and in the same environment, bar-type elements and the fixation and load conditions were defined. The final simulation was performed in Abaqus CAE.

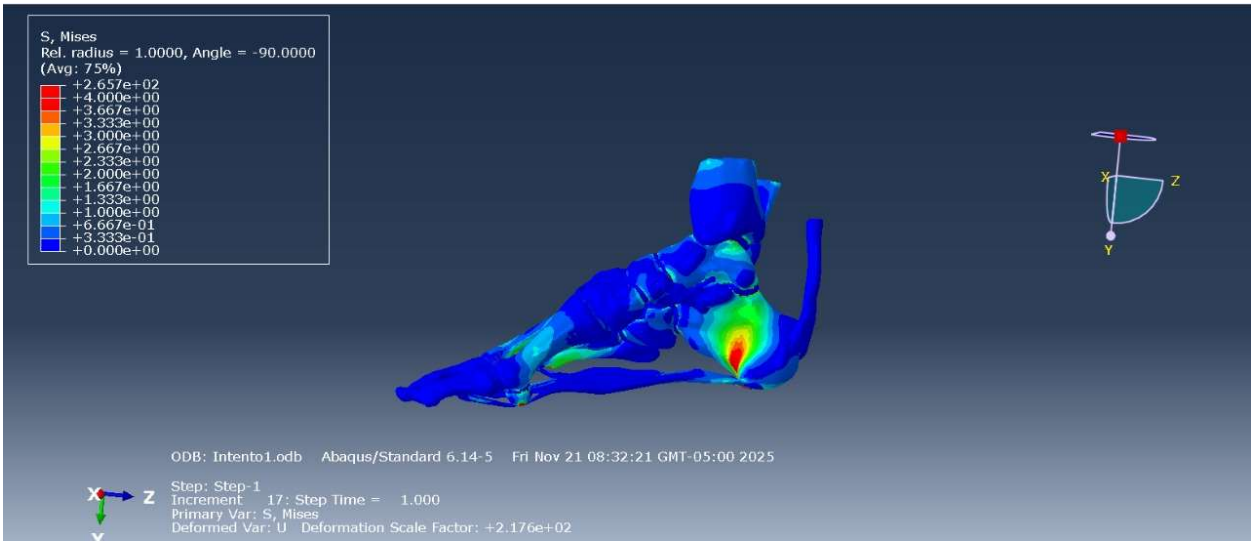
Results

Preliminary results show that, as expected, the size of the wedge is directly related to the increase in the longitudinal arch, affecting not only the position of the first metatarsal but also tissues such as the plantar fascia. A concentration of stress is also observed in the calcaneus, rearfoot, and metatarsals, while no significant stress is evident in the midfoot, possibly due to the fixation conditions applied.

Discussion

These findings suggest that osteotomy could reduce stress in medial areas, particularly in the hallux, by redistributing the load thanks to the restoration of the arch. In accordance with the literature, an increase in stress in the medial and middle regions of the ankle joint and a decrease in the lateral and posterior areas would be expected [6].

Images (Optional)



References (Optional)

[1] Kobayashi Y, et al. Morphology and loading changes after medial displacement calcaneal osteotomy via patient-specific FEM. Sci Rep. 2024;14:14766.

Session Category

Orthopaedic Biomechanics: Lower Extremities

P3-243

Total Knee Arthroplasty Rehabilitation Augmented with Electroencephalogram Biofeedback Training to Accelerate Achievement of Delayed Functional Milestones: A Case Study

Mr Matthew Varano BA[1], Mr. Henry Eilen BA[1], Ms. Camilla Antognini MS[2], Dr. Felipe Gonzalez MD MS[2], Dr. Christopher Knowlton PhD[2], Dr. Johnathan Gustafson PhD[2], Dr. Markus Wimmer PhD[2], Dr. Craig Della Valle MD[1], Dr. Brian Forsythe MD[1]

[1]Midwest Orthopaedics at RUSH, Chicago, IL, United States. [2]RUSH University Medical Center, Chicago, IL, United States

Introduction

Total knee arthroplasty (TKA) is an effective treatment for advanced degenerative joint disease, yet a subset of patients experience delayed functional recovery despite appropriate postoperative rehabilitation. Visualization-based therapies have shown potential to enhance strength, motor control, and functional outcomes when used with standard physiotherapy, although their role in patients with persistent postoperative deficits remains unclear. This case study describes the clinical course of a patient who failed to meet rehabilitation milestones after TKA and subsequently underwent EEG biofeedback training as an adjunct to therapy.

Methods

A 55-year-old female developed persistent quadriceps weakness, anterior knee pain, and restricted terminal knee extension four months after an uncomplicated TKA. She completed eight EEG biofeedback training sessions over four weeks while continuing standard physiotherapy. Training uses an EEG-based brain–computer interface to quantify neural engagement during visualization of functional movements. Biomechanical assessment, surface EMG, and isokinetic and isometric strength testing were performed immediately before and after the EEG biofeedback intervention. PROMs included KOOS JR., IKDC, and TSK-11.

Results

Motion analysis demonstrated increased external knee flexion moments across gait, squat, and lunge tasks after biofeedback, accompanied by improved knee flexion angle during loading response and more symmetrical bilateral loading. Hip flexion moments and contralateral knee loading decreased. Strength testing revealed consistent gains in knee extension torque, total work, and power at both 60°/s and 120°/s, along with improved muscular endurance. EMG showed increased vastus medialis activation and reduced

rectus femoris overreliance, although quadriceps avoidance and compensatory hamstring recruitment persisted. PROMs improved modestly but did not reach minimal clinically important difference thresholds.

Discussion

Four weeks of EEG biofeedback training combined with physiotherapy produced measurable biomechanical and strength improvements in a patient with delayed recovery following TKA. Enhanced knee loading capacity, improved symmetry, and early correction of stiff-knee gait characteristics suggest that EEG biofeedback training may support restoration of more physiologic movement patterns. Although findings are limited to a single case and natural recovery may have contributed, this preliminary evidence indicates that EEG biofeedback training may serve as a valuable adjunct for patients who fail to progress with standard rehabilitation. Further controlled studies are warranted.

Images (Optional)

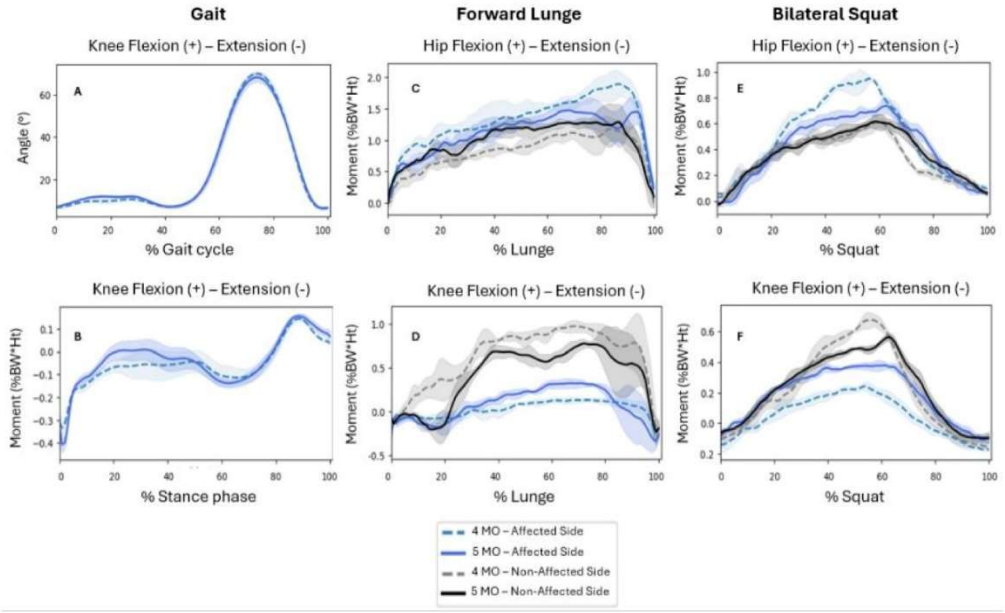


Fig. 1 Comparison of hip and knee kinematics and kinetics between the involved limb (dashed blue = 4 months, solid blue = 5 months) and the non-involved limb (dashed black = 4 months, solid black = 5 months). Mean signals ± standard deviation (shaded areas) across all trials are presented as a percentage of the movement task. Knee angels through gait cycle (A), Knee moments through stance phase (B), Hip (C) and Knee (D) moments during lunge, Hip (E) and Knee (F) moments through squat

Session Category

Orthopaedic Biomechanics: Lower Extremities

P3-244

Biomechanical Analysis of Secondary Stability in Cementless Femoral Hip Stems: An Ex Vivo Post-Mortem Study Part 2

Prof. Matthias Woiczinski[1], Dr. Manuel Kistler[1], Dr. Lena Hirtler[2], Dr. Gilbert Schwarz[2,3]

[1]Experimental Orthopaedics University Hospital Jena, Campus Eisenberg, Waldkliniken Eisenberg, Germany, Jena, Thüringen, Germany. [2]Center for Anatomy and Cell Biology, Medical University Vienna, Vienna, Austria, Vienna, Vienna, Austria. [3]Department of Orthopedics and Trauma-Surgery, Medical University of Vienna, Vienna, Austria, Vienna, Vienna, Austria

Introduction

Secondary stability, particularly with respect to micromotion, is a critical determinant of the long-term survival of cementless femoral hip stems following osseointegration.[1,2] This study investigates micromotion at the bone–implant interface in proximally loosened total hip arthroplasty (THA) stems ex vivo and compares these findings with Part 1 of the study, in which fully integrated stems were analysed. The results are further interpreted in the context of the established 150-micron threshold[3], commonly regarded as the upper limit for successful osseointegration. These insights aim to support the refinement of validation criteria for implant performance and long-term durability.

Methods

12 fresh-frozen human femora from body donations with cementless hip stems (Alloclassic® Zweymüller®) were analyzed. Standardized force alignment was ensured with a 17° adduction and 11° flexion angle, and micromotion at the bone-implant interface was measured in Gruen zones 8–10 using a 3D optical system (ARAMIS accuracy: 11.2 µm in-plane). Specimens underwent dynamic loading (11Hz, 300–1186.5N) and corresponding to body weight. Data analysis included MATLAB and GraphPad, with significance set at $p<0.05$. Ethics Committee of the Medical University of Vienna (2111/2017).

Results

For the fully integrated stems, the mean 3D micromotion was 209.7 µm ± 147.9 µm, with the highest values occurring in Gruen zone 8 and the lowest in zone 9. Stems that were radiologically loosened in the proximal region exhibited notably higher micromotion, particularly in zone 8, with a mean of 287 µm ± 104 µm.

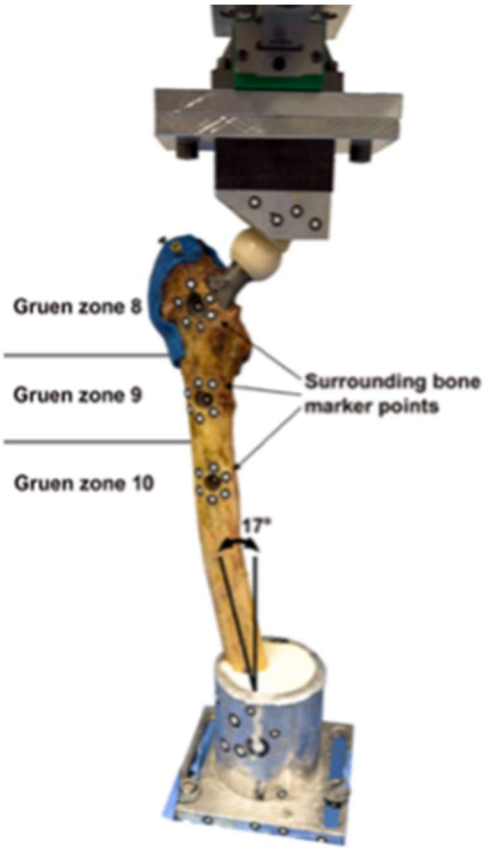
Discussion

Micromotion analysis revealed significant differences among Gruen zones, underscoring the critical influence of localized load transmission at the bone–implant interface on secondary stability. In fully integrated stems, micromotion frequently exceeded the classical 150-µm osseointegration threshold described by Pilliar yet without documented clinical complications, highlighting that this limit may be more nuanced under physiological anchorage conditions.

In contrast, proximally loosened stems demonstrated substantially higher micromotion, where values were markedly elevated.

The micromotion patterns observed across both test series provide essential insights for optimizing implant and further emphasise the diagnostic relevance of recognising fixation deficits.

Images (Optional)



References (Optional)

Session Category

Orthopaedic Biomechanics: Lower Extremities

P3-245

Center of Pressure Displacement and Plantar Pressure in Individuals With a Minor Lower Extremity Amputation.

PhD(c) Maxime Acien, PhD(c) Ahmed Dami, DPM Pier-Luc Isabelle, DPM, Pr. Virginie Blanchette, DPM, Pr. Gabriel Moisan

Université du Québec à Trois-Rivières, Trois-Rivières, Québec, Canada

Introduction

Minor lower extremity amputation (LEA) prevalence is increasing worldwide, mainly driven by diabetes-related neuropathic and vascular complications. Minor LEAs induce biomechanical alterations affecting postural control and plantar pressure distribution, with repercussions on mobility and reamputation risks [1,2]. Foot orthoses (FOs) are commonly prescribed to redistribute loads and improve stability, but their effectiveness in this population remains unclear due to limited evidence [3]. This study aimed to assess FOs-induced changes in center of pressure (CoP) and plantar pressure.

Methods

Nine participants with a minor LEA (65.9 ± 8.9 years) performed six 15-seconds quiet-standing trials, each foot on a force plate (AMTI) while plantar pressure was recorded using instrumented insoles (Pedar-NovelX). Ankle joint centers were determined using two kinematic markers to normalize CoP. Two conditions were compared: shoe-only and with custom-FOs. Outcomes included CoP length, root mean square (RMS), range and position in anteroposterior (AP) and mediolateral (ML) directions, as well as contact area, mean and peak plantar pressure. Data were summarized using medians (interquartile) and compared using rank-based mixed-effects models assessing the two conditions while accounting for repeated measures.

Results

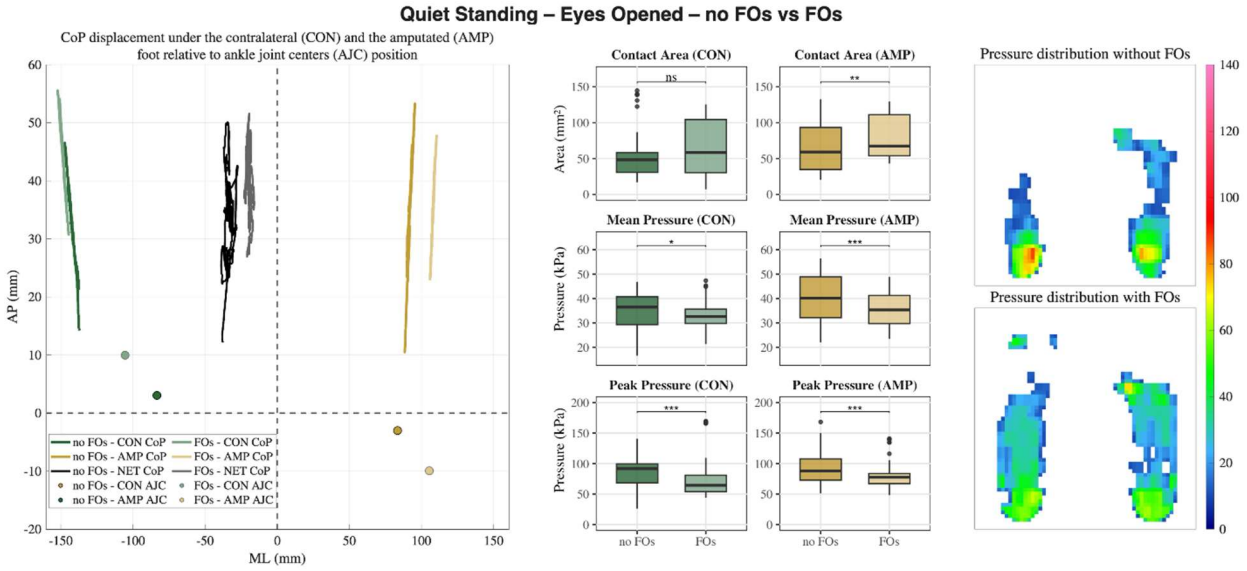
No significant changes were observed in CoP outcomes across AP/ML directions when using FOs ($p>0.05$), except for a reduction in CoP-ML-RMS (23.7 (21.4) to 19.3 (17.3) mm, $p=0.039$).

On the LEA side, FOs increased contact area (59.1 (58.6) to 67.4 (57.2) mm^2, $p=0.003$), while decreasing global mean plantar pressure (40.1 (16.7) to 35.3 (11.5) kPa, $p<0.001$) and global peak pressure (88.0 (34.8) to 77.6 (16.6) kPa, $p<0.001$). On the contralateral side, there was no change in contact area ($p=0.128$), but both global mean and peak plantar pressures decreased significantly ($p=0.010$ and $p<0.001$, respectively).

Discussion

FOs induced limited changes in postural sway but modified plantar pressure distribution. On the LEA side, the larger contact area redistributed pressure away from the rearfoot towards more distal regions, reducing global mean and peak values. On the contralateral side, global pressure also decreased despite any area changes, which may suggest reduced loading and improved bilateral charge distribution.

Images (Optional)



References (Optional)

[1] Kanade et al., *Clinical biomechanics*, 2008.

[2] El-Hilaly et al., *The Foot*, 2013.

[3] Acien et al., *Gait and Posture*, 2025.

Session Category

Orthopaedic Biomechanics: Lower Extremities

P3-246

Which Uncemented Stem Designs Used in Total Hip Replacement Do Benefit From a Collar?

Prof. Michael Morlock, Dr.-Ing. Gerd Huber, Dr.-Ing. Katja Brand

Institute of Biomechanics, TUHH Hamburg University of Technology, Hamburg, Hamburg, Germany

Prof. Michael Morlock

Dr.-Ing. Gerd Huber

Introduction

A collar has been shown to be beneficial in reducing peri-prosthetic femur fractures (PPF) and revisions in uncemented total hip arthroplasty using tapered press-fit stems (revision rate at 15 years 4.8% compared to 6.1% for collarless [1]). The purpose of this study was to develop a numerical model to quantify the benefit of a collar and to apply it to different designs.

Methods

Collared and collarless CORAIL stems (DePuy Synthes) were inserted into two human cadaveric femurs until failure using a material testing machine (constant velocity 0.1 mm/s). Shear, axial compressive, tangential tensile strains and fracture loads were recorded using Digital Image correlation and compared between the two conditions. A finite element model (FEM) based on a CT scan of one femur was used to estimate numerically the same parameters for three different stem types with vs. without collar (CORAIL, EMPHASYS, ACTIS all DePuy Synthes).

Results

The collar increased axial compressive strains and reduced the critical tangential tensile strains (hoop strains), which can cause a PPF during loading for all designs [2]. This results in substantially higher loads required for a PPF (Figure 1). In the experimental part of the study, the collar increased the fracture load for the CORAIL stem by nearly 100% (6824N vs. 3465N, benefit ratio 1.96). The results of the FEM model yielded a similar tendency for the

CORAIL stem but overestimated the benefit ratio (3.37). The EMPHASYS stem showed very similar results (3.24), whereas the ACTIS stem showed a smaller benefit ratio (1.67).

Discussion

All stem designs investigated did benefit from a collar reducing the hoop strains for a given load. As a consequence higher loading can be sustained before a critical strain magnitude is reached. The ACTIS stem benefits less from the collar due to its fit-and-fill design in the metaphyseal region, which is associated with a larger width compared to the other stem designs investigated. The presented approach can be used to investigate the benefit of a collar for other uncemented stem designs.

Images (Optional)

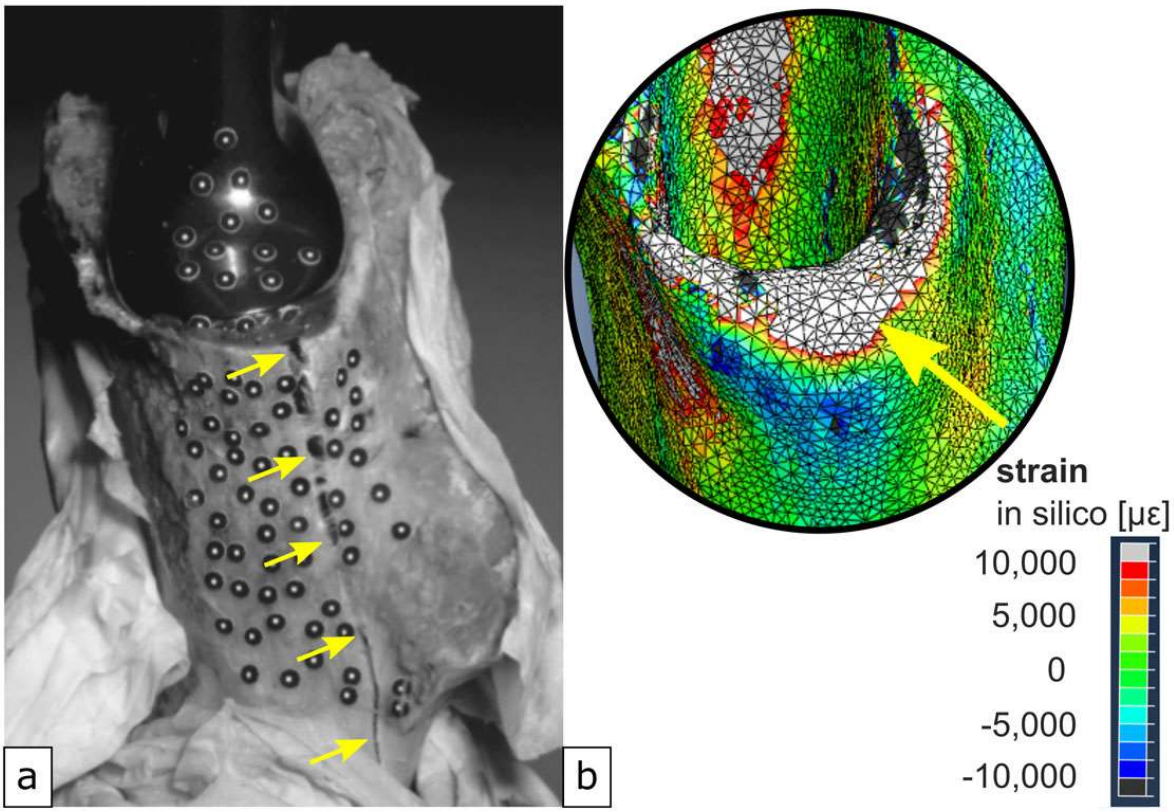


Figure 1: (a) Fracture during *in-vitro* testing;
(b) Tangential *in silico* strain distribution. Elements shown in gray exceed the failure limit of 10,000 με (yellow arrows indicate the position of the *in-vitro* fracture).

References (Optional)

1 AOA-NJRR, Annual report 2025
2 Brand K. et al., ClinBio 130, 2025

Acknowledgements (Optional)

The study was financially supported by DePuy Synthes.

Session Category

Orthopaedic Biomechanics: Lower Extremities

P3-247

Estimating Contact Pressure via Strap Tension in Rehabilitative Devices

Ms. Natasha Anderson, Dr. Qingguo Li

Queen's University, Kingston, Ontario, Canada

Introduction

Osteoarthritis (OA) is a common knee disease, that causes significant pain and functional impairment. Unloader braces are often prescribed to alleviate stress on the joint through strap tension. However, excessive pressure at the skin-brace interface can cause patient discomfort [1]. Direct pressure measurement methods such as force sensing resistors (FSRs) are often inaccurate, noisy, and costly [2]. This study aimed to investigate the relationship between strap tension and contact pressure, proposing strap force sensors (SFSs) as an alternative measurement approach for controlling pressure distribution around an injured knee.

Methods

Pressure and tension measurements were collected simultaneously in two experiments: first, on a curved surface apparatus (CSA) that simulated the skin, and second, with a knee brace on a participant. FSRs were placed between the skin and the brace, and SFSs on the straps. CSA testing explored the pressure-tension relationship at three locations from the direct point of load application (0, 20, 40 degrees). This was then validated in the second experiment, where direct and derived pressure measurements were compared to test for interchangeability.

Results

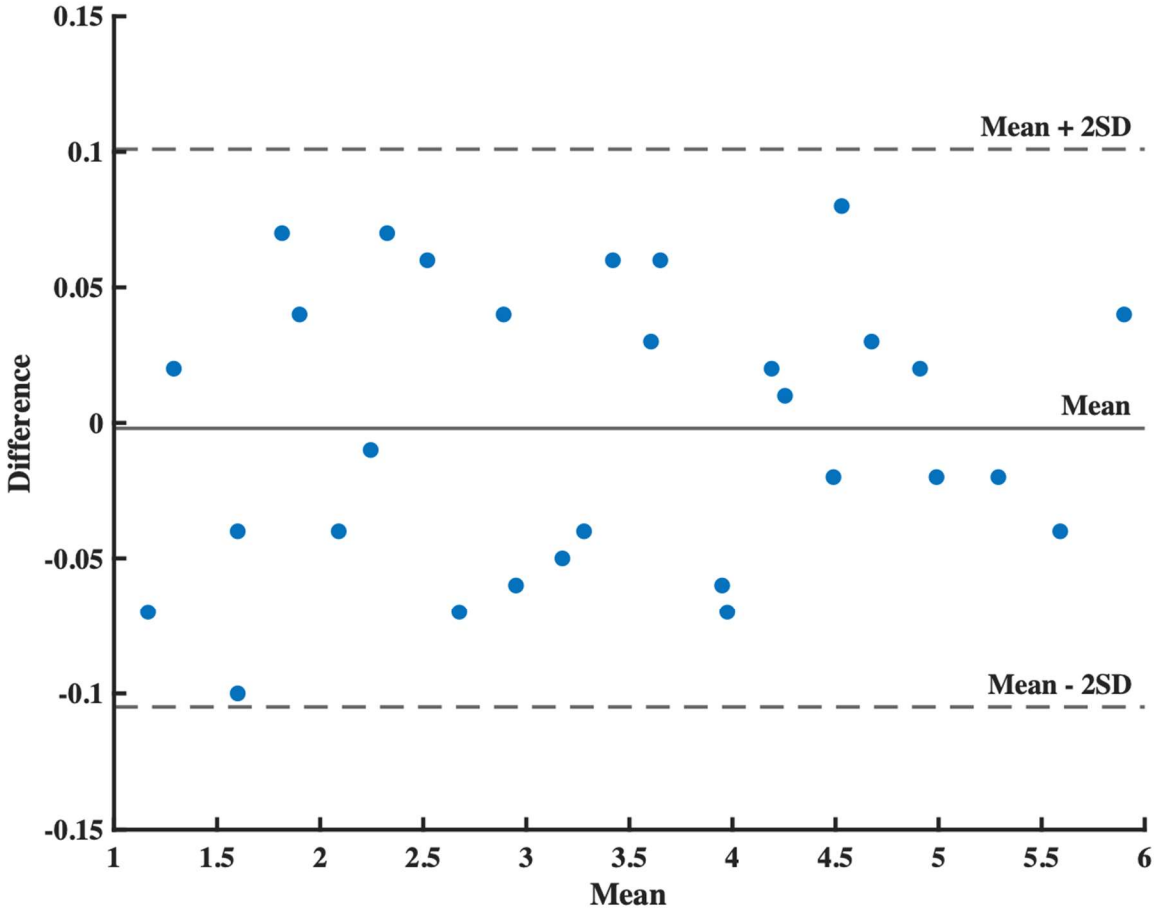
Tension and pressure show a linear relationship, in which proportionality depends on proximity to the point of load application. Bland-Altmann analysis showed narrow limits of agreement (full range=0.206 kPa) and no significant bias (grand mean difference=-0.002 kPa). A two-tailed t-test showed no significant differences in the means of SFS and FSR pressure values ($p=0.19$).

Discussion

The results confirm that pressure predictions from strap tension measurements are interchangeable with direct pressure measurements. These findings suggest that SFSs can be effectively used to monitor and control pressure in knee braces and other rehabilitative

devices, enabling the development of smart braces that optimize therapeutic outcomes while minimizing risks associated with excessive pressure. However, the study was performed under static loading conditions and in real-world applications, dynamic movements would alter strap tensions and pressure distributions, potentially changing the determined relationships. Further work should include comprehensive pressure mapping around the entire knee and consider more diverse conditions, to simulate real-world conditions.

Images (Optional)



References (Optional)

[1] Huda Alfatafta *et al.,* BMC Musculoskelet Disord, 2021.

[2] Eric C Swanson *et al.,* J Biomech Eng, 2019.

Session Category

Orthopaedic Biomechanics: Lower Extremities

P3-248

Surgical Releases During Direct Anterior Approach for Total Hip Arthroplasty: Impact on Surgical Exposure

Mr. Joshua Bland MBME, Dr. John Kelly MD, Dr. Brandon Cabarcas MD, Mr. Alexander Hooke MA, Dr. Mario Hevesi MD, Nathan Flath BS

Mayo Clinic, Rochester, MN, United States

Introduction

The direct anterior approach has considerably increased in popularity among total hip arthroplasty surgeons in the past 10-15 years. Proponents of the direct anterior approach cite its muscle-sparing nature, faster recovery, and decreased risk of postoperative dislocation as potential advantages compared to more conventional posterolateral or direct lateral approaches. Obtaining adequate surgical exposure when utilizing the direct anterior approach is critical to obtaining optimal surgical efficiency and successful outcomes. The goal of this study is to investigate the biomechanical impact of sequential soft tissue releases on femoral surgical exposure during this approach.

Methods

8 fresh-frozen cadaveric hip and full lower extremity specimens (4 left hips and 4 right hips) were obtained and prepared for dissection. A direct anterior approach was carried out, and the following sequential soft tissue releases were performed: inferomedial capsular release, superior capsular release, obturator internus followed by piriformis or piriformis followed by obturator internus, obturator externus, quadratus femoris, tensor fasciae latae, sartorius, and rectus direct head. Directly following each release, the femur was lifted from an eyelet screw placed in the medial calcar of the proximal femur using a pneumatic actuator based system. During the lift, a load cell and linear potentiometer measured the vertical load and displacement.

Results

When the obturator internus was released before the piriformis, the average femur displacement at 70 N of load was over 15 mm greater than when the piriformis was released first; at 110 N of load, this difference was just over 12 mm (Figure 1). After the obturator internus and piriformis were both released, the increase in displacement per sequential release became noticeably less.

Discussion

This study and future work will be important to understand the minimum number and optimal order of soft tissue releases required to adequately access the femur during direct anterior total hip arthroplasty.

Images (Optional)

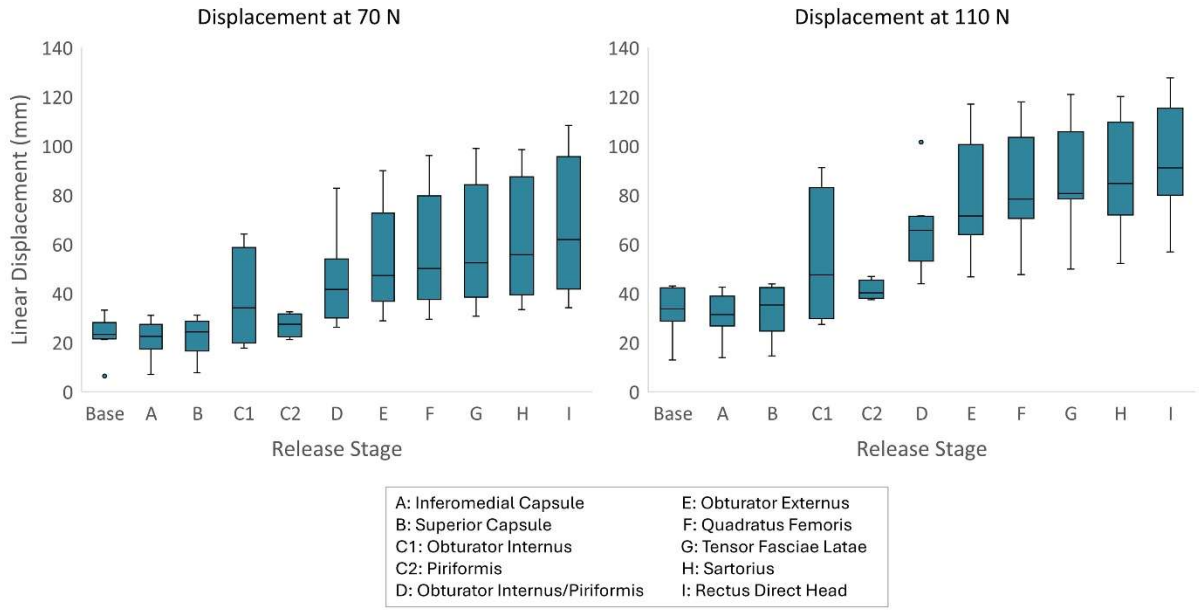


Figure 1. Linear displacements of femur during sequential release stages at 70 N and 120 N loads.

Session Category

Orthopaedic Biomechanics: Lower Extremities

P3-249

PTH Does Not Attenuate Joint Damage Due to Daily Compression of the Mouse Tibia

Mr. Omar Dervisevic, Dr. Ana Witkowski, Dr. Marjolein C. H. van der Meulen

Cornell University, Ithaca, NY, United States

Introduction

Early-stage osteoarthritis (OA) is characterized by increased bone remodeling, motivating interest in subchondral bone–targeted therapies. Parathyroid hormone (PTH), an FDA-approved anabolic osteoporosis treatment, promotes bone formation and reduces joint degradation and pain in surgical OA models. We investigated whether PTH, administered concurrently with daily mechanical loading, could reduce pain-related behaviors, attenuate cartilage damage, and increase bone mass in a load-induced OA model.

Methods

With IACUC approval, 26-week-old male C57BL/6J mice underwent 6 weeks of daily cyclic compression (9N, 1200 cycles, 4 Hz) on the left tibia; right limbs were contralateral controls. Mice were randomized to saline (VEH, n=8–10) or PTH (40 μg/kg/day, n=8–10) administered subcutaneously 5 days/week immediately after loading. Static weightbearing was assessed biweekly. After 6 weeks, knees were collected for microCT analysis of epiphyseal cancellous bone and subchondral cortical bone, and for Safranin-O staining with OARSI scoring. Treatment and loading effects were analyzed using linear mixed-effects models with Tukey post-hoc tests.

Results

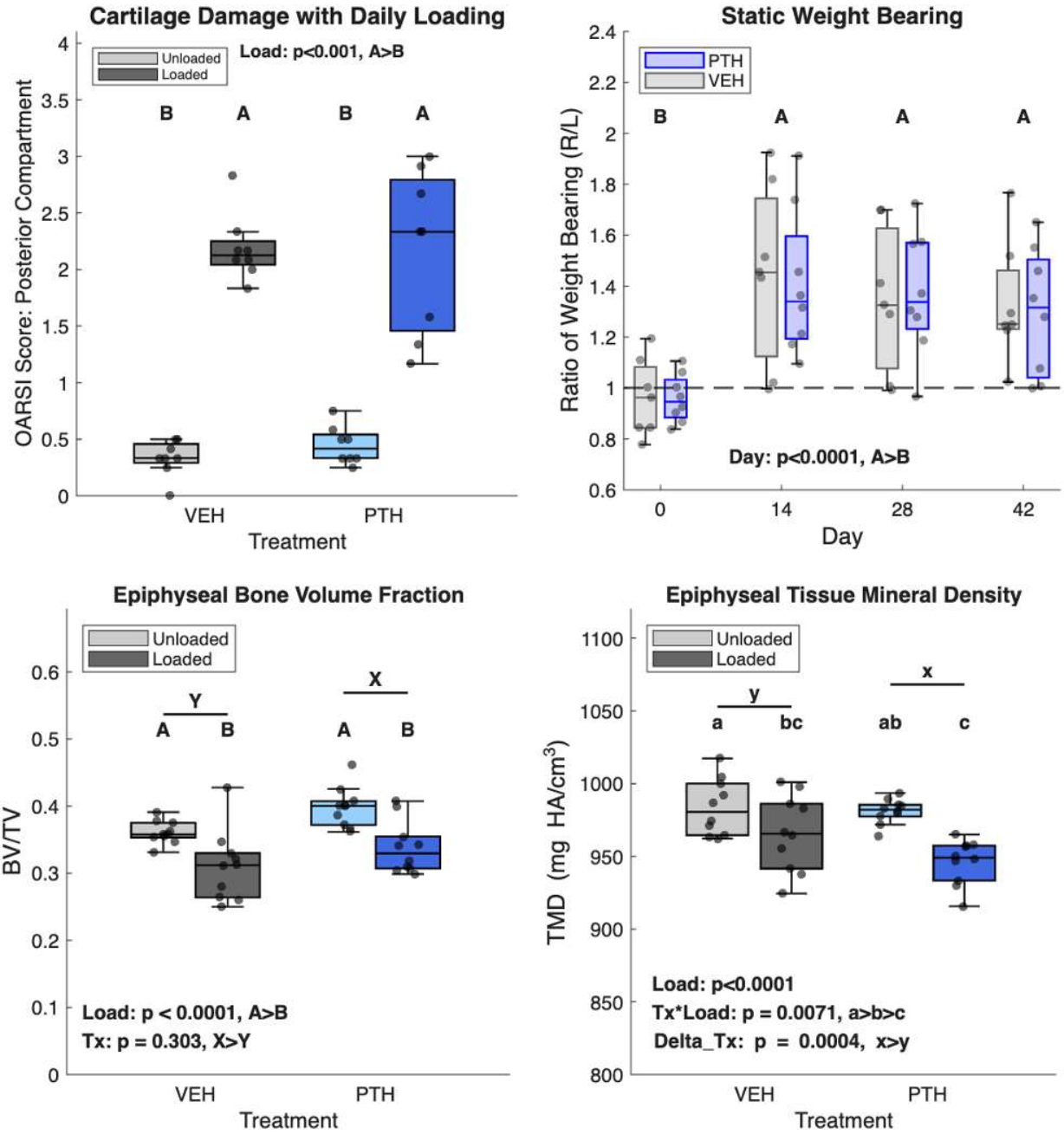
Daily loading produced significant cartilage damage, and PTH treatment did not alter the severity. Hindlimb weightbearing progressively shifted towards the control limb, and PTH did not reduce this pain-related behavior. As expected, PTH increased epiphyseal bone volume fraction (BV/TV). Loading reduced epiphyseal tissue mineral density (TMD); the reduction of TMD was greater in PTH-treated limbs.

Discussion

While PTH reduced pain and cartilage degeneration in surgical OA models, concurrent administration with compressive loading did not attenuate cartilage damage or pain behaviors. Differences across OA models may reflect differential effects of mechanical loading on cartilage biology or the interaction of PTH and loading to influence joint health.

PTH increased epiphyseal bone mass, whereas loading reduced TMD—an effect amplified with PTH—indicating enhanced remodeling under combined treatment. Despite these bone changes, joints were not protected from damage, suggesting distinct mechanisms through which PTH and loading act in joint damage. Ongoing work to define the early transcriptomic pathways will provide additional insights into the mechanisms by which PTH modulates cartilage responses to mechanical loading.

Images (Optional)



Acknowledgements (Optional)

Funding provided by NIH R01-AR081943

Session Category

Orthopaedic Biomechanics: Lower Extremities

P3-250

Changes in Knee Kinematic Gait Scores from Pre to Post Knee Arthroplasty

Mr. Owen Falkenham[1], Ms. Stephanie Civiero[2], Dr. Michael Dunbar[1,2], Dr. Jennifer Leighton[1,2], Dr. Glen Richardson[1,2], Dr. David Wilson[1,2], Dr. Janie Astephen Wilson[1,2]

[1]Dalhousie University, Halifax, NS, Canada. [2]Nova Scotia Health Authority, Halifax, NS, Canada

Introduction

The adoption of markerless motion capture in clinic spaces reduces participant burden for gait capture, and therefore increases the feasibility of clinical uptake of gait biomechanics to support clinical decisions. Understanding variability in patients' gait biomechanics response to arthroplasty can support efforts toward personalized surgical decisions that account for joint-level mechanics. The purpose of this study was to develop a multivariate knee kinematics gait score that can be captured readily in-clinic, and to examine differences and subgroups of patients based on pre-to-post-surgical changes.

Methods

Overground gait kinematics were collected in an orthopaedic clinic hallway using markerless motion capture (Theia 3D; 10-Sony RX0II cameras) pre-surgery and 3-months after surgery. Stepwise linear discriminant analysis (LDA; 2% improvement step condition) combined with waveform principal component analysis [1] was used to select gait features that optimally separated pre-operative from non-OA participant gait patterns, with discriminant scores representing the severity of knee OA gait. Individuals were classified as either 'improving', 'declining', or 'stable' if their pre-to-post-surgery score change exceeded the minimal detectable change of the non-OA participants subset who underwent three repeatability trials [2]. Subgroup differences in pre-operative kinematics were evaluated with ANOVA or Kruskal-Wallis tests, and where appropriate, with a Tukey HSD assessment (α=0.05).

Results

Fifty-three patients with advanced knee OA were included (F/M: 35/18; age = 63 +/- 9.6; BMI = 34 +/- 7.5). There were no significant group-level score changes pre-to-post-surgery. Significantly higher pre-operative gait scores (i.e. less severe gait) were found in those declining than those improving ($p<0.01$), dominated by significantly higher knee flexion/extension ranges of motion (PC2) during walking ($p<0.05$). No significant differences in anthropometrics or demographics were found among subgroups.

Discussion

These results highlight the variability in knee function response to arthroplasty among patients, and how it links to pre-operative gait function. Accounting for this variability in personalized decisions can have important implications for clinical outcomes, which we will characterize with further longitudinal assessment of clinical and gait recovery trajectories.

Images (Optional)

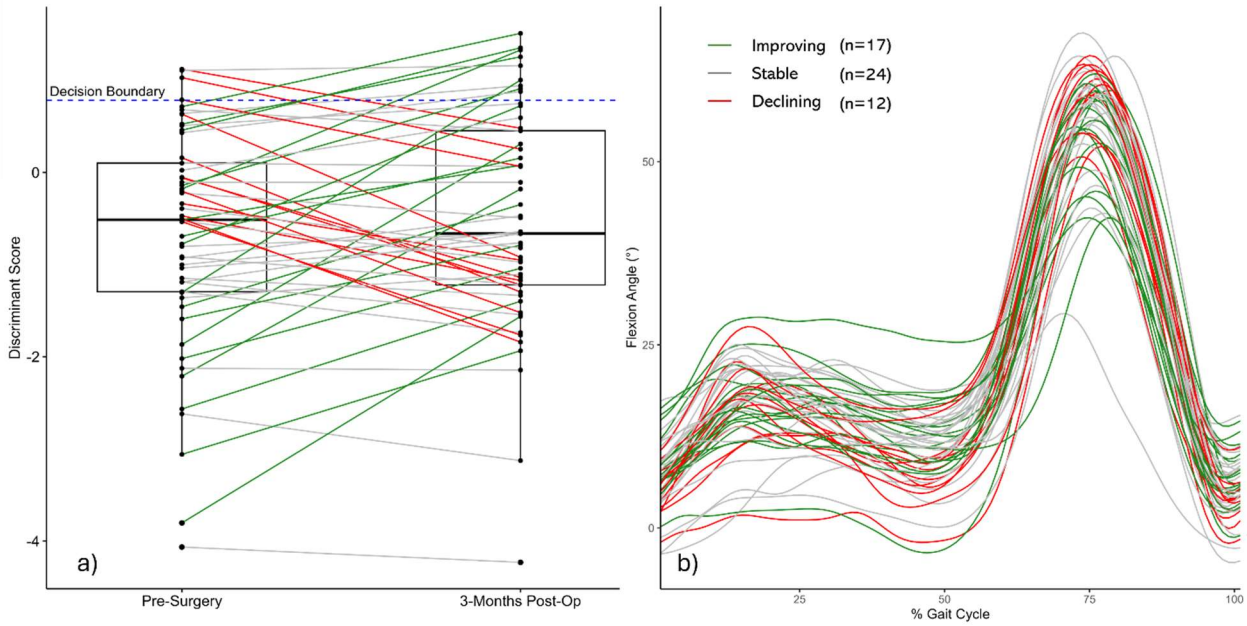


Figure 1: a) Pre-to-Post-Surgery Change in Knee Kinematic Gait Scores. Decision boundary denotes the threshold between OA/non-OA gait classification. b) Pre-Operative Overground Walking Flexion Angles,

References (Optional)

[1] Outerleys et al, J Appl. Biomechanics, 2020

[2] Civiero et al, J Appl. Biomechanics, 2025

Session Category

Orthopaedic Biomechanics: Lower Extremities

P3-251

Physical Activity Fragmentation in Patients with Knee Osteoarthritis before and after Arthroplasty

Mr. Owen Lindsay MSc[1], Mr. Adam Dorrance BEng[2], Mr. Arsh Singh BEng[1], Dr. Janie Wilson PhD[1,3], Dr. Jennifer Leighton MD[1,3], Dr. Michael Dunbar MD[1,3], Dr. Glen Richardson MD[1,3], Dr. David Wilson MD[1,3]

[1]Dalhousie University, Halifax, Nova Scotia, Canada. [2]Dalhousie, Halifax, Nova Scotia, Canada. [3]Nova Scotia Health, Halifax, Nova Scotia, Canada

Introduction

Physical activity monitoring in knee osteoarthritis (OA) traditionally emphasizes volume-based metrics, yet patients accumulating similar daily steps may exhibit markedly different movement patterns relevant to disease severity and surgical recovery. Activity fragmentation, quantified as the Active-to-Sedentary Transition Probability (ASTP), reflects the probability of transitioning from activity to rest. In aging populations, higher fragmentation is associated with adverse health outcomes [1,2] independent of activity volume. Despite potential as a clinical indicator, fragmentation remains largely uncharacterized in knee OA. This study examined relationships between ASTP and clinical status in end-stage knee OA and evaluated its responsiveness to change following arthroplasty.

Methods

Patients with end-stage knee OA undergoing knee arthroplasty surgery (KAS) wore lower-leg inertial measurement units (Axivity AX6, 100Hz) continuously for seven days pre - and 12-months post-surgery. Mean amplitude deviation thresholds (0.0167g [3]) classified one-minute epochs as active or sedentary. ASTP was calculated as the inverse of mean active bout length, expressed as a percentage. Patient-reported outcome measures (PROMs) included the Oxford Knee Score (OKS), Numerical Pain Rating Scale (NPRS), and EQ-5D-5L. Pearson correlations assessed pre-operative associations between ASTP and PROMs (n=43), while paired t-tests compared pre- to post-operative changes in ASTP (n=14) and PROMs (n=10).

Results

Pre-operatively, ASTP showed no significant correlations with NPRS ($r(41) = 0.23$, $p = 0.14$), EQ-5D-5L ($r(41) = -0.20$, $p = 0.19$), and OKS ($r(41) = -0.19$, $p = 0.21$). ASTP remained unchanged from pre-surgery (M=46%, SD= 10.8) to 12-months post-surgery (M=43.4%,

SD=10.4; t(13)=1.35, p=0.20). Conversely, significant improvements occurred in NPRS (t(10)= 4.9, p<0.001), EQ-5D-5L (t(10)= -6.0, p<0.001), and OKS (t(10)= -7.9, p<0.001).

Discussion

Activity fragmentation demonstrated limited sensitivity to self-reported clinical status and surgical intervention in end-stage knee OA, despite patient-reported improvements post-arthroplasty (Figure 1). Compared to similarly aged adults (M=20-34%) [2], fragmentation levels were elevated both before (M=46%) and after surgery (M=43.4%), suggesting that ASTP may reflect a dimension of OA not captured by PROMs or corrected by joint replacement.

Images (Optional)

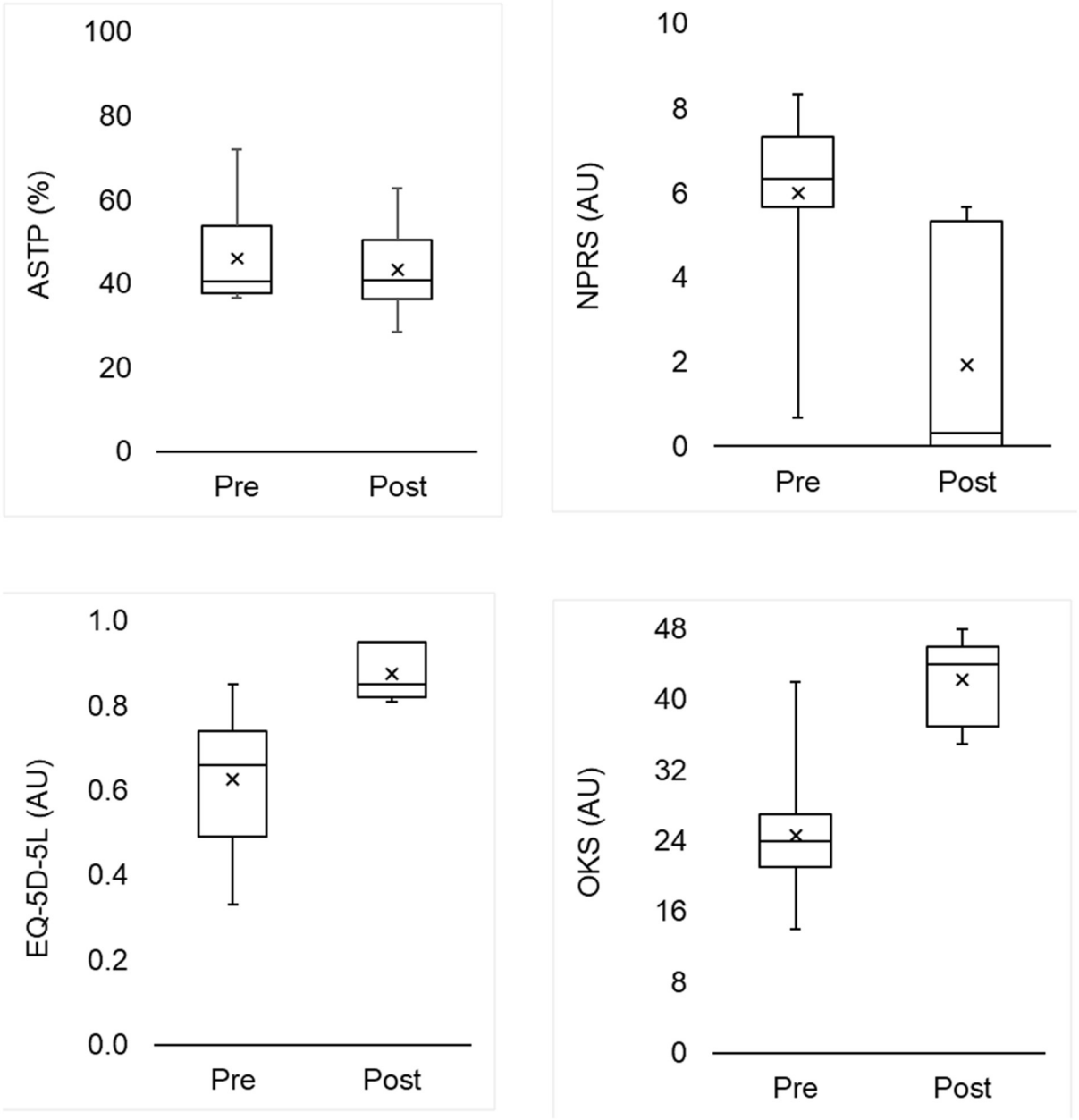


Figure 1. Activity and patient-reported outcome measures before and 12-months after total knee arthroplasty. ASTP = Active-to-Sedentary Transition Probability. NPRS = Numerical Pain Rating Scale (0 [no pain] - 10 [worst pain imaginable]). EQ-5D-5L = EuroQol five-dimensional questionnaire, five-level version (-0.148 [worst]-0.949 [best]). OKS = Oxford Knee Score (0 [worst]-48 [best]). Significantly different at α=0.05.*

References (Optional)

[1] del Polo-Cruz et al., J Gerontology, 2023

[2] Schrack et al., J Gerontology, 2019

[3] Turunen et al., Clinical Rehabilitation, 2020

Session Category

Orthopaedic Biomechanics: Lower Extremities

P3-252

Quantifying Ligament Parameter Uncertainty in the KneeHub Consensus Model

Ms. Maryam Nazem[1], Dr. Peter Laz[1], Dr. Jason Halloran[2], Ms. Nancy Kim[3], Ms. Kate Moyle[3], Ms. Snehal Chokhandre[4], Dr. Thor Besier[3], Dr. Carl Imhauser[5], Dr. Ahmet Erdemir[4]

[1]University of Denver, Denver, CO, United States. [2]Washingston State University, Spokane, WA, United States. [3]Auckland Bioengineering Institute, Auckland, Auckland, New Zealand. [4]Cleveland Clinic, Cleveland, OH, United States. [5]Hospital for Special Surgery, New York, NY, United States

Introduction

The current focus of the KneeHub project is on enhancing reproducibility and credibility in computational knee modeling through the development of consensus-based workflows [1]. Models, typically developed with anatomy from imaging, are calibrated to available experimental data. However, wide variations in reported ligament stiffness and reference strain values lead to a broad search space. The objective of this study is to quantify bounds for ligament properties from the literature and to assess how sensitive an uncalibrated model is to these variations, with the potential to inform subject-specific tuning.

Methods

A representative model of the knee was developed per the consensus-based workflow. Bone, cartilage, and ligament structures were segmented from MR images. Ligaments were modeled using multiple bundles of one-dimensional nonlinear spring elements. To define the design space for optimization, ligament properties describing the force-elongation data were aggregated from various studies [2-6]. To explore sensitivity, an initial finite element model (uncalibrated) was subjected to a simulated anterior tibial translation test with varying ACL bundle stiffness and reference strain at minimum, mean, and maximum levels from the literature.

Results

Mean, lower, and upper bounds derived from the literature are summarized (Figure 1) and represent plausible initial estimates for developing a running model. An initial sensitivity study explored changes in the ACL properties. Variations in the reference strain produced significantly larger differences in the kinematics (4.6 mm difference in anterior tibial translation between upper and lower bounds, Figure 1) than variations in stiffness (0.7 mm difference).

Discussion

Ligament properties in the literature are highly variable and known to significantly influence knee joint mechanics. When developing a knee model for a clinical context of use, data are often limited. In vivo and intraoperative measurements of joint laxity may be available, but direct measurement of ligament properties is not possible. The literature values and their bounds ensure physiological accuracy in patient-specific calibration of models and/or enable sensitivity quantification when calibration is not possible.

Images (Optional)

Ligament	Number of Springs	Stiffness [N/mm] mean (lower, upper)	Reference Strain mean (lower, upper)
ACL	4	118.5 (189.2, 47.0)	0.971 (1.05, 0.90)
PCL	4	91.8 (219.0, 4.7)	0.975 (1.10, 0.76)
MCL	3	59.9 (169.4, 0.0)	1.010 (1.08, 0.80)
LCL	1	63.5 (197.0, 7.8)	0.974 (1.05, 0.97)

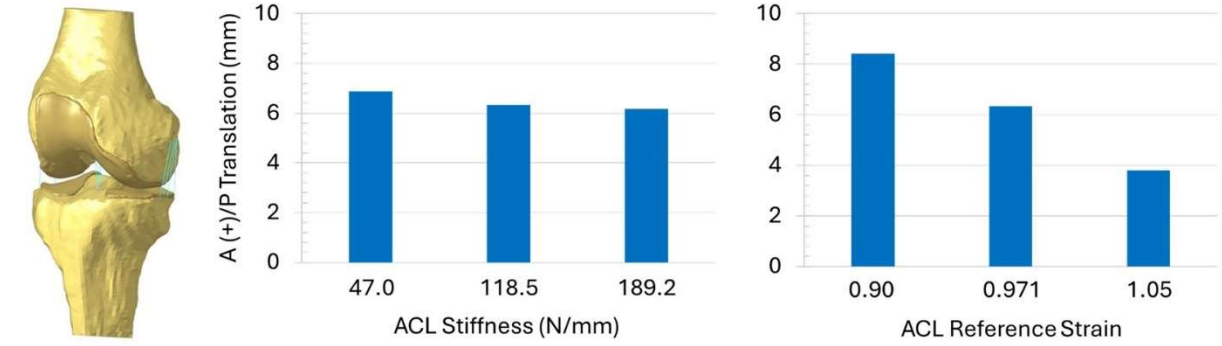


Figure 1: Summary of ligament properties derived from the literature for the ACL, PCL, MCL, and LCL (top). Influence of changes in ACL stiffness and reference strain on anterior tibial translation in an initial finite element model (bottom).

References (Optional)

[1] https://simtk.org/projects/kneehub. [2] Mommersteeg et al., 1996. [3] Kia et al., 2016. [4] Harris et al., 2016. [5] Galbusera et al., 2014. [6] Cho and Kwak, 2020.

Acknowledgements (Optional)

NIH-NIBIB R01EB024573

Session Category

Orthopaedic Biomechanics: Lower Extremities

P3-253

Paradoxical Kinematics at the Tibial Plateau After Total Knee Arthroplasty Does Not Necessarily Indicate Non-Physiological Kinematics at the Anterior Articular Surface

Dr.-Ing. Philippe Moewis[1], Dr. Rainald Ehrig[2], MS Leonie Krahl[1], Dr. Adam Trepczynski[1], PD.-Dr. Hagen Hommel[3], Prof. Georg Duda[1]

[1]Julius Wolff Institute, Berlin Institute of Health at Charité – Universitätsmedizin Berlin, Berlin, Berlin, Germany. [2]Zuse Institut Berlin, Berlin, Berlin, Germany. [3]Krankenhaus Märkisch-Oderland, Wriezen, Brandenburg, Germany

Introduction

Total knee arthroplasty (TKA) is a well-established and successful treatment for advanced osteoarthritis of the knee. However, approximately 10% of patients remain dissatisfied with the postoperative outcome. Anterior knee pain remains as one of the most cited causes of patient's dissatisfaction after total knee arthroplasty, with non-physiological knee joint kinematics patterns during flexion and patellar maltracking being frequently associated with it. The analysis of in vivo knee joint kinematics after TKA can provide objective insights into how specific TKA-design characteristics influence motion patterns—both at the anterior articular surface and at the tibial plateau.

Methods

Results

All TKA-systems demonstrated some degree of anterior translation in the medial compartment. These compartment-specific translation patterns resulted in an external rotation of the femoral component relative to the tibia (Figure-1B). The anterior aspect of the femoral component displayed a posterior translation toward maximum flexion. Both distal and anterior motion patterns produced comparable overall external rotation across all implant groups.

Discussion

Although a pronounced anterior translation in the medial compartment and a reduced posterior rollback of the lateral condyle were observed, phenomena that are typically considered as paradoxical kinematics, a consistent posterior translation of the anterior femoral aspect was also present.

While this posterior translation represents an indirect indicator of patellar motion, the combination of this motion with the femoral external rotation on the tibia plateau may potentially contribute to improved patellar-tracking. Accurate interpretation of knee joint kinematics may therefore assist in selecting the most appropriate TKA-system to properly address the specific needs of the wide range of individual patients.

Images (Optional)

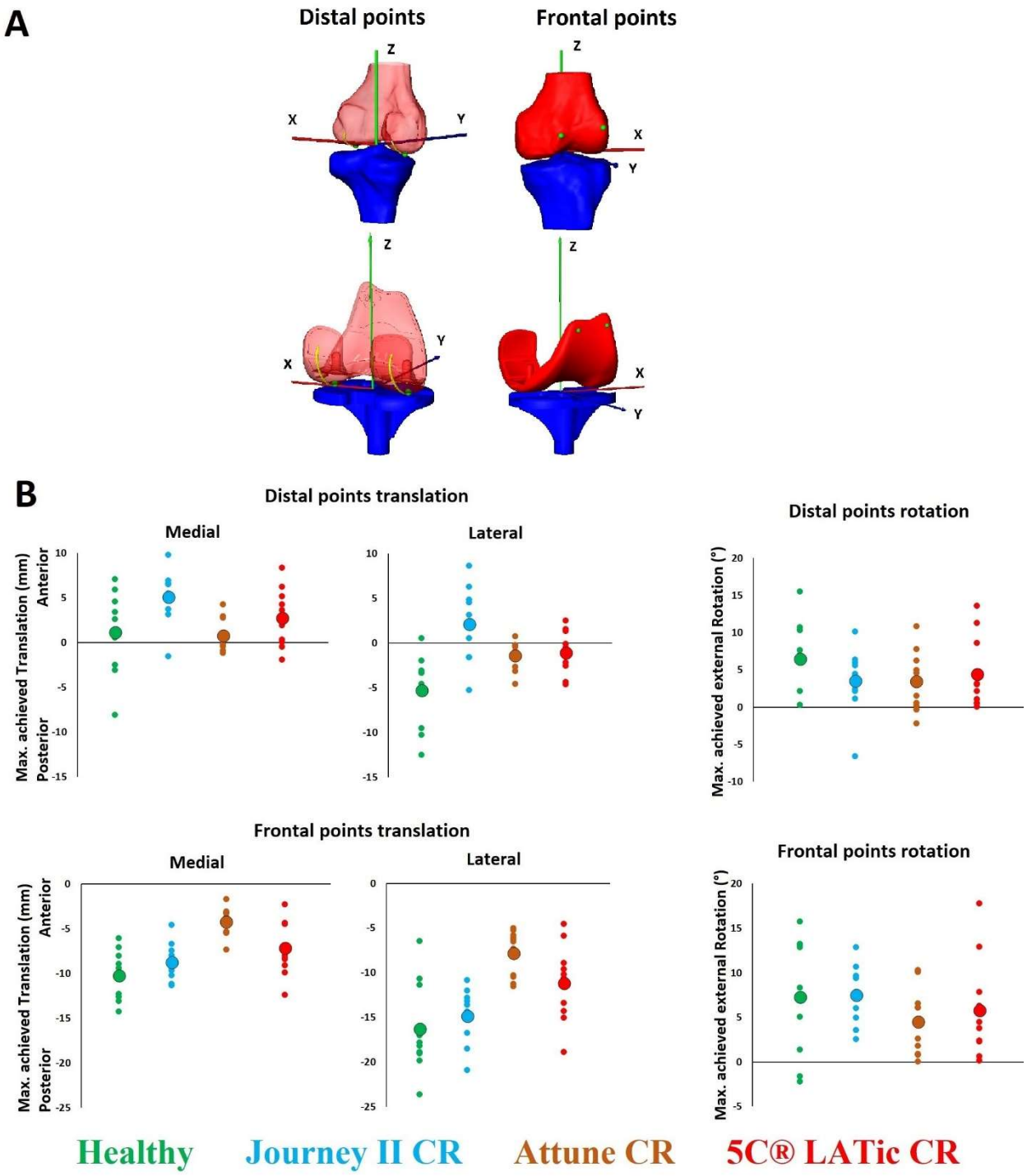


Figure 1: (A) Identification of anterior and distal reference points. (B) Maximum translations/rotations (all patients; large circles represent means).

Acknowledgements (Optional)

DFG (EH 422-2-1/MO 3865-1-1), OrthoLoad Club.

Session Category

P3-254

OpenSim JAM-based Subject-Specific Standardized Biomechanical Simulations of ACL Forces during a Standardized Test

Mr. Pratham Singh[1,2], Mrs. Anoosha Pai[2], Dr. Marianne Black[2], Dr. Katherine A. Young[2], Dr. Seth Sherman[2], Dr Constance Chu[2], Dr. Brian Hargreaves[2], Dr. Garry Gold[2], Dr. Feliks Kogan[2], Dr. Akshay Chaudhari[2], Dr. Timothy Burkhart[1], Dr. Anthony Gatti[2]

[1]University of Toronto, Toronto, ON, Canada. [2]Stanford University, Stanford, CA, United States

Introduction

Anterior cruciate ligament (ACL) injuries remain a challenge clinically, with reconstruction outcomes varying across patients. MRI imaging and computational modeling offers a powerful approach to understanding the biomechanical factors influencing ACL loading. Biomechanical simulations have identified bone features that are correlated to ACL loading during a standardized test [1]. The purpose of this study was to simulate the same standardized test using an open-source simulation pipeline comparing ACL forces in three groups: ACL-reconstructed (ACLR, n=5), contralateral limbs of ACL-injured patients (CLAT, n=5), and healthy controls (CTRL, n=7).

Methods

We used an automated MRI segmentation and neural shape modeling pipeline to generate 12 degree of freedom knee models (6 tibiofemoral, 6 patellofemoral) from 3D DESS knee MRIs. Forward dynamic simulations were performed to simulate an ACL injury mechanism using OpenSim Joint Articular Mechanics (JAM) toolkit [2]. OpenSim JAM models cartilage-cartilage contact, enabling simulation of contact pressures and ligament strains and forces. The loading protocol flexed the knee from 0 to 15° of flexion over 2 seconds while ramping up tibial compression (0-100N from 0-0.25s), a valgus moment (0-8Nm from 0.25 to 1.0s), and an anterior shear force (0-30N from 1-1.25s). After the ramp, each force/moment was held constant. The total ACL force over 12 strands representing the two ACL bundles was summed. Time histories of the ACL forces and the peak ACL force was compared between groups.

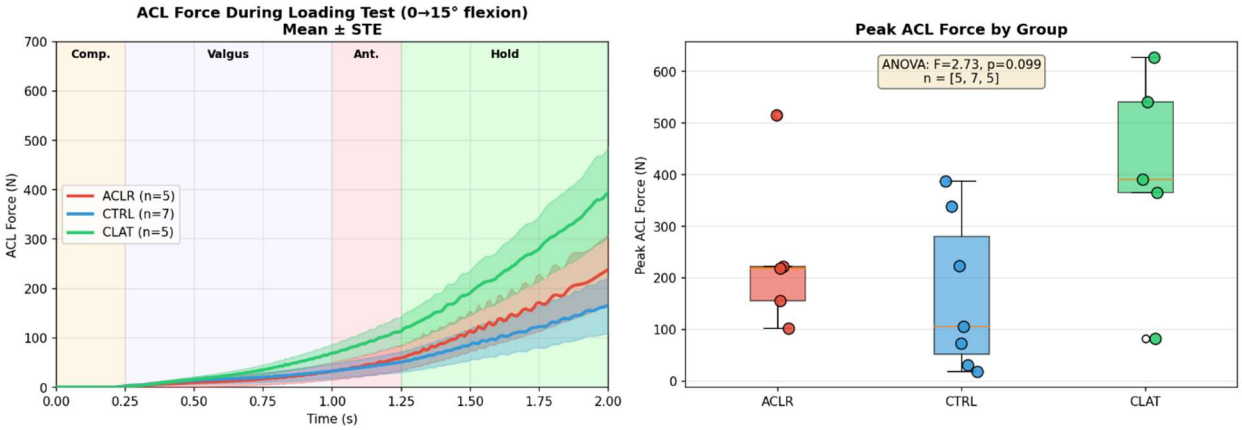
Results

During the simulation, ACL forces gradually increased from the start of the valgus moment (0.25s) until the end of the simulation. One-way ANOVA did not reveal statistically significant differences in peak ACL force between groups ($p>0.05$); the contralateral group had the greatest ACL force.

Discussion

The results show that when applied using an open-source toolkit, previously developed standardized simulations of ACL forces gradually stress the ACL. Our peak forces were higher than the previous investigation (~50-600N vs. ~25-200N) [1]. Counter to our hypothesis, the CLAT group had the highest forces. Future work will unlock tibial-meniscus degrees of freedom, explore alternative ACL reference strain normalization techniques, and increase the sample size.

Images (Optional)



References (Optional)

[1] Wheatley et al., J. Biomech. 2024

[2] Smith et al., J. Biomech. 2019

Session Category

Orthopaedic Biomechanics: Lower Extremities

P3-255

Dose-Response Effect of Toe Spring on the Running Biomechanics of Foot-Ankle Complex

Associate Professor Qichang Mei[1,2], Ms Chen Liu[1]

[1]Ningbo University, Ningbo, Zhejiang, China. [2]The University of Auckland, Auckland, Auckland, New Zealand

Introduction

Toe spring, featured by the upward curvature in the forefoot region, is a key structure in the footwear that facilitate the forward rolling and propulsion during push off of stance. However, the biomechanical effects of varying toe-spring angles in the AFT (advanced footwear technology) shoes at different running speeds remain unclear. Prior studies link forefoot stiffness and plantar tissue strain to propulsion efficiency and overuse injuries, underscoring the need for optimal structural design. This study investigates how toe-spring angle variations affect the foot biomechanics during jogging and racing.

Methods

Eighteen elite runners performed jogging (3.3 m/s) and race (4.0 m/s) running in a motion capture lab while collecting marker trajectories and ground reaction force. Running shoes with systematically developed toe-spring angles (TQ1: 28.6°, TQ2: 27.4°, TQ3: 26.1°, TQ4: 24.9°) was employed with consistent features and properties across all footwear. Joint kinematics (IK), kinetics (ID), Achilles tendon force (static optimization), and plantar fascia strain (point kinematics) were analysed using OpenSim based musculoskeletal modelling. Two-way repeated-measures ANOVA and statistical parametric mapping were applied for statistical analysis.

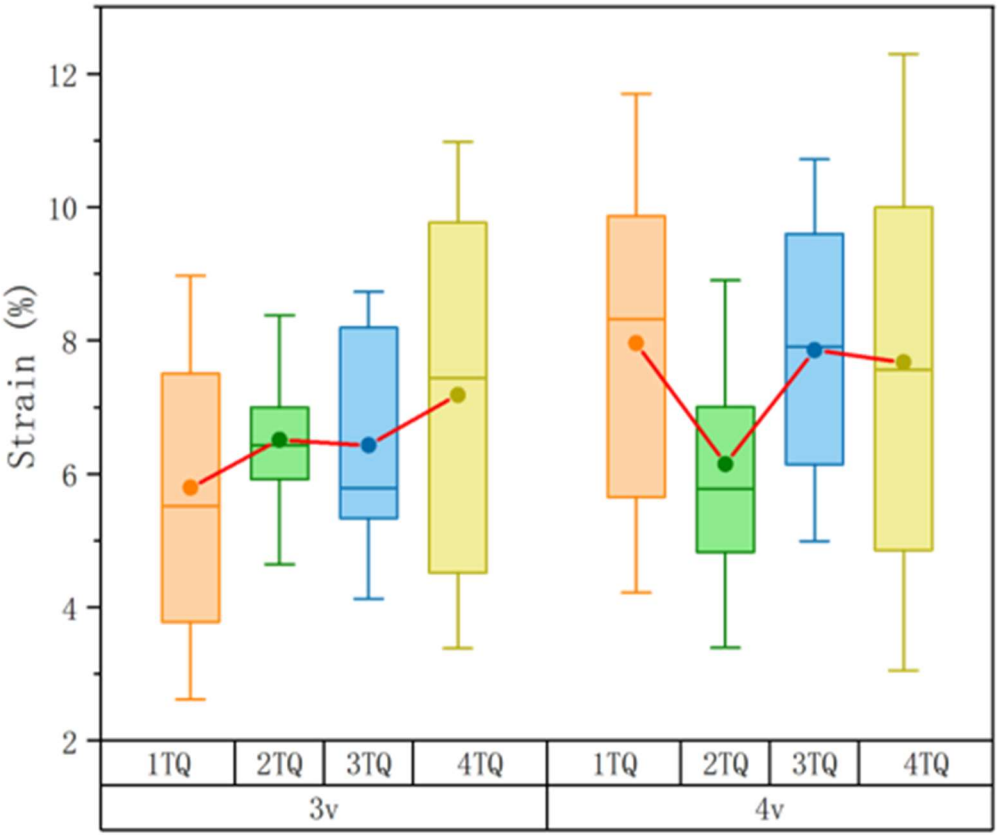
Results

The increased running velocity from 3.3 m/s to 4.0 m/s significantly elevated peak Achilles tendon force, with TQ1 showing the largest increase (+0.55 ± 0.21 BW) and TQ2 the smallest (+0.06 ± 0.27 BW). PF strain amplitude generally increased from 3.3 m/s to 4.0 m/s, with the largest percentage rise observed in TQ1 (+37.4%) and TQ3 (+22.2%). In contrast, TQ2 showed a slight decrease (–5.6%) (Figure 1).

Discussion

In this study, moderate designs (TQ2, TQ3) demonstrated superior regulation of plantar fascia strain and Achilles tendon loading, reducing excessive peaks at higher speeds. Subtle differences in toe-spring may contribute to the mechanical variations by altering roll-over mechanics and anterior lever arm function. These findings emphasize the importance of optimizing toe-spring design to balance performance benefits with reduction of injury risks.

Images (Optional)



Session Category

Orthopaedic Biomechanics: Lower Extremities

P3-256

Online Sensorimotor Control Pre- and Post-Fatigue Following ACL Reconstruction

Mr. Quinn Mulligan, Dr. Timothy Burkhart

University of Toronto, Toronto, Ontario, Canada

Introduction

ACL reconstruction (ACLR) patients often present with impaired sensorimotor function of the lower extremity, characterized by impaired proprioception, inhibition of the quadriceps, and increased excitation of the hamstrings of the reconstructed limb [1]. Sensorimotor impairments may compromise dynamic knee stability and contribute to the increased risk of secondary injury following primary ACLR [2], especially in fatigued conditions [3]. Therefore, the purpose of this study is to quantify sensorimotor control in ACLR patients pre- and post-fatiguing exercise.

Methods

Preliminary data has been collected on two ACLR patients (one male, one female), and five healthy controls (two male, three female) with the goal of recruiting 18 of each. Inertial measurement units (IMUs; Xsens, Enschede, NL) placed above the midfoot sampled acceleration data at 100Hz. A leg extension task was completed before and after a fatigue protocol consisting of isometric quadriceps contractions, vertical jumps, and high knees at 140BPM. Electromyography (EMG) data of the quadriceps were collected bilaterally, and the real-time mean power frequency (MnPF) was monitored for signs of fatigue, defined as a 10% decrease from baseline. Accelerations from the leg extensions in both the X and Z axes were fit with a fifth-order polynomial and the residuals, which represent trajectory-correcting accelerations, were isolated and converted to the frequency domain using a fast Fourier Transform. The proportional power spectrum (pPower) of the residuals was computed (Fig. 1), and the relative power of corrective accelerations at specific frequencies (i.e., latencies) were assessed as a representation of online sensorimotor control processes.

Results

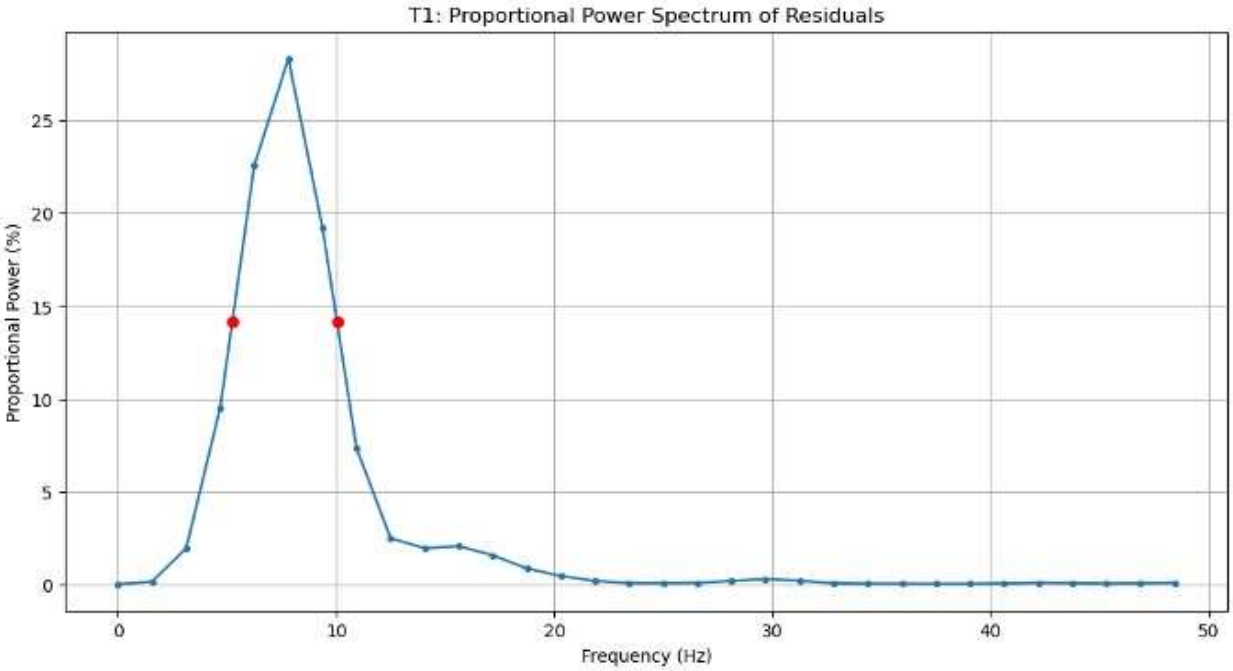
There were no significant differences between groups or fatigue condition for frequency content nor distribution in the X and Z axes ($p > 0.05$).

Discussion

Online sensorimotor control does not appear to be affected by ACLR or fatigue in this preliminary sample This initial work suggests that sensorimotor control mechanisms of the

lower extremity may remain functional, and the integration of proprioceptive information is unimpaired following ACL injury and reconstruction.

Images (Optional)



References (Optional)

[1]Smeets et al., (2021). Gait & Posture, 83, 44-51. [2] Paterno et al., (2014). The American journal of sports medicine, 42(7), 1567-1573. [3] Kim et al., (2023). Knee Surgery, Sports Traumatology, Arthroscopy, 31(12), 5428-5437.

Session Category

Orthopaedic Biomechanics: Lower Extremities

P3-257

Fatigue-Induced Changes in Jumping Mechanics Following ACL Reconstruction

Mr. Quinn Mulligan, Dr. Timothy Burkhart

University of Toronto, Toronto, Ontario, Canada

Introduction

Following ACL reconstruction (ACLR), patients have an increased susceptibility to fatigue, as neuromuscular impairments are exacerbated and kinematics deteriorate at a greater rate compared to healthy controls [1]. It is possible that the fatigue-induced kinematic changes may contribute to the six-fold increase in risk of injury following primary ACLR [2]. Therefore, the purpose of this study is to quantify jump kinematics pre- and post-fatigue in ACLR patients and healthy controls.

Methods

Preliminary data has been collected on one male ACLR patient, and five healthy controls (two male, three female) with the goal of recruiting 18 of each. Knee valgus angles were quantified using a set of seven inertial measurement units (IMUs; Xsens, Enschede, NL) sampling at 100Hz. Participants were instrumented with six electromyography (EMG) sensors placed bilaterally over the quadriceps muscles. Knee valgus angles (KVA) were computed during three vertical jumps before and after a fatiguing exercise circuit at initial contact, and 200ms post-contact. The circuit was completed until a 10% decrease in the mean power frequency (compared to the start of the first cycle) of the EMG signals was detected.

Results

Results At initial contact, mean KVA of the ACLR participant increased post-fatigue from 24.2º to 30.2º, and 19.2º to 24.4º in the involved and non-involved limbs, respectively, compared to a decrease from 27.2º (± 13.3) to 23.5º (± 9.6) of the dominant limb of the healthy controls. At 200ms post-contact, KVA increased from 71.6º to 83.4º and 73.4º to 86.6º in the involved and non-involved limbs, respectively, compared to a decrease from 70.3º (± 10.9) to 68.4º (± 6.8) of the dominant healthy control limb. These differences were non-significant ($p > 0.05$).

Discussion

This initial work shows that the KVAs of the ACLR participant increased following fatiguing exercise, whereas mean KVAs decreased in healthy controls. Greater KVAs have been

associated with higher risks of injury [3], suggesting a potential fatigue-induced decrease in movement quality.

References (Optional)

[1] Kim et al., (2023). Knee Surgery, Sports Traumatology, Arthroscopy, 31(12), 5428-5437. [2] Paterno et al., (2014). The American journal of sports medicine, 42(7), 1567-1573. [3] Hewett et al., (2005). The American Journal of Sports Medicine 33, 492–501.

Session Category

Orthopaedic Biomechanics: Lower Extremities

P3-258

Stress-Shielding Reduction and Fatigue Reliability: Topological Optimization of a TPMS Hip Prosthesis

Ms. Roberta Cromi[1], Ms. Michela Paola Miuccio[1,2], Mr. Mattia Concari[1,2], PhD Francesca Berti[1], Prof. Stefano Foletti[2], Prof. Tomaso Villa[1]

[1]Department of Chemistry, Materials and Chemical Engineering "Giulio Natta" (LaBS) – Politecnico di Milano, Milan, Italy, Italy. [2]Department of Mechanical Engineering (MetaMAT Laboratory) – Politecnico di Milano, Milan, Italy, Italy

Introduction

Total hip arthroplasty remains the gold-standard treatment for several hip pathologies, yet over 35% of implants encounter stress-shielding [1]. Anatomical stems enhance physiological load transfer; however only the advances in architected materials, particularly triply periodic minimal surface (TPMS) structures, allow microscale tailoring of mechanical properties [2]. In this context, this work aims to design a stem balancing stiffness reduction and fatigue resistance by optimizing the TPMS density distribution.

Methods

CT scans of an adult female patient's femur were used to reconstruct the geometry and map the bone's Young modulus (E). A titanium anatomical stem was designed with a core TPMS zone, while preserving both neck and distal end solid, for mechanical and surgical compatibility. Diamond, Gyroids and Schwartz sheet-based TPMS were computationally tensile-tested to assess their E-tensile fatigue strength ratio at multiple density level. Stress-shielding reduction and fatigue resistance were assessed both under a 70kg physiological gait [3] and ISO7206-4 loading configuration. Three stem designs were compared: bulk, homogeneous TPMS-distribution (H-TPMS) and optimized TPMS-distribution (O-TPMS). The optimization algorithm was based on [4] (Fig.1): starting from a H-TPMS, given the inputs and constraints, the algorithm distributes TPMS density obtaining an O-TPMS solution that optimizes fatigue performance under ISO loading condition.

Results

The CT-based mapping resulted in a E range of 0.5-22GPa. The H-TPMS stem, even with a non-ideal Diamond relative density of 0.5, achieved a stress-shielding reduction higher than 60%. However, regarding fatigue resistance, H-TMPS failed in both tensile and compressive regions under ISO loading conditions: to ensure compliance to the standard, the O-TPMS solution included high density subzones, corresponding to solid at manufacturing level, partially compromising the stiffness reduction request.

Discussion

A homogenized TPMS-distribution within a partially porous hip stem is proper in terms of bone loss reduction, yet the structure undergoes fatigue failure. A TPMS-optimized density distribution ensures ISO7206-4 fatigue resistance; nevertheless, the inclusion of quasi-solid subzones limits its potential to achieve substantial stress-shielding reduction.

Images (Optional)

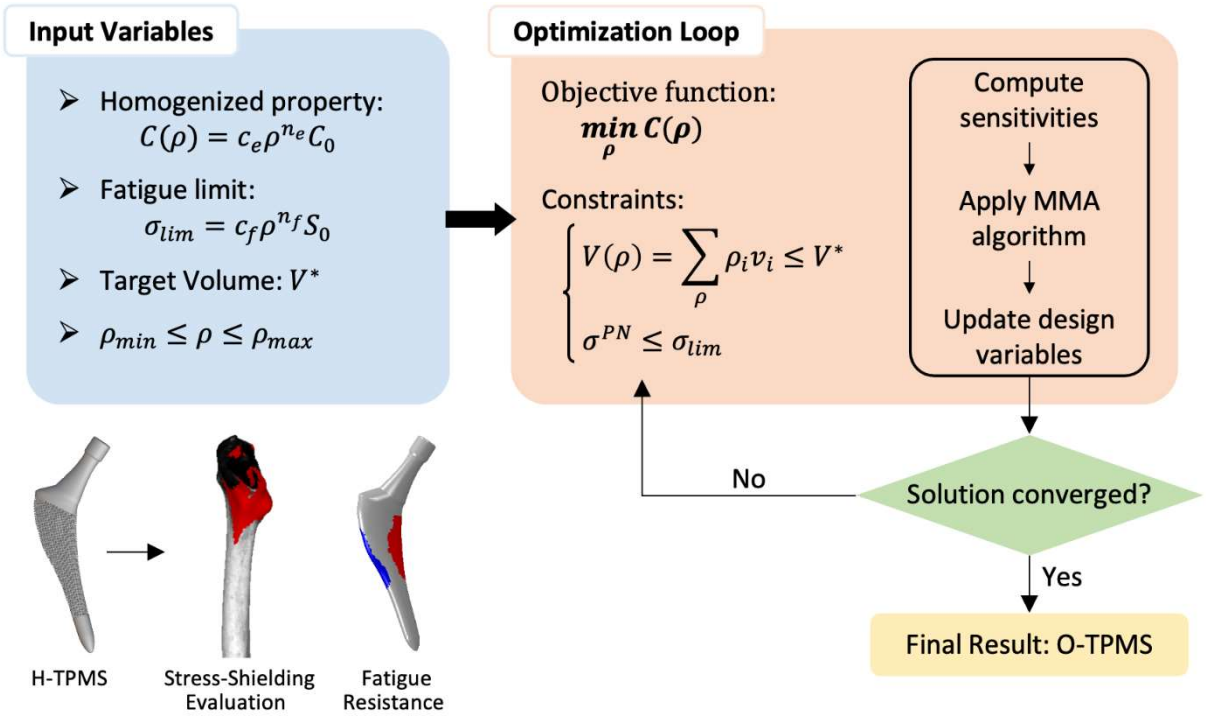


Fig.1: Using the optimization MMA method, the algorithm updates elements' densities -modeled as TPMS- to achieve minimum compliance under target volume and fatigue-stress limit constraints.

References (Optional)

1. W-dahl Annette *et al.*, AIMS Materials Sci, 2024
2. Ma Jiaqi *et al.*, J. Tissue Eng, 2024
3. Behrens Bernd-Arno *et al.*, Proc Inst MECH Eng H, 2008
4. Fernandes Pedro *et al.*, Appl Sci, 2023

Acknowledgements (Optional)

Thanks are due to orthopaedic surgeons Dr. Massimo Franceschini and Dr. Jacopo Menini, for their clinical support both in positioning the femoral stem and perform surgical cuts.

Session Category

Orthopaedic Biomechanics: Lower Extremities

P3-259

Cadaveric Proof-of-Concept of Soft Tissue to Metal Attachment in a Biosynthetic Knee Endoprosthesis

Ms. Sachi Bansal, Dr. Sean Thomas, Mr. Keval Bollavaram, Dr. Brian K. Zukotynski, Dr. Lauren E. Wessel, Dr. Michael Delong, Dr. Tyler R. Clites

University of California Los Angeles, Los Angeles, CA, United States

Ms. Sachi Bansal

Dr. Sean Thomas

Mr. Keval Bollavaram

Dr. Brian K. Zukotynski

Dr. Lauren E. Wessel

Dr. Michael Delong

Introduction

The patellar tendon (PT), a thick fibrous structure connecting the patella to the proximal tibia, enables extension of the knee [1]. Loss of the PT insertion during endoprosthetic reconstruction can compromise the knee extensor mechanism, negatively impacting knee function [2]. Current surgical interventions include reattaching the PT to a metal prosthesis [3]; however, achieving a robust interface between soft-tissue and metal remains challenging [4]. We propose a biosynthetic endoprosthesis that incorporates bone and ligament, acting as a bridge between the PT and prosthesis. Our objective was to validate surgical feasibility in a cadaver and then identify the first point of mechanical failure under load.

Methods

We designed the prosthesis (fig.1A) to house a bone block in the antero-proximal aspect of the tibial component and conducted a cadaveric dissection to verify prosthesis morphology. We then harvested i) the vascularized medial femoral condyle (MFC) bone block with the medial collateral ligament (MCL) intact and ii) the patella with the PT intact (fig.1B). The MFC was screwed onto a stainless-steel bracket to simulate attachment of bone to the prosthesis (fig.1C). The PT and MCL were whipstitched together. The patella was potted in polymethyl methacrylate, and a manipulator robot (KR-210, KUKA) pulled on the construct until failure.

Results

The implant fits within the geometric envelope of a standard knee endoprosthesis. The MFC bone block was successfully harvested with its vasculature intact and secured to the bracket (fig.1D). The MCL-to-PT attachment failed first at 30.2 mm displacement with a load of 160.1 N from suture rupture, while the tissue remained intact (fig.1E). No failure was observed in the MFC-to-bracket or MCL-to-MFC interfaces.

Discussion

The tendon-ligament rupture occurred at a relatively low force, demonstrating the importance of long-term healing between the MCL and PT in supporting sustained quadriceps loading. Robustness of the MFC bone block through screw-anchoring indicates this may have sufficient primary stability as a landing pad for soft-tissue attachment. Next steps will focus on understanding relative strength of MFC-to-implant and MCL-to-MFC interfaces.

Images (Optional)

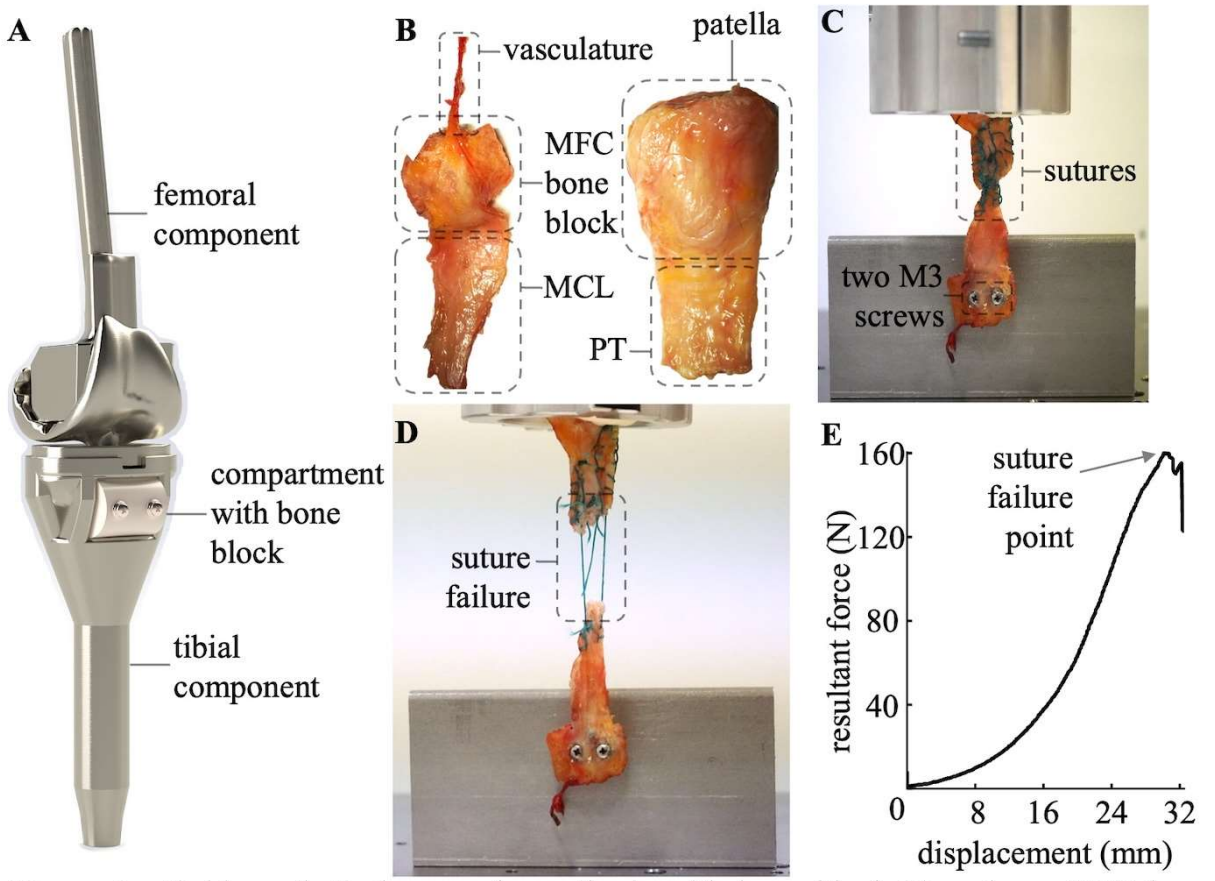


Figure 1: A) biosynthetic knee endoprosthesis with bone block B) cadaver MFC bone block with intact vasculature and MCL; dissected patella with intact PT C) KUKA testing of cadaver specimen construct D) failure of suture interface E) force displacement curve

References (Optional)

[1] Basso et al., KSSTA, 2001; **[2]** Rosteius et al., The Knee, 2021; **[3]** Calori et al., JBJS, 2016; **[4]** So et al., JBMR-A, 2010

Acknowledgements (Optional)

The authors thank those individuals who donate their bodies for research.

Session Category

Orthopaedic Biomechanics: Lower Extremities

P3-260

Ex Vivo Study on Porcine Knees under Physiological Loads to Evaluate an Innovative Synthetic Anterior Cruciate Ligament Augmentation

M.Sc. Saskia Hesse[1], M. Sc. Julietta Bandel[1], B. Sc. Alina Farchmin[1], Dr. Ing. Benedict Bauer[1], Dr. med. Sabine Roth[2], Mr. Rald Groven[2], Mr. Deniz Özman[2], M. Sc. Viktoria Kiaulehn[2], Dr. Ing. Maximilian Praster[2], Univ.-Prof. Thomas Gries[1], Prof. Dr. med. Christian Weber[2], Dr. Ing. Caroline Emonts[1]

[1]Institut für Textiltechnik of RWTH Aachen University, Aachen, NRW, Germany. [2]Department of Orthopaedic, Trauma and Reconstructive Surgery, RWTH University Hospital, Aachen, NRW, Germany

Introduction

Nowadays autologous implants are still the most common used anterior cruciate ligament (ACL) replacements. Previous work has shown the great potential of braided structures regarding their mechanics [1]. The aim of this study is to perform an ex vivo study to evaluate the performance of these structures under physiological conditions and cyclical loading in porcine knees.

Methods

The scaffolds are made of Poly-e-caprolactone (PCL) filaments which are 3D-braided into a multilayered interlaced structure. The porcine knees are prepared by removing tissue except menisci and the cruciate ligaments. The study includes four groups (five samples each): native tissue, the reconstructed native ligament, the scaffold as augmentation and the scaffold as total replacement. The testing protocol includes cyclical and load-to-failure tests and enables a comparison of each knee with itself before and after surgery. The cyclical test simulates 10,000 steps per knee with 1 Hz and a loading range of 30 N to 210 N [2]. The load-to-failure test has a testing speed of 40 mm/min.

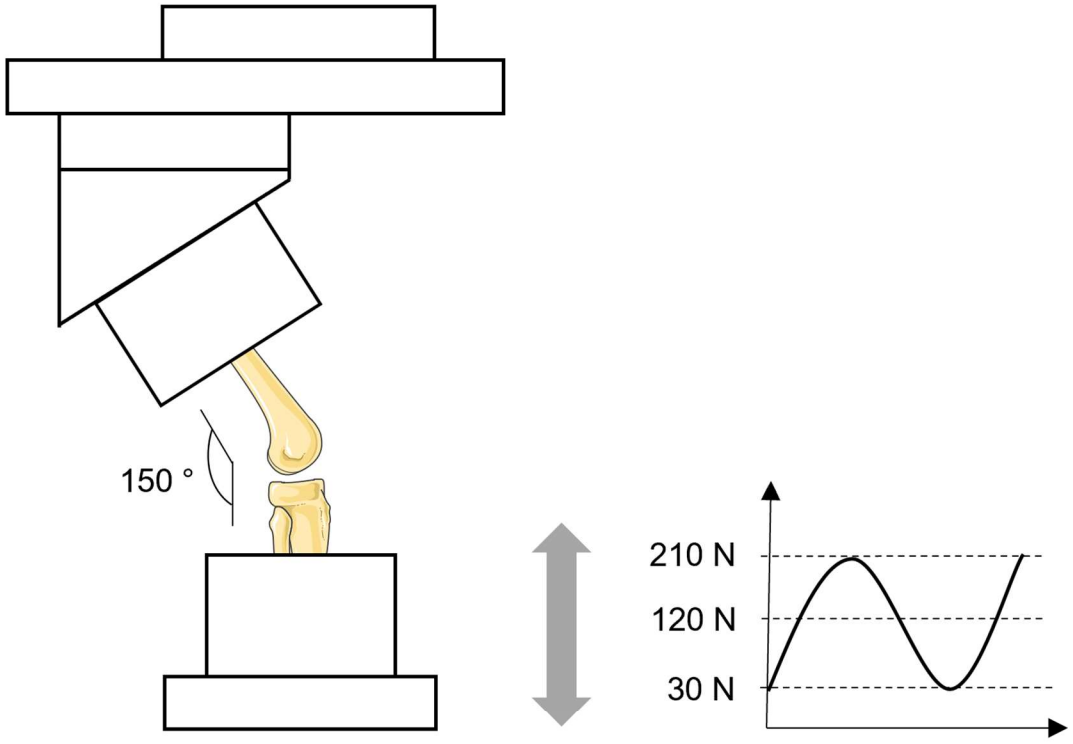
Results

Each knee is tested with native tissue first and then according to the testing group configuration. The native tissue shows no plastic deformation during the cyclical testing and maximal loads over 2000 N during the load-to-failure. The focus of further experiments lays in analyzing the elastic and plastic deformation of the scaffolds during the cyclical testings and evaluating the stress-strain-behavior of the load-to-failure.

Discussion

This ex vivo study contains cyclical and load-to-failure tensile testings with native tissue and scaffold variations. This evaluates the initial mechanics of the scaffolds under physiological load and further parameters as scaffold-bone friction. Furthermore, it shows the interaction of fixation systems with the innovative scaffold and their loading limit. Due to a high degree of individuality of each porcine knee this study has some limitations. These are minimized by preventing multiple freezing cycles in preparation and documentation of variations due to natural variations in knee geometry.

Images (Optional)



References (Optional)

[1] Emonts, 10.18154/RWTH-2024-08389, 2024

[2] Matava et al., 10.1016/j.arthro.2021.04.053, 2021

Acknowledgements (Optional)

This project is partially funded by: Federal Ministry of Research, Technology and Space (LigaBraid 2, 16LW0632K).

Session Category

Orthopaedic Biomechanics: Lower Extremities

P3-261

Inappropriate Reference Configuration Leads to Overestimation of ACL Strain:Evidence from High-Resolution 3D Scanning in Robotic Knee Loading Tests

Dr. Satoshi Yamakawa PhD[1], Dr. Shoji Konda PhD[1], Dr. Tomoya Ono MD, PhD[2], Dr. Jumpei Inoue MD, PhD[2], Dr. Issei Ogasawara PhD[1], Dr. Tomoki Ohori MD, PhD[1], Dr. Akira Tsujii MD, PhD[1], Prof. Ken Nakata MD, PhD[1], Prof. Volker Musahl MD[2], Prof. Richard E. Debski PhD[2]

[1]Graduate School of Medicine, The University of Osaka, Suita, Osaka, Japan. [2]University of Pittsburgh, Pittsburgh, PA, United States

Introduction

Because the non-uniform structure of the anterior cruciate ligament (ACL) makes experimental stress distribution analysis difficult, strain analysis—used as an indirect indicator of stress—has been widely employed to assess its mechanical function. However, although the reference configuration is fundamental to strain-based deformation analyses, its definition has remained ambiguous in many ACL studies. Without a consistent and mechanically reasonable definition of the initial ACL length, interpretations of ligament behavior may be substantially distorted.

Thus, the objective was to examine the effect of the choice of reference configuration on the ACL strain distribution by combining a robotic testing system with a hand-held 3D scanner—a novel approach that enables high-resolution analyses.

Methods

Porcine knees (n = 4) were mounted on a robotic testing system at 30° of flexion, and two reference configurations were defined: the unloaded neutral position (Unloaded group) and the position under 10 N anterior tibial loading (ATL group), selected to impose modest pretension and create a physiologically reasonable initial state. After applying 50 N anterior tibial loading as the main test, the resulting knee position was recorded. These two reference configurations and the 50 N loading condition were then reproduced following removal of the medial femoral condyle, and the ACL in each condition was scanned using a hand-held 3D scanner (Figure). ACL strain distribution was calculated from the deformation between each reference configuration and the loaded condition.

Results

Both groups showed higher fiber strain near the attachment sites than in the mid-substance; however, the ATL group exhibited markedly smaller strain values, with

differences reaching approximately fivefold in Unloaded group (5.6%) compared to ATL group (1.1%).

Discussion

That such a small load difference (10 N) produced such a large discrepancy in strain demonstrates how easily strain can be overestimated when the reference configuration lacks adequate pretension. Although previous studies have used full extension as the reference configuration, the present findings suggest that additional loading is necessary to achieve an appropriate initial state. Collectively, these results highlight the importance of defining the initial ACL length under a physiologically meaningful level of loading to avoid misinterpretation of ligament mechanics.

Images (Optional)

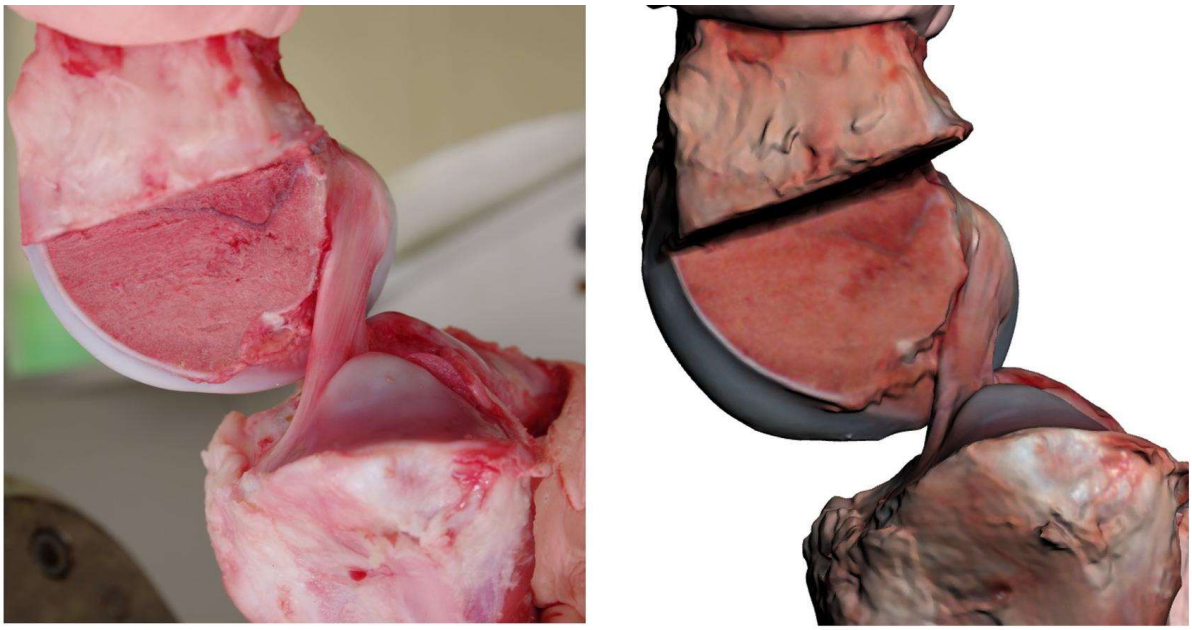


Figure. Representative comparison between the native appearance of the ACL (left) and the corresponding 3D-scanned mesh model with texture mapping (right). The scanned geometry was used for strain analysis based on deformation between reference configurations and the loaded condition.

Session Category

Orthopaedic Biomechanics: Lower Extremities

P3-262

Non-Uniform Strain Distribution of the Anterior Cruciate Ligament Under Pivot Shift loading: A Three-Dimensional Surface Scanning Study in Cadaveric Knees

Dr. Shoji Konda PhD[1], Dr. Satoshi Yamawaka PhD[1], Dr. Tomoya Ono MD, PhD[2], Dr. Jumpei Inoue MD, PhD[2], Dr. Issei Ogasawara PhD[1], Dr. Tomoki Ohori MD, PhD[1], Dr. Akira Tsujii MD, PhD[1], Prof. Ken Nakata MD, PhD[1], Prof. Volker Musahl MD[2], Prof. Richard Debski PhD[2]

[1]Graduate School of Medicine, The University of Osaka, Suita, Osaka, Japan. [2]University of Pittsburgh, Pittsburgh, PA, United States

Introduction

The anterior cruciate ligament (ACL) is thought to restrain complex multi-planar knee loads, however, the three-dimensional (3D) distribution of the non-uniform surface strain has not been fully characterized. This study determined the principal strain distribution and orientation in the ACL during simulated pivot shift loading in a cadaveric knee using 3D surface scanning.

Methods

Two fresh-frozen cadaveric knees were prepared, and the ACL was exposed by removing the medial femoral condyle and soft tissues. Small reference dots were drawn along the ACL fibers, then the knee was mounted on a robotic joint testing system with the knee fixed at 0 degree of flexion. A 10 N anterior drawer force was applied as a pre-loading reference condition, and a combined tibial internal rotation and valgus torque (pivot shift loading) was then applied. Under both conditions, the shape and texture of the ACL were captured with a hand-held 3D scanner. The coordinates of reference dots were semi-automatically extracted from the scanned models using color thresholding and used to construct triangular surface meshes. Green–Lagrange strain tensors were computed for each element, and the magnitude and direction of the maximum principal strain were obtained by eigen decomposition and mapped onto the ACL surface.

Results

Across all surface elements of the two knees, maximum principal strain ranged from −0.0139 to 0.0970 (median 0.0261, mean 0.0311 ± 0.0245). In the femoral and tibial attachment regions, maximum principal strain was higher and decreased with increasing distance from the attachment, and the corresponding eigenvectors were primarily aligned with the macroscopic fiber orientation (Figure 1). In the tibial-side mid-substance, principal strains were also higher, but the eigenvectors of maximum principal strain tended to be oriented approximately perpendicular to the macroscopic fiber direction (Figure 1).

Discussion

These findings indicate that pivot shift loading does not produce a uniform axial elongation of the ACL but rather regionally distinct deformation patterns. The observed differences in principal strain magnitude and direction between the attachment regions and the tibial-side mid-substance may be due to the interaction between regional fiber organization and multi-planar loading.

Images (Optional)

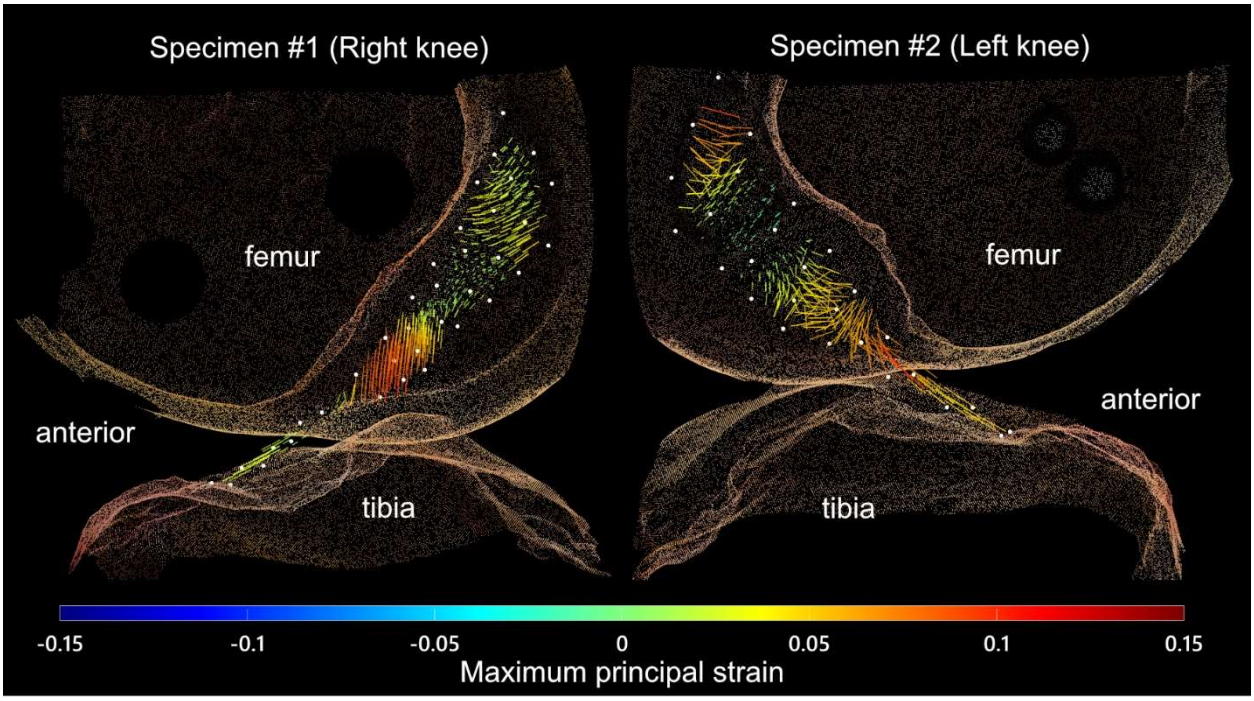


Figure 1. Maximum principal strain magnitude and direction on the ACL surface during pivot-shift loading in two cadaveric knees at 0° of flexion. Colored line segments indicate the direction of the maximum principal strain at each surface element; both their color and length represent the strain magnitude according to the scale bar.

Session Category

Orthopaedic Biomechanics: Lower Extremities

P3-263

Establishing Consensus for Knee Modeling and Simulation: A Delphi Study

Ms Snehal Chokhandre MSc[1], Dr Ahmet Erdemir PhD[1], Dr Jason Halloran PhD[2], Dr Thor Besier PhD[3], Ms Nancy Kim[3], Ms Kate Moyle[3], Dr Carl Imhauser PhD[4], Dr Peter Laz PhD[5], Ms Maryam Nazem[5]

[1]Cleveland Clinic, Cleveland, OH, United States. [2]Washington State University, Pullman, WA, United States. [3]University of Aukland, Aukland, Aukland, New Zealand. [4]Hospital for Special Surgery, New York, New York, United States. [5]University of Denver, Denver, CO, United States

Introduction

There is a lack of standardized workflows for computational knee biomechanics studies making reproducibility, credibility and clinical application challenging.
The *KneeHub* project showed that variability in modeling decisions influences M&S outcomes even if the target simulations and source data were controlled [1]. KneeHub now aims to develop consensus-based workflows for computational M&S through a structured Delphi process involving experts across knee biomechanics, computational modeling, musculoskeletal care, and regulatory science. Our first goal is to recruit and qualify a panel of experts involved in a consensus-based Delphi study, which we summarize in this abstract. The experts will identify an impactful context of use and establish workflows for the given context.

Methods

The study is divided into 5 sub-studies (Figure 1): context of use (Study 1), consensus for decisions on broad simulation study design (Study 2), model development and calibration (Study 3), model benchmarking and credibility (Study 4), and model use and communication (Study 5). Each Delphi study (Studies 1 to 5) will rely on structured rounds of surveys to achieve a data-driven consensus.

Before these studies, we reached out to experts to take a survey (Study 0) establishing their expertise to qualify participation in one or more studies. Expertise area include knee biomechanics research, computational musculoskeletal joint biomechanics research, knee- or extremity joint-focused musculoskeletal care, science of reproducibility, verification, validation and credibility as applied to physics-based modeling, and regulatory science (or regulation) of musculoskeletal joint medical devices.

Results

We identified 213 experts and invited them to participate in Study 0. The ongoing survey has gathered commitment from 50 experts so far. At least 26 experts are interested in participating in each sub-study. All respondents have advanced degrees, 10+ years of experience and at least 5 relevant publications. Studies 1-5 are scheduled to be completed within an 18 month period.

Discussion

Consensus-based workflows built with the experts' perspectives pave a path forward for improving reproducibility and credibility of M&S in knee biomechanics. The outcomes of the consensus-based workflows would serve to incease confidence in M&S use for scientific explorations and clinical applications.

Images (Optional)

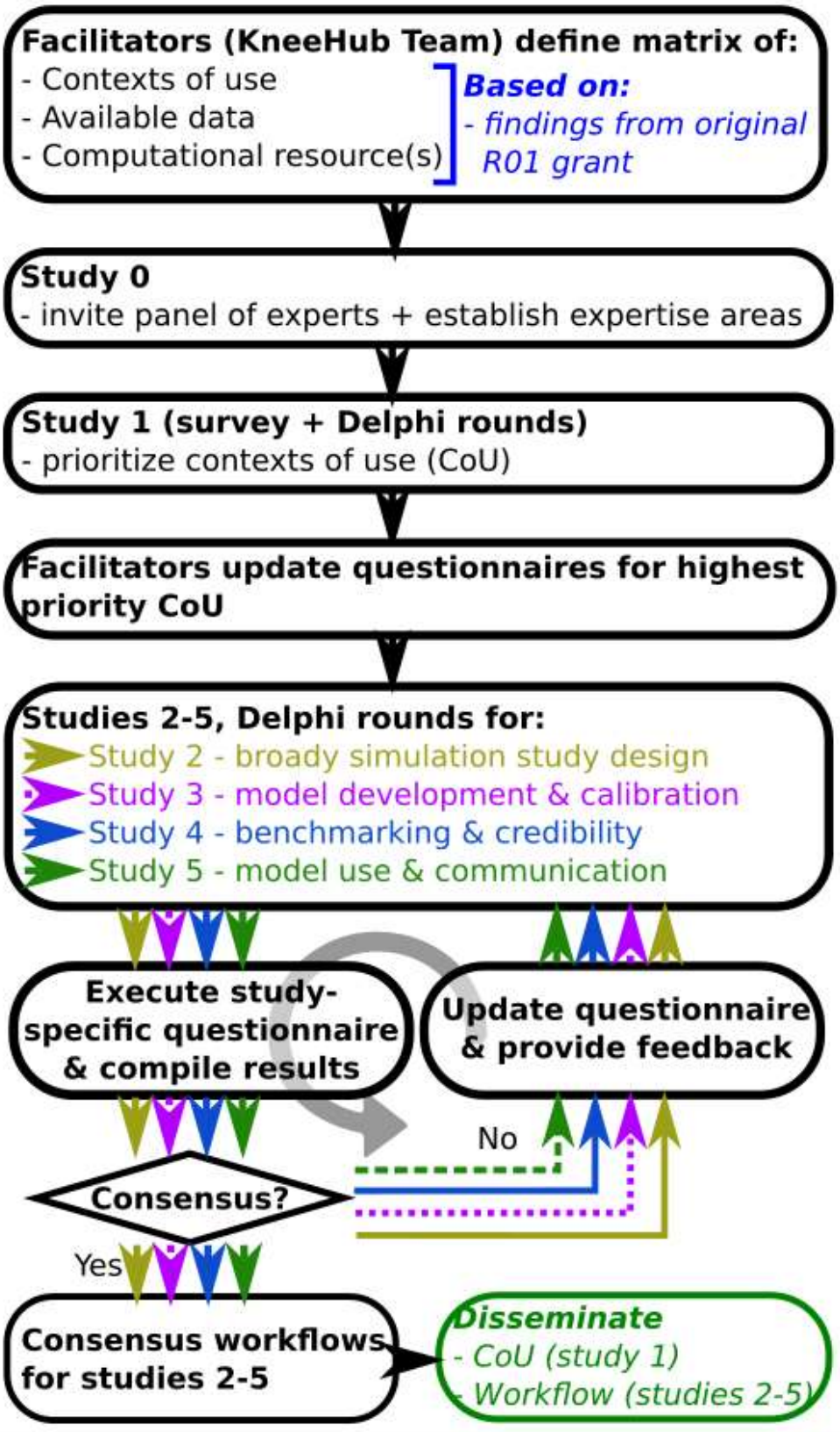


Figure 1. Study overview

References (Optional)

1. Andreassen T. (2023). *J Biomech Eng*, **145**

Acknowledgements (Optional)

Funding: NIBIB, NIH (Grant No. R01EB024573)

Session Category

Orthopaedic Biomechanics: Lower Extremities

P3-264

Experimental and Numerical Evaluation of Hinge Fracture in Open-Wedge Distal Femoral Osteotomy Using Sawbones

Mr. Sohrab REZAEI LAFMEJANI [PhD Candidate][1,2], Dr Massamaesso BILASSE [Assistant Professor][1,2], Dr Yamen OTHMANI [Assistant Professor][1,2], Pr Matthieu EHLINGER [Full Professor][1,3]

[1]ICube Laboratory, University of Strasbourg, Illkirch-Graffenstaden, Grand-Est, France. [2]Icam-Strasbourg, Schiltigheim, Grand-Est, France. [3]Hôpital de Hautepierre, Strasbourg, Grand-Est, France

Introduction

Opening-wedge distal femoral osteotomy (DFO) is a primary surgical intervention for correcting valgus knee malalignment. However, the procedure carries a risk of hinge fracture, which can compromise postoperative stability and outcomes. This study aimed to experimentally simulate the opening stage of DFO using Sawbones composite femurs and to develop a numerical model capable of predicting hinge fracture incidence.

Methods

Fourth-generation Sawbones femurs were prepared, using a patient-specific cutting guide and oscillating saw to create the osteotomy cut. The epiphysis was fixed, and a vertical load was applied to the diaphysis to simulate the opening (Figure 1). Opening angles and forces were recorded up to fracture. Standard material characterization tests including uniaxial tension/compression, shear, and single-edge notch bend (SENB), were conducted to define the properties of the cortical and trabecular analogues for numerical modeling. Finite element models using two fracture simulation methods including a transversely isotropic phase-field (PhaFi) model and the Extended Finite Element Method (XFEM), were developed to simulate fractures in both SENB and DFO tests.

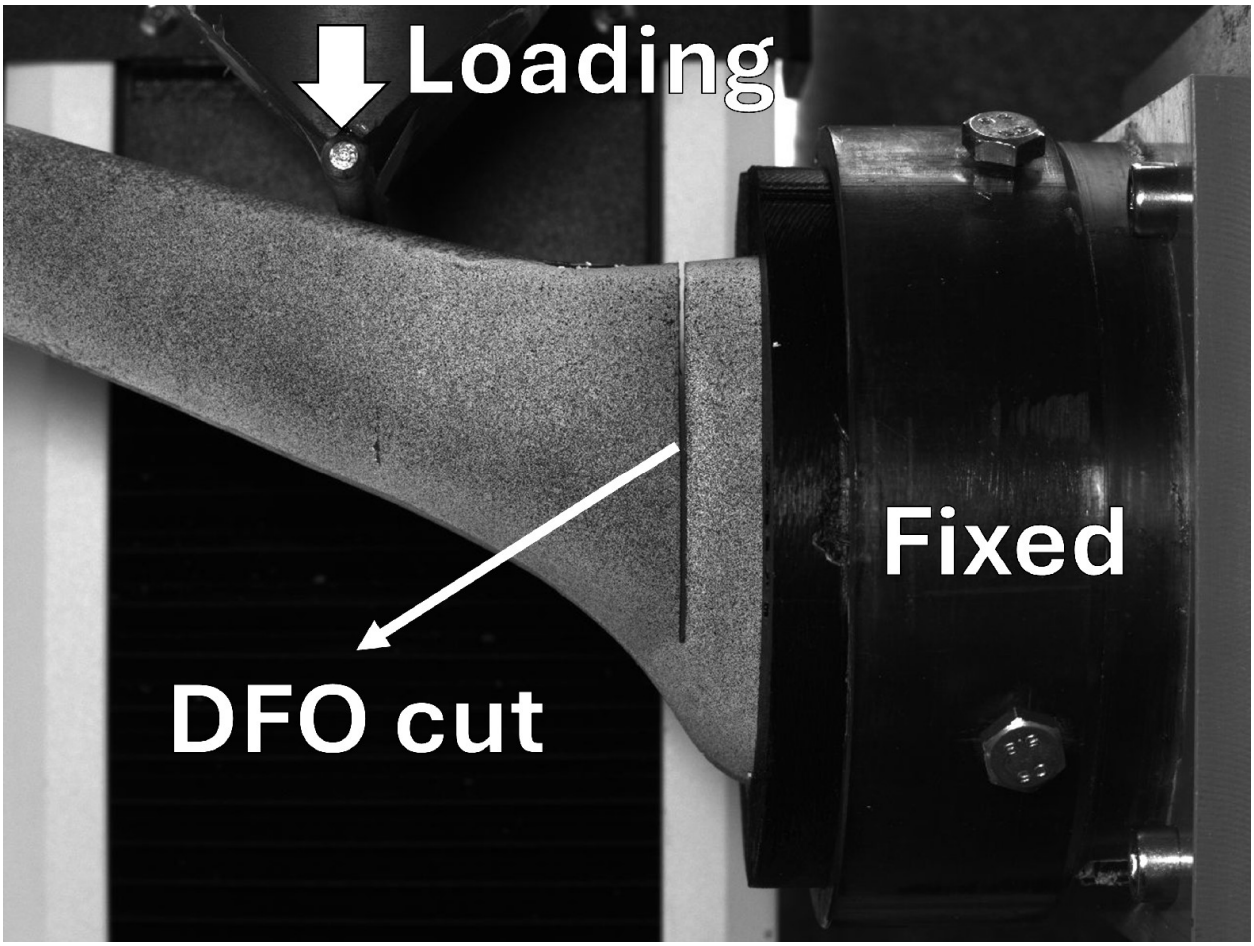
Results

A total of five DFO opening tests were performed. The maximum force recorded was 63.4±5.7N. Fracture initiated at opening angle of 1.5°±0.1° and completed at 4.4°±0.2°. Characterization of the cortical material (58 samples) revealed strong transverse isotropy, with tensile elastic moduli of 15.3±2.7GPa (longitudinal) and 10.5±1.3GPa (transverse). The trabecular material (37 samples) was isotropic with compressive modulus of 278.3±18.0MPa. Both PhaFi and XFEM numerical models successfully predicted cortical fractures in SENB tests, with crack completion angle errors of ±0.5° and ±0.7°, respectively.

Discussion

Experimental data from DFO opening tests showed results comparable to both a human cadaveric study on wedge-opening in high tibial osteotomy[1] and an experimental study on porcine femurs on DFO[2]. The characterization tests revealed strong anisotropic behavior in the cortical layer of Sawbones femurs, which aligns with the expected behavior of native bone. Regarding the numerical simulations, both PhaFi and XFEM methods demonstrated promising results in SENB tests and will be applied to the final DFO opening simulations.

Images (Optional)



References (Optional)

[1] Meisterhans et al., The Knee, 2024

[2] Didier et al., Orthop Traumatol Surg Res. 2022

Acknowledgements (Optional)

This work of the Interdisciplinary Thematic Institute HealthTech, as part of the ITI 2021-2028 program of the University of Strasbourg, CNRS and Inserm, was supported by IdEx Unistra (ANR10-IDEX-0002) and SFRI (STRAT'US project, ANR-20-SFRI-0012) under the framework of the French Investments for the Future Program.

Session Category

Orthopaedic Biomechanics: Lower Extremities

P3-265

The Associations Between Pre-Operative Knee Joint Kinematics During Walking with Frontal Plane Knee Laxity Measured Intra-Operatively Through Robotic Arthroplasty Surgery

Ms. Stephanie Civiero MASc[1,2], Dr. Jennifer Leighton MD[1,2], Dr. Michael Dunbar MD, PhD[1,2], Dr. Glen Richardson MD, MSc[1,2], Dr. David Wilson MD, MASc[1,2], Dr. Janie Astephen Wilson PhD, MASc[1,2]

[1]Dalhousie University, Halifax, Nova Scotia, Canada. [2]Nova Scotia Health, Halifax, Nova Scotia, Canada

Introduction

Many patients continue to walk with deficits after knee arthroplasty surgery (KAS)[1]. KAS planning approaches account for anatomical and morphological variability, but not joint dynamics despite their relevance to outcomes[2]. We aimed to examine the associations between preoperative knee kinematics during gait and intra-operative joint laxity measures as a step toward more mechanics-informed surgical planning.

Methods

Patients awaiting robot-assisted KAS (MAKO, Stryker; n=45; age: 67.7 +/- 8.0 years, BMI: 32.8 +/- 7.4 kg/m^2, 26 female) participated in pre-operative gait assessments using a 10-camera optical motion capture system (Sony-RX0II; Theia3D) installed in the clinic hallway using a repeatable protocol[3]. Clinically relevant sagittal and frontal plane knee angle features[3] were computed (Visual3D; HAS-motion).

Intra-operative variables included: passive maximum knee extension; passive frontal plane knee alignment; and frontal plane knee laxities (relative motion from passive alignment) under maximal varus and valgus stresses in extension (10° flexion) and flexion (90° flexion). Correlations between intra-operative variables and pre-operative kinematics were examined ($\alpha = 0.05$).

Results

Greater varus alignment was associated with larger knee adduction angles during stance (PC1: $r=0.74$; $p < 0.00001$), and a trend toward lower stance phase flexion range of motion (ROM)(PC4: $r=-0.28$; $p=0.06$). Lower maximal knee extension angles (intra-operatively) were associated with lower knee flexion ROM from late stance to swing (PC2: $r=0.46$; $p=0.001$).

Greater valgus laxity in extension was associated with lower knee flexion angles (PC1: $r=0.30$; $p < 0.05$) and greater range of adduction angles in stance (PC3: $r=-0.29$; $p=0.05$).

Greater valgus laxity in flexion was associated with less stance flexion ROM (PC4: $r=0.36$; $p=0.015$). Greater varus laxity in flexion was associated with higher knee adduction angles in early and late stance relative to more abducted knees mid-stance (PC2: $r=0.29$; $p=0.05$).

Discussion

Kinematic gait assessments may capture clinically relevant joint instability responses that passive pre-operative tests miss (due to pain/guarding). Future work will combine joint biomechanics data with morphology and alignment data in larger samples to inform surgical planning strategies to optimize dynamic joint function.

References (Optional)

[1] Hatfield et al. *J Arthro*, 26(2):309-18 (2011).

[2] Young-Shand et al. *JBJS*, 5(2):e0038 (2020).

[3] Civiero. MASc thesis, Dalhousie University. (2024).

Session Category

Orthopaedic Biomechanics: Lower Extremities

P3-266

Optimal Stem Spacing to Prevent Inter-Prosthetic Femoral Fractures in Ipsilateral Hip and Knee Arthroplasty: A computational study

Prof. Tae Soo Bae[1], Mr. Jin Ho Kim[1], Prof. Dai-Soon Kwak[2], Prof. Woowon Jeong[3]

[1]Jungwon University, Goesan-gun, Chungbuk, Korea, Republic of. [2]The Catholic University of Korea, Seoul, Seoul, Korea, Republic of. [3]Yonsei University Mirae Campus, Wonju, Kangwon, Korea, Republic of

Introduction

Ipsilateral total hip replacement and total knee replacement are increasingly performed in elderly patients, and recent clinical observations have reported a rise in inter-prosthetic femoral fractures among individuals receiving both implants. This study aims to quantify how the inter-prosthetic distance influences femoral stress distribution and to identify spacing conditions that may reduce fracture risk during combined arthroplasty.

Methods

A three-dimensional femur model and four-point bending jig were constructed from a single patient CT dataset, and finite element analysis was performed using homogeneous material properties for both normal and osteoporotic bone. The total hip replacement stem length was held constant, whereas the total knee replacement stem length was varied across 9 configurations (22~102 mm with 10 mm intervals) to generate corresponding inter-prosthetic distances. Multidirectional bending was simulated by applying loads perpendicular to the jig in four directions: lateral-to-medial, medial-to-lateral, anterior-to-posterior, and posterior-to-anterior. Stress values at the distal femoral isthmus were extracted to evaluate the effect of implant spacing on mechanical demand related to fracture susceptibility.

Results

The finite element analysis showed that an inter-prosthetic distance of 32 mm produced the highest maximum stress values in both normal and osteoporotic femora across all simulated loading directions. In contrast, an inter-prosthetic distance of 62 mm consistently resulted in the lowest maximum stress values under all loading conditions. These trends indicate that reduced spacing between stems increases stress concentration in the isthmus region, whereas greater spacing mitigates stress regardless of bone quality.

Discussion

The findings demonstrate that inter-prosthetic distance is a critical determinant of femoral stress in cases involving simultaneous hip and knee arthroplasty, with shorter distances substantially elevating the mechanical conditions associated with fracture. The results suggest that maintaining larger implant separation may contribute to biomechanical safety by reducing stress amplification in the isthmus region. The use of homogeneous bone models represents a limitation, and future studies incorporating heterogeneous bone properties are expected to enhance the clinical applicability of these conclusions.

Images (Optional)

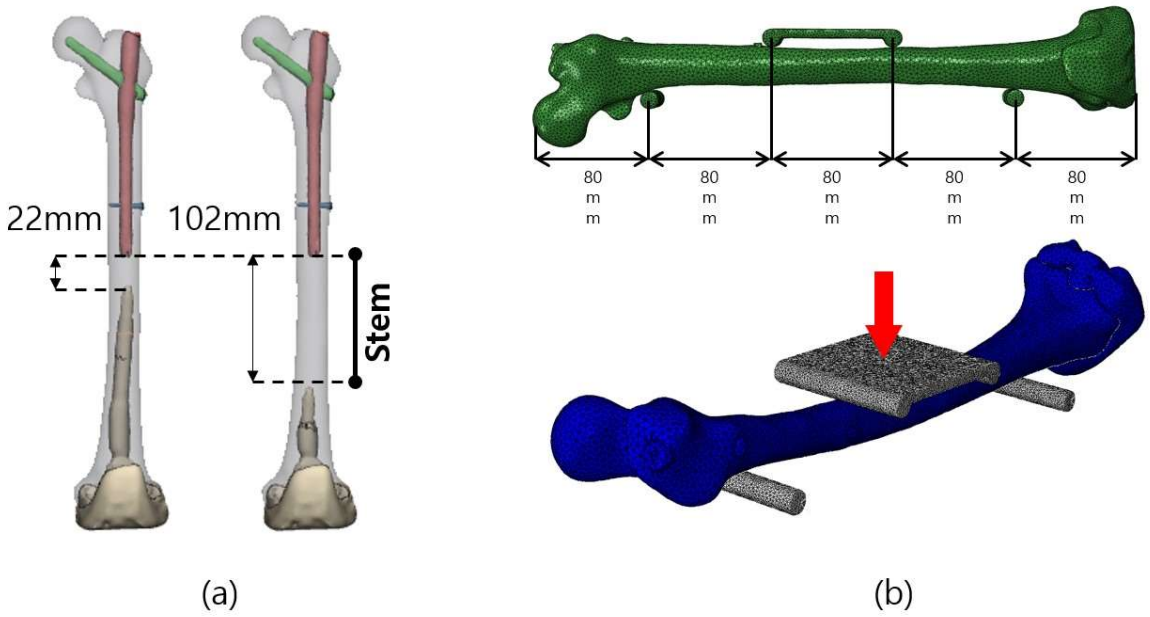


Figure 1. Ipsilateral hip and knee arthroplasty model with 9 configurations (a) and finite element analysis for combined THR–TKR model under 4-point bending test. (b)

Acknowledgements (Optional)

This research was supported by Basic Science Research Program through the National Research Foundation of Korea (NRF) funded by the Ministry of Education (NRF-2022R1A2C1009995)

Session Category

Orthopaedic Biomechanics: Lower Extremities

P3-267

Correction angle optimization in high tibial osteotomy based on patient-specific musculoskeletal models.

M.Sc Talha Üzümcü[1], Dr. habil. Alexander Pugachev[2], Dr. Stefan Zachow[3], PD Dr. med. Peter Balcarek[4], Dr. Johannes Funken[1], Prof. Dr. Wolfgang Potthast[1], Dr. Igor Komnik[1]

[1]German Sport University, Cologne, North Rhine-Westphalia, Germany. [2]Simq GmbH, Munich, Bavaria, Germany. [3]Zuse-Institute Berlin, Berlin, Berlin, Germany. [4]R + E ARCUS Klinik GmbH, Pforzheim, Baden-Württemberg, Germany

Introduction

Knee osteoarthritis (KOA) is a fast-growing global public health condition affecting 1-in-5 people over the age of forty. Open-wedge High Tibial Osteotomy (OWHTO) is a preferred treatment option for young and active patients. Despite its advantages, the outcomes largely depend on surgical planning decisions and current approaches are unsatisfactory.

This study aims to develop a surgical planning tool that determines the optimal patient-specific correction angle using musculoskeletal (MSK) modelling, considering individual knee loading profiles during activities of daily living.

Methods

Motion data will be collected from 10-12 patients planned to undergo OWHTO during daily tasks, both pre- and post-surgery. It will be used as an input to create individualized MSK models in addition to using three distinct scaling approaches.

First, a basic scaling approach will be implemented based on marker distances. Next, an accurate model will be generated from CT/MRI imaging data to produce 3D meshes. Finally, for a patient-specific planning of OWHTO, a partially-individualized 3D anatomy will be approximated based on clinical 2D X-ray images and statistical 3D shape and intensity models.

The scaled models will be used to perform virtual surgeries and to predict post-surgery knee adduction moments (KAM). Actual post-surgery data will serve as a validation for the prediction accuracy of different scaling approaches.

Results

As this is an ongoing research project, the following outcomes are the expected results. The primary outcome is the validation of the simulation process, with high correlations

expected between predicted KAM values from simulations and actual post-surgery measurements.

Additionally, the study aims to compare different scaling approaches. It is anticipated that the partially-individualized scaling method will achieve accuracy levels comparable to CT/MRI-based models, offering a more cost-effective alternative.

Discussion

OWHTO is an important treatment option for young and active patients with KOA. However, current planning methods remain insufficient, relying on oversimplified one-size-fits-all static approaches to a dynamic problem. There is a need to translate advances in computational modeling into clinical practice. Accurate prediction of KAM could significantly enhance OWHTO longevity and improve functional outcomes. Furthermore, 2D-to-3D reconstruction techniques developed in this project have the potential to be applied to other orthopedic interventions.

Images (Optional)

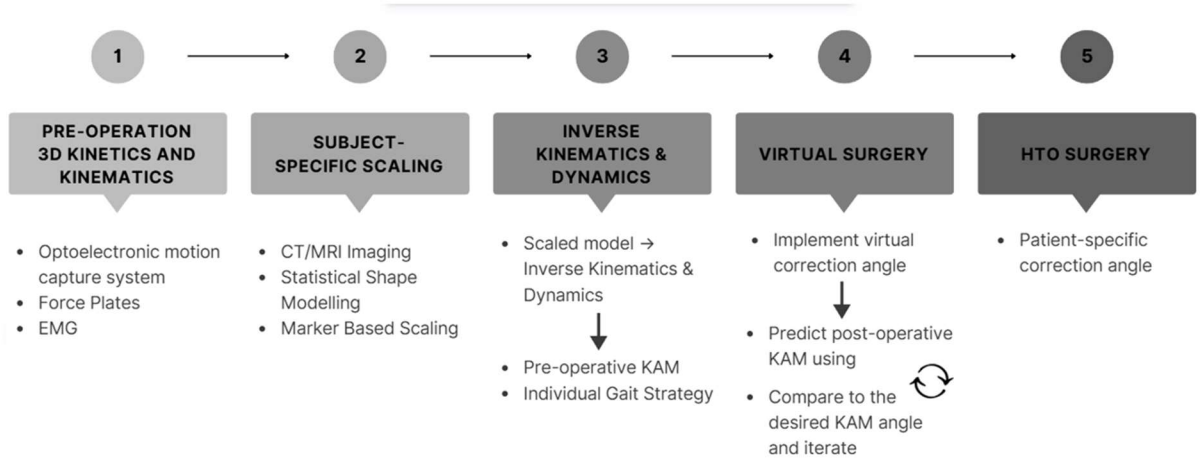


Figure 1: Individualized KAM-based HTO correction angle planning approach showing a five-step outline, comprising the inherently connected essential phases (grey-shaded blocks) and their respective subsets.

References (Optional)

Session Category

Orthopaedic Biomechanics: Lower Extremities

P3-268

Establishing an Open-Chain Squat Protocol to Identify Biomechanically Optimal Toe-Out Angles: Preliminary Reliability Results

Dr. Teresa Szu-Hua Chen PT, PhD, Mr. Ethan Gray SPT, Miss Holly Geyer SPT, Miss Kiersten Gravuer SPT, Miss Lily Holden SPT, Mr. Matthew Mitros SPT

Ithaca College, Ithaca, NY, United States

Introduction

Squats are a fundamental exercise in physical training and rehabilitation, offering significant benefits for function, strength, and injury prevention. During deep squats, external rotation of the feet ("toe-out") is frequently observed, particularly when foot-floor friction is low. This “toe-out” is thought to be linked to anatomical features such as tibial torsion and soft tissue restrictions (e.g., tight calves). Since squats are performed closed-chain with fixed feet, limiting toe-out can create torsional loads at the knee or hip that may strain structures not designed to resist them. The purpose of this study was to establish an open-chain squat protocol to determine optimal toe-out angle during squats. We hypothesized the protocol would demonstrate moderate to good test-retest reliability.

Methods

Five individuals with pronated feet participated (2 females; age: 21.6±0.6 years; height: 174.4±7.6 cm; mass: 83.1±18.7 kg). Pronated foot was confirmed by navicular drop test >9mm. Each participant stood on two footprint devices that allow foot rotation and performed five bodyweight squats at two time points on the same day. Each device consisted of two wooden plates, with the top footprint-shaped plate attached to the bottom plate via a rotational mechanism at the rearfoot. The spacing of two footprint devices matched each participant's natural squat width. Three-dimensional motion analysis captured squat movements using reflective markers on the plate's front and rear edges, representing toes and heels. Maximum toe-out angle was calculated using VBA Excel. Test-retest reliability was assessed using intraclass correlation coefficient (ICC), minimal detectable change at 95% confidence (MDC_{95}), standard error of measurement (SEM), and Bland-Altman analysis.

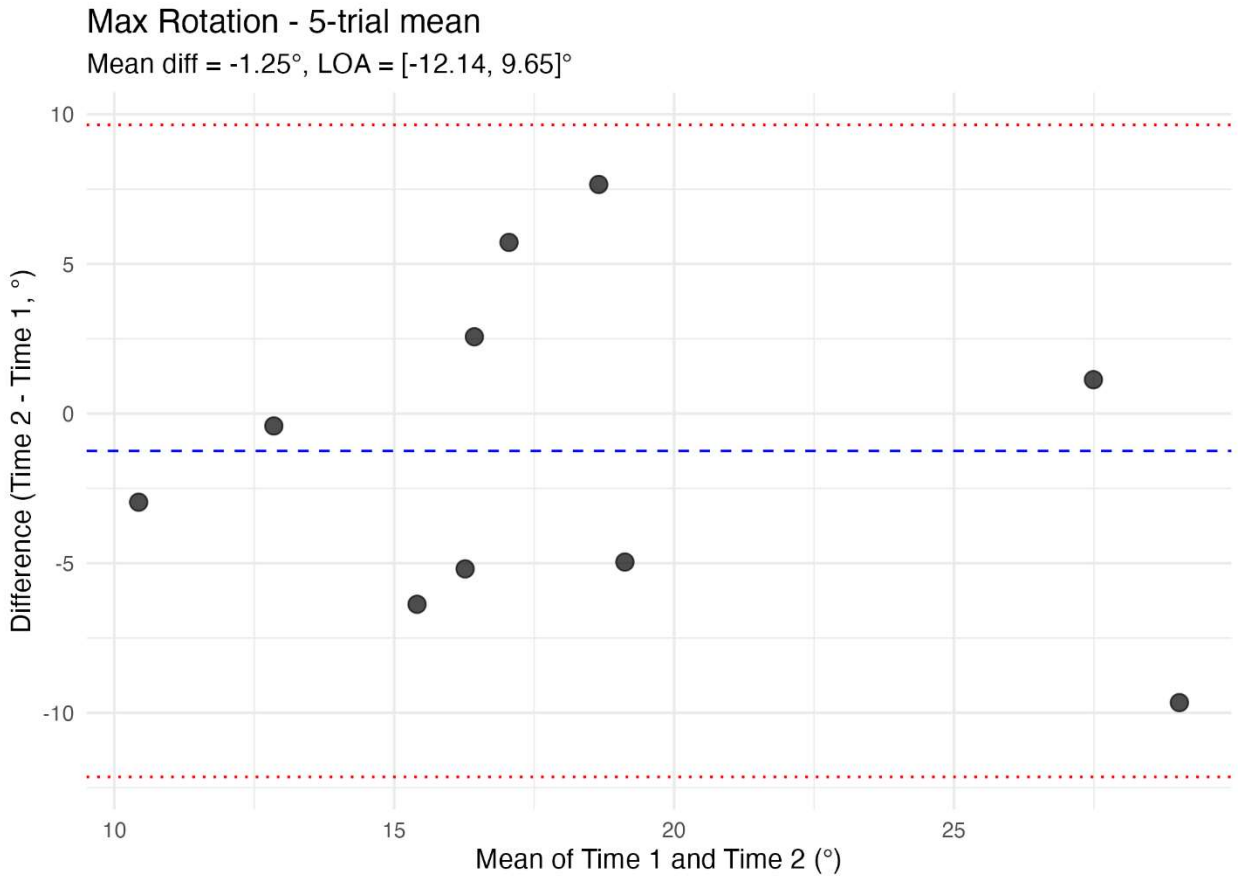
Results

Toe-out angle measurement showed moderate test-retest reliability (ICC = 0.64, 95% CI [0.07, 0.90]) with SEM of 3.78° and MDC_{95} of 10.48°. Bland-Altman analysis revealed minimal systematic bias between sessions (Figure).

Discussion

These findings support that the open-chain squat protocol using footprint devices is moderately reliable for quantifying toe-out angle. This measurement may help individuals who naturally adopt greater toe-out angles during squats—such as those with tight calves, abnormal tibial torsion, or pronated feet—identify their optimal foot position during squats without imposing torsional loads up the kinetic chain.

Images (Optional)



Session Category

Orthopaedic Biomechanics: Lower Extremities

P3-269

Effects of Traumatic Muscle Injury to Adjacent Tendon Mechanics and Structure

Mr. Trent Hardwick[1], Mr. Patrick Hinkle[1], Mr. Fuad Bin Enam[1], Dr. Jeremy Eekhoff[2], Ms. Elena Woo[1], Mr. Evan Fry[1], Mr. Brady Huggins[1], Dr. Koyal Garg[1], Dr. Alex Reiter[1]

[1]Saint Louis University, St. Louis, MO, United States. [2]Pennsylvania, Philadelphia, PA, United States

Introduction

Volumetric muscle loss (VML) is characterized by an irrecoverable loss of skeletal muscle, resulting in chronic functional deficits.[1] The inflammatory response and altered mechanical environment following injury and throughout recovery could lead to concomitant detrimental changes to the entire musculotendinous unit. However, tendinous changes due to adjacent VML injury have not been explored. The purpose of this study was to characterize the mechanical and structural changes to the Achilles tendon in a rat model of gastrocnemius VML injury.

Methods

Female Sprague Dawley rats (n=9, 10-12 weeks old, 200-275g, Inotiv) received a surgically induced VML injury bilaterally in the gastrocnemius, followed by four weeks of cage activity. Aged-matched controls (n=7) were included. Animals were euthanized and Achilles tendons were prepared for mechanical testing (n=7-12 limbs) and histological analysis (n=6-7 limbs). Mechanical testing consisted of preconditioning, 10-minute stress relaxation at 6% strain, and a quasistatic ramp-to-failure. Data were analyzed in MATLAB. Unpaired t-tests assessed group differences in mechanical outcomes (p<0.05). Histological analysis is ongoing.

Results

No significant differences were found between control and VML-injured tendons in maximum force, stiffness, maximum stress, tangent modulus, cross-sectional area, or percent relaxation (Fig. 1).

Discussion

These preliminary results suggest VML injury does not induce concomitant mechanical changes in the adjacent tendon. It should be noted that this injury model allows full weight-bearing activity immediately following VML. While a substantial inflammatory response is present, the mechanical loading environment may be only partially altered. Furthermore, pending histological analysis may reveal structural changes in the tendon that do not manifest as mechanical changes at the 4-week post-injury timepoint. However, if further investigation confirms tendons are unaltered, then research should remain focused on treating the primary VML injury with little concern for uninjured adjacent tissues in this model.

Images (Optional)

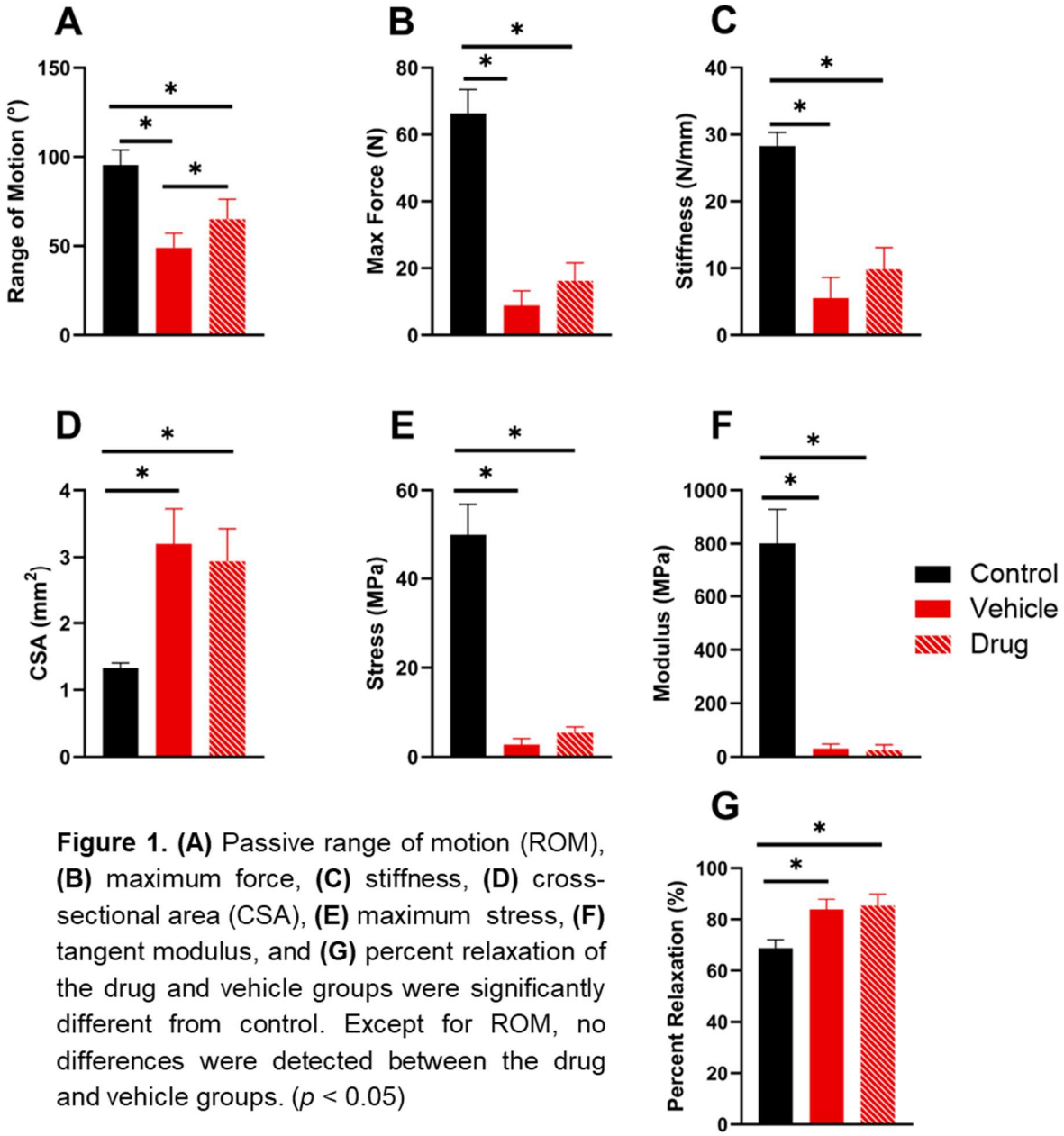


Figure 1. (A) Passive range of motion (ROM), **(B)** maximum force, **(C)** stiffness, **(D)** cross-sectional area (CSA), **(E)** maximum stress, **(F)** tangent modulus, and **(G)** percent relaxation of the drug and vehicle groups were significantly different from control. Except for ROM, no differences were detected between the drug and vehicle groups. ($p < 0.05$)

References (Optional)

[1] Corona, *Cells Tissues Organs*, 2016.

Acknowledgements (Optional)

Funding from the NIH (R03HD115731 and 1R15GM129731-02).

Session Category

P3-270

Metamorphic Compliant Total Knee Arthroplasty

Ms. Alyssa Tomkinson[1], Dr. Cameron Taylor PhD[2], Mr. Will Flanagan[1], Dr. Jonathan Hopkins PhD[1], Dr. Alexandra Stavrakis MD[1], Dr. Tyler Clites PhD[1]

[1]University of California Los Angeles, Los Angeles, CA, United States. [2]University of North Carolina at Chapel Hill, Chapel Hill, NC, United States

Introduction

Total knee arthroplasty (TKA) is an effective treatment for advanced osteoarthritis; however, as primary TKA volume has increased, so has revision TKA incidence. Primary causes of failure include aseptic loosening, tibiofemoral instability, and polyethene wear. Compliant mechanisms are a promising solution to mechanical implant failure because they are wear-free and inherently stable. However, they cannot typically support the full range of knee motion needed for activities of daily living [1]. To address this, we developed a *metamorphic* compliant TKA implant. This implant functions as a wear-free compliant mechanism during high-cycle-count activities, such as walking, then transitions to a conventional mechanism for activities that require larger ranges of motion.

Methods

A rotary metamorphic flexure bearing was designed using off-the-shelf components and a 3D printed housing. The compliant central mechanism was optimized in FEA (Abaqus, Dassault Inc.) to operate under loads and displacements typical of walking. Torque vs. angular displacement was recorded for two different retention mechanisms (magnetic and spring-based) using a motorized test-bench (Fig. 1C). We used the resultant data to design a metamorphic knee implant.

Results

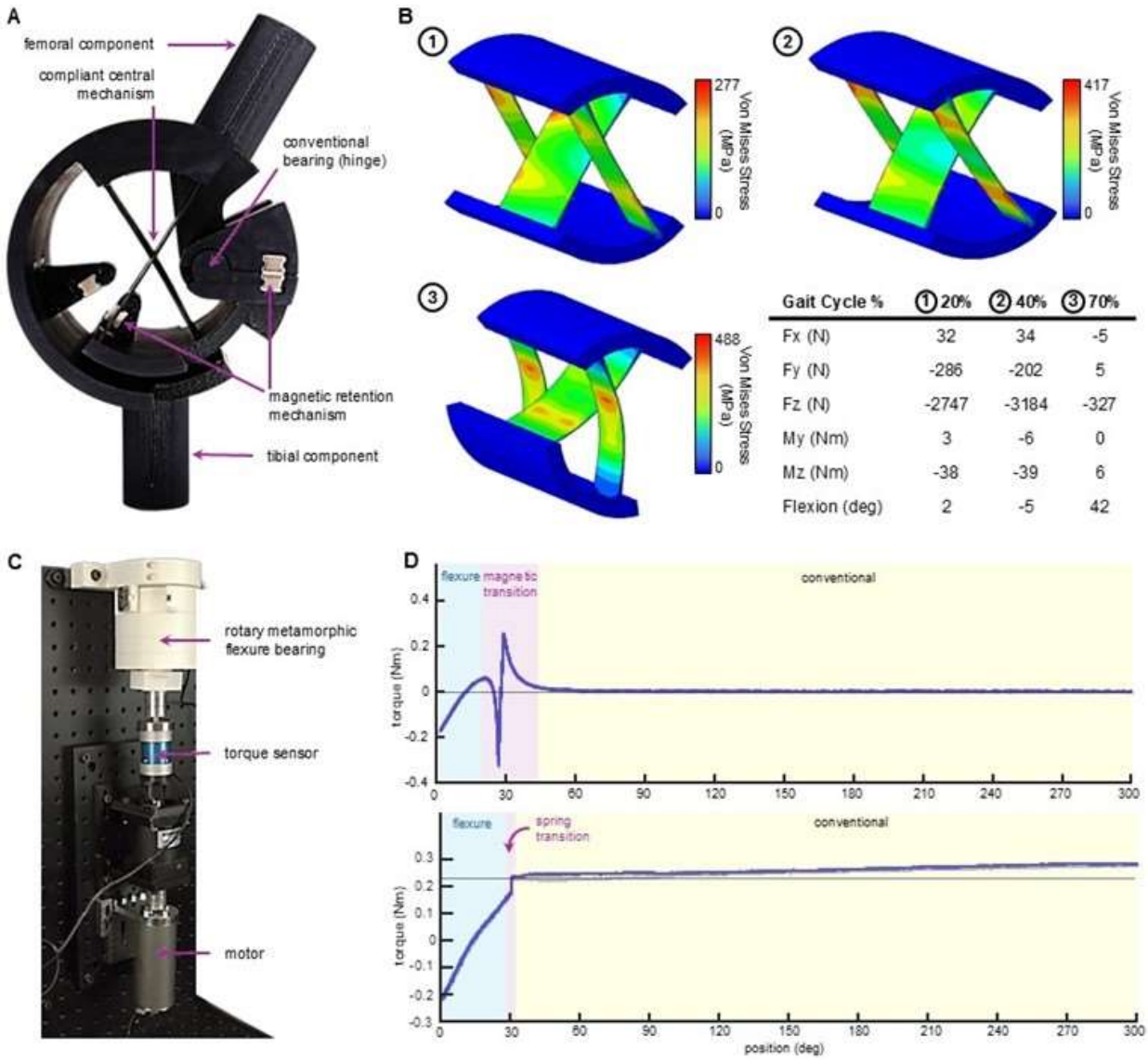
Peak stress in the central mechanism remained below 490 MPa during simulated walking (Fig. 1B), consistent with an almost 100-year fatigue life. The magnetic retention mechanism exhibited large torque perturbations at the transition zone but did not introduce sustained retention torques during flexure or conventional modes (Fig. 1D). The constant stiffness retention mechanism did not exhibit large torque perturbations at the transition zone but introduced a sustained torque during conventional-bearing mode (Fig. 1D). From these observations, we designed a metamorphic knee implant with a magnetic

retention mechanism (Fig. 1A); this was chosen to avoid sustained resistive torque during conventional-bearing mode.

Discussion

These results demonstrate mechanical feasibility of a metamorphic compliant TKA implant. We packaged the system within the envelope of a conventional revision TKA implant. Our FEA results show that the central mechanism can potentially withstand decades of gait-relevant loading within the body, and our experimental testing shows smooth and reliable transition between the two bearing modes. This approach has the potential to create lifetime TKA implants.

Images (Optional)



Gait Cycle %	① 20%	② 40%	③ 70%
Fx (N)	32	34	-5
Fy (N)	-286	-202	5
Fz (N)	-2747	-3184	-327
My (Nm)	3	-6	0
Mz (Nm)	-38	-39	6
Flexion (deg)	2	-5	42

Figure 1. (A) Metamorphic knee implant prototype **(B)** FEA from Abaqus displaying maximum stress **(C)** Motorized test-bench with rotary metamorphic flexure bearing **(D)** Torque-position plots for a retention handoff mechanism and a constant stiffness retention mechanism

References (Optional)

[1] Huxman *et al.*, Journal of Medical Devices, 2021

Session Category

Orthopaedic Biomechanics: Lower Extremities

P3-271

A Multiscale Computational Framework for Investigating Blood-Induced Cartilage Degradation in Haemophilic Arthropathy

Mr Venkata Sai Mahesh Peddapeta, Dr Hazel Fermor, Dr Greg de Boer, Dr Marlène Mengoni

University of Leeds, Leeds, England, United Kingdom

Introduction

Haemophilic arthropathy (HA) results from recurrent joint bleeds triggering inflammatory cascades and rapid cartilage degradation [1]. However, the quantitative progression from acute molecular events to tissue-scale mechanical failure remains poorly understood. This study introduces a multiscale framework integrating validated biochemical dynamics with poroelastic tissue mechanics to quantify disruptions in cartilage biomechanics.

Methods

At the biochemical scale, a 32-species ODE network simulated the inflammatory response to blood exposure. Model parameters were calibrated within literature-derived ranges to ensure physiological steady-state stability. The model was validated against experimental data [1, 2, 3, 4] for acute cytokine activation [4] (1–3h) and cumulative matrix depletion [1, 2, 3] (4 days). At the tissue scale, a 2D axisymmetric poroelastic FE model simulated confined compression. Tissue permeability and hygroscopic swelling were defined as empirical functions of glycosaminoglycan (GAG) content [5], linking mechanical function to biochemical degradation.

Results

The biochemical model reproduced acute inflammatory profiles observed in literature (Figure 1A). Over a 4-day bleeding window (Figure 1A, Inset), the simulation indicated 18% GAG loss and 26% proteoglycan synthesis inhibition, aligning with explant studies [1, 2, 3] (18–40% loss; 22–45% inhibition). Mechanically, this GAG loss increased intrinsic permeability 1.6-fold and reduced relaxation time by ~30% (Figure 1C). Consequently, the aggregate modulus decreased by ~8% (Figure 1B).

Discussion

This framework captures haemarthrosis kinetics, validating inflammation and matrix suppression against experimental data. Linking these outputs to poroelastic mechanics reveals that early GAG depletion initiates a transition towards a mechanically unstable

tissue: the corresponding increase in permeability and reduction in relaxation time signify a compromised capacity for load support. This framework provides a mechanistic understanding of the disease, establishing a quantitative tool to evaluate therapeutic strategies.

Images (Optional)

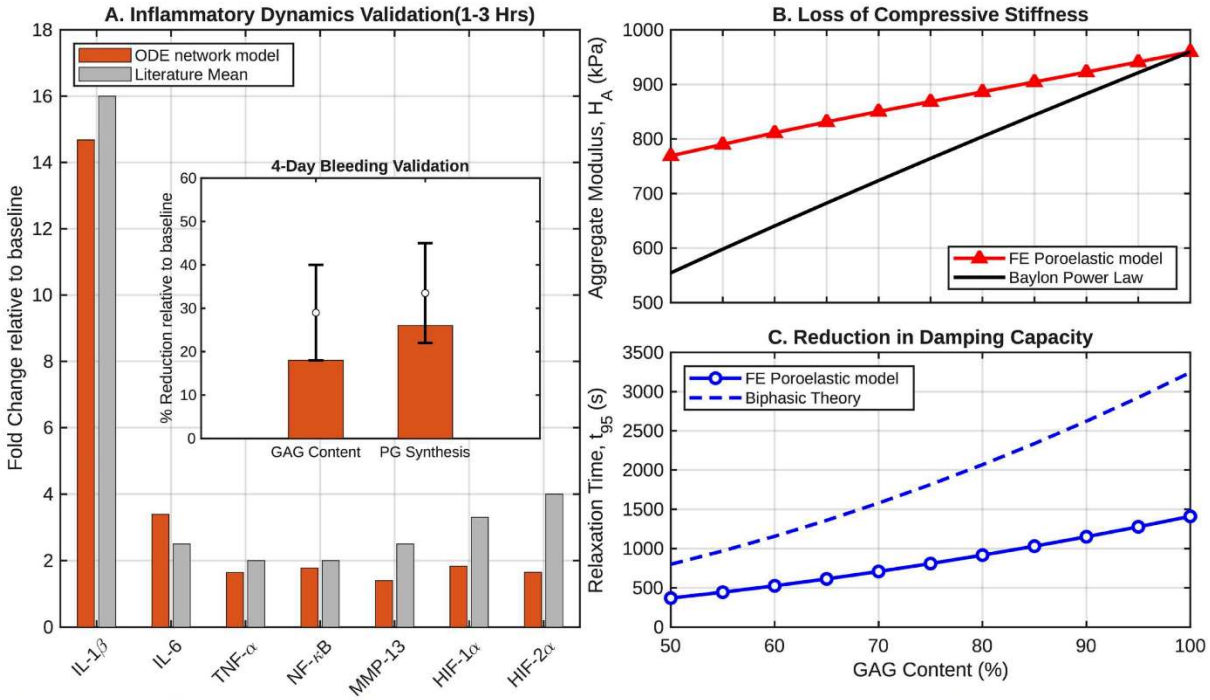


Figure 1 (A) Verification of acute (1–3h) inflammatory dynamics against literature means. (Inset) Day-4 matrix degradation simulations align with experimental (error bars) explant ranges [1, 2, 3]. (B) Loss of aggregate modulus (HA). The FE model (red) captures the qualitative trend of the Baylon power law [6] ($HA \propto GAG^{0.791}$, black), with quantitative deviations attributed to the stabilizing effect of the intact collagen network in confined compression. (C) Reduction in relaxation time (t_{95}). The FE simulation follows the trend of the 1D analytical biphasic theory [7] (dashed), with offsets resulting from realistic 2D flow and boundary effects inherent to the finite element formulation.

References (Optional)

[1] Hooiveld MJJJ *et al.*, Rheumatology, 2003

[2] Pulles AE *et al.*, Haemophilia, 2020

[3] Roosendaal G *et al.*, Arthritis Rheum, 1999

[4] Sen D *et al.*, J Thromb Haemost, 2013

[5] Zamparo O *et al.*, Arch Biochem Biophys, 1989

[6] Baylon EG *et al.*, J Orthop Res, 2020

[7] Miller GJ *et al.*, Osteoarthritis Cartilage, 2010

Acknowledgements (Optional)

Institute of Medical and Biological Engineering, University of Leeds, Leeds, United Kingdom.
Engineering Physical Sciences Research Council, UKRI, UK fund this work.

Session Category

Orthopaedic Biomechanics: Lower Extremities

P3-272

Differentiation between gait and non-gait weightbearing tasks using plantar pressure insole data: procedures for task-differentiation during daily tasks

Dr. Willa Ma, Dr. Susan Sigward

University of Southern California, Los Angeles, California, United States

Introduction

Insole measures of surgical loading during daily weightbearing activities suggest individuals following anterior cruciate ligament reconstruction practice underloading behaviors ecologically. However, it's not clear how types of daily activities influence these behaviors as current procedures do not differentiate loading across tasks. The purpose is to determine the accuracy, reliability, and validity of a gait detection algorithm that differentiates gait and non-gait activities from using plantar pressure insole data by quantifying force impulse and limb loading symmetry.

Methods

Twelve healthy participants performed gait at five speeds intermixed with non-gait daily activities for 12 minutes on two testing days. Vertical ground reaction force (Bertec: treadmill force plates) and plantar force (Novel Electronic: loadsol pro) were collected concurrently. A gait detection algorithm differentiated gait from non-gait using the following parameters to identify stance: threshold of 50N for heel-strike and toe-off, peak stance force >0.85x bodyweight, force duration 0.25-1.5 seconds, time between strides <1.5 seconds, and ≥5 consecutive strides. Time (minutes) classified as gait and non-gait for each system determined sensitivity and specificity relative to force plate-derived gait events (gold standard). Force impulse (area under force-time curve) for each limb and system were used to calculate limb loading symmetry (LLS: non-dominant/dominant). Intraclass correlation coefficients (ICC3,k) assessed between-system validity and between-day reliability for impulse and LLS. Bias, standard error of measure (SEM), and limits of agreement (LOA) were calculated.

Results

Sensitivity and specificity were 99.4% and 99.3% respectively (Figure 1). Impulse ICCs were 0.91 for gait and 0.86 for non-gait activities, whereas LLS demonstrated ICCs of 0.38 and 0.86. Bias between systems was ±2% for LLS and LOA within ±9% for gait and ±12% for non-gait. Reliability ICCs were 0.93 and 0.24 for gait and non-gait impulse and 0.37 and

0.65 for LLS. SEM was 0.01 BW*s for gait and 12.1 BW*s for non-gait impulse, and 0.03-0.05 for LLS.

Discussion

Accurate detection of gait and non-gait activities with only 4.1/622.1 minutes misclassified, excellent between-day reliability for gait impulse, and small LOA and bias between systems for impulse and LLS support the use of insoles to detect loading asymmetries differentiated by activity in ecological environments.

Images (Optional)



References (Optional)

Session Category

Orthopaedic Biomechanics: Lower Extremities

P3-273

Increases in Finite Element-Based Bone Strength Metrics Post Partial Volume Correction Evaluated at the Proximal Tibia of Persons With Spinal Cord Injuries

Mr. William Kuo[1], Dr. Christopher M. Cirnigliaro[2], Dr. William A. Bauman[3], Dr. Saikat Pal[1]

[1]New Jersey Institute of Technology, Newark, New Jersey, United States. [2]James J. Peters Veterans Affairs Medical Center, Bronx, New York, United States. [3]Icahn School of Medicine at Mount Sinai, New York City, New York, United States

Introduction

Persons with spinal cord injuries (SCI) experience rapid bone loss and are at high risk of fragility fractures, with the most common site being the knee joint (proximal tibia and distal femur) [1]. Studies have described computed tomography (CT)-based finite element (FE) methods to be better than radiographic measurements in evaluating the mechanical competence of bone [2]. However, 3-D models from CT imaging are prone to partial volume effects (PVE) and result in errors at the morphological boundaries. One specific error is reduction of cortical bone density due to averaging of bone and soft tissue pixels' greyscale values at the boundaries (Figs. 1A-B). Such PVEs directly affect the surface-based failure criteria used to determine FE-based bone strength metrics: torsional stiffness (K_t), torsional strength (T_{ult}), compressive stiffness (K_c), and compressive strength (C_{ult}) [2, 3]. The effects of partial volume correction (PVC) on FE-based bone strength metrics remain unclear. As such, the **goal** of this study was to quantify the increases in FE-based bone strength metrics due to PVC evaluated at the proximal tibia of persons with SCI.

Methods

We recruited 22 participants with SCI (15M, 7F) and 5 AB controls (4M, 1F) with procedures approved by our IRB. FE-based bone strength metrics were computed from 43 SCI and 10 AB proximal tibias through torsional (K_t, T_{ult}) and compressive displacement (K_c, C_{ult}). We applied element-based PVC, where local surface elements were converted to the highest density of adjacent elements. We quantified the increases in FE-based bone strength metrics following PVC at the proximal tibias of all participants.

Results

From all participants, PVC resulted in an average increase of 32%, 41%, 30%, and 61% for K_t, T_{ult}, K_c, and C_{ult}, respectively (Fig. 2). The increases in FE-based bone strength metrics were greater in the SCI compared to the AB participants.

Discussion

This study highlights the importance of PVC when quantifying FE-based bone strength metrics from persons with severely osteoporotic bones, such as those with SCI.

Images (Optional)

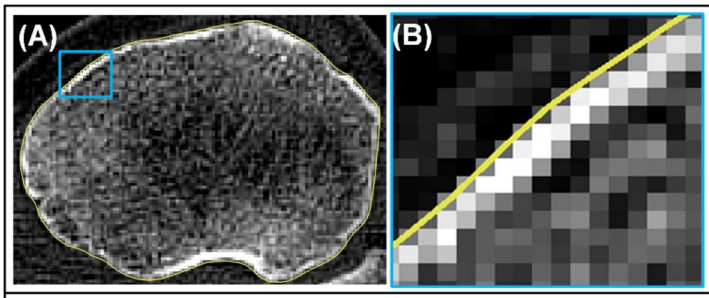


Figure 1: (A) The cross-sectional area of the tibia shows (B) partial volume effects at the yellow boundary where pixels do not show the highest greyscale intensity at the cortical surface.

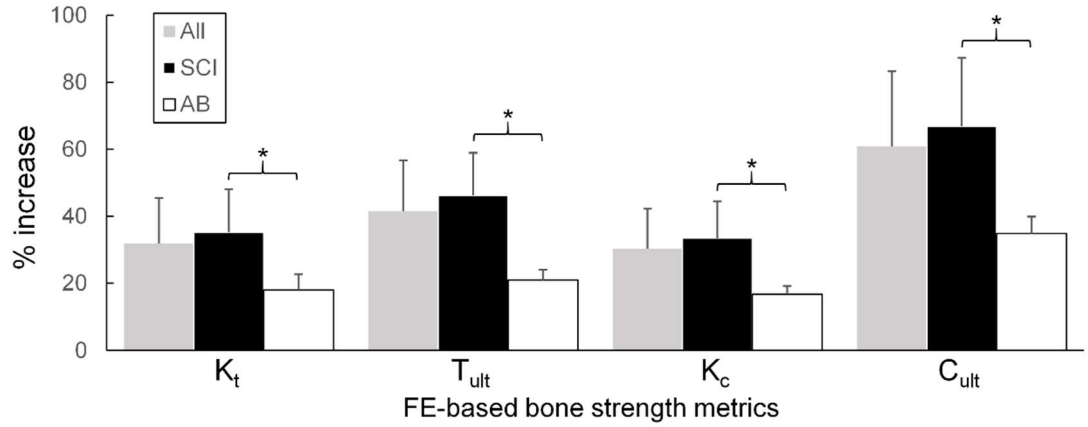


Figure 2: Increases in FE-based bone strength metric (K_t, T_{ult}, K_c, and C_{ult}) due to partial volume correction. * represents significant differences in percent increase between tibias from SCI and AB participants (Mann-Whitney U test, $p<0.05$).

References (Optional)

[1] Grassner *et al.* , J Spinal Cord Med, 2017; [2] Edwards *et al.* , J Biomech, 2013; [3] Haider *et al.* , Osteoporos Int, 2018

Acknowledgements (Optional)

VA RR&D #1 I01 RX003561

Session Category

Orthopaedic Biomechanics: Lower Extremities

P3-274

Do Implant Designs React Differently to Malalignment? Clinical Implications for TKA Stability and Longevity

Ms. Simone Sommer, Prof. William R. Taylor, Dr. Seyyed Hamed Hosseini Nasab

ETH Zurich, Zurich, Zurich, Switzerland

Ms. Simone Sommer

Prof. William R. Taylor

Introduction

Component alignment strongly influences total knee arthroplasty (TKA) function, stability, and longevity. Although malalignment affects joint mechanics, implant designs may differ in their mechanical tolerance to alignment errors. This study quantifies the sensitivity of three contemporary TKA designs – ultra-congruent (UC), posterior-stabilised (PS), and medial-stabilised (MS) – to implantation errors and identifies design-dependent risks for instability, abnormal joint loading, and implant failure.

Methods

A previously validated musculoskeletal model [1] was implanted with UC, PS, and MS configurations (Fig.1). A Monte Carlo framework introduced random perturbations up to ±5° to the femoral and tibial component alignments in all planes, producing 500 simulated implantation scenarios per design. Skin-marker trajectories and ground reaction force data from a walking trial were used as input to the COMAK algorithm [2] to estimate tibiofemoral kinematics, joint loading, and muscle activations. Mechanical sensitivity was quantified by correlating component implantation angles with joint kinematics at peak tibiofemoral force.

Results

Although MS was the most sensitive design overall, kinematic responses to malalignment were highest in MS and UC. However, the highest axis-specific kinematic sensitivity occurred in the PS design, which showed the largest anterior-posterior (AP) translation response to tibial sagittal malalignment (up to 1.16 mm/°). PS also demonstrated the

greatest sensitivity in medio-lateral (ML) loading, particularly under tibial coronal perturbations (up to 26.9 N/°). Muscle activations were largely insensitive to alignment variation; the only consistent deviation occurred near toe-off, where activation levels increased to stabilise the joint, particularly in PS and MS configurations.

Discussion

These findings reveal distinct, design-specific responses to malalignment. While MS and UC showed broad kinematic sensitivity, the PS design demonstrated pronounced axis-specific changes, which may increase asymmetric tibial loading and thereby elevate the risk of tibial component loosening. The higher muscle activation demands near toe-off in PS and MS further indicate reduced intrinsic stability. Therefore, surgeons should be aware that certain designs are less tolerant to alignment variability, meaning that meticulous surgical technique and accurate instrumentation are critical to reduce the risk of instability, abnormal wear, and early revision.

Images (Optional)

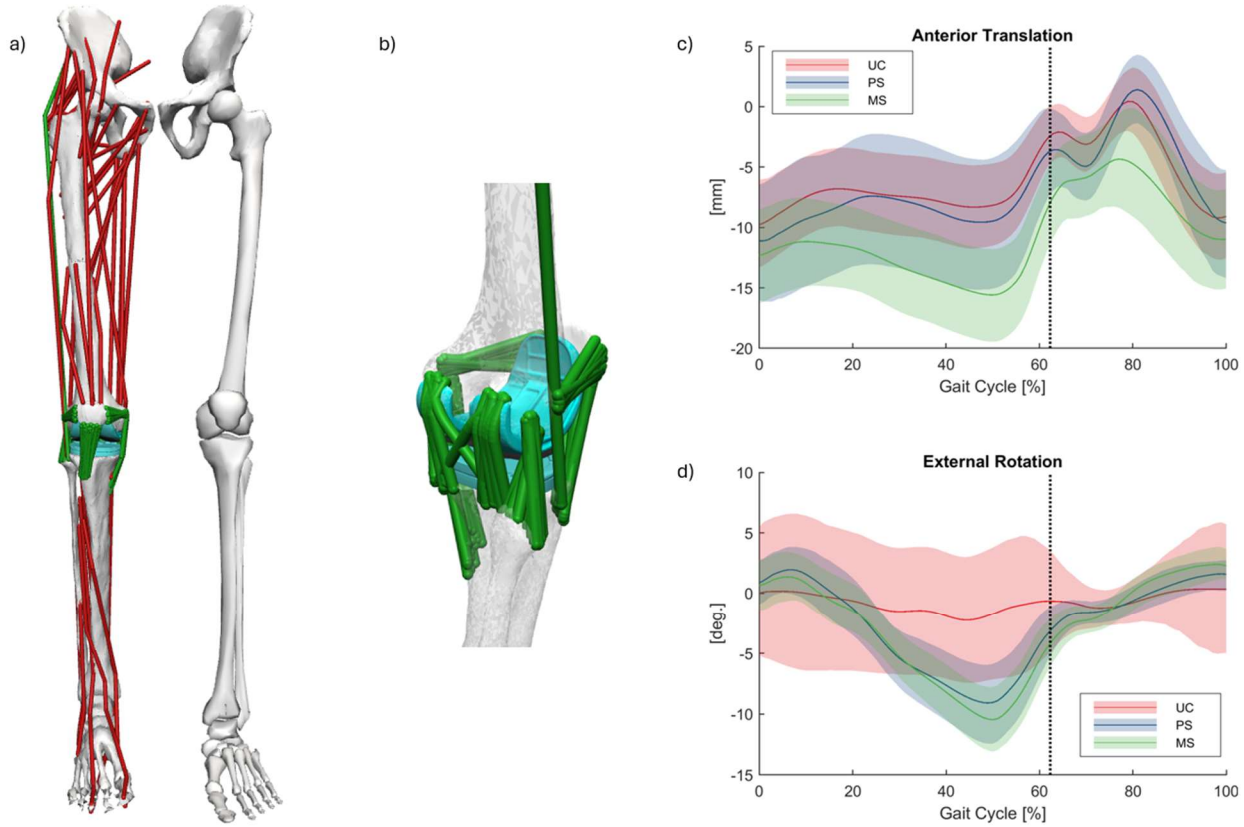


Figure 1: a) Subject-specific musculoskeletal model with muscles (red), ligaments (green) and implant (blue); b) Detail of subject-specific musculoskeletal model with ligaments (green) and implant (blue); c) Simulation results (mean and 5-95th percentile range) of anterior translation changes of all 3 implant designs; d) Simulation results of external rotation changes

References (Optional)

[1] Brandon, S. C. E. *et al.*, Handbook of Human Motion, 2017

[2] Guo, N. *et al.*, Front. Bioeng. Biotechnol., 2024

Session Category

Orthopaedic Biomechanics: Lower Extremities

P3-275

Finite Element Analysis of the Optimal Plate Positioning and Screw Length in Medial Open-Wedge High Tibial Osteotomy

Dr. Yasushi Oshima MD, PhD[1], Dr. Kohei Murase Ph.D[2], Dr. Makoto Hirao MD, Ph.D[1]

[1]Nippon Medical School, Tokyo, Tokyo, Japan. [2]The University of Osaka, Osaka, Osaka, Japan

Introduction

In medial open-wedge high tibial osteotomy (MOWHTO), the fixation plate is typically positioned on the medial tibial surface, and the most proximal screws are ideally inserted to reach beyond the lateral intercondylar eminence without penetrating the lateral cortex. However, the biomechanical implications of anteromedial plate placement and shortened screw length have not been fully clarified. We hypothesized that excessive anteromedial plate positioning, particularly when combined with shorter screws, would reduce fixation strength and increase the risk of implant failure and loss of alignment correction. This study aimed to evaluate mechanical loading changes in the proximal tibia and implants associated with variations in plate positioning and screw length using finite element analysis.

Methods

A simulated adult tibia model (Sawbones, USA), consisting of separated cortical and cancellous bone layers was generated with an average element size of 0.8 mm. An MOWHTO model with a postoperative proximal tibial medial angle of 93° was created. Finite element models were constructed using the TriS medial HTO plate purple (OSferion Biomaterials, Japan) placed on the true medial surface and at 10°, 15°, 20°, and 30° anteromedial orientations. Screw length conditions included long (reaching near the lateral cortex), short (ending just beyond the lateral intercondylar eminence), and intermediate lengths. Tibial mechanical loads of 750 N medially and 1250 N laterally were applied in vertical and 30° posterior-oblique directions. Young's modulus and Poisson's ratio of the titanium plate and screws were assigned according to the previous literature (Murase K, 2007). Stress distribution was analyzed using LS-DYNA software (Ansys, USA).

Results

Compared with true medial plate placement with long screws, anteromedial plate positioning with the combinations of shorter screws resulted in stress concentration around the proximal second-row screw hole. Moreover, changing the load direction from

vertical to oblique shifted the stress concentration from the anterior to the posterior portion of the plate.

Discussion

The plate breakage around the second-row screw hole has recently been reported. In this study, the stress concentration increased with anteromedial plate placement and shorter screws, and the plate stress location shifted with load direction. Thus, excessive anteromedial plate placement combined with shortened screws should be avoided in MOWHTO.

References (Optional)

Session Category

Orthopaedic Biomechanics: Lower Extremities

P3-276

In Silico Analysis of Etiology-Dependent Cortical and Cancellous Bone Remodeling in Osteoporosis

Dr Yoshitaka Kameo, Mr Hiroki Kazuno, Mr Yuto Niwayama

Shibaura Institute of Technology, Koto-ku, Tokyo, Japan

Introduction

Osteoporosis is a metabolic bone disease characterized by cortical thinning and a reduction in cancellous bone density, resulting from an imbalance between bone resorption and bone formation. Major etiological factors include reduced mechanical loading due to disuse and the accumulation of bone resorption–promoting factors associated with decreased sex hormone levels. These distinct etiologies are known to lead to different pathological patterns. Therefore, understanding and predicting morphological changes in cortical and cancellous bone via remodeling in response to mechanical environments is essential for developing effective preventive and therapeutic strategies for osteoporosis. This study aimed to elucidate the effects of osteoporosis-inducing factors on cortical and cancellous bone morphology from molecular and cellular perspectives by using bone remodeling simulations based on a mathematical model of bone metabolism.

Methods

A bone remodeling simulator, V-Bone, which integrates a mathematical model of bone metabolic processes and links microscopic molecular/cellular interactions to macroscopic tissue/organ adaptation, was employed [1, 2]. Bone remodeling simulations were performed using a mouse femur model to analyze changes in cortical and cancellous bone morphology under conditions of reduced mechanical loading and increased expression of RANKL, a signaling molecule that promotes osteoclast activation and bone resorption.

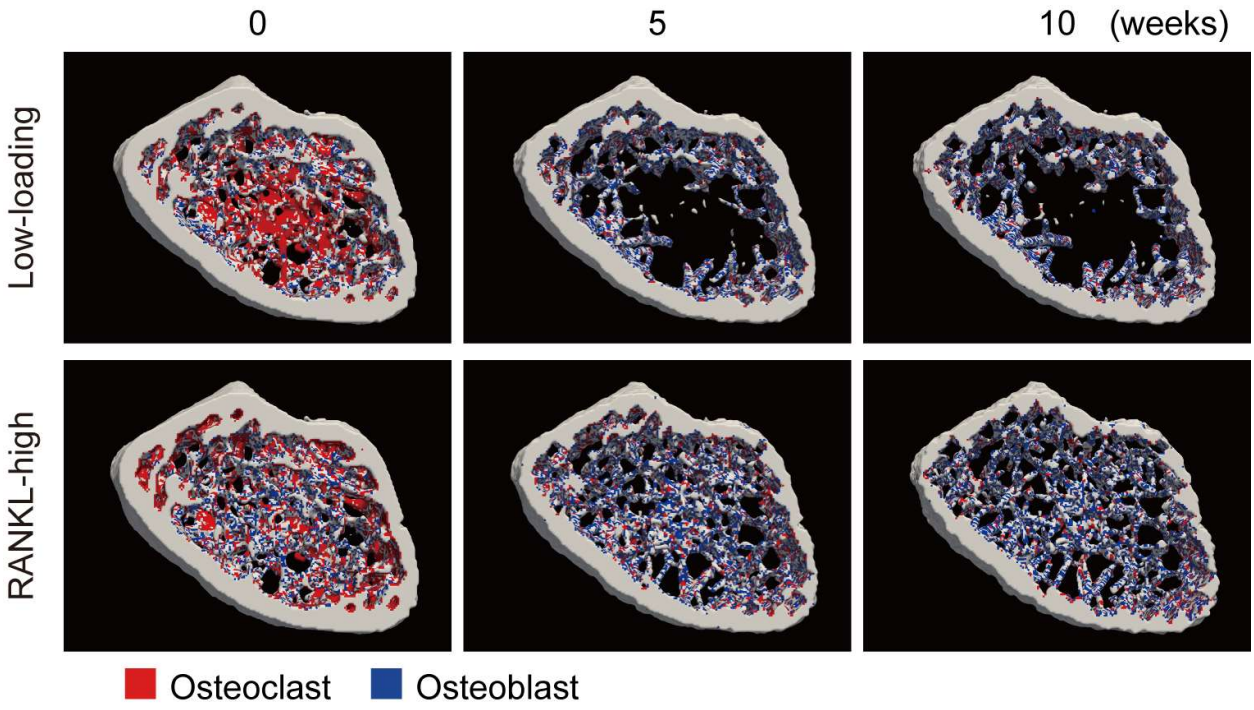
Results

The simulations showed that in osteoporosis caused by reduced mechanical loading (Low-loading model), cancellous bone volume rapidly decreased while cortical bone was relatively preserved. In contrast, in osteoporosis induced by elevated RANKL expression (RANKL-high model), both cortical and cancellous bone exhibited chronic and progressive loss (Figure).

Discussion

The etiology-dependent differences in pathological responses were qualitatively consistent with clinical and experimental observations. In RANKL-induced osteoporosis, only enhancement of bone resorption occurred, whereas in osteoporosis caused by reduced mechanical loading, both increased bone resorption and suppressed bone formation were observed due to elevated levels of sclerostin, a mechanosensitive signaling molecule. These distinct molecular mechanisms are considered to underlie the differences in cortical and cancellous bone abnormalities observed in osteoporosis.

Images (Optional)



References (Optional)

[1] Yoshitaka Kameo et al., Sci Adv, 2020

[2] Young Kwan Kim et al., JBMR Plus, 2024

Session Category

Orthopaedic Biomechanics: Lower Extremities

P3-277

A Novel Robotic System for Hip Joint Biomechanical Testing: Visualization and Three-Dimensional Analysis of Articular Contact

Mr. Yuta Sakamoto B.S.[1], Mr. Ryui Kumagai B.S.[2], Mr. Fumiya Kizawa P.T.[3,4], Prof. Daisuke Suzuki Ph.D.[5,4], Prof. Atsushi Teramoto Ph.D.[4], Prof. Hiromichi Fujie Ph.D.[1,4,6]

[1]Graduate School of Systems Design, Tokyo Metropolitan University, Hachioji, Tokyo, Japan. [2]Faculty of Systems Design, Tokyo Metropolitan University, Hachioji, Tokyo, Japan. [3]Division of Rehabilitation, Hokkaido University Hospital, Sapporo, Hokkaido, Japan. [4]Department of Orthopaedic Surgery, Sapporo Medical University School of Medicine, Sapporo, Hokkaido, Japan. [5]Department of Rehabilitation, Hokkaido Chitose College of Rehabilitation, Chitose, Hokkaido, Japan. [6]Research Center for Medicine-Engineering Collaboration, Tokyo Metropolitan University, Hachioji, Tokyo, Japan

Introduction

Internal rotation in flexion is believed to increase the loads applied to the acetabular labrum, and induce labral tears and subsequent osteoarthritis. Quantitative evaluation of labral loading and subluxation is needed for the prevention and improved treatment of those clinical problems. This study aimed to develop a framework combining robotic testing and computational modeling to reconstruct 3-D contact states, quantify subluxation, and assess acetabular labral load and stress in porcine hip joints.

Methods

Porcine hip joints were fixed to a 6-DOF robotic system (FRS-2015, Technology Service, Japan), and the hip joint coordinate system was defined according to the ISB recommendation [1]. During internal-external rotation applied up to ±600 Nmm at 0°, 20°, and 40° of flexion, hip kinematics were recorded, followed by digitization of joint surface geometry with a 3-D scanner (EinScan Pro HD, SHINING 3D, China). By combining the measured kinematics and surface geometry, a detailed hip joint model was reconstructed. This model allowed for the visualization of relative 3-D joint motion using custom-made Python programming software. To assess subluxation, the distance between the centers of curvature of the femoral head and acetabulum was determined.

Results

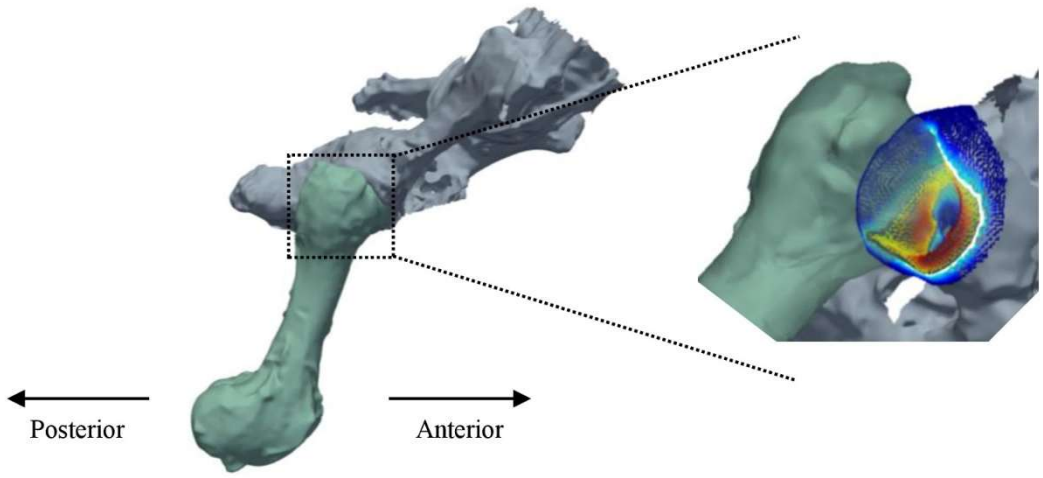
Subluxation distance varied with flexion and internal-external rotation. At 0° of flexion, the distance remained less than 1.2 mm regardless of rotation. However, at 20° of flexion, subluxation increased compared to that at 0°, with the largest value of 3.2 mm in internal rotation. At 40° of flexion, the distance took intermediate values, between those at 0° and

20° of flexion. Visualization indicated a severe, concentrated contact of the femoral head with the acetabular labrum in internal rotation at 600 Nmm.

Discussion

This study successfully conducted a hip joint loading test relative to the hip joint coordinate system and visualized the contact between the femoral head and acetabulum. Results indicated that internal rotation at light flexion poses the greatest risk to the hip, aligning with clinical findings [2]. Further research is required to examine load and stress on the acetabular labrum during this motion.

Images (Optional)



Visualization of the hip joint during 600 Nmm internal rotation at 20° of flexion with an enlarged view of the acetabulum indicating the distribution of the distance to the femoral head.

References (Optional)

[1] Ge Wu et al. , J Biomechanics, 2005

[2] Cara Lewis et al. , Phys Ther, 2006

Acknowledgements (Optional)

This research was supported by TERUMO life Science foundation 2025-2029.

Session Category

Orthopaedic Biomechanics: Lower Extremities

P3-278

Characterization of Lumbar Spine Biomechanics Using Multidimensional Motion Trajectories

Dr. Emma Coltoff PhD[1], Mr Alexander Hooke MA[2], Dr. Asghar Rezaei PhD[3,2], Dr. Philip Brown PhD[1]

[1]Department of Biomedical Engineering, Wake Forest School of Medicine, Winston-Salem, NC, United States. [2]Mayo Clinic Department of Orthopedic Surgery, Rochester, MN, United States. [3]Mayo Clinic 2Department of Physiology and Biomedical Engineering, Rochester, MN, United States

Introduction

Spinal motion and deformities occur in multiple dimensions, yet conventional biomechanical assessment largely relies on uniaxial bending kinetics and kinematics. Coltoff et al.[1] introduced a multidimensional cervical spine testing method using compound, multidirectional bending to link path directionality with biomechanical response. This study aimed to adapt that technique for the lumbar spine, with a future goal of utilizing it to correlate imaging-detected bone deformities with biomechanical function.

Methods

Two lumbar cadaveric spines from L1-L5 were used for this study: one “intact” spine with no evidence of deformities and one “deformed” spine with severe degradation and 3D deformities from L3 to L5, confirmed by CT imaging. Specimens were mounted to a 6-DOF robotic system. A set of 7.5Nm torque-limit boundary condition trajectories were run to determine each spine’s unique range of motion in the transverse plane. These results were used to create 5 multidimensional trajectories to move the spine through its full range of motion: “petals” clockwise (CW) and counterclockwise (CCW), “circles” CW and CCW, and rays (Figure 1A). Specimen kinematics and kinetics were recorded throughout each test. ARCMap[2] was used for statistical analysis between both specimens and between CW and CCW loading of the circles and petals trajectories.

Results

The deformed spine showed a 73% decrease in the multidimensional ROM versus the intact spine. The resultant load and stiffness behavior associated with each trajectory was plotted and normalized to a unit circle for comparison and calculation of differences between specimens and trajectories (Figure 1B). Resultant load differences reached 4.9Nm between specimens with the largest differences occurring in extension-driven

poses. Path directionality also indicated significant differences ($p < 0.05$) identified between the CW and CCW petals trajectories for the deformed specimen.

Discussion

The multidimensional loading presented highlights biomechanical behavior of the spine that traditional planar loading cannot identify. This includes a significant effect of bending path direction and its ability to highlight functional limitations due to deformity.

Images (Optional)

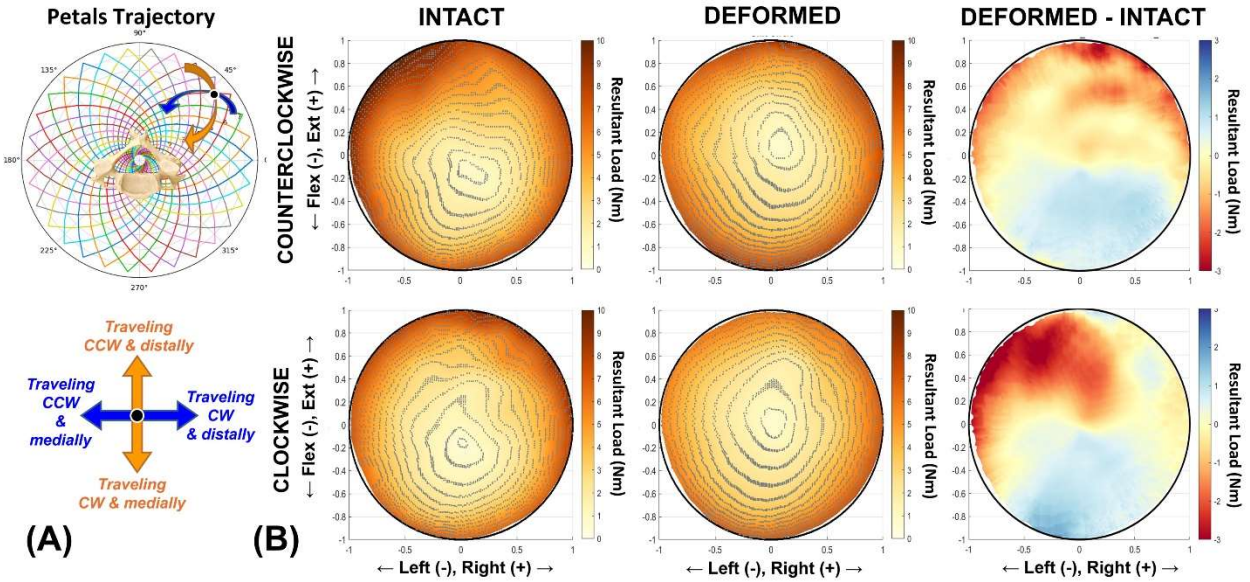


Figure 1: A) Visual representation of petals trajectory. B) Resultant load heatmaps normalized to unit circles with flexion/extension position (y-axis) versus lateral bending position (x-axis) during petals clockwise (bottom) and counterclockwise (top) loading. Contours indicate every 0.5 Nm. Intact specimen (left column), deformed specimen (middle), and difference between deformed and intact (right). Blue indicates deformed stiffness > intact. Red indicates intact stiffness > deformed.

References (Optional)

1. Coltoff, E.C., et al., Journal of Engineering and Science in Medical Diagnostics and Therapy, 2025. **8**(4).

2. Hartlen, D.C., et al., Annals of Biomedical Engineering, 2025. **53**(10).

Acknowledgements (Optional)

Supported by the National Institute on Aging and Mayo Clinic Biomechanics Core

Session Category

P3-279

Strain Based Structural Optimization of Highly Porous Bioresorbable Cages for Spinal Fusion

MsC Aline Gouveia[1], Dr. Joeri Kok[1], Dr. Claire Villette[2], Prof dr. Keita Ito[1,3], Dr. Bert van Rietbergen[1], Dr Miguel Dias Castilho[1]

[1]Eindhoven University of Technology, Eindhoven, N/A, Netherlands. [2]Queen Mary University of London, London, N/A, United Kingdom. [3]University Medical Center Utrecht, Utrecht, N/A, Netherlands

Introduction

Existing cages for spinal fusion surgery are typically made from non-resorbable materials and often fail to stimulate bone ingrowth, increasing risks of delayed fusion and complications. Fusion rates can be improved by creating a biomechanical environment that mimics native bone to favour quick bone growth, while the use of bioresorbable materials may reduce late-stage stress-shielding and enable stable fusion. 3D-printable trussed cage designs can be tuned to reach optimized mechanical and resorption characteristics through topology optimization. The aim of this project is the structural optimization of fully bioresorbable interbody cages to maximize initial bone ingrowth through mechanical stimulation.

Methods

A spinal fusion cage made from a biomimetic polymer-ceramic composite [1] was designed with a repeating body-centered cubic lattice unit cell. The design was iteratively adjusted using a strain optimization method based on finite element (FE) simulations with beam elements [2]. In each iteration, patient-specific loading was simulated using a FE model of the spine from a cohort of patients eligible for spine fusion, and the strut strains were calculated. The cross-sectional area of each beam was then adjusted until convergence to a target strain value of 2250με, within the bone apposition range according to the Mechanostat hypothesis [3].

Results

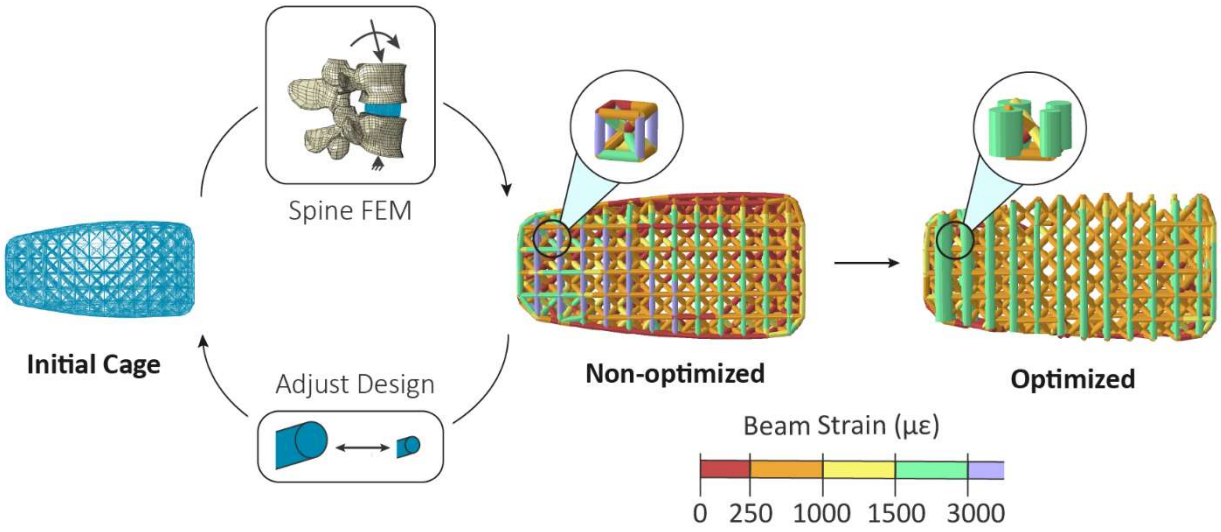
The converged strut design produced a total cage porosity of 60% while ensuring mechanical integrity under spinal loading. Preferential directionally of strut thickening was evident, and aligned with the expected trajectory of load transfer. During the optimization,

undeformed beams were removed and remaining elements converged to either the target strain or the extremes of the acceptable diameter range (Figure).

Discussion

The results indicate that a considerable increase in struts in the target strain is possible, while keeping adequate overall cage stiffness and strength. Compared to earlier topology optimization studies, the use of a strut adaptation approach simplifies the optimization workflow and applicability, as initial cage shape, unit cell size, topology, and acceptable strut thickness can be adjusted to ensure manufacturability and prevent material failure. It also enables easy implementation of resorption to simulate later fusion stages.

Images (Optional)



References (Optional)

[1] Yonggang Zhang, ACS Nano, 2021

[2] Andrew Phillips, Int Biomechanics, 2015

[3] Harold Frost, Anatomy Record, 2003

Acknowledgements (Optional)

This project is part of the Advanced Healthcare Materials call, formed by the São Paulo Research Foundation (FAPESP) and the Dutch Research Council (NWO).

Session Category

Orthopaedic Biomechanics: Spine

P3-280

Simulating Scoliosis Movement with a 1000 Degrees-of-freedom Joint-link Mechanism

Dr Athena Jalalian, Dr Soheil Arastehfar

University of Twente, Enschede, Overijssel, Netherlands

Introduction

Scoliosis is a complex 3-dimentional structural deformity of the spine. It causes wedged intervertebral discs resulting in S and C shape spines. Such deformity introduces asymmetry in the tissues surrounding the spine, e.g. stronger muscles in one side of the trunk compared to the other side. Therefore, the analysis of spine response to load becomes very complicated. In our previous work [1], we showed that simply introducing asymmetry in the spine models might not properly simulate scoliosis condition. We introduced an articulated mechanism with 1000 degrees-of-freedom that outperformed an existing model in reconstructing the spine in different positions in the coronal plane. However, we are yet to show if the mechanism can accurately simulate the spine under loads.

Methods

We added non-linear torsion springs at the rotary joints of the mechanism to capture the spine stiffness. We produced patients-specific scoliosis models for our cohort of 18 patients. For each patient, the stiffness of these springs was set by using lateral bending test, where an optimization problem was solved to define the stiffness that resulted in best reconstruction of the spine in the left and right bending positions. X-rays of five spine positions were available: erect, left bending, right bending, neutral, and traction. The first three were used for personalization and the latter two for testing the model capability for reconstruction of the spine in these positions. We compared the results with a benchmark model based on an existing scoliosis model. Root-mean-square-errors (RMSE) of the location and orientation of the vertebrae were used indicators of accuracy spinal column reconstruction.

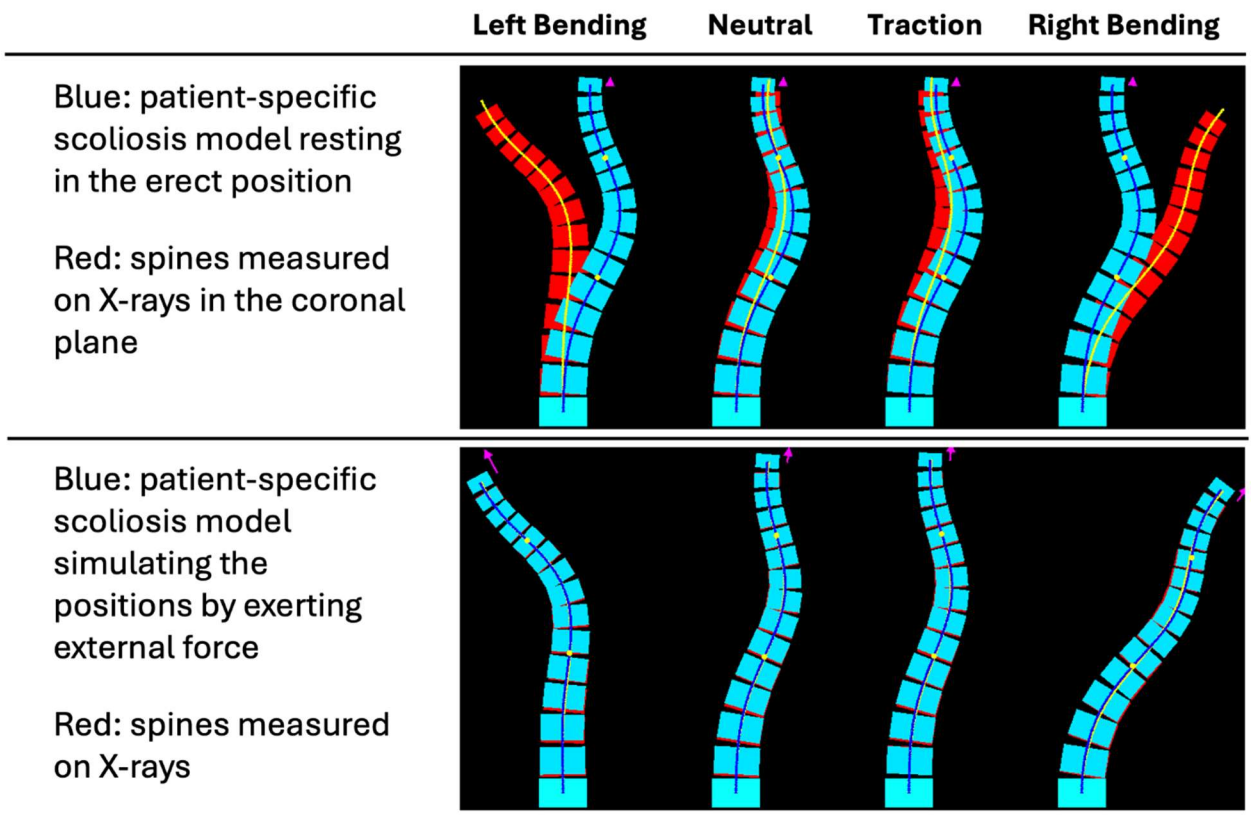
Results

RMSE for the benchmark model was 1.8 mm and 2.4 degrees for the location and orientation respectively. Our model was significantly more accurate with RMSE of 0.5 mm and 1.0 degrees, respectively.

Discussion

This can show that to simulate scoliosis we do not need to incorporate all the elements, such as muscles, ligaments and facet joints to create a complex model with questionable values for the geometry and stiffness, but rather we can capture the responses accurately through a simplified and out-of-the-box approach.

Images (Optional)



References (Optional)

[1] Soheil Arastehfar *et al.*, *IEEE Trans Med Robot Bionics, 2025*.

Session Category

Orthopaedic Biomechanics: Spine

P3-281

CT-Like MRI as a Novel, Radiation-Free Alternative for Personalized Modelling and In Vivo Kinematics Estimation of the Healthy and Deformed Spine

Ms Birgitt Peeters[1], Mr Tom Leppens[1], Prof. MD. PhD. Sebastiaan Schelfaut[2], Prof. MD. PhD. Lieven Moke[2], Prof. PhD. Lennart Scheys[1]

[1]Institute for Orthopaedic Research and Training, KU Leuven, Leuven, Flemish Brabant, Belgium. [2]Department of Orthopaedics, UZ Leuven, Leuven, Flemish Brabant, Belgium

Introduction

Personalized spine models are essential for understanding spine biomechanics in pathological spines, but remain challenging to create. Conventional approaches rely on palpation-dependent skin-marker scaling, or ionizing imaging, such as CT and biplanar radiography (BiXR). This study introduces an efficient, radiation-free workflow based on MRI to create personalized spine models for motion simulation and pilots its use in both healthy and pathological subjects.

Methods

A patient with degenerative spinal deformity and a healthy subject were studied. The pipeline integrates supine CT-like MRI with MRI-visible motion capture markers, automated bone segmentation, spinal joint and alignment definition, and semi-automatic marker definition in CT-like MRI. Postural changes from supine to standing (free-standing & SRS-pose) and walking were simulated. Model accuracy was evaluated by comparing vertebral positions and orientations with BiXR.

Results

Vertebral position and orientation errors were low (7.4 mm, 6.1°). Both subjects showed increased pelvic anteversion from supine to stance, with overall trunk extension in the healthy and flexion in the deformity subject. The healthy subject also showed the opposite flexion-extension intersegmental distribution compared to the deformity subject. Interestingly, the deformity subject demonstrated a redistribution of lateral bending in the lumbar segments (Fig.1).

In the SRS-pose, the deformity subject shifted into pelvic retroversion with increased spine flexion compared to the healthy subject.

During walking, the deformity subject showed increased pelvic anteversion and a drop toward the swing leg with trunk flexion and lateral trunk bending against the coronal deformity compared to the healthy subject.

Discussion

This CT-like MRI workflow accurately reconstructed 3D spinopelvic alignment and captured *in-vivo* kinematics. The deformity subject exhibited static and dynamic asymmetries, especially at the lumbar region. Increased pelvic anteversion and trunk flexion indicated an inability for malignment compensation, and the combined spine-pelvis lateral tilt contributed to a waddling gait. Pelvic retroversion in the SRS-pose was artificially introduced due to limited BiXR space, as the hands had to be placed on the wall. The healthy subject maintained a stable posture and uniform motions. These findings highlight the functional impact of spinal deformities and demonstrate the value of this radiation-free, patient-specific pipeline for assessing compensatory mechanisms and motion in clinical practice.

Images (Optional)

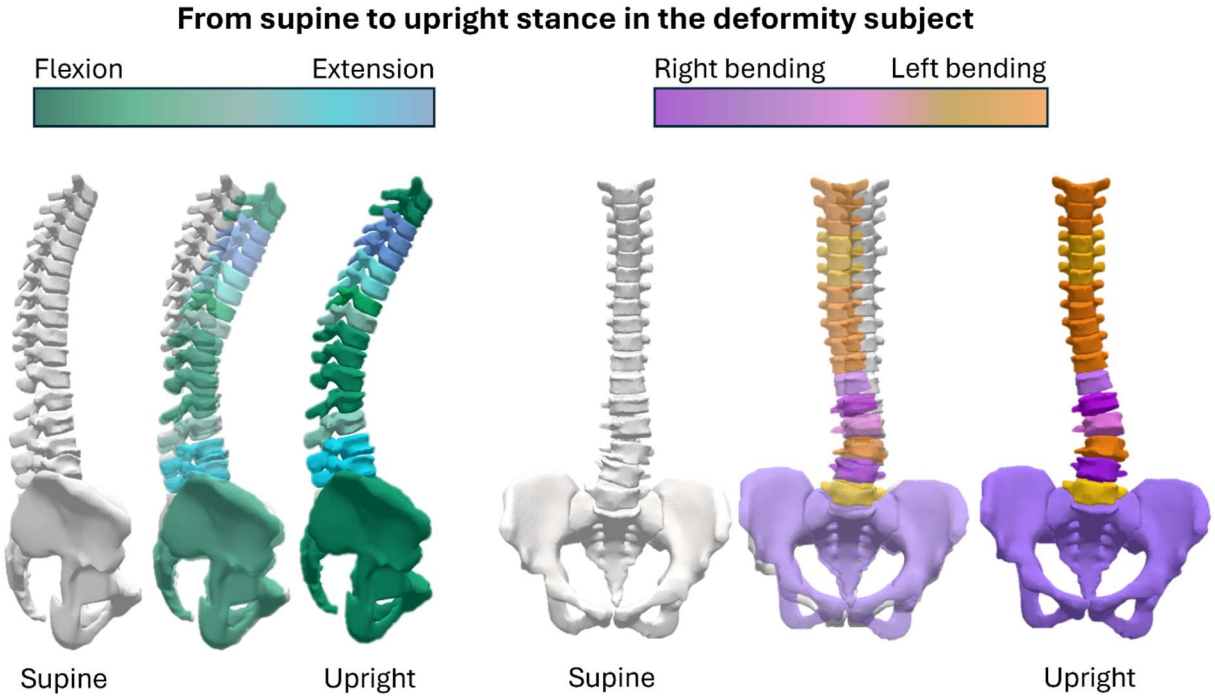


***Figure 1**: Changes in spinopelvic kinematics going from a supine to free-standing position in the spinal deformity subject.*

Acknowledgements (Optional)

The authors would like to thank Flanders' Fund for Scientific Research (1SE6225N), Internal KU Leuven C2 funds, and Medtronic for financial support.

Session Category

Orthopaedic Biomechanics: Spine

P3-282

Effects of Cervical Support Height on Neck Muscle Activity and Stiffness in Individuals With and Without Chronic Neck Pain

Mr. Chongpeng Wang

University of Michigan - School of Kinesiology, Ann Arbor, Michigan, United States

Introduction

Chronic neck pain (CNP) is a common musculoskeletal disorder that negatively impacts sleep [1]. Pillow design may modify symptoms by altering cervical alignment and neck muscle loading, yet there is little evidence to guide pillow height selection. The Set-up for Spinal Sleep (SSS) personalizes pillow height based on alignment, but its effects on neck muscle mechanics are unclear [2]. We examined how pillow heights around each person's SSS value influence neck muscle stiffness and activity during side-lying.

Methods

We examined 12 side-sleeping adults (8 with idiopathic CNP and 4 pain-free controls). Participants laid on their preferred side with individualized SSS pillow heights at 0.5×, 1.0×, and 1.5× in a randomized order. Each 5-minute side-lying trial was followed by 5 minutes of seated rest. Ultrasound shear-wave elastography quantified the change in shear-wave velocity (SWV) of the contralateral upper trapezius, levator scapulae, and sternocleidomastoid during the 5-minute trial. Surface electromyography (EMG) recorded contralateral upper-trapezius and sternocleidomastoid activity relative to relaxed sitting. Repeated-measures ANOVAs examined the effect of pillow height on these outcome measures.

Results

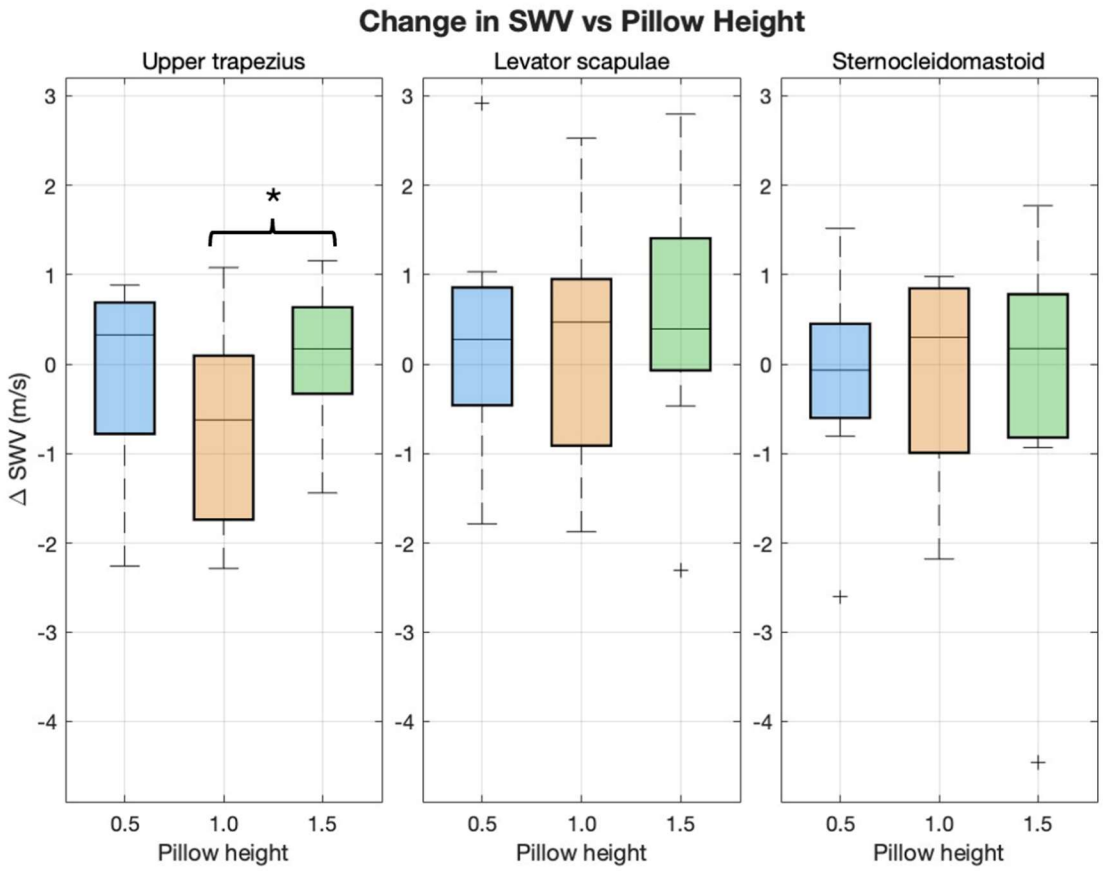
Changing pillow height between 0.5×, 1.0×, and 1.5× SSS produced small changes in ΔSWV and ΔEMG. For the upper trapezius, there was a main effect of height ($p = 0.045$), with post-hoc tests indicating greater stiffness at 1.5× than 1.0× SSS ($p = 0.013$). Pillow height did not significantly affect any other muscles' SWV or EMG measures.

Discussion

Within an individualized SSS-based range, pillow height during a short side-lying session affects the stiffness of the upper trapezius muscle. The lower ΔSWV at 1.0× and higher values at 1.5× are consistent with an intermediate height being better for preserving neutral alignment, while higher pillows may increase passive tension in the upper cervical muscles. Interpretation is limited by the small sample and pooled CNP/control data.

Ongoing recruitment will increase the total sample size to 30 participants to clarify whether individuals with CNP respond differently.

Images (Optional)



References (Optional)

[1] Chun-Yiu JP et al., Clinical Biomechanics, 2021;[2] Yamada S et al., Journal of Physical Therapy Science, 2023

Session Category

Orthopaedic Biomechanics: Spine

P3-283

A Virtual Distributed Fiber Model to Reproduce the Lumbar Intervertebral Disc Response in Experimental Spine Testing

Ms Claire Thompson[1], Dr Ryan Willing[2], Dr Stewart McLachlin[1]

[1]University of Waterloo, Waterloo, ON, Canada. [2]Western University, London, ON, Canada

Ms Claire Thompson

Dr Ryan Willing

Introduction

Pre-clinical experimental testing of spinal implants is necessary to characterize device efficacy [1]. However, a key gap in benchtop testing is the simplification of the intervertebral disc (IVD) response, which is poorly represented in pre-clinical tests like ISO12189 [2]. The goal of this study was to develop a virtual distributed fiber model that is parameterized to reproduce the IVD response of the lumbar spine in experimental spine testing. It was hypothesized that a configuration of virtual ligaments (VL) within the AMTI VIVO software could be designed to reproduce the six degree-of-freedom (6DOF) response of the IVD.

Methods

Non-linear VL fibers within the VIVO control system are represented by 1DOF springs and governed by four parameters: proximal and distal insertion coordinates, stiffness (K), and laxity (E_ref). The summed response of the individual fibers act as a 6DOF constraint in the VIVO control system.

To generate a virtual IVD, the geometry was defined based on proximal (superior) and distal (inferior) endplate coordinates using clinical CT measurements. To enable generation of 6DOF constraint forces and moments, paired VL coordinates were placed equidistantly around concentric ellipses representing the endplate surfaces with two anti-parallel VL connecting the proximal and distal coordinates at a prescribed angle to represent fibers of the annulus fibrosus. A generalized stiffness matrix of the IVD response was used to create a single targeted 6DOF force profile based on an input displacement waveform that included flexion-extension (up to ±1 deg), lateral

bending (±1.5 deg), and axial rotation (±1 deg) [3]. A custom MATLAB optimization script, informed by previous data for the IVD response, identified the best K and E_ref parameters to match the summed VL constraint forces and moments with the targeted force profile.

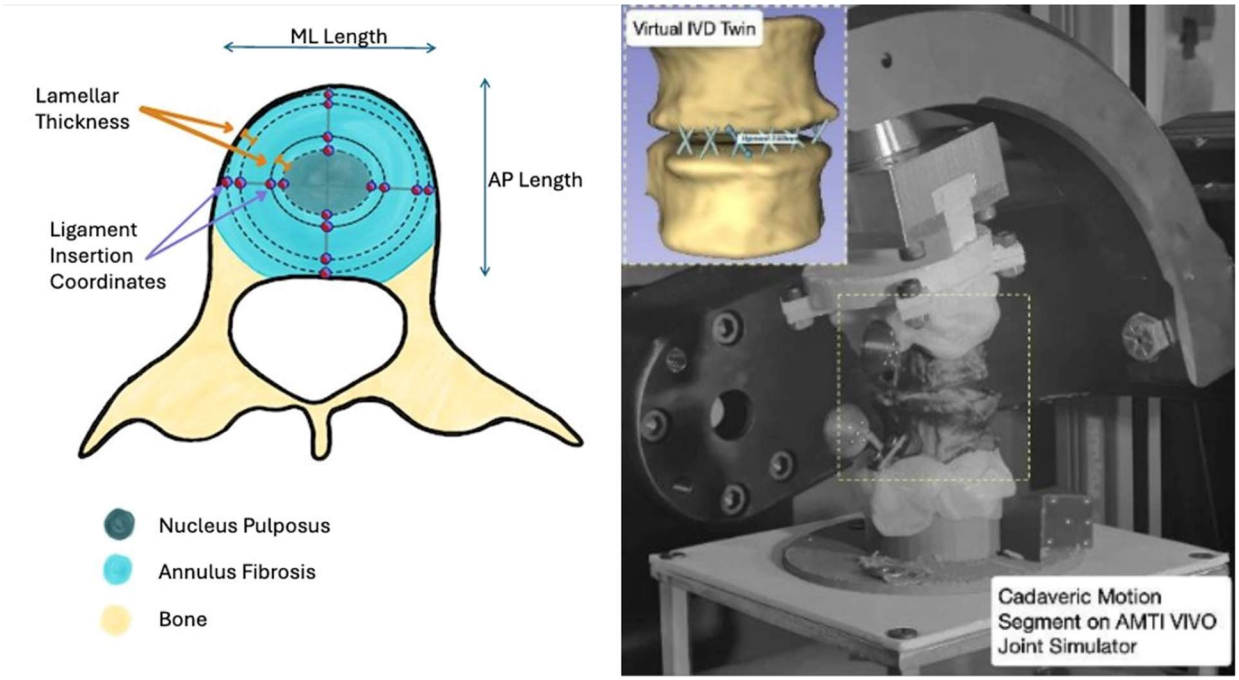
Results

At the peak displacements, the error was 0Nm for flexion/extension, 0.84Nm for lateral bending, and 0.51Nm for axial rotation between the target and the generated VL constraint moments.

Discussion

These results indicate potential of a virtual IVD in spine experiments; however, future work is needed to investigate the sensitivity of the model parameters.

Images (Optional)



References (Optional)

[1] Graham & Estes. *SAS J. (2009)*.

[2] ISO12189. International Standards (*2016*).

[3] Stokes & Gardner-Morse. J.Biomech. (*2016*).

Session Category

Orthopaedic Biomechanics: Spine

P3-284

In Vivo Assessment of Mechanical Stresses within Cervical Intervertebral Discs in One-Level and Two-Level Fusion Subjects

Ms Soumaya Ouhsousou, Mrs Clarissa M. LeVasseur, Dr. Jeremy Shaw, Dr. William Anderst, Dr. John C. Brigham

University of Pittsburgh, Pittsburgh, PA, United States

Introduction

Intervertebral disc degeneration is often related to aging and mechanical factors. Spinal fusion is the most common surgical procedure to treat symptomatic disc degeneration. However, post-surgery, patients may experience adjacent segment disease, which is assumed to be linked to the altered mechanical stresses within the cervical spine due to the fusion. To better understand how mechanical stresses change after fusion surgery and their impact on individual intervertebral discs, we developed a novel approach to estimate the intervertebral disc stresses *in vivo* using subject-specific finite element models.

Methods

3D geometries of the cervical vertebrae (C2 to C7) were extracted from CT scans. Then, intervertebral disc geometries, including annulus with embedded fibers and nucleus, facet cartilage, and ligaments were approximated. Each tissue component was assumed to be homogeneous with isotropic material properties, and material parameters were assigned to each component based on published values. Intervertebral motion data from multiple motion trials, acquired with submillimeter accuracy using biplane radiography, were then used to estimate the subject-specific spine loading to reproduce the flexion motion of the subject. Stresses within the intervertebral discs were computed and compared between pre-surgery and post-surgery spine models for both one-level (C56) and two-level (C567) fusion subjects.

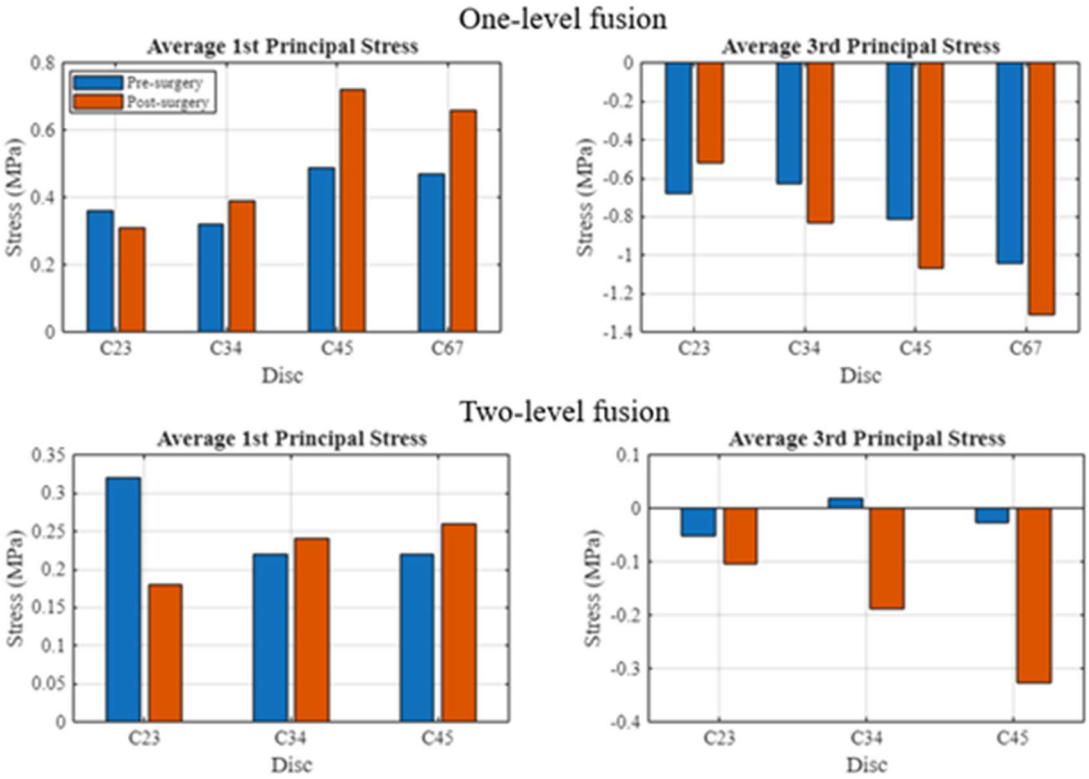
Results

Tensile and compressive stresses within the adjacent discs were higher in post-surgery compared to pre-surgery both in one-level and two-level fusion patients (Figure 1). A greater increase in the compressive stresses was observed superior to the two-level fusion compared to the one-level fusion.

Discussion

This study demonstrates an advancement in the effort to estimate *in vivo* stresses within the discs using bone kinematics obtained from biplane radiography as input to subject-specific finite element analysis. The increase of biomechanical stress within the adjacent discs in the post-surgery subject could be an important factor driving adjacent disc degeneration.

Images (Optional)



Acknowledgements (Optional)

Funding: This project was supported by a Seed/Starter Award from the Cervical Spine Research Society and a grant from the National Institutes of Health (R01AR069543).

Session Category

Orthopaedic Biomechanics: Spine

P3-285

Evaluation of Upper Instrumented Vertebra Anchor Strategies to Prevent Proximal Junctional Fracture Following Adult Spinal Deformity Surgery Using Bone Microfracture Analysis

Mr. Tomoya Aki MS[1], Dr. Yusuke Hori PhD, MD[2], Dr. Takashi Namikawa PhD, MD[2], Dr. Akira Matsumura PhD, MD[2], Mr. Humiaki Oomoto[3], Prof. Daisuke Tawara PhD[4]

[1]Graduate School of Advanced Science and Technology, Ryukoku University, Otsu, Shiga, Japan. [2]Scoliosis Center, Osaka City General Hospital, Osaka, Osaka, Japan. [3]Department of Mechanical Engineering and Robotics, Otsu, Shiga, Japan. [4]Department of Mechanical Engineering and Robotics, Ryukoku University, Otsu, Shiga, Japan

Introduction

Proximal junctional fracture (PJFr) is a critical complication following adult spinal deformity (ASD) surgery and often leads to vertebral collapse requiring revision surgery [1]. Although surgical techniques have advanced, the optimal fixation strategy at the upper instrumented vertebra (UIV) remains unclear. We hypothesized that both the length and direction of pedicle screw (PS) insertion at the UIV significantly affect stress distribution and the risk of microfracture. This study aimed to biomechanically evaluate UIV screw configurations using finite element (FE)–based bone microfracture analysis.

Methods

Four finite element (FE) models of ASD surgery from T7 to the pelvis, with posterior instrumentation from T9 to the pelvis, were constructed based on patient CT data. At the UIV, three different screw lengths (short, medium, and long for horizontal direction) and different insertion direction (caudal direction) were simulated. Vertebrae were assigned a heterogeneous Young's modulus distribution to reflect realistic bone quality [2]. Microfracture analysis was performed [3] using gradually increasing compressive loads applied to the cranial endplate, while the pelvis was constrained [4] using Mechanical Finder software (RCCM Co., Ltd., Japan).

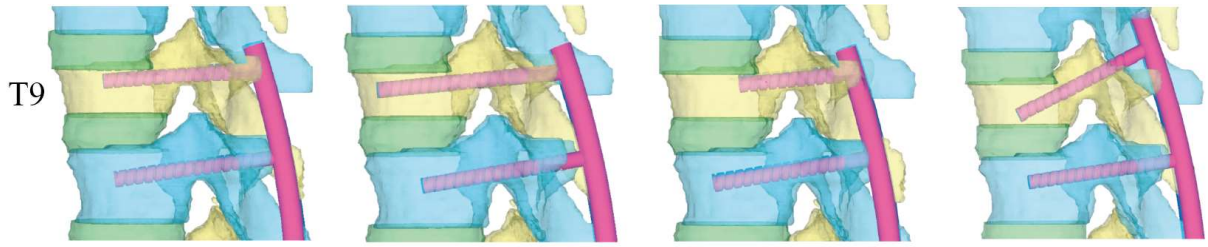
Results

Short screw models showed widespread occurrence of microfracture elements across T9, whereas long screw models demonstrated limited and localized failure. Caudally directed screws distributed mechanical stress more broadly within the vertebra, leading to a lower concentration at the bone–screw interface. In contrast, horizontally directed and shorter screws exhibited increased stress concentration and greater accumulation of microfracture elements.

Discussion

Longer pedicle screws inserted in a caudal direction at the UIV may reduce the risk of PJFr by enhancing load distribution and decreasing stress concentration due to wider contact area of bone and the screw where they are important for load transfer and support. This fixation strategy may contribute to improved mechanical stability at the proximal junction and represents a promising approach for preventing PJFr in ASD surgery.

Images (Optional)



Four FE models of ASD surgery (Types of (a): medium, (b): long and (c): short lengths for horizontal direction, and (d): caudal direction)

References (Optional)

[1] A. Matsumura *et al.*, Asian Spine J, 2018

[2] Joyce H. Keyak *et al.*, J Biomechanics, 1998

[3] M. Bessho *et al.*, J Biomechanics, 2007

[4] T. Hato *et al.*, J Orthop Sci, 2007

Session Category

Orthopaedic Biomechanics: Spine

P3-286

qCT-Based Nonlinear Finite Element Modelling Reveals Hidden Mechanical Vulnerability Patterns in Vertebrae with Metastatic Lesions

Dr Rajdeep Ghosh PhD, Postdoctoral Research Associate[1,2], Mr Eddie Shearman MEng[1,2], Dr Marco Palanca PhD, Associate Professor in Biomechanics[3], Dr Enrico Dall'Ara PhD, Professor of Musculoskeletal Biomechanics[1,4], Dr Damien Lacroix PhD, Professor of Mechanobiology[1,2]

[1]Insigneo Institute, University of Sheffield, Sheffield, South Yorkshire, United Kingdom. [2]School of Mechanical, Aerospace and Civil Engineering, University of Sheffield, Sheffield, South Yorkshire, United Kingdom. [3]Department of Industrial Engineering, Alma Mater Studiorum-University of Bologna, Bologna, Emilia-Romagna, Italy. [4]Division of Clinical Medicine, School of Medicine & Population Health, University of Sheffield, Sheffield, South Yorkshire, United Kingdom

Dr Rajdeep Ghosh

Mr Eddie Shearman

Dr Marco Palanca

Dr Enrico Dall'Ara

Introduction

Spinal Instability Neoplastic Score (SINS) helps to assess the effect of lesion on vertebral instability when the score is either low (0–6; stable) or high (13–18; unstable). It has less clinical value in the intermediate range. Biomechanical computational studies [1-2] have been limited to isolated lesion types or vertebral bodies, lacking direct comparison between metastatic vertebrae and their controls (adjacent healthy vertebrae). This study introduces **densitometrically calibrated quantitative Computed Tomography (qCT)-to-Finite Element (FE) pipeline** to assess how lytic, blastic, and mixed metastatic

phenotypes differentially modulate vertebral strength and strain distribution using a unique paired design.

Methods

Twelve human spine segments, each containing one metastatic vertebra and one adjacent lesion-free control, were scanned using qCT. Lesions were classified: lytic (n=6), blastic (n=1), or mixed (n=5). Subject-specific vertebral geometries were segmented and meshed (10-noded tetrahedra). Heterogeneous, density-dependent elasto-plastic isotropic material properties were assigned using qCT-calibrated Bone Mineral Density (BMD) [3]. Models were subjected to quasi-static axial compression until 1.9% apparent strain [1]. **Failure load(FL)** and **strain distributions** were computed. **Normalised intra-segment strength metric** (metastatic'FL/control'FL) was used to isolate lesion-specific biomechanical effects from inter-patient variability.

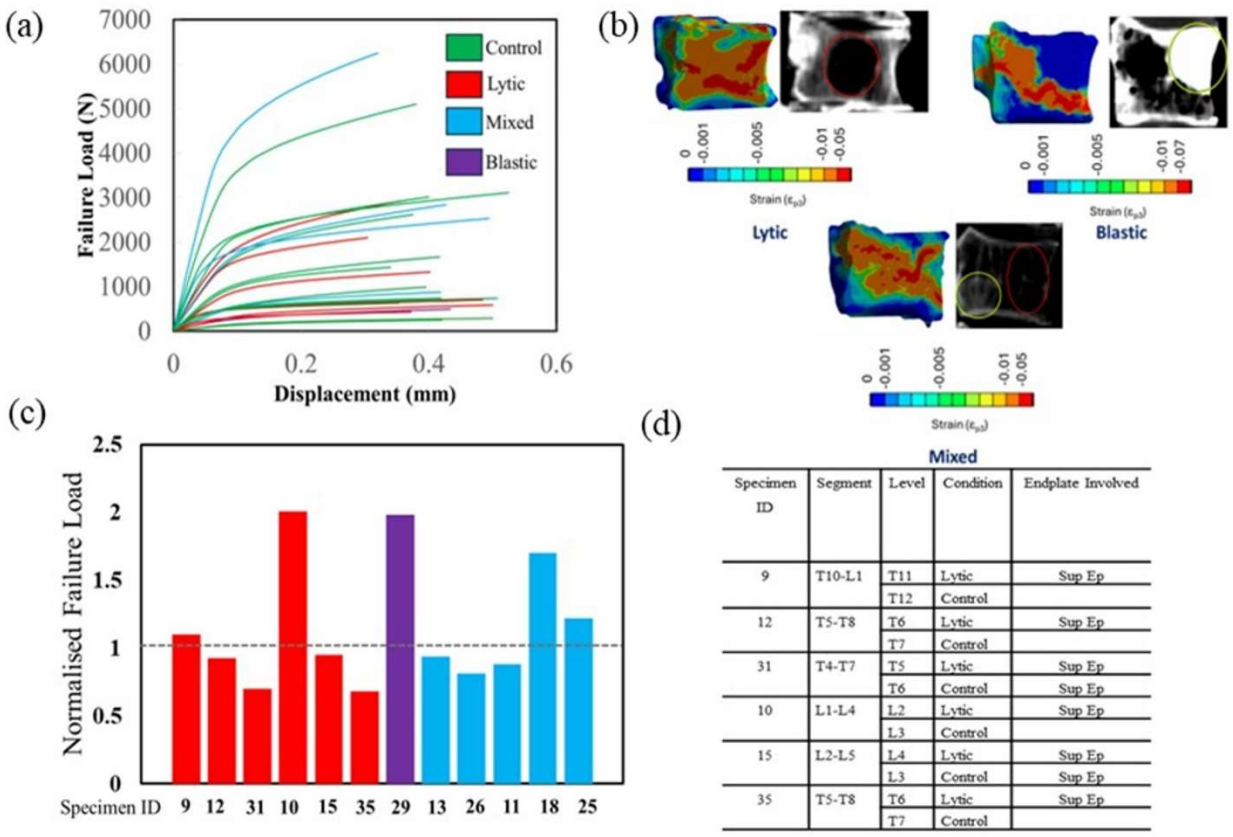
Results

Predicted failure loads between metastatic and controls showed no significant differences overall ($p>0.05$), but varied by lesion type (Lytic: 1.3±0.9 kN; Mixed: 2.6±2.2 kN; Blastic: 0.5 kN). However, **Normalised Failure Load** (Fig.1) varied widely **(−32% to +102%)**, reflecting lesion-specific behaviour. Lytic lesions predominantly reduced strength (<1 in 4/6 cases); the blastic case showed marked strength increase, and mixed lesions were variable. High compressive strains (>0.019) were **frequently concentrated near endplates** (14/24 vertebrae), especially in lytic cases, indicating under-recognised failure mechanism not captured by current clinical scoring. Notably, in blastic lesion, high-strain regions clustered away from sclerotic areas due to local load-shielding.

Discussion

This study shows lesion-induced load redistribution governing vertebral strength, revealing vulnerabilities like endplate-driven failure. These insights highlight SINS limitations and support subject-specific FE modelling as more robust quantitative tool for fracture-risk evaluation and digital-twin-based personalised oncology.

Images (Optional)



Specimen ID	Segment	Level	Condition	Endplate Involved
9	T10-L1	T11	Lytic	Sup Ep
		T12	Control	
12	T5-T8	T6	Lytic	Sup Ep
		T7	Control	
31	T4-T7	T5	Lytic	Sup Ep
		T6	Control	Sup Ep
10	L1-L4	L2	Lytic	Sup Ep
		L3	Control	
15	L2-L5	L4	Lytic	Sup Ep
		L3	Control	Sup Ep
35	T5-T8	T6	Lytic	Sup Ep
		T7	Control	

Figure 1. (a) Response of the tested vertebra to compression; (b) Representative strain distribution plots with peak strain initiation; (c) Normalised failure load; (d) Endplate involvement in vertebrae with lytic lesions

References (Optional)

[1]Costa *et al.*, JMBBE, 2019

[2]Stadelmann *et al.*, Bone, 2020

[3]QRM European Spine Phantom

Acknowledgements (Optional)

METASTRA(EU H2022:101080135;UK Guarantee: 10075325), Metaspine(MSCA-IF-EF-ST, 832430/2018).

Session Category

Orthopaedic Biomechanics: Spine

P3-287

Pre-Clinical Assessment of a New Bioceramic Cage for Spinal Interbody Fusion

Mr Davide Ninarello MSc.Eng., Associate Professor Luigi La Barbera PhD

Deptartment of Chemistry, Materials and Chemical Engineering “G.Natta”, Politecnico di Milano, Milan, Italy, Italy

Introduction

Lumbar interbody fusion (LIF) is the gold-standard treatment for severe degenerative disc conditions. Bioceramics are a promising emerging alternative to address the limitations of standard Ti6Al4V and PEEK materials. However, their brittleness requires careful design to ensure sufficient strength under complex spinal loadings. This study aims to perform a comprehensive in-silico pre-clinical assessment of a new bioceramic cage both under realistic post-surgical conditions and standard testing.

Methods

A calibrated transversely isotropic constitutive model described the ceramic’s mechanical behaviour. The cage geometry, previously optimized, consisted of a lateral LIF cage featuring one longitudinal and one transverse hole. Two finite element models were developed to assess its mechanical resistance.

(1) A lateral LIF surgery at the L4–L5 undergoing combined functional loadings (Fig.1A)[1]. Range of Motion (RoM) and the percentage of cage failed volume, comparing numerical strain with the material limit, were extracted.

(2) An in-silico replica of ASTM F2077-18 standard tests (Fig.1B) evaluating cage strength under axial compression, torsion, and shear, yielding the corresponding failed volume percentage.

Results

The LIF model, validated against experimental in-vitro data [2], demonstrated that surgery reduced RoM by over 85% relative to the intact model (Fig.1C). Failed volume remained below 5% across all motions, with flexion being the most critical (Fig.1D).

In standard testing conditions, the cage showed <1% failed volume (Fig.1E), considering the forces acting on the cage obtained from LIF model and in-vitro tests [2].

Discussion

The bioceramic cage withstood typical post-surgical loads, showing minimal failed volume, mainly influenced by the sharp cage–vertebra interface. Under standard testing, the cage exceeded ISO 23089-2:2021 acceptability criteria, based on over-dimensioned titanium cages, imposing unrealistically high forces. Under realistic loads, the ceramic cage consistently showed <1% failed volume.

In conclusion, the bioceramic cage successfully passed both functional spinal loadings and the in-silico standard tests, supporting its suitability for prototyping and further experimental validation.

Images (Optional)

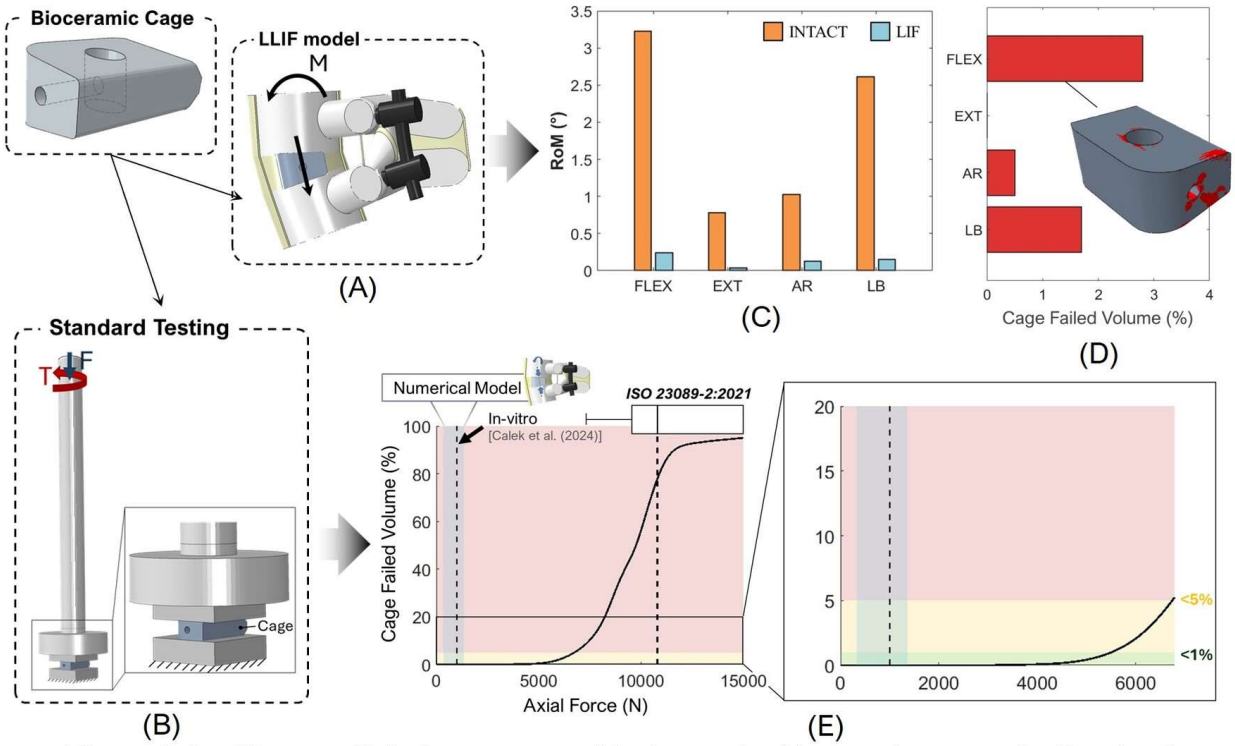


Figure 1: In-silico pre-clinical assessment of the innovative bioceramic cage under functional loadings and standard testing (representative results under axial compression).

References (Optional)

1. Dreischarf et al., J Biomech, 2014

2. Calek et al., Spine J, 2024

Session Category

Orthopaedic Biomechanics: Spine

P3-288

Rapid intradiscal pressurization consistently induces clinically relevant posterior ring fractures in the spine

Dr John McMorran PhD[1], Ms Olena Klahsen MSc[2], Ms Aliza Siebenaller MSc[3], Mr Andra Neptune BSc[1], Mr Noah Chow MSc[1], Dr Stephen Brown PhD[3], Dr Diane Gregory PhD[1]

[1]Wilfrid Laurier University, Waterloo, Ontario, Canada. [2]University of Ottawa, Ottawa, Ontario, Canada. [3]University of Guelph, Guelph, Ontario, Canada

Dr John McMorran

Introduction

Apophyseal ring fractures occur primarily in adolescent populations and are typically associated with high-loading scenarios such as sports participation or motor vehicle accidents. Although these injuries are externally driven, the underlying fracture mechanism is thought to involve rapid intradiscal pressurization that develops in response to sudden external loading. The aim of this study was to determine whether ex vivo rapid intradiscal pressurization led to fracture patterns assessed using micro computed tomography (CT) that mirrored clinical observations.

Methods

Six motion segments were excised from porcine cervical spines and further dissected to remove the posterior elements. Each motion segment then underwent a previously established rapid intradiscal pressurization protocol [1]. Briefly, a needle attached to a hydraulic pump was inserted anteriorly into the disc and positioned at the centre of the nucleus pulposus. Fluid was slowly injected until resistance was felt, then additional fluid was rapidly injected by forcefully depressing the pump handle. An in-series pressure transducer recorded intradiscal pressure throughout testing. Following pressurization, each motion segment was scanned using micro-CT and three independent raters classified fracture types according to the Takata classification [2] using reconstructed volumes and 3D renders.

Results

All six motion segments developed Type I apophyseal ring fractures following rapid intradiscal pressurization. Type I is defined as an arc-shaped (arcuate) fracture of the posterior cortical rim of the vertebra, without extension into the cancellous bone of the vertebral body (Figure 1). Further, all fractures occurred in the superior vertebra of the motion segment.

Discussion

These findings demonstrate that rapid intradiscal pressurization reliably produces posterior apophyseal ring fractures ex vivo, and that the resulting injuries closely mirror clinically observed Type I fractures in CT imaging. The consistent reproduction of arcuate cortical rim fractures strongly favours the use of this model for future inquiry into this fracture pattern and provides further evidence to support the hypothesis that sudden external loading such as that experienced during sports or trauma, results in a transient spike in disc pressure that concentrates stress at the posterior vertebral rim leading to failure.

Images (Optional)

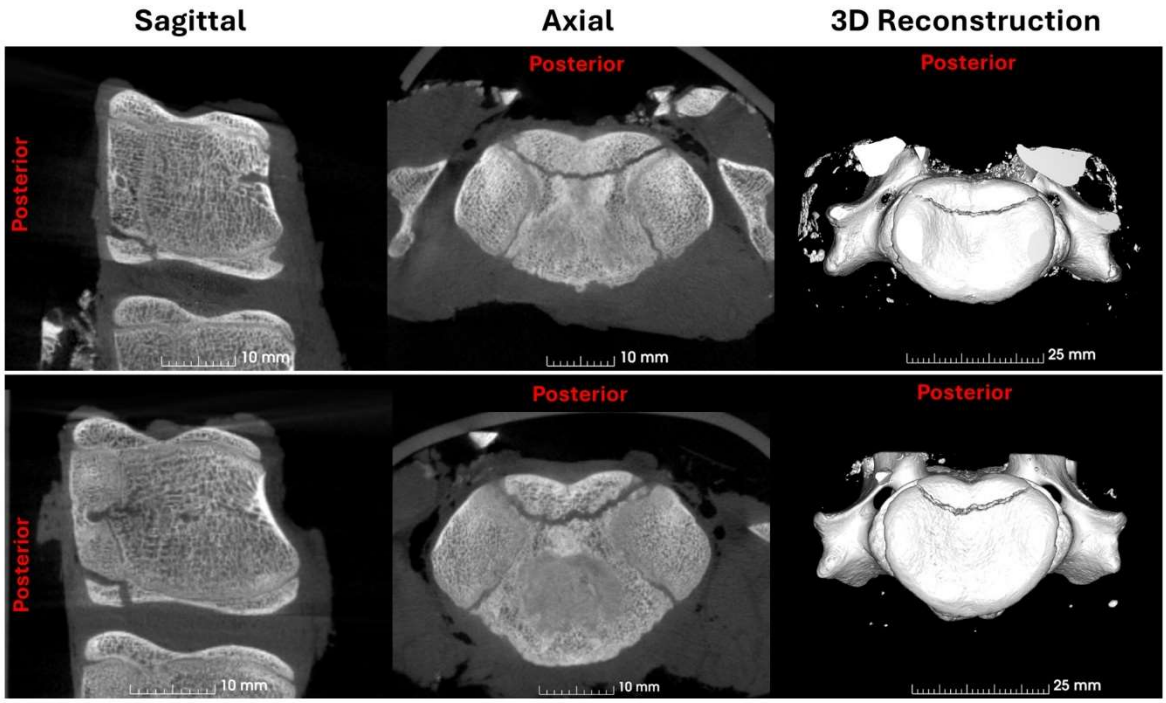


Figure 1. Two samples with Type I posterior apophyseal ring fractures. The arcuate fracture line is visible in both the axial and 3D reconstruction views. In the sagittal view, the fracture is in the posterior region of the superior vertebra and confined to the cortical rim.

References (Optional)

[1] Stephen Brown *et al.,* J. Biomech. 2008

[2] Keiichi Takata *et al*., J Bone Joint Surg. 1988

Session Category

Orthopaedic Biomechanics: Spine

P3-289

Impact of Retroverted Tilt on Facet Joint Stability and Annulus Fibrosus Microdamage in a Porcine Model

MSc Parisa Akhlaghi[1], PhD Remco Doodkorte[1], PhD Bert van Rietbergen[1], MD, ScD Keita Ito[1,2], Mrs. Federica Incatasciato[1]

[1]Eindhoven University of Technology, Eindhoven, Noord Brabant, Netherlands. [2]University Medical Center Utrecht, Utrecht, Utrecht, Netherlands

Introduction

Adolescent idiopathic scoliosis (AIS) involves asymmetric adaptation that alters posture and produces a three-dimensional deformity. As the disease and our upright posture are unique to humans, the latter may initiate the former by retroverting spinal segments and imposing dorsal shear loads on it. Although facet joints normally stabilize spinal rotation, dorsal shear forces may disengage them and amplify the rotational instability. During adolescence, increased loading with retroversion and rotational instability may accelerate annulus fibrosus (AF) microdamage and eventual deformity of the intervertebral disc. This study aimed to investigate whether retroverted tilt (1) promotes facet joint unlocking and (2) induces microdamage in the AF.

Methods

18 fresh-frozen porcine spines (T10-13) are tested in a 6-DOF spine testing system to apply 200 N load and ±7.5 Nm cyclic axial rotation with three inclination angles: 0°, 15° and 25° to induce retroversion (Fig 1). Range of Motion (RoM), Neutral Zone (NZ) and NZ stiffness are measured. Individual vertebrae are tracked by LED-marker triplets over the entire RoM to calculate the instantaneous center of rotation (ICR) and level-specific rotations. Rotational instability is defined as increased RoM and NZ, reduced NZ stiffness, and larger shifts in ICR. T11–T12 segments are fixed in 3.7% formaldehyde, decalcified in 0.5 M EDTA, paraffin embedded and sectioned for microdamage analysis using F-CHP staining. The correlation between mechanical outcomes and AF damage is studied to evaluate associations between retrotilt and damage.

Results

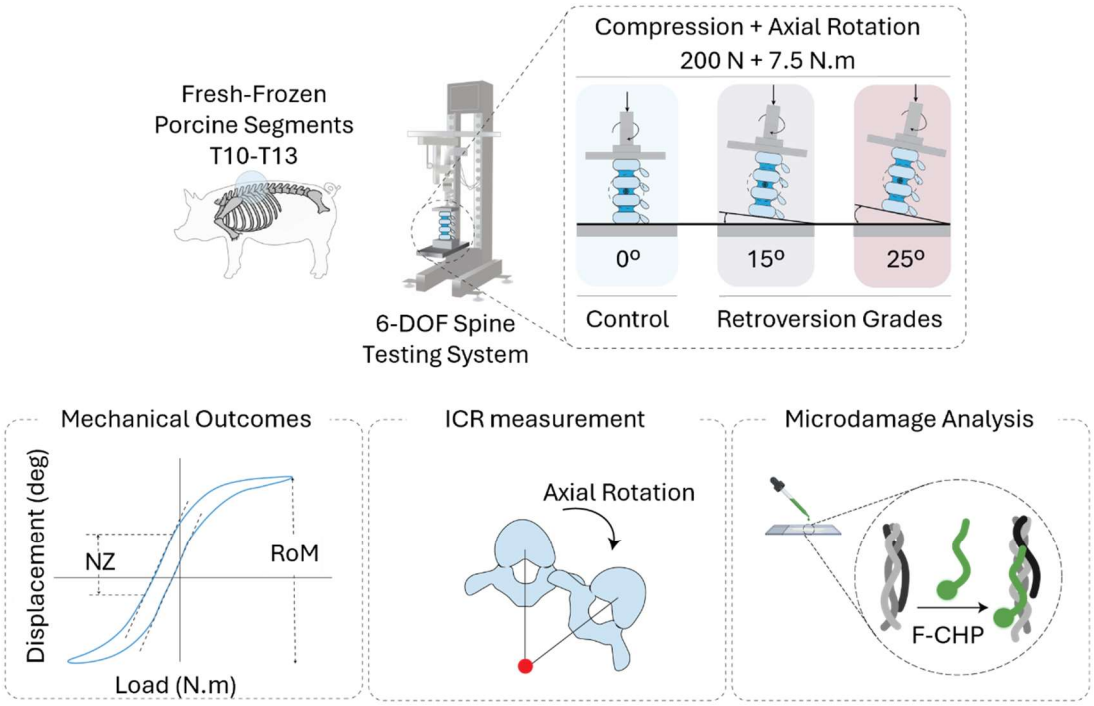
In initial testing, inclining the spine by 15° only slightly increased total RoM but substantially, increased the NZ (2.4° to 8.0°) and reduced NZ stiffness (0.37 to 0.29

N·m/deg). Comparing adjacent-level rotations showed a shift in the location of maximum rotation; T10–T11 at 0° (ROM=15°), whereas T12–T13 at 15° inclination (ROM=10°).

Discussion

Introducing 15° retroversion changed both the magnitude and distribution of motion by increasing NZ, decreasing NZ stiffness, and shifting max rotation from the upper to the lower adjacent level. Currently, more samples and inclusion of 25° retroversion are being conducted. Quantification of the ICR and assessment of microdamage in AF, to better connect the mechanical changes to the structural deformity, will complete the study.

Images (Optional)



Session Category

Orthopaedic Biomechanics: Spine

P3-290

Translating Spine Biomechanics From Animal Trials to Humans Through Parametric Finite Element Models

Dr. Joeri Kok[1], Dr. Bert van Rietbergen[1], Prof. Dr. Moyo Kruyt[2], Prof. Dr. Gabriëlle Tuijthof[3], Dr. Malte Asseln[3]

[1]Eindhoven University of Technology, Eindhoven, N/A, Netherlands. [2]University Medical Center Utrecht, Utrecht, N/A, Netherlands. [3]University of Twente, Enschede, N/A, Netherlands

Introduction

The biomechanical performance and safety of spinal implants, e.g., growing rods for scoliosis correction, or cages for intervertebral fusion, are typically evaluated in preclinical animal experiments. However, due to the unique anatomy and function of the human spine, it is not ultimately valid to transfer results from animal models directly. Finite element (FE) models can be employed to study spinal biomechanics in animals and humans. However, differences in models can easily lead to variation in predicted outcomes.

In this study, we aimed to develop a parametric model that can be used to generate meshes for FE models of human and porcine spines. This way, transferability is improved. This can help us translate preclinical data to clinical to improve safety for both humans and animals.

Methods

A parametric model previously developed to create FE models of the human spine has been adapted to also allow for the replication of porcine spines. In the updated model, the number of vertebrae are not limited, and angles and height of the transverse processes and curvature of the facet joints can be added as input. One CT of an adult human with available segmentation of vertebrae [1] and one CT of an 8-month-old Göttingen minipig, where vertebrae were semi-automatically segmented, were used (figure). Morphological parameters were measured from the segmentations and used to automatically generate a mesh of the spine, including vertebrae, intervertebral discs, endplates, and facet joints.

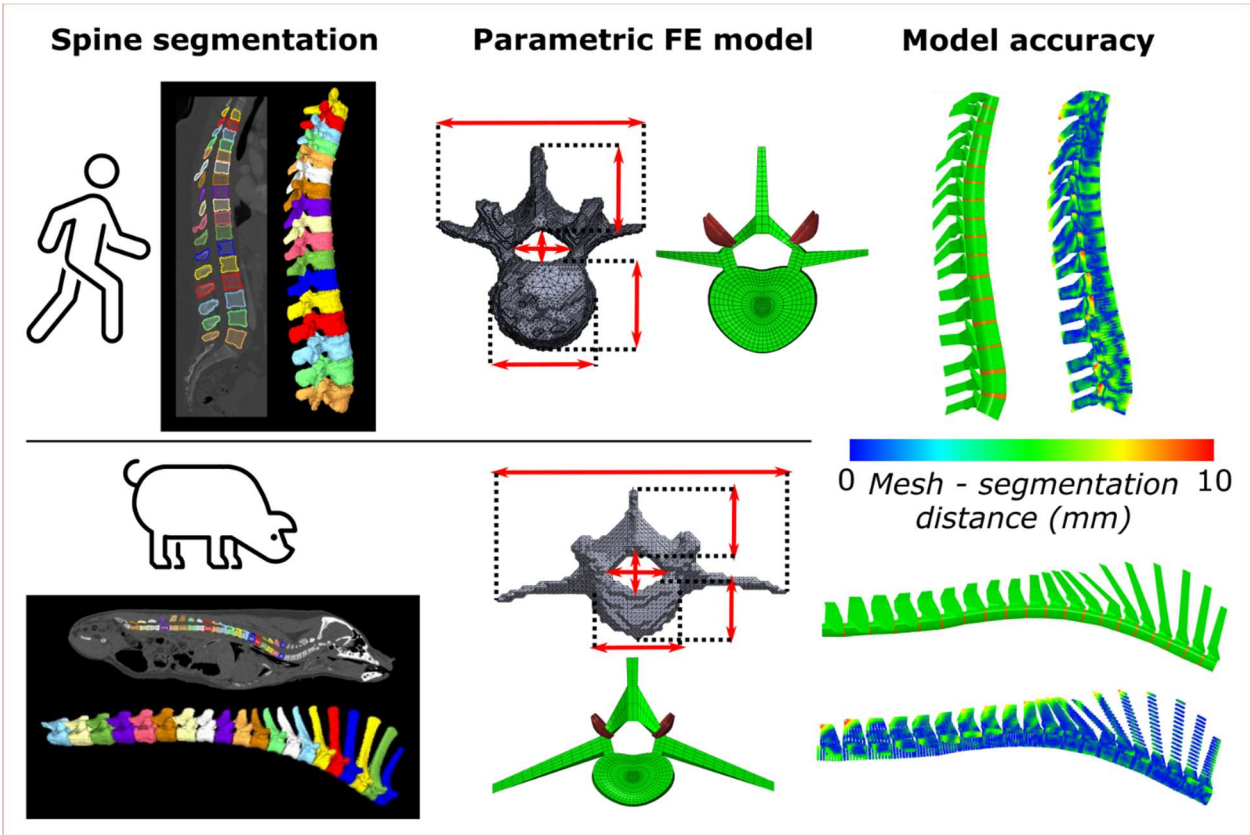
Results

The mean distance remaining between the resulting mesh and the original segmentation was 2.8 ± 2.0 mm for the human spine and 1.3 ± 0.9 mm for the minipig spine (figure). Largest deviations occurred at the ends of the spinous and transverse processes.

Discussion

The multispecies parametric model gives good geometric correspondence for the whole spine, most importantly also capturing changes in spinal curvature and axial rotation, enabling the study of spinal deformities. Furthermore, a robust option for including subject-specific facet joints, including asymmetry, has been added. This way, the accuracy of the modelled load transfer between vertebrae is ensured.

Images (Optional)



References (Optional)

[1] Jianhua Yao et al., Comput Med Imaging Graph. 2016

Acknowledgements (Optional)

This work is part of the project DYNACURE (20832) of the open technology programme financed by the Dutch Research Council (NWO).

Session Category

Orthopaedic Biomechanics: Spine

P3-291

Predicting Growth and Correction of Scoliosis With a Double Spring Reduction System

Dr. Joeri Kok[1], Dr. Bert van Rietbergen[1], Mr. Abdiqani Abdi[2], Ms. Marieke Wesselink[3], Prof. Dr. Moyo Kruyt[2], Prof. Dr. Gabriëlle Tuijthof[3], Dr. Malte Asseln[3]

[1]Eindhoven University of Technology, Eindhoven, N/A, Netherlands. [2]University Medical Center Utrecht, Utrecht, N/A, Netherlands. [3]University of Twente, Enschede, N/A, Netherlands

Introduction

Adolescent idiopathic scoliosis (AIS) is a progressive 3D deformity of the spine often ending in some treatment through correction and spinal fusion. In the past years, non-rigid fixation through a spring distraction system allowing for continuous growth and correction of the curvature has reached the clinics. As a recent advancement, torsional springs have been added to create a double spring reduction (DSR) system, countering axial rotation in addition to correcting the coronal curvature. Currently, no method exists to patient-specifically predict how much force is required to obtain optimal correction. This is partly due to the complexity of predicting the early adaptations of the spine after surgery.

In this study, we aim to calibrate and validate a 3-step finite element (FE) modelling approach to predict scoliosis correction with a DSR system. Models are calibrated and validated against an *in vivo* Göttingen minipig scoliosis model.

Methods

The FE model is created from CT images after induction of scoliosis, before surgical correction. Individual vertebrae are segmented, reconstructed in 3D, measured, and meshed using a previously developed parametric model [1]. The simulations consist of 3 steps (figure): immediately post-surgery, where the spine deforms due to elasticity following 75 N distraction forces and 2 Nm torsion applied through the springs; relaxation and remodelling of the soft tissue, represented with viscoelastic material properties; and asymmetric growth due to pressure on the growth plates. Each step is independently validated, respectively, through post-op x-ray images and a CT at termination.

Results

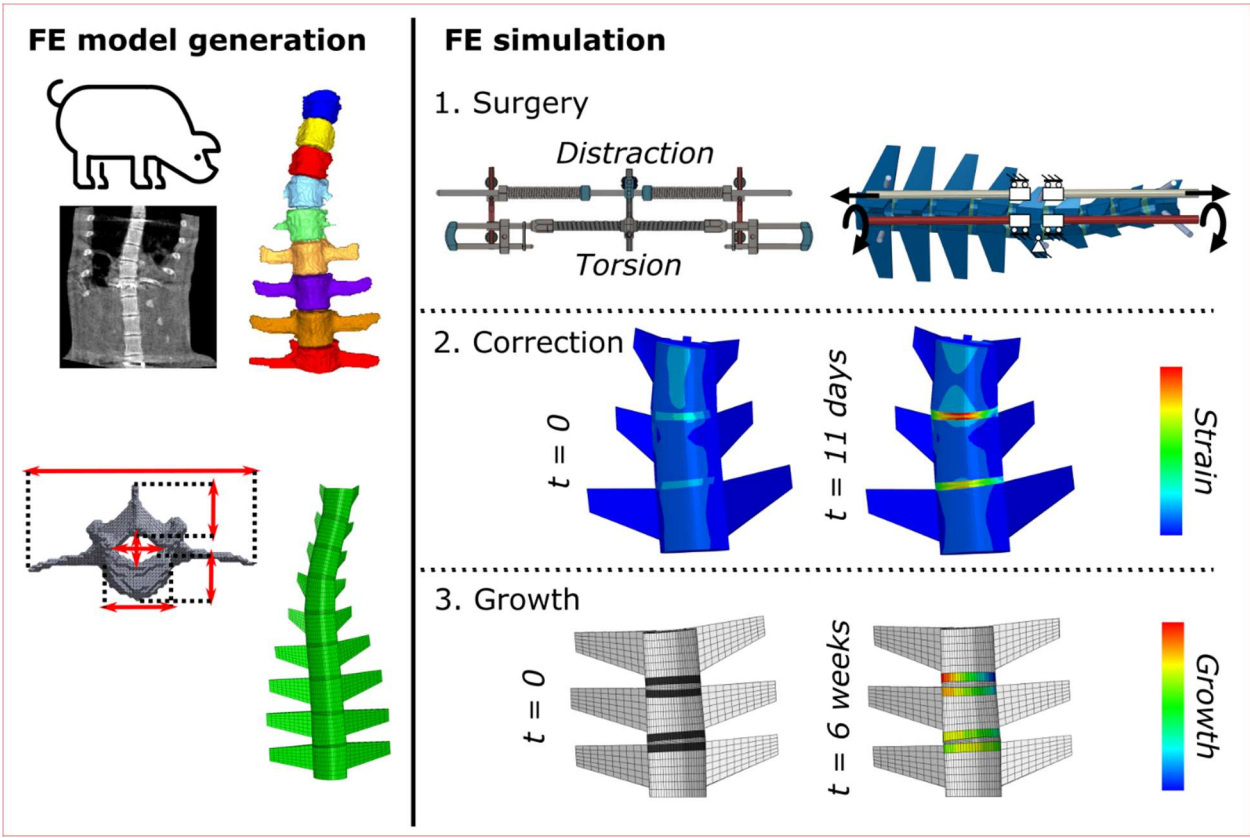
Before calibration of the correction and growth parameters in the FE model, from a baseline Cobb angle (22.9°) and axial rotation (11.8°), reduction was calculated directly

post-surgery (20.3° and 9.7°), after 11 days of correction (17.3° and 7.2°), and after 6 weeks of growth (16.8° and 7.1°).

Discussion

Calibration of the correction and growth steps in the FE model will follow from planned *in vivo* studies in the first half of 2026. With more insight into the individual correction phases, patient-specific optimization of the spring loads to be applied can be performed. This way, patient outcomes will improve, and complications can be prevented.

Images (Optional)



References (Optional)

[1] Gerdine Meijer et al., Spine, 2011

Acknowledgements (Optional)

This work is part of the project DYNACURE (20832) of the open technology programme financed by the Dutch Research Council (NWO).

Session Category

Orthopaedic Biomechanics: Spine

P3-292

Biomechanical Design and Analysis of Porous Compliant Flexures for Cervical Artificial Disc Replacement

Mr Jonah Leinwand, Dr Mihaela Vlasea, Dr Stewart McLachlin

University of Waterloo, Waterloo, Ontario, Canada

Introduction

Adjacent segment disease (ASD) is a common problem following spinal fusion surgery, where the mechanical mismatch between the stiffness of rigid implant materials and the surrounding bone and joint tissues can accelerate degeneration at the untreated levels. To address this, we have previously explored design of compliant implants for cervical artificial disc replacement (c-ADR), consisting of thin flexural members, to reduce stiffness [1]; however, to date, there have been no biomechanical investigations combining this concept with porous structures. The goal of this study was to design, manufacture, and test porous compliant flexures (PCF), additively manufactured in a titanium alloy using laser powder bed fusion (PBF-LB), to explore the mechanical response of PCF-based implants under physiologically-relevant loads.

Methods

PCF were designed using nTopology software (nTop, NY). Hollow, gyroid-, schwarz- and auxetic-latticed flexures were printed (n=3) in Ti6Al4V via PBF-LB (EOSM290). Implants were designed with PCF elements 1mm-thick in diameter, with a 0.3mm shell filled with latticed material or a hollow gap. Depowdering holes were added on endplates for removal of loose powder. The implants' mechanical response were tested based on applied physiologic loading values reported for the cervical spine to mimic the targeted application of c-ADR. Designs were tested in compression (up to 30% strain) and flexion-extension bending (up to 6°) on the AMTI VIVO joint motion simulator. Flexural displacements and strains were measured using the ARAMIS 3D digital image correlation system.

Results

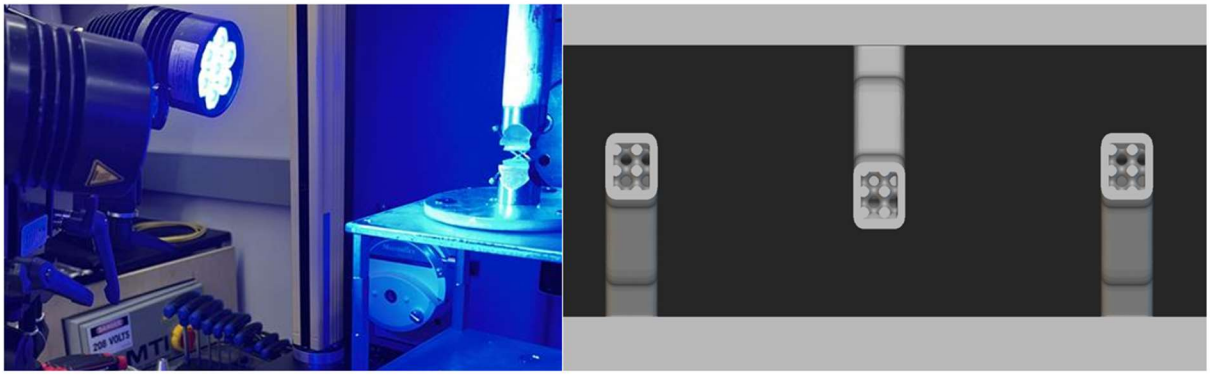
Latticing and hollowing the PCF elements' interior maintained the strength of the implant compared to a solid infill design. All three latticed infills increased the compressive stiffness of the PCF elements compared to the solid infill design. Solid (11.4kN/mm), gyroid

(17.6kN/mm), schwarz (26.7kN/mm), auxetic (37kN/mm), and hollow (3.8 kN/mm). All flexures could bend 6° in both flexion and extension without signs of failure or cracking.

Discussion

Ongoing work is investigating failure mechanisms of the flexures, including finite-element modelling of crack propagation **in the PCF** titanium structures under physiologically-relevant loading. This failure analysis **is a critical step before future clinical studies,** aimed at addressing issues related to ASD following spine surgery**.**

Images (Optional)



Testing setup for measuring stiffness of the porous compliant flexures (left) and an example of their external structure for a schwarz-latticed PCF sample (right)

References (Optional)

[1] J Leinwand et al., HI-AM Conf. Proceedings, 2025

Session Category

Orthopaedic Biomechanics: Spine

P3-293

Pelvic Rigidity and Gait Performance in Older Adults With Degenerative Lumbar Disease

PT Jr-Shiuan Lin

National Taiwan University, Taipei, Taipei, Taiwan

Introduction

Elders with degenerative lumbar disease (DLD) often limit pelvic movement during walking because of pain. Since pelvic motion plays a key role in dynamic stability and gait control, reduced pelvic mobility could impact overall walking performance. The purpose of this study was to compare pelvic rigidity, pelvic tilt excursion, and spatiotemporal gait characteristics between elders with DLD and healthy elders.

Methods

Twenty-five DLD patients and twenty-five healthy elders performed a ten-meter walk at a self-selected pace. Pelvic motion was assessed using an inertial measurement unit placed over the pelvis that recorded accelerations in the anteroposterior, mediolateral, and vertical directions. Pelvic rigidity was quantified using root mean square acceleration. Pelvic tilt excursion in anteroposterior, mediolateral, and rotational directions was calculated as the angular range within each gait cycle. Spatiotemporal gait parameters, including cadence, step length, stride length, step width, and velocity, were obtained using OpenCap motion capture. Group differences were examined with the Mann-Whitney U test(alpha=0.05).

Results

Pelvic RMS acceleration showed significant group differences in all directions. The DLD group exhibited lower anteroposterior RMS acceleration (2.81 ± 1.60 vs. 4.59 ± 1.01 m/s^2, $p < .001$), mediolateral RMS acceleration (1.80 ± 1.03 vs. 2.57 ± 0.54 m/s^2, $p = .002$), and vertical RMS acceleration (8.09 ± 4.32 vs. 15.04 ± 2.02 m/s^2, $p < .001$). Pelvic mediolateral excursion was significantly smaller in the DLD group (12.21 ± 3.36° vs. 14.28 ± 3.56°, $p = .040$), as was pelvic rotational excursion (6.09 ± 1.31° vs. 7.91 ± 1.56°, $p < .001$). Cadence was significantly lower in the DLD group compared with controls (108.74 ± 12.85 vs. 119.41 ± 13.13 steps/min, $p = .007$). Stride length was also significantly reduced in the DLD group (1.21 ± 0.12 vs. 1.31 ± 0.16 m, $p = .011$).

Discussion

Elders with DLD showed lower pelvic RMS acceleration and reduced mediolateral and rotational excursion, indicating more restricted pelvic motion during walking. These mobility limitations were accompanied by lower cadence and shorter stride length. Therefore, these findings suggest that DLD is associated with decreased pelvic movement and alterations in gait strategy. Interventions aimed at improving pelvic mobility may be beneficial for enhancing gait function in patients with DLD.

Acknowledgements (Optional)

This work was supported by the National Science and Technology Council (NSTC 114-2221-E-002 -086 -MY3) awarded to Dr. Wei-Li Hsu.

Session Category

Orthopaedic Biomechanics: Spine

P3-294

Biomechanical Evaluation of Anti-Migration Performance of an Expandable Lumbar Interbody Cage With Different Expansion Degrees

Research Fellow Kuo-Chih Su

Taichung Veterans General Hospital, Taichung, Taiwan, Taiwan

Introduction

Lumbar interbody fusion combined with pedicle screw fixation is a common surgical treatment for spinal instability [1]. However, postoperative complications such as cage migration, subsidence, and adjacent segment degeneration remain clinical concerns. Expandable lumbar interbody cages have been developed to restore disc height and enhance segmental stability, yet the biomechanical effectiveness of different expansion degrees in preventing cage migration has not been fully clarified. Understanding how expansion degree influences cage fixation is essential for optimizing implant design and reducing postoperative failure.

Methods

In this in vitro biomechanical study, three custom-designed lumbar interbody cages with different expansion degrees were fabricated using metal 3D printing (titanium alloy): non-expandable (0 mm), mildly expandable (1 mm), and highly expandable (2 mm). For each group, ten repeated pull-out tests were performed. Each cage was clamped between two polyurethane foam blocks (Sawbone, 20 PCF density) to simulate normal vertebral bone quality. A compressive preload of 200 N was applied to replicate physiological conditions. Pull-out tests were conducted using a small-scale mechanical testing system [2], and the maximum pull-out force was recorded as an indicator of anti-migration performance, following established testing approaches.

Results

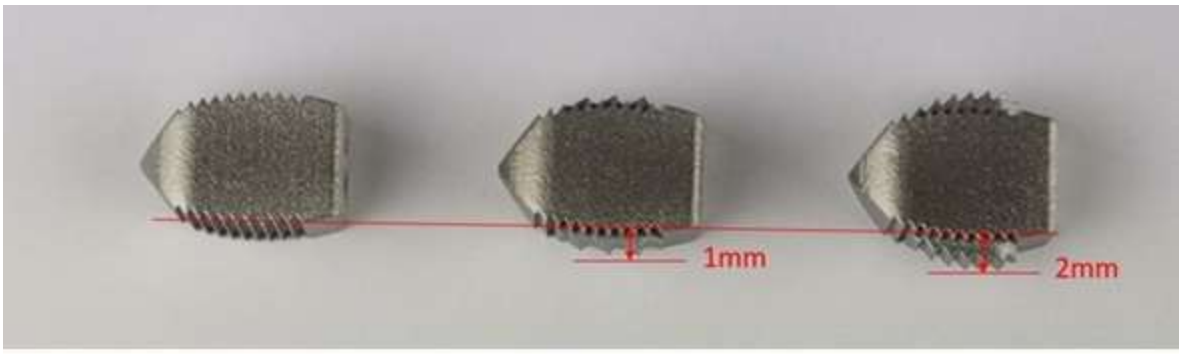
The highly expandable cage (2 mm) demonstrated the highest mean pull-out force (282.07 ± 63.05 N), indicating superior resistance to migration. The non-expandable cage (0 mm) exhibited a moderate pull-out force (242.34 ± 54.71 N). In contrast, the mildly expandable cage (1 mm) showed the lowest pull-out force (221.56 ± 37.75 N), which was lower than

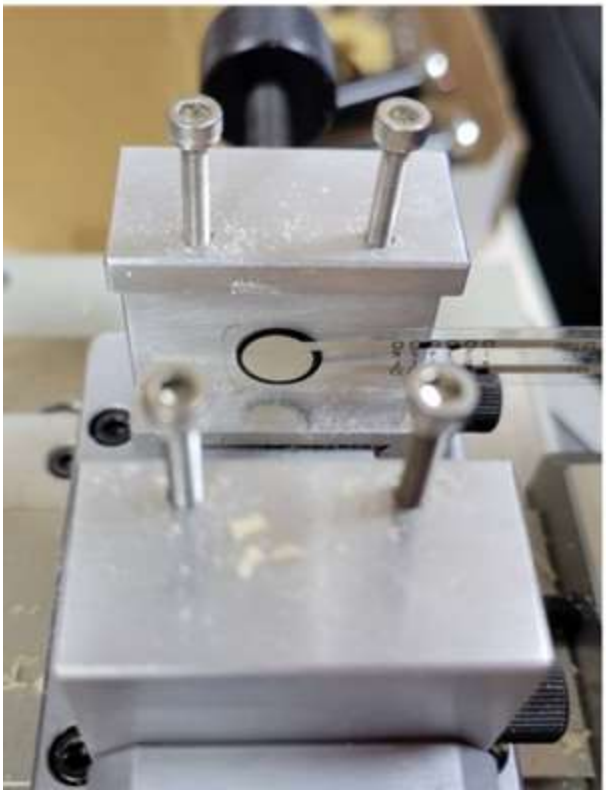
that of the non-expandable group. These findings suggest that limited expansion may reduce effective contact area or mechanical engagement between the cage and the surrounding bone surrogate.

Discussion

The results indicate that cage expansion does not necessarily improve anti-migration stability unless sufficient mechanical interlocking is achieved. Insufficient expansion may compromise fixation by reducing effective structural engagement. Adequate expansion appears critical for enhancing cage stability and preventing migration. These preliminary findings provide valuable biomechanical insight for the design optimization of expandable lumbar interbody cages. Ongoing work includes further biomechanical evaluation under additional loading conditions.

Images (Optional)







References (Optional)

[1] Sim HB et al., Journal of Neurosurgery: Spine, 2010.

[2] Kienle A et al., Spine Journal, 2016.

Acknowledgements (Optional)

We would like to thank the National Science and Technology Council of Taiwan (114-2221-E-075A-006, and 111-2221-E-075A-002).

Session Category

Orthopaedic Biomechanics: Spine

P3-295

Biomechanical Evaluation of Different Fixation for Oblique Lumbar Interbody Fusion Using Finite Element Analysis

Research Fellow Kuo-Chih Su

Taichung Veterans General Hospital, Taichung, Taiwan, Taiwan

Introduction

Oblique lumbar interbody fusion (OLIF) is increasingly used to restore disc height and spinal alignment while minimizing posterior soft tissue injury. Conventional OLIF is commonly supplemented with posterior pedicle screw fixation to ensure stability; however, the combined anterior posterior approach increases operative time, surgical invasiveness, and postoperative morbidity. Alternative anterior or lateral fixation strategies using lateral plates or anterior pedicle screws have been proposed, but their biomechanical effectiveness has not been fully evaluated. This study aimed to compare the biomechanical performance of different OLIF fixation strategies using finite element analysis.

Methods

A three-dimensional finite element model of the lumbar spine (L1–S1) was developed based on computed tomography images of a lumbar Sawbone model. The model included cortical and cancellous bone, intervertebral discs with nucleus pulposus and multilayered annulus fibrosus, vertebral endplates, posterior elements, and major spinal ligaments. Three fixation constructs were analyzed: (1) OLIF with posterior traditional pedicle screw fixation, (2) OLIF with an anterior locked lateral plate system, and (3) OLIF with anterior pedicle screw fixation. All implants were virtually implanted following clinical surgical techniques. The sacrum was fully constrained, and physiological loading conditions were applied using follower loads and moments to simulate flexion, extension, lateral bending, and axial rotation. Total deformation and von Mises stress at adjacent endplates were evaluated.

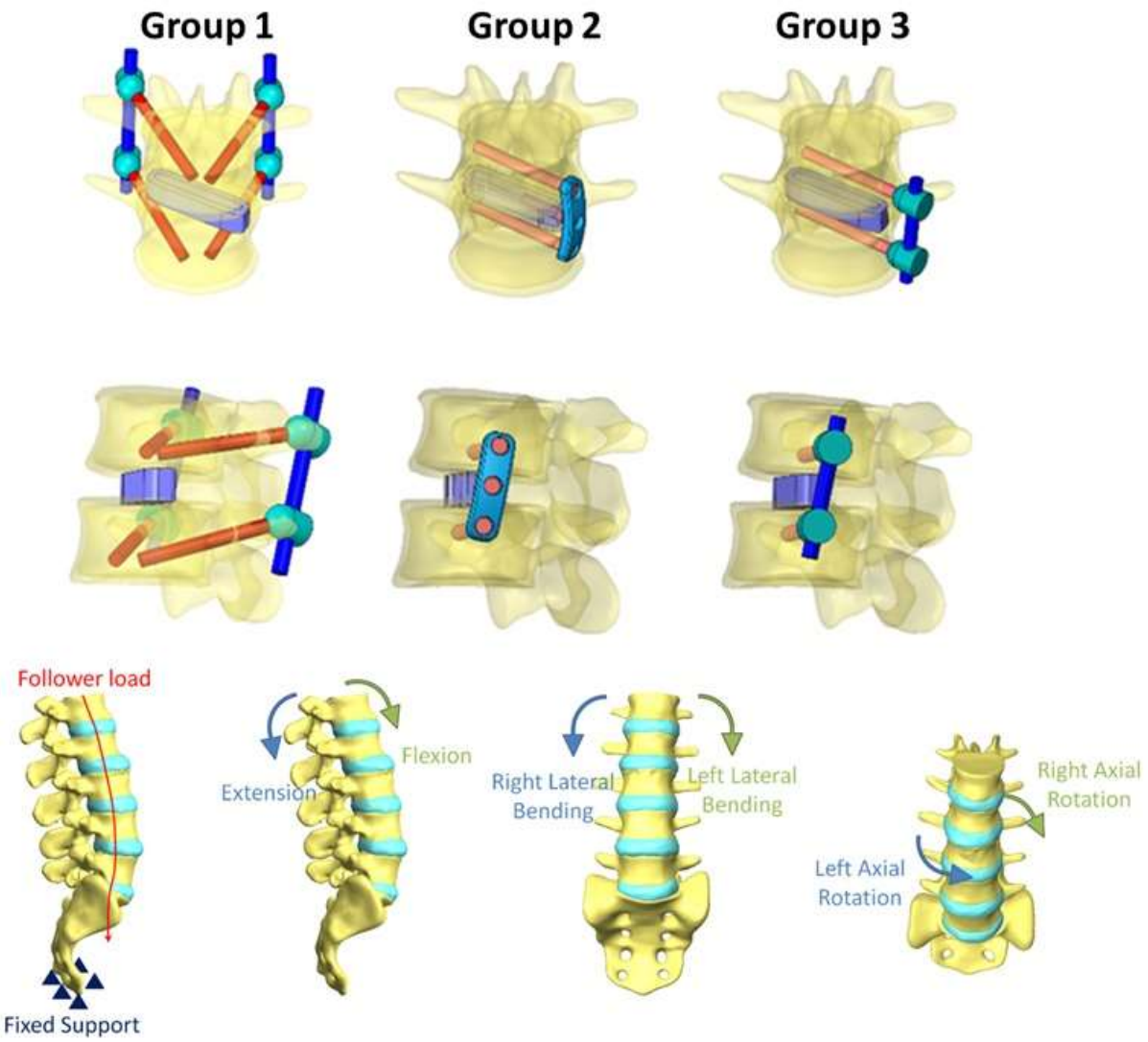
Results

The anterior locked lateral plate construct demonstrated the smallest total deformation under most loading conditions. Flexion produced the greatest deformation in all models, whereas extension resulted in the least deformation. Peak von Mises stresses at the inferior endplate of L2 and the superior endplate of L5 were generally lower in the anterior locked lateral plate group than in the other constructs, particularly during flexion, lateral bending, and axial rotation. Differences among groups were minimal under extension.

Discussion

The results indicate that OLIF supplemented with an anterior locked lateral plate provides biomechanical stability comparable to, or better than, conventional posterior pedicle screw fixation. The locked lateral plate effectively restricts motion and reduces adjacent endplate stress without posterior instrumentation. These findings suggest that a single-approach OLIF fixation strategy may achieve adequate stability while potentially reducing surgical invasiveness.

Images (Optional)



Acknowledgements (Optional)

We would like to thank the National Science and Technology Council of Taiwan (114-2221-E-075A-006, and 111-2221-E-075A-002).

Session Category

Orthopaedic Biomechanics: Spine

P3-296

Combining Validated Data-Driven and Mechanistic Models to Predict the Risk of Vertebral Fracture in Metastatic Patients

Prof Luca Cristofolini[1], Dr Giovanni Barbanti-Bròdano[2], Dr Vincenzo Carbone[3], Prof Dall'Ara Enrico[4], Dr Rudolf Ferenc[5], Prof Stephen J Ferguson[6], Prof JoseManuel Garcia-Aznar[7], Dr Niccole Germscheid[8], Dr Aron Lazary[9], Dr Marco Palanca[1], Dr Sanja Sale[10], Dr Emmanuelle Voisin[11], Prof Peter Vajkoczy[12], Prof Jorrit-Jan Verlaan[13], Prof Laszlo Vidacs[14]

[1]University of Bologna, Bologna, Italy, Italy. [2]IRCCS Rizzoli Orthopedic Institute, Bologna, Italy, Italy. [3]InSilicoTrials Technologies, Trieste, Italy, Italy. [4]University of Sheffield, Sheffield, United Kingdom, United Kingdom. [5]Frontendart Szoftver kft, Szeged, Hungary, Hungary. [6]Eidgenoessische Technische Hochschule Zürich, Zurich, Switzerland, Switzerland. [7]University of Zaragoza, Zaragoza, Spain, Spain. [8]AO Foundation, Davos, Switzerland, Switzerland. [9]Budai Egeszsegkozpont, Budapest, Hungary, Hungary. [10]Eurice, St.Ingbert, Germany, Germany. [11]Voisin Consulting Life Sciences, Boulogne, France, France. [12]Charite - Universitaetsmedizin Berlin, Berlin, Germany, Germany. [13]Universitair Medisch Centrum Utrecht, Utrecht, Netherlands, Netherlands. [14]University of Szeged, Szeged, Hungary, Hungary

Introduction

Metastatic vertebrae can be significantly weaker than healthy ones, exposing patients to critical fracture risk. About 30% metastatic patients suffer vertebral fractures, and another 30% undergo unnecessary surgeries. The standard-of-care is the Spine Instability Neoplastic Score (SINS). However, the SINS provides unclear indications for ≈60% patients, mainly because it gives limited consideration to the structure of the vertebrae and to spine biomechanics. The METASTRA project aims to improve the evaluation of the fracture risk through a combination of credible AI and physiology-based biomechanical virtual human twin (VHT) models.

Methods

We are developing and validating two types of models to be deployed in cascade (Figure 1) to assess the fracture risk. The first step relies on Explainable AI, combining parameters semi-automatically extracted from medical records and images. The AI models also provide an indication of confidence. Patients which are not reliably stratified through AI, are examined through detailed VHT models, capturing the subject-specific anatomy, material properties etc. To test the model credibility, the METASTRA project includes large

multicentric retrospective (2000+ cases), prospective (200+ cases) and cadaveric (120+ specimens) studies.

Results

The AI models for identifying spinal structures and metastases, and predicting fractures, are being trained on data from the retrospective study (nearly complete). They will be validated using data from the prospective study (recently initiated). Personalised VHT models with dedicated sub-models for the healthy and metastatic tissues, disc, interfaces and biomaterials implanted were developed [1]. They are under validation against data obtained from the cadaveric study [2], which is measuring properties (morphology, strains, displacements, failure loads and mode) at different scales (from spine- to tissue-level).

Discussion

METASTRA is in its third year (of five). The METASTRA decision support system is expected to cut the indeterminate diagnoses from the current 60% down to 20% cases, with significant benefits for the patients in terms of quality of life and risk reduction. METASTRA will allow better use of resources by preventing fractures (expected saving: ≈1'000M€/year in EU, thanks to timely instead of late surgery), and reducing unneeded surgeries (expected saving: ≈1'400M€/year).

Images (Optional)

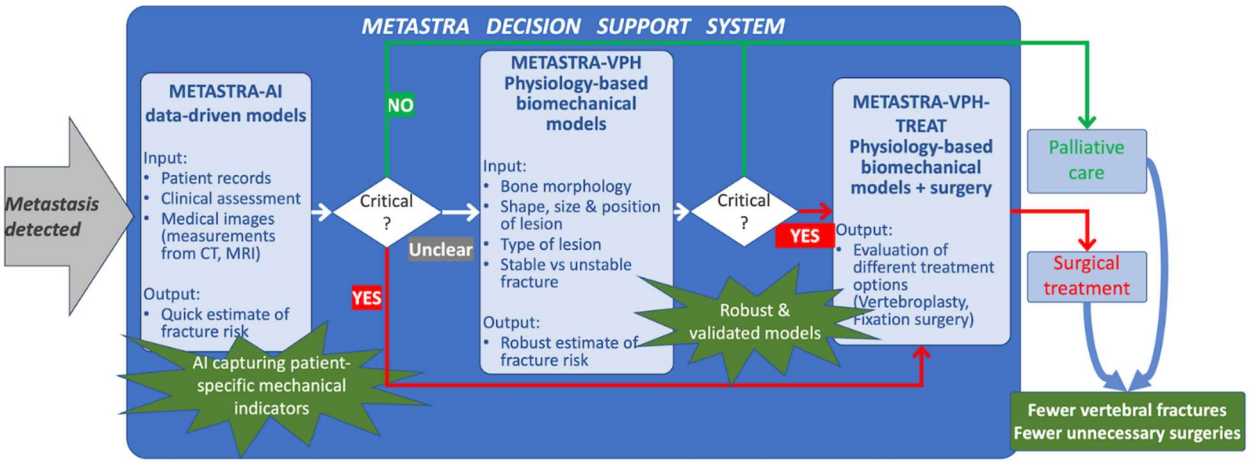


Fig. 1 - Foreseen workflow exploiting the different models of the METASTRA decision support system.

References (Optional)

[1] Ghosh_et_al, WCB2026, submitted

[2] Palanca_et_al, WCB2026, submitted

Acknowledgements (Optional)

METASTRA project funded by the European Union, HEU topic HLTH-2022-12-01, grant 101080135

Session Category

Orthopaedic Biomechanics: Spine

P3-297

Temporal Changes in Sagittal Spinal Alignment After Fusion and Nucleotomy in a Large-Animal Model

Dr. med.vet. Sandra Reitmaier, Mr. Marcel Simon Reich, Mr. Maxim Bashkuev, Ms. Nicole Bormann, Univ.- Prof. Dr. biol. hum. Hendrik Schmidt

Julius-Wolff-Institute, Berlin Institute of Health at Charité – Universitätsmedizin Berlin, Berlin, Berlin, Germany

Introduction

Surgical interventions that influence segmental stiffness, such as fusion and nucleotomy, can affect load distribution and spinal posture. While fusion limits motion and may provoke compensatory alignment changes, nucleotomy preserves mobility but may induce localized hypermobility or altered disc pressurization. How they affect global sagittal alignment remains unclear. This study quantified time-dependent postural adaptations after spinal fusion and nucleotomy in an ovine model using radiation-free surface topography combined with Statistical Parametric Mapping (SPM), providing a biomechanical perspective on procedure-specific alignment changes.

Methods

Twenty-four female Merino-mix sheep were randomized to fusion, nucleotomy, or sham. Fusion utilized an interbody cage with pedicle-screw fixation, nucleotomy removed approximately 0.2 g of nucleus pulposus, and sham animals underwent surgical exposure only. Posture was assessed via surface topography from the first thoracic vertebra to the lumbosacral junction. Posture was measured twice preoperatively (baseline), on day 1, and at weeks 1, 4, 8, and 12, with three trials per time point averaged for analysis.

Results

Healthy sheep have an inverted sagittal profile relative to humans, thoracic lordosis and lumbar kyphosis. Fusion produced an increase in lumbar kyphosis on day 1, with cranial extension of the kyphotic segment (SPM(t)-max=10; d-max=3.2; Fig. 1a). By week 1, significant clusters were limited to L1–L4, and by weeks 4–12 alignment returned to baseline. Nucleotomy did not change global alignment early, but by week 12 a thoracic cluster displayed increased lordosis (SPM(t)-max=5.8; d-max=1.6; Fig. 1b). Between groups, fusion showed greater lumbar kyphosis than sham on day 1 and week 1 (SPM(t)-max=12.3; d-max=3.7). At week 12, nucleotomy resulted in higher lumbar kyphosis than fusion or sham (SPM(t)-max=8.0; d-max=2.5; Fig. 1c-d). These changes indicate procedure-specific adaptations.

Discussion

Fusion induced an acute lumbar kyphotic shift with later thoracic compensation, likely driven by pain-avoidance postures and cranial load transfer around the rigid construct. Nucleotomy caused delayed increases in thoracic lordosis and lumbar kyphosis, suggesting reduced disc pressurization, enlarged neutral zone, and enhanced neuromuscular stabilization demands. Integrating surface topography with SPM provides a sensitive, radiation-free framework to detect alignment changes relevant for validating surgical techniques and translational spine biomechanics.

Images (Optional)

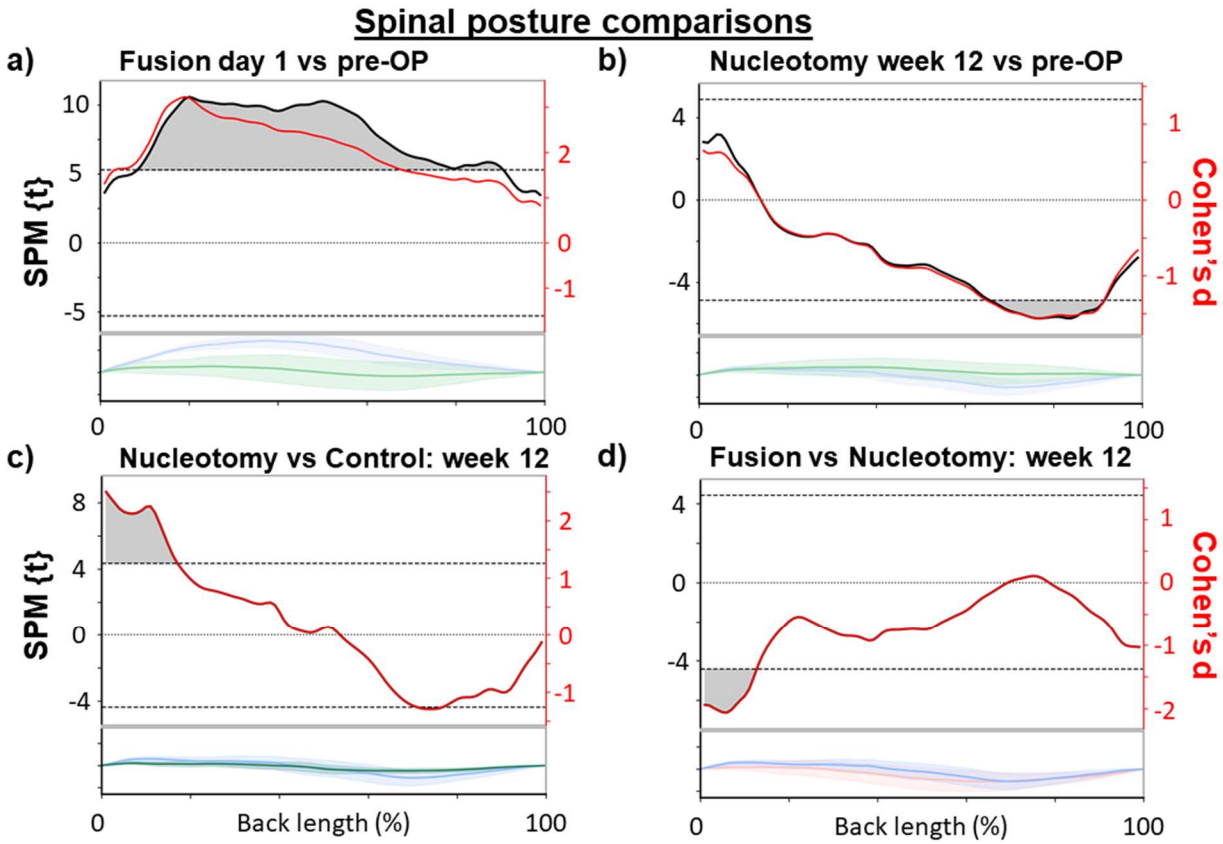


Fig. 1 Statistical parametric mapping (SPM{t}) comparison of sagittal spinal posture. (a) Fusion group one day after surgery vs presurgical baseline. Fusion shows a broad suprathreshold positive cluster over the mid-to-caudal back, showing increased lumbar kyphosis with cranial extension of the kyphotic region; **(b)** nucleotomy at twelve weeks vs baseline. Nucleotomy at week 12 exhibits an extended negative cluster in the thoracic spine, reflecting increased thoracic lordosis;**(c)** fusion vs sham on postoperative day 1. Compared with sham, nucleotomy shows greater lumbar kyphosis at week 12; **(d)** nucleotomy vs sham at week 12. Compared with fusion, nucleotomy likewise displays a more pronounced lumbar kyphosis at week 12; All significant clusters were associated with large effect sizes (Cohen's d > 1). In each panel, the lower graph shows mean spinal posture (a,b: blue = postsurgical, green = presurgical; c,d: red = fusion, blue = nucleotomy, green = sham). The x-axis represents normalized back length (0 = lumbopelvic junction, 100 = withers), the y-axis spinal curvature. The upper graph displays SPM{t} and Cohen's d (red line); horizontal dashed lines indicate the critical SPM{t} threshold for significance. Positive values show a more kyphotic posture in the first-named group, negative values a more lordotic posture.

Acknowledgements (Optional)

This study is part of a Research Unit FOR 5177, funded by the German Research Foundation (GZ RE 4292/3-1; SCHM 2572/11-1; SCHM 2572/13-1).

Session Category

Orthopaedic Biomechanics: Spine

P3-298

Intervertebral disc degeneration alters the strain patterns and failure location in the adjacent vertebrae

Miss Margherita Pasini[1], Miss Giulia Cavazzoni[1], Prof Christine Le Maitre[2], Prof Luca Cristofolini[1], Prof Enrico Dall'Ara[2], Dr Marco Palanca[1]

[1]University of Bologna, Bologna, Italy, Italy. [2]University of Sheffield, Sheffield, United Kingdom, United Kingdom

Introduction

Prediction of the risk of fracture in pathological vertebrae, whether osteoporotic or metastatic, remains a challenge. Although multiple mechanical factors influence vertebral failure, the contribution of the intervertebral disc (IVD) and the impact of its degeneration are often neglected. We hypothesize that IVD degeneration has a pivotal role in altering the load transfer across the vertebrae and drives failure mechanisms.

We aimed to quantify how vertebral strain patterns and failure locations differ when loaded through healthy and degenerated IVDs.

Methods

Eleven thoracic spine segments, consisting of a healthy (control) vertebra and a vertebra with lytic metastases, were prepared to be tested in axial compression while imaged inside a microCT (VivaCT80,Scanco,Switzerland; isotropic voxel size=0.039mm).

Six specimens had healthy IVDs, whereas five underwent enzymatic degeneration using collagenase to induce severe nucleus degradation[1,2]. All specimens were imaged and mechanically tested both in the elastic regime—reaching a minimum principal strain of 2000 microstrain[3]—and to failure. Volumetric strains were measured by global Digital Volume Correlation (BoneDVC).

Strain distributions and magnitudes in the healthy-IVD group were compared with the degenerated-IVD group (Mann-Whitney U test). Failure locations were identified by rigid registration of unloaded and post-failure scans.

Results

Similar loads were necessary to reach the target strains (1238N-degenerated vs 1050N-healthy) and to induce the failure (1917N-degenerated vs 1626N-healthy) in the metastatic vertebra.

The vertebrae loaded through healthy IVDs exhibited relatively homogeneous strain patterns, whereas degenerated IVDs showed marked strain concentrations.

Imaging revealed different failure locations: healthy IVDs predominantly led to endplate failure, degenerated IVDs increased cortical shell strain, triggering cortical failure [Fig. 1].

Discussion

These findings highlight the pivotal role of the IVD in directing load transfer and triggering different vertebral fracture patterns. Both IVD degeneration and trabecular/cortical integrity are essential parameters in vertebral failure prediction. Neglecting IVD condition and applying generalized boundary conditions may hide clinically relevant mechanical behaviour and jeopardise fracture risk prediction.

Images (Optional)

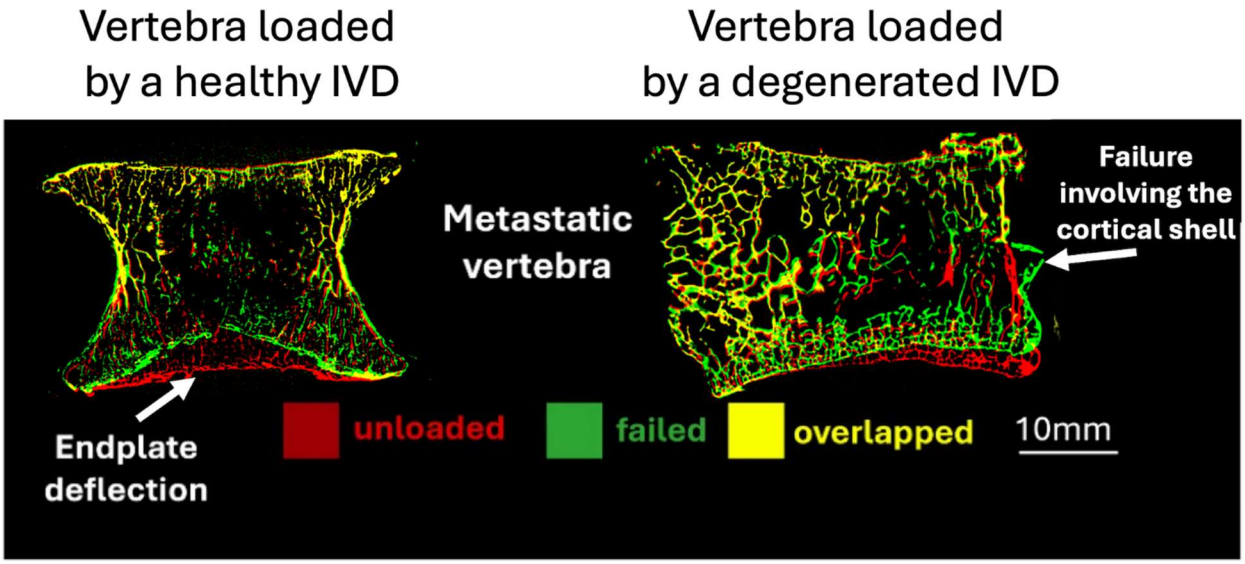


Fig. 1: failure location in a vertebra loaded by a healthy IVD (left) and in a vertebra loaded by a degenerated IVD (right).
In red, the unloaded scan, in green the scan at failure and in yellow the overlapped regions after rigid registration.

References (Optional)

Bibliography

1. Pasini,2025,107109,JMBBM
2. Cavazzoni,2025,194(258-269),ActaBiomat
3. Palanca,2021,116028,Bone

Acknowledgements (Optional)

HEU-Funded METASTRA project (grant 101080135)

Session Category

Orthopaedic Biomechanics: Spine

P3-299

Biomechanical effects of Erector Spinae Role in Sagittal Balance of Adolescent Idiopathic Scoliosis using Patient-specific and Parametric Finite Element Models

Eng. Maria Alejandra Velasquez, Eng Cristian Nikolas Morales Garcia, M.Sc. David Felipe Landinez Leon, Ph.D Christian Cifuentes-De La Portilla

Department of Biomedical Engineering, Bogota D.C, Bogota, Colombia

Introduction

Adolescent idiopathic scoliosis (AIS) is a three-dimensional deformity in which thoracic curve severity strongly correlates with loss of thoracic kyphosis ($r = -0.75$) [1]. The Lenke classification explicitly uses sagittal thoracic alignment as a key modifier of progression and treatment strategy. Despite this clinical relevance, the biomechanical role of erector spinae muscles — the primary sagittal stabilizers — in counteracting sagittal imbalance in AIS remains unquantified using realistic spinal anatomy.

Methods

Two finite element models were developed. (1) A patient-specific model of the complete spine–pelvis complex (C4–sacrum) was reconstructed from clinical CT scans and geometrically corrected in Blender to restore physiological standing alignment. Scoliosis was induced by asymmetric reduction of intervertebral disc stiffness (1000-fold in damaged partitions) following the validated protocol of Landinez et al. [2]. (2) A fully parametric model was designed in Fusion 360, considering anatomical parameters for systematic validation. Longissimus and spinalis muscles were explicitly modeled with forces applied at their anatomical insertions, together with body weight and follower load. Four scenarios were simulated in Abaqus: healthy spine ± muscle activation, scoliotic spine ± muscle activation.

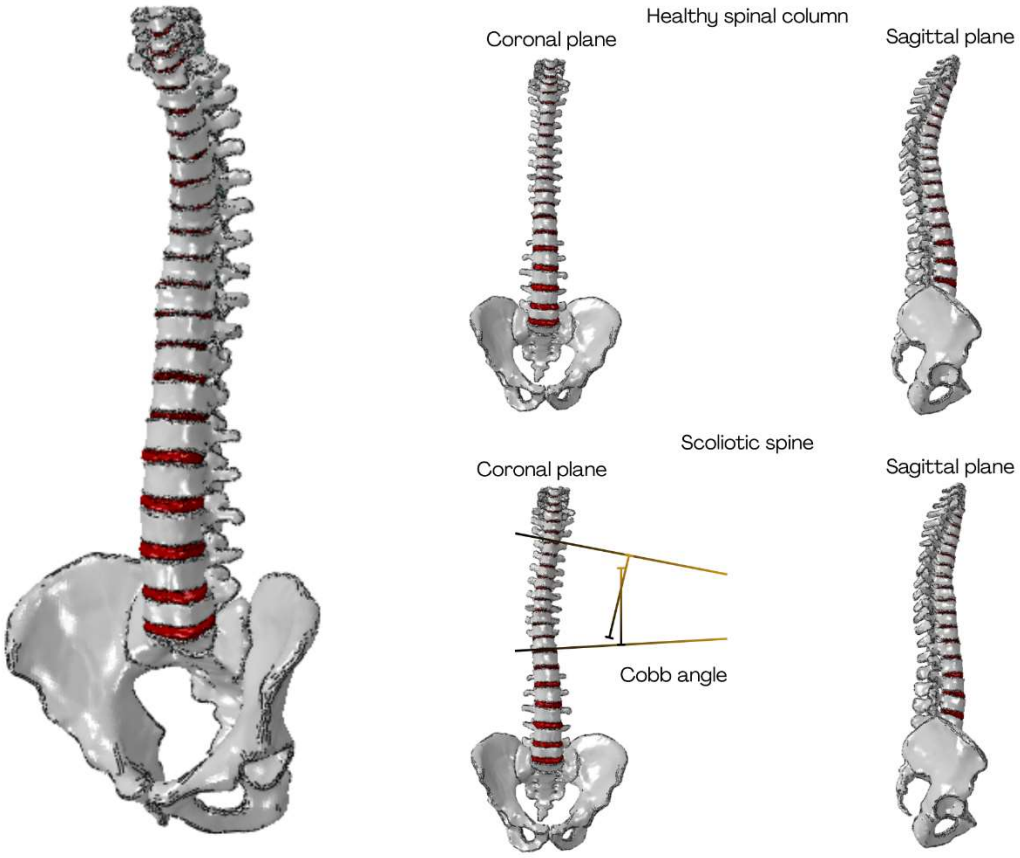
Results

Both models successfully generated deformation in the coronal plane and reproduced the characteristic thoracic hypokyphosis of AIS. Results clearly demonstrate that erector spinae muscles play a very important role in modifying sagittal curvature: in the scoliotic configuration, muscle activation visibly restored thoracic kyphosis and markedly improved global sagittal alignment compared to the scoliotic case without muscle action. Minimum principal compressive stress distribution in apical vertebrae and discs was significantly reduced with muscle activation. The parametric model confirmed identical behavior.

Discussion

This is the first study combining an anatomically detailed model derived from clinical images with a parametric model to demonstrate that erector spinae muscles generate sufficient posterior loading to actively induce thoracic flattening and sagittal decompensation caused by scoliosis. These findings provide biomechanical evidence supporting the clinical correlation reported by Sullivan et al. [1], reinforce the importance of Lenke sagittal modifiers, and strongly justify muscle-strengthening and motor-control rehabilitation in conservative AIS management.

Images (Optional)



References (Optional)

[1] Sullivan TB et al. J Bone Joint Surg Am. 2017;99(11):e54.

[2] Landinez D et al. J Orthop Surg Res. 2025;20:39.

Session Category

Orthopaedic Biomechanics: Spine

P3-300

Topology Optimization for Spinal Fusion Cages: Local Strain Constraints to Promote Bone Ingrowth

MsC Martina Paganelli[1], Dr. Remco J.P. Doodkorte[1], Dr. Bert van Rietbergen[1], Dr. Ondrej Rokos[1], Prof. Dr. Keita Ito[1,2], Prof. Dr. J. J. Chris Arts[1,3], Dr. Joeri Kok[1]

[1]Eindhoven University of Technology, Eindhoven, N/A, Netherlands. [2]University Medical Center Utrecht, Utrecht, N/A, Netherlands. [3]Maastricht University Medical Center+, Maastricht, N/A, Netherlands

Introduction

Topology optimization (TO) has been used to improve implant designs such as for lumbar interbody fusion (LIF) cages. Common TO strategies aim at maximizing stiffness under given mass. However, for optimal fusion and cage stability, enhancing bone ingrowth while maintaining structural integrity should be the goal. As mechanical strains are known to be an important stimulus for bone formation [1], an optimization procedure aimed at favoring strains in the osteogenic range may help to improve fusion outcomes. Therefore, the purpose of this study is to develop a new strain-based TO strategy and to elucidate how cage geometries and strain distribution differ when optimized with a default and local strain-based TO approach.

Methods

This two-stage study evaluated two TO strategies: a default approach minimizing overall strain energy density under a mass/volume constraint (max. 30%) and an in-structure local-strain constrained approach with total volume minimization. The TO strategies were first applied to a 30x50 elements 2D structure simulating compression for algorithm verification. Subsequently, the algorithm was applied to a 3D design representing a titanium posterior LIF cage (41x120x49 elements) subjected to an evenly distributed load in axial compression and two transverse directions of shear [2].

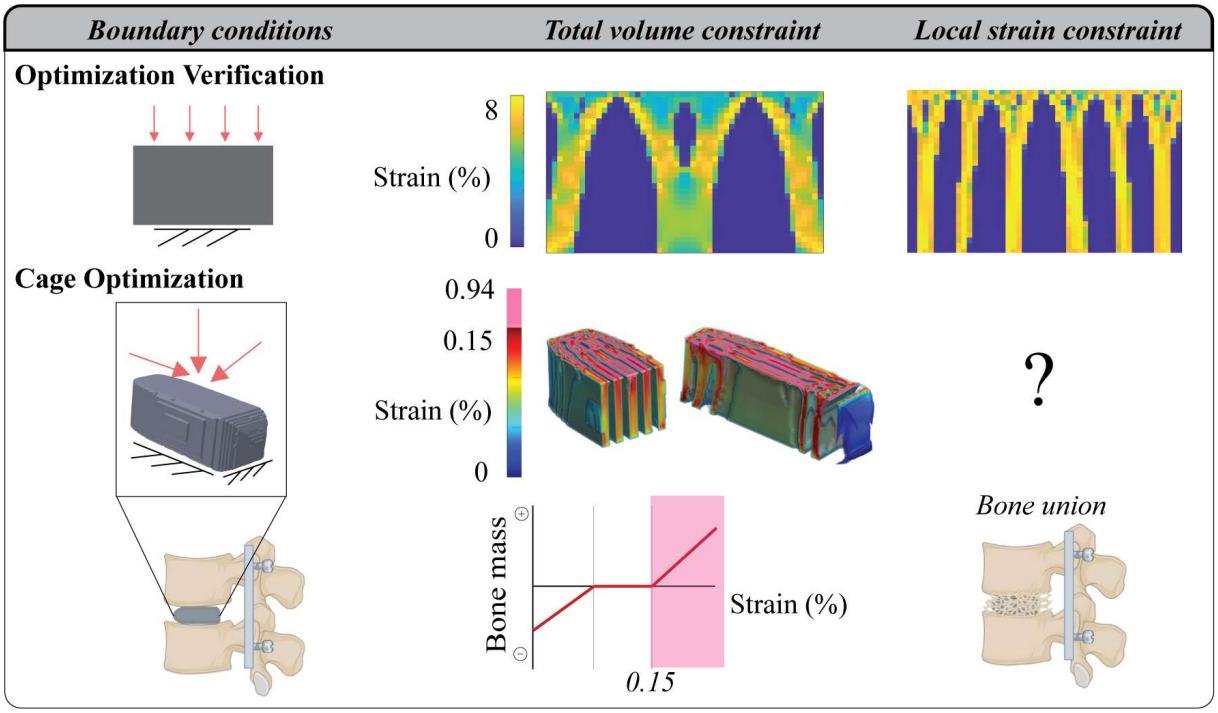
Results

The 2D optimization showed distinct differences in final topology. Moreover, the novel approach resulted in a more homogeneous structural strain distribution, i.e., a lower coefficient of variation (12% vs. 22%). The 3D optimization with the default approach resulted in a structure with a peak stress (423.5 MPa) below the ultimate stress. Strains in the osteogenic range were mostly present on the loaded surface of the structure (Figure).

Discussion

Although 3D local strain-based approach results are still pending, the 2D outcomes demonstrate that incorporating local strain control yields a more homogeneous and targeted strain pattern within the optimized structure. This suggests that geometries optimized with local constraints may better achieve target strain levels. In contrast, the 3D cage optimized with mass/volume constraint exhibit non-homogeneous strain patterns, with limited regions reaching the osteogenic range.

Images (Optional)



References (Optional)

[1] Harold M. Frost, Anat Rec, 2003

[2] Junpeng Wang et al., Struct Multidisc Optim, 2025

Acknowledgements (Optional)

Financially supported by PRosPERoS-II project, funded by Interreg VA Flanders – the Netherlands program (2021TC16RFCB041).

Session Category

Orthopaedic Biomechanics: Spine

P3-301

The Role of the Deep Multifidus During Static and Dynamic Activities in a Healthy Population: A Pilot Study

Dr Mona Fre, Dr John Charles Snow, Dr Greg Pearcey, Dr Diana DeCarvalho

Memorial Univeristy of Newfoundland, St. John's, NL, Canada

Introduction

The deep lumbar multifidus (DLM) has been proposed to be crucial for spinal stability [1]. However, since surface electrodes cannot measure muscle activity of deep LM fibers [2], little is known about the activity of DLM during functional tasks. We hypothesized that the DLM shows greater activity during tasks that challenge spinal stability while the SLM showed greater activation during tasks requiring extension. **Our purpose was to characterize the muscle activation of the deep multifidus using intramuscular EMG in comparison to the superficial LM (SLM) using surface EMG.**

Methods

Data from five (4M, 1F) asymptomatic participants was collected using intramuscular and surface EMG. Fine wire electrodes were inserted unilaterally (right side) at the L3, L4 and L5 levels, and surface electrodes were placed bilaterally at the L4 level. Participants completed three trials of fifteen different movements (Table 1) in a randomized order. Presented here are the mean, peak and minimum electromyography signals expressed as %MVC for each task (averaged across the 3 trials).

Results

Normalized EMG for the DLM and SLM at L4 for each task can be seen in table 1. Within each category, tasks are sorted in ascending order of DLM activity highlighting the increase in DLM but not SLM activity with increasing lateral and rotational demands. Average SLM activity ranged from 1-6%MVC while a larger spread was found for DLM. Similarly, a higher range (minimum to peak) of activity was observed for DLM for each task, as well as greater within-subject variability between the three trials of each task. Additionally, we observed between-level differences of the DLM with higher variability at L3.

Discussion

Our findings support that the DLM may contribute to spinal stability varying in activity depending on the task demand while the SLM was less variable. This highlights the importance of considering the DLM for low back pain rehabilitation and modelling of complex tasks using spinal finite element models. Additional analyses will investigate the

roles of the DLM and SLM throughout dynamic movement tasks and pilot motor unit decomposition for the DLM.

Images (Optional)

Table 1. Normalized muscle activation of the right deep and superficial multifidus at L4.

	Muscle Activity (%MVC)		Average		Peak		Min	
	Task	Muscle at L4	DLM	SLM	DLM	SLM	DLM	SLM
Core Exercises	Unstable plank		0.61 ±0.65	2.34 ±2.04	3.12	5.61	0.30	1.67
	Bird dog		2.23 ±2.38	1.12 ±0.49	4.76	2.35	1.82	0.71
	Plank ipsil. leg lift		4.93 ±4.02	1.22 ±0.63	9.64	1.84	3.86	0.77
	Plank		4.96 ±3.37	1.89 ±1.81	10.97	3.61	3.93	0.87
	Plank contral. leg lift		6.10 ±5.97	1.54 ±1.54	24.79	3.43	3.46	0.75
	Side plank L		7.67 ±11.38	2.79 ±1.34	27.92	7.57	5.70	1.02
	Side plank R		8.54 ±9.04	2.30 ±2.15	64.04	4.35	4.18	1.16
Carry	Suitcase carry L		4.13 ±4.31	5.49 ±1.90	18.73	9.37	1.93	2.82
	Suitcase carry R		4.26 ±4.11	2.78 ±2.11	11.54	4.45	2.79	1.81
Sit/Stand	Sitting		17.17 ±28.4	3.52 ±1.44	40.37	5.45	12.90	2.27
	Sit-to-stand		26.98 ±29.49	4.32 ±1.74	42.49	6.00	22.03	3.00
	Standing		29.50 ±43.21	3.80 ±2.36	44.23	7.29	23.17	2.21
Lifting	Box lift straight		14.80 ±22.32	5.89 ±3.31	20.35	8.51	14.30	2.71
	Box lift ipsil. rotation		29.74 ±28.72	4.43 ±1.30	39.32	7.16	20.99	2.71
	Box lift contral. rotation		38.61 ±47.61	4.49 ±2.47	45.58	7.57	34.03	2.57

References (Optional)

[1] David MacDonald et al. , Manual Therapy, 2006

[2] Ian Stokes *et al.* , Clinical biomechanics, 2003

Acknowledgements (Optional)

Funding: Natural Sciences and Engineering Research Council (NSERC) Discovery Grant

Session Category

Orthopaedic Biomechanics: Spine

P3-302

Trunk Muscle Activation in Adolescent Idiopathic Scoliosis: EMG-based Comparison of Braced and Unbraced Conditions

Mr. Philippe Bähler[1,2], Mr. Salvatore Conticello[3,1], Prof. Dr. Moritz Deml[4], Prof. Dr. Carol-Claudius Hasler[5], Prof. Dr. Philippe Büchler[3], Prof. Dr. Stefan Schmid[1,6]

[1]Spinal Movement Biomechanics Group, Division of Physiotherapy, School of Health Professions, Bern University of Applied Sciences, Bern, Bern, Switzerland. [2]University of Bern, Bern, Bern, Switzerland. [3]Computational Bioengineering Group, ARTORG Center for Biomedical Engineering Research, Faculty of Medicine, University of Bern, Bern, Bern, Switzerland. [4]Department of Orthopaedic Surgery and Traumatology, Inselspital, University Hospital Bern, University of Bern, Bern, Bern, Switzerland. [5]Orthopaedic Department and Spine Surgery, University Children's Hospital Basel, Basel, Basel, Switzerland. [6]Faculty of Medicine, University of Basel, Basel, Basel, Switzerland

Introduction

Brace treatment is a common second-line intervention for adolescents idiopathic scoliosis (AIS) in continental Europe. It is usually indicated when the curve progression persists despite physical therapy, and the Cobb angle exceeds 20°-30° [1]. Bracing applies corrective forces to the trunk and supports posture but restricts trunk mobility during daily activities. This study aimed to compare trunk muscle activation during an object lifting task performed with and without a brace.

Methods

Five female adolescents with main thoracic right convex mild to moderate AIS (Cobb angle: 34°±11°, age: 13.6 ±1.5 years) performed an object lifting task five times with and without wearing their personal customized braces, all manufactured by the same company using 3D scanning and printing. Surface electromyography (EMG) electrodes were placed bilaterally over the upper longissimus thoracic, the lower longissimus thoracic, and the iliocostalis lumborum (T5, T9, and L3 levels, respectively), as well as over the obliquus externus and rectus abdominus muscles. Muscle activity was recorded using a 16-channel telemetric EMG system. Signals were filtered, rectified, smoothed, and normalized to percentages of maximum voluntary contractions (%MVC). Mean muscle activity during the lifting and lower phases was computed for each trial and averaged across repetitions. Condition-specific differences were calculated by subtracting braced from unbraced values and considered if they were larger than 5 %MVC.

Results

Two participants showed changes in upper thoracic longissimus (left side) and lower thoracic longissimus (right side) activation when wearing the brace, but these changes were reciprocal across subjects: one exhibited higher activation, the other lower. Three participants showed no thoracic muscle changes. All subjects tended to activate the iliocostalis lumborum more when braced, while abdominal activity remained unchanged.

Discussion

This exploratory analysis revealed no consistent changes in trunk muscle activation when wearing a brace. The individual responses observed, particularly the reciprocal thoracic longissimus patterns, could not be linked to age, curve type, curve severity, or other characteristics. Overall, bracing may modulate neuromuscular activation in some individuals but not others. The absence of differences in abdominal muscle activity likely reflects their comparatively minor contribution to the lifting task assessed.

Images (Optional)

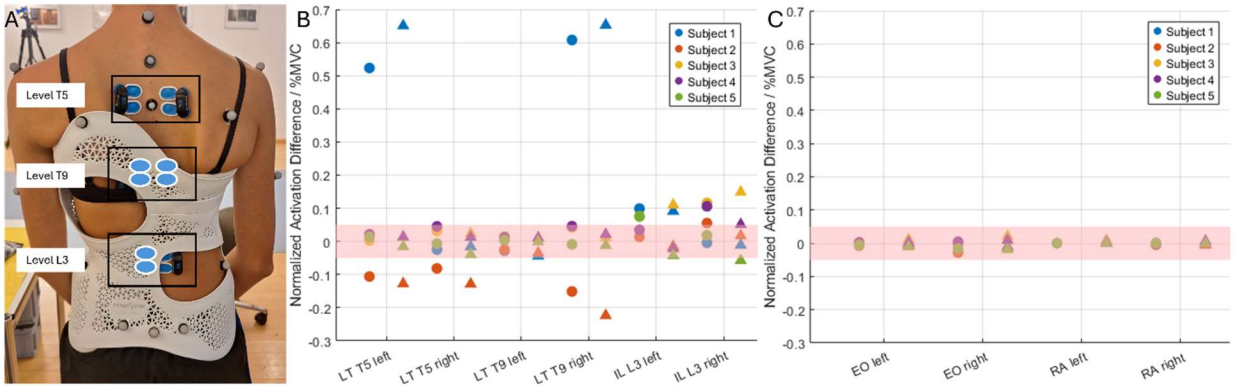


Figure 1: A) Electrode placement on the spine while the participant is wearing the brace. B) Scatter plot of the averaged activation differences per subject for the spinal muscles while lifting (●: lift down, ▲ : lift up) in braced and unbraced condition. C) Scatter plot of the averaged activation differences per subject for the spinal muscles while lifting (●: lift down, ▲: lift up) in braced and unbraced condition. The red area indicates the ±5% MVC limits. LT: Longissimus Thoracis, IL: Iliocostalis Lumborum, EO: External oblique, RA: Rectus Abdominis

References (Optional)

[1] Negrini et al. , Cochrane Database Syst, 2015

Acknowledgements (Optional)

This work was supported by the Swiss National Science Foundation (SNSF; Grant-no.: 214986).

Session Category

Orthopaedic Biomechanics: Spine

P3-303

Discriminative Morphable Shape Modeling of Lumbar Spine Geometry in Spondylolisthesis Assessment

Mr. Reza Rahimi PhD Student, Dr. Allison Clouthier Assistant Professor

University of Ottawa, Ottawa, Ontario, Canada

Introduction

Quantifying how 3D lumbar shape varies with demographics and pathology is crucial for understanding dysfunction. Statistical shape models (SSMs) are widely used to quantify geometric variation; however, typical methods impose a single, linear relationship between shape and pathology. This likely oversimplifies the complex variation existing within different populations. We present a decision-informed morphable SSM that encodes nonlinear shape–diagnosis dependencies as coherent, anatomically plausible deformation patterns across populations.

Methods

Participants and data processing:

We retrospectively analyze 87 lumbar CT scans from The Ottawa Hospital (2013–2018), approved by the University of Ottawa and Ottawa Hospital Research Institute REBs. Each case is labeled for the presence or absence of spondylolisthesis. High-resolution vertebral meshes are extracted, quality-controlled, and brought into dense point-wise correspondence (CPD) through standardized alignment and non-rigid registration, forming the basis for robust shape analysis.

Method Pipeline: (i) learn a label-informed, low-dimensional shape space with partial least squares (PLS) regression; (ii) train a nonlinear support vector machines (SVM) decision boundary on PLS scores, evaluated with nested cross-validation to avoid selection bia; and (iii) obtain morphs by sampling the SVM boundary, then from each boundary seed stepping a small margin into each class along the gradient of the decision function, and mapping the latent difference back to vertex displacements.

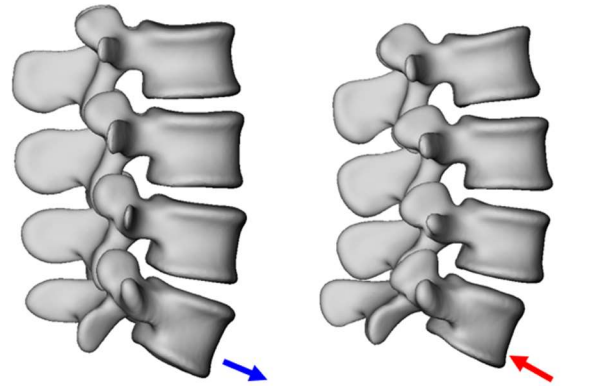
Results

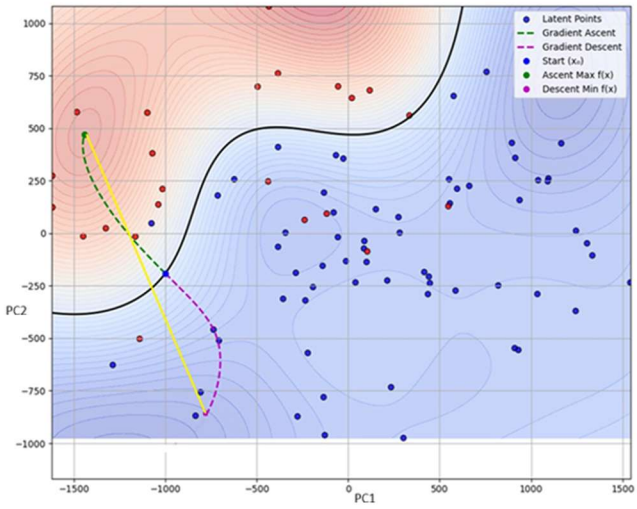
On 87 aligned, corresponded meshes, the model achieved accuracy 87.2%, AUC 0.88, and F1 67.8% for spondylolisthesis classification. Learning curves showed training and validation performance rising and converging with sample size, indicating good generalization. Performance exceeded the proposed PLS and PCA baselines

Discussion

Decision-aligned morphs emphasize pathology-specific changes (vs variance-driven methods) and, unlike a single linear PLS discriminant, reveal multiple, distinct deformation pathways actually used by the classifier. Recovered patterns matched known morphology—anterior L4/L5 slip with disc-height loss and foraminal narrowing, facet sagittalization, and dysplastic signs such as a trapezoidal L5—supporting face validity and clinical interpretability

Images (Optional)





SVM Decision Boundary with Gradient Ascent and Descent

References (Optional)

[1] Lekadir K et al., *Statistical Shape Modeling Using Partial Least Squares: Application to the Assessment of Myocardial Infarction*, Springer, 2015.

[2] James G et al., *An Introduction to Statistical Learning: With Applications in Python*, Springer, 2023.

[3] Clouthier AL et al., *J. Biomech.*, 2023.

Session Category

Orthopaedic Biomechanics: Spine

P3-304

Increased Mineralization and Decreased Collagen Alignment Occurs in Remineralization of Bone Resulting From Denosumab Treatment

Ms. Robyn Birch[1,2], Dr. Felipe Eltit[2,3], Dr. Nicolas Dea[4], Dr. Charles Fisher[5], Dr. Tony Ng[6], Dr. Raphaële Charest-Morin[4], Dr. Rizhi Wang[1,7]

[1]Materials Engineering, University of British Columbia, Vancouver, BC, Canada. [2]Centre for Aging SMART, Vancouver, BC, Canada. [3]Vancouver Prostate Centre, Vancouver, BC, Canada. [4]Combined Neurosurgical and Orthopedic Spine Program, Department of Orthopedics Surgery, University of British Columbia, Vancouver, BC, Canada. [5]Combined Neurosurgical and Orthopedic Spine Program, Department of Orthopedics Surgery, University of British Columbia, Vancovuer, BC, Canada. [6]Department of Pathology, University of British Columbia, Vancovuer, BC, Canada. [7]School of Biomedical Engineering, University of British Columbia, Vancovuer, BC, Canada

Introduction

Giant cell tumor of bone (GCTB) is a rare, locally aggressive but benign tumor that typically arises near joint surfaces. Spinal GCTB is even rarer, accounting for ~1% of cases. These tumors erode bone turning it into a soft tumor, compromising stability of a joint, also overtaking vital structures such as arteries and nerves. Denosumab, a monoclonal antibody delivered by subcutaneous injection, inhibits RANKL and suppresses osteoclast activity, promoting mineralized bone formation within the tumor. Although denosumab has been used clinically for over a decade, its long-term effects on bone remineralization in spinal GCTB remain unclear.

Methods

We compared five denosumab-treated samples to five region-matched vertebral controls. Bone microarchitecture was assessed by microCT. Mineralization and lacunar morphology were evaluated using quantitative backscattered electron microscopy (6–16 regions per sample) to measure calcium weight percent and two-dimensional lacunar shape. Collagen organization was quantified using second harmonic generation imaging (3 regions per sample) across a 15 μm depth to assess collagen alignment changes with depth. Group differences were tested using Mann–Whitney U and Kruskal–Wallis tests for unpaired data.

Results

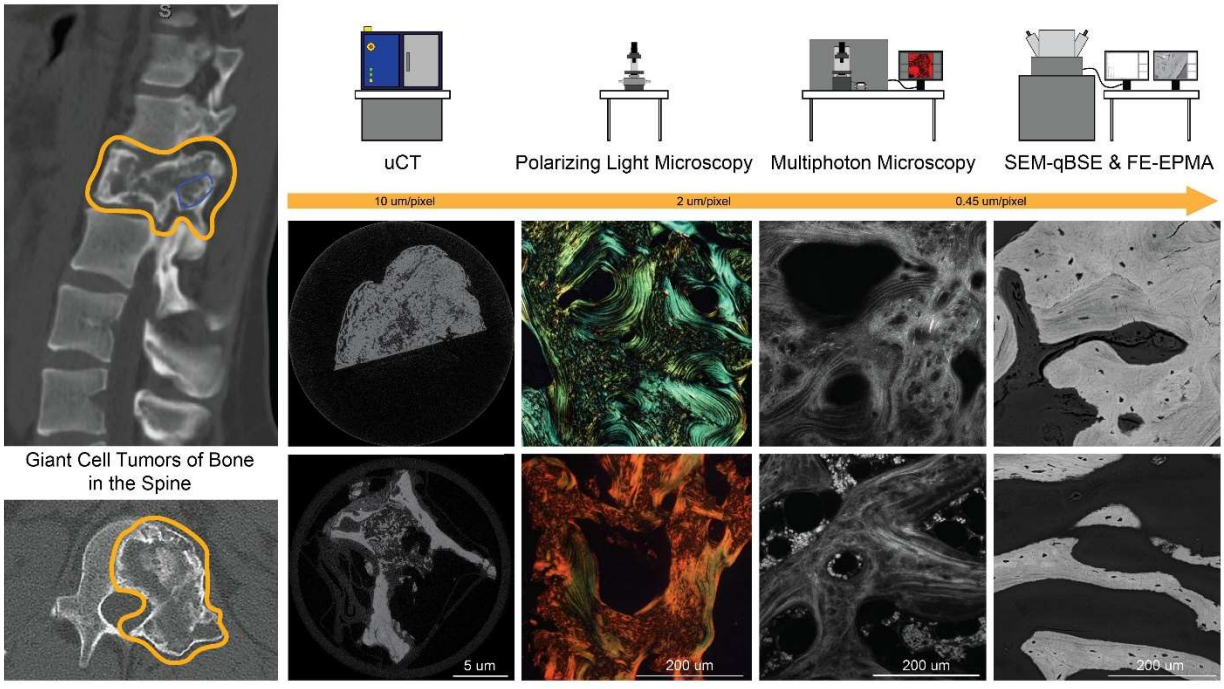
Denosumab treatment produced two bone phenotypes (woven and lamellar) and appeared to alter the mineralization process. qBSE demonstrated increased calcium weight percentage with extended treatment durations ($p<0.001$). Furthermore, the weight calcium

percentage between the lamellar and woven bone showed significant increases ($p<0.001$). The woven bone exhibited increased lacunar density ($p<0.001$) and greater circularity($p<0.05$). Additionally, the woven bone showed a decrease in the collagen alignment compared to lamellar bone ($p<0.001$), with large deviations in the angle of alignment with depth.

Discussion

Overall, denosumab-treated bone was more highly mineralized but showed disorganized collagen alignment and increased lacunar density—features consistent with a mixed woven/lamellar structure. Based on established relationships between bone composition and mechanics, these microstructural changes are expected to alter material properties such as modulus and hardness and may influence long-term vertebral strength and stability in patients receiving prolonged denosumab therapy. Future work will focus on linking these structural findings to functional mechanical outcomes, clarifying inter-patient variability, and defining whether there is an optimal treatment window that balances tumor control with bone quality.

Images (Optional)



Acknowledgements (Optional)

Session Category

Orthopaedic Biomechanics: Spine

P3-305

Development of Seating Device Focused on Pelvic Mechanical Environment for Reducing Low Back Pain During Sitting

Dr. Ryota Toyohara, Mr. Tsubasa Takahashi, Mr. Chihiro Wakamatsu, Prof. Toshiro Ohashi

Hokkaido University, Sapporo, Hokkaido, Japan

Introduction

Mechanical environments of pelves differ between standing and sitting postures. In standing, loads are transmitted from femora to pelves and lumbar spines via hip joints, whereas in sitting, loads are transferred from ischial tuberosities of buttocks to lumbar spines [1]. This difference implies that standing produces slightly lateral load direction, creating a mechanical environment in which the hip bones compress the sacroiliac joints. A clinical report [2] demonstrated that compression applied to femoral greater trochanters can relieve low back pain and extend sitting time. Therefore, in order to reduce low back pain by improving the mechanical stress environment in lower backs, we aim to develop a seating device that applies lateral loads to pelves by incorporating slopes into a seat pan.

Methods

Seating devices were designed using finite element analysis (FEA) to evaluate stress environments on lower backs. Subsequently, seat pressure distributions were measured in participants using prototypes of the seating device and the stress environments were analyzed again using FEA based on the measure pressure distributions.

Results

The FEA results showed that the seat pan with slopes altered the direction of the seat reaction force to produce lateral compression on the pelves. The seating pressure distribution measured in participants exhibited a similar pattern to the FEA predictions; however, in the prototype used in this study, lateral loads did not increase.

Discussion

The concept of a seating device that compresses the pelves laterally using slopes on seat pans was supported by the FEA results. However, in the pressure measurements obtained with the prototype, loads were mainly applied to the ischial tuberosities, producing a mechanical environment in which pelvic bones were distracted at the sacroiliac joints, which was opposite to the intended effect. These findings suggest that the pelvic contact position on the seat pan may be critical for achieving the desired load transmission in the proposed seating device.

References (Optional)

[1] Kapandji, The physiology of the joints 3, Churchill Livingstone, 1974.

[2] Sasaki et al., Clin Biomech, 2025.

Acknowledgements (Optional)

This work was supported by JSPS KAKENHI Grand Number JP24K21074.

Session Category

Orthopaedic Biomechanics: Spine

P3-306

In Vivo Spinal Stiffness Quantification in Adolescent Idiopathic Scoliosis

MSc Salvatore Conticello[1,2], MSc Noelia Bracher[1], MSc Philippe Bähler[1,2], Dr. Stefan Schmid[2,3], Dr. Philippe Büchler[1]

[1]ARTORG Center for Biomedical Engineering Research, University of Bern, Bern, Bern, Switzerland. [2]Spinal Movement Biomechanics Group, School of Health Professions, Bern University of Applied Sciences, Bern, Bern, Switzerland. [3]Faculty of Medicine, University of Basel, Basel, Basel, Switzerland

Introduction

A detailed understanding of spine biomechanics is essential for better understanding the progressive behavior of adolescent idiopathic scoliosis (AIS). Standard clinical assessments measure only displacement and therefore cannot determine true mechanical stiffness, which depends on both applied load and resulting deformation. To address this limitation, we developed a spinal traction device (Figure), which is compatible with EOS radiographic imaging system. The device delivers controlled axial traction through a head halter while a force-sensor platform simultaneously records load, enabling quantitative assessment of spinal mechanical response. The objective of this study was to derive patient-specific spinal stiffness in a patient with AIS.

Methods

A 15-year-old patient with mild thoracolumbar AIS underwent EOS imaging with and without spinal traction. Spinal stiffness was evaluated by reconstructing patient-specific 3D vertebral configurations in standing and traction conditions. Vertebral geometry was segmented from MRI images from the same patient and incorporated into an articulated spine model. This model was fitted to EOS imaging data for both loading states to recover full 3D vertebral positions and intervertebral motions (Figure1). For each vertebra, translation and rotation matrices were extracted and used as inputs for stiffness estimation. A simplified finite element representation of the spine was built using rigid connectors linked by rotational stiffness elements. Stiffness values along the three anatomical axes (Kx, Ky, Kz) were identified through Nelder–Mead optimization, which minimized the rotational and translational discrepancies between the simulated and reconstructed traction configurations.

Results

Vertebral positions were successfully reconstructed in both standing and traction conditions from EOS imaging data. The stiffness estimation revealed higher rotational

stiffness in the thoracic region (Kx=1.44 Nm/deg, Ky=2.85, Kz=1.36) compared with the lumbar region (Kx=0.21, Ky=0.72, Kz=0.68).

Discussion

The quantified stiffness values align with previously reported ranges (0.7–3.7 Nm/deg), indicating validity of our measurement and modeling framework. These results show that traction-based stiffness estimation offers supplementary quantitative data beyond standard radiographic measurements. Overall, this pilot analysis suggests that combining traction imaging with model-based reconstruction is a promising approach to better characterize individual spinal responses. Future work will include a larger cohort to further assess the variability of stiffness patterns across patients.

Images (Optional)

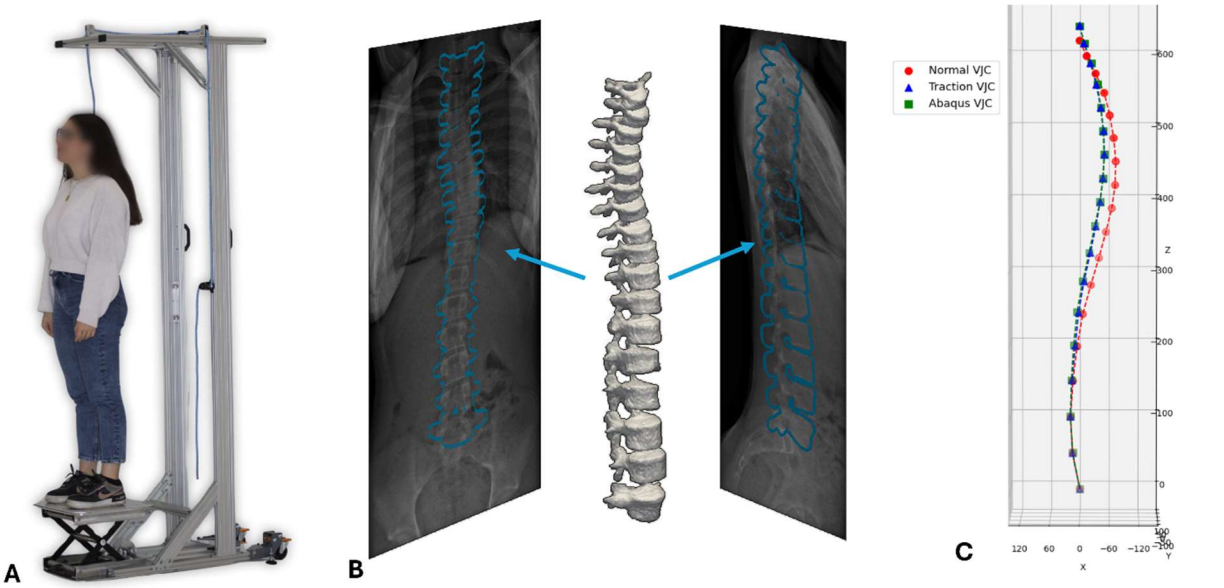


Figure 1. A) Spinal traction device and subject positioning. B) Reconstructed 3D spinal alignment, with the projections of the 3D model overlaid on the coronal and lateral EOS images. C) 3D optimization: the red model represents the spine in the normal (non-traction) condition, the blue model represents the vertebrae in the traction condition, and the green model represents the FE model created in Abaqus at the end of the optimization. Good overlap of the FE model with the traction condition.

References (Optional)

Acknowledgements (Optional)

This work was supported by the Swiss National Science Foundation (#214986).

Session Category

P3-307

In Vitro Experimental Validation of Human-Spine Finite Element Models: A Narrative Review

Ms. Sophie Beauchesne[1,2], Ms. Ariane Parisien MASc[1], Dr. Eugene Wai MD MSc[1], Dr. Matthew Coyle MD MSc[1]

[1]The Ottawa Hospital Department of Orthopaedic Surgery, Ottawa, Ontario, Canada. [2]The University of Victoria, Victoria, British Columbia, Canada

Introduction

Finite element analysis (FEA) enables evaluation of spinal mechanics, including segmental kinematics, stiffness, and implant or tissue stress. Because FEA uses simplified anatomy and material properties, in vitro testing is essential to verify accuracy, confirm clinical relevance, and provide realistic loading conditions and specimen-specific behavior. Cadaveric testing provides direct measurements of spinal motion and loading but is limited by specimen variability, non-physiological loading, and the restricted number of implants or configurations. This review summarizes how FEA and cadaveric experiments complementary characterize spinal biomechanics.

Methods

A systematic review included publications from January 2010 to September 2025. Searches targeted studies combining FEA with in vitro cadaveric testing, using keywords such as “finite element,” “FEA,” “spine,” “lumbar,” “fusion,” “cadaveric,” and “in vitro.” Titles and abstracts were screened by one author, followed by full-text review of eligible studies; inclusion required human-spine FEA studies with cadaveric validation, whereas studies restricted to computational models or involving non-human or synthetic specimens were excluded.

Results

The search yielded 356 records and 335 unique articles; five studies met all inclusion criteria. These studies examined multi-rod constructs after pedicle subtraction osteotomy, interbody fusion approaches (LIF, TLIF, ALIF), hybrid pedicle screw/cortical bone trajectory fixation, and interspinous process devices. Validated FE models reproduced experimental kinematics and loading responses, enabling evaluation of stress distributions, implant strain, and construct stability. In vitro tests used between 6 and 8 fresh-frozen lumbar segments (L1–S2, T12–S1, or L2–L5), with motion capture quantifying intact and

instrumented ROM across flexion–extension, lateral bending, and axial rotation. Rotational loading ranged from ±5 to ±10 Nm, with some aligning with the standardized ±7.5 Nm pure-moment protocol. Axial loading included physiologic preloads of 400–500 N and compressive forces up to 600 N. Across all studies, instrumentation reduced ROM relative to intact spines, and FE models consistently reproduced these reductions while identifying internal stress concentrations not measurable experimentally.

Discussion

Combined FEA and cadaveric testing provides a thorough approach for evaluating spinal mechanics. Remaining challenges include small sample sizes, bone-quality variability, simplified anatomy, and inability to model long-term adaptation. Advancing specimen-specific modeling and physiologic multi-loading will strengthen clinical relevance.

Session Category

Orthopaedic Biomechanics: Spine

P3-308

Biomechanical Investigation of the Effects of Different Cage Heights and Posterior Compressions on the Cage Migration in Transforaminal Lumbar Interbody Fusion Surgery.

Mr. Chi-Sheng Li BS[1], Dr. Ming-Kai Hsieh MD, PhD[2], Dr. Ching-Lung Tai PhD[3], Dr. Weng-Pin Chen PhD[1]

[1]Department of Mechanical Engineering, National Taipei University of Technology, Taipei, Taiwan, Taiwan. [2]Department of Orthopaedic Surgery, Spine Section, Bone and Joint Research Center, Chang Gung Memorial Hospital and Chang Gung University College of Medicine, Taoyuan, Taiwan, Taiwan. [3]Department of Biomedical Engineering, Chang Gung University, Taoyuan, Taiwan, Taiwan

Introduction

In TLIF(Transforaminal lumbar interbody fusion) surgery, suboptimal cage height due to endplate morphology can lead to posterior cage migration, often requiring posterior compression. This study uses finite element analysis to evaluate how different cage heights and posterior compression forces affect biomechanical stability.

Methods

In this study, a lumbar spine model was established using CT images imported into Amira (TGS, San Diego, CA, USA) for vertebral reconstruction. The intervertebral discs were then modeled in SolidWorks (SolidWorks Corp., Boston, MA, USA), and the full geometric model was constructed in HyperMesh (Altair Engineering, Inc., Troy, MI, USA). The implanted device used in this study was a Banana Cage (Wiltrom, Taiwan) with three size variations of 30 × 8/9/10 × 10 mm, as shown in the figure. The completed finite element model was subsequently imported into Abaqus/CAE (Simulia, Providence, RI, USA) for analysis.

The loading conditions were defined based on the work by Yamamoto et al. (1989) [1]. Displacement-controlled loads of 0, 1, 2, and 3 mm were applied at the L3 pedicle screw heads to simulate posterior compression preload. Flexion was selected as the primary physiological motion for biomechanical evaluation.

Results

Based on our analysis results, the stress distribution shifts toward the posterior region of the cage as the posterior fixation compression increases, and the stress magnitude rises

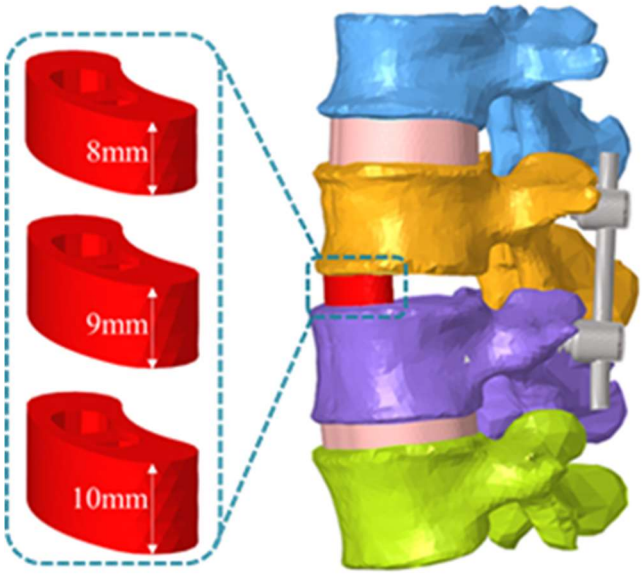
accordingly. In contrast, implanting a higher-sized cage does not produce a significant increase in stress.

The stress distribution on the endplate shows that, with greater compression, the stress shifts posteriorly, which contributes to improved cage stability.

Discussion

Based on the findings of this study, when surgeons encounter endplate anatomy that prevents the insertion of an appropriately sized cage during TLIF procedures, applying compression through the posterior fixation system can effectively stabilize the cage and reduce the risk of posterior cage migration during physiological activities. Our analysis also indicates that using a higher-sized interbody cage does not substantially improve resistance against migration. Therefore, it is recommended that surgeons may opt for a lower-sized cage combined with posterior compression to achieve better stability in clinical practice.

Images (Optional)



References (Optional)

[1] Yamamoto I *et al*. , Spine, 1989

Acknowledgements (Optional)

This research was supported by funding from National Science and Technology Council, Taiwan (NSTC 114-2221-E-182A-006)

Session Category

Orthopaedic Biomechanics: Spine

P3-309

Biomechanical Evaluation of Spinal Fixations Using Novel Dual-Trajectory, Traditional-Trajectory, and Cortical-Bone-Trajectory Screw Systems Under Normal and Osteoporotic Bone Conditions

Mr. Sin-Yan Lee BS[1], Dr. Yun-Da Li MD, PhD[2], Dr. Ching-Lung Tai PhD[3], Dr. Weng-Pin Chen PhD[1]

[1]Department of Mechanical Engineering, National Taipei University of Technology, Taipei, Taiwan, Taiwan. [2]Department of Orthopedic Surgery, New Taipei Municipal TuCheng Hospital, New Taipei City, Taiwan, Taiwan. [3]Department of Biomedical Engineering, Chang Gung University, Taoyuan, Taiwan, Taiwan

Introduction

Improving pedicle screw fixation in osteoporotic spines has long been a clinical challenge. While combining the traditional trajectory (TT) with the cortical bone trajectory (CBT) increases screw number and enhances stability, this approach is limited by pedicle anatomy and the need for additional fixation components. [1,2] To overcome these limitations, this study proposes a dual-trajectory (DT) pedicle screw system composed of a primary screw and an adjustable-angle auxiliary mini-screw, aiming to improve anatomical adaptability and fixation performance.

Methods

A finite element model of L3–S1 was developed from 1-mm CT slices of a 55-year-old male. Vertebrae, discs, endplates, and ligaments were reconstructed, meshed, and assigned literature-based material properties. Four screw constructs were modeled: TT, CBT, and DT systems with 10° and 15° auxiliary mini-screws as shown in figure. Pure moments of 10 N·m in all motion directions, gravitational loading, and a 400 N follower load were applied. Outcomes included segmental range of motion (ROM), adjacent-disc equivalent stress, and auxiliary screw stress, under both normal and osteoporotic bone conditions.

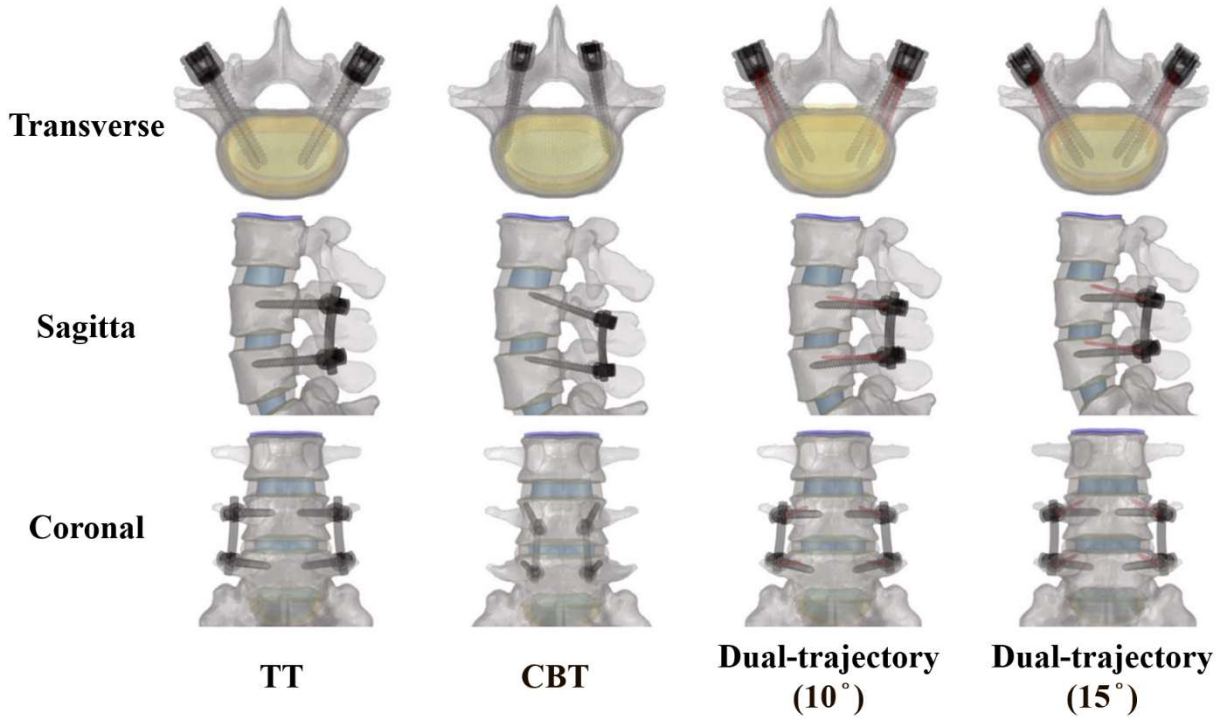
Results

Under normal bone density, the TT and DT systems showed similar ROM, indicating comparable stabilization. In osteoporotic conditions, the 15° configuration provided the greatest ROM reduction in all directions. Adjacent-disc stresses were similar among TT and DT models, whereas CBT produced lower stress in extension but higher stresses in flexion, lateral bending, and axial rotation. Peak stresses in auxiliary screws occurred at the screw-to-screw interface but remained well below the yield strength of Ti-6Al-4V; the 15° model showed lower and more uniform stresses than the 10° model.

Discussion

The DT system offers meaningful benefits primarily in osteoporotic bone, whereas the 15° auxiliary screw improves multi-axial stability and reduces micromotion without increasing adjacent-segment loading. In contrast, the higher stiffness of CBT constructs may elevate adjacent-level stress. The more favorable stress distribution in the 15° configuration suggests improved fatigue resistance and long-term reliability. Overall, the optimized DT system represents a promising strategy for enhancing fixation in osteoporotic spines.

Images (Optional)



References (Optional)

[1] Matsukawa, et al. ,Orthopaedic Surgery, 2015

[2] Mullin, Jeffrey P., et al. , Journal of Neurosurgery: Spine, 2016

Acknowledgements (Optional)

This research was supported by funding from National Science and Technology Council, Taiwan (NSTC 114-2221-E-182A-003)

Session Category

Orthopaedic Biomechanics: Spine

P3-310

Biplane Videoradiography Reveals Segmental Motion Changes Following Spinal Manipulation Therapy: Preliminary Results

Mr. Yaqoub Yusuf MS[1], Mr. Wyatt Cheney[1], Ms. Susan Burnap[1], Dr. Richard Hills PT, DC[2], Dr. Paul Osterbauer DC, MPH[3], Dr. Arin Ellingson PhD[1]

[1]University of Minnesota, Minneapolis, MN, United States. [2]Institute for Orthopedics & Chiropractic, Minneapolis, MN, United States. [3]Lexington Square Chiropractic Center, Minneapolis, MN, United States

Introduction

Spinal Manipulative therapy (SMT) is a commonly used force-based manipulation approach used by chiropractors, physical therapists, and osteopaths to treat back and neck pain by applying force to mobilize a spinal joint and improve function. While research supports its clinical effectiveness, little is known about its mechanism of action, which has been long theorized to normalize spinal motion, particularly at the intersegmental level.

The overall goal of this randomized clinical trial (RCT) is to determine the extent to which SMT can modulate, or normalize, intersegmental motion in patients with neck pain.

Methods

A single participant's (39-year-old male) data, randomized to the SMT arm, is presented herein as a case study. The remaining RCT is ongoing. The participant was evaluated by a licensed Chiropractor (RAH) and intended treatment level (C6-C7) was identified. The participant performed two kinematic assessment sessions, one before and one after SMT. The participant received a low velocity (Maitland grades 3-4) posterior-anterior (AP) glides of C6. Each kinematic assessment included two trials of flexion–extension, lateral bending, axial rotation, and protraction–retraction (FE, LB, AR, PR). Intersegmental kinematics at C4–C5, C5–C6, and C6–C7 were derived from biplane videoradiography. Summary statistics herein include on-axis rotational ROM for each motion (FE, LB, AR, PR) and associated AP translations for FE and PR.

Results

Results suggest a consistent increase in intersegmental motion across all activities (FE, LB, AR, PR) following treatment (SMT). Pain decreased from 4/10 (7/10 worst in past week) to 3/10, with the patient noting less sub-axial restriction and resolution of radicular symptoms.

Discussion

This case study provides preliminary evidence that SMT may positively influence cervical intersegmental motion concomitant with an improvement in self-reported pain and function. The observed increases in ROM across all movement trials suggest that even a single mobilization session can produce measurable biomechanical changes. Although currently limited to one participant with short-term follow-up, we can see that SMT may normalize or enhance segmental mobility, offering insight into its potential mechanism of action. Ongoing RCT data will be essential to confirm these trends and determine their clinical relevance for patients with neck pain.

Images (Optional)

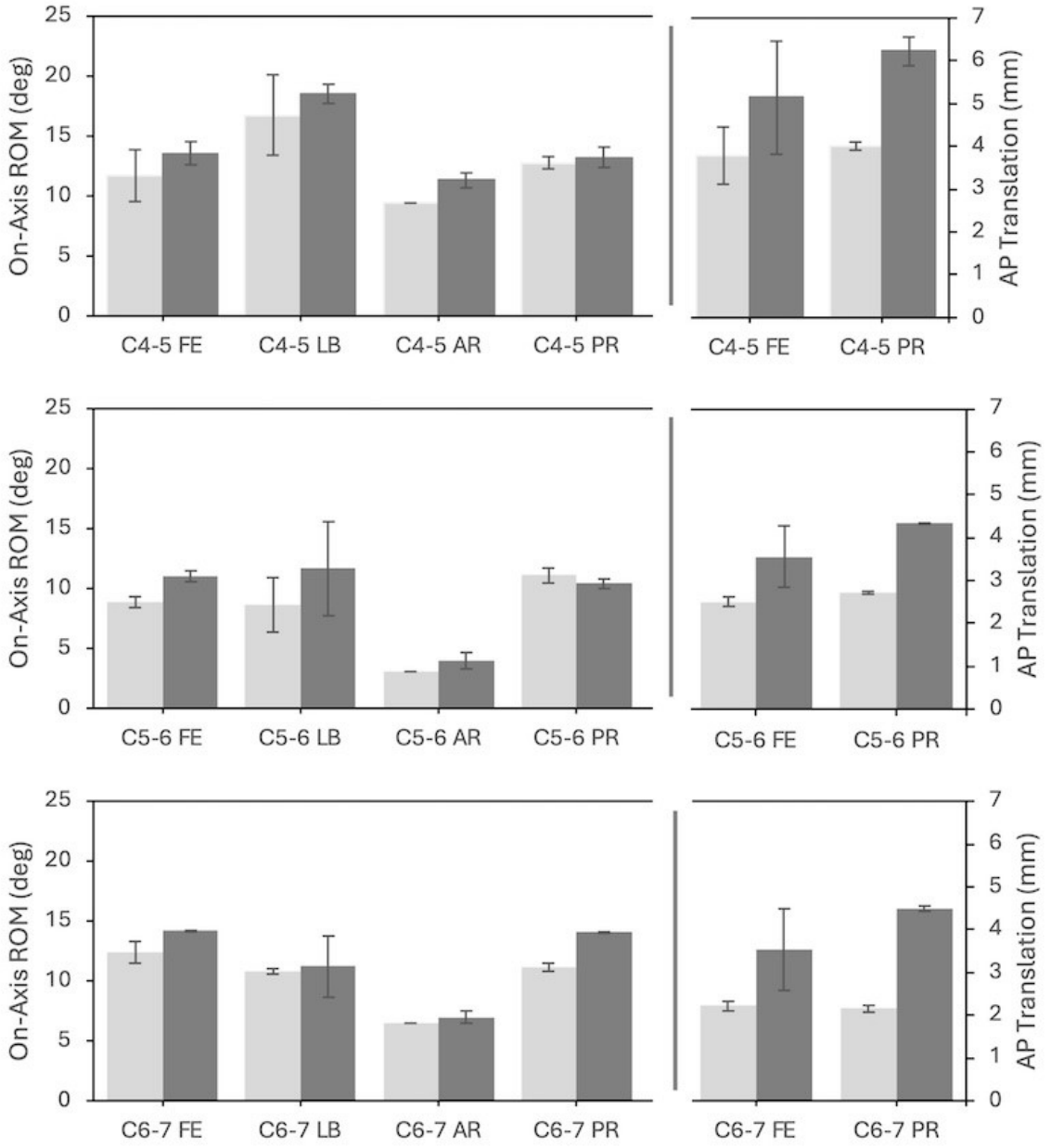


Figure 1. Results demonstrating the Average ROM occurring before and after SMT at the C4-C5 level for all motions; Flexion-Extension (FE), Lateral-Bending (LB), Axial-Rotation (AR), Protraction-Retraction (PR), and Translations (FE-T and PR-T). (E) Similar to D, E demonstrates our findings at the C5-C6 level for the average ROM occurring pre-and post-SMT. (F) Also shows our findings, reporting the average ROM at the C6-C7 level for pre- and post-SMT.

Session Category

Orthopaedic Biomechanics: Spine

P3-311

Do Craniovertebral Angle Measurements Accurately Reflect Forward Head Posture in School-Aged Children?

Ms. Zahra Heydari PhD Student, Biomedical Physiology & Kinesiology (BPK), Simon Fraser University

Simon Fraser University, Burnaby, British Columbia (BC), Canada

Introduction

Children spend many hours each day using smart devises. This increasing screen use appears to be positively associated with a higher frequency of Forward Head Posture (FHP). For school-aged populations, simple and reliable tools that can screen for FHP are therefore clinically important. Two common approaches are photogrammetric measurement of the Craniovertebral Angle (CVA; with FHP often defined as CVA < 50°), and visual posture index (the New York Posture Rating (NYPR) scale) which are still widely used in educational and clinical environments.

Methods

Within the framework of a cross-sectional study, baseline data from 260 school students (130 boys aged 10–14 years and 130 girls aged 13–15 years) were analysed. Markers were attached to the spinous process of the seventh cervical vertebra, the tragus of the ear and the acromion process. For each participant, three standardized lateral photographs were obtained using a fixed camera distance (D5600, Canon Camera). CVA and Shoulder Angle (SHA) were derived from the images using AutoCAD software (release 33), and students were categorized according to FHP status. In parallel, the same images were scored by three specialists independently, using the NYPR scale (scores of 1, 3 or 5) to describe the presence and severity of FHP. All statistical analyses were performed using Principal Component Analysis (PCA) implemented in Mathematica (Wolfram 10.0) to examine the correlation structure among the variables. This study was approved by the relevant ethics committee with the ethical code: IR.ATU.REC.1400.012.

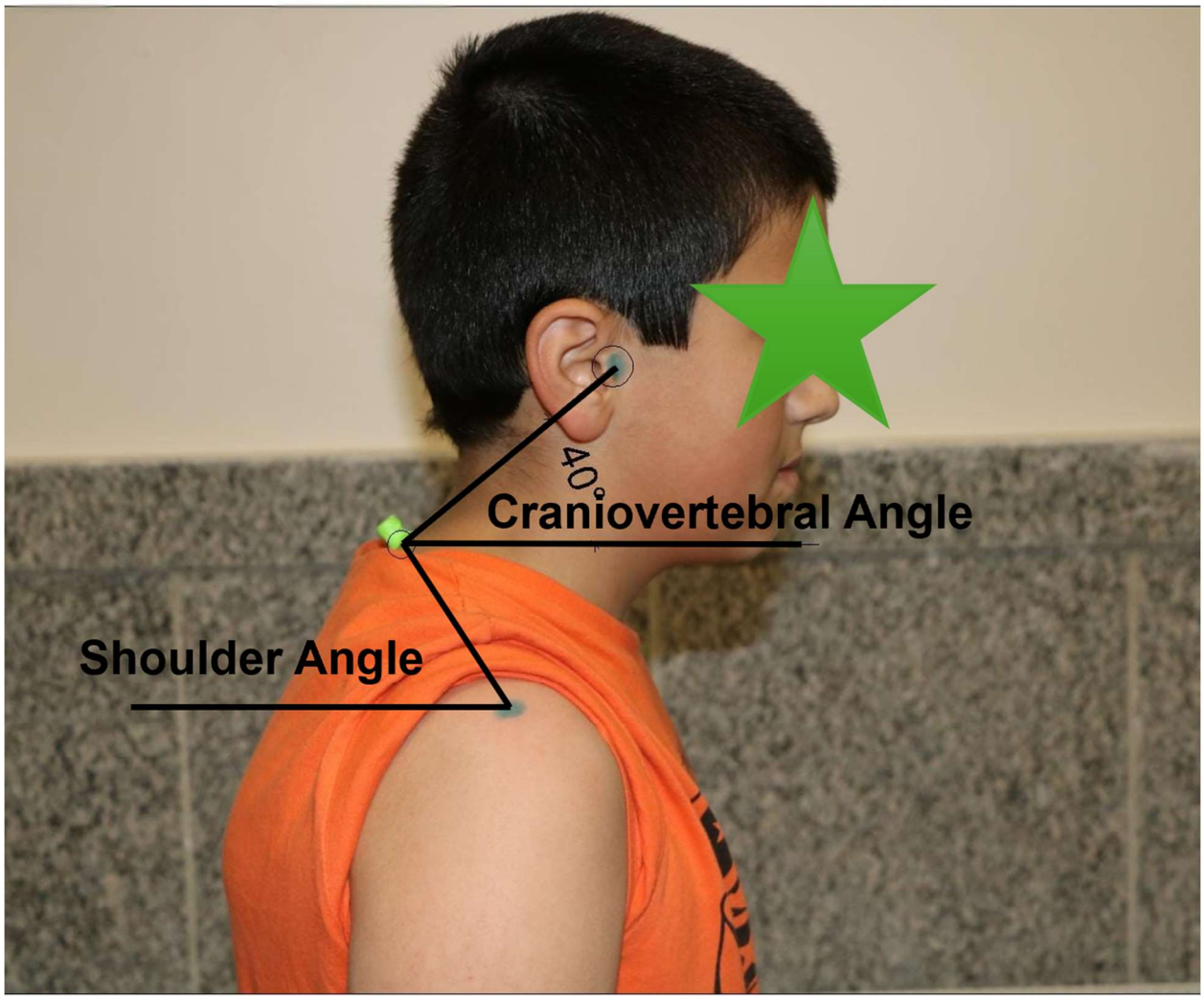
Results

The correlation between CVA and the visual posture scores was r = 0.423, whereas the correlation between SHA and the visual scores was r = -0.302, indicating only moderate agreement between angle-based and observational methods.

Discussion

These results indicate that commonly used clinical and visual tools for FHP do not fully align and that determining the presence or absence of FHP likely requires additional postural measures, such as Shoulder Angle, to categorize children more effectively. Further work is needed to refine angular cut-off values and to develop complementary or composite assessment strategies that enhance FHP screening in school and clinical settings

Images (Optional)



Session Category

Orthopaedic Biomechanics: Spine

P3-312

Differences in Overhead Throwing Biomechanics in Youth Softball Players Based on Age

Dr. Jonathan Santana DO[1], Ms. Abigail Padilla BS[1], Mr. Raul Arrioja BS[1], Mr. Shawn Roberts MS[1], Dr. Tishya Wren PhD[1,2]

[1]Children's Hospital Los Angeles, Los Angeles, CA, United States. [2]Viterbi School of Engineering, University of Southern California, Los Angeles, CA, United States

Introduction

Injury rates in fastpitch softball exceed those in baseball, but there is a dearth of research on biomechanics in softball, especially the development of overhead throwing mechanics. This study examines differences in overhead throwing biomechanics between younger and older youth softball players.

Methods

Players from local youth softball teams completed a throwing session captured by a Theia3D markerless motion capture system. Players threw 5 times to a target 60 feet away. The three fastest throws that hit the target were analyzed. Kinematics were compared between younger (<12 years) and older (≥12 years) players at foot strike, maximum shoulder external rotation (MaxER) during the late cocking phase, and ball release using Wilcoxon Rank Sum tests.

Results

Nineteen female softball players with a median age of 14 years (IQR 5), six <12 and thirteen ≥12 years old, completed the biomechanical assessment. The younger players demonstrated greater shoulder external rotation (73.2 vs. 46.8 deg, p=0.04), greater shoulder elevation (-106.1 vs. -76.4, p=0.04), and less elbow flexion (96.8 vs. 122.1 deg, p=0.01) at the time of foot strike. The younger group also showed more external rotation at MaxER (181.1 vs.168.3 deg, p=0.06). However, shoulder external rotation excursion from foot strike to MaxER was smaller in the younger group (105.2 vs. 126.0 deg, p=0.22). The average throwing velocity in the younger players was significantly lower than older players (37.7 vs. 46.0 mph, p<0.01).

Discussion

Younger softball players demonstrated less efficient throwing mechanics, including less pelvis-to-arm dissociation, which reduces energy transfer and decreases throwing velocity. To compensate, they rely more on shoulder external rotation and elevation earlier in the

throwing cycle, which may increase stress on the shoulder and elbow. These findings highlight developmental differences that may elevate injury risk in youth softball. Recognizing these compensatory mechanics is important for developing age-appropriate training, injury prevention, and rehabilitation strategies.

Images (Optional)

N = 19, all values are median (IQR)	Younger (N = 6)	Older (N = 13)	P value
Average Throwing Speed (mph)	37.7 (4.0)	46.0 (8.0)	**<0.01***
Horizontal Shoulder Abduction (deg)			
Foot Strike	-21.1 (21.7)	-27.2 (27.0)	0.79
Max External Rotation	8.8 (17.1)	13.7 (10.9)	0.93
Release	37.2 (22.6)	22.3 (11.9)	0.08
Shoulder External Rotation (deg)			
Foot Strike	73.2 (28.2)	46.8 (57.9)	**0.05***
Max External Rotation	181.1 (14.2)	168.3 (21.5)	0.06
Release	122.1 (13.1)	105.9 (31.5)	0.22
Shoulder Elevation (deg)			
Foot Strike	-106.1 (35.5)	-76.4 (14.3)	**0.02***
Max External Rotation	-93.4 (35.2)	-96.2 (16.5)	0.86
Release	-94.4 (39.9)	-96.3 (14.0)	1.00
Elbow Flexion (deg)			
Foot Strike	96.8 (40.8)	122.1 (14.0)	**0.04***
Max External Rotation	114.8 (16.8)	110.8 (21.4)	0.66
Release	60.5 (29.3)	35.3 (15.3)	0.08
Lead Knee Angle (deg)			
Foot Strike	32.4 (9.3)	27.6 (23.4)	0.60
Max External Rotation	35.6 (13.3)	35.6 (10.4)	0.86
Release	26.1 (12.6)	22.1 (17.8)	0.93
Trunk Tilt (deg)			
Foot Strike	-11.4 (8.9)	-11.5 (5.0)	0.33
Max External Rotation	6.4 (8.3)	-0.2 (8.3)	0.16
Release	15.9 (7.4)	1.2 (9.6)	**0.02***

Session Category

Orthopaedic Biomechanics: Sports Medicine

P3-313

Using Inertial Sensors to Detect Clinically Meaningful Knee Kinematic Landing Asymmetries

Mr. Adam Dorrance[1], Dr. Scott Landry[1,2], Mr. Ben MacDonald[1], Dr. Nathan Urquhart[3,1], Dr. Janie Astephen Wilson[1,3]

[1]Dalhousie University, Halifax, NS, Canada. [2]Acadia University, Wolfville, NS, Canada. [3]Nova Scotia Health Authority, Halifax, NS, Canada

Introduction

Between-limb asymmetries in knee flexion and knee abduction motion during landing are thought to increase the risk of anterior cruciate ligament (ACL) reinjury after reconstruction surgery [1].

Inertial measurement units (IMUs) enable feasible in-clinic assessment of landing mechanics. Therefore, evaluating whether IMU-derived measures can accurately detect meaningful knee movement asymmetries during landings is important for clinical uptake.

This study examined agreement in knee flexion and knee abduction excursions during drop vertical jump (DVJ) landings, and between-limb asymmetries in excursions, between optoelectronic and IMU systems, as well as the sensitivity and specificity of detecting clinically meaningful excursion asymmetries with the IMU-based system.

Methods

Patients six months to two years post-ACL reconstruction (ACLr) completed three DVJs while knee kinematics were computed using processed data from IMUs secured to both shanks and thighs, (Opal, APDM), and an optoelectronic motion capture system (Motion Analysis; processing through Visual3D, HAS-Motion). IMU processing included sensor-to-segment alignment and sensor fusion [2,3]. Primary outcomes included knee flexion and abduction excursions and their surgical/non-surgical limb asymmetries during the deceleration phase of landing [4]. Bland–Altman analysis assessed agreement between systems. Clinical thresholds for excursion asymmetry were assumed at 9 and 8 degrees (flexion, abduction respectively) based on [1,5], calculated from the optoelectronic data, with sensitivity and specificity of categorizing clinically-meaningful asymmetry with the IMU system calculated.

Results

Nine ACLr patients (6M/3F;age=28±9 years;BMI=25±2 kg/m^2;12±5 months post-ACLr) were recruited (Table 1).

Discussion

The systems showed good agreement for flexion and abduction excursions, with biases and LOA falling within the joint angle error range previously suggested for clinical interpretation [6]. Across 27 DVJs, the IMU system detected between-limb differences exceeding the thresholds with 100% sensitivity and specificity (Table 1).

These findings support the feasibility of novel IMU-based assessments for out-of-lab monitoring of biomechanical deficits relevant to ACL re-injury risk and clinical decision-making. While sensitivity and specificity were excellent, further confirmation with larger samples and stronger validation links of these thresholds with longitudinal clinical outcomes is needed.

Images (Optional)

Table 1: Agreement in knee flexion and abduction excursion outcomes on the surgical (^{S}) and non-surgical (^{N}) limb and the inter-limb asymmetries (calculated as between limb differences) during the deceleration phase of DVJ captured by an IMU and an optoelectronic motion capture. Sensitivity and specificity outcomes based on clinical thresholds of asymmetry are presented as true positive (TP), false positive (FP), true negative (TN), and false negative (FN) classifications. Sensitivity and specificity are calculated using the ratios TP/(TP+FN) and TN/(TN+FP), respectively.

Outcome	Measurement System		Agreement		Sensitivity, Specificity (TP,FP,TN,FN)
	Optoelectronic	IMU	Mean Bias (SD)	LOA	
Flexion Excursion^S (°)	54.3 (9.0)	53.5 (8.7)	1.8 (1.6)	0.3 - 3.3	
Flexion Excursion^N (°)	54.8 (8.5)	53.8 (8.9)	1.9 (1.5)	0.5 - 3.3	
Abduction Excursion^S (°)	3.2 (3.5)	4.8 (4.3)	1.8 (1.7)	0.2 - 3.4	
Abduction Excursion^N (°)	6.5 (4.6)	6.9 (5.0)	1.2 (1.2)	0.1 - 2.3	
Flexion Excursion Asymmetry (°)	0.5 (3.7)	0.2 (3.7)	0.7 (2.1)	-1.3 - 2.7	1, 0, 26, 0
Abduction Excursion Asymmetry (°)	3.3 (5.0)	2.2 (5.3)	1.8 (1.4)	0.5 - 3.1	5, 0, 22, 0

References (Optional)

[1] Meyer et al.,*KSSTA,2018*

[2] Hafer et al.,*JBiomech,2020*

[3] Madgwick,University of Bristol,2010

[4] Dowling et al.,*JBiomechEng,2011*

[5] Ithurburn et al.,*AmJSportsMed,2019*

[6] Cuesta-Vargas et al.,*pTr,2010*

Session Category

Orthopaedic Biomechanics: Sports Medicine

P3-314

Total Hip Arthroplasty Loading Library: In Silico Joint and Muscle Forces for 21 Functional and High-Impact Tasks

Dr Ahmed Soliman[1], Dr Bernard X.W. Liew[2], Prof. Dr. med. Torsten Gerich[3], Prof. Dr. med. Jens Kelm[4], Dr Leiming Gao[5], Prof Stephen McDonnell[6], Dr Wenxing Guo[7], Dr Zainab Altai[2], Prof Nelson Cortes[2], Prof Stefan Maas[1]

[1]Department of Engineering, Faculty of Science, Technology and Medicine, University of Luxembourg, Luxembourg, Luxembourg, Luxembourg. [2]School of Sport, Rehabilitation and Exercise Sciences, University of Essex, Colchester, Essex, United Kingdom. [3]Centre Hospitalier de Luxembourg, Luxembourg, Luxembourg, Luxembourg. [4]Chirurgisch-Orthopädisches Zentrum Illingen, Illingen, Saarland, Germany. [5]Department of Engineering, Nottingham Trent University, Nottingham, Nottingham, United Kingdom. [6]Division of Trauma and Orthopaedic Surgery, University of Cambridge, Addenbrooke's Hospital, Cambridge, Cambridge, United Kingdom. [7]School of Mathematics, Statistics and Actuarial Science, University of Essex, Colchester, Essex, United Kingdom

Introduction

Total hip arthroplasty (THA) is increasingly offered to active patients who wish to resume sport. Yet most in silico and in vitro THA analyses use few loading scenarios, typically walking and stair-climbing. This work presents a THA loading library with mean joint and muscle forces for 21 tasks to support in silico and in vitro biomechanical assessment of implants and periprosthetic bone integrity, and to guide graded return-to-sport protocols.

Methods

Eleven adults with unilateral THA (55.9±9.8 years, 68.9±10.7 kg), ≥1-year post-surgery and cleared for exercise, performed 21 tasks spanning walking, running, hops, jumps, landings and 45–180° change-of-direction cuts. Marker-based motion capture and force plates drove a scaled AnyBody musculoskeletal model to compute operated-hip contact and muscle forces in body-weight-normalised and absolute units. Hip joint contact forces were the primary metric to compare tasks; muscle-force cycles were also provided. Multivariate Dynamic Time Warping Barycenter Averaging (DTW-DBA) yielded cohort-representative waveforms; loading cycles with the highest peak resultant defined “worst-case” loading.

Results

Peak resultant hip joint contact forces (Figure 1) ranged from ≈4.7 body weights (BW) during walking to ≈7.5–8.2 BW during unilateral hopping; running and 45–180° cuts produced ≈6.8–7.9 BW. Ranking subjects by BW-normalised peaks identified a normal-BMI participant as worst case for most walking and running tasks, whereas ranking by absolute forces shifted treadmill and bilateral hopping conditions to the heaviest subject, thereby illustrating how joint demands vary with body mass. Normalised peak hip joint contact forces were benchmarked against in vivo telemetric THA measurements and in silico simulations and were consistent with previously reported hip loading [1, 2].

Discussion

This loading library provides DTW-DBA averaged and worst-case joint and muscle load histories that can be implemented as boundary conditions for in silico and in vitro implant biomechanical tests, complementing instrumented-implant resources such as OrthoLoad while including multi-muscle forces rather than joint contact forces alone. It offers a resource for implant benchmarking and periprosthetic bone assessment. Additionally, it may inform graded, evidence-based return-to-sport counselling for THA patients with sporting ambitions in routine clinical practice.

Images (Optional)

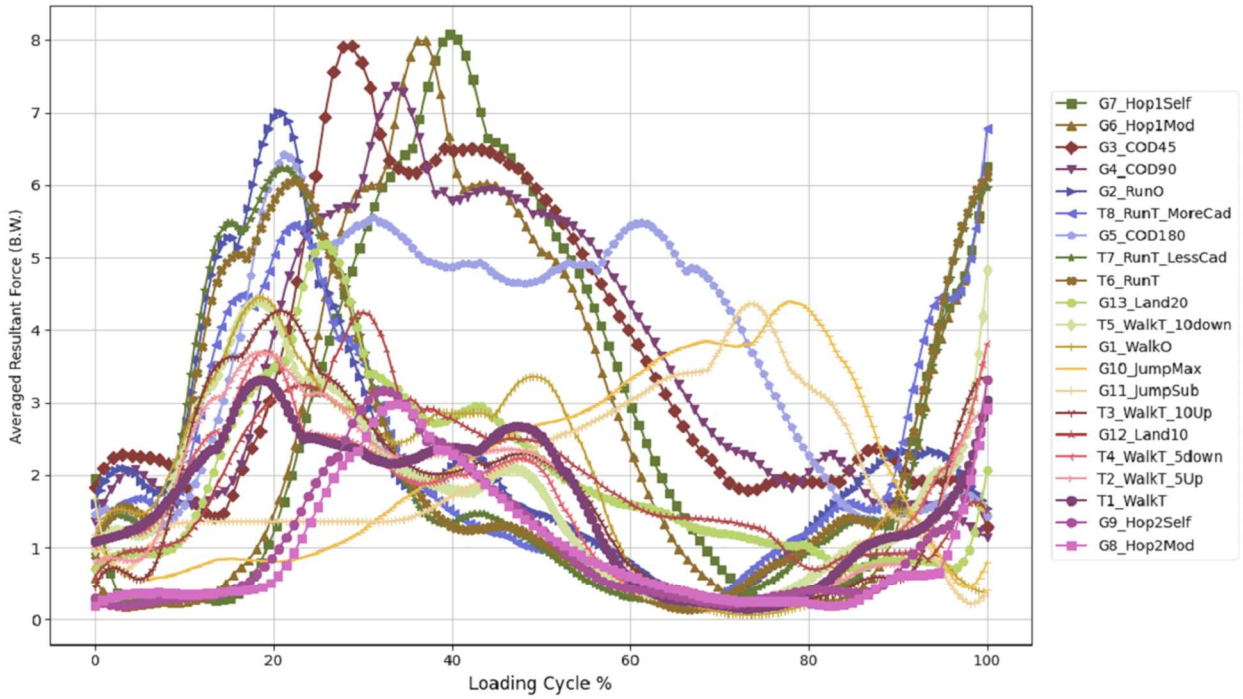


Figure 1 Averaged hip joint contact force (HJCF) data from 11 subjects across 21 movements *(prefixes: over-ground movements G1–G13, treadmill movements T1–T8). Dynamic legend of movements is ordered by maximal peak HJCF. Movement labels: level walking and running (WalkO: over-ground walk; WalkT: treadmill walk; RunO: over-ground run; RunT: treadmill run; RunT_LessCad/MoreCad: treadmill running at fixed speed with - 10%/+10% cadence), inclined treadmill walking (WalkT_5Up/10Up: +5°/+10° upslope; WalkT_5Down/10Down: - 5°/- 10° downslope), hopping (Hop1Mod/Hop1Self: unilateral hopping at moderate/self-selected cadence; Hop2Mod/Hop2Self: bilateral hopping at moderate/self-selected cadence), jumping/landing (JumpMax/JumpSub: maximal/submaximal countermovement jump; Land10/20: landing from 10/20 cm), and change-of-direction cuts (COD45/90/180: 45°/90°/180° cuts).*

References (Optional)

[1] Bergmann et al., PLoS One, 2016.

[2] Varady et al., J Biomech, 2015.

Acknowledgements (Optional)

Supported by SafeJOINTs, funded by UKRI – FNR.

Session Category

Orthopaedic Biomechanics: Sports Medicine

P3-315

Using Jumping Tasks to Identify Biomechanical Risk Factors for Musculoskeletal Injuries and Clinical Outcomes: A Scoping Review

Dr. Felipe F. Gonzalez MD, MSc[1,2], Ms. Aleksandra Kozicka BS[1], Dr. Marcos Amstalden Barros MD[1,2], Mr. Rithik Palaniappan BS[1], Mr. Poojan Thakkar MS[1], Dr. Renato Miyadahira MD[1,2], Dr. Tiago Zimerman MD[1,2], Dr. Carolline Popovicz Nunes MD[1,2], Dr. Jonathan A. Gustafson PhD[1,2], Dr. Leonardo Metsavaht MD, PhD[2], Dr. Jorge Chahla MD, PhD[1,3], Dr. Gustavo Leporace PhD[2]

[1]Rush University Medical Center, Chicago, IL, United States. [2]Instituto Brasil de Tecnologia da Saúde – IBTS, Rio de Janeiro, RJ, Brazil. [3]Midwest Orthopaedics at Rush, Chicago, IL, United States

Ms. Aleksandra Kozicka

Introduction

Orthopedic injuries account for approximately 1 million hospital visits annually, as well as considerable physical, psychological, and socioeconomic burdens. Various studies have explored valid and low-cost screening tools to identify biomechanical risk factors for musculoskeletal (MSK) injuries and unfavorable clinical outcomes. Jumping tasks have emerged as a prominent option within these assessments. However, existing findings remain fragmented or focus primarily on anterior cruciate ligament (ACL) injuries. This review aimed to determine whether jumping tasks can identify biomechanical risk factors for musculoskeletal injuries beyond ACL tears and whether they can also reveal factors associated with unfavorable clinical outcomes.

Methods

This systematic scoping review followed PRISMA guidelines and was registered in PROSPERO. Searches were conducted with support from an experienced librarian in PubMed/MEDLINE, Scopus, Cochrane CENTRAL, IEEE Xplore, and Google Scholar. Eligible studies included longitudinal designs evaluating jumping tasks as a predictive screening tool for MSK injuries. Exclusion criteria were ACL-focused studies, nonhuman or robotic models, and case reports/series. Three reviewers independently screened studies, extracted data, and assessed risk of bias using the NIH quality assessment tool. The primary outcome was MSK injury risk associated with biomechanical factors

identified during jumping tasks; secondary outcomes included other clinical outcomes linked to these biomechanical factors.

Results

A total of 60 studies were included. Most (51) evaluated young, healthy people. In 37 of these studies, jumping tasks identified individuals at higher risk of sustaining MSK injuries, such as traumatic injuries, overload injuries, and low back pain (Table 1). The remaining 9 studies involved participants with baseline orthopedic conditions, such as Achilles tendinopathy and ankle sprain; 6 of these studies linked poor performance on jumping tasks to worse clinical outcomes, including prolonged recovery times and higher risk of chronicity.

Discussion

Jumping tasks are a promising tool for identifying higher risk of MSK injuries, beyond ACL tears, in healthy, young, athletic populations. In individuals with pre-existing orthopedic pathologies, poor performance on jumping tasks is associated with unfavorable clinical outcomes. However, given the heterogeneity and methodological limitations of the included studies, clinicians should interpret these findings with caution and use jumping tasks alongside other clinical assessments.

Images (Optional)

Table 1a.

Jumping task as a prognostic factor	Population condition at baseline	Number of Studies
Significant	Healthy	37
	Orthopedic Pathology Present	6
Non- Significant/ Cannot Assess	Healthy	14
	Orthopedic Pathology Present	3

Table 1b.

Assessed Variables		Outcomes - association with injury (number of studies)	
		Significant	Non-significant
Joint Kinematics	*Knee*	*7*	*3*
	Ankle	*2*	*5*
	Hip & Pelvis	*6*	*4*
	Total	15	12
Kinetics		9	3
Asymmetry metrics		7	3
Jump height & distance	*Height*	*5*	*7*
	Distance	*6*	*5*
	Total	9	12
Other		3	0

Table 1a: Summary of included studies categorized by study population
Table 1b: Summary of included studies categorized by assessed variables

Session Category

Orthopaedic Biomechanics: Sports Medicine

P3-316

Quadriceps Muscle Imbalance in Patients with Unilateral Patellofemoral Pain- A Pilot Study

Mr. Charles Scheuermann[1], Dr. Hyun Kim Ph.D.[1], Dr. Efthymios Papadopoulos Ph.D.[1], Ms. Megan Gordon[1], Mr. Derek Calvert ATC[2]

[1]School of Kinesiology, Louisiana State University, Baton Rouge, Louisiana, United States. [2]Louisiana State University Athletics, Baton Rouge, Louisiana, United States

Introduction

Patellofemoral pain (PFP) is common among physically active individuals. Previous research has highlighted the importance of the balance between the vastus medialis oblique and vastus lateralis [1], as mal-tracking may contribute to PFP. The study aimed to investigate quadriceps muscle imbalance in individuals with unilateral PFP against healthy controls. We hypothesize that participants with PFP would show greater quadriceps imbalance.

Methods

Four individuals with unilateral PFP (2M, 2F; 24.5±4.8yrs; 178.8±16.6cm; 78.8±11.3kg; diagnosed < 2 months; data collection ongoing) and 25 healthy controls (15M, 9F; 22.4±4.2yrs; 173.7±11.1cm; 80.5±19.8kg) without lower-limb injuries participated; four matched individuals were used for statistical analysis. Muscle thickness (cm) of rectus femoris (RF), vastus medialis (VM), and vastus lateralis (VL) on both sides was measured using a handheld ultrasound (Clarius L15 HD3) with participants supine. Measurements followed the previously described protocol [2,3]. Each muscle was measured three times, and the mean value was analyzed. Within-group comparisons (injured vs. non-injured sides) used paired t-tests, and between-group (PFP vs control) differences in VL/VM ratios and symmetry index (SI%; Xinjured-Xnon-injured)/0.5(Xinjured+Xnon-injured)×100) were tested with independent t-tests.

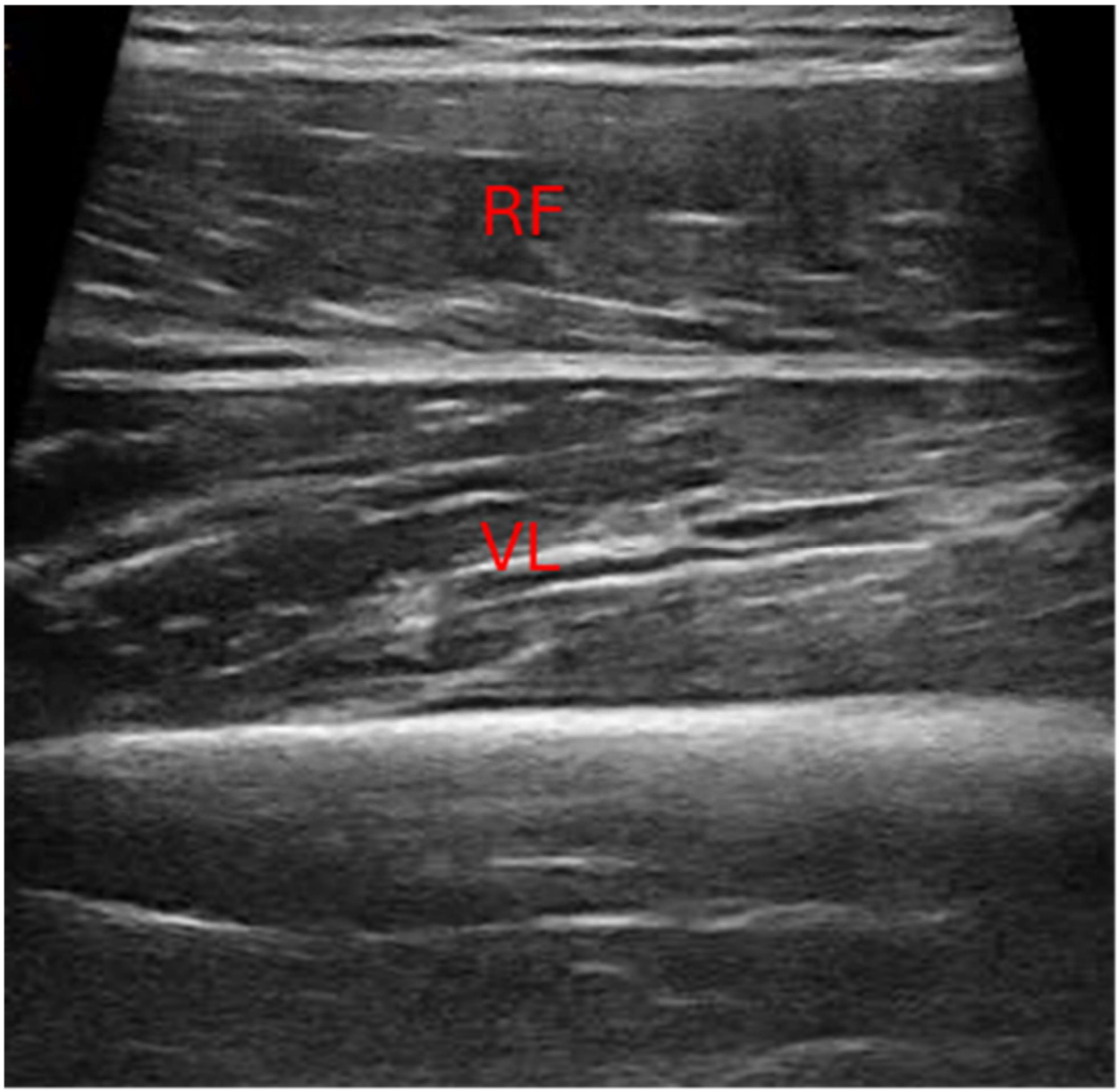
Results

The injured side showed a significantly lower VL/VM ratio than the non-injured side in PFP patients (0.71±0.04 vs. 0.77±0.05, p=0.01). The PFP group also demonstrated a significantly higher SI% for the VL than healthy controls (8.81±1.70 vs. 2.90±3.14, p=0.02), indicating greater asymmetry. No significant differences were found in individual muscle thickness between groups or between legs.

Discussion

The lower VL/VM ratio on the injured side suggests quadriceps imbalance, with reduced lateral relative to medial development in individuals with PFP. This imbalance may contribute to altered patellar tracking and increased joint stress. The higher symmetry index indicates greater side-to-side asymmetry, supporting that imbalance and asymmetry are key features of PFP. However, the absence of significant differences in absolute thickness suggests that relative proportion, not overall muscle size, may be more relevant to PFP-related adaptations.

Images (Optional)



References (Optional)

[1] Song CY et al., Phys Ther Sport, 2011; [2] Emerson C et al., J Funct Morphol Kinesiol, 2025; [3] Benjafield A et al., Clin Anat, 2015.

Session Category

Orthopaedic Biomechanics: Sports Medicine

P3-317

Ankle Laxity Quantified via Optical-Flow Based Bone-Tracking Relates to Clinically Relevant Characteristics After Ankle Sprains in Division-I Collegiate Basketball Athletes

Ms Claire Tanaka MS[1], Dr. Matthew Blomquist PhD[1], Dr. Naoaki Ito DPT, PhD[1], Ms Katharine Carter MSc[2], Dr. Bryan Heiderscheit PT, PhD, FAPTA[1]

[1]University of Wisconsin, Madison, WI, United States. [2]GE HealthCare, Waukesha, WI, United States

Introduction

Ankle sprains are highly prevalent in sports, with ~75% involving the anterior talofibular ligament (ATFL). Assessments such as the reverse anterolateral drawer test (RALD) classify ATFL laxity, but their binary interpretation limits quantification of joint displacement. Advancements in ultrasound (US) bone-tracking enable measurement of the talus-fibula displacement at the ATFL during RALD, yet its relationship to symptoms is unknown. This study aimed to compare US-derived maximum ankle displacement (i.e., laxity) with clinical RALD grading and to examine the relationship between displacement and athlete-reported chronic ankle instability using the Cumberland Ankle Instability Tool (CAIT).

Methods

CAIT scores and B-mode US cine loops of the ATFL (Figure 1a) during RALDs were collected bilaterally in 29 Division I basketball athletes (Female|Male: n=14|15, age= 20.9±1.3|20.8±1.6years, BMI= 23.4±1.5|24.9±1.7kg/m^2). RALDs were graded by one of two physical therapists. Maximum ATFL displacement was quantified using an optical-flow bone-tracking algorithm that measured talus-fibula distance across cine loop frames during RALD. Linear mixed effects models assessed (1) the fixed effect of RALD grade (+/-) on maximum displacement (mm), and (2) the fixed effect of maximum displacement on CAIT score (0-30, lower = worse symptoms). Both models included random effects of rater and athlete, with sex included as a covariate.

Results

Positive RALD grade related to greater ATFL displacement ($p < 0.001$; mean difference [95%CI] = 0.92 [0.46, 1.37] mm; Figure 1b). Greater ATFL displacement also related to worse CAIT score ($p = 0.03$, estimate [95%CI] = -1.1 [-2.1, -0.14]), with the marginal R^2 of the model limited to 0.086 (Figure 1c).

Discussion

A positive RALD was associated with 1mm greater ATFL displacement, however, the large spread in displacement within the positive and negative groups must be acknowledged. Similarly, 1mm greater displacement of the ATFL was related to 1-point lower CAIT score, but the fixed effects of the model only explained 9% of the variance. Quantifying ATFL laxity with US bone-tracking may provide an objective metric to inform prognosis for recovery, refine injury risk, and enhance injury-prevention strategies with greater precision than has previously been considered.

Images (Optional)

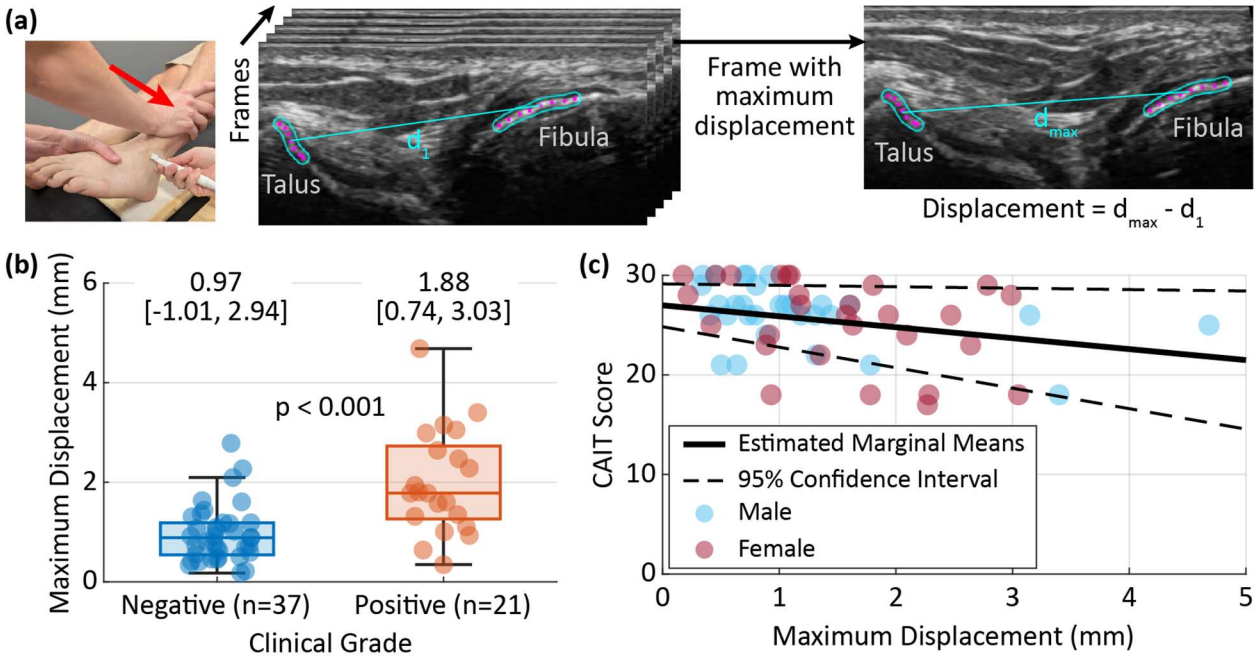


Figure 1: (a) Maximum anterior talofibular ligament (ATFL) displacement quantified via ultrasound (US) bone-tracking of talus-fibula distance (d) across US cine frames. **(b)** Box plots of raw ATFL maximum displacement by reverse anterolateral drawer (RALD) grade, with model-estimated means [95% confidence intervals]. **(c)** A linear mixed effects model assessed the effect of maximum displacement on Cumberland Ankle Instability Tool (CAIT) score (marginal $R^2 = 0.086$, conditional $R^2 = 0.55$).

References (Optional)

Acknowledgements (Optional)

This project was made possible by the BIM study group. Funding was provided by the NBA, NBPA, and GE HealthCare, who had no role in the study or decision to share results.

Efforts for author NI was in part supported by by the National Institute Of Arthritis And Musculoskeletal And Skin Diseases of the National Institutes of Health under Award

Number K99AR085752. The content is solely the responsibility of the authors and does not necessarily represent the official views of the National Institutes of Health.

Session Category

Orthopaedic Biomechanics: Sports Medicine

P3-318

Anterior Cruciate Ligament Reconstruction with Orthobiologic Injections Improves Muscle and Joint Function

Dr Colin Smith PhD, Mr Austin Carcia BS, Ms Kristen Seballos MS, Ms Rachel Conley BS, Dr Armando Vidal MD, Dr Johnathan Godin MD, Dr Thomas Hackett MD, Dr Peter Millett MD, Dr Matt Provencher MD, Dr Johnny Huard PhD, Dr Scott Tashman PhD

Steadman Philippon Research Institute, Vail, CO, United States

Introduction

Despite advances in surgical technique and rehabilitation, recovery from anterior cruciate ligament reconstruction (ACLR) still requires over one year. Orthobiologic injections such as Platelet Rich Plasma (PRP) and Bone Marrow Aspirate Concentrate (BMAC) aim to accelerate healing, however, evidence for their benefits is mixed [1]. We performed a clinical trial to evaluate whether PRP and BMAC accelerate healing and improve muscle and joint function after ACLR.

Methods

We recruited 43 unilateral anatomical bone-patellar-tendon-bone ACLR patients (22 Female, Age = 29±7) for a three-arm (PRP, BMAC, control) randomized clinical trial. Injections were performed at the time of surgery. At 6 and 12 months post-surgery, each participant underwent a CT Scan, MRI, blood test, muscle strength test, Dynamic Stereo Xray (DSX) assessment of knee function, and answered pain surveys. DSX imaging was collected at 120 Hz during downhill running. CT bone models were registered to the biplane x-ray images to assess knee joint kinematics and ACL strain. Group differences in limb asymmetry were assessed separately at 6 and 12 months using one-way ANOVA, followed by Tukey's post hoc tests for pairwise comparisons. Statistical Parametric Mapping (SPM) was used to perform an ANOVA to assess the differences in ground reaction forces, knee kinematics, and ACLR graft strain between the treatment groups.

Results

At 6 months post-ACLR, the PRP group exhibited significantly smaller quadriceps peak torque asymmetries compared to the controls (mean difference=−19.80%, p=0.046). During downhill running, SPM revealed significantly increased ground reaction forces in the BMAC group compared to the controls (p<0.001) across 14–48% of the stance phase. Compared to the control group, the ACL strain was increased during running at 6 months in both the PRP (p<0.001, 6-30% stance) and BMAC (p<0.001, 12-30% stance) groups. No

differences were found between the PRP and BMAC groups in any of the statistical comparisons.

Discussion

The results of our clinical trial indicate that both PRP and BMAC injections accelerated healing and loading of the injured knee at 6 months. This suggests that these orthobiologic treatments may compliment early-loading rehabilitation to improve recovery of function.

Images (Optional)

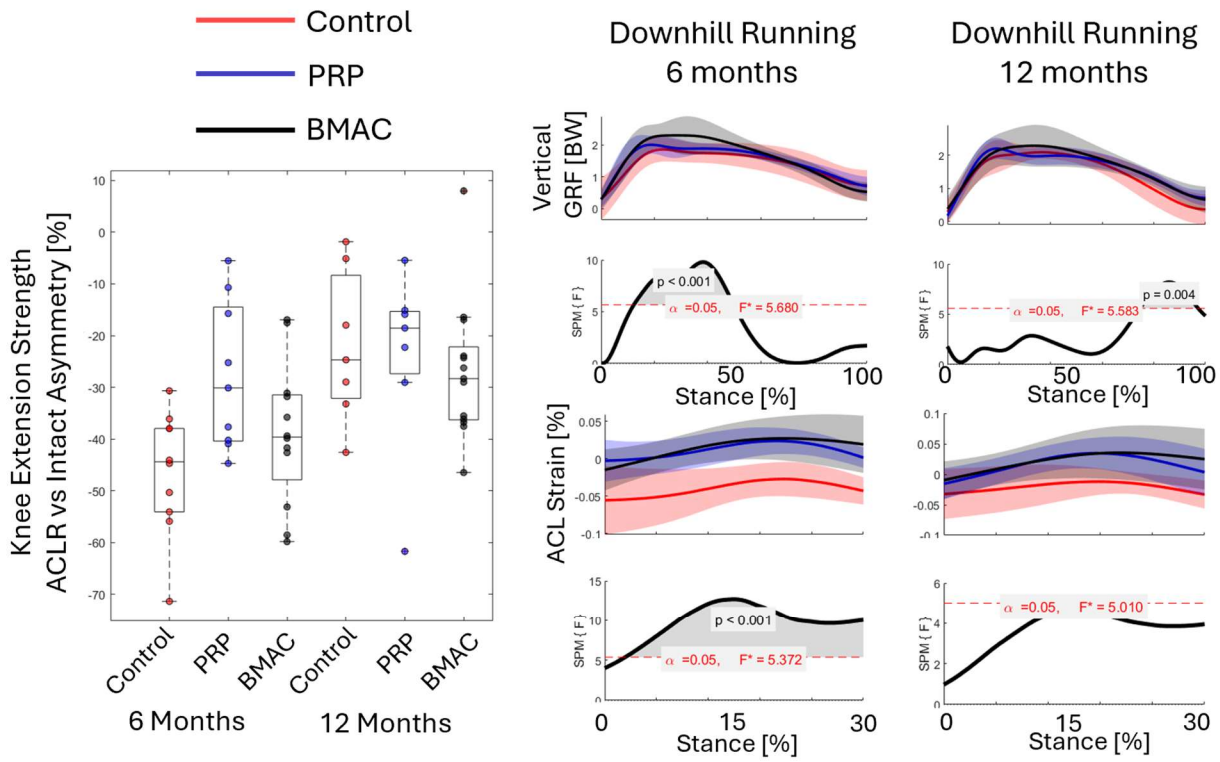


Figure 1 – (Left) The PRP and BMAC groups showed improved strength in the ACLR limb compared to the control at 6 months. (Right) Compared to the control, the PRP and BMAC groups showed increased ground reaction forces on the ACLR limb and strain in the ACLR graft during downhill running at 6 months indicating an accelerated recovery of function.

References (Optional)

[1]Kon, Orthop. Res, 2021

Acknowledgements (Optional)

Office of Naval Research, Contract # N00014-19-C-2052

Session Category

Orthopaedic Biomechanics: Sports Medicine

P3-319

Biomechanical Evaluation of Orthopedic Suture Knot Constructs: A Comparative Analysis

Dr David Rouault, Ms Cameron Scott, Dr Lindsay Westover, Dr Ahmed Samir Ead, Ms Stephanie Nathanail, Mr Richard Roberts, Dr Abdulrehman Abuhaimed, Dr Martin Bouliane, Dr Joseph Cavanagh

University of Alberta, Edmonton, Alberta, Canada

Introduction

Suture knot constructs are fundamental in Orthopedic surgery and are often used for soft-tissue fixation, bone block stabilization, and fracture cerclage. The performance of these constructs depends on suture material and knot security under both dynamic and static loads, yet comparative biomechanical data combining both knot types and different suture materials in physiological environments remains limited. The objective of this study was to evaluate how suture material, testing environment, and knot configuration influence creep behavior and the force required to reach a clinically relevant failure threshold (3 mm of displacement) after dynamic loading.

Methods

Ninety-six constructs (n = 3 per condition) were tied using four knot types (Standard Nice, Modified Nice 1, Modified Nice 2, Surgeon's knot) with #4 Ultrabraid or #5 Ethibond. Constructs were tested in air or phosphate-buffered saline at room temperature (22°C). Two load protocols were applied: (1) static creep at 100 N for 10 minutes and (2) cyclic loading (10–45 N, 1.8 Hz, 1,000 cycles) followed by load until failure. Outcomes were creep rate and force at clinical failure. Linear regression and ANOVA assessed main and interaction effects.

Results

Our testing revealed that environment (air vs fluid) had no significant effects on our outcomes; thus, results from both environments were pooled for further comparison. Material and knot configurations were strong predictors of creep and failure performance. For creep testing, Ethibond and Modified Nice 2 had the lowest creep rate ($1.37\pm0.41\times10^{-4}$mm/s), while Ultrabraid and Surgeon's knot had the highest ($3.58\pm0.52\times10^{-4}$ mm/s; difference 2.21×10^{-4} mm/s, 95% CI 1.58–2.83, $p<0.001$). After

cyclic loading, Ultrabraid and Modified Nice 2 produced the highest force at 3 mm failure (404.8±86.1 N), exceeding Ethibond and Surgeon's knot (136.2±30.3 N; difference 268.7 N, 95% CI 187.2–350.1, $p<0.001$).

Discussion

Suture material and knot configuration significantly affected construct performance, whereas testing environment did not. No suture material demonstrated consistent superiority during our testing protocols, while the modified Nice 2 knot consistently demonstrated increased performance. These findings support evidence-based selection of suture-knot constructs and warrant further investigation including additional suture types.

Images (Optional)

Table 1. Suture and Knot Testing Results

Material	Knot	Average Force at Clinical Failure (N)	Standard Deviation (N)	Average creep rate (x 10^{-4} mm/s)	SD (x 10^{-4} mm/s)
Ethibond	Modified Nice 1	178.80	16.56	1.46	0.31
Ethibond	Modified Nice 2	209.47	16.37	1.37	0.41
Ethibond	Regular Nice	171.17	4.41	1.49	0.39
Ethibond	Surgeon's knot	136.18	30.31	2.24	0.80
Ultrabraid	Modified Nice 1	292.80	160.91	3.06	0.79
Ultrabraid	Modified Nice 2	404.83	86.13	2.66	0.27
Ultrabraid	Regular Nice	210.42	42.03	2.94	0.55
Ultrabraid	Surgeon's knot	236.57	48.80	3.58	0.52

Acknowledgements (Optional)

CORE research department University of Alberta

Session Category

Orthopaedic Biomechanics: Sports Medicine

P3-320

Accuracy of Markerless Motion Capture for Clinical Hop Testing: An OpenCap Validation Study

Dr. Deborah King Ph.D., Dr. Teresa Chen PT, Ph.D., Dr. Karen Lomond Ph.D.

Ithaca College, Ithaca, NY, United States

Introduction

After anterior cruciate ligament reconstruction only 66% of athletes return to pre-injury level [1] and risk of re-injury is 40%[2]. Return to activity (RTA) 'hop-test' performance inconsistently predicts successful RTA warranting movement quality assessment for RTA decision making [3]. OpenCap (OC), an opensource iPad/iPhone motion capture system, may provide clinicians with objective measures of movement quality. Hop-test kinematics using OC have good to moderate validity; joint kinetics were not examined [4]. The purpose of this study was to validate OC knee and hip biomechanics during hop landings.

Methods

Three vertical hop landings from 15 healthy adults were analyzed to compare sagittal plane knee angles ($\theta_{K_FL/EX}$) and moments ($M_{K_FL/EX}$) and tri-planar hip angles ($\theta_{H_FL/EX}$, $\theta_{H_AB/AD}$, θ_{H_ROT}) and moments ($M_{H_FL/EX}$, $M_{H_AB/AD}$, M_{H_ROT}) between OC and Vicon. Vicon and OC data were processed in Visual3D and Python, respectively. Matlab was used to synchronize, filter, and average all trials for each participant and calculate peak angles, moments, cross correlations (R_{xy_max}), and mean absolute error (MAE). Intraclass correlations (ICC) were calculated (Jamovi).

Results

Maximum $\theta_{K_FL/EX}$ and $\theta_{H_FL/EX}$ had moderate to good agreement (ICC_{Knee}=0.769 & ICC_{Hip}=0.619) averaging 6° difference between systems for θ_{K_FL/EX_MAX} and 13° for θ_{H_FL/EX_MAX}; OC underestimated θ_{H_FL/EX_MAX} (Table). $\theta_{K_FL/EX}$ and $\theta_{H_FL/EX}$ MAE and R_{xy} were moderate to good (Table). θH_AB/AD, θ_{H_ROT}, and all moments had poor to moderate agreement (ICC=0.080 – 0.619) with large MAE. R_{xy} was moderate ($\theta_{H_AB/AD}$, θ_{H_ROT}), good ($M_{H_FL/EX}$), and excellent ($M_{K_FL/EX}$, $M_{H_AB/AD}$, M_{H_ROT}) (Table).

Discussion

OC provided acceptable $\theta_{K_FL/EX}$ measures during hop landings supporting previous findings [4]. Hip flexion accuracy was less consistent, though cross-correlations were excellent. Joint moments and non-sagittal hip angles had unacceptable accuracy for clinical decision making. Calculating moments was time-consuming, required computer

expertise, and seems currently untenable for clinical use. Further research into OC is warranted for kinematic data and RTA applications.

Images (Optional)

Table. Knee and hip joint angles and net muscle moment peak values, mean absolute error, and cross correlations.

	Angles			
	$\theta_{K_FL/EX}$	$\theta_{H_FL/EX}$	$\theta_{H_AB/AD}$	θ_{H_ROT}
OC_p (°)	53.2±13.3	37.3 ±21.8	1.1 ±4.5	4.3 ±3.9
$Vicon_p$ (°)	59.3±10.8	50.4 ±22.6	3.7 ±4.2	4.0 ±10.0
MAE (°)	7.64 ±3.4	14.6 ±10.4	5.3 ±3.9	8.8 ±5.98
R_{xy_max}	0.99 ±.01	0.95 ±0.12	0.63 ±0.33	0.50 ±0.35
	Moments			
	$M_{K_FL/EX}$	$M_{H_FL/EX}$	$M_{H_AB/AD}$	M_{H_ROT}
OC_p (Nm/BWHt)	0.11 ±-0.16	0.06 ±0.04	0.06 ±0.01	0.02 ±0.01
$Vicon_p$ (Nm/BWHt)	0.15 ±0.21	0.08 ±0.05	0.11 ±0.04	0.04 ±0.02
MAE (Nm/BWHt)	0.03 ±0.01	0.03 ±0.02	0.03 ±0.02	0.01 ±0.01
R_{xy_max}	0.96 ±0.04	0.82 ±0.27	0.96 ±0.09	0.92 ±0.08

Note. OC_p = OC peak values, $Vicon_p$ = Vicon peak values. All values are Mean ±SD . Angles, Flexion = +, Adduction = +, Internal Rotation = +. Moments are internal moments. Extension = +, Abduction = +, Internal rotation = +.

References (Optional)

[1] *Clare Ardern, et al.,* Br J Sports Med, 2014

[2] *Kate Webster & Julian Feller*, Orthop J Sports Med, 2020

[3] *William Davies, et al.,* Sports Med, 2020

[4] *Jeffrey Turner, et al.,* J Biomechanics, 2024

Session Category

Orthopaedic Biomechanics: Sports Medicine

P3-321

Identifying Sport-Specific Kinematic Drivers of Primary Cam Morphology-Associated Impingement Using a Computational Hip Model

Mr Harry Manship[1], Professor Amy Zavatsky[1], Professor Stephen Mellon[2,1], Professor Siôn Glyn-Jones[1]

[1]University of Oxford, Oxford, Oxfordshire, United Kingdom. [2]University of Southern Denmark, Odense, Region Syddanmark, Denmark

Introduction

Femoroacetabular impingement syndrome (FAIS) due to primary cam morphology causes hip pain and osteoarthritis in young athletes [1]. Early identification facilitating activity management and treatment relies on static imaging and range-of-motion tests but misses dynamic femoroacetabular joint interactions [2]. An open-source computational model [3] has been developed to evaluate the role of individual hip kinematics on impingement, but previously studied motions were not sport-specific. We applied this model to test the hypothesis that impingement incidence, location, and severity across sport-specific motions are systematically associated with characteristic combinations of hip rotations.

Methods

The model [3] was used to simulate four cam positions, each with a peak alpha angle of 80° at varying anterosuperior femoral head-neck locations. Impingement risk was determined using a 3D motion capture dataset curated by Zhao et al. [4] of 183 athletes (153 males, 30 females; age = 20.35 ± 4.20 years) performing 25 athletic exercises. Linear mixed-effects regression quantified the relationship between hip orientation and impingement severity (defined as angular overlap of structures).

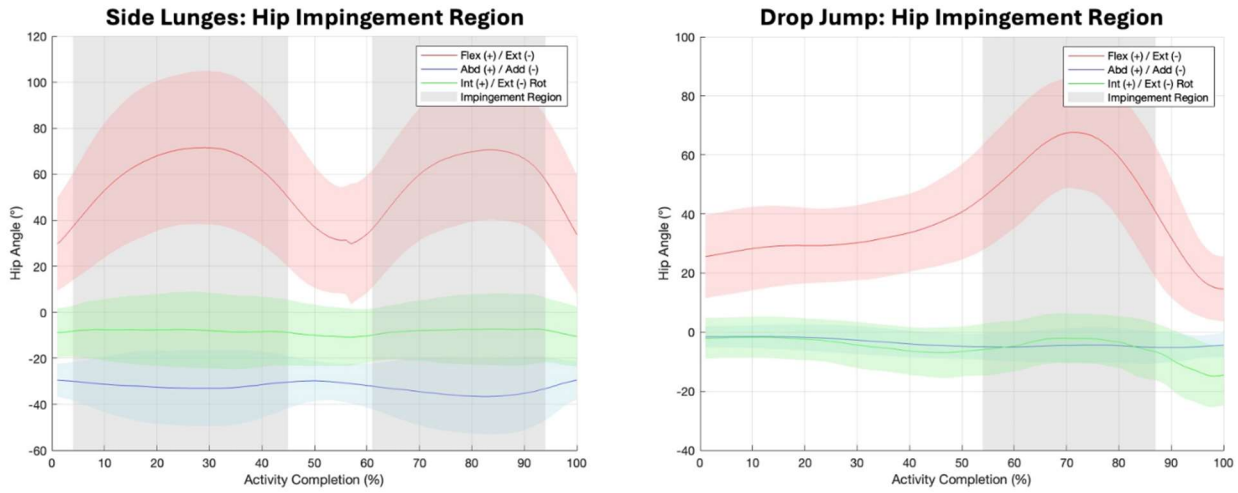
Results

For all activities, all cam positions impinged primarily in the anterosuperior region of the acetabular rim. The anterior cam position produced the most frequent impingement and exercises involving lateral movement and greater hip flexion, such as side lunges (shown in figure), showed higher impingement incidence. Across cam positions, mixed-effects regression indicated that impingement severity was most strongly driven by adduction (Main effect: ß = -7.98 ± 0.71), with flexion-internal rotation coupling also increasing severity (Interaction effect: ß = 2.71 ± 0.43). As the cam position was moved more anteriorly, flexion became an increasingly dominant contributor to impingement severity.

Discussion

Across cam positions, the model identified position-specific rotational patterns that produced bony impingement. This demonstrates its capacity for use to identify the precise rotational conditions that cause impingement and, following suitable validation, it may contribute to the establishment of a pipeline aimed at supporting the clinical management of patients with suspected FAIS.

Images (Optional)



Plots of hip rotations for **side lunges** and **drop jump**. Coloured shaded regions denote ±1SD for each hip degree of freedom. Mean impingement region across all participants for anterior cam position denoted by grey region.

References (Optional)

[1] Rintje Agricola *et al.*, Am J Sports Med, 2014

[2] Scott Fernquest *et al.*, Bone Joint J, 2017

[3] Alison Jones *et al.*, Clin Orthop Relat Res, 2023

[4] Xiong Zhao *et al.*, Sci Data, 2023

Session Category

Orthopaedic Biomechanics: Sports Medicine

P3-322

Hierarchical Clustering Analysis Suggests a Relationship between Hamstring Muscle Cross-Sectional Area Profiles and Injury Risk

Dr. Jack Martin PhD[1], Prof. Silvia Blemker PhD[2], Prof. David Opar PhD[3], Dr. Brett Mortensen PhD[4], Prof. Bryan Heiderscheit PT, PhD[1]

[1]University of Wisconsin-Madison, Madison, WI, United States. [2]University of Virginia, Charlottesville, VA, United States. [3]Australian Catholic University, Melbourne, VIC, Australia. [4]Brigham Young University, Provo, UT, United States

Introduction

Hamstring injury (HSI) risk in athletes has remained challenging to predict, and simple metrics like overall hamstring size and strength have not proven useful. While the four individual hamstring muscles (BFLH, BFSH: biceps femoris long, short heads; SM: semimembranosus; ST: semitendinosus) are generally highly redundant, relative force production between them is affected by joint angles [1], and they have distinct activation patterns during sprinting [2]. Hence, it is possible that the relative size and strength of individual hamstring muscles may affect force distribution during various tasks, thereby affecting injury risk. The purpose of this analysis is to assess the relationship between HSI incidence and relative differences in cross-sectional area (CSA) profiles of the hamstring muscles.

Methods

This analysis used data from 443 Division-I collegiate football athletes in the HAMIR study [3]. MRI examinations were performed and the hamstring muscles were segmented. Hamstring CSAs were normalized to the maximum value across all four muscles. CSA profiles for each muscle were interpolated from 0-100% femur length. Principal component (PC) analysis was performed on collated CSA profiles. Hierarchical clustering was performed on PC scores to reveal distinct hamstring CSA profile phenotypes. Clusters were inspected to determine metrics of interest and these were compared with HSI incidence.

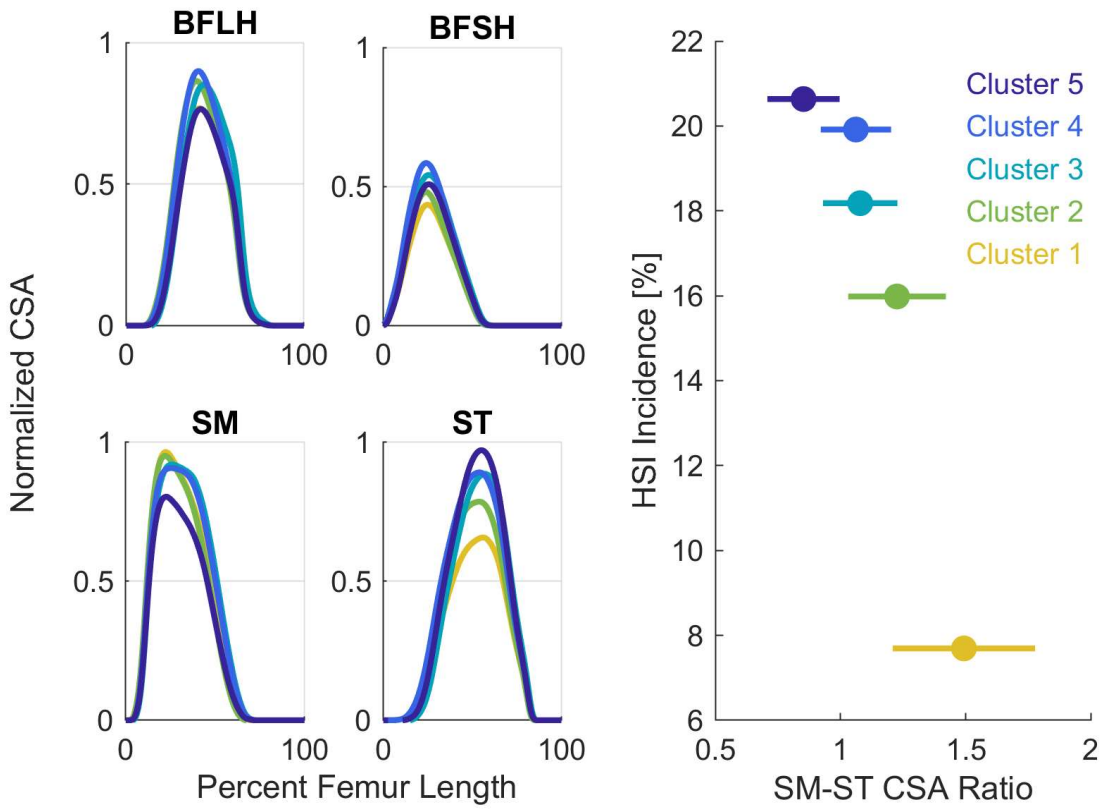
Results

HSI occurred in 74 athletes (17%). Five distinct clusters of athletes exhibited differing hamstring CSA profiles. Peak CSA of the SM and ST muscles differed across clusters, as did the ratio between them. HSI incidence and the mean SM-ST ratio differed by factors of 2.7 and 1.8, respectively, across clusters. HSI incidence was correlated with the SM-ST CSA ratio (R^2=0.45).

Discussion

The results of this analysis indicate that relative size of the individual hamstring muscles may affect injury risk. Interestingly, despite the BFLH being the most often injured muscle, the SM and ST CSA profiles differed more across clusters and were more strongly related to HSI incidence. The reasons for this are unclear and will require further mechanistic investigation.

Images (Optional)



References (Optional)

[1] Beyer et al., *Int J Sports Phys Ther*, 2019; [2] Suskens et al., *Scand J Med Sci Sports*, 2023; [3] Heiderscheit et al., *BMC Sports Sci Med Rehabil*, 2022.

Acknowledgements (Optional)

This project was made possible by the HAMIR study group. Funding was provided by the NFL, who had no role in the study or the decision to share results.

Session Category

Orthopaedic Biomechanics: Sports Medicine

P3-323

Knee Brace Function Throughout Flexion in Response to a Valgus Torque: A Cadaveric Study

Dr. Luke T. Mattar PhD[1], Mr. Tianyu Chen MS[1], Dr. Jumpei Inoue MD[1], Dr. Martin Fagerström PhD[2], Dr. Volker Musahl MD[1,3], Dr. Richard E. Debski PhD[3,1]

[1]Department of Orthopaedic Surgery, University of Pittsburgh, Pittsburgh, PA, United States. [2]Department of Industrial and Material Science, Chalmers University of Technology, Gothenburg, Västra Götaland County, Sweden. [3]Department of Bioengineering, University of Pittsburgh, Pittsburgh, PA, United States

Introduction

Although knee braces are prescribed to protect ligamentous structures in the tibiofemoral joint, injuries to the medial collateral ligament (MCL) often occur. The objective of this study was to determine how the resultant force in a knee brace changes throughout flexion in response to a valgus torque in uninjured and MCL deficient (MCLD) cadaveric knees.

Methods

Seven fresh-frozen cadaveric knees (age 37-77 years) were utilized. A 10Nm valgus torque was applied to each knee using a 6-DoF robotic testing system in two knee states during continuous flexion: 1) Native Ideal Brace and 2) MCLD Ideal Brace. To create the “ideal brace”, the knee brace was rigidly fixed to the tibial and femoral clamps on the medial and lateral sides of the knee. Utilizing the principle of superposition, the resultant force in the ideal knee brace was quantified. Spearman’s correlations were then used to determine the association between flexion angle and resultant force in the ideal knee brace for each state (significance $P<0.05$).

Results

In the Native Ideal Brace state, no association was found between flexion angle and resultant force ($P>0.05$, Figure 1A). However, a positive association between flexion angle and resultant force in the knee brace was observed in the MCLD Ideal Brace state ($P<0.05$, Figure 1B). Thus, as knee flexion angle increased, the resultant force in the ideal knee brace increased.

Discussion

The major finding was that the resultant force in the ideal knee brace increased with flexion angle in the MCLD knee, but not in the Native knee. The implications of the finding are that ideal knee bracing carries similar low magnitude loads in the Native knee throughout flexion, however, the knee brace carries increased loads throughout flexion in response to a valgus torque when the MCL is injured. Thus, knee brace function may change with flexion angle and injury state. Based on this data, practitioners may consider custom braces to address different functional limitations in uninjured and MCL injured knees.

Images (Optional)

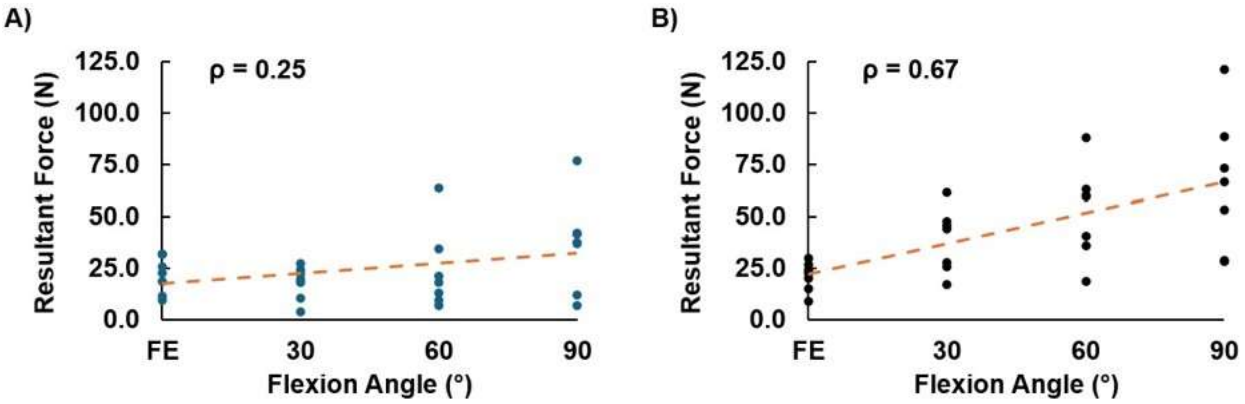


Figure 1: The association between tibiofemoral flexion angle and resultant force in the ideal knee brace in response to a valgus torque in the A) Native and B) MCLD knee (MCLD, medial collateral ligament deficient).

Acknowledgements (Optional)

Support from the National Institutes of Health grant 1F32AR084845 and Departments of Orthopaedic Surgery and Bioengineering is gratefully acknowledged.

Session Category

Orthopaedic Biomechanics: Sports Medicine

P3-324

On-field assessment of performance and joint coordination in ACL-reconstructed football players: expanding the ACL-IRD algorithm

Dr. Stefano Di Paolo[1], Dr. Margherita Mendicino[1], Dr. Pietro Margheriti[1], Dr. Marianna Viotto[2], Dr. Chiara Valastro[1], Prof. Alberto Grassi[1,3], Prof. Stefano Zaffagnini[1,3]

[1]2nd Orthopaedic and Traumatologic Clinic, IRCCS Rizzoli Orthopaedic Institute, Bologna, Emilia Romagna, Italy. [2]Pediatric Orthopaedic and Traumatology, IRCCS Rizzoli Orthopaedic Institute, Bologna, Emilia Romagna, Italy. [3]Department of Biomedical and Neuromotor Sciences, University of Bologna, Bologna, Emilia Romagna, Italy

Introduction

The “Anterior Cruciate Ligament Injury Risk profile Detection” (ACL-IRD) algorithm is a clinician-friendly kinematic-based method for quantifying biomechanical risk in ACL-reconstructed (ACLR) football players during on-field cutting tasks [1], based on kinematics. Considering the “performance-injury conflict” [2], indicating that risky biomechanics cannot be interpreted in isolation, this study extends the ACL-IRD framework by integrating joint coordination and performance with kinematics, to better assess functional movement quality during return-to-sport in ACLR players.

Methods

Sixty-one football players (40 healthy, 21 ACLR; 16.2±2.2 years) performed pre-planned Agility T-test and unplanned football-specific cutting tasks (FS deceiving action) [1]. Lower limb and trunk kinematics was collected through 8 validated inertial sensors (100Hz, MTw Awinda, Movella). Cut braking strategy and propulsive ability performance were assessed through approaching deceleration and exit velocity. ACLR trials were classified against healthy normative data (1st and 3rd terciles) for binary indications of “adequate”/“non-adequate” execution for approaching deceleration, kinematics, and exit velocity. Joint coordination was evaluated through vector coding technique of lower limb angle–angle couplings.

Results

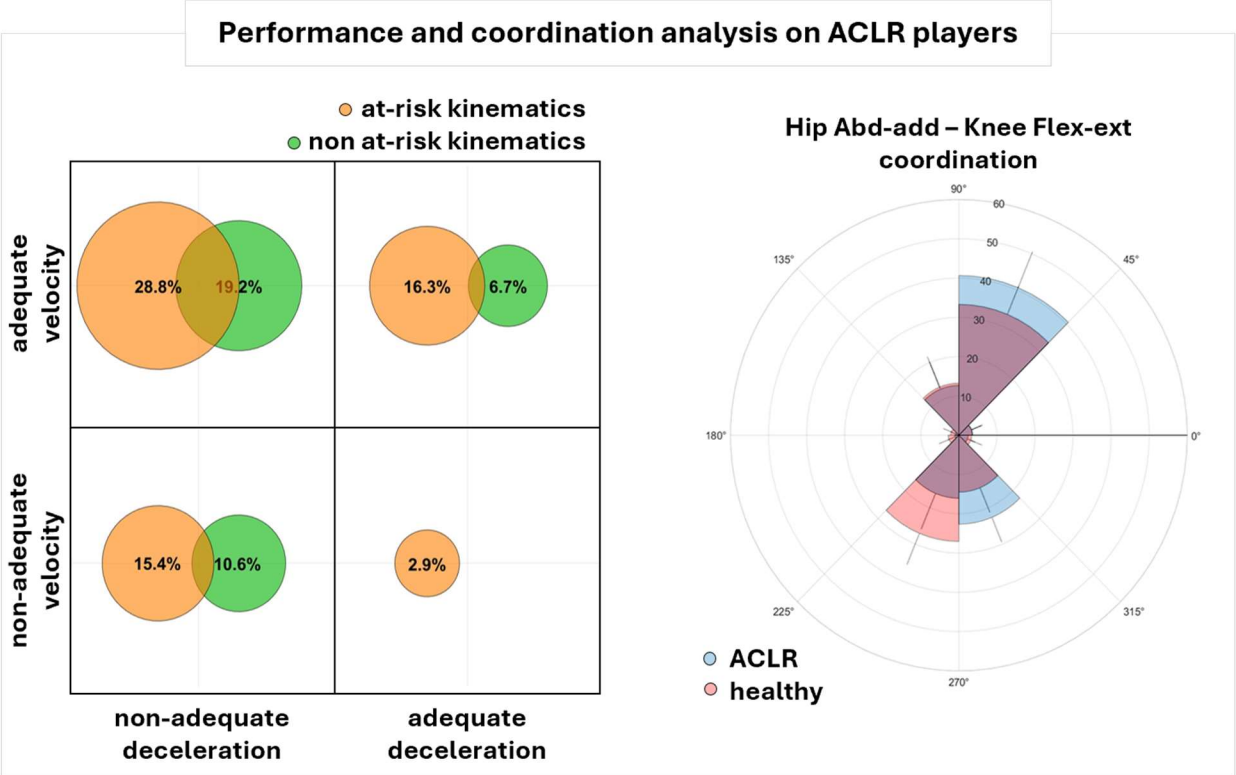
The ACL-IRD algorithm detected at-risk biomechanics in ~35% of trials in both Agility T-test and FS deceiving action. Knee/hip flexion ratio, knee valgus, and hip abduction frequently emerged as risk factors regardless of the task. Nearly 48% of ACLR clustered into a performance profile characterized by suboptimal braking strategy but preserved propulsive ability. Overall, 74% of ACLR trials exhibited inadequate approaching deceleration, 60% of which also presented at-risk kinematics, indicating altered patterns predominantly

emerging with braking deficits. Coordination analysis revealed greater deviations of the ACLR players from the normative in FS deceiving action vs. Agility T-test (9 vs. 3 of 16 angle-angle couplings). The main difference highlighted a greater hip abduction – knee flexion distal-dominant coordination of ACLR players ($p<0.001$, $d=0.68$).

Discussion

This study advances the ACL-IRD algorithm by introducing joint coordination and integrating on-field performance alongside risk profile analysis, providing a holistic interpretation of ACLR football players cutting technique. This approach could help clinicians target key factors during rehabilitation continuum, to optimize performance while minimizing injury risk.

Images (Optional)



References (Optional)

[1] Stefano Di Paolo *et al.*, Sports, 2025

[2] Thomas Dos'Santos *et al.*, Sports Medicine, 2021

Session Category

Orthopaedic Biomechanics: Sports Medicine

P3-325

Development of Simulated Osseointegration to Reduce Age and Sex-Based Disparities with In-Vitro Orthopedic Biomechanics Research

Mr. Logan Shannon, Ms. Elizabeth Pace, Dr. Tara Nagle PhD, Robb Colbrunn

Cleveland Clinic, Cleveland, Ohio, United States

Introduction

Poor bone quality of some cadaveric specimens, which can be exacerbated in female and elderly specimens, can lead to in vitro biomechanics research not accurately reflecting the patient population of interest. Studies aiming to compare surgical interventions relying on secure fixation of devices into the bone (e.g. suture anchors, buttons, etc.) are often compromised due to fixture loosening, which is rarely observed clinically and can be attributed to poor bone quality in cadavers and lack of device osseointegration.

Methods

Two male fresh frozen matched pair cadaveric knees, with a mean age of 74 years, were utilized to explore the application of two commercially available adhesives. The two adhesives (SB02 and SB150) were cyanoacrylate based and were modified with the addition of silica nanoparticles (1.5 wt%). Surrogate PEEK suture anchors were inserted into the bone of the cadaveric knees using a digital torque wrench. The bones were placed on an Instron MTS 858 to perform anchor pull-out tests. Maximum insertion torque and failure force was recorded.

Results

Twenty-eight pullout tests and insertion torque measures (n=14 per donor) were evaluated. The matched pair treated with the polymer adhesive SB02 experienced an average increase of 200N in pullout force across the seven insertion sites compared to the control side (Fig. 1a). The second matched pair, treated with the polymer adhesive SB150, experienced an average increase of 379N in pullout force across the seven insertion sites compared to the control side. Both treatment groups displayed an average 51% increase in maximum insertion torque compared to the matched control (Fig. 1b).

Discussion

Cyanoacrylate-based polymer adhesives modified with silica nanoparticles show potential to be a feasible solution to improve device fixation for in vitro biomechanics testing.

Cyanoacrylate glues form strong polymer matrices and provide quick cure times in addition to their low viscosities, allowing them to infiltrate and improve the density of the bone. This is displayed by the increase in both maximum pullout force and maximum insertion torque of PEEK anchors. Future research in this area will focus on evaluating various wt% additions of silica nanoparticles and optimize the application technique.

Images (Optional)

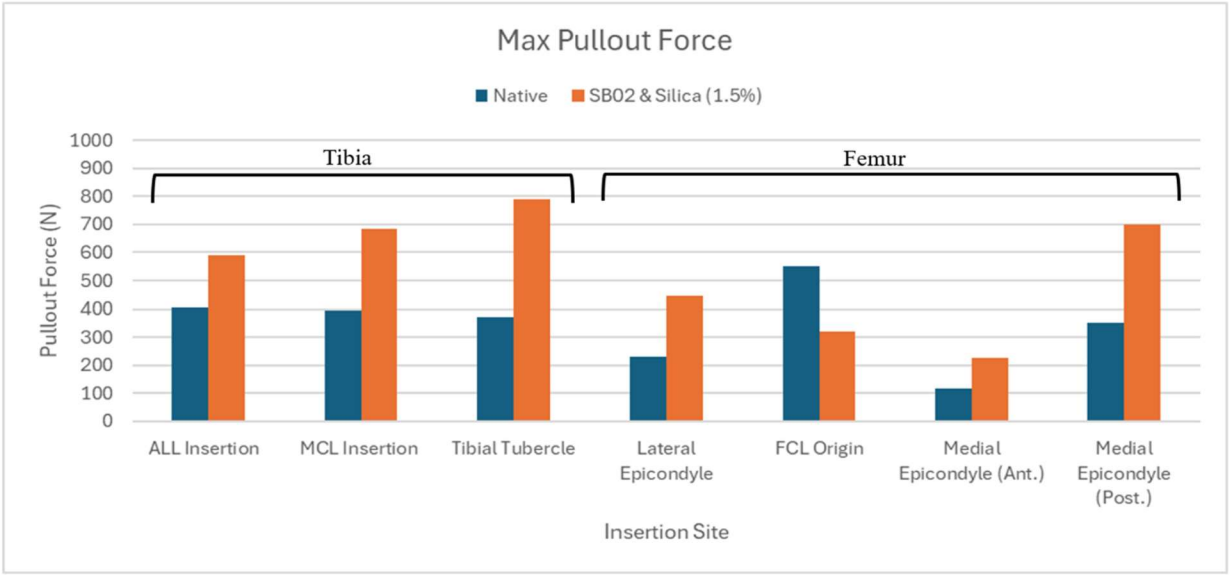


Figure 1a: Maximum pullout force of the SB02 and Silica (1.5%) adhesive for various insertion sites.

References (Optional)

Session Category

Orthopaedic Biomechanics: Sports Medicine

P3-326

The Effectiveness of Wrist Bracing for Reducing Biomechanical Risk Factors Associated With Gymnast Wrist

Miss Stefania DiLeo[1], Miss Erin Day[2], Dr. Ashley Stirling[1], Dr. Ryan Paul[3], Dr. Andrea Chan[3], Dr. Timothy Burkhart[1]

[1]Faculty of Kinesiology and Physical Education, University of Toronto, Toronto, Ontario, Canada. [2]Temerty Faculty of Medicine, University of Toronto, Toronto, Ontario, Canada. [3]Divisions of Orthopaedic and Plastic Surgery, University of Toronto, Toronto, Ontario, Canada

Introduction

Gymnasts often feel pressured to conceal pain and injury to support their likelihood for success, leading to long term health consequences. As such, preventative measures that safeguard gymnasts against common biomechanical injuries are critical. Distal radius physeal stress reaction, or Gymnast Wrist (GW), is prevalent in adolescent gymnasts due to repeated high force loading at the extended wrist. Wrist braces have shown to attenuate such forces. However, their efficacy for reducing GW risk in young female gymnasts is unknown. Therefore, this research aimed to establish the effectiveness of anti-hyperextension wrist braces for reducing biomechanical GW risk factors in young female gymnasts.

Methods

Wrist biomechanics were quantified in 14 adolescent female artistic gymnasts (mean [SD] age = 13.6 [2.4] years; gymnastics level 6-8) who performed three floor tasks (front handspring, round-off, back handspring) and the front handspring vault with and without bilateral anti-hyperextension wrist braces (Tiger Paws, Albuquerque, USA). Gymnasts' lead (LH) and non-lead (nLH) hand extension angles and impact forces were measured using inertial measurement units (Xsens MVN Awinda, Enschede, the Netherlands) and pressure sensors (Tekscan Flexiforce 5260, Norwood, USA), respectively. ANCOVAs were conducted. Exit surveys were administered to obtain feedback on brace use.

Results

During all tasks, wrist braces significantly reduced ($p < .05$) the magnitude of wrist extension at initial hand contact with the apparatus for the LH and nLH (mean reduction across tasks = 33.0° and 35.7°, respectively). Wrist braces also significantly reduced wrist extension at the time of peak hand impact force for the LH (Fig. 1) and nLH (mean reduction across tasks = 43.1° and 43.0°, respectively). However, braces did not significantly

influence the magnitudes of hand impact force ($p > .05$). In general, gymnasts perceived wrist braces to decrease wrist pain and/or increase wrist support, while causing little to no perceived changes in performance.

Discussion

This research is foundational as it provides support for wrist bracing as a potential strategy to reduce GW risk in young female gymnasts, an athlete population largely underrepresented within current literature. Focused research efforts on GW are not only imperative for protecting the growing gymnast, but also for safeguarding these vulnerable athletes.

Images (Optional)

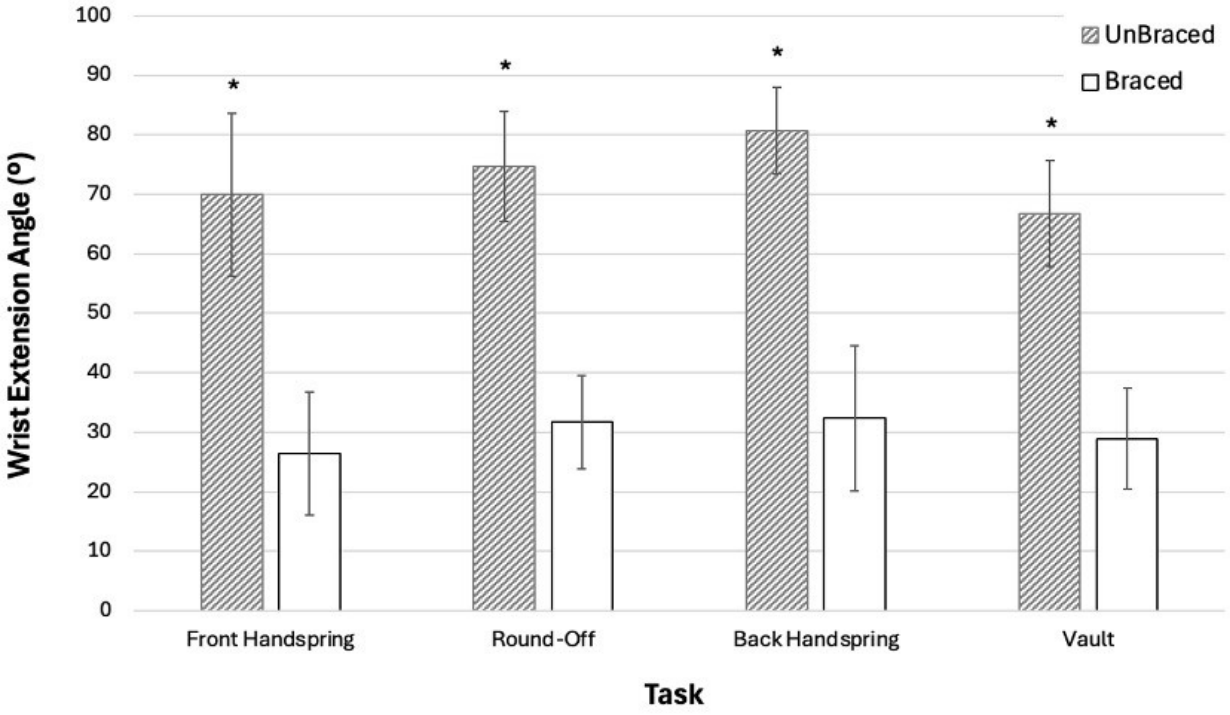


Figure 1: Braced vs unbraced wrist extension angles at peak hand impact force of the lead hand. Mean (SD) wrist extension angles are depicted in degrees (°) for each task. Asterisks denote a statistically significant difference between bracing conditions at $p < .05$.

Session Category

Orthopaedic Biomechanics: Sports Medicine

P3-327

Development of an Instrumented *in Vitro* and *in Silico* Knee Joint Model to Measure Cruciate Ligament Forces

professor António Ramos University of Aveiro[1], Professor José Simões ESAD[2], Msc Ana Matos University of Aveiro[1]

[1]University of Aveiro, Aveiro, Aveiro, Portugal. [2]ESAD-ID, Matosinhos, Porto, Portugal

Introduction

The anterior cruciate ligament (ACL) and posterior cruciate ligament (PCL) play fundamental biomechanical roles in knee stability. Among young and physically active individuals, particularly athletes exposed to rapid changes in direction and rotational loads, ACL injuries are highly prevalent worldwide. This study presents the development of an experimental instrumented in vitro knee model and in silico to designed to replicate native knee joint mechanics and quantify forces transmitted through the ACL and PCL.

Methods

An in vitro knee model (Figure 1) was constructed using synthetic composite bone structures of the left tibia, femur, and patella (Sawbones). Articular cartilage was reconstructed from MRI data using CAD tools to realize the in-silico model. Realistic geometries and anatomical insertion points for the menisci, ACL, PCL, medial collateral ligament (MCL), and lateral collateral ligament (LCL). The cartilage and menisci were manufactured using additive manufacturing. The ACL and PCL were simulated using tensioned cable assemblies to reproduce ligament-like behaviour. Knee flexion was driven in experiment under position control from full extension to 90° at 50 mm/min.

Results

A representative ACL force–flexion curve is shown in Figure 2. The curve morphology is consistent with patterns reported in cadaveric experiments [1,2], although the peak measured force was higher (≈255 N). The experimental model exhibited some instability during flexion, likely due to condylar contact dynamics and alignment variations between the tibia and femur.

Discussion

This in vitro model demonstrates good agreement with published ACL loading behaviour, supporting its potential for biomechanical evaluation of knee ligament function. However, improvements are needed, particularly in reducing friction within ligament tunnels and optimizing cartilage mechanical behaviour, as slight displacement during testing increased joint friction. Additionally, refining the stiffness properties of collateral ligaments will further enhance the model's accuracy for biomechanical simulation and testing.

Images (Optional)

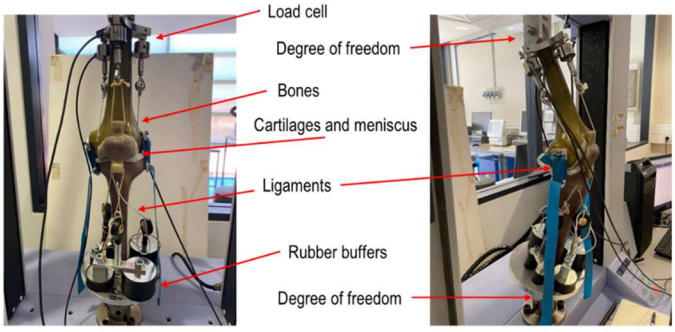


Fig. 1. Experimental in vitro model of knee joint CAD model, frontal and sagittal view.

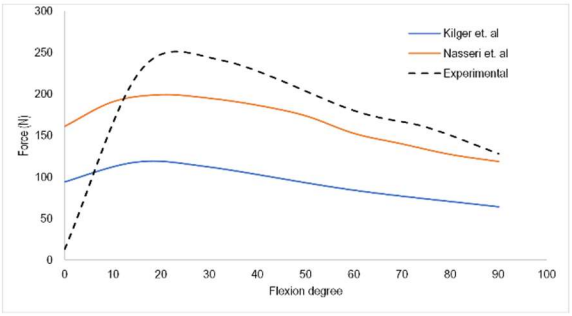


Fig. 2. Force measured in the ACL for the knee in flexion.

References (Optional)

[1] 1- R.H.P. Kilger, at. al., American Journal of Sports Medicine 34 (2006).

[2] 2 - A. Nasseri, H. et al., Comput Methods Programs Biomed 184 (2020).

Acknowledgements (Optional)

This work was supported by national funds from FCT – Fundação para a Ciência e a Tecnologia, I.P., under the project AIDAC (COMPETE2030-FEDER-00867200), and by the Centre for Mechanical Technology and Automation, https://doi.org/10.54499/UID/00481/2025

Session Category

Orthopaedic Biomechanics: Trauma and Repair

P3-328

Design of an Overlay Restoration Using 3D Functionally Graded Materials

Dr. Laurent Tapie[1], Dr. Ariane Martin[2], Dr. Vincent Fouquet[3], Pr. Elsa Vennat[2], Dr. Aurélie Benoit[3]

[1]Université Sorbonne Paris Nord, Paris, Ile-de-France, France. [2]CentraleSupélec, Gif-sur-Yvette, Ile-de-France, France. [3]Université Paris Cité, Paris, Ile-de-France, France

Introduction

The main cause of failure in bonded ceramic restorations is material fracture due to excessive stress concentration at the base of the prosthesis [1]. The design of restorative functionally graded materials (FGM) could represent a major advance in dissipating mechanical stresses during occlusal contacts. Using a biomimetic approach, an optimal configuration of FGM was defined on a simplified finite element model (FEM) of an overlay, considering constraints related to additive manufacturing of the material [2]. However, the more complex geometry of a clinical restoration may influence stress distribution. The aim of the present work is to evaluate the influence on FGM efficiency of three parameters: gradient orientation, the presence of an external protective shell, and the design of the preparation required to remove damaged dental tissues before restoration.

Methods

A topological decomposition based on anatomical entities was applied on segmented cone beam data of a healthy molar to build a 3D computer aided design (CAD) model (Fig.1) using 3DExperience (Dassault Systèmes). Different FEM were created from this healthy tooth by introducing multilayer FGM with different gradient orientations (1D/3D), preparation designs, with/without including an external shell. The FGM consisted of five 0.1mm-thick layers with linearly increasing Young moduli from 30 to 70 GPa towards the occlusal surface. The external shell's Young modulus is set at 80 GPa. All materials are considered isotropic and linear elastic. The external surface of the root is fixed and the tooth is vertically loaded up to 120 N with a rigid spherical indenter in contact with a soft food bolus.

Results

With more realistic 3D geometry, FGM continues to reduce stress at the basis of the prosthesis with no significant difference between a unidirectional and a 3D gradient. Stress

reduction improves with a protective shell and is more pronounced for realistic dental preparations that result in thinner thicknesses.

Discussion

The external shell both transmits forces more effectively to the stiffer enamel and ensures the prosthesis is sealed. FGM ceramics offers clinical potential for more lasting and less invasive dental restorations.

Images (Optional)

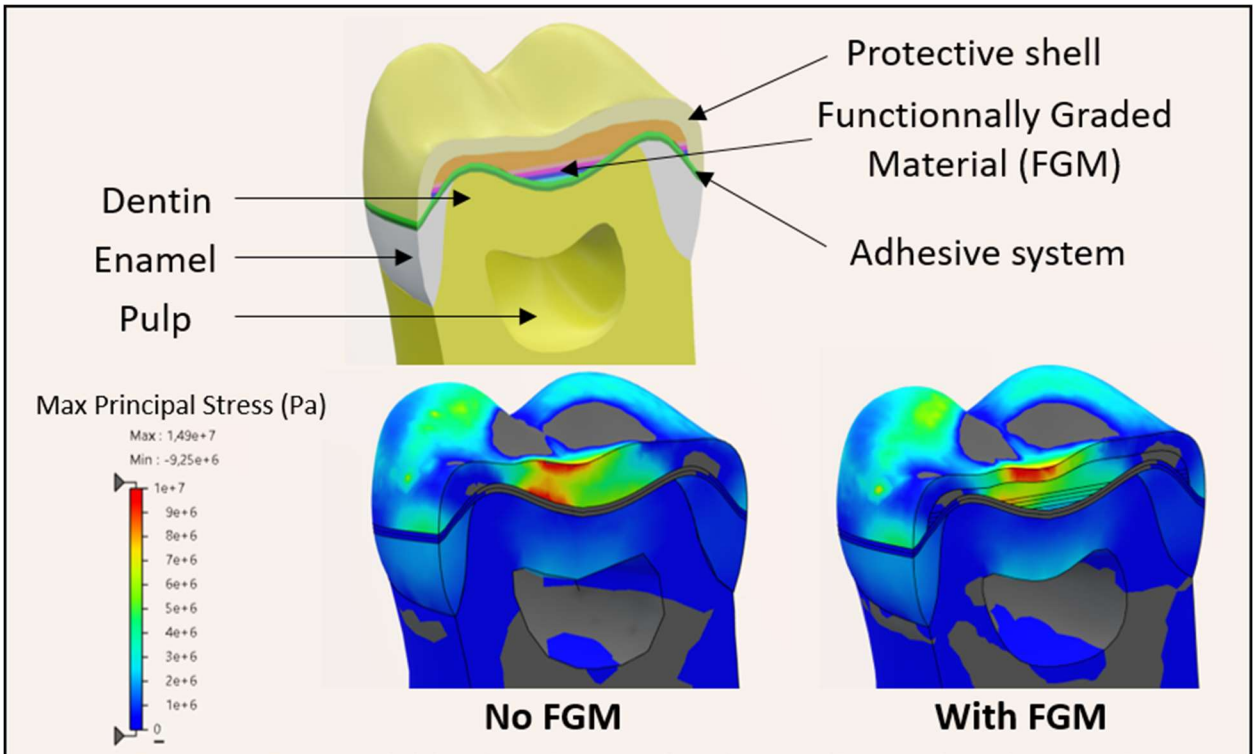


Figure 1: CAD model (top) and stress distribution (bottom) without and with a functionnally graded material

References (Optional)

[1] Vishal B Naik et al., J Conserv Dent, 2022
[2] Vincent Fouquet et al., JMBBM, 2024

Session Category

Orthopaedic Biomechanics: Trauma and Repair

P3-329

From Non-Union to Union: Computational Modeling of Magnesium-Enhanced Bone Healing

Dr. Sakip Onder[1], Dr. Leyla Noroozbabaee[2], Ms. Matilde Marradi[2], Dr. Aurélie Carlier[2]

[1]Yildiz Technical University, Istanbul, Istanbul, Turkey. [2]Maastricht University, Maastricht, Maastricht, Netherlands

Dr. Sakip Onder

Dr. Leyla Noroozbabaee

Ms. Matilde Marradi

Introduction

Magnesium (Mg^{2+})-based biomaterials are being explored for the treatment of bone fractures. As their effect on bone regeneration is dose dependent, a more mechanistic understanding of Mg^{2+}-mediated effects on the bone healing process is required to optimize the timing and spatial distribution of controlled Mg^{2+} release.

Methods

In this study, we extend a previously published bone healing model [1] (Figure 1). The inflammatory and repair phases of bone fracture healing are modeled by a system of nonlinear ordinary differential equations (ODEs) based on mass-action kinetics, assuming spatially homogeneous concentrations within a fixed volume. To better mimic Mg^{2+} concentrations at the fracture site three time-dependent Mg^{2+} release functions were defined: (1) a constant release profile, (2) a high burst release profile, and (3) a precisely controlled delayed release profile with a low initial burst. A local sensitivity analysis was conducted to evaluate the effects of Mg^{2+} delivery profiles and concentrations on bone mass dynamics in both union and non-union cases. All simulations were performed using Jupyter Notebook.

Results

We identified 1–5 mM Mg^{2+} as the optimal concentration range that promotes anti-inflammatory macrophage polarization, stem cell proliferation, and effective bone matrix formation. In contrast, Mg^{2+} concentrations ≥10 mM disrupted regeneration. Our analysis further reveals that controlled release strategies mitigate the cytotoxic effects of Mg^{2+} while preserving regenerative sensitivity in key parameters such as bone and stem cell proliferation.

Discussion

In summary, our results demonstrate that Mg^{2+} exerts concentration- and profile-dependent effects on key biological processes across all healing phases—from early immune activation to later-stage bone formation. As such this study offers a mechanistic basis to optimize Mg^{2+}-based therapies. Future work will focus on incorporating the role of angiogenesis and mechanical stimulation.

Images (Optional)

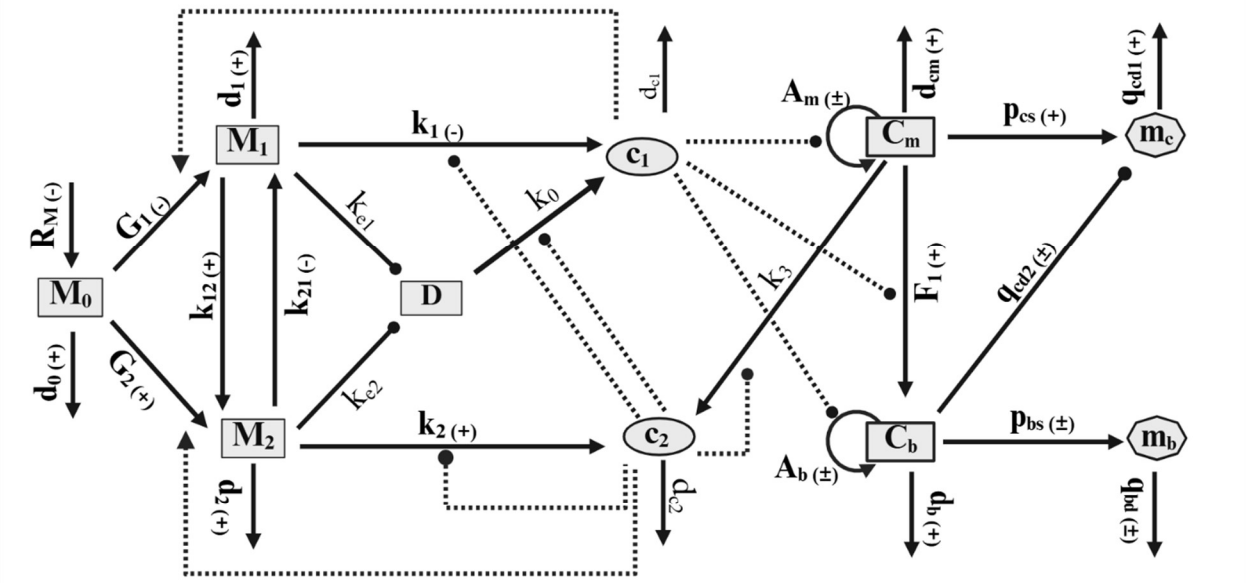


Fig 1. Schematic of the *in silico* Mg^{2+} model. M0: undifferentiated macrophages, M1: M1 polarized macrophages, M2: M2 polarized macrophages, D: debris, c1: pro-inflammatory cytokines, c2: anti-inflammatory cytokines, cm: mesenchymal stem cells, cb: osteoblasts, mc: fibrocartilage, mb: bone. Dot-ended solid arrows represent debris removal and inhibitory interactions among variables. The signs (+), (−), and (±) denote the influence of Mg^{2+} on each parameter: (+) indicates an activating effect, (−) indicates an inhibitory effect, and (±) indicates a biphasic effect.

References (Optional)

[1] Trejo I et al., Math Comput Appl, 2019

Acknowledgements (Optional)

This work was financially supported by the Gravitation Program “Materials Driven Regeneration”, funded by the Netherlands Organization for Scientific Research (024.003.013) and by the Scientific and Technological Research Council of Turkey (TÜBİTAK) under the 2219 Program (1059B192402615).

Session Category

Orthopaedic Biomechanics: Trauma and Repair

P3-330

RNASeq Links Therapeutic Exercise Response in Fatigue Injured Tendon to Differentially Regulated Cell-Matrix Connection Genes

Mr. Benjamin Johnston[1], Dr. Nelly Andarawis-Puri PhD[1,2]

[1]Cornell University, Ithaca, New York, United States. [2]Hospital for Special Surgery, New York, New York, United States

Introduction

Tendinopathy treatment efficacy is limited by a lack of markers to optimally time therapeutic intervention. Our lab has developed an in-vivo model to induce sub-rupture patellar tendon (PT) fatigue injury and observed that while resuming physiological exercise 14-days-post-injury (dpi) is beneficial, resuming 1-dpi is detrimental[1]. Mechanisms driving this phenomenon remain unclear. This study identifies genes and pathways which may determine the capacity to respond positively to physiological exercise. We hypothesize that cell-extracellular matrix (ECM) interactions are transiently disrupted post-injury, shifting exercise toward a degenerative stimulus when resumed prematurely.

Methods

Left PTs of 9–10-month-old female Sprague-Dawley rats underwent fatigue loading per IACUC approved protocol[2]. Animals were sacrificed as uninjured controls (n=3) or at 1-, 4-, 7-, or 14-dpi (n=3-4). RNA was isolated and sequenced to a depth of 20 million raw reads. DEGs between groups were calculated using DESeq2, with limits $|\log2(FC)| \geq 1$, p-adjusted < 0.05, and ncounts > 100. Analysis was performed with Qiagen Ingenuity Pathway Analysis and R.

Results

Principal component analysis demonstrates clustering within timepoints (Fig. 1A). 14-dpi and 1-dpi samples show distinct genetic profiles, but 7-dpi and 14-dpi profiles overlap heavily (Fig. 1B-D). Top up- and downregulated pathways 14-dpi vs. 1-dpi dictate cell-ECM interactions and cell-cycle regulation, respectively (Fig 1E).

Discussion

Upregulation of both collagen synthesis and degradation pathways 14-dpi vs. 1-dpi may indicate a homeostatic-like turnover wherein damaged collagen is effectively replaced by properly aligned collagen. *Cdk1*, a gene essential for cell-ECM connectivity during cell

division, is transiently downregulated 1-dpi vs. control and returns to baseline 14-dpi, exhibiting a similar temporal pattern to cell-cycle regulation[3]. Immediately post-injury, cells divide rapidly without producing genes required to maintain cell-ECM connections. This may generate a large population of aberrantly loaded cells, which supports our hypothesis. Overlap between the therapeutic 14-dpi profile and 7-dpi profile suggests that resuming exercise 7-dpi will yield similar therapeutic outcomes, confirmation of which will identify key markers which could be used to diagnose when injured tendons will respond positively to exercise.

Images (Optional)

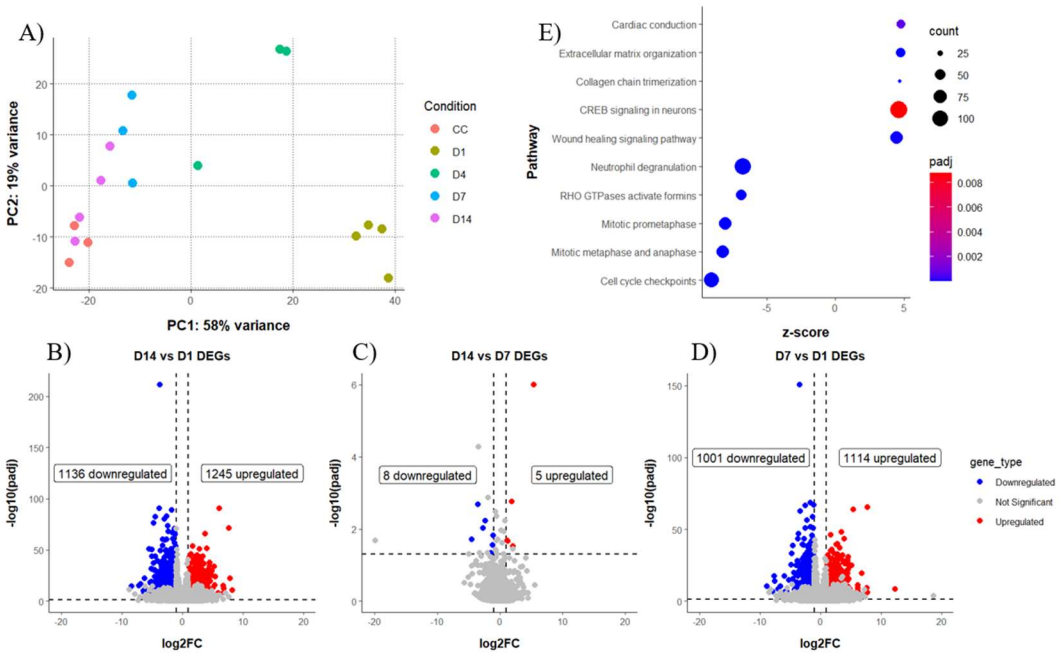


Figure 1) A) Principal component analysis of variance across all timepoints showing clustering within each group. PC1 accounts for 58% of the variance and PC2 accounts for 19%. Volcano plots show DEGs between **B)** 14-dpi and 1-dpi, with 1136 downregulated and 1245 upregulated genes, **C)** 14-dpi and 7-dpi, with 8 downregulated and 5 upregulated genes, and **D)** 7-dpi and 1-dpi, with 1001 downregulated and 1114 upregulated genes. **E)** Dot plot of the 5 most up- and downregulated pathways by z-score between 14-dpi and 1-dpi. Molecular counts ranged from 22 to 122, while adjusted p-values ranged from $3.17*10^{-14}$ to $8.78*10^{-3}$.

References (Optional)

[1] Rebecca Bell, *et al*. J Orthopedic Research, 2015. [2] David Fung, *et al*. J Biomechanics, 2010. [3] Matthew Jones, *et al*. J Cell Biology, 2018.

Acknowledgements (Optional)

We thank the Cornell Biotechnology Resource Center. NIHR56AR077239, NIHR21AR074602, NSF/CCMI2038057, NIHR01 AR084173

Session Category

P3-331

Preliminary Investigation into Optimizing Injection Molding Techniques for a Novel Universal Talus Bone Implant

Ms. Cameron Scott M.Sc., Mr. Nadr Jomha Dr., Mrs. Lindsey Westover Dr., Mr. Ahmed Ead Dr.

University of Alberta, Edmonton, Alberta, Canada

Introduction

Total talar replacements (TTR's) aim to restore both ankle mobility and weight bearing capacity after injury. TTRs involve replacing the damaged talus with a custom metal implant. However, the metal implants against biological cartilage have been found to cause joint deterioration. A coated talus implant could address this challenge.

This research investigates the preliminary prototyping methods required to make a coated talus bone implant, utilizing universal talus shapes proposed by our group. The presented work highlights the iterative process of the injection mold design.

Methods

The foundation of the implant started with Size 5 universal talus bone [1]. The Size 5 talus model was imported into SolidWorks® with feature recognition enabled. A draft angle of 3° was set to ensure that the implant could be removed from the die easily. Two parting lines were found, one that ran horizonal to the bone and another that ran through the talus-calcaneus joint. The injection mold die was designed around the parting lines and aimed to achieve a minimum coating of 2 *mm* [2].

For prototyping purposes, high-density polyethylene was used as the coating. The die was 3D printed and its ability to coat the talus bone was tested. The design was tested by qualitatively observing the coating on the implant.

Results

The initial design of the mold was able to coat six implants successfully; however, issues appeared during the injection mold process that necessitated addressing for future versions. The qualitative inspections of the prototype showed the coating thickness was, on average, 2 *mm* as targeted. There were regions of insufficient coating in the superior neck of the talus and the articular surface for the navicular (Figure 1).

Discussion

The second version of the injection mold die aimed to fix the areas of absent coatings through the addition of three internal support pins. This resulted in the neck of the implant being coating, however, insufficient coating on the navicular joint was still present. Another version of the injection mold is required prior to large scale manufacturing.

Images (Optional)

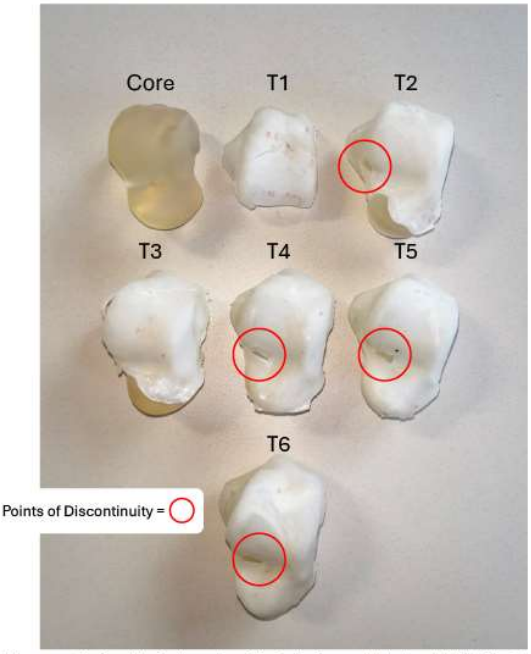


Figure 1: Prototype results from the first version of the injection mold design, highlighting the discontinuities between the implant and coating

References (Optional)

[1] T. Liu et al., *Med Biol Eng Comput*, 2022.

[2] M. Ead *et al.*, Eng. In Med. 2025.

Acknowledgements (Optional)

We would like to thank David DeJong and Dr. Abiy Wubneh for their assistance and guidance through the injection mold design process. We would also like to thank Arielle O'Brien for assisting in the injection mold process.

Session Category

Orthopaedic Biomechanics: Trauma and Repair

P3-332

The Role of the Deltoid and Syndesmotic Ligaments on the Ankle Joint Kinematics

Dr. Daniela Warnecke[1], MD Sebastian Baumbach[2], MD Nasef Abdelatif[3], M.Sc. Samuel Bachmaier[1]

[1]Arthrex GmbH, Munich, Bavaria, Germany. [2]OrthoPlus Munich, Munich, Bavaria, Germany. [3]Orthopedic Foot and Ankle Department, OrthoClinic, Cairo, al-Qahira, Egypt

Introduction

The deltoid ligament (DL) complex on the medial side of the ankle joint comprises superficial (SDL) and deep layers (DDL) and plays a crucial role in joint stabilization [1]. A previous study showed that DL and syndesmotic injuries had a similar effect on rotational ankle instability [2]. This study aimed to analyze changes in the ankle kinematics following syndesmotic and DL injuries.

Methods

Twenty-eight distal tibia amputee cadaver specimens were assigned to 3 groups. Sequential dissections of the anterior inferior tibiofibular and interosseous ligaments (AiTFL+IOL), SDL, and DDL were performed in varying orders (Figure 1). Specimens were initially loaded up to 7Nm to evaluate time-zero rotation at 2.5, 4.0, 5.5, and 7Nm, representing intact conditions, followed by rotation-controlled loading after each dissection. 3D motion was captured using an optical system (ZEISS ARAMIS) with marker sets placed on the proximal tibia and fibula, and virtual points on anatomical landmarks. Outcome parameters also included the fibular rotation angle (FRA) and anterior tibiofibular distance (aTFD) [3]. After initially confirming no group differences within the same dissection stage by one-way ANOVA, data were pooled and further analyzed using RM ANOVA with Bonferroni post-hoc t-tests.

Results

Each dissection step increased fibular and tibial internal rotation, with significant differences between intact and “unstable ankles”. DL injury shifted both bones laterally, while AiTFL+IOL dissection shifted them medially. Additionally, posterior fibular translation was observed for syndesmotic injuries, which further increases with DL involvement. No significant changes were observed for tibial anterior-posterior translation or FRA. In contrast, aTFD increases threefold after syndesmotic dissection, while DL injury alone had no effect.

Discussion

This study supports previous findings that both a two-ligament syndesmotic injury or a complete DL rupture have comparable effects on ankle joint (in)stability [2]. By adding kinematic measurements, current results complete the analysis of these injuries and demonstrate that sequential ligament dissection significantly alters ankle kinematics. Although no differences were observed between syndesmotic injuries with concomitant SDL or DDL involvement, the data underline DL's functional relevance as a medial stabilizer of the ankle joint.

Images (Optional)

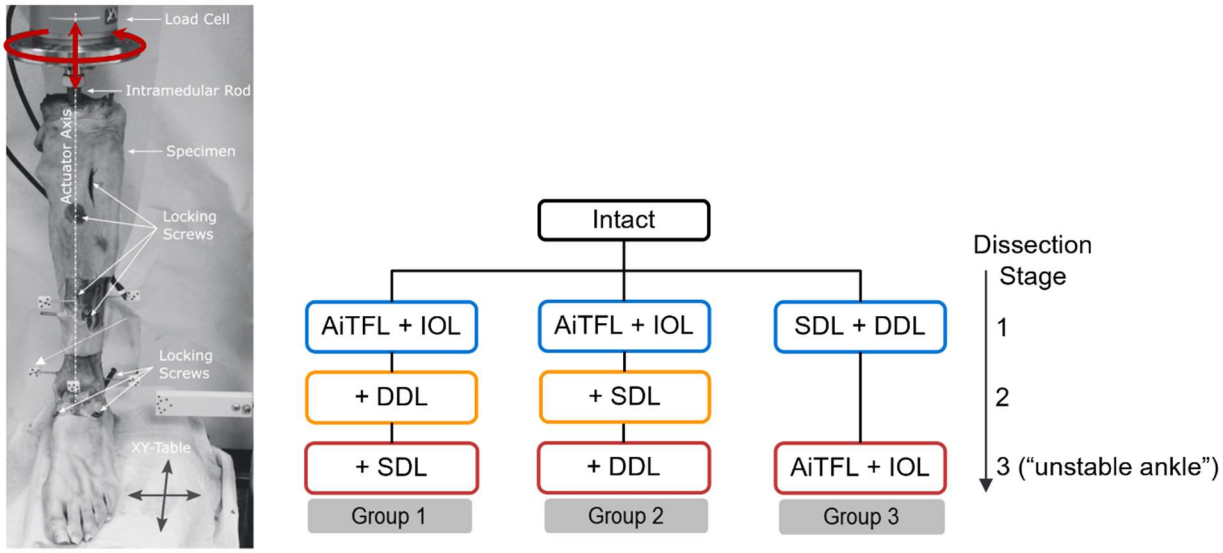


Figure 1: Test setup (left) and test protocol (right) with the intact ankle as a reference, followed by the sequential dissection steps.

References (Optional)

[1]Butlers et al.,AJSM,2020
[2]Bachmaier et al.,AJSM,2025
[3]Takahashi et al.,OJSM,2022

Session Category

Orthopaedic Biomechanics: Trauma and Repair

P3-333

Simulation-Based Assessment of Magnesium vs. Titanium Fixation Using Human Mandibular Magnesium Mini Plates

Mr. Dawei Zhang[1], Dr. -Ing Songyun Ma[1], Prof. Dr. med. Dr. med. dent. Carsten Rendenbach[2], Mr. Thomas Kött[3], Univ.-Prof. Dr.-Ing. Dr. h. c. (PSACEA) Bernd Markert[1], Dr. -Ing Agnes Beckmann[3]

[1]Institute of General Mechanics, RWTH Aachen University, Aachen, NRW, Germany. [2]Department of Oral and Maxillofacial Surgery, Charité - corporate member of Freie Universität Berlin, Humboldt-Universität zu Berlin, Berlin, Berlin, Germany. [3]KLS Martin SE & Co. KG, Mühlheim an der Donau, BW, Germany

Introduction

Titanium osteosynthesis is the current standard treatment for mandibular reconstruction. However, in cases of osteoradionecrosis, healing efficacy and implant integration remain challenging, motivating the development of resorbable biomedical materials such as magnesium alloys. In particular, PEO-coated WE43 magnesium alloys have emerged as promising biodegradable materials for mandibular reconstruction, and their successful first clinical application represents an important milestone in resorbable implant technology [1]. This study presents a computational approach to evaluate the degradation behaviour of PEO-coated WE43 implants and their interaction with tissue differentiation during fracture repair. Specifically, the biomechanical performance of these magnesium miniplates is numerically assessed over six weeks and compared with conventional titanium instrumentation, based on a first-in-human clinical case.

Methods

The finite element model of an instrumented mandible by Rendenbach et al. was extended to a mechano-regulation framework incorporating biphasic stimuli for tissue differentiation and a continuum damage model to simulate pitting corrosion in magnesium [1, 2]. A bite force of 100 N was applied perpendicular to the occlusal plane at the first right molar, with muscle forces ensuring equilibrium. Both condyles were fully constrained to ensure static determinacy of the model [3]. Screws were modelled as cylinders with screw heads and tied to the bone, while frictional contact was defined at implant-bone and screw head-implant interfaces. Implant stresses were evaluated using von Mises criteria relative to material yield strengths.

Results

The predicted corrosion process of the implants is shown in Fig. 1. On day 14, minimal corrosion occurred due to the protective coating. On day 42, the corrosion damage of the bone plate and screws had extended to many elements on the corrosion surface, reducing load-bearing areas and compromising mechanical integrity.

Discussion

The simulation demonstrates that PEO-coated magnesium implants maintain sufficient mechanical integrity during the early healing stage, supporting the potential of resorbable magnesium implants as a viable alternative to permanent titanium devices in mandibular reconstruction.

Images (Optional)

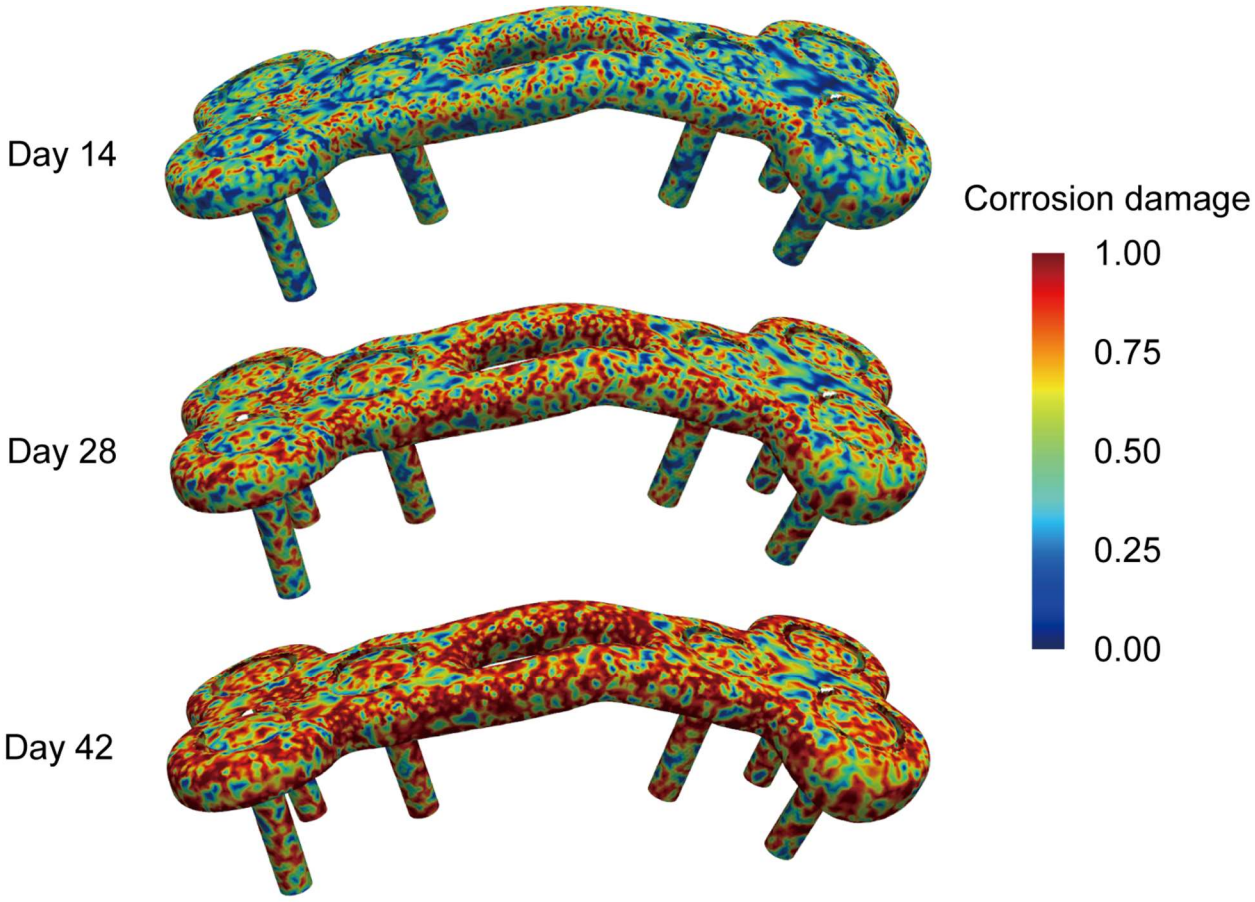


Fig. 1: The simulation results of the degradation process of the magnesium implants.

References (Optional)

[1] Rendenbach *et al.*, DGZMK Berlin, 2025

[2] Ma *et al.*, Zamm, 2017

[3] Andres, A. *et al.*, Bioengineering, 12:5, 2025

Session Category

Orthopaedic Biomechanics: Trauma and Repair

P3-334

In Vivo Assessment of Distal Femur Fracture Motion via Weightbearing Computed Tomography

Dr. Eric D. Thorhauer PhD[1,2], Dr. William R. Ledoux PhD[1,2], Mr. Nick Entress BS[1], Dr. Scott Telfer EngD[1,2], Dr. William D. Lack MD[1,2]

[1]Center for Limb Loss and MoBility (CLiMB), Seattle, WA, United States. [2]University of Washington, Seattle, WA, United States

Introduction

Distal femur fractures are associated with a high risk of delayed and/or failed healing that has been qualitatively associated with suboptimal fracture site mechanics [1,2]. We developed a method of quantifying in vivo distal femur fracture motion via weightbearing computed tomography (CT) to allow further investigation of the role of mechanoregulation in distal femur fracture healing.

Methods

Distal femur fracture patients (N = 9) were recruited and enrolled from an orthopaedic clinic; 8 subjects completed the protocol and data for 6 has been processed (5 male; 1 female; age 48.3 ± 24.9 yrs; body weight 79.8 ± 12.9 kg). Non-weightbearing (NWB) and weightbearing as tolerated (WBAT) CT scans of the distal femur were acquired using a CurveBeam LineUp conebeam CT scanner while novel pedar in-shoe sensors recorded vertical ground reaction forces bilaterally. Subject-specific fracture fragment models were generated using the Mimics segmentation suite. Using MATLAB, anatomical coordinate systems were established, and the poses of relevant fragments in the NWB and WBAT positions were reconstructed in Geomagic to determine fracture site kinematics. The volumetric nature of CT allows for analysis of the interfragmentary displacement fields (Figure 1A) and the deflection of the fixation hardware (Figure 1A) in response to weightbearing.

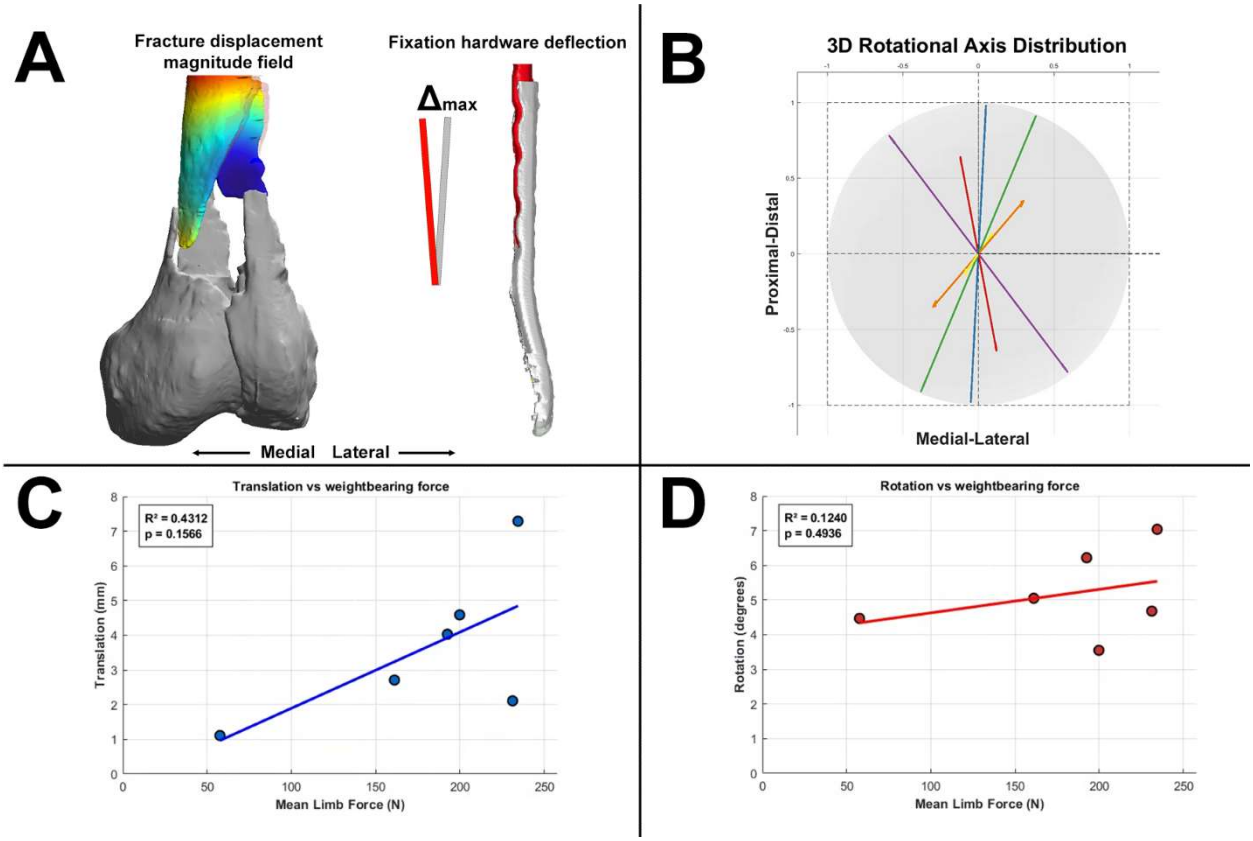
Results

The mean magnitude of fracture motion across subjects was 3.64 ± 2.19 mm for translations and 5.17° ± 1.26° for rotations. Orientation of the axes of motion varied between subjects, but transverse and frontal plane rotations were the two primary modes observed (Figure 1B). The magnitudes of fracture site translation and rotation trended toward increasing magnitudes of motion with greater limb loading (Figure 1C, 1D).

Discussion

These results demonstrate feasibility of quantifying in vivo distal femur fracture mechanics under physiological loading. Load-dependent motion patterns may inform clinical care and our understanding of osseo-biomechanics. Limitations include a small, heterogeneous sample, and natural variability in loading tolerance. Recently awarded funding will facilitate a larger cohort study correlating dynamic fracture kinematics with radiographic evidence of healing progression and outcomes.

Images (Optional)



References (Optional)

[1] Henderson CE, et al. JOT. 2011;25:S8–14
[2] Elkins, J. et al. J Bone Joint Surg Am. 2016 Feb 17;98(4):276-84.

Acknowledgements (Optional)

This research was supported by Department of Veterans Affairs grants RX003608 and RX002970 and by Seattle Institute of Biomedical and Clinical Research (SIBCR) Intramural Funds.

We would like to thank Aerie Grantham, Corey Wukelic, and Melanie Bakin for their assistance in this study.

Session Category

Orthopaedic Biomechanics: Trauma and Repair

P3-335

Subject-Specific Finite Element Modeling of KANON Cohort Reveals Individualized Mechanical Consequences of Anterior Cruciate Ligament Deficiency

Postdoc Researcher Sana Jahangir[1], Postdoc Researcher Amir Esrafilian[1], Professor Martin Englund[2], Academy Research Fellow; Adjunct Professor Petri Tanska[1,3], Professor Rami K. Korhonen[1], Professor Hanna Isaksson[2]

[1]University of Eastern Finland, Kuopio, North Savo, Finland. [2]Lund University, Lund, Skåne, Sweden. [3]Kuopio University Hospital, Wellbeing Services County of North Savo, Kuopio, North Savo, Finland

Introduction

The KANON trial[1] compared early anterior cruciate ligament (ACL) reconstruction with exercise therapy versus exercise therapy with optional delayed reconstruction in young adults. While the cohort is well characterized, mechanical consequences of ACL deficiency remain poorly understood. Both abnormally high and low joint loading have been reported after ACL injury. This proof-of-concept study uses subject-specific finite element (FE) knee models from KANON participants to quantify how ACL deficiency alters tibiofemoral contact mechanics and tissue loading during gait—providing insight into mechanical factors relevant to longer-term joint health.

Methods

MRIs from five KANON cohort subjects[1] (ACL rupture treated non-operatively; age 22–28 years) were used to generate subject-specific FE knee models with a validated atlas-based framework[2]. All subjects had no baseline cartilage damage (anterior cruciate ligament osteoarthritis (ACLOAS) score = 0). Literature-based gait kinematics and kinetics[2] were applied to simulate walking. Each subject was evaluated with (1) intact ACL and (2) ACL-deficient, modeled by reducing ACL stiffness to 0.1% of its intact value. Model outputs included posterior–anterior translation, tibiofemoral and meniscal contact areas, location of center-of-pressure (COP) on tibial plateau, and maximum principal cartilage stress (mean of upper quartile).

Results

ACL deficiency increased posterior femoral translation during mid-stance, reduced medial and lateral tibiofemoral and meniscal contact areas, and shifted the COP posteriorly.

Group-averaged mean of upper-quartile values of cartilage stress at the cartilage-cartilage contact area showed only modest differences between intact and ACL-deficient knees (Fig. 1). In contrast, lateral tibial cartilage peak-stress increased 7.2 ± 3.0 MPa across five subjects (Fig. 1).

Discussion

ACL deficiency consistently altered tibiofemoral contact mechanics, with reduced contact area and a posterior COP shift, indicating load transfer to smaller, more posterior regions. Peak cartilage stress generally increased, but the magnitude varied widely, likely due to anatomical differences under identical gait loading. Overall, although peak stress increased in some individuals, contact mechanics remained most consistent indicator of altered joint loading. These subject-specific insights provide a basis for investigating loading-related mechanisms after ACL injury.

Images (Optional)

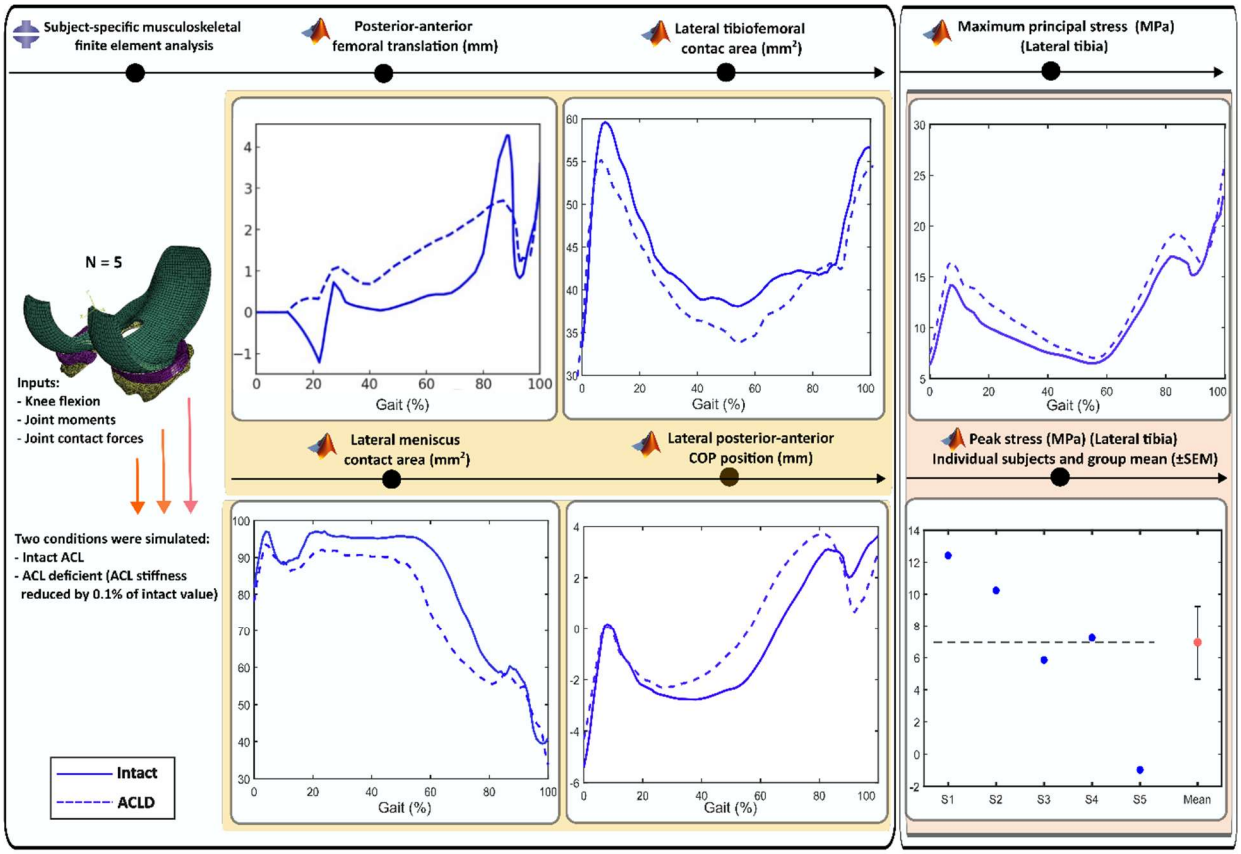


Fig 1: FE-derived changes with ACL deficiency (N = 5) over the stance phase of gait. The knees showed reduced lateral contact area and posterior COP shift. Grouped-averaged mean of upper quartile of maximum principal stress at lateral tibia is shown. Individual subjects' peak-stress changes (blue dots) and group mean ± SEM are also presented.

References (Optional)

1 Frobell, R. B. *et al. N. Engl. J. Med.* 363, 331–342 (2010)

2 Esrafilian, A. *et al. IEEE Trans. Biomed. Eng.* 69, 2860–2871 (2022)

Session Category

Orthopaedic Biomechanics: Trauma and Repair

P3-336

Bovine Osteochondral Plug Viability in Explant Culture Maintained for Up to 14 Days Post Injurious Loading

Doctoral Researcher Ida Antikainen[1,2], Doctoral Researcher Sanna Hakonen[1], Postdoctoral Researcher Özge Karadaş[1,2], Doctoral Researcher Alara Kara[1,2], Doctoral Researcher Siiri Keränen[3], Postdoctoral Researcher Atte Eskelinen[1], Professor Rami Korhonen[1], Academy Research Fellow Petri Tanska[1,2], Professor Petteri Nieminen[3], Senior Researcher Anne-Mari Mustonen[3], Senior Researcher Mikael Turunen[1,2]

[1]Department of Technical Physics, University of Eastern FInland, Kuopio, North Savo, Finland. [2]Kuopio University Hospital, Wellbeing Services County of North Savo, Kuopio, North Savo, Finland. [3]Institute of Biomedicine, University of Eastern Finland, Kuopio, North Savo, Finland

Introduction

Post-traumatic osteoarthritis (PTOA) can be initiated by injurious overloading[1]. Experimental explant models are therefore needed to investigate how excessive loading affects disease progression, cell metabolism and viability. As simultaneous changes in cartilage and bone during PTOA are underexplored, we aimed to establish an experimental PTOA model using osteochondral, cartilage-on-bone plugs subjected to traumatic injury and cultured up to 14 days. Specifically, we focused on assessing post-injury metabolic activity and chondrocyte viability.

Methods

Osteochondral plugs were harvested from bovine tibiae and femora by drilling (N=3 animals, Figure 1A) and divided into free-swelling control (n=12) and impact injury groups (n=11). Impact injury was performed on day 0 with a previously established drop-tower protocol by imposing a momentum of 0.387 kgm/s (500 g weight from height of 15 cm) onto the sample[2]. Explants were then cultured for up to 14 days in supplemented, low-glucose, serum-free DMEM, and the media were changed every three days. Metabolic activity was analyzed from culture media on days 1, 4, 7, and 14 with alamarBlue™ HS assay (Ex/Em: 570/600 nm). Cell viability was qualitatively assessed from the plugs using confocal microscope on days 1 and 14 (Zeiss LSM700; calcein AM/propidium iodide live/dead staining). Paired t-test was used for statistical analysis.

Results

Mean metabolic activity increase in control and impact injury groups was 164% and 136%, respectively, with no significant differences between the groups ($p > 0.05$) (Fig. 1B).

Qualitative cell viability was lower in the injury group compared to control, exhibiting substantial cell death but retaining a viable cell population until day 14 (Fig. 1C).

Discussion

Our findings suggest that bovine osteochondral, cartilage-on-bone plugs remain metabolically active and retain chondrocyte viability over a 14-day culture, indicating post-harvest recovery and adaptation, possible extracellular matrix synthesis and proliferation of progenitor cells. This provides a suitable explant model for studying mechanoinflammatory cell responses related to PTOA in both cartilage and bone.

Images (Optional)

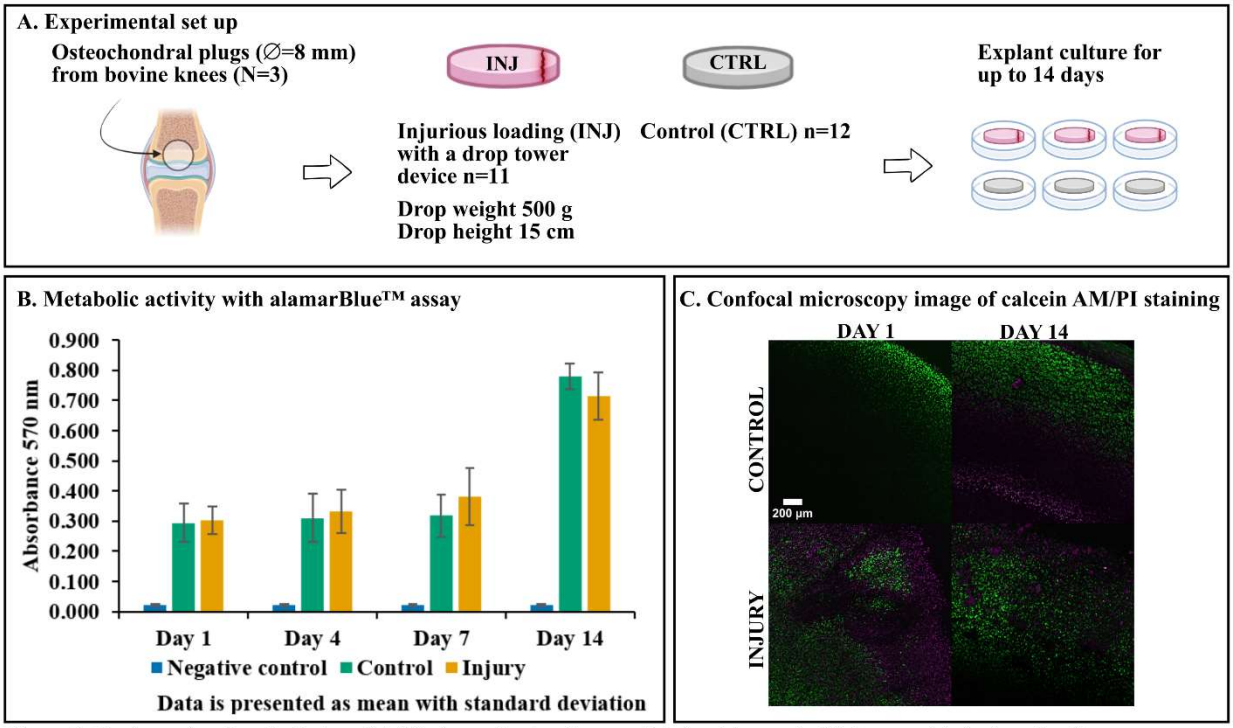


Figure 1. Bovine osteochondral plug viability in explant culture maintained for up to 14 days post injurious loading.
A. Experimental setup. B. Metabolic activity with alamarBlue™ assay: a higher absorbance value indicates greater metabolic activity and thus higher cell viability. C. Confocal microscopy image of chondrocyte calcein AM/PI staining: visualization of live (green) and dead (magenta) cells.

References (Optional)

[1] JE Dilley et al., Bone Rep, 2023

[2] HT Kokkonen et al., Osteoarth Cartil, 2011

Acknowledgements (Optional)

RCF (362247, 363459, 354916), State Research Funding for university-level health research, Kuopio University Hospital (50TP011), NNF, DREAM pilot

Session Category

Orthopaedic Biomechanics: Trauma and Repair

P3-337

Mechanical Modeling of Distraction Osteogenesis

Mr Alexandre Hamma[1], Associate Professor Jean Boisson[1], Professor Natacha Kadlub[1,2], Dr Cortet Pierre-Philippe[3], Prof Poulard Christophe[4], Prof Picard Arnaud[2]

[1]Laboratory of Mechanics and its Interfaces, ENSTA, IP-Paris, Palaiseau, Ile de France, France. [2]Maxillofacial and Plastic Surgery, Necker Children Hospital, APHP, Paris, Ile de France, France. [3]FAST, Saclay, Ile de France, France. [4]LPS, Saclay, Ile de France, France

Mr Alexandre Hamma

Associate Professor Jean Boisson

Introduction

Osteogenic distraction is a surgical procedure that has been widely used since the 1950s. It enables gradual bone lengthening by elongating a callus following a surgical fracture. This technique is now essential for treating congenital facial malformations in children. Indications are either functional, such as occlusal or respiratory issues, or morphological. Since its introduction to maxillofacial surgery, technical improvements have focused on reducing iatrogenic complications, increasing patient comfort, and improving effectiveness. However, many studies are based on cadaveric or animal models without considering the origin of the forces involved in distraction. Here, based on experimental tests and numerical simulations, we propose a complete description of the mechanical process of mandibular distraction that can be extended to any osteogenic distraction.

Methods

This study used the finite element method to simulate numerically a mandibular distraction osteogenesis. All simulations were performed using Abaqus (Dassault Systèmes). After validation of a simplified mandibular geometry, we simulated a complete 20-mm distraction. The cortical bone was modeled as an isotropic, linear, elastic material, while, the periosteum as a custom visco-hyperelastic, transversely isotropic constitutive law. We modeled the periosteum attachment to the bone using a bilinear traction-separation law to simulate the initiation and propagation of contact damage. The parameters of this law were identified through a series of periosteum peeling tests on pig

mandibles, along with a sensitivity analysis. Finally, we modeled the complex interface between the periosteum and bone to account for surgically manipulated and undisturbed adhered regions.

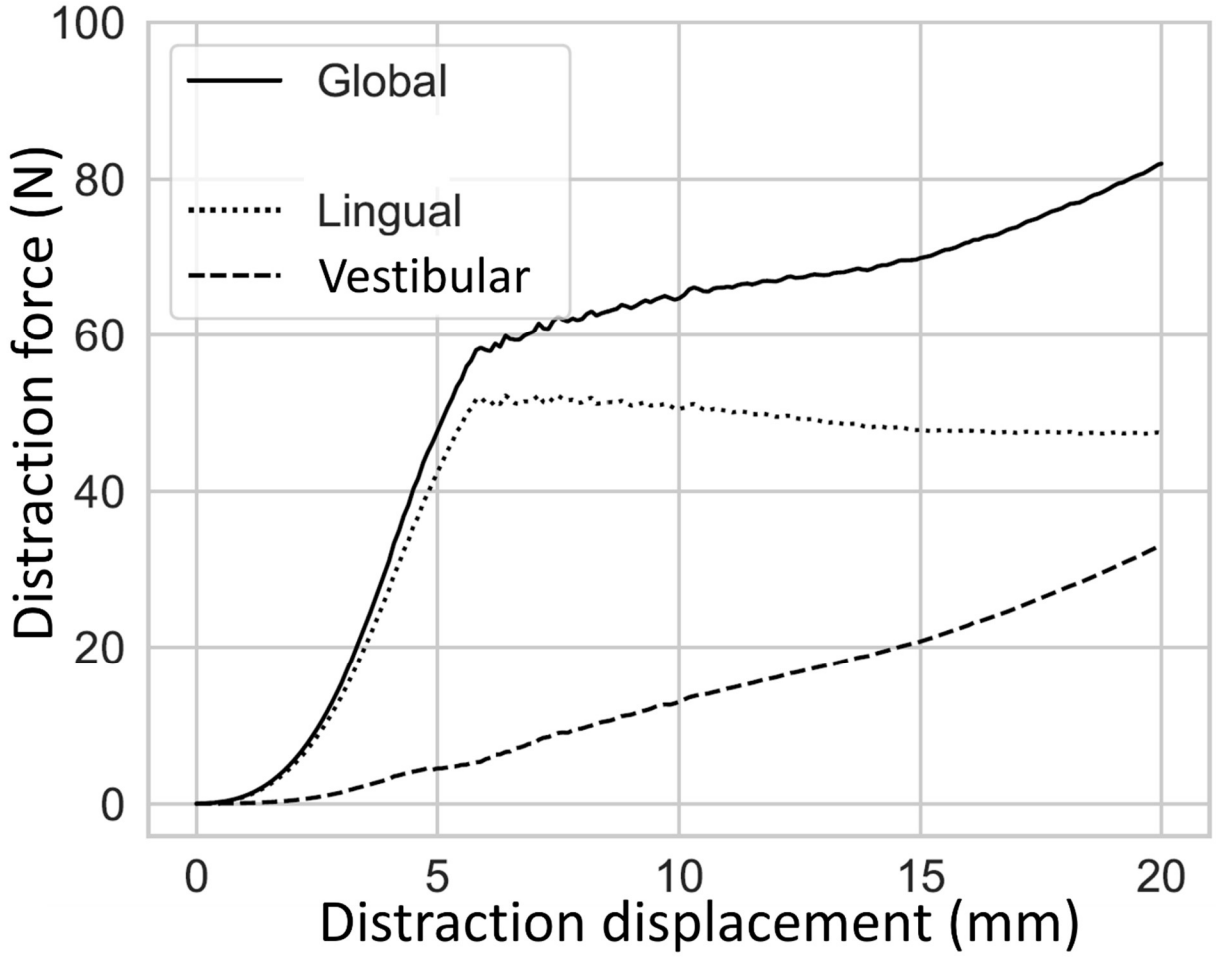
Results

The evolution of the resulting force of distraction is in very good agreement with an experimental campaign conducted on cadaveric subjects, which showed an increase in force for the first five millimeters, followed by a plateau characteristic of a peeling phenomenon. The force distribution is also greater on the lingual side than on the vestibular side.

Discussion

These results validate the entire study and highlight the important role of the periosteum in distraction osteogenesis. Additionally, we demonstrate that surgical dissection geometry controls the plateau of force level, as well as the distraction vector, which is critical in cases of craniofacial dysjunction, for example.

Images (Optional)



Acknowledgements (Optional)

The authors thanks the Ecole de Chirurgie, APHP, for the anatomic subject supply, the Fondation des Gueules Cassées for their support. This work is fully supported by funds from Agence Innovation Défense.

Session Category

Orthopaedic Biomechanics: Trauma and Repair

P3-338

Analysis of the Influence of Spinal Screw Length in Spinal Fusion in Young People and Those With Osteoporosis

Dr Krzysztof Jankowski, Dr Roman Grygoruk

Warsaw University of Technology, Warsaw, Mazovia, Poland

Introduction

Vertebral fractures are serious injuries that prevent normal functioning. In young and middle-aged individuals, these injuries may be caused by traffic accidents or sports-related accidents, while in older individuals, especially those with osteoporosis, a fall from a height may be sufficient. These fractures are treated with the use of fixators, which are secured with screws inserted into the vertebrae located above and below the fractured vertebra. This relieves the load on the fractured vertebra. The aim of this study was to determine whether, from a biomechanical perspective, it is better to use longer or shorter screws, taking into account the condition of the cortical and trabecular bone (healthy tissue and osteoporotic) in the vertebrae.

Methods

Based on computed tomography (CT) scans of patients with a fractured vertebra, 3D models of the vertebrae were created, divided into cortical and trabecular bone. The rods and screws of different sizes were modelled based on the catalogue and used in various configurations of virtual spinal fusion. These models were used in finite element simulations of uniaxial compression of the spine with a fixator performed in ANSYS. The variable between configurations was the screw length, as well as the material properties of cortical and trabecular bone (healthy and osteoporotic).

Results

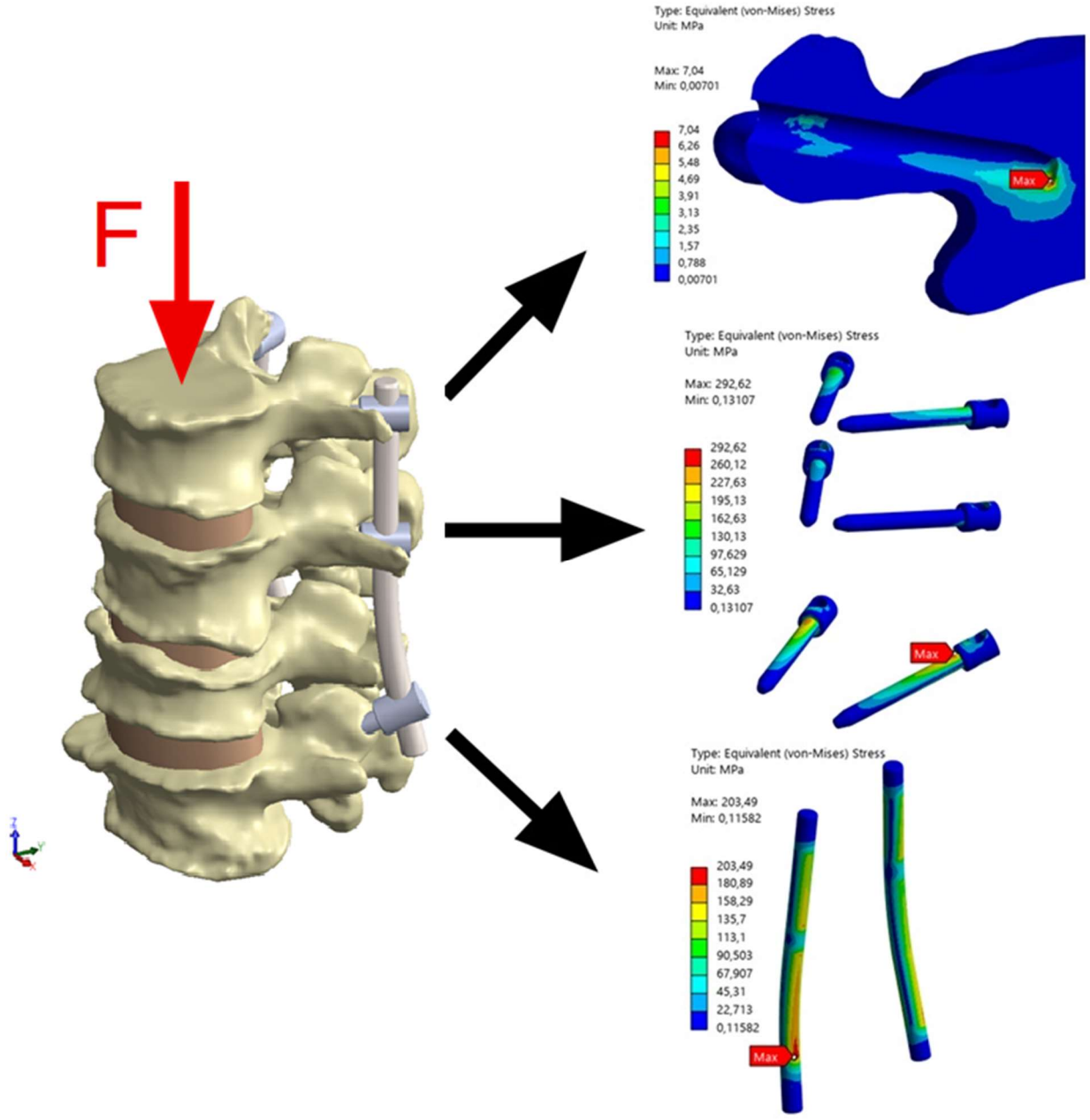
As a result of the simulations, stress and strain distributions in the vertebrae (cortical and trabecular bone structures), rods and screws were obtained (Fig. 1), which were compared and analysed.

Discussion

Simulations showed the differences in stress and strain distributions in healthy and osteoporotic vertebrae. In ‘healthy spine’, longer screws caused lower values of max stress and strain in bone tissues than shorter, but greater in rods and screws. In ‘osteoporotic spine’, longer screws caused greater values of max stress and strain in bone tissues, but smaller values on rods and screws. It was caused by the condition of osteoporotic

trabecular bone, which is much weaker in the middle of the vertebrae. Hence, the screws have a greater chance of causing damage to it and loosening themselves.

Images (Optional)



Session Category

Orthopaedic Biomechanics: Trauma and Repair

P3-339

The Effect of Braid Parameters on Soft Tissue Repair Devices

Miss Lydia Jordan[1], Professor Sam Evans[1], Dr Hayley Wyatt[1], Ms Vicky Graham[2]

[1]Cardiff University, Cardiff, UK, United Kingdom. [2]Lockdown Medical Ltd, Redditch, UK, United Kingdom

Introduction

Successful artificial ligament and tendon repairs depend on restoring joint strength and stability while preventing re-rupture or over-constraint of the joint. Braided artificial ligaments and tapes are widely used in orthopaedic reconstruction, yet the relationship between braid structure and mechanical behaviour remains poorly quantified. This study investigates how variations in braiding manufacture influence mechanical performance and develops predictive models to optimise the design of soft tissue repair devices.

Methods

Nine groups of braided samples, based on the LockDown Shoulder Stabilisation System, were produced with systematic variations in:

1. Manufacturing speed
2. Number of cores (sub-structures running vertically through the braid)
3. Core material
4. Number of bobbins (the threads that are braided around each other and the cores).
5. Fibre material

Each group contained multiple samples tested in uniaxial tension to failure, with strain measured using video extensometry. Mechanical outputs - ultimate load (N), stiffness (N/mm), engineering stress (N/mm^2), and strength efficiency ratio (actual failure load/theoretical failure load) - were analysed to identify relationships between structure and mechanical behaviour. Linear regression models were then developed to predict mechanical performance from design parameters, with goodness of fit evaluated using the coefficient of determination (R^2).

Results

Increasing total strand count produced an increase in strength and stiffness while reducing local stress, indicating there may be a more efficient load distribution within the braid as the strand count increases. Manufacturing speed had limited influence on stiffness but

affected mechanical response variability, suggesting a more complex relationship that cannot be immediately identified with these methods. Figure 1 shows the correlation map with significance indicated for each factor. Predictive models achieved strong fits ($R^2 > 0.8$) for most groups, allowing reliable estimation of mechanical behaviour from most braid inputs.

Discussion

The study demonstrates how predictive modelling can be used as an effective design tool. It links braid-manufacture parameters to mechanical behaviour, providing a quantitative framework for optimising soft tissue repair devices. These models enable intentional design of constructs with mechanical properties that better replicate native tissue behaviour, improving joint stability and long-term device performance. Ultimately, such optimisation can help maintain joint biomechanics, preventing excessive laxity or over-restriction following reconstruction.

Images (Optional)

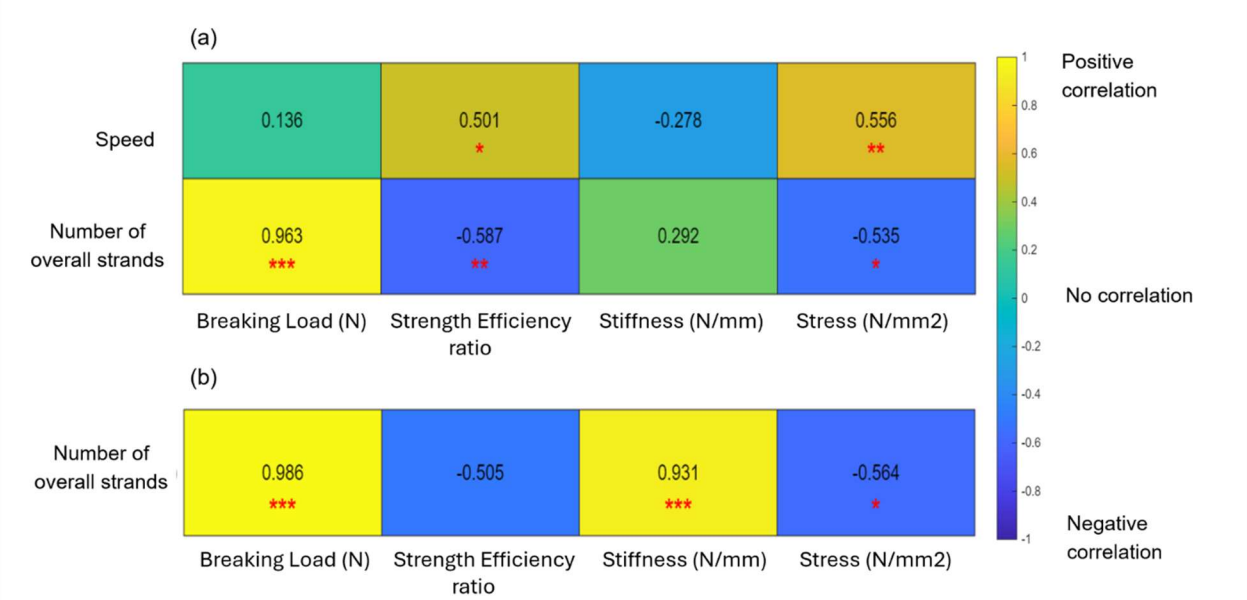


Figure 1 Shows the correlation map for the input parameters against output measurements. (a) The take-up speed varied groups; (b) the groups where another non-speed factor was varied. The correlation coefficient R is shown in each section and significance is indicated (P<0.05, **P<0.005, ***P<0.001). The heat map shows negative and positive or no correlation.*

Session Category

Orthopaedic Biomechanics: Trauma and Repair

P3-340

Finite Element Modeling of Cranial Suture Using 3D Anisotropic Material Properties

PhD Candidate Mahzad Sadati[1], MSc Kavya Weerasinghe[1], MSc student Nikala E Bochinski[2], Associate Professor Karyne N Rabey[2,3], Professor Michael R Doschak[4], Associate Professor Lindsey Westover[1,5], Associate Professor Dan L Romanyk[1,5,6]

[1]Department of Mechanical Engineering, University of Alberta, Edmonton, AB, Canada. [2]Neuroscience and Mental Health Institute, University of Alberta, Edmonton, AB, Canada. [3]Department of Surgery, University of Alberta, Edmonton, AB, Canada. [4]Faculty of Pharmacy and Pharmaceutical Sciences, University of Alberta, Edmonton, AB, Canada. [5]Department of Biomedical Engineering, University of Alberta, Edmonton, AB, Canada. [6]Mike Petryk School of Dentistry, University of Alberta, Edmonton, AB, Canada

Introduction

Cranial sutures are fibrous joints that connect skull bones and contribute to cranial growth and load transfer throughout life. Their complex interdigitated morphology and heterogenous collagen fibre architecture produces anisotropic mechanical behaviour. However, many finite element (FE) models have assumed isotropic or oversimplified anisotropic properties, limiting the understanding of how local fiber orientation influences suture mechanics. This study developed a 3D anisotropic FE model of the swine internasal suture and applied a response surface methodology (RSM) to optimize anisotropic material model constants using experimental data. It is hypothesized that using anisotropic material modeling will produce significant differences in strain distribution from isotropic modeling.

Methods

Internasal sutures from three swine were scanned using micro-computed tomography (9 resolution) to establish FE geometry, and three samples were extracted along the posterior-anterior axis for each specimen. Tensile testing was performed at 0.2 mm/min. Bone was modelled as isotropic (E= 2000 MPa, Poisson ratio=0.27), while the suture was assigned an orthotropic linear elastic material model with nine independent constants governing stiffness in the principal fibre directions. Fibre orientations in coronal and transverse planes were quantified from Masson's trichrome staining and mapped into the FE model using region-specific coordinate systems. A central composite design (CCD) was generated to explore nine independent anisotropic parameters and determine their optimum value within physically-relevant bounds. A 0.0001 mm displacement simulated

physiological strain. RSM was used to build response surfaces and identify parameter combinations minimizing error between simulated and experimental force-displacement curves.

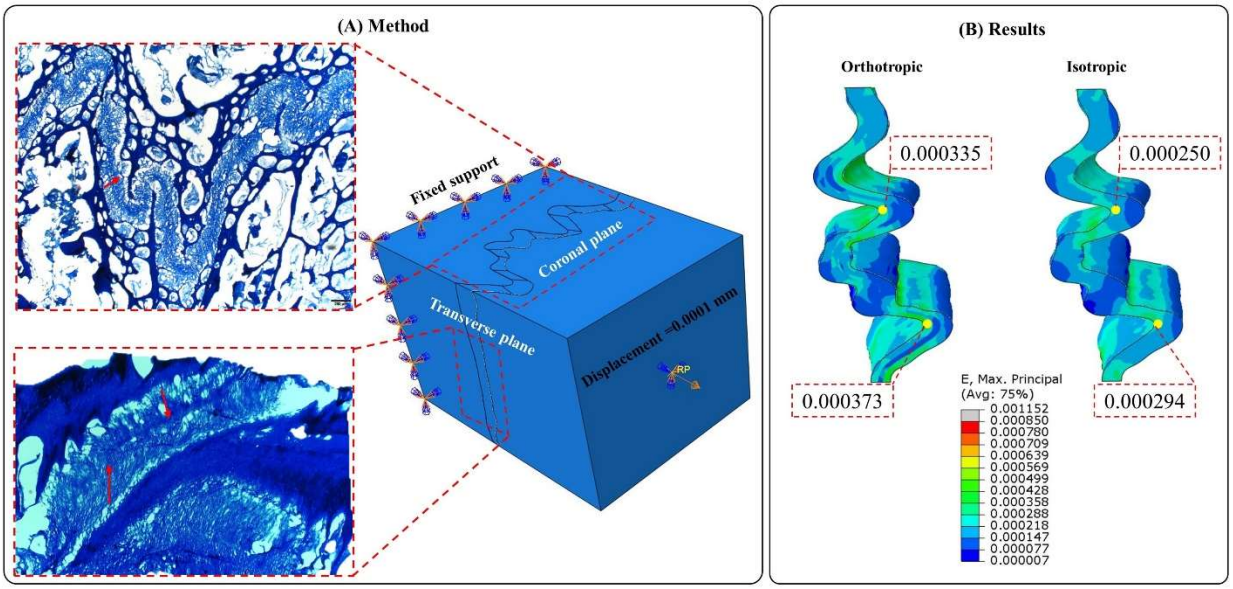
Results

The RSM identified an optimal set of anisotropic parameters for each sample, with FE outcomes closely mimicking experimental measurements. Anisotropic models produced distinct stress and strain distributions compared to isotropic models. Regions where fibers aligned with loading showed reduced strain energy, while oblique orientations caused greater deformation.

Discussion

The comparison between anisotropic and isotropic models showed that utilizing anisotropic properties altered both the magnitude and spatial distribution of stress and strain, enabling the FE model to capture localized mechanical behaviour that isotropic properties could not reproduce. Results confirmed that collagen fibre alignment influences load-bearing response and demonstrated the value of optimization-based anisotropic modeling for characterizing suture mechanical behaviour.

Images (Optional)



Session Category

P3-341

Influence of Depression Elevation on the Force Distribution of Tibia Plateau

Mr. Mahziyar Darvishi PhD candidate, Mr James Campbell Orthopaedic Surgery Resident, Dr. David Wasserstein Assistant Professor, Dr. Joseph Schatzker Professor Emeritus, Dr. Timothy Burkhart Assistant Professor

University of Toronto, Toronto, Ontario, Canada

Introduction

Schatzker type II tibial plateau fractures often involve an articular depression, where elevation during reduction influences tibiofemoral biomechanics. Although surgical thresholds of approximately 4–5 mm of depression correction are widely used [1], they rely largely on clinical consensus rather than biomechanical evidence. Consequently, the effects of under- and over-correction beyond native alignment remain poorly defined. Therefore, the objective of this study was to evaluate biomechanical effects of varying tibial plateau elevation by comparing stress and displacement across under-corrected, naturally corrected, and over-corrected configurations using finite element modeling (FEM).

Methods

A patient-specific finite element model was generated from a CT image of a Schatzker type II lateral tibial plateau fracture. Five fracture reduction conditions were evaluated: natural correction, 2.5-mm and 5-mm under-correction, and 1-mm and 2.5-mm over-correction. Each model was subjected to standardized physiological axial displacement. Von Mises stress and displacement in the tibial cartilage and subchondral bone were calculated and compared across correction conditions.

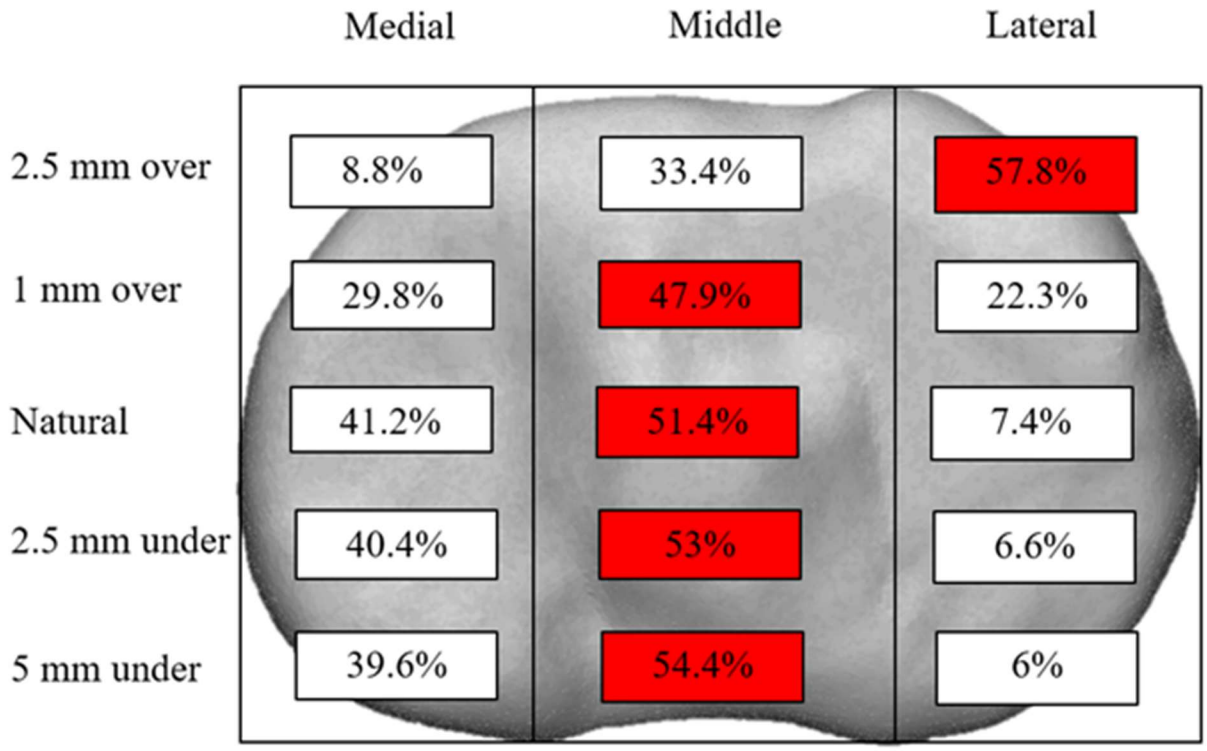
Results

The naturally corrected model showed stress and displacement values consistent with literature. The 2.5-mm over-correction yielded the highest cartilage displacement (1.34 mm) and stress (9.59 MPa). Under-correction increased cartilage stress relative to natural correction (up to 9.19 MPa vs. 7.56 MPa); however, load distribution remained predominantly medial, consistent with physiological load sharing in a healthy knee. Figure 1 demonstrates progressive lateralization with increasing correction, with lateral stress rising from 6–7% in under-corrected and naturally corrected models to 22.3% at 1 mm and 57.8% at 2.5 mm of over-correction, accompanied by reductions in medial and middle stress contributions.

Discussion

These findings indicate that over-correction disrupted native load distribution, producing lateral overload and greater biomechanical alterations compared to the under-correction. Although under-correction increased stress relative to natural alignment, it preserved more physiological medial loading patterns. The results are limited by model simplifications, including a single patient-specific geometry and omission of soft tissues. Future studies incorporating additional subjects and experimental validation are needed to define safe correction margins.

Images (Optional)



References (Optional)

[1] T. P. Vaartjes et al. *Clin Orthop Relat Res*, 2022.

Session Category

Orthopaedic Biomechanics: Trauma and Repair

P3-342

A Translatable Tribological In Vitro Model to Assess Cartilage-Biomaterial Compatibility for Hemiarthroplasty

Ms Francesca De Vecchi[1], Ms Victoria Marino[1], Dr. Thomas Schmid[1], Ms Afton K. Limberg[2], Dr. Douglas Van Citters[2], Dr. Joseph J. Crisco[3], Dr. Markus A. Wimmer[1]

[1]Rush University Medical Center, Chicago, IL, United States. [2]Dartmouth College, Hanover, NH, United States. [3]Rhode Island Hospital, Providence, RI, United States

Ms Francesca De Vecchi

Ms Victoria Marino

Introduction

Ethical and regulatory constraints continue to limit animal use in preclinical testing, increasing the need for physiologically relevant in vitro systems in biomechanics and orthopedic research. Joint-preserving procedures such as hemiarthroplasty further underscore the importance of models capable of replicating native cartilage mechanics when articulating against implant materials. Because only one surface is replaced, long-term success depends on how the biomaterial interacts with living cartilage under complex tribological loading. Existing in vitro systems rarely capture the combined rolling–gliding motion, cyclic compression, nutrient transport, and biochemical responses characteristic of in vivo articulation. The objective of this study was to develop and validate an in vitro cartilage wear model that reproduces key biomechanical features of the joint environment, enabling systematic evaluation of cartilage–biomaterial compatibility while reducing reliance on animal testing.

Methods

A multi-station joint articulation system applied physiological rolling-gliding motion under 2 MPa compressive load. Fresh bovine patellofemoral cartilage explants (14 × 20 mm) from a slaughterhouse were articulated against spherical samples of cobalt–chromium (CoCr), zirconia-toughened alumina (ZTA) ceramic, hydrophobic and hydrophilic UHMWPE, titanium nitride (TiN), PEEK, and PEKK (n = 8 per material). Culture medium served as lubricant and nutrient source and was renewed at standardized intervals. Samples

experienced 5,400 cycles/day at 0.5 Hz for five days; free-swelling controls received identical handling without loading. Outcomes included chondrocyte viability, histological matrix integrity, and biochemical wear quantified through collagen (hydroxyproline) and sGAG release. Wear rates were obtained from linearized release curves.

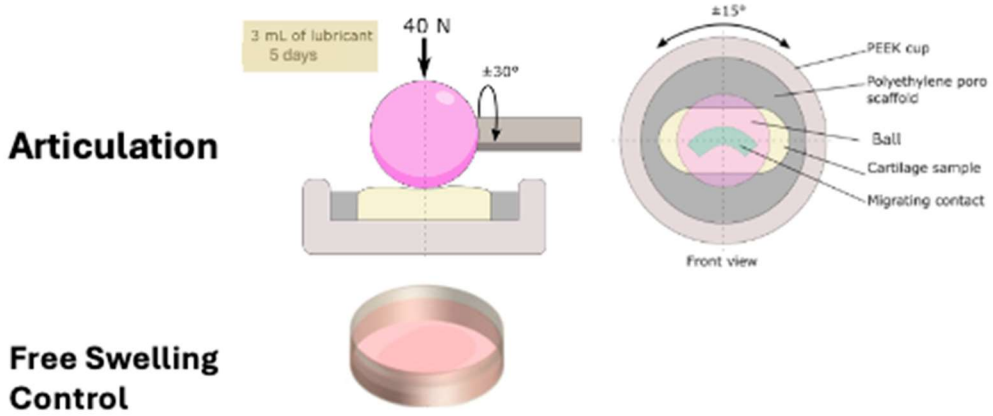
Results

The model maintained >80% viability and produced reproducible wear signatures across materials. Polyethylene-based surfaces caused the greatest superficial matrix disruption and cell loss, accompanied by 30–100× higher collagen and 2.5–3× higher sGAG release relative to CoCr and ZTA. TiN and PEEK induced intermediate wear, whereas PEKK produced moderate wear. CoCr and ceramic maintained smooth surfaces with only mild superficial cell death.

Discussion

The model reproduced key features of tribological loading and effectively distinguished cartilage compatibility among materials. Findings aligned with clinical and biomechanical evidence identifying CoCr and ceramics as gold-standard articulating surfaces. This system offers a translational platform for preclinical biomaterial screening and the development of joint-preserving technologies.

Images (Optional)



Session Category

Orthopaedic Biomechanics: Trauma and Repair

P3-343

Additively Manufactured Patient-Specific Trabecular Bone Imitations in Anatomical Bone Models for Preoperative Planning and Surgical Training: A Manufacturing Framework

Mr. Maximilian Pestel[1,2], Dr. Gerhard Hobusch[1], Dr. Jürgen Alphonsus[1,3], Dr. Gregor Wollner[1], Dr. Madeleine Willegger[1], Mr. Andreas Strassl[4], Prof. Iris-Melanie Nöbauer-Huhmann[4], Prof. Reinhard Windhager[1], Prof. Maximilian Lackner[2,5], Dr. Emir Benca[1]

[1]Department of Orthopedics and Trauma Surgery, Medical University of Vienna, Vienna, Vienna, Austria. [2]Department of Industrial Engineering, University of Applied Sciences Technikum Wien, Vienna, Vienna, Austria. [3]Karl Chiari Lab for Orthopaedic Biology, Department of Orthopedics and Trauma Surgery, Medical University of Vienna, Vienna, Vienna, Austria. [4]Department of Biomedical Imaging and Image-guided Therapy, Medical University of Vienna, Vienna, Vienna, Austria. [5]Polymer Institute SAS, Bratislava, Bratislava, Slovakia

Introduction

Additively manufactured anatomical bone models are used for medical education and surgical training. Manufacturing of patient-specific anatomies and rare pathologies has advanced rapidly, enabling training opportunities previously restricted to limitedly available anatomic specimens. [1] However, imitating patient-specific trabecular bone microstructure in printed bone models remains inadequately addressed. [2] This study aimed to evaluate the feasibility of imitating patient-specific trabecular bone structures by linking bone mineral density (BMD) assessed by clinical computed tomography (CT) to manufacturing parameters of fused filament fabrication (FFF) 3D-printing (i.e., infill densities, materials and lattice structures).

Methods

Test specimens in form of Gyroid and Voronoi lattice cubes were manufactured via FFF-printing at varying densities with polylactide (PLA), polylactide/carbon fiber composite and polyamide (PA6)/glass fiber composite filaments, and submerged in gelatin. Additionally, trabecular bone cubes were removed from bovine femoral specimens and the bone mineral density (BMD) assessed utilizing quantitative CT. Subsequently, haptic drill resistance and realism were evaluated by four orthopedic and trauma surgeons, and the mechanical drill resistance was assessed using a load frame (see Figure).

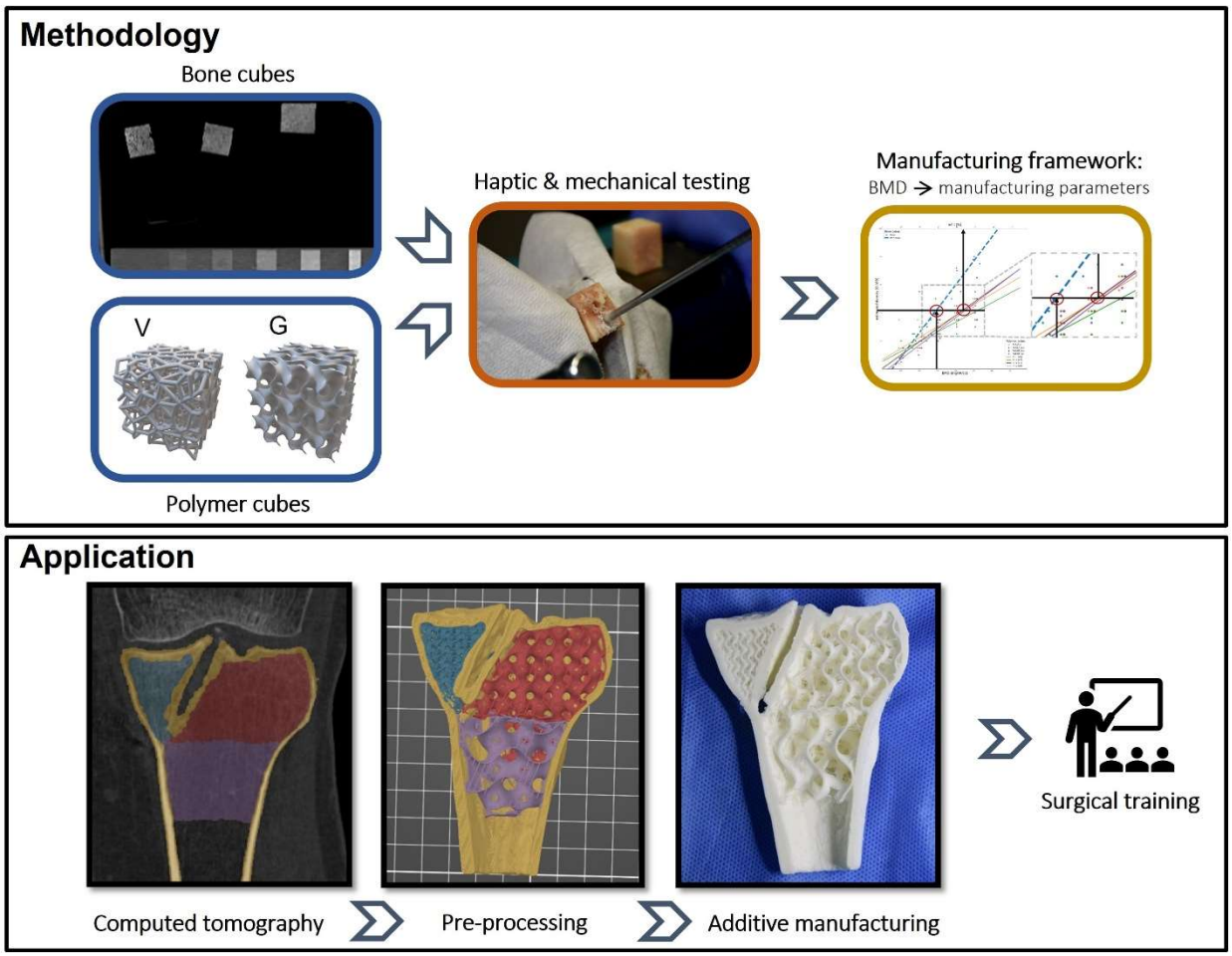
Results

Multiple polymer lattice structures and material configurations were evaluated by the surgeons with average Likert scores regarding haptic realism between 2.60 and 3.00. Correlation between the maximum indentation depth (mechanical testing) and the surgeons' drill-resistance assessments revealed a strong correlation ($R^2 = 0.82$). Regression analysis of the surgeons' evaluations of trabecular bone ($0.75 \leq R^2 \leq 0.98$) and the polymer lattice cubes ($0.66 \leq R^2 \leq 0.89$) enabled the extraction of practical manufacturing guidelines, linking patient-specific BMD with manufacturing parameters for FFF-printers.

Discussion

The strong correlation between the mechanical testing and surgeons' haptic assessments supports the feasibility of trained surgeons accurately estimating haptic material density. Likert score evaluations further demonstrate that trabecular bone structures can be effectively imitated in anatomical bone models produced via FFF-printing. By linking patient-specific BMD values with manufacturing parameters, the proposed framework enables a reproducible, cost- and time efficient production of anatomical bone models with patient-specific haptic feedback, which can be used for preoperative planning and surgical training.

Images (Optional)



References (Optional)

[1] A. Ganguli et al., Biomedical microdevices, 2018

[2] E. Benca et al., 3D printing in medicine, 2024

Session Category

Orthopaedic Biomechanics: Trauma and Repair

P3-344

Quantifying early biomechanical changes in an equine model of intra-articular soft tissue injury

Ms Olivia Kenny, Dr Kasara Toth, Dr W. Michael Scott, Dr W. Brent Edwards, Dr Thilo Pfau, Dr Roman Krawetz, Dr Holly Sparks

University of Calgary, Calgary, Alberta, Canada

Introduction

Post-traumatic osteoarthritis (PTOA) is common amongst human and animal athletes alike. While murine models of destabilizing joint injury have improved our understanding of PTOA, the risk for development of PTOA in clinical cases is difficult to predict. Further, PTOA has been reported to develop after considerably more mild forms of joint injury. Therefore, this work seeks to understand early biomechanical change both within the joint and affecting gait following mild intra-articular injury using an equine model.

Methods

In four horses, a minimally invasive technique was used to unilaterally create a defect along the length of the craniomeniscotibial ligament in the medial femorotibial joint mimicking a naturally occurring injury in equine athletes. As in other species, intra-articular injury can initiate chronic synovitis potentially predisposing the animal to PTOA [1]. Objective gait analysis data was collected using body-worn inertial measurement units (IMUs) (EquiGait, Cheshunt, UK) to quantify and compare vertical movement asymmetry throughout the study. A Mach-1 mechanical tester (Biomomentum Inc, Laval, Canada) was used for thickness and indentation tests on the intact medial femoral condylar (MFC) surfaces ex vivo. Cartilage tissue parameters, including thickness and instantaneous modulus were analyzed on the injured and sham-operated MFCs.

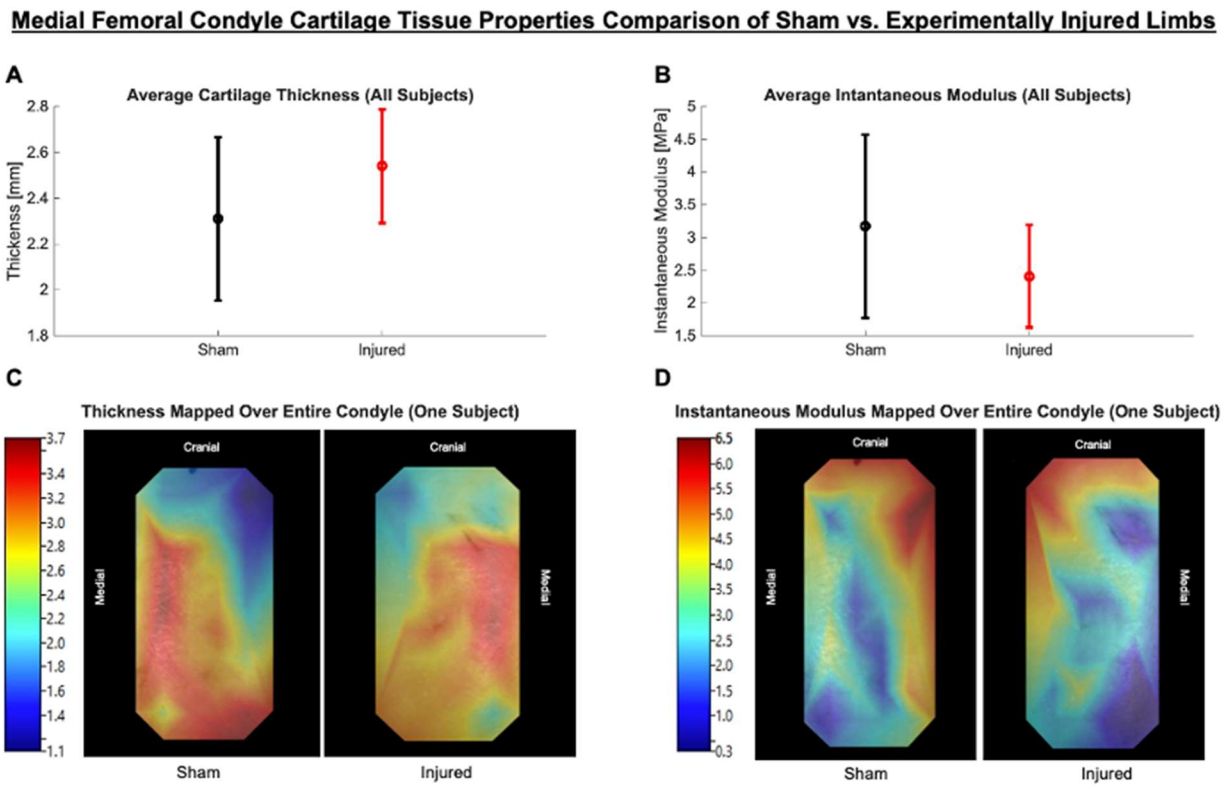
Results

Objective gait analysis showed an average difference in vertical displacement asymmetry of 5.3 mm compared to baseline, throughout the duration of the study. On average, the cartilage thickness was higher on the experimentally injured MFC, and the instantaneous modulus was lower, shown in Figure 1.

Discussion

This injury model produced minimal vertical displacement asymmetry changes, correlating with the absence of overt clinical lameness. Additional IMU data analysis is ongoing to evaluate if lower limb kinematics differ between the injured and sham limbs. Biomechanical properties mapped across the condylar surface are being further analyzed. As part of a larger study, histological methods are being used to describe the tissue response at a cellular level. The combined effects of potential differences in joint loading and changes in cartilage tissue properties will be explored as prospective indicators of early PTOA development.

Images (Optional)



References (Optional)

[1] Bolam *et al.*, AM J Vet Res, 2006

Session Category

Orthopaedic Biomechanics: Trauma and Repair

P3-345

Microdamage in Cortical Bone Induced by Screw Insertion and Pull-Out Revealed by Sequential Fluorescent Staining

MSc Saeideh Saeidi[1], PhD Mina Petrovic[2], Univ.Prof. Dieter Pahr[1]

[1]Institute of Lightweight Design and Structural Biomechanics, TU Wien, Vienna, Vienna, Austria. [2]Institute of Materials Science and Technology, TU Wien, Vienna, Vienna, Austria

Introduction

In orthopaedic implants, primary stability is significantly affected by bone damage induced during implantation procedures. This study explores the relationship between screw insertion, pull-out loading, and microscopic bone damage. We visualize and characterize various damage stages, aiming to enhance the predictive accuracy of finite element models and ultimately improve implantation outcomes.

Methods

Seven cortical bone samples were dissected from fresh frozen ovine tibia diaphysis. The sequential fluorescent staining approach [1] is adapted including xylenol orange, calcein and calcein blue to label bone damage in different stages from pre-drilling to tensile loading. First, specimens were drilled and stained with xylenol. A locking screw (Medartis, Switzerland) was implanted, then unscrewed, followed by calcein staining to identify damage caused by screw insertion. Following screw re-insertion, a tensile test was conducted until a 5% drop in measured force was detected. After screw removal, specimen was stained with calcein blue to identify load induced damage. Samples were glued on microscope slide, milled using an ultramiller till the hole centerline, and imaged using a confocal laser scanning microscope (CLSM).

Results

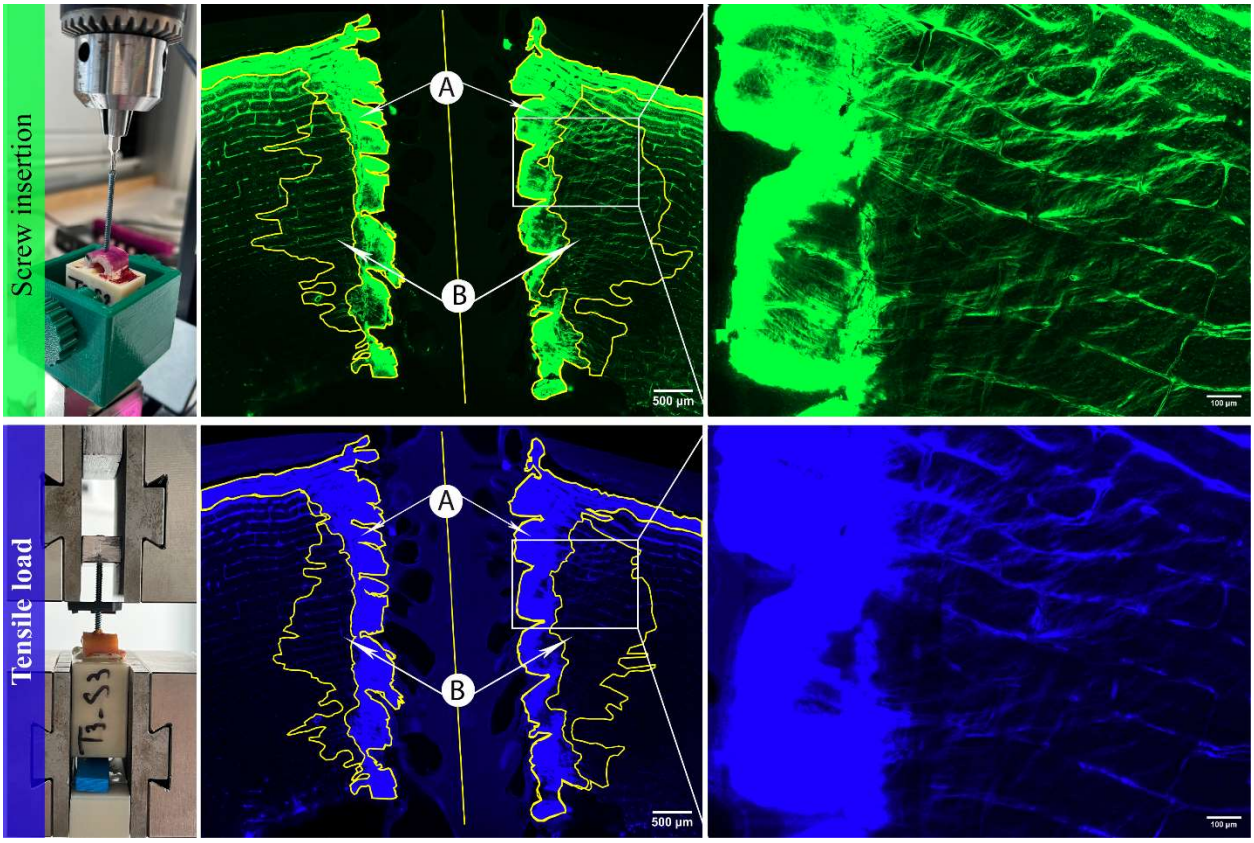
Force-displacement curves showed maximum force as 956.9 ± 175.6N. CLSM results revealed negligible damage due to drilling. Figure presents CLSM images illustrating bone damage induced by screw insertion (green) and tensile loading (blue). Both show complex damage including diffuse damage (region A) occurred in a narrow area adjacent to bone-screw interface, followed by a dense area of elongated bundles of linear cracks (region B) propagating along the weakest planes of lamellar sheets with specific orientation. Damage percentage is calculated as area of damage divided by pilot hole area. Total damage of 98.3

± 13.0% was caused by screw insertion, including 43.4 ± 6.8% diffuse damage and 54.9 ± 14.1% linear cracks. Total damage of 83.2 ± 12.3% was caused by tensile loading, including 48.2 ± 5.8% diffuse damage and 33.3 ± 12.4% linear cracks.

Discussion

Screw insertion generated the significant damage, dominated by more linear cracks. Despite causing less total damage, tensile loading expanded diffuse damage rather than linear crack growth. Our study highlights the critical role of bone damage in refining finite element models accuracy.

Images (Optional)



References (Optional)

[1] Fergal J. O'Brien, et al. , J Biomechanics, 2002

Session Category

Orthopaedic Biomechanics: Trauma and Repair

P3-346

Bendable Osteochondral Allografts for Carpometacarpal Arthritis Treatment Eliminate Sex-based Differences in Contact Pressures in Computational Model

Ms. Sarah Deiters, Dr. Katherine Spack PhD, Mr. Thomas Gardner, Dr. Clark Hung PhD, Dr. Melvin Rosenwasser MD, Dr. Gerard Ateshian PhD

Columbia University, New York, NY, United States

Introduction

A Bendable Osteochondral Allograft (BOCA) from a donor's femoral trochlea offers a potential treatment for carpometacarpal (CMC) osteoarthritis (OA), which disproportionately impacts women, by providing a thicker articular cartilage layer[1,2]. Females experience higher healthy CMC contact pressures than males[3,4], which must be considered when evaluating BOCA treatment. We hypothesize that male and female metacarpals experience comparable contact pressures when in contact with BOCA.

Methods

Finite element contact analyses in FEBio[5] simulated male and female metacarpal contact with a BOCA to determine average joint contact pressure during simulated pinch. Prior stereophotogrammetry scans[6] of 5 female and 4 male human metacarpals with Stage IV OA were used, and the BOCA model was constructed as described previously[1]. Metacarpal bone surfaces and BOCA were meshed with Quad8/Tri6 and Tet10 quadratic elements then aligned neutrally. 1000N contact force was applied in the proximal-distal direction. We calculated average contact pressure from the ratio of force and contact area. After determining data normality (Shapiro-Wilk) and equal variances (F-test), we used a two-tailed Student's t-test (α=0.05) to determine if a difference exists between male and female joints.

Results

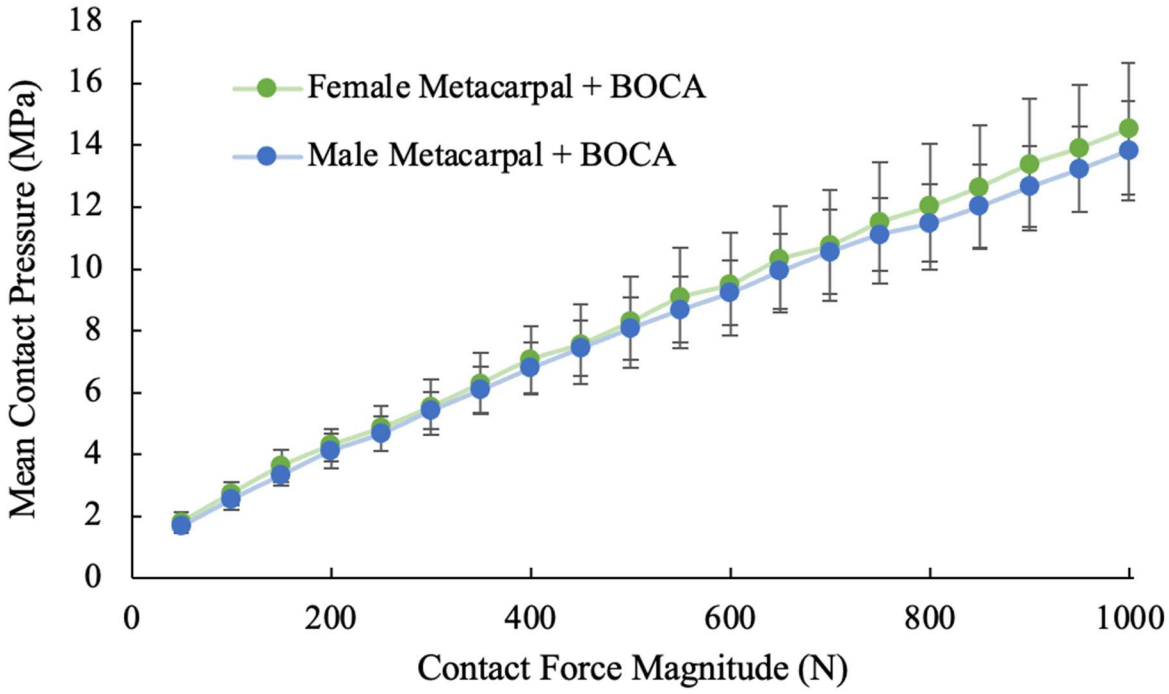
Male and female metacarpals in contact with BOCA at 1000N experienced mean contact pressures of 13.84 ± 1.61 MPa and 14.54 ± 2.12 MPa, respectively, which were not statistically different (p=0.603). For comparison, we recently showed that contact pressures for healthy male and female CMC joints are significantly different (Male 26.1 ± 6.7 MPa versus Female 38.6 ± 4.9 MPa, p=0.014)[4].

Discussion

Our previous analyses[1,4] indicated that BOCA-treated joints experience lower contact pressures than healthy CMC joints, and healthy female CMC joints experience higher

contact pressures than male joints, which may explain higher OA incidence in women[7]. Results of the current study indicate that BOCA treatment for CMC OA may eliminate sex differences in contact pressures, supporting the potential benefits of this novel treatment.

Images (Optional)



References (Optional)

[1] Deiters et al.,SBC,2025. [2] Petersen et al.,J Biomech,2022. [3] Ateshian et al.,J Biomech,1992. [4] Deiters et al.,in press (ORS),2026. [5] Maas et al.,J Biomech Eng,2012. [6] Koff et al.,J Hand Surg,2003. [7] Segal et al.,Sex Differ Osteoarthr,2024.

Session Category

Orthopaedic Biomechanics: Trauma and Repair

P3-347

Analysis of the Design Freedom of Round Braided Resorbable Synthetic Ligament Augmentation Scaffolds

M.Sc. Saskia Hesse, Dr. Ing. Benedict Bauer, Univ.-Prof. Thomas Gries, Dr. Ing. Caroline Emonts

Institut für Textiltechnik of RWTH Aachen University, Aachen, NRW, Germany

Introduction

Ligament augmentation implants have gained renewed interest to enhance the mechanical stability of reconstructed ligaments. Contemporary techniques integrate synthetic or hybrid materials to address graft elongation and postoperative laxity [1]. But there remains a need for bioresorbable and mechanically designed augmentations. Therefore, bioresorbable synthetic textile implants are developed. The aim of this study is to show the design freedom of morphological and mechanical variations of round braided augmentation scaffolds to design biomimetic load carrying implants. Previous work has shown the great potential of this braided textiles regarding their mechanics [2].

Methods

The synthetic scaffolds are made of Poly-e-caprolactone (PCL) monofilaments which are braided into multilayered structures on a round braiding machine with 48 yarn carriers. For morphological analysis µCT-scans and diameter measurements are performed. The mechanical behavior is tested in tensile load to failure testings with a gauge length of 40 mm and a testing speed of 40 mm/min.

Results

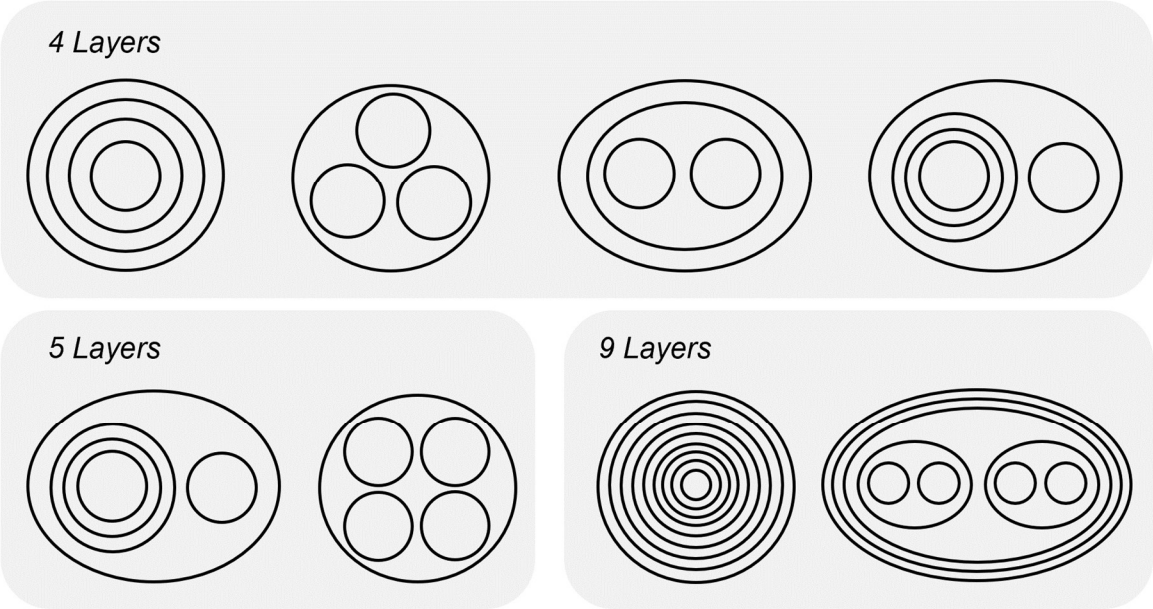
The textile round braiding process brings great design freedom to design ligament scaffolds. Multilayered designs made of bundles can be used as approach to match the structure of native ligament tissue. The trials show that the number of layers and their arrangement can be varied in different ways (Fig. 1). Depending on the arrangement the cross-sectional shape can be altered. The testings show that with constant process parameters but changing layer arrangements the mechanical performance differ. The ultimate tensile strength can vary by up to 10 % within a group with the same number of layers.

Discussion

Round braided multilayered scaffolds offer design freedom for developing biomimetic ligament augmentation implants. By varying the number of layers and their arrangement

the morphology and mechanical performance can be tailored. Future work will explore additional layer arrangements and braiding configurations. Extended mechanical testing will show the stability under physiologically conditions. Ultimately, adapting scaffold architecture to replicate the structural features of native ligament tissue may enable the development of next-generation augmentation implants.

Images (Optional)



References (Optional)

[1] Alexeev et al., 10.1016/j.jisako.2023.04.003, 2023

[2] Emonts, 10.18154/RWTH-2024-08389, 2024

Acknowledgements (Optional)

This project is partially funded by: Federal Ministry of Research, Technology and Space (LigaBraid 2, 16LW0632K).

Session Category

Orthopaedic Biomechanics: Trauma and Repair

P3-348

In Silico Design of Degradable Joint Implants for Optimal Balancing of Tissue Formation and Implant Degradation

Ms. Sophie Nguyen[1], Dr Mojtaba Barzegari[2], Prof. Dr. Liesbet Geris[1,3]

[1]Biomechanics Section, Department of Mechanical Engineering, KU Leuven, Leuven, Flemish Region, Belgium. [2]TU Eindhoven, Eindhoven, North Brabant, Netherlands. [3]Biomechanics Research Unit, GIGA In Silico Medicine, University of Liège, Liège, Walloon Region, Belgium

Ms. Sophie Nguyen

Dr Mojtaba Barzegari

Introduction

Successful bone regeneration after joint arthroplasty requires both stability and sufficient regenerative capacity. Clinical data show that 20 years after the primary total hip arthroplasty placement, revision rates reach up to 40% for patients younger than 50 years [1]. Revision surgeries inevitably remove additional surrounding bone, resulting in critical-size defects that cannot repair spontaneously. A promising strategy involves the design of composite implants consisting of a permanent component to ensure joint integrity and a porous biodegradable component to fill the defect and stimulate bone ingrowth. The degradable structure will gradually be replaced by newly formed bone, mitigating defect enlargement after each revision. Here we developed a multi-factorial *in silico* model to study the balance between the kinetics of porous scaffold degradation and the rate of bone formation.

Methods

A set of partial differential equations (PDEs) was established describing the chemistry of corrosion of a magnesium implant, as well as bone ingrowth through the spatio-temporal concentration of bone cells. The model implicitly tracks the degradation and bone formation fronts in a phase-field framework, including curvature-based effects. The PDEs are solved numerically using the finite element method and implemented in FreeFEM [2]. The interface between the scaffold and bone is refined over time through a mesh

adaptation procedure, allowing accurate tracking of the moving interfaces. The model outputs are the concentration of bone cells and magnesium ions, the geometry of the degrading scaffold, and the density of new bone over time.

Results

The model is applied to a gyroid scaffold, investigating various differences in speed between the bone formation and implant degradation. Fig. 1 shows the results of the simulation where both processes occur at comparable speed, showing scaffold degradation while new bone is forming at the scaffold surface and filling the pores.

Discussion

The presented *in silico* model, once validated, is intended be used as a design tool, providing longitudinal data to assess the interplay between scaffold degradation and bone ingrowth, and the optimized geometry to promote bone regeneration.

Images (Optional)

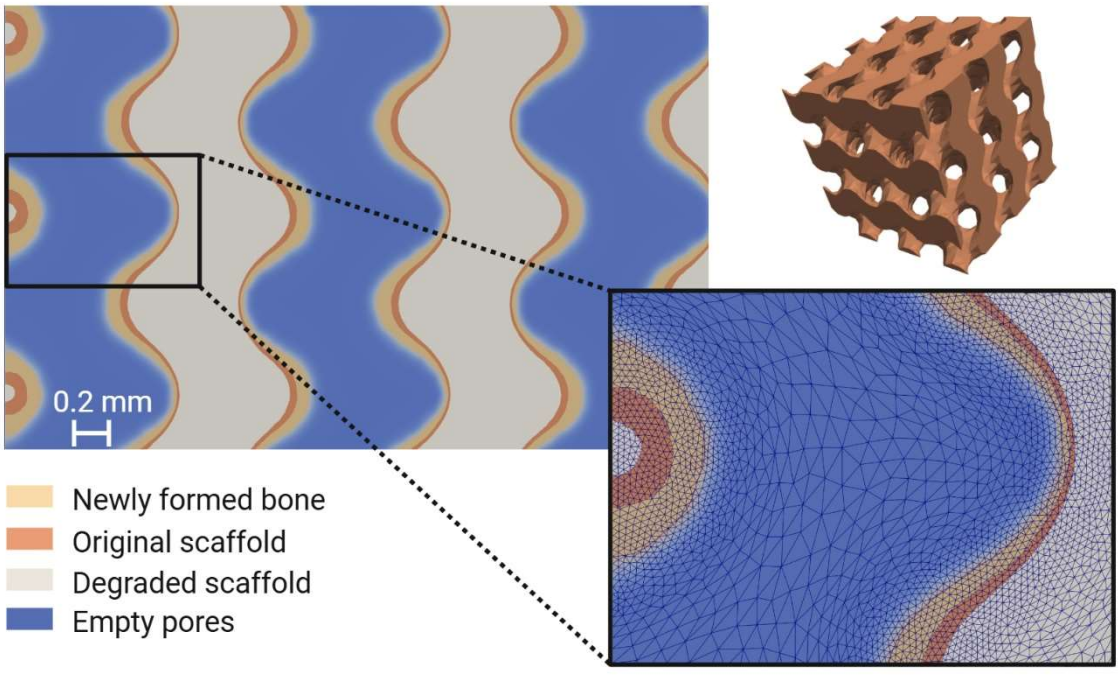


Fig.1: bone ingrowth (yellow) into pores (blue) of a degrading (beige) gyroid scaffold. Orange regions are the initial scaffold shape. Zoom illustrating the fine finite elements capturing the moving interfaces and mesh adaptation over time.

References (Optional)

[1] Christof Pabinger *et al.*, Hip Int., 2018

[2] Frederic Hecht, J Num Math, 2012

Acknowledgements (Optional)

The research was financially supported by the PRosPERoS-II project, funded by the Interreg VA Flanders - the Netherlands program, CCI grant no. 2021TC16RFCB041.

Session Category

Orthopaedic Biomechanics: Trauma and Repair

P3-349

Do Novel Dynamizers Designed to Increase Axial Interfragmentary Motion at the Fracture Site Increase Unwanted Shear in Trauma Frames?

Mr Thomas Irish MEng, BEng[1], Dr Hemant Sharma MCh (Trauma & Orthopaedics), FRCS (Trauma & Orth)[2], Dr Ross Muir FRCS[2], Dr Todd Stewart PhD[1], Dr Marlène Mengoni PhD[1], Dr Peter Watson PhD[1]

[1]Institute of Medical and Biological Engineering, Leeds, West Yorkshire, United Kingdom. [2]Department of Trauma and Orthopaedics, Hull University Teaching Hospitals NHS Trust, Hull, East Yorkshire, United Kingdom

Introduction

Circular external fixators are used for long bone fractures to control micromotion at the fracture site and promote axial interfragmentary motion, stimulating healing, while simultaneously limiting shear which is known to hinder healing [1]. Two new devices (dynamizers) have been introduced that are intended to increase axial interfragmentary motion and thus promote faster healing. However, the effect of dynamizers on changes in shear is unknown. This study measured, for the first time, axial and shear interfragmentary motion in comparable frames with and without dynamizer technology offered from two manufacturers.

Methods

Frames were constructed with central polycarbonate tubes, 4 rings, pins and wires to represent a fixated transverse fracture. Frames were loaded separately in axial (+/- 700N), torsion (+/- 25Nm) and bending (+/- 20Nm) regimes to represent bodyweight load. Ten cycles were completed for each regime providing a measure of variance. Load was held for 5 seconds at distinct loading steps. The movement at the fracture site was tracked optically for each step using a OptoTrak camera system with an accuracy of 0.1mm.

Results

Under axial loading comparison of interfragmentary motion between the classic and dynamized frames showed that both frames had increased axial deformation by 1mm with dynamizers. However, shear increased in FrameA (+0.25mm) but decreased in FrameB (-0.35mm).

Under torsion, axial motion was low (<0.4mm) in both frames. The dynamized FrameB produced negligible shear compared to the classic FrameB while the dynamized FrameA produced 2mm greater shear than FrameB and 0.7mm more than the classic FrameA.

Under bending, dynamizers introduced 0.5mm and 0.2mm increased shear for the FrameA and FrameB respectively but all frames maintained low axial motion (<0.4mm).

Discussion

This is first time that frames incorporating Dynamizers have been compared mechanically. The Dynamizers investigated were from 2 companies and were entirely different in their construction, hence, it was not surprising that variations were observed in their performance. With associated increases in axial motion and predominantly low values of shear across loading regimes, the dynamizers likely achieve their goal. Variability observed in torsion suggests that correct implementation of dynamizers is still paramount.

Images (Optional)

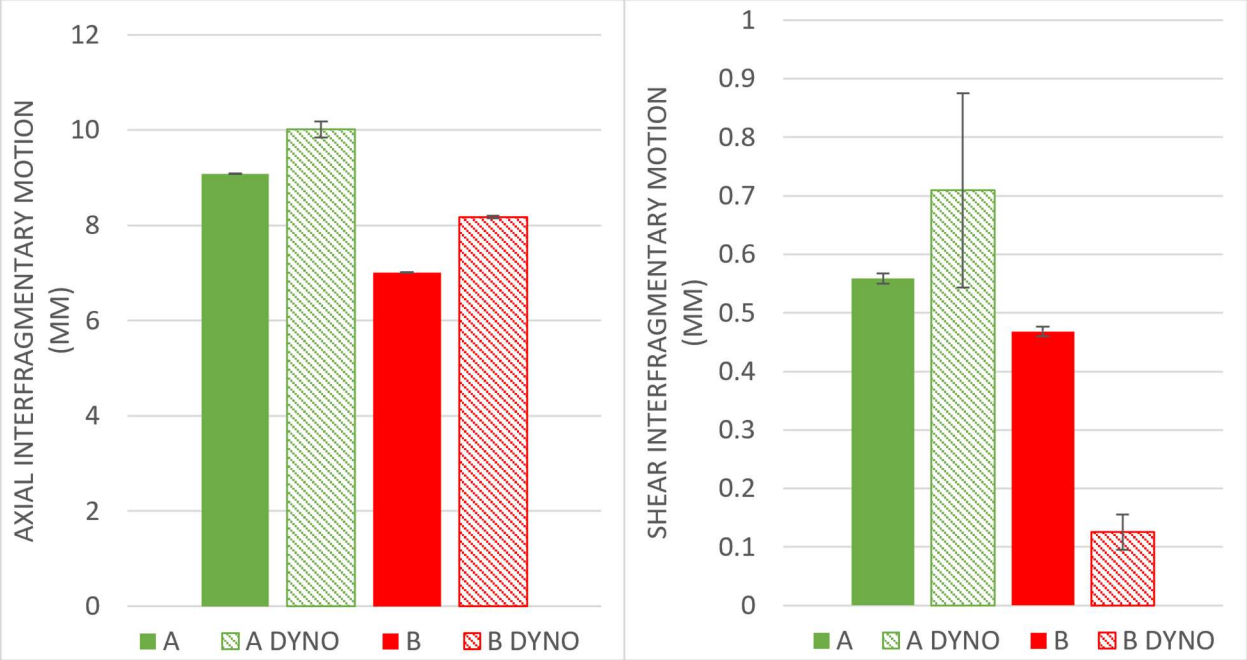


Figure 1. Interfragmentary motion Axial (left) and Shear (right) measured at 700N compression for each frame setup. Error bars represent standard deviation across 10 cycles for each frame.

References (Optional)

[1] P. Augat et al., J Orthop Res, 2003

Session Category

P3-350

Biomechanical Evaluation of Fixation Strategies for Complex Mandibular Fractures: A Finite Element and Experimental Study

Prof. Ting-Sheng Lin[1], Dr. Chien-Chung Chen[2], Mr. Kai-Chieh Chuang[1]

[1]I-Shou University, Kaohsiung, Yanchao District, Taiwan. [2]E-Da Hospital, Kaohsiung, Yanchao Distric, Taiwan

Introduction

Complex mandibular fractures involving simultaneous condylar and symphyseal/parasymphyseal regions present significant clinical challenges. Optimal fixation strategies remain controversial, with inadequate reduction potentially leading to malocclusion, temporomandibular joint dysfunction, and facial deformity. This study systematically evaluates the biomechanical stability of various plate-screw configurations for complex mandibular fractures using finite element analysis (FEA) validated by experimental testing.

Methods

Synthetic mandible models (Synbone 8950, Switzerland) were CT-scanned and reconstructed into 3D models incorporating cortical and cancellous bone. Two fracture patterns were analyzed: (1) unilateral condylar with parasymphyseal fractures, and (2) bilateral condylar with symphyseal fractures. Thirty-five combinations of titanium mini-plates (2.0mm) and micro-plates (1.2mm) with corresponding screws (Stryker, Germany) were evaluated. FEA simulations incorporated physiological muscle forces (masseter, temporalis, medial pterygoid) with bilateral condyles fixed. Stress distribution, strain, and displacement were analyzed. Three-dimensional digital image correlation (3D-DIC) was employed for experimental validation.

Results

For unilateral fractures, dual three-hole micro-plates at 120° arrangement at the condyle combined with vertical dual four-hole plates at the parasymphysis demonstrated optimal stress distribution. Parametric analysis revealed condylar fixation methods had greater influence on overall stress distribution than symphyseal/parasymphyseal fixation ($p<0.001$). For bilateral fractures, condylar combinations C and D significantly reduced plate and screw stress compared to combinations A and B ($p<0.001$). Dual plating with at least four screws at the condylar site provided superior biomechanical stability.

Discussion

Complex mandibular fracture fixation requires strategic consideration of both fracture sites, with condylar fixation being the primary determinant of overall construct stability. Dual plating with appropriate screw distribution provides optimal biomechanical stability while potentially reducing complications and healthcare costs. These findings provide evidence-based guidelines for clinical decision-making in treating complex mandibular fractures.

Acknowledgements (Optional)

This research was funded by the Ministry of Science and Technology, Taiwan, grant number NSTC 112-2221-E-214-003-MY2.

Session Category

Orthopaedic Biomechanics: Trauma and Repair

P3-351

Novel Investigation of the Biomechanical Properties of Circular Frames for the Foot

Professor Todd Stewart PhD, BSc[1], Doctor Sarah Johnson-Lynn FRCS (T&O)[2], Mr. Tom Irish MEng[1], Doctor Peter Watson PhD, BSc[3], Doctor Paul Harwood FRCS (T&O)[4]

[1]The University of Leeds, Leeds, West Yorkshire, United Kingdom. [2]South Tees Hospitals NHS Foundation Trust, Middlesbrough, South Teeside, United Kingdom. [3]University of Leeds, Leeds, West Yorkshire, United Kingdom. [4]Leeds Teaching Hospitals Trust, Leeds, West Yorkshire, United Kingdom

Introduction

The most frequently used foot frame constructs are a Charcot frame with a flat foot plate, used to commonly to offload the ankle, a Butt frame controlling the hindfoot with a U-plate allowing correction across the midfoot with a forefoot ring, and a Mitre frame with 2 rings at 45 degrees, independently controlling the hindfoot and midfoot.

The aim was to test, for the first time, the deformation and stiffness of the three most common trauma foot frame configurations.

Methods

Three frames of each geometry were constructed using Orhofix TL-HEX components (Orthofix Medical inc., USA). All frames were constructed with 2 tibial rings with 2 wires on each ring, foot elements were attached with 2 calcaneal wires and 2 forefoot wires. The Mitre frame foot was additionally tested sectioned vertically across the calcaneus and cuboid. To investigate relative stiffness an 8mm gap between the distal tibia and the proximal talus was adopted. A max vertical axial load of 700N was applied to simulate standing using an Instron E10000 Universal Testing machine (Instron, UK) . A base platform was constructed such that the 1st and 5th metatarsals and calcaneus contacted at the base forming 3 points of inferior support (Figure 1).

Results

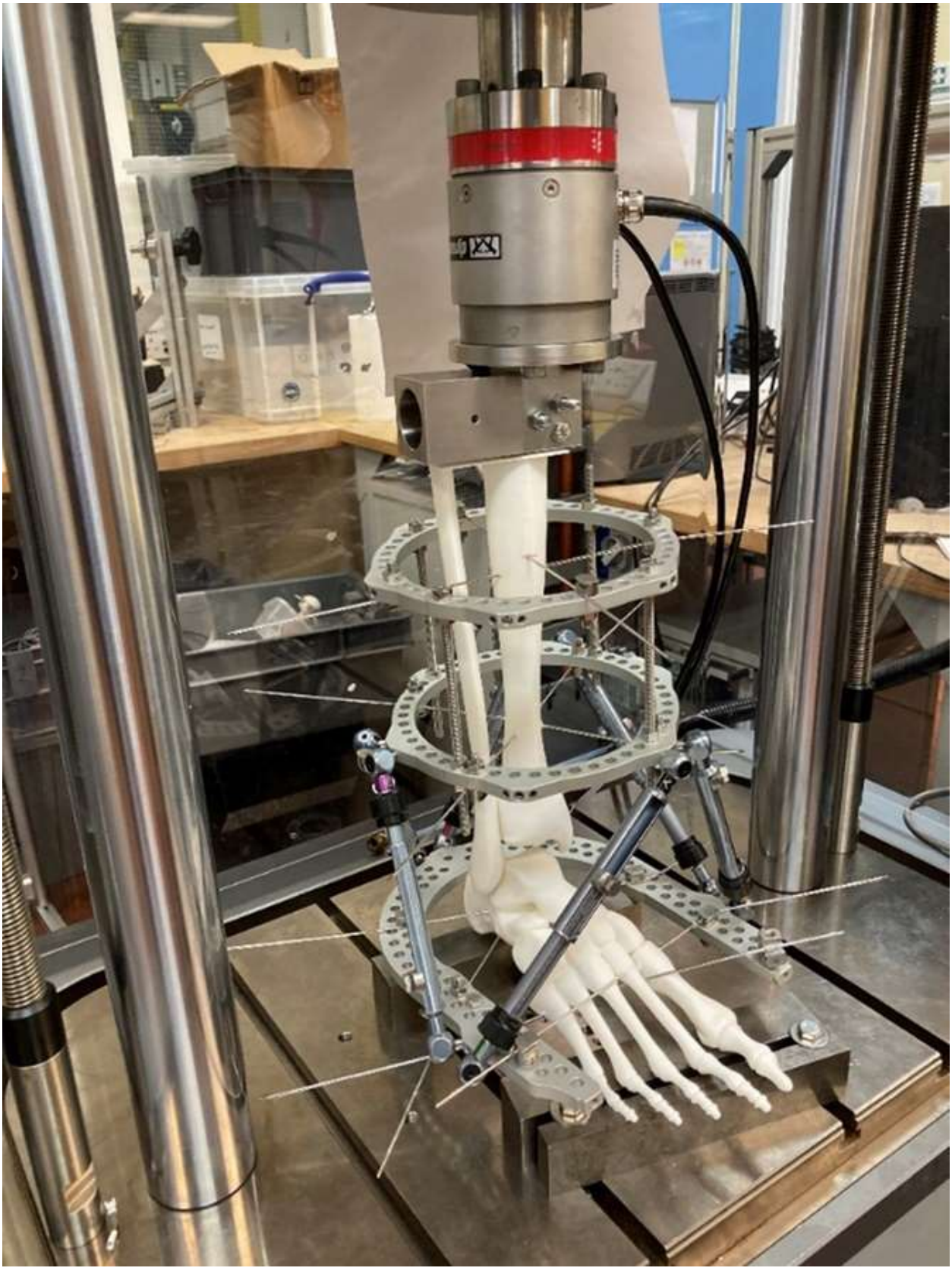
Maximum average deformation found that the Butt frame had the least deformation (7.1mm) whereas the Charcot frame had the greatest deformation (10.2mm) . Sectioning the foot showed an increase in deformation by 10% and the most variability.

All frames increased in stiffness as the applied load increased. The Charcot frame showed the least construct stiffness of 93N/mm at a load of 700N, whereas the Butt frame generally produced the greatest construct stiffness of 122N/mm. The Mitre frame with sectioned foot had a reduced stiffness under the lower loads (32N/mm), but the stiffness was comparable to the non-sectioned foot at 700N (104N/mm).

Discussion

The response of the frames to load provides key information to surgeons to inform frame construction for foot and ankle pathologies. The Charcot frame having the lowest stiffness is an important finding as these frames are frequently used in patients with peripheral neuropathy, where increased robustness is required to encourage bone healing.

Images (Optional)



Session Category

Orthopaedic Biomechanics: Trauma and Repair

P3-352

A Robotic Evaluation of Posterior Shoulder Stability in Cadaveric Specimens: Bipolar Bone Loss and Allograft Reconstruction

Mr Alex Brady MS

Steadman Philippon Research Institute, Vail, CO, United States

Introduction

Posterior shoulder instability is a challenging condition, frequently associated with posterior glenoid bone loss (GBL) and Reverse Hill-Sachs Lesions (RHSL). Objective: to characterize the decrease in dislocation force associated with GBL and RHSL and the benefits of distal tibial allograft (DTA), and talus allograft (TA) reconstruction, respectively.

Methods

Eight fresh-frozen cadaveric shoulders were dissected free of all soft tissue (mean age: 62.3, 5F,3M). Each specimen was mounted to a 6-degrees-of-freedom robotic arm and tested across nine states: 1) Native, 2) Posterior labrum removed, 3) Small GBL (12.5%) 4), Large GBL (25%), 5) DTA 6) DTA +Small RHSL 7) DTA + Large RHSL 8) DTA + TA, 9) LGBL + LRHSL. Posterior dislocation testing was performed at 90° of shoulder flexion with the arm internally rotated by 30 degrees. The humerus was translated postero-inferiorly along the 7 o'clock axis of the glenoid clockface by one humeral head radius, while maintaining an 80 N compressive load, and sagittal plane dislocation force was measured. The data were analyzed using a one-factor linear mixed effects model in three groups: A: Glenoid (states 1-5); B: Humerus (states 5-8); C: Bipolar (states 1, 7-9).

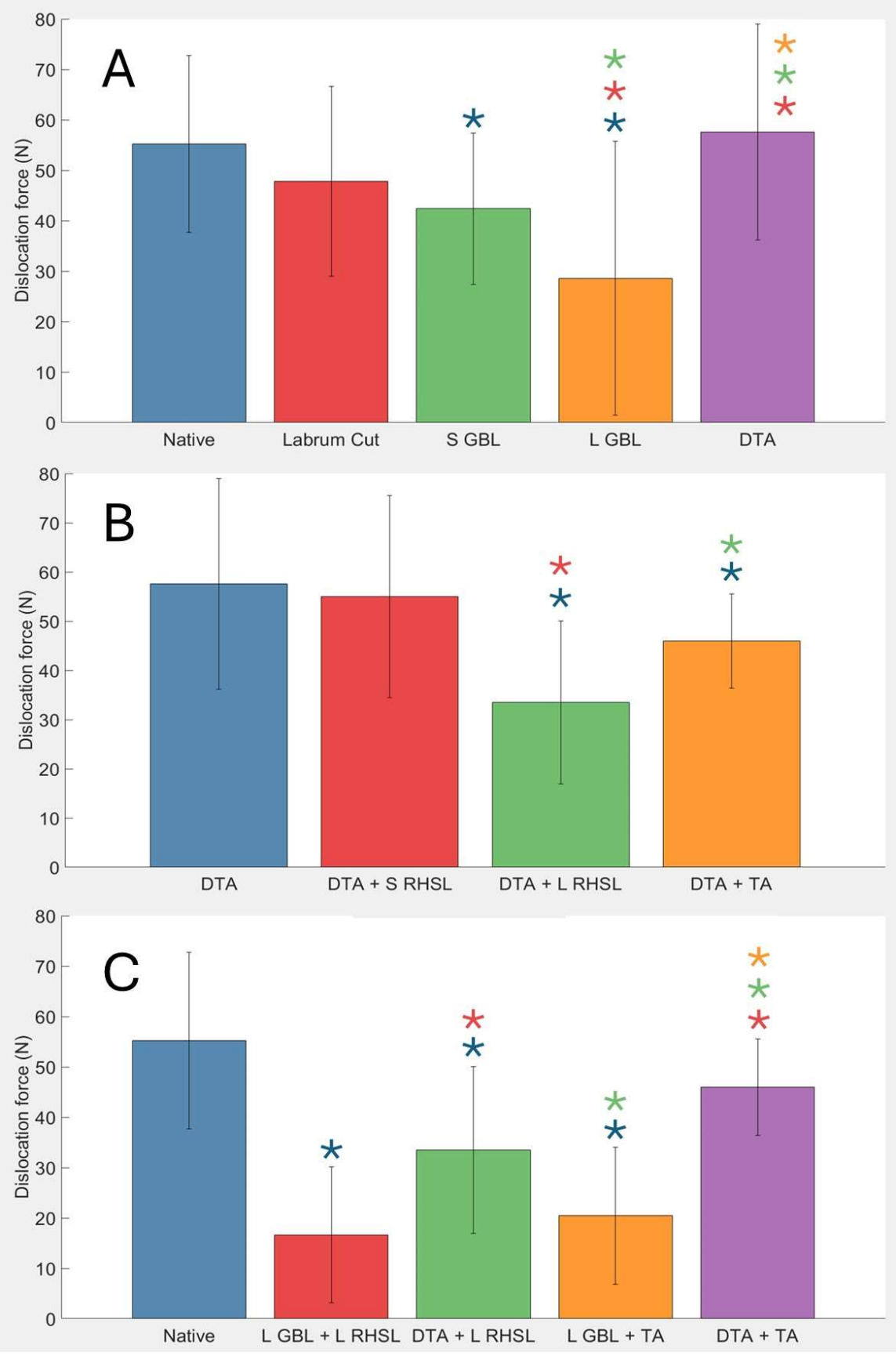
Results

Figure 1 shows dislocation force by state in each group. Stars show significant differences ($p<0.05$) from the state of associated color. Group A showed, decreasing force with progressive glenoid bone loss, and restored native force with DTA. Group B showed no significant change with small RHSL, decreased force with large RHSL and partial restoration with TA. Group C showed a severe decrease in force with bipolar bone loss, partial restoration with DTA alone, no significant improvement with TA alone, and restored native force with DTA+TA.

Discussion

Posterior instability with bipolar bone loss remains a difficult problem, and surgical decision-making is often based on limited evidence. This investigation provides the first robotic analysis of posterior dislocation across a range of clinically relevant lesion sizes and reconstructions and demonstrates that DTA and TA can improve stability in shoulders with significant bone loss. These findings support the use of structural allografts to manage posterior bipolar lesions and provide a biomechanical foundation for guiding surgical treatment algorithms.

Images (Optional)


A
Dislocation force (N)
0
10
20
30
40
50
60
70
80
Native
Labrum Cut
S GBL
L GBL
DTA
B
Dislocation force (N)
DTA
DTA + S RHSL
DTA + L RHSL
DTA + TA
C
Dislocation force (N)
Native
L GBL + L RHSL
DTA + L RHSL
L GBL + TA
DTA + TA

Session Category

Orthopaedic Biomechanics: Upper Extremities

P3-353

Does Age or Pathology Drive Changes in Thumb Muscle Architecture?

Ms. Alexis Benoit MS, Dr. Jennifer Nichols PhD

University of Florida, Gainesville, FL, United States

Introduction

Thumb motion is driven by nine muscles that cross the carpometacarpal (CMC) joint. Fascicles influence a muscle's force-generating capacity and range-of-motion, and small changes in length can alter performance on the force-length and force-velocity curves. Common CMC osteoarthritis (OA) symptoms (e.g., weakness, reduced motion) are likely related to changes in fascicle length. However, in the thumb, fascicle lengths have only been quantified in small cadaveric studies or young healthy adults using extended field-of-view ultrasound (EFOV-US). Thus, this study aimed to quantify thumb muscle fascicle lengths in older adults and evaluate whether changes relative to young adults were due to age versus OA.

Methods

Twelve older adults (6 female, age=67.8±10.3 years) were stratified by symptomatic and radiographic CMC OA. Symptomatic cohorts were classified by average Australian Canadian Hand Osteoarthritis Index (AUSCAN) pain scores: non-symptomatic (AUSCAN<1; n=6) vs. symptomatic (AUSCAN≥1; n=6). Radiographic cohorts were defined by modified Eaton-Littler stages: healthy (0-I; n=5) vs. pathologic (II-IV; n=7). EFOV-US images of six thumb muscles were taken from the dominant/affected arm of each participant. Ten fascicle lengths per muscle were measured as the distance between superficial and deep aponeuroses. Unpaired t-tests compared older adult to published young adult data. Two separate two-way analyses of variance assessed the effects of cohort and muscle on fascicle length.

Results

Significant differences in fascicle length were observed between young and older adults in five muscles ($p<0.05$) (Fig. 1A). When stratified by symptomatic cohorts, fascicle lengths differed between young and symptomatic groups in three muscles ($p<0.05$) and between young and non-symptomatic groups in one muscle ($p<0.05$) (Fig. 1B). When stratified by radiographic cohorts, fascicle lengths differed between young and pathologic groups in three muscles ($p\leq0.01$) (Fig. 1C).

Discussion

These results suggest that aging alone does not fully account for changes in thumb muscle architecture. The most pronounced differences in fascicle length occurred in individuals with symptomatic or radiographic CMC OA, indicating that pathology-related factors likely influence these changes. Given the importance of both age- and pathology-related components, continued investigation of thumb muscle fascicles is needed to advance our understanding of muscle function in the context of CMC OA.

Images (Optional)

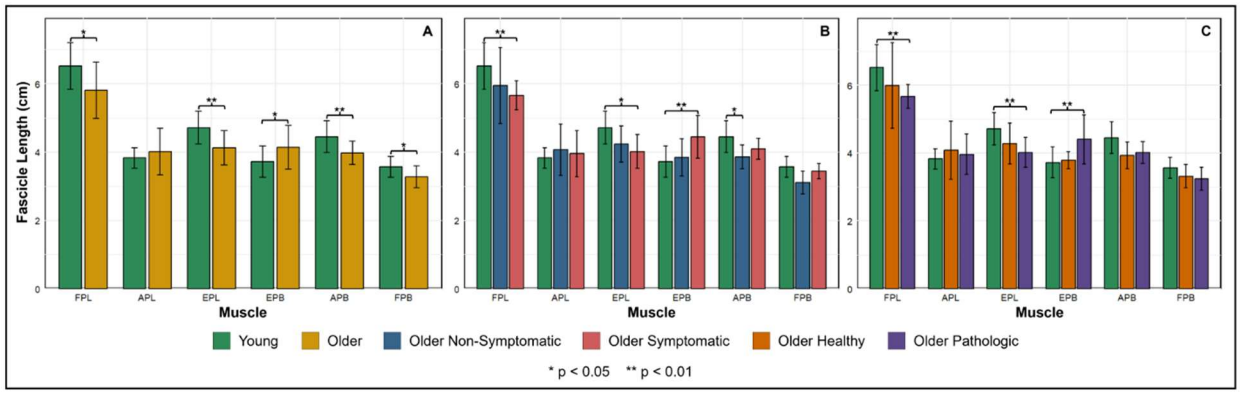


Figure 1: Comparison of thumb muscle fascicle lengths in (A) young vs. older participants, and older participants stratified by (B) symptom status (non-symptomatic vs. symptomatic) and (C) radiographic status (healthy vs. pathologic). Young adult data were obtained from Benoit et al. (2025) *Journal of Biomechanics* 192:112964. Error bars represent standard deviation. Asterisks denote statistical significance.

Acknowledgements (Optional)

Funding from NIH R01 AR078817.

Session Category

Orthopaedic Biomechanics: Upper Extremities

P3-354

Identification of Key Factors Affecting Primary Stability of Short Humeral Stems in Reverse Shoulder Arthroplasty: A QCT-Based Finite Element Analysis of the Prima Stem Prosthesis

Ms. Annalisa Bertoni[1], Mr. Cristiano Pizzamiglio[1], Mr. Andrea Fattori[1], Mr. Alex Drew[2], Mr. Michele Pressacco[1]

[1]Enovis, Villanova, Italy, Italy. [2]Enovis, Austin, Texas, United States

Introduction

Short humeral stem implants in shoulder arthroplasty preserve proximal bone and facilitate future revisions through metaphyseal fixation while sparing the diaphysis. However, there is limited knowledge on how bone mineral density (BMD) and patient-specific factors affect primary stability in reverse shoulder arthroplasty (RSA). The aim of this study is to evaluate through finite element analysis (FEA) how these factors correlate to primary stability of the Prima Stem in RSA.

Methods

Three-dimensional bone models of 45 post-mortem white adult humeri (23 male, 22 female) were segmented from anonymized CT scans calibrated with a hydroxyapatite phantom for spatial bone properties assignment using quantitative CT. Proximal resections were performed at 135° neck-shaft angle and 20° retroversion; distally cut at mid-diaphysis. Implant (Prima Stem, Enovis, US) positioning was computed automatically using Figura, a proprietary research and implant development tool. FE models were distally fixed, and abduction loads (216.46N at 45°, 321.17N at 75°) with no hand weight were applied via a semi-spherical actuator, based on prior biomechanical RSA simulations. Mesh convergence resulted in a 1.2mm second-order mesh for bone and implant. Primary stability was assessed at the trabecular titanium ring by calculating relative displacement between implant and corresponding bone nodes. BMD was measured in this trabecular region.
Donors were grouped by age (U60, 60-80, 80+). Micromotion values were log-transformed and a two-way ANCOVA was performed to evaluate sex and age effects on micromotions, with BMD and BMI as covariates.

Results

Average maximum micromotions slightly increased with abduction (45°: 32.59±9.01µm; 75°: 43.30±10.43µm).
ANCOVA indicated that BMD was the only significant predictor (45°: $p<0.001$, $\omega^2_p = 0.379$; 75°: $p<0.001$, $\omega^2_p=0.405$), with lower BMD associated with higher micromotions [Fig.1]. BMI had a marginal effect (45°:$p=0.039$, $\omega^2_p=0.073$; 75°:$p=0.051$, $\omega^2_p=0.064$); sex and age were not significant.

Discussion

Primary stability of the studied design in RSA is largely determined by BMD, with minimal influence from age or sex and only a minor effect of BMI. For the analyzed loading conditions, micromotions remained below the critical threshold of 150µm, supporting the mechanical reliability of short-stem designs across a wide range of bone qualities and patient profiles.

Images (Optional)

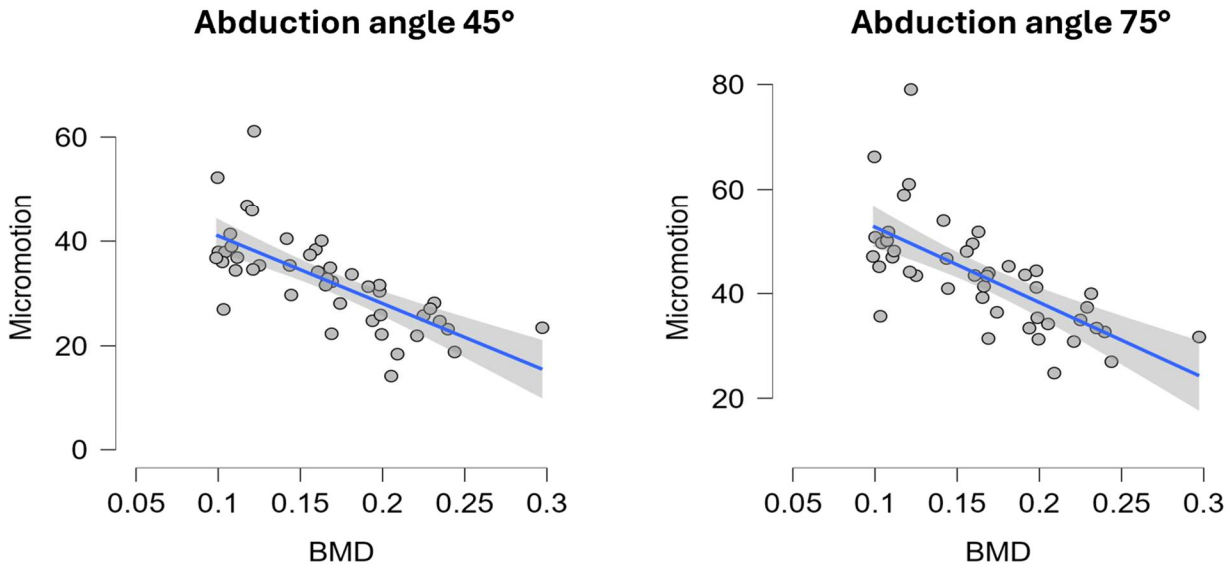


Fig. 1: BMD and non-transformed micromotions: scatterplot with regression line

Session Category

Orthopaedic Biomechanics: Upper Extremities

P3-355

The Influence of Different Radiation Therapies Regimens on Upper Extremity Nerve Tension in Breast Cancer Survivors

Mr. Chun-Kai Tang PT, MSc.[1,2], Dr. Josiah Nieto MD.[3], Prof. Yi-Fen Shih PT, Ph.D.[2], Dr. David B. Lipps Ph.D.[1]

[1]School of Kinesiology, University of Michigan, Ann Arbor, Michigan, United States. [2]Department of Physical Therapy and Assistive Technology, National Yang Ming Chiao Tung University, Taipei, Taiwan, Taiwan. [3]Department of Radiation Oncology, University of Michigan, Ann Arbor, Michigan, United States

Introduction

Breast cancer survivors (BCS) often experience chronic shoulder pain and dysfunction due to treatment-related musculoskeletal and neural changes, including fibrosis. Breast radiation therapy (RT) can expose the brachial plexus to incidental dose, particularly in standard regimens that target the whole breast or chest wall (WB), or by adding regional nodal irradiation (RNI) for more advanced cases. While research has predominantly examined musculoskeletal factors, neural tissue responses remain less explored in BCSs following RT. Standard neurodynamic tests often cannot distinguish nerve tension from adjacent tissue stiffness. This study compared brachial plexus and median nerve stiffness between healthy controls and BCSs treated with different RT regimens.

Methods

We studied BCSs who completed RT 1–3 years ago: 10 received WB (Age: 59.50±8.54, BMI: 27.39±4.11), eight received WB+RNI (Age: 62.75±10.71, BMI: 30.86±9.46), alongside 16 healthy controls (HC) (Age: 58.31±10.15, BMI: 27.50±5.97). Ultrasound shear wave elastography assessed shear wave velocity (SWV) at the brachial plexus (neck) and median nerve (elbow, mid-forearm, and wrist) during the Upper Limb Neurodynamic Test (ULNT1) at initial, submaximal (end-range minus 5°), and end-range positions. The use of SWE during neurodynamic testing provides a novel assessment of both nerve stiffness and mechanical properties under standardized limb positioning [1]. End-range ROM was recorded during the ULNT1 test. Group differences in ROM, initial SWV, and changes in SWV (ΔSWV) were analyzed using Kruskal-Wallis tests.

Results

Both WB and WB+RNI groups had significantly decreased elbow and wrist extension ROM during ULNT1 (standard: $p<0.001$; proximal: $p=0.026$). The WB group had greater initial C5 nerve stiffness compared to the HC and WB+RNI groups ($p=0.024$). The ΔSWV between the submaximal and end-range wrist position was larger in WB and WB+RNI groups than HCs ($p=0.015$).

Discussion

This study is the first to directly characterize nerve stiffness in BCSs using elastography during neurodynamic testing across different RT regimens. Both RT groups demonstrated increased nerve tension—manifesting as reduced ROM and greater nerve stiffness changes—suggesting RT reduces neural compliance. These findings underscore the need for targeted interventions that address neural fibrosis in BCSs following RT.

Images (Optional)

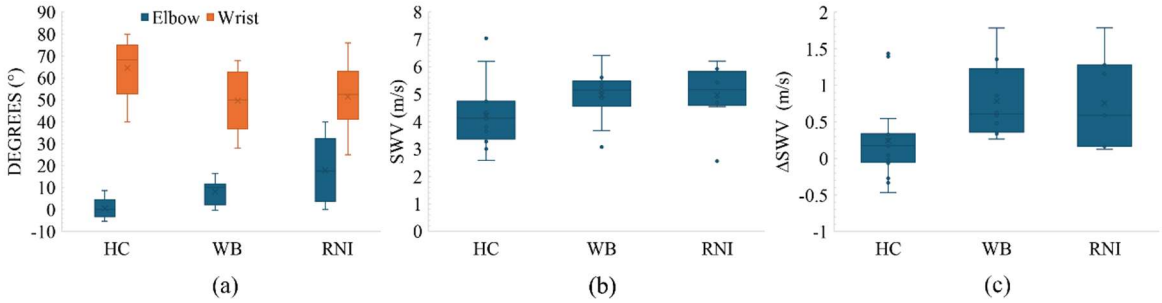


Figure: (a) End-range ROM of ULNT 1 tests, (b) SWV of C5 at initial position, (c) ΔSWV between the submaximal and end-range position at the wrist

References (Optional)

[1] Ciuffreda et al., MusculoskeletSciPract, 2025

Session Category

Orthopaedic Biomechanics: Upper Extremities

P3-356

The Secondary Stabilizers Preventing Scapholunate Instability During Wrist Movements

Prof. Dai-Soon Kwak[1], MS. Seonjin Shin[1], Prof. Il-Jung Park[1], Prof. TAE SOO BAE[2]

[1]The Catholic University of Korea, Seoul, Seoul, Korea, Republic of. [2]Jungwon University, Goesan, Chungcheongbuk-do, Korea, Republic of

Introduction

Isolated injury of the scapholunate interosseous ligament (SLIL) will not produce static instability of the scapholunate joint. For this, secondary stabilizers also must be compromised. There is no consensus on the secondary stabilizer most critical in preventing static scapholunate instability (SLI), but many studies have reported the importance of dorsal intercarpal (DIC), scaphotrapeziotrapezoid (STT), and long radiolunate (LRL) ligaments.

Methods

Thirty-six fresh-frozen upper extremity cadaveric specimens were prepared. A wrist simulator with a linear guide rail system (tendon load/motion-controlled system) and five motion capture systems were used. The experimental groups were as follows: (1) intact wrist and ligaments, (2) SLIL transection, (3) DIC transection, (4) STT transection, and (5) LRL transection. The DIC, STT, and LRL ligament transections were randomly assigned. The scapholunate distance, radioscaphoid angle (RSA), radiolunate angle (RLA), and scapholunate angle (SLA) were measured during continuous flexion-extension and ulnar deviation–radial deviation movements.

Results

Isolated transection of the SLIL was not sufficient to alter the normal kinematics of the SL joint. However, when the DIC ligament was transected in the first stages, a significant increase in the scapholunate distance was observed, and significant changes were observed in the RSA and SLA. Furthermore, when the DIC was transected in the second and third stages, the increase in scapholunate distance was significantly greater than that with transection of the other ligaments.

Discussion

The DIC ligament demonstrated the greatest influence on both distraction and rotational stability of the scapholunate joint. During treatment of scapholunate dissociation,

intraoperative assessment of the DIC ligament is crucial, and its repair or reconstruction should be considered for surgical management.

Session Category

Orthopaedic Biomechanics: Upper Extremities

P3-357

From Kinematics to Coordination: Modelling Scapular Dyskinesis and Periscapular Muscle Activation

Ms Delaney Meek[1], Dr Peter Pivonka[1], Dr Wolbert van den Hoorn[2], Dr Maxence Lavaill[1]

[1]Queensland University of technology, Brisbane, QLD, Australia. [2]University of Queensland, Brisbane, QLD, Australia

Introduction

Scapular dyskinesis (SD), defined by abnormal scapular function, is commonly associated with shoulder pain and injuries [1]. SD is typically classified into four abnormal scapulothoracic kinematic patterns: increased anterior tilt (pattern 1), increased internal protraction (pattern 2), excessive (pattern 3a) or insufficient (pattern 3b) scapular upward rotation [1]. Limited studies showed altered activations of serratus anterior (SA), upper (UT), middle (MT), and lower (LT) trapezius muscles for patterns 1 and 2 only. This study aims to describe periscapular muscle activation for each dyskinetic pattern by simulating healthy and SD motions with musculoskeletal (MSK) modelling.

Methods

A control shoulder flexion motion was developed from bi-plane fluoroscopy kinematic data [2]. For each SD pattern, the control motion was modified by altering posterior tilt, protraction, or upward rotation based on literature values. These motions drove a shoulder MSK model [3] with a 4-degree-of-freedom scapulothoracic joint actuated by 33 muscle-tendon units. Static optimisation estimated muscle activations, particularly of UT, MT, LT and SA. Each dyskinetic motion was evaluated against control to determine estimated muscle activation differences.

Results

Pattern 1 displayed decreased SA (6%) and LT (2%) activation, and increased UT (8%) activation. Pattern 2 (Figure 1) displayed decreased SA (2%), LT (2%), and UT activations (4%). Pattern 3a exhibited increased SA (2%) and LT (5%) activations, with decreased UT (3%) activation. Pattern 3b demonstrated decreased SA (8%), UT (4%) and LT (2%) activations.

Discussion

The muscular activations of patterns 1 and 2 align with literature values. Novelly, for pattern 3a, increased SA and LT activation was shown to be biomechanically consistent with increased upward rotation and reduce UT activation. In pattern 3b, decreased activation of SA and LT is consistent with reduced upward rotation. Instead of typical increased compensatory UT activation, pattern 3b displayed increased activation of the infraspinatus and coracobrachialis muscles. Understanding muscle alterations for each SD pattern can inform targeted rehabilitation strategies. The relationship between SD pattern and muscle activation will be further examined through upcoming biplane fluoroscopic data collection of SD kinematics.

Images (Optional)

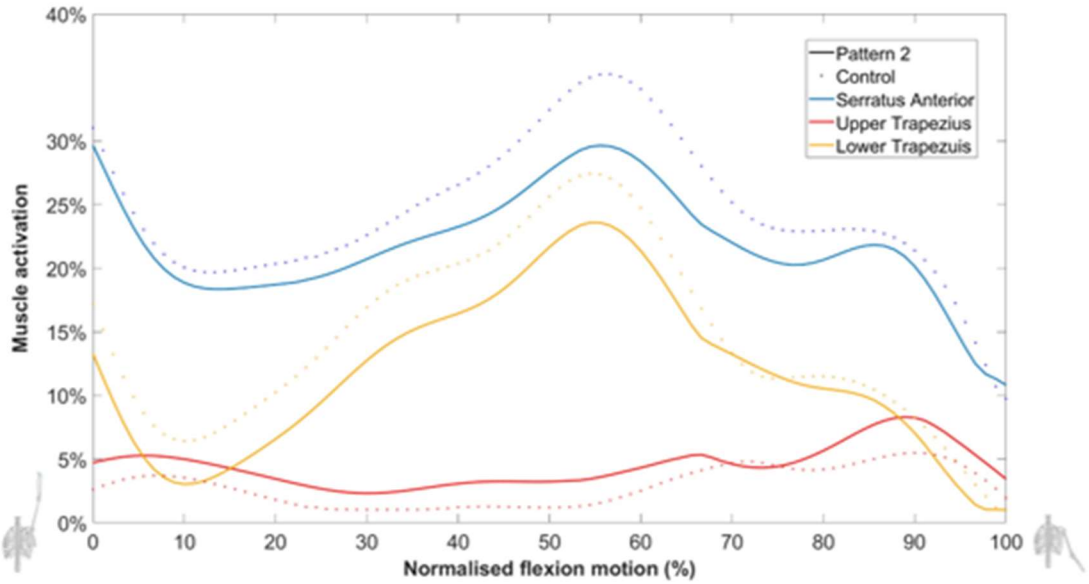


Figure 1 – Pattern 2 muscle activations against controls

References (Optional)

[1] Kibler et al., *JSES*, 2002

[2] Henninger, *Zenodo,* 2024

[3] Seth et al., *Frontiers Neurorobotics,* 2019.

Session Category

Orthopaedic Biomechanics: Upper Extremities

P3-358

Using Wavelet Coherence To explore the Relationships Between Scapular Kinematics and Muscle Activation

Ms. Denise Balogh MSc, Dr. Angelica Lang PhD

University of Saskatchewan, Saskatoon, Saskatchewan, Canada

Introduction

Evaluating the coherence (similarity in frequency content) between the continuous wavelet transforms (CWTs) of electromyography and kinematic signals provides a means of quantifying how the relationship between muscle activation and kinematics evolves over time [1,2]. This study is the first to apply wavelet coherence as a tool to explore the relationship between scapular kinematics and muscle activation.

Methods

Electromyography (EMG) of the upper trapezius (UT), lower trapezius (LT), and serratus anterior (SA) and motion of the scapula were assessed on the dominant side of 11 healthy participants. Participants performed repeated frontal plane arm elevations for 60s at a frequency of 30bpm (full cycle frequency = 0.25Hz). Using a modified version of the Wavelet Coherence Toolbox [3], the CWT coherence between scapular upward rotation (UR) and the linear enveloped muscle activations were computed. The mean coherence (value of 0 – 1) and mean phase angles across the 60s at the 0.25Hz frequency were calculated. Linear regression was also applied to determine if the coherence at 0.25Hz significantly changed across time during the task.

Results

Strong coherence between each muscle and scapular UR at the 0.25Hz frequency (Figure 1) was present across the full 60 seconds (mean coherence ± std: UT=0.99±0.004; LT=0.97±0.037; SA=0.99±0.022). Regression analysis demonstrated no significant change in coherence across time between any of the muscles and scapular UR. A task with a greater fatiguing element may generate changes or greater variability in coherence as muscle recruitment strategies change. Mean phase angles indicated that the UT (19.97º) and SA (22.81º) preceded the UR movement, while the LT (-46.28º) activated after movement initiation.

Discussion

This study provides proof of concept for the application of wavelet coherence to scapular kinematics and muscle activation. Future research should employ CWT and CWT

coherence methods to a scapular fatiguing protocol to better understand how muscle activation and recruitment patterns change relative to kinematics with fatigue.

Images (Optional)

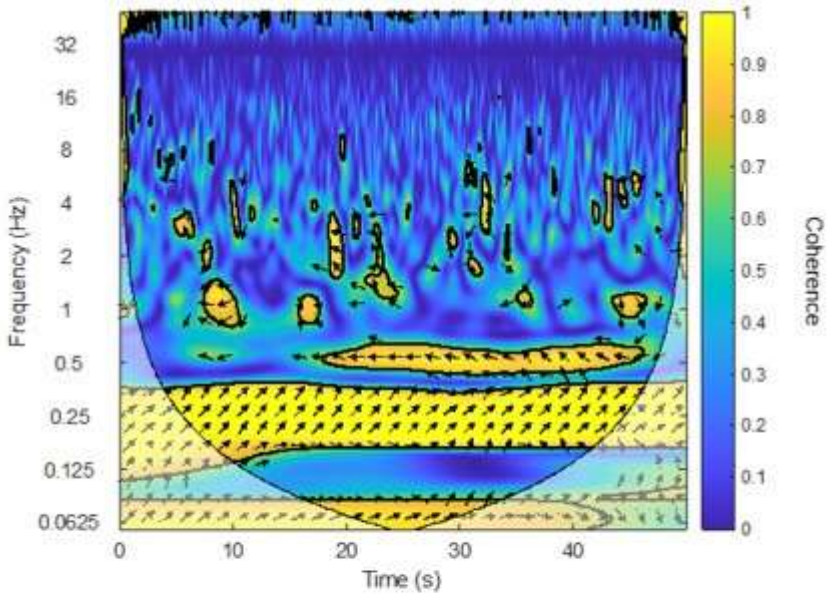


Figure 1. Coherence and phase plot for scapular upward rotation and UT from one representative subject. Strong coherence is seen at 0.25Hz frequency. Up-right direction of arrows indicate muscle activation leads kinematics by less than 90°.

References (Optional)

[1]Ivo Hostens *et al*., J Electromyogr Kinesiol, 2004. [2]Dean Hay *et al*., J Applied Biomechanics, 2016. [3]Aslak Grinsted *et al*., Nonlinear Process Geophys, 2004.

Acknowledgements (Optional)

The authors acknowledge Andrea Fernandez for assistance in data collection.

Session Category

Orthopaedic Biomechanics: Upper Extremities

P3-359

Do Subscapularis Integrity and Posterosuperior Cuff Tear Severity Affect Osseous Impingement and Joint Subluxation in Reverse Total Shoulder Arthroplasty?

Mr. Donghwan Lee BSc[1], Prof. Joo Han Oh MD, PhD[2], Prof. Choongsoo Shin PhD[1,3]

[1]Department of Mechanical Engineering, Sogang University, Seoul, Mapo-gu, Korea, Republic of. [2]Department of Orthopaedic Surgery, Seoul National University Bundang Hospital, Seongnam, Bundang-gu, Korea, Republic of. [3]Research Institute for Smart Design & Manufacturing Technology, Sogang University, Seoul, Mapo-gu, Korea, Republic of

Introduction

Osseous impingement and joint subluxation during external rotation (ER) are commonly observed in patients with reverse total shoulder arthroplasty (RTSA) [1]. However, how subscapularis and posterosuperior cuff (supraspinatus and infraspinatus) tear (PCT) severity in RTSA affects impingement and joint stability remains unclear. This study aimed to investigate the effects of subscapularis integrity and PCT severity on osseous impingement stress and joint subluxation in RTSA.

Methods

The RTSA model was developed by importing prosthetic bone geometries (Coralis® Reverse Shoulder System; Corentec Co., Ltd., Seoul, Republic of Korea) into a previously validated anatomical shoulder model [2]. Twelve male *in vivo* experimental datasets, collected during 45° of ER, were used as consistent inputs for the RTSA model. Model simulations were performed under subscapularis-repaired and -torn conditions, across three stages of PCT severity: Stage I, isolated supraspinatus tear; Stage II, complete supraspinatus tear and superior half infraspinatus tear; and Stage III, complete supraspinatus and infraspinatus tears. Post hoc paired t-tests were conducted to compare peak osseous impingement stress and peak joint subluxation between subscapularis-repaired and -torn conditions across three PCT stages.

Results

Subscapularis repair in Stages I–III significantly reduced peak impingement stress by 16.7–26.2% ($P < 0.05$ for all comparisons). The same repair stages also significantly decreased peak joint subluxation by 27.5–58.9% ($P < 0.001$ for all comparisons).

Discussion

The main finding of this study is that subscapularis repair in RTSA can reduce osseous impingement stress and joint subluxation during ER, even in the presence of PCTs. Joint subluxation is commonly associated with impingement and arises from an unbalanced force couple between the anterior (subscapularis) and posterior (infraspinatus and teres minor) cuffs caused by cuff deficiency [3]. Therefore, our results suggest that subscapularis repair in RTSA can mitigate osseous impingement and improve joint stability in patients with PCT deficiencies.

References (Optional)

[1] Kolmodin et al., *J Bone Jt Surg.*, 2018. [2] Lee et al., *Front Bioeng Biotechnol.*, 2023. [3] Boileau et al., *Orthop Traumatol Surg Res.*, 2016.

Acknowledgements (Optional)

This research was supported by the National Research Foundation of Korea grant funded by the Ministry of Science and Information Communication Technology (RS-2024-00342681).

Session Category

Orthopaedic Biomechanics: Upper Extremities

P3-360

Patient-Specific Biomechanical Modeling of Scapular Forces Following Reverse Total Shoulder Arthroplasty

Medical Student Ecem Kilic[1], Medical Student Zachary Rickmeyer[1], Medical Student Nathan Harward[1], Medical Student Kaleb Barker[1], Associate Professor Lucas Timmins PhD[2], Orthopedic Surgeon Bradley Edwards MD[3]

[1]Texas A&M School of Engineering Medicine, Houston, Texas, United States. [2]Texas A&M University, Houston, Texas, United States. [3]Fondren Orthopedic Hospital, Houston, Texas, United States

Introduction

Scapular spine stress fractures are a complication following reverse total shoulder arthroplasty (rTSA). The implant reconfigures shoulder center of rotation (COR), increasing deltoid loading across the scapular spine. The changes raise concern for stress concentrations that may predispose patients to fracture. This study evaluates a patient-specific finite element (FE) workflow designed to predict potential fracture regions in the scapula after rTSA.

Methods

Muscle force vectors, registered to the implant COR, were extracted from an open-source shoulder model for abduction and applied to a scapular FE model generated from preoperative CT scans. Bone density and Young's modulus were mapped to each FE element using CT Hounsfield units. FE model outputs were processed to quantify first principal (FP) stresses and strains within Levy zones (LZ) I–III, and compared to the postoperative fracture site. Model stability was assessed through mesh convergence, and sensitivity to muscular boundary condition (BC) selection was evaluated across six independent observers using Intraclass Correlation Coefficient (ICC) and Linear Mixed-Effects Model (LMM).

Results

Stresses and strains were highest in LZ-II, with highest values during 10-20% abduction (peak FP stress I/II/III:17.4/34.6/24.6 MPa; peak FP strain: 0.00788/0.00875/0.00563) (Figure 1). Mean FP stresses followed (1.25/4.36/3.14 MPa), as did mean FP strains (0.00125/0.00212/0.00178). Max FP stress demonstrated the closest spatial agreement with the postoperative fracture site (<5mm), while FP strain was less accurate. Observers

showed agreement in overall FEA patterns (ICCs: 0.93-0.99), though the LMM detected differences in absolute magnitudes ($p<0.05$). BC selections showed moderate similarity (DICE: 0.653).

Discussion

Patient-specific FE modeling differentiated loading patterns across LZs with LZ-II exhibiting the highest stresses. This zone-dependent behavior mirrors reports identifying the scapular spine and acromial base as vulnerable regions after rTSA. FP stress localized most accurately to the fracture site, supporting its potential as a biomechanical risk marker. BC variability had minimal influence on overall patterns, supporting robust zone-level predictions. Expanding the number of scapulae analyzed will strengthen model generalizability and further validate zone-specific trends.

Images (Optional)

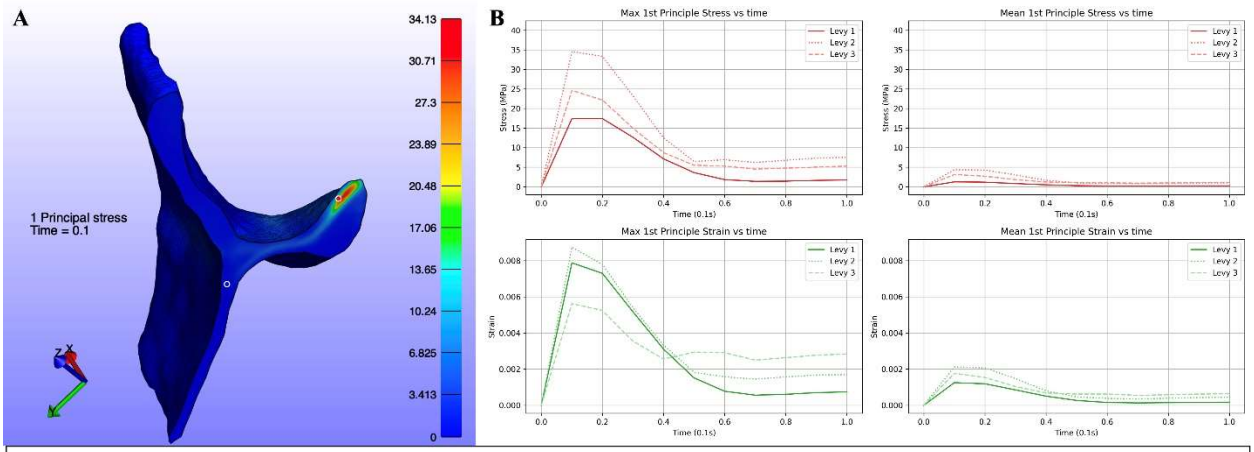


Figure 1. Stress and strains in scapula. A) Maximum (red) and minimum (blue) FP stresses within scapular spine. B) Maximum and mean FP stress and strain vs time in all three LZs.

Session Category

Orthopaedic Biomechanics: Upper Extremities

P3-361

Biomechanical Performance Assessment of Anatomical Scapula Body Fracture Fixation Plates – A Comparative Finite Element Analysis

Dr. Habtamu Yimam[1,2], Dr. Roopam Dey[1], Prof. Stephen Roche[1], Prof. Sudesh Sivarasu[1]

[1]University of Cape Town, Cape Town, Western Cape, South Africa. [2]Addis Ababa University, Addis Ababa, Addis Ababa, Ethiopia

Introduction

Displaced and unstable scapular body fractures are commonly treated with surgical fixation, primarily using plates and screws. Anatomically contoured plates serve as a template during fracture reduction and maintain fixation stability. The purpose of this study was to compare the biomechanical performance of new anatomical scapula body plates with commercial plates using the finite element analysis method.

Methods

First, a two-part osteotomy of the scapula body fracture was created, and three fixation constructs were performed using the new long lateral & medial border plates (LBP-L & MBP-L), short lateral & medial border plates (LBP-S & MBP-S), and ACUMED's ten-hole lateral & nine-hole medial border plates (SLB10 & SMB09). Then, the glenohumeral joint contact force of 400 N was applied at 90° arm abduction with a fixed boundary condition at the medial border. Finally, the response of the fixation constructs was assessed based on stress in the plates, strain in the bone around the screw holes, and fracture gap displacement (interfragmentary strain).

Results

The maximum stresses of the lateral border plates: LBP-L, LBP-S, and SLB10 were 166.0 MPa, 108.4 MPa, and 175.0 MPa, respectively. Similarly, the maximum stresses of the medial border plates: MBP-L, MBP-S, and SMB09 were 88.0 MPa, 65.0 MPa, and 86.6 MPa, respectively. Additionally, the maximum strains of the LBP-L, LBP-S, and SLB10 fixation constructs were 0.22%, 0.16%, and 0.28%, respectively, in the lateral border. In the medial border, the maximum strains of the MBP-L, MBP-S, and SMB09 fixation constructs were 0.49%, 0.36%, and 0.29%, respectively. Furthermore, the interfragmentary strain (fracture gap displacement) of the new long and short scapula body fixation constructs and the ACUMED plate fixation construct were 2.81%, 2.25%, and 3.48%, respectively.

Discussion

This study evaluated the biomechanical performances of anatomical scapula body plates using the FEA method. The results of the maximum stress in the plates, maximum strain in the bone around the screw holes, and fracture gap displacement in the three fixation constructs demonstrated that the new plates achieved better results compared to the ACUMED plates. The new plate designs with long and short size options could be a viable option for the fixation of challenging scapula body fractures.

Session Category

Orthopaedic Biomechanics: Upper Extremities

P3-362

Influence of Cup Positioning of Dual Mobility Thumb Carpometacarpal Joint Replacement on Principal Stress Projection in Trapezium

Ms Hind Alyahya, Dr Angela Kedgley

Department of Bioengineering, Imperial College London, London, Greater London, United Kingdom

Introduction

Dual mobility is the latest innovation in the design of thumb carpometacarpal (CMC) implants [1]. Its primary goal is to restore the balance between joint stability and mobility. The success of CMC joint replacement surgery is influenced by surgeon-related factors. To regain the full functionality of the thumb, implant position is critical [2]. We hypothesised that the inclination of the implant cup influences stress on the trapezium, risking postoperative complications.

Methods

An FE model of the thumb CMC joint with a dual-mobility implant simulating lateral pinch was developed. The geometry of the trapezium and first metacarpal were modelled with linearly elastic, isotropic material properties. A Maia (Groupe Lepine, France) implant was inserted into the bones, where the cup was placed at the centre [2-3]. Ligaments were modelled as 1D elements with rotational stiffness obtained from an in-house study conducted on healthy volunteers. A compressive load was applied to the top surface of the metacarpal bone, resulting from a 2.7 kg lateral pinch [4]. Simulations were run in MSC.Marc (MSC Software Corporation, USA).

Results

Cup inclination relative to the trapezium surface affected the minimum principal stress distribution in the trapezium under lateral pinch force (Fig.1). This parameter was used as an indicator of the primary compressive load transmitted to the CMC joint.

Discussion

Groupe Lepine advises that the implant's cup should be placed at the centre of the trapezium with no requirement for inclusion [3]; however, centring the cup may not be achievable, leading to placement with some degree of inclination and/or off-centre [2]. This study is ongoing to investigate the complications associated with these parameters, including the potential for PE liner wear and/or cup loosening. The results will be validated

against an in vitro experiment. This study is expected to help define standards, develop products, and guide surgeons for better clinical outcomes.

Images (Optional)

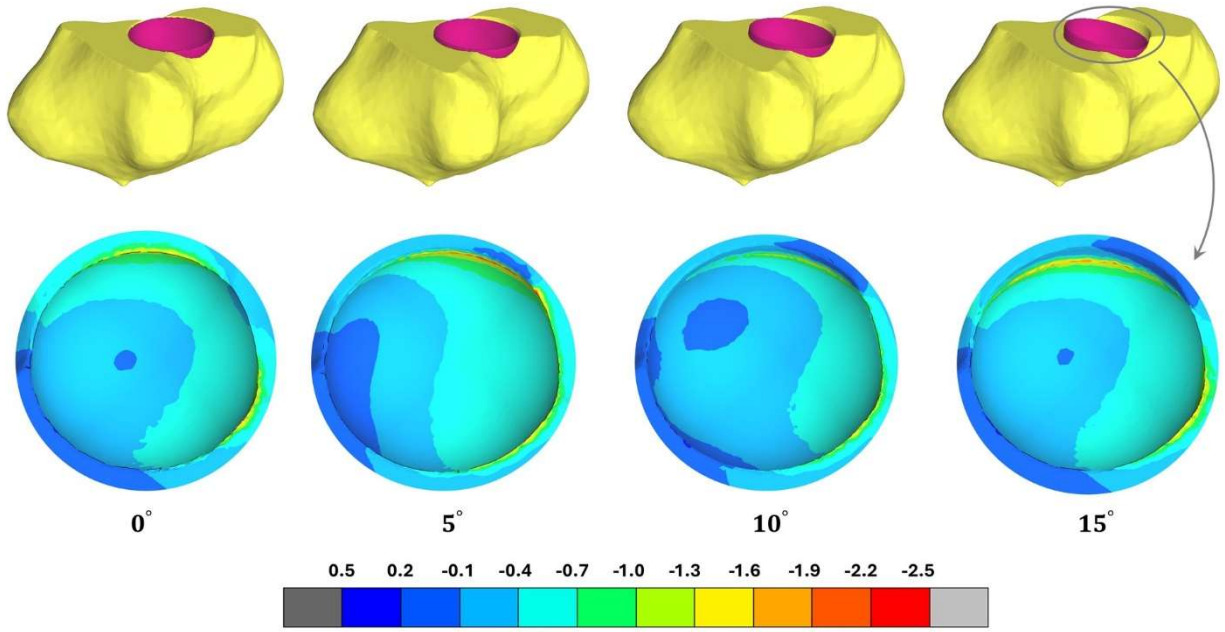


Fig.1: Contour bands of minimum principal value of stress (MPa) for the trapezium surface underneath the cup at 0°, 5°, 10°, and 15° cup inclination.

References (Optional)

[1] Lerebours Augustin *et al.*, J Hand Surg Am, 2020

[2] Edwards Dafydd. Personal Communication, 2024

[3] Groupe Lepine. Surgical Technique V4, 2022

[4] Cooney III William *et al.*, J Bone Joint Surg Am, 1977

Acknowledgements (Optional)

HA is funded by Imam Abdulrahman Bin Faisal University, Dammam, Saudi Arabia.

Session Category

Orthopaedic Biomechanics: Upper Extremities

P3-363

Stiffness of Thumb Carpometacarpal Joint: an In-vivo Study

Ms Hind Alyahya, Dr Angela Kedgley

Department of Bioengineering, Imperial College London, London, Greater London, United Kingdom

Introduction

The thumb carpometacarpal (CMC) joint is a primary contributor to hand dexterity due to its unique biconcave-convex shape [1]. Seven primary ligaments passively support the joint, all unique in morphology and mechanical properties [2-3]. Quantifying joint stiffness, which may differ by age and sex, helps understand, diagnose, and treat diseases effectively. In this study, we measured in-vivo thumb CMC joint stiffness. We hypothesised that rotational stiffness is a direction-dependent property due to the nonuniformity of the joint geometry and variations in the intrinsic properties of the passive tissues.

Methods

The dominant hand of 12 younger (5 men, 7 women; aged 27.6±3.2 years) and 8 older (4 men, 4 women; aged 58±3.7 years) participants were tested in a custom-designed setup for measuring moment-rotation response. Measurements were taken from three primary directions of thumb CMC joint motion: extension, flexion and abduction. Five thumb muscles were monitored during testing using surface electromyography to ensure relaxation. Rotational stiffness was quantified as the slope of the linear portion of the moment-rotation response. Nonparametric Wilcoxon signed rank and Wilcoxon rank sum tests were used for analysis.

Results

Results indicated differences between flexion and extension, and between flexion and abduction within each group, with flexion being less stiff (Fig.1). Sex had a significant effect on extension stiffness in the older group only. Age had no effect on the stiffness in any direction.

Discussion

The rotational stiffness for flexion is the lowest compared to extension and abduction, implying that the structure of the joint and the moment arm play a role, even though Young's modulus of the dorsal ligaments is reported to be higher than that of the volar and ulnar ligaments [2]. In the older group, women exhibited greater stiffness than men, which

may be due to post-menopausal hormonal changes [1]. Data will support developing a computational model of the joint to investigate new surgical techniques.

Images (Optional)

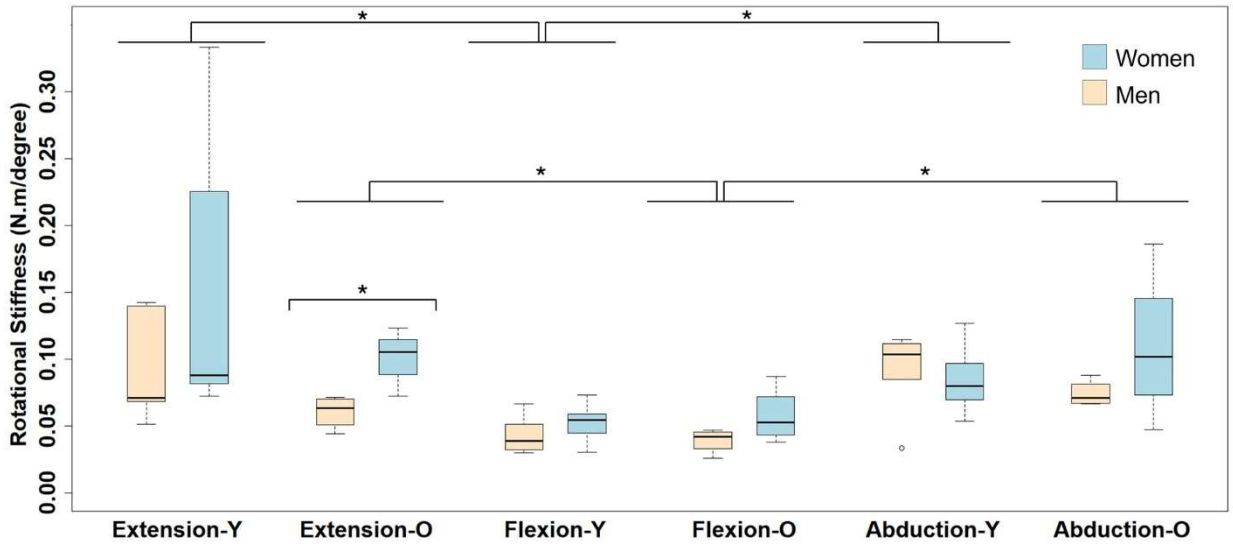


Fig.1: Median with interquartile range of the rotational stiffness in each direction of motion for younger (Y) and older (O) groups. (*p<0.05).

References (Optional)

[1] Komatsu Issei *et al.,* Oper Tech Orthop, 2018

[2] Bettinger Paul *et al.*, J Hand Surg Am, 2000

[3] Ladd Amy *et al.*, J Bone Joint Surg Am, 2012

Acknowledgements (Optional)

HA is funded by Imam Abdulrahman Bin Faisal University, Dammam, Saudi Arabia.

Session Category

Orthopaedic Biomechanics: Upper Extremities

P3-364

Biomechanical Rationale and Functional Impact of the External Rotation Torsional Humeral Osteotomy on Shoulder Kinematics in Older Children With Obstetric Brachial Plexus Palsy

Prof JAGDISH MENON MS(Ortho), MRCS(Edin), FACS, PGDHQM, Dr Ragavendra K MS(Ortho)

JIPMER, Pondicherry, Pondicherry, India

Prof JAGDISH MENON

Introduction

A significant number of children with upper trunk type of obstetric brachial plexus palsy (OBPP) have persistent residual motor deficit that extends into late childhood, leading to secondary effects like progressive internal rotation contracture, posterior subluxation of the humeral head and glenoid dysplasia, profoundly altering shoulder kinematics and upper limb function. The torsional derotation osteotomy of the humerus is a corrective surgery optimizing the mechanical alignment of the arm in space thereby improving joint function. We examined the biomechanical rationale and functional consequences of humeral derotation osteotomy in older children with OBPP focusing on shoulder kinematics, muscle mechanics, and clinical outcomes.

.

Methods

Torsional humeral external rotation osteotomy was performed on children with upper trunk OBPP with fixed internal rotation deformity of the shoulder Manual muscle testing, active/passive range of motion and functional assessment by the modified Mallet score was recorded. Radiological evaluation was performed by standard X-rays and MRI. Preoperative and post operative range of motion, strength and functional scores were measured. Compensatory mechanism like changes in the scapulothoracic rhythm and forward body lean was also recorded.

Results

14 children (5 males and 9 females) with a mean age of 12.6 +/- 2.15 years were treated by the torsional derotation external rotation osteotomy of the humerus. Significant improvements were observed in active and passive external rotation (mean gains of 33° and 53°, respectively; $p < 0.01$) and in abduction (mean increase 44°; $p < 0.01$). Pre-operative Modified Mallet score improved from 11.81 +/- 2.1 to 16.4 +/- 1.8 post operatively. All domains of the modified Mallet score showed significant improvement. All children reported an increase in power of elbow flexion. A reduction of compensatory winging was seen in 11 out of 17 patients. Excessive forward lean improved from 18° +/-6° to 8° +/-4°. No major complications were recorded and all osteotomies healed uneventfully.

Discussion

The external rotational torsional humeral osteotomy improves shoulder function in older children with obstetric brachial plexus palsy with internal rotation contracture, and/or advanced glenohumeral joint deformity. The surgery enhances rotational range of motion, increases external rotation strength, and reduces compensatory trunk flexion, leading to more efficient and functional upper limb use.

Images (Optional)



Session Category

Orthopaedic Biomechanics: Upper Extremities

P3-365

Comparison of Upper Extremity Anthropometry among Manual Wheelchair Users using Marker-Based and Markerless Biomechanical Models and Radiographic Imaging Segmentation

Mr Jeremy Lohmann[1], Ms Hannah Panchal[1], Ms Jungsun Moon[1], Dr Matthew Hanks PhD, ATC[1,2,3]

[1]Department of Health and Kinesiology, University of Illinois Urbana-Champaign, Urbana, IL, United States. [2]Beckman Institute for Advanced Science and Technology, University of Illinois Urbana-Champaign, Urbana, IL, United States. [3]Disability Resources and Educational Services, University of Illinois Urbana-Champaign, Champaign, IL, United States

Introduction

Upper extremity anthropometry is necessary to optimize manual wheelchair setup and reduce propulsion pathomechanics and risk of musculoskeletal injury. Motion analysis and radiographic imaging are systematic methods that can be used to measure upper extremity anthropometry, yet little research has compared measurements derived from these different methods. The purpose of this study was to evaluate the level of agreement in humerus and forearm segment lengths measured using marker-based and markerless biomechanical models and radiographic imaging segmentation.

Methods

Twenty-two manual wheelchair users (n=22; 12 male/10 female; age: 20.74±1.78 years) participated. Participants were affixed with 34 passive markers on their trunk and upper extremities then propelled their wheelchair overground while three-dimensional (3D) marker trajectories (120 Hz) and two-dimensional (2D) videos (60Hz) were obtained simultaneously using a 14-camera Qualisys system. Marker and video data were processed in Qualisys Track Manager and Theia3D software then exported into Visual 3D software to construct marker-based and markerless biomechanical models, respectively. In each model, humerus length was measured as the distance between the shoulder and elbow joint centers, and forearm length was measured as the distance between the elbow and wrist joint centers. Participants then underwent dual energy x-ray absorptiometry, and the scans were analyzed in ImageJ software. Humerus length was measured as the distance between the top of the humeral head and elbow joint center, and forearm length was measured as the distance between elbow and wrist joint centers. Intraclass correlation (ICC) and repeated measures MANOVA were used to assess the agreement among the methods.

Results

Strong ICC values were observed among the methods for the humerus (ICC3k=0.95) and forearm (ICC3k=0.98) segment lengths. A significant main effect of measurement method was observed (Wilks' Lambda=0.17, $F_{8,78}$=13.92, p<0.001, ηp^2=0.59). Post hoc analyses are presented in Table 1.

Discussion

Though significant differences in segment lengths were observed between the methods, the magnitudes of differences were small (≤1.5cm) with the markerless model consistently yielding the smallest measures. Additionally, ICC values were very strong indicating that all methods were highly reliable. These findings suggest that any of these methods could be used to reliably measure upper extremity anthropometry in manual wheelchair users.

Images (Optional)

Table 1. Post hoc pairwise comparisons of differences between measurement methods (mean±SD).

Segment (cm)	[1]Image Segmentation	[2]Marker-Based	[3]Markerless	$p_{1,2}$	$p_{2,3}$	$p_{1,3}$
Left Humerus	30.2±2.4	29.8±2.3	28.9±1.7	0.31	**0.003**	**< 0.001**
Right Humerus	30.5±2.1	30.0±1.8	29.1±1.6	0.07	**< 0.001**	**< 0.001**
Left Forearm	26.5±2.1	25.6±2.3	25.0±1.9	**0.001**	**0.002**	**< 0.001**
Right Forearm	26.5±2.1	25.7±2.5	25.1±1.8	**0.001**	**0.012**	**< 0.001**

Session Category

Orthopaedic Biomechanics: Upper Extremities

P3-366

Determinants of Supraspinatus Occupation Ratio During the Bench Press: The Role of Shoulder Elevation Kinematics and Sex

Ms. Jodi Motlagh[1], Dr. David Lipps[2]

[1]Wayne State University, Detroit, MI, United States. [2]University of Michigan, Ann Arbor, MI, United States

Introduction

Optimal form during the bench press is vital for injury prevention. Shoulder injuries are common in powerlifters, and anatomical factors such as an increased supraspinatus occupation ratio are associated with greater shoulder impingement [1]. In a standard bench press position, biological females have a higher supraspinatus occupation ratio than males, along with altered glenohumeral kinematics during bench press sets. Combined, these factors may put female lifters at increased risk of shoulder impingement and instability. Therefore, this study aimed to investigate whether glenohumeral elevation and biological sex could help predict the supraspinatus occupation ratio among competitive powerlifters.

Methods

Nineteen competitive powerlifters (8M, 11F) consented to participate in this study. Ultrasound imaging of the acromiohumeral distance and supraspinatus tendon was completed in the standard bench press position. The ratio of supraspinatus tendon thickness to acromiohumeral distance (e.g., supraspinatus occupation ratio) was calculated. Markerless motion capture (Theia) was used to calculate the peak glenohumeral elevation (corresponding to the highest bar position) across three bench press sets. Linear regression analysis predicted the supraspinatus occupation ratio based on glenohumeral elevation angle and biological sex.

Results

The overall regression model was significant, $F_{(2, 16)} = 15.73$, $p < 0.001$, explaining 66.3% of the variance ($R^2 = 0.663$). Both glenohumeral elevation angle (B = -0.008, SE = 0.002, t = -3.44, p = 0.003) and biological sex (B = -0.146, SE = 0.051, t = -2.89, p = 0.011) significantly predicted supraspinatus occupation ratio in a standard bench press position.

Discussion

The supraspinatus occupation ratio was strongly predicted by peak glenohumeral elevation angles during bench press sets and biological sex. By quantifying these relationships, our

model provides a practical framework for optimizing bench press form and developing targeted injury-prevention strategies—particularly for female athletes. A limitation was the inability to capture dynamic ultrasound images while athletes lowered the barbell, due to physical obstructions from the bench. Future research should explore the impact of different techniques, training volumes, and rehabilitation strategies on the supraspinatus occupation ratio, ideally across longitudinal datasets.

Images (Optional)

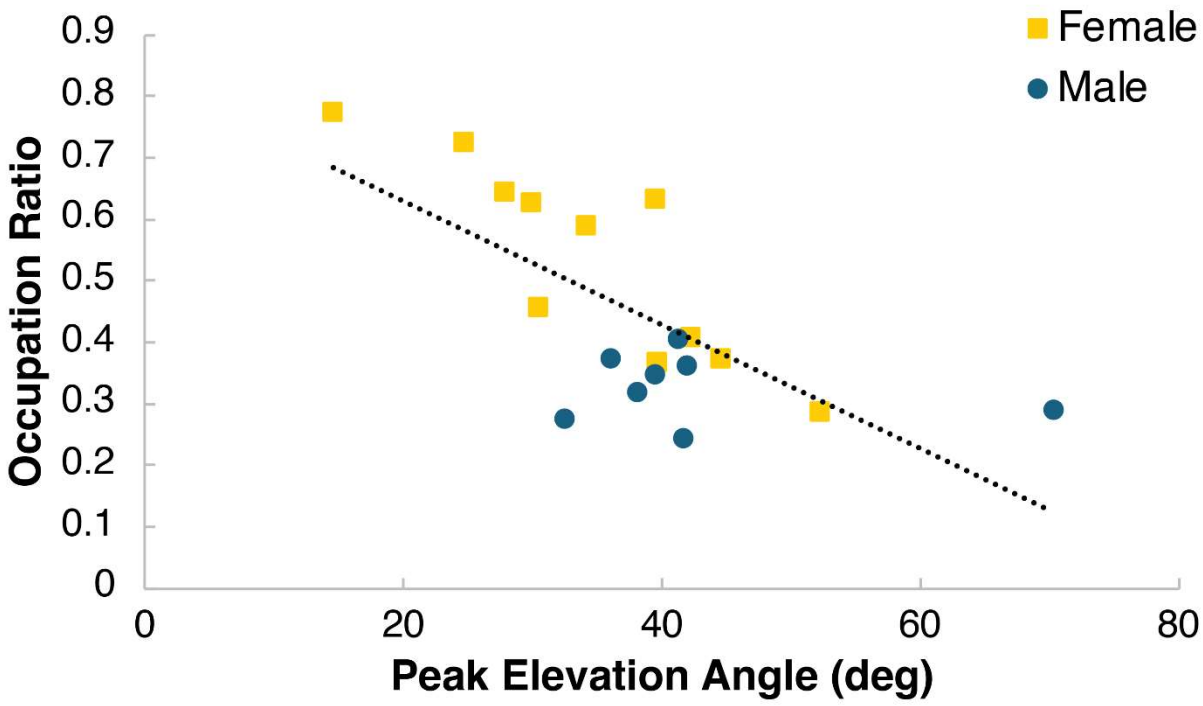


Figure 1: Peak elevation angle during bench press sets compared to supraspinatus occupation ratio in a standard bench press position. Data is striated by biological sex (Female - yellow square; Male: blue circle)

References (Optional)

[1] Michener et al., Knee Surgery, Sports Traumatology, Arthroscopy, 2015

Session Category

Orthopaedic Biomechanics: Upper Extremities

P3-367

Subject Specific Micro Finite Element Modeling of Proximal Humeral Neck Trabecular Bone: Validation and Structure Function Insights.

MSc. Eng. Johannes Eichwalder, PhD Mahsa Zojaji, PhD Nikolas Knowles

University of Waterloo, Waterloo, Ontario, Canada

Introduction

Stemless humeral head components are a popular choice for patients undergoing shoulder arthroplasty for end-stage osteoarthritis (OA).[1] OA is known to alter bone density in the humeral head, which can compromise implant stability and increase the need for surgical revision.[2] However, quantitative structure function data for humeral neck trabecular bone remain limited compared with the hip and spine. Micro-finite element (micro-FE) analysis has proven effective in linking trabecular architecture to mechanical properties in other skeletal sites. This study evaluated how local trabecular microarchitecture in the lateral proximal humeral neck relates to stiffness and apparent elastic modulus.

Methods

A 10 mm section was extracted directly below the humeral anatomic neck of cadaveric humeri, micro CT scanned, and tested in uniaxial compression obtain apparent elastic modulus. Trabecular cores (13 mm x 13 mm) from the superolateral region were segmented from each micro CT image. Bone morphometry was quantified for each core. Micro FE models were generated with linear elastic isotropic homogeneous tissue modulus and boundary conditions reproducing the experimental protocol to compute apparent elastic modulus.

Results

Trabecular cores BV/TV ranged from 4.4 to 19.7%, with corresponding FE-based apparent elastic modulus from 21.5 to 689.2 MPa. Experimental apparent modulus of the entire 10 mm humeral sections ranged from 7.3 to 37.7 MPa. FE apparent modulus showed strong positive correlations with BV/TV ($r = +0.93$), degree of anisotropy ($r= +0.72$), trabecular thickness ($r = +0.83$), and connectivity density ($r = +0.56$), and a negative correlation with trabecular separation ($r= -0.63$).

Discussion

Local trabecular architecture of the lateral proximal humeral neck strongly governs apparent stiffness and modulus, with BV/TV, degree of anisotropy, trabecular thickness, trabecular separation and connectivity density emerging as key predictors, consistent with prior structure function work in the humeral head.[3]

Images (Optional)

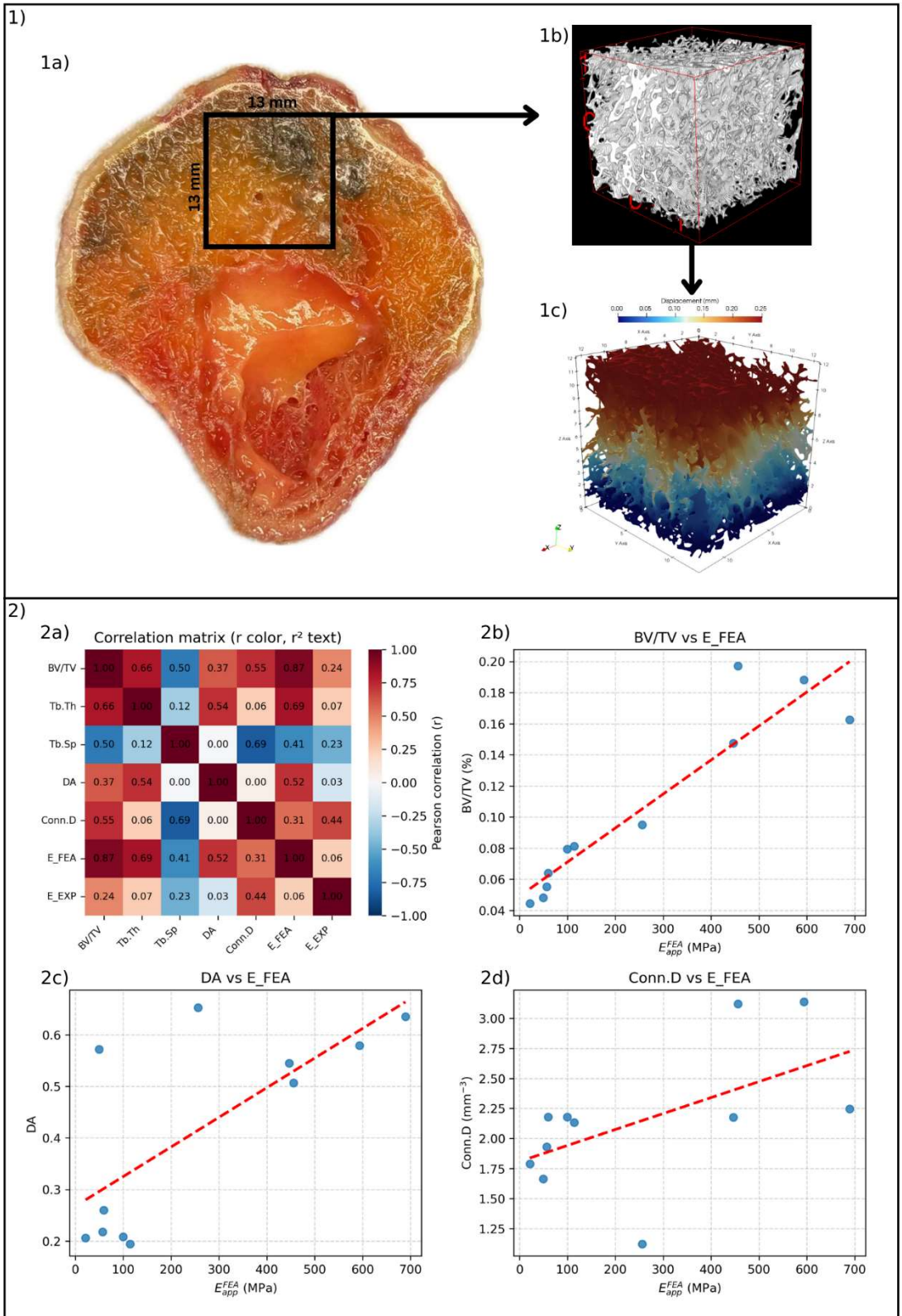


Figure: Trabecular core extraction, micro-FE modelling, and structure–function relationships in the proximal humeral neck. 1)Specimen preparation and modelling. 1a) Transverse slice of the proximal humerus showing the superolateral trabecular core region (13×13 mm) extracted distal to the anatomic neck. 1b) Corresponding micro-CT–based trabecular volume used for morphometric analysis and micro-FE modelling. 1c) Example micro-FE simulation output illustrating compressive displacement and heterogeneous apparent strain distribution within the trabecular core. 2)Structure–function relationships. 2a) Pearson correlation matrix for bone volume fraction (BV/TV), trabecular thickness (Tb.Th), trabecular separation (Tb.Sp), degree of anisotropy (DA), connectivity density (Conn.D), FE-based apparent elastic modulus (E_FEA), and experimentally measured apparent modulus (E_EXP); colour indicates Pearson r and overlaid values indicate r². 2b–2d) Linear regressions between E_FEA and BV/TV (2b), DA (2c), and Conn.D (2d). Dashed red lines denote best-fit relationships; in-plot legends report regression equations and coefficients of determination (R^2).

References (Optional)

[1] G. Athwal, Bone & Joint Surgery, 2016

[2] G. Li, Arthritis Research & Therapy, 2013

[3] J. Kussins, Mech Behav Biomed Mater., 2022

Session Category

Orthopaedic Biomechanics: Upper Extremities

P3-368

Assessing Accuracy of Glenohumeral Joint Center of Rotation Estimates Using Traditional Motion Capture Versus Bi-Plane Fluoroscopy

Dr. Julia Dunn PhD, Ms. Ola Alsaadi MS, Dr. Kevin Shelburne PhD, Dr. Michelle Sabick PhD

University of Denver, Denver, CO, United States

Introduction

The glenohumeral joint (GHJ) is located deep below skin and muscle, so its center of rotation (CoR) cannot be located by palpation alone. Accurate estimation of the GHJ CoR is essential for modeling of shoulder motion. While prediction methods using bony landmarks are commonly used, their accuracy throughout the entire range of shoulder motion has not been fully assessed. This study compared three predictive approaches for locating the CoR to results obtained from bi-plane fluoroscopy.

Methods

Five healthy adults performed controlled shoulder abduction, flexion, and external rotation movements in adducted and 90° abducted positions. Optical motion capture was used to estimate GHJ CoR via three predictive methods: acromion offset, midpoint of two technical markers, and center point of acromion plus technical markers. Bi-plane fluoroscopy was used to establish the reference location of the CoR. Absolute and axial errors were calculated across normalized ranges of motion. Statistical parametric mapping and repeated measures ANOVA assessed differences in error among methods compared to the reference location from bi-plane fluoroscopy.

Results

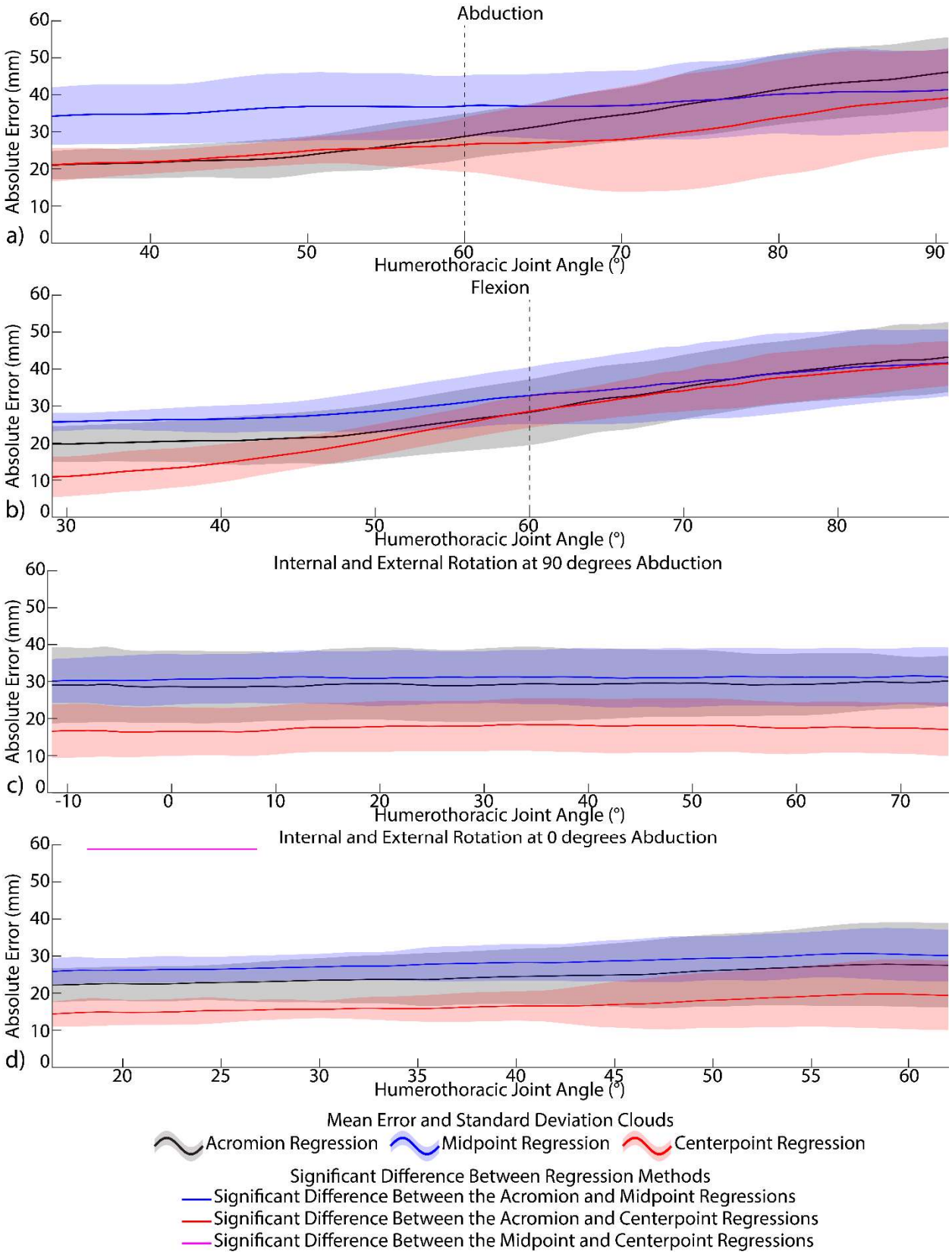
None of the predictive methods met clinically relevant thresholds for accuracy (absolute error >10mm; axial error >±5mm). Absolute error increased significantly with humeral elevation beyond 60°, reaching up to 46mm during abduction and 43mm during flexion. In contrast, error remained stable during internal/external rotation. The use of technical markers slightly reduced axial error but did not substantially improve overall accuracy. In addition to error magnitude, directional biases were observed: the acromion method produced anterior, medial, and superior errors, while the midpoint and center point methods tended toward medial and inferior errors.

Discussion

All of the commonly used predictive methods for determining GHJ CoR are unreliable for high-elevation tasks, such as overhead sports, due to significant increase in error with

elevation and susceptibility to soft tissue artifact. They may remain suitable for low-elevation activities (e.g., gait), but adjusting the offsets will be critical. Future work should explore humeral marker placement and functional methods to mitigate soft tissue artifact and improve estimation accuracy. Validating optical motion capture-based methods against bi-plane fluoroscopy will enhance consistency in calculating and reporting outcomes in shoulder biomechanics research.

Images (Optional)



References (Optional)

Session Category

Orthopaedic Biomechanics: Upper Extremities

P3-369

EMG Validation of Subject-Specific RTSA Musculoskeletal Models in Dynamic Tasks

Ms. Kaitlyn B. Kuchinka[1,2], Dr. Heath B. Henninger PhD[2], Dr. Joshua W. Giles PhD[1]

[1]University of Victoria, Victoria, British Columbia, Canada. [2]University of Utah, Salt Lake City, Utah, United States

Introduction

Reverse Total Shoulder Arthroplasty (RTSA) produces altered muscle activations, and compensatory movement patterns characterized by shifted glenohumeral and scapulothoracic contributions. Previous RTSA musculoskeletal models (MSkM) used kinematics from controls, or large reserve actuators. Crucially, these assumptions prevent considering interactions between kinematics, activations, and loading. This work parametrically generated subject-specific RTSA MSkMs. Open-source distribution of the dataset is planned following validation.

Methods

Participants (N=3) with RTSA performed scapula abduction (SA) and forward elevation (FE). Optical motion capture, biplane fluoroscopy (BF), and both surface and fine-wire electromyography (EMG) were recorded.

A generic MSkM [1] was modified using the OpenSim 4.4 MATLAB API. Pre-operative Computed-Tomography segmentations were registered to respective body-segment frames. Non-rigid point-cloud registration determined subject-specific muscle attachments. Wrapping objects and via-points were adjusted according to attachments and defined anatomic landmarks. Post-operative least-squares glenohumeral joint centres were calculated, and deltoid wrapping geometry modified accordingly.

Bilevel optimization minimizing scapula tracking error specified scapulothoracic joint ellipsoid geometry. An iterative approach calculating musculotendon (MTU) properties used strict criteria to determine optimal muscle fibre and tendon slack lengths that produce normalized fibre lengths within [0.5,1.5], and initial lengths within ±0.10 in similar motions in the target model. Computed Muscle Control (CMC) determined muscle activations.

Results

Inverse Kinematics RMSE distances were 4.5±0.6mm. Fig.1 shows CMC-calculated deltoid activations. Peak glenohumeral Joint Reaction Forces (JRF) were 95.1±21.0%BW for FE and

94.1±15.8%BW for SA. JRFs at 90° humerothoracic elevation were 71.5±11.1%BW for FE and 74.8±13.7%BW for SA.

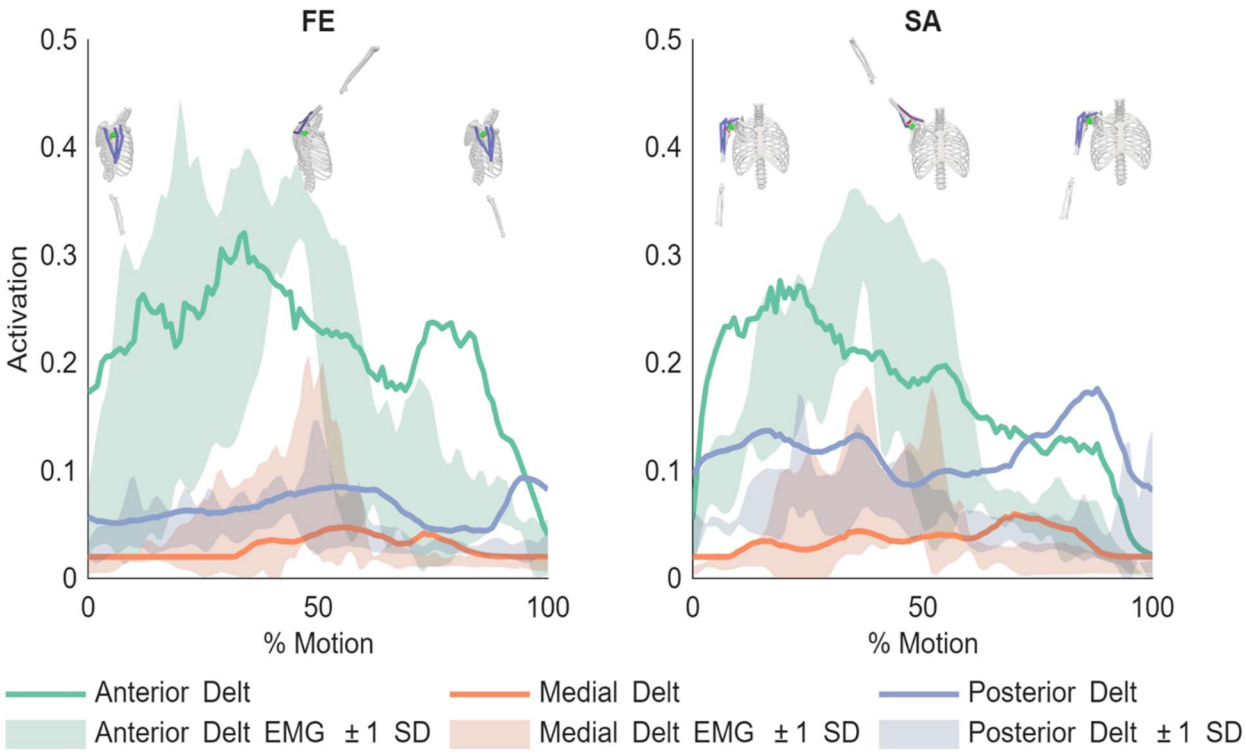
Discussion

CMC-EMG activations show moderate agreement. Peak JRFs fall within reported ranges for controls, and 90° JRFs are within RTSA ranges.

Strengths of this work are the automation of a commonly manual process and comparison against EMG. Quantifiable, measurable workflows are required for elucidating clinical conclusions, and understanding how methodological parameterization vs. personalization affect outputs.

Findings emphasize key areas to direct efforts developing clinically relevant upper-limb MSkMs. Geometric personalization alone is insufficient. MTU calibration requires improvement through suitable mapping of fibre lengths or collecting experimental measures of passive force. These varying limitations are insurmountable in isolation, and increased multi-disciplinary collaborative efforts are encouraged.

Images (Optional)



References (Optional)

[1] Ajay Seth *et al.*, Front Neurorob, 2019

Acknowledgements (Optional)

Session Category

Orthopaedic Biomechanics: Upper Extremities

P3-370

Effect of Glenoid Lateralization and Humeral Offset on Acromial and Scapular Spine Strains: Preliminary Results of an In-Vitro Active Shoulder Motion Simulator

Mrs Inês Santos[1], Ms Lea-Marie Ocker[1], Mr Daniel Ritter[1], Mrs. Maxi Tengler MD[1], Mr Patrick Raiss MD[2]

[1]Arthrex Department of Orthopedic Research, Munich, Bavaria, Germany. [2]OCM, Munich, Bavaria, Germany

Mrs Inês Santos

Ms Lea-Marie Ocker

Introduction

Acromial and scapular spine fractures after reverse total shoulder arthroplasty (RSA) can lead to substantial functional impairments, and the few biomechanical studies investigating this effect do not show consistent results. The purpose of this ongoing cadaveric biomechanical simulator study was to evaluate the role of glenoid lateralization and humeral offset on scapular spine strain.

Methods

Two fresh-frozen cadaveric shoulders with an implanted RSA were mounted to an active motion shoulder simulator (Fig.1A). The three portions of the deltoid were individually sutured with FiberTape to ensure force distribution along each insertion and routed to electric linear actuators with force transducers. The subscapularis and infraspinatus/teres minor were each loaded with 10 N, and the supraspinatus was removed to simulate rotator cuff tear. Four strain gauges were placed in Levy scapular spine fracture zones [1] (Fig.1B) to measure microstrain (strain $x10^{-6}$). Optical tracking markers were attached to the humerus and scapula, allowing the acquisition of physiological kinematic data [2]. Abduction at 7°, 20°, 40°, 60°, and 90° was simulated in the scapular plane and a glenohumeral to scapulothoracic motion ratio of 2:1 was applied [3], for three RSA design configurations: (1) 0 mm glenoid and humeral offset, (2) +4 mm glenoid offset and (3) +6 mm humeral offset.

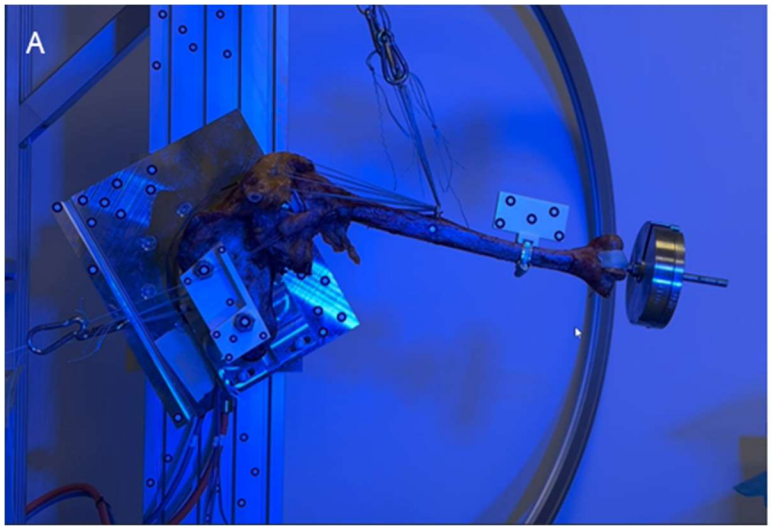
Results

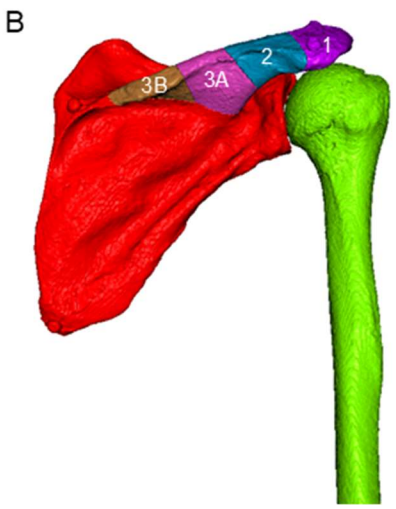
Strains measured in Levy zones 1 and 2 were higher than all other regions. The greatest increases in strain due to RSA design change were observed in Levy zones 3A and 3B. Increased humeral offset resulted in higher strain increases in zone 3A than glenoid lateralization. Increasing humeral offset led to an average increase of 36.79±4.95 in Levy zone 3A and 28.88±5.54 in Levy zone 3B. Strains in all regions were associated with increases in arm elevation.

Discussion

Increasing glenoid lateralization and humeral offset, despite its advantages in improving range of motion, increases scapular spine strains. Understanding the relationships between RSA implant design and acromial and scapular strains is crucial for optimizing outcomes and avoiding complications.

Images (Optional)





References (Optional)

[1] Levy et al., J Bone Joint Surg Am, 2013

[2] Wu et al., J Biomech, 2005

[3] Inman et al., Clin Orthop Relat Res, 1996

Session Category

Orthopaedic Biomechanics: Upper Extremities

P3-371

Differences in Glenohumeral Joint Function in Individuals with Symptomatic Isolated Supraspinatus Tears and Healthy Controls

Ms. Lidya Canturk BS[1], Ms. Clair Smith MS[2], Dr. Luke Mattar PhD[3], Dr. Adam Popchak PhD[2,3], Dr. William Anderst PhD[3,1], Dr. Volker Musahl MD[3,1], Dr. James Irrgang PT PhD FAPTA[2,3], Dr. Richard Debski PhD[1,3]

[1]Department of Bioengineering, University of Pittsburgh, Pittsburgh, PA, United States. [2]Department of Physical Therapy, University of Pittsburgh, Pittsburgh, PA, United States. [3]Department of Orthopaedic Surgery, University of Pittsburgh, Pittsburgh, PA, United States

Introduction

Individuals with a rotator cuff tear experience impaired shoulder function, such as restricted range of motion (ROM), decreased strength, and posterior capsule tightness [1]. The objective was to determine the differences in maximum active glenohumeral elevation, isometric strength, and passive ROM in individuals with a symptomatic isolated supraspinatus tear in comparison to healthy controls up to 5 years after a 12-week personalized exercise therapy program.

Methods

One hundred and nine individuals with symptomatic isolated supraspinatus tear (age 60.9 ± 9.9 years, BMI 28.7 ± 5.0 kg/m^2, 48.6% females), and 63 sex-, age-, and hand-dominance frequency matched healthy controls (age 61.4 ± 9.9 years; BMI 26.6 ± 5.6 kg/m^2; 46.0% females) were enrolled in the study. Maximum glenohumeral elevation was quantified during active scapular plane abduction using biplane radiography; isometric strength measured with a dynamometer; and passive glenohumeral ROM measured with a goniometer were determined at 3-time points for subjects with a tear and at a single time point for healthy controls [2]. Outcomes were compared between groups with independent samples t-tests (two-sided, α=0.05)

Results

The maximum active elevation in healthy controls was significantly greater than individuals with a symptomatic isolated supraspinatus tear at baseline ($p<0.01$), 12 weeks ($p<0.01$), and 5 years ($p<0.01$) (Figure 1A). At baseline ($p<0.001$) and 12 weeks ($p<0.01$), isometric strength was decreased in comparison to controls across both tasks; however, at 5 years,

no differences were found between the tear and control groups (Figure 1B). Differences in passive ROM for abduction ($p<0.03$) and internal rotation at 90° abduction ($p<0.02$) between the tear group and healthy controls were observed (Figure 1C).

Discussion

The findings indicate that even though similar isometric strength was observed in individuals with a supraspinatus tear at 5 years compared to healthy controls, differences in active in-vivo glenohumeral elevation and passive ROM may imply impaired neuromuscular control of the shoulder complex and passive glenohumeral joint function, respectively. Thus, activity limitations and participation restrictions need to be further investigated and may warrant changes in and/or additional personalized exercise therapy.

Images (Optional)

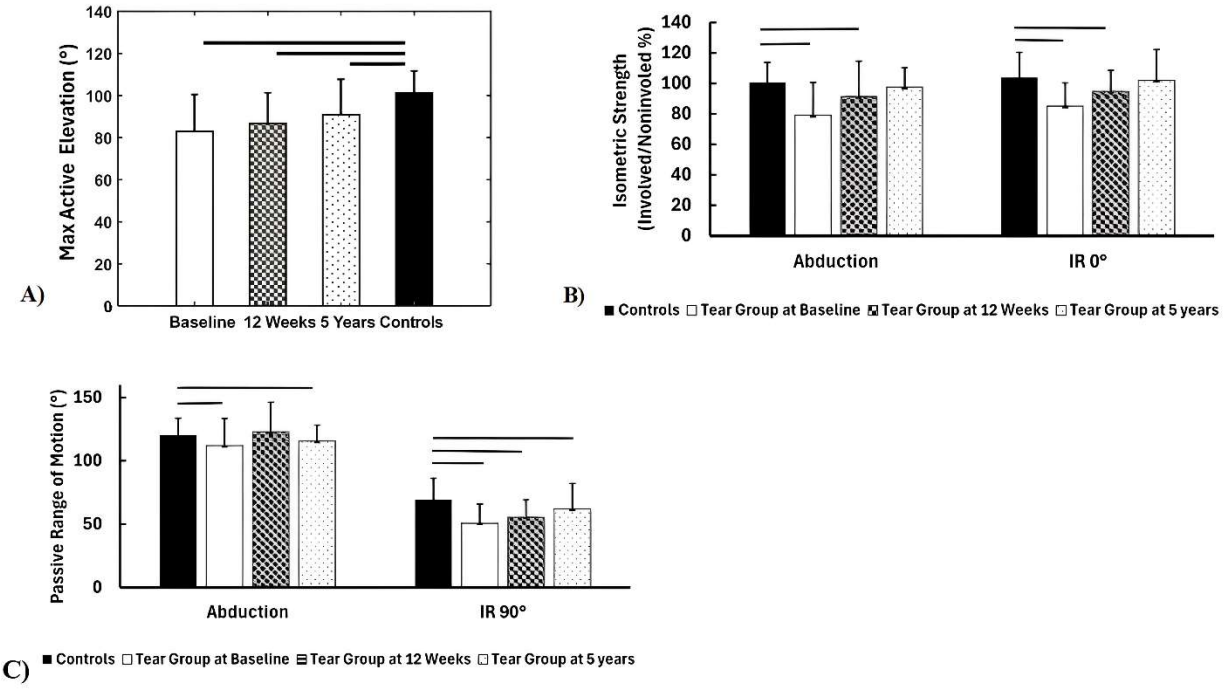


Figure 1. A-B-C) Maximum active elevation, isometric strength, and passive ROM at baseline (n=102,109,109), 12 weeks (n=96,95,95), and 5 years (n=67,76,76) for individuals with an isolated supraspinatus tendon tear and at baseline for healthy controls (n=61,63,63) (Sample sizes differed from the total number of participants in the study due to lost to follow-up and missing data).

References (Optional)

[1] Dirkjan van Schaardenburg et al. Ann Rheum Dis 1994, [2] Luke T. Mattar et al. Clin Biomech 2024

Session Category

P3-372

Unveiling Control Strategies in Fundamental Piano Keystrokes: A Wavelet Analysis of Skilled versus Amateur Pianists

Ms. Lu Yen[1], Assistant Professor Chieh-Hsiang Hsu[2], Assistant Researcher Fellow Charlie Chen Ma[3], Chair Professor Fong-Chin Su[1,3]

[1]Department of Biomedical Engineering, College of Engineering, National Cheng Kung University, Tainan, Taiwan, Taiwan. [2]Department of Electronic Engineering, Southern Taiwan University of Science and Technology, Tainan, Taiwan, Taiwan. [3]Medical Device Innovation Center, National Cheng Kung University, Tainan, Taiwan, Taiwan

Ms. Lu Yen

Assistant Professor Chieh-Hsiang Hsu

Assistant Researcher Fellow Charlie Chen Ma

Introduction

True motor expertise lies in the mastery of fundamental elements. While traditional metrics (e.g., standard deviation) capture overall stability, they miss the temporal-spectral dynamics of motor variability. This study utilizes Discrete Wavelet Transform (DWT) to investigate whether skilled pianists (SS) employ distinct neuromuscular strategies during fundamental tasks (T1-T4) compared to amateurs (SA), hypothesizing that experts demonstrate superior "spectral efficiency."

Methods

Two groups (fifteen subjects each), Skilled (SS, >10 years training) and Amateur (SA, <5 years), performed fundamental tasks on a force-instrumented piano (1000 Hz) [1]. Tasks included single-finger tapping (T1), simultaneous chords (T2-T3), and sequential movements (T4). We applied DWT to decompose vertical force signals into Approximation (low-frequency) and Detail (high-frequency) bands. Key features extracted were Wavelet Energy Ratio and Wavelet Entropy to quantify control complexity and spectral energy distribution. Independent t-tests compared groups ($p < 0.05$).

Results

Analysis revealed distinct control signatures even in the simplest tasks. In T1 (single-finger), Amateurs exhibited a significantly higher Energy Ratio in the low-frequency A5 band compared to Skilled pianists ($p < 0.05$), alongside higher force variability (SD_A5). This indicates Amateurs rely on "reactive" gross motor corrections to maintain stability. Conversely, Skilled pianists displayed a balanced energy profile across T1-T4, achieving stability with optimized spectral energy, reflecting a "predictive" and automated control strategy free from excessive corrective noise.

Discussion

We successfully identified a "spectral signature" of expertise in fundamental movements. Amateurs' reliance on low-frequency energy suggests an inefficient, feedback-dependent strategy, while experts exhibit high spectral efficiency. These findings validate wavelet-based metrics as sensitive biomarkers for motor skill. Clinically, this protocol offers a simplified assessment tool for detecting fine motor deficits (e.g., in Parkinson's disease) by analyzing spectral properties of basic tapping, eliminating the need for complex testing tasks.

References (Optional)

[1] Lai, K. Y., Hsu, C. H., Lin, Y. C., Tsai, C. H., Lin, C. F., Kuo, L. C., & Su, F. C. (2023). Practically Feasible Sensor-Embedded Kinetic Assessment Piano System for Quantifying Striking Force of Digits During Piano Playing. *Journal of Medical and Biological Engineering*, *43*(6), 749-757.

Acknowledgements (Optional)

We thank the participants, the Motion Analysis Laboratory at National Cheng Kung University, and advisor Fong-Chin Su for their support.

Session Category

Orthopaedic Biomechanics: Upper Extremities

P3-373

The Role of Palmaris Longus in the Generation of Wrist Flexion-Extension Torque: What Is the Consequence of Harvesting It for a Tendon Graft?

Mr. Mahdi Mohseni, Dr. Angela Kedgley

Department of Bioengineering, Imperial College London, London, Greater London, United Kingdom

Introduction

The palmaris longus (PL) tendon is widely harvested as a graft for surgical procedures [1]. PL has the largest wrist flexion moment arm; however, its physiological cross-sectional area is small compared to other forearm muscles [2]. This study aimed to determine the effect of PL tendon removal on the wrist flexion-extension torque (FET). We hypothesised that due to PL's large moment arm, the subsequent changes in other muscle forces in the absence of PL would increase the wrist FET.

Methods

An 11-muscle dynamic physiologic hand simulator was used with a three degree of freedom (two for wrist and one for fingers) custom-made hand model. The hand was mounted with the fingers pointed vertically upward. Kinematics were input into a PID-based cascade controller to recreate six cycles of 40° wrist flexion-extension, with the fingers held in a neutral posture. Simulated muscle forces were applied via cables by servo-linear actuators and were controlled with feedback from loadcells. FET and optimised muscle forces were calculated with and without the PL.

Results

Kinematic root mean square (RMS) errors of flexion-extension for both conditions were ≤ 0.35°. The maximum of the mean force applied by PL was 8.2 N, resulting in an 18.0 N.cm FET (Figure 1). After PL removal, the forces applied by two other wrist flexor muscles, flexor carpi ulnaris and radials, were increased (RMS of mean changes = 6.8 N and 9.1 N, respectively). Consequently, the RMS of the mean FET difference between the two conditions was 30.3 N.cm. The changes in other muscle forces increased the FET by 8.5% of its maximum value.

Discussion

Wrist flexion is a fundamental part of everyday activities. As a repetitive task, the increase in the wrist flexor forces and FET in the absence of PL may increase the risk of wrist injury. PL plays an important role in reducing the other wrist flexor muscle forces and, therefore, reducing the total wrist FET. Thus, it is recommended to harvest tendon grafts from other donor sites, such as plantaris [1].

Images (Optional)

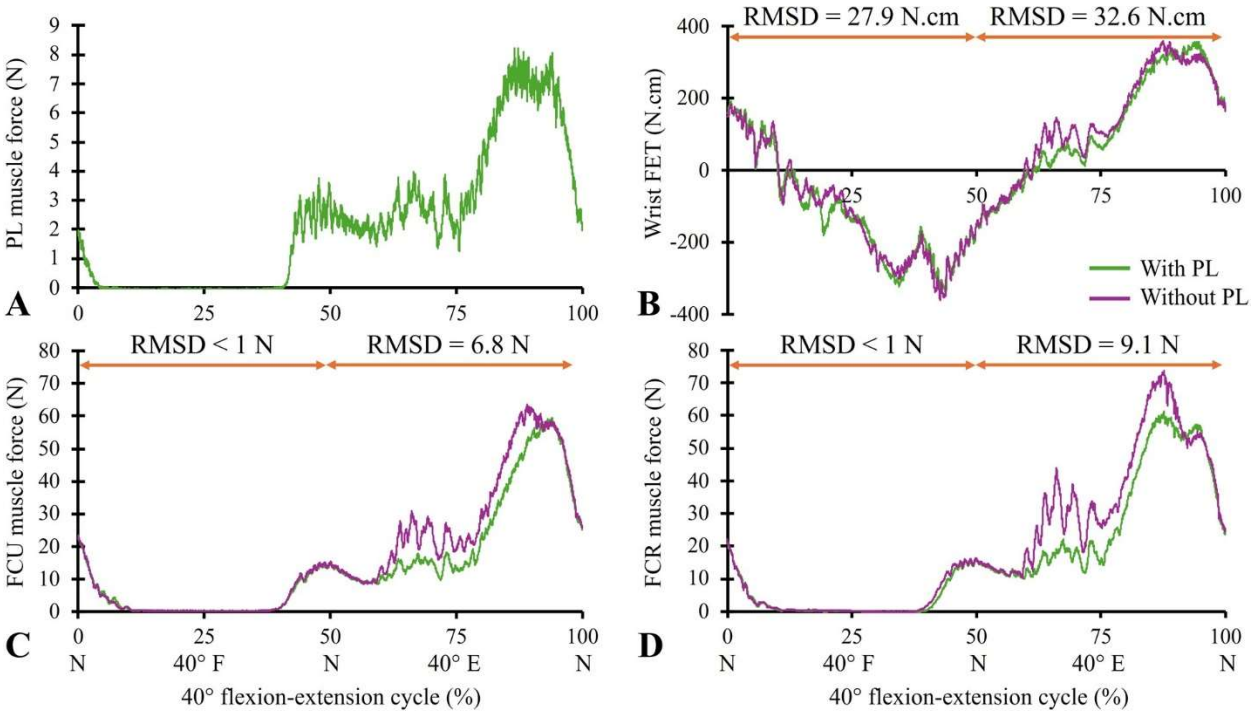


Figure 1: Mean (A) palmaris longus (PL) muscle force, (B) wrist flexion-extension torque (FET), and (C) flexor carpi ulnaris (FCU) and (D) flexor carpi radialis (FCR) muscle forces during six cycles of 40° wrist flexion-extension with and without PL.
N: neutral, F: flexion, E: extension, RMSD: root mean square difference.

References (Optional)

[1] Gregory Carlson *et al.*, J Hand Surg Am, 1993.

[2] Katherine Holzbaur *et al.*, J Biomechanics, 2007.

Session Category

Orthopaedic Biomechanics: Upper Extremities

P3-374

The Impact of Pectoralis Minor Tightness and Subsequent Interventions on Scapular Kinematics: A Systematic Review

Dr. Marcos Amstalden Barros MD[1,2], Dr. Renato Miyadahira MD[2], Ms. Vennela Challagondla BS, MPH[3], Dr. Caroline Popovicz Nunes MD[1,2], Dr. Tiago Zimerman MD[1,2], Dr. Felipe F. Gonzalez MD[1,2], Dr. Jonathan A. Gustafson PhD[1,2], Dr. Grant E. Garrigues MD[1,4], Dr. Gregory Nicholson MD[1,4], Dr. Jorge Chahla MD, PhD[1,4], Dr. Gustavo Leporace MSc, PhD[2], Dr. Leonardo Metsavaht MD, PhD[2]

[1]Rush University, Chicago, IL, United States. [2]Instituto Brasil de Tecnologias da Saúde (IBTS), Rio de Janeiro, RJ, Brazil. [3]The University of Illinois Chicago, Chicago, IL, United States. [4]Midwest Orthopaedics at Rush, Chicago, IL, United States

Introduction

Pectoralis minor (PM) tightness contributes to altered scapular mechanics, postural deviations, and shoulder dysfunction. Muscle shortening may increase scapular anterior tilt and internal rotation, restricting scapulothoracic motion and narrowing the subacromial space. However, the extent of scapular and spinal compensation remains unclear, and the comparative effectiveness of stretching, manual therapy, exercise, and surgical release has not been systematically reviewed. This systematic review aimed to evaluate biomechanical and postural alterations associated with PM tightness and determine whether targeted interventions improve scapular kinematics and thoracic alignment.

Methods

This review followed PRISMA 2020 guidelines. Eligible studies included clinical or biomechanical investigations assessing PM tightness, scapular motion, thoracic or cervical alignment, or targeted interventions. Databases searched included PubMed/MEDLINE, Scopus, Embase, CINAHL, CENTRAL, and Google Scholar (2004–2024). Screening, data extraction, and risk-of-bias assessment were performed using NIH/NHLBI tools. Given substantial heterogeneity, results were synthesized qualitatively.

Results

Forty-nine studies met inclusion criteria, representing 2,644 analyzed shoulders (Table 1). Cross-sectional research showed that PM tightness was associated with greater scapular anterior tilt and internal rotation, scapular dyskinesis, and altered postural patterns.[1,2] Interventional trials indicated that PM stretching, proprioceptive neuromuscular

facilitation, self-myofascial release, and scapular stabilization exercise increased PM length and improved scapular kinematics, pain, and function.[3] Multimodal exercise programs produced longer-term improvements in forward shoulder posture, pain, and mobility.[3] External supports such as figure-8 bracing acutely improved scapular alignment and muscle activation patterns. Surgical PM release was effective for refractory cases.[4]

Discussion

Across diverse populations and methodologies, PM tightness was associated with altered scapular kinematics and postural deviations. Interventions targeting PM length, including stretching and stabilization programs, demonstrated improvements in scapular motion, posture, and symptoms. Surgical release was effective for select refractory cases. Future research should standardize measurement methods and intervention parameters to improve comparability and guide clinical application.

Images (Optional)

Table 1. Summary of Included Studies on Pectoralis Minor Tightness and Interventions

Category	Key Focus	Main Outcomes / Findings
Overall Sample	49 studies; 2,644 shoulders	Clinical and biomechanical investigations of pectoralis minor tightness, scapular motion, posture, and interventions
Cross-sectional Studies	PM tightness vs scapular & postural variables	Increased scapular anterior tilt, internal rotation, scapular dyskinesis, and forward shoulder posture
Stretching & Manual Therapy	PNF stretching, self-myofascial release, soft-tissue mobilization	Immediate increases in PM length; improvements in scapular kinematics, pain, and function
Exercise Programs	Scapular stabilization & flexibility training	Longer-term improvements in posture, pain, and shoulder mobility
External Supports	Figure-8 bracing and postural supports	Acute improvements in scapular alignment and muscle activation patterns
Surgical Intervention	Pectoralis minor release for refractory cases	Improved pain, motion, and function in persistent scapular dyskinesis

Table 1. Summary of biomechanical and clinical findings from 49 studies (2,644 shoulders) evaluating pectoralis minor tightness and related scapular and postural alterations. Cross-sectional studies consistently associated PM tightness with increased scapular anterior tilt, internal rotation, and dyskinesis. Interventional studies demonstrated that stretching, manual therapy, exercise programs, and external supports improved PM length, scapular mechanics, posture, and symptoms. Surgical pectoralis minor release was effective for refractory cases.

References (Optional)

1. Yeşilyaprak SS. J Bodyw Mov Ther. 2016.
2. Borstad JD, Ludewig PM. J Shoulder Elbow Surg. 2006.
3. Birinci et al., 2020; Laudner et al., 2019; Ciğercioğlu et al., 2022; De Groef et al., 2017.
4. Provencher MT. Arthroscopy Techniques. 2014; Elhassan BT et al. J Shoulder Elbow Surg. 2022.

Session Category

Orthopaedic Biomechanics: Upper Extremities

P3-375

Design and Preliminary Validation of an In-Vitro Elbow Joint Simulator for Quantitative Assessment of Injury-Related Kinematics

MSc. Mateus Enzenberg, Dr. med. Lukas Dankl, Curator Romed Hoermann, Univ.-Prof. Dr. med. Rohit Arora, Univ.-Prof. Dipl.-Ing. (FH) Dr. Werner Schmoelz

Medical University of Innsbruck, Innsbruck, Tyrol, Austria

Introduction

Elbow injuries can alter joint motion and affect upper limb function. Understanding these effects supports decisions on the need for surgical intervention and rehabilitation planning. Existing test setups that aim to identify such changes often lack the ability to produce repeatable physiological motions. In vitro simulators that apply controlled muscle-driven actuation offer a platform to study elbow kinematics under defined conditions.

Methods

An active elbow joint simulator was developed to reproduce flexion and extension by applying physiologically driven muscle forces. Tendons of a cadaveric elbow specimen were connected to electromechanical actuators through high strength braided suture strands routed along anatomical paths (see Figure 1). Actuators were moved using a cascaded control strategy based on estimated muscle forces and activation profiles. Each actuator features a defined elastic element to more closely mimic physiological muscle behavior. The humerus was mounted in a defined orientation, and an angle sensor attached to the wrist was used to capture joint kinematics. Flexion-extension cycles were performed at different forearm rotations and loading conditions. Following intact testing, a radial neck osteotomy was performed to simulate a radial head fracture and enable preliminary evaluation of the injured state.

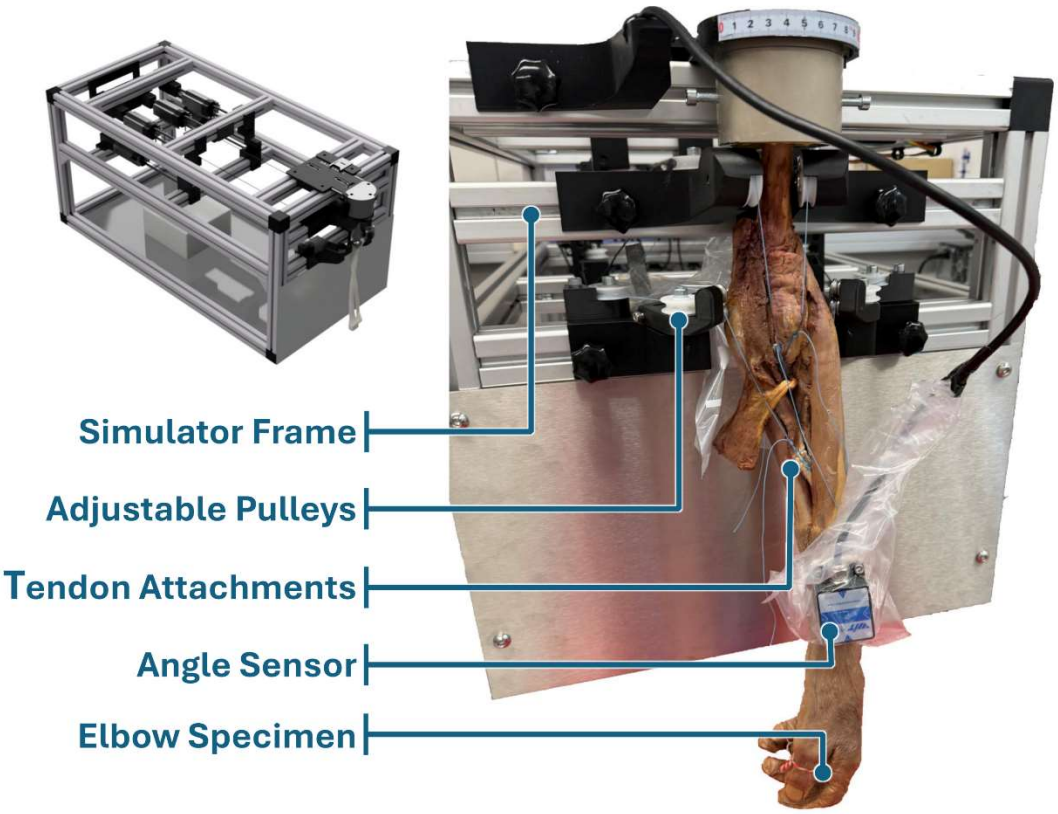
Results

The simulator reproduced controlled elbow flexion between 0° and 120° while maintaining forearm orientations at neutral, pronated, and supinated targets. Rotational positioning remained within ±3° of the intended angles. Muscle force trajectories were highly repeatable, with mean cycle-to-cycle RMSE values between 0.14 and 1.23 N across actuators (maximum 3.3 N) in neutral configuration. After the radial neck osteotomy, the specimen demonstrated similar flexion profiles while rotational deviations increased, suggesting that the system can detect changes in forearm motion associated with the simulated injury.

Discussion

The designed and constructed simulator was able to produce consistent elbow motion and enabled continuous measurement of joint kinematics and muscle forces. The intact tests demonstrated stable control of flexion and forearm orientation. The injured configuration showed altered rotational behavior, indicating that the setup can detect the changes in joint mechanics. Ongoing work focuses on expanding tests across multiple specimens and incorporating defined external joint loading to investigate additional clinically relevant injury patterns.

Images (Optional)



Session Category

Orthopaedic Biomechanics: Upper Extremities

P3-376

Validation of an Upper Limb musculoskeletal Model Against Cadaverix Muscle Moment Arms and Instrumented Implant Data

Dr Maxence Lavaill PhD[1,2], Prof Peter Pivonka PhD[1], Dr Ehsan Sarshari PhD[2]

[1]Queensland Univerisity of Technology, Brisbane, QLD, Australia. [2]Stryker GmbH, Selzach, Solothurn, Switzerland

Introduction

Accurate estimation of shoulder muscle forces and glenohumeral (GH) joint loading is essential for understanding shoulder function, guiding rehabilitation, and informing implant design. While musculoskeletal (MSK) models provide powerful non-invasive estimates, their validity remains dependent on comparisons with high-quality experimental data. This study validates an upper-limb MSK model, previously developed by Sarshari et al. [1], through two complementary approaches: (1) comparison of model-derived muscle moment arms against cadaveric reference datasets [2], and (2) direct validation of predicted GH joint reaction forces using *in vivo* measurements from an instrumented shoulder prosthesis (OrthoLoad) [3].

Methods

The MSK model (Figure 1A-1B) was adapted to match the anatomy of six OrthoLoad patients implanted with an instrumented hemi shoulder arthroplasty. A 2.4 kg weighted abduction task was simulated to drive the model. Muscle moment arms for major shoulder muscles were computed across the elevation range and compared to published cadaveric values [2]. Predicted GH joint reaction forces were then compared to *in vivo* implant data [3], with detailed analysis presented for the representative patient S8R.

Results

Model-predicted moment arms of patient S8R showed strong agreement with established cadaveric datasets, capturing both magnitude and functional trends across elevation angles (Fig1C). Validation against the OrthoLoad implant demonstrated high correspondence between predicted and measured GH joint forces during weighted abduction (Fig1D). Model–implant agreement remained consistently close across the full task, with errors ranging from –104 to +68 N and an average absolute error of 53 N.

Discussion

This study provides robust validation of the upper-limb MSK model [1] through comparison with cadaveric moment arm data and *in vivo* implant data. The high agreement observed,

particularly the close replication of GH joint forces in S8R, supports the model's ability to accurately estimate shoulder muscle mechanics and joint loading in arthroplasty patients. These findings strengthen the model's translational potential for clinical evaluation, implant optimisation, and personalised rehabilitation planning. Future work will expand the validation to more patients and a broader range of shoulder tasks.

Images (Optional)

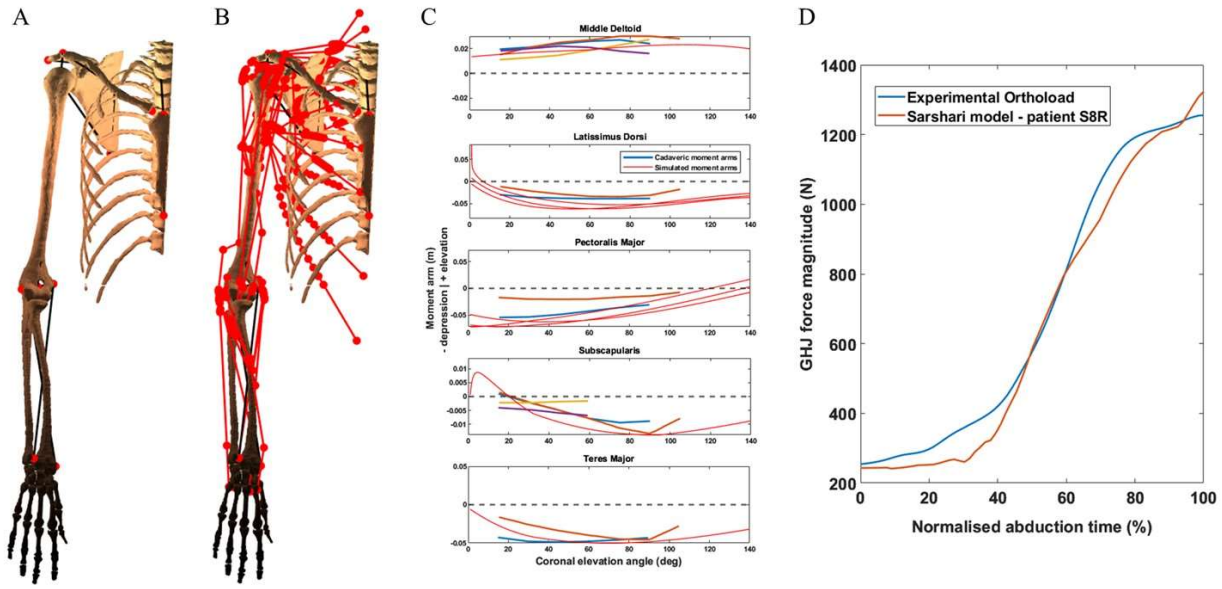


Figure 1: Sarshari upper-limb model without (A) and with muscles (B). C) Validation of model moment arms (red lines) against cadaveric moment arms from [2] (coloured lines) during an abduction task. D) Validation of the scaled model's glenohumeral joint (GHJ) force during a weighted abduction task against OrthoLoad instrumented implant data of patient S8R [3].

References (Optional)

[1] Sarshari et al., Scientific Reports, 2021

[2] Hik et al., J Anat, 2019

[3] Veeger et al., data.4tu.nl, 2023

Acknowledgements (Optional)

This work was supported by an Advance Queensland Industry Research Fellowship. ML and PP also acknowledge support from the Australian Research Council (IC190100020).

Session Category

Orthopaedic Biomechanics: Upper Extremities

P3-378

Capturing Wrist Kinematics Using Principal Component Analysis

Mr. Daniel McDermott Sc.B.[1], Dr. Nicola Sancisi Ph.D.[2], Dr. Michael Rainbow Ph.D.[3], Dr. Michele Conconi Ph.D.[2]

[1]Harvard Medical School, Boston, MA, United States. [2]University of Bologna, Bologna, BO, Italy. [3]Queen's University, Kingston, ON, Canada

Introduction

Principal component analysis (PCA) enables the compact description of the motion of a complex group of bones by intrinsically capturing the kinematic coupling introduced by fibrous tissues and articular contacts. The benefits of this approach have been recently demonstrated for the foot [1], where four motion synergies explained more than 95% of the total mobility. In this work, we test the same approach to represent wrist kinematics.

Methods

We used segmented CT scans of 9 wrists in 11 postures [2]. We defined a novel anatomical reference system (ARS) for each carpal bone in the neutral scan, using a morphological approach designed to optimize kinematic description by minimizing the cross-talk among motion components. Neutral bones were registered on all the other postures, expressing the bone's relative pose using a variation of the Grood and Suntay convention for the wrist. Like the foot [1], we performed PCA on the bone poses, searching for the minimum number of synergies that explain more than 90% of the total variability. We used correlation coefficients to test if synergies are constant within the population.

Results

Two synergies explained more than 91.9% of the total motion variability in all 9 subjects. The first synergy maps flexion and extension, and the second the radial-ulnar deviation (Fig. 1). Both synergies are highly correlated across wrists: 0.96 for the first synergy and 0.89 for the second synergy.

Discussion

Synergies allow a compact description of intrinsic kinematic coupling of carpal bone motion: PCA results suggest that the wrist can be considered as a 2-degree system, which aligns with the clinical perspective, to which all the bones participate at once. This information may help identify abnormal carpal bone motion in patients and support

treatment and device innovation to advance patient care, for instance by the definition of detailed musculoskeletal models of the wrist.

Images (Optional)

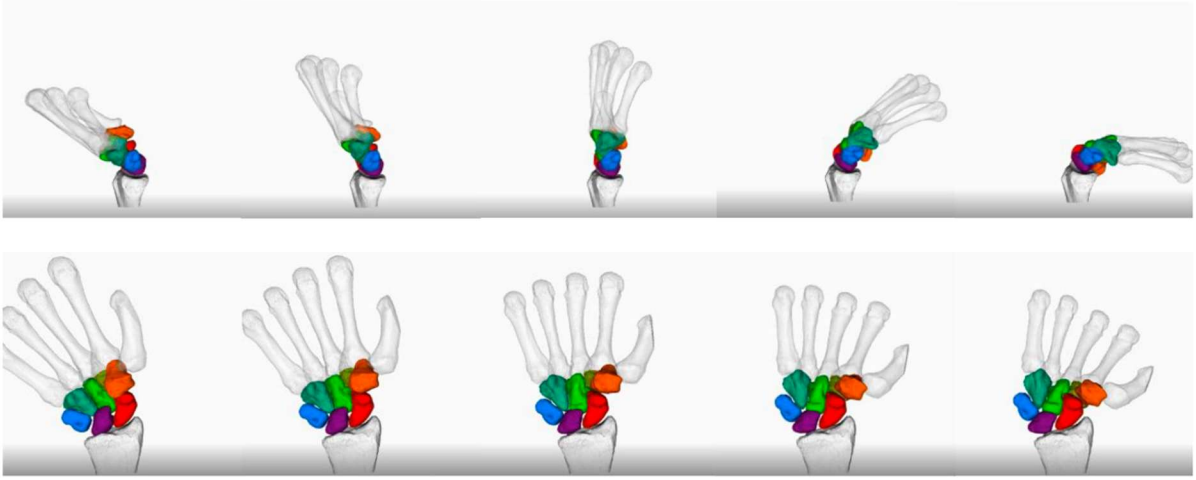


Figure 1: First synergy (top row) mapping flexion/extension and second synergy (bottom row) mapping radial/ulnar deviation.

References (Optional)

[1] Michele Conconi *et al.* , J Orthop Res, 2024

[2] Rainbow *et al.* , J Hand Surg Eur Vol, 2016

Session Category

Orthopaedic Biomechanics: Upper Extremities

P3-379

Reliability and Concurrent Validity of a Commercially Available Load Cell Dynamometer in Measuring Shoulder Rotational Torque and Rate of Torque Development

Lieutenant Commander Pollyanna Crane PT, DPT[1], Dr. Shawn Stout PT, DPT, DSc[1], Dr. Gregory Freisinger PhD[2], Dr. Jamie Morris PT, DPT, DSc[1], Dr. Will Pitt PT, DPT, PhD[3]

[1]Keller Army Community Hospital - Baylor University Division 1 Sports Physical Therapy Fellowship, West Point, NY, United States. [2]United States Military Academy, West Point, NY, United States. [3]University of Pittsburgh, Pittsburgh, PA, United States

Introduction

Shoulder rotational strength deficits are common in individuals with shoulder injuries or who have undergone shoulder surgery. Both strength and rate of force development (RFD) are important considerations when determining athletes' readiness to return to sport or activity. Manual muscle tests are commonly used in clinical practice, however only provide categorical strength ratings and demonstrate a ceiling effect in stronger individuals. Isokinetic dynamometers (IKD) are considered the gold standard in muscle testing, but are rare in clinics due to high costs. Hand-held dynamometers (HHD) are useful alternatives, but do not measure RFD. The Tindeq-Progressor (TP) (BLIMS, AS, Norway) is an inexpensive dynamometer that measures peak force and RFD. The TP has demonstrated accuracy and repeatability in measuring tension loading, and is superior to the HHD in assessing knee extension torque. Reliability and validity using the TP for shoulder rotational strength has not been assessed.

Methods

External (ER) and internal rotation (IR) neuromuscular function were assessed in 12 healthy participants (24 limbs) using the TP and IKD (HUMAC NORM, Stoughton, MA) in the seated position. Order of device testing and side tested were randomized. Three 2-second isometric warm-up repetitions were completed at 50%, 75% and 90% effort. This was followed by three 2-second maximal isometric contractions with 30-seconds of rest between repetitions. Participants were cued to push as hard and as fast as possible. Force and RFD were converted to torque and RTD to compare values with the IKD. Reliability and concurrent validity were assessed with intraclass correlation.

Results

The TP had excellent intra-rater reliability for all shoulder peak torque measures, and for ER RTD. The TP had poor to moderate intra-rater reliability for shoulder IR RTD. Agreement with

the gold standard was good to excellent for all peak torque measures. Concurrent validity for RTD was poor for all measures.

Discussion

The TP showed excellent reliability and validity for measuring shoulder rotational peak torque, indicating it may serve as a practical alternative to traditional strength assessments. RTD showed substantial variability between assessments, indicating the need for more controlled testing conditions to improve measurement accuracy.

Images (Optional)

Table 1:

Intraclass correlation for Tindeq Progressor intra-rater reliability

	Tindeq Peak Torque			Tindeq Rate of Torque Development		
	ICC (3,1)	(95% CI)	p-value	ICC (3,1)	(95% CI)	p-value
ER Right Shoulder	.979	(.949-.993)	<.001	.900	(.764-.967)	<.001
ER Left Shoulder	.964	(.905-.989)	<.001	.887	(.734-.963)	<.001
IR Right Shoulder	.943	(.852-.982)	<.001	.337	(-.016-.702)	.033
IR Left Shoulder	.954	(.869-.986)	<.001	.686	(.389-.884)	<.001

Intraclass correlation for Tindeq Progressor versus Humac comparison

	Peak Torque			Peak Rate of Torque Development		
	ICC (2,1)	(95% CI)	p-value	ICC (2,1)	(95% CI)	p-value
ER Right Shoulder	.880	(.637-.964)	<.001	.275	(-.328-.719)	.181
ER Left Shoulder	.782	(.404-.932)	<.001	.306	(-.298-.734)	.155
IR Right Shoulder	.890	(.655-.967)	<.001	.088	(-.490-.611)	.388
IR Left Shoulder	.839	(.533-.951)	<.001	.034	(-.529-.576)	.456

ER, external rotation. IR, internal rotation.

References (Optional)

Session Category

Orthopaedic Biomechanics: Upper Extremities

P3-380

Stemmed Pyrocarbon in Shoulder Hemiarthroplasty: Functional Outcomes and Complications Compared With CoCrMo Alloy—a Systematic Review and Meta-analysis

Dr. Renato Miyadahira MD[1], Mr. Robin Pelia[2], Dr. Marcos Amstalden Barros MD[3,1], Dr. Robin Pourzal PhD[3], Dr. Marcus A. Wimmer PhD[3], Dr. Grant E. Garrigues MD[3,4], Dr. Jonathan A. Gustafson PhD[3,1]

[1]Instituto Brasil de Tecnologias da Saúde (IBTS), Rio de Janeiro, RJ, Brazil. [2]University of Illinois Chicago (UIC), Chicago, IL, United States. [3]Rush University Medical Center, Chicago, IL, United States. [4]Midwest Orthopaedics at Rush, Chicago, IL, United States

Introduction

Conventional metal hemiarthroplasty is often complicated by painful glenoid erosion between cobalt–chromium–molybdenum (CoCrMo) alloys and cartilage. Pyrocarbon (PyC), with an elastic modulus closer to bone and favorable tribological properties, has been proposed as a bone-preserving alternative. The clinical performance of stemmed PyC implants, however, remains uncertain. We aimed to systematically review and meta-analyze the outcomes of stemmed PyC hemiarthroplasty, evaluating functional improvements compared with preoperative status and summarizing complications.

Methods

This review was registered with PROSPERO (CRD420251028801) and conducted following PRISMA guidelines. PubMed, Scopus, and Cochrane Library were searched on September/2023. Eligible studies included adult patients undergoing stemmed PyC hemiarthroplasty with ≥6 months follow-up, reporting range of motion (ROM), functional scores, complications, or revision causes. Random-effects models pooled pre to postoperative changes in ROM and Constant-Murley scores. Complications were summarized qualitatively. Risk of bias was assessed using the NIH Quality Assessment Tool.

Results

Twelve studies met inclusion criteria. Meta-analysis demonstrated significant postoperative improvements with stemmed PyC: active elevation +45.6° (95% CI 35.0–56.3), external rotation +18.0° (95% CI 11.3–24.7), internal rotation +9.0° (95% CI 0.4–17.6), and Constant-Murley score +42.8 points (95% CI 36.6–49.0) (all $p < 0.05$) (Table 1). Across

studies, gains ranged from +34.1° to +68.0° elevation, +5.5° to +27.0° external rotation, and +31.0 to +54.0 points Constant score. Heterogeneity was considerable for all outcomes (I^2=77–93%). Reported complications most frequently included rotator cuff insufficiency (n=10) and pain/overstuffing (n=8), followed by infection (n=4), humeral migration (n=2), glenoid erosion (n=1), and trauma (n=1).

Discussion

Stemmed PyC hemiarthroplasty provides clinically meaningful functional improvements compared with baseline, supporting its role as a bone-preserving option in younger, active patients. Nevertheless, high heterogeneity, small observational cohorts, and variable outcome definitions limit the certainty of these findings. While registry and in-vitro evidence suggest potential advantages over metal implants, consistent clinical superiority remains unproven. Stemmed PyC hemiarthroplasty improves range of motion and functional scores compared with preoperative status, with complications most often related to cuff insufficiency and implant sizing. High quality prospective studies with standardized outcome reporting and long term follow-up are required to clarify its comparative role against conventional metal implants.

Images (Optional)

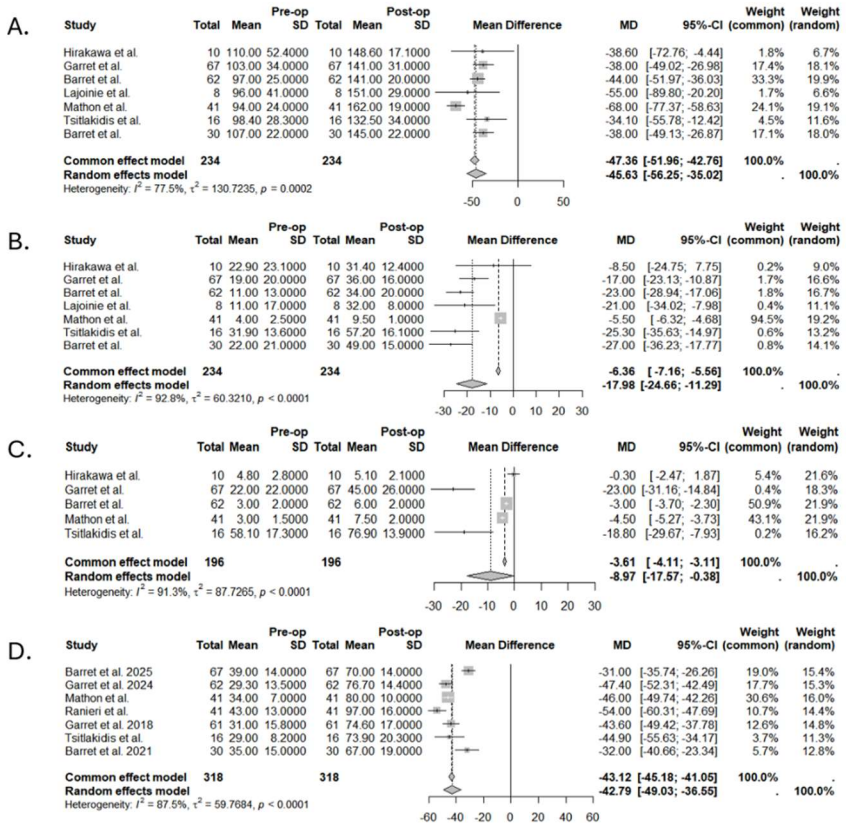


Figure 1A: Meta-analysis of Active Elevation across studies

Figure 1B: Meta-analysis of Active External Rotation across studies

Figure 1C: Meta-analysis of Active Internal Rotation across studies

Figure 1D: Meta-analysis of Constant-Murley improvement after pyrocarbon arthroplasty.

Session Category

Orthopaedic Biomechanics: Upper Extremities

P3-381

Validation of Upper Extremity Marker-Based and Markerless Motion Capture Models for Elbow Extension and Flexion

Miss Scarlett Farrar[1,2], Miss Farah Azim BASc[1], Ms Diane Wickenheiser BScPT[1], Ms Karen Davies MSc[1,3], Dr. Lise Leveille MD, PhD, FRCSC[1,4,5,6], Mr Jake Harris MOT[7], Ms Mami Okada BSc[4], Dr. Jeffrey Pike MD, MPH, MBA, FRCSC[4,5,6], Dr. Timothy Bhatnagar PhD[1,5,6]

[1]The Motion Lab, BC Children's Hospital, Vancouver, British Columbia, Canada. [2]School of Biomedical Engineering, Faculty of Applied Science, UBC, Vancouver, British Columbia, Canada. [3]Department of Physical Therapy, Faculty of Medicine, UBC, Vancouver, British Columbia, Canada. [4]Department of Orthopedics, BC Children's Hospital, Vancouver, British Columbia, Canada. [5]Research Institute, BC Children's Hospital, Vancouver, British Columbia, Canada. [6]Department of Orthopedics, Faculty of Medicine, UBC, Vancouver, British Columbia, Canada. [7]Outpatient Orthopedic Clinic, BC Children's Hospital, Vancouver, British Columbia, Canada

Introduction

The Motion Lab (TML), BC Children's Hospital performs gait analysis using motion capture (MoCap), focusing on lower extremities. As TML delves into upper extremity research, a suitable MoCap model is required. Pre-existing models require numerous markers [1], which can cause discomfort, hinder movements, and there may be insufficient space on a child's arm for all markers. Other models are complex, involving shoulder and trunk kinematics [2], which is beyond TML's interest in elbow range of motion (eROM). Comparison studies between marker-based and markerless MoCap for upper extremities are limited [3]. This project aims to compare simplified marker-based upper extremity models with markerless data for future research.

Methods

Retro-reflective markers are placed on anatomical landmarks on the arms. Participants performed elbow extension-flexion movements. Data was collected using Qualisys MoCap system (12 Oqus, 12 Miqus cameras). Two variations of marker models were explored: (1) markers were placed at three shoulder landmarks (anterior acromion (AA), posterior acromion (PA), Neviaser's Portal (NP)) to define the humeral vector; (2) two combinations of tracking markers were used to track the humerus ((a) one upper arm cluster, medial and lateral humeral epicondyles; (b) two upper arm clusters and lateral humeral epicondyle), resulting in six models. Markerless data was processed with Theia. All data was analysed using Visual3D. Each model's eROM was compared to clinical exam for validation.

Results

Participant 1 (female, 20y) had 0.0° extension and 145.0° flexion during clinical exam (Figure 1). At extension, Variation 2a's marker-based angles were 8.0° (AA), -1.0° (PA) and 4.0° (NP); variation 2b found 9.0° (AA), 0.0° (PA) and 5.0° (NP); markerless was 5.0°. At flexion, Variation 2a's marker-based angles were 141.0° (AA), 133.0° (PA) and 137.0° (NP); variation 2b found 148.0° (AA), 138.0° (PA) and 143.0° (NP); markerless was 155.0°.

Discussion

Compared to clinical eROM, PA and Variation 2a were the closest at flexion; NP and Variation 2b closest at extension. Markerless data presented flexion bias at both end ranges. Additional participant data is required for further analysis.

Images (Optional)

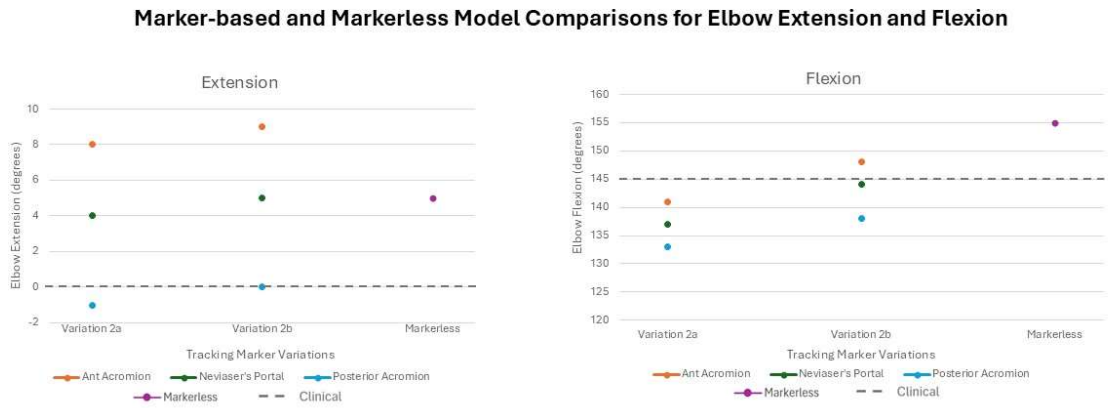


Figure 1 – Elbow extension and flexion using various marker-based models and markerless MoCap compared to clinical exam (grey dotted line). Combinations of each variation: shoulder markers (Anterior Acromion: orange, Navieser's Portal: green, Posterior Acromion: blue), markerless (purple) and tracking markers (Variations 2a and 2b). Positive/larger angles represent flexion and negative/smaller angles represent extension.

References (Optional)

[1] Laitenberger et al., Multibody Syst Dyn, 2015

[2] Rab et al., Gait and Posture, 2002

[3] Hansen et al., Biomedical Engineering Advances, 2024

Session Category

Orthopaedic Biomechanics: Upper Extremities

P3-382

Three-Dimensional Movement Variability is Not Associated with Fastball Accuracy in High School Baseball Pitchers

Ms. Tzu-Hsin Han, Mr. Yi-Hsuan Weng, Mr. Jiu-Jenq Lin

School and Graduate Institute of Physical Therapy, College of Medicine, National Taiwan University, Taipei, Taiwan, Taipei, Taipei, Taiwan

Introduction

Proprioception is crucial for coordinating the rapid, multiplanar motions required in baseball pitching. Pitchers often show altered shoulder position sense, impaired scapular control, and increased movement variability. These adaptations stem from conditions like glenohumeral internal rotation deficit. Proprioceptive deficits are linked to changes in muscle activation and pitching mechanics. However, it remains unclear if 3-Dimensional Movement Variability (3DMV) contributes to throwing accuracy. Given the accuracy's importance in both performance and injury prevention, this study examined the relationship between scapular/humeral 3DMV and fastball accuracy in high school pitchers.

Methods

One hundred and seven male high school players were recruited, with data from 68 players used for the final analysis. 3DMV was quantified as the trial-to-trial angular deviation of segmental kinematics. Variability was extracted at two key phases: 3DMVC (Cocking phase at maximum external rotation) and 3DMVA (Acceleration phase at ball release). Accuracy was determined using mediolateral (X-axis) and anteroposterior (Y-axis) absolute errors and constant errors in a controlled target task. Pearson correlations were used to test the associations between 3DMV and throwing accuracy.

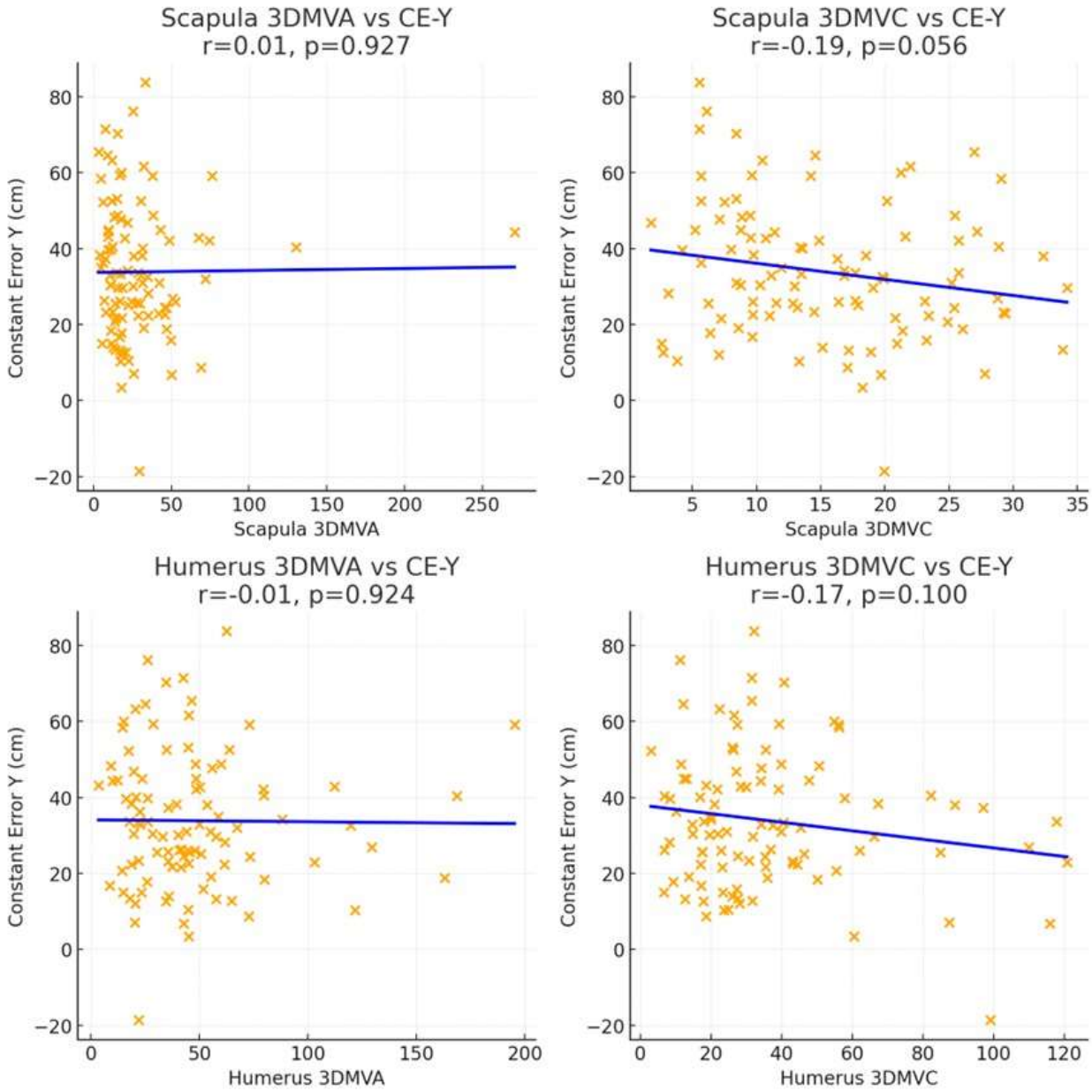
Results

Scapular 3DMVC and 3DMVA averaged 15.1 ± 8.1° and 27.4 ± 32.8°, respectively. Humeral values were 35.9 ± 24.5° and 45.1 ± 31.4°, respectively. Average accuracy errors were 32.5 ± 8.8 cm (absolute X), 42.6 ± 13.4 cm (absolute Y), 15.5 ± 17.9 cm (constant X), and 33.6 ± 17.9 cm (constant Y). Correlations between 3DMVC and throwing accuracy were small and non-significant ($r \leq 0.19$, all $p \geq 0.056$). The strongest observed trend was between scapular 3DMVC versus anteroposterior constant error ($r = -0.19$, $p = 0.056$), suggesting that lower variability might be associated with a greater directional bias.

Discussion

Proprioception-related 3-dimensional movement variability was not clearly associated with throwing accuracy in high school pitchers. Pitching accuracy is likely a more complex skill, potentially depending more on factors such as visual-motor integration, tactical execution, or whole-body kinetic-chain coordination. Therefore, a multifactorial approach is necessary for performance assessment and the design of pitching training strategies.

Images (Optional)



Session Category

P3-383

Three-Dimensional Shoulder Biokinetics and Passive Range of Motion in "Strong" Versus "Weak" Shoulders With Subacromial Pain Syndrome and Contralateral Healthy Shoulders

Dr. Renato Miyadahira MD[1], Dr Felipe F. Gonzalez MD, MSc[2,1], Dr. Eliane Guadagnin PhD[1], Dr. William Felipone MD[1], Dr. Matheus Vilela MD[1], Dr. Marcos Amstalden Barros MD[2,1], Dr. Carolline Popovicz Nunes MD[2,1], Dr. Tiago Zimerman MD[2,1], Dr. Vitor La Banca MD[1], Dr. Grant E. Garrigues MD[2,3], Dr. Gustavo Leporace MSc, PhD[1], Dr. Leonardo Metsavaht MD, PhD[1], Dr. Jonathan A. Gustafson PhD[2,1], Dr. Jorge Chahla MD, PhD[2,3]

[1]Instituto Brasil de Tecnologias da Saúde (IBTS), Rio de Janeiro, RJ, Brazil. [2]Rush University Medical Center, Chicago, IL, United States. [3]Midwest Orthopaedics at Rush, Chicago, IL, United States

Introduction

Subacromial pain syndrome (SAPS) is a prevalent cause of shoulder dysfunction, frequently associated with rotator cuff weakness and altered kinematics. While strength deficits are well documented, the interplay between weakness and movement adaptations remains unclear. Our objective was to verify the effects of shoulder strength (weak and strong) and pathology (affected and contralateral healthy shoulder), and their interaction on passive mobility and shoulder kinematics.

Methods

Thirty-eight patients (24 were male and 14 female, with a mean age of 42 ± 11.8 years) with unilateral SAPS underwent bilateral biokinetic assessment, including passive range of motion with a digital inclinometer, isometric rotator cuff strength with handheld dynamometry (external and internal shoulder rotators), and three-dimensional motion capture during shoulder elevation in the scapular plane. Shoulders were classified as weak or strong using median splits of strength values from external rotators. A two-way repeated-measures analysis of variance was applied to evaluate the effects of pathology (affected and healthy) and strength (weak and strong) on glenohumeral, scapular, and humerothoracic kinematics, with post hoc tests conducted where appropriate. Effect sizes and 95% confidence intervals (CI) were reported.

Results

There was a significant interaction between Strength and Pathology for scapulohumeral rhythm below 90° during the eccentric phase ($F = 4.36$, $P = 0.040$) (Table 1). Post hoc analysis showed that this interaction was driven by differences between the affected-strong and affected-weak groups, with a moderate effect size (Cohen's d = 0.687, 95% CI [0.03, 1.34]). No additional main effects or interactions were observed for shoulder kinematics or passive range of motion, indicating preserved passive mobility across groups.

Discussion

Shoulder weakness amplifies the kinematic alterations associated with SAPS, particularly during eccentric lowering below 90° of elevation, whereas passive motion remains unaffected. These findings indicate that SAPS associated with weakness primarily disrupts dynamic motor control rather than structural mobility, emphasizing the clinical relevance of targeted strengthening and eccentric training to restore normal scapulohumeral coordination. Identifying whether targeted external rotator strengthening in SAPS can optimize shoulder mechanics offers a promising direction for future rehabilitation strategies.

Images (Optional)

Table 1. Summary of two-way ANOVA results for the effects of Strength and Pathology on shoulder kinematics

Movement	Pathology				Strength				Pathology x Strength			
	F	**P**	**ηp^2**	**ω^2**	**F**	**P**	**ηp^2**	**ω^2**	**F**	**P**	**ηp^2**	**ω^2**
HumElev max	2.070	0.155	0.028	0.014	1.061	0.307	0.015	0.001	0.331	0.567	0.005	-0.009
Concentric Phase Below 90°												
GlenHumElev	1.472	0.229	0.020	0.006	3.531	0.064	0.047	0.032	0.245	0.622	0.003	-0.010
ScaUpRot	0.27123	0.604	0.004	-0.010	0.03631	0.849	0.001	-0.013	0.00492	0.944	0.000	-0.014
ScaTilt	0.6048	0.439	0.008	-0.005	2.5670	0.113	0.034	0.021	0.0796	0.779	0.001	-0.012
ScaExtRot	0.6915	0.408	0.010	-0.004	0.0690	0.794	0.001	-0.013	0.3953	0.532	0.005	-0.008
ScaVert	0.2677	0.606	0.004	-0.010	1.3670	0.246	0.019	0.005	0.0985	0.754	0.001	-0.012
SHR	0.1377	0.712	0.002	-0.012	0.5622	0.456	0.008	-0.006	0.0551	0.815	0.001	-0.013
Concentric Phase Above 90°												
GlenHumElev	2.3501	0.130	0.032	0.018	1.0321	0.313	0.014	0.000	0.0697	0.793	0.001	-0.012
ScaUpRot	3.5505	0.064	0.047	0.033	0.7667	0.384	0.011	-0.003	0.0224	0.882	0.000	-0.013
ScaTilt	0.0939	0.760	0.001	-0.012	1.1642	0.284	0.016	0.002	0.8110	0.371	0.011	-0.003
ScaExtRot	1.2579	0.266	0.017	0.003	0.0315	0.860	0.000	-0.013	0.2160	0.644	0.003	-0.011
ScaVert	0.0231	0.880	0.000	-0.013	3.2373	0.076	0.043	0.029	0.0891	0.766	0.001	-0.012
SHR	2.9689	0.089	0.040	0.026	1.1426	0.289	0.016	0.002	0.0825	0.775	0.001	-0.012
Excentric Phase Above 90°												
GlenHumElev	2.3501	0.130	0.032	0.018	1.0321	0.313	0.014	0.000	0.0697	0.793	0.001	-0.012
ScaUpRot	2.762	0.101	0.037	0.023	0.201	0.655	0.003	-0.010	0.447	0.506	0.006	-0.007
ScaTilt	0.365	0.548	0.005	-0.008	3.747	0.057	0.049	0.035	0.552	0.460	0.008	-0.006
ScaExtRot	0.4415	0.508	0.006	-0.008	0.6874	0.410	0.009	-0.004	0.0216	0.883	0.000	-0.013
ScaVert	0.0140	0.906	0.000	-0.013	1.3830	0.243	0.019	0.005	0.4856	0.488	0.007	-0.007
SHR	2.508	0.118	0.034	0.020	0.454	0.503	0.006	-0.007	0.361	0.550	0.005	-0.008
Excentric Phase Below 90°												
GlenHumElev	0.462	0.499	0.006	-0.007	0.128	0.722	0.002	-0.012	0.298	0.587	0.004	-0.010
ScaUpRot	0.00283	0.958	0.000	-0.013	0.80028	0.374	0.011	-0.003	3.18575	0.078	0.042	0.028
ScaTilt	1.1993	0.277	0.016	0.003	2.8929	0.093	0.039	0.025	0.0218	0.883	0.000	-0.013
ScaExtRot	0.00721	0.933	0.000	-0.013	0.99153	0.323	0.014	-0.000	0.00278	0.958	0.000	-0.013
ScaVert	0.0456	0.832	0.001	-0.013	0.1638	0.687	0.002	-0.011	0.0613	0.805	0.001	-0.013
SHR	0.00043	0.984	0.000	-0.013	0.814	0.370	0.011	-0.002	4.357	**0.040**	0.057	0.043

HumElev max = maximum humerothoracic elevation; GlenHumElev = glenohumeral elevation; ScaUpRot = scapular upward rotation; ScaTilt = scapular tilt; ScaExtRot = scapular external rotation; ScaVert = scapular vertical displacement; SHR = scapulohumeral rhythm (ScaUpRo/GlenHumElev). Concentric and eccentric phases refer to the raising and lowering phases of arm movement, respectively

Session Category

Orthopaedic Biomechanics: Upper Extremities

P3-384

Fascicle-Level Adaptation in SLAP Lesion Surgical Repairs

Dr. Wendy Murray PhD[1,2], Ms. Jorie Budzikowski MS[1,2]

[1]Northwestern University, Evanston, IL, United States. [2]Shirley Ryan AbilityLab, Chicago, IL, United States

Introduction

Superior labrum anterior to posterior (SLAP) lesion is an orthopaedic injury where the labrum and attached long head of the biceps tendon (LHBT) become detached from their glenoid origin. Three surgical repair options exist: (1) SLAP repair reattaches the labrum and LHBT to their glenoid origin, (2) tenotomy releases the LHBT and allows for distal retraction, and (3) tenodesis repair reattaches the tenotomized LHBT distally on the humerus. The rationale for choosing one intervention over another is debated; standardized functional assessment scores find few differences between interventions despite different patient reported outcomes for both satisfaction and return to activity [1]. Because biceps muscle-tendon geometry differs post-operatively, we hypothesize fascicle adaptation can differentiate surgical repair groups.

Methods

24 participants were enrolled (n=6 SLAP repair, n=6 tenotomy, n=8 tenodesis, and n=4 controls). EFOV-US images of the biceps were obtained, and fascicle lengths were measured in both arms using established methods [2]. We compared interlimb differences in fascicle length between the surgical and nonsurgical arms in participants with unilateral repairs and between dominant and nondominant arms in control participants.

Results

Our data suggest that surgical repair strategy influences chronic fascicle adaptation. Tenotomy exhibited the largest difference relative to the non-surgical limb (-18.2 +/- 4.3%). Fascicle lengths were also shorter (-10.1 +/- 3.7%) in the surgical limb for tenodesis, but less severely ($p < 0.003$). Interlimb differences in the SLAP repair (+4.5 +/- 5.0%) were not significantly different ($p = 0.982$) than controls (+4.5 +/- 7.1%).

Discussion

Surgical under-tensioning could be the impetus for shorter fascicle lengths observed in the tenotomy and tenodesis groups [3]. We observed larger interlimb differences in the control

group in this study than we observed in two previous studies where control participants did not participate in arm-dominant sports. Understanding fascicle adaptation and concomitant functional strength differences may help resolve debate about choice of surgical intervention. Our data also identifies fascicle adaptation associated with athletic activity as a potential confounding factor to be considered.

Images (Optional)

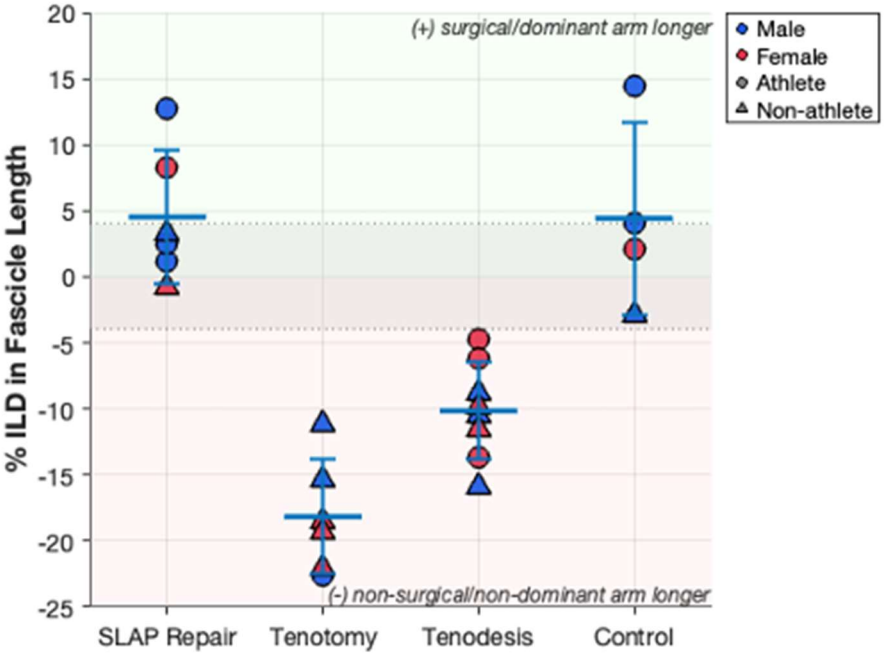


Figure 1: Interlimb difference in fascicle length. Circles indicate participants with a history of participation in unilateral, arm-dominant sports (e.g., baseball, softball, tennis, volleyball). Interlimb differences between ±4% fall within the resolution of our measurement methods [2].

References (Optional)

[1] Civan et al., J Orthop Surg (Hong Kong), 2021.

[2] Adkins et al., J Biomech, 2017.

[3] Budzikowski and Murray, SSRN, 2023.

Acknowledgements (Optional)

We would like to thank our participants and the collaborating orthoapedic surgeons. We acknowledge the ASB Grant in Aid Award, ISB Matching Dissertation Grant, and Northwestern University Alumnae Grant for their support of this study. We would also like to acknowledge the NSF GRFP (DGE-1842165), NIH TPMRI T32 (T32EB025766), and NIH F31 (1F31AR084860) fellowships which supported this work.

Session Category

Orthopaedic Biomechanics: Upper Extremities

P3-385

Total Deltoid Force Magnitude Alone Is Insufficient to Predict Physiological Shoulder Motion

MS. Woonhoe Goo, Prof. Namkeun Kim

Sogang University, Seoul, Kyeonggi-do, Korea, Republic of

Introduction

Current cadaveric shoulder biomechanics protocols often simplify deltoid loading by focusing solely on total force magnitude. However, the deltoid consists of distinct anterior, middle, and posterior heads that act with unique moment arms [1]. We hypothesized that the vector distribution of force among these heads is the primary determinant of kinematic trajectory rather than the scalar total force. This study demonstrates that ignoring physiological force ratios leads to significant kinematic divergence even under identical total force conditions.

Methods

We utilized a custom force-controlled shoulder simulator with human cadaveric specimens. The anterior, middle, and posterior deltoid tendons were independently actuated to isolate the effect of force distribution. We applied three force profiles while keeping the total force constant. These conditions included a balanced profile with equal pulling force across all, an anterior-dominant profile where the anterior head force was predominant, and a posterior-dominant profile where the posterior head force was predominant. Real-time tendon forces were measured using load cells, and glenohumeral abduction angles were recorded using inertial measurement unit sensors.

Results

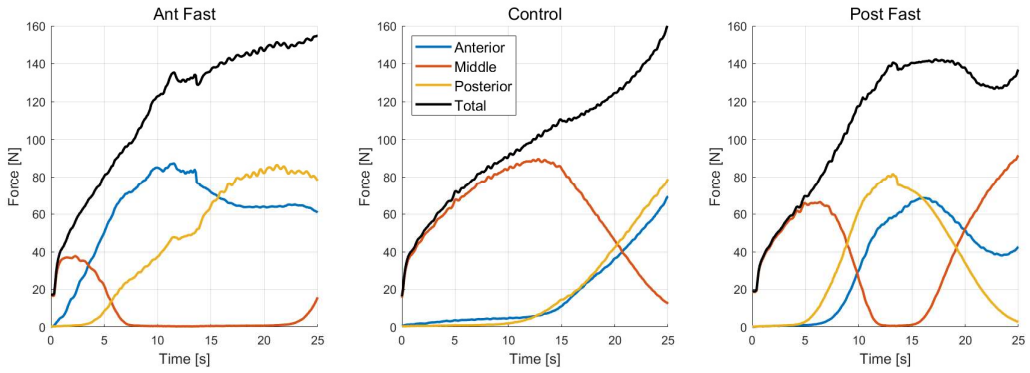
Despite comparable peak total forces across all three conditions, the resulting kinematics exhibited drastic divergence. The anterior-dominant condition caused significant deviation into the anterior plane and shifted away from the scapular plane. Conversely, the posterior-dominant condition led to significant external abduction. Only the balanced condition maintained a stable and physiological abduction trajectory. Analysis of total force versus abduction angle revealed distinct motion patterns and confirmed that identical total force magnitudes can produce opposing motions depending on the force ratio.

Discussion

These findings challenge the validity of using total deltoid force as an independent variable in cadaveric experiments. Mechanically, the deltoid acts as a vector sum, so neglecting the

physiological balance between the anterior and posterior heads generates erroneous kinematics. We conclude that force distribution ratio is the primary determinant of motion direction independent of force magnitude. Consequently, future cadaveric protocols must standardize target force ratios to ensure clinical relevance and the accurate reproduction of physiological shoulder kinematics.

Images (Optional)



References (Optional)

[1] Kuechle, David K., et al. "Shoulder muscle moment arms during horizontal flexion and elevation." *Journal of Shoulder and Elbow Surgery* 6.5 (1997): 429-439.

Acknowledgements (Optional)

This work has been supported by the National Research Foundation of Korea (NRF) grant funded by the Korea government (MSIT) (RS-2025-00563369)

Session Category

Orthopaedic Biomechanics: Upper Extremities

P4-001

Porcine Coronary Arteries as a Surrogate for Human Cerebral Arteries for Endovascular Device Testing

Ms. Bhavana Pulipaka[1,2,3], Dr. Caitríona Lally[1,2,4], Ms. Alyssa McCulloch[5], Dr. Jason Walkingshaw[3], Dr. Brooke Tornifoglio[1,2]

[1]Trinity Centre for Bioengineering, Trinity Biomedical Sciences Institute, Trinity College Dublin, Dublin, Dublin, Ireland. [2]Department of Mechanical and Manufacturing Engineering, School of Engineering, Trinity College Dublin, Dublin, Dublin, Ireland. [3]Stryker Neurovascular, Cork, Cork, Cork, Ireland. [4]Advanced Materials and Bioengineering Research (AMBER) Centre, Royal College of Surgeons in Ireland & Trinity College Dublin, Dublin, Dublin, Ireland. [5]Stryker Neurovascular, Research and Development, Fremont, California, United States

Introduction

Ischemic strokes, caused by cerebral vessel occlusions, account for 55–90% of global stroke cases [1]. Mechanical thrombectomy is the gold-standard treatment; however, its impact on vessel mechanics and function remains poorly understood. Age-related changes in cerebral arteries, including increased stiffness and reduced vasodilatory capacity, further influence post-thrombectomy vessel behaviour [2]. Mechanical irritation from stent retrievers or aspiration catheters can induce vasospasms: transient constrictions that may affect device performance [3]. Therefore, tissue models that replicate the microstructural, mechanical, and functional properties of human cerebral arteries are needed to improve device testing as existing models inadequately capture this complexity. This study investigates whether porcine coronary arteries can serve as surrogates by characterising their microstructural, mechanical and functional properties

Methods

Uniaxial ring tests were conducted on left porcine coronary arteries (N = 5; n > 8 rings/animal). Each vessel was sectioned into 3-mm rings from the proximal to the distal regions. Testing began with a 0.05 N preload followed by five preconditioning cycles (0–10% strain at 10 mm/min) and then the samples were loaded to failure. Stress–strain curves were generated, and the initial and final moduli were calculated from the first and last 10% strain intervals, respectively. Linear regression analysis in GraphPad was used to determine coefficients of determination (R^2) for both moduli. Histology of proximal and distal

segments were stained with H&E, Picrosirius Red, Alcian Blue, and Verhoeff's to evaluate microstructural differences.

Results

Mechanical testing revealed a gradient along vessel length: distal segments exhibited lower failure strains and increased stiffness, with higher initial and final moduli. Histology showed reduced wall thickness in distal segments, especially in the medial layer.

Discussion

hese findings support further evaluation of porcine coronary arteries as models for aged cerebral vessels. Future work will compare these properties with human cerebral vessels [4] and quantify vasoactivity, providing a physiologically relevant tissue model for device testing.

Images (Optional)

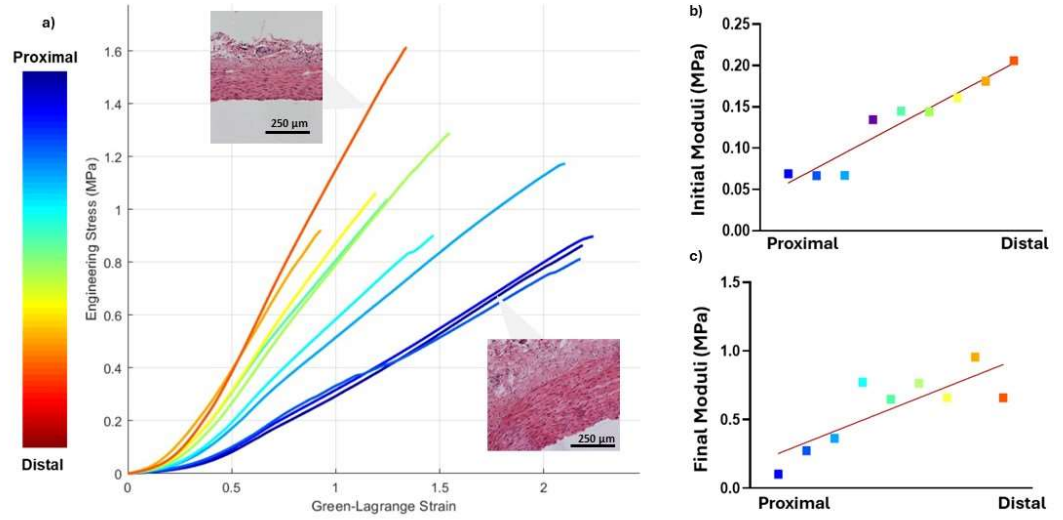


Figure 1: (a) Stress–strain curves of the left porcine coronary artery along its length. Representative H&E-stained images of the most proximal and distal segments are shown. (b) The initial (R^2 = 0.9190) and (c) final moduli (R^2 = 0.6581) along the vessel length are also presented (N = 1; n = 10).

References (Optional)

[1] Yannick Béjot et al., Presse Med, 2016

[2] Kathleen B. Miller et al., Front Aging Neurosci, 2019

[3] Jessica Jesser et al., Eur Stroke J, 2023

[4] Nele Demeersseman et al., SSRN, 2025 (Preprint)

Acknowledgements (Optional)

This project has received funding from the Irish Research Council (IRC) and Stryker Neurovascular under the Employment-based Postgraduate Programme.

Session Category

Cardiovascular/Cardiorespiratory Biomechanics: Materials and Devices

P4-002

Optimizing ultrashort-pulsed laser cutting of magnesium coronary stents for improved cut quality and mechanical performance

MSc João Cruz[1,2], MSc Diego Blunda[1,3], MSc Benedikt Bornschlegel[2], MSc Simon Pöstges[1], Dr.-Ing. Christian Rüdiger Hinke[2], Prof. Dr. rer. nat. Constantin Leon Häfner[2], Dr.-Ing. Alexander Kopp[1]

[1]Meotec GmbH, Aachen, Nordrhein-Westfalen, Germany. [2]Chair for Laser Technology (LLT), RWTH Aachen University, Aachen, Nordrhein-Westfalen, Germany. [3]School of Engineering and Institute for Health Discovery and Innovation, College of Science and Engineering, University of Galway, Galway, Galway, Ireland

MSc João Cruz

Introduction

Bioabsorbable magnesium (Mg) stents are a promising alternative to permanent implants, where mechanical performance is critical to maintaining vessel patency during early healing [1]. This performance is strongly influenced by the fabrication process, which affects geometry, corrosion, and material properties [2]. Ultrashort-pulse (USP) laser cutting offers the required precision but remains largely unexplored for Mg. This study establishes a systematic, mechanics-driven optimization framework for USP laser cutting of Mg alloy WE43MEO coronary stents, linking process parameters to cut quality and radial mechanical performance.

Methods

Experiments were performed on WE43MEO microtubes using femtosecond laser cutting and a two-step design of experiments. The first step used a fractional factorial screening design (n = 21) to evaluate six process parameters and identify main effects. The second step applied a Central Composite Design (n = 29) to model parameter interactions and enable process optimization. Both ring samples and stents were produced, with cut features assessed via laser-scanning microscopy and SEM. All stents were crimped, balloon-deployed, and radially compressed according to ASTM F3067-14.

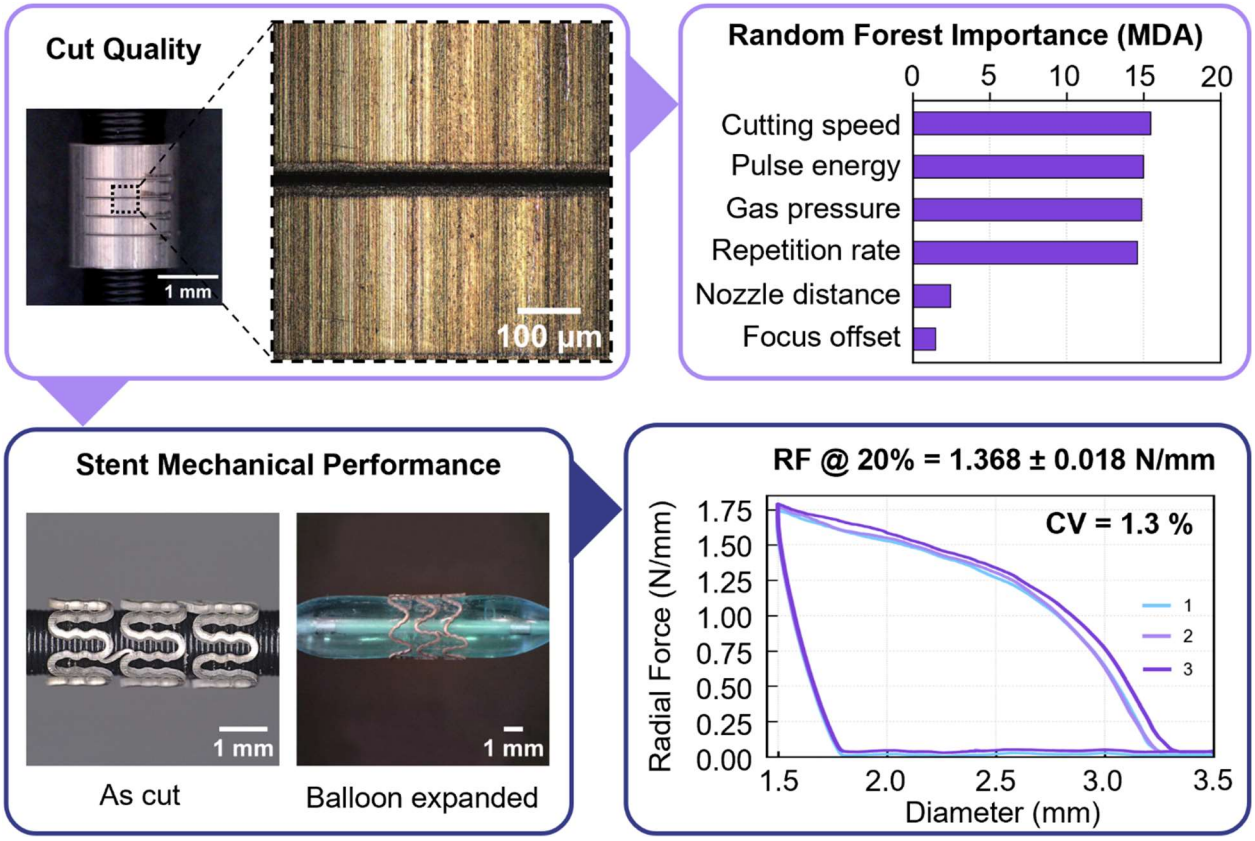
Results

Random-forest variable-importance analysis of cut quality outcomes, based on mean decrease in accuracy (MDA), identified pulse energy, cutting speed, repetition rate, and assist gas (argon) pressure as the dominant parameters (MDA = 14.6–15.5), whereas focus offset and nozzle distance showed minimal influence (MDA = 1.5–2.4). A central parameter set within the feasible window was selected to manufacture prototype stents (n = 3), which were successfully crimped, balloon-deployed, and radially compressed. Radial force curves showed a consistent behavior, with a mean radial strength at 20 % diameter reduction of 1.368 ± 0.018 N/mm and low variability (CV = 1.3 %).

Discussion

These results establish a clear pathway for linking laser processing parameters to cut quality outcomes and, ultimately, to the mechanical behavior of WE43MEO coronary stents. The strong separation between high- and low-influence parameters defines a focused region of interest, while the consistent radial performance from centrally selected settings confirms the mechanical relevance of this window. This foundation enables upcoming modeling to quantify parameter interactions and guide multi-objective optimization.

Images (Optional)



References (Optional)

[1] Bossard *et al*., Front. Cardiovasc. Med., 2022

[2] Korei *et al.,* Mater. Today Commun., 2022

Acknowledgements (Optional)

This project has received funding from the European Union's Horizon Europe research and innovation programme under Marie Sklodowska-Curie grant agreement ID No 101120006.

Session Category

Cardiovascular/Cardiorespiratory Biomechanics: Materials and Devices

P4-003

In-Silico Patient-Specific Model of Diastolic Filling Through a Mitral Valve Model With Transcatheter-Edge-to-Edge Repair

MSc Valérie Kulka[1], Dr. Natalie Simonian[2], Prof. Dr. Michael Sacks[2], Prof. Dr. Dominik Obrist[1]

[1]ARTORG Center, University of Bern, Bern, Bern, Switzerland. [2]James T. Willerson Center for Cardiovascular Modeling and Simulation, The Oden Institute for Computational Engineering and Sciences and the Department of Biomedical Engineering, The University of Texas at Austin, Austin, Texas, United States

Introduction

With mitral regurgitation (MR), blood flows pathologically back into the left atrium during systole, affecting approximately one in twelve people above the age of 75 [1]. Particularly for these potentially high-risk patients, transcatheter-edge-to-edge repair (TEER) offers a minimally invasive repair option.

The impact of TEER during diastolic filling of the left ventricle remains unclear, especially on the changed blood flow dynamics and the reduction in the open mitral valve area (MVA).

To address this question, we developed a patient-specific in-silico model with TEER to simulate the interaction between the valve tissue and blood flow during diastole, thereby gaining further insights.

Methods

We use a fluid-structure-interaction code [2] to couple blood flow and structural mechanics of the valve tissue.

The mitral valve (MV), segmented from an Echocardiogram and fitted with B-spline curves, is modelled using the Holzapfel-Gasser-Ogden material model. The MV is then attached to a plane, separating the fluid domain into the left atrium and the left ventricle. An expanding left ventricle simulates the diastole. For the TEER, the two leaflets of the MV are brought together (“clipped”) before the simulation of the diastolic phase. Five different MV geometries and four different clip positions are tested.

Results

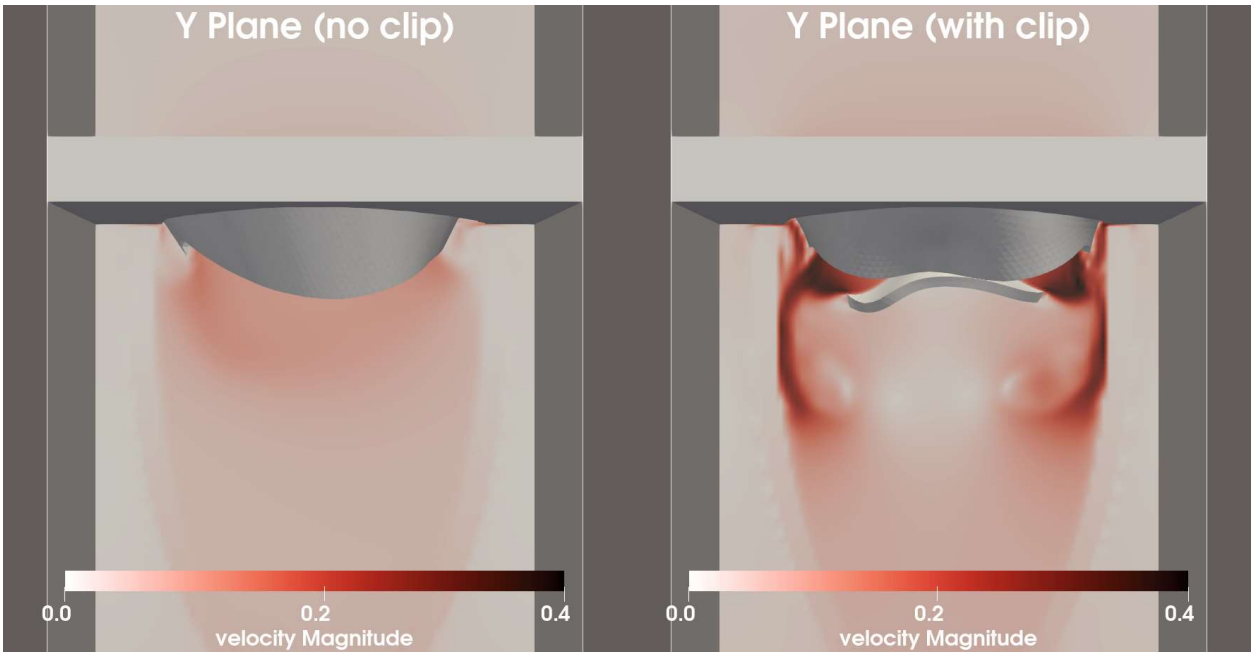
Measurement of the MV opening area (MVA) and of the pressure drop across the clipped MV shows how different TEER positions affect the MV function. Furthermore, we study how

the turbulence characteristics of the filling jet change before and after TEER. This enables us to determine specific MV characteristics, before and after clipping.

Discussion

With the patient-specific fluid-structure-interaction model, changes in the MV function due to TEER can be characterized. We can examine how the clip position is changing the MVA and fluid dynamics during diastole. Comparison of different simulations provides a causal relationship between clipping position and MV function for every individual MV. Despite the small sample size, this study may provide some initial insights that can potentially guide future TEER interventions.

Images (Optional)



References (Optional)

1. Cahill et al., Heart, 2021.
2. Nestola et al., Journal of Computational Physics, 2019.

Acknowledgements (Optional)

This work was supported by the Platform for Advanced Scientific Computing (PASC) project "MitrAccel" and received computational resources from CSCS through project sm84.

Session Category

Cardiovascular/Cardiorespiratory Biomechanics: Materials and Devices

P4-004

Intraventricular Hemodynamics under Impella implantation: effect of placement, power setting and pre and after load. An in vitro experimental study using Particle Image Velocimetry

Dr Fanette Chassagne[1], Dr. Claudio Bravo[2], Ms Jennifer Beckman[3], Dr Claudius Mahr[4], Dr Alberto Aliseda[3]

[1]Ecole de Mines, Saint Etienne, Rhone-Alpes, France. [2]UCSF, San Francisco, CA, United States. [3]University of Washington, Seattle, WA, United States. [4]Medical City Hospital System, Dallas, TX, United States

Introduction

Mechanical circulatory support is an effective therapy for heart failure, including for acute cardiogenic shock. Impella is a novel catheter-based ventricular assist device that has emerged as a clinically-preferred therapy, from hours to weeks. There is, however, a strong need to understand intraventricular hemodynamics under Impella support. Specifically, very little is known about how Impella positioning and operating conditions affect intraventricular hemodynamics.

Methods

We placed Impella through the ascending aorta into a silicone flow phantom created from segmented medical imaging of a patient's left ventricle (LV). This was connected to a flow loop where a reservoir and pulsatile pump can modify intraventricular pressure, mimicking residual native contractility. High resolution, time-resolved stereoscopic Particle Image Velocimetry provides the three components of the velocity in a coronal plane that cuts the ventricle including the mitral valve and the aortic valve annuli.

Results

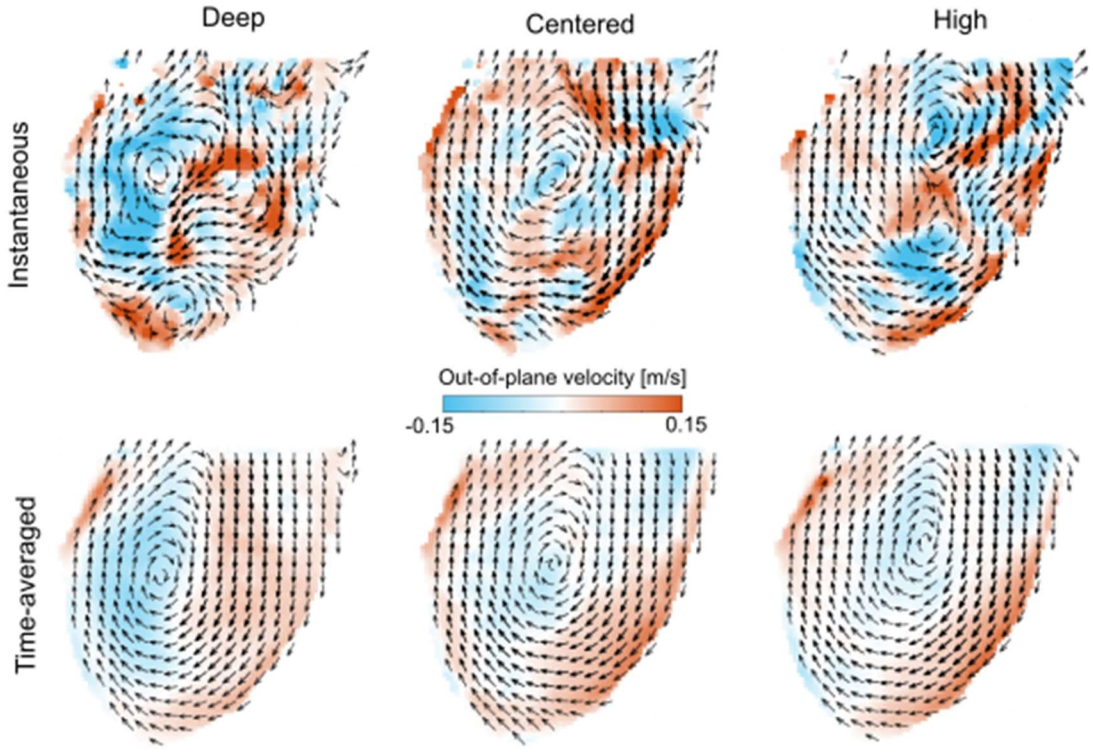
Ultrasonic flow rate measurements show the inaccuracy of the Impella-reported output and pressures. Impella output depends strongly on power, with a 35% increase between the two cases tested. Intraventricular hemodynamics under Impella support shows a strong dependency on pump placement and power setting on the mitral vortex formation and propagation. This modification of the filling vortex and its propagation inside the ventricle towards the ventricular apex has a marked influence on residence time of blood near the apex, a common site of thrombus formation in ventricles under Mechanical

Circulatory Support. Likewise, the placement of Impella at different distances from the Left Ventricle Outflow Tract influences flow near the LVOT exiting the Left Ventricle via the Impella, as opposed to via the opening aortic valve.

Discussion

Impella-induced hemodynamics creates recirculation in the LVOT, under the non-opening valve, and this can lead to thrombus formation intraventricle. Native contractility of the failing Left Ventricle results in increased pre-load, which contributes significantly to pump output and intraventricular flow circulation, with reduced residence times, at a given pump power setting. Quantitative metrics such as ventricular circulation and Ventricular Stagnation Index are provided as means to quantify placement and power dependency, suporting development of better guidelines for Impella placement and power setting personalized for each patient's anatomy and support needs.

Images (Optional)



References (Optional)

Acknowledgements (Optional)

F.C. acknowledges support from the International Federation for Artificial Organs, the American Heart Association and the Société de Biomécanique.

Session Category

Cardiovascular/Cardiorespiratory Biomechanics: Materials and Devices

P4-005

Mechanical Characterization of Retrieved Cerebral Thrombi Reveals Occlusion Site–Dependent Stiffness Influencing Endovascular Thrombectomy Success

Mr. Luca Bontempi[1,2], Ms. Janneke Cruts[1], Dr. Rachel Cahalane[1,3], Dr. Nikki Boodt[1], Dr. Daniel Bos[1], Dr. Behrooz Fereidoonnezhad[2], Mr. Pieter Jan van Doormaal[1], Prof. Aad van der Lugt[1], Prof. Diederik Dippel[1], Prof. Frank Gijsen[1,2]

[1]Erasmus MC, University Medical Center, Rotterdam, South Holland, Netherlands. [2]Delft University of Technology, Delft, South Holland, Netherlands. [3]University of Limerick, Limerick, Limerick, Ireland

Introduction

Endovascular thrombectomy (EVT) is the standard treatment for acute ischemic stroke (AIS), yet nearly 40% of patients fail to achieve complete revascularization on the first EVT attempt. Differences in the mechanical properties of cerebral thrombi may underlie these variations in procedural efficacy. [1] This study aimed to characterize AIS thrombus stiffness, identify its clinical and histological determinants, and assess its influence on EVT success.

Methods

Thrombi retrieved during EVT from 73 patients were sectioned for mechanical testing and prepared for histology within six hours. Unconfined quasi-static compression tests were performed using a custom-made compression tester to determine bulk stiffness (low-strain secant modulus). [2] A total of 346 thrombus sections (median number per patient = 6.5, IQR = 4–11) were compressed to 80% strain for 20 cycles, at a strain rate of 10%. Histological composition was quantified using Martius-Scarlett-Blue staining and $CD42b^+$ immunostaining for RBCs and platelets, respectively. Linear mixed-effects regression (LMR) identified predictors of stiffness, while generalized LMR evaluated associations with first-pass EVT success (eTICI≥2b), accounting for age, sex, occlusion site, and first-pass EVT technique (stent retriever only or combination with aspiration catheters).

Results

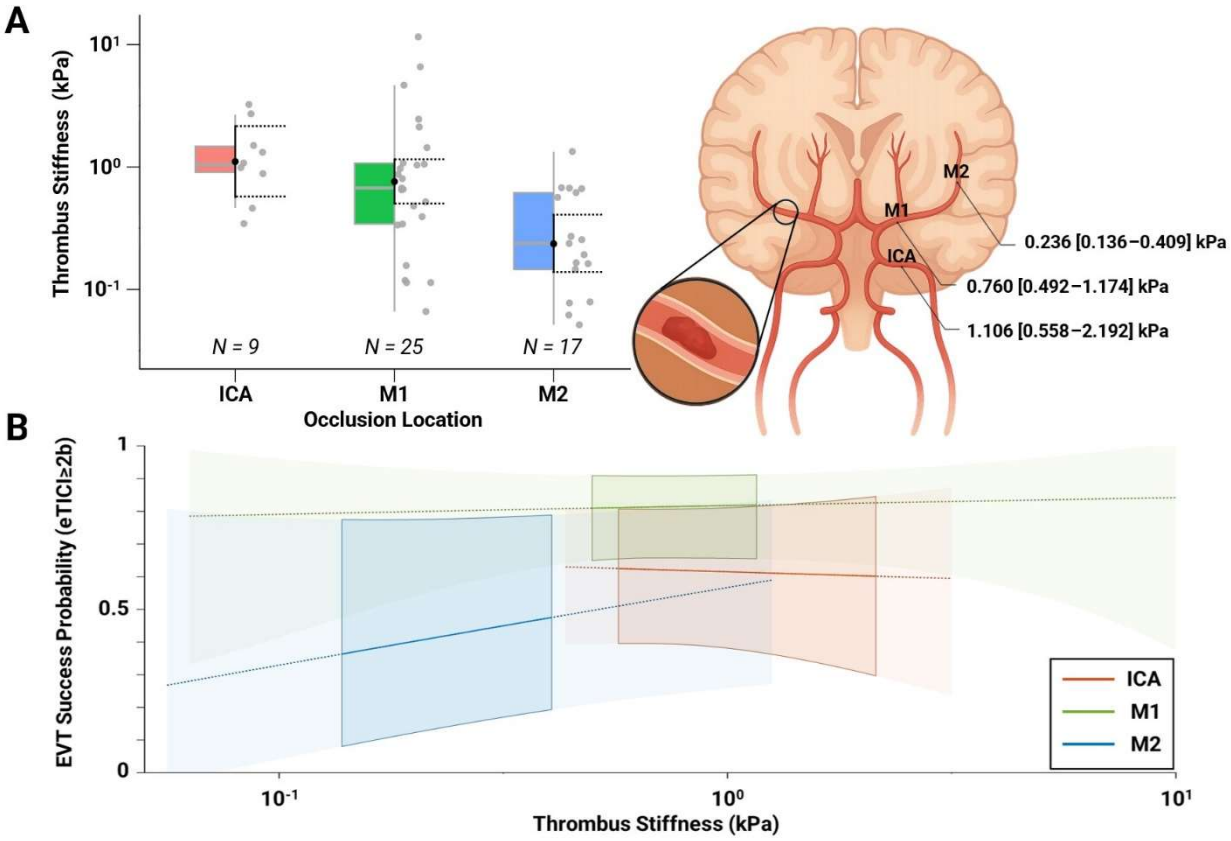
Thrombus stiffness decreased with more distal occlusions: internal carotid artery (ICA) 1.106 kPa (95% CI, 0.558–2.192), M1 segment 0.760 kPa (95% CI, 0.492–1.174) and M2 segment 0.236 kPa (95% CI, 0.136–0.409) of the middle cerebral artery (Fig. 1A). Multivariable analysis confirmed these differences were independent of thrombus composition and patient factors, with occlusion location explaining 14.3% (95% CI, 0.2–34.8) of thrombus stiffness variance. The probability of first-pass EVT success reflected

occlusion site-dependent thrombus stiffness (Fig. 1B): M1 thrombi showed consistently high first-pass success rates, while stiffer ICA thrombi and softer M2 thrombi had lower success probabilities, reflecting distinct mechanical thrombus-device interaction challenges during EVT.

Discussion

Distal thrombi are significantly softer than proximal ones, qualifying occlusion site as a clinical surrogate for thrombus stiffness. The relationship between stiffness and recanalization success varies by occlusion site, underscoring the need for stiffness-specific EVT techniques and device designs.

Images (Optional)



References (Optional)

[1] N. Boodt *et al.*, *Stroke*, 2021

[2] R.M.E. Cahalane *et al.*, *Ann Biomed Eng*, 2023

Acknowledgements (Optional)

LB, BF, and FG are supported by GEMINI, funded by the European Union’s Horizon Europe research and innovation programme under grant agreement No. 101136438.

Session Category

Cardiovascular/Cardiorespiratory Biomechanics: Materials and Devices

P4-006

Planning Acute Ischemic Stroke Treatment With Combined High-Fidelity Knowledge-Driven Modelling and Machine Learning

Dr. Sara Bridio[1,2], Prof. Giulia Luraghi[2], Dr. Virginia Fregona[2], Prof. Francesco Migliavacca[2,3], Prof. David González[4], Prof. Pedro Díez[5,6], Prof. Alberto García-González[5], Prof. Jose Felix Rodriguez Matas[2]

[1]European Commission, Joint Research Centre (JRC), Ispra, Lombardia, Italy. [2]Department of Chemistry, Materials and Chemical Engineering "Giulio Natta", Politecnico di Milano, Milano, Lombardia, Italy. [3]Fondazione IRCCS Cà Granda Ospedale Maggiore Policlinico, Milano, Lombardia, Italy. [4]Aragon Institute of Engineering Research, Universidad de Zaragoza, Zaragoza, Aragon, Spain. [5]Laboratori de Càlcul Numèric, E.T.S. de Ingeniería de Caminos, Universitat Politècnica de Catalunya-BarcelonaTech, Barcelona, Catalonia, Spain. [6]International Center for Numerical Methods in Engineering, CIMNE, Barcelona, Catalonia, Spain

Introduction

Endovascular thrombectomy (EVT) is the primary treatment for acute ischemic stroke, which involves using a stent-retriever to remove the blood clot from a cerebral artery. This procedure must be performed rapidly, leaving limited time for pre-procedural planning. While patient-specific high-fidelity computational simulations can predict EVT outcomes [1,2], they are computationally intensive and time-consuming. To address this challenge, this study proposes a machine learning-based classification model, trained on high-fidelity knowledge-driven EVT simulations, that can rapidly predict the probability of a successful procedure.

Methods

Cerebrovascular anatomies from 94 stroke patients were reconstructed from medical images and used to run finite-element simulations of the EVT procedure, as described in [1]. Results showed 81 successful (clot removed) and 13 unsuccessful outcomes (clot not removed) (Fig.1A). These simulation results were used to train a classification model, built with a two-step approach. Firstly, a dimensionality-reduction technique was applied to condense the complex vascular anatomies into a limited number of parameters (Fig.1B). Secondly, a kernel-function was trained using a restricted semidefinite-positive optimisation method, which considered the anatomy and clot properties of each virtual patient. The optimised kernel-function groups patients into clusters based on EVT success.

The resulting model can then classify data from new patients, providing an estimate of the likelihood of success of an EVT intervention.

Results

Results of the classification were evaluated using 70% of the samples for training the model and 30% for testing, and a 10-fold cross-validation was performed by changing the testing group at each iteration. Training samples were correctly clustered at each iteration (Fig.1C). The average rate of correct predictions of testing samples was 83%, with 10%false-negatives and 7%false-positives rates.

Discussion

The kernel-optimisation approach used to train the classification model appears promising, as it effectively clustered cases based on EVT outcomes and yielded good results when classifying test samples. However, the model proved weak in classifying samples with unsuccessful outcome, likely because this group is underrepresented in the training dataset. This limitation highlights the need for a significantly larger dataset of high-fidelity simulations to improve the model's performance, particularly in capturing the complex physical mechanisms underlying EVT procedures.

Images (Optional)

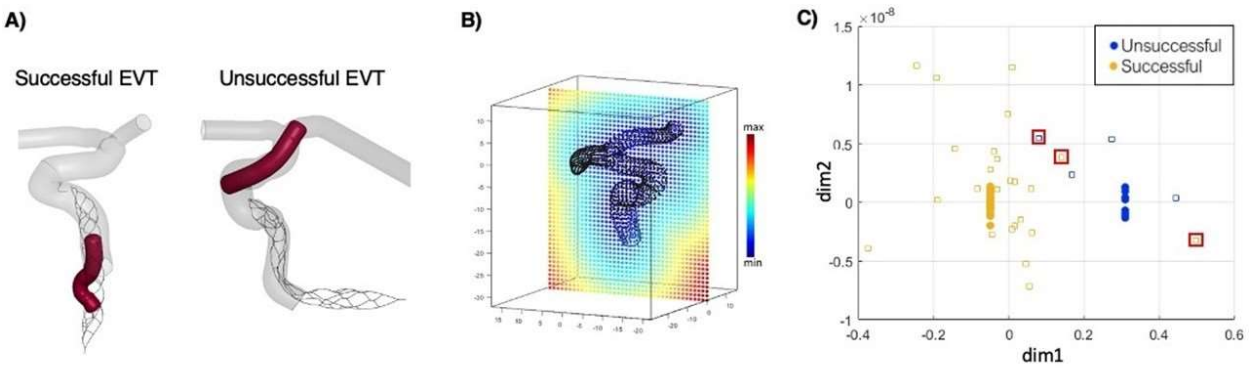


Figure 1. A) Examples of virtual patients with successful and unsuccessful EVT outcome. B) Parametrization of vascular anatomy. C) Clusterisation of training samples (yellow and blue dots) and projections of test samples (yellow and blue squares); the red squares indicate misclassified samples.

References (Optional)

[1] Luraghi,Bridio,et-al,J.Biomechanics,2021-126:110622

[2] Luraghi,Bridio,et-al,J.Biomechanics,2021-126:110631

Acknowledgements (Optional)

This project received funding from the European Union's Horizon Europe research and innovation programme under the grant agreement No:101136438.

Session Category

Cardiovascular/Cardiorespiratory Biomechanics: Materials and Devices

P4-007

Influence of Blade Flexibility on LVAD Hydrodynamic Performance & Hemocompatibility

Ms Shweta Karnik[1], Dr. Maryam Bagheri[1], Ms Shobana Santhanam[1], Dr. Huang Chen[2], Dr. Lakshmi Prasad Dasi[1]

[1]Georgia Institute of Technology, Atlanta, GA, United States. [2]University of Las Vegas, Las Vegas, NV, United States

Introduction

Left ventricular assist devices (LVADs) are widely used in patients with end-stage heart failure as both destination therapy and bridge-to-transplant support. To match LVAD output with a patient's native cardiac output, pump speeds are frequently adjusted, which can adversely affect device hemocompatibility and long-term durability.

To overcome these limitations, we have developed a novel LVAD prototype incorporating flexible rotor blades. We hypothesize that the mechanoresponsive behavior of these blades will allow them to deform in response to complex, time-varying inflow conditions. With optimized geometry and flexural properties, this design is expected to enhance hemocompatibility while expanding the operational range over which the pump maintains high efficiency. In this study, we evaluate the hemocompatibility and hydrodynamic performance of flexible rotor blades in a centrifugal LVAD under adult physiological conditions (5 L/min, 90 mmHg).

Methods

A preliminary rotor prototype was developed, with the rigid rotor fabricated from acrylic and the flexible blades cast from polyurethane. Hydrodynamic performance was characterized in a benchtop flow loop using a 40% glycerin–water mixture, where pressure–flow behavior and efficiency were measured under adult physiological operating conditions.

High-speed 2D particle image velocimetry with fluorescent particles was used to visualize flow fields, enabling identification of stagnation zones and regions of elevated shear stress. Hemocompatibility was assessed using a recirculating blood loop.

Results

Flexible and rigid blades achieved comparable pressure–flow performance, but the flexible blades exhibited higher hydraulic efficiency.

Discussion

Initial results support our hypothesis, indicating promising performance of the flexible rotor blades.

Acknowledgements (Optional)

Research supported by DoD CDMRP PR221487

Session Category

Cardiovascular/Cardiorespiratory Biomechanics: Materials and Devices

P4-008

On the Use of Nonlinear Elastic Membrane Analysis for Estimating Abdominal Aortic Aneurysm Wall Stress

Graduate research student Simon Rios Deossa[1], Master Vivian Reyna[1], MD Satish C. Muluk[2], PhD Ender Finol[1]

[1]UT San Antonio, San Antonio, Texas, United States. [2]ANH, Pittsburgh, Pennsylvania, United States

Introduction

Abdominal aortic aneurysm (AAA) is a dilatation of the infrarenal aorta, usually detected incidentally. Elective repair is guided by sex-specific maximum diameter thresholds (≥ 5.0 cm women, ≥ 5.5 cm men), which may not be sufficient to assess individual rupture risk. As wall stress is a direct biomechanical driver of failure, we evaluated the use of nonlinear elastic membrane analysis (NEMA) as an alternative to finite element analysis (FEA) for wall biomechanics.

Methods

Contrast-enhanced abdominal computed tomography (CT) scans from 16 AAA patients were used to identify the wall boundaries and build patient-specific wall and intraluminal thrombus (ILT) volume meshes with a uniform wall thickness (1.5 mm). FEA models used mean arterial pressure and six combined wall and two ILT constitutive material laws, yielding 420 simulations. The corresponding wall surface meshes were used for NEMA to compute first principal wall stress distributions and the 99th percentile wall stress (99thWS) for direct comparison with FEA.

Results

For all AAAs, NEMA yielded 99thWS estimates that were generally similar to their FEA counterparts, with notable discrepancies in two cases. The relative difference in 99thWS between NEMA and FEA was 15%-45% for all constitutive material combinations. The radar plot shows good agreement between NEMA and FEA in the distribution of 99thWS across the AAA cohort, with both methods highlighting the same aneurysms as having elevated peak wall stress, although FEA tended to predict slightly higher stresses in regions of significant asymmetry. Overall, a thin-membrane formulation, such as that used for NEMA, approximated FEA-based 99thWS reasonably while substantially reducing complexity.

Discussion

NEMA assumes the AAA wall is a thin membrane, neglects bending stresses and stress gradients through the wall, and operates directly on the deformed, pressurized CT-derived geometry. It does not require estimating patient-specific constitutive material properties or deriving an unloaded reference state. This shortens the setup and solution time compared to FEA, while supporting potential clinical translation. However, membrane-based assumptions may underrepresent the local mechanics in highly tortuous or thick-walled regions. Since true wall stress is unknown *in vivo*, broader benchmarking against high-fidelity models and clinical outcomes is needed before NEMA can be used for routine rupture risk assessment.

Images (Optional)

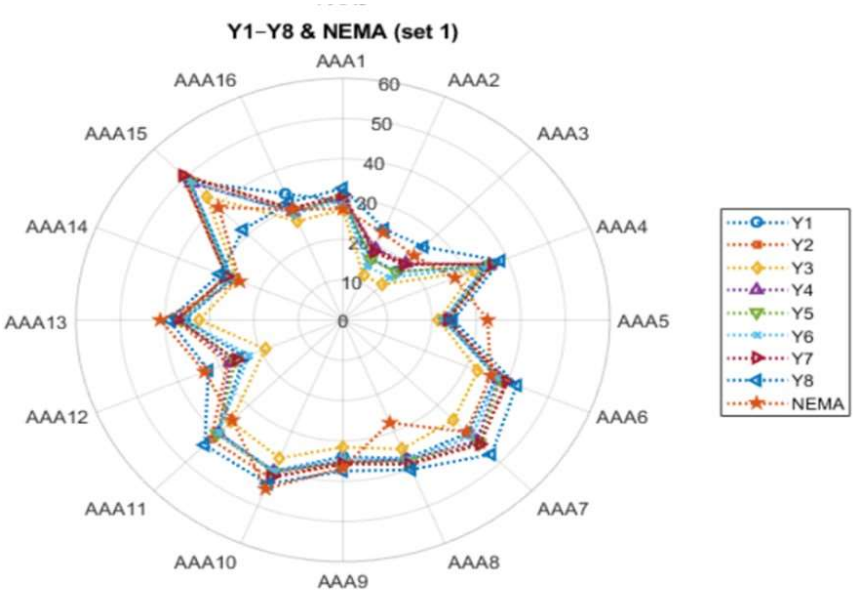


Figure 1. Radar plot of 99thWS across 16 AAAs for eight FEA material formulations (Y1–Y8) compared with NEMA, demonstrating consistent AAA-dependent stress patterns.

Acknowledgements (Optional)

NIH #1R01HL159300 funded this work.

Session Category

Cardiovascular/Cardiorespiratory Biomechanics: Materials and Devices

P4-009

In Vitro Hemodynamics of a Bio-Inspired Polymeric TAVR with 3D-Shaped Leaflets

Ms Srujana Joshi BS, Ms. Kenia Zuniga-Gallegos BS, Dr. Lakshmi Prasad Dasi PhD

Georgia Institute of Technology, Atlanta, Georgia, United States

Introduction

Although transcatheter aortic valve replacement (TAVR) is widely used to treat aortic stenosis in older patients, current commercial devices still face major clinical challenges. Bioprosthetic leaflets are prone to calcification and thrombosis, leading to reinterventions and limiting their use in younger patients. Their reliance on animal-farming and labor-intensive hand-sewing also increases production costs. Thus, there is a clear need for a durable, biocompatible, and easy-to-manufacture leaflet material that addresses both performance and production limitations. This study investigates the hemodynamic performance of 3D shaped leaflets made from a novel bio-inspired polymer composed of an interpenetrating network of hyaluronan (HA) – a naturally occurring biomolecule with anti-thrombotic and anti-calcific properties – and linear low-density polyethylene (LLDPE), a polymer known for high tensile and tear strengths and excellent durability.

Methods

A 26mm outer diameter LLDPE leaflets were manufactured through vacuum thermoforming (Figure 1A) to produce 3D shaped leaflets, then assembled onto a balloon expandable stent frame (Figure 1B). The prototype was mounted in an idealized aortic chamber connected to an in vitro left heart simulator to test under physiological aortic conditions (120/80 mmHg, 5 L/min cardiac output). A 60/40 water/glycerin mixture was used as a blood analog. Bulk hemodynamic performance metrics, mainly mean pressure gradient and effective orifice area were evaluated. Additionally, particle image velocimetry (PIV) data was performed to characterize downstream flow. All measurements were repeated using a 26mm SAPIEN 3 for comparison.

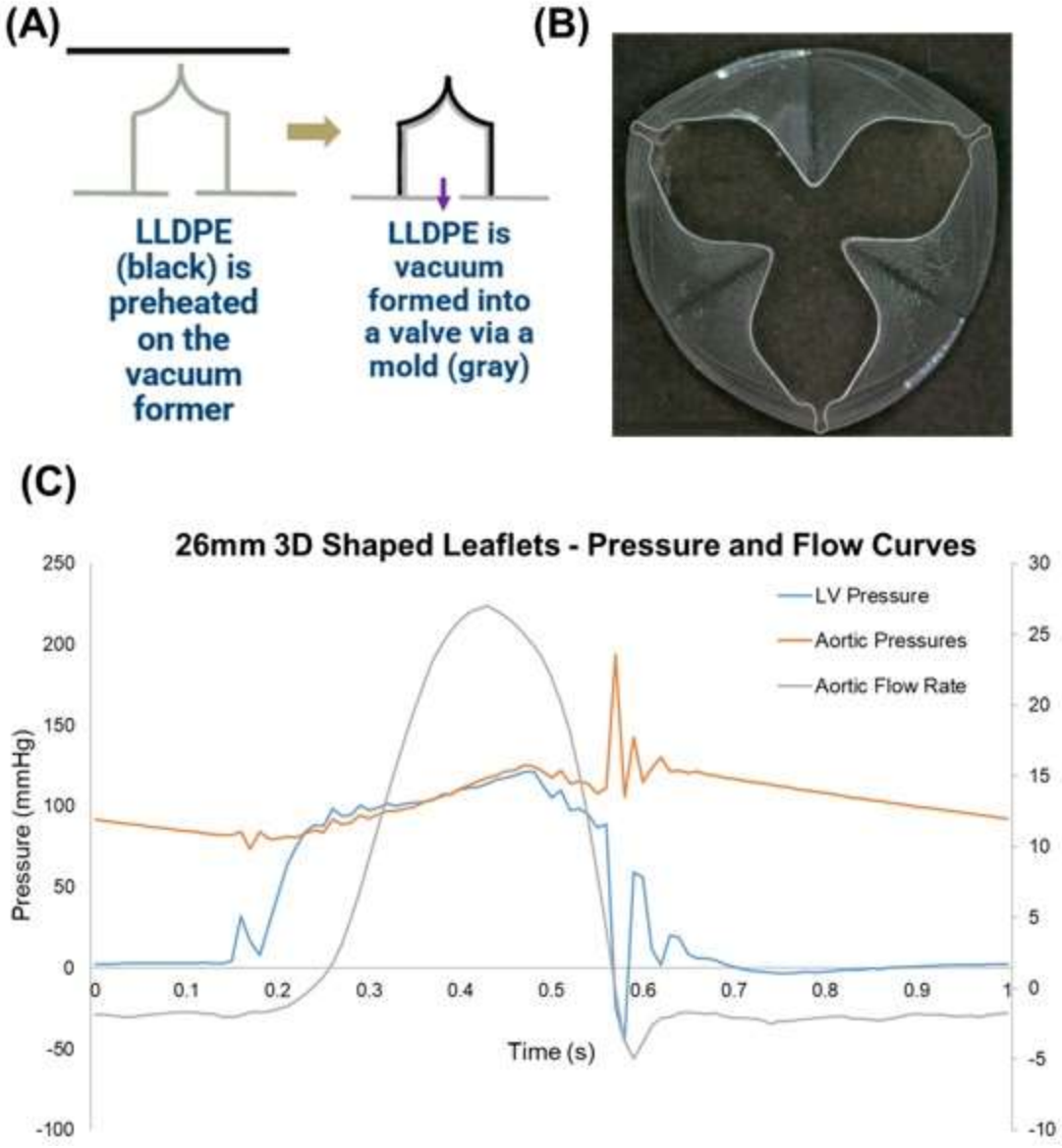
Results

The 3D-shaped polymeric leaflets demonstrated favorable hemodynamics, with a mean pressure gradient of 3.62 mmHg and an effective orifice area of 2.02 cm^2, compared with 4.93 mmHg and 2.23 cm^2 for the SAPIEN 3. At peak systole, the polymeric TAVR exhibited a lower peak velocity (1.63 m/s) than the SAPIEN 3 (1.81 m/s).

Discussion

3D-shaped polymeric leaflets exhibited excellent hemodynamic performance, achieving an effective orifice area comparable to the SAPIEN 3 while generating a lower pressure gradient. PIV measurements showed that the polymeric TAVR produced lower peak systolic velocities than the SAPIEN 3. Overall, these results highlight the strong potential of 3D-shaped polymeric leaflets to deliver hemodynamics on par with current commercial devices.

Images (Optional)



Session Category

Cardiovascular/Cardiorespiratory Biomechanics: Materials and Devices

P4-010

Digital-Twin Technology to Derive Mechanical and Morphological Predictors of In-Stent Restenosis in the Femoropopliteal Segment

R&D Engineer Mar Alonso Chornet[1,2], Dr. David Perrin[2], Professor Jean-Noel Albertini[2], Professor Yann Goueffic[3], Dr. Alexandra Hauguel[4], Professor Stéphane Avril[1]

[1]École National Supérieure des Mines de Saint-Étienne, SAINBIOSE, U 1059, Saint-Étienne, Loire, France. [2]PrediSurge, Saint-Étienne, Loire, France. [3]Vascular Surgery Department, Saint-Joseph Paris Hospital Group, Paris, Île-de-France, France. [4]Vascular Surgery Department, Marie Lannelongue Hospital, Le Plessis -Robinson, Île-de-France, France

R&D Engineer Mar Alonso Chornet

Dr. David Perrin

Professor Jean-Noel Albertini

Professor Yann Goueffic

Dr. Alexandra Hauguel

Introduction

Atheromatous lesions of the femoropopliteal segment are commonly treated with endovascular revascularization techniques involving the implantation of stent devices. The long-term results of these procedures are often impacted by the outcome of in-stent restenosis (ISR), a condition that leads to lumen re-narrowing. Despite recent research, the identification of ISR predictors remains a challenge as ISR is a complex multifactorial condition in which the influence of the mechanical environment is not yet fully understood, and the outcomes depend on each patient's anatomical characteristics. The objective of this study is to develop a digital-twin-based approach to assess potential mechanical and morphological predictors of ISR.

Methods

First, patient-specific 3D arterial models were reconstructed from contrast-enhanced preoperative CT scans. Digital models of two stent designs were then crimped and deployed in the targeted region of the artery model through numerical simulations in Abaqus® software. The final stent geometries obtained from the simulations were compared with the corresponding stent reconstructions from post-interventional CT scans. The mean absolute error of the average stent diameter at each cross-section (MAE_{avg}) and the offset were computed. Finally, potential predictors were extracted from simulation results. A preliminary analysis with 10 patients was carried out to assess the reliability of the models.

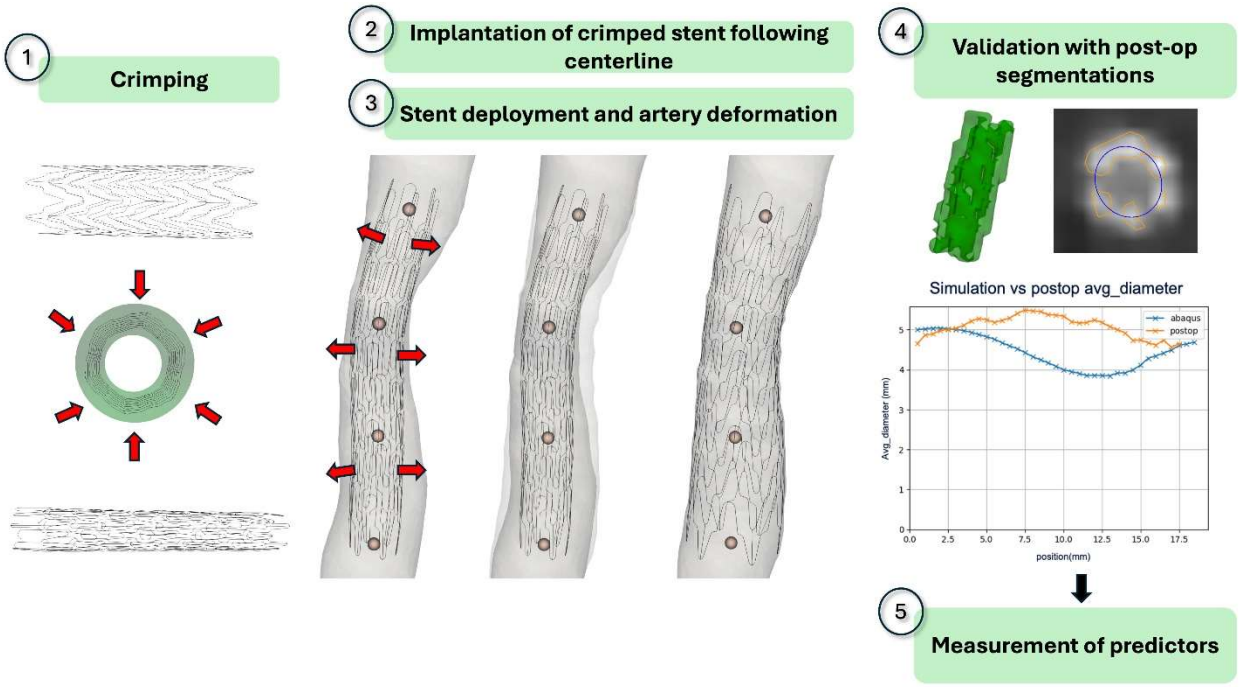
Results

The general process was successfully simulated for all cases, involving the implantation of 14 stents ranging from 5 to 8 mm in diameter. The mean MAE_{avg} for all stents is 13.79 ± 5.6% relative to their reference diameter and an average offset of 11.18 ± 7.7% was observed in the models. The cross-sectional diameters of the femoropopliteal lumen and the final stent were measured from the models as potential ISR morphological predictors.

Discussion

The proposed approach provides a personalized tool designed for clinical application, enabling the estimation of ISR predictors which cannot be easily obtained from in-vivo measurements. However, the morphological differences between the postoperative and simulation results might indicate the influence of an additional factor, such as vessel preparation, e.g. angioplasty. The future scope of this study involves the inclusion of 30 patients for tool optimization, mechanical predictors measurement and the analysis of external factors generating the offset.

Images (Optional)



Session Category

Cardiovascular/Cardiorespiratory Biomechanics: Materials and Devices

P4-011

Mechanical and Physical Evaluation of the In Vitro Degradation of Layer-by-Layer Silk Fibroin Vascular Grafts

M.Sc. Maike Bittner[1,2], Dr. Benedetta Isella[2], Dr.-Ing. Alexander Kopp[2], Prof. Ted Vaughan[1]

[1]School of Engineering and Institute for Health Discovery and Innovation, University of Galway, Galway, County Galway, Ireland. [2]Fibrothelium GmbH, Aachen, North Rhine-Westphalia, Germany

M.Sc. Maike Bittner

Introduction

Silk fibroin (SF) offers favourable mechanical and degradation behaviour with respect to other natural polymers [1] and could represent a promising material for vascular grafts, which often lack appropriate mechanical properties [2]. Layer-by-layer SF-based fabrication method could enable the modular and versatile production of vascular grafts, and this study will investigate for the first time their in-vitro degradation focusing on the mechanical and physical properties.

Methods

An in vitro degradation study of SF samples, produced through a layer-by-layer dip-coating process, was conducted over a period of 28 days (eight timepoints, four specimen types, n=4) in PBS + Protease XIV at 37 °C. References samples in only PBS were included as controls. Physical, structural (FTIR), thermal (DSC), and mechanical characterisation in hydrated state (burst pressure, uniaxial tensile tests, and circumferential tensile tests based on ISO 7198:2016) were performed.

Results

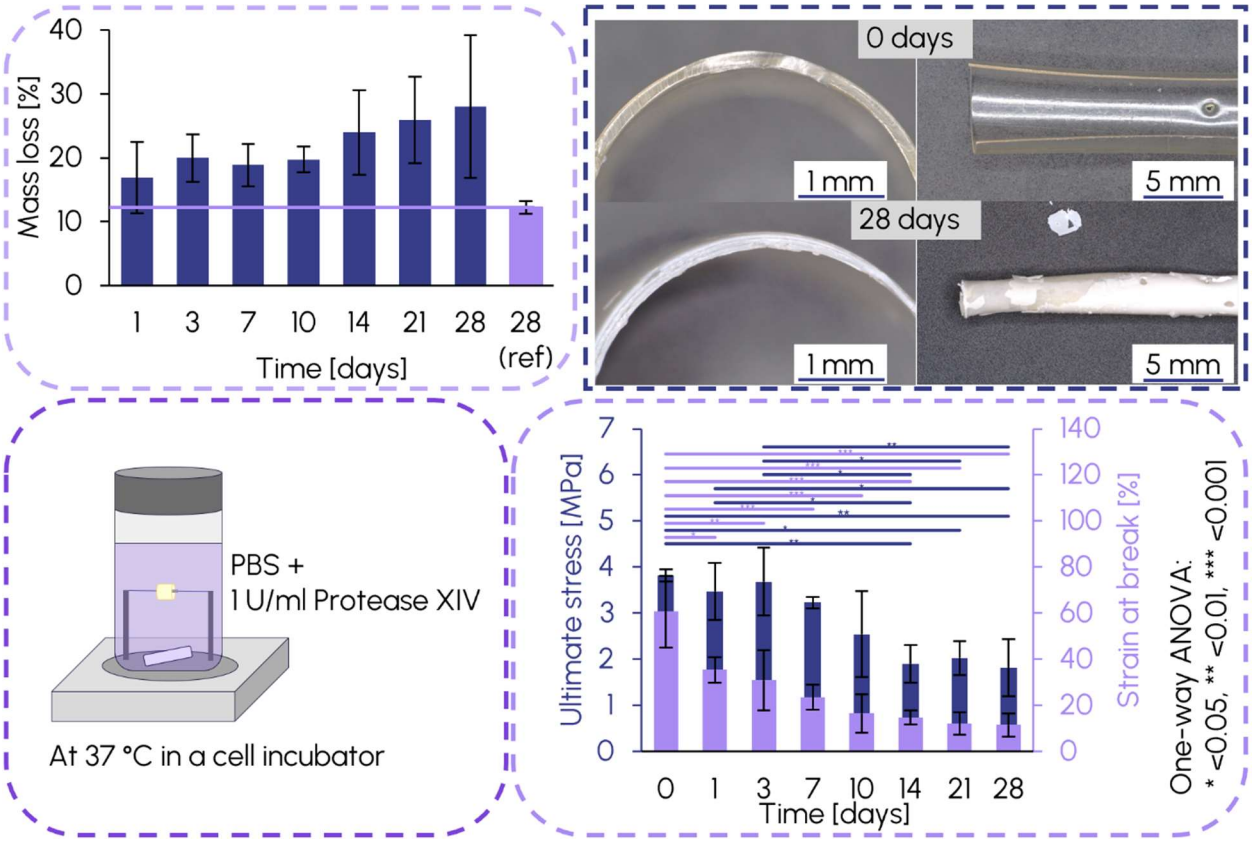
Mass loss increased from the first day across all samples, with mass loss in reference samples attributable to glycerol leaching. A gradual separation of the layers due to the degradation process was found starting from the first day. After one day, a significant decrease (p-value <0.05) in strain from 60.66 ± 15.66 % to 35.31 ± 5.53 % was observed in the uniaxial tensile test results and further decreases evident throughout the degradation. A decreasing trend was also observed for the ultimate stress after three days with a statistical difference (p-value <0.01) between day zero and 14 of 3.81 ± 0.14 MPa to 1.9 ±

0.41 MPa. This behaviour was observed throughout the entire mechanical characterisation.

Discussion

This study presented the first detailed mechanical characterisation of the in-vitro degradation process of SF. The mechanical properties especially showed that the material became progressively more brittle over time, with a more rapid decrease in strain. This suggests that the amorphous domains of the SF degrade earlier than the crystalline domains [1]. This study allows a more sophisticated understanding of the degradation mechanism of SF layer-by-layer structures, paving the way to a better design for these medical devices.

Images (Optional)



References (Optional)

[1] Guo Chengchen *et al.*, Biomacromolecules, 2020

[2] Fukayama Toshiharu *et al.*, Ann Vasc Surg, 2015

Acknowledgements (Optional)

This project has received funding from the European Union's Horizon Europe research and innovation programme under Marie Skłodowska-Curie grant agreement No.101120006.

Session Category

Cardiovascular/Cardiorespiratory Biomechanics: Materials and Devices

P4-012

A personalized FSI model of complex congenital heart disease

Dr. Aaron Brown[1,2], Ms. Elena Martinez[1,2], Dr. Michael Ma[1,2], Professor Alison Marsden[1,2]

[1]Stanford University, Stanford, CA, United States. [2]Stanford Cardiovascular Institute, Stanford, CA, United States

Introduction

Understanding intracardiac blood flow is critical in congenital heart disease (CHD), where structural defects can profoundly disturb normal hemodynamics. Although advanced imaging methods such as 4D flow MRI, or computational approaches like image-based moving-boundary CFD, can reconstruct patient-specific flow, they remain limited to preoperative conditions. Postoperative prediction requires fluid–structure interaction (FSI) modeling, in which wall motion arises from a biophysically accurate myocardial mechanic model. Such FSI models enable virtual surgical planning, which could greatly enhance decision-making for complex CHD cases that currently depend heavily on surgeon experience. Towards this goal, we develop a patient-specific FSI model of a borderline single ventricle patient undergoing a Rastelli baffle procedure [1] and compare our model to preoperative and postoperative clinical data.

Methods

A patient-specific mesh of the myocardium and blood pool is constructed from clinical imaging using a semi-automatic pipeline based on our previous work [2]. We use the arbitrary Lagrangian-Eulerian (ALE) formulation to couple blood flow to myocardial mechanics, incorporating the Holzapfel–Ogden material law, active stress, and spatially varying epicardial boundary conditions. Valves are modeled with unfitted resistive immersed surfaces (URIS) [3]. We further couple the heart to a closed-loop LPN circulation, and all parameters are personalized to preoperative clinical data using a multistep calibration strategy inspired by our previous approach [2].

Results

A preliminary FSI model of a healthy left heart with a simple open-loop circulatory model was developed as a proof of concept. Figure 1 shows velocity arrows colored by pressure results at late diastole, mid systole, and early diastole. Blood flow, valve opening and closing, and myocardial deformation all follow expected patterns for normal left heart function.

Discussion

The preliminary model demonstrates the feasibility of patient-specific FSI modeling. Next, we will build a borderline single ventricle heart, couple it to a closed-loop circulatory model, personalize myocardial and circulatory parameters to match preoperative clinical data, and virtually insert the Rastelli baffle to compare predicted postoperative function with clinical data.

Images (Optional)



References (Optional)

[1] Christian Kreutzer et al., Journal Thoracic and Cardiovascular Surgery, 2000

[2] Aaron L. Brown et al., 2025 (in prep)

[3] Marco Fedele et al., Biomechanics and modeling in mechanobiology, 2017

Acknowledgements (Optional)

NIH (R01HL12972) and NSF (1663671)

Session Category

Cardiovascular/Cardiorespiratory Biomechanics: Methods, Models and Applications

P4-013

Reduced order model for fully coupled 3D Fluid Structure Interaction of transvalvular flow affected by Aortic valve stenosis

Ms Akshita Sahni MS[1,2], Dr. Imran Shah PhD[1], Dr. Thangam Natarajan PhD[1], Dr. Alessandro Veneziani PhD[2], Dr. Karthik Menon PhD[1], Dr. Lakshmi Prasad Dasi PhD[1,2]

[1]Georgia Institute of Technology, Atlanta, Georgia, United States. [2]Emory University, Atlanta, Georgia, United States

Introduction

Full order computational biomechanics simulations, such as computational fluid dynamics models of arterial flow or fluid-structure interaction (FSI) models of transvalvular flow, are increasingly used for pre-surgical planning. However, exploration of patient specific parameter variations is difficult due to high computational time. Model order reduction can accelerate such simulations while retaining key flow features. We develop a 3D reduced order model (ROM) of aortic transvalvular flow based on fully coupled FSI simulations.

Methods

An idealized aortic valve geometry was modeled with a two-way coupled FSI where leaflet motion is described by an ODE coupled to the flow solver through a stiffness parameter K and symmetric leaflet geometry; aortic wall was assumed rigid. High fidelity simulations using a sharp-interface immersed boundary method with 8.4 million points were run for leaflet stiffness values of 10 (normal), 15.9 (31% stenosis), 42.4 (47% stenosis), and 100 kPa/m (early thrombus like stiffening), each with reduced leaflet motion (RLM) in one, two, and three leaflets [1,2]. The combination of 15.9 kPa/m, RLM in one leaflet was used as test case for prediction. The remaining 9 combinations were used for training. A non-intrusive proper orthogonal decomposition (POD) based ROM was constructed using singular value decomposition on velocity snapshots at peak systole (t = 0.15s) from 9 FSI simulations. Radial basis function (RBF) interpolation in 2D parameter space (K, # stiff leaflets) was used to map parameters to POD coefficients.

Results

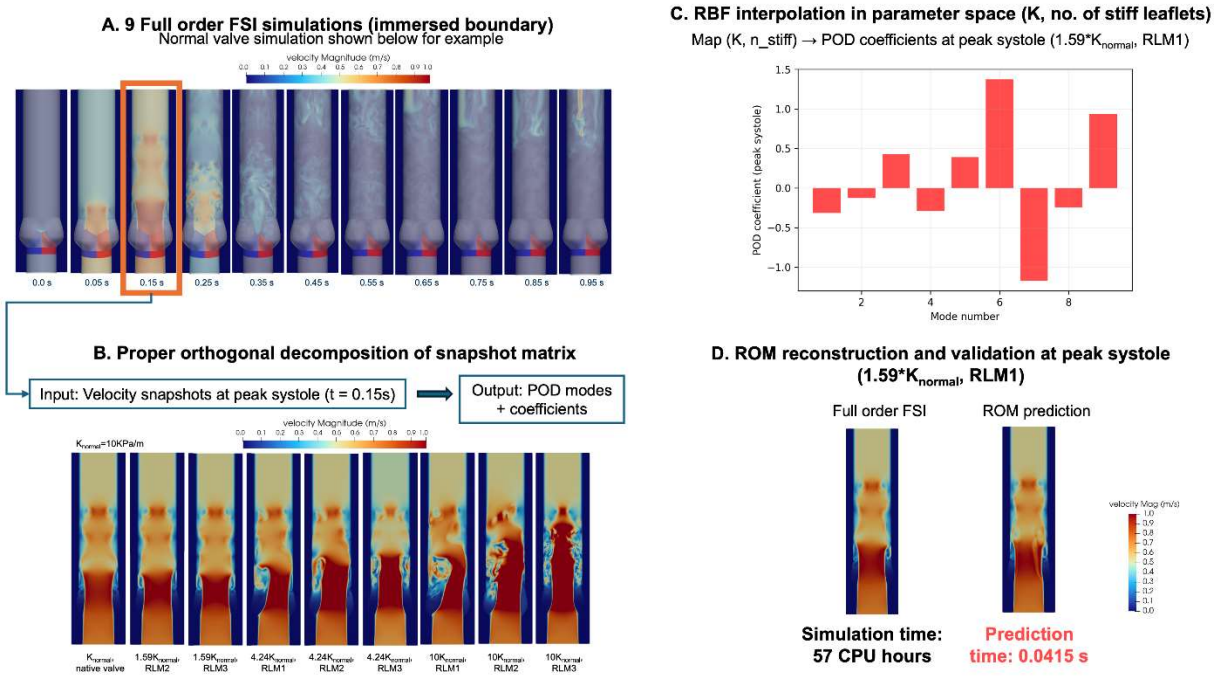
POD fitting required 2.07 s and RBF training was negligible, while ROM prediction + velocity field reconstruction required 0.0415s on a 48GB RAM laptop. In comparison, FSI simulation

of peak systole required ~57 CPU hours (576 cores) on supercomputing cluster. The ROM leads to ~5×10^6 speedup, with 18.6% relative L2 error on the 3D velocity field (Figure 1).

Discussion

The ROM recovered dominant transient flow structures over peak systole. Because the training data are fully coupled FSI simulations, the ROM predictions reflect coupled valve dynamics. We will showcase this framework for patient specific geometries and bioprosthetic transcatheter valves with RLM. We plan to include time varying hemodynamics and pressure gradient predictions by incorporating dynamic mode decomposition for large datasets.

Images (Optional)



References (Optional)

Acknowledgements (Optional)

We acknowledge the use of the ezyrb Python library for model order reduction. Computing resources were provided by the Partnership for an Advanced Computing Environment (PACE) at the Georgia Institute of Technology. This work was supported by Georgia Tech startup funds (Dr. Lakshmi Prasad Dasi and Dr. Karthik Menon, separate awards).

References – [1] Seo JH et al. J Biomech. 2014;47(11):2720–2729., [2] Zhu C et al. Ann Biomed Eng. 2018;46(11):1641–16537.

Session Category

Cardiovascular/Cardiorespiratory Biomechanics: Methods, Models and Applications

P4-014

Structural and Fluid Mechanics Analysis of Renal Artery Stenting - Effect of Stent Placement and Respiratory-Induced Motion

Dr Alessandra Corvo[1], Dr Stephane Avril[1], Dr Lucie Derycke[2], Dr Stephan Haulon[3], Dr Alberto Aliseda[4], Dr Fanette Chassagne[1]

[1]Ecole de Mines, Saint Etienne, Rhone Alpes, France. [2]Department of Vascular Surgery, Hôpital Paris Saint-Joseph, Paris, Isle de France, France. [3]Hôpital Marie Lannelongue, Université Paris Saclay, Saclay, Paris - Isle de France, France. [4]University of Washington, Seattle, WA, United States

Introduction

Endovascular Aneurysm Repair (EVAR) complications related to stent-grafts (SG) deployment in the renal arteries are poorly understood and diagnosed. They compromise short and long-term surgical outcomes. Predicting these complications (stenosis, occlusion, kink) pre-surgical intervention is challenging. Finite Element (FE) simulations of SG deployment in the renal arteries have not been conducted, and the hemodynamics changes induced by the procedure are only partially understood. Integrated structural-hemodynamics simulations can shed light on the link between procedural parameters, renal artery physiology and patients' outcomes.

Methods

This study covers five fenestrated-EVAR patients, two did not develop renal complications, and three who did. FE simulations analyzed SG deployment in the renal arteries, while CFD simulations assessed hemodynamics changes. We investigate variations in cross-sectional area along the artery, flow rate, and TAWSS, together with specific clinical metrics (Renal-Aortic Ratio or RAR) used to diagnose renal stenosis. We compare clinical and hemodynamics metrics between patients with and without complications.

Results

Renal artery lumen analysis showed decrease in cross-sectional area due to the stenting, resulting in a reduction in renal flow after fEVAR. Large TAWSS reduction post-fEVAR corresponded with regions where patients developed complications. Recirculation regions were detected downstream of the SG (Figure 1), corresponding to the stenosed area in Patient 1. High RAR values (>3.5) were found for all the patients who

suffered complications. We compared post-operative imaging against CFD simulation visualizations, to provide confidence in the validation of CFD results. Finally, CFD metrics were correlated with clinical RAR values and patient outcomes, in an effort to formulate metrics from computations that can complement or eventually replace highly uncertain and unspecific current clinical diagnosis metrics.

Discussion

This study integrates structural and fluid simulations of renal artery fenestrated stent graft placement, in patient-specific cases. The results from cases without complication are compared against those who did develop complications. The results show the potential of computational hemodynamics metrics to support prediction of complication risk, preoperatively. Clear differences exist between hemodynamics of patients with and without complications. Validation of these metrics on a much larger cohort is needed to demonstrate clinical translation of these hemodynamics simulation metrics for prediction of surgical complications.

Images (Optional)

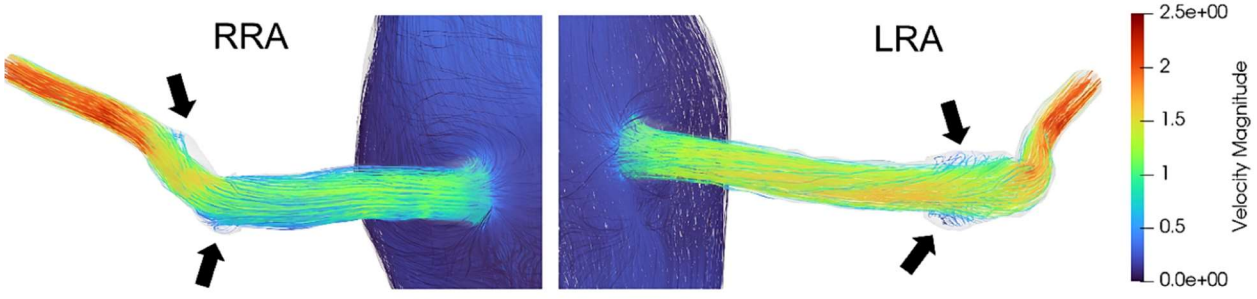


Figure 1. Recirculation in left (LRA) and right (RRA) renal arteries of Patient 2.

Session Category

Cardiovascular/Cardiorespiratory Biomechanics: Methods, Models and Applications

P4-015

Modeling the Effects of Right Ventricular Remodeling on Intramural Stress and Cardiac Outflow in Pulmonary Arterial Hypertension

Mr. Alex Barr, Dr. Jason Szafron

Carnegie Mellon University, Pittsburgh, Pennsylvania, United States

Introduction

Pulmonary Arterial Hypertension (PAH) is a chronic condition with narrowed distal pulmonary arteries, causing increased resistance. To maintain cardiac output, the right ventricle (RV) remodels, resulting in long-term maladaptive changes in size, thickness, and material behavior. [1] Thin-walled models of the ventricle do not predict changes in wall stress distribution during remodeling. [2] Additionally, research directly linking concomitant changes in cardiac microstructure to flow in the pulmonary arteries is sparse. We investigated the effects of cardiac remodeling in PAH to analyze stress distributions in the vascular wall and predict changes in outflow to the pulmonary arteries.

Methods

We gathered cardiac data from prior studies that induced PAH in Sprague Dawley rats through monocrotaline or Sugen/hypoxia. A thick-walled, hollow cylinder model was used to capture right ventricular behavior by including both active and passive constituents of the heart wall. [3] Internal pressures and volumes were simulated for each phase of the cardiac cycle by varying load and contraction. By iteratively altering material parameters, the differences between the calculated Pressure-Volume (PV) loop and the cardiac data from the literature were minimized to simulate each stage of disease progression. Simulated cardiac data consistently fell within the standard deviation of the literature values. This pressure-volume data was used to generate flow inputs for reduced order models of pulmonary hemodynamics through recapitulation of an input pressure waveform for a lumped parameter model of the heart.

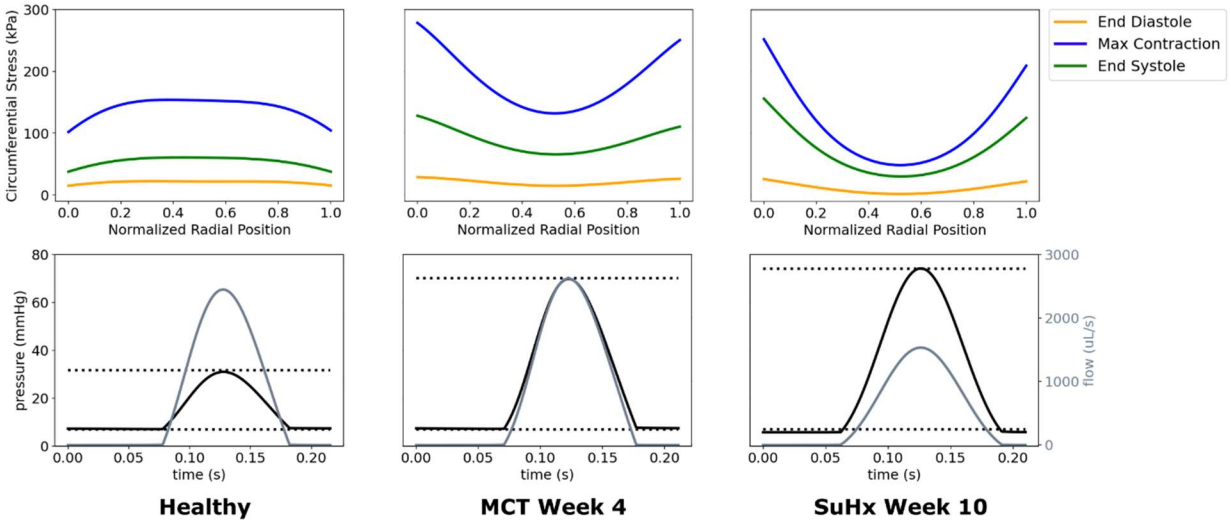
Results

PAH hearts exhibited increased circumferential stress at end systole and max contraction compared to healthy controls. While healthy hearts exhibited their highest stress in the midpoint of the wall, diseased models had a higher circumferential stress at the inner and outer wall compared to the midpoint. Additionally, we simulated changes in flow in the reduced order model across PAH progression and compared changing vascular parameters, such as compliance, with cardiac material properties.

Discussion

These simulations helped to identify the time-varying effects of different RV constituents in PAH and their relation to heart remodeling.

Images (Optional)



References (Optional)

[1] Avazmohammadi et al., J. Biomech Eng, 2019.

[2] Hood et al., Circ, Res., 1969.

[3] Larry Taber, Continuum modeling in mechanobiology. Vol. 10. New York: Springer, 2020.

Acknowledgements (Optional)

Session Category

Cardiovascular/Cardiorespiratory Biomechanics: Methods, Models and Applications

P4-016

In-Vivo Comparison between Computational Fluid Dynamics Simulations and Xenon MRI of the Upper Airways in Obstructive Sleep Apnea

Assistant Professor Qiwei Xiao Ph.D[1,2], Assistant Professor Neil Stewart Ph.D[3], Assistant Professor Matthew Willmering Ph.D[1], Mr Keith McConnell[1], Dr Robert Fleck MD[1], Dr Raouf Amin MD[1], Assistant Professor Alister Bates Ph.D[1]

[1]Cincinnati Children's Hospital, Cincinnati, OHIO, United States. [2]University of Cincinnati, Cincinnati, OHIO, United States. [3]University of Sheffield, Sheffield, Sheffield, United Kingdom

Introduction

Computational fluid dynamics (CFD) simulations of upper airway airflow offer potential for identifying sites of obstruction contributing to respiratory symptoms in obstructive sleep apnea (OSA). Previous studies comparing CFD to hyperpolarized ^{129}Xe phase contrast (PC) MRI velocimetry have been limited to healthy subjects. However, OSA patients present complex airway geometries with multiple obstruction sites at the soft palate, retroglossal region, and epiglottis. Since both CFD and ^{129}Xe PC MRI have inherent limitations, demonstrating good agreement between these two independent techniques in OSA patients would provide reassuring consistency and support confidence in using CFD for clinical decision-making.

Methods

We performed subject-specific CFD simulations and hyperpolarized ^{129}Xe PC MRI velocimetry during normal breathing in one patient. Airway anatomies were derived from ^{1}H MRI, and respiratory flow rates were recorded during ^{129}Xe inhalation. CFD simulations employed large eddy simulation turbulence modeling with boundary conditions matching MRI acquisition. Velocity fields from CFD were spatially averaged to match PC MRI resolution. Agreement was assessed using Bland-Altman analysis.

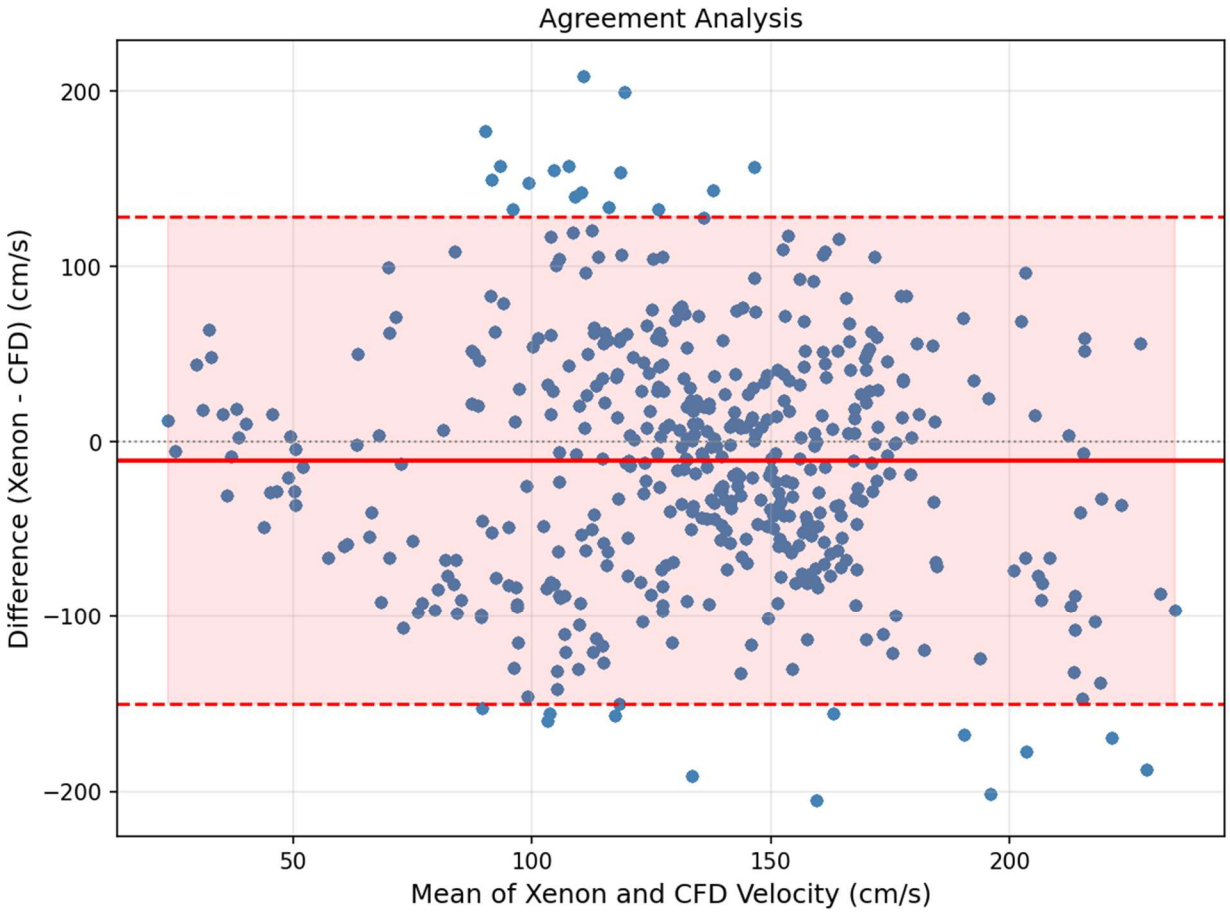
Results

Bland-Altman analysis revealed a small mean bias of -10.9 cm/s (-8.1% of mean velocity), indicating CFD velocities were slightly higher than ^{129}Xe PC MRI measurements.

Discussion

This preliminary comparison of CFD and hyperpolarized ^{129}Xe PC MRI in OSA patients demonstrates initial feasibility of comparing the two techniques in a challenging population, supporting translation of CFD toward clinical application in OSA management.

Images (Optional)



Session Category

Cardiovascular/Cardiorespiratory Biomechanics: Methods, Models and Applications

P4-017

Modeling Respiratory Mechanics in Neonatal Lung Disease: MRI–CFD Framework for Regional Work of Breathing Analysis

Dr Chamindu Gunatilaka PhD[1], Mr Christopher Boles BS[2], Dr Qiwei Xiao PhD[1], Dr Hamideh Hayati PhD[1], Mr Keith McConnell MS[1], Dr Samal Munidasa PhD[1], Dr Matthew Willmering PhD[1], Dr Nara Higano PhD[1], Dr Paul Kingma MD[1], Dr Erik Hysinger MD, MS[1], Dr Jason Woods PhD[1], Dr Alister Bates PhD[1,2]

[1]Cincinnati Children's Hospital Medical Center, Cincinnati, OH, United States. [2]University of Cincinnati, Cincinnati, OH, United States

Introduction

Bronchopulmonary dysplasia (BPD) is a chronic lung disease that primarily affects premature infants. In addition to impaired lung development, many patients with BPD also present with central airway abnormalities. These overlapping airways and parenchymal impairments make it challenging to determine how much each component contributes to a patient's symptoms. Computational fluid dynamics (CFD) simulations based on magnetic resonance imaging (MRI), enable regional quantification of the kinetic energy required to move air through the airways, providing a noninvasive assessment of the resistive work of breathing (WOB). Overall respiratory workload was also calculated. Therefore, this analysis provides both the total respiratory effort, and calculates where and how that effort is spent, allowing precise phenotyping and targeted treatment plans.

Methods

A healthy respiratory control and a subject with BPD were imaged near term age using MRI to acquire three-dimensional images of the thorax. Esophageal pressure and nasal flow were recorded concurrently with MRI. Four respiratory-gated images throughout the breath were retrospectively reconstructed. Airway surfaces spanning from the nostrils to main bronchi were segmented at end-expiration, and image registration captured airway deformation across the respiratory cycle. Subject-specific geometry, motion, and measured airflow rates were used as CFD boundary conditions. The mesh consisted of polyhedral and prism cells, totaling approximately 5 million cells. Unsteady simulations employed second-order temporal discretization with a 0.8ms time step. The Large-Eddy Simulation (LES) turbulence model was used to model subgrid-scale effects. Simulations provided resistive WOB components for the upper airway, trachea, and proximal bronchi. Total resistive and elastic WOB values were integrated from lung pressure-volume loops.

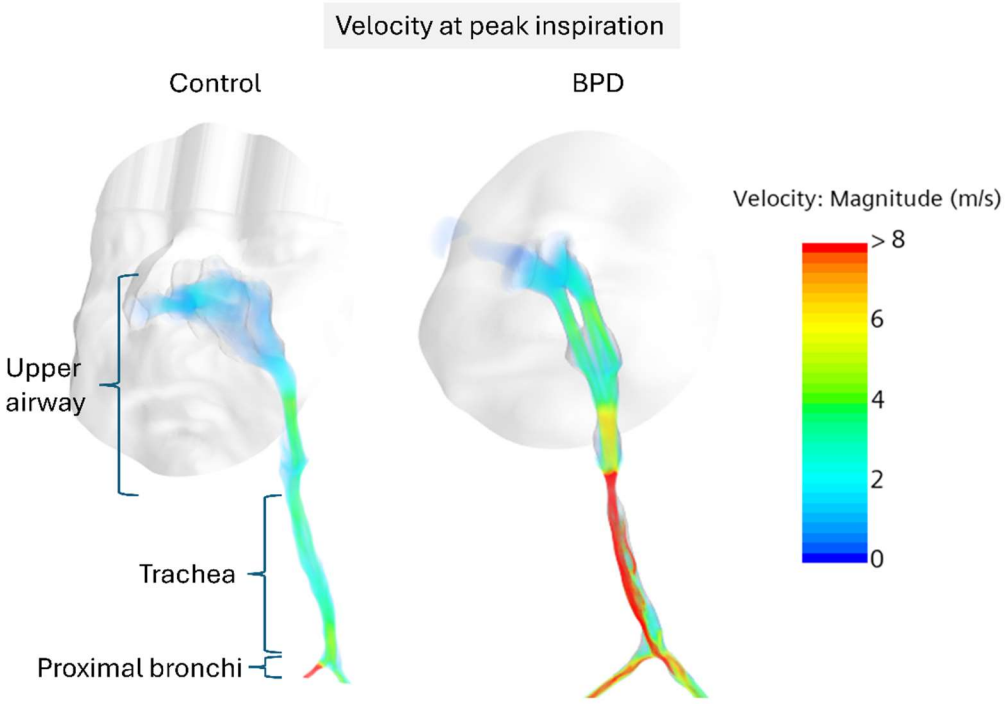
Results

Relative to the control, the subject with BPD showed markedly elevated upper airway and tracheal resistive WOB, increasing by 1293% and 408%, respectively (figure). Resistive WOB in the proximal bronchi and distal airways decreased by 54% and 45%. Overall, total WOB (562%) and elastic WOB (1927%) were substantially higher in the BPD subject.

Discussion

These findings illustrate how integrated CFD and imaging methods can support phenotype-specific, computationally informed treatment strategies for neonatal respiratory disease. With additional cases, this approach could facilitate the development of patient-specific therapeutic plans.

Images (Optional)



Session Category

Cardiovascular/Cardiorespiratory Biomechanics: Methods, Models and Applications

P4-018

Accelerated finite element analysis of patient-specific atherosclerotic coronary arteries using a locally refined structured-mesh-based surrogate meshing approach.

Mr Amear Mohammed[1], Dr Retesh Bajaj[2], Dr Nathan Yap[2], Dr Thamil Kumaran[2], Professor Jouke Dijkstra[3], Mr Pieter Kitslaar[4], Professor Andreas Baumbach[5], Professor Christos Bourantas[6,2,5], Professor Ryo Torii[1]

[1]Department of Mechanical Engineering, University College London, London, Europe, United Kingdom. [2]Centre for Cardiovascular Medicine and Devices, William Harvey Research Institute, London, Europe, United Kingdom. [3]Department of Radiology, Leiden University Medical, Leiden, Europe, Netherlands. [4]Medis Medical Imaging, Lieden, Europe, Netherlands. [5]Department of Cardiology, Barts Heart Centre, Barts Health NHS Trust, London, Europe, United Kingdom. [6]Institute of Cardiovascular Science, University College London, London, Europe, United Kingdom

Introduction

Biomechanical analysis of coronary atherosclerosis in 2D cross-sectional models have been shown to complement image-based assessment of plaque progression and identification of culprit lesions [1]. However, 2D models cannot appreciate complex vessel curvature and plaque volume distribution in patients [2]. Though, 3D reconstruction itself poses challenges in accurate plaque geometry recreation, time-consuming pre-processing and computational efficiency in typical workflows that limit large-cohort studies. This work aims to develop a fast structured-mesh-based reduced-order model of atherosclerotic coronary arteries as a practical computational method to facilitate the processing of large patient datasets, including demonstration of its efficacy to identify plaque progression.

Methods

10 patient-specific atherosclerotic coronary arteries were reconstructed from the fusion of X-ray angiogram, intravascular ultrasound and optical coherence tomography using end-diastolic frames during pull-back. All vessels were meshed using a conventional tetrahedral approach and the proposed grid-based method. Patient-specific intracoronary pressure at systole (98±24 mmHg) were used in stress analysis of each model. Because patient vessels are stressed by diastolic pressure at the time of imaging, pre-stress was calculated using inverse-elastostatics. Fibrotic tissue, calcium and lipid-rich tissue were modelled as hyperelastic materials and Von Mises stresses in the fibrotic tissue were used to assess the agreement between the two computational approaches.

Results

Tetrahedral and hexahedral approaches showed good agreement in lumen surface stress distribution, particularly in stress shielding regions caused by the calcium (Figure 1a), and cross-sectional stress distributions along the vessel (Figure 1b). The absolute agreement of the 95th centile stress was CCC = 0.93 (Figure 1c), with quantitative difference of 9.6% ± 10.2%. The time taken to produce results using the proposed method is four times faster than the conventional tetrahedral mesh.

Discussion

The proposed structured-grid-based approach was found to correlate well to the conventional approach in the estimation of stress distribution, which is produced in significantly faster time. Future analysis will extend the dataset to include 24 patients for the proposed method to investigate 3D atherosclerotic modelling in its ability to distinguish progressive and regressive patient vessels.

Images (Optional)

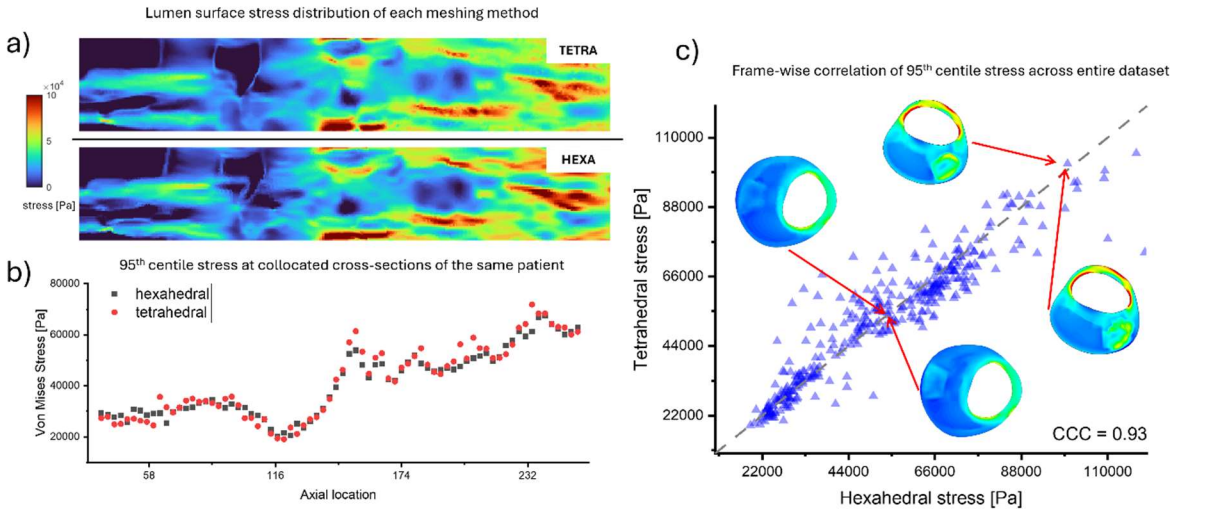


Figure 1. a) Lumen Von Mises stress distribution in both tetrahedral and the developed gridded mesh method, b) 95th centile stress at collocated cross-sections along the axial direction of an atherosclerotic artery for the same model in a). c) all collocated cross-sections for all models simulated, highlighting 2 cross-sections sampled from the same axial location for each meshing method.

References (Optional)

[1] Costopoulos et al. JACC: Cardiovascular Imaging, 13, 1206-1218, 2020.

[2] Huang et al. Journal of Biomechanics, 47, 1465-1471, 2014.

Acknowledgements (Optional)

This project is funded by the Engineering and Physical Sciences Research Council (EP/W524335/1).

Session Category

Cardiovascular/Cardiorespiratory Biomechanics: Methods, Models and Applications

P4-019

Impact of Reference State on Estimates of Passive Myocardial Stiffness in Hypertensive Patients

Mr Amirhossein Manzouri[1], Dr Debbie Zhao[1], Mr Stephen Creamer[1], Ms Mathilde Verlyck[1], Dr Vicky Wang[1], Dr Thiranja Babarenda Gamage[1], Prof Martyn Nash[1,2]

[1]Auckland Bioengineering Institute, University of Auckland, Auckland, Auckland, New Zealand. [2]Department of Engineering Science and Biomedical Engineering, University of Auckland, Auckland, Auckland, New Zealand

Introduction

Hypertension is a major driver of adverse cardiac remodelling and heart failure, yet clinical assessment still relies largely on chamber-level measures. Subject-specific biomechanical analysis has the potential to provide tissue-scale measurements of myocardial stiffness, offering mechanistic insights into disease processes. A key requirement for these models is a well-defined load-free (LF) reference state; however, this state cannot be directly observed in vivo because the left ventricle (LV) is typically exposed to load. It is often assumed that the ventricle reaches an LF configuration during diastole. In hypertensive patients, however, diastolic pressures are often elevated, meaning this assumption neglects substantial non-zero pressure at the assumed reference state. In this study, we investigate the impact of different reference state assumptions on myocardial stiffness estimates in patients with hypertension, using clinical data.

Methods

Clinical data from 34 hypertensive patients, comprising 3D echocardiography (3DE) and LV pressure recordings, were analysed. LV models were constructed by fitting finite element models to deep-learning-based segmentations of the LV myocardium. Myocardial stiffness (C) was estimated by minimising projection errors between model-predicted geometries and 3DE-derived surface data at end-diastole (ED).

Three approaches for handling the reference state were compared: (1) LF geometry estimation using the Rajagopal inverse method [1] with measured pressure at diastasis (DS); (2) “DS-offset” method, which subtracts the measured DS pressure from the measured ED pressure; and (3) “zero-pressure” method, which assumes DS pressure is zero, while using the measured ED pressure.

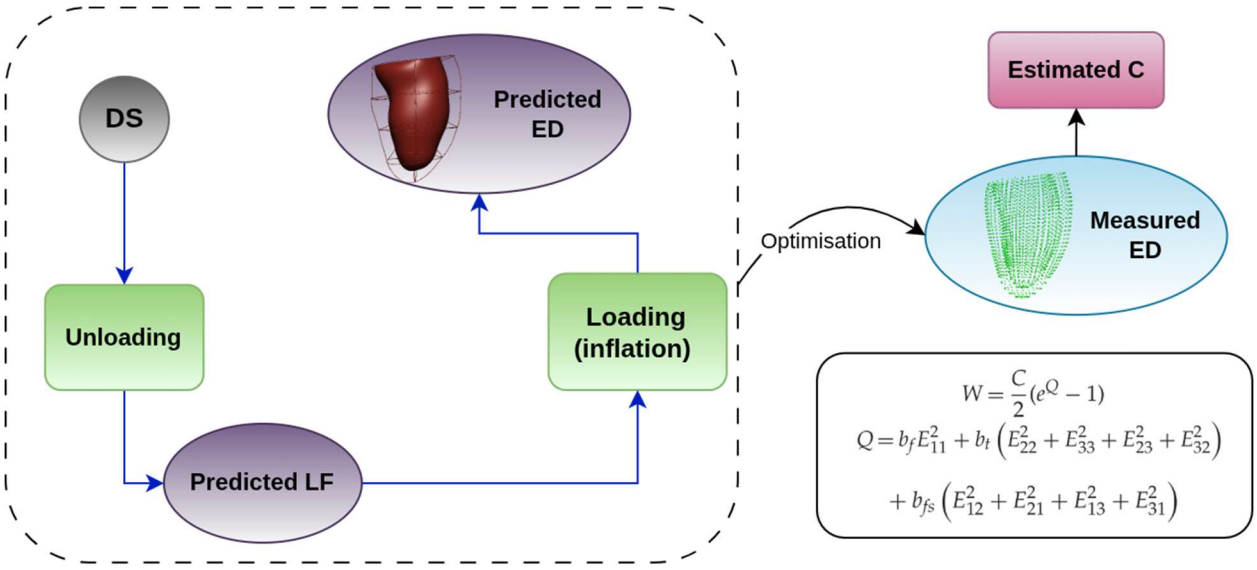
Results

The DS-offset and zero-pressure methods led to consistent overestimates of myocardial stiffness (C) compared to the LF-geometry approach. The zero-pressure approach yielded the largest bias, with stiffness values approximately 170% greater on average. The DS-offset method also showed systematic overestimation, with a more moderate but still notable mean overestimate of around 30%.

Discussion

In hypertensive patients, our clinical data show that simplifying assumptions about early diastolic pressures and neglecting the LF geometry introduce a systematic bias towards overestimating myocardial stiffness estimates. These findings highlight that accurate estimation of myocardial mechanical properties requires explicit estimation of the LF reference geometry, particularly in patients with elevated diastolic pressures.

Images (Optional)



References (Optional)

[1] Rajagopal et al., Int J Numer Methods Eng, 2007

Acknowledgements (Optional)

Health Research Council of NZ (23/527)

Session Category

Cardiovascular/Cardiorespiratory Biomechanics: Methods, Models and Applications

P4-020

Inverse Identification of mitral valve leaflet properties and chordal forces using a Physics-Informed Neural Network (PINN)

Ms. Anling Zhu[1], Dr. Ram Rohatgi[2,3,4], Dr. Pirooz Eghtesady[3,2], Dr. Fanwei Kong[1]

[1]Washington University in St. Louis, St. Louis, MO, United States. [2]Barnes-Jewish Hospital, St. Louis, MO, United States. [3]St. Louis Children's Hospital, St. Louis, MO, United States. [4]WashU Medicine, St. Louis, MO, United States

Introduction

Computational modeling demonstrates potential in simulating patient MV biomechanics. Standard- of- care imaging, echocardiograms, primarily resolve the geometry and motion of major leaflet structures, while chordal architecture remain partially visible. Thus, most established models assumed material properties and sub-valvular structures obtained from ex-vivo experiment data[1]. Recent machine learning developments allow inverse prediction of leaflet material properties using PINNs and leaflet motion[2,3]. However, these models are not yet applicable for MV because they do not account for the chordal forces. Thus, we explore a PINN framework to jointly estimate MV material properties and chordal forces by enforcing traction balance on the visible leaflet surfaces extracted from echocardiograms.

Methods

The PINN employs a quasi-static formulation assuming valve reaches near-mechanical equilibrium at peak systole. The network takes the nodal coordinates at mid-diastole as input and predicts displacements at peak systole. The predict displacement and Cauchy stress are computed using a Mindlin thick shell model. Losses enforcing momentum equilibrium, surface traction balance, and consistency with displacement data are incorporated. The leaflet material properties and nodal chordal traction are learnable parameters and jointly optimized with neural network parameters by minimizing the total loss function. The predicted parameters are tested in FEBio. The framework is tested on 3D TEE images of a pediatric patient with MV stenosis mainly in sub-valvular area.

Results

Our PINN demonstrates convergence in all losses and the predicted displacements match closely with ground truth at peak systole. MV structure simulated in FEBio coincides with mid-systole segmentation. Our current predicted chordal traction map does not yet reproduce physiologically realistic distributions.

Discussion

Because MV inverse biomechanics is inherently ill-posed, reliable parameter estimation requires strong regularization and the incorporation of prior knowledge. Ongoing work includes assimilating prior knowledge of chordal force patterns into the PINN framework and incorporating time-series dynamical models. Nonetheless, this approach may offer an alternative to manual, iterative parameter tuning and may substantially reduce the time required to build patient-specific mitral valve computational models.

Images (Optional)

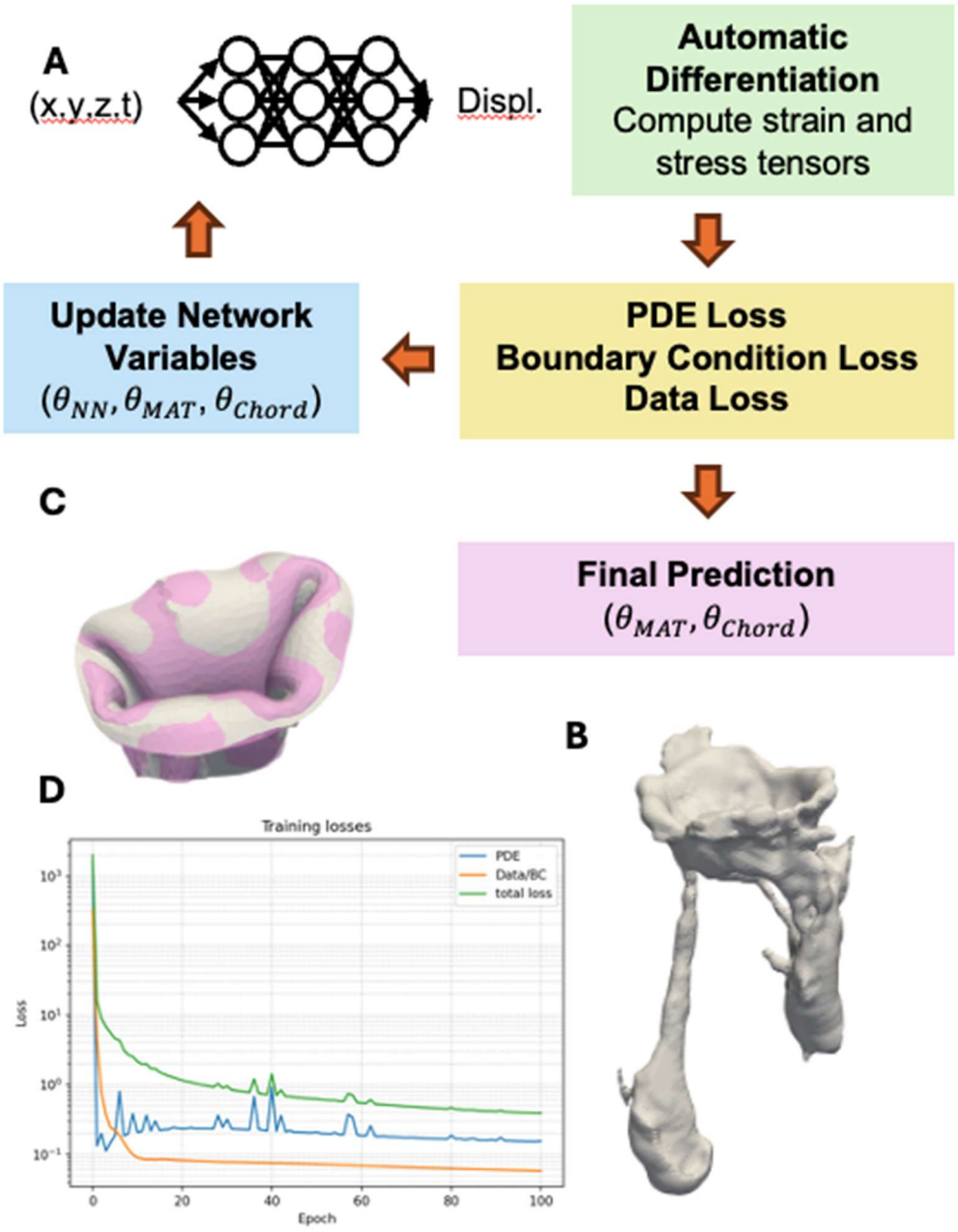


Figure 1. (A) Proposed PINN Architecture. **(B)** Patient mitral valve segmentation. 3D TEE images obtained from the Pediatric Cardiothoracic Surgery Department of St. Louis Children's Hospital. **(C)** FEBio simulation with predict material properties (pink) and ground-truth material properties (white). **(D)** Loss curve converge for both PDE and Data losses.

References (Optional)

[1] Hao Liu *et al.*, Journal of Biomechanical Engineering, 2023

[2] Federica Caforio *et al.,* Comput Mech, 2024

[3] Wensi Wu *et al.,* Acta Biomaterialia, 2025

Session Category

Cardiovascular/Cardiorespiratory Biomechanics: Methods, Models and Applications

P4-021

Blood pressure modulation during heart-paced walking is explained by vertical body acceleration

PhD Candidate Aurora Rosato[1], Dr. Emanuele Perra[2], Dr. Seraina A. Dual[1]

[1]Intelligent Heart Technology Lab, Department of Biomedical Engineering and Health Systems, KTH Royal Institute of Technology, Stockholm, Stockholm, Sweden. [2]Getinge, Acute Care Therapies, Maquet Critical Care AB, Solna, Stockholm, Sweden

Introduction

Heart-paced walking can improve exercise capacity, but the underlying biomechanical mechanisms are not fully understood. During walking, blood pressure (BP) is influenced by cardiac pumping, skeletal muscle pumping, and vertical body acceleration (VBA). Here, we investigate how inertial forces induced by VBA peaks contribute to BP modulation using a computational model of the cardiovascular system and experimental measurements during heart-paced treadmill walking.

Methods

The cardiovascular model consisted of a 25-compartment lumped parameter network incorporating a four-chamber heart, pericardial and intrathoracic pressures, and baroreflex. Inertial effects were mechanistically modeled as hydrodynamic pressure sources in all vertically aligned vessels without additional parameters. We recorded data from 36 healthy participants (19 younger adults: 28±3 years; 17 older adults: 71±5 years), who performed bouts of phase-locked heart-paced walking guided by auditory cues in a randomized cross-over design. We non-invasively acquired continuous brachial BP, electrocardiogram, and stroke volume (SV), time-synchronized to VBA using a chest-worn sensor (Cometa Srl., Italy). We imposed the recorded heart rate and VBA from two subjects (P1: 31 years and P2: 26 years) onto the model and compared the morphology of the simulated aortic BP to the measured BP. In the full cohort, we analyzed the correlation between the maximum modulation of systolic BP across phases (ΔSBP) and mean VBA.

Results

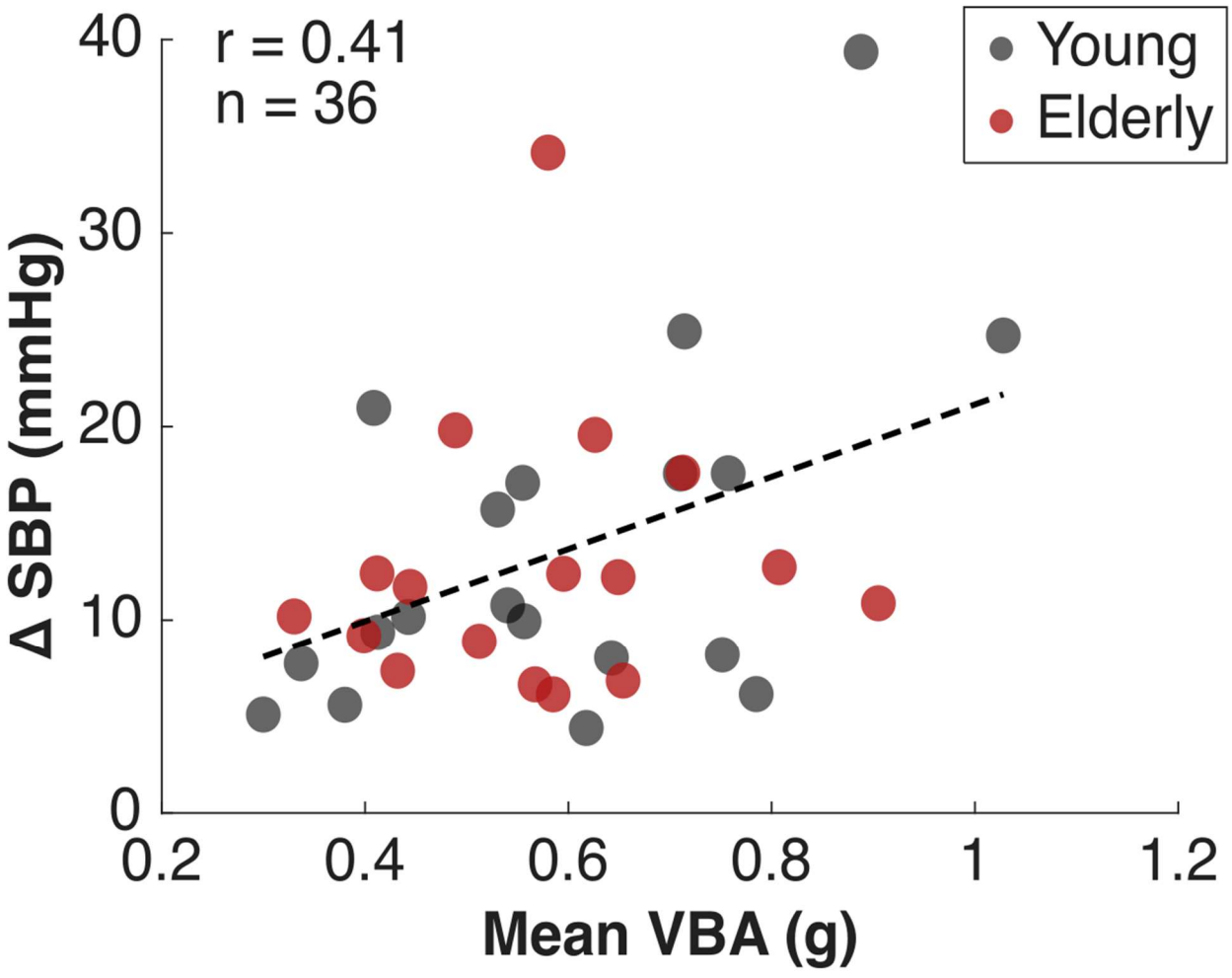
The model successfully reproduces the distinct pressure waveform morphology observed experimentally during phase-locked heart-paced walking in the two subjects we simulated. Measured stepping timing across phases led to a substantial SBP and SV change in P1 (-25 mmHg ΔSBP, +68.9 mL SV), in contrast to P2 (-5mmHg ΔSBP, +15.6 mL ΔSV). These strong

effects were associated with higher measured VBA (0.71± 0.07 g vs. 0.29±0.05 g) and peak VBA (1.4±0.06g vs. 1.1±0.03g) in P1 vs. P2, respectively. ΔSBP exhibited a moderate positive correlation (R=0.41, p<0.05, n=36) with the mean VBA, Figure 1.

Discussion

Our findings suggest that VBA is a significant biomechanical player in the BP modulation observed during walking. The magnitude of VBA appears directly related to the observed hemodynamic effects. Future work will extend the computational modeling analysis across the full cohort, incorporating subject-specific effects.

Images (Optional)



References (Optional)

Session Category

P4-022

Non-invasive, High-Resolution, and Quantitative Assessment of Cerebrovascular Reactivity Using a Whole-Brain 3D-1D-0D Geometric Multiscale Model

Graduate Student Zijie Wang, Professor Youjun Liu, Professor Liyuan Zhang, Professor Bao Li, Professor Mingai Li

Beijing University of Technology, Beijing, Chaoyang District, China

Introduction

Cerebrovascular Reactivity (CVR) is a core indicator for assessing ischemic stroke. Existing technologies face bottlenecks: MRI, despite high resolution, struggles to provide absolute quantitative measures of blood flow; TCD has low spatial resolution, missing whole-brain fine perfusion details. Furthermore, standardized gas induction (CO2 inhalation) is operationally complex and imposes a significant physiological burden on patients. Thus, developing a non-invasive, high-resolution, absolutely quantitative numerical simulation method is urgently required.

Methods

This study constructed a whole-brain 3D-1D-0D geometric multiscale model: a 3D model (Willis loop and major branches) reconstructed from CTA data; a 1D model (distal arteriolar tree) based on allometric scaling algorithms; and a 0D lumped parameter model characterizing microcirculation impedance. Based on standardized breath-holding experiments (52 volunteers), two key quantitative parameters—the mean resistance variation coefficient (R_v) and the diameter variation coefficient (D_v)—were derived via fluid dynamics. These parameters drive the model to simulate the hypercapnic state and calculate BHI. Crucially, the convection-diffusion equation was introduced to model blood transport within 3D brain tissue, achieving not only data calculation for 68 functional regions (DK atlas) but also precise millimeter-level voxel-wise analysis of whole-brain perfusion and BHI distribution.

Results

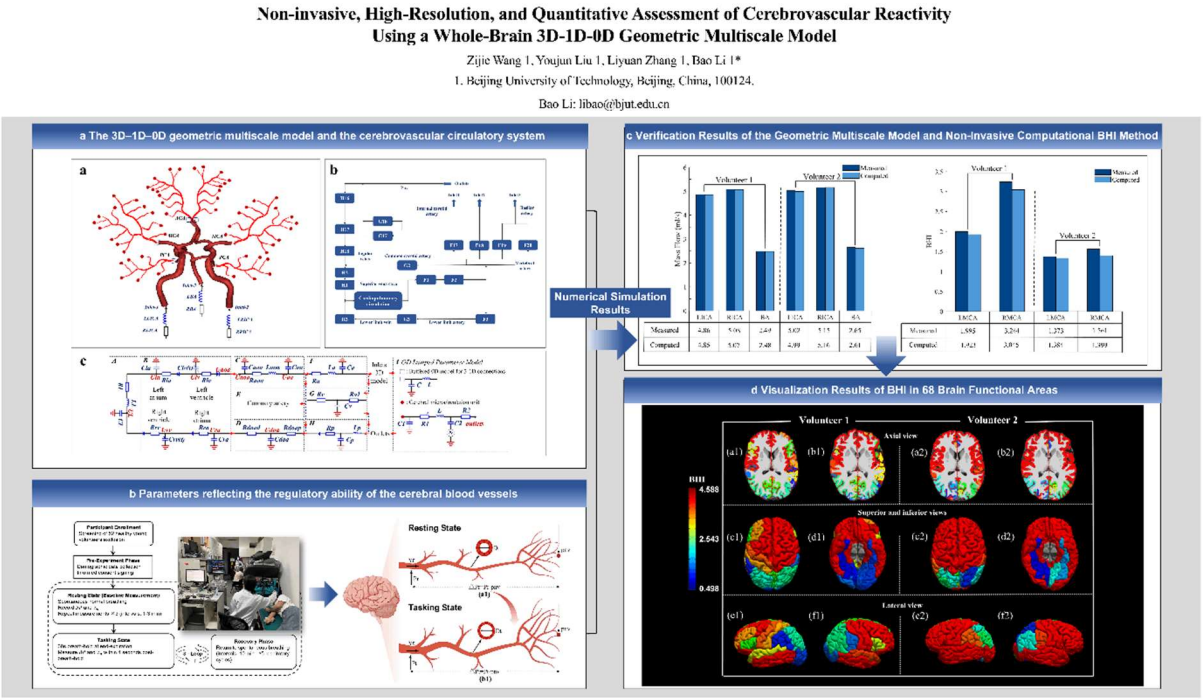
Resting flow validation showed high consistency with TCD (Mean Absolute Error, MAE = 0.0183). Inputting R_v = 0.5878 and D_v = 1.3286, the model successfully reproduced the hypercapnia-induced hemodynamic response, matching TCD BHI (MAE = 0.11925). The visualization of BHI and cerebral perfusion across the 68 functional regions confirmed the

model's high spatial resolution. Subsequent pathological simulation (MCA stenosis) verified the model's applicability in disease assessment.

Discussion

This study first quantitatively characterized the regulation of microcirculatory resistance and arteriolar diameter under hypercapnia. We propose a novel 3D-1D-0D geometric multiscale BHI calculation method driven by parameters reflecting cerebrovascular regulation capability. This approach overcomes traditional imaging limits in quantification and resolution, providing a non-invasive, high-resolution (functional region and voxel-level), and absolutely quantitative CVR assessment tool, offering a valuable technical pathway for individualized stroke intervention.

Images (Optional)



Acknowledgements (Optional)

Acknowledgements

This work was supported by the National Key Research and Development Program of China (Grant No. 2021YFA1000202), the National Natural Science Foundation of China (Grant Nos. 12202022, 32271361, and 12572064), and the Beijing Natural Science Foundation (Grant Nos. 4242032 and L246057).

Session Category

Cardiovascular/Cardiorespiratory Biomechanics: Methods, Models and Applications

P4-023

Real-Time Prediction of Stent Deployment for Brain Aneurysms Treatment Using Statistical Shape Modelling and Finite-Element-Based Surrogate Modelling

PhD Beatrice Bisighini[1], PhD Baptiste Pierrat[1], Prof Stéphane Avril[1], PhD Miquel Aguirre[2,3]

[1]Sainbiose, Mines Saint-Étienne, Saint-Étienne, Auvergne-Rhône-Alpes, France. [2]Universitat Politècnica de Catalunya, Barcelona, Catalunya, Spain. [3]CIMNE, Barcelona, Catalunya, Spain

Introduction

The growing adoption of minimally invasive procedures has intensified the need for fast and reliable planning tools capable of predicting both operative outcomes. Finite-element-based surrogate modelling has emerged as a promising approach [1], yet significant challenges persist in cardiovascular applications. These challenges stem from the complexity of parametrising vascular anatomy, the limited availability of clinical data, and the substantial computational cost of high-fidelity simulations. In this study, we present a framework that integrates finite element modelling with statistical shape modelling and machine learning to achieve real-time prediction of stent deployment for the treatment of cerebral aneurysms.

Methods

We based our work on a clinical database of cerebral aneurysms and their associated parent arteries. Due to their substantial morphological variability, we focused on small-neck cases, where the effect of the aneurysm shape on stent behaviour is minimal. For each patient-specific geometry, the parent artery was reconstructed and used to build a statistical shape model, later used to parametrise the anatomies and augment the dataset through the generation of synthetic cases. Stent deployment was simulated for every synthetic artery using EndoBeams.jl, our open-source finite element software previously validated through benchmark studies and experimental tests [2]. A surrogate model, combining proper orthogonal decomposition with gaussian process regression, was trained to map statistical shape features of the arteries to their corresponding deployed stent configurations.

Results

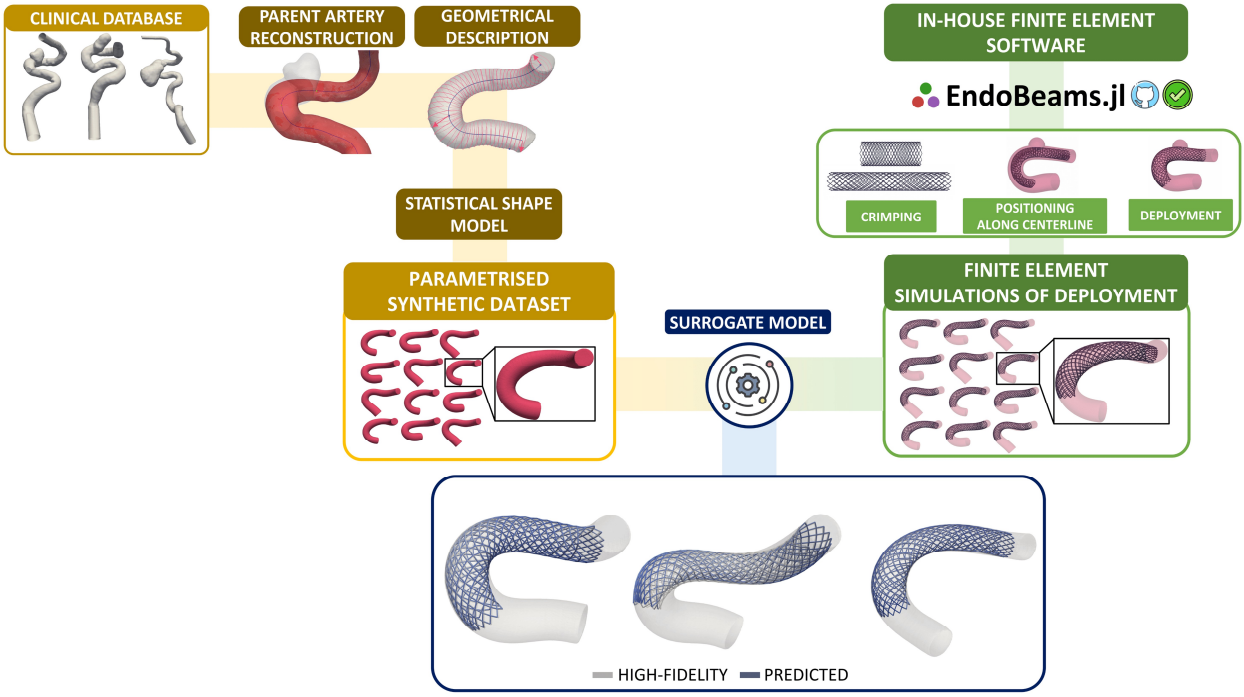
Even with 400 samples, prediction accuracy remained high, with average positional errors below 8.6% and median errors around 1.6%. Expanding the training set to 4900 samples further improved performance, yielding a median positional error under 0.1 mm (0.97%)

and a maximum error of 0.5 mm (4.8%). The largest discrepancies appeared in the radial direction, whereas deployed stent length was consistently predicted with high accuracy.

Discussion

These findings demonstrate that surrogate modelling offers a robust and clinically meaningful solution for real-time prediction of stent deployment, even in complex scenarios. Future work will incorporate aneurysm–artery intersection features into the parametrisation, enabling extension of the method to large-neck aneurysms.

Images (Optional)



References (Optional)

[1] Bridio et al., J. Mech. Behav. Biomed. Mater., 2023.

[2] Bisighini et al., Adv. Eng. Softw., 2022.

Session Category

Cardiovascular/Cardiorespiratory Biomechanics: Methods, Models and Applications

P4-024

High Speed Acute Cardiac Infarct Simulations using High Fidelity Heart Data and the Neural Network Finite Element Approach

Mr. Benjamin Thomas, Prof. Michael Sacks Ph.D.

University of Texas at Austin, Austin, Texas, United States

Introduction

Simulations of cardiac disease remains a cornerstone of discovery and treatment development, yet current cardiac simulations remain unsuitable for near real-time clinical decision making due to time-intensive methods. To address this, simulations need to execute in a tractable clinical timeframe (execution times on the order of minutes). Scientific Machine Learning (SciML) exploits recent advances in machine learning to solve physics-based models. We utilized our neural network finite element SciML approach to perform realistic high-speed simulations of the normal and infarcted heart using a comprehensive heart model dataset. We demonstrate the ability to generate high fidelity pressure-volume (PV) and wall stress responses in a matter of 2-4 seconds.

Methods

We utilized a high-fidelity ovine heart dataset, including geometry, fiber structure, surface action potentials, and pressure-volume from a single heart. We extended our SciML "Neural Network Finite Element (NNFE)" method that utilized a finite elements mesh for problem geometry and directly solves the parameter-to-solution map by learning the displacement solution over the complete physiological range. To simulate myocardial infarction, the training regime was extended to include a range of infarct sizes and anatomical locations. The final JAX-based software platform, termed 'CARDIAX,' required no data as the NNFE method solves the same governing equations by minimizing the same residual that is used in the traditional finite element method.

Results

The NNFE neural networks for healthy and infarcted models were trained until the errors over the physiological range were within 0.1% error of the standard FE simulation displacements. This is checked after training and is not used during training. Once trained was completed, the time to evaluate the NNFE cardiac model was approximately 0.15 seconds, with a complete pressure-volume loop in about 1 second. In additional accurate displacement, stress, and strain tensors, the NNFE method was able to accurately predict the effects of randomly size/placed infarcts.

Discussion

We demonstrated the ability to learn the normal and acutely infarcted PV loop using a high-fidelity heart model using the ‘CARDIAX’ NNFE method. We are currently incorporating B-spline geometries allowing patient specific geometries and reduce the problem size to reduce training and execution times.

Session Category

Cardiovascular/Cardiorespiratory Biomechanics: Methods, Models and Applications

P4-025

In Vivo Deformation of the Human Single Ventricle

Mr. Benjamin Thomas[1], Dr. Radomir Chabiniok M.D., Ph.D.[2], Prof. Michael Sacks Ph.D.[1]

[1]University of Texas at Austin, Austin, Texas, United States. [2]UT Southwestern Medical Center, Dallas, Texas, United States

Introduction

Single ventricle (SV) disease is a congenital condition where the ventricles fuse during in utero development. The abnormal shape of the SV directly influences the underlying biomechanics of the patient's heart and can lead to increased mortality.
We determined the local in vivo SV deformations over a single cardiac cycle to obtain regional strains fields and area changes. By determining the *in vivo* deformation, we can better understand this disease and develop better metrics to characterize the severity of the disease.

Methods

3D in vivo images of 3 patients with SV were segmented over the cardiac cycle, with 15-20 frames total per heart. To compute the 3D wall strains, we use truncated hierarchical B-splines (THB-spline) to encapsulate the SV endocardial and epicardial surfaces. Cubic order was used for the in-surface directions and linear order for the transmural direction. As in previous surface-based studies, we exploited the local support nature of B-splines to compute local deformations. Use of THB-splines further allowed local mesh refinement for regions of more complex geometry and deformation that are common to the SV. The resulting personalized mesh convects with the SV over the cardiac cycle, allowing 3D shape and strains to be directly computed.

Results

Use of THB splines resulted in high fidelity fits with far fewer control points than our previous NURBS based method, with no loss of accuracy. Results from all three patients demonstrated very complex, asymmetric, and generally very abnormal deformations patterns. These included focal regions of high deformation (>30% strain), irregular shape, and pronounced irregular end-diastole to end-systolic deformations. Some transmural shearing was also observed, especially mid-ventricle.

Discussion

We have shown the unique ability to compute the in vivo deformations of the single ventricle. This gives key insights into the local strain patterns that the ventricle undergoes.

An improvement to this method would be to also take into account the biomechanics of the tissue when tracking over time to fill in the 3D volume and give more accurate estimates throughout the ventricle. Use of THB-splines will facilitate direct translation to efficient computational modeling already in progress.

Session Category

Cardiovascular/Cardiorespiratory Biomechanics: Methods, Models and Applications

P4-026

Equivalent Stress-to-Strength Ratio for Assessing Rupture Risk of Abdominal Aortic Aneurysms

Ms. Chanhee An[1], Mr. Sukheon Kang[1], Mr. Hyeonbin Moon[1], Mr. Wonjin Choi[1], Dr. Hongmin Oh[2], Dr. Gyu-Han Lee[2], Prof. Dong Hyun Yang[2], Prof. Seunghwa Ryu[1], Prof. Doosang Kim[3], Prof. Simon Song[4], Prof. Seungyong Shin[5], Prof. Hyun Jin Kim[1]

[1]Korea Advanced Institute of Science and Technology, Yuseong-gu, Daejeon, Korea, Republic of. [2]Asan Medical Center, Songpa-gu, Seoul, Korea, Republic of. [3]Veterans Health Service Medical Center, Gangdong-gu, Seoul, Korea, Republic of. [4]Hanyang University, Seongdong-gu, Seoul, Korea, Republic of. [5]Korea University Ansan Hospital, Ansan, Gyeonggi-do, Korea, Republic of

Introduction

Abdominal aortic aneurysm (AAA) is a prevalent cardiovascular disease in which rupture remains a major cause of morbidity and mortality. Reliable prediction of rupture risk and location is essential for effective clinical management. However, commonly used indices do not adequately capture the biomechanical behavior of the aneurysmal wall and the underlying mechanisms of rupture.

Methods

We present a biomechanical metric - the equivalent stress-to-strength ratio (ESSR) – that incorporates both arterial wall strength and pulsatile loading conditions. The performance of ESSR was evaluated across a broad range of biomechanical, morphologic, and physiologic conditions and compared against conventional stress- and strain-based indices. Twenty-two idealized AAA models with systematically varied geometric, material, and physiological parameters were analyzed using three-dimensional, one-way fluid–structure interaction simulation. ESSR, stress, and strain distributions were quantified and assessed in the context of clinically reported rupture scenarios.

Results

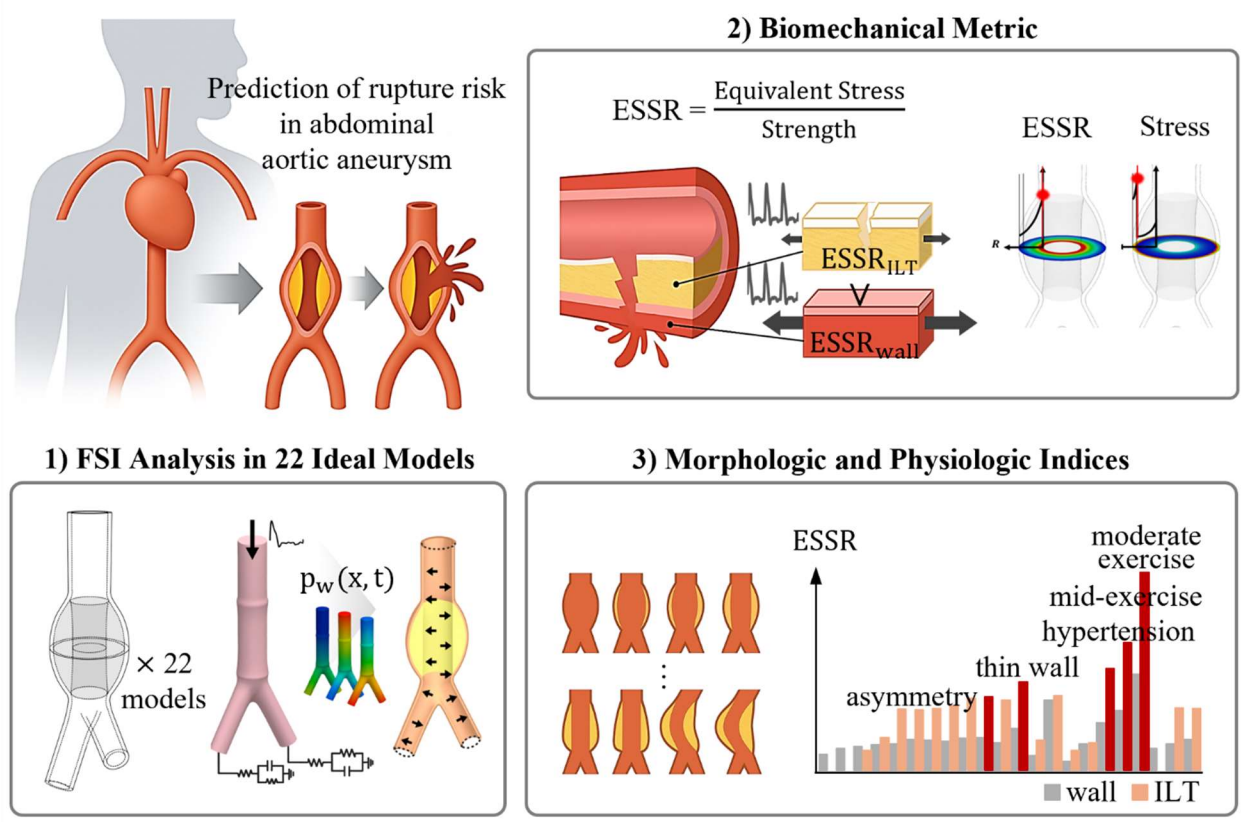
ESSR consistently predicted all clinically observed rupture-prone locations, whereas traditional biomechanical indices aligned with only a subset of these observations. ESSR indicated elevated rupture risk within regions of thick intraluminal thrombus (ILT) or in thrombus-free wall segments when ILT was thin. In cases with sagging ILT, the predicted rupture-prone region shifted toward areas of maximal thrombus thickness. Exercise and

hypertension increased overall rupture susceptibility, and aortic asymmetry and reduced wall thickness elevated localized rupture risk.

Discussion

ESSR effectively captures the interplay between mechanical loading and tissue strength, enabling more accurate prediction of AAA rupture scenarios than stress- or strain-based metrics. The results highlight the importance of ILT thickness, blood pressure, wall thickness, and geometric asymmetry in governing rupture risk. ESSR shows strong promise as a clinically useful biomechanical indicator for identifying high-risk AAA conditions.

Images (Optional)



Acknowledgements (Optional)

This work was supported by the National Research Foundation of Korea (NRF) grant funded by Ministry of Science and ICT (MSIT) (2022R1A5A1022977), Ministry of Food and Drug Safety (MFDS) (RS-2023-00215667), and Samsung Research Funding and Incubation Center for Future Technology (SRFC-IT2401-04). We would like to acknowledge the technical support from ANSYS Korea.

Session Category

Cardiovascular/Cardiorespiratory Biomechanics: Methods, Models and Applications

P4-027

Predicting Postoperative Cerebral Perfusion in Chronic Internal Carotid Artery Stenosis Through Patient-Specific Inference of Leptomeningeal Anastomoses

Mr. Chi Hang To MSc[1], Mr. Yuki Kotani BSc[1], Dr. Shigeki Yamada PhD[2], Dr. Marie Oshima PhD[1]

[1]The University of Tokyo, Tokyo, Tokyo, Japan. [2]Nagoya City University, Nagoya, Aichi, Japan

Introduction

Predicting regional cerebral perfusion under chronic carotid stenosis after surgery is crucial to prognosis [1], but remains challenging because leptomeningeal anastomoses (LMAs) and distal autoregulatory capacity cannot be imaged directly [2]. This study develops and validates a computational framework that (1) infers patient-specific LMA connectivity under distal vascular uncertainty, (2) incorporates autoregulation, and (3) integrates inferred collaterals into a 1D–0D whole-body circulation model to enable preoperative prediction of postoperative distal perfusion.

Methods

Ensembles of distal arterial networks were generated by probabilistic sampling of anatomical parameters constrained by Murray's law and projected onto the cortical surface. LMA connectivity was inferred per patient by minimising mismatch between simulated and preoperative SPECT perfusion using a genetic algorithm with preoperative 4D Flow MRI inflows as boundary conditions and LMA configuration as the decision variable. Postoperative perfusion was simulated using pre-optimised vasculature with postoperative inflows, incorporating a simplified flow-dependent autoregulation model. Inferred LMA characteristics were mapped to a lumped-parameter representation and incorporated into a 1D–0D whole-body circulation model.

Results

Four patients with internal carotid artery stenosis were analysed. For each, an ensemble of 200 optimised peripheral vascular configurations converged toward a coherent functional mode of collateral redistribution. Inferred redistribution patterns, LMA radii and counts were physiologically plausible and consistent with reported ranges. Postoperative simulations captured cerebral perfusion in three patients. In the remaining patient, perfusion was not fully captured, and incorporation of the simplified autoregulation model did not improve agreement. Initial tests indicate that the lumped LMA model can reproduce flow patterns consistent with detailed LMA simulations under baseline conditions.

Discussion

Results demonstrate that the framework produces physiologically plausible distal perfusion predictions, and that ensemble-based inference covers the range of possible collateral configurations without overfitting, enabling lumped 1D–0D representation. The mismatched case reflects pronounced autoregulatory impairment and non-uniform pial pressure under extreme stenosis. Limitations include small cohort and lack of patient-specific measurements for intracranial boundary conditions. Future work will validate predictive accuracy across more patients, refine autoregulation using acetazolamide-challenge data, and explore virtual-surgery scenarios to assess potential of model for preoperative planning.

References (Optional)

[1] Bradac et al., Clin Neuroradiol, 2017

[2] Brozici et al., Stroke, 2003

Session Category

Cardiovascular/Cardiorespiratory Biomechanics: Methods, Models and Applications

P4-028

A Multi-scale Modeling Approach for Understanding Cardiovascular Remodeling in Gender-Affirming Hormone Replacement Therapy

Mx. Christian Andrade Herrera, Mrs. Adhithi Lakshmikanthan M.S., Dr. Pim Oomen PhD

Department of Biomedical Engineering, Edwards Lifesciences Foundation Cardiovascular Innovation and Research Center, University of California, Irvine., Irvine, California, United States

Introduction

Gender-affirming hormone therapy (GAHT) induces physical changes by introducing or suppressing sex hormones. These treatments are lifesaving for transgender individuals, preventing suicide and depression. As GAHT becomes increasingly accessible, we are just beginning to observe and understand its long-term consequences across the lifespan. However, there is limited understanding of how GAHT impacts the heart, despite estrogen and testosterone's well-established impact on cardiac remodeling and function. Therefore, we use a novel multi-scale modeling approach to test the hypothesis that GAHT causes cardiac remodeling.

Methods

We created a multi-scale model by combining our recently published models of organ-scale cardiovascular mechanics [2] and cell-scale mechanobiology model of cardiomyocyte signaling [3]. The organ-scale sub-model employs a reduced-order model approach to simulate cardiac mechanics and hemodynamics. The cell-scale mechanobiology sub-model uniquely incorporates sex hormone-driven cardiomyocyte hypertrophic signaling. The sub-models were coupled using linear transfer functions [4], as shown in Fig. 1, creating a closed-loop system of organ-to-cell mechanics and cell-to-organ hypertrophy.

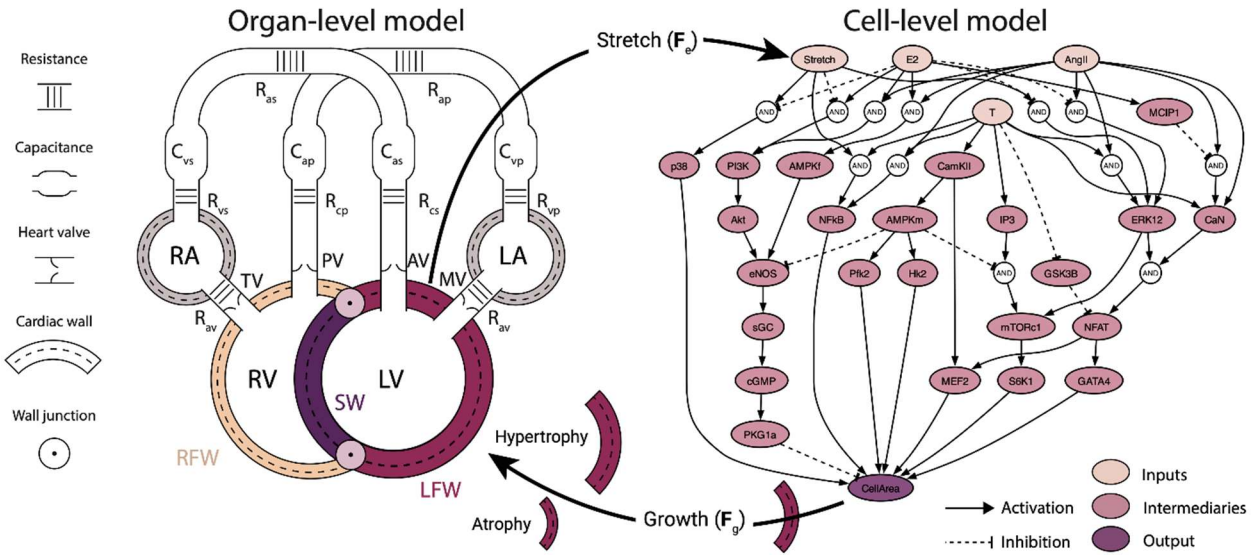
Results

We fine-tuned the organ-level model parameters to match the baseline volumes for trans-males and trans-females [5]. We prescribed the hormone dose (estrogen or testosterone) and calibrated the linear transfer function to match the 6-month post-GHRT change in LVESV and LVEDV: an 8.9% increase for transgender men and a 1.9% decrease for trans-females [5].

Discussion

Our preliminary findings align with reported data showing changes in LVEDV and LVESV. The more pronounced remodeling observed in transgender men compared to transgender women is consistent with testosterone's greater hypertrophic effect compared to estrogen. However, multiple assumptions were also made due to the available data. Future work will focus on matching individual patient data to further validate our model. In conclusion, we developed a multi-scale model that can match cardiac remodeling 6 months post-GHRT. Ultimately, our multiscale model could be used to elucidate whether changes in cardiovascular mass are due to hormonal, mechanical, or a combination of both factors.

Images (Optional)



References (Optional)

[1] Naoya Masumori *et al.*, Circ Rep. 2023

[2] Clara Jones, Pim Oomen. Comput Biol Med. 2025

[3] Adhithi Laksmikanthan *et al.*, bioRxiv. 2025

[4] Ana Estrada *et al.*, Biomech Model Mechanobiol. 2021

[5] Carola Deischinger *et al.*, Euro J Endocronol. 2025

Acknowledgements (Optional)

We want to acknowledge the BEAT lab members, Dr. Ajanta Naidu, and Brit Cervantes for their excellent discussions.

Session Category

Cardiovascular/Cardiorespiratory Biomechanics: Methods, Models and Applications

P4-029

Novel Method to Quantify Tracheal Work of Breathing During Exercise Using MRI-Derived CFD

Mr. Christopher Boles B.Sc.[1,2], Dr. Chamindu Gunatilaka Ph.D.[3], Mr. Keith McConnell M.Sc.[1], Dr. Qiwei Xiao Ph.D.[1], Dr. Hamideh Hayati Ph.D.[1], Dr. Alister Bates Ph.D.[1,2]

[1]Cincinnati Children's Hospital Pulmonary Medicine, Cincinnati, Ohio, United States. [2]University of Cincinnati Biomedical Engineering, Cincinnati, Ohio, United States. [3]Cincinnati Children's Hospital Medical Center, Cincinnati, Ohio, United States

Introduction

Exercise intolerance from dynamic airway obstruction is common and frequently overlooked in youth. Inducible laryngeal obstruction and large airway collapse affect ~7.5% of youth and up to 34% of youth athletes, where increased ventilation reveals hidden collapse. Additionally, exercise-induced bronchospasm occurs in up to 90% of patients with asthma, and exercise-induced bronchoconstriction affects ~15% of youth athletes, further increasing the mechanical burden of breathing. Conventional cardiopulmonary exercise testing cannot localize obstruction location. Work of breathing (WOB) quantifies the effort needed to move air through the respiratory system and can be regionally decomposed using subject-specific computational fluid dynamics (CFD) informed by imaging. Cine magnetic resonance imaging (MRI) sequences visualize the airway mechanics. This study represents the first integration of exercise MRI and CFD to measure tracheal resistive WOB during exercise.

Methods

A healthy young male adult underwent MRI during moderate exercise and at rest. Moderate exercise was defined as achieving ≥100 bpm heart rate while operating an MRI-compatible stepper with resistance bands opposing motion. Imaging included e-THRIVE for cine imaging across the respiratory cycle and FLORET for static anatomy. The airway from nostrils to main bronchi was segmented using ITK-SNAP. Nasal airflow was collected and applied as the inlet boundary condition. CFD simulated a full respiratory cycle and calculated resistive WOB from regional kinetic energy losses between planes at the distal and proximal ends of the upper airway and trachea.

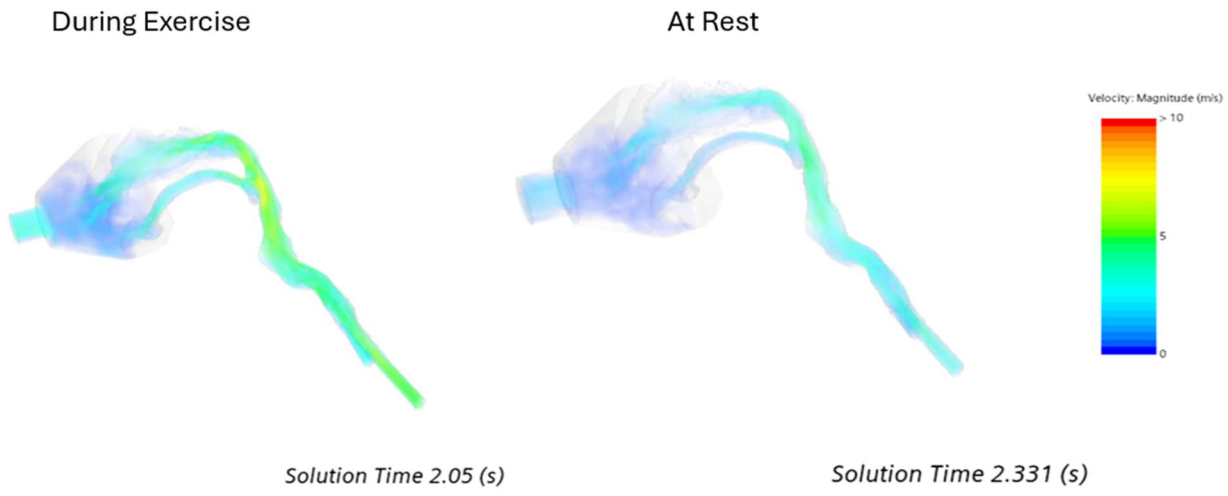
Results

MRI acquisition during exercise was successfully performed without significant motion artifact. Tidal Volume increased from 489 mL at rest to 690 mL during exercise. Tracheal resistive WOB per breath increased from 3.32 mJ at rest to 11.02 mJ during exercise. Tracheal WOB increased from 1.69 mJ/s to 4.48 mJ/s, demonstrating a 165% increase in breathing effort during exercise.

Discussion

This study represents the first demonstration of combining MRI and CFD to assess airway WOB during exercise. This framework enables quantification of how exercise stress alters airflow mechanics and may reveal ventilatory inefficiencies not present at rest. Future studies will include participants with a history of exercise intolerance to understand how to provide more accurate treatment and surgical procedures.

Images (Optional)



Session Category

Cardiovascular/Cardiorespiratory Biomechanics: Methods, Models and Applications

P4-030

Changes in Heart Rate and Heart Rate Variability Pre, During, and Post a 6-Minute Walk Test in Older Adults based on Physical Activity Level

Ms Chyenne Neath BSc (Hons), Dr. Stephen Klassen PhD, Dr. Kimberley Gammage PhD, Dr. Nicole Chimera PhD, CAT(C), ATC, CSCS

Brock University, St Catharines, Ontario, Canada

Introduction

Heart rate (HR) and root mean square of successive differences (RMSSD) are inversely related parameters that assess cardiovascular health and cardiac autonomic regulation, respectively. Both provide insight into overall fitness levels. RMSSD differences have been explored across rest and exercise, but few studies have explored changes across physical activity (PA) levels in older adults. Understanding these differences is important as decreased autonomic function and fitness are associated with aging. This study aims to explore the impact of fitness level on HR and RMSSD pre-, during-, and post-6-minute walk test (6MWT) in older adults.

Methods

A quasi-experimental time-series design assessed HR and RMSSD in adults ≥55 years. The independent variables were PA (low, moderate, high) and time (pre-,during-,post-6MWT); Godin-Shephard Leisure-Time PA Questionnaire identified PA groups. Participants rested supine for 10 minutes pre- and post-6MWT; HR and RMSSD were recorded using Firstbeat Bodyguard 3 (BG30039243, Firstbeat Technologies Ltd, Jyväskylä, Finland) and calculated during a five-minute window in each timepoint. A two-way repeated-measures ANOVA (RM-ANOVA; $p<0.05$) determined HR and RMSSD differences across timepoints and between PA; Holm post-hoc tests assessed interactions. Analyses were performed in JASP (version 0.95.4).

Results

Twenty-eight older adults (16 females, 12 males;55-78 years) had HR and RMSSD assessed pre-, during-, and post-6MWT (Table 1). RM-ANOVA for RMSSD demonstrated statistically significant main effects for time ($p<0.001$); post-hoc tests demonstrated RMSSD was lower during- (12ms±6) versus pre- (26ms±17, $p<0.001$) and post- (26ms±24, $p=0.005$) 6MWT. RM-ANOVA for HR demonstrated statistically significant main effects for time ($p<0.001$); post-hoc tests demonstrated HR was larger during- (115bpm±21) versus pre- (61bpm±9, $p<0.001$) and post- (64bpm±11, $p<0.001$), and post- versus pre- (64bpm±11 vs. 61bpm±9, $p=0.012$) 6MWT. Despite no current significant interaction, there is a trend

towards significance in the main effect of PA (p=0.053) and the interaction between time and PA (p=0.051).

Discussion

Preliminarily, RMSSD is lower and HR is higher during- compared to pre- and post-6MWT and HR is lower pre- compared to post-6MWT; there are no differences between PA or between time and PA interactions. This suggests RMSSD and HR may vary similarly pre-, during-, and post-6MWT across PA groups.

Images (Optional)

Table 1. Average heart rate and RMSSD pre-, during-, and post-6MWT for participants in low, moderate, and high PA groups.

	HR			RMSSD		
	Pre	**During**	**Post**	**Pre**	**During**	**Post**
Low (n=6)	64±7	128±17	69±10	19±10	10±4	16±7
Moderate (n=9)	60±7	102±16	60±8	35±24	11±7	43±35
High (n=13)	61±11	118±21	64±13	23±10	13±6	20±12
Total	61±9	115±21	64±11	26±17	12±6	26±24

Session Category

Cardiovascular/Cardiorespiratory Biomechanics: Methods, Models and Applications

P4-031

Cerebral Collateral Development Alters Circle of Willis Hemodynamics and Forces Experienced by the Occlusive Clot During Acute Ischemic Stroke - A Computational Fluid Dynamics Study

Mr. Cody Kubicki[1], Dr. Scott Simon[2], Dr. Keefe Manning[1,3]

[1]Department of Biomedical Engineering, The Pennsylvania State University, University Park, PA, United States. [2]Department of Neurosurgery, Penn State College of Medicine, Hershey, PA, United States. [3]Department of Surgery, Penn State College of Medicine, Hershey, PA, United States

Introduction

Cerebral collateral assessment has become a common metric for treatment planning in acute ischemic stroke patients [1] due to clinical evidence that well-developed collateral networks are correlated with favorable patient outcomes for reperfusion therapies [2]. However, the mechanisms driving these outcome disparities are not well clarified.

Methods

A computational fluid dynamics model developed in OpenFOAM was used to assess hemodynamic changes during large vessel occlusion (LVO) and to relate these changes to the mechanisms governing reperfusion therapy susceptibility. Blood flow and clot forces were quantified in a Circle of Willis model with varying collateral development levels during middle cerebral artery (MCA) occlusion. A lumped resistor model represented the collateral network based on the total applied hemodynamic resistance (R_{CN}). Five collateral development conditions were simulated, ranging from favorable (CS4 – R_{CN}=1x10^9 Pa·s/m^3), to poor (CS1 – R_{CN}=18x10^9 Pa·s/m^3), to absent (CS0 – R_{CN}=Inf Pa·s/m^3).

Results

MCA occlusion caused up to a 30% increase in systemic mean arterial pressure (MAP) but was less severe in favorable collateral cases. The ipsilateral collateral flow increased up to 20-fold following LVO, which elevated blood flow distal to the LVO. Favorable collaterals showed a 66% lower pressure drop across the clot compared to poor collaterals, which was modulated primarily by distal pressure changes. Lower pressure drops led to a linear decline in distal compaction forces experienced by the clot, ranging from 116.3 mN to 47.8 mN, similar to force estimates on clots *in vivo* [3] (see table).

Discussion

Our study indicated that collaterals serve multiple functions during stroke. First, collaterals compensate for lost blood flow to the affected brain region by permitting retrograde flow toward the distal end of the occluded vessel. Second, collaterals reduce the pressure forces on the clot, which can improve reperfusion therapy susceptibility. Overall, this study showed that we can leverage our computational model to better understand the importance of cerebral collateral circulation during stroke and the influence of collaterals on therapeutic outcomes in a realistic simulated physiological environment.

Images (Optional)

	Collateral Development Level	Proximal MAP (mmHg)	Distal MAP (mmHg)	Mean ΔP (mmHg)	F_{mean} (mN)	F_{max} (mN)
Absent	*In Silico* – CS0	117.8	0.0	117.8	116.3	172.7
Poor	*In Silico* – CS1	113.3	12.4	100.9	101.3	154.5
↓	*In Silico* – CS2	106.5	33.0	73.2	77.0	126.1
↓	*In Silico* – CS3	101.5	48.8	52.3	58.7	99.4
Favorable	*In Silico* – CS4	99.2	58.8	39.6	47.8	82.5
	In Vivo – Mean (95% C.I.) [3]	95.8 (69.8-121.8)	32.7 (3.7-61.7)	63.1 (24.9-101.3)	58.0 (22.9-93.1)	-

References (Optional)

[1] G. Maguida *et al.*, Journal of Stroke, 2023

[2] H. Saber *et al.*, Neurology, 2021

[3] T. Sorimachi, Journal of NeuroInterventional Surgery, 2011

Acknowledgements (Optional)

Research was supported by the NIH through Grant HL146921, T32 Fellowship Grant 5T32NS115667, NSF ACCESS program allocation MDE250008 (NSF grants 2138259, 2138286, 2138307, 2137603, and 2138296), and the Purdue University Rosen Center for Advanced Computing.

Session Category

Cardiovascular/Cardiorespiratory Biomechanics: Methods, Models and Applications

P4-032

Controlled Intramural Fluid Injection Reveals Biomechanical Drivers of Thoracic Aortic Dissection

Dr Cristina Cavinato[1,2], Dr Baptiste Pierrat[3], Dr Ehsan Ban[2], Dr Mathieu Simon[3], Pr Jay D. Humphrey[2,4]

[1]LMGC, Univ. Montpellier, CNRS, Montpellier, France, France. [2]Department of Biomedical Engineering, Yale University, New Haven, CT, United States. [3]Mines Saint-Etienne, Univ Lyon, Univ Jean Monnet, INSERM, U 1059, Sainbiose, Centre CIS, Saint-Etienne, France, France. [4]Vascular Biology and Therapeutics Program, Yale School of Medicine, New Haven, CT, United States

Introduction

Thoracic aortic dissection remains a devastating clinical event whose progression depends on the interplay between global mechanical loads, local wall structure, and the morphology of an initiating tear [1]. Yet, the biomechanical conditions that govern intramural propagation— particularly the pressure and structural thresholds required to extend an existing lesion—remain poorly defined, largely due to difficulties in observing this process *in vivo* or reproducing it under physiologically relevant ex vivo conditions.

Methods

Controlled extension–distension loading was combined with intramural injection to quantify how mechanical and injection parameters modulate dissection initiation and propagation in intact porcine descending thoracic aortas (DTAs). DTAs were mounted in a controlled extension–distension system, equilibrated at physiological pressure, and mechanically characterized via a comprehensive protocol. A validated four-fiber family model captured their nonlinear, anisotropic behavior. Intramural injections were performed under fixed luminal pressure while varying axial stretch (1.1vs.1.3), injection rate (1 vs. 2 mL/min), and needle gauge (25Gvs.30G).

Results

Pressure–volume curves exhibited a steep rise followed by stepwise fluctuations, reflecting successive medial micro-failures before depressurization of the false lumen. Higher axial stretch increased peak pressures and injected volumes (Fig.1), whereas faster injection rates produced sharp pressure elevations at lower volumes, consistent with prior injection-

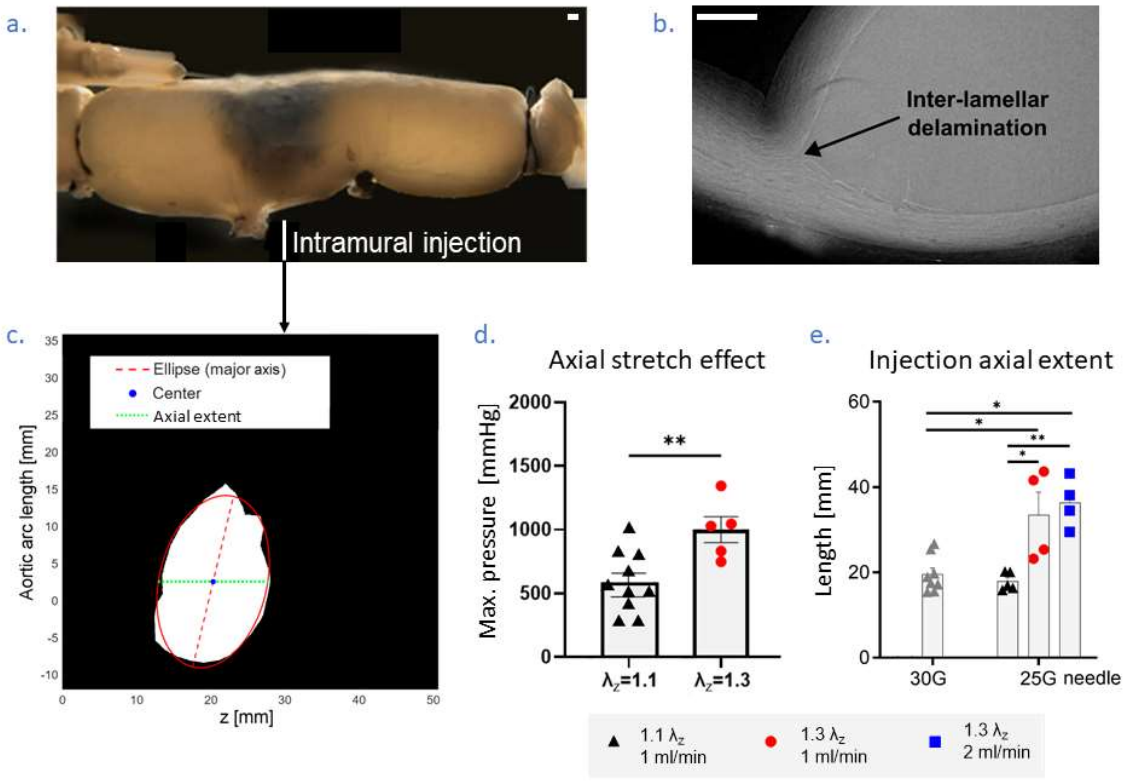
based delamination studies [2]. Smaller needles generated higher pressures for equivalent volumes, reflecting greater local stress concentration.

Quantitative image analysis—using synchronized orthogonal cameras, cylindrical surface reconstructions, and morphometric metrics—showed that axial stretch and injection rate are dominant regulators of dissection morphology. Increased axial stretch produced larger, elongated, and more anisotropic intramural patches, while higher injection rates promoted circumferential propagation and extensive interlamellar separation, corroborated by histomorphology. Synchrotron X-ray phase-contrast imaging of non-tensioned DTAs with contrast-agent injections revealed the interaction of the liquid with the lamellar structure before propagation and the subsequent dissection path, consistent with camera-based and histological measurements, reinforcing result robustness.

Discussion

Together, these findings demonstrate that axial loading and intramural flow rate critically modulate dissection propagation thresholds and morphology. Future work will integrate these results with computational modeling to refine criteria for tear progression.

Images (Optional)



References (Optional)

[1]Nienaber *et al.*, *Nat. Rev.*, 2016

[2] Roach et al., *Can. J. Cardiol.*, 1999

Acknowledgements (Optional)

This work was supported by the US National Institutes of Health (U01 HL142518), French Agence National de la Recherche (ANR-22-CPJ1-0090-01), and the Leducq Foundation (22CVD03 – erAADicate).

Session Category

Cardiovascular/Cardiorespiratory Biomechanics: Methods, Models and Applications

P4-033

Fractional Viscoelastic Modeling for the Heart and Arteries

Dr Will Zhang[1], Prof Daniel Beard[1], Prof Alexey Kamenskiy[2], Prof Gerhard Holzapfel[3], Prof David Nordsletten[1]

[1]University of Michigan, Ann Arbor, MI, United States. [2]University of Nebraska, Omaha, NE, United States. [3]TU Graz, Graz, Styria, Austria

Introduction

Cardiovascular tissues exhibit nonlinearity, anisotropy and viscoelasticity as hallmarks of their mechanical function, allowing for preferential distribution of load, progressive recruitment, and energetic dampening. Nonlinear fractional viscoelasticity theory provides mechanisms for characterizing this constitutive behavior across cardiovascular tissues – including muscular / elastic arteries and the heart.

Methods

In this work, we leverage mechanical data from arteries and the heart. Human femoropopliteal and thoracic aortic samples were cut from cadaveric arteries and tested with varying biaxial stretch experiments followed by stress relaxation experiment. Human myocardial data was tested cubic samples and biaxial sheets, examining shear, shear relaxation, and stretch. Finally, data considered in this presentation was acquired from mouse trabeculae and examined for passive mechanical response under uniaxial stretch, focusing on stress relaxation phenomena at varying calcium levels. All data was analyzed using nonlinear fractional viscoelasticity theory, providing a framework for the characterization of the response of the tested cardiovascular tissues.

Results

We show that for all three considered cardiovascular tissue types – including muscular arteries, elastic arteries and heart muscle – that the nonlinear anisotropic viscoelastic response can be well captured using nonlinear fractional viscoelastic theory (with errors for compounded stress responses typically below 9%). We also highlight the sensitivity of passive mechanics, particularly in the myocardium, to calcium which can amplify stresses 6-fold and significantly enhance hysteresis.

Discussion

This work demonstrates that nonlinear fractional viscoelasticity provides a unified and compact constitutive framework capable of capturing the complex mechanical behaviors of cardiovascular tissues. This suggests, while arteries and cardiac muscle exhibit different structural organization, their hierarchical organization yields power spectrum behavior well-suited for fractional operators, capturing the effects of multiscale mechanics without explicit modeling at each scale. This balance between model fidelity and parsimony is advantageous for both experimental interpretation and integration into large-scale computational simulations. This work also highlights the strong need for revising the theory of passive mechanics as a static state of tissue, highlighting that the biochemical response of tissue heavily influences its mechanical state.

References (Optional)

Session Category

Cardiovascular/Cardiorespiratory Biomechanics: Methods, Models and Applications

P4-034

RT3DE-Derived Finite Element Analysis of Functional Tricuspid Regurgitation and RV Free Wall Approximation

Mr. Davide Tondi[1,2], Prof. Francesco Sturla PhD[3,1], Prof. Riccardo Vismara PhD[1], Prof. Alberto Redaelli PhD[1], Prof. Emiliano Votta PhD[1]

[1]Politecnico di Milano, Milano, Italy, Italy. [2]ESB Member, Milano, Italy, Italy. [3]3D and Computer Simulation Laboratory, IRCCS Policlinico San Donato, San Donato Milanese, Italy, Italy

Introduction

Tricuspid valve (TV) regurgitation (TR) affects approximately 1.6 million individuals in the USA [1], yet its pathophysiology and biomechanics remain underexplored. Recent evidence associating TR with increased mortality [1] has spurred interest in its biomechanical evaluation. We present a finite element modeling framework based on real-time 3D echocardiography (RT3DE) that enables 3D reconstruction and simulation of the TR condition, and prediction of TV biomechanics following TR treatment through right ventricular free wall approximation (FWA) along three directions.

Methods

RT3DE was performed on six explanted porcine hearts on a pulsatile test-bench in TR conditions and following FWA [1].

From pre-FWA RT3DE, the 3D geometry of TV annulus, leaflets and papillary muscles (PMs) tips was reconstructed at end-diastole (ED) and peak-systole (PS).

The ED TV configuration was complemented by a parametric chordae tendineae (CT) template [2]. Leaflet and CT tissues were described as anisotropic hyperelastic through the Holzapfel and Weiss model, respectively. CT initial lengths were calibrated by minimizing the mismatch between simulated and reconstructed leaflet configurations at PS in TR conditions [3]. For TR conditions, TV closure from ED to PS was simulated by prescribing physiological pressure conditions and annulus and PMs motion from RT3DE tracings. In post-FWA simulations, TV closure was preceded by the reduction of inter-PMs distance by 30% and 60% along three approximation directions. Predicted post-FWA configurations at PS were validated against post-FWA RT3DE reconstructions.

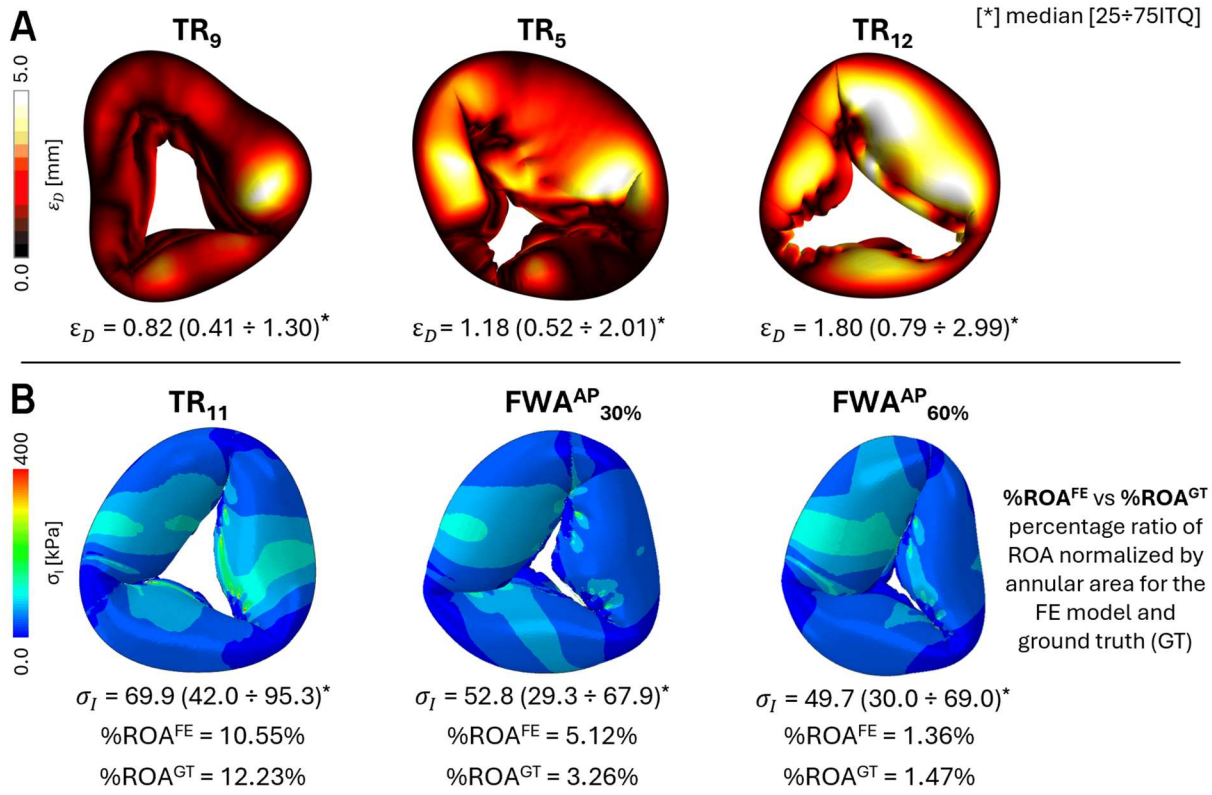
Results

Across the 6 TR configurations at PS, the median distance from simulated to ground-truth leaflet surface (ε_D) ranged between 0.82 and 1.80 mm (Fig.1A); leaflets median maximum principal stresses (σ_I) ranged from 42.6 to 69.9 kPa. FWA simulations predicted reduced regurgitant orifice area (ROA) at PS, consistent with *in-vitro* data, and a decrease in σ_I by up to 28.9% (Fig.1B) relative to baseline TR.

Discussion

Simulations closely replicated TV geometry at PS in TR conditions. The predicted reduction in ROA in post-FWA conditions was consistent with ground-truth evidence. The associated reduction in leaflet stresses suggests a beneficial biomechanical effect of FWA.

Images (Optional)



References (Optional)

[1] Jaworek et al., STRUCTURAL HEART, 2020

[2] Stevanella et al., Med Eng Phys., 2010

[3] Tondi et al., Comput Methods Programs Biomed, 2026

Acknowledgements (Optional)

IRCCS Policlinico San Donato is a clinical research hospital partially funded by the Italian Ministry of Health.

Session Category

Cardiovascular/Cardiorespiratory Biomechanics: Methods, Models and Applications

P4-035

Assessing Potential Adjunct Medications such as Hydroxocobalamin and Methylene Blue, with REBOA, in the Management of Hemorrhage in a Large Animal (Sus scrofa) Model of Polytrauma

PhD Candidate Dena Norouzi

UThealth, San Antonio, Texas, United States

Introduction

Resuscitative Endovascular Balloon Occlusion of the Aorta (REBOA) is a critical lifesaving technique used to temporarily halt blood flow in the aorta to control severe hemorrhage. However, balloon deflation poses significant challenges, including cardiovascular collapse and the systemic release of ischemic metabolites such as nitric oxide, which can further destabilize the patient. We hypothesized that adjunctive therapies such as hydroxocobalamin (HOC) and methylene blue (MB), when administered alongside REBOA, may mitigate these risks and improve outcomes following Zone 1 REBOA.

Methods

Twenty-two male and female Yorkshire swine were anesthetized, intubated, and subjected to traumatic brain injury (TBI) using a commercially available powder-actuated device, followed by tibial fracture and controlled hemorrhage equivalent to 30–40% of total blood volume. After 60 minutes of aortic occlusion with REBOA and 5 minutes of balloon deflation, animals were randomized into three groups: (1) whole blood (WB) only, (2) WB plus HOC, or (3) WB plus MB. Physiological and laboratory parameters were monitored and analyzed.

Results

At 120 minutes post-balloon deflation, animals treated with WB+MB demonstrated significantly higher pH and lower lactate levels compared to controls ($p < 0.05$), indicating improved acid-base balance and metabolic recovery.

Discussion

Adjunctive MB significantly improved metabolic and acid-base parameters following REBOA balloon deflation compared to HOC or WB alone. These findings highlight MB's potential to enhance REBOA outcomes in severe hemorrhagic trauma, warranting further investigation into its long-term effects and prehospital applications.

References (Optional)

n/a

Session Category

Cardiovascular/Cardiorespiratory Biomechanics: Methods, Models and Applications

P4-036

4D CT-Based automated quantification of RVOT 3D geometry and strain field to support TPVI planning

MSc Davide Astori[1], MSc Francesca Mariani[1], MSc Elena Odinelli[1], MSc Davide Milesi[1], MD Giulia Pasqualin[2], MD Karima Tissir[3], MD Francesco Secchi[4], Prof Alberto Redaelli[1], MD Mario Carminati[2], PhD Francesco Sturla[5,1], Prof Emiliano Votta[1]

[1]Politecnico di Milano, Department of Electronics Information and Bioengineering, Milano, Milano, Italy. [2]Department of Pediatric and Adult Congenital Cardiology, IRCCS Policlinico San Donato, San Donato Milanese, Milano, Italy. [3]Unit of Radiology, IRCCS Policlinico San Donato, San Donato Milanese, Milano, Italy. [4]Unit of Cardiovascular Imaging, IRCCS Multimedica, Sesto San Giovanni, Milano, Italy. [5]3D and Computer Simulation Laboratory, IRCCS Policlinico San Donato, San Donato Milanese, Milano, Italy

Introduction

Transcatheter Pulmonary Valve Implantation (TPVI) is performed in adult patients originally born with severe congenital defects and surgically treated when infants. Implant success and stability depend on the reliable pre-procedural quantification of right ventricle outflow tract (RVOT) size and deformability for correct device sizing, especially when treating complex anatomies with heterogeneous wall mechanical properties. Currently, pre-procedural analyses rely on static size measurements from computed tomography (CT) images; semi-automated methods based on time-resolved (4D) CT imaging have been recently proposed to quantify frame-by-frame RVOT size at multiple cross section [1] or 3D wall strains [2]. We present a fully automated method to quantify RVOT geometry and 3D wall strains from 4DCT imaging.

Methods

At each frame of the 4DCT dataset, the 3D geometry of right ventricle and pulmonary artery (PA) is automatically reconstructed via segmentation by TotalSegmentator, and remeshing and smoothing of the isosurfaces. At end-systole (ES), the isosurface (S_{ES}) is automatically trimmed to isolate RVOT and PA walls. Starting from S_{ES}, a non-rigid registration is iteratively performed between consecutive time-frames using Deformetrica, yielding the time-dependent perimeter (2p) at relevant cross-sections and displacement field over S_{ED}, which is used to compute the strain field. The method was applied to 30 patients: 19 TPVI recipients and 11 patients redirected to open-chest surgery (SPVR). 2p quantifications

were compared vs. those provided by [1] for 5 subjects from each group at the landing zone.

Results

2p quantifications well compared to those obtained by [1], with mean mismatches by 4.2% and 12.7% in TVPI and SPVR patients, respectively. Student t-test highlighted statistically significant differences ($p<0.0001$) in time-averaged perimeter between the two groups (Figure 1.a). Strain maps highlighted the heterogeneous extensibility of the wall (Figure 1.b). The entire workflow required 88 minutes on average.

Discussion

Our preliminary data suggest the reliability of the proposed approach and its potential to provide an exhaustive quantification of RVOT geometry and deformability to support TPVI planning. Full automation paves the way towards integration into the clinical workflow, although time-expense should be reduced by code optimization.

Images (Optional)

a)

Parameter	TPVI group	SPVR group
$\overline{2p}_{time-avg}$	36.4 mm	44.7 mm *
$\overline{\Delta 2p}$ vs. [1]	4.2%	12.7%

b)

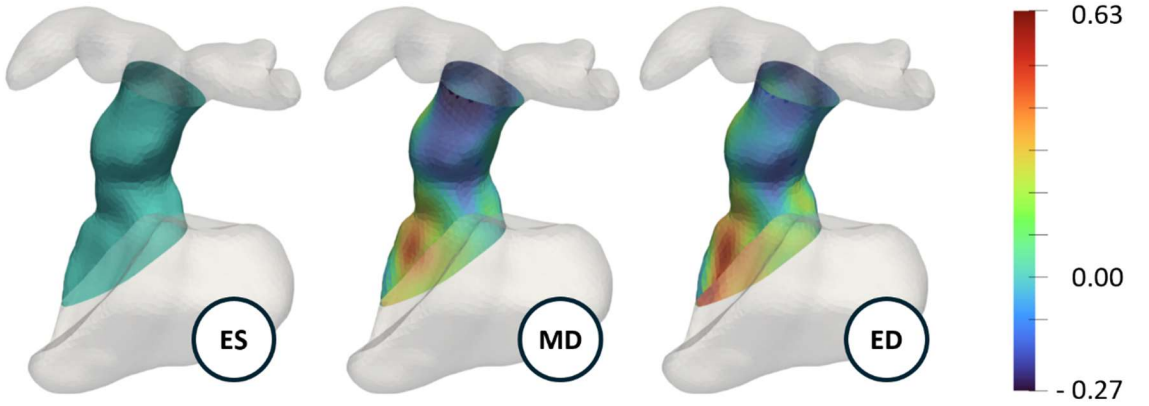


Figure 1: a) table reporting results on the landing zone perimeter (2p) - mean mismatch ($\overline{\Delta 2p}$) vs. ground truth measurements from [1], and mean time-averaged value obtained for the TPVI and SPVR groups; * = statistically meaningful difference vs. TPVI group ($p<0.0001$). **b)** Example of time-dependent axial strains (ε_{11}) for one patient (ES=end-systole, MD=mid-diastole, ED=end-diastole).

References (Optional)

[1] Sturla *et al.*, Comput Methods Programs Biomed 2025

[2] Swanson *et al.*, J Cardiovasc Dev Dis 2024

Acknowledgements (Optional)

IRCCS Policlinico San Donato is a clinical research hospital partially funded by the Italian Ministry of Health.

Session Category

Cardiovascular/Cardiorespiratory Biomechanics: Methods, Models and Applications

P4-037

Personalized Computational Fluid Dynamics Simulations of Transarterial Embolization for Liver Cancer Treatment Planning

Mr. Enrico Sangiorgio MSc[1,2], Dr. Valentina Mazzi PhD[1], Dr. Giuseppe De Nisco PhD[1], Dr. Giuseppe Isu PhD[3], Prof. Diego Gallo PhD[1], Prof. Umberto Morbiducci PhD[1]

[1]Politecnico di Torino, Torino, TO, Italy. [2]Università degli Studi di Palermo, Palermo, PA, Italy. [3]Medics Srl, Torino, TO, Italy

Introduction

Transarterial embolization (TAE) is an established treatment modality for patients with unresectable liver cancer. It involves the localized injection of microspheres via a catheter to selectively obstruct tumor-feeding hepatic arteries [1]. Embolization outcomes depend on procedural variables, such as catheter position and injection flow rate, as well as the clinical case, including tumor burden and hepatic arterial anatomy. In this study, we propose a computational framework that enables virtual TAE in personalized hepatic models.

Methods

Computational fluid dynamics simulations are performed on a patient-specific 3D anatomical reconstruction of the hepatic arterial vasculature, incorporating a virtually positioned catheter. Personalized boundary conditions are derived from liver and tumor perfusion analysis [2], adopting a distance-based method for vascular territory approximation [3]. Microparticles are virtually injected uniformly from the catheter tip and tracked over multiple simulated cardiac cycles. Alternative TAE modelling approaches are compared for outlet-to-outlet particle distribution estimation. Specifically, an Eulerian-Lagrangian approach that concurrently solves blood flow equations and predicts particle trajectories using Newton's second law is evaluated, considering both one-way and two-way coupling between continuous and discrete phases. We also examine a simplified approach that tracks massless particles by integrating the fluid velocity field. The impact of simplification strategies, including arterial geometry truncation and non-explicit modeling of injection fluid, is assessed.

Results

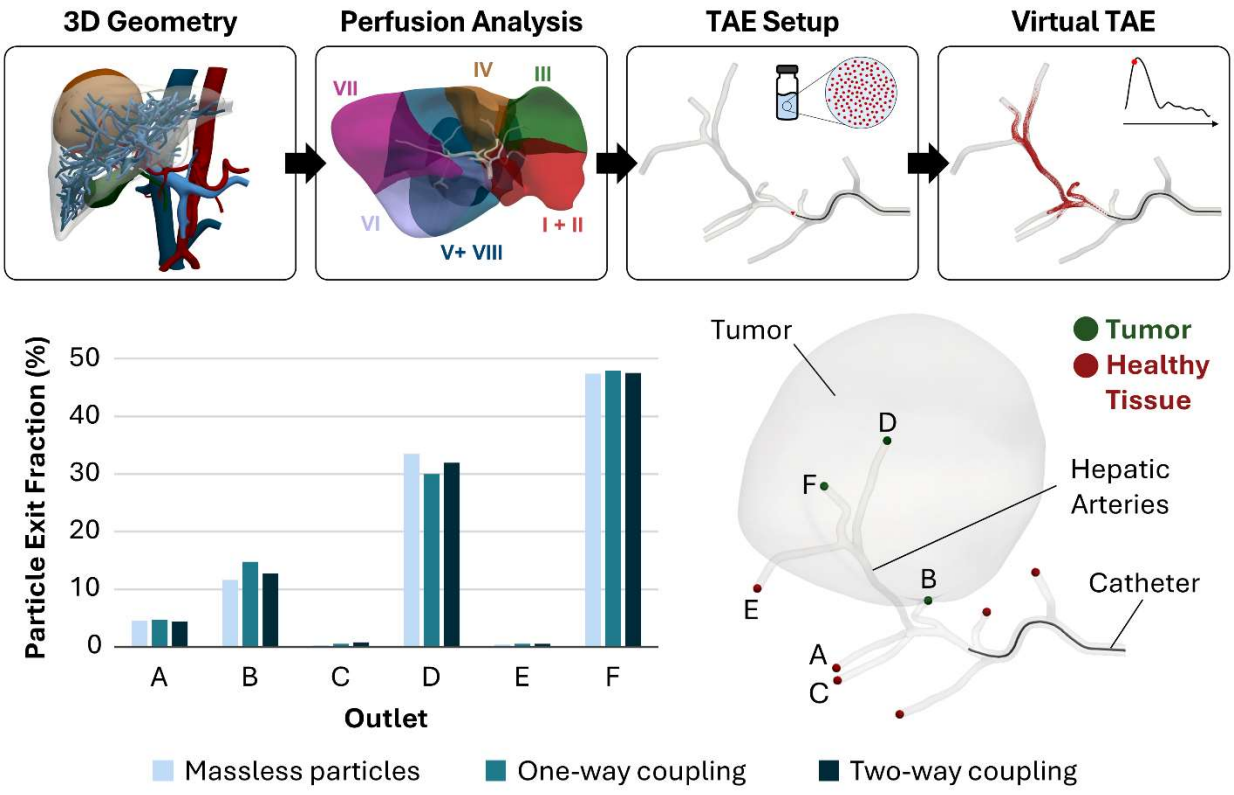
The *in silico* platform successfully replicated the embolization procedure in a patient-specific 3D truncated model of the hepatic arterial tree. Comparison of TAE modeling approaches revealed consistent predictions with a maximum 2% deviation from the two-way coupling strategy (used as reference approach) in outlet-to-outlet particle distribution.

Implemented simplification assumptions showed negligible impact on predicted TAE outcome.

Discussion

The proposed computational framework demonstrates potential to facilitate personalized treatment planning by enabling virtual testing of clinically relevant parameters in a digital twin of the patient. It is currently being refined and extended to additional patient-specific cases. Future developments will entail the integration of pharmacological models to estimate local drug exposure from simulation-predicted microsphere distribution.

Images (Optional)



References (Optional)

[1] Alexandre Pérez-López *et al.*, Acta Biomat, 2022

[2] Jorge Aramburu *et al.*, Int J Numer Meth Biomed Engng, 2016

[3] Dirk Selle *et al.*, IEEE T-MI, 2002

Acknowledgements (Optional)

This work is part of the TEPSIM project, which has received funding from the cascade funding calls of the NODES Program, supported by the MUR – M4C2 1.5 of PNRR, which is funded by the EU – NextGenerationEU (GA No. ECS00000036).

Session Category

Cardiovascular/Cardiorespiratory Biomechanics: Methods, Models and Applications

P4-038

Computational Framework Identifies Optimal Neural Operator for Forecasting Aortic Aneurysm Outcomes

Dr. Erica Schwarz[1], Dr. Qianying Cao[2], Dr. David Li[3], Mr. Colin Means[1], Dr. Roland Assi[4], Dr. George Karniadakis[2], Dr. Jay Humphrey[1]

[1]Yale University, New Haven, CT, United States. [2]Brown University, Providence, RI, United States. [3]University of Nebraska, Omaha, Omaha, NE, United States. [4]Yale School of Medicine, New Haven, CT, United States

Introduction

Thoracic aortic aneurysms (TAAs) develop through a combination of biological and biomechanical mechanisms. Current clinical risk stratification relies on size and expansion rate, which do not reliably predict whether an aneurysm will stabilize, enlarge, dissect, or rupture. Large-data models have the potential to provide additional predictive capabilities, but are limited by the scarcity of clinical data. Mechanistic computational models can simulate clinically relevant phenotypes across a range of disease trajectories, and thus represent an alternative source of data for developing robust forecasting models. Here, we use a validated computational model of TAA development to identify the optimal neural operator for outcome forecasting.

Methods

We employed a constrained mixture theory framework to model aortic wall growth and remodeling under physiologic loading. The model incorporates rate-dependent processes that drive aneurysmal progression, including elastin fiber injury and reduced mechanosensitivity. We varied the mechanisms of progression to produce distinct aneurysm phenotypes. We then developed neural operator surrogates to perform short-term forecasting, long-term forecasting, and outcome categorization. Three neural operator architectures were evaluated, with a Laplace neural operator and two distinct temporal bundling strategies proposed for long-term prediction.

Results

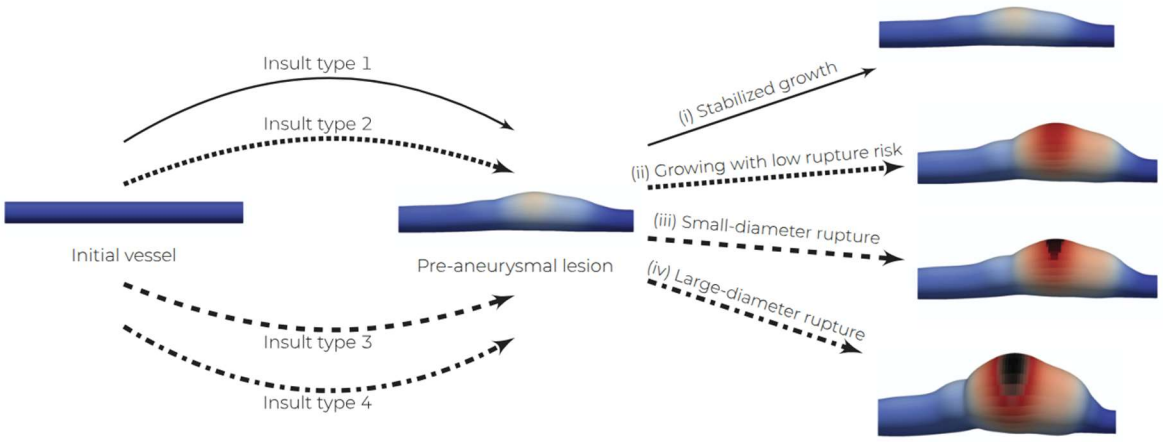
The growth and remodeling framework reproduced clinically relevant phenotypes, including situations where aneurysms with initially similar dilatations later diverged to have diverse outcomes. Simulations distinguished stable, growing, and rupture trajectories. Neural operators were able to successfully forecast aneurysm outcomes, with accuracy

increasing with additional biomechanical data, greater longitudinal sampling, reduced sampling intervals, and use of temporal bundling.

Discussion

By integrating mechanistic simulations of aortic behavior with machine learning, this framework has potential to aid the translation of large-data models for aneurysm forecasting to the clinic. Ongoing work will incorporate uncertainty quantification and patient-specific data to further develop this approach.

Images (Optional)



Session Category

Cardiovascular/Cardiorespiratory Biomechanics: Methods, Models and Applications

P4-039

An Innovative Real-time Windkessel-Based System for Dynamically Loading Isolated Heart Preparations

Mr Esau Mhandu

Auckland Bioengineering Institute, Auckland, Auckland, New Zealand

Introduction

The heart in vivo experiences beat-to-beat changes in cardiovascular load driven by dynamic vascular properties such as compliance, characteristic impedance, and peripheral resistance (R_p). These factors can be represented using a three-element Windkessel model. In *ex vivo* heart studies, however, afterload is typically imposed by adjusting the height of a pressure head, creating a constant-pressure load that fails to replicate physiological dynamics and prevents independent manipulation of vascular parameters. To overcome this limitation, we developed a system that delivers intrabeat dynamic loads to isolated hearts, modelling vascular impedance based on *in vivo*-derived Windkessel parameters. The system integrates a software-encoded Windkessel model with a feedback-controlled electromechanical valve to simulate arterial hydraulic impedance in real time. The model predicts instantaneous aortic pressure and flow from real-time left-ventricular pressure (LVP), while a control algorithm continuously adjusts valve aperture to match measured aortic pressure to model predictions.

Methods

We validated the system using isolated rat hearts (n = 10), recording pressure–volume loops, stroke volume, cardiac output, ejection fraction, and aortic flow under varying impedance conditions. Sudden changes in Rp were introduced to evaluate transient cardiac biomechanical responses.

Results

The system successfully reproduced physiologically realistic cardiac biomechanics. Pressure-volume loops closely resembled in vivo profiles. Increasing R_p elevated LVP and reduced stroke volume, cardiac output, ejection fraction, and aortic flow. Rapid step changes in R_p revealed transient cardiac responses, offering insights into the heart's intrinsic adaptive capacity on a beat-by-beat basis to fluctuating hemodynamic demands.

Discussion

This work establishes a real-time impedance-based loading system that addresses the limitations of static afterload models in isolated heart experiments. By enabling independent control of Windkessel parameters and capturing transient responses, the system provides a physiologically grounded tool for investigating cardiac function under realistic vascular loading. A current limitation is the use of constant preload; future integration of preload control to complement afterload modulation will further enhance physiological fidelity.

Session Category

Cardiovascular/Cardiorespiratory Biomechanics: Methods, Models and Applications

P4-040

Fluid-Structure Interaction Modeling of the Intracranial Carotid Artery for Cerebrovascular Events and Treatments

Ms Federica Fontana[1,2], Prof. Frank Gijsen[1,2], Dr. Daniel Bos[2], Dr. Ali Akyildiz[1,2], Dr. Selene Pirola[1]

[1]Delft University of Technology, Delft, South Holland, Netherlands. [2]Erasmus Medical Center, Rotterdam, South Holland, Netherlands

Introduction

The Intracranial Carotid Artery (ICA) is a key site for cerebrovascular disease and intervention, from atherosclerosis and aneurysm formation to endovascular procedures such as thrombectomy. Fluid Structure Interaction (FSI) models can help elucidate biomechanical factors that contribute to disease initiation and progression or procedural success, supporting studies addressing plaque vulnerability, initiation of wall remodeling, or interaction with medical devices. However, uncertainty remains on key modeling aspects, which are often overlooked or not obtainable from clinical imaging. In this study, a patient-specific FSI framework for the ICA is developed, and the effect of different model assumptions is evaluated to provide guidelines for robust modeling.

Methods

From Computed Tomography Angiography images of 100 stroke patients, the arterial lumen and calcifications of 200 ICAs were reconstructed. Morphometric features were quantified for each artery[1], and used to identify population-representative arteries via k-means clustering. For these, FSI models were built using FEBio (Fig.1a). Physiological pulsatile blood velocity was prescribed at the inlet; outlet boundary conditions were defined as fluid resistances, tuned to achieve physiological pressures. The following modeling choices were assessed: (1) surrounding bone and soft tissues, (2) arterial wall thickness, (3) inclusion of calcifications in the wall. Simulations were compared to a baseline scenario (Fig.1b).

Results

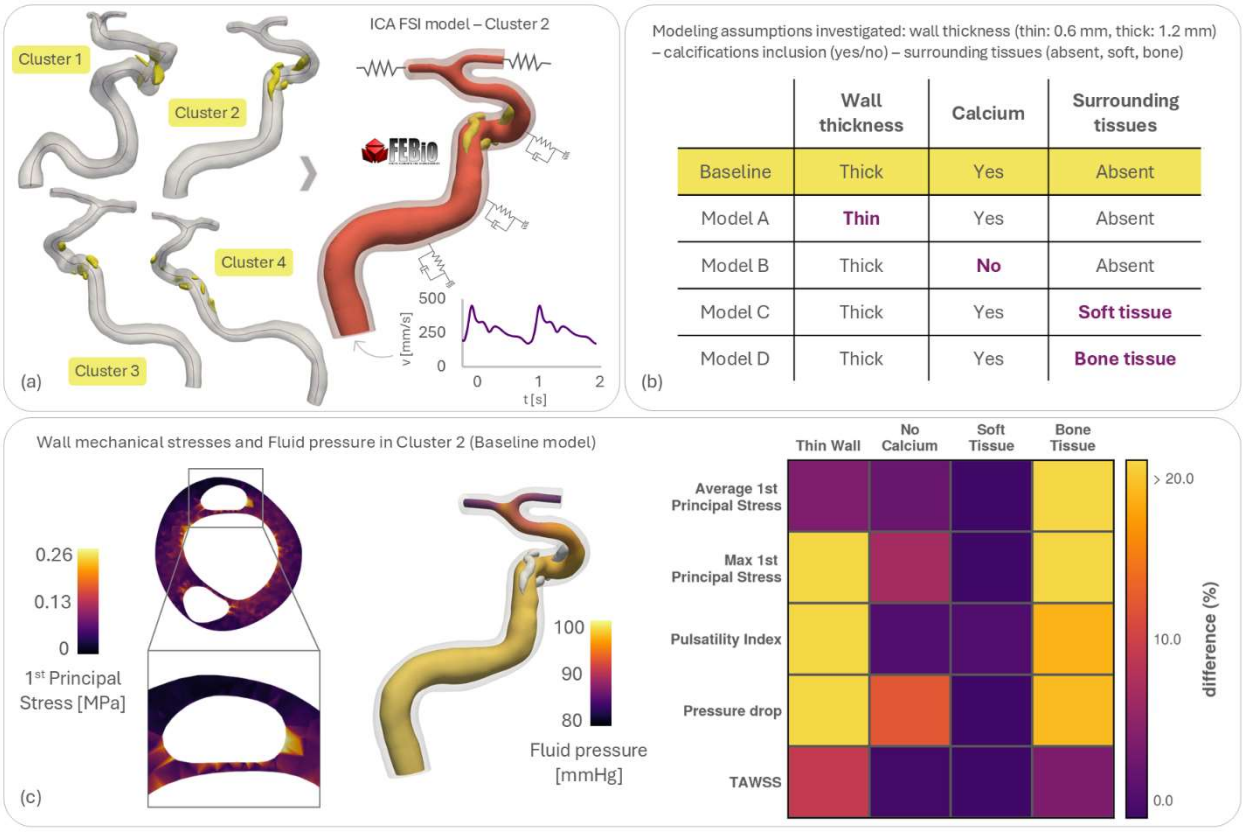
Initial results on one population-representative artery (Fig.1c) show that including surrounding bone tissue significantly alters all considered biomechanical factors, compared to simulating the artery in isolation (+42% in 1st Principal Stresses, +18% in Pulsatility Index and Pressure drop, +5% in TAWSS). Varying the wall thickness produces a

similar effect. Incorporating calcifications affects hemodynamic variables and mechanical stresses in the wall (+12% in Pressure drop, +10% in max 1st Principal Stresses).

Discussion

Surrounding bone tissue, typically neglected in FSI models, must be included to accurately capture both wall stresses and flow pulsatility in the ICA. Similarly, wall thickness is a crucial parameter. ICA calcifications present high shape complexity and variability, with varying impact on ICA hemodynamics and wall stresses. Currently, the work is being extended to include all four subgroups and additional outlier cases to capture the full spectrum of ICA anatomical variability.

Images (Optional)



References (Optional)

1. BP.Berghout & F.Fontana *et al., J. Clin. Med* (2025)

Acknowledgements (Optional)

For the contribution to this study, we acknowledge the patients and investigators from the Plaque At RISK (PARISK) multicenter study and the Erasmus Stroke Study (ESS) registry. The PARISK study was supported by the Dutch Heart Foundation and performed within the

framework of the Center for Translational Molecular Medicine (www.ctmm.nl), project PARISK (Plaque At RISK; grant number 01C-202)

Session Category

Cardiovascular/Cardiorespiratory Biomechanics: Methods, Models and Applications

P4-041

Predicting Rhythm-Dependent Cardiac Remodeling in Atrial Fibrillation using a Novel Computational Model

Dr. Felix Plappert[1], Dr. Aasima Khan[2], Dr. Arnljot Tveit[2], Dr. Pim Oomen[1]

[1]University of California, Irvine, Irvine, California, United States. [2]University of Oslo, Oslo, Oslo, Norway

Introduction

Atrial fibrillation (AF) increases heart failure risk 4-5 fold, yet predicting which AF patients will develop cardiac dysfunction remains challenging. We developed a computational biophysics model to mechanistically investigate how different AF rhythm patterns drive cardiac remodeling. Unlike existing cardiac remodeling models that assume a regular rhythm represented by one heartbeat per day, AF-induced remodeling studies must account for beat-to-beat variations in the irregular rhythms characteristic of AF.

Methods

We developed a reduced-order computational model integrating cardiac mechanics, electrophysiology [1], and mechanics-driven growth [2]. Simulations compared normal sinus rhythm (NSR) with coordinated atrial contraction 120ms before ventricular activation, versus AF with uncoordinated and irregular atrial activity. For both heart rhythms, we simulated 50 heartbeats daily (96bpm average) over 60 days using three rhythm patterns: 1) regular rhythm without RR variability/irregularity, 2) low RR variability with low irregularity, 3) high RR variability with high irregularity.

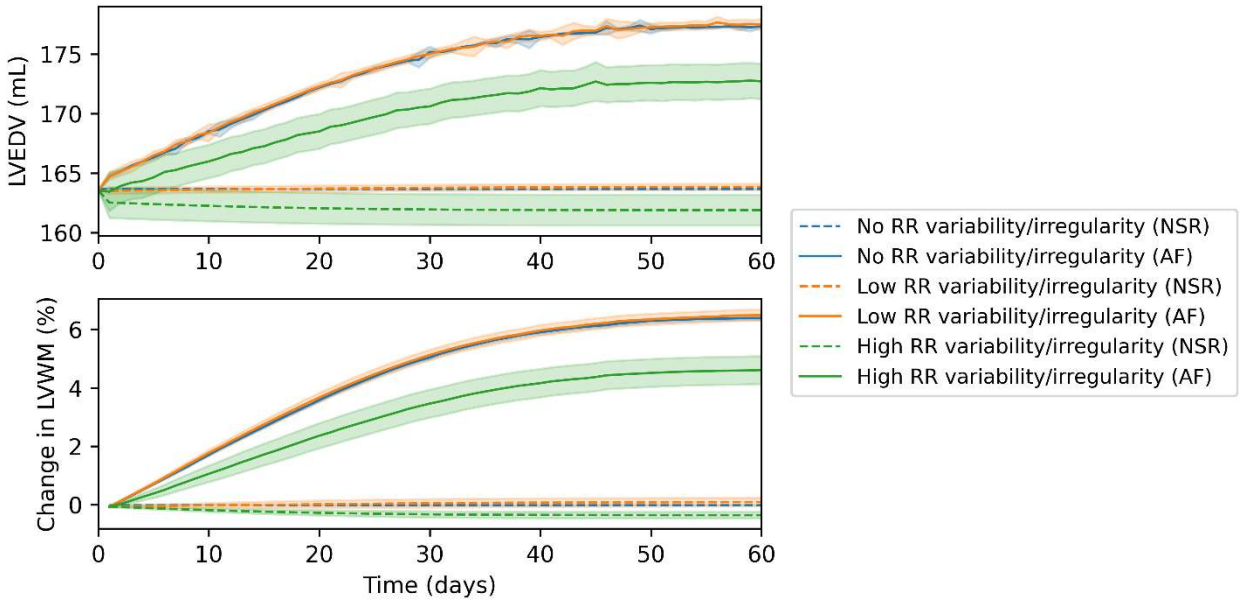
Results

Left ventricular end-diastolic volume (LVEDV) and left ventricular wall mass (LVWM) increased markedly during AF across all rhythm patterns, suggesting that loss of atrial kick plays an important role in LV remodeling. Critically, the magnitude of remodeling varied with rhythm characteristics: regular rhythms and low RR variability with low irregularity produced greater cardiac growth than high RR variability with high irregularity. AF by itself leads to mild hypertrophy, and increase in cardiac hemodynamics. Interestingly, our model predictions suggest that high RR variability and irregularity mitigate AF-driven remodeling.

Discussion

Our computational model is the first of its kind that combines cardiac remodeling in response to different heart rhythms and atrial activation patterns. Our model's prediction of mild hypertrophy following AF matches with clinical data [3], thus validating our model formulation. The mitigation of AF-induced remodeling by high variability and irregularity can be explained by changes in preload: higher RR variability leads to less optimal filling of the heart, which thus mitigates the increased preload caused by AF. Our next step is to validate model predictions with patient-specific data from previously conducted clinical trials.

Images (Optional)



References (Optional)

[1] Felix Plappert et al., bioRxiv, 2025.

[2] Clara Jones et al., Comput. Biol. Med., 2025.

[3] Qin et al., Circ. Arrhythm. Electrophysiol., 2019.

Session Category

Cardiovascular/Cardiorespiratory Biomechanics: Methods, Models and Applications

P4-042

Improving the Quantification of Tricuspid Regurgitation Through 4D Flow MRI

Dr. Alessandra Riva[1], Dr. Giulia Pasqualin[2], Dr. Francesco Sturla[1,3], Dr. Lara Tondi[4,5], Dr. Simone Saitta[6,7], Dr. Davide Tondi[3], Dr. Jessica Zannoni[8], Dr. Giandomenico Disabato[4], Dr. Daniel Giese[9], Prof. Massimo Chessa[2,10], Dr. Pietro Spagnolo[11], Prof. Alberto Redaelli[3], Dr. Massimo Lombardi[4], Prof. Emiliano Votta[3]

[1]3D and Computer Simulation Laboratory, IRCCS Policlinico San Donato, San Donato MIlanese, Lombardia, Italy. [2]Pediatric and Adult Congenital Disease Heart Centre, IRCCS Policlinico San Donato, San Donato MIlanese, Lombardia, Italy. [3]Department of Electronics, Information and Bioengineering, Politecnico di Milano, Milano, Lombardia, Italy. [4]Multimodality Cardiac Imaging, IRCCS Policlinico San Donato, San Donato MIlanese, Lombardia, Italy. [5]Department of Radiology, IRCCS Foundation Ca' Granda Ospedale Maggiore Policlinico, University of Milan, Milano, Lombardia, Italy. [6]Department of Biomedical Engineering and Physics, Amsterdam UMC, Amsterdam, Noord-Holland, Netherlands. [7]Informatics Institute, University of Amsterdam, Amsterdam, Noord-Holland, Netherlands. [8]Department of Clinical and Interventional Cardiology, IRCCS Policlinico San Donato, San Donato MIlanese, Lombardia, Italy. [9]Research & Clinical Translation, Magnetic Resonance, Siemens Healthineers AG, Erlangen, Bayern, Germany. [10]Università Vita e Salute San Raffaele, Milano, Lombardia, Italy. [11]Department of Radiology, IRCCS Policlinico San Donato, San Donato MIlanese, Lombardia, Italy

Introduction

Current techniques for quantifying tricuspid regurgitation (TR) based on magnetic resonance imaging (MRI) or transthoracic echocardiography (TTE) all suffer from limitations [1]. To address these, we proposed a new approach that directly quantifies tricuspid regurgitant volume (TR_V) by combining 4D Flow MRI with retrospective tracking of the tricuspid valve (TV) annulus. We assessed the reproducibility of this method and its agreement in terms of TR grading compared with standard MRI- and TTE-based strategies.

Methods

A cohort of patients (n=30) with TR was prospectively enrolled. TR_V was quantified implementing four MRI-based approaches into an in house Matlab pipeline [2]: i) indirect quantification, obtained by subtracting the total forward volume through the pulmonary valve (FV_{PV}) from the right ventricular stroke volume (SV_{RV}); direct quantification as time-integral of the regurgitant flow through the TV orifice measured from ii) 2D phase-contrast (PC) MRI on a plane positioned at the level of TV annulus (π_{TV}); iii) 4D Flow MRI using the

same static plane π_{TV} to project the TV orifice; iv) 4D Flow MRI with frame-by-frame update of π_{TV} position and direction based on the automated tracking of the TV annular landmarks.

Results

The dynamic 4D Flow MRI method showed strong correlations with all other MRI methods (r = 0.80-0.84, p<0.001), but consistently yielded higher TR_V estimates (Figure 1). Agreement in TR severity grading based on regurgitant fraction was poor across methods (kappa ≤ 0.07), with dynamic 4D Flow MRI classifying more cases as moderate or severe. Compared with TTE, dynamic 4D Flow MRI showed slight agreement (kappa = 0.17). Inter-observer reproducibility was excellent (r = 0.91, bias = 0.7ml, kappa = 0.80).

Discussion

TR_V quantification from 4D Flow MRI with dynamic update of π_{TV} demonstrated superior reproducibility; its tendency to yield larger TR_V estimates may provide a more sensitive quantification for TR_V compared with conventional MRI techniques. Although alignment with TTE remains limited, it may help overcome key imaging limitations and improve TR evaluation, especially in complex clinical scenarios.

Images (Optional)

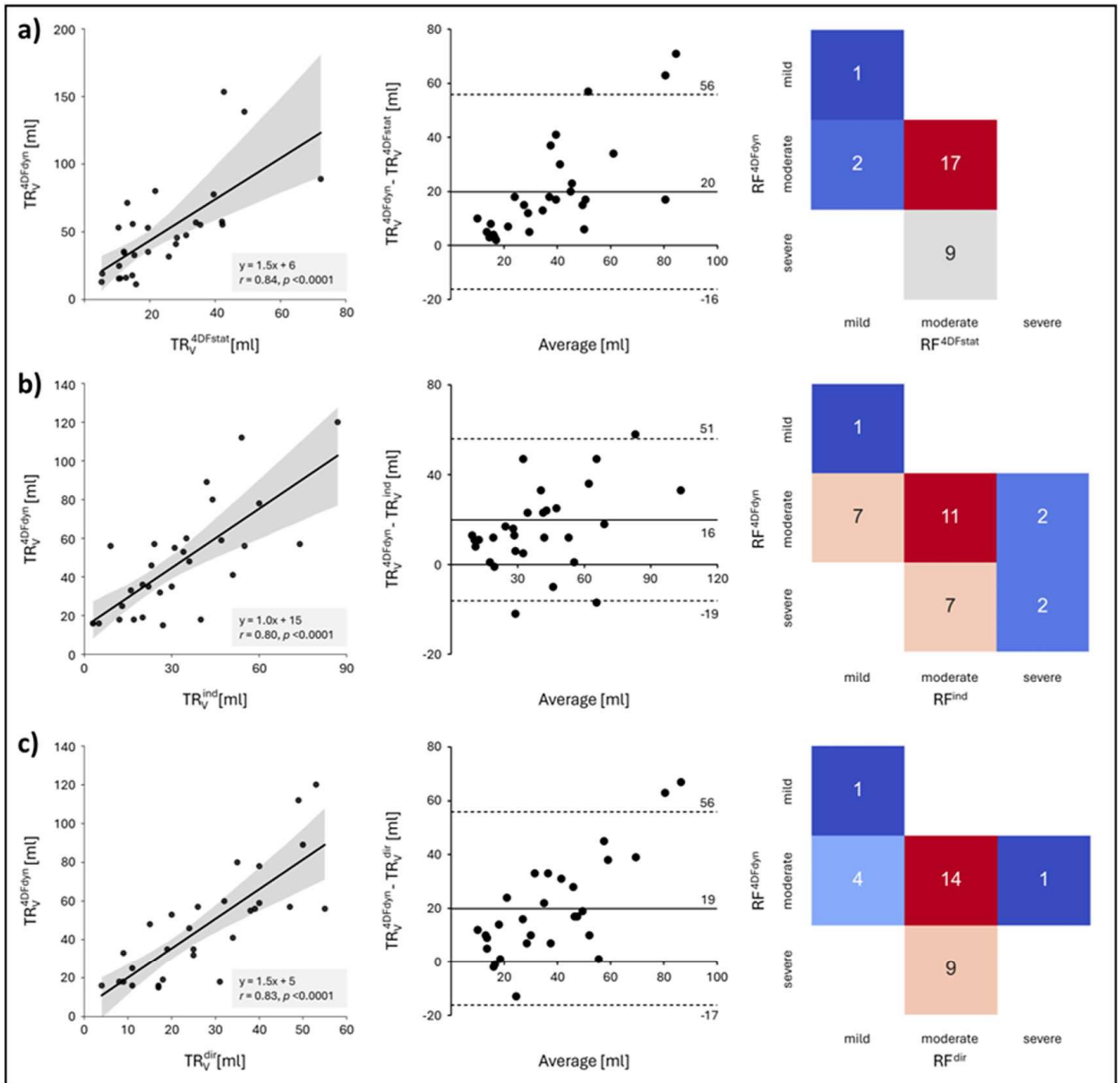


Figure 1: Comparison of 4D Flow-based TR_V with dynamic TV tracking and a) 4D Flow-based TR_V with static plane, b) indirect conventional TR_V and c) direct conventional TR_V, respectively. Linear regression plot with Spearman correlation, Bland-Altman agreement with bias and limits of agreement and confusion matrix for agreement of TR severity are reported for each comparison.

References (Optional)

[1] Hahn *et al.*, JACC Cardiovasc Imaging, 2019

[2] Riva *et al.*, J Magn Reson Imaging, 2022

Acknowledgements (Optional)

IRCCS Policlinico San Donato is a clinical research hospital partially funded by the Italian Ministry of Health.

Session Category

Cardiovascular/Cardiorespiratory Biomechanics: Methods, Models and Applications

P4-043

Physiologically Grounded CFD of Hyperemic Coronary Flow: Velocity and Wall Shear Stress Insights

Mr. Francisco Pinto de Oliveira MSc[1,2], Ms. Maria Fernandes MSc[1,2], Dr. Nuno Dias Ferreira MSc[3], Dr. Diogo Santos-Ferreira MSc[4,3], Prof. Ricardo Ladeiras-Lopes PhD[4], Prof. Nuno Bettencourt PhD[4], Prof. Luísa Costa Sousa PhD[1,2], Prof. Sónia Pinto PhD[1,2]

[1]Engineering Faculty of University of Porto, Porto, N/A, Portugal. [2]Institute of Science and Innovation in Mechanical and Industrial Engineering (LAETA-INEGI), Porto, N/A, Portugal. [3]Cardiology Department, Unidade Local de Saúde de Gaia e Espinho, Vila Nova de Gaia, N/A, Portugal. [4]UnIC@RISE, Department of Surgery and Physiology, Faculty of Medicine, University of Porto, Porto, N/A, Portugal

Introduction

Coronary artery disease is a major cause of morbidity, and assessing the functional impact of stenoses remains challenging. Fractional flow reserve (FFR) is the clinical reference for identifying flow-limiting lesions but offers only a single value and lacks spatial detail on hemodynamic factors such as velocity or wall shear stress (WSS) [1]. Computational fluid dynamics (CFD) based on coronary CT provides a noninvasive alternative, though many methods lack physiological realism. This study evaluates whether a physiologically grounded CFD workflow can relate patient-specific systolic velocity and WSS patterns to stenosis severity defined by invasive FFR.

Methods

Three right coronary arteries representing significant (Patient A, FFR = 0.63), non-significant (Patient B, FFR = 0.93), and borderline/significant (Patient C, FFR = 0.76) lesions were reconstructed from CT and transformed to hyperemic conditions. Unsteady CFD simulations incorporated viscoelastic blood rheology, Womersley pulsatile inflow and Windkessel outlet models. Physiological consistency was confirmed by comparing CFD-derived and invasive FFR values, yielding a mean relative error of 6.2% (SD = 4.2%).

Results

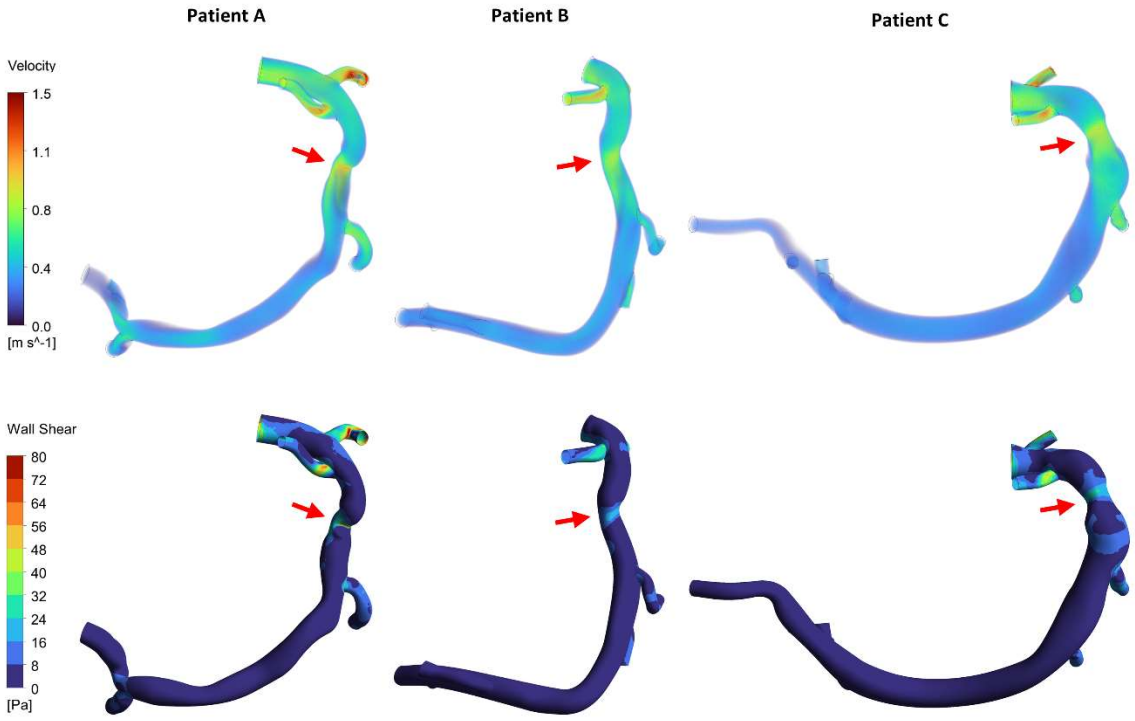
Hemodynamics differed markedly between cases. Patient A showed a pronounced systolic jet (1.45 m/s) and high focal WSS (70–75 Pa) distal to the stenosis, consistent with a flow-limiting lesion. Patient C exhibited slightly lower velocities (1.40–1.45 m/s) and WSS (65–70 Pa) but retained a concentrated high-shear band characteristic of borderline severity.

Patient B presented reduced peak velocity (0.90 m/s) and WSS (35–40 Pa), with no shear amplification, reflecting a non-significant lesion. These patterns aligned with invasive FFR and demonstrated sensitivity to anatomical and functional variation.

Discussion

Pronounced jets and focal WSS peaks reliably differentiated significant and borderline lesions from non-significant ones, supporting established mechanisms of pressure loss and shear-mediated vascular response [2,3]. The physiologically informed CFD workflow offered spatial information unavailable from FFR alone and may aid assessment of stenoses. Limitations include the small cohort, motivating future validation in larger populations and potential integration into clinical decision-support pathways.

Images (Optional)



References (Optional)

[1] De Bruyne B. et al., N Engl J Med, 2012.
[2] Morris P.D. et al., J Biomech Sci Eng, 2016.
[3] Kim H.J., Vignon-Clementel I.E., Annu Rev Biomed Eng, 2010.

Acknowledgements (Optional)

The authors gratefully acknowledge the financial support of FCT, the Foundation for Science and Technology, (Portugal) regarding the R&D Project “CADS-FACT – PTDC/EMD-EMD/0980/2020”, the Engineering Faculty of University of Porto (FEUP), the Institute of Science and Innovation in Mechanical and Industrial Engineering (INEGI), the Cardiovascular R&D Unit of the Medicine Faculty of University of Porto (FMUP), and the Cardiology Department of Gaia/Espinho Hospital Center (CHVNG/E).

Session Category

Cardiovascular/Cardiorespiratory Biomechanics: Methods, Models and Applications

P4-044

Relationship Between Portal Vein Thrombosis and Wall Shear Stress After Hepatectomy: Computational Fluid Dynamics Analysis

Mr. Yoshiki Iijima, Dr. Mamoru Takada, Mr. Shunsuke Nakajima, Dr. Hisato Kobayashi, Dr. Isamu Hosokawa, Prof. Masayuki Ohtsuka, Prof. Gaku Tanaka

Chiba University, Chiba, Chiba, Japan

Introduction

Portal vein thrombosis (PVT) is a severe complication that can occur after hepatectomy. While the association between wall shear stress (WSS) and thrombus formation has been suggested, its relationship with post-hepatectomy PVT remains unclear. Additionally, the relationship between WSS and the portal vein bifurcation angle, which is considered a risk factor for post-hepatectomy PVT, has not been fully elucidated. In this study, we used computational fluid dynamics analysis to examine the relationship between PVT and WSS, as well as between bifurcation angle and WSS.

Methods

Hemodynamics were analyzed using patient-specific models reconstructed from CT images and simplified models with only the bifurcation angle modified. Preoperative and postoperative portal vein models were reconstructed from patients who underwent right hepatectomy. This study involved seven patients, two of whom developed postoperative portal vein thrombosis and five patients who did not. Blood flow simulations were conducted based on the continuity and Navier-Stokes equations for steady, laminar, non-Newtonian flow.

Results

The results showed that patients who developed PVT had higher WSS at the left portal vein bifurcation than those who did not. The maximum postoperative WSS at the bifurcation was 82% higher in PVT patients, and the postoperative increase in spatially averaged WSS was 3.7 times greater. Furthermore, WSS tended to increase as the bifurcation angle became more acute.

Discussion

The findings of this study provide new insights in the portal venous system, suggesting that elevated WSS postoperatively plays a crucial role in the development of post-hepatectomy PVT. Unlike typical venous thrombosis, which is generally associated with low WSS, this study demonstrated a substantial postoperative increase in WSS, with localized regions

exhibiting high WSS. This suggests that post-hepatectomy PVT may follow a different thrombus formation mechanism, driven by high rather than low WSS. Additionally, surgical planning to increase the bifurcation angle may help mitigate postoperative WSS elevation and reduce the risk of PVT.

Session Category

Cardiovascular/Cardiorespiratory Biomechanics: Methods, Models and Applications

P4-045

Visualization of Transitional Flow in Nasal Cavities During a Sniff

Mr. Yasuyuki Hirai[1], Prof. Toshihiro Sera[2], Dr. Hideo Yokota[3], Prof. Gaku Tanaka[1]

[1]Chiba University, Chiba, Chiba, Japan. [2]Tokyo University of Science, Katsushika-ku, Tokyo, Japan. [3]RIKEN, Wako, Saitama, Japan

Introduction

The nasal cavity is characterized by extremely complex three-dimensional structure, and its small size and structural complexity prevents detailed in vivo airflow measurements. Airflow patterns in the nasal cavity strongly affect the uptake and deposition of inhaled pollutants, airborne particles, and odorant molecules across the nasal mucosa. The aim of this study is to investigate the airflow instability in the nasal cavity during a sniff based on the in vitro experiment.

Methods

Particle image velocimetry (PIV) was performed using a realistic bilateral nasal model that fully replicates the internal and external nasal airways. The transparent silicone nasal model was reconstructed from CT slices of a healthy male with no clinical disorders. The working fluid was an aqueous solution of glycerin with concentration adjusted to match the refractive index of the silicone model. Experiments were conducted under both steady and unsteady flow conditions using an inverter pump. Flow instability was evaluated by turbulent kinetic energy (TKE).

Results

PIV measurements confirmed that the jet through the nasal valve plays an important role in the occurrence of flow instability. It was also found that significant differences were observed between flow in the right and left cavities, indicating strong dependence on the local geometry. In the left cavity, which has larger cross-sectional area and TKE values than the right cavity, the maximum TKE during deceleration phase was 1.2 times that in steady flow at the same Reynolds number, while the TKE during acceleration phase was 0.5 times.

Discussion

The results show that the occurrence of flow instability strongly depends on the geometry of the right and left cavities, and on the flow acceleration and deceleration, rather than the Reynolds number. The TKE values in the left nasal cavity was highest near the upper nasal passages where olfactory cells exist. This unstable flow appears to be related to olfactory function.

Session Category

Cardiovascular/Cardiorespiratory Biomechanics: Methods, Models and Applications

P4-046

Pre-Transcatheter Aortic Valve Replacement Prediction of Hypoattenuated Leaflet Thickening using CT-Derived Measurements

Ms. Gauri Anil Student[1], Ms. Courtney Ream Student[2], Mr. Aniket Venkatesh Student[2], Dr. Lakshmi.P Dasi Professor[2]

[1]Dublin Jerome High School, Dublin, OH, United States. [2]Georgia Institute of Technology, Atlanta, GA, United States

Introduction

Aortic stenosis is the narrowing of the aortic valve which restricts blood flow, and the only effective treatment is aortic valve replacement. Instead of performing an open-heart Surgical Aortic Valve Replacement, the newer Transcatheter Aortic Valve Replacement (TAVR) offers a less invasive alternative for patients at high surgical risk. However, there exists a high likelihood of developing prosthetic leaflet thrombosis post-TAVR, which can reduce valve mobility, durability, and increase stroke risk. On post-procedure CT scans, this complication appears as Hypoattenuated Leaflet Thickening (HALT). In this study, we conducted a logistic regression test to investigate whether measurements taken from pre-TAVR CT scans could help detect HALT post-procedure.

Methods

A cohort of 19 patients who received the Evolut R TAV was selected from CT databases from GVM Care & Research, Palermo, Italy. The patients were recruited based on the presence of leaflet thrombosis after TAVR as scored by radiologists (n=10 HALT+, n=9 HALT-). Each patient's annulus area, average sinus diameter, left and right coronary arteries, and average sinotubular junction (STJ) height, along with other features, was measured using Radiant DICOM Viewer (Poznan, Poland), and the multiplanar reconstruction of patient CT scans were manipulated and measured with the length tool (Figure 1). These pre-TAVR anatomical dimensions were used as input parameters into a logistic regression model to identify any possible correlations indicating prediction of HALT post-TAVR.

Results

Using the selected predictors in the logistic regression analysis, we found that the AUC=0.7 (p=0.142). From a Hosmer and Lemeshow Test, we fail to reject the null hypothesis that the model is a good fit (p=0.096). Furthermore, our t-test results indicate that the most

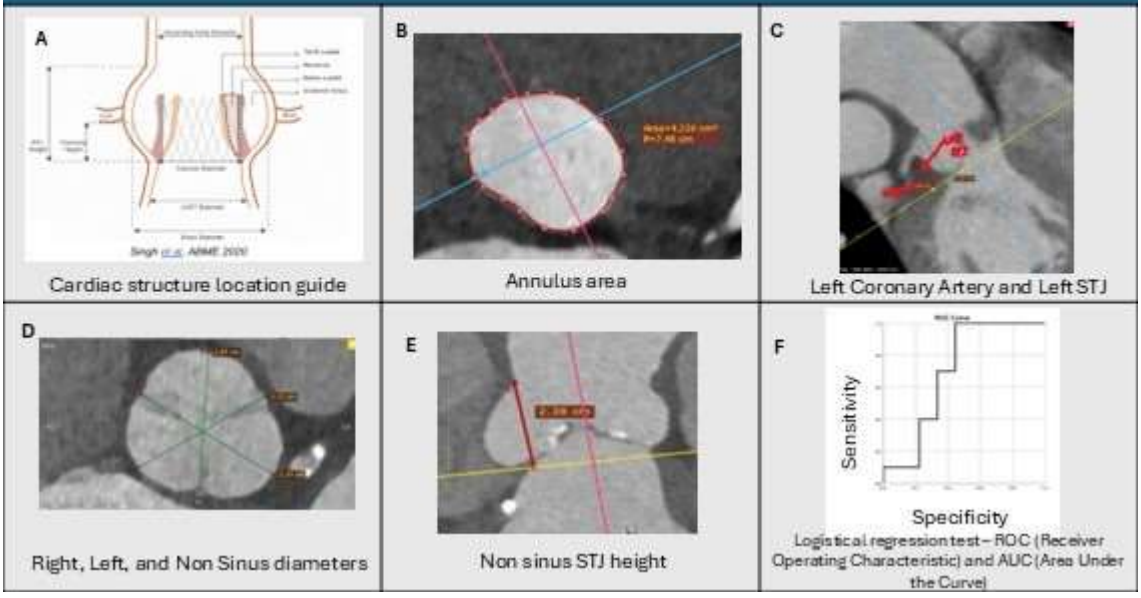
significant variable was the average sinus diameter, with a mean difference of 0.219mm between HALT+ and – groups (p=0.26).

Discussion

Although the model does calibrate reasonably with the observations, the data failed to correctly distinguish the difference between the HALT+ and HALT- patients. However, we aim to increase sample size and add flow-related variables from echocardiography to our analysis. Such predictive capabilities could provide valuable clinical insight in identifying high risk post-TAVR thrombosis patients for whom proactive antithrombotic therapy is required.

Images (Optional)

Figure 1: *Example CT cardiac measurements taken using RADIANT, structure location guide, and logistical regression test conducted*



Session Category

Cardiovascular/Cardiorespiratory Biomechanics: Methods, Models and Applications

P4-047

Model-Based Methods for Characterising Kinematics Following Myocardial Infarction: Application of Mobstr3D

Mr George Harpur[1], Mr Robin Laven[1], Dr Vicky Wang[1], Dr Debbie Zhao[1], Prof Alistair Young[1,2], Dr Thiranja Prasad Babarenda Gamage[1], Prof Martyn Nash[1,3]

[1]Auckland Bioengineering Institute, University of Auckland, Auckland, Auckland, New Zealand. [2]School of Biomedical Engineering an Imaging Sciences, King's College London, London, London, United Kingdom. [3]Department of Engineering Science and Biomedical Engineering, University of Auckland, Auckland, Auckland, New Zealand

Introduction

Regional differences in left ventricular (LV) kinematics, such as strain and torsion, have been highlighted as early indicators of cardiovascular disease, particularly ischemic heart disease. Non-invasive cardiac magnetic resonance (CMR) displacement encoding with stimulated echoes (DENSE) [1] is widely considered the gold standard for intramyocardial tracking. Accurate kinematic assessment requires reliable reconstruction of 3D displacement fields; however, existing tools are generally restricted to 2D in-plane kinematic analyses. We have developed a novel, open-source software package, mobstr3D (MOdel-Based STRains in 3D, v1.0.0) for analysing cardiac geometry and 3D displacement fields by reconstructing 3D patient-specific kinematic models, from which regional strains can be estimated.

Methods

mobstr3D was used to characterise regional distributions of circumferential strains (ECC) for infarct, neighbouring and remote AHA segments in a swine with myocardial infarction (MI), and a healthy control swine as a reference. Three mid-LV short-axis DENSE with 3D displacement encoding images were preprocessed using the existing 2D analysis tool, DENSEanalysis [2]. An end-systolic model was created by fitting the surfaces of a bi-cubic Hermite quadratic Lagrange cylindrical template model (with 8 elements circumferentially) to the segmented contour data. The phase-unwrapped displacements informed a free-form deformation fit, defining the end-diastolic model. Peak systolic Lagrangian ECC was then estimated and separated into six mid-LV AHA regions (R7-R12).

Results

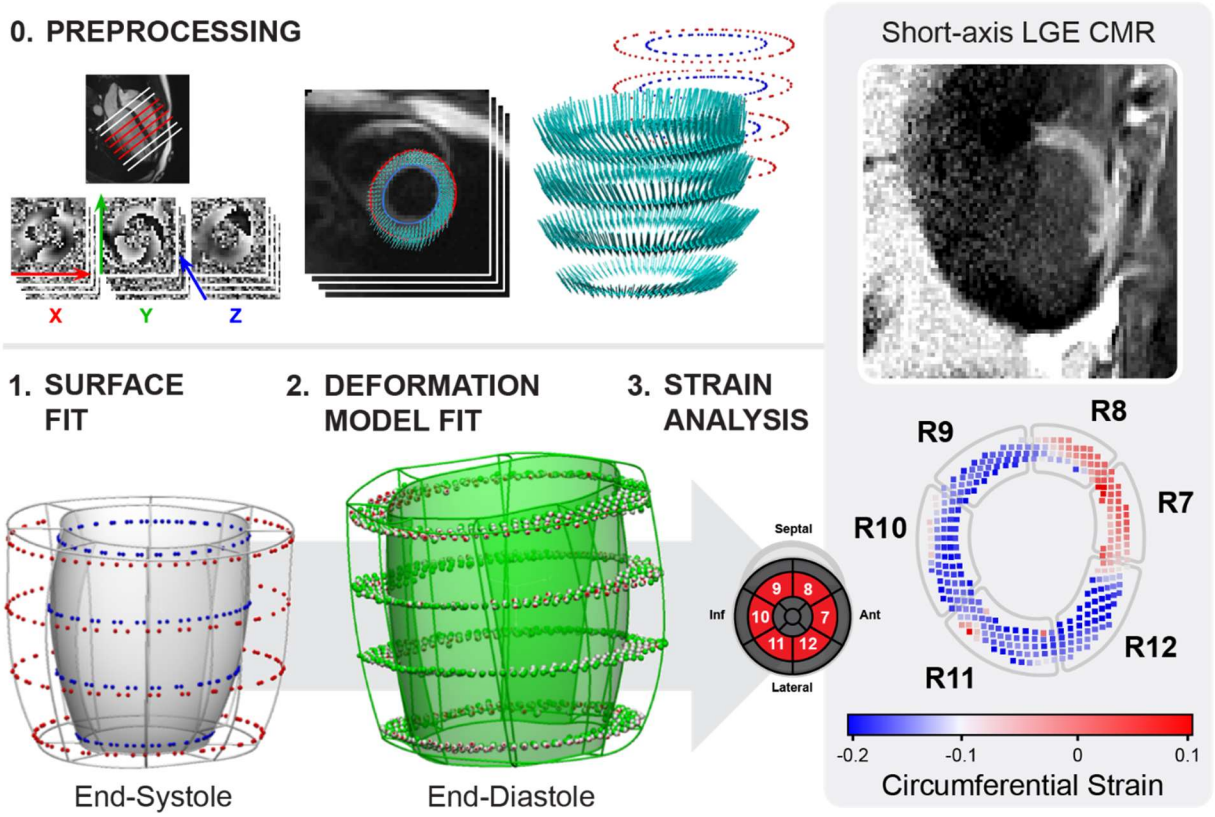
Late gadolinium enhancement (LGE) imaging indicated infarction in R7/R8. R9/R12, and R10/R11 were labelled as neighbouring and remote, respectively. Mean ECC was significantly smaller in the infarct regions, compared with the same regions in the control

case (-0.05±0.10 versus -0.12±0.04, p<0.001). ECC values in remote regions were similar to control (-0.16±0.06 versus -0.15±0.04, p=NS), while neighbouring regions were significantly larger than control (-0.17±0.05 versus -0.13±0.03, p<0.001). ECC differences can be attributed to variable infarct extent observed via LGE.

Discussion

Model-based mapping of regional circumferential strain can indicate infarct regions without the need for invasive contrast agents, which are contraindicated for some patients. Non-invasive kinematic characterisation can improve patient outcomes when monitoring disease progression.

Images (Optional)



References (Optional)

[1] Aletras et al., J Magnetic Resonance, 1999

[2] Spottiswoode et al., IEEE TMI, 2007

Session Category

Cardiovascular/Cardiorespiratory Biomechanics: Methods, Models and Applications

P4-048

Modelling Parameterised Left Atrial Appendage Morphologies Under Sinus and Atrial Fibrillation Conditions With Fluid-Structure Interaction

Mr. Matthew Tsu-En Lee[1], Dr. Giulio Musotto PhD[2], Prof. Gaetano Burriesci PhD[1,2,3], Prof. Ryo Torii PhD[1], Dr. Giorgia Maria Bosi PhD[1]

[1]UCL Mechanical Engineering, University College London, London, Greater London, United Kingdom. [2]Bioengineering Group, Ri.MED Foundation, Palermo, Sicily, Italy. [3]Department of Engineering, University of Palermo, Palermo, Sicily, Italy

Introduction

The left atrial appendage (LAA) is known for its high morphological diversity, where complex shape features contribute to increased thrombotic risk under irregular heart conditions such as atrial fibrillation (AF). While general haemodynamic trends related to LAA shape are well analysed clinically [1], the specific relationship between individual shape features and thrombotic risk remains poorly understood. This study seeks to elucidate this relationship with the development of a novel parametric morphology, where individual shape features may be deliberately adjusted within clinical ranges. The specific thrombogenicity of the chosen features is then modelled with fluid-structure interaction (FSI) under both sinus and AF conditions and categorised accordingly.

Methods

32 FSI simulations have been run on a novel LAA parametric model. The fully-adjustable morphology was built in SolidWorks, with anatomical measurements from literature [2] to generate 16 different variations. FSI boundary conditions included simulation of LAA contraction and pressure over 3 cardiac cycles of sinus rhythm and AF. Haemodynamic indices of velocity, shear strain rate (SSR), time-averaged wall shear stress (TAWSS), oscillatory shear index (OSI) and endothelial cell activation potential (ECAP) were obtained and correlated with different anatomical features.

Results

FSI results were obtained for each of the 32 simulations and compared to those of median 2-lobe morphology under sinus and AF conditions. A subset of these comparisons, focusing on the effect of morphological bending on LAA velocity, volume change, wall SSR and body SSR, is presented in Figure 1. As shown, bending in the distal LAA region, an understudied anatomical feature, leads to the lowest risk of thrombosis. Other understudied features that are evaluated by this model include trabeculae and secondary lobe distribution.

Discussion

The developed parametric FSI model can help identify the extent to which specific anatomical features lead to a higher probability of blood stagnation, thus helping clinicians better identify high thrombosis-risk patients for therapy selection. A limitation of the current setup is that blood is defined as Newtonian and single-phase. Multi-phase blood modelling will be evaluated with future collaboration.

Images (Optional)

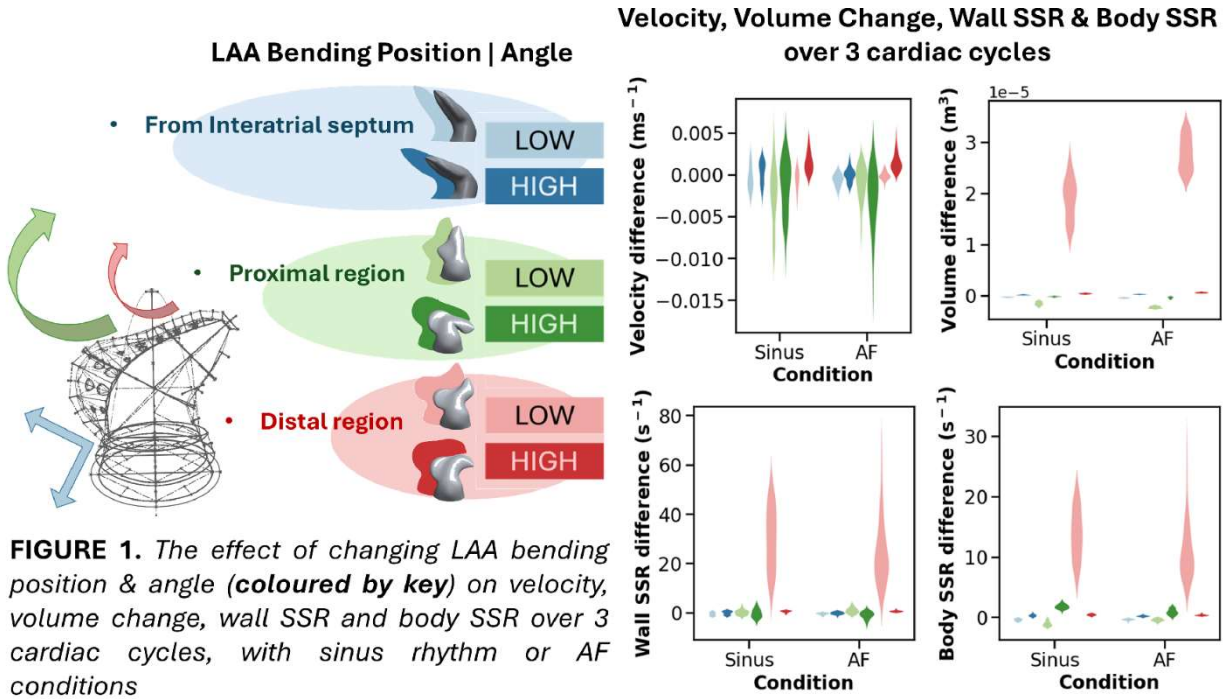


FIGURE 1. *The effect of changing LAA bending position & angle (**coloured by key**) on velocity, volume change, wall SSR and body SSR over 3 cardiac cycles, with sinus rhythm or AF conditions*

References (Optional)

[1] Yaghi S et al. Journal of cardiovascular computed tomography, 14.1: 27-33, 2020.

[2] Rajiah P et al. Radiographics, 41(3):680-98, 2021.

Acknowledgements (Optional)

The authors would like to thank the Royal Academy of Engineering (RF/201920/19/221) for providing financial support to this project.

Session Category

Cardiovascular/Cardiorespiratory Biomechanics: Methods, Models and Applications

P4-049

A computational model of chemically- and mechanically-induced thrombus formation: application to hepatectomy

PhD Giulia Cardillo[1], PhD Morgane Garreau[2], Inria Research Director Irene Vignon-Clementel[2], Professor Abdul I Barakat[1]

[1]École polytechnique de Paris, Palaiseau, Essonne, France. [2]Inria Saclay Île-de-France Research Center, Palaiseau, Essonne, France

Introduction

Thrombosis is a leading cause of death worldwide. Experiments have demonstrated that spatial changes in blood shear rate, i.e. shear gradients, play a dramatic role in thrombogenesis by controlling the process of platelet aggregation [1]. Our broad objective is to develop a computational model capable of reliably predicting thrombus formation in complex flow environments. The specific goal of the present work is to apply a validated computational thrombosis model that we had previously developed and that incorporates the impact of spatial shear gradients to a particular clinical scenario. The model is applied to cohort of 17 patients subjected to hepatectomy, a procedure involving the surgical resection of part of the liver and the consequent reconfiguration of the liver vasculature. One of the major complications associated with hepatectomy is thrombus formation inside the modified portal vein.

Methods

The 2D computational model represents the biochemical component of thrombosis as a set of coupled convection-diffusion-reaction equations and accounts for resting and activated platelets as well as various pro- and anti-thrombotic biochemical species. Platelet adhesion and aggregation to the blood vessel surface are modeled via different flux boundary conditions, implementing both chemical- and shear gradient-mediated platelet aggregation. The impact of thrombus growth at on the blood flow field is incorporated into the analysis. A simplified model of the coagulation cascade allows us to account for the role of fibrin fibers. Starting from computed tomography scan data, patient-specific geometries of the portal vein were reconstructed, and the thrombosis model was applied to the most relevant vascular sections.

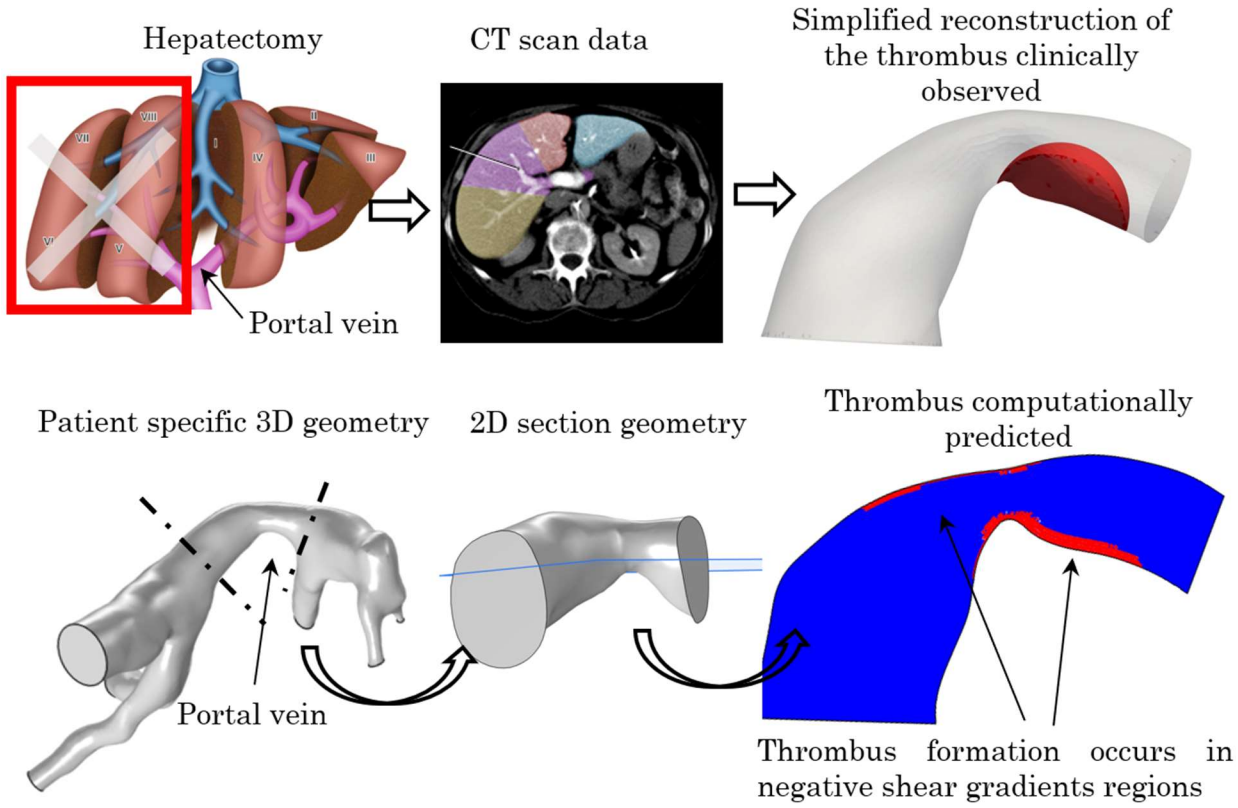
Results

The computational predictions for thrombus formation and localization demonstrated agreement with clinical observations in different patients after hepatectomy. The results suggest that, even though the post-operative vessel inflammation plays an important role, thrombus formation is driven principally by negative shear gradients.

Discussion

Despite some limitations of the model, such as its 2D nature, it has shown promising results. The model promises to constitute a tool capable of predicting thrombus formation and evolution in different clinical scenarios, providing medical doctors with meaningful insights into disease onset and progression.

Images (Optional)



References (Optional)

[1] Nesbitt et al. *Nature medicine,* 2009.

Session Category

Cardiovascular/Cardiorespiratory Biomechanics: Methods, Models and Applications

P4-050

Detecting Root Causes of Airway Obstruction Using Patient-Specific Cine Magnetic Resonance Images Based Computational Fluid Dynamics Modeling Approach Between a Stable and Collapsing Breath.

Visit Researcher Hisato Kobayashi M.D., Ph.D.[1], Instructor Qiwei Xiao Ph.D.[1,2], Sr Biomed Engineer Keith McConnell[1], Associate Professor Robert J Fleck M.D.[3], Professor Raouf S Amin M.D.[1], Assistant Professor Alister Bates Ph.D.[1,2,3,4]

[1]Division of Pulmonary Medicine, Cincinnati Children's Hospital Medical Center, Cincinnati, Ohio, United States. [2]Department of Pediatrics, University of Cincinnati, Cincinnati, Ohio, United States. [3]Department of Radiology and Medical Imaging, Cincinnati Children's Hospital Medical Center, Cincinnati, Ohio, United States. [4]Department of Biomedical Engineering, University of Cincinnati, Cincinnati, Ohio, United States

Introduction

Obstructive sleep apnea (OSA) occurs when the balance between the aerodynamic load due to airflow and the neuromuscular forces that maintain upper-airway patency fails. However, clinical metrics do not characterize the mechanisms of collapse. Even in children with severe OSA, most breaths remain stable and existing clinical metrics cannot explain why collapse occurs only intermittently. Here, we integrated cine MRI with computational fluid dynamics (CFD) to simultaneously evaluate time-resolved airway morphology, wall motion, airflow, and pressure to identify the root cause of airway collapse.

Methods

A 9-year-old with OSA (oAHI 11.9 events/hour) and trisomy 21 underwent high-resolution static MRI and cine MRI with synchronized airflow measurement. The upper airway was segmented from static MRI, then registered with cine MRI to generate dynamic airway geometry during one typical and one obstructed breath. CFD simulations quantified the power transferred between air and tissue when the airway wall moved, and distinguished between pressure and neuromuscular driven motion.

Results

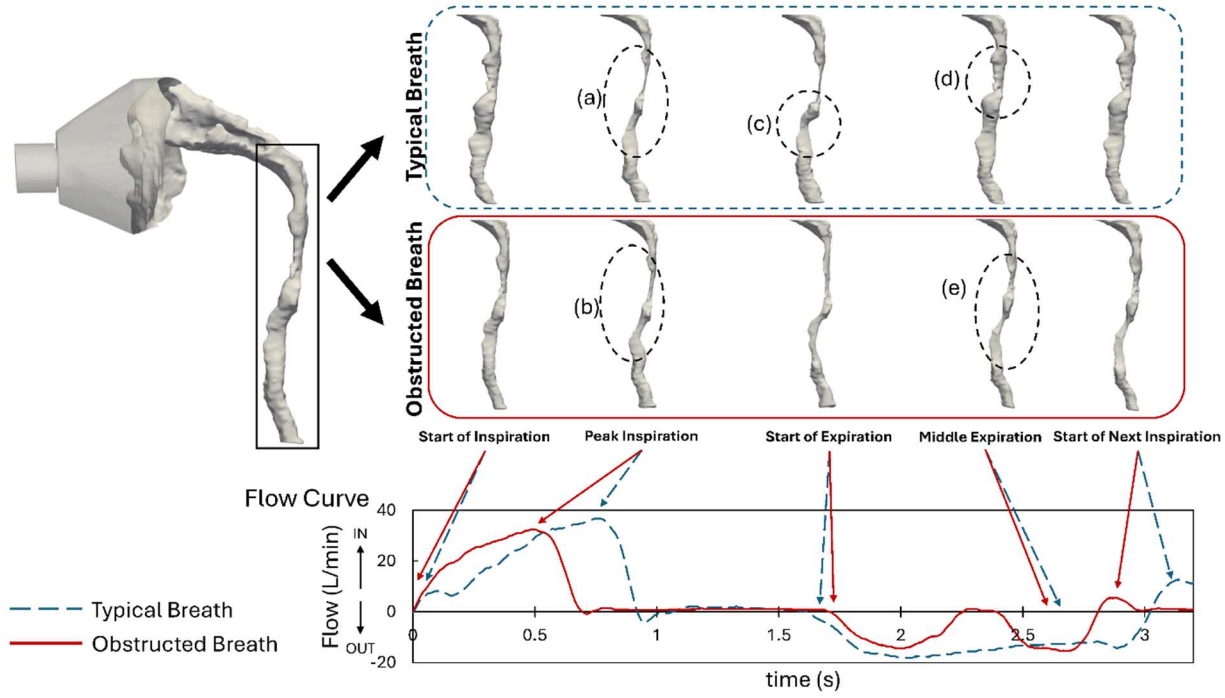
Both breaths demonstrated a respiratory pattern of inspiration, pause, and expiration. However, in the obstructed breath, the expiration and following inspiration failed due to obstruction and normal breathing resumed at the third attempted breath. Airway collapse started around peak inspiration in both breaths (Fig. a, b). In the typical breath, the

larynx dilated around expiration onset (Fig. c) followed by the oropharynx by the middle of expiration (Fig. d). In the obstructed breath, however laryngeal dilation started around the middle of expiration (Fig. e) and the oropharynx did not dilate in this period. In the larynx, the ratio of neuromuscular-driven collapsing force to pressure-driven expansion force was stronger in the obstructed breath than in the typical breath during exhalation (1.3vs.0.4).

Discussion

In this patient, successful reopening after collapse during inspiration requires an initial dilation of the larynx during the post-inspiratory pause, followed by subsequent expansion of the pharynx. Power-transfer analysis suggested that the absence of this initial laryngeal dilation during the obstructed breath was associated with inappropriate neuromuscular activation, not pressure-driven. This patient-specific approach allows evaluation of OSA mechanisms alongside anatomical variability and may facilitate personalized assessment of airway collapsibility.

Images (Optional)



Session Category

Cardiovascular/Cardiorespiratory Biomechanics: Methods, Models and Applications

P4-051

Integrating Statistical Shape Modelling and Finite Element Simulation to Evaluate the Effect of Anatomical Variation on Mitral Valve Mechanics

Dr Hyab Mehari Abraha[1,2,3], Dr Chris Goddard[2], Dr Rebecca Bryan[2], Dr George Hyde-Linaker[2], Dr Claire Conway[1,3]

[1]Royal College of Surgeons, Dublin, Dublin, Ireland. [2]Synopsys NE Ltd, Exeter, Devon, United Kingdom. [3]Trinity Centre for Biomedical Engineering, Trinity College Dublin, Dublin, Dublin, Ireland

Introduction

Statistical shape modelling (SSM) provides a quantitative description of anatomy and enables the generation of virtual patient cohorts for in silico simulation [1] . We built a SSM of the adult mitral valve (MV) from ECG-gated coronary computed tomography angiography (CCTA) scans. Here, we extend the framework by coupling the SSM to a finite-element (FE) workflow to examine how realistic anatomical variation affects MV closure mechanics under load.

Methods

Prospectively gated CCTA volumes from 72 adults were obtained from the orCaScore dataset [2]. We used a semi-automated pipeline in Synopsys Simpleware to segment the mitral leaflets and the papillary posts. We are currently using this SSM to generate a cohort of virtual valves spanning the range of anatomical variability. Each MV will be converted to a volumetric finite element mesh for solution in Abaqus Explicit Solvers. The leaflet annulus and papillary post will be fixed against translation in all directions. Healthy pressure loads (80mmHg diastolic, 120mmHg systolic) will be applied to atrial and ventricular leaflet surfaces to approximate transvalvular pressure. Coaptation and leaflet stress/strain measures will be extracted from each virtual anatomy.

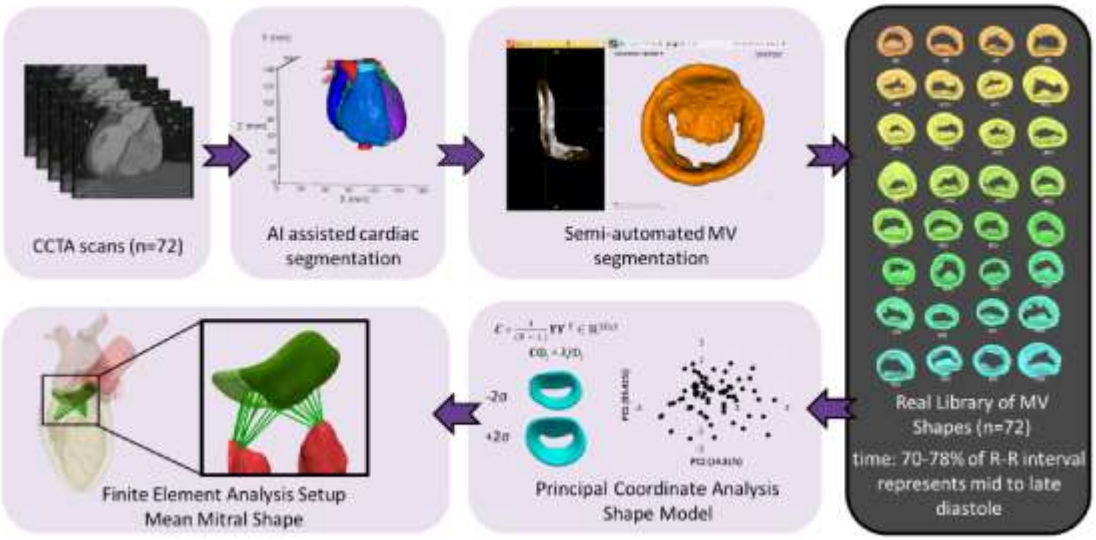
Results

The SSM of 72 CT-derived MVs captured a wide range of anatomical variation in the cohort, with the first 10 principal components describing >90% variability in annular size and shape, leaflet height and area (Fig.1). Initial statistical shape models including papillary muscle segmentations markedly restricted the spread of leaflet shapes in morpho-space, thus the SSM was re-constructed from the annulus and leaflets, and papillary tips were treated as fixed landmark points (Fig.1).

Discussion

Our created SSM results provide a compact, quantitative description of the key morphological patterns observed in the clinical dataset, and results are concordant with similar work that has been done on a paediatric transoesophageal echocardiography dataset of the mitral annulus [3]. Integrating our SSM results with the proposed FE workflow will broaden the understanding of the link between mitral mechanics and anatomical variation.

Images (Optional)



References (Optional)

[1] Martijn Hoeijmakers et al., Int. J. Numer. Method. Biomed. Eng, 2020

[2] Jelmer. M. Wolterink et al., Med Phys, 2016

[3] Silvani Amin et al., J Am Soc Echocardiogr, 2024

Acknowledgements (Optional)

The authors thank Synopsys Simpleware for providing software access and technical guidance throughout. Thanks to the data owner of orCaScore, Dr. Jelmer Wolterink, for facilitating access to the raw CCTA data. This work was supported by funding from the Research Ireland RD&I Fellowship to H. Mehari Abraha (23/IRDIFB/12075) and the Science Foundation Ireland Frontiers for the Future Programme (C. Conway - 20/FFP-P/8588).

Session Category

Cardiovascular/Cardiorespiratory Biomechanics: Methods, Models and Applications

P4-052

Automating FSI Simulations to Uncover the Downstream Effects of Ascending Aortic Grafts: A Prospective Analysis of 20 patients

Ms Ione Ianniruberto MSc[1,2], Mr Davide Astori MSc[1], Mr Davide Tondi MSc[1], Dr. Pablo Villar Calle[3], Prof. Emiliano Votta PhD[1], Dr. Jonathan Weinsaft[3], Prof. Alberto Redaelli PhD[1]

[1]Politecnico di Milano, Milano, Italy, Italy. [2]European Society of Biomechanics (ESB), Milano, Italy, Italy. [3]Weill Cornell College, New York, New York, United States

Introduction

Replacing the ascending aorta with a synthetic graft is a well-established surgical intervention for aortic aneurysms, yet it can lead to long-term degeneration of the descending aorta[1]. Compliance mismatch between the graft and the native aorta is one of the main risk factors, as it alters the hemodynamic in the distal regions[2]. We propose a novel fully automated FSI-based approach that incorporates comprehensive patient-specific data to evaluate the biomechanical impact of graft implantation.

Methods

For each patient, MRA, 4D flow MRI, and cine-MRI scans are collected both before and after surgery and used to set two different simulations: i) real pre-operative scenario, ii) Dacron graft implantation. The vessel geometry is reconstructed from MRA and meshed with an in-house Python code. Patient-specific inlet velocity profile is derived from 4D flow MRI, while outlet boundary conditions use a three-element Windkessel tuned to in-vivo pressures. The aortic wall is modelled as an incompressible, hyperelastic, anisotropic material with regional properties for ascending aorta, arch, and descending aorta. Regional compliance values are extracted from cine-MRI, while the material parameters are determined by fitting constitutive models from literature to the measured compliance. Two preliminary simulations, a fluid simulation to compute inner pressure and a structural simulation to determine prestress, provide initial conditions for the final FSI simulation.

Results

The workflow has been tested on 20 patients, (40 FSI simulations) each simulation requiring about two days. Significant differences in Wall Shear Stress (WSS) distributions were observed between pre- and post-operative models, with higher WSS values (~10 Pa) consistently appearing in the post-graft simulations in the isthmus region. Strain and oscillatory shear index (OSI) increased in almost all patients (~95%) post-graft implantation, in the proximal descending aorta.

Discussion

This automated framework enables large-scale patient-specific FSI analyses and highlights the significant biomechanical changes induced by aortic grafts. Because WSS values rise in nearly all post-operative cases, notably in the isthmus, these findings suggest that WSS could serve as a key metric for designing next-generation compliant grafts aimed at mitigating downstream disease progression.

Images (Optional)

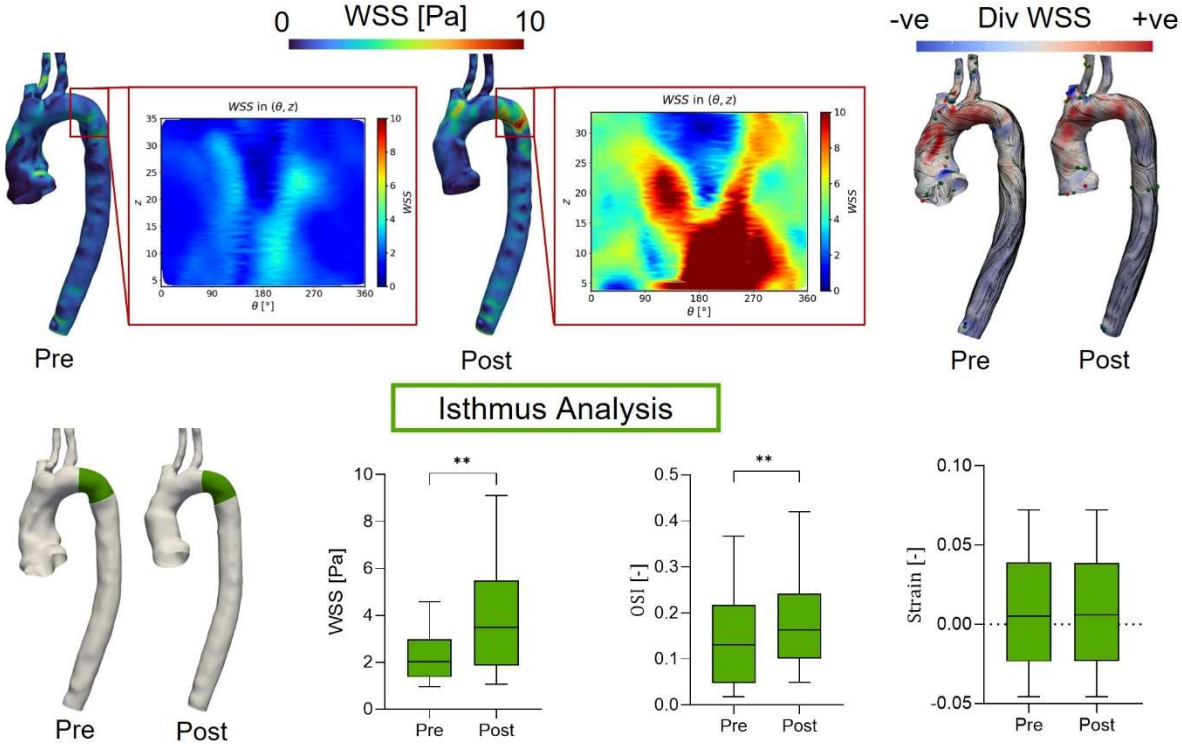


Figure 1: Analysis performed for each patient of the population

References (Optional)

[1] Palumbo et al, *EJ of Cardiothoracic Surgery*, 2022

[2] Gaudino et al, *EJ of Cardiothoracic Surgery*, 2019

Acknowledgements (Optional)

This paper is funded by NIH project #1R01HL170570-01 “Towards Personalized Prosthetic Graft Replacement for Genetically Triggered Thoracic Aortic Aneurysms”.

Session Category

P4-053

A Poroelastic Model of Lymphatic Massage

Prof. James Baish[1], Prof. Timothy Padera[2], Prof. Lance Munn[2]

[1]Bucknell University, Lewisburg, PA, United States. [2]Massachusetts General Hospital, Boston, MA, United States

Introduction

Lymphatic massage is a common treatment for lymphedema, a condition often resulting from lymphatic dysfunction or surgical interventions. A form of lymphatic massage, called Gua Sha, is also employed in traditional Chinese medicine, self-care or cosmetic contexts. However, the precise mechanics by which massage impacts interstitial fluid flow and lymphatic vessel function remain poorly understood. Here we use a computational model to examine the relevant mechanical processes.

Methods

The computational model simulates lymphatic massage with a moving compressive pressure applied to the skin (Fig. 1A). Under the skin, interstitial fluid is driven by local pressure gradients through a poroelastic subcutaneous layer into an initial lymphatic vessel, and subsequently carried away by a collecting lymphatic vessel featuring one-way valves and contractile walls. The model incorporates extrinsic forces from the massage and intrinsic pumping by the contracting collecting lymphatic vessel that is modulated by calcium from vessel stretch and nitric oxide released from wall shear stress [1]. Solution for flow, pressure, deformation, and concentrations is obtained using COMSOL Multiphysics®. Using literature parameter values our results were found to be qualitatively similar to those obtained experimentally in mice [2].

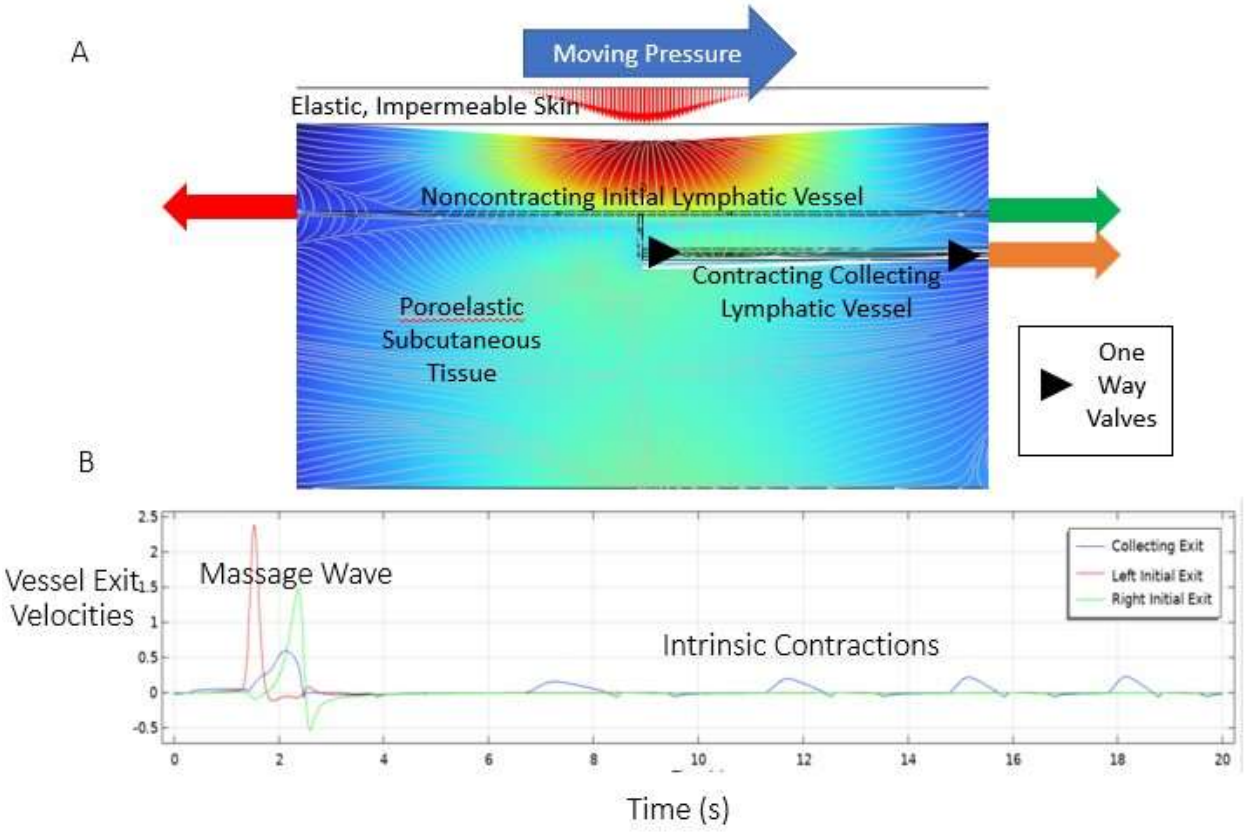
Results

Massage transiently produces localized increases in interstitial pressure, facilitating fluid entry into the initial lymphatic vessel (Fig. 1A). The collecting lymphatic vessel then clears interstitial fluid through three primary mechanisms: (1) passive conduit flow to regions of lower pressure, (2) extrinsic pumping via massage-induced vessel wall compression, and (3) intrinsic pumping through lymphatic muscle contractions (Fig. 1B). A parametric study of the model shows that there is an optimal speed for the massage wave and that massage in the orthograde direction relative to the valves is somewhat more effective than retrograde.

Discussion

The model shows how massage can modulate intrinsic pumping. Specifically, vessel wall deformation appears to stimulate intrinsic pumping, while fluid shear stress from the massage-induced flow tends to temporarily inhibit muscle contractions. The model promises to be useful as a tool to suggest further optimization of lymphatic massage techniques, as well as for prediction of tracer and antigen movement from manual stimulation.

Images (Optional)



References (Optional)

[1] Kunert, *et al.*, PNAS, 2015.

[2] Jin, *et al.*, Nature, 2025.

Acknowledgements (Optional)

We gratefully acknowledge the support of NCI grant R01-CA284603.

Session Category

Cardiovascular/Cardiorespiratory Biomechanics: Methods, Models and Applications

P4-054

Discrete Fiber–Continuum Framework for Patient-Specific Modeling of Aneurysmal Wall Microstructure

Mr. Yamnesh Agrawal[1], Dr. James R. Thunes[2], Dr. Ronald N. Fortunato[1], Dr. Anne M. Robertson[1], Dr. Spandan Maiti[1,3]

[1]Department of Mechanical Engineering and Materials Science, University of Pittsburgh, Pittsburgh, PA, United States. [2]Synopsys, Waterloo, ON, Canada. [3]Department of Bioengineering, University of Pittsburgh, Pittsburgh, PA, United States

Introduction

Aneurysm rupture risk assessment remains limited by biomechanical models that neglect tissue wall microstructure. Collagen fiber organization governs the mechanical integrity of aneurysmal tissue, yet the physiological representation of fiber architecture within patient-specific aneurysm geometries remains unresolved. This study introduces a discrete fiber–continuum framework that integrates microstructural architecture into finite element modeling of cerebral aneurysms which provides a fuller representation of the stress-state experienced by the wall tissue.

Methods

Patient-specific aneurysm geometries (N=2) were reconstructed from clinical angiographic data and extruded into multilayered hexahedral meshes representing the wall thickness. Fibers were stochastically seeded and chosen to be propagated conformally along the principal curvature directions (though this framework can also accommodate arbitrary fiber orientation vector fields) with angle dispersion of ±30° forming 1D embedded rod elements within continuum matrix. The matrix was modeled as neo-Hookean solid (**Eq.1**) and fibers as linear reinforced elastic elements (**Eq.2**).

$$\Psi_{matrix} = 1/2\mu(J^{-2/3}I_1 - 3) + 1/2K(J-1)^2 \qquad (1)$$

$$\Psi_{fiber}=1/2E_f(\lambda_f-1)^2 \qquad (2)$$

Results

The matrix and fiber stress for both samples using fiber-reinforced finite element (FE) method [1] are shown in **Fig.1**. FE analysis revealed that the mean Von-Mises stress for Sample 1 & 2 in the non-collagenous matrix was 38.99±11.96 kPa and 73.89±27.62 kPa, while the corresponding fiber stresses were 0.33±0.20 MPa and 0.72±0.44 MPa respectively. Furthermore, fiber stress maps demonstrated significant heterogeneity at

local scales where adjacent fibers exhibited varying load-bearing states (inset, right column of **Fig.1**) which cannot be captured by homogenized anisotropic models.

Discussion

The presented framework bridges the gap between physiological microstructural data and computational biomechanics by incorporating individual fiber-matrix level mechanics. Unlike homogenized anisotropic models, our discrete approach elucidates how different fiber architecture within the aneurysm geometry dictates local stress concentrations, offering a mechanistic explanation for wall failure distinct from averaged wall stress. Observed heterogeneities and attendant focal elevation in fiber stress can initiate sub-tissue scale tears revealing novel biomechanical pathways leading to wall rupture; Such failure mechanisms cannot be captured through continuum scale homogenized tissue models. Consequently, this methodology offers a scalable route for improving patient-specific rupture risk prediction.

Images (Optional)

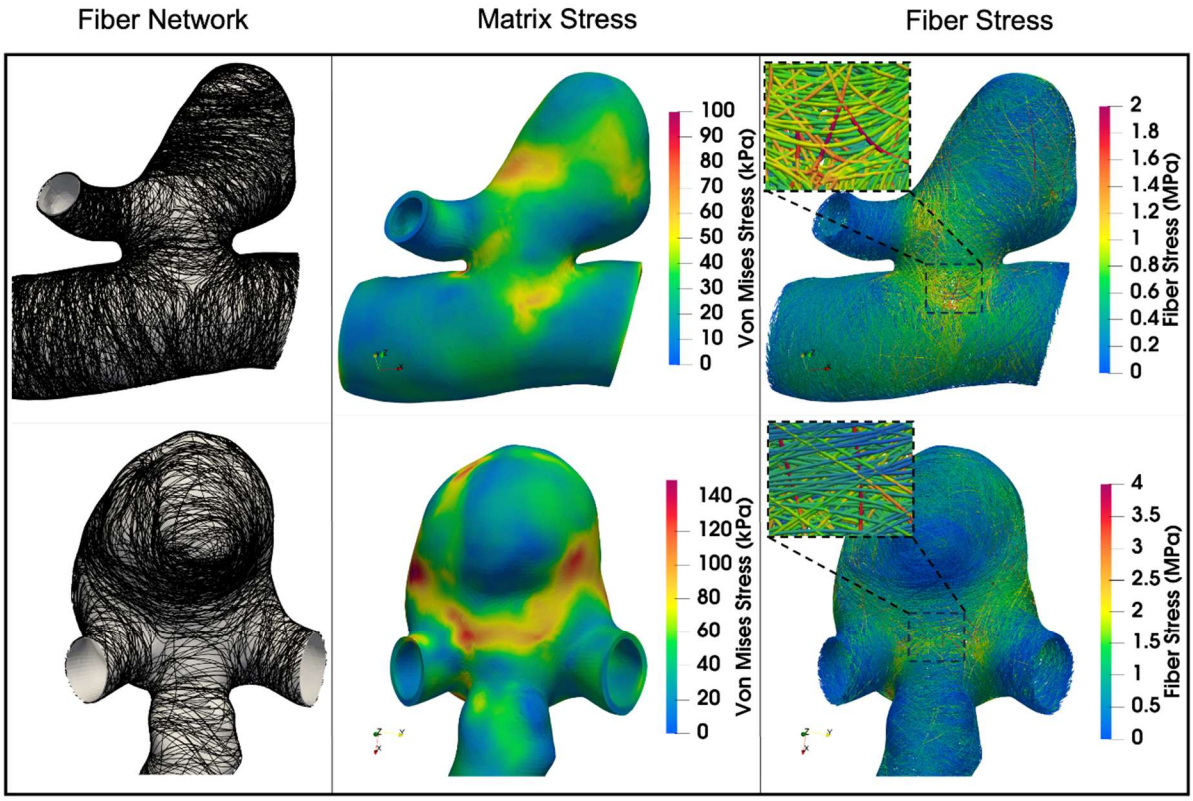


Figure 1. Discrete collagen fiber architecture and FE results on Sample 1 & 2. **(Left Column)** Generated discrete fiber networks aligned along principal curvature directions. **(Middle Column)** Von Mises stress distribution in the matrix. **(Right Column)** Fiber stress distribution from discrete fiber-reinforced FE model. Insets detail the heterogeneous fiber stress distribution at local region.

References (Optional)

[1]Thunes *et al.*, J Biomech. 2018

Acknowledgements (Optional)

Funding Support from NIH Grant No. **2R01NS097457** is gratefully acknowledged.

Session Category

Cardiovascular/Cardiorespiratory Biomechanics: Methods, Models and Applications

P4-055

A Sparse Sampling Framework for High-Fidelity Reconstruction of Aortic Fiber Architecture

Dr James Thunes PhD[1], Mr Yamnesh Agrawal[2], Dr Julie Phillippi PhD[3,2], Dr Thomas Gleason MD[4,2], Dr Spandan Maiti PhD[2,5], Mr Oleg Chernukhin MS[1]

[1]Synopsys, Waterloo, ON, Canada. [2]Department of Bioengineering, University of Pittsburgh, Pittsburgh, PA, United States. [3]Department of Cardiothoracic Surgery, University of Pittsburgh, Pittsburgh, PA, United States. [4]Asheville Heart, Asheville, NC, United States. [5]Department of Chemical and Petroleum Engineering, University of Pittsburgh, Pittsburgh, PA, United States

Introduction

Patient-specific prefailure and failure biomechanics of aorta is governed by collagen and elastin fiber network of wall tissue. Accurate biomechanical modeling requires high fidelity representation of the fiber architecture across the aortic wall. However, substantial spatial heterogeneity exists in this network (**Fig.1a**). While multiphoton microscopy (MPM) can capture fiber organization, imaging is limited to discrete locations. We propose a sparse-sampling framework to reconstruct the complete fiber architecture from limited measurements enabling spatial mapping of microstructure-induced wall stress fluctuations.

Methods

Reconstruction of aortic fiber architectures properties from limited discrete measurements was obtained by Radial Basis Function (RBF) mapping between sampling locations and the discretized geometry using Ansys System Coupling (v2025R2). To validate our sparse-sampling methodology, we constructed a synthetic “ground-truth” reference fiber direction field on a patient-specific aorta mesh with 24,502 triangle elements (**Fig.1b**) guided by the principal curvatures of the aortic surface. We sampled the field at 20 random points using Poisson disc method and reconstructed the complete fiber direction field. This process was repeated 100 times to assess reproducibility. Angular difference between the reference and reconstructed vector at each element centroid for each run was used for error estimation of the interpolation. A custom discrete embedded-fiber finite element analysis [1] was performed with the “ground-truth” and reconstructed fiber network.

Results

The average angular difference between reference and reconstructed fields was $6.6^{o}\pm8.7^{o}$ (**Fig.1c**). FE analyses using discrete fiber networks generated from the reference

and reconstructed fields (**Fig.1d,e**) showed that the fiber stress predicted from the reconstructed field (1.03±0.56 MPa) is comparable to that from the reference field (1.04±0.51 MPa).

Discussion

We demonstrated that a sparse distribution of sampling locations can approximate fiber orientation across complex aortic geometries with high fidelity. Beyond fiber orientation, this framework offers a generalized method to spatially interpolate other critical microstructural parameters such as wall thickness, fiber crimp, and material stiffness from limited local data. Future work includes optimal sampling number and placement and uncertainty quantification.

Images (Optional)

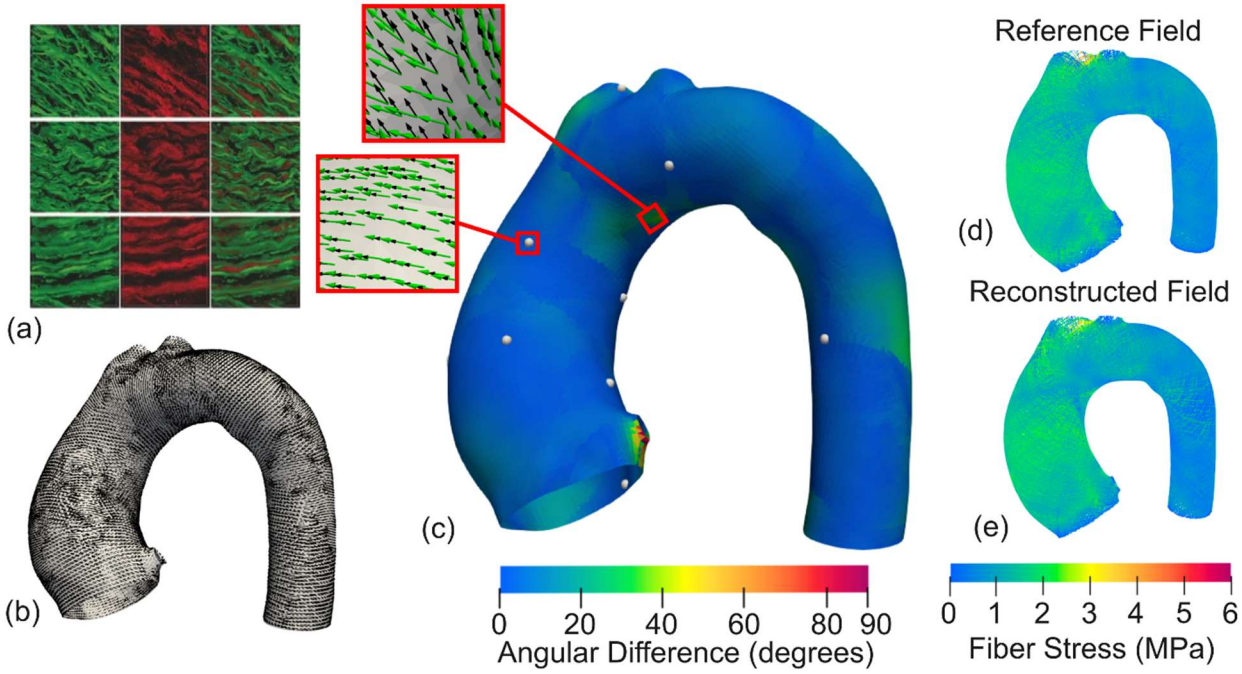


Figure 1: (a) Representative MPM images [2], (b) reference field on aorta geometry, (c) angular difference between reference and reconstructed fields (insets: regions of high and moderate agreement; black vectors: reference, green: reconstructed). Fiber stress under internal pressure of 20 kPa (~150mmHg) using (d) reference field and (e) reconstructed field.

References (Optional)

[1] Thunes *et al.*, J Biomech (2018)

[2] Fritze *et al.*, J Vasc Res (2011)

Acknowledgements (Optional)

Partial support from NIH R01HL109132 (TGG) is gratefully acknowledged by JAP, TGG, and SM.

Session Category

Cardiovascular/Cardiorespiratory Biomechanics: Methods, Models and Applications

P4-056

Finite Element Investigation of Mandibular Advancement and Hyoid Mechanics in Modulating Upper Airway Stability

Dr Wedad Saab[1,2], Dr Joseph Ghafari[2,3], Dr Jason Amatoury[4,1]

[1]Sleep and Upper Airway Research Group (SUARG), American Unviersity of Beirut, Beirut, Beirut, Lebanon. [2]Department of Dentofacial Medicine, American University of Beirut Medical Centre, Beirut, Beirut, Lebanon. [3]Department of Orthodontics, University of Pennsylvania, Philadelphia, Beirut, United States. [4]Biomedical Engineering Program, Maroun Semaan Faculty of Engeering and Architecture, American University of Beirut, Beirut, Beirut, Lebanon

Dr Wedad Saab

Dr Joseph Ghafari

Introduction

Mandibular advancement (MA) is used in the treatment of obstructive sleep apnea (OSA); however, it is not effective in all individuals. The hyoid bone serves as a key anchor point for multiple upper airway dilator muscles, including those connected to the mandible, and its position and mobility are therefore expected to influence airway stability under MA. Despite this, the combined biomechanical effects of natural (baseline) hyoid position, hyoid mobility, and surgical hyoid repositioning on MA-induced airway stabilization remain poorly understood. This study aimed to quantify these effects using computational modeling.

Methods

A validated two-dimensional mid-sagittal finite element model of the rabbit upper airway was used to simulate MA under a range of hyoid conditions. Simulations incorporated progressively more caudal baseline hyoid positions (OSA phenotype), a hyoid that was either free to move or mechanically fixed, and anterior–cranial surgical hyoid repositioning with fixation. For each simulated condition, upper airway collapsibility was quantified using closing pressure (Pclose). Mid-sagittal airway cross-sectional area (CSA), anterior–posterior diameter (APD), and stress/strain distributions were determined.

Results

At the initial (healthy) baseline hyoid position, MA reduced Pclose and increased CSA and APD, particularly at the hyoid region, indicating improved airway stability. A more caudal baseline hyoid position increased airway collapsibility and attenuated the mechanical benefits of MA, regardless of whether the hyoid was free to move or fixed. Hyoid fixation mostly reduced the effectiveness of MA in lowering Pclose and enlarging the airway, with the greatest regional APD increase shifted from the hyoid to the tongue region. Anterior–cranial surgical repositioning of the hyoid consistently reduced Pclose, increased CSA, and enhanced regional APDs across all baseline hyoid positions. Stress and strain distributions increased non-uniformly and varied across simulated conditions.

Discussion

Baseline hyoid position and mobility influence the biomechanical response of the upper airway to MA. A caudal and/or mechanically constrained hyoid limits MA-induced airway stabilization, whereas anterior-cranial hyoid repositioning enhances airway patency and compensates for unfavorable baseline anatomy. These findings highlight the importance of incorporating hyoid biomechanics into personalized OSA treatment planning and support the potential value of combined MA–hyoid interventions in selected anatomical phenotypes.

Session Category

Cardiovascular/Cardiorespiratory Biomechanics: Methods, Models and Applications

P4-057

Biomechanical Modeling of Postnatal Growth of Large Arteries

Professor Jay Humphrey PhD[1], Professor Abhay Ramachandra PhD[2], Dr. Erica Schwarz PhD[1]

[1]Yale University, New Haven, CT, United States. [2]Iowa State University, Ames, IA, United States

Introduction

Arteries undergo dramatic changes during prenatal and postnatal development. Notwithstanding the importance of both, understanding early postnatal development is critical for it is during this period that surgeons intervene to palliate congenital defects. Although there is accumulating data on transcriptional, histological, and biomechanical changes throughout postnatal development of large arteries, detailed computational biomechanical models needed for surgical planning remain wanting.

Methods

With IACUC approval, we collected RNA-sequencing, histological, geometrical, and biomechanical data on the right pulmonary artery from 50 wild-type mice at postnatal days P2 (perinatal), P10, P21 (weaning), P42, and P84 (maturity). These data provided time-course changes in key transcripts (e.g., cell proliferation, matrix synthesis), composition (elastic and collagenous fibers), dimensions (radius, wall thickness, axial stretch), and mechanical metrics (biaxial wall stretch, stress, stiffness, and elastic energy storage). To understand how these many contributors to development work together, we formulated a novel constrained mixture model of growth (changes in mass) and remodeling (changes in microstructure) and focused on changes in elastic fibers (including deposition, compaction), fibrillar collagens (deposition, orientation, maturation), and smooth muscle cells. Applied loads included a near constant distending blood pressure following closure of the ductus arteriosus and near sigmoidal increases in blood flow and axial force.

Results

Transcriptional data revealed monotonic decreases in cell proliferation and the aggregating proteoglycans that support proliferation and migration, but transient increases in elastin and collagen production that peaked at ~P10 and ~P21 respectively. Using these data to inform a model of early genetically-driven transients in mass production/removal to augment a long-term model of mechanical homeostasis based on intramural and wall shear stresses allowed the model to capture simultaneously the measured time-course

changes (many sigmoidal) in luminal radius, axial length, biaxial wall stretch and stress, energy storage, and even mass fractions for elastin, collagen, and cells. The model similarly captured the more modest changes in wall thickness and biaxial material stiffness.

Discussion

Whereas prior computations have focused on the hemodynamics during development (often assuming rigid walls at individual ages), we submit that the present multiscale growth and remodeling model promises to enhance computer-based surgical planning by including the underlying mechano-genetics.

Session Category

Cardiovascular/Cardiorespiratory Biomechanics: Methods, Models and Applications

P4-058

Towards Single-Access, Contrast-Free TAVR Guidance using PINN Hemodynamics

Mr. Jerome Gosselin[1], Professor Rosaire Mongrain[1], PhD. Frédéric Couët[2], Mr. Sébastien Lalancette[2], Dr. Renzo Cecere[1], PhD. Caroline Wagner[1]

[1]McGill University, Montreal, Quebec, Canada. [2]Haemonetics, Québec, Québec, Canada

Introduction

Aortic Stenosis (AS) is the most common valvular heart disease in developed countries, typically treated with Transvalvular Aortic Valve Replacement (TAVR). Vascular access complications can lead to increased early mortality, with bleeding as a key predictor. To achieve a minimalist approach—a single-access, contrast-free procedure—we aim to generate essential physiological data, like a coplanar view, traditionally obtained invasively with a pigtail catheter. We propose using a Digital Twin (DT) based on Physics-Informed Neural Networks (PINN) to model flow hemodynamics and accurately identify the coplanar view.

Methods

The approach uses PINNs to create the core computational engine for the single-access Digital Twin (DT) procedure. Unlike traditional methods, PINNs rely on governing equations to complement existing data. We initiated with modeling steady-state, incompressible, non-viscous 1D flow (the Bernoulli equation) as a foundational step.

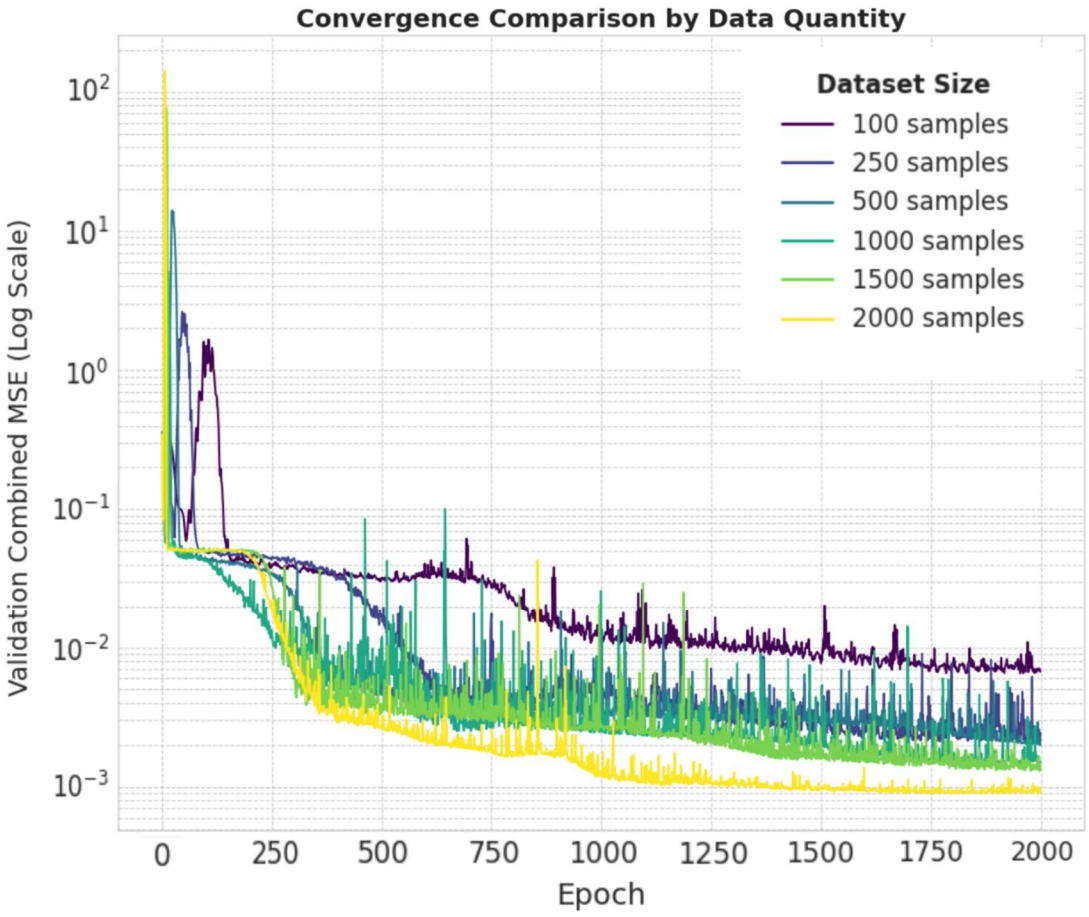
Results

The PINN model is an MLP that addresses three key residuals: the Momentum equation, the Continuity equation (with varying pipe diameter), and Simulation data. To establish model reliability, we focused on the impact of the quantity of upstream training data. We tested PINN's prediction accuracy across a dataset range of 100 to 2000 samples, fixing the physical complexity at a 30% stenosis severity. Model accuracy and stability were assessed using Root Mean Square Error (RMSE) for the pressure and velocity fields. Initial trials confirmed that performance was already highly robust with only 100 training samples, yielding a Mean RMSE Pressure of 7.19×10^{1} Pa. This RMSE, approximately 0.54 mmHg (0.45% of a 120 mmHg range), is comparable to the ±1 mmHg fidelity of the SavvyWire™ pressure sensor. Increasing the dataset size further dramatically reduced underfitting (as seen in the figure 1).

Discussion

The results show that PINN provides reliable predictions with physics-based residuals, depending on the quantity and diversity of training data. Initial high accuracy was achieved with a fixed architecture and training duration, indicating room for further improvement. It highlights the need for a multimodal dataset of TAVR cases to enable the Digital Twin (DT) to generate reliable pressure information for the coplanar view, thereby supporting the single-access minimalist TAVR procedure.

Images (Optional)



Session Category

Cardiovascular/Cardiorespiratory Biomechanics: Methods, Models and Applications

P4-059

A Hybrid Multi-Scale 3D Computational Model to Explore the Origins of Atherosclerosis

PhD candidate Mané Sarkissian[1], Professor Vasileios Vavourakis[2], Professor Jérome Noailly[1]

[1]Pompeu Fabra University, Barcelona, Catalonia, Spain. [2]University of Cyprus, Nicosia, Nicosia, Cyprus

Introduction

Atherosclerosis (AS) is influenced by inflammation, biomechanics and characterized by foam cell (FC) formation. AS has no cure beyond a very early stage. New approaches are necessary for subclinical characterization. We aimed to create a model of early AS, including key atherogenic processes for early biomarker identification with mechanistic risk stratification.

Methods

A regulatory network model (RNM) was combined with an agent-based model (ABM). The RNM was solved at each time step with a set of ordinary differential equations [1]. RNM interacted with higher-level agent rules integrating oxidative stress; inflammation; LDL oxidation & aggregation; wall shear stress (WSS); reverse cholesterol transport (RCT). WSS mechanobiology activated specific endothelial cell signaling pathways: normal WSS activated ERK5-KLF2; low WSS activated NF-kB. RCT was modelled via ABCA1 kinetics in macrophages (MC) & FC. The model was implemented in BioDynaMo. 18 cases were simulated with 6 combinations of HDL and WSS levels, each for three levels of LDL: high (200 mg/dL); borderline (150 mg/dL); normal (90 mg/dL). Each simulation was repeated 10 times. A sensitivity analysis (SA) explored the effects of the: LDL uptake rate by CD36, SR-A1 & LRP1 receptors; RCT rate by ABCA1; LDL modification rate.

Results

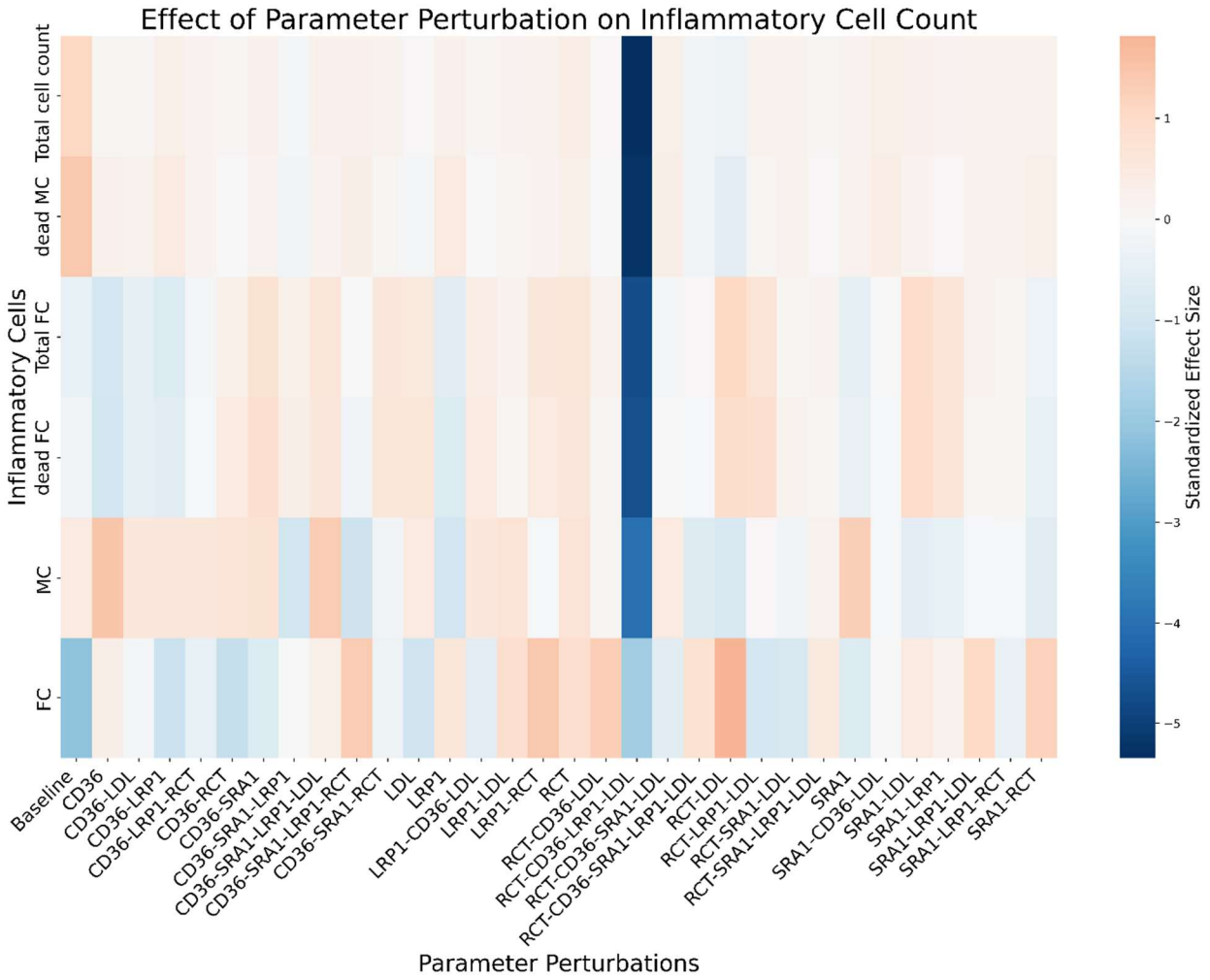
Normal LDL and WSS with high HDL showed no atherogenesis. For the hypercholesterolemic case, the SA revealed the parameter combination resulting in lowest levels of inflammation: the simultaneous upregulation of CD36, RCT and LRP1 along with increased LDL modification rate significantly reduced MC & FC ($p_value < 0.05$). Remarkably, though, the increase of CD36 alone increased oxLDL uptake and MC accumulation. However, when this upregulation was combined with increased RCT, LRP1 &

LDL modification a strong reduction in inflammatory cell counts was observed (Fig.). These results could potentially explain controversial findings on the role of CD36 in AS [2].

Discussion

This unique AS model provided realistic simulations of key atherogenic processes in the artery. The results underscore the multifactorial nature of AS highlighting the dual role of CD36. In conclusion, functional MC with effective LDL uptake and efflux are crucial for halting AS.

Images (Optional)



References (Optional)

[1] Mendoza et al., J Theor Biol Med Model., 2006

[2] Yuasa-Kawase et al., J Atheroscler Thromb., 2012

Acknowledgements (Optional)

This project has received funding from the European Research Council (ERC) under the Horizon Europe research and innovation program of the European Union (ERC-2021-CoG-O-Health-101044828).

Session Category

Cardiovascular/Cardiorespiratory Biomechanics: Methods, Models and Applications

P4-060

CFD-Agent-Based Model Reveals Spatial Clustering of Inflammatory markers in Low Shear Arterial Regions

Dr. Veera Venkata Satya Varaprasad Jakka, PhD Candidate Mané Sarkissian, PhD Candidate Yalemzerf Motbaynor Alemu, Prof. Jérôme Noailly

Universitat Pompeu Fabra (UPF), Barcelona, Catalonia, Spain

Introduction

Atherosclerotic plaques develop preferentially in arterial regions with disturbed flow and low wall shear stress [1]. The NLRP3 inflammasome, a critical mediator of atherosclerotic inflammation, responds to shear stress [2], hypoxia [3], and oxidized lipids. However, spatial relationships between hemodynamics and inflammasome activation remain unclear. We coupled CFD and agent-based simulations to investigate monocyte inflammatory signaling regulation by arterial flow.

Methods

Blood flow through a curved iliac artery was simulated using OpenFOAM with Lagrangian tracking of 4,000 monocytes over 10 hours. BioDynaMo agent-based modeling integrated hemodynamics with monocyte processes: (i) chemokine sensing, (ii) selectin-mediated rolling, (iii) integrin-dependent adhesion, (iv) state-dependent NFκB activation, (v) NLRP3 activation by NFκB and environmental stimuli (hypoxia, oxidized LDL, low shear), and (vi) subtype-specific transmigration. Monocytes were assigned classical (85%), intermediate (5%), or non-classical (10%) phenotypes.

Results

Simulations predicted 8.0% adhesion (321/4000 cells) and 9 transmigration events. Regional NFκB (Fig 1B-C) showed state-dependence: adhered cells exhibited 5.2-fold higher activity (0.800) than rolling cells (0.155). Population NLRP3 reached 0.066, while activated cells achieved near-maximal NLRP3 (0.83-0.99). NLRP3 exhibited pronounced spatial heterogeneity (Fig 1A,C,E): the middle vessel region (lowest flow velocity 27.2 μm/s, Fig 1D) showed 2.63-fold enrichment versus inlet. The middle showed highest cell density (139 cells, Fig 1F) versus inlet (55) and outlet (127).

Discussion

This multiscale framework links arterial hemodynamics to cellular inflammatory signaling. The 2.63-fold NLRP3 clustering in low-shear regions, where flow recirculation and hypoxia co-localize, provides mechanistic insight into preferential plaque development in curved

vessels [1]. The 5.2-fold NFκB amplification upon adhesion reveals that hemodynamic forces promoting capture trigger inflammatory cascades. Population-average NLRP3 (0.066) reflects that only adhered monocytes (8%) activate inflammasomes. The framework successfully models monocyte biology, enabling testing of atherosclerosis mechanisms and interventions. This arterial simulation represents a first step toward whole-body vascular modeling. Scaling from 3D segments to body-wide vasculature enables growth from ~4,000 to ~350×10^6 agents, permitting patient-specific vascular mapping to track inflammation system-wide and support precision cardiovascular interventions.

Images (Optional)

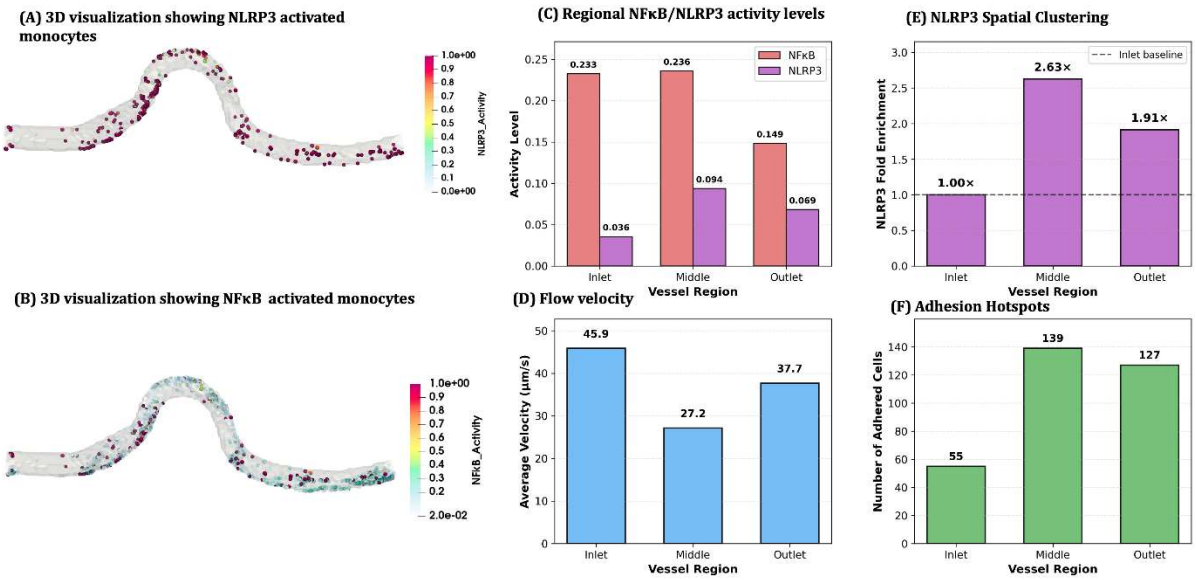


Figure 1. Spatial distribution and hemodynamic coupling: (A-B) 3D visualizations of NLRP3 and NFκB activated monocytes. (C) Regional NFκB/NLRP3 activity levels. (D) Flow velocity distribution. (E) 2.63 times NLRP3 enrichment in middle region. (F) Adhesion hotspots.

References (Optional)

[1] Chiu & Chien (2011). Physiol Rev, 91(1):327-387.

[2] Xiao H, et al. Circulation. 2013; 128(6):632-642.

[3] Wang X, et al. FASEB J. 2024; 38(15):e23854.

Acknowledgements (Optional)

European Research Council (ERC-2021-CoG-O-Health-101044828).

Session Category

Cardiovascular/Cardiorespiratory Biomechanics: Methods, Models and Applications

P4-061

Patient-Specific Fluid-Structure-Interaction Simulations Suggest Endothelial Cell Activation Potential (ECAP) as a Biomarker for Aortic Events in Marfan syndrome

Miss Yufan Wu[1], Dr. Krashn Dwivedi[1], Dr. Hadi Wiputra[2], Dr. Marisa Bazzi[3], Dr. Alan Braverman[4], Dr. Victor Barocas[2], Dr. Jessica Wagenseil[1]

[1]Dept of Mechanical Engineering, Washington University, St. Louis, Missouri, United States. [2]Dept of Biomedical Engineering, University of Minnesota, Minneapolis, Minnesota, United States. [3]Dept of Pediatrics, School of Medicine, Stanford University, Palo Alto, California, United States. [4]Department of Medicine, Cardiovascular Division, Washington University School of Medicine, St. Louis, Missouri, United States

Introduction

Marfan syndrome (MFS) is a connective tissue disorder whose cardiovascular complications include thoracic aortic aneurysm and dissection. Current surgical guidelines for intervention rely on maximum aortic diameter, failing to capture patient-specific hemodynamics. We performed fluid-structure interaction (FSI) simulations on pre-dissection and post-Type B dissection MFS aortas to identify potential hemodynamic biomarkers of aortic events.

Methods

Seven MFS patients with CT imaging before and after dissection were analyzed. Aortic geometries were reconstructed and meshed in SimVascular. FSI simulations incorporated patient-specific heart rate and blood pressure, a three-element Windkessel model at the lumen outlets, and a neo-Hookean constitutive equation for the wall and dissection flap (if applicable). Hemodynamic metrics including time-averaged wall shear stress (TAWSS), oscillatory shear index (OSI), endothelial cell activation potential (ECAP), and relative residence time (RRT), were extracted from the simulation results. Functional principal component analysis (FPCA) assigned patient-level scores for each metric. Bayesian posterior and probability models assessed the likelihood and strength of the scores' association with aortic events (i.e. dissection).

Results

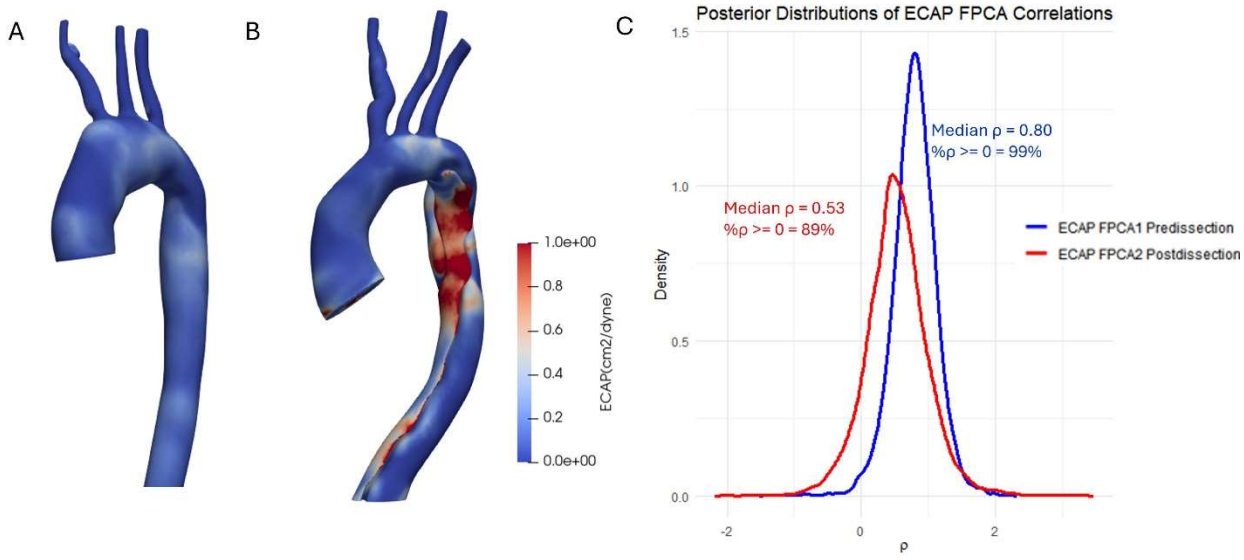
Compared to pre-dissection states, post-dissection aortas showed reduced TAWSS and elevated OSI, ECAP, and RRT (Fig.1 A-B). In dissected aortas, the true lumen, which is significantly smaller than the false lumen, demonstrated higher OSI, ECAP, and RRT. In pre-dissection models, ECAP peaked at the proximal descending aorta, anatomically matching

the future dissection site despite negligible dilation. Across all patients, ECAP showed the highest likelihood of positive correlation with aortic events (Fig.1 C).

Discussion

High ECAP indicates regions with low shear stress and highly oscillatory flow – conditions that promote endothelial dysfunction and degeneration of the intimal layer, where dissections originate [1]. Clinicians identified the start of the descending aorta as a highly dissection-prone site, coinciding with the location where ECAP peaks in our study [2]. For the dissection case, elevated ECAP in the true lumen suggests disturbed flow that may contribute to malperfusion of downstream vessels and organs [2]. Because ECAP can be estimated noninvasively from 4D-flow MRI, it holds potential as a biofluidic biomarker of aortic events in MFS.

Images (Optional)



References (Optional)

[1] Bazzi et al., Cardiovascular Engineering and Technology, 2022

[2] Crawford et al., Vasc Med, 2017

Acknowledgements (Optional)

NIH R01164800

Session Category

Cardiovascular/Cardiorespiratory Biomechanics: Methods, Models and Applications

P4-062

Multi-Phase CFD Simulations of cAVM Embolizations: Impact of Catheter Location on Liquid Embolic Agent Transport

ir. Jessie Duquesne[1], dr. Elisabeth Dhondt[2], ir. Mohammadjavad Sedghizadeh[1,3], Prof. dr. ir. Vincent Keereman[4], dr. ir. Danilo Babin[3], Prof. dr. Peter Vanlangenhove[2], Prof. dr. ir. Charlotte Debbaut[5]

[1]BioMMedA @iBME, Ghent, East Flanders, Belgium. [2]Vascular and Interventional Radiology, Ghent, East Flanders, Belgium. [3]imec-TELIN-IPI, Ghent, East Flanders, Belgium. [4]MEDISIP-IBiTech, Ghent, East Flanders, Belgium. [5]BioMMedA @iBME-IBiTech, Ghent, East Flanders, Belgium

Introduction

Cerebral arteriovenous malformations (cAVMs) are high-flow vascular anomalies in the brain characterized by an abnormal tangle of blood vessels (nidus). This poses an increased risk of intracranial hemorrhage (1-4% annual rupture rates [1]). Endovascular embolization (EE) using liquid embolic agent (LEA) is a viable treatment option. The efficacy of EE is largely dependent on the LEA's interaction with the local blood flow and the treatment-related parameters including the microcatheter position. This study uses patient-specific multiphase computational fluid dynamics (CFD) to investigate how variations in catheter position influence the LEA distribution and targeted flow occlusion within the cAVM.

Methods

A patient-specific cAVM geometry was 3D-reconstructed (Mimics, Materialise) and meshed with 10.9 million tetrahedral elements (Fluent, Ansys, USA). The Apollo microcatheter (0.33mm inner diameter) was virtually inserted into the feeding artery (Discovery, Ansys; Fig. 1A). Blood flow (ρ:1060kg/m^3, μ:3.5mPa·s) and LEA injections (ρ:1104kg/m^3, μ:18mPa·s) were modeled using transient multiphase CFD. Boundary conditions included a cerebral inlet velocity profile derived from the Reymond model [2] scaled to patient data, and 2-element Windkessel models at the draining veins (Fig. 1B). LEA progression was modelled for two distinct axial catheter tip positions to quantify filling efficiency and potential reflux.

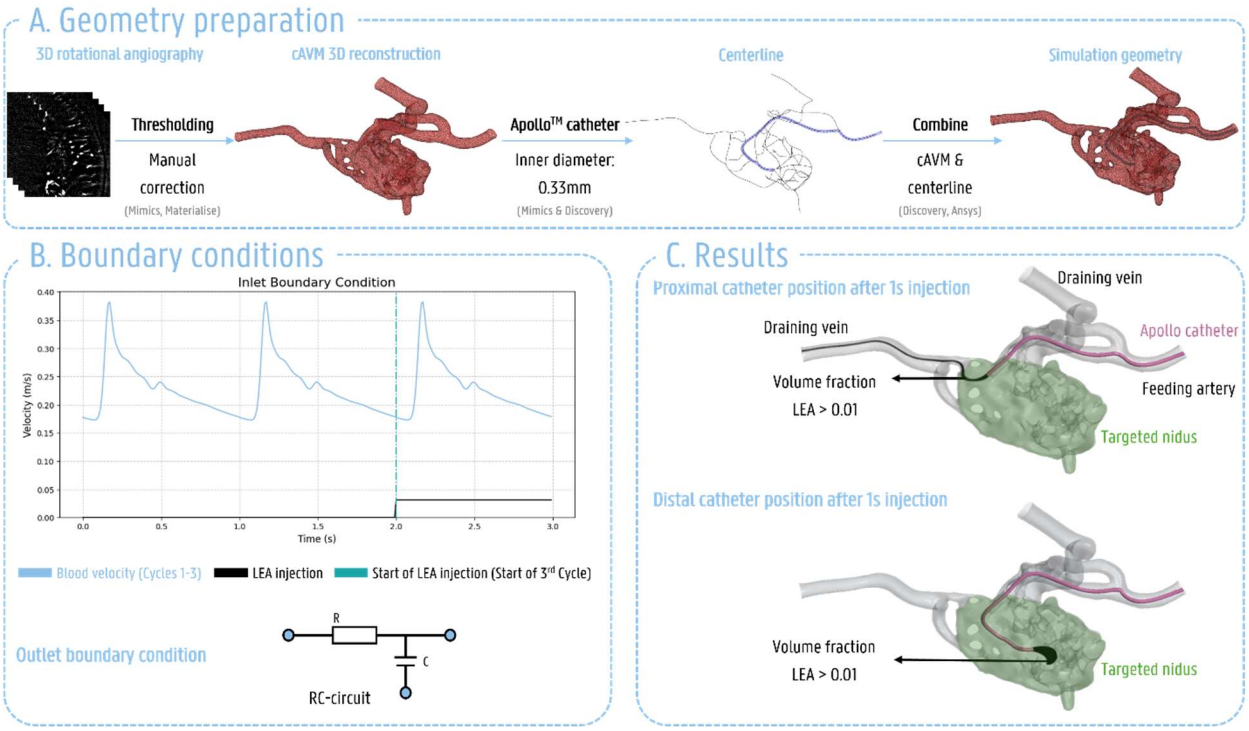
Results

Fig. 1C illustrates the LEA progression, showing the embolization extent. When the catheter tip was positioned proximally near the entrance of the feeding artery, the LEA progression was directly shunted towards the draining vein (42.97% of injected LEA volume in targeted nidus). When the catheter tip was advanced more distally in the feeding artery, it immediately targeted the nidus (100% of injected LEA volume in targeted nidus).

Discussion

The simulation results show that distal microcatheter placement maximizes targeted nidus occlusion and minimizes unintentional shunting to the draining veins. These findings suggest that a more distal catheter tip penetration into the AVM nidus may support maximizing therapeutic efficacy. Future work will focus on quantifying targeted occlusion metrics and analyzing nidus hemodynamics for multiple patients. Ultimately, these CFD-models will be extended to simulate multi-injection sequences (i.e. longer injection times, etc.).

Images (Optional)



References (Optional)

[1] Denise Brunozzi *et al.,* J NEUROINTERV SURG, 2025

[2] Phillipe Reymond *et al.*, AM PHYSIOL-HEART, 2009

Acknowledgements (Optional)

This work was financially supported by the Research Foundation Flanders (FWO, No. G034724N, FWO, No. 1105926N) and BOF funding (BOFSTG2019010701). The authors thank Amith Balusubramanya for his assistance with the boundary conditions implementation.

Session Category

Cardiovascular/Cardiorespiratory Biomechanics: Methods, Models and Applications

P4-063

Validation Pipeline for Subject-Specific Bone Conduction Finite Element Models

M.Sc. Johannes Niermann[1], M.Sc. Linus Taenzer[2], Dr. Ivo Dobrev[1], Dr. Bart Van Damme[2], Prof. Dr. Christof Röösli[1], Dr. Flurin Pfiffner[1]

[1]Department of Otorhinolaryngology, Head and Neck Surgery, University Hospital Zurich, University Zurich, Zurich, Zurich, Switzerland. [2]Laboratory of Acoustics/Noise Control, Empa, Dübendorf, Zurich, Switzerland

Introduction

Bone conduction (BC) hearing refers to the transmission of sound to the cochlea via skull vibrations. Individual anatomies and material properties cause variations in BC response [1,2].

Individualized full head BC models offer the potential for advancements in basic research, hearing aid development, and personalized treatment. A hierarchical experimental framework for the development and validation of these models has been formulated [3].

This study shows preliminary comparisons of experimental measurements with simulation predictions of the dynamic response of a dried bone piece.

Methods

CT and motion data were collected as described in [3]. The CT scan of the bone piece was segmented semi-manually into cortical and trabecular bone. A finite element (FE) mesh was generated using Synopsis Simpleware (Fig. A). Material properties were defined based on a combination of measurements, literature [2], and model tuning. A custom automatic registration and interpolation method was developed to align simulation with experimental data on a common grid of points. The modal assurance criterion (MAC) was used as a comparison metric.

Results

The registration method showed robust results with an average error of less than 0.45 mm across fiducials. The MAC showed agreement of simulation and experiment of over 98 % for multiple mode shapes of the dried bone piece (Fig. B).

Discussion

The presented validation methodology can be used in several scenarios within the development of individualized bone conduction models, including:

1. validation across large sample sizes within an individual as well as across multiple individuals
2. validation of bone piece conditions (wet and dry)
3. variation of model definitions for sensitivity studies or identification of material properties.

Additionally, the methodology can be extended towards validation of more complex model geometries (i.e., full heads), by using similar measurement methods. Furthermore, spatial registration of datasets from different hierarchies (e.g. pieces to heads) will allow application of identified properties.

References (Optional)

[1] Surendran et al., J. Acoust. Soc. Am., 2025

[2] Kohtanen et al., J Mech Behav Biomed Mater., 2021

[3] Niermann et al., Biomimetics, 2025

Acknowledgements (Optional)

This work was supported by grant 213127 from the Swiss National Science Foundation.

Session Category

Cardiovascular/Cardiorespiratory Biomechanics: Methods, Models and Applications

P4-064

Influence of Onyx Injection Rate during Endovascular Embolization of Cerebral Arteriovenous Malformations: A Computational Fluid Dynamics Study

ir. Kaat Wille[1], ir. Jessie Duquesne[1], ir. Mohammadjavad Sedghizadeh[1,2], dr. ir. Danilo Babin[2], prof. dr. ir. Vincent Keereman[3], dr. Elisabeth Dhondt[4], prof. dr. Peter Vanlangenhove[4], prof. dr. ir. Charlotte Debbaut[1]

[1]iBME-BioMMedA, Ghent University, Ghent, Flanders, Belgium. [2]imec-TELIN-IPI, Ghent University, Ghent, Flanders, Belgium. [3]iBME-MEDISIP, Ghent University, Ghent, Flanders, Belgium. [4]VINRAD, University Hospital Ghent, Ghent, Flanders, Belgium

Introduction

Cerebral arteriovenous malformations (AVMs) are vascular anomalies in the brain that increase hemorrhage risks. Endovascular embolization using catheter-based liquid embolic agent injections (e.g. Onyx) can reduce AVM flow and risks, but outcomes can be operator-dependent, influenced by parameters like injection rate and catheter position/direction. Despite an FDA-recommendation of 0.16 ml/min (with 0.30 ml/min upper limit due to angionecrosis and vasospasm in animals), flow rate is rarely monitored [1]. Hence, this study used computational fluid dynamics to assess injection rate effects on Onyx distribution and local pressure differences in an AVM.

Methods

One patient-specific AVM model was reconstructed from 3D rotational angiography in Mimics (Materialise, Belgium) and meshed in ANSYS Fluent (Ansys, USA) with ~$11 \cdot 10^6$ tetrahedral elements. Blood (density=1063 kg/m^3, viscosity=4 cP) and Onyx (density=1103.9 kg/m^3, viscosity=18 cP; mass-weighted properties of two phases of Onyx-18: 6 m% ethylene vinyl alcohol and 94 m% dimethyl sulfoxide) were modeled as incompressible, Newtonian fluids under transient conditions (time step size 0.01 s and assuming heart rate of 75 bpm) using a multiphase Volume-of-Fluid approach, with blood inlet velocity waveforms (mean 0.0920 and 0.1325 m/s for inlet 1 and 2), outlet-pressures based on patient-specific fractional outflows, and varying Onyx injection rates (0.08, 0.16, and 0.32 ml/min).

Results

Preliminary results indicate that faster injections accelerated Onyx propagation and shifted Onyx distribution from 74.35% to 39.06% of injected Onyx mass towards branch 1 over

three cardiac cycles (2.40 s) for 0.08 versus 0.32 ml/min, indicating notable Onyx spread changes, likely attributed to elevated flow resistance in branch 1 from faster delivery of viscous Onyx (Fig. 1). Maximum pressure differences over a 4 mm downstream segment rose from 3.61 Pa without Onyx to 4.47 Pa, 5.95 Pa, and 8.85 Pa at 0.08, 0.16, and 0.32 ml/min, respectively.

Discussion

Based on the AVM studied, Onyx injection rates affect embolization dynamics, suggesting need for closer clinical attention to this parameter. Future work should quantify sensitivity for various procedural parameters, as well as include larger patient cohorts, optimized boundary conditions, and experimental validation for generalizability.

Images (Optional)

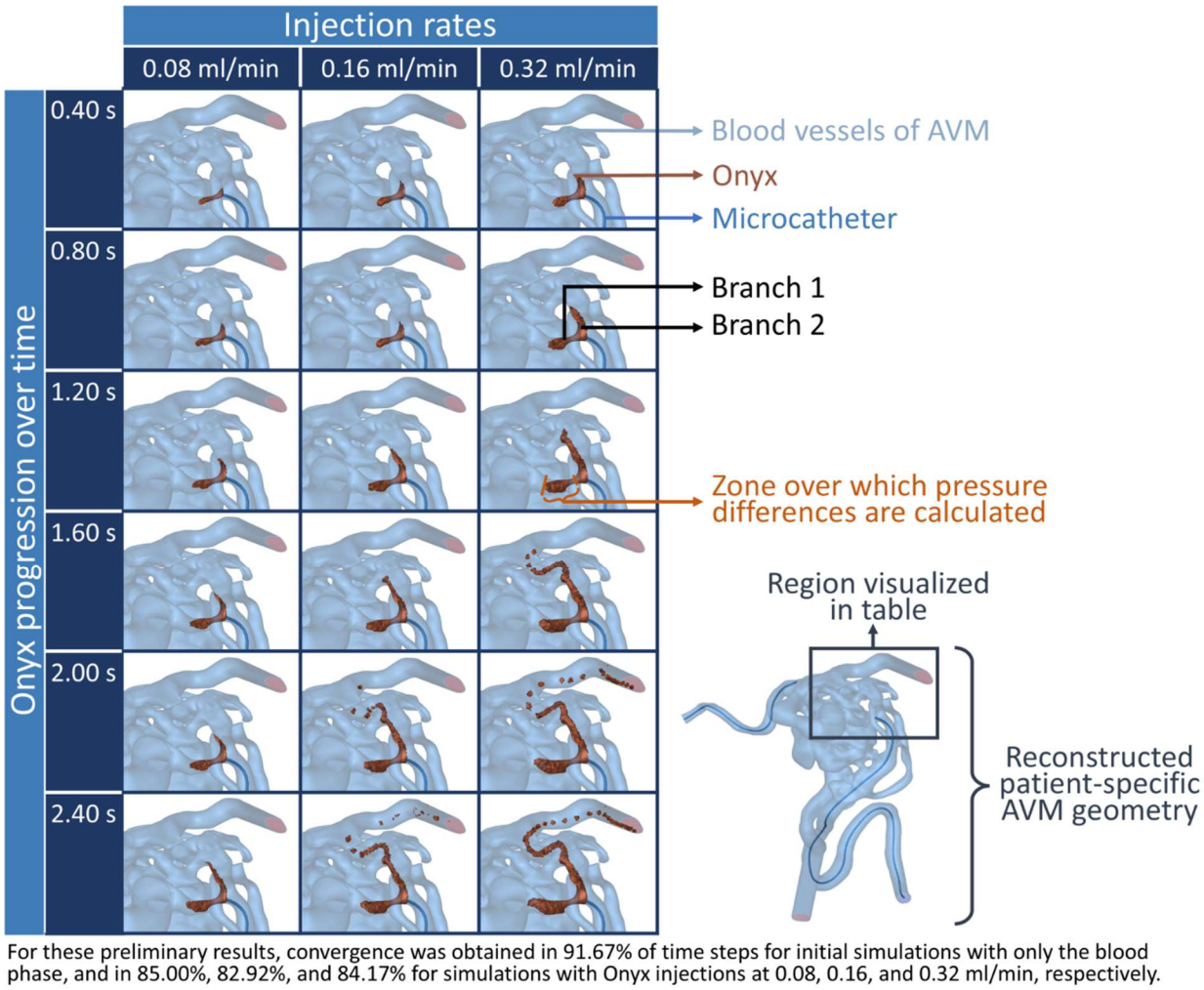


Figure 1. *Onyx progression over time (2.40 s) for various injection rates (0.08, 0.16, and 0.32 ml/min). The brown color indicates cells that contain Onyx, but are not necessarily fully filled with Onyx (criterion of volume fraction for Onyx phase > 10^{-6}).*

References (Optional)

[1] Micro Therapeutics, Inc., *Onyx® Instructions for Use*, 2023

Session Category

Cardiovascular/Cardiorespiratory Biomechanics: Methods, Models and Applications

P4-065

Investigation of Plastic Deformation and Fracture of Ischemic Stroke Clots

Ms. Kila Bein Snee[1], Ms. Alessia Ruzzier[2], Dr. Behrooz Fereidoonnezhad[2], Dr. Ray McCarthy[3], Prof. Patrick McGarry[1]

[1]Biomedical Engineering, University of Galway, Galway, Co. Galway, Ireland. [2]Biomechanical Engineering Department, TU Delft, Delft, South Holland, Netherlands. [3]Johnson & Johnson MedTech Neurovascular, Galway, Co. Galway, Ireland

Introduction

Stroke clot composition (fibrin and RBC content) strongly influences thrombectomy outcomes [1]. A deeper understanding of clot biomechanics during lodging and retrieval is critical for improving device design and clinical strategies.

This study provides the first evidence of clot permanent plastic deformation, non-linear volumetric behaviour, and composition-dependent fracture. We demonstrate that these features are key determinants for thrombectomy outcomes.

Methods

Uniaxial tension and unconfined compression tests were performed on platelet-contracted clot analogues (0-40% hematocrit). A novel hyperelastic-plastic model with non-linear volumetric stress was implemented in Abaqus (UMAT) and calibrated to axial stress-strain (σ_{axial} - ε_{axial}) and volumetric strain (ε_{vol}) data.

Benchtop tests and finite element models were developed to investigate the biomechanics of clots lodging in bifurcated vessels under physiologically relevant pressures. Friction coefficients (μ) were determined by matching lodged positions.

To evaluate clot fracture, we developed a phase field fracture model.

Results

Calibration of the initial tangent bulk modulus (κ) was essential for realistic aspiration lengths and strain distributions (Fig. 1A).

Plastic volumetric (ε^p_{vol}) and isochoric (ε^p_{iso}) deformations decreased with increased %H and increased deformation duration t_{hold} (Fig. 1B).

RBC-rich 20-40 %H clots lodged more distally and exhibited shorter lodged lengths than fibrin-rich 5 %H clots (Fig. 1C). Lodging induced strains sufficient for plastic deformation

and large volumetric compaction. Purely hyperelastic material models underpredicted clot shrinkage over time, underscoring the importance of plastic deformation.

RBC-rich 20 %H and 40 %H clots showed localised fracture ($\phi>0$) due to contact with vessel bifurcations (Fig. 1D) and catheters, whereas fibrin-rich clots exhibited no fracture ($\phi=0$).

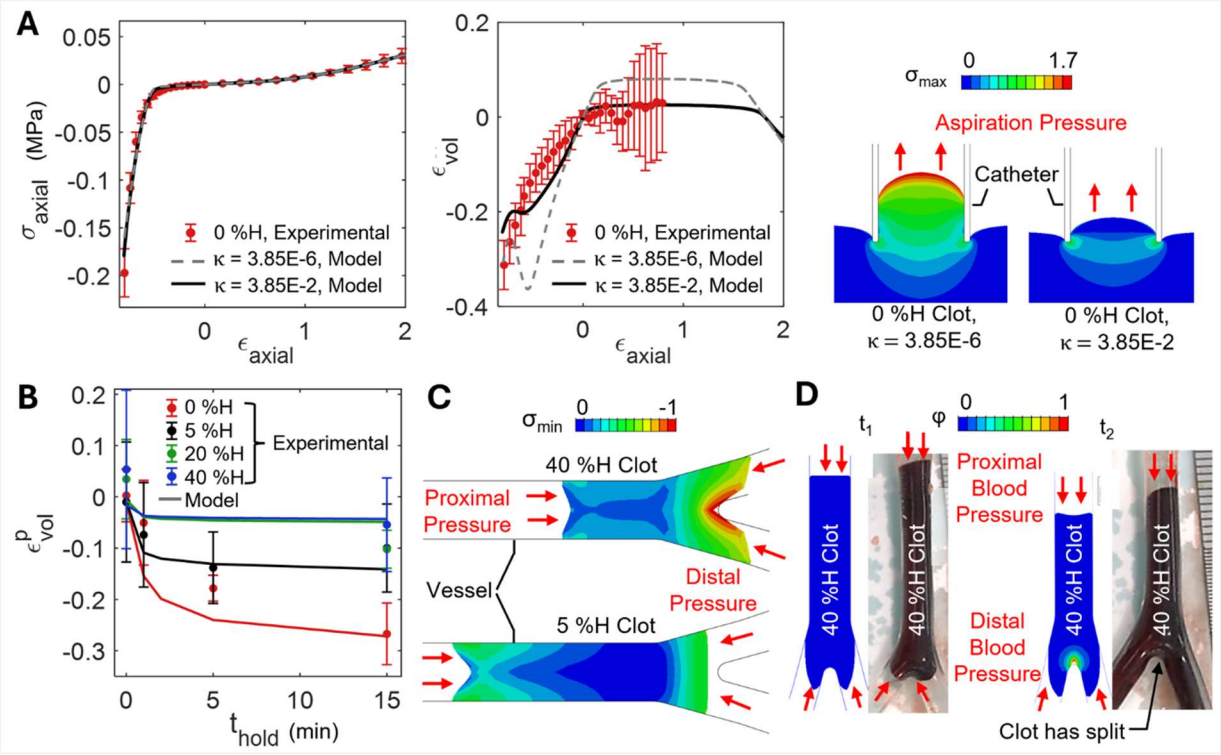
Discussion

Our findings significantly advance the understanding of clot biomechanics with implications for clinical practice and device design:

(i) Volumetric deformation significantly influences fracture in RBC-rich clots and aspiration lengths in fibrin-rich clots. Our non-linear volume change and fracture model should guide catheter tip design;

(ii) The plastic behaviour of fibrin-rich clots contrasts sharply with the predominantly hyperelastic behaviour of RBC-rich clots, motivating the development of composition specific thrombectomy devices and the advancement of imaging techniques to determine clot composition *in vivo* [2].

Images (Optional)



References (Optional)

[1] Huang et al., Neurol. Int.,14:748-770, 2022

[2] Gurary et al., Clin. Transl. Neurosci., 9(1):17, 2025

Acknowledgements (Optional)

Funding: Taighde Éireann – Research Ireland, and Johnson & Johnson MedTech Neurovascular (EPSPG/2022/379).

Session Category

Cardiovascular/Cardiorespiratory Biomechanics: Methods, Models and Applications

P4-066

Left-to-Right Ventricular Interaction: Insights From an Ex-Vivo Beating Heart Model

Mr. Chenghan Cai, Dr. Lei Fan

Michigan State University, East Lansing, Michigan, United States

Introduction

Interventricular interaction, where changes in the loading condition of one ventricle affect the diastolic and systolic function of the other, is critical for overall ventricular performance. For example, unloading of the left ventricle (LV) due to left ventricular assist device implantation affects right ventricular (RV) function through the interventricular septum. Previous animal experiments using isolated hearts have shown that LV contractility is augmented with an increase in RV pressure and vice versa, indicating systolic interdependence. Similarly, LV volume is increased at a given filling pressure when the RV is unloaded, indicating diastolic interdependence. However, the effects of ventricular loading conditions (e.g., preload and afterload) remain unquantified. The ex-vivo beating heart model provides a controlled platform to study these dynamics though most existing work focus on LV function within systemic circulation, often neglecting RV function.

Methods

To address these limitations, we further developed the ex-vivo beating heart apparatus by allowing precise manipulation of preload, afterload, and coronary perfusion, as well as direct measurement of aortic function, and ventricular pressures and volumes in both LV and RV. This beating heart setup enables detailed investigation of how ventricular interdependence shapes normal and pathological biventricular function. The gain factor is used as a quantitative measure of interventricular interaction, reflecting how changes in loading or pressure in one ventricle are transmitted to the other through interventricular septum.

Results

Our results suggest that under physiological baseline condition, LV and RV developed pressures linearly vary with coronary blood flow with a steeper gradient in the LV than in the RV. When LV preload and afterload were varied in the working heart antegrade perfusion mode, the gain factor for developed pressure and ventricular systolic pressure was below 1 whereas the gain factor of ventricular diastolic pressure was close to 0.

Discussion

In this study, we developed an ex-vivo beating heart model to measure biventricular function. The results demonstrate that changes in one ventricle significantly influence the systolic function of the other whereas diastolic effects are minimal. These findings highlight the importance of considering biventricular mechanics in studies of cardiac function and interventions, particularly when modulating ventricular loading conditions.

Session Category

Cardiovascular/Cardiorespiratory Biomechanics: Methods, Models and Applications

P4-067

Computational Fluid Dynamics for Determining the Pressure Gradient in Renal and Femoral Artery Stenosis

Dr. Lennart van de Velde[1,2,3], Dr. Thomas Bouwmeester[4], Dr. Didier Collard[4], Ms. Lisa Rutten[3], Dr. IJsbrand Zijlstra[4], Mr. Michiel van Werkum MBA[2], Dr. Paul Cernohorksy[2], Ms. Ellen van Hulst[4], Mr. Armand Lamers[4], Dr. Erik Groot Jebbink[3,2], Prof.dr. Michel Versluis[3], Prof.dr. Liffert Vogt[4], Prof.dr. Michel Reijnen[2,3], Prof.dr. Bert-Jan van den Born[4]

[1]AmsterdamUMC, Amsterdam, Noord Holland, Netherlands. [2]Rijnstate hospital, Arnhem, Gelderland, Netherlands. [3]University of Twente, Enschede, Overijssel, Netherlands. [4]AmsterdamUMC, Amsterdam, Noord-Holland, Netherlands

Introduction

In renal artery and femoropopliteal artery stenotic disease, treatment decisions could be improved using pressure gradients instead of anatomic grading. However, invasive pressure measurements in peripheral arteries require equipment that is commonly not available and that demand additional lesion crossings and procedural time. An attractive alternative is the use of computational fluid dynamics (CFD). We performed two separate studies to validate the use of CFD for estimating the pressure gradient in patients with renal or femoropopliteal stenotic disease.

Methods

For study 1, fifteen patients with two or more lesions in the femoropopliteal artery (multi-segmental) scheduled for angioplasty were enrolled. For study 2, twenty patients scheduled for renal angiography were recruited. In both studies, the pressure gradient in resting condition was measured using simultaneous sheath and pressure-wire measurements. Based on pre-operative computed tomography angiography (CTA), the pressure gradient was simulated with CFD. For study 1, CFD was performed (CFD_{US}) using a patient-specific flow rate derived from Duplex ultrasound. For study 2, the CFD flow rate was set based on the distal renal artery diameter (renal, CFD_D) or the segmented kidney cortical volume (renal, CFD_C).

For statistical analysis, a Pearson's correlation and Bland-Altman analysis between the measured and CFD-simulated pressure gradient were performed.

Results

For the femoral study, the mean pressure gradient over the multi-segmental lesions was 12.8 mmHg. An example simulation is shown in Fig. 1a. CFD_{US} closely approximated the measured gradient with a 0.1 ± 3.1 mmHg difference (R^2= 0.91).

For the renal lesions, the mean pressure gradient was 13.5 mmHg. A simulation example is provided in Fig. 1b. CFD_D showed a reasonable agreement of the pressure gradient with a difference of 3.1 ± 7.5 mmHg (R^2 = 0.91). Using kidney cortex volume information, CFD_C showed an excellent agreement with a difference of 1.1 ± 5.3 mmHg (R^2 = 0.95).

Discussion

The results support the use of CFD for hemodynamic assessment of renal artery and femoropopliteal stenotic lesions. External validation studies are indicated. For femoral disease with multiple lesions, pre-intervention CFD could help prevent overtreatment. For renal artery disease, CFD can be a valuable method for deciding on the indication for endovascular treatment.

Images (Optional)

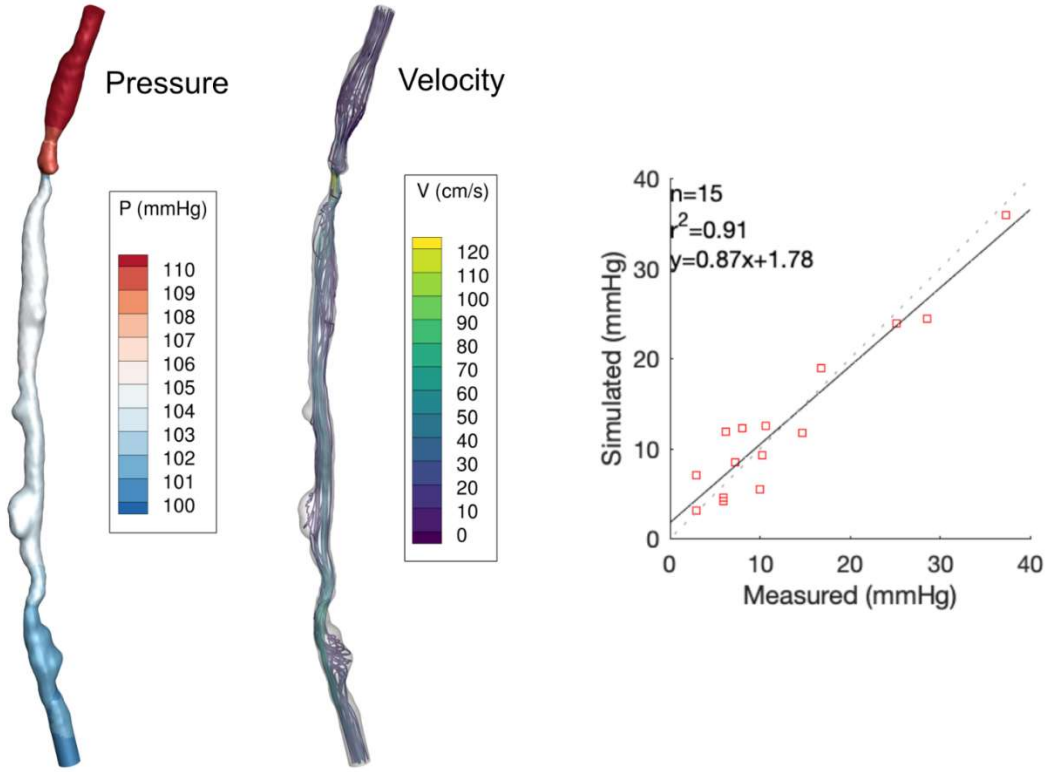


Figure 1a: a CFD simulation of a femoropopliteal artery with diffuse disease. Left: the simulated CFD pressure and velocity streamlines. Two lesions with a pressure drop are visible. Right: Pearson's correlation plot of the agreement between the simulated pressure gradient by CFD_{US} and the measured pressure gradient.

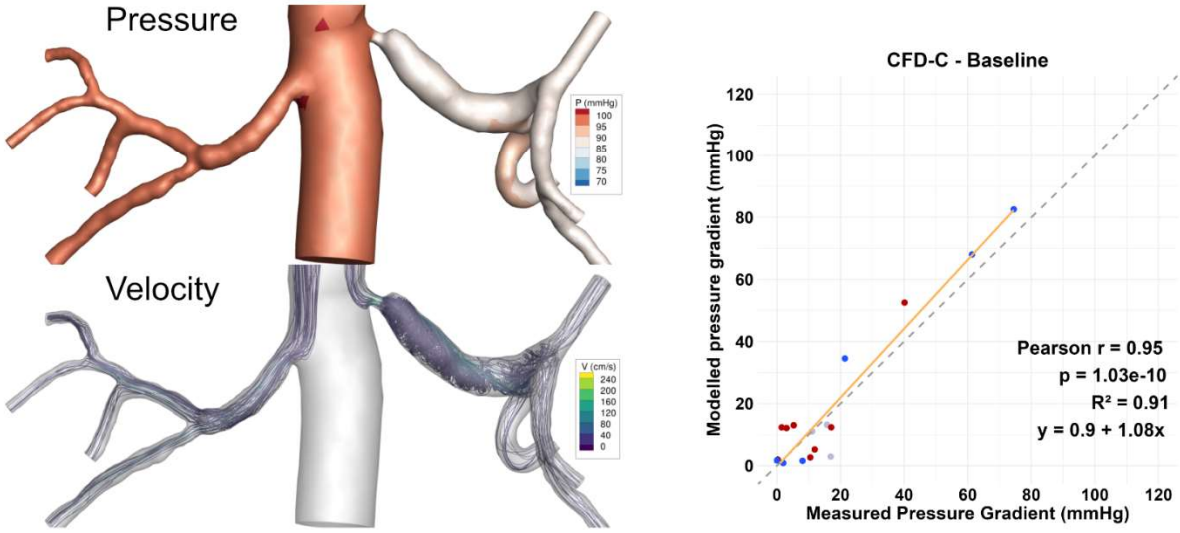


Figure 1b: a CFD simulation of a patient with an ostial stenosis in the left renal artery. Left: the CFD-simulated pressure and velocity streamlines. Right: Pearson's correlation plot of the simulated pressure gradient by CFD_C compared to the measured pressure gradient.

Acknowledgements (Optional)

The study for renal artery stenosis was funded by a Dutch Kidney Foundation Innovation Grant (19OI18) to LvdV, LV and BvdB. Pressurewires for the studies were supported in-kind by Abbott and Phillips-Volcano.

Session Category

Cardiovascular/Cardiorespiratory Biomechanics: Methods, Models and Applications

P4-068

Coherent Point Drift-Based in Vivo Mechanical Characterisation of Intracranial Aneurysms

Ms Lise Fontalirant[1], Dr Jolan Raviol[1], Dr Guillaume Plet[1], Mr Jean-Baptiste Langlois[2], Dr Salim Si-Mohamed[3,4], Dr Hélène Magoariec[1], Dr Cyril Pailler-Mattei[1,5]

[1]Laboratoire de Tribologie et Dynamique des Systèmes, CNRS UMR 5513, Université de Lyon, École Centrale de Lyon, Lyon, Auvergne-Rhône-Alpes, France. [2]CERMEP - Imagerie du Vivant, Lyon, Auvergne-Rhône-Alpes, France. [3]Université de Lyon, INSA Lyon, Université Claude Bernard Lyon 1, UJM-Saint Etienne, CNRS, Inserm, CREATIS UMR 5220, U1206, F-69621, Lyon, Auvergne-Rhône-Alpes, France. [4]Département de Radiologie, Hôpital Louis Pradel, Hospices Civils de Lyon, Lyon, Auvergne-Rhône-Alpes, France. [5]Université de Lyon, Université Claude Bernard Lyon 1, ISPB-Faculté de Pharmacie, Lyon, Auvergne-Rhône-AlpesAuvergne-Rhône-Alpes, France

Introduction

Intracranial aneurysm (IA) is a life-threatening pathology related to arterial wall deterioration. Although these mechanical alterations are a key factor in the rupture mechanism, no reliable method currently exists to predict rupture risk using in vivo biomechanical data. Developing tools to characterise these properties non-invasively is therefore essential for improving clinical risk assessment and guiding treatment decisions. This work, conducted on an animal model of aneurysm, represents a first step towards better understanding of vascular wall rupture risk. It presents the application of a procedure based on the Coherent Point Drift (CPD) algorithm to quantify the strain fields induced by a non-destructive vascular wall deformation device (DDP), enabling the acquisition of mechanical data to build a database for IA analysis.

Methods

A saccular aneurysm was induced on the bifurcation of a rabbit carotid artery to mimic a human IA. The DDP was designed as a catheter repurposed from its original use [1]. The Spectral Photon Counting Computed Tomography prototype system (SPCCT) was used for imaging. Two configurations were considered for the images acquisition: Configuration 1 (C1) with the DDP positioned in the aneurysm without flow, and Configuration 2 (C2) with flow applied by the DDP (Figure 1). An original procedure was implemented to determine the mechanical properties of the aneurysm using the CPD algorithm, which aligns two point clouds by assuming that one is a probabilistic transformation of the other [2]. Extracting the aneurysm from SPCCT images as point clouds allows a direct comparison of the two configurations and provides mechanical characterisation of the aneurysm.

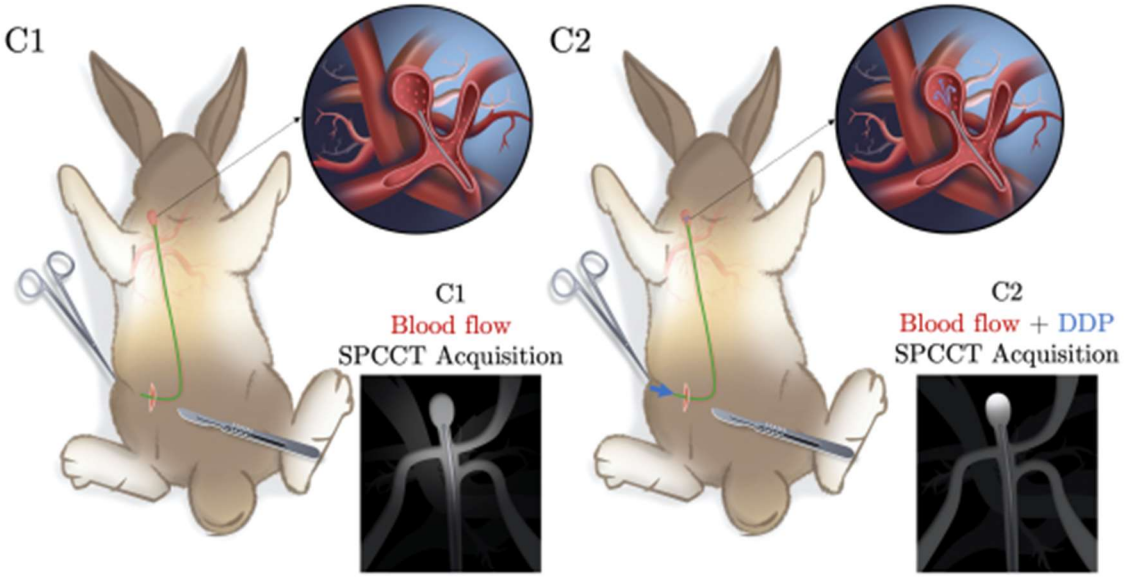
Results

Among the rabbits tested, several aneurysms were successfully created. Using the numerical procedure, it was possible to quantify the strain fields for a known mechanical loading. The average strain of aneurysms ranged from 1.5% to 3.7%.

Discussion

By combining the strain fields with material parameters representative of rabbit arteries, it would be possible to determine the corresponding stress fields, thereby pointing toward the definition of a rupture criterion.

Images (Optional)



References (Optional)

[1] Raviol, J. *et al.* , Royal Society Open Science, 2024

[2] Xie, H. *et al.* , Journal of Biomechanics, 2024

Acknowledgements (Optional)

This work was funded by the French ANR (PRAnevrisme, ANR-23-CE19-0034-01).

Session Category

Cardiovascular/Cardiorespiratory Biomechanics: Methods, Models and Applications

P4-069

Asymmetric Leg Blood Flow Regulation Before and After Walking in Individuals with Unilateral Transtibial Amputation

Dr. Logan Faux-Dugan PhD[1], Mr. Jose Anguiano-Hernandez MS[1], Dr. Jenna Burnett PhD[1], Dr. Colby Hansen MD[1], Dr. Rakesh Srivastava PhD[2], Dr. Song-young Park PhD[3], Dr. Kota Takahashi PhD[1]

[1]The University of Utah, Salt Lake City, Utah, United States. [2]Innovative Prosthetics & Orthotics, Omaha, Nebraska, United States. [3]University of Nebraska Omaha, Omaha, Nebraska, United States

Introduction

Leg blood flow (LBF) supplies oxygen to muscles during walking, especially in response to positive muscle work production (higher energetic demand [1]). One approach to examine how muscle work relates to LBF is by studying individuals with unilateral transtibial amputation (TTA) because their residual limb (RL) has less muscle mass overall to perform mechanical work. Individuals with TTA have less blood distributed to their RL when cycling [2], but it is unclear whether this asymmetry exists with walking. We, therefore, investigated the relationship between positive mechanical work done during walking and LBF, when accounting for the inter-limb asymmetry in TTAs. We hypothesized that the intact limb (IL) would have greater change in LBF (pre vs post walking) than the RL, and the inter-limb asymmetry in LBF will be correlated with asymmetry in positive work.

Methods

Eight TTAs (2F/6M) walked at a comfortable speed (1.0 ± 0.2 m/s) for ten minutes on an instrumented treadmill. Pre- and post-walking LBF, as well as the change in LBF, were measured via Doppler ultrasonography of the common femoral artery. Total positive work was computed on the IL (sum of foot, ankle, knee and hip) and the RL (sum of knee and hip). Inter-limb asymmetries were calculated as (IL-RL/IL+RL)*100 [2]. Two-sample t-tests compared LBF and work between limbs, and linear regression examined the correlation between inter-limb asymmetries in positive work and LBF change.

Results

The IL generated more positive work during walking ($p=0.002$, Figure 1) and received greater LBF post-walking ($p=0.034$). Differences in pre-walking LBF ($p=0.059$) and LBF change

(p=0.052) trended toward significance. Positive work asymmetry was not associated with LBF change asymmetry (p=0.374).

Discussion

Despite no correlation between asymmetries of work and LBF change, more post-walking blood was supplied to the IL. These findings are supported by the asymmetric LBF responses found during cycling in TTAs [2]. This growing knowledge may inform clinical practices aimed at preserving and improving tissue health in TTAs.

Images (Optional)

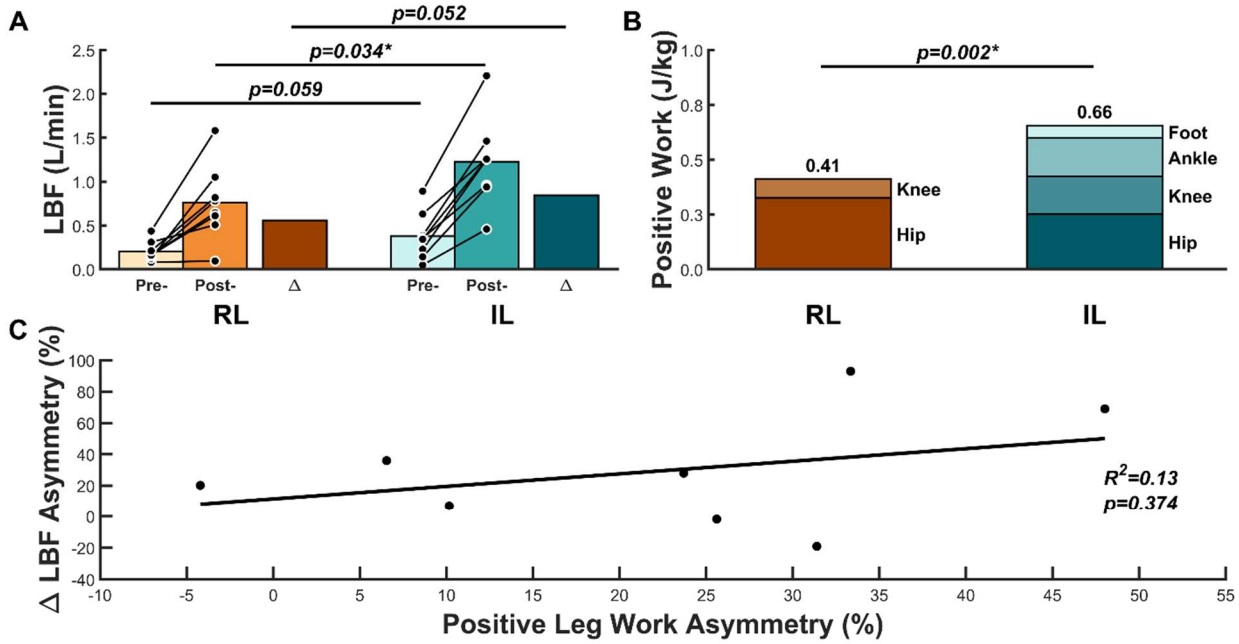


Figure 1 (**A**) Leg blood flow (LBF) before (Pre-) and after (Post-) walking with the change in blood flow (Δ) for the residual limb (RL) and intact limb (IL), (**B**) positive mechanical leg work for the RL (Hip + Knee) and IL (Hip + Knee + Ankle + Foot), and (**C**) positive mechanical leg work asymmetry regressed with LBF change asymmetry.
**Significance at α=0.05*

References (Optional)

[1] Bernard Abbott *et al.*, J. Physiol., 1952; [2] Anna Pedrinolla *et al.*, Eur. J. Appl. Physiol., 2025

Acknowledgements (Optional)

Supported by NIH R01HD106911 and 1T32DK11096601

Session Category

Cardiovascular/Cardiorespiratory Biomechanics: Methods, Models and Applications

P4-070

Restoring Tissue Anisotropy and Contractility Synergistically Supports Sustained Structural Repair After Myocardial Infarction

Mr. Luuk H.F. Souren[1,2], Dr. Hesam Hoursan[1,2], Dr. Tommaso Ristori[1,2], Dr. Peter H.M. Bovendeerd[1], Prof. Carlijn V.C. Bouten[1,2], Prof. Sandra Loerakker[1,2]

[1]Department of Biomedical Engineering, Eindhoven University of Technology, Eindhoven, Noord-Brabant, Netherlands. [2]Institute for Complex Molecular Systems, Eindhoven University of Technology, Eindhoven, Noord-Brabant, Netherlands

Introduction

Restoring cardiac structure and function after infarction remains a central challenge in regenerative medicine. Strategies focusing solely on restoring infarct tissue composition and contractility (e.g., cardiomyocyte injections) have shown limited success, shifting attention toward a combined restoration of tissue anisotropy. An aligned extracellular matrix (ECM) may improve injected cardiomyocytes' alignment, retention, and contractile efficiency, thereby supporting restoration of anisotropic tissue properties [1]. However, it remains unclear whether therapeutically induced ECM re-alignment is sustained or altered by remodeling under infarcted heart mechanics [2]. Here, we use computational modeling to investigate how induced infarct ECM (an)isotropy adapts under mechanical loading in the acutely infarcted left ventricle, with or without injected cardiomyocytes aligned with the ECM.

Methods

A finite element (FE) model of the acutely infarcted left ventricle with opposing helical fiber alignment (reference, REF) was used to compute strains at four transmural locations (Fig. 1a) [3]. Infarct properties were varied in anisotropy, either isotropic (ISO) or anisotropic aligned with REF (ANISO), and in contractility (0% or 25%) to mimic partial restoration via cardiomyocyte injections. Computed strains served as input for a mechanobiology-informed ECM remodeling model predicting in-plane collagen alignment from uniform starting conditions (Fig. 1b) [4]. Remodeling parameters were calibrated so that, under healthy conditions (ANISO-100%), predicted collagen alignment approximated REF (Fig. 1c).

Results

Collagen in untreated infarcted tissue (ISO-0%) remodeled toward transmurally uniform longitudinal alignment (Fig. 1d). Similar alignment developed when either contractility (ISO-25%) or tissue anisotropy (ANISO-0%) alone was restored. Strikingly, combining anisotropy with partial contractility restoration (ANISO-25%) preserved the induced ventricular alignment.

Discussion

Our computational findings indicate that cardiac regenerative strategies focusing solely on restoring infarct contractility through cardiomyocyte injections do not lead to favorable infarct ECM remodeling and recovery of ventricular anisotropy. Instead, therapeutically inducing infarct ECM re-alignment in combination with modest restoration of contractility is sufficient to sustain anisotropy, critical for ventricular mechanics. Future work will expand the model's design space by including diverse infarct geometries and properties.

Images (Optional)

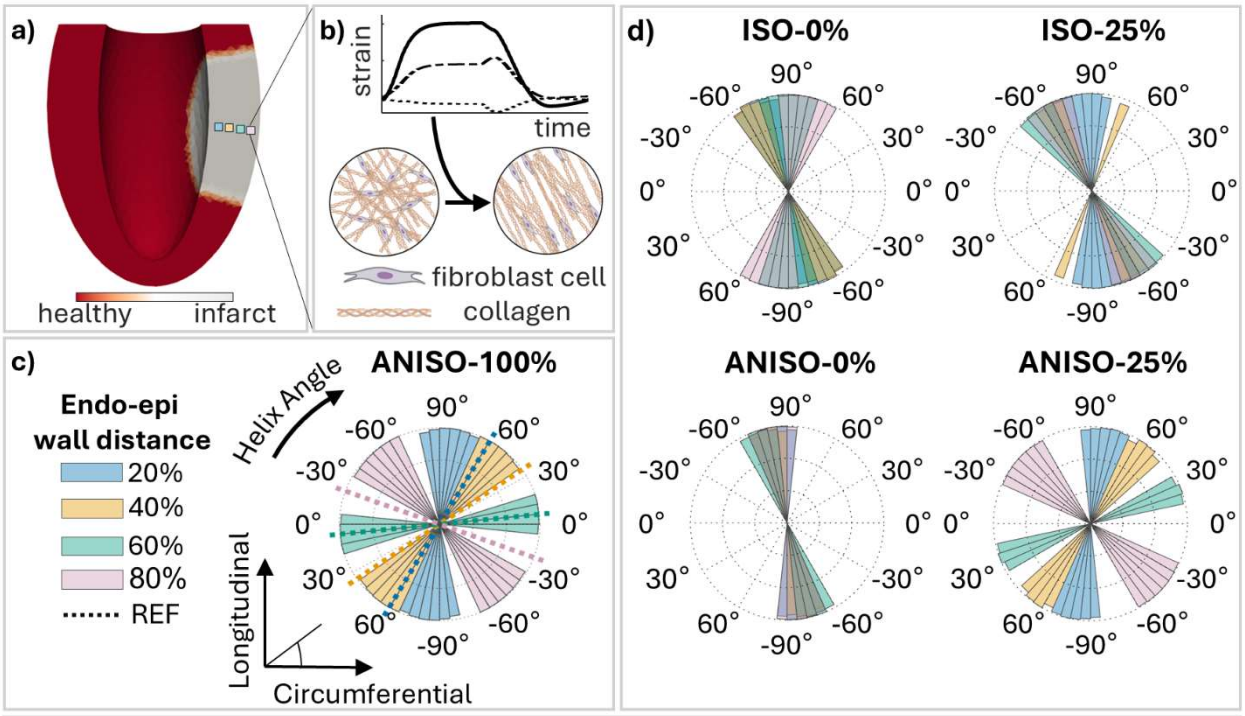


Fig. 1: a) left ventricle FE model; b) coupling with a mechanobiology-informed ECM remodeling model; collagen alignment after remodeling in c) healthy and d) varying infarct conditions

References (Optional)

1. Pijnappels et al., Ann NY Acad Sci., 2010.
2. Mostert et al., Nat. Rev. Bioeng., 2025.

3. Janssens & Bovendeerd., J. Biomech. Eng., 2025.
4. Ristori et al., Acta Biomater., 2018.

Acknowledgements (Optional)

Research funded by the European Research Council (ERC) RE-ALIGN grant (ID: 101054726) to C.V.C.B.
Elements of Fig. 1b were created with BioRender.com.

Session Category

Cardiovascular/Cardiorespiratory Biomechanics: Methods, Models and Applications

P4-071

Phase Contrast Four-Dimensional Magnetic Resonance Imaging for Obtaining Aortic Flow Boundary Conditions in Healthy Volunteers

Ir. M.E. Krommendijk[1], Dr. H. Mirgolbabaee[1,2], MSc I.D. Kikkert[1], H. R. Liefers[3], BSc J.G.M. Greve[3], MEng E. Hestermann[1], Dr. E. Groot Jebbink[1,4], Prof. Dr. M.M.P.J. Reijnen[1,4], Prof. Dr. R.H. Geelkerken[1,5]

[1]Multi-Modality Medical Imaging group, TechMed Centre, University of Twente, Enschede, Overijssel, Netherlands. [2]Physics of Fluids group, University of Twente, Enschede, Overijssel, Netherlands. [3]TechMed Centre, University of Twente, Enschede, Overijssel, Netherlands. [4]Department of Vascular Surgery, Rijnstate Hospital, Arnhem, Gelderland, Netherlands. [5]Department of Vascular Surgery, Medisch Spectrum Twente, Enschede, Overijssel, Netherlands

Introduction

Research into healthy aortic blood flow and anatomy is valuable for understanding and treating cardiovascular diseases. In many cases, general flow boundary settings are applied when studying physical or digital models of the aorta. Applying localised boundary conditions – for example, flow waveforms at the suprarenal aorta and iliac arteries – is crucial for obtaining reliable results. This study aims to obtain aortic flow boundary conditions in healthy volunteers using phase contrast four-dimensional magnetic resonance imaging (4D-flow MRI) by studying blood flow in the whole aorta and its main side branches.

Methods

4D-flow MRI scans were acquired in healthy volunteers (n=20) using a custom sequence (WIP 1106B, MAGNETOM Aera 1.5T, Siemens Healthineers) to obtain volumetric MRI data over 24 phases of the cardiac cycle. Data was acquired with a spatial resolution of 2.5x.2.5 mm^2, slice thickness of 2.5 mm, and temporal resolution of 37 ms. Separate thoracic and abdominal acquisitions were performed to capture the full aortic geometry from the ascending aorta to the iliac bifurcations, including side branches. An in-house pipeline was developed (MATLAB R2025b, MathWorks) for manually segmenting the aorta and obtaining flow velocity vectors. Flow velocity fields were visualised, and flow waveforms were plotted (Tecplot 360, Tecplot, Inc.).

Results

Preliminary results of aortic blood flow analysis in the aorta of one healthy volunteer are presented in figure 1. The segmented aortic geometry is shown (A) and four regions of interest – at the ascending aorta, descending aorta, suprarenal aorta, and left common iliac artery – are indicated. Peak systolic flow velocity magnitude and direction are shown in flow velocity fields (B). Flow waveforms are plotted to demonstrate how the flow velocity magnitude changes over the cardiac cycle, showing different flow profiles in the four regions of interest.

Discussion

4D-flow MRI was used to obtain preliminary healthy aortic blood flow boundary conditions in the aorta and its main side branches. Using the methods presented here, the effect of age and gender on aortic flow will be studied in a cohort of 70 healthy volunteers. Results will be presented as an atlas of healthy aortic flow as a base for future in-vitro and in-silico studies.

Images (Optional)

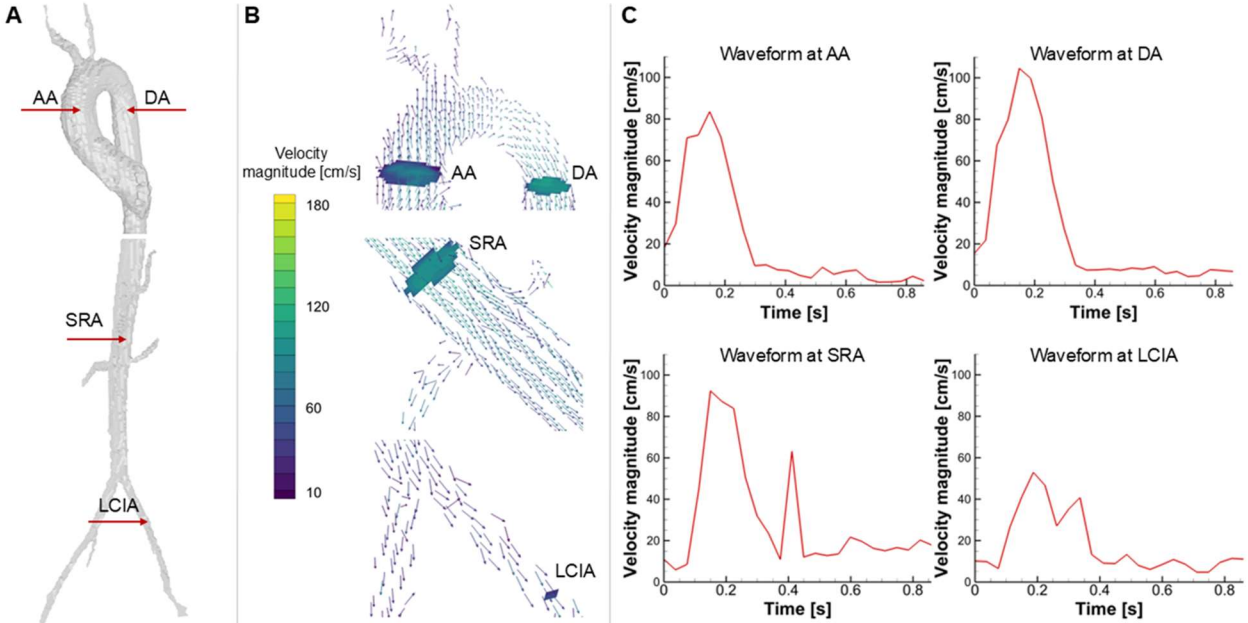


Figure 1: *Blood flow in the aorta and main side branches of a healthy volunteer studied using 4D-flow MRI. The segmented aortic geometry is shown (A). Regions of interest at the ascending aorta (AA), descending aorta (DA), suprarenal aorta (SRA), and left common iliac artery (LCIA) are indicated. Flow velocity fields (B) are shown for these regions of interest. Arrows indicate the direction of the velocity vectors, and the colour bar indicates the magnitude of the velocity vectors at peak systole. Cross-sections are drawn at the four regions of interest and flow waveforms (C) are plotted for the centre points of these cross sections.*

Session Category

Cardiovascular/Cardiorespiratory Biomechanics: Methods, Models and Applications

P4-072

Characterization of Cerebral Artery Hemodynamics in a Circle of Willis Model for Optimizing Thrombectomy Outcomes

Ms. Mackenzie Moser First Year PhD Student Biomedical Engineering, Dr. Bryan Good PhD in Bioengineering

University of Tennessee, Knoxville, Tennessee, United States

Introduction

Mechanical thrombectomy (MT) outcomes vary widely, and growing evidence suggests collateral flow and pressures distal to an arterial occlusion play a critical role in clot retrieval. An overall poor understanding of downstream intracranial hemodynamics, including distal perfusion pressure and pressure gradients across an occlusive clot, has limited the ability to optimize MT strategies. Our hypothesis is that collateral flow patterns and distal pressures significantly influence clot removal forces and these parameters can be manipulated to improve MT success. To test this using a combination of novel experimental and computational models informed by patient-specific acute ischemic stroke data, a physiologically accurate benchtop platform must first be established. The objective of this study was to characterize a silicone Circle of Willis (CoW) model and pulsatile pump by measuring pulsatile pressures in the ACA, MCA, and PCA and comparing them to invasive human intracranial data.

Methods

A CoW-Neuro Test silicone model (United Biologics) was integrated into a closed-loop pulsatile flow system. Pulsatile hemodynamics were generated using a FlowTek 125 pump (United Biologics), and pressures measured with Millar Mikro-Tip catheter transducers positioned in bilateral ACA, MCA, and PCA branches. Mean pressures were analyzed over multiple cardiac cycles and compared with published human intracranial data to evaluate physiological fidelity.

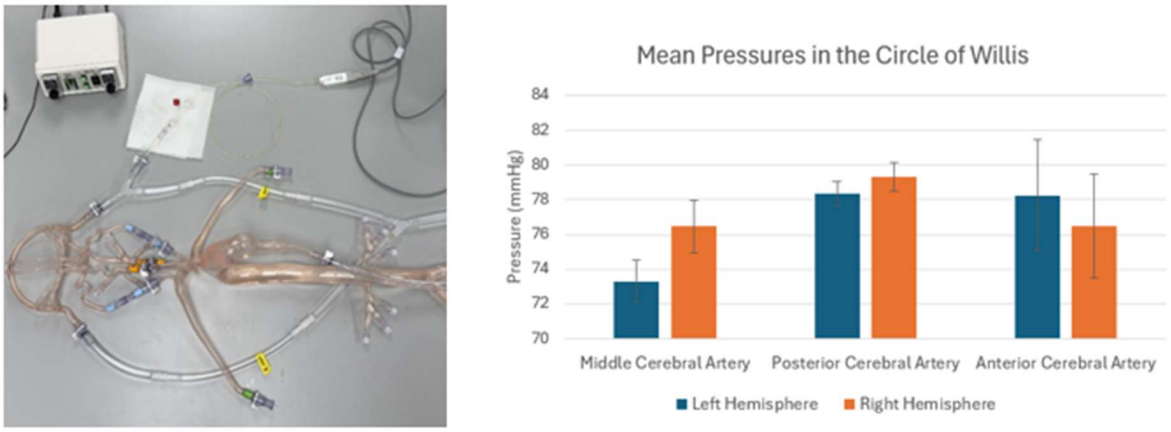
Results

Model pressures closely matched in vivo intracranial measurements. MCA average pressures were 73.3 mmHg (left) and 76.46 mmHg (right), consistent with reported human data (62 ± 29 mmHg and 72.8–75.5 mmHg). Average ACA pressures measured 78.25 mmHg (left) and 76.48 mmHg (right), while average PCA pressures were 78.36 mmHg (left) and 79.32 mmHg (right). Hemispheric variation was minimal (1–5%).

Discussion

This study provides the first vessel-specific pressure characterization of the CoW-Neuro Test model under pulsatile flow conditions. The agreement with human intracranial pressure data validates the system as physiologically accurate. This characterization is essential for upcoming studies designed to investigate how collateral pathways, distal pressures, and pressure gradients across clots influence MT mechanics, areas currently lacking experimental data yet central to improving stroke outcomes.

Images (Optional)



(A) (B)

Figure 1: (A) Silicone Circle of Willis model integrated into the pulsatile flow loop. Millar Mikro-Tip Catheters were inserted in the MCA, PCA, and ACA branches for vessel-specific pressure measurements. (B) Mean pressures measured in the left and right MCA, PCA, and ACA branches under pulsatile flow. Error bars represent the standard deviation across repeated measurements in the same branch.

Session Category

Cardiovascular/Cardiorespiratory Biomechanics: Methods, Models and Applications

P4-073

Computational Hemodynamic Analyses of Left Ventricle Segmentation in Bicuspid Aortic Valve Patients: A Comparison with Normal Valve Morphology

Ms. Malvika Sawant, Dr. Lakshmi Dasi, Mr. Aniket Venkatesh

Georgia Institute of Technology, Atlanta, Georgia, United States

Introduction

Bicuspid aortic valve (BAV) anatomy modifies aortic flow and increases the risk of structural alterations after transcatheter aortic valve replacement (TAVR). Previous predictive models use post-TAVR imaging and don't incorporate patient specific pre-procedural hemodynamics. This study aims to compare left ventricular (LV) function in BAV patients and tricuspid aortic valve (tri-AV) patients using computational modeling based on pre-TAVR computed tomography (CT).

Methods

Pre-procedural CT images of 30 BAV and 30 tri-AV patients were segmented to assess left ventricular (LV) geometry and function, using a previously validated computational pipeline. The LV was segmented using an intensity-based approach with manual adjustment in areas of significant anatomical complexity (Figure 1A). CT images underwent the proximal process of the cardiac phase selection, conversion from DICOM to numpy, motion stabilization, blood mask generation, segmentation, and volume extraction (Figure 1B). A variety of hemodynamic parameters were calculated, and two-sample t-tests assuming unequal variances were used to compare the groups ($p<0.05$) (Figure 1C).

Results

Valve morphology was most strongly associated with higher ejection fraction in tri-AV patients (58.9% vs 19.4%, $p<0.001$), lower end-diastolic volumes in tri-AV patients (148.7 mL vs 1108.5 mL, $p<0.001$), shorter ejection times in tri-AV patients (0.35s vs 0.44s, $p<0.01$), and higher peak systolic flow rates in tri-AV patients (438.9 mL/s vs 312.9 mL/s, $p<0.05$).

Discussion

This hemodynamic study offers a strong model for differentiating cardiac function for tricuspid and bicuspid aortic valves, and consequently, predicting functional outcomes in patients with different valve variants, once validated in a larger group.

Images (Optional)

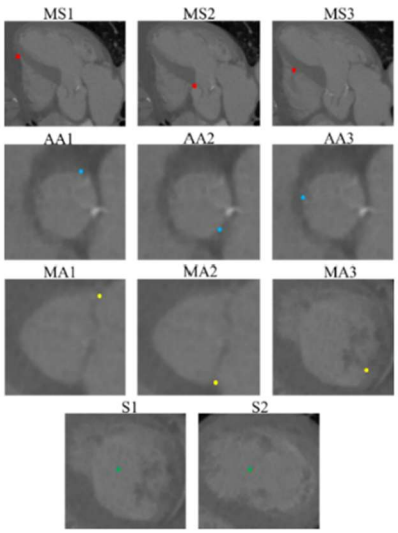


Figure 1A. Manual Landmark Refinement



Figure 1B. Left Ventricular Mesh Processing Pipeline

Hemodynamic Parameter	TAV Mean ± SD (n=30)	BAV Mean ± SD (n=30)	P-value	Statistical significance	Clinical Relevance
Average Flow Rate (mL/s)	222.1 ± 58.3	194.0 ± 83.3	0.395	Not Significant	Similar Cardiac Output
End Diastolic Volume (mL)	136.4 ± 50.2	293.4 ± 53.8	<0.001	Highly Significant	Ventricular Remodeling
Ejection time (s)	0.34 ± 0.05	0.44 ± 0.03	<0.001	Highly Significant	Systolic Duration
Peak Systolic Flow Rate (mL/s)	463.1 ± 149.5	333.7 ± 104.3	0.039	Significant	Hemodynamic Performance
Ejection Fraction (%)	62.5 ± 9.5	23.8 ± 16.7	<0.001	Highly Significant	Ventricular Function
Ejection Volume (mL)	88.2 ± 23.6	65.4 ± 33.2	0.096	Not Significant	Stroke Volume

Figure 1C. Summary Statistics

References (Optional)

[1] Pujari, S H et al., StatPearls, 2023.
[2] Fukui, M et al., Circulation, 146(6), 480-493, 2022.
[3] Hatoum, H et al., Cardiovasc Eng Technol, 12(6), 576-588, 2021.
[4] Shah, l et al., Ann Biomed Eng, 52(2), 208-225, 2024.
[5] Moscarelli, M et al., Eur J Cardiothorac Surg, 67, 2024

Session Category

Cardiovascular/Cardiorespiratory Biomechanics: Methods, Models and Applications

P4-074

Multi-Disciplinary Approach for the Characterization of Carotid Plaque

Dr Gabriele Greco[1], Ms Giulia Formenton[1], Mr Luca Romizi[1], Mr Marco Bellotti[1], Prof Ferdinando Auricchio[1], Prof Michele Conti[1,2], Prof Francesco Migliavacca[3], Prof Luca Mainardi[3], Ms Irene Fulgheri[4], Mr Jasper De Koort[4], Prof Santi Trimarchi[4,5], Dr Anna Corti[3], MD Maurizio Domanin[5], Dr Alessandro Caimi[1]

[1]University of Pavia, Pavia, Lombardy, Italy. [2]IRCCS Policlinico San Donato, San Donato Milanese, Lombardy, Italy. [3]Politecnico di Milano, Milan, Lombardy, Italy. [4]IRCCS Ca' Granda Ospedale Maggiore Policlinico, Milano, Lombardy, Italy. [5]University of Milan, Milano, Lombardy, Italy

Introduction

Annually affecting 1.1 million people in Europe, stroke remains a significant health concern, with 20% of cases attributed to vulnerable carotid plaques. However, even though plaques detection is crucial for stroke prevention, current strategies often fail to identify high-risk patients [1]. A comprehensive multi-disciplinary predictive strategy for the assessment of any possible complications related to vulnerable carotid plaques, enabling any effective patient stratification and overcoming the limits of current approaches is still lacking.

Methods

From the acceptance of the ethical committee 5 patients underwent to an endarterectomy procedure in which the anatomical district affected by the pathology is substituted by a synthetic graft. The fresh harvested sample is acquired through micro-CT in order to detail the shape and the density of the different regions of the plaque. After the acquisition, the plaque is stored at -80°C. The part of the tissue characterized by the presence of the plaque is indented (Chiaro, Optics11 Life) with a fixed depth of 10 μm, using a spherical tip (diameter 103 μm, stiffness 0.53 N/m) at a speed of 5 μm/s. Finally, extracting non-invasive functional information, a completely automatic python-based numerical pipeline, is under development to perform fluid dynamic simulations for the assessment of patient-specific hemodynamic parameters.

Results

The micro-CTs show very detailed images of the carotid plaque, highlighting the morphology of high-density deposits, that consisted of an assembly of different small and detached deposits, that cannot be observed from CT data. From a mechanical point of view, healthy tissue exhibits a higher Young's modulus than non-calcified plaque tissue. Both healthy tissue and non-calcified plaque, however, show lower stiffness than calcified plaque regions. Measurements taken in its proximity suggest that early stages of calcification or the presence of nearby calcium deposits may already increase local stiffness.

Discussion

This study, based on few patients, aims to develop a sound basis for a new multi-disciplinary analysis of the characteristics of the carotid arteries in a larger cohort of patients. Moreover, any imaging-based information can be very important for radiomic or AI-based strategy.

Images (Optional)

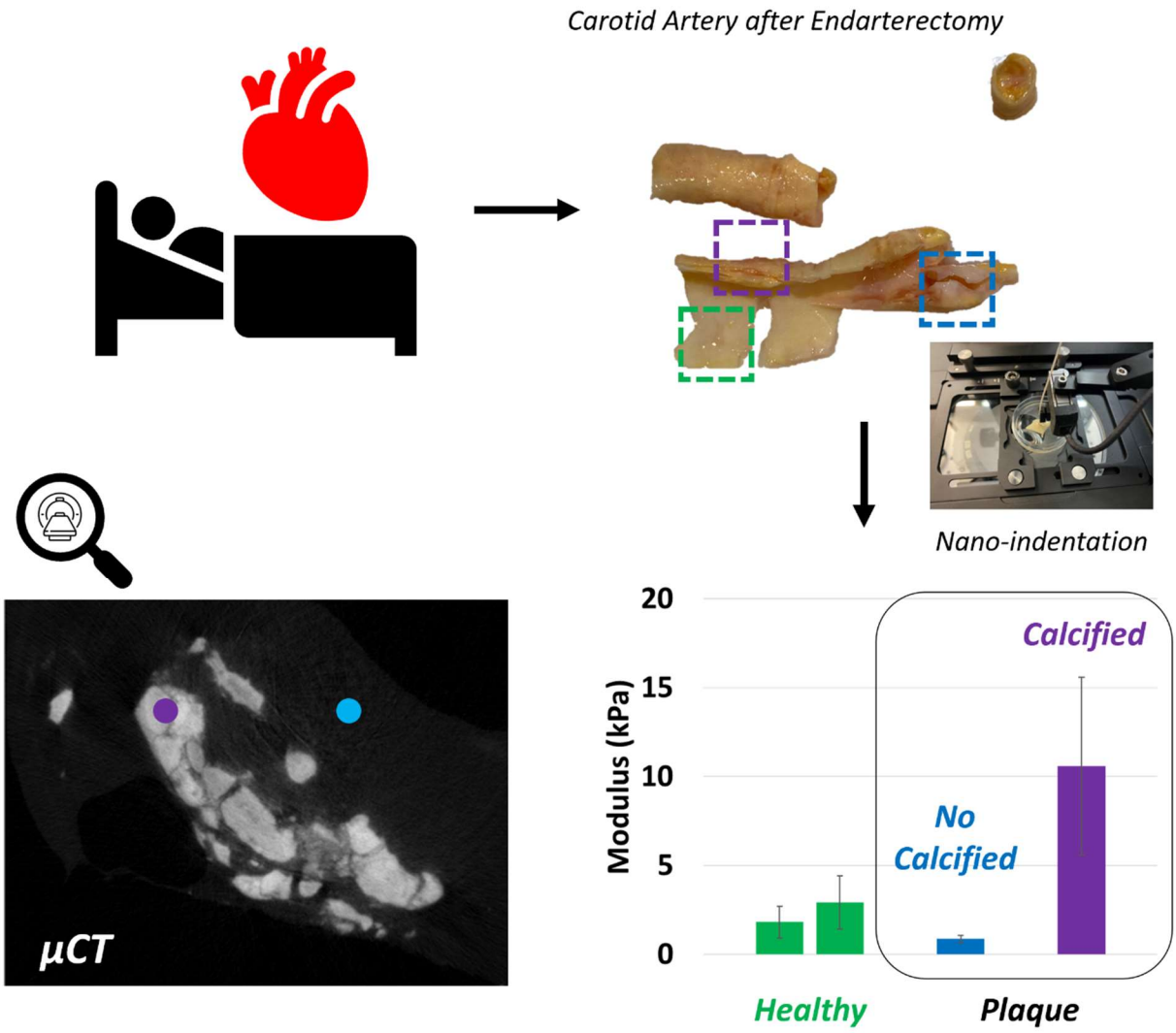


Figure *Schematic representation of the work; from the patient the carotid artery affected by the stenosis is extracted and after studied through nano-indentation and micro tomography*

References (Optional)

1. Aboyans V. et al., Eur. Heart J., 2018.

Acknowledgements (Optional)

This work was funded by the National Plan for NRRP Complementary Investments, project n. PNC0000003 - AdvaNced Technologies for Human-centrEd Medicine (project acronym: ANTHEM - Cascade Call launched by SPOKE 3 POLIMI: "PRIME").

Session Category

Cardiovascular/Cardiorespiratory Biomechanics: Methods, Models and Applications

P4-075

Machine Learning Model for Predicting the Risk of Thrombotic and Haemorrhagic Complications in Patients Supported by the Impella CP Device

Prof. Marek Pawlikowski[1], Prof. Aleksandra Gąsecka[2], PhD Ewelina Błażejowska[2], PhD Zbigniew Gulbinowicz[1], PhD Janusz Domański[1]

[1]Warsaw University of Technology, Warszawa, mazowieckie, Poland. [2]Medical University of Warsaw, Warszawa, mazowieckie, Poland

Introduction

Patients supported by the Impella CP pump due to cardiogenic shock or undergoing high-risk percutaneous coronary interventions are at risk of significant bleeding and thromboembolic complications, which are among the most commonly observed adverse events in this population. Modern versions of the Impella device, equipped with the SmartAssist function, enable continuous recording of haemodynamic parameters, pressure signals, and information related to pump operation. Although these data theoretically allow for early detection of changes conducive to bleeding or thrombosis, their systematic use in risk analysis remains limited.

Methods

Retrospective data were collected from over 300 patients supported with the Impella CP pump. The following data were obtained from electronic and paper documentation: demographic data, baseline clinical characteristics, comorbidities, medications, laboratory test results (including coagulation parameters and haemolysis), haemodynamic parameters, details of the procedure (vascular access, duration and settings of support, device type), data on anticoagulation used, and occurrence of complications. The main endpoints analysed were: clinically significant haemorrhagic complications, thromboembolic complications, including device thrombosis and ischaemic stroke, and haemolysis related to pump operation. All data were anonymised prior to analysis.

Preliminary models of artificial neural networks were created and trained using data adapted for machine learning. Various neural networks (with different structures, numbers of neurons and layers, activation functions) were examined. Several machine learning algorithms of the SGD type, Adam Optimizer, or eXtreme Gradient Boosting were used for training the artificial neural networks.

Results

Discussion

The application of machine learning algorithms can be very useful for assessing the significant bleeding and thromboembolic complications in cardiovascular procedures.

Until now, no research has been carried out to thoroughly evaluate the potential of predicting haemorrhagic and thromboembolic complications in patients treated with Impella CP using machine learning algorithms. Addressing this research gap could facilitate earlier detection of high-risk patients, personalise anticoagulant therapy, and improve management of mechanical support treatment.

Session Category

Cardiovascular/Cardiorespiratory Biomechanics: Methods, Models and Applications

P4-076

Coupling Pulmonary Arterial Hypertension Growth and Remodeling Models

Ms. Margaret Millar[1], Dr. Edward Manning[2], Dr. Jay Humphrey[3], Dr. Ana Estrada[4]

[1]Fairfield University, Fairfield, Ct., United States. [2]Yale University, New Haven, Ct., United States. [3]Yale University, New Haven, Ct, United States. [4]Fairfield University, Fairfield, Ct, United States

Introduction

When exposed to stressors, such as hypertension, the cardiovascular system goes through complex cellular and sub-cellular changes that result in the deposition, organization or removal of tissue to maintain homeostasis in response to wall and shear stress. Computational models of growth and remodeling (G&R) can be used to better understand these adaptations. In this study, we are combining G&R models of the pulmonary arteries with logic-based models of intracellular cell signaling to create a more accurate multiscale model of pulmonary artery adaptation.

Methods

We adapted a classical bilayered constrained mixture model of arterial G&R for pulmonary arterial applications, following methods established by Latorre et al. (2019). The model uses the 4-fiber family model for collagen material properties. The script utilizes data collected at two timepoints, taken 28 days apart, and interpret the G&R progression between. The material parameters were optimized using a particle swarm to find the best-matched growth model, compared to experimental data. The optimized parameters were used in a coupled multi-cell, multiscale model of vascular G&R in which individual cell-signaling network models of smooth muscle cells, fibroblasts, and macrophage drive adaptation. The G&R predicted by the coupled model was then compared to a previously published model [2] to compare differences between predictions of pulmonary vs. aortic G&R.

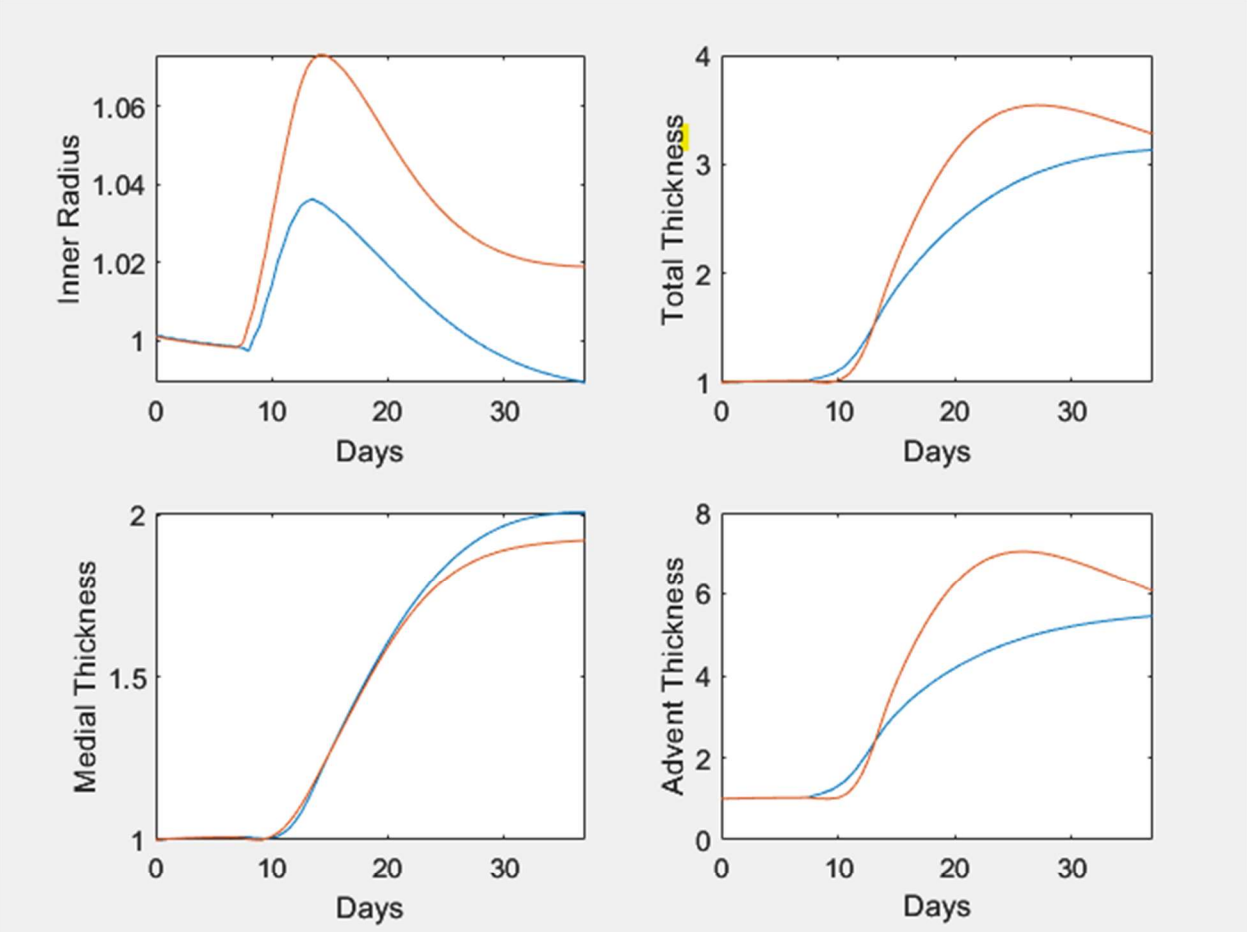
Results

The predictive model found the optimal values for the mass fraction of the medial layer to be 0.483886634314232 on day 0 and 0.427618001141548 on day 28. The model is optimized for AngII presence to be evaluated at 0.35 in the medial layer and 0.53 in the adventitial layer. The tissue-resident macrophage reaction weight is 0.85 and the recruited weight is 0.75.

Discussion

The circulatory system is a network of connected pieces. These pieces do not work separately but affect and are affected by each other so properly predicting adaptation requires models that can capture this biological complexity. By combining these models of tissue- and cell-level remodeling, we can create a more accurate predictive model and generate a better understanding of how the circulatory system remodels in response to stress.

Images (Optional)



Pulmonary Artery Growth Progression from day 0 to 28.
The blue line represents the original parameters and the red line is the current adjusted parameters so they can be used in another model.

References (Optional)

Acknowledgements (Optional)

Acknowledgement goes to Marcos Latorre who had originally written the code we are developing.

Session Category

Cardiovascular/Cardiorespiratory Biomechanics: Methods, Models and Applications

P4-077

Characterization of the Arterial Deformation During Endovascular Procedures Using 3D-Printed Aortic Aneurysm Models: A Pilot Study

Ms. Marie Julien[1,2], Dr. Alexandre Oliny[1,3], Dr. Lucie Derycke[1,3], Dr. Abdul Barakat[2], Dr. Stephan Haulon[1,3]

[1]Aortic Center, Hôpital Marie Lannelongue, Groupe Hospitalier Paris Saint Joseph (GHPSJ), Le Plessis-Robinson, Hauts-de-seine, France. [2]Laboratoire de l'Hydrodynamique, École Polytechnique, Institut Polytechnique de Paris, Palaiseau, Essonne, France. [3]INSERM UMR_S 999, Université Paris Saclay, Le Plessis-Robinson, Hauts-de-seine, France

Introduction

During endovascular procedures, arteries undergo deformations induced by the insertion of devices. In tortuous anatomies, the iliac arteries are straightened by stiff guidewires and sheaths which can influence endograft positioning and adequate sizing. This work presents preliminary results from a pilot study, using flexible 3D-printed aortic aneurysm models to characterize these deformations.

Methods

Three infra-renal aortic aneurysm models, including aneurysmal and non-aneurysmal iliac arteries, were 3D-printed in silicone using Dynamic Moulding technology. The vascular geometries were derived from patient CT scans and subsequently modified to fit the experimental setup. Using a test bench including a pulsatile pump, the models were integrated into a flow loop with controlled flow rate, pressure and temperature. Endovascular devices, namely a stiff guidewire, a 16Fr sheath and an 18Fr sheath, were inserted through dedicated puncture points within the test bench. At each step, 2D fluoroscopy and 3D CT scans were acquired using a GE hybrid-room scanner (Figure 1A). DICOM data were processed using 3D slicer. Each anatomy was segmented, and centreline models were generated using the Vascular Modelling Toolkit (Figure 1B). Extracted coordinates were processed in MATLAB (Figure 1C). For the least aneurysmal common iliac artery, the iliac tortuosity index [1] (ITI) was calculated at each step. Change in ITI, along with maximal and mean Hausdorff distance [2] between steps were quantified.

Results

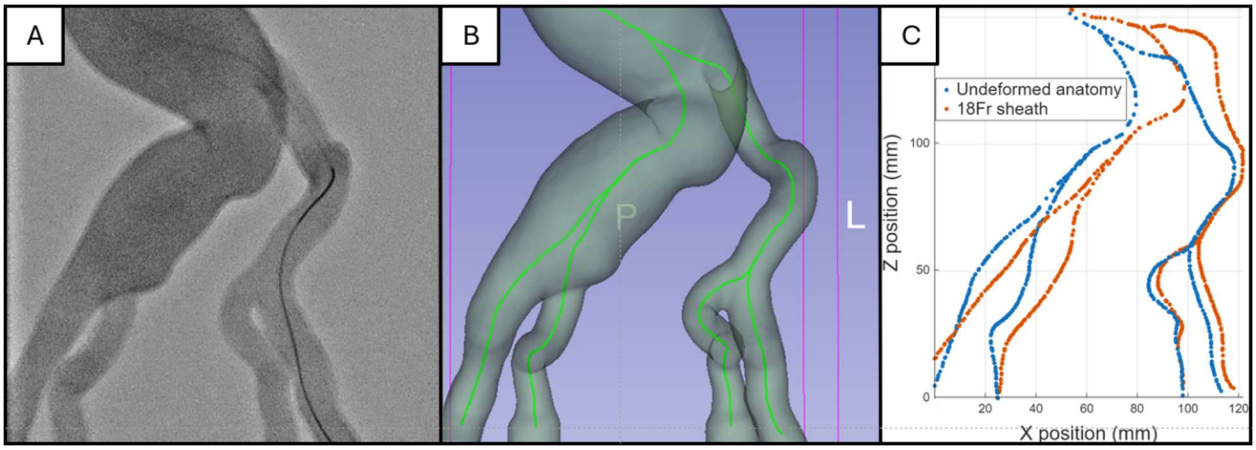
Initial ITI ranged between 1.02 and 1.45 (1.22 ± 0.22, N=3). In the anatomy with the lowest initial ITI, no change in ITI was detected, despite visually observable deformation, suggesting ITI change alone does not fully capture geometric changes. Across all models,

increases in device size produced larger changes in both maximal and mean Hausdorff distances.

Discussion

These early results demonstrate the feasibility of the proposed experimental and computational workflow. Further experiments are required to verify the statistical robustness of the findings. Future work will quantify post-endograft deployment deformation and compare model behavior to clinical EVAR data to evaluate the realism of the 3D-printed models.

Images (Optional)



References (Optional)

[1] G. Oderich et al., J Vascular Surgery, 2021.

[2] P. Dubuisson et al., Proc. International Conference on Pattern Recognition, 1994.

Acknowledgements (Optional)

Session Category

Cardiovascular/Cardiorespiratory Biomechanics: Methods, Models and Applications

P4-078

Ovine Postnatal Venous Remodeling Informs Pediatric Tissue-Engineered Vascular Graft Design

Dr Marisa Bazzi Postdoctoral Scholar[1], Dr Cole Anderson[2], Dr. Gavin Mays[3], Prof Christopher Breuer[2], Prof. Jay Humphrey[3], Prof. Alison Marsden[1]

[1]Stanford University, Palo Alto, CA, United States. [2]Nationwide Children's Hospital, Columbus, OH, United States. [3]Yale University, New Heaven, CT, United States

Introduction

Growth and remodeling (G&R) models are increasingly used to predict medium- and long-term vascular responses to changing mechanical loads and to optimize tissue-engineered vascular grafts. Yet most model parameters and design criteria are calibrated using adult vessels, even though pediatric patients undergo rapid somatic growth, evolving cardiac output, and changes in venous return that fundamentally alter hemodynamics and wall mechanics. We aimed to quantify age-dependent changes in venous structure, mechanics, and flow to provide data-driven targets for future pediatric TEVG G&R simulations.

Methods

Postnatal ovine inferior vena cava (IVC) were studied at 3, 10, 16, and 28 weeks of age (n=3 per time point). At each age, catheterization provided angiography used to reconstruct 3D lumen geometry (Fig.1A). Intravascular ultrasound (IVUS) was used to obtain wall and lumen geometry and derive a non-uniform wall thickness map (Fig.1B). At the same time, 2D phase-contrast MRI measured through-plane flow waveforms for inflow boundary conditions (Fig.1C). Biaxial mechanical testing of excised IVC segments was performed. Linearized stiffness parameters were computed around the in vivo pressure range. Subject-specific fluid–structure interaction simulations were performed in SimVascular's svMultiPhysics solver, with wall mechanics represented by a neo-Hookean model whose elastic modulus was calibrated to match in vivo compliance (Fig.1D-E).

Results

With growth, all components of the stiffness matrix increased (Fig.1F), with the largest changes occurring in the circumferential direction. Vessel diameter and wall thickness also increased (Fig.1G-H), consistent with postnatal growth and remodeling. Simulations showed that time-averaged wall shear stress decreased with age (Fig.1I), whereas oscillatory shear index increased from 3–16 weeks and declined at 28 weeks (Fig.1J).

Endothelium activation potential, defined as the ratio of oscillatory shear index to time-averaged wall shear stress, increased monotonically with age (Fig.1K).

Discussion

These data demonstrate coupled growth-dependent changes in venous geometry, material stiffness, and hemodynamics during early life in an ovine model. The age-resolved stiffness parameters, wall thickness, and shear metrics provide mechanistically grounded targets and boundary conditions for future pediatric TEVG G&R simulations. Incorporating these growth-dependent benchmarks into TEVG design and optimization frameworks may reduce graft maladaptation and failure in children undergoing venous reconstruction.

Session Category

Cardiovascular/Cardiorespiratory Biomechanics: Methods, Models and Applications

P4-079

Integrating 0D Pressure-Volume Dynamics Into Hybrid 3D-0D Cardiovascular Models in Abaqus

MSc Marta Zattoni[1,2], Dr. Annette Caenen[1,3], Prof. Patrick Segers[1], Prof. Mathias Peirlinck[2]

[1]Ghent University, Ghent, East Flanders, Belgium. [2]TU Delft, Delft, South Holland, Netherlands. [3]KU Leuven, Leuven, Flemish Brabant, Belgium

Introduction

0D cardiovascular hemodynamics models provide a computationally efficient research tool and solid basis for human virtual twin research, but lack the ability to study localized biomechanical tissue phenomena, where higher-fidelity 3D-0D hybrid models are required. Nevertheless, their implementation requires careful tuning of the underlying functional parameter set. We present a methodology to map 0D outputs to a hybrid 3D-0D left ventricular (LV) model and a two-step optimization framework to calibrate model parameters.

Methods

To demonstrate the workflow, reference 0D pressure-volume (pV) data for a healthy subject was generated in CircAdapt from vanOsta2024. For the hybrid model, a LV hexahedral mesh was parametrically designed in pyFormex. In Abaqus, passive myocardial behavior was represented by Holzapfel-Ogden (2009) constitutive law and active contraction following Guccione *et al.* (1993). Interaction with the systemic circulation was captured through a three-element Windkessel model equivalent coupled to the LV cavity. An additional proximal resistance was implemented to decouple aortic valve effects from the contribution of aortic characteristic impedance to the afterload. Two least square optimization algorithms were sequentially applied. Firstly, passive material properties were adapted against reference single-beat estimations of the end-diastolic pV relationship (Peirlinck *et al.*, 2018) (Fig-1,step-1). Then, Windkessel and contractility parameters were updated through a penalty function including LV pressure-, volume- and aortic pressure-time CircAdapt curves (Fig-1,step-2).

Results

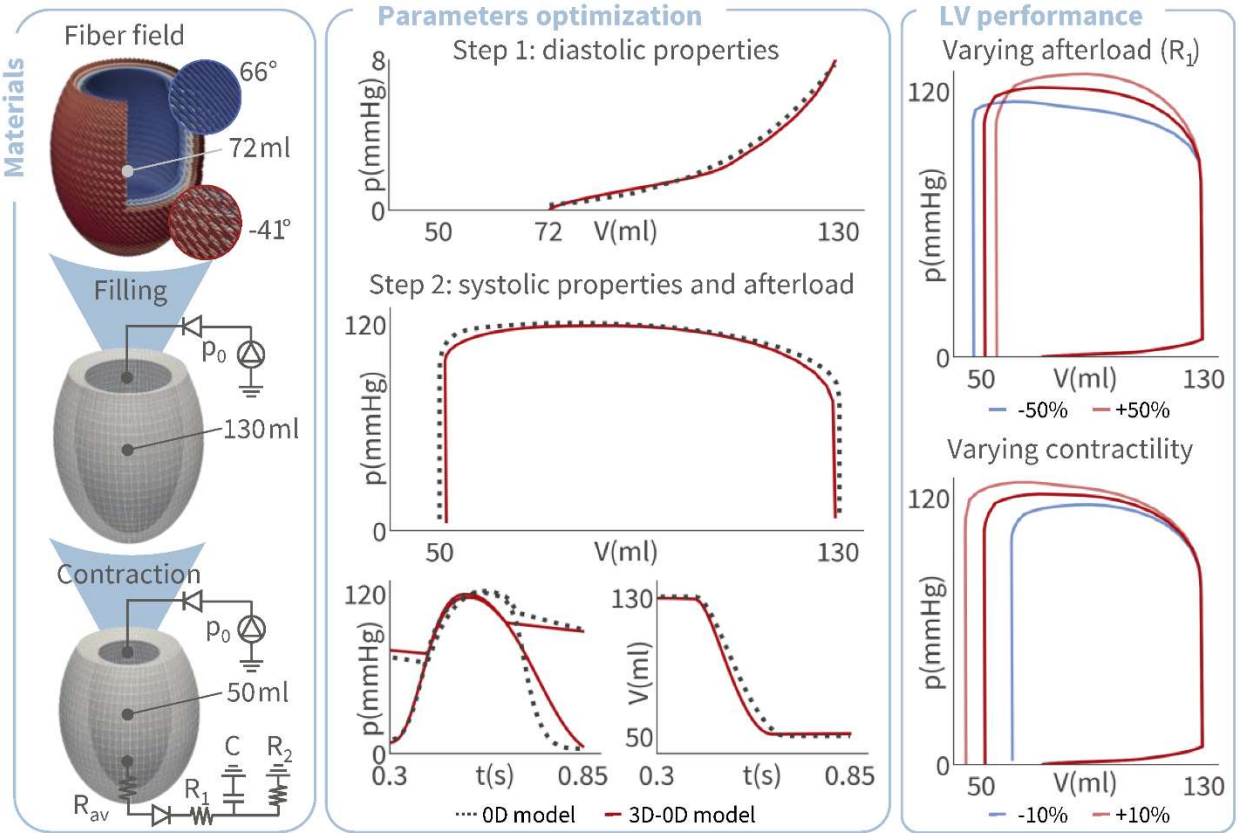
The 3D-0D implementation incorporating aortic valve effects reproduced the behavior of the three-element Windkessel formulation. The two optimization routines yielded results consistent with reference curves for pV and volume-time, while a mismatch remained

present in the pressure-time curves in the relaxation phase. The model reproduced physiological responses: 50% variations in contractility increased stroke volume by 8.9% or reduced it by 12%, while changes in afterload resistance produced a decrease and an increase of 8.9% and 5.1%, respectively (Fig-1).

Discussion

The proposed 3D-0D modelling framework captures key features of healthy LV physiology and can be reasonably well calibrated on 0D data. Further work should include better matching for the contraction-relaxation dynamics and pressure-time data, and extend to a closed-loop formulation to simulate multiple heartbeats. Overall, our model provides a simple yet robust platform for studying spatially varying cardiac mechanical phenomena.

Images (Optional)



Acknowledgements (Optional)

M.Z. acknowledges the funding provided by the European Union within project 101169278 — InSilicoHealth — HORIZON-MSCA-2023-DN-01. Views and opinions expressed are however those of the authors only and do not necessarily reflect those of the European

Union, which cannot be held responsible for them. A.C. acknowledges the support of the Research Foundation Flanders under grant 12B3124N.

Session Category

Cardiovascular/Cardiorespiratory Biomechanics: Methods, Models and Applications

P4-080

Estimation of Passive Myocardial Stiffness From Non-Invasive Pressure Estimates

Ms. Mathilde Verlyck[1], Mr. Amirhossein Manzouri[1], Dr. Joao Fernandes[2], Ms. Gina Quill[1], Dr. Thiranja Babarenda Gamage[1], Dr. Debbie Zhao[1], Prof. Martyn Nash[1,3]

[1]Auckland Bioengineering Institute, University of Auckland, Auckland, Auckland, New Zealand. [2]School of Biomedical Engineering and Imaging Sciences, King's College London, London, Greater London, United Kingdom. [3]Department of Engineering Science and Biomedical Engineering, University of Auckland, Auckland, Auckland, New Zealand

Introduction

Personalised cardiac parameters, such as passive myocardial stiffness, are not routinely available in the clinic, despite their potential to provide a more specific understanding of myocardial properties. Passive myocardial stiffness can be estimated through modelling approaches that often rely on the availability of invasive pressure measurements. This study leverages a recent non-invasive method for estimating diastolic pressures to derive myocardial stiffness estimates and assess their accuracy.

Methods

Invasive left heart pressures and 3D echocardiography (3DE) were recorded on the same day for patients referred for coronary angiography. Patients with valve diseases and atrial fibrillation were excluded from this study. Twenty-eight patients were included. We implemented a method by Smiseth et al. [1] to non-invasively estimate diastolic pressures using data derived from 2D and 3DE. We used our local biomechanics pipeline relying on diastasis (DSP) and end-diastolic (EDP) pressures to derive passive myocardial stiffness by minimising the projection error between the measured shape from 3DE and the model-predicted shape at end-diastole using non-linear optimisation.

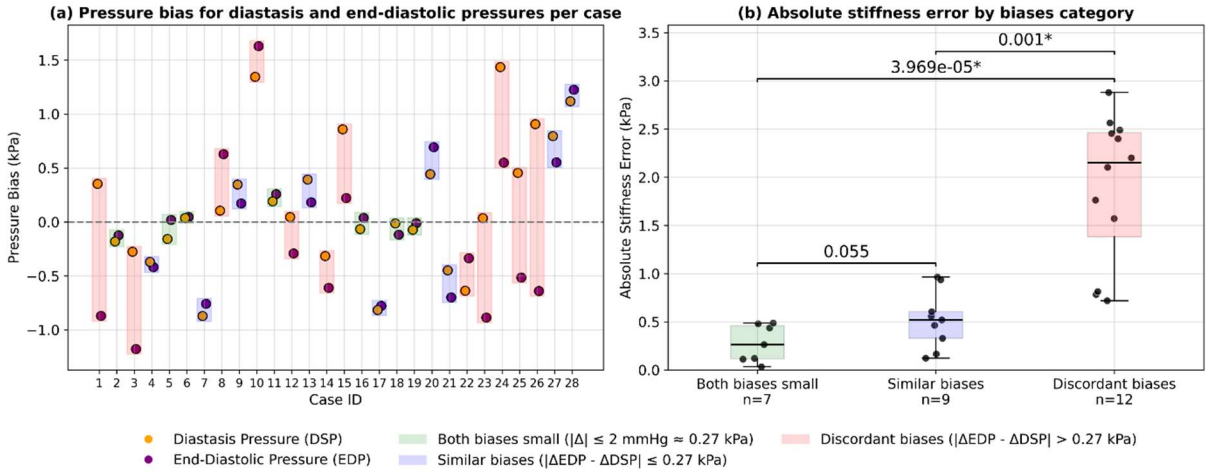
Results

Using the non-invasive pressure estimates to derive myocardial stiffness yielded a root mean square difference (RMSD) of 1.38 kPa compared to the estimates derived from invasive pressure measurements. Nine cases exhibited similar biases for the EDP and DSP, reflecting a consistent underestimation or overestimation of both pressures compared to the invasive reference (Figure a). The stiffness RMSD for these latter cases was 0.59 kPa, while cases with discordant biases in pressure estimation (n = 12) resulted in an RMSD of 2.03 kPa (Figure b).

Discussion

We found that consistent underestimates or overestimates of both the non-invasive diastasis and end-diastolic pressures yielded stiffness estimates that were similar to those derived from the invasive pressure measures. These preliminary results show the potential of deriving intrinsic myocardial parameters from non-invasive measures. These results also highlight the sensitivity of passive myocardial stiffness estimates to left ventricular pressure measurements. Future work will focus on refining the implementation of the non-invasive pressure estimation method, and assessing the potential for non-invasive tissue property estimates to better characterise phenotypes of heterogeneous conditions such as heart failure.

Images (Optional)



References (Optional)

[1] Otto Smiseth et al. , Eur. Heart J. Cardiovasc. Imaging, 2025

Session Category

Cardiovascular/Cardiorespiratory Biomechanics: Methods, Models and Applications

P4-081

Modeling Longitudinal Adaptation of the Infarcted Left Ventricle using Cardiac Magnetic Resonance and Ex-Vivo Biomechanics

Mr. Emilio Mendiola[1], Mr. Tanmay Mukherjee[1], Mr. Rana Raza Mehdi[1], Mr. Md Ajwad Mohimin[1], Dr. Qian Xiang[2], Dr. Robia Paulter[3], Dr. Peter Vanderslice[2], Dr. Reza Avazmohammadi[1]

[1]Texas A&M University, College Station, Texas, United States. [2]Texas Heart Institute, Houston, Texas, United States. [3]Baylor College of Medicine, Houston, Texas, United States

Introduction

Regional structural, biomechanical, and functional remodeling of the left ventricle (LV) post-myocardial infarction (MI) are dynamic time-evolving processes, yet our understanding of their true longitudinal evolution remains limited. Previous studies relied on cross-sectional data to characterize the progression from acute ischemia to late-stage remodeling. These approaches fail to capture the continuous, subject-specific trajectories that guide the heart towards an adaptive state or progressive decline and heart failure (HF). To elucidate individual mechanisms and interactions that drive functional outcomes, longitudinal remodeling must be characterized on a subject-specific basis to observe the gradual shift from an adaptive to a maladaptive state.

Methods

We developed longitudinal, subject-specific finite-element models of rodent hearts pre- and post-MI. Mild and severe MI were induced in six (n=3 for each group) rodent subjects via partial and complete ligation of the left anterior descending artery. Cine cardiac magnetic resonance imaging was acquired before MI and at 1-wk and 3-wks post-MI. After sacrifice, hearts were excised and the LV free wall underwent biomechanical testing. Histological analysis was performed to characterize the fibrous architecture and delineate the infarct, border zone, and remote regions of the LV. By integrating image-based geometries with in-vivo volumetric data, ex-vivo mechanical characterization, and detailed histological analyses, we offer a multiscale, longitudinal view of the post-MI remodeling process.

Results

Substantial kinematic alterations, altered ejection fraction, and region-specific variations in tissue stiffness and architecture were observed, suggesting early kinematic decompensation may prompt late-stage maladaptation. Inverse modeling and ex-vivo results demonstrated an increase in regional stiffness within the infarct and border zone

regions, with an accelerated rate of stiffening in the severe MI group. The estimated time-course regional stiffness showed that subjects progressing to maladaptation exhibited distinct, early mechanical and structural remodeling in the border zone.

Discussion

Continuous tracking of structural, biomechanical, and functional adaptations through time-course regional inverse modeling not only enhances our mechanistic understanding of post-MI adaptation but also lays the groundwork for improved, patient-specific prognostic tools and therapeutic strategies. Ultimately, our study represents a critical step towards bridging the existing gap in longitudinal cardiac assessment, with the potential to inform more personalized approaches in assessing HF risk post-MI.

Images (Optional)

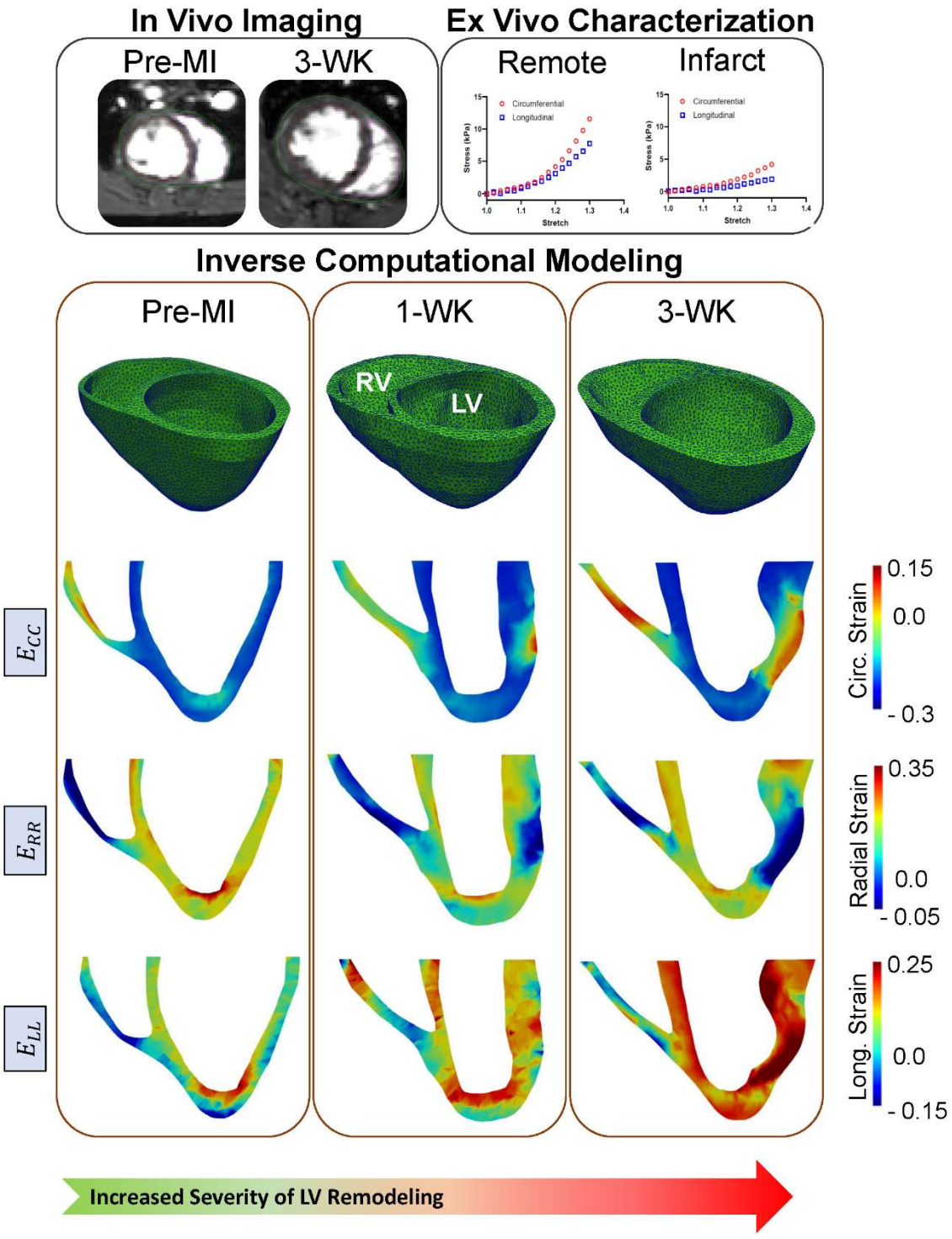


Figure 1: Longitudinal in vivo cardiac magnetic resonance imaging and ex vivo biomechanical and structural data were integrated to develop rodent computational cardiac models of a single subject at the pre-MI, 1-WK, and 3-WK post-MI timepoints. Finite-element meshes shown here are reconstructed at the end-diastolic state. Simulations revealed substantial regional alterations in end-systolic circumferential, radial, and longitudinal strain evolving over time.

Session Category

Cardiovascular/Cardiorespiratory Biomechanics: Methods, Models and Applications

P4-082

Pre- and Post-Operative Hemodynamic Assessment of Mitral Valve Prolapse Using Image-Derived Moving-Wall CFD

Mr. Md Ajwad Mohimin[1], Mr. Tanmay Tanmay Mukherjee[1], Mr. Emilio Mendiola[1], Dr. Dipan Shah[2], Dr. Reza Avazmohammadi[1]

[1]Texas A&M University, College Station, TX, United States. [2]Houston Methodist DeBakey Heart and Vascular Center, Houston, TX, United States

Introduction

Mitral valve prolapse (MVP) significantly disrupts intracardiac hemodynamics, creating abnormal flow patterns that may result in ventricular remodeling. Accurately characterizing these fluid dynamics is critical for evaluating surgical efficacy and predicting post-repair outcomes. However, standard imaging often lacks the resolution to fully capture complex flow structures within the left ventricle. To address this need, we employed a patient-specific moving-wall computational fluid dynamics (CFD) framework derived from standard cine cardiac magnetic resonance (CMR) and phase-contrast magnetic resonance imaging (MRI). By incorporating accurate endocardial wall motion without relying on complex tissue modeling, this study aims to investigate the changes in flow characteristics within the left ventricle pre- and post-mitral valve repair (MVR).

Methods

This project studies a cohort of eight MVP patients (n=8) pre- and post-surgery. We are developing patient-specific CFD models for all the subjects (16 models total). Standard cine CMR and phase-contrast MRI (PC-MRI) were acquired from the patient before and after mitral valve repair. We utilized a non-rigid image registration (NRIR) algorithm to extract the endocardial wall motion from cine images. This wall motion was prescribed as a moving boundary condition, eliminating the need for complex solid mechanics modeling of the endocardial wall. Patient-specific mitral inflow rates were derived from PC-MRI and used as the inlet condition for the CFD model. Finally, the three-dimensional Navier-Stokes equations were solved to simulate intracardiac blood flow under the assumption of Newtonian fluid and laminar flow.

Results

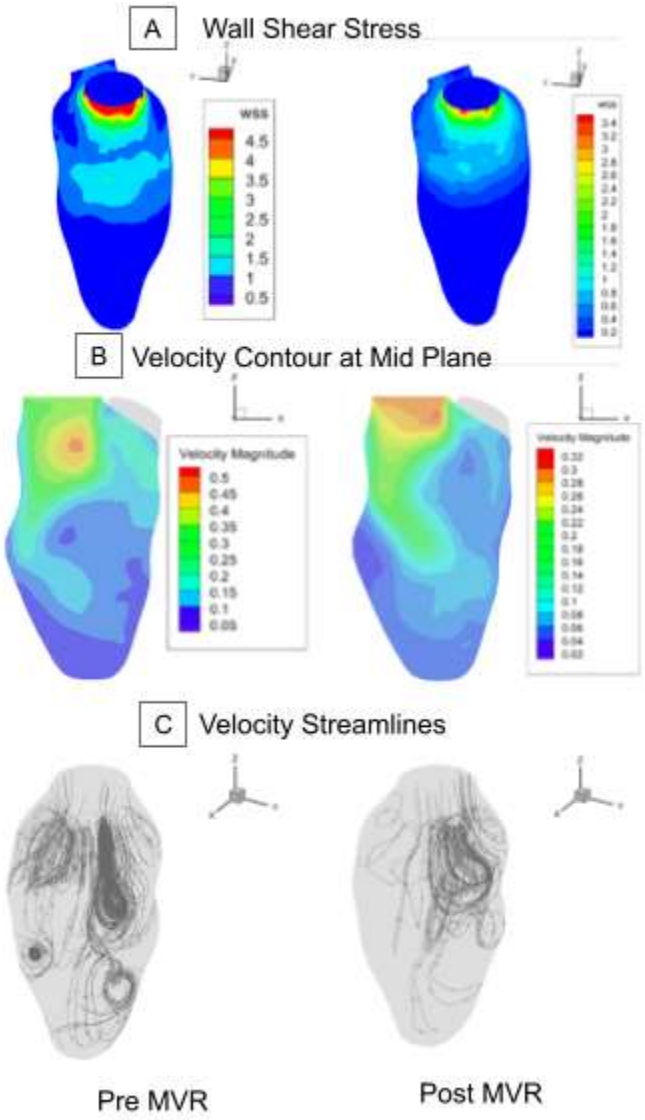
Preliminary simulations (n=1) demonstrated distinct hemodynamic alterations following mitral valve repair. Pre-operative analysis revealed elevated wall shear stress (WSS) peaking at approximately 4.5 Pa. Following repair, peak WSS decreased by 24%. Similarly, mid-plane velocity contours showed a 36% reduction in peak flow velocity, indicating a

quantitative decrease in hemodynamic parameters. In addition, a reduction in swirling motion is observed in the post-MVR case.

Discussion

The preliminary findings from our CFD study show a significant reduction in WSS and peak velocity after MVP repair. In the next phase of this study, these findings will be investigated for all the subjects in the cohort. In addition, the linkage between the structural remodeling and hemodynamic alterations will be evaluated.

Images (Optional)



Session Category

Cardiovascular/Cardiorespiratory Biomechanics: Methods, Models and Applications

P4-083

Wall Shear Stress Signatures Across Pulmonary Arterial Branching Orders Reveal Mechanistic Links from Acute Pulmonary Embolism to CTEPH and Post-Endarterectomy Haemodynamics

Dr Behdad Shaarbaf Ebrahimi[1], Dr Misha Dagan[2], Professor David Kaye[2], Mr Atsuo Doi[2], Dr Timothy Joseph[2], Professor David McGiffin[2], Professor Merryn Tawhai[1]

[1]Auckland Bioengineering Institute - University of Auckland, Auckland, Auckland, New Zealand. [2]The Alfred Hospital, Melbourne, Victoria, Australia

Introduction

Acute pulmonary embolism (PE) can progress to chronic thromboembolic pulmonary hypertension (CTEPH), yet the haemodynamic mechanisms linking initial obstruction to distal microvascular remodelling remain poorly defined. In particular, how wall shear stress (WSS) changes in CTEPH across different arterial orders in non-occluded territories - and how these patterns evolve after pulmonary endarterectomy (PEA) - has not been quantified in a spatially resolved manner. Because low time-averaged WSS (TAWSS) or high oscillatory shear index (OSI) promotes endothelial dysfunction and vascular remodelling, characterising order-specific shear disturbances may help explain why microvascular disease may persist after PEA.

Methods

Using a detailed patient-specific pulmonary arterial model and a one-dimensional (1D) haemodynamic framework, we examined WSS across Horsfield orders under four key scenarios: baseline (healthy), acute PE (proximal occlusions only), CTEPH (occlusion plus fitted microvascular remodelling in non-occluded regions), and a post-PEA state (occlusions removed but distal remodelling retained in non-occluded regions). TAWSS and OSI were computed for all vessels and aggregated by order to quantify how shear signatures shift between proximal and distal branches.

Results

Relative to baseline, acute PE produced substantial reductions in TAWSS in non-occluded mid-distal orders - typically falling by ~30–60% - while OSI increased in several orders, reflecting disturbed redistributed flow. CTEPH caused a far more pronounced collapse of shear, with >70–90% reductions in TAWSS across most orders and uniformly low OSI, indicating globally diminished pulsatility due to microvascular narrowing and pruning. In

the post-PEA state, lower-order vessels showed partial TAWSS recovery (~20–40%), but proximal branches remained markedly suppressed, consistent with clinical observations that microvasculopathy drives residual pulmonary hypertension.

Discussion

Overall, the results suggest that acute PE generates abrupt shear deficits in specific non-occluded arterial generations, providing a plausible mechanobiological trigger for distal remodelling. CTEPH amplifies these disturbances into a pan-arterial low-shear environment, whereas PEA restores proximal haemodynamics but cannot reverse microvascular disease, leaving persistently abnormal shear in high-order vessels. These order-specific WSS signatures offer mechanistic insight into CTEPH progression and may help identify vascular regions most vulnerable to remodelling, incomplete postoperative recovery, and targeted future intervention.

Acknowledgements (Optional)

We gratefully acknowledge the New Zealand Ministry of Business, Innovation and Employment (MBIE) for their support and the Auckland Bioengineering Institute for providing the essential infrastructure that made this project possible. This study was supported by the Catalyst Strategic Fund, administered by the New Zealand Ministry of Business, Innovation and Employment (MBIE) and the Auckland Bioengineering Institute. We are also grateful for our collaborators in the Alfred Hospital that provided the data and clinical insight on this study.

Session Category

Cardiovascular/Cardiorespiratory Biomechanics: Methods, Models and Applications

P4-084

Towards the Validation of Arteriovenous Fistula Sounds Using An in-Vitro vascular Flow Simulator

Dr Sofia Poloni[1], Dr Elia Pederzani[2], Dr Luca Soliveri[3], Eng Alessia Sofia Bolandrina[2], Prof Monica Soncini[2], Prof Gianfranco Beniamino Fiore[2], Prof. Andrea Remuzzi[3], Prof Chiara Emma Campiglio[3], Dr Michela Bozzetto[1]

[1]Istituto di Ricerche Farmacologiche Mario Negri IRCCS, Bergamo, Italy, Italy. [2]Politecnico di Milano, Milan, Italy, Italy. [3]Università degli Studi di Bergamo, Bergamo, Italy, Italy

Introduction

The arteriovenous fistula (AVF) remains the vascular access of first choice for hemodialysis, although primary patency at one year after surgery is about 60%, largely due to maladaptive vascular remodeling. Our recent work has shown that turbulent-like flow patterns can induce vibrations of the AVF venous wall [1]. Disturbed hemodynamics is also related to AVF-generated audible sounds [2], which can be used to monitor AVF functional status. The aim of the present study was to validate the occurrence of flow-induced sounds using an *in-vitro* vascular flow simulator.

Methods

A 3D-printed silicone AVF phantom was fabricated starting from MR images of a 6-week AVF. The phantom was housed in an advanced vascular flow simulator [3] and perfused with a patient-specific flow waveform derived from Doppler Ultrasound acquired at the same timepoint. Sounds produced by the AVF phantom were recorded positioning an electronic stethoscope 3M Littmann 3200 at the anastomosis. The recorded signals were cut to three cardiac cycles and high-pass filtered at 50 Hz. Sound processing included FFT-based spectral analysis and spectrogram representation. Spectral features were then compared with those derived from a typical sound of a matured well-functioning AVF of a dialysis patient.

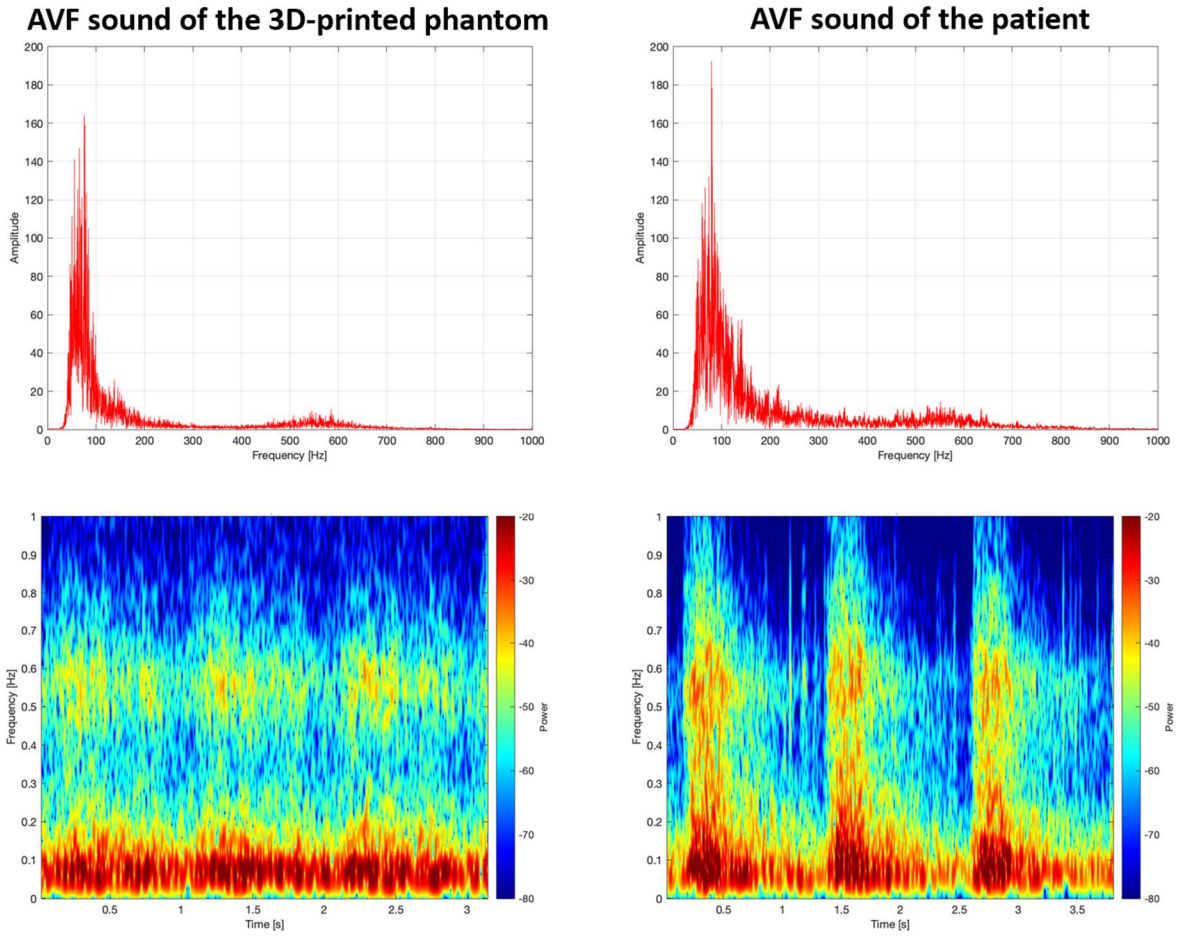
Results

The spectral analysis revealed strong agreement between the sounds acquired in the 3D-printed phantom and those acquired in the patient (see FFT analysis and spectrograms in Figure 1). Indeed, both experimental and clinical sound recordings exhibited a dominant low-frequency component between 50–100 Hz, along with a secondary, lower-amplitude contribution between 500-700 Hz. Interestingly, the amplitude values of the corresponding spectral peaks also fell within the same order of magnitude.

Discussion

These results represent a step forward towards the validation of the occurrence of hemodynamically induced AVF sounds. The versatility of the in-vitro vascular flow simulator allows the housing of different AVF geometries associated with distinct hemodynamic conditions, enabling a deeper understanding of the relationship between flow phenotypes and AVF sounds, ultimately improving the knowledge on the mechanisms of AVF failure.

Images (Optional)



References (Optional)

[1] Luca Soliveri et al., Biomech Model Mechanobiol, 2024

[2] Sofia Poloni et al. Ann Biomed Eng, 2025

[3] Elia Pederzani et al. Conference paper GNB, 2023

Session Category

Cardiovascular/Cardiorespiratory Biomechanics: Methods, Models and Applications

P4-085

Quantifying the Role of Vasoactivity on Arterial Hemodynamics Using a Spatially Multiscale, One-Dimensional Fluid Models

Dr. Mitchel Colebank Ph.D.

University of South Carolina, Columbia, South Carolina, United States

Introduction

Systemic and pulmonary arterial hemodynamics are governed by multiple factors, including ventricular function, arterial stiffness, and microvascular function. The latter two components can be modulated by the vasomotor tone of vascular smooth muscle cells (VSMCs) within the arterial walls. In particular, an imbalance between extracellular matrix (ECM) stiffness, VSMC stiffness, and vasoactivity contribute to systemic and pulmonary hypertension, and may make it difficult to identify whether treatment via vasodilators is optimal for a given patient. Computational, one-dimensional (1D), pulse-wave propagation models can help investigate these possible confounders. Here we introduce a 1D model that combines nonlinear stress-strain dynamics under vasomotor tone with a microcirculation model to identify the role of ECM and VSMC stiffness and VSMC tone on arterial wave propagation.

Methods

The 1D model is applied to a 34-vessel systemic arterial circulation and 15-vessel pulmonary circulation network. The 1D model includes a spatially averaged mass conservation and momentum balance equation. The model provides predictions of pressure, flow, and area; thus, we introduce a third equation describing the pressure-area relationship. This relationship includes ECM and VSMC stiffness, as well as VSMC tone (Fig. 1(a)). We use the structured tree model [1] to describe the downstream vasculature, allowing us alter microvascular reactivity in addition to the large vessels.

Results

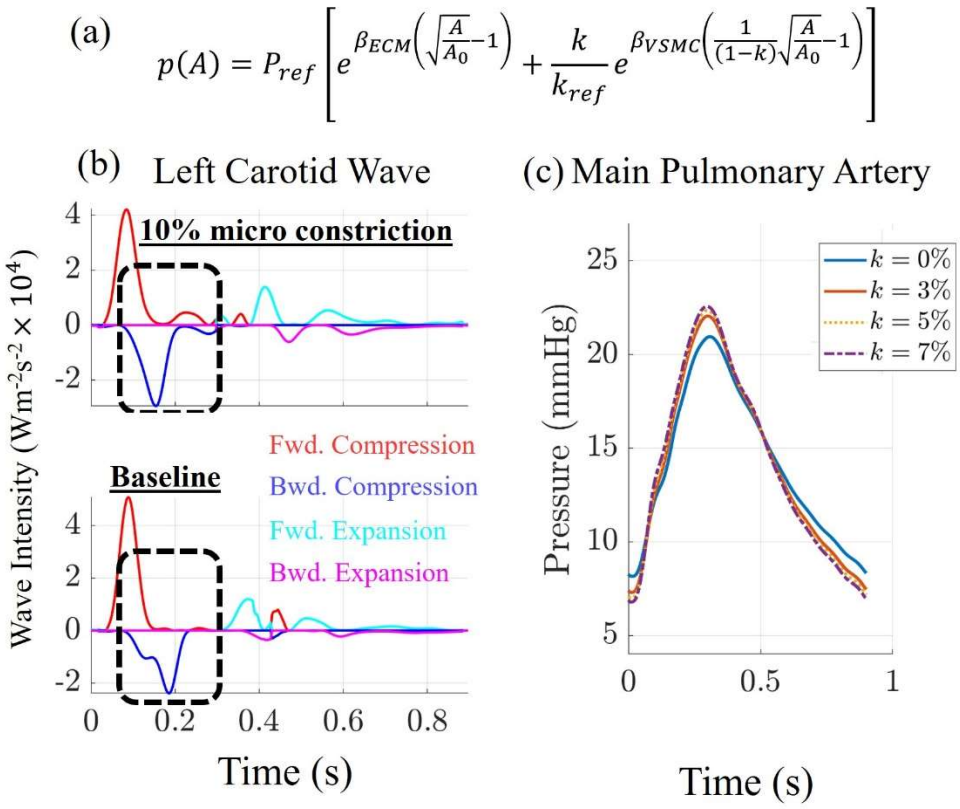
Results show that vasoconstriction of the microvasculature has large impacts on wave propagation, as shown in Fig. 1(b). Left carotid backward waves amplify with a 10% reduction in microvascular radii. In the pulmonary circulation (Fig. 1(c)), vasodilation (as k goes to zero) reduces blood pressure when ECM stiffness is comparable to VSMC stiffness. In contrast, vasodilation is ineffective when ECM stiffness is substantially larger,

as the ECM of the vessel is loaded. Thus, a combination of small and large vessel vasodilation is necessary to reduce blood pressure when ECM stiffness is high.

Discussion

We developed an interpretable hemodynamic framework for quantifying the interactions between VSMC, ECM, and pulse-wave propagation in the large and small arteries. This provides a new tool for examining the mechanisms of high-blood pressure and possible avenues for subject-specific treatment.

Images (Optional)



References (Optional)

[1] Olufsen, M, *Am J Physiol Heart Circ,* 1999

Session Category

Cardiovascular/Cardiorespiratory Biomechanics: Methods, Models and Applications

P4-086

Development of an Integrated Systemic–Coronary Closed-Loop Pulsatile Simulator with Actively Controlled Coronary Impedance

Ms. Mone Katagiri B.Eng., M.S. student[1], Dr. Kaoru Hattori MD, PhD[1,2], Mr. Katsuyoshi Suzuki[2], Prof. Kiyotaka Iwasaki PhD[3,1,2]

[1]Department of Integrative Bioscience and Biomedical Engineering, Graduate School of Advanced Science and Engineering, Waseda University, Shinjuku-ku, Tokyo, Japan. [2]Waseda Research Institute for Science and Engineering, Waseda University, Shinjuku-ku, Tokyo, Japan. [3]Department of Modern Mechanical Engineering, School of Creative Science and Engineering, Waseda University, Shinjuku-ku, Tokyo, Japan

Introduction

Coronary blood flow is maintained within a specific range through coronary autoregulation. However, this mechanism becomes impaired under low pressures, resulting in a pressure-dependent reduction in flow. Consequently, in conditions such as cardiogenic shock, reduced coronary prefusion pressure (CPP) causes a vicious cycle of declining flow and worsening myocardial ischemia. Coronary impedance fluctuates due to extravascular myocardial pressure, producing characteristic biphasic waveforms. This study aimed to develop a systemic-coronary integrated pulsatile simulator capable of reproducing physiological coronary pressure-flow relationships, including autoregulation, to quantitatively evaluate the effects of low cardiac output and mechanical circulatory support (MCS) on coronary hemodynamics.

Methods

We constructed a closed-loop pulsatile circulation system comprising a silicone elastic left ventricle, an aortic valve with coronary arteries, an aortic arch, and venous models. Two actuator-driven variable-resistance units were incorporated into the coronary arteries. We simulated coronary pressure–flow relationships by implementing: (i) phase-dependent impedance via beat-synchronized coronary artery compression, and (ii) feedback-controlled impedance adjustment based on measured mean coronary flow to track CPP-derived target flow. Target flow values were obtained by interpolation of the steady-state CPP–coronary flow curve reported by Mosher et al. (1964). Systemic conditions were set to aortic pressure 120/80 (90) mmHg, cardiac output 5 L/min, and left ventricular pressure 120/10 mmHg. The target autoregulation range was set to 70–140 mmHg.

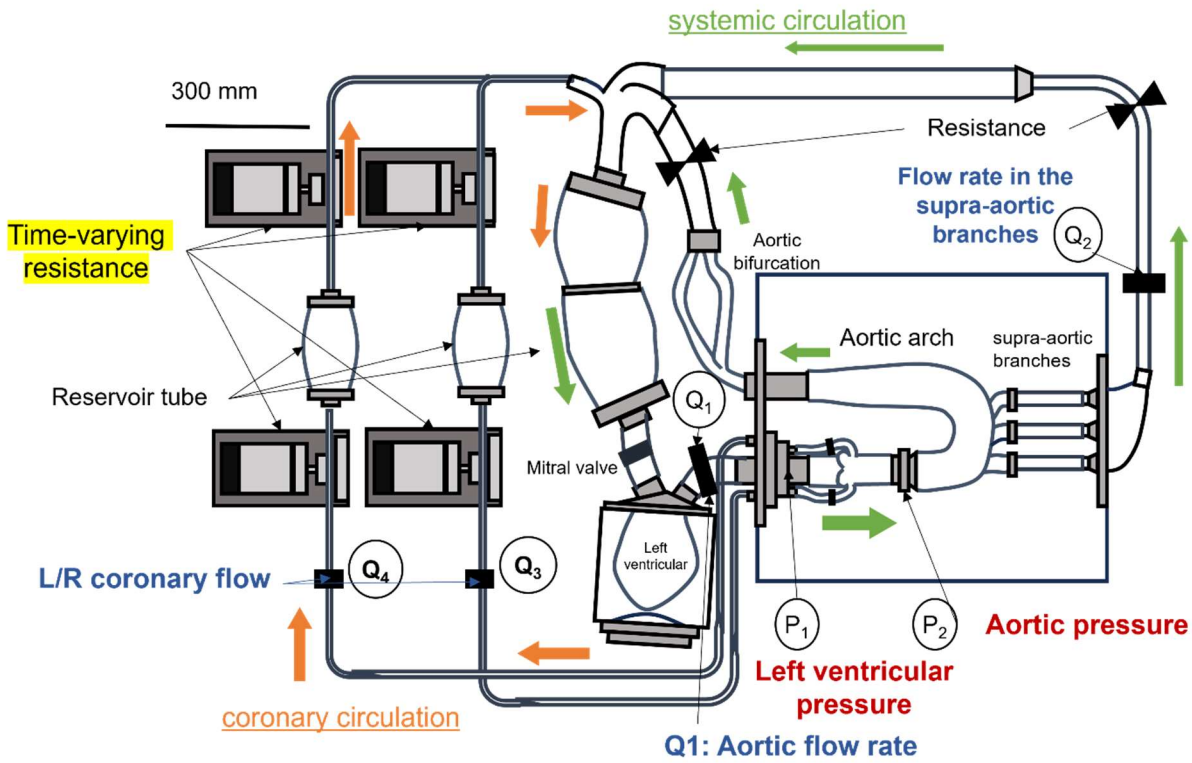
Results

Under baseline conditions, physiological biphasic coronary flow waveforms (left: diastolic-dominant; right: systolic-dominant) were generated. Initial coronary flows were 88 mL/min/100g (left) and 44 mL/min/100g (right). When CPP (aortic diastolic pressure) was varied within the autoregulation range (70–140 mmHg), left coronary flow was maintained within 82–105 mL/min/100g, successfully simulating autoregulation. Conversely, in the low CPP range below the set limit (30–70 mmHg), pressure-passive characteristics were confirmed, with flow decreasing alongside pressure drops.

Discussion

We successfully developed a systemic-coronary integrated simulator capable of reproducing physiological coronary hemodynamics via active impedance control. This system uniquely simulates the dynamic transition from a pressure-passive flow during cardiogenic shock to restored autoregulation under MCS. It serves as a valuable platform for quantitative evaluation of cardiovascular devices in complex hemodynamic scenarios.

Images (Optional)



References (Optional)

[1] Mosher *et al.* , Circulation Research, 1964

Session Category

Cardiovascular/Cardiorespiratory Biomechanics: Methods, Models and Applications

P4-087

Predicting Cardiovascular Events in Turner Syndrome Patients: Validation of the Hemodynamics Digital Twin Through 4D and 2D-Flow MRI

Dr Monika Colombo[1], MD Line Balsby Valsted[2], Prof. Steffen Ringgaard[2], Prof. Claus Højbjerg Gravholt[2]

[1]Department of Mechanical and Production Engineering, Aarhus University, Aarhus, Jutland, Denmark. [2]Department of Clinical Medicine, Aarhus University Hospital, Aarhus, Jutland, Denmark

Introduction

Turner Syndrome (TS) [1] is associated with a substantially increased risk of congenital and acquired cardiovascular complications. Early identification of individuals at risk remains challenging, highlighting the need for reliable, non-invasive biomarkers derived from hemodynamic assessment. We aim to develop a predictive hemodynamic and remodelling score using clinical MRI flow data and computational modelling.

Methods

The study included 30 women with TS, 15 of which followed over a 10-year period and healthy age- and sex-matched controls (CN) examined once (Fig.1). Participants underwent 2D- and 4D-flow MRI, with 3D-flow data available for baseline assessment. These imaging datasets were used to construct personalized moving-boundary computational fluid dynamics (CFD) models. Manually segmented geometries were used for the analysis of the wall remodelling [2] and discretized for unsteady, laminar simulations. Near-wall (wall shear stress, WSS) and bulk-flow (helicity) descriptors were computed. Clinical variables, wall remodelling, and haemodynamic data were integrated into a statistical model to generate a local event risk score (LERS).

Results

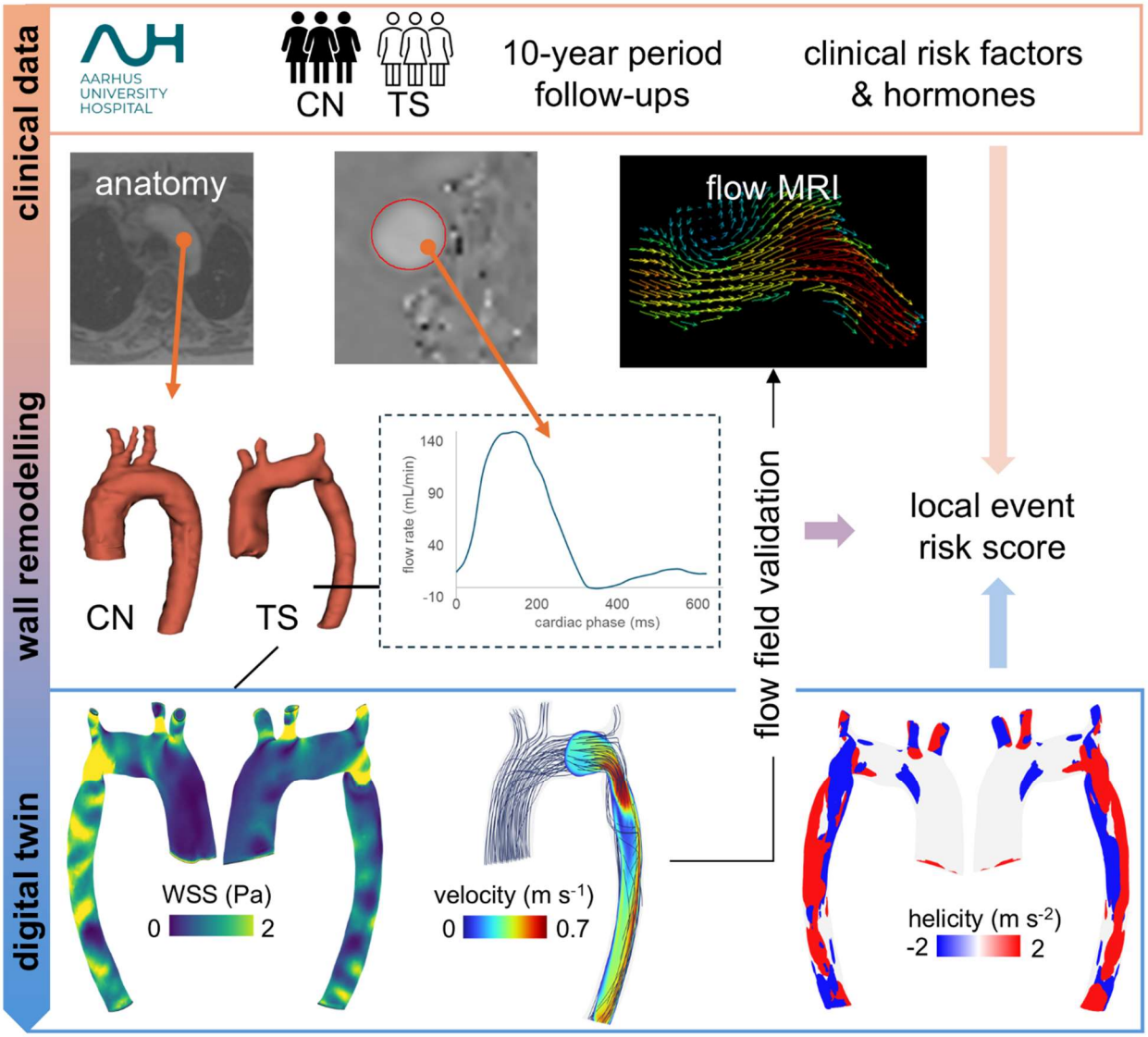
MRI-derived flow measurements were used to validate the computed flow field across multiple anatomical levels of the model [3]. LERS was significantly higher in the TS group, with considerable inter-individual variability. Bicuspid aortic valve and coarctation of the aorta remained strong predictors of elevated risk. The haemodynamic burden and wall remodelling markers were consistent with their known association with adverse cardiovascular outcomes. These findings suggest that combined imaging and modelling

metrics capture clinically relevant differences in cardiovascular risk among women with TS.

Discussion

This study introduced the first integrated model in TS that combines patient-specific moving-boundary CFD-derived hemodynamics, wall remodelling, and clinical history to estimate cardiovascular risk. The results revealed substantial variability in haemodynamic burden among women with TS, reflecting heterogeneity in clinical risk. These findings demonstrate the potential of combined imaging and modelling approaches to inform future strategies for risk stratification and personalised management.

Images (Optional)



References (Optional)

[1] Gravholt, et al., *European Journal of Endocrinology*, 2024

[2] Subramaniam, et al. *Journal of Cardiovascular Magnetic Resonance*, 2017

[3] Bontempi, et al. *Computers in Biology and Medicine*, 2025

Session Category

Cardiovascular/Cardiorespiratory Biomechanics: Methods, Models and Applications

P4-088

Effect of Artery and Tissue Compliance on Oscillometric Blood Pressure Measurement

Mr Muhammad Azhar[1], Dr Zia ul Rehman Tahir[2], Dr Philip Lewis[3,1], Dr Parthasarathi Mandal[1]

[1]The University of Manchester, Manchester, Greater Manchester, United Kingdom. [2]University of Engineering and Technology, Lahore, Punjab, Pakistan. [3]Stockport NHS Foundation Trust, Stockport, Greater Manchester, United Kingdom

Introduction

Oscillometric blood pressure (BP) measurement is a widely used non-invasive technique, but its accuracy is markedly influenced by certain biomechanical factors. Prior studies attempted at examining their influence on oscillometric BP but were limited by uniform pressure transmission assumption [1] and improper representation of arterial mechanics [2]. To address these limitations, our study develops an improved FE model that systematically investigates the effect of surrounding tissue and artery compliance on oscillometric BP.

Methods

Geometry of human upper arm and hyperelastic material properties of brachial artery were sourced from literature [1, 2]. Arterial pressure was modulated to reflect the heart rate of 1.2 Hz and BP of 120/70 mmHg. An FE model in Abaqus® simulated the oscillometric BP measurement by quick arm loading (0 to 150 mmHg) followed by 40s unloading. Oscillometric waveforms were generated by tracking brachial artery lumen area changes for unloading period. For systematic analysis the arterial stiffness was varied from compliant artery (ST1) to stiff artery (ST4) and surrounding tissue stiffness from 30 to 60 kPa [1].

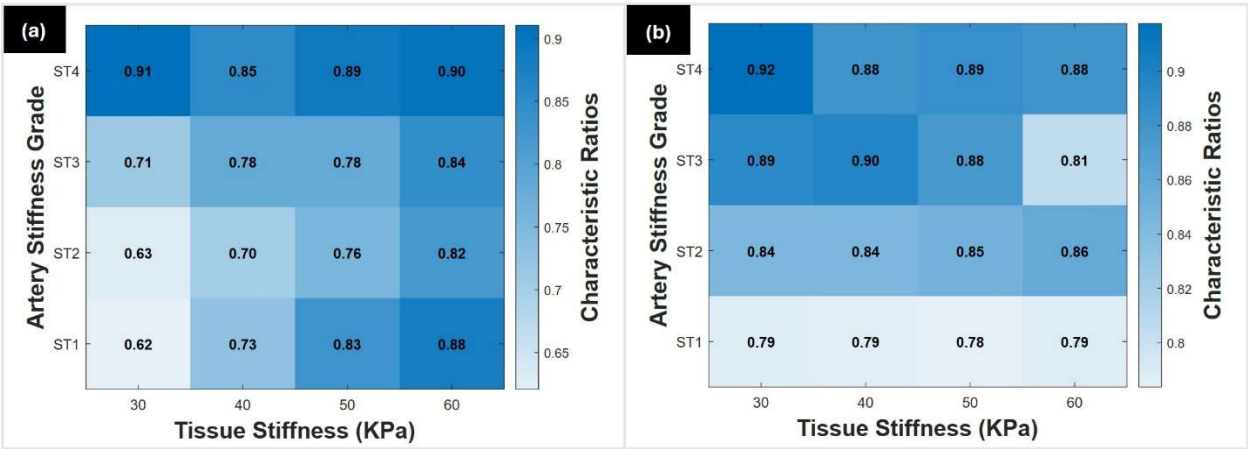
Results

Evaluation of envelope profiles for baseline data showed that the stiff artery produced wide and gradual envelope while compliant artery exhibited steeper one. Maximum amplitude fell at 85.2 mmHg for compliant artery, and 84.48 mmHg for stiff artery; the values were close to MAP of 86.7 mmHg yet differences in envelope shapes indicate potential differences in SBP and DBP estimations. This is further corroborated by systematic analysis of artery and surrounding tissue stiffness that shows variation from 0.62-0.91 for SBP [Figure (a)] and 0.79-0.92 for DBP [Figure (b)] characteristic ratios.

Discussion

Our study accounts for tissue stiffness effect on pressure transmission, a factor overlooked by Ref. [1], and evaluates its effect on oscillometric BP. Further, our proposed model demonstrates the effect of arterial compliance, addressing the limitations of earlier FE model [2], providing insights aligned with clinical evidence. These findings highlight the need to improve design and calibration of BP monitoring devices, to improve clinical accuracy.

Images (Optional)



References (Optional)

[1] Ursino,M. and C.Cristalli, IEEE Transactions on Biomedical Engineering,1996.

[2] Lan, H., et al., Medical engineering & physics,2011.

[3] Bank, A.J., et al., Circulation,1995.

Session Category

Cardiovascular/Cardiorespiratory Biomechanics: Methods, Models and Applications

P4-089

Numerical Investigation of Oscillometric Waveforms Using Non-linear Two-Way Fluid-Structure Interaction

Mr Muhammad Azhar[1], Mr Hafiz Zeeshan Ali Sardar[2], Dr Zia ul Rehman Tahir[2], Dr Philip Lewis[3,1], Dr Parthasarathi Mandal[1]

[1]The University of Manchester, Manchester, Greater Manchester, United Kingdom. [2]University of Engineering and Technology, Lahore, Punjab, Pakistan. [3]Stockport NHS Foundation Trust, Stockport, Greater Manchester, United Kingdom

Introduction

Blood pressure (BP) in oscillometric devices is estimated by detecting pressure oscillations measured by cuff during controlled deflation. Complex interaction between blood flow and arterial deformations, influences these oscillations. Flow variables, such as velocity and pressure, dynamically change as the artery deforms that affects the measured signal; traditional FE [1,2] models assume constant pulse on arterial wall, overlooking this important coupling. To simulate an oscillometric signal considering the two-way interaction of arterial wall mechanics and blood flow dynamics, this study develops a fluid-structure interaction (FSI) model.

Methods

Geometry of human upper arm and brachial artery's hyperelastic properties were selected in consistency with literature [1,2]. A two-way FSI model was implemented in ANSYS, structural deformations were solved in ANSYS Mechanical and ANSYS Fluent was used to determine fluid mechanics; Carreau constitutive model was employed to model blood. Pressure and velocity profiles for flow conditions were accessed from the data bank [3] and BP was setup at 120.5/82.2 mmHg. Arm loading representing cuff pressure was raised from 0 to 150 mmHg followed by 14s deflation; arterial wall deformations were frequently saved to generate lumen area changes and oscillometric waveform.

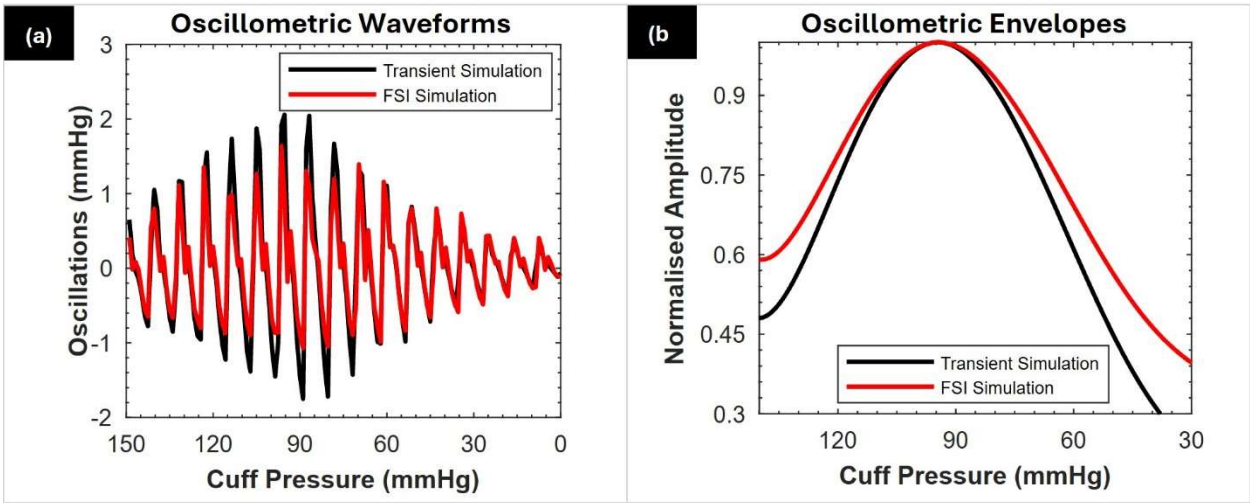
Results

The resulting waveform [Figure (a)] exhibits the expected pattern of gradual increases and decrease, closely resembling the realistic physiological oscillations. Its envelope [Figure (b)] follows a bell-shaped trend, yielding a mean arterial pressure (MAP) estimate of 94.30 mmHg, that is close to actual value of 94.99 mmHg. Comparison with FE model (Transient-Simulation) shows noticeable difference between two; FSI envelopes are wider with gradual transitions.

Discussion

Close agreement of estimated MAP with actual value demonstrates accuracy and reliability of the model. FE model considers constant pulse pressure applied on arterial wall; in FSI model artery's effective pressure is different as structure feedback to fluid domain that results in varied pressure on wall. This effect is not considered in reported literature [1,2]. Overall, the model provides a robust framework for future investigations of flow-related variables and their influence on oscillometric BP.

Images (Optional)



References (Optional)

[1] Azhar, M., et al International Society of Biomechanics (ISB),2025.

[2] Lan, H., et al., Medical engineering & physics,2011.

[3] Willemet, M., British Heart Association, Editor.2015.

Session Category

Cardiovascular/Cardiorespiratory Biomechanics: Methods, Models and Applications

P4-090

Study of Thrombus Adhesion on Fluttering Bioprosthetic Aortic Valve Leaflets

MSc Nataliya Sevryugina, Prof. Dr. Dominik Obrist

ARTORG Center for Biomedical Engineering Research, University of Bern, Bern, Bern, Switzerland

Introduction

Bioprosthetic valve thrombosis (BPVT) is a possible failure mode for bioprosthetic heart valves (BHVs). BPVT could be related to leaflet fluttering [1].

To understand the effect of leaflet fluttering on BPVT, wall shear stress (WSS) patterns are analysed in fluttering and non-fluttering BHV models, as WSS could affect thrombus adhesion.

Methods

Systolic flow in two simplified BHV models (Edwards Intuity Elite and Edwards Perimount) was simulated with a high-fidelity fluid-structure interaction solver [2].

First, the flow was analysed by Lagrangian particle tracing combined with the computation of the Blood Damage Index (BDI). The particles are then categorised into advected, sinus-washout, and lingering particles that remain in the sinus at the end of the systole [1].

Second, WSS was computed on the aortic side of the leaflets. This created a map on the leaflet area indicating where the lingering particles are likely to adhere to the leaflet to form thrombi.

Results

The non-fluttering Perimount valve (<0.5mm amplitude, >200Hz vibrations of the leaflet tips) presents low amplitude WSS with a chaotic and high frequency oscillating pattern. Suggesting the existence of small-scale vortical structures that can trap the thrombi at the end of the systole.

In contrast, in the fluttering Intuity valve (40Hz leaflet fluttering) we found structured WSS with higher amplitudes, that show an oscillatory pattern aligned with the fluttering. This implies larger scale vortical structures that can promote the recirculation on the leaflet and prevent thrombus deposition.

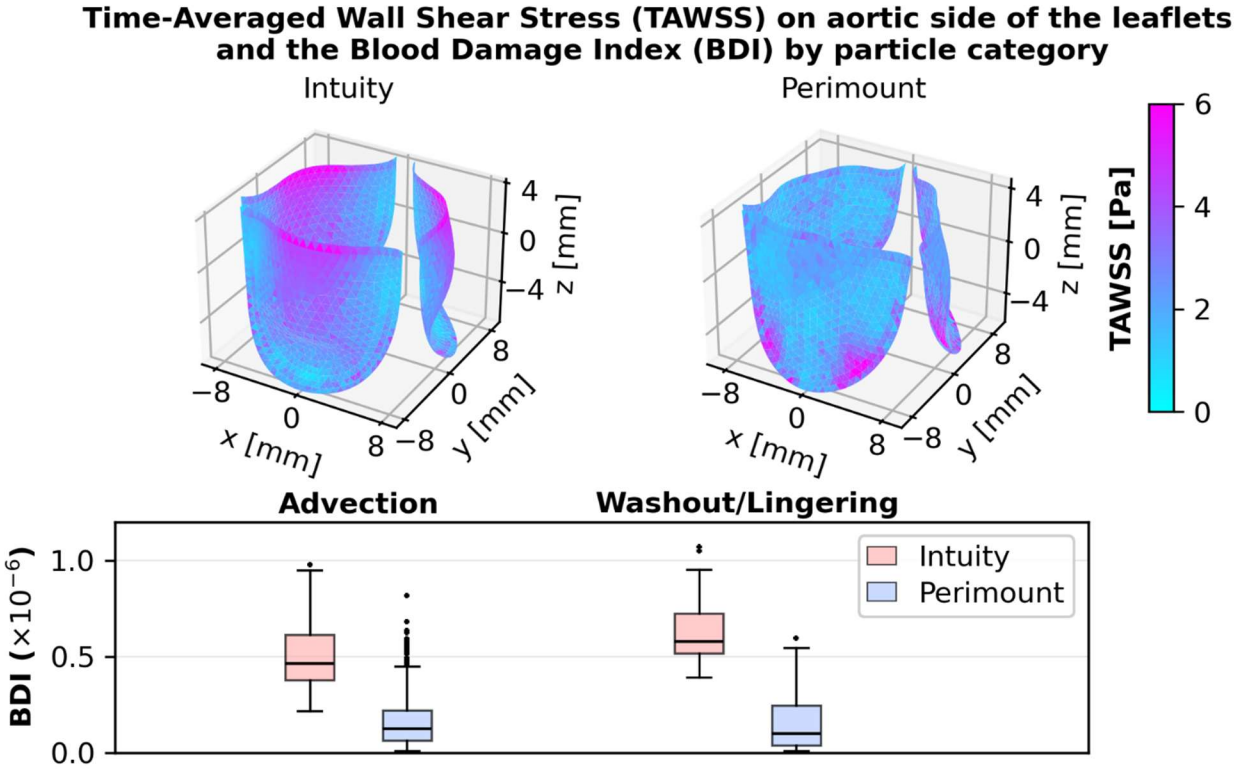
For a single release of 1025 particles, Intuity showed 3.7x higher BDI for advection and 5.9x higher BDI for sinus-washout and lingering, indicating high shear stress experienced by particles.

Discussion

Fluttering does increase WSS, this could be linked to a lower probability of thrombus deposition on the aortic side of the leaflets.

This result makes fluttering a contradictory phenomenon: on the one hand it increases the BDI which favours BPVT, and, on the other hand, fluttering elevates WSS, possibly decreasing the thrombus deposition on the leaflets. Further research will be required to resolve this contradiction.

Images (Optional)



References (Optional)

1. K.M. Bornemann, et al. , Computers in Biology and Medicine, 2024
2. M.G.C. Nestola, B. Becsek, et al. , J. Comput. Phys., 2019

Session Category

Cardiovascular/Cardiorespiratory Biomechanics: Methods, Models and Applications

P4-091

An Automated Method of Centerline Computation in Vascular Anatomies with Loops

Ms. Nhien Tran-Nguyen MASc[1], Dr. Stephen Fremes MD[2,3,4], Dr. Laura Jimenez-Juan MD[5,6,4], Dr. Piero Triverio PhD[1,7,8]

[1]Institute of Biomedical Engineering, University of Toronto, Toronto, Ontario, Canada. [2]Department of Surgery, University of Toronto, Toronto, Ontario, Canada. [3]Sunnybrook Health Sciences Centre, Toronto, Ontario, Canada. [4]Sunnybrook Research Institute, Toronto, Ontario, Canada. [5]Department of Medical Imaging, University of Toronto, Toronto, Ontario, Canada. [6]St. Michael's Hospital, Toronto, Ontario, Canada. [7]Department of Electrical and Computer Engineering, University of Toronto, Toronto, Ontario, Canada. [8]Department of Mechanical and Industrial Engineering, University of Toronto, Toronto, Ontario, Canada

Introduction

The Vascular Modeling Toolkit (VMTK) is an open-source library that enables the processing of cardiovascular models for computational fluid dynamics (CFD) simulations [1]. Crucial to the library's functionality is the computation of centerlines from a surface through the *vmtkcenterlines* method, which traces paths from target points to source points. While this method works well for vascular surfaces with a tree-like topology, it cannot identify all vessels in a loop. In such cases, manual interventions are required to clip and merge multiple centerlines generated separately, increasing the time required to process CFD models. While existing methods like *vmtknetworkextraction* can capture the topology of an arbitrary vessel network, the output is sometimes inaccurate at bifurcations and incompatible with other VMTK methods. In this work, we present an algorithm to automatically compute centerlines in vascular anatomies with loops.

Methods

The *vmtkcenterlines* method utilizes the Voronoi diagram, consisting of many points interior to the original surface. Each Voronoi point is associated with a radius derived from the largest inscribed sphere centered at that point and with a radius-weighted distance to the nearest source point, obtained by solving the Eikonal equation. This distance is used to compute the minimum-energy path from each target point to the nearest source point.

We propose a more general method to detect multiple paths from target to source. Using the centerlines and associated radii, untraced regions of the Voronoi diagram are identified, which represent vessels missing from the centerlines. Based on the Eikonal

solution, new target points are automatically selected to repeatedly compute and merge additional centerlines until the Voronoi diagram is fully traced.

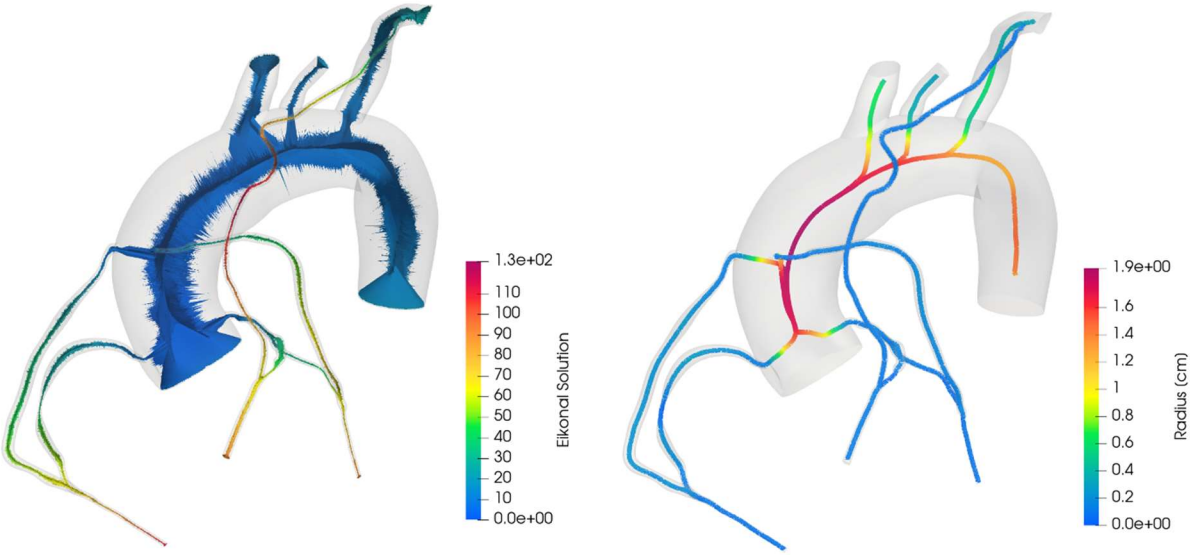
Results

The algorithm was validated on multiple patient-specific models of vascular anatomies with loops, including coronary artery bypass grafts and the Circle of Willis. Centerlines were successfully traced in every vessel for all tested models.

Discussion

An algorithm is presented to compute centerlines from vascular anatomies with loops, requiring no additional user input. Significantly, the generated centerlines are compatible with other VMTK functions, enabling the direct application of state-of-the-art processing tools to a wider range of complex vascular anatomies.

Images (Optional)



References (Optional)

[1] Richard Izzo *et al.*, J Open Source Software, 2018

Session Category

Cardiovascular/Cardiorespiratory Biomechanics: Methods, Models and Applications

P4-092

Fabrication of Calcific Aortic Valve Phantoms for I*n-Vitro* Assessment of Stenosis

Eng Nicoletta Curcio[1], MD Luigi Bernardi[1], Eng Antonio Rosato[1], Eng Fabio Pappalardo[2], Eng Martina Schembri[3], Prof Michele Conti[3], Prof Riccardo Vismara[2], MD Riccardo Gorla[4], MD Pietro Spagnolo[5], MD Lorenzo Menicanti[6], MD Alessandro Parolari[6,7], MD Giacomo Bortolussi[6], PhD Francesco Sturla[1]

[1]3D and Computer Simulation Laboratory, IRCCS Policlinico San Donato, San Donato Milanese, Milan, Italy. [2]Department of Electronics, Information and Bioengineering, Politecnico di Milano, Milan, Milan, Italy. [3]Department of Civil Engineering and Architecture (DICAR), University of Pavia, Pavia, Pavia, Italy. [4]Department of Clinical and Interventional Cardiology, IRCCS Policlinico San Donato, San Donato Milanese, Milan, Italy. [5]Department of Radiology, IRCCS Policlinico San Donato, San Donato Milanese, Milan, Italy. [6]Department of Cardiac Surgery, IRCCS Policlinico San Donato, San Donato Milanese, Milan, Italy. [7]Department of Biomedical Sciences for the Health, Università Degli Studi Di Milano, Milan, Milan, Italy

Introduction

Aortic stenosis (AS) is characterized by leaflet thickening and calcification, which markedly increase stiffness and restrict cusp mobility, ultimately reducing the aortic valve area (AVA) and increasing transvalvular pressure gradients (ΔP) [1]. Preclinical evaluation of new valvular prostheses as well as the optimization of existing devices and implantation strategies, require *in vitro* benchmarking under controlled and reproducible hemodynamic conditions. We proposed a methodology to fabricate stenotic aortic root (AR) phantoms and reproduce the *in vitro* hemodynamic AS conditions.

Methods

A parametric AR model was reconstructed from averaged computed tomography angiography (CTA) measurements of 40 patients with small aortic annuli and severe AS (Fig.1a). Modular molds were designed from this geometry (Fig.1b-c), 3D-printed and filled with silicone (Fig.1d). Calcifications (50 vs. 100 mg) were reproduced by embedding calcium phosphate crystals into the leaflet during silicone casting, while the resulting fusion of leaflet free-margin was fully or partially (50%) released. Four AR phantoms (AR1-AR4) were fabricated and tested for three repeated sessions in a pulsatile mock circulatory loop (heart rate, 60 bpm; stroke volume, 70 mL; systolic/diastolic pressures, 120/80 mmHg). ΔP was measured using pressure transducers while AVA was recorded and quantified employing a downstream camera. Compression tests quantified the mechanical response of the silicone-calcium mixture.

Results

Both calcium content and free-margin incision impacted on the hemodynamic behaviour of the tested AS configurations, with the pattern of free-margin incision being the predominant factor. Phantoms AR1, AR2 and AR4 reproduced hemodynamic conditions clinically consistent with moderate to severe AS severity (mean ΔP, 33-56 mmHg; AVA, 0.6-1.9 cm) [2]. AR3 (100 mg calcium load, full-margin incision) showed decreasing ΔP and increasing AVA. The silicone-calcium composite exhibited stiffness values (0.3-2 MPa) comparable to *ex vivo* calcified leaflet tissue [3]. The overall material cost per model is inferior to € 3.

Discussion

This methodology enables reproducible and low-cost fabrication of stenotic AR phantoms that reproduce the hemodynamic of AS. Our experimental framework makes the models a valuable tool for preclinical device testing, procedural planning, and surgical training.

Images (Optional)

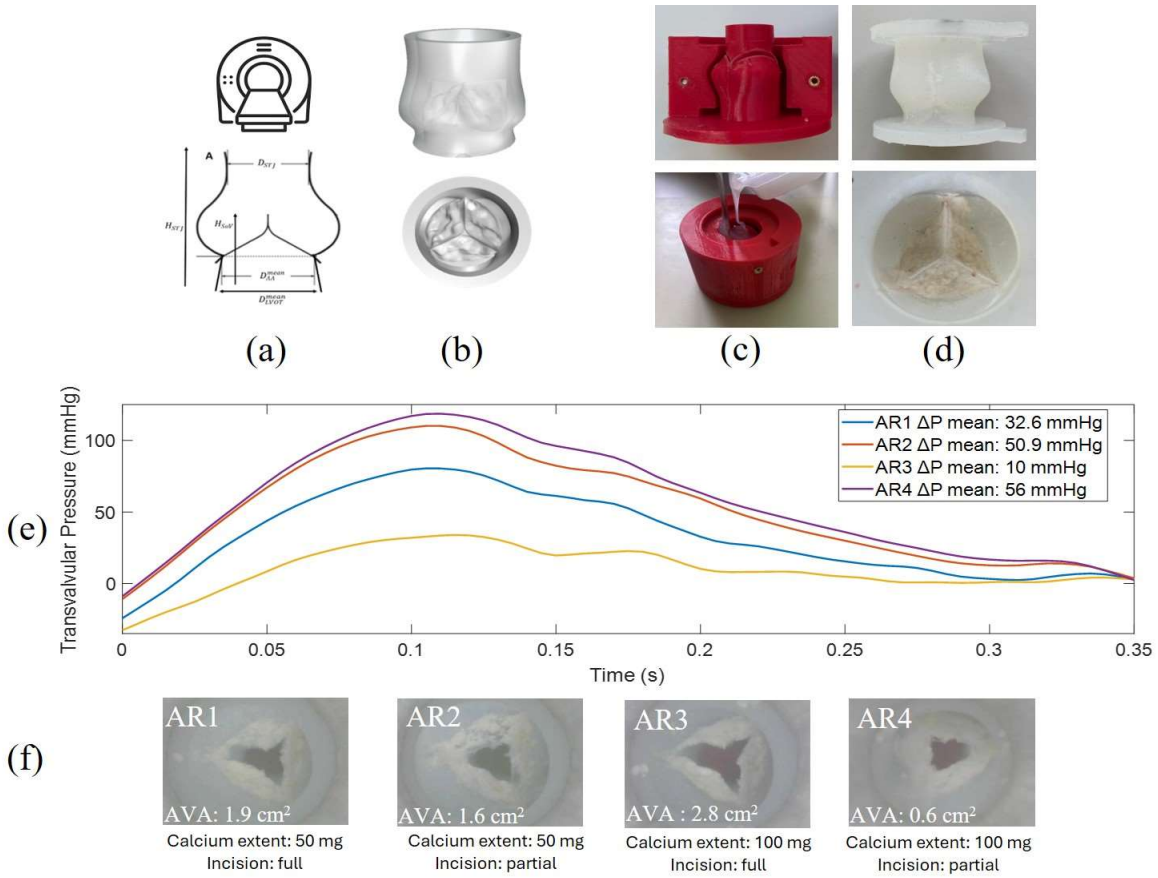


Figure. Framework for the modelling and fabrication of AR phantoms for in-vitro assessment of AS hemodynamics. (a) Geometric parameters were extracted from CTA data to generate (b) the 3D digital AR model. (c) Molds were designed for silicone casting, enabling (d) fabrication of the final AR phantoms, including calcifications .The phantoms were then tested in vitro, recording (e) mean systolic transvalvular pressure gradients, averaged over six cardiac cycles, and (f) the valve leaflets configurations at systolic peak.

References (Optional)

[1] Freitas-Ferraz *et al.*, Circulation, 2019

[2] Praz *et al.*, Eur Heart J, 2025

[3] Shirakawa *et al.*, Ann Biomed Eng, 2025

Acknowledgements (Optional)

This study was supported by the PNRR-MCNT2-2023-12378350 project, funded within the national recovery and resilience plan promoted by the Italian Ministry of Health.

Session Category

Cardiovascular/Cardiorespiratory Biomechanics: Methods, Models and Applications

P4-093

Computational Fluid Dynamics Aided Hemodynamic Analysis of Transarterial Radioembolization Treatment

Dr Nisanth Kumar Panneer Selvam Ph.D

University of California Davis, Davis, California, United States

Introduction

Liver cancer remains one of the leading causes of cancer-related deaths worldwide. Transarterial radioembolization (TARE) is a well-established minimally invasive procedure in which Y^{90} microspheres are injected through the hepatic artery to deliver targeted radiation to tumors. However, treatment outcomes are highly dependent on complex patient-specific hemodynamics that govern microsphere transport and deposition. High-fidelity computational fluid dynamics (CFD) simulation is a promising method to enhance TARE outcomes by pretreatment planning, yet still facing modeling and computational challenges to achieve high fidelity [1]. This study presents a CFD-based hemodynamic analysis designed to predict blood flow behaviour and microsphere transport during selective and lobar TARE injections.

Methods

The patient-specific 3D geometric model of hepatic artery tree is generated from the cone beam computed tomography (CBCT) images (Fig 1(a)). Tumor feeding artery is marked in red in Fig 1(a). The reconstructed 3D hepatic arterial tree was imported into COMSOL Multiphysics environment for meshing and blood-flow CFD analysis. The material property of the blood is considered as Newtonian incompressible fluid with density and viscosity as 1.06 g cm^{-3} and 0.04 g cm^{-1} s^{-1}, respectively [1]. The complex flow field within patient-specific hepatic artery tree was obtained by solving Navier-Stokes equations. Microsphere transport was modelled using two-way coupling (particle fluid interaction). The number of microspheres injected during selective and lobar injection was set to 547200 and 645800, respectively based on our previous patient studies [2].

Results

The results show that selective injection alters the blood flow more strongly than the lobar injection, as shown in the streamline plot of Fig 1(b). This flow disturbance develops higher

Time Averaged Wall Shear Stress (TAWSS) on the tumour feeding artery wall, as shown in Fig 1(c).

Discussion

The effects of flow disturbance created during selective injection influence the TAWSS developed on the tumour feeding artery. The results demonstrate that patient-specific hemodynamics analysis using CFD simulation could enhance the pretreatment planning of TARE by estimating the flow modifications in the tumour feeding artery after injection of microspheres.

Images (Optional)

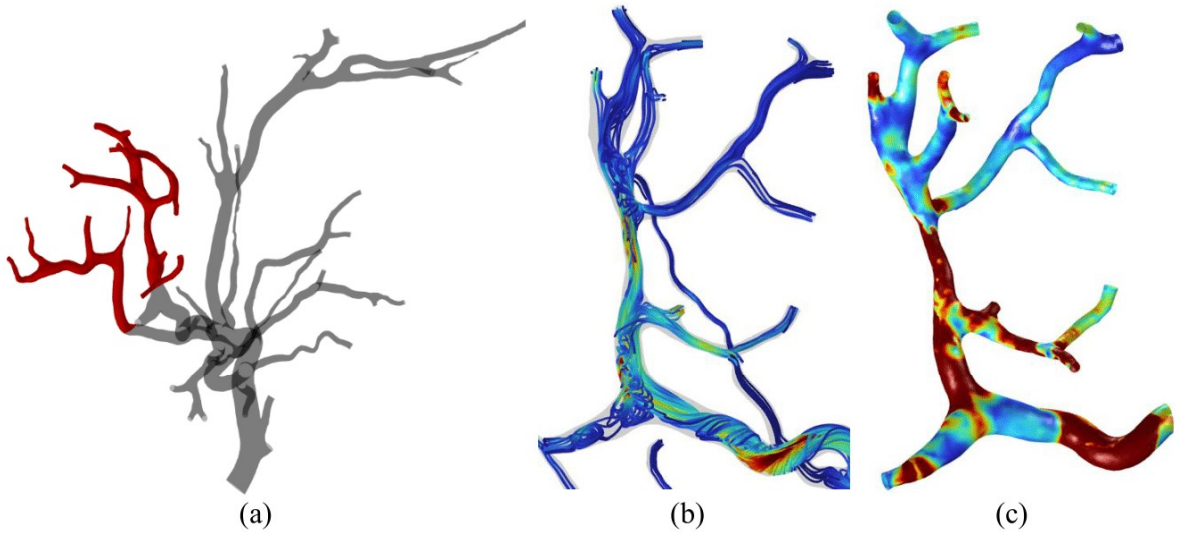


Fig 1. (a) Generated 3d model of hepatic artery tree. (b) Streamline plot after selective injection. (c) TAWSS developed after selective injection

References (Optional)

[1] A. Taebi et al. , *J. Vasc. Interv. Radiol.*, 2022,

[2] E. Roncali et al. , *Ann. Biomed. Eng,* 2020.

Acknowledgements (Optional)

This work is funded by the NCI ITCR grant U01CA289068". The authors thank Dr. Amirtaha Taebi for the segmentation of the hepatic arterial structure.

Session Category

Cardiovascular/Cardiorespiratory Biomechanics: Methods, Models and Applications

P4-094

Personalized Cerebrovascular Modeling: Comparing Generalized and Patient-Specific Boundary Condition Approaches for Sickle Cell Disease

Miss Lara Abdelmohsen, Mr. Joel Dis, Mr. Nahom Mossazghi, Miss Elizabeth Meinert-Spyker, Dr. Sossena Wood, Dr. Noelia Grande Gutiérrez

Carnegie Mellon University, Pittsburgh, PA, United States

Introduction

Accurate cerebral hemodynamic modeling depends critically on physiologically realistic boundary conditions (BCs). However, many computational studies of the Circle of Willis (CoW) rely on generalized assumptions of total cerebral blood flow (CBF) distributions, or lumen-area-based flow splits, rather than patient-specific perfusion data. These simplifications may limit the accuracy and clinical relevance of predicted hemodynamics, particularly in disease cases where the microvasculature may be compromised. In this work, we evaluate how different methods for determining outlet BCs influence simulated pressure drops from inlets to outlets in different vascular territories, time-averaged mean of the maximum velocity (TAMMV), outlet mean flow, and spatially resolved time-averaged WSS (TAWSS) across patient-specific cerebrovascular models.

Methods

A healthy control and a patient with sickle cell disease (SCD) post-stroke were included in this study. For each subject, we generated 3D models of the CoW in SimVascular and ran simulations using three different methods to prescribe outlet BCs: (1) ASL-based, using territorial perfusion from arterial spin labeling (ASL); (2) area-based, distributing total CBF by outlet lumen area; and (3) volume-based, distributing CBF by the relative volume of each vascular territory using a vascular territory atlas. Flow waveforms measured using phase contrast MRI were prescribed at the inlets.

Results

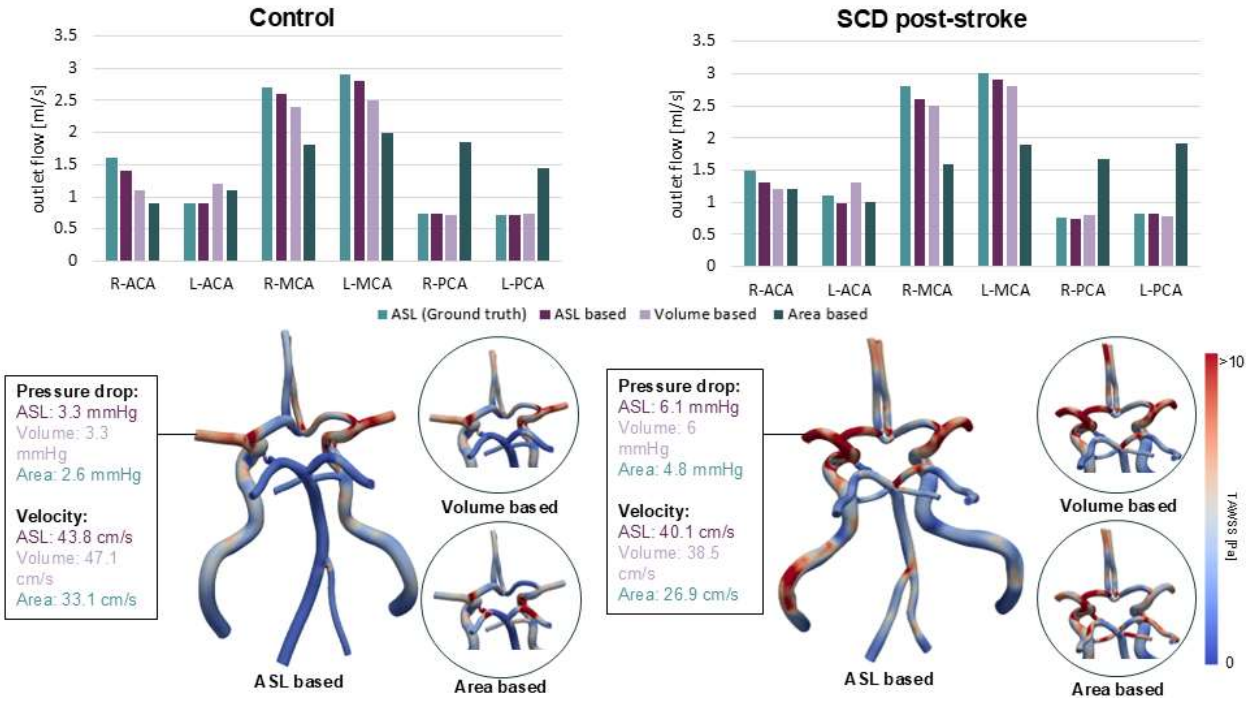
Across both subjects, volume-based BCs best reproduced ASL-derived pressure drops, with errors typically within 1–14%. Area-based BCs showed much larger pressure-drop deviations, particularly in the posterior circulation (−38% to −130%). For outlet flows, volume-based BCs again closely matched ASL perfusion (<14% error), while area-based BCs produced large posterior flow errors, often exceeding 100%. TAMMV in the MCA followed the same pattern: volume-based BCs remained within ~8% of ASL values, whereas area-based BCs deviated by up to 33%. Spatially resolved TAWSS maps from

volume-based and ASL-based simulations were similar, while area-based BCs overestimated anterior TAWSS.

Discussion

These findings show that area-based BCs can substantially distort cerebrovascular hemodynamics, whereas territorial volume-based BCs provide a more accurate and practical surrogate for patient-specific perfusion when perfusion imaging is unavailable. This comparison highlights the importance of physiologic BC selection in patient-specific cerebrovascular modeling, particularly for diseases such as SCD, with altered regional perfusion.

Images (Optional)



Session Category

Cardiovascular/Cardiorespiratory Biomechanics: Methods, Models and Applications

P4-095

A Closed Loop 2D Hemodynamic and Thermoregulation Model for Total Circulating Blood Volume Estimation in Circulatory Systems

Msc. Noëlle Gerards, Dr. Simona Turco, Prof. Dr. Frans van de Vosse, Dr. Marcel Rutten

Eindhoven University of Technology, Eindhoven, Noord-Brabant, Netherlands

Introduction

Accurate assessment of the total circulating blood volume (TCBV) is clinically important for managing trauma, major surgery and acute heart failure. Thermodilution is widely used for cardiac output measurement and enables TCBV estimation when both first-pass and recirculating thermodilution curves (TDCs) are captured [1]. However, this approach overestimates volumes [2], indicating that interpreting these TDCs requires models describing the spatiotemporal transport of an injected cold bolus.

Existing thermoregulation models often assume a centralized blood pool and do not represent TDC dynamics, while convection–diffusion models typically focus on small vascular segments. So, no suitable model exists for analyzing TDC measurements.

Methods

We developed a novel two-dimensional coupled circulation–thermoregulation model simulating a cold bolus traveling through a closed-loop circulation under steady flow conditions. The model describes axial convection, vessel wall heat exchange and radial diffusion while prescribing a developing velocity profile (Fig. 1a).

Model results were compared to experimental TDCs obtained from a mock circulatory loop (MCL) during cold bolus injections using a clinically accepted thermometer (Fig. 1a). The MCL consists of a centrifugal pump connected to flexible tubing. Measurements were performed at 37°C with varying total circulating volume (1-5L, 1L increments) and injection volumes.

Results

The mathematical model accurately reproduced the experimentally observed TDCs, capturing both their timing and amplitude (Fig. 1b). The model results agreed closely with the measurements. Deviations at the downslope of the TDCs were attributed to additional diffusion in the experimental setup.

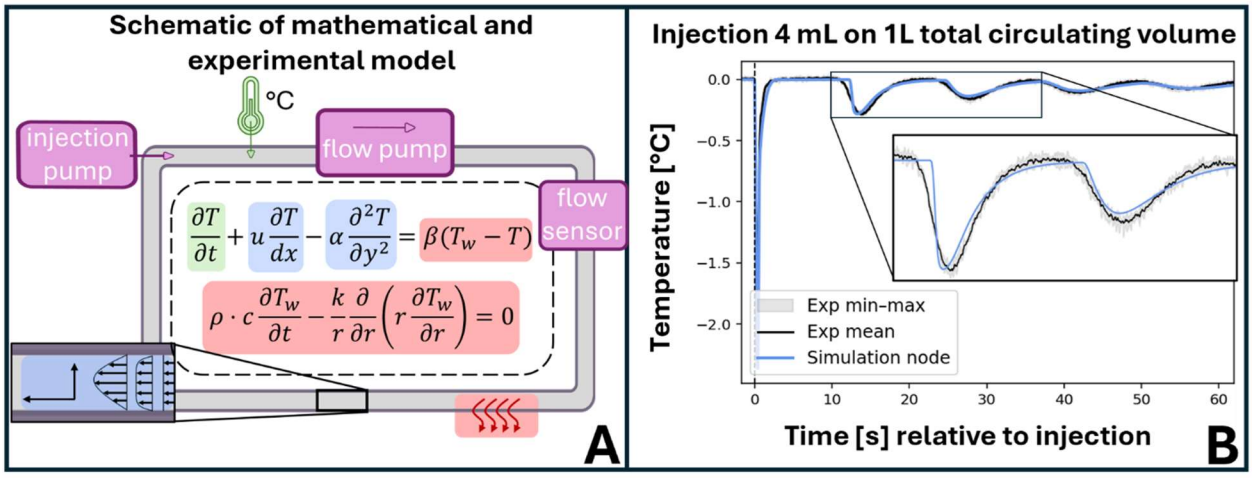
The model reproduced the experimental temperature transients with a mean RMSE of 0.087°C (R=0.97). This RMSE was higher than the inter-experiment RMSE (0.045°C),

reflecting the consistency of experiments and indicating the model performed close to the reproducibility limit of the experimental measurements. This confirms that the model captures essential TDC dynamics.

Discussion

This first closed-loop model describing full thermodilution bolus dynamics including recirculation, was successfully validated in an MCL. The model provides a useful tool to interpret and optimize future thermodilution-based TCBV assessment and is a first step towards TCBV measurements in vivo.

Images (Optional)



References (Optional)

[1] N.P.C.M. Gerards *et al.* , IEEE MeMeA, Eindhoven, Netherlands, 2024

[2] I.H. Herold *et al.* , Cardiovascular Ultrasound, 2013

Session Category

Cardiovascular/Cardiorespiratory Biomechanics: Methods, Models and Applications

P4-096

Quantifying Thrombogenic Shear Stress Distributions in Carotid Artery Web Patients Using Computational Fluid Dynamics Simulations

Mr. Patrick Jones M.S.[1], Dr. Retta El Sayed Ph.D.[1], Dr. Stephane Olindo M.D.[2], Dr. Diogo Haussen M.D.[3], Dr. Jason Allen M.D. Ph.D.[4], Dr. John Oshinski Ph.D.[1]

[1]Emory University School of Medicine/Georgia Institute of Technology, Atlanta, GA, United States. [2]University Hospital of Bordeaux, Bordeaux, Gironde, France. [3]Emory University School of Medicine, Atlanta, GA, United States. [4]Indiana University School of Medicine, Indianapolis, IN, United States

Introduction

Carotid artery web (CaW) is an important cause of embolic stroke in young patients without traditional vascular risk factors [1]. CaW is a shelf-like projection into the proximal internal carotid artery lumen which creates a pocket region distal to the shelf where clots form [2, 3]. In this study, we quantified shear rate (SR) in 20 CaW patients with clots using computational fluid dynamics (CFD) simulations to assess thrombosis risk.

Methods

Paired CT angiography (CTA) studies from two clinical sites were acquired in 20 CaW patients (18 female, mean age 51) -- one study during initial symptomatic presentation with CTA-confirmed clot superimposed in the web pocket ("*clot*" scan) and one without superimposed clot ("*no-clot*" scan). *Clot* and *no-clot* images were co-registered non-linearly to identify the clot volume (FSL v.6.0.7). CFD simulations were performed in the *no-clot* scans for each patient (SimVascular v.2023.03.27). Segmented clot volumes from the *clot* scans were superimposed over CFD results, and the carotid wall area in direct contact with the clot volume was isolated. Within this clot-wall region, we identified the contiguous patch of 100x100 μm where peak SR over the full cardiac cycle was minimized. SR below 100 s^{-1} was chosen as our thrombogenic threshold [4].

Results

Across 20 patients, SR in the clot-wall region remained low during diastole (mean 72.5 ± 56.1, max 359.0 ± 306.7) but increased during systole (mean 155.1 ± 145.0, max 644.6 ± 563.5). In the 100x100 μm minimum SR region, SR remained below 100 s^{-1} across the cardiac cycle (mean 24.3 ± 18.7, peak systole 29.6 ± 22.9).

Discussion

Spatial correlation of SR with known clot-vessel wall contact regions allowed us to assess SR values associated with cot formation in CaW patients. We examined SR in a small region within the clot-wall with low SR values across the entire cardiac cycle to identify potential nidus regions for thrombosis initiation. SR metrics may help guide clinical intervention to prevent stroke in CaW patients.

Images (Optional)

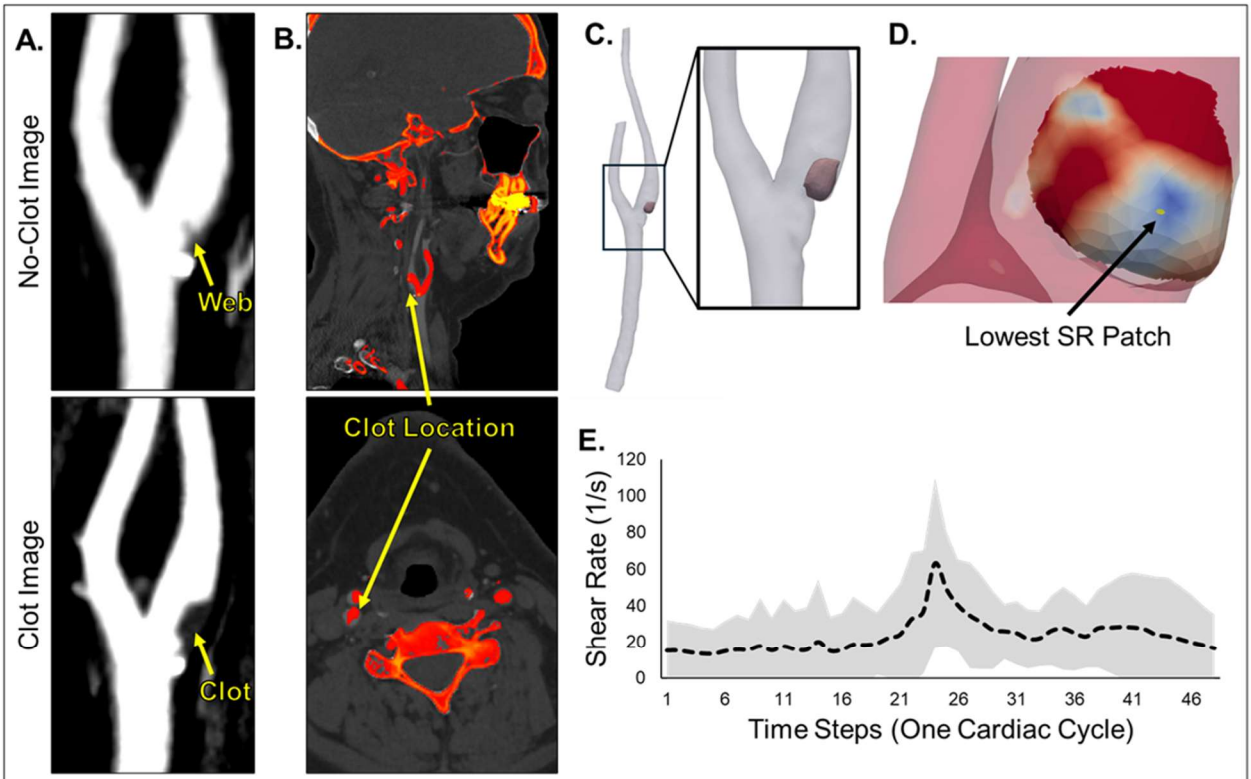


Figure 1: (**A**) Paired head and neck CTA studies showing carotid web morphology alone (*top*) and with superimposed clot (*bottom*). (**B**) Visualization of non-linear registration of *clot* volume in red with *no-clot* volume in grayscale. (**C**) Example location of clot in carotid bifurcation. (**D**) Shear rate (SR) visualized across the clot-wall interface with lowest SR patch highlighted. (**E**) SR vs time in lowest SR patch across 20 patients

References (Optional)

[1] Chen, H. *et al.*, J Neurointerv Surg, 2024

[2] El Sayed, R. *et al.*, Sci Rep, 2024

[3] El Sayed, R. *et al.*, J Magn Reson Imaging, 2024

[4] Goel, M.S. *et al.*, Blood, 2002

Session Category

Cardiovascular/Cardiorespiratory Biomechanics: Methods, Models and Applications

P4-097

Automated Breath Detection in Infants Using 1-Dimensional Convolutional Autoencoder

Mr Paul Bokelman, Ms Holly Olvera, Dr Erin Mannen, Dr Clare Fitzpatrick

Boise State University, Boise, Idaho, United States

Introduction

Lack of foundational knowledge in the relationship between respiratory and biomechanical factors (e.g., body position in seated inclined products) likely contributes to avoidable deaths attributed to sudden expected infant death (SUID). Collecting biomechanics and respiratory data from infants can help elucidate these relationships. CO_2 waveforms and chest expansion biomechanics offer a rich representation of respiratory behavior. However, these studies generate large volumes of data (i.e., temporal data streams), making it time-intensive to manually annotate individual breaths. Automated techniques capable of learning and identifying normative patterns could substantially accelerate analysis and improve the reliability of infant respiratory assessment.

Methods

Five infants were placed supine in two conditions: 0° flat (baseline) and 45° thoracic flexion, representative of common infant products. For each infant we collected end-tidal carbon dioxide (EtCO2) using a Medtronic Capnostream 35 and positional chest data of 23 reflective markers using an eight-camera motion capture system during 2-5 minutes of calm breathing. A manual observer extracted “normative” breaths from the CO_2 waveform (clean peaks with sufficiently long plateaus) to generate training data. A 1-dimensional convolutional autoencoder was trained to reconstruct normative breathing patterns with a threshold-based classifier constructed from the 95^{th} percentile of validation reconstructions being used to classify future samples (Fig-1A).

Results

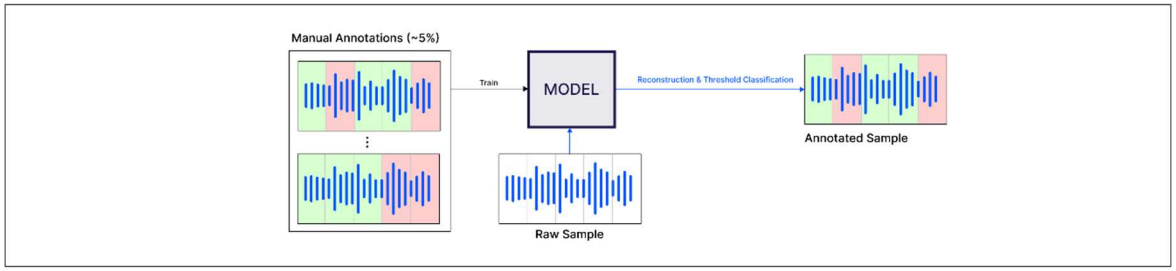
The model successfully identified normative CO_2 breathing patterns, with mean validation reconstruction error of 0.00262 for normal units. Using a conservative threshold-based classifier (MSE<0.00079), the model achieved 93.2% accuracy for normal units (Fig-1B) and 100% accuracy for abnormal units. Mean reconstruction error was 0.000335 for normal units and 0.033617 for abnormal units. 11.2 hours of data was classified in just 0.59 seconds.

Discussion

Our novel approach provides researchers with a tool to efficiently and reliably annotate large volumes of respiratory and biomechanics data, facilitating faster and more accurate analysis of infant respiration. We are extending this framework to automatically synchronize CO_2 waveforms with motion-capture chest expansion data, enabling data-driven investigation of relationships between respiratory and biomechanical factors. Ultimately, our objective is to generate robust, high-volume data that will support product design improvements that will reduce preventable infant mortality.

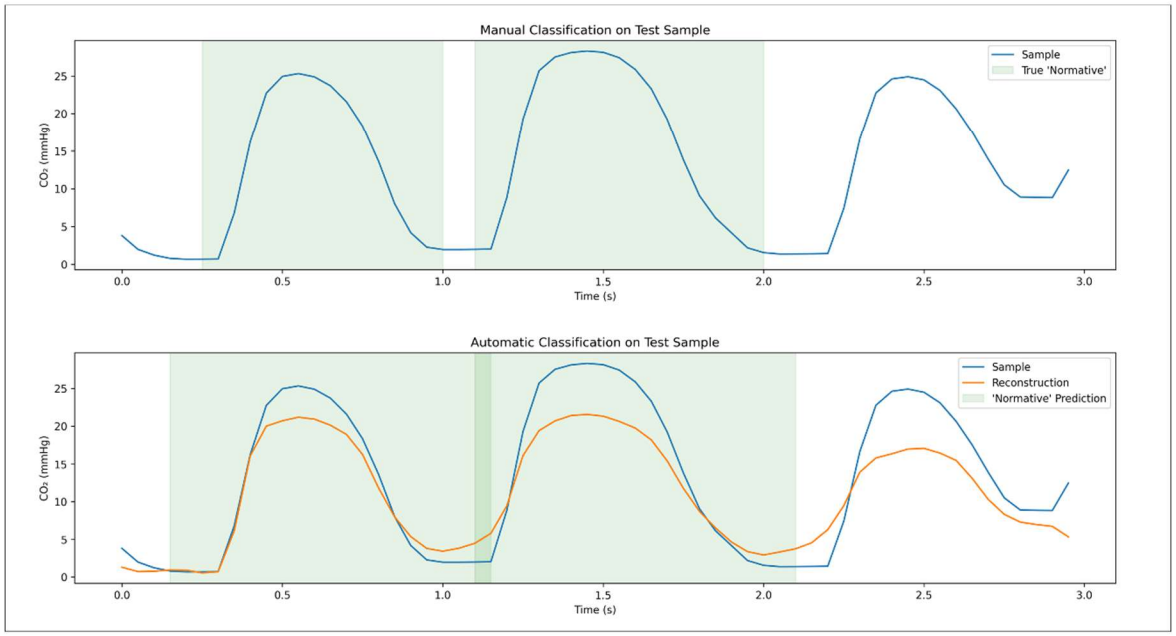
Images (Optional)

FIGURE 1A



Data pipeline and model flowchart showing the process of going from a raw sample to an automatically annotated sample.

FIGURE 1B



Comparison of a manually annotated sample to the same sample with automatic classification and its reconstruction.

Acknowledgements (Optional)

This research is supported by the National Institutes of Health, Eunice Kennedy Shriver National Institute of Child Health and Human Development, NIH Grant No. 1R01HD113921. EMM owns Mannen Bio, LLC, an engineering and expert consulting company.

Session Category

Cardiovascular/Cardiorespiratory Biomechanics: Methods, Models and Applications

P4-098

In-Silico Analysis of Tensile and Compressive Stress-Strain in Idealized Arteries

Undergraduate Student Unnathi Peri[1], Ph.D. Student Paulina Trevino[1], Postdoctoral Associate Jeremy Warren Ph.D.[2], Professor of Instruction Clark Meyer Ph.D.[1], Associate Professor Heather Hayenga Ph.D.[1]

[1]University of Texas at Dallas, Richardson, Texas, United States. [2]Yale University, New Haven, Connecticut, United States

Introduction

Atherosclerotic plaque rupture is a primary trigger of fatal cardiovascular events. Because rupture occurs in regions of high mechanical stress, characterizing arterial stress–strain patterns is essential for identifying rupture-prone regions [1]. Our laboratory previously examined arterial curvature using IVUS imaging, evaluating effective von Mises stress and Lagrange strain. However, this work did not assess how circumferential plaque location in curved arteries affects loading and rupture risk. This study aims to analyze stresses and strains in curved, idealized arteries across various curvature parameters.

Methods

The model contains two arterial layers, adventitia and media, and a homogeneous plaque layer of either necrotic core or calcium. Each layer was assigned physiologically relevant material properties [3]. A 120-mmHg load was applied to simulate blood pressure.

185 simulations were run with combinations of six percent-stenosis values, four curvature magnitudes, and nine curvature directions. For each simulation, median von Mises stress, Lagrange strain, and axial and radial tensile–compressive components were computed [4, 5].

Results

Preliminary results show that increasing percent stenosis decreases effective stress–strain in the arterial wall. Plaques on the outer curvature exhibited lower stress–strain magnitudes, while plaques on the inner curvature experienced higher loading, primarily compressive.

Discussion

The decrease in stress–strain with increasing stenosis suggests redistribution of mechanical loading into plaque regions, consistent with prior work [6]. The influence of circumferential plaque location aligns with angiography-based findings showing plaque

accumulation along the inner curvature where mechanical stresses are elevated [7]. These trends suggest that compressive loading may drive rupture mechanisms for plaques on the inner curvature, whereas tensile loading may be more relevant for plaques on the outer curvature.

Limitations include mesh density and plaque-generation variability. Future work will refine mesh resolution and plaque modeling to verify these trends.

References (Optional)

[1] C. Costopoulos et al., JACC Cardiovascular Imaging, 2017

[2] J. Warren et al., Frontiers in Medical Technology, 2022

[3] P. Paritala et al., Engineering Fracture Mechanics, 2018

[4] FEBio Documentation, FEBio Theory Manual, 2021

[5] K. Gashi et al., J Biomechanics, 2018

[6] D. Tang et al., J Biomechanical Engineering, 2004

[7] O. Smedby et al., Atherosclerosis, Thrombosis, and Vascular Biology, 1995

Session Category

Cardiovascular/Cardiorespiratory Biomechanics: Methods, Models and Applications

P4-099

Multi-scale Hemodynamic Finite Element and Agent-Based Modeling Framework with Estrogen-Related Factors in Atherogenesis

PhD Student Paulina Trevino[1], Postdoctoral Associate Jeremy Warren PhD[2], Undergraduate Student Unnathi Peri[1], Professor of Instruction Clark Meyer PhD[1], Associate Professor Heather Hayenga PhD[1]

[1]The University of Texas at Dallas, Richardson, TX, United States. [2]Yale University, New Haven, CT, United States

Introduction

Cardiovascular disease remains the leading cause of mortality in the United States, largely by plaque rupture. Because plaque rupture is influenced by both mechanical and biological factors, attention has turned on molecular regulators such as the sex hormone 17β-estradiol, shown to have cardio-protective effects [1]. Although hormone replacement therapy may slow disease progression, the continued high incidence of major adverse cardiovascular events after acute coronary syndrome highlights the need for more individualized therapeutic strategies. Our laboratory developed CAFe [2], an in-silico framework integrating agent-based modeling (ABM), computational fluid dynamics, and finite element analysis. To enhance predictive power, we propose an optimized 3D-multiscale computational approach incorporating hormones to understand their impact in plaque behavior. We hypothesize that integrating sex hormone dynamics into CAFe will reveal critical mechanisms driving plaque remodeling.

Methods

We will conduct a literature review to extract quantitative relationships describing estrogen's effects on endothelial function and inflammatory signaling. Dose-response curves will be generated using candidate functional forms and selected on goodness-of-fit criteria. Fits from literature-derived in-vitro data provide quantitative equations that are implemented directly in the ABM. These biological updates then modify the mesh geometry, leading to recalculated mechanical and hemodynamical measurements.

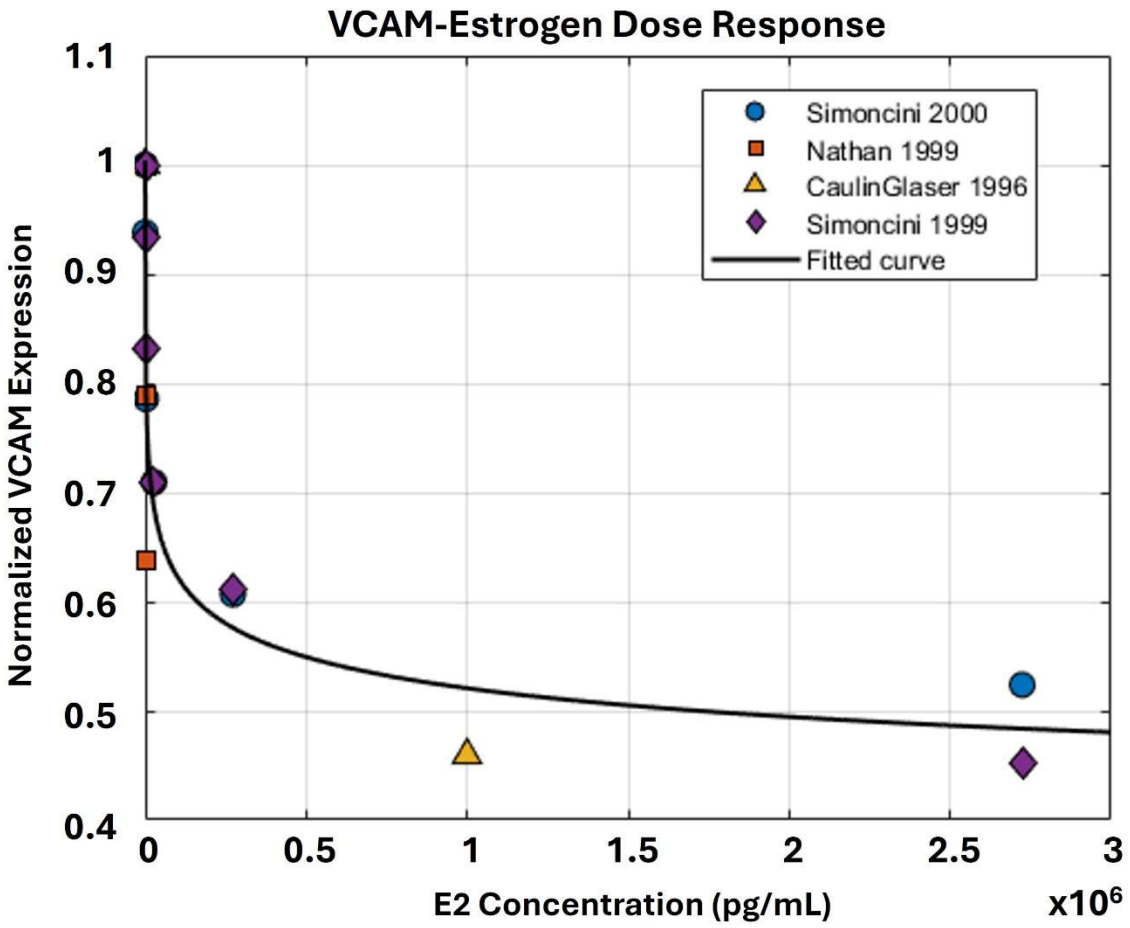
Results

Preliminary results suggest a potential correlation, using the regression model established from the data presented in Figure 1; higher circulating estrogen levels correspond to a decrease in atherogenic processes. This relationship supports the hypothesis that estrogen exerts protective effects on vascular endothelial function, potentially by reducing inflammatory signaling or modulating leukocyte trans-endothelial migration.

Discussion

The early observations highlight a biologically plausible mechanism which estrogen may contribute to improved vascular health. A limitation is potential biological mismatch when integrating heterogenous datasets; sensitivity analyses will be used to assess robustness. Future work will extend the framework to additional sex hormones, advancing CAFe toward a comprehensive, sex-specific hormonal platform.

Images (Optional)



$$\text{VCAM}-1\ \text{Expression} = 1.004 + (0.3318 - (1.004))/(1 + (\frac{E2}{39710})^{-0.2912})$$

Figure 1. ABM rule for 17β-estradiol modeled as a function of VCAM-1 expression on endothelial cells [3-6]. VCAM-1 expression was normalized to the baseline value at E2 = 0 within each respective group.

References (Optional)

1. E. Morselli, *et al.,* Nat Rev Endocrinol, 2017
2. J. Warren *et al.,* J Biomechanics, 2025
3. L. Nathan *et al.,* Circulation Research, 1999
4. T. Caulin-Glaser *et al.,* J Clinical Investigation, 1996
5. T. Simoncini *et al.,* J Clinical Endocrinology & Metabolism, 1999
6. T. Simoncini *et al.,* Circulation Research, 2000

Session Category

Cardiovascular/Cardiorespiratory Biomechanics: Methods, Models and Applications

P4-100

Small Changes in Venous Tube-Laws Significantly Alter Flow Patterns: Insights From 1D Modeling

MSc. Pauline Haulez[1], Dr. Marcel Rutten[1], Dr. Arjen van der Horst[2], Dr. Wouter Huberts[1]

[1]Eindhoven University of Technology, Eindhoven, Noord-Brabant, Netherlands. [2]Royal Philips, Eindhoven, Noord-Brabant, Netherlands

Introduction

Venous hemodynamics are strongly influenced by small perturbations in anatomy and physiologic state, making diagnosis of venous diseases difficult. Respiration induces changes in abdominal pressure, altering the cross-sectional area of abdominal veins [1], which leads to distinct flow patterns in the infrarenal inferior vena cava (IVC) of healthy volunteers: cardiac-driven, respiration-driven, and a combination of both.[2] How this respiratory–cardiac interplay exactly shapes flow patterns is still not fully understood. To address this, a 1D wave propagation model capturing venous collapse, valves, respiratory-induced transmural pressure and right atrial pressure is developed to investigate how mechanical properties influence collapse and flow patterns under respiratory pressure variations.

Methods

The Shapiro tube-law [3] is applied to capture the transmural pressure-area relation:

$P_{tr}=K_v(\alpha^m-\alpha^{-3/2})$, $\alpha=A/A_0$

With m, a fitting parameter, set to 10, and K_v the effective stiffness. Parameter Kv is scaled with vessel radius, resulting in stiffnesses ranging from 153 Pa (IVC) to 814 Pa (small veins).[4] Figure 1A illustrates the tube-laws for these stiffnesses, showing that increasing K_v from 200 Pa to 800 Pa decreases the amount of collapse at -10 mmHg from 70% to 30%, relative to A_0. To assess the effect of increased stiffness on flow patterns, all stiffness values in the system are increased fourfold.

Results

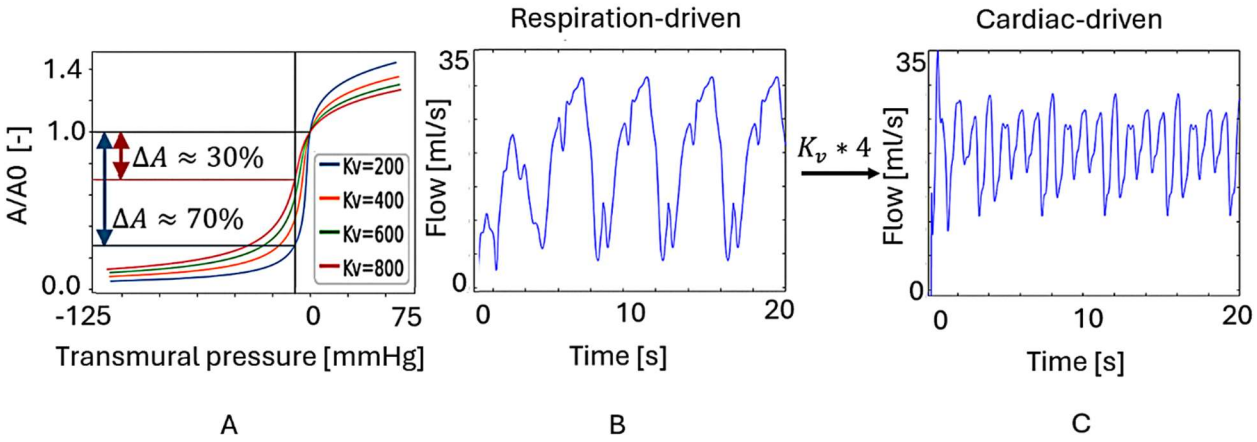
Increasing K_v fourfold alters the infrarenal IVC flow pattern from respiration-driven, Figure 1B, to cardiac-driven, Figure 1C. Intermediate K_v values result in a combined pattern. In

addition, simulations show that the amount of collapse decreased from 52% to 32% when shifting the respiratory pressure range from 0 to -10 mmHg towards -5 to -15 mmHg.

Discussion

These findings show that variations in transmural pressure and effective stiffness strongly influence vein collapse and flow patterns, resembling respiration-driven and cardiac-driven flow. Accurate modeling of venous hemodynamics requires improved tube-laws and quantification of respiratory-induced transmural pressures. Therefore, future work will assess the IVC tube-law and estimate transmural pressure during respiration using ultrasound.

Images (Optional)



References (Optional)

[1] Miller JD et al., J Physiol, 2005
[2] Joseph AA et al., NMR Biomed, 2020
[3] Shapiro AH, J Biomech Eng, 1977
[4] Müller LO et al., Front Physiol, 2023

Session Category

Cardiovascular/Cardiorespiratory Biomechanics: Methods, Models and Applications

P4-101

Hemodynamic Insights Into TIPS Intervention for Portal Hypertension: A Comprehensive Computational Study

Mr. Pavlos Varsos[1], Dr. Friederike Schäfer[1], Dr. Cristina Ripoll[2], Dr. Nicolas Golse[3,4,5], Dr. Irene Vignon-Clementel[1]

[1]Inria Saclay, Palaiseau, Île-de-France, France. [2]Jena University Hospital, Jena, Thüringen, Germany. [3]AP-HP Hôpital Paul-Brousse, Villejuif, Île-de-France, France. [4]Université Paris-Saclay, Inserm, Physiopathogénèse et traitement des maladies du Foie, UMR-S 1193, Villejuif, Île-de-France, France. [5]FHU Hepatinov, Villejuif, Île-de-France, France

Introduction

The Transjugular Intrahepatic Portosystemic Shunt (TIPS), is a well-established treatment tool in liver cirrhosis, shown to prolong transplant-free survival. It is a stent-graft connecting the portal vein to the hepatic vein within the liver parenchyma, thus reducing the portal pressure gradient (PPG) [1]. However, excessive shunting with larger graft diameters can increase systemic ammonia levels, predisposing patients to hepatic encephalopathy (HE), and may also lead to cardiac complications such as right heart failure [2]. Computational modeling can therefore serve as a valuable predictive tool for patient selection and preprocedural planning, optimizing shunt diameter and location to assess the portosystemic pressure gradient.

Methods

In this study, patient-specific TIPS geometries are segmented from CT images and analyzed using computational fluid dynamics with realistic boundary conditions to investigate the influence of geometrical and flow-related factors. Boundary conditions consider patient-specific liver volumetry as well as pre-TIPS catheterization for PPG measurement. This study includes variations in shunt positioning (right, left, and main portal vein) and diameter (8, 9, 10 mm). Flow investigations assess inflow-outflow variations and liver volume effects. A multiscale (3D-0D) model of the hepatic circulation is constructed to evaluate hepatofugal and -petal flow states.

Results

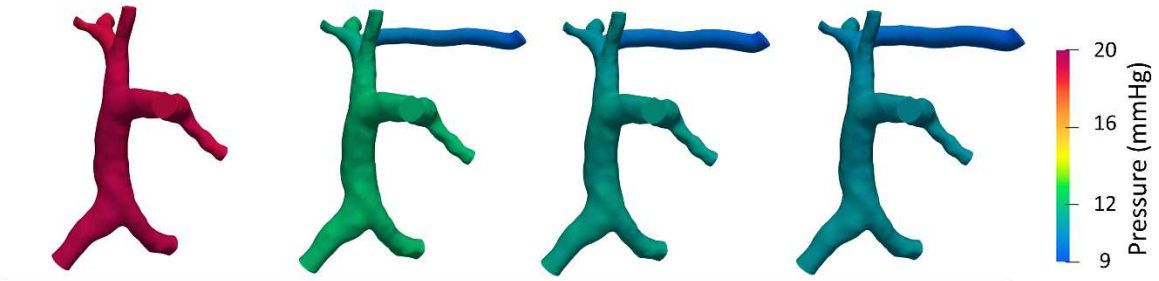
Larger shunt diameters reduce the PPG below the 50% clinically required threshold, and increase TIPS flow and steal (Shunt Index, see Figure). Shunt location affects flow distribution and the contribution of the ammonia-rich blood from the mesentery into the TIPS. Left portal puncture reduces the mesenteric flow in the TIPS, potentially lowering HE

risk. Hepatofugal and -petal flow patterns reflect disease severity and are governed by intrahepatic portal and hepatic vein resistances.

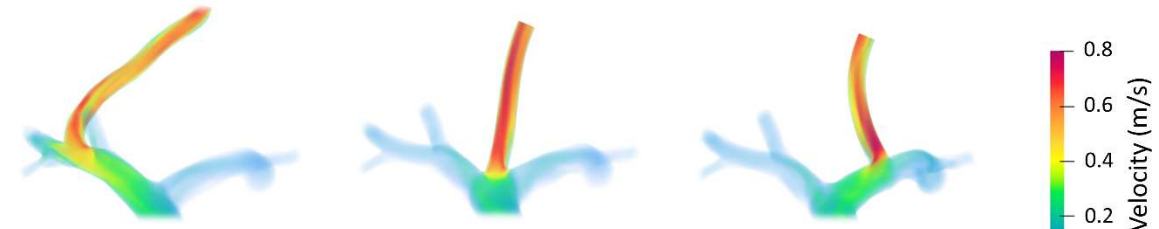
Discussion

It is clear that hemodynamic responses vary strongly with shunt configuration and patient-specific parameters. Future work will include portal vein flow measurements to validate predictions and extension of the model to include the heart and the rest of the circulation to asses brain ammonia levels and potential cardiac complications.

Images (Optional)



Pre-TIPS	D_{TIPS} = 8 mm	D_{TIPS} = 9 mm	D_{TIPS} = 10 mm
P_{PV} = 19.2 mmHg	P_{PV} = 11.8 mmHg	P_{PV} = 11 mmHg	P_{PV} = 10.6 mmHg
-	SI = 0.70	SI = 0.77	SI = 0.82



Right PV Puncture	Main PV Puncture	Left PV Puncture
SI = 0.70	SI = 0.75	SI = 0.72
SMV_f / $TIPS_f$ ≈ 49 %	SMV_f / $TIPS_f$ ≈ 54 %	SMV_f / $TIPS_f$ ≈ 45 %

References (Optional)

[1] Boyer & Haskal, Hepatology, 2005

[2] Vizzutti et al., Intern Emerg Med, 2020

Acknowledgements (Optional)

We acknowledge funding from the ERC grant no. 864313 – MoDeLLiver under the EU Horizon 2020 program, and from the EU Horizon Europe program (grant no. 101136299 – ARTEMIs).

Session Category

Cardiovascular/Cardiorespiratory Biomechanics: Methods, Models and Applications

P4-102

From Birth to Adulthood: Modeling Long-Term Cardiac Effects in Preterm Born Individuals

Ms. Judith Weng Zhu B.S.[1], Mr. Christian J. Andrade Herrera B.S.[1], Dr. Kara N. Goss M.D.[2], Dr. Naomi C. Chesler Ph.D.[1], Dr. Colleen Witzenburg Ph.D.[3], Dr. Pim J.A. Oomen Ph.D.[1]

[1]University of California, Irvine, Irvine, CA, United States. [2]University of Texas Southwestern Medical Center, Dallas, Texas, United States. [3]University of Wisconsin - Madison, Madison, Wisconsin, United States

Introduction

Survival of preterm birth, defined as a delivery before 37 weeks of gestation, is a relatively recent medical advance, and those who have reached adulthood show several long-term cardiopulmonary effects. However, because the oldest preterm born individuals are just reaching their 40s, our understanding of lifelong manifestations remains limited. A well-known complication in preterm infants is bronchopulmonary dysplasia (BPD), which is a chronic lung disease that occurs following ventilator use and oxygen therapy. BPD includes worse respiratory function and pulmonary hypertension which may lead to changes in right ventricular geometry and function. However, the long-term effects on cardiac growth and function remain poorly understood. Computational modeling has emerged as a tool to address this gap, allowing researchers to simulate long-term trajectories by integrating experimental and clinical data. This study aims to model preterm long-term cardiac growth, and provide mechanistic insights on how cardiac growth differs under somatic and BPD conditions.

Methods

We used our previously published reduced-order model to simulate cardiac mechanics and hemodynamic circulation [1]. We assumed that cardiac growth from birth through adulthood in healthy females and males is purely driven through somatic processes, so this was simulated by allometrically scaling cardiac and circulation parameters based on body weight. We then simulated the lung injury in BPD by increasing the pulmonary vasculature resistance, and simulated growth by combining allometric somatic growth with a strain-driven growth model, driven by the difference in elastic strain between the healthy and BPD simulation.

Results

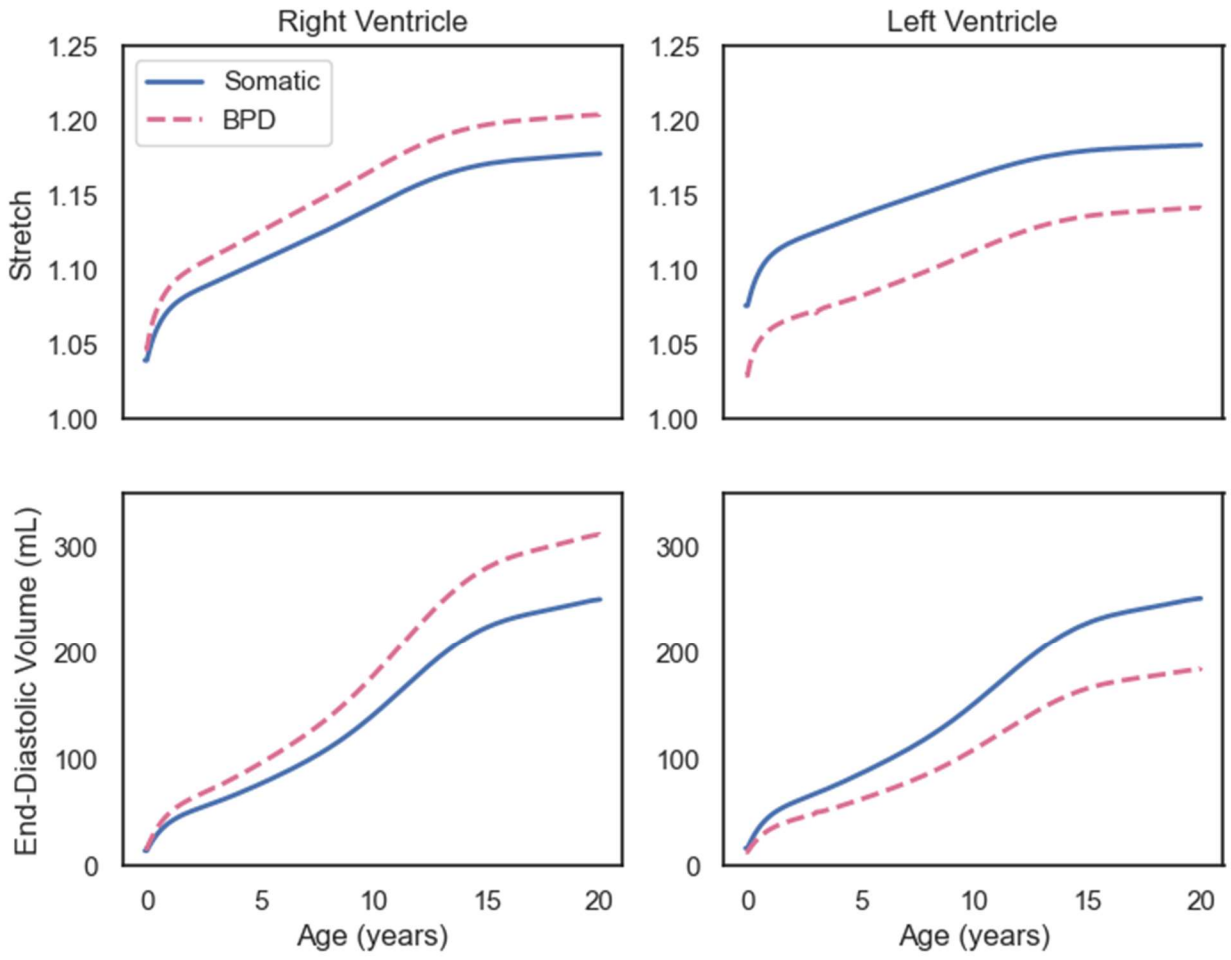
Our model demonstrates that BPD induces right ventricular hypertrophy via increased wall stretch, driven by elevated preload secondary to heightened pulmonary arterial resistance.

Conversely, our model shows that BPD lowers left ventricular volume compared to the healthy case.

Discussion

While several studies have measured changes in the right ventricle following BPD, less is known about the left ventricle. Our results showed contradicting growth patterns under BPD, where the right ventricle grows larger while the left ventricle smaller compared to somatic growth. Future work will focus on testing mechanisms other than, or in combination with, pulmonary resistance, such as vascular compliance and contractility.

Images (Optional)



References (Optional)

[1] Oomen et al.,Biomechanics and Modeling in Mechanobiology,2021

Session Category

Cardiovascular/Cardiorespiratory Biomechanics: Methods, Models and Applications

P4-103

Computational Modeling of Stent-Induced Mechanical Stimuli in Pediatric Pulmonary Vein Stenosis

Mr. R Patrick McCarthy[1], Dr. Edward Kirkpatrick DO[2,3,4], Dr. John LaDisa PhD[1,2,3,4]

[1]Biomedical Engineering, Marquette University and the Medical College of Wisconsin, Milwaukee, WI, United States. [2]Pediatric Cardiology, Medical College of Wisconsin, Milwaukee, WI, United States. [3]Cardiovascular Medicine, Medical College of Wisconsin, Milwaukee, WI, United States. [4]Herma Heart Institute, Children's Wisconsin, Milwaukee, WI, United States

Introduction

Progressive pulmonary vein stenosis (PVS) represents ~2 cases/100,000 children under 2 years old and has a ~55% 2-year untreated survival rate[1]. Stenting is a common treatment, but restenosis occurs in >50% of cases at 6 months and 5-year survival is <50%[1]. Adverse mechanical stimuli have been implicated in restenosis[2]. Unfortunately, there are no studies including stent geometry, physiologic boundary conditions and local blood flow patterns within stented pulmonary veins (**PV**). Hence, it's unknown whether optimizing mechanical stimuli after stenting will benefit PVS outcomes. Our objective was to characterize stent-induced changes in wall shear stress (**WSS**) indices from data of patients treated for PVS.

Methods

Patient-specific stented PV geometries were reconstructed from computed tomography imaging using SimVascular. Geometries included the left atrium, PV and branches influencing local flow patterns. The make and model of stents used for each patient were then virtually implemented. PV-specific boundary layer meshes were created using Simmetrix to resolve complex flow features near stent struts. Inlet boundary conditions included multiple waveforms from clinical Doppler data. Pressure was tuned to available clinical data using Windkessel approximations. Time-average WSS (**TAWSS**) and oscillatory shear index (**OSI**) were calculated for each stented and unstented (control) PV.

Results

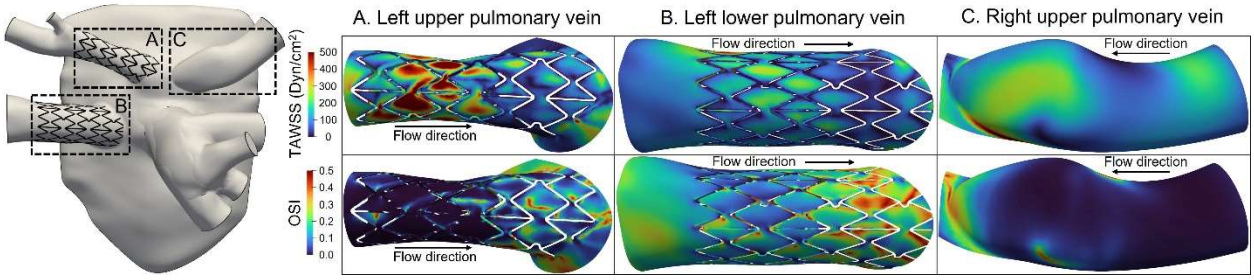
The accompanying figure shows a representative patient-specific stented model and WSS results with left upper and left lower PV stented (Cook Formula 418: 4x12 and 7x16 mm, respectively). TAWSS and OSI ranges align with unstented values from literature[3]. The right upper PV highlights normal values, which are PV-specific due to flow distributions and local area. Stent-induced changes in TAWSS and OSI patterns were most pronounced near

the atrial ostia. Additional quantification is underway across multiple patients for association with PV experiencing restenosis.

Discussion

To our knowledge, this is the first study of pediatric PVS to include stent-induced changes in WSS. Expanded results to be presented at WCB2026 will further serve as a foundation for ultimate use in optimizing stent selection and predicting the likelihood of restenosis for future PVS patients.

Images (Optional)



References (Optional)

[1] McLennan, D.I. *et al.* , FPED, 2021.

[2] LaDisa Jr, J.F. *et al.* , AJP-Heart, 2005.

[3] Hammer, P.E. *et al.* , Children, 2021.

Session Category

Cardiovascular/Cardiorespiratory Biomechanics: Methods, Models and Applications

P4-104

How to Choose Left Atrial Appendage Occlusion Devices depending on implantation site morphology.

Mr Rafizul Islam Md[1], Mr Matthew Lee[2], Mr Yuvraj Juttla[3], Prof. Andrew C. Cook[4], Dr Sandeep Panikker[5], Prof. Gaetano Burriesci[2,6,7], Dr Giorgia Bosi[2]

[1]Medical Physics and Biomedical Engineering, University College London, London, London, United Kingdom. [2]Deparment of Mechanical Engineering, University College London, London, London, United Kingdom. [3]Medical School, University College London, London, London, United Kingdom. [4]UCL Institute of Cardiovascular Science, University College London, London, London, United Kingdom. [5]Cardiology Department, Royal Brompton and Harefield, London, London, United Kingdom. [6]Bioengineering Group, Ri.Med, Palermo, Sicily, Italy. [7]Department of Mechanical Engineering, University of Palermo, Palermo, Sicily, Italy

Mr Rafizul Islam Md

Mr Matthew Lee

Mr Yuvraj Juttla

Prof. Andrew C. Cook

Dr Sandeep Panikker

Prof. Gaetano Burriesci

Introduction

The left atrial appendage (LAA) is a heterogeneous structure and the predominant site of thrombus formation, causing thromboembolic strokes in atrial fibrillation patients [1].

Percutaneous deployment of LAA occlusion devices (LAAODs), such as the Amplatzer Amulet (AA) and Watchman FLX (WFLX), has become a popular intervention to reduce thromboembolism and stroke risk [2]. Yet, selection criteria between these devices and their sizing still rely on clinician preference [3], even though WFLX and AA achieve sealing through different mechanisms. Moreover, the effect of LAA morphometric parameters on device deployment remains unclear. This study aims to identify quantifiable selection criteria between the most popular LAAODs by virtually implanting them into different LAA anatomies. The objectives are:

- Develop and calibrate computational models of both LAAODs
- Create an experimental pipeline to generate different LAA anatomies
- Build a physical set-up to mimic and validate the virtual procedure
- Investigate mechanical parameters (e.g., contact pressure and gap area) for deployed devices in varied anatomical configurations.

Methods

The AA and WFLX were CAD-designed via centrelines derived from micro-CT scans of the physical devices (Figure 1a). Various LAA models were CAD-generated for key parameters, including ostium diameter, eccentricity, and LAA bending angle (Figure 1b). These were 3Dprinted in Elastic 50A material on a FormLabs SLA machine. Finite Element simulations were run in Abaqus, modelling devices as Nitinol beam structures. Material properties were derived from radial compression tests performed on both devices at 37 °C (±1 °C) with the RX675 Machine Solutions. Virtual LAAs were modelled as shell elements with linear elastic behaviour.

Results

LAAODs virtual implantations were evaluated in terms of gap area between the device and the anatomy, landing zone and contact pressure, and compared qualitatively against corresponding experiments. The WFLX device generates higher local contact pressure than the AA.

Discussion

Numerical simulations of the LAAO procedures can anticipate peri- and post-procedural complications and guide a more effective device selection. Further analyses considering device orientation via the fossa ovalis are ongoing.

Images (Optional)

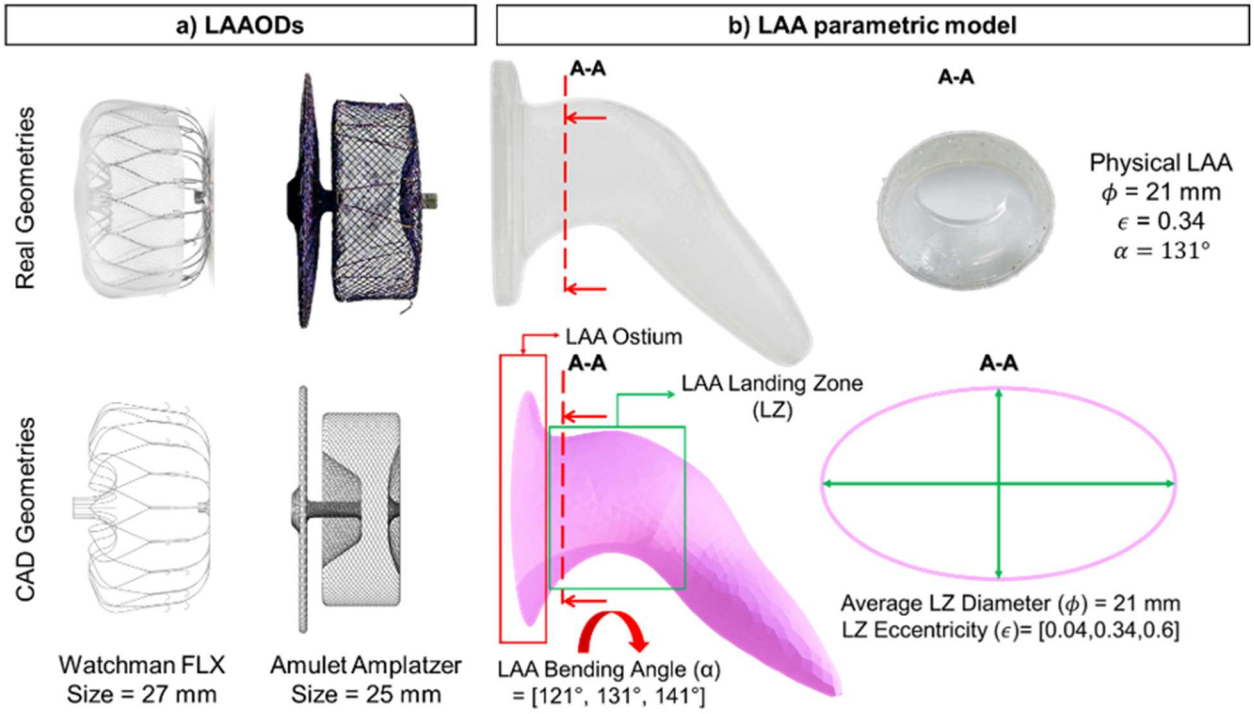


Figure 1: a) Illustration of the physical LAAODs at the top and corresponding CAD geometries at the bottom. b) Illustration of an example of a physical LAA at the top from the parametric virtual LAA at the bottom

References (Optional)

[1] Blackshear JL. et al., Ann Thorac Surg.,1996.

[2] Wang Y. et al., J of Cardiovascular Electrophysiology, 2010.

[3] Frazzetto M. et al., J Clinical Medicine, 2024.

Session Category

Cardiovascular/Cardiorespiratory Biomechanics: Methods, Models and Applications

P4-105

Rheological Comparison of Biological Fluids and Simulant Mixtures for Biomedical Flow Modeling

Mr. Rakib Hasan MS, PhD Candidate, Mr. Joby Job MS, Dr. Connor J. Evans PhD, Dr. Robert A. De Lorenzo MD, MSCI, MSM, FACEP, Dr. Alan Whitington PhD, Dr. R. Lyle Hood PhD

The University of Texas at San Antonio, San Antonio, Texas, United States

Introduction

Accurate replication of biological fluid behavior is essential for validating biomedical devices. However, many existing fluid simulants fail to capture *in vivo* rheological properties. This study compares the rheological profiles of biological fluids—including saliva, sputum, blood, and vomit—with simulant mixtures designed to emulate their flow characteristics. Benchmarking simulants against biological counterparts allows assessment of their suitability for biofluid modeling.

Methods

Rheological testing used an Anton Paar MCR 302 rheometer across 10^{-2}–10^{4} s^{-1}. Two simulant formulations were evaluated: (1) an ISO Vomit Simulant Mix composed of 10 g xanthan gum, 1000 mL distilled water, and 100 g glass beads; and (2) a Blood Phantom Mix (Akhter et al., 2019) consisting of 276 mL glycerol and 1224 mL distilled water. Reference data for saliva, sputum, and blood samples were obtained from the literature (Rantonen & Meurman 1998; Nader et al. 2019; Sturgess et al. 1971). Viscosity was plotted as a function of shear rate to assess non-Newtonian behavior and temperature sensitivity.

Results

The ISO (10079-4) vomit simulant exhibited strong shear-thinning behavior (Figure 1), with viscosity decreasing by approximately three to four orders of magnitude across 10^{-2}–10^{4} s^{-1}. Its viscosity remained far greater than sputum (10–100×) and saliva (100–10,000×). Temperature variation from 22 to 38°C produced minimal changes (<10%). The glycerol–water blood phantom showed only mild non-Newtonian behavior in 20–250 s^{-1} and displayed lower viscosity than reported whole-blood values, indicating limited physiological fidelity.

Discussion

This study presents the first known rheological characterization of the ISO vomit simulant and demonstrates its strong shear-thinning behavior across a wide shear-rate range. Here, the ISO's 1 mm glass beads were replaced with 0.1 mm beads while keeping the 100 g loading unchanged, and the simulant was tested both with and without beads (beads used only at 25°C). However, its viscosity remained far higher than saliva or sputum. The glycerol–water blood phantom mixture showed near-Newtonian behavior at shear rates >100 s^{-1} and maintained a lower viscosity than reported values for whole blood. Future studies should improve simulants to more closely reflect biological rheology.

Images (Optional)

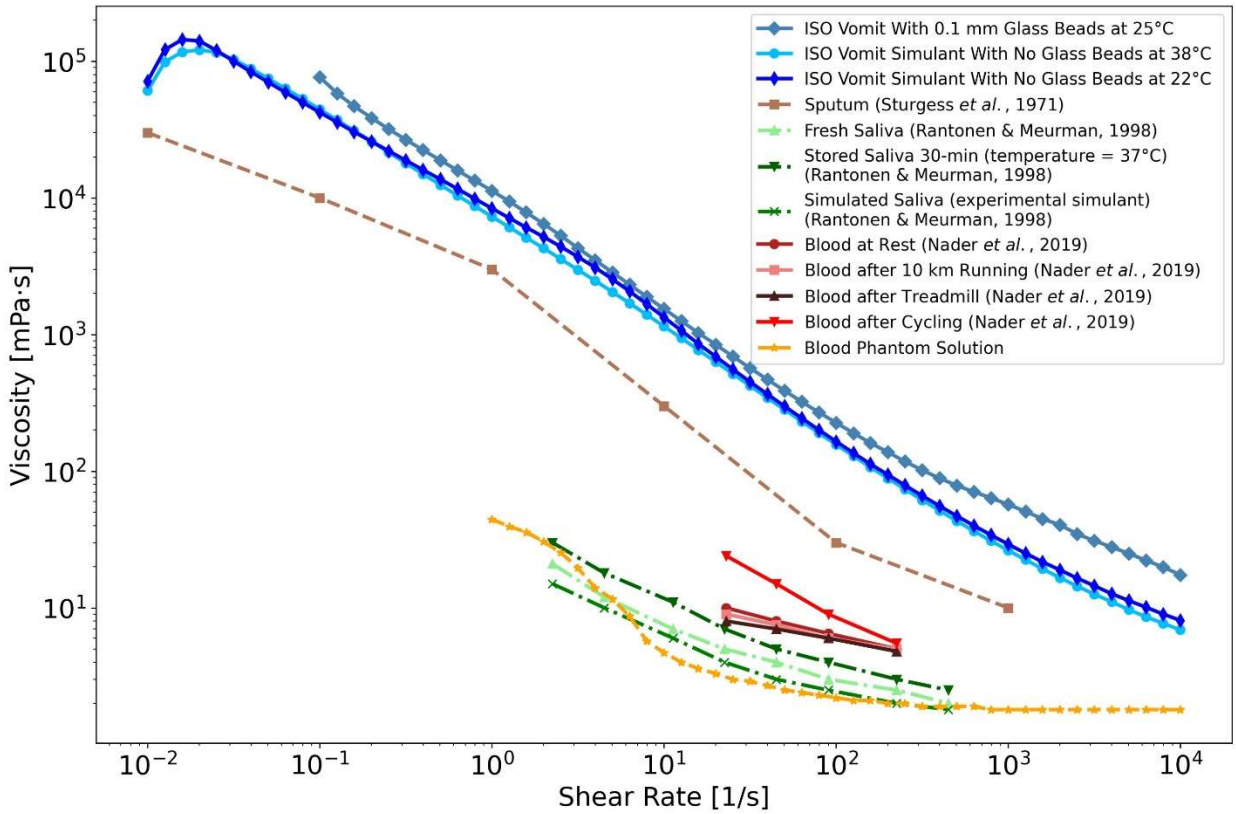


Figure 1: Comparison of Shear-rate–dependent viscosity data for multiple biological fluids (fresh saliva, stored saliva, stimulated saliva, sputum, and blood under different physiological conditions) and representative simulant materials, including ISO vomit simulants at 22 °C and 38 °C without glass beads, and a 25 °C formulation containing 0.1 mm glass beads.. Data compiled from Rantonen & Meurman (1998), Sturgess et al. (1971), Nader et al. (2019), and Akhter et al. (2019).

References (Optional)

Acknowledgements (Optional)

This work was supported by the AFWERX Direct to Phase II SBIR contract (FA864922P0928) and by EmergenceMed, LLC, a San Antonio–based university startup.

Session Category

Cardiovascular/Cardiorespiratory Biomechanics: Methods, Models and Applications

P4-106

Optimal Transport by Gradient-Based Optimization for Synthetic Vascular Tree Generation

PhD Raoul Sallé de Chou[1,2,3], PhD irène Vignon-Clementel[2], PhD Hugues Talbot[3], PhD Laurent Najman[4,5]

[1]University of Texas at Austin, Austin, Texas, United States. [2]Inria, Palaiseau, Ile de France, France. [3]CentraleSupelec, Université Paris-Saclay, Gif sur Yvette, Ile de France, France. [4]Univ Gustave Eiffel, CNRS, LIGM, Marne la Vallée, Seine et Marne, France. [5]Khalifa University, Abou Dab, Abou Dab, United Arab Emirates

Introduction

To create useful blood-perfusion models with non-invasive diagnostic tools, it is important to generate realistic vessel networks efficiently and effectively. A widely adopted method is the Constrained Constructive Optimization (CCO) tree algorithm, which iteratively builds trees by adding new segments one by one while minimizing tree volume. We recently introduced a blood transport–based cost function for CCO, offering a more optimal and physically coherent alternative to volume minimization. For a fixed tree topology, optimizing branching point positions and vessel radii under transport cost becomes a convex problem, allowing globally-optimal solutions. Building on this, the present study develops a gradient descent–based method to generate synthetic trees from terminal nodes. We aimed to identify optimal tree topologies that minimize transport cost and improve upon limitations of traditional CCO approaches.

Methods

To facilitate comparisons between the two methods, we generated trees with 100, 200, 300, and 400 terminal nodes using the transport-constrained CCO approach. The resulting terminal node distributions were then reused as inputs for tree generation with our new terminal node–based method. We first initialized the tree topologies using the dendrograms from a single-linkage clustering of terminal nodes. Optimal branching point positions, associated with the dendrogram’s internal nodes, were determined by minimizing the transport cost. A gradient-based clustering optimization method was applied to refine dendrogram's altitudes and thus the tree topology, by minimizing altitude differences between nodes closest in Euclidean distance. After each gradient update, geometric optimization of branching point positions was performed accordingly.

Results

The gradient-based method reduced transport cost compared to volume-based CCO by 9.0%, 8.7%, 9.2%, and 9.3% for trees with 100, 200, 300, and 400 terminal nodes, respectively.

Discussion

Although simulated annealing has been used for topology optimization of CCO trees, a key novelty of our method is that it is fully differentiable. It could be integrated into deep learning frameworks for synthetic tree generation or used to solve inverse problems of identifying optimal tree topologies to better match simulated blood flow with patient-specific perfusion images. The method also enables exploration of diverse terminal node geometries. Further work should focus on enabling the method to generate multiple trees.

Images (Optional)

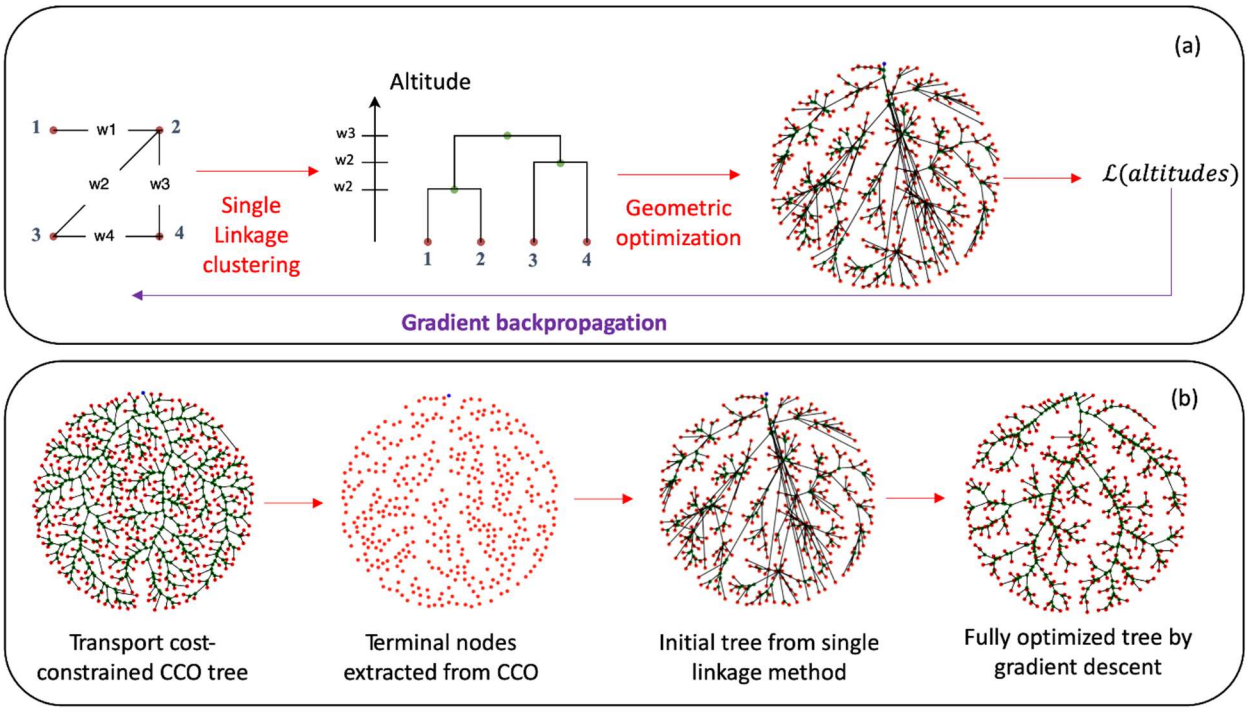


Figure: (a) Illustration of the gradient-based optimization pipeline. (b) Illustration of the topology optimization on terminal nodes extracted from a CCO tree

Acknowledgements (Optional)

This work was supported by an industrial grant by Heartflow, inc.

Session Category

Cardiovascular/Cardiorespiratory Biomechanics: Methods, Models and Applications

P4-107

Validation of Diffeomorphic Image Registration for Regional Lung Biomechanics Using an In-Silico CT Phantom

Mr. Prathmesh Bhatt, Dr. Reza Avazmohammadi1, Dr. Sunder Neelakantan

Texas A&M University, College Station, Texas, United States

Introduction

Regional lung mechanics derived from deformable image registration provide insights into heterogeneous lung injuries. Biomechanical metrics, including the Jacobian for volume change and distortion indices for shape change, quantify local tissue deformation during respiration. However, large deformations between end-expiration and end-inspiration challenge registration accuracy, and the absence of in-vivo ground truth data limits confidence in the computed biomechanical fields. We propose validation framework combining finite-element-based computed tomography phantoms with manual landmark tracking to assess registration accuracy in lung biomechanics.

Methods

Our framework uses finite element simulations of lung parenchyma to generate in-silico CT phantoms, with nodal displacements serving as ground truth for deformation. The phantom images replicate clinical acquisition parameters and enable controlled assessment of registration algorithms. We use two different image registration algorithms to register images from end-expiration to end-inspiration. We compute the deformation gradient **F** from the displacement field, use **F** to compute the Jacobian *J*, and define the distortion index D as the ratio of the maximum to the minimum isochoric principal stretches. To extend validation beyond voxelwise comparisons, we identify anatomical landmarks, vessel bifurcations, and bronchial branch points, and track their positions in both finite element simulation and registration results. Comparison of landmark displacements between these methods quantifies registration, where imaging artifacts and anatomical complexity may influence performance.

Results

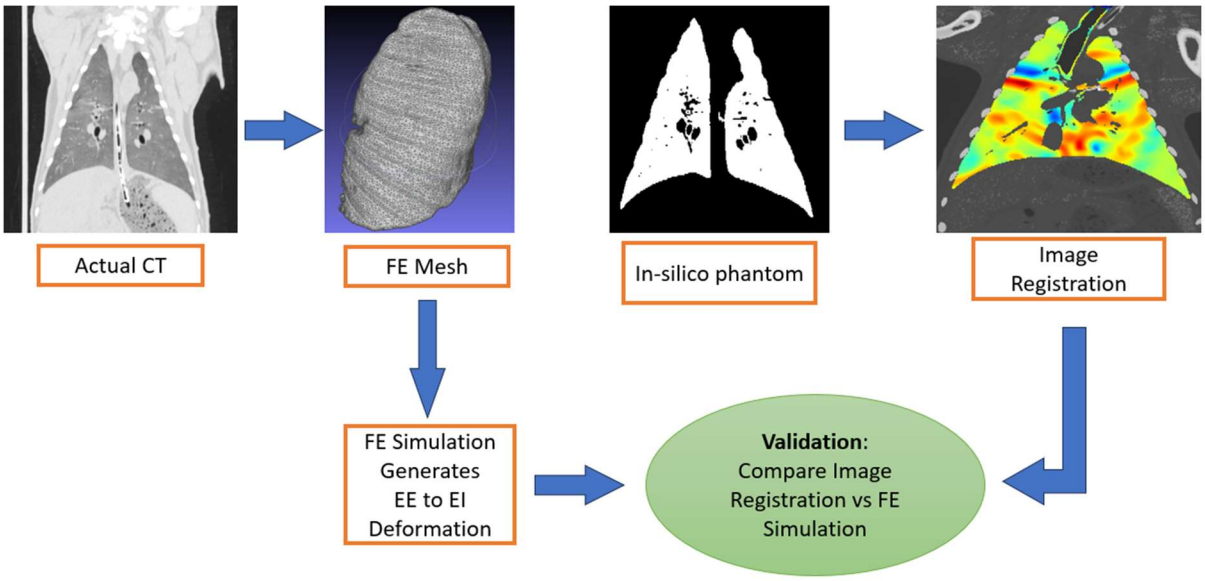
Phantom-based validation enables quantification of registration accuracy by directly comparing it with finite-element ground truth, revealing mean errors and spatial patterns of failure modes. We will compare the results for two commonly used image registration algorithms: ANTs and NiftyReg, and additionally use manual landmark tracking to provide

independent verification and further assessment. The combined approach identifies parameter regimes where registration reliably estimates regional biomechanics and reveals limitations near anatomical boundaries and regions with complex motion patterns.

Discussion

This validation framework establishes confidence in registration-derived biomechanical metrics for lung mechanics studies. By integrating computational ground truth with manual anatomical landmarks, the approach enables reliable quantification of regional deformation for applications in mechanical ventilation and lung injury assessment. The framework identifies accurate parameter regimes and limitations to inform proper use of registration for computing strain and stress fields in respiratory biomechanics.

Images (Optional)



References (Optional)

Session Category

Cardiovascular/Cardiorespiratory Biomechanics: Methods, Models and Applications

P4-108

Role of Hemodynamic Factors in the Development of Cerebral Aneurysms

Mr. Riki Kobari, Prof. Yuji Shimogonya PhD

Nihon University, Koriyama, Fukushima, Japan

Introduction

Wall shear stress (WSS) is thought to be involved in the development of cerebral aneurysms. While blood flow simulation based on actual patient vessel geometry is effective for quantifying WSS, obtaining patient vessel geometry data prior to aneurysm development is difficult. Therefore, we aimed to reproduce pre-aneurysm vascular geometry by virtually removing the aneurysm, perform blood flow simulations on the vascular geometry of 10 such cases, and investigate the relationship between WSS and cerebral aneurysm development.

Methods

For the 10 cerebral aneurysm cases provided in the Aneurisk dataset repository[1], the aneurysms were virtually removed using the Vascular Modeling Toolkit (VMTK) (Fig. 1(a)). CFX 2022 (ANSYS) was used to perform the blood flow simulations. From the obtained results, time-averaged wall shear stress (TAWSS) and Normalized transverse wall shear stress (NtransWSS)[2], an indicator of temporal disturbances of WSS, were calculated. By comparing values between the entire vessel and the aneurysm site (Fig. 1(b)), the relationship between hemodynamic factors and cerebral aneurysm development was investigated.

Results

The values shown below represent the mean and standard deviation for the 10 cases. The TAWSS for the entire vessel was 4.12 ± 0.94 Pa, while the TAWSS at the aneurysm site was 4.66 ± 2.83 Pa. In 5 of the 10 cases, the TAWSS at the aneurysm site was higher than that for the entire vessel. Meanwhile, the NtransWSS for the entire vessel was 0.0412 ± 0.0104, and the NtransWSS at the aneurysm site was 0.0544 ± 0.0220. In 9 of the 10 cases, the NtransWSS at the aneurysm site was higher than that for the entire vessel.

Discussion

The results suggest that temporal disturbances of WSS may be associated with cerebral aneurysm development. It has been reported that strong WSS disturbances induce

inflammatory responses in vascular endothelial cells[3]. Furthermore, chronic inflammation in vascular endothelial cells may trigger cerebral aneurysm development[4]. The findings obtained in this study are consistent with these previous experimental results.

Images (Optional)

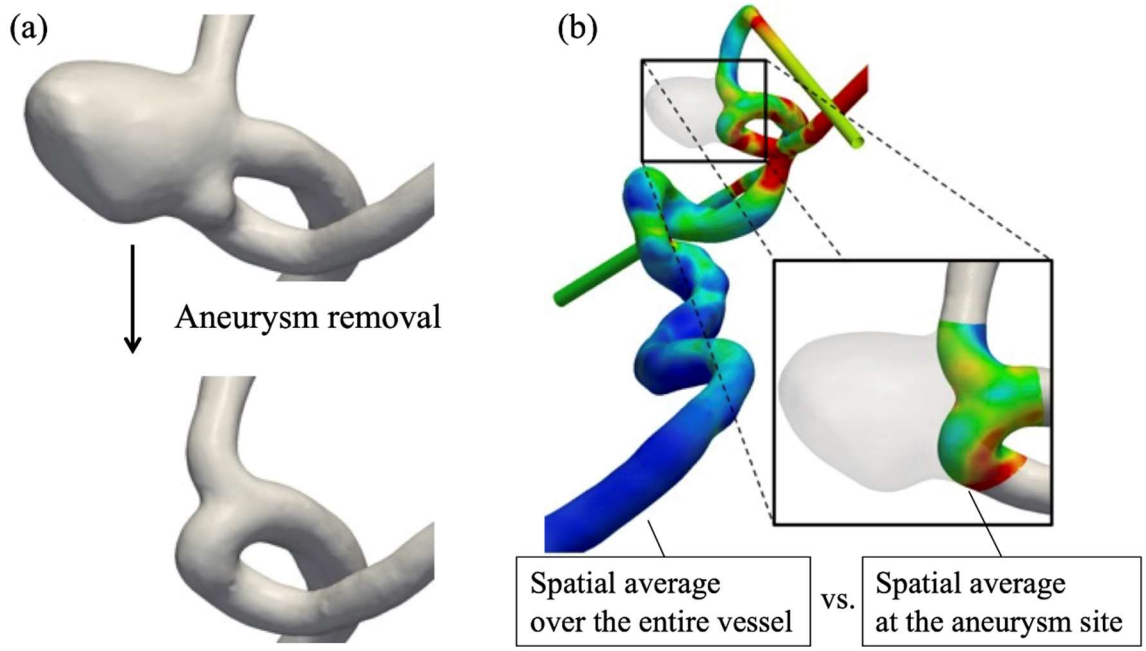


Fig. 1 (a) Pre-aneurysm vascular geometry. (b) Comparing the hemodynamic metrics.

References (Optional)

[1] http://ecm2.mathcs.emory.edu/aneuriskweb/index

[2] Shimogonya *et al.*, J Biomech, 2024

[3] Yamamoto *et al.*, Am J Physiol Cell Physiol, 2024

[4] Aoki *et al.*, Sci Signal, 2017

Session Category

Cardiovascular/Cardiorespiratory Biomechanics: Methods, Models and Applications

P4-109

CCR2+ Cells Are Critical for Normal Aortic Development

Ms Rira Choi BS, MS, Professor Jay Humphrey PhD

Yale University, New Haven, CT, United States

Introduction

Whereas it is well known that endothelial cells, smooth muscle cells, and fibroblasts contribute to the growth of the aortic wall during postnatal development, recent findings by others showed that tissue resident macrophages (Lyve1+) also contribute to normal development. In the absence of these macrophages, the aortic wall exhibits excessive stiffness, due in part to the absence of MMP-9 production by these cells. By contrast, it has been generally thought that bone marrow derived, recruited macrophages (CCR2+) contribute primarily to host defense and injury response. Here, we show that absence of CCR2+ macrophages results in unexpected aortic vulnerability.

Methods

All live animal care and use was approved by the Yale IACUC. Briefly, following euthanasia, the thoracic aorta was excised from both CCR2 null and age- and sex-matched wild-type (WT) control mice. Vessels were cleaned of loose perivascular tissue, cannulated, mounted within a custom computer-controlled biaxial testing device, and subjected to a series of isobaric-axially isometric active protocols and seven passive cyclic pressure-distension and axial force-extension protocols. The passive data were fit with a four-fiber family constitutive relation that allowed calculation of biaxial stresses and material stiffness as well as elastic energy storage. Data were collected at 6 developmental ages: P2, P10, P28, P42, P56, and P84.

Results

Amongst the many findings, three stood out. First, the rate of increase of blood pressure during development was normal despite an apparent difference in homeostatic values of multiple passive metrics. Second, aortas from CCR2 null mice exhibited a reduced vasoconstrictive capacity. Third, aortas from CCR2 null mice across age and sex exhibited an unexpected susceptibility to intramural delamination ex vivo under simulated physiological loading despite the absence of in vivo dissections or ruptures.

Discussion

CCR2+ macrophages contribute to the normal development of the structural integrity of the thoracic aorta. There is, therefore, a need for further studies of interactions between recruited macrophages and host cells and determination of the mechanisms by which these macrophages impact homeostatic targets for the mechanics of the wall.

Session Category

Cardiovascular/Cardiorespiratory Biomechanics: Methods, Models and Applications

P4-110

Influence of Bifurcation Angle and Rewiring Configuration on Double Kissing Crush Performance: A Computational Study of Mechanical and Hemodynamic Outcomes

Mr Andrea Colombo[1], Dr Dario Carbonaro[2], Dr Mingzi Zhang[1], Dr Chi Shen[1], Dr Ankush Kapoor[1], A/Prof Claudio Chiastra[2], A/Prof Mark Webster[3], Mr Robert Verdoes[1], A/Prof Nigel Jepson[1], A/Prof Susann Beier[1]

[1]University of New South Wales, Sydney, NSW, Australia. [2]Politecnico di Torino, Torino, Piedmont, Italy. [3]Auckland City Hospital, Auckland, Auckland, New Zealand

Introduction

The Double Kissing Crush (DKC) technique is widely used for complex coronary bifurcation lesions. Clinical practice favors proximal rewiring to reduce the risk of technical failure, yet the biomechanical consequences of this choice remain poorly understood. The effect of bifurcation angle on deployment quality is also unclear. This study investigates how bifurcation angle and rewiring configuration interact and influence DKC outcomes.

Methods

Twelve DKC procedures were modelled by combining three bifurcation angles (45°, 70°, 100°) with four rewiring configurations: proximal-proximal, proximal-distal, distal-proximal, and distal-distal. Finite element simulations reproduced all procedural steps, including stent crushing, two kissing balloon inflations, and proximal optimization technique, enabling quantification of malapposition, arterial wall stress, and side branch ostium clearance. Computational fluid dynamics simulations were then conducted on the final deployed geometries to evaluate regions of low endothelial shear stress and the burden of high shear rate, providing complementary insight into post procedural flow conditions.

Results

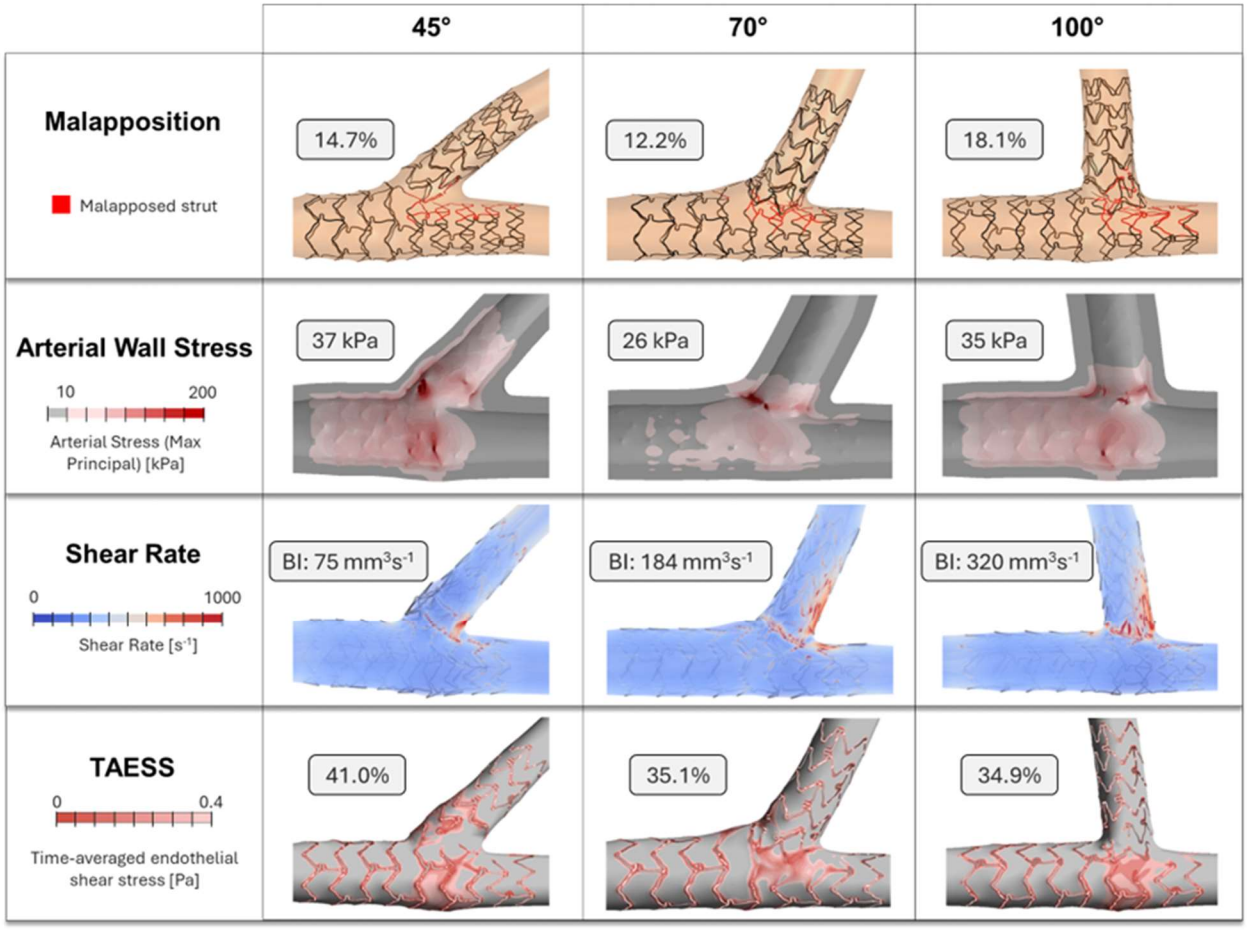
Bifurcation angle strongly affected mechanical and flow outcomes. Malapposition increased from 12.0% to 14.2% at 70° to as high as 18.1% at 100°. Side branch clearance declined with angle, from 54 to 65% at 45° to as low as 23% at 100°. High shear rate burden increased markedly in wide angles, from 75 to 140 mm^3s^{-1} at 45° up to 320 mm^3s^{-1} at 100°, driven mainly by larger high shear volumes. Average arterial wall stress varied modestly across angles, ranging between 26 and 44 kPa. Rewiring strategy influenced results in an angle-dependent manner. Proximal-proximal performed best at 70°, distal-distal at 45°,

and distal-proximal gave the most favourable balance at 100°. Low endothelial shear stress showed minimal variation and did not discriminate between strategies.

Discussion

DKC performance depended jointly on bifurcation angle and rewiring strategy. Wide bifurcations produced the worst malapposition, scaffolding, and shear conditions, indicating that DKC is not equally suited to all anatomies. No rewiring configuration was optimal across angles, and the standard proximal-proximal approach did not consistently yield the most favorable outcomes. These findings support tailoring rewiring strategy to anatomy and highlight the relevance of intravascular imaging to guide cell entry and improve procedural precision.

Images (Optional)



Session Category

Cardiovascular/Cardiorespiratory Biomechanics: Methods, Models and Applications

P4-111

A Method for Generating Realistic and Demographic-Specific Populations of Synthetic Coronary Artery Models

Mr Robert Verdoes[1], Dr Mingzi Zhang[1], Dr Diogo Ferreira de Almeida[2], Mr Miro Březík[2], A/Prof Susann Beier[1]

[1]School of Mechanical and Manufacturing Engineering, University of New South Wales, Sydney, New South Wales, Australia. [2]Virtonomy GmbH, Munich, Bavaria, Germany

Introduction

Coronary artery disease (CAD) remains a leading cause of mortality and morbidity across all demographics, with risk and incidence varying across populations. Understanding population-specific coronary anatomy and local haemodynamics is essential for accurate CAD risk assessment, yet comprehensive patient datasets are scarce. To address this gap, this study develops and validates a method for generating synthetic artery models representative of distinct populations.

Methods

From a ground truth population of 112 bifurcating left coronary arteries, we isolated sex-specific shape modes of the first three major bifurcations by statistical shape modelling. By correlating the dimensional deviation in each of the shape modes summing to 95% explained variance, a correlation matrix between each dimension was established. Ground truth linearity was used for each non-bifurcation dimension, on a branch-specific basis, so that the matrix could encapsulate 32 dimensions, including branch-specific diameters, tortuosities, and bifurcation angles. Using these correlations, sex-specific synthetic populations were generated and evaluated against the ground truth by comparing the error of all dimensions and dimensional correlations. Additionally, using morphMan [1], we constructed a pipeline to generate synthetic left coronaries models.

Results

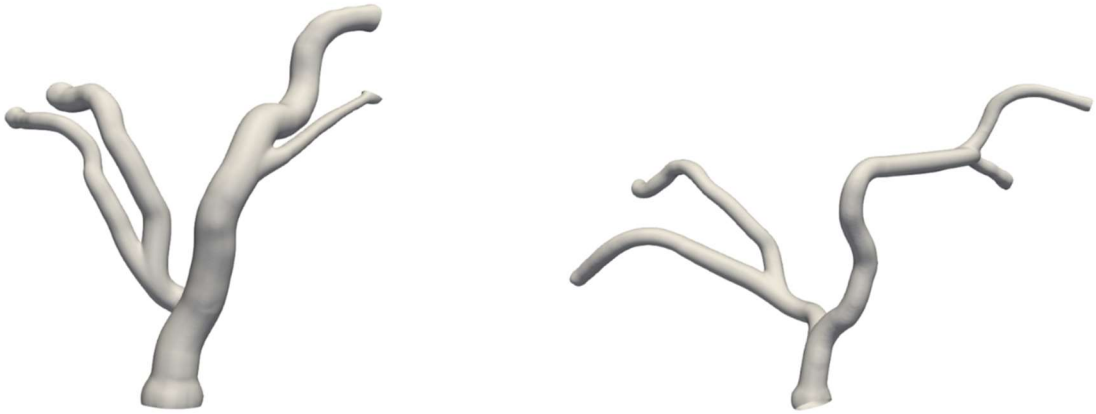
Based on the ground truth population, we generated a dimension set for a synthetic population of 200 left coronaries. For the 32 synthesized dimensional averages the error relative to the ground truth was 1.1% and 2.4% for male and female respectively. The average error for dimensional correlations between ground truth and synthetic populations, recorded as coefficients of determination, was 27% and 33%, whereas the

error when comparing the sex-specific ground truth populations against the entire population was 36% and 23%.

Discussion

These methods enable the realistic generation of synthetic left coronary artery datasets for distinct populations, based on their specific dimensional averages. The results demonstrate somewhat improved accuracy of anatomical correlation nuances than a less specific real dataset. Utilizing the generated coronary models, the haemodynamic significance of anatomical features can be evaluated on a population-specific basis. Furthermore, with reasonable assumptions regarding additional populations, input adjustments may allow for the study of underreported demographics.

Images (Optional)



Synthetic left coronary trees representative of low and high left main bifurcation angle

References (Optional)

"[1] Aslak W. Bergersen, et al., International Journal for Numerical Methods in Biomedical Engineering, 2020"

Session Category

Cardiovascular/Cardiorespiratory Biomechanics: Methods, Models and Applications

P4-112

A Deep Learning and Synthetic Data Framework for Rapid Wall Shear Stress Prediction and Clinical Risk Stratification in Stenotic Coronary Arteries

Mrs Salwa Alamir[1], Dr Vincenzo Tufaro[2], Dr Christos Bourantas[3,2], Dr Andreas Baumbach[3,2], Dr Qianni Zhang[4], Dr Joseph Jacob[5,6], Prof Ryo Torii[1]

[1]Department of Mechanical Engineering, University College London, London, London, United Kingdom. [2]Centre for Cardiovascular Medicine and Devices, Queen Mary University of London, London, London, United Kingdom. [3]Department of Cardiology, Barts Heart Centre, Barts Health NHS Trust,, London, London, United Kingdom. [4]School of Electronic Engineering and Computer Science, Queen Mary University of London, London, London, United Kingdom. [5]Satsuma Lab, Centre for Medical Image Computing, University College London, London, London, United Kingdom. [6]UCL Respiratory, University College London, London, London, United Kingdom

Introduction

Endothelial wall shear stress (WSS) derived from computational fluid dynamics (CFD), has been shown as a promising risk stratification metric for atherosclerotic coronary arteries. The use of deep learning (DL) based surrogate models has attracted attention towards clinical adaptation, with initial successes including ours [1], but large required data sizes remain a challenge. To address this, we present an integrated framework combining synthetic coronary artery data generation and DL–based WSS prediction with validation using clinical outcomes.

Methods

Fifty patient-specific stenosed coronary geometries reconstructed from X-ray angiography and CFD-derived WSS data served as the foundation for training data. The WSS was computed with two types of synthetic vessels: (1) geometrical reorientation and inflow-velocity modification of patient data, and (2) parametrically-described fully synthetic vessel geometries. A combination of real and synthetic data (440 synthetic, 40 real) was used to train a U-net–based neural network, to predict WSS from vascular anatomy and inflow velocity. Model performance was evaluated using five-fold cross-validation and normalized mean absolute error (NMAE). For preliminary clinical validation, DL-predicted WSS values were used to identify high-risk patients, i.e. experienced cardiac death or revascularization in a long-term follow-up (57 ± 20 months) in an independent test cohort (n=10 real patients) using a 4.95 Pa WSS threshold [2].

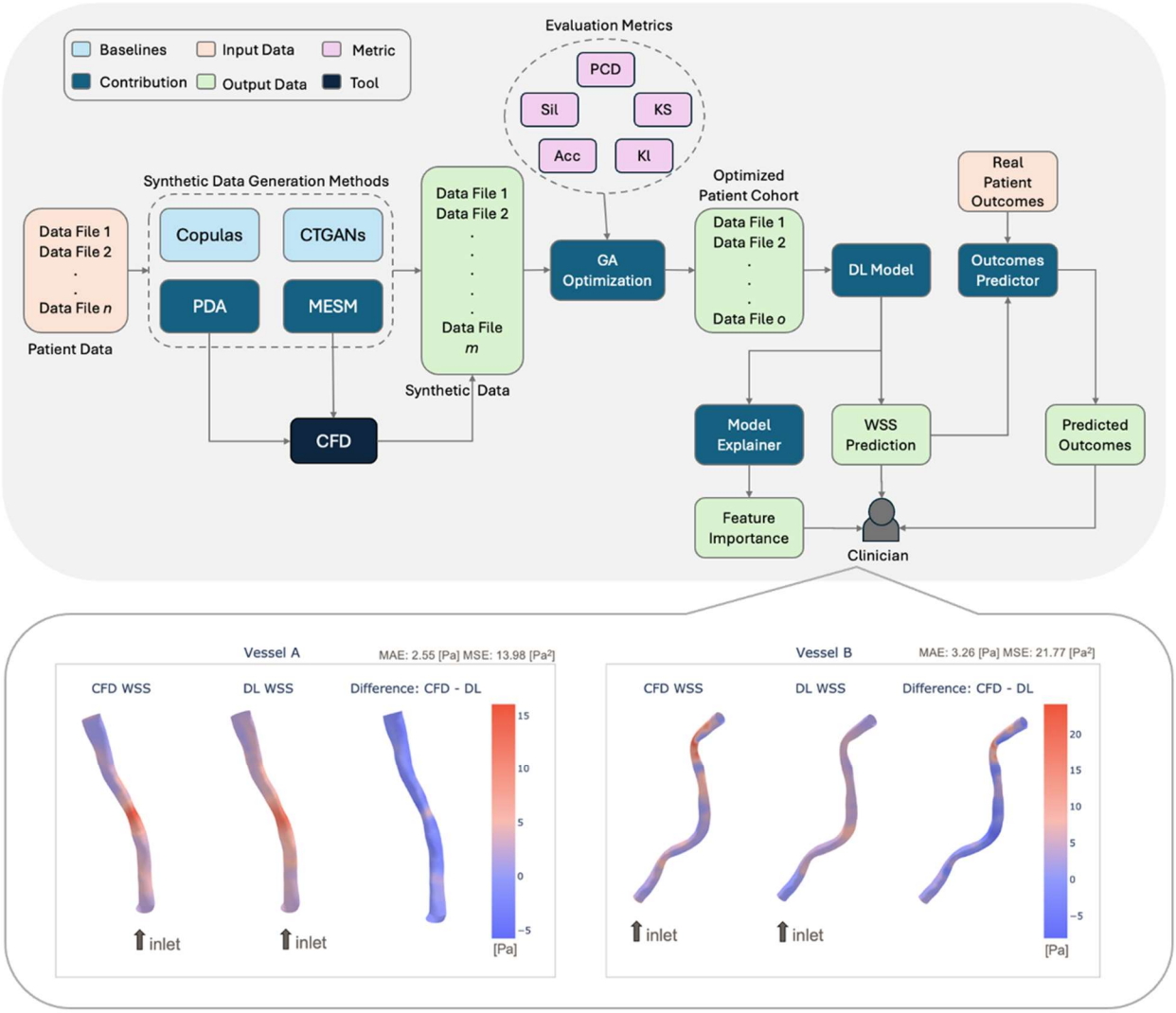
Results

The deep learning model achieved an NMAE of 6.0% and inference times of 0.35 seconds per vessel. Synthetic data augmentation improved predictive accuracy relative to training on real-patient data alone, and synthetic data optimization using genetic algorithm achieved a 21.1% better alignment with real patient data. In the clinical test cohort, predicted mean WSS across patients ranged from 3.93–11.90 Pa, and no events occurred in the low-WSS group (<4.95 Pa), compared with four events among seven high-WSS patients (57%).

Discussion

This framework demonstrates that DL-predicted WSS correlates well with cardiac deaths and/or revascularization, and WSS prediction can be enhanced using high-fidelity synthetic data. Our framework and findings support the potential for real-time, image-based biomechanical risk stratification, via fast and reliable CFD-free WSS prediction.

Images (Optional)



References (Optional)

[1] Alamir et al. Frontiers in Bioengineering and Biotechnology, 2024.

[2] Bourantas et al. JACC: Cardiovascular Imaging, 2020.

Session Category

Cardiovascular/Cardiorespiratory Biomechanics: Methods, Models and Applications

P4-113

Mitigating Material Uncertainty: A Framework for Fluid-Structure Interaction Simulations of Aneurysmatic Ascending Aorta

Ms. Sabrina Nocerino MSc[1], Dr. Chiara Catalano PhD[2], Dr. Sara Zambon PhD[1], Dr. Karol Calò PhD[1], Prof. Salvatore Pasta PhD[2], Prof. Umberto Morbiducci PhD[1], Prof. Diego Gallo PhD[1]

[1]Politecnico di Torino, Torino, Piemonte, Italy. [2]Università degli Studi di Palermo, Palermo, Sicilia, Italy

Introduction

Computational fluid-structure interaction (FSI) simulations enable to investigate biomechanical drivers of ascending thoracic aortic aneurysm (ATAA) progression [1, 2]. However, their predictive value is limited by uncertainties in the mechanical properties of the aortic wall. This study presents an FSI framework designed to mitigate this limitation via inverse identification of patient-specific wall properties.

Methods

Aortic geometries at peak systole and late diastole were reconstructed from retrospectively gated CTA [1]. The wall was modeled as a hyperelastic Neo-Hookean solid. Patient-specific material properties were estimated via an iterative inverse procedure using the CTA-measured systolic volume of the ascending aorta (AAo) as calibration target. First, finite-element structural simulations were performed to compute the diastolic stress state [3]. Then, patient-specific systolic pressure was applied, and the Young's modulus of the aortic wall was updated through a bisection method until the simulated AAo systolic volume matched the target within a 1% tolerance. Subsequently, fully coupled FSI simulations were run using the Arbitrary Lagrangian-Eulerian formulation, imposing zero displacement at ring-shaped boundaries of the solid domain. As for fluid boundary conditions, inflow waveforms were scaled using Doppler-measured transaortic jet velocities and patient-specific pressures enforced through zero-dimensional outlet models.

Results

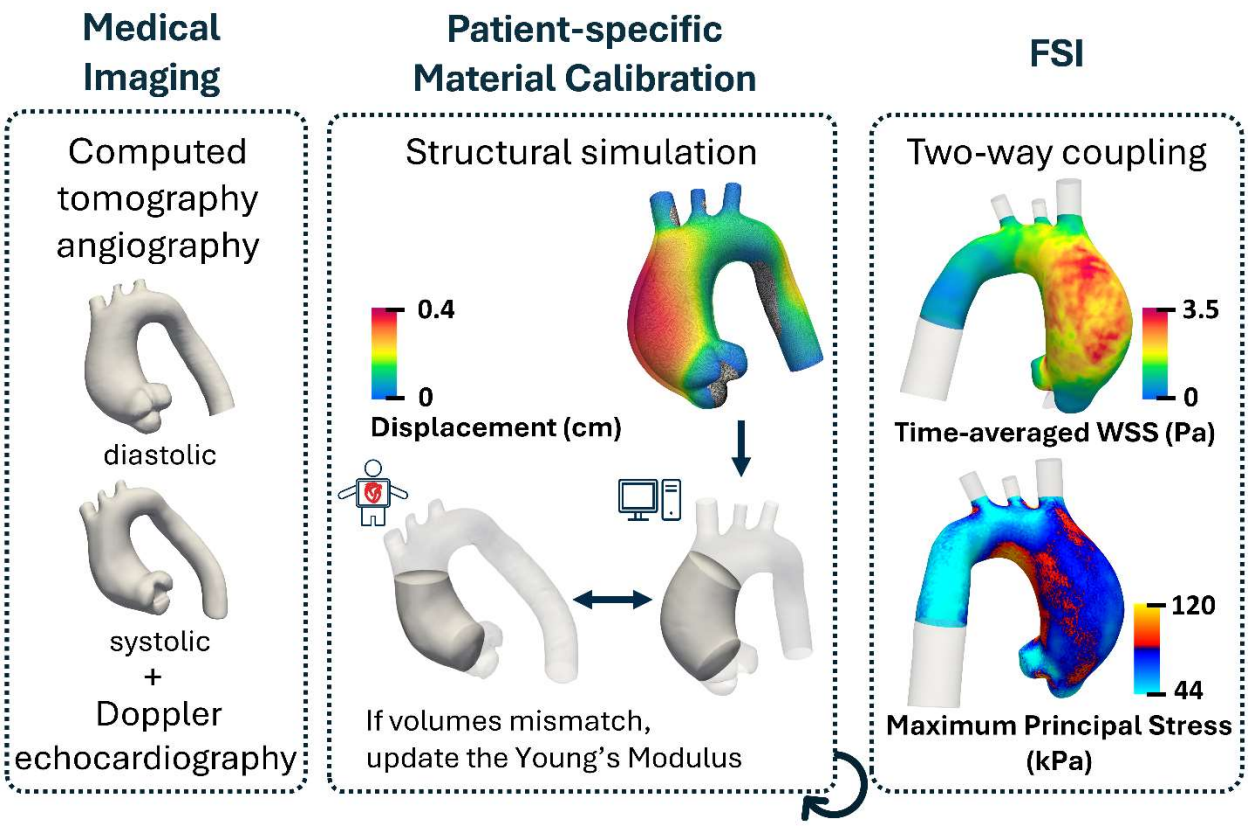
We preliminarily applied the method to three ATAAs. Identified patient-specific Young's moduli ranged from 1.25 to 3.20 MPa, capturing the expected inter-individual variability in aortic stiffness. Peak wall stresses localized along the inner aortic curvature, with secondary foci along the outer curvature. FSI simulations captured complex

hemodynamics, including flow impingement and wall shear stress (WSS) topology associated with localized contraction/expansion dynamics—potential biomechanical markers of adverse wall remodeling [2].

Discussion

This framework enables a more accurate assessment of the interplay between hemodynamic and structural drivers of ATAA progression, reducing uncertainty about aortic material properties. Limitations include the assumption of spatially uniform wall properties and the use of a global volumetric calibration target. Ongoing studies are incorporating regional material heterogeneity and distinguishing between tricuspid and bicuspid valve morphologies, both potentially relevant for improving ATAA risk stratification.

Images (Optional)



References (Optional)

[1] Pasta et al., Ann Thorac Surg, 2020

[2] De Nisco et al., Med Eng Phys, 2020

[3] Bäumler et al., Biomech Model Mechanobiol, 2020

Session Category

Cardiovascular/Cardiorespiratory Biomechanics: Methods, Models and Applications

P4-114

Investigating the Impact of Balloon Post-Dilatation on Transcatheter Heart Valve Expansion after Self-Expanding TAVI in the Bicuspid Aortic Valve: A Patient-Specific Multiphysics Modelling Approach

Mr. Sam Boxwell[1], Dr. Rachel Cahalane[1,2], Mr. Dylan Armfield[3], Mr. William Hickey[4], Dr. Philip Cardiff[3], Prof. Laoise McNamara[1]

[1]University of Galway, Galway, Connacht, Ireland. [2]Harvard Medical School, Boston, MA, Ireland. [3]University College Dublin, Dublin, Leinster, Ireland. [4]Boston Scientific Corporation, Galway, Connacht, Ireland

Introduction

Transcatheter aortic valve implantation (TAVI) is increasingly utilised to treat bicuspid aortic valve (BAV) stenosis [1]. However, BAV calcification restricts transcatheter heart valve (THV) deployment causing underexpansion, which is associated with paravalvular leakage (PVL), structural degeneration and thrombosis [2]. To address suboptimal expansion and mitigate these complications, balloon post-dilatation may be conducted. In this study, we develop and validate a novel patient-specific multiphysics modelling framework to investigate the impact of balloon post-dilatation on THV expansion following self-expanding TAVI in the BAV.

Methods

A type-1 BAV patient-specific model with severe aortic stenosis was reconstructed from pre-TAVI computed tomography (CT). We simulated the complete TAVI procedure, including crimping, deployment, balloon post-dilatation (Fig. 1A) and then applied normotensive conditions to simulate post-implantation cardiac cycle loading. Models were validated against (1) post-TAVI CT (Fig. 1B) and (2) hydrodynamic testing conducted in 3D-printed patient-specific models (Fig. 1C). Next, we investigated the impact of balloon post-dilation and balloon sizing on THV expansion, ellipticity and PVL-risk at distinct regions. We assessed bioprosthetic leaflet stress at full balloon inflation, an indicator of structural degeneration.

Results

Our approach predicted frame expansion and ellipticity in excellent alignment with post-TAVI CT (within ±10% across all planes – Fig 1B). Moreover, the predicted geometric orifice area and stent deflection were comparable to hydrodynamic testing (Fig. 1C). Balloon post-

dilatation was effective at increasing frame expansion (+4%) and circularity (+16%), whilst also reducing PVL-risk (-53%) (Fig. 1D). Although balloon size did not affect THV expansion, the 23 mm balloon (labelled THV diameter) resulted in higher leaflet stresses (σ_{mean}=1.51MPa) compared to the undersized 22 mm balloon (σ_{mean}=0.38MPa) (Fig. 1E) at full balloon inflation (3 atm).

Discussion

Utilizing a novel computational framework, we predicted that balloon post-dilation improved frame expansion and reduced PVL in a challenging case of BAV stenosis. Moreover, balloon undersizing may reduce biomechanical stress-related leaflet degeneration. Ongoing work utilizes computational fluid dynamics (CFD) to assess thrombogenic risk associated with balloon post-dilatation [3], whilst also extending the analysis to a larger BAV cohort.

Images (Optional)

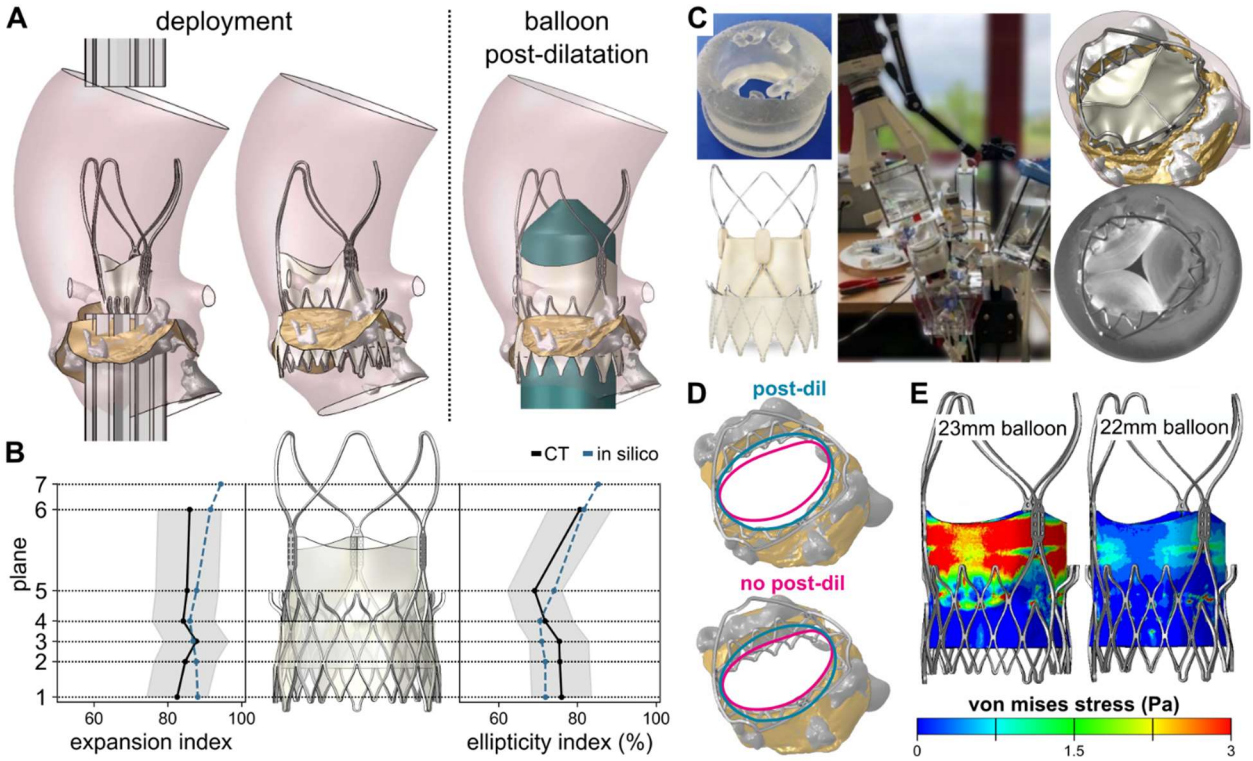


Fig. 1: (A) TAVI Simulation. Validation with (B) Post-TAVI CT and (C) Hydrodynamic Testing in 3D-Printed BAV Model. (D) Impact of Post-Dilatation on THV Expansion. (E) Leaflet Stress at Full Balloon Inflation.

References (Optional)

[1] Xiong et al., Nat Rev Cardio, 2022. [2] Makkar et al., JACC, 2025. [3] Boxwell et al., medRxiv, 2025.

Acknowledgements (Optional)

This study was funded by Taighe Éireann – Research Ireland (GOIPG/2022/2032).

Session Category

Cardiovascular/Cardiorespiratory Biomechanics: Methods, Models and Applications

P4-115

Mechanical and Microstructural Analysis of Human Umbilical Arteries

Ms. Sanaz Farmani BS, Mr. Bahman Kargarbahrkhazar, Dr. Sayed Ahmadreza Razian

University of Nebraska Omaha, Omaha, Nebraska, United States

Introduction

The mechanical properties of human umbilical arteries (UAs) are critical for maintaining placental perfusion and fetal health. Furthermore, vascular stiffness at birth may serve as a marker for fetal programming, potentially predisposing individuals to cardiovascular disease later in life. Despite this importance, mechanical characterizations of UAs have often relied on uniaxial testing, which may not fully capture the complex, anisotropic behavior of the vessel under physiological multiaxial loads. Consequently, the relationship between UA multiaxial mechanics and wall microstructure has not been comprehensively studied. This study provides a comprehensive analysis coupling biaxial mechanical testing with quantitative histomorphometry on the same tissue specimens.

Methods

Umbilical cords were collected from 30 term deliveries. UA segments were isolated and subjected to planar biaxial tensile testing using a Biaxial BioTester (CellScale). Specimens underwent preconditioning followed by equibiaxial loading up to 80 mN to characterize stress-stretch behavior in longitudinal and circumferential directions. Following mechanical testing, tissues were fixed and stained with Movat's Pentachrome and Masson's Trichrome. High-resolution whole-slide imaging and machine learning-based image analysis were employed to quantify the density and orientation of collagen, elastin, and smooth muscle cells in the extracellular matrix.

Results

Preliminary analysis demonstrated characteristic nonlinear, pseudo-elastic stress-stretch behavior. At 15 kPa equibiaxial stress, mean longitudinal and circumferential stretches were similar (1.25 ± 0.13 vs. 1.25 ± 0.19). While the average behavior was relatively isotropic, we saw significant variability between samples with different risk factors, and some subjects displayed significant anisotropy. Histologically, samples from pregnancies complicated by preeclampsia exhibited distinct structural remodeling, characterized by a marked increase in collagen density and a reduction in elastic fibers within the inner tunica media compared to healthy controls.

Discussion

This study establishes that human UAs exhibit complex, heterogeneous mechanical behaviors that are intrinsically linked to their microstructural composition. The structural alterations observed in pathological pregnancies suggest that adverse intrauterine environments trigger vascular remodeling, leading to stiffening. These findings provide a baseline for understanding fetal vascular development and support future studies aimed at understanding the specific roles of different risk factors on UA biomechanics and fetal cardiovascular programming.

Session Category

Cardiovascular/Cardiorespiratory Biomechanics: Methods, Models and Applications

P4-116

Personalized Multiphysics Four-Chamber Heart Modeling Framework for Simulating Heart Failure and Treatments

Dr Sandra Hager[1], Dr Vahid Ziaei-Rad[1], Dr Jenny Choy[2], Dr Mengjun Wang[2], Dr Ghassan Kassab[2], Dr Lik Chuan Lee[1]

[1]Michigan State University, East Lansing, Michigan, United States. [2]California Medical Innovations Institute, San Diego, California, United States

Introduction

Computational cardiac modeling is an important tool for understanding heart function, enabling personalized therapies, and developing digital twins. While frameworks for left-ventricular and biventricular mechanics are well established, physiologically realistic four-chamber models that include the Purkinje fiber network, however, remain limited. To address this issue, we developed a computational model framework that integrates a fractal-tree-based Purkinje fiber network and a patient-specific four-chamber heart geometry coupled to a closed-loop circulatory model. The computational framework was used to simulate left-branch bundle block (LBBB) and cardiac resynchronization therapy (CRT).

Methods

A patient-specific four-chamber myocardial model was generated and subsequently used to project a fractal-tree-based Purkinje fiber network onto the endocardial surfaces [1]. Electrical propagation within both the Purkinje system and the myocardium was simulated using a modified FitzHugh–Nagumo (FHN) formulation, with a modified diffusion tensor to reflect electrophysiological activation characteristics of the heart [2-4]. Electromechanical coupling was through active and passive components of a transversely isotropic constitutive law, combined with a rule-based fiber field [5,6]. Closed-loop hemodynamic coupling was incorporated using a lumped circulatory model enabled by pressure-driven contraction [7]. LBBB was simulated by setting diffusion parameters to zero at a network junction near the His bundle. To simulate CRT, two additional activation sites, lateral LV and apical RV, were introduced, reflecting the clinically accepted gold-standard approach [8].

Results

The baseline model produced activation and deformation patterns consistent with expected ventricular physiology, with total myocardial activation after 115ms an ejection

fraction (EF) of 47% and a peak LV pressure of 147mmHg. LBBB resulted in delayed LV depolarization, reduced EF to 24% and lowered peak pressure to 104mmHg. CRT pacing partially restored synchronous activation with a 28% reduction in activation time and improved global pump function (43%), with peak LV pressure of 125mmHg.

Discussion

This preliminary model offers a foundation for studying LBBB-related activation abnormalities and evaluate CRT strategies. Although quantitative metrics such as conduction velocities may require further calibration, the qualitative activation sequence and resynchronization response align with clinical observations. Its modular structure will facilitate future integration of atrial electrophysiology and refined conduction parameters, with the long-term potential to support patient-specific predictions of CRT response.

Images (Optional)

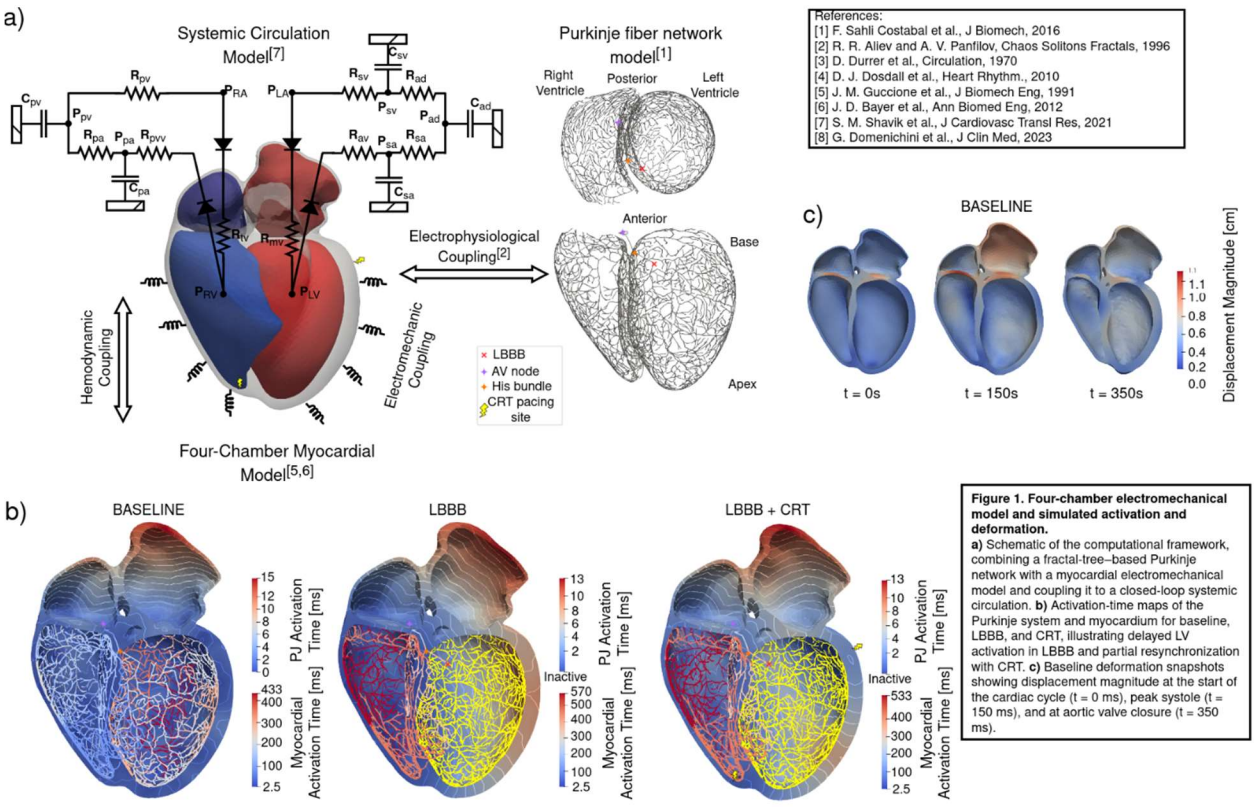


Figure 1. Four-chamber electromechanical model and simulated activation and deformation.
a) Schematic of the computational framework, combining a fractal-tree–based Purkinje network with a myocardial electromechanical model and coupling it to a closed-loop systemic circulation. **b)** Activation-time maps of the Purkinje system and myocardium for baseline, LBBB, and CRT, illustrating delayed LV activation in LBBB and partial resynchronization with CRT. **c)** Baseline deformation snapshots showing displacement magnitude at the start of the cardiac cycle (t = 0 ms), peak systole (t = 150 ms), and at aortic valve closure (t = 350 ms).

Session Category

Cardiovascular/Cardiorespiratory Biomechanics: Methods, Models and Applications

P4-117

Computational Analysis of Cerebral Hemodynamics Under Variations in Circle of Willis Anatomy and Autoregulation Capacity

Ms. Seo Yeon Kim[1], Mr. Chang Min Lee[1], Prof. Keun-Hwa Jung[2], Prof. Hyeyeon Chang[3], Prof. Hyun Jin Kim[1]

[1]Korea Advanced Institute of Science and Technology, Daejeon, Daejeon, Korea, Republic of. [2]Seoul National University Hospital, Seoul, Seoul, Korea, Republic of. [3]Konyang University Hospital, Daejeon, Daejeon, Korea, Republic of

Introduction

The brain is highly sensitive to reductions in cerebral blood flow (CBF) and relies on compensatory mechanisms such as cerebral autoregulation (CA) and the Circle of Willis (CoW). CA stabilizes CBF across a range of arterial pressures by dynamically modulating arteriolar resistance, whereas the CoW provides collateral pathways for redistributing flow when primary vessels are compromised. Both mechanisms exhibit substantial inter-individual variability, which may influence disease progression and susceptibility to ischemia. This study investigates the combined impact of CoW anatomical variation and CA impairment on cerebral hemodynamics using three-dimensional vascular models with progressive stenosis on the left internal carotid artery.

Methods

A patient-specific cerebrovascular geometry was reconstructed from MRI data and multiple CoW variants were generated to examine the effect of anatomical configurations. CA was implemented by modulating downstream resistances within physiologically informed bounds, based on arterial spin labeling measurements from ten healthy subjects before and after acetazolamide administration. Blood flow was modeled as an incompressible Newtonian flow governed by the Navier–Stokes equations and solved using a stabilized finite-element formulation. Simulations were performed across increasing stenosis severities while varying both CoW anatomy and CA capacity.

Results

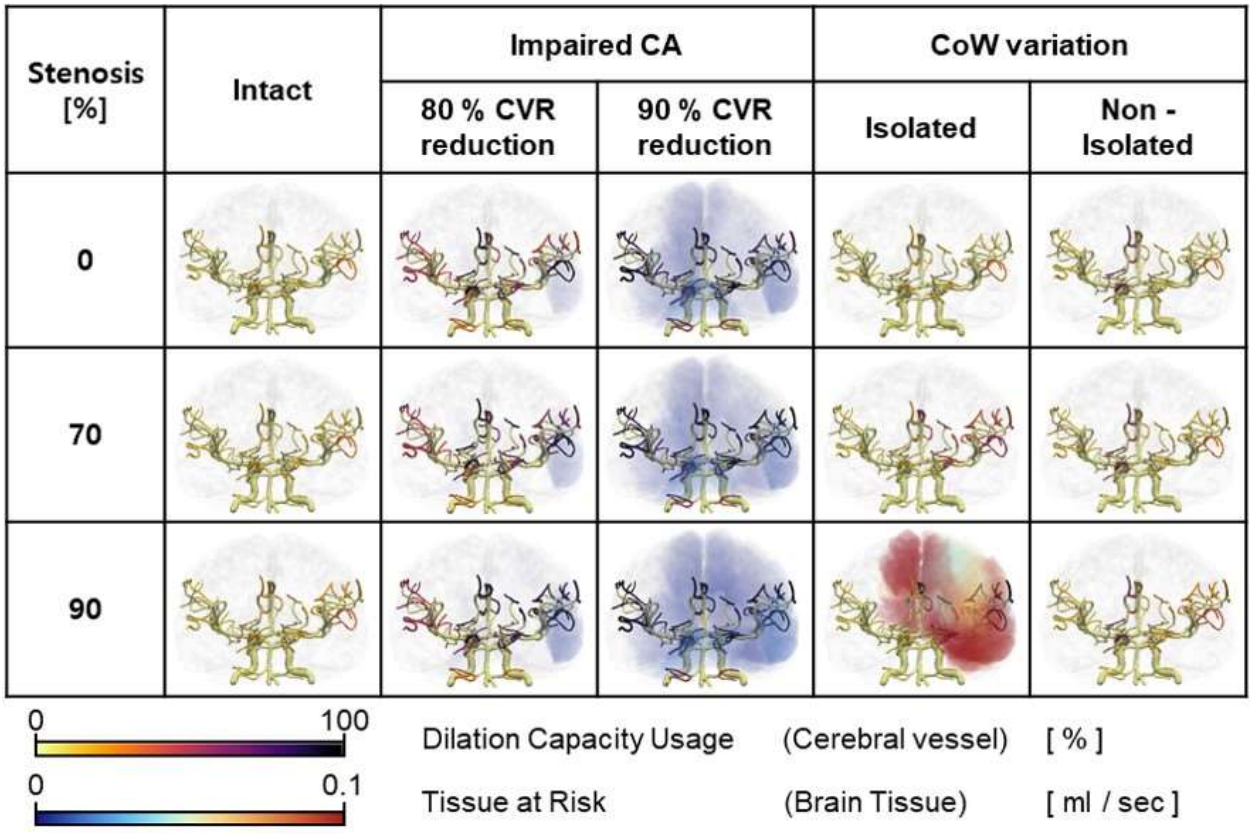
Under reduced cerebrovascular reserve (CVR<80%), models with a complete CoW exhibited only modest flow deficit of 0.07~1.93% across stenosis levels. In contrast, CoW variations produced substantially larger flow deficits of 2.83~33.61%, particularly in isolated configurations where perfusion territories depended on a single ipsilateral artery.

Impaired CA produced gradual increases in Dilation capacity usage (DCU) with worsening stenosis, whereas CoW variations induced abrupt spikes in DCU for isolated configurations. Even in non-isolated configurations, certain CoW configurations redistributed hemodynamic burden and created localized regions of vulnerability despite preserved global flow.

Discussion

Reduced CVR produces progressive increases in DCU, whereas the collateral pathways of CoW mitigate substantial flow loss. However, anatomical variability in the CoW can trigger sudden increases in DCU and precipitate acute hemodynamic vulnerability, particularly in isolated configurations. These findings highlight that CA impairment contributes to gradual hemodynamic instability, whereas CoW anatomical variation represents a conditional but potential risk factor capable of triggering abrupt cerebrovascular compromise.

Images (Optional)



References (Optional)

Acknowledgements (Optional)

This work was supported by Samsung Research Funding & Incubation Center for Future Technology of Samsung Electronics under Project Number SRFC-IT2401-04

This research was supported by a grant (RS-2023-00215667) from Ministry of Food and Drug Safety in 2025

This research was supported by the National Research Foundation of Korea (NRF) grant funded by the Korea government (MSIT) (No. 2022R1A5A1022977)

Session Category

Cardiovascular/Cardiorespiratory Biomechanics: Methods, Models and Applications

P4-118

Evaluation of Automated nnUNet Convolutional Neural Network (CNN) Segmentation of Coronary Arteries and Ascending Aorta from Coronary CT Angiography

Mr. Seraphim Fahmy, Ms. Anahita Seresti MS, Dr. M. Owais Khan PhD, P.Eng.

Toronto Metropolitan University, Toronto, Ontario, Canada

Introduction

Coronary artery segmentation from coronary computed tomography angiography (cCTA) has received increasing interest, driven primarily by non-invasive fractional flow reserve (CT-FFR) using computational fluid dynamics simulation (CFD). However, reconstructing complete coronary trees from cCTA is labor-intensive, with few open-source deep-learning coronary-specific segmentation tools, particularly for CFD. nnUNet is an open-source self-configuring convolutional neural network framework designed to automatically segment anatomical structures from various imaging modalities (e.g. CT, MRI). In this work, we evaluated the accuracy of detailed nnUNet segmentations of coronary artery trees and aorta from cCTA.

Methods

We used N=71 cCTA images. Detailed coronary arteries were segmented in SimVascular software to generate 3D label maps, which included the left/right coronary arteries and aorta. A separate dataset of N=29 test cases were used for testing with pre-existing labels. Images and coronary/aorta labels were fed into nnUNetv2 using default nnUNetTrainer, Residual Encoding Medium preset, default pre- and postprocessing, and 3d_cascade_fullres configuration. Dice scores were evaluated using nnUNetv2's built-in evaluation script. Visual Identification of true/false extensions of vasculature and disconnected regions was performed via comparison to original image.

Results

Mean Dice Scores were 0.87+-0.06 for Aorta, 0.71+-0.07 for the left coronary tree, and 0.74+-0.12 for the right coronary tree. After preliminary analysis of 6 selected cases, 14 regions were found in ground truth but disconnected, 12 regions demonstrated correct extension of vasculature, and 4 included segmentation of vasculature outside of coronaries. Mean inference time was ~10 minutes on Nvidia RTX4090. Inference dice exceeded cross-validation, indicating high model generalizability.

Discussion

nnUNet has been applied to many medical imaging tasks with high success (e.g., tumors, kidneys, liver). However, extending nnUNet to coronary arteries presents challenges due to their finer structures. Our results demonstrate that while nnUNet can segment aorta reliably, left and right coronary arteries present discontinuities and fragmentation. Post-processing techniques, including Sequential Segmentation (SeqSeg) that infer along vessel centerlines, could further improve performance. In daughter branches of epicardial coronary arteries, the segmented lumen was typically narrower than ground truth. nnUNet could provide fast initial reconstruction of coronary arteries that could be refined with post-processing, ultimately streamlining cCTA-based analysis.

Images (Optional)

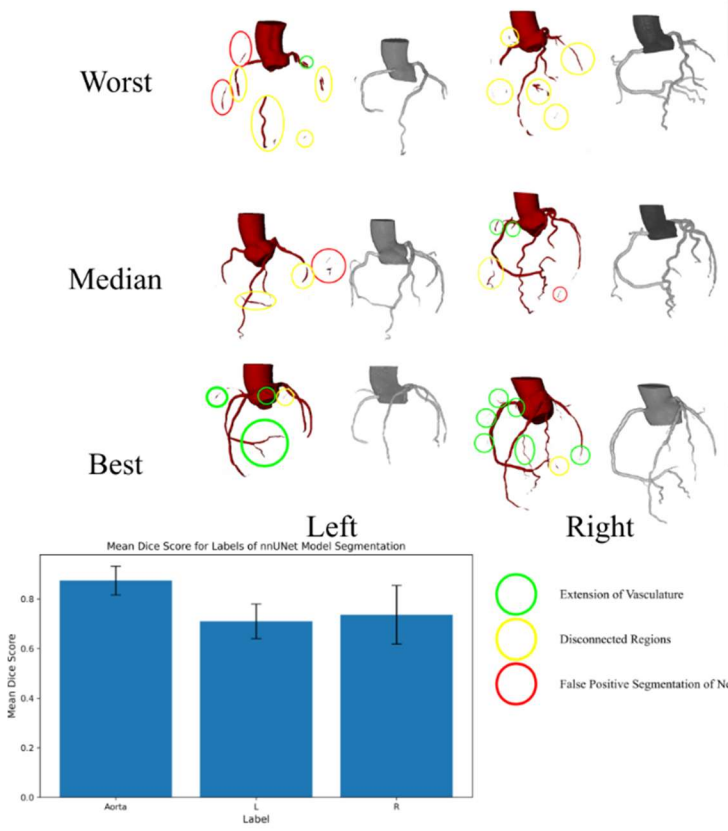


Table 1a): Mean Dice Score for Each Fold Validation and Total Cross-Validation
Table 1b): Mean, Standard Deviation, Best, Worst, and Median Prediction Dice

	Validation Dice Score (DSC)					
Label	Fold 1	Fold 2	Fold 3	Fold 4	Fold 5	Cross Val
Aorta	0.83	0.86	0.87	0.89	0.86	0.87
Left Tree	0.46	0.61	0.52	0.51	0.43	0.51
Right Tree	0.49	0.61	0.49	0.52	0.46	0.51

	Evaluation DSC				
Label	Mean	Standard Deviation	Best	Worst	Median
Aorta	0.87	0.06	0.94	0.70	0.89
Left Tree	0.71	0.07	0.80	0.52	0.71
Right Tree	0.74	0.12	0.88	0.35	0.75

Table 2: Count of False Positive Segmented Regions, Vasculature Extension, and Disconnected Regions for Selected Cases

	Case						
Feature	Worst DSC		Median DSC		Best DSC		Total
	L	R	L	R	L	R	
Disconnected Region	4	5	2	1	1	1	14
False Positive	2	0	1	1	0	0	4
Vasculature Extension	1	0	0	2	3	6	12

Session Category

Cardiovascular/Cardiorespiratory Biomechanics: Methods, Models and Applications

P4-119

Structural Biomarkers from FSI in Hyperemic Coronary Arteries: Wall Stress and Deformation Across Lesion Severities

Mr. Francisco Pinto de Oliveira MSc[1,2], Prof. Concepción Paz PhD[3,4], Prof. Eduardo Suárez Porto PhD[3,4], Prof. Christian Gil Pereira PhD[3,4], Dr. Nuno Dias Ferreira[5], Dr. Diogo Santos-Ferreira MSc[5,6], Prof. Ricardo Ladeiras-Lopes PhD[6], Prof. Nuno Bettencourt PhD[6], Prof. Luísa Costa Sousa PhD[1,2], Prof. Sónia Pinto PhD[1,2]

[1]Engineering Faculty of University of Porto, Porto, N/A, Portugal. [2]Institute of Science and Innovation in Mechanical and Industrial Engineering (LAETA-INEGI), Porto, N/A, Portugal. [3]CINTECX, University of Vigo, Vigo, N/A, Spain. [4]Biofluids Research Group, Galicia Sur Heath Research Institute (IIS Galicia Sur), Vigo, N/A, Spain. [5]Cardiology Department, Unidade Local de Saúde de Gaia e Espinho, Vila Nova de Gaia, N/A, Portugal. [6]UnIC@RISE, Department of Surgery and Physiology, Faculty of Medicine, University of Porto, Porto, N/A, Portugal

Introduction

Coronary artery disease remains a major cause of mortality, and current diagnostic tools struggle to describe the structural impact of stenoses. Fractional flow reserve (FFR) identifies flow-limiting lesions but provides only a global pressure index and neglects local wall mechanics [1]. Fluid–structure interaction (FSI) modelling estimates wall stress and deformation under hyperemic conditions, potentially revealing structural features linked to stenosis severity. This study examines whether patient-specific FSI-derived metrics correspond to invasive FFR classification.

Methods

Three right coronary arteries were selected to cover different lesion severities: two non-significant cases (Patients 1 and 3, FFR = 0.90 and 0.97) and one borderline/significant case (Patient 2, FFR = 0.75). Patient-specific geometries were reconstructed from CT and adapted to hyperemic anatomy. Blood was modeled as viscoelastic with Womersley pulsatile inflow and Windkessel outlets. Arterial walls were assumed linearly elastic and FSI simulations were run. The methodological consistency was confirmed by comparing FSI-derived with invasive FFR, yielding a mean relative error of 7.87% (SD 6.14%).

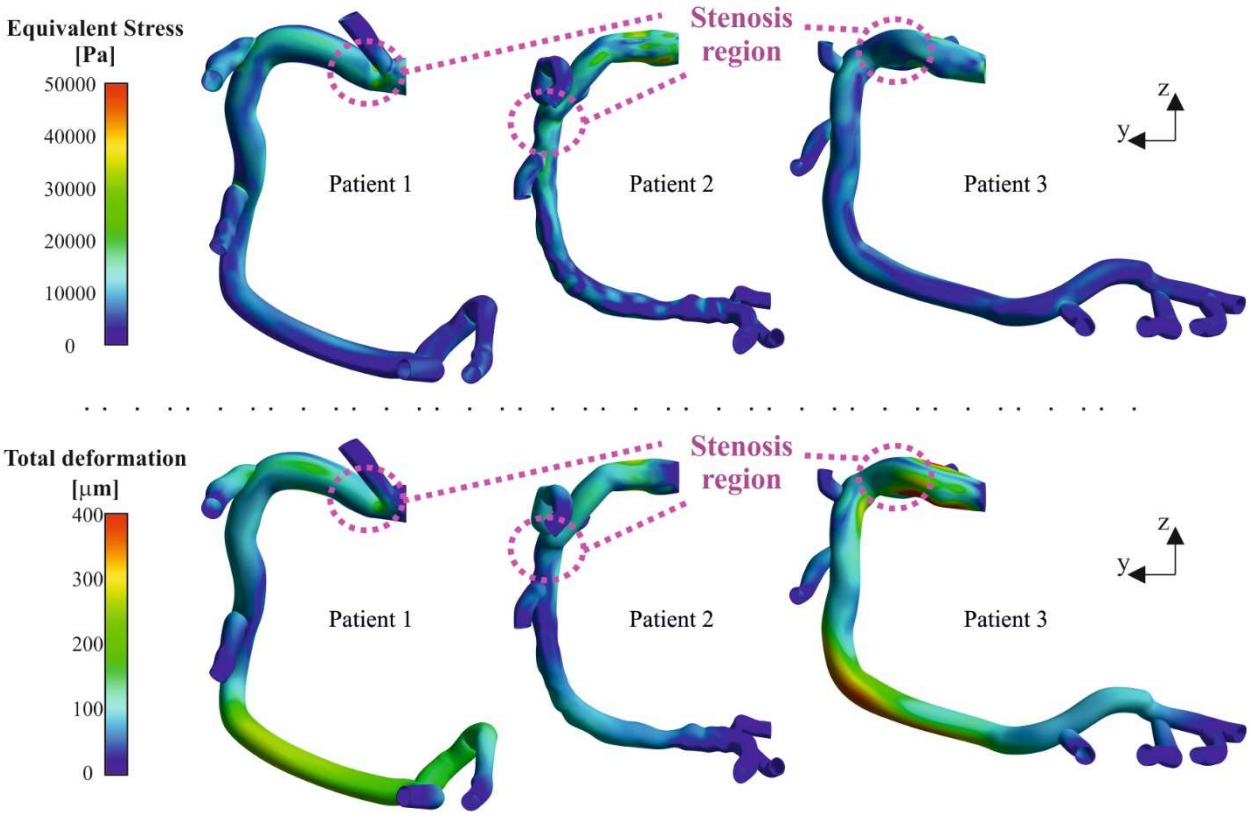
Results

Peak hyperemic structural responses differed across patients. In Patient 1, the stenotic region exhibited 10,000–50,000Pa of equivalent stress and 80–200 μm deformation, confined locally without downstream propagation. Patient 2 showed marked stress concentration (8,000–28,000 Pa) and deformation of 50–130 μm, forming a focal mechanical pattern aligned with borderline functional severity. Patient 3 demonstrated the lowest stress (5,000–12,000 Pa) and diffuse deformation (60–180 μm), indicating a geometrically irregular yet mechanically benign lesion. Stress increased over 200% from Patient 3 to Patient 2, whereas deformation showed no linear relationship with FFR.

Discussion

FSI-derived structural biomarkers distinguished lesions by mechanical relevance, identifying features not captured by pressure-based indices. Stress amplification was the clearest marker of severity, particularly in the borderline case, supporting evidence that local mechanical forces drive plaque evolution [2,3]. FSI therefore complements FFR by revealing wall loading patterns. Larger cohorts and refined wall models are required to assess prognostic value and enable clinical translation.

Images (Optional)



References (Optional)

[1] De Bruyne B. et al., N Engl J Med, 2012.

[2] Morris P.D. et al., J Biomech Sci Eng, 2016.

[3] Kim H.J., Vignon-Clementel I.E., Annu Rev Biomed Eng, 2010.

Acknowledgements (Optional)

The authors gratefully acknowledge the financial support of FCT – Fundação para a Ciência e a Tecnologia (Portugal) through the R&D Project CADS-FACT – PTDC/EMD-EMD/0980/2020, as well as the institutional support of the Faculty of Engineering of the University of Porto (FEUP), the Institute of Science and Innovation in Mechanical and Industrial Engineering (INEGI), the Cardiovascular R&D Unit of the Faculty of Medicine of the University of Porto (FMUP), and the Cardiology Department of the Vila Nova de Gaia/Espinho Hospital Centre (CHVNG/E).

The authors also acknowledge the collaboration and technical support from CINTECX, University of Vigo, and the Biofluids Research Group, Galicia Sur Health Research Institute (IIS Galicia Sur) whose contribution was essential for the development of the fluid–structure interaction simulations.

Session Category

Cardiovascular/Cardiorespiratory Biomechanics: Methods, Models and Applications

P4-120

GPU-Accelerated Cardiovascular FSI in SimVascular

Dr. Sujal Dave, Dr. David Codoni, Dr. Alison Marsden

Stanford University, Stanford, CA, United States

Introduction

High–fidelity fluid-structure interaction (FSI) simulations are central to advancing cardiovascular biomechanics, however, their computational cost remains a major barrier to rapid design, uncertainty quantification, and clinical translation. In this work, we present ongoing efforts to accelerate cardiovascular FSI and CFD simulations within the *SimVascular* [1,2] framework through GPU-enabled computing and investigation of preconditioning strategies.

Methods

Using Trilinos linear algebra libraries with Kokkos for on-node GPU parallelization, we evaluate the performance of several state-of-the-art preconditioners for representative cardiovascular test cases. Our investigation focuses on comparisons between CPU-only and GPU-enabled execution, as well as behaviour of different Trilinos preconditioners at a fixed configuration of eight MPI ranks for both FSI and rigid-wall CFD simulations.

Results

GPU-accelerated solvers provide substantial reductions in wall time compared to CPU-only runs, enabling more efficient parameter sweeps and reduced turnaround times for patient-specific analyses. For a representative Abdominal Aorta Aneurysm FSI case with Diagonal preconditioning, GPU (Ampere80 architecture) execution reduced the wall time from approximately 2200 seconds on CPUs to about 700 seconds, corresponding to a reduction of roughly 65%. For a rigid-wall CFD case with a RILUK(0) preconditioner, GPU (Ampere80) execution yields speedups of 3-4x at the same rank count. Preliminary results indicate that customized preconditioners, particularly algebraic multigrid variants optimized for coupled FSI systems, yield robust convergence and significant wall-time reductions. On the rigid-wall Navier--Stokes system, algebraic multigrid (ML) reduced GPU wall time by approximately 60% compared with Diagonal or ILUT preconditioning under GMRES. For FSI runs, the difference between Diagonal and ML remains modest to a few percentage but still favorable to multigrid.

Discussion

These results indicate that GPU-enabled cardiovascular solvers, combined with carefully selected preconditioners, can deliver significant improvements in computational efficiency. The insights gained here provide a pathway towards routinely deploying large-scale FSI simulations on GPU clusters, ultimately enhancing the modeling capabilities available to the cardiovascular biomechanics community. This work builds on the established open-source ecosystem of *SimVascular* and contributes new directions for its integration with diverse HPC systems.

References (Optional)

[1] Adam Updegrove et al., Ann. Biomed. Eng. , 2017

[2] Chi Zhu et al., JOSS, 2022

Session Category

Cardiovascular/Cardiorespiratory Biomechanics: Methods, Models and Applications

P4-121

Biphasic Modeling of a Water-Permeable Arterial Wall Under Steady Axisymmetric Deformation

Graduate Student Takeo Fujiwara MEng student[1], Associate Professor Tomohiro Otani PhD[1], Professor Shukei Sugita PhD[2], Professor Shigeo Wada PhD[1]

[1]The University of Osaka, Toyonaka, Osaka, Japan. [2]Nagoya Institute of Technology, Nagoya, Aichi, Japan

Introduction

Arterial tissue has conventionally been treated as incompressible, while recent experiments have reported large apparent compressibility [1,2]. In vitro arterial inflation tests showed volume increases of up to 40% [1], although the mechanism underlying this behavior remain unclear. In this study, we aimed to clarify the underlying mechanism of arterial compressibility using biphasic modeling approach, in which arterial compressibility arises from interstitial fluid flow driven by pressure differences across the arterial wall.

Methods

Arterial deformation was assumed to be steady, axisymmetric, and in a plane strain state following [1]. The artery wall with permeable nature was modeled as a biphasic porous media composed of incompressible solid and fluid phases. Their mechanical behavior was formulated following [3]. The constitutive law of the solid skeleton was modeled as Fung-type strain-energy density function for distortional part [4]. For volumetric deformation, we applied Simo-type logarithmic function [4,5] in compression and an exponential function in expansion (Fig. (a)). Interstitial fluid flow was modeled using Darcy's law. The governing equations were solved with an in-house finite element solver, and pressure differences ranging from 15 to 160 mmHg were examined (Fig. (a)).

Results

The pressure-total volume relationship showed good agreement with the experimental results of [1] (Fig. (b)). Figures (c) and (d) illustrate the radial distributions of fluid volume fraction and radial Cauchy stress at the pressure differences of 100 mmHg. Fluid volume fraction increased throughout the arterial region, resulting in positive radial stress across the artery wall, with the maximum occurring near the mid-wall.

Discussion

These results demonstrated that biphasic modeling could express the large arterial compressibility observed in recent experiments. Because this behavior cannot be captured using conventional single-phase, incompressible models, the biphasic framework provides a useful basis for understanding the mechanical responses in the artery under physiological loading.

Images (Optional)

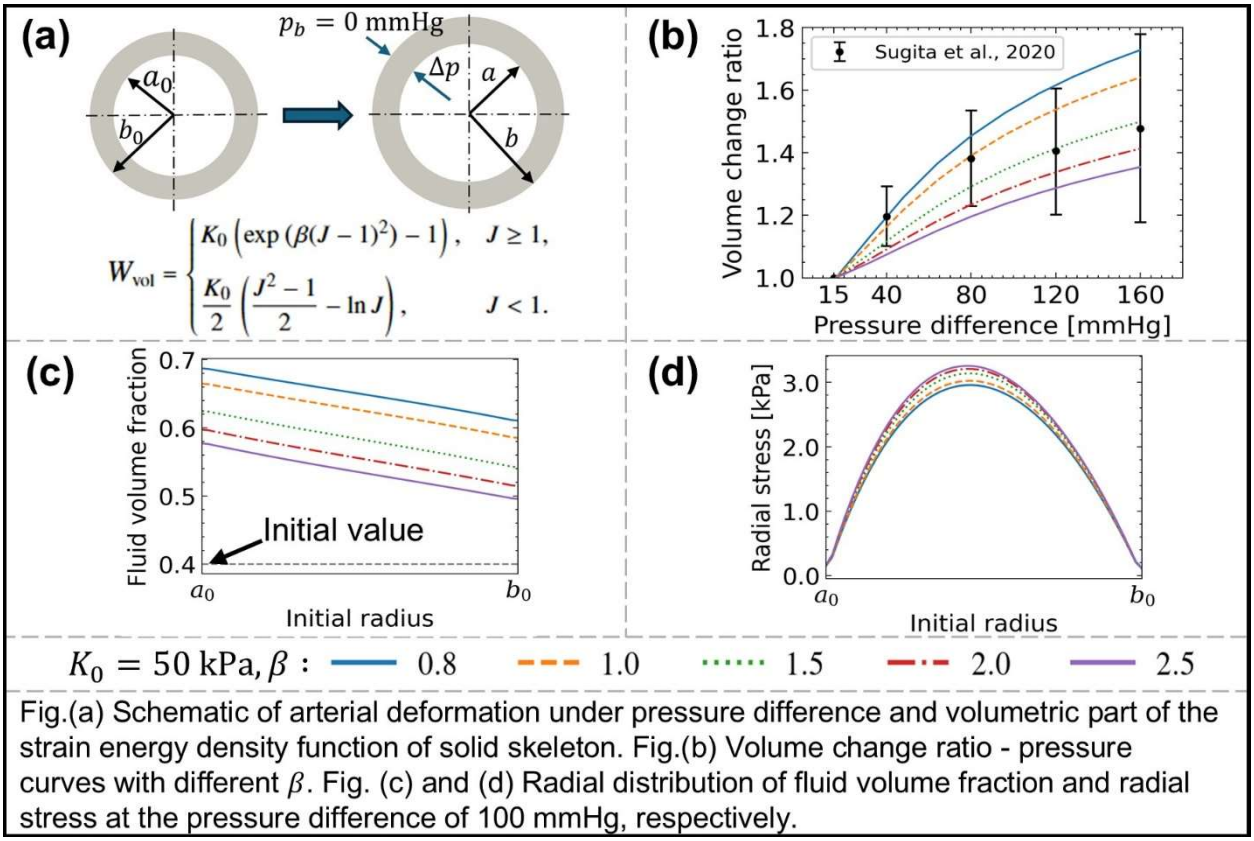


Fig.(a) Schematic of arterial deformation under pressure difference and volumetric part of the strain energy density function of solid skeleton. Fig.(b) Volume change ratio - pressure curves with different β. Fig. (c) and (d) Radial distribution of fluid volume fraction and radial stress at the pressure difference of 100 mmHg, respectively.

References (Optional)

[1] Sugita et al., Biomech. Model. Mechanobiol., 2020

[2] Yosibash et al., J. Mech. Behav. Biomed. Mater., 2014

[3] Auton et al., Proc. R. Soc. A, 2017

[4] Ateshian and Costa, J. Biomech., 2009

[5] Simo and Armero, Int. J. Numer. Methods Eng., 1992

Acknowledgements (Optional)

This study is partly supported by JSPS Scientific Research (25K03452) and MEXT program for promoting research on the Supercomputer Fugaku (JPMXP1020230118).

Session Category

Cardiovascular/Cardiorespiratory Biomechanics: Methods, Models and Applications

P4-122

An Analytical Fluid-Structure Interaction Framework for Biomechanical Behaviour of Common Carotid Artery

Mr Muhammad Azhar[1], Mr Hafiz Zeeshan Ali Sardar[2], Mr Muhammad Sohail Ashraf[2], Mr Muhammad Shehryar Naeem[2], Mr Talha Akhtar[1], Mr Muhammad Fasih Iqbal[2], Dr Zia ul Rehman Tahir[2], Dr Parthasarathi Mandal[1]

[1]School of Engineering, University of Manchester, Manchestrer, Greater Manchester, United Kingdom. [2]Department of Mechanical Engineering, University of Engineering and Technology, Lahore, Punjab, Pakistan

Introduction

Common Carotid Artery (CCA) is major vessel responsible for carrying oxygenated blood to human brain, which is susceptible to atherosclerotic plaque formation and aneurysm development, resulting in increased risk of stroke, making its analysis important for advancing clinical understanding. Previous studies on investigation of diameter changes over cardiac cycle, often assume the arterial wall as rigid, neglecting physiological compliance of the artery, limiting assessment of its biomechanical behavior. Fluid-Structure Interaction (FSI) analysis of CCA is necessary to fully understand its biomechanical behavior. Novel analytical models using one-way-FSI and two-way-FSI are developed to determine diameter changes over cardiac cycle at any location along CCA.

Methods

Experimental data for CCA were taken from [1]. Inner radius, thickness, length, and modulus of elasticity of the artery was 0.3 cm, 0.7 mm, 10 cm, and 1.0 MPa, respectively [2]. The velocity and pressure profiles of blood over cardiac cycle from Ref. [2] were used to determine diameter changes. Two novel models (one-way-FSI and two-way-FSI) were developed to determine diameter changes. Numerical analysis was performed using ANSYS, structural changes were computed in Transient Structural, whereas changes due to blood flow were computed in Fluent, and both coupled through Coupling System Module.

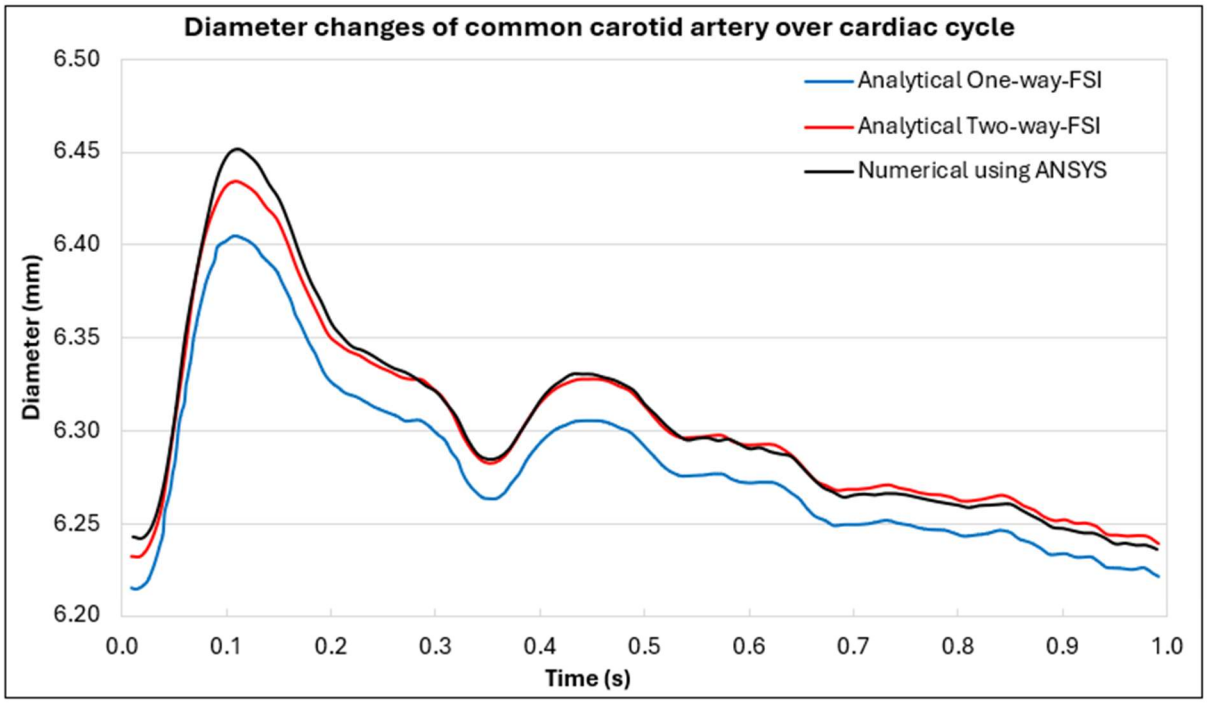
Results

The diameter changes over cardiac cycle using analytical models (one-way-FSI and two-way-FSI) and numerical analysis are presented in Figure. Three curves follow same physiological trend, with maximum diameter (6.41-6.45 mm) at systole and minimum diameter (6.22-6.24 mm) at diastole, except that analytical one-way-FSI underestimate diameter throughout the cycle.

Discussion

A comparison of results is presented in Table, and percentage difference with respect to experimental results is presented in parentheses. Analytical and numerical systolic diameters fall within range of experimental data, whereas diastolic diameter is slightly higher, with about 2% difference. Analytical one-way-FSI is simpler, yet its results are in close agreement with experimental data. Analytical two-way-FSI model gives similar results compared to computationally intensive numerical analysis. These results support validity of proposed analytical framework and provide real-time assessment of CCA without iterative computation, while retaining underlying physics.

Images (Optional)



Carotid Artery Diameter (mm)	Experimental Data	Analytical One-way-FSI	Analytical Two-way-FSI	Numerical using ANSYS
Systolic	6.4 ± 0.4	6.41 (0.2%)	6.43 (0.5%)	6.45 (0.8%)
Diastolic	6.1 ± 0.4	6.22 (2.0%)	6.23 (2.1%)	6.24 (2.3%)

References (Optional)

1. Sugawara, J., et al., Hypertens Res, 2007.

2. Bukač, M. and Čanić, S., Math Biosci Eng, 2013.

Session Category

P4-123

Effect of Cuff Compliance on Oscillometric Blood Pressure Measurements: A Finite-Element Study

Mr Muhammad Azhar[1], Mr Muhammad Fasih Iqbal[2], Mr Muhammad Sohail Ashraf[2], Mr Talha Akhtar[1], Dr Zia ul Rehman Tahir[2], Dr Parthasarathi Mandal[1]

[1]School of Engineering, University of Manchester, Manchestrer, Greater Manchester, United Kingdom. [2]Department of Mechanical Engineering, University of Engineering and Technology, Lahore, Punjab, Pakistan

Introduction

Cuff-based oscillometric devices have become standard way of measuring blood pressure (BP) in clinics and at home, yet concerns regarding their accuracy persist. The cuff remains critical component of BP devices, as it is primarily responsible for pressure transmission to brachial artery, thereby influencing BP estimations. However, limited literature addresses effects of cuff on oscillometric signals. Ursino and Cristalli [1] evaluated effect of cuff elastance for oscillometric BP; however, their assumption of uniform inner wall and omission of cuff buckling constrained the study. The present study instead explicitly considers cuff buckling to systematically evaluate effect of cuff compliance on oscillometric BP using fixed ratios.

Methods

Three-dimensional model of human upper arm was developed in Abaqus CAE, with geometry, material properties, and bladder-less cuff modelling adopted in accordance with literature [2]. The model was analysed using dynamic explicit scheme; cuff was inflated to 150 mmHg over 5 seconds and deflated over 25 seconds. The cuff compliance sensitivity analysis was performed by varying modulus of elasticity from 50 to 500 MPa. For each simulation, oscillometric envelope was obtained by plotting amplitude against cuff-pressure, and characteristic ratios were obtained for respective systolic/diastolic (120/70 mmHg) values.

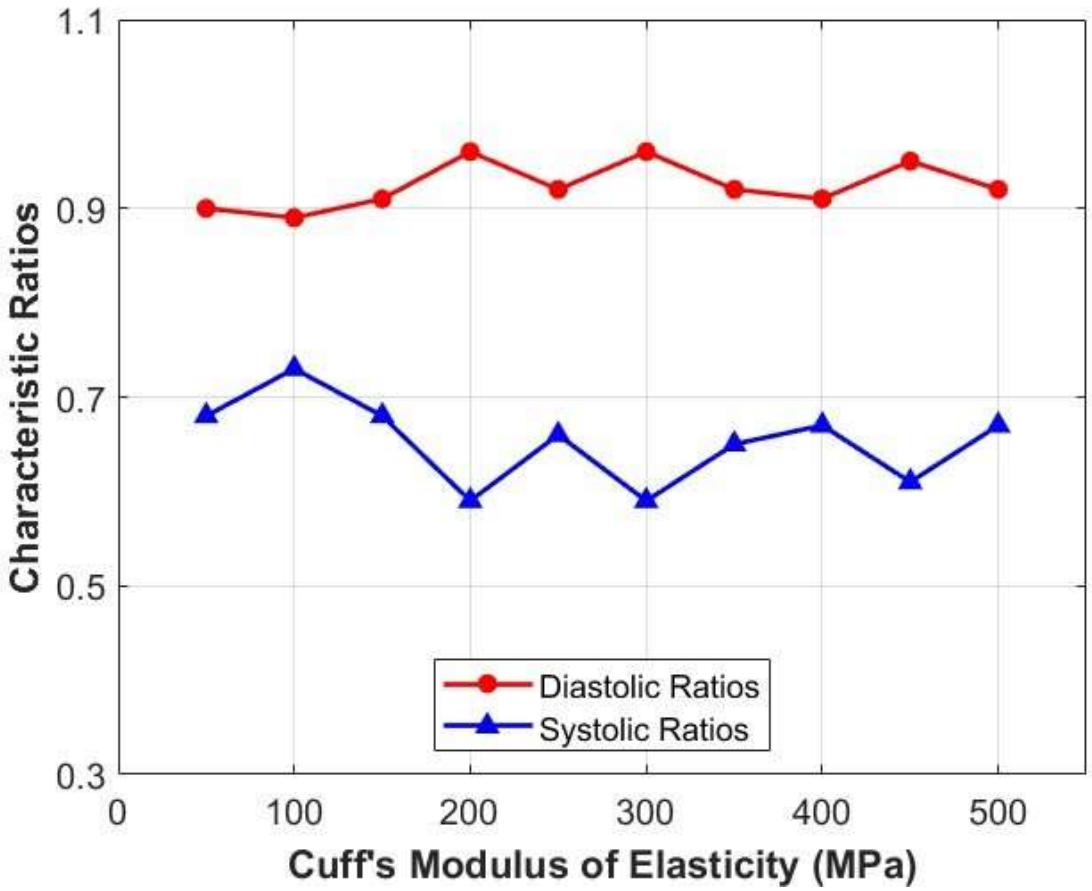
Results

Change in cuff compliance led to noticeable differences in characteristic ratios; these variations were not systematic, reflecting nuanced influence of cuff compliance. Diastolic ratios ranged between 0.89-0.96 and systolic ratios ranged between 0.59-0.73, as shown in Figure. These variations could be attributed to changes in cuff buckling wave around arm that result in axial redistribution of cuff-arm contact pressure.

Discussion

Ursino and Cristalli [1] reported negligible effect of cuff compliance on characteristic ratios, primarily because of uniform cuff-pressure distribution on arm did not account for cuff buckling. Present study demonstrated that cuff buckling, tends to concentrate loads near fabric folds, and is influenced by fabric compliance. Such load concentrations affect arterial deformations and resulting oscillometric signal used for BP estimations. These findings emphasise need for cuff-specific calibrations that account for cuff compliance given its influence on BP measurements.

Images (Optional)



References (Optional)

[1] Ursino, M. and Cristalli, C., IEEE Transactions on Biomedical Engineering, 1996.

[2] Azhar, M. et al., ESB-2025, 2025.

Session Category

P4-124

Surgical Planning for Neonatal Pediatric Heart Surgery – Optimizing the Configuration of BTT Shunts to Prevent Post-operative Complications

Mr. Tanmay M. Khare MS[1], Dr. Mohan John MD[2], Dr. Kevin O. Maher MD[2], Dr. Subhadra Shashidharan MD[2], Dr. Lakshmi Prasad Dasi PhD[1]

[1]Georgia Institute of Technology, Atlanta, Georgia, United States. [2]Children's Healthcare of Atlanta/Emory University School of Medicine, Atlanta, Georgia, United States

Introduction

The Blalock Taussig Thomas (BTT) shunt is used in the surgical palliation of cyanotic congenital heart diseases. In 30% of the cases, post-operative complications like stenosis or thrombosis develop inside the shunt. Our initial studies on a cohort of 39 patients have identified distinct differences between patients who had complications and those who did not, based on: (a) the location and angle of attachment of the shunts, and (b) flow patterns in the shunt. Using these guidelines, we have developed an in-silico surgical planning pipeline to determine optimal shunt configurations and prevent post-operative complications.

Methods

CT scans done prior to shunt implantation are used to build a 3D patient-specific model of pre-operative geometry. Using CAD software, all surgical steps are performed virtually on this model, and a shunt is constructed to generate a post-operative geometry (Figure 1c). Multiple such geometries are created for each patient by parametrically varying quantities like the location and angle of attachment of the shunts (Figure 1e, 1g). CFD simulations are performed on these new geometries (Figure 1f, 1h) using patient-specific boundary conditions adopted from echocardiogram scans and catheterization lab data. Simulations reveal the presence/absence of a region of recirculating, thrombogenic flow patterns that may develop inside the shunt for each shunt configuration. Similarly, for each patient, CFD simulations are also performed on actual post-operative geometries (Figure 1a).

Results

First, we observed that the flow patterns in the pre-operative geometry with shunt (Figure 1d) are similar to those observed in the actual post-operative geometry (Figure 1b). This demonstrates the ability to mimic the surgical shunt insertion procedure using in silico techniques. The case shown had stenosis near the shunt inlet and flow recirculation region

was also observed near the inlet. Therefore, we demonstrate that we can generate alternative shunt configurations where the flow recirculation regions are eliminated (Figure 1f) or reduced in size (Figure 1h), thus reducing the chances of complication development.

Discussion

This pipeline can serve as a predictive modeling tool for post-surgical hemodynamics and help clinicians design more informed treatment for each patient. It can also help to improve the success rate of this procedure.

Images (Optional)

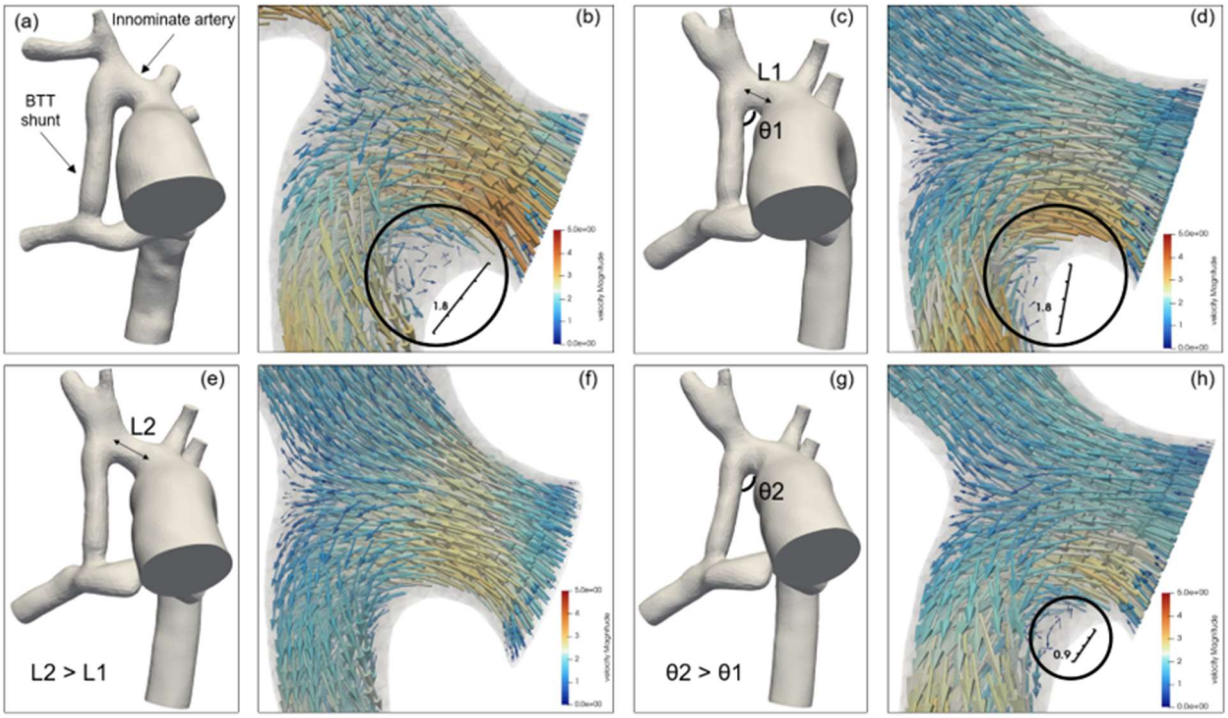


Figure 1: (a) actual post-operative geometry; (b) velocity vectors near shunt inlet of (a) – flow recirculation region highlighted by black circle; (c) shunt constructed in pre-operative geometry; (d) velocity vectors near shunt inlet in (c) – similar flow recirculation region highlighted by black circle; (e) new shunt configuration 1 where the inlet end is attached more distal along the innominate artery as compared to (c); (f) velocity vectors near shunt inlet in new configuration 1 – flow recirculation not observed; (g) new shunt configuration 2 where shunt is attached at a larger angle at the inlet end as compared to (c); (h) velocity vectors near shunt inlet in new configuration 2 – smaller flow recirculation region than original configuration (d) was observed.

Session Category

Cardiovascular/Cardiorespiratory Biomechanics: Methods, Models and Applications

P4-125

Deep Learning Estimation of Pulsatile Intracranial Aneurysm Wall Shear Stress

Mr. Wenhao DING, Dr. Choon Hwai Yap

Imperial College London, London, London, United Kingdom

Introduction

Intracranial aneurysm (IA) involves a weakness in the cerebral arterial wall that bulges and carries a potentially lethal risk of rupture. Despite extensive biomechanics studies and meta-analysis suggesting a correlation between fluid mechanics markers and aneurysm instability, these markers have yet to be adopted by physicians, who continue to rely on simple morphological markers to assess risks, even though this is inaccurate (false-positive rates up to 56%). Key reasons for this are that computational fluid dynamics (CFD) simulations are time-consuming and require specialized expertise. So physicians are unable to obtain sufficiently large samples of fluid dynamics data to evaluate their clinical utility.

We developed a deep learning (DL) framework to address this. We built a DL aneurysm generator to overcome scarce clinical data and used it to create a large CFD dataset for training a WSS predictor, which can be used without CFD skills for real-time, high-throughput predictions.

Methods

Our DL IA shape generator is a two-stage conditional VAE trained with 109 patient-specific IA morphologies [1], producing both the aneurysm pouch and its parent vessels suitable for CFD simulations. Next, mass shape generation and CFD simulations produced a large dataset with 16,000 steady and 730 transient simulations on diverse morphologies [2]. Finally, we utilized a graph Transformer to predict WSS over a full cardiac cycle, using cotangen-Laplacian eigenvectors as positional encoding. Codes and datasets are publicly shared (figure's QR codes).

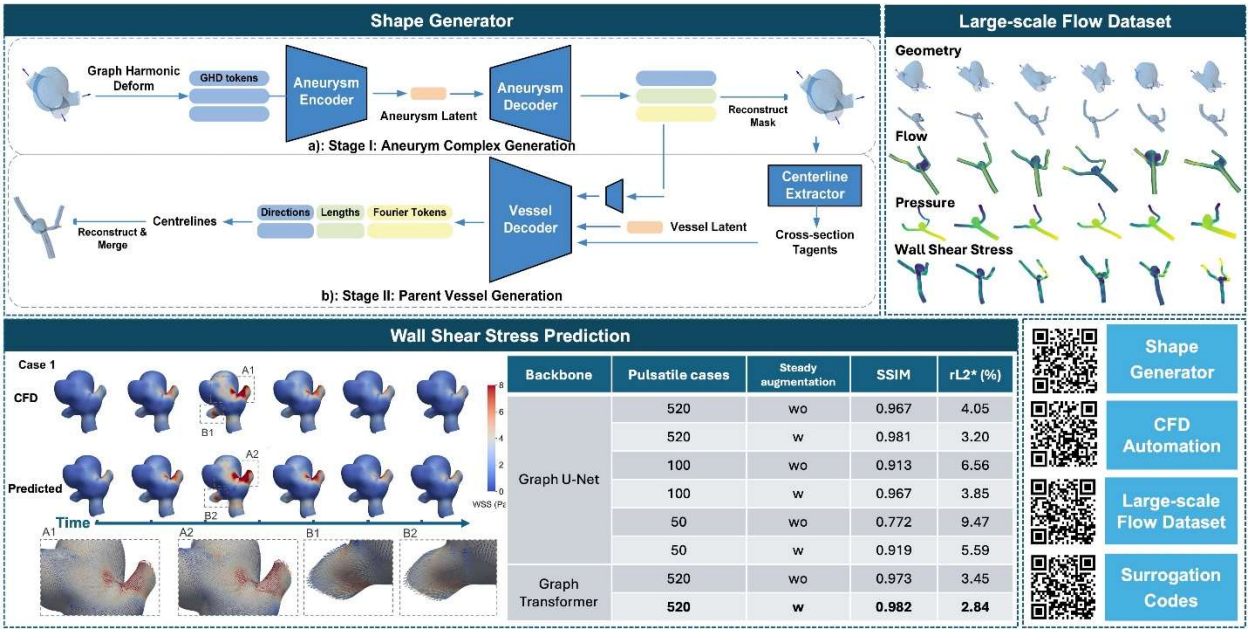
Results

Our model captures WSS pattern evolution across diverse geometries, achieving excellent spatial pattern (SSIM =0.981) and WSS magnitude accuracy (maximum-normalized relative L2 error = 2.84%). The augmentation with steady data substantially improves generalization, and allowed very few transient training data (even with <100) to achieve decent accuracy.

Discussion

We present the first DL model for pulsatile IA WSS prediction, and will also work for other parameters (OSI, pressures). Future work includes expanding boundary conditions and including IAs with different topologies.

Images (Optional)



References (Optional)

[1] Ding, W., *et al.*, Two-Stage Generative Model for Intracranial Aneurysm Meshes with Morphological Marker Conditioning, MICCAI 2025

[2] Ding, W., *et al.*, AneuG-Flow: A Large-Scale Synthetic Dataset of Diverse Intracranial Aneurysm Geometries and Hemodynamics, NeurIPS 2025 (San Diego, Poster #121403)

Session Category

Cardiovascular/Cardiorespiratory Biomechanics: Methods, Models and Applications

P4-126

Numerical Assessment of Collateral Circulation for Ischemic Relief in Coronary Chronic Total Occlusion

Mr. Wonjin Choi[1], Mr. Se Hyeog Kim[1], Mr. Hyeok Sul Kwon[1], Prof. Jung-Kyu Han[2], Prof. Bon-Kwon Koo[2,3], Prof. Hyun Jin Kim[1]

[1]Korea Advanced Institute of Science and Technology, Daejeon, Daejeon, Korea, Republic of. [2]Seoul National University Hospital, Seoul, Seoul, Korea, Republic of. [3]Seoul National University College of Medicine, Seoul, Seoul, Korea, Republic of

Introduction

Coronary chronic total occlusion (CTO) can lead to severe myocardial ischemia, and clinical outcome depends not only occlusion site and lesion length but also the extent and functional effectiveness of collateral circulation. However, current clinical assessments rely largely on imaging findings or coarse clinical measurements, offering limited quantitative insight into the hemodynamic contribution of collaterals. In this work, we quantify the role of collateral vessels in ischemia relief using numerical modeling applied to both idealized and patient-specific CTO configurations.

Methods

Coronary arteries were reconstructed as 1D vascular trees from clinical imaging. CTO lesions were artificially introduced in proximal, mid, and distal segments of major arteries [1]. We generated 500 collateral configurations per scenario, uniformly sampling the number of collaterals (1-20) and diameters (0.01-0.10 cm). Donor–recipient segment pairs followed clinical distributions [1], with anatomically realistic paths along ventricular epicardial surfaces. Hemodynamics was simulated using an in-house reduced-order solver for 1D vascular networks, enabling efficient evaluation of thousands of CTO-collateral combinations. Fractional flow reserve (FFR) was computed as the primary indicator of collateral efficacy. Gaussian process regression was employed for sensitivity analysis to identify key determinants of collateral performance.

Results

Collateral diameter was the dominant factor influencing FFR improvement and ischemia relief in the idealized model. When collateral diameter fell below a critical threshold, ischemic relief was minimal regardless of the number of collaterals. Beyond specific thresholds in diameter and vessel count, FFR improvements reached saturation, indicating diminishing hemodynamic benefit with further enlargement or collateral addition. In the

patient-specific model, collaterals reconstructed from angiographic data contributed only marginally to perfusion support, consistent with trends observed in idealized simulations.

Discussion

This study quantitatively demonstrates that angiographically visible collaterals provide limited perfusion support unless their diameters exceed a critical threshold. While functional variations existed across proximal, mid, and distal lesions, FFR rarely exceeded the clinical threshold, implying that collateral circulation alone does not guarantee clinically meaningful perfusion improvement. The proposed *in silico* framework enables an efficient, patient-specific evaluation of collateral function and provides a computational foundation for future decision-support tools in the management of coronary CTO.

References (Optional)

[1] McEntegart et al. , EuroIntervention, 2016

Acknowledgements (Optional)

This work was supported by the National Research Foundation of Korea (NRF) grant funded by Ministry of Science and ICT (MSIT) (2022R1A5A1022977), Ministry of Food and Drug Safety (MFDS) (RS-2023-00215667), and Samsung Research Funding and Incubation Center for Future Technology (SRFC-IT2401-04).

Session Category

Cardiovascular/Cardiorespiratory Biomechanics: Methods, Models and Applications

P4-127

The Influence of Viscoelasticity on the Transition to Turbulence in Blood Flow: An in Vitro Study Using Ultrasound Particle Imaging Velocimetry

Ms Ying Hu, Dr Lee Nissim, Dr Katharine Fraser

University of Bath, Bath, England, United Kingdom

Ms Ying Hu

Dr Lee Nissim

Introduction

Blood is viscoelastic, combining shear-thinning viscosity and elasticity. Experimentally a delayed transition-to-turbulence in comparison with Newtonian rheology is clear, however, the source of contribution is obscure. Studies assessing the influence of shear-thinning rheology have conflicting conclusions.

To investigate the independent influence of elasticity on the transition-to-turbulence, viscoelastic blood analogues were studied in a pipe flow rig using ultrasound particle imaging velocimetry (echo-PIV).

Methods

A pump supplied continuous flow through an 8 mm pipe flow geometry, measured by a flowmeter (em-tec GmbH). Two blood analogues with matched shear-thinning viscosity corresponding to real blood were prepared: xanthan gum solution (XG, 500 ppm, w/w) with a relaxation time of 3.8 ms; and polyacrylamide solution (PAA, 125 ppm, w/w) with a relaxation time of 38 ms. Deionised water was used as a Newtonian control.

An ultrasound research platform (Vantage 256, Verasonics) with linear transducer (GE Healthcare) was used for high-temporal-spatial-resolution B-mode image acquisition. A low concentration of Hollow Glass Spheres (Dantec Dynamics, 10 um) was used as contrast agent for motion tracking.

A custom iterative cross-correlation with correlation plane averaging, window size-reduction and image-deformation features was applied. The calculated 2D vector fields

have temporal resolution of 17.63 fps (Newtonian) and 8.5 fps (XG and PAA), and spatial resolution of 1.6 x 4.14 mm (depth x lateral).

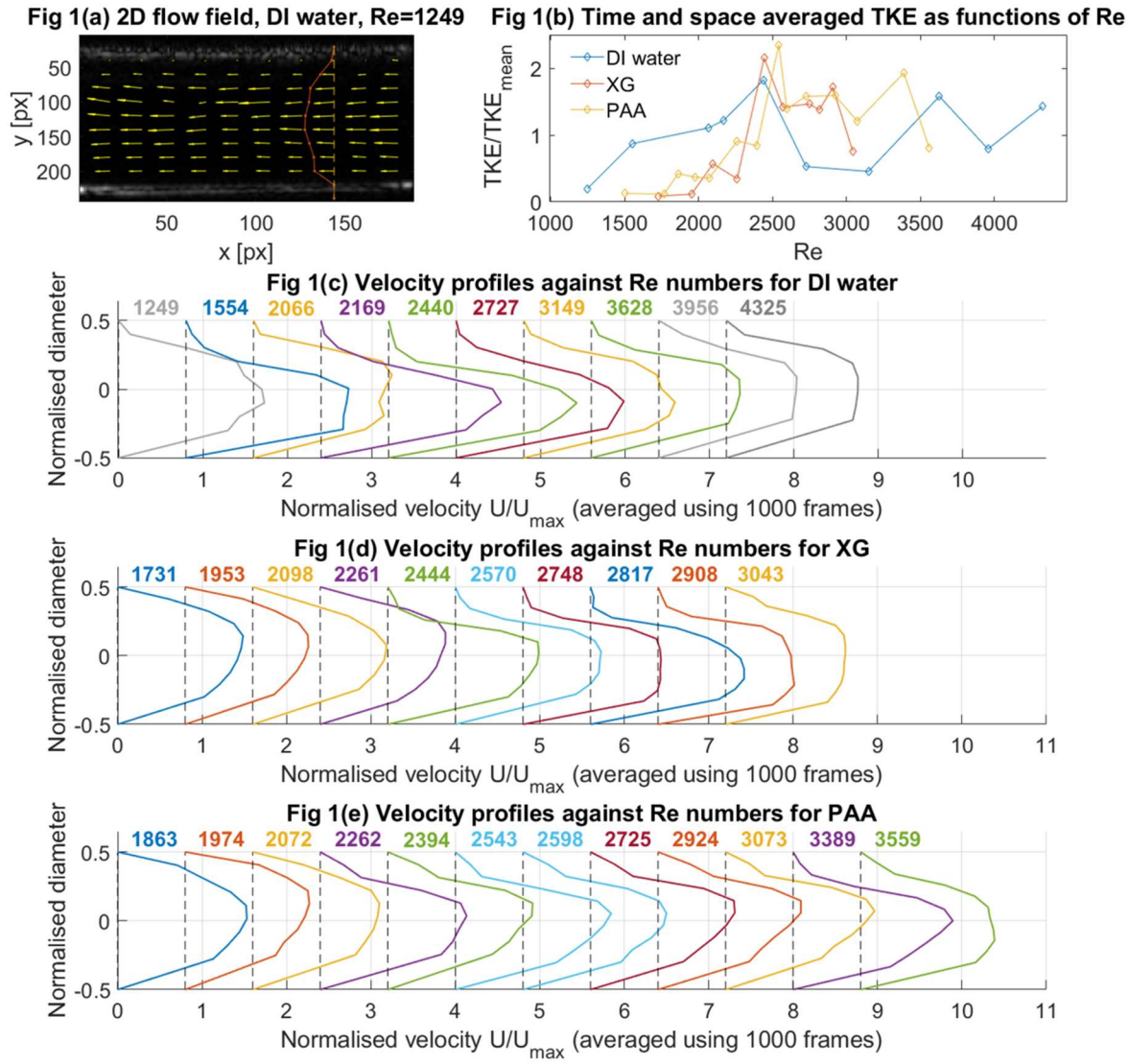
Results

Transient vector fields (example Fig1(a)) were used to calculate turbulent kinetic energy (TKE), used as the marker of the transition-to-turbulence (Fig 1(b)). Peaks of TKE (Fig 1(b)) show that elastic analogue (PAA) delays transition-to-turbulence, in comparison with shear-thinning (XG) and Newtonian (water). The evolution of the velocity profiles with Re (Fig 1(c–e)) further distinguishes the behaviour of water, low-elasticity-shear-thinning, and high-elasticity-shear-thinning analogues.

Discussion

Although the elasticity of blood, caused by the deformation of blood cells and aggregation, is small compared to high-elastic polymer solutions, this study found blood's elasticity caused a measurable delay in transition-to-turbulence, consistent with the drag-reduction phenomenon found in high-elastic flows. This work contributes to the knowledge on the interaction between haemorheology and haemodynamics, which is the key to improve current design of blood contacting medical devices.

Images (Optional)



Session Category

Cardiovascular/Cardiorespiratory Biomechanics: Methods, Models and Applications

P4-129

Production Of viable cardiac muscle strips From frozen tissue for Mechanical Experimentation

Mr Zisen Zhou[1,2], Prof Andrew Taberner[1,2], Dr June-Chiew Han[1,2], Dr Julia Musgrave[1,2], Associate Professor Kenneth Tran[1,2]

[1]University of Auckland, Auckland, AKL, New Zealand. [2]Auckland Bioengineering Institute, Auckland, AKL, New Zealand

Introduction

Human cardiac tissue biorepositories provide an invaluable resource for studying cardiac physiology and pathology, offering samples linked to detailed clinical records. These repositories enable retrospective, large-scale investigations of disease mechanisms. However, mechanical experiments often require homogenisation of tissues into multicellular preparations, which can be challenging to handle and manipulate for mechanical experimentation. To overcome these limitations, we propose a method for generating cardiac muscle strips from frozen tissue samples that preserves structural integrity and enables high-throughput mechanical testing.

Methods

Cardiac tissue blocks were excised from the left ventricular free wall of healthy rats (n = 6) and frozen at –80 °C. After storage, blocks were thawed in Tyrode's solution (4 °C) containing 2,3-butanedione monoxime to inhibit cross-bridge cycling. Each block was mounted in a custom vibratome oscillating at 80 Hz with 1 mm peak-to-peak amplitude to produce 300 µm-thick slices. Parallel blades spaced 1.2 mm apart cut each slice into muscle strips (1.2 mm wide, 3–4 mm long). Prior to cutting, slices were oriented so fibres were parallel to the blades. Strips were permeabilised in 1% Triton solution at 4 °C for 20 hours before mounting in our custom muscle mechanometer [1], consisting of a length motor for precise muscle length control and a force transducer. Strips were stretched to 2.2 µm sarcomere length, activated in pCa 4.5 solution, and subjected to sinusoidal length perturbations (amplitude 0.25% of muscle length) at frequencies from 0.1–200 Hz to determine complex modulus. This measurement allows quantification of actively cycling cross-bridge kinetics. Passive and active force–length relationships were also measured by varying muscle length.

Results

Frozen muscle strips exhibited force–length characteristics and complex moduli comparable to those of fresh cardiac trabeculae. The preparation method consistently produced viable strips suitable for mechanical testing.

Discussion

We developed a reliable system for producing muscle strips from frozen cardiac tissue samples, routinely available in biorepositories. This approach enables high-throughput mechanical experiments without reliance on fresh tissue, significantly expanding opportunities for large-scale studies of cardiac mechanics in health and disease and facilitating integration with clinical datasets.

References (Optional)

1. Choi DH *et al.*, Exp Mech, 2020.

Session Category

Cardiovascular/Cardiorespiratory Biomechanics: Methods, Models and Applications

P4-130

The Effects of Femoral Anteversion/Retroversion on Squatting Biomechanics in a Straight and Externally Rotated Foot Position

Dr Scott Lynn PhD[1,2], Mr Logan Kaptis DPT[2], Mr Dylan Darling DPT[2], Ms Abigail Brittain MS[2], Dr Abigail Schmitt PhD[3,2]

[1]California State University, Fullerton. Center for Sport Performance., Fullerton, California, United States. [2]University of Arkansas Medical School (UAMS), Little Rock, Arkansas, United States. [3]University of Arkansas. Health, Human Performance and Recreation., Fayetteville, Arkansas, United States

Introduction

The squat is a fundamental movement pattern requiring large contributions from the hip joint. Optimal squatting technique may need to vary based on an individual's anatomical hip structure. One aspect of hip structure that should be considered is hip version, as malalignments have been associated with various pathologies of the lower extremity[1-2]. Individuals with anteverted hips may avoid squats that require significant external rotation, while those with retroverted hips may struggle with a standard squat set-up (feet pointed straight forward). This study examined the differences in squat biomechanics between a more anteverted (ANT) and retroverted (RET) group in two squatting tasks: feet forward (STR) & feet externally rotated (EXT). We hypothesized that the ANT group would squat deeper in the STR condition, and the RET group would squat deeper in the EXT condition.

Methods

46 healthy participants volunteered for this study (24 male, age: 31.1±5.5 years). Participants wore a full body marker set and performed two sets of 5 squats in two different conditions in random order: STR and EXT. Craig's Test was then performed by a single experienced clinician to determine hip version for each subject. Kinematic data was used to calculate the center of mass displacement during the squat and normalized to standing height. Participants were split into 2 groups (ANT & RET) based on their Craig's Test results. A 2x2 mixed model ANOVA (group x condition) compared squat depth.

Results

Craig's Test results for the ANT and RET group (n=23/group) were 33.7±6.3 deg and 19.0±5.2 deg, respectively. Squat depth results are shown in Table 1. The interaction effect was not significant (p=.327).

Discussion

Our hypothesis was not supported, indicating other factors need to be considered to better understand these squat patterns. Compensations such as forward trunk lean and knee valgus could be used to lower the center of mass in an unfavorable alignment condition and should be investigated. Further research should also consider using medical imaging to better quantify hip version alignments.

Images (Optional)

Table 1. Squat depth for the more anteverted and more retroverted groups in both the straight and externally rotated foot position.

Anteverted (n=23)		Retroverted (n=23)	
Straight	External	Straight	External
47.0 ±5.4%	46.8 ±5.5%	48.7 ±6.1%	49.1 ±5.3%

- All numbers presented as the maximum depth of the center of mass (CoM) during the squat presented as a percentage of standing height. Calculated as % = (CoM standing height – Lowest position achieved by the CoM during the squat)/ (CoM standing height)
- Note: No significant group (anteverted/retroverted) x squat condition (straight foot position/externally rotated foot position) interaction (p=.327).

References (Optional)

[1] Lerch *et al.,* Orthop J Sports Med, 2021. [2] Eckhoff *et al.,* J Pediatr Orthop, 1994.

Session Category

Clinical Biomechanics: N/A

P4-131

Spatiotemporal Gait Parameters and Cancer: Preliminary Data From Clinical Patients With Cancer

Dr Abigail Schmitt PhD, Mr. Yale Hughes MS, Dr Nicholas Greene PhD

University of Arkansas, Fayetteville, AR, United States

Introduction

Despite acceptance of clinical gait assessments in some fields, including orthopaedics, widespread adoption of gait and functional assessments in oncology are lacking. Cancers and cancer treatments can negatively impact the musculoskeletal and nervous systems, yielding diminished muscular strength and physical function related to adverse outcomes and reduced overall survival. Chemotherapy-induced neurotoxicity is associated with sensory and motor symptoms leading to poorer physical function and gait and balance impairments. Collectively, these symptoms and side-effects reduce functional independence, increase fall risk, and reduce quality of life.

Clinical trials and cancer research recognize the need to evaluate physical function but debate how to best characterize impairment. Preclinical evidence suggests gait speed as a potentially viable biomarker for functional decline, but very few cancer clinical trials include a gait outcome. Thus, we developed a clinical partnership incorporating comprehensive gait assessments into the clinical workflow of a large, regional oncology center to evaluate the viability of spatiotemporal gait data to serve as a biomarker of physical function. Herein, we provide a preliminary assessment of gait data from a clinical population with cancer.

Methods

Gait assessments are available to all cancer patients at a major, local oncology clinic. Patients are recruited, consented, and subsequently administered a gait assessment on a 16’ instrumented pressure-sensing Zeno Walkway. Electronic medical records (EMR) data are used to align cancer diagnoses and stage to gait assessments.

Results

As of this report, gait data has been collected for 213 unique patients, 43 of which have complete gait and EMR data with staging available. The sample was 54% female, 68±11

years (range: 38-91), across 22 cancer types, with 27% Stage I, 17% Stage II, 15% Stage III, 33% Stage IV, 8% other/unavailable. For this initial report, patients were grouped by cancer severity (Stage I-II vs Stages III-IV) due to low staging data availability and compared using *t*-tests (Table 1, alpha= .05).

Discussion

These preliminary data demonstrate feasibility and practicality of integrated gait assessments in an oncology setting. These pilot data are collapsed across types and stages of cancer; subsequent analyses will disaggregate data for cancer type and stages as additional data allows.

Images (Optional)

Table 1. Mean ± standard deviation of spatiotemporal gait variables for Stages I-II (*n*= 20) compared to Stages III-IV (*n*= 23). Cadence differed significantly between groups; patients with more advanced disease took fewer steps per minute.

	Stride Length (cm)	Cadence	Double Support %	Velocity (cm/s)	Stride Length SD (cm)
Stage I-II	120.6 ± 17.7	105.0 ± 7.3	31.5 ± 3.5	105.9 ± 18.5	4.6 ± 2.3
Stage III-IV	115.7 ± 16.2	99.7 ± 8.5	32.3 ± 4.0	96.2 ± 15.5	4.0 ± 1.4
p-values	.354	**.034**	.508	.067	.346

References (Optional)

Session Category

Clinical Biomechanics: N/A

P4-132

Biomechanical Evaluation of Cervical Degeneration Using Patient-Specific Finite Element Models

Mr Afonso Silva[1], Dr Fábio Fernandes[1], Dr Alfredo Calheiros[2], Dr Ricardo Alves de Sousa[1]

[1]TEMA - Centre for Mechanical Technology and Automation, University of Aveiro, Aveiro, Aveiro, Portugal. [2]CHUSA - Centro Hospitalar Universitário de Santo António, Porto, Porto, Portugal

Introduction

Cervical spondylotic myelopathy (CSM) is frequently encountered in middle-aged and elderly patients. Aging may lead to the development of bone spurs, thickened ligaments, and herniated discs, ultimately causing spinal cord compression that can progress to spinal cord injury [1]. Despite an estimated prevalence of 1 in 50 adults, fewer than 20% receive a formal diagnosis, largely due to the nonspecific presentation of early symptoms [2]. Surgery remains the only effective treatment but is generally reserved for patients with moderate-to-severe or progressive disease because of associated risks. Given these limitations, there is a need for methods that enable detailed biomechanical assessment of the spine under varying pathological conditions. This work aims to develop finite element (FE) models to improve understanding of CSM dynamics.

Methods

Two patients with different degrees of cervical degeneration were selected. Model geometries were reconstructed using CT-scans and MRIs. Each FE model included vertebrae, intervertebral discs (IVDs), facet joints, and ligaments. Isotropic linear elastic material properties were assigned to rigid structures (bone and cartilage), whereas hyperelastic formulations were applied to IVDs and ligamentous tissues to more accurately represent physiological behavior under degenerative conditions. Both models were subjected to pure moments of 1 Nm in flexion, extension, axial rotation, and lateral bending, and the range of motion (ROM) was quantified for each loading scenario.

Results

Model validations were conducted by comparing FE results with published in-vitro data [4]. Further comparison with a previously developed healthy cervical FE model [5] enabled assessment of degenerative effects. Degenerated levels demonstrated reduced ROM and increased stress in adjacent IVDs.

Discussion

Preliminary findings indicate increased stiffness in the cervical spine associated with degeneration, with elevated IVD stress likely reflecting compensatory biomechanical responses. Limitations arise from the use of healthy-subject experimental data for initial validation, an aspect currently being refined. Overall, this work establishes a promising framework for advancing computational tools that may support clinicians in optimizing treatment strategies.

References (Optional)

[1] Kushchayev et al, Insights Imaging, 2018

[2] Smith et al., Global Spine J, 2020

[3] Fehlings et al., Global Spine J, 2017

[4] Panjabi et al, Spine, 2001

[5]Silva et al., J Mech Behav Biomed Mater, 2023

Acknowledgements (Optional)

The authors acknowledge the support given by Fundação para a Ciência e a Tecnologia (FCT) through the project PTDC/EME-EME/1239/2021 (BAFHTA). Afonso Silva acknowledge the support of the Portuguese Science Foundation, grant 2024.00600.BDANA.

Session Category

Clinical Biomechanics: N/A

P4-133

Altered Organization of Muscle Synergies during Forward Bending in People with Low Back Pain and Preliminary Evidence of Exercise Efficacy for Restoring Neuromuscular Control

Assistant Professor Ahyoung Song Ph. D.[1], Post-Doctoral Research Associate John Gillilam DPT, Ph. D.[2], Associate Professor Sheri Silfies PT, Ph. D.[3]

[1]Texas State University, Round Rock, Texas, United States. [2]University of Florida, Gainesville, Florida, United States. [3]University of Delaware, Newark, Delaware, United States

Introduction

Although prior literature has identified alterations in the activation and timing of individual trunk muscles in low back pain (LBP) [1], the neuromuscular control strategies that manifest these alterations remain unclear. This study aimed to elucidate the underlying structure of trunk muscle synergies in persons with LBP during an active forward-bending task, to compare these synergies with those of healthy adults (HA), and to examine changes in neuromuscular control following an 8-week motor-learning-based lumbar stabilization program (MLB-LSP).

Methods

Surface electromyography (EMG) of 16 trunk muscles of 25 HA and 25 persons with LBP was recorded during 6 repetitions of forward bending and return to standing. EMG signals were time- and amplitude-normalized and averaged. Non-negative matrix factorization was performed to extract muscle synergies, and the best-matching scalar product of weighting coefficients was used to calculate the similarity between synergies.

Results

5 synergies explained over 95% of the variance in both groups (Figure 1). In HA, 3/5 synergies were dominated by the trunk extensors, 1 by the trunk flexors, and 1 was mixed. In the LBP group, we observed the merging of 2 synergies present in the HA into a single mixed synergy, suggesting increased co-contraction as a strategy for trunk control. While 4/5 synergies were consistent across groups, there were significant differences in weighting coefficients and temporal patterns within these synergies. The LBP group's muscle contributions were predominantly reduced in lumbar multifidus and internal oblique with a redistribution to other extensor and flexor muscles. Following the MLB-LSP, the LBP group's 5 synergies aligned more closely with those of the healthy group, including splitting

the previously merged synergy into separate and aligned trunk flexor and extensor synergies.

Discussion

These data provide evidence of altered muscle-synergy structure in persons with LBP and preliminary evidence that MLB-LSP may alter the synergies used during a common functional task. Changes in muscle synergies aligned with improvements in patient-reported symptoms and function. Data from this study moves beyond identifying individual muscle impairments to consider how movement strategies differ in the presence of pain and change with targeted treatment.

Images (Optional)

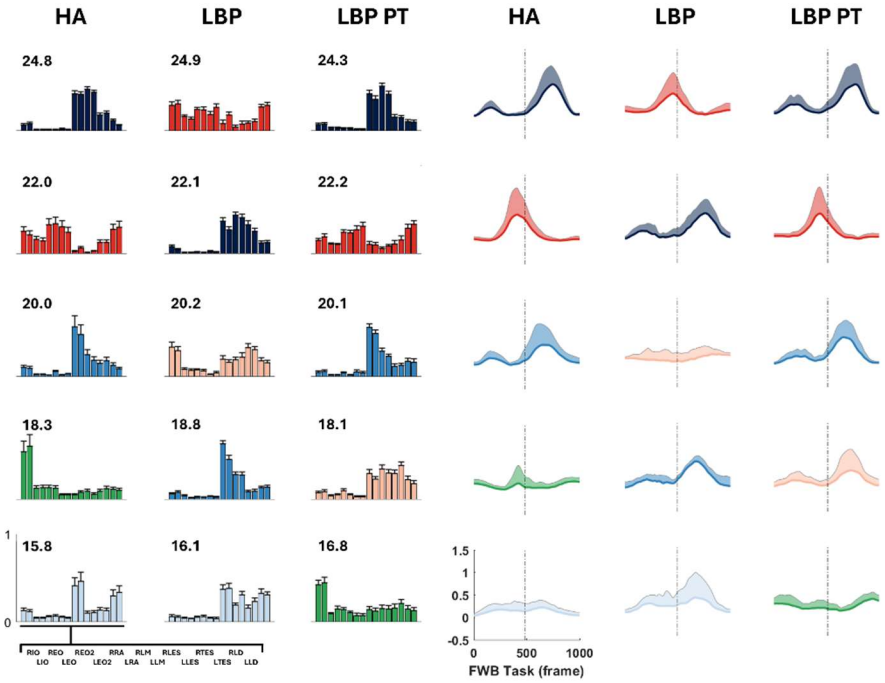


Figure 1. Summary of muscle synergy patterns of the HA and LBP groups at baseline and post-intervention (LBP PT). (Left) Group averaged weighting coefficients and standard error (+SE) of extracted muscle synergies with the same color indicating representing the same synergy (mean scalar product greater than 0.8). Averaged variance accounted for in EMG reconstruction is presented in the upper left corner of each weighting coefficient bar graph. (Right) Temporal activation patterns of extracted synergies, with group standard deviation. The vertical line separates the forward bending phase from return to standing. Extensor synergies presented in blue color scheme (dark blue, blue and light blue). Mixed synergies presented in red color scheme (dark red, light red). Flexor synergy presented in green.

References (Optional)

[1] F. Moissenet *et al.*, Scientific Reports, 2021

Session Category

Clinical Biomechanics: N/A

P4-134

Exploring the Knee Loading Variability in Parkinson's Disease With the Stochastic Modelling Approach

Mr. Alex Bersani Ph.D. candidate, Mr. Marco Viceconti Ph.D., Professor, Mr. Giorgio Davico Ph.D., Assistant professor

University of Bologna, Bologna, Italy, Italy

Introduction

Parkinson's disease (PD) is a neurodegenerative disorder affecting about 1-2 % of the population over the age of 65. People with PD exhibit a wide range of mobility disabilities, including tremor, rigidity, and freezing of gait. As there is no cure for PD, current treatments aim to reduce physical and functional impairments. However, novel wearable sensors allow to monitor disease status and progression, providing clinicians with objective assessments in real world conditions. In addition, computer models and simulations can provide further insights by allowing to explore how suboptimal is the motor control in people with PD. In particular, the use of stochastic approaches to estimate the effect of multiple control strategies onto muscle and joint biomechanics, may allow to study neuromuscular control in PD.

The aim of this work was to explore the effect of dopaminergic medication on the knee joint loads experienced during walking and predicted by a stochastic approach [1], in a group of people with PD.

Methods

Motion capture and force plates data from a publicly available dataset [2] were employed in this preliminary analysis on four subjects with PD (age: 46-74 year-old, Hoehn & Yahr, H&Y: I-IV). The generic "Full Body Model" [3] was scaled to match subjects' anthropometry and used to perform stochastic simulations within Myobolica to estimate 200k feasible solutions.

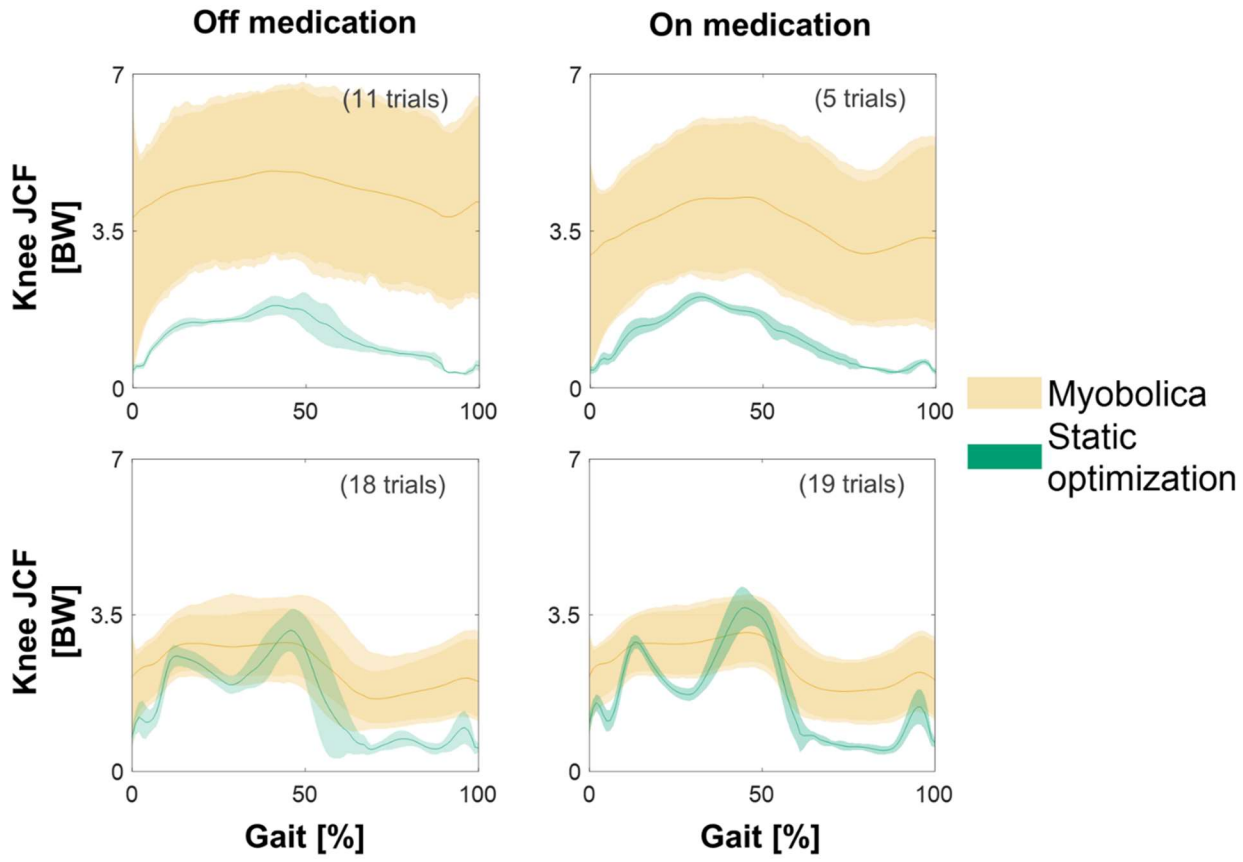
Results

Preliminary results showed marginally larger solution bands and higher values in the "off" medication trials, especially true for the most impaired case (Figure 1 shows results for two selected subjects compared to the static optimization solution; line 1: H&Y IV, line 2: H&Y II).

Discussion

The stochastic approach showed joint load and neuromotor control variability reduction in the preliminary subjects (Figure 1) as well as deviations from a typical healthy gait, underlining the impact of impaired kinematics on joint loading. This work provides an initial foundation for evaluating PD-related joint loading, showing that quantitative modelling of altered neuromuscular control may offer deeper insights into disease mechanisms and provide valuable information.

Images (Optional)



References (Optional)

[1] A. Bersani, *et al.*, *TNSRE*, 2024.

[2] T. K. F. Shida *et al.*, *Fnins*, 2023.

[3] A. Rajagopal, *et al.*, *TBME*, 2016.

Session Category

Clinical Biomechanics: N/A

P4-135

9-Month Test-Retest Reliability of the Shoulder 3D Kinematics in an Asymptomatic Control Group to Support RCRSP Evaluation

Dr Aliah F Shaheen Reader in Biomechanics, Miss Alexa McCloskey Medical Student, Mr Harry Ford Doctoral Researcher and Physiotherapist

Brunel University London, Uxbridge, London, United Kingdom

Introduction

Reliable shoulder motion assessment is critical for monitoring recovery and guiding return to sport decisions in individuals with rotator cuff-related shoulder pain (RCRSP). Limited standardization and reliability data restrict accurate interpretation of longitudinal outcomes. This study evaluates the test-retest reliability of a 3D shoulder motion protocol used within a larger investigation comparing healthy participants with individuals recently rehabilitated from RCRSP. The objective is to assess the reliability of the range of motion (ROM) and joint kinematic measures for control participants between sessions, separated by 9 months.

Methods

Nine healthy controls performed 30 standardized upper-limb movements, including glenohumeral abduction, glenohumeral flexion, and functional tasks. Reflective markers were placed on the upper and lower limbs to allow the construction of coordinate systems for the pelvis, thorax, scapulae, humeri, forearms, hands, the right thigh, shank, and foot. 3D motion was collected using Qualisys Track Manager and processed and analyzed in Visual3D to calculate 3D kinematics based on the ISB recommendations. Reliability metrics were computed using Excel (means, standard deviations, and calculation of minimal detectable change [MDC]) and SPSS (intraclass correlation coefficients [ICC 3,1] with 95% confidence intervals). ICC interpretation followed established thresholds (ICC >0.75 = good reliability).

Results

Most movements demonstrated excellent reliability (ICCs >0.9). Two of the computed joint angles, glenohumeral flexion and maximum hip flexion, demonstrated lower reliability (ICCs < 0.60). MDC values ranged from 0.5° to 23°, reflecting variability in measurement reliability and error across motion parameters.

Discussion

This analysis confirms excellent test-retest reliability for the majority of shoulder kinematic variables, supporting their use for longitudinal biomechanical assessment. Establishing MDC values enables differentiation between true change and measurement error, strengthening their clinical application. Movements with lower reliability suggest opportunities for refinement, such as improving marker placement or reducing movement variability by providing clearer instructions. Certain movements, such as hip flexion, were expectedly low as they are designed to assess variation in movement strategy between individuals in activities of daily living. Overall, the validated measures provide a stable reference for the broader study examining RCRSP recovery trajectories.

Session Category

Clinical Biomechanics: N/A

P4-136

Influence of Pectoralis Minor Tightness on Scapular Kinematics and Shoulder Strength in Subacromial Pain Syndrome: A Cross-Sectional Analysis

Dr. Renato Miyadahira MD[1], Dr. Felipe F. Gonzalez MD, MSc[2,1], Mr. Alexandre Maioli MD Candidate[1,3], Dr. Eliane C. Guadagnin PhD[1], Dr. Marcos A. Barros MD[2,1], Dr. Vitor La Banca MD[1], Dr. Jorge Chahla MD, PhD[2,4], Dr. Leonardo Metsavaht MD, PhD[1], Dr. Jonathan A. Gustafson PhD[2,1], Dr. Gustavo Leporace PhD[1]

[1]Instituto Brasil de Tecnologias da Saúde (IBTS), Rio de Janeiro, Rio de Janeiro, Brazil. [2]Rush University Medical Center, Chicago, Ilinois, United States. [3]Universidade Federal do Rio de Janeiro (UFRJ), Rio de Janeiro, Rio de Janeiro, Brazil. [4]Midwest Orthopaedics at Rush (MOR), Chicago, Ilinois, United States

Introduction

Scapular dyskinesis has been recognized as a key biomechanical factor contributing to shoulder pain and dysfunction in individuals with subacromial pain syndrome (SAPS). Among the contributors, pectoralis minor tightness has been proposed as a determinant of altered scapular kinematics, though its impact on three-dimensional scapular kinematics and shoulder strength remains unclear. The objective of this study was to investigate the influence of pectoralis minor tightness and the presence of SAPS on shoulder kinematics and strength.

Methods

A cross-sectional analysis was performed using a biokinetic database of 38 participants (24 males, 14 females; mean age 42±12 years) diagnosed with SAPS and presenting healthy contralateral shoulders. Patients were stratified according to pectoralis minor index (PMI) median (<8.24 vs. ≥8.24) and both shoulders of each patient were analyzed. Kinematic assessment included active abduction in the scapular plane (0–120°). Primary outcomes were scapulohumeral rhythm, scapular upward rotation, posterior tilt, and internal rotation across elevation. Secondary outcomes were isometric strength in flexion, internal and external rotation. Two-way ANOVA assessed the effects of pathology and PMI on kinematic and strength outcomes.

Results

When all shoulders were analyzed together using a two-way ANOVA with Pathology (SAPS vs. healthy) and PMI group (tight vs. normal) as factors, a significant main effect of PMI group was observed for scapular vertical excursion. Post-hoc analyses showed that “tight” shoulders demonstrated greater vertical excursion than “normal” shoulders during the

concentric phase of scaption—below 90° (mean difference=3.3°, p=0.03; Cohen's d=0.54) and above 90° (mean difference=5.6°, p=0.04; d=0.51) (Table 1). No significant main effects of Pathology were found for any scapular or humeral variables (p>0.05). Passive range of motion and isometric strength also did not differ significantly between groups (p>0.05).

Discussion

The results suggest that shorter muscles were associated with increased vertical scapular displacement during elevation, whereas strength and passive mobility were minimally affected. These findings suggest that altered scapular coordination may occur independently of substantial strength deficits and without consistent changes in traditional movement planes. The preserved isometric strength in this cohort indicates that scapular kinematic alterations in subacromial pain syndrome can occur without marked strength deficits, particularly in early or moderate stages.

Images (Optional)

Table 1: Two-Way ANOVA Results for the Effects of Pathological Status (Subacromial Pain Syndrome [SAPS] vs. Non-Affected Shoulder) and Pectoralis Minor Index (PMI) (Tight: <8.24 vs. Normal: ≥8.24) and interactions between Pathological Status and PMI on Shoulder Kinematics during arm elevation (scaption)

Movement	Effect	p
Scapular Vertical Excursion Below 90° – Concentric Phase	Pathological Status	0.703
	PMI	**0.031**
	Pathological Status ✻ PMI	0.84
Scapular Vertical Excursion Above 90° – Concentric Phase	Pathological Status	0.87
	PMI	**0.042**
	Pathological Status ✻ PMI	0.651

PMI: Pectoralis Minor Index; p: p-value.

Session Category

Clinical Biomechanics: N/A

P4-137

Spatiotemporal Responses to Various Dual-Tasks in Children with Autism

Dr Alyssa O Vanderlinden PhD, Ms Alyssa Moreno MS

New Mexico State University, Las Cruces, NM, United States

Introduction

Autism Spectrum Disorder (ASD) affects approximately 1 in 36 children in the United States and is characterized by behavioral symptoms [1]. Recent research has also identified motor, gait, and cognitive impairments associated with ASD [2,3]. Dual-task paradigms may be particularly relevant for this population, who often present with comorbid conditions that affect attentional resources [4]. Executive function and attention play key roles in gait control [5], and dual-task effects on gait are more pronounced in children with deficits in these domains [6]. However, the relationship between cognitive abilities and gait in children with ASD remains underexplored. Therefore, the purpose of this study was to examine the impact of various dual-task conditions on gait in children with ASD.

Methods

20 children (13 males, 12.35±2.49 years, 1.57±0.14 m, 52.64±14.30 kg) with ASD participated. Participants were instrumented with retroreflective markers on their lower extremities and trunk, and kinematic data was collected (10 camera; 200 Hz; Vicon Motion Systems, Ltd., Oxford, UK). Participants walked at a self-selected speed under three conditions: normal walking, a cognitive dual-task (Stroop Color Word Test), and a motor dual-task (balancing three tennis balls on a tray). Data were smoothed using a low-pass Butterworth digital filter (6Hz) using Visual3D (HAS-Motion, Kingston, Ontario). Mean and standard deviation values were calculated for step length, stride length, stride width, stride velocity. A repeated measures ANOVA ($\alpha = 0.05$) was used to examine differences across conditions, with Bonferroni-adjusted post hoc comparisons when appropriate.

Results

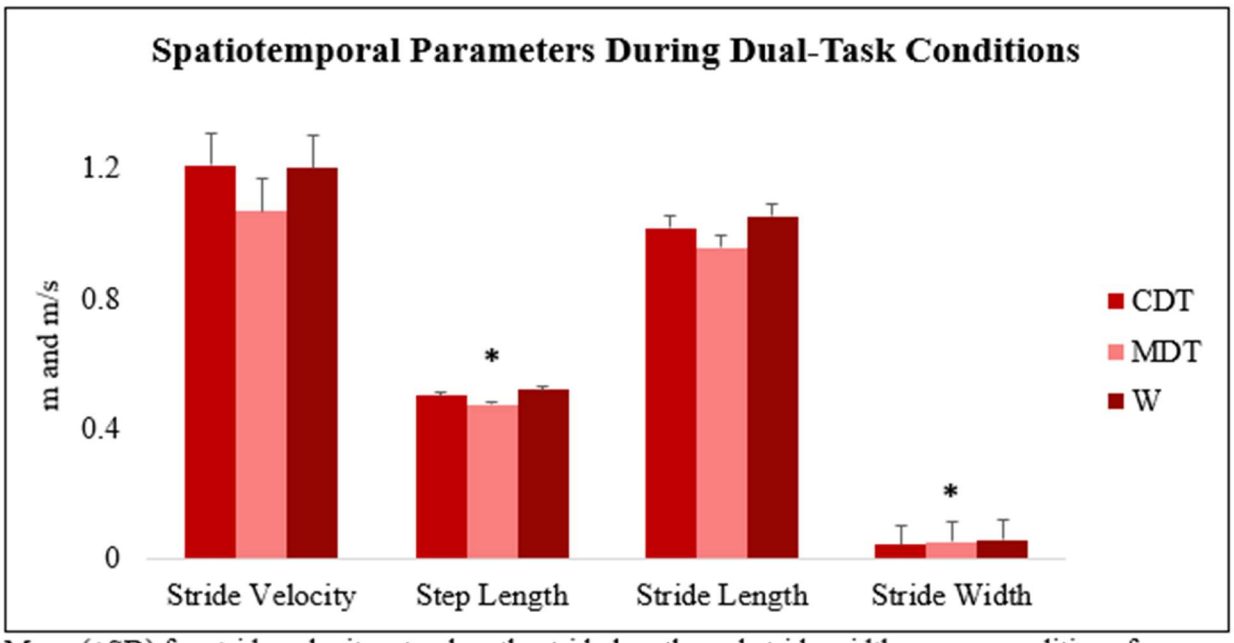
Analysis revealed that children with ASD displayed statistically different stride widths: $F(2,22)=3.70$, $p=0.041$, and step lengths: $F(2,22)=3.47$, $p=0.039$ among conditions. There was no statistical differences in stride velocity: $F(2,22)=1.39$, $p=0.270$, or stride length: $F(2,22)=2.21$, $p=0.134$ (Figure 1).

Discussion

These findings suggest that dual-tasking selectively impacts certain spatiotemporal gait parameters in children with ASD rather than producing a global effect. This work represents

a preliminary analysis and will be compared with an age- and sex-matched neurotypical group to further characterize dual-task gait differences. Understanding these patterns may help inform interventions aimed at improving functional mobility and independence.

Images (Optional)



Mean (+SD) for stride velocity, step length, stride length, and stride width among conditions for children with ASD. (*) denotes significance $p<0.05$. CDT: Cognitive Dual (Ctrl) DT: Motor Dual-Task; W: Overground Walking

References (Optional)

Acknowledgements (Optional)

This research was supported by New Mexico State University's College of HEST Emerging Scholars Grant.

Session Category

Clinical Biomechanics: N/A

P4-138

Aging Adults with Hip Osteoarthritis Ambulate with Lower Joint Power During a 30-Minute Walking Task

Ms Amara Sharp MS, ATC[1], Dr. Jaimie Roper PhD[2], Dr. Aaron Fain MD[1], Dr. Stephen Duncan MD[1], Dr. Anthony Mangino PhD[1], Dr. Kate Jochimsen PhD, ATC[3,4], Dr Michael Samaan PhD[1]

[1]University of Kentucky, Lexington, Kentucky, United States. [2]Auburn University, Auburn, Alabama, United States. [3]Massachusetts General Hospital, Boston, Massachusetts, United States. [4]Harvard Medical School, Boston, Massachusetts, United States

Introduction

Approximately 25% of all adults will develop hip osteoarthritis (HOA) across the life span. During the course of healthy aging, the power required for forward propulsion shifts from the distal to proximal joints. Aging adults with HOA walk slower and with lower ankle joint power compared to aging adults without HOA, yet the impact of slower gait speeds on power production in HOA is understudied. Although aerobic exercise is used in HOA rehabilitation, the impact of prolonged walking on ankle joint power and the underlying impact of slower gait speeds on ankle joint power during aerobic exercise in HOA is understudied. Therefore, we assessed changes in lower extremity joint power in aging adults with and without HOA and the corresponding impact of gait speed on joint power during a prolonged walking task.

Methods

Fourteen asymptomatic individuals without radiographic HOA (9 females, 55.60±10.01 years, 27.10±2.50 kg•m^{-2}) and fourteen individuals with radiographic HOA (6 females, 61.40±9.75 years, 25.70±3.54 kg·m^{-2}) underwent 3D motion capture while walking at a self-selected speed on an instrument split-belt treadmill for 30 minutes. The peak total power (sum of the lower extremity joint powers) was calculated at the start and the end of the 30-minute walking task. Gait speed was compared using Welch's t-test. Changes in peak total power and the corresponding hip, knee, and ankle power at the peak total power were compared using a gait speed adjusted and non-gait speed adjusted repeated measures analysis of variance.

Results

The HOA group walked significantly slower than the control group (HOA: 0.77±0.18m·s^{-1}, Control: 0.94±0.17m·s^{-1}, p=0.02). No within-subject effects were found for any of the joint power-based parameters (ps>0.05). The HOA group exhibited significantly lower peak total power and lower knee and ankle power at the peak total power regardless of gait speed.

Discussion

Regardless of gait speed, the HOA group exhibited lower peak total power throughout the entire 30-minute walking task and was driven by lower knee and ankle joint powers. HOA-related rehabilitation should target knee and ankle joint power production to improve total lower extremity power and function during aerobic exercise.

Images (Optional)

	Adjusted for Gait Speed					Non-Adjusted for Gait Speed				
	HOA		Control		p-value	HOA		Control		p-value
	T0	T30	T0	T30		T0	T30	T0	T30	
Peak Total Power	1.85 ±0.21	1.92 ±0.20	2.52 ±0.21	2.37 ±0.20	0.040	1.76 ±0.20	1.69 ±0.23	2.60 ±0.20	2.60 ±0.23	0.003
Hip Power	0.52 ±0.05	0.58 ±0.05	0.55 ±0.05	0.53 ±0.52	0.89	0.45 ±0.06	0.50 ±0.07	0.62 ±0.06	0.61 ±0.07	0.10
Knee Power	0.65 ±0.11	0.60 ±0.11	0.95 ±0.11	0.88 ±0.11	0.05	0.66 ±0.10	0.58 ±0.10	0.64 ±0.10	0.90 ±0.10	0.02
Ankle Power	1.31 ±0.15	1.43 ±0.11	1.82 ±0.15	1.73 ±0.11	0.017	1.23 ±0.15	1.22 ±0.16	1.90 ±0.15	1.95 ±0.16	<0.001

Table 1: Between-subject estimated marginal means±standard error and corresponding p-values for the gait speed adjusted and non-gait speed adjusted total peak power and corresponding joint powers at the peak total power (Nm·kg^{-1}) at the start (T0) and end (T30) of the 30-minute walking task.

Acknowledgements (Optional)

Funding support from the National Institutes of Health (K01-AG073698, K23-AT011922)

Session Category

Clinical Biomechanics: N/A

P4-139

Dynamic Imaging-Based Instantaneous Femoral Head Center Location As An Indicator Of Hip Microinstability

Ms. Ada Ayechu[1], Dr. med. Julien Hirt[2], PD. Dr. med. Keivan Daneshvar[3], Mr. Mirko Blaettler[1], PD. Dr. Annapaola Parrilli[4], Dr. Camilla Calastra[4], Prof. Dr. med. Moritz Tannast[2], Prof. Dr. Ameet Aiyangar[1,3]

[1]Mechanical Systems Engineering, Empa - Swiss Federal Laboratories for Materials Science and Technology, Duebendorf, Zurich, Switzerland. [2]Department of Orthopaedic Surgery and Traumatology, Inselspital, Bern, Bern, Switzerland. [3]Department of Diagnostic Interventional and Paediatric Radiology, Inselspital, Bern, Bern, Switzerland. [4]Center for X-ray Analytics, Empa - Swiss Federal Laboratories for Materials Science and Technology, Duebendorf, Zurich, Switzerland

Introduction

We introduce the application of a novel, validated high-speed dynamic biplanar radiographic imaging (DBRI) system to acquire femoro-acetabular (hip) arthrokinematrics with sub-millimetre accuracy to develop a new, dynamic metric for characterising micro-instability in patients with femoral torsion abnormalities

Methods

Two 3D-printed hip joints recreated from two patient CTs with different pathological (abnormal femoral torsion) conditions were the study objects. A DBRI system consisting of two pairs of x-ray tubes and digital flat image intensifiers along with a marker less model-based bone tracking system (DSX Suite, Has-Motion Inc., CA) was employed to capture 3D hip arthrokinematics during two defined nominal movements. "Bones" were tracked in 3D space during a nominal flexion-extension (70° ROM) and external rotation (50° ROM) recorded at 60 frames per second (fps). Three metal beads were embedded on each "bone" of one of the hips in order to validate the system and marker less model-based tracking accuracy against the gold standard radiostereometric analysis technique. Local reference frames were defined for the femur (origin at femoral head centre) and acetabulum with the femoral motion expressed relative to the acetabular reference frame. Bounding boxes for the loci of instantaneous femoral head centre (iFHC) position for each abnormal torsion condition were computed.

Results

First, the model-based marker less tracking process was validated against the bead-tracked instantaneous poses with an average accuracy of ≤ 0.83mm.

In the second step, iFHC loci of the two hips were mapped within bounding boxes, first for nominal rotation motion and then for nominal flexion-extension motion. The bounding box range for each condition and each motion varied between 1x1x1 mm^3 to 2x2x4 mm^3. Furthermore, there was no overlap between the instantaneous femoral head centre bounding boxes for the two conditions computed during the nominal rotational motion.

Discussion

iFHC bounding boxes obtained using DBRI imaging may be exploited to diagnose and quantify pathological microinstability in the hip.

References (Optional)

1. Wong et al., Curr Rev Musculoskelet Med, 15(2):38-52, 2022.
2. Cohen et al., Knee Surg, Sports Traum, Arthr, 31(1):16-32, 2023.
3. Wu et al., J Biomechanics, 35(4):543-548, 2002.
4. Martin et al., J. Arthroplasty, 2011.

Session Category

Clinical Biomechanics: N/A

P4-140

Differences in Landing Strategies during a Choice Reaction Forward Hop-to-Stabilization in Individuals With and Without Chronic Ankle Instability

Dr. Amelia Bruce Leicht PhD, CSCS[1], Ms. Amelia Johnson BS[1], Dr. Phillip Gribble PhD, ATC, FNATA[1], Dr. Nicholas Heebner PhD, ATC[1], Dr. Johanna Hoch PhD, MPH, ATC[1], Dr. Kyle Kosik PhD, ATC[1], Ms. Ilana Patlan MSc[1], Dr. Ke'La Porter PhD, ATC[1], Dr. Danielle Torp PhD, ATC[1], Dr. Bridget Walsh PhD, ATC[2], Dr. Matthew Hoch PhD, ATC, FNATA[1]

[1]University of Kentucky, Lexington, KY, United States. [2]Ohio University, Athens, OH, United States

Introduction

Physical activity commonly occurs in chaotic environments and requires cognitive-loading during dynamic tasks (e.g. jump-landing). The combination of these activities can alter movement strategies, increasing the risk of injury. However, applications of dual-tasking activities in populations with chronic ankle instability (CAI), known for having biomechanical alterations during functional movements, has seen limited investigation. The choice-reaction forward hop-to-stabilization (CR-FHTS) task is a dynamic cognitive-loading task. The purpose of this study was to compare landing kinematics during a CR-FHTS in individuals with and without CAI.

Methods

Ninety-one volunteers (CAI: 19F/27M, 21.0±5.1yrs, 172.4±10.5cm, 74.9±13.1kg; Healthy: 25F/20M, 21.4±5.2yrs, 169.8±9.4cm, 68.8±13.8kg) completed the CR-FHTS. From a double-limb stance, volunteers hopped forward over a 30cm hurdle positioned at 20% of their height, to a single-limb landing in a zone beginning at 40% of their height. Volunteers were instructed to hop as quickly as possible in response to an illuminated sensor (red/green) that indicated which limb (left/right) to land on. Upon landing, volunteers balanced for 5-seconds with hands on hips. Lower extremity joint angles in the frontal and sagittal planes were collected via inertial measurement units at 100Hz from 200ms pre-initial contact (IC) to 200ms post-IC (40 frames, IC occurring at frame 20). Outcomes from the injured limb within the CAI group and dominant limb within the healthy group were compared for using statistical parametric mapping.

Results

Significant differences were observed between groups in the frontal plane across all joints in periods prior to IC (p<0.05). Significant group differences were identified at the ankle between frames 14-17 (p=0.03), at the knee between frames 0-4 and 13-18 (p=0.01, p=0.003), and at the hip between frames 12-14 (p=0.04, Figure 1). No group differences occurred in the sagittal plane across any joints (p>0.05).

Discussion

Volunteers with CAI utilized more ankle adduction, less knee adduction, and more hip abduction immediately prior to IC. The addition of cognitive-loading during a CR-HTS may elicit risky frontal plane landing strategies prior to IC. Dynamic landing tasks paired with cognitive-loading components may provide utility as an assessment tool and mimic real-world scenarios for patients with CAI to decrease re-injury.

Images (Optional)

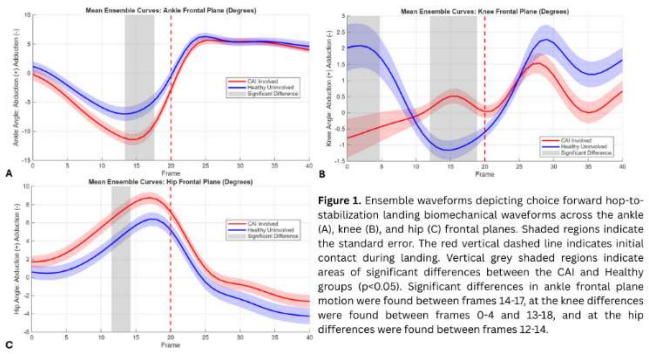


Figure 1. Ensemble waveforms depicting choice forward hop-to-stabilization landing biomechanical waveforms across the ankle (A), knee (B), and hip (C) frontal planes. Shaded regions indicate the standard error. The red vertical dashed line indicates initial contact during landing. Vertical grey shaded regions indicate areas of significant differences between the CAI and Healthy groups (p<0.05). Significant differences in ankle frontal plane motion were found between frames 14-17, at the knee differences were found between frames 0-4 and 13-18, and at the hip differences were found between frames 12-14.

References (Optional)

Session Category

Clinical Biomechanics: N/A

P4-141

Biomechanics-Informed Virtual Surgical Planning for Tongue Reconstruction

Dr. Amir Isazadeh[1], Dr. Daniel Aalto[1], Dr. Lindsey Westover[2], Dr. Hadi Seikaly[3]

[1]Faculty of Rehabilitation Medicine, University of Alberta, Edmonton, Alberta, Canada. [2]Faculty of Engineering, University of Alberta, Edmonton, Alberta, Canada. [3]Faculty of Medicine and Dentistry, University of Alberta, Edmonton, Alberta, Canada

Dr. Amir Isazadeh

Introduction

In tongue reconstruction, virtual surgical planning improves anatomical and functional outcomes. However, unified digital workflows are required to integrate virtual planning more widely into tongue reconstruction surgery. To address this, we present a patient-specific Virtual Surgical Planning (VSP) framework with a twofold objective: to bridge the gap in free flap design via biomechanical optimization and to deploy high-fidelity, high-throughput surgical simulations to transform the current intuition-driven, surgeon-dependent paradigm into data-driven decision-making.

Methods

To address the challenge of optimal flap geometry, we developed the hyperelastic inverse Finite Element Method (hiFEM), an algorithm to generate flap designs that minimize tissue stretch. Second, we established an automated, end-to-end finite element simulation pipeline, incorporating virtual reconstruction and long-term postoperative atrophy, to estimate long-term outcomes. This virtual testbed was deployed in a 120-virtual-case factorial study to systematically isolate the independent and interactive effects of two surgical decisions: donor site (Radial Forearm vs. Anterolateral Thigh) and flap overbulking on the final neotongue biomechanics.

Results

Comparative analysis demonstrated that hiFEM minimized tissue deformation, maintaining maximum area stretches between 1.10–1.12, outperforming a clinically validated geometric flattening (1.19–1.38). In the factorial study, statistical analysis quantified a mechanical trade-off: flap overbulking was the primary driver for anatomical restoration

($p<0.001$), yet it incurred a predictable penalty in imposed deformation on the native tongue ($p<0.001$). Furthermore, donor-site stiffness significantly modulated this relationship; stiffer thigh flaps imposed higher baseline strains ($p<0.001$) and exhibited diminished anatomical tunability from overbulking compared to pliable forearm flaps ($p<0.001$). This finding aligns with the clinical preference for forearm flaps in tongue reconstruction.

Discussion

This work transforms the art of surgical judgment into a data-driven science. By shifting the planning objective to biomechanical optimization, the framework enables surgeons to identify patient-specific strategies that optimally balance surgical decisions. Ultimately, the integration of active muscle contraction models will further enable function simulation for speech and swallowing, and establish a risk-aware digital ecosystem for soft-tissue reconstruction VSP.

References (Optional)

Acknowledgements (Optional)

This work was supported by the Alberta Cancer Foundation (grant number 27 601).

Session Category

Clinical Biomechanics: N/A

P4-142

The Effects of Neuromuscular Control Exercises Versus Strengthening on Clinical and Biomechanical Outcomes in the "Strong" Subgroup of Individuals With Patellofemoral Pain: A Randomized Controlled Trial

Ms. Ana Luiza Cabral[1], Mr. Victor Hugo V. Carrijo[2], Dr. J. Paulo Vilas-Boas[3], Dr. Jim Richards[4]

[1]Research Centre in Physical Activity, Health and Leisure (CIAFEL), Porto Biomechanics Laboratory (LABIOMEP), Faculty of Sport, University of Porto, Porto, Porto, Portugal. [2]Center of Research, Education, Innovation and Intervention in Sport (CIFI2D), Porto Biomechanics Laboratory (LABIOMEP), Faculty of Sport, University of Porto, Porto, Porto, Portugal. [3]Center of Research, Education, Innovation and Intervention in Sport (CIFI2D), Porto Biomechanics Laboratory (LABIOMEP), Faculty of Sport, University of Porto, Porto, Porto, Portugal. [4]Allied Health Research Unit, University of Lancashire, Preston, Lancashire, United Kingdom

Introduction

The existence of Patellofemoral Pain (PFP) subgroups has been proposed to explain inconsistencies in longitudinal studies showing high symptom recurrence after strength-focused interventions. Interestingly, one subgroup demonstrated normal strength compared to others [1], suggesting neuromuscular control may play a key role in this subgroup. This study compared the effects of two 6-week protocols based on neuromuscular control vs. strengthening on clinical and biomechanical outcomes.

Methods

Twenty-four individuals from the "strong" subgroup of PFP were randomly allocated into two groups: neuromuscular control exercises (NMC) (n = 12; 27.5 y; BMI 23.8 kg/m^2) and strengthening exercises (STG) (n = 12; 29.98 y; BMI 23.7 kg/m^2). All volunteers performed 3 sessions per week, totaling 18 sessions. The NMC group performed exercises based on proprioception and balance, and the STG group performed strengthening exercises for the quadriceps, hamstrings, hip abductors, and lateral rotators. Pain, function, kinesiophobia and biomechanics were assessed pre and post intervention. Three-dimensional kinematics were captured with a 12-camera Qualisys system (100 Hz), and kinetics were recorded during stair descent using a four-step instrumented staircase (2000 Hz). Knee angles and moments were extracted using Visual3D. Statistical analysis was conducted in SPSS version 29 (IBM, USA). A mixed-model method (two groups x two time points) was performed. Where significant main effects were seen, pairwise comparisons using LSD were performed.

Results

The table below shows the results of the clinical and biomechanical outcomes.

Discussion

Both interventions produced relevant clinical improvements, highlighting the therapeutic value for individuals in the “strong” PFP subgroup. Nevertheless, STG led to greater improvements in knee specific function and reductions in kinesiophobia, indicating a broader clinical impact even when baseline strength is not compromised. The NMC still contributed meaningful symptom relief and may target coordination and sensorimotor aspects not directly addressed by strengthening. The lack of biomechanical changes may reflect the already high baseline strength and relatively short intervention duration.

Images (Optional)

Mean and Standard Deviation of clinical outcomes and knee angles and moments during the stair descent of an instrumented stair.

			MCID†	NMC protocol Mean (SD) N = 12		Change based on MCID‡	STG protocol Mean (SD) N = 12		Change based on MCID‡	Time (p)	Group (p)	Interaction Time x Group (p)
				Pre	Post		Pre	Post				
Clinical outcomes	Pain (NPRS)		1	4.75 (1.6)	2.91 (1.44)	–1.84¥	4.16 (1.4)	1.25 (.75)	–2.91¥	<.001*	.006*	.169
	Function (KOOS-PS)		8	30.05 (16)	19.34 (15.5)	–10.71¥	25.29 (14.6)	9.22 (12.7)	–16.07¥	.003*	.089	.534
	Function (AKPS)		10	61.08 (3.72)	63.91 (8.02)	+2.83	62.25 (74.25)	74.25 (9.59)	+12.00¥	.001*	.011*	.038*
	Kinesiophobia (Tampa Scale)		6	28.5 (4.81)	24.16 (5.76)	–4.34	28.58 (5.61)	21.58 (5.69)	–7.00¥	<.001*	.434	.404
				NMC protocol Mean (SD) N = 12			STG protocol Mean (SD) N = 12			Time (p)	Group (p)	Interaction Time x Group (p)
				Pre	Post		Pre	Post				
Biomechanical outcomes	Minimum knee angle (°)	Sagittal plane		7.26 (3.98)	6.08 (4.31)		8.90 (5.48)	7.24 (3.28)		0.259	0.270	0.849
		Frontal plane		-1.42 (4.86)	-3.35 (4.36)		-4.62 (5.78)	-6.12 (6.03)		0.268	0.058	0.888
		Transverse plane		-10.04 (6.37)	-7.85 (7.80)		-6.21 (7.90)	-6.60 (7.17)		0.673	0.236	0.546
	Maximum knee angle (°)	Sagittal plane		94.36 (4.93)	92.14 (5.56)		95.09 (5.70)	93.26 (5.53)		0.205	0.560	0.901
		Frontal plane		8.47 (6.20)	5.57 (5.84)		4.22 (8.07)	4.15 (7.30)		0.462	0.162	0.482
		Transverse plane		3.72 (7.09)	4.59 (6.95)		4.86 (9.37)	6.00 (9.59)		0.525	0.457	0.776
	Knee ROM (°)	Sagittal plane		87.10 (4.95)	86.06 (3.92)		86.18 (4.56)	86.01 (4.56)		0.644	0.716	0.740
		Frontal plane		9.89 (4.19)	8.93 (3.58)		8.84 (4.80)	10.27 (3.71)		0.843	0.900	0.318
		Transverse plane		13.77 (4.00)	12.45 (5.73)		11.07 (5.55)	13.74 (5.18)		0.654	0.639	0.188
	Minimum knee moment (N·m/kg)	Sagittal plane		-0.17 (0.08)	-0.24 (0.13)		-0.15 (0.09)	-0.17 (0.07)		0.152	0.122	0.413
		Frontal plane		-0.21 (0.18)	-0.18 (0.21)		-0.14 (0.15)	-0.15 (0.18)		0.952	0.351	0.689
		Transverse plane		-0.08 (0.03)	-0.06 (0.03)		-0.06 (0.03)	-0.08 (0.04)		0.669	0.728	0.183
	Maximum knee moment (N·m/kg)	Sagittal plane		1.35 (0.26)	1.22 (0.26)		1.33 (0.30)	1.27 (0.23)		0.266	0.837	0.661
		Frontal plane		0.19 (0.19)	0.25 (0.25)		0.27 (0.23)	0.23 (0.18)		0.864	0.679	0.470
		Transverse plane		0.02 (0.01)	0.03 (0.02)		0.02 (0.02)	0.02 (0.02)		0.778	0.864	0.339
	Knee moment amplitude (N·m/kg)	Sagittal plane		1.52 (0.30)	1.47 (0.29)		1.48 (0.30)	1.47 (0.27)		0.592	0.729	0.902
		Frontal plane		0.41 (0.13)	0.44 (0.18)		0.41 (0.14)	0.39 (0.10)		0.855	0.570	0.559
		Transverse plane		0.10 (0.04)	0.09 (0.03)		0.10 (0.01)	0.10 (0.03)		0.792	0.794	0.444

*: Group difference ($p < 0.05$).
†: Pain (NPRS) - Salaffi et al., 2004; Function (KOOS-PS) - ElMelhat et al., 2022; Function (AKPS) - Heijden et al., 2015; Kinesiophobia (Tampa Scale) - Monticone et al., 2017.
‡: Post – Pre (negative values mean improvement, as the scales are "the lower the better", except for AKPS, where higher is better).
¥: Reached or exceeded known Minimal Clinical Important Differences (MCID).

References (Optional)

[1] J. Selfe *et al.*, “Are there three main subgroups within the patellofemoral pain population? A detailed characterisation study of 127 patients to help develop targeted intervention (TIPPs),” *Br. J. Sports Med.*, vol. 50, no. 14, pp. 873–880, July 2016, doi: 10.1136/bjsports-2015-094792.

Session Category

Clinical Biomechanics: N/A

P4-143

Biomechanical Impacts Of Multidisciplinary Intervention For Youth With Chronic Musculoskeletal Pain

Dr. Anna H Bailes PT, DPT, PhD[1], Dr. Samuel M Lyons PhD[2], Dr. Lauren E Harrison PhD[1], Dr. Laura E Simons PhD[1]

[1]Department of Anesthesiology, Perioperative and Pain Medicine, Stanford School of Medicine, Palo Alto, CA, United States. [2]Department of Kinesiology, Whittier College, Anaheim, CA, United States

Introduction

One is four youth have chronic musculoskeletal (MSK) pain, leading to functional impairments and altered movement biomechanics. Although multidisciplinary interventions lead to improvements in self-reports of function, impacts on movement biomechanics remain unknown. Aims of this study were to 1) identify differences in movement biomechanics pre-/post-treatment and 2) determine the impact of multidisciplinary intervention on relationships between self-report measures and biomechanics.

Methods

This secondary analysis was performed ancillary to a clinical trial (1R21AR072921) in youth (8-17 y.o.) with chronic MSK pain. Youth engaged in 12 sessions of multidisciplinary treatment with a physical therapist and pain psychologist. Participants visited the motion capture laboratory for study visits pre-/post-intervention. They performed functional tasks (double leg squat, 6-minute-walk test). Optoelectronic motion capture was used to collect primary outcomes: hip/knee kinetics/kinematics, spatiotemporal gait metrics. Participants completed the Numeric Pain Rating Scale and Functional Disability Index as secondary outcomes. To address Aim 1, paired t-tests were used to compare movement biomechanics pre-/post-treatment. To address Aim 2, mixed linear regression models with ‘timepoint’ (pre-/post-treatment) interaction effects were used to determine changes in relationships between self-report and biomechanical measures pre-/post-treatment.

Results

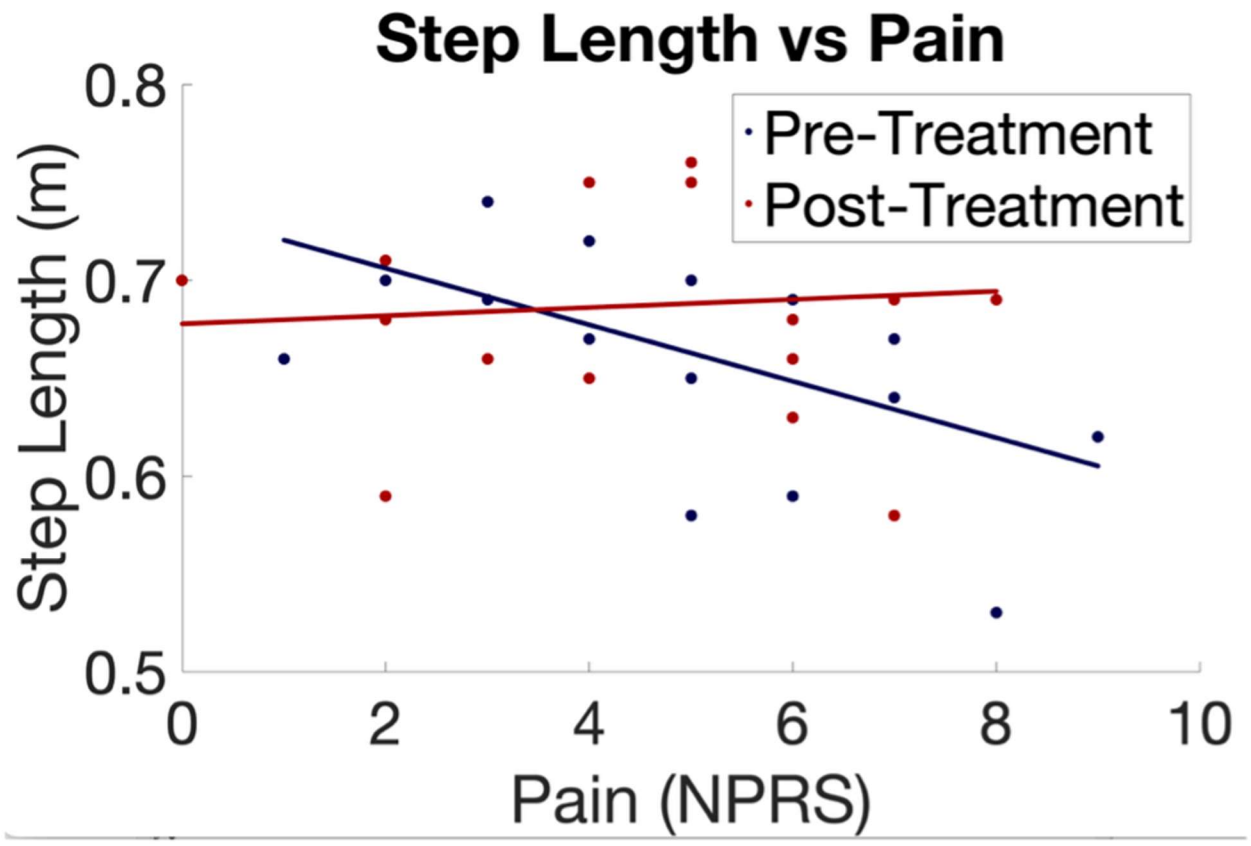
Of the 59 youth completing the clinical trial, 21 (13.8±2.6 y.o., 18% M) participated in motion capture assessment. There were no significant differences in joint kinetics/kinematics or spatiotemporal gait metrics pre-/post-treatment ($p>.05$). Aim 2 revealed a significant pain × timepoint interaction for predicting step length ($p<0.05$). Specifically, there was a moderate negative correlation between pain and step length pre-

treatment (r = -0.54) but not post-treatment (r=0.11). Plainly, participants with more pain took shorter steps pre-treatment, but the association disappeared post-treatment. There were no other significant main or interaction effects in predicting biomechanics.

Discussion

Multidisciplinary intervention did not result in biomechanical changes in youth with chronic MSK pain. The negative association between pain and step length that was observed pre-treatment was eliminated post-treatment, suggesting that high pain was no longer associated with gait impairments (reduced step length). This 'decoupling' of pain and step length is the first biomechanical evidence to corroborate existing findings that functional restoration precedes pain reduction following multidisciplinary intervention.

Images (Optional)



Acknowledgements (Optional)

Session Category

Clinical Biomechanics: N/A

P4-144

Toward Adaptive and Predictive Digital Twins in Orthopedics: A Multimodal Patient-Specific Database

Dr. Annchristin Andres, Dr. Michael Roland, Dr. Kerstin Wickert, Prof.Dr.-Ing. Stefan Diebels

Applied Mechanics, Saarland University, 66123 Saarbrücken, Saarland, Germany

Introduction

The ongoing digitization of medicine is opening up new perspectives for patient-specific modeling, simulation, and prognosis of orthopedic healing processes. This study presents a unique database built up over five years that includes patients with fractures of the long bones of the upper and lower extremities. The database currently contains 100 fully documented cases, based on a standardized, specially developed workflow [1].

Methods

Each data set includes multimodal information (see Figure 1), including imaging data (CT images, X-ray), motion analyses using the Xsens™ motion capture system, and musculoskeletal simulations using AnyBody™ software. For patients with fractures of the lower extremities, the team additionally recorded ground reaction forces using instrumented soles. Andres et al. [2] describe the methodological principles and technical capabilities of these combined measurement systems.

Based on this data structure, the creation of digital twins for orthopedic-traumatological applications was established [3]. This human digital twin approach enables patient-specific mapping of biomechanical analyses and the simulation of individual stress scenarios. In addition, these models can be used to predict healing processes and provide quantitative support for therapy decisions. For example, the workflow enabled prediction of the effects of individual partial loads on mechanical stability and healing progress in tibial head fractures [4].

Results

The database presented here thus provides a basis for developing adaptive and predictive digital twins, which are highly relevant to both research and clinical decision-making. By linking imaging, motion data, and biomechanical simulation, patient-specific factors influencing fracture healing can be systematically analyzed and quantified. In addition, the database opens new possibilities for the use of machine learning and artificial intelligence methods.

Discussion

This unique data basis thus represents an important step toward data-driven, personalized orthopedics and trauma surgery. In the future, it will be continuously expanded and supplemented with additional measurement methods to further improve the precision of digital twins and open new clinical fields of application.

Images (Optional)

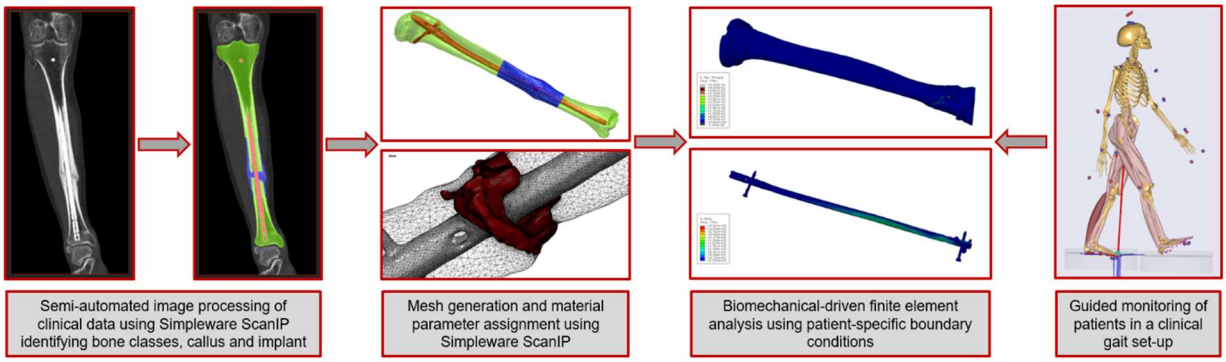


Figure 1: From clinical imaging via segmentation and model generation to personalized biomechanical finite element analysis based on patient-specific monitoring data.

References (Optional)

[1] Annchristin Andres et al., *Clin. Biomechanics,* 2025

[2] Annchristin Andres et al., S*ensors,* 2025

[3] Annchristin Andres et al., *Sci. Reports,* 2025

[4] Annchristin Andres et al., Front. Bioengineering and Biotechnology, 2025

Acknowledgements (Optional)

Session Category

Clinical Biomechanics: N/A

P4-145

A Biomechanical Framework for Assessing Evidence of Joint Stability across the Symptomatic and Asymptomatic Generalized Joint Hypermobility Spectrum

Ms. Susan Burnap[1], Dr. Rebecca Abbott PT, DPT, PhD[2], Mr. Yaqoub Yusuf MS[1], Dr. Aaron Hellem[1], Dr. Arin Ellingson PhD[1]

[1]University of Minnesota, Minneapolis, MN, United States. [2]University of Colorado, Aurora, CO, United States

Introduction

Generalized joint hypermobility (GJH)—excessive joint range of motion (ROM) throughout the body—affects up to 30% of the general population, and is frequently asymptomatic (aGJH) [1–3]. Symptomatic GJH (sGHJ) describes a subset who experience severe chronic pain and debilitating functional limitations including hypermobile Ehlers-Danlos Syndrome (hEDS) and Hypermobility Spectrum Disorder (HSD). Although joint instability is proposed as the biomechanical mechanism underlying pain in sGJH, direct evidence remains lacking.

The objective herein was to synthesize the indirect evidence of joint stability in aGJH and sGJH using White & Panjabi's [4] biomechanical framework, which conceptualizes joint stability as the interaction of passive (non-contractile tissues), active (muscle), and neural (nervous system) subsystems.

Methods

In this structured narrative review, we identified peer-reviewed studies through targeted searches across multiple databases. Evidence comparing sGJH, aGJH, and non-GJH control groups was qualitatively synthesized and mapped to passive, active, and neural subsystems. The direction and consistency of findings were summarized to characterize subsystem-specific patterns of joint stability.

Results

There was a clear and consistent pattern of impairment in sGJH compared to controls across all subsystems (↑ laxity, ROM; ↓ strength, endurance, proprioception, tissue stiffness). Findings for aGJH compared to controls were more variable, though more studies reported differences mirroring the impairment patterns observed in sGJH. Direct comparisons between sGJH and aGJH were limited, with available studies generally reporting greater impairments in sGJH. **Table 1** summarizes the number of studies (n=51) and direction of reported differences.

Discussion

Taken together, these findings demonstrate consistent impairments across multiple subsystems in sGJH compared to non-GJH. Evidence in aGJH was more variable and may reflect partially preserved active and neural subsystem function. The limited comparisons between aGJH and sGJH further support the concept of a continuum, in which symptom status corresponds to subsystem impairment. Key limitations include inconsistent definitions of GJH, heterogeneity in study populations, and a lack of direct evidence linking these to true mechanical instability. The underlying drivers of subsystem impairment—and the extent to which they can be modified—remain unclear, and may reflect complex interactions among pain, connective tissue properties, and other unmeasured contributors.

Images (Optional)

Table 1. Summary of Evidence for each joint stability subsystem (active, neural, and passive) for comparisons between symptomatic GJH (sGJH), asymptomatic GJH (aGJH), and non-GJH healthy controls (control). *The number of studies reporting outcomes in each domain are listed before the symbol indicating the direction of the finding. For example, "8<" in the "sGJH vs control" column indicates that 8 studies reported that the sGJH had a significantly lower outcome than controls in the domain.*

Subsystem	Domain	sGJH vs control	aGJH vs control	sGJH vs aGJH
Active	Strength	8 < | 1 =	5 < | 6 =	1 < | 2 =
	Endurance	3 <	0	1 <
Neural	Motor Control	2 < | 1 =	1 < | 3 =	1 < | 1 =
	Proprioception	8 < | 1 =	1 < | 3 =	1 <
	CNS/Other	1 =	1 =	0
Passive	Joint Laxity	2 >	7 > | 3 =	0
	Joint ROM	3 >	3 > | 2 =	2 =
	Tissue Stiffness	3 < | 1 =	2 < | 1 =	0

References (Optional)

[1]ReddyRS,PeerJ,2022. [2]EwertowskaP,PLOSONE,2020.
[3]NicholsonLL,Physiotherapy,2021. [4]PanjabiMM,JSpinalDisord,1992.

Session Category

Clinical Biomechanics: N/A

P4-146

Modeling First-Stage Hypoplastic Left Heart Syndrome Strategies Using a Zero-Dimensional Closed-Loop Framework

Dr. Aseem Milind Pradhan[1], Dr. Sophie Malekzadeh-Milani[2], Dr. Chiara Sacchi[2], Dr. Damien Bonnet[2,3], Dr. Irene Vignon-Clementel[1]

[1]INRIA Saclay, Palaiseau, Île-de-France, France. [2]M3C-Necker, Hôpital Necker-Enfants malades AP-HP, Paris, Île-de-France, France. [3]Université de Paris Cité, Paris, Île-de-France, France

Introduction

Hypoplastic Left Heart Syndrome (HLHS) is a complex congenital cardiac condition which needs a series of surgeries to ensure the survival of the patient. The first-stage palliation (Norwood procedure) is especially critical, as it establishes the physiological conditions necessary for both immediate survival and eligibility for subsequent surgeries. Clinicians employ a variety of surgical and interventional strategies informed by individual patient data, institutional preference, and surgeon experience. Currently morbidity and mortality remain substantial. Early reintervention rates vary with 20–40% of patients requiring additional procedures before the stage two intervention. There is, thus, an opportunity for improving outcomes with the aid of virtual human twins.

Methods

We constructed zero-dimensional (lumped parameter) computational models representing the entire HLHS circulation before and after the first-stage intervention. We evaluated four potential strategies for this stage, including the traditional Norwood procedure with either a Blalock-Thomas-Taussig or Sano shunt, Hybrid Norwood approach, and fully catheter-based interventions as practiced at Hôpital Necker-Enfants Malades, Paris. Rather than the usual time-varying elastance cardiac chamber model, we have used the single fiber heart model that is more mechanistic and capable of improved patient-specific modeling [1]. The model incorporates key cardiovascular compartments, allowing assessment of how different procedural strategies affect relevant biomarkers (shown in **Figure 1**).

Results

These virtual models enable systematic exploration of these interventions by introducing targeted modifications to each strategy, for example, the length and diameter of the cardiopulmonary shunts, the degree of banding of the pulmonary arteries, etc. By quantifying clinically meaningful biomarkers such as systemic and pulmonary flows, load on the single ventricle, coronary and cerebral perfusion, and flow to other vital organs, the

model provides insights into which approaches are most likely to produce favorable outcomes and reduce the need for reinterventions.

Discussion

This virtual human twin modeling framework could help optimize surgical and catheter-based strategies and support personalized intervention planning.

Images (Optional)

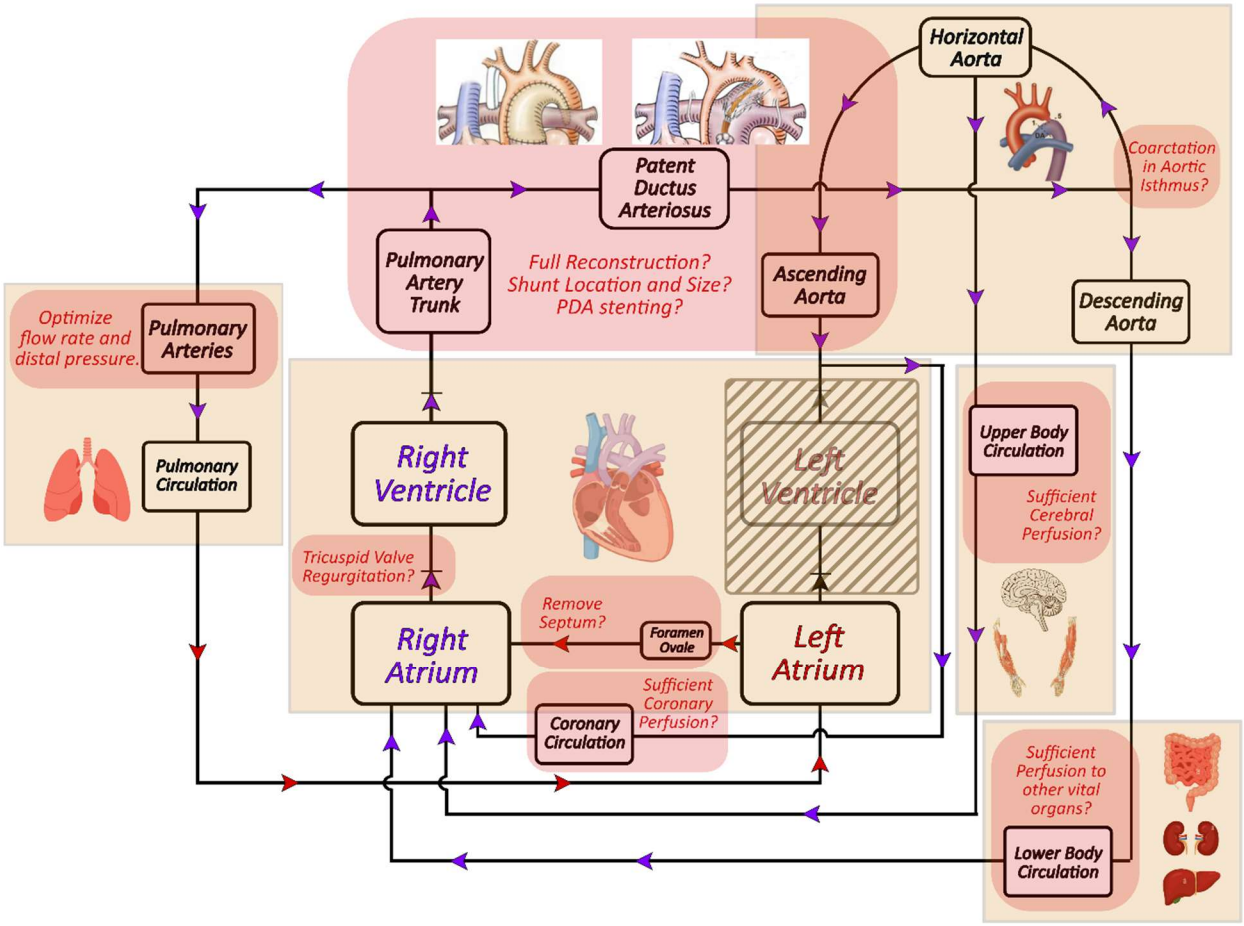


Figure 1: *Closed-loop network model of the Hypoplastic Left Heart Syndrome circulation, highlighting key physiological compartments and the primary clinical questions. (PDA – Patent Ductus Arteriosus)*

References (Optional)

[1] Haghebaert, et al., The Journal of Physiology, 2025.

Session Category

Clinical Biomechanics: N/A

P4-147

A comparison of obstacle crossing measures among older adults with and without total hip or total knee arthroplasty.

Dr. Ashlyn M. Jendro[1], Ms. Abby Brittain[2], Dr. Abigail C. Schmitt[1,2]

[1]The MOVE Lab, Exercise Science Research Center, University of Arkansas, Fayetteville, AR, United States. [2]Biomechanics Laboratory, Department of Orthopaedics, University of Arkansas for Medical Sciences, Little Rock, AR, United States

Introduction

Most falls among older adults occur due to tripping, most commonly over objects in plain sight. To successfully cross obstacles and avoid trips, sufficient clearance is needed in both the vertical (i.e., toe/heel clearance) and horizontal (i.e., approach/landing distance) directions. However, it's largely unknown how these measures might change after lower extremity total joint arthroplasty. This study sought to compare obstacle crossing measures between individuals with and without total joint arthroplasty at the hip or knee.

Methods

Fourteen older adults (7 men, 69±7 years) were included in this preliminary analysis of an ongoing study. Five older adults served as a control group and were compared to individuals with total hip (n=4) or total knee (n=5) arthroplasty. Participants completed 10 obstructed walking trials at a comfortable speed stepping over a dowel (height: 150mm) while barefoot. Participants crossed with their self-selected limb while 3D motion capture recorded marker trajectories over the 8-meter walkway.

Vertical clearance was measured as the distance between the obstacle and the toe/heel marker when directly over the obstacle. Approach and landing distance were defined as the horizontal distance between the obstacle and the toe or heel marker, respectively. Crossing step length was defined as the horizontal distance between the lead and trail heel markers during the crossing step and gait velocity was collected during the middle 4-meters of the walkway. ANOVAs were used to compare means between groups (alpha=.05).

Results

Although none of the variables examined reached significance (all $p>.08$), large effect sizes for approach distance ($p=.15$, $\eta^2=.29$), landing distance ($p=.08$, $\eta^2=.37$) and obstructed gait velocity ($p=.15$, $\eta^2=.21$) suggest meaningful group effects.

Discussion

Our findings indicate, although there were no significant differences between groups in this preliminary data, significance may be found with a larger sample, based on the large effect sizes. This would suggest individuals with total hip or total knee arthroplasty utilize different obstacle crossing strategies than older adults without joint replacements. This can help better inform fall risk and rehabilitation strategies for patients with total joint replacements. This study is ongoing, and we expect a larger sample size by the time of the conference.

Images (Optional)

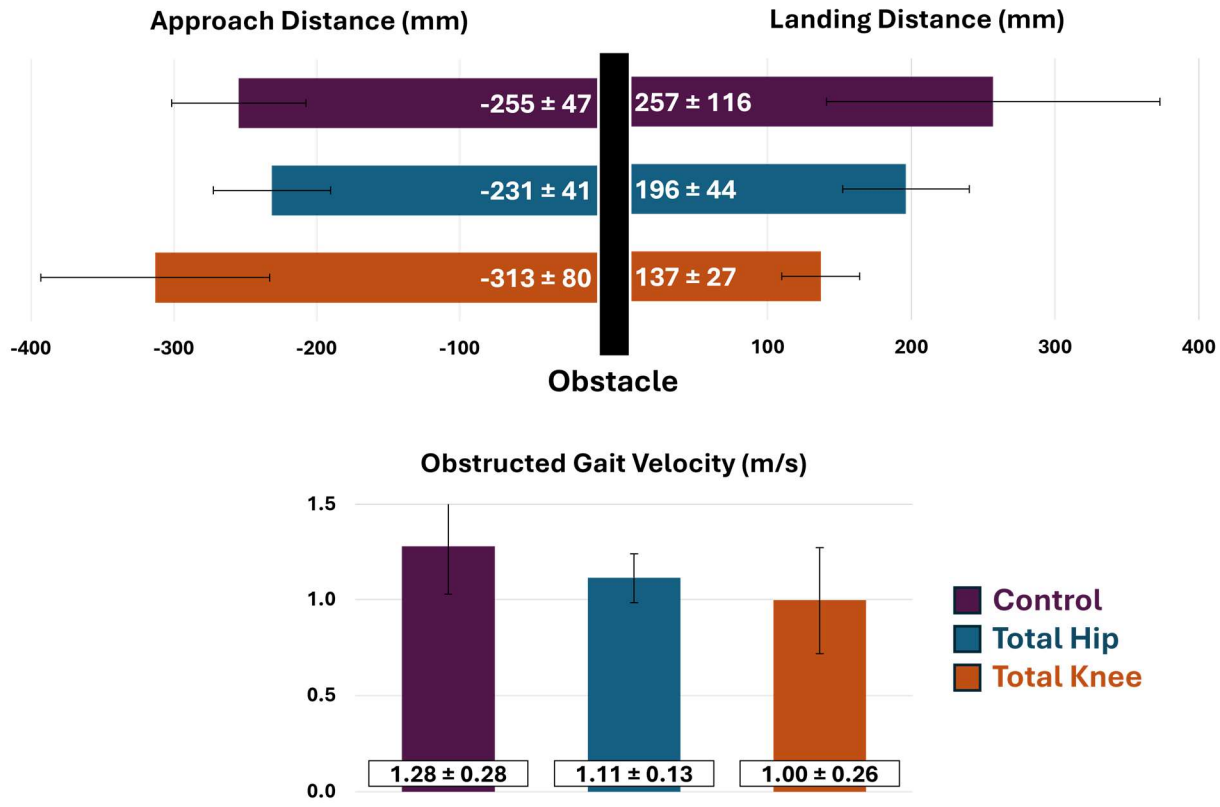


Figure. Select variable means ± standard deviations across groups.

Session Category

Clinical Biomechanics: N/A

P4-148

Evaluation of Deep Learning-Based Event Detection for Complex Gait Analysis in Parkinson's Disease

Research Engineer Avocet Nagle-Christensen BS[1], Regulatory Scientist Anthony Anderson PhD[2,3], Regulatory Scientist Michael Gonzalez PhD[2], Fellow Physician Siegfried Hirczy MD PhD[4], Associate Professor Valerie Kelly PT, PhD[5], Biomedical Engineer Kimberly Kontson PhD[2], Principal Investigator Brittney Muir PhD[1,3]

[1]VA Puget Sound Healthcare System, Seattle, Washington, United States. [2]US Food and Drug Administration, Silver Spring, Maryland, United States. [3]University of Washington, Department of Mechanical Engineering, Seattle, Washington, United States. [4]University of Washington, Department of Neurology, Seattle, Washington, United States. [5]University of Washington, Department of Rehabilitation Medicine, Seattle, Washington, United States

Introduction

Parkinson's disease (PD) often impairs gait and balance; however, clinical assessments offer limited, subjective insight into real-world mobility. Inertial measurement units (IMUs) enable quantitative gait analysis but have mainly focused on steady-state gait (SSG), overlooking transition strides like turns, gait initiation (GI), and gait termination (GT), which are difficult to segment. Deep learning methods, particularly Temporal Convolutional Networks (TCN), show promise in identifying gait events in complex, non-cyclic movement where traditional methods are limited. The study aims to evaluate the accuracy of a pipeline combining a novel TCN-based stride segmentation algorithm and established functions for quantifying simple to complex gait tasks in people with PD.

Methods

All analyses used data from our open-access dataset, WearGait-PD, which includes recordings from gait and balance from 76 individuals with PD and 78 healthy controls. A subset of data was used for training TCN models, while the remaining data was used for analysis against a pressure walkway. Acceleration and gyroscope data from dorsal foot sensors and a lower back sensor were processed via a processing pipeline using our TCN models for stride segmentation and pre-established functions to reconstruct the stride and extract gait metrics. Bland-Altman plots and Spearman correlation were used to evaluate the performance of the IMU pipeline against the pressure walkway.

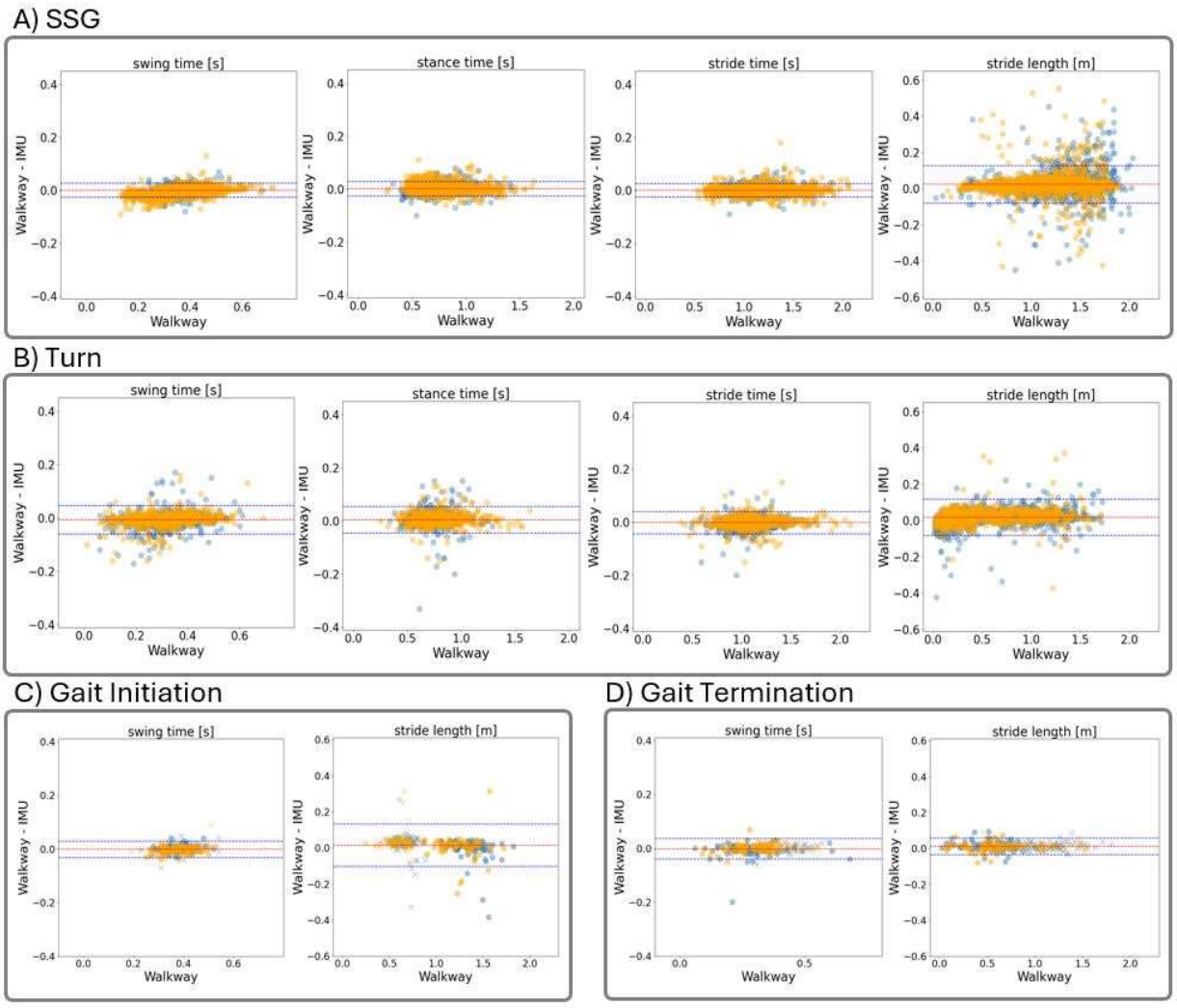
Results

For SSG strides, our method demonstrated small mean errors when calculating spatial and temporal parameters (≤ 2.3cm and ≤ 1.0ms, respectively) and strong correlation ($r \geq 0.96$) with the walkway. Performance for turns, GI, and GT was comparable, with small temporal and spatial mean errors (≤7ms and ≤2.9cm) and correlations (≥0.95).

Discussion

The IMU sensor analysis pipeline was able to effectively derive gait outcomes with high accuracy when compared to the gold standard. The outcomes are consistent with prior analyses for SSG and extend this capability to more complex tasks of gait initiation, turns, and gait terminations. Although the high accuracy of our method heavily relies on the performance of TCN models and the training data, the proposed framework is a reliable method to quantify complex walking tasks, allowing for a more complete understanding of mobility.

Images (Optional)



Session Category

Clinical Biomechanics: N/A

P4-149

Inertial Sensor-Based Gait Parameters During Complex Walking Tasks in Parkinson's Disease Beyond Steady-State Walking

Research Engineer Avocet Nagle-Christensen BS[1], Regulatory Scientist Anthony Anderson PhD[2,3], Regulatory Scientist Michael Gonzalez PhD[2], Fellow Physician Siegfried Hirczy MD PhD[4], Associate Professor Valerie Kelly PT, PhD[5], Biomedical Engineer Kimberly Kontson PhD[2], Principal Investigator Brittney Muir PhD[1,3]

[1]VA Puget Sound Healthcare System, Seattle, Washington, United States. [2]US Food and Drug Administration, Silver Spring, Maryland, United States. [3]University of Washington, Department of Mechanical Engineering, Seattle, Washington, United States. [4]University of Washington, Department of Neurology, Seattle, Washington, United States. [5]University of Washington, Department of Rehabilitation Medicine, Seattle, Washington, United States

Introduction

Parkinson's disease (PD) is a progressive neurodegenerative disorder that often impairs gait and balance. The most common way to assess motor symptoms is through clinical examinations, however they are infrequent, subjective, and provide limited quantifiable information. Inertial measurement units (IMUs) enable quantitative gait analysis but have mainly focused on steady-state gait (SSG), overlooking transition strides such as turns, gait initiation (GI), and gait termination (GT), which potentially hold valuable clinical information. The purpose of this study is to evaluate gait metrics of simple and complex walking and their association with disease status and progression.

Methods

All analyses used data from our open-access dataset, WearGait-PD, which includes recordings from gait and balance from 76 individuals with PD and 78 healthy controls. These tasks captured gait initiation, gait termination, steady-state gait, and 180-degree turns. Acceleration and gyroscope data from dorsal foot sensors and a lower back sensor were processed via a pipeline using Temporal Convolutional Network models for stride segmentation and pre-established functions [5] to reconstruct the stride and extract gait metrics. A linear mixed-effects model was used to evaluate gait metrics across PD and control populations and Hoehn & Yahr (HY).

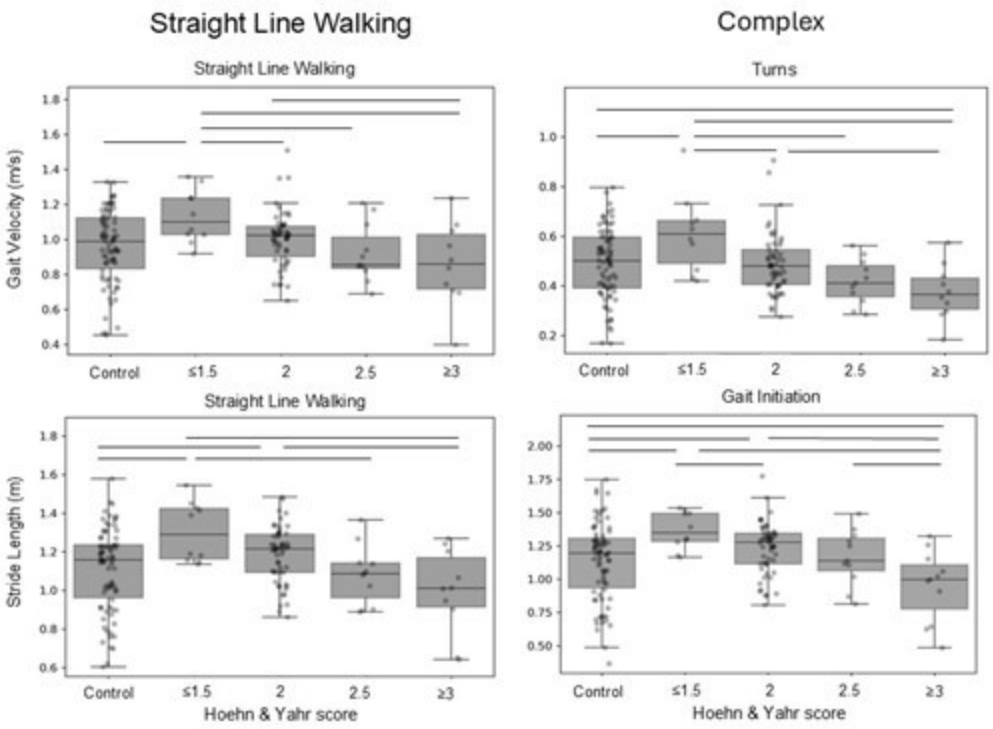
Results

Stride length was significantly different between HY groups 2.5 and ≥3, <2, and 2, and controls and HY ≥3 and <2 when evaluating SSG along with complex strides. Gait velocity was significantly different between HY groups <2 and 2, 2.5, and ≥3, and controls and HY ≥3 in SSG along with complex strides. Max foot height showed significant differences across several HY scores and control during all complex strides, however none during SGG.

Discussion

Several gait metrics suggest that complex strides have more sensitivity to changes in gait across disease status and progression compared to SSG. Metrics such as turn duration and number of strides taken during a turn have been associated with PD status and falls. Gait initiation and termination have also been associated with freezing, balance, and falls. However, stride-level metrics for turns, GI, and GT are often not published. This study proposes potential sensitive gait metrics that could be used to better characterize and understand movement in people with PD.

Images (Optional)



Session Category

Clinical Biomechanics: N/A

P4-150

Development of a 3D Visualization and Quantification System for Dynamic Evaluation of Shoulder Joint

Ms. Aya Nakamura[1], Prof. Takeshi Shimoto[1], Prof. Satoru Ikebe[2], Ms. Ayano Maehara[1], Mr. Takumi Nakano[1], Mr. Hiroya Monji[1], Ms. Hanae Myotsuzono[3], Prof. Naoya Kozono[4], Prof. Hidehiko Higaki[3], Prof. Yasuharu Nakashima[4]

[1]Fukuoka Institute of Technology, Fukuoka, Fukuoka, Japan. [2]Yamaguchi University, Ube, Yamaguchi, Japan. [3]Kyushu Sangyo University, Fukuoka, Fukuoka, Japan. [4]Kyushu University, Fukuoka, Fukuoka, Japan

Introduction

Postoperative evaluation of arthroscopic rotator cuff repair (ARCR) has primarily relied on qualitative assessments by physicians, limiting the ability to evaluate joint dynamics in a three-dimensional and quantitative manner. Our research group has established a high-precision image-matching technique for dynamic analysis[1] and obtained novel insights through visualization.[2,3] However, visualization was performed using 3D-CAD software, restricting its application to research purposes. The aim of this study was to develop a dedicated software system that visualizes and quantitatively evaluates three-dimensional dynamics during scapular plane elevation for clinical application of these findings.

Methods

One postoperative ARCR patient performed scapular plane elevation, and continuous X-ray images were acquired using a flat-panel detector. Three-dimensional models of the scapula and humerus were reconstructed from the patient's CT scan, and six-degree-of-freedom motion data were calculated using an image-matching technique. Based on these data, we developed a dedicated software system to visualize the three-dimensional relative motion of the humerus with respect to the scapula. The system loads multiple bone models and displays multiple motion postures in different colors simultaneously. Additionally, it quantifies glenoid-humeral head distance and three-dimensional displacement of the humeral head center relative to the glenoid.

Results

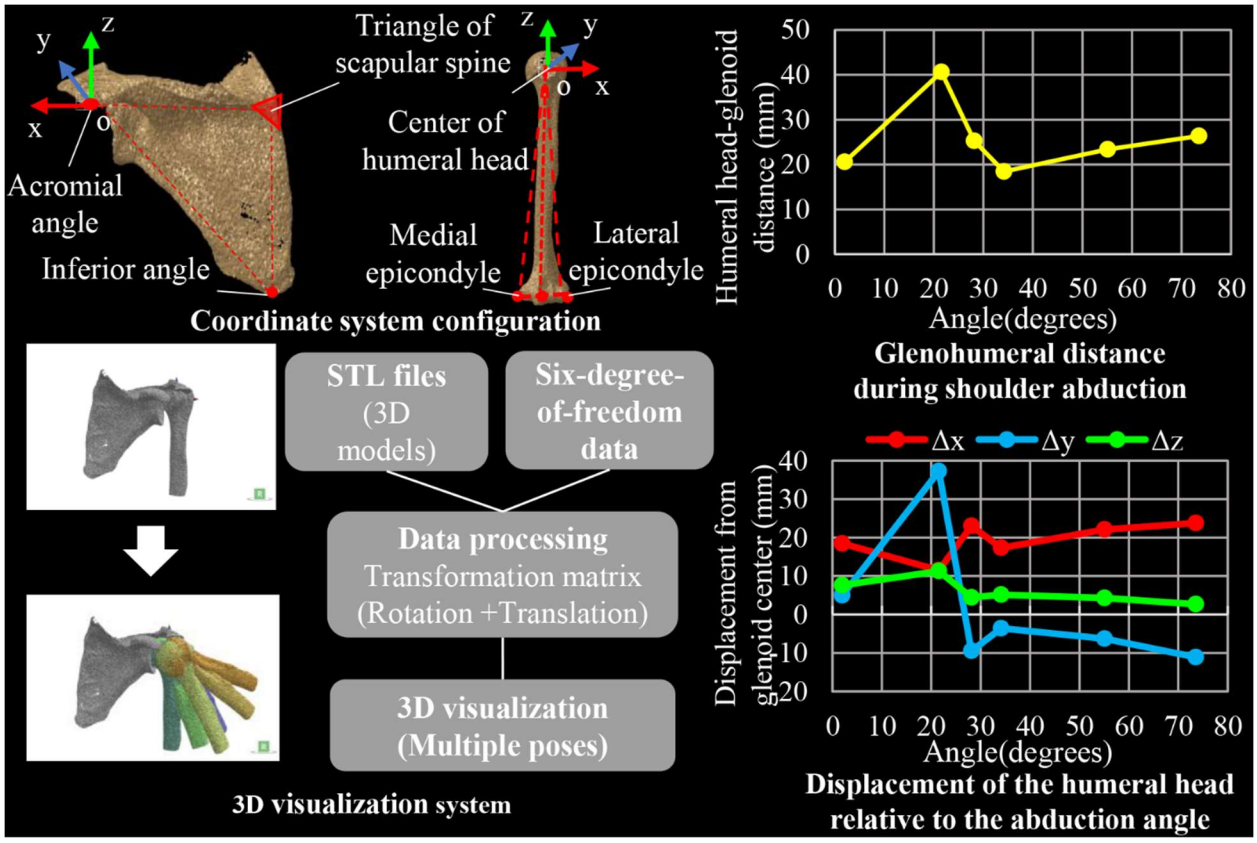
The developed system visualized the three-dimensional relative motion of the humerus with respect to the scapula using six-degree-of-freedom data obtained from image-matching. Validation using data from one postoperative ARCR patient demonstrated that simultaneous color-coded display of six motion postures throughout the elevation movement enabled observation of dynamic positional changes at each elevation angle and

quantification of glenoid-humeral head distance and three-dimensional displacement of the humeral head center relative to the glenoid.

Discussion

This system demonstrated the potential to quantitatively evaluate dynamic impingement and changes in bone-to-bone distance, which were difficult with conventional qualitative assessments. This enables more objective and accurate evaluation of joint dynamics after ARCR, potentially contributing to improved postoperative assessment. Further validation using a larger patient population is necessary to establish the clinical utility of this system.

Images (Optional)



References (Optional)

[1] Kozono N, et al. Knee Surg Sports Traumatol Arthrosc. 2017

[2] Kozono N, et al. J Orthop Surg Res. 2018

[3] Kozono N, et al. J Orthop Surg (Hong Kong). 2020

Session Category

Clinical Biomechanics: N/A

P4-151

Joint Power Redistribution and Reduced Mechanical Efficiency in Adults with Knee Injury During User-Controlled Walking

Mr. Brandon Peoples MS, EP-C, Ms. Bria Smith MS, Ms. Isabella Helm, Mr. Keven Santamaria-Guzman MS, Mr. Kenneth Harrison MS, Ms. Damaris Cifuentes MS, Ms. Silvia Campos-Vargas MS, Dr. Jaimie Roper PhD

Auburn University, Auburn, Alabama, United States

Introduction

Self-selected walking (SSW) speeds are optimized to minimize energy expenditure while maximizing muscle-tendon mechanics[1,2]. However, lower extremity injuries disrupt this balance, leading to compensatory adjustments in joint mechanics that may reduce walking efficiency[3]. User-controlled treadmill technology preserves natural SSW gait patterns and offers a valuable method to study how injury affects walking efficiency[4]. Therefore, this study examines walking efficiency and lower-extremity joint power during user-controlled SSW in adults with and without knee injury.

Methods

Eight adults (5 experimental with knee injury and 3 controls, 29±11 years) performed user-controlled treadmill SSW while outfitted for motion capture and indirect calorimetry. The treadmill algorithm used real-time pelvic marker data to regulate belt speed (SSW speeds: 1.1–1.5 m/s). Walking efficiency, efficiency of positive work, is defined as the ratio of positive joint work to the sum of net metabolic power and negative joint work. Preliminary results are presented descriptively since this is part of an ongoing study with a larger sample.

Results

Preliminary evidence suggests that injured participants had lower metabolic power (2.41±0.51 W/kg) than controls (2.97±1.07 W/kg) during SSW. Positive work was reduced at the ankle (0.58±0.21 vs. 0.91±0.29 W/kg) and the knee (0.34±0.18 vs. 0.48±0.21 W/kg), with smaller differences observed at the hip (0.59±0.19 vs. 0.65±0.26 W/kg). Negative work patterns revealed greater ankle absorption in the injured group (-0.35±0.21 vs. −0.30±0.04 W/kg), reduced knee absorption (-0.44±0.10 vs. -0.60±0.14 W/kg), and slightly greater hip absorption (-0.14±0.14 vs. -0.10±0.08 W/kg). Efficiency was modestly lower in the injured group (0.45±0.05 vs. 0.52±0.15).

Discussion

In our sample, adults with knee injury exhibit altered joint power distribution and reduced efficiency, suggesting compensatory patterns may incur a metabolic penalty. Larger sample and inferential analyses will clarify the mechanisms underlying these preliminary trends and determine whether the observed effects are unlikely to occur by chance.

Images (Optional)

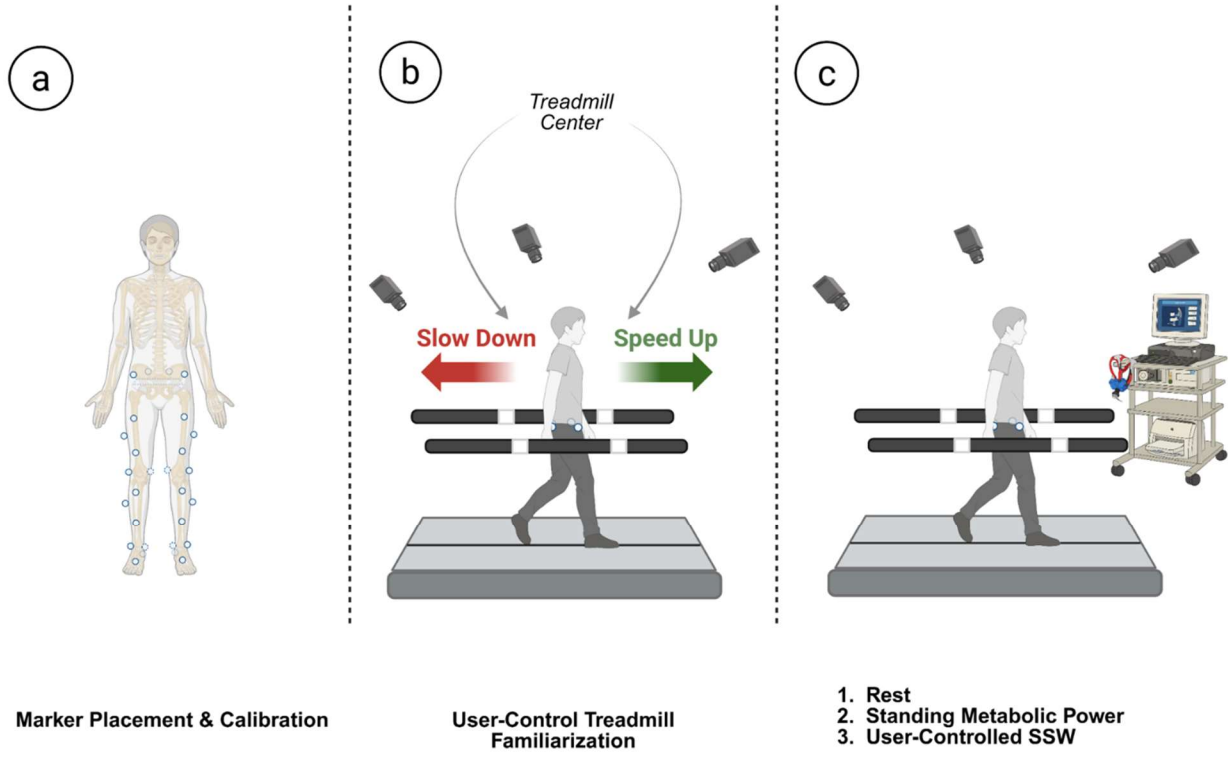


Figure 1. Experimental setup for assessing joint power and metabolic efficiency during self-selected walking (SSW) on a user-controlled split-belt treadmill. *(a)* Reflective markers placed on anatomical landmarks enable motion capture calibration. *(b)* Participants familiarize themselves with a split-belt treadmill that adjusts speed in real time based on pelvic marker displacement. *(c)* The protocol included a rest period followed by capture of standing metabolic power and user-controlled, self-selected walking (SSW) metabolic power. Joint mechanics were measured from each leg.

References (Optional)

[1]Ralston, Int.Z.Angew.Physiol.Einschl.Arbeitsphysiol., 1958

[2]Umberger & Martin, J Exp Biol, 2007

[3]Boyer et al., Exp Ger, 2023

[4]Holmes et al., J App Biomech, 2021

Session Category

Clinical Biomechanics: N/A

P4-152

Physical and Behavioral Trajectories and Cognitive Outcomes: A Longitudinal Analysis of the Health and Retirement Study

Ms. Breanna Morales MS[1], Dr. Harlan Sayles PhD[2], Dr. Jennifer Yentes PhD[1]

[1]Texas A&M Univeristy, College Station, Texas, United States. [2]University of Nebraska, Omaha, Nebraska, United States

Introduction

Alzheimer's disease and related dementias (ADRD) are preceded by subtle physiological changes that may appear years before clinical diagnosis. Declines in gait speed and daily activity have been proposed as early indicators of neurodegenerative vulnerability, yet longitudinal evidence remains limited. The Health and Retirement Study (HRS) is a nationally representative cohort of U.S. older adults, aged 51 years and older, re-interviewed biennially. This dataset provides longitudinal data to examine how trajectories of physical function and lifestyle behaviors predict cognitive outcomes. This study evaluated whether longitudinal changes in gait speed and physical activity serve as early, modifiable indicators of Alzheimer's disease and dementia in a nationally representative cohort of older adults.

Methods

Data were obtained from the Health and Retirement Study (HRS). Participants with at least two assessments of gait speed or physical activity and no diagnosis of Alzheimer's disease or dementia at baseline were included. Alzheimer's and dementia status were determined through self- or proxy-reported physician diagnosis. Annual rates of change for each variable were calculated as the slope between available waves (2004–2022), with missing intervals estimated under the assumption of linear change. These slopes represented the yearly trajectory of change in gait speed and physical activity. Generalized estimating equation logistic regressions and Cox proportional hazards models were used to test associations with subsequent Alzheimer's or dementia diagnosis, adjusting for baseline age.

Results

Gait speed was a significant predictor of Alzheimer's and dementia diagnosis. Each one-second per year slowing in gait speed increased the odds of Alzheimer's by 3.7 times and dementia by 2.8 times ($p < .001$). Annual declines in physical activity were also associated with a greater risk, while maintaining higher activity levels was protective (OR = 0.95, $p < .001$).

Discussion

Findings were consistent across Cox models, indicating that steeper yearly declines were linked to earlier disease onset. Even after adjusting for age, gait speed remained the strongest predictor. These results align with prior evidence linking slower gait to cognitive decline and suggest that subtle, measurable decreases in gait and physical activity may serve as early, modifiable indicators of neurodegenerative risk.

Session Category

Clinical Biomechanics: N/A

P4-153

Gait Speed Reserve of Young Adults Is Not Affected by a Sleep Extension Intervention

Ms. Bria Smith[1], Mr. Brandon Peoples[1], Mr. Kenneth Harrison[1], Dr. Meral Culver[1,2], Mr. Keven Santamaria Guzman[1], Ms. Silvia Campos Vargas[1], Dr. Austin Robinson[3], Dr. Jaimie Roper[1]

[1]Auburn University, Auburn, AL, United States. [2]Texas A&M University- Kingsville, Kingsville, Texas, United States. [3]Indiana University - Bloomington, Bloomington, Indiana, United States

Introduction

Gait speed reserve (GSR), which describes the difference between an individual's maximum and preferred gait speeds, is regarded as an indicator of physiological reserve, cognitive reserve, and functional capacity [1,2]. Inability to increase one's gait speed is linked to decreases in mobility and cognitive functioning [2]. While sleep plays an important role in physiological and cognitive functioning, little is known about the relation between sleep and GSR. Based on recent literature demonstrating sleep extension does not affect the single-task gait speed in young adults, we hypothesized that sleep extension would not affect GSR in young adults [3].

Methods

Thirty-nine young adults (16M/23F; SD = 22±2 years) who self-reported sleeping <7 hours per night completed two lab visits. Participants were split into a control group (N=10), who maintained their typical sleep for two weeks, and an intervention group (N=29), who were instructed to extend their sleep by one hour for two weeks. The Pittsburgh Sleep Quality Index (PSQI) was used to assess self-reported sleep duration and quality. Participants completed the instrumented 2-minute walk test (i2MWT) at preferred and fast gait speeds during laboratory visits before and immediately after their respective intervention. Relative GSR capacity was calculated using the following equations: (fast speed-preferred speed)/fast speed. A linear mixed model was used to compare changes across group and visit.

Results

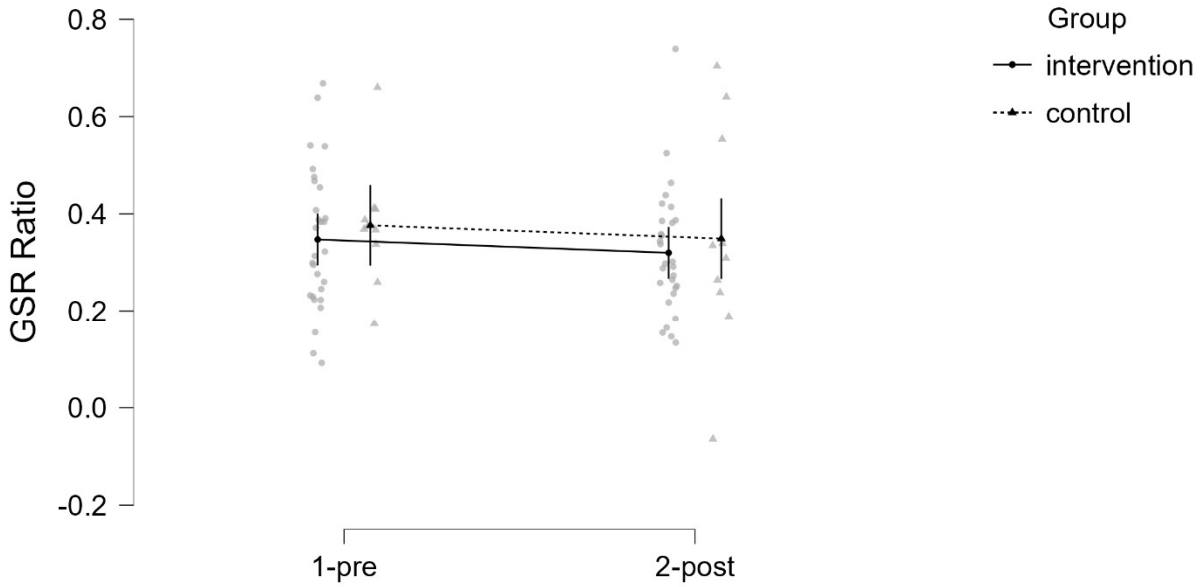
While the control group reported no improvements in sleep duration ($p>.05$) or quality ($p>.05$), the sleep extension intervention group reported increases in sleep duration (6.2 ± 0.9 vs. 7.3 ± 1.0 hours, $p<.001$) and improvements in sleep quality (5.4 ± 1.6 vs. 3.4 ± 1.4,

p<.001). However, no significant differences in GSR were found when comparing across groups or visits (p>.05).

Discussion

In our study, we found that sleep extension does not affect GSR in apparently healthy young adults. However, improvements in cognitive and physical performance associated with increased GSR and sleep extension may be more drastic in older adults due to age-related decreases in cognitive ability and sleep health.

Images (Optional)



Changes in GSR Across Visits for Intervention and Control Groups

References (Optional)

[1] Lindholm *et al.,* GeroScience, 2024

[2] Callisaya *et al.,* GeroScience, 2017

[3] Boolani *et al.*, Sensors, 2022

Session Category

Clinical Biomechanics: N/A

P4-154

Sex Differences in Running Biomechanics in Knee Injured Adults: A Systematic Review and Meta-Analysis

Mr Brody McCarthy, Ms Stephanie Tamer, Dr Danilo De Oliveira Silva, Dr Marcella Ferraz Pazzinatto, Prof Kay Crossley, Mr Matthew Savage, Dr Brooke Patterson, Ms Juanita Low, Dr Benjamin Mentiplay

La Trobe University, Melbourne, Victoria, Australia

Introduction

Running is a popular way for individuals to exercise, with female participation increasingly on the rise. Injuries are common among those who participate in running, especially at the knee joint, with female runners more likely to sustain an injury compared to their male counterparts. Altered running biomechanics (e.g., higher hip adduction) are often associated with increased knee injury risk and are more prevalent in females. To aid understanding of disease progression and prevention, it is important to consider how running biomechanics differ between males and females with knee injuries, a topic which has not been systematically reviewed. Therefore, we aimed to systematically review the literature to compare running biomechanics between males and females with knee injuries.

Methods

Six online databases were searched from inception to October 2025. We included studies that reported biomechanical running data split by males and females in individuals with knee injuries (e.g., patellofemoral pain (PFP), iliotibial band syndrome (ITBS), anterior cruciate ligament reconstruction (ACLr)) using three-dimensional motion capture and/or force plates. Variables reported in at least three studies were pooled and analysed using random-effects meta-analyses.

Results

Sixteen studies involving 517 participants (389 PFP, 78 ITBS, 50 ACLr) were included, with females representing 51% of the sample (n = 262). Meta-analyses were conducted for eight biomechanical variables (six kinematic, two kinetic). Females exhibited significantly greater peak hip adduction and hip internal rotation angles during running than males (MD = 3.84°, 95% CI = 2.82–4.86; MD = 2.88°, 95% CI = 1.35–4.41, respectively). No sex-specific

differences were found for knee joint angles (flexion, abduction, rotation), ankle eversion, or external knee joint moments (flexion, adduction).

Discussion

Our review found that females with knee injuries had higher peak hip adduction and hip internal rotation angles during running than males, while no sex-specific differences were observed for knee or ankle angles or knee joint moments. It is important to consider sex differences in running biomechanics when examining relationships with injury status and rehabilitation outcomes, and future research should account for these differences in both reporting and analysis.

Session Category

Clinical Biomechanics: N/A

P4-155

Concurrent validity of a 2D versus 3D markerless system for frontal-plane kinematics in single-leg landing tests

Mr. Jean Marlon Machado[1], Ms. Kauane de Farias Andrade[1], Dr. Danilo De Oliveira Silva[2], Dr. Heiliane de Brito Fontana[3], Dr. João Paulo Vilas-Boas[4], Dr. Caroline Ruschel[1]

[1]College of Health and Sport Science, University of the State of Santa Catarina, Florianópolis, Santa Catarina, Brazil. [2]La Trobe Sport and Exercise Medicine Research Centre (LASEM), La Trobe University, Melbourne, Victoria, Australia. [3]BSiM-UFSC Musculoskeletal Biomechanics Research Group, Federal University of Santa Catarina, Florianópolis, Santa Catarina, Brazil. [4]Porto Biomechanics Laboratory (LABIOMEP), Faculty of Sport, CIFI2D, University of Porto, Porto, Porto, Portugal

Introduction

Markerless motion capture systems are increasingly used to quantify human movement, but the validity of 2D pose-estimation approaches (e.g., MediaPipe) relative to 3D markerless systems remains unclear. This study investigated the concurrent validity of a 2D MediaPipe-based system against Theia3D in estimating frontal-plane trunk, pelvis, hip, and knee angles during a single-leg landing test.

Methods

In this study, 31 physically active adults (19 men; 29.3±8.1 years; 25.1±3.2 kg/m^2) performed single-leg landings from a 30 cm height onto a force platform. Two video datasets were simultaneously collected: an eight-camera Miqus setup processed with Theia3D (Theia, Canada) and a mobile phone frontal-plane video processed with a custom 2D pipeline based on MediaPipe pose estimation (version 0.10.14, Google, USA). Both datasets were captured at 120 Hz. Frontal-plane trunk, pelvis, hip, and knee angles at the deepest point of the landing were extracted. Both lower limbs were analyzed. Concurrent validity was assessed using Pearson correlation coefficients and Bland-Altman analysis (between-system mean differences and 95 % limits of agreement).

Results

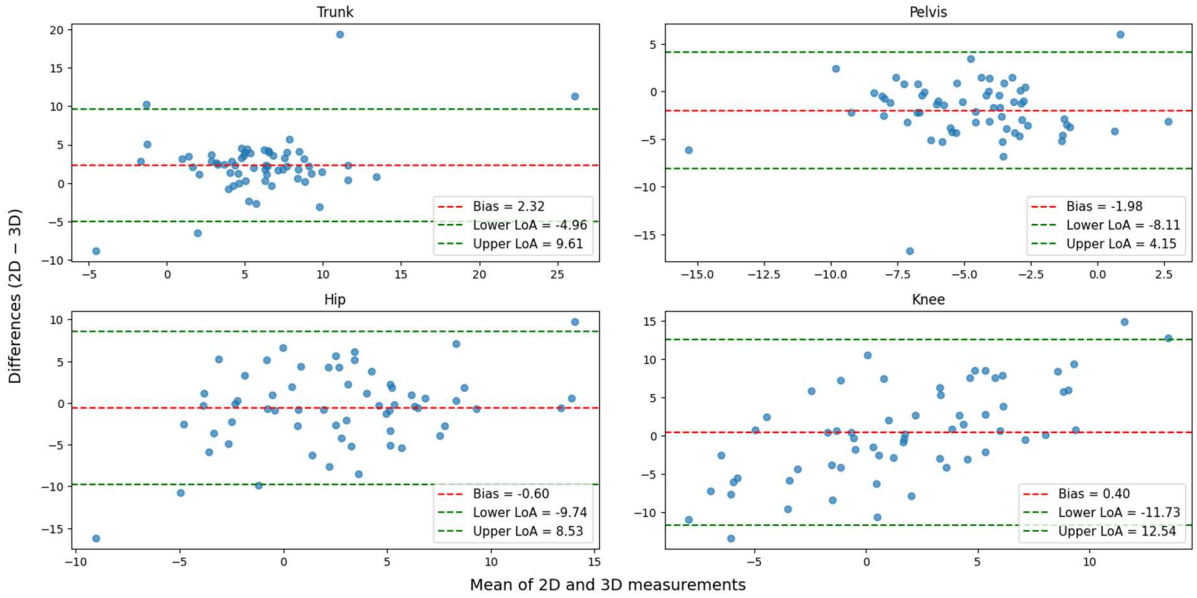
For the trunk, the correlation between 2D and 3D measurements was strong ($r = 0.71$; $p < 0.001$). For the pelvis ($r = 0.59$; $p < 0.001$), hip ($r = 0.67$; $p < 0.001$), and knee ($r = 0.57$; $p < 0.001$), the correlation was moderate. Bland-Altman analysis revealed moderate bias for the trunk (2°; LoA: -5 to 10°) and small bias for the pelvis (-2°; LoA: -8 to 4°), hip (-1°; LoA: -10 to 9°), and knee (0°; LoA: -12 to 13°). There was a moderate correlation between the

mean values and the differences between methods for the knee (r = 0,67; p < 0,001). Bland-Altman plots are presented in Figure 1.

Discussion

Although measurements were correlated, the wide limits of agreement reveal considerable between-method variability. Even so, the excellent reliability suggests that this 2D approach may be suitable for tracking within-subject changes and standardized screening in clinical or field settings.

Images (Optional)



Acknowledgements (Optional)

CAPES and UDESC for the scholarships (JMM and KFA) and FAPESC for financial support the research group (2025TR001430).

Session Category

Clinical Biomechanics: N/A

P4-156

Is the Dynamic Knee Valgus During Single-Leg Tasks Associated With Knee Disorders? a Systematic Review With Meta-Analysis

Mr. Jean Marlon Machado[1], Ms. Kauane de Farias Andrade[1], Dr. Danilo De Oliveira Silva[2], Dr. Heiliane de Brito Fontana[3], Dr. João Paulo Vilas-Boas[4], Dr. Caroline Ruschel[1]

[1]College of Health and Sport Science, University of the State of Santa Catarina, Florianópolis, Santa Catarina, Brazil. [2]La Trobe Sport and Exercise Medicine Research Centre (LASEM), La Trobe University, Melbourne, Victoria, Australia. [3]BSiM-UFSC Musculoskeletal Biomechanics Research Group, Federal University of Santa Catarina, Florianópolis, Santa Catarina, Brazil. [4]Porto Biomechanics Laboratory (LABIOMEP), Faculty of Sport, CIFI2D, University of Porto, Porto, Porto, Portugal

Introduction

There is conflicting evidence on the association between knee disorders and dynamic knee valgus (DKV) during functional tasks, possibly because different tasks generate different biomechanical demands. We conducted a systematic review to synthesize the evidence on whether DKV in single-leg tasks is associated with knee disorders and whether this association differs between single-leg squats and landings.

Methods

Systematic searches were conducted in Web of Science, CINAHL, Embase, PubMed, and Scopus. We included studies comparing DKV during single-leg tasks between individuals with knee disorders (or who later developed these disorders) and asymptomatic controls. We extracted data on participants, tasks, disorders, and DKV measures (type and magnitude). DKV measures were converted to standardized mean differences (SMD) and pooled in two meta-analyses: landings and squats. Subgroups were defined by disorder type. PROSPERO: CRD420251006257.

Results

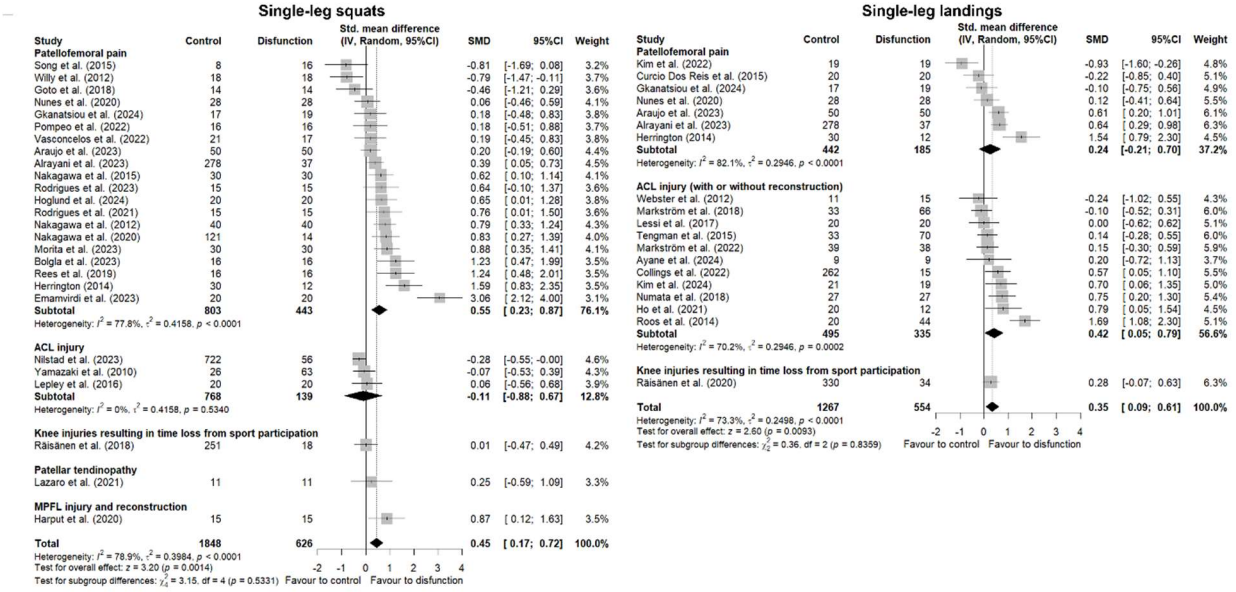
Of 10204 records, 40 studies were included. The knee disorders identified were patellofemoral pain (k=22), ACL injuries with or without reconstruction (k=14), Knee injuries that resulted in time loss from sports participation (k=2), patellar tendinopathy (k=1), and medial patellofemoral ligament (MPFL) injury with reconstruction. For single-leg squats, DKV was greater in individuals with patellofemoral pain (SMD=0.55; 95%CI=0.23–0.87; p<0.001), but not different in individuals with ACL injuries compared to control, with a small overall effect (SMD=0.45; 95%CI=0.17–0.72; p<0.001). For single-leg landings, DKV was greater in individuals with ACL injuries (SMD=0.42; 95%CI=0.05–0.79; p<0.001), but

not different in individuals with patellofemoral pain compared to controls, with a small overall effect (SMD=0.35; 95%CI=0.09–0.61; p=0.009).

Discussion

The results reveal a task-specific association between knee disorders and dynamic knee valgus, suggesting that the sensitivity of DKV to differentiate disorders may depend on the biomechanical demands of the task. Individuals with patellofemoral pain exhibited greater DKV during single-leg squats, a slow and controlled task that demands proximal control and altered movement strategies commonly reported in PFP. In contrast, individuals with ACL injuries demonstrated greater DKV primarily during single-leg landings, a high-demand, impact-driven task that challenges neuromuscular control, knee stability, and trunk–hip coordination. Based on our findings clinicians should choose tasks that biomechanically challenge the clinical population they are managing.

Images (Optional)



Acknowledgements (Optional)

CAPES and UDESC for the scholarships (JMM and KFA) and FAPESC for financial support the research group (2025TR001430).

Session Category

Clinical Biomechanics: N/A

P4-157

Functional Relevance of Radiographic Alignment Measures in Reverse Total Shoulder Arthroplasty: A 3D Kinematic Analysis

Dr. João A. Bonadiman MD[1], Dr. Renato Miyadahira MD[1], Dr. Vitor La Banca MD[1], Dr. Felipe F. Gonzalez MD[2,1], Dr. Carolline P. Nunes MD[2,1], Dr. Gregory Nicholson MD[2], Dr. Brian Forsythe MD[2], Dr. Nikhil N. Verma MD[2], Dr. Jorge Chala MD[2], Dr. Leonardo Metsavaht PhD[1], Dr. Gustavo Leporace PhD[1], Dr. Grant E. Garrigues MD[2], Dr. Jonathan Gustafson PhD[2]

[1]Instituto Brasil de Tecnologias da Saúde (IBTS), Rio de Janeiro, Rio de Janeiro, Brazil. [2]Department of Orthopaedics, Rush University Medical Center, Chicago, Illinois, United States

Introduction

Reverse total shoulder arthroplasty (RTSA) is widely used for cuff tear arthropathy, glenohumeral osteoarthritis, and complex proximal humerus fractures. Radiographic parameters such as the lateralization shoulder angle (LSA), distalization shoulder angle (DSA), acromiohumeral interval (AHI), and reverse shoulder arthroplasty angle (RSA beta) have been proposed as indicators of implant positioning, yet their relevance to postoperative function remains uncertain. This study evaluated associations between radiographic alignment parameters and in vivo shoulder kinematics in patients with medialized and lateralized glenosphere designs.

Methods

Twenty-five RTSA cases (11 medialized, 14 lateralized; mean age 71.0 ± 6.0 years) were analyzed. True anteroposterior radiographs were used to measure LSA, DSA, AHI, and RSA beta. Dynamic shoulder kinematics were recorded during abduction, scaption, and forward flexion. Range of motion was segmented into glenohumeral, scapulothoracic, and humerothoracic components, and scapulohumeral rhythm was calculated during scaption. Associations between radiographic parameters and kinematic outcomes were examined using Pearson or Spearman correlations and multivariable regression ($p < 0.05$).

Results

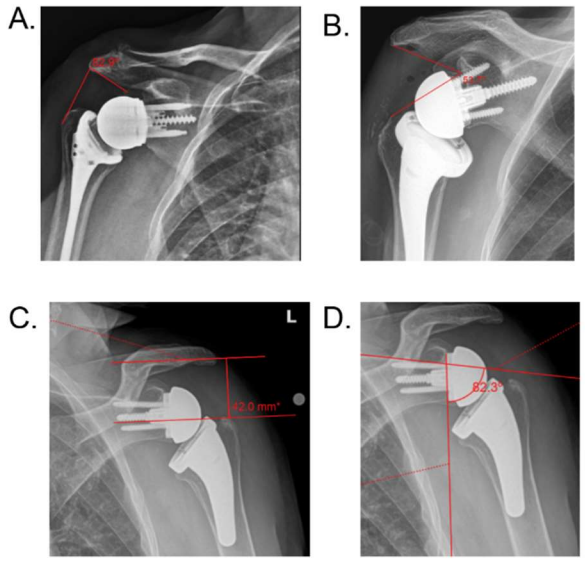
During abduction, glenohumeral abduction correlated with RSA beta ($r = 0.415$; $P = 0.049$), while glenohumeral internal/external rotation correlated with DSA ($r = 0.407$; $P = 0.054$) and AHI ($r = 0.487$; $P = 0.018$). Humerothoracic elevation and humerothoracic rotation correlated with RSA beta ($r = 0.479$; $P = 0.021$ and $r = 0.426$; $P = 0.043$). During scaption,

RSA beta correlated with humerothoracic rotation (r = 0.462; P = 0.026). During forward flexion, scapulothoracic rotation correlated with LSA (r = 0.470; P = 0.024). Regression analyses identified AHI as a predictor of glenohumeral rotation (r^2 = 0.15; P = 0.036) and LSA as a predictor of scapulothoracic rotation (r^2 = 0.17; P = 0.028).

Discussion

RSA beta showed the most consistent moderate correlations with kinematic variables, suggesting it may reflect aspects of implant positioning relevant to postoperative motion. Although these associations did not persist in multivariable models, the overall pattern indicates that RSA beta may capture alignment features related to dynamic behavior. These findings underscore the complexity of linking static radiographic measures to shoulder motion after RTSA and support the need for larger studies incorporating dynamic imaging and neuromuscular assessments.

Images (Optional)



E.

Abduction correlation matrix

		LSA (Correlation)	DSA (Correlation)	RSA Beta (Correlation)	AHI (Correlation)
GlenHum abduction (coronal-plane elevation)	Spearman's rho	-0.015 (Very Weak)	0.078 (Very Weak)	**0.415 (Moderate)**	0.254 (Weak)
	P-value	0.946	0.723	**0.049**	0.242
GlenHum internal/external rotation	Pearson's r	-0.246 (Very Weak)	**0.407 (Moderate)**	-0.198 (Very Weak)	**0.487 (Moderate)**
	P-value	0.258	**0.054**	0.364	**0.018**
HumThor elevation in sagittal plane	Spearman's rho	0.203 (Weak)	-0.566 (Very Weak)	**0.479 (Moderate)**	-0.409 (Very Weak)
	P-value	0.354	0.005	**0.021**	0.053
HumThor internal/external rotation	Spearman's rho	-0.059 (Very Weak)	-0.032 (Very Weak)	**0.426 (Moderate)**	0.023 (Very Weak)
	P-value	0.788	0.887	**0.043**	0.916

Scaption correlation matrix

		LSA (Correlation)	DSA (Correlation)	RSA Beta (Correlation)	AHI (Correlation)
HumThor internal/external rotation	Spearman's rho	-0.281 (Very Weak)	0.024 (Very Weak)	**0.462 (Moderate)**	0.17 (Very Weak)
	P-value	0.194	0.916	**0.026**	0.439

Forward flexion correlation matrix

		LSA (Correlation)	DSA (Correlation)	RSA Beta (Correlation)	AHI (Correlation)
ScapThor internal/external rotation	Spearman's rho	**0.47 (Moderate)**	-0.198 (Very Weak)	-0.124 (Very Weak)	-0.346 (Very Weak)
	P-value	**0.024**	0.364	0.574	0.106

Figure 1: A. An example of Lateralization Shoulder Angle (LSA) measured having three landmarks as reference: the superior glenoid tubercle, the most lateral border of the acromion, and the most lateral border of the greater tuberosity. **B.** Distalization Shoulder Angle (DSA) was defined using the superior glenoid tubercle, the most lateral border of the acromion, and the most superior border of the greater tuberosity. **C.** An example of Acromial humeral interval (AHI) measured having two landmarks as reference: perpendicular distance between the most lateral portion of the undersurface of the acromion and a line parallel to the superior border of the greater tuberosity. **D.** Reverse Shoulder Arthroplasty angle (RSA) was determined by the intersection of a line running along the baseplate of the glenosphere and the supraspinatus fossa line
E: Abduction, Scaption and forward flexion correlation matrix.
Legends. LSA: Lateralization Shoulder Angle; DSA: Distalization Shoulder Angle; RSA: Reverse Shoulder Angle; AHI: Acromiohumeral Interval; GlenHum: Glenohumeral; ScapThor: Scapulothoracic; HumThor: Humerothoracic

Session Category

Clinical Biomechanics: N/A

P4-158

Systematic Characterization of the Magnitude of Tremulous Joint Rotations Throughout the Upper Limb

Mr. Thomas Alley[1], Mr. Chayse Wright[1], Dr. Steven Charles PhD[1,2]

[1]Department of Mechanical Engineering, Brigham Young University, Provo, UT, United States. [2]Neuroscience, Brigham Young University, Provo, UT, United States

Introduction

Essential Tremor (ET) is one of the most prevalent movement disorders, affecting millions of people worldwide and often impairing activities of daily living [1]. Many efforts to improve tremor suppression methods (such as the development of tremor-suppressing orthoses) would benefit from a characterization of the magnitude of tremulous rotations in the joints of the upper limb. Although tremulous joint rotation (TJR) has been characterized in terms of power [2], a systematic characterization of the magnitude of TJR (in terms of degrees or radians) is not currently available.

Methods

Using motion capture data previously collected throughout the upper limbs of 23 participants with ET while they performed various postural and kinetic tasks [2], we calculated joint angles in the 7 main joint degrees of freedom (DOF) from the shoulder to the wrist [3], and applied a 6th order high-pass Butterworth filter with cut-off frequency at 2 Hz to remove voluntary motion. The root mean square (RMS) amplitude and the maximum amplitude, defined as the largest instantaneous deviation from the mean, were computed for each 30-second trial across all DOF and tasks.

Results

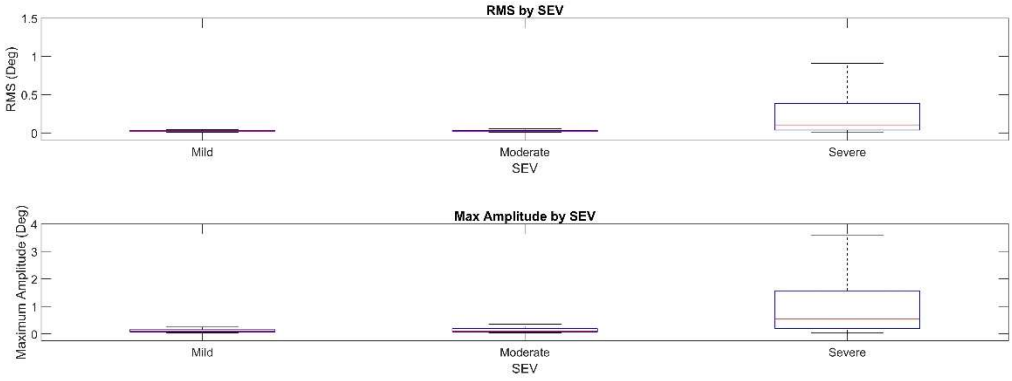
Across all participants and DOF, the mean ± SD of RMS amplitude of postural and kinetic tremor was 0.10 ± 0.33 deg and 0.53 ± 0.46 deg, and the maximum amplitude of postural and kinetic tremor was 0.42 ± 0.93 deg and 2.25 ± 1.95 deg. As expected, these magnitudes varied significantly by tremor severity (see figure) and DOF (not shown).

Discussion

This study provides the first systematic quantification of the magnitude of TJR throughout the upper limb, providing insight into where (which muscles/joints) to best intervene with peripheral tremor suppression methods. Considering the disabling nature of tremor, TJR

magnitudes were surprisingly small, especially for participants with mild and moderate tremor. The small rotation magnitudes provide partial justification for linear models of tremor propagation, which describe the effect of the peripheral neuromusculoskeletal dynamics on tremor [4].

Images (Optional)



References (Optional)

[1] ED Louis et al., TOHM, 2021.

[2] AC Pigg et al., Clin Neurophysiol, 2020.

[3] R Clark et al., J Biomech Eng, 2020.

[4] SA Baker et al., TOHM, 2025.

Session Category

Clinical Biomechanics: N/A

P4-159

A More Accurate Method to Quantify Tremorogenic Muscle Activity

Mr. Chayse Wright[1], Mr. Noah Francom[1], Dr. Dario Farina[2], Dr. Steven Charles[1,3]

[1]Department of Mechanical Engineering, Brigham Young University, Provo, UT, United States. [2]Bioengineering, Imperial College London, London, Greater London, United Kingdom. [3]Neuroscience, Brigham Young University, Provo, UT, United States

Introduction

Although many studies have analyzed surface electromyographic (sEMG) signals in persons with tremor, there is a lack of standardization in how tremorogenic muscle activity is quantified. Researchers commonly quantify features of peaks in the tremor band (4-8 Hz) of the power spectral density (PSD) of processed sEMG using Welch's method, but Welch's method produces many spurious peaks unrelated to tremor, especially in persons with mild and moderate tremor. We explore two methods to reduce the presence of spurious peaks, providing a more robust estimation of tremorogenic muscle power.

Methods

We previously recorded sEMG from the 15 major superficial muscles of the upper limb in 24 persons with Essential Tremor and 10 control subjects as they performed a variety of tasks [1]. In the first method (W+), after estimating the PSD of the linear envelope of sEMG using Welch's method, we identified tremor-band peaks that were both significant and consistent (peaks whose amplitude was statistically significantly different from side windows, and whose frequency was consistent across the participant's muscles and trials). In the second method (YW), we estimated the PSD of the linear envelope using an autoregressive method (Yule-Walker) known to minimize the number of PSD peaks, and then identified the tallest peak. The two estimates were optimized by finding the transform parameters that minimized the variance in peak frequency within a participant, which was assumed to be constant in similar experimental tasks.

Results

Both W+ and YW methods greatly reduced the presence of spurious peaks compared to Welch's method by itself. Furthermore, the W+ method accurately predicted clinical tremor severity. That said, the YW method resulted in 5-10 times lower variance in peak frequency that the W+ method (see table).

Discussion

Developing PSD estimation practices that are sensitive to tremor in persons with mild and moderate tremor allows more accurate quantification of tremorogenic muscle activity in all persons with tremor. This opens the door for future studies comparing tremorogenic activation patterns between muscles, tasks, persons, and tremor types, paving the way for improved tremor suppression.

Images (Optional)

	Mean Variance of Peak Frequency (Hz^2)	Mean Peak Amplitude ($\times 10^{-4}\ V^2/Hz$)	Mean Peak Frequency (Hz)
Welch's +	0.91	3.94	5.99
Yule-Walker	0.14	3.99	6.09
p-value (Paired Samples t-test)	<0.01	0.90	0.06

References (Optional)

[1] DJ Standring *et al.* , Clin Neurophysiol, 2022.

Acknowledgements (Optional)

This work was supported by NIH grant R15 NS087447-02.

Session Category

Clinical Biomechanics: N/A

P4-160

Changes In Trunk Flexion During Five Times Sit-To-Stand In Post-Operative Ventral Hernia Repair Patients Measured Using Single-Camera Markerless Motion Capture

Mr. Cheikh Tandiang B.A.[1], Ms. Kiana Shannon B.S.[2], Mr. Peter Edwards B.S.[3], Dr. Benjamin Poulose MD/MPH[2], Dr. Stephanie Di Stasi PT, PhD[2], Dr. Ajit Chaudhari PhD, FACSM[2]

[1]Ohio State University, Columbus, OH, United States. [2]Ohio State University, Columbus, Ohio, United States. [3]Case Western Reserve University, Cleveland, Ohio, United States

Introduction

The Five Times Sit to Stand Test (5XSTS) is a widely utilized test of physical function for a range of clinical populations, with time to complete as the primary outcome [1]. Studies regarding the biomechanics of 5XSTS have focused on populations with neuromuscular and degenerative joint diseases [2] to better understand compensations to overcome weakness, lack of control, or pain. The purpose of this study was to evaluate the biomechanics of 5XSTS in a novel population of ventral hernia repair patients to assess how they move their trunk, and how this changes as they progress through recovery.

Methods

This study included 58 participants aged 18–70 enrolled from the ABVENTURE-P trial [3] (aged 18-70) scheduled for elective ventral hernia repair. De-identified video recordings of 5XSTS were uploaded to Sit2stand.ai [4] to extract peak trunk flexion and peak trunk acceleration. Video collection was initiated part way through the trial, so not all participants had videos for all timepoints. Peak values were compared across the five timepoints using a mixed-effects model with timepoint as fixed ordinal effect and participant as a random effect, with Tukey HSD post-hoc comparisons.

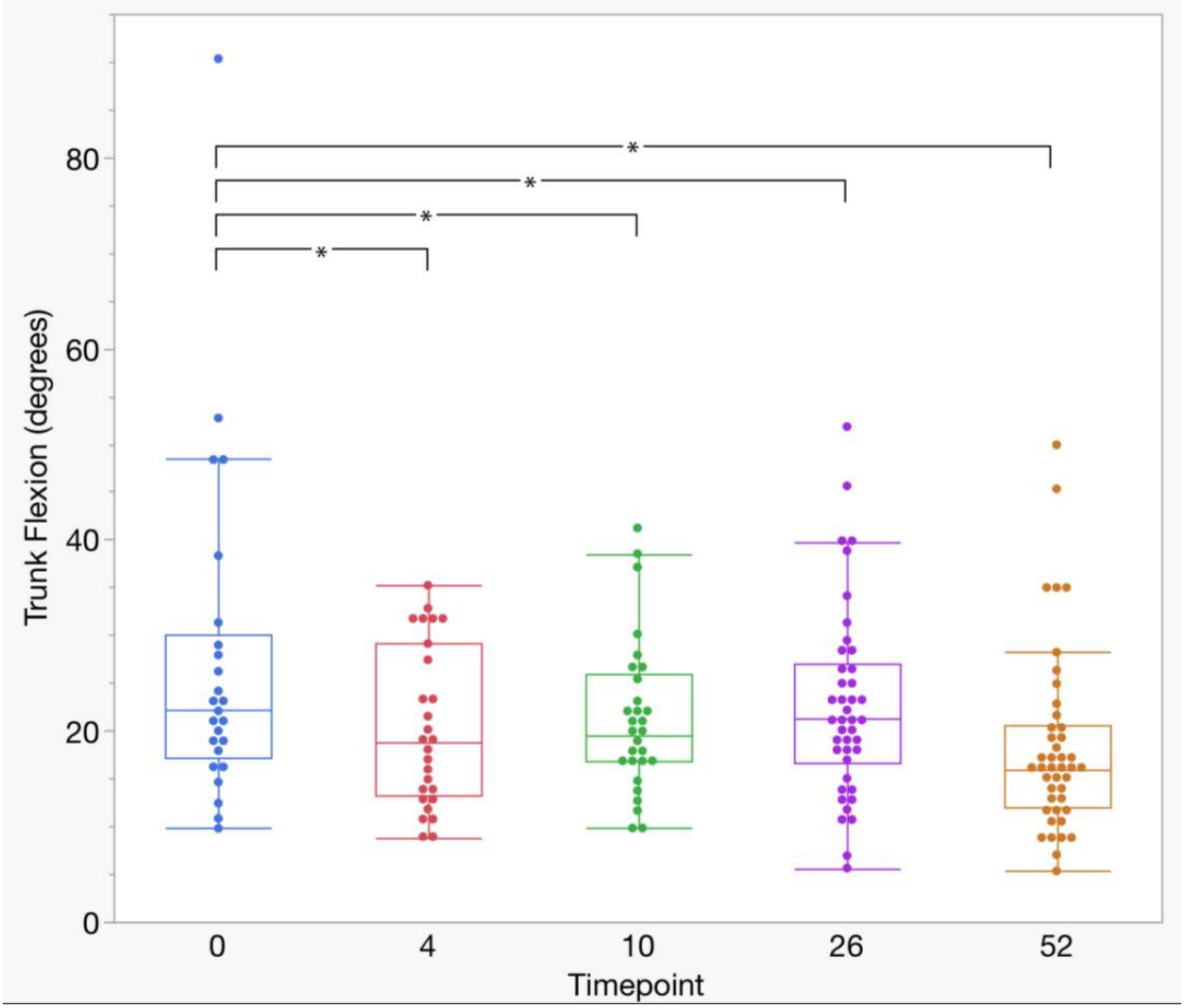
Results

Peak trunk flexion significantly decreased (i.e. more upright) between pre-operative baseline and the other timepoints (-9.7±2.3° @ 1y, $p<0.0001$). Peak trunk acceleration significantly increased between 4 weeks post-op and 1-year post-op (+128±45°/s^2, $p=0.03$).

Discussion

This study demonstrates that trunk biomechanics during 5XSTS change during recovery from ventral hernia repair. More work is needed to determine the trajectory of these changes, whether they are associated with perceived functional or quality-of-life improvements, and how they may be influenced by post-operative rehabilitation. These findings highlight the value of biomechanical analysis for identifying functional changes beyond just time to complete, and they identify a potential tool to guide development of more targeted rehabilitation for ventral hernia repair patients in clinical and telehealth environments.

Images (Optional)



References (Optional)

[1] Howarth (2021), *J Manip Phys Ther* 44(6):487.

[2] Baer (1995), *Arch Phys Med Rehab* 76(9):844.

[3] Di Stasi (2023), *PLoS One* 18(7):e0289038.

[4] Boswell (2023), *NPJ Digital Med* 6:32.

Acknowledgements (Optional)

*Corresponding author: chaudhari.2@osu.edu

Session Category

Clinical Biomechanics: N/A

P4-161

Estimating Joint Moments with Marker-less Motion Capture and Pressure Insoles

Ms. Christina Kyriacou

University of Rochester, Rochester, NY, United States

Introduction

Joint moments are important to consider in gait characterization, supporting injury prevention and rehabilitation assessment. Marker-based motion capture and 3D force plate data form the gold standard for joint kinetic estimation, but these modalities are confined to motion analysis labs, limiting accessibility and scalability. Alternatives such as marker-less motion capture and in-shoe pressure insoles offer increased portability, enabling assessment of movement mechanics outside of a research lab. This study evaluates the feasibility of estimating joint moments using marker-less motion capture and pressure insoles.

Methods

3D marker-based and marker-less (Theia3D) motion capture, force plate, and pressure insole (XSENSOR X4) data were collected during 252 stance phases (93 walking, 67 jogging, 70 drop vertical jump landing). Sagittal plane joint moments were estimated using (1) marker-based motion capture and force plates (gold standard), (2) marker-less motion capture and force plates, and (3) marker-less motion capture and in-shoe pressure insoles. After estimation, an algorithm was developed and validated to adjust alternative method outputs to the gold standard; the training subset was extracted evenly across the dataset to avoid uneven training/validation (85%/15%) distribution across participants. Within the adjustment algorithm, dynamic time warping was used to temporally align each alternative method curve with the gold standard curve. Then, the alternative method curve was scaled in magnitude to match that of the gold standard curve. Methodological agreement was assessed before and after adjustment through discrete analysis of peaks and continuous analysis using Statistical Parametric Mapping (SPM).

Results

Before adjustment, peak moments computed by alternative methods differed from the gold standard, and incorporating insoles produced larger and more variable biases. After adjustment, continuous joint moments from the alternative methods did not significantly differ throughout the stance phase compared to the gold standard (Figure 1).

Discussion

These results demonstrate feasibility to estimate sagittal plane joint moments using 3D marker-less motion capture and pressure insoles, although an adjustment algorithm is necessary to interpret outputs alongside gold standard data. This supports the possibility of joint kinetic analysis outside of a lab environment using alternative modalities, driving community-based data collection and supporting a representative population.

Images (Optional)

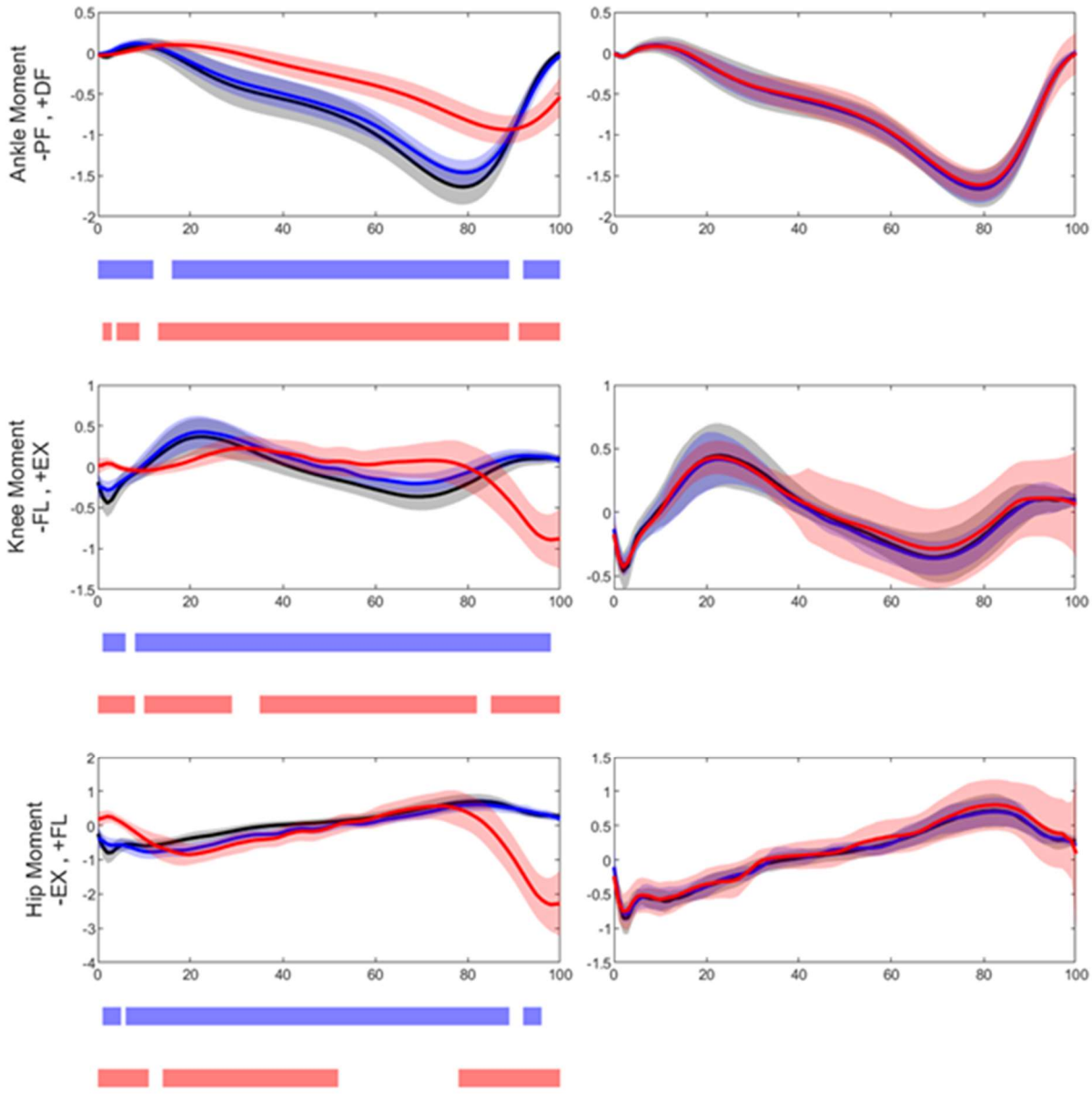


Figure 1: Sagittal plane joint moments during walking stance phase. Gold standard: black, Theia3D+Force Plates: blue, Theia3D+Insoles: red. Original (no adjustment) curves on left, curves after adjustment algorithm applied on right. Shading bars below each plot indicate regions where alternative methods significantly differ from gold standard.

Session Category

Clinical Biomechanics: N/A

P4-162

Sacral Tissue Risk Under Wearable Devices: Effects of Contact Geometry and Person-Specific Tissue Mechanics

A/Prof. Daphne Weihs[1,2,3], Ms. Anastasiia Simonova[1], Dr. Aleksei Orlov[1]

[1]Technion-Israel Institute of Technology, Haifa, Haifa, Israel. [2]Gent University, Gent, Belgium, Belgium. [3]Hasselt University, Hasselt, Belgium, Belgium

Introduction

The mechanical stability of loaded human skin tissues is central to understanding thresholds that may lead to pressure injuries. Soft-tissue thickness and mechanics vary widely across individuals, affecting stress and strain development beneath wearable devices. Despite this variability, the combined influence of device geometry and tissue material properties is not fully understood. Using computational modeling, we quantify the mechanical loads generated by simple devices, e.g. sensors and cables on sacral soft tissues.

Methods

A multi-layer sacral model was developed in Abaqus/CAE 2024, incorporating epidermis, dermis, adipose tissue, and muscle with literature-based thicknesses and mechanical properties [1], [2]. Stiffness was reduced or increased to represent aging, tissue degeneration, or rigid conditions. Two device configurations were simulated: a round, flat sensor and an elongated cable. Pressures of 2-10 kPa were uniformly applied beneath each device, and stress and strain were evaluated in all tissues in a 30 mm region of interest (ROI). The top quartile of stresses and strains was evaluated within the ROI, allowing device-specific comparisons independent of externally defined strain limits.

Results

With 10 kPa loading, the two devices exhibited distinct tissue exposure to high strains. The sensor's flat contact generated smoother, more uniform strain fields without localized peaks. In contrast, the cable's narrow elongated footprint created concentrated strain regions, yielding 1.25 times greater tissue exposure in the highest strain quartile than the sensor. Softened tissues amplified these effects, increasing high-strain exposure to 1.4 times the initial level for the sensor and 1.6 times for the cable. In stiffened tissues, high-strain exposure decreased for both devices, becoming 1.1 times lower for the sensor and 1.3 times lower for the cable, indicating reduced mechanical vulnerability.

Discussion

Device geometry and tissue stiffness together influence mechanical tissue-risk in the sacral region. The cable created localized high strains, while the flat sensor produced smoother fields across most tissue layers. These effects increased with tissue softening and diminished as tissues stiffened, emphasizing importance of consideration of tissue variability in device design, application, and in assessing pressure-injury risk.

References (Optional)

[1] Lustig et al., 19:1111-1120, 2022.

[2] Zeevi et al., 15:402-416, 2017.

Session Category

Clinical Biomechanics: N/A

P4-163

Effect of Starting Position on Shoulder Orientation Error Across Various Target Angles

Professor David Suprak PhD, Student Grace Truesdale MS, Professor Nathan Robey PhD, Professor Jun San Juan PhD

Western Washington University, Bellingham, WA, United States

Introduction

Previous research indicates that joint position sense (JPS) is affected by muscle activation and torque. Researchers have required repositioning from a single neutral starting position. Further, constant error has only considered planar errors.

This study was conducted to assess the effect of starting position on directional repositioning errors at the shoulder. It examined the effect of starting position (at side (AS) vs. 90º of abduction (ninety) vs. full elevation (FE)) on orientation error at four different target positions (50º, 70º, 90º, and 110º of scapular plane elevation).

Methods

Twenty-four healthy participants (21.79 ± 1.67 yrs, 172.10 ± 9.52 cm, 71.95 ± 14.31 kg) completed a single JPS testing session.

The Polhemus Fastrak 3Space electromagnetic tracking system (Colchester, VT), integrated with custom LABVIEW software (National Instruments, Austin, TX), collected humerothoracic kinematics.

Participants were guided to target positions via a head-mounted display, concentrated on the position, returned to start, and tried to replicate the position. Participants lay supine on a custom apparatus with back support and minimal skin contact to reduce tactile stimulation. Participants completed two trials to each target angle, from each starting position. Kinematic data were used to calculate orientation error, with 0° indicating reproduced position to the right, 90° directly above, 180° to the left, and 270° directly below the target position.

A Harrison-Kanji test was run via custom MATLAB code (CircStat Toolbox) to examine the interaction and main effects of starting position and target angle on orientation error.

Results

There was a significant starting position-by-target angle interaction effect on orientation error (p = .017). The follow-up Watson-Williams test indicated no effect of target angle on orientation error starting from the at-side position (p = .116), but a significant effect when starting at 90° (p = .0007) and from full elevation (p < .001) (Table).

Discussion

Participants overshot most, but not all, target angles. They overshot each target angle starting AS. From ninety, they overshot 70° and 90°, missed anterior at 50°, and missed high at 110°. From FE, participants undershot 50° and overshot higher angles. These results may help elucidate contributions from peripheral receptors and motor command.

Images (Optional)

Starting Position	At-side				Ninety				Full Elevation			
Target Angle	50°	70°	90°	110°	50°	70°	90°	110°	50°	70°	90°	110°
Mean Orientation (°)	44.25	14.62	11.17	40.35	167.93	234.42	222.71	68.20	174.24	279.24	296.97	294.80
Angular Dispersion (°)	55.07	50.19	47.83	56.78	61.47	66.17	72.60	65.73	69.95	56.12	46.95	55.32

Table. Mean orientation error (°) and angular dispersion (°) across target angles and starting positions.

Session Category

Clinical Biomechanics: N/A

P4-164

Impaired Control of Whole-Body Angular Momentum During Gait in Chronic Ankle Instability

Ms. Diane Malenfant[1], Mr. Chems-eddine Hakmi[2], Dr. Charlotte Le Mouel[1], Dr. Rosemary Dubbeldam[2]

[1]Institut des Systèmes Intelligents et de Robotique (ISIR), Sorbonne Université, CNRS, Paris, Paris F-75005, France. [2]Dept. of Movement Science, University of Münster, Horstmarer Landweg 62b, Münster, North Rhine-Westphalia, Germany

Introduction

Musculoskeletal injuries can severely disrupt the motor strategies of human balance, increasing the risk of falls and health costs. Dynamic balance during walking is maintained by controlling the range of Whole-Body Angular Momentum (WBAM). This range is increased in patients with lower limb injuries and/or neural pathologies.

Chronic Ankle instability (CAI) is one of the most common and disabling balance disorders, developing in up to 40–70 of individuals after a lateral ankle sprain. It combines mechanical instability – tissue laxity and altered joint kinematics – and functional instability, including proprioceptive deficits, delayed neuromuscular response and impaired postural control. Ankle torque during gait is altered in CAI patients, and this alteration at the ankle level might affect their control of the angular momentum. Considering previous works, we expect the range of WBAM to be increased in CAI patients, reflecting impaired control of WBAM.

Methods

We recorded the kinetics and kinematics of thirteen CAI patients and thirteen healthy controls while they walked barefoot on force plates, at self-selected comfortable speed, with reflective markers for 3D motion capture. We then computed the net torque around the Center of Mass (CoM) – the WBAM being its integration over time –, the mean walking speed over each gait cycle and step length and width.

Results

The results indicate that patients walked significantly slower than controls, with shorter steps. After correcting for walking speed, patients had larger range of WBAM. This was due to a significantly increased net torque around the CoM in both the sagittal and frontal

planes only during the single stance phase of gait. In contrast, during the double stance phase, patients had significantly lower torque than controls.

Discussion

This suggests that patients regulate their WBAM more tightly than controls during double stance, possibly because both feet touching the ground simultaneously facilitates torque control. Such better regulation at the hip level in patients may then be a compensation for impaired control of the ankle due to CAI. However, double stance compensation alone does not seem to be sufficient to fully correct for impaired control, since the range of WBAM on the whole gait cycle it is still increased.

Session Category

Clinical Biomechanics: N/A

P4-165

Bilateral Impairments in the Stability of Center of Pressure Control During One-Limb Stance in Chronic Ankle Instability

Mr. Chems-eddine Hakmi[1], Ms. Diane Malenfant[2], Dr. Rosemary Dubbeldam[1], Dr. Charlotte Le Mouel[2]

[1]Dept. of Movement Science, University of Münster, Horstmarer Landweg 62b, Münster, North Rhine-Westphalia, Germany. [2]Institut des Systèmes Intelligents et de Robotique (ISIR), Sorbonne Université, CNRS, Paris, Paris F-75005, France

Introduction

Lateral ankle sprains are amongst the most prevalent injuries in the general population. In 40 to 70% of patients, symptoms persist more than 1 year after the injury, with sensations of the ankle “giving way” and increased re-injury risk. In such Chronic Ankle Instability (CAI), bilateral alterations in the neural control of standing balance have been identified, suggesting that maladaptive neural changes play a role in the chronification of symptoms. We hypothesise that CAI patients have a bilateral deficit in the control of the Centre of Pressure (CoP), impacting their balance.

Methods

Thirteen CAI patients and thirteen matched healthy controls completed one-limb stance with eyes open and closed. The CoP was recorded using force plates. Full body kinematics were recorded using motion capture, and used to estimate the Centre of Mass (CoM) position. The CoP was reconstructed as a linear sum of the delayed CoM position and velocity in the frontal plane, yielding the proportional and derivative gains. The stability of the CoP controller on a given trial was determined analytically, depending on whether a controller with these gains can stabilise an inverted pendulum. Balance errors were detected whenever the raised foot touched the ground.

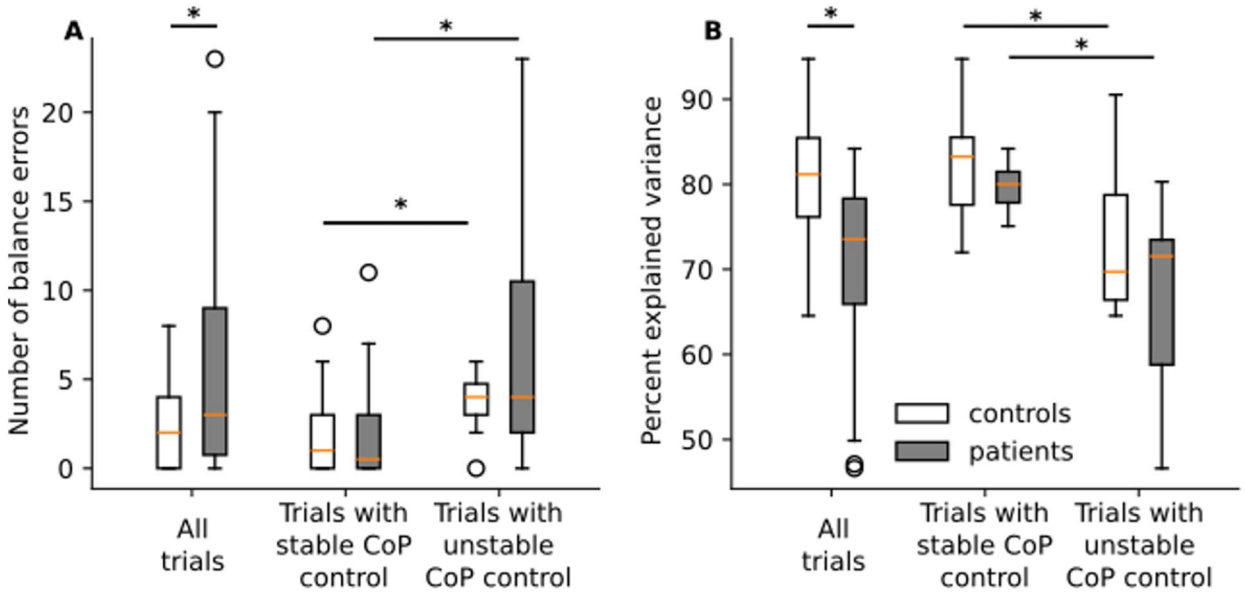
Results

There were no significant differences between the injured and uninjured limb in either balance errors or CoP control. Balance errors increased when closing the eyes for both patients and controls, and were larger in patients than controls. With eyes closed, CoP control was impaired in patients relative to controls, with a reduction of both the variance of the CoP explained by CoM state, and the proportion of trials with stable controllers. When comparing trials with stable (respectively unstable) controllers between patients and controls, we found no differences in either explained variance or balance errors.

Discussion

The ability to maintain balance on one limb with eyes closed is impaired bilaterally in CAI patients, due to a bilateral impairment in CoP control, specifically a reduction in the proportion of trials with stable CoP control. This ability to adopt a stable CoP controller seems critical for balance, as differences between patients and controls disappeared when controlling for CoP controller stability.

Images (Optional)



Influence of CoP controller stability on balance with eyes closed. Number of balance errors (A) and Percent explained variance of the CoP in the frontal plane (B). There are significant difference between controls (white) and patients (grey) when considering all trials (left), but these differences disappear when considering only trials with stable (middle) or unstable (right) CoP control.

Session Category

Clinical Biomechanics: N/A

P4-166

Tibiofemoral Loading Shifts Following Combined ACL Reconstruction and Meniscus Treatment: A Weight Bearing CT Study

Mr. Tyce C. Marquez, Mr. Travis Zhang, Dr. Richard VanTienderen, Ms. Shannon Ortiz, Prof. Brian R. Wolf, Prof. Donald D. Anderson

University of Iowa, Iowa City, IA, United States

Introduction

Failure to fully restore native knee kinematics with ACL reconstruction (ACLR) is theorized to shift tibiofemoral loading to unconditioned cartilage regions, contributing to later osteoarthritis (OA) development [1]. ACL-injured knees often have concurrent meniscal injuries, with certain pathologies known to accelerate OA [2,3]. This study analyzed shifts in the tibiofemoral center of contact (CoC) in ACLR knees with concurrent meniscal injuries.

Methods

Bilateral knee weight bearing CT (WBCT) scans were acquired for 58 patients (26M/32F, Age=22.9±8.9) at 12.5±0.8 months post-ACLR in semi-flexed (~20°) and fully extended poses. 3D joint space width (JSW) distributions in the knee were computed from WBCT using semi-automated methods [4]. The CoC was defined as the centroid of the narrowest 10% of JSW values measured in each compartment. CoC location and translation between poses for patients with ACLR+meniscus treatment were compared to their intact contralateral knee and ACLR only knees. Group differences in CoC translations were assessed using one-way ANOVA with post-hoc Bonferroni correction, significance set at p=0.05.

Results

A meniscus tear was concurrently treated in 36 patients, with 22 patients receiving ACLR only. A medial meniscus tear resulted in a more medially positioned CoC in the medial compartment during full extension compared to ACLR only and intact knees (Figure 1). This resulted in a significant difference (p=0.02) in medial-lateral translation between ACLR+meniscus and ACLR only knees and a trend, although not significant (p=0.08), between ACLR+meniscus and intact knees. No significant differences were observed for anterior-posterior translations in the medial compartment or for any translations in the lateral compartment.

Discussion

As the knee moves from semi-flexed to fully extended, a medial meniscus tear, although treated, shifted medial compartment tibiofemoral loading medially. This shift in tibiofemoral loading to unconditioned cartilage regions may contribute to later OA development. Utilizing WBCT and new biomarkers, such as the CoC, may enable earlier OA risk stratification, allowing for timely intervention.

Images (Optional)

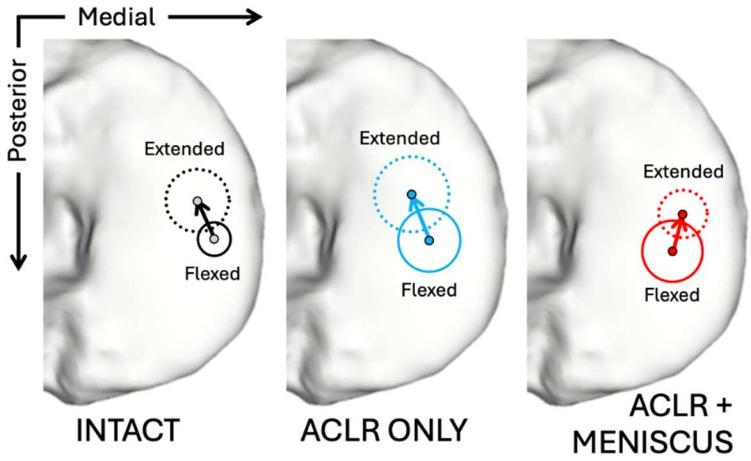


Figure 1. Medial compartment Center of Contact (CoC) locations plotted on top of the tibial plateau for the semi-flexed (Flexed) and fully extended (Extended) poses. Circle centers are plotted at the group mean CoC location with their radii reflecting their standard deviations.

References (Optional)

[1] Andriacchi TP, *et al*., J Bone Joint Surg, 2009. [2] Crema MD, *et al*., Osteoarthritis Cartilage, 2014. [3] Jones MH, *et al*., Osteoarthritis Cartilage, 2015. [4] Segal NA, *et al*., Osteoarthritis Cartilage, 2023.

Acknowledgements (Optional)

This research was supported by a grant from the Arthritis Foundation (Award #851789) and the University of Iowa Summer Research Fellowship.

Session Category

Clinical Biomechanics: N/A

P4-167

Assessing Biomechanical Risk Factors for Knee Osteoarthritis in Patients With Medial Meniscus Posterior Root Tears and Repairs: A Three-Dimensional Gait Analysis Study

Dr. Felipe F. Gonzalez MD, MSc[1,2,3], Dr. Enzo Mameri MD[4,2], Ms. Aleksandra Kozicka BS[5], Dr. Lucas Pallone MD[1,2], Ms. Eleonora Cabai MS[1], Dr. Tiago Zimerman MD[2,1], Dr. Cameron Gerhold BS[1], Dr. Renato Miyadahira MD[1,2], Dr. Matthew Henriques MD[1], Dr. Leonardo Metsavaht MD, PhD[2,3], Dr. Gustavo Leporace PhD[2,3], Dr. Jonathan A. Gustafson PhD[1,2], Dr. Jorge Chahla MD, PhD[1,5]

[1]Rush University Medical Center, Chicago, IL, United States. [2]Instituto Brasil de Tecnologias da Saúde (IBTS), Rio de Janeiro, RJ, Brazil. [3]Departamento de Diagnóstico por Imagem, Escola Paulista de Medicina, Universidade Federal de São Paulo, São Paulo, SP, Brazil. [4]Departamento de Ortopedia, Escola Paulista de Medicina, Universidade Federal de São Paulo, São Paulo, SP, Brazil. [5]Midwest Orthopaedics at Rush (MOR), Chicago, IL, United States

Dr. Felipe F. Gonzalez

Ms. Eleonora Cabai

Introduction

A large proportion of individuals with medial meniscus posterior root (MMPR) tears progress to knee osteoarthritis even after surgical repair. Gait analysis can help identify modifiable biomechanical risk factors to optimize knee joint loading through gait modification interventions. The objective of this study was to define gait kinematics and kinetics in patients with MMPR tears and those with MMPR repairs, compared to healthy, age-matched controls. We hypothesized that patients with MMPR tears and repairs would exhibit altered gait characteristics associated with joint degeneration.

Methods

In this cross-sectional study, 58 knees were analyzed: MMPR tear (n=20), MMPR repair (n=21), and healthy controls (n=17). MMPR repair patients underwent transtibial pullout repair performed by a single fellowship-trained surgeon. Gait analysis was conducted using a marker-based 3D motion capture system and force plates. Primary outcomes included

knee joint kinematics and kinetics. Statistical comparisons of discrete metrics and time-series data via Statistical Non-Parametric Mapping were evaluated across the gait cycle. Patient-reported outcomes were also assessed using IKDC, KOOS Jr., VR-12, and VAS pain scores. Group comparisons were performed using the Kruskal–Wallis test. The significance level was set at $p<0.05$.

Results

Both MMPR tear and repair groups exhibited increased knee varus thrust (Tear: 5.0° ± 2.1; Repair: 5.2° ± 2.0; Control: 3.3° ± 0.9; $P < 0.01$), decreased tibial internal rotation at loading response (Tear: –6.2° ± 5.3; Repair: –2.1° ± 3.6; Control: 2.2° ± 5.8; $P < 0.01$), and greater knee adduction angle (varus) at midstance (Tear: 0.1° ± 3.9; Repair: –0.1° ± 5.0; Control: –5.9° ± 4.1; $P < 0.01$) (Figure). The MMPR repair group exhibited higher functional scores (IKDC: 75.3 ± 19.9 vs. 43.6 ± 14.2; KOOS Jr.: 84.7 ± 15.4 vs. 59.7 ± 8.9; $P < 0.01$), lower pain levels (VAS: 1.5 ± 2.1 vs. 3.8 ± 2.4; $P < 0.01$), and higher tibial internal rotation compared to the tear group ($P < 0.05$; ES: 0.95).

Discussion

The repair group showed more favorable clinical and biomechanical variables than the tear group. However, both groups exhibited established biomechanical risk factors for knee OA progression, such as varus thrust. Motion analysis can be used to detect early biomechanical issues and may help identify MMPR tear and repair candidates for timely gait-modification interventions to improve long-term joint health.

Images (Optional)

A.

Variables	Control	Repair	Tear	P-value	Post hoc test
Kinematics (Peaks)(°)					
Knee Extension Angle at Midstance (30–50% of stance)	-1.4 ± 5.5	-4.4 ± 6.0	-6.9 ± 6.3	**0.03**	Control > Tear (P = 0.001; ES: 0.95)
Knee Abduction Angle at Terminal Stance (60%-100% of stance)	10.1 ± 4.3	6.0 ± 5.5	5.4 ± 4.2	**0.02**	Control > Repair (P = 0.019; ES: 0.64); Control > Tear (P = 0.006; ES: 1.01)
Knee Adduction Angle at Midstance (20–40% of stance)	-5.9 ± 4.1	-0.1 ± 5.0	0.1 ± 3.9	**< 0.01**	Repair>Control (P = 0.003; ES: 0.93); Tear>Control (P = 0.002; ES: 1.23)
Knee Internal Rotation Angle at Loading Response (0–20% of stance)	2.2 ± 5.8	-2.1 ± 3.6	-6.2 ± 5.3	**<0.01**	Control > Repair (P = 0.048; ES: 0.81); Control > Tear (P <0.001; ES: 1.43); Repair > Tear (P = 0.028; ES: 0.95)
Kinetics (Peaks)(%BW*HT)					
Knee Extension Moment at Midstance (20–40% of stance)	2.8 ± 0.9	2.3 ± 0.8	1.8 ± 1.0	**0.01**	Control>Tear (P = 0.001; ES: 1.05)
Knee Adduction Moment at Terminal Stance (40–60% of stance)	1.6 ± 0.7	2.2 ± 0.7	2.3 ± 0.8	**0.04**	Tear>Control (P = 0.013; ES: 0.80)
Knee External Rotation Moment at Terminal Stance (40–60% of stance)	0.1 ± 0.1	0.1 ± 0.1	0.1 ± 0.1	**0.03**	Control > Tear (P = 0.011; ES: 0.70)
First Peak Vertical Ground Reaction Force (%BW)	109.3 ± 7.4	111.2 ± 10.5	104.3 ± 6.9	**0.03**	Control>Tear (P = 0.047; ES: 0.77) Repair>Tear (P = 0.014; ES: 0.76)
Second Peak Vertical Ground Reaction Force (%BW)	111.3 ± 6.6	106.7 ± 6.8	104.9 ± 7.1	**0.02**	Control>Tear (P = 0.004; ES: 0.92)
Varus Thrust (ROM and Velocity)					
Varus Thrust ROM (initial contact to peak knee adduction)(°)	3.3 ± 0.9	5.2 ± 2.0	5.0 ± 2.1	**<0.01**	Repair>Control (P<0.001; ES: 1.18); Tear>Control (P<0.001; ES:1.00).
Varus Thrust ROM (min to max frontal plane angle during 0–20% of gait cycle)(°)	3.3 ± 1.0	5.2 ± 2.0	4.9 ± 2.2	**<0.01**	Repair>Control (P<0.001; ES: 1.16); Tear>Control (P<0.001; ES: 0.94).
Varus Thrust Peak Velocity (initial contact to peak knee adduction)(°/s)	18.4 ± 10.3	34.1 ± 18.0	33.3 ± 22.4	**<0.01**	Repair>Control (P<0.001; ES: 1.04); Tear>Control (P<0.001; ES: 0.83).
Varus Thrust Peak Velocity (min to max frontal plane angle during 0–20% of gait cycle)(°/s)	28.4 ± 14.6	43.9 ± 22.8	39.5 ± 22.8	**<0.01**	Repair>Control (P<0.001; ES: 0.79); Tear>Control (P<0.001; ES: 0.57).

B.

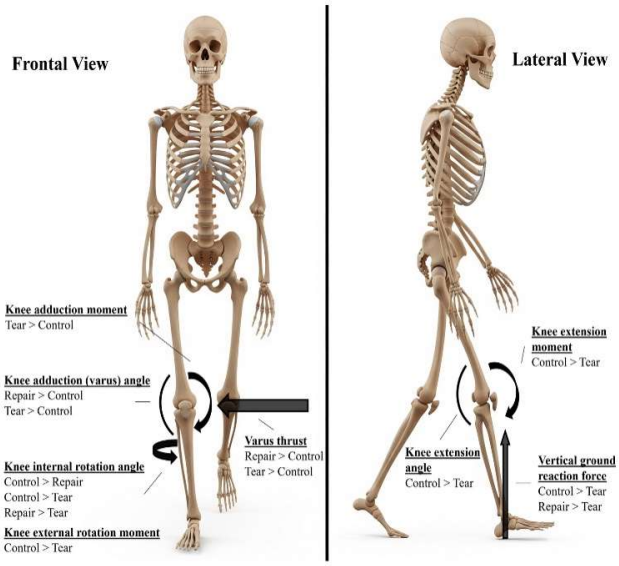


Figure 1: A. The table displays peak values of selected gait kinematic and kinetic parameters extracted from specific phases of the gait cycle. Values represent group means with corresponding standard deviations (SD) for the control, MMPR repair, and MMPR tear groups. Between-group comparisons were performed using the Kruskal–Wallis test and post-hoc comparisons with Dunn test. Statistically significant p-values ($p < 0.05$) indicate group differences for the corresponding discrete variable.BW: Body weight; HT: Height; S: Second; N/a: Not applicable; ROM: Range of motion).
B: Frontal and lateral views depict the biomechanical differences between the medial meniscus posterior root (MMPR) repair, tear, and control groups. ">" denotes a statistically significant higher value.

Session Category

Clinical Biomechanics: N/A

P4-168

Characterizing Ipsilateral Temperature Differentials in Wearable Foot Monitoring for Ulcer Prevention

Dr. Emily Matijevich PhD[1,2], Dr. Maryam Hajizadeh PhD[1], Ms. Emily Bray MBA[1], Ms. Erin Barrett MScHQ[1], Dr. Evan Minty MD[3], Dr. Breanne Everett MD[1]

[1]Orpyx Medical Technologies, Calgary, Alberta, Canada. [2]Faculty of Kinesiology, University of Calgary, Calgary, Alberta, Canada. [3]Department of Medicine, University of Calgary, Calgary, Alberta, Canada

Introduction

Since 1979, foot temperature monitoring has been used to detect tissue inflammation in individuals with neuropathy at risk of foot ulceration [1]. Guidelines recommend identifying temperature differences between corresponding plantar regions on the left and right foot that exceed a threshold (2.2°C) [2].

Contralateral differentials help reduce confounding that impacts both limbs (environmental temperatures), but cannot be used in individuals with one foot or when one foot is obscured (bandages, offloading devices). Although unilateral monitoring methods exist [3], accuracy may be enhanced by relating ipsilateral and contralateral differentials in individuals with data from both feet.

The purpose of this analysis was to compare ipsilateral (within foot) to contralateral differentials in individuals at risk for diabetic foot ulceration.

Methods

Twelve months of plantar temperature data were analyzed from patients using the Orpyx® Sensory Insole system, which monitors temperature continuously at high-risk bony prominences.

For each patient-day, contralateral differentials were computed between corresponding locations on left and right feet and ipsilateral differentials between a single location and the average temperature of that foot. Correlations were evaluated using Pearson's r.

Data were categorized as left contralaterally warm, right contralaterally warm, or contralaterally symmetric. Differences in ipsilateral differentials among groups were analyzed with Kruskal-Wallis tests, and significant results ($p<0.05$) were followed by Mann-Whitney tests with Bonferroni correction.

Results

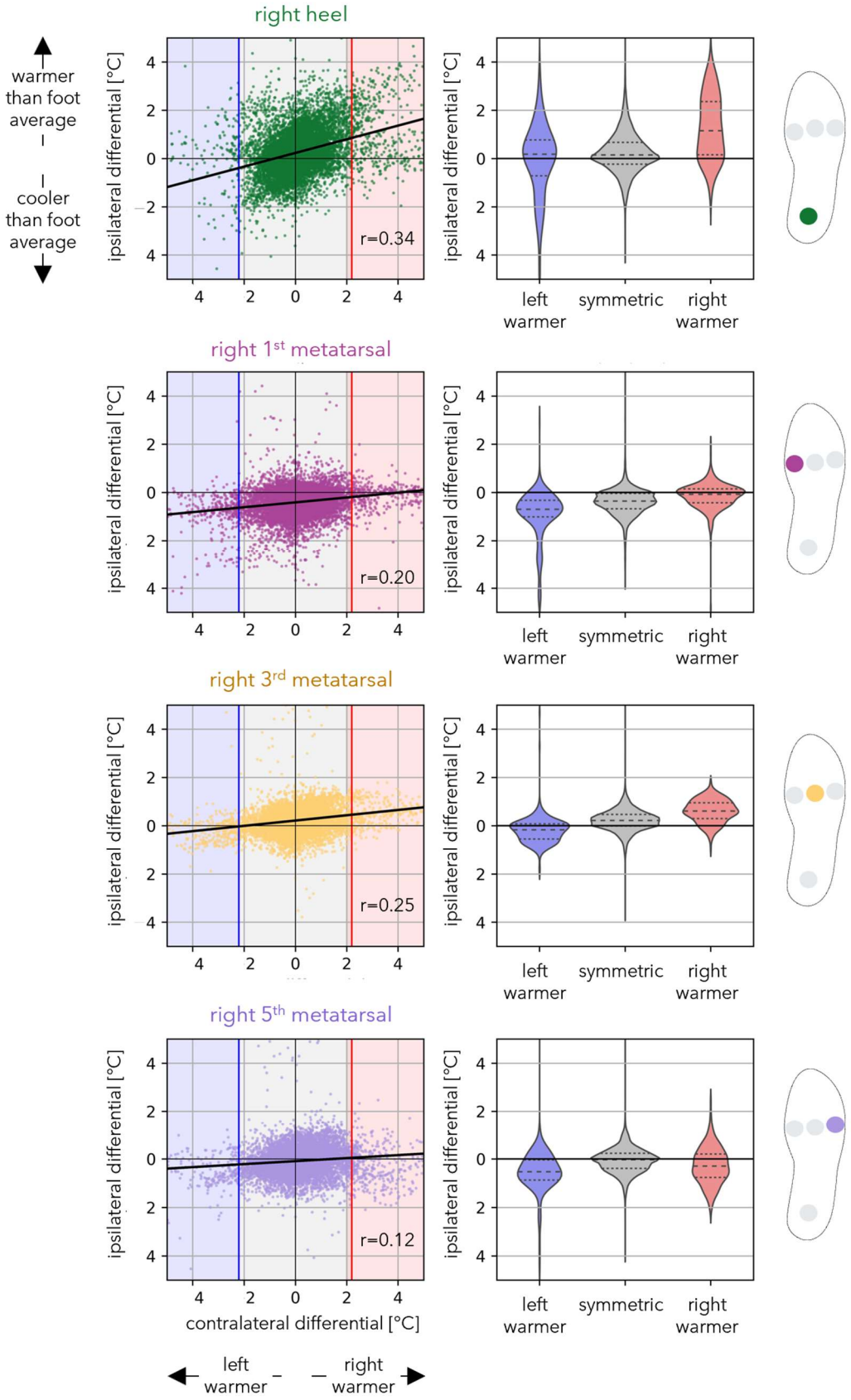
11,165 patient-days were analyzed (Figure 1). Contralateral-ipsilateral correlations were significant for all regions except the left heel (p=0.29). Significant correlations were weak (r = 0.12 to 0.34).

Significant group-wise differences were found across all regions. Pairwise comparisons were significant except for the left heel (symmetric vs. left warmer, p=0.10) and right heel (right cooler vs. symmetric, p=0.77). Median ipsilateral differentials ranged from 0.05-0.73 °C (contralaterally cool), 0.03-0.36 °C (contralaterally symmetric), and 0.07-1.15 °C (contralaterally warmer).

Discussion

Ipsilateral differentials varied across contralateral groups, though the magnitude of difference was small. Robust unilateral monitoring may require detecting deviations from an individual's personalized temperature profile, while also considering factors such as angiosome-level perfusion and activity dependent foot loading.

Images (Optional)


right heel
warmer than foot average
cooler than foot average
ipsilateral differential [°C]
r=0.34
left warmer
symmetric
right warmer
right 1st metatarsal
r=0.20
right 3rd metatarsal
r=0.25
right 5th metatarsal
r=0.12
contralateral differential [°C]
left warmer
right warmer

References (Optional)

[1] H. Bergtholdt, Phys. Ther., 1979

[2] S. Bus et al., Diabetes Metab. Res. Rev., 2024

[3] L. Lavery, et al., 2019

Acknowledgements (Optional)

Figure 1. (Left column) Ipsilateral versus contralateral temperature differentials for the right foot for 11,165 patient-days. Vertical red and blue lines indicate contralateral differential threshold of 2.2°C. Black line indicates the linear fit. (Right column) Distribution of ipsilateral differentials for three contralateral groups: left warmer (blue), symmetric (gray), and right warmer (red). Dashed lines on violin plots indicate quartiles of data.

Session Category

Clinical Biomechanics: N/A

P4-169

Acute Cartilage Deformation Following Walking Differs With Radiographic Severity in Clinical Knee Osteoarthritis

Dr. Erin C.S. Lee PhD[1], Dr. Kendal A. Marriott PT, PhD[1], Dr. Anthony A. Gatti PhD[2], Ms. Natasha K. Ivanochko MSc[1], Dr. Jacquelyn M. Maciukiewicz PhD[1,3], Dr. Lauren Straatman PhD[1], Ms. Emily Wiebenga[1], Dr. Jonathan D. Adachi MD[4], Dr. Michael D. Noseworthy PhD[4], Mr. Paul W. Stratford MSc[4], Dr. Monica R. Maly PT, PhD[1]

[1]University of Waterloo, Waterloo, ON, Canada. [2]Stanford University, Palo Alto, CA, United States. [3]Waterloo Regional Health Network, Waterloo, ON, Canada. [4]McMaster University, Hamilton, ON, Canada

Introduction

Knee osteoarthritis (OA) severity is commonly classified by Kellgren-Lawrence (KL) grade. While KL grade indirectly accounts for cartilage loss by categorizing joint space narrowing, cartilage also varies in quality and function. Compliant cartilage may have a compromised ability to withstand loading [1] but it is unknown whether compliance differs across OA severity. The objective of this study was to compare tibiofemoral cartilage thickness, composition (T2 relaxation time), and acute deformation following walking across KL grades in adults with clinical knee OA.

Methods

89 adults aged 45-75 with clinical knee OA received an x-ray of their most symptomatic knee. KL grade was determined by a musculoskeletal radiologist. Participants underwent magnetic resonance imaging before and immediately after a 25-minute walk at a standardized speed [2]. We computed mean thickness and T2 (reflecting free-water content) in the medial and lateral tibia and weight-bearing femur. Acute deformation was the change in thickness from pre- to post-walk scans. For each region, we performed ANCOVAs and post hoc Tukey tests to compare thickness, T2, and deformation between KL grades cross-sectionally, after adjusting for covariates.

Results

15 participants were classified as normal (KL0) or doubtful (KL1), 25 as mild (KL2), 24 as moderate (KL3), and 25 as severe (KL4) OA. Thickness and acute deformation of the medial tibia, medial femur, and lateral femur varied across KL grade. In the medial regions, knees with severe OA (KL4) had thinner cartilage ($p<0.001$) and greater deformation ($p<0.01$) than

less severe knees (KL0-KL3). In the lateral femur, severe knees had thicker cartilage ($p<0.05$) and greater deformation ($p<0.05$) than mild knees (KL2). Thickness and deformation did not differ among KL0-KL3. There was no difference in T2 in any region; or in thickness or deformation in the lateral tibia.

Discussion

Compared to KL0-3, acute cartilage deformation in the medial tibia and weight-bearing femur is greater in KL4, suggesting that more compliant cartilage is a feature of severe knee OA disease. Thickness, composition, and function were highly variable in KL0-3. Future work will explore whether greater cartilage compliance and lower thickness predict future worsening in KL0-3.

Images (Optional)

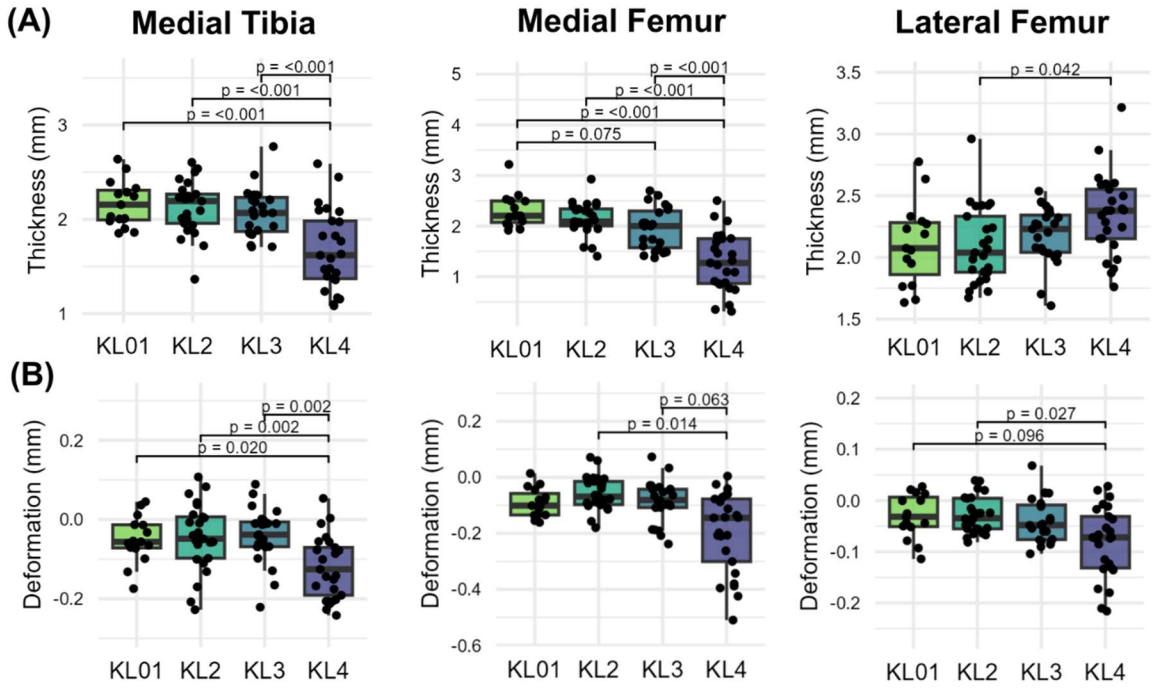


Figure 1: (A) Thickness and **(B)** acute deformation across KL grades for the medial tibia, medial femur, and lateral femur. Negative deformation indicates a reduction in thickness after walking.

References (Optional)

[1] Brenneman Wilson, Gait Posture, 2021. [2] Paranjape, Sci Reports, 2018.

Acknowledgements (Optional)

Arthritis Society Canada Training Postdoctoral Fellowships (TPF 24-117, TPF 21-39), Canadian Institutes of Health Research (CIHR) Fellowship, CIHR Project #175169.

Session Category

Clinical Biomechanics: N/A

P4-170

Electromyography Activation Comparison of a Novel Deceleration Upper Extremity Exercise Compared to Traditional Thrower's Ten Exercises

Dr. FJ Goodwin PT, PhD, DPT, Dr. Angela Stagliano PT, DPT, PhD, OCS, GTS, CSCS, Dr. Grant Drenning PT, DPT, Dr. Davis Jackson PT, DPT, Dr. Garrett Sicard PT, DPT

Charleston Southern University, Charleston, SC, United States

Introduction

Current throwing rehabilitation programs attempt to restore shoulder neuromuscular control and function. Deceleration training has emerged as a novel exercise to improve ball throwing velocity however it is not utilized in Throwers Ten programs. We hypothesize that a novel deceleration brake training (DBT) upper extremity exercise will demonstrate greater muscular activation levels assessed via electromyography (EMG) compared traditional Thrower's Ten exercises.

Methods

24 individuals (14 M, 10 F; 24.7±2.1 y.o; 1.73±0.06 m; 74.1±11.8 kg) free from upper extremity pathology volunteered for this study. Subjects completed dominant arm external rotation MVIC with EMG sensors placed on supraspinatus and infraspinatus with a handheld dynamometer in the 90/90 position. Peak EMG values were recorded and averaged across 3 trials. Subjects then completed 2 sets of 4 exercises via a balanced Latin Square: Sidelying ER with 5#, Standing D2 Flexion with Theraband, Standing ER with arm at side with Theraband, & Seated DBT with arm in 90/90 position. The DBT exercise involved rapidly pulling a strap attached to a 5# weighted pendulum and then catching as the pendulum swung back down. EMG was collected during each exercise and average EMG peaks were determined from 3 consecutive repetitions. These were calculated as percentages with the peak EMG values from the MVIC trials. ANOVAs were completed to determine the difference between exercises in relative peak EMG activation in the supraspinatus and infraspinatus muscles.

Results

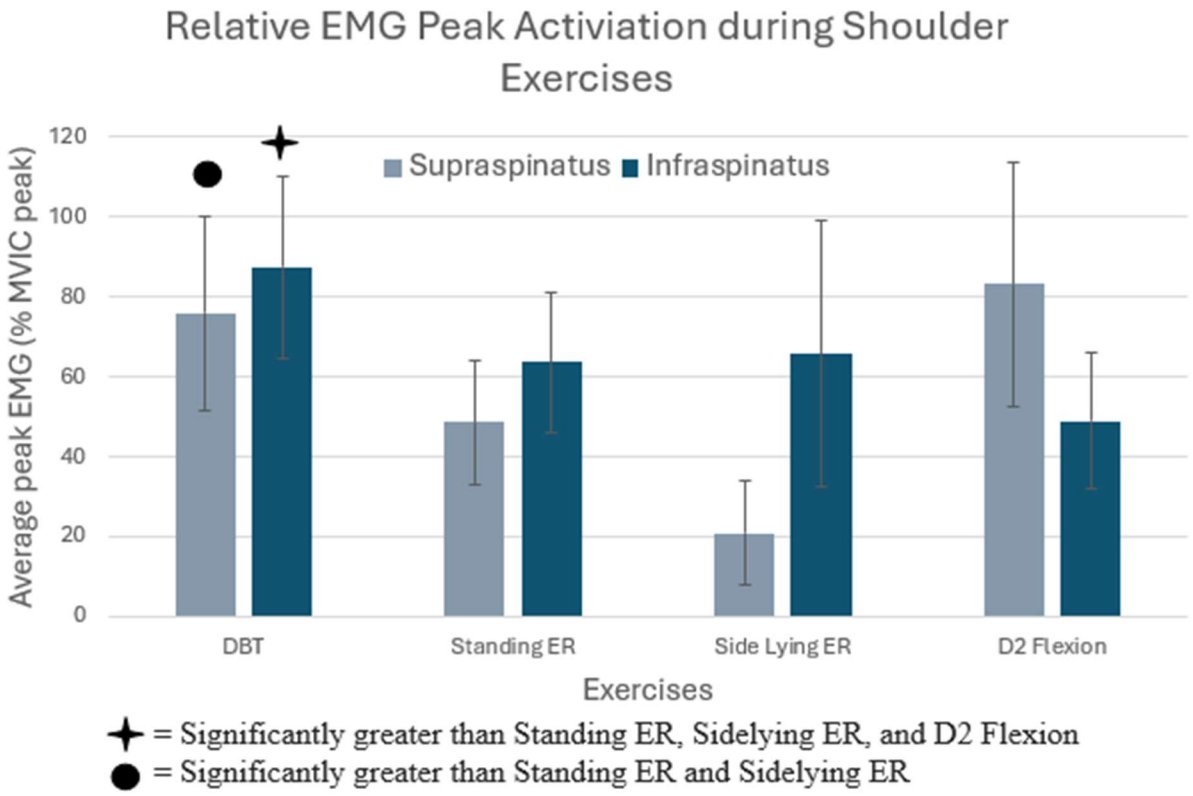
1-way ANOVA of Infraspinatus EMG peaks was significant ($F=12.36$, $p<0.001$) with Tukey's HSD post-hoc revealing the DBT exercise (87.45±22.83%) was significantly higher than Sidelying ER (54.66±33.29%, $p<0.001$), Standing ER (63.54±17.77%, $p=0.003$), and D2 Flexion (49.0±16.87%, $p<0.001$).

1-way ANOVA of Supraspinatus EMG peaks was significant (F=39.79, p<0.001) with Tukey's HSD post-hoc revealing the DBT exercise (75.88±22.12%) was significantly higher than Sidelying ER (20.79±13.06%, p<0.001) and Standing ER (48.54±15.67%, p<0.001) but not different from D2 Flexion (83.08±30.75%)

Discussion

The DBT exercise appears to elicit greater EMG activation compared to traditional rehabilitation exercises. Clinically, DBT could be a higher skilled exercise which indicates its use for later phase rehabilitation protocols when athletes are ready for ballistic exercises.

Images (Optional)



Session Category

Clinical Biomechanics: N/A

P4-171

Phase Shift of Brain Tissue and Cerebrospinal Fluid Motion in Chiari Type 1 Malformation

Bioengineering PhD Student Hannah Higgins B. S. E.[1], Bioengineering PhD Candidate Mahsa Karamzadeh M.S., B. S. E.[1], Associate Professor of Radiology Rafeeque Bhadelia D. M. R., M. B., B. S.[2], Pediatric Neurosurgeon Petra Klinge MD, PhD[3], Professor of Radiology and Imaging Sciences John Oshinski PhD[4], Associate Professor of Bioengineering and Mechanical and Industrial Engineering Rouzbeh Amini PhD[1], Professor of Bioengineering and Mechanical and Industrial Engineering Francis Loth PhD[1]

[1]Northeastern University, Boston, MA, United States. [2]Harvard University, Cambridge, MA, United States. [3]Brown University, Providence, RI, United States. [4]Emory University, Atlanta, GA, United States

Introduction

Chiari Malformation Type I (CMI) is a neurological disease characterized by herniation of the cerebellar tonsils into the spinal canal and symptoms such as headaches, dizziness, and brain fog, with an incidence of 1/1000 patients. Researchers have been searching for measurable biomechanics that are predictive of CMI symptomatology. Studies have shown that CMI patients exhibit 52% higher compression strains in the cerebellum compared with healthy subjects. We hypothesize that there is a statistically significant difference in the timing of caudal (away from the brain) motion between brain tissue (BT) and cerebrospinal fluid (CSF) in CMI subjects. The goal of this preliminary study is to evaluate timing differences between BT and CSF using phase-contrast magnetic resonance imaging (PC-MRI) data.

Methods

10 CMI subject midsagittal-plane tissue-gated PC-MRI datasets were selected based on image resolution and non-surgical status. Four regions of interest were selected to evaluate the velocity of BT and CSF (see figure). Two regions of interest were selected on the spinal cord and cerebellum, respectively, with a five-voxel radius mask. The two remaining regions of interest were selected in the anterior and posterior CSF of the spinal canal, with a two-voxel radius mask. A paired two-tailed t-test was conducted for the beginning, end, and duration of caudal movement for the CSF and BT.

Results

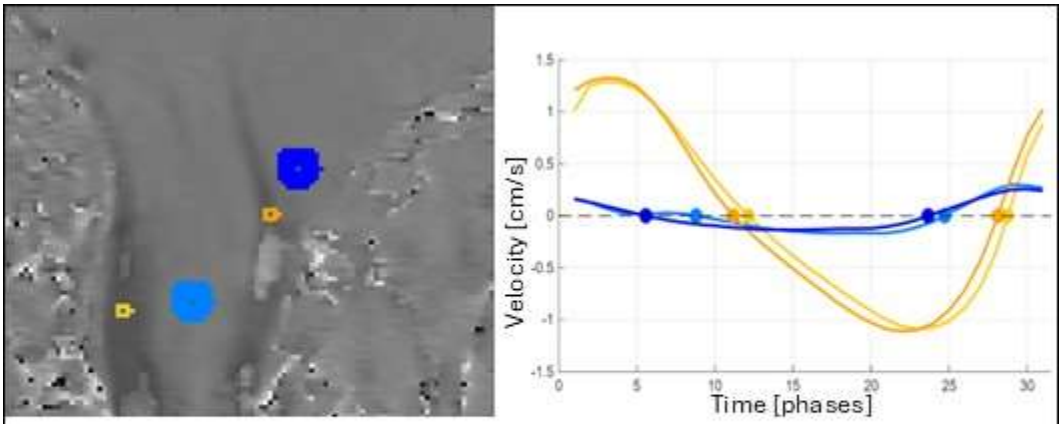
The results showed an average of 94 and 84 ms delay in the beginning and ending of caudal motion in the CSF compared to the BT ($p < 0.001$). However, there was no significant

difference between the overall duration of caudal movement in the BT and CSF. The project is ongoing to evaluate if this behavior is observed in a larger CMI population.

Discussion

The findings suggest that motion in the cranial vault and spinal canal originates in the BT, most likely due to an initial influx of fluid volume into the hyper-vascularized BT during the cardiac cycle, which is then transmitted to the CSF. The findings of this preliminary study suggest that further investigation in a larger sample size should be conducted to see if delays could be a factor in CMI symptomatology.

Images (Optional)



LEFT - PC-MRI image at peak systole at the midsagittal plane showing the location of the ROIs for cerebrospinal fluid (CSF) and brain tissue (BT). RIGHT - Velocity trace over the cardiac cycle showing the difference in phase shift for caudal motion between the CSF and BT.

References (Optional)

Session Category

Clinical Biomechanics: N/A

P4-172

Damage Accumulation at the Taper of Modular Hip Revision Implants

MSc Lennart Rogoll, Prof. Sara Checa, Dr.-Ing. Gerd Huber

TUHH Hamburg University of Technology, Hamburg, Hamburg, Germany

Introduction

Modular hip revision implants separate distal fixation of the stem from proximal patient-specific intraoperative reconstruction through the neck segment. Although rare, serious fractures have been reported at this intermediate taper connection, which has the smallest diameter of the implant.

Load pattern along the implant axis significantly depend on the performed activity [1]. Thus, the taper should be placed in a low-load position with respect to all activities, bringing the length-ratio between neck segment and shaft under debate.

The aim was to combine the contribution of daily activities for damage accumulation, to determine the favorable length of neck segments.

Methods

Three mobility profiles (low, medium, high) containing different daily activities were defined. For each activity and two body weights (75 kg, 100 kg) von Mises equivalent implant stress for a taper diameter of 13 mm was calculated [1] based on in-vivo measured hip joint forces [2]. Wöhler's curve of TiAl6V4 and Miner's rule enabled to combine the activities of each profile to determine the damage accumulation and hence taper junction's fatigue life for each potential neck segment length.

Results

Stair descent and jogging impose the greatest impact on accumulated damage, while cycling, walking and other daily activities have a minimal effect. Taper fatigue life is highly sensitive to patient weight (medium activity: 100 kg / 75 kg -> 4 y / 29.5 y) and activity (75 kg: low / medium / high -> 8.4 y / 29.5 y / 116.5 y). The hereby determined favorable neck length lies between 70 mm to 90 mm.

Discussion

This study emphasizes the need to consider patient-specific factors such as activity level and body weight, when selecting implants and surgical planning.

Results are limited by not considering osseous implant support on one side and extreme events such as stumbling on the other side.

Revision implants are available in various lengths and shaft thicknesses. For compatibility reasons, a uniform tapered cone is often used at the end of the shaft. In order to be able to treat large and heavy patients, however, this uniform cone size should be questioned.

Images (Optional)

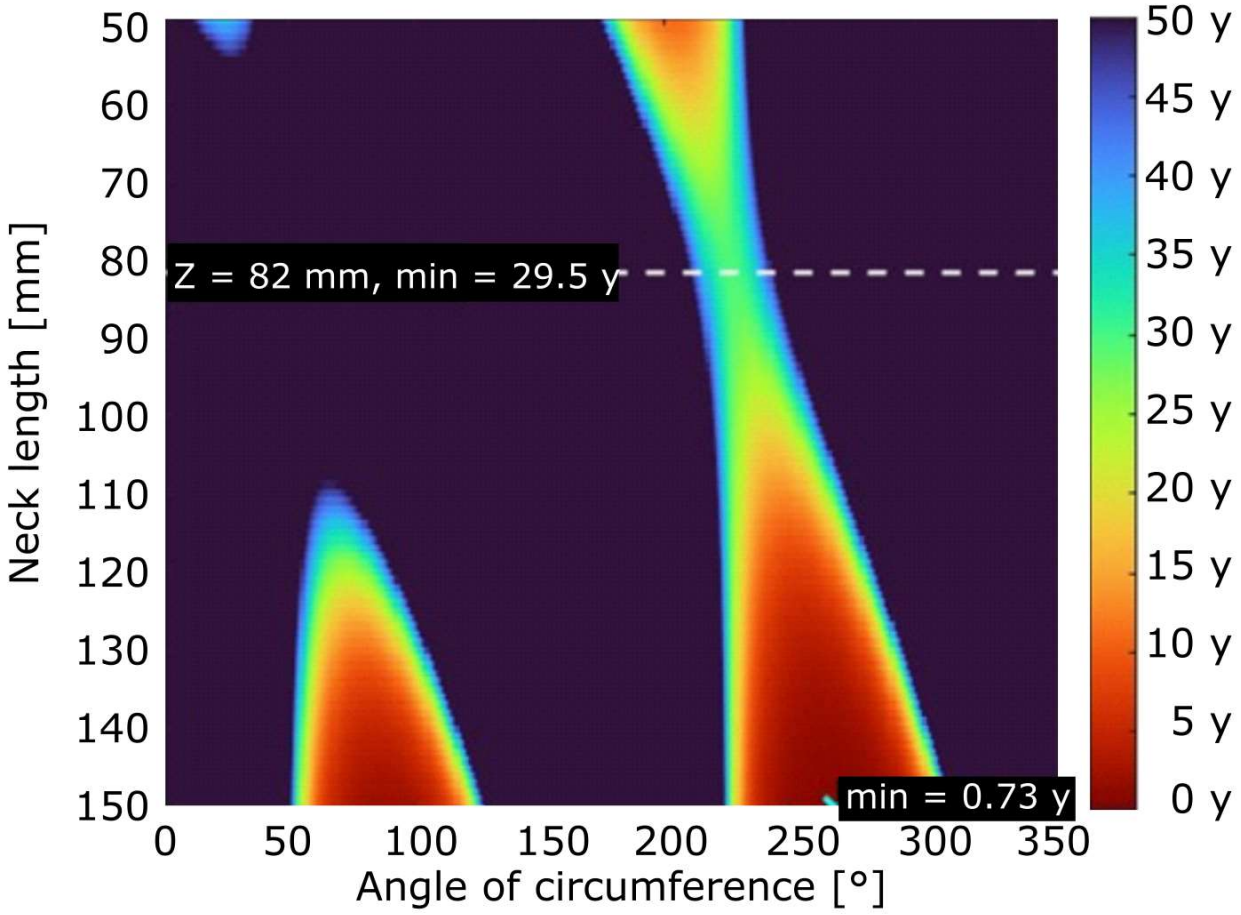


Fig. 1: Time to failure (years) based on the accumulated loading of a 75 kg person with medium activity profile. A neck segment length of 82mm reveals the highest survival time.

References (Optional)

[1] Gerd Huber *et al.*, Clinical Biomechanics, 2021

[2] Georg Bergmann *et al.*, PLOS One, 2016

Session Category

Clinical Biomechanics: N/A

P4-173

Test–Retest Reliability of 4DCT-Derived Wrist Kinematics in Healthy and Scapholunate-Injured Wrists

ir. Hanne Vries, Ms. Maranda Haenen MSc, Ms. Erin Teule MSc, dr. Stefan Hummelink, prof.dr. Ioannis Sechopoulos, prof. dr. Brigitte van der Heijden

Radboudumc, Nijmegen, Gelderland, Netherlands

Introduction

Four-dimensional CT (4DCT) provides quantitative in-vivo evaluation of carpal motion and is increasingly used to characterize wrist kinematics. Its ability to capture carpal bone movement throughout motion makes it a promising tool for evaluating wrist injuries, such as scapholunate (SL) instability. To support its use in both biomechanical and clinical contexts, the repeatability of 4DCT-derived kinematic parameters must be evaluated in healthy and unstable wrists. This study therefore evaluated the test–retest reliability of 4DCT-based wrist kinematics in healthy wrists and in wrists with suspected scapholunate (SL) injury.

Methods

Patients with a unilateral suspicion of scapholunate (SL) injury underwent bilateral 4DCT scanning, with the contralateral wrist used as a healthy reference. Each scan included one static acquisition and two dynamic sequences during radial–ulnar deviation (RUD) and flexion–extension (FE). To assess test–retest reliability, both dynamic sequences were repeated. An automated pipeline segmented and registered all carpal bones across time frames. Kinematic parameters of the scaphoid and lunate were extracted, including 3D scapholunate distance (SLD), 3D translation (norm of x,y,z), and 3D rotation (axis angle magnitude). Reliability was evaluated using the coefficient of multiple correlation (CMC) and root mean square difference (RMSD), and differences between motion directions were tested with a paired t-test.

Results

Dynamic 4DCT scans from eighteen patients were analyzed. Both RUD and FE showed high reliability, with median CMC values of 0.90 for scapholunate distance and above 0.90 for scaphoid and lunate translation and rotation, accompanied by low RMSD values across all parameters (Figure 1). For both movements, no significant differences were found between directions for any kinematic parameter.

Discussion

This study demonstrated high test–retest reliability of scaphoid and lunate kinematics, indicating that 4DCT can consistently quantify key motion parameters relevant to scapholunate instability. Across both FE and RUD, rotational and translational measures showed stable motion patterns on repeated scans, with no direction-dependent differences. While these findings confirm the repeatability of 4DCT-derived kinematics, further work is needed to determine whether this consistency translates into sufficient accuracy for specific clinical diagnostic tasks.

Images (Optional)

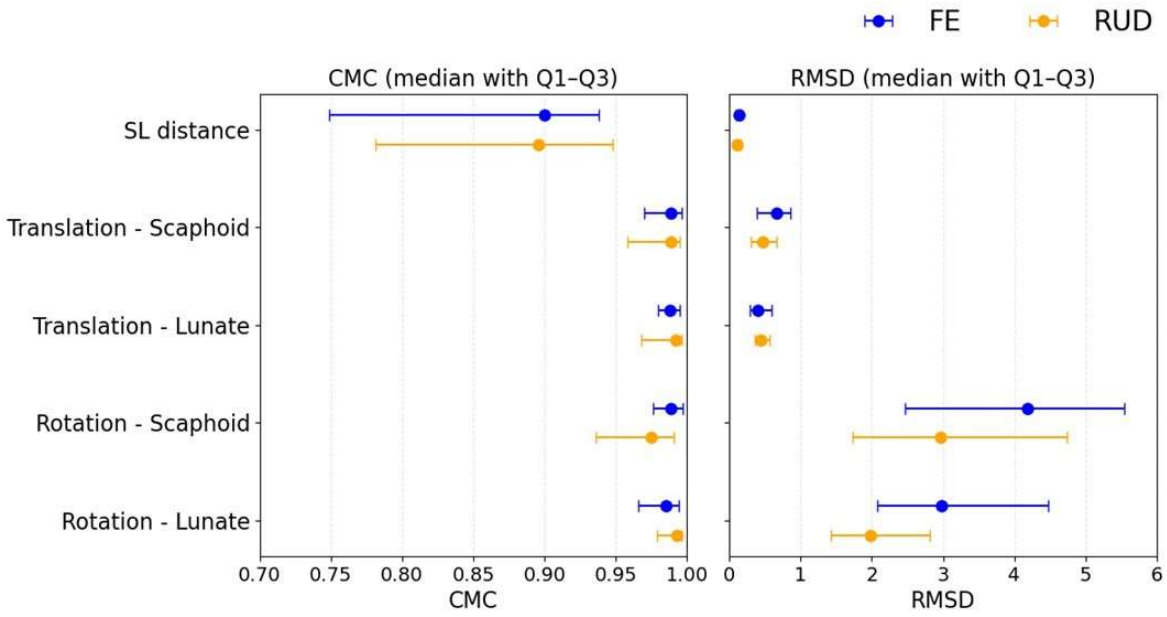


Figure 1. CMC and RMSD values (median with Q1–Q3) for SLD, scaphoid and lunate translation, and rotation during FE and RUD. Both movements show high reliability with CMC values near 1.0 and low RMSD across all parameters. RMSD is shown in millimeters for translations and SLD, and in degrees for rotations.

Session Category

Clinical Biomechanics: N/A

P4-174

Hysteresis in 4DCT-Derived Wrist Kinematics: A Comparison of Healthy and Scapholunate-Injured Wrists

ir. Hanne Vries, Ms. Maranda Haenen MSc, Ms. Erin Teule MSc, dr. Stefan Hummelink, prof. dr. Ioannis Sechopoulos, prof. dr. Brigitte van der Heijden

Radboudumc, Nijmegen, Gelderland, Netherlands

Introduction

Four-dimensional CT (4DCT) enables detailed, non-invasive quantification of wrist kinematics. Despite this capability, wrist motion is often interpreted using simplified, unidirectional models that overlook direction-dependent behavior. Hysteresis, the change in carpal motion that depends on movement direction, may therefore be an important but under-recognized aspect of wrist mechanics. It is unclear whether hysteresis is different for healthy wrists and injured wrists like those with a scapholunate ligament injury. Therefore, this study aims to investigate the difference in hysteresis on dynamic CT-derived wrist kinematics between healthy and scapholunate ligament-injured wrists.

Methods

Dynamic CT scans from healthy wrists and wrists with complete scapholunate ligament rupture (arthroscopically confirmed) were analyzed. Each dataset included a static scan and two motion sequences: radial–ulnar deviation (RUD) and flexion–extension (FE Carpal bones were segmented, registered, and analyzed using a fully automated algorithm, which extracted five kinematic metrics at each wrist position: radioscaphoid (RSA), scapholunate (SLA), capitolunate (CLA), and radiolunate (RLA) angles, plus the 3D scapholunate distance (SLD). Motion curves were generated for both directions of FE and RUD, and hysteresis was calculated as the area between direction-specific curves, normalized to range of motion. Group differences were assessed using unpaired t-tests ($p < 0.05$).

Results

In FE, twenty SL4 and seventy-one healthy wrists were analyzed. Only the SLD showed a significantly greater hysteresis area in SL4 wrists (0.24 [0.17 – 0.30] deg^2; median [25^{th} percentile – 75^{th} percentile], $p < 0.001$) compared with healthy wrists (0.10 [0.07 – 0.14] deg^2). In RUD, SL4 wrists showed significantly higher hysteresis for both SLA (2.15 [1.46 – 3.43] deg^2 vs. 1.35 [1.04 – 1.78] deg^2, $p = 0.00$) and SLD (0.18 [0.10 – 0.24] deg^2 vs. 0.08 [0.05 – 0.11] deg^2, $p < 0.001$). The remaining kinematic parameters showed no significant differences during RUD (Figure 1).

Discussion

Automated motion analysis of dynamic wrist CT showed significantly greater hysteresis in scapholunate-injured wrists, particularly for scapholunate distance across both motions and for scapholunate angle during RUD. Since hysteresis captures direction-dependent carpal mechanics that are not visible in static or single-direction assessments, these results highlight its potential as a sensitive biomechanical marker for pathology like scapholunate instability.

Images (Optional)

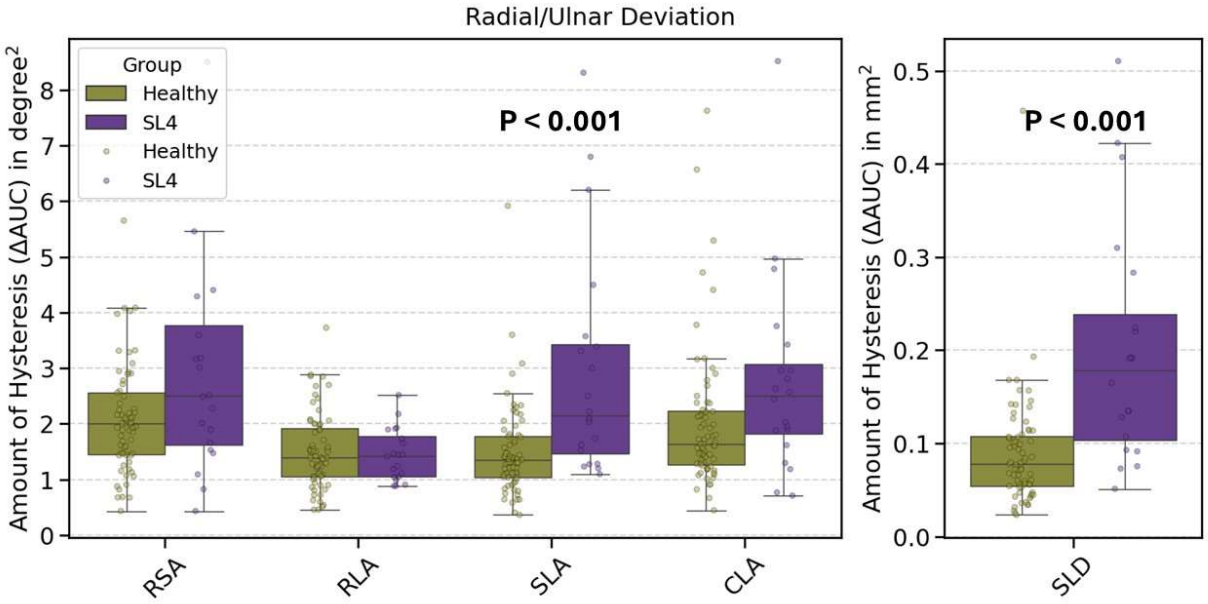


Figure 1. Hysteresis during RUD was greater in SL4 wrists across all kinematic parameters. Only the scapholunate angle and scapholunate distance showed statistically significant differences compared with healthy wrists.

Session Category

Clinical Biomechanics: N/A

P4-175

Effects of Maximal 1500-m Running on Relative Stiffness of the Biceps Femoris Long Head and Semitendinosus in Trained and Untrained Individuals

Sr. Thiago de Souza da Silva[1], Sr Heinrich Leon Souza Viera[2], Dr. Fabio Juner Lanferdini[3], Dr Heiliane de Brito Fontana[1]

[1]BSiM-UFSC - Musculoskeletal Biomechanics Research Group, Federal University of Santa Catarina, Florianopolis, Santa Catarina, Brazil. [2]Federal Universiy of Santa Maria, Santa Maria, Rio Grande do Sul, Brazil. [3]Federal University of Santa Maria, Santa Maria, Rio grande do Sul, Brazil

Introduction

The hamstrings play a key role in running, particularly in generating horizontal propulsion and controlling limb deceleration during terminal swing—the phase in which hamstring strains most frequently occur. The biceps femoris long head (BFlh) is injured two to four times more often than the semitendinosus (ST). Because muscle injury risk is mechanically linked to the magnitude of fiber strain, understanding how the relative stiffness of these muscles responds to fatiguing running may help explain differential injury susceptibility. This study evaluated whether a maximal 1500-m effort alters the BFlh/ST stiffness ratio in trained and untrained individuals.

Methods

Twenty-three participants were assigned to a trained group (n=14; athletes with >1 year of running experience) or an untrained group (n=9; healthy individuals without systematic training). Muscle stiffness was assessed with shear-wave elastography (Siemens Acuson S2000) at 55% of femur length, with participants positioned prone on a dynamometer (hip 0°, knee 30°). For each muscle, three passive and three active measurements at 20% maximal voluntary contraction were obtained. Participants then completed a maximal 1500-m track run, after which stiffness and torque were reassessed. Active stiffness values were normalized to passive stiffness. Pre–post comparisons used paired tests; between-group differences used independent t-tests ($\alpha=0.05$).

Results

In untrained individuals, the BFlh/ST stiffness ratio decreased significantly (–19%; $p=0.039$; median from ~1.26 to ~1.02). In trained individuals, the ratio remained unchanged ($p=0.983$). Ratio data showed normal distribution and homogeneous variances.

Discussion

A maximal 1500-m effort reduced the relative stiffness of the BFlh only in untrained individuals. Lower BFlh stiffness may increase muscle fiber strain by reducing the contribution of series elastic components, potentially heightening susceptibility to strain injury—particularly relevant given the high incidence of BFlh injuries during running. Trained individuals maintained stiffness stability, suggesting protective neuromuscular or structural adaptations. Future studies should explore whether training interventions can modulate these stiffness responses and reduce strain risk.

Acknowledgements (Optional)

This study was supported with a CNPq scholarship awarded to TSS.

Session Category

Clinical Biomechanics: N/A

P4-176

Force Variability in Low-Level Demands and Functional Deficits as Markers of Neuromuscular Impairments in Chronic Ankle Instability

P.T. Milena F. Murari[1], P.T. Lucas S. Fernandes[1], P.T. Guilherme S. C. Rego[1], P.T. Leticia A. Böttcher[1], PhD Maria Isabel V. Orselli[2,1,3], BME Graziele Silva[2], PhD Eneida Y. Suda[3], PhD Isabel C.N. Sacco[1]

[1]School of Medicine, University of São Paulo, São Paulo, São Paulo, Brazil. [2]Israeli College of Health Sciences Albert Einstein, São Paulo, São Paulo, Brazil. [3]Universidade Cidade de São Paulo (UNICID), Graduate Program in Physical Therapy, São Paulo, São Paulo, Brazil

P.T. Milena F. Murari

P.T. Lucas S. Fernandes

P.T. Guilherme S. C. Rego

P.T. Leticia A. Böttcher

PhD Maria Isabel V. Orselli

BME Graziele Silva

PhD Eneida Y. Suda

Introduction

Acute lateral ankle sprain is highly prevalent among active individuals, with an incidence of 50%[1]. One of its long-term consequences is chronic ankle instability(CAI), which affects 46% and leads to sensorimotor and mechanical deficits, episodes of giving-way, perceived

instability, pain, and reduced functional performance[2]. Considering inconsistencies in the literature on neuromuscular control, we aimed to analyze and compare the magnitude (Coefficient of variation CV, standard deviation SD) and structure (Sample Entropy, SE) of force performance during isometric tasks at different force levels (10%, 30%, 50% and 70% of MVIC), between individuals with CAI and healthy controls.

Methods

This cross-sectional study approved by the ethical committee (CAEE:80722924.7.0000.0068) included 42 adults (26 CAI; 16 controls). CAI was defined based on the International Ankle Consortium criteria[3], in addition to functional tests scores (Y-Balance Test). Participants were asked to perform three submaximal isometric tasks (eversion, inversion and plantarflexion) at four force levels. Ankle force was recorded using a dynamometer (OTBioelettronica) @2048Hz, 500x gain. Signals were digitally low-pass filtered using a zero-lag 8th order Butterworth filter (10Hz cutoff). Force CV, SD and SE were compared between groups by mixed ANOVAs followed by Newman Keuls post hoc ($p<0.05$).

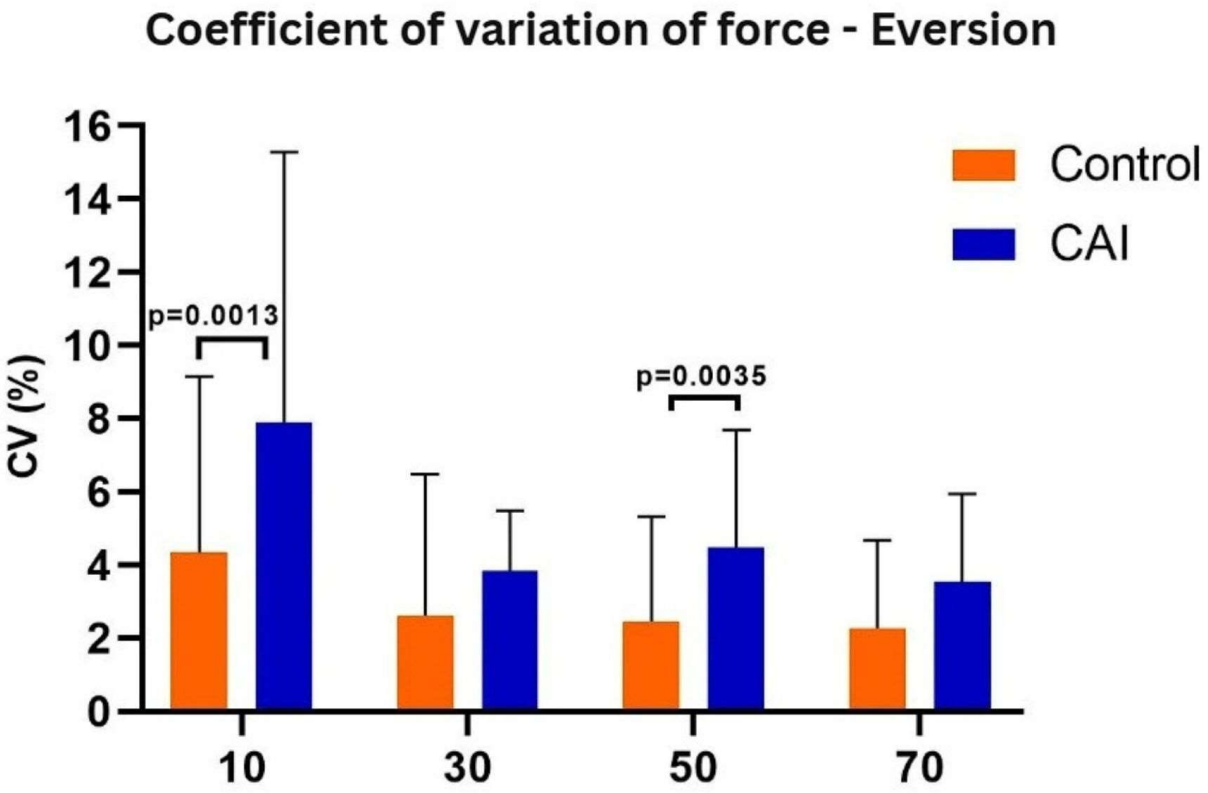
Results

CAI group showed a significantly worse performance on functional tests ($p=0.010$ for YBT posteromedial direction). They also showed greater eversion force (peroneus longus) CV at 10% and 50% of MVIC (fig.1). No group differences were found for force SD or SE. However, within both groups, greater force levels resulted in reduced force CV and SD ($p<0.05$). Fig.1: CV (mean±standard deviation) of eversion force for both groups.

Discussion

The increased eversion force CV at low-level tasks in CAI indicates reduced force consistency possibly due to irregular MU recruitment, impairing ankle control and performance in precision tasks, such as Y-Balance Test. These findings may represent markers of neuromuscular impairments in CAI, which support rehabilitation emphasizing proprioception, balance, evertor strength, and submaximal isometric control.

Images (Optional)



References (Optional)

[1] Waterman BR, et al. J Bone Joint Surg Am. 92:2279-84, 2010.

[2] Fong DTP, et al. Sports Med. 37:73-94, 2007.

[3] Gribble et al. J. Orthop. Sports Phys. Ther. 43: 585-591, 2013.

Acknowledgements (Optional)

Sao Paulo Research Foundation FAPESP (2024/16019-7; 2025/10622-6), CNPq/Brazil (302558/2022-5); and the USP Unified Scholarship Program (PUB).

Session Category

Clinical Biomechanics: N/A

P4-177

What Strategies Do Healthy Adults Use to Alter Foot Progression Angle During Gait?

Ms. Antoinette Torsij[1], Dr. Erin Macri[2], Dr. Martin Schepers[3], Dr. Jos Runhaar[2], Dr. Ignazio Aleo[3], Dr. Selma Papegaaij[3], Dr. Eline van der Kruk[1], Prof. Jaap Harlaar[2,1], Dr. Mariska Wesseling[2]

[1]Delft University of Technology, Delft, South-Holland, Netherlands. [2]Erasmus MC University Medical Center, Rotterdam, South-Holland, Netherlands. [3]Moveshelf Labs B.V., Utrecht, Utrecht, Netherlands

Introduction

Altering foot progression angle (FPA) has been shown to reduce pain, reduce knee adduction moment, and slow down structural progression in knee osteoarthritis. It is not well understood what lower limb kinematic strategies individuals employ to achieve different FPAs. Therefore, the aim of this study was to explore how pelvic, hip, and subtalar joint kinematics differ between natural walking and walking with different FPAs among healthy adults.

Methods

Fourteen healthy participants were included (9 women, age: 57.8 ± 12.1 years; BMI: 23.7 ± 2.7 kg/m^2). We performed three-dimensional gait analysis using an instrumented treadmill while participants walked under five conditions: natural FPA (self-selected pace) and 5° and 10° toe-out and toe-in (at same speed) relative to their natural FPA. The FPA was calculated using an inertial measurement unit on the shoe. Participants received visual and audio feedback on their altered FPA every five steps. Pelvic, hip and subtalar joint angles were obtained via OpenSim using a generic musculoskeletal model. We performed statistical parametric mapping on the last 20 gait cycles of each condition, to compare joint angles throughout stance between each FPA condition and natural walking.

Results

Compared with natural walking, 10° toe-out involved ~6-8° greater hip external rotation and 5-10° more subtalar eversion (significant in late stance). Toe-out 5° showed a similar pattern but with smaller magnitudes. Toe-in conditions produced similar changes but in opposite directions, again larger with toe-in 10°. For example, subtalar inversion was significant only with toe-in 10°. Toe-in gait also involved contralateral transverse pelvic rotation (i.e. forward translation of the ipsilateral pelvis) that reached significance for 10° toe-in only (standard deviations were large for all conditions).

Discussion

Hip and subtalar joint angles were consistently and significantly altered for different FPAs, compared to natural walking. Pelvic rotation was more varied, possibly reflecting individual anatomical differences (e.g. pelvic rotation may help overcome limited hip internal rotation) or movement strategies. Investigating these adaptations may help clarify what strategies individuals employ to achieve different FPAs, which could support the development of predictive models to estimate the effects of gait modifications based on natural gait.

Images (Optional)

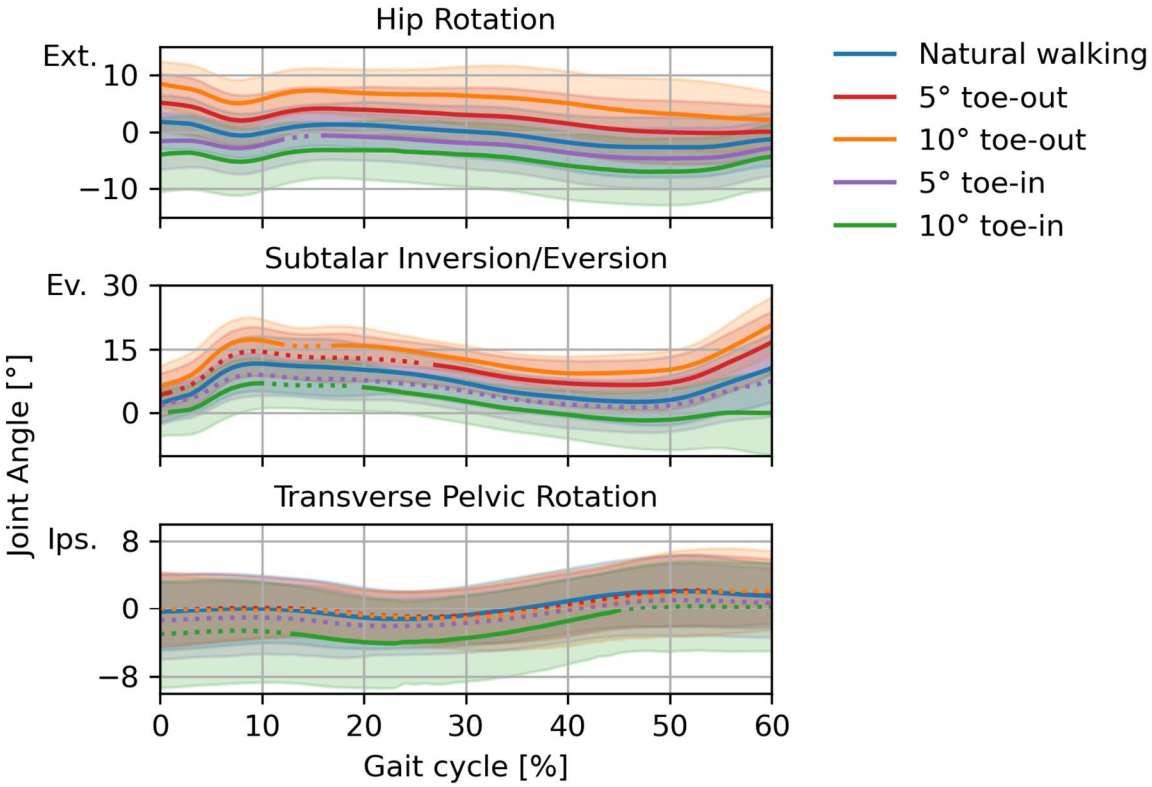


Figure. Joint angles for different FPA conditions (mean[SD]). Solid = p<0.05 vs natural walk; Dotted = not significant. Ext = external rotation; Ev = eversion; Ips = ipsilateral.

Acknowledgements (Optional)

This project was supported by a Health Holland Public Private Partnership grant (#EMCLSH23038).

Session Category

Clinical Biomechanics: N/A

P4-178

Comparison of Static Alignment with and without X-Ray Metrics in Pediatric Foot Deformities

Ms. Janet Le[1,2], Dr. Joseph Krzak PT, PhD, PCS[3,4], Dr. Karen Kruger PhD[1,2,4]

[1]Marquette University, Milwaukee, Wisconsin, United States. [2]Medical College of Wisconsin, Milwaukee, Wisconsin, United States. [3]Midwestern University, Downers Grove, Illinois, United States. [4]Shriners Children's, Chicago, Illinois, United States

Introduction

Segmental foot models (SFM) have been widely used in clinical gait analysis to assess foot deformities and differentiate between flexible and rigid deformities for intervention planning. The Shriners Children's Model (SCM) has been shown to be amongst the most repeatable and reproducible SFM [1]. While the SCM can be utilized with marker and goniometer-based definitions or in combination with radiographic offset inputs, prior studies have not examined the alignment differences between the two input conditions for pediatric foot deformities.

Methods

Segmental foot data was collected from 16 pediatric patients with foot deformities. The SCM was analyzed between marker-based and radiographic inputs. Deformity severity was taken from the absolute value of the radiographic offsets. Pearson's correlation coefficients (r) were calculated to test the hypothesis that greater differences between model outputs would be associated with increasing deformity.

Results

A strong correlation (r=0.89) was found between deformity severity and SCM input measure differences for the coronal hindfoot (Figure 1A). Transverse midfoot alignment (Figure 1B) showed a moderate correlation (r=0.50) between measurement differences. Sagittal hindfoot alignment measurement differences exhibited a moderate correlation (r=0.48) with hindfoot pitch (Figure 1C). A negative correlation (r=-0.19) was observed between measurement differences for sagittal forefoot alignment and pitch (Figure 1D).

Discussion

The static alignment results show that as deformity increased, there was increased disagreement between static alignment from marker/goniometer and x-ray inputs,

particularly for the coronal hindfoot. While marker-based inputs for the coronal hindfoot provide appropriate measurements for typical feet, the physical exam may underestimate the deformity compared to x-ray inputs with increased severity. Even with less differences for transverse midfoot and sagittal hindfoot alignment, it is suggested that forefoot and hindfoot progression be examined separately to determine the specific segment contributions. Sagittal forefoot alignment showed an inverse correlation, where decreased deformity displayed better agreement between input conditions. This confirms that SCM input measure differences for smaller deformities can be examined by either goniometer or x-ray inputs, but as severity increases, these differences increase, indicating x-ray inputs should be considered, especially when used for presurgical assessment.

Images (Optional)

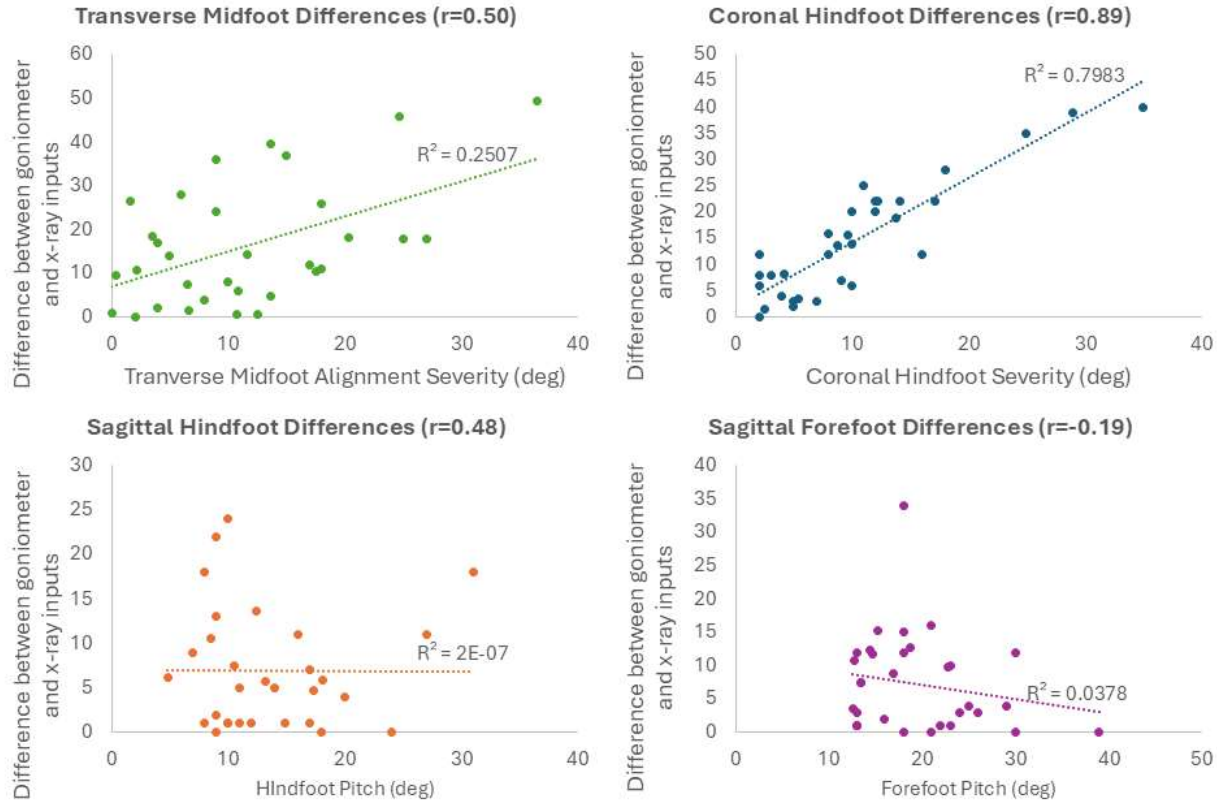


Figure 1. Measurement differences between goniometer and x-ray SCM inputs against deformity severity (deg) for A) coronal hindfoot and B) transverse midfoot. C) Sagittal hindfoot measurement differences against hindfoot pitch (deg). D) Sagittal forefoot measurement differences against forefoot pitch (deg).

References (Optional)

[1] Yoo, H. J. *et al. Journal of Foot and Ankle Research* 15, 1 (2022)

Session Category

Clinical Biomechanics: N/A

P4-179

Altered Relationships between Lower Limb Torques and Limb Loading during Speed Modulation after Stroke

Mr. Zekun Liu, Mr. Jason Tsai, Dr. Hao-Yuan Hsiao

The University of Texas at Austin, Austin, Texas, United States

Introduction

Individuals post-stroke commonly exhibit impaired limb loading, which is associated with reduced walking speed and mobility limitations. Limb loading during walking depends on coordinated sagittal-plane knee extension and frontal-plane hip abduction torque production. This study compared how knee extension and hip abduction torques contribute to changes in limb loading with increasing walking speed in individuals post-stroke and healthy controls.

Methods

Nine individuals more than 6 months post-stroke and nine age-matched healthy control individuals walked on an instrumented split-belt treadmill (Motek Medical, Amsterdam, Netherlands) at self-selected and maximal speeds. Kinematic data were collected using a 10-camera motion capture system (Vicon-USA, Denver, USA), and inverse dynamics was used to estimate hip abduction and knee extension torques for the paretic limb in stroke and the non-dominant limb in controls. Peak vertical ground reaction force (vGRF) during the 1st half of the stance phase was used to characterize limb loading.

Results

Compared with stroke, controls showed greater increases in speed, peak knee extension torque, and peak vGRF ($p < 0.05$). In controls, changes in peak hip abduction torque and peak knee extension torque were both positively correlated with changes in peak vGRF as walking speed increased. In contrast, only changes in peak hip abduction torque were correlated to changes in peak vGRF in individuals post-stroke. In addition, changes in peak knee extension and hip abduction torques were correlated in controls but not in stroke.

Discussion

Persons with chronic stroke and healthy controls adopted different strategies to change limb loading as walking speed increased. Specifically, healthy controls modulated both hip abduction and knee extension torques to increase limb loading. In contrast, knee extension torque did not contribute to changes in paretic limb loading in individuals post-stroke. Moreover, the strong coupling between knee extension and hip abduction torques in

controls suggests coordinated modulation of both joints. This coupling was not observed in individuals post-stroke. Therefore, knee extension torque may be an important target for improving coordinated joint torque modulation to restore limb loading after stroke.

Images (Optional)

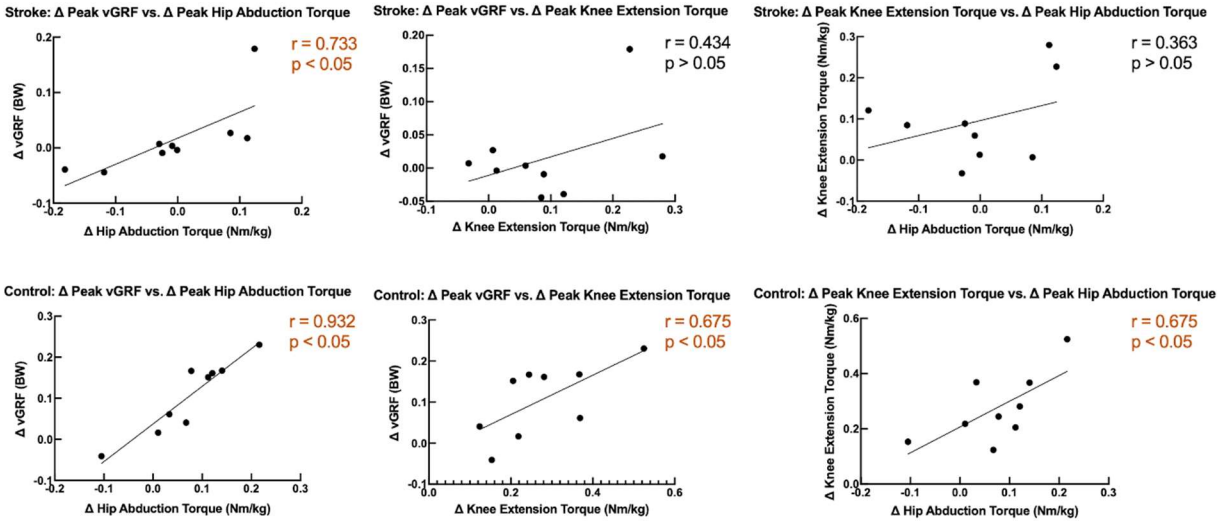


Figure 1. Relationships between changes in peak hip abduction torque, peak knee extension torque, and peak vGRF in stroke and control groups from self-selected to maximal walking speed.

Session Category

Clinical Biomechanics: N/A

P4-180

Effect of Strut Stiffness on Peak Push-Off Powers Using Two Approaches in Carbon Fiber Custom Dynamic Orthoses

Ms. Kaitlyn deBlois[1], Dr. Kirsten Anderson PhD[1], Dr. Kota Takahashi PhD[2], Dr. Jason Wilken PT, PhD[1]

[1]The University of Iowa, Iowa City, Iowa, United States. [2]The University of Utah, Salt Lake City, Utah, United States

Introduction

Carbon fiber custom dynamic orthoses (CDOs) improve gait and function after limb trauma.[1] CDOs have a cuff below the knee, a footplate, and a stiff carbon fiber posterior strut. CDOs reduce pain and control limb position during gait but reduce ankle motion and peak sagittal plane ankle rotational push-off power by nearly 50%. This decrease contrasts with positive patient perceptions of energy return reported with CDO use. The unified deformable (UD) model, which quantifies contributions from all structures distal to the shank (ankle+foot),[2] is thought to better represent CDO energetics than the traditional assessment of rotational ankle power (ankle). The purpose of this study was to determine the effect of strut stiffness on ankle and ankle+foot powers.

Methods

Participants walked at a controlled speed without an orthosis (NoCDO) and with different stiffness CDOs in randomized order: Compliant 3.9(1.2)Nm/deg, Moderate 5.4(1.4)Nm/deg, Stiff 7.0(2.1)Nm/deg. Peak ankle and ankle+foot power were calculated using Visual3D (HAS Motion) and MATLAB (The MathWorks Inc.). One-way repeated measures or Friedman ANOVA were used to determine main effects. Post-hoc analysis included paired sample t-tests or Wilcoxon signed rank tests with Bonferroni Holm correction.

Results

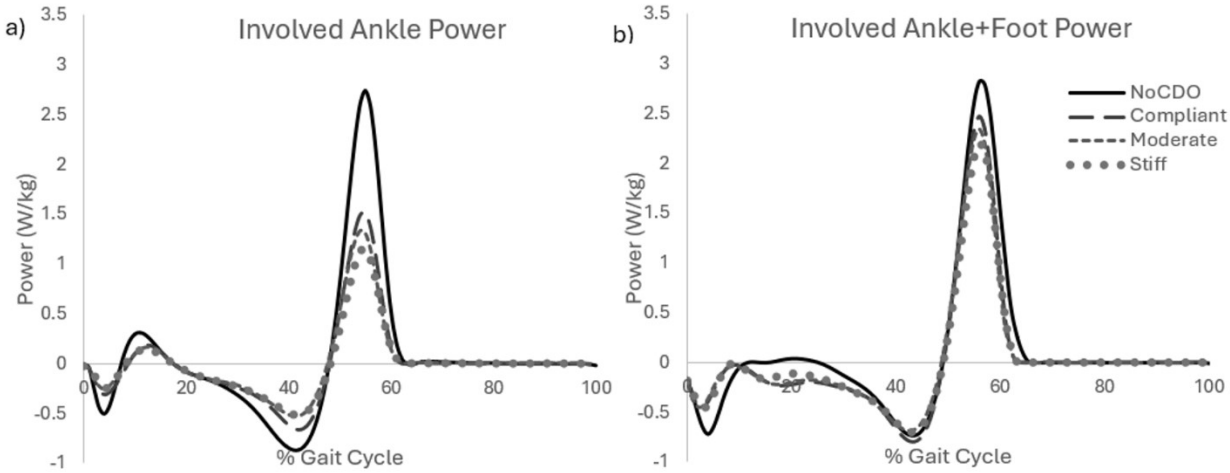
Seven individuals with limb trauma participated (1 Female, 35.9(10.1)yrs, 1.8(0.1)m, 92.2(19.4)kg). Differences were not observed between stiffnesses for ankle or ankle+foot power. Ankle power for all stiffnesses was significantly reduced ($p<0.001$) compared to NoCDO, with reductions greater than 47% (Figure 1a). Ankle+foot power for all stiffnesses was also significantly reduced ($p<0.001$) compared to NoCDO, but differences ranged from 17-24% (Figure 1b).

Discussion

Ankle and ankle+foot powers did not differ between stiffnesses, however, both were lower with CDO use compared to NoCDO. Accounting for contributions distal to the ankle joint (ankle+foot) resulted in a 50% smaller deficit in peak power with CDOs than indicated by peak ankle power. This difference highlights the potential importance of CDO footplate energy storage and return, and importance of accounting for contributions distal to the ankle joint.

Images (Optional)

Figure 1.



References (Optional)

[1] Grunst et al. ProsthetOrthotInt, 2023.

[2] Takahashi et al. J Biomech, 2012

Acknowledgements (Optional)

This project was supported in part by the Department of Defense (Award No. W81XWH-18-1-0658) and by the National Center for Advancing Translational Sciences of the National Institutes of Health (Award Number UM1TR004403).

Session Category

Clinical Biomechanics: N/A

P4-181

The Effects of Proximal Cuff Tightness on Hindfoot and Forefoot Forces During Gait With Carbon Fiber Custom Dynamic Orthoses

Dr. Kirsten Anderson PhD, Mr. Matthew Nachtman, Dr. Jason Wilken PT, PhD

The University of Iowa, Iowa City, Iowa, United States

Introduction

Carbon fiber custom dynamic orthoses (CDOs) reduce pain, restore function, and alter foot loading for individuals after limb trauma.[1-4] CDOs include a proximal cuff, posterior strut, and footplate. The CDO cuff is tightened around the limb every time the CDO is donned, however, the impact of cuff tightness on foot loading is not well understood. The purpose of this study was to determine the effect of cuff tightness on foot loading during gait.

Methods

This study was institutional review board approved. 15 unimpaired individuals (9 Female, 29.6(12.6)yrs, 1.7(0.1)m, 72.5(13.3)kg) provided informed consent. Loadsol insoles were placed under the foot and loadpad sensors were placed inside the cuff to measure forces acting on the limb (Novel Electronics Inc.). Participants completed testing without an orthosis (NoCDO) and in a CDO (Biomechanical Composites Inc.) tightened to 30N, 50N, and 70N in a randomized order. Peak force and force impulse, the indefinite integral over stance, were calculated for the hindfoot and forefoot as participants walked at a controlled speed. Repeated measures or Friedman's ANOVAs were performed to determine main effects, and post-hoc paired sample t-tests or Wilcoxon signed rank tests with Bonferroni Holm correction were performed.

Results

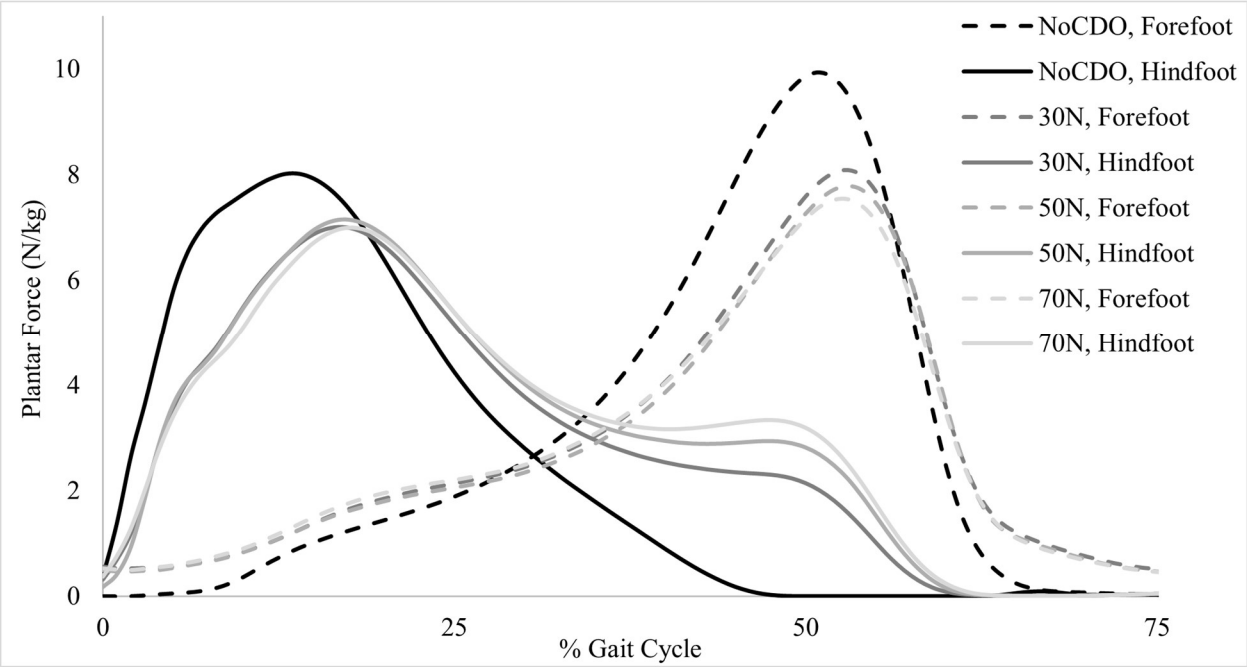
Hindfoot impulse increased significantly in 50N and 70N compared to NoCDO (23%) and 30N (8%). Peak hindfoot force (12-13%), peak forefoot force (21-26%), and forefoot impulse (20-24%) decreased significantly with CDO use compared to NoCDO, but there was no significant effect of tightness for these measures.

Discussion

Similar to previous work[1-4] study CDO altered foot loading at each tightness compared to NoCDO. Force was redistributed from the forefoot to the hindfoot in late stance (Figure 1). While cuff tightness had a limited effect, hindfoot impulse demonstrated a trend toward increased hindfoot loading with increased cuff tightness. This may be due to the stiffer

cuff-limb interface and suggests that rather than decreasing loading, a tighter cuff may increase hindfoot foot loading.

Images (Optional)



References (Optional)

[1] Anderson DD *et al*. JOR, 2024.

[2] Anderson, KM *et al*. GaitPosture, 2024.

[3] Anderson, KM *et al*. GaitPosture, 2025.

[4] Feng, J *et al*. FootAnkleOrthop, 2023.

Acknowledgements (Optional)

This project was supported in part by the National Center for Advancing Translational Sciences of the National Institutes of Health (Award Number UM1TR004403).

Session Category

Clinical Biomechanics: N/A

P4-182

Investigating Lower and Upper Body Shock Attenuation Across Walking Speeds in Middle-Aged Adults with Obesity

Dr. Julie Rekant PT, DPT, PhD[1,2], Dr. Odessa Addison DPT, PhD[1,2], Dr. Mark Redfern PhD[3], Dr. Jennifer Brach PhD, PT, FAPTA[3], Dr. April Chambers PhD[3]

[1]University of Maryland, Baltimore, Baltimore, MD, United States. [2]Baltimore VA, Baltimore, MD, United States. [3]University of Pittsburgh, Pittsburgh, PA, United States

Introduction

Shock attenuation – the absorption of accelerations as they propagate through the body – is linked to musculoskeletal injury risk, with greater attenuation at a segment indicating higher exposure to potentially injurious forces there. Adults with obesity walk more slowly than their normal-weight counterparts and experience higher rates of musculoskeletal injuries, likely due to greater mechanical loading and altered gait mechanics. This pilot study examined shock attenuation during walking at different gait speeds in middle-aged adults with obesity and explored relationships with temporal gait characteristics.

Methods

Six participants (3 male/3 female; age:49.7±7.1years; BMI:37.1±2.3kg/m^2) completed overground walking at self-selected and fast speeds while wearing accelerometers at the shanks, pelvis, and head. The ratio of vertical acceleration power spectral densities of the proximal to distal segment quantified shock attenuation for the shank-to-pelvis (ATT_{SP}) and pelvis-to-head (ATT_{PH}) across steps. Step timing identified from shank accelerations was used to derive temporal gait characteristics.

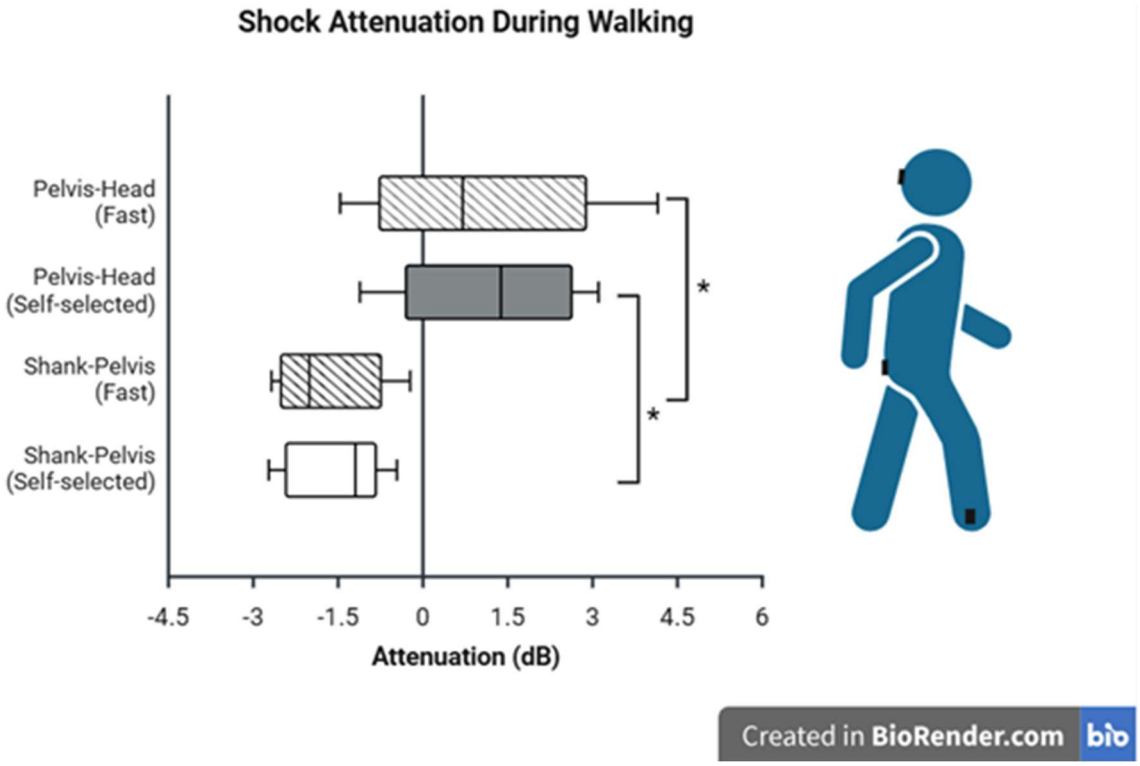
Results

Fast gait speeds exceeded self-selected speeds (1.9±0.2 vs. 1.2±0.0m/s,$p<0.01$), achieved through shorter step times (0.43±0.05 vs 0.54±0.03 s, $p<0.01$), higher cadence (137±12 vs. 111±8steps/min, $p<0.01$) and reduced terminal double support (0.12±0.02 vs. 0.19±0.02s,$p=0.03$). At self-selected speeds, attenuation was greater in the lower (ATT_{SP}=-1.5±1.0dB) versus upper body (ATT_{PH}=1.2±1.8dB,$p=0.03$); a similar trend was seen for fast walking ($p=0.07$). No meaningful differences in attenuation were observed across conditions for ATT_{SP} ($p=0.62$) and ATT_{PH} ($p=0.86$). ATT_{PH} was related with terminal double support time during fast walking (Rho=0.951,$p=0.01$) and inversely related with walking speed for self-selected walking (Rho=-0.97,$p=0.03$).

Discussion

Middle-aged adults with obesity demonstrate greater shock attenuation in the lower compared to upper body while walking at fast and self-selected speeds, suggesting the knees and hips may be at greater risk for injury than the back in these individuals. Walking speed and terminal double support time helped explain a large amount of variance in ATT_{SP} at self-selected and fast speeds, respectively. These preliminary findings support the feasibility of accelerometry to capture speed-dependent differences in shock attenuation and gait and suggest interventions targeting walking speed and mechanics may help reduce exposure to potentially injurious acceleration propagation in this population.

Images (Optional)



Session Category

Clinical Biomechanics: N/A

P4-183

The Impact of Pregnancy on Whole Body Angular Momentum During Walking

Ms. Kaitlyn Kleeman BS, Mrs. Maryam Golmohammadi MS, Dr. Amanda Paluch PhD, Dr. Sarah Roelker PhD

University of Massachusetts Amherst, Amherst, MA, United States

Introduction

More than 25% of pregnant individuals experience a fall [1,2], most often in months 6-8 of gestation [1]. Regulation of the whole-body angular momentum (WBAM) about the body's center of mass is required to maintain dynamic balance and prevent a fall during gait [3]. Larger peak-to-peak ranges of WBAM are associated with poor balance control and increased fall risk [4]. This study aims to determine the effects of pregnancy on peak-to-peak range of WBAM during gait. For each anatomical plane, we hypothesize that 1) WBAM range will be larger in trimester 3 (P-T3) than trimester 2 (P-T2), indicating reduced balance control later in pregnancy, and 2) pregnant participants will show larger WBAM range than age-matched nulligravida individuals, reflecting poorer balance control.

Methods

12 pregnant (PREG) (n=12, 34 ± 3.8 yrs) and 8 nulligravida (NG) (n = 8, 34 ± 4.6 yrs) participants performed 5 overground walking trials at a self-selected speed, at two timepoints in PREG (P-2T and P-3T) and once in NG. Motion capture and ground reaction force data were collected to quantify WBAM in the sagittal, frontal, and transverse planes. The WBAM range in each plane was calculated as the average peak-to-peak range from all 5 trials at each time point and normalized to mass, height, and gait speed. A mixed-model ANOVA with a Bonferroni correction assessed for differences in WBAM range across groups.

Results

Compared to NG, frontal plane WBAM range was significantly lower in P-T2 ($p = 0.008$) and PT-3 ($p = 0.009$) (Fig. 1). There were no differences in WBAM range in the sagittal and transverse planes, or between trimesters.

Discussion

The lower range of WBAM in P-T2 and P-T3 indicates greater balance regulation in PREG in the frontal plane, which may indicate a more cautious mediolateral gait strategy. Future work will determine the relationship between WBAM, strength, and neuromuscular control

while walking during pregnancy, and whether physical activity levels might modulate these changes.

Images (Optional)

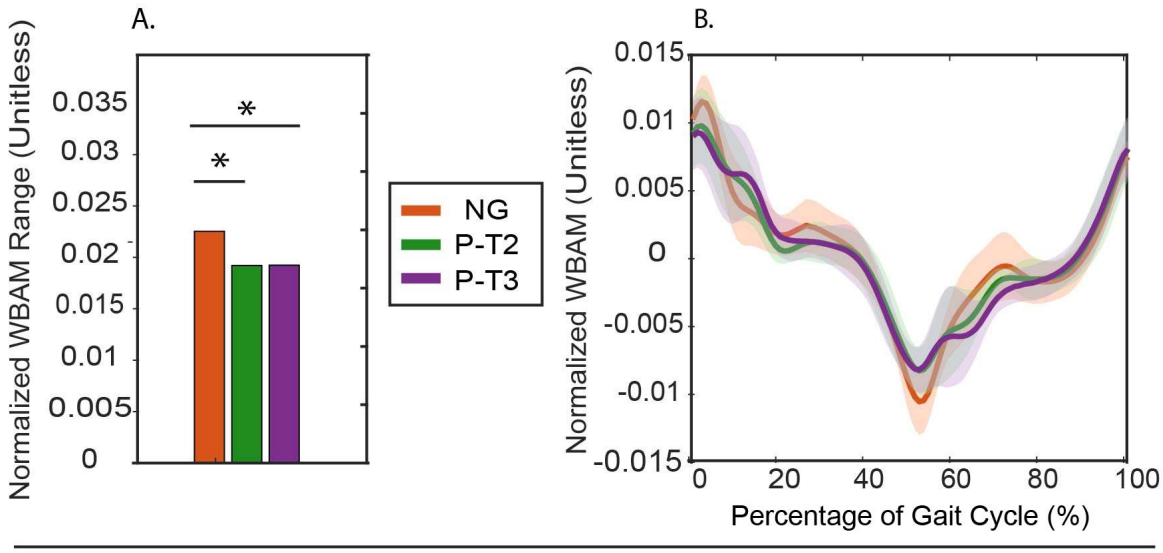


Figure 1: (A) A boxplot of the normalized peak-to-peak range of WBAM for each group in the frontal plane. * denotes a statistically sigificant difference between groups. (B) The mean (solid lines) and standard deviation (shaded areas) of normalized WBAM for one gait cycle for each group in the frontal plane.

References (Optional)

[1] Dunning, Am J Ind Med. 2003. [2] Dunning, Matern Child Health J. 2010. [3] Herr & Popovic, J Exp Biol. 2008. [4] Nott, Gait Posture. 2014.

Acknowledgements (Optional)

Funding: UMass Amherst IALS Midi Grant

Session Category

Clinical Biomechanics: N/A

P4-184

Metatarsal Injury Study: Hormonal, Energetic, & Activity-Related Determinants (MISHEARD)

Dr. Andrew Wilzman PhD, Ms. Julia Nicolescu, Dr. Karen Troy PhD

Worcester Polytechnic Institute, Worcester, Massachusetts, United States

Introduction

Metatarsal Bone Stress Injuries (BSI) are common in women and youth athletes, yet links among bone structure, strength, and BSI risk remain limited [1]. This study tested if metabolic and biomechanical metrics could classify recent metatarsal BSI.

Methods

Thirty-six female runners (17-40 y; >10 mi/wk) were assigned to healthy or injured groups (n=7). Questionnaires quantified past activity and RED-S risk [2,3,4]. DXA quantified lean mass and mineralization. Micro-CT measured metatarsal and tibial geometry and density [5]. Each injured runner was matched with two unique controls by running performance. We predicted injury status based on load history, foot arch, metabolism, foot strength, and bone strength. The two strongest predictors per category (Hedges' g) were pooled and the top five were entered in a Linear Discriminant Analysis, using leave-one-out cross-validation.

Results

Injury status aligned with longer metatarsals, higher RED-S risk (low energy availability and bone density), lower age of menarche, and greater activity levels, particularly when increased after age 15 (Table 1). The same three participants were misclassified between the validation and final model.

Discussion

Findings indicate elevated risk in individuals who had lower physical activity during adolescence but high bone loading in early adulthood. Mechanical loading during adolescence has a large influence on peak adult bone mass and structure [6]. Suboptimal bone adaptation may also reflect age, overuse, reduced energy availability, or genetic factors. Combined metabolic and structural markers form a risk model suitable for screening if confirmed in larger cohorts.

Images (Optional)

Table 1: Linear Discriminant Analysis results, units scaled to 0-1 using the dataset minimum and maximum.

Validation Results	*Predicted Control*	*Predicted Injured*	Final Results	*Predicted Control*	*Predicted Injured*
Actual Control	**13**	1	*Actual Control*	**13**	1
Actual Injured	2	**5**	*Actual Injured*	2	**5**

	RED-S Risk Score	Age of Menarche	BPAQ < 15 years	BPAQ Total	Longest Metatarsal Length
Dataset Minimum	0	11	0.2	21	0.067
Dataset Maximum	6	16	426	442	0.082
Coef. Mean	10.97	-8.95	-4.03	15.32	1.79
Coef. SD	1.31	1.02	8.46	8.09	0.83
Coef. Minimum	9.65	-11.61	-22.83	-3.43	0.39
Coef. Maximum	14.88	-7.83	20.54	35.00	4.59
Final Model	10.72	-8.82	-4.59	15.56	1.67

References (Optional)

[1] Troy KL, et al., 2020; [2] Dolan S, 2003; [3] Weeks BK & Beck BR, 2008; [4] Mountjoy M, et al., 2018; [5] Chaplais E, et al., 2014; [6] Troy KL et al, 2018

Acknowledgements (Optional)

The data from this work was supported by NIH R15HD104169 grant (to KLT).

Session Category

Clinical Biomechanics: N/A

P4-185

Comparison of Markerless and Marker-Based Motion Capture for Pediatric Gait in Typically Developing and Clinical Populations

Mr. Karson Fitzsimons MSc[1,2], Mrs. Amanda Rande MSc[2], Ms. Mahika Sharma BSc[3], Mr. Ion Robu MSc[4], Mrs. Gina Ursulak PT, BScPT, MSc[4], Mrs. Amanda Beaudin PT, MSc[4], Dr. Gregor Kuntze PhD[5], Mr. Jereme Outerleys BEng, MASc[6,7], Dr. Elise K. Laende PhD[8,6], Dr. Ranita H. K. Manocha MD, MSc, FRCPC (PM&R), CSCN (EMG)[2], Dr. Rubini Pathy BScPT, MD, FRCSC[9], Dr. Elizabeth G. Condliffe PhD, MD, FRCPC[2,10,4]

[1]Schulich School of Engineering, University of Calgary, Calgary, Alberta, Canada. [2]Department of Clinical Neurosciences, Cummings School of Medicine, University of Calgary, Calgary, Alberta, Canada. [3]Department of Biomedical Engineering, Georgia Institute of Technology, Atlanta, Georgia, United States. [4]Alberta Children's Hospital, Calgary, Alberta, Canada. [5]Cummings School of Medicine, University of Calgary, Calgary, Alberta, Canada. [6]Faculty of Engineering and Applied Sciences, Queen's University, Kingston, Ontario, Canada. [7]Theia Markerless Inc., Kingston, Ontario, Canada. [8]Faculty of Engineering, University of Waterloo, Waterloo, Ontario, Canada. [9]Department of Surgery, Cummings School of Medicine, University of Calgary, Calgary, Alberta, Canada. [10]Department of Pediatrics, Cummings School of Medicine, University of Calgary, Calgary, Alberta, Canada

Introduction

Markerless motion capture has the potential to facilitate pediatric clinical gait analysis by eliminating the difficulties associated with marker placement. This study aims to evaluate markerless motion capture compared to the marker-based clinical standard for children with and without mobility impairments.

Methods

Two cohorts were recruited for this study: 26 (11 female/15 male) children with mobility impairments (20 cerebral palsy) who had been referred for clinical gait assessment and 30 (15 female/15 male) typically developing (TD) children. Participants walked barefoot while marker-based (12 Motion Analysis Eagle4 cameras with modified Helen-Hayes approach) and markerless (Theia3D with 8 Sony Cameras) data were captured concurrently. For each participant, lower body joint angles normalized to 100% of the gait cycle were statistically compared using root-mean-square-deviation (RMSD). The RMSDs for each subject were then averaged across multiple strides for each side of the body. The TD cohort values were calculated with 7 strides per individual, while the clinical cohort used 3-6 strides per individual due to factors including fatigue and marker occlusion.

Results

Table 1 shows the median and 25th-75th percentiles for the RMSD of the left side. In both groups the frontal and sagittal planes showed better agreement between marker-based and markerless approaches than the transverse plane across all joints, except for the pelvis. The clinical group had higher median RMSD values all plane-joint-side combinations except the right hip frontal plane. The largest difference between the two groups was seen at the frontal and transverse plane ankle angles.

Discussion

The transverse plane poses challenges for marker-based systems due to its higher sensitivity to soft-tissue artifacts and marker placement. The larger RMSD values in the transverse plane indicate disagreement between systems, but not which system is closer to a true measurement. The larger RMSD values in the clinical group could be caused by anatomic differences including foot deformities being underrepresented in Theia3D's training dataset or fewer strides contributing to the participant's average. These results indicate potential systematic differences between how clinical and TD individuals are measured using markerless motion capture that should be explored prior to implementation in a clinical pediatric gait laboratory.

Images (Optional)

Table 1: Median and 25th-75th percentile RMSD between Marker-based and Markerless motion capture for left side lower body joint angles

Plane / Joint	Typically Developing			Clinical		
	Sagittal	Frontal	Transverse	Sagittal	Frontal	Transverse
Pelvis	4.0° 2.8-6.0°	2.6° 2.3-3.2°	2.8° 2.1-3.2°	5.1° 3.0-8.8°	3.8° 3.0-4.7°	3.0° 2.3-3.5°
Hip	5.7° 3.4-8.3°	3.4° 2.4-4.2°	7.5° 5.8-9.7°	5.8° 4.9-7.5°	3.8° 3.2-6.1°	8.7° 6.9-15.8°
Knee	4.6° 3.7-6.2°	5.5° 3.5-6.3°	8.4° 6.6-11.1°	5.0° 3.9-6.5°	6.7° 5.6-11.0°	9.8° 7.3-12.3°
Ankle	3.1° 2.6-4.3°	3.9° 2.7-5.3°	11.3° 9.3-13.5°	4.2° 3.3-4.7°	6.4° 4.1-9.9°	13.9° 10.9-24.4°

Acknowledgements (Optional)

Session Category

Clinical Biomechanics: N/A

P4-186

Foot Strategies Used During Y-Balance Tests may be Influenced by Suboptimal Postural Control in Adolescents Post-Anterior Cruciate Ligament Reconstruction

Ms. Kasey Stammen BS[1,2], Dr. Elliot Greenberg DPT, PhD[3], Ms. Madeleine McCreary BS[1,4], Mr. Stone Streeter BS[3], Mr. Kevin Xu BA[3], Dr. Theodore Ganley MD[3], Dr. Valentina Graci PhD[1]

[1]Center for Injury Research and Prevention, Children's Hospital of Philadelphia, Philadelphia, PA, United States. [2]Department of Human Sciences, Ohio State University, Columbus, OH, United States. [3]Department of Orthopaedic Surgery, Children's Hospital of Philadelphia, Philadelphia, PA, United States. [4]Department of Mechanical Engineering, University of Washington, Seattle, WA, United States

Introduction

Prior research has identified that three months after anterior cruciate ligament reconstruction (ACLR), adolescents will utilize different movement strategies to perform the anterior reach portion of the Y-balance test (antYBT) by remaining more flatfooted (FF) on their operated limb (OPL) and moving onto the ball-of-foot (BoF) on the non-operative limb (NOPL). It remains unclear if the foot strategy (FS) is influenced by postural control and/or strength. Understanding which factors influence FS can help guide precise rehabilitation during recovery. This study aimed to assess how FS and leg strength impact the center-of-pressure (CoP) entropy of adolescents post-ACLR while maintaining balance during the antYBT.

Methods

Adolescent athletes three months post-ACLR, completed two trials of the antYBT, which involves balancing on one limb, reaching their opposing limb forward as far as possible, and returning to a single-leg balanced position. Video recordings on their OPL and NOPL were reviewed and classified as either FF or BoF strategy on the balancing limb. The complexity index (CI; CoP entropy measure) in the anterior-posterior (AP) and medial-lateral (ML) direction was calculated for each trial. Hamstring/quadriceps strength ratios were extracted from medical records. Wilcoxon test was used to compare strength and CI between FS ($p<=0.05$).

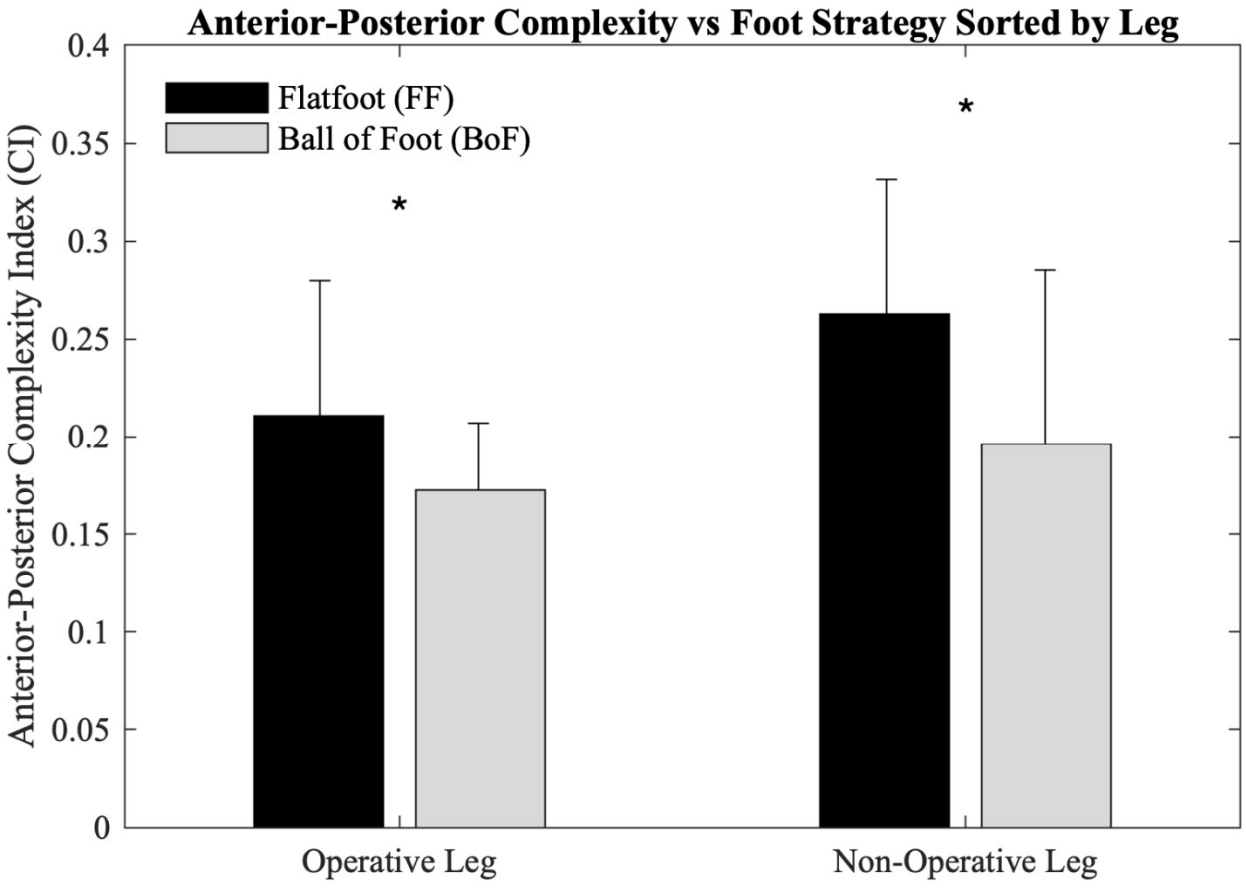
Results

23 patients (15.53 ± 1.98 years old, 65% female) completed 45 OPL and 46 NOPL trials. CI in the AP direction was statistically significantly lower when using BoF strategy for both OPL and NOPL (OPL: 0.21±0.06 vs 0.17±0.03 p=0.05, NOPL: 0.26±0.06 vs 0.19±0.08 p=0.03, Figure 1). There was no significant difference in CI in the ML direction between FS. There was no significant difference in hamstring/quadriceps strength ratios between FS.

Discussion

Lower AP CoP entropy in the BoF than the FF strategy suggests less refined postural control and adaptability in both legs in adolescents post-ACLR during this dynamic balance task. Patient's hamstring/quadriceps strength ratio did not show differences between FS, suggesting that FS may be more influenced by postural control than strength. Future studies should seek to better understand how CoP entropy may affect movement strategies, recovery, and reinjury risk in adolescents post-ACLR.

Images (Optional)



Session Category

Clinical Biomechanics: N/A

P4-187

Passive Smartphone Gait Monitoring in Ankle Fracture Recovery: Feasibility in a Prospective Cohort of 91 Patients

Dr. Daniel Fitzpatrick MD, MS[1], Dr. Michael Hahn PhD[2], Dr. Blake Dowdle MD[1], Dr. Brandon Wilkinson MD[1], Dr. Nicholas Strasser MD[3], Ms. Tessa Kirkpatrick BS, CCRC[4], Ms. Cindy Headlee[4], Ms. Ellie DeLoretto BS[4], Ms. Leila Hollis MS[5], Dr. Kate Spitzley PhD[4]

[1]Slocum Center for Orthopedics and Sports Medicine, Eugene, OR, United States. [2]University of Oregon, Eugene, OR, United States. [3]Vanderbilt University Medical Center, Nashville, TN, United States. [4]Slocum Research and Education Foundation, Eugene, OR, United States. [5]University of Nevada Reno School of Medicine, Reno, NV, United States

Introduction

Smartphone-based gait monitoring presents clinicians with a low-burden opportunity to objectively compare pre- and post-injury gait patterns and offers individualized baselines for functional recovery. This study evaluated the feasibility of passively collecting iPhone gait metrics to track functional recovery after ankle fracture in both a private orthopedic practice and university medical center setting.

Methods

A cohort of 91 patients with isolated ankle fractures was enrolled. Thirty days of pre-injury baseline gait data was captured retrospectively at enrollment, and gait data was prospectively captured for 6 months following treatment. Gait metric data was passively collected on the HealthKit app and transferred to the research team using an app designed for this study. Metrics included step count, walking distance, double support percentage, walking speed, step length, and walking asymmetry. Data completeness was determined relative to the subgroup of patients with valid preinjury baseline data for each metric.

Results

Preinjury baseline data was present in 62 of 91 patients (68.1%) for walking speed; in 45 of 91 patients (49.5%) for step count, walking distance, double support, and walking asymmetry; and in 54 of 91 patients (59.3%) for step length. Among those with valid preinjury baseline data, complete follow-up was achieved in 47 of 62 patients (75.8%) for walking speed, in 38 of 45 patients (84.4%) for step count, walking distance, and double support, in 46 of 54 patients (85.2%) for step length, and in 29 of 40 patients (72.5%) for

walking asymmetry. In contrast, among participants lacking preinjury baseline data, complete follow-up rates ranged from 0% for step length to 31.3% for step count.

Discussion

Passive collection of iPhone gait metrics is a feasible approach for monitoring functional recovery following orthopedic trauma in a subset of the patient population. Our findings demonstrate that when preinjury baseline data are available, follow-up data completeness is relatively high across multiple gait parameters. Conversely, patients without baseline data show significantly lower follow-up completeness, underscoring the necessity for researchers to confirm the availability of pre-injury measurements prior to longitudinal analysis. This study supports the broader utility of passive smartphone monitoring as a tool in clinical research and practice.

Acknowledgements (Optional)

The authors would like to thank the Orthopaedic Trauma Association for funding this work through their Research Grants Program [OTA Grant Number: 6703] and acknowledge Dr. Erin Owen for her work on the project.

Session Category

Clinical Biomechanics: N/A

P4-188

Markerless Pose Estimation to Assess Functional Mobility Before and After Focused Ultrasound Ablation in Individuals With Essential Tremor

Dr. Kavya Katugam-Dechene PhD[1,2], Mr. Ethan Simaitis[1,2], Dr. Daniel Roque MD[1], Dr. Aaron Gelinne MD[1], Dr. Vibhor Krishna MD[1], Dr. Jason Franz PhD[1,2]

[1]University of North Carolina at Chapel Hill, Chapel Hill, NC, United States. [2]North Carolina State University, Raleigh, NC, United States

Introduction

Essential tremor (ET) is a common neurologic disorder that disproportionately impairs upper-limb control but is frequently associated with balance and gait dysfunction. Focused ultrasound ablation (FUSA) is a treatment option that targets the ventral intermediate nucleus of the thalamus to disrupt central nervous system excitatory pathways that perpetuate ET pathology. Although generally safe, FUSA can lead to post-treatment gait dysfunction or imbalance in ~33% of patients. Traditional neurological tests may miss subtle changes in locomotor function necessitating the need for more objective means to evaluate gait following FUSA. In this study, we used markerless pose estimation to assess pre-post changes in spatiotemporal gait patterns, joint kinematics, and center-of-mass (CoM) control following FUSA in people with ET.

Methods

ET patients (males and females) aged 22 years and older with moderate to severe ET refractory to at least two medications were included. Five adults with ET have completed a battery of functional and locomotor tasks immediately before and immediately after FUSA. The battery included: walking at preferred speed and fast speeds, walking with head turns, a figure-8 walking test, and a sit-to-stand task. Standard 2-camera videos were processed using OpenCap to extract 3D joint kinematics (hip, knee, ankle flexion-extension) and keypoint and CoM trajectories.

Results

Most participants adopted slower preferred (n=3/5), maximum (n=4/5), and figure-8 (n=4/5) walking speeds with shorter and wider steps and, when walking with head turns, larger path deviations (n=4/5) following FUSA. Across most tasks, participants tended to adopt smaller peak leg joint angles and lesser CoM peak jerk, the latter interpreted as a “smoother” pattern (preferred: n=4/5; fast: n=3/5; figure-8: n=3/5; walk with head-turn: n=3/5). These changes may be unique to locomotion; n=4/5 participants completed the sit-to-stand more quickly following FUSA.

Discussion

Early findings suggest that FUSA in patients with ET may promote smoother walking patterns yet precipitate a more cautious, stability-oriented gait strategy. Together, these findings demonstrate the clinical feasibility of markerless pose estimation to quantify gait and mobility after FUSA, providing an objective complement to standard neurological assessments to fully capture functional recovery.

Images (Optional)

Table 1: Individual walking speeds (m/s) for five participants during four gait tasks in the Pre and Post treatment conditions. Tasks include preferred-speed walking, maximum-speed walking, figure-8 walking, and walking with head turns.
* indicates decreased walking speed Post treatment compared to Pre treatment within a given subject and task.

Subject	Condition	Preferred Walking Speed (m/s)	Maximum Walking Speed (m/s)	Figure-8 Walking Speed (m/s)	Walking Speed with Head Turn (m/s)
S1	Pre	0.922	1.265	0.587	0.827
	Post	1.048	1.272*	0.535*	0.901
S2	Pre	1.055	1.414	0.570	0.879
	Post	0.832*	1.026*	0.419*	0.676*
S3	Pre	0.793	1.211	0.402	0.663
	Post	0.775*	1.136*	0.465	0.740
S4	Pre	0.835	1.410	0.483	0.868
	Post	0.864	1.255*	0.430*	0.882
S5	Pre	0.904	1.468	0.480	0.721
	Post	0.685*	1.044*	0.374*	0.434*

Acknowledgements (Optional)

Authors KKD and EGS contributed equally to this work and share co-first authorship. The authors gratefully acknowledge the clinical and support staff whose efforts made this work possible. Supported by NIH Grant 5R01NS125386-03.

Session Category

Clinical Biomechanics: N/A

P4-189

Effectiveness of Stochastic Resonance Electrical Stimulation on the Timed Up-and-Go Test Performance in Individuals with Cerebral Palsy

Dr. Khushboo Verma BPT, Ph.D.[1], Dr. Michele A. Lobo PT, Ph.D.[1], Dr. Eman Alsaqabi PT, Ph.D.[2,3], Dr. Stephen DiBianca Ph.D.[2], Dr. M. Wade Shrader MD[4], Dr. Alice Taylor BS, MACPR, MBChB[5], Dr. Jeremy Crenshaw Ph.D.[2], Dr. Laura Prosser PT, Ph.D.[6,7], Dr. Stuart Binder-Macleod PT, Ph.D.[1], Dr. Samuel C.K. Lee PT, Ph.D.[1]

[1]Department of Physical Therapy, University of Delaware, Newark, DE, United States. [2]Department of Kinesiology, University of Delaware, Newark, DE, United States. [3]Department of Physical Therapy, College of Allied Health Sciences, Kuwait University, Kuwait City, Capital Governorate, Kuwait. [4]Nemours Children's Health, Wilmington, DE, United States. [5]Department of Orthopedics, Alfred I. duPont Hospital for Children, Wilmington, DE, United States. [6]Division of Rehabilitation Medicine, Children's Hospital of Philadelphia, Philadelphia, PA, United States. [7]Department of Pediatrics, Perelman School of Medicine, University of Pennsylvania, Philadelphia, PA, United States

Introduction

Individuals with cerebral palsy (CP) have somatosensory deficits that contribute to balance impairments and postural challenges, leading to increased fall risk and poorer quality of life. Effective sensory-motor interventions may enhance somatosensory perception and balance. Stochastic Resonance (SR) electrical stimulation improves somatosensation, standing, and walking balance, predominantly in individuals with poorer sensory perception, by utilizing sub-sensory noise to elicit the detection of weak sensory input. While SR has shown promising results in improving balance during standing and walking in individuals with CP, its effect on more complex tasks, such as the Timed Up-and-Go test (TUG), is unknown. Thirty-five percent of falls in individuals with CP occur during walking-related activities such as turning and trunk bending, which are components of the TUG. We investigated the immediate effects of SR stimulation on TUG in individuals with CP.

Methods

Twenty individuals with spastic diplegic CP performed three trials of TUG each with and without SR stimulation. The optimal SR intensity was used to simultaneously stimulate the muscles and ligaments of the ankle and hip joints. We segmented the TUG into five phases, i.e., sit-to-walk, walk forward, turn, walk back, and turn-and-sit. The time taken to complete TUG and its phases was calculated. Paired-samples T-tests were performed to

evaluate changes in the time taken to complete the TUG and its phases in individuals with CP in response to SR.

Results

SR stimulation did not shorten the time it took to complete the TUG in individuals with CP. SR stimulation similarly did not affect the time required to complete any phase of the TUG in individuals with CP (**Table)**. Although TUG performance times did not significantly differ, all time measurements showed a slight increase with the use of SR.

Discussion

SR-enhanced somatosensory information may not be immediately utilized by the central nervous system to improve performance in more complex tasks. SR may not be effective to change performance, it may initially act as a distraction, or it may require training for individuals with CP to learn to use the enhanced sensory information to change their motor performance.

Images (Optional)

Table: Mean difference in total time taken to complete the Timed-Up-and-Go test (TUG) and its phases with the use of stochastic resonance electrical stimulation (SR) for individuals with cerebral palsy (CP). Significance is Bonferroni corrected to be at $p < 0.008$.

	No-SR Mean ± SD (s)	ΔSR Mean difference (s)	p-value
Sit-to-walk	2.55 ± 0.66	0.07	0.596
Walk-forward	5.73 ± 1.54	0.07	0.772
Turn	2.50 ± 0.57	0.01	0.844
Walk-back	5.12 ± 1.37	0.05	0.727
Turn-to-sit	4.50± 1.23	0.06	0.838
Total time	19.37 ± 4.29	0.14	0.781

* No-SR, without stimulation; ΔSR, Mean change in time with stochastic resonance stimulation; SD, standard deviation; s, seconds.

Session Category

Clinical Biomechanics: N/A

P4-190

Dynamic Visual Acuity in A Pediatric Population: Differences between Sexes

Dr. Kiara Barrett[1], Dr. Anastasia Kyvelidou[2], Dr. Kathryn Lucas[3], Dr. Kamran Barin[1]

[1]Bertec Corporation, Columbus, OH, United States. [2]Creighton University, Omaha, NE, United States. [3]Creighton University, Phoenix, AZ, United States

Introduction

The Dynamic Visual Acuity (DVA) test is a functional measure of the vestibulo-ocular (VOR) reflex that measures visual acuity during head movements. Although the DVA test is used routinely in adults, testing in children is less popular. Normative values have been established for children using the same optotypes used for adult testing [1], however pediatric-friendly optotypes have recently become available. Normal limits for such optotypes have yet to be reported. The purpose of this study is to determine the DVA normative values and compare sex differences in developing children using child-friendly optotypes.

Methods

39 participants (M=23, F=16) under the age of 18 were tested at two Creighton University campuses; characteristics are reported in Table 1. Computerized assessments were administered using the Bertec Vision Advantage system™. During testing, participants were asked to identify pediatric optotypes with the head at rest (baseline) and with the head moving horizontally at about 100°/s (dynamic). Passive instructor-led testing was performed if the participant was unable to maintain consistent head velocities independently. Trials with different optotype sizes continued until acuity thresholds were established. Responses were tabulated then statistically analyzed using a non-parametric Kruksal-Wallis test with an alpha level of .05.

Results

No significant differences were found between sexes in Baseline Visual Acuity (BLVA) (p=.076) or between right (p=.061) and left (p=.617) directions in DVA. Means and standard deviations for each group are provided in Table 1.

Discussion

This study provides normative pediatric values for the child-specific optotypes in the DVA test. The NIH toolbox reported an average DVA score of 0.116 for children aged 3-17 [1] using a “tumbling E” optotype, which is consistent with our results; however, no comparison of sexes was made. The lack of sex differences in our findings suggests early

development of the VOR is not influenced by this variable. Future research should investigate the impact of passive and active head movements in a pediatric population to determine if a disparity in methodology influences results.

Images (Optional)

Table 1. Participant Characteristics and DVA Results

Sex	Age (yr)	Height (m)	Weight (kg)	BLVA	DVAL	DVAR
Male	12 (4)	1.64 (0.21)	56.82 (20.32)	-0.076 (0.245)	0.073 (0.276)	0.035 (0.234)
Female	10 (3)	1.45 (0.19)	38.77 (13.95)	0.054 (0.181)	0.107 (0.236)	0.141 (0.175)

Note: All values are displayed as Mean (SD). BLVA: Baseline Visual Acuity (head at rest); DVAL: Dynamic Visual Acuity Left; DVAR: Dynamic Visual Acuity Right

References (Optional)

[1] Li *et al.*, Front. Neurology, 2014

Session Category

Clinical Biomechanics: N/A

P4-191

Evaluating MRI-Derived Predictors of Hamstring Strength in Facioscapulohumeral Muscular Dystrophy

Ms. Kimberly M. Steininger[1], Dr. Seth D. Friedman[2], Dr. Silvia S. Blemker[1]

[1]University of Virginia, Charlottesville, VA, United States. [2]Seattle Children's Hospital, Seattle, WA, United States

Introduction

Facioscapulohumeral muscular dystrophy (FSHD) causes progressive muscular degeneration and intramuscular fat infiltration, reducing force-generation capacity. Muscle force depends on structure and quality, but as the heterogeneous spatial distribution of fat in FSHD impacts muscle composition, this structure-function relationship is complicated. This study aims to evaluate which MRI-derived muscle features best predict knee-flexion strength from manual muscle testing (MMT) and whether changes in contractile volume (CV) influence functional decline independently of fat fraction (FF).

Methods

We analyzed longitudinal MRI and clinical manual muscle testing (MMT) data for the biceps femoris long head (BFLH), semimembranosus (SM), and semitendinosus (ST) in FSHD patients [n=11, 7, 6 at t=1, 2, 3yrs]. For each hamstring and as a group, we calculated total volume (TV) and CV, FF, mean and max cross-sectional area (CSA), and length. Log-Pearson correlations assessed associations between absolute and normalized CV and MMT, with p-values were corrected using Benjamini–Hochberg FDR. Random forest models ranked feature importance. Longitudinal changes were evaluated via within-subject deltas (Δ) of MRI features and side-matched ΔMMT using linear regression models adjusted for timepoint and clustered by subject. P-values were FDR-corrected.

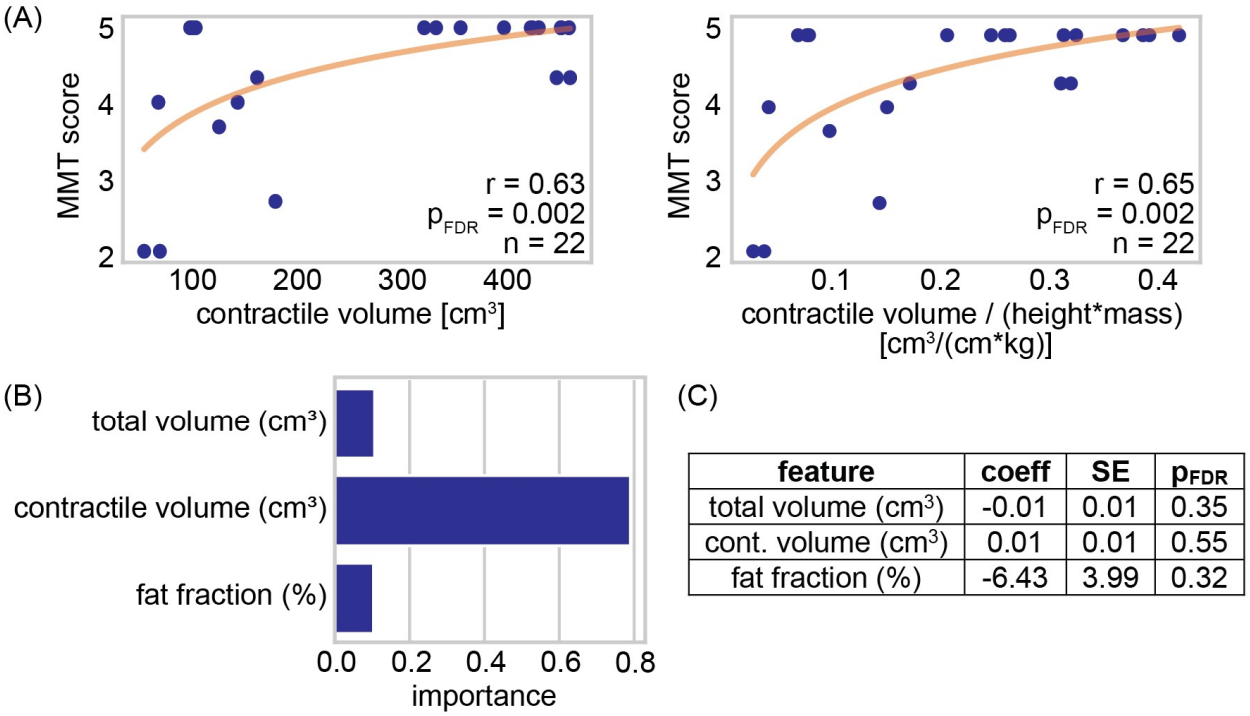
Results

Log-Pearson correlations revealed significant associations between CV and MMT scores at the first timepoint: r = 0.63, p_{FDR} = 0.0019 for abs(CV) and r = 0.65, p_{FDR} = 0.0019 for norm(CV), indicating modest improvements with normalization. Random forest models showed that CV (importance = 0.79) was the top predictor, followed by TV (0.11) and FF (0.10). Longitudinal Δ analyses indicated no MRI feature was significant after FDR correction: FF, −6.43 (3.99), p_{FDR}=0.32; TV, −0.0069 (0.0058), p_{FDR}=0.35; CV, 0.0046 (0.0076), p_{FDR}=0.55.

Discussion

Overall, CV emerged as the primary MRI determinant of strength, with secondary contributions from TV and FF. While longitudinal Δ associations were not significant, the direction of effects aligned with cross-sectional findings. Body-size normalized metrics modestly improve strength prediction and highlight CV as a key MRI biomarker. Future studies with larger cohorts are warranted to better characterize temporal relationships between MRI features and functional decline and inform objective outcome measures for FSHD clinical trials.

Images (Optional)



feature	coeff	SE	p_{FDR}
total volume (cm^3)	-0.01	0.01	0.35
cont. volume (cm^3)	0.01	0.01	0.55
fat fraction (%)	-6.43	3.99	0.32

(A) Log-Pearson correlations between absolute (left) and normalized (right) contractile volume and MMT score. (B) Random forest feature importance. (C) Longitudinal Δ analyses results, including coefficient, standard error (SE), and p_{FDR}.

References (Optional)

Session Category

Clinical Biomechanics: N/A

P4-192

Effect of Carbon Fiber Custom Dynamic Orthosis Cuff Design on Foot Loading During Gait With Unimpaired Individuals

Dr. Kirsten Anderson PhD, Ms. Molly Pacha MS, ATC, Dr. Jason Wilken PT, PhD

The University of Iowa, Iowa City, Iowa, United States

Introduction

Carbon fiber custom dynamic orthoses (CDOs) include a footplate, posterior strut, and cuff that wraps around the leg under the knee. The cuff is a primary interface between CDO and patient. CDOs reduce pain, improve quality of life, and alter foot loading during gait following lower limb trauma.[1-3] Multiple cuff designs are available for clinicians to choose from, based on their patient's needs. However, the effect of cuff design on foot loading is not well understood. This study was completed to determine the effects of cuff design on foot loading in a group of unimpaired individuals.

Methods

Activities were approved by the local institutional review board and participants provided informed consent. 15 individuals with no history of injury (9 Female, 25.5 (7.1)yrs, 1.7 (0.1)m, 73.0 (13.1)kg) participated. Loadsol insoles (novel electronics inc.) measured forces acting on the foot as participants walked at a controlled speed without a CDO (NoCDO) and with a CDO using four interchangeable cuffs (Figure 1; BOA, ChiScrew, AntShell, Flex) in a random order. Peak force and force-time integral (impulse) were calculated for the hindfoot and forefoot. One-way repeated measures ANOVAs were used to test for main effects of condition and post-hoc testing included paired sample t-tests and Wilcoxon signed rank tests with Bonferroni Holm correction.

Results

Peak forefoot force (43-45%) and impulse (32-36%) decreased significantly and hindfoot impulse (47-63%) increased significantly with CDO use compared to NoCDO. There were no significant differences between cuffs. Peak hindfoot force was not significantly different between conditions.

Discussion

Similar to previous work,[1-3] CDOs in this study significantly altered foot loading compared to NoCDO. The reductions in peak forefoot force and impulse, combined with the increased hindfoot impulse, indicate that forces are redistributed from the forefoot to the hindfoot within the CDO footplate. The lack of significant differences between cuffs

indicates that cuff design plays a limited role in foot loading and that clinicians can choose from multiple cuff designs to alter foot loading during gait.

Images (Optional)



BOA: Patellar tendon bearing design with mechanical ratcheting system



ChiScrew: Patellar tendon bearing design with fixed point and Velcro straps



AntShell: Anterior/ posterior shell with Velcro straps



Flex: Flexible cuff with anterior Velcro strap

References (Optional)

[1] Anderson, KM *et al*. Gait Posture, 2024.

[2] Anderson, KM *et al*. Gait Posture, 2025.

[3] Feng, J *et al*. Foot Ankle Orthop, 2023.

Acknowledgements (Optional)

This project was supported in part by the Department of Defense (Award No. W81XWH-22-1-0464) and by the National Center for Advancing Translational Sciences of the National Institutes of Health (Award Number UM1TR004403).

Session Category

Clinical Biomechanics: N/A

P4-193

EFFECT OF CUFF DESIGN ON HINDFOOT AND FOREFOOT LOADING DURING GAIT WITH CARBON FIBER CUSTOM DYNAMIC ORTHOSES IN INDIVIDUALS WITH ANKLE ARTHRITIS

Dr. Kirsten Anderson PhD, Ms. Molly Pacha MS, ATC, Dr. Jason Wilken PT, PhD

The University of Iowa, Iowa City, Iowa, United States

Introduction

Limb trauma often results in post-traumatic osteoarthritis (PTOA), leaving patients at risk for poor outcomes including weakness and pain with loading.[1] Carbon fiber custom dynamic orthoses (CDOs) alter foot loading, reduce pain, and address limitations associated with limb trauma and PTOA.[2-4] CDOs consist of a cuff below the knee, posterior strut, and footplate. Clinicians can choose between cuff designs to best meet the needs of their patients. However, the effect of cuff design on foot loading is not well documented. This study recruited individuals with ankle PTOA to determine the effects that cuff design has on foot loading during gait.

Methods

This study was institutional review board approved. 14 individuals with injury resulting in ankle PTOA (9 Female, 47.8 (12.3)yrs, 1.8 (0.1)m, 88.5 (21.8)kg) provided consent. Forces acting on the hindfoot and forefoot were measured using loadsol insoles (Novel Electronics Inc.). Peak force and force-time integral (impulse) were calculated as participants walked at a controlled speed without a CDO (NoCDO) then with a CDO using four interchangeable cuffs (Figure 1; AntShell, BOA, ChiScrew, Flex) in a randomized order. Main effects of condition were tested for using one-way repeated measures ANOVAs. Paired sample t-tests and Wilcoxon signed rank tests with Bonferroni Holm correction were completed for post-hoc analysis.

Results

Peak hindfoot force did not significantly differ between conditions. Hindfoot impulse significantly increased (39-50%) while peak forefoot force (32-34%) and impulse (19-22%) significantly decreased with CDO use compared to NoCDO. There were no significant differences between cuffs.

Discussion

Results indicate that all cuffs altered foot loading compared to NoCDO. Reductions in forefoot loading, combined with increased hindfoot impulse, indicate redistribution of

forces from the forefoot to hindfoot, which aligns with previous work.[2-3] There were no significant differences between cuffs, which indicates that cuff design plays a limited role in foot loading. This may allow clinicians to use multiple cuff designs to alter foot loading for individuals with ankle PTOA.

Images (Optional)



References (Optional)

[1] Anderson DD *et al*. JOR, 2024.

[2] Anderson, KM *et al*. Gait Posture, 2024.

[3] Anderson, KM *et al*. Gait Posture, 2025.

[4] Feng, J *et al*. Foot Ankle Orthop, 2023.

Acknowledgements (Optional)

This project was supported in part by the Department of Defense (Award No. W81XWH-22-1-0464) and by the National Center for Advancing Translational Sciences of the National Institutes of Health (Award Number UM1TR004403).

Session Category

Clinical Biomechanics: N/A

P4-194

Adaptations to Unilateral Dorsiflexor Fatigue in Walking

Mr John Kerr BEng, MSc[1,2], Dr Luca Modenese PhD[1], Dr Key Nahan BPodMed, MSc, PhD[3,1,2], Dr Lucy Armitage BAppSci, BEng, MBiomedE, PhD[1], Associate Professor Lauren Kark BE (Hons), MBiomedE, PhD[1], Dr Martin Héroux BSc PT, MSc, PhD[4], Dr Kirsty McDonald BSc (Hons), PhD[5,1,2]

[1]University of New South Wales, Sydney, NSW, Australia. [2]Neuroscience Research Australia, Sydney, NSW, Australia. [3]University of Massachusetts Amherst, Amherst, MA, United States. [4]University of Sydney, Sydney, NSW, Australia. [5]Edith Cowan University, Perth, WA, Australia

Introduction

Humans without pathology walk symmetrically in stable environments to improve energetics and stability [1, 2]. We aimed to determine whether symmetric gait is conserved under conditions of unilateral dorsiflexor fatigue, given the importance of local muscle effort in dictating gait strategy [3].

Methods

The study was approved by the University of New South Wales Human Research Ethics Committee. Able-bodied adults (8M/8F; age: 28.1±5.8 years; mass: 68.4±11.2kg; mean±SD) provided informed consent. Trunk and lower limb markers were tracked (200Hz; Bonita, Vicon) as participants walked on a split-belt instrumented treadmill (1000Hz; M-Gait, Motek Medical). They performed 30s of baseline unfatigued walking, followed by maximum voluntary contractions (MVCs) and a unilateral dorsiflexor fatiguing protocol involving isometric contractions. This led to a 30.5% [26.7, 34.2] (mean [95%CI]) reduction in MVC dorsiflexor torque. Participants then completed a 30s fatigued walk and another MVC. Linear mixed-effects models were developed for step time, step length, first and second peak vertical ground reaction force (vGRF), peak swing dorsiflexion angle and peak stance dorsiflexor moment, with trial (baseline, fatigued) and limb (unfatigued, fatigued) as fixed factors, and participant as a random intercept. MVC torque was compared using paired t-tests.

Results

Fatigue recovered slightly (2.7%) during the fatigued walk ($p=0.022$). Spatiotemporal parameters showed no interaction effect ($p\geq0.602$), and main effects of trial (step time: $p=0.015$; step length: $p=0.049$) but not limb ($p\geq0.09$), indicating symmetry was conserved despite bilateral gait adaptations. First and second vGRF peaks showed no trial, limb, or

interaction effects ($p \geq 0.051$). Peak dorsiflexor moment asymmetries existed (limb effect: $p=0.012$) and persisted between baseline and fatigued trials (interaction effect: $p=0.220$; trial effect: $p=0.045$). Peak dorsiflexion angle showed an interaction effect ($p=0.025$), as the only variable asymmetrically altered.

Discussion

These findings suggest that while minor (<2°) kinematic changes occurred in the fatigued limb, high-level symmetry was maintained, possibly prioritising energetic/stability benefits over asymmetric offloading. This contrasts with recent experimental work suggesting fatigue (or local muscle effort) minimisation represents a principal locomotor objective [3].

References (Optional)

[1] Ellis, R. *et al.*, Proc. B., 2013

[2] Hill, A., & Nantel, J. PLOS ONE, 2019

[3] McDonald *et al.*, Proc. B., 2022

Session Category

Clinical Biomechanics: N/A

P4-195

Effective Body Stiffness Estimation During Falls Using a Customized Hand-Held Indentation Device for Hip Fracture Risk Prediction

Dr. Kitaek Lim PT, PhD, Ms. Soyeon Yoon PT, Mr. Junwoo Park PT, MSc, Dr. Seyoung Lee PT, PhD, Mr. Sungmin Chun PT, Mr. Donggeon Kim PT, Prof. Woochol Joseph Choi PT, PhD

Injury Prevention and Biomechanics Laboratory, Dept of Physical Therapy, Yonsei University, Wonju, Gangwon, Korea, Republic of

Introduction

Hip fracture risk is defined as a ratio of hip impact force to femoral strength, where the impact force (F) is given by $F = v*(m*k)\text{^}(1/2)$, with v denoting impact velocity, m effective body mass, and k effective body stiffness [1]. If k can be readily estimated, an individual's hip fracture risk during a fall can be predicted easily. To estimate the k at impact, we developed a customized hand-held indentation device designed to measure the trochanteric soft tissue stiffness.

Methods

Nine young adults mimicked older adults' falls, with different landing configurations (Figure 1a). Impact force was measured with a force plate underneath the mat, and pelvic deformation was tracked with a motion capture system. Effective body stiffness (k_b) was calculated from total stiffness (k_t) and mat stiffness (k_m) using a series spring model ($1/k_b = 1/k_t - 1/k_m$). A customized hand-held indentation device was also used to record force and deformation data under cyclic forces (>100 N) at 30 and 60 cycles per minute. Then, trochanteric soft tissue stiffness was determined as the tangent slope at maximum deformation from first and second order polynomial and exponential fits (k_{sc_30}, k_{sc_60}), and also measured with a MyotonPro (k_{sm}), which were normalized by body weight and trochanteric soft tissue thickness [2]. Linear regression analyses were used to predict k_b with trochanteric soft tissue stiffness.

Results

Descriptive statistics are summarized in Table 1. Correlation analysis indicated that normalized k_b in the knee-on-mat configuration was associated with normalized k_{sc_30} derived from both first and second order fits ($p < 0.05$). Furthermore, linear regression analysis suggested that the normalized k_b decreased 2041.9 and 777.9 for every

increase in k_{sc_30} derived from both first and second order fits, respectively (Figure 2). However, no significant correlations were found for other variables ($p > 0.05$).

Discussion

Our results suggest that the effective body stiffness can be predicted with trochanteric soft tissue stiffness measured by the customized hand-held indentation device, suggesting its potential for hip fracture risk assessment without complex laboratory experiments.

Images (Optional)

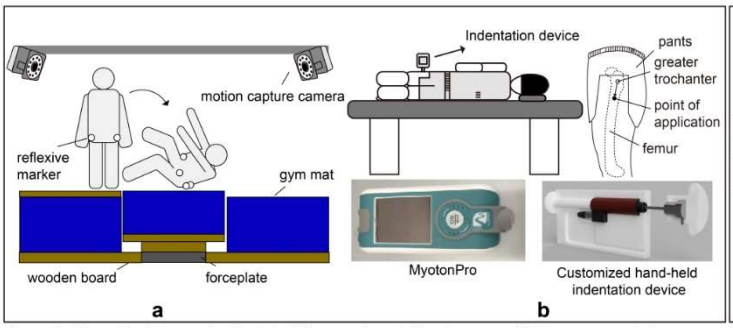


Figure 1. Schematic diagrams showing (a) a falling experiment with a human, and b) a measurement of trochanteric soft tissue stiffness and two indentation devices

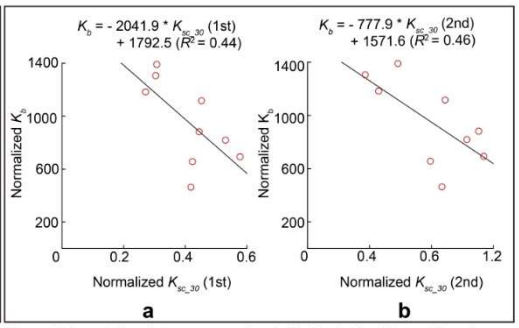


Figure 2. Associations between normalized effective body stiffness (K_b) and normalized trochanteric soft tissue stiffness derived from the customized hand-held indentation device at 30 bpm (K_{sc_30}) using (a) a first-order polynomial fit and (b) a second-order polynomial fit.

Table 1. Average stiffness values with SD shown in parentheses for all 9 participants

Subject ID	Gender	Body weight (kg)	Body height (m)	Trochanteric soft tissue thickness (mm)	Trochanteric soft tissue stiffness (kN/m)							Body stiffness (kN/m)			
					k_{im}	k_{sc_30}			k_{sc_60}						
						Linear	Quad	Exp	Linear	Quad	Exp	Knee-on -mat	Knee -together	Knee-free	Mean
1	Male	62.8	1.7	13.1	0.3 (0)	24.96 (6.76)	48.4 (6.16)	59.85 (16.09)	14.77 (0.35)	23.69 (5.66)	24.58 (6.64)	38.49 (7.63)	69.87 (37.25)	68.35 (38.56)	58.91 (17.69)
2	Male	86.7	1.8	24	0.35 (0.01)	10.78 (1.17)	13.21 (6.76)	15.25 (7.23)	11.85 (0.64)	19.05 (6.71)	21.19 (8.53)	46.28 (3.93)	155.75 (146.66)	88.8 (33.98)	96.94 (55.19)
3	Female	59.7	1.63	26.5	0.27 (0)	9.25 (1.62)	19.20 (4.15)	22.09 (4.93)	8.80 (3.17)	21.44 (12.98)	27.76 (19.79)	10.25 (1.12)	25.17 (4.11)	24.26 (6.89)	19.89 (8.36)
4	Male	70.8	1.65	33.4	0.29 (0)	8.81 (0.28)	16.51 (1.10)	18.46 (2.28)	10.85 (0.72)	10.8 (4.61)	12.82 (2.65)	13.65 (2.79)	22.77 (9.11)	30.35 (4.11)	22.26 (8.36)
5	Male	80.2	1.7	42.2	0.34 (0.01)	8.45 (0.61)	16.57 (0.2)	19.19 (0.9)	6.98 (0.06)	11.14 (0.73)	11.83 (0.94)	20.82 (13.89)	28.29 (8.04)	22.02 (3.28)	23.71 (4.01)
6	Male	90.7	1.82	40.3	0.28 (0.01)	6.8 (0.19)	12.89 (1.02)	14.76 (2.07)	5.36 (0.19)	9.66 (0.77)	10.47 (1.27)	30.7 (13.81)	268.71 (0)	73.18 (16.73)	124.2 (126.94)
7	Male	74.1	1.67	40	0.26 (0.01)	8.09 (0.71)	20.1 (0.63)	26.27 (3.47)	7.52 (0.77)	11.02 (5.57)	12.5 (6.26)	16.03 (2.99)	113.22 (72.4)	146.36 (76.37)	91.87 (67.74)
8	Male	89	1.77	37	0.29 (0)	6.41 (0.29)	10.85 (0.47)	11.58 (0.42)	9.31 (0.64)	14.92 (1.35)	15.69 (2.19)	27.93 (5.43)	120.7 (93.6)	64.93 (39.44)	71.19 (46.7)
9	Male	66.7	1.68	37.1	0.34 (0.01)	10.19 (1.17)	20.08 (2.16)	22.25 (2.99)	4.18 (0.37)	6.97 (0.5)	7.6 (0.83)	12.23 (2.12)	25.01 (0.96)	14.59 (4.78)	17.27 (6.8)
Mean		75.63	1.71	32.6	0.3	10.42	19.76	23.3	8.85	14.3	16.05	24.04	92.17	59.2	58.47
SD		11.58	0.07	0.96	0.03	5.64	11.24	14.42	3.31	5.81	6.89	12.62	82.81	42.15	39.97

References (Optional)

[1] Robinovitch et al., *Osteoporos Int, 2009*. [2] Lim et al., *J. App. Biomech, 2025*.

Acknowledgements (Optional)

This research was supported by Basic Science Research Program (RS-2023-00270689) and by the Brain Korea 21 FOUR Project" (F21SH8303039) and the National Research Foundation of Korea (NRF) grant funded by the Korea government (MSIT) (RS-2025-16071808), and by the Regional Innovation System & Education (RISE) program through the Gangwon RISE Center, funded by the Ministry of Education (MOE) and the Gangwon State (G.S.), Republic of Korea (2025-RISE-10–006).

Session Category

Clinical Biomechanics: N/A

P4-196

Acute Effects of Reactive Agility Training on ACL injury Risk Factors in Collegiate and Recreational Athletes

Dr Kristamarie Pratt PhD, Mr Wesley Johnson DPT, Mr Daniel Reynolds DPT, Mr Noah Ackerman DPT, Ms Julia Chapell DPT, Ms Lindsay Coffey DPT, Ms. Ashlyn Tavares DPT, Ms Victoria Jedrychowski DPT, Ms Amanda Warner DPT, Ms Aarohi Patel DPT

University of Hartford, West Hartford, CT, United States

Introduction

Collegiate and recreational athletes participating in sports involving reactive movements like defense cutting and sudden directional changes are susceptible to ACL-injuries. Contributing risk factors include lower neurocognitive function leading to poor knee and hip biomechanics. Research has shown that reactivity agility training (RAT) drills have notable improvements on overall performance of cutting mechanics and deceleration during game time decisions for athletes. Acute effects of RAT drills on risk factors are unknown; therefore, the purpose is to investigate the real time effects of RAT drills, ultimately providing valuable insights into how RAT drills can reduce ACL-injury risk.

Methods

18 recreational or collegiate athletes (10 offensive/10 defensive) over 18 years old with no current injuries were tested. 3D motion capture data and forces were collected during pre-training and post-training test sessions which involved an unanticipated 45° cuts on both left and right limbs; Participants completed an acute bout of RAT using a Mirror Drill in between testing sessions. Knee and hip kinematics and kinetics were recorded and calculated.

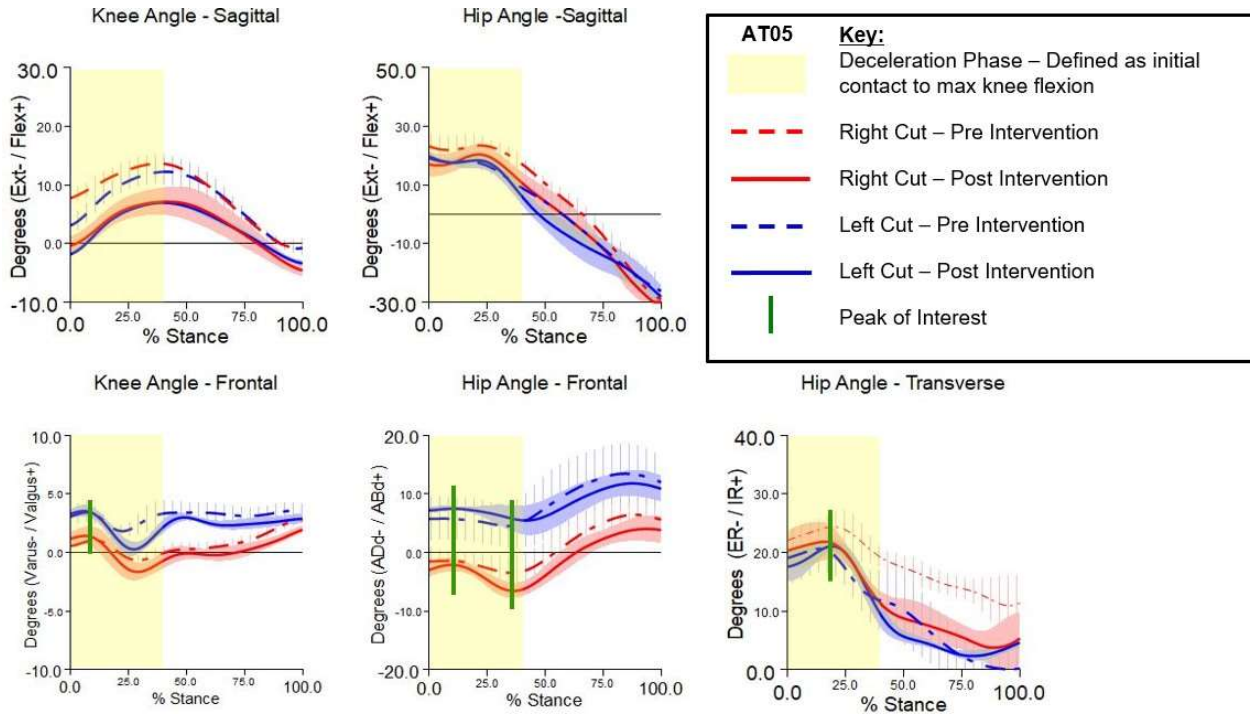
Results

Initial findings indicate athletes performed cutting with greater knee and hip flexion following an acute bout of RAT. We anticipate improvements in ACL injury risk factors for defensive player between pre-drill testing and post-drill testing, suggesting that use of reactive agility drills as a pregame warm up can reduce risk factors related to in game injuries. This result will be further supported if there is no significant change observed in offensive players ACL injury risk factors. We also expect to find a greater statistical change in ACL injury risk factors of recreational athletes compared with collegiate athletes.

Discussion

Understanding acute effects of RAT may reduce ACL-injury risk factors. Coaches, and clinicians could benefit from incorporating such functional drills into warm-up routines pre-game or pre-practice, potentially offering a more effective approach than traditional drills. Although further analysis is warranted to validate these anticipated findings, stage for a potential breakthrough in ACL-injury prevention strategies for athletes.

Images (Optional)



References (Optional)

Porter et al., J Sci Med Sport 2022

Mijatovic et al. Healthcare 2022

Boden et al., Orthop 2021

Session Category

Clinical Biomechanics: N/A

P4-197

Relating Head Impacts to Pupillary Light Reflex Metrics and Symptom Reporting in Collegiate Rugby Players

Ms. Lauren Duma, Dr. Nicole Stark, Dr. Steve Rowson

Virginia Tech, Blacksburg, VA, United States

Introduction

Concussions are a common sports-related injury, and athletes in contact sports will also sustain several subconcussive head impacts throughout their career. Previously, studies have observed measurable changes in the pupillary light reflex (PLR) in response to concussion [1]. The objective of this study was to relate changes in PLR metrics and symptom reporting to subconcussive head impacts experienced throughout a semester of collegiate rugby games.

Methods

Twenty-one male collegiate rugby players were observed during seven 15s rugby games across a semester. Before and after each game, players completed a symptom survey and PLR measurement. The total number of reported symptoms and the Symptom Severity Score (SSS), the sum of all symptom ratings, were calculated for each survey. Pupil measurements were taken with a PLR-4000 pupillometer (NeurOptics). Players wore instrumented mouthguards (Prevent Biometrics) during each game, and the recorded head impacts were video-verified. For each player, the number of head impacts sustained in each game was counted, and the change in SSS, number of symptoms, and PLR metrics were calculated by subtracting baseline measurements from post-game measurements.

Results

Data collection and analysis is ongoing. Preliminary results show no correlation between the number of head impacts sustained in a game and change in SSS, number of symptoms, or any PLR metric (SSS: $r^2 = 0.02$, $p = 0.24$; Number of symptoms: $r^2 = 0.02$, $p = 0.22$; Average constriction velocity: $r^2 = 0.01$, $p = 0.32$; Average dilation velocity: $r^2 = 0.14$, $p < 0.01$). Further, there is no significant correlation between change in SSS and change in any PLR metric (Average constriction velocity: $r^2 = 0.02$, $p = 0.21$; Average dilation velocity: $r^2 = 0.01$, $p = 0.30$).

Discussion

In this study, we assessed the ability of the PLR to quantify the effects of repetitive subconcussive head impacts. Preliminary results show that the head impacts experienced

throughout this study were likely not severe enough to result in measurable changes in the PLR as observed in previous studies with concussed athletes. Future directions include relating head impact severity to PLR changes and including women's rugby players.

References (Optional)

[1] Christina L. Master *et al.*, JAMA Ophthalmology, 2020

Session Category

Clinical Biomechanics: N/A

P4-198

Association of Intramuscular Fat Fraction with Knee Extensor Strength in Adults with Clinical Knee Osteoarthritis

Postdoctoral Fellow Lauren Straatman PhD[1], Postdoctoral Fellow Anthony A. Gatti PhD[2], Postdoctoral Fellow Jacquelyn M. Coyne PhD[1,3], Lab Tech Braeden Cowbrough[4], Postdoctoral Fellow Kendal A. Marriott PT, PhD[1], PhD Student Natasha I. Ivanochko MSc[1], Lab Coordinator Emily Wiebenga[1], Professor Dawn E. Bowdish PhD[4], Professor Marina Mourtzakis PhD[1], Professor Monica R. Maly PT, PhD[1]

[1]University of Waterloo, Waterloo, ON, Canada. [2]Stanford University, Palo Alto, CA, United States. [3]Waterloo Regional Health Network, Waterloo, ON, Canada. [4]McMaster University, Hamilton, ON, Canada

Introduction

Quadriceps weakness is a hallmark of knee osteoarthritis (KOA). While lean muscle loss contributes to weakness, accumulating evidence suggests adiposity, a metabolically active tissue, may further impair muscle function through inflammatory mechanisms [1]. In parallel, anti-inflammatory cytokines have a protective influence on muscle strength in females with KOA [2]. The purpose of this study was to determine if serum inflammatory cytokines mediate the association between quadriceps and adipose tissue volumes with knee extensor strength in adults with clinical KOA.

Methods

Forty participants (20 male-female pairs matched on age (± 3 years) and BMI (±3 kg/m^2)) with clinical KOA were included. The most symptomatic limb was examined. Knee extensor strength was the average peak torque from five maximal voluntary isometric contractions measured using an isometric dynamometer (Biodex System 4). Thigh MRIs were captured using the IDEAL sequence on a 3T magnetic resonance imaging scanner, auto-segmented using an open-source program [3], and manually edited in 3D Slicer for total volumes of quadriceps intramuscular fat (IMAT), and quadriceps lean tissue (QV). Fat fraction was calculated as IMAT divided by QV. Fasting venous blood samples were collected after 30-minutes of rest to assess C-reactive protein (CRP, proinflammatory) and interleukin-10 (IL10, anti-inflammatory). Hierarchical linear regression models assessed direct associations between tissue volumes with knee extensor strength (adjusting for age, sex, and step count); followed by mediation analyses with CRP and IL10 in separate models.

Results

After adjusting for covariates, greater fat fraction associated with lower knee extensor strength ($t = -2.21$, $p = 0.03$); and larger QV associated with greater knee extensor strength ($t = 3.7$, $p < 0.001$). Inflammatory cytokines did not mediate these associations.

Discussion

In clinical knee OA, serum cytokines did not mediate associations between thigh tissue volumes with knee extensor strength. However, quadriceps fat fraction and QV associated with lesser and greater knee extensor strength respectively, highlighting the importance of both muscle quality and quantity in knee strength. This work complements existing data showing quadriceps fat fraction associated with self-reported disability [4].

Images (Optional)

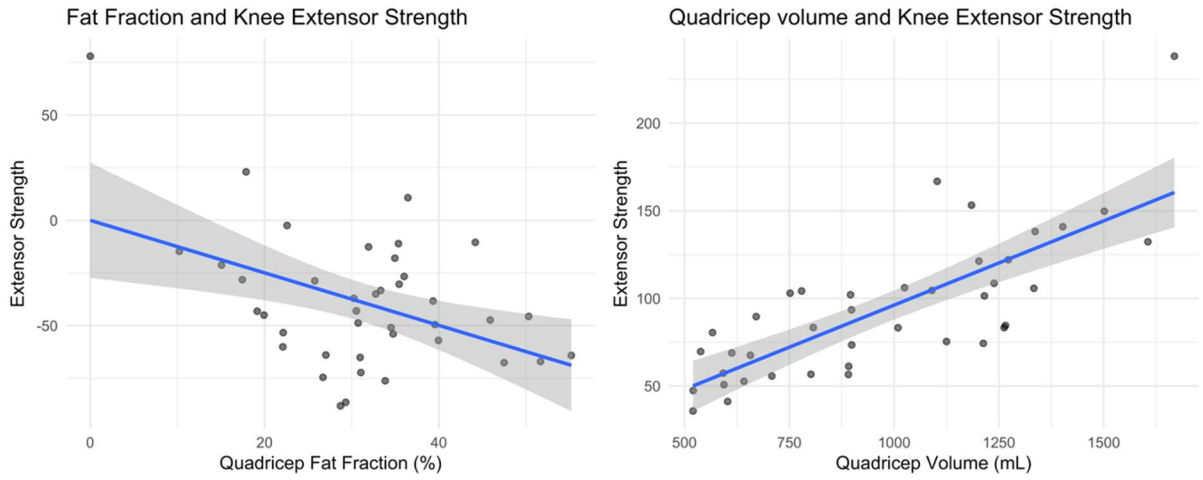


Figure 1. Associations of fat fraction (left) and quadriceps lean mass volume (right) with knee extensor strength.

References (Optional)

[1] Tuttle, J Aging Research Reviews, 2020, [2] Straatman, J Clinical Biomechanics, 2025, [3] McKay, J Imaging, 2024, [4] Kumar, Osteoarthritis and Cartilage, 2014.

Acknowledgements (Optional)

Arthritis Society Canada Training Postdoctoral Fellowship (TPF #21-39)

Session Category

Clinical Biomechanics: N/A

P4-200

Unique Frontal Plane Gait Biomechanical Features in Lateral Knee Osteoarthritis

Dr. Kendal Marriott PT PhD, Dr. Erin Lee PhD, Mrs. Emily Wiebenga BSc, Dr. Monica Maly PT PhD, Leah Williams

University of Waterloo, Waterloo, Ontario, Canada

Introduction

Knee osteoarthritis (OA) affects the medial tibiofemoral compartment most often. OA that primarily affects the lateral compartment may reflect unique biomechanical features, but little is known. The purpose of this study was to compare hip and knee angles and moments between medial and lateral tibiofemoral OA and between sexes.

Methods

Baseline data from a longitudinal study of clinical knee OA were used. Participants completed gait analyses and knee radiographs. Biomechanical features measured included peak knee (adduction, flexion) and hip (adduction) moments and knee (adduction) and hip (adduction) angles. Standing radiographs were acquired in a standardized position. From these radiographs, joint space in the medial and lateral compartments was assessed separately using the Osteoarthritis Research Society International (OARSI) atlas; with greater joint space narrowing defining the primary OA compartment (medial or lateral). Those with equal narrowing in the medial and lateral compartments were excluded from analyses. For each of the five peak biomechanical features, a two-way (OA compartment, sex, OA compartment × sex) ANCOVA (covariates: age, BMI) was completed.

Results

Data from 92 participants (age=65.4 years, body mass index (BMI)=29.0 kg/m^2, females/males=61/31) were used. For each biomechanical feature, there was no interaction (OA compartment × sex). For both the peak knee adduction moment and peak knee adduction angle, there were main effects for OA compartment ($F=31.44$, $p<0.001$ and $F=6.59$, $p<0.02$, respectively) and sex ($F=14.87$, $p<0.001$ and $F=9.95$, $p<0.003$), with those with medial compartment disease and males demonstrating higher peak knee adduction moments and angles. For the peak hip adduction angle, there were main effects for OA compartment ($F=14.91$, $p<0.001$) and sex ($F=13.11$, $p<0.001$), with those with lateral compartment disease and females demonstrating higher peak hip adduction angle. For both the peak knee flexion moment and peak hip adduction moment, there were no main effects.

Discussion

In lateral OA, the pattern of peak knee moments and peak knee and hip angles in the frontal plane reflect greater mechanical loading of the lateral tibiofemoral compartment; and higher moments in males compared to females. These differences in frontal plane gait biomechanics may indicate different underlying biomechanical mechanisms for lateral versus medial knee OA.

Images (Optional)

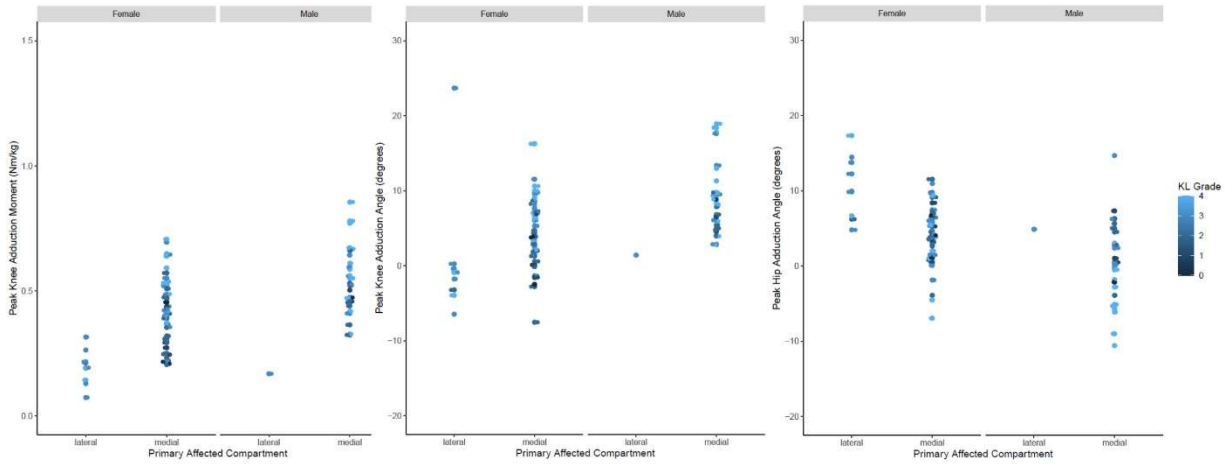


Figure 1. Distribution of peak values for knee adduction moment (Nm/kg), knee adduction angle (degrees) and hip adduction angle (degrees) across primary compartment affected by osteoarthritis (medial versus lateral) and across sex (female versus male). Osteoarthritis severity is represented by Kellgren-Lawrence (KL) grade with darker blue indicating greater disease severity (ranging from 0-4).

Acknowledgements (Optional)

Arthritis Society Canada Training Postdoctoral Fellowships (TPF 21-39, TPF 24-117), Canadian Institutes of Heath Research (CIHR) Fellowship.

Session Category

Clinical Biomechanics: N/A

P4-201

Markerless Motion Capture Hardware for Biomechanical Assessment in Compact Clinical Spaces

Dr. Ryan Rykhus PhD, Dr. Lisa MacFadden PhD

University of South Dakota, Sioux Falls, SD, United States

Introduction

Quantifying human movement through biomechanical assessments provides objective metrics for evaluating rehabilitation progress and assessing functional movements of patients. Traditional motion capture systems provide accurate results but have significant barriers that limit clinical integration, including high costs, space requirements, and time required to perform assessments. Recent advances in markerless motion capture methods have reduced some barriers but have yet to address all three simultaneously. Despite these advances, there remains no clinical movement assessment tool that fits into the small spaces present in existing healthcare settings.

This study presents CloseCap, a markerless motion capture system designed to enable motion capture close to the participant by integrating wide field-of-view (FOV) cameras into a calibration-driven 3D reconstruction workflow. The objective was to evaluate the feasibility of performing gait assessments in compact clinical environments while maintaining clinically interpretable kinematics.

Methods

CloseCap uses low-cost, synchronized, wide field-of-view, global-shutter cameras mounted with fixed relative geometry to enable 3D reconstruction at close proximity (approximately 1m). Camera calibration was performed using distortion-aware methods optimized for wide-angle lenses. Using Facebook Research's Sapiens pose estimation algorithm, 2D body keypoints were identified us and triangulated into 3D coordinates.

The performance of CloseCap was assessed against OpenCap using thirty simultaneously recorded treadmill walking trials for two participants. Kinematics for both methods were computed using an OpenSim inverse kinematics pipeline, and lower-limb joint angles were compared. This study was deemed not human subject research by IRB.

Results

CloseCap successfully captured full-body gait data within a substantially reduced spatial footprint. Wide FOV imaging ensured consistent visibility of lower-limb landmarks at close range, and calibration-based distortion modeling supported stable 3D triangulation.

Comparisons revealed mean joint-angle differences of 6-8 degrees, depending on the joint measured. Despite higher-than-expected differences, kinematic trajectories were temporally consistent for gait analysis.

Discussion

These results demonstrate clinical movement assessments can be performed in spaces much smaller than previously possible by prioritizing wide FOV imaging and calibration-driven processing. Although joint-angle differences exceed commonly cited benchmarks, CloseCap produces clinically interpretable kinematics in environments where traditional motion capture is infeasible. Future work will focus on formal validation, repeatability, and expansion to additional movements and clinical populations.

Session Category

Clinical Biomechanics: N/A

P4-202

The Effect of an Integrated Personalized Multimodal Intervention on Footwear Adherence and Cumulative Mechanical Stress in People With Diabetes at High Foot Ulcer Risk: A Multicenter Randomized Controlled Trial (DIASSIST)

Ir. Lisa Vossen[1,2], Dr. Jaap van Netten[1,2], Dr. Chantal Hulshof[1,2], Drs. Natasja Jelsma[3], Drs. Anne Slootman[4], Dr. Maarten Merkx[5,6], Prof. Dr. Sicco Bus[1,2]

[1]Department of Rehabilitation Medicine, Amsterdam UMC, University of Amsterdam, Amsterdam, Amsterdam, Netherlands. [2]Amsterdam Movement Sciences, Rehabilitation & Development, Amsterdam, Amsterdam, Netherlands. [3]Department of Rehabilitation Medicine, Red Cross Hospital/Heliomare, Beverwijk, Beverwijk, Netherlands. [4]Department of Rehabilitation Medicine, Spaarne Gasthuis, Hoofddorp, Hoofddorp, Netherlands. [5]Department of Clinical and Development Psychology, University of Amsterdam, Amsterdam, Amsterdam, Netherlands. [6]Mental Care Group, Woerden, Woerden, Netherlands

Introduction

Pressure-optimized custom-made footwear helps prevent foot ulcer recurrence in people with diabetes. This footwear protects the foot from high mechanical loads, by redistributing pressure underneath the foot. Adherence to wearing such footwear is essential for its biomechanical function to affect clinical outcome, yet is often too low. There is limited evidence for adherence-improving interventions. We assessed the effectiveness of an integrated personalized multimodal intervention on footwear adherence in people with diabetes at high risk of ulceration, aiming to reduce cumulative mechanical stress on the foot.

Methods

In a multicenter randomized controlled trial, we randomized 126 participants with diabetes, peripheral neuropathy, ulcer history and custom-made footwear to usual care or enhanced treatment. Enhanced treatment consisted of pressure-optimized custom-made footwear, provision of pressure-optimized indoor-specific custom-made footwear, foot temperature monitoring, structured education, and motivational interviewing including personalized feedback. The primary outcome was adherence, calculated as percentage of steps wearing prescribed footwear, and objectively measured using a temperature sensor in the shoe and a physical activity monitor. Adherence was measured at baseline (before intervention), at 6 and 12-months follow-up, and statistically tested using a linear mixed model. Secondary outcomes included objectively measured wearing time in hours/day,

compared before and after study events, and cumulative mechanical stress, statistically tested using (paired) t-tests.

Results

Adherence to wearing custom-made footwear was significantly higher in enhanced treatment compared to usual care (75% (SD:10) vs 56% (SD:22) at 6 months, and 58% (SD:18) vs 49% (SD:20) at 12 months, $p<0.001$), with a relative improvement of 34% at 6 months (Fig.1). Wearing time was significantly increased after the provision of indoor-specific footwear (mean 7.7 to 9.4 hours/day, $p<0.001$), and structured education (mean 7.8 to 8.2 hours/day, $p=0.049$). Cumulative mechanical stress results will be presented at WCB.

Discussion

An integrated personalized multimodal intervention significantly increased footwear adherence compared to usual care. This increased adherence in combination with pressure-optimized footwear will likely lead to decreased cumulative mechanical loads underneath the foot, currently investigated as a secondary analysis of the trial and expected to finish in due time. The results support emphasizing indoor-specific footwear and structured education in foot care, as adherence-improving interventions.

Images (Optional)

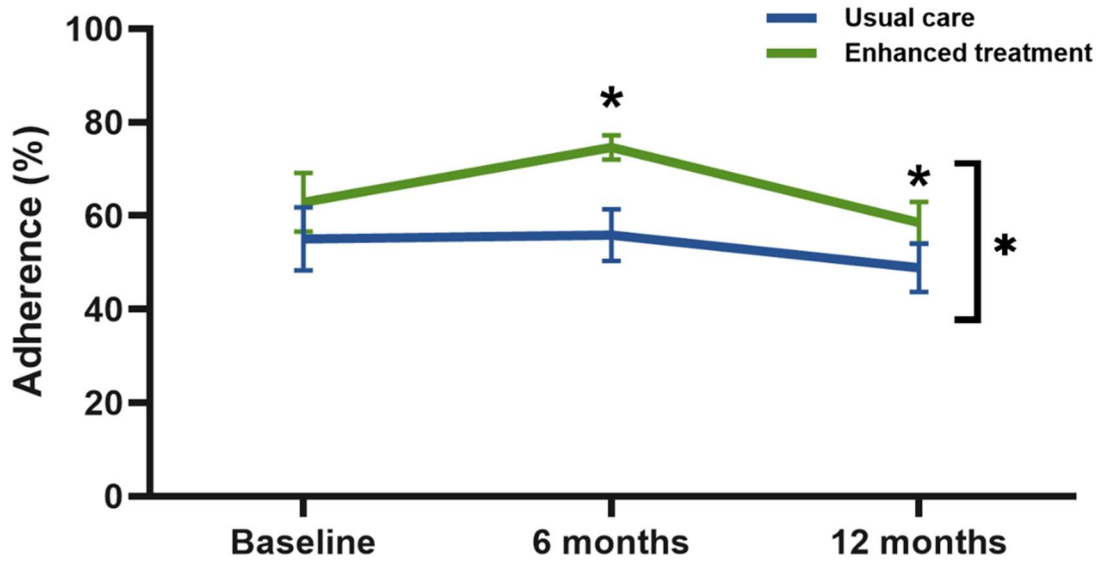


Fig.1: Adherence over the study period for usual care (blue) and enhanced treatment (green), measured at baseline (before intervention), and at 6 and 12 months after start of the multimodal intervention. Asterisks indicate significant differences between groups ($p<0.05$).

Session Category

Clinical Biomechanics: N/A

P4-203

A Dynamical Model of the Pendulum Test in Stroke Patients with Quadriceps Spasticity: Parameter Identification and Correlation with Clinical Scales

Prof. Luciano Menegaldo[1], Dr. Joeana Withers[2], Dr. Veronica Silva[2], Dr. Carla Rinaldin[2], Prof. Maria Isabel Orselli[3], Prof. Elisângela Manffra[2]

[1]Universidade Federal do Rio de Janeiro, Rio de Janeiro, RJ, Brazil. [2]PUC-PR, Curitiba, PR, Brazil. [3]Faculdade Israelita de Ciências da Saúde Albert Einstein, São Paulo, SP, Brazil

Introduction

Stroke often leads to muscle spasticity, characterized by velocity-dependent resistance to stretch beyond a specific threshold. The pendulum test is a simple assessment for monitoring spasticity. This study proposes a model for the knee pendulum test that incorporates nonlinear rotational springs and dampers. Model parameters were identified from kinematics of stroke patients. We hypothesized that parameters correlating with clinical scales could serve as biomarkers for spasticity.

Methods

Ten individuals with post-stroke quadriceps spasticity (51.6 ± 15.9 years; 65.9 ± 10.1 kg; 163.5 ± 8.7 cm) participated. The protocol was approved by the PUC-PR Ethics Committee. Participants underwent the Timed Up and Go test (TUG), the Modified Ashworth Scale (MAS), and the Fugl–Meyer Assessment (FMA). They performed two pendulum tests while seated on a chair, ensuring 70° hip flexion. Knee kinematics were recorded with a Vicon system.

Segment inertia was computed using regression equations. The model incorporated elastic and damping torque actuators for flexion and extension. Elastic torques used an inverse-logit formulation with parameters for maximum torque, stiffness, and threshold angle. Velocity-dependent damping was defined as the product of a damping coefficient and the normalized inverse-logit term. A linear damper acting throughout the motion simulated passive soft-tissue effects. Nine parameters were estimated.

Hybrid constrained optimization (particle swarm followed by *fmincon*) in MATLAB identified parameters by minimizing the L2 error between measured and simulated absolute leg angles. Pearson correlations were computed between parameters, clinical scales and years since stroke.

Results

For seven participants, simulations matched measured angles with a mean error of 1.9 ± 1.1°. But the model failed to reproduce kinematics for three participants, who were excluded from the analysis. Significant correlations ($p < 0.05$) between model parameters and clinical measures are shown in Table 1.

Discussion

The proposed model successfully represented the kinematics of pendulum tests in most participants. Poor fits in three cases may reflect experimental inconsistencies or patient-specific neuromuscular characteristics not captured by the model. Preliminary findings suggest that higher reflex extension stiffness and damping are associated with better clinical status, whereas increased maximum flexion torque and reflex stiffness may reflect worse impairment. Larger samples are required to validate these trends.

Images (Optional)

Table 1 – Significant ($p<0.05$) Pearson correlation between identified model's parameters and clinical scales. C – whole joint span damping; K_E – Extensors reflex stiffness; Tor_E – maximum reflex torque; Tor_F – maximum reflex flexor torque, θ_E – extensors' reflex threshold angle; θ_F-flexors' reflex threshold angle; C_E – extensors' reflex damping; K_F – flexors' reflex stiffness; TUG - Timed Up and Go Test; MAS - Modified Ashworth Scale; FMA - Fugl-Meyer Assessment. Years – years of disease at the test; (-) – not significant correlation.

variable	C	K_E	Tor_E	Tor_F	θ_E	θ_F	C_E	K_F
FMA	-0.77	-	-	-	-	-	0.58	-
TUG	-	-0.65	-	-	-	-	-	0.63
MAS	-	-0.73	-	0.64	-	-	-0.76	-
Years	-	-	-0.64	-	-0.59	-	-	-

References (Optional)

Acknowledgements (Optional)

The authors thank the financial support from CNPq, CAPES, FINEP, and FAPERJ.

Session Category

Clinical Biomechanics: N/A

P4-204

Numerical Analysis of the Biomechanical Behavior of Patient-Individual Root Analogue Implants Compared With Conventional Threaded Dental Implants

Dr. Ludger Keilig, Ms. Farah Al-Obaidi, Dr. Mostafa Aldesoki, PD Dr. Istabrak Dörsam, Prof. Dr. Christoph Bourauel

Oral Technology, Medical Faculty, University of Bonn, Bonn, NRW, Germany

Introduction

Single tooth replacements with conventional threaded dental implants (CI) cannot be in inserted directly into the empty alveolus, but require a sufficiently solid bony anchorage. Root analogue implants (RAI), which mimics the shape of the root of the lost teeth, may offer an alternative if the alveolus is still intact. We investigated the biomechanical behavior of both implant types at different positions in both jaws, compare them with each other and with the natural dentition.

Methods

CT scan of a jaw with full dentition and healthy bone was used as modelling basis. Further models were generated where selected teeth were replaced by implants (one incisor, canine, premolar, molar each in the upper and lower jaw). For the CIs we filled the alveolus with spongious bone, covered with thin layers of cortical bone. RAIs were modelled from the original geometry of the alveolus, removing undercuts that might hinder the insertion. A central node on each natural crown was identified, transferred to the corresponding model with an implant, and connected to that implant using a rigid body element. Each natural tooth and each implant was then loaded separately at this node with forces between 130 N (incisor) and 500 N (molar) in vertical direction.

Results

Displacements at the loaded node differed between the implant types (e.g. at the upper canine 0.03 mm and 0.02 mm for CI and the RAI, respectively; and 0.11 mm and 0.05 mm for the same implants in the lower jaw). This was lower than the movement of the natural teeth (0.05 mm and 0.12 mm in the upper and lower jaw) due to the absence of the PDL. Stresses around the RAIs were lower than for the CIs, where sharp corners at the threads resulted in localized, increased stresses.

Discussion

The larger support of the RAIs in the alveolus as well as the absence of sharp geometric features seem to be advantages for the RAI. While this type of implant is only applicable if

the alveolus is still intact, such implants might offer a suitable alternative to the conventional threaded implants.

Session Category

Clinical Biomechanics: N/A

P4-205

Entropy of the center of pressure during dynamic balance tasks in adolescents post-anterior cruciate ligament reconstruction surgery

Ms. Madeleine McCreary BS[1,2], Dr. Elliot Greenberg PT, DPT, PhD, OCS, CSCS[2,3], Mr. Kevin Landrum BS[2], Dr. Theodore Ganley MD[2,3], Dr. Valentina Graci PhD[2,4]

[1]University of Washington, Seattle, Washington, United States. [2]Children's Hospital of Philadelphia, Philadelphia, Pennsylvania, United States. [3]University of Pennsylvania, Philadelphia, Pennsylvania, United States. [4]Drexel University, Philadelphia, Pennsylvania, United States

Ms. Madeleine McCreary

Dr. Elliot Greenberg

Mr. Kevin Landrum

Dr. Theodore Ganley

Introduction

Due to risk of re-injury after anterior cruciate ligament reconstruction (ACLR) in adolescents, return to sport decisions may need to include new metrics of dynamic postural control. Entropy is a nonlinear parameter that assesses temporal variability, looking at the overall structure found within signals such as the center of pressure (COP) by analyzing the regularity and predictability of the signal. Thus, the aim of this study was to understand if entropy of the COP while performing a Y-balance test could detect differences between the operative and uninjured limbs in adolescents three-months post-surgery.

Methods

Twenty-four adolescents completed the anterior, posterior-medial, and posterior-lateral directions of the Y-balance test on their operative and uninjured limbs while standing on a

force plate. Y-balance maximum reach distance was recorded, and entropy (*i.e.,* complexity index) of the anterior-posterior and medial-lateral COP traces was calculated for each trial. Maximum reach distance was normalized by participant height. Wilcoxon signed-rank tests evaluated differences between limbs (p<0.05) and the correlation between maximum reach distance and complexity index was calculated.

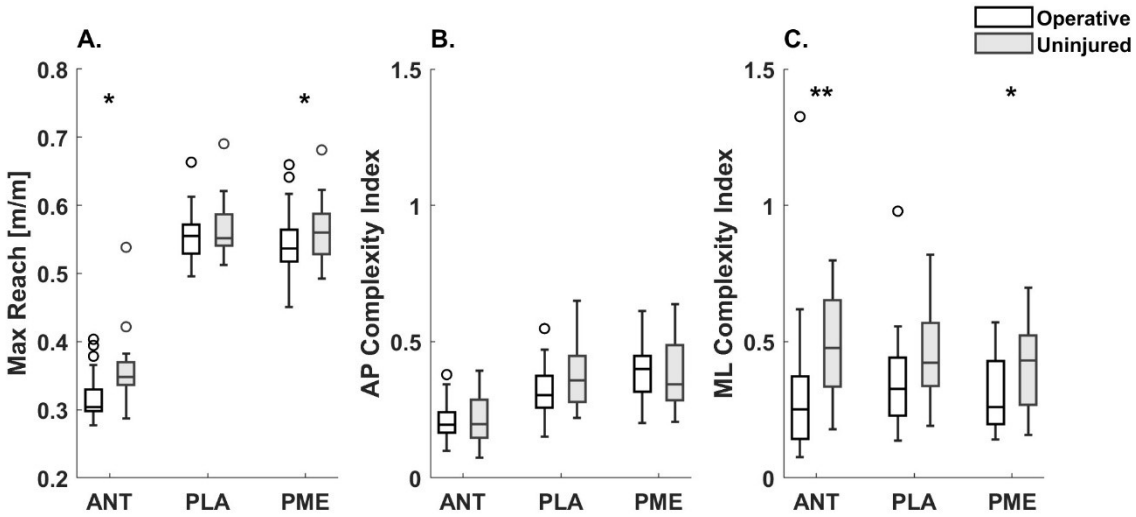
Results

Maximum reach distance and the medial-lateral COP complexity index of the operative limb were statistically significantly lower in the anterior (p=0.001, < 0.001; Effect Size = 0.81, 0.74) and posterior-medial (p=0.01, 0.006; Effect Size = 0.37, 0.59) directions of the Y-balance test, respectively. There were no significant differences in the anterior-posterior complexity index between limbs (p > 0.06; Effect Size < 0.54). The complexity index was weakly correlated with maximum reach distance (|r|<0.32).

Discussion

The results of this study suggest that COP entropy can differentiate between operative and uninjured legs three-months after ACLR in the frontal plane of motion. Decreased frontal plane COP entropy and maximum reach distance in the operative limb indicates a less adaptive postural control strategy compared to the uninjured limb. The lack of correlation between complexity index and maximum reach distance shows that these measures quantify different aspects of postural control during dynamic balance tasks post-surgery. Using the complexity index, in addition to other clinical assessments, may allow practitioners to tailor rehabilitation strategies to meet a participant's individual needs, marking an improvement towards precision medicine in ACLR recovery.

Images (Optional)



Acknowledgements (Optional)

This work was supported by the Children's Hospital of Philadelphia Department of Orthopedic Surgery and is based upon work supported by the National Science Foundation [Grant Number EEC-2149555]. The views presented here are solely those of the authors and not necessarily the views of the NSF.

Session Category

Clinical Biomechanics: N/A

P4-206

Simulated Plantarflexor Strength Differences in Osteogenesis Imperfecta Gait

Ms. Maeve McDonald MS[1,2], Dr. Rachel Lenhart MD, PhD[1], Dr. Jessica Fritz PhD[1,2]

[1]Medical College of Wisconsin, Milwaukee, WI, United States. [2]Marquette University, Milwaukee, WI, United States

Introduction

Osteogenesis imperfecta (OI) is a rare genetic disorder caused by defective type I collagen production. Type I OI, the mildest and most common form, is characterized by bone fragility, mild long bone bowing, and reduced muscle mass and force generation, leading to weakness, fatigue, gait impairments, and increased fracture risk. Although strengthening programs benefit children with OI, isolated strengthening may increase fracture risk from increased tensile forces and moments applied to weakened bones and joints. The goal of this study was to simulate varying plantarflexor strength and compare resulting muscle force (MF) outputs during gait in OI and control subjects.

Methods

Deidentified motion analysis data from a previously conducted, IRB-approved study was used to create ten OI and ten age- and sex-matched control models in OpenSim. Models were scaled using anthropometric measurements and maximum isometric force (MIF) for each muscle was scaled using subject-specific body mass. Baseline kinematics, kinetics, muscle activation (MA), and MFs were simulated using subject-specific motion analysis data. MIF of the gastrocnemius and soleus muscles was adjusted from baseline (−5%, +5%, +10%, +15%) to model plantarflexor strength changes, and simulations were rerun (Figure 1). Baseline kinematics, kinetics, and MAs between the OI and control group were compared using a Student's t-test (α=0.05). Peak MFs of the lower extremities at each strength level during stance were compared within groups using one-way repeated measures ANOVA (α=0.05).

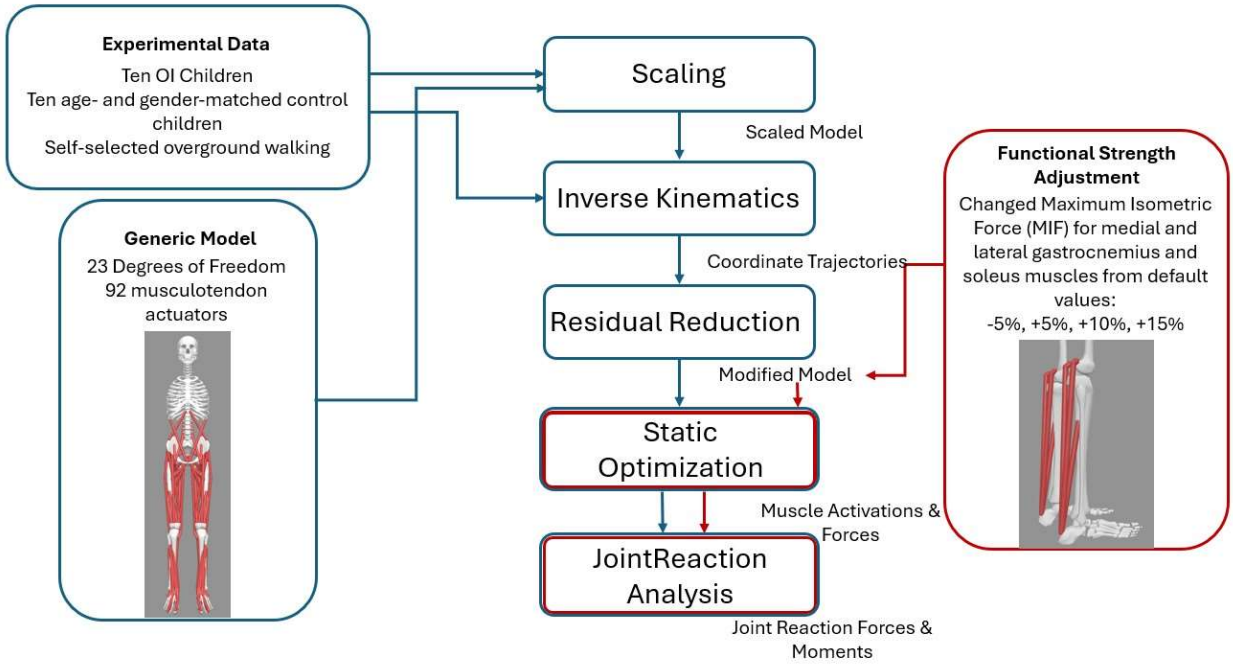
Results

When plantarflexor strength was increased, OI patients showed increased peak gastrocnemius and tibialis anterior MF ($p<0.02$). No differences were seen in controls. Differences in MF outputs between the OI and control groups may be a result of significantly increased hip flexion ($p<0.05$) in OI patients, reflective of neuromuscular strategies to compensate for muscular weakness and bone fragility.

Discussion

Though not significant, the differences seen in kinematics, kinetics, and MA in OI patients may contribute to the MF differences with varied strength. Although minimal MF differences with plantarflexor strength level were seen, fracture risk may still be affected due to the altered material properties in OI bone. Further analysis includes development of subject-specific finite element models to study how changes in plantarflexor strength affect fracture risk.

Images (Optional)



Session Category

Clinical Biomechanics: N/A

P4-207

Lower Limb Proprioception Assessed in Free-Standing, Standing-Braced and Lying

Dr Martin Héroux[1], Ms Linda Wang[2], Dr. Annie Butler[1], Prof Janet Taylor[1], Mr Amin MohammadiNasrabadi[3], Prof Jean-Sébastien Blouin[3], Prof Simon Gandevia[1]

[1]Neuroscience Research Australia, Randwick, NSW, Australia. [2]University of New South Wales, Kensington, NSW, Australia. [3]University of British Columbia, Vancouver, BC, Canada

Introduction

Lower limb proprioceptive tests are typically performed unilaterally at a single joint with participants seated or supine. Such approaches do not reflect how the lower limbs are used during everyday activities like standing and walking. Preliminary evidence suggests proprioceptive acuity is better in bipedal stance than in single-joint, supine tests [1]. This study examined which factors associated with standing and balance might contribute to improved proprioceptive ability when upright.

Methods

Fifteen healthy adults (8 males, 7 females; mean age 30.1±9.1 yr) were tested in three conditions: free standing (Stand), standing with support (Braced), and lying supine (Lying). Braced reduced sway and lower-limb muscle activity; Lying further removed joint compression and most foot-sole forces. Movements were delivered using two motorised platforms: 0.8 mm inward/outward displacements at 0.1–5 mm/s. Proprioceptive velocity thresholds were obtained using a 2-alternative forced-choice protocol. Linear mixed models estimated effects of condition and direction, with mean differences reported alongside 95% CIs for planned contrasts.

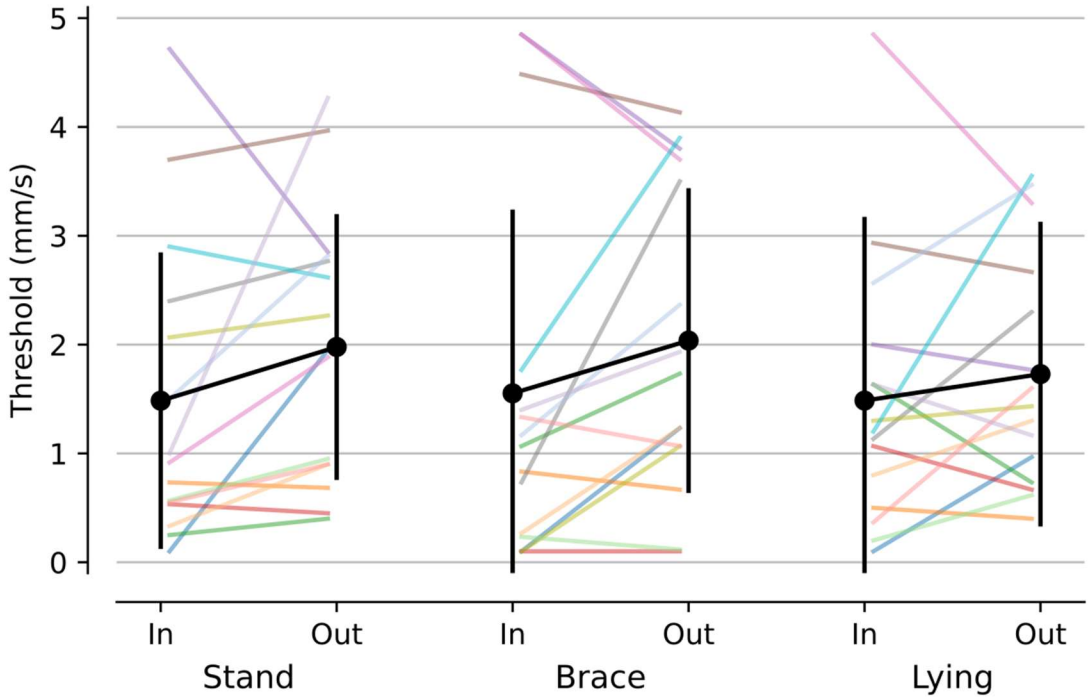
Results

Across conditions and directions, thresholds ranged from 1.46–2.04 mm/s. Thresholds differed minimally between In and Out movements: Stand: –0.49 mm/s [–1.12, 0.13]; Braced: –0.48 mm/s [–1.11, 0.15]; Lying: –0.24 mm/s [–0.87, 0.39], with negative values indicating lower thresholds for In movements. Unexpectedly, condition had little influence on threshold values, and this for both In movements (Stand vs Braced: –0.07 mm/s [–0.70, 0.56]; Stand vs Lying: –0.001 mm/s [–0.63, 0.63]; Braced vs Lying: 0.07 mm/s [–0.56, 0.70]) and Out movements (Stand vs Braced: –0.06 mm/s [–0.69, 0.57]; Stand vs Lying: 0.25 mm/s [–0.38, 0.88]; Braced vs Lying: 0.31 mm/s [–0.32, 0.94]).

Discussion

Compared with published single-joint thresholds, thresholds here were approximately ten-fold better across all three conditions. Available evidence suggests this enhanced acuity likely reflects the integration proprioceptive input (muscle spindles, joint receptors, foot-sole tactile receptors) from multiple joints and body regions. These findings indicate that single-joint tests underestimate lower-limb proprioceptive ability during real-world tasks involving coordinated bilateral limb use.

Images (Optional)



References (Optional)

[1] Liu A **(2024). Assessing Lower Limb Proprioception With A Novel Mechatronics Device [Master's thesis]. UBC.**

Session Category

Clinical Biomechanics: N/A

P4-208

Sensorimotor Synchronization in Children With and Without Down Syndrome During Two-Legged Hopping

Dr. Matthew Beerse Ph.D.[1], Dr. Jianhua Wu Ph.D.[2]

[1]University of Dayton, Dayton, Ohio, United States. [2]Georgia State University, Atlanta, Georgia, United States

Introduction

Methods

Results

Discussion

The sensorimotor synchronization of children with DS follows a similar control mechanism as TD peers. Whole-body vertical stiffness is not controlled on a cycle-by-cycle basis to maintain consistent cycle times. Moreover, children with DS responded to the external cue of the metronome by increasing the regularity of their stance time parameters.

Images (Optional)

Table 1: Mean coefficient of variation (sd) of force-time parameters during the *free* condition and the *preferred* condition. † indicates that the DS group was significantly different from the TD group. * indicates that the *preferred* condition was significantly different from the *free* condition. Note that at the *free* condition the participant hopped at their self-selected frequency without a metronome. At the *preferred* condition the participant hopped at a metronome-cued frequency which was equal to their self-selected frequency.

Variable	Group	Free condition	Preferred condition
Cycle time	TD	0.06 (0.03)	0.05 (0.01)
	DS	0.13 (0.07)†	0.11 (0.05)†
Stance time	TD	0.08 (0.02)	0.07 (0.02)*
	DS	0.13 (0.09)	0.11 (0.07)*
Flight time	TD	0.11 (0.04)	0.10 (0.03)
	DS	0.25 (0.09)†	0.22 (0.08)†
Peak GRF IRI	TD	0.05 (0.03)	0.04 (0.01)*
	DS	0.13 (0.07)†	0.11 (0.05)†*
Time to peak GRF	TD	0.11 (0.04)	0.09 (0.02)*
	DS	0.21 (0.14)†	0.17 (0.10)†*
Time to takeoff	TD	0.18 (0.06)	0.14 (0.04)
	DS	0.19 (0.11)	0.19 (0.12)
Whole-body vertical stiffness	TD	0.16 (0.09)	0.14 (0.05)
	DS	0.29 (0.15)†	0.30 (0.15)†
Peak GRF	TD	0.08 (0.02)	0.07 (0.01)
	DS	0.10 (0.04)†	0.10 (0.03)†
Peak vertical COM displacement	TD	0.12 (0.05)	0.10 (0.04)
	DS	0.23 (0.09)†	0.23 (0.06)†
Rate of force development	TD	0.16 (0.05)	0.14 (0.03)*
	DS	0.22 (0.09)	0.20 (0.07)*

References (Optional)

Repp & Steinman, J Mot Beh, 2010

Farley et al., J App Phys, 1991

Horvat et al., Perc Mot Skills, 2012

Session Category

Clinical Biomechanics: N/A

P4-209

Investigating Neuromuscular Coordination and Adaptations from Knee-Ankle-Foot Orthosis (KAFO) Assisted Gait Training in Post-Stroke Individuals

Mr. Matthew De Guzman B.S.[1], Dr. Shuo-Hsiu Chang PhD[2], Dr. Gerard Francisco MD[2], Dr. Mohammad S. Shourijeh PhD[2]

[1]McGovern Medical School, Houston, TX, United States. [2]UTHealth Department of Physical Medicine and Rehabilitation, Houston, TX, United States

Introduction

Stroke survivors with hemiparesis often experience abnormal gait patterns and high energy cost due to impaired neuromuscular coordination. Muscle synergy analysis provides insight in pathological neuromuscular control and adaptations during and after rehabilitation. Advanced stance and swing control knee-ankle-foot orthoses (KAFOs), such as the C-Brace, improve gait mechanics and efficiency, but their effects on neuromuscular control remain poorly understood. This study will evaluate changes in muscle synergy organization following C-Brace gait training in individuals with post-stroke hemiparesis.

Methods

Five participants with chronic hemiparesis completed 12 sessions of gait training with the C-Brace KAFO. Surface EMG was collected from major lower-limb muscles before training, after training without using the KAFO (PostWO), and after training with using the KAFO (PostWT). Muscle synergy weights and activations were extracted using non-negative matrix factorization, and similarities across conditions were compared using statistical parameter mapping (SPM) and cosine similarity metrics.

Results

At baseline, the paretic limb demonstrated fewer synergies (3.6 ± 1.14) compared to the nonparetic limb (4.6 ± 0.55), consistent with impaired motor control. In the post-training, KAFO assisted trial (PostWT), synergy counts increased in the paretic limb and decreased slightly in the nonparetic limb (3.8 ± 1.10 paretic; 4.4 ± 0.55 nonparetic). In the post-training, KAFO unassisted trial (PostWO), paretic and nonparetic synergy counts were slightly lower (3.2 ± 0.84 paretic; 4.2 ± 1.10 nonparetic). Importantly, compared to baseline, the paretic limb demonstrated the emergence of 2 ± 0.8 unique synergies PostWO and 1.6 ± 0.7 unique synergies PostWT, suggesting enhanced neuromuscular organization.

Discussion

Preliminary findings suggest that C-Brace–assisted gait training may promote more complex and adaptive neuromuscular control in stroke survivors. The increase in synergy number and the emergence of unique synergies with KAFO use point to potential neural reorganization, beyond mechanical assistance alone. These results support the role of advanced KAFOs not only in improving gait mechanics but also in driving neuroplasticity. Ongoing work will expand this sample and assess how synergy changes relate to long-term functional outcomes.

Images (Optional)

		P1	P2	P3	P4	P5	Mean	STD
Paretic Limb	PreWO	3	5	4	2	4	3.6	1.14
	PostWO	3	3	4	2	4	3.2	0.84
	PostWT	4	4	4	2	5	3.8	1.10
Nonparetic Limb								
	PreWO	4	5	5	4	5	4.6	0.55
	PostWO	3	5	5	3	5	4.2	1.10
	PostWT	4	5	4	4	5	4.4	0.55

Table 1: Summary of number of synergy groups needed to achieve both 90% VAF and <5% VAF improvement with an additional synergy in the paretic and nonparetic limb of the PreWO, PostWO, and PostWT conditions.

Acknowledgements (Optional)

This study was supported by the UTHealth Houston SRP Program and Mary H. Cain Foundation via Mission Connect, a program of TIRR Foundation.

Session Category

Clinical Biomechanics: N/A

P4-210

Feasibility of Utilizing a Robotic System to Deliver Physical Therapy-based Exercises to Individuals with Parkinson's Disease: A Pilot Study

Dr. Meredith Wells PhD[1,2], Mr. Matthew Lamsey[3], Ms. Arielle Wallenstein[2], Mr. Jerry Feldman[4], Dr. Charles Kemp PhD[5], Dr. Madeleine Hackney PhD[2,3,6,7]

[1]Exponent, Inc., Farmington Hills, MI, United States. [2]Emory University School of Medicine, Atlanta, GA, United States. [3]Georgia Institute of Technology, Atlanta, GA, United States. [4]The Parkinson's Foundation, New York, NY, United States. [5]Hello Robot, Inc., Martinez, CA, United States. [6]Atlanta VA Health Care System, Decatur, GA, United States. [7]Dept. of Veterans Affairs Birmingham/Atlanta Geriatric Research Education and Clinical Center, Brookhaven, GA, United States

Introduction

Parkinson's disease (PD) is the fastest growing neurodegenerative disease with approximately 10 million people living with PD worldwide [1]. Physical therapy (PT) can slow the functional decline associated with PD through cardiovascular endurance, strength, balance and flexibility training [2,3]. However, patients may not achieve the full benefits of PT due to therapist availability and time limitations. To overcome this barrier, robotic exercise systems have been introduced into PT for certain populations. This study aimed to determine if a custom-programmed robotic system could lead individuals with PD through movements at different joints.

Methods

Eleven participants with PD (7 female; age: 68.2 ± 6.2 yrs; time since diagnosis: 7.1 ± 5.1 yrs; Hoehn &Yahr stage: I-II.5) completed 6 exercises with a Stretch-with-Stretch robot (Hello Robot, Inc.). The robot-guided activities included 3 seated (calf raises, forward reach, knee extensions) and 3 standing (contra-body reach with rotation, windmills, high knees) exercises. The robot (Figure 1) was programmed to present a target at specific locations for each exercise and to provide instructions. Range of motion (ROM) was collected via inertial sensors (APDM). Participants also completed a standing forward reach immediately before and after the session to assess any immediate improvement in mobility.

Results

Participants completed all exercises with the robot. ROM was dependent upon the exercise and joint of interest. For example, hip ROM during the standing reach was 8.2±2.2 degrees, while hip ROM during high knees was 71.4±9.2 degrees. Standing forward reach improved by an average of 1.7 inches, demonstrating immediate benefits of exercising with the robot. Additionally, when asked if the robotic system would be useful in their daily exercise, 8 of the 11 participants agreed, indicating a positive experience.

Discussion

Results demonstrated potential benefits of exercising with a robotic exercise system, such as functional mobility gains. The number of sessions spent with a PT can be limited by time and availability, so this system could be a fun way to encourage individuals with PD to consistently complete their PT exercises at home.

Images (Optional)



Figure 1. The Stretch-with-Stretch system consists of a mobile manipulator with a soft-bubble that serves as an external cue for participants to reach towards with different parts of their body, such as their hand or foot. The location of the bubble relative to the participant is personalized for each exercise.

References (Optional)

1. Parkinson's Disease Foundation. Available online: Statistics | Parkinson's Foundation
2. Goodwin, et al. Movement Disorders, 2008.
3. Salgado, et al. Brain Sciences, 2013.

Acknowledgements (Optional)

The authors would like to thank all the individuals who participated for their assistance in completing this study.

Session Category

Clinical Biomechanics: N/A

P4-211

Physiological Strain Windows as Drivers of Fracture Healing: A Simulation-Based Framework for Site-Specific Modeling

Dr Michael Roland[1], Prof. Dr.-Ing. Stefan Diebels[1], Dr. Thorsten Tjardes[2]

[1]Saarland University, Applied Mechanics, Saarbrücken, Saarland, Germany. [2]Hospital of the German armed forces Berlin, Berlin, Berlin, Germany

Introduction

Fracture healing is governed by mechanobiological regulation, in which local mechanical stimulus is the primary driver of cell differentiation, tissue formation, and remodeling in the callus. Existing mechanobioregulatory models and Frost's mechanostat define strain "windows" for healing and bone formation but thresholds mainly come from animal lower-limb data and are poorly specified across human bones and anatomical sites. Because loading and mechanosensitivity are site-specific, it is unclear whether strain ranges at one region can be transferred to others without bias. We hypothesize that the strain window for bone formation in fracture callus corresponds to Frost's physiological usage window at the same anatomical site, and that this relationship can be quantified via simulations.

Methods

We constructed subject-specific finite element models of healthy and fractured long bones (lower and upper extremity) based on clinical imaging. Physiological activities (walking, stair negotiation, and a palm-leaning task) were applied using musculoskeletal simulations based on motion capturing data to estimate joint and muscle forces. For healing scenarios, callus tissue was represented by time-varying material properties and mechanobioregulatory rules adapted from literature models [1,2]. For each site and activity, distributions of different strains were quantified. The strain-states were then compared to the corresponding physiological usage windows [3].

Results

Across all subjects and activities, the peak and median strains in the regions of bone formation were within the callus or only slightly deviated from the physiological usage window derived for the corresponding healthy bone site. In addition, for the different bones considered and the different probands, there was also an inter-individual strain variability observable.

Discussion

Our simulations support a quantitative overlap between the physiological usage window and the strain ranges that drive osteogenesis in fracture healing at matched anatomical sites. This linkage can provide a pathway to generate mechanically driven site-specific differentiation rules.

References (Optional)

1. Claes *et al.*, J Biomech **32**(3): 255-266, 1999.

2. Prendergast *et al.*, J Biomech **30**(6): 539-548, 1997.

3. Frost, *Anat Rec A Discov Mol Cell Evol Biol.* **275**(2): 1081-1101 (2003).

Session Category

Clinical Biomechanics: N/A

P4-212

Mimicking Daily-Life Loading: A Hexapod-Driven, 6-Axis Experimental Setup for Fracture–Implant Mechanics

Dr. Michael Roland, Laboratory manager Danijel Crepulja, M.Sc. Kerstin Wickert, Prof. Dr.-Ing. Stefan Diebels

Saarland University, Applied Mechanics, Saarbrücken, Saarland, Germany

Introduction

Multi-axis physiological loading is essential for evaluating bone-implant constructs, yet most experimental setups still apply simplified uniaxial or planar loading. This limits their ability to reproduce the complex 3D force and moment patterns occurring during daily activities. We present a new hexapod-based test system capable of applying controlled six-degree-of-freedom (6-DOF) loading to long-bone fracture-implant systems while simultaneously measuring forces, moments and interfragmentary mechanics. To our best knowledge, this is one of the first systems designed to mimic daily-life loading scenarios in a biomechanically realistic way.

Methods

The testing device consists of a hexapod with flexible mold clamping system for long bones, equipped with two 6-axis force/moment sensors at the proximal and distal interfaces. A four-camera digital image correlation setup records full-field surface displacements and strains across the fracture region. Artificial composite bones and human cadaveric specimens were prepared with standardized AO-classified diaphyseal fractures and stabilized using clinically relevant implants. Hexapod motions were programmed to reproduce kinematics representative of daily-life activities and partial weight-bearing. Time-resolved interfragmentary movement, local strain distributions, and global load paths were quantified and compared to ranges reported in mechanobiological literature for fracture healing cell differentiation. In parallel, specimen-specific finite element models with identical boundary conditions were used to validate the simulations against DIC and load cell measurements.

Results

The hexapod system reproduced complex multi-axis load paths, including combined axial loading, bending, torsion, and shear, with good repeatability of boundary forces and kinematics. DIC revealed heterogeneous strain fields and interfragmentary movement patterns that were dependent on implant configuration and fracture type. For selected loading conditions, measured interfragmentary strains fell within stimulus ranges reported

in the literature, supporting the physiological relevance of the test protocols. FE predictions showed good agreement with experimental displacement and strain fields, confirming the suitability of the setup for validating numerical models.

Discussion

This new hexapod-based testing platform enables 6-DOF, activity-mimicking loading of fracture-implant systems with concurrent measurement of interfragmentary mechanics. The combination with validated FE models provides a framework for designing implants, optimizing loading protocols, and linking experimental data to mechanobiological healing models in future digital-twin applications.

Session Category

Clinical Biomechanics: N/A

P4-213

Gait Kinematics of Children With Severe Motor Impairments Using Conventional Gait Trainers Versus a Motorised Robotic Rehabilitation Trainer

Miss Miray Kirollos, Dr Angela Kedgley

Imperial College London, London, Greater London, United Kingdom

Miss Miray Kirollos

Introduction

Gait trainers, also known as walkers, are conventionally used to assist the mobility of children with severe motor impairments. More recently, a novel motorised robotic rehabilitation trainer, thought to simulate gait-like patterns and help maintain musculoskeletal health, has been prescribed [1]. This study aimed to compare the kinematics of typical, walker-assisted and motorised device-simulated gaits. It was hypothesised that using the motorised device would improve lower-limb movement symmetry and produce consistent joint angle trajectories.

Methods

Participants comprised five children with severe motor impairments (aged 10.2 ± 3.9 years; three males and two females) who performed assisted walking using their walker, and five typically developing children (aged 10.4 ± 3.8 years; two males and three females) who performed unassisted walking on a level surface at a self-selected speed. Simulated gait using the motorised device (Innowalk Pro, Made for Movement GmbH) was performed by all participants. Lower-body kinematic data were acquired via eight inertial measurement units (Xsens, Movella Inc.) and analysed in the sagittal plane for five continuous gait cycles. The lower limbs were categorised into more and less flexed sides for symmetry comparison.

Results

Children with severe motor impairments showed greater gait variability than typically developing children (Figure 1). The motorised device produced increased asymmetry for typically developing children; however, improved symmetry, especially in the ankle (from 14.8° ± 8.2° to 2.7° ± 2.1°), for children with motor impairments. The motorised device

(compared to typical and walker-assisted gaits, respectively) resulted in decreased hip (62.2%; 57.0%), knee (71.21%; 59.8%,) and ankle (82.93%; 73.9%) ranges of motion.

Discussion

The motorised device did not produce gait-like patterns, instead it resulted in more constrained movement, limiting both hip and knee flexion and extension. The device reduced excessive plantarflexion and improved limb movement symmetry for children with severe motor impairments. This can assist with posture and muscle contracture management, supporting the improvements in passive joint extension after device use shown previously [2]. Walkers continue to encourage a greater range of motion, but the robotic rehabilitation trainer could form a complementary therapy to improve walker-assisted gait.

Images (Optional)

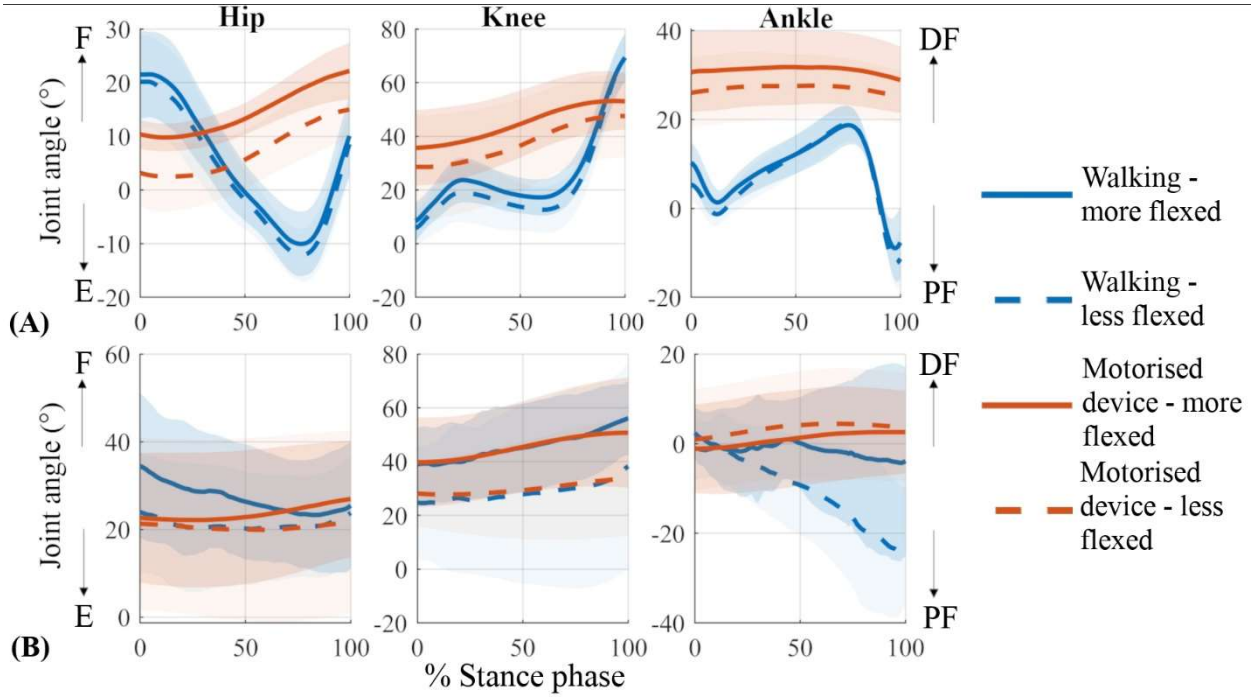


Figure 1: Mean hip, knee and ankle angles ± one standard deviation, showing flexion (F), extension (E), dorsiflexion (DF) and plantarflexion (PF) for (A) typically developing children and (B) children with motor impairments during unassisted or assisted walking (blue) compared to motorised device use (orange) for both more flexed (solid) and less flexed (dashed) limbs determined during walking.

References (Optional)

[1] Caroline Schmidt-Lucke et al., PeerJ, 2019

[2] Clare Grodon et al., Child Care Health Dev., 2023

Acknowledgements (Optional)

Miray Kirollos was supported by the Engineering and Physical Sciences Research Council, Orthopaedic Research UK and British Society for Children's Orthopaedic Surgery.

Session Category

Clinical Biomechanics: N/A

P4-214

Bilateral External Knee Adduction Moment During Cycling in People With and Without Knee Pain From Osteoarthritis

Mr Dan Currie, Ms Dalia Grad, Ms Kathryn Webster, Ms Huaning Liu, Dr Stacey Acker, Dr Nikolas Knowles, Dr Monica Maly

University of Waterloo, Waterloo, ON, Canada

Introduction

Knee osteoarthritis (OA) is one of the most common chronic conditions in Canada [1]. Commonly, the pain caused by knee OA is unequal between knees, which can lead to asymmetry of movement in daily activities. External knee adduction moment (KAM) is linked to the progression and severity of knee OA [2]. The effect of seat height and workload on KAM during cycling has been explored in a single leg analysis in healthy adults [3]. Bilateral analyses are rare. The objective of this secondary analysis is to compare peak KAM between seat heights, workloads and knees (more versus less painful knee; or dominant versus non-dominant when there was no knee pain or the same pain intensity in both knees) in people with and without symptomatic knee OA.

Methods

Twenty-six participants aged 45-75 years, with and without symptomatic knee OA completed six cycling bouts at three seat heights and two workloads on a commercial fit-bike (Pro 1, Purely Custom, USA). Each bout was performed for two minutes at a cadence of 60 rpm. Self-reported knee pain on the Numeric Pain Rating Scale (NPRS) was recorded before the first and after each bout. Synchronized three-dimensional kinematics and kinetics were collected with a commercial motion capture system (Optotrak Certus, NDI, Canada) and a commercial instrumented three-axis pedals (Science to Practice, Slovenia). The KAM waveform for both knees was calculated in Visual3D (HAS-Motion, Canada). From the full waveform, a one-minute portion was selected and averaged to one pedal cycle. A three-factor repeated-measures analysis of variance was used to compare the peak external KAM values.

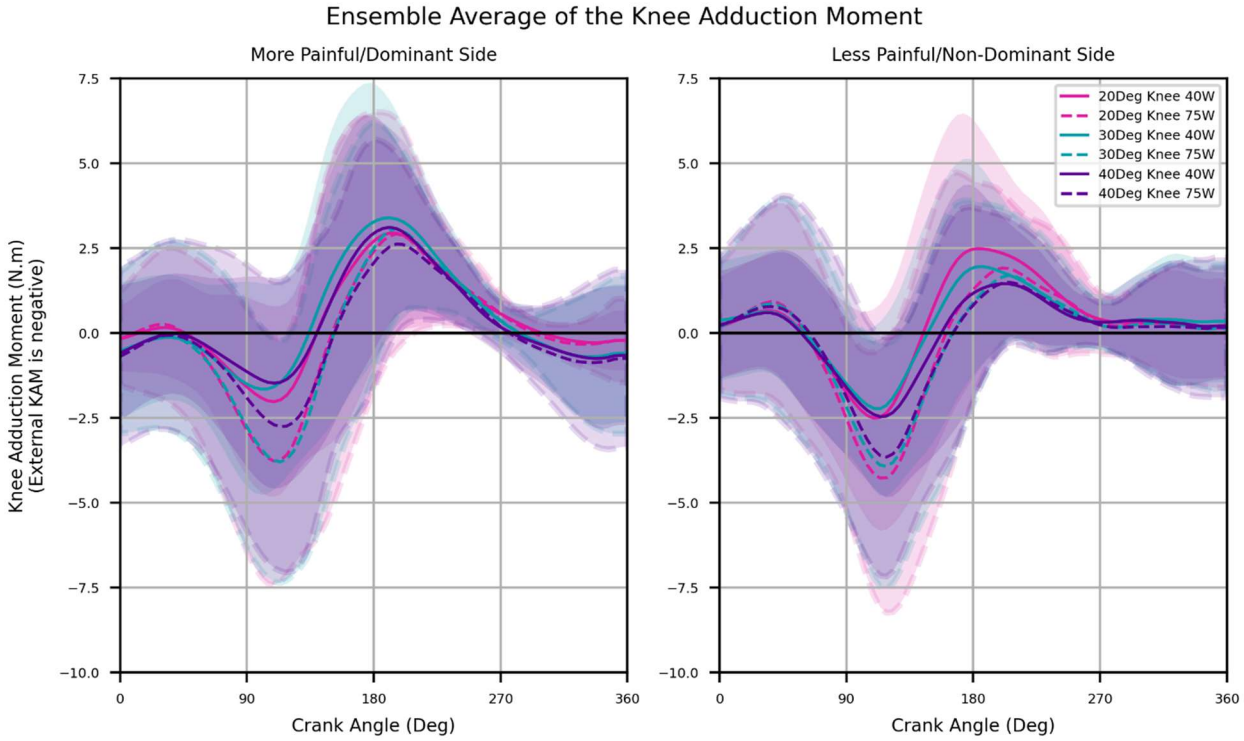
Results

A significant effect of workload was found ($p < 0.01$) where peak KAM was greater with greater workload. No difference in peak KAM was observed between seat heights or between knees ($p > 0.05$).

Discussion

The peak KAM, on average, is the same in both knees in this bilateral task. The increase in demand from the higher workload appears to increase the external peak KAM. This result is in line with previous research [3].

Images (Optional)



Session Category

Clinical Biomechanics: N/A

P4-215

Effects of Prolonged Walking on Toe Clearance and Stability Margins in Older Adults With and Without Knee Osteoarthritis

Ms. Nancy Nguyen, Ms. Fany Alvarado, Ms. Millissia Murro, Ms. Grace Kellaher, Ms. Mayumi Wagatsuma, Dr. Jocelyn Hafer, Dr. Jeremy Crenshaw

University of Delaware, Newark, DE, United States

Introduction

Fatigability, defined as an individual's susceptibility to fatigue with activity, may underlie the elevated fall risk of individuals with knee osteoarthritis (OA) because 1) those with knee OA do not always have worse balance or gait stability when unfatigued, 2) fatigue affects balance and walking mechanics, and 3) knee OA is associated with high fatigability. If prolonged walking induces disproportionate fatigue in those with knee OA, fatigue-related gait changes may explain their elevated fall risk. The purpose of this study was to determine how prolonged walking changes gait in adults with and without knee OA. Falls in this population often result from a trip during walking, so we focused on measures that characterize the likelihood of a trip (i.e., toe clearance) and the initial stability conditions should a trip occur (i.e., anterior stability margins).

Methods

Eight participants with knee OA (4F/4M, 64.3±3.0 years, 25.1±4.2 kg/m^2) and ten without knee OA (4F/6M, 63.0±3.6 years, 26.3±4.2 kg/m^2) walked on a treadmill (OA=1.38±0.08 m/s, non-OA=1.44±0.17 m/s) with full-body motion capture for 34 minutes, including three one-minute challenge periods at +50% speed. Four-minute periods were analyzed at the beginning and end of the walk. Using a 3-way ANOVA, we assessed the effects of GROUP (OA, non-OA), LIMB (more/less affected, right/left), and TIME (beginning, end) on each individual's lower quartile of minimum toe clearance and corresponding anterior stability margins.

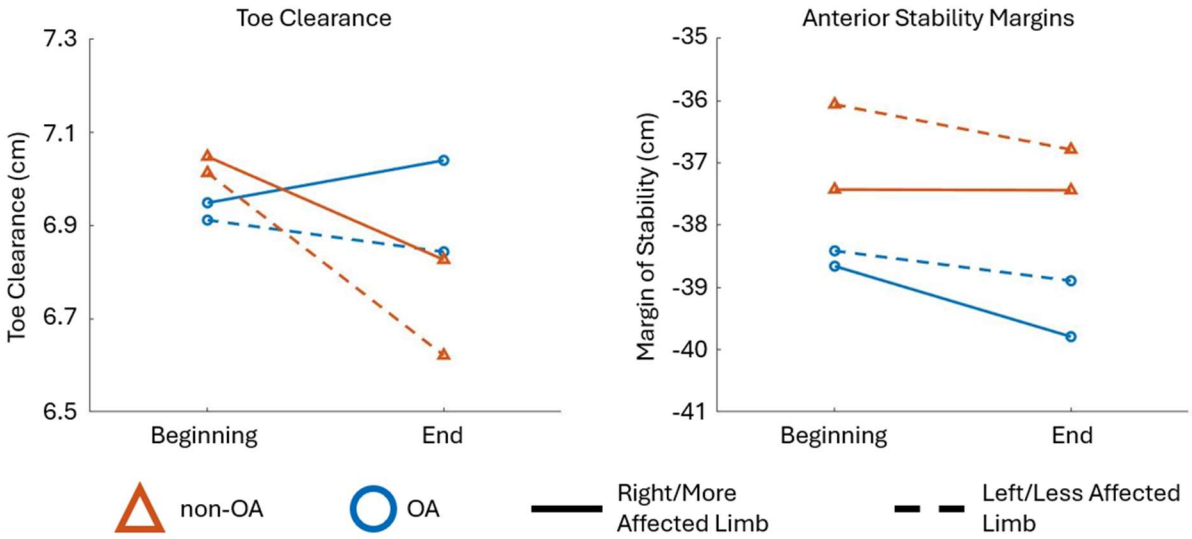
Results

We observed a significant GROUP*TIME interaction on toe clearance ($p=0.025$). The non-OA group decreased toe clearance with prolonged walking (-0.3±0.1cm, $p=0.001$, Figure). No between-group differences were observed ($p>0.5$). No main effect or interactions containing LIMB were significant ($p>0.09$). A significant effect of TIME was observed on anterior stability margins, with margins becoming more negative with prolonged walking (-0.6±0.3cm, $p=0.048$). No main effects or interactions containing GROUP or LIMB were significant ($p>0.06$).

Discussion

We cannot conclude that OA-related fatigability affects gait in a manner that increases the risk of trip-related falls. Changes in dynamometer-measured, knee-extensor power were not different between groups (OA=-12.7±19.8%, non-OA=-2.2±20.3%), suggesting that our premise of OA-related fatigability was not supported.

Images (Optional)



Session Category

Clinical Biomechanics: N/A

P4-216

Estimating Spinal Loads of Clinicians in Real-Time Using Machine Learning

Ms. Natasha Anderson[1], Mr Samuel Brost[1], Dr Cari Whyne[2], Dr Qingguo Li[1]

[1]Queen's University, Kingston, Ontario, Canada. [2]Sunnybrook Health Sciences Centre, Toronto, Ontario, Canada

Introduction

Back-related musculoskeletal disorders are a common injury among clinicians because of the prolonged non-neutral postures they maintain in the operating room [1]. We investigate whether machine learning can be used to estimate the spinal load in real-time, as previously developed models do not have this ability, limiting their practical applications [2]. This can be integrated with wearable sensor systems to provide feedback to promote postural awareness in clinicians, thus reducing their risk of injury.

Methods

The spinal load was estimated from data collected from 4 IMUs placed along the spines of 20 participants (8F/12M) at Sunnybrook Health Sciences Centre, using the spine equivalent beam model [2]. The algorithm used was a neural network with 2 hidden layers (sizes: 128 and 64). The model had four inputs (from each IMU), and two outputs, the compressional loads at C6/C7 and L4/L5 vertebra. It was trained on 16 datasets, with 10% set aside for validation, and 4 datasets left unseen for testing.

Results

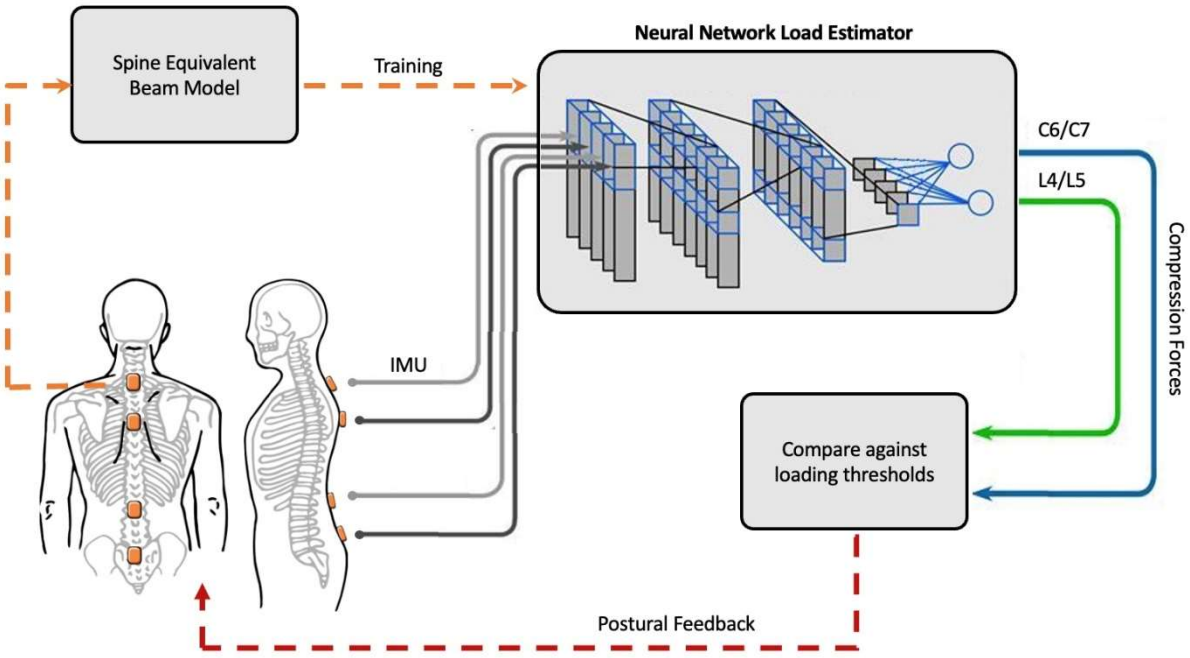
Comparison between the true and predicted compressional forces showed mean average percent errors of 25.7±5.6% and 28.5±7.3% for the C6/C7 and L4/L5 locations, respectively. Calculating the cumulative load per participant at the same locations resulted in errors of 4.3±1.9% and 6.2±2.9%. This model had an average run-time of 0.5±0.1 seconds.

Discussion

The model’s accuracy is not sufficient for estimating instantaneous loads, however, it has significantly less error when estimating cumulative load. Cumulative load has higher injury contributions since it leads to repeated stresses and overuse [3]. Therefore, the cumulative load-based algorithm is an effective method for delivering postural feedback to clinicians, as it can accurately estimate loads in real-time. The model will be further explored to compute the shear and internal moment, for a more robust loading profile. Additional inputs, such as gender and height will be added to allow the model to learn more features

that impact spinal loading thresholds, leading to future development of individualized models with reduced error margins.

Images (Optional)



References (Optional)

[1] Jacob Seagull, Work, 2012.

[2] Samuel Brost *et al.,* Comput Methods Biomech Biomed Engin [submitted], 2025.

[3] William Marras *et al.,* Hum Factors, 2014.

Session Category

Clinical Biomechanics: N/A

P4-217

Obesity Increases Muscle Capacity Utilization in Those With Clinical Knee Osteoarthritis

Ms. Natasha K. Ivanochko MSc[1], Dr. Jacquelyn M. Maciukiewicz PhD[1,2], Dr. Kendal A. Marriott PT, PhD[1], Dr. Lauren Straatman PhD[1], Ms. Kathryn F. Webster MSc[1], Mrs. Emily G. Wiebenga[1], Dr. Monica R. Maly PT, PhD[1]

[1]University of Waterloo, Waterloo, Ontario, Canada. [2]Waterloo Regional Health Network, Waterloo, Ontario, Canada

Introduction

Obesity and weakness are common features of knee osteoarthritis (OA). However, the impact of these features on demands to the musculoskeletal system during activities of daily living, and how weakness might interact with obesity, is not fully understood. The objective of our study was to investigate the association between obesity and muscle capacity utilization (MCU), which represents the proportion of maximal muscle capacity required to perform a task, in those with clinical knee OA.

Methods

Participants with clinical knee OA were recruited and the most symptomatic knee was studied. Obesity was represented by body mass index (BMI) (kg/m^2) from measured height and weight while barefoot, wearing a t-shirt and shorts. MCU was the ratio of knee flexion moment during walking and maximal knee extensor strength. Level, barefoot walking at a self-selected speed was completed. Kinematics were collected using 5 infrared camera banks at 100 Hz. Kinetics were collected with a synchronized, floor-embedded force plate at 1000 Hz. From these data, the mean peak external knee flexion moments (Nm) during stance phase from 5 trials was calculated. Maximal knee extensor strength (Nm) was the mean of the 3 largest peak values during maximal voluntary isometric contractions on a commercial dynamometer. Multiple hierarchical linear regressions (adjusted for covariates age, gait speed, accelerometry-based step count, and self-reported comorbidity) evaluated the association between BMI and MCU. Regressions were then stratified by sex.

Results

Data from 83 (57 female/26 male/0 intersex) participants were included. Mean (SD) age was 65.0 (6.2) years and mean BMI was 28.5 (4.9) kg/m^2. Obesity related with MCU (R^2 increased 0.140 from the covariate model to 0.191, p = 0.03), such that a greater

BMI related with greater MCU. For females, BMI was positively associated with knee extensor strength (R^2 increased 0.389 to 0.439, p = 0.038). No other associations were found.

Discussion

Obesity was related to greater MCU, suggesting a greater functional demand during level walking in adults with clinical knee OA. Also, contrary to previous findings, greater BMI was associated with greater knee extensor strength in females [1].

Images (Optional)

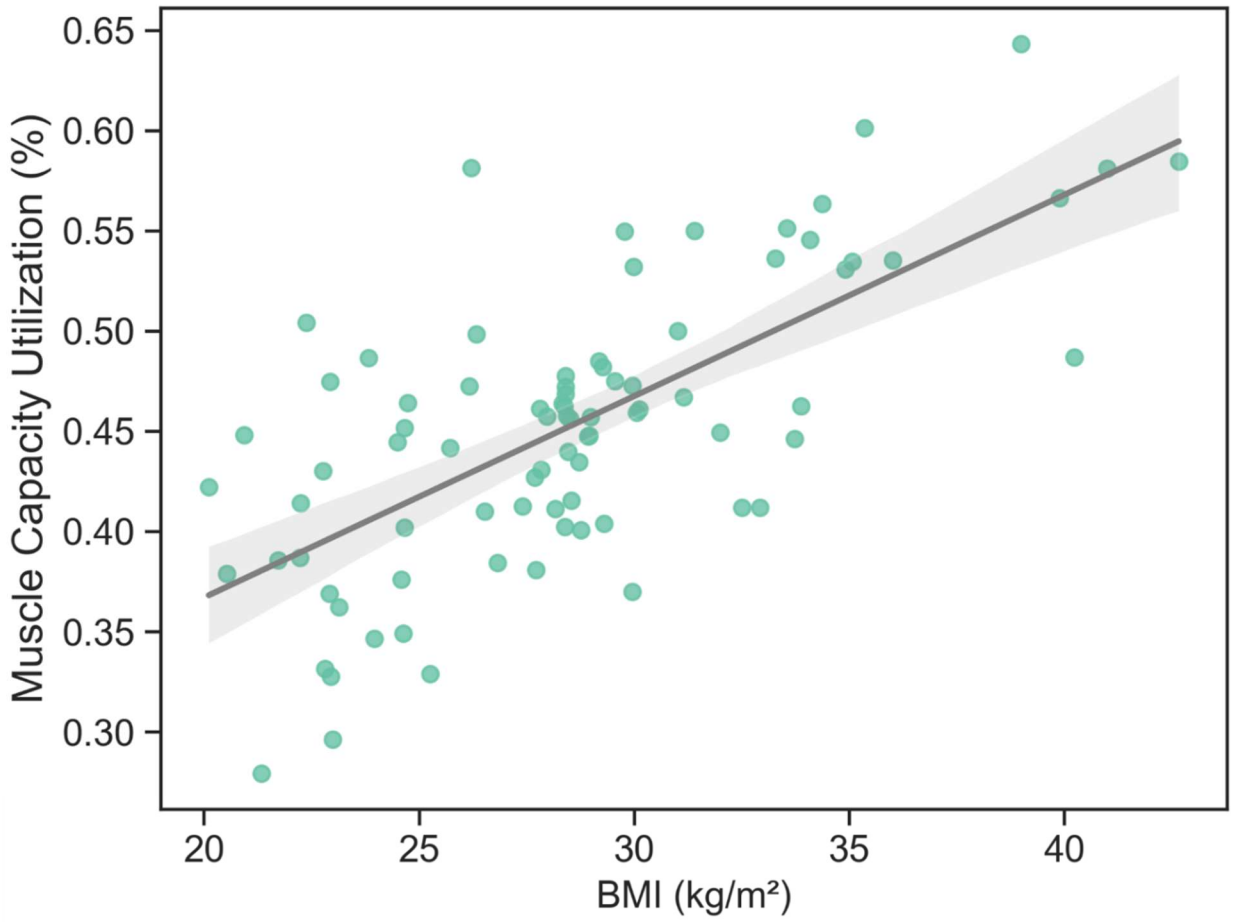


Figure 1. Scatterplot of the association between BMI (kg/m^2) and muscle capacity utilization (%) adjusted for age, gait speed, accelerometry-based step count, and self-reported comorbidity. The grey line represents the best linear fit with 95% confidence intervals.

References (Optional)

[1] Culvenor, AC&R, 2017

Session Category

Clinical Biomechanics: N/A

P4-218

Immediate Biomechanical and Symptomatic Effects of 3D Printed Lateral Wedge Insoles in People With Knee Osteoarthritis and Foot Pain

Ms. Natasha M. Krowchuk BSc[1], Mr. Haocheng Zhang MSc[1], Ms. Jessica M. Millan Alvarez BASc[2], Dr. Jesse M. Charlton PhD[1], Dr. Michael A. Hunt PhD, PT[1]

[1]University of British Columbia, Vancouver, BC, Canada. [2]Universidad Iberoamericana, Mexico City, Mexico, Mexico

Introduction

Lateral wedge insoles (LWIs) are shoe-worn insoles that represent an inexpensive, non-surgical approach to manage knee osteoarthritis (KOA). LWIs reduce the external knee adduction moment (KAM) – a biomarker associated with KOA disease progression – by approximately 6% on each step. Though effective at the knee, little is known about their effects at the foot – the location in which they interact with the body. Addressing this knowledge gap is especially relevant for certain subgroups, including those with KOA and concomitant foot pain given the large prevalence of this clinical presentation (25%). The purpose of this study was to examine the immediate biomechanical and clinical effects of LWIs in people with KOA and foot pain.

Methods

Individuals with foot pain and KOA in the same limb were recruited. They underwent a single gait analysis session to compare outcomes from two gait-speed matched, randomly-ordered conditions: with and without 3D printed 6-degree LWIs. Participants wore slip-resistant socks during both conditions, and the LWIs were secured underfoot with tape before donning the socks. Synchronized kinematic (120 Hz) and kinetic (1200 Hz) data were collected from five trials per condition. Participants rated pain in the foot, ankle, and knee after each condition (0 = “no pain”, 10 = “worst pain imaginable”). Commercially-available software (Orthotrak) was used to calculate joint kinematics and moments, and paired t-tests were used to test for any statistical differences between conditions.

Results

51 individuals participated (36 females, mean (sd) age: 63 (8) years; BMI: 28.6 (5.6) kg/m^2). Walking with LWIs produced significant reductions in the KAM impulse (p<0.001), knee flexion angle at initial contact (p=0.035), and knee valgus angle during midstance (p=0.003), as well as significant increases in toe-out angle (p=0.015) and peak ankle eversion moment (p<0.001). Foot pain was significantly reduced with LWIs (p=0.015).

Discussion

LWIs produce significant immediate improvements in foot pain and lower limb biomechanics relevant to KOA (i.e. knee adduction moment, knee valgus, and toe-out angles) in people with both KOA and foot pain. Though our findings are positive, future research is needed to understand the longer-term effects of LWIs in this clinical subgroup of the KOA population.

Session Category

Clinical Biomechanics: N/A

P4-219

Three-Dimensional Distance and Coverage Mapping in Adolescents with Idiopathic Flatfoot and Flatfoot Secondary to Cerebral Palsy

Mr. Nathan Nichols[1], Mr. Nick Slavik[2,1], Dr. Amanda Whitaker MD[3], Dr. Amy Lenz PhD[4], Dr. Kevin Dibbern PhD[5], Dr. Karen Kruger PhD[1,2,6]

[1]Marquette University, Milwaukee, Wisconsin, United States. [2]Medical College of Wisconsin, Milwaukee, Wisconsin, United States. [3]Shriners Children's Northern California, Sacramento, California, United States. [4]University of Utah, Salt Lake City, Utah, United States. [5]University of Nebraska Medical Center, Omaha, Nebraska, United States. [6]Shriners Children's Chicago, Chicago, Illinois, United States

Introduction

Pediatric flatfoot can occur either idiopathically or as a secondary neurological disorder such as cerebral palsy (CP). Physiologically, idiopathic flatfoot arises from a multitude of factors while flatfoot in cerebral palsy specifically develops through impaired neuromuscular control, spasticity, and weakness.

High variability in subtalar joint alignment relating to pediatric flatfoot may be attributed to differences between idiopathic flatfeet or flatfeet secondary to CP. The objective of this work was comparing distance and coverage mapping of CP and idiopathic participants to discern potential differences within the flatfoot population.

Methods

This IRB approved study contained a CP group (n=5, mean=13.7 years, range=12-16 years) and an idiopathic group (n=10, mean=12.83 years, range=11-17 years). Weightbearing CT scans were collected, and talar/calcaneal bone segmentations were generated using BoneLogic, Mimics 25.0, and 3D Slicer v5.8.0. Joint distances and bony coverage percentage ratios were calculated using methods described by Dibbern [1]. Statistical differences were assessed with t-tests at $\alpha=0.05$.

Results

Distance and coverage mapping analysis yielded significant results in the sinus tarsi region. Distance mapping significance showed $p=0.043$ with CP sinus tarsi mean distance 6.22mm±0.47mm and idiopathic sinus tarsi mean distance 5.44mm±0.64mm. Coverage mapping significance showed $p=0.012$ with CP sinus tarsi coverage of 20.9%±4.9% and idiopathic sinus tarsi coverage of 33.6%±9.1%. Increased joint space distances and higher

uncoverage in sinus tarsi region of the CP group are indicative of subluxation. Decreased distances in the sinus tarsi region of the idiopathic group suggest impingement in the subtalar joint.

Discussion

This data reports an objective measure of CP participants having higher spacing and less coverage in the sinus tarsi region compared to the idiopathic group. All other facets were not statistically significant, but this may be due to low participant numbers. Since significance occurred at the sinus tarsi region, differences in this region may be the primary driver of subtalar joint coverage differences between these two flatfoot populations. Our ongoing work aims to increase sample sizes to confirm these findings. These improved metrics can aid in earlier, less invasive intervention recommendations targeted at specific types of flatfeet.

Images (Optional)

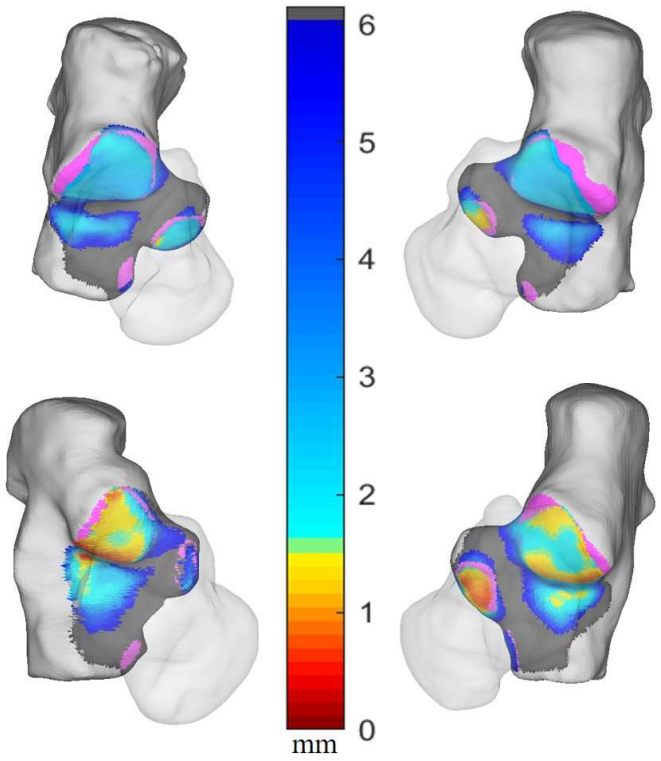


Figure. Example distance mapping on calcaneus and opaque talus overlayed. Top models are a CP participant, bottom models are an idiopathic participant. Warmer colors indicate smaller joint space (impingement) and cooler colors indicate larger joint space (subluxation).

References (Optional)

[1] Kevin Dibbern *et al*. , Foot & Ankle International, 2021

Acknowledgements (Optional)

This work was supported by Shriners Children's grant #79135. We would also like to acknowledge Tracy O'Brien and Nikki Mittel in the Shriners Children's Radiology Department.

Session Category

Clinical Biomechanics: N/A

P4-220

Classification of Inflammatory Arthritis Patients Based on Forearm Muscle Activity Patterns During Cylinder-Grasping using traditional Machine Learning Methods

B. Sc. negin javaheri[1,2,3], Dr. rer. biol. hum. Birte Coppers[1,2], Prof. alp. PhD Verónica Gracia Ibáñez[4], M. Sc. Simon Heinrich[5], Dr. med. Sara Bayat[1,2], Dr.-Ing. Robert Richer[3], Prof. Dr. med. Arnd Kleyer[1,2,6], Prof. Dr.-Ing. habil. Sigrid Leyendecker[5], Prof. Dr. Björn Eskofier[3], Prof. Dr. Georg Schett[1,2], PD Dr. sport.science Dr. habil. med. Anna-Maria Liphardt[1,2]

[1]Friedrich-Alexander-Universität (FAU) Erlangen-Nürnberg & Universitätsklinikum Erlangen, Internal Medicine 3 - Rheumatology and Immunology, Erlangen, Bavaria, Germany. [2]FAU Erlangen-Nürnberg & Universitätsklinikum Erlangen, Deutsches Zentrum Immuntherapie, Erlangen, Bavaria, Germany. [3]Machine Learning and Data Analytics Lab Department Artificial Intelligence in Biomedical Engineering FAU Erlangen-Nürnberg, Erlangen, Bavaria, Germany. [4]Department of Mechanical Engineering and Construction, Universitat Jaume I, Castellón de la Plana, Valencian Community, Spain. [5]FAU Erlangen-Nürnberg, Lehrstuhl für Technische Dynamik, Erlangen, Bavaria, Germany. [6]Charité - Universitätsmedizin Berlin, Med. Klinik mit Schwerpunkt Rheumatologie und Klinische Immunologie, Berlin, Berlin, Germany

Introduction

Hand function is impaired in rheumatoid arthritis (RA) and psoriatic arthritis (PsA), even in the absence of acute inflammation [1,2]. The contribution of muscle activity and motor control to loss of function in RA and PsA is unclear. Surface electromyography (sEMG) enables objective, non-invasive quantification of neuromuscular activity. By using machine learning, we aimed to classify RA, PsA, and healthy controls (HC) and identify the most discriminative sEMG features from forearm muscles during standardized cylinder-grasping.

Methods

RA (ACR/EULAR 2010) and PsA (CASPAR) patients (MED3 clinics Erlangen, Germany) and HC performed cylinder-grasping (four varying diameters, three repetitions each), while sEMG (Noraxon, USA, 1500Hz) was recorded using two sEMG sensors (n-electrodes, Ambu, Denmark) from flexor digitorum superficialis (flexor) and extensor digitorum communis (extensor) (Ethics #357_20B). After standard post-processing [3], signals were normalized task-specific (participant-specific peak across all grasps) or to the maximum voluntary contraction (MVC; isometric grip strength). Time- and frequency-domain features were extracted from a one-second segment around the peak sEMG and classified using Linear Discriminant Analysis (LDA), Random Forest, and Support Vector Classifier with stratified k-fold cross-validation by participant.

Results

Data from 64 HC (58% female, 46.3±18.9 years), 71 PsA (52% female, 52.1±14.4 years), and 57 RA patients (72% female, 54.4±14.5 years) were analyzed. The highest accuracy was achieved for HC vs PsA using LDA on female-only extensor sEMG signals during the largest cylinder-grasp with task-specific normalization, while binary classifications outperformed the three-class model in other comparisons. The most informative features (descending order) were: Root Mean Square, Mean/Median Frequency, Enhanced Wavelength.

Discussion

Female extensor muscle activity during the largest-cylinder grasp best distinguished PsA from HC. RA was less separable from both HC and PsA, reflecting more overlapping activation patterns. The three-class model showed poor performance due to shared EMG characteristics. Results suggest the extensor digitorum communis as the most discriminative muscle in our data set. Sex-specific activation patterns strengthen disease discrimination, supporting sEMG's potential to identify disease-specific muscle activation patterns.

Images (Optional)

Table 1: Classification performance for female participants using task-specific normalization, the largest-cylinder grasp, and extensor muscle data.

Groups	Features	Classifier	Accuracy	F1-Score
HC vs PsA	RMS, MNF, MDF, EWL	LDA	0.7973	0.7969
HC vs RA	MAV, MNF, MDF	LDA	0.7436	0.7393
RA vs PsA	ZC, EWL, NZC	KNN	0.7051	0.7051
HC vs RA vs PsA	RMS, ZC, EWL, NZC	RF	0.5217	0.5216

Healthy Controls, HC; Psoriatic Arthritis, PsA; Rheumatoid Arthritis, RA; Root Mean Square, RMS; Mean Absolute Value, MAV; Zero Crossings, ZC; New Zero Crossings, NZC; Mean Frequency, MNF; Median Frequency, MDF; Enhanced Waveform Length, EWL; Extensor Digitorum Communis, extensor; Linear Discriminant Analysis, LDA; k-Nearest Neighbors, KNN; Random Forest, RF.

References (Optional)

[1] Coppers et al., MSSE, 2025.

[2] Liphardt et al., ACR Open, 2020.

[3] Jarque-Bou et al., Sensors, 2023.

Acknowledgements (Optional)

Funding: German Research Foundation, CRC-1483-Project-ID 442419336, EmpkinS.

Session Category

Clinical Biomechanics: N/A

P4-221

Ipsi- And Contra-Lateral Neural Connectivity Among Arm MusclesIs Disrupted by Muscle Weakness: A Computational Neuromechanical Study of Force Production in the Two-Handed Tennis Backhand

Ms. Neva Manas, Ms. Giulia Zandri, Mr. Suhail Hooker, Mr. Nwachukwu Anene, Dr. Francisco Valero-Cuevas

University of Southern California, Los Angeles, CA, United States

Ms. Neva Manas

Ms. Giulia Zandri

Mr. Suhail Hooker

Mr. Nwachukwu Anene

Introduction

Musculoskeletal models of limb function often assume that muscles are controlled independently of each other. However, ipsi- and contra-lateral neural interconnections among muscles are well documented by mutual inhibition/facilitation [1] and force-sharing of neural origin among fingers [2] . Here, we investigate the functional interactions between muscle connectivity and coordination in arm muscles for force production during the two-handed tennis backhand (with the left arm in the rear as the power-arm) before and after simulated injury.

Methods

A coupled neuro-muscular computational 3D model of two arms simulated instantaneous force production at the moment of ball impact. The model included 17 muscles per arm [4], plus alpha motor neurons, commissural interneurons, Ia pathways and gamma motor neurons, linked via a connectivity matrix W ([170 x 170]) representing synaptic weights between -1 and 1. Starting from a random W_0, synaptic weights and muscle activations

were iteratively adjusted via simple Hebbian plasticity to reduce the Euclidean norm between the predicted and target 3-D force at the racquet {300, 100, 200} N. Injury was implemented by reducing the maximal isometric force (F_0) of 3 left-arm muscles (*Ant. Delt, Post. Delt and Tri)* by 50%, simulating disuse atrophy from rotator cuff injury. Principal Component (PC) analysis of the converged W identified dominant connectivity patterns, Fig. 2, with a threshold of $|w_i| \geq 0.2$.

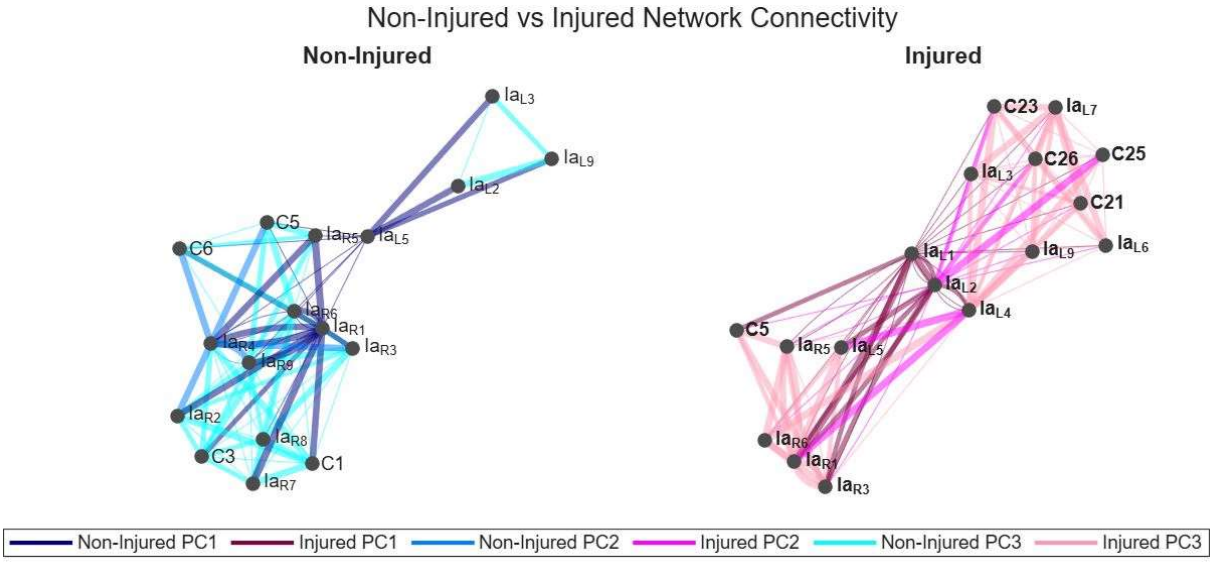
Results

For the 'un-injured' case, 40 PCs explained 80% of the variance in W, but PCs 1, 2 and 3 accounted for 38% (18%, 13%, and 7%, respectively) in a representative case shown in Fig. 2. These PCs reveal dominant interconnections from Ia pathways and commissural interneurons, underscoring the functional relevance of reflex and contralateral pathways. Results for the 'injured' case showed increased Ia and commissural interconnectivity compared to the 'un-injured' case.

Discussion

This pilot study computationally demonstrates adaptive and maladaptive neural plasticity in post-injury cross-muscle and cross-limb interconnectivity. Our results suggest rehabilitation strategies should consider neural plasticity and target possible maladaptive plasticity to optimize return-to-sport performance.

Images (Optional)



References (Optional)

[1] Hortobágyi T. Exerc Sport Sci Rev. 2005 [2] Zatsiorsky VM et al. Exp Brain Res. 2000 [3] Valero-Cuevas FJ et al. J Biomech. 2015

Acknowledgements (Optional)

Thanks to Grace Niyo for her feedback during the development of this project.

Session Category

Clinical Biomechanics: N/A

P4-222

Baseline Knee Flexion Moment Is Associated With Short-Term Infrapatellar Fat Pad Volume Change After Anterior Cruciate Ligament Reconstruction

Dr. Nicholas Brisson PhD[1], Dr. Matej Skrobot[1], Dr. Stephan Oehme[2], Dr. Tobias Jung[2], Prof. Jürgen Reichenbach[3], Prof. Georg Duda[1], Dr. Martin Krämer[3]

[1]Julius Wolff Institute, Berlin Institute of Health, Charité – Universitätsmedizin Berlin, Berlin, Berlin, Germany. [2]Center for Musculoskeletal Surgery, Charité – Universitätsmedizin Berlin, Berlin, Berlin, Germany. [3]Medical Physics Group, Institute of Diagnostic and Interventional Radiology, Jena University Hospital, Friedrich Schiller University Jena, Jena, Thuringia, Germany

Introduction

Anterior cruciate ligament (ACL) injury increases post-traumatic osteoarthritis (PTOA) risk, and this risk persists after reconstruction (ACLR) due to aberrant gait mechanics. The infrapatellar fat pad (IPFP) is mechanosensitive; cyclic deformation during walking – primarily from sagittal-plane knee loading – may influence its structure and composition, which can be assessed using magnetic resonance imaging (MRI)-based volume and T1 measures. Whether sagittal-plane knee moments relate to early IPFP remodeling after ACLR is unknown. This study tested whether baseline peak knee flexion and extension moments (KFM, KEM) predicted 6-month changes in IPFP volume or T1.

Methods

Ten ACLR patients (4 women; age 34±9 y) and ten age- and sex-matched controls underwent baseline gait analysis and knee MRI; with repeat scans at 6 months. For ACLR, baseline was 6.2±0.7 months after ipsilateral four-strand semitendinosus reconstruction (9.6±1.9 months post-injury). Gait data (45 s) were collected during self-paced treadmill walking using motion capture (Vicon) and force plates (Motek). Peak external KFM and KEM were averaged across gait cycles. MRI (3T Siemens Vida) acquired ultrashort echo-time images and T1 maps ($0.6\times0.6\times1.5\ mm^3$). The IPFP was segmented to extract volume and mean global T1. Between-group differences were tested with independent t-tests; 6-month changes with paired t-tests. In ACLR, linear regression tested whether baseline KFM or KEM predicted ΔVolume or ΔT1. Significant results were followed by a multivariate model including all participants, adjusting for baseline volume. All tests were two-tailed ($\alpha=0.05$).

Results

Groups were similar in age, sex, and walking speed. Baseline KFM, KEM, and IPFP volume were comparable; T1 was higher in ACLR ($p=0.003$). IPFP volume and T1 showed no group-

level change over 6 months. In ACLR, baseline KFM predicted ΔVolume (β =–6.51, p=0.027). In the multivariate model, both KFM (β=–4.17, p=0.001) and baseline volume (β=–0.06, p=0.040) were significant predictors (Figure 1).

Discussion

Group-level IPFP volume and T1 remained stable over 6 months, yet individual ΔVolume variability allowed loading–volume associations to emerge. Baseline KFM was related to ΔVolume, suggesting sagittal-plane loading influences short-term IPFP behavior. Larger, longer-term studies should determine whether early loading-related IPFP responses are relevant to PTOA development.

Images (Optional)

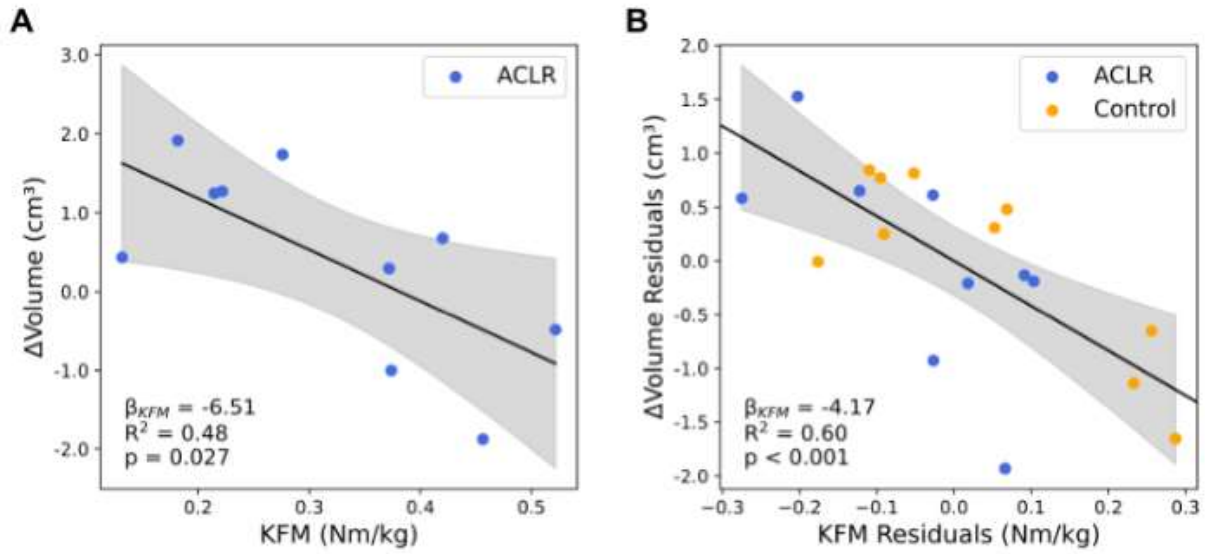


Figure 1: (A) Univariate association between baseline KFM and 6-month ΔVolume in ACLR, and **(B)** partial regression plot from the multivariate model including ACLR and controls showing the adjusted KFM–ΔVolume association after controlling for baseline volume. Individual data points are displayed with regression lines and 95% confidence bands.

Session Category

Clinical Biomechanics: N/A

P4-223

Three-Dimensional Biomechanics of Bilateral Squats After Medial Meniscus Posterior Root Tear and Repair: A Cross-Sectional Motion Analysis Study.

Dr. Tiago Zimerman MD[1,2], Dr. Felipe F. Gonzales MD, MSc[1,3,2], Dr. Enzo Mameri MD[4,1], Ms. Aleksandra Kozicka BS[5], Ms. Nicole Potter MA[2], Dr. Leonardo Metsavaht MD, PhD[1,6], Dr. Gustavo Leporace PhD[1,6], Dr. Jorge Chahla MD, PhD[2,5], Dr. Jonathan A. Gustafson PhD[2,1]

[1]Instituto Brasil de Tecnologia da Saúde (IBTS), Rio de Janeiro, Rio de Janeiro, Brazil. [2]Rush University Medical Center, Chicago, Illinois, United States. [3]Universidade Federal de São Paulo (UNIFESP), Escola Paulista de Medicina, Departamento de Diagnóstico por Imagem, São Paulo, São Paulo, Brazil. [4]Departamento de Ortopedia, Escola Paulista de Medicina, Universidade Federal de São Paulo, São Paulo, São Paulo, Brazil. [5]Midwest Orthopaedics at Rush (MOR), Chicago, Illinois, United States. [6]Departamento de Diagnóstico por Imagem, Escola Paulista de Medicina, Universidade Federal de São Paulo,, São Paulo, São Paulo, Brazil

Dr. Tiago Zimerman

Introduction

Medial meniscus posterior root (MMPR) tears disrupt stress transmission in the knee and may change limb coordination during bilateral functional tasks. Understanding how MMPR tears and repairs affect bilateral squat (BLS) biomechanics, a highly functional movement, could help clarify how this pathology contributes to long-term joint degeneration. The purpose of this study was to examine BLS kinematics and kinetics in patients with MMPR tears and those with MMPR repairs, compared to healthy, age-matched controls. We hypothesize that patients with MMPR tears and repairs will exhibit altered BLS biomechanics associated with knee osteoarthritis.

Methods

Our cross-sectional cohort consisted of 56 knees: MMPR tear (n=20), MMPR repair (n=20), and healthy controls (n=16). Each patient performed eight bilateral squats with standardized instructions in our Motion Analysis Lab. Lower-limb kinematics (120 Hz) were estimated using a point cluster technique, and kinetics were measured via force plates (3000 Hz). Statistical comparisons of discrete metrics and time-series data via Statistical Non-Parametric Mapping (SnPM) were evaluated across the BLS cycle. Group comparisons

were performed using the SPM1D nonparametric one-way ANOVA test, and post hoc pairwise t-tests (permutation inference), and Bonferroni correction was employed for multiple comparisons ($\alpha = 0.05$).

Results

Significant differences were observed for knee adduction throughout 0.1-16.6% (P=0.021) and 92.2-95.7% (P=0.046) of the squat cycle (%SC). Group comparisons revealed a significant main effect of group knee external rotation over 12.5-16.2% and 78.6-94.7% of the squat cycle; however, post-hoc analysis did not identify any individual pairwise group differences. The MMPR tear and repair groups displayed increased knee internal rotation moment at 0-5.7%SC (P=0.0149) compared to control (Tear: 0-9.1%SC, P=0.0015; Repair: 0-2.8%SC, P=0.0382). (Figure 1)

Discussion

Distinct group differences appeared during bilateral squats. Both MMPR tear and repair groups exhibited altered kinematics and kinetics linked with increased osteoarthritis risk. Still, the repair group showed patterns closer to those of controls, indicating partial restoration of knee biomechanics. These findings highlight the value of assessing squat mechanics to help guide targeted specific movement interventions and to identify the patients who may benefit from earlier surgical management to reduce long-term joint degeneration.

Images (Optional)

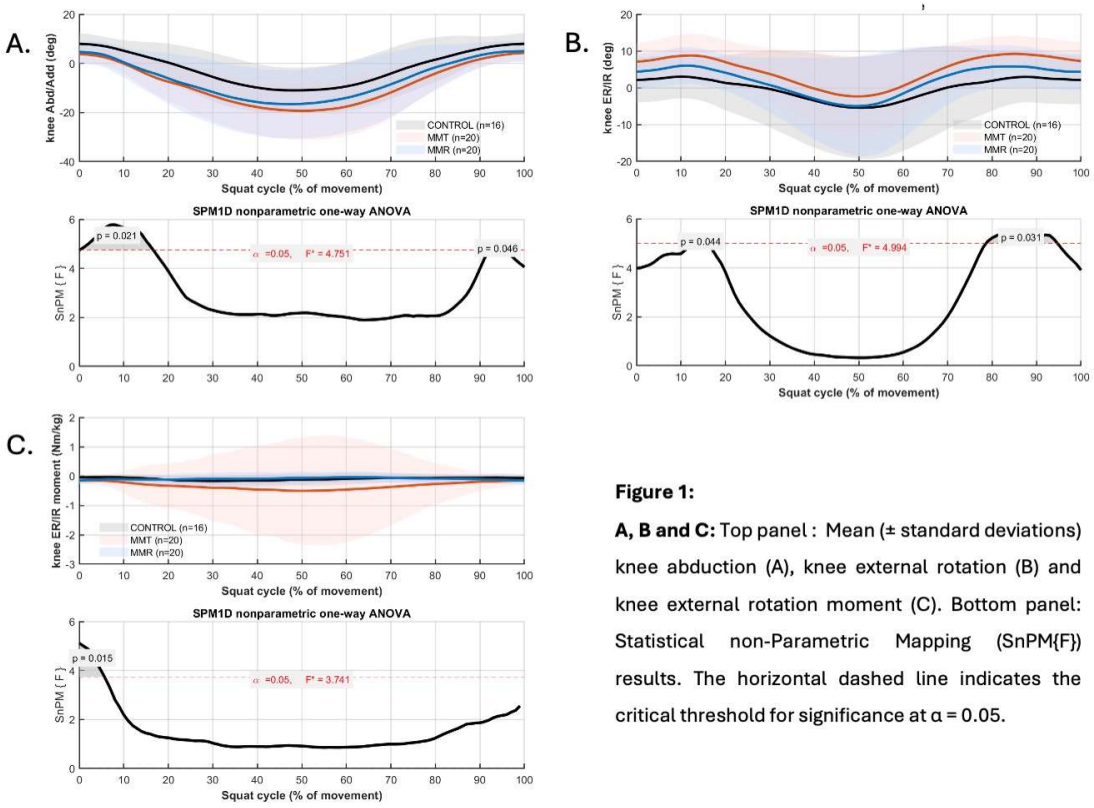


Figure 1:

A, B and C: Top panel : Mean (± standard deviations) knee abduction (A), knee external rotation (B) and knee external rotation moment (C). Bottom panel: Statistical non-Parametric Mapping (SnPM{F}) results. The horizontal dashed line indicates the critical threshold for significance at α = 0.05.

Session Category

Clinical Biomechanics: N/A

P4-224

Smartphone-Based Spinal Kinematic Measures in Low Back Pain Patients and Asymptomatic Individuals: Reliability and Group Differentiation

Dr. Niels Brouwer[1], MSc. Arlene von Aesch[1], Dr. Adrien Cerrito[1,2], Dr. Lucas Moulin[3], Prof. Dr. Laura Raileanu[3], Prof. Dr. Guillaume Christe[4], Prof. Dr. Stefan Schmid[1,5]

[1]Spinal Movement Biomechanics Group, Division of Physiotherapy, Department of Health Professions, Bern University of Applied Sciences, Bern, Bern, Switzerland. [2]HE-ARC Santé, HES-SO University of Applied Sciences and Arts Western Switzerland, Delémont, Jura, Switzerland. [3]School of Engineering and Management Vaud (HEIG-VD), HES-SO University of Applied Sciences and Arts Western Switzerland, Yverdon-Les-Bains, Vaud, Switzerland. [4]Department of Physiotherapy, HESAV School of Health Sciences, HES-SO University of Applied Sciences and Arts Western Switzerland, Lausanne, Vaud, Switzerland. [5]Faculty of Medicine, University of Basel, Basel, Basel, Switzerland

Introduction

Individuals with LBP typically show altered spinal motor behaviour [1,2], which has been associated with clinical outcomes, such as changes in pain and disability [1]. However, spinal motor behaviour assessments in clinical practice are typically based on visual evaluation [3], possibly since objective measurements are predominantly laboratory-constrained. Inertial sensors, integrated in most smartphones, allow ambulatory spinal kinematic measurements [4]. However, for smartphone-based spinal kinematic measures, reliability amongst LBP individuals and ability to differentiate between LBP and asymptomatic groups, remain unknown, and we therefore aimed to evaluate these in this study.

Methods

Spinal kinematics were collected using a custom-made smartphone application amongst eighteen LBP (female=14; age=43±17y) and seventeen asymptomatic (female=11; age=37±13y) individuals. Participants performed, at their preferred speed, eight repetitions of maximum trunk flexion, extension, left/right lateral flexion, and a natural pen-pickup movement in two sessions (5±2 days apart) while holding the smartphone against their sternum. Since spinal movement amplitude and speed are generally altered in LBP [1,2], average maximum trunk inclination and root-mean-square (RMS) angular velocity were computed across the eight repetitions for each movement task. Within- and between-

session reliability were determined using intra-class-correlation (ICC) coefficients and group discrimination using a 2x2 repeated-measures ANOVA.

Results

Within- and between-session reliability was near-excellent to excellent for both maximum inclination and RMS angular velocity across all movements (generally ICC>0.86; Table 1). Both measures yielded significant (p-value<0.05) differences between groups for all movements, indicating lower maximum inclination and RMS angular velocity in LBP. Furthermore, both reliability and discrimination outcomes suggested that similar ICCs and p-values were reached after three repetitions.

Discussion

This study demonstrates that, with a smartphone, clinically relevant spinal kinematic measures can be measured that yield near-excellent to excellent reliability in individuals with LBP and effectively discriminate them from asymptomatic individuals. This enables objective, ambulatory assessment of spinal movement and paves the way for including such assessments in longitudinal studies on LBP.

Images (Optional)

Table 1. Outcomes of within- and between-session reliability analyses amongst LBP individuals (Intra-class correlation coefficient; ICC), and discrimination analyses (2x2 repeated measures ANOVA). ηp^2: effect size; ns: non-significant; Ext: Extension; L Lat Flex: Left lateral flexion; R Lat Flex: right lateral flexion; Pick: picking up a pen.

	Maximum Inclination					Root-mean-square Angular Velocity				
	Flexion	**Ext**	**L Lat Flex**	**R Lat Flex**	**Pick**	**Flexion**	**Ext**	**L Lat Flex**	**R Lat Flex**	**Pick**
Reliability LBP (ICC)										
Within-session 1	0.96	0.96	0.91	0.93	0.95	0.93	0.91	0.86	0.87	0.93
Within-session 2	0.96	0.94	0.91	0.93	0.92	0.96	0.89	0.94	0.93	0.91
Between-session	0.91	0.97	0.88	0.91	0.88	0.88	0.88	0.86	0.74	0.89
Discrimination (p-value)										
Group (LBP vs. asymptomatic)	<0.001	<0.001	<0.001	<0.001	0.014	0.006	0.003	0.002	<0.001	0.030
Session (1 vs. 2)	ns	ns	ns	ns	ns	ns	ns	ns	ns	ns
Group:Session	ns	ns	ns	ns	ns	ns	ns	ns	ns	ns
Discrimination (ηp^2)										
Group (LBP vs. asymptomatic)	0.31	0.30	0.36	0.41	0.17	0.21	0.25	0.28	0.34	0.14
Session (1 vs. 2)	-	-	-	-	-	-	-	-	-	-
Group:Session	-	-	-	-	-	-	-	-	-	-

References (Optional)

[1] Nzamba *et al.*, EJP, 2024
[2] Moissenet *et al.*, Sci Rep, 2021
[3] Van Dijk *et al.*, BMC Musculoskelet Disord, 2017
[4] Brouwer *et al.*, Scand J Med Sci Sports, 2021

Acknowledgements (Optional)

This work was supported by the Swiss National Science Foundation (SNSF; Grant No.: 220434).

Session Category

Clinical Biomechanics: N/A

P4-225

Smartphone-embedded Inertial Sensors Detect Postural Control Changes in Low Back Pain Not Evident from Motion Capture or Centre of Pressure

Dr. Niels Brouwer[1], MSc. Arlene von Aesch[1], Dr. Adrien Cerrito[1,2], Dr. Lucas Moulin[3], Prof. Dr. Laura Raileanu[3], Prof. Dr. Guillaume Christe[4], Prof. Dr. Stefan Schmid[1,5]

[1]Spinal Movement Biomechanics Group, Division of Physiotherapy, Department of Health Professions, Bern University of Applied Sciences, Bern, Bern, Switzerland. [2]HE-ARC Santé, HES-SO University of Applied Sciences and Arts Western Switzerland, Delémont, Jura, Switzerland. [3]School of Engineering and Management Vaud (HEIG-VD), HES-SO University of Applied Sciences and Arts Western Switzerland, Yverdon-Les-Bains, Vaud, Switzerland. [4]Department of Physiotherapy, HESAV School of Health Sciences, HES-SO University of Applied Sciences and Arts Western Switzerland, Lausanne, Vaud, Switzerland. [5]Faculty of Medicine, University of Basel, Basel, Basel, Switzerland

Introduction

Trunk motor control, commonly evaluated through postural tasks, is altered in individuals with low back pain (LBP), potentially reflecting clinically relevant phenotypes [1]. Conventional assessments are often laboratory-constrained. Inertial measurement units (IMUs), integrated in most smartphones, enable ambulatory assessments of trunk kinematics [2]. We examined the use of smartphone-embedded IMUs to evaluate postural control in LBP.

Methods

Eighteen LBP (female=14; age=43±17y) and seventeen asymptomatic (female=11; age=37±13y) individuals performed standing with eyes closed for 90 seconds twice, 5±2 days apart, while holding a smartphone against their sternum. Trunk kinematics were recorded using a smartphone and with an optoelectronic motion capture system (Mocap). The Centre of Pressure (CoP) was measured using a force plate. We assessed smartphone- and Mocap-based root-mean-square trunk angle and angular velocity (anterior-posterior (AP), medial-lateral (ML), and AP-ML vector norm), and root-mean-square CoP position [1,3]. We also assessed these measures' spectral content using frequency bands (<0.5Hz, 0.5-2Hz, >2Hz), based on CoP literature associating the lowest and highest band with visual/vestibular- and proprioceptive control, respectively [3]. Group differences were evaluated with a two-by-two repeated-measures ANOVA.

Results

Smartphone- and Mocap-based kinematics showed greater overall sway (vector norm) in individuals with LBP (Fig. 1A), while AP and ML sway and root-mean-square angular velocity did not differ. Smartphone-based angular velocity spectral analysis revealed group differences in AP at <0.5Hz and >2Hz (Fig. 1B) and in ML at <0.5Hz, with a reduction in high-frequency and an increase in low-frequency content in LBP. Mocap-based spectral measures and all CoP measures showed no between-group differences across both sessions.

Discussion

We found increased smartphone- and Mocap-based trunk sway in LBP, in line with previous findings [1]. Only smartphone-based angular velocity revealed spectral content differences, possibly reflecting decreased proprioceptive and increased vestibular weighting in postural control in LBP [3]. These findings suggest smartphone-embedded IMUs may detect postural control changes not captured by Mocap or CoP measures, providing insight into potential mechanisms underlying altered postural control in LBP.

Images (Optional)

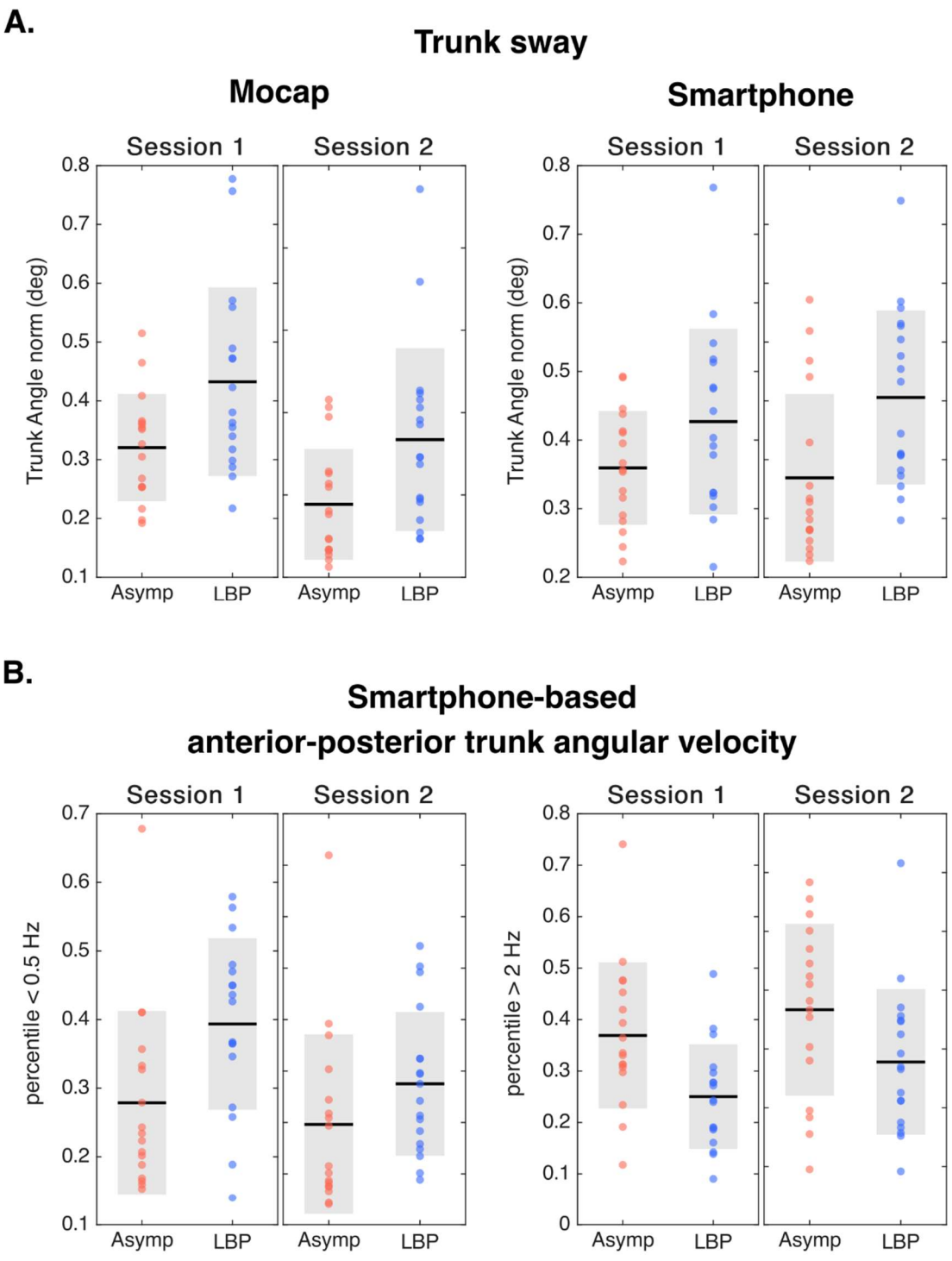


Figure 1. (A) Mocap- and IMU-based overall trunk sway (root-mean-square of vector norm) for asymptomatic (Asymp) and low back pain (LBP) individuals for both sessions. Both showed significant group differences across the two sessions (Mocap-based: *p*-value = 0.011; IMU-based: *p*-value = 0.017). (B) IMU-based spectral analysis of anterior-posterior trunk angular velocity: percentile of normalized power < 0.5 Hz and > 2 Hz. Both showed significant group differences across the two sessions (< 0.5 Hz: *p*-value = 0.037; > 2 Hz: *p*-value = 0.013). Black line: mean; grey rectangle: standard deviation.

References (Optional)

[1] Van Dieën *et al.*, J. Orthop. Sports Phys. Ther., 2019
[2] Brouwer *et al.*, Scand. J. Med. Sci. Sports, 2021
[3] Gilfriche *et al.*, Front. Physiol., 2018

Acknowledgements (Optional)

This work was supported by the Swiss National Science Foundation (SNSF; Grant No.: 220434).

Session Category

Clinical Biomechanics: N/A

P4-226

3D Morphometric Analysis of Maxillary Arch Remodeling Following Primary Cheiloplasty in Newborn Cleft Patients Using a Novel Software Tool

MD, PhD Olga Koskova[1,2], Ing, PhD Libor Borak[3], MD, PhD Alena Brysova[4,2], MD Magda Novakova[4], PhD Katerina Vymazalova[5], Ing, PhD Petr Marcian[3]

[1]Department of Burns and Plastic Surgery, University Hospital Brno, Brno, Czech Republic, Czechia. [2]Masaryk University, Faculty of Medicine, Brno, Czech Republic, Czechia. [3]Brno University of Technology, Faculty of Mechanical Engineering, Institute of Solid Mechanics, Mechatronics and Biomechanics, Brno, Czech Republic, Czechia. [4]Clinic of Dentistry, St. Anne's University Hospital Brno, Brno, Czech Republic, Czechia. [5]Department of Anatomy, Masaryk University, Faculty of Medicine, Brno, Czech Republic, Czechia

Introduction

The growth of the craniofacial skeleton is influenced by genetic factors and biomechanical forces (Wolff's Law). In healthy infants, a balance between tongue pressure and the containment from lips and cheeks guides the development of the maxillary arch. In newborns with cleft lip and palate, the absence of anterior muscular continuity leads to pathological displacement of alveolar segments.
Primary cheiloplasty re-establishes the anterior muscular sling, introducing new biomechanical forces that trigger bone remodeling. While this effect is recognized, its precise 3D nature remains insufficiently quantified.
This study aimed to use the 3D morphometric tool CleftPoint to quantify the vectors of bone remodeling vectors and changes in maxillary arch geometry between lip and palate surgeries. We hypothesized significant medial remodeling in anterior segments post-cheiloplasty, with posterior regions maintaining innate growth.

Methods

A retrospective study was conducted on 14 patients with non-syndromic unilateral cleft lip and palate (UCLP). All underwent modified Fischer cheiloplasty (~7 days of age) and one-stage palatoplasty (~8 months). No presurgical orthopedics were used.
Silicone impressions were taken before each surgery. 3D dental models were digitized and spatially aligned using a quaternion-based algorithm. Landmarks according to Seckel were identified on both timepoints using CleftPoint [1].
Four morphometric parameters (P-L, C-C', Q-Q', T-T') were calculated and compared using the Wilcoxon signed-rank test ($p < 0.05$).

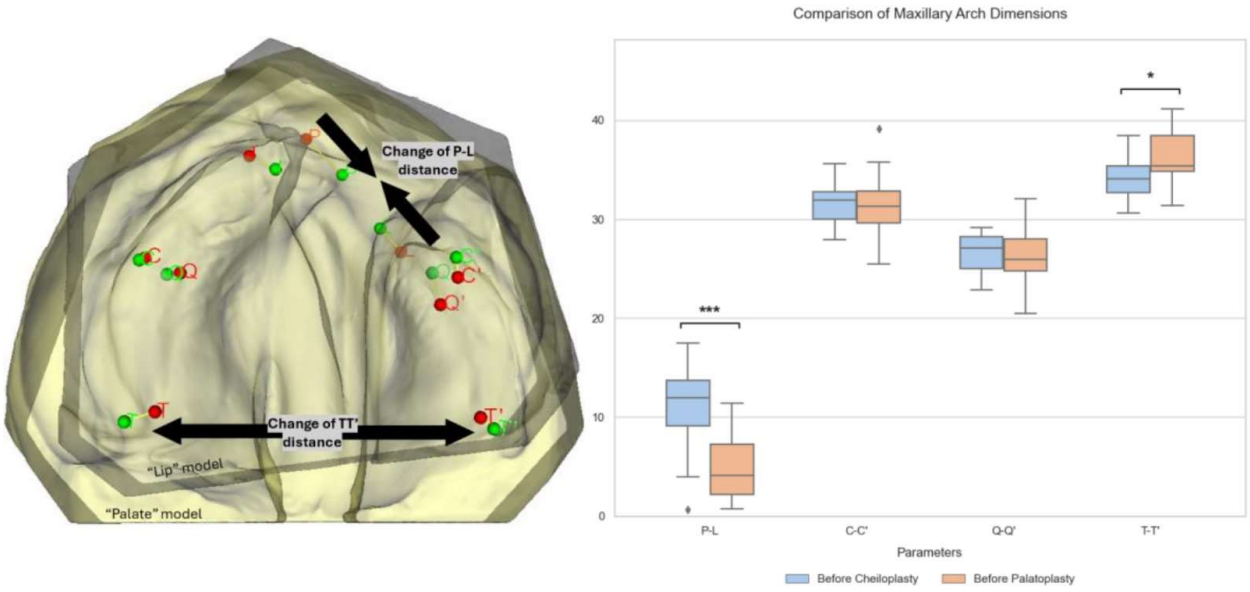
Results

The anterior alveolar cleft width (P-L) showed a significant median decrease of 7.82 mm (from 11.94 mm to 4.11 mm; $p < 0.001$), representing a >60% reduction. Transverse dimensions (C-C', Q-Q') remained stable ($p = 0.808$ and $p = 0.670$), while the posterior width (T-T') significantly increased (from 34.05 mm to 35.42 mm; $p = 0.020$).

Discussion

Primary cheiloplasty induces significant remodeling of the maxillary arch. Reconstructing the orbicularis oris muscle restores anterior pressure, which contributes to the medial shift of anterior alveolar segments and initiates a cascade of biomechanical adaptations. The resulting remodeling pattern—anterior constriction with posterior expansion—reflects a new functional equilibrium of forces. CleftPoint enables precise quantification of these 3D morphological changes, highlighting the role of cheiloplasty as a catalyst for functional, not just aesthetic, normalization.

Images (Optional)



Typical comparison of pre-cheiloplasty ("Lip"; red dots) and pre-palatoplasty ("Palate"; green dots) models of one specific patient; Comparison of maxillary arch dimensions (* p<.05, ** p<.01, ***, p<.0001).

References (Optional)

[1] https://doi.org/10.5281/zenodo.16970749

Acknowledgements (Optional)

This research was supported by AZV—Czech Health Research Council (NU23–06-00301), Czech Republic.

Session Category

Clinical Biomechanics: N/A

P4-227

Unilateral Arm Restriction Affects Dynamic Balance Recovery in Response to Unanticipated External Treadmill Perturbations

Dr. Paige Paulus PT, DPT, PhD[1], Mr. Bradley Moore MS[2], Mr. Paul Hammond II MS[3], Ms. Rebecca Stine MS[3], Dr. Noah Rosenblatt PhD[4], Dr. Matthew Major PhD[1,2,3]

[1]Northwestern University Department of Physical Medicine and Rehabilitation, Chicago, IL, United States. [2]Northwestern University Department of Biomedical Engineering, Evanston, IL, United States. [3]Jesse Brown VA Medical Center, Chicago, IL, United States. [4]Rosaland Franklin University, Chicago, IL, United States

Introduction

Research suggests that unilateral arm restriction (UAR) during steady-state walking, due to upper limb casting/bracing, can increase fall risk. Less is known about how UAR affects perturbation recovery. This study aimed to (1) assess the influence of UAR on reactive balance control in healthy individuals, (2) observe the effect of UAR on muscle activation during recovery to assess motor adaptations. We hypothesized that individuals would experience greater dynamic balance disturbance during perturbation recovery with UAR.

Methods

Ten able-bodied individuals provided informed consent to participate in this IRB-approved study. Participants donned a ceiling-mounted harness and walked on an instrumented treadmill for ten randomly presented perturbation trials (5 per foot) per condition: non-dominant UAR and unbound. Kinematic data were collected by an optical motion capture system (120Hz). Wireless EMG sensors collected bilateral posterior deltoids (PD), tibialis anterior (TA), and medial gastrocnemius muscle activity (960Hz). Perturbations were defined as unexpected treadmill acceleration-deceleration (6.5m/s^2) from 1.0m/s to 3.3m/s and back. Kinematic and EMG data were processed following previous methodology using Visual3D. Whole body angular momentum (*L*) was calculated as the sum of the instantaneous angular momentum of each segment about the center of mass and normalized by treadmill speed and participant mass and height. *L* range (L_{range}) was calculated as the global range (max-min) over the first five post-perturbation strides. EMG data was integrated over the first five post-perturbation strides (*iEMG*). The effects of perturbation side and arm binding on L_{range} and *iEMG* were evaluated using a two-way repeated-measures ANOVA (α=0.05).

Results

UAR caused increased transverse plane L_{range} (p=0.05)(Fig.1A), with non-dominant side perturbations causing greater coronal-plane L_{range} (p=0.04)(Fig.1A). Participants had less non-dominant arm PD activation with UAR (p=0.04)(Fig.1B). There was an interaction effect (condition×side) on nondominant TA activation (p=0.04), and although non-significant, post hoc simple main effects analyses revealed greater TA activation with UAR in response to nondominant perturbations (p=0.08).

Discussion

Study findings suggest that UAR causes an increased challenge to regulating body spin and avoiding falls when recovering from trip-like perturbations. This provides some justification for clinicians to screen their patients' balance when access to natural arm dynamics is unilaterally absent.

Images (Optional)

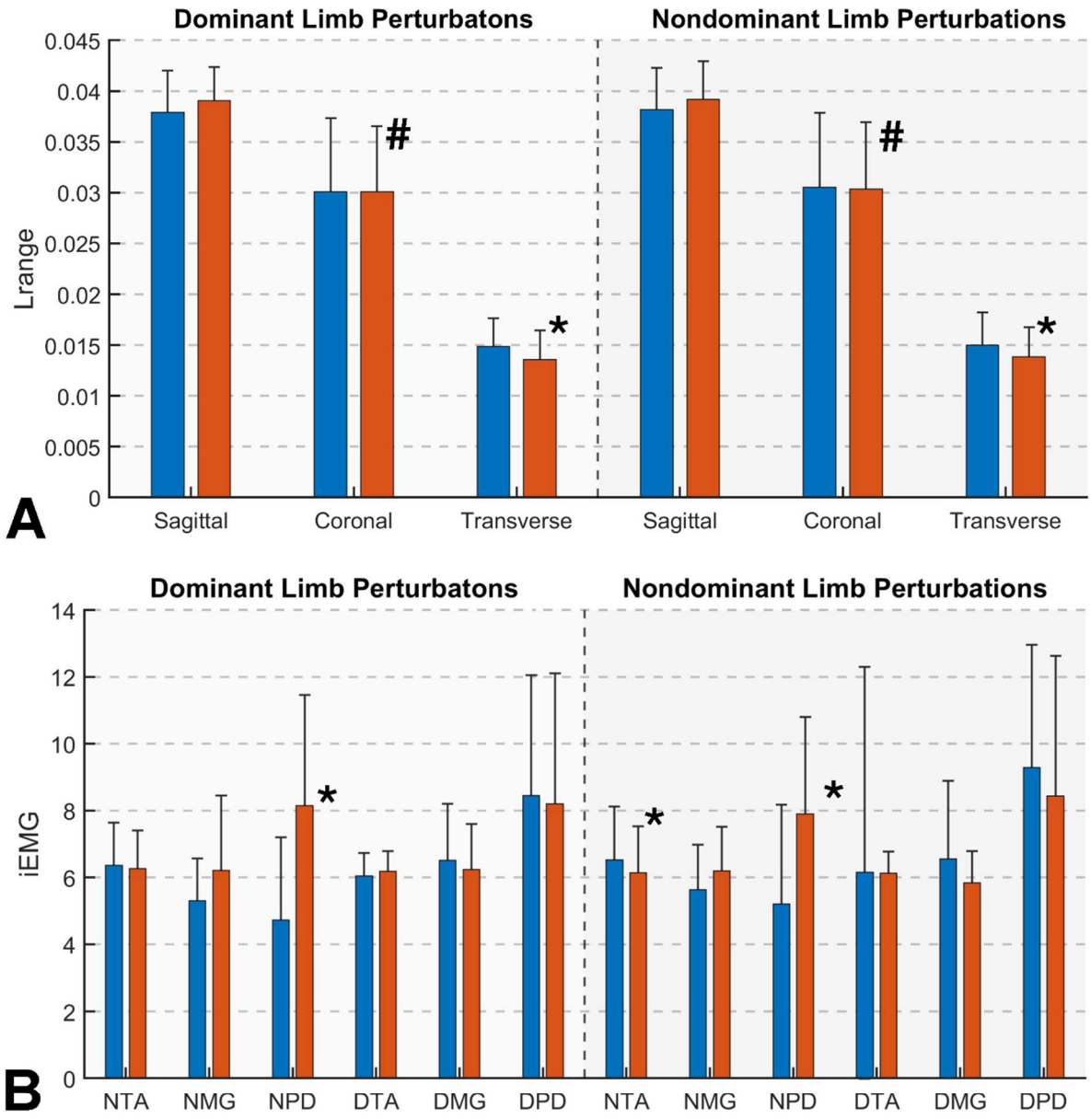


Figure 1: (A) Whole body angular momentum range (L_{range}) and (B) integrated EMG (iEMG) data for perturbation trials. *Dominant limb perturbations are included on the right and nondominant limb perturbations are on the left. Blue bars indicate bound arm data and orange indicate unbound data. *indicates significant differences based on bound vs. unbound arm conditions. #indicates significant differences based on perturbation side.*

References (Optional)

Session Category

Clinical Biomechanics: N/A

P4-228

Integrating Kinematic and Morphometric Data for the Functional Characterization of Lower Limb Joints in Individuals With Multiple Osteochondromas

MEng Giulia Rogati[1], PhD Marina Mordenti[1], MEng Roberto Ramaglia Amadasi[1], Eng Letizia Barbi[2], MD, PhD Luca Sangiorgi[1], PhD Zimi Sawacha[2], DPhil Leardini Alberto[1], PhD Paolo Caravaggi[1]

[1]IRCCS Istituto Ortopedico Rizzoli, Bologna, Emilia-Romagna, Italy. [2]Università di Padova, Padova, Veneto, Italy

MEng Giulia Rogati

Introduction

Multiple Osteochondromas (MO) is a rare hereditary skeletal disorder characterized by benign bone tumors (osteochondromas, OCs) arising primarily from the metaphyses of long bones. These lesions can cause severe complications, such as skeletal deformities, limb length discrepancies, restricted joint motion, and functional impairments of the upper and lower limbs. This study aims to functionally characterise individuals with MO in relation to age-matched healthy populations.

Methods

Approval was obtained from the local ethics committee (333/2024/Sper/IOR) to enrol 30 young adults and children with MO and 30 age-matched healthy subjects. Lower-limb kinematics was measured during gait and in specific motor tasks (e.g. active knee and hip flexion/extension) using 8 IMUs (Ultium Motion, Noraxon). Full-body radiographic evaluation was performed using a micro-dose EOSedge (EOS imaging), and body shape was captured using 3D scanners (InBody, BeyondShape; Artec Leo, 3DZ). Spatiotemporal parameters, joint ROM, and temporal profiles of joint rotation angles were evaluated. OCs location and dimensions, as well as skeletal alignment of the spine and lower limbs, were analysed from imaging. The effect of MO on relevant spatiotemporal and kinematic parameters was investigated using the Mann–Whitney test.

Results

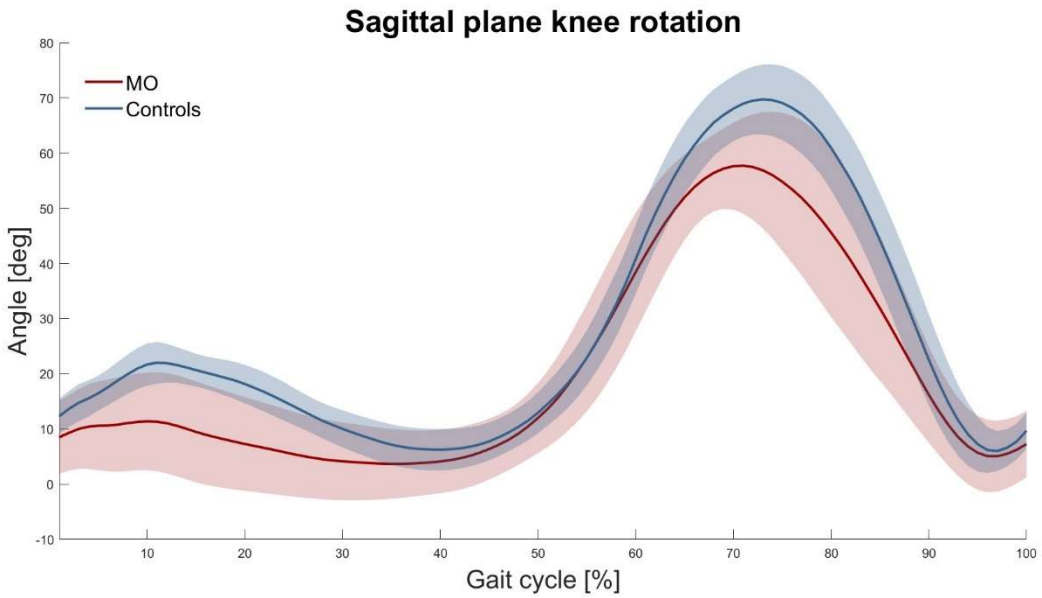
Sagittal plane knee joint rotations over normalized gait cycle for 7 young adults with MO (5F, 2M; 22.0±3.1 years; 22.4±4.3 kg/m^2) and 7 healthy subjects (5F, 2M; 26.6±1.7 years;

24.1±3.6 kg/m^2) are reported in Fig.1. According to the Mann–Whitney test, no statistically significant differences in ROM (deg) between the MO and controls were found in the sagittal plane for the hip (MO=47±6, CONTROL=47±3; p=1.000) or the ankle (MO=39±5, CONTROL =38±3; p=0.714), whereas a significant decrease in knee ROM was detected in the MO population (MO=59±3, CONTROL=65±2; p=0.007).

Discussion

While the recruitment of both MO and healthy individuals is still ongoing, preliminary results on lower-limb joint kinematics suggest a reduced knee ROM and a greater variability in knee kinematics for the MO population in the sagittal plane (Fig.1). These data will be combined with radiographic findings to assess possible correlations between bone deformities and functional alterations.

Images (Optional)



Acknowledgements (Optional)

This research is funded by the Italian Complementary National Plan PNC-I.1 "Research initiatives for innovative technologies and pathways in the health and welfare sector" D.D. 931 of 06/06/2022, "DARE - Digital Lifelong Prevention" initiative, code PNC0000002, CUP B53C22006230001.

Session Category

Clinical Biomechanics: N/A

P4-229

Achilles Subtendon Behaviour and Foot Biomechanics Following Rupture: Preliminary Findings From Heel-Rise Analysis

Dr. Andreas Brand[1,2], B.Sc. Inga Kröger[1,2], M.Sc. Honoka Ishihara[3], M.Sc. Markus Greinwald[1,2], Dr. Johannes Gabel[4], Prof. Peter Augat[1,2]

[1]Institute for Biomechanics, BG Unfallklinik Murnau, Murnau am Staffelsee, Bavaria, Germany. [2]Institute for Biomechanics, Paracelsus Medical University, Salzburg, Salzburg, Austria. [3]Department of Sports Rehabilitation, Hiroshima University, Hiroshima, Chugoku, Japan. [4]Department of Foot and Ankle Surgery, BG Unfallklinik Murnau, Murnau am Staffelsee, Bavaria, Germany

Introduction

The Achilles tendon (AT) is composed of distinct muscle-specific subtendons that enable non-uniform displacements and differential force transmission to the foot [1]. Following rupture, severe impairments of foot function are common, often accompanied by morphological and mechanical changes of the tendon [2]. Little is known about how individual subtendons adapt after rupture and surgical repair. This study aims to investigate the functional adaptations of different Achilles subtendons during dynamic plantar flexion of the foot following AT rupture.

Methods

AT movements of the medial (MG) and lateral gastrocnemius (LG) tendon portions were prospectively analysed in 13 patients with unilateral traumatic AT rupture (10M/3F; age 45±12 y; BMI:26±2 kg/m^2; AT Rupture Score: 40/100), 10-12 weeks post-surgery. Motion capture and synchronized portable ultrasound were used to analyse repetitive bipedal heel-rise performance. Subtendon elongation, sagittal ankle kinematics, weight bearing levels and local AT stiffness using tendotonometry were compared intra-individually between the ruptured and intact side. As the data are preliminary, descriptive results are reported.

Results

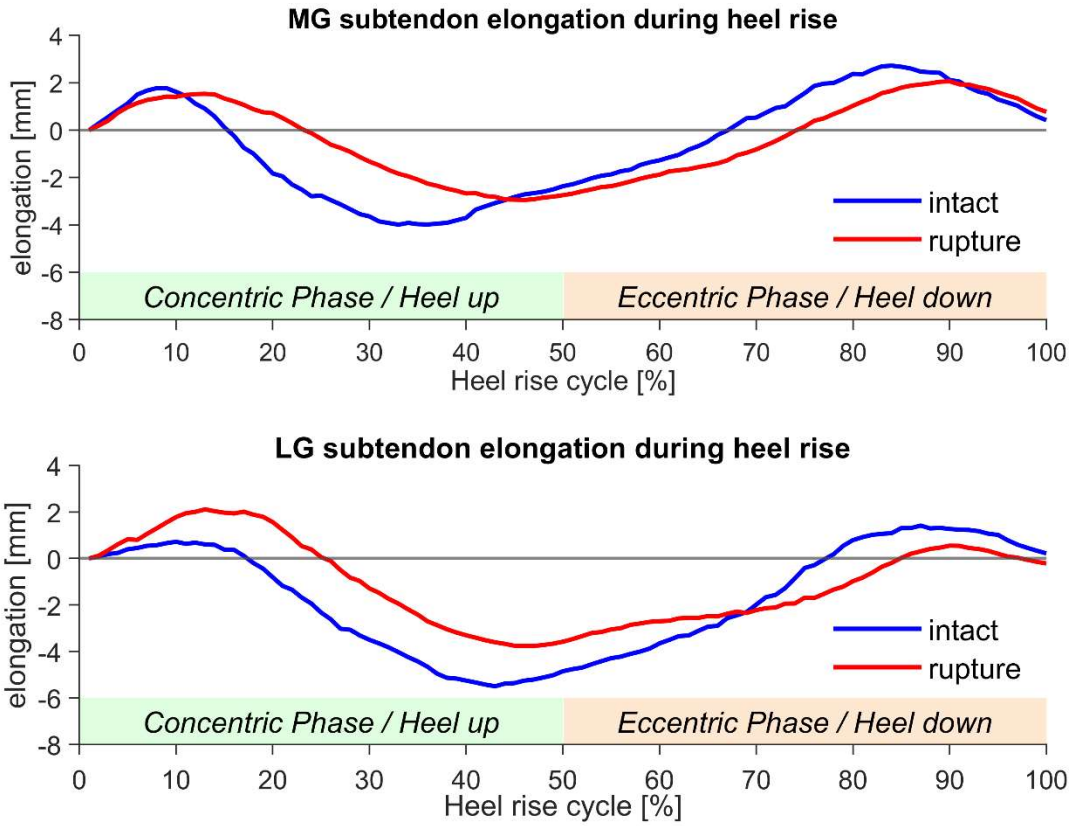
At the ruptured side, a prolonged LG and MG subtendon elongation during the intial phase of concentric plantar flexion was observed. Over the entire heel-rise cycle, LG subtendon elongation showed larger side-to-side differences compared to the MG subtendon (Fig. 1). Average ankle plantar flexion during bipedal heel-rise was 14° (range: 3-25°). Weight-

bearing (% bodyweight) at the foot was lower on the ruptured side (31%; range: 28–35%) compared to the intact side (66%; range: 62–69%). Local stiffness of the ruptured AT was reduced by 26% (range: 8-41%).

Discussion

Preliminary findings indicate early functional adaptations of AT subtendons following trauma and surgical repair. Altered elongation patterns of ruptured subtendons, combined with reduced weight bearing at comparable ankle kinematics, is consistent with changes of biomechanical compliance (loss of stiffness) at the entire AT. Altered elongation patterns further suggest a heterogenous AT adaptation, with the LG subtendon appearing more susceptible to functional alterations than the MG subtendon. Additional data acquisition and analysis are required to confirm these observations and their clinical significance.

Images (Optional)



References (Optional)

[1] Handsfield et al. , J Biomechanics, 2017

[2] Khair et al. , Clin Biomechanics, 2022

Acknowledgements (Optional)

Funded by the German Research Foundation (DFG-Project-Number: 552605231).

Session Category

Clinical Biomechanics: N/A

P4-230

Biomechanical Stability of Neonatal Cleft Lip and Palate Obturators: Effect of Thickness and Surface Roughness on Laryngoscope-Simulated Loading

Ing Petr Marcian[1], MD Olga Koskova[2,3], MD Michaela Richtrova[4,3], Ing Pavel Skacel[1], prof. Petr Stourac[4,3,5], Ing Libor Borak[1]

[1]Brno University of Technology, Brno, Czech Republic, Czechia. [2]Department of Burns and Plastic Surgery, University Hospital Brno, Brno, Czech Republic, Czechia. [3]Faculty of Medicine, Masaryk University, Brno, Czech Republic, Czechia. [4]Department of Paediatric Anaesthesiology and Intensive Care Medicine, University Hospital Brno, Brno, Czech Republic, Czechia. [5]Department of Simulation Medicine of the Faculty of Medicine, Masaryk University, Brno, Czech Republic, Czechia

Introduction

Palatal obturators facilitate feeding and airway management in neonates with cleft lip and palate, a condition that also presents significant challenges for safe neonatal intubation. These challenges arise from a combination of typical neonatal airway anatomy and cleft-related disruptions, which together hinder visualization and increase the risk of trauma during laryngoscope manipulation. Protective obturators—silicone devices covering the cleft—may ease intubation and reduce soft tissue injury [1,2]. While digital workflows enable precise customization, the biomechanical influence of design parameters remains unclear. This study evaluated the mechanical resistance of 3D-printed silicone obturators, hypothesizing that increased thickness and surface roughness enhance load-bearing capacity under laryngoscope-simulated forces.

Methods

Patient-specific obturators (medical-grade silicone) were obtained via 3D-printed molds derived from a digital workflow. Four groups (n=3 each) were tested, varying thickness (1.5 vs. 2.5 mm) and surface finish (smooth vs. rough). A custom setup utilized a maxillary alveolus-simulating lower fixture and a laryngoscope-mimicking upper mandrel. Samples were compressed vertically until failure. Maximum load was analyzed, and Cohen's *d* was calculated to quantify effect sizes given the sample size.

Results

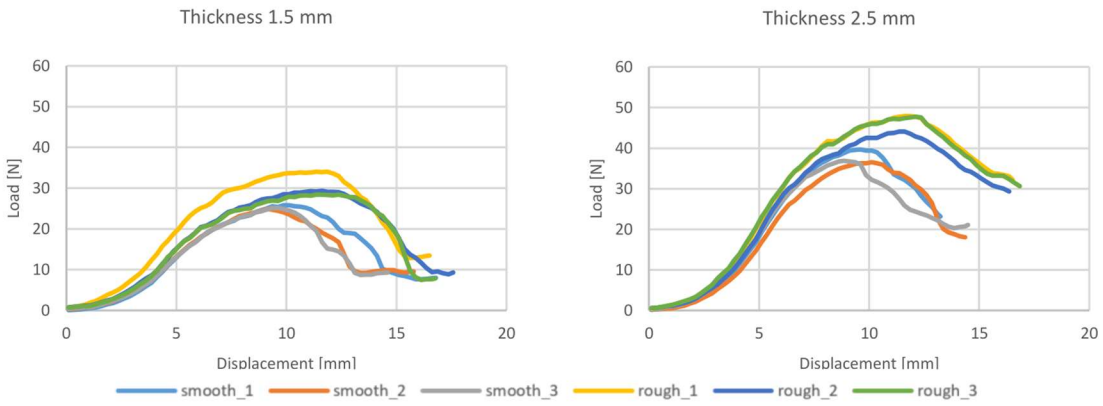
Thickness was the primary determinant of stability. The 2.5 mm samples withstood significantly higher loads (Smooth: 37.7±1.7 N; Rough: 46.6±2.1N) compared to 1.5 mm samples (Smooth: 25.3±0.5 N; Rough: 30.6±3.0 N). This represented an extremely strong effect size for both finishes (d=9.81 and d=6.13, respectively). Surface texture was also

critical; rough surfaces consistently outperformed smooth ones (d=2.46 for 1.5 mm; d=4.57 for 2.5 mm), increasing load capacity by approximately 20–24% and preventing premature slippage.

Discussion

The very large Cohen's d values confirm that thickness is the dominant contributor to mechanical resistance, providing essential bulk stiffness under vertical loading. However, the substantial effect of surface roughness demonstrates a complementary mechanism: friction-mediated retention. The larger effect size observed in thicker samples suggests a synergistic interaction, where enhanced structural rigidity amplifies the stabilizing influence of a textured surface. These findings strongly support incorporating controlled surface roughness into digitally designed neonatal obturators to improve safety during laryngoscope manipulation without changing material formulation.

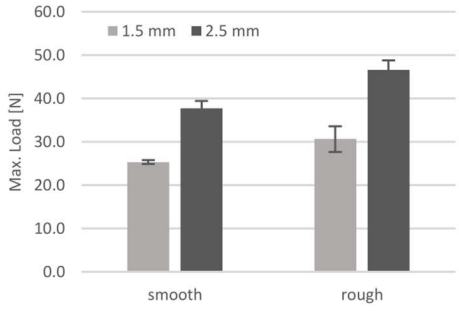
Images (Optional)



Force–displacement curves for all obturator groups



Compressive test



Maximum load to failure across design groups (mean ± SD)

References (Optional)

[1] Richtrova et al., BJA, 2023

[2] Richtrova et al., Annals of Medicine, 2025

Acknowledgements (Optional)

This research was supported by AZV—Czech Health Research Council (NU23–06-00301), Czech Republic. This publication was supported by the 'Mechanical Engineering of Biological and Bio-inspired Systems' project, funded as project No. CZ.02.01.01/00/22_008/0004634 by Programme Johannes Amos Comenius, call Excellent Research.

Session Category

Clinical Biomechanics: N/A

P4-231

Biomechanical Analysis of the Effect of Different Alignment Techniques in Total Knee Arthroplasty in Patients with Valgus Deformities: A Finite Element Study

Mr. Mattia Sisella[1], Mr. Fabiano Bini[2], Mr. Pietro Margheriti[2], Mr. Nicolò Monticelli[2], Mr. Franco Marinozzi[2], Mr. Bernardo Innocenti[1]

[1]BEAMS Department, Brussels, Brussels, Belgium. [2]Department of Mechanical and Aerospace Engineering, Roma, Italy, Italy

Introduction

Achieving optimal alignment in Total Knee Arthroplasty (TKA) is essential for long-term joint function and implant durability, yet the ideal alignment strategy remains debated, particularly in patients with valgus deformities. Mechanical Alignment (MA) and Kinematic Alignment (KA) are based on different concepts, raising questions about their relative biomechanical consequences. The aim of this study is to numerically compare effects of MA versus KA in valgus knees (8° and 11° deformity), aiming to identify a superior patient-specific strategy.

Methods

Patient-specific FE models were developed, following previous validated studies. A Genus FB PS (Adler Ortho, Cormano, Italy) prosthesis was virtually implanted, following the surgical guidelines. A 0°–120° squat motion was simulated under specific loading condition. Key outputs were extracted from only the flexion motion including tibio-femoral and patello-femoral joints kinematics and kinetics, polyethylene stresses and contact areas, and mean collateral ligament stresses, comparing MA and KA for each patient.

Results

For the tibio-femoral joint, polyethylene contact areas and stresses were similar between the two alignment strategies, with notable differences observed in the post-cam interaction, particularly at 60° of flexion, distinguishing the 8° and 11° valgus knees. Regarding the patello-femoral joint, KA showed reduced contact forces compared to MA in both patients, while contact areas were similar, with regional differences dictated by patellar bone anatomy. Finally, KA consistently resulted in lower mean stress values on the collateral ligaments for both patients, though the 11° valgus patient exhibited generally greater overall ligament stress.

Discussion

Despite few differences in polyethylene contact characteristics at the tibio-femoral joint, this study conclusively demonstrates that Kinematic Alignment yields a biomechanical advantage across the rest of the knee. KA consistently results in a reduction in mean collateral ligament stress and lower patello-femoral contact forces compared to Mechanical Alignment in valgus TKA patients. This evidence strongly supports KA as a superior patient-specific approach for soft tissue balancing and patellar tracking, offering a robust solution to improve functional outcomes and potentially enhance implant longevity in complex knee deformities.

Session Category

Clinical Biomechanics: N/A

P4-232

Dynamic Postural Control Reveals Adaptations to Postpartum Infant Carriage

Ms. Rachel Berns BS, Dr. Kornelia Kulig PhD, PT, FAPTA, Mr. Melvin Leon BS, Dr. Kathryn Havens PhD

University of Southern California, Los Angeles, CA, United States

Introduction

Postpartum individuals face significant musculoskeletal pathologies and mass distribution changes that impact gait, balance, and postural control [1]. These biomechanical shifts are compounded by physical demands of infant carrying [2]. This case study followed two individuals from pre-pregnancy to early postpartum, examining changes in spatiotemporal gait and dynamic stability during various infant carriage conditions.

Methods

Two healthy women participated in data collection pre-pregnancy (32 yrs, 1.7 ± 0.018 m, 89 ± 9.3 kg), and 3-4 months postpartum (33 yrs, 1.7 m, 92 ± 9.7 kg). Participants completed self-selected speed walking trials under three carrying conditions (Fig. 1A), holding an infant mannequin (6.7 kg) pre-pregnancy, and holding their own infant (7.1 ± 1.1 kg) postpartum. Reflective markers tracked lower extremity and trunk 3D-motion and were used to compute spatiotemporal gait parameters. Dynamic postural control was assessed in the anteroposterior (AP) and mediolateral (ML) directions using margin of stability (MoS): the minimum distance between the velocity-extrapolated center of mass and base of support, defined by lateral and distal heel markers. Data were averaged across trials per condition and expressed as percent change pre-pregnancy to postpartum.

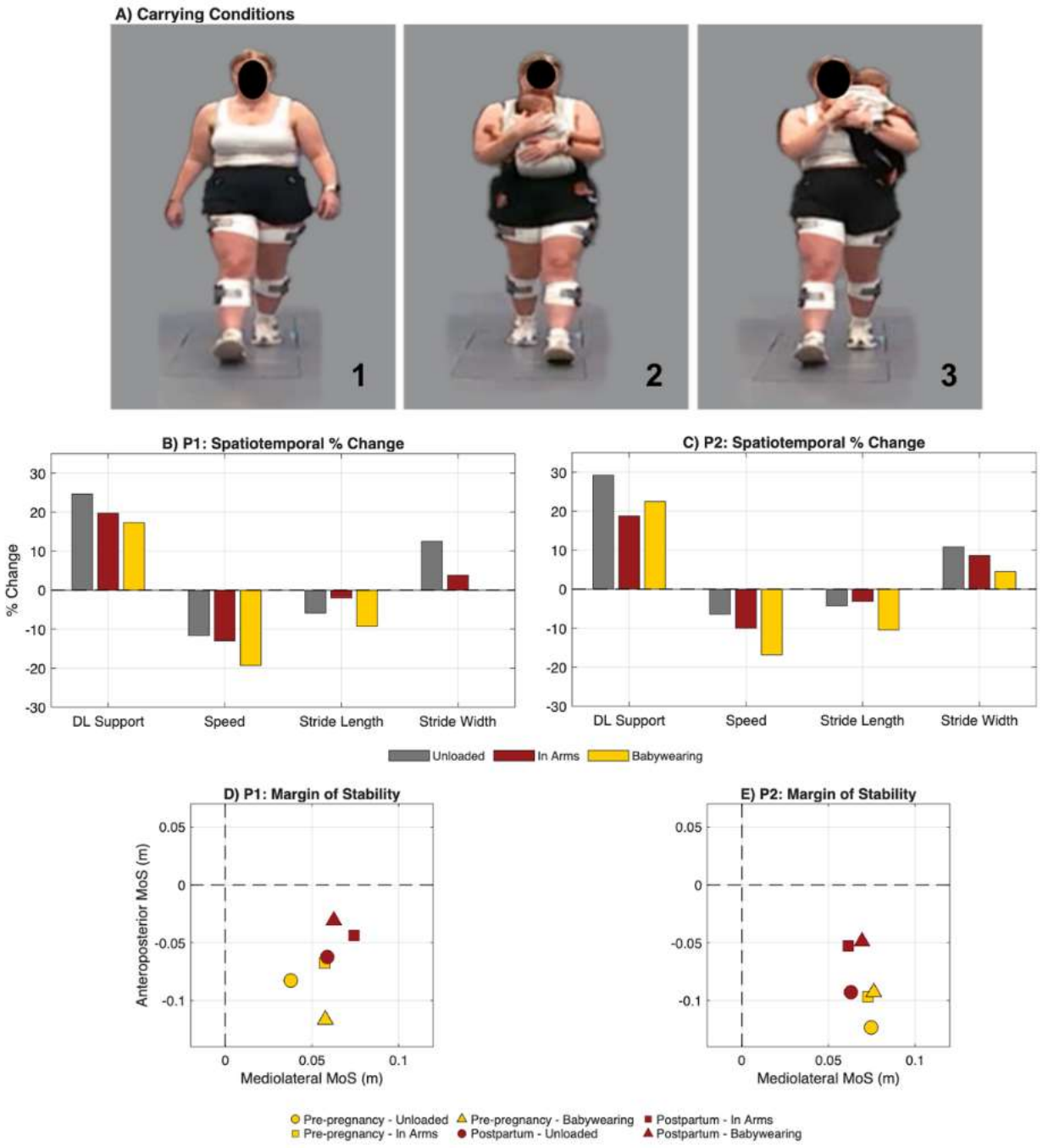
Results

Consistently across carrying conditions, increased speed and double-limb support time, with decreased stride length and width, indicated a cautious gait pattern postpartum (Fig. 1B-C). AP MoS became less negative in all conditions, suggesting greater comparative stability driven by slower postpartum walking speed. Mediolateral stability control diverged: Participant 1 experienced an 8-55% increase in lateral stability, while Participant 2 had 8-16% decreased lateral stability across all conditions (Fig. 1D-E). Interestingly, for double-limb support time, stride width, and ML MoS, the largest changes were observed walking unloaded.

Discussion

Adapted spatiotemporal gait indicates a stability-favoring strategy postpartum, consistent with AP MoS. Infant carriage either amplified or mitigated the observed changes, suggesting fundamental effects of pregnancy on gait, not solely responses to infant carriage. Notably, opposing changes in ML MoS suggest that cautious postpartum gait may mask distinct control mechanisms for lateral stability. Postpartum recovery may involve individualized compensatory strategies for dynamic stability, challenging the notion of a single postpartum gait pattern.

Images (Optional)



References (Optional)

[1] Bagwell, et al., Gait & Posture, 2020

[2] Havens, et al., J Applied Biomechanics, 2024

Session Category

Clinical Biomechanics: N/A

P4-233

Estimating the Centre of the Humeral Head Using Five Humeral Anatomical Landmarks: An Exploratory Study on Dry Bones

Mr. Marc-Olivier St-Pierre PhD[1], Mr. Philippe Paquette PhD[2], Mr. Guillaume Desroches PhD[2], Mr. Rachid Aissaoui PhD[1]

[1]École de technologie supérieure, Département Génie des sytèmes, Montréal, Québec, Canada. [2]Université du Québec à Trois-Rivières, Département d'anatomie, Trois-Rivières, Québec, Canada

Introduction

Estimating the centre of the humeral head has great implications in kinematics and dynamic research as it represents the centre of rotation of the glenohumeral joint. Three-dimensional ultrasound-imaging contour-based methods have shown promising results. However, the reported 14 mm error exceeds both intracortical pins (4.2 ± 0.6 mm) and Rab equation (5.5 ± 4.0 mm). This study aimed to develop a regression-based model to predict the centre of the humeral head using five humeral landmarks.

Methods

Fifty-five dry humeri (n=55) were scanned using an Artec Eva 3D scanner (±0.1 mm). The data set was divided into training (n=35), validation (n=10), and test sets (n=10). Specimens presenting large osteophytes on the greater or lesser tubercles were excluded. The centre of the humeral head was obtained using a sphere-fitting technique. Five landmarks (lateral/medial epicondyles, lesser and greater tubercles, deltoid tuberosity) were digitized to define their centre and used as the independent variables in model (Ordinary least square (OLS) algorithm). The mean 3D Euclidean distance between the predicted and sphere-fitted humeral head centre was calculated (mm). Regression equations and errors were expressed in the ISB-recommended coordinate system.

Results

Landmark identification has shown an error of less than 1.9 ± 1.0 mm. The mean Euclidean distance between the predicted and sphere-fitted CoR was 3.4 ± 1.2 mm. The greater tubercule (GT) was the primary contributor for the superior-inferior (Y) (0.883 GT_y) and anterior-posterior (Z) (− 0.342 GT_y, + 0.879 GT_z**)** coordinates. For the X axis (latero-medial), the lesser tubercule (LT) (0.939 LT_x) influenced the position of the CoR helped with the lateral (− 0.433 LE_x) and medial (0.302 ME_x**)** epicondyles (Table 1).

Discussion

Five anatomical humeral landmarks predict the centre of the humeral head with sub-4 mm accuracy on dry bone. These findings are clinically relevant because the greater and lesser tubercules are easily accessible using ultrasound imaging. Conversely, the deltoid tuberosity contributed minimally, which may be advantageous given its less prominent bony relief and limited applicability with ultrasound. External validation of this model using 3D ultrasound-imaging is needed to quantify the error with soft tissue.

Images (Optional)

Table 1. Linear regression equations, expressed in the ISB-recommended reference frame of the humerus, and R2 obtained using the Ordinary least square algorithm

Coordinates (mm)	Equations	R^2
x	-1.131 + **0.302 ME_x** − 0.093 ME_y + 0.012 ME_z − **0.433 LE_x** + 0.094 LE_y − 0.037 LE_z − 0.151 GT_x − 0.027 GT_y − 0.135 GT_z + **0.939 LT_x** + 0.048 LT_y + 0.108 LT_z + 0.292 DT_x − 0.008 DT_y + 0.027 DT_z	0.979
y	-10.143 + 0.011 ME_x − 0.000 ME_y + 0.066 ME_z + 0.024 LE_x − 0.074 LE_y − 0.010 LE_z + 0.033 GT_x + **0.883 GT_y** + 0.021 GT_z − 0.039 LT_x + 0.092 LT_y + 0.232 LT_z − 0.000 DT_x + 0.091 DT_y − 0.258 DT_z	0.999
z	8.883 − 0.004 ME_x + 0.135 ME_y + 0.058 ME_z − 0.071 LE_x + 0.007 LE_y − 0.038 LE_z − 0.098 GT_x − **0.342 GT_y** + **0.879 GT_z** + 0.005 LT_x + 0.273 LT_y + 0.055 LT_z + 0.161 DT_x − 0.084 DT_y + 0.082 DT_z	0.992

R^2, ME: medial epicondyle, LE: lateral epicondyle, GT: greater tubercule, LT: lesser tubercule, DT: deltoid tuberosity

Acknowledgements (Optional)

Marc-Olivier St-Pierre is supported by the Natural Sciences and Engineering Research Council of Canada (NSERC)

Session Category

Clinical Biomechanics: N/A

P4-234

Feasibility of Estimation of Femoral Bone Strength in Fibrous Dysplasia of Bone with the MEKANOS Tool

Dr Helene Follet[1,2], Dr Cyrille Confavreux[3,4], Dr Deborah Gensburger[3,5], Ms Nadege Trehet-Mandel[3], M Thibault Gandet[3], Ms Marine Grandin[3,6], Dr Aurelie Levillain[6], Dr Marc Gardegaront[6], Dr Raphael Dumas[6], Dr Emile Saillard[3,7], Dr Thomas Grenier[7], Dr David Mitton[6], Dr Roland Chapurlat[3,5]

[1]INSERM, Lyon, Auvergne-Rhône-Alpes, France. [2]Univ Lyon, Université Claude Bernard Lyon 1, INSERM, LYOS UMR 1033, lyon, Auvergne-Rhône-Alpes, France. [3]Univ Lyon, Université Claude Bernard Lyon 1, INSERM, LYOS UMR 1033, Lyon, Auvergne-Rhône-Alpes, France. [4]Centre Expert des Métastases Osseuses (CEMOS), Service de Rhumatologie Sud, Hôpital Lyon Sud, Institut de Cancérologie des Hospices Civils de Lyon, Lyon, Auvergne-Rhône-Alpes, France. [5]Rhumathology department, Hôpital Lyon Sud, Hospices Civils de Lyon, Lyon, Auvergne-Rhône-Alpes, France. [6]Univ Lyon, Univ Gustave Eiffel, Univ Claude Bernard Lyon 1, LBMC UMR_T9406, Lyon, Auvergne-Rhône-Alpes, France. [7]INSA-Lyon, Universite Claude Bernard Lyon 1, CNRS, Inserm, CREATIS UMR 5220, U1294, Lyon, Auvergne-Rhône-Alpes, France

Dr Helene Follet

Introduction

Fibrous dysplasia of bone (FD) is a rare, congenital bone disease due to a post-zygotic mutation of GNAS, (guanine nucleotide-binding protein, alpha stimulating, an imprinted gene) causing bone pain, deformities and fractures. Mechanically speaking, FD lesions, which are often lytic and heterogeneous, can be compared to those of bone metastases. The assessment of mechanical strength and fracture risk in FD lesions, however, remains a significant unresolved issue for clinicians.

Methods

We have developed MEKANOS, a digital simulation tool for calculating the mechanical strength of tumor bone based on routine scans using a dedicated protocol[2,3,4,5]. Briefly, we wanted to determine whether this tool can be used to quantify bone strength in FD, with routine CT scanning? To this end, we used scanned images of patients with FD (15 patients)

obtained by the Fibrous Dysplasia National Reference Center. For each patient images, mid-length femur lengthening was done, calibration of Hounsfield Units (HU) to density was performed using (i) a patient-specific method and (ii) an asynchronous method. Femurs were automatically segmented[2], meshed using tetrahedral elements, and assigned linear elastic material properties using a model implemented in Lyon[3,6] Femurs were loaded in axial compression, and their failure load was computed using a failure criterion based on a volume of contiguous failed elements. protocol[2,3,4,5,6].

Results

We compared the fracture strength of femurs obtained numerically using the two calibration methods (n=28 from 14 patients). Both methods showed a strong correlation (R^2=0.92), but a relative bias of 12% (SD=5.56%, and IC95% [1.2 to 23%]). Between pathological bone and healthy bone, for 6 patients, both models were able to show a significant difference of bone strength between them (*resp* p=0.0278 for patient-specific method and p=0.0377 for asynchronous method).

Discussion

These preliminary results are very encouraging for the continuation of the study and to elaborate a fracture risk criterion for this type of rare disease.

Images (Optional)

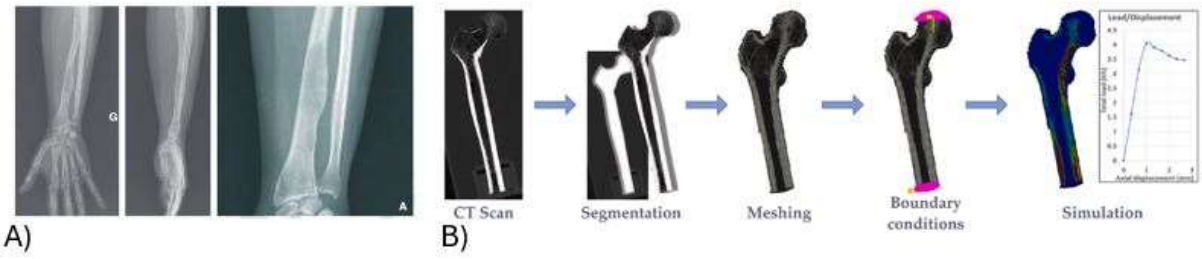


Figure A) Examples of fibrous dysplasia lesions of radius in standard radiography B) Global process to obtain the failure load of a femur based on its CT scan (Gardegaront et al. 2024)

References (Optional)

1-Gensburger et al 2024 10.1016/S0246-0521(21)41573-1,2-Saillard, E. et al. 2024 10.1038/s41598-024-66934-w, 3-M. Gardegaront,2024, 10.1016/j.jmbbm.2024.106676,4- A. Levillain, 2023, 10.1016/j.mtla.2022.101555,5- C. B. Confavreux, 2021 10.3390/cancers13225711, 6-L.Duchemin, 2008 10.1080/10255840701535965

Acknowledgements (Optional)

Keywords: Fibrous dysplasia, Femur, Bone strength, Fracture risk

Session Category

Clinical Biomechanics: N/A

P4-235

Knee Joint Hyperextension is Associated with an Increased Prevalence of Knee Pain in Young Adults

Dr. Rebecca Abbott DPT, PhD[1], Ms. Susan Burnap[2], Dr. Arin Ellingson PhD[2]

[1]University of Colorado Anschutz, Aurora, Colorado, United States. [2]University of Minnesota, Minneapolis, Minnesota, United States

Introduction

Knee pain poses a major health, societal, and economic burden. Biomechanical factors, such as knee joint hypermobility, are consistently cited as potential risk factors for the development of knee pain and osteoarthritis (OA) [1]. However, there is conflicting evidence supporting [2] and refuting [3] the role of knee hyperextension in knee pain. This study investigates the relationship between knee hyperextension and pain within each individual knee in a large sample of the general population.

Methods

This data was collected as part of a larger cross-sectional study that took place at the Research Facility at the Minnesota State Fair. Participants self-reported demographics and recorded individual painful joints. Each knee was assessed for hyperextension >10 degrees as a component of the Beighton Score, a clinical measure of generalized hypermobility. Participants were dichotomized by age (young: 18-40 yrs, older: 40+ yrs) due to known effects on joint mobility. The results are stratified by individual knees, allowing us to directly link hyperextension and pain.

Results

555 participants (219 males, 336 females, age 18-86 years) were enrolled. While knee hyperextension and knee pain were more prevalent in females than males, subsequent analyses include both sexes combined because associations between hyperextension and pain were similar. The results are reported in **FIGURE 1**. Knee hyperextension was more common in young adults (28.2%) than older adults (11.6%). The association between knee hyperextension and knee pain differed by age group: in young adults, hyperextension was associated with a 2.3-fold higher prevalence of knee pain, whereas in older adults, hyperextension was associated with a 2.7-fold lower prevalence.

Discussion

Knee hyperextension is common in young adults and reflects altered biomechanical patterns associated with an increased prevalence of knee pain. Individuals with painful

knee hyperextension may lose mobility with age due to joint degeneration, leading to the inverted relationship between knee hyperextension and knee pain in older adults. Clinicians should be aware that excessive knee hyperextension in young adults may be a risk factor for knee pain.

Images (Optional)

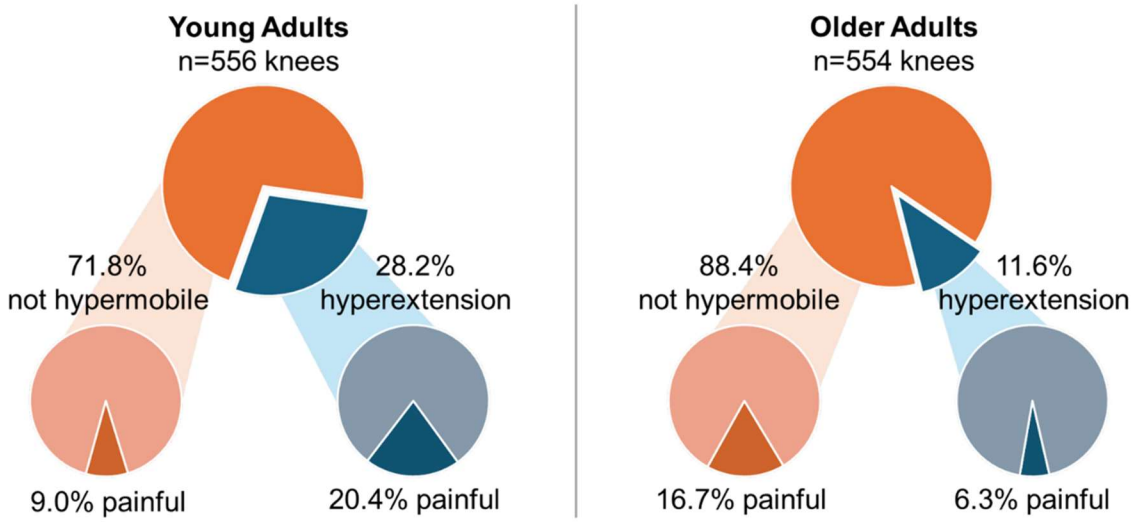


FIGURE 1. Percentage of knees exhibiting hyperextension and reported as painful in young adults <40 years old (left) and older adults 40+ years old (right). Top row: The percentage of knees exhibiting hyperextension. Bottom row: The percentage of knees within each subgroup that were reported as painful.

References (Optional)

[1] D'Souza et al., Osteoarthr Cartil, 2022

[2] Junge et al., Int J Rheum Dis, 2019

[3] Chan et al., Int J Rheum Dis, 2021

Acknowledgements (Optional)

Sources of Grant Support: RA TL1 TR002493, F32 AR082276. Participant recruitment and data collection were completed at the University of Minnesota's Driven to Discover Research Facility at the Minnesota State Fair.

Session Category

Clinical Biomechanics: N/A

P4-236

Generalized Joint Hypermobility Modifies the Relationship Between Neck Pain Burden and Neck Function in Women

Dr. Rebecca Abbott PT, DPT, PhD[1], Dr. Andrew Leroux PhD[1], Dr. Carly Molenaar PT, DPT[2], Dr. Kyle Dalske PT, DPT, MS[2], Dr. Arin Ellingson PhD[2]

[1]University of Colorado Anschutz, Aurora, Colorado, United States. [2]University of Minnesota, Minneapolis, Minnesota, United States

Introduction

Generalized joint hypermobility (GJH; excessive joint range of motion (ROM) throughout the body) is present in up to 30% of young women and associated with increased risk of injury and joint pain [1,2]. Despite evidence that neck pain (NP) is particularly prevalent and debilitating [2], little is known about the presentation of NP in GJH, which is a barrier to effective clinical management. The objective of this study was to determine the relationships between GJH, NP burden, and neck function (ROM and strength).

Methods

Females (18+) were enrolled at the research facility at the Minnesota State Fair as part of a larger cross-sectional study. All participants were assessed for GJH with the Beighton Score (BS) and Five-Part Questionnaire [3]. A subset completed neck function measures (ROM and strength) and the Neck Disability Index (NDI). Multivariable regression models were created for each neck function outcome with predictors: GJH (BS) and NP burden (NDI), covariates: age and BMI, and an interaction term: BSxNDI.

Results

336 participants were enrolled. GJH prevalence was 23.5%. NP was more prevalent in GJH (24.1%) than non-GJH (16.0%), and most prevalent in GJH age 18-40 years (29.3%). Regression analyses were performed on 182 participants (GJH: 71, non-GJH: 111) who completed all neck function measures. Controlling for age, BMI, and NP burden, GJH was associated with increased neck ROM (flexion, extension, sidebending, rotation) and increased strength (flexion, extension, sidebending). Most outcomes showed a significant positive BS×NDI interaction (**FIGURE 1**), indicating that GJH was linked to reduced deficits in ROM and strength with increasing NP burden.

Discussion

GJH plays a role in NP, disability, and function. NP is common in women with GJH, who may present with less ROM and strength impairments than typical NP patients. These results

should be interpreted within the context of our relatively healthy and mobile study population: community members who approached the research facility at a bustling State Fair. Individuals with more severe pain and disability may not be represented.

Images (Optional)

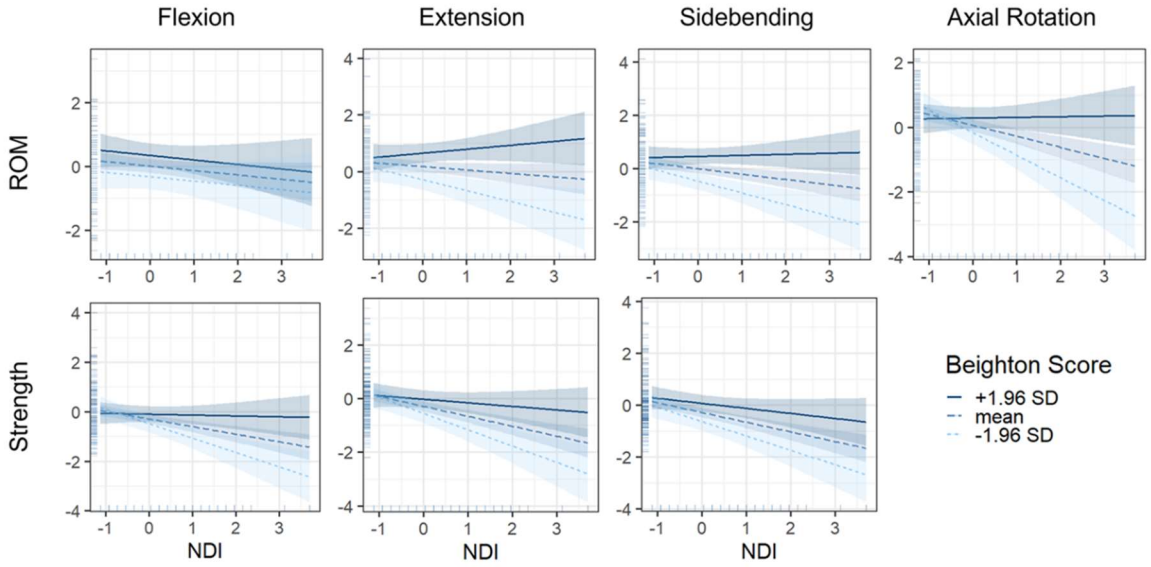


FIGURE 1: Interaction plots illustrating the interaction between Beighton Score and Neck Disability Index (NDI) as a predictor of neck range of motion (ROM) (top row) and strength (bottom row), adjusted for age and BMI. All continuous variables are centered and standardized. The interaction was significant ($p<.05$) and positive for extension, sidebending, and axial rotation ROM and neck flexion and extension strength.

References (Optional)

[1] Pacey et al., Am J Sports Med, 2010

[2] Juul-Kristensen et al. BMC Musculoskelet Disord 2017

[3] Malfait et al. American Journal of Medical Genetics 2017

Acknowledgements (Optional)

Sources of Grant Support: RA TL1 TR002493, F32 AR082276, R03HD097715. Participant recruitment and data collection were completed at the University of Minnesota's Driven to Discover Research Facility at the Minnesota State Fair.

The study protocol was approved by the Institutional Review Board of the University of Minnesota in Minneapolis, Minnesota, USA.

Session Category

Clinical Biomechanics: N/A

P4-237

Changes in Gait Kinematics and Surgical Outcomes after Proximal and Distal Femoral Derotational Osteotomy in Children with Cerebral Palsy

Dr. Reiko Hara PhD[1], Dr. Susan Rethlefsen DPT[1], Ms. Nerissa Chin[1], Ms. Alyssa Ponratana[1], Dr. Tishya Wren PhD[1,2], Dr. Robert Kay MD[1,2]

[1]Children's Hospital Los Angeles, Los Angeles, California, United States. [2]University of Southern California, Los Angeles, California, United States

Introduction

It remains unclear whether proximal or distal femoral derotational osteotomy (FDRO) is preferable for correcting excessive internal hip rotation and foot progression in children with cerebral palsy (CP). This study compares kinematic and surgical outcomes between the two types of FDRO.

Methods

Retrospective data of children with CP who underwent FDRO with pre-and post-operative gait analysis were evaluated to compare proximal and distal FDROs. Patient and surgical characteristics were compared between groups using Mann-Whitney rank sum and Fisher's exact tests. Mean hip rotation and foot progression angles during the stance phase of gait were compared between groups before and after surgery using linear mixed models accounting for repeated measures. The relationship between amount of surgical correction and change in hip rotation angle during gait was examined using Pearson's correlation.

Results

The analysis included 125 FDROs in 75 patients. 41 patients underwent proximal FDRO (25 bilateral), and 34 underwent distal FDRO (25 bilateral). Both groups improved significantly in hip rotation and foot progression angles post-operatively ($p<0.0001$). Hip rotation changed similarly between groups (Table). Foot progression changed more in the distal group because foot progression angle was more internal in the distal group pre-operatively and both groups were similar post-operatively.

The change in hip rotation angle was moderately correlated with the amount of anatomic rotation for proximal osteotomies ($r=0.44$, $p=0.0005$) but not distal osteotomies ($r=0.18$, $p=0.15$).

Total number of surgical procedures per patient was similar between groups, suggesting similar surgical complexity. Estimated blood loss was greater in the proximal group, but use of pain medication on the day after surgery measured as morphine milligram equivalents

(MME) was lower (0.42 vs. 0.65MME/kg, p=0.0003). Complication rate trended higher in the distal group (11 vs. 2%, p=0.07), mostly due to cast problems like pressure sores. Recurrence rate did not differ between groups.

Discussion

Both proximal and distal FDROs are similarly effective in reducing excessive hip internal rotation and normalizing foot progression during gait in children with CP. However, proximal rotation produces changes more consistent with the surgical correction and has a lower complication rate and reduced need for pain medication post-surgery.

Images (Optional)

Table: Comparison of Proximal and Distal FDROs

	Proximal	**Distal**	p
	n=34 patients	*n=41 patients*	
Age (years)	9.7 (2.7)	8.4 (2.3)	0.02
Sex, female	15 (44%)	16 (39%)	0.81
Time pre-op to surgery (months)	10.3 (7.6)	7.7 (4.1)	0.29
Time surgery to post-op (months)	17.9 (8.9)	21.5 (17.8)	0.69
CP distribution, bilateral	29 (85%)	34 (83%)	1.00
FDRO sides, bilateral	25 (74%)	25 (61%)	0.33
Total number of surgical procedures	5.4 (3.3)	6.3 (2.7)	0.12
Estimated blood loss (ml)	97.3 (54.5)	48.3 (36.6)	<0.0001
Pain medication (MME/kg)	0.421 (0.229)	0.654 (0.278)	0.0003
	n=59 limbs	*n=66 limbs*	p
Mean hip rotation in stance (deg)			
Pre-operative	14.4 (1.6)	16.5 (1.5)	0.34
Post-operative	1.8 (1.6)	4.4 (1.5)	0.24
Change	-12.6 (1.5)	-12.1 (1.4)	0.82
Mean foot progression in stance (deg)			
Pre-operative	8.8 (2.6)	20.4 (2.4)	0.001
Post-operative	-9.0 (2.6)	-6.3 (2.4)	0.44
Change	-17.8 (2.5)	-26.6 (2.4)	0.01
Complications	1 (2%)	7 (11%)	0.07
Recurrence	4 (7%)	7 (11%)	0.54
Continuous variables: mean (SD) or model predicted mean (SE), categorical variables: n (%)			

Acknowledgements (Optional)

The authors would like to thank Shashank Coorapati for his contributions to data collection.

Session Category

Clinical Biomechanics: N/A

P4-238

Effect of Adaptive Training on Joint Coordination in Recreational Runners: A Pilot Clinical Trial

Dr. Vaibhavi Rathod PT, PhD, Mr. Scotty Hardwig MFA, Dr. Julia Basso PhD, Dr. Robin Queen PhD, FACSM, FIOR, FASB, FAIMBE

Virginia Tech, Blacksburg, VA, United States

Introduction

Running is one of the most popular recreational activities with numerous health benefits. However, it is associated with a high incidence of overuse injuries. Safe and efficient running mechanics require coordinated motion across hip, knee, and ankle joints with joint coordination playing a key role in load distribution, movement efficiency, and the ability to adapt to changing environments. Adaptive training incorporates variable, unpredictable task demands that cultivate diverse whole-body motor responses and promote neuromuscular adaptability. Therefore, the purpose of this pilot clinical trial was to examine the effects of an adaptive training movement practice on joint coordination during running and standing lunges in runners.

Methods

26 recreational runners (13F/13M; age 26.2±9.2 years; BMI 23.2±3.5 kg/m^2) completed 12 group-based movement training sessions over 4 weeks (3x/week). Training included unpredictable, game-like tasks (e.g., reaching, catching, dynamic balancing, avoiding unpredictable externally controlled obstacles) to promote diverse movement responses. Markerless motion capture (85 Hz) was used to analyze Hip-Knee (proximal) and Knee-Ankle (distal) sagittal and frontal plane coupling angles pre- and post-intervention, during running and standing lunges. A linear mixed-effects model was used to examine the effects of Time (Pre vs Post), Joint Pair (Hip–Knee vs Knee–Ankle), and their interaction on coupling angle, with participant included as a random effect.

Results

During the running task (sagittal plane), the Time × Joint Pair interaction was significant ($p< 0.001$) with a significant increase in proximal coupling ($p< 0.001$) post intervention (Table 1). Similarly, for the left-lunge task (sagittal plane), the interaction was significant ($p= 0.025$), with proximal coupling increasing post-intervention ($p= 0.017$). No significant interactions ($p= 0.856$) or main effect ($p= 0.817$) were observed for the right lunge task (sagittal plane). Additionally, no significant main effects or interaction were observed for running or lunges in the frontal plane ($p >0.05$).

Discussion

These pilot study findings suggest that adaptive training promotes greater proximal coordination during functional tasks such as running and lunging. Increased proximal engagement may indicate improved ability to control the limb using a hip-dominant strategy, important for absorbing load and stabilizing the lower extremity during dynamic movement.

Images (Optional)

Table 1: Pre- and post-intervention Mean and Standard Deviation (SD) of coupling angles during the stance phase of each movement (*Denotes significant pre-post intervention differences ($p < 0.05$))

Joint Pair	Plane	Run Pre	Run Post	Lunge Left Pre	Lunge Left Post	Lunge Right - Pre	Lunge Right - Post
Hip-Knee	Sagittal	218.11 (93.1)	238.98 (82.9)*	177.51 (111.2)	200.84 (111.8)*	183.59 (114.2)	181.25 (116.1)
	Frontal	175.06 (85.0)	168.30 (79.7)	174.69 (110.1)	172.47 (104.9)	165.77 (118.6)	169.48 (108.5)
Knee-Ankle	Sagittal	222.01 (76.2)	221.49 (64.7)	192.63 (110.3)	187.60 (109.5)	195.26 (110.5)	190.59 (111.6)
	Frontal	127.37 (93.3)	124.50 (94.07)	174.21 (110.4)	171.62 (108.6)	169.3 0(112.1)	185.69 (112.1)

Session Category

Clinical Biomechanics: N/A

P4-239

Investigating How Pregnancy Weight Gain Impacts Achilles Tendon Load

Ms. Robyn de Wet, Dr. Lauren Welte PhD

University of Alberta, Edmonton, Alberta, Canada

Ms. Robyn de Wet

Introduction

Pregnant individuals undergo substantial hormonal and weight changes that impact the musculoskeletal system, leading to compensatory walking patterns such as wider stance and increased stride time [1], and larger ankle moments [2]. However, which plantarflexors are responsible for the increased moments remains unclear, as the compensatory strategies may preferentially recruit smaller plantarflexors – like the posterior tibialis – to accommodate a wider stance, instead of the larger triceps surae and Achilles tendon. This pilot study aims to simulate pregnancy weight gain to understand how these compensations alter Achilles tendon load.

Methods

To isolate the effects of increased weight from pregnancy-related hormonal fluctuations, five non-pregnant female participants were recruited (mean±SD, 24.6±4.2 y; 166.6±4.2 cm; 64.4±9.4 kg). Participants walked on a treadmill for 5 minutes at 1.0 m/s at a self-selected cadence, which was measured and kept constant with a metronome. Participants walked without added weight and with a 20 lb simulated pregnancy belly. Shear wave tensiometry, which non-invasively measures tendon wave speed [3], measured tendon loading patterns. Strides were averaged within conditions and normalized to the gait cycle.

Results

Stride times were consistent between trials; the difference between weighted and non-weighted trials was 0.006 ± 0.001 s. Four subjects experienced an average 4.7% higher peak wave speed (2.6 ± 0.8 m/s), and therefore tendon load, in weighted trials compared to non-weighted trials (Figure 1), while one subject experienced a decrease in peak tendon wave speed (3.2 m/s).

Discussion

Preliminary results suggest that simulated pregnancy may increase Achilles tendon load during walking; however, compensation responses may be subject-specific. Participants reported poorer balance and increased forefoot pressure during weighted trials, indicating compensatory gait strategies. Ongoing work includes additional subject recruitment, and collection and analysis of plantar pressure data and motion capture to quantify gait compensations and the effects on tendon load during simulated pregnancy. Understanding tendon adaptations during pregnancy could help guide exercise programming aimed at reducing lower-limb muscle and tendon strain, helping to promote healthier pregnancies.

Images (Optional)

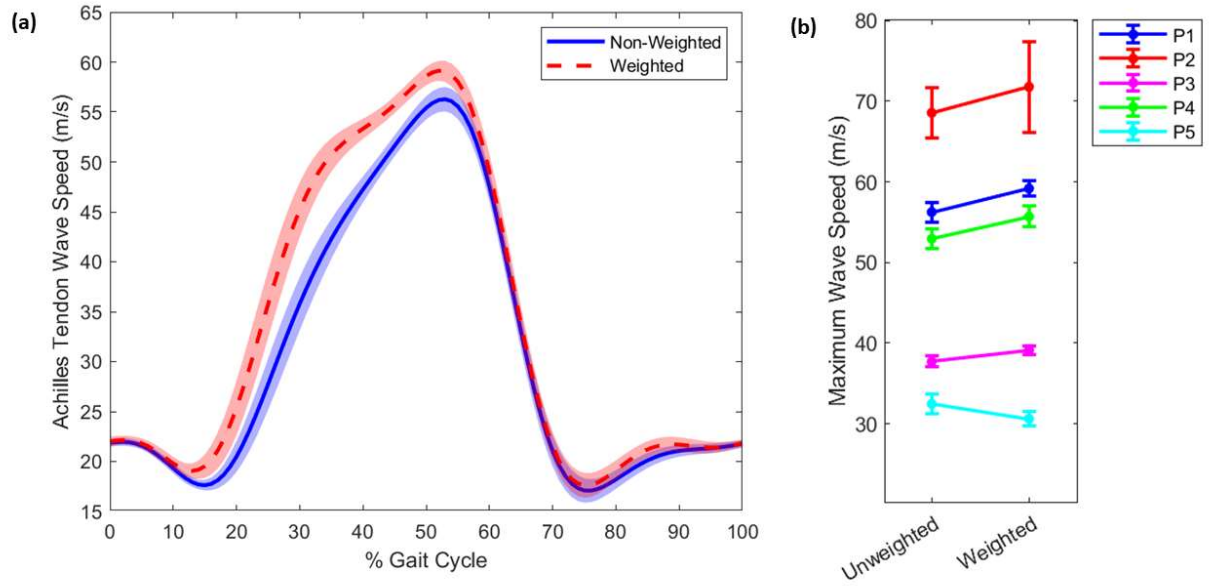


Figure 1. (a) Mean Achilles tendon wave speed with one standard deviation for a representative subject between weighted and unweighted conditions.
(b) Peak Achilles tendon wave speed for all participants.

References (Optional)

[1] Zarko Krkeljas *et al.*, BMC Sports Science., *2018*

[2] Theresa Foti *et al.,* JB&JS, 2000

[3] J. Martin *et al.*, N Communications, *2018*

Session Category

Clinical Biomechanics: N/A

P4-240

Benchmarking AI Pose Estimators: How Well Do Markerless Pose Estimators Reproduce 3D Gait Kinematics?

Dr Romain Feigean, Mr Thomas Marques, PT Pauline Santmarty, Dr Jean-Yves Hogrel, Mr Frederic Fer

Institut de myologie, Paris, Ile de France, France

Introduction

Optical motion capture with reflective markers is a widely used and highly accurate method for assessing human movement, particularly in gait impairment analysis. However, it requires extensive setup time, technical expertise, and costly equipment, which limits its applicability in routine clinical or home settings (Rode et al., 2025). Recent advances in markerless pose estimation from a handled monocular smartphone camera offer a promising alternative for accessible gait assessment. This study aims to evaluate the accuracy of several state-of-the-art pose estimation algorithms for gait analysis.

Methods

Twenty gait trials were recorded simultaneously using a smartphone video following the participant and a 3D marker-based motion capture system (Vicon, Oxford, UK). Hip and knee flexion–extension angles were extracted from both sources. Joint angles were computed from 2D key points (MediaPipe: 33 landmarks; HRNet: 17 landmarks), and gait cycles were identified using the method by Zeni et al. (2007). Signals from video and 3D reference data were synchronized. Range of motion (RoM) and root-mean-square error (RMSE) were calculated to evaluate model accuracy. Preliminary analysis was performed on one participant and eight gait cycles as proof of concept.

Results

For the knee, the reference system reported a median range of motion (RoM) angle of 66.1°, while MediaPipe overestimated it at 94.7° (RMSE 30.4°); HRNet produced a more accurate estimate with a median of 73.4° and RMSE of 22.8°. At the hip, the reference RoM median was 42.8°; MediaPipe again overestimated (62.3°, RMSE 16.7°), while HRNet showed better alignment (35.9°, RMSE 14.0°).

Discussion

Preliminary results indicate systematic overestimation of joint angles by MediaPipe across hip and knee flexion-extension, while HRNet provides more accurate estimates. However, HRNet does not detect foot landmarks, which limits its use in full gait analysis. Given the

persistent RoM errors, interpretation should be approached with caution. Further investigation is required to determine whether these markerless methods can reliably assess gait impairments, particularly in clinical populations such as those with neuromuscular disorders.

References (Optional)

Session Category

Clinical Biomechanics: N/A

P4-241

Probabilistic detection of initial contact and toe-off from adults with impaired gait kinematics using a harmonic hidden markov model

Mr Thomas MARQUES[1], Mr Frédéric Fer[2], PT Pauline Santmarty[1], Dr Jean-Yves Hogrel[1], Dr Romain Feigean[1]

[1]Institute of Myology, Neuromuscular Exploration and Evaluation Center, Neuromuscular Physiology and Evaluation Laboratory, Paris, Île-de-France, France. [2]Institute of Myology, MyoData center, Paris, Île-de-France, France

Introduction

Precise detection of gait events such as heel strike (HS) and toe-off (TO) is crucial for evaluating gait impairments and tracking disease progression in neuromuscular disease (e.g. muscular dystrophies). Despite the wide availability of detection algorithms, some user-friendly gait analysis tools often rely on proprietary "black boxes" algorithms, limiting the interpretation and may fail in people with gait impairments. In particular, compensatory movements in neuromuscular patients can alter kinematic signals (inertial vs. optical), challenging standard detection methods. This study aims to present an innovative probabilistic approach based on harmonic Hidden Markov Models to identify HS and TO events in adults with neuromuscular gait impairment – a method not previously explored in this population.

Methods

Performances has been validated on 27 patients with neuromuscular disease (NMD) and 18 healthy controls. All completed a Two-Minute Walk Test. Kinematics were recorded using 8 sensors from IMU system (APDM Opal sensor), providing synchronized inertial signals and joint angles from which gait events were extracted. Four detection approaches were evaluated to identify HS and TO:

(1) Probabilistic joint-angle modelling, using preliminary segmentation based on knee-crossing, followed by HS and TO inference from joint-angle transitions (knee flexion–extension and hip extension patterns).

(2) Zeni's kinematic method (Zeni et al., 2008),

(3) Wavelet-based detection (Hafer et al., 2020),

(4) Ghoussayni's velocity-threshold method (Ghoussayni et al., 2004).

Comparison focused on event timing, stride variability, and spatiotemporal outcomes.

Results

Our preliminary investigation indicate that all methods can be consistently applied to IMU-derived kinematics in both healthy and neuromuscular cohorts. Notably, the probabilistic HMM-based approach successfully detected HS and TO with timing consistency comparable to or exceeding that of traditional methods, especially in NMD group. Differences in algorithm behavior led to modest variations in calculated stride time and gait speed. These findings suggest that signal modality and algorithmic strategy influence gait-cycle segmentation outcomes.

Discussion

This study demonstrates how different detection strategies and sensing modalities affect gait-event identification in heterogeneous gait patterns. Comparing our probabilistic model with standard algorithms in healthy and pathologic walkers, we highlight the impact of neuromuscular compensation on method performance and guide the development of robust segmentation pipelines across sensing technologies.

References (Optional)

Session Category

Clinical Biomechanics: N/A

P4-242

Altered Neuromuscular Control of the Quadriceps in Patellofemoral Pain: Evidence From HD-EMG and Force Variability

P.T Max W. Roizman[1], PhD Ronaldo H. Cruvinel-Júnior[1], PhD Maria Isabel V. Orselli[1,2,3], PhD Jane S. S. P. Ferreira[1], PhD Fábio M. Azevedo[4], PhD Eneida Y. Suda[3], PhD Isabel C. N. Sacco[1]

[1]School of Medicine, University of São Paulo, São Paulo, São Paulo, Brazil. [2]Israeli College of Health Sciences, Albert Einstein, São Paulo, São Paulo, Brazil. [3]Universidade Cidade de São Paulo (UNICID), Graduate Program in Physical Therapy, São Paulo, São Paulo, Brazil. [4]Physical Therapy Department, School of Science and Technology, São Paulo State University, Presidente Prudente, São Paulo, Brazil

P.T Max W. Roizman

PhD Ronaldo H. Cruvinel-Júnior

PhD Maria Isabel V. Orselli

PhD Jane S. S. P. Ferreira

PhD Fábio M. Azevedo

PhD Eneida Y. Suda

Introduction

Patellofemoral pain (PFP) is a condition whose etiology is multifactorial and poorly understood. Still, there is evidence that there are alterations in the quadriceps motor control. Given PFP unfavorable long-term prognosis[1], we aimed to investigate additional neuromuscular and motor control parameters of the quadriceps in people with PFP, based on HD-EMG and force.

Methods

This cross-sectional study, approved by the ethics committee (CAAE:80722924.7.0000.0068), included 22 adults with PFP (PFPG) and 13 controls (CG). Vastus medialis (VM) and lateralis (VL) activities were assessed by 64-electrode matrices during submaximal isometric knee extension (10%, 30%, 50% 70% of maximum force), synchronized with force data from a dynamometer (OTBioelettronica). Muscle fiber conduction velocity(MFCV) was estimated following[2]. The amount of force variability was quantified as standard deviation (SD) and coefficient of variation(CV), and the structure of variability of force and EMG was estimated by sample entropy(SaEn). Groups were compared by Generalized Estimating Equations with Bonferroni-adjusted pairwise comparisons (α=0.05).

Results

EMG SaEn and force CV were higher for PFPG across all force levels and muscles. Force SD and VM MFCV at 10% were higher for PFPG (Table 1).

Discussion

Higher force levels reduced force SaEn but increased EMG SaEn in both groups. PFPG showed greater motor control redundancy (higher EMG SaEn at 10–50% for VM and 30% and 70% for VL) despite similar force regularity, suggesting disrupted MU recruitment linked to chronic pain–related central inhibition[3]. Such inhibition[3] and cortical imprecision[4] may impair MU recruitment efficiency during sustained isometric force, requiring extra neural input to maintain force. This may explain the higher MFCV at 10% for VM due to greater control demand and poorer force maintenance in PFPG. These findings highlight PFP mechanisms that are often overlooked in guideline-oriented exercise therapies [1]. The study is ongoing, and further analyses will refine these conclusions.

Images (Optional)

Table 1: Descriptive statistics (mean ± SD) and between-group differences of neuromuscular variables of the vastus medialis and vastus lateralis for PFPG and CG.

	PFPG (n=22)	CG (n=13)	p
SaEn VM 10%	1.74 (0.03)	1.57 (0.04)	0.002
SaEn VM 30%	1.44 (0.03)	1.30 (0.03)	0.006
SaEn VM 50%	1.30 (0.03)	1.20 (0.03)	0.035
SaEn VL 30%	1.38 (0.03)	1.27 (0.011	0.011
SaEn VL 70%	1.30 (0.03)	1.17 (0.03)	0.004
Force CV 10%	0.08 (0.02)	0.01 (0.004)	0.005
Force CV 30%	0.02 (0.003)	0.01 (0.0007)	<0.001
Force CV 50%	0.01 (0.001)	0.009 (0.0007)	<0.001
Force CV 70%	0.01 (0.001)	0.01 (0.001)	0.004
Force SD 10%	0.70 (0.06)	0.47 (0.05)	0.009
MFCV VM 10%	4.88 (0.08)	4.60 (0.09)	0.029
MFCV VL 10%	4.74 (0.06)	4.56 (0.11)	0.185
MFCV VM 30%	4.80 (0.09)	4.64 (0.09)	0.216
MFCV VL 30%	4.76 (0.08)	4.59 (0.10)	0.185

References (Optional)

[1] Willy RW, et al. J Orthop Sports Phys Ther. 49(9), 2019.

[2] Farina et al. Gait & Posture, 114:152-159, 2024.

[3] de Oliveira Silva D, et al. Arch Phys Med Rehabil. 98. p. 114-9, 2017.

[4] Te M, et al. Pain Med. 18(11):2224-34, 2017.

Acknowledgements (Optional)

São Paulo Research Foundation FAPESP (2025/16045-0, 2024/19928-8, 2024/20974-4) and CNPq/Brazil (302558/2022-5).

Session Category

Clinical Biomechanics: N/A

P4-243

Hallux grip strength as a neuropathy-related marker of foot-ankle function decline in people with diabetes

P.T., PhD Jane Suelen S.P. Ferreira[1], PhD Carla B. Rodrigues[1], P.T. Giovana P. Carlos[1], P.T. Danielle A. Maze[1], PhD Panagiotis E. Chatzistergos[2], PhD Nachiappan Chockalingam[3], PhD Maria L. Lucoveis[1], P.T, MSc Paula N. C. Soares[1], PhD Ana C. B. Schmitt[1], PhD Ronaldo H. Cruvinel-Júnior[1], PhD Isabel C. N. Sacco[1]

[1]School of Medicine, University of São Paulo, Sao Paulo, Sao Paulo, Brazil. [2]University of Dundee, Dundee, Scotland, United Kingdom. [3]Reading Central Primary Care Network (PCN), Reading, England, United Kingdom

P.T., PhD Jane Suelen S.P. Ferreira

PhD Carla B. Rodrigues

P.T. Giovana P. Carlos

P.T. Danielle A. Maze

PhD Panagiotis E. Chatzistergos

PhD Nachiappan Chockalingam

PhD Maria L. Lucoveis

P.T, MSc Paula N. C. Soares

PhD Ana C. B. Schmitt

PhD Ronaldo H. Cruvinel-Júnior

Introduction

Foot muscle weakness is a frequent complication of diabetes mellitus (DM), particularly in individuals with diabetic peripheral neuropathy (DPN). These deficits contribute to altered gait biomechanics, impaired balance, and increased ulceration risk. Although changes in intrinsic foot muscles are well documented, clinical guidelines still do not include strength assessment as a marker of functional decline in people with DPN. Moreover, how DPN severity independently contributes to foot strength loss remains unclear. This study aimed to identify determinants of strength reduction in adults with DM and DPN.

Methods

This cross-sectional study approved by the local ethics committee (CAAE:63457822.0.0000.0068) included 68 healthy adults and 404 individuals with DM. Participants completed foot strength testing using the Enhanced Paper Grip Test, which measures hallux grip strength as a proxy for foot-ankle strength and function. Between-group comparisons (68 controls and 100 DM) were performed by t-tests, and differences across DPN severity levels were analyzed by one-way ANOVAs (404 DM) ($p<0.05$). Spearman correlations examined associations between strength and DPN severity, and multiple linear regression tested independent effects of DPN severity, body mass, height, and age on normalized strength (404 DM subjects).

Results

Healthy participants presented greater hallux strength than those with DM (0.51 ± 0.27N/kg vs. 0.25 ± 0.17N/kg; $p<0.0001$). In the expanded cohort, increasing DPN severity was associated with progressively lower strength (ANOVA $p<0.0001$), and the largest reduction was observed between absent and severe DPN (mean diff=0.19; $p<0.0001$). Strength correlated negatively with DPN severity ($r=-0.28$; $p<0.0001$). Regression analysis identified DPN severity as the strongest independent predictor of reduced normalized strength ($\beta=-0.0276$; $p<0.0001$), while height showed a positive association ($\beta=0.716$; $p<0.0001$). The model, including DPN severity, body mass, height, and age, explained 18% of the variance in foot strength ($R^2 = 0.18$).

Discussion

This study showed that hallux strength is reduced in individuals with DM, especially as DPN severity increases, and could be a DPN-related marker for foot-ankle function decline. These deficits are easily detected with a simple, low-cost test, supporting the inclusion of foot strength assessment in routine clinical practice.

Acknowledgements (Optional)

São Paulo Research Foundation FAPESP (2025/16045-0, 2023/09860-4, 2024/20974-4) and CNPq/Brazil (302558/2022-5).

Session Category

Clinical Biomechanics: N/A

P4-244

When Neuro Meets Ortho: Assessing Knee Joint Loading Patterns during Gait in People Post-Stroke

Dr. Russell Johnson PhD[1], Ms Ria Bakshi[2], Dr. Natalia Sánchez PhD[3]

[1]Northwestern University, Chicago, IL, United States. [2]Illinois Math and Science Academy, Aurora, IL, United States. [3]Chapman University, Orange, CA, United States

Introduction

Stroke survivors experience gait impairments, including impaired muscle control and kinematic deviations [1], which likely alter knee joint loads, and may accelerate the development of knee osteoarthritis [2]. Osteoarthritis can further limit mobility for people post-stroke, compounding the burden of stroke-related disability [3]. We developed novel musculoskeletal models that use each participant's gait data to estimate knee loading during gait in people post-stroke and age-matched controls.

Methods

Fifteen people post-stroke (time post-stroke > 6 months, ability to walk independently for 5 minutes) and 12 age- and sex-matched controls participated in our study (Chapman University IRB 23-57). We recorded gait mechanics using marker-based motion capture, ground reaction forces, and electromyography while participants walked on an instrumented treadmill at their self-selected speed. A scaled 3-D model and the recorded gait data were inputs for an OpenSim Moco [4] Inverse optimization to compute muscle forces, which allow us to estimate medial- and lateral-compartment knee joint compressive forces. We compared these knee joint forces between groups and limbs.

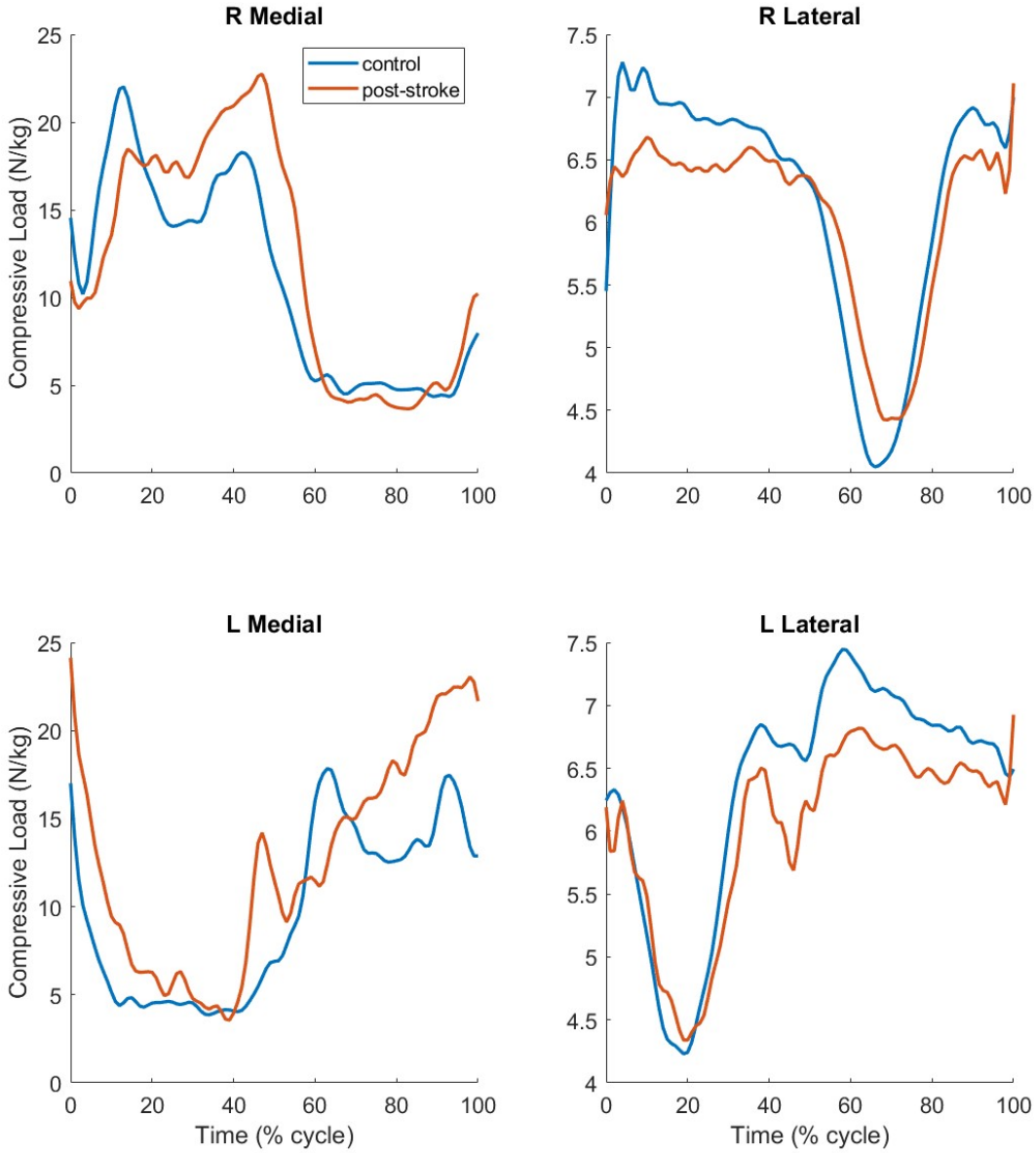
Results

We have completed data analysis for two people post-stroke (right paresis, speeds 0.99 and 0.75 m/s) and two controls (speeds 1.5 and 1.4 m/s). Despite slower speeds, the average peak magnitude of the right (paretic) medial knee load in people post-stroke was comparable to that of controls (stroke=22.7 N/kg; control=22.0 N/kg), while the left (non-paretic) medial knee joint load was greater than that of controls (stroke=24.1 N/kg; control=17.8 N/kg). Future work will assess loading across the full sample and compare the speed dependence of knee joint loads.

Discussion

These preliminary findings suggest that knee joint loads are altered in people post-stroke, particularly on the non-paretic side. This may indicate an over-reliance on the non-paretic limb, which increases the risk of cartilage degeneration over time. Overall, this work addresses a critical gap in stroke gait rehabilitation and has the potential to reduce long-term disability and improve mobility for millions of stroke survivors.

Images (Optional)



References (Optional)

[1] Chen et al., Gait & Posture, 2005.

[2] Andriacchi and Favre, Curr Rheumatol Rep, 2014.

[3] Nguyen-Oghalai et al., Arthritis Rheum, 2005.

[4] Dembia et al., PLOS Computational Biology, 2021.

Acknowledgements (Optional)

Andrian Kuch, PhD and Evan Shrier for help with data collection.

NIH NCMRR R03HD107630 to N Sánchez for clinical trial number NCT06034119.

Session Category

Clinical Biomechanics: N/A

P4-245

Lower Limb Muscle Fatigue During Dry and Wet Treadmill Walking in Children with Cerebral Palsy

Mr. Sangyup Lee M.A., Mr. Joseph Harrington M.S., Dr. David Kingston Ph.d.

University of Nebraska Omaha, Omaha, Nebraska, United States

Introduction

Children with cerebral palsy (CP) experience local muscle fatigue during walking due to impaired neuromuscular control and reduced endurance[1,2]. Local muscle fatigue can be observed as a lowered surface EMG median frequency (MDF) over time[3,4]. This study compared lower-limb MDF changes across treadmill walking speeds and environments between children with CP and typically developing (TD) peers. We hypothesized that greater impairment (GMFCS II) would exhibit larger MDF decreases compared to less impaired (GMFCS I) and TD groups across walking environments.

Methods

Fifteen typically developing and 12 CP (GMFCS I = 7, II = 5) children walked for 3 minutes on a dry and wet treadmill at 75%, 100%, and 125% of their self-selected speed. Water depth was at the subject's xiphoid level. Surface EMGs were recorded from the tibialis anterior (TA), medial gastrocnemius (MG), rectus femoris (RF), and semitendinosus (ST) following SENIAM guidelines using waterproof sensors[5]. Each trial was divided into five time segments to quantify MDF changes, but segments 1 and 5 were compared here.

Results

The GMFCS II group had decreased MDF across all speeds and muscles on a dry treadmill (Left: - 4.7 Hz; Right: - 5.8 Hz; both p <.001). The TD group also had decreased MDF values, whereas GMFCS I had MDF increases in MG and ST in several conditions (Table 1). In the wet treadmill environment, the TA had decreased MDF across almost all conditions, while the left MG showed the largest change in GMFCS II at fast speeds. TD displayed minimal RF fatigue in water, whereas the CP groups showed increased left RF fatigue at both normal and fast speeds (Table 1).

Discussion

The GMFCS II group demonstrated consistent MDF declines across muscles and speeds during dry treadmill walking. This finding is similar to prior work where CP gait had a – 3.3

Hz MDF reduction at normal walking speed[6]. However, wet treadmill walking demonstrated fatigue in specific muscles likely due to aquatic modifications to gait mechanics[1-4,7]. These findings support that buoyancy and hydrodynamic resistance challenge neuromotor control and could suggest wet treadmill walking as a beneficial rehabilitation for children with CP[8].

Images (Optional)

Dry treadmill		GMFCS II	ΔMDF [Hz]	*p*-value	GMFCS I	ΔMDF [Hz]	*p*-value	TD	ΔMDF [Hz]	*p*-value
Slow	Left TA	103.1 / 98.4	-4.8	0.313(W)	98.1 / 94.4	-3.6	0.057	79.8 / 78.4	-1.3	0.015*
	Left MG	120.2 / 113.3	-6.9	0.045*	100.5 / 105.6	+5.1	0.406(W)	79.5 / 78.2	-1.3	0.044*
	Left RF	89.0 / 84.9	-4.1	0.030*	46.4 / 38.2	-8.2	0.030*	58.3 / 54.9	-3.4	0.141
	Left ST	71.9 / 63.4	-8.5	0.032*	72.8 / 70.6	-2.2	0.289(W)	50.1 / 49.6	-0.5	0.076(W)
	Mean	96.1 / 90.0	-6.1	<.001***	79.4 / 77.2	-2.2	0.008(W)**	66.9 / 65.3	-1.6	0.004(W)
Normal	Left TA	103.3 / 101.2	-2.1	0.252	101.9 / 96.1	-5.8	0.039(W)*	79.4 / 78.1	-1.4	0.056
	Left MG	117.7 / 113.8	-3.9	0.073	99.9 / 106.2	+6.3	0.711(W)	80.5 / 80.4	-0.1	0.490
	Left RF	84.5 / 82.0	-2.6	0.126	44.3 / 36.1	-8.2	0.125	51.2 / 46.1	-5.1	0.047*
	Left ST	67.1 / 59.9	-7.2	0.038*	72.2 / 72.2	-0.1	0.485	45.7 / 42.1	-3.6	0.036*
	Mean	93.1 / 89.2	-3.9	0.003**	79.6 / 77.6	-1.9	0.093(W)	64.2 / 61.7	-2.5	0.002(W)
Fast	Left TA	104.6 / 100.7	-3.9	0.031(W)*	103.9 / 96.7	-7.2	0.023(W)*	80.9 / 78.2	-2.7	<.001***
	Left MG	113.8 / 110.3	-3.5	0.193	101.1 / 109.2	+8.0	0.766(W)	81.5 / 80.7	-0.8	0.237
	Left RF	85.0 / 81.0	-3.9	0.040*	41.5 / 31.2	-10.3	0.009**	42.6 / 37.0	-5.6	0.049*
	Left ST	66.3 / 61.2	-5.2	0.199	71.7 / 60.9	-10.8	0.016(W)*	46.2 / 42.6	-3.6	0.076(W)
	Mean	92.4 / 88.3	-4.1	0.010*	79.6 / 74.5	-5.1	<.001(W)***	62.8 / 59.6	-3.2	<.001(W)***
Total	Left M.	93.9 / 89.2	-4.7	<.001(W)***	79.5 / 76.4	-3.1	<.001(W)***	64.6 / 62.2	-2.4	<.001(W)***
	Right TA	128.0 / 119.5	-8.5	0.054	98.4 / 92.8	-5.6	0.344(W)	80.7 / 78.0	-2.7	<.001(W)***
Slow	Right MG	114.0 / 112.6	-1.3	0.181	94.5 / 94.3	-0.2	0.471	82.9 / 81.4	-1.5	0.062
	Right RF	84.8 / 76.3	-8.5	0.062	52.8 / 45.9	-6.9	0.078(W)	42.4 / 38.9	-3.5	0.033*
	Right ST	64.5 / 53.7	-10.8	0.125(W)	64.2 / 71.9	+7.7	0.984(W)	45.7 / 42.6	-3.1	0.179(W)
	Mean	97.8 / 90.5	-7.3	<.001(W)***	77.5 / 76.2	-1.3	0.539(W)	62.8 / 60.4	-2.4	<.001(W)***
Normal	Right TA	119.4 / 110.1	-9.3	0.013*	100.7 / 94.7	-6.0	0.500(W)	80.8 / 80.2	-0.6	0.239
	Right MG	118.7 / 114.9	-3.8	0.146	92.6 / 94.5	+1.9	0.781	82.7 / 81.6	-1.2	0.115
	Right RF	81.0 / 76.0	-5.0	0.092	52.4 / 39.8	-12.6	0.035*	38.0 / 33.9	-4.1	0.018*
	Right ST	56.7 / 53.9	-2.8	0.005**	65.1 / 68.1	+3.0	0.756	40.3 / 39.4	-0.9	0.178
	Mean	94.0 / 88.7	-5.2	<.001***	77.7 / 74.3	-3.5	0.195(W)	60.4 / 58.8	-1.7	0.005(W)**
Fast	Right TA	122.8 / 114.6	-8.2	0.028*	102.9 / 94.3	-8.6	0.156(W)	83.2 / 80.2	-3.0	0.001*
	Right MG	113.1 / 110.8	-2.3	0.270	92.7 / 93.9	+1.2	0.779	86.0 / 83.9	-2.1	0.080
	Right RF	79.6 / 73.3	-6.4	0.080	51.7 / 37.9	-13.8	0.023*	34.3 / 30.3	-4.0	0.086(W)
	Right ST	58.6 / 54.9	-3.7	0.262	61.9 / 70.9	+9.0	0.953(W)	41.6 / 41.9	+0.3	0.679
	Mean	93.5 / 88.4	-5.1	0.007**	77.3 / 74.3	-3.0	0.228(W)	61.3 / 59.1	-2.2	0.002(W)**
Total	Right M.	94.9 / 89.1	-5.8	<.001(W)***	77.5 / 74.9	-2.6	0.179(W)	61.5 / 59.4	-2.1	<.001(W)***

Wet treadmill		GMFCS II	ΔMDF [Hz]	*p*-value	GMFCS I	ΔMDF [Hz]	*p*-value	TD	ΔMDF [Hz]	*p*-value
Slow	Left TA	91.7 / 81.7	-10.0	0.143	59.7 / 53.3	-6.4	0.030(W)*	75.1 / 76.0	+0.8	0.151(W)
	Left MG	89.8 / 115.9	+26.0	0.893	74.2 / 75.2	+0.9	0.544	64.8 / 72.4	+7.6	0.979
	Left RF	48.8 / 57.7	+8.9	0.813	55.5 / 56.2	+0.7	0.688	62.3 / 61.2	-1.2	0.211(W)
	Left ST	92.7 / 86.1	-6.6	0.083	69.1 / 70.1	+1.0	0.971	58.5 / 58.2	-0.3	0.533(W)
	Mean	80.8 / 85.4	+4.6	0.779	64.6 / 63.7	-0.9	0.476(W)	65.2 / 66.9	+1.7	0.669(W)
Normal	Left TA	97.9 / 91.6	-6.3	0.005**	59.6 / 56.5	-3.1	0.163	74.4 / 74.0	-0.3	0.415
	Left MG	103.4 / 110.9	+7.5	0.842	83.0 / 88.5	+5.5	0.862	72.0 / 70.1	-2.0	0.201
	Left RF	49.4 / 38.7	-10.7	0.049*	55.1 / 53.5	-1.6	0.078	60.9 / 62.3	+1.4	0.897
	Left ST	91.5 / 88.7	-2.8	0.313(W)	69.5 / 69.8	+0.3	0.647	59.9 / 59.3	-0.6	0.304
	Mean	85.6 / 82.5	-3.1	0.035(W)*	66.8 / 67.1	+0.3	0.442(W)	66.8 / 66.4	-0.4	0.292(W)
Fast	Left TA	97.7 / 90.5	-7.2	0.035*	66.7 / 59.1	-7.6	0.028*	78.3 / 75.8	-2.6	0.036*
	Left MG	111.1 / 95.7	-15.4	0.406(W)	90.7 / 87.1	-3.6	0.374	72.3 / 65.3	-7.0	0.006(W)
	Left RF	65.7 / 52.2	-13.5	0.117	56.1 / 52.4	-3.8	0.109(W)	61.0 / 61.2	+0.3	0.596
	Left ST	90.8 / 85.2	-5.5	0.125	77.8 / 69.0	-8.7	0.109(W)	59.3 / 58.1	-1.2	0.119
	Mean	91.3 / 80.9	-10.4	0.007(W)**	72.8 / 66.9	-5.9	0.012(W)*	67.7 / 65.1	-2.6	0.003(W)
Total	Left M.	85.9 /82.9	-3.0	0.004(W)**	68.1 / 65.9	-2.2	0.032(W)*	66.6 / 66.1	-0.4	0.057(W)
	Right TA	114.8 / 106.2	-8.5	0.053	59.2 / 58.6	-0.6	0.350	78.1 / 76.9	-1.2	0.164
Slow	Right MG	88.3 / 89.0	+0.7	0.628	91.1 / 90.4	-0.7	0.331	83.9 / 87.6	+3.7	0.964(W)
	Right RF	95.4 / 87.2	-8.1	0.016*	89.5 / 84.9	-4.6	0.092	52.4 / 52.8	+0.4	0.582
	Right ST	82.8 / 82.4	-0.4	0.425	68.0 / 72.2	+4.2	0.531(W)	42.7 / 44.7	+2.0	0.862
	Mean	95.3 / 91.2	-4.1	0.011*	77.0 / 76.6	-0.4	0.105(W)	64.3 / 65.5	+1.2	0.871(W)
Normal	Right TA	114.7 / 105.6	-9.1	0.213	60.4 / 58.3	-2.1	0.239	81.2 / 80.5	-0.7	0.234
	Right MG	88.9 / 89.9	+1.0	0.797	91.4 / 93.2	+1.8	0.693	85.3 / 87.2	+1.8	0.904
	Right RF	93.3 / 86.7	-6.6	0.070	88.9 / 83.8	-5.1	<.001***	52.0 / 52.8	+0.8	0.720
	Right ST	80.5 / 75.2	-5.2	0.264	67.9 / 68.1	+0.3	0.544	45.9 / 44.6	-1.3	0.211(W)
	Mean	94.3 / 89.4	-5.0	0.018*	77.2 / 75.9	-1.3	0.162	66.1 / 66.3	+0.2	0.609(W)
Fast	Right TA	110.7 / 95.9	-14.8	0.033*	61.0 / 57.4	-3.6	0.018*	83.4 / 81.6	-1.7	0.089
	Right MG	89.1 / 90.1	+0.9	0.585	85.3 / 95.7	+10.4	0.977(W)	84.4 / 85.6	+1.3	0.533(W)
	Right RF	92.9 / 87.0	-5.9	0.071	87.1 / 88.1	+1.0	0.594 (W)	54.7 / 56.2	+1.5	0.423(W)
	Right ST	72.9 / 75.5	+2.6	0.837	71.4 / 72.1	+0.7	0.590	46.5 / 39.6	-6.9	0.009(W)**
	Mean	91.4 / 87.1	-4.3	0.049*	76.2 / 78.3	+2.1	0.619(W)	67.2 / 65.8	-1.5	0.016(W)*
Total	Right M.	93.7 / 89.2	-4.5	<.001(W)***	76.6 / 76.9	+0.1	0.094	65.9 / 65.8	-0.0	0.335

Table 1. Median frequency (MDF) values for segment 1 and segment 5 are presented for each muscle across the three groups, along with ΔMDF, which represents the difference between the two segments. Negative ΔMDF values indicate a reduction in MDF and therefore suggest muscle fatigue. TD; typically developing, TA; tibialis anterior, MG; medial gastrocnemius, RF; rectus femoris, ST; semitendinosus. *$p < 0.05$, **$p < 0.01$, ***$p < 0.001$. (W) indicates results obtained using the Wilcoxon signed-rank test.

References (Optional)

Session Category

Clinical Biomechanics: N/A

P4-246

Ertl and Non-Ertl balance strategy differences during quiet standing

Dr. Sara A. Mannello PhD, Dr. Abbie E. Ferris PhD

University of Northern Colorado, Greeley, CO, United States

Introduction

Traditional transtibial amputation methods have been associated with reduced loading of the prosthetic limb that may reduce stability. Improved loading and reduced asymmetries have been demonstrated in individuals with amputations that include a bone bridge (Ertl) compared to Non-Ertl amputations [1]. It is unknown how the Ertl method influences stability and balance. We hypothesize that postural stability measures will reveal differences between amputation techniques that exhibit reduced postural sway and improved interlimb symmetry during quiet standing in those with Ertl amputation.

Methods

Ertl (n = 11, 79.4 ± 16.7 kg, 1.77 ± 0.08 m) and Non-Ertl (n = 7, 88.3 ± 16.0 kg, 1.78 ± 0.08 m) participants stood with feet on separate force plates (AMTI, Watertown, MA) with or without a foam mat and with eyes open or closed for 20s. COP, Rambling-Trembling, and symmetry measures were calculated and compared between groups and conditions.

Results

Compared to the Non-Ertl group, the Ertl group had significantly greater overall COP RMS values (Ertl Prosthetic = 514.74 ± 213.65 mm, Intact = 485.54 ± 176.99 mm vs. Non-Ertl Prosthetic = 358.96 ± 56.12 mm, Intact = 374.02 ± 50.22 mm) for prosthetic and intact limbs. Symmetry indices indicated small prosthetic dominance in the Ertl group in the ML and RMS Rambling/Trembling mean velocities while the Non-Ertl group had greater asymmetry with preference for the intact limb especially for COP mean velocity (-11.44 ± 21.64% vs. Ertl 7.20 ± 33.13%). Examination of Rambling-Trembling measures revealed significantly increased Rambling across in the Ertl group (Table 1). Trembling only showed increases in the Ertl prosthetic limb AP velocity and RMS with more variability across individuals.

Discussion

Overall, the groups appear to use different strategies to maintain balance in quiet stance. The non-Ertl group had less postural sway and preference for the intact limb, while the Ertl

group had greater sway with a preference for the prosthetic limb. It appears that the additional manipulation of the internal structure as part of the Ertl method provides the opportunity for more loading and results in individuals utilizing different strategies for balance control.

Images (Optional)

Table 1: Mean Rambling and Trembling metrics for quiet standing for Ertl and Non-Ertl groups.

Group	Limb	Rambling			Trembling	
		AP velocity (mm/s)	ML velocity (mm/s)	RMS (mm)	AP velocity (mm/s)	RMS (mm)
ERTL	Prosthetic	646.6 ± 647.5*	692.9 ± 786.6*	514.73 ± 213.64*	568.8 ± 604.8*	1.47 ± 1.17*
	Intact	661.4 ± 672.9*	672.6 ± 652.3*	485.53 ± 176.99*	586.4 ± 622.3	1.15 ± 1.08
Trad	Prosthetic	373.9 ± 63.8*	452.2 ± 55.8*	358.97 ± 56.13*	309.3 ± 64.1*	0.61 ± 0.40*
	Intact	403.5 ± 114.7*	533.4 ± 113.8*	374.02 ± 50.22*	339.7 ± 105.5	0.71 ± 0.59

Note: *Indicates significant group difference (p = 0.05)

References (Optional)

[1] Abbie E. Ferris *et al.* , Clinical Biomechanics, 2017

Session Category

Clinical Biomechanics: N/A

P4-247

Muscle Activation Patterns During Lifting in Individuals with Large to Massive Rotator Cuff Tears: Adaptive vs. Limited Responders

Ms. Sarah Remedios MSc[1,2], Dr. Ivan Wong MD FRCS(C), Dip. SPORTS MED, MACM, FAANA[1], Dr. Kathleen MacLean PhD[1], Dr. Janie Astephen Wilson PhD[1], Dr. Derek Rutherford PT, PhD[1]

[1]Dalhousie University, Halifax, Nova Scotia, Canada. [2]Nova Scotia Health, Halifax, Nova Scotia, Canada

Introduction

Rotator cuff tears (RCT) result in altered shoulder function, such as limited range of motion (***limiters)***. However, some adults with RCTs adapt and demonstrate full shoulder motion (***adapters)***. This study aims to determine muscle activation patterns and range of motion during a lifting task between asymptomatic older adults (ASYM) and patients with a large-to-massive RCT (***adapters***, ***limiters***).

Methods

ASYM were recruited from the community (n=20). Patients with >3cm RCT were recruited from an orthopaedic clinic (N=39). The RCT group was divided into ***adapters*** *(*n=21*)* if peak active thoracohumeral flexion measured with optoelectronics was within one standard deviation of the ASYM average. Remaining RCT were classified as ***limiters*** (n=18) (Fig1). Electromyography of six shoulder muscles and optoelectronics were collected during flexion with a 2.5% body mass load to a shoulder height target. Signals were low pass filtered, time normalized to 100% of the lift cycle, and amplitude normalized to percent peak muscle activity. Principal component analysis (PCA) was used to analyze all %peak waveforms, and principal patterns (PP) were assessed for differences between groups and interactions with muscle (2-way ANOVA, =0.05).

Results

No significant thoracohumeral angle differences were found between ***adapters*** and ***limiters*** (54.4º±19.4 vs. 48.4 º±14.3,p>0.05) and both less than ASYM (78.5º±5.2,p<0.05). Three PPs were identified to represent >95% of variance. Significant group by muscle interactions were found for all *PP-scores*. RCT groups showed greater anterior deltoid *PP1-scores* (more activity) (p<0.05), only ***limiters*** had smaller lower trapezius *PP1-scores* (less activity) (p<0.05) than ASYM. ***Limiters*** had lower infraspinatus

and lower trapezius *PP2-scores* (smaller lift phase differential) than both ***adapters*** and ASYM ($p<0.05$). Upper trapezius and supraspinatus *PP2-scores* were smaller in RCT groups than ASYM ($p<0.05$). RCT groups exhibited greater deltoid *PP3-scores* than ASYM ($p<0.05$) (bigger lower phase differential).

Discussion

Limiters consistently demonstrated restricted motion and elevated activation demands in agonist and synergist muscles. a***dapters*** often resembled ASYM patterns. Findings suggest some distinct activation strategies between RCT subgroups compared to asymptomatic individuals during lifting. Clinically, the similarity of ***adapters*** to asymptomatic patterns and the heightened demands in ***limiters*** indicate RCT patients may require subgroup-specific rehabilitation approaches.

Images (Optional)

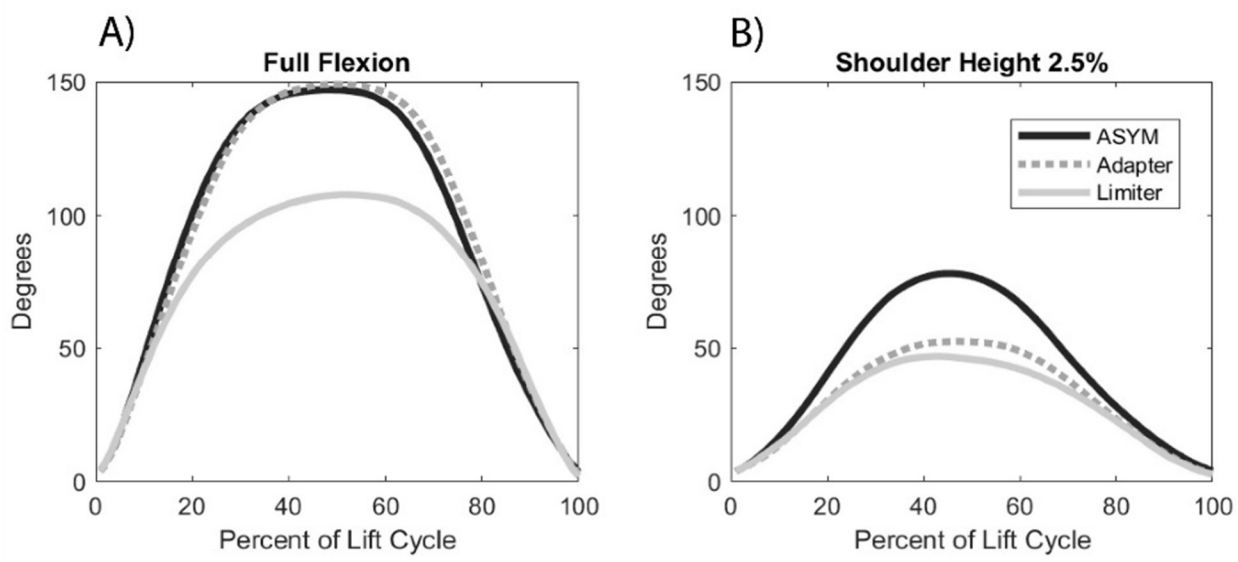


Figure 1. Thoracohumeral angles for (A) maximal forward flexion, and (B) flexion with 2.5% load to shoulder height for the entire lift cycle (lift, lower) for all three groups: asymptomatic (ASYM), Adapters and Limiters.

References (Optional)

Session Category

Clinical Biomechanics: N/A

P4-248

40 Hz Transcranial Vibration Enhances CSF Hydrodynamics: A Finite Element Study of the Entire Head

Ms. Seo Hyun Lee student, Mr. Taehyun Kim student, Prof. Namkeun Kim Professor

Sogang University, Seoul, Seoul, Korea, Republic of

Introduction

Current research on Alzheimer's disease (AD) depends heavily on clinical trials. However, these trials often lack a clear explanation of the physical mechanisms. Therefore, we need a computational head model to simulate physical interactions inside the head. Specifically, modeling the hydrodynamics of cerebrospinal fluid (CSF) is critical. CSF dynamics play a key role in removing toxic proteins. This study analyzes the hydrodynamic effects of 40 Hz vibration on waste transport in CSF using a whole-head finite element model.

Methods

We constructed a whole-head finite element model and validated it using magnetic resonance elastography data.[1] We defined brain tissue as a linear viscoelastic solid. We modeled the CSF using the linearized Navier-Stokes equations to represent fluid behavior. After validation, we applied 40 Hz vibration to the skin. This replicated the parameters of the AriBio HERZION device. Our analysis was based on Taylor Dispersion Theory, which suggests that high velocity gradients help mix and remove waste.[2] We measured velocity gradients and energy intensity in the CSF to evaluate potential for waste clearance.

Results

The simulation results showed distinct velocity gradient hotspots in the lateral CSF regions under 40 Hz stimulation. We compared 40 Hz vibration with 50 Hz and 60 Hz. The 40 Hz vibration generated significantly higher energy intensity and larger velocity gradient hotspots. Also, we found a direct positive correlation between energy intensity and the size of velocity gradient hotspots. These findings confirm that external vibration creates internal velocity gradients needed for fluid mixing.

Discussion

This study is the first to quantitatively show the mechanical impact of 40 Hz vibration on CSF hydrodynamics. The main contribution is the structure of the model. Unlike other studies that simplify CSF as a solid, our model treats CSF as a fluid. This allows us to observe how substances move. Also, including the skin and skull allows accurate

simulation of vibration from the outside to the inside. Future research will build models with AD pathologies to compare them with healthy brain models.

References (Optional)

[1] Li et al., J Mech Behav Biomed Mater, 2021

[2] Asgari et al., Sci Rep, 2016

Session Category

Clinical Biomechanics: N/A

P4-249

Proposed Symptom-Avoidance Strategies in Femoroacetabular Impingement Syndrome Identified Through 3D Shape-Kinematic Correlates

Mr. Seth Kussow MS, Dr. Jared Zitnay PhD, Mr. Rich Lisonbee MS, Dr. Stephen Aoki MD, Dr. Travis Maak MD, Dr. Andrew Anderson PhD

University of Utah, Salt Lake City, Utah, United States

Introduction

Cam morphology is prevalent in femoroacetabular impingement syndrome (FAIS), yet ~35% of the general population exhibits cam morphology without symptoms [1], indicating morphology alone does not dictate pathology. Combining statistical shape modeling (SSM) with biplane fluoroscopy (BF) enables precise 3D characterization of morphology and in vivo motion, overcoming limitations of traditional methods. Herein, we aimed to identify hip shape-motion relationships underlying FAIS symptom-avoidance strategies.

Methods

Symptomatic FAIS patients (n=23) and asymptomatic individuals with (positive controls; n=14) and without (negative controls; n=11) cam morphology were recruited. CT/MRI data were segmented to reconstruct 3D femur and pelvis surfaces for SSMs (femur: 2048 particles; pelvis: 4096 particles; ShapeWorks) and to measure 3D hip and pelvis kinematics from BF data while treadmill walking. Group mean SSM principal component (PC) score contributions were compared and group kinematics differences were assessed at push-off (PO) and heel-strike (HS) using ANOVA (α=0.05). Linear regression was evaluated between groupwise different PC scores and kinematic metrics across the cohort and within groups.

Results

FAIS patient femurs exhibited a more prominent cam region and greater neck-shaft angle, reflected in higher femur PC mode 4 scores versus negative controls (**Figure 1**). Patients demonstrated greater hip external rotation at PO (3.61° ± 5.78°) and less relative posterior pelvic tilt at HS (-0.57° ± 3.25°) than negative controls (hip ext. rotation: -2.03 ± 4.59°, p=0.02; pelvic tilt: -3.39 ± 2.73°, p=0.04), but not positive controls (hip ext. rotation: 2.92 ± 5.72°; pelvic tilt: -0.39 ± 2.86°). Femur mode 4 displayed a strong, negative correlation with pelvic internal rotation at PO across positive controls (**Figure 1**) and a negative correlation with hip flexion across the cohort at HS.

Discussion

FAIS patients had distinct femoral morphology and altered hip and pelvis kinematics compared to negative controls, aligning with prior work [2]. Positive controls with patient-like femurs may avoid FAI symptoms by increasing pelvic internal rotation at PO. Findings highlight pelvic mobility as a therapeutic target in FAIS treatment and support phenotyping FAIS for patient-specific interventions.

Images (Optional)

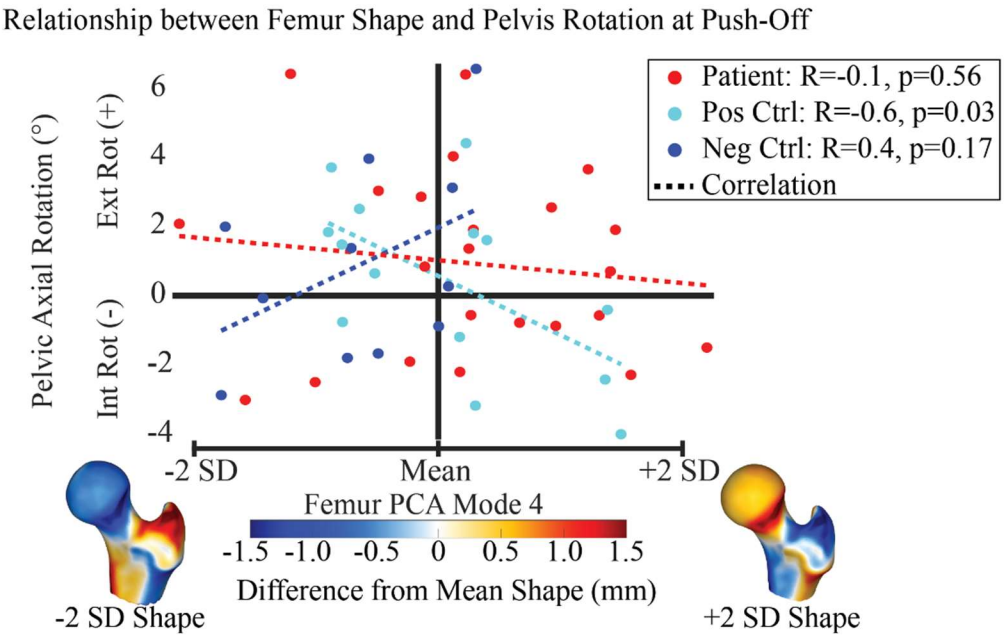


Figure 1: Positive controls with more patient-like femurs displayed a more internally rotated pelvis at push-off, as indicated by a strong correlation between PC score and internal pelvis rotation. Regression lines (top) highlight a stronger correlation for positive controls than patients. Shape variation along ±2 SD of femur PC mode 4 (bottom) that significantly differs between patients and negative controls ($p<0.05$) where patients had more positive PC scores. Red and blue in colormaps indicate regions where bone is more or less prominent compared to the population mean femur shape, respectively.

References (Optional)

[1] Frank JM et al., Arthroscopy, 2015 [2] Atkins PR et al., J Orthop Res, 2020

Acknowledgements (Optional)

National Institutes of Health (R01AR077636, U24EB029011, R01AR076120, R01HL135568, R01EB016701).

Session Category

Clinical Biomechanics: N/A

P4-250

Gait Gear Shifting: Age and Perception Modulate Walking Speed

Ms. Silvia Campos-Vargas[1], PhD Kenneth Harrison[1], PhD Redden David[2], PhD Jaimie Roper[1]

[1]Auburn University, Auburn, Alabama, United States. [2]VCOM-Auburn, Auburn, Alabama, United States

Introduction

Gait speed is a crucial marker of mobility and falls risk in older adults (OA), but how individuals adjust gait speed with aging and verbal instructions remains unclear. In younger adults (YA), gait speed varied (0.91–2.16 m/s) across 24 prompts [1], showing high adaptability. Extending this to OA, verbal instructions explained 76.1% of variance, suggesting modulation strategies change with age [2]. This study examines age-related differences in gait speed adaptability, hypothesizing that YA exhibit more gait groupings while OA show reduced variability and stronger cue dependence.

Methods

49 Auburn University participants. 26 YA (21±2 years) and 23 OA (70±5 years), completed gait trials on a 5.8-meter walkway following 24 randomized walking instructions. Inclusion required no lower extremity injuries for 6+ months. K-means clustering identified gait-speed patterns with and without verbal instruction consideration. Silhouette analysis validated cluster quality, and relative instruction contributions were calculated using the distance of each instruction from its specific cluster center.

Results

Without instructions, YA exhibited 4 gait-speed clusters (average 1.1–1.4 m/s) versus 3 in OA (1.1–1.2 m/s) in the clusters, indicating reduced speed range. With instructions, cluster numbers remained stable but revealed distinct modulation patterns. YA, explaining 79% variance, showed Low Demand, Comfortable, Hustle, and Maximal (as fast as possible, 100% loading) clusters. Older adults demonstrated three clusters, accounting for 77% of the variance: Comfortable, Hustle, and Maximal (Figure 1). Critically, the "fast as possible" instruction was only in YA but was in Maximal for OA with urgency cues.

Discussion

This study highlights age-related differences in gait-speed modulation. Younger adults exhibited 4 distinct speed clusters, whereas older adults showed only 3, indicating decreased adaptability with age. Notably, the "fast as possible" instruction triggered a separate cluster solely in younger adults (100% loading). In older adults, this cluster

merged with the contextual urgency cues to form the Maximal cluster. It is worth considering whether this absence reflects an actual limitation or a decline in rarely-used reserve capacity, as meaningful comparisons should focus on real-world speeds.

Images (Optional)

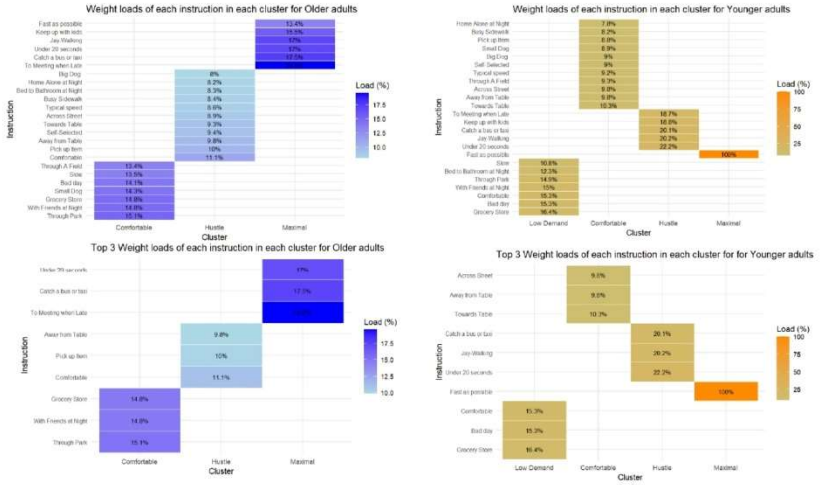


Figure 1. Gait Speed Modulation: Weight Load Distribution of Walking Instructions by Age Group *(Top panel: All instructions; Bottom panel: Top 3 instructions per cluster)*

References (Optional)

[1] Brinkerhoff, S.A., et al., Gait & Posture, 2022.

[2] Harrison, K., et al., bioRxiv, 2025.

Session Category

Clinical Biomechanics: N/A

P4-251

Instrumented Timed Up and Go in Younger Adults: Variability of Neuromechanical and Spatiotemporal Parameters Using an 18-Sensor Inertial Measurement System

Prof. Slawomir Winiarski DSc, Associate Professor, Eng[1], Doctor Mateusz Kowal PhD in Medical Sciences, PT[2], Doctor Ewa Morgiel PhD in Medical Sciences[2]

[1]Wroclaw University of Health and Sport Sciences, Wroclaw, -, Poland. [2]Wroclaw Medical University, Wroclaw, -, Poland

Introduction

Quantifying neuromechanical control during functional mobility tasks is essential for clinical biomechanics. The instrumented Timed Up and Go (iTUG) test enables detailed assessment of movement phases relevant to balance, gait and transitional control [1]. However, normative data for younger adults remain limited [2]. This study characterises the variability of spatiotemporal and kinematic parameters of the iTUG in healthy younger adults to inform clinical interpretation and contribute reference values for research and therapeutic monitoring.

Methods

Seventy-three physically active adults (20–40 years) performed a standardised iTUG under laboratory conditions. Eighteen inertial measurement units (Noraxon MyoMotion) recorded 3-dimensional trunk and limb kinematics @200 Hz. The test was segmented into sit-to-stand, walking, turning and stand-to-sit phases. Descriptive statistics, ranges of motion (ROM) and coefficients of variation (CV) quantified variability across temporal, spatial and kinematic metrics.

Results

Total iTUG time demonstrated low variability (13.1 ± 1.9s, CV 14.8 %). Walk 1 and Walk 2 phases showed average variability (CV 20–23%), whereas Turn 1 exhibited low variability (CV 19,5%). Most gait parameters, including stride time (CV 7.7 %), stance and swing proportions (CV 3–6%), and foot pitch at foot -off (CV 12–14 %), were highly consistent across individuals. In contrast, derived asymmetry indices showed markedly elevated variability, particularly the double-support ratio (CV 271.5 %). Trunk-related variables displayed phase-dependent behaviour: ROM values presented average to high variability (eg, trunk rotation ROM CV 43.1%), while trunk velocity parameters during sitting transitions showed very high to extremely high variability (CV up to 373.6 %).

Discussion

Neuromechanical performance during the iTUG is highly consistent in younger adults for key temporal and gait-cycle parameters, supporting their use as normative biomechanical references. Elevated variability in trunk ROM and trunk speed metrics suggests individual movement strategies during transitional phases, indicating sensitivity to motor control differences. Extremely variable asymmetry indices demonstrate limited utility for normative interpretation but potential value as markers of pathology. The findings support the iTUG as a trastwothy, sensor-based assessment for clinical biomechanics and research requiring precise functional mobility characterisation[3].

Images (Optional)

Table 1. Key iTUG parameters in healthy younger adults.

Parameter	Mean ± SD	Coefficient of Variation (CV%)
Total iTUG time (s)	13.1 ± 1.9	14.8
Walk 1 duration (s)	4.1 ± 1.0	22.4
Walk 2 duration (s)	3.2 ± 0.7	20.5
Stride time (s)	1.1 ± 0.1	7.7
Cadence (steps/min)	107.6 ± 8.3	7.7
Stance phase left (%)	60.3 ± 2.0	3.3
Stance phase right (%)	59.6 ± 2.3	3.9
Double support left (%)	9.7 ± 2.0	20.3
Double support ratio (R–L)/(R+L) (%)	4.1 ± 11.0	271.5
Turn 1 duration (s)	2.0 ± 0.4	19.5
Trunk rotation ROM during sit phase (°)	163.5 ± 70.4	43.1
Trunk flexion speed avg (deg/s)	36.3 ± 44.3	122.1
Trunk extension speed avg (deg/s)	8.5 ± 31.7	373.6

References (Optional)

[1] Mao et al. J.Neuroeng.Rehabil. 2024, 21, 85.

[2] Kobsar et al. J.Neuroeng.Rehabil. 2020, 17, 62.

[3] Kowal Winiarski, et al. J.Clin.Med. 2025, 14, 1944.

Acknowledgements (Optional)

We acknowledge the Ministry of Education and Science in Poland for funding support (SUBZ.E060.23.037).

Session Category

Clinical Biomechanics: N/A

P4-252

Fundamental Study on a Predictive Diagnostic Method for Abdominal Aortic Aneurysm Expansion Using Thermal Expansion Analysis

Professor Sota Yamamoto[1], Mr. Ziyi Ye[1], Mr. Masayuki Kamada[1], Dr. Katsuyuki Hoshina[2], Dr. Ken Kimura[3]

[1]Shibaura Institute of Technology, Koto-ku, Tokyo, Japan. [2]The University of Tokyo Hospital, Bunkyo-ku, Tokyo, Japan. [3]Kyorin University Hospital, Mitaka, Tokyo, Japan

Introduction

Abdominal aortic aneurysms (AAAs) primarily affect older adults and require annual imaging follow-ups to monitor growth, imposing burdens on patients and healthcare systems. A predictive diagnostic method estimating future expansion could reduce these burdens by extending follow-up intervals without compromising safety. However, CT imaging provides only static geometry, posing challenges for predictive diagnosis.
We propose a novel framework combining finite element analysis (FEA) with thermal expansion modeling to predict future AAA geometry. Patient-specific CT data are used to reconstruct aneurysm geometry, inflate a cylindrical finite element model (FEM) within the lumen, and compute local expansion rates from node displacement and strain invariants. These rates are converted into thermal expansion coefficients, enabling time-dependent prediction by simulating temperature change.

Methods

AAA geometry was reconstructed from annual CT scans. A rigid wall model was generated, and a cylindrical shell-element FEM was positioned inside and inflated under controlled pressure. Local expansion rates were estimated by projecting FEM nodes onto the aneurysm wall and calculating strain invariants. Rates were translated into thermal expansion coefficients, with time modeled as temperature change. Calcified regions identified by Li et al. (2008) were assigned zero expansion. Two prediction strategies were tested: element-wise local rates and uniform average rates. Predicted third- and fourth-year geometries were compared with actual CT data using diameter and surface deviation metrics.

Results

The proposed predictive method was applied to longitudinal CT data from one AAA patient over four years. The constructed FEM consisted of 8,540 elements spanning from the renal artery bifurcation to the iliac bifurcation. The FEM-based approach successfully estimated local expansion rates between the first and second years and predicted the third-year

geometry using thermal expansion analysis. The element-wise expansion approach showed substantially higher accuracy than the uniform expansion model.

Furthermore, the fourth-year geometry predicted from second-year expansion rates closely matched the actual CT-derived geometry, especially in the regions of maximal expansion.

Discussion

This framework demonstrated feasibility for predicting AAA progression and clinically relevant indices such as maximum diameter. Incorporating spatial heterogeneity and calcification enhanced accuracy. Future work will expand patient cohorts, optimize mesh resolution.

Images (Optional)

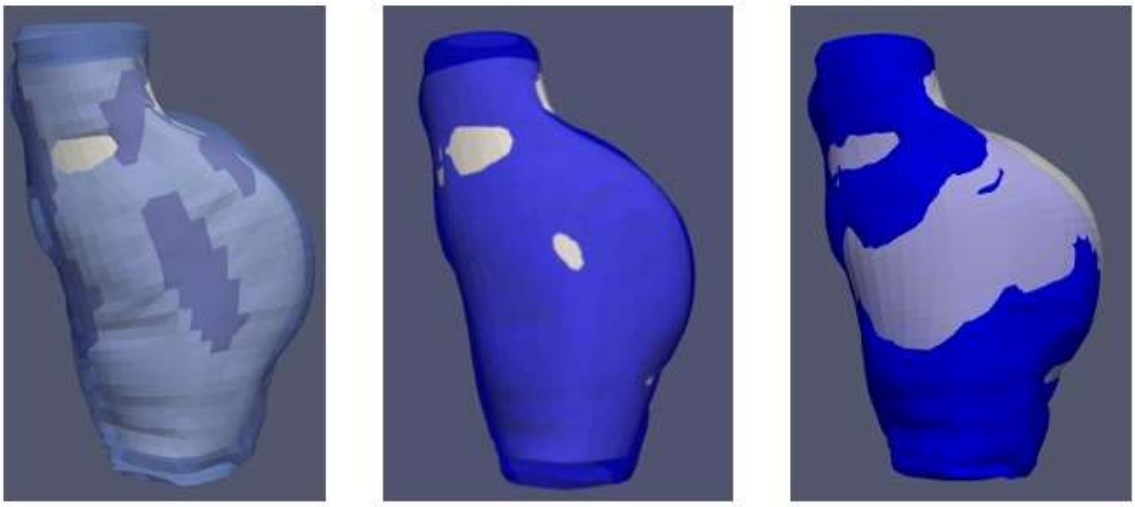


Figure Predictive Simulations for AAA Expansion

References (Optional)

Z.Y. Li et al., *J Vasc Surg*, 2008

Acknowledgements (Optional)

This study was supported by JSPS KAKENHI Grant-in-Aid for Scientific Research (C), Grant Number 24K11948.

Session Category

Clinical Biomechanics: N/A

P4-253

Assessment of Fall Risks With Multi-Directional Perturbations in Young, Older Adults, and Older Adults With High Fall Risk

Ms Soyoung Lee PhD[1], Mr Wei Yin PhD[2], Mr Zongpan Li PhD[1], Ms Peiwen Fu[1], Mr Matteo Pergami-Peries PhD[1], Mr Li-Qun Zhang PhD[1]

[1]University of Mryland Baltimore, Baltimore, Maryland, United States. [2]New Jersey Institute of Technology, Newark, New Jersey, United States

Introduction

Reactive balance to perturbations is important for preventing falls, yet how multidirectional responses differ with aging and fall risk remains unclear. We compared center-of-pressure (COP) stability, COM (center of mass) acceleration, and COP trajectory orientation between young healthy (HY), healthy older (HO), and high fall-risk older (HFR) adults during multidirectional footplate perturbations.

Methods

Thirty-one adults stood on a moveable platform delivering horizontal translations in eight directions at 45° intervals under eyes-open conditions. COP trajectories were recorded by force plates and COM acceleration by an IMU at L5. For each trial we calculated COP stability index (SI), peak COM acceleration (pACC), and COP angular deviation from the perturbation direction. SI was the farthest COP distance from the base-of-support center normalized to the distance from center to boundary (range 0–1). COP angle deviation (AD) was the angle between the reversely extended perturbation line and the line from the base-of-support center to the farthest COP location. One-sample t-tests tested AD against 0° within each group and direction. One-way ANOVA with Tukey post-hoc tests compared SI and pACC across groups.

Results

Across all three groups, COP AD during four oblique perturbations was consistently deviated to the lateral direction (~10–20°, $p < 0.05$), whereas AD for anterio-posterior and left-right perturbations did not differ from 0° (Figure 1). SI showed significant group effects in lateral and posterior-oblique directions (lateral: $p = 0.03$; postero-medial: $p = 0.03$; postero-lateral: $p = 0.01$), with older groups, particularly HFR, exhibiting less COP movement than HY. pACC differed by group for anterior ($p < 0.001$) and postero-lateral ($p = 0.031$) perturbations; HY showed smaller peak accelerations than both HO and HFR, while HO and HFR were similar.

Discussion

Multidirectional perturbations revealed a common pattern of COP lateral deviation during oblique perturbations across groups, suggesting higher risk in lateral than AP directions. Aging and high fall risk showed reduced ability to change COP with perturbations and greater COM accelerations and instability in specific directions. Combining COP SI, COM acceleration, and COP AD provides a direction-resolved approach to detect lateral instability and design oblique- and lateral-focused fall-prevention training for older adults at risk of falls.

Images (Optional)

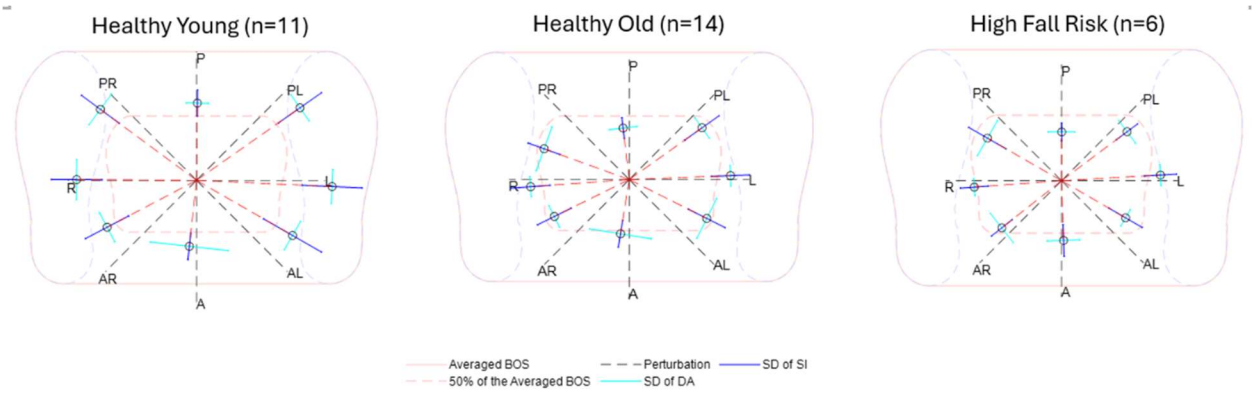


Figure 1. SI and DA across all groups during perturbations in the 8 directions. Along the radial distance, the circles and the lines show the mean and standard deviation (SD) of SI across all subjects, respectively. On the polar angle, the circles and the lines show the mean and SD of DA across all subjects, respectively. A, AR, R, PR, P, PL, L, and AL correspond to linear perturbations in Anterior, Anterior-Right, Right, Posterior-Right, Posterior, Posterior-Left, Left, and Anterior-Left directions, respectively. Participants Characteristics: Age (HY=28.7±4, HO= 73.5±3.7, HFR= 22.7±2.9), BMI (HY=23.1±3.7. HO=27.6±3.9, HFR=22.7±2.9).

Session Category

Clinical Biomechanics: N/A

P4-254

Application of Lateral Pressure to the Buttocks Improves Tissue Perfusion in the Seated Patient

Miss Maegan Spiteri[1], Professor Peter Worsley[2], Professor Spyros Masouros[1]

[1]Imperial College, London, London, United Kingdom. [2]University of Southampton, Southampton, Hampshire, United Kingdom

Introduction

Prolonged sitting increases pressure-ulcer (PU) risk for individuals with limited mobility such as the elderly and wheelchair users. During loading, blood vessels are occluded, O_2 is obscured, and CO_2 accumulates causing PUs [1]. Current prevention methods used in healthcare aim to reduce underbody pressure by increasing contact area through compliant surfaces, but evidence suggests that these devices don't reduce the tissue stresses deeper, at the bone-tissue interface [2]. Finite-element studies have shown that applying lateral pressure (LP) can mitigate the internal stresses [3]. Transcutaneous oximetry is commonly used in PU research as a surrogate measure of local tissue perfusion and ischaemic burden [4]. This study compares the ability of a novel LP device with a standard static foam chair to maintain baseline transcutaneous gas tensions during sitting.

Methods

Transcutaneous CO_2 and O_2 were recorded at the ischial tuberosity in 30 healthy adults using an oximeter. Participants underwent 20 minutes sitting on static-foam, 10 minutes standing to re-establish baseline, then 20 minutes sitting with the LP device. Percentage deviations from physiological baseline were determined and interpreted using Chai and Bader's classification [5]. Underbody pressure was obtained with a pressure-sensing mat. Statistical comparisons were performed using paired, one-tailed Student's t-tests.

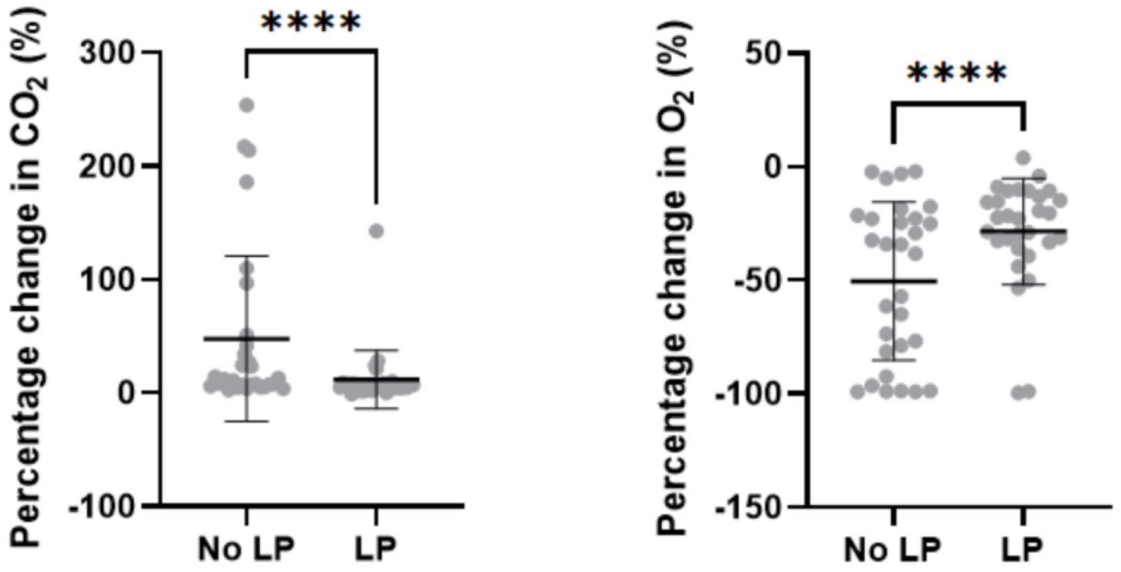
Results

The cohort (mean age 28.9 years, 20–59; mean BMI 25.5 kg/m^2, 18.7-40.9) showed substantially improved tissue gas responses with LP. CO_2 elevations fell from +47.8% on foam to +11.9% with LP ($p < 0.0001$), while O_2 deficits improved from –50.4% to –28.5% ($p < 0.0001$). LP produced significantly lower mean and peak underbody pressures ($p < 0.0001$).

Discussion

These results suggest that lateral pressure may be more effective than static-foam in PU prevention for seated individuals. While underbody pressure decreased in every participant, the inconsistent gas-tension changes further demonstrates that pressure does not reliably represent tissue perfusion. Nonetheless, the young, healthy sample limits generalisability to higher-risk clinical populations.

Images (Optional)



Average percentage change of (left) carbon dioxide and (right) oxygen for all participants during sitting periods on static foam and lateral pressure interventions, where **** denotes $p < 0.0001$

References (Optional)

[1] Amit Gefen, J Wound Care, 2024

[2] Eran Linder-Ganz et al. , J Biomechanics, 2007

[3] Colin Boyle et al. , PLoS One, 2020

[4] Dan Bader et al. , Clinical Physics and Physiological Measurement, 1988

[5] Chanyuan Chai et al. , J Mechanical Behavior of Biomedical Materials, 2013

Session Category

Clinical Biomechanics: N/A

P4-255

Afferent feedback increases simulated upper-limb tremor but has little effect on tremor propagation patterns

Mr. Ian Syndergaard BS[1], Dr. Daniel Free PhD[1], Prof. Dario Farina PhD[2], Prof. Steven Charles PhD[1]

[1]Brigham Young University, Provo, UT, United States. [2]Imperial College London, London, Greater London, United Kingdom

Introduction

Tremor is the most common movement disorder, often impairing daily activities [1]. Many peripheral tremor suppression techniques have been proposed, including injections of botulinum toxin, low-level electrical stimulation, and low-pass filtering orthoses. However, optimally implementing these techniques requires a deeper understanding of tremor propagation, i.e. how tremorogenic excitation to muscles creates tremor throughout the upper limb. Past simulations of tremor propagation have yielded important principles [2], but these simulations did not include afferent feedback, which may have a significant effect on tremor. The purpose of this study was to simulate the effect of short-loop afferent feedback on tremor propagation.

Methods

We used a recently developed closed-loop model of the upper limb [3] to simulate tremor propagation (see figure). Model inputs were tremorogenic excitation to the 15 major superficial muscles of the upper limb, and model outputs were tremulous rotation in the seven main joint degrees of freedom of the upper limb. Short-loop afferent feedback was modeled as homonymous feedback via Golgi tendon organs (GTO), homonymous and heteronymous feedback via muscle spindles, and neural transmission delays. Simulations across four postures and varied physiological parameters assessed tremor under different feedback conditions.

Results

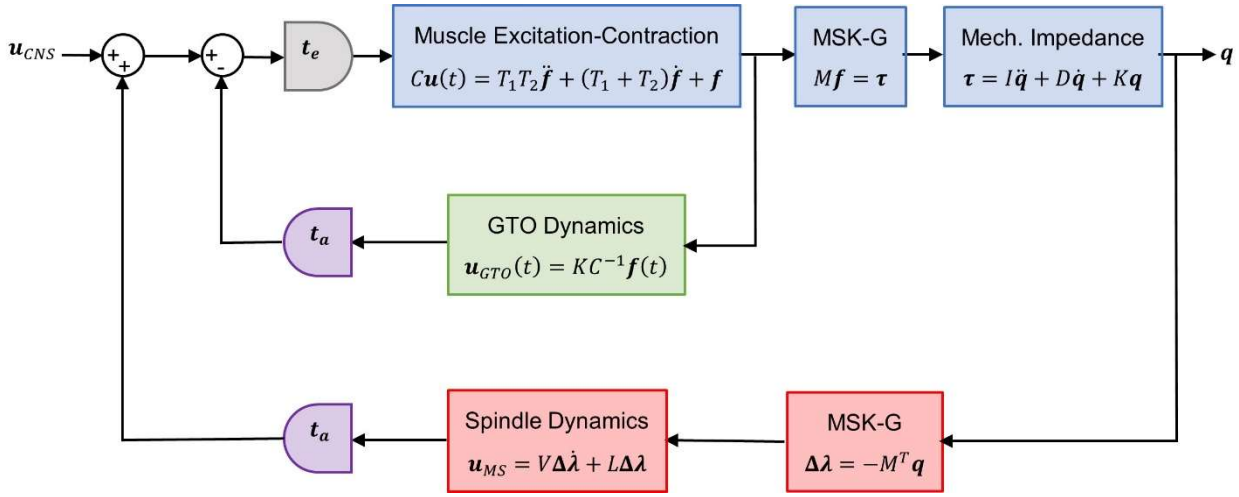
Simulated GTO-mediated feedback amplified responses at tremor frequencies by 44% on average (range 11-95%). This amplification increased with transmission delay, so the greatest amplification occurred for tremor caused by distal muscles. In contrast, spindle-mediated feedback had minimal impact at tremor frequencies. Combined feedback effects were approximately additive. Tremor propagation patterns remained consistent across conditions; as without feedback, wrist muscles contributed most prominently to

simulated tremor, which appeared greatest in wrist degrees of freedom. Trends were robust across postures and physiological parameter ranges.

Discussion

According to our simulations, afferent feedback amplifies tremor by about 50% but does not significantly alter propagation patterns. Therefore, tremor propagation (how tremorogenic excitation of a given muscle creates tremor throughout the upper limb) depends primarily on mechanical coupling (multi-articular muscles and interaction torques), not neural coupling (heteronymous feedback).

Images (Optional)



References (Optional)

1. KP Bhatia et al., Mov Disord, 2018.

2. SA Baker et al., TOHM, 2025.

3. I Syndergaard et al., PLoS Comput Biol, 2025.

Acknowledgements (Optional)

This work was funded by NIH grant R15NS087447 and NSF grant 1806056.

Session Category

Clinical Biomechanics: N/A

P4-256

Age-Dependent Biomechanical Properties of Japanese Children's Skulls: Implications for Injury Risk and Protection Strategies

A. Prof Suguru Torimitsu

The University of Tokyo, Bunkyo-Ku, Tokyo, Japan

Introduction

Head injuries are a leading cause of death in children worldwide. Pediatric skull fractures, often resulting from falls, traffic accidents, or abuse, require accurate biomechanical understanding for forensic and clinical evaluation. However, data on skull strength and thickness in children remain limited.

Methods

Skull samples were collected from 42 Japanese deceased individuals aged 0–19 years during autopsy. Bone specimens from frontal, parietal, and occipital regions were collected using calipers. Three-point bending tests were performed to assess mechanical properties, including Young's modulus, 0.2% proof stress, and maximum stress. Linear regression analysis was conducted using age (log-transformed) as the independent variable.

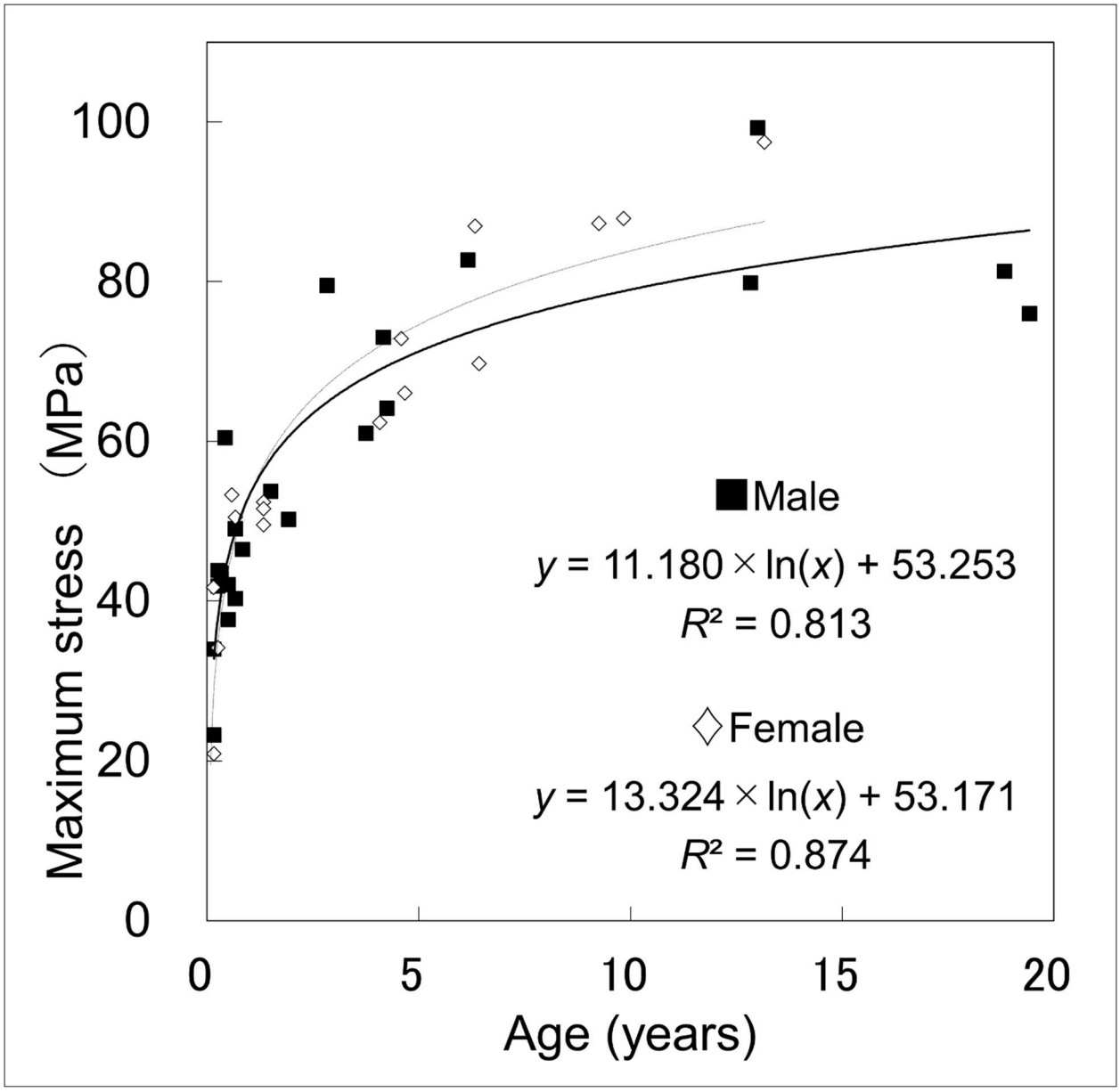
Results

A total of 170 samples were analyzed. In children under 1.5 years, 34 out of 86 samples did not fracture under testing, indicating low stiffness. No significant sex differences were found in thickness or mechanical properties. All parameters—thickness, Young's modulus, 0.2% proof stress, and maximum stress—increased significantly and logarithmically with age (R^2 = 0.761–0.899).

Discussion

This study demonstrates that preschool children's skulls are thin and mechanically weak, making them highly susceptible to fractures from minor external forces. The absence of sex differences contrasts with adult skull biomechanics. These findings provide essential data for injury prevention, forensic analysis, and finite element modeling of pediatric head trauma.

Images (Optional)



Session Category

Clinical Biomechanics: N/A

P4-257

A Scoping Review of the Utility of Low-Cost Markerless Motion Capture in Clinical Practice

MSc. Thiago Vidal Pereira[1,2], PT. Romina Perrotti[1,2], Dr. Guillaume Durandau[3,2], Dr. Joyce Fung[1,2]

[1]McGill University School of Physical and Occupational Therapy, Montreal, Quebec, Canada. [2]Feil/Oberfeld/CRIR Research Centre, Laval, Quebec, Canada. [3]McGill University Department of Mechanical Engineering, Montreal, Quebec, Canada

Introduction

Low-cost markerless motion capture (MMC) is emerging as a practical alternative to observational gait analysis because it is portable, inexpensive, quick to use, and requires less technical expertise than conventional marker-based systems. Although the technology is progressing rapidly, its use in clinical decision-making remains limited. This review synthesizes the current practice of MMC, its feasibility in clinical settings, and the remaining gaps that must be addressed for successful clinical integration.

Methods

We conducted a scoping review of MMC for gait analysis by searching PubMed and Ovid MEDLINE for peer-reviewed studies published in 2022 or later. Eligible studies used smartphones or other mobile devices and required minimal to no manual processing. We also screened open-source systems available through GitHub and arXiv preprints. We extracted information on the technology, study design, relevant clinical measures, factors that affect implementation, and any evidence supporting integration into clinical decision-making workflows.

Results

Nine peer-reviewed studies and one preprint were selected after critical appraisal. Four studies used single-camera smartphone systems and consistently reported small joint-angle differences compared with marker-based or multi-view systems during walking in healthy or athletic populations. The remaining studies used multi-view approaches with two or more smartphone cameras, in conjunction with open source, cloud-based applications such as OpenCap. These systems generally showed smaller or similar 3D errors than single-view systems, had a good consistency across repeated measurements and also included participants with neurological conditions.

Discussion

Most studies focus on whether MMC can replicate measurements from marker-based systems, but evidence on clinical utility remains limited. Advancing toward real-world adoption will require research conducted in close collaboration with clinicians to determine how MMC outputs can meaningfully support rehabilitation decision-making and successful integration into clinician routines. Such partnerships are essential for understanding how these technologies can meaningfully inform clinical decision-making in rehabilitation settings and for determining whether clinicians can effectively integrate MMC into their routines. Future work should evaluate alignment with clinical workflows, optimize presentation of results to guide decisions, explore integration with electronic health records, and examine whether MMC-informed assessments lead to better clinical outcomes than observational gait analysis.

Session Category

Clinical Biomechanics: N/A

P4-258

Biokinetic Profiles in Single-Leg Horizontal Landing After ACL Reconstruction: An Artificial Intelligence-Driven Biomechanical Classification for Return-to-sports.

Dr. Gustavo Leporace PhD[1,2], Dr. Leonardo Metsavaht MD, PhD[1,2], Dr. Tiago Zimerman MD[1,3], Dr. Felipe F. Gonzalez MD, MSc[1,2,3], Dr. Eliane C. Guadagnin PhD[1,4], Dr. Carolline Popovicz Nunes MD[1,3], Dr. Marcos Amstalden Barros MD[1,3], Dr. Nilton G. Filho MD[5], Dr. Jonathan A. Gustafson PhD[3,1], Dr. Jorge Chahla MD, PhD[6,3], Dr. Moises Cohen MD, PhD[5]

[1]Instituto Brasil de Tecnologia da Saúde (IBTS), Rio de Janeiro, Rio de Janeiro, Brazil. [2]Universidade Federal de São Paulo (UNIFESP), Escola Paulista de Medicina, Departamento de Diagnóstico por Imagem, São Paulo, São Paulo, Brazil. [3]Rush University Medical Center, Chicago, Illinois, United States. [4]Universidade Federal de Goiás (UFG), Goiânia, Goiás, Brazil. [5]Departamento de Ortopedia e Traumatologia, Escola Paulista de Medicina, Universidade Federal de São Paulo (UNIFESP), São Paulo, São Paulo, Brazil. [6]Midwest Orthopaedics at Rush (MOR), Chicago, Illinois, United States

Introduction

Return-to-sports (RTS) criteria after anterior cruciate ligament reconstruction (ACLR) usually focus on strength, patient-reported outcomes, and hop distance, but fail to predict outcomes accurately. Biomechanics are increasingly used to determine RTS readiness and reinjury risk. However, there is no classification that can help with RTS assessment. This study aimed to create a biomechanics-based classification using artificial intelligence to improve the RTS evaluation.

Methods

Forty-four physically active subjects, 7-9 months post-ACLR, performed a single-leg horizontal hop test. Kinematics were collected using an 8-camera motion analysis system with reflective markers. Participants also completed isometric hip and knee strength tests, the International Knee Documentation Committee (IKDC) questionnaire, and the visual analogue scale for pain. Profiles were identified using principal component analysis to extract variables from the landing phase, followed by self-organizing maps and k-means clustering. Profiles were compared using the Kruskal-Wallis test ($\alpha=0.05$). Differences were considered significant when having large effect sizes (Cohen's $d > 0.8$).

Results

Four profiles were identified (Figure 1). Profile 1 (Dynamic Valgus): good hop performance (63.4 %Ht [percentage of height) and high IKDC scores, but presented a quadriceps-dominant strategy and knee valgus (2.2°) at landing. Profile 2 (Return to Play): good hop performance (64.3 %Ht), adequate knee flexion (48.7°) and trunk flexion (31.1°), with excellent pelvic and hip control, the highest muscle strength, and mild/no pain. Profile 3 (Weak Group): adequate hop performance (59.6 %Ht), but with hip and knee weakness, moderate IKDC scores, and compensatory landing mechanics such as hip abduction (2.2°) and knee varus (3.6°) and internal rotation (-4.2°). Profile 4 (Low Performance): worst hop performance (45.3 %Ht), minimal knee (34.8°) and trunk flexion (17.1°), increased hip adduction (4.4°) and knee varus (3.4°), weak extensors, and potential kinesiophobia.

Discussion

Machine learning identified four distinct landing strategies in ACLR patients, providing a biomechanical classification to help with RTS decisions. Profile 1 has an increased risk of reinjury and requires neuromuscular training; Profile 2 is ready for RTS depending on pain management; Profile 3 needs strength training; Profile 4 must address both physical and psychological barriers. Biokinetic profiling may optimize RTS assessment and enable personalized rehabilitation strategies, potentially reducing reinjury risk.

Images (Optional)

Results Characterizing the Horizontal Landing Profiles in Patients with ACL Reconstruction Based on Demographics, Biomechanics, Strength, and Patient-Reported Outcome Measures (PROMs). Continuous variables are presented as mean (95% confidence interval).

	Profile 1 (P1)	Profile 2 (P2)	Profile 3 (P3)	Profile 4 (P4)	p-value	Effect Size
Demographic						
Sex (n (%))	5M (62.5%) / 3F (37.5%)	9M (69.2%) / 4F (30.8%)	10M (100%) / 0F (0%)	9M (69.2%) / 4F (30.8%)		
Age (years)	34.1 ± 16.6	32.9 ± 13.0	29.4 ± 7.6	36.2 ± 10.9	P > 0.05	ES < 0.8
Mass (kg)	68.8 ± 13.2	73.0 ± 15.4	84.1 ± 8.8	78.3 ± 16.3	P > 0.05	ES > 0.8 (P3 > P1; P2)
Height (cm)	170.8 ± 9.2	173.7 ± 9.9	174.9 ± 5.0	170.8 ± 8.3	P > 0.05	Not significant
BMI (m/kg²)	23.5 ± 3.5	24.0 ± 3.2	27.5 ± 3.0	26.6 ± 3.7	P > 0.05	P3 > P1; P2 | P4 > P1
Biomechanics						
Distance (%Ht)	63.4 ± 18.5	64.3 ± 16.5	59.6 ± 10.4	45.3 ± 9.9	P > 0.05 - P4 < P1; P2; P3	P4 < P1; P2; P3
Trunk Flexion (°)	23.6 ± 15.3	31.1 ± 14.2	24.1 ± 8.9	17.1 ± 10.3	P > 0.05 - P2 > P1; P4	P2 > P4
Trunk Lateral Lean (°)	-5.1 ± 5.4	-12.5 ± 7.0	-7.9 ± 3.2	-8.3 ± 4.0	P > 0.05 - P1 > P2	P1; P3 > P2
Pelvic Drop (°)	2.5 ± 3.3	-7.6 ± 4.7	-2.5 ± 3.5	-0.0 ± 3.0	P > 0.05 - P1 > P2; P3 / P4; P3 > P2	P1 > P2; P3; P4 / P3; P4 > P2
Hip Adduction (°)	6.6 ± 4.0	1.2 ± 4.7	-2.2 ± 3.4	4.4 ± 4.9	P > 0.05 - P1 > P2; P3 / P4 > P3	P1 > P2; P3 / P3 < P2; P4
Hip Internal Rotation (°)	-5.7 ± 5.3	2.1 ± 5.9	-5.2 ± 2.6	0.5 ± 4.7	P > 0.05 - P1; P3 < P2; P4	P1; P3 < P2; P4
Knee Flexion (°)	48.7 ± 7.4	48.7 ± 12.2	42.9 ± 16.3	34.8 ± 11.7	P > 0.05 - P4 < P1; P2	P4 < P1; P2
Knee Varus (°)	-2.2 ± 3.9	2.3 ± 3.8	3.6 ± 4.3	3.4 ± 3.5	P > 0.05 - P3; P4 > P1	P1 < P2; P3; P4
Knee Internal Rotation (°)	-7.9 ± 5.9	-16.7 ± 5.1	-4.2 ± 5.4	-18.0 ± 5.2	P > 0.05 - P1; P3 > P2; P4	P1; P3 > P2; P4
Biomechanical Classification	**Dynamic Valgus**	**Return to Play**	**Weak Group**	**Low Performance**		
PROMs						
IKDC Score (0-100)	79.3 ± 13.4	78.5 ± 14.2	74.3 ± 18.0	73.2 ± 16.1	P > 0.05 - P4; P3 < P1	Not significant
VAS Pain (0-10)	1.0 ± 1.5	1.8 ± 1.7	2.0 ± 2.4	2.4 ± 2.8	P > 0.05	Not significant
Isometric Strength						
Hip Abductors (%BW)	39.2 ± 8.4	38.3 ± 9.2	33.0 ± 7.0	37.2 ± 9.3	P > 0.05 - P3 < P2	P1 > P3
Hip Extensors (%BW)	41.9 ± 14.6	33.9 ± 16.0	30.5 ± 10.5	33.4 ± 11.9	P > 0.05 - P4; P3 < P1; P2	P1 > P3
Hip Ext Rotators (%BW)	19.4 ± 4.7	19.9 ± 3.3	17.5 ± 4.0	16.8 ± 4.4	P > 0.05	P2 > P4
Knee Extensors (%BW)	55.2 ± 10.9	69.6 ± 15.3	55.5 ± 16.0	54.2 ± 15.9	P > 0.05 - P4; P3 < P2	P2 > P1; P3; P4
Knee Flexors (%BW)	20.9 ± 9.1	18.0 ± 7.3	16.1 ± 7.9	16.6 ± 6.7	P > 0.05 - P3 < P1	Not significant

%Ht: Percentage of Height; %BW: Percentage of Body Weight; BMI: Body Mass Index; Trunk Flexion: Flexion (+)/Extension (-); Trunk Lateral Lean: Contralateral Lean (+)/Ipsilateral Lean (-); Pelvic Drop: Contralateral (+)/Ipsilateral (-); Hip Adduction: Adduction (+)/Abduction (-); Hip Internal Rotation: Internal Rotation (+)/External Rotation (-); Knee Flexion: Flexion (+)/Extension (-); Knee Varus: Varus (+)/Valgus (-); Knee Internal Rotation: Internal Rotation (+)/External Rotation (-).

Session Category

Clinical Biomechanics: N/A

P4-259

Community-Dwelling older Adults use Different Gait Strategies During Dual-Task and Fast Gait, but Strategies Are Not Affected by Timed Up and Go Time, Handgrip Strength, or Fall History

Dr. Tiphanie E Raffegeau PhD[1], Dr. Kelly Poretti PhD[1], Ms Eter Mjavandze MS[2], Ms Dieanna C Prudholme MS[1], Mr Ahmadreza Souri MS[1], Dr. Emily S Ihara PhD, MSW, FGSA[2], Dr. Catherine J Tompkins PhD, MSW[2], Dr. Angela Miller PhD[2], Dr. Jatin Ambegaonkar PhD, ATC OT[1]

[1]George Mason University, Manassas, VA, United States. [2]George Mason University, FaIrfax, VA, United States

Introduction

Community fall prevention partnerships may reveal more ecologically valid results than controlled laboratory-based projects. We provided community-based health assessments via our Balance for Wellness program and examined fall-risk factors in older adults (>55 years) in a large metropolitan region. Our purpose was to determine how common clinical measures, e.g., Timed Up and Go (TUG) time (seconds, high>12, low<12), fall history in the previous 6 months (yes, no), handgrip strength (kilograms, strong > 22, weak < 22), affect gait strategies during challenging gait tasks.

Methods

In addition to common clinical tests, 129 participants (106 women, Mean(SD), Age =75.3 (7.7) years) completed three walking trials: self-paced (ST), self-paced during a verbal fluency dual-task (Dual Task-DT) (e.g. list zoo animals) and fast walking (FW) in a fixed order along a 16-foot long pressure-sensitive mat (Protokinetics, Zeno mat). We calculated DT and FW gait strategies by determining the combined percent change in step length and step time relative to ST (Length-time difference, LTD), a positive value indicates a step length dominant strategy and negative values indicate a step time dominant strategy. We used two-way mixed ANOVAs to analyze differences in LTD between clinical factors (i.e. TUG time: lower limb strength, handgrip strength, and falls history) across conditions (DT, FW) ($p<.05$).

Results

LTD differed across walking conditions ($p <.001$). During DT (LTD = 5.6 (22.1)) participants used a step length dominant strategy to accomplish the DT by taking shorter steps.

During FW (LTD = -4.3 (13.2)) participants showed a time-dominant strategy by taking faster steps. LTD did not differ between high and low lower limb function (TUG), weak or strong handgrip, or falls history (Table 1).

Discussion

Overall, older adults used a step length dominant strategy during DT, which is in contrast to previous studies showing time-dominant strategies during a DT in older adults with high lower limb strength. Contrary results may be because gait strategies differ for motoric versus verbal DTs in older adults. Dichotomizing TUG times, handgrip strength, or fall history did not explain differences in gait strategies, warranting additional research.

Images (Optional)

Table 1. Comparison of gait strategies (LTD) in dual-task (DT) and fast walking across clinical group comparisons

Sample ***n***		**DT LTD** Mean (SD)		**Fast LTD** Mean (SD)		Group ***F-value***	Group ***p-value***
TUG Time *(>12s = Low function, ≤12 s = High function)*							
Low	High	Low	High	Low	High		
n = 21	***n*** = 94	-0.33 (22.9)	7.44 (22.7)	-1.94 (10.3)	-5.15 (13.7)	0.443	.501
Handgrip *(weak ≤22kg, strong >22 kg)*							
Weak	Strong	Weak	Strong	Weak	Strong		
n =64	***n*** =61	5.81 (23.4)	5.45 (21.4)	-4.95 (11.8)	-3.78 (14.6)	0.002	.964
Fall-history *(1 or more falls in previous 6 months)*							
1+ fall	None	1+ fall	None	1+ fall	None		
n =24	***n*** =99	5.04 (23.6)	5.99 (22.3)	-4.93 (13.7)	-3.93 (13.2)	0.071	.789

Notes: LTD = Length-time difference where a positive value indicates a step dominant strategy and negative value a step time dominant strategy, s = seconds

Acknowledgements (Optional)

We thank and acknowledge our community partners, volunteer participants, and student research

Session Category

Clinical Biomechanics: N/A

P4-260

Using Ankle Kinematics to Differentiate Contracture as a Cause of Excessive Plantarflexion in Swing in Charcot-Marie-Tooth Disease

Dr. Tishya Wren PhD[1,2], Dr. Reiko Hara PhD[1], Dr. Eva Ciccadicola PT, DPT, PCS[1], Dr. Alison Hanson MSPT, OCS[1], Dr. Susan Rethlefsen PT, DPT[1], Dr. Emmanuelle Tiongson MD[1,2], Dr. Kristan Pierz MD[3], Dr. Jennifer Rodriguez-MacClintic PT, DPT[3], Dr. Gyula Acsadi MD, PhD[3], Ms. Sylvia Ounpuu MSc[3]

[1]Children's Hospital Los Angeles, Los Angeles, CA, United States. [2]University of Southern California, Los Angeles, CA, United States. [3]Connecticut Children's, Hartford, CT, United States

Introduction

Charcot-Marie-Tooth disease (CMT) is the most common inherited neuropathy and often causes distal muscle weakness. Lack of dorsiflexion during the swing phase of gait can cause tripping and is usually attributed to weakness of the anterior tibialis. However, calf muscle tightness or contracture can also contribute to excessive plantarflexion in swing. It is important to distinguish between excessive plantarflexion in swing due to plantarflexor contracture versus anterior tibialis weakness (true drop foot) since these have different causes and warrant different treatment. This study examines differences in ankle kinematics to distinguish between excessive plantarflexion in swing due to contracture versus anterior tibialis weakness in children with CMT.

Methods

Kinematic and video data were analyzed for children with CMT who had undergone instrumented gait analysis as part of an ongoing natural history study. Walking videos were reviewed independently by three experienced gait laboratory physical therapists. Cases in which all reviewers identified excessive plantarflexion in swing of the same type (true drop foot or contracture) were included in the analysis. Ankle kinematics of the right limb were compared between groups (contracture versus true drop foot) using statistical parametric mapping.

Results

The reviewers identified 3 patients with excessive plantarflexion in swing due to contracture and 7 with true drop foot. Ankle kinematic patterns differed significantly between the two groups across almost the entire gait cycle (Figure). The drop foot group exhibited a more typical pattern of increasing ankle dorsiflexion through terminal stance, but without the first rocker. The contracture group exhibited a “double bump” pattern in stance reflecting

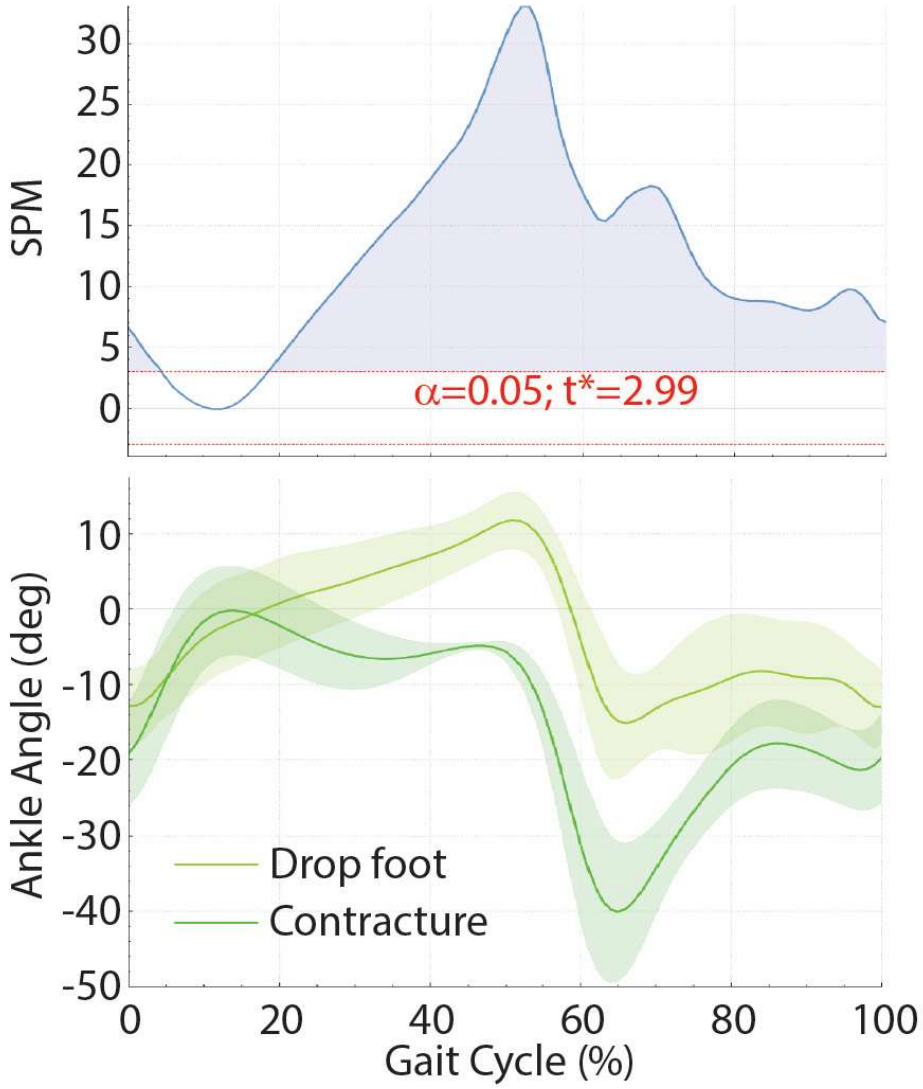
forefoot contact and lack of dorsiflexion in mid to terminal stance. Peak plantarflexion in initial swing was significantly greater in the contracture group although both groups showed less dorsiflexion in mid to terminal swing and at initial contact than typical.

Discussion

Ankle kinematics in stance and swing can help distinguish excessive plantarflexion in swing due to contracture from true drop foot in children with CMT. This distinction is important to identify patients whose dorsiflexion in swing will likely improve after surgical lengthening of the plantarflexors compared with those needing bracing to counteract dorsiflexor weakness.

Images (Optional)

Figure: Statistical parametric mapping (SPM) results comparing ankle sagittal plane kinematics (dorsi/plantarflexion) after time registration based on foot contact and foot off events



Session Category

Clinical Biomechanics: N/A

P4-261

Effects of Asymmetric Crank Arm Length Adjustments on Knee Biomechanics During Recumbent Cycling in Early Rehabilitation Following Total Knee Replacement: A Case Study

Mr. Tsung-Lin Lu MS[1], Mr. Alejandro Ovispo-Martinez MS[1], Ms. Yufei Sun MS[1], Dr. Katie Stevens DPT[2], Dr. Harold Cates MD[2], Dr. Songning Zhang PhD[1]

[1]The University of Tennessee, Knoxville, TN, United States. [2]Tennessee Orthopaedic Alliance, Knoxville, TN, United States

Introduction

Patients with total knee replacement (TKR) often exhibit biomechanical deficits in the replaced limb during upright stationary cycling in early rehabilitation [1]. Postoperative physical activity is critical for long-term recovery, but pain, swelling, and stiffness can limit adherence [2]. Shortening the crank arm on the replaced limb may accommodate reduced knee range of motion (ROM), and recumbent cycling may improve comfort, encouraging earlier pedaling. Therefore, this study investigated the biomechanical effects of shortened crank arm lengths on the replaced limb during recumbent cycling in early rehabilitation.

Methods

One male participant (71 years, 183 cm, 84 kg), 26 days post-TKR, was recruited from a local physical therapy clinic. Cycling was performed on a recumbent ergometer (RE7, Kettler, Germany) equipped with 3D Kistler force-sensing pedals and crank arm shorteners. Three crank-length conditions were tested for the replaced/non-replaced limbs: C1 (170/170 mm), C2 (155/170 mm), and C3 (140/170 mm). The participant cycled at 70 W and 70 rpm for 2 minutes and rated knee pain (0–10, VAS) and perceived exertion (RPE 6–20, Borg scale) per condition. The last 10 seconds were recorded and truncated into five consecutive crank cycles. Kinematic (240 Hz) and kinetic (1,200 Hz) data were collected using a 12-camera Vicon system and analyzed in Visual3D.

Results

Sagittal ROM in the replaced limb decreased with shorter cranks, while the non-replaced limb showed minimal reductions. Peak extension moment and power increased in the replaced limb. In the non-replaced limb, extension moment decreased from C1 to C2 with a slight rebound at C3, whereas power declined progressively across conditions. Pain in the replaced limb and RPE decreased with crank shortening (Table 1).

Discussion

Crank arm shortening of the replaced limb during recumbent cycling accommodated limited knee ROM and reduced pain and RPE, while enhancing peak extension moments and power, suggesting this intervention may support earlier engagement in cycling and improve post-TKR rehabilitation outcomes.

Images (Optional)

Table 1: *Knee Sagittal ROM (°), Peak Extension Moment (Nm), Peak Power (W), Pain, and RPE across crank length conditions: Mean ± SD*

Variable	Limb	C1 (170/170 mm)	C2 (155/170 mm)	C3 (140/170 mm)
Sagittal ROM	R	65.54 ± 1.01	61.31 ± 0.88	55.97 ± 0.53
	NR	82.25 ± 2.09	80.16 ± 2.80	76.95 ± 2.01
Peak Extension Moment	R	4.33 ± 1.21	9.63 ± 2.84	18.17 ± 0.65
	NR	21.01 ± 6.90	16.90 ± 3.99	17.05 ± 2.18
Peak Power	R	14.68 ± 5.10	35.28 ± 11.15	63.03 ± 2.17
	NR	100.93 ± 33.95	83.09 ± 19.26	80.00 ± 9.51
Pain (1-10)	R	6	3	2
RPE (6-20)	–	14	10	9

Note: "R" = replaced limb; "NR" = non-replaced limb; "–" = not limb-specific.

References (Optional)

[1] Hummer et al., 2021. *J Biomech* **115**, 110111.

[2] Bakaa et al., 2022. *Disabil Rehabil* **44**, 6348-6355.

Acknowledgements (Optional)

This research was funded by the 2025 Graduate Student Research Grant from the American Society of Biomechanics.

Session Category

Clinical Biomechanics: N/A

P4-262

Frontal Plane Jerk Cost and Fluctuation Analysis for Individuals With ACL Reconstruction and Osteoarthritis

Mr. Nicholas Hunt, Dr. Tyler Brown

Boise State University, Boise, ID, United States

Introduction

Following ACL injury and subsequent reconstruction (ACL-R), altered neuromuscular function and control may accelerate knee osteoarthritis (OA) development [1]. Altered neuromuscular function following ACL injury may provoke joint instability that promotes knee OA progression. The purpose of this study is to compare jerk magnitude, cost, and fluctuation analysis between ACL-R, knee OA and healthy controls to assess smoothness of knee joint motion and provide a biomechanical measure of dynamic neuromuscular control at the joint.

Methods

Three cohorts (1: 14 ACL-R, 2: 9 knee OA, and 3: 14 healthy control) had knee biomechanics quantified during a 10-meter walk. Using filtered marker data, peak, minimum, and range (peak minus minimum) of frontal plane jerk (third time derivative of knee abduction-adduction angle during stance) and, jerk cost (area under the logarithmically transformed jerk-time curve according to [2]) were quantified during weight acceptance (initial contact to peak knee flexion angle) and full stance phase (initial contact to toe off) phases. After the jerk-time curve was submitted to a fast-Fourier transform, mean, median, and peak power frequency (PPF) as well as total signal power were calculated according to [3]. Time and frequency domain jerk measures were submitted to a one-way ANOVA to assess cohort differences.

Results

ACL-R and knee OA cohort exhibited greater range of frontal plane jerk ($p=0.002$and $p=0.035$), but smaller mean frequency ($p=0.014$ and $p=0.042$) and peak power frequency ($p=0.043$ and $p=0.029$) than controls. Knee OA also exhibited greater peak jerk than controls ($p=0.019$). No cohort differences were observed for weight acceptance or full stance jerk cost ($p=0.124$ and $p=0.107$).

Discussion

Increased jerk magnitude (peak and range) in the ACL-R and OA cohorts may indicate greater, more abrupt postural knee changes resulting in joint instability that promotes knee

OA progression. Yet, the ACL-R and knee OA cohorts may reduce fluctuation frequency in attempt to restrict frontal plane motion and protect the joint from further injury. However, this neuromuscular strategy may alter knee joint loading and may exacerbate knee OA symptoms.

Images (Optional)

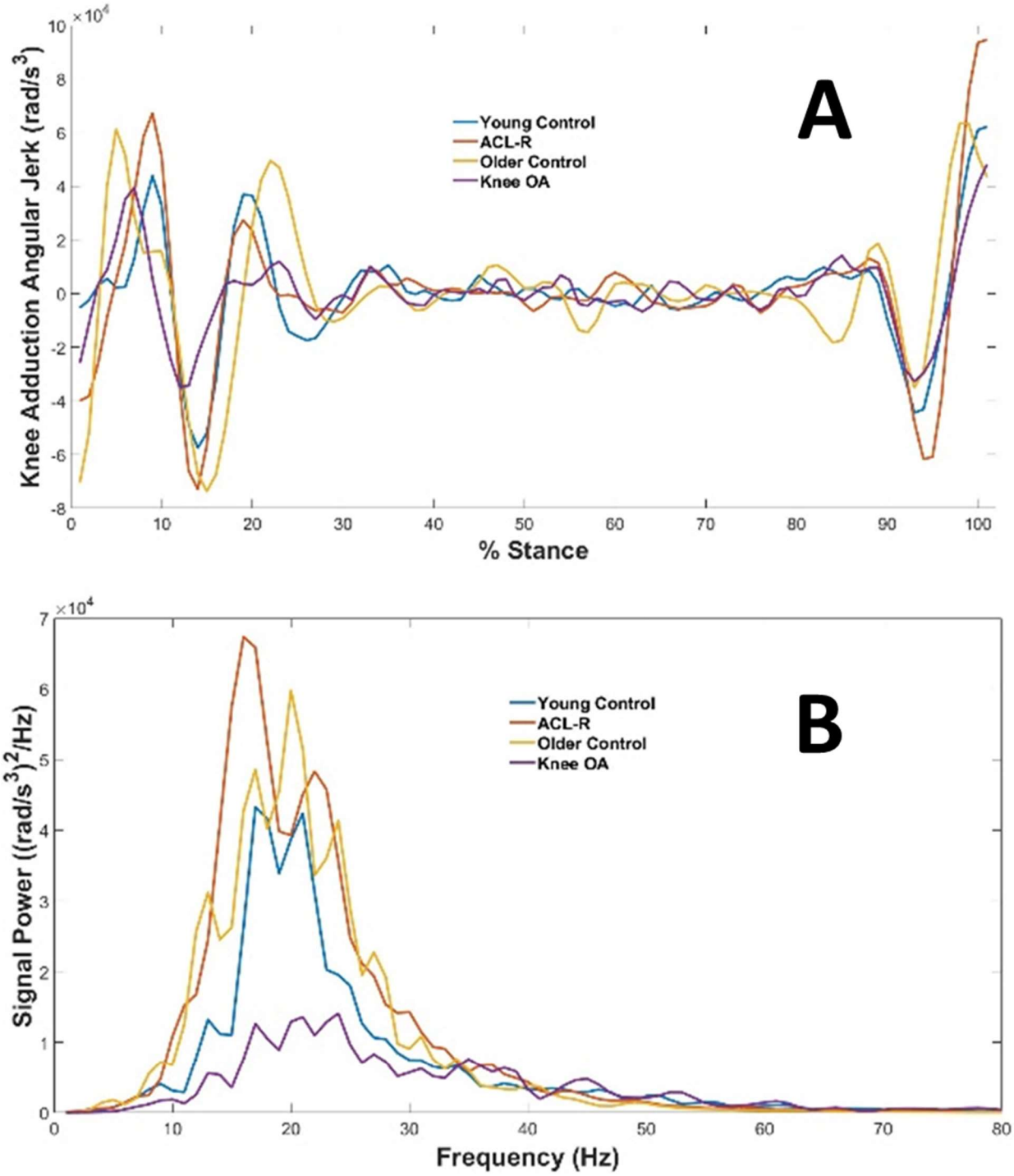


Figure 1: (**A**) Mean jerk-time curve and (**B**) mean power spectral density by cohort.

References (Optional)

[1] Tayfur et al., Sports Medicine, 2021

[2] Krammer et al., Gait & Posture, 2018

[3] Hunt et al., Clinical Biomechanics, 2024

Acknowledgements (Optional)

NIH NIA (R15AG059655) and NIH NIGMS (2U54GM104944, P20GM109095, P20GM148321) supported this work.

Session Category

Clinical Biomechanics: N/A

P4-263

Effects of Aquatic Versus Land-Based Exercise on Static Postural Sway in Older Adults With Multimorbidity: A Randomized Controlled Trial

Mr. Victor Hugo V. Carrijo[1,2], Ms. Ana Luiza Cabral[3,2], Mr. Johan Robalino[1,2], Dr. Catarina C.Santos[4], Dr. Daniel Moreira-Gonçalves[3], Dr. Mário J. Costa[1,2]

[1]Centre for Sports Research, Education, Innovation and Intervention in Sport, CIFI2D, Faculty of Sport, University of Porto, Porto, Porto, Portugal. [2]Porto Biomechanics Laboratory (LABIOMEP), Faculty of Sport, University of Porto, Porto, Porto, Portugal. [3]Research Center for Physical Activity, Health and Leisure, CIAFEL, University of Porto, Porto, Porto, Portugal. [4]University of Trás-os-Montes and Alto Douro, Vila Real, Vila Real, Portugal

Introduction

Aging reduces balance and postural control, increasing fall risk. Physical exercise mitigates these impairments, but its usefulness for older adults with multimorbidity still requires optimization. This study aimed to verify the effects of aquatic versus land exercise programs on static postural sway in older adults with multimorbidity.

Methods

Forty-eight older adults were enrolled in a randomized controlled trial (NCT06879639), and 40 completed the 10-week intervention. The participants were allocated to a water group (n = 10; 60% women; age = 71.6 ± 5.3 years; BMI = 32.9 ± 3.5 kg/m^2), a land group (n = 15; 53% women; age = 69.8 ± 3.6 years; BMI = 31.7 ± 4.1 kg/m^2) and a control group (n = 15 66% women; age = 69.4 ± 3.1 years; BMI = 30.4 ± 3.2 kg/m^2). Both land-based and aquatic groups completed three supervised 45-minute sessions per week. Exercise intensity was monitored using heart rate (Polar®), perceived exertion (Borg scale), or a percentage of 1RM. Training load increased by 20% in weeks 3 and 7. Pre and post-test measurements of anteroposterior and mediolateral sway range (mm), total sway velocity (mm/s), and sway area (mm^2) with eyes open and closed were assessed using a force plate system by AIMT®. Statistical analysis (in SPSS 29.0) used GEEs to assess pre vs post changes across groups, with Bonferroni-adjusted post hoc tests and a significance level of $p \leq 0.05$.

Results

The comparison between groups and pre and post 10 weeks of intervention in postural sway is shown in Figure 1.

Discussion

A previous study showed that aquatic exercise improved balance in older adults using dynamic functional tasks [1]. In contrast, our static force-platform assessments revealed only small tendencies toward change, although each modality indicated distinct sensory and mechanical influences on postural control in older adults with multimorbidity. These results suggest that both interventions may have the potential to assist in managing balance in this population.

Images (Optional)

Figure 1. Changes in static postural sway variables in both groups pre and post 10 weeks.

	Pre	Post	*p* Group	*p* Time	*p* Group x Time	Hedges´*g*
Eyes Open (normalized x 1000)						
Sway Range AP						
Water fitness	13.8 ± 5.7	14.3 ± 3.3				0.08
Combined exercise	13.0 ± 5.9	14.6 ± 6.4	0.83	**0.005**	**0.03**	0.21
Control	10.6 ± 3.4	16.1 ± 7.5				0.82
Sway Range ML						
Water fitness	8.7 ± 3.8	7.4 ± 4.1				-0.27
Combined exercise	7.1 ± 4.5	4.8 ± 2.3	0.18	0.08	0.17	-0.68
Control	7.8 ± 5.3	8.0 ± 6.4				0.03
Total Sway Velocity						
Water fitness	4.7 ± 1.6	4.0 ± 1.3				0.28
Combined exercise	4.1 ± 1.3	4.1 ± 1.4	0.35	0.33	0.76	0.006
Control	4.0 ± 2.2	4.4 ± 1.1				0.17
Sway Area						
Water fitness	0.09 ± 0.05	0.08 ± 0.05				-0.08
Combined exercise	0.09 ± 0.10	0.07 ± 0.06	0.76	0.78	0.15	-0.27
Control	0.07 ± 0.69	0.11 ± 0.14				0.30
Eyes Closed (normalized x 1000)						
Sway Range AP						
Water fitness	17.4 ± 4.7	14.7 ± 4.5				-0.46
Combined exercise	14.8 ± 6.5	14.6 ± 8.0	0.81	0.16	0.62	-0.03
Control	16.6 ± 10.5	15.0 ± 4.3				-0.16
Sway Range ML						
Water fitness	9.2 ± 4.2	7.2 ± 4.9				-0.59
Combined exercise	8.0 ± 5.8	5.5 ± 3.1	0.37	**0.007**	0.33	-0.46
Control	9.2 ± 6.0	8.6 ± 6.5				-0.10
Total Sway Velocity						
Water fitness	6.9 ± 3.1	6.2 ± 2.8				-0.55
Combined exercise	5.6 ± 2.7	5.0 ± 2.0	0.45	**0.02**	0.98	-0.33
Control	6.1 ± 3.7	5.6 ± 2.1				-0.20
Sway Area						
Water fitness	0.12 ± 0.09	0.08 ± 0.11				0.74
Combined exercise	0.10 ± 0.10	0.07 ± 0.08	0.71	**0.02**	0.85	0.82
Control	0.14 ± 0.22	0.09 ± 0.11				0.78

Note: AP: Anteroposterior; **ML:** Mediolateral; **normalized x 1000:** All variables were normalized by participants' height to reduce the influence of anthropometric differences on postural sway measures and multiplied by 1000 for presentation.

References (Optional)

[1] Y. Deng *et al.*, "Comparing the effects of aquatic-based exercise and land-based exercise on balance in older adults: a systematic review and meta-analysis," *Eur. Rev. Aging Phys. Act.*, vol. 21, p. 13, May 2024, doi: 10.1186/s11556-024-00349-4.

Session Category

Clinical Biomechanics: N/A

P4-264

A development framework for a physical simulator of minimally invasive surgery in gynecology and obstetrics: from procedure modelling to posture assessment.

Mr Vincent Lemarteleur[1,2], Mrs Aurélie Benoit[1,2], Mrs Floriane Laverne[3,2], Mr Thomas Provot[4,5], Mr Laurent Tapie[3,6], Mr Pierre-François Ceccaldi[1,2,7]

[1]Université Paris Cité, Paris, 75006, France. [2]UMRS-1333, Oral Health, Montrouge, 92120, France. [3]Université Sorbonne Paris Nord, Villetaneuse, 93430, France. [4]EPF, Cachan, 94230, France. [5]Institut de Biomécanique Humaine Georges Charpak, Paris, 75013, France. [6]UMRS-1333, Oral Health, Montrouge, 75006, France. [7]Beaujon Hospital , AP-HP, Clichy, 92110, France

Introduction

Surgical operators are among the occupational groups most susceptible to developing joint pain and musculoskeletal disorders, largely due to the adoption of constrained postures [1]. In gynecological laparoscopy, the operator's posture is shaped by interactions with operating room equipment [2], as well as by the patient's morphological characteristics. In particular, patients with a high body mass index (BMI) require adjustments of the trocar insertion site to ensure safe surgical access [3].

The aim is to develop an educational tool that incorporates the placement of secondary trocars with improved physical fidelity, achieved through the treatment of anatomical data acquired directly at the operating room.

Methods

The acquisition and processing of both internal and external anatomical data serve to account for inter-patient variability in body morphology. Internal anatomical structures are derived from preoperative computed tomography (CT) scans obtained with the patient in a supine position. External geometry is captured intraoperatively by scanning the abdominal wall under pneumoperitoneum, following prior validation of the measurement instruments.

The two resulting 3D anatomical datasets are subsequently realigned through geometric feature matching and merged into a single model. This procedure yields a virtual patient that integrates all relevant anatomical characteristics. The primary and secondary surfaces constructed to represent the envelope of the abdominal wall incorporate these fidelity parameters and constitute the basis for designing the volumes required for simulator fabrication using suitable haptic materials.

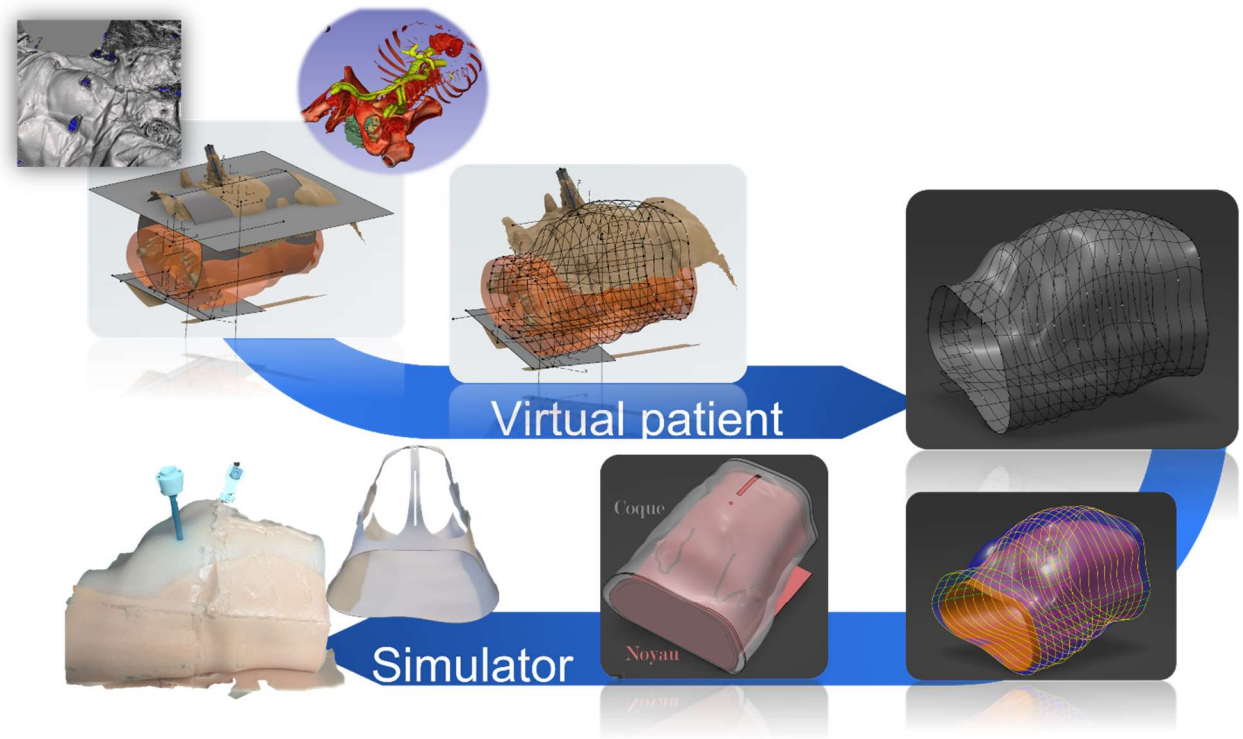
Results

A simulator for a patient with a BMI of 25 kg/m^2 was manufactured from the virtual patient, demonstrating the feasibility of the methodology based on anatomical data.

Discussion

The next step is to validate the data using an ergonomic criterion to assess the efficiency of the movements performed on the simulator. The posture data from operators using our simulator will be compared across different contextual variables (type of simulator used, participants with varying competency levels), as well as with posture data collected from surgeons in the operating room.

Images (Optional)



References (Optional)

[1] Epstein, S. *et al. ,* T *Ann. Surg.,* 2019

[2] Schlussel, A.T. & Maykel, J.A.,*Clin. Colon Rectal Surg.,* 2019

[3] Sers, R. *et al., Appl. Ergon.,* 2021

Session Category

Clinical Biomechanics: N/A

P4-265

Explainable AI Uncovers Hidden Neuromuscular Efficiency Driving Individual Functional Performance in Complex Eccentric Hamstring Control Tasks

Mrs. Yanan YOU PhD Candidate, ACSM-EP[1], Prof. Norikazu Hirose PhD, JSPO-AT[2]

[1]Graduate School of Sport Sciences, Waseda University, Tokorozawa, Saitama-ken, Japan. [2]Faculty of Sport Sciences, Waseda University, Tokorozawa, Saitama-ken, Japan

Mrs. Yanan YOU

Introduction

Although strength testing is central to hamstring injury assessment, it does not explain why individuals with comparable strength can show markedly different eccentric control. Such discrepancies suggest that traditional models may overlook a hidden layer of neuromuscular regulation. This study used a hierarchical explainable machine learning approach (XGBoost + SHAP) to disentangle these factors. An ablation design—removing all absolute strength metrics—was implemented to isolate the independent contribution of neural coordination strategies to eccentric performance.

Methods

High-density sEMG, kinematics, and body composition data were collected from 25 healthy adults during eccentric tasks; individuals with recent lower-limb pathology were excluded. Using a comprehensive scoring system, we developed a hierarchical XGBoost–SHAP model targeting Global Hamstring Efficiency (GHE). Determinants were evaluated across three layers: global features, EMG-based neuromechanical mechanisms, and kinematic performance.

Results

Global determinants (Figure 1a)*:* Hip Smoothness was the strongest predictor of neuromuscular efficiency (35.3%, shown as relative Importance), surpassing morphological indicators such as body fat percentage. Greater semitendinosus (ST) involvement (14.0%) also characterized higher GHE.
Neuromuscular mechanisms (Figure 1b)*:* A dominant ST-driven activation strategy improved GHE (28.3%). High-efficiency performers showed stable coordination between mid-belly and distal ST regions (15.8%), emphasizing the importance of regional activation

consistency. Differential BF–ST recruitment at mid and distal sites further influenced performance (19.9%).

Kinematic characteristics (Figure 1c)*:* Greater knee range of motion and stable hip–knee coupling were shared features of high-efficiency performers, whereas compensatory hip-flexion strategies were ineffective (43.3%).

The Injury Link (Figure 1d)*:* SHAP interactions revealed that prior injury alters neuromuscular strategy. Participants without injury flexibly adopted an ST-dominant pattern that enhanced GHE, whereas previously injured individuals showed strategy rigidity, remaining locked into BF-dominant activation.

Discussion

By quantifying the neural cost–benefit relationship, this study shows that post-injury deficits arise from impaired strategy flexibility rather than weakness. Loss of ST compensatory capacity may trap individuals in a "high-cost, low-efficiency" cycle. These findings support shifting rehabilitation toward neuromuscular strategy remodeling, emphasizing BF-downregulation, ST spatial activation, and smooth movement. Limitations include modest sample size and task specificity. Future work should validate these neural signatures in larger cohorts and test targeted neuromuscular retraining.

Images (Optional)

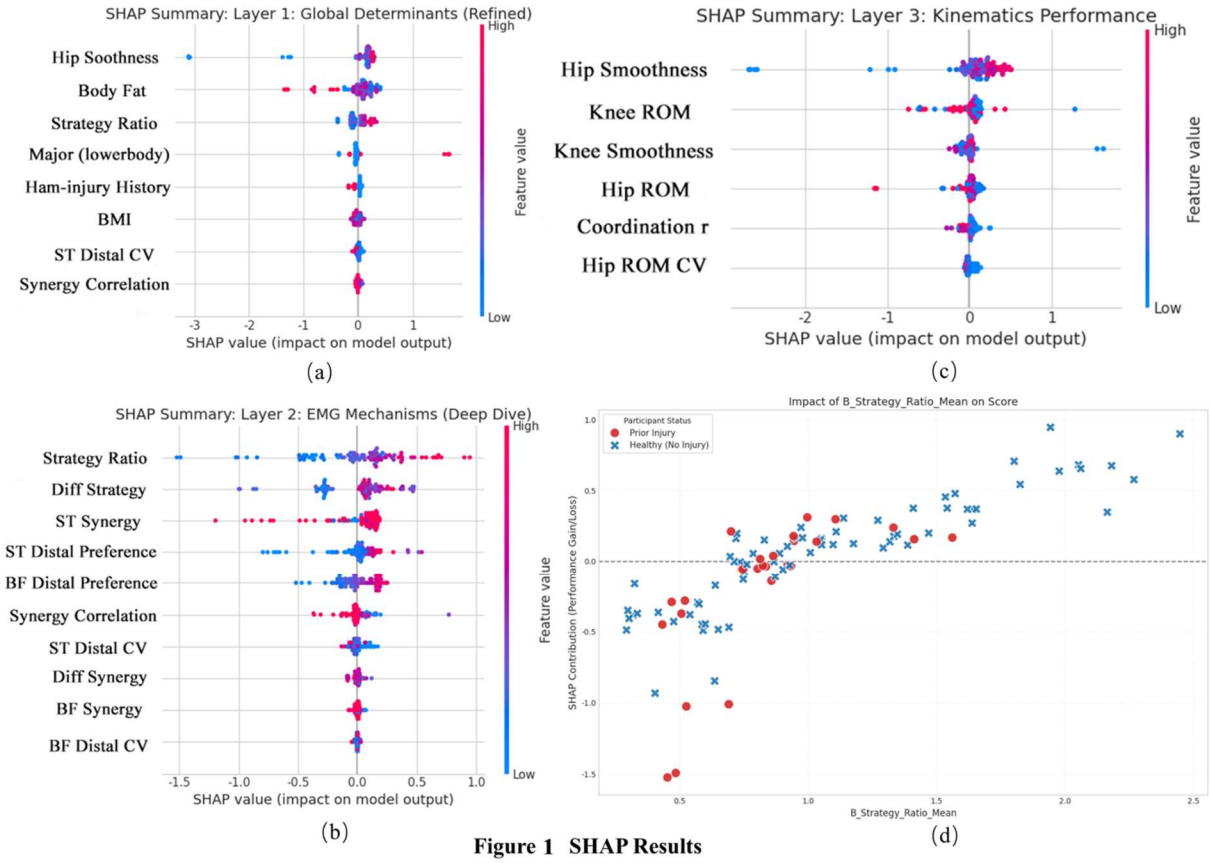


Figure 1 SHAP Results

Acknowledgements (Optional)

This work was supported by JST BOOST, Grant Number JPMJBS2429.

Session Category

Clinical Biomechanics: N/A

P4-266

Lower Back Strain Associated with Functional Activities in People with and People without Low Back Pain Using Motion Tape

Ms. Yasmin Velazquez MS[1], Mr. Elijah Wyckoff MS[2], Dr. Santiago Ortega DPT, MS[1], Dr. Kevin Patrick MD[2], Dr. Emilia Farcas PhD[2], Dr. Kenneth Loh PhD[2], Dr. Sara Gombatto PT, PhD[1]

[1]San Diego State University, San Diego, CA, United States. [2]University of California San Diego, San Diego, CA, United States

Introduction

Chronic low back pain (CLBP) is highly prevalent and associated with altered movement, yet existing methods for monitoring lumbar spine biomechanics are limited outside laboratory settings. Motion Tape (MT) is a flexible fabric-based device, made with multi-walled carbon nanotube piezoresistive sensors, that offers a potential solution for real-world lumbar strain monitoring. The primary purposes of this study were to: (1) determine whether MT can measure differences in lower back strains across different functional activities in a free-living environment, and (2) assess usability and acceptability of MT. A secondary purpose was to explore differences in lower back strain between people with and without CLBP.

Methods

Seventeen participants (9 with CLBP, 8 controls) completed a series of mid- and end-range functional tasks in flexion, extension, and lateral bending, and walking and stair climbing while wearing six MTs placed bilaterally on the upper, middle, and lower lumbar spine. Lumbar strain was quantified using normalized peak resistance during each task, and LBP was assessed with the Visual Analog Scale. Usability and acceptability were evaluated using the System Usability Scale (SUS) and a MT questionnaire.

Results

Significant differences in peak strain were observed across tasks ($p < .001$) and sensors ($p < .01$); significant differences in peak strain also were observed between mid- and end-range tasks for extension and lateral bending ($p < .01$), but not flexion ($p = 0.17$). Uphill walking produced greater lumbar strains than flat walking ($p < .05$). No significant differences in peak strain were observed between CLBP and control groups ($p > .05$), but the effect size for group differences was large for the mid-range lateral bending task (partial $\eta^2 = .33$). SUS ratings for usability were high (mean(SD)=77.2(14.7)), and participants reported sensors were comfortable, easy to use, and were confident in using MT.

Discussion

MT is acceptable for measuring differences in lumbar strain across functional tasks and ranges of lumbar movement and reported usability was high. MT shows promise as a wearable sensor to characterize real-world lumbar strain. MT did not distinguish between participants with CLBP and controls, but heterogeneity within the CLBP group suggests subgroup analysis may be needed.

Images (Optional)

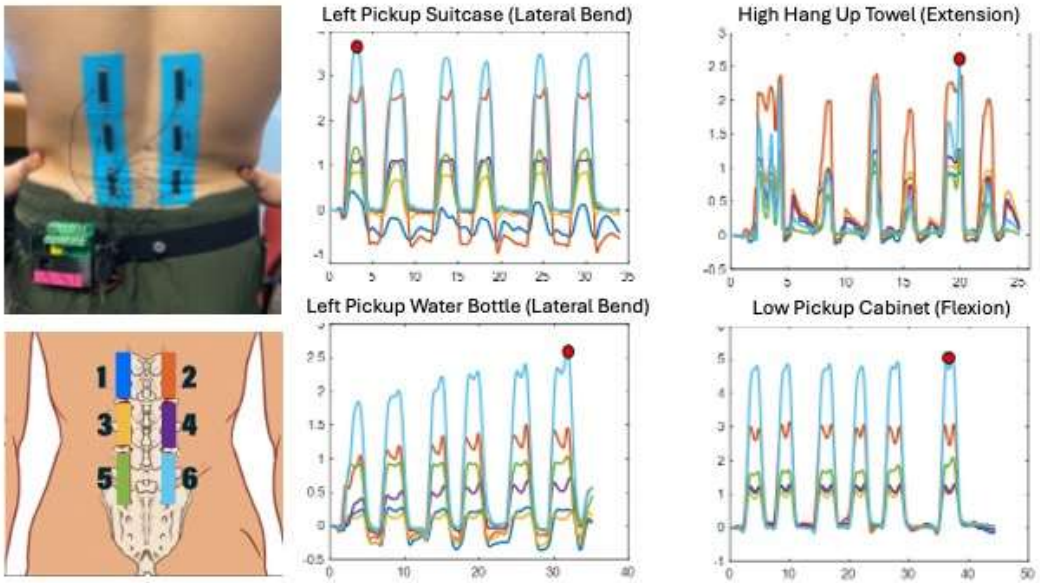


Figure 1. Motion Tape Sensor Placement (left) and Lower Back Strains (right) During Representative Functional Tasks. Red dots represent peak strains for one sensor (#6) for each task.

References (Optional)

Acknowledgements (Optional)

Thank you to student volunteers and research assistants who supported this project, including Christopher Alfaro, Jay Barolo, Alexandra Guzzardo, Sarah Konig, Jeremy La Rosa, Katya Pushka, and Walker Rost Kruger.

Session Category

Clinical Biomechanics: N/A

P4-267

Biomechanics of Functional Preservation in Full-Thickness Rotator Cuff Tears: A Study on Compensatory Strategies

Dr. Yi-Hsuan Weng[1], Mr. Chon-Kio Wong[1], Ms. Yang-Ting Chien[1], Ms. Kuan-Yun Liu[1], Mr. Yu-Cheng Weng[1], Dr. Chung-Hsun Chang[2], Dr. Jiu-Jenq Lin[1,3]

[1]School and Graduate Institute of Physical Therapy, College of Medicine, National Taiwan University, Taipei, Taipei, Taiwan. [2]Department of Orthopedic Surgery, College of Medicine, National Taiwan University Hospital, Taipei, Taipei, Taiwan. [3]Physical Therapy Center, National Taiwan University Hospital, Taipei, Taipei, Taiwan

Introduction

Full-thickness rotator cuff tears (FT-RCTs) often result in pain, weakness, and limited shoulder function. However, a subset of patients remains functional and pain-free despite substantial structural damage. This study aimed to determine which clinical and biomechanical factors differentiate functional from impaired FT-RCTs, thereby providing insight into compensatory mechanisms that may preserve performance.

Methods

From the fifty-three patients with full-thickness rotator cuff tears (FT-RCTs), fourteen were selected to form the good function group (top 25% by functional score) and fourteen formed the poor function group (bottom 25% by functional score). The two groups were well-matched, showing no statistically significant differences ($p>0.05$) in most baseline demographic and clinical variables, including age, sex, height, mass, arm dominance, tear size, pain level, symptom duration, range of motion, and structural measurements. Assessments included ultrasonography to evaluate tear size and humeral head migration. Clinical outcomes measured shoulder strength, range of motion, pain intensity, and self-reported disability. Three-dimensional scapular kinematics and electromyography of the upper trapezius, lower trapezius (LT), serratus anterior (SA), and teres major (TM) were recorded during controlled arm elevation tasks.

Results

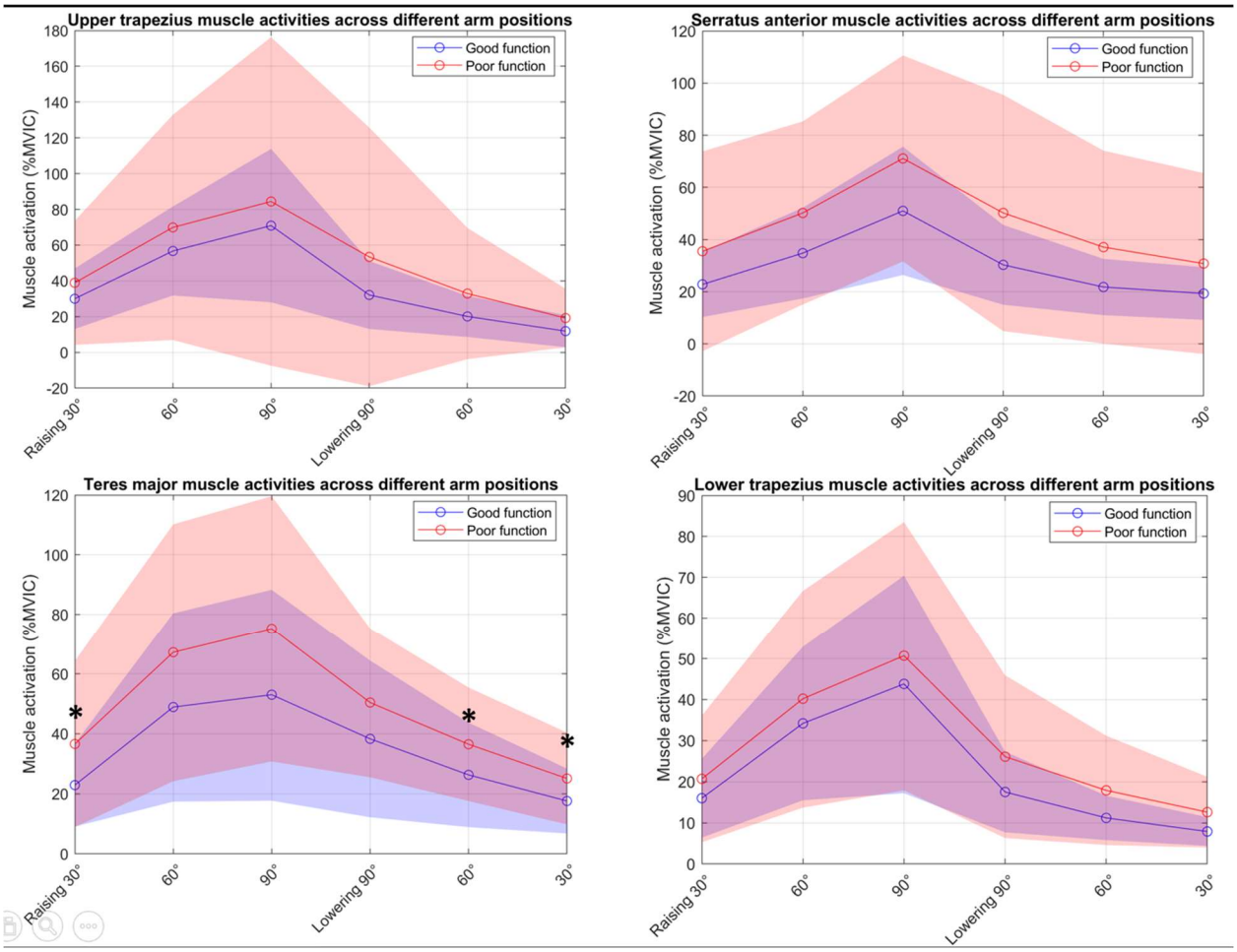
The good function group demonstrated greater shoulder flexor strength (11.2±3.2%, $p=0.001$) and lower activation of the TM (8.0-13.4%, $p=0.015$-0.028). Poor function was associated with decreased strength in the shoulder flexors ($r=0.485$, $p<0.001$) and LT ($r=0.376$, $p=0.007$), reduced humeral head migration ($r=0.311$, $p=0.028$), and increased

activation of the SA (r=-0.338 to -0.335, p=0.017) and LT (r=-0.318 to -0.347, p=0.014-0.024). Pain correlated with larger tear size (r=0.317, p=0.025), thinner coracohumeral ligaments (r=-0.365, p=0.009), narrower acromiohumeral distance (r=-0.340, p=0.016), and reduced scapular upward rotation (r=-0.308 to -0.371, p=0.008-0.029).

Discussion

This study demonstrates that functional capacity in individuals with FT-RCTs largely depends on their compensatory strategies. The primary distinction between patients with preserved and impaired function lies in muscle strength and activation profiles. Those maintaining better function exhibit stronger shoulder flexors and reduced recruitment of the TM muscle. Conversely, impaired individuals display deficits in key muscle groups and compensatory overactivation of muscles such as the SA. These findings suggest that rehabilitation could emphasize strengthening compensatory muscle groups and optimizing neuromuscular coordination, rather than focusing solely on the torn tendon.

Images (Optional)



Acknowledgements (Optional)

This study was supported by the Ministry of Science and Technology, Taiwan (110-2314-B-002-054-MY3). Additionally, the authors would like to thank the patients who participated in the study.

Session Category

Clinical Biomechanics: N/A

P4-268

3D-Printed Hip Protectors to Enhance User Compliance in Older Adults: Protocol of A Cluster Randomized Controlled Trial

Prof. Yijian Yang, Prof. Xu Song

The Chinese University of Hong Kong, Shatin, NT, Hong Kong

Introduction

95% of hip fractures in older adults are caused by falls. Although hip protectors have been promoted for hip fracture prevention, user compliance (acceptance and adherence) is generally low mainly due to discomfort (e.g., bulky, unbreathable, and unisize design). To address this issue, we developed and evaluated the effects of customized 3D-printed hip protectors on biomechanical performance and user compliance in older adults residing in care homes.

Methods

This study includes two stages. During stage one, we recruited 32 older adults (80.3±9, 55% females) with different body shapes from care homes and scanned their pelvis using a portable scanner. Data were used to generate 3D-printed hip protectors. Biomechanical performance of protectors was evaluated by measuring force attenuation in an impact test on a force plate. Physical performance of older adults was assessed to examine whether wearing hip protectors affect their balance and mobility. During stage two, we will conduct a 12-month cluster randomized controlled trial to evaluate user compliance with hip protectors. 300 older adults from 30 care homes will be recruited and randomly assigned to an intervention group (receiving 3D-printed hip protectors) or a control group (receiving conventional hip protectors). User compliance of wearing protectors and fall-related hip injuries (e.g., pain, bruises and fractures) will be measured over the study period. Generalized linear models will be applied to compare the acceptance, adherence and injury outcomes between the two groups.

Results

The dropping test showed that the 3D-printed hip protector attenuated 42.9% of impact forces compared to the non-protector condition. 3D-printed hip protectors did not adversely alter gait, mobility, and balance compared to no wearing of protectors ($p > 0.05$). Recruitment of older adults for the clinical trial is currently ongoing. We anticipate that participants in the intervention group will show higher acceptance and adherence to hip protectors and have a lower risk of hip injury.

Discussion

The 3D-printed hip protectors demonstrate lightweight and breathable features, with satisfied force attenuation and comfort for performing daily activities. By enhancing user compliance, our results will guide future scale-up implementation of 3D-printed hip protectors for the prevention of hip fracture in frail older adults.

References (Optional)

Session Category

Clinical Biomechanics: N/A

P4-269

Passive-Dynamic Ankle Foot Orthosis Can Offload the Achilles Tendon during Dynamic Tasks in a Patient with Achilles Tendinopathy

Ms. Zahra McKee, Dr. Stephanie Cone, Dr. Karin Grävare Silbernagel, Dr. Elisa Arch

University of Delaware, Newark, DE, United States

Introduction

Achilles tendinopathy is a common and chronic overuse injury of the Achilles tendon. Managing the load experienced in the Achilles tendon is important during rehabilitation as underloading precludes tendon remodeling and overloading induces pain and possible reinjury, but there is currently no way to control loading during daily living beyond pain monitoring [1]. Passive-dynamic ankle foot orthoses (PD-AFOs) may be able to partially offload the Achilles tendon during dynamic tasks by providing eccentric plantarflexion assistance through dorsiflexion stiffness and concentric plantarflexion assistance through energy release. PD-AFO use has previously been linked to reduced biological ankle moment and soleus activity [2,3]. This study aimed to investigate if PD-AFOs can offload the Achilles tendon for individuals with Achilles tendinopathy.

Methods

One individual with unilateral right Achilles tendinopathy (37 y.o., Female, Right VISA-A: 47, Left VISA-A: 85) was fitted for a PD-AFO, that only provided dorsiflexion resistance, on their right leg. Two PD-AFO conditions were tested: unengaged (no stiffness), and stiff (1.5 Nm/deg). Under the PD-AFO conditions, the participant performed bilateral heel raises at 60 bpm, and walking and running at self-selected speeds. Shear wave tensiometry data was collected to assess Achilles tendon loading as squared shear wave speed is a proxy for tendon loading [4]. Peak squared shear wave speed in the tendinopathic leg was averaged for each activity and compared between the PD-AFO conditions.

Results

Average peak squared shear wave speed was lower in the stiff PD-AFO condition than the unengaged condition for all three activities (Figure 1).

Discussion

The PD-AFO reduced peak Achilles tendon loading during walking, running, and bilateral heel raises in an individual with Achilles tendinopathy. If results are consistent with additional participants (being recruited), our findings may indicate that PD-AFOs enable tendinopathic patients to return to activity sooner without overloading their Achilles tendon. Future work will also explore if adjusting PD-AFO stiffness can fine-tune the level of assistance provided.

Images (Optional)

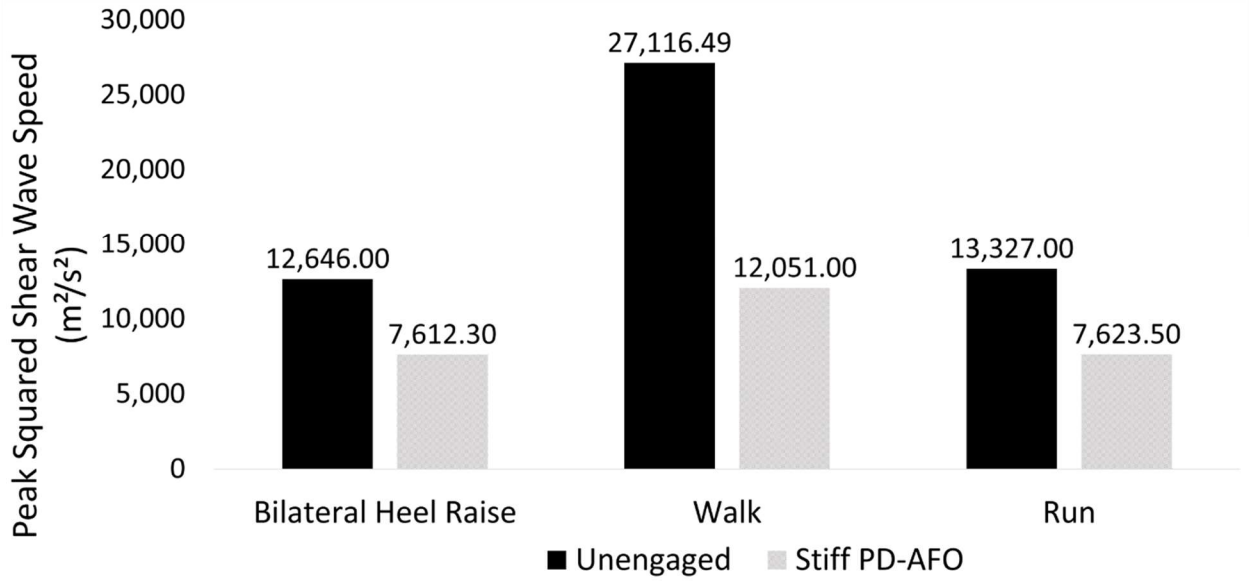


Figure 1. Peak squared shear wave speed during bilateral heel raises, walking (1.27 m/s), and running (2.60 m/s) and under unengaged and stiff PD-AFO conditions

References (Optional)

[1] Karin Grävare Silbernagel et al., J Athl Train, 2020

[2] Elisa S. Arch et al., Prosthet Orthot Int, 2015

[3] Elisa S. Arch et al., Ann Biomed Eng, 2015

[4] Jack A. Martin et al., Nat Commun, 2018

Session Category

Clinical Biomechanics: N/A

P4-270

Beyond Blood: Exploring Musculoskeletal and Neuromotor Phenotypes in Fragile X Syndrome

PhD Student Federica Beghetti[1], Dott.ssa Fabiola Spolaor[1,2], PhD Roberta Polli[3,2], PhD Elisa Betella[3,2], Dott.ssa Valentina Liani[4], Associate Professor Elisa Di Giorigio[5], Mr Francesco Campulla[1], Prof. Stefano Sartori[6], Prof Giorgio Perilongo[2,4], Prof Damiano Varagnolo[1,7], Associate Professor Zimi Sawacha[1]

[1]Department of Information Engineering, University of Padova, Italy, Padova, ITA, Italy. [2]Fondazione Istituto di Ricerca Pediatrica (IRP), Città Della Speranza,, Padova, ITA, Italy. [3]Molecular Genetics of Neurodevelopment, Department of Woman and Child Health, University of Padova, Padova, ITA, Italy. [4]Department of Women's and Children's Health, University of Padova, Padova, ITA, Italy. [5]Department of Developmental Psychology and Socialization, University of Padova, Padova, ITA, Italy. [6]Child Neurology and Clinical Neurophysiology Unit, Padova University Hospital,, Padova, ITA, Italy. [7]Department of Engineering Cybernetics, University of Science and Technology, Trondheim, Norway, Norway

Introduction

Fragile X syndrome (FXS) is a rare genetic condition and the most common monogenic cause of autism [1] characterized by two main phenotypes: Full Mutation (FXSFull) and somatic mosaicism (FXSMos). FXS children show hypotonia and joint hyperlaxity, however as the diagnosis relies on blood-based molecular testing, the impact of FMRP deficiency on muscle and connective tissues is still unclear. Recent evidence indicates preferential recruitment of fast-twitch muscle fibers [2], suggesting delayed muscular maturation. In this study, we integrated gait biomechanics and surface electromyography (sEMG) with clinical and neurocognitive assessments [1] to examine how neuromuscular patterns relate to the FXS phenotype. Unsupervised machine-learning approaches were used to identify data-driven subgroups.

Methods

FXS affects males more frequently due to their single X chromosome, therefore fifty-five FXS boys (age: 10.48 ± 3.42; BMI: 19.25 ± 4.38) and 14 age- and BMI-matched control subjects (CS) were enrolled. Markerless gait analysis was performed through GoPro Hero cameras (60 fps) and a Cometa sEMG system (2000 Hz) recording bilateral activity from Tibialis Anterior , Gastrocnemius Lateralis , Rectus Femoris , and Biceps Femoris . Spatiotemporal parameters and EMG-derived features were extracted as in [2] and used as inputs for DBSCAN, K-means, and Hierarchical Clustering. Feature subsets were evaluated

through a grid-search procedure, and the optimal configuration for each model was selected using the Silhouette score. Clusters were subsequently characterized using all biomechanical and neuropsychiatric measures and correlation analyses were performed within each cluster.

Results

K-means using muscle activation durations yielded the best performance, identifying two clusters. Children with FXS in cluster 1 showed higher Total Intelligence Quotient (TIQ) scores and biomechanical features more aligned with the CS group. Representative boxplots illustrate differences in selected EMG-based and gait parameters.

Discussion

Findings indicate that neuromuscular alterations in FXS do not fully align with blood-based diagnostic categories, suggesting that FMRP deficiency may differentially affect blood and muscle tissues. Lower anxiety scores on the Child Behavior Checklist in FXS children from Cluster 1, compared to Cluster 2, may explain why some FXS children fall into Cluster 1.

Images (Optional)

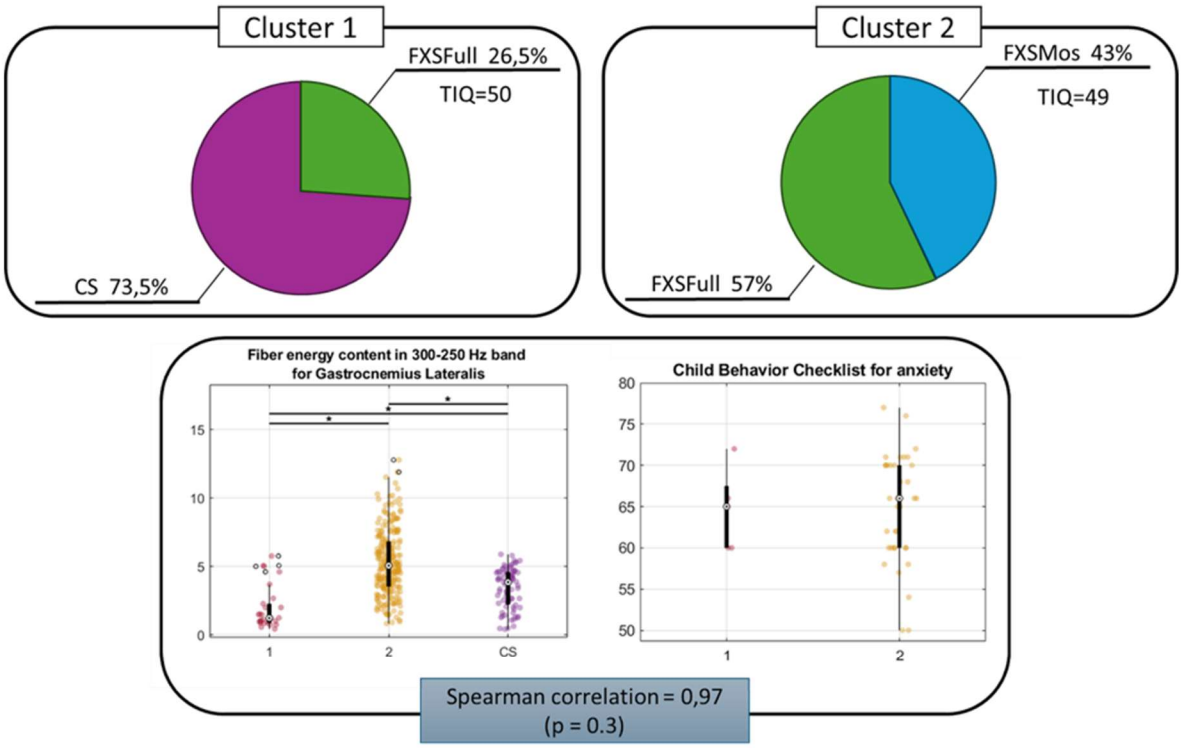


Figure 1 Top: pie charts showing the percentage composition of Cluster 1 and Cluster 2. **Bottom left**: comparison among clusters and the control group (CS) for fiber energy content in the 300–250 Hz band of the Gastrocnemius Lateralis; horizontal bars indicate statistically significant differences. **Bottom right:** Child Behavior Checklist anxiety scores for the two clusters. The lower panel reports the Spearman correlation between the two measures (ρ = 0.97, p = 0.3).

References (Optional)

[1] Hagerman RJ, et al.Front Psychiatry. 2018

[2] Sawacha Z, et al. Sensors. 2021

Acknowledgements (Optional)

In memory of Prof. Alessandra Murgia. This work was supported by FRAXA Foundation and PRIN project (2022, Prot. 20227JA8R3).

Session Category

Clinical Biomechanics: N/A

P4-271

3D Printing Enables Custom-Shaped Hydrogel–Elastomer Soft Sensing Skins for Next-Generation Sensate Prosthetics

Mr. Arman Arezoomand, Dr. Heather Baltzer, Dr. Fae Azhari

Univesity of Toronto, Toronto, ON, Canada

Introduction

Hydrogel-elastomer hybrids [1] are promising materials for soft robotic skins due to their tunable mechanical properties and inherent ionic electrical conductivity. Their mechanical compliance can be tuned to match that of soft tissues and their piezoresistive behaviour enables self-sensing by relating changes in electrical resistivity to applied pressure or strain. Despite their potential, casting the thin elastomeric layer that covers and protects the hydrogel layer is time-consuming and requires custom molds for different shapes. 3D printing can facilitate the elastomer fabrication for applications that require high flexibility and shape customization such as pressure-sensitive digits for partial hand prostheses. We propose a new fabrication method for digit-like hydrogel-elastomer hybrid sensors and demonstrate its application for tactile sensing using a customized compact impedance measurement system.

Methods

A 1-mm-thick elastomeric protective layer in the shape of a thumb was fabricated using an SLA 3D printer. A PCB that acts as the backing and houses the sensor electrodes was treated with an adhesion promoter and inserted into the elastomeric protective layer. The elastomeric cavity was then filled with the hydrogel precursor and cured with UV light. We used a custom-designed wearable impedance measurement board [2] for impedance measurements under arbitrary surface indentations. Baseline measurements were continuously compared to the latest measurements to determine the amount of applied deformation, which was then used to actuate a vibrotactile unit for feedback purposes.

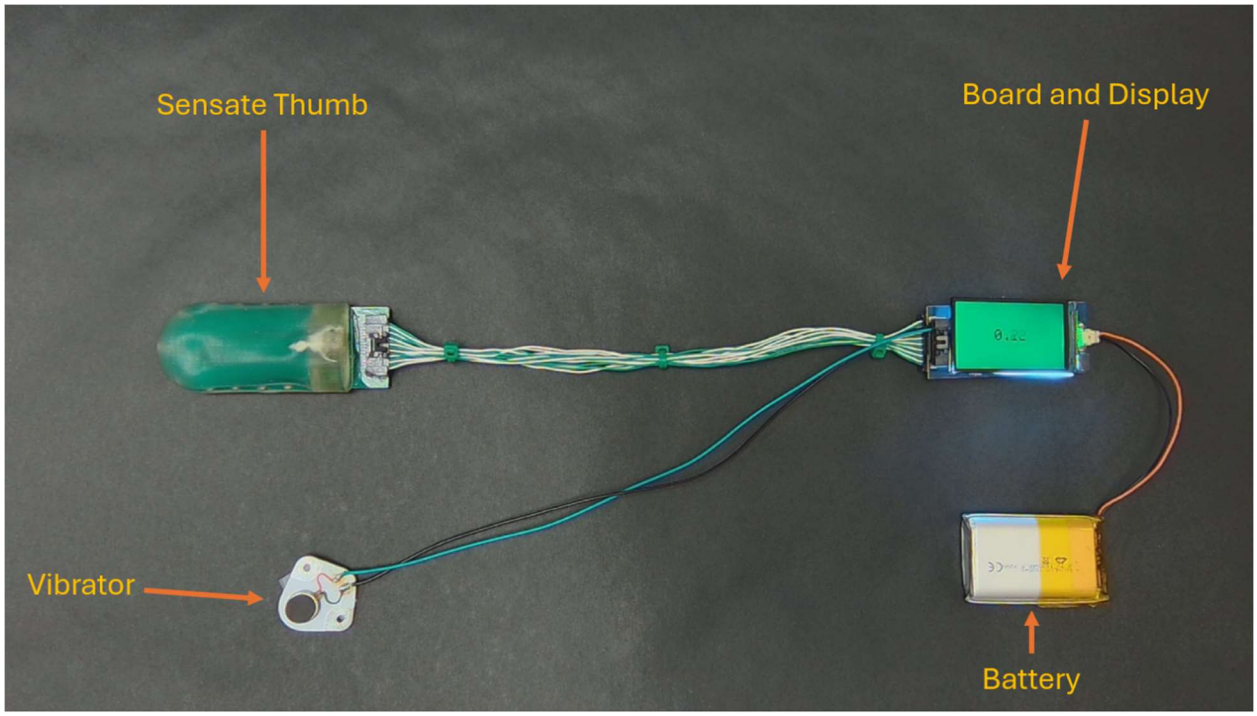
Results

The resulting sensate digit has a Shore A hardness of 15±3, which is comparable to the pad of a human thumb. The hydrogel was effectively bonded to the elastomeric layer and the PCB backing. The system distinguished light (indentation<3 mm) and deep (indentation>3 mm) contact using a thresholding method applied to the sensor output and provided vibrotactile feedback.

Discussion

The sensate digit prototype demonstrates, as a proof of concept, the feasibility of integrating hydrogel-elastomer hybrid sensors into prosthetic and robotic devices with a high degree of shape customizability. Such devices can support tactile sensing architectures ranging from the simple configurations presented here to advanced, tomography-based distributed sensing.

Images (Optional)



References (Optional)

1. Kim Park *et al.* , Science Robotics, 2022
2. Arman Arezoomand *et al.* , IEEE Humanoids, 2024

Acknowledgements (Optional)

This work was supported by The War Amps, the New Frontiers through research fund NFRFE-2020-01171, and the Data Sciences Institute at the University of Toronto through grant number DSI-DSFY4R1P13.

Session Category

Imaging and Biomedical Devices: Artificial Organs, Devices

P4-272

Broadband Axial and Shear Testing Device for Heterogeneous Soft Materials

Mr. Brandon Chelstrom[1], Dr. Corinne Henak[1,2,3]

[1]Department of Biomedical Engineering, University of Wisconsin-Madison, Madison, Wisconsin, United States. [2]Department of Mechanical Engineering, University of Wisconsin-Madison, Madison, Wisconsin, United States. [3]Department of Orthopedics and Rehabilitation, University of Wisconsin-Madison, Madison, Wisconsin, United States

Introduction

Complete mechanical characterization of soft materials remains a considerable challenge due to the local variation in mechanical properties across length scales. Heterogeneous tissue structures and material boundaries give rise to stark gradients or discontinuities often incorrectly captured using standard mechanical testing. To address these gaps, we developed a device capable of applying multi-axial loading while simultaneously capturing full-field displacements.

Methods

Two perpendicular linear actuators interface with a custom CNC machined microscope well to apply normal and shear loading to samples within the well (Fig. 1A). The well sits atop an inverted bright field microscope to visualize small scale displacement fields. Actuator displacements, loads and displacement fields are captured synchronously.

After tuning the actuators, 200μm step displacements were verified against high-speed video data across the microscope field of view (FOV). Experimental validation compared elastic properties of PDMS (1:10) in uniaxial tension and shear against an established test frame (TA Electroforce). Samples were loaded at 10 mm/min to 4 mm with a preload of 0.07 N. One batch of samples (n = 10) cured for 6 days prior to mechanical testing. Various gauge strain tracking methods, including both static and dynamic line tracking and digital image correlation (DIC), were used for each test set up due to the difference in image resolution and FOV. The average elastic modulus for each test type was compared between samples tested on both devices.

Results

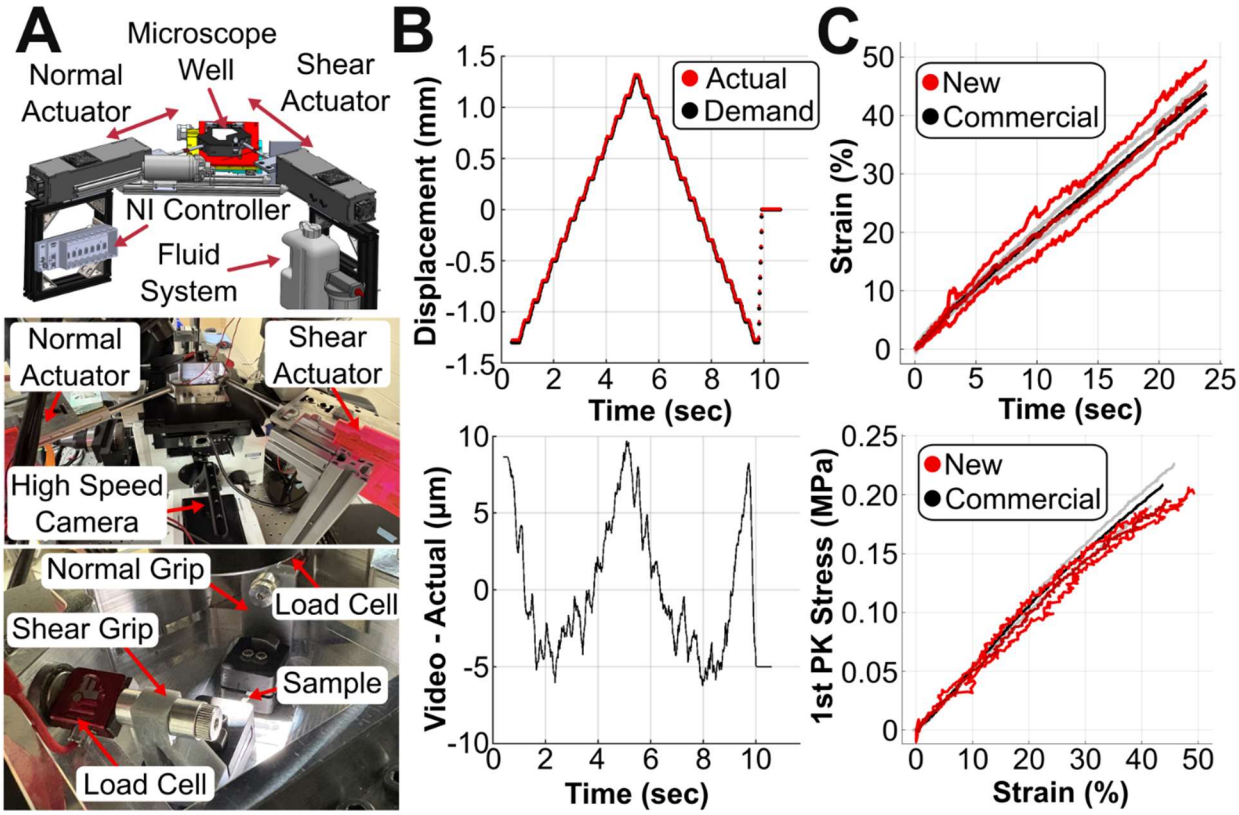
Optical displacements were ±10μm of the demand position across the entire FOV (Fig. 1B). The difference in stress-strain distribution for tensile samples is within 1% across test frames (Fig. 1C). Average elastic moduli are within 5% across all tensile and shear samples.

Discussion

The proposed device can visualize local strain fields under multi axial loading using multiple strain tracking methods. Mechanical testing of PDMS samples indicates a consistent elastic response when compared to an established test device (Fig. 1B). However, mechanical analysis failed to consider out of place deformation and DIC based tracking methods were noisier due to the smaller FOV (Fig. 1C). The consistent response between standard uniaxial tests lays the foundation to further characterize local heterogeneity in soft materials.

.

Images (Optional)



References (Optional)

Session Category

Imaging and Biomedical Devices: Artificial Organs, Devices

P4-273

Load-Induced Internal Relative Motion Between Cementless Tibial Trays and Cadaveric Proximal Tibiae in Stair Descent: A Micro-CT and DVC Study

Dr Kieran Bennett[1], Dr Lauren Wearne[2], Dr Sophie Rapagna[1], Dr Sunil Reddy[3], Mr Julius Dohm[4,5], Dr Cristoph Schilling[4], Dr Berna Richter[4], Professor Dr Dr Thomas Grupp[4,5], Associate Professor Egon Perilli[1]

[1]Medical Device Research Institute, College of Science and Engineering, Flinders University, Adelaide, South Australia, Australia. [2]Lund University, Lund, Skåne County, Sweden. [3]The Joint Replacement Clinic, Adelaide, South Australia, Australia. [4]Aesculap AG Research and Development, Tuttlingen, Baden-Württemberg, Germany. [5]Department of Orthopaedic and Trauma Surgery, Musculoskeletal University Center Munich (MUM), Munich, Bavaria, Germany

Introduction

Cementless knee implants rely on interference to achieve primary stability. Previous studies quantified the relative motion between tibial bone and implant under load using digital image correlation (DIC) [1], however, they were limited to external motion measurements. In this study, we aimed to quantify the internal relative motion between bone and implant under stair descent loads, using micro-CT imaging and digital volume correlation (DVC).

Methods

Five human cadaver proximal tibiae were implanted with in-development cementless tibial components (Aesculap AG) by an orthopaedic surgeon (ethics HREC 223.23). These tibiae were micro-CT scanned at 46 µm/pixel (Nikon XT H 225ST) [2] under increasing loads representing stair descent, from 0 to 2.5 kN. Internal bone displacements were quantified using DVC on micro-CT datasets (DaVis v8.4, subvolume side length 24 pixels, 1,104 µm), and implant displacements calculated by segmenting and aligning the implant position in each scan (MATLAB r2024b). Relative motion was determined as the difference between bone and implant displacement at the centroids of subvolumes closest to the implant, and decomposed into normal and shear motion relative to the implant surface.

Results

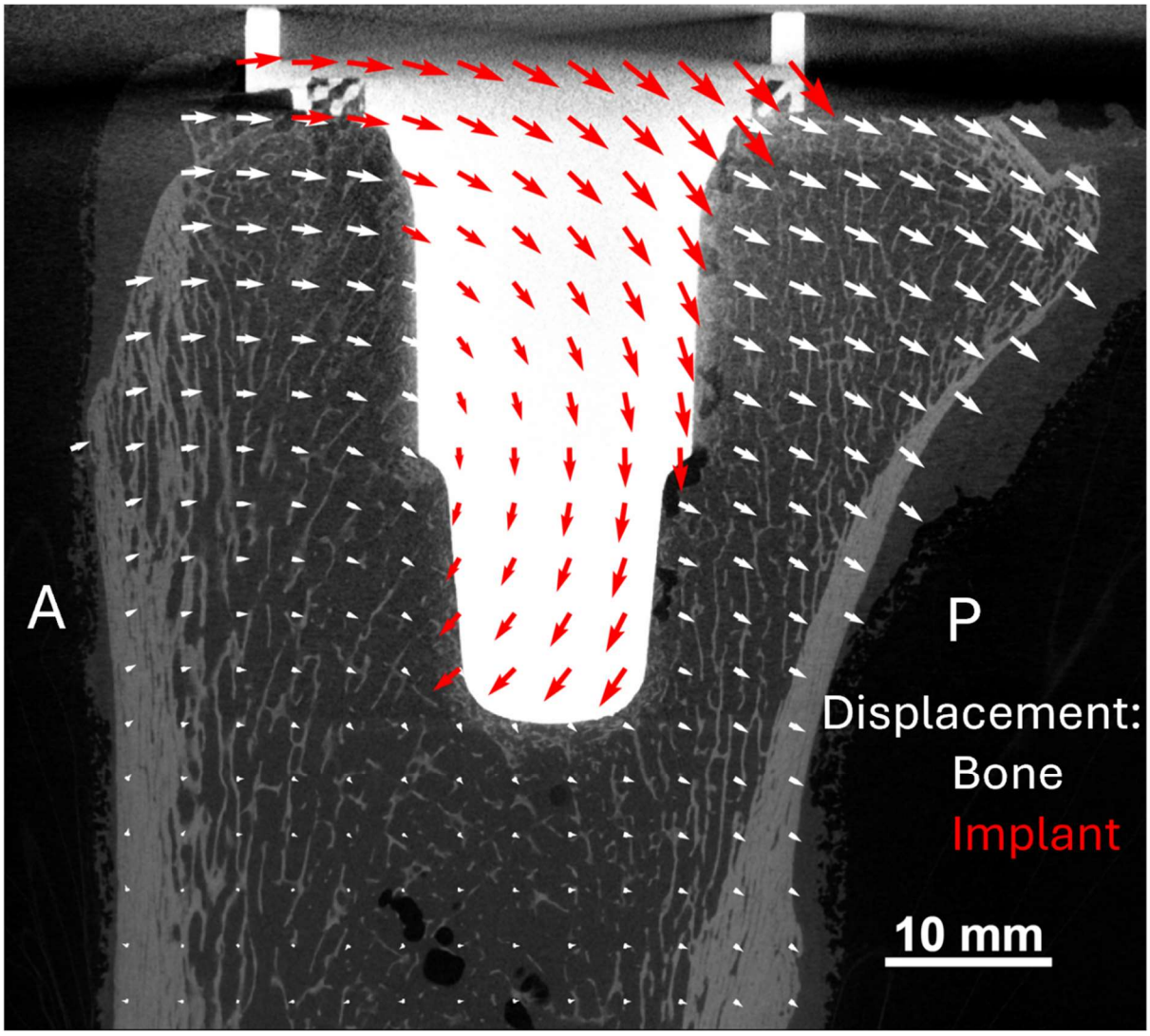
Relative motion increased linearly with applied load. With 2.5kN applied, maximum observed relative motion was between 78 and 295 µm, dominated by posterior bone-

implant gap closing beneath the tray baseplate (range 77-293 μm). Interestingly, in all specimens, to posterior gap closing under the tray baseplate corresponded also a gap opening on the posterior side of the keel and wings (Figure 1). Maximum gap opening was primarily observed at the most inferior and posterior point of the keel/wings (range 60-251 μm).

Discussion

The internal relative motion between implanted cementless tibial trays and bone, a measure of primary stability, has been quantified under progressive stair descent loads. Our DVC measurements around the tibial tray align with DIC measurements from literature [1], and reveal previously unreported internal relative motion at the bone-implant interface on the posterior side of internal implant geometries (keel/wings). These results improve our understanding of cementless tibial tray primary stability, informing surgical technique and implant designs.

Images (Optional)



References (Optional)

[1] Sánchez E, *et al.*, JMBBM, 2021

[2] Wearne LS, *et al.*, JMBBM, 2022

Acknowledgements (Optional)

Aesculap AG and Flinders Microscopy and Microanalysis.

Session Category

Imaging and Biomedical Devices: Artificial Organs, Devices

P4-274

A Mechanotherapeutic Implant for Delivery of Immunotherapy to Treat Ovarian Cancer

Dr Hannah Prendeville[1], Ms Parand Shokrani[2], Prof Garry. P Duffy[3,4], Dr Eimear. B Dolan[1,3]

[1]Biomedical Engineering, School of Engineering, College of Science and Engineering, University of Galway, Galway, Connaught, Ireland. [2]Biomedical Engineering, School of Engineering, College of Science and Engineering, University of Galway, Galway, Connaught, India. [3]CÚRAM, Centre for Research in Medical Devices, University of Galway, Galway, Connaught, Ireland. [4]Anatomy and Regenerative Medicine Institute (REMEDI), School of Medicine, University of Galway, Galway, Connaught, Ireland

Introduction

Ovarian Cancer is the most lethal gynaecological malignancy. There is an urgent need for innovative strategies to improve therapeutic outcomes and increase patient survival. We previously described a mechanotherapeutic implant that uses actuation to modulate the foreign body response (FBR)[1,2]. Actuation significantly reduced the thickness of the fibrous capsule around subcutaneous implants[1], and improved drug transport for up to 8 weeks in immunocompetent mice[2]. More recently, we used a non-actuatable version of this implant to deliver Natural Killer (NK) cells to the peritoneal cavity in immunocompromised mice bearing OVCAR-8 tumours. Delivering NK cells through our therapeutic implant led to superior control of ovarian tumours, as compared to intraperitoneal injection of therapy[3]. We are now evaluating whether actuation of our peritoneal implant can enhance therapeutic efficacy in an ID8 immunocompetent mouse model of ovarian cancer.

Methods

We have redesigned our actuatable implant for implantation in the peritoneal space. We first assessed if actuating our implant is suitable for delivery of cell therapies. Therapeutic implants were loaded with NK cells *ex vivo* and connected to a pneumatic control system. The implants were actuated to a peak pressure of 27.57kPa for 20 or 40 seconds. Cell number and viability post-actuation were analysed using a cell counter.

Results

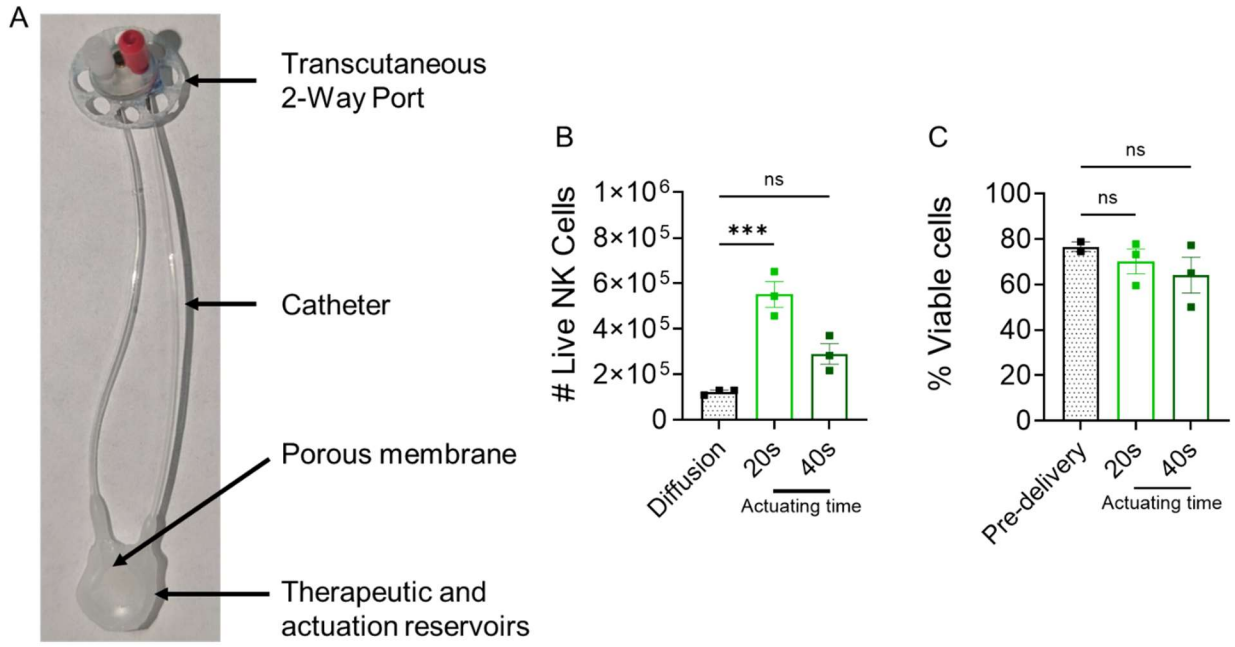
Actuation enhanced NK cell ejection from the therapeutic implant but did not affect cell viability, indicating that actuation can improve cell delivery efficacy without compromising cell integrity.

Ongoing work in our group is focused on establishing the ID8 mouse model of Ovarian Cancer and examining if actuation can modulate the FBR towards a peritoneal implant. Future work will use this actuatable implant to deliver immunotherapy to the peritoneal cavity and assess its ability to control tumour growth.

Discussion

Here we describe a mechanotherapeutic implant that allows for effective delivery of therapy to the peritoneal space. By combining actuation with cellular immunotherapies, our strategy has the potential to overcome the clinical challenges and shortcomings associated with intraperitoneal treatment of Ovarian Cancer.

Images (Optional)



References (Optional)

[1] Eimear B. Dolan *et al.*, *Sci. Robot,* 2019.

[2] William W. Whyte *et al.*, *Nat. Commun* 2022.

[3] Aoibhín M. Sheedy *et al.*, *Device* in press

Session Category

Imaging and Biomedical Devices: Artificial Organs, Devices

P4-275

Neonatal venoarterial extracorporeal life support: large-eddy simulations of the return cannula

MSc Hanna Hörwing[1], MD Jan Svoboda[2], Associate Professor Lars Mikael Broman[3,4], Professor Lisa Prahl Wittberg[1]

[1]Dept. of Engineering Mechanics, FLOW, KTH Royal Institute of Technology, Stockholm, Stockholm, Sweden. [2]Dept. of Pediatric Radiology, Karolinska University Hospital, Solna, Stockholm, Sweden. [3]ECMO Centre Karolinska, Pediatric Perioperative Medicine and Intensive Care, Karolinska University Hospital, Solna, Stockholm, Sweden. [4]Department of Physiology and Pharmacology, Karolinska Institute, Solna, Stockholm, Sweden

Introduction

In patients with respiratory and cardiac failure, venoarterial extracorporeal membrane oxygenation (VA ECMO) can relieve the heart and lungs of the patient, offering life support. The ECMO system drains de-oxygenated blood from the patient's venous system, pumps the blood through an oxygenator outside the body, then returns oxygenated blood to the patient's arterial system**.** In the system, blood and vessels are exposed to unphysiological conditions, promoting thrombosis and reduced oxygen delivery to the brain. In this work, CFD was used to study the return cannula in neonatal patients on VA ECMO. The aim was to investigate the effect of flow rates and cannula positioning on flow structures and stress dynamics, and thus, potentially reducing complication risks.

Methods

Computed tomography (CT) imaging of 12 neonatal patients (age 2-25 days; weight 2.5-4.5 kg) were collected during ECMO treatment (Approved by the Swedish Ethical Review Authority). 3D geometries of the aorta and major connecting vessels were reconstructed for each patient. Anatomical variations typical in neonates were identified, including a ductus in 8 out of 12 patients. A cannula was inserted into the Brachiocephalic artery according to clinical practice, applying large eddy simulations to simulate the blood flow. The Quemada (Das) viscosity model was used to account for the shear-thinning characteristic of blood. An ECMO flow rate of 90 mL/kg/min was applied as baseline, applying a pulsatile inflow profile at the aortic valve.

Results

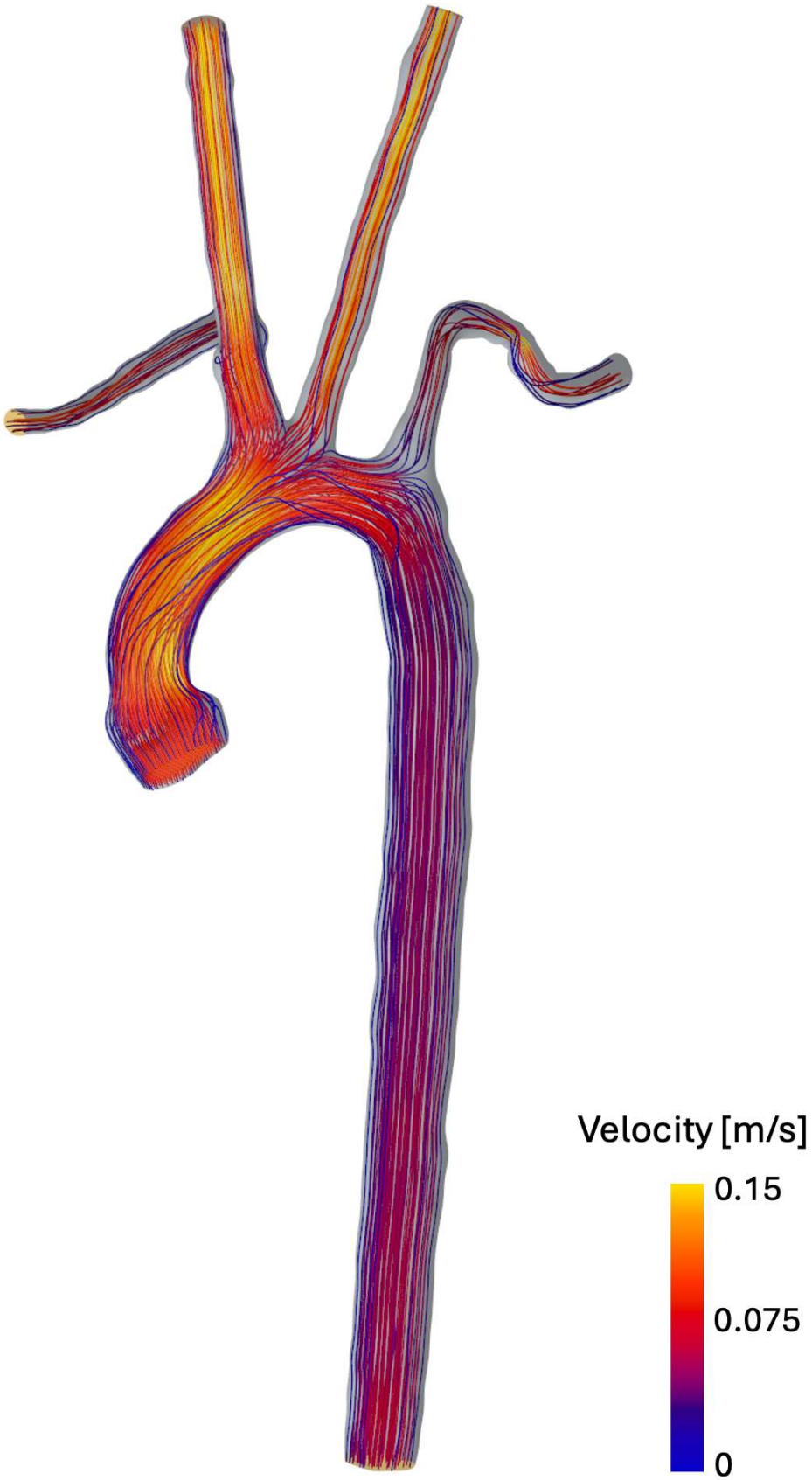
Oxygen transport and distribution was assessed, along with flow structures linked to thrombogenicity, including shear stresses and stagnation of blood. The preliminary results indicate that the cannula return flow formed a jet colliding with the wall of the aortic arch.

Reducing the ECMO flow rate decreased wall shear stresses at the location of the impinging jet. In addition, lower ECMO flow rate decreased oxygen transport.

Discussion

While neonates represent a large group among ECMO patients, most computational fluid dynamics (CFD) studies have been centered around adult geometries. With these findings, we aim to increase knowledge on cannula flow dynamics in neonatal patients, and provide a foundation supporting clinical decision-making in neonatal practice.

Images (Optional)


Velocity [m/s]
0.15
0.075
0

References (Optional)

Acknowledgements (Optional)

The research was founded by the European Union (ERC CoG 2021: Project 101045453 - fitsCAN). Views and opinions expressed are however those of the author(s) only and do not necessarily reflect those of the European Union or the European Research Council Executive Agency. Neither the European Union nor the granting authority can be held responsible for them.

Session Category

Imaging and Biomedical Devices: Artificial Organs, Devices

P4-276

Advancement in Endotracheal Intubation: Fabrication and Preliminary Characterization of An Improved Robotic Cuff System

Mr. Jacob Provencio, Mr. Orlando Favela, Mr. Mohammad Nikmehr, Dr. Connor J. Evans Ph.D., Dr. Robert A. De Lorenzo M.D., Dr. R. Lyle Hood Ph.D.

The University of Texas at San Antonio, San Antonio, Texas, United States

Introduction

Endotracheal (ET) intubation is a common procedure, with an estimated 13–20 million cases annually in the United States. Despite its frequency, clinicians must navigate small apertures and complex anatomical curvatures. A controlled system is needed to improve ET intubation, especially in prehospital settings where first-pass success may be as low as 46.4%. This work aimed to develop and characterize a multi-channeled soft robotic steerable cuff system capable of directional actuation and radial expansion.

Methods

A soft robotic maneuverable cuff was fabricated using a multi-mold process to produce a four-channel silicone structure. Ecoflex 00-30 was mixed in equal parts and injected into 3D-printed molds designed to create pneumatic channels for steering and radial expansion. After a four-hour cure, mold components were removed, with a secondary sealing step implemented to enclose the pneumatic channels. The completed cuff was bonded to an 8 mm inner diameter silicone tube using Sil-Poxy.

Benchtop testing was performed using a lab stand with a protractor behind the tube and a stylet inserted for alignment. A 60 mL syringe—actuated via syringe pump—was connected in line with a pressure gauge and the channel being tested. Channels were pressurized and angular deflection was recorded to generate pressure–angle profiles. Four cuff prototypes were evaluated, with each channel actuated ten times.

Results

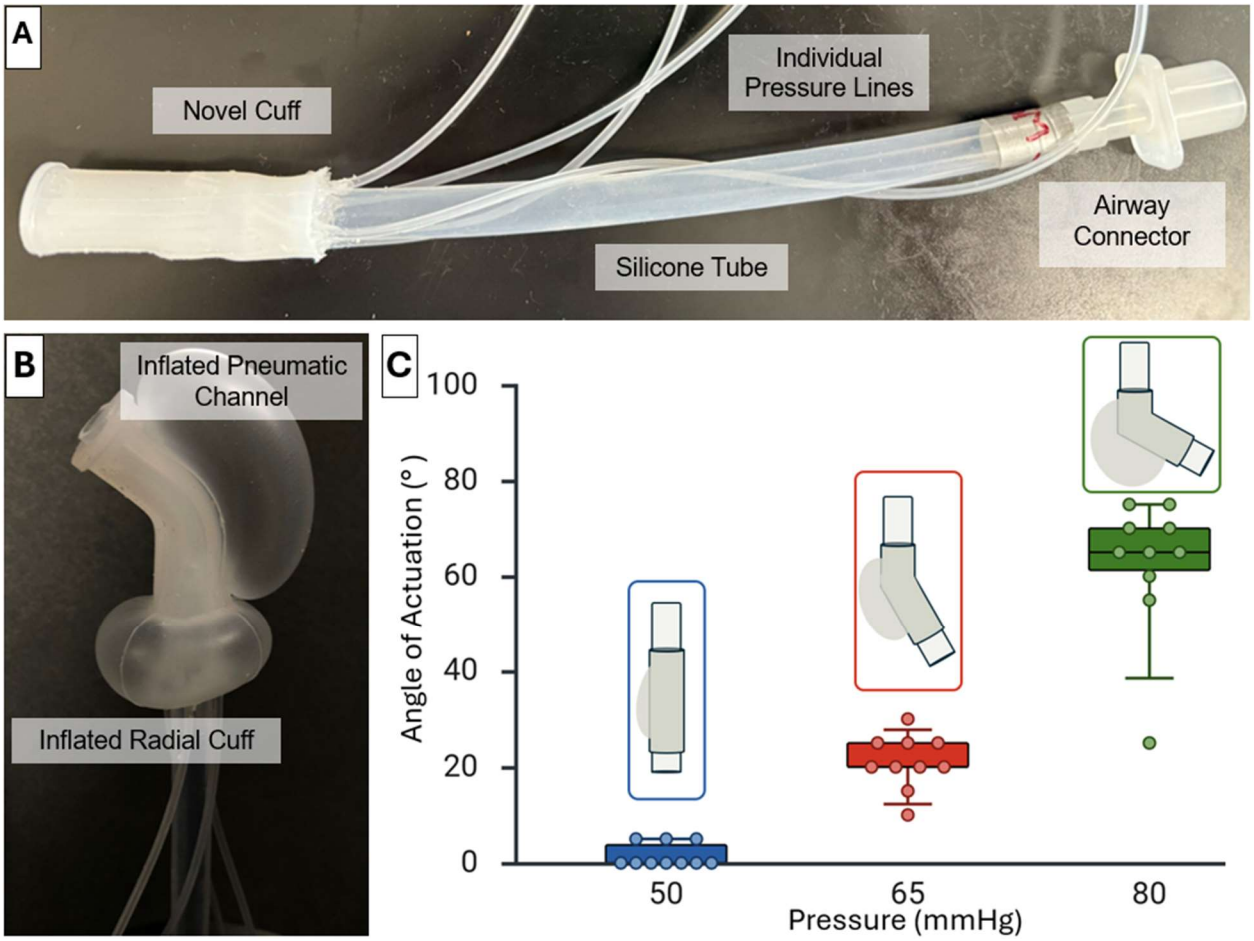
Through quality assessment, each of the fabricated tubes exhibited the ability to radially expand the pneumatic cuff channel. Across prototypes, initial angular displacement occurred between 40–50 mmHg. Three cuffs achieved anatomically relevant bending, reaching angles up to 40°, while an average tracheal tilt is approximately 20°. Three of the four cuffs produced 20° of deflection under 70 mmHg, and two tubes withstood

pressurization to 80 mmHg, achieving max bending angles of 62.5° ± 13.83° and 36.6° ± 10.6°.

Discussion

The cuff prototypes demonstrated the ability to generate both radial cuff expansion and controlled angular displacement through independent pneumatic actuation. While all prototypes produced measurable bending, further refinement is needed to achieve consistent outcomes. Future work will aim to reduce unintended channel expansion and develop a user-controlled pneumatic system for next-generation steerable cuffs.

Images (Optional)



Session Category

Imaging and Biomedical Devices: Artificial Organs, Devices

P4-277

Experimental Evaluation of the Geometry of Stepped Catheters on Backflow During Infusion into Agarose Gel

Professor Joshua Smith Ph.D., Mr. Elliott Godin, Ms. Sophia Gaysinskiy

Lafayette College, Easton, PA, United States

Introduction

One of the challenges of convection-enhanced delivery into brain tissue is backflow, where the infused fluid flows preferentially along the shaft of the catheter away from the targeted tissue. Stepped catheters, in which there is a sudden increase in the diameter of the shaft a few millimeters away from the tip, have been proposed as a means to minimize backflow. While a few studies have established the utility of stepped catheters, this study examines the effect of variations in the diameters of the tip and the shaft on backflow.

Methods

Stepped catheters were manufactured using 304 stainless steel needle tubing in combinations of shafts of 26, 20, and 16 gauge with 5-mm-long tips of 33, 30, and 26 gauge. Infusions were conducted with a custom-built infusion rig into 0.6% (w/v) agarose gel. Infusion flow rates from 1 to 10 μL/min were investigated and a total of 25 μL of 0.05% (w/v) bromophenol blue was infused. Backflow lengths were determined by analysis of images of the infusions. At least three infusions were conducted for each stepped catheter at each flow rate.

Results

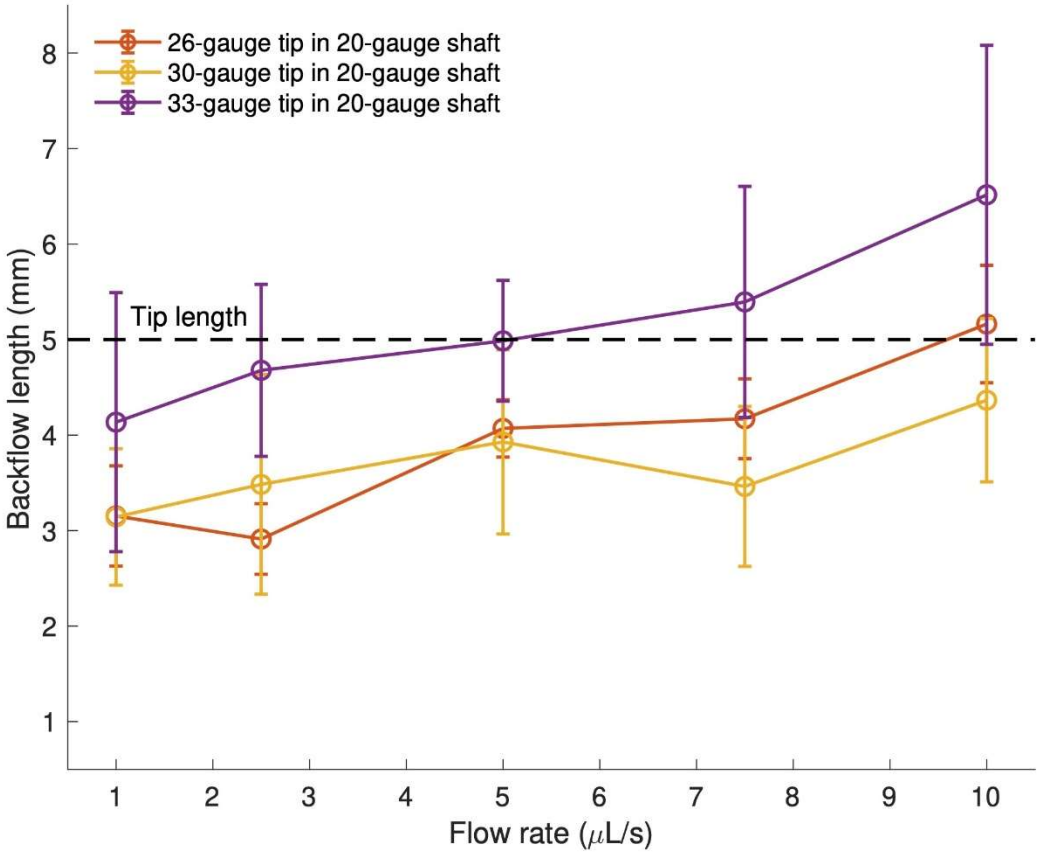
For all catheters, it was found that lower infusion rates yielded backflow shorter than the step location, but higher flow rates for some tip/shaft combinations yielded backflow beyond the step. For stepped catheters with 30-gauge tips, it was found that the smallest shaft of 26 gauge experienced the most backflow and that the larger 20- and 18-gauge shafts did not have backflow beyond the step. For stepped catheters with 20-gauge shafts, it was found that the smallest tip of 33 gauge experienced the most backflow, with the larger 30- and 26-gauge tips not having backflow beyond the step.

Discussion

Increasing the shaft diameter for a fixed tip diameter, thereby increasing the size of the step, yielded a reduction in the backflow length. In contrast, decreasing the tip diameter for a fixed shaft diameter, which also increases the step size, yielded an increase in the

backflow length. This difference may be explained since a smaller tip diameter yields a larger infusion pressure at the tip, which may increase backflow.

Images (Optional)



Acknowledgements (Optional)

J. Smith thanks Lafayette College's Clare Boothe Luce Scholars Program for the support of E. Godin during Summer 2025.

Session Category

Imaging and Biomedical Devices: Artificial Organs, Devices

P4-278

Piezoelectric Peptide/Ionic Hybrid Platforms with Tunable Biodegradability for Self-Powered Biomedical Stimulation

Prof. JUHYUCK LEE

Daegu Gyeongbuk Institute of Science and Technology, Daegu, N/A, Korea, Republic of

Introduction

Diphenylalanine (FF) peptide nanotubes have recently emerged as a compelling class of bio-piezoelectric materials for implantable biomedical devices due to their strong shear piezoelectric responses, biocompatibility, and ability to self-assemble into aligned tubular architectures. Advances in meniscus-driven processing have enabled large-area, unidirectionally polarized FF nanotube films with high crystallinity, while eco-friendly ethanol–water solvent systems now allow scalable fabrication suitable for biomedical translation. Concurrently, the intrinsic rapid biodegradability of FF in physiological fluids has been addressed through incorporation of hydrophobic porphyrins, enabling controlled degradation kinetics without sacrificing piezoelectric performance. Furthermore, embedding FF nanotubes within biodegradable polymer matrices allows mechanically induced piezoelectric stimulation to directly influence cell alignment and proliferation, highlighting their potential as electromechanically active biomaterials.

Methods

Aligned FF nanotube films were fabricated using solvent-engineered self-assembly, optimizing crystallinity, orientation order, and nanotube density. Porphyrin molecules were co-assembled with FF to modulate hydrophobicity and degradation rate while retaining the non-centrosymmetric crystal phase required for piezoelectricity. To enhance mechanical robustness and biological compatibility, FF nanotubes were integrated into polymer matrices such as PLGA, PCL, PLA, and PHBV. Electromechanical outputs, degradation behavior, and cellular responses were assessed using piezoelectric measurements, biodegradation tests, FEM simulations, and in-vitro cell culture.

Results

The aligned FF nanotube scaffolds exhibited strong unidirectional polarization with shear piezoelectric coefficients exceeding 46–60 pm/V. Device platforms generated voltages in the range of 1.6–2.8 V and stable power outputs under biomechanical stimulation. Porphyrin incorporation increased hydrophobicity and extended degradation times from

minutes to beyond 15 minutes while maintaining voltage outputs above 2 V. FF–polymer nanocomposites demonstrated stable performance over more than 1000 mechanical cycles and produced local piezoelectric potentials sufficient to guide fibroblast alignment and enhance proliferation, even under cell-generated mechanical forces.

Discussion

These results establish a multifunctional platform combining aligned bio-piezoelectric nanotubes, degradation-controlled hybrid structures, and biodegradable polymer integration to create self-powered electromechanical interfaces. The ability to sustain piezoelectric output, modulate biodegradation, and regulate cellular behavior presents promising opportunities for next-generation implantable biomedical devices, including self-powered sensors, bioelectronic stimulators, and smart tissue engineering scaffolds.

Session Category

Imaging and Biomedical Devices: Artificial Organs, Devices

P4-279

Deformable Graphene-Based Electrodes That Transmit Electrical Nerve Impulses

Prof. Marek Pawlikowski, PhD Zbigniew Gulbinowicz, PhD Rafał Drobnicki, PhD Daniel Janczak

Warsaw University of Technology, Warszawa, mazowieckie, Poland

Introduction

One of the main challenges in modern neurosurgery is activating damaged nerve fibres. The complex structure and function of nervous tissue mean that materials used for nerve electrodes must meet specific requirements related to the electrical charge delivered. These emerging demands have led to the development and adoption of innovative electrode materials, along with a deeper understanding of how electrode materials influence neuron stimulation. Carbon and its allotropes are regarded as some of the best materials for neural interfaces. Their chemical inertness, biocompatibility, good electrical performance, and electrochemical stability make them superior to other materials for implantable neural electrodes.

Methods

The electrodes were produced using a screen printing method on thin, biocompatible, flexible foil with a thickness of 0.125 mm. The impulse-conducting pathway was formed from a carbon-based paste. This paste mainly comprised fine-grained graphite micropowder, conductive carbon black, and graphene.

To evaluate the basic electrical properties of the electrodes, resistance and their response to the transmission of a rectangular signal were measured. During the experiments, we applied electrical impulses to the electrodes. We tested the printed electrodes at various flexion angles to assess how different angular deformations influenced their electrical conductance. Additionally, we examined their durability and electrical stability by subjecting them to cyclic deformation.

Results

The results show that graphite- and carbon-black-based electrodes offer better electrical signal transmission, while graphene electrodes perform worse. This suggests new directions for future research on printable neural interfaces using carbon. It was also found that the electrode's electrical performance was not influenced by the flexion angle or cyclic deformation.

Discussion

In our studies, we concentrated on electrical impulse conductors printed with three types of pastes: fine-grained graphite micropowder, conductive carbon black, and graphene. The aim was to establish a correlation between the shape (length and width) of the printed electrodes and their ability to conduct electrical impulses, as measured at the different angular deformations. Since carbon and carbon-derived materials demonstrate excellent biocompatibility and low toxicity, we examined two carbon allotropes, graphite and graphene, as well as black carbon.

Session Category

Imaging and Biomedical Devices: Artificial Organs, Devices

P4-280

Utilizing Computational Models in Evaluating Exposure Risk of Implanted Medical Devices

Dr. Martin L. Tanaka PhD, PE[1], Dr. David M. Saylor PhD[2], Dr. David D. Simon PhD[2]

[1]Western Carolina University, Cullowhee, North Carolina, United States. [2]US Food and Drug Administration, Silver Spring, Maryland, United States

Introduction

Computational models are valuable tools often used to develop engineered products. They can be used to predict performance of a device before building the first prototype. They are particularly well suited for evaluating long term performance of a medical device because they can predict behavior spanning weeks or years in just minutes. This work examines several methods that may be used to quantify the long-term exposure and discusses the advantages of each approach.

Methods

Three methods to quantify leaching of potentially hazardous materials from implanted medical devices were examined. The **conservative model** estimates material leached from a polymeric implant by modeling diffusion of a leachable substance through the polymer matrix. The **polymer/tissue model** expands on the conservative model by also considering migration of leachable materials across the polymer tissue interface and diffusion through the tissue [1]. This enables solubility differences in the polymer and tissue to be captured. It also accounts for the influence of diffusion on leachable accumulation. The **phase field model** adds to the prior model capabilities by also considering the foreign body response, a cascade of events that can occur when medical devices are implanted.

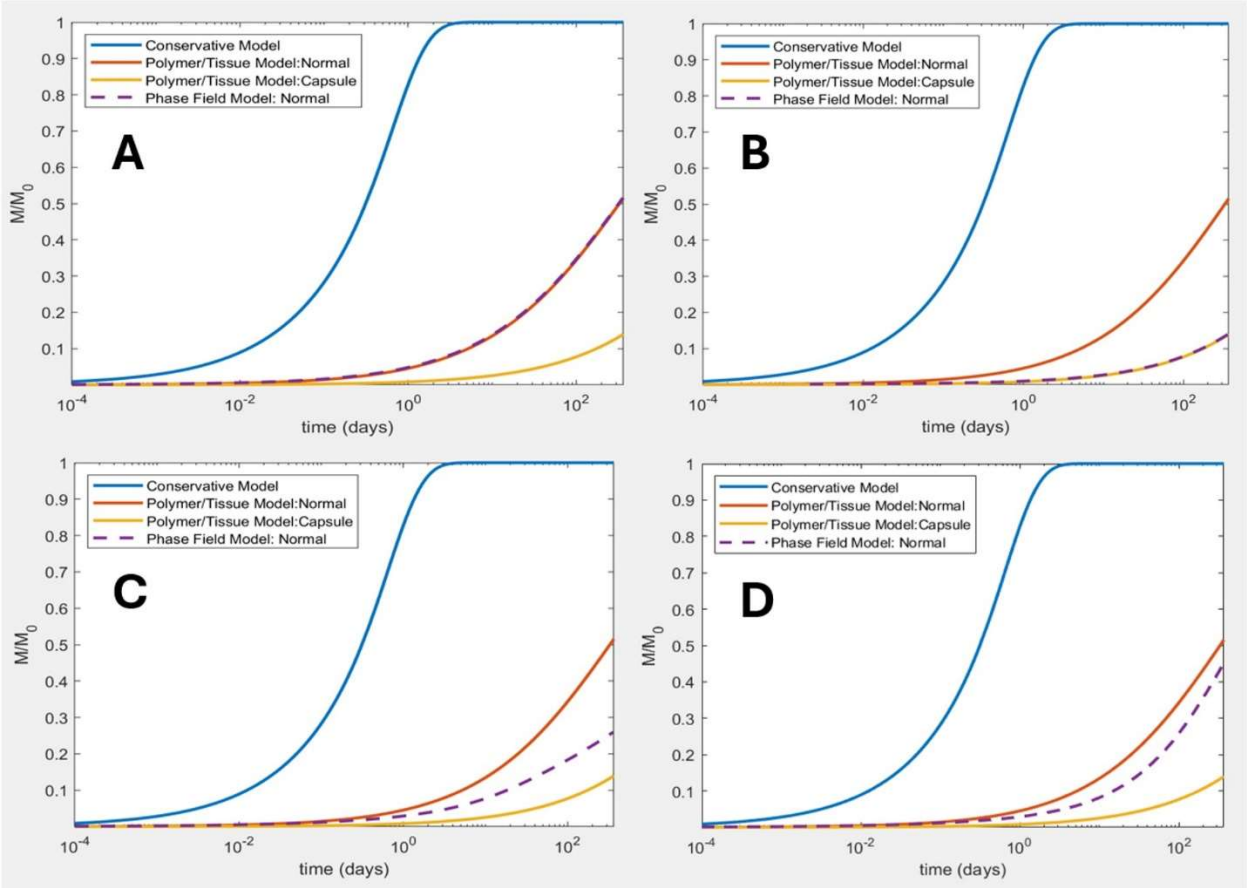
Results

Mass release as a function of time is shown for the three models (Figure 1). The conservative model showed ~100% mass release by day four. The polymer/tissue model showed a mass release of approximately 52% in one year when set to values of normal tissue and about 14% when set to values of a capsule. The phase field model yielded results between the polymer/tissue models showing the effect of tissue transformations during wound healing.

Discussion

Performance of the three models were compared. Some are simpler to implement, while others consider more system parameters or model parameters that change over time. Each has its advantages and disadvantages. The best model to use will depend on the specific application.

Images (Optional)



References (Optional)

[1] Tanaka, M. L., Saylor, D. M., and Elder, R. M., 2024, "Polymer-interface-tissue model to estimate leachable release from medical devices," Mathematical Medicine and Biology: A Journal of the IMA, 41(4), pp. 382-403.

Acknowledgements (Optional)

ACKNOWLEDGEMENTS: This research was supported by awards from the National Science Foundation – 2309538 and 2149517. Both awards were the NSF/FDA Scholar in Residence at the FDA which supported summer research by MLT at FDA headquarters on the White Oak Campus during the summers of 2022, 2024, and 2025 where he worked closely with DMS and DDS.

DISCLAIMER: The findings and conclusions in this manuscript have not been formally disseminated by the Food and Drug Administration and should not be construed to represent any agency determination or policy. The mention of commercial products, their sources, or their use in connection with material reported herein is not to be construed as either an actual or implied endorsement of such products by the Department of Health and Human Services.

Session Category

Imaging and Biomedical Devices: Artificial Organs, Devices

P4-281

Development of High-Porosity Radiopaque Shape Memory Polymer Scaffolds for Personalized Cerebral Aneurysm Therapy

Mr. Tanner Cabaniss[1], Dr. Yingtao Liu PhD[1], Dr. Chung-Hao Lee PhD[2], Dr. Bradley Bohnstedt MD[3]

[1]University of Oklahoma, Norman, Oklahoma, United States. [2]University of California, Riverside, Riverside, California, United States. [3]Indiana University School of Medicine, Indianapolis, Indiana, United States

Introduction

Cerebral aneurysms (CAs) are balloon-like protrusions of blood vessel walls in the brain, affecting approximately 4% of the population [1]. While typically harmless when unruptured, CA rupture can cause subarachnoid hemorrhage, resulting in mortality rates exceeding 50%. Current endovascular solutions, including metal coiling and flow-diverting stents, are effective in many cases but demonstrate limited efficacy for wide-necked or irregular aneurysms. To address these shortcomings, we are developing personalized shape memory polymer (SMP) scaffold-based implants with spatial and compositional tailorability to optimally treat each patient's unique aneurysm. In this study, we present an improved fabrication method for radiopaque SMP scaffolds featuring high porosity and exceptional surface area-to-volume ratios.

Methods

Polyvinyl alcohol (PVA) sacrificial templates were 3D printed and coated with a polyurethane-based SMP prepolymer mixed with powdered barium sulfate to impart radiopacity. Coated templates were shaken for uniform coverage, then centrifuged to remove excess SMP solution at varying speeds (0–100% of maximum, in 20% increments), generating g-forces up to 2500 G. Samples were subsequently cured under vacuum in a nitrogen atmosphere, and the PVA templates dissolved in a heated, circulating water bath. Cylindrical scaffolds (8 mm × 10 mm, n = 6) were evaluated both with and without barium sulfate to determine the effects of centrifugal extraction on porosity and structure.

Results

Neat (no barium sulfate) scaffold porosity increased from 83.1% to 91.5% across the centrifuge speed range, while barium sulfate–loaded scaffolds reached 87.1–94.3%. Reduced structural collapse in the barium sulfate scaffolds accounted for both higher porosity and lower surface area-to-volume ratios compared to neat scaffolds. Scaffolds

fabricated with lower infill density achieved porosities exceeding 97.5%, indicating further tunability of structural design.

Discussion

The integration of a centrifugal extraction stage substantially increased achievable scaffold porosities, enhancing compressibility, a key determinant of treatable aneurysm size. This improvement expands the potential clinical applicability of SMP scaffolds and represents a critical step toward customizable, patient-specific endovascular implants for safer and more effective cerebral aneurysm treatment.

Images (Optional)

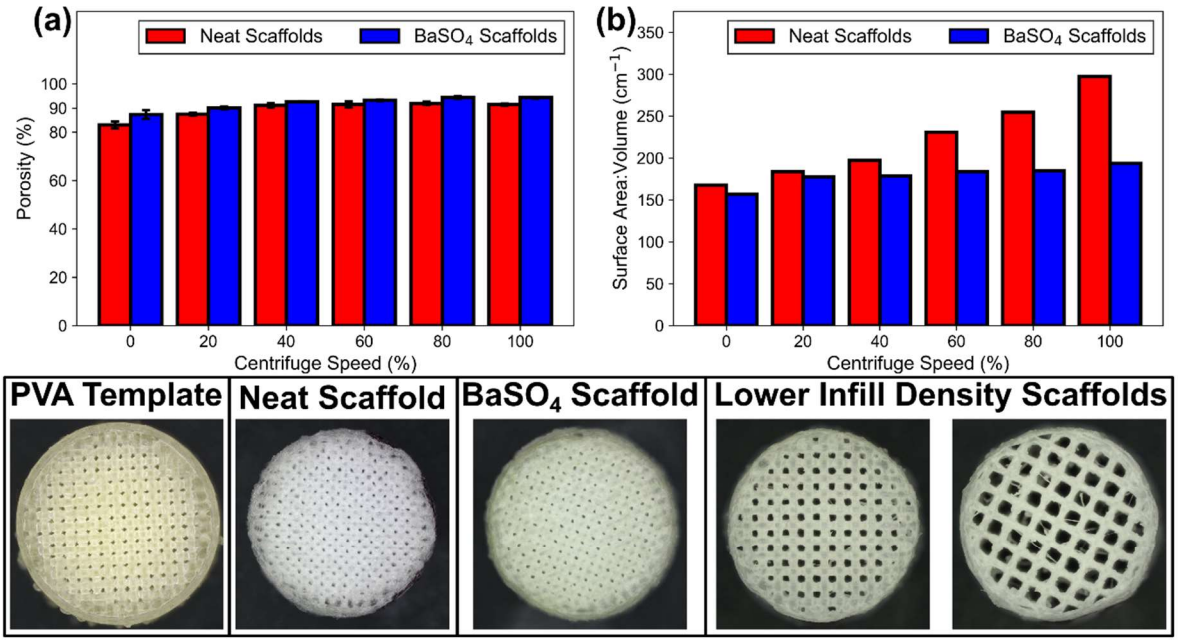


Figure 1: Bar graph summaries of (a) porosity (%) vs. centrifuge speed (%) and (b) surface area : volume ratio (cm^{-1}) vs. centrifuge speed (%). Micrographs of cylindrical (8 mm diameter, 10 mm height) PVA template and various SMP scaffolds showing 90% (left three samples), 70%, and 50% infill densities.

References (Optional)

[1] Keedy, A. *et al., Mcgill J Med,* 9:141-146, 2006.

Acknowledgements (Optional)

NIH R01 HL159475

Session Category

P4-282

Toward a 3d Superelastic Corotational Beam Model for Nitinol Stents Simulations

PhD Student Thach-Hoang NGUYEN[1], Professor Mikaël Barboteu[1], Professor Serge Dumont[1], Associate Professor Francesco Bonaldi[1], Professor Franck Jourdan[2]

[1]Laboratoire de Modélisation Pluridisciplinaire et Simulations, Université de Perpignan Via-Domitia, Perpignan, Occitanie, France. [2]Laboratoire de Mécanique et Génie Civil, Université de Montpellier, Montpellier, Occitanie, France

Introduction

Flow-diverter (FD) stents have revolutionized the treatment of intracranial aneurysms, yet simulating such braided structures remains computationally demanding due to large number of wire contacts and material nonlinearity. To address the latter, we developed a 3D beam model specifically for Nitinol, one of the most widely used superelastic alloys in stent fabrication. Within the EndoBeams.jl [1] corotational framework, we developed a superelastic beam model based on Auricchio's model [2] to efficiently simulate stent wires.

Methods

The model in [2] relies on an additive strain decomposition and employs a 3D elastic constitutive law. However, for 3D beam formulation, the transverse strain and stress components (indices 22, 33, and 23) are neglected. To ensure physical consistency, the linear elastic response is defined as $\sigma_{11} = E\,\varepsilon_{11}^{e}$ for the axial component while the shear terms are governed by $\sigma_{12} = 2G\,\varepsilon_{12}^{e}$ and $\sigma_{13} = 2G\,\varepsilon_{13}^{e}$.

The superelastic model is governed by a linear evolution of the martensite fraction, updated via a return mapping algorithm. Stress and consistent tangents are evaluated at Gauss points to compute the local internal force and stiffness, which are subsequently transformed to the global system.

Results

A first simulation was conducted on a single circular beam element (radius of 0.035 mm and length of 0.1 mm) under pure tension using 27 Gauss points. Adopting material properties from [2] (E = 60000 MPa, v = 0.3, σ^{S}_{AS}=520 MPa, σ^{F}_{AS}=600 MPa , σ^{S}_{SA}=300 MPa, σ^{F}_{SA}=200 MPa), the computed Von Mises stress-strain response (Fig. 1) demonstrates initial consistency with the result in [2].

Discussion

In this study, we successfully implemented superelasticity in the EndoBeams.jl corotational framework and achieved coherent initial results. Future work focuses on validating the model with various geometries and full stents, benchmarked against commercial 3D solid solvers.

Images (Optional)

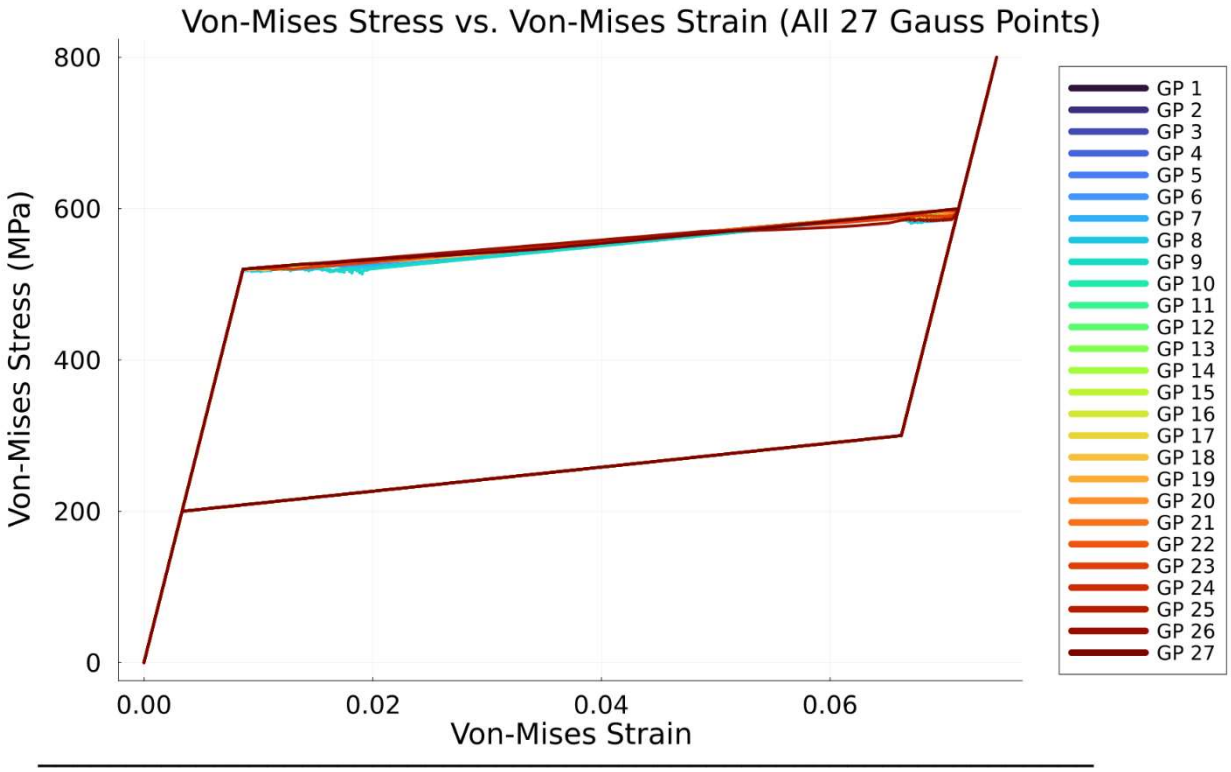


Fig.1. Von-Mises Stress vs. Von-Mises Strain during tensile simulation

References (Optional)

[1] Bisighini, B., Aguirre, M., Pierrat, B., Perrin, D., & Avril, S. (2022). EndoBeams. jl: A Julia finite element package for beam-to-surface contact problems in cardiovascular mechanics. *Advances in Engineering Software*, *171*, 103173.

[2] Auricchio, F., Taylor, R. L., & Lubliner, J. (1997). Shape-memory alloys: macromodelling and numerical simulations of the superelastic behavior. *Computer methods in applied mechanics and engineering*, *146*(3-4), 281-312.

Session Category

Imaging and Biomedical Devices: Artificial Organs, Devices

P4-283

Human-in-the-Loop Optimization of Hip Exoskeleton Assistance During Incline Walking

Postdoctoral Fellow Jae-Ryeong Choi, Visiting Student Yinkai Dong, Visiting Student Catherine Rohner, Doctoral Student Anh Nguyen, Assistant Professor Patrick Slade

Harvard University, Boston, MA, United States

Introduction

Exoskeletons have the potential to substantially reduce the energetic cost of human locomotion, particularly during physically demanding tasks such as uphill walking. Although many portable exoskeletons have been developed and shown promising results, achieving substantial metabolic benefits during incline walking remains challenging. A key challenge is that providing the high assistive torques required for intensive tasks often leads to discomfort, instability, or excessive device mass.

Methods

Here, we introduce a fully portable hip exoskeleton that addresses this challenge by combining rigid structural components with a soft brace, effectively enhancing torque transmission. Using this platform, we conducted a multi-day human-in-the-loop optimization study with eight participants to identify personalized assistance profiles for incline walking.

Results

This hybrid structural component enables one of the most torque-dense portable hip exoskeletons reported to date, capable of delivering up to 45 N·m of peak hip assistance. The optimized assistance reduced the metabolic cost of 10° incline walking by an average of 21%, corresponding to a 2.1 W/kg reduction in net metabolic cost compared with walking without an exoskeleton. This absolute reduction in metabolic cost exceeds previously reported benefits across all portable exoskeletons.

Discussion

These results demonstrate that personalization combined with high-torque assistance can provide substantial metabolic benefits during uphill walking. More broadly, our findings establish a framework including exoskeleton design, optimization, and validation, which emphasizes the importance of personalizing assistance using the appropriate boundary conditions to identify optimality.

Session Category

Imaging and Biomedical Devices: Assistive Technologies

P4-284

The Effect of Distributed Practice on Learning to Walk with Robotic Ankle Exoskeletons

Miss Caitlyn Baliki, Dr. Anthony Chen, Dr. Gerome A. Manson, Dr. Jessica C. Selinger

Queen's University, Kingston, Ontario, Canada

Introduction

Robotic ankle exoskeletons can reduce metabolic expenditure by decreasing the biological work required to walk. However, to achieve these savings, users must first adapt to the device, for example by reducing muscle activity [1]. This can require long and taxing periods of walking [2]. User adaptation often improves with multi-day sessions [1, 2]. This may simply be due to additional practice time, or distributed practice (where sessions are separated by extended rest periods) may offer benefits compared to massed practice (where a single, lengthy session with minimal rest occurs) [3]. Here, our aim was to test whether distributed practice better facilitates motor adaptation during exoskeleton walking compared to massed practice, when practice time is kept constant.

Methods

We instrumented participants with indirect calorimetry to measure metabolic expenditure and electromyography (EMG) sensors on the tibialis anterior, medial gastrocnemius, and soleus muscles (Fig. 1A). Participants also wore bilateral robotic ankle exoskeletons that applied assistive plantarflexion torques during the stance phase of the gait cycle. We randomized participants (n=20) into two practice groups: Massed and Distributed. The Massed group completed two 15-minute powered walking (Exo-On) trials in one day (separated by 15-minutes), while the Distributed group did so over two consecutive days (separated by 24-hours). We analyzed net metabolic expenditure and EMG peak activity using mixed ANOVAs to test for differences in adaptation magnitude for practice time and/or group.

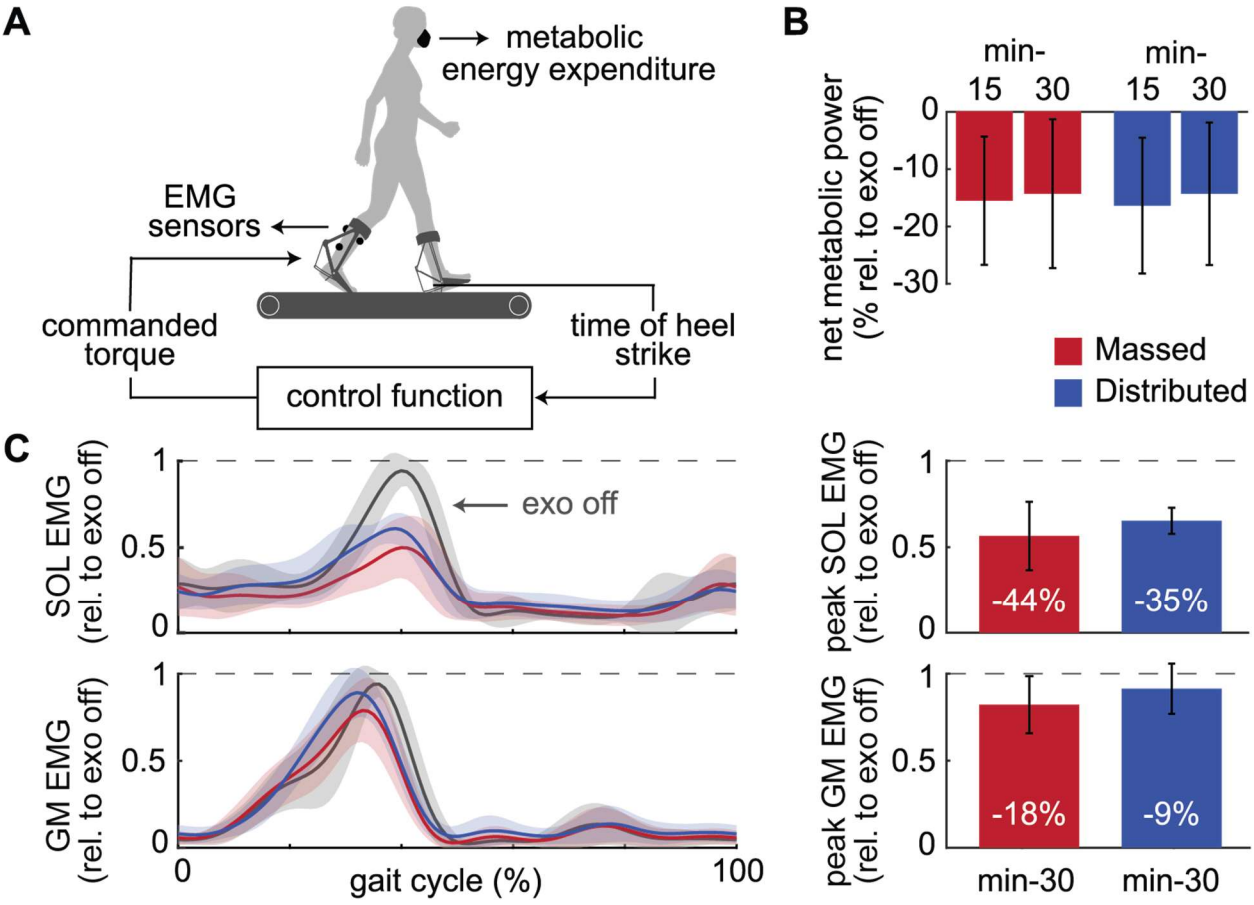
Results

We found metabolic savings relative to the exoskeleton powered off, but no significant differences or interactions in time points (15-minute vs. 30-minute) or groups (Massed vs. Distributed) for our outcome metrics: metabolic expenditure, peak tibialis anterior, peak medial gastrocnemius, and peak soleus activity (all $p > 0.05$; Fig 1B, C).

Discussion

We were unable to determine whether distributed practice better facilitates user adaptation compared to massed practice because we observed no improvements from 15- to 30-minutes. This suggests that 15-minutes of practice is sufficient to achieve significant adaptations, but more than 30-minutes may be required to overcome an early adaptation plateau and detect further improvements.

Images (Optional)



References (Optional)

[1] Sawicki & Ferris., J Experimental Biology, 2008

[2] Poggensee & Collins., Science Robotics, 2021

[3] Baddeley & Longman., Ergonomics, 1978

Session Category

Imaging and Biomedical Devices: Assistive Technologies

P4-285

Development of a MyoBionic Actuator for Musculoskeletal Rehabilitation

Mr. Chenghao Xing[1], Dr. Sean Thomas[2], Dr. Gregory Sawicki[3], Dr. Jonas Rubenson[1]

[1]The Pennsylvania State University, State College, PA, United States. [2]University of California, Los Angeles, Los Angeles, CA, United States. [3]Georgia Institute of Technology, Atlanta, GA, United States

Introduction

Muscle-tendon weakness is ubiquitous in aging and is common in many neuromusculoskeletal conditions. The ensuing loss of mobility is a leading cause of poor quality of life and has been linked to morbidity and even mortality (e.g., in aging [1]). Most assistive devices remain simple aids (e.g., walkers, braces, orthoses). While advanced wearable robotics are making inroads into musculoskeletal rehabilitation, both simple aids and advanced wearable devices suffer from poor user adoption, leading to the problem of non-adherence to treatment. An alternative but much less explored solution is implantable assistive devices. Here, we benchtop test a prototype assistive MyoBionic actuator aimed to be implantable in a bipedal animal model (fowl) of muscle impairment.

Methods

The Myobionic actuator was designed to provide isometric force and allow for spring elastic energy storage and return at the ankle during gait [2]. A robotic dual-mode force–length transducer was used in a linear rig to assess actuator mechanical characteristics including maximal resistance to motor back-drive (isometric force), stroke rate, and maximal contraction force. Work to simulate gait in a cadaveric preparation is ongoing.

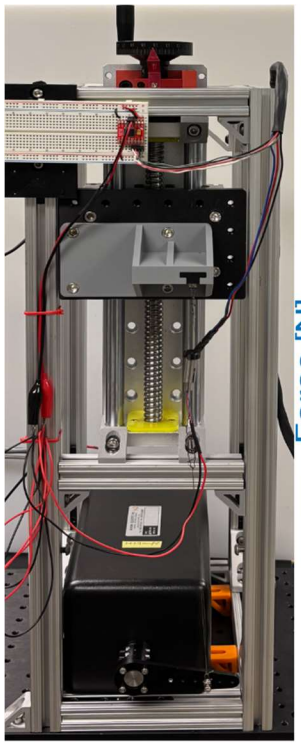
Results

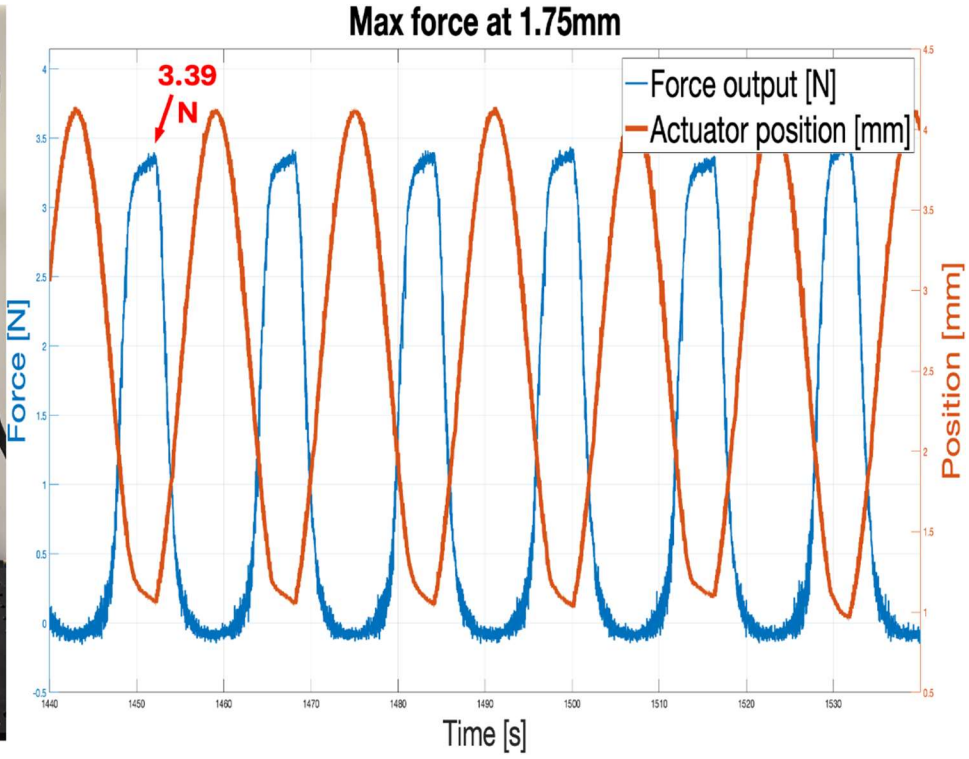
Actuator back-drive strength was estimated at over 25N, similar to the maximal in vivo ankle extensor muscle force expected during gait in fowl. Contraction strength was assessed to be 3 N, sufficient to overcome passive biological tissue resistance during length modulation. Actuator speed was assessed at 4.8 mm/sec. With these characteristics, the actuator was shown to be capable of modulating force assistance profiles for walking gait.

Discussion

Our preliminary data show that the MyoBionic actuator is suitable for meeting the functional requirements for assisting ankle torque during walking in our animal model, and for the level of assistive force to be adjustable over only a few gait cycles.

Images (Optional)





References (Optional)

[1] Fritz S et al. , J Geriatr Phys Ther. 2009

[2] S. Thomas et al., IEEE/RSJ International Conference on Intelligent Robots and Systems (IROS), 2023

Session Category

Imaging and Biomedical Devices: Assistive Technologies

P4-286

Investigating Methods for Safely Securing Mobility Devices in Aircraft Cargo Areas During Air Travel: A Motion Simulation Study

Mr. Davood Dadkhah[1,2], Mr. Amir Babazadehjoudi[1,2], Mr. Zeyad Ghulam[2], Dr. Tilak Dutta[1,2]

[1]University of Toronto, Toronto, Ontario, Canada. [2]University Health Network, Toronto, Ontario, Canada

Introduction

Damage to mobility devices (e.g. wheelchairs, mobility scooters) during air travel remains a surprisingly common problem that prevents many from recognizing the many benefits that air travel has to offer. There are currently no standards on how these devices should be secured when placed in aircraft cargo areas, and some of this damage has been caused by inappropriate securement. The objective of this project was to investigate current methods for securing these devices in aircraft cargo areas and develop recommendations for methods that prevent the risk of damage.

Methods

This simulation study took place in a 6 m by 6 m self-contained laboratory mounted on top of a six-degree-of-freedom motion platform. The platform was programmed to simulate 6 motions, including taxing, takeoff, turbulence, and landing, using four different aircraft. Mobility devices tested included power wheelchairs, manual wheelchairs, power scooters, strollers, and walkers, secured using different methods (Q'STRAINT self-tightening straps, conventional ratchet straps, as well as straps currently used by a major national airline). Overall, 150 different scenarios were simulated. Instrumentation included high-fidelity accelerometers and IMUs on the platform and device frames, along with calibrated load cells for measuring the tension at each strap anchor. Video recordings documented device behaviour throughout.

Results

Preliminary review of trials indicates visually stable device positioning and no evidence of slip, tip, or structural compromise across the range of test conditions, including high-vibration simulated flight. Initial results suggest that Q'STRAINT straps produced lower average loads on the devices, but slightly higher vibration transmission compared to other tie-down methods, though no failures were observed in any case.

Discussion

These early results demonstrate the feasibility and practical value of a biomechanics-informed protocol for experimentally assessing the mechanical safety of mobility devices in air travel. The protocol provides a robust foundation for future quantitative analysis and evidence-based improvement of tie-down standards, with ongoing work planned to expand data processing, evaluate load and vibration metrics in detail, and inform real-world training and policy.

Session Category

Imaging and Biomedical Devices: Assistive Technologies

P4-287

Quantifying Trip Risk and Recovery Demands of Ankle-Foot Orthoses Using Pendulum Testing

Ms Elaina Van Dorp, Mr Tom Cotton, Mr Mark Roser, Dr Nataliya Rokhmanova

Motive Labs, Hebron, CT, United States

Introduction

Slips and trips are leading causes of falls, particularly among older adults and individuals with neurodegenerative conditions who rely on ankle-foot orthoses (AFOs). While AFOs provide critical gait support, their interaction with footwear can alter ground clearance and trip recovery dynamics. Standardized methods to quantify shoe-AFO performance across surface conditions are needed to guide clinical prescription and improve fall prevention strategies.

Methods

We developed an anatomically correct manikin foot-ankle system with an articulating joint mounted to a pendulum apparatus calibrated to swing at 2 m/s. Testing was conducted on smooth concrete and rocky pavement surfaces. A Converse shoe was tested alone and with three AFO designs (Blue Rocker, Semi-Rigid Leaf Spring, Adjustable Drop Foot Brace) at 0°, 5°, 10°, and 15° plantarflexion (5° increments). Minimum ground clearance was set at 1.12 mm using a gauge block. For each condition (3 trials per angle), we recorded trip occurrence and measured the peak force required to pull the shoe clear of the obstacle using a calibrated scale.

Results

At 0° plantarflexion, all configurations cleared both surfaces successfully. At 5°, only Converse tripped on smooth pavement requiring 2.39 kg clearance force, which increased to 5.16 kg on rocky terrain. The Adjustable Brace also tripped on rocky surfaces (5.50 kg). At 10°, the Converse and Adjustable Brace impacted both surfaces, with clearance force significantly higher on rocky terrain for the Brace (0.25 kg vs 5.78 kg). All configurations tripped at 15°. On smooth concrete, clearance forces were: Converse (8.85 kg), Adjustable Brace (5.85 kg), Semi-Rigid Leaf Spring (7.18 kg), and Blue Rocker (4.06 kg). On rocky pavement: Converse (13.00 kg), Adjustable Brace (12.41 kg), Semi-Rigid Leaf Spring (6.16 kg), and Blue Rocker (4.67 kg). The Blue Rocker consistently required lowest clearance forces across conditions.

Discussion

Surface texture critically influences trip recovery demands, with rigid AFO designs more vulnerable on irregular terrain. The Blue Rocker's compliant design facilitated lower clearance forces, suggesting material properties significantly affect fall risk. This pendulum method provides objective benchmarking for AFO-footwear systems. Future work should examine additional footwear styles, real-world obstacle geometries, and validation with human gait data to enhance clinical relevance.

Session Category

Imaging and Biomedical Devices: Assistive Technologies

P4-288

A Powered Step Forward: Developing an Active Prosthetic Knee for Children

Mr. Elijah Birley BASc[1,2], Mr. Charles Haliburton BEng[3], Mr. Clive Mullins BASc[3], Dr. Gualtiero Guadagni PhD[3], Dr. Jan Andrysek PhD[1,2]

[1]University of Toronto, Toronto, Ontario, Canada. [2]Holland Bloorview Kids Rehabilitation Hospital, Toronto, Ontario, Canada. [3]Bionic Power, Vancouver, British Colombia, Canada

Introduction

Prosthetic knees enhance mobility, balance, and independence for individuals with above-knee amputations. Active prosthetic knees (APKs)—which use powered actuation to replicate muscle-driven movement—have demonstrated improvements in gait efficiency, symmetry, and stability in adults; however, no pediatric APK currently exists. Children with limb loss have fewer device options and unique needs due to growth, high activity levels, and size constraints. The Agilik assistive device, developed for children with cerebral palsy, features a compact, high-torque actuator. Preliminary testing suggests that this could be adapted into an APK. Considerations requiring evaluation include whether torque output and battery life are sufficient for prosthetic use.

Methods

This project will develop and evaluate the first known pediatric APK using the Agilik actuator. The five objectives are: (1) Evaluate actuator torque capacity and battery life under simulated prosthetic use, using inertial measurement units, a load cell and comparative walking trials tracking battery depletion over time and extrapolating. (2) Design and fabricate a prototype APK, through requirements definition, 3D modelling, finite element analysis, rapid prototyping, and mechanical refinement. (3) Verify safety and durability through structural testing following ISO 10328. (4) Evaluate performance using A simulated walking rig before preliminary able-bodied trials. (5) Conduct a clinical pilot study assessing gait kinematics, kinetics, spatiotemporal parameters, metabolic cost, and user satisfaction.

Results

Estimated knee torque, using able-body adult data scaled to older children, peaks at 15–21 Nm. The Agilik can be amplified up to 20 Nm; sufficient alongside the users own ability. The battery is sufficient for 1+ days use and smaller batteries, appropriate for integration, can be used. The initial 3D modelling has been completed and validated using FEA and

manufacturing has started. Assembly, structural and performance testing, and the start of pilot testing will be complete by the conference.

Discussion

This work aims to produce a functional prototype addressing a critical gap in pediatric rehabilitation technology and establish the foundation for future APK development tailored to growing users. We anticipate demonstrating that an existing assistive device can be adapted for pediatric prosthetic application, while also creating a highly controllable platform to better study pediatric gait.

Session Category

Imaging and Biomedical Devices: Assistive Technologies

P4-289

Foot Progression Angle Gait Retraining: Within-Session Response to a Real-Time Feedback Algorithm in Healthy Participants

Dr. Erin Macri PT PhD[1], Dr. Mariska Wesseling[1], Dr. Martin Schepers[2], Dr. Selma Papegaaij[2], Dr. Ignazio Aleo[2], Dr.ir. Eline van der Kruk[3], Ms. Antoinette Torsij[3], Prof.dr.ir. Jaap Harlaar[1,3], Dr. Jos Runhaar[1]

[1]Erasmus MC University Medical Center Rotterdam, Rotterdam, Zuid Holland, Netherlands. [2]Moveshelf Labs BV, Utrecht, Utrecht, Netherlands. [3]Technische Universiteit Delft, Delft, Zuid Holland, Netherlands

Introduction

Altering foot progression angle (FPA) can reduce pain, reduce knee load, and slow structural progression in knee OA. Though studies have investigated FPA gait-retraining programs, it is not clear how individuals adapt to real-time feedback within a single-session. Therefore, we explored how individuals adapted their FPA in response to a single session of real-time feedback.

Methods

We developed a device with a foot-mounted sensor, and a mobile app with a previously-validated algorithm to estimate FPA and real-time audio feedback based on five-stride mean FPA. The feedback signal indicated “Good”, “Move Outward” (toe-out) or “Move Inward” (toe-in) to guide individuals towards the target FPA. We enrolled 14 healthy adults aged ≥45 years. Individuals wore the sensor on the right foot and walked on a treadmill in 3-minutes bouts, beginning with self-selected speed and natural FPA. Subsequently, individuals maintained walking speed at four target FPAs: toe-out or toe-in at 5º or 10º relative to natural FPA. To evaluate the appropriateness of a 4º feedback range (i.e., ±2º) and 5-stride feedback set-up, we calculated: FPA variance during the first and last 50 strides of each condition; overall proportion of 5-stride mean FPAs and total strides within the 4º range; and how long it took to achieve 80% adherence.

Results

Participants (57% women, mean age 59 [9.7] years, BMI 24.0[2.2] m/kg^2) naturally walked at mean 1.0 (0.2) m/s with 12.1 (6.6)º FPA, and 76% of natural strides fell within a 4º range (Table). On average, participants achieved mean FPAs close to target conditions. Variance increased substantially when learning a new FPA, but reduced during each 3-minute bout.

Most participants achieved 80% adherence within 15 feedback signals (75 strides) for each condition.

Discussion

A 4º feedback range was appropriate for this sample. Participants achieved target FPA adherence with 5-stride mean FPA feedback frequency, though this overestimated stride-by-stride performance, possibly due to regression to mean or measurement error. Adjustable feedback algorithms (range, frequency) may be useful when prescribing initial FPA targets. Some individuals may require longer walking bouts to learn a new target FPA. These findings should be confirmed in a larger, clinical population.

Images (Optional)

Table: Foot progression angles - performance during natural, toe-out and toe-in treadmill walking, n=14

	Target FPA: Toe Out 10±2°	**Target FPA: Toe Out 5±2°**	**Natural gait (no feedback)**	**Target FPA: Toe In 5±2°**	**Target FPA: Toe In 10±2°**
Grand Mean Relative FPA, *mean (SD)°*	9.2 (7.0)	4.5 (7.3)	0 (6.6)	-4.6 (6.9)	-9 (7.1)
Variance 1st 50 steps, *mean (SD)°²*	11.3 (8.9)	9.9 (6.7)	4.0 (4.3)	13.2 (13.7)	9.3 (4.4)
Variance last 50 steps, *mean (SD)°²*	6.6 (3.5)	4.4 (2.6)	2.8 (1.6)	5.4 (3.6)	6.9 (3.6)
Proportion feedback signals within window, *mean (SD) [min, max]*	0.72 (0.11) *[0.50, 0.87]*	0.81 (0.10) *[0.56, 0.93]*	n/a	0.72 (0.18) *[0.24, 0.93]*	0.62 (0.14) *[0.35, 0.8])*
Proportion steps within window, *mean (SD) [min, max]*	0.53 (0.10) *[0.35, 0.70]*	0.62 (0.08) *[0.43, 0.74]*	0.76 (0.12) *[0.50, 0.88]*	0.57 (0.14) *[0.28, 0.75]*	0.50 (0.09) *[0.34, 0.67]*
Number feedback signals (5-stride average) to first achieve 80% adherence [<=15 | >15 | never], *(n)*	13 | 1 | .	14 | . | .	n/a	10 | 4 | .	10 | 3 | 1
Number of strides to first achieve 80% adherence [<=75 | >75 | never], *(n)*	1 | 4 | 9	5 | 2 | 7	n/a	4 | 1 | 9	1 | 3 | 10

Acknowledgements (Optional)

This project was supported by a Health Holland Public Private Partnership grant (#EMCLSH23038)

Session Category

Imaging and Biomedical Devices: Assistive Technologies

P4-290

Physiological vs. Perceptual Exercise Intensity Targeting in Spinal Cord Injury Users: A Pilot Comparison Study

Ms Hyunji Kim[1], Ms Yoojin Choi[1], Ms Gaju Shin[1], Ms Chae Lynne Kim[1], Prof Jooeun Ahn[1,2]

[1]Seoul National University, Seoul, Seoul, Korea, Republic of. [2]Institute of Sport Science, Seoul, Seoul, Korea, Republic of

Ms Hyunji Kim

Introduction

Regular moderate-to-vigorous exercise performed for at least 20 minutes is recommended to reduce the risk of cardiovascular disease, a major secondary complication in individuals with spinal cord injury (SCI). Monitoring exercise intensity in SCI is challenging because common physiological indicators show reduced reliability due to autonomic and sensory impairments [1]. Talk-test and speed-zone approaches require substantial experience or expertise. Consequently, rating of perceived exertion (RPE) is often used for self-directed exercise. This study compared an only RPE-guided session with an individualized power-target session derived from metabolic thresholds to evaluate feasibility and differences in achieved intensity across injury levels and activity profiles.

Methods

Four SCI manual wheelchair users from a previous fitness assessment cohort (n=23) participated: tetraplegia-active, tetraplegia-inactive, paraplegia-active, and paraplegia-inactive. Participants completed two 20-minute propulsion sessions on a custom torque-sensor ergometer: (1) self-regulated using RPE 12-16 (Borg 6-20), and (2) guided to maintain individualized target power between ventilatory thresholds determined from prior assessment. Normalized peak stroke power (peak power relative to VT2 power) was computed for six 3-minute stages following a 2-minute warm-up and used to evaluate perceptual- versus physiological-based intensity targeting.

Results

Monitoring-based exercise produced more stable and target-aligned intensity profiles. Normalized peak stroke power increased across stages with relatively small between-participant variation and group means approaching the VT2 target. By contrast, RPE-only

exercise consistently underestimated the intended workload: group means remained at ~0.7-0.8 times VT2 power with greater variability, and several participants showed sustained under-target performance throughout the session. This trend was most evident among individuals with tetraplegia or lower physical activity. These patterns indicate that perceived exertion alone did not reliably reflect the physiological intensity required to reach individualized metabolic thresholds.

Discussion

Findings highlight a systematic mismatch between perceptual and physiological intensity regulation. Monitoring-based feedback improved alignment with VT-derived targets and reduced variability, suggesting enhanced feasibility for achieving prescribed intensities. Although based on a small heterogeneous cohort, the consistent underestimation clarifies the need for integrating objective workload cues into exercise prescription for SCI populations.

Images (Optional)

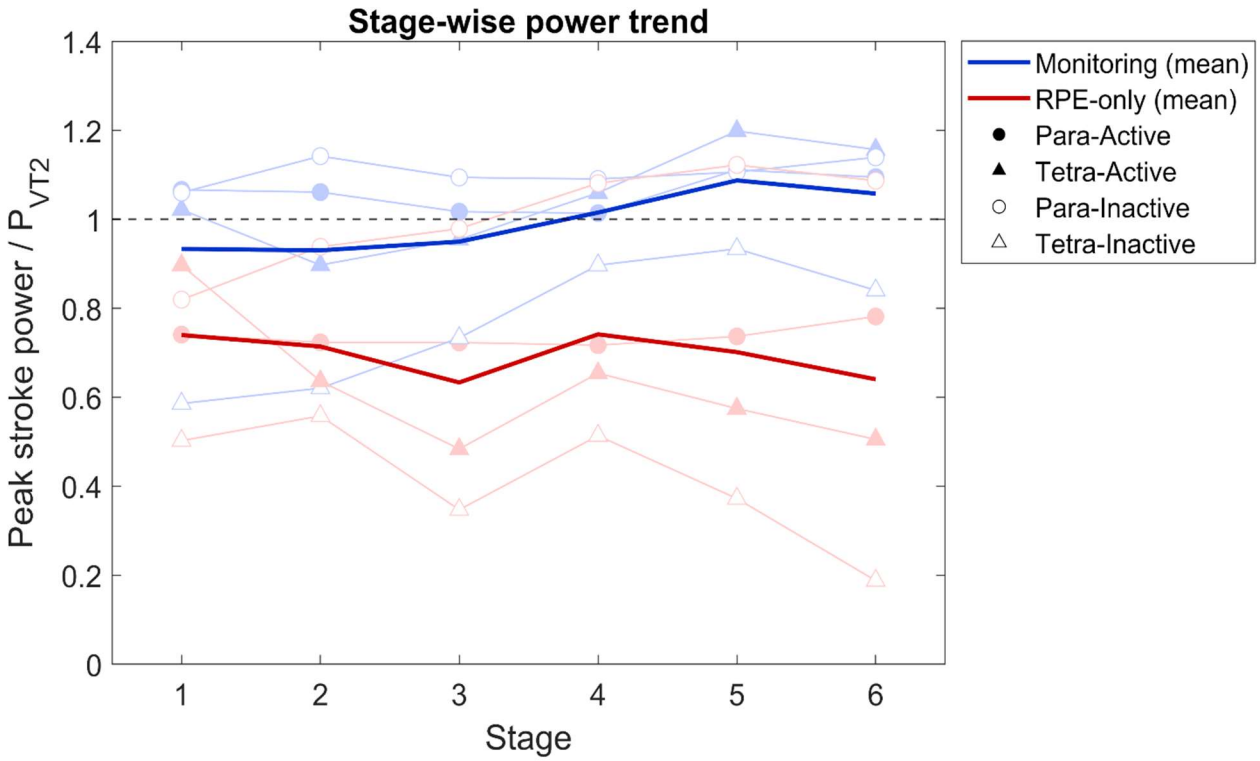


Figure 1. Stage-wise peak stroke power (normalized by target power ; VT2) across monitoring-based and RPE-only exercise conditions

References (Optional)

[1] Goosey-Tolfrey et al, BJSM, 2023.

Acknowledgements (Optional)

This work was supported by the Ministry of Education (NRF-2024S1A5B5A17035174) and the Ministry of Culture, Sports and Tourism (RS-2024-00396700).

Session Category

Imaging and Biomedical Devices: Assistive Technologies

P4-291

Towards Intelligent Assistive Aids: An Imaging-Based Rollator Walker for Posture Analysis

Ms Ivanna Kramer[1], Dr Sabine Bauer Rhineland-Palatinate[2], Prof. Dr. Dietrich Paulus[2]

[1]University of Koblenz, Koblenz, RLP, Germany. [2]University of Koblenz, Koblenz, Rhineland-Palatinate, Germany

Introduction

Poor upper-body posture during rollator use can increase discomfort and fall risk, highlighting the need for continuous and objective monitoring. This work introduces an imaging-based extension to our previously developed sensor-based rollator walker, enhancing its capability for posture classification [1].

Methods

A rollator walker was equipped with two Intel RealSense D435i RGB-D cameras, mounted using custom 3D-printed brackets to capture synchronized RGB and depth data during usage. Eight participants walked a 10-meter path twice: once with an upright posture and once with intentionally poor posture induced by lowering rollator handles. Hip joints were detected using YOLO Pose on each RGB frame to define a region of interest (RoI) in the corresponding depth map (Fig. 1). Within each RoI, multiple feature categories were extracted: (1) structural depth features using Sobel gradients to capture depth discontinuities, (2) contour-based descriptors representing shape complexity, and (3) statistical depth measures (mean depth and standard deviation). These features were used to train Support Vector Machines, Logistic Regression, Random Forest (RF), and an ensemble of XGBoost and RF (XGRF). Performance was evaluated using accuracy, precision, recall, F1-score.

Results

A total of 3,380 valid RoIs (1,787 poor and 1,593 good posture) were extracted. Using only geometric depth features resulted in moderate classification performance (accuracy 0.64–0.71), with RF and XGRF already outperforming linear models. Including statistical depth metrics enhanced separability between posture classes, increasing RF and XGRF performance to an accuracy of 0.85, precision of 0.88–0.89, recall of 0.83, and F1-score of 0.86. The SVM model showed the highest recall (0.86), indicating strong sensitivity to poor

posture, although precision was lower due to increased false alarms. Overall, ensemble approaches achieved the most stable and reliable performance across all metrics.

Discussion

Although the number of participants in this study is limited, the findings demonstrate that analyzing RGB-D data integrated into a smart rollator can reliably distinguish posture quality during walking. The accompanying RGB-D dataset further supports ongoing research in intelligent posture-aware rollator systems, showing the potential of the presented methodology.

Images (Optional)

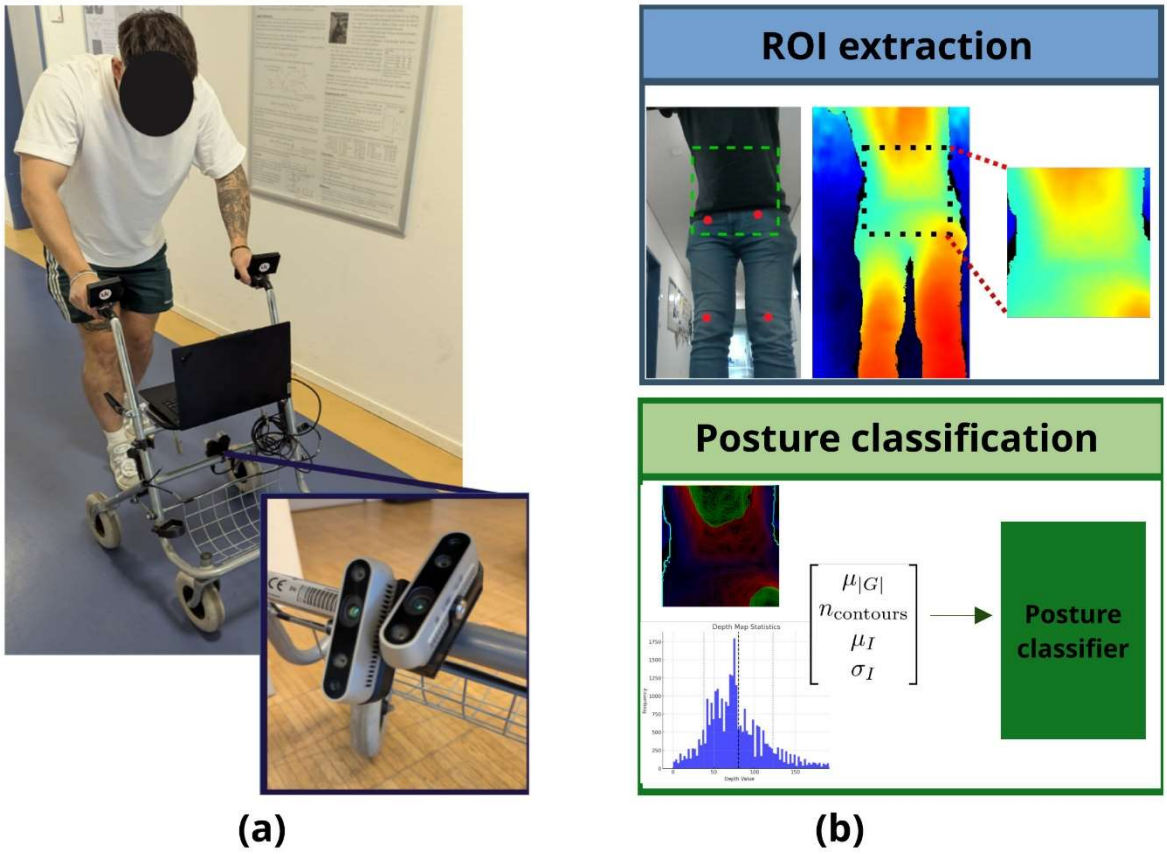


Fig.1 Recording of the training dataset using two mounted Intel RealSense cameras to capture hip and knee region (a), and the presented pipeline for posture classification (b).

References (Optional)

[1] ***I. Kramer et al., International Conference on Advanced Machine Learning and Data Science, 2025***

Session Category

Imaging and Biomedical Devices: Assistive Technologies

P4-292

Novel Sensor Fusion of Ultrasound and Pressure Sensing Insoles Enables Lower Limb Future Kinematic Predictions Across Ambulation Modes

Ms. Juliana Iverson, Ms. Marissa Pirritano, Mr. Finn Eagen, Dr. Nicholas Fey

The University of Texas at Austin, Austin, TX, United States

Introduction

Real-time prediction of lower limb joint kinematics can improve wearable robotics and rehabilitation. Ultrasound imaging provides spatiotemporal information on muscle tissue dynamics, indirectly measuring neuromotor processes that drive movement. Pressure-sensing insoles capture spatiotemporal patterns of foot-ground contact and are increasingly used in biomechanical research. There is minimal overlap between the spatial information each sensing modality provides making them suitable for convolutional neural networks (CNNs). This study integrates unilateral ultrasound images with bilateral insole pressure maps to predict lower-limb joint kinematics and evaluates subject-specific future prediction performance. Unlike most prior work focusing on mode-dependent gait, we also include noncyclic activities, hypothesizing that these complementary modalities enable accurate kinematic forecasts across diverse movements.

Methods

Six able-bodied adults completed trials while wearing pressure-sensing insoles and an ultrasound probe positioned across the rectus femoris of the nondominant leg. Joint kinematics were computed using markerless motion capture data. Trials included cyclic (ambulation circuit) and noncyclic tasks (non-phase-dependent activities such as pick-and-place). Subject-specific CNNs were trained on three datasets: all trials, cyclic only, or noncyclic only. Synchronized ultrasound images and pressure maps served as inputs, with CNNs predicting sagittal-plane hip, knee, and ankle angles 160 ms in the future. Performance was assessed using RMSE and Pearson correlation on held-out test sets. Permutation importance quantified each sensor's contribution.

Results

Baseline models trained on both cyclic and noncyclic trials outperformed those trained on a single trial type. Mean prediction errors (Table 1) were lower across joints for both cyclic (RMSE = 8.08°, R = 0.87) and noncyclic (RMSE = 21.56°, R = 0.35) data. Permutation

importance revealed that disrupting pressure insole data caused the largest performance drop.

Discussion

Integrating ultrasound and pressure insole data, along with including both cyclic and noncyclic movements, improves lower limb kinematic predictions. Foot-ground contact information primarily drives accuracy, while ultrasound provides complementary insight into finer muscle dynamics. Predictions for noncyclic movements remain challenging, though results across five ambulation modes in cyclic data are promising. These findings suggest that multi-sensor fusion can yield robust, subject-specific forecasts across diverse activities, extending beyond traditional mode-based models. Future work with more subjects and leave-one-subject-out validation is planned to assess generalizability.

Images (Optional)

Table 1: Mean±SD RMSEs (degrees) across subjects for each model and test data type (cyclic and noncyclic).

Training Data	Hip		Knee		Ankle	
	Cyclic	Noncyclic	Cyclic	Noncyclic	Cyclic	Noncyclic
No Permutation						
Both	7.42±0.82	27.30±4.38	11.31±1.30	28.05±3.87	5.51±0.40	9.31±1.10
Cyclic	7.83±0.94	27.48±4.55	12.02±1.66	26.38±2.83	5.62±0.39	10.60±1.11
Noncyclic	16.82±2.48	28.11±4.17	26.04±1.86	28.97±3.89	10.15±1.10	9.35±0.90
Insole Permutation						
Both	21.04±1.87	31.08±4.37	28.01±2.73	32.19±4.52	11.92±0.58	10.59±1.19
Cyclic	21.58±2.18	30.57±4.50	28.34±2.70	30.03±3.36	12.13±0.70	11.58±1.32
Noncyclic	20.86±1.91	31.42±4.06	29.83±2.18	33.00±4.91	11.94±0.70	10.76±1.07
Ultrasound Permutation						
Both	11.48±0.92	28.46±4.17	18.47±2.52	28.73±3.31	7.92±0.79	9.52±1.03
Cyclic	10.78±1.27	27.71±4.24	17.40±2.67	26.79±2.86	7.56±0.54	10.55±1.06
Noncyclic	17.27±2.61	28.84±3.96	26.28±1.53	29.62±3.76	10.26±1.08	9.59±0.77

Session Category

Imaging and Biomedical Devices: Assistive Technologies

P4-293

Intraoperative Sensor-Based System for Simultaneous Dynamic Evaluation of Tibiofemoral and Patellofemoral Joint Balance in Total Knee Arthroplasty

Mr. Kosuke Tokashiki[1], Prof. Takeshi Shimoto[1], Mr. Chihiro Takaki[1], Prof. Shinya Kawahara[2], Prof. Yasuharu Nakashima[2]

[1]Fukuoka Institute of Technology, Fukuoka, Fukuoka, Japan. [2]Kyusyu University, Fukuoka, Fukuoka, Japan

Introduction

Patient dissatisfaction following Total Knee Arthroplasty (TKA) is linked to load instability in medial and lateral condyles [1]. While optimal tibiofemoral (TF) soft-tissue balance is crucial, intraoperative assessments remain largely qualitative [2]. Furthermore, despite the impact of patellofemoral (PF) complications on QOL, standardized dynamic PF evaluation is lacking [3]. We aimed to develop a surgical support system for Posterior Stabilizer (PS) prostheses that quantitatively evaluates TF-PF interaction via real-time feedback of TF load balance and PF 3D load vectors.

Methods

We developed a system for PS prostheses using a compact 2-axis moment sensor in the tibial insert and a 3-axis force sensor in the femoral trial to quantify TF balance and PF loads. Sensors were embedded in custom acrylic monomer trials; the insert featured a sliding mechanism for easy exchange. Custom software visualized real-time load vectors. Validation used a knee model with acrylic bones and artificial ligaments under a dynamic flexion/extension (0[deg]–90[deg]) protocol.

Results

PF compression from 0 N at extension to ~20 N at 10[deg], plateaued at 40-50[deg], and peaked at ~48 N at 90[deg]. Proximal-distal shear shifted distally after 20[deg], reaching -13 N at 70[deg]. TF medial-lateral load balance fluctuated with flexion angle, reversing at 40[deg] and reaching -0.5 N at 90[deg]. In contrast, TF anterior-posterior load remained negligible (~0 N), indicating high conformity and stability.

Discussion

The system successfully quantified dynamic behavior undetectable by static assessment. PF compression increase aligns with the patella engaging the trochlear groove as a biomechanical pulley. The distal shear shift reflects patellar tendon vector influence in deep flexion. Negligible TF anterior-posterior load confirms implant conformity, while

medial-lateral fluctuations relate to physiological motion. Limitations include acrylic models that do not replicate articular friction; future validation with biofidelic systems is needed. By visualizing these dynamics, the system enables intraoperative optimization of implant positioning to ensure stability throughout the range of motion, contributing to safer, more physiological dynamic stability.

Images (Optional)

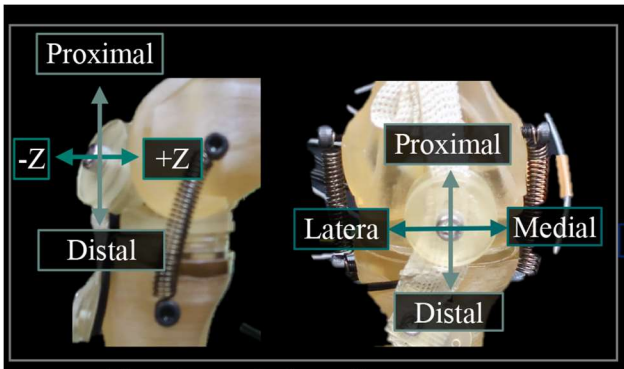


Fig.1 Anatomical coordinate system

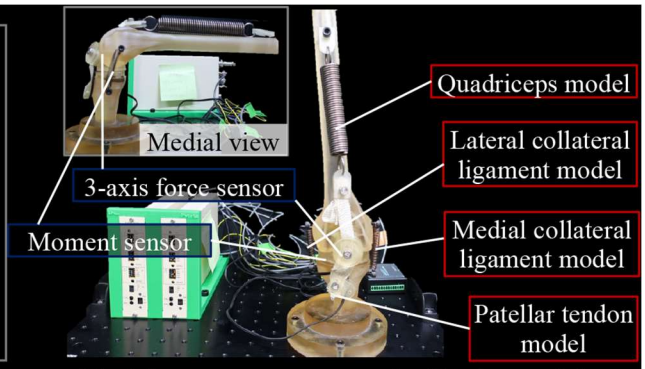


Fig.2 System components and validation model

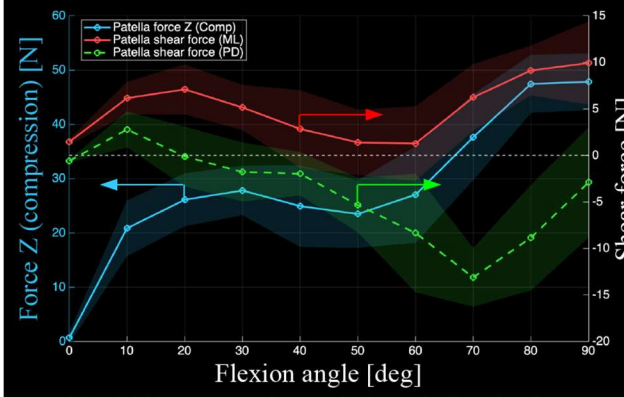


Fig.3 PF compression and shear during flexion

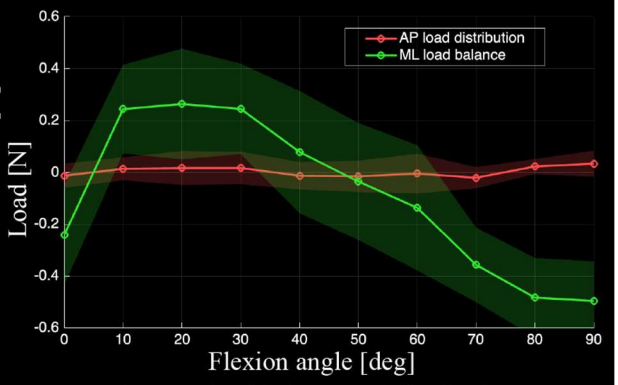


Fig.4 TF load balance and distribution

References (Optional)

[1] Shalhoub S et al., Arthroplasty Today, 2019

[2] Elmallah RK et al., J Arthroplasty, 2016

[3] Matz J et al., Can J Surg, 2019

Session Category

Imaging and Biomedical Devices: Assistive Technologies

P4-294

Active Walking Assistive Device Considering the Anatomical Axis of Metatarsophalangeal Joint to Improve Push Off During Level Walking

Mr. Sang Woo Jung BSc, Mr. Joonsoo Kwak HS, Post Doc. Pankwon Kim PhD, Prof. Choongsoo Shin PhD

Department of Mechanical Engineering, Sogang University, Seoul, Mapo-gu, Korea, Republic of

Introduction

Anatomical axis of metatarsophalangeal (MTP) joint has not been considered in most current active walking assistive devices even though it can improve their effect on human during push off. The purpose of this study was to develop an active walking assistive device considering the anatomical axis of the MTP joint and investigate its effect on human push off performance.

Methods

The non-anatomical MTP axis was defined as a line from the first metatarsal center perpendicular to the sagittal plane, whereas the anatomical axis connected the first metatarsal center to the fifth metatarsal head. Forefoot and metatarsal segments were divided along each axis, with FSRs positioned as two on the forefoot and one on the metatarsal segment. A rear-mounted motor was adopted to emulate plantar fascia–like tensioning. A trigger-based control strategy was implemented to operate the motor by detecting heel contact, tracking the rise and peak of forefoot pressure, and determining the stance-phase duration up to toe-off. Using the normalized timing ratio extracted from these pressure events, the motor was activated so that maximal assistance was operated to the MTP joint during push-off phase.

Three healthy male subjects walked barefoot at a self-selected speed on a flat surface while ground-reaction forces were recorded using a 1200-Hz force plate synchronized with a 400-Hz motion-capture system with markers placed at anatomical landmarks. Kinematic and kinetic data were collected for a single gait cycle and processed using a fourth-order Butterworth low-pass filter frequency of 10Hz.

Results

Walking speed, device range of motion, anterior ground reaction force, and force sensing reaction value of the anatomical axis of the MTP joint rate of increase 10.33%, 30.69%,

25%, and 17.47% respectively, compared to the non-anatomical axis of the MTP joint (Table 1).

Discussion

Applying the anatomical axis brought the device behavior closer to normal MTP joint function and suggested improved human–device interaction during gait. The anatomical condition increased walking speed and anterior GRF, suggesting enhanced interaction that improved push-off. In conclusion, considering the anatomical axis in the design of walking assistive device can improve human-device interaction, ultimately improving gait performance during push off.

Images (Optional)

Table 1 Mean results for spatiotemporal, kinematics, and kinetics parameters during walking with MTP joint assistive device under non-anatomical condition, anatomical condition, and rate of increase in the anatomical condition compared with the non-anatomical condition

Variables	Walking assistive device conditions		Rate of increase (%)
	Non-anatomical	Anatomical	
Walking speed (m/s)	0.87	0.96	+ 10.33
Device ROM (°)	25.64	33.51	+ 30.69
Max. Anterior GRF (N/BW)	0.12	0.15	+ 25.00
Max. FSR value (mV/BW)	7.84	9.21	+ 17.47

MTP: metatarsophalangeal; ROM: range of motion; GRF ground reaction force; FSR: force sensing resistor

Acknowledgements (Optional)

This work was supported by the National Research Foundation of Korea (NRF) grant funded by the

Korea government (RS-2024-00342681)

Session Category

Imaging and Biomedical Devices: Assistive Technologies

P4-295

Quantitative Analysis of Autonomous Wheelchair Navigation Stability: A ROS2-Based Framework for Pediatric Mobility Assistance

Ms. Uchechi Ukaegbu Ph.D. Student, Mr. Jesuloluwa Zaccheus Ph.D. Student, Dr. John Andersen Professor, Dr. Mahdi Tavakoli Professor, Dr. Hossein Rouhani Professor

University of Alberta, Edmonton, Alberta, Canada

Introduction

Children with severe motor disabilities often cannot operate power wheelchairs due to an inability to use joysticks or alternative control methods. Autonomous navigation can offer safer mobility, but its effectiveness depends on tuning navigation parameters to achieve stable path tracking, minimal unnecessary rotations, and predictable behaviour in indoor clinical spaces. Without proper tuning, sudden corrections can cause postural perturbations, increasing user discomfort and anxiety. This study presents a ROS2-based autonomous pediatric wheelchair and evaluates its navigation performance following structured parameter optimization.

Methods

A conventional pediatric wheelchair (0.86 × 0.53 × 0.60 m) was equipped with an RPLidar A12, wheel encoders, and a custom ROS2 hardware interface. The ROS2 navigation stack [1] guided the wheelchair using the regulated pure pursuit controller [2] for path tracking. Baseline trials using default parameters produced excessive rotations, overshoots, and poor tracking. Five critical navigation parameters were experimentally tuned and examined individually to characterize their effects on controller stability, goal convergence, and rotation behaviour. Tuning proceeded sequentially to isolate first-order sensitivities. The resulting configuration provides a clinically practical parameter set for indoor pediatric mobility, rather than a provably global optimum. Navigation was tested using the default NavFn and the Theta star planners on a 12-meter course, followed by ten repeated trials with the optimized configuration.

Results

The optimized Theta star configuration reduced mean absolute error by 42.5% and root mean square error by 35.6% compared to baseline, as shown in Table 1. Tracking variability decreased, and the resulting paths were smoother. Across 6172 tracking points, 60% had

errors below 0.15 m. The NavFn planner performed worse, with MAE of 0.336 0.048, RMSE of 0.445 0.063 m, and spurious rotations despite parameter adjustments.

Discussion

Parameter threshold analysis showed that XY tolerances above 0.3 m and yaw tolerances above 0.785 rad produced repeated in-place rotations at navigation onset. Minimum lookahead distances below 0.25 m caused instability, while distances above 0.35 m increased overshoot. Lookahead values below 0.4 m also allowed erratic rotations. Systematic tuning improved stability, predictability, and clinical suitability, establishing validated parameters that support future user-focused trials.

Images (Optional)

Table 1: Navigation performance comparison

Parameter	Baseline parameters	Optimized parameters
rotate_to_heading_angular_vel	1.8 rad/s	1.0 rad/s
lookahead_distance	0.6 m	0.8 m
min_lookahead_distance	0.4 m	0.28 m
xy_goal_tolerance	0.25 m	0.15 m
yaw_goal_tolerance	0.25 rad	0.75 rad
Mean absolute error	0.254 ± 0.179 m	0.146 ± 0.046 m
Root mean square	0.303 ± 0.144 m	0.195 ± 0.037 m

References (Optional)

[1] Macenski, Steve et al., *IROS,* 2020.

[2] Macenski, Steve et al., *Autonomous Robots*, 2023.

Acknowledgements (Optional)

This research was supported by NSERC SMART CREATE, the Women and Children's Health Research Institute, MITACS, A-MEDICO, and the Glenrose Hospital Foundation. The authors thank the research and clinical teams at the Glenrose Rehabilitation Hospital for their guidance and collaboration.

Session Category

Imaging and Biomedical Devices: Assistive Technologies

P4-296

Biomechanics of Yawning: Insights Into Cranio-Cervical Fluid Dynamics and Kinematic Consistency

Dr Adam Martinac PhD

Neuroscience Research Australia, Sydney, NSW, Australia

Introduction

Yawning is a stereotyped orofacial–respiratory behaviour whose physiological role remains uncertain. A range of hypotheses have been proposed: physiological hypotheses suggest that yawning may play a role in regulating blood oxygen/CO_2 levels and airway patency, brain thermoregulation, arousal/attentional state, and cerebral metabolic waste clearance. Because cerebrospinal fluid (CSF) movement contributes to solute transport and waste removal and is strongly influenced by respiratory pressure dynamics, this study evaluated whether yawning alters neurofluid flow relative to normal and deep breathing, and whether yawning kinematics are reproducible within individuals.

Methods

In a single MRI session in healthy adults (N = 22), real-time phase-contrast imaging at the upper cervical level (C3) was combined with mid-sagittal real-time cine imaging to quantify CSF and internal jugular venous flows during normal breathing, forceful oral inspirations (“deep breaths”), yawns, and stifled yawns, and to derive tongue-motion trajectories. The real-time PC-MRI protocol used turbo-field echo-planar imaging and was not cardiac gated. The encoding velocities were set to 10-20cm/s for CSF flow and 60-90cm/s for arterial and internal jugular flow. CSF and blood flow were measured in separate, sequential scans rather than simultaneously due to velocity encoding constraints

Results

Both deep breaths and yawns increased CSF and venous flow compared with normal breathing; despite similar flow magnitudes (Figure 1), yawns more frequently produced co-directional caudal CSF and jugular outflow during inspiration, whereas deep breaths typically showed counter-directional CSF–venous profiles. Yawning kinematics were highly reproducible within individuals across repeated events. Once triggered, yawns proved difficult to suppress completely. While participants could modify the yawn by keeping their lips closed and reducing jaw movement, they could not prevent the yawn entirely (Figure 1).

Discussion

These observations show that yawning is not simply an intensified breath but a distinct cardiorespiratory manoeuvre that reorganizes neurofluid flow. The inspiratory alignment of CSF with venous outflow during yawns suggests a transient caudal advection that could influence solute transport and heat exchange within the cranial–cervical system. In addition, yawns within individuals also exhibited highly stereotyped orofacial tongue kinematics across repeated events, compatible with, but not proof of, control by a central pattern generator.

Images (Optional)

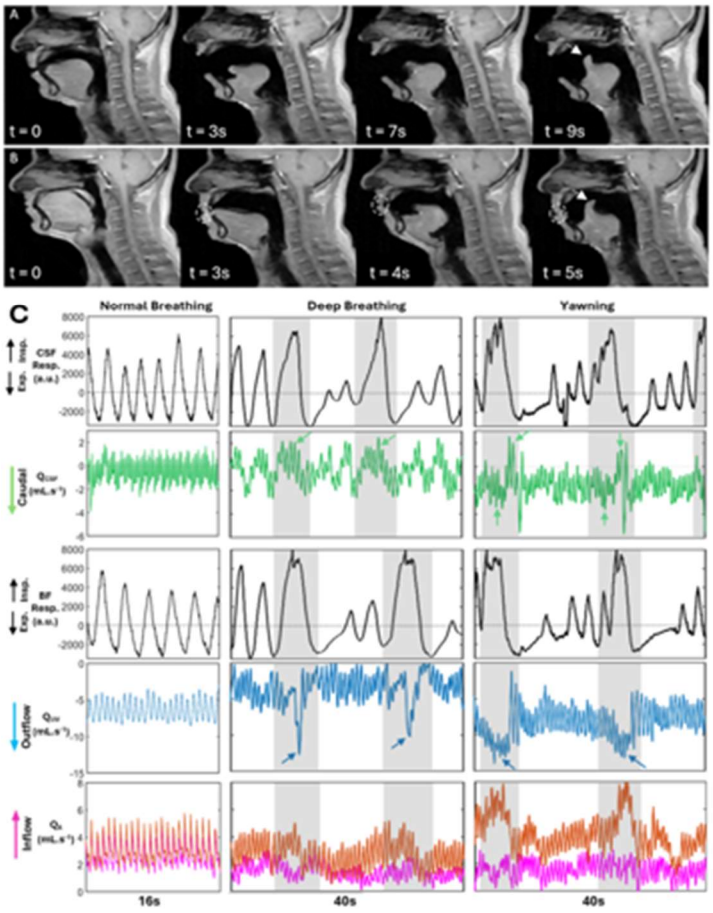


Figure 1. Yawning, stifled yawning, and associated CSF/vascular flows. **(A)** Sagittal real-time montage of a full yawn in representative participant. After inspiration, the tongue retracts and rapidly alternates between horizontal and vertical orientations at the yawn apex (white arrows), then returns to rest with expiration. **(B)** Montage of a stifled yawn in the same participant. Despite a voluntarily closed mouth (dashed white circle), tongue movements closely resemble the full yawn. **(C)** CSF (green) and vascular flows from the internal jugular vein (blue), vertebral artery (orange), and internal carotid artery (magenta) during normal breathing, deep breaths, and yawns (Q, ml·s^{-1}; positive = cranial, negative = caudal), with respiration shown in black (arbitrary units). Deep breaths produce bidirectional shifts with cranial CSF inflow and increased jugular outflow on inspiration that reverse on expiration (counter-directional); yawns produce the largest changes, often with caudal CSF flow and jugular outflow aligned during inspiration (co-directional).

References (Optional)

Acknowledgements (Optional)

NHMRC

Session Category

Imaging and Biomedical Devices: Imaging Fundamentals and Applied Research

P4-297

Digital volume correlation at the voxel level for the study of mineralised tissues

Dr Alissa Parmenter PhD, MEng[1], Dr Elis Newham[2], Dr Aikta Sharma[1], Dr Joseph Brunet[1], Dr Nick Terrill[3], Dr Federico Bosi[1], Professor Andrew Pitsillides[4], Dr Brian Bay[5], Professor Himadri S Gupta[2], Professor Peter D Lee[1]

[1]University College London, London, London, United Kingdom. [2]Queen Mary University of London, London, London, United Kingdom. [3]Diamond Light Source, Harwell, Oxfordshire, United Kingdom. [4]Royal Veterinary College, London, London, United Kingdom. [5]Oregon State University, Corvallis, Oregon, United States

Introduction

Digital Volume Correlation (DVC) enables quantitative experimental measurements of strain in mineralised tissues. Improving spatial resolution of DVC strain fields is critical for probing microscale mechanics with lower-dose X-ray imaging and for validating finite element models. We previously showed accurate strain measurement in bone and calcified cartilage with points spaced every 4–5 voxels [1]. Here, we show that accurate voxel-wise strain measurements can be achieved in both synchrotron and lab-based microCT images of mineralised tissues.

Methods

In situ microCT datasets from multiple animal models (rat, mouse, pig, zebrafish) and imaging systems (Diamond I13-2, ESRF BM18, Skyscan 1270) with 1–10 µm voxel sizes were analysed. Mineralised tissue was segmented by thresholding. Local DVC was performed using the open-source software iDVC [2], with spherical sub-volumes (~30-voxel diameter, optimised per dataset) centred on every mineralised voxel, resulting in >90% sub-volume overlap. Lagrangian strain was derived from the displacement field via a least-squares second-order Taylor expansion.

Results

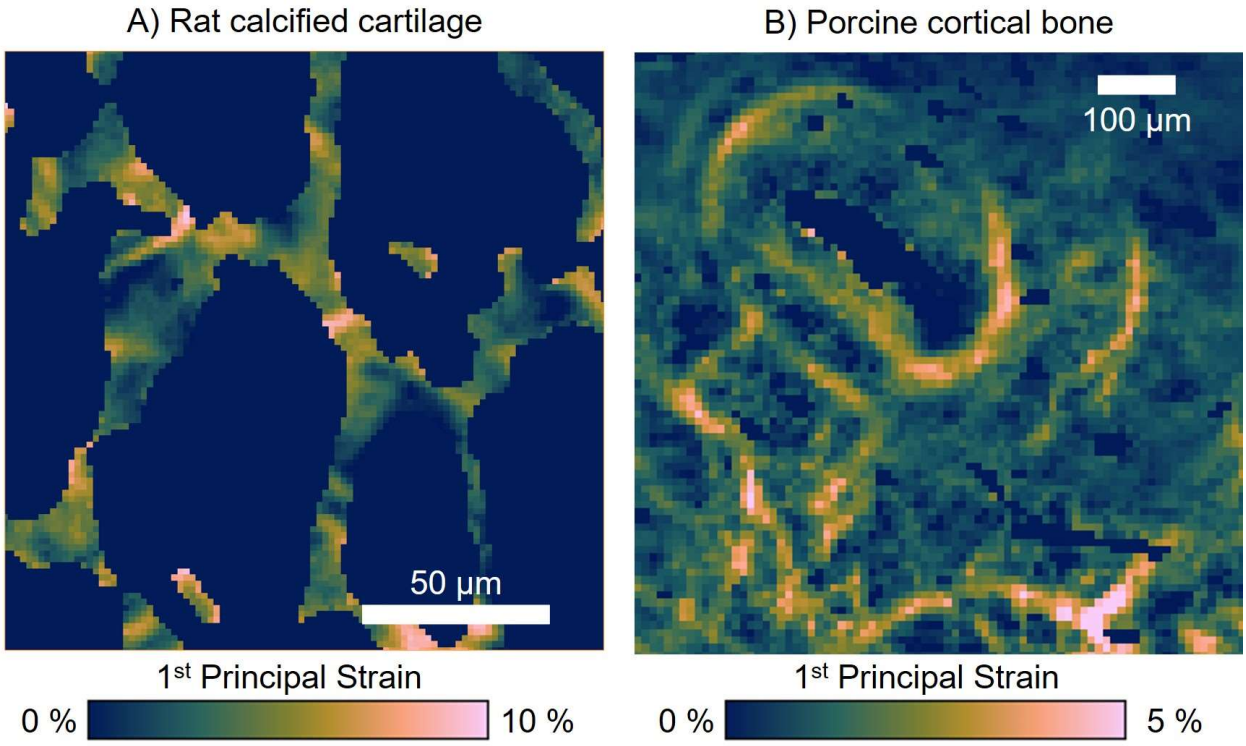
Zero-strain and virtual deformation tests showed displacement accuracy of 0.01-0.1 voxels and strain accuracy of 0.01-0.2% (image-dependent). DVC strain fields resolved tissue-level deformation in features <10 voxels thick, such as mineralised cartilage septa (Fig. A). Strain patterns generated by features smaller than the image resolution were seen, including strain around cement lines in cortical bone in images with a 10µm voxel size

(Fig.B). The presence of these features was confirmed by scans at 2µm voxel size within the same sample.

Discussion

This work substantially advances the achievable strain-measurement resolution in microCT/sCT imaging of mineralised tissues. Although smoothing means the strain field cannot fully match the underlying image resolution, we show that strain localisation driven by sub-resolution features can still be detected. This capability opens new possibilities for investigating microscale biomechanics while reducing required imaging resolution—and therefore X-ray dose—for studies of mineralised tissues. The analysis pipeline is fully open-source and we have demonstrated it's applicability across a range of synchrotron and lab-based imaging systems, as well as a range of sample types.

Images (Optional)



References (Optional)

[1] Alissa Parmenter *et al.*, 2025, Cell Biomaterials

[2] https://tomographicimaging.github.io/iDVC

Acknowledgements (Optional)

We acknowledge funding from Back to Back, the UK Engineering and Physical Sciences Research Council (EP/V011235/1, EP/V011006/1, EP/V011383/1, EP/V011065/1), UK Medical Research Council (MR/R025673/1 and MR/V033506/1), Royal Academy of Engineering (CiET 1819/10), Chan Zuckerberg Initiative (CZIF2022-316777), ESRF HOAHub MD-1389, MD-1290, Diamond Light Source long-term project (SM29784), & the i4health Centre for Doctoral Training.

Session Category

Imaging and Biomedical Devices: Imaging Fundamentals and Applied Research

P4-298

Unraveling Bone Remodeling: A Topological and Tensor-Field 4D Analysis of Remodeling Spaces from In-Vivo Synchrotron Micro-CT

Mr. Amine Lagzouli[1,2], Dr. Kim Harrison[3], Dr. Lindsay Loundagin[3], Prof. Davide Fontanarosa[4], Dr. Maria Antico[5], Prof. Vittorio Sansalone[2], Prof. David Cooper[3], Prof. Peter Pivonka[1]

[1]School of Mechanical, Medical, and Process Eng., Queensland University of Technology, Brisbane, Queensland, Australia. [2]Univ Paris Est Creteil, Univ Gustave Eiffel, CNRS, UMR 8208, MSME, Creteil, Ile de France, France. [3]Department of Anatomy, Physiology, and Pharmacology, University of Saskatchewan, Saskatoon, Saskatchewan, Canada. [4]School of Clinical Sciences, Queensland University of Technology, Brisbane, Queensland, Australia. [5]CSIRO Health and Biosecurity, Brisbane, Queensland, Australia

Introduction

Bone remodelling maintain skeletal integrity through the activity of Basic Multicellular Units (BMUs), composed of osteoclasts, osteoblasts, and progenitor cells. Synchrotron-based *in-vivo* micro-CT now enables direct 4D visualization of cortical remodeling and access to dynamic resorptive parameters such as the Longitudinal Erosion Rate (LER) [1], which previously was only measured indirectly using histology. However, current analyses rely on manual BMU identification, which is time-consuming, operator-dependent, and difficult to scale, especially within the highly interconnected cortical porosity where vascular canals form complex branching networks, often amplified under drug treatment.

To overcome these limitations, we developed a novel method integrating porosity segmentation, topological graph modeling, and scale-tensor field analysis to extract local structural features, quantify network complexity over time, disentangle branched BMUs, and track BMU progression in 4D to compute LER.

Methods

Using longitudinal *in-vivo* (t=5,10,15 days) synchrotron micro-CT (13 µm) of tibiae of New Zealand White rabbits (n = 7) treated with intermittent PTH (1–34, 30 µg/kg/day × 15 days), followed by *ex-vivo* micro-CT (t=20 days), we proposed a novel 4D analysis pipeline (Fig. 1): (1) preprocessing and segmentation of cortical porosity; (2) topological and graph-based characterization of the vascular canal network; (3) scale-tensor estimation of local anisotropy and orientation; (4) tensor-topology disentanglement to extract branched BMUs; (5) 4D tracking of BMUs to compute LER.

Results

The method enabled detailed topological characterization of the vascular canal network, revealing increased branching and complexity following PTH treatment. Scale-tensor analysis captured heterogeneous BMU orientations and morphologies. The disentanglement stage identified substantially more branched BMUs than isolated ones, consistent with the biological emergence of new BMUs from existing canals. Median LER values were 22.6 µm/day (t1–t2), 26.3 (t2–t3), 21.8 (t3–t4), and 23.1 (t1–t4). Kruskal–Wallis testing ($p = 0.138$) showed no significant temporal differences, consistent with manual measurements.

Discussion

This automated 4D method provides robust topological and structural descriptors of cortical remodeling *in-vivo*. It overcomes limitations of manual BMU identification and is adaptable to other microstructures, skeletal sites, and high-resolution imaging modalities, offering a scalable platform for studying remodelling dynamics and evaluating therapeutic interventions.

Images (Optional)

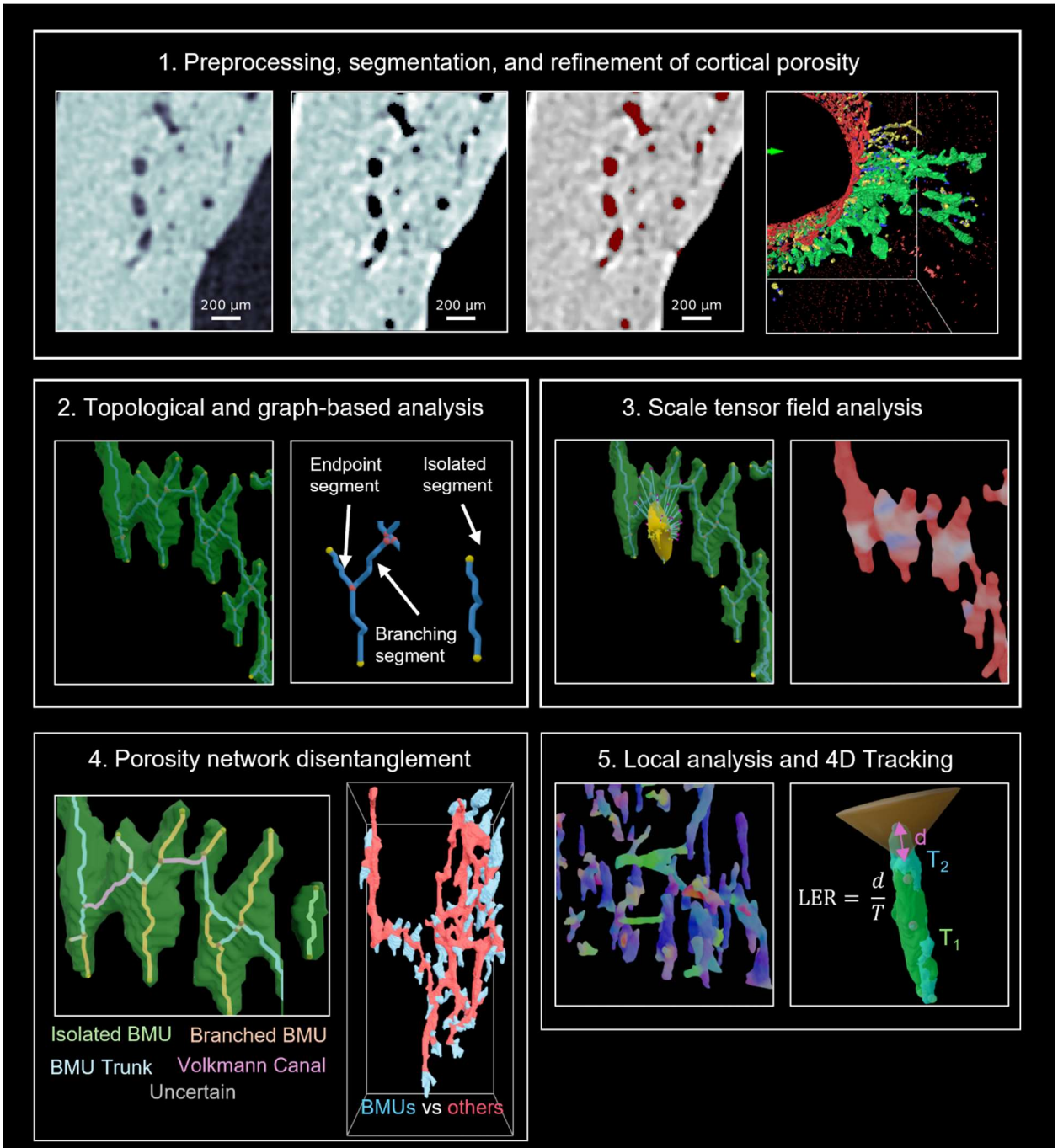


Fig. 1: Overview of the proposed 4D analysis pipeline for of the complex vascular canal network in the cortical bone of rabbit tibiae from high-resolution multi–in vivo Sr-microCT.

References (Optional)

[1] K. Harrison et al., *JBMR, 2020*

Session Category

Imaging and Biomedical Devices: Imaging Fundamentals and Applied Research

P4-299

Tissue-Specific Optical Signatures: Comparing Dermis and Pancreas for Thermal Therapy Design

Ms. Anjelyka Fasci

University of Texas at San Antonio, San Antonio, Texas, United States

Introduction

Thermal therapies are minimally invasive treatments achieving effects through controlled heat delivery. A core challenge is achieving precise thermal effects while preserving surrounding structures. Dermis provides an excellent model due to its organized architecture dominated by collagen scattering, allowing reproducible measurements and predictable responses. Conversely, the pancreas presents substantial challenges: deeply situated, highly heterogeneous with irregular arrangements, and exhibiting complex optical properties due to variable lipid, fibrosis, and vascular density, particularly in pancreatic cancer with fibrotic stroma.

Methods

Optical characterization utilized a dual integrating sphere system with tungsten halogen illumination. Porcine dermis and pancreas specimens were mounted between fused silica windows for optical measurements using Inverse-Adding-Doubling analysis. Tissue thickness was measured using a dial indicator with thousandths of a millimeter precision. System calibration used a reference polyurethane phantom. This methodology enabled rigorous optical property comparison.

Results

Pancreatic tissue exhibited higher absorption coefficients, particularly near hemoglobin peaks (540-580 nm), but substantially lower scattering coefficients compared to dermis. Dermal tissue demonstrated higher baseline scattering from its dense collagen matrix. Dermal tissue's elevated scattering indicates more dramatic structural changes. These distinct signatures suggest tissue-specific calibration and predictive models are necessary for safe, effective therapy.

Discussion

This study reveals fundamental optical differences critically impacting thermal therapy design. Pancreatic tissue's higher absorption yet lower scattering demonstrates that

extrapolating protocols from superficial to deep tissues is problematic without tissue-specific characterization. These findings have implications for pancreatic cancer treatments. Future investigations should characterize optical property evolution during thermal exposure and extend this framework to diseased pancreatic tissue.

Acknowledgements (Optional)

Views expressed are those of the author and do not reflect official policy of the Department of War, Department of the Air Force, or U.S. Government. Discussion of non-federal entities, methods, products, or services does not imply endorsement. Study protocol was approved by IACUC and conducted in an AAALAC-accredited facility in compliance with Animal Welfare Act and Guide for Care and Use of Laboratory Animals. Work was supported by Air Force Research Laboratory Minority Leaders Collaborative Research Program through The Ohio State University (FA8650-20-2-5823, SPC-1000013899|GR137125) and SAIC (FA8650-19-C-6024).

Session Category

Imaging and Biomedical Devices: Imaging Fundamentals and Applied Research

P4-300

An In Silico Biomechanics Framework for Ultrasound Shear Wave Elastography to Measure Myocardial Stiffness

Dr. Eng. Annette Caenen[1,2], Eng. Marta Zattoni[3,4], Dr. Eng. Mathias Peirlinck[4], Prof. Dr. Eng. Jan D'hooge[2], Prof. Dr. Eng. Patrick Segers[1]

[1]Ghent University, Ghent, East-flanders, Belgium. [2]KU Leuven, Leuven, Flemish Brabant, Belgium. [3]Ghent University, Ghent, East Flanders, Belgium. [4]Delft University Of Technology, Delft, South Holland, Netherlands

Introduction

Ultrasound shear wave elastography (SWE) can non-invasively assess myocardial stiffness by inducing shear waves with focused ultrasound and tracking their propagation in real time. Since shear wave speed reflects tissue stiffness, SWE holds promise for improving diagnosis and treatment. However, shear wave speed increase can result not only from pathology but also fiber orientation, wave-guiding, and pressurization. To address these confounders, we developed a finite element framework of the left ventricle (LV) tailored for SWE. The framework has been refined and validated in previous work through gradually increasing complexity of models and experiments. Building on this foundation, the framework was extended to incorporate myocardial contraction, enabling a more comprehensive evaluation of myocardial mechanics.

Methods

The LV was modeled as a truncated ellipsoid in Abaqus, connected to a closed-loop lumped parameter system. The passive material response followed a nonlinear, anisotropic Holzapfel-Ogden law (2009), and active response a time-varying elastance function [1]. Material parameters were tuned to obtain realistic pressure-volume response: (92ml, 12mmHg) in end-diastole and (43ml, 125mmHg) in end-systole. Operational stiffness was derived from pressure-volume and shear stress-stretch analysis. Shear waves were simulated in a refined submodel by applying a body force for 300µs at end-diastole (fig. A). Wave speeds were estimated at the mid-wall in long-axis view using Radon transform. Simulations were repeated for various LV stiffnesses (x1, x2, x5) and filling pressures (8, 20, 30mmHg).

Results

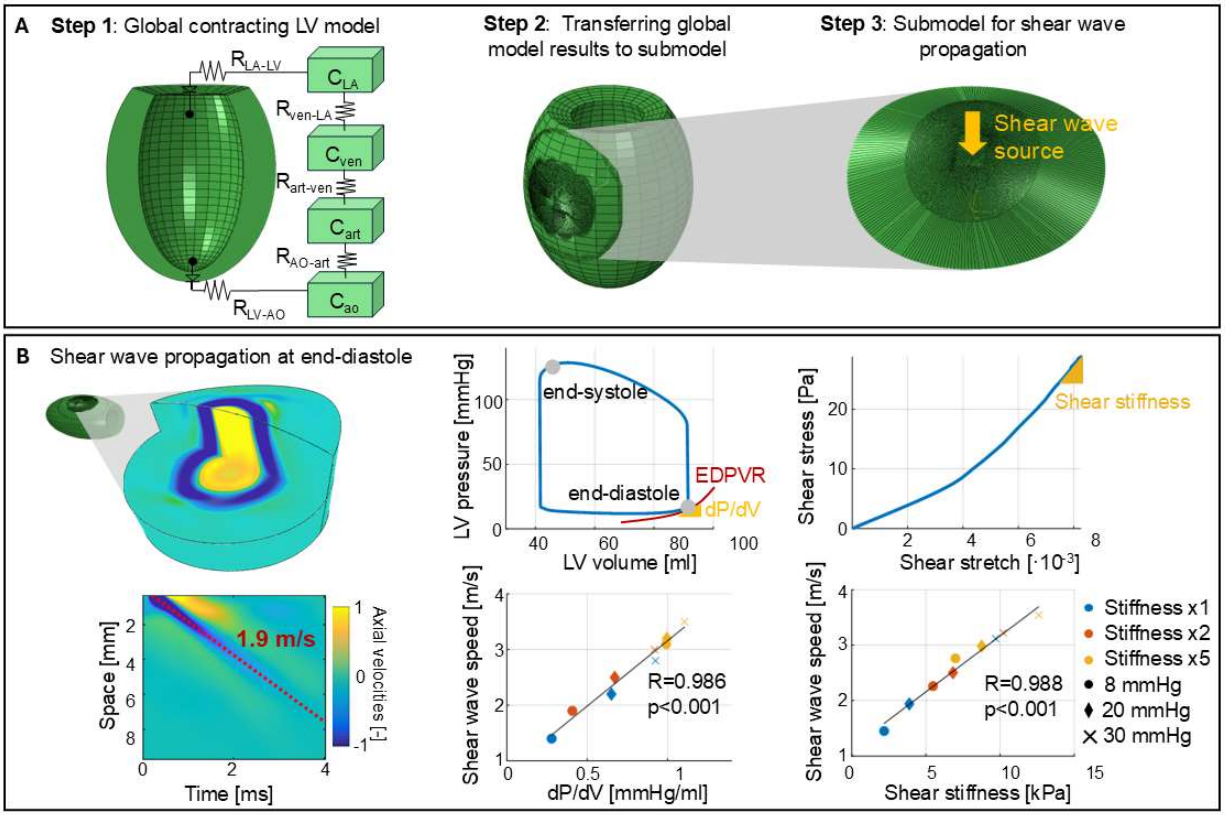
Shear wave speed increased with pressure and stiffness (fig. B). At higher stiffness levels, however, the rate of increase in speed diminished with increasing pressure (Δ1.34 vs. 0.36m/s at stiffness factor x1 and x5 for Δ22mmHg). Shear wave speed showed a strong

correlation with operational stiffness derived from pressure-volume analysis (R=0.989, p<0.001), consistent with animal experiments [2], and shear stress-stretch analysis (R=0.988, p<0.001).

Discussion

This work presents a biomechanics framework for virtual cardiac SWE measurements, enabling both validation of the technique, and mechanistic insights into the relationship between shear wave speed and myocardial stiffness. Future developments will extend the framework to end-systolic wave speed as a marker of contractility.

Images (Optional)



References (Optional)

[1] Guccione et al., TASME, 1993.

[2] Caenen et al., Sci. Rep., 2023.

Session Category

Imaging and Biomedical Devices: Imaging Fundamentals and Applied Research

P4-301

Anatomically Accurate Shape Correspondence for Statistical Shape Modelling of Human Bones

Dr Soheil Arastehfar, Dr Athena Jalalian

University of Twente, Enschede, Overijssel, Netherlands

Introduction

In statistical shape modelling, shape correspondence is the crucial step of establishing a mapping between structurally similar points across a population of shapes. In groupwise correspondence, these points are aligned iteratively through converging to a mean shape. Thus, the correspondence is biased to the converged mean shape. We hypothesize that the correspondence can represent the bone anatomy more accurately if the convergence criterion defines discrepancies between the shapes.

Methods

We created statistical shape models of three different bones, Femur, Tibia, and Hip. Per bone, 10 images were available. Two sets of models were produced based on iterations on mean shape and deviations of aligned shapes. We then tested these models to determine their capability of bone shape reconstruction. We did this in a leave-one-out cross validation setting. Next, the errors of the reconstructions based on the mean shape convergence and minimized alignment deviations were paired. We carried out one-way paired *t*-test at statistical significance level of 1%. The alternative hypothesis stated reduction in the mean of errors, and the null hypothesis stated the inequality in the opposite direction.

Results

The results showed error improvement from 5.5±1.3mm to 0.8±0.1mm for Femur, from 4.4±1.3mm to 0.7±0.2mm for Tibia, and from 2.2±0.5mm to 2.1±0.2mm for Hip. As for the *t*-tests, we found strong statistical evidence to reject the null hypotheses for Femur and Tibia, p=.000, while we failed to reject the null hypothesis for Hip, p=0.466. We achieved better correspondence establishment with Femur and Tibia bones, but for the hip the results were comparable.

Discussion

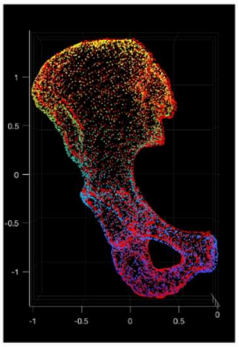
In bones with elongated shapes, the variations are mainly in the proximal and distal bones rather than in the bone shaft. For a good correspondence establishment, it is important that the two end parts are well aligned. Our approach by measuring the shape deviations

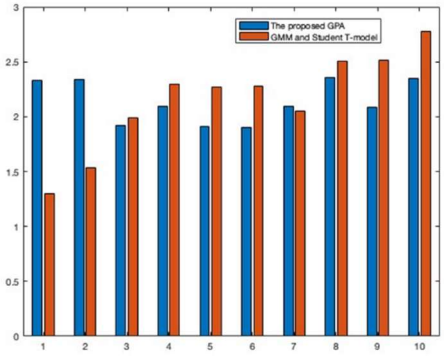
tries to minimize the discrepancies between the shapes especially in the proximal and distal bones. Whereas the groupwise approach based on mean shapes is significantly affected by the shaft because it is a big part of the point clouds of these bones, while carrying significantly less information about the bone shape.

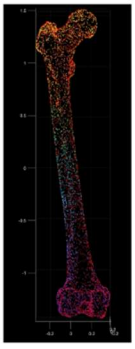
Images (Optional)

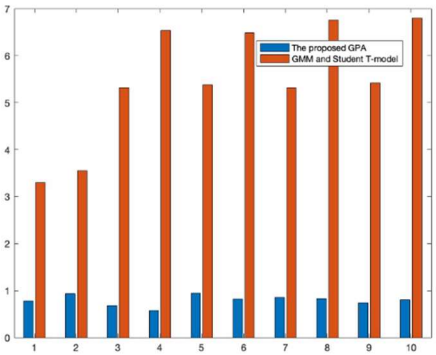
Orange: minimization of the deviations between the shapes resulted in significantly more accurate correspondence especially for elongated bones

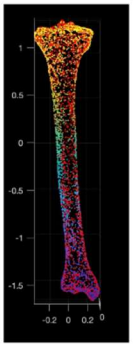
Blue: groupwise correspondence based on convergence of mean shape

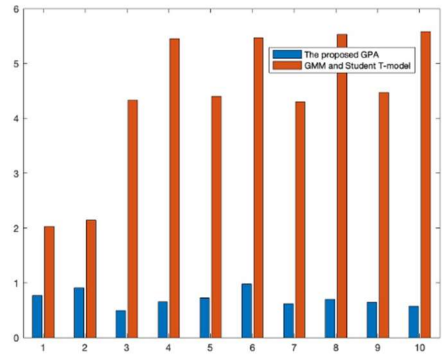












Session Category

Imaging and Biomedical Devices: Imaging Fundamentals and Applied Research

P4-302

Regional Arterial Timing and Pulsatile Motion Signatures in the Human Brain Parenchyma

Ms. Caitlin Neher MS, Mr. Tyson Lam BSME, Dr. Fargol RezayAraghi PhD, Dr. Mehmet Kurt PhD

University of Washington, Seattle, WA, United States

Introduction

Vascular health is crucial to the functioning human brain, with impairments leading to cognitive decline, stroke, and neurodegenerative diseases. This is due in part to the fact that precise cerebral blood flow requirements are needed to support the brain's functional activity and restful states, and that arterial pulsation drives glymphatic clearance. These essential functions motivate the ability to measure cerebrovascular function in the human brain *in vivo*, which poses challenges but has shown increased promise in aging and vascular dementia research. Here, we propose a multimodal magnetic resonance imaging (MRI) framework to measure regional arterial timing and parenchymal pulsatile motion during the cardiac cycle, and use this framework to quantify distinct vascular signatures of proximal and distal structures along the middle cerebral artery (MCA).

Methods

Thirty-one subjects (15F/16M, age 20-57) with no known neurological disorders underwent a multimodal MRI protocol including T1-weighted structural imaging, multi-delay pseudo-continuous arterial spin labeling (pCASL) and phase-contrast cine MRI. The pCASL data was postprocessed using Bayesian Inference for Arterial Spin Labeling (BASIL) to quantify perfusion and arterial transit time for each voxel of the brain; the cine MRI was postprocessed with an amplification algorithm and bandpass filter to isolate the frequency of the heartbeat. Regional segmentation of T1 images was done with FreeSurfer.

Results

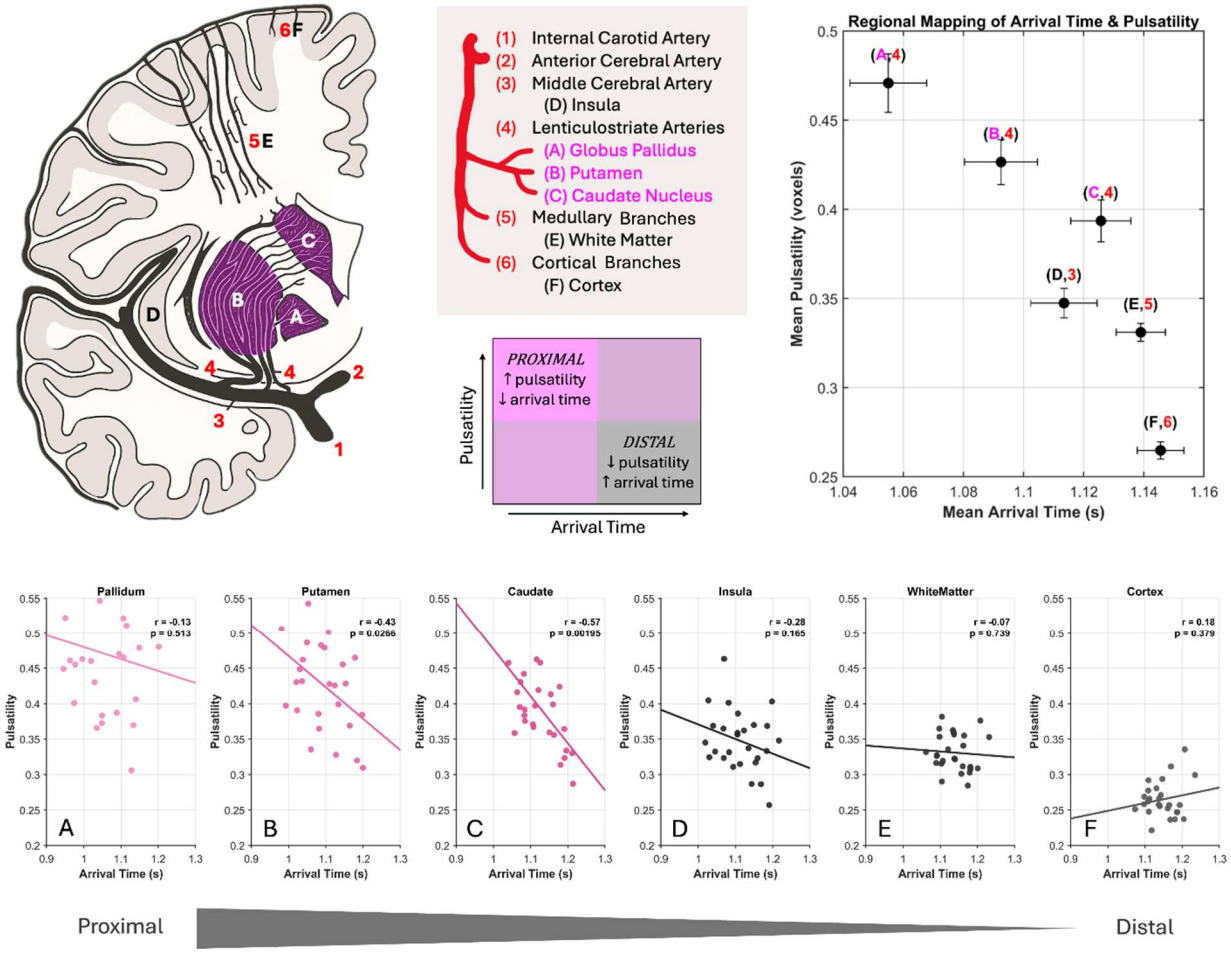
A data-driven mapping of cerebrovascular dynamics emerged in the combined arterial timing and pulsatile motion 2D space, with spatial alignment to the branching MCA. Distinct vascular signatures were observed across subjects in the globus pallidus, putamen, and caudate nucleus, which are supplied by the lenticulostriate arteries, indicating a high spatiotemporal accuracy achieved by the framework. Furthermore, pulsatile motion and arterial transit time correlated across subjects in the putamen

(p<0.05) and caudate nucleus (p<0.005), potentially indicative of the known relationship between mean arterial pressure and pulse transit time in the cerebral vasculature.

Discussion

These preliminary findings introduce a noninvasive *in vivo* mapping of how arterial input propagates through the brain using multimodal MRI. Future work will investigate the framework's specificity to arterial pressure and aging, with the goal of quantifying the vascular changes which modulate the severity of cerebral small vessel disease.

Images (Optional)



Session Category

Imaging and Biomedical Devices: Imaging Fundamentals and Applied Research

P4-303

A Novel Extraction and Description of Patellofemoral Joint Kinematics From the Fusion of Freehand Ultrasound and Motion Capture

Miss Caterina Vanelli Coralli[1], Dr Shihfan Jack TU[2], Prof Stephen Mellon[3,2]

[1]University of Oxford, Oxford, Oxfordshire, United Kingdom. [2]Botnar Institute for Musculoskeletal Sciences, NDORMS, University of Oxford, Oxford, Oxfordshire, United Kingdom. [3]Biomedical Engineering Centre, Department of Technology and Innovation, University of Southern Denmark, Odense, Region of Southern Denmark, Denmark

Introduction

Accurate quantification of patella tracking is crucial to the clinical assessment of abnormal kinematics, such as in post-operative maltracking following total knee arthroplasty; however, current diagnostic techniques remain limited. CT and MRI provide morphological detail but inadequately describe motion, while gait analysis imprecisely tracks patellar movement due to soft tissue artefacts. This study aimed to establish the feasibility of a novel ultrasound and motion capture fusion technique for quantifying patellofemoral kinematics across loaded knee flexion.

Methods

Eight healthy volunteers (22-57) participated in the study at the Oxford Gait Laboratory. Two five-marker plates were placed on the proximal thigh and distal shin of the right leg. The knee joint was scanned with a hand-held ultrasound in one reference (9 sweeps, 10 minutes) and up to five semi-dynamic positions (6 sweeps, 3 minutes). The latter represented flexion angles (10º – 75º) and loading covering the joint's range of motion during step-climbing. A Vicon motion-capture system tracked the ultrasound probe and participants' legs.

A custom segmentation algorithm extracted bony profiles from ultrasound images, creating detailed reference point-clouds and sparse semi-dynamic ones. Point-cloud registration recreated bony morphology at semi-dynamic positions. A femoral-based coordinate system enabled quantification of patellar shift and tilt.

Results

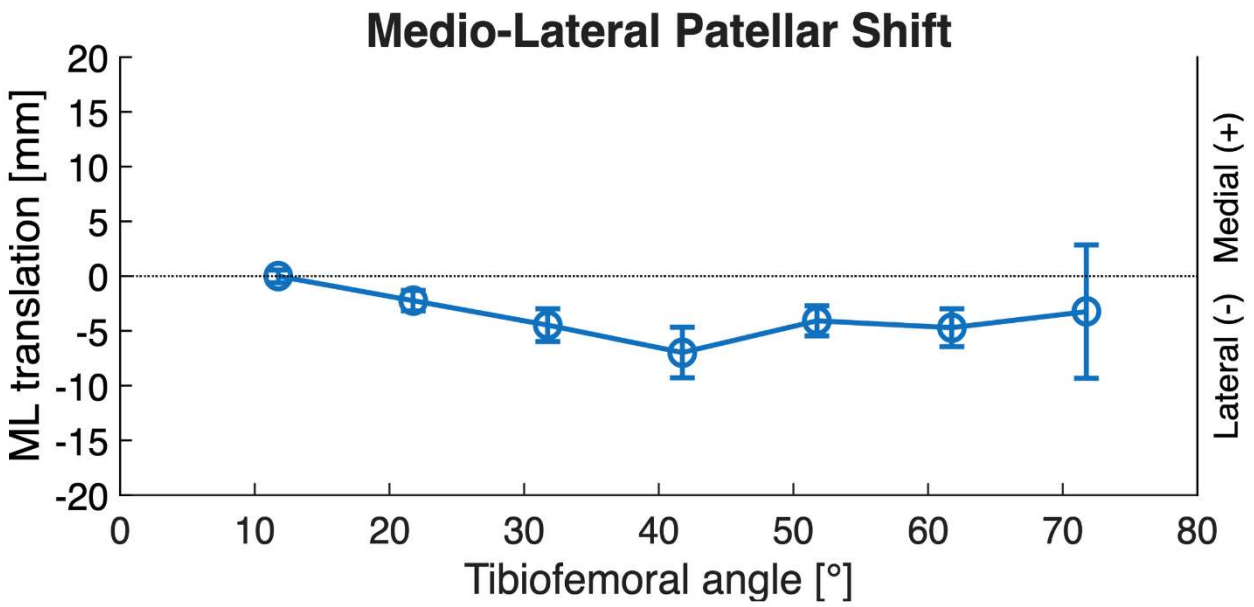
The custom algorithm was applied to a subset of participants (n = 4) for whom the scanning protocol had been optimised, yielding high-fidelity reconstructions of the bone surfaces. The point-cloud registration yielded root mean square errors of 0.47-1.41 mm, representing

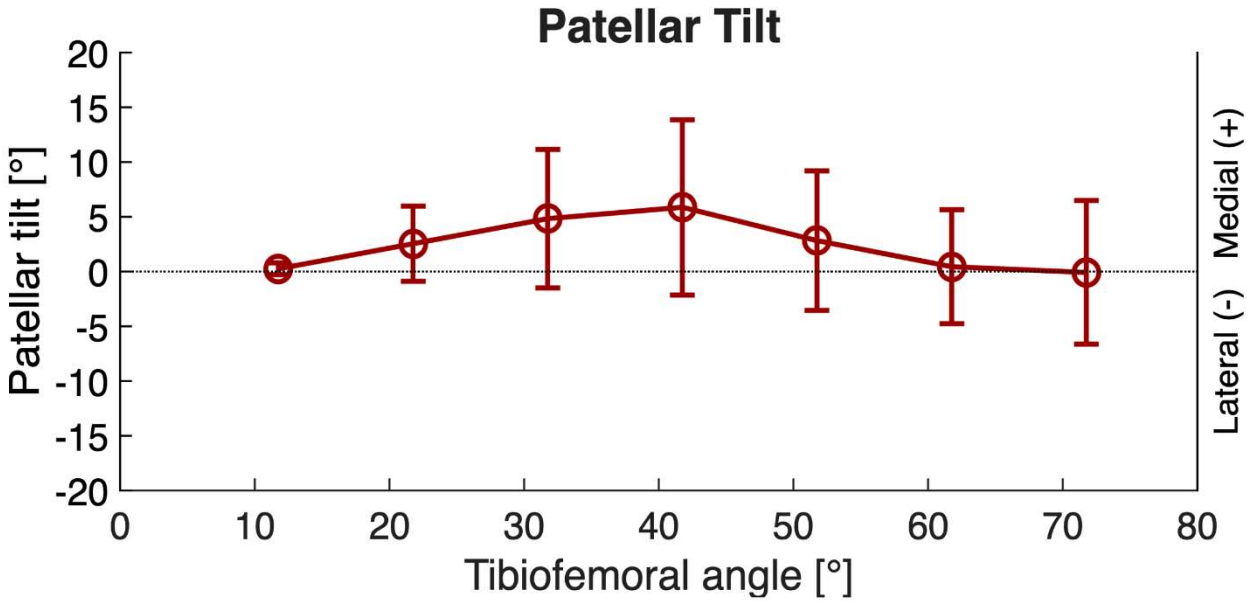
the average deviation between reconstructed and reference clouds. On this basis, medio-lateral translations (-6.98 to 0 mm) and patellar tilt angles (0º to 5.87º) were extracted across the range of knee flexion. The resulting kinematic patterns were consistent with values previously reported in the literature.

Discussion

This study introduces a novel approach to patella tracking that enables extraction of clinically relevant parameters across a pseudo-dynamic range of motion, overcoming the limitations of current marker-based and imaging methods. Ongoing work aims to translate this framework into a quantitative tool for assessing patellofemoral kinematics in both healthy and pathological populations, with the longer-term objective of enabling fully dynamic assessments.

Images (Optional)





Session Category

Imaging and Biomedical Devices: Imaging Fundamentals and Applied Research

P4-304

Early Subchondral Bone Remodeling after Destabilization of the Medial Meniscus (DMM) and Sham Surgery in Mice

Miss Cecilia Liberati, Prof. Harry van Lenthe

Department of Mechanical Engineering, KU Leuven, Leuven, Vlaams-Brabant, Belgium

Introduction

Osteoarthritis(OA) is characterized by progressive subchondral bone (SB) degeneration [1], yet the early alterations are not well documented. Longitudinal microCT is the gold-standard for tracking SB remodeling but detecting the pathological onset remains a challenge. Hence, this study developed an open-source, voxel-to-voxel analysis pipeline to track longitudinal SB changes in a microCT dataset of a mouse OA model to detect early pathogenic alterations.

Methods

A custom image-processing pipeline was developed in Jupyter Notebook (v7.0.8) environment to standardize processing of longitudinal microCT datasets, incorporating rigid-registration for voxel-to-voxel comparison and quantification of dynamic bone parameters in the murine tibial SB (Fig.1a). The pipeline was tested on a MicroCT dataset of C57BL/6 mice that underwent destabilization of the medial meniscus (DMM) or Sham surgery (n=10/group). Operated and contralateral limbs were imaged in vivo (Viva80, Scanco Medial AG,10.3 m, 70 kVp, 114 A) at baseline (Week 0), weekly for the first month (Weeks 1–4), and at Week 8 post-operation.

Results

Application of the pipeline revealed distinct remodeling patterns. Abnormal bone formation was primarily localized along the edges of the tibial plateaus in operated limbs across both groups. Dynamic bone morphometry showed no significant differences between DMM and Sham groups in the operated limb over the analyzed period (Fig.1b). Larger differences were observed when comparing operated and contralateral limbs within each group. Specifically, the operated limb showed increased (BV/TV), prominently in the medial compartment from 4 weeks post-operation (Fig.1c-d). The responses at the medial and lateral side appeared similar, although at two weeks a small difference in (BV/TV) was noticed.

Discussion

Using a custom, open-source pipeline, this study provided a detailed temporal and spatial visualization of SB adaptation in the early stages following DMM surgery. Analysis revealed that early post-operative changes were generally similar between DMM and Sham mice, suggesting this phase is dominated by a shared remodeling response to surgical invasiveness. Consequently, within this time window, the use of the contralateral limb as an internal control is essential to localize and quantify early site-specific pathogenic alterations characteristic of OA.

Images (Optional)

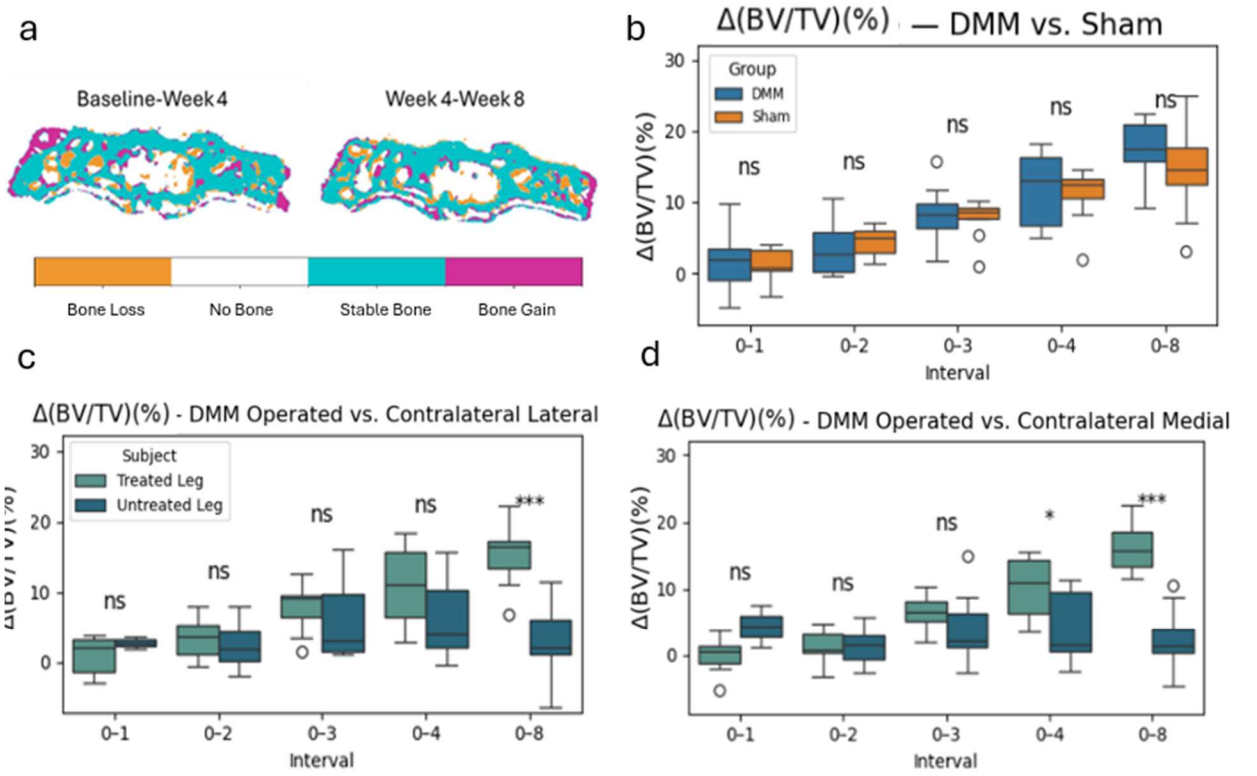


Figure 1 a) Voxel-to-voxel difference map comparing bone structure at baseline to Week 4 and comparing Week 4 and 8. Orange indicates bone loss and fuchsia bone gain localized in the tibial plateau. b) Δ(BV/TV) (%) comparison between Sham and DMM group operated limbs. c-d) Internal control comparison of Δ(BV/TV) (%) in DMM subjects comparing operated limb vs contralateral across time intervals. Lateral compartment is shown in c while Medial in d.

References (Optional)

[1] H. Fang *et al, Sci Rep*,**8**, no.1(2018)

Acknowledgements (Optional)

The authors thank Kathryn Stok, Jemima Schadow, and Emma Boersma (Department of Biomedical Engineering, The University of Melbourne) for performing the animal study and providing the microCT dataset, and the Biosciences Animal Facility at the University of

Melbourne for assistance with animal care and housing. This work was supported by funding from FWO and F.R.S.-FNRS under the Excellence of Science (EOS) program (EOS No. 40007553).

Session Category

Imaging and Biomedical Devices: Imaging Fundamentals and Applied Research

P4-305

Decoding Exercise Intensity Through Facial Action Units in Older Adults

Prof Chih-Chun Lin[1,2], Prof Yu-Sheng Lin[3], Prof Li-Chieh Kuo[4,2], Prof Fong-Chin Su[5,2], Prof James Jenn-Jier Lien[6], Prof Chi-Lun Cyrus Lin[7], Mr Bo-Sheng Chen[2], Dr Yung-Kuo Lee[8]

[1]Department of Physical Therapy, I-Shou University, Kaohsiung, Taiwan, Taiwan. [2]Medical Device Innovation Center, National Cheng Kung University, Tainan, Taiwan, Taiwan. [3]Department of Mechanical Engineering, Southern Taiwan University of Science and Technology, Tainan, Taiwan, Taiwan. [4]Department of Occupational Therapy, National Cheng Kung University, Tainan, Taiwan, Taiwan. [5]Department of Biomedical Engineering, National Cheng Kung University, Tainan, Taiwan, Taiwan. [6]Department of Computer Science and Information Engineering, National Cheng Kung University, Tainan, Taiwan, Taiwan. [7]Department of Mechanical Engineering, National Cheng Kung University, Tainan, Taiwan, Taiwan. [8]Medical laboratory, Medical Education and Research Center, Kaohsiung Armed Forces General Hospital, Kaohsiung, Taiwan, Taiwan

Introduction

Facial recognition technologies are increasingly used for identification and medical assessment. The Facial Action Coding System (FACS) categorizes facial movements into Action Units (AUs), but existing AU databases mostly include younger adults, and studies on AU responses to exercise or fatigue are limited. With population aging, promoting health and functional capacity in older adults has become an increasingly important priority. To address this gap, this study investigates changes in facial AUs in older adults by graded intensity exercise.

Methods

Facial expression data were collected from six older adults (68 ± 2.8 years; 1 male and 5 females) during exercise tasks. Participants completed three 7.5-minute lower-limb exercise sessions on the EIOT-ergo system[1] at predefined intensities: low (resistance level 2; 17.97 W; 40 RPM), moderate (level 5; 68.20 W; 60 RPM), and high (level 7.2; 81.64 W; 50 RPM). Video recordings were captured at 30 frames per second, resulting in a total of 243,000 frames. A YOLOv4-based model was trained and applied to detect and extract facial regions, with only frames achieving a face-detection confidence of at least 50% retained for analysis. OpenFace 2.0 was then applied to extract facial AUs.

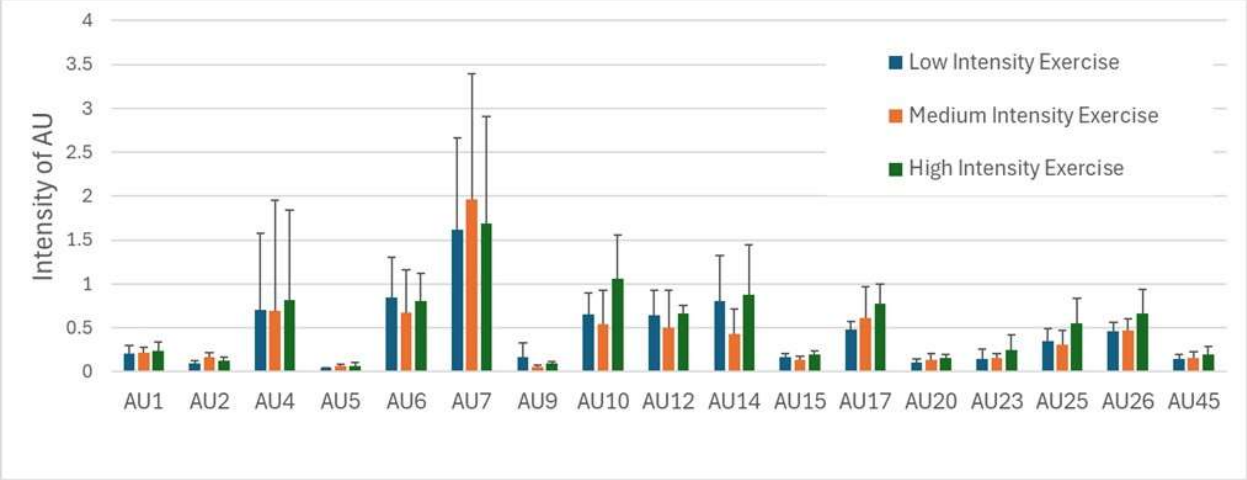
Results

The percentage of maximum heart rate (%MHR) is widely recognized as a strong indicator of exercise intensity. In this study, the %MHR increased with graded intensity exercise, and several facial Action Units—AU10 (Upper-Lip Raiser), AU17 (Chin Raiser), AU 23 (Lip Tightener), AU 25 (Lips Part), and AU26 (Jaw Drop)—showed progressive increases across intensity levels (see Figure 1). Among these, AU 17 exhibited the most pronounced elevation.

Discussion

AU12 (Lip-Corner Puller), previously linked to fatigue in young adults, showed no significant change in this study. Musculoskeletal pain after knee replacement has been associated with increased AU10, AU17, AU25, and AU26 activation. In our findings, older adults exhibited similar patterns in the above-mentioned AUs. Notably, AU23, which emerged in our analysis, has not been previously described. These results highlight distinctive facial AU patterns in older adults during exercise, underscoring the need for larger studies to better characterize these responses and advance intelligent exercise-monitoring for aging populations.

Images (Optional)



References (Optional)

1. Lin, C.C., et al., Gerontology, 2023

Session Category

P4-306

Associations Between Head Impact Kinematics and Regional Cortical Morphometry in Collegiate Ice Hockey Athletes

Mr. Daniel Bondi[1], Mr. Alex Jaffray[1], Mr. Zaryan Masood[1], Mr. David Luke MASc[1], Dr. Rebecca Kenny PhD[1], Dr. Adam Clansey PhD[1], Dr. Paul van Donkelaar PhD[2], Dr. Songbai Ji PhD[3], Dr. Alex Rauscher PhD[1], Dr. Lyndia Wu PhD[1]

[1]University of British Columbia, Vancouver, BC, Canada. [2]University of British Columbia, Kelowna, BC, Canada. [3]Worcester Polytechnic Institute, Worcester, Massachusetts, United States

Introduction

Alterations in cortical morphometry have been correlated with head impact exposure in contact sport athletes. However, the nature and extent of these alterations remain poorly characterized due to a lack of prospective longitudinal studies linking impact biomechanics to brain structure. This study examines cortical morphometric changes using neuroimaging and associates these with cumulative head impact exposure quantified through wearable sensor technology and independent risk factors.

Methods

Collegiate male ice hockey athletes underwent pre- and post-season neuroimaging across three competitive seasons (n = 42; UBC ethics: H21-00400). Athletes wore custom-fitted instrumented mouthguards (iMGs) throughout each season, with year-one kinematic data fully verified with missing data imputed, and available for analysis (n = 26). Linear mixed-effects models examined relationships between cortical morphometric measures (cortical thickness, cortical volume, sulcal depth, mean and Gaussian curvature) and independent variables across 14 frontotemporal regions-of-interest and 4 subcortical structures. The first model tested longitudinal associations between morphometric changes and independent risk factors including prior concussion history, alcohol consumption, and cannabis use over three years. Following, cumulative kinematic values were individually added to a second model restricted to year-one data to test associations with morphometric changes over a single season. These included peak linear acceleration (PLA), peak angular acceleration (PAA), and peak angular velocity (PAV). This model also tested the association of independent risk factors with morphometric changes.

Results

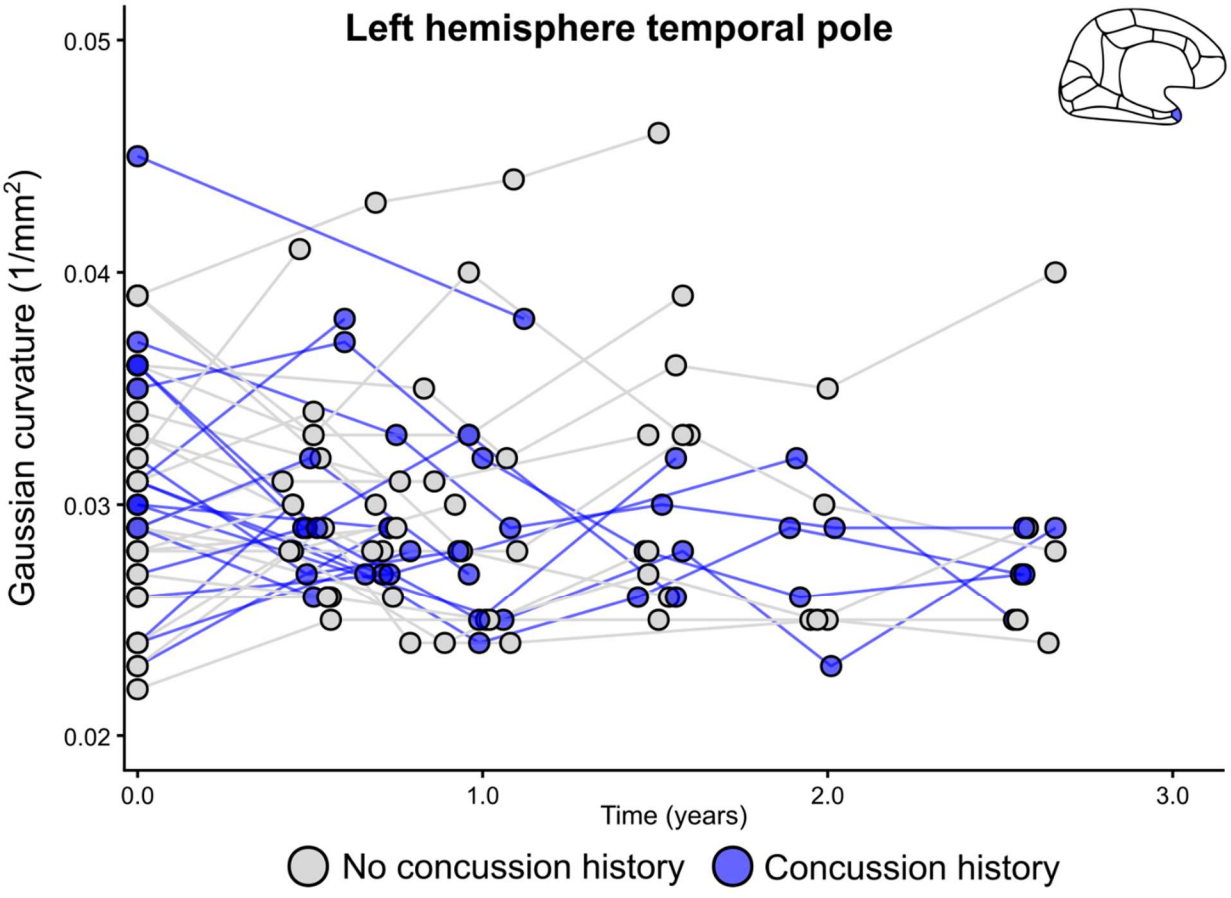
Over three years, athletes with prior concussion history demonstrated decreased Gaussian curvature in the left temporal pole compared to athletes without [-2.3E-03 mm^{-2}/yr; FDR-

corrected p = 0.03]. Over a single season, no statistically significant associations (FDR-corrected p < 0.05) were observed between any independent risk factor or cumulative kinematic measure and cortical morphometry across any region examined.

Discussion

The only longitudinal change observed was progressive flattening in the left temporal pole associated with prior concussion history, defined as a clinically-diagnosed concussion sustained within three years of study entry. No significant associations emerged over a single season for any independent risk factor or kinematic measure. These findings suggest that detectable morphometric changes may require sustained exposure beyond a single competitive season, and future studies should investigate kinematic associations across multiple years.

Images (Optional)



Session Category

Imaging and Biomedical Devices: Imaging Fundamentals and Applied Research

P4-307

MRI Diffusion Predicts Power Across the Lifespan

Dr. Daniel Desroches PhD, Dr. Janessa Drake PhD, Daniel Sheffield

York University, Toronto, Ontario, Canada

Introduction

Diffusion MRI Fractional anisotropy (FA) has been reported to non-invasively predict structural and functional changes such as muscular power with variable success – Scheel and colleagues [1] found a strong correlation (r=-0.85, p=0.0015) while Takao and colleagues [2] found no linear relationship (r=0.04, p=0.907). The ability to serially monitor changes over time may improve our understanding of age-related physical disability. This research evaluated the relationship between FA and ankle power output measured via countermovement jump (CMJ) with age as a crucial factor.

Methods

36 participants (23m & 13f, age 57.8 years) completed a warmup followed by three maximum effort repetitions. 3D optoelectronic motion capture (NDI 3D Investigator; 100Hz) and two 6DOF force plates (AMTI OR6-7;1200Hz) yielded ankle power. At a subsequent visit, participants underwent MRI diffusion of the soleus. Multiple linear regression was used to determine if age and FA of the soleus could predict ankle power.

Results

Age and FA of the soleus generated a statistically significant predictive model of ankle power (Figure 1; $F_{2,35} = 9.700$, $p < 0.001$, $R^2_{adj} = 0.332$). Both age and FA made significant contributions to the model age ($r_{Age} = -0.555$, $p < 0.001$; $r_{FA\ Sol} = -0.356$, $p = 0.036$). FA of the gastrocnemii and the tibialis anterior did not contribute significantly to the remaining three regression models ($p > 0.292$).

Discussion

This work is the first to demonstrate the combined effects of age and FA on ankle power. Previous work by Scheel and colleagues [1] found a strong negative correlation ($r_s = -0.85$) between FA of the soleus and ankle power measured via Biodex, likely due to their narrower and lower age range (27.2 ± 10.7 years). By comparison, our results showed a weaker effect of FA ($r_{FA\ Sol} = -0.356$) but a strong age effect on power ($r_{Age} = -0.555$) suggesting that effect of age should be a factor in future MRI diffusion investigations either in broadly-aged samples or investigations involving serial measurements.

Images (Optional)

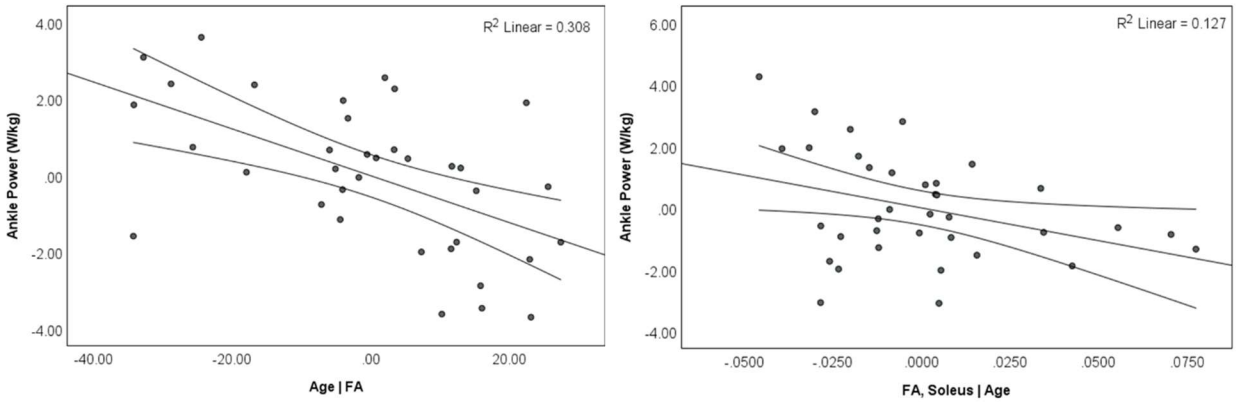


Figure 1 - The partial regressions showing the effects of age (left) and FA of the soleus muscle (right) on ankle power output during a CMJ. Age shows roughly twice the effect size in predicting ankle power, suggesting it should be included in future investigations if serial measurement or large age-spans are of interest. Error bands represent 95% confidence intervals.

References (Optional)

[1] Scheel et al., J Fortschr Röntgenstr, 2013

[2] Takao et al., Jpn J Radiol, 2022

Session Category

Imaging and Biomedical Devices: Imaging Fundamentals and Applied Research

P4-308

Interrogating Amplified Femtosecond Laser Ablation to Induce Controlled Microvessel Rupture and Localized Bleeding in Mouse Patellar Tendon

Ms. Diane Stonestreet, Dr. Nelly Andarawis-Puri

Cornell University, Ithaca, New York, United States

Introduction

Tendinopathies are common injuries that heal ineffectively with dysregulated inflammation.[1] Dry needling is a treatment that intends to disrupt the tendon's chronic degeneration by inciting inflammation and localized bleeding, though its clinical success varies.[2] Our current work uses Amplified Femtosecond Laser (AFL) ablation to isolate damage mechanisms of cell necrosis, extracellular matrix (ECM) microdamage, and vascular rupture, mimicking dry needling. Our prior studies have optimized cell and ECM ablation. This study examines AFL ablation for microvessel rupture in mouse patellar tendon in vivo.

Methods

Under IACUC approval, animals were anesthetized and injected with FITC dextran (50µL, 1% v/v, RO) and propidium iodide (50µL, 1.5mg/mL, SQ) <1 hour prior to imaging. Imaging and ablation were conducted simultaneously using a custom two-photon microscope. Z-stacks of the targeted region were obtained immediately before and after ablation, and animals were euthanized after imaging concluded. Using ImageJ, fluorescent intensity of FITC in a 15µm radius surrounding the blood vessel was compared before versus after ablation using a paired t-test (*p<0.05, #p<0.10).

Results

Blood vessels within the peritendinous tissue ruptured at a laser energy of 50-250nJ and 1-100 pulses. Timelapse images show leakage from the targeted vessel immediately post-injury, and death of endothelial cells in the vessel wall (Fig 1A-1D). There was a trend towards decreased FITC signal surrounding the vessel after ablation (Fig 1E). No tenocytes underneath the targeted vessel exhibited increased propidium iodide signal after ablation, indicating tenocyte survival.

Discussion

This is the first study using AFL ablation to induce precise microvessel rupture in tendon in vivo. As dextran binds to blood plasma, FITC signal decreasing following ablation indicates presence of red blood cells flooding the space surrounding the vasculature. Targeted

ablation of blood vessels causes localized bleeding without inducing tenocyte necrosis or ECM microdamage, allowing precise interrogation of each damage modality. Isolating the impacts of these damage mechanisms on tendon inflammation and healing is critical in the development of precision therapies for chronic musculoskeletal disorders with dysregulated inflammatory responses.

Images (Optional)

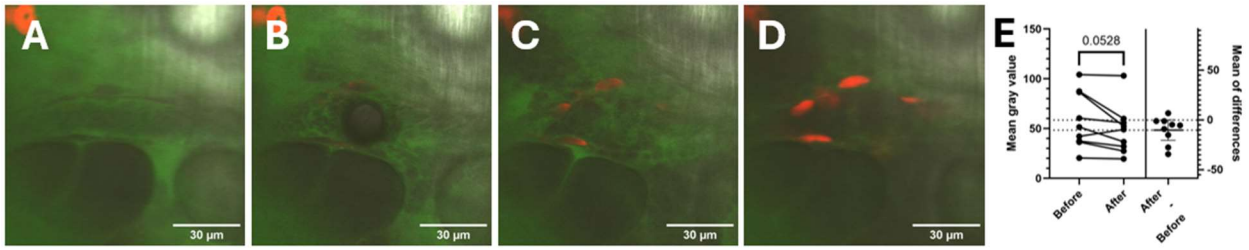


Figure 1: Blood vessel (A) before, (B) during, (C) 20s after, and (D) 2mins after ablation. (E) Mean signal intensity surrounding blood vessel before versus after ablation.

References (Optional)

[1] George Jomaa et al., *BMC Musculoskelet Disord,* 2020. [2] Vladimir Stoychev et al., *Curr Rev Musculoskelet Med,* 2020.

Acknowledgements (Optional)

NIH R01AR084173, NIH R01EB033179, NSF DGE 2139899, Cornell SPROUT.

Session Category

Imaging and Biomedical Devices: Imaging Fundamentals and Applied Research

P4-309

Comparison of In-Shoe and Barefoot Plantar Pressure Maps for High-Pressure Region Identification in Diabetic Adults

Research Engineer Dylan Heino MS[1,2], Principal Investigator Scott Telfer EngD[1,2,3], Research Engineer Avocet Nagle-Christensen BS[1], Principal Investigator William Ledoux PhD[1,2,3], Principal Investigator Brittney Muir PhD[1,2]

[1]VA RR&D Center for Limb Loss and MoBility (CLiMB), Seattle, WA, United States. [2]Department of Mechanical Engineering, University of Washington, Seattle, WA, United States. [3]Department of Orthopaedic Surgery and Sports Medicine, University of Washington, Seattle, WA, United States

Introduction

Foot ulceration is a serious complication of diabetes, often linked to elevated forefoot pressures. Custom accommodative insoles can reduce peak plantar pressures, with greater reductions achieved when dynamic pressure data informs design. While in-shoe and barefoot pressure data are used independently to guide insole fabrication in research, their agreement in pressure distribution and location of high-pressure regions (HPRs) has not been evaluated. This study compares plantar pressure distribution and HPR mapping between in-shoe and barefoot walking in individuals with elevated forefoot pressures.

Methods

In-shoe and barefoot plantar pressures were collected during walking for 25 feet from 16 individuals with elevated forefoot peak plantar pressure (PPP). Pressures were captured using pedar-X insoles and an emed platform. In-shoe and barefoot pressure maps were averaged across trials and trimmed to the distal 50% of the foot. Barefoot trials were aligned using a global grid for averaging. Both maps were normalized by PPP thresholds (>200 kPa in-shoe; >450 kPa barefoot), overlaid at corresponding midpoints, and pressure differences for overlapping sensels were visualized. HPRs were identified, masked, and labeled by anatomical region. Barefoot HPRs within the same region but separated by one sensel were merged. For matched HPRs between systems, PPP, contact area, and centroid location were compared. Regions appearing in only one system were classified as unmatched, and PPP and contact area were averaged across trials.

Results

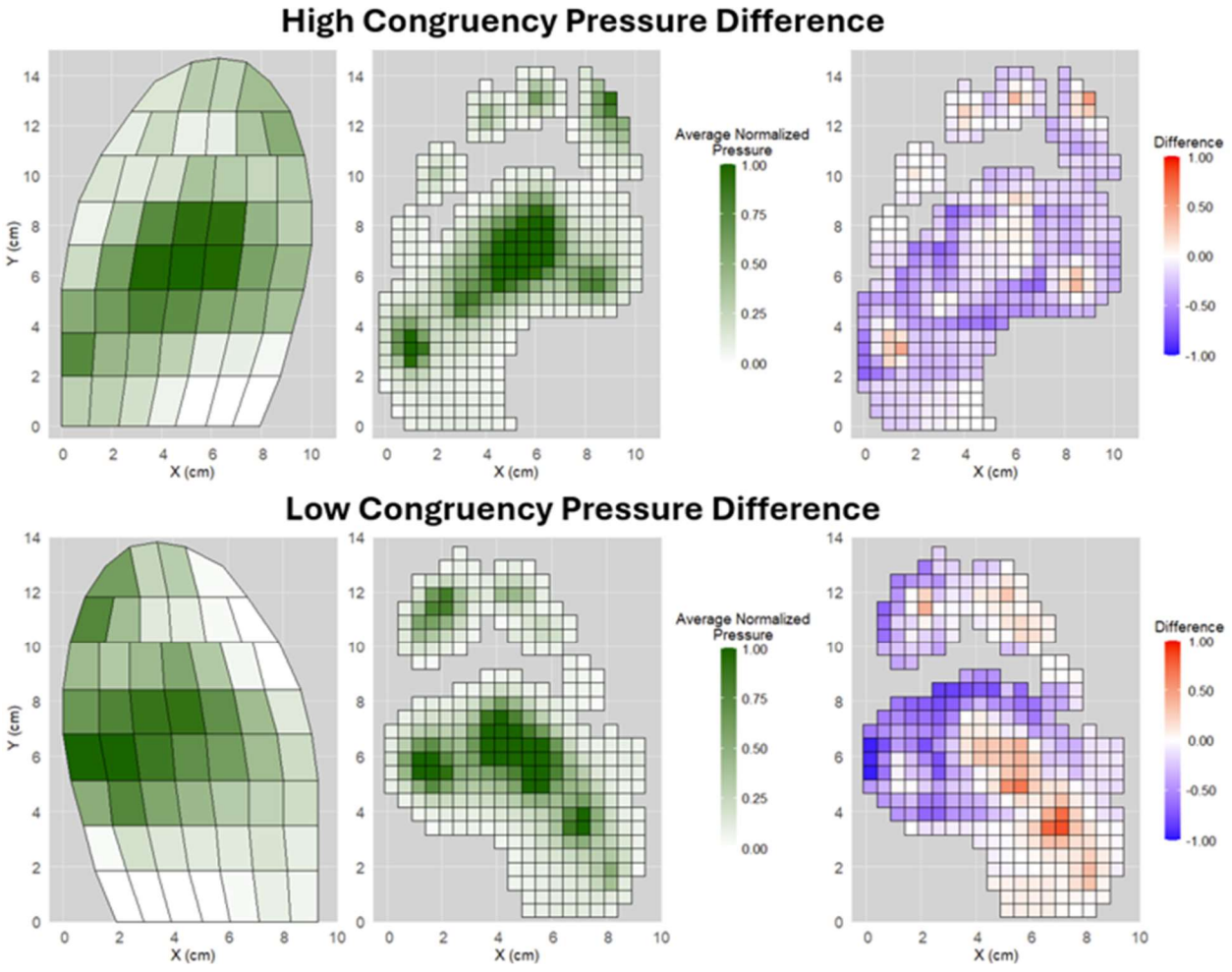
In-shoe high-pressure regions (>200 kPa) were typically observed in similar locations to barefoot walking, while barefoot maps often identified additional regions (>450 kPa) in the

toes and lateral forefoot. For in-shoe data, matched regions had lower peak pressures and larger contact areas. For matched regions, centroid positions differed by 0.23–0.60 cm.

Discussion

Key loading areas were spatially consistent between systems, though unmatched regions were common, particularly in barefoot data, reflecting greater sensitivity to localized pressures. Using barefoot data for insole design may help identify a broader set of high-risk regions, supporting a more conservative ulcer-prevention strategy. However, it may introduce excessive offloading that compromises performance in other regions. Future work comparing pressure offloading capabilities of insoles designed from in-shoe and barefoot plantar pressure is needed.

Images (Optional)



Acknowledgements (Optional)

We acknowledge Kimberly A. Nickerson, Mathew Sunil Varre, Christina Carranza, Ellen Y. Li, Ellen Clarissimeaux, and Leo Gagnon from the Department of Veterans Affairs for their contributions to data collection.

Session Category

Imaging and Biomedical Devices: Imaging Fundamentals and Applied Research

P4-310

Dynamic In-Vivo Pulsatility Analysis for W-Stent Graft Rings in Abdominal Aortic Aneurysm Patients After Endovascular Aneurysm Repair

Miss Elke Hestermann MEng[1], Ir Marleen Krommendijk[1], dr. Hadi Mirgolbabaee[1], dr. Erik Groot Jebbink[1,2], Prof. dr. Michel M.P.J. Reijnen[1,2], Prof. dr. Robert H. Geelkerken[1,3]

[1]University of Twente, Enschede, Overijssel, Netherlands. [2]Rijnstate Hospital, Arnhem, Gelderland, Netherlands. [3]Medisch Spectrum Twente, Enschede, Overijssel, Netherlands

Introduction

Endovascular aneurysm repair (EVAR) is the preferred method to treat abdominal aortic aneurysms (AAA), although EVAR still has a reintervention rate of up to 20% due to complications such as stent migration and endoleaks. One third of the reinterventions occur because of endoleaks, with type 1 endoleaks resulting from improper sealing or fixation at the proximal or distal stent locations, exposing the aortic wall to arterial pressure and pulsatile flow. This highlights the importance of understanding the dynamic behavior of stent graft fixation to improve post-operative patient care.

Methods

Electrocardiogram (ECG)-gated computed tomography (CT), a validated method used previously for saddle-shaped stent rings, was employed in this study to analyze interactions between the aortic wall and implanted stent grafts in 10 patients at discharge, 6 months, and 12 months after receiving the E-tegra stent graft within the EASYII study. To segment the stent rings, the established algorithm was adapted to fit the W-rings of the E-tegra; allowing quantification of the proximal sealing rings' pulsatility and displacement during the cardiac cycle. Pulsatility is defined as the change in diametric distance in the anterior-posterior (AP) or left-right (LR) direction determined by fitting ellipses through the four strut levels of the W-rings.

Results

The results showed that the proximal sealing rings demonstrated no significant change over 12 months. Figure 1A shows both rings experienced a higher AP pulsatility than LR pulsatility, with values of 0.38±0.22mm, 0.40±0.18mm, 0.37±0.15mm and 0.17±0.07mm, 0.20±0.06mm, 0.20±0.07mm for Ring 1 and 0.40±0.19mm, 0.36±0.15mm, 0.35±0.15mm and 0.15±0.06mm, 0.20±0.11mm, 0.17±0.07mm for Ring 2 at discharge, 6 months, 12 months, respectively. Mean 3D displacement (Figure 1B) was 0.95±0.32mm at discharge, 0.96±0.41mm at 6 months and 1.09±0.32mm at 12 months, with overlapping data points.

Discussion

This interim analysis of 10 patients with 12-month follow-up after EVAR demonstrated minimal change in E-tegra‘s proximal sealing rings. Using stent graft segmentation, in vivo pulsatility and displacement were quantified and indicated no significant change. These results confirm limited motion within the first post-operative year and imply stable stent behavior over this period.

Images (Optional)

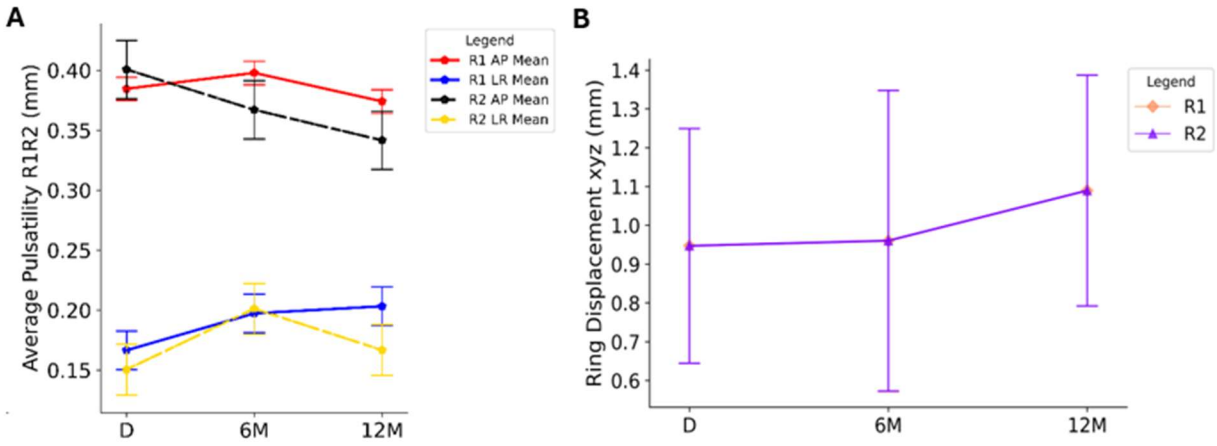


Figure 1: (A) The average pulsatility in the anterior-posterior (AP) direction and in the left-right (LR) direction for both the first stent ring (R1) and second stent ring (R2) over the cardiac cycle, throughout the follow-up period. (B) The 3D displacement over the cardiac cycle for the first stent ring (R1) and second stent ring (R2) during the follow-up period. D, discharge; 6M, 6 months after EVAR; 12M, 12 months after EVAR.

Session Category

Imaging and Biomedical Devices: Imaging Fundamentals and Applied Research

P4-311

Longitudinal Structural Changes to Whole Knee Joint With Progression of OA Using *in Vivo* Micro Computed Tomography Imaging

Dr Han Liu PhD, Ms Emma Boersma, Dr Julia Gregory PhD, Dr Mateus Silva PhD, Dr Cathrine Davey PhD, Dr Kathryn Stok PhD

Department of Biomedical Engineering, The University of Melbourne, Melbourne, Victoria, Australia

Introduction

Structural alteration of the whole knee joint has an important role in the progression of musculoskeletal disorders [1]. Longitudinal data can provide spatial-temporal information on disease progression that can be linked to mobility and biomechanics. This proof-of-concept study aims to establish a longitudinal *in vivo* microCT imaging protocol to track mechanical alteration in whole joint structure in a mouse osteoarthritis (OA) model.

Methods

Eight nine-week-old male C57BL/10 mice were evenly assigned to control (CT) and OA groups. To induce OA, a single intra-articular injection of collagenase was administered to the right knee joints of mice in the OA group at ten-week-old. *In vivo* micro-computed tomography (microCT) scans (vivaCT80, Scanco Medical, 10.4 µm, 70 kVp, 350 ms, 114 µA, 1000 projections) were performed one day prior to collagenase injection and then weekly for eight weeks (nine scans per animal). A positioning device was used for consistent joint pose.

Lateral and medial joint space width $JSW_{L/M}$ (mm), volume $JSV_{L/M}$ (mm^3)and the orientation angle, β°, defined by the femur-tibia centre-of-mass vector relative to the animal's transverse axis, were measured [2]. To examine the differences between CT and OA group at each time point, a one-way ANCOVA was used.

Results

Representative three-dimensional visualization of joint space regions of CT and OA groups over time are shown in **Figure 1A**. Joint alignment was altered following collagenase injection in the OA group. Specifically, three weeks post OA-induction, a significantly smaller JSW was observed in the medial OA joint (**Figure 1B**). This corresponded with increasing JSW on the lateral side, and a decrease in β (**Figure 1C**).

Discussion

This study, for the first time, demonstrated the application of a longitudinal *in vivo* microCT imaging protocol for tracking structural changes in the whole knee joint in a mouse OA model. Joint malalignment, indicated by reduced JSW on the medial side and femur shifting to the animal's transverse axis, was detected three weeks post collagenase injection. Combined with future mechanical loading tests, this work has the potential to provide deeper insights into the mechanisms of musculoskeletal disorders.

Images (Optional)

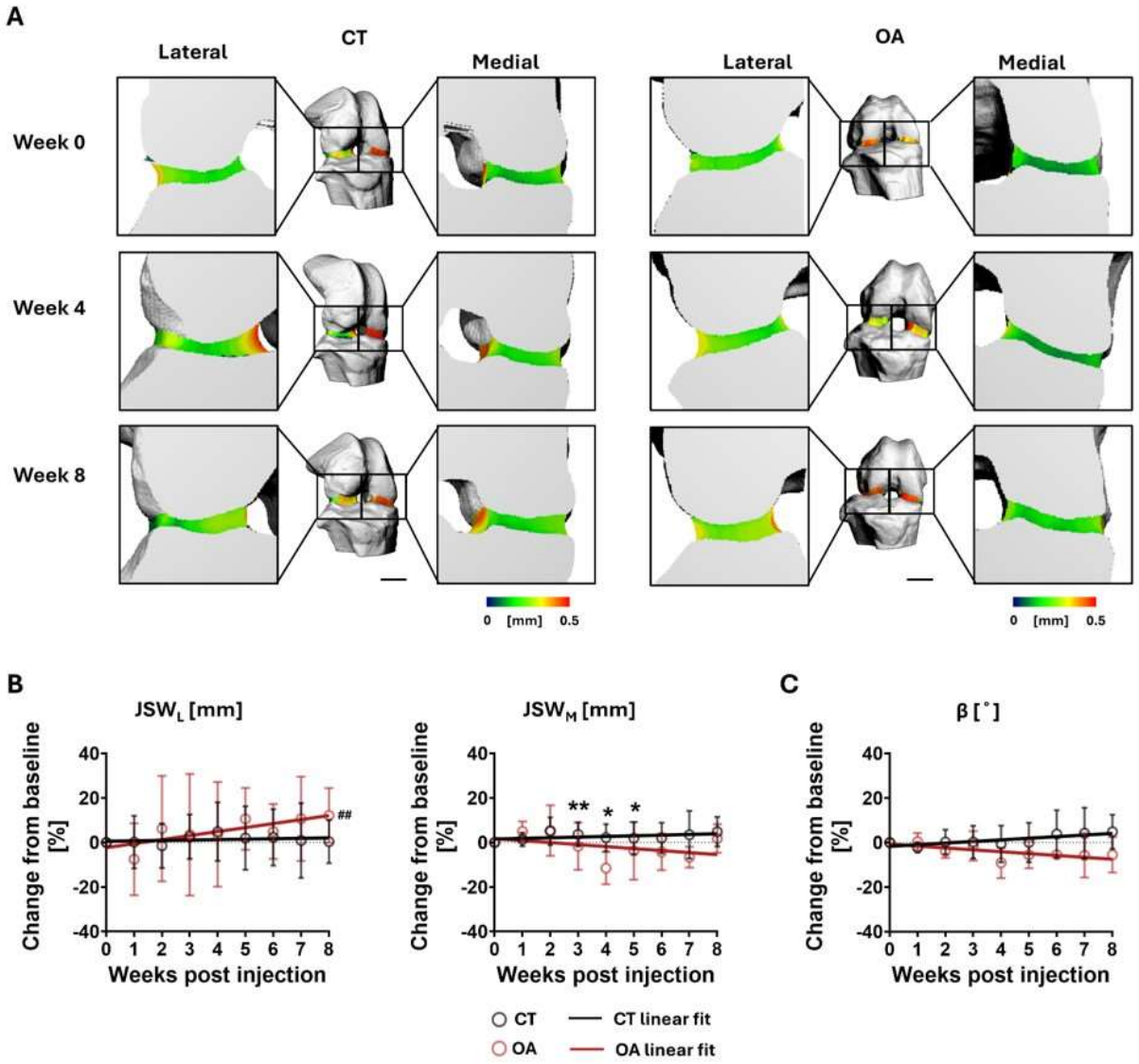


Figure 1. (A) Representative three-dimensional visualization of joint space regions of CT and OA groups at multiple time points with femur (top) and tibia (bottom). Inset: cross-sectional view of joint space region enlarged on both lateral and medial sides. (B) Joint space width measures from both lateral, JSWL, and medial, JSWM, and (C) Centre of mass measure of transverse axis alignment, β, from CT and OA groups, expressed as percent change from week 0 (baseline) with linear fits. ## indicates significant effect of time within OA group, $p < 0.01$. * indicates significant difference between CT and OA group, $p < 0.05$; **, $p < 0.01$.

References (Optional)

[1] Man GS et al., 2014.

[2] Durongbhan P et al., 2023.

Acknowledgements (Optional)

This project is supported by the Discovery Project scheme of the Australian Research Council (DP180101838), and China Scholarship Council stipend (Han Liu). Our thanks to animal facility staff for their training in mice handling, expertise in the welfare of animals, advice and technical help (Melbourne Bioresources Platform, The University of Melbourne, Australia); Dr Pholpat Durongbhan for his technical help with data analysis (Integrative Cartilage Research Group, Department of Biomedical Engineering, The University of Melbourne, Australia).

Session Category

Imaging and Biomedical Devices: Imaging Fundamentals and Applied Research

P4-312

Contrast-Enhanced 3D Ultrasound for Real-Time Iterative Catheter Placement During Radioembolization, A Proof of Concept

MSc. Jan van der Hoek[1], BSc. Nikita de Haan[1], MSc. Shannen Ubbink[1], Msc. Marleen Krommendijk[1], MSc. Remco Liefers[2], Dr. Erik Groot Jebbink[1]

[1]Multi-Modality Medical Imaging Group, TechMed Centre, University of Twente, Enschede, Overijssel, Netherlands. [2]Simulation Centre, TechMed Centre, University of Twente, Enschede, Overijssel, Netherlands

Introduction

Worldwide, hepatocellular carcinoma (HCC) ranks as the third leading cause of cancer-related deaths [1]. For advanced HCC palliative treatment via transarterial radioembolization (TARE) is routinely used [2]. During the procedure, radioactive microspheres are injected intra-arterially and lodge in the tumor vasculature. It was shown that patient survival improves with increasing tumor radiation-absorbed dose, however, realizing high radiation doses at the tumor is challenging as limited feedback is available during the procedure, while the microsphere injection location is of high importance [3]. Therefore, our goal is to use 3D ultrasound and contrast microbubbles as harmless precursors of the microspheres to real-time and iteratively improve the catheter position and maximize the tumor dose.

Methods

A microcatheter was advanced under fluorscopy (ARTIS Pheno, Siemens Healthineers) in the arterial system of normothermic, machine perfused, ex-vivo, non-tumorous porcine livers. A low concentration (1:40 diluted clinical dose) ultrasound contrast microbubbles (Sonovue, Bracco Suisse) was continuously injected. Simultaneously freehand, electromagnetically tracked (NDI Aurora, NDI Europe GMBH) ultrasound contrast-mode sweeps (9L4 probe, Siemens Acuson S2000, Siemens Healthineers) were recorded to obtain 3D reconstructions of the microbubble distributions in the liver, using the Plus toolbox. After several iterations, non-irradiated holmium-165 microspheres (Quirem Medical B.V.) were injected at the optimal catheter position. Thereafter, the microsphere biodistribution was visualized using a $T2^*$ multi-gradient MR scan (1.5T Aera, Siemens Healthineers) to evaluate the microbubble prediction.

Results

Fluoroscopy allowed catheter navigation (Figure 1A), followed by three iterations of contrast injections and 3D ultrasound sweeps (Figure 1B) to isolate the target location.

Subsequent MRI scanning confirmed the injected holmium-165 microspheres lodged predominantly at the target location, corresponding to the microbubble prediction (Figure 1C).

Discussion

Our proof-of-concept shows the feasibility of using 3D ultrasound sweeps to support catheter placement during TARE procedures. Future pilot patient studies should prove clinical feasibility.

Images (Optional)

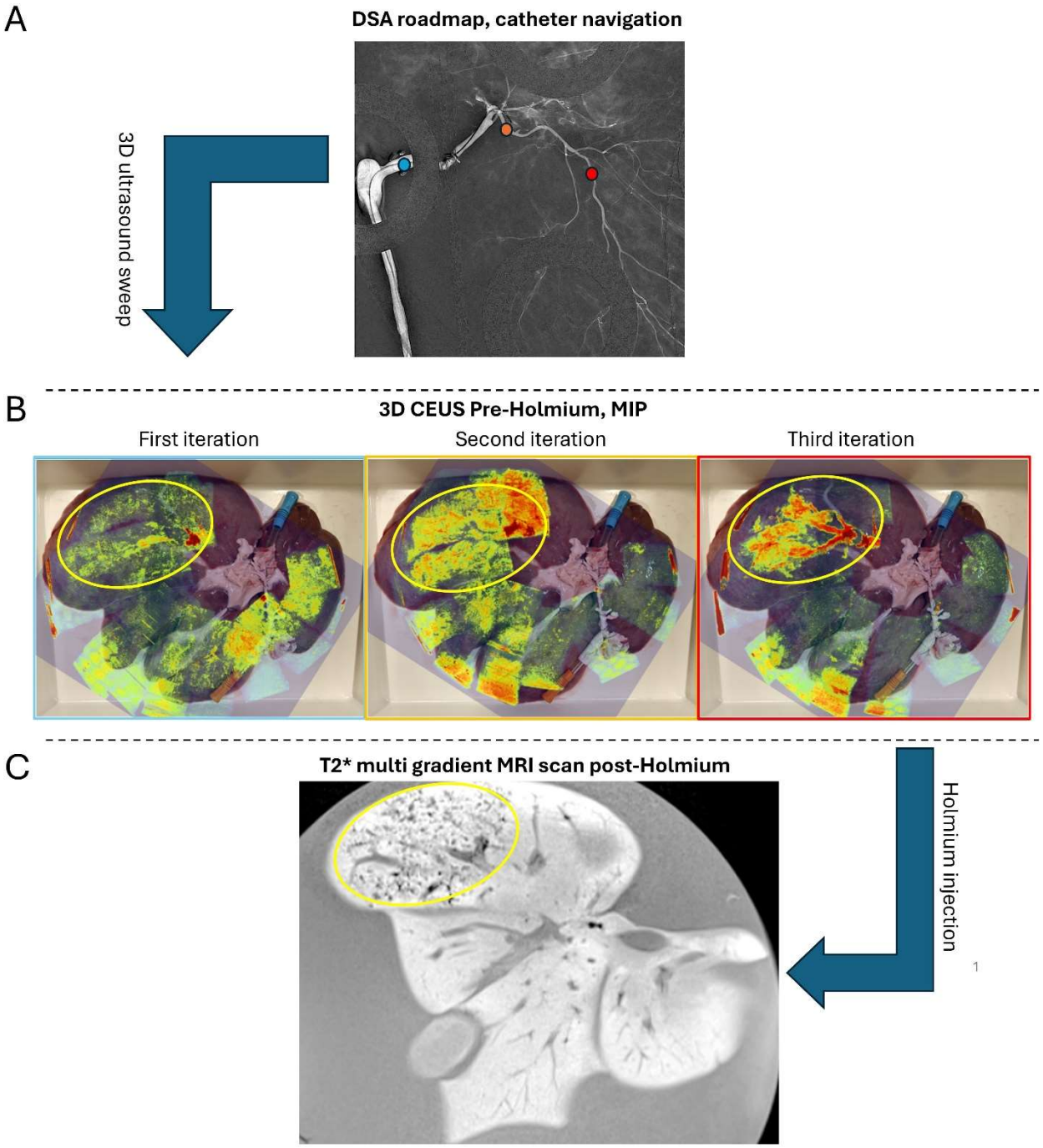


Figure 1, A. Catheter locations indicated by the blue, orange and red dots on the digital subtraction angiography (DSA) roadmap. B. Target area indicated by the yellow circle. After each catheter displacement, a contrast-enhanced 3D ultrasound sweep was performed, border color corresponds with the catheter location from A, maximum intensity projection (MIP) results are shown. C. T2 MRI scan showing a matching distribution between the ultrasound and MRI data.*

References (Optional)

[1] National Cancer Institute. Liver cancer causes, risk factors, and prevention. 2024.

[2] Nicholas Voutsinas et al. Treatment of primary liver tumors and liver metastases, part 1: nuclear medicine techniques. Journal of Nuclear Medicine, 2018.

[3] Jorge Aramburu et al. Computational particle-haemodynamics analysis of liver radioembolization pretreatment as an actual surrogate. Int J Numer Method Biomed Eng, 2017

Session Category

Imaging and Biomedical Devices: Imaging Fundamentals and Applied Research

P4-313

Associations Between Echo Intensity and Isometric Strength in Lower Extremity Musculature in an Active Population

Dr. FJ Goodwin PT, PhD, DPT, Dr. Josie Clary PT, DPT, Dr. Hermes Gomez PT, DPT, Dr. Amanda Harris DPT, Dr. Carrie LaBonte DPT

Charleston Southern University, Charleston, SC, United States

Introduction

Diagnostic ultrasound provides insight into tissue composition by using echo intensity (EI) to reflect tissue brightness. Greater EI brightness in skeletal muscle is associated with lesser contractile elements and increased intramuscular fat and connective tissue. Greater EI brightness is also associated with lesser force generating capacity. Subsequently, lower EI values are associated increased muscular force generating capability. However, these relationships are most often seen in older subjects. The purpose of this study is to observe the relationship between EI and muscular strength in young, athletic individuals. The hypothesis was that lower EI values (i.e. better muscle quality) would correlate with greater muscular performance.

Methods

Twelve active individuals (4 M, 8 F; 25.7±2.6 y.o; 1.71±0.06 m; 70.3±20.1 kg) participated in this study. Subjects were free from injury and meet the minimum level of activity per the ACSM Guidelines. Cross-sectional diagnostic ultrasound images were captured of the right vastus medialis oblique (VMO) and right lateral gastrocnemius (LG). EI was then calculated via ImageJ. Subjects then completed maximal voluntary isometric contractions via a HUMAC dynamometer seated at 90 degrees of knee flexion and prone with ankle in neutral to capture right knee and right ankle plantarflexion torque respectively. Pearson correlations were calculated for R VMO EI and average right knee isometric peak torque and time to peak torque. Correlations was repeated for R LG EI and muscular performance measures.

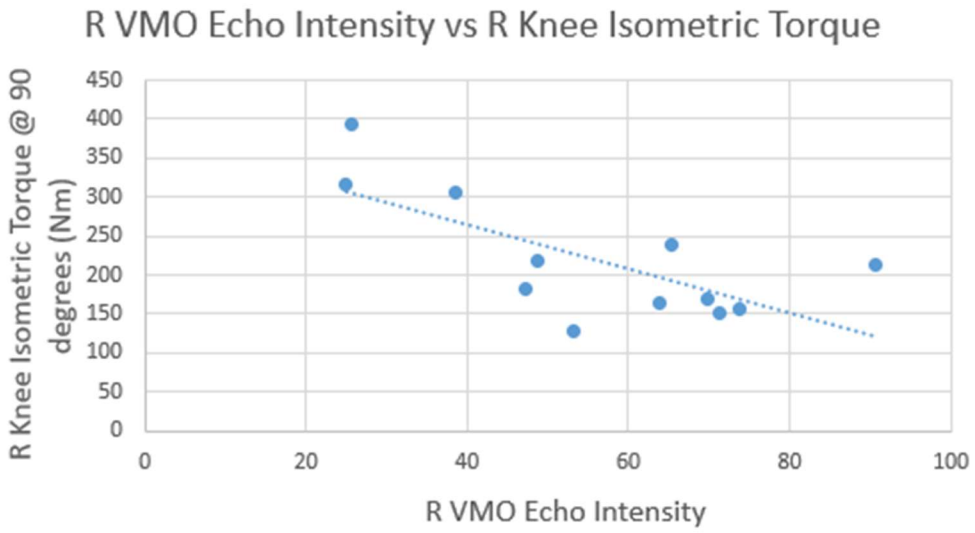
Results

There was a significant, negative correlation between R VMO EI (56.08±19.1) and average right knee peak isometric torque (219±77.34 Nm) ($r = -0.702$, $p=0.01$). There were no statistically significant associations with R VMO EI and time to peak ($p=0.52$). There were also no statistically significant associations with R LG EI and average right ankle plantarflexion torque ($p=0.50$) and time to peak ($p=0.69$).

Discussion

Our findings support our hypothesis that lower EI would reflect greater torque capability in a younger population in the R VMO. However, this was not reflected in the R LG or time to peak torque. These findings suggest assessments of muscular quality (EI) and muscular performance may differ across varied muscle groups in a younger population.

Images (Optional)



References (Optional)

Session Category

Imaging and Biomedical Devices: Imaging Fundamentals and Applied Research

P4-314

Diffusion MRI Method for Estimating Architecture-Based Physiological Cross-Sectional Area in Skeletal Muscle

Mr Zhenhao Liu M.S.[1], Dr Geoffrey Handsfield PhD[1,2]

[1]University of North Carolina at Chapel Hill, Chapel Hill, NC, United States. [2]North Carolina State University, Raleigh, NC, United States

Mr Zhenhao Liu

Introduction

Physiological cross-sectional area (PCSA) is a determinant of force capacity in muscle [1] and is fundamentally defined as the combined cross-section of all fibers in parallel [2]. Presuming fibers are at optimal length, PCSA may be computed as:

(1) PCSA = muscle volume / mean fiber length

We refer to this as the VFL equation, which is sensitive to mean fiber length measurement. While convenient, the VFL equation (1) may also not accurately capture PCSA for muscles with complex architecture. Diffusion tensor imaging (DTI) enables *in vivo* characterization of muscle architecture and allows for a more robust estimation of PCSA derived from fiber tractography [3]. Here, we present a method to compute PCSA as the combined cross-sectional area of its fibers in parallel, using DTI tractography data. Using a similar method, we compute the related geometrical cross-sectional area (GCSA) [2] and compare both metrics to PCSA computed with the VFL equation.

Methods

DTI and T1 MRI data from a previous study were used, approved by the University of Auckland Human Participant Ethics Committee [4]. Muscles were manually segmented, and fiber tractography performed with DSI Studio. We developed an algorithm that

computed PCSA by estimating the global fiber direction, projecting all fiber points onto the orthogonal plane, and calculating the convex-hull area of the projection. GCSA was calculated by estimating local fiber orientations, generating perpendicular slicing planes along each muscle, intersecting them with the segmented mesh, and identifying the maximum interior slice area.

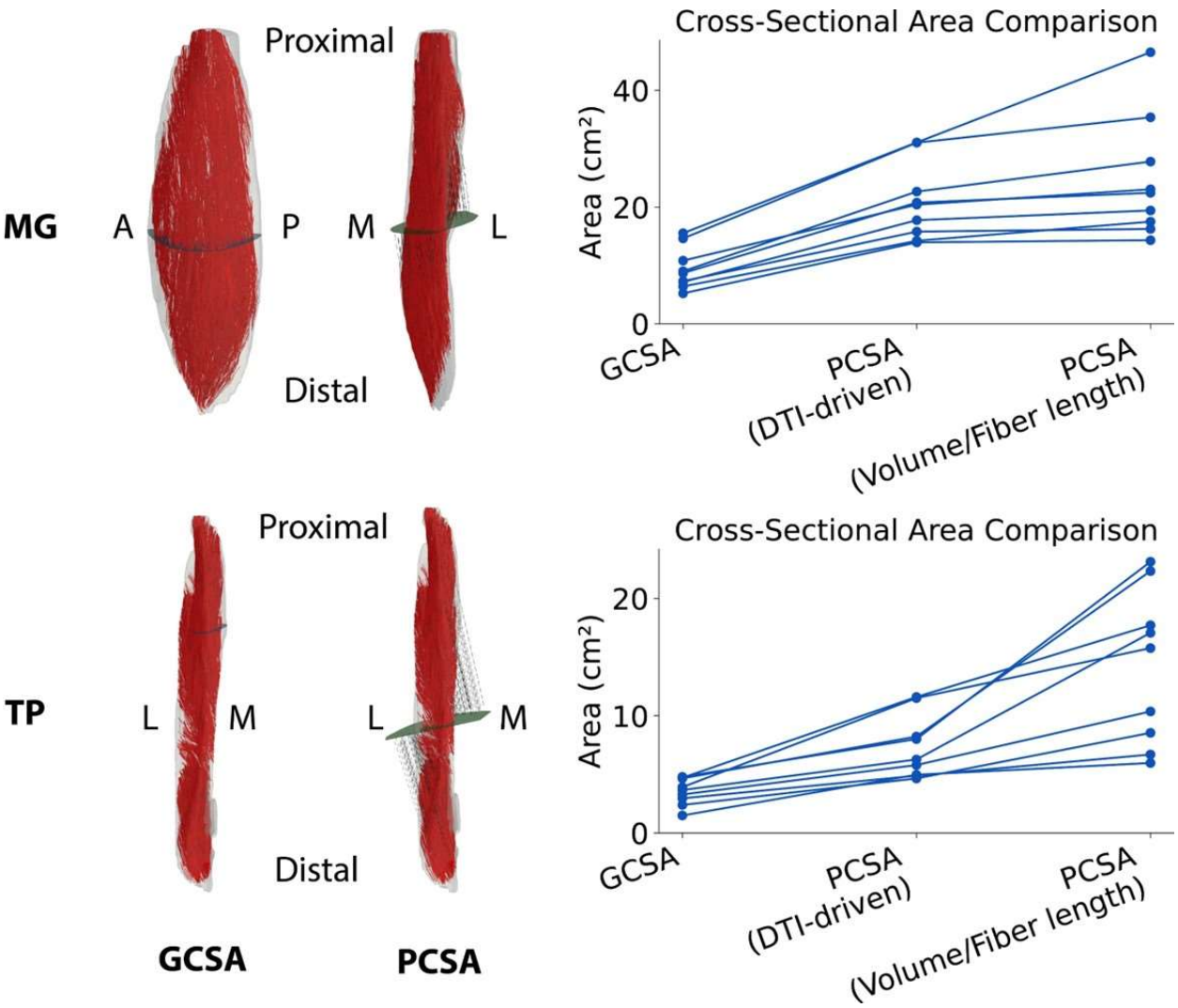
Results

DTI-derived PCSA and GCSA were anatomically consistent and reasonable, aligning with previous literature [2]. For the medial gastrocnemius (MG), PCSA was 20.85 ± 6.50 cm^2 and GCSA was 9.42 ± 3.59 cm^2, while for the tibialis posterior (TP), PCSA was 7.33 ± 2.72 cm^2 and GCSA was 3.54 ± 1.13 cm^2. DTI-based PCSA values were lower than VFL values, with percentage differences of 12.84% for MG and 42.98% for TP (Fig. 1).

Discussion

The VFL equation may over-estimate PCSA. With increasingly accurate digital data, more sophisticated methods may be used to determine muscle architectural parameters. We plan to extend this to additional muscles and empirically measured isometric force.

Images (Optional)



References (Optional)

Session Category

Imaging and Biomedical Devices: Imaging Fundamentals and Applied Research

P4-315

Physics-Informed Anisotropic Laplacian Modeling Enables Muscle Fiber Architecture Estimation from Conventional MRI Slices

Ms Negar Mehrabi M.S., Dr. Geoffrey Handsfield PhD

University of North Carolina, Chapel Hill, NC, United States

Ms Negar Mehrabi

Introduction

Characterizing skeletal muscle fiber architecture is important for estimating force-generating capacity. Diffusion Tensor Imaging (DTI), although widely adopted, suffers from low spatial resolution, signal instability, orientation bias, and partial-volume effects [1]. Laplacian-based fiber-generation methods can estimate muscle fiber fields but are unable to capture architectural deviations, as may be seen in pathological muscle. To overcome these limitations, we present a **physics-informed neural PDE framework that learns a patient-specific anisotropic Laplacian operator directly from MRI-derived structure-tensor representations** [2]**,** providing a novel approach to infer fiber architecture from structure-tensors derived from conventional MR images.

Methods

Segmented axial T1-weighted MRI slices of the medial gastrocnemius from one adolescent with cerebral palsy (CP) were used from previous study [3]. Local image-gradient structure was quantified using Sobel derivatives and assembled into a smoothed structure tensor, yielding a spatially varying base anisotropy field We then formulated a generalized anisotropic Laplacian PDE:

$$\partial/\partial x(Dxx\ \partial\phi/\partial x + Dxy\ \partial\phi/\partial y) + \partial/\partial y(Dyy\ \partial\phi/\partial y + Dxy\ \partial\phi/\partial x) + YS(x) = 0$$

$$\text{Where: } D(x) = D_{base}(x) + \Delta D_{net}(x)$$

A physics-informed neural network (PINN) optimized the fields ΔD_{net}, Y_{net} using PDE residual as physics loss, allowing the network to **discover the differential operator best reflecting slice-specific muscle conduction anisotropy**. Fiber orientations were extracted from principal eigenvectors of learned operator field *D(x)* (Figure 1). Spatially averaged coefficients were assembled into a **patient-specific slice-wise anisotropic operator**.

Results

Our method produced smooth, continuous, and anatomically coherent [4] fiber trajectories that captured patient-specific fiber architecture (here in an adolescent with CP) when compared to DTI (Figure 1). Example coefficient values given below:

$$\partial/\partial x(0.6008\ \partial\phi/\partial x - 0.2445\ \partial\phi/\partial y) + \partial/\partial y(0.6289\ \partial\phi/\partial y - 0.2445\ \partial\phi/\partial x) + 0.0022S(x) = 0$$

Discussion

This work introduces **patient-adaptive anisotropic Laplacian operators learned from structure-tensor fields**, demonstrating that conventional MRI contains sufficient information to generate fiber directions when coupled with physics-informed learning. Extension to 3D will enable volumetric fiber continuity and establish a path toward high-resolution fiber modeling directly from standard clinical MRI.

Images (Optional)

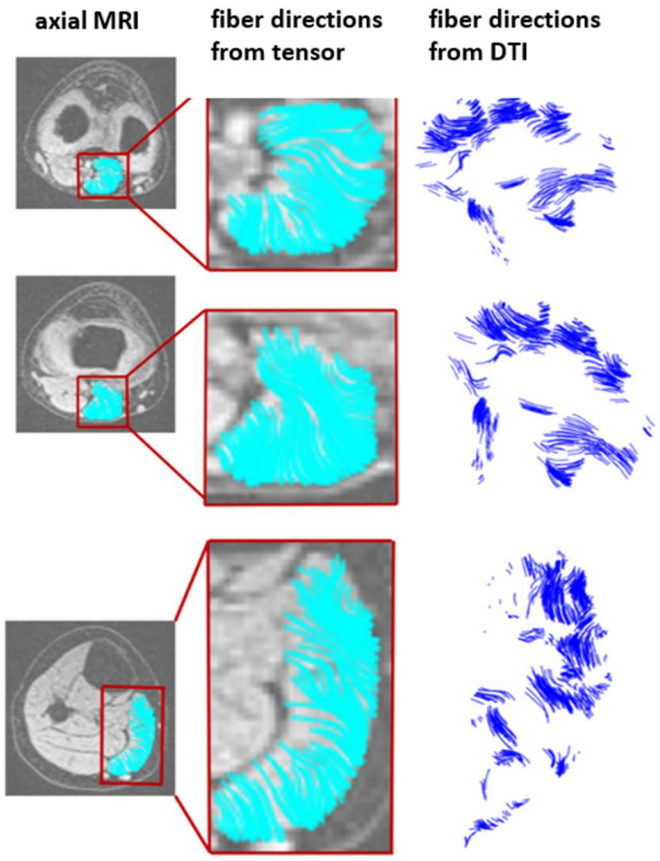


Figure 1 *Comparison of MRI-derived fiber architecture (inset) with DTI data projected into matched 2D slices. The structure-tensor method shows consistency with DTI where tracts are available in the noisy DTI dataset. Fiber directions from the structure-tensor are smoother and continuous and are consistent with fascicle patterns from the anatomical literature [4].*

References (Optional)

[1] Heemskerk et al. (2007) *CurrMedImagRev*; [2] Otake et al. (2017) *MICCAI;* [3] Sahrmann et al. (2019) *PLOSOne* [4]; Dalmau-Pastor, et al. (2014) *FootAnkleClinic*

Acknowledgements (Optional)

Session Category

Imaging and Biomedical Devices: Imaging Fundamentals and Applied Research

P4-316

µCT and HR-pQCT Texture and Finite Element Analysis as Imaging Biomarkers for Quantifying Diseases Related Bone Phentoypes: A Example in Iron-Deficiency Anemia.

MSc. BSc. Gerald Degenhart[1], MSc. Sonja Wagner[2,3], MSc. Johannes Bereiter-Payr[1], BSc. Thomas Ausserer[1], MSc. Elke Pertler[2,3], Prof. Dr. Heinz Zoller[2,3], Dr. Martina Saretto[2,3]

[1]Core Facility MicroCT Univ. Clinic. for Radiology Medical University Innsbruck, Innsbruck, Tirol, Austria. [2]Gastroenterology, Hepatology and Endocrinology, Department of Medicine I, Medical University Innsbruck, Innsbruck, Tirol, Austria. [3]Christian Doppler Laboratory on Iron and Phosphate Biology, Innsbruck, Tirol, Austria

Introduction

This study investigates a characteristic bone phenotype associated with iron-deficiency anemia (ID) using micro-computed tomography (µCT) in mice and high-resolution peripheral quantitative CT (HR-pQCT) in patients. We demonstrate how texture analysis (TA) and micro finite element analysis (µFEA) can function as imaging biomarkers to detect ID-related bone alterations. In the mouse model, we additionally compare treatment effects of three iron-replacement therapies.

Methods

Tibiae from 10-week-old mice were scanned using a vivaCT 40 (Scanco Medical AG). TA was performed in an 80-slice region below the proximal tibial growth plate. Five groups (n = 5/group) were analyzed: healthy controls (Ctrl), untreated ID, and ID mice treated from week 6 onward with ferric carboxymaltose (ID+FCM), ferric derisomaltose (ID+FDI), or low-molecular-weight iron dextran (ID+LMWID). ID was induced via a reduced-iron diet.

Two male ID patients (ages 35 and 64) with a chronic clinical history of iron deficiency were scanned at the distal radius and tibia using an XCT-2 system (Scanco Medical AG). In both species, cortical and trabecular TA metrics were quantified, and µFEA simulations of axial compression were performed to estimate bone mechanical competence.

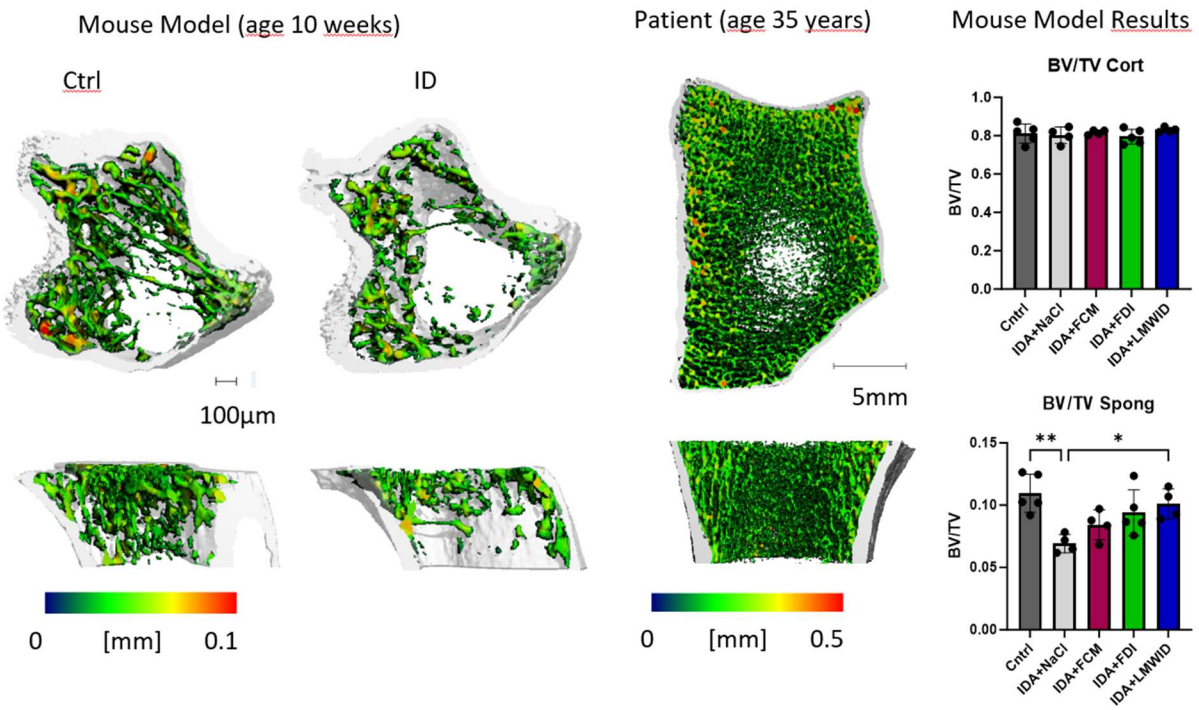
Results

In both mice and patients, cortical bone parameters showed no significant deterioration. However, the ID condition resulted in pronounced trabecular degradation compared to controls. Treatment partially restored trabecular structure, with the greatest improvement observed in ID+LMWID, followed by ID+FDI, and the smallest effect in ID+FCM. µFEA detected no statistically significant differences between mouse groups, although stiffness trends mirrored the TA findings. Patients displayed similar trabecular texture impairment but additionally reduced µFEA-derived mechanical stability.

Discussion

This study shows that TA and µFEA are suitable imaging biomarkers for detecting desease related bone phenotypes. Because ID can impair bone quality without overt structural collapse. Identifying disease-specific phenotypes is valuable beyond fracture prediction as overlooked deseases may be found. Therefore ability to non-invasively characterize bone alterations provides an opportunity to recognize and monitor metabolic and hematologic conditions with skeletal involvement at earlier stages. Moreover, the agreement between mouse and human observations supports the relevance of the ID mouse model for translational research and treatment evaluation.

Images (Optional)



Session Category

Imaging and Biomedical Devices: Imaging Fundamentals and Applied Research

P4-317

Non-Invasive Cartilage Histology: A Microscopy-Informed Machine-Learning Model for MRI-Based Proteoglycan Mapping in Osteoarthritis

MSc Ikram Mohout[1], Dr. Seyed Ali Elahi[1], Dr. Shannon Helsper[1], Dr. Willy Gsell[2], Prof. Uwe Himmelreich[1], Prof. Ilse Jonkers[1]

[1]KU Leuven, Leuven, Flanders, Belgium. [2]Bruker Preclinical Imaging, Kontich, Flanders, Belgium

Introduction

Cartilage degeneration is *the* hallmark of osteoarthritis (OA), characterized in early disease stages by extracellular matrix changes, including alterations in proteoglycan (PG) concentration [1]. Quantitative MRI (qMRI) can link image parameters to tissue composition; however, the exact relationship remains unclear [2]. This *in vitro* study applies a microscopy-informed machine learning approach to predict PG content from non-invasive qMRI data of cartilage, ultimately applicable *in vivo*.

Methods

Osteochondral cylindrical plugs (1cm diameter) were harvested from 14 hip arthroplasty OA patients; one plug per subject was snap-frozen. After thawing, plugs were imaged in PBS using a 7T scanner (Bruker Biospec) with T1, T2, and T1ρ mapping sequences [3]. Samples were processed for histology: cut at the imaging plane, fixed in formaldehyde, decalcified in EDTA, embedded in paraffin, sectioned at 3µm, stained with Safranin-O, and mounted for microscopy. Brightfield microscopy (Zeiss Axio Scan.Z1) was performed, and three sections per sample were analyzed.

Microscopy data of cartilage (~9 µm/pixel) were downsampled to match MRI resolution (0.313 x 0.156 mm/pixel) and semi-automatically registered using in-house code. A bagged regression tree model was trained pixel-wise on normalized qMRI parameters (T1, T2, and T1ρ) to predict PG content, using leave-one-out cross-validation and evaluated by Pearson's r and RMSE. Three plugs were excluded due to presumed staining artefacts or limited tissue overlap. Model fitting used 3,444 training and 1,663 testing pixels, with each plug used exclusively for training or testing to avoid bias.

Results

The model showed strong training performance (r= 0.878, RMSE= 0.162) and maintained predictive ability on the independent test set (r=0.623, RMSE=0.279), as shown in Figure

1a. Predicted PG maps reproduced key spatial patterns observed in microscopy (Figure 1b).

Discussion

This MRI-based, microscopy-informed machine-learning approach predicts cartilage PG content with moderately strong correlations. It advances earlier low-field studies with limited pixel counts [2] by using high-field MRI for the first time. This non-invasive method may support future assessment of cartilage constituents in OA using clinical imaging.

Images (Optional)

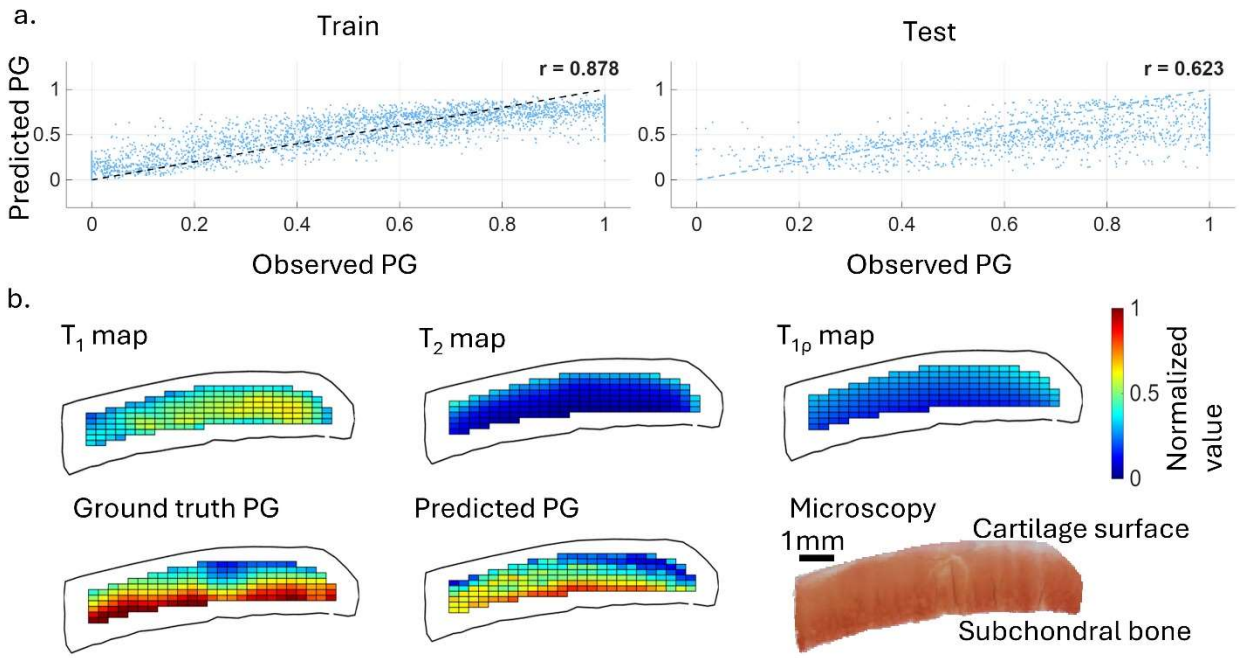


Figure 1. *(a)* Pixel-wise correlation between observed and predicted PG content for the training and independent test sets (bagged regression trees). *(b)* Example section showing normalized qMRI inputs (T1, T2, T1ρ), the corresponding Safranin-O histology, and the resulting ground-truth and predicted PG maps, illustrating spatial agreement between microscopy and model output.

References (Optional)

[1] S. A. Elahi, *et al.,* Osteoarthritis and Cartilage, 2023

[2] K. Linka *et al.,* Osteoarthritis and cartilage, 2021

[3] L. Zevenbergen *et al.,* Osteoarthritis and Cartilage, 2018

Acknowledgements (Optional)

This work was supported by the FWO fundamental fellowship (11M9422N). We gratefully acknowledge the Skeletal Biology and Engineering Research Center and VIB Bioimaging Core Leuven for assistance with histology.

Session Category

Imaging and Biomedical Devices: Imaging Fundamentals and Applied Research

P4-318

Hierarchical Phase-Contrast Tomography Reveals Multi-Scale Hard-Soft Tissue Architecture in the Intact Human Spine

Miss Isla Henderson[1], Dr Aikta Sharma[1], Dr Alissa L. Parmenter[1], Dr Joseph Brunet[1,2], Dr Theresa Urban[1,2], Dr Joanna Purzycka[2], Dr Hector Dejea Velardo[2], Dr Stefan Zwingenberger[3], Dr Timothy J. P. Bray[4,5], Dr Alexandre Bellier[6], Dr Paul Tafforeau[2], Professor Peter D. Lee[1]

[1]Department of Mechanical Engineering, University College London, London, London, United Kingdom. [2]European Synchrotron Radiation Facility, Grenoble, Auvergne-Rhône-Alpes, France. [3]University Centre of Orthopaedic, Trauma and Plastic Surgery, University Hospital Carl Gustav Carus at Technische Universität Dresden, Dresden, Saxony, Germany. [4]Centre for Medical Imaging, University College London, London, London, United Kingdom. [5]Department of Imaging, University College London Hospital, London, London, United Kingdom. [6]University Grenoble Alpes, Department of Anatomy (LADAF), Grenoble, Auvergne-Rhône-Alpes, France

Introduction

The spine has a highly complex hierarchical structure, with its biomechanical function critically reliant upon the integrated behaviours of its bone and soft tissue components. The current understanding of the structure-function relationships between these tissues in the healthy spine is limited by the low spatial resolution of conventional imaging modalities such as MRI. Hierarchical Phase-Contrast Tomography (HiP-CT) [1] is a novel synchrotron X-ray imaging technique that is capable of resolving both hard and soft spinal tissues at unprecedented resolution and was used herein to image an intact human spine for the first time.

Methods

The spine, from a 62-year-old male donor, was chemically fixed in formalin and mounted in a formalin-agar solution. HiP-CT images were acquired at voxel size of 16.26 µm using BM18 beamline at the European Synchrotron Radiation Facility (MD1290), with local regions of interest imaged at a voxel size of 2.2 µm. Vascular networks and nerve bundles were segmented using region-growing in VG Studio Max, and collagen fibres in the intervertebral disc (IVD) were traced using the XFiber module in Avizo 3D.

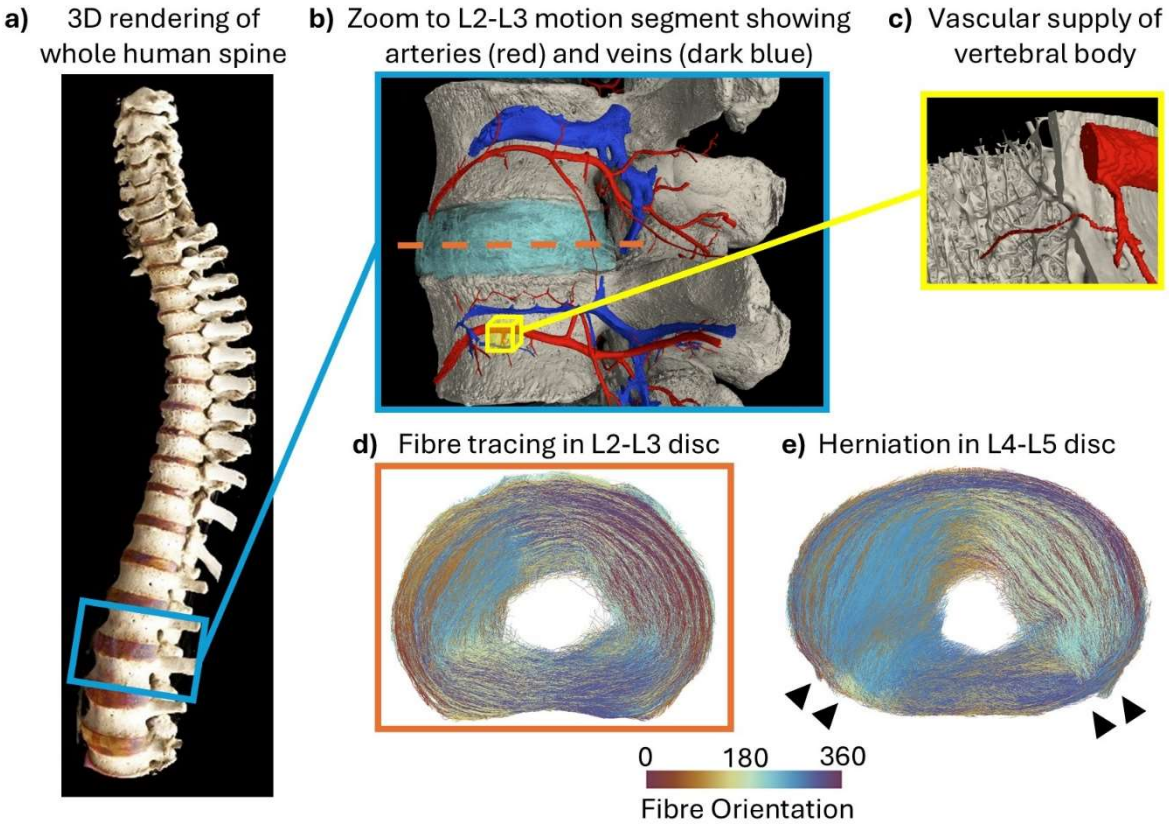
Results

HiP-CT enabled high-resolution visualisation of mineralised vertebral bodies, IVDs, vasculature, and nerve bundles without exogenous contrast agents. Virtual sectioning and 3D renderings of segmented structures provide valuable insight into spinal anatomy, including vascular supply and innervation of the vertebral body and IVDs (Figure 1). Fibre tracing revealed collagen fibre orientation within the IVD (Figure 1d) and identified disruption of the lamellar architecture in herniated discs (Figure 1e).

Discussion

Our methodology resolves the multi-scale anatomy of the human spine, enabling investigation into structural changes characteristic of healthy ageing and degenerative diseases. Future work aims to perform anatomically guided microarchitectural analyses on these images which will inform the development of finite element models that better capture disease progression.

Images (Optional)



References (Optional)

[1] Claire L. Walsh *et al.* Nat. Methods, 2021

Acknowledgements (Optional)

We kindly acknowledge funding from ESPRC (EP/T517793/1, EP/W524335/1), the Royal Academy of Engineering (CiET 1819/10), the Chan Zuckerberg Initiative Foundation (CZIF2022-316777), and ESRF (BM18, proposals MD1290/1389).

Session Category

Imaging and Biomedical Devices: Imaging Fundamentals and Applied Research

P4-319

VMamba-Pose: Efficient Multiperson Pose Estimation Using Visual State Space Models

Mrs Ivanna Kramer, Dr Sabine Bauer, Mr Jan Herschel, Prof. Dr. Dietrich Paulus

University of Koblenz, Koblenz, RLP, Germany

Introduction

Accurate Human Pose Estimation (HPE) from RGB-images is essential for biomechanical research, rehabilitation technologies and the development of assistive devices, as it enables markerless kinematics. This study introduces VMamba-Pose: a novel deep learning framework for the efficient processing of RGB images in biomechanics-related environments, specifically for multiperson HPE.

Methods

The presented model is derived from VMamba visual state space architecture [1], replacing computationally expensive self-attention with state space models that enable linear-time training and constant-time inference. VMamba-Pose follows a top-down approach partitioning input images into patches and processing through hierarchical Visual State Space blocks combining normalization, selective 2D scanning (SS2D), and feed-forward layers. The SS2D module performs four-directional scanning for efficient spatial feature extraction under complex motion and occlusions. The resulting representations are decoded into 2D-joint heatmaps, producing keypoint locations.

Results

Experiments were conducted on the MS COCO dataset using AdamW optimization, and four model scales -Tiny, Tinier, Small, and Base - were trained without any pre-training.

VMamba-Pose achieved accuracy comparable to state-of-the-art transformer models requiring significantly fewer parameters and substantially reduced computational load. VMamba-Pose-S reached 77.26% AP on COCO at 576×768 resolution, matching HRFormer and ViTPose-B. The lightweight VMamba-Pose-TR (6.99M parameters) delivered 75.34% AP, outperforming YOLOv5l6-Pose and GMamba, demonstrating its suitability for real-time embedded systems (see Table 1). Importantly, the models maintained stable performance across varying image resolution. Across evaluated VMamba models (VMamba-Pose-B), increasing the input resolution resulted in an average AP improvement of approximately 1.93%. The Tiny and Tinier variants further highlight the efficiency of the

architecture: VMamba-Pose-T, with 21.05M parameters, achieved an AP of 76.89%, while the more compact VMamba-Pose-TR, using only 6.99M parameters, still reached 75.34% AP.

The implementation of VMamba-Pose, along with visual results, is available in our open-source repository : https://github.com/VisSim-UniKO/VMamba-Pose.

Discussion

The model's linear-time computation and low parameter count make it well-suited for real-time imaging systems, wearable sensors, and assistive devices, where fast inference and minimal hardware load are essential. It provides an efficient alternative to transformer-based HPE, and its computational efficiency makes it appealing for real-time clinical monitoring, sports applications, and integration with biomechanical devices.

Images (Optional)

Model	Backbone	Image resolution (H×W)	Param (M)	AP (%)	AR (%)	FLOPS
ViTPose-B [16]	Vit-B	192×256	90.59	75.8	81.1	17.86G
ViTPose-B [16]	Vit-B	288×384	90.18	76.9	81.9	40.19G
ViTPose-B [16]	Vit-B	576×432	89.99	77.8	82.6	90.44G
HRNet [23]	HRNet-W32	256×192	29	74.4	78.9	7.69G
HRNet [23]	HRNet-W32	384×288	29	75.8	81.0	17.29G
YOLOv5l6-pose	CSP-darknet	960×960	87	69.4	75,9	11.71G
HRFormer[13]	HRFormer-B	256 × 192	43	75.6	80.8	14.11G
HRFormer [13]	HRFormer-B	384×288	43	77.2	82.0	30.89G
MambaPose [22]	GMamba	640×640	20.1	72.2	78.6	13.3G
VMamba-Pose-B	VMamba	384×288	93.83	74.95	80.29	36.11G
VMamba-Pose-B	VMamba	576×768	93.83	76.88	81.95	0.14T
VMamba-Pose-S	VMamba	576×768	54.6	77.26	82.28	85.91G
VMamba-Pose-T	VMamba	576×768	21.05	76.89	82.02	34.88G
VMamba-Pose-TR	VMamba	576×768	6.99	75.34	80.68	15.25G

Table 1. Comparison of VMamba-Pose and SOTA methods on MS COCO val set. VSMamba-Pose models are trained on COCO train set only, no pre-training settings used.

References (Optional)

Liu, Yue, et al., *Advances in neural information processing systems*, 2024

Session Category

Imaging and Biomedical Devices: Imaging Fundamentals and Applied Research

P4-320

Clinical Translation of Magnetic Resonance Quantitative Susceptibility Mapping (MR-QSM) to Characterise Carotid Plaque Composition and Predict Rupture Risk

Ms Jessica Bagnall[1,2], Mr Francesco Digeronimo[1,2], Professor Brooke Tornifoglio[1,2], Dr Niamh Hynes[3], Professor Sherif Sultan[3], Professor Caitríona Lally[1,2,4]

[1]Trinity Centre for Biomedical Engineering, Trinity College Dublin, Dublin, Leinster, Ireland. [2]Discipline of Mechanical, Manufacturing and Biomedical Engineering, Trinity College Dublin, Dublin, Leinster, Ireland. [3]Department of Vascular and Endovascular Surgery, Western Vascular Institute, University Hospital Galway, University of Galway, Galway, Connacht, Ireland. [4]Advanced Materials and Bio Engineering Research (AMBER) Centre, Royal College of Surgeons in Ireland and Trinity College Dublin, Dublin, Leinster, Ireland

Introduction

Stroke is the second leading cause of death worldwide [1]. 87% of all strokes are ischemic [2], with 23% of these linked to large-vessel atherosclerosis, such as the carotid [3]. Recent guidelines have emphasised the importance of assessing plaque composition to inform plaque rupture risk [4]. Multi-contrast MRI is the clinical gold standard for assessing plaque composition *in-vivo;* however, it is limited by long acquisition times [5]. In this study, we assess the feasibility of running a single-sequence MR-QSM technique *in-vivo* to fully characterise carotid plaque composition and inform rupture risk [6].

Methods

Ex-vivo ME-GRE MRI (7T-Bruker-BioSpec-70/30) for QSM was acquired for excised human carotid plaques (n=4). MicroCT (μCT) was acquired to validate the presence of calcification. Histological validation of plaque composition was carried out using Movat's pentachrome (MP) and Prussian Blue (PB). *In-vivo* MRI and Computed Tomography Angiography (CTA) were acquired for a female undergoing a carotid endarterectomy. A thrive sequence was acquired on a Philips Ingenia 3.0T scanner and postprocessed to generate the QSM data.

Results

A representative *ex-vivo* QSM image is outlined in Figure.1.a, and demonstrates that calcification, the lipid-rich necrotic core (LRNC) and intraplaque hemorrhage (IPH) can be clearly distinguished. The media, intimal thickening (IT), the LRNC and calcification appeared diamagnetic, whereas IPH appeared paramagnetic, Figure.1.b. A significant difference ($P<0.05$) in susceptibility was observed for all components with the exception of

the media and IT and the LRNC and IT. *In-vivo* QSM identifies a diamagnetic region indicative of calcification that is validated by CTA, Figure.1.c and d. Heterogeneous susceptibility was observed within the calcification region, which could be due to noise artefacts or other plaque constituents, such as IPH in close proximity causing partial voluming.

Discussion

Clinical translation of MRI-QSM from *ex-vivo* to *in-vivo* was achieved. Although somewhat limited by lower resolution and motion-related artefacts, this work presents a ground-breaking first step towards using this powerful imaging for plaque risk stratification.

Images (Optional)

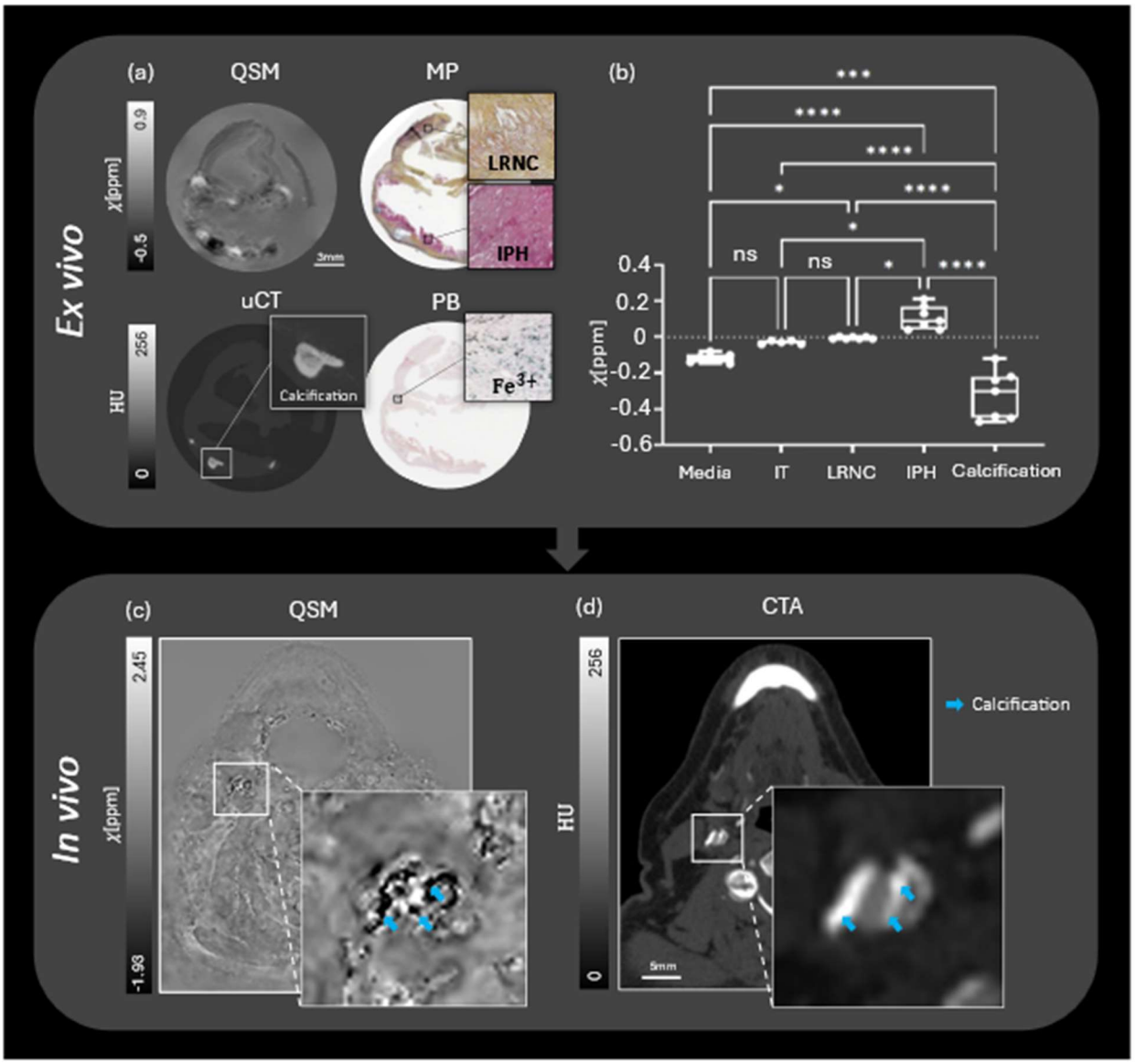


Figure 1A (a) *Ex vivo* QSM differentiates a LRNC, calcification, and chronic IPH. (b) Box and whisker plot displaying the mean, minimum, and maximum values for each plaque component (n=7). Statistical analysis was performed using one-way ANOVA (*P < .05, **P < .01, ***P < .001, ****P < .0001). **B** (a) *In vivo* QSM of a right carotid plaque identifies diamagnetic regions, indicative of calcification. (b) Registered CTA validates the presence of calcification.

References (Optional)

[1] Feigin *et al.,* Int.J.Stroke, 2025.

[2] Virani *et al.,* Circulation , 2020.

[3] Ornello *et al.,* Stroke, 2018.

[4] Naylor *et al.,* Eur.J.Vasc.Endovasc.Surg, 2023.

[5] Saba *et al.,* ASNJ, 2018.

[6] Shmueli *et al., Adv.in Mag.Res.Tech.and App*, 2020.

Session Category

Imaging and Biomedical Devices: Imaging Fundamentals and Applied Research

P4-321

Tracking Wrist Bones from Sequential 3DCT using 3DH, an Open-Source Hierarchical 3D Registration Module in SlicerAutoscoper^{M}

Ms Amy Morton[1], Ms Shelly Belsky[2], Mr John Holtgrewe[1], Mr Jean-Christophe Fillion-Robin[2], Mr Douglas Moore[1], Prof Beatriz Paniagua[2], Prof JJ Trey Crisco[1]

[1]Brown University, Providence, RI, United States. [2]Kitware, Clifton Park, NY, United States

Introduction

Kinematic tracking of *in vivo* joint and implant motion is indispensable for addressing a wide range of questions in musculoskeletal research. Projective imaging tools, such as biplane videoradiography, are established for studying the arthrokinematics of large joints. However, they can be technically challenging to implement for the small overlapping bones in the wrist and foot. In this work, we present Hierarchical 3D Registration (3DH), a 3DSlicer module for efficient, semi-automated registration of multiple bones imaged with sequential 3DCT or 4DCT.

Methods

3DH facilitates semi-automatic registration via an intelligent bone hierarchy sub-volume extraction, boundary-tests, and forward registration propagation. ITKElastix (https://elastix.dev/) is used for optimal registration between target and source sub-volumes. To validate the method, data from nine (9) hands/wrists scanned in neutral and 10 thumb ROM and task poses was used. The same dataset was previously registered via tissue-classified distance fields (TCDF) [1]. The radius, first metacarpal (MC1), and trapezium (TPM) were segmented and registered using 3DH. Bone motion was expressed as helical axis of motion rotation and translation. Bias, bias standard deviation (SD), and the 95% limits of agreement (LOA) between TCDF and 3DH motion parameters were quantified using Bland-Altman analysis.

Results

Across all subjects and tasks, the bias (SD) of the radius, MC1, and TPM rotation between TCDF and 3DH was 0.01°, -0.20°, 0.00° (0.15°, 2.30°, 0.36°), respectively, and the 95%LOA of the rotations across all bones averaged -1.87° and 1.74°. The bias (SD) of the 3DH-calculated translation for the radius, MC1, and TPM was -0.37mm, 0.01mm, and 0.00mm (1.90mm, 0.40mm, 0.91mm), respectively, and the 95%LOA for translation across all bones averaged -2.23mm and 2.00mm.

Discussion

We have developed a free, open-source software solution for musculoskeletal registration of 3D and 4DCT datasets. Our new Hierarchical 3D Registration module in 3DSlicer enables tracking of multiple small bones in 3DCT or 4DCT. The accuracy of the TCDF method was previously established as less than 0.3 mm and less than 0.4°. The agreement between TCDF and 3DH was better than 1/10 of these values. Our overarching goal is to provide a platform for sharing tracking algorithms.

References (Optional)

[1] Marai et al., IEEE 2006

Acknowledgements (Optional)

Supported by NIMAS/NIH Award Number R01AR078924 and NIH AR059185. The content is solely the responsibility of the authors.

Session Category

Imaging and Biomedical Devices: Imaging Fundamentals and Applied Research

P4-322

Investigation of Phase-Contrast micro-CT for Design Characterization of the Cervical Intervertebral Disc Space

Mr Jonah Leinwand, Ms Claire Thompson, Dr Stewart McLachlin

University of Waterloo, Waterloo, Ontario, Canada

Introduction

Understanding the design space is critical to spinal implant development, where knowledge of the geometry and properties of the vertebral bone and connecting soft tissues is needed to improve outcomes for devices like cervical artificial disc replacements (c-ADR). Imaging techniques, such as MRI or X-ray computed tomography (CT) are useful in characterization of these joints; however, detailed understanding of the tissue microstructure is often lacking. Use of micro-computed tomography (mCT) presents a potential option but is typically limited for understanding the intervertebral disc (IVD) space without staining [1]. The goal of this study was to investigate a phase-contrast mCT to better delineate the microstructure of the vertebral endplates towards characterization of c-ADR design constraints.

Methods

Cadaveric cervical spine motion segments were prepared for phase-contrast mCT imaging (InCiTe 3D X-ray Microscope, KA Imaging, Waterloo, Canada) by cutting through the superior and inferior vertebrae. Excess soft tissue and the posterior elements were removed. Samples were scanned at varying voltages (40-80kV), currents (100-150uA), integration times (800-2000ms), and both projection and frame count to determine optimal parameters for imaging and characterizing the IVD space and adjacent bony endplates of the vertebral joint. Scans were pre-processed with ImageJ to despeckle and normalize to an air gap measurement, then reconstructed in VGStudio (Hexagon, Sweden). Further processing was done in Fiji, an open-source image processing software, to create a volumetric thickness map of the endplates above and below the IVD.

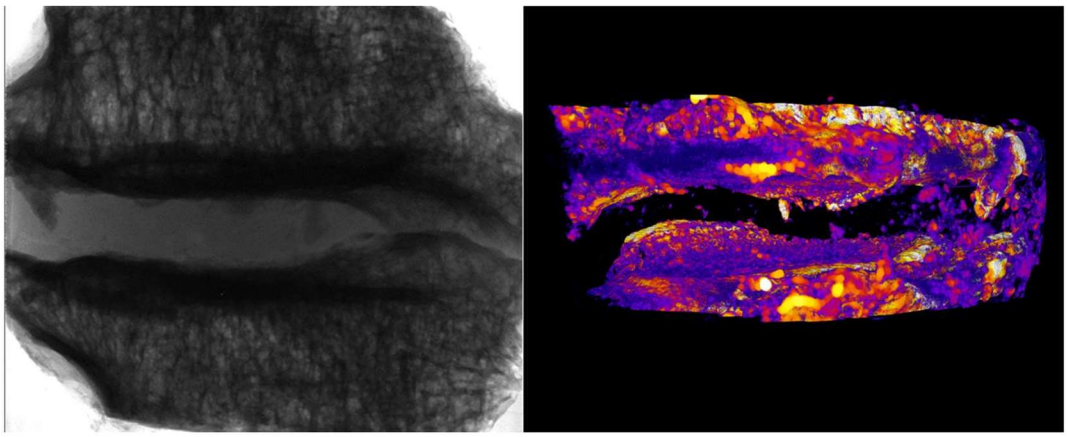
Results

The volumetric thickness map, and the pre-processed mCT scan of the sample, with an effective pixel size of 6.15um, are shown (attached) for a representative specimen that had an overall width of 30mm and height of 22mm, with an IVD width of 25mm and height of 5mm. Scan time was approximately 5 hours.

Discussion

Further design metrics and constraints for c-ADR will be quantified based on the vertebral endplate thickness and geometric density distribution through post-processing of the 3D reconstructions. These results provide the basis for quantifying design constraints for a c-ADR to fill the envelope left by the removed IVD, while promoting attachment to the densest regions of adjacent bone.

Images (Optional)



A 40kV m-CT scan with high integration time of the C6-C7 vertebral joint in a cadaveric specimen (left) and a volumetric thickness map of the same joint with high density regions shown in bright white and low density in dark purple (right)

References (Optional)

[1] C Disney et al., Scientific Reports, 2017

Session Category

Imaging and Biomedical Devices: Imaging Fundamentals and Applied Research

P4-323

Changes in Supraspinatus Tendon Structural and Material Properties during Manual Wheelchair Handrim Loading

Ms Jungsun Moon[1], Ms Savanna Rudy[1], Mr Dustin Tran[1], Ms Denali Hutzelmann[1], Dr. Matthew Hanks PhD, ATC[1,2,3]

[1]Department of Health and Kinesiology, University of Illinois Urbana-Champaign, Urbana, Illinois, United States. [2]Beckman Institute for Advanced Science and Technology, University of Illinois Urbana-Champaign, Urbana, Illinois, United States. [3]Disability Resources and Educational Services, University of Illinois Urbana-Champaign, Champaign, Illinois, United States

Introduction

Manual wheelchair use places repetitive stress on the shoulder, which may contribute to shoulder pain and tendinopathy. Supraspinatus tendon properties and three-dimensional (3D) scapular kinematics are associated with these musculoskeletal conditions. However, scapular kinematics and supraspinatus tendon structural properties (e.g., cross-sectional thickness) have been evaluated independently despite their anatomical link, and studies evaluating supraspinatus tendon material properties (e.g., stiffness) among manual wheelchair users are limited. Therefore, the purpose of this study was to examine changes in supraspinatus tendon structural and material properties during two handrim loading conditions.

Methods

Twenty-three manual wheelchair users (n=23, 12M/11F, age: 21.5±3.5 years, duration of wheelchair use: 14.1±4.5 years) participated. Participants, in their personal wheelchair, assumed a natural, static position simulating propulsion with their hands atop the wheel aligned vertically with the axle. Participants then underwent shoulder musculoskeletal imaging in two conditions: (1) resting their hands on the handrim and (2) exerting a mock propulsion force on the handrim. Tendon thickness and acromiohumeral distance (AHD) were measured using B-mode ultrasound, and tendon occupation ratio (thickness divided by AHD) was computed. Tendon shear velocity, a surrogate measure of stiffness, was measured using shear wave elastography. Participants, in the same static position, were affixed with 34 passive markers on their upper body, 3D marker trajectories were tracked using motion analysis, and a biomechanical model was constructed to quantify 3D scapular kinematics. Repeated-measures MANCOVA was used to explore the effect of handrim loading condition on supraspinatus tendon properties, adjusting for scapular kinematics.

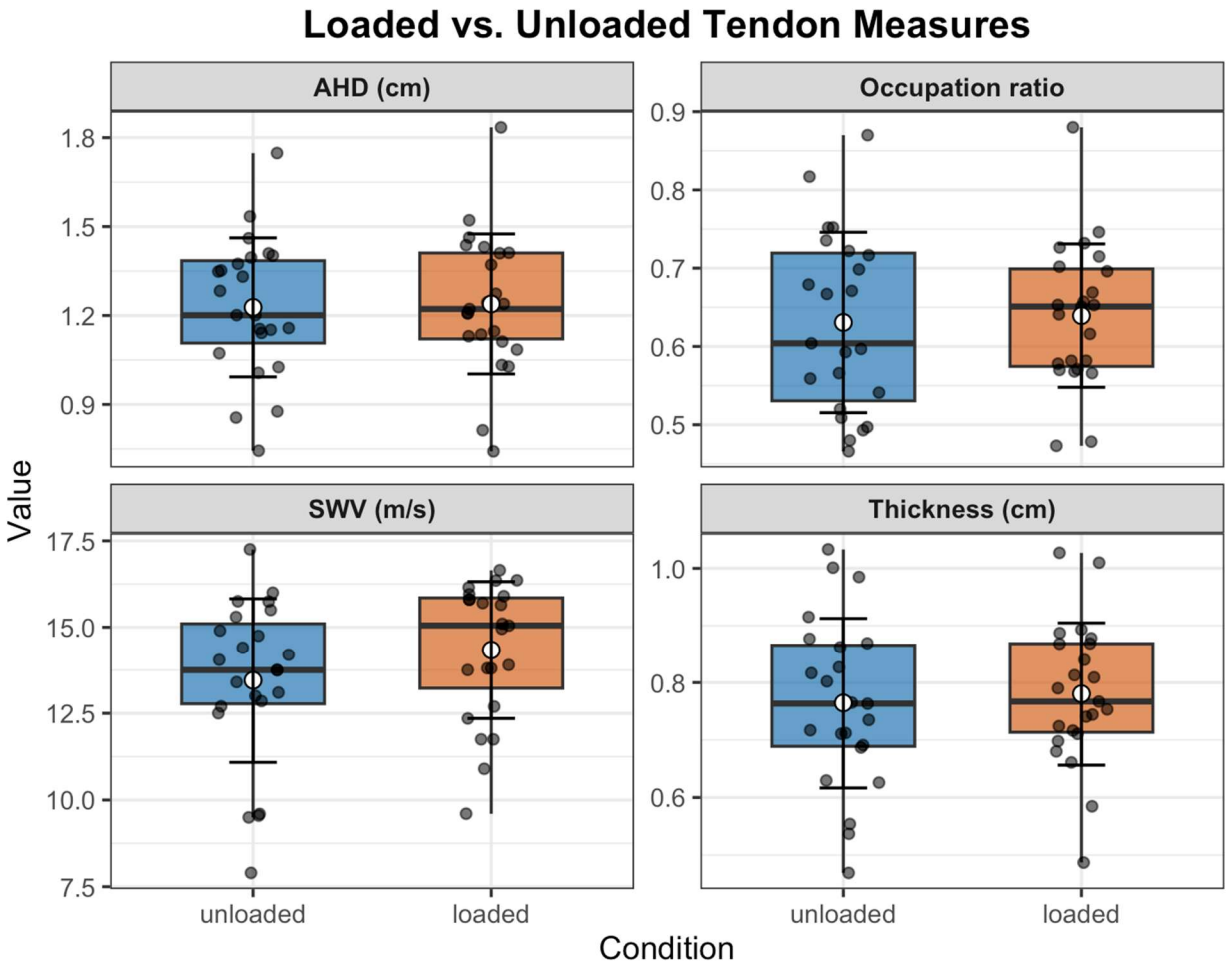
Results

No significant main effect of loading condition was observed (*Pillai's Trace*=0.036, $F_{4,19}$= 2.68, p=0.063; Figure 1), and only a small-to-moderate effect of loading condition was observed for shear velocity (η_p^2=0.05). We observed statistical significance and large effects of scapular upward/downward rotation on tendon shear velocity (p=0.017; η_p^2=0.18) and AHD (p=0.04; η_p^2=0.18) though tendon thickness was nonsignificant (η_p^2=0.17, p=0.05).

Discussion

Supraspinatus tendon structural and material properties were not different between loading conditions after controlling for scapular kinematics. However, increased scapular downward rotation was associated with smaller tendon shear velocity, thickness, and AHD. Our findings suggest that scapular kinematics may influence tendon health more than handrim loading alone.

Images (Optional)



Session Category

Imaging and Biomedical Devices: Imaging Fundamentals and Applied Research

P4-324

FiberFit: A Web Application for Fiber Orientation Analysis with Comparative Assessment to Existing Software Tools

Ms. Katherine Fors, Mr. Cody Willson, Mr. Kyle Shannon, Dr. Trevor Lujan PI

Boise State University, Boise, ID, United States

Introduction

Accurate quantification of fiber network structures is essential for advancing a mechanistic understanding of biomaterials. Research groups have therefore developed software applications that quantify structural parameters from two-dimensional images, including mean fiber orientation and fiber alignment (dispersion). These applications include: OrientationJ, Directionality, CurveAlign, Cytospectre, and FiberFit, which was developed by our group [1]. However, adoption of these tools has been limited by two factors: accessibility and accuracy. Although free to use, these applications require users to download and run standalone executables, limiting accessibility. Additionally, no study has directly compared their accuracy because each program quantifies alignment using a different metric. Therefore, this study had two goals: convert FiberFit into a web-based application and objectively evaluate the accuracy of different software applications.

Methods

FiberFit's original Python code was installed on a server, and a web interface was developed in standard HTML, JavaScript, and CSS (Fig. 1A). A set of 72 unique images with known mean fiber orientations and alignments were generated using a custom MATLAB program. Each binary image was populated with line segments based on a semicircular von Mises probability function. Images were analyzed using the five software applications. The fiber angle distribution histograms produced by each tool were extracted and processed to compute the mean orientation and alignment by fitting each histogram to a von Mises distribution. Errors between known and measured parameters were computed. To ensure each program was evaluated under optimal conditions, a sensitivity analysis was conducted to identify the settings that minimized error for each application.

Results

FiberFit showed the lowest mean error for orientation (1.11°) and alignment (3.34%; $p<0.05$). Across all tools, disordered networks produced substantially greater measurement error than aligned networks (Fig. 1B-C).

Discussion

FiberFit demonstrated the highest overall accuracy among the applications analyzed, with its performance especially robust at analyzing networks of different alignments. Accuracy differences across applications reflect differences in the algorithms used to generate histograms. Importantly, this analysis was performed using optimal parameters for each specific application. FiberFit is now available as a web application providing an accurate and accessible option for fiber network analysis.

Images (Optional)

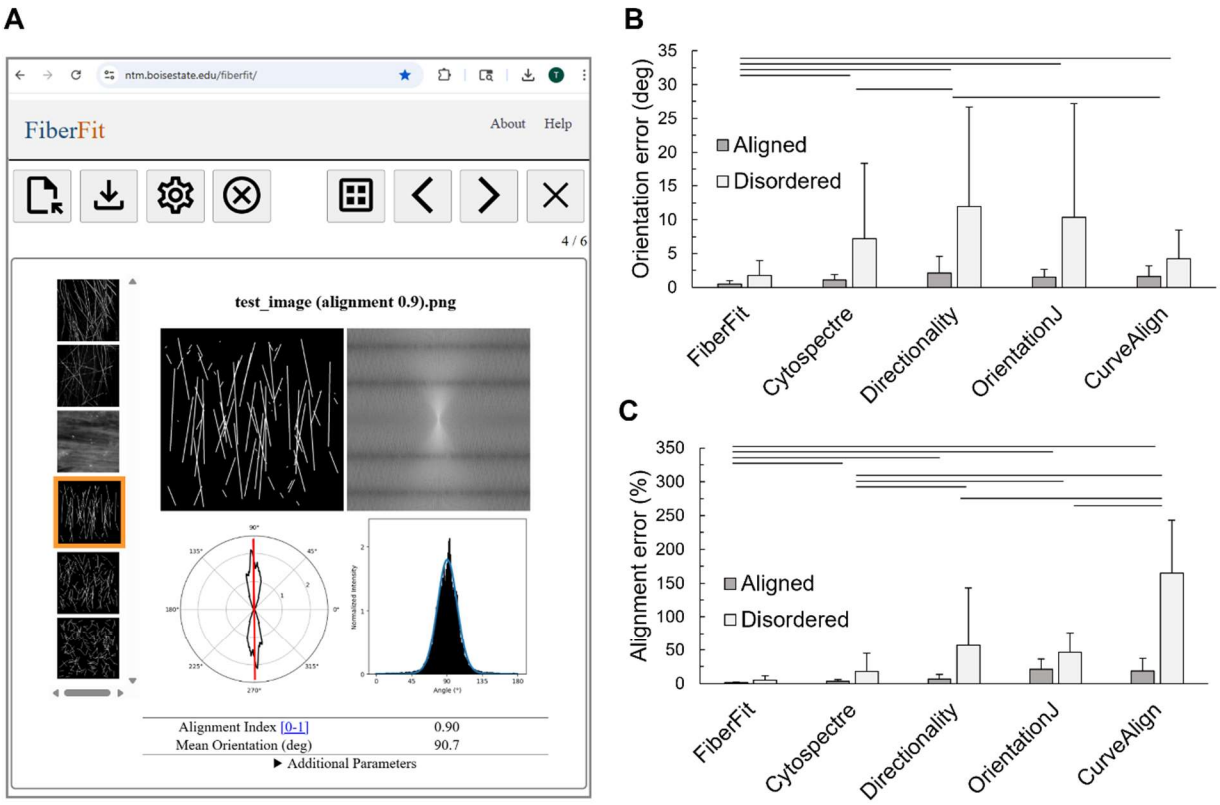


Figure 1: A) FiberFit web application. **(B-C)** Comparison of software orientation and alignment error for aligned and disordered fiber networks, where bars = ($p < 0.05$). Aligned networks had significantly lower error than disordered networks in all cases ($p < 0.05$).

References (Optional)

[1] Morrill et al., BMMB, 2016

Session Category

Imaging and Biomedical Devices: Imaging Fundamentals and Applied Research

P4-325

Quantification of Vastus Lateralis Obliquus Muscle Volume Using MRI and its Implication on Identifying the Boundary Between the Vastus Lateralis and Vastus Intermedius

Dr Geoffrey Handsfield PhD[1,2], Dr Katherine Knaus PhD[3], Dr Joe Hart PhD[1], Dr Silvia Blemker PhD[4]

[1]University of North Carolina, Chapel Hill, NC, United States. [2]North Carolina State University, Raleigh, NC, United States. [3]Colorado School of Mines, Golden, CO, United States. [4]University of Virginia, Charlottesville, VA, United States

Dr Geoffrey Handsfield

Dr Katherine Knaus

Dr Joe Hart

Introduction

Among the quadriceps femoris muscle group, the vastus lateralis (VL) and vastus intermedius (VI) play key roles in knee extension. The VL occupies the lateral superficial aspect of the thigh and the VI lies deep to the rectus femoris (RF). Despite these clear locations, the boundary between these muscles is not consistently identified in radiological cross-sectional studies [1]. The greatest ambiguity concerns the posterolateral inferior portion of the quadriceps, which is variably described as part of the VI in radiological studies [1] or as part of the VL in gross anatomical studies [2]. A third interpretation identifies this tissue as a distinct subdivision of the VL, termed the vastus lateralis obliquus (VLO). Despite references to the VLO in the literature [3-5], no prior study has assessed its structure in radiological cross-section and quantified its volume in a group of healthy adults.

Methods

To address this gap, we used high-resolution MRI to examine quadriceps in a group of healthy adults that included elite NCAA sprint runners (6F/4M) and non-sprinter controls

(6F/6M). Data were collected under IRB from the University of Virginia; all participants provided informed consent. We manually segmented axial images, defining the VLO as the region between the deep and superficial septum, posterolateral to the femur (Figure 1A), thus generating 3D geometries of the VLO, vastus lateralis longus (VLL), VI, vastus medialis (VM), and RF.

Results

We found that the VLO is consistently present, extends three-quarters of the femoral length, comprises 18% of the VL volume (Figure 1B), and is not significantly larger (p=0.08) in elite sprinters, though all other quadriceps heads were significantly hypertrophied in sprinters (p<0.05) (Figure 1C).

Discussion

Muscle boundary definitions impact downstream biomechanical variables such as predicted force. Our results suggest a correction factor of 18% could be applied to VL volume when comparing studies with different VL–VI definitions, offering a practical way to reconcile methodological differences without compromising internal consistency.

Images (Optional)

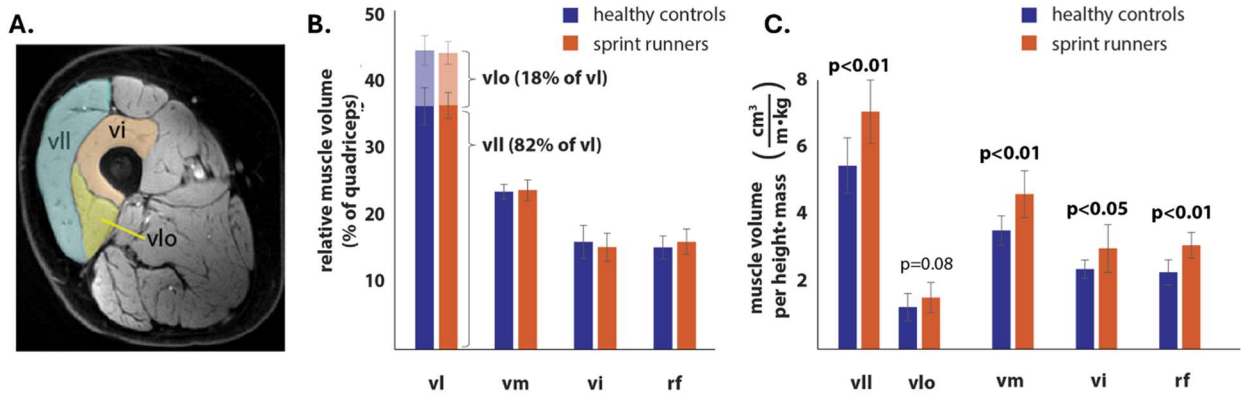


Figure 1. The vastus lateralis obliquus (VLO) was consistently identifiable across participants. (A) In axial MRI, the VLO occupied the posteromedial aspect of the vastus lateralis, superficial to the posterolateral aspect of the vastus intermedius. (B) The VLO represented 18% of the vastus lateralis, which was consistent across our population. (C) Height-mass normalized muscle volumes were higher for the sprinter group in all quadriceps heads.

References (Optional)

[1] Barnouin et al. (2014), *JMRI*; [2] Moore et al. (2013), *Clin Orient Anat*; [3] Vieira (2011), *J Morph Sci*; [4] Hallisey et al. (1987), *J Bone Joint Surg*; [5] Farahmand et al. (1998) *J Orth Res*.

Session Category

Imaging and Biomedical Devices: Imaging Fundamentals and Applied Research

P4-326

Positional Accuracy Assessment of 3D Gaussian Splatting from Monocular Video for Medical Image Registration

Mr Hewamannege Sudam, Ms Kanon Sato, Prof Koich Kobayashi, Prof Makoto Sakamoto

Graduate School of Health Sciences, University of Niigata, Niigata, Niigata, Japan

Introduction

Meniscal injury diagnosis relies on both Magnetic Resonance Imaging, which suffers from limited accuracy for subtle tears, and invasive arthroscopy - the diagnostic gold standard. There is opportunity for training an AI model capable of achieving diagnostic accuracy closer to arthroscopy, by using novel 3D Gaussian Splatting (3DGS) as a generator of 3D anatomical images from knee arthroscopy video. However, accuracy of 3DGS should be assessed first.

Methods

A short video sequence, under 1 minute was captured using consumer camera of a custom-made triangular prism, in which 34 small metal balls with known coordinates were embedded (ground truth). Structure-from-Motion (Colmap) and 3DGS were employed to generate a 3D point cloud from the video frames. This is imported to CloudCompare software, and an initial scale calibration was performed using a reference distance of 120.575mm, yielding a scale factor of 0.7296. Then x,y,z coordinates of each ball was obtained. Using minimization of the least squares and by iterative translation(x,y,z); Rotation; Scaling, obtained point cloud was aligned so that it achieved the best fit with known coordinates. Aligned point cloud coordinates of each ball was compared against the ground truth, displacement (error) was recorded in each direction. 34 sets of records were obtained. Summery statistics of error was calculated.

Results

Mean three dimensional alignment error was 0.806 ± 0.337mm. The median error was 0.873mm, with a range of 0.161mm to 1.294mm. Per-axis error analysis revealed maximum single axis errors of 1.127mm (x), 0.983mm (y), and 0.978mm (z). The interquartile range was 0.072mm, indicating consistent error distribution across the reconstructed volume.

Discussion

Since metal balls are not point objects, care was taken to pick coordinates so that they represent the middle of each ball, yet there could have been human error. This pre assessment shows that monocular video derived 3D structures show acceptable

positional accuracy to be used for gross 3D-anatomy generation. Having mostly submillimeter accuracy just from an under one minute video is promising and the accuracy could be improved further by using longer videos. This validated pipeline is scheduled to be used to synthesize the 3D knee inner capsule from arthroscopy video.

Session Category

Imaging and Biomedical Devices: Imaging Fundamentals and Applied Research

P4-327

Automated and Reproducible FE Patient-Specific Modeling of the TMJ Based on Medical Imaging

PhD Student Lilian Baugnon[1], Full Professor and Hospital Practitioner Romain Nicot[1,2], Research Engineer Nicolas Béthune[1], Associate Professor Pauline Lecomte-Grosbras[1], Research Engineer Jean-François Witz[1], Associate Professor Olivier Mayeur[1]

[1]Univ. Lille, CNRS, Centrale Lille, UMR 9013 LaMcube Laboratoire de Mécanique, Multiphysique, Multiéchelle, Lille, Nord, France. [2]Univ. Lille, CHU Lille, Department of Oral and Maxillofacial Surgery, Lille, Nord, France

Introduction

The temporomandibular joint (TMJ) connects the mandible to the skull and enables chewing, speech, and swallowing. It is composed of a disc that separates synovial cavities. The joint combines rotation and translation to generate movements of retraction, protrusion, elevation, lowering, and lateral excursions via the temporal, masseter, and pterygoid muscles. Nearly 34% of the population shows signs of TMJ disorders according to the State Of The Art. Finite Element (FE) models driven by displacements or forces, analyze stresses and strains. The study presents a personalized model of the TMJ, automated and reproducible, that can be used for diagnostic purposes and therapeutic planning in cases of TMJ disorders and surgical correction.

Methods

The study uses algorithms for the generation of FE models, following a standardized workflow of patient-specific digital twins. The CT data in DICOM format were segmented automatically for bones and muscles, producing FE-compatible volumes. The tissues are modeled as linear elastic with generic properties or derived from medical imaging. The parametric model incorporates contacts, muscle forces according to different orientation methods, with the realistic mandibular position in inter cuspation position. This enables detailed and personalized FE simulations to analyze physiological and pathological conditions.

Results

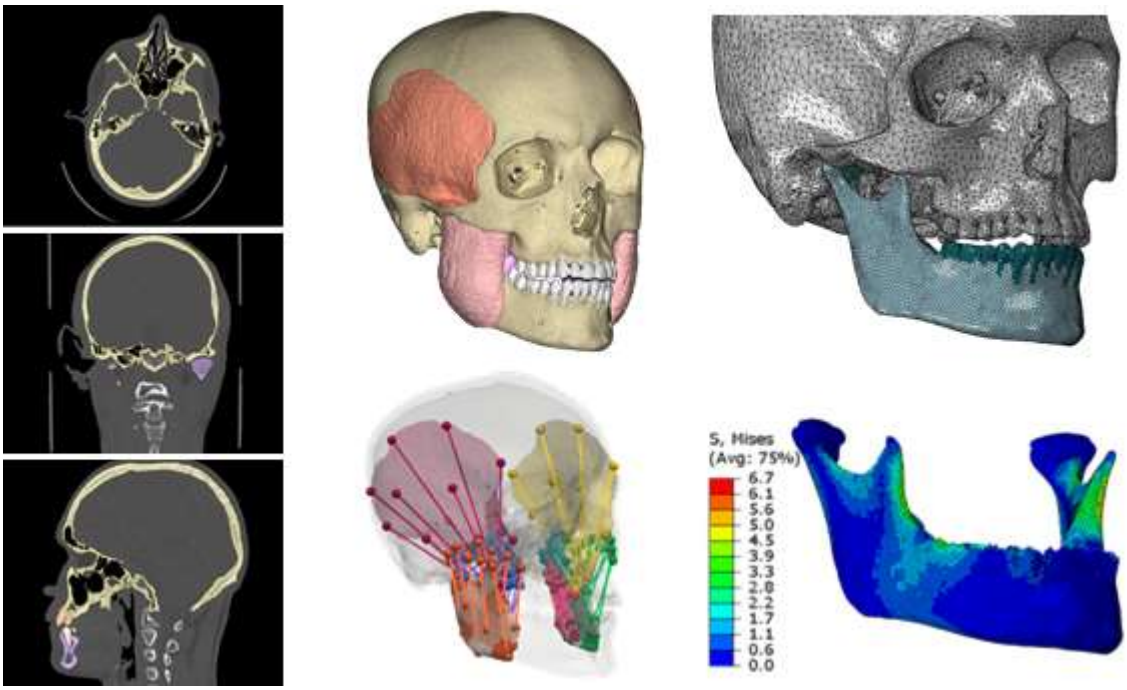
Material assignment via HU values improves spatial resolution and mechanical consistency with the literature (mandibular Young's modulus: 11.4GPa vs 11.6GPa) and Von Mises stresses (<0.1% difference). Sensitivity analysis shows that seven cortical

classes and two trabecular classes are sufficient for convergence and highlights the limitation of assigning a single material. Increasing friction reduces overall stresses but locally doubles the stresses in the condyles, revealing a left–right asymmetry. Finally, muscle representation influences mechanical response: the multivector method provides the most accurate and stable results, with stress predictions stabilizing beyond 10 directional loads per muscles.

Discussion

This study provides a fully automatic and parameterized, patient-specific TMJ model consistent with literature, enabling diagnostic insights through stress maps, asymmetry patterns, and muscle load effects. It opens perspectives for pathological analysis and surgical planning. Future work will validate against experiments, extend to multiple patients to assess variability, and integrate automated workflows for personalized prosthesis design and evaluation.

Images (Optional)



Session Category

Imaging and Biomedical Devices: Imaging Fundamentals and Applied Research

P4-328

In-vitro Investigation of Stress-Relaxation Behavior in Orthodontic Aligners

Mr. Lingyu Bu[1], Dr. Paul Major[2], Dr. Dan Romanyk[1,2,3]

[1]Department of Mechanical Engineering, University of Alberta, Edmonton, Alberta, Canada. [2]Mike Petryk School of Dentistry, University of Alberta, Edmonton, Alberta, Canada. [3]Department of Biomedical Engineering, University of Alberta, Edmonton, Alberta, Canada

Introduction

Orthodontic aligners are commonly polymeric-based, exhibiting viscoelastic behavior leading to inconsistent orthodontic forces applied to teeth over time. Previous studies have explored stress-relaxation behavior of aligner materials through mechanical tests. However, the effects of hydration are often missing in such studies. Also, most experiments were performed over planar aligner sheets, while the highly complicated 3D geometry of aligners can significantly influence their force delivery. Therefore, the present study aims to quantify the time-dependent decay of orthodontic forces in aligners using in-vitro measurements under clinically relevant tooth displacements.

Methods

In-vitro tests were performed on aligners using an Orthodontic Simulator (OSIM), which can measure the 3D forces generated by the aligner on each tooth through the connected loadcells [1]. Aligners were inserted on OSIM, and the right central incisor was displaced 0.5 mm outward to generate an initial force of ~1.5 N. Five consecutive 8-hour dry tests (DT) were performed. Hydration tests (HT) were performed after soaking the aligners for 48 hours, and aligners were tested 2 hours to avoid excessive dehydration, based on previous results showing most force decay occurs within 2 hours.

Results

A force decay of 0.15–0.38 N was observed in DT samples, with a decreasing rate of force decay over time (Test 1: 0.38 N, Test 2: 0.26 N). The averaged DT force decay was 15.40% in 8 hours and 7.67% in 2 hours. HT exhibited similar behavior but showed reduced force decay (average of 4.67% in 2 hours).

Discussion

This study bridges the gap between material and in-vitro viscoelastic behavior of orthodontic aligners. Most in-vitro studies ignored the stress-relaxation of aligner materials, which was shown to have a significant effect on force delivery. One key

limitation is that the aligners cannot be tested while immersed in fluid due to instrumentation positioning on OSIM, which limits the ability to test hydration effects. However, short-term tests showed that hydration affects the relaxation behavior. Future work will focus on developing a constitute material model based on these results to enhance FEA simulations of aligner behavior.

Images (Optional)

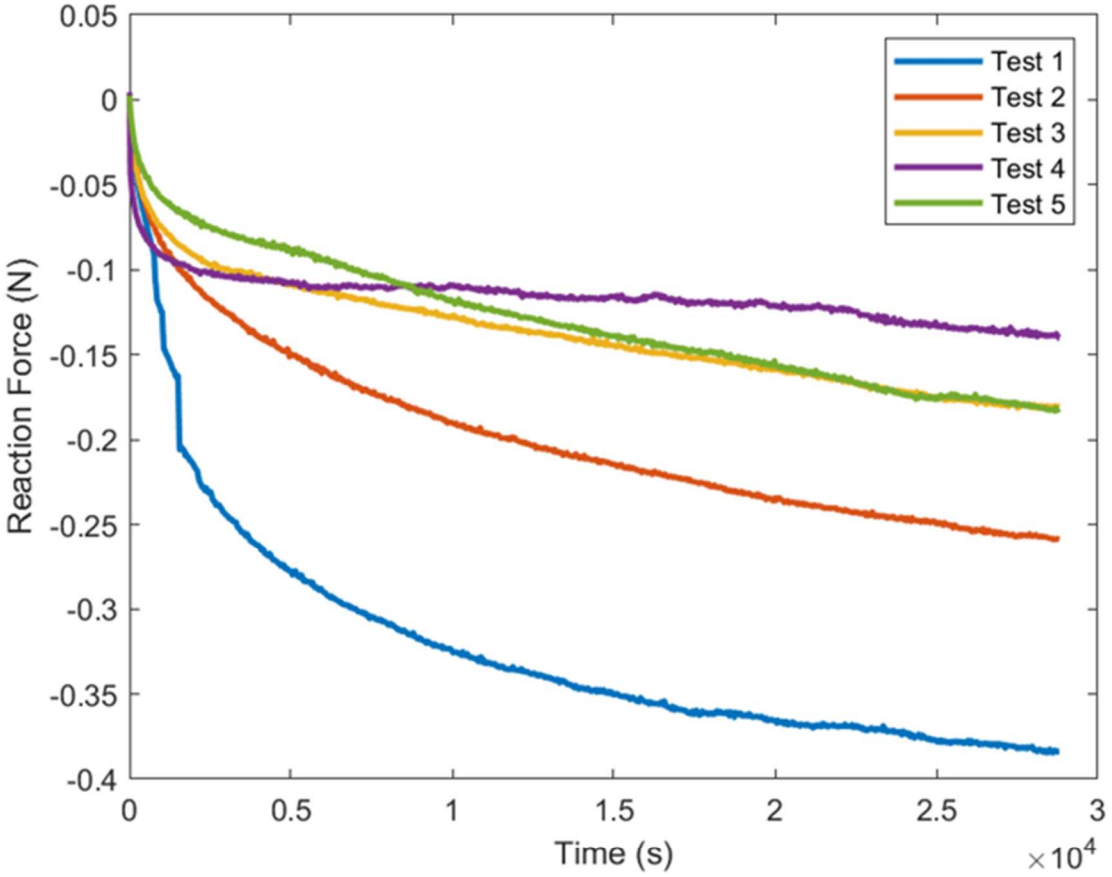


Figure 1: The force decay results from DT sample tested on OSIM with an outward displaced central incisor presented for 5 tests, where Test 1 is the first experiment and Test 5 is the final; original measurements from the loadcell were filtered by a 4th order Butterworth low-pass filter to eliminate noise, and starting points were normalized to 0 for comparison.

References (Optional)

[1] Harsimrat Kaur *et al.* , J Biomed Mater Res B Appl Biomater, 2022

Acknowledgements (Optional)

The authors acknowledge financial contributions from the McIntyre Fund (Mike Petryk School of Dentistry, University of Alberta) and the NSERC Discovery Grant Program towards completion of the presented research.

Session Category

Imaging and Biomedical Devices: Imaging Fundamentals and Applied Research

P4-329

Design of a Dual-Probe Setup for Experimental Assessment of Multi-Mode Shear Wave Propagation in Transversely Isotropic Tissues

Ph.D. candidate Lorena Claeys[1,2], Ph.D Tim Nordenfur[1,2], Ph.D Zhongzheng Wang[1], Ph.D Ruoli Wang[1], Ph.D Matilda Larsson[1]

[1]Kungliga Tekniska högskolan, Stockholm, Stockholm, Sweden. [2]Karolinska Institutet, Stockholm, Stockholm, Sweden

Introduction

Shear wave elastography (SWE) measures tissue stiffness but is limited for transversely isotropic (TI) tissues, which require three elastic parameters for characterization. Conventional SWE captures two parameters related to shear anisotropy (SH mode), while the third, linked to tensile anisotropy (SV mode), cannot be measured directly. This study introduces a dual-probe setup allowing full parameters characterization. This design was tested on ex-vivo muscle tissue and SWE results were compared with mechanical testing.

Methods

SWE was performed on ex-vivo bovine semitendinosus tissue using a Verasonics V1 (L7-4). For shear anisotropy, a vertically positioned probe was aligned with the fiber direction (Figure 1a) and used for both pushing (5 MHz, 70 V, F#2) and imaging (5 MHz, PRF 10 kHz) every 10° over 360°. Axial velocities were computed via 2D autocorrelation and SH velocities were extracted using a Radon-sum algorithm. Rheology was performed five times on 10×10×2 mm^3 transverse and longitudinal samples using a frequency sweep (0.1–100 Hz) with 10% compressive preload. For tensile anisotropy, the vertical probe generated the push while a second, orthogonally positioned probe aligned with the fibers was used for imaging (Figure 1b); SV group velocities were manually tracked from the axial velocity maps. The extracted SH and SV velocities were fitted to a theoretical TI model to estimate the mechanical parameters (Figure 1c). Compression testing was performed on 20×20×20 mm^3 samples (transverse and longitudinal) using 1 N preload and 3 mm ramp over 2 min (±5 kN load cell), with two preconditioning cycles prior to data acquisition on the third cycle.

Results

The results demonstrate that the mechanical parameters assessed by SWE are comparable to those obtained through mechanical testing. The μ_l/μ_t ratio measured by SWE was 1.84, compared to 1.34±0.11 from mechanical testing, while the E_t/E_l ratio was 0.53 for SWE and 0.68 for mechanical testing.

Discussion

The same-range agreement between SWE-derived and mechanically measured parameters demonstrates that the dual-probe setup enables full elastic characterization of TI tissue by estimating both shear and tensile anisotropy. Future work will improve compression test robustness and extend validation to ex-vivo and in-vivo tissues.

Images (Optional)

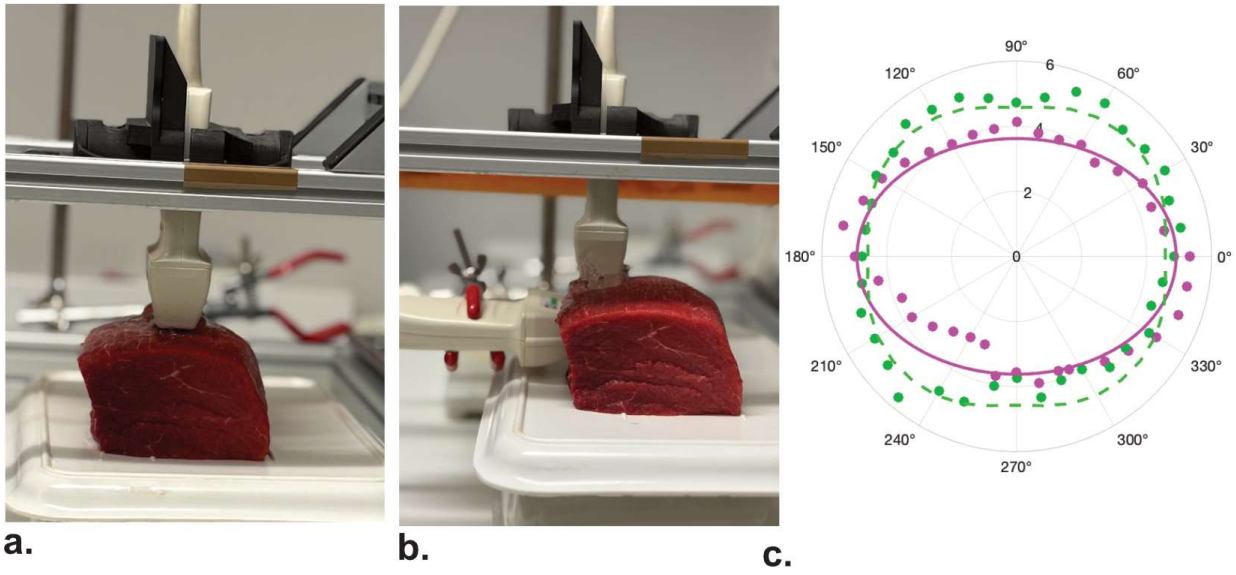


Figure 1: (a) Single probe setup. (b) Dual probe setup. (c) SH (purple) and SV (green) velocity points measured with SWE and their mathematical fits.

Session Category

Imaging and Biomedical Devices: Imaging Fundamentals and Applied Research

P4-330

MRI-Based Pressure Gradient Mapping in Patient-Specific Models of Aortic Coarctation

- Priya Nair[1], Dr. Lorenzo Ferrari[1], Dr. Michael Loecher[1], Dr. Charles McGrath[1], Dr. Carlos Castillo Passi[1], Dr. Doff McElhinney[1], Dr. Alison Marsden[1], Dr. Daniel Ennis[1,2]

[1]Stanford University, Stanford, CA, United States. [2]VA Palo Alto Healthcare System, Palo Alto, CA, United States

Introduction

Coarctation of the aorta (CoA) is a congenital narrowing of the aorta affecting ~3 per 10,000 births [1]. Clinical decision-making relies on estimation of the pressure gradient (ΔP) across the stenosis, with invasive cardiac catheterization serving as the reference standard. Non-invasive estimation using phase-contrast MRI is feasible with 3D+time (4D) velocity-encoding methods such as 4D-Flow, where ΔP is calculated from measured velocity fields using the Navier-Stokes equations. This approach is sensitive to noise due to reliance on temporal and spatial derivatives of velocity. We developed 4D-FlowP, a novel MRI sequence that directly encodes velocity and acceleration to improve ΔP accuracy [2]. We evaluated the robustness of 4D-FlowP using *in vitro* experiments and fluid-structure interaction (FSI) simulations in patient-specific 3D-printed CoA models.

Methods

MRI and catheterization data from two patients with CoA (obtained under IRB) were retrospectively analyzed. Patient-specific aortic geometries were segmented in SimVascular, with an additional higher-severity stenosis geometry generated per patient. Compliant phantoms were 3D-printed using Agilus30 (E = 1.2 MPa) and integrated into a mock circulatory loop driven by a programmable pump (Shelley CardioFlow 5000) [3]. Pulsatile flow waveforms from clinical 4D-Flow MRI (Q1) were prescribed, with resistance and capacitance tuned to match in vivo pressures; a reduced-flow condition (Q2 = 0.5Q1) was also studied. Time-resolved 3D images (1.8 mm isotropic) were acquired on a 3T MRI (Vida Fit, Siemens) using conventional 4D-Flow and 4D-FlowP with comparable scan times. ΔP was computed via the incompressible Navier-Stokes equations, with acceleration derived from velocity gradients (4D-Flow) or directly encoded (4D-FlowP). Corresponding FSI simulations were performed using SimVascular.

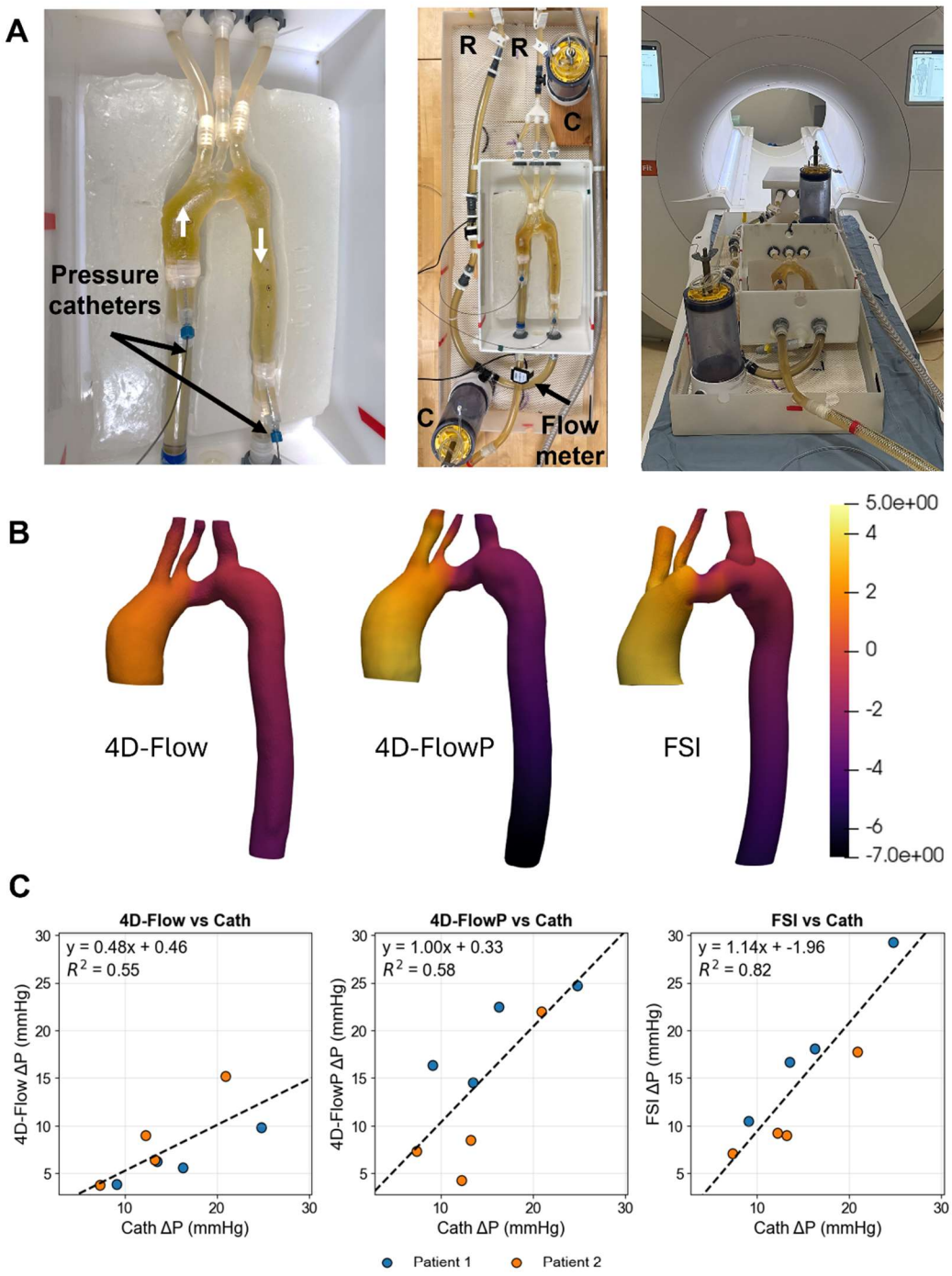
Results

Conventional 4D-Flow underestimated ΔP relative to catheter measurements ($y = 0.48x + 0.46$, $R^2 = 0.55$), while 4D-FlowP demonstrated near-unity agreement with reduced bias ($y = 1.00x + 0.33$, $R^2 = 0.58$). FSI showed the strongest correspondence ($y = 1.14x + 1.96$, $R^2 = 0.82$).

Discussion

Patient-specific compliant phantoms provide a controlled framework for validating MRI-based ΔP estimation. Direct acceleration encoding with 4D-FlowP improves robustness and can enhance non-invasive hemodynamic assessment.

Images (Optional)



(A) MRI-compatible in vitro flow loop with an embedded 3D-printed compliant patient-specific CoA model instrumented for direct pressure and flow rate measures. The system includes tunable fluid capacitors and resistors to match patient-specific hemodynamics.

(B) Relative pressure fields and ΔP measures across the CoA demonstrating excellent agreement between 4D-FlowP and FSI.

(C) Comparison of 4D-Flow, 4D-FlowP, and FSI ΔP estimates to those obtained directly with a pressure catheter. Both 4D-FlowP and FSI show very good agreement with catheter-based estimates of ΔP.

References (Optional)

[1] Ringel, R.E. et al., *Am Heart J*, 2012.
[2] Loecher, M. et al., *ISMRM Annual Meeting*, 2023.
[3] Zimmermann, J. et al., *Sci Rep*, 2021.

Session Category

Imaging and Biomedical Devices: Imaging Fundamentals and Applied Research

P4-331

Development of a 3-D Knee Joint Instability Testing System Using Image Analysis Technology

Mr. Manato Hayashi B.S.[1], Mr. Naoya Kuroyama B.S.[1], Prof. Norio Tagawa Ph.D.[1,2], Assistant Professor Yohei Okada M.D., Ph.D.[3], Prof. Atsushi Teramoto M.D., Ph.D.[3], Prof. Hiromichi Fujie Ph.D.[1,2]

[1]Graduate School of Systems Design, Tokyo Metropolitan University, Hachioji, Tokyo, Japan. [2]Research Center for Medicine-Engineering Collaboration, Tokyo Metropolitan University, Hachioji, Tokyo, Japan. [3]School of Medicine, Sapporo Medical University, Sapporo, Hokkaido, Japan

Introduction

It is important to quantitatively assess knee joint instability to improve the treatment of knee ligament injuries and total knee arthroplasty. However, commercially available knee arthrometers have several limitations: (i) the use of contact displacement sensors, which may cause errors due to skin deformation; (ii) the inability to measure the femoral three-dimensional motion, making varus–valgus testing in flexion impossible; and (iii) displacement measurement restricted to only one degree-of-freedom (DOF), although knee motion occurs in 6-DOF. To address these problems, we developed a novel knee joint instability test system using image analysis techniques.

Methods

A tibial loading device and a depth camera(RealSense D435if, Intel) were fixed in a knee-fixation plate. The accuracy of three-dimensional shape tracking with this camera using the iterative closest point (ICP) algorithm was 0.35mm in translation and 0.34° in rotation[1]. Young healthy male (n=5, age 28.8±8.2) were selected. The femoral coordinate system and tibial coordinate system were defined using bony landmarks following the ISB recommendation[2] and related to point cloud data of the patella and tibia, respectively. During the anterior drawer test and varus-valgus rotation test of the knee, the patellar and tibial surface were recorded by the camera, and the relative location between the coordinate systems was determined using the ICP with the fast point feature histograms. Finally, the 3-D knee displacement during the tests was determined with respect to the knee joint coordinate system referred from the ISB recommendation[2]. Note that a Python-based program for measurement and analysis was developed and used.

Results

At 20° of flexion, the tibial anterior displacement was 2.1 ± 1.4mm and the internal rotation was 3.7 ± 2.5° in response to 100N of anterior force. The varus–valgus rotation was 3.7 ± 2.0° in response to ±10Nm of varus–valgus moments. A good correlation between the obtained displacement and X-ray-measured true displacement was found with the intraclass correlation coefficient of 0.73-0.80.

Discussion

A novel 3-D knee instability test system was successfully developed in this study, though further accuracy improvements are needed.

Images (Optional)

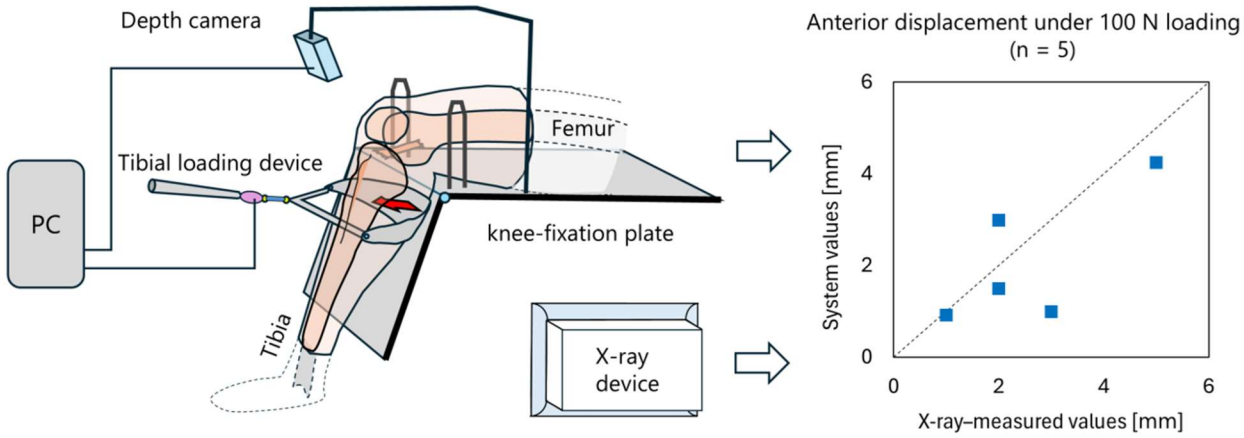


Fig. Overview of the novel 3-D knee instability test system and correlation between system values and X-ray–measured values under 100 N loading.

References (Optional)

[1] Kuroyama N *et al.*, Jpn Clin Biomech, 2025.

[2] Grood E. S *et al.*, J Biomech Eng, 1983.

Acknowledgements (Optional)

この研究はテルモ生命科学財団2025-2029の支援を受けて行われました。

Session Category

Imaging and Biomedical Devices: Imaging Fundamentals and Applied Research

P4-332

Quantification of Skeletal Dissolution of Cold-Water Corals in a Changing Ocean

Dr Marta Peña Fernández[1], Dr Kristina Beck[2], Prof J. Murray Roberts[2], Dr Sebastian Hennige[2], Prof Uwe Wolfram[3]

[1]School of Engineering and Physical Sciences, Heriot-Watt University, Edinburgh, Scotland, United Kingdom. [2]School of GeoSciences, University of Edinburgh, Edinburgh, Scotland, United Kingdom. [3]Institute of Materials Science and Engineering, Clausthal University of Technology, Clausthal-Zellerfeld, Lower Saxony, Germany

Introduction

Cold-water corals (CWCs) form complex habitats supporting high biodiversity in the deep sea [1]. Their structural complexity is at risk from ocean acidification (OA) which leads to reduction of seawater pH and aragonite saturation. While *live* corals continue to calcify under projected climate conditions, *dead* coral is prone to dissolution [2] which may result in habitat collapse and loss of biodiversity [3]. Here, we quantify the skeletal dissolution of the CWC Lophelia pertusa under projected OA conditions.

Methods

Dead skeletons were exposed for one year to (i) present-day oceanic pH (pH8.1); (ii) extreme end-of-century OA scenarios (pH7.7 and 7.8); (iii) OA projections beyond 2100 (pH7.6); and (iv) multiple stressors (high temperature, low oxygen and pH 7.7). We used time elapsed µCT (7µm) to quantify skeletal changes after 3, 4.5, 6, 9 and 12 months. Additionally, we performed high-resolution multi-scale SR-µCT (2.6µm to 0.325µm) at beamline I13-2 (Diamond Light Source) to quantify skeletal porosity.

Results

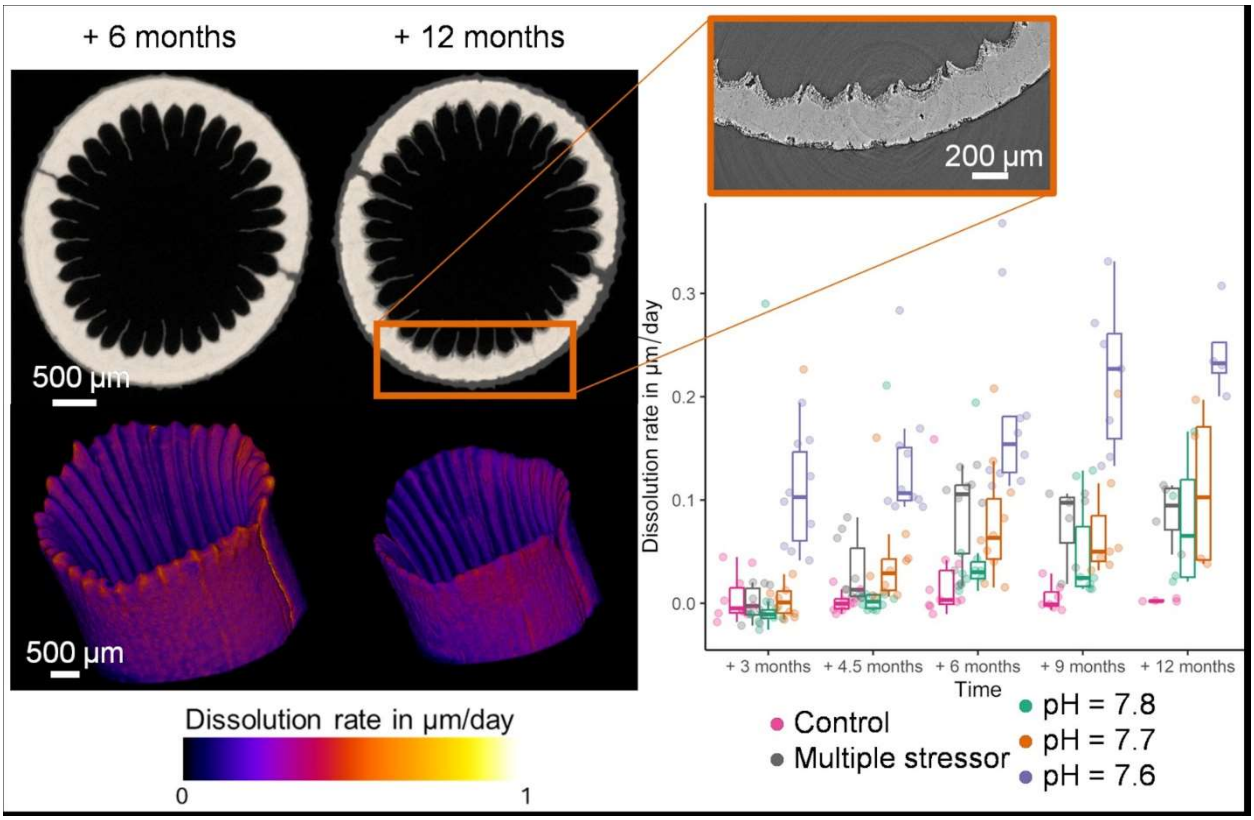
µCT images confirmed skeletal dissolution after 3 months that increased exponentially (Figure). Dissolution increased with reduced pH, with volume loss ranging from 1% to 83% for present-day pH and OA projections beyond 2100, respectively. The dissolution rate was not equal throughout the surface. Multi-scale SR-µCT images provided detailed dissolution and porosity information.

Discussion

We acquired the first µCT dataset on the dissolution process and its extent of *dead* CWC skeletons under present and projected OA scenarios. By investigating samples that have been exposed to a range of pH conditions over time, we can establish an exposure trajectory of aragonite saturation and OA-induced dissolution. This can be used to inform *in*

silico models [4,5] to investigate the increased risk of reef crumbling and consequent habitat loss under future OA projections.

Images (Optional)



References (Optional)

[1] Roberts et al., Science, 2016; [2] Hennige et al., Proc R Soc B, 2015; [3] Hennige et al., Front. Mar. Sci. , 2020; [4] Wolfram et al., Sci Rep, 2022; [5] Peña Fernández et al., Front. Mar. Sci., 2025

Acknowledgements (Optional)

We thank Shashi Marathe, Kaz Wanelik, Ruby Bader, Zoe Burns, Sarah Kaye, Blair Easton, Ian Butler, Kelsey A Barnhill, Brianna Ibarrola, Emma House, Anabel Alderson, Ann Larsson, Susana Strömberg, and St Abbs Marine Station for support with samples, experiment and µCT imaging. This research is funded by Leverhulme Trust RPG-2020-215, Horizon 2020 (Grant 818123), UKRI (Grant NE/S 008950 1), and Diamond Light Source (MG34205).

Session Category

Imaging and Biomedical Devices: Imaging Fundamentals and Applied Research

P4-333

In Silico Investigation of Natural Shear Wave Elastography in the Left Ventricle

MSc Marta Zattoni[1,2], Prof. Mathias Peirlinck[2], Prof. Patrick Segers[1], Dr. Annette Caenen[1,3]

[1]Ghent University, Ghent, East Flanders, Belgium. [2]TU Delft, Delft, South Holland, Netherlands. [3]KU Leuven, Leuven, Flemish Brabant, Belgium

Introduction

Altered left ventricular (LV) myocardial stiffness is a hallmark of several cardiac pathologies. Shear wave elastography (SWE) provides a non-invasive tool to assess stiffness from shear wave speed (SWS) propagation. Cardiac SWs can be generated by an impulsive acoustic radiation force (ARF) or naturally (NAT) following mitral valve closure (Fig-1A). Both techniques show promise in preclinical stiffness assessment, but the physics governing NAT SW propagation remain poorly understood. We developed an *in silico* framework to investigate key mechanisms underlying NAT SW behavior: (i) excitation duration, (ii) time instant of evaluation, and (iii) LV contractility.

Methods

An idealized LV hexahedral mesh was parametrically designed using pyFormex. Myocardial mechanics were modelled in Abaqus by combining passive Holzapfel-Ogden (2009) and active Guccione *et al.* (1993) formulations. Coupling with a three-element Windkessel model equivalent allowed to reproduce healthy pressure-volume behavior. SWs were excited with an impulsive body force and their propagation was analyzed through a submodelling technique focusing on the parasternal long-axis view of the LV wall (Fig-1B). This approach has been validated for ARF SWs, and it was adapted to induce NAT-alike SWs by applying a 1-, 2.5- or 5-ms body force. Simulations were performed at end-diastole, and 30 ms after, corresponding with experimentally observed SW propagation after mitral valve closure (Papangelopoulou *et al.,* 2024). SWS was estimated using a Radon transform on the pathlength-time plot at mid-wall (Fig-1C).

Results

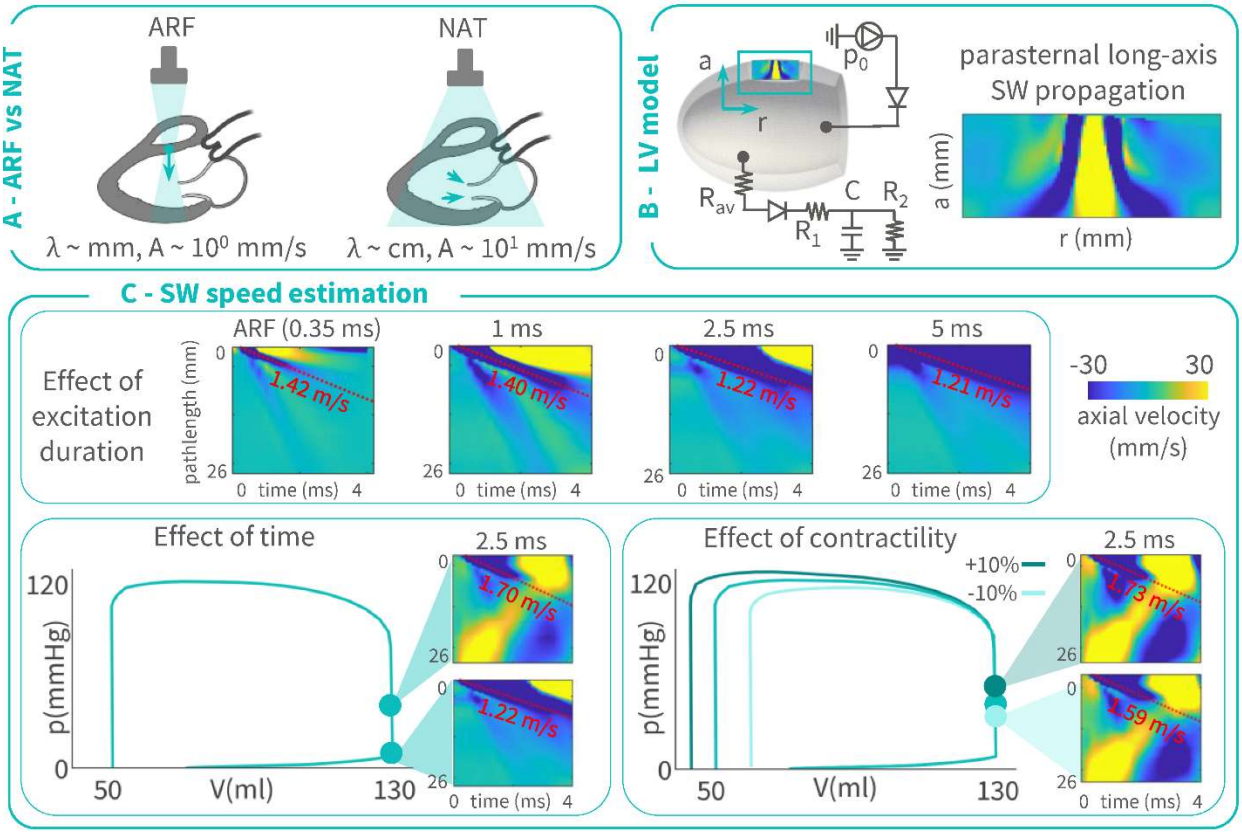
Longer excitation duration produced progressively longer wavelengths (λ_{ARF}=0.88mm; λ_{5ms}=6.5mm), consistent with *in vivo* reported results, and reduced SWS (-15%). NAT-alike SW assessed 30 ms after end-diastole aligned more closely with the timing of an actual SWE measurement and showed increased SWS (+39%), due to contractility effects. Averaged SWS across the wall was then 2.55±1.65 m/s, resembling averaged *in vivo* values

reported in literature. Similarly, increasing contractility resulted in higher SWS (+9%) 30 ms after end-diastole, due to pressure increase.

Discussion

Current study shows the added value of the modelling framework to study the effect of confounding factors on myocardial stiffness measurements. Ongoing work will redefine the body-force-based excitation by incorporating higher-fidelity modelling of valve closure, for a more physiological representation of NAT SW generation.

Images (Optional)



Acknowledgements (Optional)

M.Z. acknowledges the funding provided by the European Union within project 101169278 — InSilicoHealth — HORIZON-MSCA-2023-DN-01. Views and opinions expressed are however those of the authors only and do not necessarily reflect those of the European Union, which cannot be held responsible for them. A.C. acknowledges the support of the Research Foundation Flanders under grant 12B3124N.

Session Category

Imaging and Biomedical Devices: Imaging Fundamentals and Applied Research

P4-334

KNEE JOINT TISSUE DAMAGE IN RESPONSE TO REDUCED MECHANICAL LOADING BY BEDREST IMMOBILIZATION ASSESSED BY MRI-BASED SEMI-QUANTITATIVE METHOD

Ms Mathilde Lepileur[1,2], Prof., Dr. Frank Roemer[3,4], Ms Ines Ebner[1,2], Ms Maren Dreiner[5], Dr. Miriam Weyers[5], Prof., Dr. Annegret Mündermann[6,7,8], Prof., Dr. Frank Zaucke[9], Prof., Dr. Felix Eckstein[10], Prof., Dr. Anja Niehoff[5,11], P.D. Anna-Maria Liphardt[1,2]

[1]Department of Internal Medicine 3 – Rheumatology & Immunology, Universitätsklinikum Erlangen & Friedrich-Alexander-Universität Erlangen-Nürnberg, Erlangen, Bavaria, Germany. [2]Deutsches Zentrum Immuntherapie (DZI), Universitätsklinikum Erlangen & Friedrich-Alexander-Universität Erlangen-Nürnberg, Erlangen, Bavaria, Germany. [3]Department of Radiology, Universitätsklinikum Erlangen & Friedrich-Alexander-Universität Erlangen-Nürnberg, Erlangen, Bavaria, Germany. [4]Quantitative Imaging Center, Department of Radiology, Boston University School of Medicine,, Boston, Massachussets, United States. [5]Institute of Biomechanics and Orthopaedics, German Sport University Cologne, Cologne, Rhine-Westphalia, Germany. [6]Department of Teaching, Research and Development, Schulthess Clinic, Zurich, Zurich, Switzerland. [7]Department of Biomedical Engineering, University of Basel, Basel, Basel-Stadt, Switzerland. [8]Department of Clinical Research, University of Basel, Basel, Basel-Stadt, Switzerland. [9]Dr. Rolf M. Schwiete Research Unit for Osteoarthritis, Department of Trauma Surgery and Orthopedics, University Hospital Frankfurt, Goethe University, Frankfurt am Main, Hesse, Germany. [10]Institute of Anatomy, Paracelsus Medical University Salzburg & Nuremberg, Salzburg, Salzburg, Austria. [11]Faculty of Medicine, Cologne Center for Musculoskeletal Biomechanics (CCMB), University of Cologne, Cologne, Rhine-Westphalia, Germany

Introduction

Mechanical loading is essential for tissue health but quantifying the harm of disuse in healthy individuals is difficult. We previously showed enhanced cartilage extracellular matrix degradation after 21 days of 6° head-down-tilt (HDT) bedrest [1]. Using the validated multi-tissue Magnetic Resonance Imaging (MRI) Osteoarthritis Knee Score (MOAKS) [2], we evaluated the impact of reduced mechanical loading by three 21-day 6° head-down-tilt (HDT) bedrest periods within 1 year on knee joint structural health in young healthy adults.

Methods

Twelve healthy male participants (age 34.2 ± 8.3 years; body mass index 22.4 ± 1.7 kg/m^2) were exposed to three 21-days HDT periods within 1 year. HDT was combined with resistive vibration exercise and/or whey protein supplementation. MRI scans (3T, Siemens Trio, Erlangen, Germany) of the left knee were acquired. For this analysis, MRI scans taken

before the first (baseline, V1) and after the last HDT period (V2) were considered. Pathoanatomical features (bone marrow lesions (BML), osteophytes, meniscus damage) were assessed with MOAKS.

Results

At baseline, 8/12 participants did not have BML in the femur. After the three 21-day HDT bedrest periods, MOAKS increased. In the central medial femoral subregion, BML size decreased in one (MOAKS −0.5), and increased in two participants (MOAKS +0.5 and +2), with the latter developing an additional BML (MOAKS +1) and >66% cystic change (MOAKS +3/3). Ten participants had no abnormalities regarding the meniscus at either visit. At V1, two participants had meniscal extrusion of 2.0 to 2.9mm in the lateral and medial meniscus, respectively (MOAKS=1/3) and one of these had an abnormal lateral tear (MOAKS=4/8). These meniscal defects remained at V2. Finally, two participants had small osteophytes (MOAKS=1/3) in the femur and one participant in the tibia at both V1 and V2.

Discussion

Overall, we found very little structural change in healthy individuals in response to reduced mechanical loading during HDT immobilization. Semi-quantitative MRI assessment allows detection of pre-existent morphologic tissue damage and change over time and a complete description of joint tissue damage; quantitative assessments may be more sensitive to detect subtle longitudinal changes.

References (Optional)

[1] Dreiner et al. OA&C Open, 2025, [2] Collins J.E. OA&C Open, 2024

Acknowledgements (Optional)

SPONSOR: Min for Economic Affairs and Climate Action, Germany & German Aerospace Centre (DLR e.V.), German Space Agency (Project #: 50WB0913, 50WB1217, 50WB1719, 50WB1520, 50WB2021, 50WB2022) and the European Space Agency

DISCLOSURE STATEMENT: FWR is CMO, Director of Research and shareholder of Boston Imaging Core Lab (BICL), LLC., a company providing image assessment services to academia and the pharmaceutical industry. He is Editor in Chief of *Osteoarthritis Imaging*

Session Category

Imaging and Biomedical Devices: Imaging Fundamentals and Applied Research

P4-335

2D Bone Morphological Changes During Normal Growth at Localized Cranial Suture Sites

Dr. Michael Baggaley[1], Ms. Alexa Wingnean[2], Ms. Daelyn Page[1], Dr. Tsolmonbaatar Khurelbaatar[3], Dr. Dan Romanyk[1]

[1]University of Alberta, Edmonton, Alberta, Canada. [2]University of South Dakota, Vermillion, South Dakota, United States. [3]University of Calgary, Calgary, Alberta, Canada

Introduction

As the skull grows during infancy, the cranial sutures connecting the bones change shape to adapt to increasing pressure resulting from brain growth; suture width narrows and suture interdigitation increases [1]. However, it is unknown how these morphological changes are achieved in local regions of interest near the bone/suture interface. An image analysis pipeline was developed to quantify coronal suture morphology during normal growth in a rat model.

Methods

10 wild-type Sprague-Dawley rats received *in vivo* µCT at 7, 9, 11, and 16 weeks old. Planar images at 2% intervals between the endo- and ectocranial surfaces were created using a curved re-slicing technique to capture the entire length of the coronal suture accounting for skull curvature [1]. Three images were extracted for analysis in the endo- and ectocranial regions, located at 6%, 12%, and 18% and 86%, 92%, and 98% of skull thickness. 2D registration was performed between time-points to align the corresponding images (Figure 1A). To quantify bone addition, the younger image was subtracted from the older image; the older image was subtracted from the younger image to quantify bone removal. The number of pixels where deposition and removal occurred was counted and normalized to the suture size. Linear regression models were fit to the data; the main effect of animal age was examined using one-way ANOVA.

Results

A main effect of age was observed for bone addition ($F(1) = 49.06$; $p<0.001$) and bone removal ($F(1) = 97.23$, $p<0.001$) ratio. Bone addition decreased ($\beta = -0.034$; $t = 7.00$, $p<0.001$; Figure 1B) as the animals aged while bone removal increased ($\beta = 0.047$; $t = 9.86$, $p<0.001$; Figure 1C).

Discussion

Morphological changes are achieved through the coupled process of bone addition and removal at the bone-suture interface. Bone addition was greatest when the animal was young but decreased with aging; alternatively, bone removal was lowest when the animal was young and increased with age. Figure 1A highlights how remodeling activity differs at local suture sites; future analysis will quantify remodeling activity at specific suture features – i.e., convex, concave, and straight limb regions.

Images (Optional)

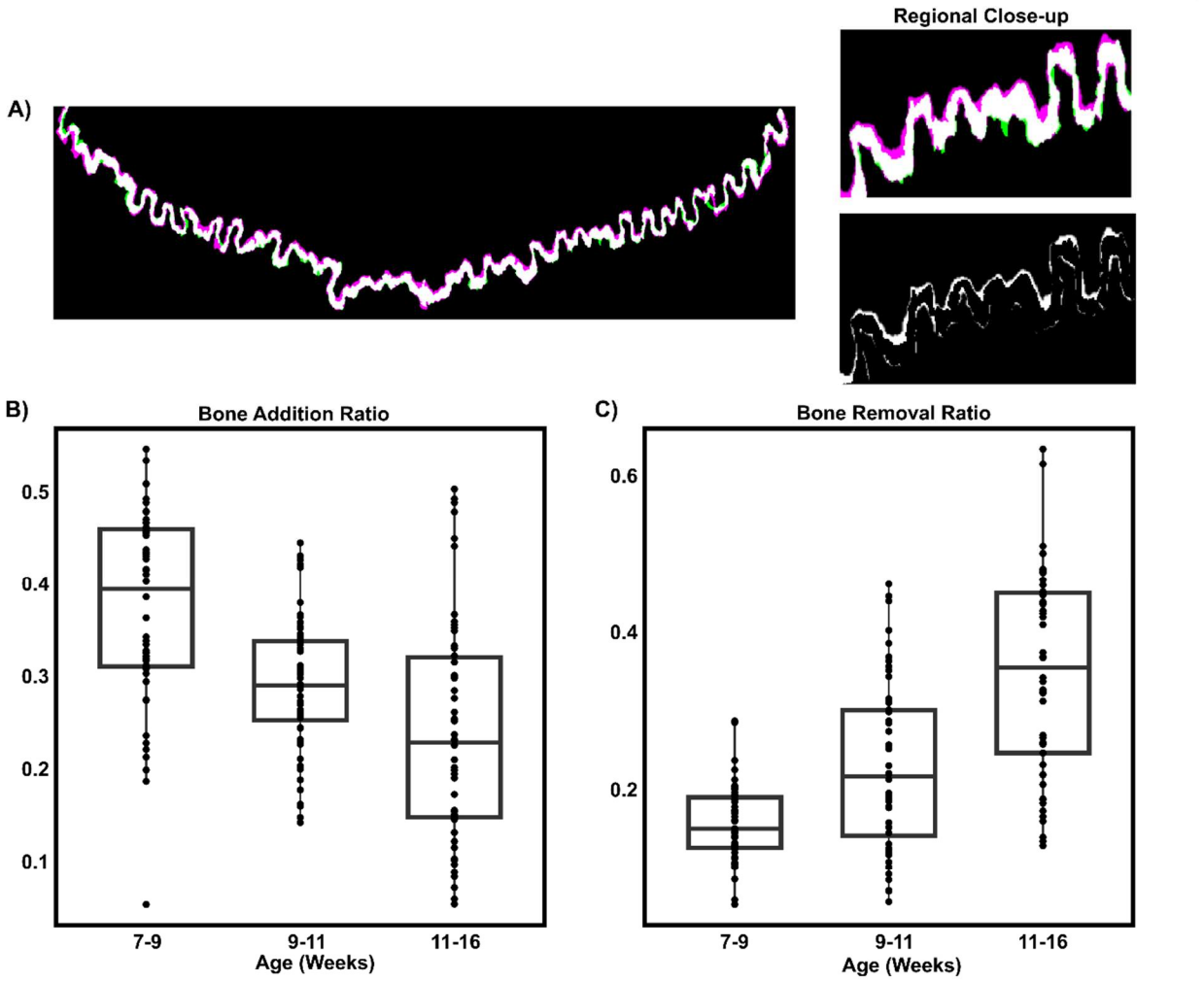


Figure 1: A) Exemplary image of the overlaid sutures. The white represents areas of mutual overlap. The pink is area unique to the older suture and green is area unique to the younger suture. The regional close up shows how changes to the suture are region specific. The black and white image indicates regions where bone addition occured. Box plots and individual data points for bone addition ratio (B) and bone removal (C) ratio vs. animal age.

References (Optional)

[1] Tsolmonbaatar Khurelbaatar *et al.* , Bone, 2025

Acknowledgements (Optional)

This work was supported by Natural Sciences and Engineering Council of Canada (NSERC) Postdoctoral Fellowship, Izaak Walton Killam Memorial Postdoctoral Fellowship, NSERC Discovery Grant, NFRF Exploration, and the Geoffrey and Robyn Sperber Craniofacial Biology Research funding programs.

Session Category

Imaging and Biomedical Devices: Imaging Fundamentals and Applied Research

P4-336

Combining Raman Spectroscopy and Optical Coherence Tomography to Assess Molar–Incisor Hypomineralization: Diagnostic Support in Dentistry

Ph.D. Nelly Vanessa Padilla Bello[1], M.Sc. Capucine Tavernier[1], Ph.D. Daniel R Neuville[2], Prof. Jean-Marc Allain[3], Prof. Elsa Vennat[4], Prof. Elisabeth Dursun[1], Ph.D. Aurélie Benoit[1]

[1]Université Paris Cité, Montrouge, Ile-de-France, France. [2]Institut de Physique du Globe de Paris (IPGP), Paris, Ile-de-France, France. [3]Ecole Polytechnique, Palaiseau, Ile-de-France, France. [4]CentraleSupélec, Gif-sur-Yvette, Ile-de-France, France

Introduction

Molar-Incisor Hypomineralization (MIH) is a dental condition affecting enamel, characterized by well-defined opacities and alterations in microstructure, chemical composition, mineral density, and mechanical properties [1].

Diagnosis of MIH is typically based on visual examination and its treatment depends on lesion severity and depth, which cannot be assessed using current clinical tools. To address these limitations, we combine two non-invasive techniques: Raman spectroscopy to assess the physico-chemical alterations [2] and optical coherence tomography (OCT) to investigate lesion location [3]. The aim is to identify reliable criteria of distinction from Raman spectra and assess the OCT's ability to delineate MIH-lesions.

Methods

180 Raman spectra were collected in vitro from two cross-sections of MIH-affected teeth and pre-processed to extract band integrals of different chemical bonds (phosphate, carbonate, amide and CH). Specific regions of interest (MIH/healthy enamel, dentin) were mapped by plotting the ratio between a selected band integral and phosphate. Statistical analysis was performed using the Kruskal-Wallis test combined with Mann-Whitney post-hoc tests.

OCT acquisitions, performed on the cross-sections and a whole premolar, were analyzed to evaluate the optical attenuation coefficient (OAC) in different tissues.

Results

Raman spectroscopy revealed more pronounced amide and CH peaks for MIH than for healthy enamel. Amide/phosphate and CH/phosphate ratios were both able to discriminate MIH from healthy enamel ($p<0.001$). CH maps also revealed low variability within MIH lesions despite the tissue heterogeneity.

OCT revealed contrast in tissue architecture, with affected enamel showing stronger surface reflection and higher OAC.

Discussion

Raman spectroscopy suggested an increased protein content and a reduction in mineral density, consistent with the structural difference observed in the MIH lesions. OCT observations agreed with the reported heterogeneity of MIH lesions causing light scattering, and opened perspectives to delineate MIH lesions.

Overall, despite the low number of samples, these findings highlight the potential of integrating OCT and Raman spectroscopy for an objective quantitative, and multi-scale characterization of MIH to enhance diagnosis accuracy in both research and clinical settings.

Images (Optional)

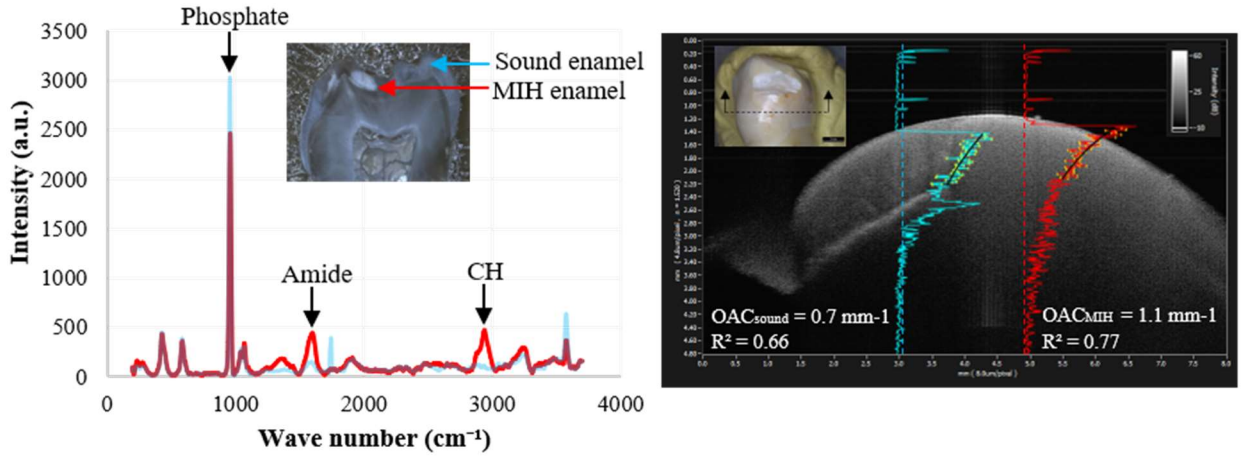


Fig. 1. Average Raman spectra of sound and MIH enamel (left) and OCT image of a premolar tooth showing the gray-level profiles with depth for sound and MIH enamel, and the regions used to calculate the optical attenuation coefficient (right).

References (Optional)

[1] Jälevik B *et al.*, JG. Int J Paediatr Dent. 2005.

[2] Fraser SJ. *et al.*, Raman Spectrosc. 2015.

[3] Popescu DP. *et al.*, J Biomed Opt. 2008.

Session Category

Imaging and Biomedical Devices: Imaging Fundamentals and Applied Research

P4-337

Semi-Automated Tracking of Tissue Thickness in Ultrasound B-Mode Images During Dynamic Deformation of the Plantar Soft Tissue

Mr. Nicholas Ozanich B.S., M.S.[1,2], Dr. Scott Telfer EngD[1,2,3], Dr. William Ledoux PhD[2,3]

[1]University of Washington Department of Mechanical Engineering, Seattle, WA, United States. [2]Center for Limb Loss and MoBility Research (CLiMB) VA Puget Sound Health Care System, Seattle, WA, United States. [3]University of Washington Department of Orthopaedics & Sports Medicine, Seattle, WA, United States

Introduction

Tissue thickness is a fundamental metric in ultrasound analysis, but manual calculation becomes inefficient and error-prone when applied to large dynamic datasets. Although tissue thickness is straightforward to measure in a single B mode image, manual measurement across continuously deforming sequences is inefficient and susceptible to operator variability. To address this, we developed a semi-automated pipeline that requires only two operator inputs: selection of the skin and a region of interest (ROI) around the bone.

Methods

B-mode ultrasound videos of the plantar surface of a single cadaver foot at the calcaneus were collected during cyclic loading of the tibia using an Instron E3000 at 200 N across three frequencies (0.5, 1.0, 1.5 Hz), with ten cycles per frequency and three trials for various speeds of sound (1540, 1600, 1660 m/s) for a total of nine videos (n=23007 frames). Images were processed by applying a bilateral filter followed by a Gabor filter bank [1] and gamma correction to distinguish bone from soft tissue. For tracking, an ROI was drawn around the bone to initialize a kernelized correlation filter (KCF) [2], which followed the bone throughout deformation. Within the tracked ROI, Otsu's thresholding [3] was applied to each frame to segment the calcaneus, followed by morphological operations to refine the segmentation. Validation was performed through visual confirmation of tracking quality and calculation of internal metrics of tracker performance.

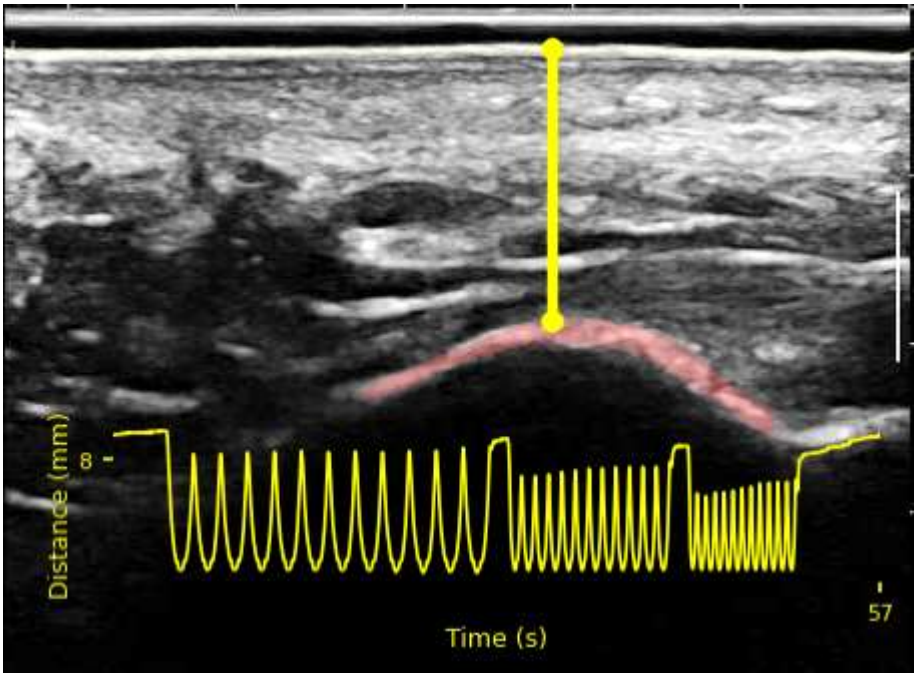
Results

KCF tracking was reliable with strong spatial agreement and minimal temporal variability, with no tracker failures in any video. Across all frames, mean ROI intersection over union was 0.979 ± 0.009, mask area coefficient of variation was 0.047 ± 0.012, and the temporal stability score was 0.996 ± 0.0008.

Discussion

This automated approach produced calcaneus segmentations that enabled calculation of tissue thickness. This work demonstrates an automated method for quantifying musculoskeletal tissue thickness and provides a framework for assessing tissue deformation over time without reliance on training data. Future work should extend this approach to other tissues and incorporate segmentation of skin undergoing deformation.

Images (Optional)



References (Optional)

[1] Daugman, J. Opt. Soc. Am. A, 1985

[2] Henriques *et al.*, CVPR, 2014

[3] Otsu, IEEE Trans. Syst. Man, Cybern.,1979

Session Category

Imaging and Biomedical Devices: Imaging Fundamentals and Applied Research

P4-338

Ultrasound-Derived Plantar Soft Tissue Deformation Using Lucas-Kanade Tracking

Mr. Nicholas Ozanich B.S., M.S.[1,2], Dr. Scott Telfer EngD[1,2,3], Dr. William Ledoux PhD[2,3]

[1]University of Washington Department of Mechanical Engineering, Seattle, WA, United States. [2]Center for Limb Loss and MoBility Research (CLiMB) VA Puget Sound Health Care System, Seattle, WA, United States. [3]University of Washington Department of Orthopaedics & Sports Medicine, Seattle, WA, United States

Introduction

This study introduces a grid-based pyramidal Lucas–Kanade (LK) [1] approach to quantify plantar soft-tissue displacement across the heel pad microchambers and macrochambers during cyclic compression. Quantifying full-field motion throughout the tissue area could further elucidate mechanical differences between the macrochambers and microchambers.

Methods

B-mode ultrasound videos of the plantar surface of a single cadaver foot at the calcaneus were collected during cyclic loading of the tibia using an Instron E3000 at 200 N across three frequencies (0.5, 1.0, 1.5 Hz), with ten cycles per frequency and three trials for various speeds of sound (1540, 1600, 1660 m/s) for a total of nine videos (n=23007 frames). The probe was positioned anteroposteriorly. The pyramidal LK optical flow estimates horizontal (U) and vertical (V) heel pad and bone displacements by tracking a grid of points that move with respect to localized features. The points are re-seeded after each period of unloading to prevent accumulation of drift. A horizontal line is used to roughly estimate the division between macrochambers and microchambers. Average peak vertical and horizontal displacements were calculated per-cycle. Point tracking was validated against known displacement of a bone mask and soft tissue motion was restricted to soft tissue above the bone and plantar fascia.

Results

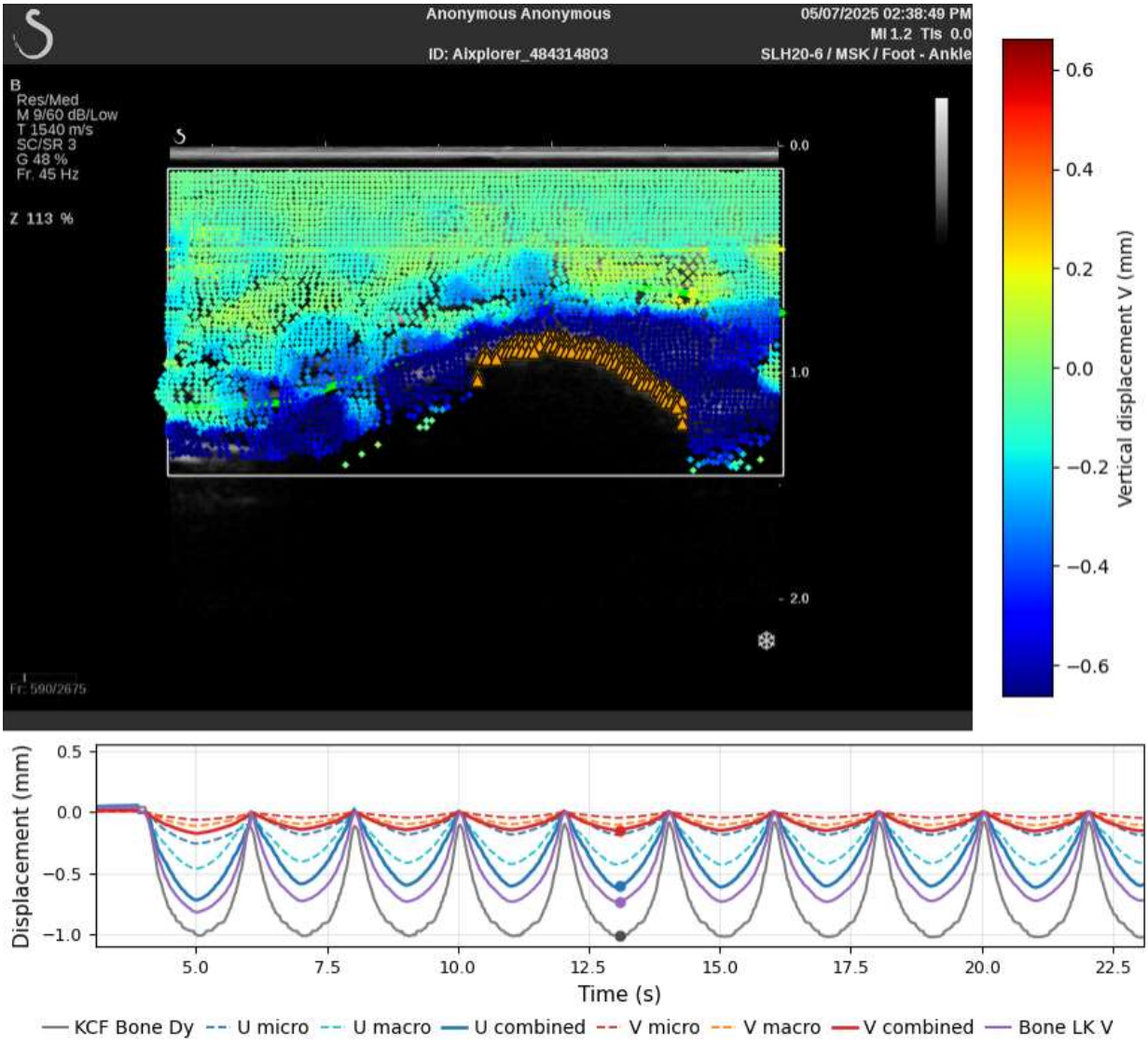
Preliminary results showed that the LK tracking of bone underestimated peak displacement (-0.276 ± 0.069 mm when compared to known peak bone mask displacement (0.831 ± 0.141 mm), alluding to systemic underestimation of displacement (Figure 1). Average horizontal peak displacement (0.205 ± 0.052 mm) was observed to be greater than average vertical peak displacement (0.0624 ± 0.011 mm). Average horizontal peak macrochamber (0.314 ± 0.090 mm) and microchamber (0.160 ± 0.029 mm)

displacements were greater than average vertical peak macrochamber (0.079 ± 0.015 mm) and microchamber (0.045 ± 0.009 mm) displacements.

Discussion

This pipeline provides a framework for quantifying soft tissue vertical and horizontal displacement. Further analyses will seek to improve tracking performance, better discrimination between two chambers, test on larger heel pad deformations seen in gait, and test on other musculoskeletal tissues. A key limitation of this work is out of plane motion from the B-mode images.

Images (Optional)



References (Optional)

[1] Bouget, Intel MRL Technical Report, 2000

Session Category

Imaging and Biomedical Devices: Imaging Fundamentals and Applied Research

P4-339

Evaluating Sensitivity of MRI-Based Porosity Index to Acute Changes in Cortical Bone Blood Flow Following Exercise

Ms. Patricia Tran, Ms. Katie Sofko, Dr. Feliks Kogan, Dr. Olivia L Bruce

Department of Radiology, Stanford University, Stanford, California, United States

Introduction

Ultrashort echo time (UTE) magnetic resonance imaging (MRI) can detect signal from cortical bone, enabling quantitative assessment not possible with conventional MRI sequences. A UTE-derived biomarker associated with bone strength, porosity index (PI), quantifies the proportion of free water in cortical pores relative to total bone water [1]. Since pore water has a longer T2* relaxation time than water bound to the bone's collagen matrix, PI is calculated by taking the ratio of proton signal acquired at the shortest possible echo time (total water image) and a longer echo time (pore water image) [1]. Changes in blood flow in the bone could alter the long T2* components and, consequently, PI, but this has not yet been investigated. The purpose of this study was to determine whether PI is sensitive to blood flow changes in cortical bone following acute exercise.

Methods

Seven physically active participants (6 female, 1 male, 26 ± 4 years, 1.70 ± 0.03 m, 66.4 ± 10.3 kg) completed a ten minute treadmill run at preferred speed (2.7 ± 0.3 m/s). Dual-echo UTE MRI scans of the lower leg (TE = 0.028 ms and 2.2 ms; hard pulse; 2:23 min per scan) were acquired immediately following exercise and approximately 20 minutes later, which was treated as the at-rest (baseline) value. For each scan, mean cortical PI was calculated across five slices at the mid-tibia. Differences between PI values at the two timepoints were evaluated using a paired-t test.

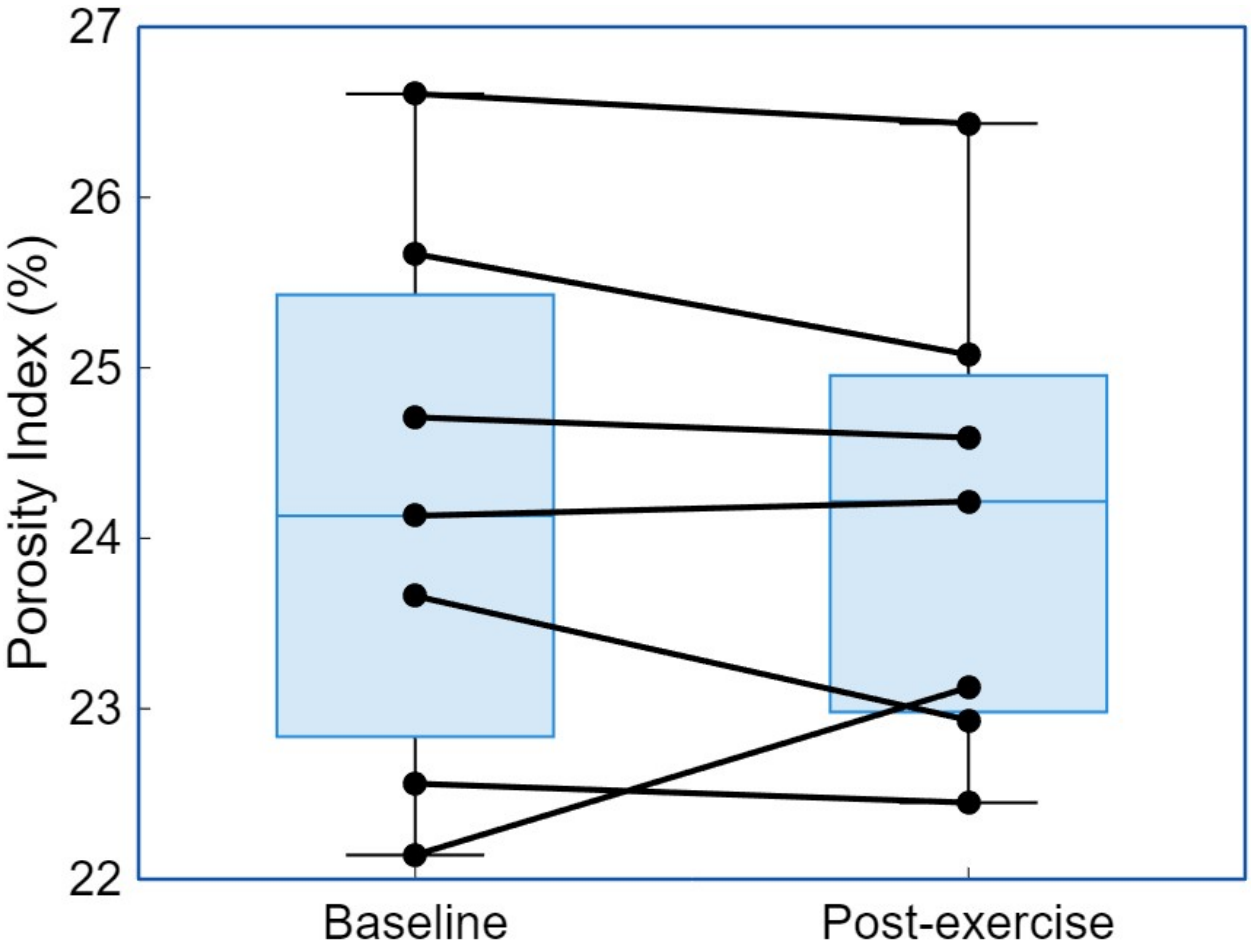
Results

Mean PI was 24.2 ± 1.60 at baseline and 24.1 ± 1.40 immediately after exercise. PI values immediately post-exercise were not significantly different when compared to baseline (mean difference = 0.1 ± 0.6, $t = 0.543$, $p = 0.607$, Figure 1).

Discussion

PI values were within the range previously reported for tibial cortical bone [1]. Our results show that PI does not change with acute exercise. Since bone blood flow increases in response to exercise [2], this suggests that bone PI measures are not sensitive to changes in bone blood flow.

Images (Optional)



References (Optional)

[1] Chamith Rajapakse *et al*. Radiol, 2015

[2] John Stabley *et al.* Med Sci Sports Exerc, 2014

Acknowledgements (Optional)

The authors would like to acknowledge funding support for this study: GE Healthcare, Stanford Medicine Department of Radiology, and the Wu Tsai Human Performance Alliance.

Session Category

Imaging and Biomedical Devices: Imaging Fundamentals and Applied Research

P4-340

Evaluating Clinically Relevant Imaging Techniques to Assess Collagen Organisation in Ex Vivo Breast Tissue

Ms. Olivia Strong[1,2], Dr. Brooke Tornifoglio[1,2]

[1]Trinity Centre for Biomedical Engineering, Trinity College Dublin, Dublin, Ireland. [2]Discipline of Mechanical, Manufacturing and Biomedical Engineering, Trinity College Dublin, Dublin, Ireland

Introduction

Ranging from non-dense to highly fibroglandular, breast density is a major risk factor for breast cancer and correlates with increased collagen deposition[1,2]. Elevated collagen content increases cancer risk, while increased alignment links with tumour aggressiveness[3,4]. No current clinical method characterises collagen in breast tissue. MRI offers a non-invasive option and particularly, diffusion tensor imaging (DTI) has shown sensitivity to collagen orientation in other tissues[5,6]. This study aims to evaluate the sensitivity of DTI to collagen alignment within ex vivo breast tissue.

Methods

Fixed cadaveric breast tissue (N=1) was obtained from the Anatomy Department at Trinity College Dublin. Ex vivo DTI was acquired on a 7T Bruker BioSpec using a 3D-spin echo sequence with parameters based off a previous study[6]. Data was pre-processed in MRtrix3 and tensor fitted in ExploreDTI[6].

Standard histological processing was performed: Picrosirius-red (PSR) stained slides were imaged using polarised light microscopy on an Olympus-BX41. Analysis was carried out using OrientationJ in FIJI.

Results

Ex vivo DTI differentiated between the main tissue types in cadaveric breast tissue (1a). First eigenvector maps, overlayed on the MD map (1b), revealed sections of alignment within fibrous tissue. Regions of increased collagen alignment were confirmed via ground-truth PSR (1c) and the corresponding fibre orientation colour map revealed 75% of fibres were orientated along the dominant direction (1d).

Discussion

Measured MD, in this study, was comparable to previous in vivo values of normal breast tissue (0.0014 ± 0.00027 mm^2/s)[7]. Regions of high alignment were identified via the

principal eigenvector and confirmed via histology. Future work will investigate fresh breast tissue of varying densities to better assess DTI as a potential non-invasive method to quantify collagen alignment in breast tissue – potentially informing BC invasiveness.

Images (Optional)

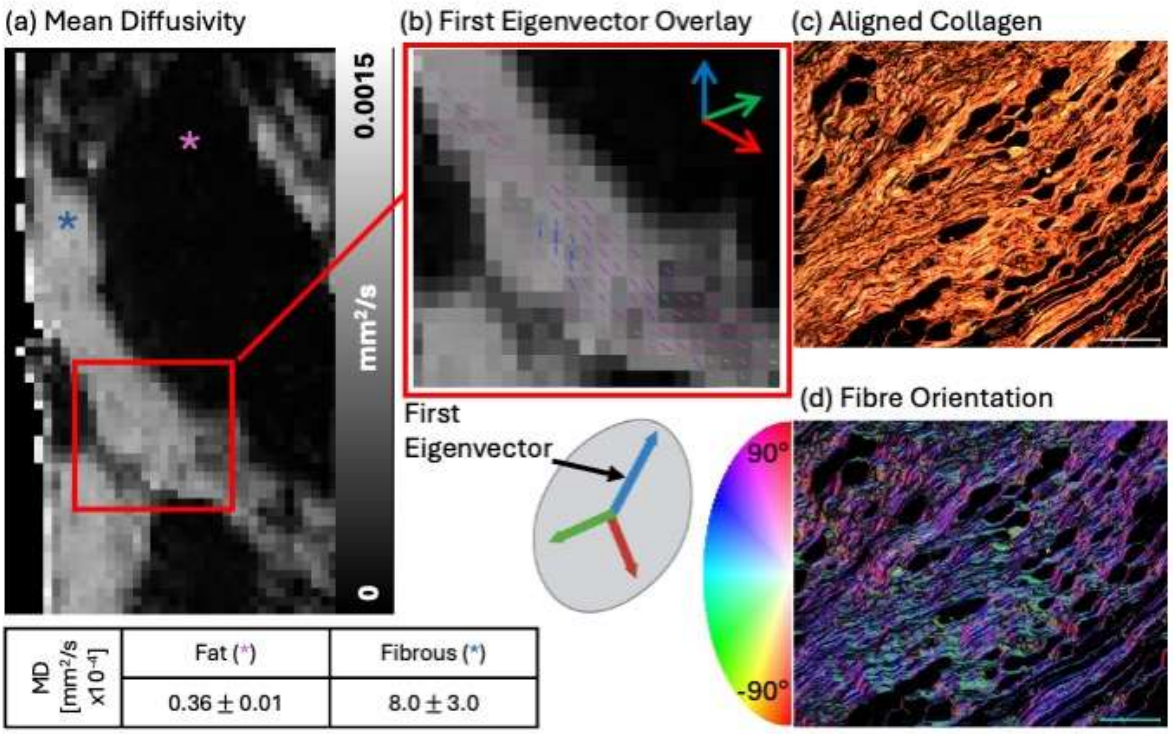


Figure 1: Ex vivo DTI metrics (a,b), PSR staining (c) and corresponding fibre orientation colour map (d) of human cadaveric breast tissue. Scale bar = 200 µm.

References (Optional)

[1] Elsebeth Lynge, et al. Int J Cancer, 2022

[2] Salem Alowami, et al. Breast Cancer Res, 2003

[3] Kun Zhang, et al. Nat Cell Biol, 2013

[4] Paolo Provenzano, et al. BMC Med, 2006

[5] Nan Wang, et al. Magn Reson Med, 2020

[6] Brooke Tornifoglio, et al. Sci Rep, 2020

[7] Ruisheng Jiang, et al. Med Sci Monit, 2016

Acknowledgements (Optional)

This project is funded by a Cancer Research Stimulus Award (CREST) from the Trinity St. James's Cancer Institute. The authors would also like to thank Claire Murphy from the Department of Anatomy at Trinity College.

Session Category

Imaging and Biomedical Devices: Imaging Fundamentals and Applied Research

P4-341

Age-Related Differences in Prefrontal Cortex Activation and Stance Time Modulation During Visually Cued Gait

Mr. Paul McDonnell MS, Mr. Adam B. Grimmitt MS, Mr. Jonaz Moreno Jaramillo MS, Dr. Wouter Hoogkamer PhD, Dr. Douglas N. Martini PhD

University of Massachusetts Amherst, Amherst, MA, United States

Introduction

Gait requires visually cued step adjustments, which involve modulating stride phase timing [1]. Older adults (OA) display longer stance times and larger stepping errors than young adults (YA) in visually complex environments [2,3]. OA exhibit more executive control of gait (higher prefrontal cortex [PFC] activity) [4], representing reduced gait automaticity. Reduced automaticity may limit flexible stride phase timing control when visuomotor demands increase. This study compared stance time, stepping error, and PFC activity in YA and OA during visually cued gait without (VC) and with perturbations (VCP). We hypothesized that OA would exhibit longer stance times, larger stepping errors, and higher PFC activity than YA, and that higher PFC activity would relate to longer stance times during VCP.

Methods

28 YA (21.9[3.4]yrs; 15F) and 54 OA (70.9[4.3]yrs; 32F) completed 3-minute treadmill walking trials (VC and VCP) at preferred speed. Stepping targets were presented, matching foot size, step length, and gait speed. During VCP, random targets shifted to a new position when approaching the participant. We quantified stepping error as the distance between foot and target center at midstance. Inertial measurement units computed stance time. Functional near-infrared spectroscopy quantified relative changes in oxygenated hemoglobin concentration in the PFC. Mixed ANOVAs assessed group and condition effects. Pearson's correlation assessed the relationship between PFC activity and stance time.

Results

Only YA reduced stance times from VC to VCP (p=.003). Across conditions, OA exhibited longer stance times (p=.014), larger stepping errors (p<.001), and higher PFC activity

(p<.001) than YA. Across participants, higher PFC activity was associated with longer stance times during VCP (r=0.26, p=.019).

Discussion

Consistent longer stance times and larger stepping errors across conditions in OA indicate age-related difficulty in adjusting gait to meet visuomotor demands. PFC activity was significantly higher in OA across conditions and was positively correlated with stance time during VCP, suggesting an age-related cortical compensatory gait control strategy that limits gait flexibility.

Images (Optional)

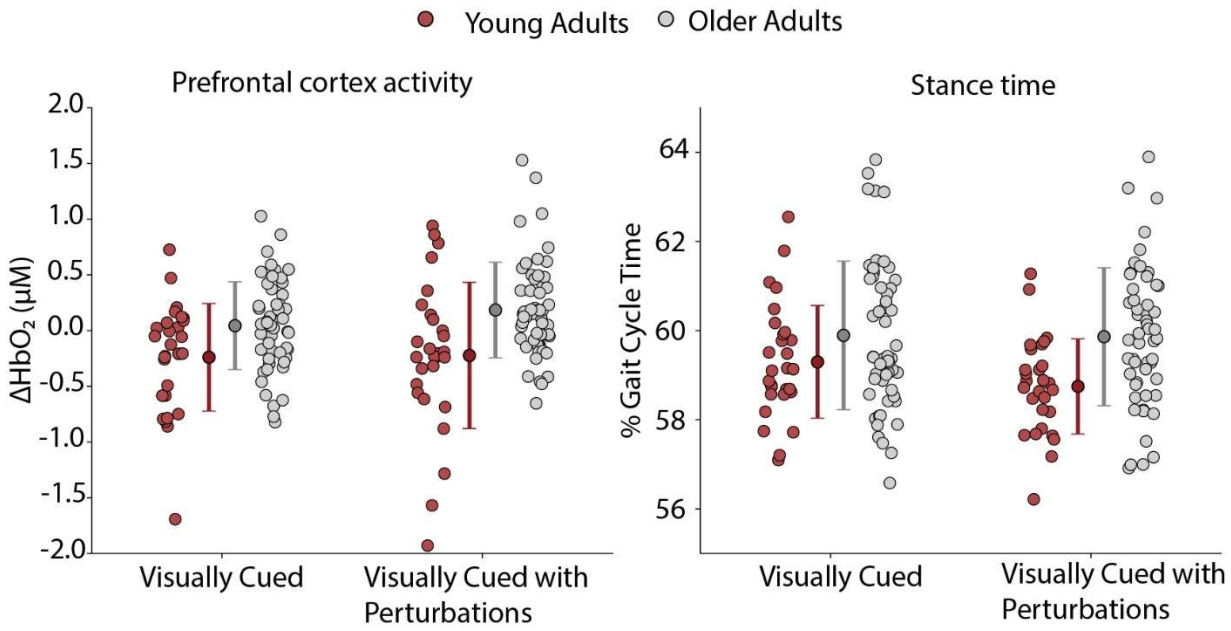


Figure: Age-related differences in PFC activity and stance time during visually cued gait and visually cued gait with perturbations. Left: individual data points represent PFC activity, measured as the relative change in oxygenated hemoglobin (ΔHbO2) concentration from baseline standing. Right: individual data points represent stance time, measured as a percentage of gait cycle time. Points with whiskers represent the mean and standard deviation for each group-condition combination.

References (Optional)

[1] Zhang et al., EJAP, 2021

[2] Yun and Park., Gait & Posture, 2022

[3] Mazaheri et al., EBR, 2015

[4] Mirelman et al., Brain & Cognition, 2017

Acknowledgements (Optional)

This work was supported by: NIA R21AG075489

Session Category

Imaging and Biomedical Devices: Imaging Fundamentals and Applied Research

P4-342

Densitometric Correction for Appendicular Soft Tissue Artefacts Measured by Second-Generation HR-pQCT

MSc Simone Poncioni[1], BSc Alexia Pollaci[1], MSc Stefan Bracher[1], Ms Silvia Owusu[2], Prof Dr Dieter Bosshardt[2], Prof Dr Philippe Zysset[1]

[1]ARTORG Centre for Biomedical Engineering Research, University of Bern, Bern, Bern, Switzerland. [2]Department of Periodontology, School of Dental Medicine, University of Bern, Bern, Bern, Switzerland

Introduction

Longitudinal monitoring of distal radius and tibia using high-resolution peripheral quantitative computed tomography (HR-pQCT) offers several advantages over the clinical standard DXA, including distinct evaluation of cortical and trabecular bone compartments, 3D registration, and shorter trend assessment intervals. However, CT methods suffer from beam hardening artefacts associated with the amount of soft tissues surrounding the bones, which may impair quantitative follow-up if concomitant with weight changes. Therefore, this study aimed to quantify the effects of increasing X-ray attenuation around *ex vivo* human distal radii using second-generation HR-pQCT.

Methods

A human cadaveric phantom of the appendicular skeleton was manufactured using three distal radius sections of 20 mm from distinct donors. Nine soft tissue-equivalent discs of PMMA (Ø=34-120 mm) were sequentially appositioned around the phantom to simulate the variation of soft tissue thickness (b,c). Images were acquired and evaluated using standard clinical settings and multi-stack protocol [1,2]. Densitometric variables, microstructural parameters such as trabecular degree of anisotropy (DA), relative cortical thickness (Rel.Ct.Th), and apparent yield stress were assessed at each thickness. A correction model was developed to relate Tot.vBMD, Ct.vBMD, and Tb.BV/TV attenuated to baseline values as a function of soft tissue area (A_{st}) and intercompartmental bone density ratio.

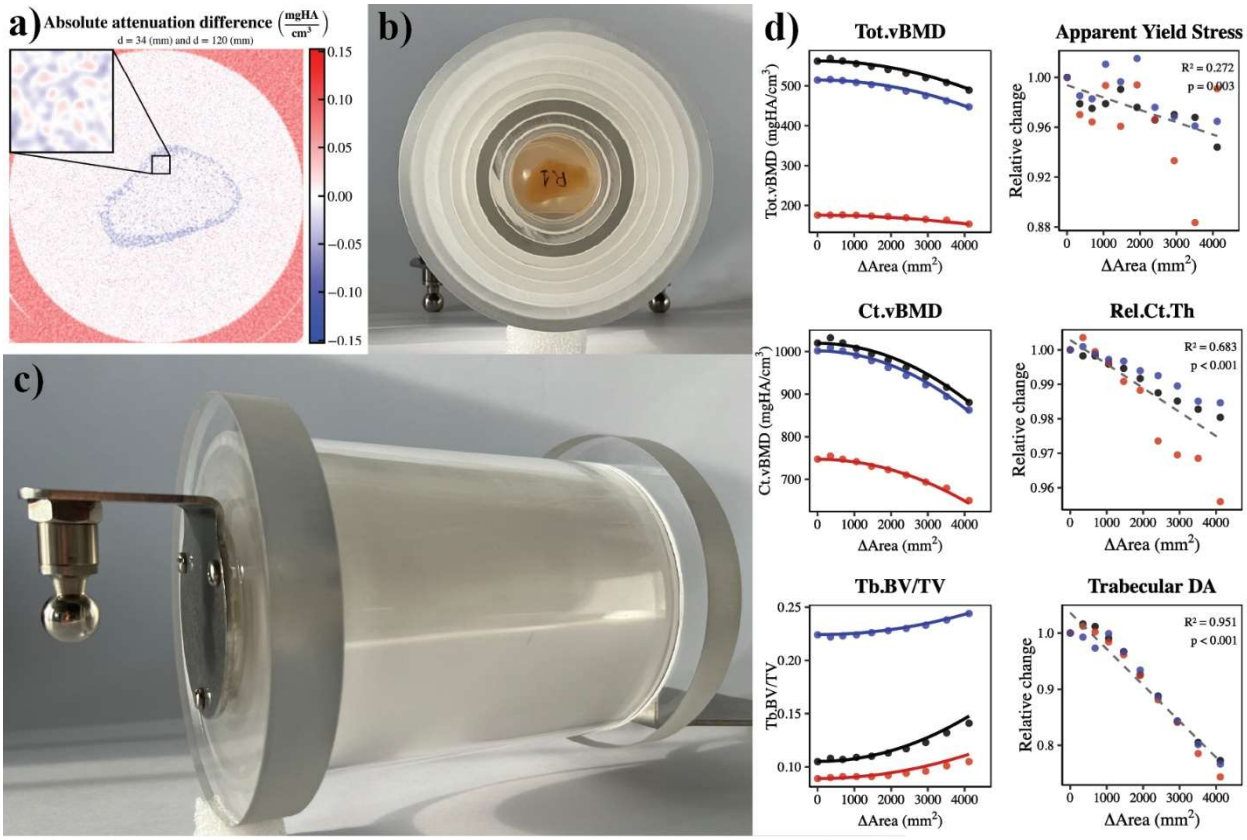
Results

The model demonstrated strong and significant relationship with A_{st} for Tot.vBMD, Ct.vBMD, and Tb.BV/TV (R^2>0.99, p<0.001). The interaction term Ct.vBMD/Tb.vBMD was significant for Tb.BV/TV (p<0.001) but not for Tot.vBMD and Ct.vBMD. Compartment-specific effects were observed, with underestimation in the cortex and overestimation in the marrow cavity for increased A_{st} (a). Geometric, microstructural, and mechanical properties decreased significantly with increasing A_{st}, strongest in Tb.DA (R^2=0.97) and Rel.Ct.Th (R^2=0.69) (d).

Discussion

These findings confirm that beam hardening artefacts in second-generation HR-pQCT cause increasing errors in bone densitometric variables as soft tissue-equivalent material increases around the bone section [3]. Future work will address generalisation by including three distal tibia sections and correction for segmented A_{st}. This will improve the accuracy of longitudinal monitoring of densitometric and biomechanical variables when substantial weight changes are involved.

Images (Optional)



References (Optional)

[1] Whittier *et al.* Osteoporos Int, 2020.

[2] Schenk *et al.* JMBBM, 2022

[3] Caksa *et al.,* Bone, 2019

Session Category

Imaging and Biomedical Devices: Imaging Fundamentals and Applied Research

P4-343

Biomechanics of the Ligamentum Flavum via 4D Contrast Enhanced Micro-CT

Ms. Raluca-Ana-Maria Barna[1,2,3], PD Dr. Jonas Widmer[4,5], Prof. Dr. Ameet Aiyangar[6,7,8], PD Dr. Annapaola Parrilli[1]

[1]Center for X-Ray Analytics , Swiss Federal Laboratories for Materials Science and Technology, Empa, Dübendorf, Zurich, Switzerland. [2]University of Bern, Bern, Bern, Switzerland. [3]Spine Biomechanics Balgrist University Hospital, Zurich, Zurich, Switzerland. [4]Spine Biomechanics, Balgrist University Hospital, Zurich, Zurich, Switzerland. [5]Department of Orthopedics, Balgrist University Hospital, Zurich, Zurich, Switzerland. [6]Department of Diagnostic, Interventional and Paediatric Radiology, Insel Gruppe, Bern, Bern, Switzerland. [7]School of Medicine, University of Bern, Bern, Bern, Switzerland. [8]Mechanical Systems Engineering, Swiss Federal Laboratories for Materials Science and Technology, Empa, Dübendorf, Zurich, Switzerland

Introduction

Lumbar spinal stenosis (LSS) is the narrowing of the spinal canal compressing the spinal cord and causing low back pain. It is often related to hypertrophy of the ligamentum flavum (LF), whose altered morphology and reduced stiffness further compromise spinal stability. Existing studies are limited to LF biopsies assessed primarily with 2D histology rather than whole-ligament imaging. Control samples often come from patients with other degenerative spinal conditions, so baseline data on healthy LF physiology are lacking. This project fills this gap by developing a method that integrates non-destructive 3D imaging with in-situ loading on intact, healthy LF to relate macro-scale properties to microstructure and mechanical behaviour.

Methods

Human lumbar ligaments are biomechanically tested both fresh and after iodine staining. Tensile tests are performed using a predicted non-destructive maximum elongation, and micro-CT scans are acquired at different loading points within the linear region of the stress-strain curves. Digital volume correlation (DVC) is then used to quantify strain distribution. Staining conditions were defined through comparisons of contrast agents, concentrations, and staining durations, leading to the selection of a 10-day protocol with 3.75% buffered Lugol's iodine.

Results

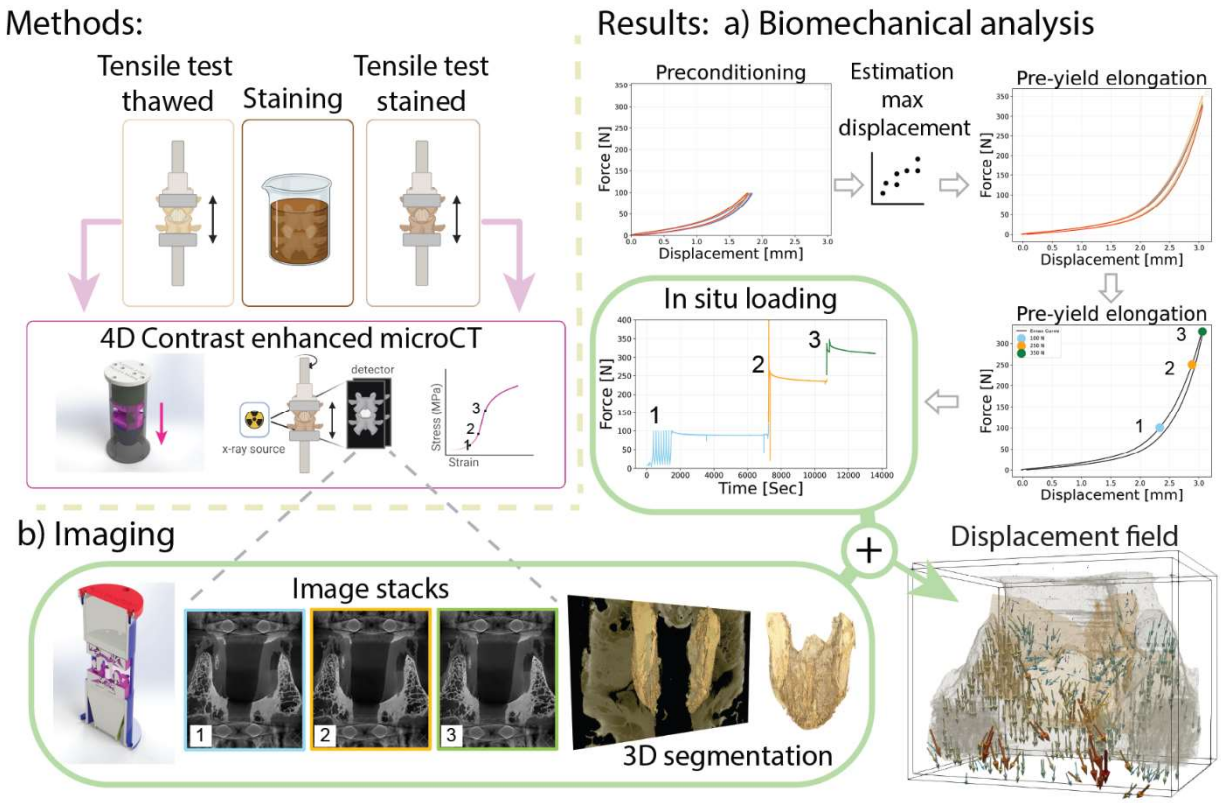
Ordinary-Least-Squares regression demonstrated a strong linear relationship between displacement at 100 N and pre-yield elongation ($R^2 = 0.836$, $p < 0.0001$). This model was

estimated on 50 ramp-to-failure datasets [1] and successfully predicted non-destructive displacement for 10 preliminary specimens. For contrast enhancement, PTA and Lugol were compared; both PTA and 8% Lugol markedly increased stiffness and were discarded. Lower-concentration Lugol (3.75%) was then tested at varying immersion times, with 10 days proving sufficient. Strain distribution was computed for both label-free and contrast-enhanced samples, capturing native behaviour and fiber spatial organization (Fig:1).

Discussion

Specimen-specific prediction of pre-yielding elongation ensured repeatable non-destructive testing. Stepwise scanning enabled assessment of contrast-enhancement benefits while tracking preparation artefacts (volume shrinkage, increased stiffness). The relationship between macroscopic biomechanical behaviour and local volumetric deformations was revealed combining high-resolution micro-CT and in situ-loading, resulting in local characterization of ligament strain distribution. This multiscale approach generates valuable baseline data on healthy LF physiology and responds to a gap in current knowledge.

Images (Optional)



References (Optional)

[1] Cornaz F. et al., Spine J, (2021)

Session Category

Imaging and Biomedical Devices: Imaging Fundamentals and Applied Research

P4-344

Fiducial Marker-Based 3D Freehand Ultrasound for *in vivo* Muscle Morphology Quantification

PhD student Ruoyu Huang[1], Master student Lorenzo De Sanctis[2,3], Postdoctoral Researcher Zhongzheng Wang[1,4], Professor Umile Giuseppe Longo[2,3], Professor Matilda Larsson[4], Associate professor Ruoli Wang[1,5]

[1]KTH MoveAbility Lab, Dept. of Engineering Mechanics, KTH Royal Institute of Technology, Stockholm, Stockholm, Sweden. [2]Fondazione Policlinico Universitario Campus Bio-Medico, Rome, Rome, Italy. [3]Research Unit of Orthopaedic and Trauma Surgery, Department of Medicine and Surgery, Università Campus Bio-Medico di Roma, Rome, Rome, Italy. [4]Dept. of Biomedical Engineering and Health Systems, KTH Royal Institute of Technology, Stockholm, Stockholm, Sweden. [5]Division of Paediatric Neurology, Department of Women's and Children's Health, Karolinska Institutet, Stockholm, Stockholm, Sweden

Introduction

Muscle morphological parameters, such as muscle volume (MV), fascicle length (FL) and pennation angle (PA), are key determinants of muscle function. 3D freehand ultrasound (3DfUS) enables their non-invasive quantification by reconstructing 2D ultrasound images into 3D using probe tracking. Infrared stereophotogrammetry offers high accuracy but requires specialized laboratory setups, limiting clinical applicability. Monocular tracking may enhance feasibility, yet its capability for muscle assessment remains unclear. This pilot study evaluated the reliability and validity of a fiducial marker–based monocular 3DfUS system for muscle morphology quantification.

Methods

Ten healthy participants underwent 3DfUS scanning of the rectus femoris using a linear ultrasound probe (5cm, Mindray M9, 19Hz) equipped with a 3D-printed dodecahedron housing twelve ArUco fiducial markers and a cluster of four reflective markers (Fig. 1A). Probe motion was simultaneously captured by a video camera (LUCID PHX-CS016, 60 Hz) and a motion capture system (Vicon V16, 100 Hz) as a reference. Each participant was scanned by two operators during the first session, and one operator repeated the scan in a second session within one week. Fiducial marker detection and pose estimation were performed using OpenCV's ArUco module solving a RANSAC-optimized Perspective-n-Point (PnP) problem. 3D images were reconstructed using a python library for 3DfUS (py3dfreehandus) and manually segmented using 3D slicer (Fig. 1B-C).

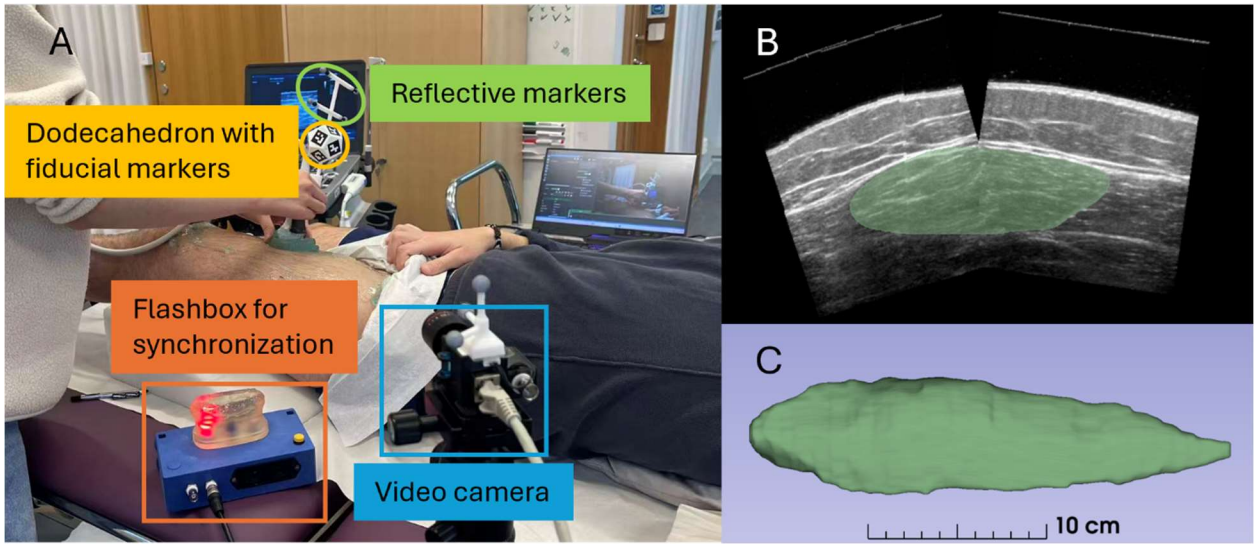
Results

Preliminary analysis of two participants showed a minor overestimation of MV compared with the reference (absolute difference = 4.7±4.0 mL, percentage difference = 2.8±2.4%), with slightly lower accuracy for FL (4.7 ± 2.9 mm, 5.6 ± 3.6%) and PA (1.3 ± 0.5°, 11.1 ± 4.3%). Inter-rater discrepancies were 5.0 ± 0.0 mL for MV, 3.5 ± 2.1 mm for FL and 0.0 ± 0.0° for PA, while inter-session discrepancies were 4.0 ± 1.4 mL for MV, 1.5 ± 0.7 mm for FL, and 1.0 ± 0.0° for PA.

Discussion

This pilot study demonstrates that fiducial marker–based 3DfUS can provide reliable and valid measurements of muscle morphology. The system yielded consistent estimates of MV, FL and PA, and showed good agreement with the reference. By substantially reducing hardware complexity and cost while maintaining good repeatability, this approach offers promising potential for clinical settings where accessible muscle morphology assessment is needed.

Images (Optional)



References (Optional)

Session Category

Imaging and Biomedical Devices: Imaging Fundamentals and Applied Research

P4-345

Standardized, Multi-modal Anisotropic Elastography Phantoms for the Elasticity Imaging Community

Ms Samyuktha Kolluru[1], Mr Kaden Bock[2], Ms Shruthi Srinivasan[2], Dr Kevin Eckstein[3], Dr Ned Rouze[2], Dr Juan Manuel Urueña Vargas[4], Dr Kathyrn R. Nightingale[2], Dr Philip V. Bayly[3]

[1]Institute of Materials Science and Engineering, Washington University in St Louis, St Louis, Missouri, United States. [2]Department of Biomedical Engineering, Duke University, Durham, North Carolina, United States. [3]Department of Mechanical Engineering & Materials Science, Washington University in Saint Louis, St Louis, Missouri, United States. [4]BioPACIFIC-MIP, UC Santa Barbara, Santa Barbara, California, United States

Introduction

Mechanical anisotropy is a promising biomarker for monitoring tissue health. Many tissues have organized fibrous structures that can be disrupted by injury or disease. Elastography can noninvasively characterize anisotropic properties in skeletal muscle, brain white matter, and reproductive tissues but validating elastography requires standardized phantoms that mimic anisotropic tissue behavior. To address this need, we developed a multimodal imaging phantom for both magnetic resonance elastography (MRE) and ultrasonic shear wave elasticity imaging (SWEI) and compared measurements with benchtop dynamic shear testing (DST).

Methods

Lattices were fabricated using PEGDA Start (CellInk) on a Lumen X+ 3D printer (CellInk). Two lattice types were printed: SD300 (300 μm struts, 2×2×4 mm unit cell) and SD240 (240 μm struts, same scaling). Lattices were embedded in polyacrylamide hydrogels to create composite anisotropic phantoms (Fig.1A). In DST (Fig.1B), shear moduli parallel (and perpendicular (to the lattice scaling direction were measured from shear force vs displacement ratios. In SWEI, shear moduli were estimated from shear wave speeds (Fig.1C), $\mu=\rho v_s^2$, parallel and perpendicular to the scaling direction using a Verasonics NXT scanner and GE9L-D transducer [1]. MRE experiments were performed on a Bruker 9.4T MRI, and anisotropic properties (baseline shear modulus, μ_2, shear anisotropy, $\phi=(\mu_1/\mu_2)-1$, and tensile anisotropy, $\zeta=(E_1/E_2)-1$) were estimated from displacement fields (Fig.1D) using TI-NLI inversion [2].

Results

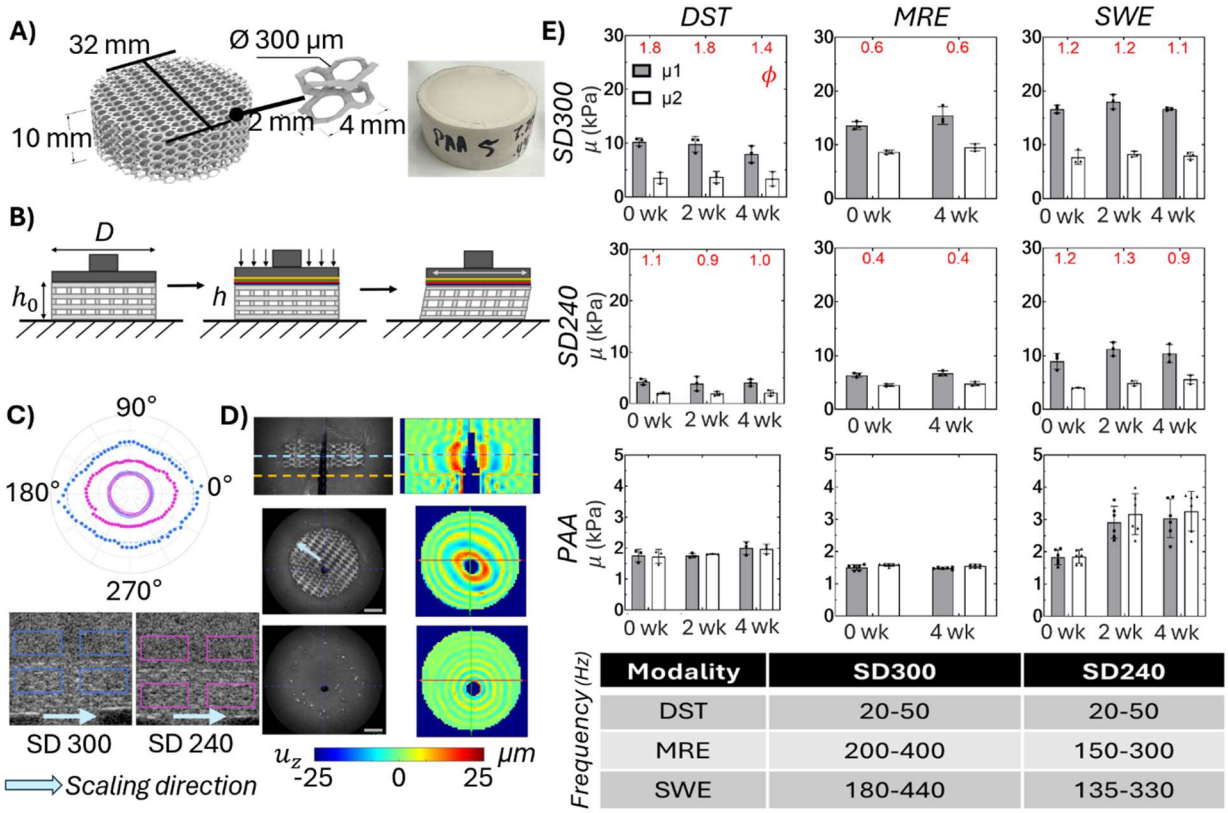
Shear stiffness measurements from DST, SWE, and MRE agreed within 20% in both directions, while shear anisotropy values were approximately 60% lower in MRE (Fig.1E).

Across modalities, SD300 had higher shear moduli and shear anisotropy than SD240, highlighting the tunability of these anisotropic phantoms. Phantoms are reproducible (n=3) and stable for four weeks (within 15% variability).

Discussion

We developed stable, tunable, multimodal phantoms to validate elastography measurements of anisotropic mechanical behavior of soft tissues. This study extends previous work [3] by comparing modalities over time, finding consistent estimates between modalities. SWEI appears more sensitive to shear anisotropy in this material than MRE; MRE with TI-NLI also accounts for tensile anisotropy.

Images (Optional)



Modality	SD300	SD240
DST	20-50	20-50
MRE	200-400	150-300
SWE	180-440	135-330

Frequency (Hz)

References (Optional)

[1] Srinivasan et al., JMBBM, 2025

[2] McGarry et al., Medical Image Analysis, 2022

[3] Eckstein et al., MRM, 2025

Acknowledgements (Optional)

R01EB033064

Session Category

Imaging and Biomedical Devices: Imaging Fundamentals and Applied Research

P4-346

Time-Lapsed Micro-CT Imaging of Calcium Phosphate Scaffolds in a Mouse Model of Heterotopic Ossification

MSc Sara Lindenmann[1], MSc Nico V. Giger[2,1], MSc Farida Elharouni[3,1], Dr. Francisco Correia Marques[1], Dr. med. vet. James Tapia-Dean[2], Dr. Dr. med. vet. Stephan Zeiter[2], Dr. Neashan Mathavan[1], Dr. Gisela A. Kuhn[1], Dr. Yassine Maazouz[3], Dr. Dr. Marc Bohner[3], Dr. Esther Wehrle[2], Prof. Dr. Ralph Müller[1]

[1]Institute for Biomechanics, ETH Zürich, Zürich, Zürich, Switzerland. [2]AO Research Institute Davos, Davos Platz, Graubünden, Switzerland. [3]RMS Foundation, Bettlach, Solothurn, Switzerland

Introduction

Heterotopic ossification (HO) is a critical prerequisite for bone graft substitutes (BGS) intended to repair large bone defects. A BGS's ability to induce HO can be assessed experimentally by implanting it into soft tissue and monitoring bone formation. Granular BGS have been shown to expand in overall volume occupied by the material in the presence of HO [1]. This study aims to use time-lapsed *in vivo* micro-computed tomography (micro-CT) to assess if material-induced HO (MIHO) can be predicted with material volume and implant thickness.

Methods

15±1 mg CaP granules mixed with NaCl solution (1.36 µl/mg) were injected intermuscularly of the right quadriceps in 10-14-week-old male C57BL/6J and FVB mice (n=3/group, license: GR/27/2023). Bi-weekly time-lapsed *in vivo* micro-CT was performed over 8 weeks [2]. The full implant formed by the granules was masked using dilation and erosion of the segmented granules (threshold=350 mgHA/cm^3), registered and cropped to define a consistent field of view (FOV) (Fig. 1A). The material volume and the implant thickness within the FOV were calculated for all weeks. Endpoint H&E stained histology sections (n=32-36/animal) were evaluated for HO. Micro-CT results were analyzed using linear mixed-effects models with week and group as fixed factors and mouse ID as a random effect to account for repeated measures.

Results

96±6% of histological sections in FVB showed HO, whereas no section did in C57BL/6J. There was significantly higher material volume at week 8 (C57BL76J: 4.79±1.42, FVB: 5.65±2.65 mm^3) compared to week 0 (C57BL76J: 3.52±0.99, FVB: 4.71±0.83 mm^3, p = 0.038) within the FOV (Fig. 1B). Implant thickness showed no significant differences over

time (Fig. 1C). There were no significant effects of group or week x group interactions for either parameter.

Discussion

In vivo micro-CT allows successful time-lapsed monitoring of a partial volume of the injected granules. Even though MIHO was successfully shown in FVB, neither the material volume or implant thickness as parameters were sensitive enough to pick up on the strain dependent differences.

Images (Optional)

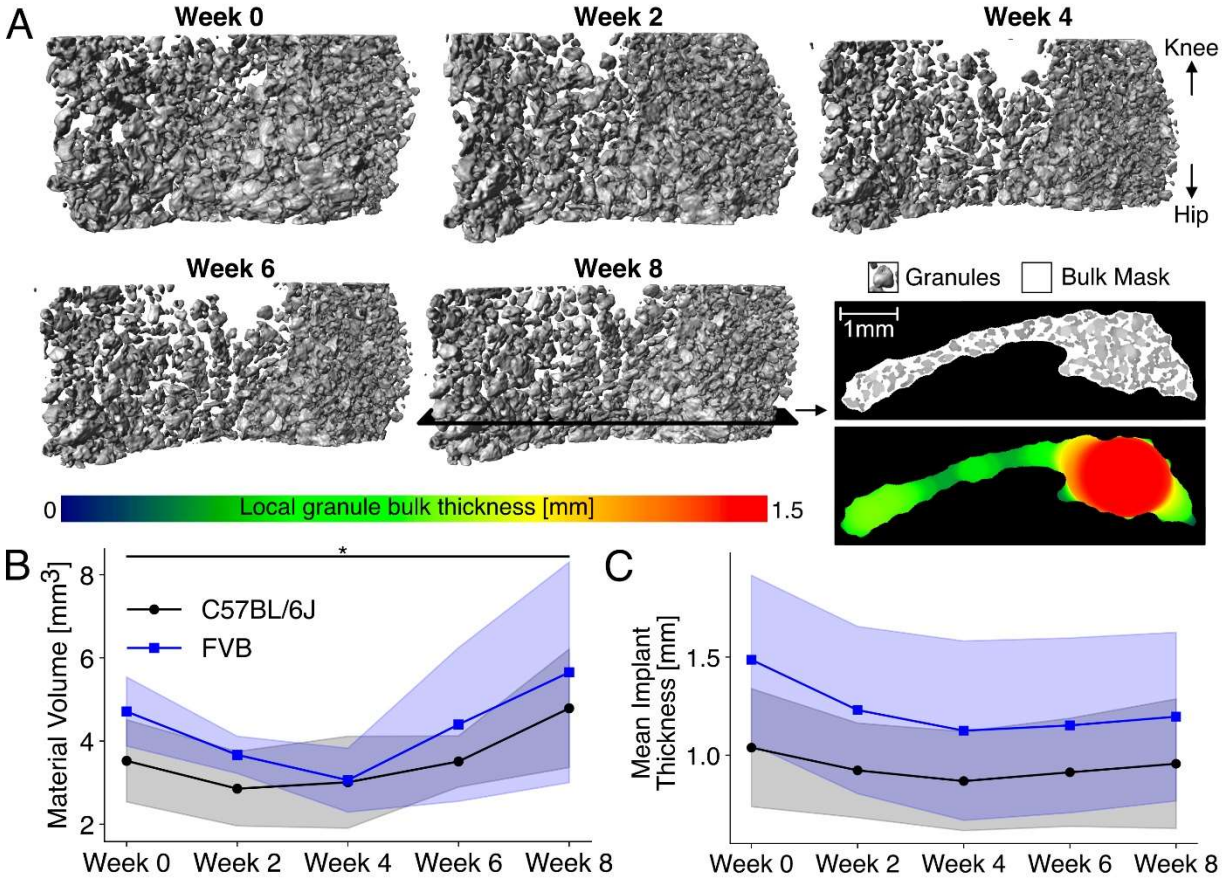


Figure 1: (A) Representative 3D visualizations of the intramuscularly implanted granules in the *in vivo* micro-CT FOV for one FVB mouse over 8 weeks. A sample 2D section at week 8 shows the granules and fitted granule bulk mask (top) and local thickness evaluation (bottom). (B) Material volume in the FOV in C57BL/6J and FVB mice presented as group mean±SD across mice. (C) Mean granule bulk thickness in the FOV in C57BL/6J and FVB presented as group mean±SD across mice. All significant differences are indicated with (*) $p<0.05$.

References (Optional)

[1] Tzu-Wei Wang *et al.*, J Biomed Mater Res A, 2015

[2] Esther Wehrle *et al.*, Sci Rep, 2019

Acknowledgements (Optional)

We thank the Swiss National Science Foundation (Sinergia Grant 213520) and Dominic Gehweiler and Alisa Hangartner for their micro-CT support.

Session Category

Imaging and Biomedical Devices: Imaging Fundamentals and Applied Research

P4-347

Reliability of 3D Scanned Breast Volume Measurements Within and Between Raters

Ms Sophia Wisotzki Bsc, Ms Ine Mylle Phd, Ms Jessica Yeoman Bsc, Mr. Christopher Napier Professor

SFU Run Lab, Department of Biomedical Physiology and Kinesiology, Simon Fraser University, Vancouver, BC, Canada

Introduction

Inadequate breast support is associated with pain and reduced physical activity participation, yet 85% of women wear an incorrect bra size [1, 2]. Accurate breast volume data are essential for designing proper-fitting bras; traditional sizing methods are limited. Three-dimensional (3D) surface scanning offers a non-invasive and reproducible alternative [1]. This study evaluated the intra- and inter-rater reliability of breast volume measurements from 3D scans to determine whether this method is reliable and usable in practice.

Methods

Healthy female participants (24.5 ± 5.7 years) underwent prone [2] 3D surface scanning (Artec Leo, Artec, Luxembourg) after breast boundaries were defined with a marker. Breast meshes were created by tracing the boundary, separating the breast from the torso, and filling the posterior chest wall in Artec Studio [1]. Volumes were calculated in cubic centimeters (cc). Two trained raters analyzed the scans of both breasts from participants to obtain volumes. Reliability was quantified using intraclass correlation coefficients (ICC; poor: <0.50, moderate: 0.50-0.75, good: 0.76-0.90, and excellent: >0.90 [3]). Precision was assessed using the standard error of measurement (SEM) and minimal detectable change (MDC; <5% considered excellent).

Results

Intra-rater (n = 35 participants/70 scans) and inter-rater (n = subset of 19 participants/38 scans) reliability analyses were performed . Intra-rater volumes ranged from 130-796 cc (left) and 108-808 cc (right). Inter-rater volumes ranged from 130-593 cc (left) and 108-596 cc (right). 3D scanning demonstrated excellent intra-rater (ICC = 0.996-0.999) and inter-rater reliability (ICC = 0.985-0.988), both with low SEM and MDC values. Mean ± SD volume, SEM, and MDC values are reported in Table 1.

Discussion

3D surface scanning demonstrated excellent reliability and high precision for breast volume measurements. Accurate breast volume data could improve bra sizing and support, addressing the high prevalence of poor bra fit and associated discomfort . Future research should evaluate the validity of 3D breast volume measurements against current sizing techniques (e.g., underband and overbust) and explore how consistent volume estimates can inform bra design, breast support, and biomechanical analyses.

Images (Optional)

Table 1. Breast volumes and reliability outcomes (Mean, ICC, SEM, MDC) for left and right breast volumes.

	Intra-rater (n = 35)			Inter-rater (n = 19)		
	Mean ± SD [cc]	SEM [cc]	MDC [cc]	Mean ± SD [cc]	SEM [cc]	MDC [cc]
Left Breast	353 ± 141	13	26	327 ± 130	10	20
Right Breast	347 ± 144	4	8	322 ± 126	7	14

References (Optional)

[1] Coltman, C. E., et al. Ergonomics, 2017

[2] Rizzone, K. H., et al. IJERPH. 2021

[3] Koo, T. K., & Li, M. Y. J Chiropr Med. 2016

Session Category

Imaging and Biomedical Devices: Imaging Fundamentals and Applied Research

P4-348

Decoding the Reynolds Stress Tensor for Turbulent Flow in a Pulsatile Total Artificial Heart using ICOSA6 4D Flow Magnetic Resonance Imaging

MSc. Twan Bakker[1,2], MD. Azad Najar[1,2,3], Dr. Sohaib Ayaz Qazi[1,2], Dr. Thomas Finocchiaro[3], Dr. Ina Laura Perkins[3], Prof. Petter Dyverfeldt[1,2,4], Dr. Jonas Lantz[1,2], Prof. Tino Ebbers[1,2,4]

[1]Department of Health, Medicine and Caring Sciences (HMV), Linköping University, Linköping, Östergötland, Sweden. [2]Center for Medical Image Science and Visualization (CMIV), Linköping University, Linköping, Östergötland, Sweden. [3]Scandinavian Real Heart AB, Västerås, Västmanland, Sweden. [4]Science for Life Laboratory, Linköping University, Linköping, Östergötland, Sweden

Introduction

Blood constituents are believed to be relatively resistive to viscous shear stresses and turbulent normal stresses but are believed to be sensitive to the rapid fluctuations in turbulent shear stresses, potentially resulting in hemolysis and thrombosis. Measurement of turbulent shear is therefore important in the development of a total artificial heart (TAH) but has shown to be challenging. In this study, we aim to assess viscous stresses, and turbulent normal and shear stresses in a TAH using 4D flow MRI.

Methods

The Realheart pulsatile TAH was made MR-compatible and scanned with an MRI-sequence from which velocities and turbulence over time were obtained. A conventional asymmetric 4-point scheme was extended to an ICOSA6 sequence with 3 additional encoding directions. This allowed the computation of the Reynolds stress tensor, partially describing the turbulent production by velocity fluctuations. The normal stresses on the diagonal of the Reynolds stress tensor were used to derive turbulent kinetic energy (TKE), while to off-diagonal characterized the turbulent shear stresses. Viscous stresses were computed from the velocity gradients.

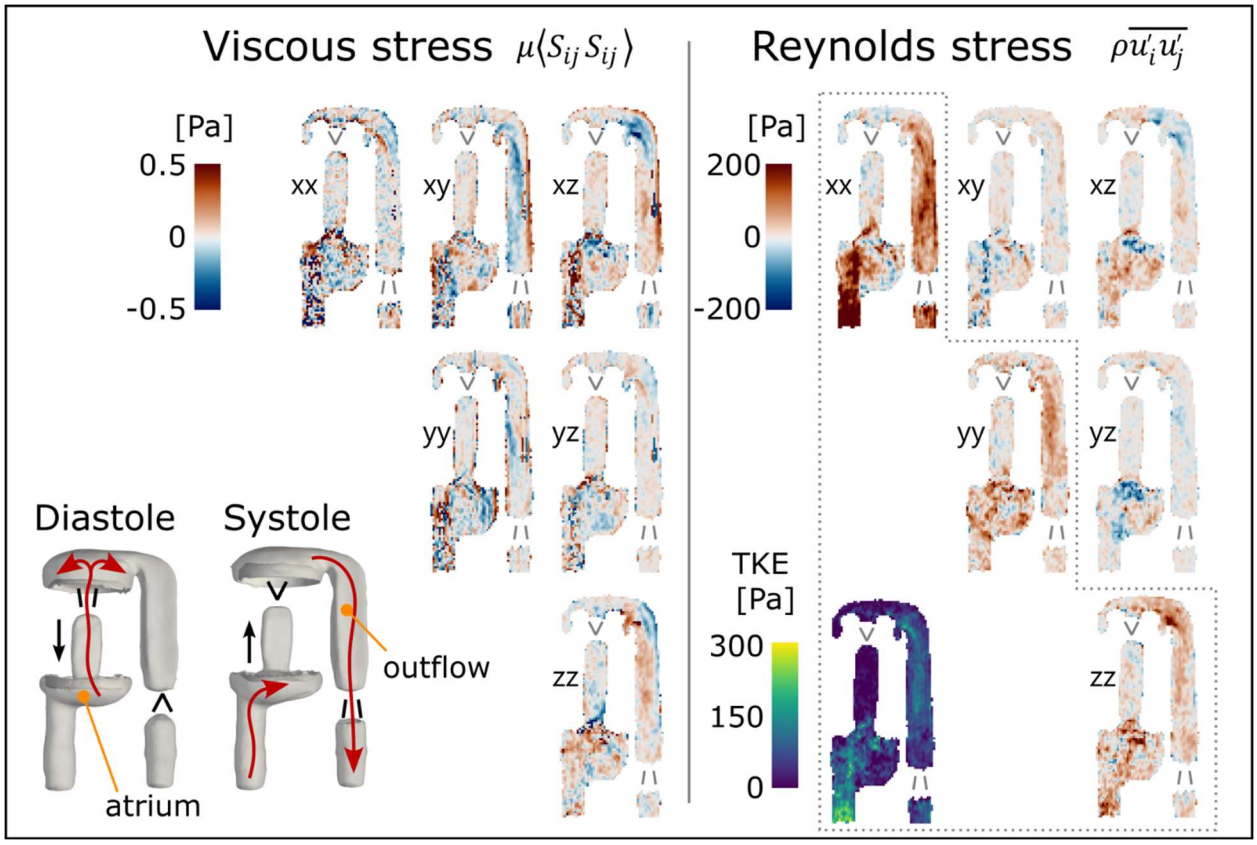
Results

TThe extra encodings resulted in a longer scan time (5min versus 9min) but with ICOSA6, we were able to determine the Reynolds stress tensor. TKE integrated across volumetric regions, yielded similar values as observed in the conventional 4-point method. Reynolds stresses showed more than an order of magnitude higher values than viscous stresses. In addition, the off-diagonal components revealed a non-negligible contribution to the Reynolds stress acting on the fluid in the atrium and outflow.

Discussion

We show that ICOSA6 can be used to study Reynolds stresses in a complex geometry like the TAH. ICOSA6 provided deeper insight into the turbulent stresses, specifically shear, by allowing direct computation of these components. The order of magnitude difference between turbulent and viscous stress denotes the importance of turbulence. Signal voids near the metal valves showed limitations of the 4D flow MRI technique. Noise can be reduced by extending the measurement time. ICOSA6 4D flow MRI can be a valuable tool to assess turbulent normal and shear stresses in a TAH and increase our understanding of the importance of turbulent shear stresses for blood damage.

Images (Optional)



References (Optional)

Acknowledgements (Optional)

The authors acknowledge funding from Scandinavian Real Heart AB, and Vinnova/Visual Sweden.

Session Category

Imaging and Biomedical Devices: Imaging Fundamentals and Applied Research

P4-349

The Lacunocanalicular Network in Subchondral Bone and the Connection Paths Between Mineralized Cartilage and Bone

Ms. Valentine Gaillard[1], Mr. Albano Malerba[1], Dr. Alexandra Tits[2], Dr. Stéphane Blouin[3], Mr. Gaëtan Lefèvre[1], Dr. Richard Weinkamer[2], Priv. Doz. Dr. Markus A. Hartmann[3], Prof. Davide Ruffoni[1]

[1]University of Liège, Liège, Wallonia, Belgium. [2]Max Planck Institute of Colloids and Interfaces, Potsdam, Brandenburg, Germany. [3]Ludwig Boltzmann Institute of Osteology, Vienna, Vienna, Austria

Introduction

The osteochondral junction transmits dynamic loads from cartilage to bone and contains mineralized cartilage, which anchors articular cartilage to the underlying subchondral bone. Both mineralized cartilage and subchondral bone maintain cells inside a mineralized extracellular matrix (ECM) where diffusion is strongly limited. In bone, osteocytes form the lacunocanalicular network (LCN), a key player in transporting matter and in regulating bone remodeling and mineralization. In mineralized cartilage, chondrocytes tend to form clusters to overcome diffusion limits. The osteochondral junction is clinically relevant, showing alterations with aging and osteoarthritis, including subchondral bone thickening and mineralization-front advancement at the tidemark. Changes in subchondral bone are driven by bone remodeling, which depends on LCN architecture. However, little is known about the organization of the LCN in subchondral bone: is it different from that of cortical bone located away from the joint? Is the LCN contributing to the possible connecting pathways between subchondral bone and mineralized cartilage? To address these gaps, we characterized the LCN in subchondral bone, comparing it with cortical bone and examining connecting pathways across the bone-cartilage interface.

Methods

We analyzed five tibiae from 10-week-old male C57Bl/6J mice, stained with rhodamine and imaged using confocal laser scanning microscopy (Stellaris 8, Leica, pixel size 0.18 µm). Network analysis was performed with the open-source software TINA [1].

Results

We found several chondrocyte lacunae reached by rhodamine, despite being surrounded by a mineralized ECM and we uncovered multiple connection patterns between chondrocyte lacunae and the underlying subchondral bone (Fig. 1f-h). The LCN in subchondral bone was disorganized, with only locally organized regions around bone

marrow and channels (Fig. 1b). Conversely, cortical bone featured larger ordered and disordered regions lying side by side (Fig. 1d). Network quantification confirmed a sparser, less connected network in subchondral bone (canalicular density Can.Dn = 0.144 ± 0.017 µm/µm^3, Fig. 1c) than in cortical bone (Can.Dn = 0.187 ± 0.022 µm/µm^3, Fig. 1e ; $p < 0.05$).

Discussion

These data provide baseline LCN metrics and highlight possible bone-cartilage connections for a widely used mouse model in pre-clinical research, enabling future comparisons of healthy, aged, and diseased states.

Images (Optional)

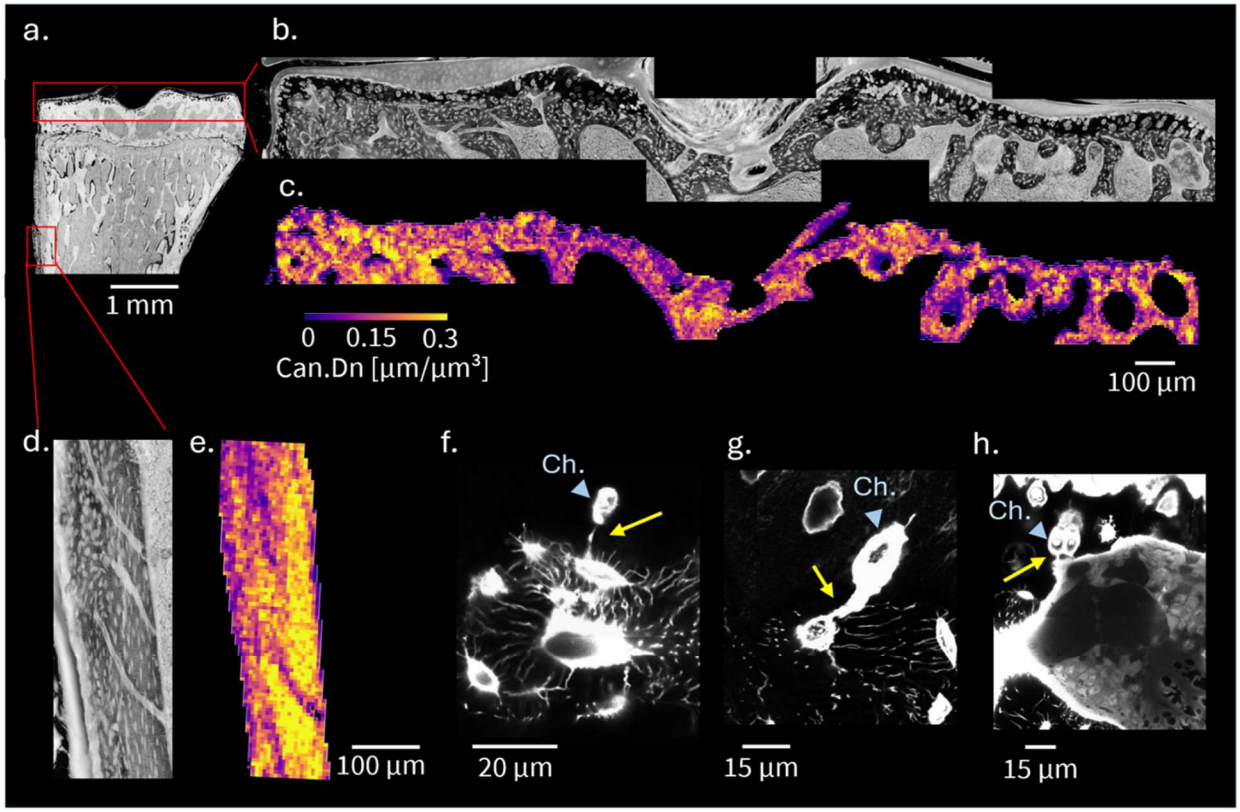


Fig. 1 (a) Scheme representing regions imaged by CLSM. (b,d) Network overview and (c,e) corresponding quantification of mean canalicular density in subvolumes of 400 µm^3 over a depth of 30 µm in subchondral bone and cortex, respectively. Overview of bone–cartilage connections (yellow arrows): (f) Chondrocyte lacuna–LCN, (g) Chondrocyte lacuna–channel, (h) Chondrocyte lacuna–bone marrow. Ch stands for chondrocyte lacuna and are highlighted by blue arrowheads.

References (Optional)

[1] Repp et al., Bone Reports, 2017

Acknowledgements (Optional)

This project has received funding from the FWO and F.R.S.-FNRS under the Excellence of Science (EOS) programme (EOS No. 40007553).

Session Category

Imaging and Biomedical Devices: Imaging Fundamentals and Applied Research

P4-350

Diffusion MRI to Predict Hip Muscle Strength After FAI Surgery

Mr William MacDonald[1], Ms Hannah Traynor[1], Dr Ryan Degen[1,2], Dr David Wang[2], Dr Corey Baron[1], Dr Geoffrey Ng[1]

[1]Western University, London, ON, Canada. [2]London Health Sciences Centre, London, ON, Canada

Introduction

Cam femoroacetabular impingement (FAI) is a leading cause of hip pain and early osteoarthritis. While hip arthroscopy aims to restore impingement-free range of motion and function, patients may still exhibit altered muscle function, illustrating the need to further investigate hip musculature. This study uses diffusion magnetic resonance imaging, which captures how water courses through muscle, and maximal isometric voluntary contractions (MVICs) to compare the muscle microarchitecture and force output in FAI patients pre- and one-year post-operative, as well as to controls.

Methods

11 FAI patients (n=11, m:f=5:6, age=28±9 years, BMI=24±4 kg/m^2) and 11 healthy controls (n=11, m:f=5:6, age=26±9 years, BMI=23±4 kg/m^2) were included. Participants underwent 3T MRI of the lower spine and hips, including bilateral T2-weighted 3D dual-echo steady-state and diffusion-weighted sequences. Patients underwent imaging prior to and one year after surgery, with controls undergoing a single imaging session. Fifteen muscles were analyzed including the flexors, abductors, extensors, and rotators. Muscles were manually segmented (Figure 1), and apparent diffusion coefficient (ADC; lower=more restricted diffusion; higher=less restricted diffusion) and fractional anisotropy (FA; lower=less directional diffusion; higher=more directional diffusion) values were extracted. MVIC was collected via handheld dynamometer. Paired-sample (FAI_{PRE} vs FAI_{POST}) and independent-sample t-tests (FAI vs controls) compared the differences in ADC and FA, and multiple linear regressions assessed the relationship between MVIC and diffusion values.

Results

TFL ADC increased post-operatively (FAI_{PRE}=1.38x10^{-3}mm/s^2, FAI_{POST}=1.50x10^{-3}mm/s^2, p=0.004). Psoas major (R^2=45%, p=0.015) and rectus femoris (R^2=14%, p=0.13) FA predicted hip flexion strength pre-operatively, whereas iliocapsularis FA (R^2=55%, p=0.006) predicted hip flexion strength post-operatively.

Discussion

The principal findings were that FAI patients demonstrated reduced TFL microarchitectural organization one year following surgery. Persistent deficits in hip flexion, abduction, and combined flexion-abduction strength have been documented in FAI patients after surgical intervention. The reduced TFL microarchitectural organization could represent a compensatory adaptation involving suboptimal muscle activation. Interestingly, iliocapsularis proved to be crucial for post-operative hip stability during flexion. Characterizing microarchitectural adaptations of periarticular hip muscles enhances the understanding of the pathomechanical consequences of cam FAI. The post-operative changes in TFL and iliocapsularis can inform targeted rehabilitation strategies.

Images (Optional)

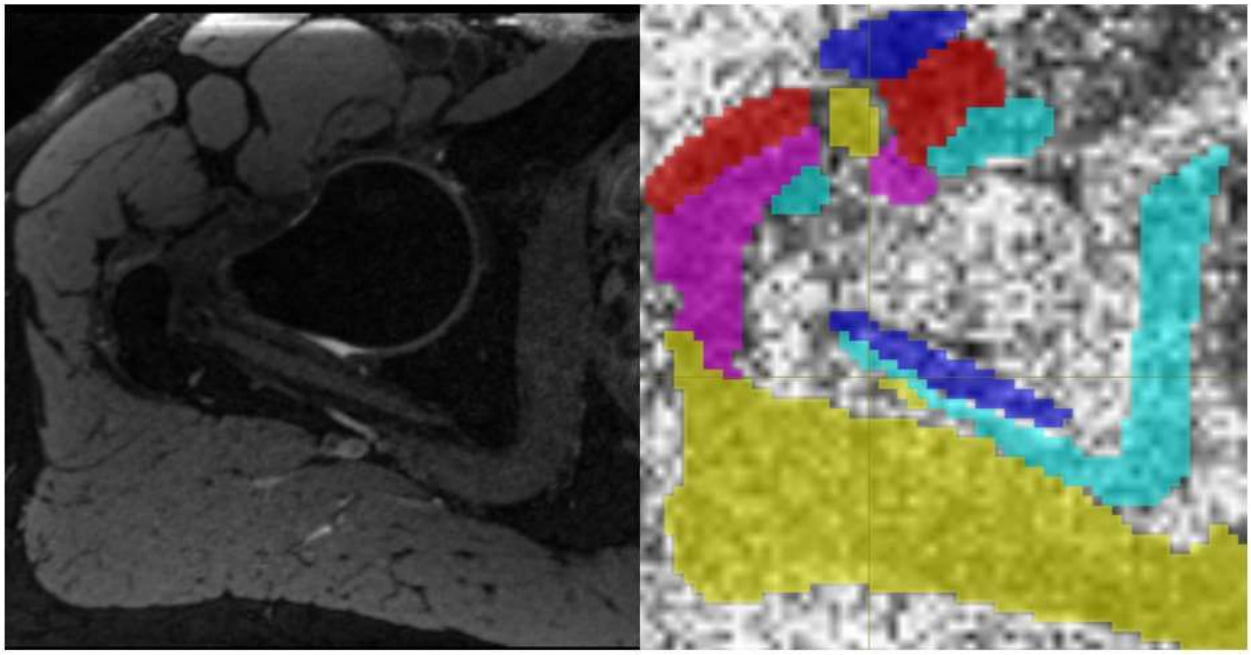


Figure 1: Axial image of the T2 3D-DESS scan used as a muscle atlas (left) and the corresponding diffusion scan (right) with manually segmented muscle masks.

Session Category

Imaging and Biomedical Devices: Imaging Fundamentals and Applied Research

P4-351

Preservation of Body Curvature Features in Visual Hull Reconstruction and Their Relevance to Markerless Motion Capture

Prof. Yoshimori Kiriyama Ph.D, Mr. Siyuan Hon B.S., Prof. Katsumasa Tanaka Ph.D

Kogakuin University, Shinjuku, Tokyo, Japan

Introduction

Video-based markerless motion capture is increasingly used in clinical evaluations. Although current systems can reliably capture large primary motions such as knee flexion and extension, their accuracy remains insufficient for detecting small secondary motions, including axial knee rotation. To address this limitation, we evaluated the curvature distribution of the body surface to examine the feasibility of estimating small axial knee rotations from reconstructed visual hulls.

Methods

Mean shape data of Japanese adults [1] were used as the true shape, and visual hulls were constructed from the mean model. A visual hull is composed of tangent curved surfaces defined by silhouette contours and forms a concave volume. Because curvature along the silhouettes is preserved, we examined how the curvature distribution of the shank shape depends on camera parameters, including the number and position. Curvature was assessed along both the circumferential direction of the shank and its longitudinal axis. The number of cameras ranged from three to twelve, arranged at regular intervals without any cameras directly facing one another. Camera positions were rotated around the model in 10-degree increments, and the visual hull and curvature distribution were recalculated for each configuration.

Results

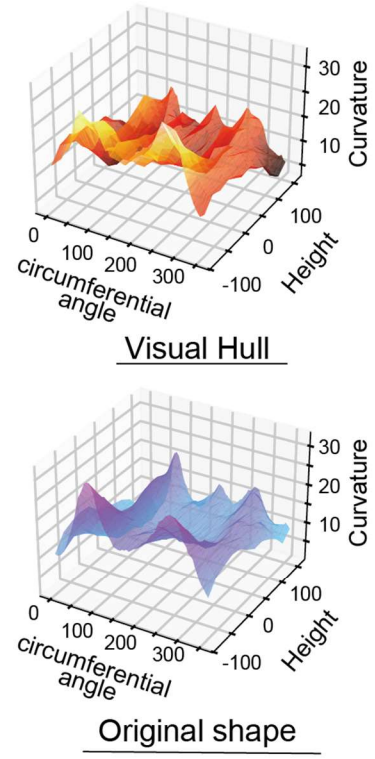
Figure 1(a) shows typical curvature distributions for the original shape and visual hulls constructed with nine cameras; the visual hull retained the characteristic curvature features of the shank. Figure 1(b) demonstrates that curvature correlation with the true shape increased as the number of cameras increased and converged near nine, with decreasing variance.

Discussion

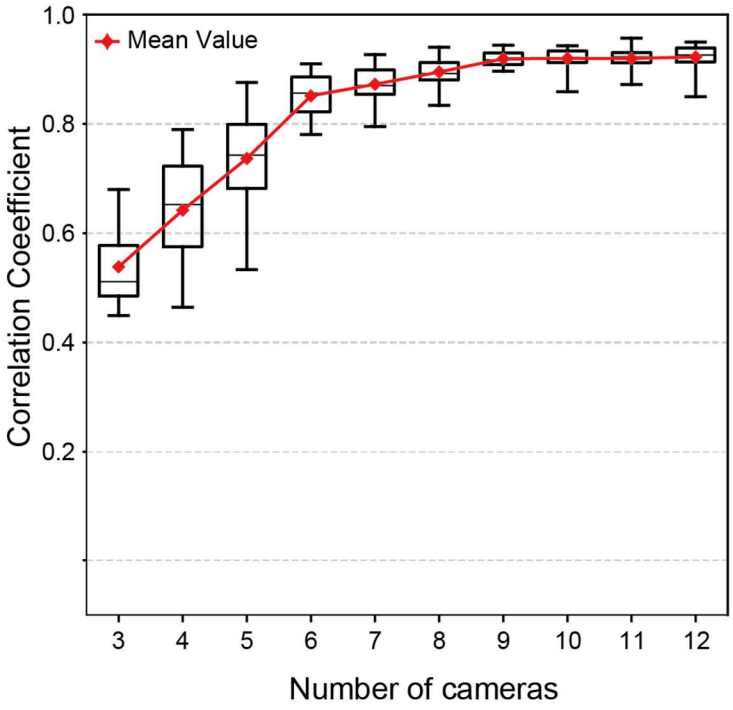
Although a visual hull inherently contains shape errors between tangent surfaces, the curvature distribution achieved a correlation coefficient of 0.9 with the true shape, indicating substantial preservation of curvature characteristics. This study demonstrated

that nine cameras are sufficient to reconstruct shank curvature from a visual hull. Consequently, visual–hull–based markerless motion capture enables tracking of anatomical landmarks and surface deformation, allowing estimation of small shank movements while reducing skin–motion artifacts. This approach therefore provides a practical method for detailed motion analysis not inferior to marker-based systems.

Images (Optional)



(a) Distribution of curvature



(b) Shape similarity depending on the number of camera

References (Optional)

[1]https://www.airc.aist.go.jp/dhrt/fbodydb/index.html (in Japanese)

Session Category

Imaging and Biomedical Devices: Imaging Fundamentals and Applied Research

P4-352

Quantitative Ultrasound Characterization of Age-Related Skeletal Muscle Changes Using Multiscale Fuzzy Entropy

Mr. Yunlin Tsai MS[1], Dr. Dang Phu Ha Nguyen MD[2], Dr. Chih-Hsiu Cheng PhD[1]

[1]School of Physical Therapy and Graduate Institute of Rehabilitation Science, College of Medicine, Chang Gung University, Taoyuan City, None, Taiwan. [2]Department of Orthopedic, Nhan dan Gia Dinh Hospital, Ho Chi Minh City, None, Vietnam

Introduction

Aging leads to skeletal muscle alterations, such as increased fat infiltration and fibrosis, which impair functional performance [1]. While these microstructural changes are difficult to detect with traditional B-mode ultrasound, raw radiofrequency (RF) ultrasound data preserve the full acoustic signature, providing superior sensitivity to tissue heterogeneity. Multiscale Fuzzy Entropy (MFE), an entropy-based measure of signal complexity, provides enhanced robustness to noise compared with conventional multiscale entropy methods [2]. This study aims to investigate whether MFE derived from RF ultrasound data can identify differences in skeletal muscle characteristics between young and older adults.

Methods

This study recruited 30 young adults (22.8 ± 2.2 years) and 23 older adults (69.0 ± 4.0 years), all capable of independent daily activities. Participants with recent musculoskeletal injuries (<3 months) or neuromuscular disorders were excluded. Raw radiofrequency (RF) ultrasound data were obtained from the gastrocnemius medialis (GM) and vastus lateralis (VL) using a 5-MHz center-frequency linear transducer (Telemed ArtUs EXT-1H) sampled at 40 MHz. Multiscale Fuzzy Entropy (MFE) was computed at scales 1–10. Group differences were examined using independent t-tests ($p < 0.05$).

Results

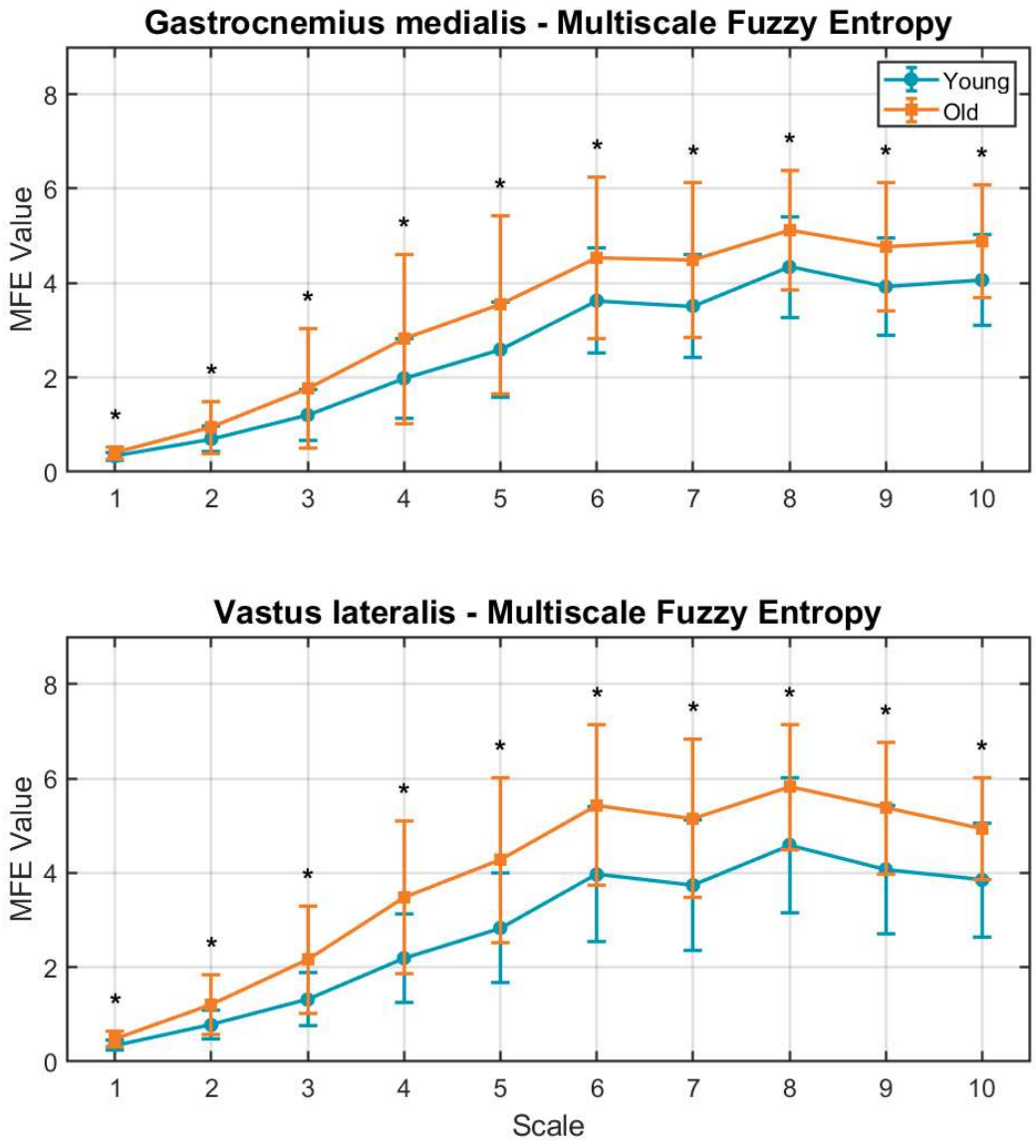
The overall mean MFE was significantly higher in older adults compared to young adults for both the gastrocnemius medialis (3.3 ± 1.2 vs. 2.6 ± 0.8, $p < 0.05$) and the vastus lateralis (3.8 ± 1.2 vs. 2.8 ± 1.0, $p<0.01$). Furthermore, older adults exhibited significantly higher MFE values across scales 1-10 for both muscles ($p<0.05$).

Discussion

This study reveals that MFE is consistently higher in older adults than in young adults within the gastrocnemius medialis and vastus lateralis muscles. The elevated MFE reflects increased signal irregularity and complexity, indicating greater muscle tissue heterogeneity.

These findings align with well-known age-related skeletal muscle changes, including intramuscular fat infiltration and fibrosis formation, which likely contribute to the increased entropy. These results support MFE as a sensitive tool for sub-visual muscle property alterations, providing diagnostic information beyond standard B-mode imaging analysis. Future large-scale and longitudinal research is needed to establish MFE as a predictive marker of muscle quality decline.

Images (Optional)



References (Optional)

[1] Tieland *et al*. , Journal of cachexia, sarcopenia and muscle, 2018

[2] Hilal *et al*. , IEEE Transactions on Biomedical Engineering, 2019

Acknowledgements (Optional)

This study was supported by research grants from the National Science and Technology Council of Taiwan (114–2221-E-182–033-MY3).

Session Category

Imaging and Biomedical Devices: Imaging Fundamentals and Applied Research

P4-353

Evaluation of commercial visual-inertial SLAM pipelines for free-hand ultrasound-probe tracking

Mr Zohar Oddes, Dr. Dana Solav

Technion – Israel Institute of Technology, Haifa, Israel, Israel

Introduction

Free-hand three-dimensional ultrasound (3D-US) relies on tracking the pose of a B-mode probe to spatially reconstruct a series of two-dimensional cross-sectional images. Outside-in optical and electromagnetic tracking systems can achieve sub-mm and sub-deg accuracy but require extensive calibration and are sensitive to line-of-sight occlusions and electromagnetic interference. Probe-mounted sensors such as stereo cameras with integrated inertial-measurement-units (IMUs) enable inside-out tracking with minimal setup. Robot-localization methods for visual-inertial odometry and visual-inertial simultaneous-localization-and-mapping (SLAM) offer robust pose-estimation, but accuracy depends strongly on both sensors and algorithms. Here, we evaluate the pose-tracking accuracy of two commercial visual-inertial SLAM pipelines based on contemporary sensors: ZED-X Mini (Stereolabs) and D455 (RealSense).

Methods

Both cameras and a set of infrared-reflective markers were rigidly mounted to a frame representing the ultrasound-probe base. Stereo and IMU data were recorded while the frame was manipulated by hand near a textured wall to mimic free-hand 3D-US scanning. A sub-mm-accuracy Vicon motion-capture system tracked the six-degree-of-freedom pose of the infrared-localizer. Visual-inertial SLAM trajectories were computed from ZED-X Mini data using ZED SDK v5.1 and from D455 data using cuVSLAM (isaac-ros v3.2). Eye-in-hand calibration was then used to derive camera trajectories in the room coordinate-frame.

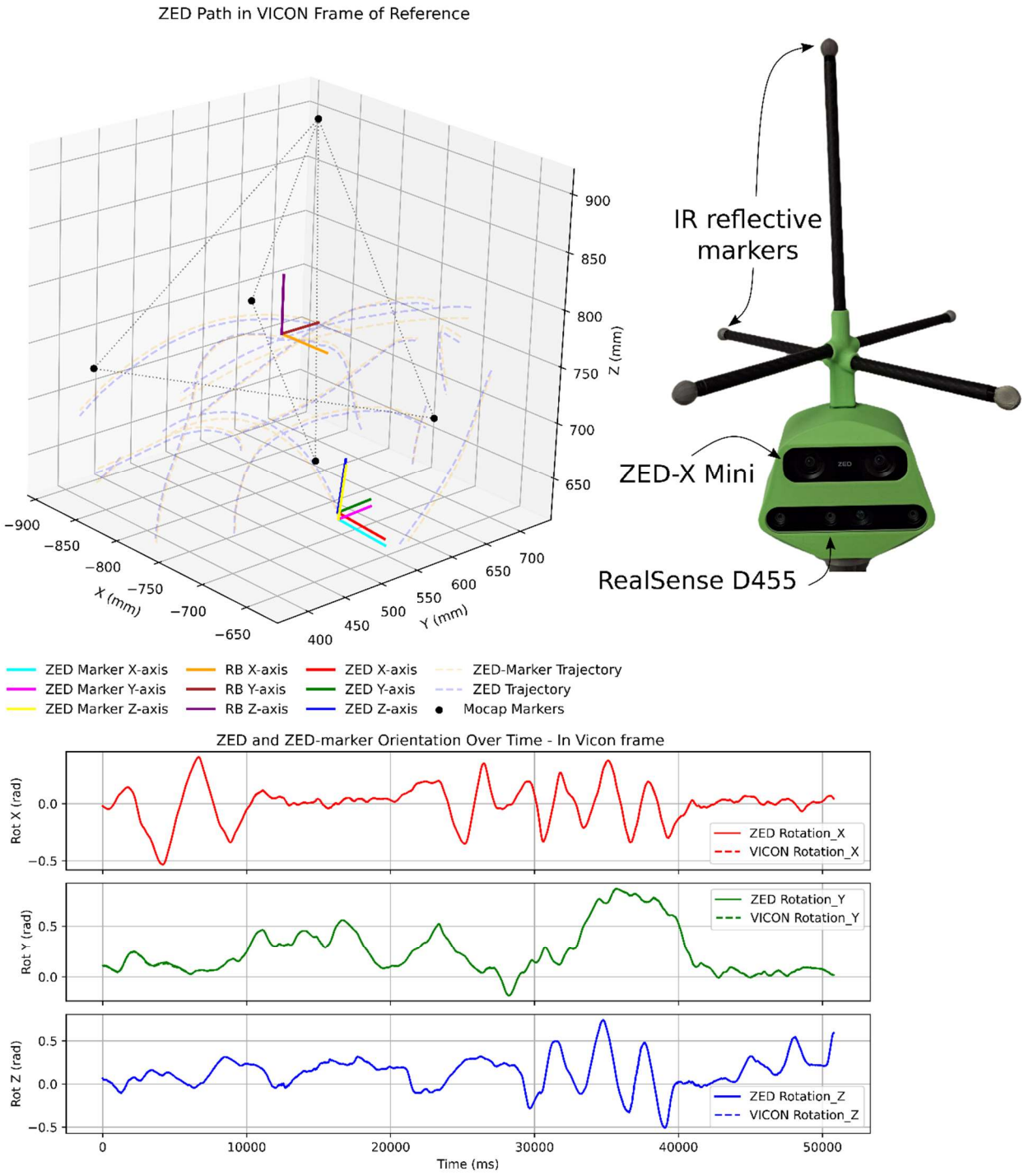
Results

Treating Vicon data as ground-truth, eye-in-hand calibration residuals were used as tracking-error measures for each pipeline. Across all frames, mean translational error was 5.19 mm (SD 2.30mm) for the ZED pipeline and 4.17mm (SD 2.11mm) for the RealSense pipeline. Negligible rotational errors were measured in both pipelines.

Discussion

This study benchmarks two recent commercial visual-inertial SLAM pipelines in a 3D-US-like setting, addressing the current lack of independent accuracy data beyond vendor datasheets. Mean translation errors of 4-5mm are roughly an order of magnitude larger than typical outside-in optical tracking, so these configurations are not suitable when sub-mm accuracy is required. The RealSense pipeline showed slightly lower translation errors, whereas the ZED-X Mini pipeline provides a higher pose-update rate (60 Hz vs 30 Hz), which is especially relevant considering typical B-mode framerates. These results are preliminary; further parameter tuning and testing are planned to assess how much accuracy can be improved and in which 3D-US scenarios visual-inertial tracking is acceptable.

Images (Optional)



Session Category

Imaging and Biomedical Devices: Imaging Fundamentals and Applied Research

P4-354

Prediction of Carpal Tunnel Boundary from Restricted Visibility Using Ultrasound Imaging

Ms. Mary Henderson MS, Dr. David Jordan PhD, Dr. Zong-Ming Li PhD

The University of Arizona, Tucson, Arizona, United States

Introduction

Accurate delineation of the carpal tunnel using point-of-care ultrasound is limited due to the interference of anatomical structures, resulting in only partial visualization of the tunnel. Therefore, the purpose of this study was to (1) develop a model to predict the non-visible landmarks of the carpal tunnel in ultrasound images and (2) estimate the area and shape of the carpal tunnel.

Methods

At the distal carpal tunnel, visible carpal tunnel landmarks were identified in cadaveric hands (n=6) using ultrasound imaging. A model was created by obtaining spatial relationships between the known MRI carpal tunnel and a few internal bone landmarks, which was validated using leave-one-out analysis. The model was then used to predict the non-visible landmarks of the carpal tunnel in ultrasound images. The area and circularity (of the MRI and ultrasound tunnel boundaries were calculated and compared using paired t-tests ($\alpha = 0.05$).

Results

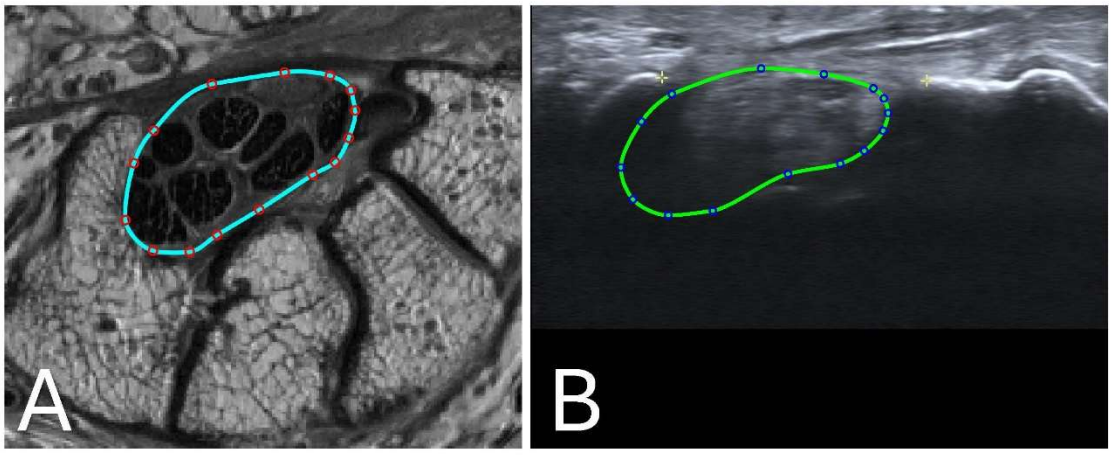
Based on the leave-one-out validation analysis, the average ultrasound carpal tunnel boundary was predicted within 7.90% and 9.71% error for area and circularity compared with MRI. Using the model, the predicted ultrasound carpal tunnel area was 145.1 ± 27.6 mm2 showing no significant difference from the MRI area of 144.2 ± 19.1 mm2 ($p = 0.857$) (95% CI: -10.84 to 12.56 mm2). The circularity of the predicted ultrasound tunnel (0.73 ± 0.06) also showed no significant difference compared with that from the MRI (0.79 ± 0.05, $p = 0.038$). The prediction errors averaged at 6% and 9% for area and circularity, respectively.

Discussion

Despite ultrasound's limited visualization of the carpal tunnel, the predictive model successfully reconstructed its boundary based on visible carpal tunnel landmarks. Future work will include in-vivo analysis using a larger sample size to further improve the predictive model. This model is a first step in estimating the carpal tunnel boundary from

ultrasound images, which can serve as a quick and non-invasive method for obtaining carpal tunnel area and shape for point of care use.

Images (Optional)



Session Category

Author Index

Author name	Presentation Number
A S, Shifin	P1-362
A. Barros, Marcos	P1-061, P4-136
A. Bauman, William	OA33-02, P3-273
A. Bonadiman, João	OA14-04, P4-157
A. Cripton, Peter	OA32-05, OA42-06
A. Gustafson, Jonathan	OA14-02, OA76-04, OA94-03, P3-374, P4-136, P4-223, P4-258
A. Prabhakar, Vibhav	OA153-01
A. Uona, Princess	P1-308
Aalto, Daniel	P4-141
Aamir, Amna	P2-209
Aarnio, Antti	OA149-04
Aathresh, Vishak Nandan	OA192-04
Abarca-Ortega, Aldo	OA88-02, P1-017
Abbadi, Moustafa	P2-211
Abbott, Rebecca	P4-145, P4-235, P4-236
Abdel-Raouf, Yousof M.A.	P1-027
Abdelatif, Nasef	P3-332
Abdelmohsen, Lara	P4-094
Abdelsalam, Aya	P1-021
Abdi, Abdiqani	P3-291
Abe, Koki	OA47-05
Abe, Mayuna	P1-026
Abedi, Ali	OA149-02
Abel, Richard	OA149-01, P1-038
Abercrombie, John	P3-073, P3-128
Ablordeppey, Eugene	P2-047
Aboodarda, Saied Jalal	P2-339
ABOU HAMDAN, Mouhamad	P2-162
Abraham, Angela	P3-076
Abrahamsson, Henrik	OA58-03
Abrams, Mitchell	P3-022, P3-102
Abramson, Alex	P3-171
Abssi, Lina	OA116-03
Abuhaimed, Abdulrehman	P3-319
Abusara, Ziad	OA65-05, P2-250
Acevedo, Claire	OA125-03, OA71-04
Acheampong, Kofi K.	P2-052
Achermann, Basil	OA3-01
Acien, Maxime	P3-245
Acker, Antoine	OA83-02
Acker, Stacey	P2-089, P4-214
Ackerman, Noah	P4-196
Ackermann, Marko	OA160-04
Ackland, David	OA15-05
Acosta, Ana Maria	P2-037
Acsadi, Gyula	P4-260
Adachi, Jonathan D.	OA117-02, P4-169
Adachi, Taiji	OA180-05, OA91-04, PL04-01
Adalid-Llansa, Laia	P1-032
Adams, Michael A.	OA113-02
Adanty, Kevin	P3-089, P3-090, P3-107

Author name	Presentation Number
Addison, Odessa	P4-182
Adeeb, Samer	OA74-05, P2-241, P3-039
ADEGBEMIGUN, OLUWAFEMI	P1-072
Adhikari, Shambhu	OA169-06
Adil, Divya	OA139-05, OA179-03
Adil, Muhammad Taimoor	P2-330
Adili, Anthony	OA128-03
Adkisson, Fisher	OA28-02, OA81-06, P2-232
Adlou, Bahman	OA68-01, P1-243, P1-311
Afara, Isaac O.	P3-049
Aflatounian, Fatemeh	OA189-05, P1-356, P2-102, P2-153, P2-189
Aftabi, Hamidreza	OA153-02
Agel, Julie	OA86-06
Agnew, Paige	P1-212, P2-291
Agoalikum, Shariphine	OA111-02
Agrawal, Yamnesh	P4-054, P4-055
Agricola, Rintje	OA96-02
Aguinaldo, Arnel	OA16-01, P1-346
Aguirre, Miquel	P4-023
Ahlström, Christer	P3-106
Ahmadi, Ali	OA198-04
Ahmadi, Reza	P1-350, P2-187
Ahmed, Alaa	OA28-05
Ahmed, Ananna	P3-085, P3-141
Ahn, Jiyun	P2-302
Ahn, Jooeun	OA111-04, OA155-06, P1-164, P2-309, P2-311, P3-005, P3-028, P4-290
Ahnaf, Vedhino Bima Aryaputra	OA127-03
Ai, Niimura	OA167-04
Aina, Peace	P3-066
Aissaoui, Rachid	P2-306, P2-335, P4-233
Aitken, Caroline	P1-048
Aitken, Holly	OA18-04
Aiyangar, Ameet	P2-368, P4-139, P4-343
Aiyangar, Ameet K.	OA38-03
Ajne, Gunilla	OA45-04
Akachi, Yusei	OA180-05
Akbarzadeh Khorshidi, Majid	P3-158
Akhlaghi, Parisa	P3-289
Akhlaghi, Pedram	P2-246
Akhtar, Talha	P4-122, P4-123
Aki, Tomoya	P3-285
Akiyama, Riku	P2-348
Akiyama, Yu	P2-357
Akpaloo, Victor	P2-198
Akyildiz, Ali	OA17-01, P4-040
Akyildiz, Ali C.	OA17-05
Akyuz, Ulas	OA120-05
Al Juboori, Ruaa	P1-062
Al-Obaidi, Farah	P4-204
Al-Saket, Shadan	OA13-04
Al-Salehi, Loay	OA19-02
Al-Shaer, Alaa	OA91-02
Al-Shimari, Banin	OA18-06
Alam, Zahin	OA20-05

Author name	Presentation Number
Alamir, Salwa	P4-112
Alamri, Mohammed	P1-204
Alaniz, Michele	P2-213
Albanese, Giulia	P1-068
Albani, Diego	OA153-03, OA26-04
Albert, Alina	OA21-03
Albert, Wayne	P2-279
Albert, Wayne J.	P2-282
Alberti, Davide	OA194-03
Albertini, Jean-Noel	P4-010
Alberto, Leardini	P4-228
Albors, Carlos	OA43-05
Albracht, Kirsten	OA154-01, OA154-04
Alderson, Jacqueline	OA190-01
Aldesoki, Mostafa	P4-204
Aldieri, Alessandra	OA18-01, OA49-05
Alemu, Yalemzerf Motbaynor	P4-060
Aleo, Ignazio	OA128-01, P4-177, P4-289
Alesi, Domenico	P3-240
Alexander, Nathalie	OA171-02, OA54-02, P2-069
Alexander, Renee	P1-349, P3-132
Alhamam, Hadeel	P2-310
Ali Sardar, Hafiz Zeeshan	P4-122
Ali, Haider	OA75-03
Ali, Jamel	OA26-02
Alijanpour, Elham	OA166-05
Aliseda, Alberto	OA69-05, P4-004, P4-014
Alizadeh, Elahe	OA113-02
Alizadeh, Elham	OA122-03, OA122-06, OA35-02
Allain, Jean-Marc	P4-336
Allard Brown, Aysha	OA193-06
Allen, Jason	P4-096
Allen, Jessica	OA160-05, OA196-03, P1-058, P1-076, P1-150, P1-180
Allen, Matthew	OA99-06
Allen, Pablo	OA12-04
Allen, Samuel	OA96-05
Allen, Sian	OA143-02, OA143-04, OA143-05
Allen, Victoria	OA161-02
Alley, Thomas	P4-158
Alli, Nurudeen	P1-071
Allison, George	OA96-06, P2-128
Alliston, Tamara	OA71-04
Allyn, Katheryn	P2-329
Almeida, Craig	OA161-02
Almutairi, Salman	OA96-06, P2-128
Alonso Chornet, Mar	P4-010
Aloy, Alexander	P1-401
Alperin, Marianna	P2-239
Alphonsus, Jürgen	P3-343
Alpkaya, Alican Tuncay	OA60-05
Alsaadi, Ola	P3-368
Alsaaran, Zaid	OA111-01
Alsaqabi, Eman	P1-065, P4-189
Alshareef, Ahmed	OA32-03, OA58-04, P3-066

Author name	Presentation Number
Alshareef, Amro	OA184-02
Alsharif, Abdelrahman	OA187-04
Alt, Wilfried	P2-028
Altai, Zainab	OA188-06, OA60-05, OA99-01, P3-314
Altaleb, Joudi	OA149-01, P1-038
Altamirano, Melanie	P1-068
Altman-Singles, Allison	OA140-04, OA142-02, OA9-05, P1-100
Alvarado, Fany	P1-144, P1-202, P4-215
Alvarado, José	P1-033
Alves de Sousa, Ricardo	P4-132
Alves de Sousa, Ricardo J.	OA169-02
Alwan, Aya	OA79-04, P1-082
Alyahya, Hind	P3-362, P3-363
Alzubaidi, Laith	P2-030
Amabile, Marilina	OA18-01
Amacker, Christine	P1-219
Amaechi, Martins	P1-219
Amatoury, Jason	P4-056
Ambegaonkar, Jatin	P4-259
Amenini, Sara	OA49-03
Amico, Enrico	OA25-02
Amicone, Alessio	P2-360
Amin, Jay	P2-052
Amin, Raouf	P4-016
Amin, Raouf S	P4-050
Amin, Stavan	P3-241
Amini, Rouzbeh	P4-171
Amiri, Arya	P3-154
Amiri, Pouya	OA70-01
Amirian, Jhaleh	P3-158
Amirtharaj, Mark	OA141-03
Amis, Andrew	P2-070
Amstalden Barros, Marcos	OA105-06, OA76-04, OA94-03, P3-374, P3-380, P3-383, P4-258
An, Chanhee	P4-026
An, Kai-Nan	P2-031
Anand, Sanjeev	OA163-03
Anania, Sandy	P2-371
Anantha Krishnan, Ahilan	OA97-01
Anbarafshan, Rojin	OA82-03
Andarawis-Puri, Nelly	OA151-02, OA96-05, P1-022, P3-330, P4-308
Anderl, William	P3-114
Andersen, John	P4-295
Andersen, Michael S	OA14-03
Anderson Lee, Maryanne	P2-235
Anderson, Andrew	OA135-04, P4-249
Anderson, Anthony	P4-148, P4-149
Anderson, Brody	OA103-05
Anderson, Cody	OA166-02
Anderson, Cole	P4-078
Anderson, Dennis	OA70-02
Anderson, Donald	OA178-03, OA86-06, P1-238, P3-219
Anderson, Donald D.	P4-166
Anderson, Kirsten	P4-180, P4-181, P4-192, P4-193
Anderson, Kirsten M.	OA65-03

Author name	Presentation Number
Anderson, Natasha	P3-247, P4-216
Anderson, Ryan	OA166-03
Anderst, William	OA165-05, OA23-01, OA23-03, OA60-04, P2-046, P3-284, P3-371
Andrade Herrera, Christian	OA4-05
Andrade Herrera, Christian J.	P4-102
Andrade, Kauane de Farias	P4-155, P4-156
Andre, Thomas	P1-062, P1-316
Andrea, Lugas	OA199-02
Andreasen, Charlotte	OA87-01
Andres, Annchristin	P4-144
Andrews, David	P1-285, P1-286
Andriotis, Orestis	P3-179
Andriotis, Orestis G.	OA122-01, OA97-02
Andrysek, Jan	P4-288
André, Julian	OA200-02
Anedda, Bastian	OA118-01, OA3-03, P1-047
Anene, Nwachukwu	P4-221
Angadi, Siddhartha	OA166-06
Angelini, Michael	OA141-04
Anglese, Serena	OA185-03
Anguiano-Hernandez, Jose	OA166-02, P1-247, P4-069
Anijs, Thomas	OA197-05
Anil, Gauri	P4-046
Annaidh, Aisling Ni	P3-121
Annasagaram, Meghna	P3-222
Anselmo, Peter	OA65-04
Ansu-Kyeremeh, Maya	P3-042
Antaki, James F	OA25-01
Antflek, Daniel	OA46-06
Antico, Maria	P4-298
Antikainen, Ida	P3-336
Antognini, Camilla	OA20-04, P1-115, P1-276, P2-321, P3-243
Antonacci, Giuseppe	OA77-03
Antoniou, John	OA195-05, P1-181
Antón, Raúl	OA39-03
Anwer, Mehwish	OA133-02
Anzai, Hitomi	OA127-03
Ao, Di	OA129-06
Aoki, Stephen	P4-249
Aoun, Rita	P3-133
Aoyama, Ryo	P2-359
Aparecida Leal, Leandra	P1-044
Appiah-Kubi, Kassidy	OA128-03
Appleton, Tom	OA195-03
Aquino, Domenico	OA197-03, OA90-05
Arab Makansi, Maya	P2-253
Aramayo Gomes Rezende, Mercedes	OA29-02
Aramburu, Jorge	OA39-03
Arami, Arash	P1-045, P1-131, P2-295
Arampatzis, Adamantios	OA200-01, P2-134
Arana Barcala, Emily	P3-089, P3-090
Arastehfar, Soheil	P3-280, P4-301
Araya, Catalina	P2-368
Arbogast, Kristy	OA19-01

Author name	Presentation Number
Arbogast, Kristy B.	OA119-01, OA3-04, OA81-03
Arce-McShane, Fritzie	OA12-05
Arch, Elisa	OA53-04, P1-225, P1-227, P2-059, P4-269
Arden, Tobin	P1-257
Ardianuari, Satria	OA80-05
Arefin, Nafis	OA157-04
Areias, Bruno	P3-048
Arensmann, Andrea	P3-202
Arezoomand, Arman	OA46-06, P4-271
Arias, Adrien A.	P2-002
Arieta, Luke	P1-249
Aristizábal Pla, Gerard	OA35-04, P3-015
Ariza-Gracia, Miguel Angel	P3-177
Armand, Stéphane	OA54-02, OA83-02
Armfield, Dylan	P4-114
Armitage, Aidan	OA186-01
Armitage, Lucy	OA66-03, P4-194
Armstrong, Kaitlyn	P1-062, P1-316
Arnaud, Picard	P3-337
Arnold, W. David	OA168-02
Arokoski, Jari	OA166-04, P2-178
Arora, Hari	P3-071
Arora, Ishi	OA61-05, P2-168, P3-042
Arora, Rohit	P3-375
Arredondo Carrera, Hector Manuel	P2-125
Arrioja, Raul	P3-312
Arruda, Ellen	OA87-01, P2-217
Arruda, Ellen M	OA100-01
Arshad, Rizwan	P2-147
Arshee, Mahmuda	OA170-05
Arts, J. J. Chris	P3-300
Arévalo, Martín	P3-060
Asadi, Amir	P3-113
Asakawa, Takumi	P2-354
Asay, Jessica L.	OA48-03
Ash, Kiichi	OA46-01, P2-320
Ashadujjaman, Md.	P2-373
Ashby, Blake	P1-272
Ashjaee, Nima	P2-169
Ashkenazi, Amit	OA7-02
Ashraf, Muhammad Sohail	P4-122, P4-123
Ashton-Miller, James	P2-234
Asif Zawad, Muhammad	P3-125
Askew, Graham	P1-369, P2-008, P2-173
Aslan, Seda	OA132-05
Asmussen, Michael	OA109-03, OA18-06, P2-039, P2-168
Assal, Mathieu	OA83-02
Asseln, Malte	P3-290, P3-291
Assi, Roland	P4-038
Assip, Bridget	OA98-04
Astephen Wilson, Janie	P3-204, P3-205, P3-250, P3-265, P3-313, P4-247
Astill, Sarah	P2-100
Astl, Markus	P2-156
Astori, Davide	OA179-05, OA191-05, OA95-03, P4-036, P4-052

Author name	Presentation Number
Asuncion, Robert	OA16-01, P1-346
Ateshian, Gerard	P2-251, P3-346
Ateshian, Gerard A.	LS1-02, P2-362
Athwal, George	P2-140, P2-367
Atkinson, Hayden	OA195-03
Au, Austin	P2-220, P2-221
Audenino, Alberto	OA199-02, OA49-05
Audu, Musa	P2-143
Auer, Timo A.	P3-027
Augat, Peter	OA175-01, P4-229
Augustin, Edouard J.	P2-052
Auricchio, Ferdinando	OA185-03, OA78-02, P4-074
Ausserer, Thomas	OA197-04, P4-316
Austin, Aaron	P1-250
Austin, Eddie	P3-123
Austin, Kieran	OA145-01
Avaz, Reza	OA191-02
Avazmohammadi, Reza	OA132-03, OA56-05, P4-081, P4-082
Avazmohammadi1, Reza	P4-107
Avedesian, Jason	OA8-05, OA94-04
Avey, Alec	OA87-03
Avila, Jacqueline	P2-347
Avila, Jacqueline L.	P2-366
Avilés-Rojas, Nibaldo	OA156-01
Avril, Stephane	OA84-01, P3-174, P4-014
Avril, Stéphane	OA129-04, OA84-04, P4-010, P4-023
Awad, Bishoy	OA99-03
Awad, Lou	OA33-04
Awosoga, Olu	P2-270
Ayaz, Hasan	P3-059
Ayazi, Mehrnoosh	P2-280, P2-326
Ayechu, Ada	P4-139
Azevedo, Fábio M.	P4-242
Azhar, Muhammad	P4-088, P4-089, P4-122, P4-123
Azhari, Fae	P1-168, P2-301, P4-271
Azhari, Faezeh	OA46-06
Azim, Farah	P1-145, P1-355, P3-381
Azim, Farah T.	OA155-05
Azzi, Charbel	P3-007
B. De Carvalho, Gabriela	OA33-02
B. Warren, Beth	OA153-04
Baaijens, Frank P. T.	OA4-02
Baaijens, Frank P.T.	OA4-01, P1-030
Baar, Keith	OA87-03
Babarenda Gamage, Thiranja	P4-019, P4-080
Babarenda Gamage, Thiranja Prasad	P4-047
Babazadehjoudi, Amir	P4-286
Babin, Danilo	P4-062, P4-064
Baca, Arnold	OA147-02, OA54-02, P1-270
Bachmaier, Samuel	OA200-02, P3-332
Bachmann, Sebastian	P2-186
Back, David A.	P3-027
Bacon, Beth	OA141-06
Badrou, Arif	OA134-04

Author name	Presentation Number
Bae, Lexie	OA183-02, OA8-03
BAE, TAE SOO	P3-356
Bae, Tae Soo	P3-266
Baek, Seungik	OA167-05, P1-400
Baekelandt, Frederic	OA25-05
Bagchi, Indrani	OA170-05
Baggaley, Michael	P4-335
Baggley, Michael	P2-241
Baghaei Oskouei, Seyedmohsen	P1-401
Bagheri, Mahan	P3-013
Bagheri, Maryam	P4-007
Bagley, Anita	P1-117, P1-235, P1-236
Bagnall, Jessica	OA10-02, P4-320
Baguyo, Jan Jethro	P1-018
Bahreinizad, Hossein	OA121-01
Baik, Seung-Min	P1-359
Bailes, Anna H	P4-143
Bailey, Olivia	OA32-04
Bailez, Alberto	OA83-02
Bailoor, Shantanu	OA120-03
Baird, Ethan	P1-139
Baish, James	P4-053
Bajaj, Retesh	P4-018
Baker, Alexander	P2-197
Baker, Claire	OA121-03, OA133-05, P3-081
Baker, Janelle	P1-165
Bakker, Chantal	OA79-05
Bakker, Twan	P4-348
Bakshi, Ria	P4-244
Balasubramanian, Ravi	OA151-05
Balcarek, Peter	P3-267
Baldwin, Ross	P1-082
Baliki, Caitlyn	P4-284
Ballinger, Karen	OA129-02
Balogh, Denise	P2-043, P3-358
Balsby Valsted, Line	P4-087
Baltzer, Heather	P4-271
Ban, Ehsan	P4-032
Bandel, Julietta	P3-260
Banfi, Giuseppe	OA64-04
Banghart, Kuper	OA192-03
Banks, Jacob	P1-162
Bansal, Sachi	OA38-02, P3-259
Bansal, Vinayak	P1-241
Bao, Yiwen	P2-118
Bar, Koushik	P2-019, P3-031
Barahona, Melanie	OA93-06, P2-280, P2-326
Barak, Meir M.	P2-186
Barakat, Abdul	OA138-03, OA157-01, P1-024, P4-077
Barakat, Abdul I	P4-049
Barati, Sara	OA127-05, OA95-02
Baratta, John	OA33-03
Barattini, Claudia	P1-189
Barbanti-Bròdano, Giovanni	P3-296

Author name	Presentation Number
Barber, Addison	OA168-02
Barbi, Letizia	P4-228
Barbosa, Guilherme	P3-048
Barboteu, Mikaël	P4-282
Bari, Elia	OA78-02
Barin, Kamran	P4-190
Barker, Kaleb	P3-360
Barna, Raluca-Ana-Maria	P4-343
Barnes-Wood, Megan	P3-121, P3-122
Barocas, Victor	P4-061
Baron, Corey	P4-350
Barr, Alex	P4-015
Barr, Alexander	OA156-04
Barrack, Adam	OA16-05, P1-252
Barrera, Olga	P2-209
Barrett, Erin	P4-168
Barrett, Kiara	P1-323, P1-338, P4-190
Barrett, Rod	OA147-02
Barrett, Rodney	OA80-01
Barros, Marcos Amstalden	P1-255, P3-315
Barrouhou, Manal	OA43-05
Baruffaldi, Fabio	OA18-01
Barzegari, Mojtaba	P3-348
Bashkuev, Maxim	OA23-05, P3-297
Bass, Cameron	OA32-02, P3-076
Bass, Cameron 'Dale'	P3-112
Bass, Cameron R. 'Dale'	P3-086, P3-087
Bass, Charles	OA32-02
Bass, Dale	OA121-02
Basso, Julia	P4-238
Bastias, Catalina	OA97-05
Bastounis, Effie	OA173-05
Bates, Alister	P4-016, P4-017, P4-029, P4-050
Bates, Karl	P2-173
Batista de Oliveira, Barbara	OA102-03
Batista, Javier	P2-061
Batista, Katherine	OA190-04
Batsis, John	OA67-02
Battersby, Harry	OA141-02, OA195-03, P2-088
Battis, Aurora	OA155-03, P2-272
Battle, Lauren	OA122-01
Baudendistel, Sidney T.	OA92-01
Bauer, Benedict	OA151-03, P3-260, P3-347
Bauer, Leandra	P1-188
Bauer, Sabine	P3-051, P4-291, P4-319
Baugnon, Lilian	P4-327
Baum, Daniel	P2-005
Baumbach, Andreas	P4-018, P4-112
Baumbach, Sebastian	P1-188, P3-332
Bause, Katharina	P1-005, P3-131
Bauser, Holly	OA43-02
Bavil, Alireza	OA80-01
Bawab, Sebastian	OA99-02
Baxter, Josh	P1-183

Author name	Presentation Number
Bay, Brian	P2-356, P4-297
Bayat, Ateayeh	P2-297
Bayat, Sara	P4-220
Bayly, Phil	P1-039
Bayly, Philip	OA152-02, OA176-02, OA32-03, P1-389
Bayly, Philip V.	P4-345
Bayne, Helen	OA13-04
Bayod, Javier	OA62-04, P3-242
Bazzi, Marisa	OA179-03, P4-061, P4-078
Beard, Daniel	P4-033
Beasley, Laina	P3-143
Beaton, Luke	OA161-05
Beattie-Edwards, Ella	OA46-05
Beauchesne, Sophie	OA193-03, P3-307
Beaudette, Shawn	OA155-03, P1-068, P1-084, P1-122, P2-272
Beaudin, Amanda	P4-185
Beaulé, Paul	OA99-04
Bechard, Vanessa	P1-286
Bechet, Romain	OA124-02, OA130-03, OA172-05
Beck, Kristina	P4-332
Beck, Owen	OA119-06, OA177-03, OA68-06, P1-208, P2-009, P2-212
Beck, Owen N.	P3-010
BECKENNY, Rebecca	P3-119
Becker, James	OA142-06, OA189-05, OA3-05, OA55-03, P1-273, P1-278, P1-304, P1-356, P2-067
Beckman, Jennifer	P4-004
Beckmann, Agnes	P3-333
Bedi, Asheesh	P2-217
Bedogni, Francesco	OA95-03
Beeche, Cameron	P3-023
Beeche, Cameron A.	OA74-04
Beerse, Matthew	P1-209, P4-208
Beghetti, Federica	OA35-05, P1-387, P3-064, P4-270
Behan, Fearghal	P3-215
Behar, Jasmin	P1-181
Behboodi, Ahad	OA123-01, P2-292
Behrman, Emma	OA105-04
Behrouzian, Mona	OA129-03
Behrouzitabar, Morteza	OA77-03
Beier, Susann	OA139-01, OA144-03, OA17-03, P4-110, P4-111
Bein Snee, Kila	P4-065
Bejaoui, Alaa	P3-027
Belibi, Francesca	P2-224
Bell, Elyssa	P1-064
Bell, Erica	P3-222
Bellemans, Johan	P3-239
Bellier, Alexandre	OA10-04, P4-318
Bellotti, Marco	OA78-02, P4-074
Belsky, Shelly	P4-321
Belvedere, Claudio	P2-079
Bemis, Caitlin	OA12-03
Benavidez, Yafa	P3-143
Benca, Emir	P3-221, P3-343
Bendell, Rosalind	OA59-03

Author name	Presentation Number
Bender, Alwina	P3-236
Bendjaballah, Mohamed	P2-200
Bendjaballah, Mohamed Z.	OA180-02
Benech, Nicolás	P2-130
Benfield, Kate	P2-063
Benjaminse, Anne	P3-129
Benna, Jacob	OA86-06
Bennett, Hunter	OA155-02, OA166-05, P1-212, P2-291
Bennett, Kieran	P4-273
Benoit, Alexis	P2-058, P3-353
Benoit, Aurélie	P3-328, P4-264, P4-336
Benoit, Daniel	OA13-03
Benoit, Daniel L.	P1-258
Bereiter-Payr, Johannes	OA197-04, P4-316
Berendsen, Heleen	OA79-05
Berestesky, Emily	OA125-02, OA180-01, 3468
Berger, André	OA181-03
Berger, Constantin	P3-183
Berggren, Caleb	OA17-04
Bernardi, Luigi	P4-092
Bernas, Riley	OA123-04
Berns, Rachel	P4-232
Berquin, Camille	OA25-05
Berryman, Katharina	OA187-04
Bersani, Alex	P4-134
Berson, Ayli	P1-355
Berteau, Jean-Philippe	OA126-05, OA71-04
Berthaimue Fox, Kayleigh	OA187-04
Berti, Francesca	OA25-03, P3-258
Berti, Lisa	P1-149
Bertoni, Annalisa	P3-354
Bertram, John	OA111-01
Bertram, John E.A.	P2-014
Bertschy, Montgomery	P2-081
Berube, Erin	OA183-02, OA188-04, OA8-03
Beschorner, Kurt	OA174-01, OA35-04, P3-015
Beschorner, Kurt E.	OA140-04
Besier, Thor	OA113-03, OA31-01, OA31-02, OA34-02, OA44-06, P2-163, P3-212, P3-230, P3-231, P3-252, P3-263
Bessen, Madeleine	P3-127
Betella, Elisa	P4-270
Bettella, Elisa	P3-064
Bettencourt, Nuno	P4-043, P4-119
Betz, Ulrich	P1-240
Beutler-Minth, Verena	OA62-02
Beverland, David	OA99-05
Beyer, Constantin	P1-076
Beynnon, Bruce	OA141-03, P2-042
Bezold, Will	OA188-03
Bhadelia, Rafeeque	P4-171
Bhagwat, Atharva	OA151-04
Bhandari, Susmita	P2-307
Bhat, Sanchita	OA102-05, OA132-04
Bhatnagar, Tim	OA129-03, OA155-05

Author name	Presentation Number
Bhatnagar, Timothy	P1-145, P1-355, P3-381
Bhatt, Akshay	OA138-05
Bhatt, Prathmesh	P4-107
Bhatt, Tanvi	OA160-02, OA40-04
Bhattacharya, Pinaki	OA18-01
Bhattacharya, Shambo	OA36-05
Bhuvanesh, Eeshana	OA151-04
Biancardi, Carlo	P1-146
Biancardi, Carlo M.	P3-060
Biancardi, Carlo Massimo	P1-148
Bianco, Nicholas	OA57-03
Bideau, Nicolas	OA29-04
Bidhendi, Amir	OA35-01
Bieri, Alex	OA125-04
Bierma-Zeinstra, Sita	OA96-02
Bieryla, Kathleen	P1-300
BILASSE, Massamaesso	P3-264
Billapaty, Bhavana	OA117-05
Billauer, Barbaram Pfeffer	OA128-06
Bilston, Lynne	OA78-01
Bin Enam, Fuad	OA151-04, OA163-05, P3-269
Binder-Macleod, Stuart	P1-065, P4-189
Binder-Markey, Benjamin	OA137-02, P2-261
Bini, Fabiano	P4-231
Bini, Stefano	OA99-06
Biondi, Giovanni	P1-387
Bir, Cynthia	OA121-02, P3-084, P3-118, P3-140
Bir, Cynthia A.	OA181-01
Birch, Robyn	OA194-02, P3-304
Birchmeier, Thomas	OA141-06
Bird, Matthew B.	P3-115
Birk, Carola	P3-098
Birk, David	P2-260
Birley, Elijah	P4-288
Birmingham, Trevor	OA183-04, OA183-05, OA195-03
Biscaglia, Simone	OA69-03
Bischof, John C.	P3-181
Bishay, Peter	OA123-02, P2-332
Bishay, Peter L	P2-336
Bisighini, Beatrice	OA108-01, P3-156, P4-023
Bissacco, Daniele	OA82-02
Bissacco, Elisa	P2-362
Bitter, Thom	OA47-02, OA9-03, P2-222
Bittner, Maike	P4-011
Bjornsen, Elizabeth	P1-211
Bjornson, Kristie F.	OA27-01
Black, Marianne	P3-254
Black, Michael J.	OA61-04
Blackburn, Laura	OA137-05
Blackburn, Troy	OA141-06
Blaettler, Mirko	P4-139
Blain, Grégory M	P1-125
Blanchette, Virginie	P3-245
Bland, Joshua	P3-248

Author name	Presentation Number
Blandford, Alexandra	OA186-01
Blanke, Philipp	OA120-03
Blemker, Silvia	OA44-02, P3-322, P4-325
Blemker, Silvia S.	OA31-06, P2-161, P4-191
Blessinger, Kathryn	OA9-04
Bliven, Emily	P3-091
Blomenkamp, Lara	P3-051
Blomquist, Matthew	P3-317
Blondeel, Phillip	OA7-04
Blouin, Jean-Sébastien	OA118-03, OA148-04, OA196-04, P1-048, P1-094, P4-207
Blouin, Stéphane	P4-349
Bluethmann, Shirley	P2-236
Blumbergs, Peter	P3-079, P3-082
Blunda, Diego	OA102-02, P4-002
Blunn, Gordon	OA149-03, P2-345
Blázquez-Carmona, Pablo	OA122-02
Bocconi, Alberto	OA11-03, OA114-04, OA187-01, OA197-03, OA199-03, OA90-05
Bochinski, Nikala	OA125-05
Bochinski, Nikala E	P3-340
Bock, Kaden	P4-345
Boers, Tom	P2-088
Boersma, Emma	P4-311
Boersma, Emma C	OA10-05
Boersma, Emma C.	OA195-02
Boettcher, Markus	OA50-01
Bogner, Sierra	P1-312
Bogner, Wolfgang	OA171-02, OA171-03
Bohlmann Kunz, Miriam	P3-167, P3-180
Bohne, Annika	P3-183
Bohner, Marc	P4-346
Bohnstedt, Bradley	P4-281
Boisson, Jean	P3-337
boisson, jean	OA5-02
Bokelman, Paul	P4-097
Bokowy, Kate	OA123-04
Bolandrina, Alessia Sofia	P4-084
Boles, Christopher	P4-017, P4-029
Bollavaram, Keval	P3-259
Bollens, Jellis	P3-023
Bolsterlee, Bart	OA1-03, OA44-01
Bombard, Evelyn	OA168-03
Bonadiman, João	OA14-01
Bonaldi, Francesco	P4-282
Bonassar, Lawrence	P2-005, P2-044, P2-249, P2-358
Bonato, Paolo	OA46-01
Bond, Colin	P1-126, P1-127
BONDI, Daniel	P3-119
Bondi, Daniel	CSB-05, OA169-06, OA6-04, P3-126, P4-306
Bonelli, Eleonora	P2-124
Bonetti, Marcello	OA138-03
Bonifas, Anne	OA121-04
Bonin, Stephanie	P3-093
Bonithon, Roxane	P2-345
Bonnet, Damien	P4-146

Author name	Presentation Number
Bonneuil, Willy	OA198-01
Bonnin, Anne	OA157-02
Bonnor, Genevieve	OA143-05, OA192-02
Bontempi, Luca	OA115-01, OA115-05, P4-005
Boocock, Mark	OA174-04, OA174-05
Boodt, Nikki	OA115-05, P4-005
Boom, Bart	P2-013
Boon-van Mossel, Nathan	OA129-02, OA13-04, P2-104
Borak, Libor	P4-226, P4-230
Bordeleau, Francois	3539
Borhani, Anita	P2-027
Borjali, Amirhossein	OA193-06
Bormann, Nicole	OA23-05, P3-297
Bornemann, Karoline-Marie	OA120-04
Bornschlegel, Benedikt	P4-002
Borovik, Michael	OA163-05
Borrelli, Simone	OA49-05
Bortolussi, Giacomo	P4-092
Bos, Daniel	OA115-05, OA17-05, P4-005, P4-040
Bosch Príncep, Ramon	P1-032
Boschetti, Federica	OA153-03, OA26-04
Bose, Alisha	OA123-04
Bosi, Federico	P4-297
Bosi, Giorgia	P4-104
Bosi, Giorgia Maria	P4-048
Bossert, Andrew	OA70-02
Bosshardt, Dieter	P4-342
Bossom, Juliana	CSB-01
Bostock, Juliana	OA106-03
Boström, Kim	P2-149
Boström, Kim Joris	P3-202
Boswell, Melissa	OA94-04
Both, Kevin	OA125-04
Botha, Tanita	OA13-04
Botsul, Sasha	P1-166
Bouchard, Anthony	OA42-03
Boudali, Mounir	OA47-05
Bouffard, Jason	OA42-03, P1-266
Boulanger, Stephen	OA131-05
Bouliane, Martin	P3-319
Bourantas, Christina	OA105-02, OA105-04, OA105-05
Bourantas, Christos	P4-018, P4-112
Bourauel, Christoph	P2-293, P2-350, P4-204
Bouten, Carlijn	PL02-01
Bouten, Carlijn V.C.	P4-070
BOUVET, Antoine	OA155-04
Bouwmeester, Thomas	P4-067
Bovendeerd, Peter	OA56-04
Bovendeerd, Peter H.M.	P4-070
Bowdish, Dawn E.	P4-198
Bowes, Matthew	P1-161
Bowman, Elizabeth	OA86-02, P2-026
Boxer, Rebecca	P1-117
Boxwell, Sam	P4-114

Author name	Presentation Number
Boyd, Steven	OA129-05
Boyd, Steven K.	CSB-02
Boyer, Alexa	OA111-01
Boyer, Katherine	OA130-01, OA16-03, OA189-03, OA73-04
Boyer, Katherine A.	P1-177
Boyes, Madeline	OA175-02
Boyle, Kyle	OA121-04
Bozoki, Andrea	OA40-03
Bozzetto, Michela	OA69-01, P4-084
Bočan, Petr	P2-351
Brach, Jennifer	P4-182
Bracher, Noelia	P3-306
Bracher, Stefan	P4-342
Bradshaw, Adam	P1-193
Brady, Alex	P3-352
Bragonzoni, Laura	OA42-01
Brama, Pieter AJ	OA113-04
Brancati, Ross J.	P1-177
Branco, Paula	P1-102
Brand, Andreas	P1-188, P4-229
Brand, Katja	OA99-05, P3-246
Branda, Maria Clara	P2-130
Brandon, Scott	P3-163
Brandon, Scott CE	OA142-04
Braun, Luca	OA118-01, OA3-03, P1-047
Braun, Steffen	P2-352, P2-353
Braunstein, Bjoern	OA154-01, OA154-04
Braverman, Alan	P4-061
Bravo, Claudio	P4-004
Bray, Emily	P4-168
Bray, Timothy J. P.	P4-318
Breen, Alex	OA23-04
Breen, Sarah	OA128-04
Brendenkamp, Jaclyn	OA151-04
Brennan, Keith	P2-146
Breton, Ismael	OA42-03
Breuer, Christopher	P4-078
Brewster, John	OA163-03
Brewster, Luke	OA4-04
Briar, Josh	OA137-05, P2-204
Briard, Nathan	P2-242
Bricarell, Katie	P2-314
Brice, Aaron	OA193-03, P3-134
Brickman, Daniel	OA155-03
Bridger, Zac	P1-251
Bridges, William	P1-218
Bridio, Sara	OA179-01, P4-006
Briggs, Haley	OA193-04
Briggs, Robert	P1-367
Brindle, Richard	P1-137
Brink, Tim Ten	OA50-04
Brinkhorst, Michelle	OA135-02
Briscoe, Adam	OA47-02
Brisson, Nicholas	P4-222

Author name	Presentation Number
Brito, João	P2-108
Brittain, Abby	P4-147
Brittain, Abigail	P3-198, P4-130
Brix, Gitte S	P3-045
Broberg, Jordan	OA5-06
Brokamp, Jacquelyn	OA48-04
Brolinson, Gunnar	P2-047
Broman, Lars Mikael	OA38-04, P4-275
Brook, Bindi	OA198-01
Brost, Samuel	P2-182, P4-216
Brouwer, Niels	P4-224, P4-225
Brown, Aaron	OA30-02, P4-012
Brown, Andy	P1-369
Brown, Ashley	OA65-02
Brown, Diane	P2-302
Brown, Philip	P2-047, P3-278
Brown, Stephen	OA137-05, P1-083, P1-084, P2-204, P2-207, P3-288
Brown, Stephen H. M.	P3-168
Brown, Susan	P1-051
Brown, Tyler	OA150-02, P3-139, P4-262
Bruccoleri, Michael	P2-203
Bruce Leicht, Amelia	P4-140
Bruce, Olivia L	OA5-04, P4-339
Bruckner, Harald	OA18-03
Bruening, Dustin	OA55-04, P1-097, P1-217, P1-225, P1-354, P1-360, P3-037
Bruggeling-Lavoie, Katie	OA155-03
Brugo, Octavio	P1-033
Brunet, Joseph	OA10-04, OA100-02, P4-297, P4-318
Bruschi, Davide	P1-387
Bruyer-Monteleone, Francois	OA31-04
Bryan, Rebecca	P4-051
Bryant, Dianne	OA141-02
Brynolf, Marcus	OA38-04
Brysova, Alena	P4-226
Brånemark, Rickard	P3-221
Bu, Lingyu	P4-328
Bubier-Hunter, Jasmaine	OA118-04
Buccino, Federica	OA64-04, P2-376, P3-033
Buccioli, Giovanni	OA11-03, OA77-03, P1-013
Buchanan, Lucy	P1-328
Bucherl, Sean	P3-136
Buchholz, Otto	P1-070
Buckley, Thomas	P1-058
Budzikowski, Jorie	P3-384
Buganza Tepole, Adrian	P3-025
Bugedo, Guillermo	OA156-01
Bui, Adam	OA137-05, P2-204
Buizer, Annemieke	P3-223
Bukhari, Muhammad Munam Mustafa	OA198-02
Bukhari, Munam	OA88-03
Bulen, Jennah	OA177-04
Bull, Anthony	P2-310
Bull, Anthony M. J.	OA70-01
Bull, Anthony MJ	P2-190

Author name	Presentation Number
Bullock, Garret D.	OA128-05
Bullock, Garrett	P3-083, P3-147
Bunch, Luke	P3-123
Bunn, Adam	OA142-05
Burden, Alexander	OA133-02, OA193-04
Burgess, Isaac	OA3-05, OA55-03, P1-273, P1-278, P1-304
Burgkart, Rainer	OA60-03
Burke, David	P1-051
Burke, Hudson	P3-018
Burke, Ryan	P1-351, P1-352
Burkhardt, Janis	OA88-04
Burkhart, Timothy	OA34-03, OA55-01, P2-027, P2-064, P2-073, P2-091, P2-121, P2-126, P3-241, P3-254, P3-256, P3-257, P3-326, P3-341
Burland, Julie	P1-253
Burn, J.F.	OA166-01
Burnap, Susan	P3-310, P4-145, P4-235
Burnett, Jenna	OA166-02, P1-247, P2-300, P4-069
Burns, Jane	OA157-03
Burriesci, Gaetano	P4-048, P4-104
Burrowes, Kelly	P1-015
Burrows, Jason	P3-085, P3-141
Burrows, Liam	P3-080
Burssens, Arne	P3-201
Burša, Jiří	OA164-05
Bus, Sicco	OA79-05, P4-202
Busa, Michael	P1-249
Busch, Ryan	OA52-03
Busse, Franziska	P1-007
Bussey, Melanie	OA172-01
Bustos Bautista, María Alejandra	P3-242
Butera, Katie	P2-059
Butler, Annie	P4-207
Butler, Sarah	OA6-05
Butowicz, Courtney	OA1-02, OA46-01, P2-320
Butowicz, Courtney M.	P3-115
Butterfield, Julia	OA178-02, OA178-05, OA67-04
Bynens, Bernard	OA25-05
Bähler, Philippe	OA62-02, P2-191, P3-302, P3-306
Béthune, Nicolas	P4-327
Böhr, Yana	OA60-02
Böttcher, Leticia A.	P4-176
Bøhme, Ida M	P3-045
Büchler, Philippe	OA62-02, OA62-05, P2-191, P3-177, P3-302, P3-306
Błażejowska, Ewelina	P4-075
Březík, Miro	P4-111
C. Anzovino, Daniel	P1-308
C. Brigham, John	P3-284
C. Guadagnin, Eliane	OA14-02, OA94-03, P1-061, P4-136, P4-258
C. Muluk, Satish	P4-008
C.Santos, Catarina	P4-263
Cabai, Eleonora	P3-012, P4-167
Cabaniss, Brandon	P1-273, P1-304
Cabaniss, Tanner	P4-281
Cabarcas, Brandon	P3-248

Author name	Presentation Number
Cabral, Ana Luiza	P4-142, P4-263
Cabral, Silvia	P2-108
Caccese, Jaclyn	OA133-03
Caenen, Annette	P3-152, P3-153, P4-079, P4-300, P4-333
Cafazzo, Marita	P2-323
Cafiero, Gioacchino	OA25-02
Cagnoni, Annunzia M	OA10-05
Cagnoni, Annunzia M.	OA195-02
Cahalane, Rachel	OA115-05, P4-005, P4-114
Cahill, Patrick	OA62-01
Cai, Chenghan	OA58-02, P4-066
Cai, Hejin	OA61-02
Cai, Yun	P3-117
Caimi, Alessandro	OA185-03, OA78-02, P4-074
Caimi, Alice	OA18-02
Cain, Stephen	OA150-04, OA52-03, OA76-03, P1-051, P1-197, P1-230, P2-059
Cairns, Ofubofu	OA137-04
Calastra, Camilla	P4-139
Calheiros, Alfredo	P4-132
Calistri, Laurine	OA111-05, OA172-04
Callaghan, Jack	CSB-01, P2-159, P2-226, P2-267, P2-273, P2-277
Callaghan, Jack P.	OA162-04, P2-057
Calvert, Derek	P3-316
Calvert, Derek D	P3-123
Calò, Karol	OA108-02, P4-113
Camara, Oscar	OA43-05
Camarillo, David	OA48-01
Camboni, Silvia	P1-376
Cameron, Emily	OA99-03
Cameron, Emily G.	OA113-02
Caminita, Mia	OA55-04, P1-354
Camomilla, Valentina	P1-376
Campbell, Evelyn	OA89-02
Campbell, James	P3-341
Campbell, Katelyn	OA57-01, P1-363, P2-144
Campiglio, Chiara Emma	OA69-01, P4-084
Campo, Gianluca	OA69-03
Campos Vargas, Silvia	P4-153
Campos, Sheridyn	P1-033
Campos-Vargas, Silvia	OA165-02, OA165-04, OA196-06, P4-151, P4-250
Campulla, Francesco	P3-064, P4-270
Camy, Claire	OA71-02
Candreva, Alessandro	OA69-03, OA82-05, P3-044
Canete, Santiago	OA33-01
Cann, Amanda	OA107-03, OA68-02
Cannariato, Maco	OA91-03
Cannon, Jordan	P1-086, P1-098, P1-156, P2-285
Cannon, Shauntelle	OA165-06
Canturk, Lidya	P3-371
Canziani, Gabriela	P2-260
Cao, Qianying	P4-038
Capalbo, Margaret	OA200-05
Capetta, Lorenzo	OA44-04
Caraan, John	P3-090

Author name	Presentation Number
Carass, Aaron	OA58-04
Caravaggi, Paolo	P1-149, P1-305, P4-228
Carballido-Gamio, Julio	CSB-02, OA27-04
Carballo, Camila	P2-249
Carbonaro, Dario	OA102-02, P4-110
Carbone, Vincenzo	P3-296
Carcia, Austin	OA195-04, P3-318
Cardiff, Philip	OA30-04, P4-114
Cardillo, Giulia	P4-049
Cardinale, Tyler	OA15-03, OA190-03, P1-373
Cardoso, Carlos	P3-077
Cardoso, Michelle	P2-279
Cardoso, Michelle R.	P2-282
Carelli, Stephana	OA77-03
Carey, David	P1-108
Carey, Hannah	OA66-05
Carey, Hannah D.	OA66-02, P1-103
Carey, Stephanie	P2-329
Carhaus, Angelica	P2-063
Caringella, Emma	P2-304
Carini, Alessandro	P2-151
Carlier, Aurelie	P1-025
Carlier, Aurélie	OA164-01, P2-017, P3-329
Carlos, Giovana P.	P4-243
Carlson, Breanne	P1-001
Carlson, Taliah	P1-234
Carman, Laura	OA31-01, OA31-02
Carminati, Mario	P4-036
Caro, Anne-Sophie	P3-156
Caroli, Anna	OA69-01
Carollo, James	OA153-04
Carollo, James J.	OA27-03
Carpenedo, Linda	OA96-03, P2-151
Carpes, Felipe	OA131-02, OA85-05, OA94-03
Carragher, Paul	OA131-03
Carrall-Worsey, Matthew	OA15-01
Carranza, Christina	OA66-04, OA72-04
Carrara, Elena	OA69-01
Carriero, Alessandra	OA122-01
Carroll, Lindsay	P1-326
Carry, Patrick	OA27-04
Carsen, Sasha	OA13-03
Carswell, Chris	OA169-04
Carter, Jade	P1-216
Carter, Katharine	P3-317
Carter, William S.	OA128-05
Carvajal Rico, Julian	OA108-04, OA191-03
Carvalho, Eduardo	P3-048
Casadei, Silvia	P3-240
Casey, Ryan	P1-229
Casler, Richard	P2-247
Castagnino, Alessia	OA138-03
Castaldi, Gian Mario	P1-376
Castillo Passi, Carlos	P4-330

Author name	Presentation Number
Castro Jr., Roberto	P2-248
Castro, William H.M.	OA18-03
Catalano, Chiara	OA185-03, P4-113
Catapano, Michael	P3-241
Catelli, Danilo	P3-226
Catena, Robert	OA124-04
Cates, Harold	OA98-02, P4-261
Cauley, Jane	P2-236
Cavanagh, Joseph	P3-319
Cavazzoni, Giulia	P3-298
Cave, Juan	OA66-04
CAVINATO, Cristina	OA146-04
Cavinato, Cristina	P2-219, P3-156, P3-165, P4-032
Cawthon, Peggy	P2-236
Cazenave, Marine	P2-186
Cazzola, Dario	OA154-01, OA154-04
Cazzola, Eliza	OA162-01, OA162-02, OA162-03, P2-271
Cañadas, Patrick	P2-219
Ceccaldi, Pierre-François	P4-264
Cecere, Renzo	P4-058
Cederna, Paul	P2-328
Cedin, Luisa	OA20-04, P2-321
Celi, Simona	OA139-04, OA144-04, OA25-03
Celik, Melih Özgür	OA113-05
Celik, Özgür	P2-134
Cerbai, Elisabetta	OA97-03
Cernohorksy, Paul	P4-067
Cerrito, Adrien	P4-224, P4-225
Cerullo, Giulio	OA114-04
Cesarovic, Nikola	OA157-02, OA157-05
Cha, Junmin	P2-313
Chabiniok, Radomir	P4-025
Chae, Minho	P1-203
Chahla, Jorge	OA105-06, OA14-01, OA14-02, OA14-04, OA76-04, OA94-03, OA98-06, P1-061, P1-255, P3-012, P3-315, P3-374, P3-383, P4-136, P4-167, P4-223, P4-258
Chaiken, Irwin	P2-260
Chaix-Eichel, Naomi	P1-069
Chakraborty, Srijan	OA11-03
Chala, Jorge	P4-157
Chalik, Alireza	P2-295
Challagondla, Vennela	OA14-02, OA76-04, P3-374
Challis, John	P2-112
Challis, JOHN H	P2-141
Challis, John H.	P2-110
Chalmers, Brian P.	P3-237
Cham, Rakié	OA118-06
Chambers, April	P4-182
Chan, Alex	OA137-05, P2-204
Chan, Andrea	P2-091, P3-326
Chan, Christy Oi-ying	OA128-01
Chan, Emily	OA6-05
Chan, Emily Yik Kwan	OA128-02, OA145-01, OA58-01
Chan, Ho-Fung	OA156-02
Chan, Ming	OA125-05

Author name	Presentation Number
Chan, Thomas	OA123-02, P2-332, P2-336
Chan, Wei Xuan	OA167-04
Chan, Zoe	P2-006
Chancey, Valeta	OA181-04
Chanda, Arnab	P1-345
Chang, Annette	P2-029
Chang, Chien-Chi	OA124-03
Chang, Chung-Hsun	P4-267
Chang, Emma	OA43-02
Chang, Hyeyeon	OA69-04, P4-117
Chang, Jia-Hao	P1-310
Chang, Shu-Hsuan	P2-377
Chang, Shuo-Hsiu	P4-209
Chang, Young-Hui	OA103-04, OA159-03, P1-059
Chantachotikul, Pirawan	OA91-05
Chao, Pen-Hsiu Grace	P2-377
Chao, Pen-hsiu Grace	OA138-01, OA77-04, P1-016, P2-354, P2-380
Chapell, Julia	P4-196
CHAPLAIN, Olivier	P3-119
Chapman, Kathryn	P2-230
Chapurlat, Roland	P4-234
Chardon, Matthieu	OA168-05
Charest-Morin, Raphaële	P3-304
Charles, Steven	OA92-02, P4-158, P4-159, P4-255
Charlton, Jesse	OA118-03, OA147-05
Charlton, Jesse M.	P4-218
Chassagne, Fanette	OA116-03, OA84-04, P4-004, P4-014
Chatzistergos, Panagiotis E.	P4-243
Chau, Tom	P2-323
Chaudhari, Ajit	OA165-06, OA9-04, P1-080, P1-339, P4-160
Chaudhari, Akshay	OA57-03, OA73-01, P3-254
Chaudhari, Akshay S	P3-203
Chaudhary, Suhani	P2-342
Chaumeil, Anais	OA2-01
Chauvet, Robert	OA5-03, P2-087, P3-134
Chavez, Chastity	P3-162
Checa, Sara	OA47-03, P2-134, P4-172
Checchia, Stefano	OA71-02
Cheek, Lila	P3-171
Chekroun, Abdennasser	OA126-05
Chelette, Amber	P1-361
Chelstrom, Brandon	P2-214, P4-272
Chemorion, Francis	OA182-03
Chen, Anthony	OA52-05, P4-284
Chen, Bo-Sheng	P4-305
Chen, Cecily X.	P2-361
Chen, Chi-Hsien	P1-279
Chen, Chien-Chung	P3-350
Chen, Danli	OA187-02
CHEN, Duzhi	OA104-04
Chen, Hsuan-Ju	OA104-02
Chen, Huang	OA120-03, P4-007
Chen, Jiasi	P2-342
Chen, Jishizhan	OA10-04

Author name	Presentation Number
Chen, Joseph	OA75-04
Chen, Junwei	OA114-02, P1-034
Chen, Karen	P1-317, P1-318
Chen, Kellen	OA187-04
Chen, Kuanting	P2-266
Chen, Liyi	P1-067
Chen, Shuting	P2-160
Chen, Siyuan	OA58-03
Chen, Teresa	P3-320
Chen, Teresa Szu-Hua	P2-193, P3-268
Chen, Tianyu	P3-323
Chen, Tony Lin-Wei	OA61-02
Chen, Wen	OA138-04
Chen, Wen-Xuan	P2-380
Chen, Weng-Pin	P3-308, P3-309
Chen, Xi	P2-356
Chen, Xiaodie	OA50-02
Chen, Xinman	OA114-02, P1-034
Chen, Yan	OA127-03
Chen, Yi-Jing	OA127-04
Chen, Yiqun	OA15-05
Chen, Yiyang	OA186-02
Chen, Yu-Ting	P3-238
Cheney, Wyatt	P3-310
Cheng, Chih-Hsiu	P4-352
Cheng, Hsin-Yi Kathy	P1-155
Cheng, Kai	OA196-05, OA79-02
Cheng, Leon	OA43-02
Cheng, Luyao	OA134-03
Cheng, Wai Hang	OA133-02
Cheng, Yi-Yun	OA106-05
Cheong, Vee San	P2-125, P2-197
Cherian, Josh	OA92-03
Chernukhin, Oleg	P4-055
Cherubin, Leonardo	OA11-03, OA114-04, OA187-01, OA199-03, OA90-05
Cheruparambil, Charles	OA36-02
Chesler, Naomi C.	P4-102
Chessa, Massimo	P4-042
Chestek, Cynthia	P2-328
Cheung, Phoebe	P2-334
Cheung, Vincent CK	OA20-03
Cheuvront, Samuel	P1-271, P1-306
Chew, Min Waye	OA46-05
Chhiba, Ryan	OA150-06, OA162-06, P2-283, P2-284
Chiaia, Theresa	OA188-04
Chiang, Ellis	P1-292
Chiang, You-Rong	OA97-02
Chiastra, Claudio	OA102-02, OA69-02, OA69-03, OA82-05, P4-110
Chickering, Graylen	P1-009
Chien, Jung Hung	P1-205
Chien, Kai-Wen	P1-181
Chien, Yang-Ting	P4-267
Chiesa, Enrica	OA78-02
Childers, Lee	P2-166, P2-167

Author name	Presentation Number
Chimedtseren, Anudari	P3-181
Chimera, Nicole	P1-206, P1-375, P4-030
Chimera, Nicole J	P1-374
Chimwaza, Jennifer	P3-169
Chin, Nerissa	P4-237
Chirico, Giuseppe	OA11-03
Chirinos, Julio A.	OA74-04, P3-023
Chirizzi, Cristina	OA197-03, OA90-05
Chirumbole, Sophia	OA165-06, P1-080
Chitnis, Parag V.	OA173-02, OA59-01
Chiu, Ching Hang	P3-014
Chmura, Nikola	P1-207
Cho, Changhee	P3-213
Cho, Haedo	OA52-02
Cho, Jaewoo	P1-164
Cho, Kyu-jin	P2-311
Cho, Minyoung D.	OA28-03
Cho, Sang Wouk	P2-197
Cho, Sanghyun	P1-171
Cho, Yebin	P2-313
Cho, Yoon Hyung	P1-299
Chockalingam, Nachiappan	P4-243
Choi, Chi-Whan	OA41-02
Choi, Ho Seon	P2-276, P2-338, P3-054
Choi, Itak	OA67-03
Choi, Jae-Ryeong	P4-283
Choi, Jongwon	P1-171, P1-176
Choi, Junyeol	P2-276
Choi, Perry S.	OA120-04, OA139-03
Choi, Rira	P4-109
Choi, Sehoon	OA199-04
Choi, Seobin	P1-232
Choi, Song Yi	P1-299
Choi, Wonjin	P4-026, P4-126
Choi, Woochel Joseph	OA172-02
Choi, Woochol	P1-359
Choi, Woochol Joseph	OA172-03, P1-085, P1-176, P2-288, P3-138, P4-195
Choi, Yoojin	P4-290
Choi, Youngjae	OA69-04
Choisne, Julie	OA113-03, OA31-01, OA31-02
Chokhandre, Snehal	OA159-04, P2-163, P3-212, P3-230, P3-231, P3-252, P3-263
Chollet, Mickaël	OA83-02
Chopp-Hurley, Jaclyn	OA131-05
Chou, Li-Shan	OA18-05, P1-066, P2-152
Choudhary, Gaurav	OA191-02
Choudhury, Mahua	OA56-05
Chow, Noah	P3-288
Chowdhury, Suman	OA121-01, P2-092, P2-192
Choy, Jenny	OA30-05, P4-116
Chrea, Bopha	OA178-03, P1-238, P3-219
Christe, Guillaume	P4-224, P4-225
Christensen, Cory	OA196-01
Christiansen, Blaine	P2-055
Christiansen, Cory	P2-080

Author name	Presentation Number
Christie, Dennis	P3-218
Christophe, Poulard	P3-337
Christopoulos, Vasileios	P2-213
Chu, Constance	OA73-01, P3-203, P3-254
Chu, Hsuan-Wei	P3-097
Chu, Jonathan	P3-056
Chuang, Kai-Chieh	P3-350
Chuang, Li-Ling	OA196-05
Chuang, Tyler	P1-357
Chun, Kyubin	P1-187
Chun, Sungmin	OA172-03, P1-085, P3-138, P4-195
chun, Sungmin	OA172-02
Chun, Young Min	P1-095
Chung, Timothy	P3-029
Chung, Vivian	P3-085, P3-141
Chénier, Félix	OA42-03, P2-297, P2-306
Cibin, Federica	P1-387
Ciccadicola, Eva	P4-260
Cieri, Robert	OA103-02
Cifuentes - De La Portilla, Christian	P3-224
Cifuentes de la Portilla, Christian Javier	P3-242
Cifuentes, Damaris	OA165-02, OA165-04, OA196-06, P4-151
Cifuentes-De La Portilla, Christian	OA62-04, P3-299
Cihan, Ariana	P3-152, P3-153
Cina, Andrea	P3-002
Cino, Claudia	OA84-04
Cirovic, Srdjan	P2-015
Civiero, Stephanie	P3-250, P3-265
Claeys, Kristl	OA197-05
Claeys, Lorena	P4-329
CLANSEY, Adam	P3-119
Clansey, Adam	CSB-05, OA169-06, OA6-04, P3-126, P4-306
Clapp, Dan	P1-377
Claquesin, Lauranne	OA172-04
Clark, Alys	OA170-01, P3-161, P3-184
Clark, James	P2-312
Clark, James D.	P3-227
Clark, Jay	P1-166
Clark, Krista G.	P3-115
Clark, Mindie	P1-074
Clark, Sophie	OA36-05
Clarke, Allyson	OA111-02, OA27-05
Clarke, Elizabeth	OA47-05, OA7-01, P3-178
Clarke, Jack	P1-161, P3-227
Clary, Josie	P4-313
Clasey, Jody L.	P2-074
Clausen, Alyssa	OA187-04
Clavica, Francesco	OA110-02
Cleary, Christopher	P1-091
Clemens, Noah	P1-209
Clements, Naomi	OA42-06
Clermont, Matthias	OA181-03
Clifton, Glenna	P1-300
Clingo, Kelly A.	OA158-02, OA181-05

Author name	Presentation Number
Clites, Tyler	OA109-04, P3-270
Clites, Tyler R.	OA38-02, P3-259
Cliver, Richard	OA77-05, P1-011
Clohisy, John	OA105-02, OA105-04
Clouthier, Allison	CSB-04, OA13-03, OA153-06, OA8-02, P3-203, P3-303
Clouthier, Allison L.	P1-258
Cluzeau, Océane	OA103-01
Coats, Brittany	OA169-01
Cobb, Stephen	P1-204
Cochran, Emma	P1-316
Cochran, Joy	P2-296
Codoni, David	P4-120
Coffey, Lindsay	P4-196
Cohen, Itai	P2-005, P2-249
Cohen, Karly	OA103-05
Cohen, Moises	P4-258
Cohen, Moisés	OA94-03
Coifman, Itay	P3-021
Colbrunn, Robb	P2-086, P3-233, P3-325
Coldman, Suzie	P3-189
Cole, Alison J.	OA92-01
Colebank, Mitchel	P4-085
Coleman, Rhima	OA64-05
Coleman, Ryan	OA152-04, OA56-02
Coleman, Thomas	OA62-01
Collard, Didier	P4-067
Collet, Carlos	OA69-03, OA82-05
Collimore-Doherty, Ashley	OA2-04
Collins, John	P1-219
Collins, Nicholas	OA144-03
Colombo, Alessandro	P2-124
Colombo, Andrea	P4-110
Colombo, Monika	P1-002, P3-044, P3-045, P4-087
Colpitts, Alyson	P2-023, P2-133
Coltoff, Emma	P3-278
Coluni, Christopher	P3-146
Colvin, James	P2-329
Colyer, Steffi	OA154-01, OA154-04
Concannon, Jamie	OA134-02, OA56-02
Concari, Mattia	P3-258
Conci, Claudio	OA11-03, OA114-04, OA153-03, OA187-01, OA197-03, OA199-03, OA77-03, OA90-05, P1-013
Conci, Sebastiano	P1-376
Conconi, Michele	OA37-02, OA44-04, P1-200, P2-079, P2-179, P3-201, P3-378
Condliffe, Elizabeth	OA5-03
Condliffe, Elizabeth G.	P4-185
Condorelli, Gianluigi	OA89-03, OA89-04
Cone, Stephanie	OA163-04, P2-055, P2-072, P3-216, P3-222, P3-228, P4-269
Cone, Stephanie G.	P2-299
Confavreux, Cyrille	P4-234
Cong, Ting	P3-199
Conley, Rachel	P3-318
Connaboy, Christopher	P3-067
Connop, Ella	OA99-03

Author name	Presentation Number
Conquergood, Nicole A.	P2-243
Conrad, Bryan	OA119-02
Conroy, Christy	P1-072
Considine, Cassidy	OA106-03
Consolini, Jack	OA188-04
Constantinou, Iordania	OA11-01, OA173-05, OA90-01
Constantinou-Simek, Athena	P1-268
Conti, Matthew	OA86-01
Conti, Michele	OA146-03, OA185-03, OA78-02, P2-372, P4-074, P4-092
Conticello, Salvatore	OA62-02, P2-191, P3-302, P3-306
Contreras Raggio, José I.	OA38-03, P3-235
Contreras, Jose Ignacio	P2-378
Contreras, José	P2-368
Conway, Claire	OA89-05, P4-051
Conway, Fiona	OA141-04
Cook, Andrew C.	P4-104
Cook, James	OA188-03
Cookson, Andrew N	P3-169
Coolbaugh, Crystal	OA168-03
Cooley, Josephine	P1-166
Coombs, Dana	OA96-01, P2-150
Cooper, David	OA185-02, P4-298
Cope, Timothy C.	OA109-05
Coppers, Birte	P4-220
Coppini, Raffaele	OA97-03
Corbin, Elise	OA32-04
Cordero, Ignacio	P2-238
Cordes, Caleb	OA161-03, P2-215, P2-216
Corey, Eva	OA194-02
Cork, Tyler	OA30-02
Cornish, Bradley	OA15-01, P3-032
Correa-Belloso, Alejandra	OA113-02, P3-148
Correia Marques, Francisco	P1-012, P4-346
Corrigan, Patrick	OA28-02, OA81-06
Cortes, Nelson	OA60-05, P3-314
Cortesi, Cristina	OA77-03, P1-013
Cortest, Nelson	OA99-01
Corti, Anna	OA17-02, P4-074
Corvo, Alessandra	P4-014
Cosgriff-Hernandez, Elizabeth	OA102-05
Cossin, Marion	OA193-05
Cossmann, Peter	OA173-04
Cosson, Michel	OA170-04
Costa Sousa, Luísa	P4-043, P4-119
Costa, Nina	P3-077
Cotariu, Stephanie	OA140-01, P1-231
Cotton, James	OA2-03
Cotton, R. James	P2-176, P3-050
Cotton, Thomas	P3-101
Cotton, Tom	P4-287
Coudyzer, Walter	OA197-05
Coulthard-Wragg, Robert	OA131-03
Cournoyer, Janie	OA153-06
Courtois, Lucie	P1-327

Author name	Presentation Number
Cousins, Daniel	OA150-02
Couët, Frédéric	P4-058
Cowan, Marissa	OA80-02
Cowbrough, Braeden	P4-198
Cowburn, James	OA154-01, OA154-04
Cowie, Raelene M	P3-209, P3-210
Cox, Michael	OA194-02
Coyle, Amy	P1-102
Coyle, Matthew	P3-307
Coyne, Jacquelyn M.	P4-198
Coyne, Lara	P1-281
Cozma, Lisa	P2-071
Cozzi, Ottavia	OA89-03
Crandall, Jeff	KN01-01
Crane, Pollyanna	P3-379
Crawford, Lauren	P1-324
Crawford, Reyna	P1-348
Creamer, Stephen	P4-019
Crenshaw, Jeremy	OA160-03, OA160-05, OA53-04, P1-058, P1-065, P1-144, P1-197, P1-202, P4-189, P4-215
Crepulja, Danijel	P4-212
Crews, Courtney	P1-280
Crews, Ryan	OA79-01
Cribbie, Teah	P1-087, P3-057
Crimaldi, Luigi	P1-024
Cripton, Peter	OA133-02, OA145-04, OA193-06, P3-079, P3-082, P3-085, P3-116, P3-141, P3-146
Cripton, Peter A.	OA19-02
Crisco, JJ Trey	OA16-04, P4-321
Crisco, Joseph J.	P3-342
Crisostomo, Dominic	P1-291
Cristina de David, Ana	P1-044
Cristofolini, Luca	OA194-03, P2-154, P3-240, P3-296, P3-298
Critchley, Meghan	P1-348
Cromi, Roberta	P3-258
Cross, Matt	P1-319
Crossley, Kay	OA117-05, OA147-04, P4-154
Crossman, Antony	OA83-01, P2-109
Crotin, Ryan	P1-250, P1-283
Crovace, Alberto Maria	OA50-04
Crovace, Antonio	OA50-04
Crowe, Lauren	OA178-03
Cruts, Janneke	OA115-05, P4-005
Cruvinel-Júnior, Ronaldo H.	P4-242, P4-243
Cruz, Jazmin	P2-103
Cruz, João	OA102-02, P4-002
Cuahtecontzi Delint, Rosalia	OA187-03
Cuddy, Benjamin	OA15-03, OA190-03, P1-373
Cudlip, Alan	OA186-01
Cui, Mingyang	P1-389
Culiver, Adam	OA133-03
Cullum, Jason	P2-009
Culver, Meral	P4-153
Cunningham, Olivia	P1-218
Curcio, Nicoletta	P4-092

Author name	Presentation Number
Curd, Evan	P2-126
Curran, Matthew	OA125-05
Curran, Patrick	P1-219
Currie, Dan	P4-214
Curry, William	P3-192
Curt, Nicolas	OA84-04
Curtze, Carolin	P1-116
Cynn, Heon-Seock	P1-359
Czajkowsky, Daniel	OA101-03
Czerpak, Cameron A.	OA158-02
Côté, Julie	OA186-02
Côté, Julie N	OA177-01
Côté, Julie N.	OA155-01
D'Amario, Domenico	OA43-04
D'Andrea, Davide	P3-175
D'Andrea, Susan	OA190-05
D'Arnese, Eleonora	P2-376
D'Ascenzo, Fabrizio	OA69-02
D'Hondt, Lars	OA41-04
D'hooge, Jan	P4-300
da Costa Barcelos, Kate	P1-044
Da Costa, Marta	OA111-05
da Rosa, Bruna	OA74-05, P3-039
da Silva Torres, Ricardo	OA98-03
Dadkhah, Davood	OA54-05, P4-286
Dagan, Misha	P4-083
Dagdeviren, Didem	OA74-01
Dahl, Jonathan N	P3-045
Dai, Xiaoqiang	P1-059
Dailey, Hannah	OA175-02
Dal Fabbro, Giacomo	OA73-05
Dalal, Sufyan	P3-188
Dalby, Mathew	OA187-03
Dale, Marian L.	P1-116
Daley, Monica	OA12-03, P1-192, P2-011, P2-095
Daley, Seth	P1-307, P1-358
Dalfito Gava, Aline	OA118-05, P1-044
Dall'Ara, Enrico	OA194-04, P2-125, P2-154, P3-286, P3-298
Dalle Vacche, Maria	OA109-06, OA35-05, P2-155
Dalman, Morgan J.	P2-161
Dalske, Kyle	P4-236
Dalton, Brian H.	P2-054
Dalton, Diane	OA33-04
Dalton, Laura	P3-076
Daly, Morgan	OA159-03
Damal Kandadai, Mythili	OA103-01
Dami, Ahmed	P3-245
Damink, Lianne	OA57-06
Damm, Philipp	P3-027, P3-236
Damon, Bruce	OA168-03
Daneshvar, Keivan	P4-139
Daneshvarhashjin, Nazanin	OA14-03, OA24-03
Dang, Ryan	P2-336
Daniels, Kat	OA166-01

Author name	Presentation Number
Dankl, Lukas	P3-375
Dannaoui, Abdul	P2-278
Danner, Simon	OA109-03
Danos, Nicole	P2-002
Dantas de Moraes, Pedro	P3-153
Dapaah, Daniel	P3-007
Darling, Dylan	P3-198, P4-130
Darling, Eric	P1-009
Darter, Benjamin	P2-123
Darvishi, Mahziyar	P2-091, P3-241, P3-341
Darvishi, Vahid	OA128-02, OA169-04, OA58-01
Darwiche, Sophie	P3-199
Dashtdar, Babak	P2-031
Dasi, Lakshmi	OA120-03, OA132-02, P4-073
Dasi, Lakshmi Prasad	OA102-05, OA132-04, OA43-02, P4-007, P4-009, P4-013, P4-124
Dasi, Lakshmi.P	P4-046
Dave, Sujal	P4-120
Davenport, Felicia	P2-103
Davey, Catherine E.	OA64-03
Davey, Cathrine	P4-311
Davey, Rachel E	OA10-05
Davico, Giorgio	P4-134
David, Michael C. B.	OA169-04
David, Redden	P4-250
Davidson, Jessa	P2-267, P2-277
Davidson, Jessa M.	P2-057
Davidson, Justin	OA174-02, OA174-06
Davidson, Justin B.	P3-111
Davies, Karen	OA155-05, P1-145, P1-355, P3-381
Davis, Andrew	P3-084, P3-118
Davis, Brittany	P2-006, P2-035, P2-036
Davis, Daniel	OA34-04, P1-220, P2-218
Davis, Daniel J.	P1-123
Davis, Elysia	OA107-03, OA68-02
Davis, Irene	P1-136, P1-173
Davis, Matthew	P2-047
Davis, Sarah	OA149-03, P2-345
Dawber, Will	OA121-03
Dawes, Helen	OA15-02
Day, Erin	P3-326
Day, Evan	OA107-01, OA81-02, P1-347
Day, Gavin	OA31-03
Day, Molly	OA188-05
Dayan, Eran	OA130-06
Dayanidhi, Sudarshan	OA168-02
De Angelis, Adrian	OA175-05
De Backer, Julie	P1-027
De Backer, Pieter	OA25-05
de Beukelaar, Toon	OA106-04
de Boer, Greg	P3-271
De Bortoli, Marzia	OA97-03
de Brito Fontana, Heiliane	P4-155, P4-156, P4-175
De Bruyne, Bernard	OA69-03
De Bruyne, Charlotte	P2-006

Author name	Presentation Number
de Bruyne, Charlotte	P2-035, P2-036
De Campo, Giulia	OA127-05, OA95-02
de Cesar Netto, Cesar	P3-201
de David, Ana	OA118-05
de França, Cassidy	OA13-04
de Graaf, Myriam	P2-149
De Groote, Friedl	OA41-04, P1-151, P2-263
De Guzman, Matthew	P4-209
de Haan, Nikita	P4-312
de Jager, Stefanie	OA123-05
De Jesus, Megan	OA120-03
De Koort, Jasper	P4-074
De Kuyper, Peter	OA25-05
de Lange, Julia	P3-078, P3-080, P3-108
De Lorenzo, Robert A.	P3-181, P4-105, P4-276
De Luca, Gianluca	P1-377
de Lussanet, Marc	P3-202
de Maleprade, Hélène	OA26-03
De Marzio, Margherita	OA63-01
De Melo, Kristen	P1-135, P1-186
De Mey, Marie	P3-020, P3-040
De Nisco, Giuseppe	OA43-04, P4-037
De Oliveira Silva, Danilo	OA117-05, OA147-04, P4-154, P4-155, P4-156
de Oliveira, Inaê	OA85-05
de Oliveira, Jorge	OA125-04
De Oliveira, Julia	P1-190
De Rosario, Helios	P1-172
de Ruijter, Joerik	OA82-04
De Sanctis, Lorenzo	P4-344
de Sousa, Ricardo	P3-077
de Souza da Silva, Thiago	P4-175
De Vecchi, Francesca	P3-342
De Visschere, Pieter	OA25-05
de Wet, Robyn	P4-239
De, Sayan	OA27-03, OA27-04
Dea, Nicolas	P3-304
Dean, Jesse	OA148-01, OA85-01
Dean, Mason	P2-005
Dean, Matthew	OA97-05
DeAngelo, Samantha	OA133-03
Deaver, Nicholas	P3-126
Debbaut, Charlotte	OA25-05, P4-062, P4-064
Debbi, Eytan M.	P3-237
Debeer, Philippe	OA14-03, OA24-03
Debenedetti, Anne	P3-225
deBlois, Kaitlyn	P4-180
Debski, Richard	P3-262, P3-371
Debski, Richard E.	P3-261, P3-323
Decaestecker, Karel	OA25-05
DeCarvalho, Diana	OA23-04, P3-301
Deegan, Paul	OA102-03
DeForest, Cole	P2-223
Degen, Ryan	OA183-04, OA183-05, P4-350
Degen, Ryan M.	OA161-05

Author name	Presentation Number
Degenhart, Gerald	OA197-04, P4-316
Deguchi, Shinji	OA126-02, OA91-05, 1385
DeHart, Kristin	OA178-02, OA178-05, OA67-04
Dehghan Hamani, Iraj	P3-168
Dehnert, Sol	P1-070
Deiters, Sarah	P2-251, P3-346
Dejea Velardo, Hector	P4-318
Dejea, Hector	OA100-02
Del Giovane, Martina	OA169-04
Del Rio, Luis	OA122-06
DeLaCruz, Dalia	P2-264
DeLancey, John	P2-234
Delaney, Connor	OA59-01
Delargy, M. Lauren	P2-002
Deleu, Paul-André	P1-200
Delfino, Florencia	P1-146
Delgado, Mauricio	OA43-03, P2-238, P3-004
Della Casa, Alice	OA188-01
Della Valle, Craig	P3-243
Della Valle, Craig J.	P3-225
Della Villa, Francesco	P1-332
Delong, Michael	P3-259
DeLoretto, Ellie	P4-187
Delp, Scott	OA148-02, OA159-02, OA57-03, OA68-05, OA73-01, OA9-02, P1-057, P1-256, P2-029, P3-099
Delp, Scott L	P3-203
Delp, Scott L.	OA48-03
Deluzio, Kevin	CSB-06, OA117-04, OA2-02, P1-077, P1-134
Demetracopoulos, Constantine	OA86-01
Deml, Moritz	P3-302
Deml, Moritz C.	P2-191
Demma, Dominic	P3-109, P3-110
Demopoulos, Bryce	OA8-03
Dempsey, Cole	P2-034, P3-075
Deng, Cheri	OA64-05
Denis, Denys	P2-116
Denisco, Joseph	P1-022
Dennis, Justin	OA141-06
Dennison, Christopher	OA193-03, P3-134
Dennison, Christopher R.	OA169-03
Denton, Alex	OA107-04, P1-353
DePaul, Vincent	P1-077
Deriu, Marco Agostino	OA91-03
Derrick, Timothy	P1-279, P1-349, P2-170, P3-132
Dervisevic, Omar	P3-249
Derycke, Lucie	P4-014, P4-077
Desai, Dhairya	OA43-03
Desai, Garui	OA46-03
Desai, Gauri	OA142-01
Desamito, Alyssa	P2-011
Desbrosses, Kévin	OA186-03
Deshpande, Aditi	OA185-01
Desloovere, Kaat	OA41-04
Desroches, Dan	P1-284, P1-405

Author name	Presentation Number
Desroches, Daniel	P4-307
Desroches, Guillaume	P4-233
Dessureault, Cédric	P1-119
Desyatova, Anastasia	OA102-03, OA127-02
Devane, Karan	OA121-02
Devert, Nicholas	OA131-04
Devismes, Morgane	OA170-04
DeVita, Paul	OA116-01
Devos, Hannes	OA79-02
Dewig, Derek	P1-288
Dewil, Sophie	OA111-03, P2-344
Dey, Priyanka	OA149-03
Dey, Roopam	P3-361
Dhondt, Elisabeth	P4-062, P4-064
Di Bacco, Vincenzo	OA128-03
Di Berardino, Federica	OA26-04
Di Filippo, Sofia	OA191-05, OA95-03
Di Giorigio, Elisa	P4-270
Di Gregorio, Alessandro	P1-376
Di Gregorio, Silvana	OA122-06
Di Paolo, Stefano	OA42-01, P1-332, P3-129, P3-324
Di Stasi, Stephanie	P4-160
Diallo, Malicki	OA178-04, P1-329, P1-339
Diamond, Laura	OA147-01, OA147-02, OA15-01, OA73-02, P2-117, P3-032
Diamond-Ouellette, Gabriel	P2-116
Diano, Alexa	OA32-04
Dias Castilho, Miguel	P3-279
Dias Ferreira, Nuno	P4-043, P4-119
Dias, Luis	OA133-02, P3-116
Diaz Armas, Gladys	OA90-04
Diaz, Roberto L	P3-188
Dibbern, Kevin	OA188-02, P1-129, P3-201, P4-219
DiBianca, Stephen	P1-065, P4-189
DiCarlo, Julie	OA144-02
Dick, Joelle	P1-059
Dick, Taylor	P2-024
Dickerson, Clark	OA131-05, OA186-01, OA186-05, P2-295, P3-056
Dickerson, Darryl	P2-363
Dickin, Clark	OA8-05, P1-050
Diebels, Stefan	OA60-02, P4-144, P4-211, P4-212
Diena, Giorgio	OA58-03
Dietz, Lindsay	P2-095
Digeronimo, Francesco	OA10-02, P4-320
Dijkgraaf, Marcel	OA79-05
Dijkshoorn, Lynn	P3-223
Dijkstra, Jouke	P4-018
DiLeo, Stefania	P2-091, P3-326
Dimbath, Elizabeth	P3-076
Ding, Julia	P3-171
DING, Wenhao	P4-125
Dinning, Phil	OA97-01
Dion, Cynthia	P2-279, P2-282
Diotalevi, Gaspard	P1-055, P1-119
Dippel, Diederik	OA115-05, P4-005

Author name	Presentation Number
Dirstaru, Silvia	P2-125
Dis, Joel	P4-094
Disabato, Giandomenico	OA95-03, P4-042
Disney, Catherine	P2-356
Disselhorst-Klug, Catherine	P1-133
Dittmer, Emily	OA190-04
Dixon, Andrew	OA83-04
Dixon, Philippe	OA42-02, P1-181, P1-360
Dixon, Philippe C.	OA143-06, P3-014
Djafar, Tatiana	OA15-03, OA190-03, P1-373
Djuraskovic, Irina	P1-158
Doan, Jasmine	OA163-02
Doan, Jon	P2-270, P2-275
Doan, Minh Khoi	OA161-05
Dobbe, Iwan	P3-223
Dobler, Florian	OA54-02
Dobrev, Ivo	P3-036, P4-063
Docaj, Anxhela	OA122-01
Doctor, Ian	OA155-03
Doehne, Brandon	P1-275
Dohm, Julius	P4-273
Doi, Atsuo	P4-083
Dolan, Eimear	OA38-01
Dolan, Eimear. B	P4-274
Domanin, Maurizio	OA82-02, OA95-02, P4-074
Domański, Janusz	P4-075
Dombrowski, Malcolm	OA165-05
Domkam, Nya	P2-020
Donahue, Nicole	P1-377
Donahue, Seth	P1-158
Donatelli, Cassandra	OA103-05, P2-013
Donatelli, Noelle	P2-245
Donelan, Max	P3-013, P3-057
Dong, Yinkai	P4-283
Dong, Zongyin	P2-358
Donlin, Margo	P1-195
Doodkorte, Remco	P2-360, P3-289
Doodkorte, Remco J.P.	P3-300
Dooley, Evan	OA3-04
Dooley, Evan A.	OA119-01, OA81-03
Dorgo, Sandor	OA128-04
Dorj, Ariunzaya	OA122-05
Dorrance, Adam	P3-204, P3-205, P3-251, P3-313
Dorscher, Sydney	P2-256
Doschak, Michael R	P3-340
Doshi, Durshil	OA133-03
Doshi, Sagar	OA59-03, P1-213
Dotov, Dobromir	OA93-04, P2-315
Douglas, Abigail	P1-272
Douglas, Fraser	P2-308
Dowdle, Blake	P4-187
Dowling, Brittany	OA94-04, P1-276, P1-295
Downer, Kaitlyn	OA196-03, P1-150, P1-180
Downey, Kiera	OA64-05

Author name	Presentation Number
Downs, Kathleen	P1-144, P1-202
Dozio, Scilla	OA62-02
Drake, Janessa	P1-284, P1-405, P4-307
Drakos, Mark	OA86-01
Drees, Philipp	P1-240
Dreiner, Maren	P1-007, P2-240, P4-334
Drenning, Grant	P4-170
Dresen, Jonas	P2-352, P2-353
Drew, Alex	P3-354
Drew, Elodie	P3-014
Drew, Stefanie	OA123-02, P2-332
Drew, Stefanie A	P2-336
Dreyer, Michael J.	P3-235
Drnec, Jakub	OA10-04
Drobnicki, Rafał	P4-279
Droual, Tamara	P2-253
Drozdov, Maya	OA128-03
Drummer, Dietmar	P1-393
Du, Xiaoyu	OA36-02, P2-098
Du, Yanan	OA114-01, OA126-04
Dual, Seraina A.	P4-021
Duarte, Camilo	OA170-02
Duarte-Cordon, Camilo	P3-160
Dubbeldam, Rosemary	P4-164, P4-165
Duca, Francesca	OA82-02
Duda, Georg	OA113-05, P2-134, P3-253, P4-222
Duda, Georg N.	P3-027, P3-236
Dufeil, Amélie	OA198-04
Duffy, Garry P.	OA38-01
Duffy, Garry. P	P4-274
Dufour, Antoine	P2-238
Dugan, Eric	OA57-01, P1-363, P2-144
Dukelow, Sean	OA111-01
Duma, Lauren	P4-197
Dumas, Raphael	OA135-05, OA172-05, OA2-01, P1-200, P2-179, P4-234
Dummer, Kirsten	OA157-03
Dumont, Georges	P1-378, P2-033
Dumont, Sarah	OA61-05, P3-052
Dumont, Serge	P4-282
Dumphart, Bernhard	OA54-02, P1-237
Dunbar, Michael	P3-204, P3-205, P3-250, P3-251, P3-265
Duncan, Ryan P.	OA92-01
Duncan, Stephen	OA99-02, P4-138
Dunn, Julia	P3-368
Duong, Tony	P1-262
Dupuis, Beau P.	OA128-04
Duque Urrego, Daniel	P1-051
Duquesne, Jessie	P4-062, P4-064
Dur, Niels	OA57-06
Duraffourg, Clément	OA172-04
Durandau, Guillaume	P2-116, P3-218, P4-257
Durnin, Ainsley	P1-098
Durongbhan, Pholpat	OA10-05
Dursun, Elisabeth	P4-336

Author name	Presentation Number
Durão, Ana Filipa	P1-078, P1-228
Dutcher, Susan	P1-389
Dutra, Jose	OA98-06
Dutta, Sanjib	P2-184
Dutta, Tilak	OA130-02, OA54-05, P4-286
Dwivedi, Krashn	OA108-03, P4-061
Dyer, Olivia	OA163-04, P2-055
Dyment, Nathaniel	OA126-03
Dyverfeldt, Petter	P4-348
Dzenutis, Paige	OA46-02
Dzewaltowski, Alex	P3-067
Dæhlin, Torstein	P2-263
Díez, Pedro	P4-006
Dörsam, Istabrak	P4-204
Düser, Tobias	P1-005, P3-131
D'Ascenzo, Fabrizio	OA43-04
d'Entremont, Agnes	P3-146
E. Garrigues, Grant	OA14-02, P3-374, P4-157
Ead, Ahmed	P3-331
Ead, Ahmed Samir	P3-319
Eagen, Finn	P4-292
Eamon, Camille	P2-035, P2-036
Earhart, Gammon M.	OA92-01
Earthman, Carrie	OA160-03
Easson, Margaret	P2-233
Ebben, William	OA128-04
Ebbers, Tino	P4-348
Ebenbichler, Maximilian	OA45-02
Eberle, Robert	OA45-02
Eberth, John F.	OA144-05, OA146-01
Ebner, Ines	P4-334
Ebrahimzadeh, Amin	OA185-01
Eckes, Beate	P2-240
Eckhardt, Maximilian	P1-393
Eckstein, Felix	P4-334
Eckstein, Kevin	P4-345
Edwards, Bradley	P3-360
Edwards, Brent	OA18-06
Edwards, Peter	P4-160
Edwards, W Brent	P2-211
Edwards, W. Brent	OA119-03, OA122-05, OA73-05, P2-039, P3-344, PL03-01
Eekhoff, Jeremy	OA151-04, P3-269
Efthymiou, Athena	OA130-04
Egawa, Hayata	P3-096
Egger, Andre	P3-077
Eghobamien, Iwi	P1-160
Eghtesady, Pirooz	P4-020
Egner, Clara	OA171-02, OA171-03, P2-069, P2-094, P3-200
EHLINGER, Matthieu	P3-264
Ehrig, Rainald	P3-253
Eibichova, Sabina	P3-183
Eichenlaub, Emily	OA160-05, OA40-03
Eichwalder, Johannes	P2-140, P2-367, P3-367
Eikelenboom, Esmee	OA44-01

Author name	Presentation Number
Eilen, Henry	P1-276, P3-243
Eisner, Charles	P1-120, P3-211
Ekdahl, Mitchell	OA196-01, P2-080, P2-136
Ekroll Jahren, Silje	OA110-02
El Abdoulli, Mohammed	P2-306
El Bahry, Mohammed	OA42-03
El Saedi, Kariem	OA97-03
El Sayed, Retta	P4-096
Elahi, Seyed Ali	OA149-01, OA149-02, P4-317
Elder, Benjamin	P2-031
Elder, Katherine	P1-182
Elena, Delgrosso	P2-372
Elharouni, Farida	P4-346
Elia, Eleni	P2-209
Elia, Stefano	OA43-04
Elias, George	OA65-03
Eliason, Travis	P2-166, P2-167
Elkhatib, Bashar L.	OA58-04
Elkin, Benjamin	P3-093
Ellingson, Arin	OA29-03, P3-310, P4-145, P4-235, P4-236
Elliot, Dawn M.	P3-199
Elliott, Dawn M	OA161-01
Elliott, Holly	OA99-02
Ellis, Scott	OA86-01
Ellison, Matthew	P2-164
Ellison, Peter	P1-161, P2-312, P2-324, P3-227
Ellmers, Toby	OA177-02, OA189-04
Elsayed, Karim	P2-203, P2-253
Elson, Elliot	OA126-04
Eltit, Felipe	OA194-02, P3-304
Eltschinger, Yannic	P3-177
Emanuele, Gasparotti	OA139-04
Embaye, Simon	P2-090
Emendi, Monica	OA38-04
Emery, Carolyn	P3-126
Emery, Carolyn A.	OA131-04
Emmenegger, Tim	OA171-02, OA171-03
Emmert, Maximilian Y.	OA4-02
Emmerzaal, Jill	OA143-06
Emonts, Caroline	OA151-03, P3-260, P3-347
Engelmann, Willi	OA21-03
Englund, Martin	P3-335
Ennis, Daniel	OA30-02, P4-330
Ennis, Daniel B.	OA25-04
Enns, Madeleine	OA155-02
Enomoto, Shota	P2-255
Enomoto, Yasushi	P1-383
Enrico, Dall'Ara	P3-296
Entress, Nick	P3-334
Enyinnaya-Okidi, Chinaza	OA119-03
Enzenberg, Mateus	P3-375
Epifanio, Jacopo	P1-078
Epp-Stobbe, Amarah	P1-261, P3-001
Erdemir, Ahmet	OA159-04, P2-163, P3-212, P3-230, P3-231, P3-252, P3-263

Author name	Presentation Number
Erhard, Cosima	OA113-05
Eriks, Keith	P2-056, P3-101
Eriksson, Thomas	P2-298
Ernst, Joel	OA6-05
Ertekin, Tayfun	P1-360
Esanu, Ioana	OA90-06
Escamilla, Rafael	OA16-01, P1-346
Escarcega, Jordan	OA32-03
Esculier, Jean-Francois	OA117-03, OA147-05
Eshaghi, Dorsa	P2-064
Eskandari, Mark	OA167-05, OA179-04
Eskandari, Mark K	P1-400
Eskandari, Mark K.	OA108-04, OA191-03
Eskandari, Mona	OA134-04
Eskelinen, Atte	OA109-02, OA19-03, OA73-02, P3-155, P3-336
Eskelinen, Atte SA	P1-021
Eskofier, Björn	P4-220
Esrafilian, Amir	OA109-02, OA41-01, OA57-03, OA73-02, P2-178, P3-155, P3-203, P3-335
Essien, Utomobong	OA99-03
Estrada, Ana	OA71-05, P3-150, P4-076
Estrada, Jon	P2-234
Ethier, C. Ross	OA101-04
Ethier, Emilie	P3-088
Evangelidis,, Pavlos E.	OA15-02
Evans, Connor J.	P4-105, P4-276
Evans, Isabel	P2-273
Evans, Lauren	OA6-05
Evans, Mary Kate	OA200-03
Evans, Ryan	OA141-02, OA178-06, P2-088
Evans, Sam	P3-339
Even, Azilis	P3-074
Everest, Stephen	P2-204
Everett, Breanne	P4-168
Eyre, Arianna	P2-266
Ezzat, Mariam	OA74-05, P3-039
F. Gonzales, Felipe	P4-223
F. Gonzalez, Felipe	OA14-02, OA14-04, OA153-01, OA76-04, OA94-03, P1-061, P3-374, P4-136, P4-157, P4-258
Fabre, Arthur	P2-030
Fabry, Ben	OA88-05
Fagan, Michael	P2-173
Fagerström, Martin	P3-323
Fahmy, Seraphim	P4-118
Fain, Aaron	OA99-02, P4-138
Faiz, Zaid	OA117-05
Fakhar, Maliheh	OA142-01, P3-038
Falcone, Samantha	OA137-04
Falcão, Manuel	P3-048
Falkenham, Owen	P3-250
Falla, Deborah	OA177-01
Fallahtafi, Farah	P2-056
Fallahtafti, Farah	P3-101
Fallon, Leah	P1-018
Fallscheer, Maggie	P2-035, P2-036

Author name	Presentation Number
Famaey, Nele	OA84-05, P1-027, P3-023
Fan, Jianjia	OA133-02
Fan, Lei	OA58-02, P4-066
Fan, Luyao	OA197-01
Fan, Mingyue	P2-260
Fan, Ruijie	P1-222
Fan, Tingting	OA95-01
Fan, Xiang	P3-194
Fang, Ying	P1-093, P3-061
Fang, Zhou	OA15-05
Fang, Zhu	P1-179, P1-248
Fanni, Benigno Marco	OA25-03
Farage-O'Reilly, Saira	P2-125
Farcas, Emilia	P4-266
Farchmin, Alina	P3-260
Farina, Dario	OA1-03, OA92-02, P4-159, P4-255
Farmani, Sanaz	P4-115
Farrag, Saifullah	P2-329
Farrar, Scarlett	P1-145, P1-355, P3-381
Farrell, Garreth	P1-281
Farris, Dominic	P2-164
Farris, Dominic J.	OA154-04
Farshad, Ali	P2-373
Fasanella Masci, Francesca	OA198-01
Fasci, Anjelyka	P4-299
FASUYI, Francis	P1-054
Fatone, Stefania	P2-314
Fattori, Andrea	P3-354
Faul, Oliver	P1-001
Faux-Dugan, Logan	P4-069
Favela, Orlando	P4-276
Federico, Salvatore	OA100-05, P2-196, P2-250, P2-364
Feeney, Daniel	OA107-05, OA131-01, P1-336
Feier, Cathrine	P1-083, P1-084
Feigean, Romain	P4-240, P4-241
Feih, Stefanie	OA80-01
Feld, Katharina	P3-131
Feldman, Jerry	P4-210
Feldman, Jordan	OA106-01, P1-076, P1-105
Feldman, William	P2-095
Feldner, Heather	OA111-02, OA123-04, P2-322
Feldner, Heather A.	OA27-01
Felipe, Jack	P3-228
Felipone, William	P3-383
Feller, Herman	OA188-05
Fels, Sidney	OA153-02, P2-169
Felton, Olivia	OA28-05
fenelon, Christopher	P3-241
Feng, Ke	P2-319
Feng, Xi-Qiao	OA126-04
Feng, Yuan	OA101-03
Fer, Frederic	P4-240
Fer, Frédéric	P4-241
Fereidoonnezhad, Behrooz	OA115-01, OA115-05, P4-005, P4-065

Author name	Presentation Number
Ferenc, Rudolf	P3-296
Ferey, Jeremie	OA168-02
Ferguson, Stephen	OA36-02, P2-098, P2-197
Ferguson, Stephen J	P3-296
Ferguson, Stephen J.	OA18-02, OA70-05, P2-360, P2-362
Fermor, Hazel	P2-355, P3-271
Fernades, Fábio	P3-077
Fernandes de Oliveira, Liliam	P2-130
Fernandes, Antonio	OA121-01
Fernandes, Eric B. P.	OA113-02
Fernandes, Fábio	P4-132
Fernandes, Joao	P4-080
Fernandes, Lucas S.	P4-176
Fernandes, Maria	P4-043
Fernandez, Amanda	OA167-05, OA179-04
Fernandez, Jake	OA4-04
Fernandez, Justin	OA145-06, OA169-05, OA190-02, OA58-05, P1-092
Ferrari, Lorenzo	OA25-04, P4-330
Ferraz Pazzinatto, Marcella	P4-154
Ferrazzi, Giulio	OA144-04
Ferreira de Almeida, Diogo	P4-111
Ferreira, Jacielle	P1-060
Ferreira, Jane S. S. P.	P4-242
Ferreira, Jane Suelen S.P.	P4-243
Ferreira, Louis	OA161-05
Ferreira, Louis Miguel	P2-140, P2-367
Ferreira-Shornack, Matheus	OA48-04
Ferrell-Olson, Julie	OA66-02, OA66-05, P1-103
Ferrigno, Christopher	OA20-04
Ferris, Abbie	P1-054, P1-064, P1-301, P1-302
Ferris, Abbie E.	P1-251, P4-246
Ferris, Daniel	P1-239
Ferris, Jamie	OA107-02, P1-271, P1-306
Ferruzzi, Jacopo	OA63-01, OA75-03, P3-162
Fewster, Kayla	P2-273
Fey, Nicholas	OA59-05, P2-083, P4-292
Fey, Nicholas P.	P3-010
Fey, Nick	P2-061, P3-046
Fiedler, Imke A. K.	OA71-04
Fillingham, Patrick	OA32-06
Fillion-Robin, Jean-Christophe	P4-321
Finch, Sadie	P2-285
Finger, Erik	P3-181
Fink, Chris	OA20-03
Fink, John	P3-034
Finley, James	OA106-02, OA53-05, P1-081
Finnerty, Caitlyn	P1-114
Finni, Taija	P2-227
Finnie, John	P3-079, P3-082
Finnilä, Mikko A.J.	OA149-04
Fino, Peter	OA184-04, P2-333
Fino, Peter C.	OA106-04, P1-118, P2-124
Finocchiaro, Thomas	P4-348
Finol, Ender	OA167-05, OA179-04, P4-008

Author name	Presentation Number
Finol, Ender A	P1-400
Finol, Ender A.	OA108-04, OA191-03
Fiore, Gianfranco Beniamino	P4-084
Fiorin, Alessio	P1-032
Firminger, Colin	P2-039
Firminger, Colin R.	OA119-03
Firouzabadi, Pouyan	P2-176
Fischer, Kenneth	P1-023
Fischer, Maximilian	OA60-03
Fischer, Patrick	P3-073, P3-128
Fischer, Steven	OA174-02, OA174-06, P2-274
Fischer, Steven L.	P3-111
Fischer-Carles, Alba	P1-032
Fischlin, Nicholas	OA18-02
Fisher, Charles	P3-304
Fisher, Matthew	P2-233
Fitzgerald, Lucy	P3-072
Fitzgerald, Sarah	OA79-03
Fitzpatrick, Clare	OA70-02, P4-097
Fitzpatrick, Daniel	P4-187
Fitzsimons, Karson	P4-185
Flahaut, Zachary A.	P1-258
Flanagan, Thea	P3-215
Flanagan, Will	P3-270
Flath, Nathan	P3-248
Flaum, Benjamin	P2-005
Flaws, Jodi	OA170-05
Fleck, Robert	P4-016
Fleck, Robert J	P4-050
Fleig, Lena	P2-134
Fleisig, Glenn	OA16-01, OA16-06, OA3-06, OA42-02, P1-295, P1-296, P1-346, P1-372
Fletcher, David	OA78-01
Fletcher, Jared	OA154-05, OA18-06, P2-071, P2-090
Fletcher, Jared R.	OA154-02, OA154-03
Flohr, Janine	OA57-05, P2-070, P2-120
Florea, Cristina	OA45-03
Florkiewicz, Erin	OA177-04
Flouri, Dimitra	P3-191
Fluit, René	P3-218
Flynn, Gregory	P2-142
Foch, Eric	P1-137
Foch, Kevin	P1-137
Foletti, Stefano	P3-258
Foley, Kristie L.	OA128-05
Foley, Landon	OA129-02
Foley, Sierra	OA85-04
Follet, Helene	P4-234
Fong, Daniel	P1-382
Fontaine, Simon	OA116-03
Fontalirant, Lise	P4-068
Fontana, Federica	P4-040
Fontanarosa, Davide	P4-298
Forczek-Karkosz, Wanda	P1-207
Ford, Allyson	P1-260

Author name	Presentation Number
Ford, Harry	P4-135
Ford, Kevin	P1-260, P1-293, P1-313, P1-322, P1-340
Forde, Nancy	OA91-02
Forde, Nancy R.	P2-019
Forer, Jarod	P3-229
Forman, Garrick	P2-267
Forman, Jason	P3-085, P3-141
Formella, Emily	P1-011
Formenton, Giulia	OA146-03, P4-074
Fors, Katherine	P4-324
Forsythe, Brian	OA14-04, P1-276, P3-243, P4-157
Fortin, Aiyana	P2-358
Fortunato, Ronald N.	P4-054
Fossan, Fredrik E	P3-045
Foster, Jacob	P2-135
Fouda, Ahmed	P2-293
Foulger, Liam	OA118-03
Fouquet, Vincent	P3-328
Fournier, Daniel	P3-056
Fournier, Lisa	OA124-04
Fox, James	OA110-02
Fragomeni, Anna	P2-322
Fragomeni, Anna M.	OA27-01
Frame, Hannah	OA178-05, OA67-04
Francisco, Gerard	P4-209
Francom, Noah	P4-159
Frank, Jesse	OA119-02
Frank, Nick	OA68-02
Frank, Rachel	OA200-03
Franks, Corbit	P1-062, P1-316
Frankston, Naomi	OA147-03, P2-164
Franz, Jason	OA130-06, OA141-06, OA160-05, OA178-01, OA184-04, OA184-05, OA28-04, OA33-03, OA34-04, OA40-03, OA53-04, OA67-02, P1-076, P1-211, P1-220, P1-221, P1-334, P2-032, P2-218, P2-227, P4-188
Franz, Jason R.	P1-123
Franz, Thomas	OA88-05
Frascella, Francesca	OA51-03
Fraser, Katharine	P3-169, P4-127
Frattolin, Jennifer	OA198-01
Frayne, Ryan	P1-358
Frazer, Lance	P2-148
Fre, Mona	P3-301
Frederick, Joni	OA138-03
Free, Daniel	P4-255
Freear, Bulut	P3-209, P3-210
Fregly, B.J.	P2-111
Fregly, Benjamin	OA70-06
Fregona, Virginia	OA115-02, OA115-03, P4-006
Freisinger, Gregory	OA177-04, P3-379
Fremes, Stephen	P4-091
French, Archer	OA179-04
French, Archer A	P1-400
Freschlin, Nikolaj	OA189-03
Frew, Kylie	OA175-02
Frewein, Moritz P.K.	OA71-02

Author name	Presentation Number
Frey, Martin	OA3-01
Frey, Mona	OA23-04
Frey, Sabrina	OA157-05
Fried, Margit	OA79-06
Friedel, Jared-Isaac	P2-274
Friedman, Seth D.	P4-191
Friesen, Andrew	P1-100
Friesen, Kenzie	OA79-03
Friesen, Kenzie B.	P1-321
Frigerio, Giulia	OA95-04
Frijia, Francesca	OA144-04
Fritz, Christian	OA60-03
Fritz, Jessica	P4-206
Froehler, Michael	OA115-04
Frondorf, Brian	OA8-03
Frossard, Laurent	OA80-01
Frostad, Sara	P2-035, P2-036
Fry, Christopher	P3-211
Fry, Christopher S.	P2-074
Fry, Evan	OA151-04, P3-269
Fu, Henry	OA26-02
Fu, Michael	OA98-04
Fu, Peiwen	OA165-03, P4-253
Fu, Yilin	P1-194
Fuchs, Magdalena	OA122-01, OA63-03
Fucile, Pierpaolo	OA50-04
Fujie, Hiromichi	OA11-04, P3-166, P3-277, P4-331
Fujii, Norihisa	P1-246
Fujimoto, Masahiro	OA136-04, P1-233, P1-254
Fujisaki, Kazuhiro	P2-231, P3-172, P3-182
Fujiwara, Takeo	P4-121
Fujiwara, Yukio	P1-398
Fukute, Jumpei	OA91-04
Fulgheri, Irene	OA127-05, OA95-02, P4-074
Funamoto, Kenichi	OA198-03, OA51-04, P1-026, P1-391
Funes Alfaro, Gerbert	OA123-02, P2-332
Fung, Joyce	P4-257
Funk, Sharon	OA153-04
Funk, Tobias	OA170-02
Funken, Johannes	P3-267
G. Andriotis, Orestis	OA97-03
G. Filho, Nilton	P4-258
G. Lloyd, David	P2-178
G. Van Straaten, Meegan	OA150-04
G.Leguia, Marc	P1-228
G.S Cardoso, Carlos	OA169-02
Gabbard, Jackson	P2-055
Gabbert, Lukas	OA66-01
Gabel, Johannes	P4-229
Gabert, Lukas	OA46-04, OA80-02, P2-303
Gabetti, Stefano	OA199-02, OA51-03
Gaboriau, David	OA46-05
Gacoin, Thierry	OA138-03
Gaddy, Dana	P2-022, P2-101

Author name	Presentation Number
Gaffino, Lisa	OA111-05
Gaffney, Brecca	OA153-04, OA196-01, OA70-03, OA99-02, P2-080, P2-136
Gafoor, Fatima	OA46-06
Gaiesky, Sean K.T.	P1-357
Gaillard, Valentine	P4-349
Gala de Pablo, Julia	P2-355
Galbusera, Fabio	P3-002
Gale, Tom	OA165-05, OA23-03, OA60-04, P2-046
Gallagher, Brittany	P1-280
Gallagher, Kaitlin	OA140-01, P1-231
Gallagher, Katie	OA182-05
Gallardo-Borràs, Noèlia	P1-032
Gallegos, Joseph	OA65-04
Gallo, Diego	OA108-02, OA25-02, OA43-04, OA51-03, OA69-02, OA69-03, OA82-05, P4-037, P4-113
Galloway, Cole	OA93-06
Galloy, Adam	P2-001
Galteri, Giulia	P3-240
Galvanetto, Ugo	P3-125
Galvin, Emily	OA187-04
Gambelli, Clement	OA124-02
Gambelli, Clément	P1-089, P1-090
Gambill, Julia	P2-166, P2-167
Gammage, Kimberley	P4-030
Gandet, Thibault	P4-234
Gandevia, Simon	P4-207
Ganley, Theodore	P3-059, P4-186, P4-205
Gao, Jeslyn	OA176-02
Gao, Leiming	OA60-05, OA99-01, P3-314
Gao, Tianxiang	P3-061
Gao, Xingqun	OA101-03
Gao, Zi Xiang	OA190-04
Gao, Zixiang	OA81-04
Gao, Zixin	OA46-06
Garant, Renee	P2-253
Garavelli, Chiara	OA100-02
Garces, Irina	OA198-04
Garcia Alamo, Karelhia	P2-035, P2-036
Garcia, Gina	P1-294
Garcia, Karelhia	P2-006
Garcia, Mario E.	OA31-06, OA44-02
Garcia, Steven	P2-258
Garcia-Aznar, JoseManuel	P3-296
García-Aznar, José Manuel	OA152-01, P1-404
García-González, Alberto	P4-006
García-Herrera, Claudio	OA146-02
García-Muro San José, Francisco	OA42-04
Gardegaront, Marc	P4-234
Gardes, Camille	OA5-01
Gardner, Adrian	OA36-06
Gardner, Thomas	P3-346
Garg, Koyal	OA151-04, OA163-05, P3-269
Garikipati, Krishna	P2-217
Garner, Ellen	OA151-02

Author name	Presentation Number
Garon, Martin	OA163-02
Garreau, Morgane	P4-049
Garrigues, Grant	OA14-01, OA14-04
Garrigues, Grant E.	P3-380, P3-383
Gasiorowski, Verushca	P3-192
Gasparotti, Emanuele	OA144-04, OA25-03
Gasser, Christian	OA199-05
Gasser, Thomas Christian	P3-186
Gassner, Heiko	OA136-02, P1-152
Gastaldi, Dario	OA49-03
Gaston, Lucas	P2-153, P2-189
Gates, Deanna	P2-328
Gather, Malte C.	P1-007
Gatti, Anthony	CSB-04, OA147-05, OA57-03, OA73-01, OA73-04, P2-029, P3-203, P3-254
Gatti, Anthony A.	OA117-02, OA117-03, P4-169, P4-198
Gaudette, Logan	P1-173
Gaudiosi, Pompeo	OA51-03
Gauss, Taylor	OA92-04
Gautam, Umesh	P3-185
Gauvin, Chantal	P1-055, P1-119
Gavazzoni, Benedetta	OA77-03
Gaweda, Boguslaw	OA4-03
Gaysinskiy, Sophia	P4-277
Gayzik, F. Scott	OA121-02, P3-068
Gazzerro, Elisabetta	P3-019
Geelkerken, Bob	OA10-03
Geelkerken, R.H.	P4-071
Geelkerken, Robert H.	P4-310
Gehling, Jane	OA21-03
Gelinne, Aaron	P4-188
Geneau, Daniel	P1-343
Generoso, Talissa	OA105-06
Genin, Guy	OA126-04
Gennart, Isabelle	OA84-05
Gensburger, Deborah	P4-234
Georgiadis, Christos	OA17-04
Georgiou, Grace	OA196-01
Gerards, Noëlle	P4-095
Gerber, Gabriela	OA96-04
Gerhold, Cameron	P4-167
Gerich, Torsten	P3-314
Geris, Liesbet	OA149-02, OA199-01, P1-021, P2-371, P3-035, P3-348
Germscheid, Niccole	P3-296
Gerus, Pauline	P1-125
Geschwender, Cole	OA8-05
Getgood, Alan	OA141-02
Geyer, Holly	P3-268
Gföhler, Margit	P1-401
Ghafari, Joseph	P4-056
Ghajari, Mazdak	OA121-03, OA128-02, OA133-05, OA145-01, OA169-04, OA58-01, OA6-01, OA6-05, P3-081
Gharibi, Orod	OA161-04
Gharleghi, Ramtin	OA144-03
Ghazouani, Clément	P2-306, P2-335

Author name	Presentation Number
Ghebryal, Justina	OA4-01, OA4-02, P1-030
Ghezelbash, Farshid	OA35-01, P2-174
Gholami, Behnam	P1-111
Gholami, Reyhaneh	P2-347
Ghomashchi, Hamed	OA54-05
Ghosh, Preetam	OA51-05
Ghosh, Rajdeep	OA194-04, P3-286
Ghulam, Zeyad	P4-286
Ghysel, Christophe	OA25-05
Giaccone, Emma	OA25-02
Giacomini, Francesca	OA50-04
Giampietro, Costanza	P1-006
Giannetti, Arianna	OA138-03
Giannopoulos, Dimosthenis	OA97-03
Giavaresi, Gianluca	OA50-04
Gibbons, Erin	P3-150
Gibson, Eric	P3-126
Giese, Daniel	P4-042
Giger, Nico V.	P4-346
Gijsen, Frank	OA115-01, OA115-05, P4-005, P4-040
Gil Pereira, Christian	P4-119
Gilchrist, Michael	P3-121
Giles, Joshua W.	P3-369
Gilet, Flavie	OA193-05
Gill, Simone V.	OA41-02
Gille, Maryse	OA50-04
Gillespie, Ciaran	OA115-03
Gillespie, Samuel	OA2-03
Gillilam, John	P4-133
Gillstrom, Diana	P2-283
Giordano, Carmen	OA153-03, OA26-04
Giorgino, Riccardo	OA50-04
Giorgio, Giorgio	P3-004
Giorgio-Serchi, Francesco	OA36-06
Girdwood, Michael	OA117-05, OA147-04
Giuffredi, Giulia	P2-049
Gizzi, Alessio	P2-196
Gizzi, Leonardo	OA177-01
Glass, Ashley	P1-322
Glaviano, Neal	P1-253
Glazer, Yaron	P2-099
Gleason, Rudy	OA4-04
Gleason, Thomas	P4-055
Gleaves, Davin	P1-099, P1-371
Glick, Andrew	OA63-01
Gliniak, Christy	P3-162
Glyn-Jones, Siôn	P3-321
Goda, Ibrahim	P2-365
Godard, Zoe	P2-265
Goddard, Chris	P4-051
Godfrey, Alan	OA124-04
Godin, Elliott	P4-277
Godin, Johnathan	P3-318
Godin, Jonathan	OA195-04

Author name	Presentation Number
Godoy-Guzmán, Carlos	OA146-02
Godoy-Santos, Alexandre	P1-255
Goertz, Alan	P3-140
Goethel, Márcio	P1-060
Goetz, Aurele	OA157-03
Goetz, Jessica	OA18-04
Goh, Siew Li	P1-267, P1-362
Goi, Filippo	P1-149, P1-376
Gokeler, Alli	P3-129
Golabchi, Ali	P2-165
Gold, Garry	OA73-04, P2-224, P3-254
Gold, Garry E.	OA48-03, P3-203
Gold, Gatti E.	OA73-01
Goldcamp, Nate	P1-337
Goldman, Haviva M.	OA144-05
Goldsberry, Kirk	OA68-06
Goldstein, Raymond E.	OA26-03
Golmohammadi, Maryam	OA189-02, P4-183
Golse, Nicolas	P4-101
Golyski, Pawel	OA46-01, P2-166, P2-167, P2-320
Golyski, Pawel R.	P3-115
Gombatto, Sara	P1-309, P4-266
Gomes Moraes, Andréa	P1-044
Gomes, Maria Clara	P1-191
Gomez Hjerthen, Isabella	OA141-03, OA183-02, OA188-04, P2-042
Gomez, Hermes	P4-313
Gomoll, Andreas	P2-249
Goncalves, Basilio	P1-270, P2-156
Gong, Shu	OA184-02
Gong, Xiaobo	OA164-03, OA64-02, OA90-03
Gong, Ze	OA129-06
Gonzalez Heit, Elsa Josefa	P1-148
Gonzalez Villasanti, Hugo	P3-034
Gonzalez Welker, Cara	OA28-05
Gonzalez, Alex	P1-256
Gonzalez, Felipe	OA14-01, OA98-06, P1-071, P1-276, P3-243
Gonzalez, Felipe F.	OA105-06, P1-255, P3-315, P3-383, P4-167
Gonzalez, Jorge	P1-281
Gonzalez, Michael	P4-148, P4-149
González Ballester, Miguel A	OA35-02
González Ballester, Miguel A.	OA182-03
González Cabrero, Jose	OA169-02
González, David	P4-006
González-Bermúdez, Blanca	OA88-02
Gonçalves, Basilio	OA44-03
Gonçalves, Basílio	OA147-02, OA70-04
Goo, Woonhoe	P3-385
Good, Bryan	OA104-03, OA115-02, OA115-04, OA157-04, P4-072
Goodding, Spencer	P1-064
Goodfriend, Karin	OA24-04
Goodwin, FJ	P4-170, P4-313
Goodyke, Austin	OA4-03
Gooyers, Chad	P3-078
Gorbet, Maud	P2-140

Author name	Presentation Number
Gordon, Karen	P3-104
Gordon, Megan	P3-123, P3-316
Gorla, Riccardo	OA95-03, P4-092
Gorniak, Stacey	P3-055
Goss, Dante	OA166-06
Goss, Kara N.	P4-102
Gosselin, Jerome	P4-058
Goswami, Bhavya Giri	P1-045
Gottschall, Jinger	OA107-02, P1-271, P1-306
Goubault, Étienne	P2-116
Goueffic, Yann	P4-010
Gourgi, George	OA63-03
Gouteron, Anais	OA172-04
Gouveia, Aline	P3-279
Govers, Megan	OA162-01, OA162-02, OA162-03, P2-271
Goy, Annika	P3-183
Grabowski, Alena	OA119-04, OA80-03, P1-113, P1-189
Grabowski, Alena M.	OA20-03
Grace, John	OA68-01, P1-243, P1-311
Graci, Valentina	P3-059, P4-186, P4-205
Gracia Ibáñez, Verónica	P4-220
Gracia-Ibáñez, Verónica	OA37-04
Grad, Dalia	P4-214
Graf, Robert	OA44-05
Graham, Claudia	P1-286
Graham, Claudia M.	P2-268
Graham, Kendra	P1-320
Graham, Robert	OA144-03
Graham, Ryan	OA153-06, P1-327
Graham, Vicky	P3-339
Grande Gutierrez, Noelia	OA167-01
Grande Gutiérrez, Noelia	P4-094
Grandin, Marine	P4-234
Grassi, Alberto	P3-324
Grassi, Lorenzo	OA100-03, OA105-03, P2-197
Grau, Raphael	P1-005, P3-131
Gravare Silbernagel, Karin	P2-299, P3-222
Gravuer, Kiersten	P3-268
Grawe, Brian	P1-265, P2-107
Gray, Aubrey	P2-032
Gray, Ethan	P3-268
Gray, Hans	OA175-05, OA83-06, P2-244
Greco, Gabriele	OA146-03, P4-074
Green, David A.	OA154-01, OA154-04
Greenberg, Elliot	P3-059, P4-186, P4-205
Greene, Katelyn	P2-197
Greene, Nicholas	P4-131
Greene, Olivia	P1-210
Greene, Trevour	OA87-02
Greenwald, Richard	OA16-04
Gregory, Diane	OA189-01, OA194-05, P3-288
Gregory, Julia	P4-311
Greiner, Katharina	OA171-02
Greiner-Perth, Ann-Kathrin	OA36-03, OA36-04

Author name	Presentation Number
Greinwald, Markus	P4-229
Grenier, Thomas	P4-234
Greve, J.G.M.	P4-071
Gribble, Phillip	P4-140
Gries, Molly	P2-329
Gries, Thomas	OA151-03, P3-260, P3-347
Griesbach, Julia K	OA122-04
Griffin, Lisa	OA177-03
Griffin, Sarah	OA174-01
Griffo, Bianca	OA82-05
Grillo, Alfio	P2-196
Grimm, Bernd	P1-181
Grimmitt, Adam	OA118-02, OA178-04, P1-210, P1-329
Grimmitt, Adam B.	P4-341
Grinspan, Gustavo	P2-130
Grison, Agnese	OA1-03
Grither, Emily	P1-128
Grittner, Ulrike	P2-134
Grodzinsky, Alan	OA19-03
Groot Jebbink, E.	P4-071
Groot Jebbink, Erik	OA10-03, P4-067, P4-310, P4-312
Grosklos, Madeline	OA142-05
Gross, Felix	OA63-03
Gross, Lauren	OA60-04
Gross, Melissa	P1-182
Grossi, Benedetta	OA89-03, OA89-04
Grote, Kyle	P2-095
Group, mTBI	OA145-06, OA58-05
Groven, Rald	P3-260
Growney, Emily	OA89-02
Groß, Felix	OA122-01
Gruenhagen, Jennifer	OA29-05, OA3-02, OA42-05
Grunblatt, Samuel	OA48-05
Grunert, Lance	P2-037
Grunkemeyer, Anna	P3-076
Grupp, Thomas	P4-273
Gruppioni, Emanuele	P3-240
Grygoruk, Roman	P3-338
Gräter, Frauke	OA126-01
Grävare Silbernagel, Karin	P4-269
Grünewald, Tilman A.	OA71-02
Grüttner, Maximilian	OA107-04
Gsell, Willy	P4-317
Gu, Jingxian	OA93-04, P2-315
Gu, Minghuan	P2-160
Gu, Yu	P1-091, P2-343
Guadagni, Gualtiero	P4-288
Guadagnin, Eliane	OA14-01, OA76-04, OA98-06, P3-383
Guadagnin, Eliane C.	OA105-06, P1-255
Guerin, Luke	OA89-02, 1564
Guerra, Ana	P3-048
Gueugnon, Mathieu	OA172-04
Guibault, Francois	OA167-02
Guiotto, Annamaria	P2-155

Author name	Presentation Number
Gulbinowicz, Zbigniew	P4-075, P4-279
Guleria, Akanksha	P1-122
Gulsin, Gaurav	OA120-03
Gumulec, Jaromír	OA164-05
Gunatilaka, Chamindu	P4-017, P4-029
Guo, Jing	P3-153
Guo, Lingzhong	OA194-04, P3-189
Guo, Ming	OA164-04, OA199-04
Guo, Wenxing	OA60-05, OA99-01, P3-314
Gupta, Amiya	P2-025
Gupta, Himadri S	OA10-04, P4-297
Gupta, Vibha	P3-045
Gurappa, Sanskriti	P2-060
Gurchiek, Reed	OA106-06, OA94-04, P1-218, P2-135
Gurtner, Geoffrey	OA187-04
Gurung, Sristi	P3-187
Gustafson, Johnathan	P3-243
Gustafson, Jonathan	OA14-01, OA14-04, OA153-01, OA98-06, P1-061, P1-071, P3-012, P4-157
Gustafson, Jonathan A.	OA105-06, P1-255, P3-315, P3-380, P3-383, P4-167
Gustafsson, Anna	OA100-03, OA100-04
Gutierrez-Farewik, Elena	OA41-03
Gutiérrez de San Miguel, Marta	OA39-03
Gutruf, Phillip	OA187-04
Gwon, Jungeun	OA168-01
Gyemi, Danielle	P1-286
Gómez-Benito, María José	P1-404
Gül, Mustafa	P2-298
Günther, Denise	P1-012
Gąsecka, Aleksandra	P4-075
Ha, Dongho	OA136-05, OA93-05
Ha, Dongwon	P1-009
Haag, Emily	OA68-03
Haan, Dimitri	P1-289, P1-290
Haberfield, Melissa	OA117-05, OA147-04
Haboba Nebel, Carolina S.	P2-052, P3-225
Hachem, Elie	OA157-03
Hackett, Thomas	OA195-04, P3-318
Hackney, Madeleine	OA79-04, P4-210
Haddy, Chelsea	P2-300, P2-304
Hadwen, Alexander	OA2-02
Haenen, Maranda	OA135-02, OA21-05, P4-173, P4-174
Hafer, Jocelyn	OA160-03, P1-058, P1-144, P1-197, P1-202, P1-230, P2-059, P4-215
Hafer, Jocelyn F	OA159-01
Hagel, Brent	P3-126
Hager, Sandra	OA30-05, P4-116
Hahn, Daniel	OA13-02, P1-325
Hahn, Michael	OA107-04, P1-337, P2-225, P2-254, P3-229, P4-187
Hahn, Mike	P1-353
Haider, Malik Salman	P3-183
Haight, Ethan	P2-107
Haines, Victoria	P2-355
Haire, Cameron	P1-051
Hajizadeh, Maryam	P1-193, P4-168

Author name	Presentation Number
Hakansson, Nils	P2-177
Hakim, May	P3-021
Hakmi, Chems-eddine	P4-164, P4-165
Hakonen, Sanna	P3-336
Hakopian, Erik	P2-213
Haliburton, Charles	P4-288
Halilaj, Eni	OA141-01, OA141-05, OA174-01, OA61-04, P2-046
Halje, Pär	P1-258
Hall, Deborah J.	P3-225
Hall, Emily	P1-008
Hall, Mary	OA48-03
Hall, Michelle	OA73-02
Haller, Justin	OA86-06
Halliday, Iona	P3-139
Hallman, Jason	P3-085, P3-141
Hallman, Sarah	P2-089
Halloran, Jason	P2-163, P2-185, P3-212, P3-230, P3-231, P3-252, P3-263
Halmai, Barbara	OA193-02
Halsne, Elizabeth	OA66-04
Hamada, Masami	OA122-03
Hamada, Moustafa	OA45-03
Hamai, Satoshi	P3-053
Hambly, Matthew	OA22-03, P2-117
Hamilton, Heather	OA166-05
Hamma, Alexandre	P3-337
Hammer, Daniel	OA88-04
Hammer, Maria	OA49-02
Hammerberg, Alexandra	OA48-05
Hammond II, Paul	P4-227
Hamner, Sam	OA68-05, OA9-02, P3-099
Hamouda, Abdelrahman	P2-031
Han, Biao	P2-260
Han, Hyemin	OA136-05, OA93-05
Han, Jun Hyun	P1-299
Han, June-Chiew	OA156-03, P4-129
Han, Jung-Kyu	P4-126
Han, Lin	OA126-03, P2-260
Han, Soo-Ji	P1-163
Han, Tzu-Hsin	P3-382
HAN, Xinmiao	OA158-03
Han, Yingzhe	OA158-04, P3-167, P3-180, P3-195
Handsfield, Geoffrey	P4-314, P4-315, P4-325
Haneda, Kazuki	P2-348
Hanks, Matthew	OA161-03, P3-365, P4-323
Hannigan, J.J.	OA119-05, P3-092
Hannigan, Lindsay	P2-258
Hansen, Andrew	OA66-04
Hansen, Colby	P4-069
Hansen, Phillip	P3-201
Hansen, Ulrich	P1-038
Hansmann, Jan	P3-183
Hanson, Alison	P4-260
Hara, Reiko	P4-237, P4-260
Haralabidis, Nicos	OA73-01

Author name	Presentation Number
Harasek, Michael	P1-401
Hardwick, Trent	OA151-04, OA163-05, P3-269
Hardwig, Scotty	P4-238
Hareendranathan, Abhilash	OA197-02
Harel, Noam	OA111-03
Hargreaves, Brian	P3-254
Harlaar, Jaap	OA128-01, OA57-06, P2-097, P4-177, P4-289
Harlander, Alexandra	P2-253
Harman, Melinda	OA60-01
Harper, Matthew	P3-083, P3-147
Harpur, George	P4-047
Harrell, Braeden	OA65-03
Harrington, Joseph	OA15-04, P4-245
Harrington, Margaret	OA55-01, P2-073, P2-126
Harris, Amanda	P4-313
Harris, Andrew	OA198-04
Harris, Dean	P3-085
Harris, Jake	P3-381
Harris, Michael	OA105-02, OA105-04, OA105-05, OA18-04
Harris, Yovana	P2-213
Harrison, Kathryn	OA107-05, OA131-01, P1-336
Harrison, Kenneth	OA165-02, OA196-06, P4-151, P4-153, P4-250
Harrison, Kim	OA185-02, P4-298
Harrison, Lauren E	P4-143
Hart, Adam	OA195-05
Hart, David	P3-004
Hart, David A.	P2-238
Hart, Harvi	OA117-05
Hart, Joe	P4-325
Hart, Justin	P3-046
Hart, Matthew	P2-237
Harter, Michelle	OA118-06
Hartley, Peter	OA117-05
Hartmann, Markus A.	P4-349
Harward, Nathan	P3-360
Harwood, Paul	P3-351
Hasan, Kamrul	OA74-02
Hasan, Rakib	P4-105
Hasegawa, Yosuke	P1-397
Hashiguchi, Rinto	P2-231
Hashim, Mahmoud	OA74-05, P3-039
Hashimoto, Jason	OA107-03
Hashlamoun, Kotaybah	OA100-05, P2-250
Hashmi, Eisha	P1-010
Hasick, Sasha M.	CSB-02
Hasler, Carol	OA62-05
Hasler, Carol-Claudius	P2-191, P3-302
Hassan, Olamide	OA168-01
Hassani, Mohsen	OA100-05, P1-394
Hassar, Abdellah	P1-266
Hasson, Christopher	OA123-03, P1-112
Hastings, Sierra	P1-363
Hatamzadeh, Mehran	OA135-05
Hatoum, Hoda	OA120-03

Author name	Presentation Number
Hatsey, Saliem	OA140-03
Hattori, Kaoru	P4-086
Hatzigeorgiou, Tony	P3-140
Hauff, Nils	OA38-04
Hauguel, Alexandra	P4-010
Haulez, Pauline	P4-100
Haulon, Stephan	P4-014, P4-077
Haussen, Diogo	P4-096
Havashinezhadian, Sara	P1-266
Havens, Kathryn	P2-286, P4-232
Haverich, Axel	OA199-05
Hawke, Ashley	OA79-04
Hawkins, Ali	OA155-05
haxhiademi, Dorela	OA139-04
Hayase, Gen	OA11-02, P3-197
Hayashi, Hidetaka	P2-225
Hayashi, Manato	P4-331
Hayati, Hamideh	P4-017, P4-029
Hayenga, Heather	OA17-02, P4-098, P4-099
Hayes, Jack	OA46-05
Hayes, Thomas	OA152-03
Hayot, Chris	OA186-03
Hazelwood, Ben	OA107-02, P1-271, P1-306
He, Ge	OA58-02
He, Jianghua	OA79-02
He, Liang	P1-328
He, Xuehuan	OA158-04, P3-180, P3-195
He, Yufan	P1-247
He, Yuqi	P1-386
He, Zhengyi	P1-179
Headlee, Cindy	P4-187
Healey, Laura	OA107-04
Healy, Chadwick	OA28-05
Heard, Barbara	P1-128
Heebner, Nicholas	OA15-03, OA190-03, P4-140
Heffernan, Kelsie	OA80-03
Heiderscheit, Bryan	OA200-04, P2-114, P3-317, P3-322
Heigold, Hannah	OA148-02, P1-057
Heijmen, Robin	OA95-02
Heilmann, Nina	P2-236
Heindel, Matthew	OA14-05, OA37-03
Heinis, Frazer	OA102-03
Heino, Dylan	OA72-04, P4-309
Heinrich, Dieter	OA45-02
Heinrich, Simon	P4-220
Heise, Gary	P1-054
Heiser, Torri	P2-262
Heitman, Kristen	P1-082
Hejrati, Babak	OA93-01
Helga Jónsdóttir, Kristín	OA46-02
Helgason, Benedikt	P2-197
Helgers, Verena	OA47-02
Hellem, Aaron	OA29-03, P4-145
Heller, Ben	P1-108

Author name	Presentation Number
Heller, Dave	P1-128
Hellman, Ellen	OA166-04
Hellmich, Christian	OA97-02
Helm, Isabella	OA196-06, P4-151
Helou, Anthony	P2-253
Helseth, Joseph	P1-260, P1-293, P1-313, P1-340
Helsper, Shannon	P4-317
Helwig, Janina	OA118-01, OA3-03, P1-047
Henak, Corinne	P2-214, P2-229, P4-272
Hendershot, Brad	OA1-02, OA46-01, P2-320
Henderson, Adrienne	P1-097, P1-217, P1-225
Henderson, Isla	P4-318
Henderson, Mary	P4-354
Heng, Elbert E.	OA139-05
Henley, Ethan	OA19-04
Hennen, Elizabeth	OA180-01
Hennige, Sebastian	P4-332
Henninger, Heath	OA161-03
Henninger, Heath B.	OA70-05, P3-369
Henriksson, Sara	OA38-04
Henriques, Matthew	P4-167
Henry, Aaron	P2-022, P2-101
Hensley, Spencer	OA111-02
Hentnik, Haley	OA106-06
Hepke, Nikolai	P1-174
Heras Rivera, Juampablo	OA74-03
Herbert, Anthony	P2-355
Herbst, Eva	OA24-01
Herbst, Eva C.	OA70-05
Herda, Ashley	P1-091
Herlah, Lara	P2-370
Herling, Lotta	OA45-04
Herrera, Emilio A.	OA146-02
Herrera, Nicolas	P1-317, P1-318
Herrin, Kinsey	P1-079
Herron, Sakura	P1-223
Herschel, Jan	P4-319
Herssens, Nolan	OA154-01, OA154-04
Hertel, Jay	OA166-06
Herve, Ophelie M.	OA38-02
Herzog, Walter	OA137-01, OA137-03, OA149-04, OA27-06, OA43-03, OA65-05, OA98-03, P1-350, P2-104, P2-187, P2-196, P2-226, P2-238, P2-243, P2-250, P2-256, P2-257, P2-262, P3-004
Hess, Garrett	P1-260, P1-293, P1-313, P1-322, P1-340
Hesse, Saskia	OA151-03, P3-260, P3-347
Hesselson, Stephanie	OA144-03
Hestermann, E.	P4-071
Hestermann, Elke	P4-310
Hevesi, Mario	P3-248
Heydari, Zahra	P2-202, P3-311
Heyl, Jennifer	P3-153
Heyland, Mark	P3-027
Heynen, Rahel	OA3-01
Heyraud, Agathe	P2-345
Hickey, James	OA6-05

Author name	Presentation Number
Hickey, William	P4-114
Hicks, Jennifer	OA57-03, OA68-05, OA9-02, P1-256, P3-099
Hicks, Jennifer L.	OA48-03
Hicks, W. Brody	OA119-01, OA3-04, OA81-03
Hidson, Georgia	P2-129
Higaki, Hidehiko	P3-053, P4-150
Higano, Nara	P4-017
Higgins, Claire	OA46-05
Higgins, Ghodeejah	OA88-05
Higgins, Hannah	P4-171
Higginson, Jill	OA59-03, P1-213
Higginson, Jill S.	OA53-02
Highsmith, M. Jason	P2-329
Hill, Cherice	P1-003, P1-101, P1-223
Hillenkamp, Jost	P3-183
Hillman, Charles	OA123-03, P1-112
Hills, Richard	P3-310
Hillstrom, Howard	OA86-01, P1-364
Hillstrom, Rajshree	OA86-01
Hiltunen, Rasmus K.	OA149-04
Hilty, Matthias P	P3-044
Himeno, Ryutaro	OA54-03
Himmelreich, Uwe	P4-317
Hinke, Christian Rüdiger	P4-002
Hinkel-Lipsker, Jacob	OA123-02, P2-332
Hinkel-Lipsker, Jacob W	P2-336
Hinkle, Patrick	OA163-05, P3-269
Hinman, AJ	OA193-03
HINO, YASUMICHI	OA32-01, P3-094
Hirai, Yasuyuki	P4-045
Hirao, Makoto	P3-275
Hirczy, Siegfried	P4-148, P4-149
Hirono, Yasuko	P1-246, P1-383
HIROSAWA, Seiji	OA94-05
Hirose, Norikazu	P4-265
Hirose, Satomi	P1-026
Hirota, Sanae	P1-392
Hirsch, Zahava	OA130-04, OA20-02, P1-053, P1-096, P1-138
Hirschberg, Edoardo	P3-240
Hirschman, Caelyn	OA20-03
Hirt, Julien	P4-139
Hirtler, Lena	P3-179, P3-221, P3-244
Hisano, Genki	OA172-05
Ho, Cheuk Yin	P1-244
Ho, Cheukyin	P1-382
Ho, Tyler	OA66-04
Hobara, Hiroaki	OA124-03, P1-178, P1-185
Hobo, Ayaka	P1-088
Hobusch, Gerhard	P3-221, P3-343
Hoch, Johanna	P4-140
Hoch, Matthew	P4-140
Hockerman, Lucia	OA200-04
Hocquet, Stéphane	P2-371
Hodgson, Antony	OA153-02

Author name	Presentation Number
Hoermann, Romed	P3-375
Hoerstrup, Simon P.	OA4-02
Hofecker, Sarah	P1-224
Hoffman, Mia	OA111-02, OA123-04
Hofsädter, Jochen	OA44-03
Hogan, Neville	P1-075
Hogan, Ryan V.	OA162-06
Hogrel, Jean-Yves	P4-240, P4-241
Hokari, Kazuki	P1-063
Holbach, Jamina	P1-393
Holcomb, Brady	P1-361
Holcomb, Ty D.	OA128-05
Holden, Lily	P3-268
Holden, Rachel M.	OA113-02
Holdsworth, Samantha	OA145-06, OA169-05, OA58-05
Holland, Galen	OA118-06
Holland, Maria	OA97-01
Holland, William	P1-280
Hollinger, David	P1-111
Hollis, Leila	P4-187
Holmes, Jack	P2-063
Holmes, Madison	P2-279, P2-282
Holmes, Michael	OA150-01, OA150-02, P1-068, P2-195, P2-267
Holmes, Skylar	OA73-04, P2-224
Holsgrove, Tim	OA135-03
Holsgrove, Timothy P	OA193-02
Holt, Cathy	OA135-03, OA57-05, P2-070, P2-120
Holtgrewe, John	P4-321
Holzapfel, Gerhard	P4-033
Hommel, Hagen	P3-253
Hon, Siyuan	P4-351
Hondzinski, Jan	OA92-04
Honert, Eric	OA107-05, OA131-01
Honert, Eric C.	P1-336
Hong, Christopher	P2-234
Hong, Eun Ji	OA85-02
Hong, Jiwon	P1-015
Hong, Juntaek	P2-313
Hong, Namki	P2-197
Hong, Seongwoong	OA136-03, OA176-01
Honkanen, Juuso T.J.	OA149-04
Hood, Lyle	ES11-01
Hood, R. Lyle	P3-181, P4-105, P4-276
Hoogkamer, Wouter	OA118-02, OA178-04, P1-210, P1-329, P2-081, P3-015, P4-341
Hooijmans, Melissa	OA168-03
Hooke, Alexander	P2-031, P3-248, P3-278
Hooker, Suhail	P4-221
Hooyman, Andrew	P1-141
Hopfner, Keiji	P2-257
Hopkins, Jonathan	P3-270
Hopkins, Quinn	P1-322
Hori, Yusuke	P3-285
Horie, Shahd	OA115-03
Horiguchi, Satoshi	OA98-05

Author name	Presentation Number
Horiuchi, Gen	OA94-02
Horiuchi, Kenta	OA98-05
Horn, Riley	P1-219
Horsak, Brian	OA54-02, P1-172, P1-237, P2-068
Hoshina, Katsuyuki	OA102-04, P4-252
Hoshizaki, Thomas	P3-088
Hoshizaki, Thomas Blaine	P3-069, P3-088
Hosokawa, Isamu	P4-044
Hosseini Nasab, Seyyed H.	P3-235
Hosseini Nasab, Seyyed Hamed	P3-274
Hosseini, Amirreza	P2-339
Hosseini, Seyedeh Fahimeh	P2-376
Hosseinitabatabaei, Seyedmahdi	OA5-05, OA74-01, P2-246
Hostler, Andrew	OA187-04
Houde, Hannah	OA150-04, OA29-05, OA3-02, OA42-05, OA76-03
Hoursan, Hesam	P4-070
Houston, Denise	P2-236
Howard, Jason	OA27-06
Howard, Sean	P1-020, P2-264
Howell, David	OA27-04
Howes, Nolan	OA92-02
Howley, Enda	OA152-05, OA176-03
Hoxao, Amadeo	P2-192
Hsiao, Hao-Yuan	OA53-03, P4-179
Hsiao-Wecksler, Elizabeth	OA124-01
Hsieh, Han-Chieh	OA86-03
Hsieh, Katherine	OA40-01
Hsieh, Ming-Kai	P3-308
Hsieh, Naomi	OA176-02
Hsieh, Zong-Han	OA16-02
Hsu, Chieh-Hsiang	P3-372
Hsu, Edward	OA17-04
Hsu, Fang-Chi	OA121-02, P2-236
Hsuen, Phoenix	OA113-02
Hu, Chia-Han	OA106-05, P3-214
Hu, David	OA103-04
Hu, Guopeng	P1-386
Hu, Jin-Jia	OA127-04, P3-170
Hu, Jingwen	OA121-04, OA121-05, OA193-01, P1-169, P3-024
Hu, Shengming	P2-363
Hu, Xiaomei	P1-382
Hu, Ying	P4-127
Hua, Xijin	OA15-02, OA182-04, OA33-05
Huang, Chun-Kai	OA196-05, OA79-02
Huang, Haoxin	OA26-02
Huang, Helene	P1-377
Huang, Hung-Chun	P3-097
Huang, Huocong	OA63-01
Huang, Po-Teng	P1-310
Huang, Qi	P3-130
Huang, Ruoyu	P4-344
Huang, Tony B.	OA64-03
Huang, Yen-Hsiang	P2-374
Huang, Yuxuan	OA126-04

Author name	Presentation Number
Huard, Johnny	OA195-04, P3-318
Huber, Colin	OA133-01
Huber, Gerd	OA99-05, P3-246, P4-172
Huber, Jay	OA120-04
Huber, Meghan	P1-329
Huberts, Wouter	P4-100
Hubertus, Jochen	P2-210
Hudecek, Laetitia	P2-219
Hudgins, Jake	P1-347
Hudson, David	P1-287
Hufft-Martinez, Brittany M.	P1-023
Hugard, Shannon	P1-337, P2-254
Hugenschmidt, Christina	OA40-01
Huggins, Brady	OA151-04, OA81-06, P3-269
Hughes, Celia	OA89-02
Hughes, Paige	OA46-06
Hughes, Yale	P1-245, P4-131
Huk, Olga	OA195-05
Hulshof, Chantal	OA79-05, P4-202
Humbert, Andrew	P2-329
Humbert, Ludovic	OA122-03, OA122-06, OA35-02
Humenay, Justin	P1-277
Hummelink, Stefan	OA135-02, OA21-05, P4-173, P4-174
Hummer, Erik	P1-351, P1-352
Humphrey, Jay	OA139-05, OA179-03, OA64-01, OA71-05, OA84-03, P4-038, P4-057, P4-076, P4-078, P4-109
Humphrey, Jay D.	P1-027, P4-032
Hundsdorfer, Lara	OA173-05
Hung, Clark	P2-251, P3-346
Hung, Clark T.	P2-362
Hunt, Grace	OA162-05, OA66-01
Hunt, Jacqueline	P2-332
Hunt, Michael	OA147-05, P2-327
Hunt, Michael A.	OA117-03, P4-218
Hunt, Nicholas	P4-262
Hunter, Dana J	OA72-05
Hunter, Iain	P1-157, P3-037
Huo, Dongfei	OA182-04
Hurtado, Daniel	OA156-01, OA191-01
Husband, Sean	OA131-03
HUSE, MORGAN	OA88-01
Hussein,, Tawfik	OA191-04
Hussey, Alice	P3-215
Hutchens, Shelby	P3-149
Hutchinson, Sophie	OA36-05
Hutchison, Keith	OA189-05, P1-356
Huthwelker, Janine	P1-240
Hutzelmann, Denali	OA161-03, P2-215, P2-216, P4-323
Hwang, Priscilla	OA101-02, OA101-05, OA51-05
Hyakutake, Toru	P1-396
Hyde-Linaker, George	P4-051
Hynes, Niamh	P4-320
Hynes, Sarah	P3-056
Hysinger, Erik	P4-017

Author name	Presentation Number
Häfner, Constantin Leon	P4-002
Héroux, Martin	P4-194, P4-207
Hölzl, Sebastian	P3-027
Hörmann, Sabrina	P2-097, P2-181
Hörwing, Hanna	P4-275
Højbjerg Gravholt, Claus	P4-087
Iacocca, Anna	OA62-01
Iaizzo, Paul A.	P3-181
Ianniruberto, Ione	OA179-05, OA191-05, P4-052
Iaquinta, Sarah	P3-156
Ibarra, Sergio	P1-309
Ibinson, Jonathan	OA156-04
Ibrahim, Celina	OA99-05
Ignasiak, Dominika	OA18-02
Ihara, Emily S	P4-259
Ii, Satoshi	OA39-02
Iljima, Lucas	OA74-02
Iijima, Yoshiki	P4-044
Iijima, Yuta	P3-197
Iizuka, Minori	OA42-02
Ikebe, Satoru	P3-053, P4-150
Iki, Masayuki	OA122-03
Ilham, Tahia	P3-125
Ilianu, Richard	P2-203
Im, Nathaniel	OA148-05
Imai, Nami	OA122-03
Imai, Yohsuke	OA110-03
Imamura, Rodney	OA16-01, P1-346
Imhauser, Carl	OA141-03, OA183-02, OA188-04, OA8-03, P2-042, P2-163, P3-212, P3-230, P3-231, P3-252, P3-263
Imhauser, Carl W.	P3-237
Imran, Syed Ali	P1-198, P1-199
Inaba, Manabu	OA153-05
Inagaki, Takashi	P1-019
Inai, Takuma	OA136-04, P1-233
Incatasciato, Federica	OA62-03, P3-289
Infante, Eric	P1-373
Innocenti, Bernardo	OA47-01, P3-207, P4-231
innocenti, bernardo	P3-208
Ino, Taiki	OA87-05
Inoue, Hayato	P3-166
Inoue, Jumpei	P3-261, P3-262, P3-323
Inoue, Takahiro	P3-053
Inui, Mariko	P3-030
Ioannou, Eleftherios	P3-191
Iordanov López, Daniel	OA42-04
Iozzo, Renato	P2-260
Ippersiel, Patrick	OA99-04, P1-181
Iqbal, Muhammad Fasih	P4-122, P4-123
Irie, Yamato	P2-060
Irish, Thomas	P2-194, P3-349
Irish, Tom	P3-351
Irrgang, James	OA141-01, P3-371
Irrgang, James J.	OA141-05

Author name	Presentation Number
Irvine, Julia	OA117-04
Isabelle, Pier-Luc	P3-245
Isaksson, Hanna	OA100-02, OA100-03, OA100-04, OA105-03, OA113-04, OA151-01, OA175-04, P2-197, P3-335
Isazadeh, Amir	P4-141
Isella, Benedetta	P4-011
Ishida, Shunichi	OA110-03
Ishida, Yudai	OA114-03
Ishida, Yusuke	OA134-03
Ishihara, Honoka	P4-229
Ishii, Daichi	P3-166
Ishikawa, Takuji	OA26-03, OA78-03
Isobe, Yuga	OA114-03
Isu, Giuseppe	P4-037
ITO, Akitoshi	P2-003
Ito, Keita	OA62-03, P2-360, P3-279, P3-289, P3-300
Ito, Kohta	P2-255
Ito, Naoaki	OA200-04, P3-317
Itou, Junya	P3-239
Ivanets, Margaryta	P2-371
Ivanochko, Natasha I.	P4-198
Ivanochko, Natasha K.	OA117-02, P4-169, P4-217
Iven, Carl	P3-146
Iverson, Jana	OA2-04
Iverson, Juliana	OA59-05, P4-292
Iwasaki, Kiyotaka	OA89-01, P4-086
Iyer, Gayatheri Mahesh Hema	P3-092
Iyer, Shridhar	P2-040
Izhiman, Yara	P1-265, P2-107
Iznat, Nurkeldi	P2-171, P3-178
İk, Tsì-Uí	P3-097
J. Costa, Mário	P4-263
J. Cyron, Christian	OA63-01
J. Grodzinsky, Alan	OA45-03
J. Hussain, Rashad	P1-308
J. Hyeamang, Lord	OA153-01
J. Ratke, Emma	P1-308
J. Thurner, Philipp	OA97-03
Jaafar, Lina	P1-189
Jabr, Mariam	P2-177
Jacchetti, Emanuela	OA11-03, OA153-03, OA187-01, OA197-03, OA199-03, OA77-03, OA90-05, P1-013
Jackson, Davis	P4-170
Jackson, Garrett	OA188-03
Jackson, Kaitlin	OA68-06
Jacob, Joseph	P4-112
Jacobs, Mariana V.	P2-074
Jadrna, Lucie	OA164-05
Jafarinia, Hamidreza	P2-017
Jaffray, Alex	P4-306
Jaffray, Alexander	CSB-05, OA169-06
Jahangir, Sana	P3-335
Jahanian, Omid	OA150-04, OA76-03
Jain, Divya	P3-059
Jakka, Veera Venkata Satya Varaprasad	OA122-06, P4-060

Author name	Presentation Number
Jakubowski, Kristen	OA148-03, P1-046
Jalali, Fatemeh	OA109-02
Jalalian, Athena	P3-280, P4-301
Jamali, Pegah	OA124-04
James, Fiona	P2-204
James, Ireen	OA46-05
James, Joanna	P3-184
Jamieson, Colin	OA120-03
Jamros, Finn	P1-133
Janczak, Daniel	P4-279
Janes, Hayley	OA186-04, P2-053
Jang, Beomsu	OA155-06
Jankowski, Krzysztof	P3-338
Janssen, Dennis	OA47-02, OA47-04, OA9-03, P2-222
Janssen, Famke	P2-222
Janssen, Renate	OA100-02, OA182-03
Janzen, Nicole	OA193-04
Jar, Chester	OA182-02
Jaremko, Jacob	OA197-02
Jarrige, Raphaëlle	OA116-03
Jarry, Charles-Edouard	OA143-06
Jasimi Zindashti, Niromand	P2-165
Javadi, Akbar	OA135-03
Javadpour, Sina	OA89-05
javaheri, negin	P4-220
Jaworski, David	OA173-05
Jayaneththi, Nisal	OA83-06, P2-244
Jayaraman, Arun	PL11-01
Jayatissa, Sahan	P3-184
Jedrychowski, Victoria	P4-196
Jehpsson, Lars	OA105-03
Jeka, John	OA160-03
Jeken Rico, Pablo	OA157-03
Jelsma, Natasja	P4-202
Jemas, Kathryn	OA2-04
Jendro, Ashlyn	OA140-01, P1-245
Jendro, Ashlyn M.	P4-147
Jenkins, Andy	P1-335
Jenkyn, Thomas	P1-250
Jennings, Louise	P2-100
Jennings, Louise M	OA163-03, P3-209, P3-210
Jensen, Cameron	P1-274, P1-275
Jensen, Michael	OA16-03
Jeon, Eun Seong	OA28-03
Jeon, Hyung Gyu	OA85-02
Jeong, Dongwon	OA72-06
Jeong, Seokhwan	OA28-03
Jeong, Woowon	P3-266
Jeong, Yun-Bae	OA107-06, P1-163, P1-385
Jepson, Nigel	P4-110
Jessup, Luke	P1-192, P2-095
Jesus, Luciana Angélica	P1-191
Jezequel, Jennifer	OA98-04
Jha, Dheeraj	P2-197

Author name	Presentation Number
Jha, Swaneet	P3-237
Jhaveri, Sanam	OA79-01
Ji, Chenyang	OA114-02, P1-034
Ji, Songbai	CSB-05, OA133-03, OA169-06, P3-137, P4-306
Jilberto, Javiera	OA30-02
Jimenez-Juan, Laura	P4-091
Jin, Huijing	OA101-03
Jin, Jiaqi	P3-114
Jin, Kazuyoshi	OA127-03
Jinha, Azim	OA65-05
Jinji, Tsutomu	P1-372
JMAL, Hamdi	P2-162
Joachim, Mikel	OA177-04
Job, Joby	P4-105
Jobeili, Lara	P2-349
Jochimsen, Kate	OA99-02, P4-138
Johansson, Helena	OA105-03
Johansson, Martin	P2-298
John, Mohan	P4-124
Johnson, Alexa	OA141-04
Johnson, Amelia	P4-140
Johnson, Benjamin	P2-355
Johnson, Caleb	P2-034, P3-075
Johnson, Camille	P3-211
Johnson, Curtis	OA32-03, OA32-04
Johnson, Darren	OA72-02, P3-211
Johnson, Holly	OA86-01
Johnson, Janie	OA77-02
Johnson, Russell	P4-244
Johnson, Sarah	P1-256
Johnson, Wesley	P4-196
Johnson-Lynn, Sarah	P3-351
Johnston, Benjamin	P3-330
Johnston, James (J.D.)	P2-137
Johnston, Peta	P1-344
Johnston, Robert	OA49-04
Jolley, Matthew	P1-008
Jomha, Nadr	OA182-02, P3-331
Jones, Alison	P3-188
Jones, Ben	OA6-03, P1-108, P3-100
Jones, Carly	P2-224
Jones, Chris	OA145-01
Jones, Claire	OA145-04, P3-079, P3-082, P3-127
Jones, Claire F.	OA171-04
Jones, Deborah	OA188-04
Jones, Derek	P2-047
Jones, Douglas	P1-262
Jones, Julian R	P2-345
Jones, Margaret	P1-341, P1-342
Jones, Margaret T.	OA173-02, OA59-01
Jones, Michael	OA55-04, P1-354
Jones, Patrick	P4-096
Jones, Ryan	P2-015
Jones, Stephanie	P1-282, P1-314

Author name	Presentation Number
Jongbloed, Koen	P1-184
Jonkers, Ilse	OA149-01, OA149-02, OA34-01, P2-062, P3-017, P4-317, PL08-01
Jordan, David	OA24-02, OA87-02, P4-354
Jordan, Jacob	OA62-01
Jordan, Lee	P3-206
Jordan, Lydia	P3-339
Jordan, Matthew	OA129-02, OA13-04, OA98-03, P2-104
Jordan, Matthew J	OA72-05
Jordan, Matthew J.	P1-348
Joseph, Timothy	P4-083
Joshi, Srujana	P4-009
Joshi, Varun	OA118-01
Joulain, Elise	P3-221
Joulin, Etienne	OA183-04, OA183-05
Joumaa, Venus	OA27-06, P2-226, P2-262
Jourdan, Franck	P4-282
João, Filipa	OA70-04
Ju, Yan-Ying	P1-155
Julien, Marie	P4-077
Julkunen, Petro	OA109-02
Juner Lanferdini, Fabio	P4-175
Jung, Bernd	OA62-02
Jung, Jinsung	OA54-04, P1-170
Jung, Keun-Hwa	OA69-04, P4-117
Jung, Kwan-Jin	OA161-03
Jung, Naomi	OA194-02
Jung, Sang Woo	P4-294
Jung, SeHee	P2-338
Jung, Tobias	P4-222
Junker, Anthony	P1-039
Junker, Philipp	OA199-05
Jurestovsky, Derek	P2-010
Jurestovsky, Derek J.	P2-248
Justen, Gabriella	OA151-05
Juttla, Yuvraj	P4-104
Jíra, Aleš	P2-351
Jönsson, Viktor	OA100-03
K, Ragavendra	P3-364
K. Korhonen, Rami	OA45-03, P3-335
Kacmarcik, Claudia	P3-216
Kaczmarczyk, Łukasz	OA122-06
Kadlub, Natacha	P3-337
kadlub, Natacha	OA5-02
Kadotani, Ayaka	OA11-02
Kagamimori, Sadanobu	OA122-03
Kageyama, Atsuki	OA94-02
Kahlenberg, Cynthia A.	P3-237
Kaholokula, J. Keawe'aimoku	P1-073
Kainz, Hans	OA147-02, OA171-02, OA171-03, OA34-05, OA44-03, P1-270, P2-068, P2-069, P2-094, P2-156, P3-200
Kairamkonda, Dheeraj	OA92-03
Kaiser, Alexander	OA120-02
Kaiser, Alexander D.	OA120-04
Kaiser, Jarred M.	OA159-03

Author name	Presentation Number
Kaiser, Mirko	OA173-04
Kait, Jason	P3-076, P3-086
Kaito, Takashi	OA11-04
Kaizu, Riona	OA98-05
Kajita, Etsuko	OA122-03
Kajiura, Hiroki	P3-194
Kalaitzi Manifrenti, Marilena	OA93-02, OA93-03, P1-196
Kalmar-Gonzalo, Alex	OA121-02, P3-068
Kamada, Masayuki	P4-252
Kamatani, Yoichiro	OA127-03
Kamenskiy, Alexey	OA102-03, P4-033
Kameo, Yoshitaka	P3-276
Kamfwa, Nkumbu	P1-081
Kaminski, Thomas	P3-077
Kamiya, Kuniyasu	OA122-03
Kamiya, Tomoe	OA114-03
Kamm, Roger	OA164-04, OA199-04
Kamm, Roger D.	OA51-02
Kampik, Daniel	P3-183
Kan, Tianyou	P1-031
Kanai, Alicia	P2-103
Kane, Meira	P1-059
Kaneda, Janelle	OA9-02
Kang, Annabelle Sung Min	OA19-05, 3359
Kang, Inseung	OA67-03, P3-010
Kang, Jae-Won	OA107-06, P1-163, P1-385
Kang, Ji-sang	P2-311
Kang, Sukheon	P4-026
Kangas, Joseph R.	P3-181
Kanikawa, Shu	OA91-04
Kanjuh, Mario	OA3-03
Kankkunen, Janne J.	P3-049
Kanuka, Charlie	P2-054
Kao, Sheng-Jie	P3-097
Kapoor, Ankush	P4-110
Kapoor, Neha	P1-323, P1-338
Kaptis, Logan	P3-198, P4-130
Kara, Alara	P3-336
Karacic, Sabina	P2-350
Karadaş, Özge	P3-336
Karali, Aikaterina	P2-345
Karali, Katerina	OA149-03
Karamifard, Fatemeh	P2-346
Karamzadeh, Mahsa	P4-171
Karavas, Blake	P1-112
Karduna, Andy	OA140-03, P3-003
Kargarbahrkhazar, Bahman	P4-115
Karimi, Alireza	OA186-01
Karimi, Pedram	OA130-02
Kark, Lauren	OA66-03, P4-194
Karki, Bishan	OA63-01
Karki, Bishant	OA75-03
Karlsson, Magnus K	OA105-03
Karniadakis, George	P4-038

Author name	Presentation Number
Karnik, Shweta	OA102-05, P4-007
Karton, Clara	P3-069
Karumbunathan, Kanthi	P2-143
Karunaratne, Angelo	P3-071
Karydis, Konstantinos	OA116-02, P2-280, P2-326
Kasai, Mari	P2-252
Kashir, Imad	OA128-03
Kashiwagi, Yu	P1-384
Kashyap, Vikram	OA167-05, OA179-04
Kassab, Ghassan	OA30-05, P4-116
Katagiri, Mone	P4-086
Katamine, Kanju	P1-036
Katthagen, J. Christoph	OA21-03
Katugam-Dechene, Kavya	OA184-05, P4-188
Katz, Eden	P3-160
Kaufman, Kenton	OA59-02, OA76-02, P2-031
Kautman, Owen	P1-238
Kawabata, Yuto	OA110-03
Kawaguchi, Takahisa	OA127-03
Kawahara, Akito	OA12-04
Kawahara, Shinya	P4-293
KAWAI, Kosei	P1-043
Kawai, Kosei	P1-040
Kawasaki, Akihiro	P1-399
Kawashima, Keita	P3-135
Kay, Robert	P4-237
Kaye, David	P4-083
Kazakia, Galateia	OA5-05
Kazuno, Hiroki	P3-276
Kearns, Zoey	OA142-01
Keckes, Jozef	OA71-02
Kedgley, Angela	OA29-02, OA37-04, OA83-01, P2-109, P2-294, P3-362, P3-363, P3-373, P4-213
Kedgley, Angela E.	OA52-04
Keene, David J.	P2-334
Keereman, Vincent	P4-062, P4-064
Keilig, Ludger	P2-293, P4-204
Keir, Peter	OA150-06, P2-245
Keir, Peter J.	OA162-06, P2-283, P2-284
Kellaher, Grace	OA53-04, P1-144, P1-202, P4-215
Keller, Brian	P2-114
Kelley, Claire	P3-171
Kelly Jr, Troy	OA1-04
Kelly, Emily	OA135-03
Kelly, John	P3-248
Kelly, Luke	OA147-03
Kelly, Valerie	P4-148, P4-149
Kelm, Jens	P3-314
Kelp, Nicole	OA143-05
Kelp, Nicole Yvette	P2-168
Kemp, Charles	P4-210
Ken, Evans	OA33-05
Kendall, Jack J.	OA185-04, P1-012
Kenneally, Mark	P1-281

Author name	Presentation Number
Kennedy, Colin	P2-142
Kennedy, Deanna	OA92-04
Kenny, Olivia	P2-014, P3-344
Kenny, Rebecca	CSB-05, OA169-06, OA6-04, P4-306
Kent, Jane	OA130-01, P1-249
Kent, Jane A.	P1-177
Kent, Jenny	P2-314
Kerckhofs, Greet	OA10-01, OA84-05
Kerfi, Raneda	P3-006
Keri, Inyani	OA169-03
Kermel, Christine	P2-371
Kernozek, Thomas	P1-368
Kerr, Carolyn	P3-163
Kerr, Graham	P2-030
Kerr, John	OA66-03, P4-194
Kerr, Katherine	P3-029
Kerrigan, Alicia	OA13-03
Kerrigan, Jason R.	OA119-01
Kersh, Mariana	OA125-01
Keränen, Siiri	P3-336
Kesar, Trisha M.	OA20-05
Kesari, Haneesh	P1-009, P3-065, P3-103
Keulen, Kelly	OA56-04
Khadivi, Sorour	OA185-04
Khair, Raad	P2-227
Khan, Aasima	P4-041
Khan, Adil	OA75-03
Khan, Asim	OA14-01
Khan, M. Owais	P4-118
Khan, Michaela	OA147-05, P2-327
Khan, Michaela C.M.	OA117-03
Khandare, Sujata	OA121-04, OA193-01
Khare, Tanmay M.	P4-124
Khatib, Nidal S	OA113-04
Khattignavong, Emilie	P2-018
Kheram, Najmeh	P3-127
Kheshti, Mohammadreza (Hooman)	OA161-05
Khiyara, Ines	OA93-01
Khoo, John	OA120-03
Khorshidparast, Setareh	P2-253
Khosrojerdi, Abed	P2-291
Khoury, Anthony	OA200-03
Khurelbaatar, Tsolmonbaatar	OA122-05, P2-241, P4-335
Kiaulehn, Viktoria	OA151-03, P3-260
Kiernan, Damien	P1-169, P3-024
Kikkert, I.D.	P4-071
Kikuchi, Keisuke	P1-392
Kikuchi, Kenji	OA26-01, OA26-03, P1-392
Kikuchi, Yuta	OA146-01
Kilic, Ecem	P3-360
Killen, Bryce	OA149-02, P2-062
Killen, Bryce A	P3-017
Kilpatrick, Bethany	OA107-05, OA131-01, P1-336
Kilzi, John	P1-322

Author name	Presentation Number
Kim, Chae Lynne	P4-290
Kim, Chaesu	OA20-01, OA72-01
Kim, Changki	P1-379
Kim, Donggeon	OA172-02, OA172-03, P3-138, P4-195
Kim, Doosang	P4-026
Kim, Doyeon	OA176-01
KIM, HAEYOUNG	OA32-01, P3-094
Kim, Haneol	P1-153
Kim, Hanjun	P1-079
Kim, Hoon	OA117-06, OA136-05, OA93-05, P3-226
Kim, Houn	P1-100
Kim, Hyeong-Sik	OA107-06
Kim, Hyun	P3-316
Kim, Hyun Jin	OA69-04, P4-026, P4-117, P4-126
Kim, Hyun K	P3-123
Kim, Hyunji	P1-164, P4-290
Kim, Hyunsoo	OA85-02
KIM, Jeonghyun	P1-043
Kim, Jeonghyun	P1-019, P1-040
Kim, Jin Ho	P3-266
Kim, Jinyoung	OA109-04
Kim, John	P2-060
Kim, Jongsu	P1-171
KIM, Jongwook	OA138-03
Kim, Joo H.	OA136-03
Kim, Julie	OA113-03
Kim, Julius	P2-042
Kim, Kang	P2-347
Kim, Kyungeon	OA85-02, P2-065
Kim, Min Jun	OA26-02
Kim, Minju	P1-357
Kim, Namkeun	OA28-03, P3-385, P4-248
Kim, Nancy	OA34-02, P2-163, P2-185, P3-212, P3-230, P3-231, P3-252, P3-263
Kim, Pankwon	OA28-03, P4-294
Kim, Sang Yup	OA28-03
Kim, Se Hyeog	P4-126
Kim, Seo Yeon	P4-117
Kim, Seok-Hyun	P1-359
Kim, Seoyoung	OA35-03
Kim, Seung Kyeom	OA130-05, OA93-02, P1-196
Kim, Seunggyu	OA164-04, OA199-04
Kim, Soo Hyeon	P1-397
Kim, Subin	OA150-03, P1-232
Kim, Taehyun	P4-248
Kim, Taehyung	P2-066, P2-093
Kim, Won	P2-316
Kim, Yoonhwan	P2-313
Kim, Young Kwan	OA180-05
Kim, Yundong	OA28-03
Kimiavi, Tara	OA33-01
Kimmel, Shameka	P2-188
Kimura, Ken	P4-252
Kindermann, Marius	OA8-04
Kindl, Zak	P2-254

Author name	Presentation Number
King, Deborah	P3-320
King, Erica	P1-341, P1-342
King, Erica L.	OA173-02, OA59-01
King, Mark	OA29-01
Kingma, Paul	P4-017
Kingsbury, Trevor	P1-373
Kingston, David	OA15-04, P1-129, P1-274, P4-245
Kiriyama, Yoshimori	P2-075, P2-364, P3-096, P4-351
Kirkpatrick, Edward	P4-103
Kirkpatrick, Tessa	P4-187
Kirkup, Alexandra Q	P2-230
Kirkup, Alexandra Q.	P2-206, P2-208
Kirollos, Miray	P4-213
Kirschke, Jan	OA44-05
Kirschke, Jan S.	OA49-03
Kirsten, Kirsten	P2-050
Kissane, Roger	P2-008, P2-173
Kistler, Manuel	P3-244
Kitagawa, Jun	OA122-03
Kitahara, Moko	OA98-05
Kitchin, Matthew	OA6-03
Kitir, Kevin	OA171-02, OA171-03, OA34-05, P2-069, P2-094, P3-200
Kitslaar, Pieter	P4-018
Kizawa, Fumiya	P3-277
Klahsen, Olena	OA168-04, P2-172, P3-288
Klassen, Stephen	P4-030
Kleeman, Kaitlyn	OA189-02, P4-183
Klein, Karina	OA188-01
Kleiven, Svein	OA133-04, OA145-03, P3-074, P3-106, P3-130
Klemm, Elizabeth	OA55-04, P1-354
Kleweno, Conor	OA86-06
Kleyer, Arnd	P4-220
Klimek, Matthias	P2-180
Klimstra, Marc	P1-261, P1-343, P3-001
Kline, Joshua	P1-377
Kline, Paul	OA66-06, OA80-04
Klinge, Petra	P4-171
Kloock, Lena	P2-149
Klotzsch, Enrico	OA138-06
Klucker, Gianna	OA54-02
Klug, Kelsey	OA42-02
Klute, Glenn	OA80-05
Kmiec Jr., Stanley	P2-150
Knarr, Brian	P1-274, P1-275, P1-366
Knarr, Brian A.	P1-290
Knaus, Katherine	P2-045, P2-077, P2-078, P2-095, P2-145, P4-325
Knaus, Katie	OA94-01
Kneissel, Michaela	OA122-04
Kness-Knezinkis, Erika	OA187-04
Kniepert, Johanna	P1-240
Knight, Christopher	P1-197
Knizley, Amanda	OA44-02
Knowles, Nikolas	P2-140, P2-367, P3-367, P4-214
Knowles, Ryan	P1-353

Author name	Presentation Number
Knowlton, Christopher	OA20-04, P1-115, P2-321, P3-243
Knudsen, Linda	OA76-01
Knutson, Kassidy	OA86-02, P2-026
Kobari, Riki	P4-108
Kobayashi, Hisato	P4-044, P4-050
Kobayashi, Kai	OA124-03, P1-185
Kobayashi, Koich	P4-326
Kobayashi, Masaharu	OA127-03
Kobayashi, Miyu	P2-252
Kobayashi, Shunichi	P2-016
Kobayashi, Shunta	OA124-03, P1-178, P1-185
Kobayshi, Kai	P1-178
Kobsar, Dylan	OA128-03, OA59-04, OA68-04
Koch, David	OA18-02
Koch, Lauren G	P3-004
Koch, Lauren G.	P2-238
Kochetkova, Tatiana	OA125-04
Koehler-McNicholas, Sara	OA66-04
Koelewijn, Anne	P3-019
Koelewijn, Anne D.	P1-124
Koff, Matthew	OA188-04
Koga, Ami	OA55-02
Koga, Takehiko	OA134-03
Kogan, Feliks	OA5-04, OA73-01, P3-203, P3-254, P4-339
Koh, Chin Rhong	P2-115
Kohombakadawala, Chamal	OA156-03
Kohyama, Keishi	P2-347
Kok, Jacob	P1-184
Kok, Joeri	OA62-03, P3-279, P3-290, P3-291, P3-300
Kok, Manon	OA192-05
Kokkoni, Elena	OA116-02, OA93-06, P2-213, P2-280, P2-326, P2-342
Kolanko, Magdalena A.	OA169-04
Kolesar, Julie	OA68-05, OA9-02, P3-099
Kolking, Pippa	OA169-03
Koller, Willi	OA171-02, OA171-03, OA183-01, P1-270, P2-068, P2-069, P2-094, P2-156, P3-200
Kolluru, Samyuktha	P4-345
Kolstad, Ash	P3-126
Komarova, Svetlana	OA71-01, P1-042, P3-173
Komeili, Amin	P1-350, P2-187, P2-339
Komnik, Igor	P3-098, P3-267
Komrakova, Alexandra	P1-042
Konda, Shoji	P3-261, P3-262
Kong, Fanwei	OA120-02, OA74-06, P3-008, P4-020
Kong, Sejin	OA107-06
Kong, Taewoong	OA117-06, OA136-05, OA93-05, P3-226
Kong, Wenyu	OA126-04
Konradi, Jürgen	P1-240
Kontaxis, Andreas	OA98-04
Kontson, Kimberly	P4-148, P4-149
Kontulainen, Saija	P2-137
Konz, Suzanne M	OA98-01
Koo, Bon-Kwon	P4-126
Koo, Seungbum	OA182-01, P1-151, P1-187, P3-232

Author name	Presentation Number
Kooiman, Vera	OA41-05
Kopp, Alexander	OA102-02, P4-002, P4-011
Koretsky, Elizabeth	OA188-04
Korhonen, Rami	OA166-04, OA19-03, OA73-02, OA8-01, OA87-03, OA87-04, P2-178, P3-155, P3-336
Korhonen, Rami K	P1-021
Korhonen, Rami K.	OA109-02
Koser, Jared	OA181-04
Koshyk, Andrew	P2-211
Kosik, Kyle	P4-140
Kositsky, Adam	OA87-03, OA87-04
Koskela, Morgan	OA3-05
Koskova, Olga	P4-226, P4-230
Kosonen, Joonas	P1-021, P3-155
Kostelnik, Colton	OA4-03
Kotani, Yuki	P4-027
Kotanko, Peter	OA180-04
Kotevski, Andrew	P1-285
Kothari, Alpesh	P3-014
Koto, Tom	P1-257
Kouda, Katsuyasu	OA122-03
Koumantou, Elena	OA145-01
Koumantou, Eleni	OA128-02
Kouvoutsakis, Georgia Roula	OA116-02
Kovacic, Jason	OA144-03
Kowal, Mateusz	P4-251
Koya, Bharath	OA121-02, P3-068
Koyama, Eiki	OA126-03
Koyama, Shuji	OA26-03
Koyiloth Vayalil, Sarathlal	OA38-04
Kozicka, Aleksandra	OA105-06, P1-255, P3-315, P4-167, P4-223
Kozono, Naoya	P4-150
Kraeutner, Sarah N.	P1-107
Kragballe, Jesper O	P3-045
Krahl, Leonie	P3-253
Krajewski, Kellen	OA27-04
Krajewski, Kellen T.	OA27-03
Krakora, Emelia	OA165-05
Kram, Rodger	P1-159
Kramer, Ivanna	P3-051, P4-291, P4-319
Kramer, Patricia	OA48-05
Kramer, Paula	OA140-04, OA184-04
Kranzl, Andreas	OA171-02, OA44-03, OA54-02, P2-069
Kratzer, Avery	OA183-03, P1-106
Kraus, Emily	P2-224
Krausz, Nili	P1-132
Krautwurst, Britta	OA54-02
Krawetz, Roman	P3-344
Kreis, Erin	OA130-04, OA20-02, P1-053, P1-096, P1-138
Kreplak, Laurent	OA91-01
Kretzer, Jan Philippe	P3-236
Kreutz, Clemens	OA122-04
Krishna, Vibhor	P4-188
Kritchevsky, Stephen	P2-236

Author name	Presentation Number
Kritzer, Tamar D.	OA59-04
Krivenko, Kate	P2-277
Krok-Schoen, Jessica	P1-080
Kromer, Daniela	P1-006
Krommendijk, M.E.	P4-071
Krommendijk, Marleen	OA10-03, P4-310, P4-312
Kronenberg, Jamie	OA129-01, OA40-01
Kronenberg, Nils M.	P1-007
Krosshaug, Tron	OA128-04, OA8-04, P1-001, P1-348
Krotine, Madeleine	P2-072
Krowchuk, Natasha	OA147-05
Krowchuk, Natasha M.	OA117-03, P4-218
Kruger, Karen	OA86-02, OA86-05, P2-026, P3-201, P4-178, P4-219
Kruse, Elizabeth	OA88-05
Kruyt, Moyo	P3-290, P3-291
Krywanio, Matilda	OA171-04
Krzak, Joseph	P4-178
Krämer, Martin	P4-222
Kröger, Heikki	OA149-04
Kröger, Inga	P4-229
Kshatriya, Eshan	P2-040
Kuan, Yi-Chun	OA106-05, OA124-05
Kubicki, Cody	P4-031
Kubo, Kinoka	OA198-03
Kubo, Soto	P3-162
Kuchinka, Kaitlyn B.	P3-369
Kudo, Asako	OA122-03
Kudo, Shoma	OA136-04, P1-233, P1-254
Kudzia, Pawel	OA32-05, OA42-06
Kuehl, Damon	OA19-04, P2-331
Kuhl, Ellen	OA179-03, P1-256
Kuhn, Gisela A	OA122-04
Kuhn, Gisela A.	OA185-04, P1-012, P1-028, P4-346
Kulakarni Prachet, Aashutosh	P3-065
Kulig, Kornelia	P2-041, P4-232
Kulka, Valérie	P4-003
Kulkarni, Amit	P2-291
Kulkarni, Ashwini	OA166-05, P1-215, P1-216
Kulkarni, Rucha	OA53-02
Kulkarni, Yuvam	OA7-03
Kumagai, Ryui	P3-277
Kumano, Akira	OA91-04
Kumar, Vatsal	OA176-03
Kumaran, Thamil	P4-018
Kumi, Isaac	P2-291
Kumpf, Davin	P2-240
Kundu, Paromita	P1-213
Kundu, Rohit	P1-220
Kuniyil, Sivapriya	OA127-02
Kuntze, Gregor	P4-185
Kunzler, Marcos	OA131-02
Kuo, Calvin	OA129-03, OA143-05, OA148-04, OA192-02, OA192-04, OA196-04, OA61-05, P1-094, P2-308, P3-042, P3-052
Kuo, En-Lin	P1-052

Author name	Presentation Number
Kuo, Li-Chieh	P4-305
Kuo, William	P3-273
Kupratis, Meghan	OA126-03
KURATA, Kosaku	P1-043
Kurata, Kosaku	P1-040
Kuriu, Satoru	P1-397
Kuroyama, Naoto	OA11-04
Kuroyama, Naoya	P4-331
Kurt, Mehmet	OA32-06, OA74-03, P4-302
Kurtcuoglu, Vartan	P3-127
Kusins, Jonathan	OA36-01
Kussie, Hudson	OA187-04
Kussow, Seth	OA135-04, P4-249
Kutch, Jason	OA37-03
Kutluk, Hazal	OA11-01
Kutulakos, Zoe	OA52-02
Kvashin, Nikolai	P3-190
Kwak, Dai-Soon	P3-266, P3-356
Kwak, Joonsoo	P4-294
Kwak, Samuel	P2-183
Kwan, Jasmine	P1-307, P1-358
Kwasek, Marek	OA123-02, P2-332
Kwei, Eric	P2-060
Kwiatkowski, Artur	OA145-02
Kwoh, C. Kent	OA24-02
Kwok, Bryan	P2-260
Kwon, Brian	OA193-06
Kwon, Daehoon	P2-118
Kwon, Eryn	OA145-06, OA169-05, OA58-05
Kwon, Hyeok Sul	P4-126
Kwon, Ohyun	P2-288
Kyriacou, Christina	P4-161
Kyvelidou, Anastasia	P4-190
Kölbl, Robert	P1-401
Kött, Thomas	P3-333
Kühne, Mareike	P1-331
L. Baltzer, Heather	OA46-06
L. Romanyk, Dan	P2-241
La Banca, Vitor	OA14-04, P3-383, P4-136, P4-157
La Barbera, Luigi	OA175-04, OA96-03, P2-151, P3-287
La Delfa, Nicholas	OA186-04, P2-053, P2-281
La Mattina, Antonino Amedeo	OA18-01
La Rosa, Jeremy	P1-309
Labberté, Margot C	OA113-04
LaBo, Connor	P3-034
LaBonte, Carrie	P4-313
Lack, William	OA163-01
Lack, William D.	P3-334
Lackner, Maximilian	P3-343
Lacroix, Damien	OA194-04, P2-119, P3-286
Ladeiras-Lopes, Ricardo	P4-043, P4-119
LaDisa, John	P4-103
LaDisa, Jr., John F.	OA102-01
Ladouceur, Michel	P1-198, P1-199

Author name	Presentation Number
Laende, Elise	OA117-04, P1-134, P2-023, P2-133
Laende, Elise K.	P4-185
Lafranca, Peter P.G.	OA62-03
Laganà, Matteo	OA90-05
Lagzouli, Amine	OA185-02, P4-298
Lai, Adrian	OA143-05, P2-168
Lai, Juntong	P2-119
Lai, Victor K.	P1-402
Laing, Andrew	P3-070, P3-151
Laing, Andrew C.	OA174-03, P2-268
Lakmazaheri, Ava	P1-105
Laksari, Kaveh	OA185-01, P3-113
Lakshmikanthan, Adhithi	OA4-05
Lal, Dveeta	P2-121
Lalancette, Sébastien	P4-058
Lallemant, Marine	OA170-04
Lally, Caitríona	OA10-02, OA89-02, P4-001, P4-320
Lally, Caitríona (Triona)	OA132-01
Lally, Caitríona (Tríona)	P3-158
Lallès, Ariane	OA130-03
Lalone, Emily	P1-250
Lam, Tyson	OA32-06, P4-302
Lamarre, Morgan	OA59-01
Lamas, Mario	P1-172
Lamb, Nikolas	P1-377
Lambers, Floor M	OA122-04
Lambers, Floor M.	P1-028
Lambert, Brad	OA190-03
Lambert, France	P2-371
Lamers, Armand	P4-067
Lamontagne, Anouk	P1-237
Lamontagne, Mario	OA99-04
Lamsey, Matthew	P4-210
Lamuta, Caterina	OA65-03
Lan, Rongxi	P1-381
Landinez Leon, David	OA62-04
Landinez Leon, David Felipe	P3-299
Landrum, Kevin	P3-059, P4-205
Landry, Scott	P3-313
Landwehr-Prakel, Katie	P2-322
Landwehr-Prakel, Katie M.	OA27-01
Lane, Brooks A.	OA144-05, OA146-01
Lang, Angelica	OA79-03, P1-321, P2-043, P2-287, P3-358
Lang, Cameron	P2-267
Lang, Jan	OA60-03
Langer, Max	OA71-04
Langford, Jordan	OA86-06
Langlois, David	P1-079
Langlois, Jean-Baptiste	P4-068
Langton, Christian	OA80-01
Lantis, Kristen	OA79-04
Lantz, Jonas	P4-348
Lanzl, Felicitas	OA181-03
Lapins, Elana	OA86-06

Author name	Presentation Number
Lapins, Renae	OA86-04, OA86-05
Larivière, Christian	P2-116
Larsen, Stain	P1-351
Larsen, Stian	P1-352
Larson, Dennis	OA174-06
Larson, Ember	OA131-04
Larson, Jaron	OA193-01
Larsson, Matilda	OA45-04, P4-329, P4-344
Lateef, Ali	OA32-04
Latifi, Lulejeta	OA187-04
Latimer, Sharon	OA80-01
Latreche, Ameur	P2-024
Lau, Teresa	P2-290
Laudo, Joel	P3-025
Laurence, Devin	P1-008
Lauret, Leon	P1-325
Lavacot, Dana Lynn	P3-008
Lavaill, Maxence	OA24-05, OA31-04, P3-357, P3-376
Laven, Robin	P4-047
Laverne, Floriane	P4-264
Lavikainen, Jere	P2-178
LaVoy, Emily	P3-055
Lawrence, J. Todd	P3-059
Lawrence, Reece	OA196-03, P1-150
Lax, Mya	OA189-01
Laz, Peter	OA81-01, P2-163, P3-212, P3-230, P3-231, P3-252, P3-263
Lazary, Aron	P3-296
Lazic, Igor	OA60-03
Lazáry, Áron	OA194-04
Le Floc'h, Simon	P2-219
Le Flao, Enora	OA133-03
LE MAIGAT, Mathias	P3-119
Le Maitre, Christine	P3-298
Le Mouel, Charlotte	P1-049, P1-121, P4-164, P4-165
LE SAGE HAKIM, Hassen	P2-132
Le, Anthony	P2-084, P2-114
Le, Janet	P4-178
Le, Peter	P1-367, P2-103
Le, Shenglong	OA131-06
Leardini, Alberto	P1-149, P2-079, P3-201
LeBar, Kristen	P3-063
Lebedeva, Aleksandra	P3-179
Lechner, Norbert	OA18-03
Lecomte-Grosbras, Pauline	P4-327
Ledoux, William	OA72-04, P2-227, P3-201, P4-309, P4-337, P4-338
Ledoux, William R.	P3-334
Lee, Beom Chan	OA111-04, P3-005
Lee, Beom Jun	OA120-03
Lee, Beom-Chan	P2-309
Lee, Breanna	P1-204
Lee, Chaeeun	OA61-04
Lee, Chang Min	OA69-04, P4-117
Lee, Cheoljae	P2-127, P2-316
Lee, Chihyeong	P2-309, P3-005

Author name	Presentation Number
Lee, Chung-Hao	P4-281
Lee, Donghwan	P3-359
Lee, Erin	OA21-02, P4-200
Lee, Erin C.S.	OA117-02, P4-169
Lee, Gahyun	P2-127, P2-316
Lee, Gyu-Han	P4-026
Lee, Hae Dong	P1-299
Lee, Hyeonyong	P2-311
Lee, Isabelle	P1-313
Lee, Jeffrey	P3-020, P3-040
Lee, Jeonghwan	OA48-02
Lee, Ji-Hyun	P1-359
Lee, Jia Jun	OA46-05
LEE, JUHYUCK	P4-278
Lee, Jun Hyuk	P3-028
Lee, Jungho	P1-248, P2-311
Lee, Kunwoo	OA61-04
Lee, Kyung-Eun	P1-359
Lee, Kyungmin	P2-066, P2-093
Lee, Lik Chuan	OA30-05, P3-063, P4-116
Lee, Matthew	P4-104
Lee, Matthew Tsu-En	P4-048
Lee, Peter	OA15-05, OA175-05, OA83-06, P2-244
Lee, Peter D	OA10-04, P4-297
Lee, Peter D.	P4-318
Lee, Po-Yi	OA158-04, P3-180
Lee, Sae Yong	OA85-02
Lee, Samuel C.K.	P1-065, P4-189
Lee, Sangyup	P4-245
Lee, Seo Hyun	P4-248
Lee, Seohyun	OA35-03
Lee, Seyoung	OA172-02, P1-176, P2-288, P3-138, P4-195
Lee, Sin-Yan	P3-309
Lee, Soyoung	OA165-03, P4-253
Lee, Sungkil	P1-029
Lee, Szu-Ping	P2-314
Lee, Taeyong	OA168-01, OA35-03
Lee, Yung-Kuo	P4-305
Lee-Confer, Jonathan	P1-312
Leestma, Jennifer	OA46-02, OA85-03
Lefèvre, Gaëtan	P4-349
LeGault, Madelyn	P1-301, P1-302
Lei, Andy Man Kit	P2-108
Lei, Yuming	OA92-04
Leighton, Jennifer	P3-204, P3-205, P3-250, P3-251, P3-265
Leija, Katie	OA111-02
Leinwand, Jonah	P3-292, P4-322
Leipsic, Jonathon	OA120-03
Lejeune, Marylène	P1-032
Lemarteleur, Vincent	P4-264
Lemasters, Tricia	P1-288
Lemineur, Clément Lemineur	P1-125
Lemos, Andressa	OA85-05
Lenchik, Leon	P2-236

Author name	Presentation Number
Lenhart, Rachel	P4-206
Lenhoff, Mark	P1-364
Lenz, Amy	OA171-01, OA86-02, OA86-04, OA86-05, OA86-06, P2-026, P2-084, P2-105, P2-114, P3-201, P3-220, P4-219
Lenzi, Tommaso	OA162-05, OA46-04, OA66-01, OA80-02, P2-303
Leon Souza Viera, Heinrich	P4-175
Leon, Melvin	P4-232
Leonard, Corinne	OA101-05
Leonard, Tim	OA27-06
Leonard, Timothy	P2-256, P2-257
Leonardis, Joshua	OA161-03, P2-215, P2-216
Leonardo Diaz, Roberto	OA31-05
Leonardo-Diaz, Roberto	P2-076
Lepileur, Mathilde	P4-334
Leporace, Gustavo	OA105-06, OA14-01, OA14-02, OA14-04, OA153-01, OA76-04, OA94-03, OA98-06, P1-061, P1-255, P3-012, P3-315, P3-374, P3-383, P4-136, P4-157, P4-167, P4-223, P4-258
Leppens, Tom	OA23-02, P3-281
Lerner, Matthew	P1-139
Lerner, Zachary	OA67-02
Leroux, Andrew	P4-236
Leung, Lester	OA123-03, P1-112
Leussink, Karlijn	OA10-03
LeVasseur, Clarissa	OA23-03
Leveille, Lise	OA129-03, OA155-05, P1-145, P1-355, P3-381
Levillain, Aurelie	P4-234
Levine, Jade	P3-085, P3-141
Levy, Robert	P1-008
Lewek, Michael	OA130-06, OA28-04, OA33-03, OA67-02
Lewis, Cara	OA183-03, P1-106, P1-114, P1-143
Lewis, Jessica	OA57-04, P2-050, P2-157
Lewis, Philip	P4-088, P4-089
Leyendecker, Sigrid	P4-220
Li Yam Nam, Heather	P2-023, P2-133
Li, Bao	OA179-02, OA197-01, P4-022
Li, Chengbin	OA145-03, P3-130, 2670
Li, Chi-Sheng	P3-308
Li, David	P4-038
Li, Guoyang	P3-193
Li, Haozhixiang	P2-145
Li, Hiayan	OA101-04
Li, Jian	OA20-06
Li, Jinfeng	P1-066
Li, Jing-Sheng	OA12-05
Li, Jingeng	OA18-05, P2-152
Li, John	OA131-05
Li, Julia	OA174-02, OA174-06
Li, Junyan	OA182-04
Li, Kang	OA197-06, P1-175
Li, Le	OA129-06
LI, LEI	OA57-02
Li, LePing	P2-171, P3-178
Li, Longyu	P3-146
Li, Mingai	OA179-02, OA197-01, P4-022
Li, Ning	OA104-01

Author name	Presentation Number
Li, Qing	P2-260
Li, Qingguo	P2-182, P3-247, P4-216
Li, Rong	PL12-01
Li, Sijia	OA141-01, OA61-04
Li, Tao	P1-205
Li, Thomas	OA126-03, P2-260
Li, Weiping	OA64-05
Li, Xiaogai	OA45-04, OA58-03
Li, Xinghan	P1-248
Li, Xinshan	OA96-06, P2-128, P3-189
Li, Xuran	OA64-02, P1-031
Li, Yi	P1-397
Li, Yun-Da	P3-309
Li, Zhixiong	OA141-01, OA141-05, OA61-04
Li, Zhiyong	OA82-01
Li, Zihui	P1-028
Li, Ziting Liz	OA20-03
Li, Zong-Ming	OA24-02, OA87-02, P4-354
Li, Zongpan	P4-253
Liang, Chunping	OA131-06
Liang, Jing-Min	P3-097
Liang, Leo Hwa	OA179-02
Liani, Valentina	P3-064, P4-270
Liao, Jing	OA127-03
Liberati, Cecilia	P4-304
Lichtenberg, Jessanne	OA101-02, OA101-05, OA51-05
Liddle, Alexander	OA149-01
Lieball, Kim	P2-191
Lieber, Richard	OA168-02, OA76-02
Liebsch, Christian	OA36-03, OA36-04
Liefers, R.	P4-071
Liefers, Remco	P4-312
Lien, Hen-Yu	OA196-05
Lien, James Jenn-Jier	P4-305
Lievre, AJ	P1-326
Liew, Bernard	OA99-01, P1-111
Liew, Bernard X.W.	OA188-06, OA60-05, P3-314
Likens, Aaron	OA130-05, OA93-02, OA93-03, P1-196
Likens, Aaron D.	P3-009
Lim, Hyerim	OA54-04, P1-170
Lim, Jeffrey	P3-104
Lim, Kitaek	OA172-02, OA172-03, P1-085, P1-176, P2-288, P3-138, P4-195
Limberg, Afton K.	P3-342
Limbu, Summik	OA46-05
Lin, Beier	P1-107
Lin, Che-Kuan	P1-155
Lin, Chi-Lun Cyrus	P4-305
Lin, Chien-Yu	OA4-03
Lin, Chih-Chun	P4-305
Lin, David	P2-012, P2-220, P2-221
Lin, Hua-Bin	P1-156
Lin, Jeng-Heng	OA106-05, P2-139
Lin, Jianhao	P1-205
Lin, Jiu-Jenq	OA16-02, P3-382, P4-267

Author name	Presentation Number
Lin, Jr-Shiuan	P3-293
Lin, Run	OA15-02
Lin, Tangdi	P1-205
Lin, Ting-Sheng	P3-350
Lin, Tsai-Ling	P2-139
Lin, Wei-Chen Leo	OA77-04
Lin, Yang-Shen	OA121-04
Lin, Yu-Sheng	P4-305
Lin, Yuan	P3-187
Lind, Henrik P	P3-045
Lind, Jonathan	P1-280
Lindenmann, Sara	P1-028, P4-346
Lindsay, Owen	P3-251
Lindsey, Bryndan	OA131-06
Lintner, Laura	P2-047
Linton, Ashley	P3-167, P3-196
Lintz, François	P3-201
Liphardt, Anna-Maria	P4-220, P4-334
Lipphaus, Andreas	P2-210
Lippitt, Victoria	P1-084
Lipps, David	OA37-05, OA79-06, P2-215, P3-366
Lipps, David B.	P3-355
Lisi, Lucia	OA18-01
Lisonbee, Rich	OA135-04, P4-249
Liu, Aiqin	OA163-03, P2-048, P2-100
Liu, Bin	OA74-02
Liu, Charles	P2-213
Liu, Chen	P3-255
Liu, Chia-Lun	OA53-01, P2-340
Liu, Chiang	P1-279
Liu, Chih-Chia	P3-170
Liu, Danmei	OA194-02
Liu, David	P1-059
Liu, Deyun	OA90-03
Liu, Dianze	OA35-01
Liu, Han	OA10-05, OA195-02, P4-311
Liu, Huaning	P4-214
Liu, Jie	OA193-04
Liu, Jingmin	OA55-02
Liu, Jun	OA130-04, P1-053, P1-138
Liu, Kristie	P2-027, P2-064
Liu, Kuan-Yun	P4-267
Liu, Min	OA193-04
Liu, Tianmian	OA64-02, OA90-03
Liu, Vienna	OA37-05
Liu, Weiqiang	OA167-02
Liu, Wenpei	P1-364
Liu, Wuhuang	OA114-02, P1-034
Liu, Xiaofan	P2-118
Liu, Yingtao	P4-281
Liu, Youjun	OA179-02, OA197-01, P4-022
Liu, Yuan	OA99-06
Liu, Yuchen	P2-260
Liu, Yuqi	P3-193

Author name	Presentation Number
Liu, Zekun	P4-179
Liu, Zhenhao	P4-314
Liukkonen, Mimmi	OA19-03
Livingood, Ethan	OA55-03, P1-273, P1-304
Lizalek, Lesley	P2-025
Lloyd, Alexandria	OA66-04
Lloyd, John E.	OA153-02, OA70-05
Lloyd, Rob	OA78-01
Lo Rito, Mauro	OA185-03
LO, I-CHIA	P1-016
Loayza-Saldaña, Mayra Alejandra	OA117-01
Lobe, Leon	OA147-02
Lobo, Michele A.	P1-065, P4-189
Lockard, Carly	OA168-03
Lockhart, Samuel	OA40-01
Locurto, Dominic	OA65-02
Lodde, Moritz	P2-180
Lodhia, Parth	OA5-06
Lodi Rizzini, Maurizio	OA69-02, OA69-03, OA82-05
Lodi, Musaddiq	OA51-05
Lodola, Giulia	OA187-01, OA197-03, OA90-05
Loecher, Michael	P4-330
Loerakker, Sandra	OA4-01, OA4-02, OA77-01, P1-030, P4-070
Loh, Kenneth	P4-266
Loh, Ping Yeap	P1-386
Lohmann, Jeremy	P3-365
Lohrenz, Gabrielle X.	OA144-05, OA146-01
Lohscheller, Jörg	OA81-05, P1-174, P1-330
Lohse, Keith	OA105-04
Loiret, Isabelle	OA111-05
Lombardi, Massimo	OA95-03, P4-042
Lomond, Karen	P2-193, P3-320
Londono, Maria	P3-181
Long, Christopher	P1-221, P2-218
Long, Christopher L.	P1-123
Long, Douglas	P3-211
Long, Mian	P3-176
Long, William J.	P3-237
Longo, Umile Giuseppe	P4-344
Lonuzzo, Gabriel	OA128-03
Loong, Aidan	OA193-04
Loosemore, Mike	OA145-01
Lopata, Richard	OA144-01, OA82-04
Lopez, Arianna	P2-009
Lorenzetti, Silvio	OA3-01
Lorenzo, Corinne	P3-165
Loria-Calderon, Tyrone	OA165-02
Loss, Jeremy	P3-233
Loth, Francis	P4-171
Lotz, Christian	P3-183
Loughlin, Naomi	P1-134
Loundagin, Lindsay	P4-298
Lourdes Rios, Jaqueline	OA149-04
Lovell, Nigel	OA1-03

Author name	Presentation Number
Lovett, Belzora	OA37-05
Low, Juanita	P4-154
Low, Lucas	OA121-03
Lowe, Kaylee	OA159-03
Lowe, Timothy	OA129-04, P1-379
Lowell, Gina	P3-143
Lu, Lichun	OA161-04, P2-031
Lu, Ming-Chen	P1-051
Lu, Shiuan-Huei	OA106-05, OA124-05, OA22-04, P3-214
Lu, Sung-Ting	P1-279
Lu, Tsung-Lin	OA98-02, P1-099, P1-371, P4-261
Lu, Tung-Wu	OA106-05, OA124-05, OA135-05, OA22-04, OA86-03, P2-139, P3-214, P3-238
Lu, X. Lucas	P2-260
Lu, Yi-Fu	OA22-04
Lu, Yuan-Chiao	P3-066
Lu, Yuankai	OA158-04, P3-167, P3-196
Lubisco, Eleonora	P1-228
Lucas, Kathryn	OA29-05, OA3-02, OA42-05, P4-190
Luchies, Carl	OA196-05, OA79-02
Luciano, Francesco	OA154-01, OA154-04
Luck, Jason	P3-022, P3-076, P3-102
Luckfiel, Tobias	P1-124
Lucoveis, Maria L.	P4-243
Ludewig, Paula	OA29-03
Ludvig, Daniel	OA168-05, P2-247
Luetkemeyer, Callan	OA168-03, OA170-05, OA7-03, OA97-05, P3-159
Luftglass, Adam	OA107-05, OA131-01, P1-336
Luginsland, Lauren A	P1-323, P1-338
Lujan, Trevor	P2-063, P2-264, P3-058, P3-164, P4-324
LUKE, David	P3-119
Luke, David	CSB-05, OA169-06, OA6-04, P4-306
Lukic, Bratislav	OA50-04
Lumen, Nicolaas	OA25-05
Lundberg, Hannah J.	P2-052, P3-225
Lunde, Ty	P2-114
Lundell, Sydney	OA59-02
Luo, Pei	OA20-06
Luo, Shuzhen	P2-319
Luo, Weiru	OA56-03
Luo, Yihao	OA74-02
Luo, Yunhua	OA71-03
Luraghi, Giulia	OA115-02, OA115-03, OA127-05, OA89-03, OA89-04, OA95-02, P4-006
Lustberg, Maryam	OA79-04
Lusvardi, Sofia	P3-167
Luxton, Gant	P1-020
Luzo, Marcus	OA98-06
Lyman, Stephen	P3-237
Lynch, Alexandra	OA189-05, P2-102, P2-153, P2-189
Lynch, Delanie	P3-109, P3-110
Lynch, Layla	OA79-06
Lynn, Scott	P3-198, P4-130
Lyons, Nathan	OA15-01, P3-032
Lyons, Samuel M	P4-143

Author name	Presentation Number
Léger, Michelle	P2-279, P2-282
López, Carlos	P1-032
López-Pascual, Juan	P1-172
M Nasrabadi, Amin	OA148-04, OA196-04
M. Beaudette, Shawn	P1-308
M. Black, Amanda	P1-308
M. Cirnigliaro, Christopher	P3-273
M. LeVasseur, Clarissa	P3-284
M. Nasrabadi, Amin	OA143-03
M. Samaniego, Joshua	OA153-01, OA76-04
M. Spungen, Ann	OA33-02
Ma, Charlie Chen	P3-372
MA, Dong	OA158-03
Ma, Dong	P1-390
Ma, Michael	P4-012
Ma, Michael R.	OA120-04, OA139-03, OA25-04
Ma, Shengyuan	OA101-03
Ma, Songyun	P3-333
Ma, Willa	P3-272
Ma, Xianghong	OA36-06
Maak, Travis	P4-249
Maas, Mario	P3-223
Maas, Stefan	OA60-05, OA99-01, P3-314
Maas, Steve	OA17-04
Maazouz, Yassine	P4-346
Mabu, Shingo	P3-053
MacDonald, Ben	P3-204, P3-205, P3-313
MacDonald, William	P4-350
MacFadden, Lisa	P4-201
Machado, Esthevan	P2-257
Machado, Jean Marlon	P4-155, P4-156
Macht, Jesse	P1-168
Macie, Annagh	CSB-04
Maciukiewicz, Jacquelyn M.	OA117-02, P4-169, P4-217
MacLean, Kathleen	P1-307, P4-247
MacPherson, Isla R. G.	P2-054
Macri, Erin	OA128-01, OA57-06, P4-177, P4-289
MacTaggart, Jason	OA102-03, OA127-02
Macwan, Isaac	P3-150
Madden, Kim	OA128-03
Maddox, Grant	OA196-03, P1-150
Maddox, Rebekah	P3-055
Madhekar, Advait S.	P3-199
Madhukaran, Priyya	OA170-02
Madinger, Alexander	OA46-02, OA85-03
Madrid, Aaron	OA65-04
Madrid, Diana	P2-236
Maeda, Eijiro	P1-019
Maehara, Ayano	P4-150
Maehlich, Daniela	P1-007
Maes, Lauranne	P1-027
Maestas, David	P2-347
Maga, Ludovica	P1-027
Magarey, Charlie	OA145-04, P3-079, P3-082

Author name	Presentation Number
Magliocco, Marco	OA185-03
Magoariec, Hélène	P4-068
Magony, Richard	OA195-03
Magruder, R. Daniel	OA48-03
Mah, Joseph	OA153-04
Mah, Niamh	OA153-04
Maharaj, Jayishni	OA80-01, P2-218
Mahendroo, Mala	OA170-02
Maher, Kevin O.	P4-124
Mahmoodi, Mohammad	OA96-02
MahmoudzadehKhalili, Sara	P2-302
Mahoney, Joseph	OA142-02, OA9-05, P1-100
Mahoney, Ryan	OA141-04
Mahr, Claudius	P4-004
Mahrous, Amr	OA168-05
Mai, Patrick	OA147-03
Mailey, Brian	OA151-04
Mainardi, Luca	P4-074
Mainieri, Giada	OA114-04, OA187-01, OA199-03
Maioli, Alexandre	OA94-03, P1-061, P4-136
Maiti, Spandan	P4-054, P4-055
Maitland, Murray	P2-329
Majdolhosseini, Maryam	OA133-04
Major, Matthew	P4-227
Major, Paul	P4-328
Maki, Koichiro	OA91-04
Makino, Akitoshi	P1-254
Malakian, Alique	P1-257
Malatesta, Davide	P1-147
Malcolm, Philippe	P2-304, P2-337
Malda, Jos	OA198-04
Malekzadeh-Milani, Sophie	P4-146
Malenfant, Diane	P4-164, P4-165
Malerba, Albano	P4-349
Malette, Molly	OA150-06
Malhotra, Paresh A.	OA169-04
Mallea, Jorge	OA156-04
Malloy, Philip	P1-115
Mally, Franziska	OA18-03
Maluckov, Teodora	P2-140, P2-367
Maly, Monica	P4-200, P4-214
Maly, Monica R.	OA117-02, P4-169, P4-198, P4-217
Mameri, Enzo	P4-167, P4-223
MAN, Hok Sum	OA57-02
Manas, Neva	P4-221
Manavis, Jim	P3-079, P3-082
Mancini, Martina	P1-116
Manco-Johnson, Marilyn	OA153-04
Manczurowsky, Julia	OA123-03, P1-112
Mandal, Parthasarathi	P2-330, P4-088, P4-089, P4-122, P4-123
Manffra, Elisângela	P4-203
Manfrim, Luciana C.	P1-305
Mang, Joshua	P2-014
Mangalgi, Chinmay	OA151-02

Author name	Presentation Number
Mangino, Anthony	OA99-02, P4-138
Mann, Matthias	P1-005
Manned, Erin	OA70-02
Mannello, Sara A.	P4-246
Mannen, Erin	P2-188, P3-143, P4-097
Manning, Edward	P4-076
Manning, Jack	OA40-02
Manning, Keefe	OA39-04, P4-031
Manocha, Ranita H. K.	P4-185
Manouchehri, Neda	OA193-06
Mansfield, Avril	OA160-01
Manship, Harry	P3-321
Manske, Sarah	CSB-03, OA129-05, OA73-05, OA76-05, P2-039
Manske, Sarah L.	CSB-02
Manson, Gerome A.	P4-284
Manzouri, Amirhossein	P4-019, P4-080
Mao, Jie	OA54-03
Mar, Merrick	P2-333
Marathe, Shashidhara	OA113-04
March, Alyson	P1-101
Marchese, Vincenzo	P2-378, P2-379
Marchetti-Deschmann, Martina	P3-179
Marchiori, Gregorio	OA50-04
Marcian, Petr	P4-226, P4-230
Margheriti, Pietro	P3-129, P3-324, P4-231
Margulies, Susan	OA133-01
Marian, Max	P3-217
Mariani, Francesca	P4-036
Mariani, Luca	OA95-04
Mariaux, Francine	OA9-01
Marin, Nadja	P1-082
Marino, Emily	P1-135, P1-186
Marino, Michele	OA17-05, OA4-01
Marino, Victoria	P3-342
Marinozzi, Franco	P4-231
Markert, Bernd	P3-333
Marks, Madison E.	OA128-05
Marne, Aniket	P1-033
Marques, Francisco C	OA122-04
MARQUES, Thomas	P4-241
Marques, Thomas	P4-240
Marquez, Tyce	OA178-03, P1-238
Marquez, Tyce C.	P4-166
Marradi, Matilde	P1-025, P3-329
Marriott, Kendal	P4-200
Marriott, Kendal A.	OA117-02, P4-169, P4-198, P4-217
Marsden, Alison	OA120-02, OA157-03, OA179-03, OA30-02, P4-012, P4-078, P4-120, P4-330, PL01-01
Marsden, Alison L.	OA120-04, OA25-04
Marsden, Alison Lesley	OA139-05
Marsh, Richard	OA137-04
Martel, François	P1-119
Martin Robinson, James L.	OA198-04
Martin, Anne	P1-104

Author name	Presentation Number
Martin, Ariane	P3-328
Martin, Jack	P3-322
Martin, Will	P2-214
Martinac, Adam	OA78-01, P4-296
Martinelli, Chiara	OA11-03, OA114-04, OA187-01, OA197-03, OA199-03, OA77-03, OA90-05, P1-013
Martinet, Katarina	P2-347
Martinez Vázquez, Rebeca	OA114-04
Martinez, Diana C.	P3-009
Martinez, Eddie	OA119-02, OA81-02
Martinez, Elena	P4-012
Martinez, Elena S.	OA25-04
Martinez, Lorenzo	OA103-05
Martinez-Vazquez, Rebeca	OA187-01
Martini, Douglas	OA118-02, P1-210
Martini, Douglas N.	P4-341
Martins e Souza, Patricia	OA105-06
Martínez Vázquez, Rebeca	OA77-03, P1-013
Marusich, Kathryn R.	P3-203
Marvin, Zachary	OA111-03, P2-344
Masaei, Mobina	P2-292
Masante, Beatrice	OA199-02, OA51-03
Maschlanka, Philip	P1-325
Mascia, Guido	OA92-03
Masen, Marc	OA46-05
Maskatia, Shiraz A.	OA120-04
Masmoudi, Ilias	P3-019
MASOOD, Zaryan	P3-119
Masood, Zaryan	CSB-05, OA169-06, OA6-04, P3-105, P4-306
Masouros, Spyros	P2-190, P2-310, P4-254
Masrouri, Milad	P3-033
Massai, Diana	OA199-02, OA51-03
Masse, Sylvia	P1-086
Massone, Valentina	P1-068
Masteling, Mariana	P2-234
Mastnardo, Diane	OA79-06
Mastrofini, Alessandro	OA17-05, OA4-01
Mastronuzzi, Girolamo	OA25-02, OA82-05
Mata Cano, Daniel	P1-032
Mata Quinonez, Luis Rene	OA132-04, OA43-02
Matagi, Chantelle	P1-073
Matan, Salman	P2-005, P2-249
Mateus, Rodrigo	OA70-04
Mathavan, Neashan	P1-012, P1-028, P4-346
Mathew, Jacob	OA145-06, OA169-05
Mathieu, Colleen	OA163-02
Mathieu, Yves	OA193-05
Matijevich, Emily	P1-193, P4-168
Matos, Ana	P3-327
Matsuda, Fumihiko	OA127-03
Matsumoto, Eiji	OA126-02, 1385
Matsumoto, Takeo	P1-019
Matsumura, Akira	P3-285
Matsunaga, Yukiko	P1-397

Author name	Presentation Number
Matsushita, Kei	P3-234
Mattar, Luke	P3-371
Mattar, Luke T.	P3-323
Matthews, Colina	P1-129
Matties, Justin R.	P1-177
Mattucci, Stephen FE	OA142-04
Maucieri, Joseph	P3-150
Mauck, Robert	OA126-03, P2-260
Mausehund, Lasse	OA8-04
Mayer, Jörg	OA188-01
Mayes, Katherine	OA19-04, P2-331
Mayeur, Olivier	OA170-04, P4-327
Mayman, David J.	P3-237
Maynard, Chelsea	P1-223
Mayo, J. Patrick	OA118-06
Mays, Gavin	OA84-03, P4-078
Mazariegos, Kenneth	P2-332
Mazariegos, Kenneth M	OA123-02, P2-336
Maze, Danielle A.	P4-243
Mazza, Edoardo	P1-006
Mazzi, Federica	OA197-03, OA90-05
Mazzi, Valentina	OA108-02, OA82-05, P4-037
Mazzola, Cecilia	P2-124
Mazzoli, Valentina	OA48-03
McAllister, David R.	OA38-02
McArthur, Adam	OA197-02
McBain, Brodwen	P1-344
McCain, Emily M.	P2-161
McCall, Blake	OA163-03
McCarthy, Abigail	OA190-05
McCarthy, Brody	OA117-05, OA147-04, P4-154
McCarthy, R Patrick	P4-103
McCarthy, Ray	OA115-03, P4-065
McCarthy, Robert	P1-281
McCartney, Megan	P3-143
McCarty, Tristan	OA93-06, P2-342
McClean, Zachary	OA13-04, OA98-03, P2-104
McClean, Zachary J	OA72-05
McClelland, Jodie	P1-344
McClintock, Rebecca	P1-262
McCloskey, Alexa	P4-135
McClure, Michael	P1-277
McConnell, Kaitlyn	P1-128
McConnell, Keith	P4-016, P4-017, P4-029, P4-050
McCoy, Annette	P2-232
McCoy-Munger, Hailey	OA50-03
McCreary, Madeleine	P2-322, P4-186, P4-205
McCreath Frangakis, Erinn	OA162-04
McCrory, Jean	P1-224
McCulloch, Alyssa	P4-001
McCullough, Sam	P1-015
McDermott, Anna	P1-211
McDermott, Daniel	OA37-02, P3-378
McDonald, Catherine	P3-059

Author name	Presentation Number
McDonald, Kirsty	OA66-03, P4-194
McDonald, Maeve	P4-206
McDonald, Monte	P1-251
McDonald, Stuart	OA6-05
McDonnell, Paul	OA118-02, P1-210, P4-341
McDonnell, Stephen	OA60-05, OA99-01, P3-314
McElhinney, Doff	OA25-04, P4-330
McEntire, B. Joseph	P3-086
McEntire, Joseph	OA181-04
McEvoy, Eoin	OA152-03, OA152-05, OA164-05, OA176-03, P1-404, P2-381
McGarry, Matthew	OA32-06
McGarry, Patrick	OA152-03, OA152-04, OA56-02, P4-065
McGeown, Josh	OA169-05
McGeown, Joshua	OA145-06, OA58-05
McGhee, Kelly	P1-064
McGiffin, David	P4-083
McGinley, Timothy	OA137-02, P2-261
McGinnis, Ryan	OA92-03
McGlasson, Xandra	OA65-03
McGowan, Craig	OA103-03, P2-012
McGrath, Charles	P4-330
McGrath-Cadell, Lucy	OA144-03
McGregor, Alison	OA180-03
McGregor, Martine	OA36-01, P2-023
McGuckin, Kaylie	P3-072
McGuirk, Theresa E.	P1-117, P1-235, P1-236
McIlroy, William E.	P1-107
McKee, Zahra	P4-269
McKenna, Eamonn	OA187-04
McKernan, Gina	OA23-03
McLachlin, Stewart	OA36-01, P3-020, P3-040, P3-056, P3-283, P3-292, P4-322
McLaughlin, Claire	P2-126
McLean, Linda	OA168-04, P2-172
McMenemy, Louise	OA180-03
McMorran, John	P3-288
McNamara, Laoise	OA176-03, OA198-02, OA88-03, P4-114, PL05-01
McNeil, Chris	P2-054
McNew, Ethan	OA187-04
McNish, David	OA81-04
Mcnitt Gray, Jill I	OA13-01
McNitt-Gray, Jill	OA29-05, OA3-02, OA42-05, P1-268, P1-384
McParland, Emily	OA12-02
McPhee, John	OA131-05, P1-045, P3-020, P3-040, P3-047
McPherson, Daniel	OA14-06
McSweeney, Orlaith	P1-404
Md, Rafizul Islam	P4-104
Meacham, J. Mark	P1-389
Meador, Benjamin	P3-062
Meakin, Jude	OA135-03
Means, Colin	P4-038
Meardon, Stacey	P2-170
Mebrahtu, Abel	OA43-03
Mecheri, Hakim	P2-116
Medeiros, Tainá	P1-191

Author name	Presentation Number
Meek, Delaney	P3-357
Megherhi, Sabreen	OA23-03
Mehari Abraha, Hyab	P4-051
Mehdi, Rana Raza	OA191-02, P4-081
Mehmeti, Leutrim	P1-367
Mehrabi, Negar	P4-315
Mehrrostami, Arman	OA6-04
Mehta, Maahika	P1-193
Mei, Qichang	OA190-02, P1-092, P3-255
Mei, Qipei	OA74-05, P3-039
Meier, David	OA120-03
Meinders, Evy	OA141-01, OA141-05, OA147-02
Meindlhumer, Michael	OA71-02
Meinert-Spyker, Elizabeth	P4-094
Meinhold, Katherine	OA77-02
Mekonnen, Ephrem	OA143-01, OA143-03
Melick, Colin	P1-082
Mellon, Stephen	P3-321, P4-303
Meloy, Angie	P2-296
Mendez, Keegan	OA43-05
Mendicino, Margherita	OA42-01, P1-332, P3-129, P3-324
Mendiola, Emilio	OA132-03, OA191-02, OA56-05, P4-081, P4-082
Mendonca Cardoso, Marcio	OA118-05
Menegaldo, Luciano	P1-191, P4-203
Menendez, Sydney	OA178-01, P1-334
Meng, Shiyang	OA121-03
Mengoni, Marlene	OA36-05, OA83-04
Mengoni, Marlène	OA49-01, OA83-03, P2-076, P2-194, P3-188, P3-271, P3-349
Menicanti, Lorenzo	P4-092
Menke, Walter	OA98-02
Menner, Skylar	P1-128
MENON, JAGDISH	P3-364
Menon, Karthik	OA157-03, P4-013
Mentiplay, Benjamin	OA117-05, OA147-04, P4-154
Mercadal, Clara	P1-281
Mercer, Vicki	OA160-05
Merfeld, Daniel	OA165-06, P1-080
Mergler, Olivia	OA170-03, 2432
Merkx, Maarten	P4-202
Mertiya, Abhimanyu	P2-203
Mesfar, Wissal	OA109-01, OA180-02, P2-200
Mestdagh, Kenzo	OA25-05
Metsavaht, Leonardo	OA105-06, OA14-01, OA14-02, OA14-04, OA153-01, OA76-04, OA94-03, OA98-06, P1-061, P1-255, P3-012, P3-315, P3-374, P3-383, P4-136, P4-157, P4-167, P4-223, P4-258
Mettler, Jeff	P1-166
Meyer, Ben	P1-109, P1-110
Meyer, Brett	OA92-03
Meyer, Clark	OA17-02, P4-098, P4-099
Meyer, Gretchen	OA168-02
Meyer, Kenneth	OA84-02, OA89-02
Meyer, Tom	P3-027, P3-153
Meza, Guadalupe	OA168-02
Mhandu, Esau	P4-039
Miah, Samuil	OA32-02

Author name	Presentation Number
Miceli, Marcello	OA91-03
Michaels, Reese	OA6-02
Michaud, Jana	OA137-05
Michel, Silvain A.	P3-235
Micheler, Carina	OA60-03
Michener, Lori	OA14-05, OA14-06, OA37-03
Michiels, Gerben	OA7-04
Mickle, Karen	OA142-03
Middendorf, Jill	OA161-02, OA73-03, P2-228
Middleton, Kane	P1-108
Miehling, Jörg	OA136-02, P1-152
Mielkozorova, Mariia	P1-042
Migliavacca, Francesco	OA115-02, OA115-03, OA127-05, OA82-02, OA89-03, OA89-04, OA95-02, P4-006, P4-074
Mihic, Anastasija	OA8-02
Mihy, Julien	P1-197, P1-230, P2-059
Milcsik, Matthew	OA188-02
Miles, Christopher M.	OA128-05
Miles, John	OA196-05, OA79-02
Milesi, Davide	OA191-05, P4-036
Milkovich, John	OA46-06
Mill, Jordi	OA43-05
Millan Alvarez, Jessica M.	P4-218
Millan, Carola	P2-378, P2-379
Millar, Margaret	P4-076
Millard, Matthew	OA165-01
Miller, Abby	OA142-02
Miller, Angela	P1-341, P4-259
Miller, Carl	OA121-04
Miller, Claire	P3-161
Miller, Emily	OA129-04, OA176-04, OA195-01, P2-303
Miller, Lee	P2-176
Miller, Michael	P2-077, P2-078, P2-145
Miller, Ross	OA142-01, OA177-03, OA46-03, P1-208, P1-269, P3-038
Miller, Spencer	P1-230, P2-059
Miller, Sue	OA65-05
Millett, Peter	OA195-04, P3-318
Mills, Megan	OA86-04, P2-105
Millán, Carola	OA38-03
Milner, Clare	P2-038, P2-122
Milone, Dario	P3-175
Milusev, Anastasia	OA157-05
Mima, Fuyu	P2-364
Mimura, Kenshi	P2-369
Min, Hong	P2-311
Min, Leon	P2-347
Min, Yunseo	P3-146
Minard, Charlie	OA81-06, OA81-06
Mindler, Gabriel	OA171-02, P2-094
Minerd, Charles	OA28-02
Mines, Daniel	P2-089
Minetti, Alberto	P1-147
Minetti, Alberto E.	OA154-01, OA154-04
Minikus, Giulia	OA175-03

Author name	Presentation Number
Mink, Zoie	P3-083, P3-147
Minnert, Christian	OA125-04
Minty, Evan	P4-168
MINVIELLE, Antonin	P3-119
Mirgolbabaee, H.	P4-071
Mirgolbabaee, Hadi	OA10-03, P4-310
Misquitta, Joanna M.	OA162-06, P2-284
Mitchell, Edward	OA94-04
Mitchell, Juliana	OA193-06
Mitra, Pratik	P1-400
Mitros, Matthew	P3-268
Mitton, David	P4-234
Miuccio, Michela Paola	P3-258
Miura, Kotaro	P2-231, P3-172, P3-182
Miutz, Lauren	P1-209
Mixon, Parker	OA170-03
Miyadahira, Renato	OA14-01, OA14-02, OA14-04, OA76-04, P3-315, P3-374, P3-380, P3-383, P4-136, P4-157, P4-167
Miyajima, Saori	P3-135
Miyamoto, Shoei	P2-252
Miyata, Shogo	P2-348, P2-357
Miyoshi, Hiromi	OA139-02
Mizrahi, Jacob	P1-335
Mizuuchi, Ikuo	P2-201
Mjavandze, Eter	P4-259
MO, Haoming	P3-095
Mochida, Ai	OA88-04
Mockensturm, Eric	P1-292
Modenese, Luca	OA1-03, OA66-03, P4-194
Moe, Avery	P1-269
Moewis, Philippe	P3-253
Mofrad, Mohammad	P2-020
Moghimifam, Hossein	OA26-02
Moglo, Kodjo	OA109-01, P2-147
Mohamed, Mostafa	P2-241, P2-298
Mohammadi Ghalehney, Sahel	OA123-01
MohammadiNasrabadi, Amin	P4-207
Mohammadzadeh Gonabadi, Arash	P3-101
Mohammed, Amear	P4-018
Mohilldeen, Heytham	OA32-02
Mohimin, Md Ajwad	P4-081, P4-082
Mohout, Ikram	OA149-02, P4-317
Mohr, Maurice	OA45-02, OA8-04, P1-331
Mohseni, Mahdi	OA37-04, P3-373
Moisan, Gabriel	P3-245
Moison, Julie	P2-306
Moissenet, Florent	OA83-02
Mojtahedzadeh, Bita	OA194-02
Mojumder, Joy	P3-066
Mok, Seungju	P3-054
Moke, Lieven	OA23-02, P3-281
Molenaar, Carly	P4-236
Molina, Jessica	P2-058
Molinari, Roberto	OA48-04

Author name	Presentation Number
Mollaei, Zahra	P1-204
Mollen, Frederik	P2-005
Mombaur, Katja	OA184-01
Monaghan, Michael G.	OA197-03
Monchaux, Romain	OA5-02
Monfort Faure, Jordi	OA182-03
Monfort, Jordi	OA117-01, OA182-05, P1-078, P1-228
Monfort, Scott	OA189-05, P1-356, P2-102, P2-153, P2-189
Mongeau, Luc	P2-370
Mongrain, Rosaire	OA167-02, P4-058
Monji, Hiroya	P4-150
Monoli, Cecilia	P1-002, P1-118, P2-124, P2-333
Mononen, Mika	P2-178
Monson, Ken	OA169-01
Monson, Kenneth	P3-114
Monteiro, Arianna S.	P3-010
MONTEL, Mathilde	OA155-04
Monteleone, Angelo	OA144-04
Monticelli, Nicolò	P4-231
Moo, Eng Kuan	OA198-04
Moon, Hyeonbin	P4-026
Moon, Jeongin	P1-167
Moon, Jungsun	P3-365, P4-323
Moon, Yaejin	OA6-02, P1-087
Moore, Axel	OA62-01, P2-259
Moore, Axel C.	P3-199
Moore, Bradley	P4-227
Moore, Connor	OA94-04
Moore, Douglas	P4-321
Moore, James	OA198-01
Moore, Jason	OA124-04
Moore, Justin B.	OA128-05
Moore, Sarah	OA113-04
Mora-Macías, Juan	OA122-02
Mora-Pinos, Maria	OA187-04
Moradi, Souren	OA32-02
Morales Garcia, Cristian Nikolas	P3-299
Morales, Breanna	OA40-02, P4-152
Moran, Jason	OA188-06
Morata Moreno, Luis	P1-113
Morata-Moreno, Luis	OA119-04
Morbiducci, Umberto	OA108-02, OA25-02, OA43-04, OA69-02, OA69-03, OA82-05, OA91-03, OA95-05, P4-037, P4-113
Mordenti, Marina	P4-228
Moreddu, Rosalia	OA90-02
Moreira-Gonçalves, Daniel	P4-263
Morel, Olivier	OA186-03
Morellato, Kavin	P3-240
Morelli, Moreno	P1-318
Moreno González, Inés	OA169-02
Moreno Jaramillo, Jonaz	P1-210, P4-341
Moreno, Alyssa	P4-137
Moreno, Eliana	P3-220
Moreno, Jonaz	OA118-02

Author name	Presentation Number
Moreno, Rodrigo	P3-186
Moreno, Tiffany	OA50-01
Moretta, Elisa	OA73-05
Morgan, Kristen	P1-120
Morgan, Kristin	OA106-03
Morgan, Mary	OA189-01
Morgaz, Juan	OA122-02
Morgenroth, David	OA66-04
Morgiel, Ewa	P4-251
Morin, Claire	OA97-02
Morishita, Katsuyuki	P2-201
Morita, Akemi	OA122-03
Morita, Yasuyuki	P2-375
Moritz, Chet T.	OA27-01
Morlock, Michael	OA99-05, P3-246
Moroder, Philipp	OA70-05
Moroni, Lorenzo	OA50-04
Morris, Jamie	OA177-04, P3-379
Morris, Keiana	OA9-05
Morris, Nathaniel	P2-104
Morris, Seamus	P2-115
Morrison, Benjamin	P2-345
Morrissey, Colm	OA194-02
Morrow, Melissa	OA29-05, OA76-03
Morrow, Melissa M. B.	OA150-04
Mortensen, Brett	P3-322
Mortenson, W. Ben	P2-327
Morton, Amy	P4-321
Moscoloni, Beatrice	OA167-03, OA74-04, P3-023
Moser, Gabrielle	P2-056, P3-101
Moser, Mackenzie	P4-072
MoslemiVaraki, Abdollah	OA122-06
Mossayebi, Ali	P2-009
Mossazghi, Nahom	P4-094
Motlagh, Jodi	P3-366
Motoi, Yugo	P3-135
Motoori, Yutaro	P2-016
Motta, Sarah	OA4-02
Moufflet, Adrien	P1-318
Moulin, Lucas	P4-224, P4-225
Moulton, Derek	P2-265
Moulton, Richard	P1-102
Mourtzakis, Marina	P4-198
Moutinho, Matheus O.	P1-305
Movahhedinia, Hosna	OA54-05
Mowla, Shaheen	OA88-05
Moy, Trina	P1-117
Moyer, Austin	OA159-03
Moyle, Kate	P2-163, P2-185, P3-212, P3-230, P3-231, P3-252, P3-263
Mu, Siyu	OA167-04
Muccini, Julie	OA68-05, OA9-02, P3-099
Muczynski, Brandon	P1-290
Mudway, Ian	P1-038
Mueller, Juliane	OA81-05, P1-174, P1-330

Author name	Presentation Number
Mueller, Steffen	OA81-05, P1-174, P1-330
Muir, Brittney	OA72-04, P4-148, P4-149, P4-309
Muir, Ross	P2-194, P3-349
Mukherjee, Mukul	P2-337
Mukherjee, Satanik	OA149-02, P1-021
Mukherjee, Shubhra	OA24-04
Mukherjee, Tanmay	OA56-05, P4-081
Mulla, Daanish M.	OA162-06
Muller, Antoine	OA2-01
Muller, David	OA144-03
Mullet, Jodi	P3-034
Mulligan, Dylan	P2-038, P2-122
Mulligan, Quinn	P2-121, P3-256, P3-257
Mullins, Clive	P4-288
Muluk, Satish	OA167-05, OA179-04
Muluk, Satish C	P1-400
Muluk, Satish C.	OA108-04, OA191-03
Munidasa, Samal	P4-017
Muniz, Adriane	P1-191
Munn, Lance	P4-053
Munoz, Nathalie	P3-114
Munro, Vicki	P1-198, P1-199
Munshi, Sayar	OA139-03
Murakoshi, Michio	OA153-05, P1-014
Muralidhar, Sriram	P1-081, P1-082
Murari, Milena F.	P4-176
Murase, Kohei	P3-030, P3-275
Murawski, Jessica	P2-010
Murphy, Ciara	OA49-04
Murphy, Colin	OA88-03
Murphy, Kaitlyn	P3-150
Murphy, Shaughnessy	P2-264
Murray, Morgan	P1-351, P1-352
Murray, Wendy	OA2-03, P2-176, P3-384
Murrell-Smith, Zhané	P2-100
Murro, Millissia	P1-144, P1-202, P4-215
Murthy, Naveen	OA76-03
Murthy, Sage	OA103-03
Musahl, Volker	OA141-01, OA141-05, P3-261, P3-262, P3-323, P3-371
Museck, Isabelle	OA148-01
Musgrave, Julia	P4-129
Music, Hallie	P1-301, P1-302
Musotto, Giulio	P4-048
Mussano, Federico	OA199-02
Mustonen, Anne-Mari	P3-336
Mutnick, Mira	P2-328
Muto, Tsuyoshi	OA180-05
Muñoz Estevez, Laura Valentina	P3-242
Myer, Gregory	OA68-05, P2-183
Myer, Gregory D.	OA128-04
Myers, Casey	OA81-01
Myers, Kristin	OA170-02, OA170-03, P3-160
Myers, Kyle	OA191-02
Myers, Sara	P3-101

Author name	Presentation Number
Myers, Sarah A.	P2-056
Mylle, Ine	OA143-01, OA143-02, OA143-03, OA143-04, P4-347
Mylonas, Vasileios	OA93-02, OA93-03, P1-196
Myotsuzono, Hanae	P4-150
Mählich, Daniela	P2-240
Mäusli, Andrea	P3-235
Ménard, Anne-Laure	OA193-05
Möller, Hendrik	OA44-05
Mühlpointner, Matis	P3-179
Müller, Ralph	OA122-04, OA185-04, P1-012, P1-028, P4-346
Mündermann, Annegret	OA18-02, P4-334
N, Jeevaraaj	P1-362
N. Verma, Nikhil	P4-157
Naaim, Alexandre	OA2-01, P1-200
Nachtman, Matthew	P4-181
Nadeau, Philippe	P2-335
Nadybal, Ryan	P3-181
Naeem, Muhammad Shehryar	P4-122
Naeini, Vahid	OA132-03
Nagane, Rin	P3-182
Nagano, Akinori	OA136-04, OA94-02, P1-254
Nagargoje, Mahesh S.	OA115-02
Nagasaki, Goki	P1-014
Nagayama, Rei	P1-040
Nagle, Tara	P2-086, P3-233, P3-325
Nagle-Christensen, Avocet	OA72-04, P4-148, P4-149, P4-309
Nahan, Key	OA178-04, OA66-03, P1-329, P4-194
Nail, Elizabeth	P1-280
Nail-Ulloa, Ivan	OA48-04
Nair, Priya	P4-330
Nair, Supriya	P1-365
Naito, Munekazu	P3-194
Najar, Azad	P4-348
Najman, Laurent	P4-106
Nakajima, Shunsuke	P4-044
Nakamura, Aya	P4-150
Nakamura, Masnaori	OA127-01
Nakamura, Taishi	P1-391
Nakamura, Taisuke	P2-016
Nakane, Masaki	OA11-04
Nakanishi, Yoshitaka	P1-398
Nakano, Takumi	P4-150
Nakashima, Yasuharu	P3-053, P4-150, P4-293
Nakashima, Yuta	P1-398
Nakata, Ken	P3-261, P3-262
Namahoro, Benit	OA67-02
Namikawa, Takashi	P3-285
Namsrai, Bat-Erdene	P3-181
Nanayakkara, Sheran	OA38-04
Napier, Christopher	OA143-01, OA143-02, OA143-03, OA143-04, OA143-05, P1-357, P4-347
Naqvi, Syeda Masooma	OA198-02, OA88-03
Narayan, Advaith	P1-389
Narayanan, Vaishnavi	OA187-04
Nardini, Alessandra	OA11-03, OA187-01, OA77-03, P1-013

Author name	Presentation Number
Nash, Martyn	OA56-01, P4-019, P4-047, P4-080
Nash, William	P2-142
Nasim, Mohammad	P3-125
Nasrabadi, Amin	P1-048
Natalucci, Valentina	OA154-01, OA154-04, P1-147
Nataraj, Raviraj	OA111-03, P2-344
Natarajan, Sai	OA182-03, OA35-02
Natarajan, Thangam	OA108-02, OA43-02, P4-013
Nathanail, Stephanie	P3-319
Nauman, Eric	P1-265, P2-107, P2-363, P3-136
Navarrete, Álvaro	OA146-02
Navratnarajah, Saranya	P1-267, P1-362
Nawabi, Danyal	OA141-03, OA183-02, OA188-04, P2-042
Naybour, John	P3-209, P3-210
Nazarahari, Milad	OA148-06, P1-201
Nazem, Maryam	P2-163, P2-185, P3-212, P3-230, P3-231, P3-252, P3-263
Ndeh, Arthur	OA88-05
Neath, Chyenne	P1-206, P4-030
Nebuya, Satoru	P1-036
Necas, David	P3-217
Needles, Bradley	OA119-04, P1-113
Neelakantan, Sunder	OA191-02, P4-107
Neeteson, Nathan	OA129-05
Negron-Fernandez, Nahir	OA79-01
Neher, Caitlin	OA32-06, OA74-03, P4-302
Neill, Matthew G.	OA131-04
Nelson, Andrew	OA74-01
Nelson, Christa	P2-037
Nelson-Wong, Erika	P1-231
Nematollahi Sanij, Seyed Mahan	P2-178
Nemecek, Daniel	P3-217
Nepe-Apatu, Tuterangi	OA58-05
Neptune, Andra	P3-288
Neptune, Richard	OA33-06, OA80-05
Nestor, Dominic	P1-326
Netzer, Cordula	OA18-02
Neu, Corey	OA129-04, OA176-04
Neu, Corey P	OA182-05
Neuenschwander, Beat	OA125-04
Neufeld, Jillian	OA141-02
Neumann, Marc	P1-004, P2-180, P2-210
Neuville, Daniel R	P4-336
Neves, Cauã	OA76-04
Newham, Elis	OA10-04, P4-297
Newman-Casey, Paula	P1-051
Nezami, Farhad	OA185-05
Ng, Geoffrey	OA183-04, OA183-05, P4-350
Ng, K.C. Geoffrey	OA161-05
Ng, Tony	P3-304
Nguyen, Anh	P4-283
Nguyen, Camille	P2-299
Nguyen, Catherine	P2-223
Nguyen, Dang Phu Ha	P4-352
Nguyen, Giang Lam	P1-281

Author name	Presentation Number
Nguyen, Kaylee	OA103-03
Nguyen, Nancy	OA160-03, P1-144, P1-202, P4-215
Nguyen, Peter	P3-034
Nguyen, Sophie	P3-348
NGUYEN, Thach-Hoang	P4-282
Nguyen, Thao	P3-174
Nguyen, Thao D.	OA158-02, OA181-05
Nguyen, Thi Bang Giao	P2-340
Nguyen, Vicky	OA158-01
Nguyen, Vivian	OA18-06, P2-168
Ngyuen, Victor	OA63-01
Nibbs, Robert	OA198-01
Nichols, Jennifer	OA1-04, P2-058, P2-198, P3-353
Nichols, Nathan	P4-219
Nicholson, Gregory	OA14-01, OA14-02, OA14-04, P3-374, P4-157
Nicholson, Kristen	OA16-04, P2-047
Nickel, Andrew	P2-104
Nickerson, Kimberly	OA72-04, P1-347
Nicolas, Bideau	P1-378
Nicolas, Guillaume	P1-378
Nicolella, Daniel	P2-148, P2-166, P2-167
Nicolescu, Julia	P1-136, P1-173, P4-184
Nicot, Romain	P4-327
Nie, Yong	OA197-06, P1-175
Niederer, Steven	PL07-01
Niehaus, Peter	P2-009
Niehoff, Anja	P1-007, P2-240, P4-334
Nielsen, Elise	OA80-02
Nieminen, Petteri	OA109-02, P3-336
Niermann, Johannes	P3-036, P4-063
Nieto, Josiah	P3-355
Nieuwenhuys, Arne	OA174-04, OA174-05
Nigam, Nilima	P2-131, P2-202, P2-263
Nigg, Benno	P1-193
Nigg, Sandro	P1-193
Nightingale, Kathyrn R.	P4-345
Nijmeijer, Eline	P3-129
Nikitina, Nina	P1-020
Nikmehr, Mohammad	P4-276
Nikoumanesh, Nikou	P2-258
Nilsson, Frida	OA38-04
Ninarello, Davide	OA175-04, P3-287
Nisa, Intan Chairun	OA91-05
Nishihira, Masako	P1-383
Nishikawa, Kiisa	P2-247
Nishina, Takuya	OA114-03
Nissi, Mikko J.	OA149-04
Nissim, Lee	P4-127
Nitschke, Marlies	P1-124
Nitta, Akemi	OA122-03
Niu, Xufeng	OA187-02
Niwayama, Yuto	P3-276
Nixon, Ryan	P2-235
Niziol, Leslie	P1-051

Author name	Presentation Number
Nkansah, Abbey	OA102-05
Noailly, Jérome	P4-059
Noailly, Jérôme	OA117-01, OA122-03, OA122-06, OA182-05, OA35-02, P1-032, P1-037, P4-060
Noaílly, Jérôme	OA182-03
NOCENT, Olivier	P2-132
Nocerino, Sabrina	P4-113
Noda, Shigeho	OA54-03
Nodes, Harrison	P1-218
Noehren, Brian	OA72-02, P1-120, P1-234, P3-211
Nolasco, Luis	P2-278, P3-117
Noma, Yuto	OA11-04
Nordenfur, Tim	P4-329
Nordsletten, David	OA30-01, P4-033
Norman, Destan	OA81-01
Noroozbabaee, Leyla	P3-329
Norouzi, Dena	P4-035
Noseworthy, Michael D.	OA117-02, P4-169
Novak, Vesna	P1-265, P2-107
Novakova, Magda	P4-226
Nowak, Benjamin	OA1-04, P2-198
Nowlan, Niamh C	OA113-04
Noyes, Frank	P2-107
Nuckols, Richard	P1-167
Nuelle, Clayton	OA188-03
Nuethong, Sittinon	OA1-01
Nuhash, Mashrur Muntasir	P1-402
Nunley, Brandon	P2-083, P3-046
Nussbaum, Maury	P2-051
Nwaokoro, Vital	P1-160
Nygårds, Kim	OA38-04
Nyman, Jeff	OA180-01
Nyman, Jeffry	OA125-02
Nöbauer-Huhmann, Iris-Melanie	P3-343
Nüesch, Corina	OA18-02
Němeček, Jiří	P2-351
O K, Sikha	OA35-02
O'Brien, Fergal	OA89-05
O'Brien, Terence	OA6-05
O'Brien, William	OA6-05
O'Cain, Cody M.	OA119-01, OA3-04, OA81-03
O'Connor, Brianna	P1-280
O'Day, Johanna	P1-256
O'Neill, Matthew	P2-004
Oana, Ghita	OA33-05
Oberdorfer, Annika	OA158-04
Oborn, Michael	OA44-06
Obrist, Dominik	OA110-02, OA157-02, OA157-05, P4-003, P4-090
Ocampo, Vianey Hortencia	P1-377
Ochocki, Katarzyna	P3-084
Ocker, Lea-Marie	OA21-04, P3-370
Oda, Toshiaki	OA54-03
Oddes, Zohar	P4-353
Odinelli, Elena	P4-036

Author name	Presentation Number
Oehme, Stephan	P4-222
Offiah, Amaka C	OA96-06, P2-128
Ogasawara, Issei	P3-261, P3-262
Ogasawara, Takato	P1-366
Ogawa, Takumi	OA26-03
Ogaya, Shinya	OA98-05
Ogbu Felix, Jordan	P3-107
Oghinan, Bettina	OA46-06
Ogihara, Naomichi	P2-079
Oguchi, Abbi	OA182-02
Oh, Hongmin	P4-026
Oh, Jeongseok	P3-232
Oh, Joo Han	P3-359
Oh, Junsik	OA155-06
Oh, Kyoung Uk	OA85-02
Ohanessian, Gary	P1-198, P1-199
Ohara, Kumiko	OA122-03
Ohashi, Toshiro	P1-029, P3-305
OHDO, KATSUTOSHI	OA32-01, P3-094
Ohira, Taisei	P2-003
Ohori, Tomoki	P3-261, P3-262
Ohta, Makoto	OA127-03
Ohtsuka, Masayuki	P4-044
Ojeda, Lauro	P3-034
Ojima, Takeru	OA94-02
Okada, Mami	P3-381
Okada, Yohei	P4-331
Okamoto, Ruth	OA32-03
OKAMURA, MASAHIRO	P3-094
Okuyama, Haruka	P1-088
Olatosi, Oluranti	OA28-04
Oldfather, Taylor	P1-288
Oleinik, Ekaterina	OA63-03, OA97-03
Oleszek, Joyce	OA27-03
Olindo, Stephane	P4-096
Oliny, Alexandre	P4-077
Olivares, Andy L.	OA43-05
Oliveira, Sara	P2-108
Oliver, Michele	OA162-01, OA162-02, OA162-03, P2-271, P3-104
Olivesi, Cécilia	P3-161
Olivier, Agnès	OA29-04
Olivier, Cecile	OA71-04
Oliviero, Sara	P2-125
Olsson, Christoffer	P3-186
Olvera, Holly	P4-097
OMalley, Colleen	OA50-01
Omata, Seiji	P2-375
Omerkhil, Latif	OA27-06
Omori, Toshihiro	OA26-03, OA78-03
Omran, Kareem	OA188-02
Onate, James	OA133-03
Onder, Sakip	P3-329
Ong, Carmichael	P3-203
Ong, Jared	OA87-03

Author name	Presentation Number
Ono, Akira	P2-359
Ono, Tomoya	P3-261, P3-262
Ono, Yoshikazu	OA139-03
Onoue, Kotaro	OA102-04
Ooba, Yosei	P3-234
Oomen, Pim	OA4-05, P4-041
Oomen, Pim J.A.	P4-102
Oomoto, Humiaki	P3-285
Op't Eynde, Joost	P3-086
Opar, David	P3-322
Opsomer, Matthias	OA197-05
Oram, Matthew	P2-076
Orban, Joe	P3-150
Orliac, Baptiste	OA172-04
Orlov, Aleksei	P4-162
Orselli, Maria Isabel	P4-203
Orselli, Maria Isabel V.	P1-305, P4-176, P4-242
Ortega, Santiago	P1-309, P4-266
Ortigas-Vásquez, Ariana	OA57-01, P1-115
Ortiz, Shannon	P4-166
Ortiz-Weissberg, David	P2-041
Osawa, Takayuki	P1-397
Osellame, Roberto	OA114-04
Oshima, Marie	OA102-04, OA127-03, P4-027
Oshima, Yasushi	P3-275
Oshinski, John	P4-096, P4-171
Oshinski,, John	OA191-04
Osman, Hassan	OA192-05
Osterbauer, Paul	P3-310
Ota, Nobutoshi	P1-395
Ota, Satoshi	P1-063
OTANI, Tomohiro	OA30-03
Otani, Tomohiro	P4-121
Othmani, Alice	OA185-02
OTHMANI, Yamen	P3-264
Otsuka, Shun	P3-194
Ott, Kelly	OA114-05
Ouellet, Raphaël	OA42-03
Ouellet, Simon	P3-134
Ouhsousou, Soumaya	P3-284
Ounpuu, Sylvia	P4-260
Ousset, Marielle	P3-165
Outerleys, Jereme	CSB-06, OA117-04, OA2-02, P1-077, P1-134, P4-185
Overby, Darryl	OA101-04
Overby, Sarah	OA53-04, P1-225
Ovispo-Martinez, Alejandro	OA98-02, P1-099, P1-371, P4-261
Owen, Cameron	OA131-04, OA6-03, P3-100
Owen, Meredith	OA72-02, P1-120, P1-234, P3-211
Owusu, Silvia	P4-342
Oxford, Julia	P2-264
Oxland, Thomas	OA193-04, P2-169, P3-116
Oxland, Thomas R.	P3-168
OYAMA, HIDEKI	P3-094
Oyama, Kotaro	OA139-02

Author name	Presentation Number
Oyama, Tomoko G.	OA139-02
Oyen, Michelle	P3-141
Ozanich, Nicholas	P4-337, P4-338
Ozel, Ali	P3-190
Ozturk, Yusuf	OA74-06
O'Keefe, Joan	P2-321
P. Kosonen, Joonas	OA45-03
P. Nunes, Carolline	OA14-04, OA153-01, OA94-03, P1-061, P4-157
P. Saad, Guilherme	P1-061
Pace, Elizabeth	P2-086, P3-233, P3-325
Pacha, Molly	P4-192, P4-193
Packer, Jacob	OA106-03
Padera, Timothy	P4-053
Padilla Bello, Nelly Vanessa	P4-336
Padilla, Abigail	P3-312
Paganelli, Martina	P3-300
Page, Daelyn	P4-335
Page, Danielle	OA107-04
Page, Dylan M.	P3-010
Pageau, Annelise Grace	P2-140, P2-367
Pagnotta, Kaley	P1-003
Pahr, Dieter	OA34-05, P3-200, P3-221, P3-345
Pahr, Dieter H.	P2-186
Pai, Anoosha	OA73-01, P3-254
Pailler-Mattei, Cyril	P4-068
Pajares, Antonia	OA122-02
Pajor, Edmond	P2-035, P2-036
Pal, Saikat	OA33-02, P3-185, P3-273
Palagani, Yellappa	OA139-03, OA25-04
Palahnuk, Hannah	OA39-04
Palanca, Marco	OA194-03, P2-154, P3-286, P3-296, P3-298
Palaniappan, Rithik	P3-315
Palanisamy, Anil	OA68-04
Palizi, Mehrdad	P2-241
Pallone, Lucas	OA105-06, P4-167
Pallone, Rebekah	P1-347
Palmieri-Smith, Riann	OA141-04
Palmquist, Anders	P2-298
Paluch, Amanda	OA189-02, P4-183
Pampu, Cristian	P3-084
Pamukoff, Derek	OA141-02, OA178-06, OA195-03, P1-160, P2-088
Pamulaparthi Venkata, Sairam	OA30-04
Pan, Boyu	P2-298
Pan, Huiming	OA131-06
Panchal, Hannah	P3-365
Panday, Siddhartha Bikram	P1-179, P1-248
Pandher, Harnoor	P1-070
Pandit, Hemant	P3-209, P3-210
Pandy, Marcus G.	OA64-03
Panero, Sara	OA49-05
Pang, Derek	P3-086
Paniagua, Beatriz	P4-321
Panikker, Sandeep	P4-104
Panneer Selvam, Nisanth Kumar	P4-093

Author name	Presentation Number
Pant, Anup	P2-148, P2-166, P2-167
Panzer, Matthew	OA32-05
Papadopoulos, Efthymios	P3-316
Papageorgiou, Elisavet	P3-191
Papamanolis, Lazaros	OA139-05
Papanikas, Christos Panagiotis	P3-191
Papastratakos, Eleni	P2-037
Pape, Philipp	OA8-03
Papegaaij, Selma	OA128-01, P4-177, P4-289
Pappalardo, Fabio	P4-092
Paquette, Caroline	OA177-01
Paquette, Philippe	P4-233
Paravisi, Elena	OA197-05
Parent, Gerald	OA193-05
Parente, Marco	P3-048
Parham, Ellsworth	P1-280
Parides, Michael	OA141-03
Parikh, Shital	P2-029
Parisien, Ariane	OA99-04, P3-307
Park, Chan-Beom	OA176-01
Park, Dongho	OA72-06
Park, Guena	P1-203, P1-298
Park, Gunwoo	P1-151
Park, Gwansik	OA3-04
Park, Hanjun	P2-051
Park, Hyunje	OA111-04
Park, Il-Jung	P3-356
Park, Ilseung	OA67-03
Park, Jihoon	P3-171
Park, Jong Chul	P1-179
Park, Junwoo	OA172-02, OA172-03, P1-085, P1-176, P3-138, P4-195
Park, Keunhwan	OA155-06
Park, Min Soo	OA28-03
Park, Sang-Kyoon	OA107-06, P1-163, P1-315, P1-385
Park, Sangyeong	OA176-01
Park, Seoung Hoon	OA111-04, P2-309
Park, Song-Young	OA166-02
Park, Song-young	P4-069
Park, Sukyung	OA136-03, OA54-04, P1-140, P1-170, P1-203, P1-298, P1-380
Park, Sukyung (Sue)	OA54-01
Park, Wooyoung	P1-380
Parker, David	OA47-05
Parker, Thomas	OA58-01, OA6-05
Parkinson, Rob	P3-078
Parmenter, Alissa	OA10-04, P4-297
Parmenter, Alissa L.	P4-318
Parolari, Alessandro	P4-092
Parr, Therese	P1-367
Parrett, Matthew	OA57-04, P2-050, P2-157
Parrilli, Annapaola	P4-139, P4-343
Parsowith, Emily	OA66-06, OA80-04
Pasanen, Kati	OA129-02, OA13-04, OA72-05, OA98-03, P1-348
Pasapula, Chandra	P3-224
Pascuet-Fontanet, Andreu	OA182-05

Author name	Presentation Number
Pasini, Margherita	OA194-03, P2-154, P3-298, 2189
Pasqualin, Giulia	P4-036, P4-042
Passos Goncalves, Carlos	OA118-05
Pasta, Salvatore	OA185-03, P4-113
Paszek, Matthew	P2-044
Pataky, Joshua	OA83-05
Patalak, John	P3-083, P3-147
Patangia, Jeetika	P3-103
Patel, Aarohi	P4-196
Patel, Alvin	OA151-04
Patel, Jainil	P3-061
Patel, Janki	P1-072
Patel, Mrital	P2-336
Patel, Neil	OA126-03, P2-260
Patel, Snehal	P1-364
Patel, Sonia	OA151-04
Pathak, Harshil	P2-131, P2-202
Pathak, Prabhat	P1-179, P1-248
Pathak, Pushparaj	P2-182
Pathare, Niharika	P2-084
Pathmanathan, Cinthuja	OA177-01
Pathy, Rubini	P4-185
Patlan, Ilana	P4-140
Patrick, Kevin	P4-266
Patrick, Shawanee'	OA165-06, P1-080
Patsch, Janina	OA171-02, OA171-03
Patten, Carloynn	OA1-05
Patten, Carolynn	P1-117, P1-235, P1-236
Patterson, Brooke	P4-154
Patterson, Jae	P1-068
Patti, Giuseppe	OA43-04
Pau, Massimiliano	OA92-05, P2-325
Paukner, Daniel	OA63-01
Paul, Roman	P1-240
Paul, Ryan	P2-091, P3-326
Paulon, Gustavo	P2-092, P2-192
Paulter, Robia	P4-081
Paulus, Dietrich	P4-291, P4-319
Paulus, Paige	P4-227
Paupert, Jenny	P3-165
Pavani, Luiz	P1-060
Pavei, Gaspare	OA154-01, OA154-04, P1-147, P1-148
Pavlovic, Nina	CSB-02, OA129-05
Pavol, Michael	OA151-05
Pawlikowski, Marek	P4-075, P4-279
Payne, Stephen	OA104-02
Paz Carvajal, Alexander	OA19-03
Paz, Adolfo A.	OA146-02
Paz, Concepción	P4-119
Pazzinatto, Marcella	OA147-04
Peach, Megan	OA142-06, OA3-05, P2-067
Pearcey, Greg	P3-301
Pearle, Andrew	OA141-03, OA183-02, OA188-04, P2-042
Pearson, Chad	P1-039

Author name	Presentation Number
Pearson, Noah	P2-234
Pecchio, Daniele	OA25-02
Pechstein, Andrew	OA141-03, P2-042
Peddapeta, Venkata Sai Mahesh	P3-271
Pederzani, Elia	P4-084
Pedraz Munoz, Jose Luiz	OA50-04
Pedretti, Anna	P2-179
Pedretti, Davide Joseph	P2-151
Peersman, Geert	P3-239
Peersman, Gérard	P3-239
Peery, Gabriel	P1-035
Peeters, Birgitt	OA23-02, P3-281
Peham, Christian	P2-007
Pei, Meng	OA143-05
Peiffer, J.D.	P2-176
Peirlinck, Mathias	OA167-03, OA74-04, P1-027, P4-079, P4-300, P4-333
Peitola, Joose	OA73-02, P3-155
Peixoto, Nathalia	OA177-02, OA189-04
Pekkan, Kerem	OA43-01
Pelah, Adar	P1-161
Peldschus, Steffen	OA181-03
Pelia, Robin	P3-380
Pellegrini, Giulio	OA144-04
Pemberton, Brock	OA50-01
Pena, Mary	OA103-03
Pendrak, Bex	OA170-02
Peng, Xiangjun	OA126-04
Peniche Silva, Carlos	OA50-04
Pennati, Giancarlo	OA25-03
Peoples, Brandon	OA165-02, OA196-06, P4-151, P4-153
Pequera, Germán	P1-146, P1-148, P3-060
Perez, Manon	P2-335
Pergami-Peries, Matteo	OA165-03, P4-253
Peri, Unnathi	P4-098, P4-099
Perilli, Egon	OA173-01, P4-273
Perilongo, Giorgio	P3-064, P4-270
Perizzolo, Marco	OA18-06
Perkins, Ina Laura	P4-348
Perkumas, Kristin	OA101-04
Perotti, Luigi	OA30-02
Perottoni, Simone	OA153-03, OA26-04
Perra, Emanuele	P4-021
Perreault, Eric	OA168-05, P2-247
Perri, Letizia Maria	OA89-03, OA89-04
Perrier Groult, Emeline	P2-219
Perrin, Ben	P2-112
Perrin, David	P4-010
Perrotti, Romina	P4-257
Perrudin, Baptiste	P2-306
Pertler, Elke	P4-316
Peskova, Mariya	P2-140
Pestel, Maximilian	P3-343
Peterson, Andrew	OA34-04, OA86-02, OA86-06, P2-026, P2-105, P3-201, P3-220
Peterson, Carrie	P1-277

Author name	Presentation Number
Peterson, Matthew	P1-262
Petrini, Lorenza	OA25-03
Petrovic, Mina	OA97-03, P3-345
Petter Rodrigues, Marina	OA168-04
Petushek, Erich	OA128-04, P1-001
Pew, Corey	OA189-05, OA192-03, P1-356, P2-142
Pexa, Brett	P1-260, P1-293, P1-313, P1-322, P1-340
Peyrin, Francoise	OA71-04
Peyton, Leo	P1-281
Peña Fernández, Marta	OA5-01, P3-190, P4-332
Peña, Mary	P2-012
Pešek, Jiří	OA104-01
Pfau, Thilo	P2-006, P2-035, P2-036, P3-344
Pfiffner, Flurin	P4-063
Pham, Dzung L.	P3-066
Pham, Toan	OA156-03
Phan, Vu	OA141-05, P2-046
Phillippi, Julie	P4-055
Phillips, Andrew	OA180-03, OA180-06, P1-264
Phillips, Andrew T M	OA188-06
Phillips, Anthony	P1-015
Phillips, Clara	P2-301
Phillips, Courtney	OA137-05
Phillips, Gemma	OA6-03
Piaia Silvatti, Amanda	P1-044
Piazza, Stephen	P2-010
Piazza, Stephen J.	P2-248
Picco, Bryan	OA107-03
Pichika2, Rajeswari	OA76-02
Piché, Nicolas	OA74-01
Piek, Lotte	OA82-04
Piekarska, Magda	OA4-03
Piella, Gemma	OA117-01, P1-032
Pierantoni, Maria	OA100-02, OA100-03, OA100-04, OA113-04
Pierce, David M	P1-021
Pierrat, Baptiste	OA116-03, OA84-04, P3-156, P4-023, P4-032
Pierre-Philippe, Cortet	P3-337
Pierz, Kristan	P4-260
Pietrosimone, Brian	OA141-06, P1-211
Pignolo, Robert	OA161-04
Pike, Jeffrey	P3-381
Pillet, Helene	OA172-05
Pillet, Hélène	OA130-03
Pillitteri, Marta	OA95-04
Pineda Guzman, Roberto	OA168-03
Pinhey, Shay	P1-227
Pinnock Branford, Kathylee	OA150-04, OA76-03
Pinto de Oliveira, Francisco	P4-043, P4-119
Pinto, Sónia	P4-043, P4-119
Pirola, Selene	P4-040
Pirritano, Marissa	OA59-05, P4-292
Pisay, Prachi	P1-215, P1-216
Pistelli, Giorgia	OA153-03
Pithioux, Martine	OA71-02

Author name	Presentation Number
Pitsillides, Andrew	P4-297
Pitt, Will	P3-379
Pitti, Estelle	OA45-04
Pitts, Jessica	OA160-02, OA40-04
Pitts, Mackenzie	OA27-02
Pivonka, Peter	OA185-02, OA24-05, P2-030, P2-069, P2-094, P3-357, P3-376, P4-298
Pizzamiglio, Cristiano	P3-354
Pizzolato, Claudio	OA15-01, OA22-03, OA80-01, P2-069, P2-094, P2-117, P3-032
Plappert, Felix	P4-041
Plate, Johannes	OA165-05
Plaza, Gustavo R.	OA88-02
Plet, Guillaume	P4-068
Ploeg, Heidi	OA113-02, OA99-03, P3-148
Ploeg, Heidi Lynn	P2-378, P2-379
Plows, Andrew	P1-373
Plummer, Mark	OA145-04
Plunet, Ward	OA193-04
Plüss, Stefan	OA173-04
Podoll, Katherine	P1-335
Poehlmann, Claudia	P1-282
Pohl, Michael	P1-335
Poitras, Isabelle	OA111-01
Poles, Isabella	P2-376
Poletto, Giorgio	P2-238
Pollaci, Alexia	P4-342
Pollard, Ryan	OA48-04
poller, Beatrice	P2-007
Polli, Dario	OA77-03
Polli, Roberta	P3-064, P4-270
Pollock, Courtney L.	OA155-05, P1-107
Pollock, Tanner	P2-188
Poloni, Sofia	OA69-01, P4-084
Poncioni, Simone	P4-342
Ponratana, Alyssa	P4-237
Pontillo, Marisa	OA142-05
Pontone, Gianluca	OA95-04
Pontonnier, Charles	OA186-03, P2-033
Pop, Alexandra	OA128-03
Popchak, Adam	P3-371
Pope, John	OA46-03
Popescu, A. Eduard	OA113-02
Popovicz Nunes, Caroline	OA76-04, P3-374
Popovicz Nunes, Carolline	OA105-06, P1-255, P3-315, P3-383, P4-258
Popovicz, Carolline	OA98-06
Poretti, Kelly	OA177-02, OA189-04, P4-259
Porta, Micaela	P2-325
Portela, Bianca M.	P1-305
Porter, Annie	P2-260
Porter, Ke'La	P4-140
Porter-Honicky, Nana	P2-082
Porto, Ryan	OA150-02
Posluszny, Kate M.	P3-111
Potluri, Ajay S.	P3-225
Potter, Hollis	OA188-04

Author name	Presentation Number
Potter, Leigh	OA58-05
Potter, Michael	P3-015
Potter, Nicole	P1-071, P4-223
Potthast, Wolfgang	P3-098, P3-267
Potvin, Jim	OA186-04
Poulos, Demitria	OA115-02, OA115-04
Poulose, Benjamin	P4-160
Pourmodheji, Reza	OA8-03
Pourmussa, Bianca	OA144-05
Pourzal, Robin	P3-225, P3-380
Pouzet, Florian	P3-165
Powar, Gouresh	P1-291, P1-297
Power, Geoffrey	P2-205
Power, Geoffrey A.	P2-208
Power, Geoffrey A	P2-230
Power, Geoffrey A.	P2-054, P2-206
Prader, Antonius	OA119-01
Pradhan, Aseem Milind	P4-146
Prahl Wittberg, Lisa	OA38-04, P3-186, P4-275
Prajapati, Om	OA123-03
Prajapati, Sunil	P1-214
Prakash, Mithilesh	P3-049
Pramudita, Jonas	P3-234
Prasad, Jakka	OA35-02
Prasanna, Angeline	P1-105
Praster, Max	OA151-03
Praster, Maximilian	P3-260
Pratt, Kristamarie	P4-196
Praz, Quentin	OA83-02
Prehar, Arandeep	P3-227
Prejean, Mabel	OA102-05
Prendeville, Hannah	OA38-01, P4-274
Prentice, Katherine	OA135-03, P2-158
Pressacco, Michele	P3-354
Pretty, Steven	P3-070, P3-151
Preuss, Richard	P1-360
Price, Mark	OA136-06
Prince, Jerry L.	OA58-04
Princelle, Domitille	P1-130
Prisman, Eitan	OA153-02
Pritchard, N. Stewart	OA128-05
Pritchard, Nicholas	P3-083, P3-147
Privet-Thieulin, Coralie	P2-349, P3-006
Proestaki, Maria	OA199-04
Prosser, Laura	P1-065, P4-189
Proudhon, Henry	OA50-04
Provencher, Matt	P3-318
Provencher, Matthew	OA195-04
Provencio, Jacob	P4-276
Provot, Thomas	P4-264
Prudholme, Dieanna C	P4-259
Pruyn, Kai	P2-303
Ptak, Mariusz	OA145-02
Pu, Xinzhu	P2-264

Author name	Presentation Number
Pudhota, Shantha Sindhu	P2-289
Puerta, Carlos	P2-005
Puetzer, Jennifer	OA114-05, OA138-05
Puetzer, Jenny	OA63-02
Pugachev, habil. Alexander	P3-267
Pujo-Menjouet, Laurent	OA126-05
Pulipaka, Bhavana	P4-001
Pumberger, Matthias	P2-134
Purcell, Philip	P2-115
Purzycka, Joanna	P4-318
Putame, Giovanni	OA199-02, OA49-05
Pydi, Yeswanth	OA100-04
Pálsson, Halldór	P2-197
Pérez Ansón, María Ángeles	P1-404
Pérez Mallada, Néstor	OA42-04
Pérez, Agustín	OA156-01
Pérez, Luis	P2-368
Pétré, Maïté	OA84-05
Pöstges, Simon	OA102-02, P4-002
Pürzel, Alexander	P1-270
Qayyum, Usama	OA38-03
Qazi, Sohaib Ayaz	P4-348
QIAN, Xiuqing	OA158-03
Qian, Xiuqing	P3-193
Qian, Zhihui	OA22-01
Qin, Zhao	P3-033
Qiu, Jiajie	P1-075
Qu, Feini	P2-223
Qu, Hang	P1-066
Quah, Kris	OA81-01
Quah, Kristin	OA178-02, OA178-05, OA67-04
Queen, Robin	P4-238, PL09-01
Queenan, Michael	P3-150
Quenneville, Cheryl	P3-080, P3-108
Quenneville, Eric	OA163-02
Quezada-Plaza, Ignacio	P1-017
Quigley, Harry A.	OA158-02
Quill, Gina	P4-080
Quin, Adam	P3-159
Quinlan, Kyran	P3-143
Quinn, Alastair	OA22-03
Quinn, Anthony	OA58-01
Quinn, Conall	OA110-04
Quintana Matoses, Carlos	OA42-04
Quintiens, Jilmen	OA197-05
Quirk, D. Adam	OA33-04
R. Booth, Gabrielle	OA32-05
R. Wong, Chloe	OA46-06
Rabey, Karyne	OA125-05
Rabey, Karyne N	P3-340
Racy, John	OA103-05
Radalov, Igor	OA182-03
Radivojevic, Olga	P2-168
Rafaels, Karin	P3-084, P3-140

Author name	Presentation Number
Rafaels, Karin A.	P3-087
Raffaele, Elizabeth	OA193-04
Raffegeau, Tiphanie	OA177-02, OA189-04
Raffegeau, Tiphanie E	P4-259
Ragu, Roshan	OA67-02, P1-076
Rahimi, Hoda	P1-015
Rahimi, Reza	OA153-06, P3-303
Rahmati, Seyed Mohammadali	OA159-03
Rahner, Marco	OA81-05, P1-330
Raileanu, Laura	P4-224, P4-225
Raimondi, Manuela	OA187-01, OA90-05
Raimondi, Manuela T	OA153-03
Raimondi, Manuela T.	OA114-04, OA197-03, OA199-03
Raimondi, Manuela Teresa	OA11-03, OA51-01, OA77-03, P1-013
Rainbow, Michael	CSB-04, OA21-02, OA37-02, OA8-02, P2-085, P2-158, P3-201, P3-378
Rainbow, Roshni	P3-148
Rainville, Marlon	OA68-02, P1-333
Raiss, Patrick	OA21-04, P3-370
Rajabifard, Abbas	OA15-05
Rajasekar, Tarini	OA143-02
Rajmalwar, Nishad	OA131-05, P3-047
Rajshekar, Mithun	OA125-05
Rakshit, Ritwik	P3-072
Ramachandra, Abhay	P4-057
Ramachnadra, Abhay	P2-373
Ramage, Stephanie	OA125-05
Ramaglia Amadasi, Roberto	P4-228
Ramakrishnan, Anand	OA175-05
Ramella, Anna	OA127-05, OA95-02
Ramião, Nilza	P3-048
Ramos, António	P3-327
Ramsey, Daniel	P1-283
Rana, Samar	P2-011
Rancourt, Denis	P1-055, P1-119
Rande, Amanda	P4-185
Randhawa, Anaikh	P1-263
Randhawa, Aniakh	OA68-04
Randrianavony, Koloina	P2-349
Rankin, Jeffery	OA3-02, OA42-05, P1-384
Rankin, Jeffrey	OA29-05
Rao Shishis, Madeline	OA128-03
Rao, R. Yogeshwar	P2-040, P2-184
Rao, Ria	OA183-03, P1-114
Raona, Valeria	OA89-03
Rapagna, Sophie	P4-273
Rappel, Hussein	P2-209
Rasalingam, Heshanth	OA113-02
Raschke, Michael J.	OA21-03
Rashedi, Mahmood	OA70-03
Raskin, Yannic	OA25-05
Rasmussen, Corbin	P1-056, P3-101
Rasmussen, Laust D	P3-045
Rasoulian, Shahram	P1-350, P2-187, P2-339
Rasouligandomani, Morteza	OA35-02

Author name	Presentation Number
Rastogi, Rish	P1-226
Rasumussen, Corbin	P2-056
Rathmair, Laura	OA171-02, OA171-03, P2-068, P2-069, P2-094
Rathod, Vaibhavi	P4-238
Ratke, Emma	P1-122, P2-272
Ratnakumar, Neethan	OA67-05
Rauch, Frank	OA5-05, P2-203
Rauch, Noah	P1-260, P1-313, P1-340
Rauch1, Frank	P2-246
Rausch, Manuel	OA4-03
Rauscher, Alex	P4-306
Rauscher, Alexander	CSB-05, OA117-03, OA169-06
Rauter, Georg	OA62-05
Raviol, Jolan	P4-068
Raviot-Derrien, Sophie	P2-018
Rawshami, Araz	P3-045
Rawson, Kerri S.	OA92-01
Razian, Sayed Ahmadreza	P4-115
Ream, Courtney	P4-046
Rebolo, Pedro	P3-048
Recchia, Reagan	OA141-04
Rector, Tradd	OA86-02, P2-026
Redaelli, Alberto	OA179-05, OA191-05, OA95-04, P4-034, P4-036, P4-042, P4-052, 3600
Reddy, Chethan	OA14-06
Reddy, Curran	OA86-06, P2-105
Reddy, Kesava	OA169-03
Reddy, Sunil	P4-273
Redfern, Mark	OA174-01, P4-182
Redmond, Joseph	OA192-03, P2-142
Reed, Alexander K.	OA120-04, OA139-03
Reed, Justin	P1-367
Reed, Matthew	OA121-04, P3-120
Reed, Nick	P3-126
Reesink, Heidi	P2-044
Regazzi, Naire	OA3-01
Regis, Claude	P3-237
Register-Mihalik, Johna	OA128-05
Regnault, Nolwenn	OA29-04
Rego, Guilherme S. C.	P4-176
Rehmani, Anoush	P2-104
Rehme, Lindsay	OA81-06, P2-232
Rehorst, Sebastian	OA118-01, OA3-03, P1-047
Reibel, Kundry	OA84-04
Reich, Marcel Simon	OA192-01, OA23-05, P3-297
Reichenbach, Jürgen	P4-222
Reichhardt, Desiree	P3-085
Reichhardt, Desirée	P3-141
Reid, Abbey	OA137-05
Reifman, Jaques	OA169-01
Reijnen, M.M.P.J.	P4-071
Reijnen, Michel	OA10-03, P4-067
Reijnen, Michel M.P.J.	P4-310
Reilly, Brianna	OA19-04, P2-331
Reimann, Hendrik	P1-058

Author name	Presentation Number
Reimer, Raylene	P3-004
Reimer, Raylene A.	P2-238
Reina-Romo, Esther	OA122-02
Reinardt, Robin	OA60-02
Reinbolt, Jeffrey	P2-138
Reisman, Darcy	OA53-04, P1-227
Reiter, Alex	OA151-04, OA163-05, OA28-02, OA81-06, P2-232, P3-269
Reiter, Leah	OA81-05, P1-330
Reitmaier, Sandra	OA192-01, OA23-05, P2-134, P3-297
Rekant, Julie	P4-182
Relloso Ortiz de Uriarte, Mikel	P1-032
Remedios, Sarah	P4-247
Remus, Robin	P1-004, P2-180
Remuzzi, Andrea	OA69-01, P4-084
Ren, Jifeng	P1-390
Ren, Muchen	P1-205
Ren, Zijie	P1-161
Renaud, Philippe	OA42-02, P1-264, P1-360
Renda, Erika	OA186-02
Rendenbach, Carsten	P3-333
Render, Anna	P2-333
Render, Anna C.	OA106-04, P1-118, P2-124
Rendos, Nicole K.	OA20-05
Requist, Melissa	P2-105, P3-220
Respicio, Konna	P1-056
RESTRAT, Victor	P1-378
Restrepo, Juan	OA167-05, OA179-04
Restrepo, Juan C.	OA191-03
Retamal, Jaime	OA156-01
Rethlefsen, Susan	P4-237, P4-260
Retzky, Julia	OA98-04
Reuter, Payton	P1-074
Revaz, Marys	OA54-02
Reverté, Laia	P1-032
Rex, Kathryn	OA83-05
Rey, Sandrine	OA111-05
Reyes, Kathy	OA119-05
Reyna, Vivian	P4-008
Reynier, Kristen	OA32-05
Reynolds, Daniel	P4-196
Rezaei Adariani, Mahdi	OA104-01
REZAEI LAFMEJANI, Sohrab	P3-264
Rezaei, Asghar	OA161-04, P2-031, P3-278
RezayAraghi, Fargol	P4-302
Rezayaraghi, Fargol	OA32-06
Reznikov, Natalie	OA171-05, OA74-01
Rha, Dong-wook	P2-313
Rhea, Christopher	OA177-02, OA189-04
Rhee, Peter	OA76-02
Rhee, Yumie	P2-197
Rhodes, Anna	OA46-05
Rhodes, Jason	OA27-04
Rhodes, Jason T.	OA27-03
Rhodes, Sidney	P1-280

Author name	Presentation Number
Riahi, Negar	P2-165
Ricard, Etienne	OA186-03
Rice, Charles L.	P2-054
Rice, Hannah	OA147-03, P2-164
Richard, Kassandra	OA91-02
Richards, Chris	OA12-01
Richards, Jim	P4-142
Richards, Peter J	OA122-04
Richardson, Glen	P3-204, P3-205, P3-250, P3-251, P3-265
Richer, Robert	P4-220
Richie, Daniel	P1-339
Richie, Robert	OA71-04
Richter, Berna	P4-273
Richtrova, Michaela	P4-230
Rickmeyer, Zachary	P3-360
Riehm, Christopher	P2-183
Riem, Lara	OA44-02
Riemer, Raziel	P3-021
Ries, Andrew	OA27-02, OA27-05
Rietzschel, Ernst	OA167-03
Riglet, Louis	OA172-04
Rigoni, Giulio	OA109-06, OA35-05, P2-155, P3-016
Rigou, Ioanna	OA187-03
Riise, Jonatan	OA147-03
Riley, Michael	OA129-01, P1-265
Rilling, Amelia	P2-206, P2-208, P2-230
Rinaldin, Carla	P4-203
Ringgaard, Steffen	P4-087
Ringleb, Stacie	P2-291
Rios Deossa, Simon	P4-008
Ripamonti, Claudio	OA18-01
Ripoll, Cristina	P4-101
Ristaniemi, Aapo	OA87-04
Ristori, Tommaso	P4-070
Ritchie, Brodie	CSB-03, OA76-05
Ritsma, Benjamin	P1-077
Ritter, Daniel	OA21-04, P3-370
Ritter, Marisa	P1-004
Ritter, Nicole	OA7-04
Rittweger, Jörn	OA154-01, OA154-04
Riva, Alessandra	OA95-03, P4-042
Rivera Calagua, Bryan	OA70-01
Rivera, Adriele	OA111-04
Rivera, Alexis	OA152-02, OA176-02
Roach, Koren	CSB-03, OA5-03, OA76-05, P2-087
Roach, Megan H.	P3-115
Roato, Ilaria	OA199-02
Robalino, Johan	P1-060, P4-263
Robb, Kelly	OA178-06
Robbins, Andrew	P2-022, P2-101
Robbins, Shawn	OA195-05, OA42-02, P1-264, P1-317, P1-318, P1-360
Robert, Thomas	OA172-05, OA2-01
Roberts, Bryant	P2-125
Roberts, J. Murray	P4-332

Author name	Presentation Number
Roberts, Richard	P3-319
Roberts, Shawn	P3-312
Roberts, Spencer	OA6-05
Roberts, Thomas	OA12-02, OA137-04
Robertson, Anne M.	P4-054
Robertson, Blake	P3-076, P3-102
Robertson, Caden	OA153-04
Robey, Nathan	P1-070, P4-163
Robinette, Allison	P1-259
Robinovitch, Stephen	P1-087, P3-057
Robinson, Austin	P4-153
Robinson, Cylus	P3-046
Robinson, Jennifer	OA77-02
Robinson, Rachel	P1-353
Robu, Ion	P4-185
Roche, Ellen	OA156-01
Roche, Ellen T.	OA38-01, OA43-05
Roche, Stephen	P3-361
Rock, Chase	P1-059
Rockford, Connor	P1-166
Rockwell, Brendan	OA99-06
Rodeo, Scott	OA188-04, P2-249
Rodrigues, Ariana	OA148-02
Rodrigues, Carla B.	P4-243
Rodriguez Matas, Jose Felix	OA115-02, OA115-03, P4-006
Rodriguez, Alondra	P3-034
Rodriguez, Angie	P1-280
Rodriguez, Maria J.	OA119-03
Rodriguez-Hernandez, Mynor	OA165-02
Rodriguez-MacClintic, Jennifer	P4-260
Rodríguez Matas, José Félix	OA69-02
Rodríguez, Benjamín	P2-368
Roe, Gregory	P3-100
Roe, Katelyn M	OA142-04
Roehrle, Oliver	OA28-01
Roelker, Sarah	OA189-02, OA189-03, OA9-04, P4-183
Roemer, Frank	P4-334
Roffino, Sandrine	OA71-02
Rogati, Giulia	P1-149, P4-228
Roger, Robert	OA194-04
Rogers, Meghan	OA190-04
Rogoll, Lennart	P4-172
Rogot, Jack	P2-362
Rohan, Pierre-Yves	P3-157
Rohatgi, Ram	P4-020
Rohleder, Claire	OA2-04
Rohner, Catherine	P4-283
Roizman, Max W.	P4-242
Rokhmanova, Nataliya	P2-056, P4-287
Rokos, Ondrej	P3-300
Rokudo, Miwa	OA91-04
Roland, Michael	OA60-02, P4-144, P4-211, P4-212
Rolston, Jesee	OA51-05
Rolston, Jesse	OA101-05

Author name	Presentation Number
Romanyk, Dan	P2-298, P4-328, P4-335
Romanyk, Dan L	P3-340
Romeo, Manuel	P2-179
Romero A., Giovanny A.	OA128-05
Romero Avila, Elisa	P1-133
Romero Delgado, Gisell Natalia	P3-224
Romizi, Luca	P4-074
Rooks, Tyler F.	OA145-05
Rootman, Daniel	OA109-04
Roper, Jaimie	OA165-02, OA165-04, OA196-06, P4-138, P4-151, P4-153, P4-250
Roque, Daniel	P4-188
Rosado-Mendez, Ivan	P3-160
Rosalia, Luca	OA139-03
Rosario, Lailah	OA142-06, P2-067
Rosato, Antonio	OA185-03, P4-092
Rosato, Aurora	P4-021
Roscher, Patrick	P2-296
Rose, Dorian	P1-072
Rose, Sean	OA133-03
Rosen, Adam	P1-274, P1-275
Rosen, Adam B.	P1-290
Rosenberg, James	OA71-04
Rosenblatt, Noah	OA160-03, OA79-01, P1-093, P4-227
Rosenbohm, Jordan	OA102-03
Rosengren, Björn E	OA105-03
Rosenwasser, Melvin	P3-346
Roser, Mark	P2-056, P3-101, P4-287
Ross, Jeremy	OA15-03, OA190-03
Ross, Stephanie	P2-024, P2-256, P2-257, P2-263
Ross, Stephanie A.	P2-243
Rossini, Alessandra	OA97-03
Rossman, Stephanie	P3-117
Rost Kruger, Walker	P1-309
Roth, Joshua	OA188-05, P2-025
Roth, Sabine	P3-260
Roth, Stephan	OA38-04
Rouault, David	P3-319
Rouhani, Hossein	P2-165, P4-295
Rouse, Elliott	P2-082
Routt, Autumn	P1-046
Routzong, Megan	P2-239
Rouze, Ned	P4-345
Rowan, Mallory	OA57-04, P2-050, P2-157
Rowe, James	OA149-01
Rowlands, Danielle	P3-085, P3-141
Rowson, Steve	OA19-04, P2-331, P4-197
Roy, Ishan	OA168-02
Roy, Serge	P1-377
Roy, Sitikantha	P3-185
Roy-Chowdhury, Amit	OA185-01
Royal, Kingsley	P3-228
Roybal, Joanna	OA153-04
Rubenson, Jonas	P2-010, P2-248, P4-285
Rubert, Marina	OA188-01

Author name	Presentation Number
Rubin, Clinton	P1-020
Rubio, Jose	OA169-01
Rubod, Chrystèle	OA170-04
Rudan, John	OA99-03
Ruder, Matthew	OA128-03
Rudski, Benjamin Zvi	OA171-05
Rudy, Savanna	P2-216, P4-323
Ruffoni, Davide	P4-349
Ruggiero, Luca	P1-147
Ruhland, Laura	OA97-04
Ruiz Alonso, Sandra	OA50-04
Runcie, Callum J.	OA122-06
Rundell, Steve	P3-109, P3-110
Rundell, Steven	P3-117
Runhaar, Jos	OA128-01, P4-177, P4-289
Rusbridge, Clare	P2-015
Ruschel, Caroline	P4-155, P4-156
Ruseckaite, Nida	OA74-02
Rusk, Nate	P2-037
Rusling, Chris	P1-348
Russell, Matthew	OA174-02, OA198-01
Russell, Serena	OA170-02
Russell, Shawn	P1-300
Rustenhoven, Justin	P1-015
Ruth, Parker	OA148-02, P1-057
Rutherford, Derek	P4-247
Rutherford, Drew	P1-368
Rutten, Lisa	P4-067
Rutten, Marcel	P4-095, P4-100
Ruzicki, Janae	OA5-03, P2-087
Ruzzier, Alessia	P4-065
Ryait, Hardeep	P2-270, P2-275
Ryan, Des	P1-281
Ryan, Micheal	OA178-06
Ryan, Nicholas S.	P1-258
Rygielski, Jacob	P1-099, P1-371
Rykhus, Ryan	P4-201
Ryu, Donghyeon	OA65-04
Ryu, Hansol	P1-046, P1-082
Ryu, Hansol X.	OA136-01
Ryu, Jeicheong	OA168-01
Ryu, Jiwon	P2-127, P2-316
Ryu, Seunghwa	P4-026
Ryu, Sihyun	P1-315, P1-385
Rzymkowski, Cezary	P3-026
Rönsch, Henriette	P1-240
Rösch, Yannick	OA157-05
Röösli, Christof	P4-063
Rügamer, David	P1-188
S. Brooks, Jeffrey	P1-308
S. Shah, Darshan	P1-362
S.A. Eskelinen, Atte	OA45-03
Sa, Yookyeong	OA150-03, P1-232
Saab, Wedad	P4-056

Author name	Presentation Number
Saadi, Irfan	P1-023
Sabelis, Louise	OA79-05
Sabick, Michelle	P3-368
Sabin, Patricia M.	OA158-02
Sacchi, Chiara	P4-146
Sacco, Isabel C. N.	P4-242, P4-243
Sacco, Isabel C.N.	P1-305, P4-176
Sachdev, Divesh	P2-052
Sachs, Emma	P2-224
Sack, Ingolf	P3-153
Sacks, Michael	OA120-05, OA84-02, P1-035, P4-003, P4-024, P4-025
Sacks, Michael S.	OA89-02
Sadati, Mahzad	P3-340
Sadeghinia, Parham	OA41-05
Sado, Natsuki	P1-088
Saeidi, Saeideh	P3-345
Saenz del Burgo, Laura	OA50-04
Saenz, Fidel	OA187-04
Safar, Adira	OA170-05
Safdar, Rahmat	P2-177
Saffuri, Eshraq	P2-305, P3-206
Safira, Isna Riski	P2-190
Saftich, Megan	OA81-02
Sagar, Samrat	OA52-04
Sagen, Sara	P2-287
Sahani, Ridhi	OA168-05, P2-247
Sahed, Md Fahad	P2-201
Sahin, Ipsita	P2-213, P2-280, P2-326
Sahni, Akshita	P4-013
Saiki, Michina	OA110-03
Saillard, Emile	P4-234
Saine, Noelle	P1-342
Saine, Noelle D	P1-341
Saini, Justen	CSB-03, OA76-05
Saito, Masato	P3-194
Saito, Takumi	OA138-02, OA91-05
Saitta, Simone	OA191-05, P4-042
Sajjad, Mona	P1-280
Sakai, Rina	P1-036, P2-369
Sakamoto, Makoto	P3-172, P4-326
Sakamoto, Yuta	P3-277
Sakellaridi, Sofia	P2-213
Sakhrani, Neeraj	P2-362
Salamunes, Ana Carla C.	P2-248
Salchak, Yana	OA15-01, P3-032
Sale, Sanja	P3-296
Salehi, Pooya	P2-174, P2-175
Salido, Tiffany	P2-296
Salizzoni, Stefano	OA69-02
Sallé de Chou, Raoul	P4-106
Salmeron-Sanchez, Manuel	OA187-03
Salome, Murielle	OA71-04
Saloner, David	OA108-02
Salsali, Mohammad	P3-124

Author name	Presentation Number
Saltzman, Charles	OA86-04
Saludar, Christian	OA169-05
Saludar, Christian John	OA145-06, OA58-05, 3092
Salvador-Lis, Sandra	P2-108
Salverda, Gaervyn	P1-373
Salzar, Robert	P3-086
Salzer, Elias	OA64-03
Samaan, Michael	OA99-02, P3-211, P4-138
Samaan, Michael A.	P2-074
Samaee, Milad	OA120-03
Samaniego, Joshua	OA98-06, P1-061, P1-071
Samarani, Francesca	P2-204
Samartzis, Dino	OA98-06
Sammel, Jacqueline	P2-136
Sampaio de Oliveira, Manuel Lucas	OA158-02, P3-174
Sample, Alanson	P1-051
San Juan, Jun	P4-163
Sanati Nezhad, Amir	P1-394
Sanati-Nezhad, Amir	OA100-05
Sanchez Marrero, Gloriani	OA4-04
Sanchez, Alex	P3-069
Sancisi, Nicola	OA37-02, OA44-04, P1-200, P2-079, P2-179, P3-378
Sanders, Quentin	OA177-02, OA189-04
Sangiorgi, Luca	P4-228
Sangiorgio, Enrico	P4-037
Sansalone, Vittorio	OA185-02, P4-298
Sansare, Ashwini	OA92-04
Santamaria Guzman, Keven	P4-153
Santamaria-Guzman, Keven	OA165-02, OA196-06, P4-151
Santana, Jonathan	P3-312
Santhanam, Shobana	P4-007
Santiago, Eduardo	OA165-04
Santis, César	OA156-01
Santmarty, Pauline	P4-240, P4-241
Santo Domingo Berzosa, Carlos	OA42-04
Santonocito, Dario Francesco	P3-175
Santos, Inês	OA21-04, P3-370
Santos, Mafalda	OA199-02
Santos-Ferreira, Diogo	P4-043, P4-119
Santos-Lopes, Oliver	OA164-02
Santuz, Alessandro	OA154-01
Sarantos, Lucas	P2-034, P3-075
Saravanakumar, Harish	P2-011
Sardar, Hafiz Zeeshan Ali	P4-089
Saretto, Martina	OA197-04, P4-316
Sarfati, Benjamin	P3-206
Sarin, Jaakko	P3-049
Sarkissian, Mané	P4-059, P4-060
Sarlak, Hadi	P1-149
Sarshari, Ehsan	OA24-05, P3-376
Sartorato, Giorgia	P1-149
Sartori, Massimo	P3-218
Sartori, Stefano	P3-064, P4-270
Sasagawa, Kazuhiko	P2-231, P3-172, P3-182

Author name	Presentation Number
Sato, Kanon	P4-326
Sato, Ren	P2-021
Sato, Takahiko	OA94-02
Sato, Yuho	OA122-03
Saucedo, Fabricio	P1-142
Sauer, Adrian	OA57-01, P1-115
Sauras-Colón, Esther	P1-032
Savage, Matthew	P4-154
Sawacha, Zimi	OA109-06, OA35-05, P1-387, P2-155, P3-016, P3-064, P4-228, P4-270
Sawant, Malvika	OA120-03, P4-073
Sawatsky, Andrew	OA122-05, P2-257
Sawczuk, Thomas	P3-100
Sawers, Andrew	OA66-02, OA66-04, OA66-05, P1-103
Sawiccy, Val	OA140-03
Sawicki, Gregory	OA148-03, OA184-02, OA33-03, OA33-06, P1-046, P2-212, P4-285
Sawicki, Gregory S.	OA109-05, OA136-01
Sawyer, Charles	OA46-05
Saxby, David	OA73-02, P2-102, P2-117, P2-178, P3-032
Saxby, David John	OA147-02
Sayal, Meera	P1-068
Saygin, Zeynep	OA133-03
Sayles, Harlan	P4-152
Saylor, David M.	P4-280
Sayre, Eric C.	OA117-03
Sbriglio, Claudia	OA145-02, 1001
Scagnetti, Ian	OA162-01, OA162-02, OA162-03, P2-271
Scanagatta, Gloria	P2-062, P3-017
Schaake, Leendert	OA41-05
Schadow, Jemima E	OA10-05
Schaeffer, Annika	P1-265, P2-107
Schaer, Thomas	OA175-02
Schaible, Eric	OA71-04
Schallig, Wouter	OA57-06, P2-097, P3-223
Schap, Jeremy	P2-047
Schappacher-Tilp, Gudrun	OA180-04
Scharnreitner, Iris	OA74-02
Schatzker, Joseph	P3-341
Schaumann, Nicole	OA66-04
Schehl, Jan Marc	P2-352, P2-353
Schelfaut, Sebastiaan	OA23-02, P3-281
Schembri, Martina	P4-092
Schepens, Benedicte	OA124-02
Schepens, Bénédicte	P1-089, P1-090
Schepers, Martin	OA128-01, P4-177, P4-289
Scherb, David	P2-269, P2-289
Scherer, Philipp	P3-162
Scherf, Felix	OA60-02
Schett, Georg	P4-220
Scheuch, Sofie-Josephine	P2-353
Scheuermann, Charles	P3-316
Scheuring, Luisa	P3-200
Scheven, Ulrich	OA87-01, P2-217
Scheys, Lennart	OA14-03, OA23-02, OA24-03, P3-239, P3-281
Schierding, William	OA145-06, OA58-05

Author name	Presentation Number
Schifino, Albino	P2-261
Schifino, Albino G.	OA137-02
Schileo, Enrico	OA73-05
Schilling, Cristoph	P4-273
Schilpp, Hannah	OA158-04
Schlager, Benedikt	OA44-05
Schlicht, Samuel	P1-393
Schlittler, Maja	OA97-03
Schlosser, Tom P.C	OA62-03
Schloßmacher, Benjamin	OA60-03
Schluse, Benedikt	OA188-01
Schmid, Stefan	OA62-02, P2-191, P3-302, P3-306, P4-224, P4-225
Schmid, Thomas	P3-342
Schmida, Elizabeth	OA200-04
Schmidt, Hendrik	OA192-01, OA23-05, P2-134, P3-297
Schmidt, Pierre	OA193-05
Schmidt, Samuel E	P3-045
Schmidt, Semjon	P1-331
Schmidt-Bleek, Katharina	OA113-05
Schmitt, Abigail	P1-231, P1-245, P3-198, P4-130, P4-131
Schmitt, Abigail C.	P4-147
Schmitt, Ana C. B.	P4-243
Schmitt, Kira	P2-005
Schmitt, Laura	OA129-01, OA9-04
Schmitt, Laura C.	OA119-01, OA3-04, OA81-03
Schmitt, Syn	OA194-01
Schmoelz, Werner	P3-375
Schnabel, Lauren	P2-233
Schneider, Anne Lotte	P1-174
Schneider, Holm	P1-393
Schneider, Julian	P3-131
Schneider, Kristin	P1-093
Schneider, Marco	OA34-02
Schneider, Noah	P1-292, P3-091
Schneider, Stephanie	OA176-04
Schneider, Stephanie E	OA182-05
Schnorenberg, Alyssa	OA24-04, P3-041
Schober, Shelby	P1-361
Schoinas, Spyridon	OA83-02
Schollenberger, Jonas	OA108-02
Schreiber, Areonna	P2-031
Schroeder, Jordyn	P2-212
Schroeder, Ryan	OA166-03
Schröder, Stefan	P3-236
Schuengel, Verena	OA154-01, OA154-04
Schulte, Friederike A	OA122-04
Schulte, Friederike A.	OA185-04, P1-012, P1-028
Schumacher, Florian	P2-257
Schuring, Lindsay	OA135-04
Schuster, Aurélien	P2-033
Schuster, Robert	OA147-03
Schwameder, Hermann	OA55-05
Schwartz, Amy	P1-262
Schwartz, Michael	OA27-02, OA27-05

Author name	Presentation Number
Schwarz, Erica	P4-038, P4-057
Schwarz, Gilbert	P3-244
Schwarz, Natalie	P1-360
Schwarz, Thomas	P3-183
Schwarzenberg, Peter	OA175-03
Schwiebert, Grant	OA57-04, P2-050, P2-157
Schwiedrzik, Jakob	OA125-04
Schäfer, Friederike	P4-101
Schär, Tim	P2-191
Schönnagel, Lukas	OA113-05
Scilla, Joey	OA59-03
Scocozza, Franca	P2-372
Scott, Cameron	P3-319, P3-331
Scott, Stephen	CSB-06, P1-077
Scott, W. Michael	P2-257, P3-344
Sculco, Peter K.	P3-237
Scurlock, Avery	P3-073, P3-128
Seagers, Kirsten	OA68-05, OA9-02, P3-099
Seballos, Kristen	OA195-04, P3-318
Sebastiani, Sara	OA64-04
Secchi, Francesco	P4-036
Sechopoulos, Ioannis	OA135-02, OA21-05, P4-173, P4-174
Seddighi, Nooshin	P2-333
Sedghizadeh, Mohammadjavad	P4-062, P4-064
Seeger, Anja	P2-028
Seelemann, Corin	P3-007
Seeley, Mark	OA70-03
Seerattan, Ruth	P2-238, P3-004
Seerattan, Ruth-Anne	OA27-06
Seethapathi, Nidhi	OA136-06, OA48-02, OA61-03, P1-069, P1-241, P1-268
Segers, Patrick	OA167-03, OA7-04, OA74-04, P1-027, P3-023, P3-152, P3-153, P4-079, P4-300, P4-333
Seifert, John	P1-257
Seikaly, Hadi	P4-141
Seiler, Theo	P3-177
Seira, Oscar	OA193-04
Seitz, Amee	OA24-04
Selbie, Scott	P1-077
Selinger, Jessica C.	OA52-05, P1-159, P4-284
Selkmann, Sascha	P2-180
Sellers, Stephanie	OA120-03
Semmler, Marion	P1-393
Semodji, Amevi	P2-264, P3-058
Sen, Indrani	P3-029
Sen, Soumyadip	OA161-04
Seno, Hoshito	P1-036
Sensini, Alberto	OA50-04
Senthil, Darshan	OA56-02
Senthilkumar, Irish	OA152-05, OA176-03
Seong, Daniel	OA61-03
Sera, Toshihiro	P4-045
Seresti, Anahita	P4-118
Sergooris, Abner	OA105-01
Serighelli, Fernanda	OA117-05, OA147-04

Author name	Presentation Number
Serina, Elaine	P1-292, P3-091
Serpieri, Jacopo	OA25-02
Serra, Corentin	OA5-02
Serrancolí, Gil	OA117-01
Seshadri, Sriranjani	OA64-05
Seth, Ajay	OA103-01, OA123-05, OA192-05, P2-097, P2-181
Seth, Praneel	P3-046
Severe, Clare	OA46-04
Sevryugina, Nataliya	P4-090
Seyler, Devin	OA30-02
Seymore, Kayla	OA14-05, OA14-06
Seynaeve, Maura	OA106-04
Sgarzi, Andrea	OA1-03
Sha, Zhanxin	P3-062
Shaarbaf Ebrahimi, Behdad	P4-083
Shabangu, Majahonkhe	OA88-05
Shadden, Shawn	OA144-02
Shafer, Mark	P3-112
Shaffer, Mason	P2-236
Shaffer, Sarah	P2-167
Shah, Alok	OA181-04
Shah, Darshan S	P2-184
Shah, Darshan S.	OA52-04, P1-267, P2-040
Shah, Dipan	OA132-03, P4-082
Shah, Imran	OA132-02, P4-013
Shah, Kunal	P2-176
Shah, Meet	P2-203
Shahard, Haziq	OA74-02
Shahbad, Ramin	OA127-02
Shaheen, Aliah F	P4-135
Shahiri, Mohammadali	OA130-02
Shahsavari, Leila	OA100-05
Shahsavari, Mohammadhamed	OA182-02
Shakir, Kamran	P1-149
Shamritsky, David	OA141-03, OA183-02, OA188-04, OA8-03, P2-042
Shamritsky, David Z.	P3-237
Shan, Xiyao	P3-194
Shanbhag, Julian	OA136-02, P1-152
Shankel, Matthew	OA134-04
Shannon, Kiana	P4-160
Shannon, Kyle	P4-324
Shannon, Logan	P3-325
Shao, Nancy	P2-160
Shao, Zhifeng	OA101-03
Shapiro, Erin	OA198-04
Sharir, Amit	OA120-04, OA139-03
Sharma, Aikta	P4-297, P4-318
Sharma, Hemant	P2-194, P3-349
Sharma, Mahika	P4-185
Sharma, Nikita	OA160-04
Sharp, Amara	P4-138
Sharp, David	OA133-05, OA169-04, OA6-05, P3-081
Shashidharan, Subhadra	P4-124
Shatila, Mohamad	OA183-05

Author name	Presentation Number
Shatila, Mohamad El Fateh	OA183-04
Shatrov, Jobe	OA47-05
Shaw, Jeremy	P3-284
Shea, Brendan S.	OA44-02, P2-113, P2-161
Shearman, Eddie	P3-286
Shebanova, Olga	OA149-01
Sheedy, Aoibhin	OA38-01
Sheehan, Dawson	OA154-05
Sheehan, Dawson S.	OA154-02, OA154-03
Sheely, Brandon	P3-072
Sheerin, Kelly	P1-319
Sheets-Singer, Alison	OA178-02, OA178-05, OA67-04, OA81-01
Shefelbine, Sandra	OA113-01
Shefelbine, Sandra J.	OA64-03
Sheffield, Daniel	P1-284, P1-405, P4-307
Shelburne, Kevin	P3-368
Shen, Chi	OA144-03, OA17-03, P4-110
Shen, Dylan	P2-044
Shen, Jiaqi K.	OA64-03, P2-361
Shen, Xinfei	P2-234
Shenker, Nicholas	P1-161
Shepherd, Max	P1-226
Shepherd, Molly	OA105-02, OA105-05, OA18-04
Sheppard, Mary B.	P2-074
Sheridan, Conal	OA134-02
Sherman, Don	OA121-02
Sherman, Donald	P3-084, P3-118, P3-140
Sherman, Seth	OA73-01, P2-029, P3-203, P3-254
Shi, Jingcheng	P2-118
Shi, Lidan	P2-017
Shi, Yu	OA111-03, P2-344
Shibata, Keisuke	P2-359
Shibata, Masafumi	OA139-03
Shibata, Shohei	OA94-02
Shieh, Wann-Yun	P1-155
Shih, Isabella	P1-159
Shih, Kao-Shang	P3-238
Shih, Tsai-Yu	OA53-01, P2-340
Shih, Yi-Fen	P3-355
Shim, Jae	P1-294
Shim, Jae Kun	P3-038
Shim, Jae-Hun	P1-359
Shim, John	P1-079
Shim, Vickie	OA145-06, OA169-05, OA190-02, OA34-02, OA45-01, OA58-05, P1-092
Shimada, Sean	P3-089, P3-090, P3-107
Shimamura, Masahiko	OA98-05
Shimogonya, Yuji	P1-399, P1-403, P4-108
Shimoto, Takeshi	P3-053, P4-150, P4-293
Shin, Choongsoo	P3-359, P4-294
Shin, Choongsoo S.	OA28-03
Shin, Gaju	P2-309, P4-290
Shin, Gwanseob	OA150-03, P1-232, P2-066, P2-093, P2-127, P2-316
Shin, Hyun Seong	OA28-03
Shin, Sangwon	P2-337

Author name	Presentation Number
Shin, Seonjin	P3-356
Shin, Seungyong	P4-026
Shin, Soyong	OA141-01, OA61-04
Shin, Ye Young	OA36-01
Shinabe, Yoshino	P1-088
Shinohara, Marie	P1-397
Shirazi-Adl, Saeed	P2-174, P2-175
Shiri, Barbod	P2-238, P3-004
Shishov, Nataliya	P1-087
Shivashankar, G.V.	OA75-01
Shiwani, Bhawna	P1-377
Shlecker, Kylie	P1-087
Shmueli, Karin	OA10-02
Shoaf, Nick	OA133-03
Shojaei, Davood	OA15-05
Shojaeianforoud, Farshid	OA169-01
Shokrani, Parand	OA38-01, P4-274
Shourijeh, Mohammad S.	P4-209
Shrader, M. Wade	P1-065, P4-189
Shrier, Evan	P1-141
Shrivastava, Apoorv	OA52-04, P1-267, P1-362
Shrive, Nigel	P2-014
Shriver, Cassandra	OA103-04
Shrotriya, Pranav	P2-373
Shull, Daniel	OA119-02
Shull, Kenneth	OA168-05
Shull, Peter	OA131-06, OA65-01, 3759
Shultz, Sandra	P2-233
Shultz, Sandy	OA6-05
Shvarts, Andrei G	OA122-06
Si-Mohamed, Salim	P4-068
Siadat, Seyed Mohammad	OA101-04
Siakallis, Loizos	P3-191
Siao, Jing-Huei	P3-238
Sibole, Scott	P2-185, P3-230, P3-231
Sicard, Garrett	P4-170
Siddicky, Safeer	P2-286
Siebenaller, Aliza	P2-207, P3-288
Siegel, Danielle	OA153-04
Siegler, Sorin	P3-201
Siegmund, Gunter	P3-093
Siegmund, Gunter P.	OA19-02
Sierra, Isabella	OA195-05
Sigaeva, Taisiya	P3-154
Sigal, Ian	P2-001, P3-167, P3-196
Sigal, Ian A.	OA158-04, P3-180, P3-195
Sigaudo-Roussel, Dominique	P2-349
Sigward, Susan	P1-165, P3-272
Sikdar, Siddhartha	OA173-02, OA59-01
Sikeler, Laila	OA118-01, OA3-03, P1-047, 1970
Silbernagel, Haylie	OA163-04
Silbernagel, Karin	P3-216
Silder, Amy	P1-262, P1-377, P2-114
Siles, Francisco	OA165-04

Author name	Presentation Number
Silfies, Sheri	OA1-02, P4-133
Silon, Nicolas	OA178-06
Silva Barreto, Isabella	OA71-02
Silva, Afonso	P3-077, P4-132
Silva, Ana	P1-191
Silva, Carolina	OA70-04
Silva, Graziele	P4-176
Silva, Joao	OA199-02
Silva, Mateus	P4-311
Silva, Saige	P1-326
Silva, Veronica	P4-203
Silva-Pereyra, Valentina	P1-148
Silverman, Anne	P2-045, P2-077, P2-078, P2-095, P2-103, P2-145
Sim, Sotcheadt	OA163-02
Simaitis, Ethan	OA28-04, OA67-02, P4-188
Siman Tov, Elad	P1-132
Simeone, Matteo	OA152-05
Simha, Surabhi N.	OA109-05, OA136-01
Simms, Ciaran	OA131-03, P1-169, P1-281, P3-024
Simms, Ciaran Knut	P3-215
Simon, David D.	P4-280
Simon, Mathieu	P4-032
Simon, Scott	P4-031
Simonelli, Carlo	OA42-01
Simonian, Natalie	P4-003
Simonova, Anastasiia	P4-162
Simons, Laura E	P4-143
Simpkins, Caroline	P2-307
Sims, Taylor	P3-088
Simões, José	P3-327
Sinclair, Brittany	P3-078
Singer, Lamia	P2-350
Singer-Fox, Laura	OA153-04
Singh, Amit	P1-012
Singh, Arsh	P3-251
Singh, Manisha	OA43-05
Singh, Pratham	OA34-03, P3-254
Singh, Sadaival	OA167-02
Singh, Sanjay	P2-125
Singh, Trisha	OA113-02
Singh-Gryzbon, Shelly	OA132-04
Singletary, Milena	OA107-05, OA131-01, P1-336
Sinnott, Thomas	P3-158
Sinopoli, Marissa	P2-029
Sinopoli, Sabrina	OA189-01, OA194-05
Siong, Mia	OA29-05, OA3-02, OA42-05
Sips, Patrick	P1-027
Sirhan, Katerena	P3-112
Sisella, Mattia	P4-231
Siston, Robert	OA9-04
Sivakumar, Sanjana	P1-117
Sivakumar, Sri Krishna	OA132-02
Sivaraj, Dharshan	OA187-04
Sivarasu, Sudesh	P3-361

Author name	Presentation Number
Siverino, Claudia	OA125-03
Siy, Isaac	OA145-01
Skacel, Pavel	P4-230
Skotarek Loch, Sara	P2-035, P2-036
Skrobot, Matej	P4-222
Skylar-Scott, Mark A.	OA139-03
Slade, Gillian	OA186-04, P2-053
Slade, Patrick	OA106-01, OA33-01, OA52-02, OA65-02, P1-105, P4-283
Sladoje, Marco	P1-285
Slavens, Brooke	OA2-03, OA24-04, P3-041
Slavik, Nick	OA86-05, P4-219
Slavin, Colin	OA106-03
Slavin, Emma	P1-136, P1-173
Slijepčević, Djordje	OA54-02
Slive, Léa	OA36-01
Sloot, Lizeth	OA165-01, OA177-05
Sloot, Lizeth H.	OA160-04
Slootman, Anne	P4-202
Slopecki, Matthew	OA155-01
Sloseris, Daniel	OA91-02
Slowik, Jon	P1-372
Slowik, Jonathan	OA16-01, OA16-06, OA3-06, P1-295, P1-296, P1-346
Smalley, Samuel	P2-211
Smeesters, Cécile	P1-055, P1-119
Smeets, Bart	OA152-05, OA176-03
Smelley, Cade	P2-052
Smirl, Jonathan D.	OA131-04
Smit, Thijs	OA36-02
Smit-Russcher, Roelien	OA192-06
Smith, Adeline	OA106-03
Smith, Benjamin	OA188-03, OA200-03
Smith, Bria	OA165-02, OA196-06, P4-151, P4-153
Smith, Clair	P3-371
Smith, Claudia	P3-163
Smith, Cole	P3-083, P3-147
Smith, Colin	OA195-04, P3-318
Smith, Corey Daniel	P2-140, P2-367
Smith, Jolinda	P3-229
Smith, Joshua	P4-277
Smith, Max	OA141-02
Smith, Ross	OA178-01, P1-221, P1-334, P2-032
Smith, Zoe	OA130-01, P1-249
Smith, Zoe H.	P1-177
Smith-Bregeda, Emily	OA5-03, P2-087
Smolic, Aljosa	P1-281
Snow, John Charles	P3-301
Snow, Tim	OA10-04
So, Kitty	OA193-06
Soares, Paula N. C.	P4-243
Sobinov, Anton	P2-176
Sofko, Katie	P4-339
Sogno, Andrea	OA26-04
Soh, Adam	P1-039
Solav, Dana	OA7-02, P2-305, P3-206, P4-353

Author name	Presentation Number
Soleimani, Meisam	OA199-05
Soliman, Ahmed	OA60-05, OA99-01, P3-314
Soliveri, Luca	OA69-01, P4-084
Sollmann, Nico	OA49-03
Solomon, Andrew	OA92-03
Soltan, Nikoo	P3-127
Soltanolkotabi, Maryam	OA86-06
Somberg, Lewis	OA181-04
Sombris-Picot, Sarah-Maud	P2-219, P3-165
Somerville, Sophia	P1-218
Sommer, Simone	P3-274
Son Hong, Gwi-Ryung	P2-288
Son, Hyesu	OA184-03
Son, Yuju	OA58-03
Soncini, Monica	P4-084
Sondhi, Yash	OA12-04
Song, Ahyoung	P4-133
Song, Changseob	P3-010
Song, Ke	P1-183
Song, Seungmoon	OA41-02, P1-154, P1-226, P1-242
Song, Simon	P4-026
Song, Wenyuan	OA120-03
SONG, Xu	P3-095
Song, Xu	P4-268
Song, Yu	P1-091, P2-343
Sonne, Mike	P2-195
Soo, Megan	OA156-02
Sopeña, Bridget	P1-347
Soroushi, Hossein	OA92-04
Sorrentino, Rita	P2-079
Sotiriou, Sofoklis	OA116-02
Soubra, Hassan	P3-006
Soulez, Gilles	OA104-01
Souppez, Jean-Baptiste R.G.	OA36-06
Souren, Luuk H.F.	P4-070
Souri, Ahmadreza	P4-259
Soutos, Konstantinos	OA116-02
Sowa, Gwendolyn	OA23-03
Spack, Katherine	P3-346
Spagnolo, Pietro	OA95-03, P4-042, P4-092
Spagnuolo, Paul Lucas	OA155-01, P1-343
Spang, Jeffrey	P2-233
Spanou, Martha	OA116-02
Sparks, Holly	P2-014, P3-344
Sparks, Neil	P2-047
Sparling, Tawnee	OA1-02
Sparrey, Carolyn	P2-290
Spartacus, Victoria	OA111-05, OA172-04
Spataro, Marta	P3-175
Speirs, Andrew	OA198-04
Spelly, Gwen	OA136-02, P1-152
Spencer, Katherine	P2-193
Spencer, Megan	OA178-01, OA184-05, P1-334
Spiers, Andrew	OA99-04

Author name	Presentation Number
Spiesecke, Paul	P3-153
Spirtos, Michelle	P1-169, P3-024
Spiteri, Maegan	P4-254
Spitz, Gershon	OA6-05
Spitzley, Kate	P4-187
Spolaor, Fabiola	OA109-06, OA35-05, P1-387, P2-155, P3-016, P3-064, P4-270
Spomer, Alyssa	OA27-02
Sponberg, Simon	OA12-04
Sponer, Yvonne	P2-240
Spradlin, William	P2-096
Sprague, Andrew	OA141-01, OA141-05
Spratley, E. Meade	OA119-01, OA81-03
Spring, Mary	P3-184
Sreedhar, Shreya	OA4-03
Srikanchana, Rujirutana	OA1-02
Srinivasan, Manoj	OA9-04, P1-082, P1-194
Srinivasan, Shriya	OA46-02, OA85-03
Srinivasan, Shruthi	P4-345
Sritharan, Prasanna	OA117-05, OA147-04
Srivastava, Rakesh	P4-069
Srivastava, Siddhartha	P2-217
Srocka, Janine	OA91-02, P2-019
St-Pierre, Marc-Olivier	P4-233
Stacey, Chloe	OA87-01
Stachelek, Stanley	P1-008
Stadelmann, Vincent	OA125-03
Stagliano, Angela	P4-170
Stamati, Olga	OA50-04
Stamer, W. Daniel	OA101-04
Stammen, Kasey	P4-186
Stammer, Moritz L.	OA71-02
Stanley, Jimmy	P2-090
Stansfield, Ekaterina	OA44-03, P1-270
Stark, Nicole	OA19-04, P2-331, P4-197
Starkey, Scott	OA73-02
Stassi, Ariel E.	P3-060
Statiri, Aliki	OA52-04, P2-294
Stauffert, Peter	OA44-05
Staumont, Bernard	P2-371
Stavrakis, Alexandra	P3-270
Stebbins, Julie A.	P2-334, P3-014
Steele, Katherine	OA111-02, OA123-04, OA27-02, OA27-05, OA67-01, P2-322
Steele, Katherine M.	OA27-01
Steer, Samantha	OA123-03
Steere, Karin	P1-335
Stefanati, Marco	OA69-02
Stefanini, Giulio	OA89-03, OA89-04
Stefanyshyn, Darren	OA190-04, OA81-04
Steib, Simon	OA160-04
Steiner, Ann-Kathrin	P1-005
Steininger, Kimberly M.	P4-191
Steinman, David A.	OA108-02, OA82-03
Steinmeier, Annika	P3-027
Steinwender, Chiara	P2-007

Author name	Presentation Number
Stemler, Sophia	P2-153, P2-189
Stemper, Brian	OA181-04, P3-192
Stenroth, Lauri	OA109-02, OA166-04, OA87-03, P2-178
Stenson, Aileen	P3-215
Stepanian, Argishti	P2-213
Stephens, Ben	OA198-01
Stepp, Olivia	P1-211
Stergiou, Nick	OA130-05, OA93-02, OA93-03
Sterling, Hazel	OA101-05
Stevens, Emma	OA73-03
Stevens, Katie	OA98-02, P4-261
Stewart, Dean	P2-270, P2-275
Stewart, Kristen	OA33-06
Stewart, Neil	P4-016
Stewart, Todd	P1-369, P2-048, P2-194, P3-209, P3-210, P3-349, P3-351
Stickley, Christopher	P1-073
Stief, Thomas	P3-202
Stiles, Chloë	OA197-02
Stimolo, Marco	OA69-02
Stine, Rebecca	P4-227
Stirling, Ashley	P3-326
Stirling, Callie	OA129-05
Stirling, Callie E.	CSB-02
Stitzel, Joel	P2-047, P3-083, P3-147
Stitzel, Joel D.	OA128-05
Stockhausen, Jessica	OA27-04
Stockhausen, Jessica L.	OA27-03
Stoecker, Ethan	OA163-04
Stoelben, Karine	OA85-05
Stoff, Jasmin	P3-121
Stok, Kathryn	P2-356, P4-311
Stok, Kathryn S	OA10-05
Stok, Kathryn S.	OA195-02, OA64-03, P2-361
Stolk, Willem R.	OA4-01, P1-030
Stone, Audrey	P2-009
Stoneback, Jason	OA196-01, P2-080
Stonestreet, Diane	P4-308
Stoodley, Marcus	OA78-01
Stourac, Petr	P4-230
Stout, Shawn	P3-379
Stovall, Jeremy	P1-361
Straatman, Lauren	OA117-02, P4-169, P4-198, P4-217
Strack, Daniel	OA49-03
Strasser, Nicholas	P4-187
Strassl, Andreas	P3-221, P3-343
Stratford, Maxum A.K	P2-230
Stratford, Paul W.	OA117-02, P4-169
Straughan, Ross	OA157-02
Streekstra, Geert	OA135-02, P3-223
Street, John	P2-169
Streeter, Stone	P4-186
Streijger, Femke	OA193-06
Strickland, Sabrina	P2-249
Stroh, Nora	P1-368

Author name	Presentation Number
Strong, Olivia	P4-340
Strotmeyer, Elsa	P2-236
Strube, Patrick	OA49-02
Struck, Emma	P2-321
Studer, Daniel	OA62-05
Sturla, Francesco	OA95-03, P4-034, P4-036, P4-042, P4-092
Stöckl, Florian	P3-131
Su, Fong-Chin	P3-372, P4-305
Su, Ken-Hsien	OA53-01
Su, Kuo-Chih	P3-294, P3-295
Su, Wanyan	P1-091, P2-343
Subburaj, Karupppasamy	OA49-03
Suda, Eneida Y.	P4-176, P4-242
Suda, Masahiko	P2-359
Sudam, Hewamannege	P4-326
Suddhir, Shraddha	P2-258
Sudo, Ryo	OA114-03, P2-359, P2-374
Sugihara-Seki, Masako	OA39-01
Sugimoto, Hisashi	OA153-05, P1-014
Sugimoto-Dimitrova, Rika	P1-075
Sugita, Shukei	P4-121
Sugiyama, Kazuyasu	OA90-03
Sulaiman, Muhammad Yusril	OA180-06
Sultan, Sherif	P4-320
Summers, Adam	OA103-05, P2-013
Sumner, Jennifer	OA119-02, OA81-02, P1-347
Sun, Xiujie	OA131-06
Sun, Yufei	P1-371, P4-261
Sun, Yumei	P2-117
Sun, Zhe	OA54-03
Sunada, Ryuki	P3-135
Sundaram, Vani	OA140-04
Sundararajan, Aravind	P2-004
Sunderlik, Olivia	OA141-04
Sunil Varre, Mathew	OA72-04
Suo, Qian	OA101-03
Suprak, David	P4-163
Surbeck, Raphael	OA173-04
Surendran, Tejus	P2-259, P3-199
Sureshkumar, Hariharan	P1-154
Sushanek, Lev	P3-173
Suter, Julia	OA3-01
Suva, Larry	P2-022, P2-101
Suzuki, Daisuke	P3-277
Suzuki, Katsuyoshi	P4-086
Suzuki, Kouichi	P1-185
Suzuki, Masaya	P2-075
Sußiek, Julia	OA21-03
Suárez Porto, Eduardo	P4-119
Sveinsson Cepero, Numi	OA144-02
Sverrisson, Atli Örn	P1-079
Svetek, Ainsley	P1-253
Svoboda, Jan	P4-275
Swain, Lauren	OA135-03, OA57-05, P2-070, P2-120, P2-158

Author name	Presentation Number
Swaminathan, Krithika	OA68-05, OA9-02, P3-099
Swanson, Christine	OA27-04
Swartz, Emma R.	P2-161
Swearinger, Ryland	P1-072
Sweeney, Sierra	P2-339
Swent, Amber	OA194-05
Syed, Faizan	OA27-06
Sylvain, Nicole	P2-081
Sylvestre, Elizabeth	OA117-05
Syndergaard, Ian	P4-255
Synek, Alexander	OA34-05, P2-186, P3-200, P3-221
Syrett, E. Daniel	P2-123
Syu, Fang-Yu	P1-143
Szafron, Jason	OA156-04, P4-015
Szczepanek, Oliva	OA186-01
Szczesny, Spencer	OA200-05
Szymeczek, Steven	P3-164
Szyszko, Julia Aleksandra	OA18-01
Sánchez Aldana, Natalia	P1-141
Sánchez, Natalia	P4-244
Sánchez-Alcántara, Tábata	P1-032
Säisänen, Laura	OA109-02
Séguin, Nathalie	OA42-03
T. Schroeder, Ryan	P1-308
Tabaie, Sean	OA57-04, P2-050, P2-157
Tabatabaei, Mohammad	OA134-05
Taberner, Andrew	OA156-03, P4-129
Taborda, Maria Camila Mejia	P1-124
Taccori, Francesca	P2-325
Tachiki, Takahiro	OA122-03
Taddei, Fulvia	OA73-05
Taenzer, Linus	P3-036, P4-063
Tafforeau, Paul	P4-318
Tafur-Oviedo, Jackeline	OA106-02
Tagawa, Norio	P4-331
Taguchi, Mitsumasa	OA139-02
Taguchi, Yoshihiro	P2-359
Tahir, Adnan	OA19-03
Tahir, Zia ul Rehman	P4-088, P4-089, P4-122, P4-123
Tahmasebi Birgani, Zeinab	OA50-04
Tahsili-Fahadan, Pouya	OA185-01
Tahvilian, Ehsan	P1-131
Tai, Ching-Lung	P3-308, P3-309
TAISHAKU, Atsuhito	OA30-03
Takada, Mamoru	P4-044
Takagi, Shu	OA39-02
TAKAHASHI, HIROKI	OA32-01, P3-094
Takahashi, Kota	OA166-02, OA178-01, OA184-04, OA184-05, OA34-04, P1-220, P1-221, P1-247, P2-032, P2-218, P2-300, P2-304, P4-069, P4-180
Takahashi, Kota Z.	P1-123
Takahashi, Tsubasa	P3-305
Takaki, Chihiro	P4-293
Takaoka, Haruki	OA94-02
Takashima, Naoyuki	OA122-03

Author name	Presentation Number
Take, Aoi	P2-016
Takeda, Hironori	OA110-03
Takeishi, Naoki	OA39-01
Takeshita, Daisuke	P1-386
Talavage, Thomas	P2-107
Talbot, Hugues	P4-106
Talbot, Simon	P3-210
Tallia, Francesca	P2-345
Tamai, Julia	P1-282, P1-314
Tamaki, Junko	OA122-03
Tamer, Stephanie	OA147-04, P4-154
Tan, Qitao	OA61-02
Tan, Shunyu	OA161-02
Tan, Tian	OA57-03
Tan, Yuanshuo	OA131-06
Tanaka, Claire	P3-317
Tanaka, Gaku	P4-044, P4-045
Tanaka, Kaito	P2-375
Tanaka, Katsumasa	P2-075, P2-364, P3-096, P4-351
Tanaka, Martin L.	P4-280
Tanaka, Nozomu	P2-170
Tandiang, Cheikh	P4-160
Tang, Chun-Kai	P3-355
Tang, Hui	OA119-06
Tang, Peng	OA114-02
Tang, Yaohui	OA101-03
Tanioka, Hiroki	P1-303
Tanmay Mukherjee, Tanmay	P4-082
Tannast, Moritz	P4-139
Tanner, Bertrand	P2-220, P2-221
Tanska, Petri	OA149-04, OA19-03, OA45-03, P1-021, P3-049, P3-155, P3-335, P3-336
Tanzi, Rudolph	OA199-04
Tao, Matthew	OA188-02
Tao, Shengce	OA101-03
Tapia-Dean, James	P4-346
Tapie, Laurent	P3-328, P4-264
Tarakhovsky, Diana D.	P3-087
Tarter, Madeleine	P3-118
Tashman, Scott	OA195-04, P3-318
Tassani, Simone	OA117-01, P1-078, P1-228
Tateishi, Kei	P1-395
Tatterton, Rory	OA107-04
Tatum, Kyndall	P3-199
Tavakoli, Mahdi	P2-165, P4-295
Tavares, Ashlyn	P4-196
Tavarone, Silvia	OA82-02
Tavernier, Capucine	P4-336
Tawara, Daisuke	P3-285
Tawhai, Merryn	OA156-02, P4-083
Tay, Edwin	P3-011
Tayebi, Maryam	OA145-06, OA169-05, OA58-05
Tayfur, Beyza	OA141-04
Taylan, Orçun	P3-239
Taylor, Alice	P1-065, P4-189

Author name	Presentation Number
Taylor, Cameron	P3-270
Taylor, Charles	OA144-02
Taylor, Janet	P4-207
Taylor, Jeffrey	P1-260, P1-293, P1-313, P1-322, P1-340
Taylor, Joshua	P1-168
Taylor, William R.	OA135-01, OA173-04, P3-235, P3-274
Taylor,, W. Robert	OA191-04
Teater, Rachel H.	OA3-04, OA81-03
Tebbetts, John	OA40-02
Tebbetts, John D.	P2-266
Teeter, Matthew G.	OA161-05
Tehrani, Minoo	OA87-04
Tejada, Marcos	OA200-03
Telfer, Scott	OA72-04, P3-334, P4-309, P4-337, P4-338
Tello, Steve	OA9-05
ten Klooster, Linda	OA9-03
Tenforde, Adam	P1-136, P1-173
Tengler, Maxi	OA21-04, P3-370
Tennison, Kyle	OA157-03
Teplitchi-Menou, Lune	OA63-03
Terada, Yu	OA39-02
Teramoto, Atsushi	P3-277, P4-331
Terhune, E. Bailey	P3-225
TerMaath, Stephanie	OA104-03
Terrill, Nick	OA10-04, OA149-01, P4-297
Terzini, Mara	OA49-05
Tetzlaff, Wolfram	OA193-04
Teule, Erin	OA47-04, P4-173, P4-174
Teuschl-Woller, Andreas H.	OA63-03
Thai, Celeste	P1-093, P3-061
Thakkar, Poojan	P3-315
Thambyah, Ashvin	P3-178
Thangadurai, Senthil	P3-190
Theeuwes, Hilco	OA44-01
Thelen, Darryl	OA200-04, P2-114
Theobald, Peter	P3-121, P3-122
Theodorou, Marilena	P3-191
Theodosiou, Eirini	OA36-06
Thewlis, Dominic	OA171-04
Thiele, Leonie	P2-352
Thiele, Tobias	OA113-05
Thomas, Benjamin	P4-024, P4-025
Thomas, Benjamin J.	OA89-02
Thomas, Jacob	OA130-01, P1-210
Thomas, Sean	OA38-02, P3-259, P4-285
Thompson, Burke	OA43-02
Thompson, Claire	P3-283, P4-322
Thompson, Ellie	P3-013
Thompson, Irwin	OA16-01, P1-346
Thompson, Jacob	P2-233
Thompson, Megan	OA81-06
Thompson, Rachel	P1-219
Thompson, Steven	OA33-03
Thomsen-Freitas, Peter	OA196-01

Author name	Presentation Number
Thorhauer, Eric	P3-201
Thorhauer, Eric D.	P3-334
Thorne, Michael	P3-043
Thornton, Andrew	P2-212
Thornton, Gail	OA182-02
Thorpe, Stephen	P1-018
Thostenson, Erik	OA59-03
Thourani, Vinod	OA120-03, OA132-02
Thunes, James	P4-055
Thunes, James R.	P4-054
Thurner, Philipp	P3-179
Thurner, Philipp J.	OA122-01, OA63-03, OA97-02
Tian, Qi	OA158-04, P3-167, P3-180, P3-195
Tiernan, Stephen	P2-115
Tierney, Isabella	P3-020, P3-040
Tiessen, Chris	OA137-03
Till, Kevin	OA6-03, P3-100
Tillman, Mitchell	OA130-04, P1-053, P1-138
Timek, Tomasz	OA4-03
Timm, Emily	P2-321
Timmermann, Scott	OA65-05
Timmermans, Annick	OA105-01
Timmins, Lucas	OA17-04, P3-360
Ting, Lena	OA148-03, P1-046
Ting, Lena H.	OA109-05, OA136-01
Tio, Laura	OA182-05, P1-078, P1-228
Tiong, Annabel	OA199-04
Tiongson, Emmanuelle	P4-260
Tiso, Paolo	P3-036
Tisserand, Romain	OA172-04
Tissir, Karima	OA95-03, P4-036
Title, Michaela	P1-198, P1-199
Tits, Alexandra	P4-349
Tiu, Tiffany	P2-341
Tizzard, Cassidy	OA153-02
Tjardes, Thorsten	P4-211
To, Chi Hang	P4-027
Tobalske, Bret	P2-253
Tobin, Nicolas	OA39-04
Todd, Rachel	P1-097, P1-217
Todt, Juraj	OA71-02
Tohfafarosh, Mariya	OA67-05
Tohidnezhad, Mersedeh	OA151-03
Tokashiki, Kosuke	P4-293
TOKUYAMA, Kenta	P2-003
Tom, Nicholas	P1-339
Tominaga, Tempei	P1-088
Tomkinson, Alyssa	P3-270
Tomlinson, Emily	P1-128
Tompkins, Catherine J	P4-259
Tompkins, Tamara	OA195-03
Ton, Vincent	OA41-02, P1-242
Tondat, Alyssa	P3-070, P3-151
Tondat, Alyssa M.	OA174-03

Author name	Presentation Number
Tondi, Davide	P4-034, P4-042, P4-052
Tondi, Lara	P4-042
Tong, Carl	OA56-05
Tong, Guoxiang Grayson	OA139-05
Tooby, James	OA131-04, OA6-03, P3-100
Toone, Jessica	P3-105
Toribio, Sherwin	P1-368
Torii, Ryo	P4-018, P4-048, P4-112
Torimitsu, Suguru	P4-256
Tornifoglio, Brooke	OA10-02, P4-001, P4-320, P4-340
Torp, Danielle	P4-140
Torres Serrato, Santiago	P3-224
Torres, Anisa	P2-160
Torres-Costa, Sónia	P3-048
Torres-Negron, Marcus	OA73-03
Torsij, Antoinette	OA128-01, P4-177, P4-289
Torta, Elena	OA25-02, OA51-03
Toscano-Angulo, Juan José	OA122-02
Tosini, Marta	OA199-02
Totah, Deema	OA65-03, P2-317
Toth, Kasara	P2-014, P3-344
TOUCHAL, Siham	P2-162
Tous, Cyril	OA104-01
Toussaint, Thibaut	P1-089, P1-090
Towles, Joseph	P2-146
Toya, Teruki	OA153-05
Toyohara, Ryota	P1-029, P3-305
Tozzi, Gianluca	OA50-04
Tracy, James	P1-058, P1-312
Trager Ridge, Sarah	OA55-04, P1-354
Trama, Robin	OA190-04, OA81-04
Tramble, Lisa	P1-198, P1-199
Tran, An J.	P1-023
Tran, Dustin	P4-323
Tran, Kenneth	OA156-03, P4-129
Tran, Patricia	P4-339
Tran-Nguyen, Nhien	P4-091
Trask, Lesley	OA38-01
Traynor, Hannah	P4-350
Tregobov, Noah	OA120-03
Trehet-Mandel, Nadege	P4-234
Tremblay, Anthony	P1-266
Trepczynski, Adam	P3-253
Trevino, Paulina	P4-098, P4-099
Trimarchi, Santi	OA127-05, OA82-02, OA95-02, P4-074
Triolo, Em	OA32-06
Triolo, Ronald	P2-143
Tripathi, Darsh	OA43-03, P2-238, P3-004
Triverio, Piero	P4-091
Trnonja, Max	OA67-02
Troop, Leia	OA63-02
Troy, Karen	P1-136, P1-173, P4-184
Truckenmüller, Roman	OA50-04
True, Lawrence	OA194-02

Author name	Presentation Number
Trueblood, Peggy	P2-296
Truesdale, Grace	P4-163
Truscott, Haley	P3-126
Tröbs, Ralf-Bodo	P2-210
Tsai, Hsiang-Yu	OA106-05
Tsai, Jason	OA53-03, P4-179
Tsai, Liang-Ching	OA159-03
Tsai, Ming-Chang	P1-261, P3-001
Tsai, Yunlin	P4-352
Tseng, Yan-Jer	P1-279
Tsimbouri, Monica	OA187-03
Tsioros, Samantha	P1-084
Tsubata, Hazuki	P1-246
Tsuchida, Wakako	P1-233
Tsuda, Kouji	OA122-03
Tsujii, Akira	P3-261, P3-262
Tsumaki, Noriyuki	OA11-04
TU, Shihfan Jack	P4-303
Tucker, Andrew	OA99-04
Tufaro, Vincenzo	P4-112
Tughra, Benafsha	OA65-05
Tuijthof, Gabriëlle	P3-290, P3-291
Tulchin-Francis, Kirsten	OA57-04, P2-157
Tulzer, Andreas	OA74-02
Tumer, Nazli	OA96-02
Tur, Bogac	P1-393
Turco, Simona	P4-095
Turcot, Katia	OA42-03
Turinske, Thomas	P2-052
Turmezei, Tom	P3-201
Turnbull, Jeannine	OA43-03
Turner, Caroline	P2-095
Turner, Charlotte	P2-381
Turner, Mandy E.	OA113-02
Turpin, Nicole	P3-076
Turunen, Mikael	P3-336
Turunen, Mikael J.	OA149-04
Tuttle, Niklas	P3-027
Tveit, Arnljot	P4-041
Tzanetis, Periklis	OA41-05, OA47-02, OA47-03, OA9-03
Tzeranis, Dimitrios	OA164-02
Tziotziou, Aikaterini	OA17-05
Tzschätzsch, Heiko	P3-027
Tío, Laura	OA117-01
Tögel, Stefan	P3-179
Töyräs, Juha	P3-049
Tümer, Nazli	P2-181, P3-011
Ubbink, Shannen	P4-312
Uchida, Satoshi	P2-021
Ueda, Akihiro	P2-375
Ueda, Yuika	OA91-05
Ueguri, Masato	P1-303
Uelner, Mathis	OA122-01
Uenaka, Norino	OA75-02, P1-026

Author name	Presentation Number
Uenishi, Kazuhiro	OA122-03
Uhlrich, Scott	OA135-04, OA61-01, OA80-02, P2-303
Uhlrich, Scott D.	OA48-03
Ujihira, Masanobu	P1-036, P2-369
Ukaegbu, Uchechi	P4-295
Ulrich, Scott	P2-114
Ulring, Lindsey	P1-288
Um, Joohno	P1-248
Um, Joonho	P1-179
Umberger, Brian	OA130-01, P2-004
Umberger, Brian R.	OA118-01
Umebayashi, Mayumi	P2-203
Umemoto, Kanae	P3-194
Unanyan, Anais	P2-336
Unglaube, Fabian	OA54-02
Uniyal, Piyush	P3-175
Unseld, Hanna	OA36-04
Upadhyay, Kshitiz	OA32-04
Uppuganti, Sasidhar	OA125-02, OA180-01
Urban, Jillian	P3-083, P3-147
Urban, Jillian E.	OA128-05
Urban, Theresa	P4-318
Urish, Kenneth	OA165-05, OA60-04
Urquhart, Nathan	P3-313
Ursulak, Gina	P4-185
Urueña Vargas, Juan Manuel	P4-345
USHIO, Fuga	OA30-03
Utrera, Andrés	OA146-02
Utz, Michael	P1-115
Uzer, Gunes	P1-020, P2-264
V. Carrijo, Victor Hugo	P4-142, P4-263
V.N.Wijayathunga@leeds.ac.uk, Nagitha	OA83-03
Vadivelu, Raja	P2-381
Vaes, Nele	P1-007
Vafaeian, Behzad	OA74-05, P3-039
Vaiciulis, Katherine	OA65-03, P2-317
Vainberg, Yael	OA48-03
Vajkoczy, Peter	P3-296
Valastro, Chiara	P3-324
Valen-Sendstad, Kristian	OA69-01
Valentine, Gianni	P3-157
Valerio, Emily	OA88-04
Valerio, Thomas	P2-125
Valero-Cuevas, Francisco	P2-060, P2-160, P4-221
Valero-Cuevas, Francisco J.	P2-118
Valeti, Chanikya	OA30-04
Valevicius, Aïda	P1-357
Vallis, Lori Ann	P1-135, P1-186, P1-190
Valtchanov, Hristo	OA167-02
van Arkel, Richard	P2-070
van Batenburg-Sherwood, Joseph	OA90-04, OA90-06
van Beers, Marian	P3-223
van Beesel, Julia	OA103-01
Van Citters, Douglas	P3-342

Author name	Presentation Number
Van Damme, Bart	P3-036, P4-063
van de Groes, Sebastiaan	OA47-04
van de Hoek, Jan	OA10-03
van de Velde, Lennart	P4-067
van de Vosse, Frans	P4-095
van de Weerd, Sjoerd	OA44-01
Van Den Anker, Sterre	P1-091
Van den Berghe, Pieter	P2-337
van den Born, Bert-Jan	P4-067
van den Broek, Joost	P2-097
van den Broek, Matthijs	P2-035, P2-036
van den Heuvel, Gaia	P3-223
Van den Heuvel, Maarten	OA18-03
van den Hoorn, Wolbert	P2-030, P3-357
Van der Heijden, Brigitte	OA135-02, OA21-05
van der Heijden, Brigitte	P4-173, P4-174
Van der Helm, Frans	P1-184
van der Hoek, Jan	P4-312
van der Horst, Arjen	P4-100
van der Krogt, Marjolein	OA123-05, P3-223
Van der Kruk, Eline	P1-184
van der Kruk, Eline	OA128-01, OA44-01, P2-045, P2-077, P2-078, P4-177, P4-289
van der Lugt, Aad	OA115-05, P4-005
van der Meulen, Marjolein C. H.	P3-249
van der Reijden, Till	OA62-05
van Donkelaar, Paul	CSB-05, OA169-06, P4-306
van Doormaal, Pieter Jan	OA115-05, P4-005
Van Dorp, Elaina	P4-287
van Griensven, Martijn	OA50-04, P1-025
Van hede, Dorien	P2-371
van Hulst, Ellen	P4-067
van Kan, Iris	OA44-01
van Kerkhof, Britt	OA56-04
Van Klei, McKinley	OA113-02
van Lenthe, G.Harry	P3-175
van Lenthe, Harry	OA197-05, P4-304
van Minnen, Karin	P2-062
Van Nes, Amber S	OA142-04
van Netten, Jaap	OA79-05, P4-202
Van Oosterwyck, Hans	P1-007
Van Osch, Gerjo J. V. M.	OA64-03
Van Praet, Charles	OA25-05
van Rietbergen, Bert	OA62-03, P3-279, P3-289, P3-290, P3-291, P3-300
van Sambeek, Marc	OA82-04
Van Straaten, Meegan	OA76-03
Van Tongel, Alexander	OA103-01
van Werkum, Michiel	P4-067
van Zyl, Jacqueline	OA164-04
Vancíková, Karin	OA113-04
Vande Geest, Jonathan	OA50-01, P2-347
Vande Geest,, Jonathan P.	P2-366
Vandekerckhove, Ines	OA41-04
Vandenberg, Megan	OA103-05, P2-013
Vandenberg, Nicholas	P2-166, P2-167

Author name	Presentation Number
Vandenberghe, Jessica	ES3-01
Vandenbulcke, Sarah	P3-186
Vander Vleuten, Reid	P1-348
Vanderlinden, Alyssa O	P4-137
Vanderslice, Peter	P4-081
Vandiver, Victoria	P1-379
Vanelli Coralli, Caterina	P4-303
Vangeneugden, Joris	OA25-05
Vangheel, Jef	OA176-03
VanKeersbilck, Luke	P1-157, P3-037
Vanlangenhove, Peter	P4-062, P4-064
Vanna, Renzo	OA77-03
Vannatta, C. Nathan	P1-368
Vanstone, Jameson	OA174-02
VanTienderen, Richard	P4-166
Vanwanseele, Benedicte	OA105-01
Varagnolo, Damiano	OA35-05, P3-016, P3-064, P4-270
Varano, Matthew	P1-276, P3-243
Varelas, Xaralabos	OA75-03
Varga, Peter	OA175-03
Vargas, Brooklyn	OA135-04
Varsos, Pavlos	OA134-01, P4-101
Vartiainen, Paavo	OA109-02
Vasavada, Anita	P2-138, P3-072
Vasilounis, Sam	P1-284, P1-405
Vassar, Jacob	P1-301, P1-302
Vaughan, Ted	P4-011
Vaughan, Ted J.	OA102-02
Vavilala, Shreya	OA120-03
Vavourakis, Vasileios	OA110-01, OA164-02, P3-191, P4-059
Vazquez Conde, Pablo	P3-221
Vedula, Vijay	OA120-01, OA170-03
Veerkamp, Kirsten	OA123-05
Veeser, Lisa	P2-352, P2-353
Velasques Stoelben, Karine	OA13-03
Velasquez, Hanz Cuevas	OA61-04
Velasquez, Maria Alejandra	P3-299
Velazquez, Yasmin	P4-266
Vellucci, Chris	P1-122
Veloso, Antonio P.	P2-108
Veloso, António	OA70-04
Ven, Line	OA14-03, OA24-03
Venetsanou, Foteini	OA116-02
Veneziani, Alessandro	OA132-02, P4-013
Venezie, Alexander	OA169-01
Venkategowda, Sunil	OA56-05
Venkatesh, Aniket	OA120-03, P4-046, P4-073
Vennat, Elsa	P3-328, P4-336
Ver-Steeg, Greg	OA185-01
Verbruggen, Stefaan	P1-010
Verdirame, Ilaria	OA25-03
Verdoes, Robert	P4-110, P4-111
Verdonschot, Nico	OA41-05, OA47-02, OA47-03, OA47-04, OA9-03, P2-222, P3-218
Vereecke, Evie	OA103-01

Author name	Presentation Number
Vergani, Laura	OA64-04, P2-376, P3-033
Vergara, Christian	OA82-02
Verhaegen, Filip	OA14-03, OA24-03
Verlaan, Jorrit-Jan	P3-296
Verlyck, Mathilde	P4-019, P4-080
Verma, Isha	P3-034
Verma, Khushboo	P1-065, P4-189
Verma, Nikhil	OA14-04
Vermijs, Saar	OA25-05
Verner, Kari	P3-109, P3-110
Vernooij, Natasha	P2-278
Versluis, Michel	P4-067
Vervenne, Thibault	OA84-05
Viceconti, Marco	OA18-01, P4-134
Vicini, Matteo	OA11-03, OA187-01
Vidacs, Laszlo	P3-296
Vidal Pereira, Thiago	P1-237, P4-257
Vidal, Armando	OA195-04, P3-318
Vidt, Meghan	OA83-05
Vidt, Meghan E.	OA37-01
Vignali, Emanuele	OA139-04, OA144-04, OA25-03
Vigneri, Marco	OA114-04, OA199-03, OA90-05
Vignon-Clementel, Irene	OA104-01, OA134-01, P4-049, P4-101, P4-146
Vignon-Clementel, irène	P4-106
Vila-Dieguez, Oscar	OA14-05, OA37-03
Vilas-Boas, J. Paulo	P4-142
Vilas-Boas, João Paulo	P1-060, P4-155, P4-156
Vilela, Matheus	OA105-06, OA98-06, P1-071, P3-383
Vilela, Matheus M.	P1-255
Villa, Alessandra	OA133-04
Villa, Tomaso	P3-258
Villacís Núñez, Carla Nathaly	P2-217
Villanova, Julie	OA50-04
Villar Calle, Pablo	P4-052
Villata, Simona	OA51-03
Villegas, Diego F.	P3-009
Villella, Julianna	P3-237
Villette, Claire	P3-279
Vinci, Valentin	OA10-04
Vinson, Amanda L.	OA27-03
Vintimilla, Antonio	P2-296
Viotto, Marianna	P3-324
Virgilio, Kelley	P3-072
Vishnu, Kavin	P3-044
Vishnubala, Dane	OA6-03, P3-100
Vismara, Riccardo	P4-034, P4-092
Visscher, Lucas	OA44-01
Visser, Valery	OA4-02
Vistamehr, Arian	P1-072
Vivanco Morales, Juan F.	OA38-03
Vivanco, Juan	P2-368
Vivanco, Juan Francisco	P2-378, P2-379
Vivekanandan, Jeevaraaj N.	P1-267
Vlasea, Mihaela	P3-292

Author name	Presentation Number
Vo, Nam	OA23-03
Voellmicke, Isabella	OA86-01
Vogel, Colleen	OA161-03, P2-215, P2-216
Vogel, Viola	OA176-05
Vogt, Liffert	P4-067
Vogt, Morten	OA36-03
Voisin, Emmanuelle	P3-296
Voloshina, Alexandra	P1-192
Volpe, Daniele	P3-016
von Aesch, Arlene	P4-224, P4-225
von Diecken, Carlo	OA118-01, OA3-03, P1-047
von Eisenhart-Rothe, Rüdiger	OA60-03
von Rechenberg, Brigitte	OA188-01
von Salis-Soglio, Marcella	OA122-04
Vong, Chun Kiet	OA145-06
Voogt, Lennard	OA128-01
Vopat, Bryan	P1-091
Vopat, Lisa	P1-091
Vorel, Jan	P2-351
Vorp, David	P3-029
Vossen, Lisa	OA79-05, P4-202
Votta, Emiliano	OA179-05, OA191-05, OA95-03, P4-034, P4-036, P4-042, P4-052
Vovchenko, Maxim	P1-007
Voziyan, Paul	OA125-02
Vraitch, Rajan S.	OA36-06
Vrbka, Martin	P3-217
Vries, Hanne	OA135-02, P4-173, P4-174
Vu, Melissa	P2-239
Vucelic, Marko	P3-041
Vuong, Sunnie	OA27-06
Vyavahare, Naren	OA146-01
Vymazalova, Katerina	P4-226
Vázquez, Rebeca Martínez	OA11-03
Väänänen, Sami	P2-197
Völkel, Lilly	P2-350
WADA, Shigeo	OA30-03
Wada, Shigeo	P4-121
Wade, Chip	P1-062, P1-316
Wade, Frankie	OA118-04
Wadsworth, Jonathan	P1-020
Wagatsuma, Mayumi	P1-144, P1-197, P1-202, P1-230, P2-059, P4-215
Wagenseil, Jessica	OA108-03, P4-061
Wagnac, Eric	OA193-05
Wagner, Andrew	P1-056
Wagner, Caroline	P4-058
WAGNER, Delphine	P2-162
Wagner, Heiko	OA18-03, P2-149, P3-202
Wagner, Sonja	OA197-04, P4-316
Wagner, William	OA50-01, P2-347
Wagoner Johnson, Amy	OA170-05
WagonerJohnson, Amy	P3-149
Wai, Eugene	P3-307
Wakamatsu, Chihiro	P3-305
Wakeling, James	P2-024, P2-131, P2-263

Author name	Presentation Number
Wakeling, James M.	P2-202
Walcott, Sam	P1-082
Walker, Karen	OA66-01, 2982
Walker, Richard	OA129-05
Walker, Richard E. A.	CSB-02
Walker, Simon	OA125-04
Walkingshaw, Jason	P4-001
Wallace, Dylan	P2-328
Wallace, Jack	OA85-04
Wallenstein, Arielle	P4-210
Wallnöfer, Elias	P2-156
Walser, Ronald	P2-296
Walsh, Bridget	P4-140
Walsh, Conor	OA33-01, OA33-04
Walter, Joseph	P1-229
Walter, William	OA47-05
Walz, Fabiola	P3-183
Wan, Zhengpeng	OA199-04
Wang, Alan	OA145-06, OA169-05, OA58-05
Wang, Anqi	OA114-02, P1-034
Wang, Bingrui	P3-167
Wang, Chao	P2-260
Wang, Chongpeng	P3-282
Wang, Chuyi	P1-124
Wang, Daniel	OA113-02
Wang, David	P4-350
Wang, Dong	OA15-02
Wang, Guangchen	OA197-03
Wang, Han	OA64-02, 958
Wang, Hao-Nan	OA20-06
Wang, Henry	OA8-05, P1-050
Wang, Jack	OA17-04
Wang, Jiahui	OA105-01
Wang, Jiefei	OA76-03
Wang, Jingyi	P2-229
Wang, Jinhang	OA95-01
Wang, Joonho	P3-232
Wang, Josephine	OA61-03
Wang, Jr-Yi	P3-214
Wang, Junqing	OA197-06, P1-175
Wang, Kangxin	P2-228
Wang, Kesheng	P3-062
Wang, Lin	OA96-01, P2-150
Wang, Linda	P4-207
Wang, Linjie	OA180-03, P2-173
Wang, Mengjun	OA30-05, P4-116
Wang, Min	OA22-02, OA50-02
Wang, Qifeng	OA168-05, OA74-02
Wang, Qiong	OA194-02
Wang, Rizhi	OA194-02, P3-304
Wang, Ruizhi	OA139-05, OA179-03
Wang, Ruoli	OA41-03, P4-329, P4-344
Wang, Shilin	OA189-06
Wang, Sophia	OA98-04

Author name	Presentation Number
Wang, Takeisha	OA125-05
Wang, Ting-Ming	OA124-05, OA22-04, P2-139, P3-214
Wang, Vicky	P4-019, P4-047
Wang, Xinyue	OA158-04
Wang, Xun	OA199-04
Wang, Yaqiong	P1-128
Wang, Yimo	OA117-05
Wang, Yugi	P1-199
Wang, Yuqi	P1-198
WANG, YUQING	1682
WANG, Yuqing	OA158-03
Wang, Zheng	OA76-02
Wang, Zhengcan	P1-082
Wang, Zhijie	P3-063
Wang, Zhongzheng	P4-329, P4-344
Wang, Zijie	P4-022
Wanniarachchi, Saduni	P2-209
Wannop, John	OA190-04, OA81-04, P1-348
Waraich, Minah	OA86-01, OA98-04
Ward, Emilie C.	OA113-02
Ward, Jared	P1-157
Ward, Lance	OA86-01
Ward, Landon	P1-280
Ward, Michael	OA135-03
Ward, Niamh	OA38-01
Ward, Rebecca	P3-215
Ward-McIntosh, Chelsea	P3-059
Warnecke, Daniela	P3-332
Warner, Amanda	P4-196
Warren, James	OA36-05, OA83-04
Warren, Jeremy	OA17-02, P4-098, P4-099
Wartzack, Sandro	OA136-02, P1-152
Washabaugh, Edward	OA85-04
Wasiak, Axelle M	P2-141
Wasiak, Axelle M.	P2-110
Wasserstein, David	P3-241, P3-341
Watamura, Tomoaki	OA39-02
WATANABE, Yoshiyuki	OA30-03
Waters, Heather	P1-219
Waters, Sarah	P2-265
Waterval, Niels	OA123-05
Watier, Bruno	OA130-03
Watkin, Ben	P1-015
Watkin, Tegid	P2-125
Watschke, Brian	P3-158
Watson, Daniel	OA198-01
Watson, Michael	P2-159
Watson, Peter	P2-173, P2-194, P3-349, P3-351
Watson, Richard	P3-073, P3-128
Watterworth, Michael	OA186-04, P2-053, P2-281
Watts, Aidan	OA178-04, P1-329
Watts, Alexander	OA65-04
Wauneka, Clay	P1-072
Waungana, Tadiwa	OA73-05

Author name	Presentation Number
Waungana, Tadiwa H	P2-211
Waxman, Susannah	P3-167
Wearne, Lauren	P4-273
Weaver, Ashley	P2-197, P2-236
Weaver, Brian	P2-278
Weber, Christian	P3-260
Weber, Tobias	OA154-01, OA154-04
Webster, Kate	P1-344
Webster, Kathryn	P4-214
Webster, Kathryn F.	P4-217
Webster, Mark	P4-110
Wechsler, Iris	OA136-02, P1-152
Weerasinghe, Kavya	P3-340
Wehrle, Esther	P1-012, P4-346
Wei, Fuxiang	OA114-02, P1-034
Wei, Linjuan	OA61-02
Wei, Qi	OA173-02, OA59-01
Weidner, Robert	P2-269, P2-289
Weigt, Claudia	OA122-04, P1-028
Weihs, Daphne	P4-162
Weimar, Wendi	OA68-01, P1-243, P1-311
Weinhandl, Joshua	P1-320
Weinkamer, Richard	P4-349
Weinsaft, Jonathan	OA179-05, P4-052
Weiss, Gera	P3-021
Weiss, Jeffrey	LS1-01, OA17-04
Weiss, Justin	P2-251
Weisse, Bernhard	OA38-03, P2-368, P3-235
Weiß, Maurice	P3-236
Wellenberg, Ruud	P3-223
Weller, Rebecca	P1-262
Weller, Renate	P2-035, P2-036
Wellington, Cheryl	OA133-02
Wells, Joel	P2-083
Wells, Meredith	P3-124, P4-210
Wellsandt, Elizabeth	OA188-02
Welsh, Piper	P3-162
Welte, Lauren	P2-129, P3-201, P4-239
Wendler, Olaf	P1-393
Wendt, Christopher	P1-280, P2-047
Weng Zhu, Judith	P4-102
Weng, Yi-Hsuan	OA16-02, P3-382, P4-267
Weng, Yu-Cheng	P4-267
Wenzel, Thomas	P3-139
Werkhoven, Conrad	OA113-03
Wermers, Jens	OA21-03
Werner, Brian	OA200-03
Wernke, Matthew	P2-329
Wertelecky, Tiana A.	OA52-05
Wessel, Lauren E.	P3-259
Wesseling, Mariska	OA128-01, OA57-06, P4-177, P4-289
Wesselink, Marieke	P3-291
West, Luke	P1-005
West, Stephen	P3-126

Author name	Presentation Number
West, Toni	P1-035
Westover, Lindsay	P3-319
Westover, Lindsey	OA182-02, OA74-05, P2-241, P2-298, P3-039, P3-134, P3-331, P3-340, P4-141
Westrich, Geoffrey H.	P3-237
Weyand, Peter	OA68-03, P1-214, P1-291, P1-297
Weyers, Miriam	P1-007, P2-240, P4-334
Weyland, David	P3-112
Whalen, Corey	P2-225
Whatley, Kayla	P1-023
Whatman, Chris	P1-319
Wheat, Jon	P1-108
Wheatley, Benjamin	OA70-03, P3-157
Wheatley, Mitchell	OA141-03, P2-042
Whitaker, Amanda	OA86-05, P4-219
Whitby, Elspeth	P3-189
Whitcomb, Charlotte	P1-278
White, Daniel K.	P3-199
White, Emma	P1-280
White, Kaylee	OA143-03
White, McKenzie S.	OA73-01, P3-203
White, Neil	CSB-03, OA76-05
Whitington, Alan	P4-105
Whitney, Peter	OA123-03, P1-112
Whittaker, Jackie	P2-327
Whyne, Cari	P4-216
Wickenheiser, Diane	OA155-05, P1-145, P1-355, P3-381
Wickert, Kerstin	P4-144, P4-212
Wickiewicz, Thomas	OA141-03, OA183-02, OA188-04, P2-042
Widmer, Jonas	P4-343
Widowski, Tina	P2-253
Wiebe, Katherine	P2-318
Wiebenga, Emily	OA117-02, P4-169, P4-198, P4-200
Wiebenga, Emily G.	P4-217
Wiesner, Ulrich	P2-358
Wiggermann, Neal	P1-162
Wijayathunga, Nagitha	OA83-04
Wijayathunga, V. Nagitha	OA36-05
Wijekoon, Sachitha	CSB-06, P1-077
Wilburn, Christopher	OA140-04, OA68-01, P1-311
Wilcox, Ruth	OA31-05, OA83-03, OA83-04, P3-188
Wilczok, Dominika	P3-181
Wilde, Fabian	P2-005
Wildenberg, Joseph	P3-029
Wilders, Lise	OA41-05
Wiles, Tyler	OA130-05, P1-239
Wilk, Julia	P3-026
Wilke, Hans-Joachim	OA36-03, OA36-04, OA44-05
Wilken, Jason	OA178-03, OA65-03, P1-238, P3-219, P4-180, P4-181, P4-192, P4-193
Wilkie, Ethan W.C.	P1-317, P1-318
Wilkins, Samuel	P1-274, P1-275
Wilkins, Samuel J.	P1-290
Wilkinson, Brandon	P4-187
Willbanks, Amber	OA168-02

Author name	Presentation Number
Wille, Kaat	P4-064
Willegger, Madeleine	P3-343
Willem, Miel	P3-017
Willems, Miel	OA149-02, P2-062
Willett, Nick	P3-229
Willett, Thomas	OA125-02, P3-007, P3-154
Williams, David	OA135-03, OA57-05, P2-070, P2-120, P2-158, P3-201
Williams, Edward	P3-122
Williams, Genevieve K R	OA193-02
Williams, Jack	P3-099
Williams, Jania	P2-056, P3-101
Williams, Jenny	OA135-03, P2-070
Williams, L. Tyler	OA32-04
Williams, Lakiesha	OA134-05
Williams, Lauren	P1-097, P1-217, P1-247, P2-218
Williams, Leah	P4-200
Williams, Nicole	OA171-04
Williams, Sophie	OA31-05, P2-076
Williams, Spencer	OA70-06, P2-111
Williamson, Jessica	OA101-02, OA51-05
Willie, Bettina	OA5-05, P2-203, P2-246
Willie, Bettina M.	P2-253
Willing, Ryan	P3-283
Williston, Zachary	P2-317
Willmering, Matthew	P4-016, P4-017
Willner, Kai	OA97-04
Wills, Carlos Ruiz	OA122-06
Wills, Neil	OA141-02, P1-160
Willson, Cody	P2-063, P3-164, P4-324
Willwacher, Steffen	OA118-01, OA3-03, P1-047
Willy, Richard	OA195-03, P2-088
Wilsom, Quinn	P1-099
Wilson, Alan	OA165-05
Wilson, Christopher	P3-143
Wilson, David	OA5-06, P3-250, P3-251, P3-265
Wilson, Don	P3-150
Wilson, Janie	P3-251, PL10-01
Wilson, Jorjie M.	OA20-05
Wilson, Patrick	OA166-05
Wilson, Quinn	P1-371
Wilson, Taylor	OA140-03, P3-003
Wilzman, Andrew	P4-184
Wimmer, Marcus A.	P3-380
Wimmer, Markus	OA153-01, OA20-04, P1-115, P1-276, P2-321, P3-243
Wimmer, Markus A.	P3-342
Winberg, Taylor B.	OA174-03
Windhager, Reinhard	P3-221, P3-343
Wingnean, Alexa	P4-335
Winiarski, Slawomir	P4-251
Winkler, Kurt	OA176-04
Winteler, Travis	P2-195
Winters, Joshua	OA15-03, OA190-03, P1-373
Winther, Simon	P3-045
Wiputra, Hadi	P4-061

Author name	Presentation Number
Wisch, Marcus	P3-077
Wisotzki, Sophia	OA143-01, P4-347
Wissman, Madison	OA105-02, OA105-05
Witbreuk, Melinda	P3-223
Withers, Joeana	P4-203
Witkowski, Ana	P3-249
Witmer, Maitland	P3-059
Witt, Spencer	P2-044
Wittstein, Jocelyn	OA200-03
Witz, Jean-François	P4-327
Witzel, Ulrich	P2-210
Witzenburg, Colleen	P4-102
Woiczinski, Matthias	OA49-02, P3-244
Wojtowicz, Agnieszka	P1-207
Wold, Ethan	OA12-04
Wolf, Brian R.	P4-166
Wolf, Jakob	P2-047
Wolfenson, Haguy	P2-017
Wolff, Whitney	P2-215, P2-216
Wolfram, Suzi	OA79-06
Wolfram, Tobias	P2-352, P2-353
Wolfram, Uwe	P3-190, P4-332
Wolfs, Hannes	OA84-05, 2661
Wolfsteiner, Sophie	P1-393
Wolint, Petra	OA157-05
Wollner, Gregor	P3-343
Wolstenholme, Mark	P2-324
Wolterink, Jelmer	OA9-03
Wong Shi Kam, Sophie	OA46-06
Wong, Chon-Kio	P4-267
Wong, Devin	P3-219
Wong, Griffin	OA43-03
Wong, Ivan	P4-247
Wong, Jasper	P1-319
Wong, Kamen	OA119-06
Wong, Martin	P2-211
Woo, Elena	OA151-04, P3-269
Woo, Junhyuck	P2-011
Wood, Leo	OA12-04
Wood, Sossena	P4-094
Woodhams, Louis	OA152-02, OA176-02, P1-039
Woods, Jason	P4-017
Wooton, Timothy	P1-280
Workineh, Zerihun G.	P1-037
Workman, Anna C.	OA3-04, OA81-03
Wormsley, Ashlyn	OA66-02, OA66-05, P1-103
Worobets, Jay	P1-333
Worsey, Matthew	P2-117, P3-032
Worsley, Peter	P4-254
Worthen-Chaudhari, Lise	OA79-04
Worthington, Kristan	OA50-03, OA77-05, P1-011
Wren, Tishya	P3-312, P4-237, P4-260
Wriggers, Peter	OA199-05
Wright, Chayse	P4-158, P4-159

Author name	Presentation Number
Wright, Jennifer L.	P3-225
Wright, Thomas	P2-058
Wright, Timothy M.	P3-237
Wright, Virginia	P2-323
Wrona, Hailey	P1-300
Wu, Chenjun	OA78-03
Wu, Ching-Yi	OA53-01, P2-340
Wu, Dengjiang	P3-189
Wu, Jianhua	P4-208
Wu, Julia	OA140-03
Wu, Kuan Hsien	OA135-05
Wu, Kuan-Hsien	OA86-03, P3-238
Wu, Kuan-Wen	OA124-05, P3-214
WU, Lyndia	P3-119
Wu, Lyndia	CSB-05, OA169-06, OA6-04, P1-048, P3-105, P3-126, P4-306
Wu, Tong-Ching Tom	P1-370
Wu, Wel-Lan	P3-097
Wu, Xueying	OA124-04
Wu, Yanglei	P3-153
Wu, Yetong	OA173-05
WU, YUEYING	P1-043
Wu, Yufan	OA108-03, P4-061
Wyatt, Hannah	P1-319
Wyatt, Hayley	P3-339
Wyatt, Juliette	P2-061
Wyckoff, Elijah	P4-266
Wüthrich, Isabelle	P2-098
Xavier, Ana Paula	P1-191
XI, Zihan	OA158-03
Xiang, Liangliang	OA41-03
Xiang, Qian	P4-081
Xiao, Bo	OA131-06
Xiao, Qiwei	P4-016, P4-017, P4-029, P4-050
Xie, Becca	OA6-05
Xie, Dennis	OA194-02
Xing, Chenghao	P4-285
Xing, Kailin	P1-179, P1-248
Xu, Jia-Cheng	P3-106
Xu, Jialiang	OA61-02
Xu, Jiawen	OA33-05
Xu, Karen	OA126-03
Xu, Kevin	P4-186
Xu, Samuel	OA194-02
Xu, Wei	P1-175
Xu, Yidan	OA31-01
Xue, Yawen	P3-114
Yadav, Aditya S.	P3-225
Yadav, Pramod	P1-345
Yadu, Neha	OA44-02
Yagi, Ippei	P2-021
Yamada, Hiroshi	OA134-03
YAMADA, SATOSHI	P3-144
Yamada, Satoshi	P2-252, P3-135
YAMADA, Shigeki	OA30-03

Author name	Presentation Number
Yamada, Shigeki	P4-027
Yamada, Yuki	OA94-02
Yamaguchi, Takeshi	OA124-03
Yamakawa, Satoshi	P3-261
Yamamoto, Shun	P3-116
Yamamoto, Sota	P4-252
Yamamoto, Yudai	P2-201
Yamanishi, Yoko	P1-395
Yamashita, Tadahiro	OA114-03, P2-359, P2-374
Yamawaka, Satoshi	P3-262
Yan, Mengning	OA64-02
Yanagita, Shohei	OA51-04
Yang, Bing-Shiang	P1-052
Yang, Che-Yi	P1-310
Yang, Dong Hyun	P4-026
Yang, Eunbean	P1-140
Yang, Fan	P1-381
Yang, Feng	OA189-06, P2-302, P2-307, P3-124
Yang, Guang	OA74-02
Yang, Guang-Zhong	OA101-03
Yang, Jingzhen	OA133-03
Yang, Ruxin	OA64-05
Yang, Shanren	P3-013
Yang, Thomas	P2-319
Yang, Xiaoqiu	P1-008
Yang, Xiaoyi	OA190-02, P1-092
Yang, Yang	OA179-02
YANG, Yi-jian	P3-095
Yang, Yijian	P1-244, P1-382, P4-268
Yang, Yu-Tung	OA10-03
Yang, Zhenhao	P3-146
Yanke, Adam B.	P2-052
Yao, Minghe	OA197-06
Yao, Yicai	P3-062
Yap, Choon Hwai	OA167-04, OA74-02, P4-125
Yap, Nathan	P4-018
Yaple, Nicholas	P1-104
Yassa, Eanas	OA167-05
Yau Shan Chan, Zoe	P2-035, P2-036
Yavari, Mohammad	OA15-05
Yazdekhasti, Saba	P3-055
Ye, Ziyi	P4-252
Yeats, Breandan	OA120-03
Yeh, Chia-Chun	OA138-01
Yelós Tellagorry, Vanessa	P1-148, P3-060
Yen, Lu	P3-372
Yen, Sheng-Che	OA123-03, P1-112
Yentes, Jenna	OA40-05
Yentes, Jennifer	OA40-02, P4-152
Yentes, Jennifer M.	P2-266
Yeoman, Jessica	OA143-01, OA143-02, OA143-04, P1-357, P4-347
Yesuf, Hannah	OA154-05
Yesuf, Hannah G.	OA154-02, OA154-03
Yetman, Quinn	P2-085

Author name	Presentation Number
Yeung, Ted	OA169-05
Yi, Chung-Hwi	P1-359
Yi, Chunghwi	P2-288
Yiannakidis, Anastasios	OA61-04
Yilmaz, Dilara	P1-012
Yimam, Habtamu	P3-361
Yin, Wei	P4-253
Yingxiao Wang, Peter	OA101-01
Yoganandan, Narayan	OA145-05, OA181-04
Yokota, Hideo	P4-045
Yokoyama, Naoto	OA39-01
Yoo, Jehyun	P2-313
Yoon, Ethan	OA16-04
Yoon, Joshua	OA120-03
Yoon, Jung-Min	P1-163, P1-315, P1-385
Yoon, Jungmin	OA107-06
Yoon, Soyeon	OA172-02, OA172-03, P3-138, P4-195
Yoon, Suji	OA85-02
Yoon, Sukhoon	P1-315, P1-385
Yoshida, Kazuhiro	P1-036, P2-369
Yoshimura, Sheryl	P1-073
Yoshino, Daisuke	OA11-02, OA198-03, OA75-02, P1-026, P3-197
Yoshizaki, Tomokazu	P1-014
You, Joshua Sung	OA20-01, OA72-01
YOU, Yanan	P4-265
Young, Aaron	OA148-03, OA33-06, OA72-06, P1-079, P1-139, P1-229
Young, Alistair	P4-047
Young, Daniel	P2-238
Young, Katherine A.	P3-254
Young, Nathaniel	P2-193
Young, Patricia	P1-073
Youssef, Gaia	OA194-03, P2-154
Yousufy, Umar	P1-374, P1-375
Yu, Boliang	OA71-04
Yu, Cheng-Hao	OA106-05, OA22-04, P2-139
Yu, Lina	OA154-02, OA154-03, OA154-05
Yu, Zhifeng	OA64-02, P1-031
Yuan, Juefei	P3-062
Yueh-Hsun Yang, Kevin	OA126-05
Yusuf, Yaqoub	P3-310, P4-145
Zabala, Michael	OA48-04
Zaccara, Gabriel	OA195-05
Zaccheus, Jesuloluwa	P4-295
Zacher, Vivienne	OA102-05
Zachow, Stefan	P3-267
Zadpoor, Amir	OA96-02, P3-011
Zadpoor, Amir A.	P2-181
Zaferiou, Antonia	OA130-04, OA20-02, P1-053, P1-096, P1-138
Zaffagnini, Stefano	OA42-01, OA73-05, P1-332, P3-129, P3-240, P3-324
Zahouani, Hassan	P2-018, P2-349
Zalaiskalns, Andrejs	OA15-03
Zaluski, Dylan	P2-137
Zambare, Keya	P3-089, P3-107
Zambon, Sara	OA43-04, P4-113

Author name	Presentation Number
Zampieri, Niccolò	OA154-01
Zandbergen, Raymond	OA192-06
Zandri, Giulia	P4-221
Zanini, Silvia	OA86-01, OA98-04, P1-364
Zannone, Manuel	OA25-02
Zannoni, Jessica	P4-042
Zanrè, Valeria	OA125-04
Zantiba, Sherif	OA31-03, OA36-05, OA83-03
Zare, Vahid	P2-196
Zattoni, Marta	P4-079, P4-300, P4-333
Zaucke, Frank	P4-334
Zavala, Anamaria	P2-264
Zavatsky, Amy	P1-328, P3-321
Zavatsky, Amy B.	P2-334, P3-014
Zazpe, Oier	OA35-05, P3-016
Zehr, Jackie	P2-159, P2-226, P2-273
Zeiter, Stephan	OA125-03, P4-346
Zekonyte, Jurgita	OA149-03
Zemel, Assaf	OA101-03
Zemp, Roland	OA173-04
Zeng, Dorothy	P2-073
Zeng, Wei	P2-199, P3-142
Zeng, Ziwei	P1-244, P1-382
Zenzeri, Jacopo	P1-068
Zeppetelli, David	P2-034, P3-075
Zero, Alexander	P2-205
Zero, Alexander M	P2-230
Zero, Alexander M.	P2-054, P2-206
Zeveleva, Svetlana	OA71-04
Zhai, Xiaojun	OA188-06, P1-111
Zhan, Shaobo	P3-149
Zhang, Aili	OA101-03
Zhang, Chaokai	CSB-05, OA133-03, OA169-06, P3-137
Zhang, ChengYue	P1-102
Zhang, Dawei	P3-333
Zhang, Fengtao	P2-048
Zhang, Guoxin	OA61-02
Zhang, Haixia	OA95-01, P3-193
Zhang, Haocheng	P4-218
Zhang, Haoyu	P2-251, P2-362
Zhang, Honglin	OA5-06
Zhang, JiangYue	OA181-05
ZHANG, Jingxi	OA158-03
Zhang, Jingzhi	P2-125
Zhang, Li	P1-205
Zhang, Li-Qun	OA165-03, P4-253
Zhang, Liyuan	OA179-02, OA197-01, P4-022
Zhang, Mengjie	OA174-04, OA174-05
ZHANG, Ming	OA57-02
Zhang, Ming	OA129-06, OA61-02, PL06-01
Zhang, Mingzi	OA144-03, OA17-03, P4-110, P4-111
Zhang, Peng	OA191-02
Zhang, Qianni	P4-112
Zhang, Ruihang	P1-402

Author name	Presentation Number
Zhang, Shanshan	P1-041
Zhang, Shenghong	OA90-03
Zhang, Songning	OA98-02, P1-099, P1-371, P4-261
Zhang, Travis	P4-166
Zhang, Weijia	P2-342
Zhang, Wenfeng	P2-139
Zhang, Will	P4-033
Zhang, Xianyi	OA52-01, P1-381
Zhang, Xinyu	OA114-02, P1-034
Zhang, Yanxin	OA174-04, OA174-05
Zhang, Yixin	P1-094
Zhang, Yixuan	OA149-01, OA149-02
ZHANG, YUELIN	P3-144
Zhang, Yuelin	P3-135
Zhang, Yujie	OA22-02, OA50-02
Zhang, Zhengyu	OA199-04
Zhang-Lea, Janet	OA20-03, OA80-03
Zhao, Debbie	P4-019, P4-047, P4-080
Zhao, Fujie	OA4-04
Zhao, Han	OA120-02
Zhao, Iris	P3-146
Zhao, Kristin	OA21-01
Zhao, Ningzhen	OA177-03, P1-208, P3-010
Zhao, Peijun	OA101-03
Zhao, Wei	OA133-03
Zhao, Xiong	OA153-06
Zheng, Jie	OA74-06
Zheng, Xiaoping	P1-244
Zhou, Chengkang	P3-061
Zhou, Di	OA153-05
Zhou, Guanglong	P3-189
Zhou, Hongyou	P3-027
Zhou, Junhong	P1-244
Zhou, Minhao	OA5-05
Zhou, Sixu	P1-079, P1-229
Zhou, William	OA6-05
Zhou, Xianlian	OA67-05
Zhou, Xin	OA164-03
Zhou, Yue	OA101-03
Zhou, Zhou	OA133-04, OA145-03, P3-074, P3-106, P3-130
Zhou, Zisen	P4-129
Zhu, Anling	P4-020
Zhu, Hongtian	OA129-04
Zhu, Kezhe	OA131-06
Zhu, Kiana	P2-241
Zhu, Liang	OA140-02
Zhu, Linyong	OA101-03
Zhu, Zijie	P2-060
Ziaei-Rad, Vahid	OA30-05, P4-116
Zierke, Julian N.	P3-027, P3-236
Zijlstra, IJsbrand	P4-067
Zimerman, Tiago	OA105-06, OA14-01, OA14-02, OA76-04, OA94-03, P1-061, P1-255, P3-315, P3-374, P3-383, P4-167, P4-223, P4-258
Zimmer, Gracie	P1-056

Author name	Presentation Number
Zimmerman, Brandon K.	OA158-02
Zimmerman, Karl	OA6-05
Zimmermann, Jan	OA181-03
Zinno, Raffaele	OA42-01
Zipser, Carl	P3-127
Zitnay, Jared	OA135-04, P4-249
Ziv-Gal, Ayelet	OA170-05
Zizzi, Eric Adriano	OA91-03
Zojaji, Mahsa	P2-140, P2-367, P3-148, P3-367
Zoldan, Janet	P1-035
Zoller, Heinz	OA197-04, P4-316
Zoni, Sheikh Umara	OA132-04
Zukor, David	OA195-05
Zukotynski, Brian K.	P3-259
Zukowski, Lisa	OA40-01, OA66-06, OA80-04
Zukowski, Matthew	P2-104
Zuniga-Gallegos, Kenia	P4-009
Zupan, Andreja	P2-363
Zurlo, Giuseppe	OA152-03
Zwingenberger, Stefan	P4-318
Zysset, Philippe	OA125-04, OA96-04, P4-342
Álvarez Gual de Torrella, Andrés	OA47-03
Özman, Deniz	P3-260
Üzümcü, Talha	P3-098, P3-267

**if no program code was given for a submission then this will show the submission serial number*